KU Leuven
Department of Mechanical Engineering
Celestijnenlaan 300 - box 2420
B-3001 Heverlee (Belgium)

Proceedings of

ISMA2018

International Conference on

Noise and Vibration Engineering

USD2018

International Conference on

Uncertainty in Structural Dynamics

17 to 19 September, 2018
Editors: W. Desmet, B. Pluymers, D. Moens, W. Rottiers.

© KU Leuven - Departement Werktuigkunde
Celestijnenlaan 300 - box 2420, B-3001 Heverlee (Belgium)

Alle rechten voorbehouden. Niets uit deze uitgave mag worden vemenigvuldigd en/of openbaar gemaakt worden door middel van druk, fotokopie, microfilm, elektronisch of op welke andere wijze ook zonder voorafgaandelijke schriftelijke toestemming van de uitgever.

All rights reserved. No part of the publication may be reproduced in any form by print, photoprint, microfilm or any other means without written permission from the publisher.

D/2018/5789/1
ISBN 9789073802995

Proceedings of

ISMA2018

International Conference on

Noise and Vibration Engineering

USD2018

International Conference on

Uncertainty in Structural Dynamics

Leuven
17 to 19 September, 2018

Organising Committee:

Prof. Dr. ir. W. Desmet,	*ISMA Conference Chairman*
Dr. ir. B. Pluymers,	*ISMA Conference Chairman*
Prof. Dr. ir. P. Sas,	*ISMA Honorary Chairman*
Prof. Dr. ir. D. Moens,	*USD Conference Chairman*
Prof. Dr. ir. D. Vandepitte,	*Programme Chairman*
Dr. ir. W. De Roeck,	*Conference Programme*
Prof. Dr. ir. K. Gryllias,	*Conference Programme*
Prof. Dr. ir. W. Heylen,	*Conference Programme*
Prof. Dr. ir. J. Swevers,	*Conference Programme*
ir. S. Vanpaemel,	*Conference Manager*
Mrs. L. Notré,	*Conference Secretary*
ir. ing. W. Rottiers,	*Conference Proceedings and database*
ir. D. Brandolisio,	*Exhibition*
ir. M. Muriel Gracia,	*Exhibition*
ir. M. Kirchner,	*Social Events*
ir. S. Ahsani,	*Webmaster*

Organised by:

KU Leuven – Department of Mechanical Engineering
Celestijnenlaan 300 - box 2420
B-3001 Heverlee (Belgium)

KEYNOTE PAPERS

Keynote

Session Keynote presentation

Shapes & DOF: on the use of modal concepts in the context of parametric non-linear studies 1
E. Balmes [1,2]
(1) Arts et Métiers Paristech, France
(2) SDTools, France

Automotive NVH – Methodology for Future Innovative Product Development 17
P.-O. Sturesson [1]
(1) AB Volvo, Sweden

ISMA2018 PAPERS

AVC

Session Active vibration control

Synthesis of vibration signals with prescribed power spectral density and kurtosis value 29
E. Pesaresi [1], M. Troncossi [1]
(1) University of Bologna, Italy

Analysis of a transport equation as boundary condition in an acoustic transmission line. 41
E. De Bono [1], M. Collet [1], S. Karkar [1]
(1) Ecole Centrale de Lyon, France.

On the noise reduction of active sidewall aircraft panels using feedforward control with embedded systems 55
M. Misol [1], S. Algermissen [1], M. Rose [1]
(1) DLR - German Aerospace Center, Germany

A multimodal nonlinear piezoelectric vibration absorber 63
G. Raze [1], B. Lossouarn [2], A. Paknejad [3], G. Zhao [3], J.-F. Deü [2], C. Collette [3], G. Kerschen [1]
(1) University of Liège, Belgium
(2) CNAM - Conservatoire National des Arts et Métiers, France
(3) Université Libre de Bruxelles, Belgium

Mechatronic control of the car response based on VFC 79
D. Antonelli [1], L. Nesi [1], G. Pepe [1], A. Carcaterra [1]
(1) Sapienza University of Rome, Italy

FLOP: feedback local optimality control of the inverse pendulum oscillations 93
G. Pepe [1], D. Antonelli [1], L. Nesi [1], A. Carcaterra [1]
(1) Sapienza University of Rome, Italy

Active noise control in pipes and ducts using carbon nanotube thermophones 107
A. Barnard [1], S. Senczyszyn [1]
(1) Michigan Technological University, United States of America

Vibration suppression using the concept of a semi-active magnetorheological inerter device 121
M. Tipuric [1], D. Wagg [1], N. D. Sims [1]
(1) University of Sheffield, United Kingdom

Active vibration reduction on a quadrocopter 131
T. Bartel [1], H. Atzrodt [1], D. Wilczynski [1]
(1) Fraunhofer Institute for Structural Durability and System Reliability, Germany

H-infinity optimization of positive position feedback control for mitigation of nonlinear vibrations 143
G. Zhao [1], A. Paknejad [1], G. Raze [2], G. Kerschen [2], C. Collette [1]
(1) Université Libre de Bruxelles, Belgium
(2) University of Liège, Belgium

Multi-input multi-output aeroelastic control using the receptance method 153
B. Mokrani [(1)], F. Palazzo [(2)], S. Fichera [(1)], L. J. Adamson [(1)], J. E. Mottershead [(1)]
(1) University of Liverpool, United Kingdom
(2) Politecnico di Torino, Italy

Minimisation of the effect of aleatory uncertainties on dynamic systems by active control using the method of receptances 165
L. J. Adamson [(1)], S. Fichera [(1)], J. E. Mottershead [(1)]
(1) University of Liverpool, United Kingdom

The effect of active vibration control on the sound field scattered from a flexible structure 175
C. House [(1)], J. Cheer [(1)], S. Daley [(1)]
(1) University of Southampton, United Kingdom

An investigation on a semi-active damping of forced structural vibrations by means of controllable structural nodes 189
G. Mikułowski [(1)], B. Popławski [(1)], R. Wiszowaty [(1)], A. Mróz [(2)], Ł. Jankowski [(1)]
(1) Institute of Fundamental Technological Research Polish Academy of Sciences, Poland
(2) Adaptronica Sp. z o.o., Poland

Design of an inertial mass actuator for active vibration control of a planetary gearbox using piezoelectric shear actuator 203
P. Zech [(1)], D. F. Plöger [(1)], T. Bartel [(2)], T. Röglin [(2)], S. Rinderknecht [(1)]
(1) TU Darmstadt, Germany
(2) Fraunhofer Institute for Structural Durability and System Reliability, Germany

Self-adaptive fluid-based absorbers for impact mitigation and vibration damping 217
C. Graczykowski [(1)], R. Faraj [(1)]
(1) Institute of Fundamental Technological Research Polish Academy of Sciences, Poland

Simulation of active control systems considering different levels of detail in the signal processing chain 229
J. Millitzer [(1)], J. Rohlfing [(2)], V. Mees [(1)], A. Döring [(1)]
(1) Fraunhofer Institute for Structural Durability and System Reliability LBF, Germany.
(2) Fraunhofer Institute for Building Physics IBP, Germany.

Control of fluctuations of a tethered unmanned-underwater-vehicle 241
E. Paifelman [(1,2)], G. Pepe [(1)], F. La Gala [(2)], A. Carcaterra [(1)]
(1) Sapienza University of Rome, Italy
(2) CNR - National Research Council, Italy

Optimization of skyhook control strategies and an alternative approach for the operational conditions 253
G. Papaioannou [(1)], D. Koulocheris [(1)]
(1) National Technical University of Athens, Greece

A compact and light acoustic transducer using dielectric elastomer films for low frequency active noise cancellation 267
A. Paradeisiotis [(1)], C. Yiakopoulos [(1)], I. Antoniadis [(1)]
(1) National Technical University of Athens, Greece

Simulink-PSpice co-simulation of Power Amplifier for driving piezoelectric actuators 279
Y. J. Park (1), T. Bartel (1), T. Röglin (1), G. Stoll (1), P. Zech (2), D. F. Plöger (2), S. Rinderknecht (2)
(1) Fraunhofer Institute for Structural Durability and System Reliability, Germany
(2) TU Darmstadt, Germany

A practical approach of active vibration control with the use of piezoelectric actuators 293
D. J. Williams (1), H. Haddad Khodaparast (1), C. Yang (1)
(1) Swansea University, United Kingdom

Wave-based control of a planar mechanical structure by piezoelectric actuators 303
P. Beneš (1), Z. Neusser (1), Z. Šika (1), M. Valášek (1), J. Zavřel (1)
(1) Czech Technical University in Prague, Czech Republic

Decentralized and distributed MIMO H-infinity robust control of vibration suppression of planar structures 309
Z. Šika (1), M. Hromčík (1), F. Svoboda (1), J. Volech (1), J. Zavřel (1), J. Karlíček (1)
(1) Czech Technical University in Prague, Czech Republic

ANT

Session Advanced training and research in energy efficient smart structures

Virtual sensing of wheel center loads on a McPherson suspension 325
E. Risaliti (1,2), T. Tamarozzi (1,2), B. Cornelis (1), W. Desmet (2,3)
(1) Siemens PLM Software, Belgium
(2) KU Leuven, Belgium
(3) Flanders Make, Belgium

Nonlinear feedback control of a stroke limited inertial actuator using a state estimation approach 341
M. Dal Borgo (1), M. Ghandchi Tehrani (1), S. J. Elliott (1)
(1) University of Southampton, United Kingdom

Piezoelectric patches with multi-resonant shunts for multiple frequency band vibration control 355
M. Zientek (1), P. Gardonio (1), L. Dal Bo (1)
(1) University of Udine, Italy

Experimental decentralised control of vibration on a plate with inertial actuators 371
S. Camperi (1), M. Ghandchi Tehrani (1), S. J. Elliott (1)
(1) University of Southampton, United Kingdom

Experimental tests of a flywheel proof mass actuator for velocity feedback control 381
A. Kras (1), P. Gardonio (1)
(1) University of Udine, Italy

Numerical modeling of a flexural displacement-converter mechanism to excite a flat acoustic source driven by piezoelectric stack actuators 397
F. Tajdari (1), A. Berkhoff (1,2), A. de Boer (1)
(1) University of Twente, The Netherlands
(2) TNO Technical Sciences, Acoustics and Sonar, The Netherlands

Active vibration control of a system subject to random excitation using impulsive parametric damping 407
M. Ghandchi Tehrani [(1)], T. Pumhoessel [(2)]
(1) University of Southampton, United Kingdom
(2) Johannes Kepler University Linz, Austria

A study on important criteria for the effectiveness of piezoelectric energy harvesters under a constant volume 415
N. Aboulfotoh [(1,2)], J. Twiefel [(1)]
(1) Leibniz University Hannover, Germany
(2) Cairo University, Egypt

Stability, performance and power consumption of a centralised and decentralised active vibration control system 431
G. Lapiccirella [(1)], J. Rohlfing [(2)]
(1) Fraunhofer Institute for Building Physics, Germany
(2) Fraunhofer Institute for Structural Durability and System Reliability, Germany

Efficient assembly of unit cells with Krylov based model order reduction 445
S. van Ophem [(1,2)], E. Deckers [(1,2)], W. Desmet [(1,2)]
(1) KU Leuven, Belgium
(2) Flanders Make, Belgium

Nonlinearity assessment of MIMO electroacoustic systems on Direct Field Environmental Acoustic Testing 457
M. Alvarez Blanco [(1,2)], P. Z. Csurcsia [(1,3)], K. Janssens [(1)], B. Peeters [(1)], W. Desmet [(2,4)]
(1) Siemens Industry Software NV, Belgium
(2) KU Leuven, Belgium
(3) Vrije Universiteit Brussel, Belgium
(4) Flanders Make, Belgium

Efficiently assessing changes in boundary conditions using vibro-acoustic information 473
P. Becht [(1,2)], S. van Ophem [(1,2)], E. Deckers [(1,2)], C. Claeys [(1,2)], B. Pluymers [(1,2)], W. Desmet [(1,2)]
(1) KU Leuven, Belgium
(2) Flanders Make, Belgium

Object-oriented model-based condition monitoring 489
M. Gonzalez [(1,2)], O. Salgado [(1)], J. Croes [(2,3)], B. Pluymers [(2,3)], W. Desmet [(2,3)]
(1) IK4-Ikerlan, Spain
(2) KU Leuven, Belgium
(3) Flanders Make, Belgium

AE

Session Aero-elasticity

Metamodel-based optimization of an energy harvester from stall-induced pitching oscillations of airfoils 505
C. R. dos Santos [(1)], M. M. da Silva [(1)], F. D. Marques [(1)]
(1) University of São Paulo, Brazil

On-line tracking of aircraft aeroelastic modes during flutter flight tests 515
B. Jacquier [1], F. Ayme [2]
(1) ONERA - Office National d'Etudes et de Recherches Aérospatiales, France
(2) Airbus, France

On the effect of control surface deflections on the aeroelastic response of an aerofoil at transonic buffet conditions 531
N. F. Giannelis [1], G. A. Vio [1]
(1) University of Sydney, Australia

Development of a nonlinear state space model of the forces acting on an aerofoil oscillating in pitch 547
M. F. Siddiqui [1], J. Ertveldt [2], J. Decuyper [1], T. De Troyer [1], J. Schoukens [1], M. C. Runacres [1]
(1) Department of Engineering Technology, Vrije Universiteit Brussel, Belgium
(2) Department of Mechanical Engineering, Vrije Universiteit Brussel, Belgium

Computationally-efficient aeroelastic analysis tool for shortwing / propeller configuration on compound helicopters 559
Z. Wang [1], A. A. Popov [1]
(1) University Of Nottingham, United Kingdom

AA

Session Aeroacoustics and flow noise

A recursive transfer admittance formulation in time domain 571
H. Denayer [1,2], W. De Roeck [1], W. Desmet [1,2]
(1) KU Leuven, Belgium
(2) Flanders Make, Belgium

Monte-carlo computation of wall-pressure spectra under turbulent boundary layers for trailing-edge noise prediction. 585
G. Grasso [1,2], P. Jaiswal [2], S. Moreau [2]
(1) Ecole Centrale de Lyon, France
(2) Université de Sherbrooke, Canada

Experimental analysis of aeroacoustic instabilities in Helmholtz resonators 601
L. Criscuolo [1,2], H. Denayer [1,2], W. De Roeck [1], W. Desmet [1,2]
(1) KU Leuven, Belgium
(2) Flanders Make, Belgium

Broadband noise from serrated UAS propellers: validation of a lattice Boltzmann approach 613
B. G. Marinus [1], D. Bontea [2], A. Halimi [3], A. Pire [1]
(1) Royal Military Academy, Belgium
(2) Military Technical Academy, Romania
(3) National Polytechnic School of Algiers, Algeria

Inverse methods in aeroacoustic three-dimensional volumetric noise source localization 621
G. Battista [1], P. Chiariotti [1], M. Martarelli [2], P. Castellini [1]
(1) Università Politecnica delle Marche, Italy
(2) Università degli studi e-Campus, Italy

Prediction of outdoor sound propagation from firearms shooting ranges: a comparison 637
B. G. Marinus [1], K. Harri [1]
(1) Royal Military Academy, Belgium

Axial propagation of flow-induced vibrations in thick walled pipes and hoses 647
I. F. Rodrigues [1], I. Lopez Arteaga [1]
(1) Eindhoven University of Technology, The Netherlands

CAM2

Session Characterisation, design and optimisation of Acoustic Materials

Predicting the sound insulation of finite double-leaf walls with a flexible frame 655
J. C. E. Van den Wyngaert [1], M. Schevenels [1], E. Reynders [1]
(1) KU Leuven, Belgium

Finite element analysis of the acoustic behavior of poroelastic materials based on experimentally determined frequency-dependent material properties 671
P. Schrader [1], F. Duvigneau [1], M. Gavila-Lloret [2], H. Rottengruber [1], U. Gabbert [1]
(1) Otto-von-Guericke-University Magdeburg, Germany
(2) BMW Group, Germany

Experimental-numerical methods for inverse characterization of the anisotropic-anelastic properties of porous materials, based on dynamic Digital Image Correlation. 687
L. Manzari [1], H. Mao [1], P. Goransson [1], J. Cuenca [1,2], I. Lopez Arteaga [1]
(1) KTH Royal Institute of Technology, Sweden
(2) Siemens Industry Software NV, Belgium

CAM

Session Characterisation, design and optimisation of acoustic materials

Microstructure based modelling of the thermal and viscous dissipation of a transversely isotropic porous fibrous insulation material. 697
B. P. Semeniuk [1], P. Goransson [1], O. Dazel [2]
(1) KTH Royal Institute of Technology, Sweden
(2) Le Mans Université, France

Modelling of nonlinear prestrain effects on the dynamic properties of viscoelastic materials 713
L. Rouleau [1], J.-F. Deü [1]
(1) CNAM - Conservatoire National des Arts et Métiers, France

Installation effects on sound absorption and flow resistivity of glass wool fibres 721
G. Petrone [1], A. Sorrentino [1], E. De Bono [1], T. Polito [1], F. Marulo [1]
(1) University of Naples Federico II, Italy

Simulations and experiments for vibro-acoustical behaviours of circular multi-layered plates 735
T. Deng [1], X. Sheng [1], Y. Ma [2], J. Li [2]
(1) Southwest Jiaotong University, People's Republic of China
(2) Sichuan University, People's Republic of China

Optimization and testing of periodic and locally resonant dead-end pores for sound absorption in frequencies below 1000 Hz 751
A. Carvalho de Sousa [1,2], M. Bartczak Camargo [3], A. Lenzi [3], C. Claeys [1,2], E. Deckers [1,2]
(1) KU Leuven, Belgium
(2) Flanders Make, Belgium
(3) Federal University of Santa Catarina, Brazil

CM

Session Condition monitoring

Detection of faulty accelerometer mounting 761
R. B. Randall [1], W. A. Smith [1]
(1) University of New South Wales, Australia

Aircraft braking dynamics and brake system modeling for fault detection and isolation 769
L. C. Navarro [1], L. C. S. Goes [1]
(1) ITA - Instituto Tecnológico de Aeronáutica, Brazil

Employment of an auto regressive moving average model for on-board knock detection of a spark ignited engine 785
D. Siano [1], M. A. Panza [1]
(1) CNR - National Research Council, Italy

Speed-dependent wet road surface detection using acoustic measurements, octave-band frequency analysis and Support Vector Machines 795
S. Kanarachos [1], M. Kalliris [1], M. Blundell [1], R. Kotsakis [2]
(1) Coventry University, United Kingdom
(2) Aristotle University of Thessaloniki, Greece

CMRM

Session Condition monitoring of rotating machinery

A diagnostic protocol for the monitoring of bearing fault evolution based on blind deconvolution algorithms 809
M. Buzzoni [1], E. Soave [1], G. D'Elia [1], E. Mucchi [1], G. Dalpiaz [1]
(1) University of Ferrara, Italy

Fleet-wide condition monitoring combining vibration signal processing and machine learning rolled out in a cloud-computing environment 823
J. Helsen [1], C. Peeters [1], T. Verstraeten [1], J. Verbeke [1], N. Gioia [1], A. Nowé [1]
(1) Vrije Universiteit Brussel, Belgium

Development and testing of health monitoring of the bearings of traction system of a regional train locomotive during commercial service 839
P. Pennacchi [1], S. Chatterton [1], A. Vania [1]
(1) Politecnico di Milano, Italy

A novelmulti-harmonic demodulation technique for instantaneous speed estimation 847
C. Peeters [1], J. Antoni [2], N. Gioia [1], P. Guillaume [1], J. Helsen [1]
(1) Vrije Universiteit Brussel, Belgium
(2) INSA Lyon, France

A comparison of different features for discrepancy analysis-based bearing diagnostics 855
S. Schmidt [1], P. S. Heyns [1], K. Gryllias [2,3]
(1) University of Pretoria, South Africa
(2) KU Leuven, Belgium
(3) Flanders Make, Belgium

Experimental validation of a bearing fault model for an independent cart conveyor 871
M. Cocconcelli [1], J. Cavalaglio Camargo Molano [1], R. Rubini [1], L. Capelli [2]
(1) University of Modena and Reggio Emilia, Italy
(2) Tetra Pak Packaging Solutions SpA, Italy

Methodologies for designing new condition indicators 883
J. Antoni [1], P. Borghesani [2], S. Kass [3], A. Raad [3], K. Gryllias [4,5]
(1) Université de Lyon, France
(2) University of New South Wales, Australia
(3) Université Libanaise, Liban
(4) KU Leuven, Belgium
(5) DMMS Lab, Flanders Make

Online fault identification for rotating machinery 891
C. E. Ludwig [1,2], U. Wever [1]
(1) Siemens AG, Germany
(2) Technical University of Munich, Germany

Cyclostationary-based tools for bearing diagnostics 905
A. Mauricio [1,2], W. A. Smith [3], R. B. Randall [3], J. Antoni [4], K. Gryllias [1,2]
(1) KU Leuven, Belgium
(2) Flanders Make, Belgium
(3) University of New South Wales, Australia
(4) Université de Lyon, France

Optimal frequency band selection via stationarity testing in time frequency domain 919
A. Michalak [1], A. Wyłomańska [1], J. Wodecki [1], R. Zimroz [2], K. Gryllias [3,4]
(1) KGHM Cuprum Ltd, Research and Development Centre, Poland
(2) Wroclaw University of Science and Technology, Poland
(3) KU Leuven, Belgium
(4) DMMS, Flanders Make, Belgium

Semi-blind Wiener filtering of mechanical source vibrations: theory and application to aircraft gearbox surveillance 929
D. Abboud [1], Y. Marnissi [1], M. El-badaoui [1,2]
(1) Safran Group, France
(2) Université de Lyon, France

Gearbox fault diagnosis based on Convolutional Neural Networks 941
Z. Chen [1,2], W. Li [1], K. Gryllias [2,3]
(1) South China University of Technology, People's Republic of China
(2) KU Leuven, Belgium
(3) Flanders Make, Belgium

Blade tip timing based condition monitoring of bladed disks in rotating machines 955
N. Jamia [1], M. I. Friswell [1], S. El-Borgi [2], P. Rajendran [3]
(1) Swansea University, United Kingdom
(2) University at Qatar, Qatar
(3) Deemed University, Tamil Nadu, India

A comparison of the prognostic approaches for rolling element bearings 971
P. Shakya [1], A. K. Darpe [2], M. S. Kulkarni [3]
(1) IIT Madras, India
(2) IIT Delhi, India
(3) IIT Bombay, India

Multi-fault diagnosis based on bi-frequency cyclostationary maps clustering 981
P. Kruczek [1], J. Wodecki [1], A. Wyłomańska [1], R. Zimroz [2], K. Gryllias [3,4]
(1) KGHM Cuprum Ltd, Research and Development Centre, Poland
(2) Wroclaw University of Science and Technology, Poland
(3) KU Leuven, Belgium
(4) DMMS, Flanders Make, Belgium

D

Session Damping

Stabilised Layer Method for linear and nonlinear spatial non classical damping identification 991
D. Lisitano [1], E. Bonisoli [1], J. E. Mottershead [2]
(1) Politecnico di Torino, Italy
(2) University of Liverpool, United Kingdom

Analysis and simulation of structures with local visco-elastic damping from elastomers 1005
M. Böswald [1], M. Gröhlich [1], J. Biedermann [1], R. Winter [1]
(1) DLR - German Aerospace Center, Germany

The effect of friction damping on the dynamic response of vibrating structures: an insight into model validation 1021
M. Umer [1], C. Gastaldi [1], D. Botto [1]
(1) Politecnico di Torino Italy

Identification of hysteretic systems for damping modelization 1037
V. Kehr-Candille [1]
(1) ONERA - Office National d'Etudes et de Recherches Aérospatiales, France

Semi-active damping of forced vibrations by means of pneumatic supports 1047
G. Mikułowski [1]
(1) Institute of Fundamental Technological Research Polish Academy of Sciences, Poland

Implementation and comparison of advanced friction representations within finite element models 1059
A. T. Mathis [1], A. R. Brink [2], D. D. Quinn [1]
(1) The University of Akron, United States of America
(2) Sandia National Laboratories, United States of America

DNRMS

Session Designs for noise reducing materials and structures

Sound transmission through checkerboard sandwich panels 1073
B. Van Damme [(1)], G. Hannema [(1)], A. Zemp [(1)]
(1) EMPA - Swiss Federal Laboratories for Materials Science and Technology, Switzerland

Design of a Kelvin cell acoustic metamaterial 1081
H. Rice [(1)], J. Kennedy [(1)], P. Goransson [(2)]
(1) Trinity College Dublin, Ireland
(2) KTH Royal Institute of Technology, Sweden

A concept demonstrator of adaptive sound absorber/insulator involving microstructure-based modelling and 3Dprinting 1091
K. C. Opiela [(1)], M. Rak [(1)], T. G. Zielinski [(1)]
(1) the Polish Academy of Sciences, Poland

The use of a benchmark periodic metamaterial to inform numerical modelling and additive manufacturing approaches. 1105
L. Dowling [(1)], L. Flanagan [(1)], H. Rice [(1)], D. Trimble [(1)], J. Kennedy [(1)]
(1) Trinity College Dublin, Ireland

Study of sound absorption capability of silencers based on the acoustic black hole effect 1121
N. L. K. Sharma [(1)], O. Umnova [(1)]
(1) University of Salford, United Kingdom

Simplification of the transfer matrix model for acoustic screens 1127
M. Gaborit [(1,2)], P. Goransson [(2)], O. Dazel [(1)]
(1) Le Mans Université, France
(2) KTH Royal Institute of Technology, Sweden

A numerical study on the shielding performance of a periodic vibration protection device 1135
L. Godinho [(1)], C. Albino [(1)], P. Alves-Costa [(2)], P. Amado-Mendes [(1)], A. Pinto [(2)], D. Soares Jr. [(3)]
(1) University of Coimbra, Portugal
(2) University of Porto, Portugal
(3) Federal University of Juiz de Fora, Brazil

Perceptual evaluation of metamaterials as insulation partitions: A listening test within the COST action DENORMS (CA15125) 1147
L. de Ryck [(1)], J. Cuenca [(1)], K. Jambrosic [(2)], C. Glorieux [(3)], M. Rychtarikova [(3,4)], V. Romero-Garcia [(5)], A. Cebrecos [(5)], N. Jiménez [(5,6)], J.-P. Groby [(5)]
(1) Siemens Industry Software NV, Belgium
(2) University of Zagreb, Croatia
(3) KU Leuven, Belgium
(4) STU - Slovak University of Technology, Slovakia
(5) Le Mans Université, France
(6) Universidad Politécnica de Valencia, Spain

A combined design-manufacturing-testing investigation of micro- to macro-scale tailoring of open poroelastic materials based on perturbed Kelvin cell micro-geometries. 1163
L. Dowling [1], H. Mao [2], L. Flanagan [1], J. Kennedy [1], H. Rice [1], D. Trimble [1], P. Goransson [2], J. Cuenca [2]
(1) Trinity College Dublin, Ireland
(2) KTH Royal Institute of Technology, Sweden

A periodic acoustic meta-material concept incorporating negative stiffness elements for low-frequency acoustic insulation/ absorption 1179
I. Antoniadis [1], A. Paradeisiotis [1]
(1) National Technical University of Athens, Greece

Influencing the wave-attenuating coupling of solid and fluid phases in poroelastic layers using piezoelectric inclusions and locally added masses 1195
T. G. Zielinski [1], M.-A. Galland [2], E. Deckers [3,4]
(1) the Polish Academy of Sciences, Poland
(2) Ecole Centrale de Lyon, France
(3) KU Leuven, Belgium
(4) Flanders Make, Belgium

DT

Session Dynamic testing: methods and instrumentation

Numerical and experimental study of first passage time of a steel strip subjected to forced and parametric excitations 1209
E. J. Delhez [1], H. Vanvinckenroye [1], J.-C. J. G. Golinval [1], V. Denoël [1]
(1) University of Liège, Belgium

Response of a curved panel subjected to local heating and base excitation 1223
D. A. Ehrhardt [1,2], B. Gockel [2], T. Beberniss [2]
(1) Ehrhardt Engineering LLC, United States of America
(2) Wright Patterson Air Force Base, United States of America

Effect of in-flight differential pressure in modal behaviour of an aircraft demonstrator using HS 3D-DIC. 1235
Á. J. Molina-Viedma [1], A. González-Centeno [1], E. López-Alba [1], L. Felipe-Sesé [1], F. Díaz [1]
(1) Universidad de Jaén, Spain

Design and validation of a nonlinear test rig with hardening stiffness in multiple degrees of freedom 1245
N. Pandiya [1], R. J. Allemang [2], A. W. Phillips [2]
(1) Robert Bosch GmbH, Germany
(2) University of Cincinnati, United States of America

Drives power reduction procedure to fill in the multipleinput multiple-output random control reference matrix 1259
G. D'Elia [1], U. Musella [2], E. Mucchi [1], B. Peeters [2], P. Guillaume [3]
(1) University of Ferrara, Italy
(2) Siemens Industry Software NV, Belgium
(3) Vrije Universiteit Brussel, Belgium

Fully automated vibration measurements of aircraft fuselages in the mid-frequency range 1271
R. Winter [1], S. Heyen [1], M. Böswald [1]
(1) DLR - German Aerospace Center, Germany

Robust algorithm for optimal configuration of a multi-type network of sensors 1281
M. Khalil [1,2], C. Heinrich [2], R. Wüchner [1], K.-U. Bletzinger [1]
(1) Technical University of Munich, Germany
(2) Siemens AG, Germany

Nonlinear system identification using digital image correlation 1295
D. R. Roettgen [1], E. M. C. Jones [1], A. R. Brink [1], P. L. Reu [1], D. P. Rohe [1], J. Wagner [1]
(1) Sandia National Laboratories, United States of America

Detecting cavitation inception in external gear pumps by means of vibro-acoustic measurements 1309
M. Battarra [1], E. Mucchi [1]
(1) University of Ferrara, Italy

Spectral optical flow imaging: measuring full-field subpixel oscillations without a high-speed camera 1323
J. Slavič [1], J. Javh [1], M. Boltežar [1]
(1) University of Ljubljana, Slovenia

Hardware in the loop testing using a hydraulic shaking table 1331
M. Böswald [1], M. Tang [1]
(1) DLR - German Aerospace Center, Germany

Statistical analysis of cup-horn ultrasonic proximity sensor output 1349
S. Jackson [1], A. J. Croxford [1], B. W. Drinkwater [1]
(1) University of Bristol, United Kingdom

Easy sensor localization using an RGB camera 1361
S. Sels [1], B. Bogaerts [1], S. Vanlanduit [1], R. Penne [1]
(1) University of Antwerp, Belgium

Optimal positioning of continuous optical fiber sensors for the modal analysis of turbine blades with optical backscatter reflectometer technology 1371
P. Pennacchi [1], G. Cazzulani [1], M. Chieppi [1], A. Colombo [1]
(1) Politecnico di Milano, Italy

Experimental evaluation of pressure dependent tangential contact stiffness 1385
M. Kreider [1], C. W. Schwingshackl [1]
(1) Imperial College London, United Kingdom

Consideration of estimation error in multiple coherence approaches: application to the inside/ outside coherence analysis of aircraft flight tests 1395
Q. Leclère [1], J. Antoni [1], E. Julliard [2], A. Pintado-Peño [2]
(1) INSA Lyon, France
(2) Airbus, France

Model validation of an aeroelastically-tailored forward swept wing using fibre-optical strain measurements 1403
Y. Govers [1], M. Y. Meddaikar [1], K. Sinha [1]
(1) DLR - German Aerospace Center, Germany

Top 10 mechanical experiments for the teaching of sound and vibration in mechanical engineering 1419
M. A. Peres [1], A. Barnard [2]
(1) The Modal Shop, Inc., United States of America
(2) Michigan Technological University, United States of America

Impact testing lightweight structures 1431
R. J. Allemang [1], A. W. Phillips [1], D. L. Brown [1]
(1) University of Cincinnati, United States of America

Vibration-based monitoring of the quality of clutch engagement in a forklift truck 1447
A. Van Campen [1], T. Ooijevaar [1], C. Mannaerts [1], C. De Buyser [2], A. Bartic [1]
(1) Flanders Make, Belgium
(2) Dana Belgium N.V., Belgium

Experimental evaluation of a new two-microphone method for the mode detection and radiation of broadband noise in ducts 1461
J. Chen [1,2], J. Melling [1], P. Joseph [1]
(1) University of Southampton, United Kingdom
(2) University of Leicester, United Kingdom

Huddle test of optical inertial sensors combined with slightly damped mechanics 1471
B. Ding [1], J. Watchi [1], C. Collette [1,2]
(1) Université Libre de Bruxelles, Belgium
(2) University of Liège, Belgium

Experimental investigation on the acoustic impedance of Helmholtz resonators using an accelerometer for the volume velocity source 1479
G. P. Guimarães [1], I. T. Ribeiro [1]
(1) UFOP - Federal University of Ouro Preto, Brazil

Compressive sensing-moving horizon estimator for periodic loads: experimental validation in structural dynamics with video-based measurements 1487
M. Kirchner [1,2], J. Croes [1,2], F. Cosco [1,2], B. Pluymers [1,2], W. Desmet [1,2]
(1) KU Leuven, Belgium
(2) Flanders Make, Belgium

Accurate structural excitation through adaptive control 1503
M. Norambuena [1], R. Winter [1], J. Biedermann [1]
(1) DLR - German Aerospace Center, Germany

Microphone random arrangements for near-field acoustic holography based on compressive sampling 1513
B. Du [1], X. Liu [1], X. Wu [1], Z. Wang [1]
(1) Kunming University of Science and Technology, People's Republic of China

CIV

Session Dynamics of civil structures

Validation of PIRAT, a novel tool for beam-like structures subject to seismic induced misalignment of guiding sleeves 1525
M. S. Bonney [1], M. Zabiégo [1]
(1) CEA, France

Influence of diaphragm modelling on the dynamic performance of a reinforced concrete high-rise building 1541
N. J. Savnik [(1)], E. I. Katsanos [(1)], S. Amador [(1)], C. E. Ventura [(2)], R. Brincker [(1)]
(1) Technical University of Denmark, Denmark
(2) University of British Columbia, Canada

Mass loading and temperature compensation for long-term ambient measurement data of a freeway bridge 1555
T. Furtmüller [(1)], C. Adam [(1)], R. Veit-Egerer [(2)]
(1) University of Innsbruck, Austria
(2) VCE Vienna Consulting Engineers ZT GmbH, Austria

Soil-structure interaction and the added-foundation effect of surface foundations with application to groundborne vibration in buildings 1567
G. Sanitate [(1)], J. P. Talbot [(1)]
(1) University of Cambridge, United Kingdom

Influence of transverse bracing beams on the dynamic behaviour of Arroyo Bracea I bridge in Madrid-Sevilla High- Speed railway line 1583
E. Moliner [(1)], P. Galvín Barrera [(2)], M. D. Martínez-Rodrigo [(1)], A. Romero Rodóñez [(2)]
(1) Universitat Jaume I, Spain
(2) Universidad de Sevilla, Spain

Specific dynamic response of truss railway bridge identified using operational modal analysis as an extension of typical dynamic load testing 1597
G. Poprawa [(1)], S. Pradelok [(1)], M. Salamak [(1)]
(1) Silesian University of Technology, Poland

Modelling of prestressed concrete bridges with 3 dimensional finite elements for structural health monitoring with model updating techniques 1607
S. Schommer [(1)], T. Kebig [(1)], V. H. Nguyen [(1)], A. Zürbes [(2)], S. Maas [(1)]
(1) University of Luxembourg, Luxembourg
(2) Bingen University of Applied Sciences, Germany

Simplified design of filler beam railway bridges for high-speed traffic 1621
H. Bigelow [(1)], B. Hoffmeister [(1)], M. Feldmann [(1)]
(1) RWTH Aachen University, Germany

Examining the impact of critical building substructural elements on the building's rail induced vibration responsiveness 1635
J. D'Avillez [(1)]
(1) WSP, United Kingdom

Dynamic effects at sudden structural rebuilding of the "beam-foundation" system 1645
V. Gordon [(1)], O. Pilipenko [(1)], V. Trifonov [(2)]
(1) Orel State University, Russian Federation
(2) GAZPROM, Russian Federation

Resonance and cancellation mechanisms in existing High-Speed railway bridges with an orthotropic plate behaviour 1655
M. D. Martínez-Rodrigo [(1)], E. Moliner [(1)], A. Romero Rodóñez [(2)], P. Galvín Barrera [(2)]
(1) Universitat Jaume I, Spain
(2) Universidad de Sevilla, Spain

HARV

Session Dynamics of energy harvesters

Ship roll control and energy harvesting using a U-tube anti-roll tank 1671
N. Alujević [(1)], I. Ćatipović [(1)], I. Senjanović [(1)], N. Vladimir [(1)], Š. Malenica [(2)]
(1) University of Zagreb, Croatia
(2) Bureau Veritas, France

Modeling of partially covered piezoelectric energy harvester connected to SEH interface circuit 1685
G. Hu [(1)], B. Zhao [(2)], L. Tang [(1)], J. Liang [(2)], R. Das [(3)]
(1) The University of Auckland, New Zealand
(2) ShanghaiTech University, People's Republic of China
(3) RMIT University, Australia

A nonlinear vibration energy harvester for spacecraft 1701
H. Liu [(1)], D. Zhou [(1)], Y. Wang [(1)]
(1) Beijing Key Laboratory of Intelligent Space Robotic System Technology and Applications, China

Tuned mass dampers as energy harvesters for railways 1713
G. Nerubenko [(1)], A. Bograd [(1)], P. Kolomier [(1)]
(1) NERMAR Limited, Canada

Analytical modeling of a cantilever beam type vibration energy harvester with a lever mechanism 1727
S. Ertarla [(1)], C. V. Karadag [(1)], N. Topaloglu [(1)]
(1) Yeditepe University, Turkey

Energy in Random Vibration – reduce, resist, recycle 1739
A. Wasenczuk [(1)], I. Corni [(2)], N. Symonds [(2)]
(1) Perpetuum, United Kingdom
(2) University of Southampton, United Kingdom

JOINT

Session Dynamics of joints

Response predictions of reduced models with whole joints 1753
R. J. Kuether [(1)], D. A. Najera-Flores [(2)]
(1) Sandia National Laboratories, United States of America
(2) ATA Engineering, United States of America

Modal impact testing for estimating bolted joint tightness 1769
M. Brøns [(1)], J. J. Thomsen [(1)], A. Fidlin [(2)], D. Tcherniak [(3)], S. M. Sah [(1)]
(1) Technical University of Denmark, Denmark
(2) Karlsruhe Institute of Technology, Germany
(3) Brüel & Kjær Sound & Vibration Measurement A/S, Denmark

Identification of contact parameters for dry friction joints 1777
K. Willner [(1)]
(1) FAU Erlangen-Nürnberg, Germany

A block-Gauss Seidel algorithm with static reduction to predict damping in bolted joints 1789
I. Zare [1], M. S. Allen [1]
(1) University of Wisconsin-Madison, United States of America

Extracting natural frequency and damping from time histories. Better than the frequency domain? 1801
H. G. D. Goyder [1], D. P. T. Lancereau [1]
(1) Cranfield University, United Kingdom

The surrogate system hypothesis for joint mechanics: statement and evaluation through empirical parameter estimation 1813
N. N. Balaji [1], M. R. W. Brake [1]
(1) Rice University, United States of America

Two types of dynamic joint behaviour: theoretical and experimental analysis 1823
H. G. D. Goyder [1], D. P. T. Lancereau [1], P. Ind [2], D. Brown [2]
(1) Cranfield University, United Kingdom
(2) AWE - Atomic Weapons Establishment, United Kingdom

Dynamic response and energy loss in jointed structures using finite element methods: application to an aero-engine casing assembly 1835
X. Chi [1], D. Di Maio [1], N. A. J. Lieven [1]
(1) University of Bristol, United Kingdom

Estimation of normal contact stiffness for different contact pairs: experiments and numerical approach 1851
D. Tonazzi [1], F. Massi [1], L. Baillet [3], M. Salipante [1], Y. Berthier [2]
(1) Sapienza University of Rome, Italy
(2) LaMCoS - INSA Lyon, France
(3) Joseph Fourier University, France

Experimental and numerical modal analysis of dry frictioninduced contact damping in assembled structures 1863
B. Magyar [1], G. Csernak [1], R. Zana [1], R. Wohlfart [1], G. Stepan [1]
(1) Budapest University of Technology and Economics, Hungary

RMD

Session Dynamics of rotating machinery

Extension of the multi-stage cyclic symmetry methodology and application to modal and dynamic response analyses 1873
N. C. Kill [1], F. d'Ambrosio [1]
(1) SAMTECH S.A., Belgium

Numerical and experimental vibration analysis of a two-pole induction motor mounted on an elastic machine test bed 1881
S. Mathes [1], U. Werner [1], B. Christian [2]
(1) University of Applied Sciences Georg Simon Ohm Nuremberg, Germany
(2) Siemens AG, Germany

Frictional effects on the synchronisation of partial contact in rotating machinery 1897
E. T. Chipato [1], A. D. Shaw [1], M. I. Friswell [1]
(1) Swansea University, United Kingdom

Balancing rotating structures using slow-speed data via optimized parametric excitation and nonlinear feedback 1907
A. Dolev [(1)], S. Tresser [(1)], I. Bucher [(1)]
(1) Technion, Israel

Rotor-to-seal rubs in a steam turbine caused by deposits of carbonized oil 1921
A. Vania [(1)], P. Pennacchi [(1)], S. Chatterton [(1)], F. Cangioli [(1)]
(1) Politecnico di Milano, Italy

Vibration dynamics in non-linear dual mass flywheels for heavy-duty trucks 1935
L. M. Wramner [(1,2)], V. Berbyuk [(2)], H. Johansson [(2)]
(1) AB Volvo
(2) Chalmers University of Technology

Dynamic characterisation of rolling-element bearings - implementation of smooth contact-state transition 1949
M. Razpotnik [(1)], G. Čepon [(1)], M. Boltežar [(1)]
(1) University of Ljubljana, Slovenia

Relative cyclic component mode synthesis and its application to nonlinear vibration analysis of mistuned bladed disks with friction joints 1965
S. M. Pourkiaee [(1)], S. Zucca [(1)], R. G. Parker [(1)]
(1) Politecnico di Torino, Italy

Solution of rotor stator contact problems with the method of normal forms 1979
A. D. Shaw [(1)], A. R. Champneys [(2)], M. I. Friswell [(1)]
(1) Swansea University, United Kingdom
(2) University of Bristol, United Kingdom

Effects of geometrical nonlinearities for a rotating intentionally mistuned bladed-disk 1993
A. Picou [(1,2)], E. Capiez-Lernout [(1)], C. Soize [(1)], M. Mbaye [(2)]
(1) Université Paris-Est, France
(2) Safran Group, France

A novel identification tool for rotors working under nonstationary conditions based on the IAS 2005
E. Sghaier [(1)], A. Bourdon [(1)], D. Rémond [(1)], J.-L. Dion [(2)], N. Peyret [(2)]
(1) Université de Lyon, France
(2) Laboratoire QUARTZ, France

Influence of internal friction dampers on global dynamics of discrete cyclic structure 2013
M. Byrtus [(1)], M. Hajžman [(1)], L. Pešek [(2)], L. Půst [(2)]
(1) University of West Bohemia, Czech Republic
(2) Czech Academy of Sciences, Czech Republic

Experimental investigation on timing belt drive dynamics with non-circular pulley 2029
S. Passos [(1,2)], L. Manin [(2)], D. Rémond [(2)], O. Sauvage [(1)], L. Rota [(1)], E. Besnier [(2)]
(1) Groupe PSA, France
(2) LaMCoS - Laboratoire de Mécanique des Contacts et des Structures, France

Improvement of instantaneous angular speed estimation based on frequency demodulation method under non stationary conditions 2043
K. Lizoul [(1)], H. Andre [(1)], F. Guillet [(1)]
(1) Université de Lyon, Université Jean Monnet, France

FSI

Session Fluid-structure interaction

Nonlinear dynamical analysis of a fluid-structure computational model with sloshing and capillarity 2057
Q. Akkaoui [(1)], E. Capiez-Lernout [(1)], C. Soize [(1)], R. Ohayon [(2)]
(1) Universite Paris-Est, France
(2) CNAM - Conservatoire National des Arts et Métiers, France

Energy dissipation due to sloshing in baffled fuel tanks 2069
F. Buck [(1,2)], H. Hetzler [(1)], E. Fruend [(2)], S. Oexl [(2)]
(1) University of Kassel, Germany
(2) Daimler AG, Germany

Efficient time-domain modeling of floating structures with fluid-structure interaction by reduced order state-space approximations 2081
Ø. W. Petersen [(1)], O. Øiseth [(1)]
(1) NTNU - Norwegian University of Science and Technology, Norway

High-speed 3D DIC random dynamic strain measurement of a panel subjected to Mach 2 flow 2095
T. Beberniss [(1)]
(1) United States Air Force Research Lab, United States of America

Experimental and theoretical characterization of a dAFM cantilever dynamics 2107
E. Pierro [(1)], F. Bottiglione [(2)], G. Carbone [(2)]
(1) Università degli Studi della Basilicata, Italy
(2) Politecnico di Bari, Italy

INV

Session Inverse methods - load identification

Using wavelet deconvolution method to determine the force applied by drops of water on dry plates and plates with shallow surface water 2119
Y. Yu [(1)], C. Hopkins [(1)]
(1) University of Liverpool, United Kingdom

Localisation, characterisation and Identification of localised nonlinearity in structural dynamics using base excitation frequency response functions 2127
J. Taghipour [(1)], H. Haddad Khodaparast [(1)], M. I. Friswell [(1)], H. Madinei [(1)], H. Jalali [(1)], X. Wang [(2)]
(1) Swansea University, United Kingdom
(2) University of Bristol, United Kingdom

Random force identification via Kalman filtering on a cantilevered structure 2139
R. P. Álvarez-Briceño [(1)], L. de Oliveira [(1)]
(1) University of São Paulo, Brazil

Inverse parameter estimation in resonant, coupled fluid-structure interaction problems 2155
J. Cuenca [1,2], P. Goransson [2], L. De Ryck [1], T. Lähivaara [3]
(1) Siemens Industry Software NV, Belgium
(2) KTH Royal Institute of Technology, Sweden
(3) University of Eastern Finland, Finland

Identification of wave forces from acceleration and wave elevation data using inverse methods and spectral wave field reconstruction 2171
Ø. W. Petersen [1], O. Øiseth [1], E.-M. Lourens [1]
(1) NTNU - Norwegian University of Science and Technology, Norway

Investigation of virtual sensing techniques on a rear twistbeam suspension by performing multiple-input/state estimation 2181
R. Cumbo [1], T. Tamarozzi [1,2], K. Janssens [1], W. Desmet [2]
(1) Siemens Industry Software NV, Belgium
(2) KU Leuven, Belgium

LW

Session Lightweight structures and materials

Linking manufacturing simulation with functional performance engineering for composites applications 2197
K. Vanclooster [1], L. Spina [2], S. Donders [1], R. Lombardi [3], R. D'Ippolito [3], L. Farkas [1], D. Mundo [2]
(1) Siemens Industry Software NV, Belgium
(2) University of Calabria, Italy
(3) Noesis Solutions, Belgium

Mesoscale structure of periodic textile composites effect on wave propagation 2213
V. Thierry [1], L. Brown [1]
(1) University of Nottingham, United Kingdom

Modal frequency and damping analysis of tow steered CFRP composite plates 2223
D. d. A. Pereira [1,3], T. A. M. Guimaraes [2], D. A. Rade [1]
(1) Division of Mechanical Engineering, ITA - Technological Institute of Aeronautics, Brazil.
(2) School of Mechanical Engineering, UFU - Federal University of Uberlândia, Brazil.
(3) Lightweight Structures Laboratory, IPT - Institute for Technological Research, Brazil.

Numerical and experimental investigation of prestress effect on natural frequencies of composite beams 2239
A. Orlowska [1], C. Graczykowski [1], A. Galezia [2]
(1) Institute of Fundamental Technological Research Polish Academy of Sciences, Poland
(2) Warsaw University of Technology, Poland

Multi-attribute evaluation of concept variants for lightweight structures 2249
C. Lopez [1], M. Boucher [1,2], B. Van Doninck [1], F. Maurin [1,2], V. Iliopoulou [1], J. Stroobants [1], S. Jonckheere [1,2], E. Deckers [1,2], S. van Poppel [1], B. Pluymers [1,2]
(1) Flanders Make, Belgium
(2) KU Leuven, Belgium

The effect of the weaving architecture of periodic composite structures on structural damping 2265
V. Thierry [1], D. Chronopoulos [1]
(1) University of Nottingham, United Kingdom

Analysis of Sound Transmission Loss of a Rectangular Plate with Acoustic Treatments 2275
S. Zhang [1], X. Sheng [1]
(1) Southwest Jiaotong University, People's Republic of China

MHF

Session Medium and high frequency techniques

Narrow band analysis of structure borne noise in complex dynamical systems using energy methods 2291
G. Borello [1], L. Gagliardini [2], T. Lambert [2], I. Abettan [2]
(1) InterAC, France
(2) Groupe PSA, France

Dynamical energy analysis modelling by using transfer path analysis 2303
S. Morita [1], T. Hartmann [2], G. Tanner [2]
(1) Yanmar R&D Europe, Italy
(2) University of Nottingham, United Kingdom

A fast and efficient approach for simulating ultrasonic waves and their interaction with defects in periodic structures 2311
M. K. Malik [1,2], D. Chronopoulos [1], G. Tanner [1], Y. Essa [2], F. de la Escalera Cutillas [2]
(1) University of Nottingham, United Kingdom
(2) Aernnova S.A., Spain

Band-averaged variance prediction in the hybrid deterministic – statistical energy analysis of vibro-acoustic systems 2323
E. Reynders [1], R. S. Langley [2]
(1) KU Leuven, Belgium
(2) University of Cambridge, United Kingdom

An experimental investigation of the three-dimensional vibration characteristics of ultrasonic irrigation tips 2337
M. Dannemann [1], M. Kucher [1], M.-T. Weber [1], N. Modler [1]
(1) Technical University of Dresden, Germany

Tunnelling corrections to wave transmissions on shell structures 2349
N. M. Mohammed [1,3], S. Creagh [1], G. Tanner [1], D. Chappell [2]
(1) University of Nottingham, United Kingdom.
(2) Nottingham Trent University, United Kingdom.
(3) University of Sulaimani, Iraq.

Connectivity in waves and vibrations: one-to-six, one-to-all, all-to-all and random connections 2363
A. Carcaterra [1], N. Roveri [1], A. Akay [2]
(1) Sapienza, University of Rome, Italy
(2) Bilkent University, Ankara, Turkey

Waves path in an elastic membrane with selective nonlocality 2371
F. Coppo [1], A. S. Rezaei [1], F. Mezzani [1], S. Pensalfini [1], A. Carcaterra [1]
(1) Sapienza University of Rome, Italy

MOR

Session Model order reduction

Model order reduction of large stroke flexure hinges using modal derivatives 2379
J. P. Schilder [1], F. M. Segeth [1], M. H. M. Ellenbroek [1], M. van den Belt [1], A. de Boer [1]
(1) University of Twente, The Netherlands

A full PGD/HBM-based algorithm for a low-dimensional NNM continuation with modal enrichment 2387
L. Meyrand [1], E. Sarrouy [1], B. Cochelin [1], G. Ricciardi [2]
(1) Aix-Marseille University, France
(2) CEA Cadarache, France

Amultivariate, well-conditioned asymptotic waveform evaluation for finite element solutions with complex parametric dependence 2403
R. Rumpler [1], R. Rodríguez Sánchez [2], P. Goransson [1]
(1) KTH Royal Institute of Technology, Sweden
(2) Technical University of Munich, Germany

Model order reduction for nonlinear dynamics engineering applications 2415
F. Naets [1,2], T. Tamarozzi [1,3], W. Rottiers [1,2], S. Donders [3], H. Van der Auweraer [3], W. Desmet [1,2]
(1) KU Leuven, Belgium
(2) Flanders Make, Belgium
(3) Siemens Industry Software NV

The application of artificial neural networks in mechatronics system development 2431
P. Mas [1], S. B. Maddina [1], F. L. Marques dos Santos [1], C. Sobie [1], H. Van der Auweraer [1]
(1) Siemens Industry Software NV, Belgium

Non-intrusive model-order reduction of geometrically nonlinear finite elements: enhancement with static augmentation 2445
M. Karamooz Mahdiabadi [1], D. J. Rixen [1]
(1) Technical University of Munich, Germany

Parametric model order reduction for efficient frequency response evaluation 2461
V. Cool [1], F. Naets [1,2], W. Rottiers [1,2], W. Desmet [1,2]
(1) KU Leuven, Belgium
(2) Flanders Make, Belgium

MTOA

Session Modeling, testing, and optimization of acoustic metamaterials

Application of the wave finite element method to the analysis of locally resonant band gaps in periodic structures with viscoelastic properties 2469
J.-M. Mencik [1], V. Denis [1], M. Caliez [1], S. Méo [2]
(1) INSA Centre Val de Loire, France
(2) Université de Tours, France

Investigating simple designs of phononic crystal plates and their influence on the wave propagation properties 2483
E. D. Nobrega [1,2], M.-L. Gobert [3], J. M. C. Dos Santos [1], J.-M. Mencik [3]
(1) State University of Campinas, Brazil
(2) Federal University of Maranhão, Brazil
(3) INSA Centre Val de Loire, France

Computing the dispersion diagramand the forced response of periodic elastic structures using a state-space formulation 2497
G. F. C. A. Assis [1], E. J. P. Miranda Jr. [2], D. Beli [1], J. F. Camino [1], J. M. C. Dos Santos [1], J. R. F. Arruda [1]
(1) Unicamp - University of Campinas, Brazil
(2) IFMA - Federal Institute of Maranhão, Brazil

MB

Session Multi-body dynamics and control

Increasing the threshold of vibration stability of soft mounted induction motors with elastic rotors and sleeve bearings using active motor foot mounts 2509
U. Werner [1]
(1) University of Applied Sciences Georg Simon Ohm Nuremberg, Germany

Separation of structural response and excitation characteristics in planetary gearboxes 2525
D. F. Plöger [1], J. Jungblut [1], P. Zech [1], S. Rinderknecht [1]
(1) TU Darmstadt, Germany

Full model multibody approach for the sound calculation of gearboxes 2533
D. Werner [1], S. Falkenberger [2], B. Graf [1], F. Wegerer [1], J. Neher [3], B. Wender [1]
(1) University of Applied Sciences of Ulm, Germany
(2) Continental Automotive, Germany
(3) MAN Diesel & Turbo SE, Germany

Comparison of finite-element methods to compute the transmission error to noise transfer function of a simple gear box. 2549
Y. Goth [1]
(1) CETIM - Centre Technique des Industries Mécaniques, France

An absolute interface coordinates floating frame of reference formulation for plates 2559
M. van den Belt [1], J. P. Schilder [1], D. M. Brouwer [1]
(1) University of Twente, The Netherlands

Topology optimization of a high-speed cutting mechanism 2567
K. Asrih [1], F. Naets [1,2], W. Desmet [1,2]
(1) KU Leuven, Belgium
(2) Flanders Make, Belgium

Modal behavior and transient dynamic analysis of a planetary gear train with time-varying mesh stiffness using a multibody model 2577
C. Alessio [1], D. Park [2], D. Mundo [1], T. Tamarozzi [2], A. Rezayat [2]
(1) University of Calabria, Italy
(2) Siemens Industry Software NV, Belgium

NL

Session Non-linearities: identification and modelling

A nonlinear energy harvester for torsional oscillations 2593
B. Gunn [1], S. Theodossiades [1], S. Rothberg [1]
(1) Loughborough University, United Kingdom

On selecting appropriate training data to model an autonomous oscillator 2601
J. Decuyper [1], T. De Troyer [1], M. C. Runacres [1], K. Tiels [2], J. Schoukens [1]
(1) Vrije Universiteit Brussel, Belgium
(2) Uppsala University, Sweden

Unsteady aerodynamics and nonlinear dynamics of freefalling rotating seeds 2615
B. A. Roccia [1,2], M. L. Verstraete [1], G. Dimitriadis [2], O. Brüls [2], S. Preidikman [1]
(1) CONICET – National Council of Scientific and Technological Research Argentina
(2) University of Liège, Belgium

Predicting nonlinear system responses without a single simulation 2631
G. Manson [1]
(1) University of Sheffield, United Kingdom

Experiments and simulations of an industrial assembly with nonlinear joints subjected to harmonic and random vibrations 2647
T. Roncen [1,2], J.-J. Sinou [2,3], J.-P. Lambelin [1]
(1) CEA, France
(2) Ecole Centrale de Lyon, France
(3) Institut Universitaire de France, France

Modal analysis of an isolated nonlinear response mode using the Nyquist circle properties: numerical case 2661
D. Di Maio [1]
(1) University of Twente, The Netherlands

Linearization of modal parameters in Duffing oscillator using the random decrement technique 2673
K. K. Vesterholm [1], R. Brincker [1], A. Brandt [2]
(1) DTU - Centre for Oil and Gas, Technical University of Denmark, Denmark
(2) University of Southern Denmark, Denmark

Computation of nonlinear modes of non-conservative mechanical systems 2687
M. Jahn [1], S. Tatzko [1], L. Panning-von Scheidt [1], J. Wallaschek [1]
(1) Leibniz University Hannover, Germany

Using the harmonic balance method to directly compute NNMs of geometrically nonlinear finite element models 2701
C. I. Van Damme [1], A. E. Madrid [1], M. S. Allen [1]
(1) University of Wisconsin - Madison, United States of America

Nonlinear time series analysis of drillstring lateral vibrations 2719
T. Kasper [1], S. Tatzko [1], J. Wallaschek [1]
(1) Leibniz University Hannover, Germany

Investigating the bi-stable behavior of a lumped system with frictional contact 2727
J. Brunetti [1], W. D'Ambrogio [1], N. Hoffmann [2], F. Massi [3]
(1) Università dell'Aquila, Italy
(2) Hamburg University of Technology, Germany
(3) Sapienza University of Rome, Italy

Investigating a mechanism which causes divergence of a resonant decay from the backbone curve 2739
A. K. M. Brown [1], T. L. Hill [1], S. Neild [1], I. Tartaruga [1]
(1) University of Bristol, United Kingdom

Manuscript preparation instructions 2749
A. J. Elliott [1], I. Tartaruga [2], A. Cammarano [1], P. S. Dobson [1], S. Neild [2]
(1) University of Glasgow, United Kingdom
(2) University of Bristol, United Kingdom

On the identification of model error through observations of time-varying parameters 2759
P. L. Green [1], E. Chodora [2], S. Atamturktur [2]
(1) University of Liverpool, United Kingdom
(2) Clemson University, United States

On NARX models using treed Gaussian processes 2775
T. Zhang [1], R. J. Barthorpe [1], K. Worden [1]
(1) University of Sheffield, United Kingdom

OMA

Session Operational modal analysis

Optimal parameters in Data-driven stochastic subspace identification in Operational Modal Analysis 2783
C.-Y. Tsai [1], Y. J. Chan [1], J.-L. Chen [1], C.-L. Chao [1], S.-Y. Chien [1]
(1) National Chung Hsing University, Taiwan

Operational modal analysis and fluid-structure interaction 2793
M. Vigsø [1], T. Kabel [1], M. Tarpø [1], R. Brincker [2], C. T. Georgakis [1]
(1) Aarhus University, Denmark
(2) Technical University of Denmark, Denmark

Fatigue damage prediction based on strain field estimates using a smoothed Kalman filter and sparse measurements 2805
U. Lagerblad [1,2], H. Wentzel [2], A. Kulachenko [1]
(1) KTH Royal Institute of Technology, Sweden
(2) Scania CV AB, Sweden

Dealing with harmonics in continuous modal analysis 2819
N. Gioia [1], C. Peeters [1], P. J. Daems [1], P. Guillaume [1], J. Helsen [1]
(1) Vrije Universiteit Brussel, Belgium

Output-only recursive identification of time-varying systems subject to gross errors 2829
Z.-S. Ma [1], Q. Ding [1], B. Wang [1]
(1) Tianjin University, People's Republic of China

Operational modal analysis of a turbine in big noise environment 2839
M. Zhao [1], L. Yue [1]
(1) Nanjing University of Aeronautics and Astronautics, People's Republic of China

Statistical error reduction for correlation-driven operational modal analysis 2851
M. Tarpø [1], P. Olsen [1], M. Juul [1], S. Amador [2], T. Friis [2], R. Brincker [2]
(1) Aarhus University, Denmark
(2) Technical University of Denmark, Denmark

Regularized time-varying operational modal analysis illustrated on a wind tunnel testing measurement 2859
P. Z. Csurcsia [1,2], B. Peeters [2], J. Schoukens [1]
(1) Vrije Universiteit Brussel, Belgium
(2) Siemens Industry Software NV, Belgium

Automated modal identification in operational conditions using 3D stabilization diagrams 2873
G. Marrongelli [1], F. Magalhães [2], C. Gentile [1], Á. Cunha [2]
(1) Politecnico di Milano, Italy
(2) University of Porto, Portugal

Operational modal analysis based on time-domain expansion of transmissibility 2887
J. Kang [1], L. Liu [1,2,3], S. D. Zhou [1,2,3], L. Yu [1]
(1) Beijing Institute of Technology, People's Republic of China
(2) Ministry of Education, People's Republic of China
(3) Ministry of Industry and Information Technology, People's Republic of China

Output-only modal parameter estimator of time-varying structures based on maximum correntropy criterion and kernelized TARMA model 2903
L. Yu [1], L. Liu [1,2,3], J. Kang [1]
(1) Beijing Institute of Technology, People's Republic of China
(2) Ministry of Education, People's Republic of China
(3) Ministry of Industry and Information Technology, People's Republic of China

PE

Session Parameter estimation

Identification of the modal parameters of systems with general damping. 2917
N. Feng [2], E. J. Hahn [1], M. Yu [3]
(1) University of New South Wales, Australia
(2) Shandong University, China
(3) Sun Yat-sen University, China

Automatic operational modal analysis using statistical modelling of pole locations 2927
S. S. Christensen [1], A. Brandt [1]
(1) University of Southern Denmark, Denmark

Variance computation of the Modal Assurance Criterion 2939
S. Gres [1], M. Döhler [2], P. Andersen [3], L. Mevel [2]
(1) Aalborg University, Denmark
(2) Inria/IFSTTAR, France
(3) Structural Vibration Solutions A/S, Denmark

Recent advances in swept sine controlled excitation and processing for Multi-Input Multi-Output FRFs estimation 2951
U. Musella [1,2,3], A. Longo [3], S. Vettori [4], S. Waimer [1,2], E. Di Lorenzo [2], B. Peeters [2], F. Marulo [3], P. Guillaume [1]
(1) Vrije Universiteit Brussel, Belgium
(2) Siemens Industry Software NV, Belgium
(3) University of Naples Federico II, Italy
(4) Sapienza University of Rome, Italy

Automatic modal parameter selection using a statistical model and a Kalman filter 2967
K. Soal [1], Y. Govers [1], J. Bienert [2], A. Bekker [3]
(1) DLR - German Aerospace Center, Germany
(2) THI - Technische Hochschule Ingolstadt, Germany
(3) Stellenbosch University, South Africa

Identification and comparison of modal parameter in a structure during the vibration test using operational modal analysis 2977
N. C. Costa [1], E. A. Camargo [2], R. Pirk [2]
(1) Brüel & Kjær Sound & Vibration Measurement A/S, Brazil
(2) ITA - Instituto Tecnológico de Aeronáutica, Brazil

Output-only damping estimation of friction systems in ambient vibrations 2989
T. Friis [1], E. I. Katsanos [1], M. Tarpø [2], S. Amador [1], R. Brincker [1]
(1) Technical University of Denmark, Denmark
(2) Aarhus University, Denmark

PBNv2

Session Pass-by noise

Approaches to the remote mapping of vehicle noise sources in a reverberant environment 3001
A. Papaioannou [1], S. J. Elliott [1], J. Cheer [1]
(1) University of Southampton, United Kingdom

Model-based acoustic characterisation of muffler components and extrapolation to inhomogeneous thermal conditions 3009
M. H. Alkmim [1], J. Cuenca [1], L. De Ryck [1], P. Goransson [2]
(1) Siemens Industry Software NV, Belgium
(2) KTH Royal Institute of Technology, Sweden

The design of a low-cost directional warning sound system for electric vehicles 3021
N. Kournoutos [1], J. Cheer [1], S. J. Elliott [1]
(1) University of Southampton, United Kingdom

PER

Session Periodic structures and metamaterials

Tailoring Phononic-like topologies for controlling the structural-acoustic coupling in fluid-filled cylinders 3033
Y. Vered [1], I. Bucher [1]
(1) Technion, Israel

Resonant metabarriers as seismic attenuators in granular media 3047
R. Zaccherini [(1)], A. Palermo [(2,3)], S. Krödel [(1)], V. K. Dertimanis [(1)], A. Marzani [(2)], C. Daraio [(3)], E. N. Chatzi [(1)]
(1) ETH Zürich, Switzerland
(2) University of Bologna, Italy
(3) California Institute of Technology, United States of America

The influence of uncertainties in periodic structures for vibro-acoustic problems 3059
J. Henneberg [(1,2)], J. S. Gomez Nieto [(1)], K. Sepahvand [(1)], A. Gerlach [(2)], H. Cebulla [(3)], S. Marburg [(1)]
(1) Technical University of Munich, Germany
(2) Robert Bosch GmbH, Germany
(3) Technical University Chemnitz, Germany

Diffusion-based design of locally resonant sub-systems using a reduced wave finite element framework 3071
C. Droz [(1)], R. F. Boukadia [(1)], M. Ichchou [(2)], W. Desmet [(1)]
(1) KU Leuven, Belgium
(2) Ecole Centrale de Lyon, France

Broadband resonance suppressions using a resonant beam damper with embedded acoustic black hole features 3085
T. Zhou [(1)], L. Cheng [(1)]
(1) Hong Kong Polytechnic University, Hong Kong S.A.R. (People's Republic of China)

Metamaterial characterization for acoustic cloaking applications 3097
A. Hanford [(1)], P. Kerrian [(1)], B. Beck [(1)], D. Capone [(1)]
(1) The Pennsylvania State University, United States of America

Attenuation of the mass-spring-mass effect in the sound transmission loss of double panel partitions using vibroacoustic resonant metamaterials 3111
N. G. Rocha de Melo Filho [(1,2)], L. Van Belle [(1,2)], C. Claeys [(1,2)], E. Deckers [(1,2)], W. Desmet [(1,2)]
(1) KU Leuven, Belgium
(2) Flanders Make, Belgium

Design tool for realisable vibro-acoustic metamaterials based on their NVH performance 3125
M. E. S. Clasing Villanueva [(1,2)], C. Claeys [(1,2)], N. G. Rocha de Melo Filho [(1,2)], E. Deckers [(1,2)], K. Geurts [(2)], I. Van de Weyenberg [(2)], P. Campestrini [(2)], B. Pluymers [(1,2)], W. Desmet [(1,2)]
(1) KU Leuven, Belgium
(2) Flanders Make, Belgium

Long-range coupling of waveguides 3135
F. Mezzani [(1)], F. Coppo [(1)], A. Carcaterra [(1)]
(1) Sapienza University of Rome, Italy

Control of edge modes in finite vibro-acoustic resonant metamaterials 3145
L. Sangiuliano [(1,2)], E. Deckers [(1,2)], C. Claeys [(1,2)]
(1) KU Leuven, Belgium
(2) Flanders Make, Belgium

Formation mechanisms of vibration bandgaps based on block diagrams of wave transmission 3159
S. Tomita [(1)], S. Nakano [(1)], R. Omote [(1)]
(1) Toyota Inc., Japan

Influence of damping on the sound insulation of infinite and finite locally resonant metamaterial plates 3171
L. Van Belle [1,2], C. Claeys [1,2], E. Deckers [1,2], W. Desmet [1,2]
(1) KU Leuven, Belgium
(2) Flanders Make, Belgium

Revisited impedance tube for standard and metamaterial testing 3185
L. A. Nascimento [1], G. K. Rodrigues [1], L. de Oliveira [1]
(1) University of São Paulo, Brazil

Small-world based interactions in elastic metamaterials 3199
n. roveri [1], s. pensalfini [1], a. carcaterra [1]
(1) Sapienza University of Rome, Italy

RAIL

Session Railway dynamics and ground vibrations

Dynamic FEM simulation of wheel-rail rolling contact with friction in an Eulerian frame - Application to curve squeal 3213
V. V. Lai [1,2], O. Chiello [2], J.-F. Brunel [1], P. Dufrénoy [1]
(1) University of Lille, France
(2) IFSTTAR, France

Apodization and phase methods applied to the seismic detection of underground objects 3227
E. Rustighi [1], Q. Leclère [2], J. M. Muggleton [1]
(1) University of Southampton, United Kingdom
(2) INSA Lyon, France

Optimization of flow restrictor diameter in high speed railway vehicle suspensions 3243
C. Ramiro Redondo [1], P. Pintado Sanjuán [1], A. L. Morales Robredo [1], A. J. Nieto Quijorna [1], J. M. Chicharro Higuera [1]
(1) University of Castilla-La Mancha, Spain

Modelling of the track supports with elements over elastic foundation together with dynamic internal degrees of freedom 3255
B. Blanco [1,2,3], L. Kari [3], N. Gil-Negrete [1,2], A. Alonso [2,4]
(1) CEIT-IK4, Spain
(2) University of Navarra, Spain
(3) KTH Royal Institute of Technology, Sweden
(4) CAF I+D, Spain

Enabling the optimisation of the primary suspension with passive components for an industrial railway vehicle model 3269
T. D. Lewis [1], Y. Li [1], J. Z. Jiang [1], S. Neild [1], G. Tucker [2], S. Iwnicki [2], R. Goodall [2], M. Smith [3]
(1) University of Bristol, United Kingdom
(2) University of Huddersfield, United Kingdom
(3) University of Cambridge, United Kingdom

An investigation on the influence of pantograph friction on its interaction with a catenary using co-simulations 3283
P. Zdziebko [1], A. Martowicz [1], T. Uhl [1]
(1) University of Science and Technology AGH, Poland

Sensitivity of dynamic responses of railway prestressed concrete sleepers with under sleeper pads to impact energy 3295
C. Ngamkhanong [1], K. Goto [1,2], S. Kaewunruen [1]
(1) University of Birmingham, United Kingdom
(2) Railway Technical Research Institute, Japan

Enhancing the dynamic performance of a pantograph-catenary system via inerter-based damping technology 3305
M. Zhu [1], S. Y. Zhang [1], J. Z. Jiang [1], J. Macdonald [1], S. Neild [1]
(1) University of Bristol, United Kingdom

SEV

Session Self-excited vibrations

Mitigation of friction-induced vibrations in braking systems: prediction of the mitigation limit 3315
B. Bergeot [1], S. Bellizzi [2], S. Berger [1]
(1) INSA Centre Val de Loire, France
(2) LMA - Laboratoire de Mécanique et d'Acoustique, France

Structural modification of tool holder geometry as a chatter avoidance method 3331
T. J. Gibbons [1], E. Ozturk [1], L. Xu [2], N. D. Sims [1]
(1) University of Sheffield, United Kingdom
(2) The Boeing Company

Bifurcations and limit cycles due to self-excitation in nonlinear systems with joint friction: Phenomena and approximation schemes 3343
J. Kappauf [1], H. Hetzler [1]
(1) University of Kassel, Germany

Flutter testing using ambient excitation 3353
J. Cooper [1]
(1) University of Bristol, United Kingdom

SD

Session Structural dynamics: methods and case studies

Developing and analysing an electromechanical model of a bio-inspired flapping wing mini UAV 3365
M. Park [1], A. Abolfathi [1], J. Biggs [2], Y. Ventikos [1]
(1) University College London, United Kingdom
(2) Politecnico di Milano, Italy

Dynamic behavior and vibration analysis of tensegrity - membrane structures 3373
P. Kurka [1], V. Paiva [1], L. Teixeira [1], J. Izuka [1], P. Gonzalez [1]
(1) Unicamp - University of Campinas, Brazil

Contactless 3D manipulation of silicon wafers using acoustic levitation 3389
I. Bucher [1]
(1) Technion, Israel

Squeal measurement with 3D scanning laser doppler vibrometer: handling of the time varying system behavior and analysis improvement using FEM expansion 3399
G. Martin [1], E. Balmes [1,3], G. Vermot des Roches [1], T. Chancelier [2]
(1) SDTools, France
(2) Chassis Brakes International, France
(3) ENSAM - École Nationale Supérieure d'Arts et Métiers, France

A periodic H2 state feedback controller for a rotor-blade system 3413
J. F. Camino [1], I. F. Santos [2]
(1) Unicamp - University of Campinas, Brazil
(2) Technical University of Denmark, Denmark

Model-based analysis of the dynamic behaviour of the wing drive line of a robotic hummingbird 3427
S. Timmermans [1], D. Vandepitte [1]
(1) KU Leuven, Belgium

Focussing flexural waves for accretion removal from a beam 3443
T. Waters [1], P. Harris [1], H. Mulchandani [1], I. Stothers [2]
(1) University of Southampton, United Kingdom
(2) Cambridge, UK.

Non-stationary random vibration modeling and analysis: kernel versus adaptable Functional Series TAR methods 3455
C. N. Kapsalas [1], S. D. Fassois [1], J. S. Sakellariou [1]
(1) University of Patras, Greece

Numerical and experimental modal analysis of structures under gyroscopic influence in ALE formulation 3467
T. Weidauer [1], K. Willner [1]
(1) FAU Erlangen-Nürnberg, Germany

Electromagnetic vibration analysis of main transformer for railway 3483
K. Fukui [1], T. Noda [1]
(1) Mitsubishi Electric Corporation, Japan

Load and deflection estimation of a fast catamaran towingtank model via reduced order modeling and optimal natural observer 3495
F. Saltari [1,2], D. Dessi [1], E. Faiella [1], F. Mastroddi [2]
(1) CNR - National Research Council, Italy
(2) Sapienza University of Rome, Italy

Characterization of reaction wheel micro-vibrations 3511
W. De Munter [1], T. Delabie [1], D. Vandepitte [1]
(1) KU Leuven, Belgium

Simulation and experimental validation of gas-engine blade dynamics during milling 3527
S. Nikolaev [1], I. Kiselev [2], V. Kuts [2], S. Voronov [2]
(1) Skolkovo Institute of Science and Technology, Russia
(2) Bauman Moscow State Technical University, Russia

Pneumatic single hit test rig for analysis of the stress wave profile of non-uniform impacting rods 3535
J. Burgert [(1)], C. Moilanen [(2)], W. Seemann [(1)], J. Montonen [(3)], J. Miettinen [(2)], P. Saarenrinne [(2)]
(1) Karlsruhe Institute of Technology, Germany
(2) TUT - Tampere University of Technology, Finland
(3) Robit Company, Finland

Simulation and digital twin for mechatronic product design 3547
H. Van der Auweraer [(1,3)], S. Donders [(1)], D. Hartmann [(2)], W. Desmet [(3,4)]
(1) Siemens Industry Software NV, Belgium.
(2) Siemens Corporate Technology, Germany.
(3) KU Leuven, Belgium.
(4) DMMS core lab, Flanders Make.

On the dynamic stiffness of air springs at medium-high frequencies 3567
N. Gil-Negrete [(1,2)], A. J. Nieto Quijorna [(1,2)], A. Pradera-Mallabiabarrena [(1)], J. Gonzalez-Prada [(1)]
(1) University of Navarra, Spain
(2) CEIT, Spain

Dynamic optimization of an electro-spindle for robotic machining 3581
A. Mora [(2)], G. Bianchi [(1)], M. Leonesio [(1)]
(1) CNR - National Research Council, Italy
(2) SUPSI University of Applied Sciences and Arts of Southern Switzerland, Switzerland

Experimental and numerical mode shape tracing from components to whole motorbike chassis 3597
E. Bonisoli [(1)], D. Lisitano [(1)], L. Dimauro [(1)]
(1) Politecnico di Torino, Italy

Accurate product model development for the simulation of the dynamic behaviour of deep drawn components 3605
F. Greco [(1,2)], E. Deckers [(1,2)], J. Stroobants [(2)], S. Van Poppel [(2)], F. Maurin [(1,2)], W. Desmet [(1,2)]
(1) KU Leuven, Belgium
(2) Flanders Make, Belgium

Transmission of vibrations between towed and towing agricultural machines 3617
J. Brunetti [(2)], W. D'Ambrogio [(2)], A. Fregolent [(1)], G. Lacerra [(1)]
(1) Sapienza University of Rome, Italy
(2) Università dell'Aquila, Italy

Modal analysis tools at V2i: improved pre- and post-processing with modified p-LSCF algorithm 3629
S. Hoffait [(1)], S. Moschini [(1)], J. Ligot [(1)], D. Simon [(1)]
(1) V2i, Belgium

Towards an application of an active tendon in rotorcraft: A numerical and experimental study of coupled bending-torsion vibration of a beam-tendon system 3645
V. Ondra [(1)], R. P. Dibble [(1)], B. Titurus [(1)]
(1) University of Bristol, United Kingdom

Dynamics and control of adaptive airbags for UAV impact protection 3661
Z. Wolejsza [1], J. Holnicki-Szulc [1], C. Graczykowski [1], K. Hinc [1], R. Faraj [1], T. Kowalski [2], G. Mikułowski [1], K. Kazmierczak [1], R. Wiszowaty [1], P. Pawlowski [1]
(1) Institute of Fundamental Technological Research Polish Academy of Sciences, Poland.
(2) Adaptronica sp. z o.o., Poland.

Structural intensity on irregular shells 3671
F. Pires [1,2], S. Vanlanduit [1,2], J. Dirckx [1]
(1) University of Antwerp, Belgium
(2) Vrije Universiteit Brussel, Belgium

SHM

Session Structural health monitoring

A multi-level uncertainty integration strategy for forward model-driven SHM 3681
P. Gardner [1], C. Lord [1], R. J. Barthorpe [1]
(1) University of Sheffield, United Kingdom

Railway suspension fault detection under variable operating conditions via random vibration signals and the stochastic Functional Model based method 3693
T.-C. I. Aravanis [1], J. S. Sakellariou [1], S. D. Fassois [1]
(1) University of Patras, Greece

On the use of pseudo-damage to represent damage to structures in population-based Structural Health Monitoring 3709
S. Walker [1], C. Lord [1], N. Dervilis [1], E. Papatheou [2], K. Worden [1]
(1) University of Sheffield, United Kingdom
(2) University of Exeter, United Kingdom

Connecting nonlinearities: damage precursors detection and control methodology 3723
E. Habtour [1,2,3], T. Dragman [2], T. Masmeije [2], D. Di Maio [2], R. Haynes [2], A. Homborg [1], T. Tinga [1,2]
(1) The Netherlands Defence Academy, The Netherlands
(2) University of Twente, The Netherlands
(3) U.S Army Research Laboratory

Modal strain identification using sub-microstrain fiber-optic Bragg grating data for damage detection of prestressed concrete structures 3731
D. Anastasopoulos [1], G. De Roeck [1], E. Reynders [1]
(1) KU Leuven, Belgium

Relations between the quality of identified modal parameters and measured data obtained by structural monitoring 3747
S. Marwitz [1], V. Zabel [1]
(1) Bauhaus University Weimar, Germany

Robust damage detection using Bayesian virtual sensing with noise reduction and environmental effect elimination capabilities 3759
J. Kullaa [1]
(1) Metropolia University of Applied Sciences, Finland

Application of H-infinity estimation and oblique projections for experimental damage identification by SP2E 3775
M. Vollmering [1], A. Lenzen [1]
(1) Leipzig University of Applied Sciences, Germany

A wave-based optimization strategy of curved joints for improved defect detection in coupled waveguides 3791
V. Denis [1], J.-M. Mencik [1]
(1) INSA Centre Val de Loire, France

Vibration integrity assessment on LNG process pipework using a combined experimental and analytical approach 3805
G. Wally [1], C. McIlwraith [1], M. Hutchinson [1]
(1) Wood PLC, United Kingdom

Virtual Distortion Method based optimal sensor placement for damage identification 3815
B. Blachowski [1], A. Swiercz [1], Ł. Jankowski [1]
(1) Institute of Fundamental Technological Research Polish Academy of Sciences, Poland

Pseudo-faults (or damage metaphors) for SHM: a discussion on their practical use 3825
E. Papatheou [1], G. Manson [2], K. Worden [2]
(1) University of Exeter, United Kingdom
(2) University of Sheffield, United Kingdom

A methodology using health and usage monitoring system data for payload life prediction 3837
P. Nalliah [1], A. Lewis [1], C. Lomax [3], C. Hawkins [2]
(1) University of Hertfordshire, United Kingdom
(2) DSTL - Defence Science and Technology Laboratory, United Kingdom
(3) MBDA UK Limited, United Kingdom

Multi-level damage identification in operational condition 3849
S. Milana [1], G. Acunzo [2], S. Gabriele [2], A. Culla [1], G. R. Argento [2]
(1) Sapienza University of Rome, Italy
(2) University Roma Tre, Italy

Transmissibility based structural assessment using deep convolutional neural network 3859
S. Cofré [1], P. Kobrich [1], E. López Droguett [1], V. Meruane [1]
(1) Universidad de Chile, Chile

Embedded optical sensors for vibration monitoring of large structures 3875
M. Pinto [1], N. Roveri [1], G. Pepe [1], A. Nicoletti [2], G. Balconi [3], A. Carcaterra [1]
(1) Sapienza University of Rome, Italy
(2) BASF, Italy
(3) SIREG GEOTECH

Vibration-based structural damage identification using sparsity constrained Extended Kalman Filter concept 3887
C.-P. Fritzen [1], D. Ginsberg [1], O. Loffeld [1]
(1) University of Siegen, Germany

Transmissibility versus damage detection 3901
N. Maia [1], M. M. Neves [1], T. A. N. Silva [2]
(1) IDMEC - Instituto Superior Técnico, Portugal
(2) NOVA UNIDEMI - Universidade NOVA de Lisboa, Portugal

On the quality of identified parameters of prestressed concrete catenary poles in existence of uncertainty using experimental measurements and different optimization methods 3913
F. Alkam [1], T. Lahmer [1]
(1) Bauhaus University Weimar, Germany

Continuous wavelet transform for structural health monitoring of a pipe 3925
S. Milana [1], N. Roveri [1], A. Carcaterra [1], A. Culla [1]
(1) Sapienza University of Rome, Italy

Damage phenomena characterization in RCF tests using image analysis and vibration-based machine learning 3935
M. Lancini [1], I. Bodini [1], C. Petrogalli [1], L. Provezza [1], M. Faccoli [1], G. Sansoni [1], L. Solazzi [1], A. Mazzù [1]
(1) University of Brescia, Italy

Model-based optimization of axisymmetric wave motion in buried plastic water distribution pipes 3947
O. Scussel [1], M. J. Brennan [1], J. M. Muggleton [3], F. C. L. de Almeida [2], A. T. Paschoalini [1]
(1) UNESP - São Paulo State University, Ilha Solteira, Brazil
(2) UNESP - São Paulo State University, Bauru, Brazil
(3) University of Southampton, United Kingdom

SC

Session Substructuring and coupling

Substructuring approach and blocked forces method: application for structure-borne vibration prediction in heavy weight assemblies 3959
D. Miguez [1,2], O. Farrell [1], M. O. Bannister [1], R. Arbabi [1], A. T. Moorhouse [2], A. S. Elliott [2]
(1) Farrat Isolevel, United Kingdom
(2) University of Salford, United Kingdom

Characterization of dynamic forces generated by an active component: experimental validation of the Block Sensor Method 3973
X. Carniel [1], J. Champain [1], T. Gardin [1], G. Pavic [2]
(1) CETIM - Centre Technique des Industries Mécaniques, France
(2) INSA Lyon, France

Contact problems in the framework of dynamic substructuring 3987
J. Brunetti [1], W. D'Ambrogio [1], A. Fregolent [2]
(1) Università dell'Aquila, Italy
(2) Sapienza University of Rome, Italy

Comparison of substructuring techniques for experimental identification of rubber isolators dynamic properties 3999
M. Haeussler [1], S. Klaassen [1], D. J. Rixen [1]
(1) Technical University of Munich, Germany

Vibration response of a solid volume of arbitrary shape using the Boundary Forming Approach 4015
G. Pavic [1]
(1) INSA, France

Experimental-analytical state-space synthesis of passenger car components 4021
A. Bylin [1,2], M. Gibanica [1,2], T. J. S. Abrahamsson [1]
(1) Chalmers University of Technology, Sweden
(2) Volvo Car Corporation, Sweden

Application of System Equivalent Model Mixing (SEMM) to model the structural dynamic properties of a complex vehicle component using numerical and experimental data 4037
E. Pasma [1], S. Klaassen [2], L. Nieuwenhuijse [1,3], M. van der Seijs [1,3], D. Lennström [4]
(1) VIBES.technology, The Netherlands
(2) Technical University of Munich, Germany
(3) Technical University of Delft, The Netherlands
(4) AB Volvo, Germany

Design of particle dampers for lightweight structures using frequency based substructuring 4049
J. Oltmann [1], T. Hartwich [1], D. Krause [1]
(1) Hamburg University of Technology, Germany

Reduced order modeling for forced response prediction of structures with large contact interfaces 4063
G. Battiato [1], C. M. Firrone [1]
(1) Politecnico di Torino, Italy

TPA

Session Transfer path analysis

Use cases for vehicle TPA: from shock absorbers to electric drive 4075
J. Freund [1], T. Vöhringer [1]
(1) ZF Friedrichshafen AG, Germany

Empirical formula for the vibration reduction index of junctions with different coplanar walls 4085
C. Crispin [1], C. Mertens [1], A. Dijckmans [1]
(1) BBRI - Belgian Building Research Institute, Belgium

A hybrid numerical and experimental approach for structural intensity analysis of stiffened lightweight structures 4101
J. Biedermann [1], R. Winter [1], M. Norambuena [1], M. Böswald [1]
(1) DLR - German Aerospace Center, Germany

Application of operational test data and transfer path analysis to a test bench for optical systems 4115
C. Schedlinski [1], C. Marzok [2], U. Wiesendahl [2]
(1) ICS Engineering GmbH, Germany
(2) Carl Zeiss SMT GmbH, Germany

Predicting vibration levels on an experimental test case by using invariant loads (e.g. blocked forces) as source characterization 4131
J. Ortega Almirón [1,2], F. Bianciardi [1], P. Corbeels [1], W. Desmet [2,3]
(1) Siemens Industry Software NV
(2) KU Leuven, Belgium
(3) Flanders Make, Belgium

TVD

Session Tuned vibration absorbers and dampers

Passive multi-mode piezoelectric shunt damping: an approach based on matrix inequalities 4147
M. Berardengo [(1)], S. Manzoni [(2)], M. Vanali [(1)], A. M. Conti [(2)]
(1) Università degli Studi di Parma, Italy
(2) Politecnico di Milano, Italy

Optimization of tuned mass damper parameters based on numerical optimization and model reduction 4159
M. Soubeyroux [(2)], C. Dumoulin [(1)], A. Deraemaeker [(1)]
(1) Université Libre de Bruxelles, Belgium
(2) ENSTA ParisTech, France

Dynamics of torsional vibration damper (TVD) pulley: implementation of elastomeric constitutive law 4175
C. A. F. SILVA [(1)], L. MANIN [(1)], R. G. RINALDI [(1)], J. AMEIL [(2)], E. Besnier [(1)], M.-A. Andrianoely [(1)]
(1) Université de Lyon, France
(2) AB Volvo, France

Effect of temperature on the tuning of a piezoelectric resonant shunt composed of variable inductance or variable capacitance 4187
R. Darleux [(1)], B. Lossouarn [(1)], J.-F. Deü [(1)]
(1) CNAM - Conservatoire National des Arts et Métiers

Optimization of multi-modal targeted energy transfer performance of nonlinear passive vibration absorbers 4197
K. Dekemele [(1)], P. Van Torre [(1)], M. Loccufier [(1)]
(1) Ghent University, Belgium

Modeling the the amplitude and magnetic dependency to the vibration isolation effect for magneto-sensitive rubber isolation system by assessing the energy flow 4211
B. Wang [(1)], L. Kari [(1)]
(1) KTH Royal Institute of Technology, Sweden

Suppression of the wind-induced vibration of high-rise buildings with inerter systems 4223
Y. Xia [(1)], R. Zhang [(2)], M. I. Friswell [(1)], Y. Cao [(2)]
(1) Swansea University, United Kingdom
(2) Tongji University, People's Republic of China

NVH

Session Vehicle noise and vibration (NVH)

Uneven vane spacing design for reducing noise emission in a variable displacement vane oil pump 4235
L. Benzoni [(1)], F. Braghin [(1)], L. Marchetti [(2)], F. Tramaglia [(2)]
(1) Politecnico di Milano, Italy
(2) Bosch VHIT SpA, Italy

Estimation of steering gear running noise using simulated excitations and measured noise transfer functions 4247
A. Scholz [(1)], P. Marinova [(1)], N. Schmidt [(1)], D. Vieker [(1)], S. Orlando [(2)], B. Van Genechten [(2)]
(1) ZF Friedrichshafen AG, Germany
(2) Siemens PLM Software, Belgium

Towards a high-fidelity simulation approach for predicting coarse road dynamic tire/road contact forces using an ALE-formulation and a-priori nonlinear hyper-reduction 4259
D. De Gregoriis [(1,2)], F. Naets [(2,3)], P. Kindt [(1)], W. Desmet [(2,3)]
(1) Goodyear Innovation Center Luxembourg, Luxembourg*
(2) KU Leuven, Belgium
(3) Flanders Make, Belgium

Analysis of experimental MT clunk with STFT and CWT to observe mode participation and reduction 4269
J. E. Furlich [(1)], J. Blough [(1)], D. L. Robinette [(1)]
(1) Michigan Technological University, United States of America

Optimising geometry and asymmetrical damping ratio to reduce vehicle vertical acceleration under stochastic road profile 4283
J. C. M. Fernandes [(1)], M. Silveira [(1)]
(1) UNESP - São Paulo State University, Brazil

Validation experiment for structural power 4293
R. Ullmann [(1,2)], S. Sicklinger [(1)], G. Müller [(2)]
(1) BMW Research, Innovations, New Technologies, Germany
(2) Technical University of Munich, Germany

Multiple-order excitation and response of centrifugal pendulum vibration absorbers 4305
E. R. Gomez [(1,2)], I. L. Arteaga [(2,3)], L. Kari [(2)]
(1) Scania CV AB, The Royal Institute of Technology, Sweden.
(2) KTH Royal Institute of Technology, Sweden.
(3) Eindhoven University of Technology, The Netherlands.

Structural power as an acoustic design criteria for the early phase of product design 4321
S. Sicklinger [(1)], R. Ullmann [(1)]
(1) BMW Research, New Technologies, Innovations, Germany

A robust design approach to optimize the vibrational comfort of automotive seats 4329
R. Barbeau [(1,2)], T. Weisser [(1)], R. Dupuis [(1)], E. Aubry [(1)], S. Baudu [(2)]
(1) Université de Haute-Alsace, France
(2) Faurecia Automotive Seating, France

Assessment of the potential of trim parts to reduce structure-borne noise in the interior of vehicles 4343
R. Stelzer [(1)], T. Delpero [(1)], R. D'Amico [(1)]
(1) Autoneum Management AG, Switzerland

Active damping of automotive driveline oscillations and its interactions with engine suspension 4359
A. Gaudin [(1)]
(1) Groupe PSA, France

Investigation of the influence of DC-bus voltage on switched reluctance machines regarding noise and vibrations 4373
Y. Mollet [1,2], F. Chauvicourt [1,2,3], J. Pelletier [2], M. Sarrazin [1], C. T. Faria [1], H. Van der Auweraer [1], J. C. Gyselinck [2]
(1) Siemens Industry Software NV, Belgium
(2) Université Libre de Bruxelles, Belgium
(3) KU Leuven, Belgium

Experimental applications of Bayesian Focusing in an industrial context 4389
T. Le Magueresse [1], O. Minck [1], J. Antoni [2]
(1) MicrodB, France
(2) Université de Lyon, INSA Lyon, France

MOR for friction induced self-excitation in jointed structures based on substructuring for nonlinear interfaces – a review of methods with application to brake squeal 4401
M. Zacharczuk [1,2], O. Stump [1], H. Hetzler [2]
(1) Daimler AG, Germany
(2) University of Kassel, Germany

Real-time assignment method of resonance frequency by change of coupling stiffness for improving road induced noise 4411
M. Komada [1,2], Y. Matsumura [2], I. Kido [2], E. Nakatsugawa [1], H. Ozaki [2]
(1) Toyota Motor Corporation, Japan
(2) Gifu University, Japan

Nonlinear modelling and simulation of impact events and validation with physical data 4427
M. Bayani [1,2], A. P. Székely [3], N. Al Hanna [3], H. Viktorsson [1], C. Wickman [1,2], R. Söderberg [2]
(1) Volvo Car Corporation, Sweden
(2) Chalmers University of Technology, Sweden
(3) KTH Royal Institute of Technology, Sweden

Alternative lamination stacking technique of stator cores for improved structural damping of electric machines 4443
F. Chauvicourt [1,2,3], C. T. Faria [1], J. C. Gyselinck [3], H. van der Auweraer [1,2], W. Desmet [3]
(1) Siemens Industry Software NV, Belgium
(2) KU Leuven
(3) Université Libre de Bruxelles

Composite phononic crystals modelling and its application in vehicle noise control 4459
C. Jin [1], T. Zhang [1]
(1) Tongji University, People's Republic of China

Test and improvement of drive axle whine for a light bus 4469
W. Shi [1], G. Liu [1], C. Gao [1], H. Shi [1], Z. Chen [1]
(1) Jilin University, People's Republic of China

Mechatronic suspension design for vehicle dynamic performance enhancement 4477
H. Yuan [1], Y. Li [1], J. Z. Jiang [1], P. H. Mellor [1]
(1) University of Bristol, United Kingdom

VAM

Session Vibro-acoustic modelling and prediction

A parametric study and modal analysis of an acoustic black hole on a beam 4489
K. Hook [(1)], J. Cheer [(1)], S. Daley [(1)]
(1) University of Southampton, United Kingdom

Robust sound transmission modelling of finite-sized layered walls and floors 4499
C. Decraene [(1)], A. Dijckmans [(2)], E. Reynders [(1)]
(1) KU Leuven, Belgium
(2) BBRI - Belgian Building Research Institute, Belgium

Validity of the transfer matrix method for modeling trim components in vibro-acoustic applications 4511
B. Van Antwerpen [(1)], S. Corveleyn [(1)], G. Lielens [(1)], B. Van den Nieuwenhof [(1)]
(1) Free Field Technologies, MSC Software Company, Belgium

Determination and optimisation of the sound reduction index of ship bulkheads through the wave propagation approach 4527
E. A. Piana [(1)], U. Carlsson [(2)], L. Feng [(2)]
(1) University of Brescia, Italy
(2) KTH Royal Institute of Technology, Sweden

Assessment of the vibro-acoustic performance of an all-electric light aircraft based on ground and in-flight measurements 4543
R. Hallez [(1)], C. Colangeli [(1)], J. Cuenca [(1)], E. Di Lorenzo [(1)], U. Musella [(1)], J. Debille [(1)]
(1) Siemens Industry Software NV, Belgium

Damping enhancement of sheet-metal components through shot peening process to improve vibro-acoustic performance 4559
V. K. Balla [(1,2)], F. Greco [(1,3)], E. Deckers [(1,3)], B. Pluymers [(1,3)], W. Desmet [(1,3)], G. Vadakkel [(1,2)]
(1) KU Leuven, Belgium
(2) TVS Motor Company
(3) Flanders Make, Belgium

Reflections from elastic wedges of different thickness profiles 4571
A. Karlos [(1)], S. J. Elliott [(1)], J. Cheer [(1)]
(1) University of Southampton, United Kingdom

Optimization of perforated plates in interaction with acoustic waves 4585
V. Lukeš [(1)], E. Rohan [(1)]
(1) University of West Bohemia, Czech Republic

Investigation of the effect of stamping process on dimpled beams 4597
V. Pendse [(1)], M. Ghazwani [(1,2)], K. Naghshineh [(1)]
(1) Western Michigan University, United States of America
(2) Jazan University, Kingdom of Saudi Arabia

Optimization of acoustic doors using laser-spectro-vibrometry and finite element methods 4609
C. C. van Dijk [(1)]
(1) Alara-Lukagro, The Netherlands

VIPER

Session Vibro-acoustic of periodic media

Wave propagation in an auxetic core embedding resonators 4617
M.-A. Campana [1], F. Scarpa [1], M. Ouisse [2], E. Sadoulet-Reboul [2]
(1) University of Bristol, United Kingdom
(2) FEMTO-ST Institute, France

Wavenumber identification technique for axial-symmetric structures 4627
G. Tufano [1,2], C. Droz [1,2], O. Bareille [1], A.-M. Zine [1], B. Pluymers [2,3], W. Desmet [2,3], M. Ichchou [1]
(1) Ecole Centrale de Lyon, France
(2) KU Leuven, Belgium
(3) Flanders Make, Belgium

Diffusion based homogenization method for one dimensional locally resonant system 4637
S. Ahsani [1,2], R. F. Boukadia [1,2], C. Droz [3], C. Claeys [1,2], E. Deckers [1,2]
(1) KU Leuven, Belgium
(2) Flanders Make, Belgium
(3) Ecole Centrale de Lyon, France

Modeling and experimental measurements of the sound transmission loss for multi-layer core topology systems 4653
N. Guenfoud [1,2], C. Droz [1], M. Ichchou [1], O. Bareille [1], B. Pluymers [2,3], E. Deckers [2,3]
(1) Ecole Centrale de Lyon, France
(2) KU Leuven, Belgium
(3) Flanders Make, Belgium

Model order reduction in unit cell modeling and its application to complex structures 4663
R. F. Boukadia [1,2,3], C. Claeys [1,2], C. Droz [3], M. Ichchou [3], E. Deckers [1,2]
(1) KU Leuven, Belgium
(2) Flanders Make, Belgium
(3) Ecole Centrale de Lyon, France

Investigation for the analysis of the vibrations of quasi-periodic structures 4679
S. Timorian [1,2], F. Franco [1], M. Ouisse [2], S. De Rosa [1], N. Bouhaddi [2]
(1) University of Naples Federico II, Italy
(2) Université Bourgogne Franche-Comté, France

Inverse characterization method of viscoelastic materials using dispersion analysis 4691
T. Bourgana [1,2,4], R. F. Boukadia [1,3,4], S. Jonckheere [1,4], C. Claeys [1,4], G. Chevallier [2], M. Ouisse [2], E. Deckers [1,4]
(1) KU Leuven, Belgium
(2) FEMTO-ST Institute, France
(3) Ecole Centrale de Lyon, France
(4) Flanders Make, Belgium

Design of a multi-scale reinforced sandwich panel with enhanced vibroacoustics performances 4707
R. Palumbo [1,2], D. Ivanov [1], C. Droz [2], O. Bareille [2], M. Ichchou [2], F. Scarpa [1]
(1) University of Bristol, United Kingdom
(2) Ecole Centrale de Lyon, France

A load approximation for the vibroacoustic analysis of periodic structures to fluid excitation 4721
F. Errico [1,2], M. Ichchou [1], S. De Rosa [2], O. Bareille [1], F. Franco [2]
(1) Ecole Centrale Lyon, France
(2) University of Naples Federico II, Italy

A study of structured uncertainties in wave characteristic of one-dimensional periodic structures 4731
R. P. Singh [1,2], C. Droz [2], S. De Rosa [1], F. Franco [1], O. Bareille [2], M. Ichchou [2]
(1) University of Naples Federico II, Italy
(2) Ecole Centrale de Lyon, France

Computation of wave dispersion characteristics in periodic porous materials modeled as equivalent fluids 4741
D. Magliacano [1,2], M. Ouisse [1], A. Khelif [1], S. De Rosa [2], F. Franco [2], N. Atalla [3]
(1) Université Bourgogne Franche-Comté, France
(2) University of Naples Federico II, Italy
(3) Université de Sherbrooke, Canada

Interlocked hybrid-cell Kirigami inspired cellular structures and their vibroacoustic performance 4753
S. Del Broccolo [1], M. Ouisse [1], E. Foltete [1], F. Scarpa [2]
(1) FEMTO-ST Institute, France
(2) University of Bristol, United Kingdom

WIND

Session Wind turbine dynamics

Integrated dynamic testing and analysis approach for model validation of an innovative wind turbine blade design 4767
M. M. Luczak [1], B. Peeters [2], S. Manzato [2], E. Di Lorenzo [2], P. Z. Csurcsia [2,5], K. Reck-Nielsen [3], P. Berring [1], P. U. Haselbach [1], K. Branner [1], V. Ruffini [4]
(1) Technical University of Denmark, Denmark
(2) Siemens Industry Software NV, Belgium
(3) CEKO Sensors ApS, Denmark
(4) University of Bristol, United Kingdom
(5) Vrije Universiteit Brussel, Belgium

Virtual prototyping of an actuator-based structural health monitoring system of wind turbine blades 4783
D. Garcia [1], D. Tcherniak [2], K. Branner [3]
(1) University of Strathclyde, United Kingdom
(2) Brüel & Kjær Sound & Vibration Measurement A/S, Denmark
(3) Technical University of Denmark, Denmark

Experimental damage detection on small wind turbines through vibration and acoustic analysis 4793
F. Castellani [1], D. Astolfi [1], M. Becchetti [1], F. Berno [1]
(1) University of Perugia, Italy

Gear tooth crack detection in a wind turbine drive train 4809
C. V. H. Gayatri [1], A. S. Sekhar [1]
(1) Indian Institute of Technology, India

Passive vibration control of offshore wind turbines using structure-immittance approach 4821
Y.-Y. Li [(1)], S. Y. Zhang [(1)], J. Z. Jiang [(1)], S. Neild [(1)], I. Ward [(2)]
(1) University of Bristol, United Kingdom
(2) SNC-Lavalin Atkins, United Kingdom

Novel phase-bound magnetic vibration absorber for improved NVH performance of a wind turbine gearbox 4833
B. Mrak [(1,2)], R. Adduci [(1,2)], S. Weckx [(1)], W. Driesen [(2)], W. Desmet [(1,2)]
(1) KU Leuven, Belgium
(2) Flanders Make, Belgium

Fatigue stress estimation of offshore wind turbine using a Kalman filter in combination with accelerometers 4847
N. Noppe [(1)], K. Tatsis [(2)], E. N. Chatzi [(2)], C. Devriendt [(1)], W. Weijtjens [(1)]
(1) Vrije Universiteit Brussel, Belgium
(2) ETH Zürich, Switzerland

USD2018 PAPERS

USDA

Session USD – applications

Experimental measurement of value and associated uncertainty of wave speed in Hopkinson bars with an accurate and robust method 4857
D. Brizard [(1)]
(1) Université de Lyon – IFSTTAR, France

Experimental study of vibration uncertainty of multilayered timber beams assembled through wood dowels 4867
T. A. Bui [(1)], P. Lardeur [(2)], M. Oudjene [(1)]
(1) Université de Lorraine, France
(2) Université de Technologie de Compiègne, France

Fatigue analysis of wind excited structures with structural parameters affected by uncertainties described by interval variables 4881
F. Giunta [(1)], G. Muscolino [(1)], A. Sofi [(2)]
(1) University of Messina, Italy
(2) University "Mediterranea" of Reggio Calabria, Italy

Efficient bolted joint modeling for industrial applications - empirical and analytical approaches 4897
K.-A. H. Hoppe [(1)], P. Langer [(1)], S. Marburg [(1)]
(1) Technical University of Munich, Germany

Experimental application of random matrix theory to quantify modal uncertainty in aircraft t-tails 4909
A. Vishwanathan [(1)], G. A. Vio [(1)]
(1) University of Sydney, Australia

Catastrophic event prediction associated with road vehicle dynamic responses and randomly uncertain suspension parameters 4921
J. A. Gonzalez Anaya [(1)], J. F. Dunne [(1)]
(1) University of Sussex, United Kingdom

The influence of the uncertainty on dynamic soil properties on the prediction of railway induced vibration 4931
M. Germonpré [(1)], M. Papadopoulos [(1)], G. Degrande [(1)], G. Lombaert [(1)]
(1) KU Leuven, Belgium

Spectral and statistical evaluation of the properties of the vibration measured at the base of an automotive seat for non-Gaussian random noise synthesis 4947
D. González [(1)], R. López-Valcarce [(2)]
(1) CTAG - Automotive Technology Centre of Galicia, Spain
(2) University of Vigo, Spain

USDM

Session USD – methods

Uncertain quantification in nonlinear dynamics with an high-dimensional computational model 4963
E. Capiez-Lernout [1], C. Soize [1]
(1) Université Paris-Est, France

Vibration analysis of a structure with an attachment at an uncertain location using parametric model order reduction with Krylov subspaces 4975
S. Li [1], B. R. Mace [1], J. S. Dhupia [1]
(1) The University of Auckland, New Zealand

Outlier analysis under uncertainty: applications to structural health monitoring 4985
R. Fuentes [1], N. Dervilis [1], D. Tcherniak [2], K. Worden [1], E. J. Cross [1]
(1) University of Sheffield, United Kingdom
(2) Brüel & Kjær Sound & Vibration Measurement A/S, Denmark

A stochastic multidomain approach for mid-frequency vibration problems 5001
S. Adhikari [1], M. I. Friswell [1]
(1) Swansea University, United Kingdom

Efficient random vibration analysis of nonlinear systems with long short-term memory networks for uncertainty quantification 5011
D. A. Najera-Flores [1], A. R. Brink [2]
(1) ATA Engineering
(2) Sandia National Laboratories, United States of America

Multilevel Monte Carlo applied to a structural engineering model with random material parameters 5027
P. Blondeel [1], P. Robbe [1], C. Van hoorickx [1], G. Lombaert [1], S. Vandewalle [1]
(1) KU Leuven, Belgium

On the non-parametric modelling of uncertain elastic joints in periodic structures 5043
A. Fabro [1], J.-M. Mencik [2]
(1) University of Brasília, Brazil
(2) INSA Centre Val de Loire, France

Vehicle model likelihood computation using a probabilistic complex FRF matrix statistical reduction 5059
J. Reyes [1,2], C. Soize [1], L. Gagliardini [2], G. Brogna [2,3]
(1) Université Paris-Est Marne-La-Vallée, France
(2) Groupe PSA, France
(3) Université de Lyon, France

High dimensional dependence via pair constructions for interval finite models 5071
M. Faes [1], D. Moens [1]
(1) KU Leuven, Belgium

A multi-fidelity approach for possibilistic uncertainty analysis 5081
M. Mäck [1], M. Hanss [1]
(1) Universtity of Stuttgart, Germany

A sensitivity-based approach for the dynamic analysis of structures with uncertain-but-bounded parameters 5095
F. Giunta [(1)], G. Muscolino [(1)], A. Sofi [(2)]
(1) University of Messina, Italy
(2) University "Mediterranea" of Reggio Calabria, Italy

A twin-mesh approach for random field analysis in highdimensional dynamic models 5111
S. Ghosh Dastidar [(1)], M. Faes [(1)], D. Moens [(1)]
(1) KU Leuven, Belgium

Unstructured uncertainty modeling for coupled vibration systems 5125
B. Dogančić [(1)], N. Alujević [(1)], M. Jokić [(1)], H. Wolf [(1)]
(1) University of Zagreb, Croatia

An efficient strategy to describe the propagation of variation through multi-stage metal forming processes 5133
B. M. de Gooijer [(1)], J. Hazrati-Marangalou [(1)], H. J. M. Geijselaers [(1)], A. H. van den Boogaard [(1)]
(1) University of Twente, The Netherlands

USDUIQ

Session USD – uncertainty identification and quantification

On inverse fuzzy arithmetical problems in uncertainty analysis 5143
D. Hose [(1)], M. Hanss [(1)]
(1) University of Stuttgart, Germany

Bayesian model updating using stochastic distances as uncertainty quantification metrics 5157
S. Bi [(1)], M. Broggi [(1)], M. Beer [(1)], Y. Zhang [(2)]
(1) Leibniz University Hannover, Germany
(2) Beijing Institute of Technology, People's Republic of China

Identification of a stochastic model for bolted joints 5169
H. Jalali [(1)], H. Haddad Khodaparast [(1)], M. I. Friswell [(1)]
(1) Swansea University

A Bayesian filtering approach to operational modal analysis with recovery of forcing signals 5181
T. J. Rogers [(1)], K. Worden [(1)], G. Manson [(1)], U. T. Tygesen [(2)], E. J. Cross [(1)]
(1) University of Sheffield, United Kingdom
(2) Ramboll Energy, Denmark

Fuzzy Model Updating: covariance updating to estimate the interval radii of the updated parameters 5195
D. Ricardo [(1)], T. A. N. Silva [(1)]
(1) NOVA UNIDEMI - Universidade NOVA de Lisboa, Portugal

Bayesian estimation of interval bounds based on limited data 5207
M. Imholz [(1)], D. Vandepitte [(1)], D. Moens [(1)]
(1) KU Leuven, Belgium

Stochastic analysis of the natural frequencies of rectangular plates under random temperature distributions 5215
R. A. Borges [1], L. F. F. Rodovalho [2], D. A. Rade [3]
(1) Federal University of Goiás, Brazil
(2) Federal University of Uberlandia, Brazil
(3) Aeronautics Institute of Technology, Brazil

Robust identification of parameters uncertainty in stochastic finite element model updating 5231
N. Sharma [1], S. V. Modak [1]
(1) IIT Delhi, India

On the efficacy of random matrix theory to quantify uncertainty in topology optimisation 5247
A. Vishwanathan [1], G. A. Vio [1]
(1) University of Sydney, Australia

Shapes & DOF: on the use of modal concepts in the context of parametric non-linear studies

Etienne Balmes [1,2]
[1]Arts et Metiers ParisTech, CNRS, PIMM
151 Boulevard de l'Hôpital, 75013, Paris, France

[2]SDTools
44 rue Vergniaud, 75013, Paris, France
e-mail: **balmes@sdtools.com**

Abstract

Physical responses tend to lie within restricted subspaces even for parametric problems. For a given subspace, the choice of a basis defines Degree Of Freedom (DOF) and this choice may give interesting meaning to the associated amplitudes. Classical modal analysis builds subspaces combining modeshapes and static responses. Parametric loads for non-linear, damped, variable, ... structures are discussed to extend the theory and illustrated for test and simulation cases. Challenges in shape extraction and basis generation techniques are then detailed. Introducing the ability to manipulate models with variable junction properties, component material and geometry, load and operating conditions, ... opens new questions on the quantification and tracking of changes and objectives throughout design exploration. The definition of a reference linear system and the use of global and/or local modal DOF are shown to provide an interesting perspective.

1 Introduction

Modal analysis has been used extensively for many decades. The base notion is that the response is dominated by modal contributions corresponding to a linear combination of shapes constant in space and associated amplitudes depending on time, which are known as Degrees of Freedom (DOF) in mechanics and states in system modeling. Linear time invariant systems are no longer considered difficult, so the focus of this paper will be on parametric problems. Non-linearities, damping treatments, junctions, geometric variability, ... are such parameters that challenge current practice. In such studies the choice of relevant shapes and associated DOF plays a useful role in both speeding computations and providing ways to analyze tests.

As illustrated by figure 1, design groups use direct problem resolution: starting from geometry in the form of CAD models, well defined mechanical model equations are generated in the form of finite element models for most industrial applications. From these models, reduction techniques are used to extract shapes and generate system models that allow the prediction of frequency or time responses.

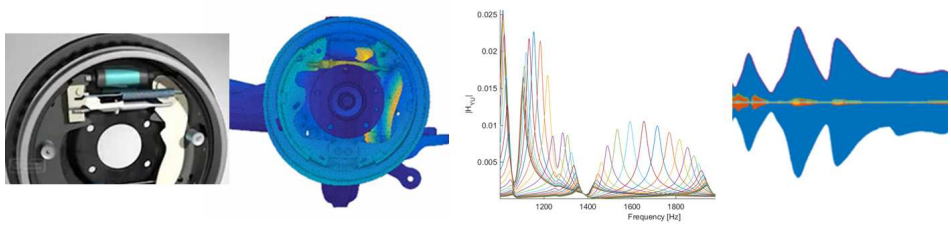


Figure 1: Direct problem: CAD, FEM modes/reduced models, transfers, time responses

Experimental groups go in the opposite direction, that is solve inverse problems. As shown in figure 2, time responses are measured, signal processing tools are then used to obtain experimental characterizations such as transfer functions, then multiple sensor reading are combined to identify system models containing shape information. Finally test and FEM models can be combined in modeshape expansion and updating processes.

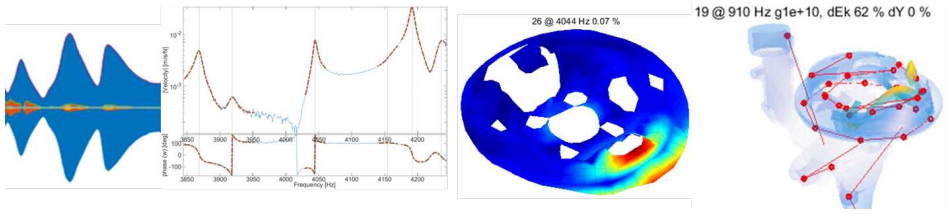


Figure 2: Inverse problem : a) time response, b) transfer function and identification, c) analysis of mode-shapes, expansion

The meeting point between computational and experimental activities is a system with inputs and outputs as detailed in section 2. A key difficulty of system modeling is the definition of states/DOF and associated shapes. Bandwidth and load objectives are introduced to allow correct system representations. Within a given subspace the ability to choose DOF is discussed. Parametric problems and associated loads are then introduced. Finally current challenges in subspace techniques are detailed: alternative learning and classification strategies, interface reduction, sparsity preservation.

Considering cases where parametric models are available, section 3 addresses tools needed to analyze their evolution. A parallel with control theory shows the relevance of "coupling" studies that correspond to the adaptation of root locus computations. The definition of a reference linear system is used to track property changes in parametric computations and test. Finally, the issue of understanding component properties when integrated in a system is discussed and illustrated.

2 A system perspective of structural dynamics

2.1 Definition of system models

Considering vibration problems through the point of view of system dynamics is a useful perspective. In a system model, one considers

- inputs $\{u(t)\}$, which in vibration problems will typically be applied loads or enforced displacements. In experiments inputs are measured as electrical signals and thus limited to a series of scalar quantities, which may a notable approximation if the true loads are non-uniform fields.
- states $\{x(t)\}$, which are all the quantities needed to write a differential equation describing the evolution of the system in time. In a fairly general setting the evolution equation can be written as a non-linear state-space equation

$$\{\dot{x}\} = f(x(t), u(t), p, t) \tag{1}$$

For mechanical engineers, displacement Degrees of Freedom (DOF) $\{q\}$ are used and the state vectors combines displacement $\{q\}$ and velocity $\{\dot{q}\}$. Additional internal states are also introduced for non-linear material laws (plasticity, viscoelasticity, ...). Figure 3 illustrates a simple modified Oberst test which can be considered as a single DOF system characterizing the feature of interest which is the frequency and damping of the first bending mode, but will require many FEM DOF to allow the prediction of the strain energy field shown as color. Modal analysis or by extension model reduction, discussed in section 2.2, provides a clean strategy to relate these two definitions of DOF for the same system.

- outputs $\{y(t)\}$, which are measurable quantities in test (displacements, strains, loads, ...) and predictable quantities in models. Since states describe all the quantities describing the evolution of the system, outputs can be estimated at a given time through an observation equation

$$\{y\} = g(x(t), u(t), p, t) \tag{2}$$

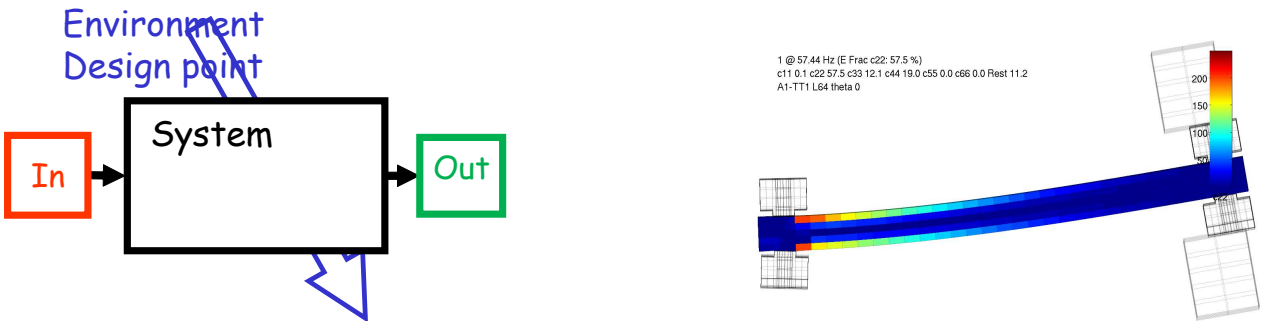


Figure 3: Left : parametric system representation. Right : sample case modified Oberst test

- environment variables or design points corresponding to parameters that are either constant or assumed to be independent of states. Section 2.3 will detail parameters of interest in vibration design problems.
- features are quantities that can be extracted from the response such as resonance frequencies, shapes, damping, mean levels, ...

The objective of a system model is to provide accurate prediction of the input/output relation and the associated features for a range of design points. Side objectives are to minimize the cost of obtaining and operating such a model and to have a proper understanding of its limitations.

2.2 Classical modal analysis/model reduction

Classical *modal analysis*, which is taken here to include Component Mode Synthesis (CMS), assumes Linear Time Invariant (LTI) systems so that the evolution equation can be written using constant matrices. Although the theory applies to all LTI problems, the paper will focus on mechanical problems of the form

$$[M]\{\ddot{q}\} + [C]\{\dot{q}\} + [K]\{q\} = [b]\{u(t)\} \tag{3}$$

In vibration problems, modeling typically considers two objectives: the accurate representation of the response to a restricted *set of loads* within a *bandwidth*. In an undamped LTI system, normal modes are harmonic solutions in the *absence of excitation* and thus verify

$$\left[-M\omega_j^2 + K\right]\{\phi_j\} = 0. \tag{4}$$

To achieve the bandwidth objective the system model must be able to represent all modeshapes within this band. Strategies to eliminate modes within the band can be based on modal participation factors or balanced

realization arguments [1, 2], but in practice such truncation is nowadays rarely necessary for performance. The argument to use modes above the bandwidth, the common 1.5 times the bandwidth or any other factor, is actually quite weak and adding more modeshapes is generally sub-optimal in terms of model size.

To achieve the *loads objective*, it is also necessary to account for the additional associated information. This is achieved by computing static responses to loads

$$[q_{Residual}] = [K_{Flex}]^{-1}[b] \tag{5}$$

or by using the common alternative of static responses to enforced displacements on the areas of load application, which is known as Guyan condensation. The need for static terms is widely acknowledged: the contribution is called upper residuals in experimental modal analysis [3], attachment mode or residual flexibility for free mode component mode synthesis [4], D term in the observation equation of state-space models, *residual vector* in many FEM solvers, ... and yet many recognize to have difficulties with the notion.

Figure 4 illustrates a case with strong static contribution [5]. A piezo-actuator is glued on a honeycomb panel. At 10 Hz, the bending of the honeycomb skin is much larger than the overall panel bending. The response can be decomposed in modal (a), (b) and static (c) contributions. The first key here is to understand that static contribution comes from the piezo load, and thus is completely independent from the structural modes which do not depend of any load.

Once the necessity of static correction/residual flexibility understood, the challenge remains in the definition of reference loads $[b]$ for which a static correction is needed, discussed in section 2.3 and the understanding of how wrong results are when it is ignored.

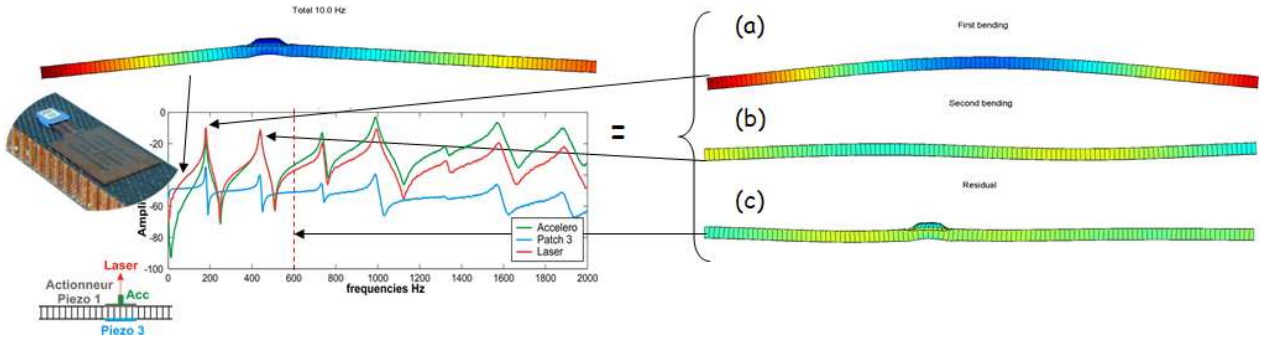


Figure 4: Sample case with strong static contribution [5]

While modes and static responses are results of interests, one of the key aspects of modal analysis is that they span the subspace where the response lies. For any basis T of that subspace, one defines generalized DOF $\{q_R\}$ and seeks an approximation of the form

$$[q_{Full}(t)] = [T]\{q_R(t)\} \tag{6}$$

leading in a Ritz-Galerkin approach to a reduced model still of the form (3) but using reduced matrices $M_R = T^T M T$, ...

The two basics bases [4, 6] are McNeal (free modes + static response to loads $\left[\phi_{1:NM} \;\; K^{-1}b\right]$) and Craig-Bampton (enforced static displacement /Guyan+ fixed interface modes), but any combination of mode and static response will give achieve the bandwidth and load objectives and thus lead to correct results. Conceptual limitations of most of the literature are

- the use of explicit formulas for bases rather than the implementation of numerical basis generation strategies to go from arbitrary sets of assumed vectors to bases [7, 8]. Thus many have rejected static corrections because it tends to generate poorly conditioned basis if iterative orthogonalization of loads b is not enforced. But the combination of free modes and Guyan vectors is also valid although rarely implemented in software packages.

- the use of modes computed on a single component rather than the trace of modes computed on a larger system (see section 2.4.3).
- the failure to recognize that the accuracy of a reduced model depends on the subspace spanned by T not on the base vectors and associated DOF used to generate that subspace. For example, a modal model in physical coordinates can be defined by taking the first few modes $[\phi_{1:NR}]$, retaining a subset of physical DOF R, and spanning the subspace with the basis defined as follows

$$[q_{Full}(t)]_N = [\phi_{1:NR}]_{N\times NR} \, [\phi_{1:NR}|_R]^{-1}_{NR\times NR} \, \{q_R(t)\}_{NR} \tag{7}$$

  Starting from physical DOF, basis generation techniques based in incomplete LU factorization will lead to generalized coordinates that still correspond to physical DOF, while eigenvalue/SVD based techniques will lead to modal coordinates.

2.3 Parametric problems of interest beyond LTI modal analysis

While LTI modal analysis remains very useful the challenge has now moved to the handling of parametric problems. The common approach is to continue using classical CMS methods and to reformulate the problem as a linear reduced model with all other aspects of interest (coupling, non-linearity, and environment) implemented as external load or feedback. This approach is well mastered for point to point connections. Thus many multi-body simulation software support flexible component reduction using Craig-Bampton reduction with residual terms for viscous loads, distributed inertia (inertial relief modes [4]). But much more should be done.

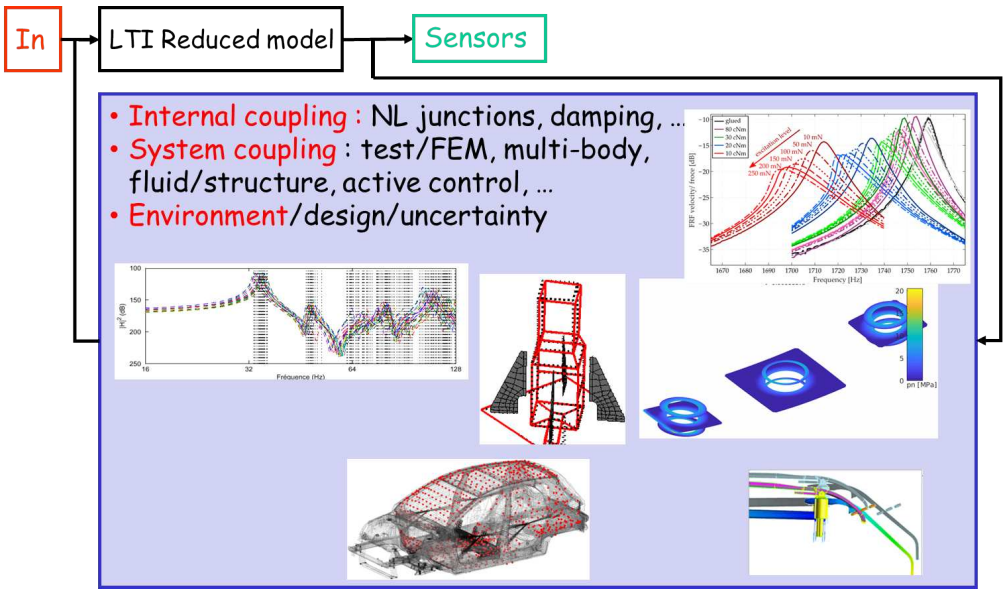


Figure 5: Formulation as a combination of LTI problem with additional loads representing parametric effects.

Selecting an underlying linear system, associated with constant matrices, M_0, C_0, K_0, one can always rewrite the equations of motion (3) by the defining a parametric load $\{f_p\}$ in the right hand side of the equation

$$[M_0]\{\ddot{q}\} + [C_0]\{\dot{q}\} + [K_0]\{q\} = [b]\{u(t)\} + \{f_p\,(M(p) - M_0, K(p) - K_0, q, \dot{q}, p)\} \tag{8}$$

Figure 12 illustrates a parametric contact problem. The contact between a main press formed plate and a small "cable guide" component is modeled at gauss points shown in (a). Due to manufacturing the contact does not occur on the whole surface and different colored dots correspond to different surfaces. In the frequency tracking, cross markers correspond to variable surface computations. They overlay nearly exactly

with solid lines which correspond to variable distributed stiffness. The selected modes illustrate that fairly flat lines correspond to global bending of the plate while the frequency traversing the full frequency range from 700 to 1900 Hz corresponds to a local bending shape of the cable guide.

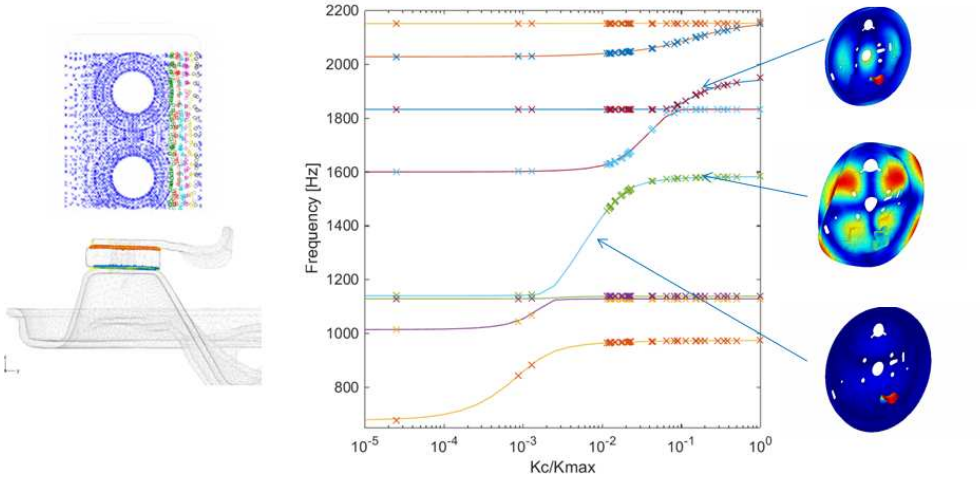


Figure 6: Influence of contact on the modal properties of a brake part [9]. Left: Zoom on cable guide, right: frequency evolution with contact surface/stiffness

The idea of parametric reduced models is to construct a basis independent of the amplitude of parameter loads just as traditional CMS is independent of the amplitude of external inputs. Here the parameter loads are forces applied on all contact points. As there are many points, computing a static correction (5) for all contact loads will lead to large reduced models. Alternatives [10] are to build a multi-model basis from modes computed using different contact conditions or the compute the static correction to contact loads found for the nominal modes (first order correction). These techniques are similar to interface reduction discussed in 2.4.1.

The representation of static correction corresponds to the use of additional out of band DOF. These have a strong impact on zeroes (by opposition to in band modes which generate poles) of transfers associated with parameter loads and thus on the prediction of closed loop configurations where these have a significant impact. A key result is that the added shapes are very different from the following modes so that seeking convergence by just adding more modes is rarely a good idea. A challenging question is the analysis of the minimum number of out of band DOF necessary to represent all configurations shown in figure 12 right.

A very partial list of problems that can be addressed by including parametric loads into classical CMS are

- Non-linear responses are parametric in the sense that local properties depend on inputs. Figure 5 thus illustrates the amplitude dependence of a junction problem [11] where the parametric loads are contact/friction forces distributed on junction surfaces also shown in the figure.
- Structures damped with viscoelastic materials have parametric volume loads associated with viscoelastic stresses which depend on temperature and frequency (figure 11 gives an illustration). Thickness variations, often used as design parameters, can also be represented as a parametric load.
- Structural dynamic modification techniques [12] seek to combine a linear test model with parametric models of possible modifications.
- Geometry variations due to design or variability in the manufacturing process are also of major interest [13, 14].

2.4 Open challenges in shape extraction and basis generation techniques

Space/time separation (6) considering bandwidth and input objectives were shown to be the base ingredients of CMS. This leaves many choices open and this section seeks to illustrate areas still under development. Section 2.4.1 addresses alternative learning and vector classification techniques. Section 2.4.2 discusses issues with interface reduction, which occur in mechanical problems where applied loads correspond to fields. Finally, section 2.4.3 touches basis sparsity and associated memory/CPU issues.

2.4.1 Alternative learning and vector classification strategies

In traditional CMS methods, shapes are obtained by a combination of simple computations of modes and static responses. Even modes are actually computed through a series of static computations in Krylov iteration based strategies such as the Lanczos algorithm.

Another category of approaches uses learning techniques where a full order response is analyzed a posteriori. Such techniques can be used both in computations (for example to compute the high frequency impedance of a piezo [16]) and experiments [17]. Figure 7 illustrates a time varying resonance found in a squeal test. From the spectrogram of each sensor, a response at the frequency of the maximum amplitude can be extracted. The set of learning vectors is thus a matrix with spatial rows (different sensors) and temporal columns associated with the maximum response at different instants.

Given a set of learning vectors or the full possible space, a natural strategy is to classify directions by their relative contribution. Here the Singular Value Decomposition is used to extract shapes, shown in red, and associated time amplitudes (DOF) shown in blue. The usefulness of these amplitudes will be further discussed in section 3.2.

$$\begin{bmatrix} y(c,t) & \rightarrow & time \\ \downarrow & & \\ sensors & & \end{bmatrix} = \sum_i \left\{ \begin{matrix} U_i \\ \downarrow \\ sensors \end{matrix} \right\} \{ a_i(t) \rightarrow time \}$$



Figure 7: Shape and amplitude extraction in a time varying squeal event [17]

Classification of vectors in a large subspace, followed by truncation, is a key ingredient of most strategies. Modal analysis considers low frequency modes which for equal kinetic energy the shapes of interest are those that minimize strain energy [18]. Using strain and kinetic energy norms is not the only possibility and Ref [19] clearly points out that the literature is full of eigenvalue based subspace classification algorithms: SVD Singular Value Decomposition, KLD Karhunen-Loève Decomposition, PCA Principal Component Analysis, ...

In parametric problems, the body of literature on Proper Generalized Decomposition arguments that rather than limiting the decomposition to space and time, variable separation can made on space, time and parameter variations [20]. Finally, many other fields, including the very active image and text classification fields, also address dimensionality reduction [21]. It should be noted however that a lot of this literature deals with data reduction (representation of a parametric surface through variable separation) rather than model reduction (generation of small differential equations).

2.4.2 Interface reduction

The global application of subspace classification algorithms without reference to loads leads to modes. To continue addressing the objective of correct representation of inputs, local or interface problems must be considered. Interfaces corresponds to the areas where external or parametric loads are applied (surfaces in junctions, volumes for viscoelastic models, volumes for geometry changes, ...).

Taking the crankshaft shown in figure 5, there are about 5 000 DOF connected to the bearing interfaces (red dots) and the FEM model contains 2 million DOF to allow accurate prediction of stresses. If no special care is taken to build vectors that are zero on large parts (possible here by considering interfaces that contain all nodes of a perpendicular surface), the static part of the basis shown in green will use $2e6 \times 5e3$ doubles $\approx 74GB$. The reduced matrix also has a full block associated with the interface leading to a $5e3 \times 5e3$ matrix requiring 120 MB storage which must be passed from computer memory to processor at each time step of a time integration thus creating a computational bottleneck.

The Craig-Bampton approach however considers unit displacements at DOF (indicated by the red identity in basis T): one of the interface nodes moves while no other does. Unit displacements guarantee independence but any basis on the interfaces will achieve the same objective. Analytic decompositions (Fourier, orthogonal polynomials) and eigenvalue problems solved on a restricted mesh close to the interface provide much more bases of independent unit displacements that are more easily truncated. Such interface modes are used in automated procedures such as AMLS [22], but can also be quite useful in analyzing loads transmitted through surfaces in contact [23, 24]. Similar techniques can be used to deal with periodic structures [8, 25].

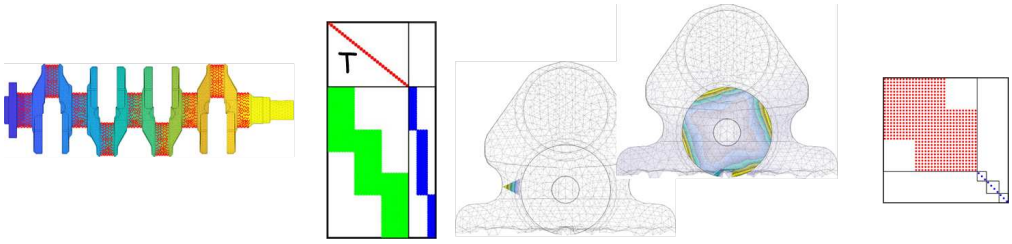


Figure 8: Redefining unit displacements : (a) sample crankshaft example, (b) topology of reduced basis, (c) unit nodal displacement/interface mode (d) topology of reduced matrix

The limited success of interface reduction methods outside automated procedures may be due to issues with the choice of coordinates (see (7) for a bypass) and the need to automate precision checks (see, for example, the work on residue iteration [26]).

2.4.3 Piece wise decompositions and sparsity

The discussion of interface modes motivated that computation and memory costs are critical objectives for computational model reduction methods. The variable separation techniques (6) need to be extended by acknowledging that piecewise decompositions will lead to much sparser matrices and thus lower memory and/or CPU costs. Figure 9a illustrates that a full model response $\{q\}$ can be represented as a combination of bases on components (here individual blade sectors shown with different colors) and associated generalized DOF $\{q_{Ri}\}$. If the DOF sets associated with each component are disjoint (this is always possible), the reduced matrix is sparse as shown in 9b. In the test case [8], reduction is essential both to allow computations and to store 1500 modes on a 60e6 DOF model which would require 670 GB.

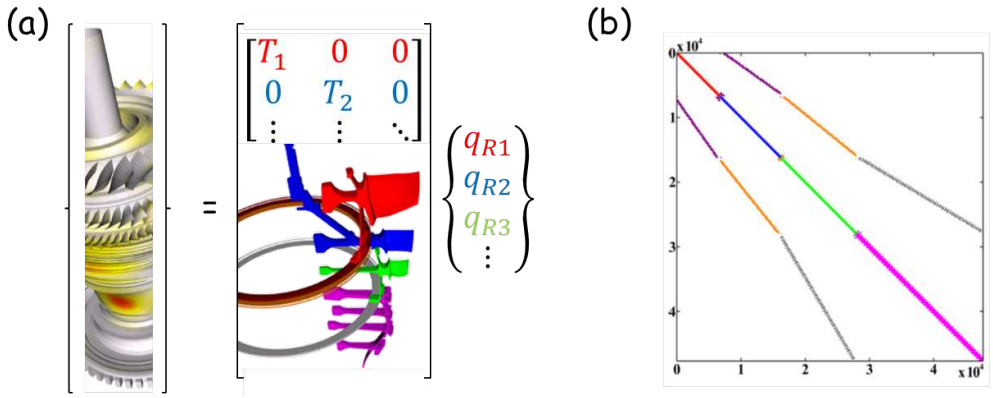


Figure 9: Reduction and sparsity: (a) reduced bases with disjoint support (b) topology of reduced matrix [8]

Obviously a model reduced this way should still achieve the general load/bandwidth accuracy objectives introduced in section 2.1. This requires fairly automated procedures to be applicable without expert knowledge. When performing a spatial decomposition, loads will be transmitted between components and if the components are reduced independently, as traditionally assumed [4], large interfaces are found and truncation, discussed in section 2.4.2, does not solve everything.

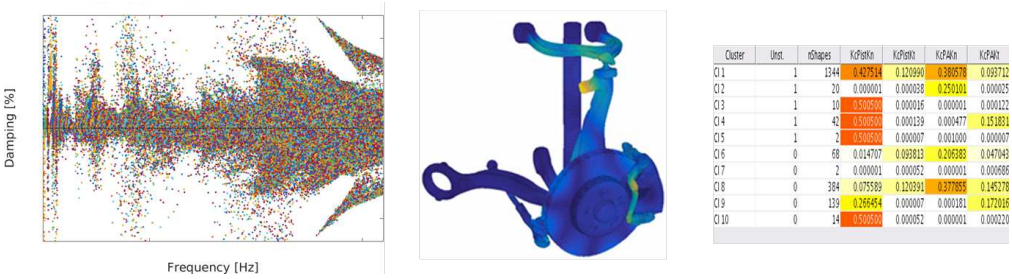
A simple procedure to obtain *exact interface reduction* in the nominal model consists in starting with a basis T valid for the full model and using the subspace generated by the trace of this basis on each component at component basis T_i. Obviously the basis is no longer exact if parameters vary, but parameter variations can be accounted for by enriching T. For more details see applications to multi-stage cyclic symmetry [8], brake squeal [27], train/track interaction [25].

It is finally interesting to note that sparsity issues can also be applied to the time domain (Harmonic Balance Method) or to PGD strategies.

3 Parametric problems :*coupling*, modal interaction, generalized DOF

While different orientations for reduced model representations were discussed in section 2.4, more interesting challenges are associated with the analysis of parametric problems.

Figure 10 illustrates a brake squeal instability study. Model complexity is due to the fact that lower squeal frequencies (1-4kHz) tend to have significant interactions with the suspension system. A state-of-the art industrial model thus features between 2 and 5 million DOF (geometric complexity), and between 300 and 600 modes in the frequency band of interest below 16 kHz (dynamic complexity). 8 to 15 components, which exhibit material and geometric variability, are coupled by interfaces whose properties vary with operating conditions requiring additional DOF (parametric complexity). Design exploration typically considers sampling over a subset of sensitive parameters to search for robust countermeasures or update parameters when test is available. A full complex eigenvalue extraction for a design point can require a few hours of computation time, challenging relevant design exploration strategies. Here computing 1000 design points would require over 80 days and generate 22 TB of data without post-treatment – clearly unacceptable in terms of design cycles timing and storage capabilities.



Cluster	Unst.	nShapes	KcPistXn	KcPistXt	KcPAXn	KcPAXt
Cl 1	1	1344	0.427514	0.120990	0.380578	0.093712
Cl 2	1	20	0.000001	0.000038	0.250101	0.000025
Cl 3	1	10	0.500500	0.000016	0.000001	0.000122
Cl 4	1	42	0.500500	0.000139	0.000477	0.151881
Cl 5	1	2	0.500500	0.000007	0.001000	0.000007
Cl 6	0	68	0.014707	0.093813	0.206383	0.047043
Cl 7	0	2	0.000001	0.000052	0.000001	0.000686
Cl 8	0	384	0.075589	0.120391	0.377855	0.145278
Cl 9	0	139	0.266454	0.000007	0.000181	0.172016
Cl 10	0	14	0.500500	0.000052	0.000001	0.000220

Figure 10: Left : poles for a 1000 design points, center : sample mode, right : tabular representation of sensitivity parameters. Test case courtesy of Daimler AG.

Model reduction is key to make the model practical in the sense that rather than doing a few hundred computations lasting a couple hours, one spends a couple hours reducing the model and computes a few thousands computations lasting tens of seconds. Another aspect of model reduction is that if you perform restitution on the fly (when you click on a point of (a) you launch the restitution of the shape in (b)), you do not deal with TB of data but just hundreds of MB. There are thus no theoretical limitations to making parametric tools accessible on workstation, rather than large cluster.

The figure however illustrates that the raw result of a parametric experiment is not very understandable. Questions of interest are : is one of those points closer to my experiment, is the experiment sensitive to small changes, is one of the designs better and robust (meaning with little sensitivity to things that are not controlled).

A key question in analyzing parametric problems is thus to have objective strategies to quantify what remains constant and what corresponds to small or large changes. Section 3.1 introduces the idea that many parametric problems can be analyzed as system *coupling* with variable stiffness studies providing very relevant information about damping, non-linear or variability effects. Tools to track shape changes are then addressed in section 3.2. Finally, section 3.3 addresses the relation between local and global modes.

3.1 *Coupling* : a measure of change in parametric dynamic problems

In control applications, it is common to compare open and closed loop performance. Taking the system perspective, the equivalent of a feedback loop is the part of the dynamics not included in the nominal LTI system. Change can thus be measured through the impact of parameter loads and the section seeks to illustrate how this applies to structural problems.

Following resonance frequencies is a measure of change that is very natural to modal analysts. Figure 11 illustrates the impact of random excitation level on steam exchanger structure with contact non-linearity and the impact of temperature and viscoelastic material thickness in a bracket junction. In both cases, the modal frequency increases with a parameter and in the range where the frequency sensitivity is highest, higher damping levels are achieved. As argumented in [10], frequency sensitivity is very much related to the level of energy in the design area (here the contact non-linearity or the viscoelastic joint). The notion is also used to estimate electromechanical coupling in active systems [28], hence the name *coupling* retained here.

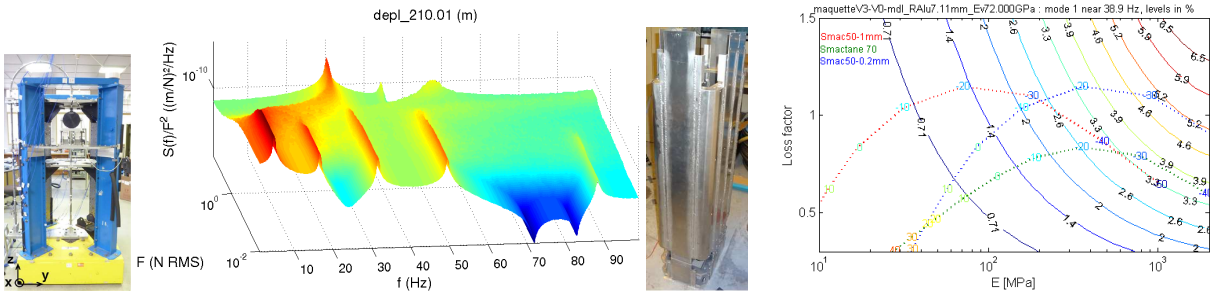


Figure 11: Left : effect of excitation level for a structure with impact non-linearity [29]. Right : effect of temperature in a structure with viscoelastic damping [10]

As motivated in section 2.3, it always possible to represent non-linear parametric problems as an underlying LTI problem (at design point p_0) with parametric loads. It is further possible to use modal states of this LTI problem to write system equations under the form

$$[I + \Delta M(p)]\{\ddot{q}_R\} + [\Delta C(p)]\{\dot{q}_R\} + \left(\left[\backslash s^2 + \omega_j^2(p_0)\backslash\right] + \Delta K(p)\right)\{q_R(s)\} = \{f_p(q_R, \dot{q}_R, p)\} \quad (9)$$

In this formulation, one distinguishes the nominal LTI model, and perturbations on mass $\Delta M(p)$, damping $\Delta M(p)$ and stiffness $\Delta K(p)$. These are however not unique since their effect can also be represented by the parametric force f_p. In the contact problem of figure 11 left, the linear system can be considered to correspond to the tube without contact, the tube in full contact or a tube with an intermediate contact stiffness that depends on amplitude. From the point of view of resonances visible in the spectra, the variable contact stiffness/damping provides a good representation of the frequency transition or an envelope for the non-linear response.

A key consequence of illustrations shown here is that in many parametric problems, initial design can simply be performed by doing multiple linear elastic computations with variable stiffness, which is much more accessible than full-fledged non-linear or damping computations.

3.2 Observing *Degree of Freedom* associated with shapes

While observing frequency shifts is very useful, properly understanding modal crossing can be very necessary to understand responses. Section 2.3 illustrated how this can be done in experiments but more efficient tools can be inspired by analysis.

Computing modal amplitudes is much more efficient than using the MAC (shape correlation) for tracking. Using the orthogonality condition for modes of the reference system $\{\phi_j(p_0)\}^T [M(p_0)]\{\phi_k(p_0)\} = \delta_{jk}$ leads to the estimation of modal amplitudes from non-reduced response $\{q\}$ as

$$\{q_{jR}(t)\} = [\phi(p_0)]^{-1}\Big|_j \{q(t)\} = \left[\{\phi_j(p_0)\}^T [M(p_0)]\right]\{q(t)\} \quad (10)$$

which corresponds to the perfect modal filter [30].

On the vibro-impact case of figure 11 left, the estimation from operational deflection shapes shown in figure 12, clearly illustrates that the shape of the dominant resonance transitions from the low frequency bending with no effect of the support plate to an high frequency shape combining the first two modes of the free-free tube. During the transition some torsion effects become visible. The shape transition corresponds directly with the resonance transition visible in 11 left (5 Hz for low amplitude to 30 Hz at high amplitude with additional damping visible during the transition).

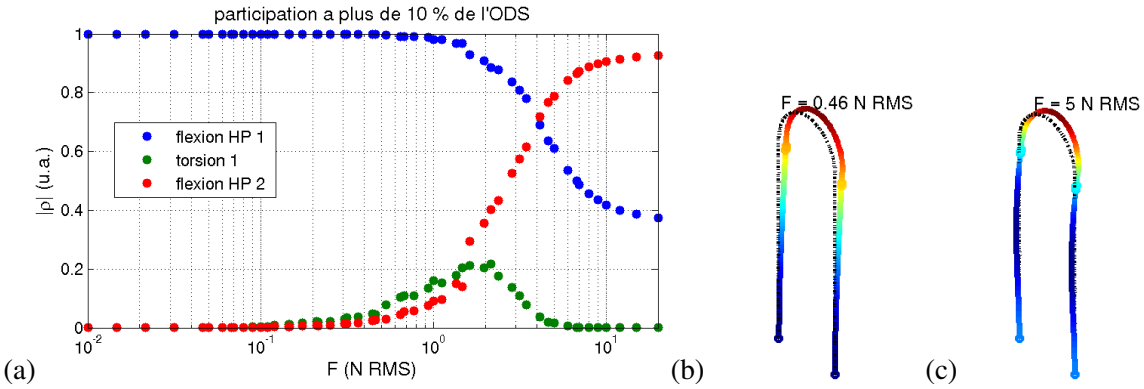


Figure 12: a) Evolution of modal participations with excitation amplitude, b) Low amplitude shape, c) high amplitude shape.

Other analysis applications of modal amplitude tracking are tracking unstable modes in time simulation of brake squeal [27], study of blade mistuning [8], tracking of waves propagating in the soil [25].

Experimentally, modal amplitude estimation was illustrated for time varying squeal (figure 7 and [17]), is applied to auto-resonance techniques in [31]. Expansion [32] in subspaces of modes or static responses are related linear observation schemes, which use the current measured shapes to estimate the generalized amplitudes. These techniques can however be usefully extended to estimate more DOF than sensors in the frequency domain (Minimum Dynamic Residual Expansion or Error in Consitutive Law) or in the time domain (Kalman Filtering possibly extended with the estimation of parameters).

3.3 Component within a system, local and global modes

The next issue of interest is that one typically redesigns a component with the objective of improving the system performance. However, the component modes of interest are usually not the fixed interface modes found in a Craig-Bampton model. The *Component Mode Tuning* (CMT) method [14, 27] was thus introduced to provide a reduced model with DOF that explicitly correspond to the amplitude of free-free component modes. In this algorithm, components are assumed disjoint (this is always possible if it is accepted to use an element layer as interface) and for each component one generates a mass and stiffness orthogonal basis spanning the subspace combining NC component free modes and NG trace on the component of system modes

$$[T_c] = \left[\left[\phi_{\text{local}}\right]_{1:NC} \quad \left[\phi_{\text{global}}\Big|_c\right]_{1:NG} \right]_\perp \tag{11}$$

Any appropriate numerical orthogonalization procedure can then be used to generate a well-conditioned basis T_c.

In this basis, the first generalized DOF of each component correspond to its retained free modes and the last to corrections needed to recover the nominal system modes exactly. Figure 13 illustrates that in the resulting basis, the mass is an identity matrix, the stiffness is diagonal with squared component mode frequencies ω_{jc}^2 for the first elements, and component coupling leads to block diagonal terms respecting the topology of component connections. The *tuning* in the name CMT reflects the fact the specific form of matrices makes it simple to perform sensitivity studies on the frequency of component modes. Similarly it is quite simple to sum modal energies to display component energies as illustrated in figure 13 right.

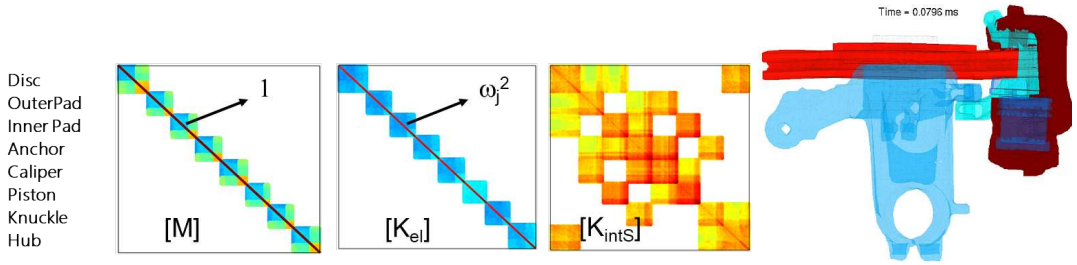


Figure 13: Left : reduced matrix topology in a CMT reduced basis. Right : sample post-processing of component energies

The idea of tracking modal amplitude is quite useful in this context. The CMT basis decomposition provides a sound basis to define local modes : significant fraction of energy associated with a given component. For small components, such as the cable guide of figure 6, free component modes may not be relevant and variants of the base CMT procedure were introduced in [14].

The notions of local and global modes shown here are very much related with the introduction of stochastic models in Ref [33, 34]. These discussions paved the way for the work in [35] which demonstrates how a large number of randomly distributed local modes can lead to significant damping : actually the major source of damping in aircraft modes. The fact that such modes come from so called *non structural* mass opens a very interesting design perspective.

4 Conclusion

The presentation sought to illustrate notions related to shapes and modes. Physical responses tend to lie within restricted subspaces even for parametric systems. DOF are amplitudes associated with base vectors generating the subspace of interest. Since a given subspace has an infinite number of bases, DOF are arbitrary in the sense that they can be changed without affecting the response. But some choices make more sense. Modal amplitude DOF can be defined at the system and component levels and tracking these amplitudes is of interest both in tests and analysis. Amplitude extraction seems particularly promising for non-linear, damped, and time varying problems which commonly share the fact that the varying parameter induces coupling. On the computation side, DOF selections leading to sparse bases can lead to gains in CPU and memory requirements which become interesting when the one or more order of magnitude is gained.

Problems of interest go beyond the traditional theory of linear time invariant systems. Extensions of traditional CMS, considers parametric loads, interface reduction, constant basis reduction for parametric models, and sparsity enhancing basis generation. With such models parametric studies with thousands of design points become routine and lead to new challenges in defining procedures to base decisions on large data sets. Finally, the possibility of state (expansion) and parameter (updating) estimation is very much linked to the ability to build a reduced parametric model but the relation between the two needs to be clarified.

This presentation will conclude with a few general comments, partially inspired by challenges in A. Pfeiffer's ISMA/USD 2016 keynote.

- The main cost of a model is not computational time but engineering time spent : preparing the right computation, navigating between results of a parametric experiment, designing and analyzing tests, progressing in a design cycle. This implies that each design group should have a digital work-flow allowing parametric studies.
- When everything goes well, the new routine practice is to deal with tens of configurations each containing thousands of computations. The need for companies to manage learning costs typically implies that software vendors pre-package GUI operated processes. But new processes devised for parametric studies typically imply the writing of custom steps (computation of criteria, automated generation

of images, ...). A trade-off thus exists between process standardization, implemented as a GUI, and adaptability implemented in the form of a script. On the academic side, the need to focus on teaching GUI or script operation will certainly continue to be an object of debate.

- Outside user process, a few software issues with parametric studies are: the need to perform reduced order computations on the fly using interaction with initial data; the computational architecture between off-line computations (cluster, background) and workstation near real time interaction; scalability of licensing models devised for a few computations rather than thousands.
- It is unlikely that any software provider will ever cover more than 50-70% needs. This is even not desirable since it would mean other groups would stop developing new intelligent strategies. Efficient inter-operability between software packages is thus key. Open source efforts are very good at broad problems with a very large number of users, but often lack vision and focus to answer very technical needs of niche markets. And the noise and vibration community is a collection of such niches. So the inter-operability impulse should come from major user companies forcing/giving incentives to the software providers to develop open API that allow access not only at pre-processing and post-processing but also at solver levels.
- Non-linearity, damping, junction surfaces, variability, local modes associated with non-structural mass, ... correspond to both challenges (they are difficult to account for in test and analysis) and opportunities (since they have a strong impact on the dynamics, they can be used to improve performance).
- Academics will not convince industry that they are dealing with real problems when using mass-spring-beam models. Distinguishing geometric complexity (a FEM with the true geometry and thus many DOF rather than analytic equations), system complexity (a CMS model accounting for both bandwidth and loads), and parametric complexity (multiple designs, boundary conditions, operating conditions, ...) is an often ignored path to demonstrating scalability.

Acknowledgements

The author would like to thank former students from Ecole Centrale Paris and Arts and Metiers ParisTech (ENSAM), whose work helped construct the perspective presented here and provided most illustrations. Special thanks also go to the SDTools engineers J.M. Leclère, J.P. Bianchi, G. Vermot des Roches, G. Martin who contributed to the development of a software environment where ideas can be tested on real life problems. As always, funding is key and thanks must go to those who funded the work presented here : PSA, Chassis Brakes International, EDF, Safran Aircraft Engines, Daimler, ... Finally, the team at KU Leuven should be recognized for the work implied in organizing the top conference on modal analysis and uncertainty.

References

[1] A. Girard, N. Roy, *Structural Dynamics in Industry*, ISTE, London, UK (2008).

[2] D. C. Kammer, M. J. Triller, *Selection of Component Modes for Craig-Bampton Substructure Representations*, Journal of Vibration and Acoustics, Vol. 118, No. 2, (1996), pp. 264.

[3] W. Heylen, P. Sas, *Modal Analysis Theory and Testing*, Katholieke Universteit Leuven, Departement Werktuigkunde (2006).

[4] R. J. Craig, *A Review of Time-Domain and Frequency Domain Component Mode Synthesis Methods*, Int. J. Anal. and Exp. Modal Analysis, Vol. 2, No. 2, (1987), pp. 59–72.

[5] E. Balmes, C. Florens, *Validation of a vibration and electric model of honeycomb panels equipped with piezoelectric patch actuators*, Revue des composites et des matériaux avancés, Vol. 19, No. 3, (2009), pp. 319–338.

[6] D. de Klerk, D. Rixen, S. N. Voormeeren, *General Framework for Dynamic Substructuring : History, Review and Classification of Techniques*, AIAA Journal, Vol. 46, No. 5, (2008), pp. 1169–1181.

[7] O. Boiteau, *Modal Solvers and resolution of the generalized problem (GEP)*, Code_Aster, Version 5.0, R5.01.01-C, (2001), pp. 1–78.

[8] A. Sternchüss, *Multi-level parametric reduced models of rotating bladed disk assemblies*, Ph.D. thesis, Ecole Centrale Paris (2009).

[9] G. Martin, E. Balmes, T. Chancelier, *Review of model updating processes used for brake components*, *Eurobrake* (2015).

[10] C. Hammami, E. Balmes, M. Guskov, *Numerical design and test on an assembled structure of a bolted joint with viscoelastic damping*, Mechanical Systems and Signal Processing, Vol. 70–71, (2015), pp. 714–724.

[11] G. Chevallier, P. Butaud, *Design of an Assembly for Nonlinear Vibration Reduction*, *IMAC*, Springer International Publishing, Cham (2017), 331–336.

[12] M. Corus, *Amélioration de méthodes de modification structurale par utilisation de techniques d'expansion et de réduction de modèle.*, Ph.D. thesis, Ecole Centrale Paris (2003).

[13] T. França de Paula, G. Rejdych, T. Chancelier, G. Vermot des Roches, B. E, *On the influence of geometry updating on modal correlation of brake components.*, *Vibrations, Chocs & Bruit* (2012).

[14] G. Martin, *Méthodes de corrélation calcul/essai pour l'analyse du crissement*, Ph.D. thesis, CIFRE SDTools, Arts et Metiers ParisTech, Paris (2017).

[15] O. Vo Van, *Introduction of variability into pantograph-catenary dynamic simulations*, Ph.D. thesis, Ecole nationale supérieure d'arts et métiers - ENSAM (2016).

[16] E. Balmes, M. Guskov, M. Rebillat, N. Mechbal, *Effects of temperature on the impedance of piezoelectric actuators used for SHM*, *14th Symposium on Vibration, Shock and Noise (VISHNO)* (2014), 1–6.

[17] G. Martin, E. Balmes, G. Vermot Des Roches, T. Chancelier, *Squeal measurement with 3D Scanning Laser Doppler Vibrometer: Handling of the time varying system behavior and analysis improvement using FEM expansion*, *ISMA*, KUL (2018).

[18] E. Balmes, *Optimal Ritz vectors for component mode synthesis using the singular value decomposition*, AIAA Journal, Vol. 34, No. 6, (1996), pp. 1256–1260.

[19] G. Kerschen, J.-c. Golinval, A. F. Vakakis, L. A. Bergman, *The method of proper orthogonal decomposition for dynamical characterization and order reduction of mechanical systems: An overview*, Nonlinear dynamics, Vol. 41, No. 1, (2005), pp. 147–169.

[20] F. Chinesta, A. Huerta, G. Rozza, K. Willcox, *Model Reduction Methods*, E. Stein, R. de Borst, T. J. R. Hughes, Editors, *Encyclopedia of Computational Mechanics Second Edition*, John Wiley & Sons, Ltd, Chichester, UK (2017), 1–36.

[21] S. T. Roweis, *Nonlinear Dimensionality Reduction by Locally Linear Embedding*, Science, Vol. 290, No. 5500, (2000), pp. 2323–2326.

[22] J. Bennighof, M. Kaplan, M. Muller, M. Kim, *Meeting the NVH Computational Challenge: Automated Multi-Level Substructuring*, International Modal Analysis Conference, (2000), pp. 909–915.

[23] G. Vermot Des Roches, E. Balmes, H. Ben Dhia, R. Lemaire, *Compatibility measure and penalized contact resolution for incompatible interfaces*, European Journal Of Computational Mechanics, Vol. 19, (2010), pp. 317–329.

[24] E. Balmes, G. V. Vermot Des Roches, *From physical to macro-models of local assemblies for predictions of global dynamics.*, *Colloque Assemblages Mécaniques*, St Ouen (2015).

[25] E. Arlaud, S. Costa D'Aguiar, E. Balmes, *Receptance of railway tracks at low frequency: Numerical and experimental approaches*, Transportation Geotechnics, Vol. 9, (2016), pp. 1–16.

[26] A. Bobillot, *Méthodes de réduction pour le recalage : Application au cas d'Ariane 5*, Ph.D. thesis, Châtenay-Malabry, Ecole centrale Paris (2002).

[27] G. Vermot Des Roches, *Frequency and time simulation of squeal instabilities. Application to the design of industrial automotive brakes*, Ph.D. thesis, Ecole Centrale Paris, CIFRE SDTools (2011).

[28] N. W. Hagood, W. H. Chung, A. V. Flotow, *Modelling of Piezoelectric Actuator Dynamics for Active Structural Control*, Journal of Intelligent Material Systems and Structures, Vol. 1, No. 3, (1990), pp. 327–354.

[29] T. Thénint, E. Balmes, M. Corus, *Definition of a linear equivalent model for a non-linear system with impacts*, *ISMA* (2012).

[30] J. Bianchi, E. Balmes, G. Vermot des Roches, A. Bobillot, *Using modal damping for full model transient analysis. Application to pantograph/catenary vibration*, *ISMA*, Leuven (2010).

[31] S. Davis, I. Bucher, *Automatic vibration mode selection and excitation; combining modal filtering with autoresonance*, Mechanical Systems and Signal Processing, Vol. 101, (2018), pp. 140–155.

[32] E. Balmes, *Review and Evaluation of Shape Expansion Methods*, IMAC, (2000), pp. 555–561.

[33] A. Arnoux, A. Batou, C. Soize, L. Gagliardini, *Stochastic reduced order computational model of structures having numerous local elastic modes in low frequency dynamics*, Journal of Sound and Vibration, Vol. 332, No. 16, (2013), pp. 3667–3680.

[34] C. Soize, *A model and numerical method in the medium frequency range for vibroacoustics predictions using the theory of structural fuzzy.*, J. Acous. Soc. America, Vol. 94, No. 2, (1994), pp. 849–865.

[35] J. Loukota, J.-C. Passieux, A. Lucchetti, G. Michon, *Modeling of Nonstructural Components in the Dynamic Behavior of Aeronautical Structures*, Journal of Aircraft, (2016), pp. 1–9.

Automotive NVH – Methodology for Future Innovative Product Development

Per-Olof Sturesson[1]
[1] Driving Dynamics and Noise & Vibration Centre
Volvo Car Group

Abstract

The automotive market is subject to not only a highly competitive environment but also facing introduction of many new technologies spanning from pure electric propulsion systems to advanced driver assistance systems. All of these new technologies together with continuously increasing customer expectations give rise to challenges in the automotive OEM product development as they require a high rate of innovation and development. Additional complexity in terms of new legal regulations, such as vehicle safety, CO_2 and noise emission reduction, which often are contradicting, needs consideration during the product development. An efficient and innovative product development organisation yields significant competitive advantages as more product can be put to the market faster for a given cost and time.

The refinement of noise, vibration and harshness (NVH) is one the most important tasks in the premium and luxury automotive segments during the vehicle development process. It strongly influences the overall perception of the vehicle together with other attributes such as styling, digital user experience, performance & drivability and vehicle dynamics.

The introduction of new technologies, such as electrification and software-controlled systems, result in numerous challenges with respect to NVH requiring cost and weight efficient countermeasures coupled with new simulation and test methods. Consideration to secondary effects caused by trade-off with other attributes is also critical and requires cross-attribute optimisation. Traditional target setting and down-cascading processes through benchmarking is not ready to be applied. Simulation and test methods as well as engineering system solutions derived during the product development relies strongly on experiences from previous programs through closed loop learning. The high rate of innovation with a smaller knowledge basis results in higher risk of failure as many issues may not be foreseen. Therefore, it is important to execute advanced research projects up-front of the ordinary product development projects to address all new concepts and technologies. Focus on closing critical knowledge gaps early in the product development is required. Knowledge gaps may not only be related to the physics of the new technologies but also to customer preferences. Strategies like application of NVH simulator technology and systems engineering and synthesis early in the product development phase should support robust decision making. The need to derive noise and vibration characteristics for critical systems, such as interior sound pressure level or radiated sound power, for different use cases are examples of necessary strategies in future automotive development. In this paper, different application cases from development of new technologies will be discussed.

1 Introduction

Volvo Cars has made several commitments to deliver sustainable products to the market; from 2019 all product launches will include electric motor propulsion, marking the end of pure internal combustion engine. By 2025 the aim is that 50% of sales will be pure electric vehicles and one third autonomous vehicles. All of these commitments yield significant challenges to the product development organisation and especially with respect to noise and vibration as new technologies have to be developed, industrialised and launched into the market in a given time with quality.

The opportunities to industrialise products with alternative propulsion concepts with higher energy efficiency than the conventional combustion engine has evolved over the last years due to improved engineering capability supported by the development of software, simulation and optimisation techniques but also due to lower price and improved performance for key technologies such as batteries, power electronics and electrical machines. The development efforts in the automotive industry for more energy efficient technologies, such as electrification have increased considerably over the last year driven by a combination of regulations, competition, political pressure and public opinion but also by the fact that products can be offered to customers with attractive attribute performances such as acceleration, range and operating costs. Often, governmental support and subsidiaries play an important role for introduction of new propulsion technologies.

Volvo Cars began its journey as many automotive OEMs towards alternatives to the conventional internal combustion engine as a response to the oil crisis in the mid 1970's and initiated research within the area of fuel efficiency and electromobility. Then, availability of economical oil was forecasted to decrease, which dramatically increased fuel prices. Low fuel consumption became more important in the competition. Innovations were developed and some were put into the market. For electromobility prototype vehicles lead acid batteries and induction electric motors were used.

The gaining awareness of the impact of the greenhouse gases on the climate in the 1990s and in the first decade of the 21st century resulted in more stringent regulations, especially in the European Union. EU Regulation No 443/2009 sets an average CO2 consumption for new passenger vehicles. This regulation enforced increased efforts in product development of more energy efficient technologies. Technologies like stop/start and hybrid electrical vehicles were put to market by many OEMs as a result of these efforts. The development efforts within Volvo Cars yielded in the introduction of the C30 Electric in 2009, which had a limited production volume and was only leased to the customer base. The V60 D6 plug-in hybrid in 2013 paved the way for plug-in hybrids in the upcoming SPA product line. Permanent magnet electric motors,

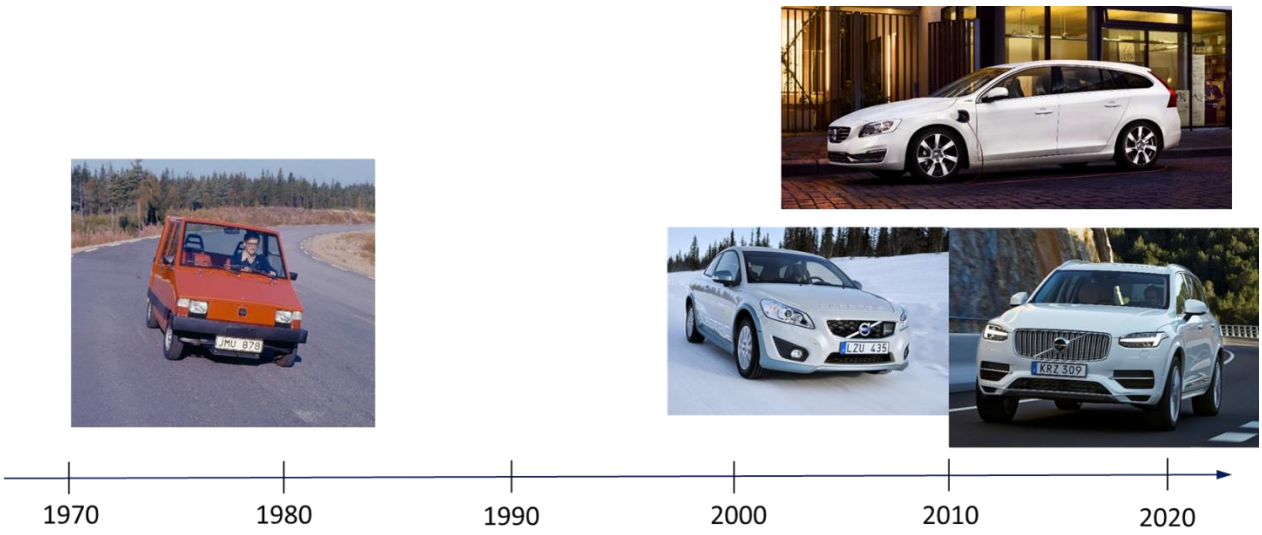


Figure 1: Retrospective overview of Volvo vehicles with alternative propulsion systems.

integrated starter generator (ISG) and Li-ion batteries were key technologies that enabled attractive attributes. In Figure 1 a retrospective summary of main efforts by Volvo Cars in development of alternative and energy efficient propulsion technologies is shown. Looking back in history one can find out that development takes time, ideas that existed were correct but were constrained in their realisation due to limitations in technology, performance and knowledge [[1]]. Today, many OEMs have multiple customer offers in terms of alternative propulsion concepts, ranging from pure/battery electric vehicles, sometimes with an optional range extender, to hybrid or plugin hybrid electric vehicles. The vehicles range from compact light weight city cars through midsized sedans, estates and SUVs to high powered performance

cars. The sizing of power source including driveline, power supply and power electronics varies depending on requirements of projected customers and concept.

The electric propulsion system adds new challenges in terms of noise and vibration refinement. Critical to consider are tonal noise components that might give rise to customer annoyance. These tonal noise components are speed dependent and generated by the electrical motor and transmission/reducer but also in the power electronics due to high voltage DC/AC conversion by means of pulse-width modulation (PWM), see Figure 2. Other noise sources can be prominent as the background masking noise in an electric vehicle

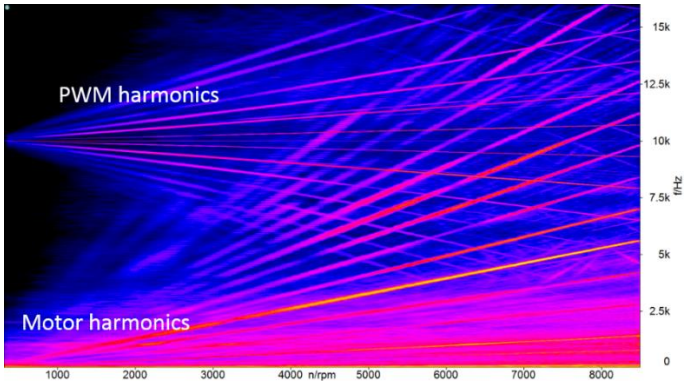


Figure 2: Surface acceleration on e-motor housing during acceleration for a vehicle with electrical propulsion system.

(EV) is low, mainly due to the absence of internal combustion engine. Examples are various auxiliary components such as electrical power storage, climate control (fans and pumps), electrical power

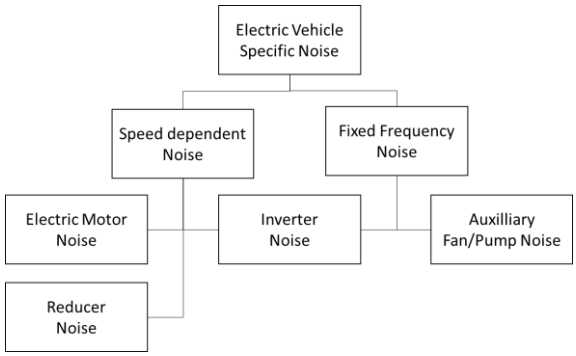


Figure 3: Electric vehicle specific noise character.

steering systems, electro-hydraulic brake controller or HVAC. The noise character may be speed dependent, fixed frequency or a mixture, see Figure 3.

In order to be successful in the process of noise & vibration refinement it is important to apply cross-attribute considerations as there are many engineering challenges in developing electric vehicles. The main engineering challenge is to industrialise and decrease cost for batteries, power electronics and electric motors [1]. As the volume of electric vehicles is expected to increase, part price will drop but cost gap to technologies for internal combustion engine may still exist, see Figure 4. From business point of view this will have an impact on the contribution margin and put constraints on opportunities for attribute engineering as there is a relationship between consumer demographics and income to car price and volume, see Figure 5.

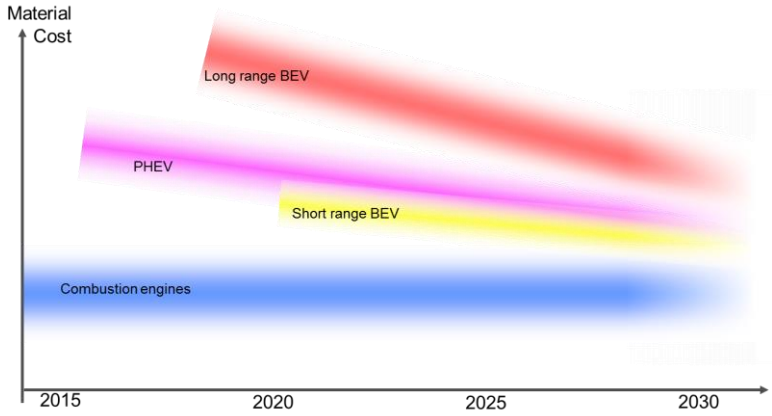


Figure 4: Comparison overview of material cost for different propulsion technologies.

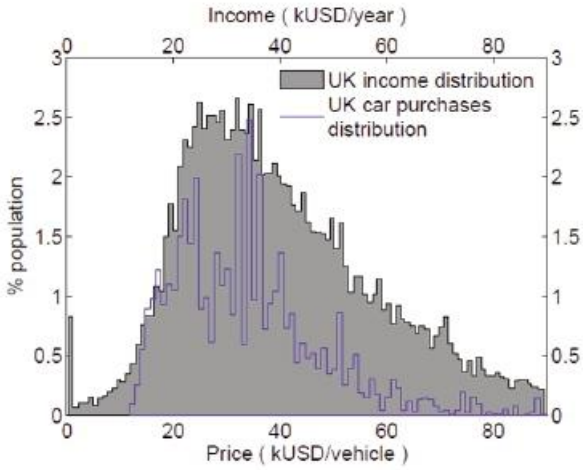


Figure 5: Comparison between distribution of income and passenger car price in UK 2012 [[2]].

Cross attribute optimisation needs to be applied upfront during the development of electrical vehicles. One key attribute for electrical vehicles to be considered is their driving range. It is dependent of road load

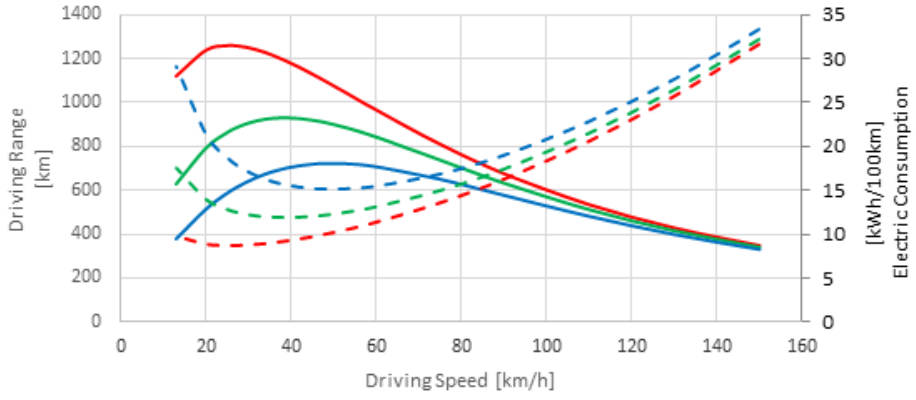


Figure 6: Driving range (solid lines) and electric consumption (dashed line) for different electric load, 500 W (blue), 1500W (green) and 3000W (red).

(aerodynamics, weight, tyre roll resistance, etc.), auxiliary loads (HVAC, electric system loads) and propulsion system losses. In an electric vehicle the propulsion losses are much lower compared to a vehicle with internal combustion engine, resulting in that auxiliary losses and road load are more important to consider, see Figure 6. Auxiliary losses strongly influences efficiency at low speeds (urban driving) while road load

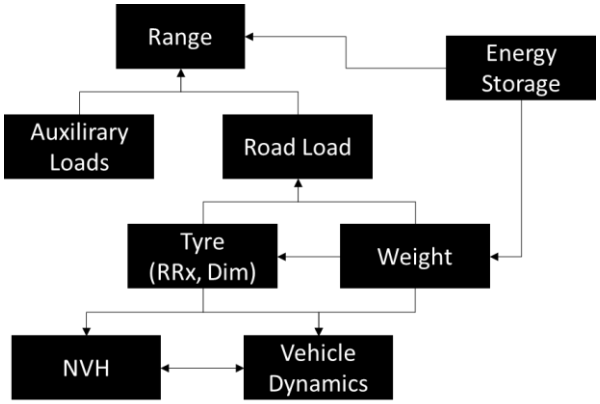


Figure 7: Example of cross attribute dependencies for electrical vehicles.

dominates the losses at highways speeds. Increasing range can be done by adding more energy storage modules (batteries), which significantly impacts weight of vehicle or reducing road load. Both vehicle weight and road load influence other attributes like safety, durability and vehicle dynamics but also NVH attributes like road noise and pass-by noise, see Figure 7.

The introduction of more software controlled systems add more complexity in the vehicle development. The NVH abatement of auxiliary systems like controllers, fans and pumps requires attention early in the concept phase. Often development experience for these new systems are low and the development logic may be purely based on testing. The final system calibration for these systems is performed in the very final stage of the development due to software functional development. Unforeseen noise and vibration issues may then occur late in the program, which will be mitigated often with a penalty on cost and quality. Additionally, the systems operate in multiple modes making system identification even more complex. Therefore it is critical to have an understanding of a system when optimising NVH performance both with means of simulation and later in the hardware development to obtain repeatable test conditions.

Further to the development challenges yielding from the introduction of new technologies, challenges during development logic may arise and must be considered and mitigated. NVH refinement becomes even more complex due to the reduction of both hardware stages and number of builds in a given hardware stage.

The classical “V”-process depicted in Figure 8: The principle of the V-process for requirement setting, target cascading to component, design and integration verification. is widely used for requirement setting and system and component target allocation and cascading. It features the logic “design first – then test”, where design decisions are made early, often without sufficient knowledge [2,3,4]. High rate of innovation needed in the development of vehicles with alternative propulsion technologies may stretch the capability of processes and result in late design loopbacks. One way of mitigating late NVH quality issues is to execute advanced or research projects up front of the ordinary product development projects in order to address all new concepts and technologies. In order to further reduce the risk of failure, method and operational development projects have to be executed in order to address increased verification efficiency and capability. The created new knowledge due to “front-loading” activities results in knowledge that can be turned into new specifications and requirements with associated assessment methods. However, too high rate of innovation driven by competitiveness may constrain the time needed for proper knowledge build-up and also result in design complexity. Design concepts may then be selected without critical concurrent physical and virtual assessment resulting in unforeseen knowledge gaps that may lead to that the complete vehicle specifications lack important information and, even more critically, the lack of knowledge may down-cascade to system and component specifications.

Verification activities later on in the development process may then reveal deviations resulting in costly design loop-backs. Application of Knowledge Based Development principles like set-based design and systems engineering yielding in trade-off relationships by means of combination of physical and virtual

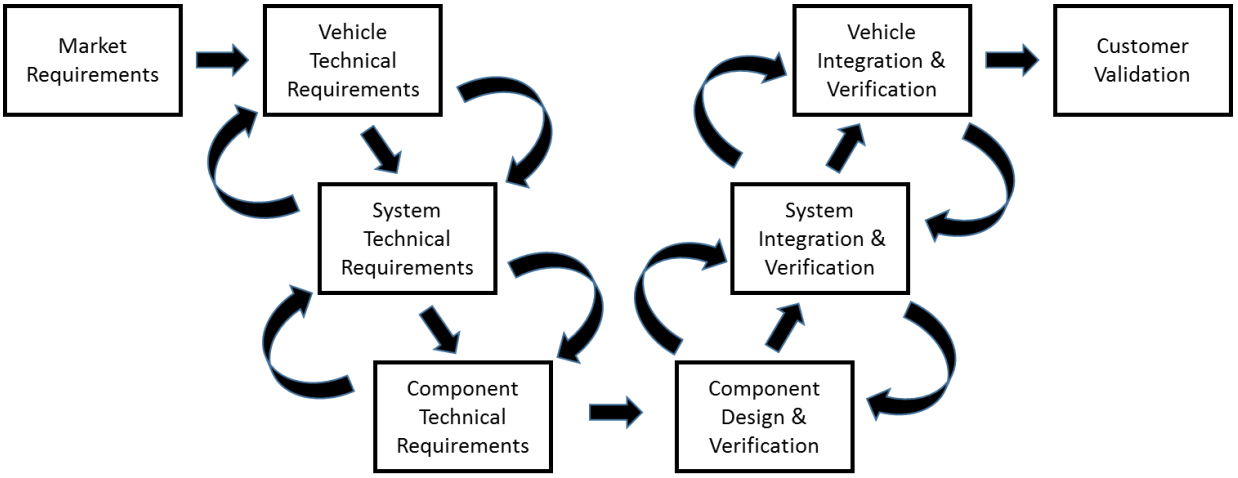


Figure 8: The principle of the V-process for requirement setting, target cascading to component, design and integration verification.

assessments between critical attributes minimises the risk of late design changes. All knowledge needs to be documented for use in the later product development projects. To be able to close the loop, the knowledge feedback during the development projects and quality issues found in running production have to be transferred back into the specifications, standards and methods.

As decision making early in projects will rely on available data including engineering knowhow the balancing of math model fidelity and complexity versus time to result is a key to address proper simulation activities to get input in order to support design directions. Additional complexity is added as the frequency range of dominant structure borne noise for electric machine noise is significantly higher than for a conventional internal combustion engine.

In this paper three different NVH development cases are discussed where method development and research in co-operation with academia have been applied to increase the development capability and knowledge.

2 Targets for vehicle interior noise and allocation of component targets

The whining noise from the electric motor is low in terms of sound pressure level but can still be potentially annoying if it cuts through masking such as road, wind and engine noise. Targets for interior noise at occupant position may be described by a metric for quantifying this tonal exposure rather than sound pressure for the fundamental harmonics of the electric drive. Different metrics such as prominence ratio (PR) which is standardized together with tone-to-noise ratio (TNR) in ECMA74 [6] have been evaluated. A comparison between those two metrics with respect to the specific electric motor noise is available in [7]. The level of prominence ratio and its relation to the perceived annoyance was mapped for different frequencies from analyses of listening tests performed on 22 non-experts (see Figure 9). The jury rated sound stimuli which were synthesized by adding authentic tones of varying intensity to ”tone-free” binaural head recorded sound files. Based on the findings from the studies targets for interior noise based on prominence ratio could be developed.

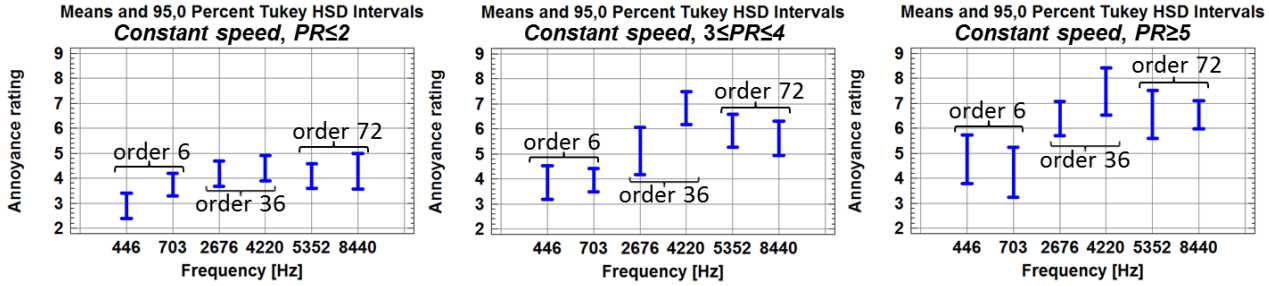


Figure 9: Annoyance rating for different frequencies/orders, constant speed driving condition. The ANOVAs are done for three ranges of PR-levels corresponding to low, middle and high audibility [[8]].

With the target for complete vehicle developed, the source and transfer path domains can be addressed. An independent quantity for allowed radiated noise is desired in order to allow for measurements in different test environments where bench tests could be performed. Sound power is standardized hence suitable to use as requirement towards suppliers. Due to the tonal character of the electromagnetic noise, narrowband smoothing filters were adopted for source and acoustic transfer functions. Research studies [8] have been done with respect to how the amount of discrete source positions including order of smoothing filters influences the mean transfer function between interior ear positions and motor and consequently the

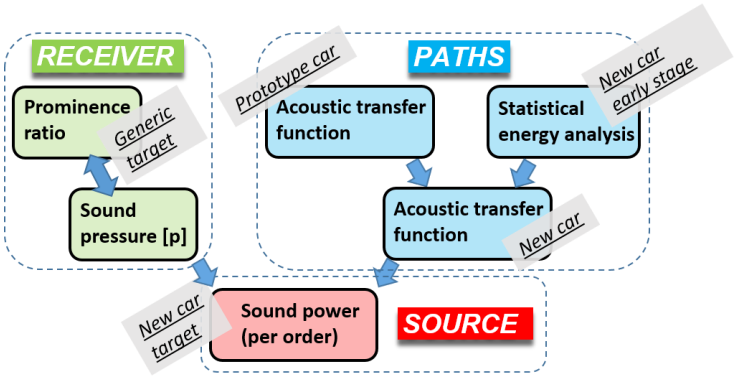


Figure 10: : Illustration of how a component requirement with respect to airborne tonal components was derived for the electric traction motor from combining complete vehicle requirements with estimations of airborne transmission properties [8].

robustness of the modelled interior noise. The working principles are summarized in Figure 10. The differences with respect to sound transmission properties between the measured vehicle and the new vehicle model that the target specifications were formulated for, can be estimated by means of statistical energy analysis (SEA) taking trim details into consideration.

3 Methods for low frequency structure-borne sound – XC90 Twin Engine

Based on the experience from different plug-in hybrid projects, ranging from Volvo V60 D6 to XC90 T8, high attention is needed in the early development phase on a low frequency noise due to tangential magnetic force excitation. This noise occurs as a fundamental torque ripple excitation order passes through the resonance frequencies in the suspension and is most prominent during mild acceleration at low speed when the vehicle is propelled by the electric drive.

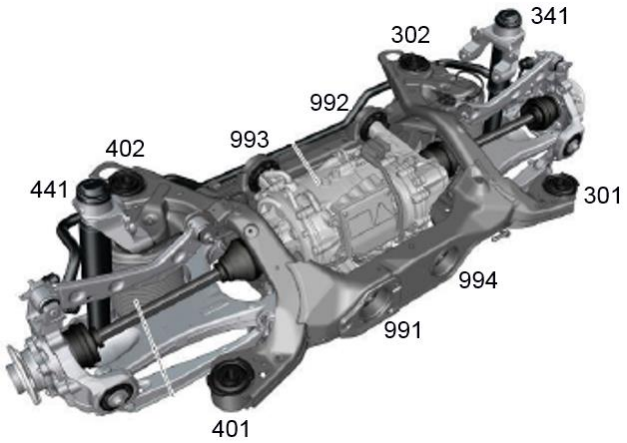


Figure 11: Positions and numbers for subframe and electric drive unit bushings and damper top mounts (XC90 T8) [9].

This structure borne noise is transferred through the subframe bushings into the body and may be disturbing in city driving. Since the electric drive unit is suspended in a subframe with bushings there is a double isolation from the electric drive unit to body, see Figure 11, above the subframe rigid body modes but a higher sensitivity at these modes.

Reducing the source strength is often the best way of dealing with a noise issue, and skewed rotor design of the electric motor is the first step. Full load acceleration is a typical load case to be used in vehicle system analysis for the electric motor torque ripple order. A finite element (FE) model can be used to calculate the interface forces into the body and the resulting interior noise levels. As this is a low frequency issue below 200 Hz both the FE model and the bushing stiffness data should be reasonably accurate. In Figure 12 the calculated interior noise for XC90 Twin Engine is shown indicating a peak at 50 Hz. The succeeding transfer path analysis of the FE results showed that the main paths are the subframe bushings in vertical direction. At this frequency there was a force peak as well as a high vehicle body noise sensitivity. A modal analysis revealed a corresponding rear suspension mode with a roll motion of the subframe/electric drive unit

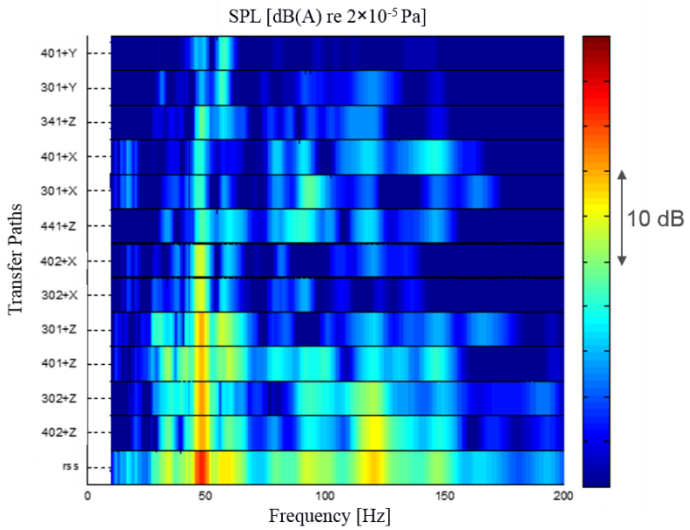


Figure 12: TPA plot for interior noise at driver's ear, indicating subframe attachments in vertical direction as main transfer paths at 50 Hz peak [9].

assembly, which could primarily be affected by the subframe bushing vertical stiffnesses. The effect of changes to the electric drive unit to the subframe bushing stiffnesses were investigated in the FE model and it was concluded that tuning the subframe bushings ±25% in vertical direction had a big effect on the 50 Hz peak. On the other hand, tuning the ERAD bushings ±25% had the expected effect above 90 Hz of increasing/decreasing the noise level but the 50 Hz peak was not affected and around 70 Hz the stiffer bushing was better, see Figure 13.

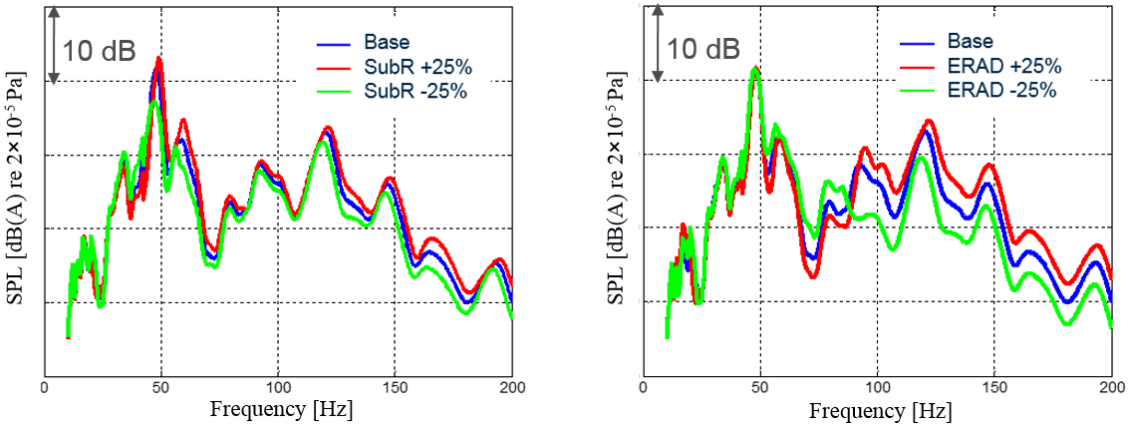


Figure 13: Effect on interior noise at the driver's ear from modified stiffnesses of either subframe or electric drive unit bushings [9].

In the early stage these analyses must be performed using only CAE data since there is no vehicle hardware available, later on both force levels and transfer functions can be measured and used for further analyses. Then, a TPA analysis was performed to further investigate the dominant transfer paths and directions as well as investigating the effect of having different body transfer functions.

4 Methods for high frequency structure borne noise - blocked force approach.

Interior high frequency noise, which can be perceived as annoying, originating from the electric powertrain can be structure borne [8]. The development of noise abatement strategies features significant challenges as the problem frequency range can be well above the capability range for vehicle system models based on finite element technology. Other approaches needs to be developed. For requirement setting of the source level (electric drive unit) an independent quantification is desirable. In essence there are two independent test methods to select – the free velocity and the blocked force. More information about the blocked force method can be found in [10].

In the final phase of the development of the XC90 plug-in hybrid, transmission of structure borne gear whine originating from the reduction transmission was examined. The reduction transmission is part of the rear electric drive unit mounted via four rubber mounts to the subframe which in turn is isolated by four rubber mounts to the body, see Figure 14.

In order to get a robust acoustic average at the interior response position ten microphones were clustered around the ear position see Figure 11. Two interfaces were analysed – 1) the blocked force points were chosen in the vicinity of the active side of each of the four electric drive unit mounts and 2) the blocked force points were allocated on the subframe close to each of the four bushes connecting to the body.

In Figure 15 and Figure 16 the comparison between the measured (original) interior noise and the reconstructed noise as well as body side acceleration from blocked forces and coupled state transfer

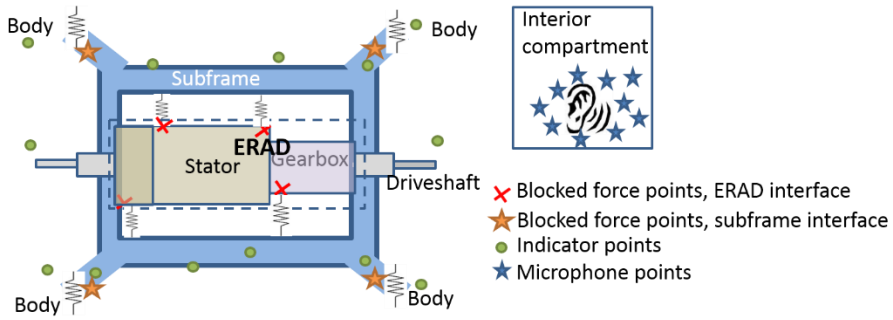


Figure 14: Schematic top view of the suspension of the XC90 rear electric drive unit (ERAD). Indicator points used for determining the blocked forces are spread out over the receiver – the subframe and body while blocked force points were allocated to the connection are [9].

functions are shown for the electric drive unit and the subframe interface respectively. Here it needs to be emphasized that, in the process of inverting matrices consisting of test data where several DOFs are included, the numerical properties play a significant role in the success of the reconstruction.

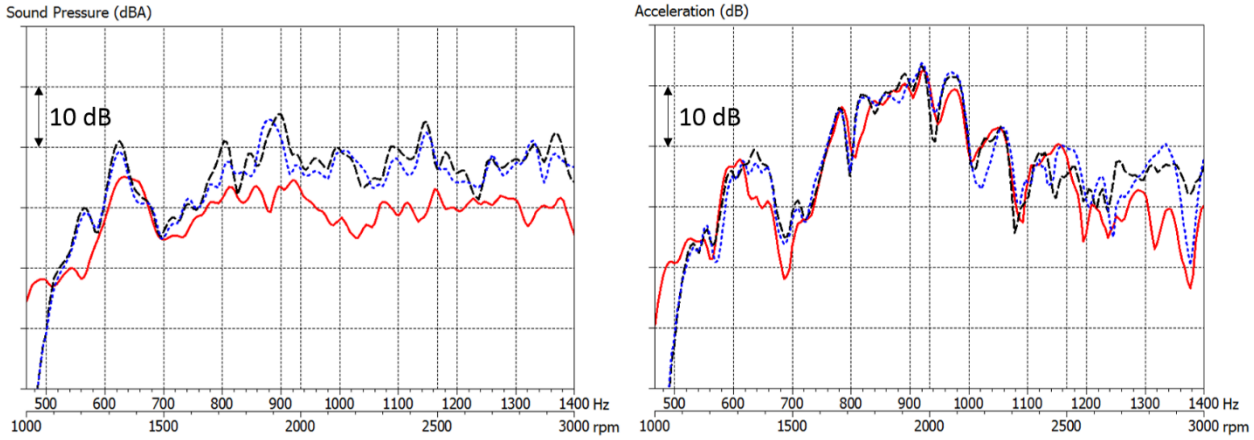


Figure 15: Measured (red, solid) and reconstructed response (black, dashed denotes no truncation and blue, dotted denotes truncated) from main gearbox order, rear seat outer ear position sound pressure level (left) and car body lateral acceleration (right), electric drive unit interface [9].

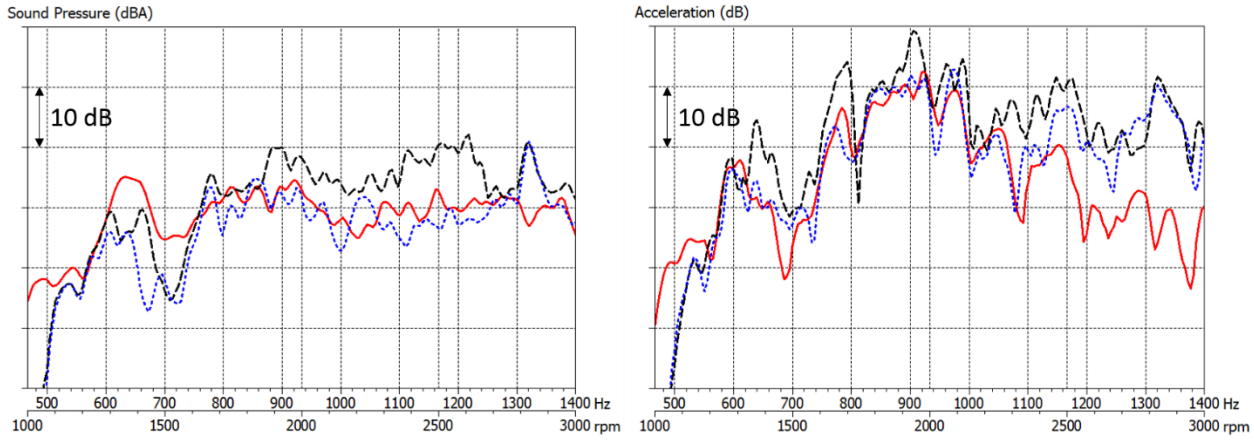


Figure 16: Measured (red, solid) and reconstructed response (black, dashed denotes no truncation and blue, dotted denotes truncated) from main gearbox order, rear seat outer ear position sound pressure level (left) and car body lateral acceleration (right), subframe interface [9].

The sound pressure from the TPA synthesis considering the electric drive unit only as source is overestimated, see Figure 15. However, the synthesized body acceleration aligns well with the measured data indicating that the estimated forces are accurate. As seen in Figure 16 the reconstructed sound pressure from the subframe interface aligns better with the measured data, especially in the case where truncation of the FRF matrix was applied.

5 Conclusions

This paper covers aspects of the methodology related to the NVH development of electric, hybrid or pure battery electric vehicles. Specifically, the need of up-front cross functional systems engineering should be applied in order to gain sufficient knowledge to direct design solutions. Development examples of low frequency torque ripple, gear whine and airborne noise from motor orders have been discussed.

The contributions from electric motors, inverters and transmission reducers need to be targeted and analysed with respect to the vehicle integration through synthesis models covering both measured and FE-modelled data as with any other noise-emitting sources in vehicles. There are several specific noise phenomena that need to be taken into account during pure electric drive.

Starting from the complete vehicle level, tonal components in the high frequency domain do not contribute to any positive perception and should be suppressed. Prominence ratio was used as a metric to set the interior noise requirements. Depending on the amount of tonal components, frequency separation and occurring frequencies, other metrics may be used such as TNR, tonality, loudness and sharpness [11,12]. Nevertheless, component targets for tolerable radiated sound power can be derived from complete vehicle requirements in combination with estimates of the acoustic transfer functions between source and response positions.

For structure borne noise, application of the principles of blocked forces are practically beneficial for both TPA and prediction. In this paper, a TPA based upon blocked forces concerning gear whine from the reducer in the frequency range 500-1400 Hz was performed. Robust data acquisition of the noise transfer functions for this double-isolated system was perhaps the most crucial.

Acknowledgement

The author is grateful for all input and contributions from all colleagues at Volvo Car Group.

References

[1] R. Eriksson, *Experience from 40 years with Volvo Cars Electrification*, *EEHE 2013*, Bamberg, 23-24 April. (2013), ISBN: 978-3-8169-3213-0.

[2] J-F Mercure and A. Lam, *The effectiveness of policy on consumer choices for private road passenger transport emissions reductions in six major economies*, Environ. Res. Lett. 10 064008, (2015)

[3] J. Lemon, *Breakthough Improvement™ in Product Validation Through Integrated Test and Analysis Lead Design, LMS User Conference for Physical and Virtual Prototyping*, Munich, (2004)

[4] M.N. Kennedy, *Product Development for the Lean Enterprise: Why Toyota's System is Four Times More Productive and How You Can Implement It*, ISBN 978-1-892-53809-3, Oaklea Press, (2010)

[5] M.N. Kennedy and K. Harmon, *Ready, Set, Dominate: Implement Toyota's Set-Based Learning for Developing Products and Nobody Can Catch You*, ISBN 978-1-892-53840-6, Oaklea Press, (2008)

[6] ECMA-74, *Measurements of Airborne Noise Emitted by Information Technology or Telecommunication Equipment*, (12th ed.), ECMA International, Geneva, (2012)

[7] D. Lennström, A. Nykänen, *Interior Sound of Today's Electric Cars: Tonal Content, Levels and Frequency Distribution", SAE Technical Paper* 2015-01-2367, (2015)

[8] D. Lennström, *Assessment and control of tonal components in electric vehicles, Doctoral thesis, Luleå Technical University*, ISBN 978-91-7583-447-4, (2015)

[9] D. Lennström, H.K.A. Olsson, P.-O. Sturesson and J.-Å. Andersson, *NVH development of the all new Volvo XC90 Twin Engine plug-in hybrid, Proceedings of Aachen Acoustics Colloquium*, (2015)

[10] A.T. Moorhouse, A.S. Elliott, T.A. Evans, *In-situ Measurement of the Blocked Force of Structure-borne Sound Sources, Journal of Sound and Vibration*, 325 (4-5), p. 679 – 685, (2009)

[11] M. Sarrazin, S. Gillijns, J. Anthonis, K. Janssens, H. Van der Auweraer, K. Verhaeghe, *NVH analysis of a 3 phase 12/8 SR motor drive for HEV applications*, *2013 World Electric Vehicle Symposium and Exhibition (EVS27)*, Barcelona, (2013)

[12] T.W. Bassett, S. Tate, M. Maunder, *Study of high frequency noise from electric machines in hybrid and electric vehicles" InterNoise*, Melbourne, (2014)

Synthesis of vibration signals with prescribed power spectral density and kurtosis value

E. Pesaresi[1], M.Troncossi[1]
[1] University of Bologna, Department of Engineering for Industry
via Fontanelle 40,1-47121, Forlì, Italy
e-mail: **marco.troncossi@unibo.it**

Abstract
In the field of vibration qualification testing, random excitations are typically set as input in terms of a PSD profile. The physical motion at the shaker head is obtained through the application of the Inverse Fourier Transform in combination with randomized phases. The overall probability distribution of the input signal tends toward Gaussian, whereas distinctive peaks are often present in real-life random excitations, causing the probability distribution to be non-Gaussian. The parameter known as kurtosis is usually exploited to quantify the feature of non-Gaussianity. Several methods have been proposed to control kurtosis, still maintaining the desired PSD profile, in order to synthesize more realistic signals. However, kurtosis control implemented by some of these methods may be ineffective. In fact, in some cases, the response of a lightly damped system can prove closer to Gaussian than the applied excitation. This work presents two novel algorithms to effectively control kurtosis in random vibration tests are.

1 Introduction

In several applications, some components are subjected to mechanical vibrations which may lead to a premature failure due to fatigue phenomena. To ensure that they operate properly during their service life, in many industrial sectors (e.g. Automotive and Aerospace Engineering) the use of qualification tests tailored in accordance with the application and/or components to be analyzed (Test Tailoring) has been consolidated over the years. This is usually preferred to Standards that propose generic test procedures and are excessively strict in general (e.g. MIL STD 810F, GAM EG13). The Test Tailoring procedure requires an appropriate definition of vibratory test profiles (Mission Synthesis) to be used as the excitation of the device under test (DUT). The synthesis of such profiles requires measuring signals in real environments and then reproducing their most important characteristics in laboratory tests, where the actual motion is generated by vibrating tables or shakers. The vibration measures of real-life applications are typically not replicated "as is" because their stochasticity would be lost. The conventional Mission Synthesis procedures implemented so far [1], provide the synthesis of a test profile in terms of Power Spectral Density (PSD). The physical motion is obtained by applying the Inverse Fast Fourier Transform (IFFT) in combination with randomized IFFT phases. As a consequence, the overall probability distribution of the input signal tends toward Gaussian. Such a kind of synthesis might be unfit to completely represent the real environment signal taken as reference in the case the latter is non-Gaussian. Consequently, the test reliability could be compromised since the "nature" of the real signal is not preserved (despite preserving the spectral content). Typical examples of non-Gaussian signals observed in real applications are the so-called Leptokurtic signals, where high amplitude peaks are present (for instance due to micro-collisions) which originate a non-Gaussian probability distribution. A dimensionless parameter called kurtosis is often employed to represent concisely the number and severity of the signal peaks. For Gaussian signals the value of kurtosis is equal to 3, while it takes higher values for Leptokurtic signals [2].

A common reference is made to "kurtosis control" whenever it is required that the reference and the synthesized signals have not only the same PSD but also the same kurtosis value. The additional control of kurtosis is aimed at shaker simulations better representing non-Gaussian excitations with the presence of

high peaks occurring in real-life applications. The control of the kurtosis value in the synthesis of random vibrations is a non-trivial task. In fact, a reformulation of the "Central Limit Theorem" [3] in the field of mechanical vibrations, better known as "Papoulis' Rule" [4, 5], states that the response of a lightly-damped linear system to a non-Gaussian signal tends to present a Gaussian probability distribution if certain conditions are met. As a result, even though the excitation presents high peaks and is characterized by a high kurtosis, the response may not present significant peaks and a lower kurtosis value can thus characterize the signal. In such cases, it is sometimes stated that the kurtosis is not transferred from the input to the output response (i.e. the peaks are filtered out).Several kurtosis control algorithms have been proposed in the literature (e.g. [5-8]) but not all of them prove to be effective in transferring the kurtosis value of the input signal to the response of the DUT.

In this work, two algorithms for kurtosis control are proposed, which effectively generate time histories with prescribed kurtosis value and PSD, avoiding the problems associated with the Papoulis' Rule.

2 Theoretical Background

In the field of random vibration testing, a test specification is typically given in the form of a PSD that is processed by the shaker controller via the IFFT technique to construct a time history.
As random time histories are required in the tests, the IFFT is performed by selecting the phases of the harmonics as uniformly distributed random variables in the interval $[0,2\pi[$, whereas the amplitude A_n of the n^{th} harmonic is related to the n^{th} PSD element G_n via the following equation:

$$A_n = \sqrt{2\, G_n\, \Delta f} \tag{1}$$

where Δf is the frequency resolution of the PSD spectrum. The time histories generated in such a way are always characterized by a distribution of their values close to Gaussian.

The statistical parameter known as kurtosis, is defined as the 4th statistical central moment of a signal, normalized by the 4th power of its standard deviation. For Gaussian signals the theoretical value of kurtosis is 3.0.

In practical applications, the theoretical definition is replaced by its discretized variant, namely:

$$k = \frac{1}{N\sigma^4}\sum_{n=0}^{N-1}(x_n - \bar{x})^4 \tag{2}$$

$$\sigma = \frac{1}{N}\sum_{n=0}^{N-1}(x_n - \bar{x})^2 \tag{3}$$

$$\bar{x} = \frac{1}{N}\sum_{n=0}^{N-1} x_n \tag{4}$$

where k, σ and $\bar{x}$ are the kurtosis, the standard deviation, and the mean value of the signal, respectively, x_n its n^{th} sample, and N its total number of samples.

The time-series can be thought of as a multi-frequency signal with a large number of harmonics N_h, namely:

$$x_n = \sum_{k=0}^{N_h-1} A_k cos\left(2\pi\, n\, k\, \frac{\Delta f}{F_s} + \varphi_k\right) = \bar{x} + \sum_{k=1}^{N_h-1} A_k cos\left(2\pi\, n\, k\, \frac{\Delta f}{F_s} + \varphi_k\right) \tag{5}$$

where F_s is the sampling frequency, φ_k the k^{th} harmonic phase and N_h is related to the number of samples N by the relation:

$$N_h = \begin{cases} \frac{N+1}{2} & if\ N\ odd \\ \frac{N}{2}+1 & if\ N\ even \end{cases} \tag{6}$$

If Eq.(5) is inserted into Eqs.(2)–(4), kurtosis can be expressed in terms of the amplitudes and phases of the signal. In order to simplify the resulting expression, Eqs.(2)–(5) can be proposed in the integral form, namely:

$$k = \frac{1}{T\sigma^4}\int_0^T (x(t)-\bar{x})^4\,dt \tag{7}$$

$$\sigma = \frac{1}{T}\int_0^T (x(t)-\bar{x})^2\,dt \tag{8}$$

$$\bar{x} = \frac{1}{T}\int_0^T x(t)\,dt \tag{9}$$

$$x(t) = \sum_{k=0}^{N_h-1} A_k cos(2\pi\ t\ k\ \Delta f\ + \varphi_k) = \bar{x} + \sum_{k=1}^{N_h-1} A_k cos(2\pi\ t\ k\ \Delta f\ + \varphi_k) \tag{10}$$

Introducing Eq.(10) in Eqs.(7) and (8), k and σ can be rewritten as [9]:

$$k = \frac{1}{\sigma^4}\left(\sum_{n+k+l=m}\frac{1}{2}A_nA_kA_lA_m\cos(\varphi_n+\varphi_k+\varphi_l-\varphi_m) + \sum_{n+k=l+m}\frac{3}{8}A_nA_kA_lA_m\cos(\varphi_n+\varphi_k-\varphi_l-\varphi_m)\right) \tag{11}$$

$$\sigma = \sqrt{\frac{1}{2}\sum_n {A_n}^2} \tag{12}$$

The formula in Eq.(11) can be written equivalently in the following form [6, 9, 10]:

$$\begin{aligned} k = \frac{1}{\sigma^4}\Bigg(& 3\sigma^4 - \frac{3}{8}\sum_n {A_n}^4 + 3\sum_{\substack{l+m=n+k \\ l<m,n<k,n<l}} A_nA_kA_lA_m\cos(\varphi_n+\varphi_k-\varphi_l-\varphi_m) \\ & + 3\sum_{\substack{n+k+l=m \\ n<l<k}} A_nA_kA_lA_m\cos(\varphi_n+\varphi_k+\varphi_l-\varphi_m) \\ & + \frac{1}{2}\sum_{3k=m} {A_k}^3A_m\cos(3\varphi_k - \varphi_m) \\ & + \frac{3}{2}\sum_{\substack{2n+l=m \\ n\neq l}} {A_n}^2A_lA_m\cos(2\varphi_n+\varphi_l-\varphi_m) \\ & + \frac{3}{2}\sum_{\substack{n+k=2m \\ n<k}} A_nA_k{A_m}^2\cos(\varphi_n+\varphi_k-2\varphi_m)\Bigg) \end{aligned} \tag{13}$$

In Eqs.(11) and (13) the sums are performed only for those quartets of indices that satisfy the relations written under the summation symbols. The kurtosis of a certain signal thus depends on both the amplitudes and the phases of its harmonics.

Since the PSD depends only on the amplitudes as in Eq.(1), kurtosis can be achieved by manipulating the phases without affecting the spectral content of the signal. The Analytical Phase Selection (APS) method was described by Steinwolf [6] and can be used for kurtosis control purposes without the limitations associated with the Papoulis' Rule if the natural frequency of the DUT is known [11]. On the contrary, if the latter is unknown the test risks suffering from the Papoulis' Rule [9], hence the response of the system could tend to Gaussian.

A different kurtosis control method described in literature is the Polynomial Transformation, which consists in generating a Gaussian signal $x(t)$ with the prescribed PSD first and then applying a transformation of the form:

$$y(t) = \alpha_1 x(t) + \alpha_3 x(t)^3 \tag{14}$$

in order to obtain a Leptokurtic signal, with the coefficients α_1 and α_3 being functions of the target kurtosis value [6]. The transformation in Eq.4 presents two disadvantages: (*i*) the PSD of the signal is affected by an unwanted disturbance and (*ii*) Papoulis' Rule is very likely to occur, thus causing the peaks present in the input signal to be filtered out and leading the response to Gaussianity.

Another approach consists in modulating a Gaussian signal $x(t)$ having the desired PSD with an appropriate function $w(t)$ as in the following equation:

$$y(t) = w(t)x(t) \tag{15}$$

in order to obtain a Leptokurtic signal with a desired kurtosis value [12, 13]. This method is effective in transferring the kurtosis value to the response of the DUT if the signal bursts of the modulating signal have greater duration than the inverse of the bandwidth of the lightly-damped system [12]. The carrier waveform $w(t)$ introduces low frequency components in the spectrum of $y(t)$ compared to that of $x(t)$, albeit negligible if $w(t)$ is properly designed.

3 Multi-Level Variance (*MLV*) algorithm

The aim of the algorithms hereinafter presented is to synthesize a vibratory profile whose kurtosis and PSD match the reference input ones.

The first algorithm named "Multi-Level Variance" (MLV), considers the signal to be synthesized as divided into n_b blocks of the same duration T_b (no overlap). The generated blocks have different standard deviation, which is suggestive of a modulation procedure, although no modulating function is explicitly used. The different levels of variance ${\sigma_i}^2$ $(i = 1, \dots, n_b)$ are produced in such a way that the synthesized signal is compliant with the kurtosis and PSD constraints as it will be shown in the following. In general, the PSD of a signal is computed by calculating the Fast Fourier Transform (FFT) over small-sized blocks and squaring their magnitude in order to obtain the so-called periodograms and then averaging the periodograms. More specifically, the periodogram could be thought of as some sort of PSD computed only for the generic block of the signal. Therefore, instead of using the word "periodogram", reference will be made hereinafter to the PSD of a certain block of the signal.

In the algorithm, the PSD $\boldsymbol{G_i}$ of the i^{th} block of the signal is imposed to be scaled with respect to the PSD $\boldsymbol{G}$ of the reference signal:

$$\boldsymbol{G_i} = \frac{{\sigma_i}^2}{{\sigma_{tot}}^2}\boldsymbol{G}, \qquad i = 1, \dots, n_b \tag{16}$$

In Eq.(16) σ_{tot} is the standard deviation of the overall signal, whereas σ_i is the standard deviation of the i^{th} block. It is to be highlighted that the σ_i parameters are the unknowns, whereas ${\sigma_{tot}}^2$ can be calculated from either the reference signal using Eq.(3) or from the reference PSD:

$$\sigma_{tot}{}^2 = \int_0^\infty G(f)df \tag{17}$$

where $G(f)$ is the PSD of a continuous reference signal. However, since the processed signal is discrete in practice, the PSD is also discrete and the theoretical computation of Eq.(17) must be discretized.

The unknown parameters σ_i are also related to the overall variance $\sigma_{tot}{}^2$ via the relation [9]:

$$\sigma_{tot}{}^2 = \frac{1}{n_b}\sum_{i=1}^{n_b}\sigma_i{}^2 \tag{18}$$

From Eqs.(16) and (18) the following relation must hold:

$$\boldsymbol{G} = \frac{1}{n_b}\sum_{i=1}^{n_b}\boldsymbol{G_i} \tag{19}$$

Since the PSD $\boldsymbol{G}$ is computed by averaging the PSD of the blocks, Eq.(19) is automatically satisfied. Hence, the constraint on the PSD spectrum is respected if n_b coefficients σ_i ($\sigma_i > 0$) that comply with Eq.(18) are found.

In addition to Eqs.(18) and (19), there is also a relation between the kurtosis values of the overall signal, k_{tot}, and of the single blocks, k_i [9]:

$$k_{tot} = \frac{\sum_{i=1}^{n_b} k_i \cdot \sigma_i{}^4}{n_b \cdot \sigma_{tot}{}^4} \tag{20}$$

The first step of the algorithm is to randomly generate the σ_i values: such that $\sigma_i \in [\sigma_{min}, \sigma_{max}]$ and $\sigma_{min} < \sigma_{tot} < \sigma_{max}$. The ratio $r_\sigma = \frac{\sigma_{min}}{\sigma_{tot}} \in]0,1[$ must be selected by the user as an input for the algorithm: the closer to 0 the more the variance of the synthesized signal will vary in time, whereas the opposite is true if closer to 1. The parameter σ_{max} is not selectable by the user because it is adjusted throughout the algorithm iterations in order to approach the target kurtosis within a certain tolerance.

The user can also choose the parameter $n_p = 0, \dots, n_b$ intended to set the number of "bursts" of high amplitude excursion of the synthesized signal. The algorithm generates n_p blocks with a standard deviation equal to σ_{max}, which is greater than that of the other blocks.

The kurtosis k_i and variance $\sigma_i{}^2$ of the blocks are calculated via Eqs.(2)–(4) only on the first iteration, whereas the discrete signal x_n is obtained by IFFT of the PSD of the single blocks with randomly generated phases and then by concatenating the blocks.

A random integer s, representing a single block, is then automatically generated in the interval $[1, n_b]$.

After the σ_i levels are generated ($i = 1, \dots, n_b, i \neq s$), the standard deviation and kurtosis of the randomly selected s^{th} block are calculated via the following relations, which stem from Eqs.(18) and (20):

$$\sigma_s = \sqrt{n_b \sigma_{tot}{}^2 - \sum_{\substack{i=1 \\ i \neq s}}^{n_b} \sigma_i{}^2} \tag{21}$$

$$k_s = \frac{n_b k_{tot} \sigma_{tot}{}^4 - \sum_{\substack{i=1 \\ i \neq s}}^{n_b} k_i \sigma_i{}^4}{\sigma_s{}^4} \tag{22}$$

Eqs.(21) and (22) are used in order to verify if the prescribed PSD and target kurtosis can be achieved: indeed σ_s is required to be greater than zero and k_s greater than a lower threshold (the lower theoretical limit of kurtosis being 1) and less than an upper threshold. The upper threshold should not be set

excessively high so as to generate unrealistic peaks in the s^{th} block exceeding by far the amplitude of those of the other blocks. Afterwards, in order to obtain the k_s given by Eq.(22), the harmonics phases of the s^{th} block are adjusted by means of a phase manipulation procedure. With a very few iterations, where the parameter σ_{max} is changed in order to converge towards the target kurtosis value, Eqs.(21) and (22) are usually satisfied.

The final step of the algorithm is to smooth the signal at the edges of the blocks (by means of special windows), in order to avoid unrealistic discontinuities among them.

In conclusion, the user has to insert:

- the reference input signal or, alternatively, reference PSD and kurtosis value;
- the parameter T_b;
- the ratio r_σ;
- the number of bursts n_p;
- the duration T of the signal to be synthesized;
- the sampling frequency of the synthesized signal (usually the same as the reference signal, thus it may not be required to be an input).

4 Variable Spectral Density (VSD) algorithm

The algorithm hereinafter called "Variable Spectral Density" (VSD) splits the signal to be synthesized into n_b blocks of the same duration T_b, as the previous algorithm. The major difference is that the PSD $\boldsymbol{G_i}$ of the i^{th} block is randomly generated.

Let the PSD matrix $\left[\ G'_{ij}\ \right]$ be defined as:

$$\left[G'_{ij}\right] = \begin{bmatrix} G_1 & G_1 & \cdots & G_1 \\ \vdots & \vdots & \ddots & \vdots \\ G_{N_h} & G_{N_h} & \cdots & G_{N_h} \end{bmatrix} \tag{23}$$

where $\mathrm{N_h}$ is the number of harmonics/PSD points.
This matrix has N_h rows and n_b columns, with the j^{th} column being the PSD vector of the j^{th} block of the reference signal $(j = 1, \dots, n_b)$. Eq.(23), where all the columns have the same elements (harmonic amplitudes), refers implicitly to a signal having a stationary PSD. On the other hand, the PSD matrix $\left[\ G''_{ij}\ \right]$ corresponding to the signal synthesized through the MLV algorithm has the following form:

$$\left[G''_{ij}\right] = \begin{bmatrix} \left(\frac{\sigma_1}{\sigma_{tot}}\right)^2 G_1 & \left(\frac{\sigma_2}{\sigma_{tot}}\right)^2 G_1 & \cdots & \left(\frac{\sigma_{n_b}}{\sigma_{tot}}\right)^2 G_1 \\ \vdots & \vdots & \ddots & \vdots \\ \left(\frac{\sigma_1}{\sigma_{tot}}\right)^2 G_{N_h} & \left(\frac{\sigma_2}{\sigma_{tot}}\right)^2 G_{N_h} & \cdots & \left(\frac{\sigma_{n_b}}{\sigma_{tot}}\right)^2 G_{N_h} \end{bmatrix} \tag{24}$$

Both the matrices in Eqs.(23) and (24) satisfy Eq.(19) that may be rewritten in this case, in conformity with the notation used in this section, as:

$$\sum_{j=1}^{n_b} G_{ij} = G_i\, n_b \qquad i = 1, \dots, \mathrm{N_h} \tag{25}$$

The VSD algorithm synthesizes a signal with a PSD variable over time, corresponding to a PSD matrix having the most general form:

$$\left[G_{ij}'''\right] = \begin{bmatrix} G_{11} & G_{12} & \cdots & G_{1n_b} \\ \vdots & \vdots & \ddots & \vdots \\ G_{N_h1} & G_{N_h2} & \cdots & G_{N_hn_b} \end{bmatrix} \tag{26}$$

where the elements must comply with Eq.(25).

The matrix in Eq.(26) is useful to generate signals whose PSD varies over time.

To understand the method, a few steps are necessary to illustrate how the generic form matrix of Eq.(26) can be derived from Eqs.(23) and (25). Let us start with the matrix as shown in Eq.(23): if, for instance, the i^{th} row is taken and changed as follows (where $p \in [0,1]$ and l is a positive integer such that ($l \leq n_b$):

$$\left[G_{ij}\right] = \begin{bmatrix} G_1 & G_1 & & G_1 & & G_1 & G_1 & G_1 \\ \vdots & \vdots & & \vdots & & \vdots & \vdots & \vdots \\ G_i & \dots pG_i \dots & [1+(l-1)(1-p)]G_i & & \dots pG_i \dots & pG_i & \dots & G_i \\ \vdots & \vdots & & \vdots & & \vdots & \vdots & \vdots \\ G_{N_h} & G_{N_h} & & G_{N_h} & & G_{N_h} & G_{N_h} & G_{N_h} \end{bmatrix} \tag{27}$$

(j^{th} column)

Eq.(25) is still respected if the terms of the type pG_i are $l-1$. If similar operations were done not only on the term G_{ij} but also on other terms and in a random manner then the PSD of each block could be varied still preserving the overall PSD.

The steps of the algorithm are the following:

0) insert a reference input signal or, alternatively, reference PSD and kurtosis value;
1) set the duration T and the sampling frequency F_s of the signal to be synthesized;
2) choose $p \in [0,1]$ (user's choice), start from a certain T_b (automatically set), and set $i = 1$;
3) start from the i^{th} row and set $s = 0$;
4) choose a random element j of that row;
5) generate a positive random integer $l \leq n_b - s$;
6) set:
   $G_{ij} = [1 + (l-1)(1-p)]G_i$ and $s = s + l$;
7) repeat $4-5-6$ with a another value for j (different from the values generated in the previous loops), and another value of l, until $s \geq n_b - 1$;
8) set
   $$G_{im} = pG_i;$$
   with m ranging over all the elements of the i^{th} row which have not been modified in point 6;
9) if $i < N_h$, set $i = i + 1$ and repeat from point 3, otherwise proceed to point 10;
10) terminate if the kurtosis of the synthesized signal matches the target value (within a certain tolerance, to be preliminarily set), otherwise repeat from point 2 without changing p but with a different T_b, automatically defined. Decreasing T_b makes the kurtosis value increase and vice versa (this is how the algorithm converges towards target kurtosis).

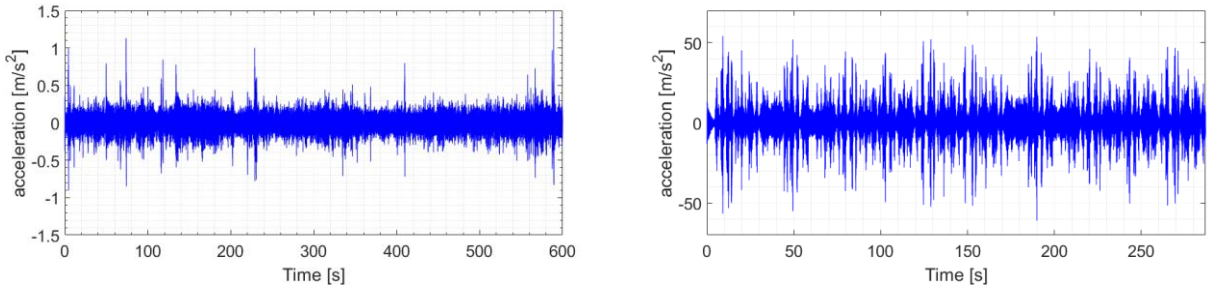
A limitation of the algorithm could be that the variation of the PSD over time (i.e. over the blocks) is not controlled but randomly generated.

As in the case of the MLV algorithm, the last step is to smooth the signal at the edges of the blocks, in order to avoid unrealistic discontinuities.

5 Simulation Results

The two algorithms were tested starting from numerous reference input profiles. For the sake of brevity, only the results of two applications will be shown. Nevertheless, general considerations can be extended to generic cases.

The starting reference signals, here denoted as *RS100* and *RS500*, are field data sampled at 100 Hz and 500 Hz, respectively, with durations of 600 and 288 seconds. Figure 1 reports their plots, whereas some statistical parameters are listed in Table 1, in particular: standard deviation, kurtosis, crest factor (i.e. the ratio between the peak value and the standard deviation). Both the reference signals prove to be Leptokurtic, i.e. their kurtosis is greater than 3.0 as numerous peaks and/or bursts are present in the time-series. The kurtosis values of the responses of four single-degree-of-freedom systems with different natural frequencies and a damping coefficient of 2%, are also reported in Table 1 to check the sensitivity to the Papoulis' Rule. The responses were obtained in terms of acceleration $[m/s^2]$, by implementing the well-known convolution between the impulse response of the system and the reference signal.



(a) (b)

Figure 1: Reference signals used in the two applications: a) *RS100*, b) *RS500*

	RS100	***RS500***
Std deviation $[\boldsymbol{m/s^2}]$	0.125	71.0
Kurtosis [-]	6.64	6.47
Crest factor [-]	14.3	9.02
Kurtosis of the response at 12 Hz [-]	5.54	13.8
Kurtosis of the response at 24 Hz[-]	12.3	12.3
Kurtosis of the response at 27 Hz [-]	5.32	10.4
Kurtosis of the response at 35 Hz [-]	3.60	19.7

Table 1: Statistical parameters of the reference signals *RS100* and *RS500*

The MLV and VSD algorithms are firstly applied to the reference signal *RS100*. The input parameters for the MLV algorithm are:

- duration of the synthesized signal $T = 600\ s$ (the same as for the reference signal);
- sampling frequency of the synthesized signal $F_s = 100\ Hz$;
- $r_\sigma = 0.5$;
- T_b= 3 s $\left(n_b = \frac{T}{T_b} = 200\right)$;
- number of bursts: n_p= 10;

The input parameters for the VSD algorithm are:

- duration of the synthesized signal: T = 600 s
- sampling frequency of the synthesized signal $F_s = 100\ Hz$;
- p=0.2.

By inspecting the plot, a dozen distinctive peaks can be approximately counted. As a consequence, the parameter related to the number of bursts was chosen equal to 10 for the *MLV* algorithm.

The parameter r_σ has been chosen equal to 0.5 to give a "moderate" amount of variability to the standard deviation over time. The signals synthesized by the two algorithms are reported in Fig.2 along with their *PSD*s. The *PSD* spectra plotted in Fig.2c were computed with a 50% overlap among the n_b blocks and using a Hamming window. On the other hand, it should be noted that both the algorithms process the signals with 0% overlap and rectangular windows.

The parameter p of the *VSD* algorithm has a similar meaning to the parameter r_σ of the *MLV* algorithm. Nevertheless in order to give the same amount of variability requires to be set to a lower value.

The statistical parameters of the synthesized signals are shown in Table 2.

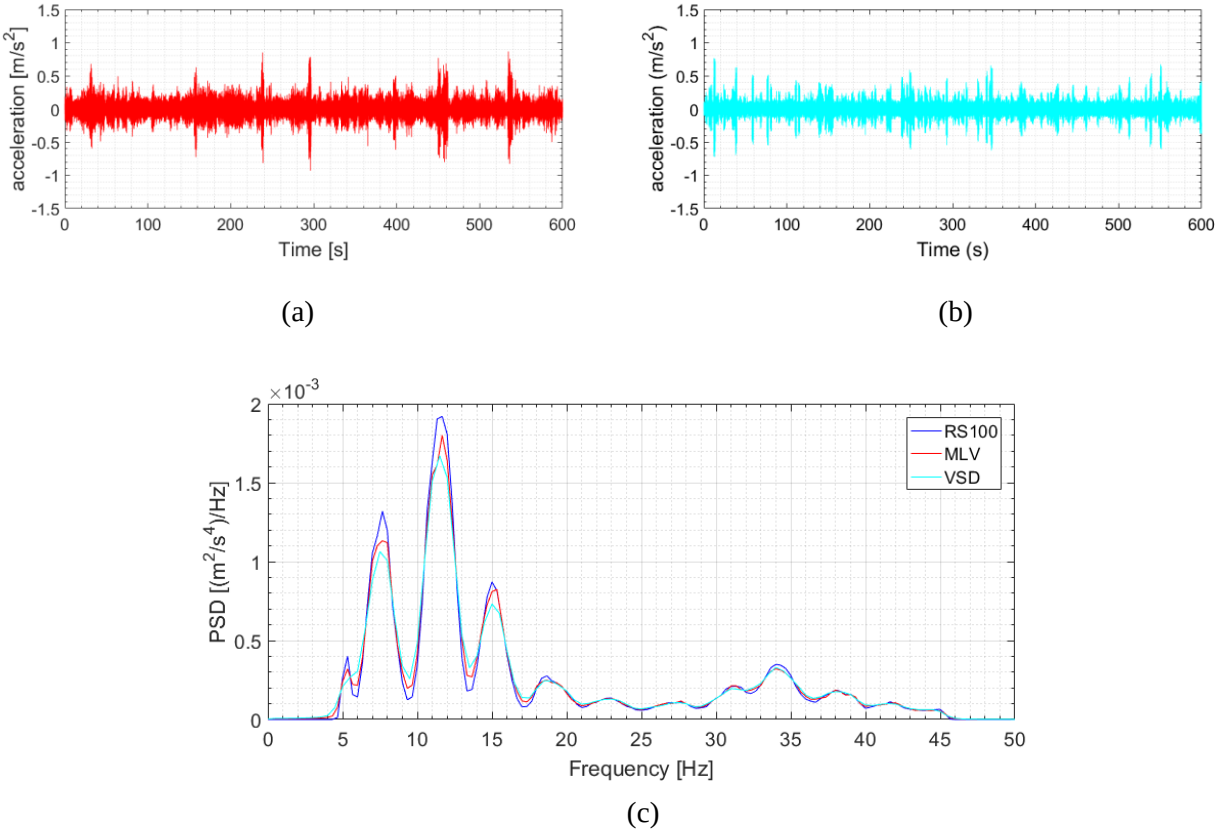


Figure 2: Synthesis results starting from the reference input profile *RS100*: a) signal synthesized by the *MLV* algorithm; b) signal synthesized by the *VSD* algorithm; c) *PSD*s comparison

	MLV signal	***VSD signal***
Std deviation $[\boldsymbol{m/s^2}]$	0.125	0.125
Kurtosis [-]	6.50	6.62
Crest factor [-]	8.32	6.85
Kurtosis of the response at 12 Hz [-]	5.25	35.7
Kurtosis of the response at 24 Hz[-]	6.48	18.6
Kurtosis of the response at 27 Hz [-]	6.46	18.0
Kurtosis of the response at 35 Hz [-]	6.46	25.8

Table 2: Statistical parameters of the signals synthesized starting from the reference input profile *RS100*

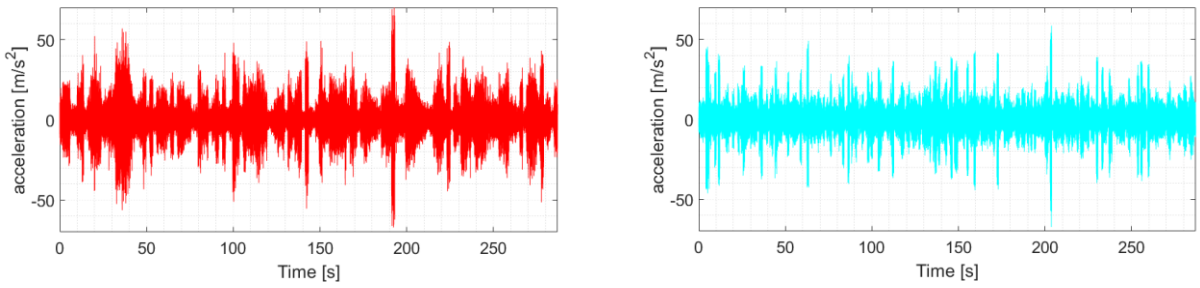
The results of the *MLV* and *VSD* algorithms applied to the reference signal *RS500* are now shown. The input parameters for the *MLV* algorithm are:

- duration of the synthesized signal $T = 288\ s$ (the same as for the reference signal);
- sampling frequency of the synthesized signal $F_s = 500\ Hz$;
- $r_\sigma = 0.25$;
- T_b= 2 s $\left(n_b = \frac{T}{T_b} = 144\right)$;
- number of bursts: n_p= 20.

The input parameters for the *VSD* algorithm are:

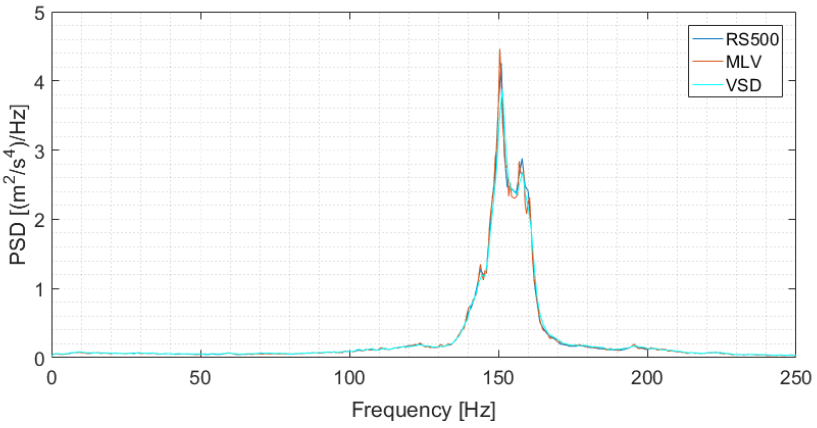
- duration of the synthesized signal: T = 288 s
- sampling frequency of the synthesized signal $F_s = 500\ Hz$;
- p=0.1.

The parameter r_σ has been chosen equal to 0.25 to give a great amount of variability to the standard deviation over time since, as it can be observed in Fig.1b, the reference signal does not simply contain isolated peaks but also the variance varies to a greater extent than in the previous example.
The signals synthesized by the algorithms are reported in Fig.3 along with their *PSDs*. The *PSD* spectra plotted in Fig.3c were computed with a 50% overlap among the n_b blocks and using a Hamming window. The statistical parameters of the synthesized signals are shown in Table 3.



(a)

(b)



(c)

Figure 3: Synthesis results starting from the reference input profile *RS500*: a) signal synthesized by the *MLV* algorithm; b) signal synthesized by the *VSD* algorithm; c) *PSD*s comparison

	MLV signal	***VSD signal***
Std deviation [$\boldsymbol{m/s^2}$]	71.0	71.0
Kurtosis [-]	6.50	6.40
Crest factor [-]	7.24	8.00
Kurtosis of the response at 12 Hz [-]	5.76	25.9
Kurtosis of the response at 24 Hz[-]	6.01	22.6
Kurtosis of the response at 27 Hz [-]	6.11	16.5
Kurtosis of the response at 35 Hz [-]	6.80	17.7

Table 3: Statistical parameters of the signals synthesized starting from the reference input profile *RS500*

As it can be observed by comparing Tables 2 and 3, the kurtosis values of the responses to the signals synthesized by the MLV algorithm are closer to the kurtosis of the reference input profile, whereas the kurtosis of the responses to the signals synthesized by the *VSD* algorithm take much larger values. These values highlight an important difference between the two algorithms: the VSD algorithm can generate signals whose system response has a (much) higher kurtosis than the input one. This is the reason why the reference signal *RS500* has been considered particularly significant to illustrate the special feature of the VSD algorithm. As it can be observed in Table 1, the kurtosis values of the four system responses are higher than that of the input excitation. This is due not only to the variation of the variance of the signal over time, but mainly to the variation of the PSD. The very high kurtosis values of the responses are due to a resonance effect: in particular, some blocks of the reference signals present a very sharp PSD around the natural frequency of the system. This implies that in those blocks the signal is approximately a sinusoid with the same frequency, leading the system to resonate. Unlike the VSD algorithm, the resonance effect does not occur by using the MLV algorithm, because all the blocks of the signal have the same shape and a wide band (the same of the reference signal).

6 Conclusion

Two novel algorithms – named Multi-Level Variance (*MLV*) and Variable Spectral Density (*VSD*) – which synthesize vibration signals with prescribed *PSD* and kurtosis value are proposed. The *MLV* algorithm varies the variance (*RMS*/standard deviation) of the blocks constituting the signal, whereas the *VSD* algorithm varies the *PSD* of the blocks. They both require as inputs: a reference vibratory profile or, alternatively, a reference *PSD* and a target kurtosis, the duration of the synthesized signal, a parameter which indicates the level of variation of the variance/*PSD* of the blocks. The *MLV* algorithm also requires to specify the duration of the blocks of the signal to be synthesized and the number of bursts of high amplitude excursion that the synthesized signal must present.

The *MLV* algorithm is particularly suited to synthesize profiles able to transfer a value of kurtosis to the DUT response close to that of the input, whereas the *VSD* algorithm is particularly suited to synthesize profiles able to transfer a value of kurtosis to the output much higher than that of the input. To obtain the same output kurtosis with the two algorithms, the second one needs a lower crest factor, thus subjecting the shaker to less severe loads. The results in output kurtosis do not depend on the natural frequency of the DUT, unlike Analytical Phase Selection (*APS*) whose output kurtosis is close to 3 if the bandwidth of the controlled phases does not contain the natural frequency of the DUT. In fact, a proper selection of the algorithm parameters permits to preserve (for the *MLV* algorithm) or even increase (for the *VSD* algorithm) the kurtosis of the reference signal. Moreover, in order to guarantee the randomness of the synthesized signals, the *MLV* algorithm manages to manipulate the variance of the blocks among n_b levels, with n_b being the number of the blocks that the signal is split into. It ensures that the overall kurtosis and *PSD* are satisfactorily close to the desired ones. Furthermore, since all the phases in the *VSD* algorithm and all the phases except for only one block in the *MLV* algorithm are randomly selected, the important characteristic of randomness in vibration tests is preserved and each synthesis run gives rise to different signals, even if the same input parameters are used.

In terms of speed, both the algorithms could be implemented in such a way that the required computational time is not burdensome: long signals can be synthesized in a few seconds.

Future works are planned to investigate the possibility of using synthesized Leptokurtic signals to carry out accelerated durability tests.

Acknowledgements

This activity was performed in collaboration with *Dana Rexroth Transmission Systems* (Trento, Italy) and *Easting S.r.l.s.* (Trieste, Italy), that are gratefully acknowledged for operative cooperation and financial support.

References

[1] C. Lalanne, *Mechanical Vibration and Shock Analysis-Volume 5: Specification Development*, John Wiley & Sons, Inc-ISTE, London (2009)
[2] C. Lalanne, *Random Vibration*, John Wiley & Sons, Inc-ISTE, London (2009)
[3] Papoulis, *Probability,Random Variables, and Stochastic Processes*, McGraw-Hill, 3rd ed. *(1991)*
[4] Papoulis, *Narrow-Band systems and Gaussianity*, IEEE Trans. On Information Theory, Vol.18, No.1 *(1972)*
[5] J. J. Van Baren, P. Van Baren, *Kurtosion*tm*-getting the kurtosis into the resonances*, SAVIAC (2007)
[6] Steinwolf, *Vibration testing of vehicle components by random excitations with increased kurtosis*, Int. J. Vehicle Noise and Vibration (2015)
[7] J. Zhang,B. Cornelis,B. Peeters,K. Janssens,P. Guillaume, *A new practical and intuitive method for kurtosis control in random vibration testing*, ISMA 2016 Conference, Leuven, Belgium (2016)
[8] D.O. Smallwood, *Generating non-Gaussian vibration for testing purposes*, Sound and Vibrations, Vol.39, No. 10 (2005)
[9] E. Pesaresi, *Leptokurtic signals in random control vibration testing*, MSc Thesis in Mechanical Engineering, University of Bologna *(2017)*
[10] Steinwolf, *Approximation and simulation of probability distributions with a variable kurtosisvalue*, Computational Statistics and Data Analysis,21 (2),163-180 (1996)
[11] Cornelis, A. Steinwolf, M. Troncossi, A. Rivola, *Shaker testing simulation of non-Gaussian random excitations with the fatigue damage spectrum as a criterion of mission signal synthesis*, Proceedings of the 2015 International Conference on Engineering, Liubljana, Slovenia *(2015)*
[12] J. Minderhoud, P. Van Baren, *Using Kurtosion® to Accelerate Structural Life Testing*, Sound And Vibration, Vol.44 (2010)
[13] F. Kihm, N. S. Ferguson, J. Antoni, *Fatigue life from kurtosis controlled excitations*, 6th Fatigue Design conference, Fatigue Design (2015)

Analysis of a transport equation as boundary condition in an acoustic transmission line.

E. De Bono [1], **M. Collet** [1], **S. Karkar** [1]
[1] Ecole Centrale de Lyon, Laboratoire de tribologie et dynamique des systèmes,
36 Avenue Guy de Collongue, 69134 Écully, France.
e-mail: **emanuele.de-bono@ec-lyon.fr**

Abstract
The acoustic coupling between the acoustic operator and a Transport operator, the latter applied as boundary condition, is numerically investigated in this paper. A transport equation, involving both the normal and the tangential derivative of the acoustic variable (pressure), is applied on the upper side of an acoustic waveguide. This boundary condition can be reproduced experimentally by a distributed impedance control of an active liner. In this paper, we numerically demonstrate the reciprocity breaking for acoustic wave propagation, caused by such boundary condition. Furthermore, several analyses are carried out in order to assess the stability conditions of the acoustic system, coupling the acoustic wave propagation domain (where the D'Alambert operator applies) and the transport operator on the boundary.

1 Introduction

In order to reduce the airborne sound transmission in a generic duct, its surfaces can be lined with materials realizing specific surface impedance conditions. Classical examples are passive absorbers whose main working principle is the viscous dissipation. The performances of this dissipative liners are poor at lower frequencies, the actual limit being governed by the cross-sectional dimensions of the duct, liner thickness and absorption properties of the lining material [1]. Opposite to the passive philosophy, is the Active Noise Control (ANC), developed after the rapid development of modern digital computers. The ANC techniques are based upon the destructive interference produced by actively controlled secondary sources with the capacity both to reflect and absorb sound [2]. Also in the realm of Control techniques, lies the concept of Acoustic Impedance Control. While the ANC strategies (both local and global) act directly on the acoustical medium by using secondary sources, the Impedance Control methodology instead tends to adjust the Impedance at the boundary interfaces for inducing suitable sound diffusion. This methodology has been developed after conceiving the loudspeaker as an electroacoustic absorber, as firstly done by Olson and May [2]. A suitable combination of both active and passive methods allows to achieve a compromise between dimensions, weight and efficiency over a wide frequency range. The idea is to get a sound pressure as low as possible behind a passive surface, by using the active control system and the Darcy's law. In this way, the device, which is then equivalent to a quarter wavelength absorber, can improve the low-frequency absorption of a thin sample of porous material. This idea was first proposed by Olson and May [2] and then experimentally investigated by Guicking and Lorentz [3]. The classical approaches used by many authors studying the implementation of active acoustic impedance based on Guicking's work, such as Galland et al. [4] for example, are based on the knowledge of the so-called optimal complex impedance, which they tend to implement experimentally using hybrid parietal ANC systems. Their purpose is to locally control a boundary interface to follow the pre-established frequency-dependent complex impedance. The proposed solutions for impedance optimization ([4] and [5]) lead to theoretical frequency-dependent impedances $Z(j\omega)$ guaranteeing efficient sound

absorption depending on the disturbances, boundary conditions, speed of sound, frequency band, structural interfaces, and geometry. These dependencies prohibit broad frequency band applications and good efficency is restricted to a specific configuration. As already said, the optimally designed impedance ([4] and [5]) appears as a frequency dependent function $Z(j\omega)$, linking acoustic pressure and velocity. While its experimental implementation allows to control these parietal quantities by using only the corresponding time operator, it appears very interesting to introduce also a wave number dependency (that is a space operator) so that $Z = Z(j\omega, jk)$ in order to improve efficiency and versatility [6]. This interest has brought about the design of a Generalized Distributed acoustic impedance $Z = Z(j\omega, jk)$. An impedance operator for total absorption of acoustic waves in 2D has been mathematically derived in [6], but this complex operator involves space and time pseudodifferential terms that prevent any possible experimental implementation as it would require an infinitely large data storage. Therefore, a first order operator has been conceived, designed and experimented in Collet et al. ([7] and [8]), which could be realistically implemented.
The generalized impedance proposed in [7] is an advection equation, where the normal acceleration at the boundary is function of both the tangential and time derivative of pressure, see Equation (1) and Figure 1.
$\forall t \in \mathbb{R}$, and all $(x, y) \in \partial\Omega_1$

$$-\rho\frac{\partial v_z}{\partial t} = \frac{\partial p}{\partial x} - \frac{1}{c_a}\frac{\partial p}{\partial t} \tag{1}$$

In Equation (1), v_z is the outward normal velocity at the boundary, x is the longitudinal direction of the duct, c_a is a parameter to be defined, corresponding to the celerity coefficient of the transport equation.
The objective of this contribution is specifically to assess the stability of the acoustic domain bounded on one side by the transport equation (1). This will be done through different analyses. First, a semi-infinite 2D acoustic domain $(x, z) \in (-\infty, \infty)x(-\infty, 0]$ (see Figure 1) will be considered, as in [7]. The analytical results of non-reciprocity, obtained already in [7] for a semi-infinite 2D acoustic domain, are reproposed with some additional remarks. In particular, it is pointed out the condition in which the control behaves as an active source, inputting energy in the acoustic domain. Then, the wave propagation in an infinite waveguide will be analyzed, and the non-reciprocity of plane wave mode demonstrated. In addition, we will show that the "active behaviour" of the control found in Section 2 will result to be a condition of possible instability in the propagation of duct modes. Finally, the cavity modes in an enclosed finite duct will be analyzed and the time stability correlated to the condition of "active" behaviour of the controlled boundary.

2 Semi-infinite acoustic domain analysis

Collet et al. ([7] and [8]), showed how the boundary condition (1) in a semi-infinite 2D acoustic domain $(x, z) \subset (-\infty, \infty)x(-\infty, 0]$ (see Figure 1), allows wave propagation only in the x<0 direction for certain values of the celerity coefficient c_a.

$$\nabla^2 p = \frac{1}{c_0^2}\frac{\partial^2 p}{\partial t^2} \qquad in \quad x \in (-\infty, \infty) \;\; z \in (-\infty, 0) \tag{2}$$

$$\hat{n} \cdot \vec{\nabla} p = \frac{\partial p}{\partial x} - \frac{1}{c_a}\frac{\partial p}{\partial t} \qquad on \quad z = 0 \tag{3}$$

In Equation (3), the normal acceleration has been substituted by the normal pressure gradient, according to linearized momentum equation $\hat{n} \cdot \nabla p = -\rho\frac{\partial v_n}{\partial t}$.

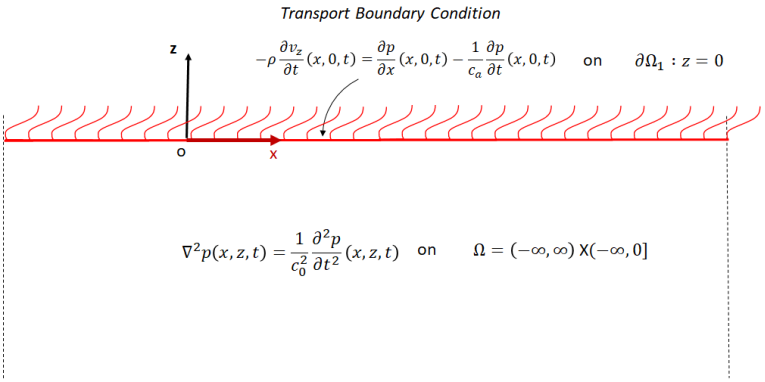
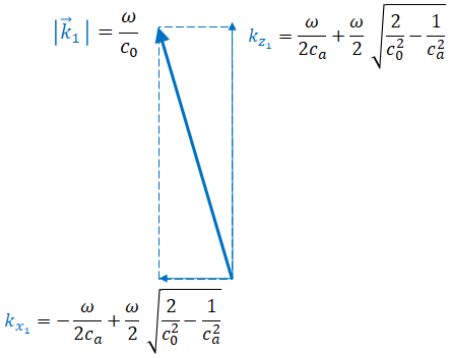


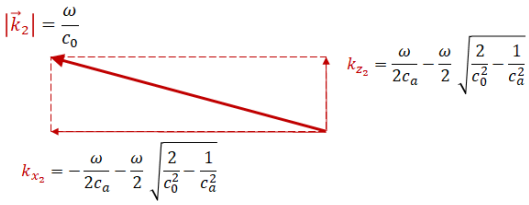
Figure 1: Semi-infinite domain bounded on one side by our Transport Equation.

The problem analyzed in [7] is described by Equations (2) and (3). If we consider the stationary regime, the above problem can also be considered as a frequency dependent eigenvalue problem, with eigenfunctions being the waves and eigenvalues being the wave numbers along the x and z directions. Indeed, as the domain is not bounded on the lower side, there will not be standing waves, but just travelling waves generated by the transport equation.

The results as reported in [7], in terms of wavenumbers, for $c_a < c_0$ and $c_a > c_0$, are reported in Figure 2 and 3 respectively.

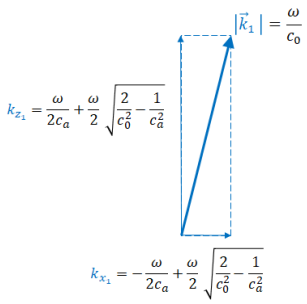


(a) Wavenumber k_1 components for $c_a < c_0$.

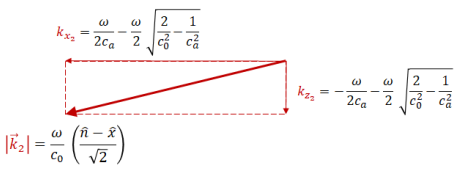


(b) Wavenumber k_2 components for $c_a < c_0$.

Figure 2: Wavenumbers for $c_a < c_0$ in the semi-infinite domain bounded on the upper side by the transport boundary condition.



(a) Wavenumber k_1 components for $c_a > c_0$.



(b) Wavenumber k_2 components for $c_a > c_0$.

Figure 3: Wavenumbers for $c_a > c_0$ in the semi-infinite domain bounded on the upper side by the transport boundary condition.

In this simplified system of a semi-infinite domain bounded on the upper side by the transport boundary condition (3), we have some important information on the effect of the transport boundary condition over the acoustic domain. From Figure 2 we can see that for $c_a < c_0$, $\vec{k}_1$ and $\vec{k}_2$ are directed toward the boundary itself (which is situated upward). If we consider the boundary as an interface between the acoustic domain and a fictitious transport domain where the equation (3) holds, the wave solutions found by imposing the boundary condition (3) on the interface between these two domains, are solutions for both the acoustic domain and the fictitious transport domain. In this perspective, in the case of $c_a < c_0$ both waves are transmitted from the acoustic domain to the fictitious domain (as they are directed toward the boundary), whereas for $c_a > c_0$ one wave (relative to $\vec{k}_2$) is transmitted from the fictitious domain to the acoustic domain (see Figure 3b).
This means that, for $c_a > c_0$ the transport boundary condition will behave as an active boundary. In a real application of the boundary condition (3) in a duct, the case of $c_a > c_0$ may lead to unstable duct modes.

3 Infinite waveguide analysis

The acoustic domain is now bounded on both the upper and lower sides.
Karkar et al. [9], in the 1D approximation of the waveguide (i.e. in the hypothesis of only plane waves propagating in the lined duct), demonstrated how the Transport Equation (1) reproduces an acoustic "diode" effect, blocking the plane wave propagation in the $x > 0$ direction. We will here demonstrate the breaking of reciprocity in the real case of a 3D waveguide.
We will consider a duct with rectangular cross section, as depicted in Figure 4. The dimensions of the rectangular cross section of the duct are as follows:

$d_y = 0.15\ m$ Dimension along y axis, normal to the rigid walls
$d_z = 0.30\ m$ Dimension along z axis, normal to the active liners

The attenuation of sound waves propagated through an infinite transmission line (as a duct) of uniform cross section, can be evaluated by knowing the wave number (in both its real and imaginary parts) along the main direction of propagation (the longitudinal axis of the duct).

3.1 Outline of the problem

The calculation of the wave number along the x-direction is achieved by solving a frequency dependent eigenvalue problem, in terms of duct modes (i.e. the distribution of pressure along the cross section of the duct) as the eigenfunctions, and wave numbers along x as the corresponding eigenvalues. The mathematical formulation of the eigenproblem, in the frequency domain, is reported in Equations (4) (refer to Figure 4).

$$\begin{aligned}
\left[\nabla^2 + \frac{\omega^2}{c_0^2}\right] p(y,z,\omega) &= k_x^2\, p(y,z,\omega) \qquad \text{in } S \\
\left[\hat{n}\cdot\vec{\nabla} - j\frac{\omega}{c_a}\right] p(y,z,\omega) &= jk_x\, p(y,z,\omega) \qquad \text{on } BS_1 \\
\hat{n}\cdot\vec{\nabla} p(y,z,\omega) &= 0 \qquad \text{on } BS_2,\ BS_3,\ BS_4
\end{aligned} \tag{4}$$

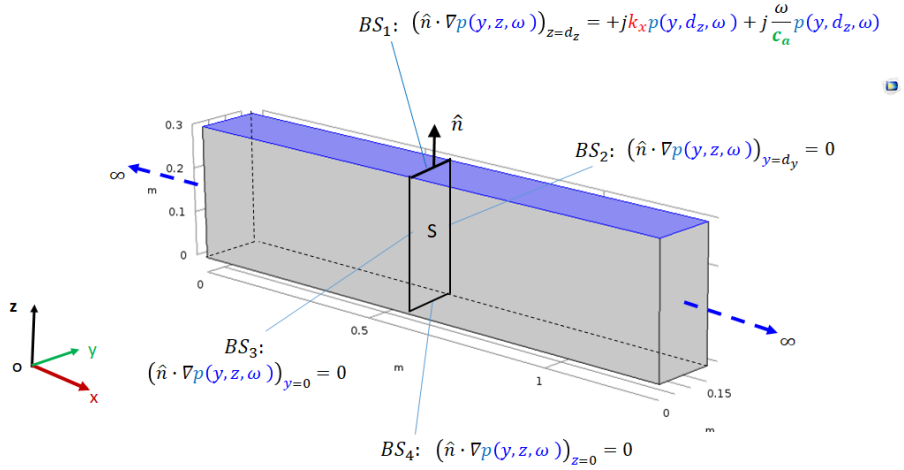


Figure 4: Infinite waveguide bounded on the upper side by our transport equation. The lateral sides are considered as rigid.

The wave number k_x will define an attenuation or an amplification of the amplitude of the corresponding duct modes (see Figure 5). In particular, the sign of the group velocity (or its inverse $\frac{\partial Realk_x}{\partial\omega}$), will determine the direction of propagation of the corresponding duct mode, and the sign of the imaginary part of k_x will determine the attenuation property. In the assumption for wave function $e^{-j\omega t+jk_x x}$ assumed here, if the two quantities $\frac{\partial Realk_x}{\partial\omega}$ and $Imag(k_x)$ keep the same sign, then the duct mode will propagate into the waveguide without increasing its amplitude, and we will say that the wave propagation is stable. Therefore we can state a wave stibility criteria:

$$\frac{\partial Real(k_x)}{\partial\omega} Imag(k_x) > 0 \tag{5}$$

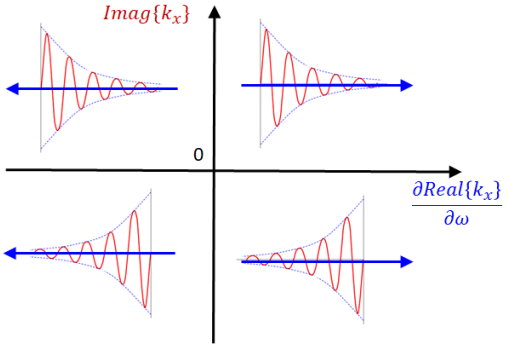


Figure 5: Duct modes propagation properties, according to the group velocity ($\frac{\partial Rek_x}{\partial\omega}$), and the imaginary part of k_x. It is based on the assumption $e^{-j\omega t+jk_x x}$.

The eigenproblem of Equation (4) is solved numerically, with Finite Elements. It is a frequency dependent eigenproblem, with non-homogeneous boundary condition (given by the transport equation). Furthermore the eigenvalue k_x itself is in the boundary transport equation. This asks for a delicate numerical treatment of the problem, as this special boundary condition must be integrated directly in a weak formulation. We will briefly summarize the steps to get to the weak formulation of the system of equations (4).
By multiplying the first of equations in (4) by a test function $\tilde{p}$ and integrating by part over the bidimensional domain S (cross section of the duct), we get:

$$\begin{aligned}&\int_S \nabla^2 p\ \tilde{p}\ dS + (\frac{\omega^2}{c_0^2} - k_x^2) \int_S p\ \tilde{p}\ dS = \\ &= -\int_S \vec{\nabla} p \cdot \vec{\nabla} \tilde{p}\ dS + \int_{BS} \hat{n} \cdot \vec{\nabla} p\ \tilde{p}\ dBS + (\frac{\omega^2}{c_0^2} - k_x^2) \int_S p\ \tilde{p}\ dS = 0\end{aligned} \tag{6}$$

In Equation 6, the integration by parts (also called Kelvin-Stokes theorem, which in 2D becomes the Green theorem) has been applied, and the differential order of the problem has been reduced by one.
In order to implement the boundary conditions reported in Equations (4), the normal derivative of pressure in the last term of Equation (6) will be substituted by the right side of the robin B.C. (on BS_1) and by zero on BS_2, BS_3 and BS_4. Finally, we arrive at the expression of the weak formulation of the system of equations (4):

$$(\frac{\omega^2}{c_0^2} - k_x^2) \int_S p\ \tilde{p}\ dS - \int_S \nabla p \cdot \nabla \tilde{p}\ dS + j(k_x + \frac{\omega}{c_a}) \int_{BS_1} p\ \tilde{p}\ dBS_1 = 0 \tag{7}$$

We can now apply the Finite Element method to solve the above eigenvalue problem written in its weak form.

3.2 Results

In order to find the conditions under which the wave propagation of the duct modes is stable, the eigenvalue problem of Equation (7) has been solved for different values of the parameter c_a. In this paper the results obtained for $c_a = 0.9c_0$, $c_a = c_0$ and $c_a = 1.01c_0$ are reported.

Figure 6 shows the dispersion curves for the case of $c_a = c_0$. We can notice the solution corresponding to the plane wave mode propagating with a wavenumber $k_x = -\omega/c_0$, therefore towards the negative x-direction. The plane wave mode propagating toward $x > 0$ instead is not an eigensolution, demonstrating that the reciprocity of plane wave propagation is broken. The other dispersion curves correspond to higher order duct modes, travelling both in the positive and negative x-direction. From Figure 6 we can see that all the higher order modes propagate since the lowest frequencies (as the real part of k_x is different from 0 even at frequencies close to 0). Nevertheless, from Figure 7, we notice that the higher order modes are always attenuated, with an attenuation which progressively decreases as frequency increases.
We must report the numerical difficulty of the eigenvalue solver in following the same dispersion curve when varying frequency, which causes the typical numerical mode crossing phenomenon.

In Figure 8 the variation of $\frac{\partial Real(k_x)}{\partial \omega} Imag(k_x)$ with ω is plotted, in order to verify the wave propagation stability criteria (see Figure 5). The numerical mode crossing we mentioned above, is the responsible of some single negative values of $\frac{\partial Real(k_x)}{\partial \omega} Imag(k_x)$ in Figure 8, as during the "mode crossing" the derivative $\frac{\partial Real(k_x)}{\partial \omega}$ will be discontinous. By excluding these "spurious" values, we can assess that the wave propagation in a waveguide, bounded on the upper side by our transport equation (3), is stable as the product $\frac{\partial Real(k_x)}{\partial \omega} Imag(k_x)$ is always positive or equal to 0.

In order to investigate the wave propagation stability when varying the value of c_a around the value of c_0, the same calculations have been repeated for $c_a = 0.9c_0$ and $c_a = 1.01c_0$. In Figure 9 the case of $c_a = 1.01c_0$

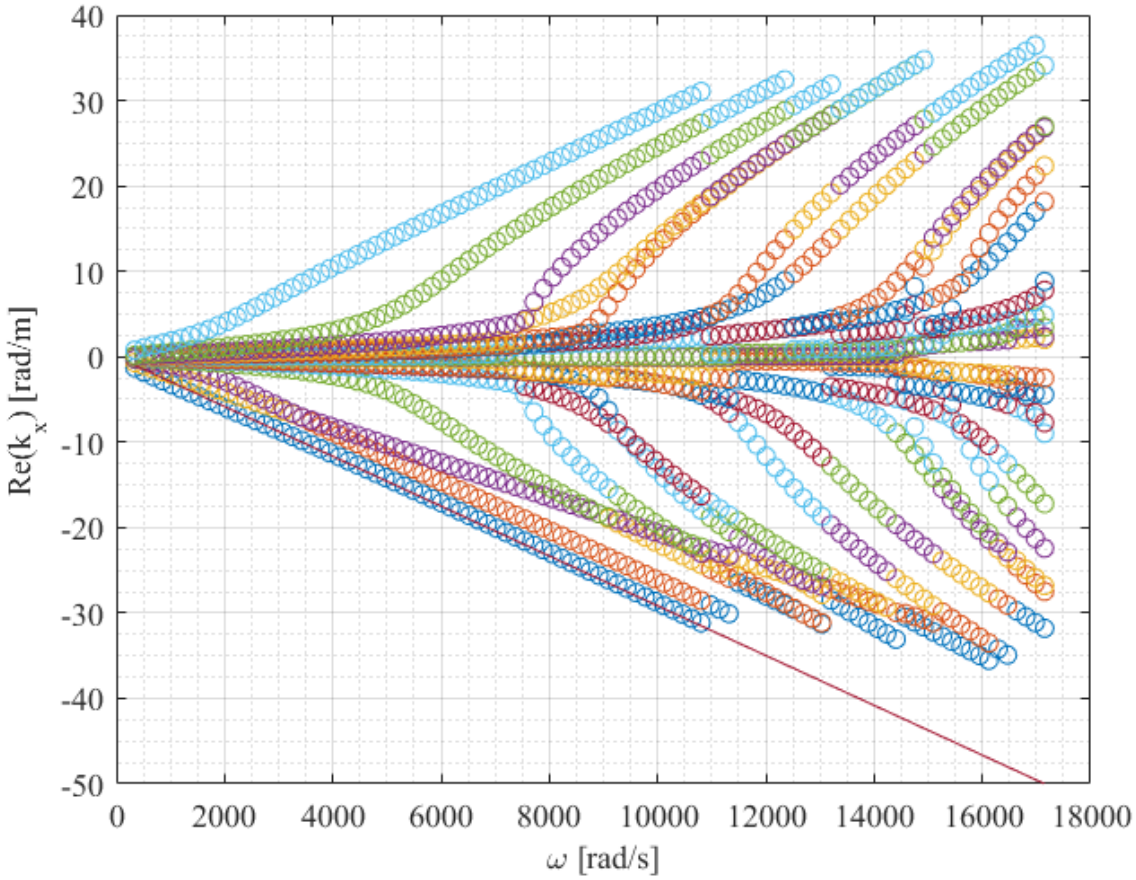


Figure 6: Numerical dispersion curves for duct modes, in the case of upper side of the duct bounded by the transport equation (3), with $c_a = c_0$. The continuous line in red, is relative to $k_x = -\omega/c_0$, and it corresponds to the back-propagating plane wave mode.

is considered. It is evident that the plane wave mode presents values of $\frac{\partial Real(k_x)}{\partial \omega} Imag(k_x)$ which are lower than 0. Same thing happens at higher frequencies for higher order modes propagating toward the negative x-direction.
Figure 10 instead, corresponding to the case of $c_a = 0.9c_0$, shows that the product between the inverse of group velocity and the imaginary part of k_x is always positive. We can therefore affirm that the value of $c_a = c_0$ is an upper limit for the wave propagation stability in a waveguide bounded on the upper side by our transport equation (3).

4 Time stability of cavity modes in a finite waveguide.

The system is now a duct of finite longitudinal length, $L = 1.3m$, see Figure 11.
According to the assumption:

$$p(x, y, z, t) = p(x, y, z)e^{-\lambda t} \tag{8}$$

The eigenproblem writes:

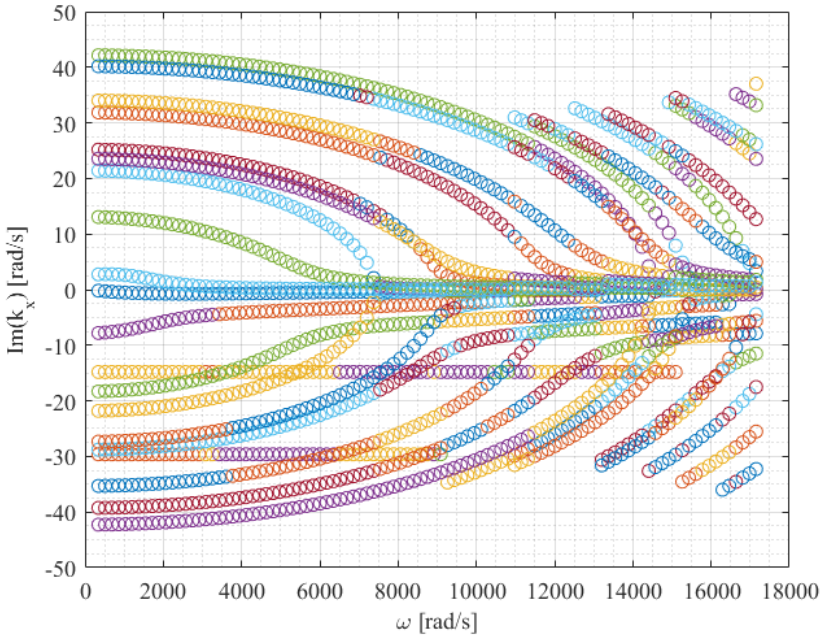


Figure 7: Imaginary part of k_x versus ω, in the case of upper side of the duct bounded by the transport equation (3), with $c_a = c_0$.

$$\begin{aligned} \nabla^2 p(x,y,z) &= \frac{\lambda^2}{c_0^2}\, p(x,y,z) && \text{in } \Omega \\ \hat{n}\cdot\vec{\nabla} p(x,y,z) &= -\frac{\lambda}{c_a}\, p(x,y,z) && \text{on B}\Omega_1 \\ \hat{n}\cdot\vec{\nabla} p(x,y,z) &= 0 && \text{on B}\Omega_2, \text{B}\Omega_3, \text{B}\Omega_4, \text{B}\Omega_5 \text{ and B}\Omega_6 \end{aligned} \tag{9}$$

The lateral sides and the input and output sections of the duct are considered as rigid (any reactive boundary condition is allowed as long as there is no damping added into the system, which would modify its stability conditions).
The real part of λ will give us the indication on stability (if $Real(\lambda) > 0 \Rightarrow$ the system is stable, if $Real(\lambda) < 0 \Rightarrow$ the system is unstable), depending upon the artificial celerity coefficient c_a.

In Figure 12 the mode which becomes unstable as soon as c_a overcomes c_0 is shown. The evolution of the $Real(\lambda)$ with c_a is shown in Figure 13.
In order to further check the convergence for the unstable eigensolution, the eigenvalue relative to cavity mode of Figure 12 for $c_a = 1.1c_0$ has been followed by varying the mesh of the FE model (see Figure 14). From Figure 14, we can affirm that the eigenvalue of the unstable cavity mode for $c_a = 1.1c_0$, converges as the mesh gets refined.

5 Conclusions

In Section 3, we have numerically demonstrated the breaking of acoustic propagation reciprocity in a 3D infinite waveguide bounded on one side by our generalized impedance (1).

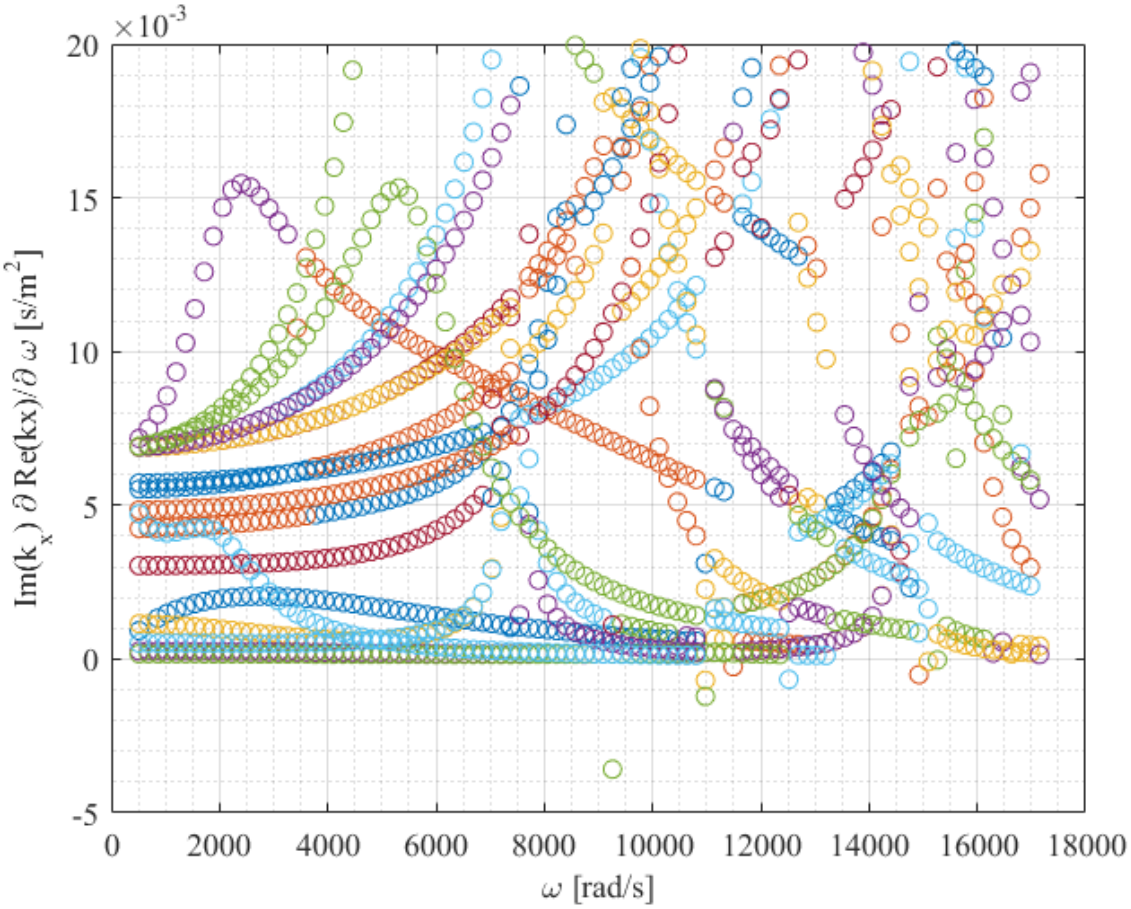


Figure 8: Plot of $\frac{\partial Real(k_x)}{\partial \omega} Imag(k_x)$, versus ω in the case of upper side of the duct bounded by the transport equation (3), with $c_a = c_0$. The numerical crossing between different eigensolutions, brings about the presence of some spurious negative values which should not be taken into account.

Moreover we have found out that for $c_a > c_0$ the transport boundary condition applied on an acoustic domain will introduce energy into the system (see Section 2), determining unstable wave propagation of duct modes (see Section 3) as well as time instability of cavity modes (see Section 4). On the other hand, for values of $c_a < c_0$ we are sure that the transport boundary condition will not introduce any instability into the system.

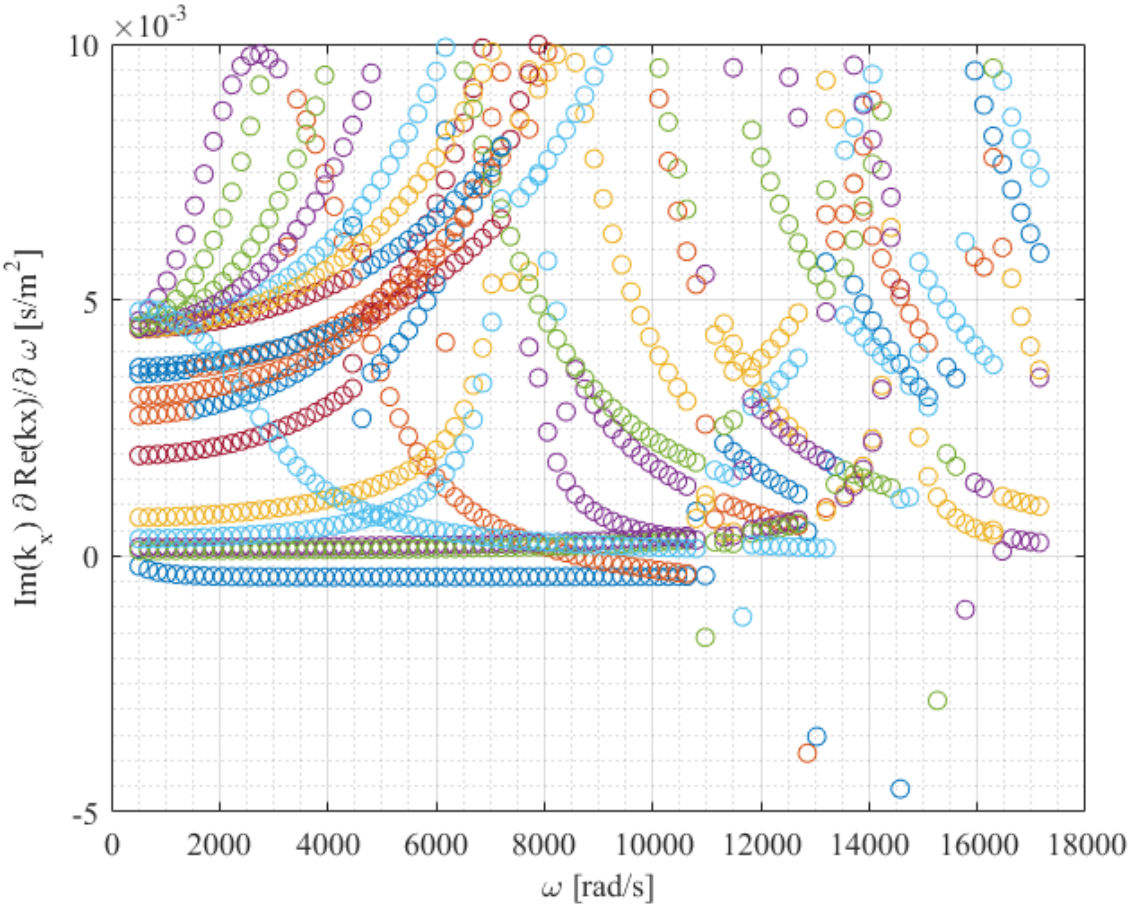


Figure 9: Plot of $\frac{\partial Real(k_x)}{\partial \omega} Imag(k_x)$, versus ω in the case of upper side of the duct bounded by the transport equation (3), with $c_a = 1.01 c_0$.

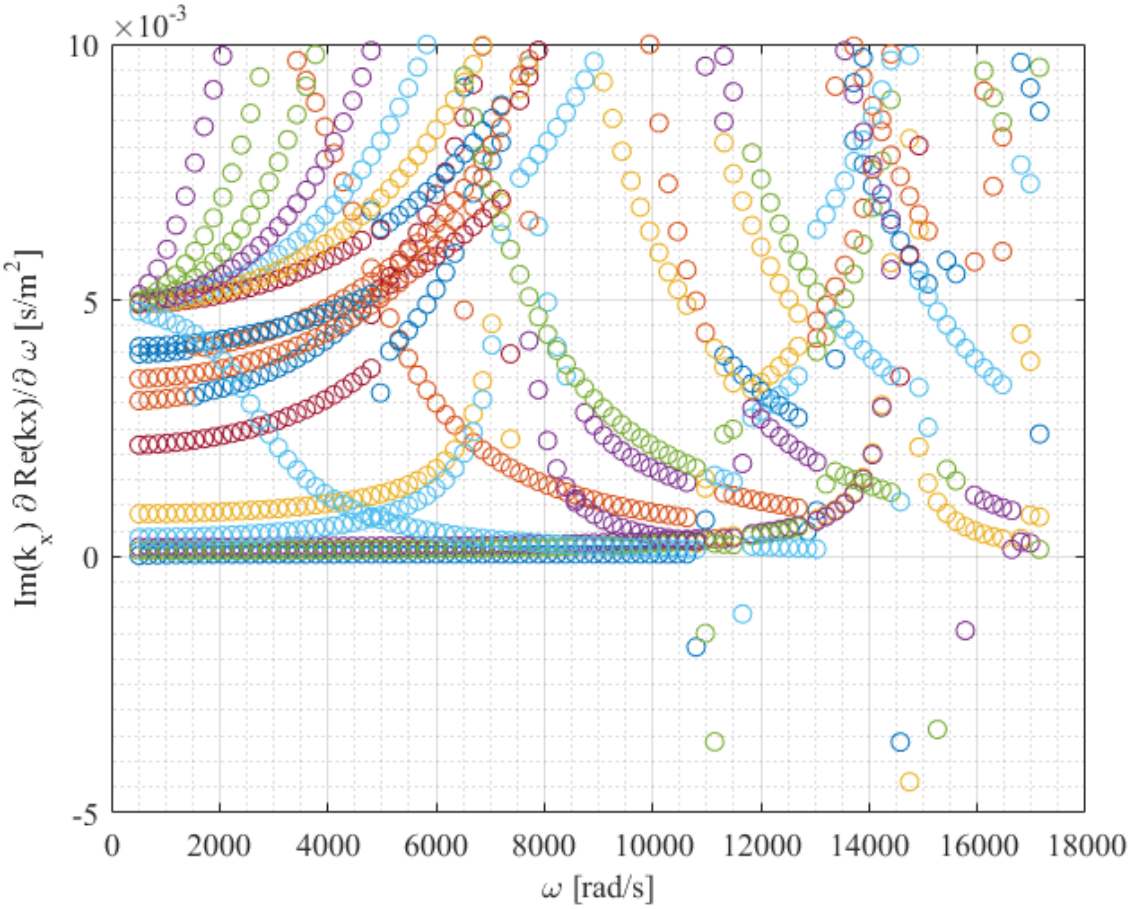


Figure 10: Plot of $\frac{\partial Real(k_x)}{\partial \omega} Imag(k_x)$, versus ω in the case of upper side of the duct bounded by the transport equation (3), with $c_a = 0.9c_0$. The numerical crossing between different eigensolutions, brings about the presence of some spurious negative values which should not be taken into account.

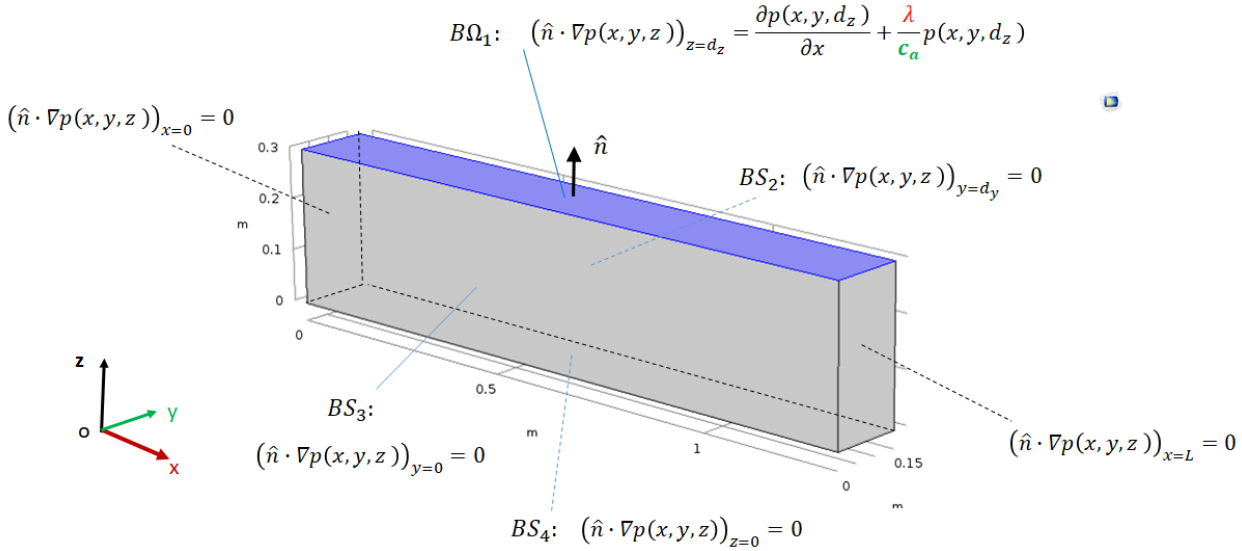
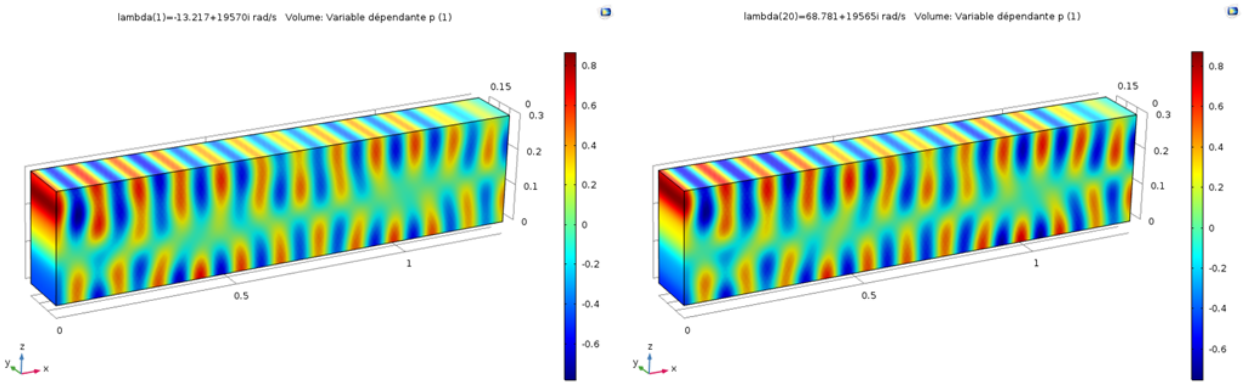


Figure 11: Finite waveguide with Transport Boundary condition applied on the upper side of the duct. The lateral sides, the input and the output sections of the duct, are considered as rigid.



(a) First unstable cavity mode for $c_a = 1.1c_0$.

(b) First unstable cavity mode for $c_a = c_0$.

Figure 12: First cavity mode becoming unstable for as soon as soon as c_a becomes bigger than c_0.

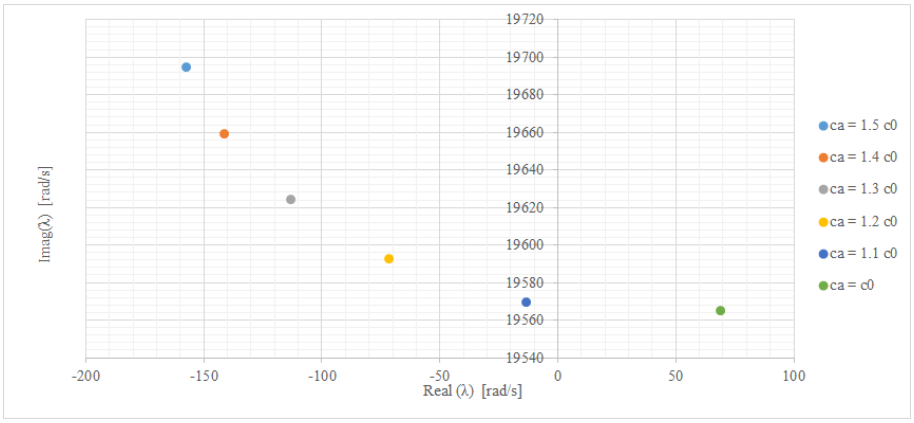


Figure 13: Root locus of the eigenvalue λ, relative to the mode of Figure 12 from $c_a = 1.5c_0$ to $c_a = c_0$.

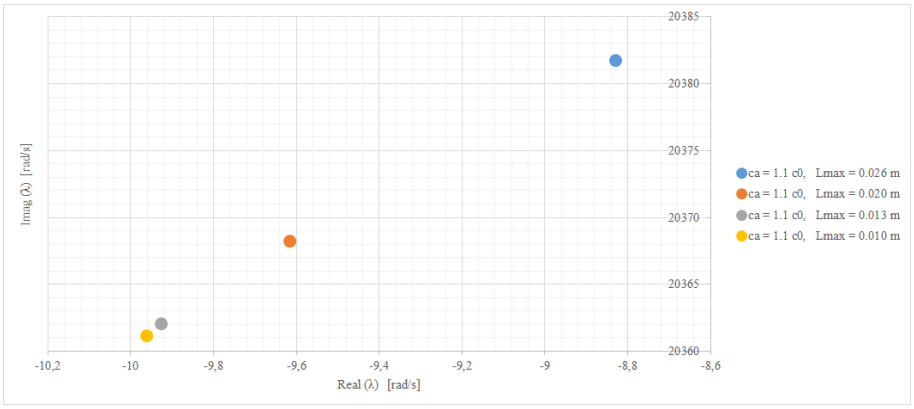


Figure 14: Unstable eigenvalue corresponding to the cavity mode of Figure 12, for $c_a = 1.1c0$, at different mesh sizes.

References

[1] M. L. Munjal, *Analysis and design of mufflers—An overview of research at the Indian Institute of Science*, J. Sound Vib. 211, 425–433 (1998).

[2] H. F. Olson and E. G. May, *Electronic sound absorber*, J. Acoust. Soc. Am. 25, 1130–1136 (1953).

[3] D. Guicking and E. Lorentz, *An active sound absorber with porous plate*, ASME J. Vib., Acoust., Stress, Reliab. Des. 106, 389–392 (1984).

[4] M. A. Galland, B. Mazeaud, and N. Sellen, *Hybrid passive/active absorbers for flow ducts*, Appl. Acoust. 66, 691–708 (2005).

[5] N. Sellen, M. Cuesta, and M. A. Galland, *Passive layer optimization for active absorbers in flow duct applications*, Ninth AIAA/CEAS Aeroacoustics Conference, AIAA Paper No. 2003-3186, (2003).

[6] G. Montseny, *Diffusive representation of pseudo-differential timeoperator*, ESAIM: Proceedings, fractional differential systems: Models, methods and applications, 5, 159–175 (1998).

[7] M.Collet, P.David, M.Berthillier, *Active acoustical impedance using distributed electrodynamical transducers*, The Journal of the Acoustical Society of America, vol. 125, no 2, p. 882-894., (2009).

[8] P. David, M. Collet, and J. M. Cote, *Experimental implementation of acoustic impedance control by 2D network of distributed smart cells*, Smart Mater. Struct., Vol. 19, no. 3, p. 035028, (2010).

[9] S. Karkar, M. Collet, *Nonreciprocal Acoustics Using Programmable Boundary Conditions: From Boundary Control and Active Metamaterials to the Acoustic Diode*. V002T03A017. 10.1115/SMASIS2017-3797 (2017).

On the noise reduction of active sidewall aircraft panels using feedforward control with embedded systems

M. Misol [1], **S. Algermissen,** [1], **M. Rose** [1]
[1] German Aerospace Center, Institute of Composite Structures and Adaptive Systems,
Lilienthalplatz 7, 38108 Braunschweig, Germany
e-mail: **malte.misol@dlr.de**

Abstract
Keeping aircraft interior noise on an acceptable level is important in modern aircraft design. There is a trade-off in the achievable transmission loss of aircraft and the additional weight of the insulation provision, especially at low frequencies. The present work focuses on narrow banded noise sources due to the rotational speed of rotors. So-called smart linings, augmented with actuators and sensors shall reduce the transmitted noise by feedforward control. Their feasibility to reduce noise at frequencies below 500 Hz (excited by a loudspeaker array) has already been tested successfully at DLR on test panels and in a fully equipped test aircraft on ground. This paper is a discussion of the recent activities to simplify the control strategies in a way that they can be implemented on small embedded systems with limited performance. In the future, such microprocessor units enable the integration of the actuators, sensors and control algorithms directly into smart lining modules, having a positive effect on maintainability and weight footprint of the smart panels.

1 Introduction

A major goal in modern aircraft design is the suppression of disturbing noise in the cabin. One promising way to reduce low frequency content is the use of active control. Different strategies have been successfully implemented in the past. The so-called active noise cancellation (ANC) uses loudspeakers to reduce the interior sound pressure by emitting anti-sound or by alternating the radiation impedance (see [1] for early results with loudspeakers and microphones in different configurations). Focusing on blade passage frequencies of around 88 Hz, reductions of 13 dB sound pressure level (SPL) have been achieved. Substituting loudspeakers by shakers or piezoelectric patch actuators in combination with the structure itself, the second major approach of active structural acoustic control (ASAC) can be used. Early results with respect to aircraft are given in [2]. In that work, a model aircraft fuselage (downscaled unstiffened aluminium cylinder) is mounted in an anechoic chamber and excited by a monopole sound source. A strong reduction of interior SPL was achieved, using as actuator one properly tuned attached mini-shaker. In this paper, a related approach for active interior noise reduction using active trim panels (linings) instead of actuated fuselage structures is investigated. In the past, experimental work of Lyle and Silcox [3] and by Tran and Mathur [4] reported unsatisfactory performance of such systems, which might be the reason, that this method has not gained much attention by researchers. In the former work, active linings are coupled to a stiffened fuselage barrel (3.66 m long with a diameter of 1.68 m) made of filament-wound graphite-epoxy composite, stiffened with frames and stringers and equipped with a plywood floor. As linings, generic sandwich structures extending from floor to floor are used. The external excitation of the fuselage barrel was realized by a loudspeaker, sealed with end caps to prevent secondary transmission pathes. The whole setup was embedded in an anechoic chamber. Augmenting the outer surface of the linings by piezoelectric patch actuators, a global SPL reduction of up to 5 dB has been documented. In view of the promising results given by Fuller and Jones [2], this was considered unsatisfactory. One explanation of the limited performance of the active linings was

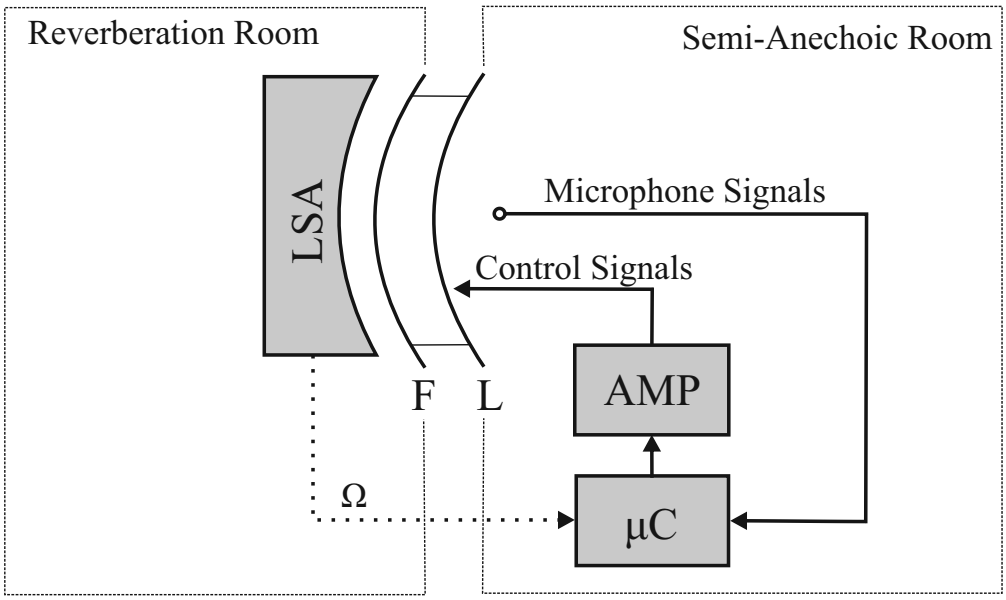


Figure 1: Schematic of the experimental setup showing the main signals and systems.

related to the different coupling of the primary excitation and the active linings into the cavity modes. In the latter work of Tran and Mathur, full-scale experiments in a McDonnell Douglas DC-9 aircraft on ground are described. As control actuators, 16 piezoelectric patches have been attached to the linings (aft section) and 32 microphones placed at the headrests and in the aisle served as sensors. Basically only one frequency out of eight have been reduced, which is not competitive to equivalent loudspeaker based ANC systems and systems with actuators on the fuselage being implemented on the same aircraft (see [4], figure 4). In conclusion, the unsatisfactory performance of the active linings is explained by the unsuitable structural dynamics of the linings, the sub-optimal actuator positions and the flanking paths. As there is no further elaboration on these possible explanations, it remains unclear, which factors are most important for the limited performance and how these limitations could be overcome. The results are very important as reference, because a real aircraft is used in the experiments with realistic structural and acoustic damping (compare also with Lyle and Silcox [3]).

In a recent publication of the lead author of this presentation [8], the noise reduction performance of active linings has been investigated in a full-scale experiment based on a Dornier Do728 aircraft. Mean SPL reductions of up to 6.8 dB are reported and in the controlled area, maximum SPL reductions of up to 11.3 dB have been achieved. In this work, the aircraft is substituted by a fuselage panel, which is mounted in a sound transmission loss facility. The aim here is to better characterize the active system in a controlled laboratory environment. A serial production Airbus A350 lining coupled to a carbon-fibre reinforced plastic (CFRP) fuselage panel with two windows was used, allowing mean SPL reductions of up to 12 dB in the anechoic room in front of the lining. A special focus of this paper is given by the control algorithm (based on Johansson [7]) and its properties to be implementable on low cost microcontroller hardware.

2 Experimental setup

The principle experimental setup is shown in figure 1. A loudspeaker array (LSA) located in the reverberation room induces the external excitation onto the primary structure (F) being a testrig of a typical aircraft fuselage segment. The active lining (L), mounted on the fuselage segment in the semi-anechoic room radiates the transmitted sound. These parts will be described in more detail in the following subsections. The real

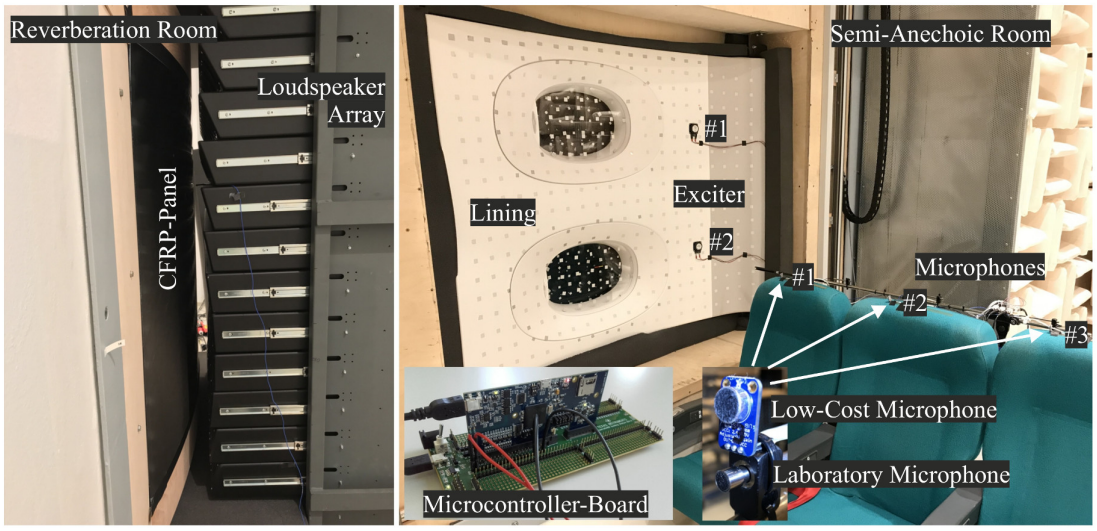


Figure 2: Excitation in reverberation room (left) and cabin side in anechoic chamber (right).

experimental setup is shown in figure 2. Three pairs of laboratory and low-cost microphones are installed at the head rest positions of the three seats in front of the lining (cp. figure 2). The signals of the three low-cost microphones are fed to the TI Delfino microcontroller unit (MCU) of the type TMS320F2837xD. These signals are A/D-converted, processed, D/A-converted and finally fed to the amplifiers (not shown) controlling the two inertial force exciters of the type Visaton EX 45 S. As can be seen in figure 2 (right), the exciters are applied at positions on the lining skin fields below the window units. The collocated laboratory microphones of the type PCB T130D21 are used for the performance evaluation of the smart lining. More details on the signal processing and the implemented control algorithm are provided in section 3.

2.1 Excitation

Currently, most aircraft are jet-driven because fuel is cheap and jet engines still have potential for improvements. Rotor engines are energy-efficient and might become more important in the future. One major drawback of rotor engines like counter-rotating open rotors (CROR) is the high sound radiation of the engines. The excitation generated by typical rotor engines of aircraft consist mainly of tonal frequencies, which are multiple of the rotational speed with respect to the number of rotor blades. These tonal frequencies induce high acoustic loads on the fuselage being transmitted into the cabin. Simulation results for a generic counter-rotating open rotor (CROR) engine suggest that the strongest excitation occurs in the frequency range of 100–500 Hz [6]. Therefore, the investigated active noise reduction system is designed for this frequency range, which contains the first five CROR frequencies: 119.4 Hz, 149.2 Hz, 268.6 Hz, 388 Hz and 417.9 Hz. The synthesis of the calculated pressure distribution on the fuselage is done with a LSA and a sound field reconstruction (SFR) method. As shown in figure 2 (left), the LSA is placed in front of the fuselage. The mean distance between the loudspeaker plane and the fuselage panel is approx. 0.14 m. The LSA has 14 rows with eight loudspeakers each. In total, there are 112 loudspeakers, which can be individually controlled to facilitate the SFR. More information on the calculation and the synthesis of the CROR pressure field can be found in [6].

2.2 Primary structure

The primary structure is defined together with DIEHL Aviation and Airbus. The main goal is the derivation of a CFRP fuselage panel that approximates the vibro-acoustic properties representative for an Airbus A350

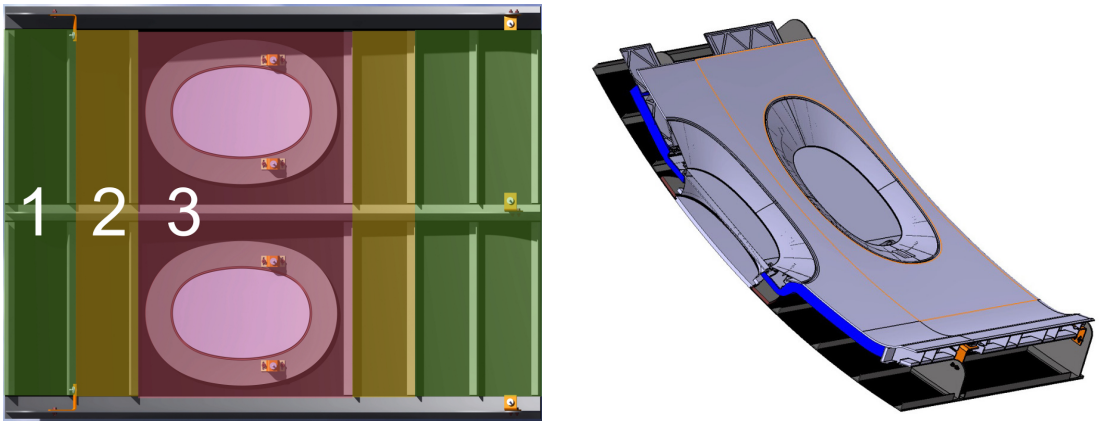


Figure 3: CFRP fuselage panel with three zones of increasing skin thickness (left) and Airbus A350 side panel coupled to fuselage with secondary thermo-acoustic isolation in blue (right). The primary isolation is suppressed in this view.

aircraft. The CFRP panel has the dimensions 1690 mm x 1300 mm (direction: frame x stringer) and a radius of 2980 mm. The skin is made of unidirectional (UD) CFRP tapes with different thicknesses in the areas 1, 2 and 3 (cp. figure 3). The skin is thinnest in area 1 and thickest in area 3. The fuselage has two windows with 15 mm thick plexiglass window panes and two 12 mm thick aluminum window frames. The window frames are glued to the CFRP skin. The stringers and frames are made of aluminum in a L- and T-shape geometry. The spacing of the stringers is 200 mm and the spacing of the frames is 635 mm. The primary structure is mounted in the test opening of the transmission loss facility by means of four shock mounts located near the corners of the panel. Each shock mount is connected to the outer frame on one side and to the embrasure of the test stand on the other side. A small air gap between the four panel edges and the test opening is sealed with flexible tape. This kind of mounting leads to a dynamic decoupling in the frequency range of interest. The lining itself is mounted to the primary structure at 9 positions near the frames or the windows (cp. figure 3). The secondary structure is a serial production sidewall panel from DIEHL Aviation for the Airbus A350 series. It has 9 structural holders which are connected to the counterparts on the fuselage. The lining is equipped with a thermo-acoustic isolation bag applied at the backside. Prior to the mounting of the lining a primary thermo-acoustic isolation is applied to the fuselage. A sectional view of the coupled system without primary isolation is shown in figure 3.

2.3 Active lining

Each smart lining is equipped with two inertial force actuators of the type Visaton EX 45 S. This type of actuator has a maximum rms power of 10 W and a mass of 0.06 kg. The number and positions of the actuators are not optimized. It is known from preliminary tests that – because of the relatively high structural damping of the double panel system – the modal behavior is weakly pronounced. Therefore, it is considered appropriate to position the actuators in a straightforward manner. The positions can be seen in figure 2. In order to ensure sufficient control authority, the structural vibration of the lining and the SPL at the seats induced by the loudspeaker array are compared to the values generated by the actuators. A more elaborate actuator placement based on genetic optimization is described in [5]. A simple approach is also followed with regard to the error microphones. Each head rest is equipped with one microphone (cp. figure 2). The control system configuration described here, uses three electret microphones with preamplifier unit of the type MAX 4466 as error sensors. The error sensor signals are processed by the TI Delfino microcontroller unit (MCU) of the type TMS320F2837xD and fed to the actuators via the amplifier. A cheap and small class D stereo audio amplifier can be used to drive the actuators. Before the integration of these components into the smart lining, the microphones have to be replaced by a number of structural sensors and a suitable

observer filter. This task is not part of the research work described here.

3 Control algorithm

In view of manageable and mostly autonomous units, it is desirable to integrate the control hardware in the active panel substructures. To additionally minimize the overall costs, the use of cheap and small microcontroller boards is of high interest. In figure 4, the choosen hardware, a TMS320F2837xD board from *Texas Instruments*, is shown. It consists of two 32 bit CPUs with 200 MHz clock frequency and has four sixteen bit analog digital converters (ADC) and three twelve bit digital analog converters (DAC). To enable quick changes in the algorithm, the use of the simulation environment *MATLAB/SIMULINK* is convenient. A suitable toolbox is available to compile and run the control algorithms via USB connection on the evaluation board. The underlying overhead using this toolbox can be avoided by coding the algorithms directly in the C language, but this was not necessary yet.

The control algorithm itself is adopted from Johansson et al. [7]. It is based on a complex filtered-x LMS algorithm, which realizes a narrowband multiple-reference feedforward controller. We have R complex reference signals $x_r(n)$ (the engine drives including their harmonics at angular frequency ω_r, $r = 1, \ldots, R$), A actuators and S sensors. n denotes the sample number in the discrete time domain. The system dynamics are described by R complex matrices $\boldsymbol{F}_r$, each of dimension $S \times A$. These matrices can be obtained from the measured frequency response functions at the given frequencies. Johansson describes a method to keep the reference signals in sync with the engines using suitable filters based on fast fourier transformations (FFT). For simplicity, in our implementation the reference signals are completely software generated and the phase drifts are also adapted by the LMS algorithm with only minor degradation in performance, if the frequencies ω_r are suitable stable. With this algorithm each actuator is individually controlled by one adaptive complex FIR filter weight per frequency. This permits a very efficient implementation even in the case of close frequencies (beating), which might arise if the rotors are not perfectly synchronized. Hence, each smart lining uses $A \cdot R = 2 \cdot 5 = 10$ adaptive complex filter weight to control the five frequencies. There are R complex weight vectors $\boldsymbol{w}_r(n)$ of dimension $A \times 1$ as parameters for the finite impulse response (FIR) filter of the x-LMS algorithm. The square $J(n) = |\boldsymbol{e}(n)|^2$ of the error signal vector

$$\boldsymbol{e}(n) = \boldsymbol{d}(n) + \sum_{r=1}^{R} \Re\left\{\boldsymbol{F}_r \boldsymbol{y}_r(n)\right\} = \boldsymbol{d}(n) + \sum_{r=1}^{R} \Re\left\{\boldsymbol{F}_r \boldsymbol{w}_r(n) x_r(n)\right\}, \quad \text{with} \quad \boldsymbol{y}_r = \boldsymbol{w}_r x_r, \tag{1}$$

should be minimized by the filtered-x LMS algorithm. Here $\boldsymbol{d}(n)$ denotes the external disturbances, which has the same dimension $S \times 1$ as the error vector $\boldsymbol{e}(n)$. The adaptation of the weight vectors

$$\boldsymbol{w}_r(n+1) = \boldsymbol{w}_r(n) - \boldsymbol{M}_r \frac{\partial J(n)}{\partial \overline{\boldsymbol{w}}_r}. \tag{2}$$

is done using some damped Newton type method or a scaled steepest descend direction in the simplest case, depending on the choice of the scaling matrix $\boldsymbol{M}_r$ of dimension $A \times A$. The gradient is simply

$$\frac{\partial J(n)}{\partial \overline{\boldsymbol{w}}_r} = 2\overline{x}_r(n) {\boldsymbol{F}_r}^H \boldsymbol{e}(n). \tag{3}$$

Here $(\cdot)^H$ denotes the conjugate transpose. The Newton-like algorithm needs a fully populated matrix

$$\boldsymbol{M}_r = \mu_0 \left(\rho_r {\boldsymbol{F}_r}^H \boldsymbol{F}_r\right)^{-1}, \quad \text{with} \quad \rho_r = E\{|x_r(n)|^2\}. \tag{4}$$

To avoid the costly matrix multiplication in equation (2), a diagonally dominant approximation

$$\boldsymbol{M}_r = \mu_0 \left(\rho_r \text{diag}\left({\boldsymbol{F}_r}^H \boldsymbol{F}_r\right)\right)^{-1} \tag{5}$$

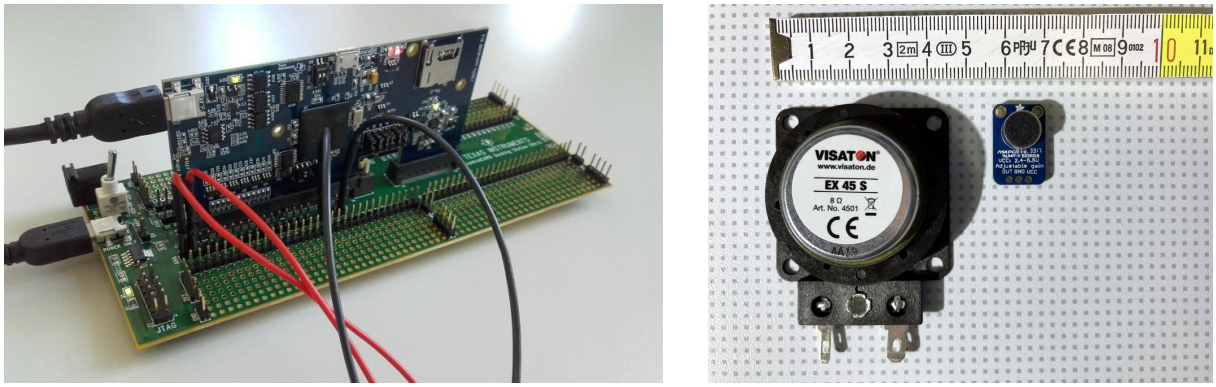


Figure 4: Evaluation board with low-cost microcontroller unit TI Delfino TMS320F2837xD (left) and exciter Visaton EX 45 S and electret microphone with preamplifier unit MAX 4466 (right).

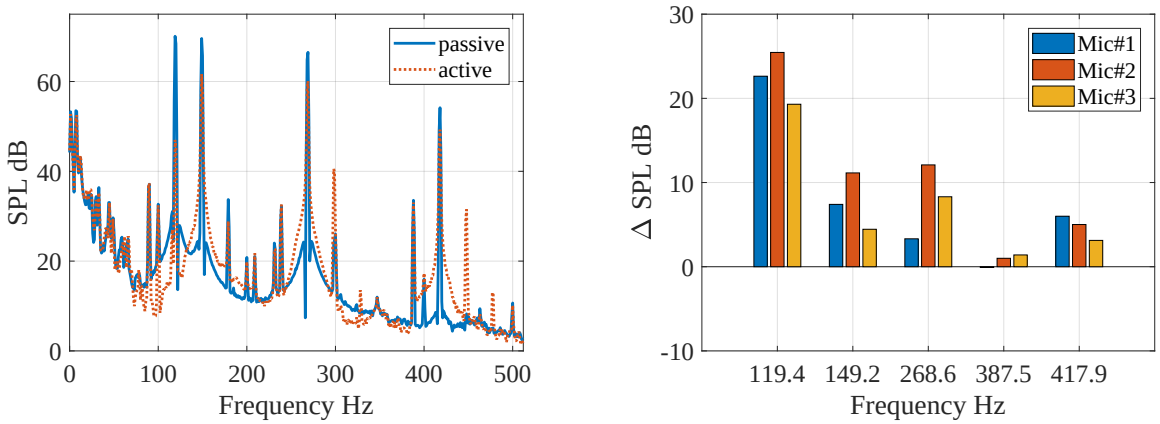


Figure 5: Mean SPL with de-activated (passive) and activated smart lining (active) (left) and SPL reductions achieved by the active system at the five CROR frequencies measured at the head rests (right).

of $\boldsymbol{M}_r$ is choosen, according to equation (8) of [7]. Stability of the algorithm can be expected for positive values μ_0 smaller then one (though not guaranteed). In fact only substantially smaller values $\mu_0 \approx 0.001$ provided convergence. One reason could be the strong coupling of the actuators to the sensors and the corresponding weak approximation of $\boldsymbol{M}_r$ by a diagonal matrix. In further studies, equation (4) will be used to investigate this hypothesis and as a result possibly increasing the performance.

4 Results

The acoustic performance of the smart lining with low-cost hardware is shown in figure 5. The main reduction occurs at the first blade-passing frequency 119.4 Hz. There, the mean SPL reduction amounts to 23 dB and the maximum SPL reduction measured at microphone 2 is 25 dB. It is shown in Misol [8] that in a real aircraft cabin, the SPL drops about 10 dB from the window to the aisle seat. Therefore, it was expected that the SPL reduction is largest at microphone 1 and smallest at microphone 3. This, however, is not the case because the results show mean SPL reductions of 8.3 dB at microphone 1, 12.2 dB at microphone 2 and 5.1 dB at microphone 3. This effect is also visible in the right hand part of figure 5 that shows the SPL reductions measured by the three microphones at the CROR frequencies. Although the smart lining processes the signals of the low-cost microphones, the results are based on the laboratory microphone signals.

5 Conclusion and Outlook

In this work, an active feedforward control system for a serial production Airbus A350 lining coupled to a CFRP fuselage panel with two windows has been discussed. The experimental setup is realized in a sound transmission loss facility with an semi-anechoic room on the cabin side. The chosen control algorithm is described and successfully realized on a low-cost microcontroller unit allowing tonal reductions up to 23 dB mean SPL and reductions up to 12 dB mean SPL for the energetic sum of all five frequencies. Further investigations will be done to enhance robustness by advanced choices of the feedforward adaptation gain factors. Ongoing research aims at the replacement of microphones by a number of structural sensors and the integration of the smart lining components suitable for production.

Acknowledgements

This project was funded by the Bundesministerium für Wirtschaft und Energie (BMWi) under grant number 20K1301D.

Supported by:

Federal Ministry for Economic Affairs and Energy

on the basis of a decision by the German Bundestag

References

[1] S. J. Nelson, P. A. Nelson, I. M. Stothers, C. C. Boucher, *In-flight experiments on the active control of propeller-induced cabin noise*, Journal of Sound and Vibration, 140 (2), 219–238, (1990).

[2] C. R. Fuller, J. D. Jones, *Experiments on reduction of propeller induced interior noise by active control of cylinder vibration*, Journal of Sound and Vibration, 112 (2), 389–395, (1987).

[3] K. H. Lyle, R. J. Silcox, *A study of active trim panels for interior noise reduction in an aircraft fuselage*, SAE Technical Paper, 05, SAE International, (1995).

[4] B. N. Tran, G. P. Mathur, *Aircraft interior noise reduction tests using active trim panels*, Proceedings of Noise-Con 96, pp. 395–400, (1996).

[5] M. Misol, T. Haase, S. Algermissen, V. Papantoni, H. P. Monner, *Lärmreduktion in Flugzeugen mit aktiven Linings*, Smarte Strukturen und Systeme – Tagungsband des 4SMARTS-Symposiums, Shaker Verlag, 329–339, (2017).

[6] S. Algermissen, S. Meyer, C. Appel, H. P. Monner, *Experimental synthesis of sound pressure fields for active structural acoustic control testing*, Journal of Intelligent Material Systems and Structures, 140 (7), 881–889, (2014).

[7] S. Johansson, P. Sjösten, S. Nordebo, I. Claesson, *Comparison of multiple-and single-reference mimo active noise control approaches using data measured in a dornier 328 aircraft*, International Journal of Acoustics and Vibrations, 5 (2), 77–88, (2000).

[8] M. Misol, *Experiments on noise reduction in aircraft with active sidewall panels*, Proceedings of 25th International Congress on Sound and Vibrations, 8-12 Juli, Hiroshima, (2018).

A multimodal nonlinear piezoelectric vibration absorber

G. Raze[1], **B. Lossouarn**[2], **A. Paknejad**[3], **G. Zhao**[3], **J.-F. Deü**[2], **C. Collette**[3], **G. Kerschen**[1]
[1] Department of Aerospace and Mechanical Engineering, University of Liège,
Allée de la Découverte 9, 4000 Liege, Belgium
e-mail: **G.Raze@uliege.be**

[2] Laboratoire de Mécanique des Structures et des Systèmes Couplés, Conservatoire national des arts et métiers, 292 Rue Saint-Martin, 75003 Paris, France

[3] Department of Bio-, Electro- and Mechanical Systems, Precision Mechatronics Laboratory, Université Libre de Bruxelles, Av. F.D Roosevelt 50, 1050 Brussels, Belgium

Abstract
This paper presents a design methodology for a piezoelectric vibration absorber able to damp multiple nonlinear resonances. The design of multimodal linear piezoelectric absorbers is first reviewed. Next, based on the dynamics of the structure to which linear absorbers are attached, the design is extended to the nonlinear regime. The methodology is inspired from a principle of similarity: if a nonlinearity of one type is present in the host structure, the same type of nonlinearity is used in the absorbers. An explicit semi-analytical expression of the nonlinear coefficients in the absorber is obtained thanks to a first-order harmonic balance and a straightforward series expansion. Numerical examples are analysed to demonstrate the efficiency of the proposed approach.

1 Introduction

Owing to stringent requirements on performance, low-emission regulations and increasing price of energy, mechanical structures in the aerospace industry are becoming more lightweight, which makes them prone to experience high-amplitude vibrations. These structures can be subjected to broadband or multiharmonic forcing excitations. For sufficiently high forcing amplitudes, the induced motion can trigger nonlinearities such as geometric nonlinearities, contact or friction in bolted connections.

Among the existing possibilities for vibration mitigation, the piezoelectric vibration absorber appears as an attractive option: it does not include additional moving parts, the absorption system can be localised away from the points where the vibratory amplitude is critical and it eases the implementation of semi-active control. The first use of a piezoelectric vibration absorber is attributed to Forward [1]. Hagood and von Flotow [2] later provided design rules for piezoelectric shunts. Ever since that pioneering work, there has been a growing body of literature on the subject.

Real-life structures exhibit multiple resonances. If the excitation spectrum is not localised around a specific frequency, several modes can be excited simultaneously. Edberg et al [3] first proposed a two-mode shunt circuit connected to a single piezoelectric patch to damp simultaneously two structural modes. Hollkamp [4] later generalised it to any number of modes. The circuit of Hollkamp is unfortunately not easy to tune. Wu [5] proposed a multimodal current blocking shunt circuit with an associated design methodology. Despite its efficiency, the number of required electrical components grows quadratically with respect to the number of mode to be controlled. It makes the use of this circuit impractical for a large number of modes. Behrens et al [6] proposed a simplified multimodal current flowing shunt circuit, requiring one RLC branch per mode to be damped. Interestingly, another approach involving the connection of a mechanical structure to its

electrical analogue through multiple piezoelectric patches can serve the same purpose, as done by Lossouarn et al [7].

A linear absorber is detuned when nonlinearities arise due to high forcing amplitudes, and its performance might be substantially reduced. Through the intentional and adequate use of nonlinearities in the absorber, this detrimental effect can be significantly mitigated. Habib and Kerschen [8] showed that the design of a general nonlinear vibration absorber can be guided by a principle of similarity. This principle states that the mathematical form of the nonlinearity in the absorber should be identical to that of the primary structure. The range of forcing amplitudes in which the absorber is efficient can therefore be extended. Soltani and Kerschen [9] applied successfully this principle to a single-mode piezoelectric absorber, the nonlinear piezoelectric tuned vibration absorber (NPTVA), which was later experimentally realised by Lossouarn et al [10].

This paper brings together the multimodal and nonlinear aspects and proposes a multimodal nonlinear piezoelectric vibration absorber for the mitigation of multiple nonlinear resonances of mechanical systems using a single piezoelectric transducer. Nonlinearities are located in a shunt circuit with multiple branches, each tuned to a specific resonance frequency. The electrical nonlinearities are implemented using nonlinear capacitors. Their mathematical form is chosen thanks to a principle of similarity. An explicit expression of the nonlinear coefficients is obtained with a first-order harmonic balance method followed by a series expansion. The resulting absorber is able to effectively damp several nonlinear resonances.

2 Linear piezoelectric vibration absorber

This section briefly reviews the concepts of single-mode and multi-mode piezoelectric vibration absorbers. The linear absorbers are designed independently of the nonlinearities in the primary structure, and serve as a baseline for the design of nonlinear absorbers.

2.1 Single-mode piezoelectric vibration absorber

The purpose of a single-mode vibration absorber is to mitigate the vibration of its host structure. In Figure 1(a), the host structure is represented by a modal spring k and a modal mass m. The classical resonant shunt, as studied by Hagood and von Flotow [2], consists in connecting an series RL circuit to the electrodes of a piezoelectric material (in this case a piezoelectric stack) as shown in Figure 1(b). The piezoelectric material is a transducer, and is represented by both a mechanical and an electrical model. Mechanically, it behaves as a spring $k_{p,oc}$ (the stiffness of the piezoelectric element when its electrodes are open-circuited) in parallel with a force source f_p proportional to the charge in the piezoelectric element (Figure 1(a)). Electrically, it may be represented as a voltage source V_p proportional to the strain in the piezoelectric material in series with a capacitor C_p^ε (the capacitance of the piezoelectric material at constant strain). By connecting an inductor L and a resistor R to the electrodes of the piezoelectric material, a resonant RLC circuit is therefore created (Figure 1(b)). The tuning of the inductance and resistance is made according to the objectives at stake. The most common objectives include the minimisation of the H_∞ norm of the receptance [11] or the maximisation of modal damping [2].

2.2 Multimodal piezoelectric vibration absorber

One of the interesting features of the piezoelectric vibration absorber is that it can simultaneously mitigate the vibration of several modes of different frequencies if properly designed. Among the proposed approaches in the literature, one of the simplest is the current flowing shunt circuit proposed by Behrens et al [6]. This circuit is depicted in Figure 2. It consists in N resonant RLC branches, each tuned to a specific mode. It can resonate at N different frequencies, providing the possibility for multimodal shunt damping with a single piezoelectric transducer.

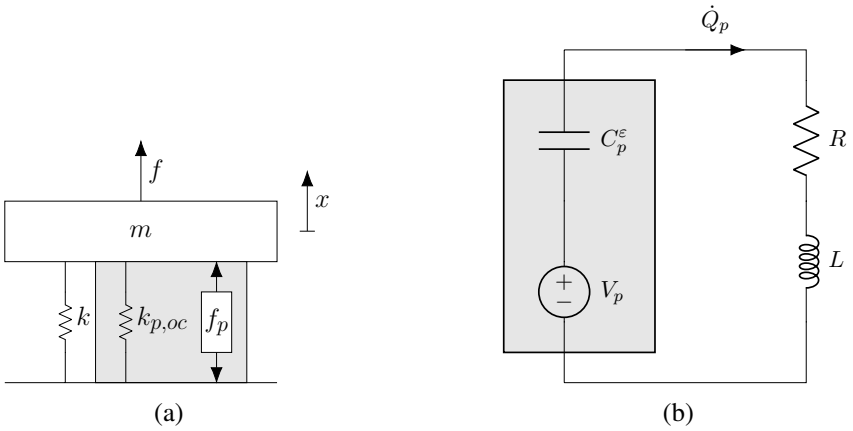


Figure 1: Single-mode resonant piezoelectric shunt: mechanical representation (a) and electrical representation (b).

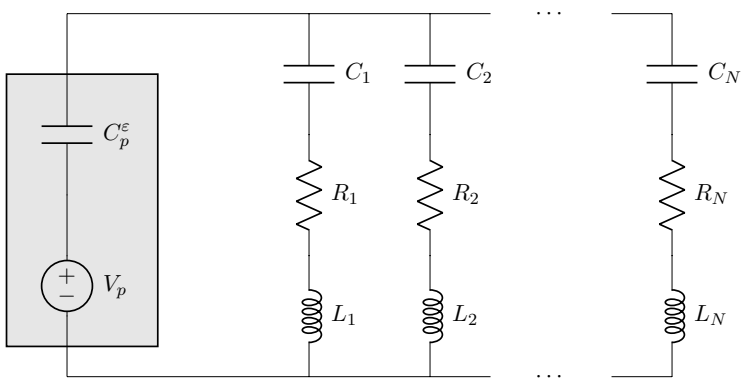


Figure 2: Current flowing shunt circuit.

The tuning methodology for this circuit relies on a model such as the one developed in the next subsection, and is therefore postponed to Subsection 2.4.

2.3 Model of a piezoelectric structure

A model of coupled second-order ordinary differential equations of the coupled electromechanical system is now derived. This model is necessary for the design of the absorbers, as discussed in the next subsection. The dynamics of the piezoelectric structure is governed by the following linear ordinary differential equations

$$\mathbf{M}_s\ddot{\mathbf{x}}_s + \mathbf{C}_s\dot{\mathbf{x}}_s + \mathbf{K}_s\mathbf{x}_s = \mathbf{f}_s + \mathbf{f}_p, \tag{1}$$

in which $\mathbf{M}_s$, $\mathbf{C}_s$ and $\mathbf{K}_s$ are the structural mass, damping and stiffness matrices (including the mechanical characteristics of the piezoelectric material), respectively, $\mathbf{x}_s$ is the vector of generalised degrees of freedom, $\mathbf{f}_s$ is the vector of generalised loading and $\mathbf{f}_p$ represents the generalised loading generated by the force source in the piezoelectric element. If Q_p is the charge in the piezoelectric material, this loading is given by

$$\mathbf{f}_p = \theta_p\mathbf{B}_pQ_p, \tag{2}$$

where $\mathbf{B}_p$ is an influence vector [12] and θ_p is a piezoelectric coupling coefficient. Since all the branches of the current flowing circuit are in parallel, they are subjected to the same voltage difference V. Then, if q_i is

the electrical charge in the i^{th} branch,

$$L_i\ddot{q}_i + R_i\dot{q}_i + \frac{1}{C_i}q_i = V_i = V, \qquad \forall i \in [1, ..., N], \tag{3}$$

where L_i, R_i and C_i respectively are the inductance, resistance and capacitance of the i^{th} branch of the current flowing circuit represented in Figure 2. The voltage difference V is also the voltage across the electrodes of the piezoelectric material. It is given by the strain-driven voltage source of the piezoelectric material V_p, minus the voltage drop across the piezoelectric capacitance $V_{C_p^\varepsilon}$.

$$V = V_p - V_{C_p^\varepsilon} = \theta_p \mathbf{B}_p^T \mathbf{x}_s - \frac{1}{C_p^\varepsilon} Q_p \tag{4}$$

The superscript T denotes a transposition. Charge conservation imposes the following equality

$$Q_p = \sum_{i=1}^{N} q_i. \tag{5}$$

Combining Equations (3), (4) and (5) and introducing the vector of electric charges $\mathbf{x}_e = [q_1, ..., q_N]^T$ yields

$$\mathbf{M}_e\ddot{\mathbf{x}}_e + \mathbf{C}_e\dot{\mathbf{x}}_e + \mathbf{K}_e\mathbf{x}_e = \theta_p \mathbf{1}_{N\times 1}\mathbf{B}_p^T\mathbf{x}_s = \mathbf{\Theta}\mathbf{x}_s, \tag{6}$$

in which $\mathbf{M}_e$, $\mathbf{C}_e$ and $\mathbf{K}_e$ are the electrical mass, damping and stiffness matrices, respectively, given by

$$\mathbf{M}_e = \mathbf{diag}([L_1, ..., L_N]), \tag{7}$$

$$\mathbf{C}_e = \mathbf{diag}([R_1, ..., R_N]), \tag{8}$$

$$\mathbf{K}_e = \mathbf{diag}\left(\left[\frac{1}{C_1}, ..., \frac{1}{C_N}\right]\right) + \frac{1}{C_p^\varepsilon}\mathbf{1}_{N\times N}, \tag{9}$$

$\mathbf{1}_{m\times n}$ is a matrix of size $m \times n$ filled with ones and $\mathbf{\Theta}$ is an electromechanical coupling matrix. Eventually, a system of coupled electromechanical equations is obtained by combining Equations (1), (2) and (6).

$$\begin{bmatrix} \mathbf{M}_s & \mathbf{0} \\ \mathbf{0} & \mathbf{M}_e \end{bmatrix} \begin{bmatrix} \ddot{\mathbf{x}}_s \\ \ddot{\mathbf{x}}_e \end{bmatrix} + \begin{bmatrix} \mathbf{C}_s & \mathbf{0} \\ \mathbf{0} & \mathbf{C}_e \end{bmatrix} \begin{bmatrix} \dot{\mathbf{x}}_s \\ \dot{\mathbf{x}}_e \end{bmatrix} + \begin{bmatrix} \mathbf{K}_s & -\mathbf{\Theta}^T \\ -\mathbf{\Theta} & \mathbf{K}_e \end{bmatrix} \begin{bmatrix} \mathbf{x}_s \\ \mathbf{x}_e \end{bmatrix} = \begin{bmatrix} \mathbf{f}_s \\ \mathbf{0} \end{bmatrix}. \tag{10}$$

Equation (10) may be written in a more compact form

$$\mathbf{M}\ddot{\mathbf{x}} + \mathbf{C}\dot{\mathbf{x}} + \mathbf{K}\mathbf{x} = \mathbf{f}, \tag{11}$$

with $\mathbf{x}^T = [\mathbf{x}_s^T \ , \ \mathbf{x}_e^T]$.

2.4 Design of the electrical circuit

In the current flowing circuit proposed by Behrens et al [6], one of the electrical elements of each branch can be chosen arbitrarily. In that paper, the choice of the filter capacitances is arbitrary, the tuning of the inductances of the current flowing circuit is straightforward, and the tuning of the resistances requires an optimisation algorithm as the one proposed by Fleming et al [13]. However, no explanation was given on the impact of the choice of the filter capacitances. The effect of placing a parallel capacitance across the terminals of the piezoelectric material was shown to influence the damping performance of a single-mode shunt circuit by Fleming et al [14]. The subsequent work of Cigada et al [15] highlighted the influence of the filter capacitances in the case of the current flowing circuit. They showed that a higher filter capacitance enables a better control capability on the mode it is associated to. Unfortunately, increasing the filter capacitance also increases the coupling between the different branches of the circuit. It was shown that the tuning rule of [6] started to fail as the filter capacitances were increased because of this increased coupling. An optimisation algorithm was also proposed in that paper to tune the inductances so as to set the resonance frequencies of the circuit properly.

In this paper, the choice of the filter capacitance is made beforehand, and a two-step optimisation algorithm is used to tune the remaining electrical parameters. First, following the proposition of Cigada et al [15], the inductances are tuned so that the undamped electrical circuit (the circuit without resistors) has the desired resonance frequencies. In the case of multimodal shunt damping, these resonance frequencies should match these of the structural modes that have to be damped. Then, the resistances are computed using the optimisation algorithm proposed in [13].

For the first step of the algorithm, the cost function is defined as

$$f(L_1, ..., L_N) = \sum_{i=1}^{N} (\omega_{e,i}^2 - \omega_{s,i}^2)^2, \tag{12}$$

where $\omega_{e,i}$ is the i^{th} resonance frequency of the electrical circuit and $\omega_{s,i}$ is its targeted value. Since the square of $\omega_{e,i}$ are the eigenvalues of the matrix $\mathbf{M}_e^{-1}\mathbf{K}_e$, their sensitivity to the inductance L_j can be computed analytically (Van der Aa et al [16]) as

$$\frac{\partial \omega_{e,i}^2}{\partial L_j} = -\mathbf{\Phi}_e^{-1}\mathbf{M}_e^{-1}\frac{\partial \mathbf{M}_e}{\partial L_j}\mathbf{M}_e^{-1}\mathbf{K}_e\mathbf{\Phi}_e, \tag{13}$$

where $\mathbf{\Phi}_e$ is the matrix of right eigenvectors of $\mathbf{M}_e^{-1}\mathbf{K}_e$. The sensitivity of the cost function is then

$$\frac{\partial f}{\partial L_j} = 2\sum_{i=1}^{N}(\omega_{e,i}^2 - \omega_{s,i}^2)\frac{\partial \omega_{e,i}^2}{\partial L_j}. \tag{14}$$

With this formulation, an unconstrained optimisation algorithm can readily be used. Once the resonance frequencies of the undamped electrical circuit are tuned, the second step of the algorithm consists in tuning the resistances values with the algorithm proposed in [13]. This algorithm is based on a state-space model of the whole structure and aims at minimising the H_2 norm of the receptance. With the model proposed in Subsection 2.3, the state-space matrices $\tilde{\mathbf{A}}$ and $\tilde{\mathbf{B}}$ can be readily built:

$$\tilde{\mathbf{A}} = \begin{bmatrix} \mathbf{0} & \mathbf{I} \\ -\mathbf{M}^{-1}\mathbf{K} & -\mathbf{M}^{-1}\mathbf{C} \end{bmatrix}, \qquad \tilde{\mathbf{B}} = \begin{bmatrix} \mathbf{0} \\ \mathbf{M}^{-1}\mathbf{f} \end{bmatrix}. \tag{15}$$

The state-space matrix $\tilde{\mathbf{C}}$ is chosen according to the choice of the degree of freedom at which the H_2 norm of the transfer function has to be minimised. The three state-space matrices can then be used in the algorithm of [13].

Another objective for the choice of the resistances could have been the optimisation of the H_∞ norm of the receptance, yielding the so-called equal-peak design. This kind of optimisation is often harder to accomplish than the H_2 optimisation and is beyond the scope of this paper. Nevertheless, the H_2 optimisation algorithm can provide nearly-equal peaks and is not that far from the H_∞ optimum.

3 Nonlinear piezoelectric vibration absorber

Real-life structures often depart from their ideal linear behaviour as the forcing amplitude increases. The inherent nonlinearities in the primary structure might have undesirable effects on the performance of the absorbers. Using nonlinearities in the absorbers as well can benefit their performance. This section proposes a design methodology for these nonlinear absorbers. It is assumed that the linear absorbers have already been tuned.

3.1 A principle of similarity

In [8], the authors showed that an intentional and adequate use of nonlinearities in a vibration absorber coupled to a nonlinear structure could substantially improve its performance. The nonlinearities have to be chosen according to a principle of similarity: they should have the same mathematical form as those of the primary structure.

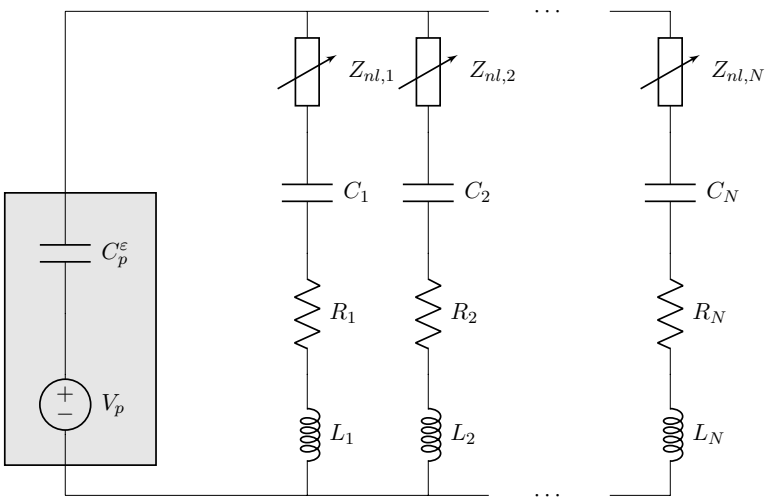


Figure 3: Nonlinear current flowing shunt circuit.

Figure 3 depicts the general arrangement of a nonlinear current flowing circuit. Essentially nonlinear impedances are considered to reflect the effect of the nonlinearities in the primary structure. Their arbitrary placement is guided by the behaviour of the linear current flowing circuit. It is expected that each nonlinear impedance will have a pronounced effect on the mode to which its branch is tuned. The physical type of the nonlinear impedance is made depending on practical considerations such as availability of the components. For instance, a nonlinear stiffness may be controlled with a nonlinear capacitor [9]. Another possibility is to use saturable inductors as in [10]. Once the type of nonlinear components has been chosen, it is necessary to determine their coefficients. In the following sections, a design methodology is proposed.

3.2 Nonlinear frequency response

Using the same formalism as Habib and Kerschen [17], the coupled nonlinear electromechanical equations are

$$\mathbf{M}\ddot{\mathbf{x}} + \mathbf{C}\dot{\mathbf{x}} + \mathbf{K}\mathbf{x} + k_{nl}\left(\mathbf{b}_{nl}(\mathbf{x}) + \sum_{i=1}^{N} b_{nl,i}\mathbf{b}_{nl,i}(\mathbf{x})\right) = \mathbf{f}(t), \tag{16}$$

where $\mathbf{b}_{nl}$ represents the nonlinearities in the primary structure, and $\mathbf{b}_{nl,i}$ are the nonlinearities in the absorbers. According to the principle of similarity, the latter are chosen to have the same mathematical form as the former. In the following, it is assumed that the nonlinearities are cubic. The remaining unknowns are the nonlinear coefficients of the absorbers, $b_{nl,i}$.

The coupled electromechanical equations are normalised considering $\mathbf{y} = \mathbf{x}/f_0$

$$\mathbf{M}\ddot{\mathbf{y}} + \mathbf{C}\dot{\mathbf{y}} + \mathbf{K}\mathbf{y} + \alpha_3\left(\mathbf{b}_{nl}(\mathbf{y}) + \sum_{i=1}^{N} b_{nl,i}\mathbf{b}_{nl,i}(\mathbf{y})\right) = \frac{\mathbf{f}(t)}{f_0}, \tag{17}$$

in which $\alpha_3 = k_{nl}f_0^2$ for cubic nonlinearities. The nonlinearity parameter α_3 quantifies the effects of both the nonlinearity and the forcing. The solution of Equation (17) under a harmonic forcing can be approximated with a first-order harmonic balance (HB) method. Using

$$\mathbf{y} = \mathbf{q}_c\cos(\omega t) + \mathbf{q}_s\sin(\omega t), \tag{18}$$

and introducing $\mathbf{q}^T = [\mathbf{q}_c^T, \mathbf{q}_s^T]$, Equation (17) becomes

$$\mathbf{W}\mathbf{q} + \alpha_3\left(\mathbf{d}_{1,nl}(\mathbf{q}) + \sum_{i=1}^{N} b_{nl,i}\mathbf{d}_{1,nl,i}(\mathbf{q})\right) = \mathbf{c}. \tag{19}$$

In Equation (19), the matrix $\mathbf{W}$ represents the linear dynamics, $\mathbf{c}$ is the forcing term, and the terms $\mathbf{d}_{1,nl}$ and $\mathbf{d}_{1,nl,i}$ represent the nonlinearities in the primary structure and in the i^{th} absorber, respectively. Thanks to the HB method, Equation (17), representing a set of nonlinear ordinary differential equations, has been transformed into a set of nonlinear algebraic equations. To find an approximate solution, it is further assumed that the nonlinearity parameter α_3 is small. Hence, the nonlinear response of the system may be expressed as a series expansion in terms of α_3 as

$$\mathbf{q} = \mathbf{q}^{(0)} + \alpha_3\mathbf{q}^{(1)} + \alpha_3^2\mathbf{q}^{(2)} + O(\alpha_3^3). \tag{20}$$

Inserting Equation (20) into (19) and equating coefficients of like powers of α_3 up to first order leads to the following explicit relations :

$$\mathbf{q}^{(0)} = \mathbf{W}^{-1}\mathbf{c}, \tag{21}$$

$$\mathbf{q}^{(1)} = -\mathbf{W}^{-1}\left(\mathbf{d}_{1,nl}(\mathbf{q}^{(0)}) + \sum_{i=1}^{N} b_{nl,i}\mathbf{d}_{1,nl,i}(\mathbf{q}^{(0)})\right) = \mathbf{q}_{nl}^{(1)} + \sum_{i=1}^{N} b_{nl,i}\mathbf{q}_{nl,i}^{(1)}. \tag{22}$$

Equation (21) indicates that $\mathbf{q}^{(0)}$ represents the response of the system when no nonlinearity is present. Equation (22) shows that first-order terms $\mathbf{q}^{(1)}$ are generated by the nonlinear forces triggered by the zeroth-order motion. These terms can be separated into terms due to the nonlinearities inside the primary structure

$\mathbf{q}_{nl}^{(1)}$ and terms due to the nonlinearities inside the i^{th} absorber $\mathbf{q}_{nl,i}^{(1)}$. The square of the frequency response function at a given degree of freedom is given by

$$H = \left(\mathbf{q}_c\right)_j^2 + \left(\mathbf{q}_s\right)_j^2 . \tag{23}$$

Inserting the solution of (21) and (22) into (23) and keeping only the first-order terms leads to

$$\begin{aligned} H &= \left(\mathbf{q}_c^{(0)}\right)_j^2 + \left(\mathbf{q}_s^{(0)}\right)_j^2 + \alpha_3 \left[2\left(\mathbf{q}_c^{(0)}\right)_j \left(\mathbf{q}_{c,nl}^{(1)}\right)_j + 2\left(\mathbf{q}_s^{(0)}\right)_j \left(\mathbf{q}_{s,nl}^{(1)}\right)_j\right] \\ &\quad + \alpha_3 \left[\sum_{i=1}^{N} b_{nl,i} \left[2\left(\mathbf{q}_c^{(0)}\right)_j \left(\mathbf{q}_{c,nl,i}^{(1)}\right)_j + 2\left(\mathbf{q}_s^{(0)}\right)_j \left(\mathbf{q}_{s,nl,i}^{(1)}\right)_j\right]\right] \\ &= H^{(0)} + \alpha_3 H_{nl}^{(1)} + \alpha_3 \sum_{i=1}^{N} b_{nl,i} H_{nl,i}^{(1)} \end{aligned} . \tag{24}$$

In Equation (24), three terms can be identified. The term $H^{(0)}$ stands for the frequency response function of the underlying linear structure. The term $\alpha_3 H_{nl}^{(1)}$ is the modification brought by the (supposedly small) nonlinear forces generated by the linear motion in the nonlinearities of the primary structure. The term $\alpha_3 b_{nl,i} H_{nl,i}^{(1)}$ is the modification brought by the (supposedly small) nonlinear forces generated by the linear motion in the nonlinearitiy i of the absorbers. Thanks to the straightforward expansion, all these effects can be separated to first order in α_3.

With Equation (24), it is now possible to impose N conditions on the first-order nonlinear FRF. This yields a linear system of size $N \times N$, where the nonlinear coefficients $b_{nl,i}$ are the unknowns. Depending on the imposed conditions, the nonlinear coefficients may or may not depend on the parameter α_3.

3.3 Imposing equal peaks in the nonlinear regime

A condition enforcing equal peaks in the nonlinear regime will now be derived. It is first assumed that in the linear regime, the linear absorbers yield the so-called equal-peak design, i. e. the peaks are equal in magnitude and located at frequencies $\omega_{j,p1}$ and $\omega_{j,p2}$. Equation (24) can be used to enforce the equality of the first-order nonlinear FRFs.

$$\begin{aligned} &H^{(0)}(\omega_{j,p1}) + \alpha_3 \left(H_{nl}^{(1)}(\omega_{j,p1}) + \sum_{i=1}^{N} b_{nl,i} H_{nl,i}^{(1)}(\omega_{j,p1})\right) \\ &= H^{(0)}(\omega_{j,p2}) + \alpha_3 \left(H_{nl}^{(1)}(\omega_{j,p2}) + \sum_{i=1}^{N} b_{nl,i} H_{nl,i}^{(1)}(\omega_{j,p2})\right) \end{aligned} \tag{25}$$

Since equal peaks were assumed in the linear regime, $H^{(0)}(\omega_{j,p1}) = H^{(0)}(\omega_{j,p2})$. Then, Equation (25) becomes independent of α_3 and can be written as

$$\sum_{i=1}^{N} b_{nl,i} \left(H_{nl,i}^{(1)}(\omega_{j,p1}) - H_{nl,i}^{(1)}(\omega_{j,p2})\right) = H_{nl}^{(1)}(\omega_{j,p2}) - H_{nl}^{(1)}(\omega_{j,p1}). \tag{26}$$

Enforcing Equation (26) for $j = 1, \cdots, N$ yields the following linear system of size $N \times N$:

$$\begin{bmatrix} \Delta_{\omega_1} H^{(1)}_{nl,1} & \Delta_{\omega_1} H^{(1)}_{nl,2} & \dots & \Delta_{\omega_1} H^{(1)}_{nl,N} \\ \Delta_{\omega_2} H^{(1)}_{nl,1} & \Delta_{\omega_2} H^{(1)}_{nl,2} & \dots & \vdots \\ \vdots & \vdots & \ddots & \vdots \\ \Delta_{\omega_N} H^{(1)}_{nl,1} & \dots & \dots & \Delta_{\omega_N} H^{(1)}_{nl,N} \end{bmatrix} \begin{bmatrix} b_{nl,1} \\ b_{nl,2} \\ \vdots \\ b_{nl,N} \end{bmatrix} = - \begin{bmatrix} \Delta_{\omega_1} H^{(1)}_{nl} \\ \Delta_{\omega_2} H^{(1)}_{nl} \\ \vdots \\ \Delta_{\omega_N} H^{(1)}_{nl} \end{bmatrix}, \tag{27}$$

in which

$$\Delta_{\omega_j} H = H(\omega_{j,p1}) - H(\omega_{j,p2}). \tag{28}$$

Note that the equality of the peaks in the linear regime is not strictly necessary for the absorbers to work efficiently. Indeed, Equation (26) expresses that the (first-order) effects of all the nonlinearities is the same at $\omega_{j,p1}$ and $\omega_{j,p2}$. Therefore, if the peaks are only approximately equal in the linear regime (which is the case with the H_2 optimisation), they will remain approximately equal in the nonlinear regime.

Because the frequency response (24) is only accurate to the first order, this approach is a local approach, in the sense that the obtained results will gradually lose their validity with increasing α_3. That is, if either the forcing amplitude or the nonlinear coefficients become large, the proposed method is likely to fail. For small α_3 however, it is expected that the nonlinear absorbers yield better result than their linear counterparts.

4 Numerical examples

The proposed approach is illustrated with two numerical examples. The frequency response functions were computed using a continuation procedure coupled with a harmonic balance formalism [18] with five harmonics.

4.1 Comparison with the Nonlinear Piezoelectric Tuned Vibration Absorber

As a verification of the proposed method, it is compared to the NPTVA proposed by Soltani and Kerschen [9]. In that paper, the nonlinearities in the absorber are chosen according to a principle of similarity as well. Their coefficients are determined thanks to a first-order HB and a homotopy perturbation method.

A single-degree-of-freedom structure to which a piezoelectric stack is attached (Figure 1) is considered as an example. A nonlinear cubic spring is attached to the mass as well. The piezoelectric stack is connected to a shunt circuit in an attempt to mitigate the vibrations. The coupling between the structure and the piezoelectric material can be characterised by the effective electromechanical coupling factor (EEMCF) defined as [19]

$$K_c^2 = \frac{\omega_{oc}^2 - \omega_{sc}^2}{\omega_{sc}^2}, \tag{29}$$

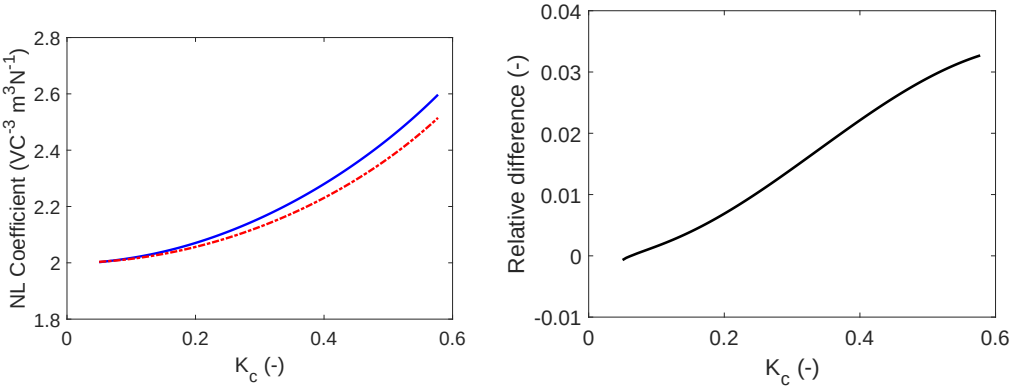
where ω_{oc} is the resonance frequency of the structure when the electrodes of the piezoelectric material are open-circuited and ω_{sc} is the resonance frequency of the structure when these electrodes are short-circuited. In this example, the numerical parameters are given in Table 1. The EEMCF is varied between 0.05 and 0.6. The optimal inductance and resistance of the linear piezoelectric shunt are computed following [11]. The nonlinear impedances are implemented with cubic capacitances. The electromechanical equations are given by

m	k	$k_{p,oc}$	k_{nl}	C_p^ε
1 kg	0.5 N/m	0.5 N/m	1 N/m^3	1 F

Table 1: Numerical parameters of the single-degree-of-freedom structure.

$$\begin{cases} m\ddot{x} + (k + k_{p,oc})x + k_{nl}x^3 - \theta_p q = f \\ L\ddot{q} + R\dot{q} + \dfrac{1}{C_p^\varepsilon} q + C_{nl}q^3 - \theta_p x = 0 \end{cases} . \tag{30}$$

The nonlinear coefficients computed using the method in [9] and the method proposed in Subsection 3 are compared.



(a) (b)

Figure 4: Comparison of the NPTVA (—) and the proposed method (– · –): nonlinear coefficients (a) and relative difference between the coefficients (b).

Figure 4 shows a comparison between the results of the proposed method and the NPTVA (a forcing amplitude of 10^{-3} N was chosen to account for the local nature of the proposed approach, and a modal damping of 1% in the host structure was assumed). A good agreement between the computed nonlinear coefficients is observed, with up to 3% relative difference for the highest coupling factor (the coefficient m_3 of the NPTVA as given in [9] has to be multiplied by $(L/m)^2$ to have consistent units). For realistic EEMCFs, that is $K_c \leq 0.2$, the relative difference is less than 1%.

Next, the EEMCF is fixed to $K_c = 0.2$ and the forcing amplitude is varied. Figure 5 shows the nonlinear frequency responses functions (NFRF) of the system with only a linear absorber, with the NPTVA and with the absorber tuned according to Subsection 3. As the hardening effects of the nonlinearity inside the structure become more prominent, the linear absorber is progressively detuned and loses its efficiency. Around $f = 0.0416$, a detached resonance curve (DRC) merges with the rightmost peak of the NFRF, leading to the possibility of high-amplitude vibrations over a broad frequency range. On the other hand, the nonlinear absorbers are able to mitigate the vibrations over a larger range of forcing amplitudes. Indeed, the difference between the maximum of the receptance with and without nonlinear absorbers is 15.73 dB at $f = 0.05$.

4.2 Two-degree-of-freedom structure

To demonstrate the ability of the method to damp multiple modes, a two-degree-of-freedom structure shown in Figure 6 is studied. A cubic spring k_{nl} attached to mass 1 is considered to introduce nonlinear effects. The characteristics of the structure as well as those of the piezoelectric stack are given in Table 2 (where $K_{c,1}$

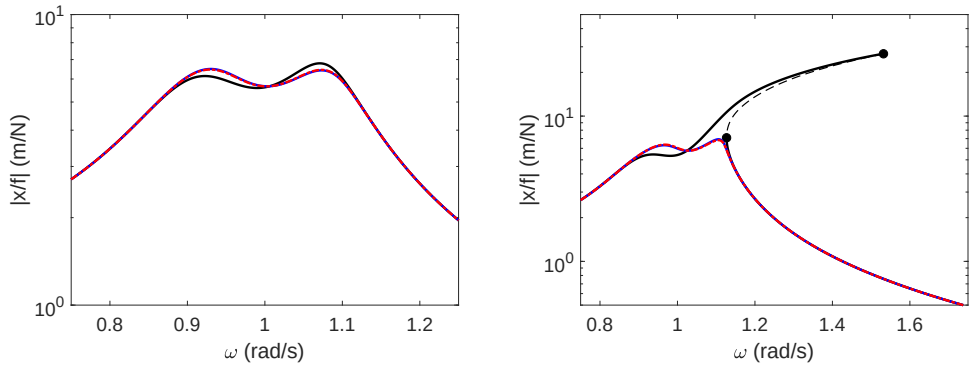


Figure 5: Comparison of the NPTVA and the proposed method: nonlinear frequency response function at $f = 0.025$ N (a) and $f = 0.05$ N (b): linear absorbers (—: stable solution, - - : unstable solution, •: fold bifurcation), NPTVA (—) and the proposed approach (– · –).

and $K_{c,2}$ are the EEMCFs of modes 1 and 2, respectively). Damping is also introduced to have 1% modal damping on both modes in the primary structure. The structure is subjected to a harmonic forcing located on the first mass and the displacement is measured as this same mass.

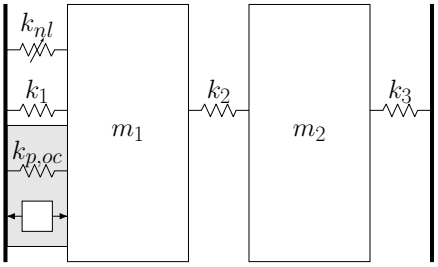


Figure 6: Two-degree-of-freedom structure.

m_1	m_2	k_1	k_2	k_3	k_{nl}	$k_{p,oc}$	C_p^ε	$K_{c,1}$	$K_{c,2}$
1 kg	1 kg	5 N/m	5 N/m	1 N/m	1 N/m^3	1 N/m	1 F	0.0774	0.0567

Table 2: Numerical parameters of the two-degree-of-freedom structure.

A two-mode current flowing shunt circuit is connected to the electrodes of the piezoelectric stack. The choice of the filter capacitances was made empirically so as to obtain approximately the same amplitude on both modes. The inductances values are initialised using the simple rule in [6]. The inductances and resistances are then tuned using the two-step algorithm described in Subsection 2.4. The obtained parameters are gathered in Table 3. The amplitude reductions of modes 1 and 2 are 16.9 dB and 18.6 dB respectively.

Figure 7 illustrates the different steps of the design algorithm with the receptance of the structure in the linear regime. It can be seen that the initialisation of the inductances provides a circuit whose resonance frequencies are not correctly tuned to those of the structure. After a correction of the inductances, the resistances are optimised to minimise the H_2 norm of the receptance.

Nonlinear cubic capacitances are then added in each branch of the current flowing shunt circuit. Their coefficient is determined using Equation (27) and is given in Table 3. The NFRFs of the structure with and without nonlinearities in the absorber are compared in Figure 8 (mode 1) and Figure 9 (mode 2) for various forcing amplitudes.

Once again, the nonlinear absorbers are able to mitigate the vibration amplitude over a broader range of

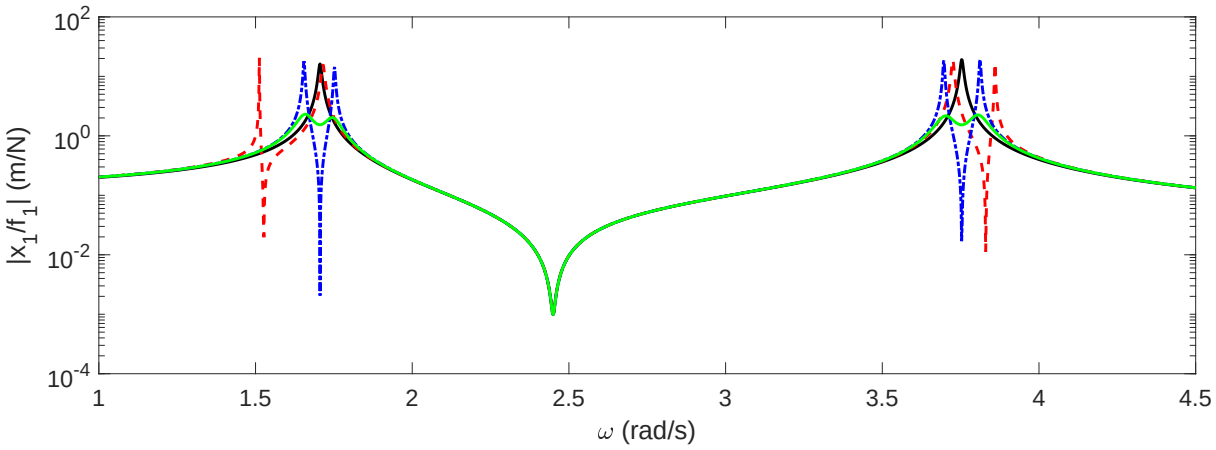


Figure 7: Steps of the design algorithm for the linear absorbers: open-circuit piezoelectric stack (—), initial guess for the inductances of the undamped circuit (- -), optimised inductances of the undamped circuit (— · —) and final design (—).

C_1	C_2	R_1	R_2	L_1	L_2	$C_{nl,1}$	$C_{nl,2}$
5 F	0.25 F	0.0316 Ω	0.0438 Ω	0.3244 H	0.3759 H	0.0169 V/C^3	0.1524 V/C^3

Table 3: Parameters of the current flowing shunt circuit.

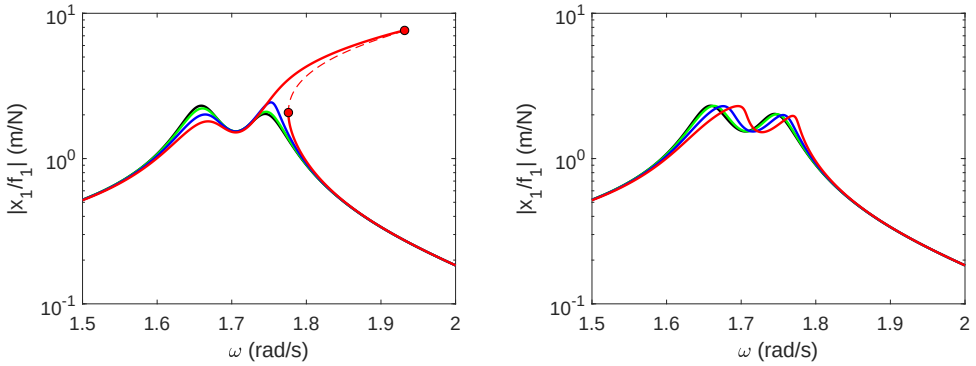


Figure 8: NFRFs of the structure with linear absorbers (a) and with nonlinear absorbers (b), close-up on mode 1: linear FRF (—), $f_1 = 0.1$ N (—), $f_1 = 0.2$ N (—), $f_1 = 0.3$ N (—: stable solution, - - : unstable solution, ●: fold bifurcation).

forcing amplitudes. Figure 8 shows that the proposed method yields nonlinear absorbers with fair efficiency even though the peaks resulting from the linear design are not perfectly equal in amplitude. In Figure 9(a), a DRC coalesced with the rightmost peak of mode 2 can be observed. The use of nonlinear absorbers delays this undesirable phenomenon to higher forcing amplitudes. A global view of the NFRF is given in Figure 10. This shows that both nonlinear resonances are damped simultaneously by the nonlinear absorbers.

The nonlinear absorbers are not fail-proof, though. At $f_1 = 0.3265$ N, a DRC merges with the rightmost peak of mode 2 with the nonlinear absorbers. At this point, the receptance amplitude around the frequency of mode 2 becomes comparable whether or not nonlinearities are used in the absorbers, as can be seen in Figure 11. This phenomenon bears a strong resemblance with that of the nonlinear tuned vibration absorber [20]. Nevertheless, mode 1 is still correctly damped with nonlinear absorbers.

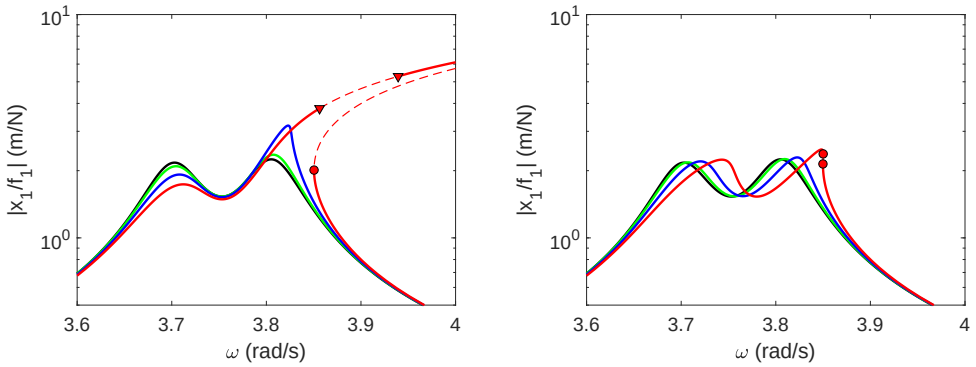


Figure 9: NFRFs of the structure with linear absorbers (a) and with nonlinear absorbers (b), close-up on mode 2: linear FRF (—), $f_1 = 0.1$ N (—), $f_1 = 0.2$ N (—), $f_1 = 0.3$ N (—: stable solution, - - : unstable solution, •: fold bifurcation, ▼: Neimark-Sacker bifurcation).

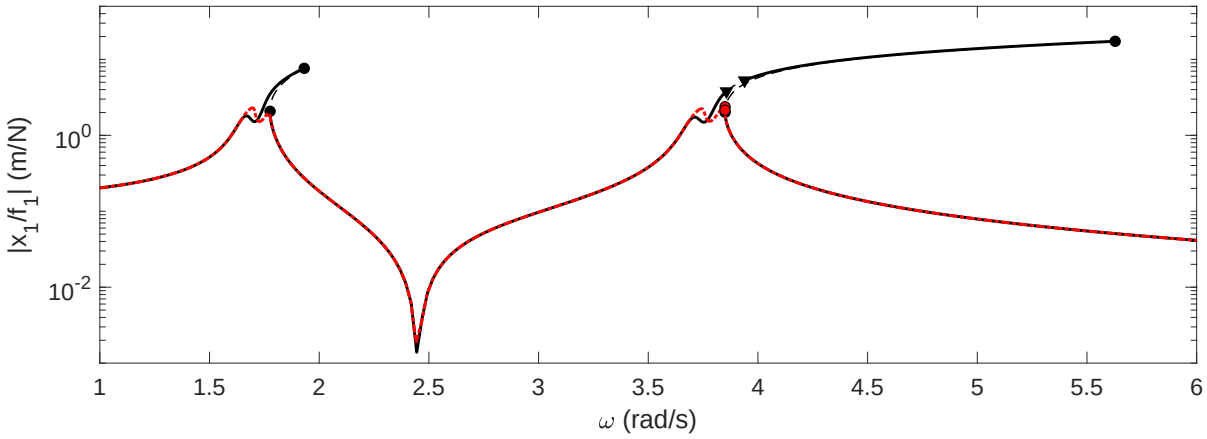


Figure 10: NFRF of the structure at $f_1 = 0.3$ N with linear absorbers (—: stable solution, - -: unstable solution, •: fold bifurcation, ▼: Neimark-Sacker bifurcation) and with nonlinear absorbers (— · — : stable solution, - -: unstable solution,•: fold bifurcation).

5 Conclusion

In this paper, a new methodology for tuning multimodal nonlinear piezoelectric vibration absorbers was proposed. A current flowing shunt circuit proposed in the literature was chosen to implement a multimodal absorber. A model of the piezoelectric structure connected to a current flowing shunt circuit was proposed, and this allowed us to revisit the tuning methodology of the shunt circuit. This methodology consists in a two-step optimisation algorithm. The inductances are first optimised to yield the correct resonance frequencies, and then the resistances are optimized to minimise the H_2 norm of the receptance.

The design of nonlinear multimodal vibration absorbers is inspired from a principle of similarity. Nonlinearities are introduced in the branches of the shunt circuit to mimic the behaviour of the structure in the nonlinear regime. Their mathematical form is chosen to be identical as these in the primary structure. Their coefficients are then found by imposing equal peaks in the nonlinear frequency response function.

The proposed design methodology was shown to be efficient both when a single mode and when two modes are to be damped. Namely, the range of forcing amplitudes in which the absorbers are efficient is substantially increased when properly tuned nonlinearities are used in the absorbers. Eventually, for very high forcing amplitudes, the nonlinear absorbers also fail and at that point the advantage of using nonlinearities becomes

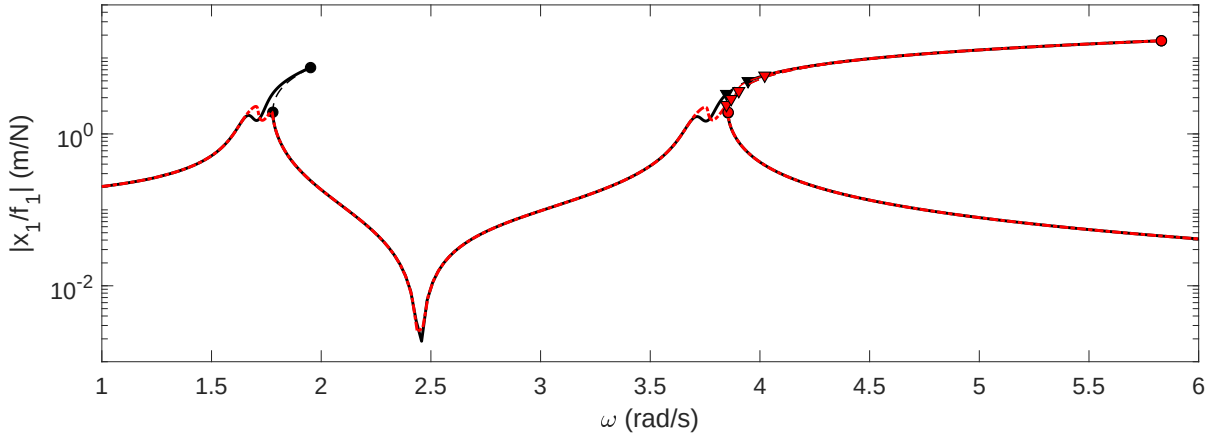


Figure 11: NFRFs of the structure at $f_1 = 0.3265$ N with linear absorbers (—: stable solution, - -: unstable solution, •: fold bifurcation, ▼: Neimark-Sacker bifurcation) and with nonlinear absorbers (– · – : stable solution, - -: unstable solution,•: fold bifurcation, ▼: Neimark-Sacker bifurcation).

less obvious.

The design of the nonlinearities relies on the presence of equal (or nearly equal) peaks in the linear receptance of the structure. Therefore, the design of linear absorbers has a strong impact on that of the nonlinearities. Future work for improving the proposed design methodology may involve choosing the inductances and the resistances in the objective of minimising the H_∞ norm of the receptance (and no longer its H_2 norm).

Acknowledgements

The authors G. Raze, A. Paknejad, G. Zhao, C. Collette and G. Kerschen would like to acknowledge the financial support of the SPW (WALInnov grant 1610122).

References

[1] R. L. Forward, *Electronic damping of vibrations in optical structures*, Applied optics, Vol. 18, No. 5, (1979), pp. 690–697.

[2] N. W. Hagood, A. von Flotow, *Damping of structural vibrations with piezoelectric materials and passive electrical networks*, Journal of Sound and Vibration, Vol. 146, No. 2, (1991), pp. 243–268.

[3] D. Edberg, A. Bicos, J. Fechter, *On piezoelectric energy conversion for electronic passive damping enhancement*, *Proceedings of Damping* (1991), pp. 717–724.

[4] J. J. Hollkamp, *Multimodal passive vibration suppression with piezoelectric materials and resonant shunts*, Journal of intelligent material systems and structures, Vol. 5, No. 1, (1994), pp. 49–57.

[5] S.-Y. Wu, *Method for multiple-mode shunt damping of structural vibration using a single PZT transducer*, *Smart structures and materials 1998: passive damping and isolation*, International Society for Optics and Photonics (1998), pp. 159–169.

[6] S. Behrens, S. R. Moheimani, A. Fleming, *Multiple mode current flowing passive piezoelectric shunt controller*, Journal of Sound and Vibration, Vol. 266, No. 5, (2003), pp. 929–942.

[7] B. Lossouarn, M. Aucejo, J.-F. Deü, *Multimodal coupling of periodic lattices and application to rod vibration damping with a piezoelectric network*, Smart Materials and Structures, Vol. 24, No. 4, (2015), p. 045018.

[8] G. Habib, G. Kerschen, *A principle of similarity for nonlinear vibration absorbers*, Physica D: Nonlinear Phenomena, Vol. 332, (2016), pp. 1–8.

[9] P. Soltani, G. Kerschen, *The nonlinear piezoelectric tuned vibration absorber*, Smart Materials and Structures, Vol. 24, No. 7, (2015), p. 075015.

[10] B. Lossouarn, J.-F. Deü, G. Kerschen, *A fully passive nonlinear piezoelectric vibration absorber*, Philosophical Transactions of the Royal Society of London A: Mathematical, Physical and Engineering Sciences (In Press).

[11] P. Soltani, G. Kerschen, G. Tondreau, A. Deraemaeker, *Piezoelectric vibration damping using resonant shunt circuits: an exact solution*, Smart materials and structures, Vol. 23, No. 12, (2014), p. 125014.

[12] A. Preumont, *Vibration control of active structures*, Springer (2011).

[13] A. J. Fleming, S. Behrens, S. R. Moheimani, *Innovations in piezoelectric shunt damping*, *Smart Structures and Devices*, International Society for Optics and Photonics (2001), pp. 89–102.

[14] A. Fleming, S. Behrens, S. Moheimani, *Reducing the inductance requirements of piezoelectric shunt damping systems*, Smart materials and structures, Vol. 12, No. 1, (2003), p. 57.

[15] A. Cigada, S. Manzoni, M. Redaelli, M. Vanali, *Optimization of the current flowing technique aimed at semi-passive multi-modal vibration reduction*, Journal of Vibration and Control, Vol. 18, No. 2, (2012), pp. 298–312.

[16] N. Van Der Aa, H. Ter Morsche, R. Mattheij, *Computation of eigenvalue and eigenvector derivatives for a general complex-valued eigensystem*, Electronic Journal of Linear Algebra, Vol. 16, No. 1, (2007), p. 26.

[17] G. Habib, G. Kerschen, *Linearization of Nonlinear Resonances Through the Addition of Intentional Nonlinearities*, *Recent Trends in Applied Nonlinear Mechanics and Physics*, Springer (2018), pp. 215–225.

[18] T. Detroux, L. Renson, L. Masset, G. Kerschen, *The harmonic balance method for bifurcation analysis of large-scale nonlinear mechanical systems*, Computer Methods in Applied Mechanics and Engineering, Vol. 296, (2015), pp. 18–38.

[19] O. Thomas, J.-F. Deü, J. Ducarne, *Vibrations of an elastic structure with shunted piezoelectric patches: efficient finite element formulation and electromechanical coupling coefficients*, International journal for numerical methods in engineering, Vol. 80, No. 2, (2009), pp. 235–268.

[20] T. Detroux, G. Habib, L. Masset, G. Kerschen, *Performance, robustness and sensitivity analysis of the nonlinear tuned vibration absorber*, Mechanical Systems and Signal Processing, Vol. 60, (2015), pp. 799–809.

Mechatronic control of the car response based on VFC

D. Antonelli[1], L. Nesi[1], G. Pepe[1], A. Carcaterra[1]
[1] Department of Mechanical and Aerospace Engineering
University of Rome "La Sapienza"
Rome, Italy
e-mail: **antonio.carcaterra@uniroma1.it ,**

Abstract
This paper is addressed to the analysis of an autonomous vehicle as a first step of an on-going project at the Mechatronic and Vehicle Dynamic Lab of Sapienza. The project is developing an experimental setup for a series city car to be equipped with a complete assisted integrated system of mechatronic type, controlling the steering and the wheel torques. In this paper we develop a complete car model for its dynamic response, including the car body dynamics, tires that can rely on the previous controls and on a control logic that is based on a new strategy, the FLOP control. This kind of control, recently developed by the Sapienza team, relies on optimal control theory of Pontryagin type, that has been revisited transforming the global optimality problem into a set of local optima along the system trajectory. This method provides a chance for an efficient feedback control of the vehicle in an environment in which moving obstacles and external noise are present. Numerical results complete the analysis.

1 Introduction

Nowadays, autonomous vehicle (AV) represents a crucial field in intelligent transportation systems. In recent years, integrated control of in-wheel motor and assisted-steering is a subject of central interest [13-14-15-16] in automotive technology, and the introduction of active devices in place of the traditional passive components can improve vehicle dynamics as in the case of the semi active suspension [2-4-5-7-9].

In this paper a new method of control for a complex mechanical systems [1-2-3-4-8-9] developed by the authors, named Feedback Local Optimality Principle (FLOP) [1], is tested on a nonlinear bike model for cars. FLOP is part of a new class of algorithms the group of Mechatronic and Vehicle Dynamic Lab of Sapienza is developing under the name of Variational Feedback Controllers (VFC) [5-6-7]. The proposed method starts from classical optimal variational principles, usually part of the Pontryagin's or Bellman's methods, but it provides the user with the possibility to implement a feedback control, even in the presence of nonlinearities. This chance is obtained by changing the optimality principle used in the classical approach [1], as it will be shown in next section. FLOP approach, respect to classical nonlinear controls, such as Sliding Mode, Lyapunov and feedback linearization controls, presents a great advantage because of the chance of a more flexible specification of the objective function.

The FLOP method is here implemented to control the steering radius in a turning maneuver. The goal is to track, at the possible maximum speed, the assigned trajectory maintaining a given steering radius. Moreover, an obstacle is introduced along the ideal trajectory, and the FLOP algorithm is capable to skip the obstacle with an avoiding maneuver introducing a local perturbation of the steering radius, regaining at the end of the obstacle avoiding operation, the prescribed curvature of the tracked trajectory. All these achievements are included within a unique objective function maintaining a unique control logic, that of FLOP.

2 Resume of VFC theory

Classical variational approach consists in the minimization (maximization) problem of a functional J [5-6-7], as in (1):

$$\begin{gathered}\bar{J} = \min J = \int_0^T E\big(x(t), u(t)\big)\, dt \\ \text{subject to} \\ \dot{x} = f\big(x(t), u(t)\big) \\ x(0) = x_0\end{gathered} \tag{1}$$

which leads to:

$$\bar{J} = \min J = \int_0^T E(x,u) + \lambda\big(\dot{x} - f(x,u)\big)\, dt = \int_0^T \mathcal{L}(\dot{x}, x, u, \lambda) dt, \tag{2}$$

In (1) x, u represent the state and the control variable, respectively, $f(x,u)$ the dynamical system and $E\big(x(t), u(t)\big)$ the cost function. From equation (2) it also follows the optimality condition implies $\lambda(T) = 0$, the final end boundary condition of the optimal problem. FLOP approach changes the global optimality condition of Pontyagin into a local optimality principle [1]. Integral (2) splits into N integrals and a local optimality condition is applied on each integral, so that:

$$\begin{gathered}J = \int_0^T \mathcal{L}(\dot{x}, x, u, \lambda) dt = \sum_1^N J_i = \int_{\tau_0}^{\tau_1} \mathcal{L}(\dot{x}, x, u, \lambda) dt + \cdots + \int_{\tau_{N-1}}^{\tau_N} \mathcal{L}(\dot{x}, x, u, \lambda) dt \\ \tilde{J} = \sum_{i=1}^N \min J_i = \sum_{i=1}^N \int_{\tau_{LB_i}}^{\tau_{UB_i}} \mathcal{L}(\dot{x}, x, u, \lambda) dt\end{gathered} \tag{3}$$

In (3) UB_i and LB_i indicates Upper Bound and Lower Bound of the $i\text{-}th$ integral, and $\tilde{J}$ the reached minimum valued, in general different from $\bar{J}$. Along each sub-interval it is required to satisfy the continuity condition for the partial sub-interval solutions, and the trasversality condition to hold at the sub-interval end:

$$\begin{gathered}x_{LB_i}(\tau_{i-1}) = x_{UB_{i-1}}(\tau_{i-1}) \\ \lambda_{UB_i}(\tau_i) = 0\end{gathered} \tag{4}$$

In general, this new criterion leads to a different minimum with respect to the Pontryagin's method, but in some conditions, specified in [1], the two solutions can collapse into the same $\tilde{J} = \bar{J}$.

FLOP algorithm and its local optimality condition provide three main advantages:

i) The dynamical system can be nonlinear.
ii) The class of the allowed cost functions $E(x,u)$ can be wider with respect the classical quadratic ones. In particular, penalty function of non-quadratic types (for example exponential) can be introduced especially useful for a target efficient reaching and for obstacle avoidance purposes. This is a remarkable advantage with respect to classical control techniques such as, for example, the LQR approach.
iii) FLOP algorithm is a feedback control. Most used optimal control based on variational methods are solved used feed-forward law with all the known associated limitations.

2.1 Resume of FLOP application strategy

From the second equation of (3), applying the variational approach to the discretized version of the equation and using the Euler first-order approximation, one obtains:

$$\begin{cases} \left.\frac{\partial E}{\partial x}\right|_{LB_i} + \left.\left(\lambda\frac{\partial f}{\partial x}\right)\right|_{LB_i} - \frac{\lambda_{UB_i} - \lambda_{LB_i}}{\Delta\tau} = 0 \\ \left.\frac{\partial E}{\partial u}\right|_{LB_i} + \left.\left(\lambda\frac{\partial f}{\partial u}\right)\right|_{LB_i} = 0 \qquad \forall\ i \in [1, N] \\ \frac{x_{UB_i} - x_{LB_i}}{\Delta\tau} = f(x_{LB_i}, u_{LB_i}) \end{cases} \tag{5}$$

Using the trasversality condition expressed in the second equation of (4), $\dot{\lambda} = \frac{\lambda_{UB_i} - \lambda_{LB_i}}{\Delta\tau} \cong -\frac{\lambda_{LB_i}}{\Delta\tau}$, this can be also written as $\dot{\lambda} \cong G\lambda_{LB_i}$, where $G = -\frac{1}{\Delta\tau}$.

3 Vehicle Dynamic Model

In this section, a standard three-DOF nonlinear bike model, depicted in Figure 1, is considered. The vehicle motion is assumed planar and including the longitudinal forward motion (u), the lateral sway (v), and the yaw (ψ). The equations of motion are expressed in the body reference frame. The rear wheel steering angle is set to zero, while the front one is δ. The center of gravity of the vehicle is CG. The distances of points A (center of front wheel) and B (center of rear wheel) from CG are l_f and l_r, respectively. The wheelbase is $L = l_f + l_r$. The velocity of CG is V, the angle between the velocity vector $of\ CG$ and the longitudinal axis of the vehicle u is β.

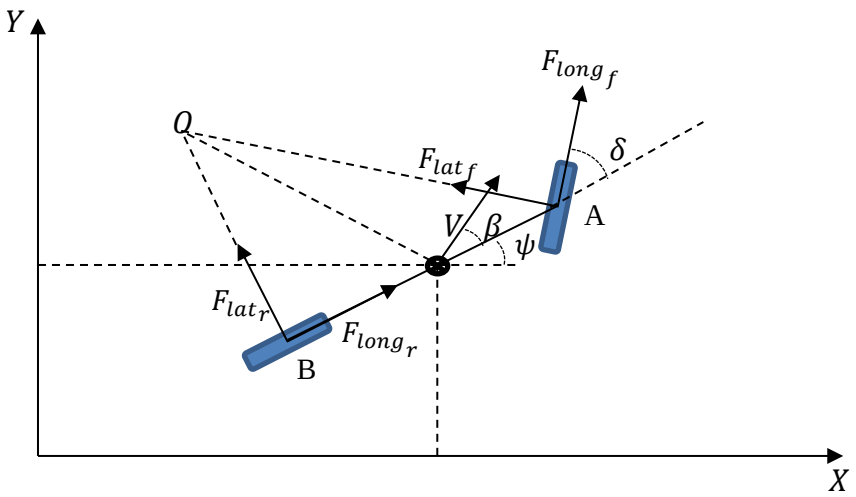


Figure 1: Vehicle model

3.1 Vehicle model

The state vector is $\boldsymbol{x} = [X; Y; \psi; u; v; \omega; \omega_r; \omega_r]$, where X, Y are the coordinates of CG in the road reference, while ψ is the yaw rotation angle, u, v, ω, are the speed components measured in the body fixed reference, representing the surge, sway, and yaw motions. The longitudinal and lateral slips of the wheels depend both on the spin speeds ω_r, ω_r , for the rear and front wheel, respectively. The equations of motion of the vehicle can be written in terms of the state defined above. The system has three degrees of control, the steering angle of the front wheel δ, the rear torque C_r and the front torque C_f. The inertia matrix can be written in terms of the body mass m_b summed with wheels masses m_w in m, the yaw moment of inertia I_z, the wheels inertia moments I_w

$$\boldsymbol{M} = diag[1; 1; 1; m; m; I_z; I_w; I_w] \tag{6}$$

This leads to the following expressions for the $\dot{\boldsymbol{x}} = \left[\dot{X}; \dot{Y}; \dot{\psi}; \dot{u}; \dot{v}; \dot{\omega}; \dot{\omega}_r; \dot{\omega}_r\right]^T$. The speeds of the vehicle, in the fixed reference can be written through the 2D rotation matrix which is function of the yaw angle ψ that converts the speeds of the vehicle from the body reference frame to the fixed reference frame.

$$\begin{bmatrix} \dot{X} \\ \dot{Y} \\ \dot{\psi} \\ \dot{u} \\ \dot{v} \\ \dot{\omega} \\ \dot{\omega}_r \\ \dot{\omega}_f \end{bmatrix} = \boldsymbol{M}^{-1} \begin{bmatrix} \cos(\psi)\, u - \sin(\psi) v \\ \sin(\psi)\, u + \cos(\psi) v \\ \omega \\ F_{long_f} \cos(\delta) - F_{lat_f} \sin(\delta) + F_{long_r} + mv\omega \\ F_{long_f} \sin(\delta) + F_{lat_f} \cos(\delta) + F_{lat_r} - mu\omega \\ F_{long_f} \sin(\delta)\, l_f + F_{lat_f} \cos(\delta)\, l_f - F_{lat_r} l_r \\ C_r - F_{long_r} R_w - F_{rolling_r} R_w \\ C_f - F_{long_f} R_w - F_{rolling_f} R_w \end{bmatrix} \tag{7}$$

The terms F_{long_f} and F_{long_r} represent the Pacejka longitudinal front and rear forces evaluated in function of the normal force acting on the tires and of the longitudinal slip ratio σ_f and σ_r

$$\begin{aligned} F_{long_f} &= f(F_{N_f}, \sigma_f(u_f, \omega_f, \delta)) \\ F_{long_r} &= f(F_{N_r}, \sigma_r(u_r, \omega_r)) \\ \sigma_f &= -\frac{u_f - \omega_f R_w}{|u_f|} \\ \sigma_r &= -\frac{u_r - \omega_r R_w}{|u_r|} \end{aligned} \tag{8}$$

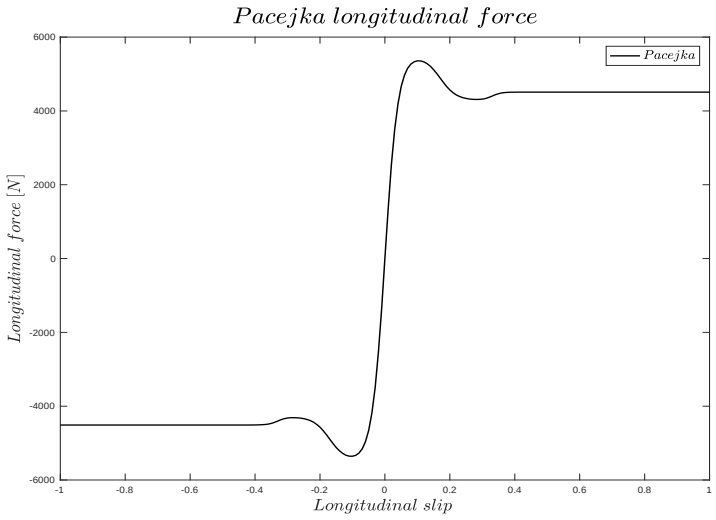


Figure 2: Pacejka longitudinal force model

The rolling resistance of the tires are represented by two forces, $F_{rolling_f}$ and $F_{rolling_r}$ defined as:

$$\begin{aligned} F_{rolling_f} &= \left(\mu_0 + \mu_1 u_f^2\right) F_{N_f} \\ F_{rolling_r} &= \left(\mu_0 + \mu_1 u_r^2\right) F_{N_r} \end{aligned} \tag{9}$$

where u_f and u_r are the longitudinal speed of the front and rear wheels, respectively, in the body fixed reference frame:

$$\begin{aligned} u_f &= \cos(\delta)\, u - \sin(\delta)\left(v + l_f \omega\right) \\ u_r &= u \end{aligned} \tag{10}$$

The lateral sway motion forces are F_{lat_f} and F_{lat_r}. They depend on the lateral slip ratios α_f and α_r

$$\begin{aligned} F_{lat_f} &= f\left(F_{N_f}, \alpha_f(\hat{u}, \hat{v}, \omega, \delta)\right) \\ F_{lat_r} &= f\left(F_{N_r}, \alpha_r(\hat{u}, \hat{v}, \omega)\right) \\ \alpha_f &= -\operatorname{atan}\left(\frac{\left(\hat{v} + \omega l_f\right)\cos(\delta) - \hat{u}\sin(\delta)}{\hat{u}\cos(\delta) + \left(\hat{v} + \omega l_f\right)\sin(\delta)}\right) \\ \alpha_r &= -\operatorname{atan}\left(\frac{(\hat{v} - \omega l_r)}{\hat{u}}\right) \end{aligned} \tag{11}$$

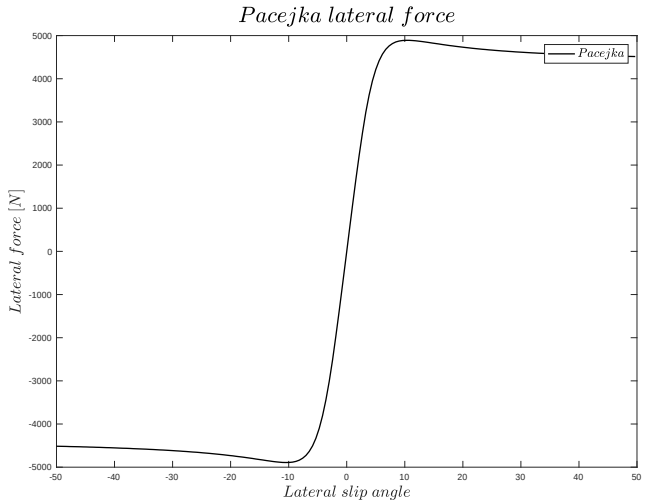


Figure 3: Pacejka lateral force model

The estimation of the tire's grip and rolling resistance, can be performed even in feedback by using advanced intelligent tires provided with sensors as shown in [10-11-12]. Finally, the vertical forces F_{N_f} and $F_{N_r}$are:

$$\begin{aligned} F_{N_f} &= \frac{m}{L}\left(g l_r - (\dot{u} - v\omega)h_g\right) \\ F_{N_r} &= mg - F_{N_f} = mg - \frac{m}{L}\left(g l_r - (\dot{u} - v\omega)h_g\right) \end{aligned} \tag{12}$$

4 Control design

The cost function in the FLOP method is assumed to be:

$$\bar{J} = \int_0^T \frac{1}{2}\boldsymbol{u}^T \boldsymbol{R}\boldsymbol{u} + g(\boldsymbol{x}) + \boldsymbol{\lambda}^T\left(\dot{\boldsymbol{x}} - \boldsymbol{f}(\boldsymbol{x},\boldsymbol{u})\right) dt \tag{13}$$

where $g(\boldsymbol{x})$ can represent any kind of possible nonlinear and continuous function. This permits the user to define $\bar{J}$ as:

$$\begin{aligned} g(\boldsymbol{x}) = g_r(\boldsymbol{x}) + \ g_s(\boldsymbol{x}) + g_c(\boldsymbol{x}) \\ = k_r\left(t_r(\boldsymbol{x}) - t_{reference}\right)^2 + \frac{ampS}{\sigma_s\sqrt{2\pi}}\exp\left(-0.5\left(\frac{V(\boldsymbol{x}) - V_{min}}{\sigma_s}\right)^2\right) \\ + \frac{ampO}{\sigma_O\sqrt{2\pi}}\exp\left(-0.5\left(\frac{\theta_{V(\boldsymbol{x};\boldsymbol{x}_{obs})} - \theta_{relativePosition(\boldsymbol{x};\boldsymbol{x}_{obs})}}{\sigma_O}\right)^2\right) \end{aligned} \tag{14}$$

$g_r(\boldsymbol{x})$ shown in fig 5 is a quadratic form of the $t_r(\boldsymbol{x}); t_{reference}$ these represent the actual turning radius and its reference value. $t_r(\boldsymbol{x})$ is function of the state $\boldsymbol{x}$, and can be easily evaluated in term of the absolute speed V of the vehicle and the yaw rate $\dot{\psi}$ using the following formula:

$$t_r(\boldsymbol{x}) = \frac{V}{\dot{\psi}} \tag{15}$$

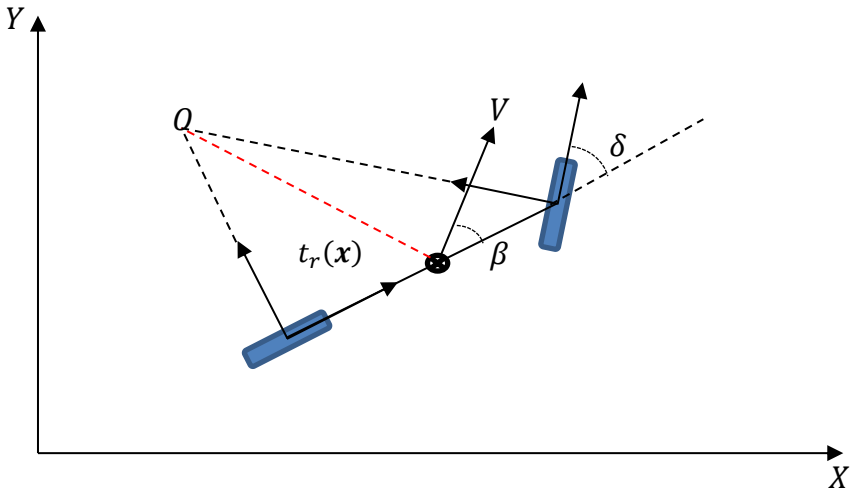


Figure 4: Actual turning radius

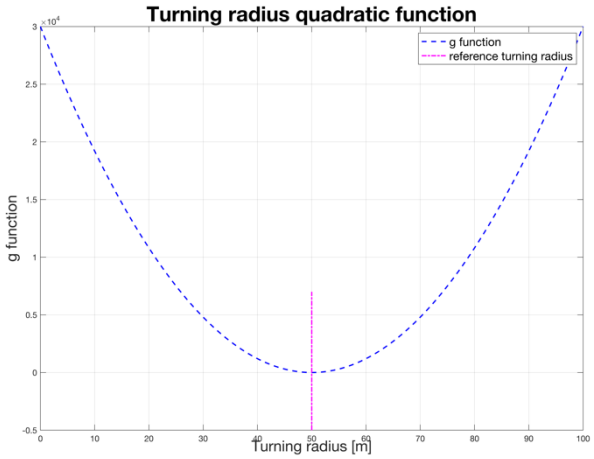


Figure 5: $g_r(\boldsymbol{x})$ function for various turning radius

The function $g_S(\boldsymbol{x})$ shown in fig 6 is a gaussian function of the vehicle absolute speed V and of a minimum speed V_{min}.

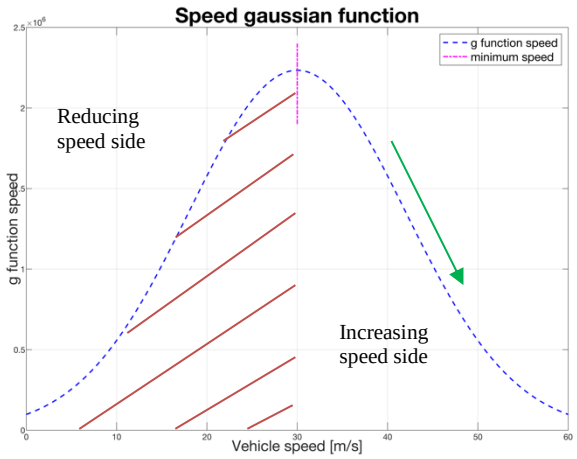


Figure 6: $g_s(\boldsymbol{x})$ function for various speed

$g_O(\boldsymbol{x})$ is shown in fig 7 and depends on the polar angles $\theta_{relativePosition(\boldsymbol{x};\boldsymbol{x}_{obs})}$ $\theta_{V(\boldsymbol{x};\boldsymbol{x}_{obs})}$ of the vector relative position $\overrightarrow{GO}$, that connects the vehicle center of gravity G with obstacle O, and of the vector relative speed $\overrightarrow{V_O V_G}$, these introduce a repulsion from the obstacle, by varying the direction of the relative speed:

$$\theta_{relativePosition(\boldsymbol{x};\boldsymbol{x}_{obs})} = \operatorname{atan}\left(\frac{y_{\overrightarrow{GO}}}{x_{\overrightarrow{GO}}}\right) \tag{16}$$

$$\theta_{V(\boldsymbol{x};\boldsymbol{x}_{obs})} = \operatorname{atan}\left(\frac{y_{\overrightarrow{V_O V_G}}}{x_{\overrightarrow{V_O V_G}}}\right)$$

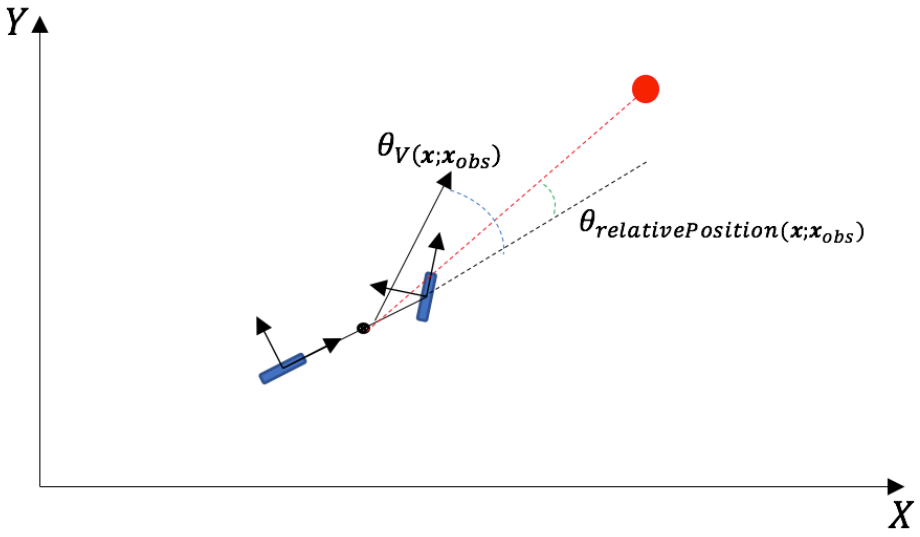


Figure 7: Vehicle obstacle interactions

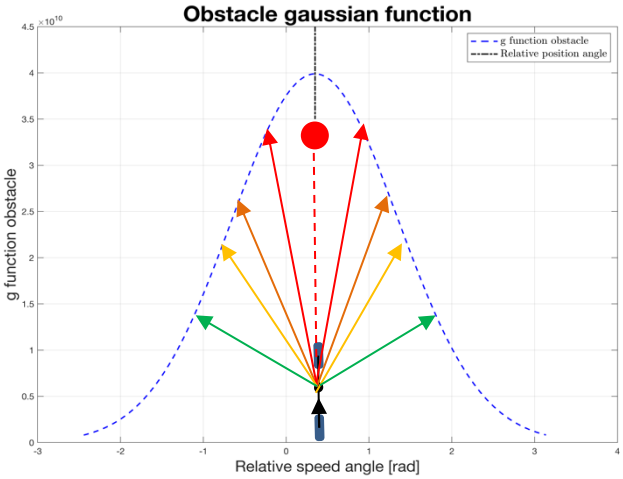


Figure 8: $g_O(\boldsymbol{x})$ function for various relative speed directions

Since the dynamic systems considered is strongly nonlinear in the state $\boldsymbol{x}$ and in the control $\boldsymbol{u}$, a linearization is required to obtain the analytically the control law

$$\dot{\boldsymbol{x}} = \boldsymbol{\phi}(\boldsymbol{x}) + \boldsymbol{h}(\boldsymbol{x}, \boldsymbol{u}) \tag{17}$$

$\boldsymbol{h}(\boldsymbol{x}, \boldsymbol{u})$ is the linearized form, obtained through a Taylor series expansion of the first order, and provides two linear terms, one in the state $\boldsymbol{x}$, the second in the control variable $\boldsymbol{u}$

$$\boldsymbol{x_0} = [0;0;0;0;0;0;0;0]^{\boldsymbol{T}} \ , \ \boldsymbol{u_0} = [0;0;0]^{\boldsymbol{T}} \tag{18}$$
$$\boldsymbol{h}(\boldsymbol{x}, \boldsymbol{u}) = \boldsymbol{h}(\boldsymbol{x_0}, \boldsymbol{u_0}) + \nabla_{\boldsymbol{x}}\boldsymbol{h}(\boldsymbol{x}, \boldsymbol{u})|_{\boldsymbol{x_0},\boldsymbol{u_0}}(\boldsymbol{x} - \boldsymbol{x_0}) + \nabla_{\boldsymbol{u}}\boldsymbol{h}(\boldsymbol{x}, \boldsymbol{u})|_{\boldsymbol{x_0},\boldsymbol{u_0}}(\boldsymbol{u} - \boldsymbol{u_0}) = \boldsymbol{A}\boldsymbol{x} + \boldsymbol{B}\boldsymbol{u}$$

where $\boldsymbol{h}(\boldsymbol{x_0}, \boldsymbol{u_0}) = [0;0;0;0;0;0;0;0]^T$, $\nabla_{\boldsymbol{x}}\boldsymbol{h}(\boldsymbol{x}, \boldsymbol{u})|_{\boldsymbol{x_0},\boldsymbol{u_0}} = \boldsymbol{A}$ and $\nabla_{\boldsymbol{u}}\boldsymbol{h}(\boldsymbol{x}, \boldsymbol{u})|_{\boldsymbol{x_0},\boldsymbol{u_0}} = \boldsymbol{B}$. The following set of equations are determined by the variational technique:

$$\begin{cases} \nabla_{\boldsymbol{x}} g(\boldsymbol{x}) - \dot{\boldsymbol{\lambda}} - \left(\nabla_{\boldsymbol{x}}\boldsymbol{\phi}(\boldsymbol{x})\right)^T \boldsymbol{\lambda} - \boldsymbol{A}^T\boldsymbol{\lambda} = \boldsymbol{0} \\ \boldsymbol{R}^T\boldsymbol{u} - \boldsymbol{B}^T\boldsymbol{\lambda} = \boldsymbol{0} \\ \dot{\boldsymbol{x}} = \boldsymbol{\phi}(\boldsymbol{x}) + \boldsymbol{A}\boldsymbol{x} + \boldsymbol{B}\boldsymbol{u} \end{cases} \tag{19}$$

The FLOP approach assumes the solution for $\dot{\boldsymbol{\lambda}} = \boldsymbol{G}\boldsymbol{\lambda}$, where $\boldsymbol{G} = -\frac{1}{\Delta\tau} I_{N\times N}$. Substituting this into the set of equations (19), permits to write the feedback control law:

$$\boldsymbol{u_{FLOP}} = \boldsymbol{\chi}(\boldsymbol{x}) \tag{20}$$

5 Numerical results

In this section some numerical simulations are shown. The first set shows the cornering capability and the obstacle avoidance performance, this last being the most challenging and critical for an autonomous vehicle.

Figure 9 illustrates the capability of the vehicle to follow a corner with specific turning radius, fixed by the user to 70 m.

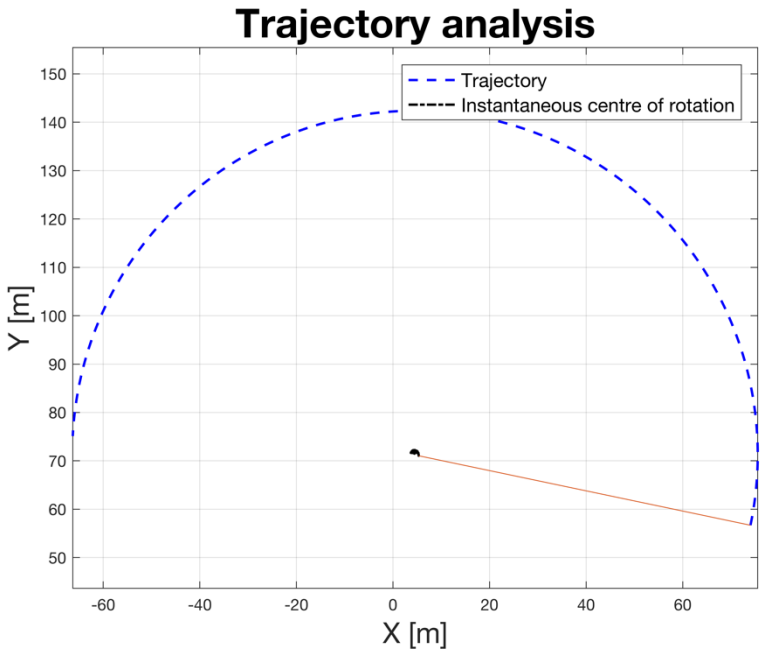


Figure 9: Trajectory analysis

Figure 10 visualizes small perturbations of the position of the center of instantaneous rotation in comparison with the radius of curvature.

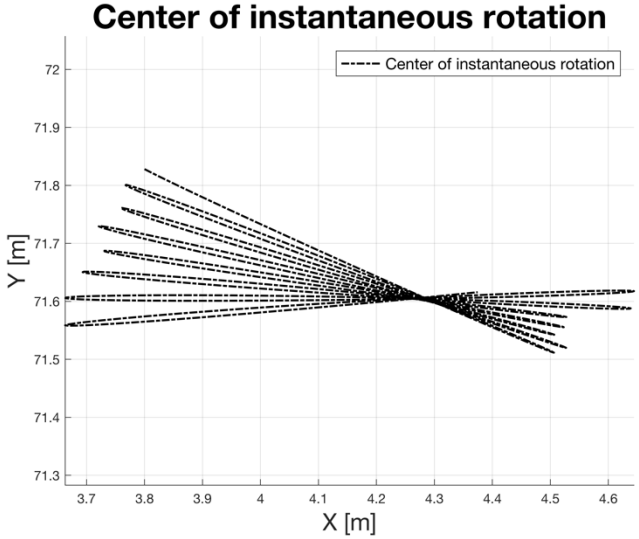


Figure 10: Center of instantaneous rotation

Figure 11 reports the highest speed reached by the vehicle for various steering angles. Moreover, the time history of the speed for one of the vehicle's maneuver is represented with the black curve to show the stability of the controlled vehicle. The blue curve represents the highest speed reached by the controlled vehicle and it is compared to the maximum speed obtained equating the maximum lateral adherence force reachable by the Pacejka's forces with the centrifugal force, for various turning radius (11):

$$F_{long_f} \sin(\delta) + F_{lat_f} \cos(\delta) + F_{lat_r} = \frac{mV^2}{R} \tag{21}$$

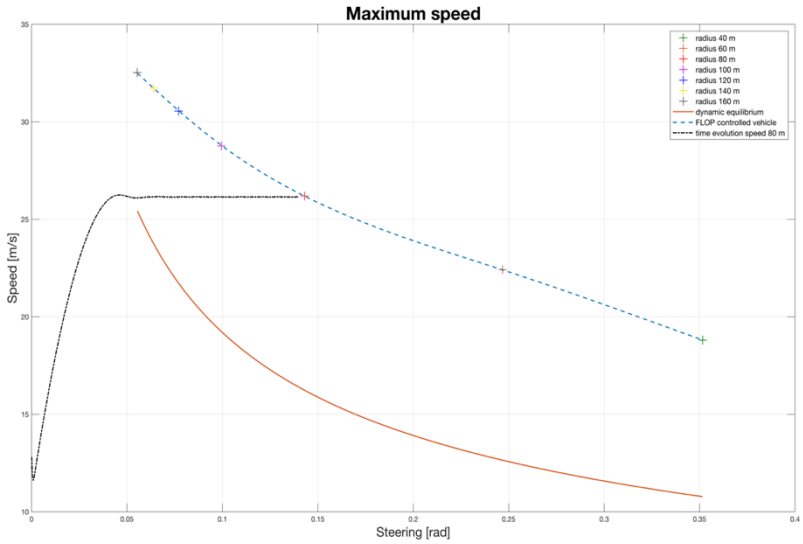


Figure 11: $g_s(\boldsymbol{x})$ function for various speed

The following figures illustrate the reaction in case of an obstacle placed along the trajectory of the vehicle, this is compared to the free-way case (compare figures 12 and 13). This shows the different trajectories, different turning radius, longitudinal and lateral speeds, lateral slip angles of the body and tires and in terms of Pacejka's forces.

The starting point of the variation is represented by the magenta marker placed within the plot. It is interesting to notice that the system, after the corrections and due to the presence of the obstacle, returns to the initial maneuver.

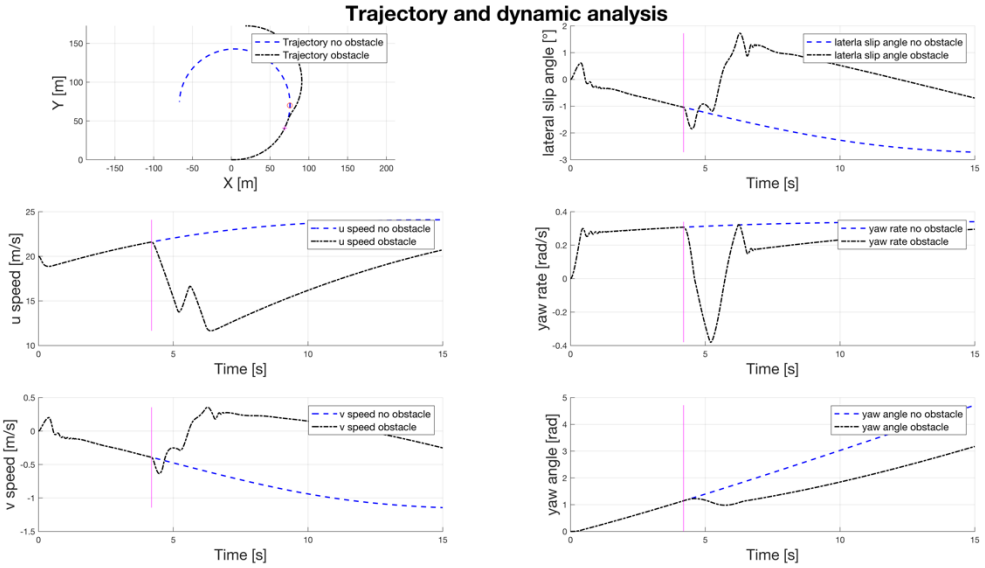


Figure 12: Trajectory comparison

It is interesting to notice in figure 13 the behavior of the control input represented by steering, rear torque and front torque when the vehicle reaches the obstacle, in fact it is noticeable that after a fist braking phase the vehicle steers to avoid the collision, then it returns to accelerate and while proceeding to the original turning radius, this particular behavior is due to the functions (14) that request to maximum speed of the vehicle while following a specific trajectory and to avoid the obstacle by varying the orientation of the speed and not only its modulus showing a great performance in terms of vehicle maneuverability.

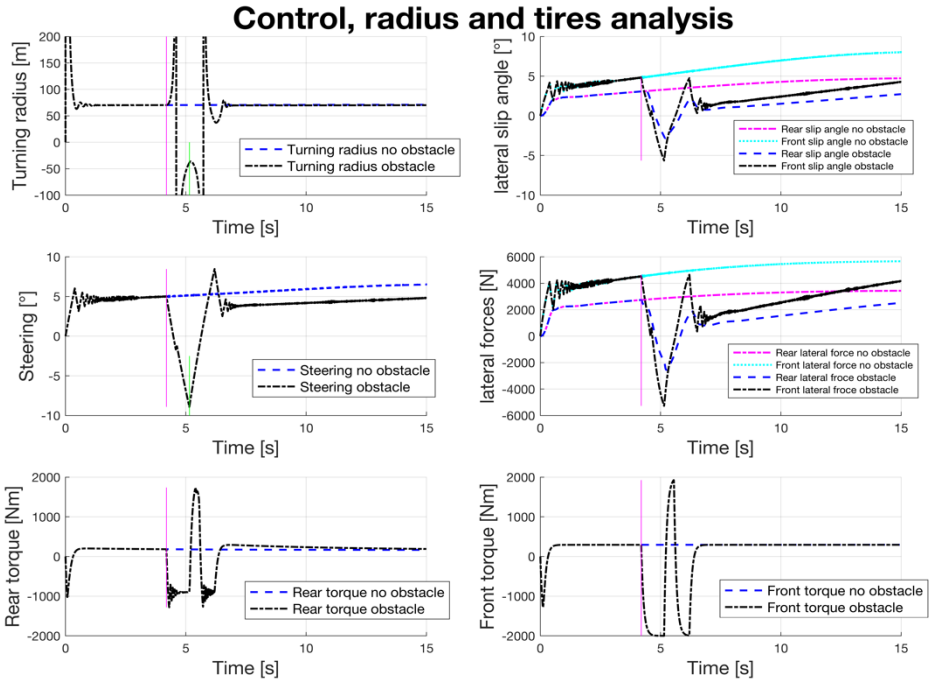


Figure 11: Control and Pacejka's forces comparison

Conclusions

The FLOP algorithm, here applied to an autonomous vehicle, provides promising results in terms of stability and robustness, even in critical scenarios, as shown in the case of the obstacle avoidance.

Most of the existing methods in the literature, have as their main drawback for engineering applications the fact their solution is represented by feed-forward law. These have an engineering weakness, that is they use only one single information on the system state: the initial condition, leading to a loss of robustness of the controlled system, except also external disturbances could be present. In this context, use of measurements by sensors is of great value, and feedback control strategies use the valuable support of measurement states. The FLOP algorithm, thanks to its feedback formulation, can rely on these information at the cost of providing a suboptimal solution, derived by the change of the optimality criterion form a global one to a local one.

References

[1] G. Pepe, D. Antonelli, L. Nesi, A. Carcaterra, *FLOP: feedback local optimality to control mechanical nonlinear systems*, (2018) under review at Mechanical Systems and Signal Processing.

[2] Pepe, G., Carcaterra, A., *VFC - Variational Feedback Controller and its application to semi-active suspensions*, (2016) Mechanical Systems and Signal Processing, 76-77, pp. 72-92.

[3] Pepe, G., Carcaterra, A., Giorgio, I., Del Vescovo, D., *Variational Feedback Control for a nonlinear beam under an earthquake excitation*, (2016) Mathematics and Mechanics of Solids, 21 (10), pp. 1234-1246.

[4] Pepe, G., Roveri, N., Carcaterra, A., *Prototyping a new car semi-active suspension by variational feedback controller*, (2016) Proceedings of ISMA 2016 - International Conference on Noise and Vibration Engineering and USD2016 - International Conference on Uncertainty in Structural Dynamics, pp. 231-245.

[5] Pensalfini, S., Coppo, F., Mezzani, F., Pepe, G., Carcaterra, A., *Optimal control theory based design of elasto-magnetic metamaterial*, (2017) Procedia Engineering, 199, pp. 1761-1766.

[6] Pepe, G., Carcaterra, A., *Semi-active damping by variational control algorithms*, (2014) Proceedings of the International Conference on Structural Dynamic, EURODYN, 2014-January, pp. 1721-1727.

[7] Pepe, G., Carcaterra, A., *A new semi-active variational based damping control*, (2014) MESA 2014 - 10th IEEE/ASME International Conference on Mechatronic and Embedded Systems and Applications, Conference Proceedings, art. no. 6935611.

[8] G. Pepe, I. Giorgio, A. Carcaterra, D. Del Vescovo, and A. Sestieri, *Semiactive vibration control via VFC-Variational Feedback by piezoelectric actuation*, (2015) in NOVEM2015.

[9] G. Pepe and A. Carcaterra, *VFC - Variational Feedback Control applied to semi-active car suspensions*, (2015) in NOVEM2015.

[10] Coppo, F., Pepe, G., Roveri, N., Carcaterra, A., *A multisensing setup for the intelligent tire monitoring*,(2017) Sensors, Article number 576.

[11] Roveri, N., Pepe, G., Carcaterra, A., *OPTYRE - A new technology for tire monitoring: Evidence of contact patch phenomena*, (2016) Mechanical Systems and Signal Processing, Volume 66-67, 2016, Pages 793-810.

[12] Roveri, N., Pepe, G., Carcaterra, A., *On line estimation of rolling resitance for intelligent tire*, (2016) Proceedings of ISMA 2016 - International Conference on Noise and Vibration Engineering and USD2016 - International Conference on Uncertainty in Structural Dynamics2016, Pages 1725-1740

[13] Haotian Cao, Xiaolin Song, and Zhi Huang, *A Switched MPC Lateral Steering Controller Which Considered Tracking Quality and Handling Quality for Autonomous Vehicle*, (2017) SAE Technical Paper 2017-01-1591.

[14] S. Çağlar Başlamişli , İ. Emre Köse & Günay Anlaç, *Handling stability improvement through robust active front steering and active differential control*, (2011) Vehicle System Dynamics, 49:5, 657-683

[15] Nobuyoshi Mutoh, *Driving and Bracking Torque Distribution Methods for Front-and-Rear-Wheel-Independent Drive-Type Electric Vehicles on Roads With Low Friction Coefficient*, (2012) IEEE 2012-2-3.

[16] Haiping Du, Nong Zhang, Fazel Naghdy, *Velocity-dependent robust control for improving vehicle lateral dynamics*, (2011) Transportation Research Part C 19 454-468.

FLOP: feedback local optimality control of the inverse pendulum oscillations

G. Pepe[1], D. Antonelli[1], L. Nesi[1], A. Carcaterra[1]
[1] Department of Mechanical and Aerospace Engineering
University of Rome "La Sapienza"
Rome, Italy
e-mail: **gianluca.pepe@uniroma1.it**

Abstract
Feedback control techniques for vibrations suppression are widely investigated in the technical literature. However, the most powerful method in this context, the optimal control theory, despites its generality and flexibility related to the user defined cost function, meets serious engineering limitations. This is due to the lack of a feedback law, because of the intrinsic formulation of the Pontryagin optimality criterion. This paper proposes a novel method of control that, still maintaining the structure of the optimal control technique, provides a feedback control. The method is applied to one of the most challenging nonlinear oscillation control, the inverse pendulum, that is a benchmark in the field.

The FLOP- Feedback Local OPtimality control, provides excellent results obtaining with a unique control law a very rapid swing-up of the pendulum and its inverse position characterized by instable vibrations is maintained by the FLOP control in a more efficient way with respect to competitor recent methods.

1 Introduction

In this paper, a new method of solution for optimal control problems, named FLOP- Feedback Local OPtimality is presented. The method is based on the use of a variational method that is modified to obtain a feedback control. In this sense FLOP is part of a new class of algorithms the group is developing under the name of VFC- Variational Feedback Controllers. The FLOP gives the possibility to control complex systems through a feedback control law. Currently, VFC methods are being tested in various engineering fields, from autonomous driving systems to intelligent suspensions [1-4] and from vibrations control to smart materials field [5-7]. This new method is based on classical variational approach based on Pontryagin's optimal problem [8, 9], but it gives the possibility to reach a form of feedback control by changing the optimality condition, as it will be seen in next section. Through the application of this new optimality condition, VFC can be applied also to non-linear dynamical systems. VFC approach belongs to the category of nonlinear controls such as Sliding Mode, Lyapunov and feedback linearization controls [10-12] but FLOP adds the possibility to perform specific objective functions respecting assigned constraints.

Pendula problems are generally used to approximate many engineering problems as vertical rocket landing, human locomotion and balancing vertical objects. These systems are typically under-actuated, hence extremely unstable and difficult to control. Therefore, pendula problems represent a useful test for new control algorithms. Nowadays, many strategies have already been proposed and implemented to such systems and usually these strategies are based on fuzzy logic by switching different type of controls e.g. [13-17] .

This paper shows that the proposed FLOP method can control both a swing up maneuver and an upward pendulum position. Moreover, it is shown the robustness of the tuned control.

2 Resume of FLOP theory

2.1 Description of the new local optimality principle

Recently the authors have developed a control strategy based on classical variational approach. This approach introduces a local optimality condition trough which is possible to obtain a feedback control law for non-linear dynamical system. Classical variational problem states the cost functional $\bar{J}$ needs to be minimized in the entire time interval $[0, T]$. The main idea of the FLOP- Feedback Local OPtimality control is to divide the original functional (1) into N functionals with a short time interval $\Delta\tau$ (equation (2)) and to minimize each one of them, creating a local optimality condition. With local optimality condition, FLOP approach creates a new scenario for the control of dynamical system, for three, main reasons:

(i) Dynamical system can be a non-linear one, and complete theory has been developed for class of dynamical system of the form $\dot{x} = \phi(x) + Bu + C$. Recently, authors are working also on non-linear dynamical system in control variable, considering also the control constraints.

(ii) A new class of non-linear functions, differentiable in the state and control variables, can be introduced in a general objective function $E(x, u)$. It can be customized to add some high/low potential zones to reach a specific target point (low potential area) and, simultaneously, avoid some obstacle points (high potential zones), as it will be shown in next section. The possibility to add this class of non-linear functions permits to overcome difficulties derived from classical quadratic cost function used in the LQR approach.

(iii) The FLOP is a feedback control based on an optimal principle and permits to overcome the main drawback of classical optimal problem solved by Pontryagin's or Bellman's method, which solutions are represented by feed-forward law.

Although, it is important to denote that FLOP approach, in general, does not leads to the optimal control but it leads to a local optimal control. Therefore, with the assumption stated in (2) for obtaining the local optimality condition, an error from the minimization problem in (1) is produced. It has been demonstrated that, in some cases, this error goes to zero but, in general, an error will be committed by using the FLOP approach.

Classical variational approach is based on a minimization problem as:

$$\begin{aligned} &\min \bar{J} = \int_0^T E\big(x(t), u(t)\big)\, dt \\ &\text{subject to} \\ &\dot{x} = f\big(x(t), u(t)\big) \\ &x(0) = x_0 \end{aligned} \tag{1}$$

$$\min J = \int_0^T E(x,u) + \lambda\big(\dot{x} - f(x,u)\big)\, dt = \int_0^T \mathcal{L}(\dot{x}, x, u, \lambda) dt,$$

In (1), x is the system state and u is the input control. The associated equation of the controlled process $\dot{x} = f(x, u, t)$ with its known initial condition $x(0) = x_0$ represents a constraint between x and u. The inclusion of the constraint is made by the Euler-Lagrange multiplier $\lambda(t)$. The problem (1) is solved by finding an optimal control $u^*(t)$ to which the optimal trajectory $x^*(t)$ is associated.

The new proposed method of control FLOP is based on a less accurate solution by solving not the entire time domain [0 T] but N-subintervals.

$$J = \int_0^T \mathcal{L}(\dot{x}, x, u, \lambda)dt = \sum_1^N J_i = \int_{\tau_0}^{\tau_1} \mathcal{L}(\dot{x}, x, u, \lambda)dt + \cdots + \int_{\tau_{N-1}}^{\tau_N} \mathcal{L}(\dot{x}, x, u, \lambda)dt \tag{2}$$

In (2) a new optimality condition is required, so that a minimization for each of time-limited functional is required:

$$\min J_i = \int_{\tau_{LB_i}}^{\tau_{UB_i}} \mathcal{L}(\dot{x}, x, u, \lambda)dt \tag{3}$$

where *UB* and *LB* pedixs are indicating *upper bound* and *lower bound*. For each integral is required to satisfy the boundary conditions for the related Pontryagin's equations, the initial and transversality conditions, so that:

$$\begin{aligned} x_{LB_i}(\tau_{i-1}) &= x_{UB_{i-1}}(\tau_{i-1}) \\ \lambda_{UB_i}(\tau_i) &= 0 \end{aligned} \tag{4}$$

The new criterion of optimality expressed by (3) leads to find the optimal local trajectory and control (x_i^*,u_i^*) and the sum of each integrals lead to the optimal local solution J'^*:

$$J'^* = \sum_{i=1}^N \int_{\tau_{i-1}}^{\tau_{i-1}+\Delta\tau_i} \mathcal{L}(x_i^*, u_i^*)dt \tag{5}$$

In general, J^* represents the optimum over the whole interval $[0, T]$, instead J'^* is based on a sequence of local optimality principles and is possible to demonstrate that $J^* \leq J'^*$ or rather:

$$\Delta J = J^* - J'^* = \sum_{i=1}^N \int_{\tau_{i-1}}^{\tau_{i-1}+\Delta\tau_i} \mathcal{L}(v^*) - \mathcal{L}(v_i^*)\ dt = \Delta\boldsymbol{\tau}^T \boldsymbol{\mathcal{J}} \Delta\boldsymbol{\tau} \tag{6}$$

The term $\Delta\boldsymbol{\tau}\,\boldsymbol{\mathcal{J}}\Delta\boldsymbol{\tau}$ is the residual term, with $\boldsymbol{\mathcal{J}}$ a $\mathbb{R}^{NxN}$ matrix depending on the couple of (x^*,u^*) and (x_i^*,u_i^*) and $\Delta\boldsymbol{\tau}$ is a $\mathbb{R}^N$ vector of $\Delta\tau_i$ elements.

The last expression shows the error is a quadratic form in terms of the smalls time intervals, neglecting higher order terms.

2.2 Resume of FLOP application strategy

Starting from (5), applying variational approach and by discretizing result using the Euler first-order approximation for $\dot{x}_i$ and $\dot{\lambda}_i$, it results:

$$\begin{cases} \left.\frac{\partial E}{\partial x}\right|_{LB_i} + \left.\left(\lambda\frac{\partial f}{\partial x}\right)\right|_{LB_i} - \frac{\lambda_{UB_i} - \lambda_{LB_i}}{\Delta\tau} = 0 \\ \left.\frac{\partial E}{\partial u}\right|_{LB_i} + \left.\left(\lambda\frac{\partial f}{\partial u}\right)\right|_{LB_i} = 0 \qquad\qquad \forall\ i \in [1, N] \\ \frac{x_{UB_i} - x_{LB_i}}{\Delta\tau} = f\left(x_{LB_i}, u_{LB_i}\right) \end{cases} \tag{7}$$

Set of equations (6) leads to a system of three equations in three unknowns for each i. By applying local optimality condition (4), it follows that $\dot{\lambda}_i = \frac{\lambda_{UB_i} - \lambda_{LB_i}}{\Delta\tau} = -\frac{\lambda_{LB_i}}{\Delta\tau}$. Looking at the continuous counterpart of this equation, it is natural to assume $\dot{\lambda} = -\frac{\lambda}{\Delta\tau} = G\lambda$. This leads to a reformulation of the Pontryagin's problem in the following augmented form:

$$\begin{cases} \dfrac{\partial E}{\partial x} + \lambda \dfrac{\partial f}{\partial x} - \dot{\lambda} = 0 \\ \dfrac{\partial E}{\partial u} + \lambda \dfrac{\partial f}{\partial u} = 0 \\ \dot{x} = f(x,u,t) \\ \dot{\lambda} = G\lambda \end{cases} \quad \forall\ t \in [0,T] \tag{8}$$

Starting from general dynamical system in the form of $\dot{\boldsymbol{x}} = \boldsymbol{\phi}(\boldsymbol{x}) + \boldsymbol{Bu} + \boldsymbol{C}$ with $\boldsymbol{\phi}(\boldsymbol{x})$ to be a generical differentiable non-linear function and writing the cost function $E(\boldsymbol{x}, \boldsymbol{u})$ with classical quadratic cost function plus a generical non-linear function in the state variable, functional in (1) is written as:

$$J = \int_0^T \frac{1}{2}\boldsymbol{x}^T\boldsymbol{Q}\boldsymbol{x} + \frac{1}{2}\boldsymbol{u}^T\boldsymbol{R}\boldsymbol{u} + g(\boldsymbol{x}) + \boldsymbol{\lambda}^{\boldsymbol{T}}\left(\dot{\boldsymbol{x}} - (\boldsymbol{\phi}(\boldsymbol{x}) + \boldsymbol{Bu} + \boldsymbol{C})\right) dt \tag{9}$$

From expression (8) it is possible to apply the FLOP method and to obtain:

$$\begin{gathered} \dot{\boldsymbol{x}} = \boldsymbol{\phi}(\boldsymbol{x}) + \boldsymbol{Bu} + \boldsymbol{C} \\ \boldsymbol{u} = (\boldsymbol{R}^T)^{-1}\boldsymbol{B}^T[\boldsymbol{\Phi}(\boldsymbol{x})^T + \boldsymbol{G}]^{-\mathbf{1}}[\boldsymbol{Q}^T\boldsymbol{x} + \boldsymbol{\gamma}^T(\boldsymbol{x})] \end{gathered} \tag{10}$$

where:

- $\boldsymbol{G} = -\frac{1}{\Delta\tau}\boldsymbol{I}$
- $\boldsymbol{\Phi}(\boldsymbol{x}) = \boldsymbol{\nabla_x}\boldsymbol{\phi}(\boldsymbol{x})$
- $\boldsymbol{\gamma}(\boldsymbol{x}) = \boldsymbol{\nabla_x} g(\boldsymbol{x})$

In equation (9), the function $g(x)$ in the cost function $E(x,u)$ is introduced, for which the only requirement is to be differentiable in the state variable. A wider class of objective functions, that goes beyond the limit of quadratic terms as usual for LQR, permits generalizations because of the chance of introducing sharp local effects, especially useful for obstacle avoidance as well as for target reaching.

3 FLOP control of inverse pendulum

3.1 The inverted Pendulum

A schematics representation of the inverted pendulum in Figure 1 is shown.

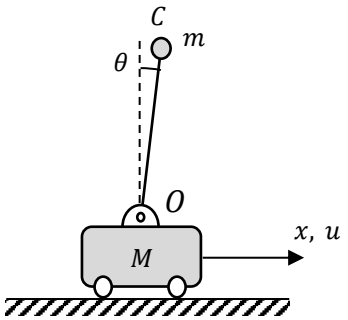


Figure 1 inverted pendulum

The variable used are described in Table 1:

Symbol	Description
M	Mass of the cart 0.5 [kg]
m	Mass of the pendulum 0.2 [kg]
l	Length of the pendulum 0.3 [m]
x	Position of the cart [m]
θ	Angular rotation [rad]
u	Force on the actuator [N]
g	Acceleration of gravity $[m/s^2]$

Table 1: Symbols and values used

The dynamic system starting from the classical Hamilton-Lagrange's equations is derived, so that:

$$\frac{d}{dt}\frac{\partial L}{\partial \dot{q}_k} - \frac{\partial L}{\partial q_k} = Q_k \qquad L = T - U \tag{11}$$

with T, U, Q_k and q_k are the kinetic, the potential energy, the generalized forces of the system and the Lagrange's variables respectively.

Considering the Lagrange's vector $\boldsymbol{q} = [x, \theta]^T$, the kinetic and potential energy are defined as:

$$T = \frac{1}{2}M\dot{x}^2 + \frac{1}{2}m\left(\dot{\theta}^2 l^2 + \dot{x}^2 + 2\dot{x}\dot{\theta}l\cos\theta\right) \qquad U = mgl(1+\cos\theta) \tag{12}$$

The resulting dynamical system is:

$$(m+M)\ddot{x} + ml\ddot{\theta}\cos\theta - ml\dot{\theta}^2\sin\theta = u \qquad l\ddot{\theta} + \ddot{x}\cos\theta = g\sin\theta \tag{13}$$

Arranging the (13) in four first order differential equations, it is obtained:

$$\dot{\boldsymbol{x}} = \boldsymbol{\phi}(\boldsymbol{x}) + \boldsymbol{h}(\boldsymbol{x})u \tag{14}$$

where:

$$\boldsymbol{x} = \left[x, \theta, \dot{x}, \dot{\theta}\right]^T \qquad \boldsymbol{\phi}(\boldsymbol{x}) = \begin{bmatrix} \dot{x} \\ \dot{\theta} \\ \boldsymbol{M}(\boldsymbol{x})^{-1}\boldsymbol{P}(\boldsymbol{x}) \end{bmatrix} \qquad \boldsymbol{h}(\boldsymbol{x}) = \begin{bmatrix} 0 \\ 0 \\ \boldsymbol{M}(\boldsymbol{x})^{-1}\boldsymbol{d} \end{bmatrix}$$
$$\boldsymbol{M}(\boldsymbol{x}) = \begin{bmatrix} M+m & ml\cos(\theta) \\ \cos(\theta) & l \end{bmatrix} \qquad \boldsymbol{P}(\boldsymbol{x}) = \begin{bmatrix} ml\dot{\theta}^2\sin(\theta) \\ g\sin(\theta) \end{bmatrix} \qquad \boldsymbol{d} = \begin{bmatrix} 1 \\ 0 \end{bmatrix} \tag{15}$$

The here presented simplified version of the FLOP requires $\boldsymbol{h}(\boldsymbol{x})$ to be linear in the state variable, therefore it is linearized in the target position, i.e. $\boldsymbol{x}_T = \boldsymbol{0}$. After the partial linearization, the dynamical system in (14) is rewritten as it follows:

$$\dot{\boldsymbol{x}} = \tilde{\boldsymbol{\phi}}(\boldsymbol{x}) + \boldsymbol{B}u + \boldsymbol{C}$$

with:

$$\begin{aligned} &\boldsymbol{B} = \boldsymbol{h}(\boldsymbol{x}_T) \\ &\tilde{\boldsymbol{\phi}}(\boldsymbol{x}) = \boldsymbol{\phi}(\boldsymbol{x}) + \boldsymbol{\mathcal{A}}\boldsymbol{x} \\ &\boldsymbol{\mathcal{A}} = \boldsymbol{\nabla}_{\boldsymbol{x}}(\boldsymbol{h}(\boldsymbol{x})u)|_{\boldsymbol{x}_T, u_T} \\ &\boldsymbol{C} = -\boldsymbol{\nabla}_{\boldsymbol{x}}(\boldsymbol{h}(\boldsymbol{x})u)|_{\boldsymbol{x}_T, u_T}\, \boldsymbol{x}_T \\ &u_T = 0 \end{aligned} \tag{16}$$

3.2 Swing up controller

The functional to be minimized is J:

$$J = \int_0^T \frac{1}{2}\boldsymbol{x}^T\boldsymbol{Q}\boldsymbol{x} + \frac{1}{2}\dot{\boldsymbol{x}}^T\boldsymbol{S}\dot{\boldsymbol{x}} + \frac{1}{2}Ru^2 + g(\boldsymbol{x}) + \boldsymbol{\lambda}^{\boldsymbol{T}}\left(\dot{\boldsymbol{x}} - \left(\tilde{\boldsymbol{\phi}}(\boldsymbol{x}) + \boldsymbol{B}u + \boldsymbol{C}\right)\right) dt \tag{17}$$

where $g(\boldsymbol{x})$ is suitably chosen θ-dependent to perform the swing up manoeuvre. Namely, $g(\boldsymbol{x})$ is shaped to create a potential-attractive function at the upward position of the pendulum, and a potential-repulsive function at the downward pendulum position. The sum of three Gaussian-like functions is useful to obtain this goal:

$$g(\theta) = -k_1 e^{-\alpha_1\theta^2} + k_2 e^{-\alpha_2(\theta+\boldsymbol{\pi})^2} + k_3 e^{-\alpha_3(\theta-\boldsymbol{\pi})^2} \tag{18}$$

the last two terms are due to the downward position can be reached for clockwise or anti-clockwise rotations, and k_i and α_i are tuning parameters.

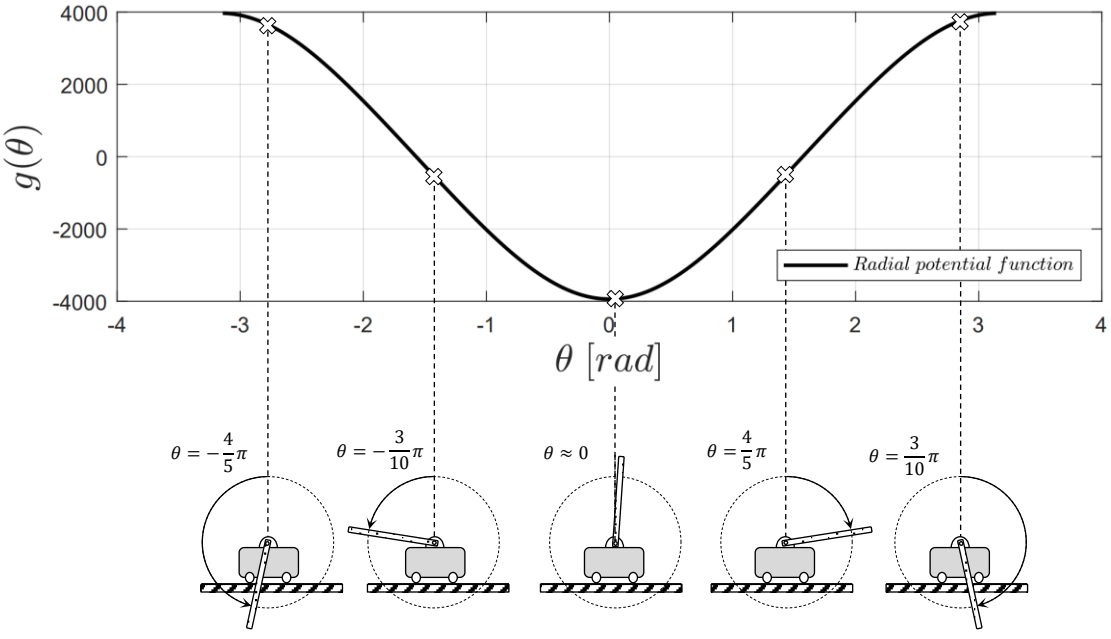


Figure 2 inverted pendulum

The FLOP formulation (10) leads to a control feedback:

$$u^* = f(\boldsymbol{Q}, \boldsymbol{S}, \boldsymbol{R}, \boldsymbol{G}, g(\theta), \boldsymbol{x}) \tag{19}$$

specifically:

$$u^* = (\boldsymbol{R}^T + \boldsymbol{B}^T\boldsymbol{S}\boldsymbol{B})^{-1}\,\boldsymbol{B}^T\left(\boldsymbol{\lambda} - \boldsymbol{S}\widetilde{\boldsymbol{\phi}}(\boldsymbol{x}) - \boldsymbol{S}\boldsymbol{B}\boldsymbol{u}_T - \boldsymbol{C}\right) + \boldsymbol{u}_T$$

with

$$\begin{aligned}
&\boldsymbol{u}_T = -\boldsymbol{B}^{+}\left[\widetilde{\boldsymbol{\phi}}(\boldsymbol{x}_T) + \boldsymbol{C}\right]\\
&\boldsymbol{\Phi}(\boldsymbol{x}) = \boldsymbol{\nabla}_{\boldsymbol{x}}\widetilde{\boldsymbol{\phi}}(\boldsymbol{x})\\
&\boldsymbol{\gamma}(\boldsymbol{x}) = \boldsymbol{\nabla}_{\boldsymbol{x}} g(\boldsymbol{x})\\
&\boldsymbol{\lambda} = \widetilde{\boldsymbol{A}}^{-1}\left[\boldsymbol{Q}^T(\boldsymbol{x} - \boldsymbol{x}_T) + \boldsymbol{\gamma}^T(\boldsymbol{x} - \boldsymbol{x}_T) + \boldsymbol{\Phi}(\boldsymbol{x})^T\boldsymbol{S}\left[\widetilde{\boldsymbol{\phi}}(\boldsymbol{x}) - \boldsymbol{B}\left[\boldsymbol{R}_1^{-1}\boldsymbol{B}^T\left(\boldsymbol{S}\widetilde{\boldsymbol{\phi}}(\boldsymbol{x}) + \boldsymbol{S}\boldsymbol{B}\boldsymbol{u}_T + \boldsymbol{C}\right) - \boldsymbol{u}_T\right] + \boldsymbol{C}\right]\right]\\
&\boldsymbol{R}_1 = \boldsymbol{R}^T + \boldsymbol{B}^T\boldsymbol{S}\boldsymbol{B}\\
&\widetilde{\boldsymbol{A}} = \left[\boldsymbol{\Phi}(\boldsymbol{x})^T\left(\boldsymbol{I} - \boldsymbol{S}\boldsymbol{B}\boldsymbol{R}_1^{-1}\boldsymbol{B}^T\right) + \boldsymbol{G}\right]\\
&\boldsymbol{G} = -\frac{1}{\Delta\tau}\boldsymbol{I}\\
&\boldsymbol{x}_T \ \textit{is the target state vector}
\end{aligned} \tag{20}$$

An optimization procedure is needed to find the best values for $\boldsymbol{Q}, \boldsymbol{S}, \boldsymbol{R}, \boldsymbol{G}$ k_i and α_i, that are tested analysing the control features in the next sections.

3.3 Numerical results

In the Table 2 the parameters values and the tuning parameter used in the numerical simulations are listed.

Tuning parameters	**Value**
$\boldsymbol{Q}$	$\begin{bmatrix} 10 & 0 & 0 & 0 \\ 0 & 0 & 0 & 0 \\ 0 & 0 & 8 & 0 \\ 0 & 0 & 0 & 0 \end{bmatrix}$
$\boldsymbol{S}$	$\begin{bmatrix} 24 & 0 & 0 & 0 \\ 0 & 100 & 0 & 0 \\ 0 & 0 & 22 & 0 \\ 0 & 0 & 0 & 7 \end{bmatrix}$
R	1
$\boldsymbol{k} = [k_1, k_2, k_3]$	[80, 4 , 4]
$\boldsymbol{\alpha} = [\alpha_1, \alpha_2, \alpha_3]$	[0.125 , 50 , 50]

Table 2: Parameters used

Numerical results for FLOP control under different conditions are obtained, showing its robustness and effectiveness in bringing the pendulum in the upper position. To test the control algorithm, limitations were imposed on both the maximum u_{max} actuation force and the 10Hz response time of the actuator for all simulations. All the following figures shows the positions of the carriage, the angular position of the pendulum and the respective speeds, finally the force control u is shown in the lower part of the figure.

Figure 3 shows four different cases of swing up. Cases 1 and 4 have the same trend and are overlapped until the 15th second in which, in case 4, the pendulum undergoes a disturbance. Both cases oscillate around the equilibrium position and carry out the ascent manoeuvre that ends after only 7 seconds of oscillation. The trolley moves only 20 cm from the origin, exploiting maximum actuator accelerations less than 0.2g. When the pendulum is now in the upper vertical position, a disturbance is applied and it is possible to notice how the cart reacts quickly in such a way to keep the upper position of the rod stable and then slowly returning to the position of the zero displacement. Case 3 is very similar to case 1, except for the inertial characteristics of the pendulum. In fact, to validate the control, random variations of 10% is introduced for the mass of the carriage, mass and length of the rod while maintaining constant the tuning parameters of the control logic. Case 2 is instead a swing up test starting from the initial pendulum conditions of π/2. This condition is very favourable, because the pendulum is already oscillating and is pulled up in less than one second, keeping the carriage travel very limited near the origin.

Finally, to verify the robustness of the presented controller, a large set of simulations with random initial conditions are performed, changing the initial speed of the cart and rod and different angular rod position (Figure 4). The control shows good results in all cases, driving both the cart and the rod to the desired positions.

The Figure 5 shows a comparison simulation with a nonlinear control logic based on energy [17]. In particular, this technique is based on the fusion of two controls, the first of Lyapunov type, used when the pendulum is in its lower configuration, and the second, LQR based, intervenes when a threshold set for the angle close to the origin is exceeded. Synthetically, energy-based control is formulated as follows:

$$u_{energy} = \begin{cases} -\boldsymbol{K}_{LQR}\boldsymbol{x} & |\theta| < \varepsilon \\ sat_{u_{max}}(\mu(E - E_r)sign(\dot{\theta}\cos\theta)) & otherwise \end{cases} \tag{21}$$

where $\boldsymbol{K}_{LQR}, E,\ E_r, \mu, \varepsilon$ are the Riccati gain of LQR, the instantaneous potential and kinetic energy of the pendulum, the reference energy of the upward position and the last two terms are tuning parameters.

In the Figure 5 and Figure 6 it is possible to observe a comparison between FLOP and Energy control based. To compare FLOP *ceteris paribus* with the method proposed in [17], the limit u_{max} must be moved up to 5N and the response time of the actuator is increased up to 100Hz because it is difficult to find tuning parameters admissible for control in energy. The switch threshold was set to ε = 30°. Both controls behave very well and the energy method is able to pull up the pendulum in a very short time if it starts from the rest condition. In the case illustrated in Figure 5, in which the pendulum starts from the π rest condition, the energy method, although very reactive in the swing up operation, moves far away from the origin, almost 2 meters. On the contrary, FLOP shows a trend of oscillations that move away the pendulum of only 50cm from the origin. FLOP control proves to be slow only starting from the rest condition; in fact, in Figure 6 it is possible to observe a much faster dynamics starting both from 3/4 π rod position. In addition, in the last simulation FLOP demonstrates an excellent control ability to rise up combining small movements. Finally, FLOP use the actuator in a smoother way, arriving only a few times to the saturation condition.

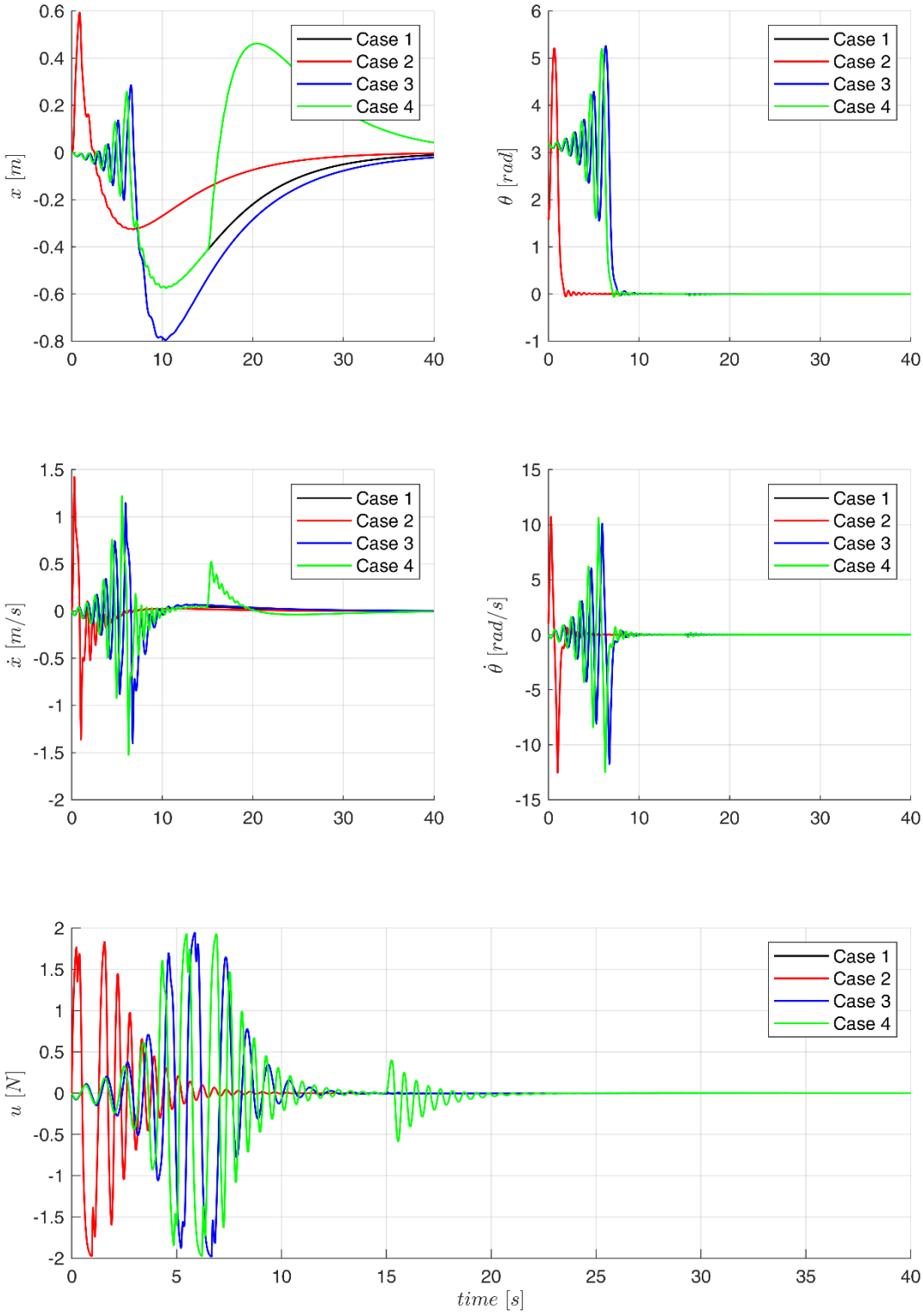


Figure 3 Swing-up maneuver with perturbed parameters

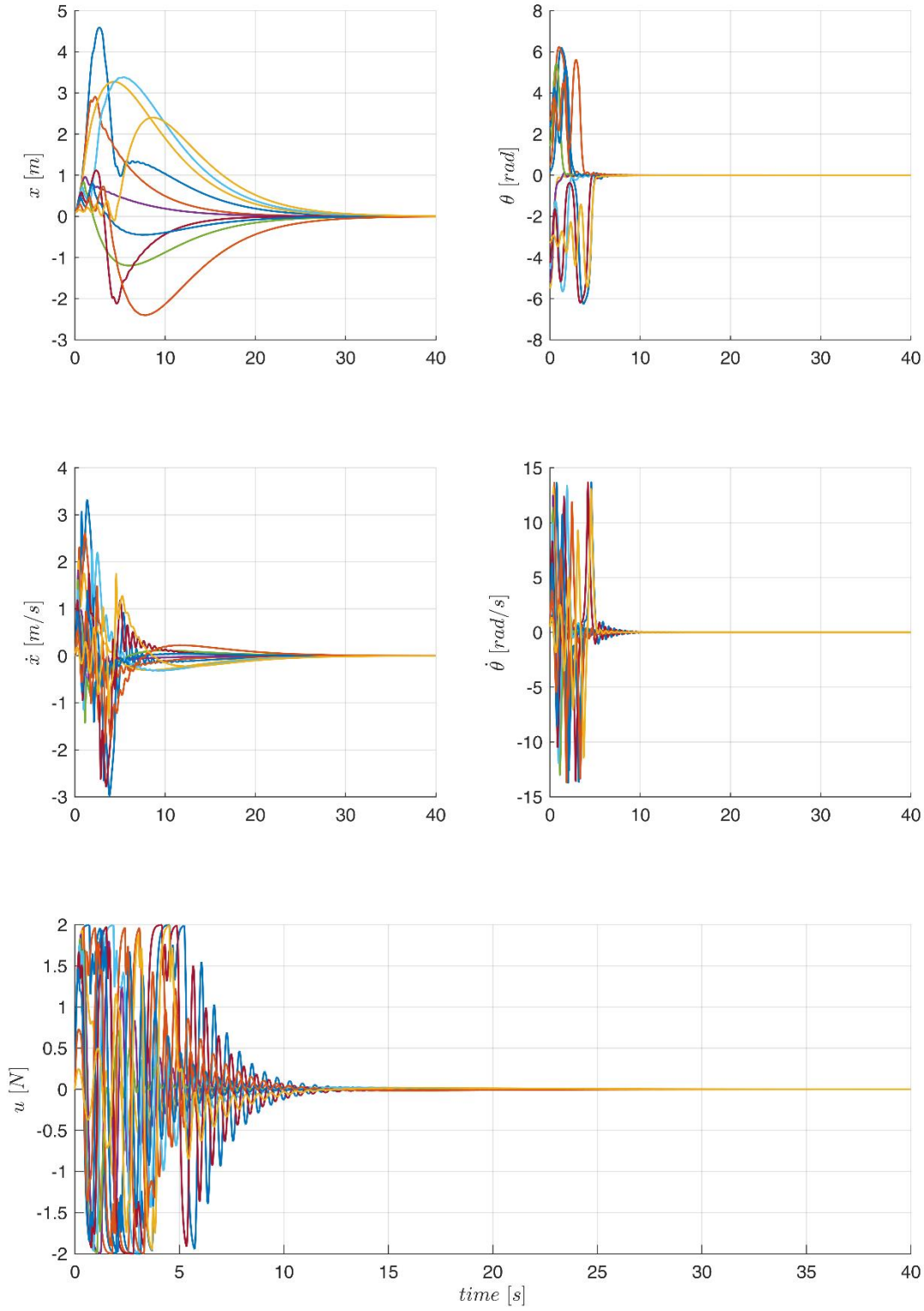


Figure 4 Swing-up maneuver with different initial conditions

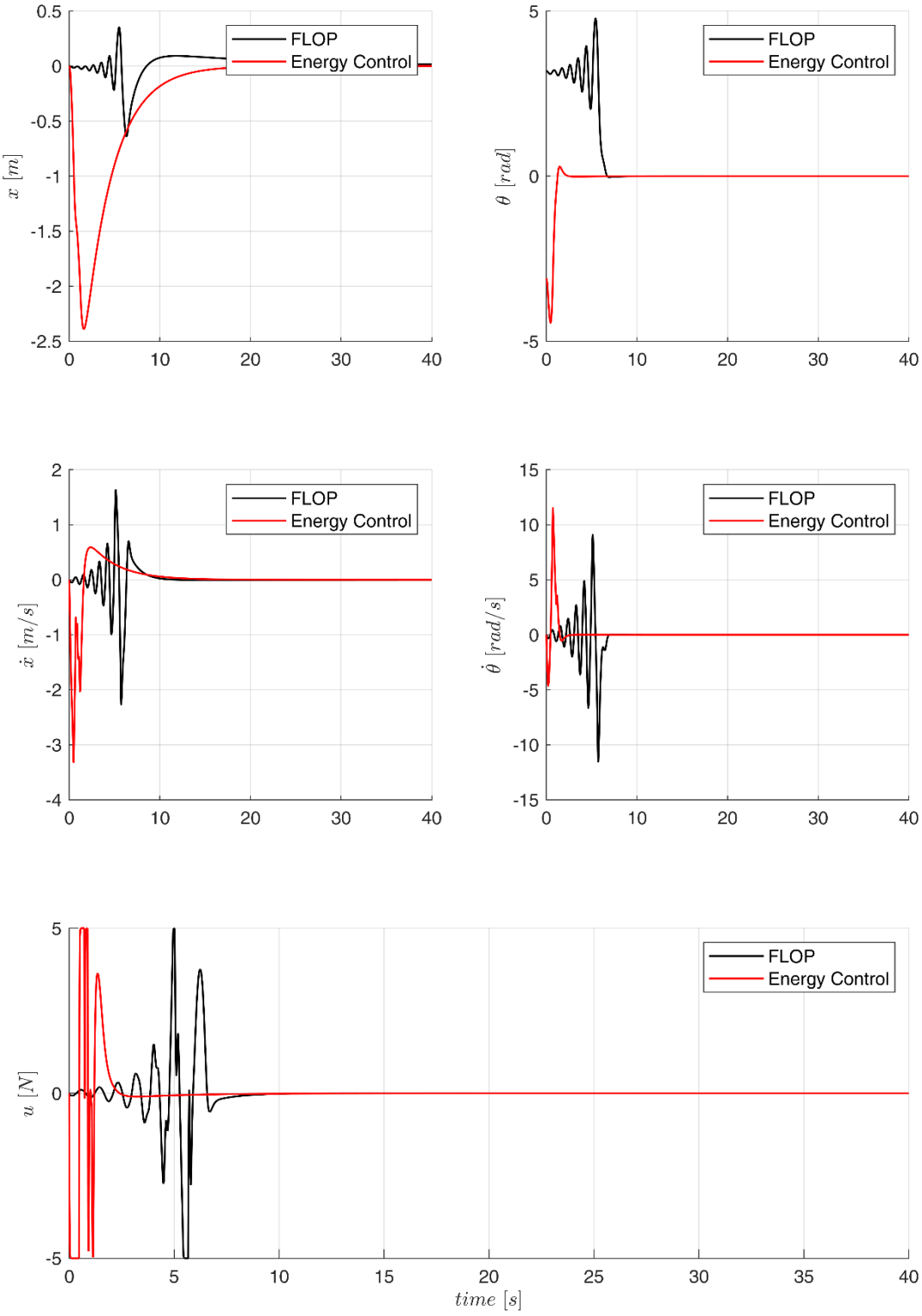


Figure 5 Swing-up maneuver vs energy method

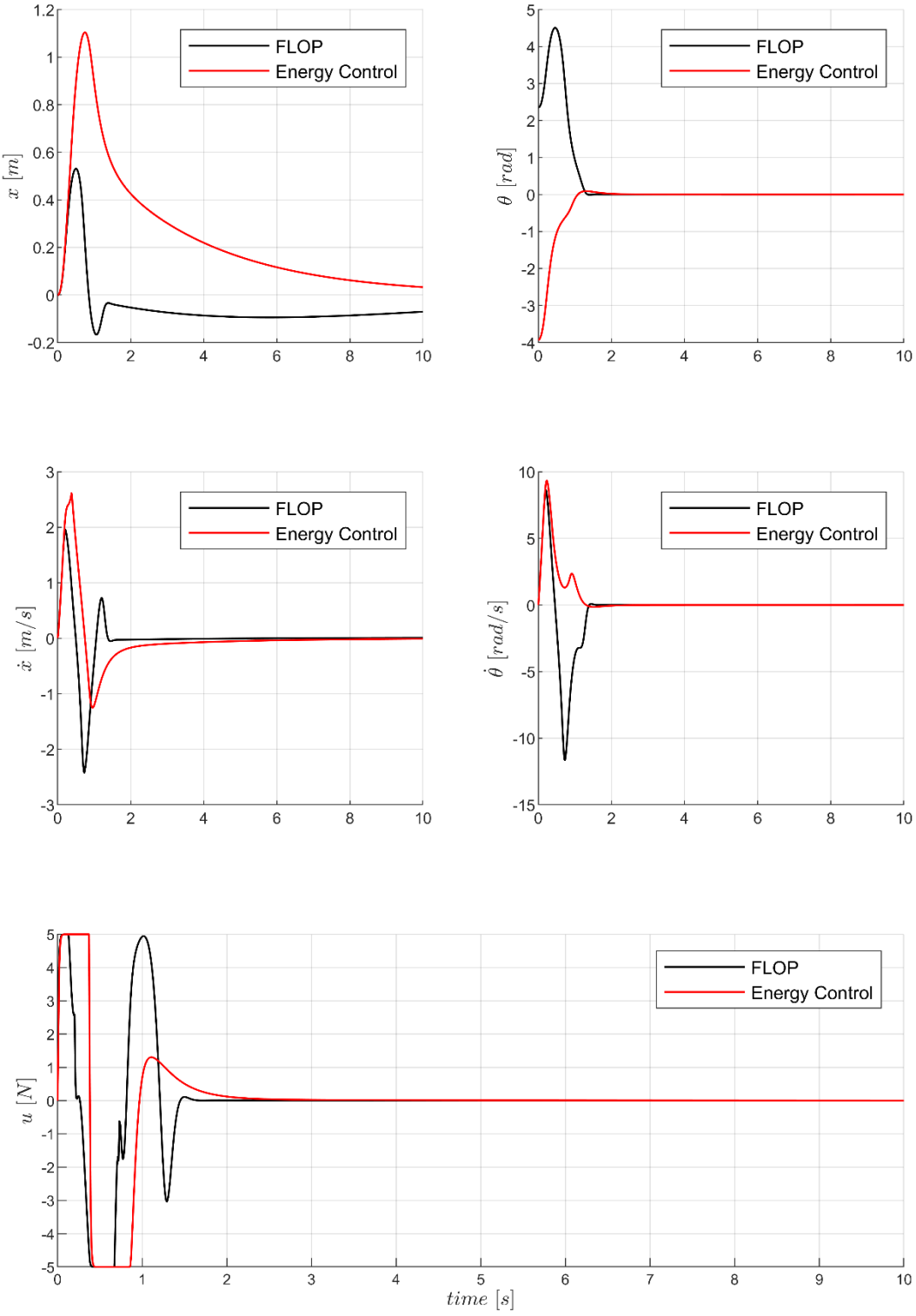


Figure 6 Swing-up maneuver vs energy method from $\theta_0 = \pi 3/4$

4 Conclusions

A new method of control for mechanical systems, named FLOP is introduced. This method belongs to a class of methods developed at the Sapienza Mechatronic Lab and named Variational Feedback Control VFC methods based on local optimality principle with the possibility to include both non-linear dynamics and to formulate a wider class of cost functions such as in the classic LQR. In fact, FLOP permits to introduce in the objective function specific requests giving the chance of introducing sharp local effects, especially useful for obstacle avoidance as well as for reaching specific targets.

In this paper the FLOP method is applied to control an inverse pendulum showing robustness and effectiveness for the swing up manoeuvre. The control, thanks to its formulation, allows to choose how the pendulum is accompanied and maintained in the upper position. In fact, in the objective function it is possible to create customized potential functions allowing different control behaviours, such as managing the initial oscillations of the pendulum in the downward position, differently from the maintenance of the upward position. The FLOP control is also compared with Lyapunov control law method mixed to LQR control and it reaches excellent results.

References

[1] G. Pepe and A. Carcaterra, *VFC – Variational Feedback Controller and its application to semi-active suspensions*, Mechanical Systems and Signal Processing, (2016).

[2] G. Pepe, N. Roveri, and A. Carcaterra, *Prototyping a new car semi-active suspension by variational feedback controller*, presented at the ISMA 2016, Leuven, Belgium, (2016).

[3] G. Pepe and A. Carcaterra, *Semi-Active Damping by Variational Control Algorithms*, presented at the Proceedings of the 9th International Conference on Structural Dynamics, EURODYN 2014, Porto, Portugal, (2014).

[4] G. Pepe and A. Carcaterra, *A new semi-active variational based damping control*, in MESA (2014 - 10th IEEE/ASME International Conference on Mechatronic and Embedded Systems and Applications, Conference Proceedings, (2014).

[5] G. Pepe, A. Carcaterra, I. Giorgio, and D. Del Vescovo, *Variational Feedback Control for a nonlinear beam under an earthquake excitation*, Mathematics and Mechanics of Solids, (2014).

[6] S. Pensalfini, F. Coppo, F. Mezzani, G. Pepe, and A. Carcaterra, *Optimal control theory based design of elasto-magnetic metamaterial*, Procedia Engineering, vol. 199, pp. 1761-1766, (2017).

[7] G. Pepe, I. Giorgio, A. Carcaterra, D. Del Vescovo, and A. Sestieri, *Semiactive vibration control via VFC-Variational Feedback by piezoelectric actuation*, in NOVEM2015, (2015).

[8] L. S. B. Pontryagin, V. G., R. V. Gamkrelidze, and E. F. Mishchenko, *The Mathematical Theory of Optimal Processes*, Interscience, ISBN 2-88124-077-1, (1962).

[9] A. E. Bryson, *Applied Optimal Control: Optimization, Estimation and Control* (Halsted Press book'). Taylor & Francis, (1975).

[10] A. Bacciotti and L. Rosier, *Liapunov Functions and Stability in Control Theory* (Communications and Control Engineering). Springer Berlin Heidelberg, (2005).

[11] V. Utkin, J. Guldner, and J. Shi, *Sliding Mode Control in Electro-Mechanical Systems*, Second Edition (Automation and Control Engineering). CRC Press, (2017).

[12] A. Isidori, Nonlinear control systems. 2 (1999), *Communications and control engineering*, Springer, (1999).

[13] S. Jadlovska and J. Sarnovsky, *A complex overview of modeling and control of the rotary single inverted pendulum system*, Advances in Electrical and Electronic Engineering, Article vol. 11, no. 2, pp. 73-85, (2013).

[14] T. Horibe and N. Sakamoto, *Optimal Swing Up and Stabilization Control for Inverted Pendulum via Stable Manifold Method*, IEEE Transactions on Control Systems Technology, Article vol. 26, no. 2, pp. 708-715, (2018).

[15] T. T. Sarkar and L. Dewan, *Application of LQR and MRAC for swing up control of inverted pendulum*, in 2017 4th International Conference on Power, Control and Embedded Systems, ICPCES 2017, 2017, vol. (2017).

[16] X. Yang and X. Zheng, *Swing-Up and Stabilization Control Design for an Underactuated Rotary Inverted Pendulum System: Theory and Experiments*, IEEE Transactions on Industrial Electronics, Article vol. 65, no. 9, pp. 7229-7238, (2018).

[17] K. J. Åström and K. Furuta, *Swinging up a pendulum by energy control*, Automatica, vol. 36, no. 2, pp. 287-295, 2000/02/01/ (2000).

Active noise control in pipes and ducts using carbon nanotube thermophones

Andrew R. Barnard[1], Steven A. Senczyszyn[1]
[1] Michigan Technological University, Department of Mechanical Engineering – Engineering Mechanics
1400 Townsend Drive, Houghton, Michigan, United States
e-mail: **arbarnar@mtu.edu**

Abstract

Carbon nanotube thin films provide the capability to rapidly oscillate their surface temperature on time scales less than 10 nanoseconds. This unique feature allows them to be used as a thermophone, or thermoacoustic heat engine. As the surface of the film is rapidly and periodically heated by an electrical input signal, the surrounding air expands and contracts with the periodic heating to create a propagating acoustic wave. This type of loudspeaker is solid state with no moving parts and lightweight because there is no need for heavy magnets. In this paper, a coaxially configured thermophone will be discussed with applications in active noise control in pipes and ducts. Design parameters will be discussed as well as preliminary active noise cancellation data. Commercialization technical challenges will be presented.

1 Introduction

Recent technological advancements have allowed for revolutionary changes to noise abatement methods within pipe and duct systems. The implementation of active noise control, or the cancellation of sound through destructive interference, has removed the restriction of using purely passive sound absorption. However, the implementation of these active systems has been inhibited due to the strict requirements imposed by the traditional moving coil loudspeaker. Moving coil loudspeakers are heavy and sensitive to temperature, which makes installation into existing pipe and duct systems, such as automotive exhaust pipes, a significant challenge. This challenge has sparked the development of a revolutionary new loudspeaker technology to create a lightweight, solid-state, and flexible loudspeaker, known as the carbon nanotube (CNT) thermophone, or CNT loudspeaker. The CNT thermophone does not operate on a velocity boundary condition, like the moving coil loudspeaker, but rather on a temperature boundary condition, using rapid fluctuations in temperature to create an acoustic wave. These flexible and lightweight loudspeakers provide significant improvements towards the commercial design and implementation of active noise control systems.

2 Carbon nanotubes

2.1 Carbon nanotube definition

Carbon nanotubes (CNTs) were first discovered in 1991 by Sumio Iijima, a Japanese physicist, who found that hexagonally latticed tubes of carbon could be created using an arc-discharge method [31]. These allotropes of carbon have been characterized as seamless cylindrical nanostructures and have been the focus of a significant amount of research since their discovery, both in application and fabrication [24]. This research has led to the discovery of additional fabrication methods, such chemical vapor deposition (CVD) and laser ablation [37]. Using these different methods can create CNTs that vary in two key ways. The first difference is the number of carbon layers, or walls, present in the nanotube structure, which can range from

single-walled carbon nanotubes (SWCNT) to multi-walled carbon nanotubes (MWCNT) [7]. The second difference is the alignment of groups of carbon nanotubes, or forests, as they grow on the substrate, which can range from randomly aligned to vertically aligned. The CNT forest can also be superaligned, which is a vertically aligned forest that is able to be dry-drawn, or pulled, into a thin-film [33]. These CNT thin-films are the enabling technology behind the CNT thermophone. Currently, the superaligned MWCNT forests needed to create the CNT thermophones are produced exclusively using the CVD production method [48]. The CNT forests used to create the CNT thermophones presented are approximately 100 nm tall and produced by Nanoworld Laboratories. These CNTs have 7-8 shells with an outer diameter of approximately 10 nm and an inner diameter of approximately 5 nm [15].

2.2 Material properties of carbon nanotubes

Carbon nanotubes possess exceptional material properties that are desirable in areas such mechanical, thermal, and electrical applications. The electrical and thermal conductivity of CNTs are among the highest of any known materials, with a thermal conductivity of approximately 2.5 ± 0.5 W m^{-1} K^{-1} at room temperature and a heat capacity per unit are (HCPUA) of approximately $7.7x10^{-3}$ J/m^2 K [32]. These properties are inversely related to the height of the CNT forest, with shorter forests having higher thermal and electrical conductivity. The CNT thin-films also possess exceptional mechanical properties, with a tensile strength of approximately 7.9 MPa and a Young's modulus of 310 MPa, while having a density of 0.039 g cm^{-1} [44]. These properties make CNT thin-films a highly applicable and versatile material.

3 Carbon nanotube thermophones

3.1 Thermophone definition

The CNT thin-films allow for the creation of a CNT thermophone. A thermophone is a loudspeaker that creates sound by rapidly oscillating the surface temperature of a material at acoustic frequencies to generate an acoustic wave. This process, known as the thermoacoustic effect, utilizes a temperature boundary condition to generate sound, unlike the traditional moving coil loudspeaker, which requires a velocity boundary condition. Ferdinand Braun discovered the thermoacoustic effect in 1898 when he passed an alternating current through a bolometer [21]. Arnold and Crandall then conducted the first scientific exploration of this concept in 1917 when they attempted to create a thermophone using 700 nm platinum thin-film [8]. However, this initial attempt was limited by the relatively high heat capacity per unit area (HCPUA) of the platinum thin-film, which restricted the frequencies generated to a maximum of 16 Hz. Without a viable material to support it, this concept was left untouched for the next 90 years. In 2008, Xiao *et al.* passed an alternating current through a carbon nanotube thin-film and found that the material was emitting sound [59]. It was found that the CNT thin-film possessed a HCPUA that was low enough to allow for the generation of acoustic frequencies over a range of 1 Hz to 100 kHz. Since this discovery, the operation and application of CNT thermophones has been widely researched as an alternative to moving coil loudspeakers.

3.2 Characterization

Arnold and Crandall were able to derive the physics behind the thermoacoustic effect during their scientific exploration using the 700 nm platinum thin-film, which can be seen in Equation 1 [8]. They found that the root-mean-square (RMS) sound pressure, P, that a thermophone generates at a distance, r, for a given electrical input, W_{in}, is a function of the HCPUA of the material, C_s, the frequency, f, the thermal diffusivity, α, the density of the material, ρ_0, and the absolute ambient temperature of the surround gas, T_K.

$$P = \frac{\sqrt{\alpha f}\rho_0 W_{in}}{2\sqrt{\pi}(T_K + \Delta T) r C_s} \tag{1}$$

When Xiao *et al.* rediscovered this effect in 2008, it was found that the theory proposed by Arnold and Crandall was not suitable to predict the response of the CNT thermophone [59]. The initial theory was expanded upon to account for the instantaneous heat exchange per unit area between the CNT thin-film and the surrounding media due to thermal conduction, which can be seen in Equation 2. In the expanded term, $f_1 = (\alpha\beta_0^2)/(\pi\kappa^2)$, $f_2 = \beta_0/(\pi C_S)$, and $\Delta T = \frac{W_{in}}{2a\beta_0} = T_f - T_K$. These terms include the thermal conductivity of the CNT thin-film, κ, the single-sided surface area of the thin-film, *a*, and the rate of heat loss per unit area of the thin-film per rise in temperature above the surrounding, β_0.

$$P = \frac{\sqrt{\alpha f}\rho_0 W_{in}}{2\sqrt{\pi}(T_K + \Delta T) r C_s} \frac{\frac{f}{f_2}}{\sqrt{\left(1 + \sqrt{\frac{f}{f_1}}\right)^2 + \left(\frac{f}{f_2} + \sqrt{\frac{f}{f_1}}\right)^2}} \tag{2}$$

The CNT thermphone is a non-linear transducer. This non-linearity occurs because the output sound pressure level is proportional to the square of the input electrical current, resulting in a doubling of the output frequency compared to that of the input frequency [2]. The non-linear response creates a noticeable distortion if not properly compensated for. The non-linearity can be offset using two prominent signal processing techniques that have been developed. The first method involves adding a direct current (DC) to an alternating current (AC) in a method known as DCAC and can be seen in Equation 3. The second method requires the amplitude modulation of an alternating current, in a method known as AMAC and can be seen in Equation 4. Although these methods can negate the non-linearity, they do require additional input power to the CNT thermophone. The DCAC method generates a sounds pressure level, *P*, as a function of time that is dependent on the peak amplitude of the signal, *A*, the DC offset provided, *B*, and the frequency of the signal, ω. The AMAC method alters the input voltage of the signal, *V*, as a function of time, which is squared because of the non-linearity. This method is dependent on amplitude modulated signal, A_M, the amplitude of the carrier signal, A_C, the frequency of the modulated signal, F_M, and the frequency of the carrier signal, F_C [19].

$$P(t) \approx B^2 + 2BA\sin(\omega t) + A^2\left[\frac{1 - \cos(2\omega t)}{2}\right] \tag{3}$$

$$V(t) = (1 + A_M\cos(2\pi F_M t)) * A_C\sin(2\pi F_C t) \tag{4}$$

3.3 Open-air efficiency

A CNT thermophone in open air has a lower overall efficiency compared to that of a moving coil loudspeaker. Bouman *et al.* found that the overall efficiency of an open-air CNT thermophone is between 1.2 E-6 and 1083E-6 percent. These values were found using a 72 W_{rms} input signal [19]. A moving coil loudspeaker typically has an efficiency near one percent. While traditional moving coil loudspeakers are not very efficiency, the CNT thermophones are multiple orders of magnitude lower in efficiency. Xiao et al. has developed a theoretical model to find the true efficiency of an open-air CNT thermophone, η, which can be seen in Equation 5 [59]. The true efficiency is the ratio of acoustic output power to the electrical power input to the system. The theoretical model utilizes the sound power, Π, the total input power, P_{input}, the frequency, *f*, the density of the surrounding gas, ρ_0, the speed of sound in the gas, *c*, the specific heat of the gas, C_P, the ambient temperature, T_0, and the mean temperature of the thin-film, T_a.

$$\eta = \frac{\Pi}{P_{input}} = \frac{\pi f^2 P_{input}}{2\rho_0 c C_P^2 (T_0 + T_a)^2} \tag{5}$$

3.4 Enclosed efficiency

Aliev *et al.* later discovered that a CNT thermophone can be encapsulated to increase the overall efficiency, however the previously determined efficiency was no longer accurate [2]. The encapsulated efficiency can be seen in Equation 6. It was found that operating the CNT thermophone at low frequencies resulted in higher efficiencies. The developed model incorporates the resonant quality factor of the vibrating surface enclosing the thermophone, Q, a correction factor to account for the gas in the enclosed cavity, γ, and the speed of sound of the gas, υ. It was determined that the encapsulated CNT thermophone could reach greater efficiencies in different environments. Efficiencies of 0.3% were attained when operated with air as the surrounding media, and 1.5% when operated underwater.

$$\eta = \frac{(\gamma - 1)^2 \rho_{air} Q^2}{2 f^2 V^2 \upsilon_g} P_h \tag{6}$$

3.5 Thermophone fabrication

CNT thermophones can be fabricated in a relatively simple manner. The core thermophone consists of the CNT thin-film suspended between a set of electrodes to the provide the input signal, a combination of alternating and direct current. The CNT thin-film must be dry-drawn from a CNT forest onto the electrodes, which are typically copper. The thin-film is then densified to the electrodes using denatured alcohol to secure the connection [14]. This process is depicted in Figure 1. The flexible and stretchable nature of the CNT thin-film allows for thermophones to be created using either free-standing CNT thin-film or the thin-film can also be supported on an underlying base material with embedded electrodes. The supporting material must be able to withstand the high temperature of the CNT thin-film during operation while also being electrically insulating to preserve the circuit being created. Traditionally, this material has been Teflon ® PTFE. These fabrication techniques have allowed for the creation of a variety of free-standing and supported CNT thermophones in complex geometries previously thought to be unattainable given the restrictions of the moving coil loudspeakers. Figure 2 depicts both the free-standing and supported CNT thermophones as well as the various geometries that have been attained.

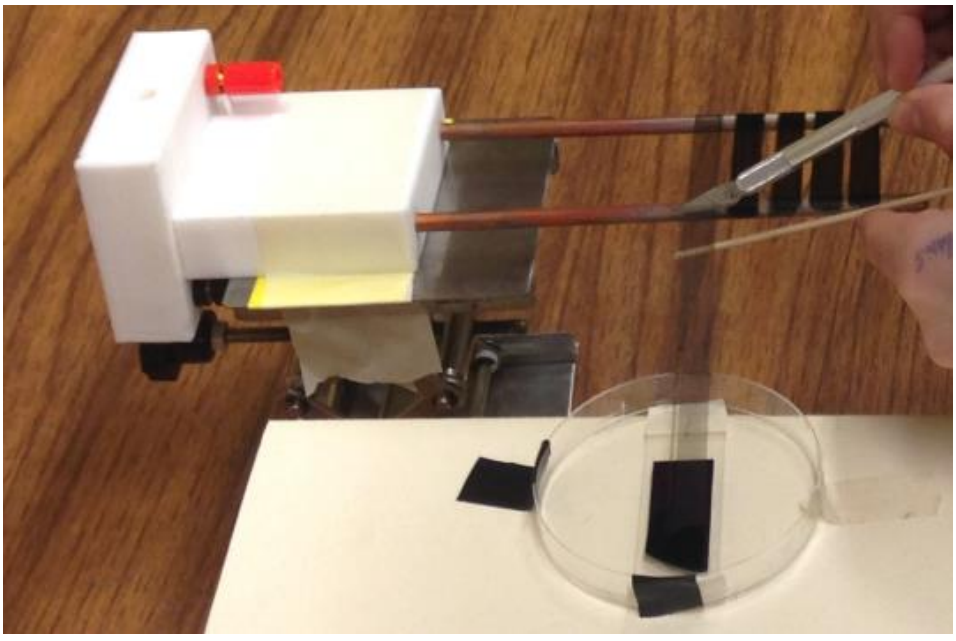


Figure 1: Dry-drawing process of CNT thin-film used to create planar CNT thermophone



Figure 2: Free-standing and supported CNT thermophones created in planar, cylindrical, and spherical geometries

3.6 Modeling

A significant amount of research has been focused on creating a multi-physics 3-D model of CNT thermophones. Asgarisabet *et al.* has created a model aimed at predicting the operation of the CNT thermophone as it transitions from the electrical domain to the thermal domain to the acoustic domain with a high amount of accuracy [11]. This model has been created using the COMSOL Multi-Physics software with the AC/DC (Joule Heating), thermoviscous and pressure acoustic modules. The analytical models presented in Equations 1-6 are necessary to properly obtain the surface temperature variations of the CNT thin-film as the current is applied, which is then converted to pressure changes in the surrounding media that then produces the acoustic waves. The model that has been created has been validated using results from the analytical models and with experimental data, which can be seen in Figure 3. Understanding this model will allow for future ease in optimizing thermophone designs.

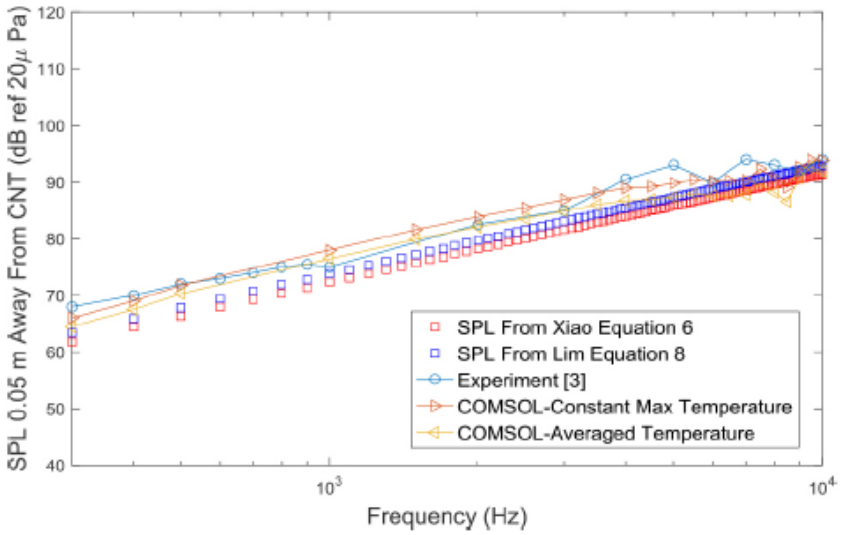


Figure 3: Comparison between COMSOL model, theoretical, and experimental data [11]

4 Coaxially configured CNT thermophone

4.1 Pipe and duct active noise control

The lightweight, flexible, and conformable nature of the CNT thermophone make it the ideal replacement for a moving coil loudspeaker in applications where weight and the restrictions of the moving coil loudspeaker are of concern. These features provide great benefit to active noise control systems within pipes and ducts. Most notably, pipe and duct active noise control is found in automotive exhaust systems as a supplement to the traditional passive muffler. However, this technology could also be used in heating, ventilation, and air conditioning (HVAC) systems to reduce the noise generated by the air handling unit, which can travel throughout the building, and has also been traditionally abated using passive methods. These active systems measure the incoming sound from the source using a microphone, then the speaker injects the same waveform back into the system with a 180-degree phase shift. This creates destructive interference, which lowers the amplitude of the acoustic wave. In vehicles, the use of moving coil loudspeakers within these active systems creates a challenge in designing them into the vehicle undercarriage. These loudspeakers are heavy due to the magnets required and must also be offset from the exhaust pipe to avoid high temperatures. To create this offset, the loudspeaker is isolated using a branch pipe angled off the exhaust pipe [4]. The need for this branch pipe system can be eliminated using a CNT thermophone in place of the moving coil loudspeaker. The flexible nature of the CNT thin-film allows for a coaxial speaker to be created, meaning that it can fit directly in-line with the given pipe or duct system. Additionally, the coaxial CNT thermophone allows for better generation of plane waves inside the pipe or duct opposed to the angle branch pipe, improving the overall performance of the noise cancellation.

4.2 Coaxial design benefits

The coaxial CNT thermophone provide three key benefits over the traditional passive pipe and duct muffler systems. First, the CNT thermophone allows for a significant reduction in both weight and volume. The lightweight and flexible CNT thin-film allow for compact designs that can reduce size by up to 80% compared to passive mufflers. Second, the coaxial thermophone does not obstruct airflow through the system. Passive mufflers force the airflow through resonant chambers and fibrous material that generates backpressure on the source. This backpressure will lower the overall performance of the system, requiring additional energy to overcome and reducing overall efficiency. Third, the coaxial CNT thermophone can adapt to changing acoustic environments unlike the passive muffler that can only be tuned to a specific operating condition. Given these benefits, the coaxial CNT thermophone can provide a competitive alternative the passive muffler.

4.3 Prototype development

An initial proof of concept coaxial CNT thermophone was designed, fabricated, and tested by Prabhu *et al.* to understand the potential benefits this technology could provide in active noise control systems [45]. The coaxial CNT thermophone was designed to optimize the resistance so that it matched that of a commercial amplifier. The theoretical resistance was 1.53 Ω, however in testing the resistance was found to be 1.98 Ω. The discrepancy in resistance is attributed to a difference in the total area of CNT thin-film. The design consisted of three rings, each containing six copper electrodes that were secured using Teflon ® PTFE end caps. Five layers of CNT thin-film were then wrapped onto the copper electrodes through the dry-drawing process. This process started with the inner most ring, and as the thin-film was applied the copper electrodes were inserted to begin the next ring until all three rings had been completed. A transparent cover was then placed over the thermophone to provide protection. A second-generation prototype was also created with several improvements over the initial prototype. Most notably, an aluminum shielding was used along with an internal slotted pipe with a Kapton coating. This coating was used to protect the CNT thin-film from the

airflow, which could easily destroy the CNT, while also remaining acoustically transparent. The initial and second-generation proof of concept coaxial CNT thermophones can be seen in Figure 4.

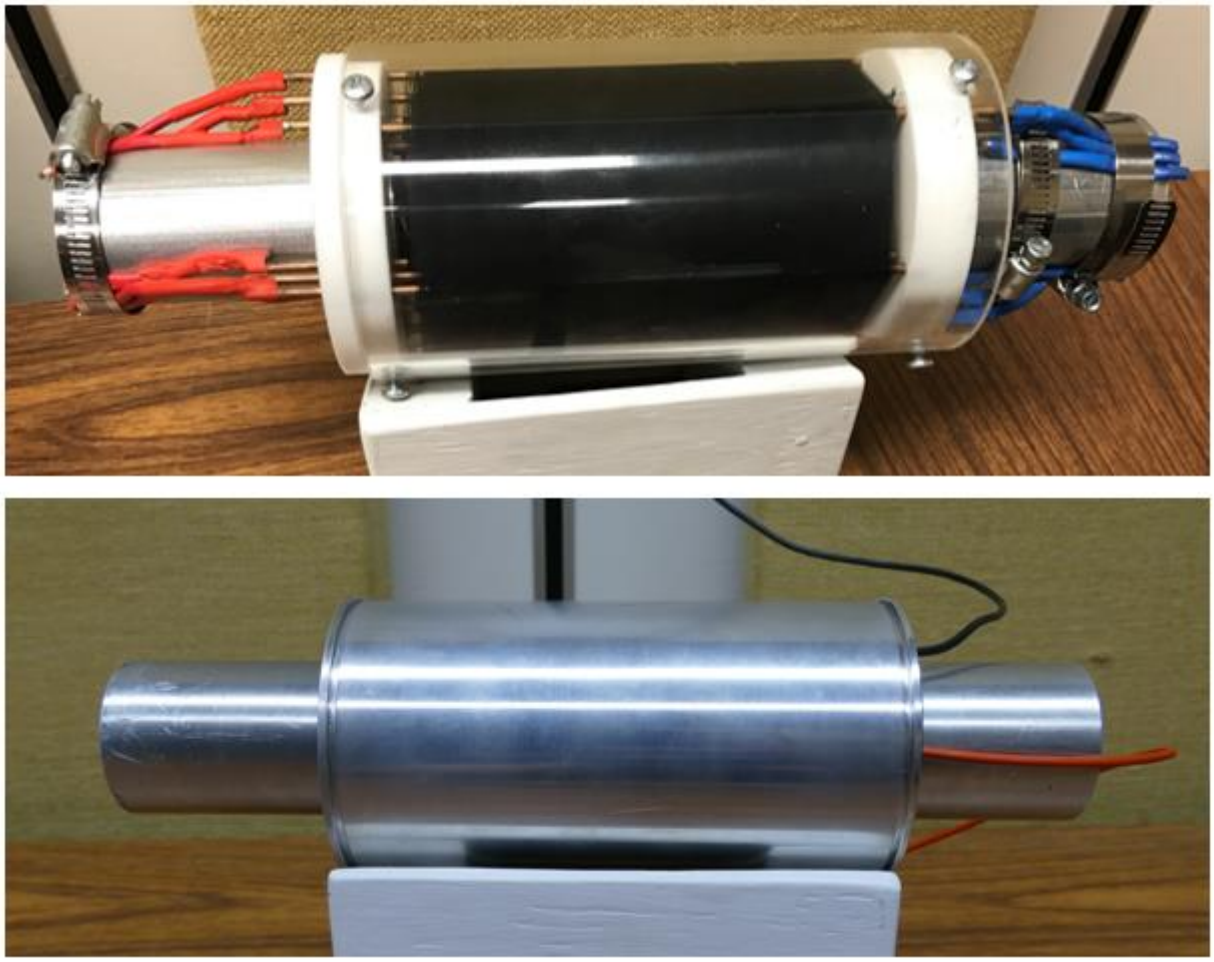


Figure 4: Initial (top) and second-generation (bottom) proof of concept coaxial CNT thermophone prototypes

4.4 Prototype validation

After the coaxial CNT thermophone had been fabricated, initial testing was needed to quantify the noise cancellation capabilities of the system compared to that of a passive muffler, which cancels approximately 30 dB of adverse noise [46]. Initial test data has shown that sound pressure levels of up to 125 dB were achieved inside the test pipe using an input power of 200 W. The noise cancellation capability was then tested using pure tones in the pipe at one-third octave frequencies. The phase of the output of the CNT thermophone was manually adjusted to cancel the sound being generated using destructive interference. The preliminary data achieved from this test can be seen in Table 1. Throughout this test an average reduction in sound pressure level of 12 dB was seen. This cancellation is expected to improve with the use of an active noise control algorithm. The test setup used to perform these tests can be seen in Figure 5.

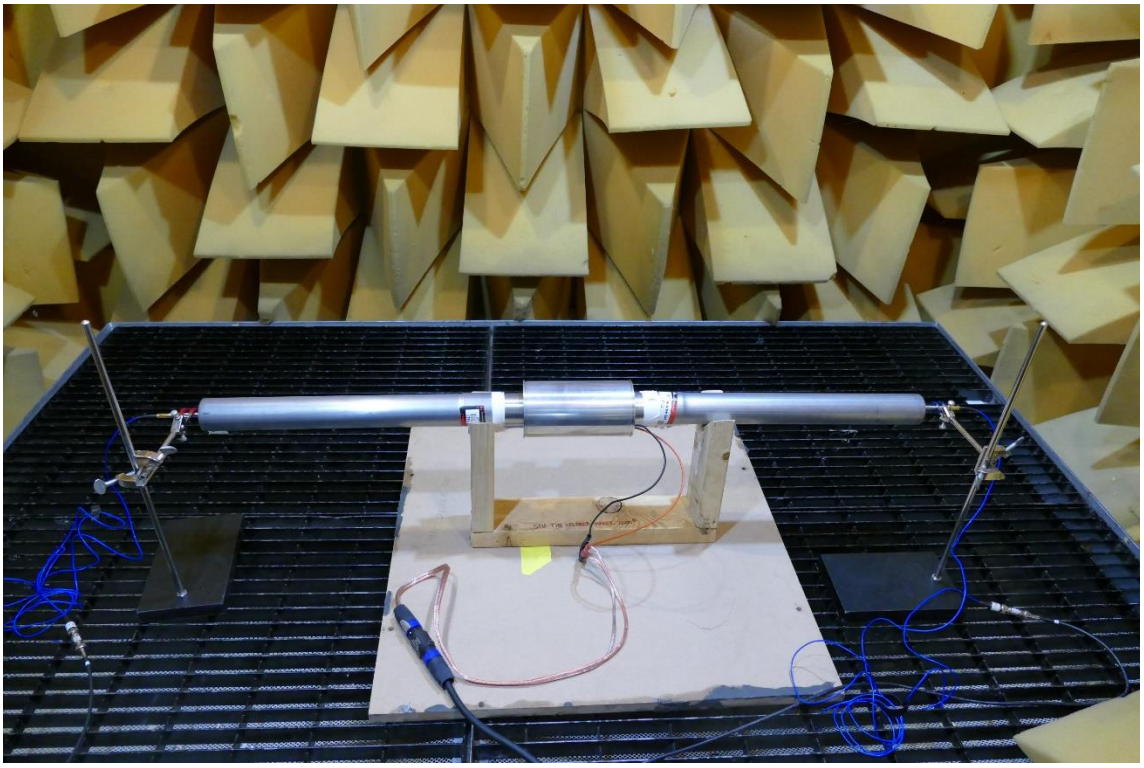


Figure 5: Exhaust pipe test setup to acquire preliminary coaxial CNT thermophone noise cancellation data [45]

Frequency (Hz)	**Sound Pressure Level in Pipe (dB re 20µPa)**	**Sound Pressure Level Reduction (dB re 20µPa)**
50	111	15
63	112.6	10
80	114	10
100	115.9	10
125	119.2	12
160	124.3	10
200	134.6	10
250	126.3	10
315	111.8	25
400	128.4	10
500	115.7	10
100	114.3	10

Table 1: Manual noise cancellation results of pure tones over one-third octave band [45]

4.5 Commercialization technical challenges

Although the proof of concept prototype has shown promising preliminary active noise cancellation data, there are still many hurdles that must be overcome in the path to commercializing this promising technology. The main challenges that must first be understood are the durability of the CNT thin-films, providing a sufficient level of noise reduction can be seen on a real-world source, and ensuring that the CNT thermophone can be produced at a cost competitive rate. The passive systems that have been used in vehicle exhaust systems and HVAC systems are expected to last for 100,000 miles and 20 years respectively, therefore a viable replacement must be able to meet or exceed these expectations. Currently, the coaxial CNT thermophones have been operated for minutes at a time. A comprehensive durability study is needed to understand the thermal cycling of the CNT thin-film, as the surface temperatures reach upwards of 300°C during operation. Traditionally, passive muffler systems are expected to abate roughly 30 dB of adverse noise in the exhaust system, whereas the coaxial CNT thermophone was able to cancel 12 dB of noise on average in preliminary testing. This must also be improved to remain competitive in the market. Finally, the production of the CNT thermophone must also be financially viable. Currently, most of the cost to producing CNT thermophones comes from the CNT forests. To meet the high demands of creating a commercial product, the CNT forests must be produced in a large enough quantity and at a competitive price. If these three challenges can be dealt with, then the path towards commercialization becomes a much more attainable goal.

5 Conclusions and future work

The introduction of the CNT thermophone has revolutionized loudspeaker design and implementation. No longer restricted to moving coil loudspeakers, the CNT thermophone provides a loudspeaker that is lightweight, flexible, and contains no moving parts. The thermophone operate using the thermoacoustic effect, which generates acoustic waves using rapid fluctuations in temperature to alter the pressure in the surrounding media. The CNT thermophone is enable by CNT thin-film which has a heat capacity low enough to allow for frequencies over a range of 1 Hz to 100 kHz to be generated. The enabling material is lightweight, flexible, and stretchable, which allows for complex and unique speaker geometries that were impossible using moving coil loudspeakers. These features have allowed for the development of a coaxial CNT thermophone that can fit directly in-line with a pipe or duct, which can provide active noise control to the system using destructive interference.

The initial proof of concept prototype coaxial CNT thermophones show great promise and benefit compared to the passive muffler systems, however there are still many challenges that must be overcome. Moving forward there are plans to conduct an in-depth durability study on the second-generation proof of concept prototype to gain a better understanding of how the CNT thin-film withstands both external vibration and extended thermal cycling. Additional work will also be done to design and fabricate a thermophone that is optimized to a specific engine to understand the potential noise cancellation in a real-world scenario. Finally, further discussion and planning is being conducted into making CNT thermophones more financially viable. Understanding and adapting to these challenges will improve the effort to commercialize the CNT thermophone and create a viable product.

Acknowledgements

The authors would like to acknowledge the sponsors of this work including the Michigan Economic Development Corporation under the supervision of Denise Graves, Ford Motor Company under the supervision of Al Frank, The National Science Foundation I-Corps program under the supervision of Steven Konsek, and the Michigan Technological University Research Excellence Fund.

References

[1] Aliev AE, Lima MD, Fang S, and Baughman RH, “Underwater sound generation using carbon nanotube projectors.” Nano Letters, 2010. 10: 2374-2380.

[2] Aliev AE, Gartstein YU, and Baughman RH, “Increasing the efficiency of thermoacoustic carbon nanotube sound projectors.” Nanotechnology, 2013. 24: 233501.

[3] Aliev AE, Lima MD, Silverman EM, and Baughman R, “Thermal conductivity of multi-walled carbon nanotube sheets: radiation losses and quenching of phonon modes.” Nanotechnology, 2010. 21: 035709.

[4] Aliev AE, Mayo NK, Baughman RH, Avirovik D, Priya S, and Zarnetske MR, “Thermal management of thermoacoustic sound projectors using a free-standing carbon nanotube aerogel sheet as a heat source.” Nanotechnology, 2014. 25: 405704.

[5] Aliev AE, “Thermophones using carbon nanotubes and alternative nanostructures for high power sound generation and noise cancellation.” InterNoise and NoiseCon Congress and Conference Proceedings: Institute of Noise Control Engineering, 2014. 3938-3947.

[6] Alvarez NT, Miller P, Haase M, Kienzle N, Zhang L, Schulz MJ, and Shanov V, “Carbon nanotube assembly at near-industrial natural-fiber spinning rates.” Carbon, 2015. 86: 350-357.

[7] Aqel A, El-Nour KMMA, Ammar RAA, and Al-Warthan A, “Carbon nanotubes, science and technology part (I) structure, synthesis and characterization.” Arabian Journal of Chemistry, 2012. 5: 1-23.

[8] Arnold H, and Crandall I, “The thermophone as a precision source of sound.” Physical Review, 1917. 10(1): 22-38.

[9] Asadzadeh SS, Moosavi A, Huynh C, and Saleki O, “Thermoacoustic study of carbon nanotubes in near and far field: Theory, simulation, and experiment.” Journal of Applied Physics, 2015. 117(9): 095101.

[10] Asgarisabet M, Barnard AR, and Bouman TM, “Near field acoustic holography measurements of carbon nanotube thin film speaker.” Journal of Acoustical Society of America, 2016. 140(6): 1-9.

[11] Asgarisabet M, and Barnard AR, “Multi-physics simulation of ultra-lightweight carbon nanotube speakers.” SAE International Journal of Materials and Manufacturing, 2017. 10 (3).

[12] Barnard AR, Brungart TA, McDevitt TM, Aliev AE, Jenkins DM, Kline BL, and Baughman RH, “Advancements toward a high-power, carbon nanotube, thin-film loudspeaker.” Noise Control Engineering Journal, 2014. 62(5): 360-367.

[13] Barnard AR, Jenkins DM, Brungart TA, McDevitt TM, and Kline BL, “Feasability of a high-powered carbon nanotube thin-film loudspeaker.” The Journal of the Acoustical Society of America, 2013. 134(3): EL276-EL281.

[14] Barnard AR, Brungart TA, McDevitt TM, and Jenkins DM, “Background and development of a high-powered carbon nanotube thin-film loudspeaker.” Proceedings of Inter Noise, 2012. 1513-1524. New York, USA.

[15] Barnard AR, Brungart TM, McDevitt TM, Jenkins DM, and Kline BL, “Advancements towards a high-powered carbon nanotube thin-film loudspeaker.” Proceedings of Noise Control, 2013. 796-802. Denver, USA.

[16] Barnard, AR, “Solid State Transducer, System, and Method,” US Patent Pending, PCT/US2018/012061, 2 Jan. 2018.

[17] Beck BS, Zugger ME, Brungart TA, Fredley JE, Kline BL, and Yoas BW, "Increasing the efficiency of carbon nanotube, thin film loudspeakers." InterNoise 2015. San Francisco, USA.

[18] Bin J, Oates WS, and Taira K, "Thermoacoustic modeling and uncertainty analysis of two-dimensional conductive membranes." Journal of Applied Physics, 2015. 117: 064506.

[19] Bouman TM, "Drive signal development for the thermoacoustic loudspeaker." Michigan Technological University, 2016.

[20] Bouman TM, Barnard AR, and Asgarisabet M, "Experimental quantification of the true efficiency of carbon nanotube thin-film thermophones." Journal of the Acoustical Society of America, 2016. 139: 1353-1363.

[21] Braun F, "Notiz über thermophonie (Note on thermophonie)." Annalen Der Physik, 1898. 65: 358-360.

[22] Cho W, Schulz M, and Shanov V, "Growth and characterization of vertically aligned centimeter long CNT arrays." Carbon, 2014. 72: 264-273.

[23] Daschewski M, Boehm R, Prager J, Kreutzbruck M, and Harrer A, "Physics of thermo-acoustic sound generation." Journal of Applied Physics, 2013. 114: 114903.

[24] De Volder MFL, Tawfick SH, Baughman RH, and Hart AJ, "Carbon nanotubes: Present and future commercial applications." Science, 2013. 339 (6119): 535-539

[25] Eklund P, Ajayan P, Blackmon R, Hart AJ, Kong J, Pradhan B, Rao A, and Rinzler A, "International assessment of carbon nanotube manufacturing and applications." World Technology Evaluation Center, 2007.

[26] Fei W, Zhou J, and Guo W, "Low-voltage driven graphene foam thermoacoustic speaker." Small, 2015. 11(19): 2252-2256.

[27] Hu L, Hecht DS, and Grüner G, "Carbon nanotube thin films: fabrication, properties, and applications." Chemical Reviews, 2010. 110(10): 5790-5844.

[28] Hu S and Rajamani R, "Carbon nanotube thin films for active noise cancellation, solar energy harvesting, and energy storage in building windows." University of Minnesota, 2014.

[29] Hu S, Rajamani R, and Yu X, "Directional cancellation of acoustic noise for home window applications." Applied Acoustics, 2013. 74: 467-477.

[30] Hu S, Rajamani R, and Yu X, "Active noise control for selective cancellation of external disturbances." American Control Conference, 2011. San Francisco, USA.

[31] Ijima S, "Helical microtubules of graphite carbon." Nature, 1991. 354: 56-58.

[32] Jakubinek MB, White MA, Li G, Jayasinghe C, Cho W, Schulz MJ, and Shanov V, "Thermal and electrical conductivity of tall, vertically aligned carbon nanotube arrays." Carbon, 2010. 48(13): 3947-3952.

[33] Jiang K, Wang J, Li Q, Liu L, Liu C, and Fan S, "Superaligned carbon nanotube arrays, films, and yarns: A road to applications." Advanced Materials, 2011. 23: 1154-1161.

[34] Keqiang L, Diange Y, Sifa Z, Xiaomin L, and Takeharu T, "Active noise control for vehicle exhaust noise reduction." Tsinghua Science and Technology, 2003. 8 (5): 577-581.

[35] Kim CS, Hong SK, Lee JM, Kang DS, Cho BJ, and Choi JW, "Free-standing graphene thermophone on a polymer-mesh substrate." Small, 2016. 12(2): 185-189.

[36] Kozlov ME, Haines CS, Oh J, Lima MD, and Fang S, “Sound of carbon nanotube assemblies.” Journal of Applied Physics, 2009. 106: 124311.

[37] Kumar M, and Ando Y, “Chemical vapor deposition of carbon nanotubes: A review on growth mechanism and mass production.” Journal of Nanoscience and Nanotechnology, 2010. 10: 3739-3758.

[38] Kuznetsov AA, Fonseca AF, Baughman RH, and Zakhidov AA, “Structural model for dry-drawing of sheets and yarns from carbon nanotube forests.” ACS Nano, 2011. 5 (2): 985-993.

[39] Lepró X, Lima MD, and Baughman RH, “Spinnable carbon nanotube forests grown on thin, flexible metallic substrates.” Carbon, 2010. 48: 3621-3627.

[40] Li G, Chakrabarti S, Schulz M, and Shanov V, “Growth of aligned multiwalled carbon nanotubes on bulk copper substrates by chemical vapor deposition.” Journal of Materials Research, 2009. 2 (9): 2813-2820.

[41] Lim CW, Tong L, and Li Y, “Theory of suspended carbon nanotube thin film as a thermal-acoustic source.” Journal of Sound and Vibration, 2013. 332(21): 5451-5461.

[42] Lu W, Liu X, Li Q, Byun JH, and Chou TW, “Mechanical behavior and structural evolution of carbon nanotube films and fibers under tension: A coarse-grained molecular dynamics study.” Journal of Applied Mechanics, 2013. 80: 051015.

[43] Mason BJ, Chang SW, Chen J, Cronin SB, and Bushmaker AW, “Thermoacoustic transduction in individual suspended carbon nanotubes.” ACS Nano, 2015. 9(5): 5372-5376.

[44] Pöhls JH, Johnson MB, White MA, Malik R, Ruff B, Jayasinghe C, Schulz MJ, and Shanov V, “Physical properties of carbon nanotube sheets drawn from nanotube arrays.” Carbon, 2012. 50(11): 4175-4183.

[45] Prabhu S, and AR Barnard, “Active noise control of automotive exhaust noise using carbon nanotube speakers.” Noise-Con, 2017.

[46] Reddy KA, “A critical review on acoustic methods & materials of a muffler.” Materials Today: Proceedings, 2017. 4: 7313-7334.

[47] Schulz M, Hou G, Ng V, Rabiee M, Cahay M, Chaudhary S, Lindley D, Chauhan D, Paine M, Vijayakumar D, Xu C, Yin Z, Haworth K, Liu Y, Sundaram M, Li W, Mast D, and Shanov V, “Science to commercialization of carbon nanotube sheet and yarn.” WSEAS Transactions on Applied and Theoretical Mechanics, 2017. 12: 41-50.

[48] Shanov V, Cho W, Malik R, Alvarez N, Haase M, Ruff B, Kienzle N, Ochmann T, Mast D, and Schulz M, “CVD growth, characterization and applications of carbon nanostructured materials.” Surface & Coatings Technology, 2013. 230: 77-86.

[49] Sidhu S, “Implementation of active noise cancellation in a duct.” Simon Fraser University, 2013.

[50] Sugimoto T and Nakajima Y, “Acoustic characteristics of a flexible sound generator based on thermoacoustic effect.” Acoustical Society of America, 2013. 1aEA4. Montreal, Canada.

[51] Suzuki K, Sakakibara S, Okada M, Neo Y, Mimura H, Inoue Y, and Murata T, “Study of carbon-nanotube web thermoacoustic loud speakers.” Japanese Journal of Applied Physics, 2011. 50: 01BJ10.

[52] Tao Z, and Seybert AF, “A review of current techniques for measuring muffler transmission loss.” SAE International, 2003.

[53] Tian H, Ren TL, Xie D, Wang YF, Zhou CJ, Feng TT, Fu D, Yang Y, Peng PG, Wang LG, and Liu LT, "Graphene-on-paper sound source devices." ACS Nano, 2011. 5(6): 4878-4885.

[54] Tong LH, Lim CW, and Li YC, "Gas-filled encapsulated thermal-acoustic transducer." Journal of Vibration and Acoustics, 2013. 135(10): 051033.

[55] Tong LH, Lim CW, Lai SK, and Li YC, "Gas separation effect on thermoacoustic wave generation by heated suspended CNT nano-thinfilm." Applied Thermal Engineering, 2015. 86: 135-142.

[56] Vesterinen V, Niskanen AO, Hassel J, and Helisto P, "Fundamental efficiency of nanothermophones: modeling and experiments." Nano Letters, 2010. 10: 5020-5024.

[57] Wei Y, Lin X, Jiang K, Liu P, Li Q, and Fan S, "Thermoacoustic chips with carbon nanotube thin yarn arrays." Nano Letters, 2013. 13: 4795-4801.

[58] Winberg M, Johamsson S, and Lagö T, "Speaking panels – new actuators for active noise control." InterNoise 2005. Rio de Janeiro, Brazil.

[59] Xiao L, Chen Z, Feng C, Liu L, Bai ZQ, Wang Y, Lan L, Zhang Y, Li Q, Jiang K, and Fan S, "Flexible, stretchable, transparent carbon nanotube thin film loudspeakers." Nano Letters, 2008. 8(12): 4539-4545.

[60] Xiao L, Liu P, Li Q, Feng Z, Fan S, and Jiang K, "High frequency response of carbon nanotube thin film speaker in gases." Journal of Applied Physics, 2011. 110(8): 084311.

[61] Yasuda T, Wu C, Nakagawa N, and Nagamura K, "Studies on an automobile muffler with the acoustic characteristic of low-pass filter and Helmholtz resonator." Applied Acoustics, 2013. 74: 49-57.

[62] Yu X, Rajamani R, Stelson KA, and Cui T, "Carbon nanotube-based transparent thin film acoustic actuators and sensors." Sensors and Actuators A: Physical, 2006. 132(2): 626-631.

[63] Yu X, Rajamani R, Stelson K, and Cui T, "Active control of sound transmission through windows with carbon nanotube-based transparent actuators." IEEE Transactions on Control Systems Technology, 2007. 15(4): 704-714.

[64] Zhang M, Fang S, Zahkidov AA, Lee SB, Aliev AE, Williams CD, Atkinson KR, and Baughman RH, "Strong, transparent, multifunctional, carbon nanotube sheets." Science, 2005. 309: 1215-1219.

[65] Zhu C, Cheng C, He YH, Wang L, Fung KK, and Wang N, "A self-entanglement mechanism for continuous pulling of carbon nanotube yarns." Carbon, 2011. 49: 4996-5001.

[66] Zhu H, Rajamani R, Dudney J, and Stelson K, "Active noise control using a distributed mode flat panel loudspeaker." ISA Transactions, 2003. 42: 475-484.

[67] Zhu Y, Zhu F, Zhang Y, and Wei Q, "The research on semi-active muffler device of controlling the exhaust pipe's low-frequency noise." Applied Acoustics, 2017. 116: 9-13.

Vibration suppression using the concept of a semi-active magnetorheological inerter device

M.Tipuric [1,2,*], **D. Wagg** [2], **N. Sims** [2]
[1] Industrial Doctoral Centre in Machining Science, Advanced Manufacturing Research Centre with Boeing, University of Sheffield, Rotherham, S60 5TZ, UK
[*]e-mail: **mrtipuric1@sheffield.ac.uk**

[2] Department of Mechanical Engineering, Sir Frederick Mappin Building, University of Sheffield, Sheffield, S1 3JD, UK

Abstract
The inerter is a mechanical analogue to a capacitor, where the force across the device is proportional to relative rather than absolute acceleration. The fact that inerters can be tuned in a similar way to a mass damper, without significantly increasing the mass of a structure makes them attractive for a range of engineering tasks. Applications that have been studied in recent years include seismic isolation of tall buildings, control of vibration in bridges, vehicle suspensions, as well as other engineering problems. The prospect of using inerters as part of a semi-active system has only recently begun to be investigated. A previous paper has demonstrated the feasibility of a semi-active inerter based on a helical fluid design, using magnetorheological fluid to create a controllable damping force. The present study will develop the potential of this device by investigating a novel device layout; making use of two helical coils to create an inertance value which can be adjusted. In addition, the properties of the semi-active damper are highly dependent on the geometry of the device. The limitations and opportunities caused by this will be investigated.

1 Introduction

The ideal inerter is a mechanical element with two terminals, which creates a force proportional to the relative acceleration of these terminals [1], in the same way that the ideal spring and damper create a force proportional to the relative displacement and velocity of their terminals, respectively. This allows for vibration absorber designs with advantages over those using a mass damper, the most obvious of which is a large saving in weight. Initially used as a part of vehicle suspension, current research is focused on expanding their application in other areas, such as civil structures [2].

Various inerter designs exist which make use of the inertia created by different elements, such as gears or flywheels. The type discussed in this paper is the fluid inerter [3]. At its simplest, this device consists of a piston, with a helical tube attached to it at both ends, as demonstrated in Figure 1. Motion of the piston causes the fluid to flow around the curves of helix, creating inertia. Due to the flow properties in the helix, resistive forces are created proportional to the velocity of the flow and its square, hence this type of inerter can be modeled as an ideal inerter in parallel with a nonlinear damper.

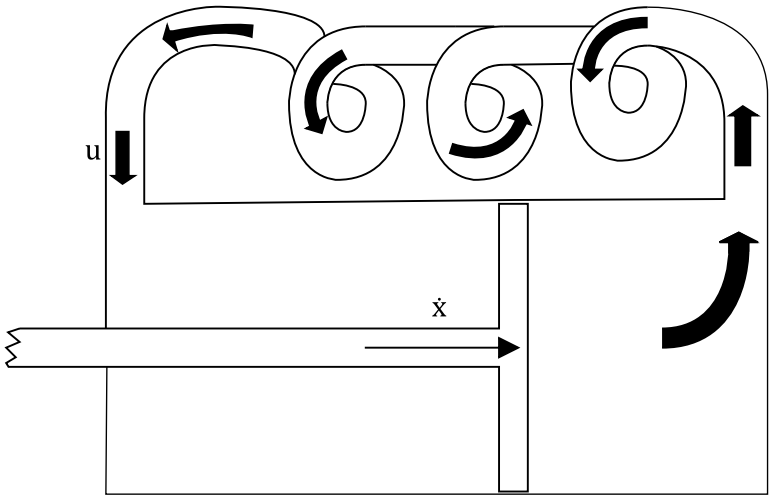


Figure 1: A highly simplified schematic of a fluid inerter.

Magnetorheological (MR) fluids are a class of smart fluid with established uses in vibration control [4]. They consist of a suspension of magnetically responsive particles in a non-magnetisable liquid. Introducing a magnetic field to the MR fluid causes the particles to link up, increasing the yield stress of the fluid. While calculating the exact flow behaviour of an MR fluid under the influence of a magnetic field is moderately complex [5], for the purposes of this paper it can be sufficiently approximated as a Bingham fluid, a class of non-Newtonian fluid which will not flow until its yield stress is overcome, at which point it will flow as a viscous Newtonian fluid.

Previous work by the authors [6] established the feasibility of a using MR fluid in an inerter to create a semi-active, controllable device. This paper builds upon that work by investigating the possibilities afforded by using multiple helixes, in particular the potential for controlling the inertance of the device. To achieve this, the effects of different geometries on the flow and the potential they offer in terms of control will be analysed and discussed.

2 Underlying Physics and Modeling Assumptions

2.1 Fluid Inerters

Figure 2 shows the nomenclature which will be initially used when discussing inerters. Note that some of this will be adapted later in the paper, to better describe inerters with novel geometry.

An ideal inerter is described by the equation $F = b\ddot{x}$, where b is the inertance and $\ddot{x}$ is the relative acceleration of the two terminals [7]. In the case of the fluid inerter, one terminal is the piston tube and the other is the piston itself. The tube will be assumed to be fixed and so $\ddot{x}$ is the acceleration of the piston. By equating the kinetic energy to the inertial energy of the fluid in the helix,

$$\frac{1}{2}b\dot{x}^2 = \frac{1}{2}J\dot{\theta}^2 \tag{1}$$

it can be seen that the inertance is proportional to the moment of inertia of the fluid, J, and the square of the ratio of its angular velocity, $\dot{\theta}$, to the velocity of the piston. For a helix which has a sufficiently large curve radius (r_4) when compared to its pitch (h), almost the entirety of the angular velocity vector is normal to the bend and so this can be approximated by a velocity vector along the flow line, u, where $u = r_4\dot{\theta}$. Due to continuity, $u = \frac{A_1}{A_2}\dot{x}$, where $A_1 = \pi(r_2^2 - r_1^2)$ is the piston tube area and $A_2 = \pi r_3^2$ is the cross sectional area

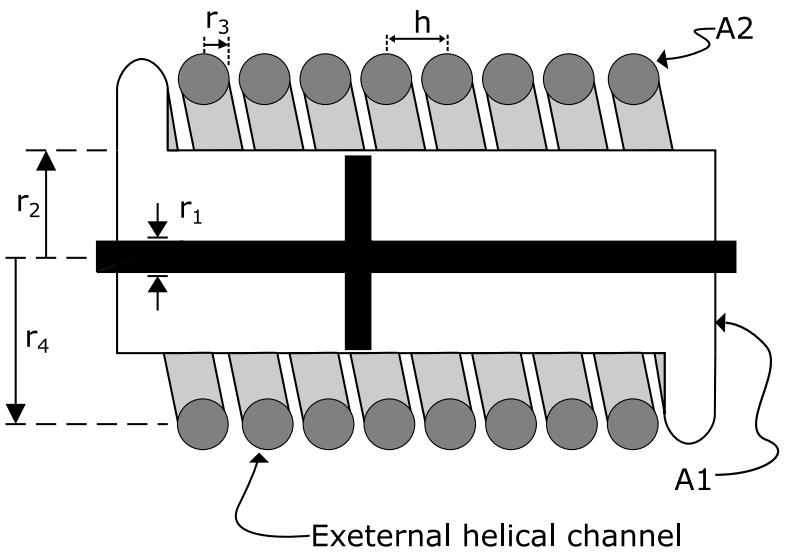


Figure 2: The key dimensions of a fluid inerter, as used in this section (not shown: helix length, l).

of the helix. Finally the moment of inertia can be approximated by $J = m_{hel}r_4$, with $m_{hel} = \rho l A_2^2$ being the mass of the fluid in the helix and l being the length of the helix. Hence, a reasonable approximation of the inertance for a typical fluid inerter designs is

$$b = m_{hel}\left(\frac{u}{\dot{x}}\right)^2 = m_{hel}\left(\frac{A_1}{A_2}\right)^2. \tag{2}$$

Viscous effects are the main contributor to pressure loss in a helical channel. In Ref. [3], an equation is derived to calculate this pressure drop:

$$p = 0.04845\frac{\rho l}{\sqrt{r_3 r_4}}u^2 + 8.77\frac{\mu l}{r_3^2}u. \tag{3}$$

Ref. [3] also demonstrated that this pressure drop was sufficiently large that other effects, such as pressure drop from sudden contraction and expansion of the flow at the inlet and outlet could be largely neglected and so the damping force on the piston is approximately

$$F_d = pA_1. \tag{4}$$

2.2 Magnetorheological valves

Conventional magnetorheological valves are annular in nature, subjecting a narrow channel to a relatively uniform magnetic field. While exact analytical solutions are unavailable for this geometry, provided the gap height is sufficiently small compared to the total diameter, the flow can be approximated as flow between two parallel plates with a width $W = 2\pi R$. The flow conditions for this type of can be found by finding the largest root of the cubic equation

$$C_f^3 - (3/2 + 6\frac{Re}{He})(\frac{He}{Re^2})C_f^2 + 1/2(\frac{He}{Re^2}) = 0, \tag{5}$$

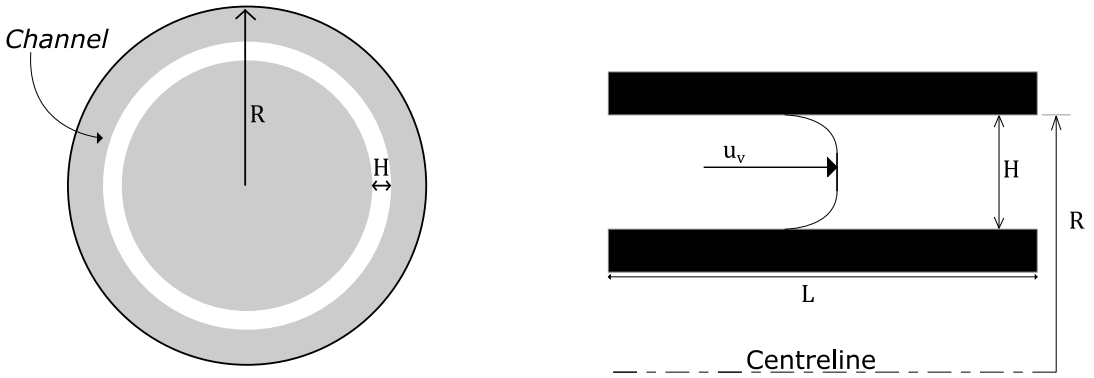
with C_f, Re and He being the friction factor, Reynolds number and the Hedstrom number, respectively, three dimensionless groups [5].

For the purposes of this paper, it is sufficient to model the MR fluid as a Bingham fluid. This approximates the pressure drop across the valve as the sum of two quantities, the Bingham shear stress, τ_y, and the pressure

drop across the valve due to Newtonian viscosity, $k_v u_v$:

$$p_v = \tau_y + k_v u_v = \tau_y + 12\frac{\mu L}{H^2}u_v, \tag{6}$$

where u_v is the flow velocity within the valve and L and H are the valve length and annular gap height, respectively. The Bingham yield stress is the minimum pressure required before the fluid will start to flow. It is equal to zero when the valve is in its off state and can be increased up to a maximum value of between 50-100kPa, depending on the fluid [8].



(a) (b)

Figure 3: Diagrams of an MR valve (a) end on and (b) side on, as two parallel plates of width $W = 2\pi R$.

2.3 Combined Device

The aim of this paper is to explore how multiple flow channels can be used to design an MR inerter with controllable inertance. This could be useful as part of a semi-active vibration absorber, which could cope with structures whose dynamics are not constant. One example of these structures are the work pieces in machining operations, where a large amount of material being removed can substantially reduce the mass and cause a traditional vibration absorber to detune; a vibration absorber which remains tuned throughout the operation could lead to improvements in productivity in this area [9].

In order to describe an inerter with two helixes, it is necessary to adapt the notation used. In this paper, the helix which does not contain the valve will be referred to as helix a, with its dimensions and values denoted by a subscript a (eg. r_a for its radius and u_a for the flow velocity), with the other helix, containing a valve being designated helix b. As the only dimension which will be varied is the radii r_a and r_b, it is useful to rewrite Equation 7 as

$$p = \frac{\alpha}{r_a^2}u_a + \frac{\beta}{r_a^{0.5}}u_a^2 \tag{7}$$

$$= \frac{\alpha}{r_b^2}u_b + \frac{\beta}{r_b^{0.5}}u_b^2 + \tau_y, \tag{8}$$

where $\alpha = 8.77\mu l$ and $\beta = 0.04845\frac{\rho l}{\sqrt{r_4}}$.

It should be noted that the density of MR fluid is significantly higher than that of either water or oil, the traditional working fluids used in inerters, this corresponds with an increase in m_{hel} and β. Unless otherwise stated, the values used to create example values are as stated in Table 1; these are based on an existing test rig at the University of Sheffield. The Newtonian pressure loss within the valve, $k_v u_v$, has been neglected; while this can affect the results and should not be ignored when designing real devices, valve design is an involved area of study in itself and so discussion of these effects are best left for later work which can give it the attention it requires.

Table 1: Default values used throughout this paper.

Variable	Value
r_1	0.0125m
r_2	0.025m
r_3, r_a, r_b	0.015m
r_4	0.1m
L	0.225m
l	4.71m
ρ	3500kgm^{-3}
μ	0.28Pas
k_v	0 Pa^{-1}s^2

3 Modeling of an inerter with two helixes, one of which contains an MR valve

3.1 Model and example values

The fluid flow in the type of device shown in figure 4 is assumed to meet three conditions:

1. Flow is continuous and incompressible:
$$A_1\dot{x} = \pi\big(r_a^2 u_a + r_b^2 u_b\big), \tag{9}$$
2. The pressure loss in both helixes is equal to one another :
$$\frac{\alpha}{r_b^2}u_b + \frac{\beta}{r_b^{0.5}}u_b^2 + \tau_y = \frac{\alpha}{r_a^2}u_a + \frac{\beta}{r_a^{0.5}}u_a^2 \tag{10}$$
3. Flow velocity in each helix is never less than zero (as the MR valve is semi-active, it will only provide a resistive force)

Initially the fluid will only flow through helix without the valve, as it would in a standard, single-helix inerter and so, from Conditions 1. and 3., the fluid velocity will be $u_a = \frac{A_1}{A_a}\dot{x}$, $u_b = 0$.

Once the piston velocity is above the critical value,
$$\dot{x}^* > \frac{A_a}{A_1}\frac{\sqrt{(\frac{\alpha}{r_a^2})^2 + \frac{4\tau_y\beta}{r_a^{0.5}}} - \frac{\alpha}{r_a^2}}{\frac{\beta}{r_a^{0.5}}}, \tag{11}$$
the pressure in helix a will be greater than the yield stress of the fluid and the flow will occur in both helixes. Beyond this point, the value of u_b can be found from the roots of
$$\left(\frac{\beta}{r_b^{0.5}} - \frac{\beta}{r_a^{0.5}}\big(\frac{r_b}{r_a}\big)^4\right)u_b^2 + \left(\frac{\alpha}{r_b^2} + \frac{\alpha}{r_a^2}\big(\frac{r_b}{r_a}\big)^2 + 2\frac{\beta}{r_a^{0.5}}\frac{r_2^2 r_b^2}{r_a^4}\dot{x}\right)u_b + p_v - \frac{\alpha}{r_a^2}\big(\frac{r_2}{r_a}\big)^2\dot{x} - \frac{\beta}{r_a^{0.5}}\big(\frac{r_2}{r_a}\big)^4\dot{x}^2 = 0. \tag{12}$$
(by combining Equations 9 and 10) and then substituted into Equation 9 to find u_a.

The flow velocities for an example device, with $r_a = r_b$ are shown Figure 5 for various values of τ_y. It can be seen that for the geometry studied here, in order to prevent any flow within helix b for the entire velocity range studied (i.e $\dot{x}^* = 0.4$), a yield stress of $\tau_y = 57.7kPa$ is required. This maximum yield stress is important to consider when designing these devices. The required value can be found by rearranging Equation 11 to reach
$$\tau_y^{max} = \frac{\left(2\frac{\beta}{r_a^{0.5}}\frac{A_1}{A_a}\dot{x}^{max} + \frac{\alpha}{r_a^2}\right)^2 - \left(\frac{\alpha}{r_a^2}\right)^2}{4\frac{\beta}{r_a^{0.5}}}. \tag{13}$$

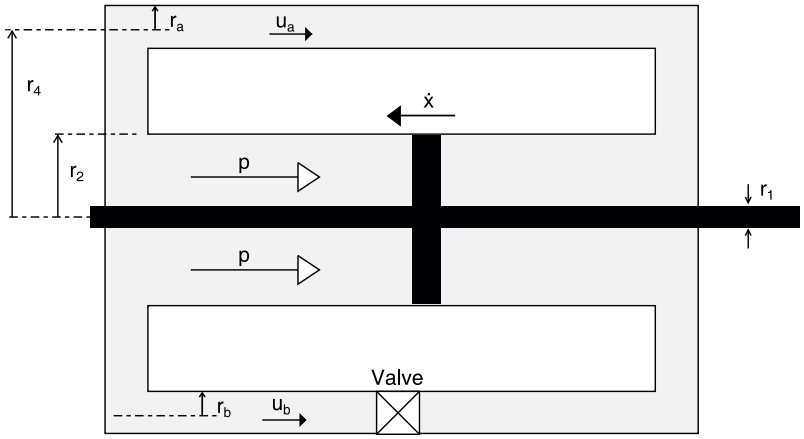


Figure 4: The key dimensions of a fluid inerter, as used in this section (not shown: helix length, l).

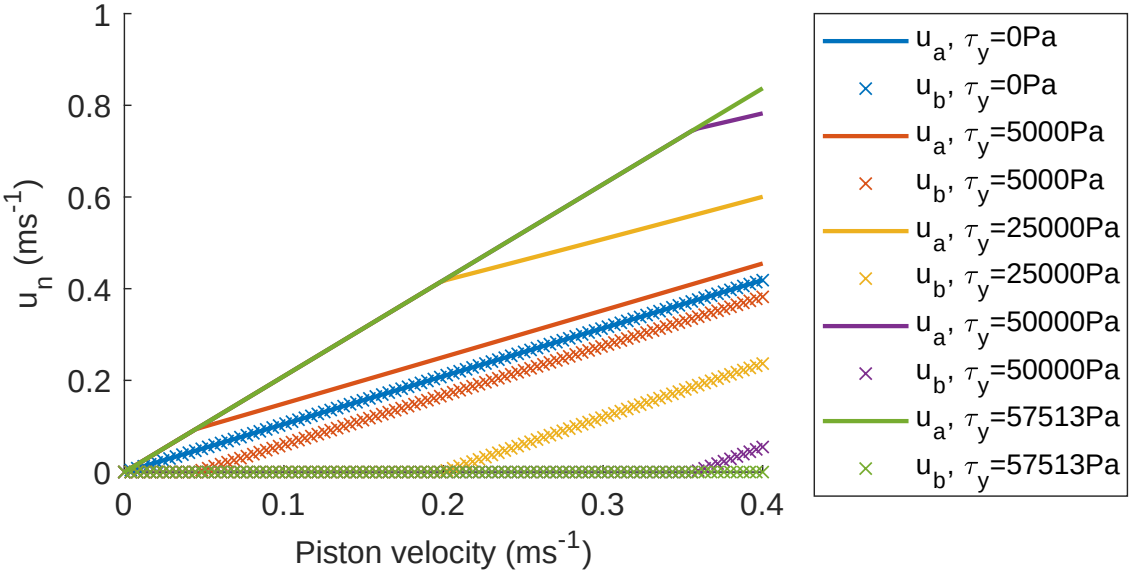


Figure 5: The velocity in the helix without a valve, u_a, scales with the piston velocity until the fluid's yield stress is overcome. Then the fluid velocity in both helixes begin to converge towards the average velocity.

Once the velocity in each helix is known, the damping force pressure in helix a can be found from Equation, 7 and thus the damping force from Equation 4, as shown in Figure 6. It can be seen that, due to the reduced flow velocity in each helix, once the yield stress of the fluid is overcome, the increase in damping force is reduced.

By considering the conservation of energy and Equation 1, it can be shown that the total inertance will be equal to the sum of the inertance in each helix,

$$b = \frac{m_{hel,a}u_a^2}{\dot{x}^2} + \frac{m_{hel,b}u_b^2}{\dot{x}^2} \tag{14}$$

As can be seen in figure 7, the device inertance is now velocity dependent. By dynamically adjusting the yield stress of fluid as the piston velocity changes, it is theoretically possible to fix the inertance to any value within this range, although a control strategy to do this in reality remains to be developed. The strategy would also need to be able to deal with the damping force, which would be some point between the bounds shown in Figure 7.

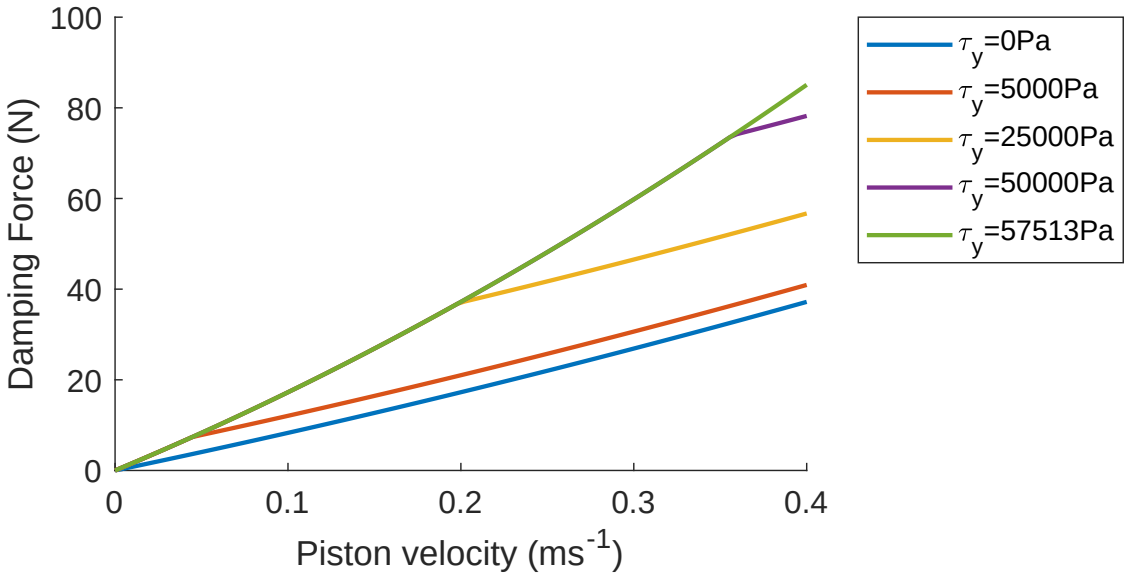


Figure 6: The damping force increases rapidly until the yield stress of the fluid is overcome and then rises more slowly beyond this point.

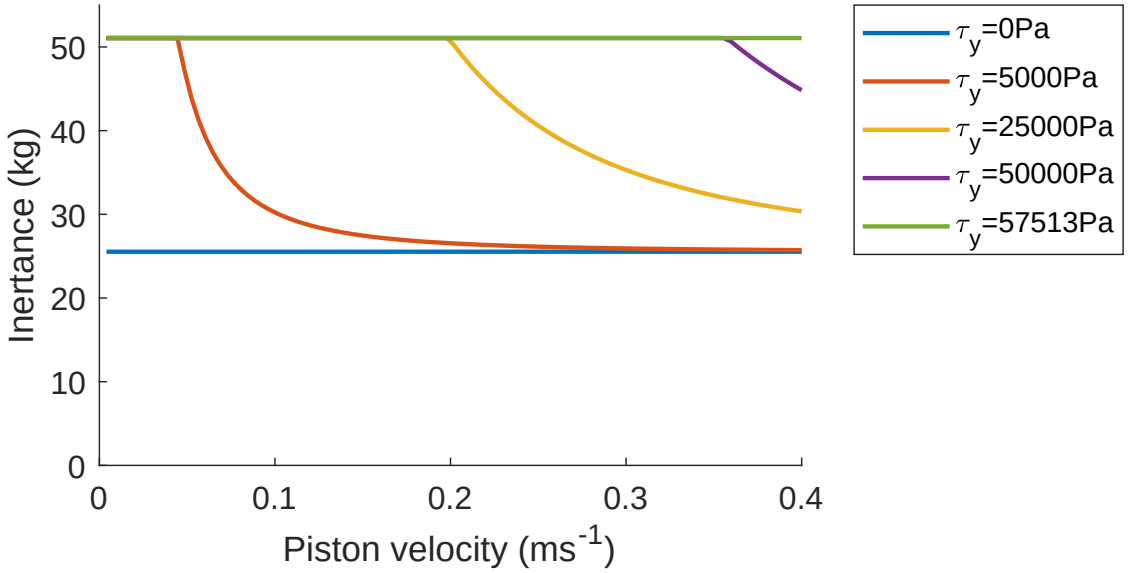


Figure 7: Once the valve pressure is overcome, the rate of increase of the damping force is slowed.

3.2 Control Range

The ratio of the radii of the helixes affects the values of inertance which can be achieved, with the upper bound being the inertance created by helix a alone and the lower bound being equal the inertance created by an equivalent, single helix inerter with a helix radius of $r_3 = r_a + r_b$. Hence, the larger the difference between the two, the larger the range which can be controlled. Figure 8 shows the range available for six different geometries, as detailed in Table 2. Geometry 3 is the case discussed in Section 3.1. Geometry 6 represents a slightly different design; here helix b is replaced with an arbitrarily large, straight tube which acts as an ideal bypass valve.

While maximising the range of achievable inertance is obviously desirable, limiting the lower bound might possess some advantage. For example, it might be useful to design a device which provides some inertance when in its off state, as a fail safe.

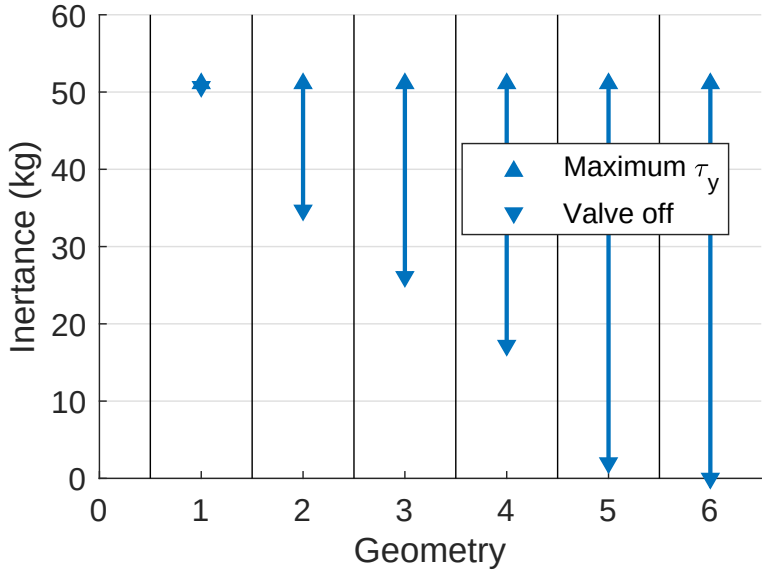


Figure 8: Comparison of inertance range for different values of $\frac{r_b}{r_a}$.

Table 2: Geometries used.

Geometry	$\frac{r_b}{r_a}$	r_a (mm)	r_b (mm)
1	0.25	15	3.75
2	0.75	15	11.25
3	1	15	15
4	1.5	15	22.5
5	5	15	75
6	-	15	-

4 Conclusion

This paper has examined a fluid inerter which uses two helical coils and a magnetorheological valve to produce a variable inertance. The underlying physics were discussed, along with some of the simplifications used in developing the analysis. An analytical model was developed and used to produce detailed results for one design of the device. Finally, the model was used to demonstrate how the relationship between the radii of the helical coils affects the range of inertance which would be achievable with such a device.

Acknowledgements

This research was supported by EPSRC (grant EP/L016257/1). The authors gratefully acknowledge this support.

References

[1] M.C. Smith, *Synthesis of mechanical networks: the inerter*, IEEE Transactions on Automatic Control, Vol. 47, No. 10, (2002) pp. 1648-1662.

[2] I.F. Lazar, S.A. Neild, D.J. Wagg *Using an inerter-based device for structural vibration suppression*, Earthquake Engineering Structural Dynamics, Vol. 43 (2014), pp. 1129-1147.

[3] S.J. Swift, M.C. Smith, A.R. Glover, C. Papageorgiou, B. Gartner, N. E. Houghton *Design and modelling of a fluid inerter*, International Journal of Control, Vol. 86, No. 11 (2013), pp. 2035–2051.

[4] X. Zhu, X. Jing, L. Chen *Magnetorheological fluid dampers: A review on structure design and analysis*, Journal of Intelligent Material Systems and Structures, Vol. 23, No. 8 (1995), pp. 609-625.

[5] R. Stanway, J.L. Sproston, A.K. El-Wahed *Applications of electro-rheological fluids in vibration control: a survey*, Smart Materials and Structures, Vol. 5 (1996), pp. 464–482.

[6] M. Tipuric, P. Deastra, D.J. Wagg, N.D. Sims *Semi-active inerters using magnetorheological fluid: a feasibility study*,in *proceedings of Active and Passive Smart Structures and Integrated Systems XII, Denver, Colorado, United States, 2018 March 16*, Denver (2018).

[7] B. J. Gartner, M. C. Smith *Damping and inertial hydraulic device*," (US20130037362 A1), patent filed 2011.

[8] J.D. Carlson *What Makes a Good MR Fluid?*, Journal of Intelligent Material Systems and Structures, Vol. 13 (2002), pp. 431-435.

[9] N.D. Sims *Vibration absorbers for chatter suppression: A new analytical tuning methodology*, Journal of Sound and Vibration, Vol. 301 (2007), pp. 592-607.

Active vibration reduction on a quadrocopter

T. Bartel[1], H. Atzrodt[1], D. Wilczynski[1]
[1] Fraunhofer LBF
Bartningstraße 47, Germany
e-mail: **torsten.bartel@lbf.fraunhofer.de**

Abstract
A major application case for drones is its usage as a flying video camera. Vibration excited by motors and wind reduces the video quality. Therefore passive and active vibration reduction mechanisms as electromotor enhanced gimbals are typically integrated. By means of these measures a good vibration reduction can be achieved. Nevertheless in certain operation conditions, still a reduced video quality is observed. As a typical phenomenon the rolling shutter effect is observed. This work presents the positive effect of a device for an active vibration reduction of a camera mounted on a quadrocopter. It focuses on the experimental identification of the vibration behaviour of the quadrocopter in different defined flight conditions. The effects of vibration excitation by wind and electromotors onto the acceleration of the camera are presented. According to the results an active vibration control system based on an electrodynamic actuator and velocity feedback is designed, realized and tested on test rig and in flight.

1 Introduction

1.1 Motivation

In recent years, the maker scene has expanded in Europe and more events are showing the increasing interest in this field. The increasing numbers of Fabrication Laboratories (FabLab's) are used by private persons and Start Up's to realize own creative ideas. These so called "Makers" can fall back on open hardware and open source platforms that offer free instructions, scripts, routines and other source code. For example, the OpenAdaptronik platform offers information, tools and instructions on the topic of intelligent systems for vibration reduction that are freely accessible to anyone interested. OpenAdaptronik is a project that prepares the adaptronics for the maker movement in photonics. Within the frame of OpenAdaptronik, simple procedures for the design and integration of adaptronic measures in photonics are developed, discussed with the maker scene and published. Within the frame of the project, the implementation of active structures was to be demonstrated with the aid of three demonstrators using understandable and interesting examples. Besides the active mounting of a telescope and the active vibration isolation on a breadboard made of Lego bricks, the third demonstrator is the vibration reduction system in the digital camera of a quadrocopter that is presented in this paper.

In drone cameras with CMOS sensor, the so-called "rolling shutter effect" or "jello effect" occurs. The cause of the effect is the functionality of the CMOS (complementary metal-oxide-semiconductor) sensor. With a CMOS sensor there is only one readout unit for reading one line of pixels. The consequence is that the lines must be read one after the other. The microcontroller of the camera determines which line is read at which time. The rolling shutter effect of the CMOS sensor is created by reading out the sensor lines at different times (at a CCD (charge-coupled device) sensor, all pixels are read simultaneously).

The rolling shutter effect on an image is inversely related to the shutter speed compared to camera movement. When moving the camera or the object, shutter speed has to be as high as possible (e.g. 1/1000 s) in order to obtain a sharp picture. The higher the shutter speed, the greater the rolling shutter effect (with the same movement). At a low shutter speed (e.g. 1 s), the readout time has relatively little influence on the image capture. Another way to avoid the rolling shutter effect is to reduce the disturbing vibration.

If the image is steady, there is no effect on the image quality by reading the lines one after the other. Mostly passive systems are used for vibration reduction. However, the isolation system reduces the high-frequency vibration of the camera, but increases the natural frequency of the isolation system. Best reduction is offered by active isolation systems. Active vibration-reducing systems on a drone occur in the form of gimbals (Figure 1). This combines gimbal mounts and brushless motor to compensate for rotary's movement and vibration of one to three axes. However, translational vibration can still lead to the rolling shutter effect, for example during fast climb or descent. Therefore, an inexpensive and simple system for active vibration reduction is developed within the scope of the OpenAdaptronik project. The aim is to implement the complete development with open source tools, to make the instructions for reproduction freely accessible and to use components that are easy to procure. The whole active vibration isolation system should not cost more than 50 euros. The quality and service life of expensive, commercial solutions cannot be achieved with the developed system, but it should still be able to be used over a longer period of time.

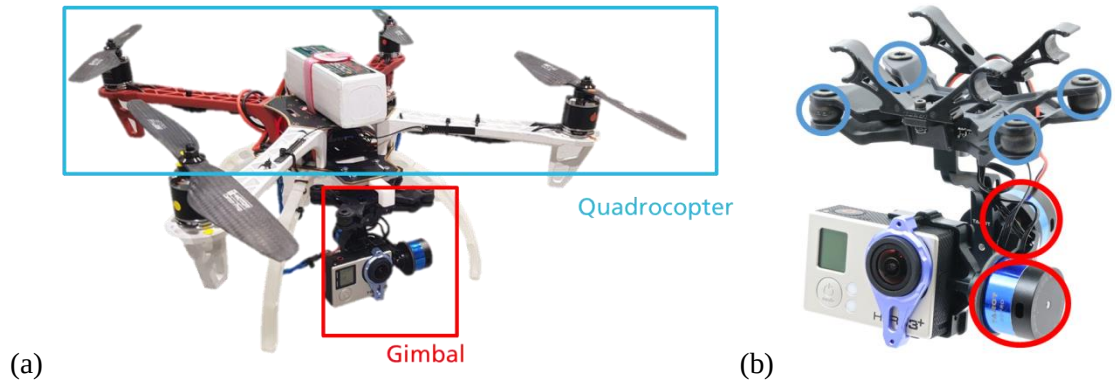


Figure 1: (a) Investigated quadrocopter with gimbal (including camera); (b) Gimbal with camera: Passive rubber mounts (marked blue) and BLDC motor (marked red)

1.2 State of the art in science and technology

In general, vibration of a camera results in a bad image quality of the camera record. In this chapter is explained how vibration of a quadrocopter arises and which solutions are being used to reduce the final vibrations of the camera recording.

There are two main sources of vibration. At first, the BLDC Motor and secondly the control strategy of the BLDC motor and the quadrocopter. These vibration sources cannot be stated in general because there are different parts used on different quadrocopter which results in different vibration characteristics.

The other aspect of vibration is the transfer path of vibration. The camera is mostly placed in a central position on the quadrocopter. How the vibrations are forwarded from the vibration sources (BLDC Motors) through the quadrocopter frame to the camera depends on the structural dynamic properties of the used frame [1].

In the following, the different solutions are presented how to reduce the vibration in the image of a camera mounted on a quadrocopter.

Firstly, there are many software solutions for cameras aiming at the removal of vibration effects of an image [2][3][4]. The advantage of this solution is that there are no additional mechanical parts which can fail over the time. On the other side, the disadvantage is that the real time correction of the vibration needs high computation power. Additionally, the software solutions work with images already disturbed by vibration. Therefore, there is already an information loss in the image before the software correction begins to work. If there is no need to remove vibration in real time, there are many solutions for video

offline processing. Some examples for the offline software tools are Adobe After Effects, Wondershare Filmora, Deshaker etc.

Secondly, the most efficient way to reduce the vibration is the prevention of vibration. The flight controller includes integrated sensors like accelerometer and gyroscope. These sensors are also measuring the unintended vibration which leads to bad control performance, increasing vibration. To reduce vibration of the sensor, a noise attenuated sensor fusion can be used [5]. Additionally, mostly used ESCs (Electronic speed controller) have a square-wave driver because they are cheaper, more simple and easier to control in comparison to a sinusoidal driver [6]. To reduce vibration caused by the ESC, an ESC with a sinusoidal driver is advantageous.

The ESC is controlling the rotation speed of the used BLDC motor which includes a propeller to transform the rotational force to a translational force. During this process the propeller produces vibration in dependency of the used material of the propeller and the structure. In general, a more stiff material like carbon fiber is advantageous with respect to vibration reduction [6]. In reference to the structure of the propeller, mostly used propellers are two bladed. A vibration reduction can be achieved using a propeller with four blades[7]. Nevertheless, the most important aspect is the proper balancing of the propeller. Vibration from an unbalanced propeller is caused by asymmetric centrifugal forces which are further caused by the asymmetrical distribution of mass and shape of the propeller. Nevertheless, there are various propeller balancers available to get a properly balanced propeller.

The vibration produced by the propeller is forwarded through all parts of the frame to the camera sensor. In dependency on the previous aspects, the propeller is exciting vibration. This vibration is in dependence to the frequency attenuated or increased in the frame. The structural analysis of a hexacopter frame [8] results in measured resonance frequencies between 86 Hz and 330 Hz. To prevent vibration increase, it is recommended to set the operational frequencies of the rotor below the resonance frequencies of the frame. To increase the resonance frequencies of the frame, a material like carbon fiber with high stiffness can be used.

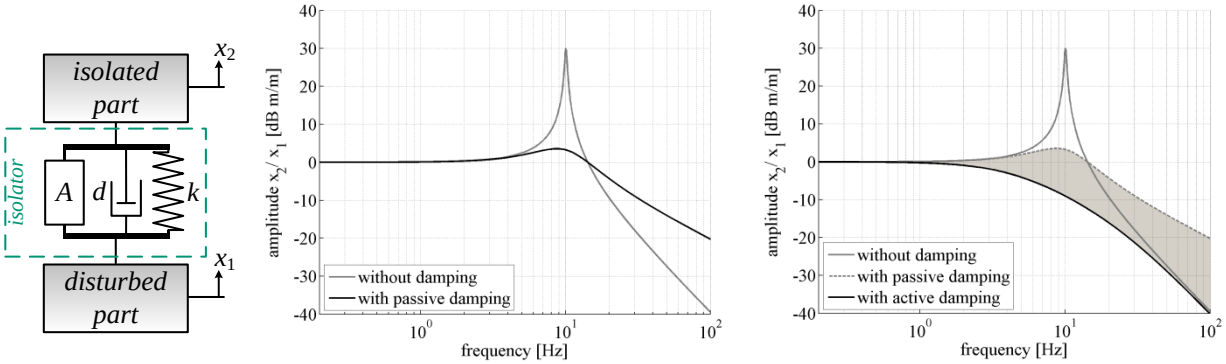
Lastly, the most widely used market solution for vibration reduction of the camera is the gimbal. Gimbal is a device, connecting camera and frame of the quadrocopter. The gimbal can be divided in active and passive parts. The passive parts are spring and damper causing a low resonance frequency of the gimbal-camera-system, thus reducing vibration at higher frequencies. On the passive suspension, the active part is disposed. For the active parts, there exist different variations with one two or three rotational axis. To reduce the vibration in one axis, a BLDC motor is used which acts against the vibration movement. The BLDC are controlled with a PID controller and the control state is the rotational velocity.

By using most of these presented solutions, a vibration reduction of the camera can be achieved and a better record of the camera can be expected. The conclusion of the state of art technology is that an active translational vibration reduction like presented in this work is not common for a quadrocopter UAV (unmanned aerial vehicle). Furthermore, there is some potential of the active translational vibration reduction.

1.3 Technical Background

The usage of lightweight construction and a higher analysing precision is specific for the development of modern products. The effect of vibration, influencing the function or even causing damages, gets in the focus of the development process. Vibration induced from a quadrocopter into an attached camera reduces picture quality. Mentioned conventional passive vibration isolation methods are limited in their effect and cannot comply all demands. For vibration isolation, the mechanical path between a disturbance source and the structure that is to be isolated has to be designed. The design follows such way that a vibration reduction is yielded in a certain frequency range. This can be achieved by adding a stiffness element k, a damping element d and, if required, an actuator element A. The scheme of an isolation system is depicted in Figure 2 (a). Regarding the transmissibility of a passive isolation system between a disturbed part and an isolated part, the typical amplitude response is given in Figure 2 (b). As shown, the undamped isolator effects an increasing vibration isolation of -40 dB per decade in the frequency range above the resonance

of the mass-spring system. An arising drawback is the vibration amplification around resonance frequency. The amplification can be reduced by the integration of a damper, which however also reduces the isolation effect at higher frequencies. In addition to passive isolation, active isolation unites the advantages of damped and undamped systems as can be seen in Figure 2 (c). While broadband isolation remains at frequencies above the resonance, the vibration amplification in the resonance can be reduced equal to the effect of a damping element [9].



(a) Scheme of an isolation system (b) passive isolation (c) active isolation

Figure 2: Operational direction of the actuators and the resulting movement

This paper shows the design process of the integration of an active isolation system into the passive Gimbal isolation of a video camera attached to a quadrocopter.

1.4 Approach for active isolation system development

In the beginning the demands on the active isolation system have to be defined. Therefore, the vibration of the camera on the quadrocopter is experimentally investigated during climb, stationary flight and descent. Furthermore the principal structural dynamic behavior of the gimbal and the camera attached to the quadrocopter is determined. On base of the experimental results, the scheme of the active isolation system is defined. A preliminary realized setup consisting of actuator, amplifier, controller and sensor is tested in laboratory. The single components as well as the active isolation system are numerically modelled and experimentally validated. The final setup of the active isolation system is integrated into the Gimbal of the quadrocopter. Its performance is tested in real flight condition.

2 Experimental vibration investigation

As reference for the active vibration control system, the quadocopter is experimentally investigated. Both operational measurements during flight condition and structural identification using hammer excitation are conducted. During all measurements, the camera is attached to quadrocopter via elastic gimbal as shown in Figure 3 b).

For structural identification of the gimbal-camera-system, the quadrocopter is excited close to the mounting point of the gimbal using hammer excitation as depicted in Figure 3 b). The responding acceleration amplitude is measured in three directions on the back side of the camera (x-direction equals horizontal flight direction, y-direction equals horizontal direction to the side, z-direction equals vertical direction) as shown in Figure 3 a). The first structural resonance of the gimbal-camera-system can be observed between 9 Hz and 20 Hz in dependence to the direction.

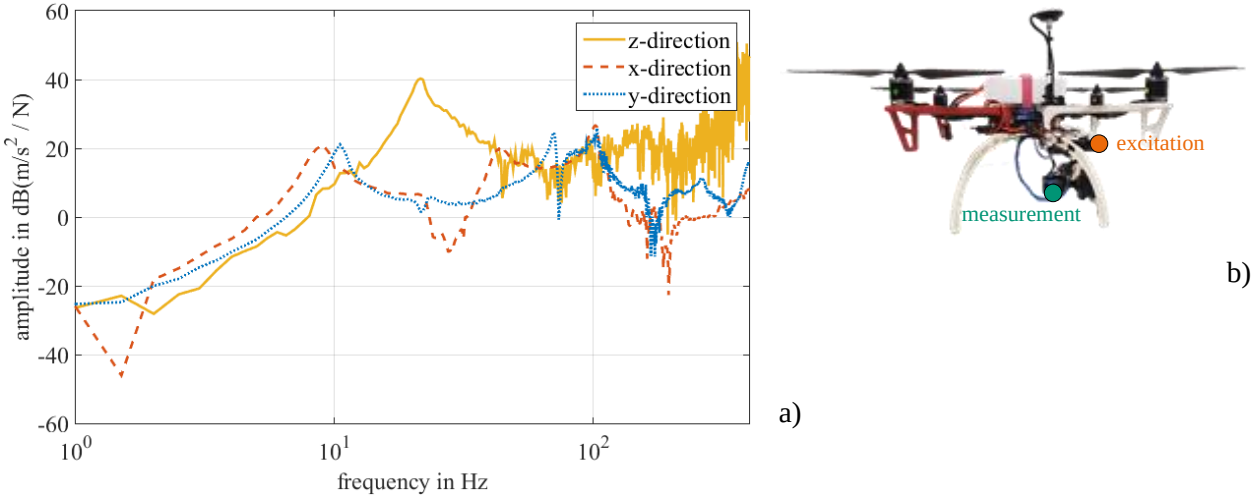


Figure 3: Natural frequencies of the gimbal-camera-system in x-, y- and z-direction.

a) Acceleration of the camera in response to hammer excitation
b) Excitation and measurement points on the quadrocopter

In flight condition, the acceleration of the camera is measured during stationary flight, descent and climb. The amplitudes of the acceleration spectra are shown in Figure 4 a). Two significant vibration amplifications are observed in the frequency range up to 400 Hz. The second amplification can be related to the rpm of the motor and becomes especially visible during stationary flight and climb, when the motor provokes highest thrust. According to datasheet, the rpm of the used motor MT2216 lies between 5600 1/m (equal to approx. 93 Hz in 1st order) and 8950 1/min (equal to approx. 149 Hz in 1st order) in dependence to the torque load.

As proven before, the first amplification can be related to the natural frequency of the gimbal-camera-system. Though, this structural resonance is excited during all flight conditions, it becomes clearly visible during descent of the quadrocopter.

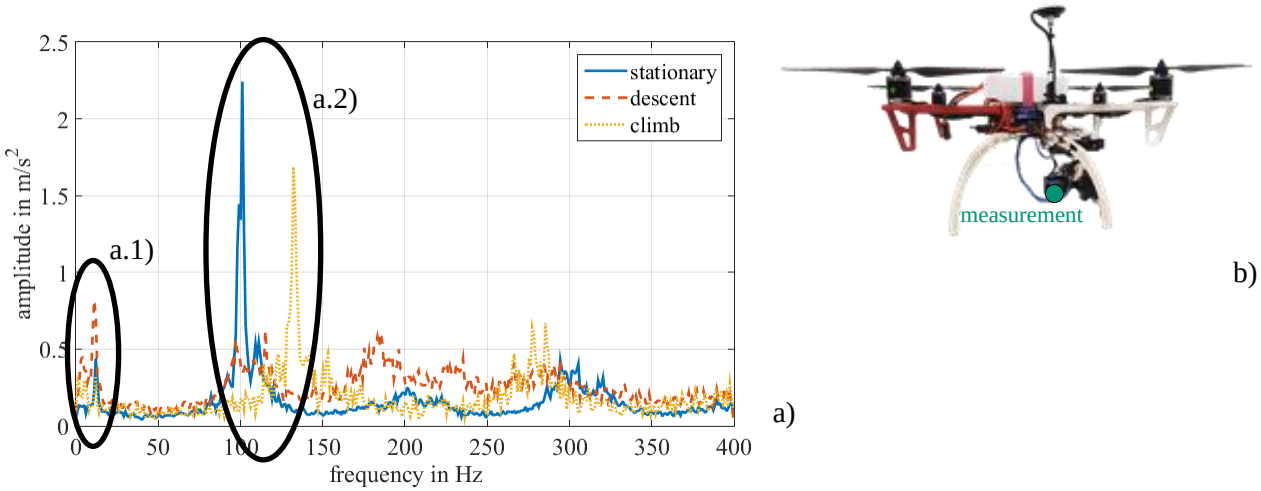


Figure 4: Camera vibration in vertical direction during stationary flight, descent and climb.

a) Acceleration spectra during different flight conditions: stationary flight, descent, climb
   a.1) Vibration amplification due to natural frequency of the gimbal rubber mounts.
   a.2) Vibration amplification due to motor excitation in accordance to rpm
b) Measurement point on the quadrocopter

Besides wind flow effects, the structural resonance of the gimbal-camera-system is excited by discontinuous motor excitation. The signal output of the flight controller is shown in Figure 5 during approx. 5 minutes of quadrocopter operation. The time intervals of climb and descent flight situations are indicated blue and red respectively, the remaining time is stationary flight. Especially during descent, the motor controller gets a discontinuous signal from the flight controller, thus causing abrupt, impulse-like changes of motor torque, which result in a broad-band vibration excitation of the quadrocopter.

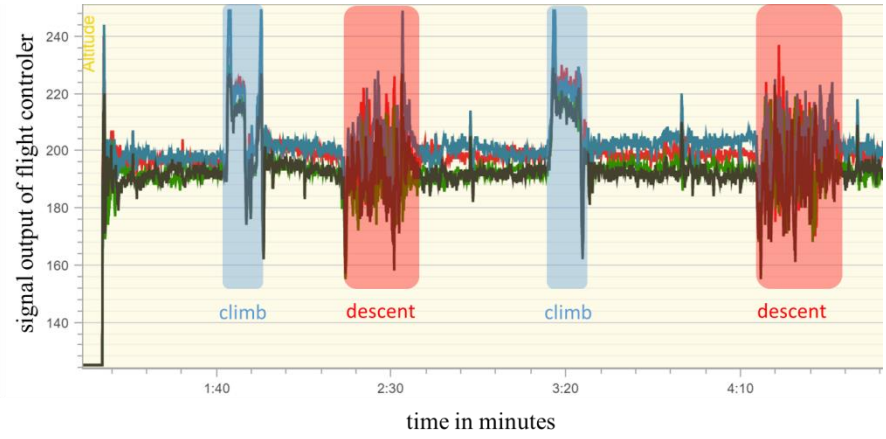


Figure 5: Controller output during climb, descent and stationary flight

3 Active isolation system layout and development

For optimization of vibration reduction, different actuator concepts as depicted in Figure 6 are investigated. The actuator itself is illustrated as a spring-damper system with actuation force F_{act}.

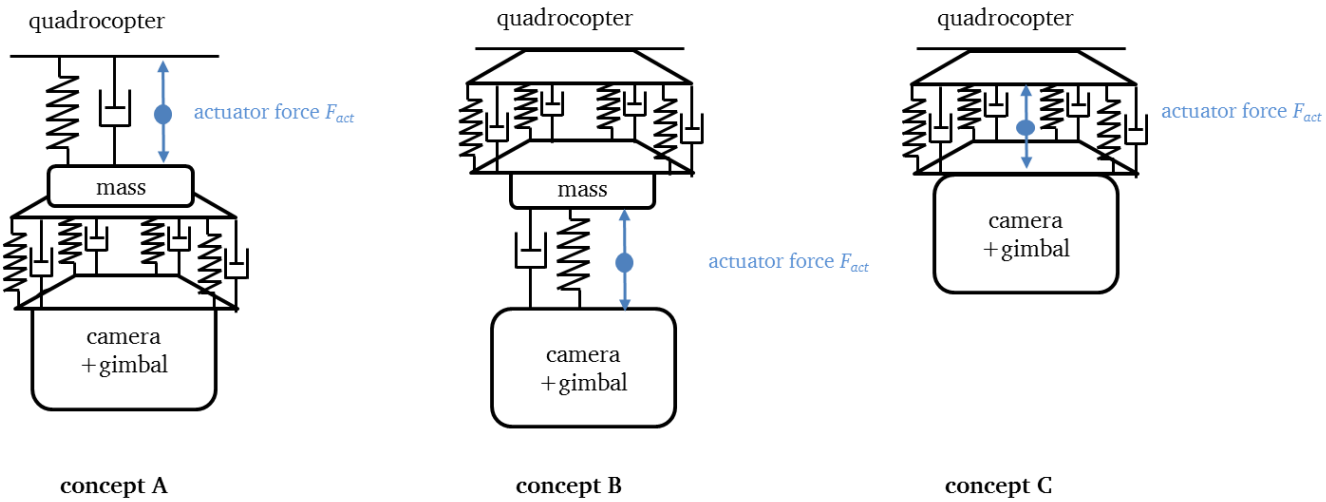


Figure 6: Concepts for the active vibration control system, integrated in the gimbal

In concept A and B, the actuator is serially connected to the passive components of the gimbal. Due to the serial connection, a lot of space is required and the lever between quadrocopter and camera is increasead. This results in a further amplification of camera acceleration due to rotatory quadrocopter vibration. The possibility of an unchanged gimbal design is the advantage of the serial connection. In the parallel configuration, shown in concept C, the actuator increases the passive stiffness and damping in the non-active direction, thus resulting in a loss of passive isolation performance. Nevertheless, the effect of active damping is highest, due to the direct coupling of the actuator force.

For the selection of a concept, numerical models of all system components are set up and experimentally validated. As controller, a velocity feedback is chosen as illustrated in Figure 7.

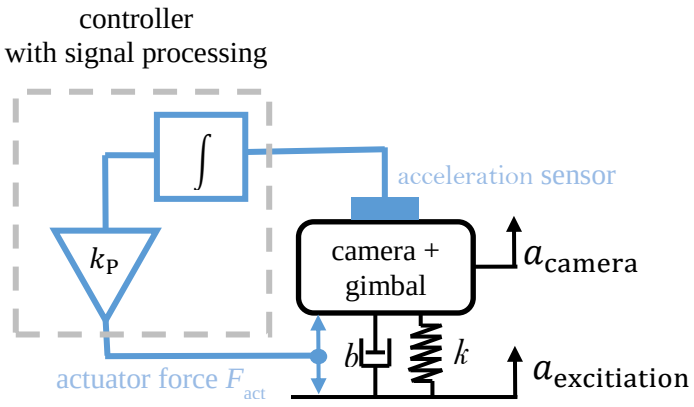


Figure 7: Scheme of velocity feedback control

The closed loop control circuit is depicted in Figure 7. The acceleration is captured using a MEMS acceleration sensor. The acceleration signal is integrated in order to achieve velocity. The velocity signal is amplidied by a P-controller in accordance to the amplification factor k_P. The actuator amplifier is driven with the output signal of the P-controller, thus finally exciting the actuator.

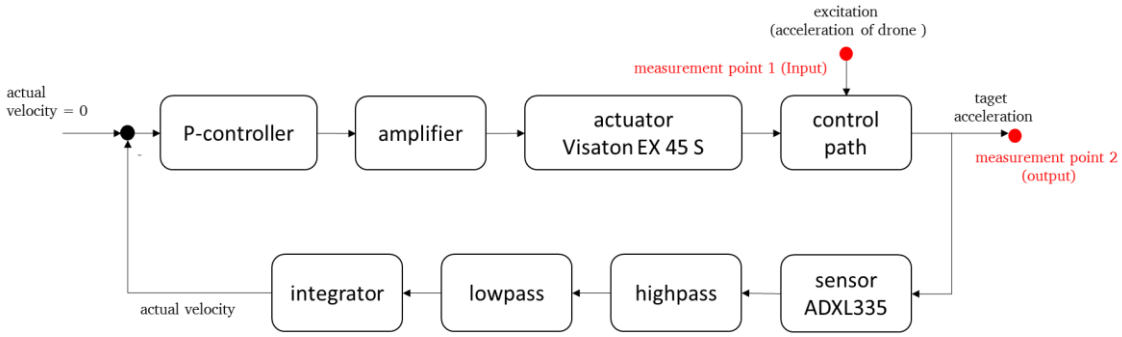


Figure 8: Closed loop control circuit of the velocity feedback vibration control

Figure 9 shows the transmissibility of the active vibration isolation between quadrocopter and camera, comparing experiment and simulation. A good agreement between numerical model and experiment up to 400 Hz can be proven. Furthermore, the acceleration amplification of the gimbal-camera-system that occurred approx. at 10 Hz can be reduced to zero.

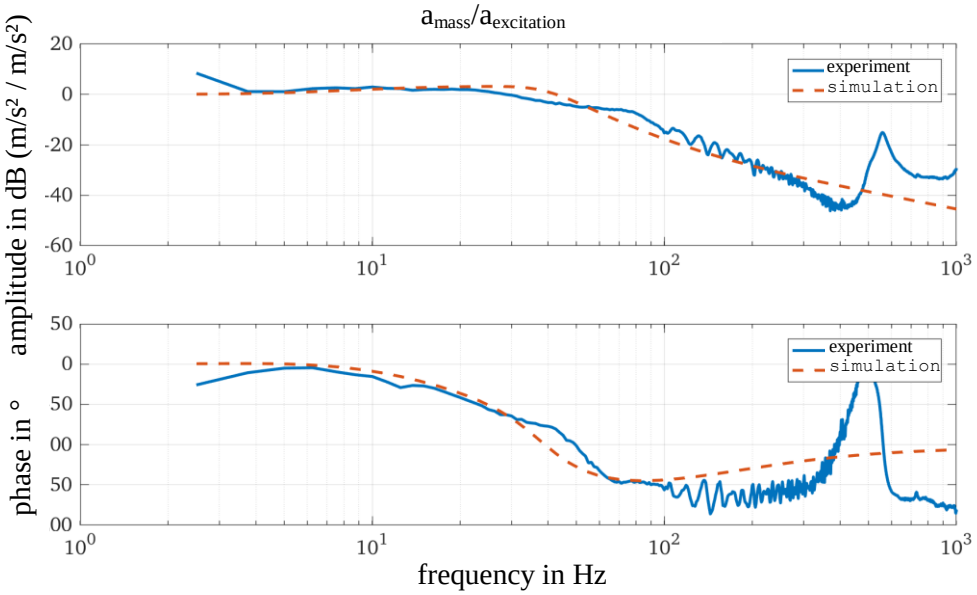


Figure 9: Transmissibility of the active vibration isolation system

After validation of the single components and the holistic system, the concepts shown in Figure 6 are numerically compared. The results are shown in Figure 10.

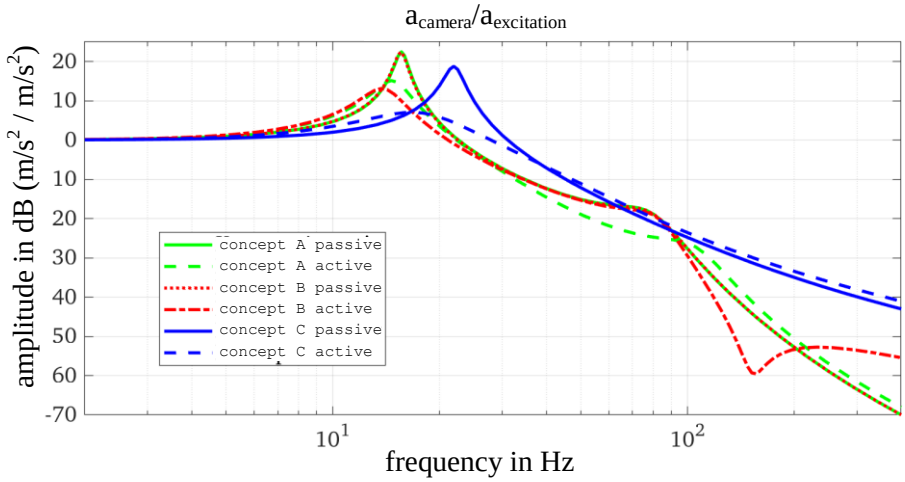


Figure 10: Transmissibility of the numerical comparison of concepts

According to the results, the highest vibration reduction (-12 dB) in comparison between all concepts can be achieved using concept C. A slight disadvantage is the reduced passive isolation effect at higher frequencies due to the one-mass isolation in comparison to the two-mass isolation.

On base of the numerical results, concept C is chosen to be preliminary designed.

4 Actuator setup and active isolation system testing

In this chapter, the actuator setup and gimbal integration is presented. Before flight test, the functionality of the active system is tested in a laboratory. Finally, the performance of the active vibration control system is discussed.

Experimental results show that the gimbal is performing rotational movements around the x-axis. Accordingly, the actuator setup is chosen. Consequently, the active vibration control system includes two actuators which are working in opposite direction in order to reduce the rotational movement of the gimbal. This relation is displayed in Figure 11.

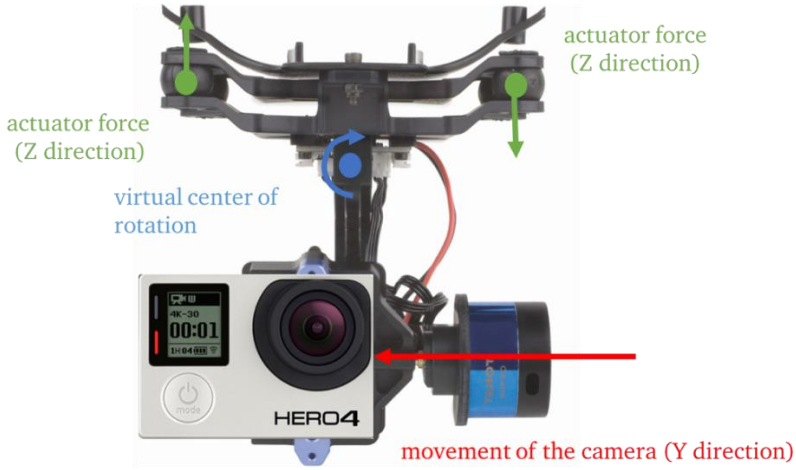


Figure 11: Operational direction of the actuators and the resulting movement

The dimensioning and the design of the actuator are displayed in Figure 12. The two actuators are designed, following the electrodynamic principle. Each coil is guided by a 3D-printed guidance though the magnetic field of two neodymium magnets, used for each actuator. The 3D-printed guidance is part of an adaptor plate, attached to the original gimbal system.

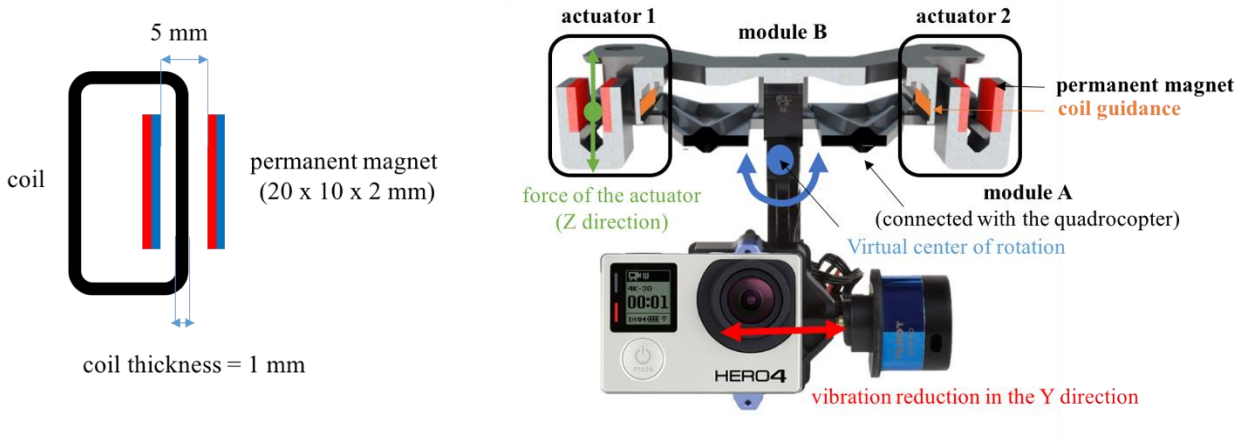


Figure 12: Dimensioning of the actuator

To test the functionality of the active vibration control system, the gimbal is clamped on a rigid breadboard and broad-band excited by electrodynamic excitation.

The results in Figure 13 show that the active vibration system achieves a damping value of -6 dB in the resonance frequency of 11 Hz of the gimbal, using only one actuator.

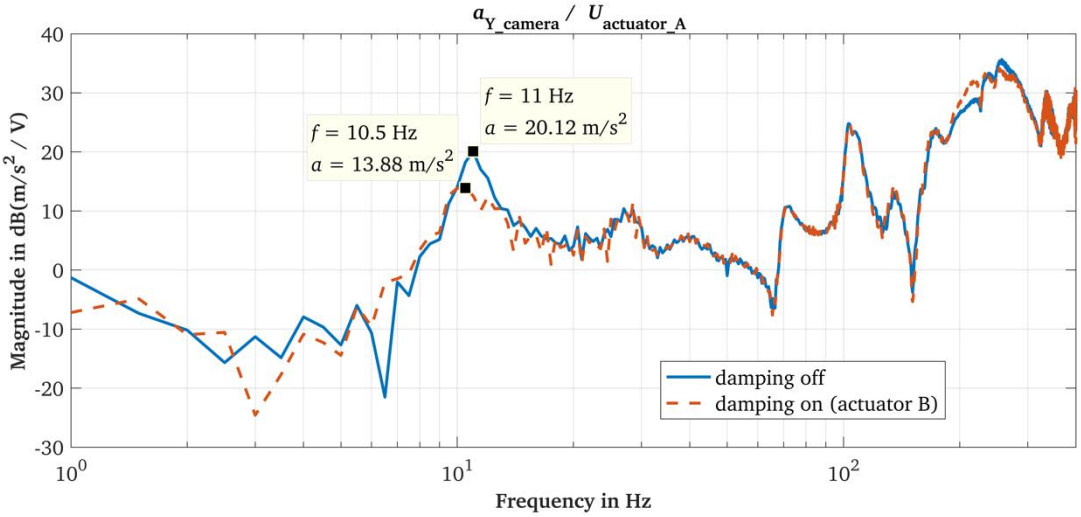


Figure 13: Performance measurement of the active vibration system on a test bench

To verify if it is possible to achieve this damping performance during real flight, the system is mounted on the quadrocopter. The active isolation performance varies from flight to flight due to unequal flight condition. Thus, the results are a mean value of 5 descending flights with the active system turned off and 5 descending flights with the active system turned on.

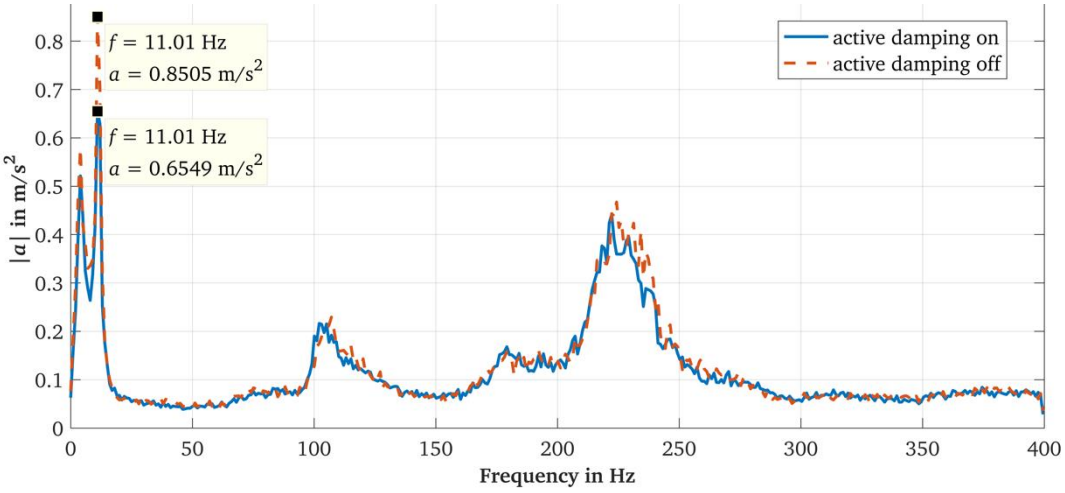


Figure 14: Average acceleration spectra of the camera with integrated active vibration control system during descending flight

The final result of the flights according to Figure 14 shows that the active control vibration system achieved a damping reduction of 24 % at the frequency of 11 Hz. However, the damping reduction of 50 % on test bench is higher. This discrepancy could be explained with the following aspects:

- Non-steady disturbances during the flight influences the performance of the active vibration control system
- The deflection of the gimbal is higher during flight

5 Summary

In this paper, the design, setup and test of an active isolation control system is described. The design is in accordance to the OpenAdaptronik project, where low cost components are used and the design as well as any programming code is published open source.

As introduction, the effect of vibration on image quality of a camera attached to a Quadrocopter is described. State-of-the-art solutions to reduce vibration are presented. A standard commercially available system to reduce vibration is the gimbal. It consists of a BLDC motor to reduce the quasi-static movement and rubber mounts for passive vibration isolation.

The vibration of a camera attached to a quadrocopter via gimbal is experimentally investigated. It is presented, that the natural frequency of the gimbal causes an increase in vibration especially during descent flight.

Concepts to actively counter this increase using active velocity feedback are depicted and numerically compared. The most promising concepts, a parallel integration of the actuator into the gimbal, is realized and tested in laboratory.

Final tests of the active vibration control system during flight prove a certain vibration reduction of the actively vibration controlled camera.

Acknowledgements

The authors acknowledge the financial support by the Federal Ministry of Education and Research of Germany in the framework of OpenAdaptronik.

References

[1] J. Verbeke, *Vibration analysis of a UAV multirotor frame*, 2016.

[2] D. Afolabi, *Monocular line tracking for the reduction of vibration induced during image acquisition*, 2015.

[3] D. Afolabi, Real-time vibration reduction in uav's image sensors using efficient hough transformation, 2013

[4] C.-K. Liang, Analysis and Compensation of Rolling Shutter Effect, 2008.

[5] Y. Cho, A QuadCopter Posture Stabilization Control using Noise Attenuated Sensor Fusion and Modified PID Control, 2014.

[6] Q. Quan, Introduction to Multicopter Design and Control, Springer Nature Singapore, 2017.

[7] S. Radkowski, Analysis of Vibration of Rotors in Unmanned Aircraft, 2015.

[8] J. Verbeke, Vibration analysis of a UAV multirotor frame, Research Gate, 2016.

[9] A. Preumont: Vibration Control of Active Structures: An Introduction, Kluwer Academic Publishers (2002)

$\mathcal{H}_\infty$ optimization of positive position feedback control for mitigation of nonlinear vibrations

G. Zhao[1], A. Paknejad[1], G. Raze[2], G. Kerschen[2], C. Collette[1]
[1] Université Libre de Bruxelles, Department of Bio-, Electro- and Mechanical Systems, Precision Mechatronics Laboratory
50, F.D.Roosevelt Av, B-1050, Brussels, Belgium
e-mail: **guoying.zhao@ulb.ac.be**

[2] University of Liège, Department of Aerospace and Mechanical Engineering
Allée de la Découverte 9, B-4000, Liège, Belgium

Abstract
This paper investigates the potential of using positive position feedback control for the mitigation of nonlinear vibrations. Closed form expressions for the $\mathcal{H}_\infty$ optimal control parameters that minimize the maximal response of the structure are firstly derived for the linear case and then extended to the nonlinear case. The resonant vibration of a Duffing oscillator is considered to illustrate the proposed tuning of the optimal control parameters and the harmonic balance method is employed to approximate the analytical solutions. Numerical simulations are performed to demonstrate and validate the proposed method.

1 Introduction

Controlling nonlinear structural vibrations is becoming increasingly important in a number range of engineering applications such as aerospace, medicine and robotics, wherein lightweight materials are considered in the construction of systems in order to meet the increasing demand for fuel efficiency or smaller actuators [1], [2]. However, this will naturally lead to the fact that the resonances are lightly damped and to the presence of some geometric nonlinearities from large deformations. The resulting unwanted nonlinear vibrations thus become the main concern, limiting the success of these applications. One key characteristic of nonlinear vibrations is their frequency-energy dependence which in other words means that the frequency of the nonlinear oscillations depends intrinsically on the motion amplitudes [3]. As a consequence, the mature linear damping-enhanced approaches based on the superposition principle such as tuned mass dampers and piezoelectric shunting [4]–[6] (passive solutions) or direct velocity feedback, integral acceleration, positive position feedback (PPF) and force feedback controllers (active solutions) [7] are no longer effective in the presence of strong nonlinearities. In order to recover their control effectiveness for a large range of excitation levels, mechanisms that can deliver nonlinear reacting forces should be included in these linear approaches. For example, Agnes [8] suggested to integrate a positive or negative cubic spring into a linear vibration absorber for compensating the softening (hardening) nonlinear effect of the primary systems. Febbo and Machado [9] explored the potential of using a nonlinear absorber with the saturation nonlinearity for vibration mitigation of nonlinear primary oscillators. Habib et al. [3] reported that the mathematical form of the nonlinear vibration absorber should be the same as that of the primary nonlinear system such that the nonlinear vibration absorber behaves as a linear vibration absorber.

In this study, a nonlinear positive position feedback (NPPF) controller as an extension of the classical PPF controller is investigated for the mitigation of Duffing oscillations. According to the similarity principle proposed by [10], the NPPF controller introduces a cubic term on top of the original PPF controller. The proposed nonlinear PPF controller is implemented by feeding the structural position directly to the nonlinear compensator, whose output is fed through a fixed gain positively back to the structure, thus achieving damping for a particular mode. In this sense, NPPF as well as PPF controllers would be well suited for the

applications where piezoelectric sensors and actuators are employed for vibration damping. This is because the voltage from the sensor is proportional to the strain of the attached structure, which can be directly measured to drive the strain-based piezoelectric actuators based on the NPPF or PPF controllers.

Although some numerical and experimental implementations of the proposed NPPF control scheme may be found in the literature, limited investigation of the optimization the NPPF controller for the Duffing vibrations exists. In this paper, an $\mathscr{H}_\infty$ optimization criterion is used to optimize the NPPF controller, and accordingly the optimal parameters are set to minimize the maximum steady state response of the structure. The objective of the study is to understand its working principle and validate the control efficiency through a harmonic balance analysis.

2 Mathematical model and $\mathcal{H}_\infty$ optimization

2.1 Modeling

The system under investigation is shown in Figure 1. The structure is modeled as an undamped single degree of freedom (dof) system, defined through a lumped mass m_1, a linear spring k_1 and a cubic spring k_3. It is excited by a harmonic force $F = F_d \cos(\omega t)$. A force actuator with its stiffness k_2 is placed in parallel to the passive mount. The control loop is implemented by feeding the displacement of the lumped mass m_1 through a nonlinear controller $h(x)$ to drive the actuator.

The governing equations of the system read:

$$m_1\ddot{x} + k_1 x + k_3 x^3 = F_d \cos(\omega t) + F_a - k_2 x \tag{1}$$

$$F_a = g_1 h(x) \tag{2}$$

where F_a is the actuating force proportional to the driving signal, g_1 represents the feedback gain and $h(x)$ is the NPPF controller.

The NPPF controller is designed based on the principle of similarity, and consequently a cubic term is included in the linear PPF controller, yielding:

$$\ddot{u}_a + 2\alpha\omega_f \dot{u}_a + {\omega_f}^2 u_a + \kappa {u_a}^3 = x \tag{3}$$

where $u_a = h(x)$, α, ω_f and κ are controller parameters.

In order to come to a more general formulation, the following parameters are introduced to normalize the system governing equations:

$$\begin{aligned} &\tau = \omega_1 t, \quad \mu = \frac{\omega_f}{\omega_1}, \quad k_t = k_1 + k_2 \quad y_1 = \frac{k_t x}{F_d}, \quad y_2 = \frac{k_t {\omega_1}^2 u_a}{F_d}, \\ &\omega_1 = \sqrt{\frac{k_t}{m}}, \quad \delta = \frac{k_3 {F_d}^2}{{k_t}^3}, \quad g = \frac{g_1}{k_t {\omega_1}^2}, \quad \beta = \frac{\kappa k_t}{k_3 {\omega_1}^6} \end{aligned} \tag{4}$$

The equations of motion with normalized parameters can then be written as:

$$y_1'' + y_1 + \delta {y_1}^3 - g y_2 = \cos(\Omega\tau) \tag{5}$$

$$y_2'' + 2\alpha\mu y_2' + \mu^2 y_2 + \delta\beta {y_2}^3 - y_1 = 0 \tag{6}$$

where Ω is the normalized frequency defined as $\Omega = \omega/\omega_1$.

It is shown that the forcing amplitude appears only in the expression of the nonlinear coefficients. The $\mathcal{H}_\infty$ optimization criterion is employed to optimize the controller $h(x)$ aiming to minimize the maximum magnitude of the frequency response of the system under consideration. In this context, the magnitude of the normalized driving point receptance $|y_1|$ is taken as the performance index.

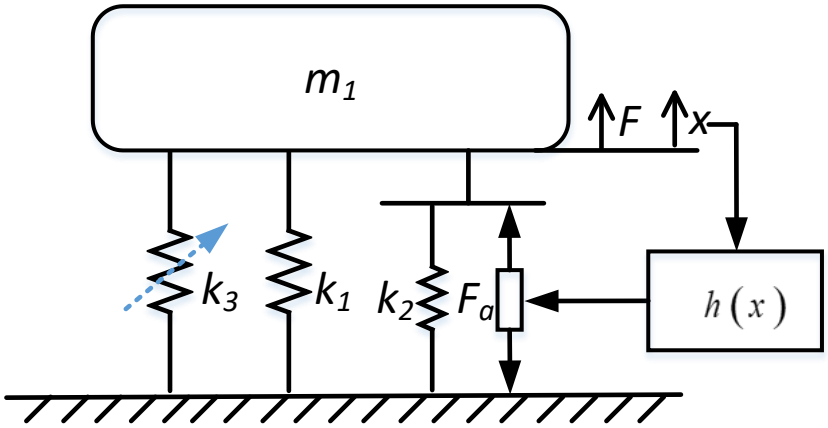


Figure 1 The scheme of the system under consideration

2.2 $\mathcal{H}_\infty$ optimization of linear PPF controller

The system with a linear PPF controller is considered first. This is done by setting the parameter δ in Eq. (5) equal to zero. The normalized driving point receptance of the primary structure is then given by:

$$y_1 = \frac{s^2 + 2\alpha\mu s + \mu^2}{s^4 + 2\alpha\mu s^3 + \mu^2 s^2 + s^2 + 2\alpha\mu s + \mu^2 - g} \tag{7}$$

where $s = j\Omega$ is the Laplace variable and the magnitude of y_1 is calculated as:

$$|y_1| = \frac{\sqrt{\Omega^4 + \left(4\alpha^2 - 2\right)\mu^2\Omega^2 + \mu^4}}{\sqrt{\left(\Omega^2 - 1\right)^2\mu^4 + 2\left(\left(2\alpha^2 - 1\right)\Omega^4 + \left(-2\alpha^2 + 1\right)\Omega^2 + g\right)\left(\Omega^2 - 1\right)\mu^2 + \left(-\Omega^4 + \Omega^2 + g\right)^2}} \tag{8}$$

From the mathematic point of view, the control effectiveness of a PPF controller according to Eq. (7) would be similar to that of a tuned Mass damper, where an additional zero is introduced to interfere with the resonance of the primary system aiming to reduce certain vibration metrics in the frequency band of interest. Following the $\mathcal{H}_\infty$ optimization procedure proposed by Den Hartog [4], the parameters of the linear PPF controller are optimally tuned such that the responses at the fixed points are minimized. Fixed point refers to the frequency location at which the magnitude of the driving point receptance of the primary structure is invariant in terms of the damping coefficient of the TMD or the parameter α of the PPF controller.

The frequencies at which the fixed points occur can be calculated by differentiating Eq. (8) with respect to the damping coefficient, α, and equating the derivative to zero, which yields:

$$\Omega_{f1} = \frac{\sqrt{2\mu^2 + 2 - 2\sqrt{\mu^4 - 2\mu^2 + 2g + 1}}}{2} \tag{9}$$

$$\Omega_{f2} = \frac{\sqrt{2\mu^2 + 2 + 2\sqrt{\mu^4 - 2\mu^2 + 2g + 1}}}{2} \tag{10}$$

The optimal μ is set to equalize the resulting performance index as defined in Eq. (8) at the two fixed points. This can be done by substituting Eqs. (9) and (10) into Eq. (8) and equating the resulting expressions for $\alpha = 0$, yields,

$$\mu_{opt} = 1 \tag{11}$$

For the optimal α, it is sought to make the performance index horizontally pass through the fixed points. Thus, two optimal damping coefficients associated with the two fixed points are obtained:

$$\alpha_1 = \sqrt{\frac{3g}{4\sqrt{2}\left(\sqrt{2}-\sqrt{g}\right)}} \tag{12}$$

$$\alpha_2 = \sqrt{\frac{3g}{4\sqrt{2}\left(\sqrt{2}+\sqrt{g}\right)}} \tag{13}$$

The optimal α can be taken in practice by calculating the average of Eqs. (12) and (13). It should be noted that this approach is an empirical method as the resulting resonance points (the derivative of (8) with respect to Ω is equal to zero) do not necessarily coincide simultaneously with the corresponding fixed points. An exact solution for this problem was proposed in [11], with which the two resulting resonance points are equally damped. In this study this exact approach is not considered because this would result in very long and therefore rather impractical polynomial expressions.

Up to now, only the parameter g (normalized feedback gain) is left un-optimized for implementing the linear PPF controller. The function of the feedback gain g can be assessed by evaluating the magnitude of driving point receptance at the fixed points. This is done by substituting Eqs. (9) and (11) into Eq. (8) for $\alpha = 0$, yields the minimal maximum response

$$y_{1mm} = \sqrt{\frac{2}{g}} \tag{14}$$

As shown in Eq. (14), the minimal maximum response is inversely proportional to the gain g, indicating that the value of the feedback gain g should be as high as possible without compromising the stability of the active system.

The stability of an active system can be studied by applying the Routh-Hurwitz stability criterion to its closed loop characteristic equation [12]. The characteristic equation of the system can be formed as:

$$A_4 s^4 + A_3 s^3 + A_2 s^2 + A_1 s + A_0 = 0 \tag{15}$$

where A_0, A_1, A_2, A_3 and A_4 are the corresponding coefficients of Laplace variable in the denominator of Eq. (7).

The Routh-Hurwitz stability criterion states that the roots of the characteristic equation have negative real parts if and only if the following conditions are satisfied:

$$A_0, A_1, A_2, A_3, A_4 > 0 \tag{16}$$

$$A_2 A_3 - A_1 A_4 > 0 \tag{17}$$

$$A_1 A_2 A_3 - A_1^2 A_4 - A_0 A_3^2 > 0 \tag{18}$$

It can be derived that the system is stable if and only if the gain g is defined:

$$g < \mu^2 \tag{19}$$

In the following, numerical studies are performed to illustrate the control effectiveness of the linear PPF controller for the system under consideration. Figure 2 shows the performance index $|y_1|$ plotted against

frequency for five different damping ratios defined as α/α_{opt} : 0, 1/4, 1, 4 and ∞, where the control parameters μ is set to its optimal value as given in Eq. (11) and the gain is set to 0.2. It can be seen that all the curves with different damping values intersect at two frequencies and only with the optimal damping the response at the two fixed frequencies become the maximum. One should also note that the system becomes dynamically softer with the application of PPF control as the control signal is positively proportional to the displacement of the system in the low frequency range whereas the PPF control effectiveness is similar to that of a negative spring. However, when the damping value approaches infinity, the stiffness softening effect disappears as the control action is lost. Figure 3 depicts the performance index $|y_1|$ plotted against frequency for four different feedback gains namely g : 0, 0.01, 0.05, and 0.5, where the control parameters μ and α are both set to their optimal values. As can be seen, the performance index indeed decreases with an increase in the gain as indicated by Eq. (14). With this respect, the feedback gain g of the PPF controller can be understood to play the same role as the mass ratio between tuned mass dampers and host primary structures, where better performance comes with a large value of this quantity. However, the approximation errors induced by estimation of the damping parameter α is more pronounced with an increase in the feedback gain. In the same fashion, the response in the low frequency range will be more amplified because of the negative stiffness effect. Therefore, the maximum feedback gain g under $\mathcal{H}_\infty$ optimization criterion is not only limited by the stability concern, but also by the amplification of the low frequency response.

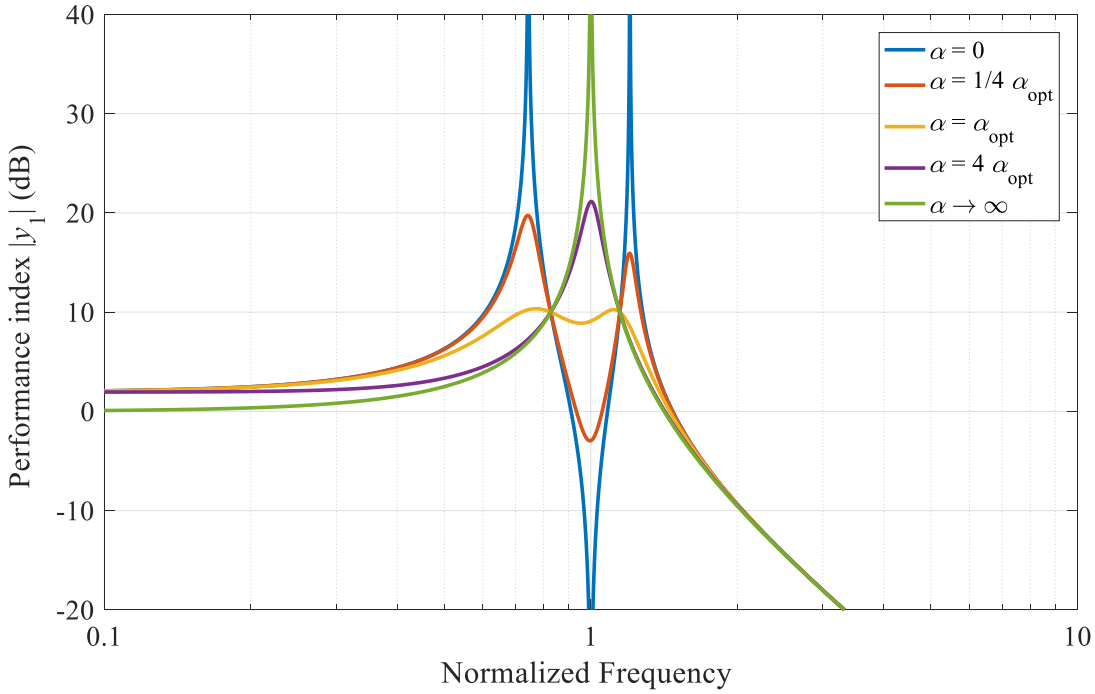


Figure 2 The driving point receptance under different active damping ratios

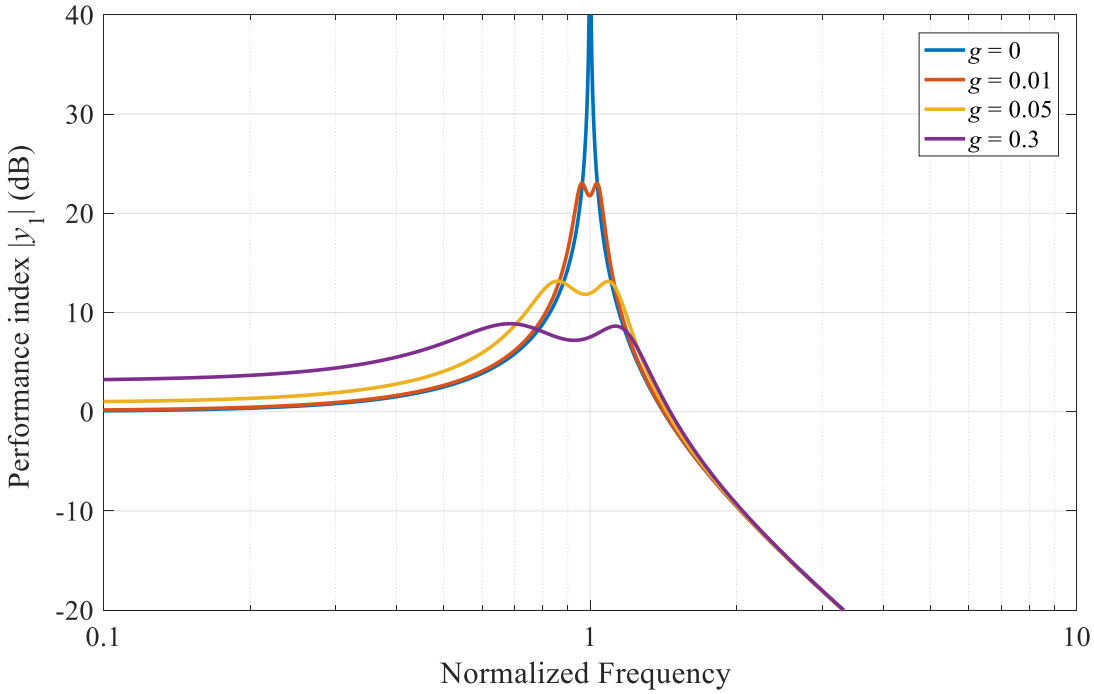


Figure 3 The driving point receptance under different feedback gains

2.3 $\mathcal{H}_\infty$ optimization of nonlinear PPF controller

In this subsection, $\mathcal{H}_\infty$ optimization of the nonlinear PPF controller is performed. Due to the cubic terms, no explicit solutions can be found for Eqs. (5) and (6). As reported in [13]–[15], harmonic solutions can be used to approximate the exact solutions with a good agreement. In the following, a pair of one-term harmonic balance approximation $y_1 = A_1\cos(\Omega\tau) + B_1\sin(\Omega\tau)$ and $y_2 = A_2\cos(\Omega\tau) + B_2\sin(\Omega\tau)$ is assumed as the solutions. Substituting the above ansatz into Eqs. (5) and (6), and applying the approximations $\cos^3(\Omega\tau) \approx 3/4\cos(\Omega\tau)$ and $\sin^3(\Omega\tau) \approx 3/4\sin(\Omega\tau)$, then balancing cosine and sine terms, yields the system of polynomial equations:

$$-A_1\Omega^2 + A_1 + g\Omega^2 A_2 + 3/4\delta A_1\left(A_1^2 + B_1^2\right) = 1 \tag{20}$$

$$-B_1\Omega^2 + B_1 + g\Omega^2 B_2 + 3/4\delta B_1\left(A_1^2 + B_1^2\right) = 0 \tag{21}$$

$$-A_2\Omega^2 + 2\alpha\mu\Omega B_2 - A_1 + \mu^2 A_2 + 3/4\delta\beta A_2\left(A_2^2 + B_2^2\right) = 0 \tag{22}$$

$$-B_2\Omega^2 - 2\alpha\mu\Omega A_2 - B_1 + \mu^2 B_2 + 3/4\delta\beta B_2\left(A_2^2 + B_2^2\right) = 0 \tag{23}$$

Up to now, it is still not possible to find explicit solutions of Eqs. (20)-(23), we thus expand the harmonic coefficients A_i and B_i into series with respect to the primary nonlinear coefficient δ, i.e. $A_1 = A_{11} + \delta A_{12}$, $B_1 = B_{11} + \delta B_{12}$, $A_2 = A_{21} + \delta A_{22}$ and $B_2 = B_{21} + \delta B_{22}$.

Substituting the above ansatz into Eqs. (20)-(23), and collecting the resulting expressions with respect to the order of the parameter δ, then after omitting the expressions whose orders are higher than δ^1, yields:

$$\left(gA_{21} - A_{11}\right)\Omega^2 + A_{11} - 1 = 0 \tag{24}$$

$$1/4\left(4gA_{22} - 4A_{12}\right)\Omega^2 + 3/4A_{11}^3 + 3/4A_{11}B_{11}^2 + A_{12} = 0 \tag{25}$$

$$\left(gB_{21}-B_{11}\right)\Omega^2+B_{11}=0 \tag{26}$$

$$1/4\left(4gB_{22}-4B_{12}\right)\Omega^2+3/4A_{11}{}^2B_{11}+3/4B_{11}{}^3+B_{12}=0 \tag{27}$$

$$1/4\left(3A_{21}{}^3+3A_{21}B_{21}{}^2\right)\beta+1/4\left(4\mu^2-4\Omega^2\right)A_{22}+2\alpha\mu\Omega B_{22}-A_{12}=0 \tag{28}$$

$$\left(\mu^2-\Omega^2\right)A_{21}+2\alpha\mu\Omega B_{21}-A_{11}=0 \tag{29}$$

$$\left(\mu^2-\Omega^2\right)B_{21}-2\alpha\mu\Omega A_{21}-B_{11}=0 \tag{30}$$

$$1/4\left(3A_{21}{}^2B_{21}+3B_{21}{}^3\right)\beta+1/4\left(4\mu^2-4\Omega^2\right)B_{22}-2\alpha\mu\Omega A_{22}-B_{12}=0 \tag{31}$$

Solving for A_{ij} and B_{ij} ($i=1,2$, $j=1,2$) from Eqs. (24)-(31), the resulting solutions are found to be in terms of the control gains α , μ, g and the normalized frequency Ω. Due to the complexity, these expressions are not given here. Nevertheless, the absolute value of the normalized frequency response $\left|y_1(\Omega)\right|$, namely the performance index, can be expressed as:

$$\left|Q(\Omega)\right|=\sqrt{A_{11}{}^2+B_{11}{}^2+2\delta\left(A_{11}A_{12}+B_{11}B_{12}\right)+\delta^2\left(A_{12}{}^2+B_{12}{}^2\right)} \tag{32}$$

Substituting Eqs. (9)-(13) into Eq. (32) and solving for β to maintain the equal peaks at the fixed points, yields

$$\beta=\frac{1}{4}g+\frac{2}{3}g^2+\mathrm{O}\left(g^3\right) \tag{33}$$

In fact, Eq. (33) represents a simpler and more easily interpretable relation which is the Taylor series expansion of the exact solution with respect to the feedback gain g given $g \ll 1$.

Up to now, the derivation of the explicit expressions for forming the NPPF controller $h(\cdot)$ is complete wherein the optimal control parameters are given in Eqs. (11), (12)-(13) and (33) respectively. Some numerical studies are performed to illustrate the control effectiveness of the NPPF controller for the system under consideration, where the feedback gain is set to 0.2 and the primary nonlinear coefficient δ is varied between 0.0001 and 0.03. Substituting the optimal control parameters into Eqs. (5) and (6), the resulting nonlinear equations are computed using a path-following algorithm combining shooting and pseudo-arclength continuation [12]. This algorithm provides a very accurate numerical solution to the equations of motion. Figure 4 (b) illustrates that the frequency response of the Duffing oscillator with the linear PPF controller is strongly detuned in the presence of strong nonlinearities i.e. $\delta=0.03$. Conversely, Figure 4 (a) shows that the nonlinear controller can compensate, to a certain extent, the detuned equal peaks for values of δ ranging from 0.0001 to 0.03. Although the control effectiveness degrades in terms of the differences between the two peaks when δ is large, Eq. (33) can be updated using approximated solutions with more harmonics.

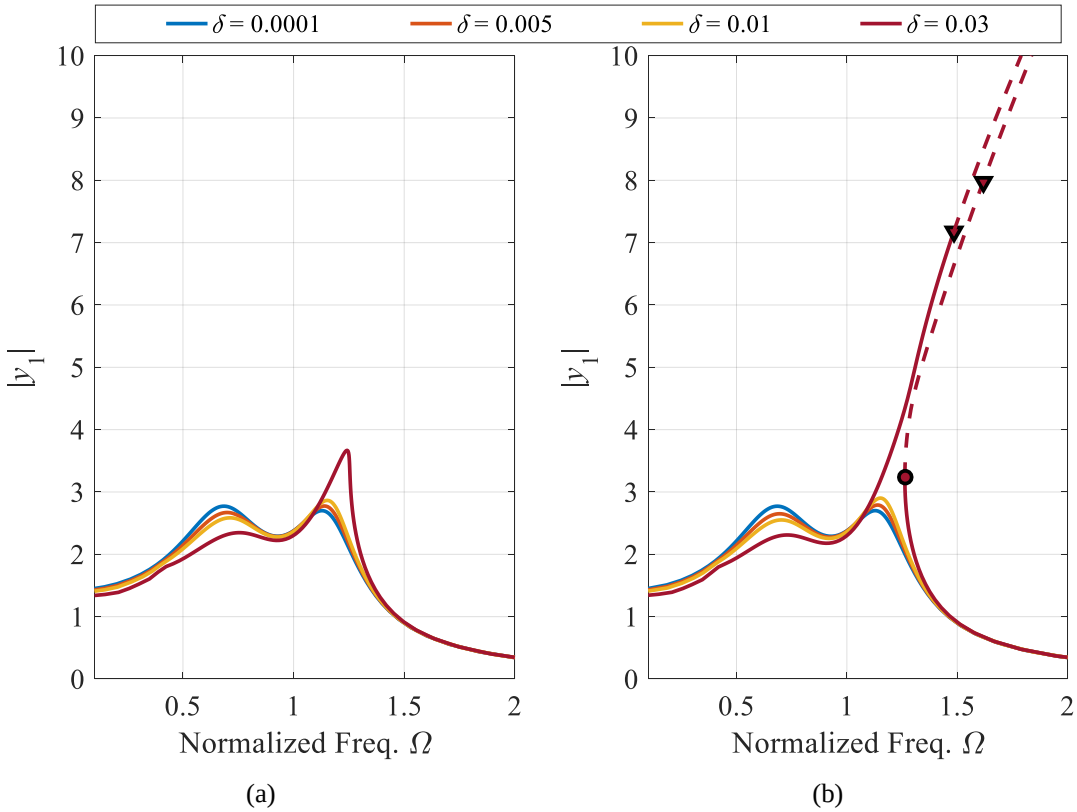


Figure 4 The performance of the system under consideration where the feedback gain is set to 0.2 and the primary nonlinear coefficient δ varies between 0.0001 and 0.03: (a) with NPPF controller and (b) with linear PPF controller (—:stable solution, --: unstable solution, •: fold bifurcation, ▼: Neimark-Sacker bifurcation)

3 Conclusion

A nonlinear active damping strategy based on positive position feedback is proposed. Closed-form expressions are derived using the $\mathscr{H}_\infty$ optimization criterion wherein the optimal control parameters are achieved to minimize the maximal response of the structure. The resonant vibration of a Duffing oscillator is considered to illustrate the proposed tuning of the optimal control gains and the harmonic balance method is employed to approximate the analytical solutions. With the proposed NPPF controller, it has been shown that the response around the resonance does not change substantially when the importance of the nonlinearity increases, which means that the response of the coupled system is almost proportional to the forcing amplitude, as it would be the case for a linear system.

Acknowledgements

The financial supports from MAVERIC (Wal'innov project 1610122) and F.R.S.-FNRS (IGOR project F453617F) are gratefully acknowledged.

References

[1] F.-Y. Wang and Y. Gao, *Advanced Studies of Flexible Robotic Manipulators*. 2003.

[2] M. Darecki *et al.*, "Flightpath 2050," *Flightpath 2050 Eur. Vis. Aviat.*, p. 28, 2011.

[3] G. Habib, T. Detroux, R. Viguié, and G. Kerschen, “Nonlinear generalization of Den Hartog’s equal-peak method,” *Mech. Syst. Signal Process.*, vol. 52–53, no. 1, pp. 17–28, 2015.

[4] J. P. Den Hartog, *Mechanical Vibrations*. Dover Publications, 1985.

[5] G. Zhao, N. Alujević, B. Depraetere, and P. Sas, “Dynamic analysis and H_2 optimisation of a piezo-based tuned vibration absorber,” *J. Intell. Mater. Syst. Struct.*, vol. 26, no. 15, pp. 1995–2010, 2015.

[6] N. W. Hagood and A. von Flotow, “Damping of structural vibrations with piezoelectric materials and passive electrical networks,” *J. Sound Vib.*, vol. 146, no. 2, pp. 243–268, Apr. 1991.

[7] A. Preumont, *Vibration Control of Active Structures, an introduction*, vol. 179. Dordrecht: Springer Netherlands, 2011.

[8] G. S. Agnes and R. D. Kriz, “Performance of Nonlinear Mechanical , Resonant-Shunted Piezoelectric , and Electronic Vibration Absorbers for Multi-Degree-of-Freedom Structures by Electronic Vibration Absorbers for Multi-Degree-of-Freedom Structures,” 1997.

[9] M. Febbo and S. P. Machado, “Nonlinear dynamic vibration absorbers with a saturation,” vol. 332, pp. 1465–1483, 2013.

[10] G. Habib and G. Kerschen, “A principle of similarity for nonlinear vibration absorbers,” *Phys. D*, vol. 332, pp. 1–8, 2016.

[11] T. Asami and O. Nishihara, “Closed-Form Exact Solution to H[sub ∞] Optimization of Dynamic Vibration Absorbers (Application to Different Transfer Functions and Damping Systems),” *J. Vib. Acoust.*, vol. 125, no. 3, p. 398, 2003.

[12] L. Meirovitch, *Dynamics and Control of Structures*. John Wiley & Sons, Inc, 1990.

[13] D. Wagg, S. Neild, C. W. S. To, and S. K. Lau, *Nonlinear Vibration with Control*, vol. 58, no. 4. 2010.

[14] T. Detroux, L. Renson, L. Masset, and G. Kerschen, “The harmonic balance method for bifurcation analysis of large-scale nonlinear mechanical systems,” pp. 1–34, 2016.

[15] G. Kerschen, K. Worden, A. F. Vakakis, and J.-C. Golinval, “Past, present and future of nonlinear system identification in structural dynamics,” *Mech. Syst. Signal Process.*, vol. 20, no. 3, pp. 505–592, 2006.

Multi-input multi-output aeroelastic control using the receptance method

B. Mokrani[1], F. Palazzo[2], S. Fichera[1], L. Adamson[1], J. E. Mottershead[1]
[1] University of Liverpool, Department Mechanical, Materials and Aerospace Engineering,
Brownlow Hill, Liverpool, L69 7ZX, United Kingdom

[2] Politecnico di Torino, Department Mechanical and Aerospace Engineering,
Torino, Italy
e-mail: **bilal.mokrani@liverpool.ac.uk**

Abstract
This paper presents the experimental validation of the Multiple-Input Multiple-Output Receptance Method on an aeroelastic rig. It addresses experimentally flutter suppression and vibration control in aerostructures and shows an effective mean for increasing the flow speed at which the flutter occurs. The experimental rig features a modular flexible wing equipped with a leading- and trailing-edge control surfaces and two displacement sensors for measuring its position in real time. The MIMO Receptance controller is designed only by using the Frequency Response Functions (FRFs), in term of receptances, measured between the the control surfaces (inputs) and the structural displacements (outputs). The MIMO Receptance controller is validated experimentally on the MODFLEX rig in the wind tunnel; both frequencies and damping are assigned (together or independently) for the first two eigenpairs, and considerations on the optimal control strategy, as well as limits of the proposed controller, are drawn for the given system.

1 Introduction

Partial pole placement for vibration control can be achieved by active or passive modification of the structure [1]. Passive structural modification, using receptance/admittance methods, have been widely used since a long time [2-4]. Active modification, using the method of receptances, has been first proposed in [5], for structures equipped with a single control input and several outputs. The method considers a proportional and derivative output feedback and relies only on the measured receptances to determine the controller gains which guarantee the placement of the system poles at desired locations. The number of complex pole pairs which can be assigned is equal to the number of available sensors.

In the last decade, the receptance method has seen an increasing interest by the community and led to several demonstrations, ranging from aero-servo-elastic systems [6], flexible structures [7], vibro-acoustic control [8] and nonlinear structures [9-10]. It relies merely on the measured receptances and does not require any numerical model or state observers. This is possible, particularly for flexible structures, because the states can be chosen to be proportional to the modal position and velocities and, thus, they are reconstructed from position or velocity measurements, by an eigenvalue spatial filter arising from the method formulation.

Recently, the receptance method has been generalised for Multi-Input Multi-Output systems by the same authors [11]. The efficiency of the generalised method was demonstrated through a series of numerical examples amongst which, the most relevant for this work is [12], where the MIMO RM is demonstrated numerically for accomplishing active aeroelastic control of a delta wing with multiple tailing edge control surfaces. However, the method in MIMO formulation has never seen any experimental validation. In this paper, the method is validated experimentally on the MODFLEX aeroelastic wing, featuring a leading and trailing edge control surfaces and equipped with two position sensors.

The paper is organised as follow: Section 2 recalls the principle of the method and the control design procedure. Section 3 describes the flexible aeroelastic test rig and the control architecture. Section 4 shows the experimental design, through a set of different pole placement objective, while section 5 shows the results for flutter control.

2 Pole placement with the receptance method

In this section, the Multi-Input Multi-Output (MIMO) receptance method is recalled for a generic dynamic system. For a system defined with its measured receptance matrix $H(s)$, i.e. transfer function matrix between the control forces and the measured displacements, the receptance method proposes a systematic control design procedure for pole placement, without any use of state observers or numerical models. It relies only on the (experimentally) measured transfer functions.

2.1 Control problem

The dynamics of a structure, modelled with its mass, damping and stiffness matrices, $M_{n\times n}, C_{n\times n}$ and $K_{n\times n}$, is governed by:

$$M\ddot{x} + C\dot{x} + Kx = Bu + d \tag{1}$$

where $u_{n\times 1}$ is the control forces vector and $d_{n\times 1}$ represents an external force vector applied on the structure (i.e. disturbances or, in the the test case considered in this work, the aerodynamic loads); $u_{n\times 1}$ is the vector of control input forces, and $B = [b_1\ b_2 \dots b_m]$ is a $n \times m$ topology matrix, describing the control force distribution over the structure. For an aeroelastic structure, the matrices M, C and K count also for the added aerodynamic mass, damping and stiffness, respectively, resulting by moving term d to the left hand side of Eq.(1).

Assuming a proportional and derivative feedback control, i.e.

$$u = F^T\dot{x} + G^T x, \tag{2}$$

Eq.(1) becomes

$$M\ddot{x} + (C - BF^T)\dot{x} + (K - BG^T)x = d. \tag{3}$$

The position vector x is assumed to be measurable. Provided that the matrices M, C and K are available, the poles of the system of Eq.(3) can be chosen arbitrarily, by properly tuning the feedback gains F and G. Nevertheless, in most of practical situations, only the transfer matrix between the control input forces and the displacement of some degrees of freedom is available; thus, a pole-placement controller with only output feedback cannot be performed, unless a state-observer is used. For such situations, the receptance method is a straightforward method aimed to determine the feedback gains F and G by using only the measured receptances. The number of pole pairs which can be placed is equal to the number of sensors, from which these poles are observable (assuming all the poles are controllable).

2.2 Control design procedure: the method

Let μ_k, $k = 1, 2, \dots, p$, be the set of desired poles to be assigned, distinct from the open loop poles λ_k, $k = p + 1, \dots, 2n$, remaining unchanged; and let $r(s) = H(s)B$ be the measured transfer matrix between the control inputs and outputs, where $H(s) = (Ms^2 + Cs + K)^{-1}$ is the receptance matrix. The control feedback gains $F = [f_1\ f_2 \dots f_m]$ and $G = [g_1\ g_2 \dots g_m]$ can be found by solving the linear equation:

$$\begin{pmatrix} P_1 \\ P_2 \\ \vdots \\ P_p \\ Q_{p+1} \\ Q_{p+2} \\ \vdots \\ Q_{2n} \end{pmatrix} \begin{bmatrix} f_1 \\ \vdots \\ f_m \\ g_1 \\ \vdots \\ g_m \end{bmatrix} = \begin{bmatrix} \alpha_1 \\ \alpha_2 \\ \vdots \\ \alpha_p \\ 0 \\ 0 \\ \vdots \\ 0 \end{bmatrix} \tag{4}$$

with

$$P_k = \begin{bmatrix} \mu_k w_k^T & 0 & \dots & 0 & w_k^T & 0 & \dots & 0 \\ 0 & \mu_k w_k^T & \dots & 0 & 0 & w_k^T & \dots & 0 \\ \vdots & \vdots & \ddots & \vdots & \vdots & \vdots & \ddots & \vdots \\ 0 & 0 & \dots & \mu_k w_k^T & 0 & 0 & \dots & w_k^T \end{bmatrix}, \tag{5}$$

$$Q_k = \begin{bmatrix} \lambda_k v_k^T & 0 & \dots & 0 & v_k^T & 0 & \dots & 0 \\ 0 & \lambda_k v_k^T & \dots & 0 & 0 & v_k^T & \dots & 0 \\ \vdots & \vdots & \ddots & \vdots & \vdots & \vdots & \ddots & \vdots \\ 0 & 0 & \dots & \lambda_k v_k^T & 0 & 0 & \dots & v_k^T \end{bmatrix}, \tag{6}$$

$$\alpha_k = \left[\alpha_{\mu_k,1}\, \alpha_{\mu_k,2}\, \dots\, \alpha_{\mu_k,m}\right]^T \tag{7}$$

and

$$w_k = \alpha_{\mu_k,1} r_{\mu_k,1} + \alpha_{\mu_k,2}\, r_{\mu_k,2} + \cdots + \alpha_{\mu_k,m}\, r_{\mu_k,m}, \tag{8}$$

where $r_{\mu_k,j}$ stand for the j^{th} column of $r(\mu_k) = H(\mu_k)B$, or alternatively $r_{\mu_k,j} = H(\mu_k)b_j$, and v_k denotes the retained eigenvectors, solution of the quadratic eigenvalue problem

$$\left(\lambda_k^2 M + \lambda_k C + K\right)v_k = 0. \tag{9}$$

The v_k eigenvectors are computed directly from the measured open-loop transfer matrix, while w_k are the eigenvectors of the closed loop system, solution of the quadratic eigenvalue problem

$$\left(\mu_k^2 M + \mu_k C + K\right)w_k = B(F^T \mu_k + G^T)w_k. \tag{10}$$

w_k can be chosen a priori, by a careful choice of the weighting parameters $\alpha_{\mu_k,j}$, $(j = 1, \dots, m)$. Indeed, the parameters $\alpha_{\mu_k,j}$ determine the participation of the j^{th} control input for the assignment of the k^{th} mode. In [11], they are chosen in such a way that the eigenvectors of the controlled system w_k remain identical to the eigenvectors of the uncontrolled system v_k; in this study we follow the same approach, and we determine the parameters $\alpha_{\mu_k,j}$ by imposing $w_k = v_k$ in Eq.(8).

Finally, once the parameters $\alpha_{\mu_k,j}$ are found, the closed loop eigenvectors w_k are constructed and the matrices P_k and Q_k are easily built. The feedback gains F and G are then found by solving Eq.(4).

Remark: In theory, the parameters $\alpha_{\mu_k,j}$ can be chosen arbitrarily; however, this may lead to a high control effort for some actuators and a smaller for the others. From Eq.(8), it is clear that $\alpha_{\mu_k,j}$ parameters are ponderation factors of the j^{th} control input contribution; if $\alpha_{\mu_k,j} = 0$, then the j^{th} actuator will not contribute to the control of the k^{th} pole; inversely, if $\alpha_{\mu_k,j} \gg \alpha_{\mu_k,i}$ $(i \neq j)$, then the k^{th} pole will be principally controlled with the j^{th} actuator. Alternatively, if the parameters $\alpha_{\mu_k,j}$ are equal, then the feedback gains of each input j, f_j and g_j, will be identical for all the control loops. An obvious way to tune $\alpha_{\mu_k,j}$ is to choose them proportionally to the control input authority over the assigned mode (e.g. proportional to the modal amplitudes at the input location). The selection of the parameters $\alpha_{\mu_k,j}$ in an optimal way (e.g. minimizing the overall control effort) remains an open problem and will not be addressed in this paper.

3 Aeroelastic system

The MIMO receptance method has been applied experimentally to an aeroelastic wing, referred to as MODFLEX [13]. The rig is composed by a main spar plus four aerodynamic sectors and a tip sector, as shown in Figure 1. The main specifications of MODFLEX are summarized in Table 1. The main spar is made by aluminium alloy and it is the only structural element of the model. By accurately shaping the cross-section of the main spar, the desired flexural, torsional and in-plane stiffness have been achieved. The main spar is covered by four sectors that provide the correct aerodynamic shape. Each sector is connected to the main spar by two pins at the mid span of the sector to not alter the stiffness distribution of the overall model. The centre of gravity and the flexural axis were designed to be coincident on the main spar. The wing model is fully constrained at the built-in end. The 4th sector is equipped with a leading and a trailing edge aerodynamic control surfaces. Each aerodynamic control surface is actuated with two identical 60W brushless motors from MAXON, supplemented with a planetary gearbox and an angular position encoder. Two contactless laser sensors (Keyence LK-500 - mounted on the top of the wind tunnel test section) measure the absolute position of the wing at two distinct points on the 3rd sector, as shown in Figure 1 and Figure 2.

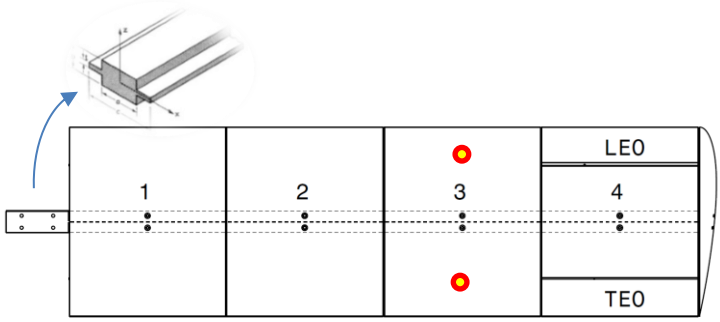


Figure 1: MODFLEX drawing.

wing data	dimension
wing span	1 m
chord (c)	0.3 m
aerofoil	NACA0018
mass axis pos.	0.5×c
flexural axis pos.	0.5×c

Table 1: MODFLEX main specifications.

The experimental campaign was carried out in a low speed wind tunnel facility at the University of Liverpool. The facility features a test section of $1.2 \times 0.6 \times 1.0$m and a maximum airspeed of 20m/s. The controller is implemented in a dSPACE system, while the transfer functions have been measured using a Siemens.PLM LMS Test.Lab acquisition system. The experimental model installed in the wind tunnel is depicted in Figure 2.

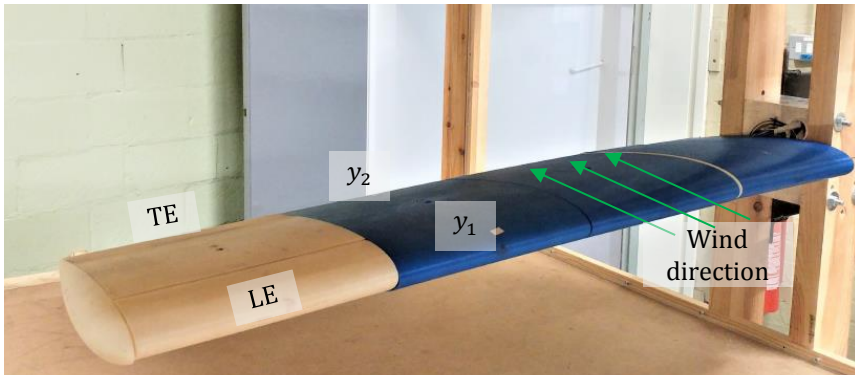


Figure 2: MODFLEX experimental setup.

MODFLEX has a twin-numerical model. Such numerical model is a beam FE model with concentrated masses and 2% structural damping, to which are added aerodynamic panels to solve the unsteady

aerodynamic with MD.Nastran DLM. A comparison between the numerical and experimental first three poles of the systems is reported in Table 2.

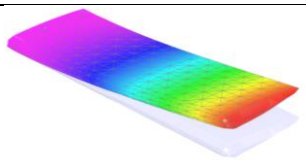
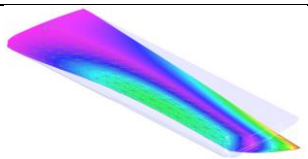
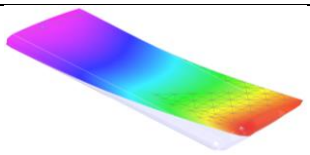
Mode	ω_i [Hz]		ξ_i [%]		Mode shape
	Num.	*Exp.*	*Num.*	*Exp.*	
1B	2.97	2.84	6.7	7.0	
1T	4.41	4.11	4.9	3.4	
1P	6.97	6.41	1.14	-	

Table 2: Modal data of the flexible wing, at wind speed $v = 10m/sec$. The numerical data are compared with the experimental data when available. The model includes the modes 1B, 1T and 1P, and ignores the high frequency modes.

3.1 Control architecture

The controller of the aeroelastic wing is made in two cascade control loops: *(i)* a low authority control loop (LAC), which controls the angular position of the aerodynamic surfaces; and *(ii)* a high authority control loop (HAC) which implements the receptance based controller for partial pole placement, Figure 3.

3.1.1 Low authority control (LAC)

Due to the rigid body dynamics of the leading-edge control surface, the aeroelastic model of the flexible wing is inherently unstable. Furthermore, the inputs of the system are the torques applied at the hinge of the control surfaces and not their angular positions, which is not convenient for aeroelastic control. To cope with these issues, a low authority control loop (LAC) featuring a PID controller is implemented for each control surface. Such PID loop uses the angular position of the control surface (measured with a position encoder) to calculate the appropriate torque to stabilize the system and maintain the control surface at a desired position (internal loop in Figure 3b). With the PID controllers, the inputs of the system become the control surface angular positions (u_{LE}, u_{TE}) and the outputs are the position of the flexible wing (y_1, y_2).

3.1.2 High Authority Control (HAC): Pole Placement

The control is targeted on the first flexible modes of the system 1B and 1T, Table 2. The receptance based controller is implemented as shown in Figure 3b. The transfer function matrix $R(s)$, relating the position of the input control surfaces (u_{LE}, u_{TE}) to the position of the wing (y_1, y_2), is used to calculate the feedback gains F and G, by following the procedure described in section 2.2. The parameters $\alpha_{\mu_k,j}$ are tuned to preserve the mode shapes of the structure, i.e. the closed loop eigenvectors w_k are chosen identical to the open loop eigenvectors v_k; they are found by solving the system of equations (8).

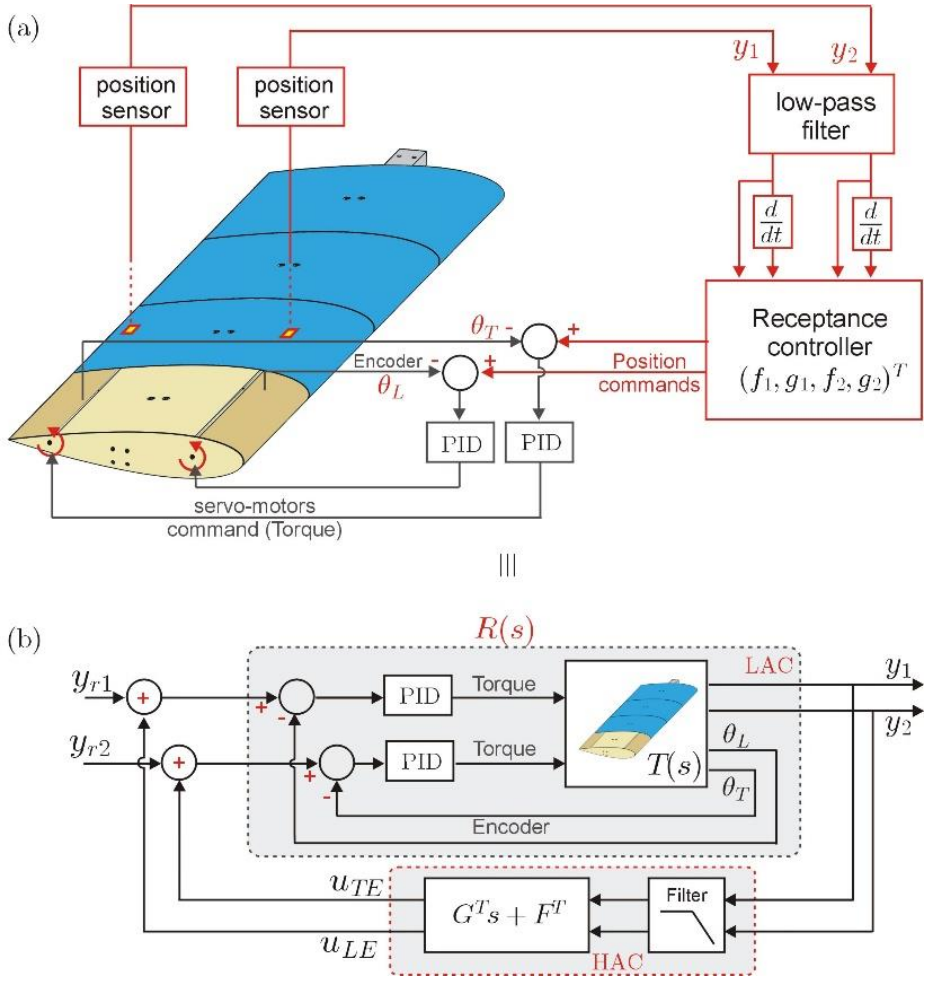


Figure 3: Bloc diagram of the HAC-LAC controller. The HAC loop involve a Butterworth low-pass to remove the high frequency noise and avoid high frequency spill-over.

3.2 Controller design

The control architecture is implemented as depicted in Figure 3b. The PID bandwidth has been checked up to 15Hz; for both loops, it is estimated around 30Hz. At a wind speed $v = 10\text{m/s}$, the transfer function matrix of the system $R(x)$ is measured between the control surface angular position (control inputs: u_{LE} and u_{TE}) and the position of the wing measured with the laser sensors (y_1 and y_2), Figure 4. The measured input-output FRFs are then fitted with stable minimum-phase transfer functions, using SDTool toolbox, while the modal data are identified using the PolyMAX technique [14].

Once the open loop transfer matrix of the system $R(s)$ is obtained, the receptance based pole placement controller is implemented exactly as described in section 2. The control is targeted on the first two modes, 1B and 1T and ignores the higher frequency modes. A second order Butterworth filter, with a cross-over frequency at 10Hz, has been placed in series with the controller; it is necessary for the stability of the system, as it limits the control bandwidth and add a roll-off at high frequencies to avoid spill-over. The closed loop transfer functions of the system are measured by exciting the control surfaces with a stepped sine oscillation (y_{r1} and y_{r2} in Figure 3b), over a frequency range of interest, 2 to 6Hz. A single control surface is excited at a time. The gain computed at a nominal speed of 10m/s are then used at higher speeds for flutter tests.

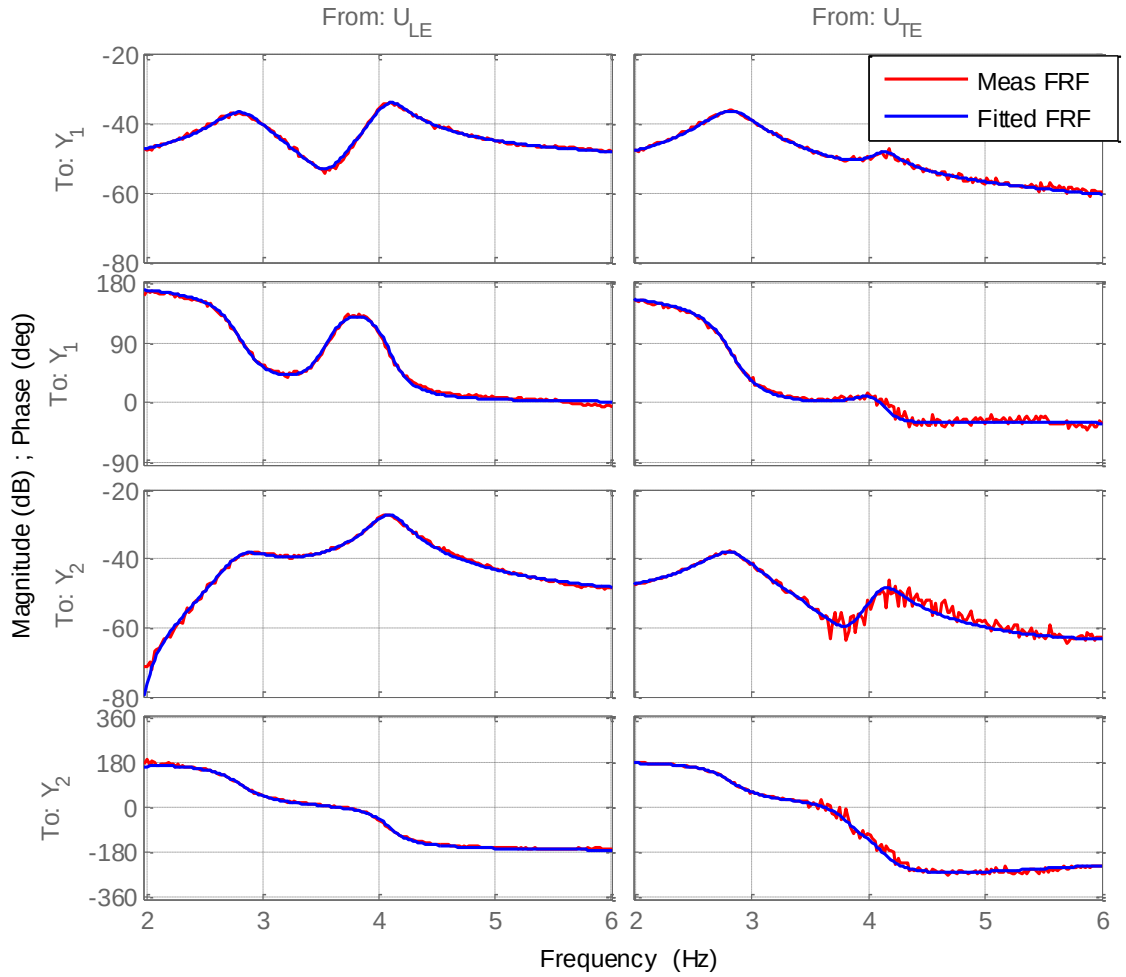


Figure 4: Measured vs. fitted open loop FRF $R(s)$, between the angular positions of the control surfaces (Inputs: u_{LE}, u_{TE}) and the position of the flexible wing (outputs: y_1, y_2).

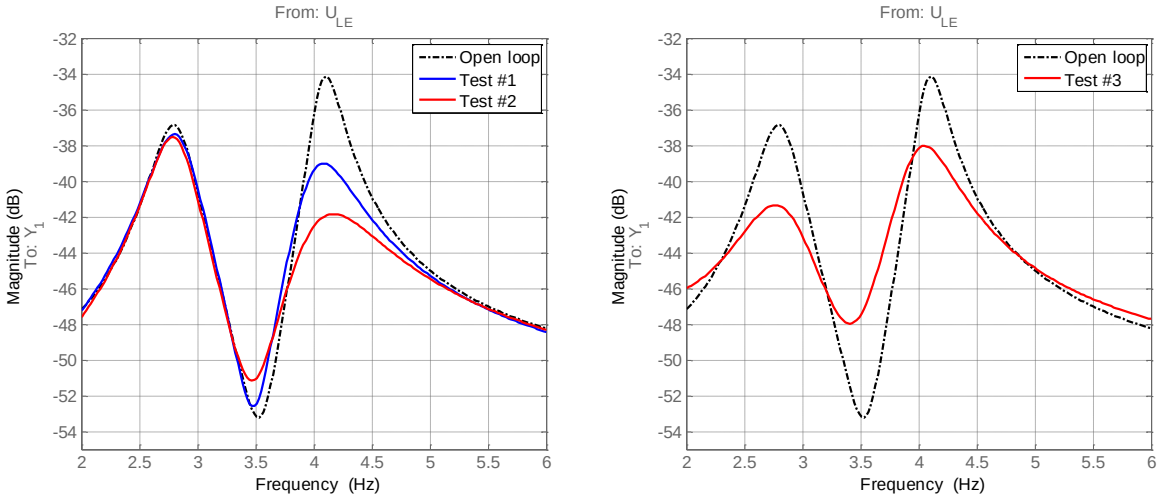
4 Experimental results

Several control scenarios are implemented, they are summarized in Table 3. Tests #1 to #3 are targeted for increasing the damping of the first bending 1B and the first torsional 1T modes, while tests #4 and #5 are targeted for modifying their resonance frequencies; the associated FRFs y_1/y_{r1} with and without control are shown in Figure 5 and Figure 6, respectively.

Test		**Desired pole location**		**New pole location (exp results)**	
		$\mu_{1,2}$	$\mu_{3,4}$	$\mu_{1,2}$	$\mu_{3,4}$
#1	$\xi_{1T} \times 2$	$-1.25 \pm 17.8j$	$-1.76 \pm 25.8j$	$-1.42 \pm 17.8j$	$-1.78 \pm 25.3j$
#2	$\xi_{1T} \times 3$	$-1.25 \pm 17.8j$	$-2.63 \pm 25.7j$	$-1.41 \pm 17.7j$	$-2.7 \pm 25.5j$
#3	$\xi_{1B} \times 2$ and $\xi_{1T} \times 2$	$-2.5 \pm 17.7j$	$-1.76 \pm 25.8j$	$-2.33 \pm 17.7j$	$-1.72 \pm 25.1j$
#4	$\omega_{1T} \times 1.2$	$-1.25 \pm 17.8j$	$-1.05 \pm 31j$	-1.67 ± 17.8	$-1.8 \pm 31.3j$
#5	$\omega_{1B} \times 0.9$ and $\omega_{1T} \times 1.1$	$-1.13 \pm 16j$	$-0.97 \pm 28.4j$	$-1.26 \pm 16j$	$-1.36 \pm 28.2j$

Table 3: Closed loop control test campaign conducted on the flexible wing. New pole location vs. desired pole location.

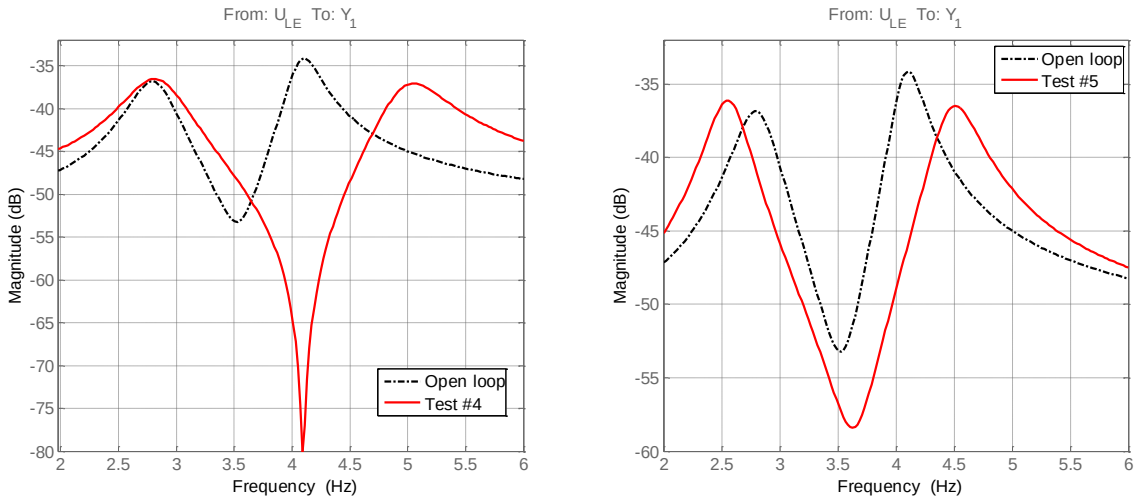
Figure 5.a shows the FRF when the control is tuned for doubling and tripling the damping of the first torsional mode 1T (2nd mode), while the 1st bending mode is kept unchanged; tests #1 and #2 respectively; Figure 5.b shows the same FRF when the damping of both modes is doubled. For the three tests, the error on the pole location is negligible, and it is mainly associated with the real part of the pole (i.e. the damping component of the pole).



(a) (b)

Figure 5: Measured FRF y_1/y_{r1} with and without control: (a) tests #1 and #2; (b) test #3.

Figure 6.a shows the FRF obtained in test #4, during which the resonance frequency of the 1st torsional mode is increased by 20%; Figure 6.b shows the same FRF when the resonance frequencies of the 1B and 1T modes are shifted by $\pm 10\%$. Once again, one can consider the error on the new poles location negligible for the imaginary part of the pole (and the resonance frequency). However, especially for these two test, the error on the damping is relatively high and may reach 66% (in test #4, $\xi_{1T} = 5.7\%$ instead of 3.4%); this may be associated to the fact that the control surface deflection is very high and may add some aerodynamic damping.



(a) (b)

Figure 6: Measured FRF y_1/y_{r1} with and without control: (a) tests #4; and (b) test #5.

5 Flutter control

A flutter test has been carried out for the five active control tests depicted in Table 4. The wing is positioned in the wind tunnel, with the control surfaces positioned at zero angular position (aligned with the wing), while the control is turned on. The wind speed is then increased progressively until the flutter speed is reached. Table 4 depicts the flutter speed for each control test; test#0 is the reference case, in which only the LAC loop is active, and the system exhibits a flutter speed of $v_f = 13.5m/s$.

	Test	Flutter speed [m/s]
#0	Open loop	13.5
#1	$\xi_{1T} \times 2$	15.5
#2	$\boldsymbol{\xi_{1T} \times 3}$	**16.5**
#3	$\xi_{1B} \times 2$ and $\xi_{1T} \times 2$	15.5
#4	$\omega_{1T} \times 1.2$	14
#5	$\omega_{1B} \times 0.9$ and $\omega_{1T} \times 1.1$	15

Table 4: Flutter speed with various control configurations.

The experimental campaign showed that increasing the damping of the torsional mode (test #2) is the most efficient way to increase the flutter speed, as the flutter occurs when the damping of this mode becomes negative. Fig.7 shows the time response of the position sensors y_1, near an air speed of $13.5m/sec$, without HAC control and when the control is turned on after the 10th sec; the control corresponds to test #2 where the damping of the torsional mode is tripled.

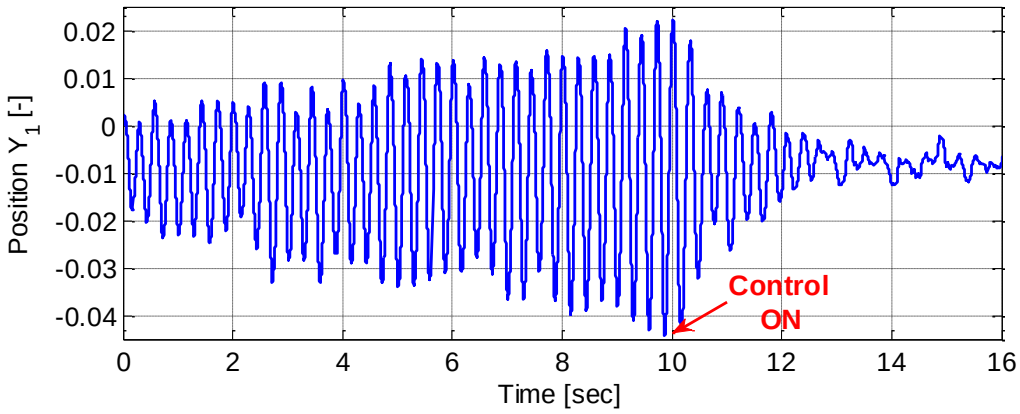


Figure 7: Measured wing position in flutter at wind speed $v_f = 13.5m/s$. The control is turned ON near the 120th second. The control is tuned to triple the damping of the torsional mode 1T (test #2).

The experimental V-f/g (velocity vs. frequency/damping – where the damping g is expressed as $g = -2\xi$) diagrams are plotted in Figure 8, with and without control. The control is tuned to triple the damping of the torsional mode 1T (test #2). As imposed by the control design, only the damping of the 1st torsional mode is increased, while the resonance frequencies of the 1B and 1T modes remain almost identical to the open loop system. It is clearly seen that the control shifts down the damping curve of the torsional mode, responsible of flutter. Notice also that even at rest, without any flow around the wing, i.e. $v = 0m/s$, the control still provides significant damping to the targeted mode; this is possible due to the relatively high inertia of the leading-edge control surface which makes it behaving as an inertial actuator.

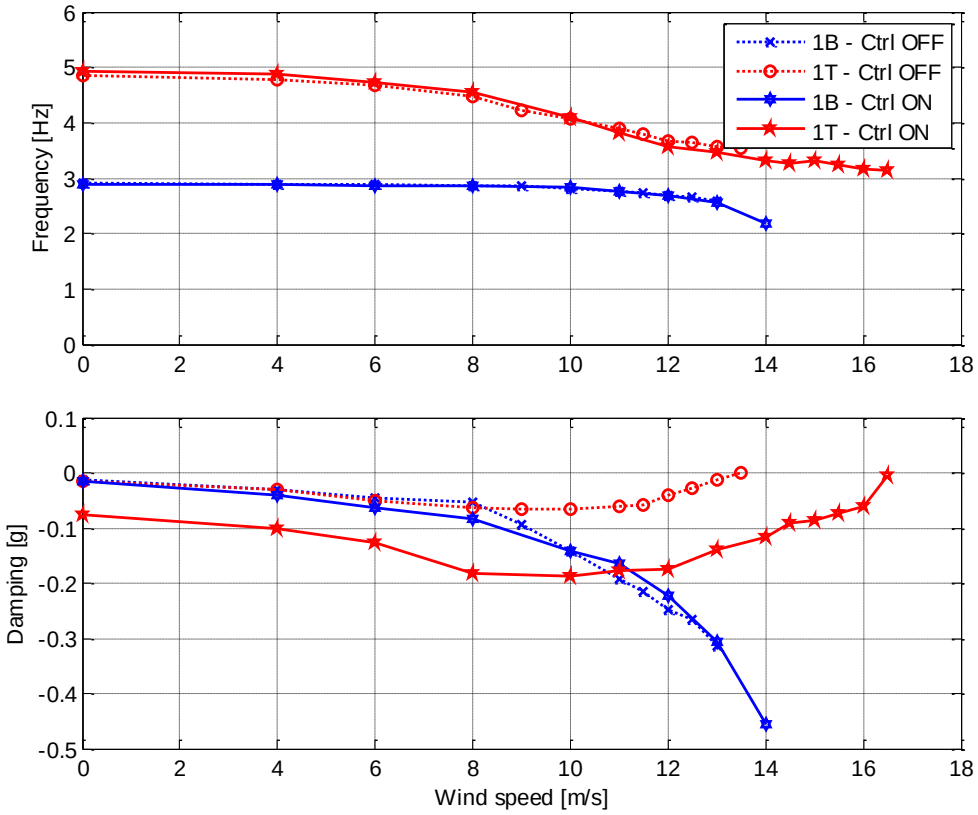


Figure 8: Measured frequency and damping ($g = -2\xi$) as a function of the wind speed, V-f/g diagram, with and without control. The control is tuned to triple the damping of the torsional mode 1T (test #2).

Finally, one should note that the controller has been tuned based on a model at wind speed $v = 10m/s$, and has not been adapted as the wind speed evolves. Although the control proves efficient, it would be worth if the feedback gains could be adapted in function of the wind speed.

6 Conclusion

In this paper, the pole placement control using the Multi-Input Multi-Output receptance method has been implement and validated experimentally for the first time. The method considers a proportional and derivative output feedback and relies only on the measured input-output frequency response functions to calculate the controller gains. The efficiency and the accuracy of the method has been demonstrated through a set of control scenarios applied on an aeroelastic wing. The presented study demonstrates the merits of the receptance method for simplifying the control design for active vibration control of flexible structures, without any need of a quantitative numerical model or the use of state observers.

Finally, the control effort is particularly sensitive to the choice of the parameters α_{μ_k}. Although imposing a modal constraint would result in reasonable feedback gains, the choice of the parameters α_{μ_k} must be made in order to minimise the control effort. Further investigations will be conducted in this sense.

Acknowledgements

This research has been supported by EPSRC grant EP/N017897/1.

References

[1] Mottershead, J. E., & Ram, Y. M. *Inverse eigenvalue problems in vibration absorption: passive modification and active control*. Mechanical systems and signal processing, *20*(1), 2006, 5-44.

[2] Bishop, R. E. D., & Johnson, D. C. *The mechanics of vibration*. Cambridge University Press, 1960.

[3] J.T. Weissenburger, *Effect of local modifications on the vibration characteristics of linear systems*, Transactions of ASME, Journal of Applied Mechanics 90, 1968, 327–332.

[4] Sadeghipour, K., Brandon, J. A., & Cowley, A. *The receptance modification strategy of a complex vibrating system.* International journal of mechanical sciences, *27*(11-12), 1985, 841-846.

[5] J. E. Mottershead, Y. M. Ram, *Receptance Method in Active Vibration Control*, AIAA Journal, Vol. 45, No. 3, 2007, pp. 562–567.

[6] E. Papatheou, N. D. Tantaroudas, A. Da Ronch, J. E. Cooper, J. E. Mottershead, and A. Da Ronch, *Active control for flutter suppression: an experimental investigation*, in *International Forum on Aeroelasticity and Structural Dynamics (IFASD), Bristol June 24-26, 2013*, UK, pp. 1-14.

[7] M. Ghandchi Tehrani, R. N. R. Elliott, J. E. Mottershead, *Partial pole placement in structures by the method of receptances: Theory and experiments*, Journal of Sound and Vibration, Vol. 329, No. 24, 2010, pp. 5017–5035.

[8] XIA, Maolong et LI, Sheng. *Active control of structural sound radiation using receptance method*. In: *INTER-NOISE and NOISE-CON Congress and Conference Proceedings*. Institute of Noise Control Engineering, 2017. p. 2218-2225.

[9] Zhen, C., Jiffri, S., Li, D., Xiang, J., & Mottershead, J. E. *Feedback linearisation of nonlinear vibration problems: A new formulation by the method of receptances*. Mechanical Systems and Signal Processing, 98, 2018, 1056-1068.

[10] Lisitano, D., Jiffri, S., Bonisoli, E., & Mottershead, J. E. *Experimental feedback linearisation of a non-smooth nonlinear system by the method of receptances.* Mathematics and Mechanics of Solids, 2017, p. 1081286517744601.

[11] Y. M. Ram, J. E. Mottershead, *Multiple-input active vibration control by partial pole placement using the method of receptances*, Mechanical Systems and Signal Processing, Vol. 40, No. 2, 2013, pp. 1–9.

[12] Singh, K. V., McDonough, L. A., Kolonay, R., and Cooper, J. E., *Receptance-based active aeroelastic control using multiple control surfaces*. Journal of Aircraft, 51(1), 2014, 335-342.

[13] S. Fichera , S. Jiffri and J. E. Mottershead, *Design and wind tunnel test of a MODular aeroelastic FLEXible wing (MODFLEX),* in *International Conference on Noise and Vibration Engineering (ISMA2016), Leuven 19-21 Sept. 2016, Belgium.*

[14] B. Peeters, G. Lowet, H. Van Der Auweraer, J. Leuridan, L. M. S. International, *A New Procedure for Modal Parameter Estimation*, Sound and Vibration, Vol. 38, 2004, pp. 24–28.

Minimisation of the effect of aleatory uncertainties on dynamic systems by active control using the method of receptances

L. J. Adamson [1], **S. Fichera** [1], **J. E. Mottershead** [1]
[1] School of Engineering, University of Liverpool,
Liverpool, L69 3GH, United Kingdom
e-mail: **l.j.adamson@liverpool.ac.uk**

Abstract

This paper presents a method to reduce the effect of uncertainties on dynamic systems by means of active control. In the proposed approach, pole placement is performed iteratively using an optimisation algorithm with an objective function that includes the variance of the real and imaginary part of each of the system's pole. The method is advantageous in that control gains are calculated using the method of receptances, which eliminates model form uncertainty since only measured receptance data is used. Moreover, variances are extracted through a polynomial chaos expansion, which requires fewer samples as opposed to other techniques. The method is demonstrated numerically on a simple multi-degree-of-freedom system. It is shown that active control can be used in a way that not only places the poles of the system but also reduces their spread. Furthermore, it is shown that it is possible to directly relate uncertainty in the poles to meaningful physical based uncertainty in the structural parameters.

1 Introduction

With the rise of increasingly complex designs and manufacturing processes, structural parameters are often difficult to predict computationally and can be highly sensitive to manufacturing defects. Consequently, the performance of many systems exhibit uncertainty. In the case of dynamic systems with narrow stability margins, potentially small parameter variations may lead to instability, which can severely damage or destroy such systems. It is important, therefore, that the effects of uncertainty are sufficiently quantified and, where possible, reduced or mitigated.

Classically, robust design optimisation (RDO) or reliability-based design optimisation (RBDO) have been used to address the aforementioned issue. Both methods typically modify a system's stiffness and damping passively such that its stability margin is increased and the probability of instability is reduced [1]. Alternatively, RDO and RBDO can be performed as feedback control to actively modify the system's stiffness and damping by means of pole placement.

Traditional pole placement requires knowledge of the $\mathbf{M}$, $\mathbf{C}$ and $\mathbf{K}$ matrices of the system, which are usually extracted from a numerical model. As a result, model-form uncertainty is introduced and therefore the optimised system may not sufficiently represent the true system. Consequently, an alternative approach for pole placement, which does not require direct knowledge of the system's structural matrices, is desired so that this further uncertainty is not introduced.

The method of receptances, first formalised by Ram and Mottershead [2,3], is a technique that enables partial pole placement using only measured receptance data. The advantage of this method is that experimental data is used directly and so there is no need to know or evaluate the $\mathbf{M}$, $\mathbf{C}$ and $\mathbf{K}$ matrices. The method has been implemented on various experimental set-ups [4] and has recently been extended to the more general

case of multiple-input-multiple-output (MIMO) systems [5]. Tehrani et. al. [6] first investigated the effect of uncertainty on this technique by considering eigenvalue sensitivities and minimising them such that poles were considered sufficiently robust. Whilst this approach successfully reduced the effects of uncertainty, it only considered local sensitivities and did not consider the uncertainty across its full domain. Moreover, the uncertainty was modelled as measurement error in the experimentally obtained receptances and did not explicitly account for physical based uncertainties in the system itself, such as the structural parameters.

In this paper, a new optimisation method is implemented using the method of receptances. An algorithm is used to recursively place the system's poles such that the effect of uncertainty due to random structural parameters is reduced. The uncertainty is modelled as a perturbation from a measured nominal system and pole variances are extracted using a polynomial chaos (PC) expansion [7–9]. In this way, the global uncertainties are minimised.

The remainder of this paper is divided as follows; first, the method is presented theoretically and is written in a form that is applicable to any generic, linear dynamic system. Next, a simple numerical example is given, which highlights the advantages of the proposed approach. Finally, the main conclusions are summarised and some suggestions of future work are provided.

2 Theory

In this section, the method is presented theoretically. First, the method of receptances, which enables pole placement using only measured receptances, is summarised. For simplicity, the method is shown using a single-input controller, although this can easily be extended to the general MIMO case. Following this, the effect of physical based uncertainties is introduced and the combined effect of the active controller and the uncertainties is studied. Next, the optimisation approach is introduced together with an outline of how to appropriately select an objective function and set of constraints. Finally, a summary of the method is illustrated diagrammatically.

2.1 Active control using measured receptances

Consider a linear, n degree-of-freedom dynamic system with single-input state feedback. The equation of motion is written in the form

$$(\mathbf{M}s^2 + \mathbf{C}s + \mathbf{K})\mathbf{x}(s) = \mathbf{b}(s\mathbf{f}^T + \mathbf{g}^T)\mathbf{x}(s), \tag{1}$$

or more compactly,

$$\mathbf{Z}(s)\mathbf{x}(s) = \mathbf{b}(s\mathbf{f}^T + \mathbf{g}^T)\mathbf{x}(s), \tag{2}$$

where $\mathbf{Z} \in \mathbb{C}^{n\times n}$ is the dynamic stiffness matrix; $\mathbf{M}$, $\mathbf{C}$, $\mathbf{K} \in \mathbb{R}^{n\times n}$ are the mass, damping and stiffness matrices respectively; $\mathbf{b} \in \mathbb{R}^n$ is the force distribution vector; and $\mathbf{f}$, $\mathbf{g} \in \mathbb{R}^n$ are vectors of control gains. Pre-multiplying (1) by the receptance matrix,

$$\mathbf{H}(s) = (\mathbf{M}s^2 + \mathbf{C}s + \mathbf{K})^{-1}, \tag{3}$$

gives that

$$\mathbf{x}(s) = \mathbf{H}(s)\mathbf{b}(s\mathbf{f}^T + \mathbf{g}^T)\mathbf{x}(s). \tag{4}$$

In order to calculate the control gains necessary to shift the system's poles from the set $\{\lambda_1, \lambda_2, ..., \lambda_{2n}\}$ to a new arbitrary set $\{\mu_1, \mu_2, ..., \mu_{2n}\}$, the method of receptances is implemented.

Denoting

$$\mathbf{r}_s = \mathbf{H}(s)\mathbf{b}, \tag{5}$$

(4) becomes

$$\mathbf{x}(s) = \mathbf{r}_s(s\mathbf{f}^T + \mathbf{g}^T)\mathbf{x}(s). \tag{6}$$

Substituting each desired closed-loop pole into (6) yields

$$\mathbf{w}_k = \mathbf{r}_{\mu_k}(\mu_k\mathbf{f}^T + \mathbf{g}^T)\mathbf{w}_k, \quad k = 1, 2, ..., 2n, \tag{7}$$

where $\mathbf{w}_k$ is the eigenvector corresponding to the k^{th} eigenvalue. Since $\mathbf{w}_k$ may be scaled arbitrarily, it is selected such that

$$(\mu_k\mathbf{f}^T + \mathbf{g}^T)\mathbf{w}_k = 1, \quad \forall k. \tag{8}$$

Substituting (8) into (7) gives that

$$\mathbf{w}_k = \mathbf{r}_{\mu_k}, \tag{9}$$

and thus (8) becomes

$$\mathbf{r}_{\mu_k}^T(\mu_k\mathbf{f} + \mathbf{g}) = 1, \quad k = 1, 2, ..., 2n, \tag{10}$$

which can be solved to find the gain vectors $\mathbf{f}$ and $\mathbf{g}$. It is important to note that the set of desired closed-loop poles must be closed under conjugation in order for the control gains to be strictly real and therefore physically realisable.

2.2 Uncertainty modelling

Suppose now that the system represented by (2) is subject to uncertainty in one or more of its structural parameters. The equation of motion is now written in the form

$$\mathbf{Z}(s, \boldsymbol{\theta})\mathbf{x}(s) = \mathbf{b}(s\mathbf{f}^T + \mathbf{g}^T)\mathbf{x}(s), \tag{11}$$

where $\boldsymbol{\theta} \in \mathbb{R}^m$ is a vector of m random parameters. The uncertainty may be modelled as a perturbation from a nominal system, and so

$$\mathbf{Z}(s, \boldsymbol{\theta}) = \mathbf{Z}_n(s) + \mathbf{Z}_r(s, \boldsymbol{\theta}), \tag{12}$$

where the subscripts n and r represent the nominal and random contributions to the dynamic stiffness matrix respectively. Substituting (12) into (11) and rearranging gives that

$$[\mathbf{Z}_n(s) + \mathbf{Z}_r(s, \boldsymbol{\theta}) - \mathbf{b}(s\mathbf{f}^T + \mathbf{g}^T)]\mathbf{x}(s) = \mathbf{0}. \tag{13}$$

Pre-multiplying (13) by the nominal receptance matrix $\mathbf{H}_n$ yields

$$[\mathbf{I} + \mathbf{H}_n(s)\mathbf{Z}_r(s, \boldsymbol{\theta}) - \mathbf{H}_n(s)\mathbf{b}(s\mathbf{f}^T + \mathbf{g}^T)]\mathbf{x}(s) = \mathbf{0}, \tag{14}$$

and thus the closed-loop, random poles are governed by the characteristic equation

$$\det[\mathbf{I} + \mathbf{H}_n(s)\mathbf{Z}_r(s,\boldsymbol{\theta}) - \mathbf{H}_n(s)\mathbf{b}(s\mathbf{f}^T + \mathbf{g}^T)] = 0. \tag{15}$$

The effect of the controller and the uncertainty on the system's poles, governed by (15), can be considered successively. First, the open-loop poles are shifted to a new set of closed-loop poles by the term

$$\mathbf{H}_n(s)\mathbf{b}(s\mathbf{f}^T + \mathbf{g}^T). \tag{16}$$

Since (16) is independent of the vector of random parameters, the closed-loop poles are non-random and are denoted the 'nominal, closed-loop poles' hereinafter. Next, the term

$$\mathbf{H}_n(s)\mathbf{Z}_r(s,\boldsymbol{\theta}) \tag{17}$$

acts to shift the poles again. Here, however, the term contains the vector of random parameters and thus the shift is random. In the case that

$$\mathrm{E}[\mathbf{Z}_r(s,\boldsymbol{\theta})] = \mathbf{0}, \tag{18}$$

the closed-loop random poles will be spread about the closed-loop nominal poles and will form so-called clusters. As will be shown later, the size and shape of the pole clusters is a function of the location of the closed-loop nominal poles. That is to say that the pole clusters may be modified by selecting different control gains. It is hypothesized, therefore, that there exists some optimum control gains such that the pole clusters are minimised in terms of size, shape, or both. In order to find this optimum controller, it is necessary to numerically quantify the geometry of pole clusters.

2.3 Pole placement optimisation

One way in which the pole clusters can be quantified is by the variance in their real and imaginary parts. Classically, the variances are found by performing a Monte Carlo simulation. This approach, however, often requires a large number of samples to obtain accurate estimations of the variances and is therefore computationally expensive. Alternatively, a polynomial chaos approach can be used, which significantly reduces the number of samples required.

PC expansions are used to form a surrogate model of a random dependent variable that is a function of one or more random independent variables. When the independent variables follow a normalised Gaussian distribution, the expansion is a sum of weighted multidimensional Hermite polynomials and is written

$$y(\boldsymbol{\theta}) = \sum_{i=0}^{\infty} a_i \Psi_i(\boldsymbol{\theta}), \tag{19}$$

where $y \in \mathbb{R}$ is the dependent variable, $a_i \in \mathbb{R}$ are constants of the expansion and Ψ_i is the i^{th} Hermite polynomial. In practice, the expansion is truncated to the first P terms and so

$$y(\boldsymbol{\theta}) \approxeq \sum_{i=0}^{P-1} a_i \Psi_i(\boldsymbol{\theta}). \tag{20}$$

The coefficients of the expansion can be obtained in two ways: intrusive and non-intrusive methods. In this work, a non-intrusive method is used; a linear regression is performed to fit the expansion to a given set of data obtained through sampling.

Once the coefficients have been found, it is relatively straightforward to obtain the output statistics. The mean is given by

$$\mathrm{E}[y(\boldsymbol{\theta})] = a_0. \tag{21}$$

Similarly, the variance is

$$\mathrm{Var}[y(\boldsymbol{\theta})] = \sum_{i=1}^{P-1} a_i^2 \mathrm{E}[\Psi_i^2(\boldsymbol{\theta})], \tag{22}$$

In this application, there are $4n$ expansions; one for the real and imaginary part of each pole. Of course, in the case where all of the poles are strictly non-real, it is unnecessary to construct an expansion for each pole. Instead, the property of symmetry about the real axis of the complex plane means that only $2n$ expansion need be constructed.

Now that expressions for the mean and variance of the pole clusters have been obtained, it is possible to modify their size and shape using an optimisation approach. For each pole, a local objective function

$$\rho_i = \alpha_i \mathrm{Var}[\mathrm{Re}(\mu_{r,i})] + \beta_i \mathrm{Var}[\mathrm{Im}(\mu_{r,i})], \quad i = 1, 2, ..., 2n \tag{23}$$

is defined, where α_i, $\beta_i \in \mathbb{R}$ are weighting constants and $\mu_{r,i}$ is the r^{th} random, closed-loop pole. This serves to weight the relative importance of the variance of the real and imaginary part of each pole. Now, a global objective function

$$\sigma = \sum_{i=1}^{2n} \gamma_i \rho_i \tag{24}$$

is written, where $\gamma_i \in \mathbb{R}$ are weighting constants. The global objective function now considers the relative importance of each pole and is to be minimised by iteratively placing the nominal, closed-loop poles. By appropriate selection of weighting constants, it is possible to modify not only the size of the pole clusters, but also their orientation in the complex plane. This will be demonstrated in the numerical example presented later.

In practice, the positions of the nominal, closed-loop poles are limited by the maximum control authority. Furthermore, large deviations from the initial set of nominal poles used in the optimisation may lead to non-physical natural frequencies and damping in the system. Consequently, constraints on the nominal poles are used.

For each pole, an upper and lower limit is defined such that

$$x_{low} \leq \mathrm{Re}(\mu_i) \leq x_{high}, \quad i = 1, 2, ..., 2n, \tag{25}$$

and

$$y_{low} \leq \mathrm{Im}(\mu_i) \leq y_{high}, \quad i = 1, 2, ..., 2n. \tag{26}$$

These constraints appear on the complex plane as rectangular boxes that the nominal poles must be placed within.

2.4 Method summary

The optimisation approach may now be summarised as follows:

Select a set of nominal, closed-loop poles such that the objective function (24) is minimised subject to constraints (25) and (26).

A more detailed overview of the method is given in figure 1.

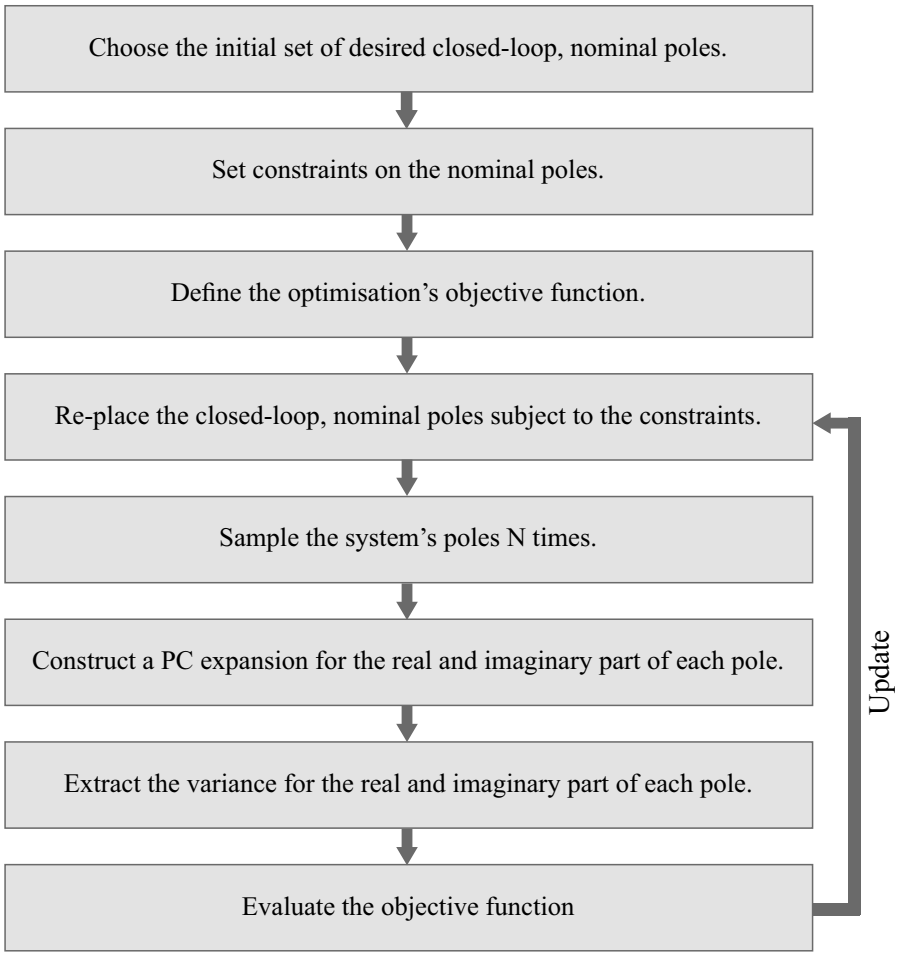


Figure 1: Method overview.

3 Numerical example

Consider the mass, spring, damper system shown in figure 2 with parameters as given in table 1.

The nominal receptance matrix is given by

$$\mathbf{H}_n(s) = \begin{bmatrix} 1.3s^2 + 0.5s + 3700 & -0.5s - 1700 & 0 \\ -0.5s - 1700 & 2.4s^2 + s + 5400 & -0.5s - 1700 \\ 0 & -0.5s - 1700 & 0.9s^2 + 0.5s + 3700 \end{bmatrix}^{-1}, \tag{27}$$

and the set of open-loop poles is

$$\lambda = \{-0.4362 \pm 67.2677i, -0.2359 \pm 54.7128i, -0.0066 \pm 33.5330i\}. \tag{28}$$

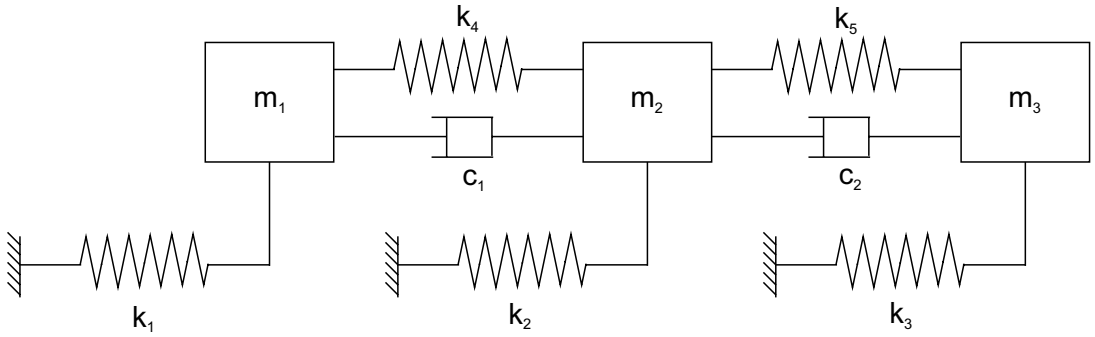


Figure 2: 3 DoF system.

Parameter	Value	Unit
m_1	1.3	kg
m_2	2.4	kg
m_3	0.9	kg
c_1	0.5	kg/s
c_2	0.5	kg/s
k_1	2000	N/m
k_2	2000	N/m
k_3	2000	N/m
k_4	1700	N/m
k_5	1700	N/m

Table 1: Nominal system parameters.

The mass m_2 is subject to uncertainty that has a distribution

$$m_2 \sim \mathcal{N}(2.4, 0.2). \tag{29}$$

The effect of the uncertainty can be modelled as a perturbation from the nominal system, in accordance with (12), using

$$\mathbf{Z}_r = \begin{bmatrix} 0 & 0 & 0 \\ 0 & m_r s^2 & 0 \\ 0 & 0 & 0 \end{bmatrix}, \tag{30}$$

where

$$m_r \sim \mathcal{N}(0, 0.2). \tag{31}$$

Suppose that it is desired to shift the nominal, open-loop poles to a new set of nominal, closed-loop poles $\mu = \{\mu_1, \mu_2, ..., \mu_6\}$, which satisfies the constraints given in table 2.

If it is required that the real part variances of the poles μ_5 and μ_6 are as small as possible, the objective function is defined as

$$\sigma = \mathrm{Var}[Re(\mu_5)]. \tag{32}$$

Note that since μ_5 and μ_6 are a conjugate pair, it is unnecessary to include both in the objective function.

Pole	$\mathrm{Re}(\mu_i)_{min}$	$\mathrm{Re}(\mu_i)_{max}$	$\mathrm{Im}(\mu_i)_{min}$	$\mathrm{Im}(\mu_i)_{max}$
μ_1	-0.55	-0.45	63	67
μ_2	-0.55	-0.45	-67	-63
μ_3	-0.3	-0.2	53	57
μ_4	-0.3	-0.2	-57	-53
μ_5	-0.2	-0.1	33	37
μ_6	-0.2	-0.1	-37	-33

Table 2: Closed-loop pole constraints.

Using a differential evolution algorithm [10, 11], the optimum set of closed-loop nominal poles are found such that (32) is minimised subject to the above constraints. Using

$$\mu_{init} = \{-0.5 \pm 65i, -0.25 \pm 55i, -0.15 \pm 35i\} \tag{33}$$

as the initial set of nominal poles, the optimum set was found to be

$$\mu_{final} = \{-0.45 \pm 64.78i, -0.2 \pm 57i, -0.1 \pm 33i\}, \tag{34}$$

which reduces to the objective function from 6.98×10^{-4} to 4.45×10^{-4}. A comparison of the initial and optimum closed-loop poles is shown in figure 3, which includes a visualisation of the nominal pole constraints shown by the rectangular boxes. It is clear that the optimisation successfully reduced the spread of the real part of the rightmost poles. In order to do so, not only has it moved the pole of interest, but also the other nominal poles. Indeed, it is shown here that the distributions of all of the pole clusters are related to the location of the set of nominal, closed-loop poles. Consequently, it is important when performing pole placement under uncertainty to consider the combined effect of all nominal poles.

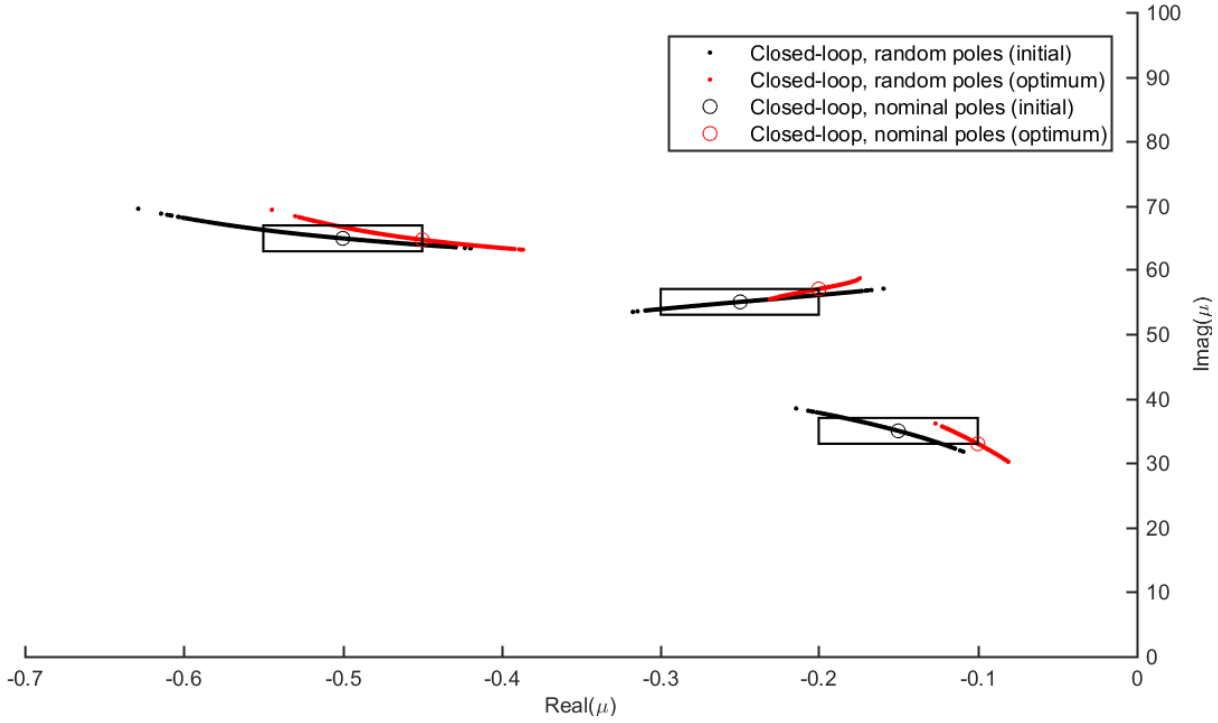


Figure 3: Optimised pole clusters in the top-left quadrant of the complex plane.

4 Conclusions

This paper has presented a method that uses active control to reduce the effects of uncertainty on dynamic systems. As has been shown, the set of closed-loop nominal poles directly affects the random spread of poles, known as pole clusters. By coupling pole placement with a global optimisation algorithm based on pole variances, the pole clusters can be modified according to specified criteria. The method is advantageous in that the method of receptances is used, which uses only measured receptance data and so does not introduce modelling error. Furthermore, it is possible to directly relate the effect of physical-based uncertainty in structural parameters to uncertainty in a system's poles. Future developments will see this method applied experimentally to various systems and will consider the case of uncertainty governed by stochastic processes that are non-stationary.

Acknowledgements

The authors wish to acknowledge the support provided by the EPSRC Doctoral Training Scholarship.

References

[1] Y. Tsompanakis, N. D. Lagaros, M. Papadrakakis, *Structural design optimization considering uncertainties*, Taylor & Francis, First edition (2008).

[2] Y. M. Ram, J. E. Mottershead, *Receptance Method in Active Vibration Control*, AIAA Journal, Vol. 45, No. 3, American Institute of Aeronautics and Astronautics (2007), pp. 562-567.

[3] J. E. Mottershead, Y.M. Ram, *Inverse eigenvalue problems in vibration absorption: Passive modification and active control*, Mechanical Systems and Signal Processing, Vol. 20, No. 1, Elsevier (2006), pp. 5-44.

[4] M. G. Tehrani, R. N. R. Elliott, J. E. Mottershead, *Partial pole placement in structures by the method of receptances: Theory and experiments*, Journal of Sound and Vibration, Vol. 329, No. 24, Elsevier (2010), pp. 5017-5035.

[5] Y. M. Ram, J. E. Mottershead *Multiple-input active vibration control by partial pole placement using the method of receptances*, Mechanical Systems and Signal Processing, Vol. 40, No. 2, Elsevier (2013), pp. 727-735.

[6] M. G. Tehrani, J. E. Mottershead, A. T. Shenton, Y. M. Ram, *Robust pole placement in structures by the method of receptances*, Mechanical Systems and Signal Processing, Vol. 25, No. 1, Elsevier (2011), pp. 112-122.

[7] R. Ghanem, P. Spanos, *Stochastic Finite Elements: A Spectral Approach*, Springer, First edition (1991).

[8] B. Sudret, *Global sensitivity analysis using polynomial chaos expansions*, Reliability Engineering & System Safety, Vol. 93, No. 7, Elsevier (2008), pp. 964-979.

[9] R. C. Smith, *Uncertainty Quantification: Theory, Implementation and Applications*, Society for Industrial and Applied Mathematics, First edition (2014).

[10] R. Storn, K. Price, *Differential Evolution: A Simple and Efficient Heuristic for Global Optimization over Continuous Spaces*, Journal of Global Optimization, Vol. 11, No. 4, Kluwer Academic Publishers (1997), pp. 341-359.

[11] M. Buehren, *Differential Evolution (Version 1.16)* [Software], MATLAB™ Central (2017).

The effect of active vibration control on the sound field scattered from a flexible structure

C. House, J. Cheer, S. Daley
Institute of Sound and Vibration Research - University of Southampton
e-mail: **c.house@soton.ac.uk**

Abstract

It is desirable, in many applications, to minimise the acoustic scattering from an object when it is subject to an incident sound field. Active Vibration Control (AVC) has been demonstrated in many applications, and can effectively reduce an unwanted disturbance signal using control sources. However, when attempting to attenuate the acoustic scattering from an object, it is not straightforward to measure, and therefore control, the scattered component of the sound field directly. In this paper, the effect that AVC has on the scattered acoustic field has been investigated for a hollow, non-rigid cylinder via a series of numerical simulations. The cylinder is excited by an acoustic plane wave incident from a single direction and the AVC system uses an array of accelerometers and an array of structural actuators to control the vibration. As expected, significant reductions in the structural velocity are predicted. The effect of AVC on the acoustic scattering is then investigated, and it is shown that, at resonance, the scattered sound power is reduced by over 5dB.

1 Introduction

Active control has now been demonstrated and applied to many applications, and has been shown to be effective at reducing a range of different disturbance signals with the introduction of secondary control sources. In the case of active acoustic cloaking, the disturbance signal to be minimised is the scattered sound pressure, as shown in Figure 1, which could be controlled using either structural or acoustic control sources. This has been demonstrated numerically by Eggler [1] and Cheer [2], who present results using computational models that predict significant reductions in the acoustic scattered field over a fairly wide frequency range by using secondary acoustic sources [2], and secondary structural sources [1]. However, the performance of an active control system is dependent on the measured disturbance signal, and in the case of acoustic cloaking it is not possible to measure the scattered component of the sound field directly in real-time. Therefore it is challenging to minimise acoustic scattering directly,

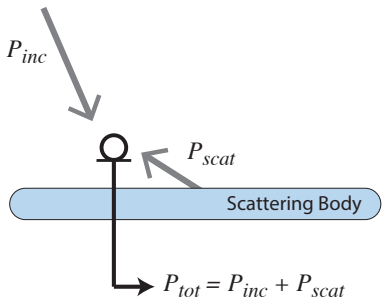


Figure 1: A schematic diagram of a microphone measuring a sound field including scattering.

Friot et al [3] have predicted and demonstrated a potential solution to this scattered field detection problem, with the development of an active control system that was two concentric rings of microphones surrounding the scattering object. The correlation between each ring was used to determine the incident signal from the scattered signal. This performs very well in the computer simulation at low frequencies, with reductions in the scattered field of an order of magnitude; however it is less effective at higher frequencies. The model was validated with a simple 1D experiment in a duct, and over 20dB of attenuation was achieved in the scattered pressure between 100Hz and 700Hz. Friot et al went on to implement a three dimensional single-tone control system based on this theory [4] with a parallelepiped scattering object, and achieved reductions in the scattered field of between 5dB and 20dB.

Although Friot et al were able to demonstrate a cloaking capability, the system required a large number of microphones positioned remotely from the structure to accurately distinguish the incident and scattered pressure waves, which may not always be practical to implement. Han et al [5] eliminate the need for the second ring of error sensors by modelling the transfer function between the scattered pressure and the total pressure with a computational model. They then use the simulated transfer function to estimate the scattered component of the microphone signals, which is then used as the disturbance signals for the active control system. The structure was implemented in a laboratory experiment using a spherical scatterer, and an 8dB attenuation in the scattered pressure was demonstrated.

It should be noted that Han's experiments were using simplified 1D active control systems, and only corrected for reflective scattering (reducing scattering in the opposite direction to the propagation of the incident wave). They did not attempt to reduce refractive scattering (scattering 'downstream' of the scattering object). They were also only excited by a single tone, single direction incident wave. In practice, there is an interest in controlling the scattering due to uncorrelated disturbance sources at multiple positions over a broad bandwidth and this would significantly deteriorate performance.

To attempt to overcome some of the practical limitations of directly controlling scattering, the effect of active vibration control on the acoustic scattering from a controlled body is investigated in this paper. The benefit of this method is that real-time adaptive active vibration control has been more extensively investigated and demonstrated, and has now matured into a robust and regularly used real-world solution to vibration problems [6, 7, 8, 9]. Initially, the development of a numerical model to predict the vibro-acoustic properties of a flexible cylinder will be discussed. A modal analysis will be carried out to identify the eigenfrequencies and mode shapes of the cylinder, before the structural response of the cylinder to an incident acoustic plane wave is modelled. The acoustic scattered field is calculated, and a formulation for the total acoustic scattered power is used at each frequency to compare the magnitude of the acoustic scattering to the magnitude of the structural response. Single tone active vibration control is simulated, and the effect that this has on the scattered acoustic field is predicted.

2 Numerical Model of Structural-Acoustic Coupled System

The COMSOL Multiphysics package has been used to model the structural-acoustic response of of a flexible hollow cylinder. The Boundary Element Method (BEM) was used to model the incident plane wave, whilst the Finite Element Method (FEM) was used to model structural vibration through the cylindrical shell, and acoustic propagation within the internal cavity of the cylinder. The use of BEM to model the incident and scattered acoustic waves in the external fluid significantly reduced the computational cost of solving the model when compared to FEM. This advantage is minimal for small problem sizes, however, therefore the interior volume of the cylinder was modelled using FEM so as to mesh well with the solid shell and therefore minimise the amount of BEM/FEM coupling required.

2.1 Model Description

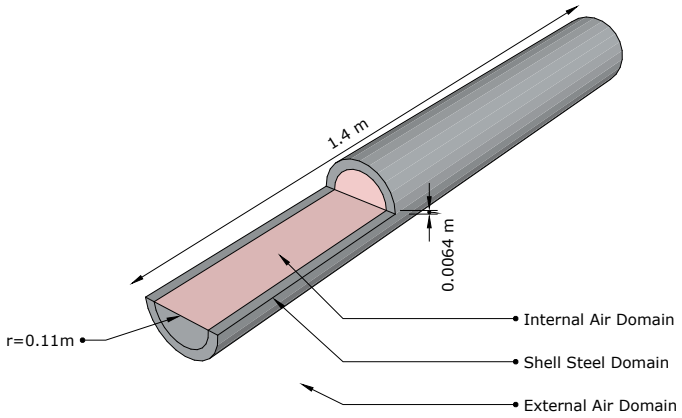


Figure 2: Cylinder Geometry

A steel cylindrical shell of thickness 6.4mm, length 1.4m and radius 0.11m has been modelled, and the geometry is shown in Figure 2. The internal volume of the cylinder was filled with air, and the the external fluid in which the cylinder was placed was also air. Acoustic propagation through both the internal and external air domains was modelled, as was structural vibration through the steel domain, with both physics being fully coupled to allow for the transfer of energy between acoustic and structural excitations. The structure was excited by a single incident acoustic plane wave, propagating from the $\theta = 45$ $\phi = 45$ direction, as shown in Figure 3.

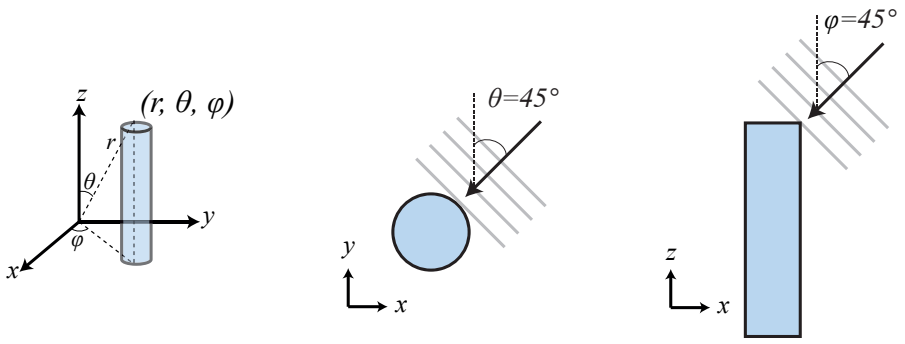


Figure 3: Schematic diagram showing the direction of the incident acoustic plane wave, in both plan view and front projection.

The model was meshed using free tetrahedral elements over the cylindrical shell, with a minimum of 6 elements per wavelength. This mesh density was selected as a result of a convergence study, which showed that 6 elements per wavelength was sufficient to obtain reliable results. The external air domain does not require meshing due to the use of BEM rather than FEM.

2.2 Modal Analysis

It is well known that the structural response of the cylinder will be greatest when it is excited at a resonance, and the work by Bobrovnitskii [10] and Williams [11] shows that the acoustic scattering of a structure

may also increase around these resonant frequencies. To identify the frequencies at which this will occur, an eigenfrequency analysis was conducted using the implemented numerical model. The modal frequencies, and corresponding mode shapes, were calculated and used to inform further analysis on the structural response of the cylindrical shell. The identified eigenfrequencies below 1kHz are shown in Table 1; axisymmetric, repeated modes have only been included once but are indicated by bold typeface.

An analytical model of a rigid walled cylindrical acoustic cavity was also solved [12] to indicate the eigenfrequencies of such a system. These results were used to distinguish whether the frequencies identified in the numerical model were caused by acoustic cavity modes, or structural modes. This has also been noted in Table 1.

Figure 4 displays the mode shapes of a selection of the modes identified in Table 1, which result in the largest structural response. As before, axisymmetric, repeated modes have only been included once but are identified by bold typeface.

Eigenfrequency (Hz)	**Cause**
122	Cavity Mode
245	Cavity Mode
353	**Structural Mode**
367	Cavity Mode
490	Cavity Mode
512	**Structural Mode**
548	**Structural Mode**
612	Cavity Mode
735	Cavity Mode
858	Cavity Mode
860	**Structural Mode**
915	**Cavity Mode**
923	**Cavity Mode**
947	**Cavity Mode**
948	**Structural Mode**
980	**Cavity Mode**
981	Structural Mode
985	**Cavity Mode**

Table 1: Modal frequencies below 1kHz, and whether they are caused by acoustic or structural resonances. Bold font represents an axisymmetric repeated mode.

The output from this modal analysis provides an indication of at which frequencies the structural velocity will be at a maxima, and therefore, at which frequencies acoustic scattering will potentially be most significant. These frequencies will be the most important to acoustic cloaking applications. The mode shapes shown in Figure 4 also assist in the future implementation of AVC, as they provide physical insight into which positions on the cylinder will be the most efficient for placement of accelerometers and actuators for the control of a particular mode.

2.3 Structural Response to an Acoustic Excitation

The vibro-acoustic model has been solved over a fine frequency sweep from 100Hz to 1kHz. At each frequency point the squared radial velocity when excited by a single incident plant wave has been integrated

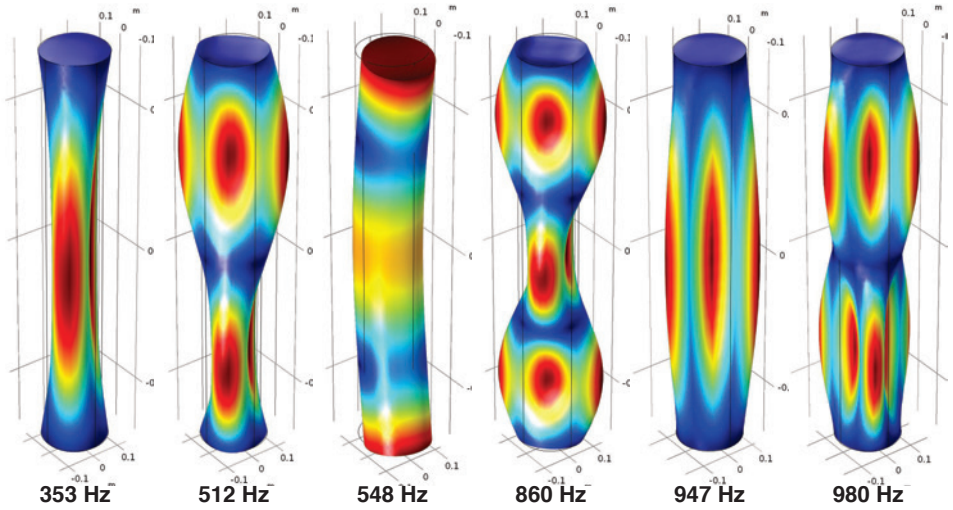


Figure 4: A selection of the modal frequencies and corresponding mode shapes of the cylinder. Frequencies in bold indicate that mode is a repeated axisymmetric mode.

over the cylindrical shell to calculate the resultant Kinetic Energy. This is shown in Figure 5, along with dashed vertical lines marking the eigenfrequencies calculated previously. It can be seen that there are 6 dominant resonances in the structure which, when compared to the mode shapes shown in Figure 4, all correspond to structural bending or acoustic breathing modes of the cylinder. The largest resonance is at 548Hz, and corresponds to the first acoustic bending mode of the cylinder.

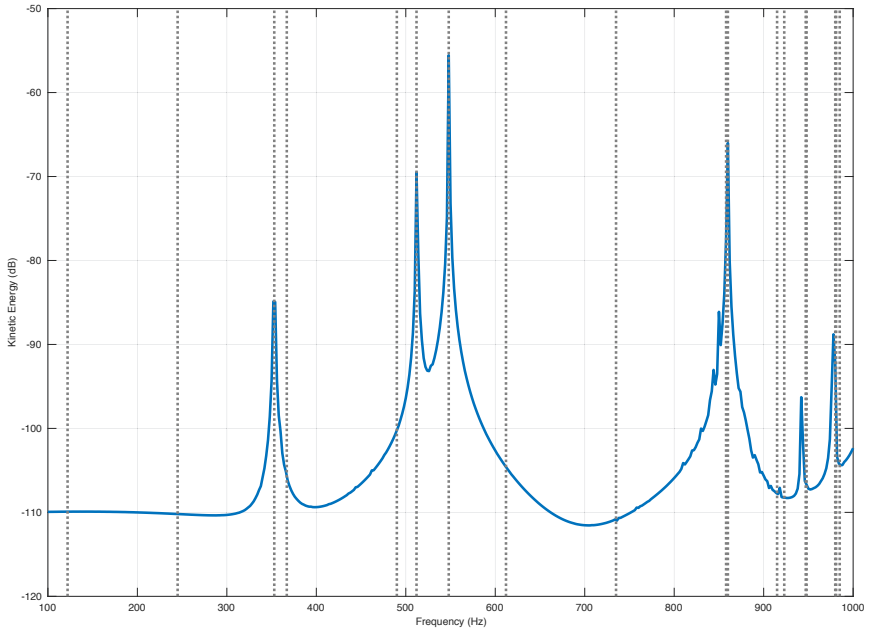


Figure 5: Kinetic energy of the cylinder as a function of frequency, when excited by an acoustic plane wave from $\theta = 45$ $\phi = 45$. Dashed vertical lines identify the frequencies of the modes of the cylinder.

2.4 Scattered Acoustic Response

The results presented above describe the structural response to an acoustic excitation. Now, the effect that this has on the acoustic pressure field will be investigated. To begin with, the computational model was solved at the four highest magnitude resonance frequencies identified in Figure 5. In each case the total acoustic pressure field p_t has been plotted over a $1\mathrm{m} \times 1\mathrm{m}$ grid with the cylinder marked in black and the angle of incidence marked with an arrow, as shown in Figure 6. These plots show that the presence of the cylinder is generating two types of acoustic scattering: acoustic reflections and acoustic shadowing, especially at the 548Hz mode.

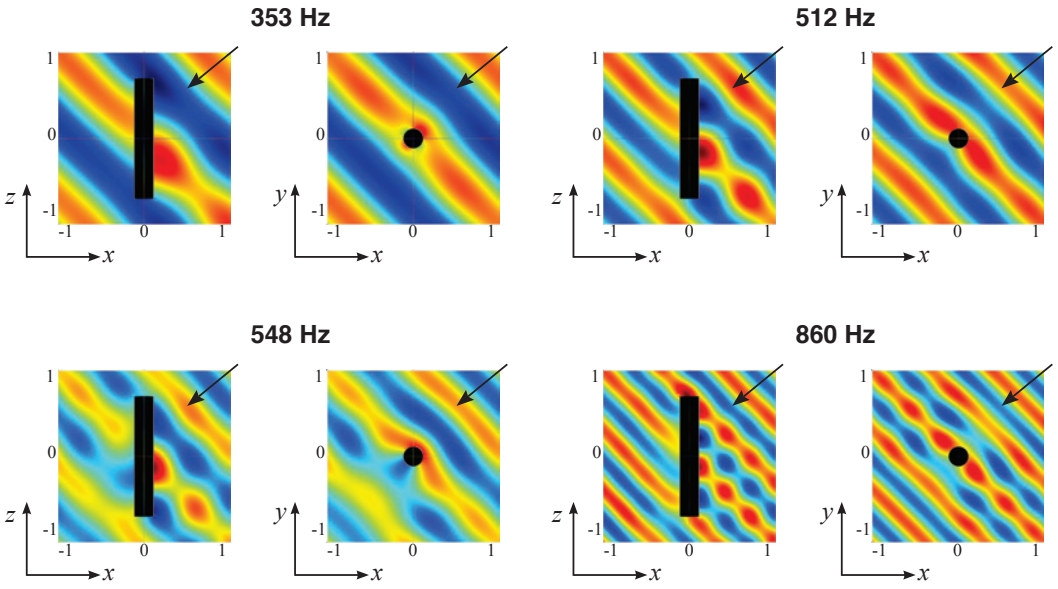


Figure 6: Predicted acoustic pressure field when the cylinder is excited by an incident plane wave at 353Hz, 512Hz, 548Hz and 860Hz. The angle of incidence of the plane wave is marked.

To further investigate the effect of the cylinder on the acoustic field, the scattered acoustic field p_s can be defined as the difference between the incident acoustic field p_{inc}, and the total acoustic field p_t:

$$p_s = p_t - p_{inc}. \tag{1}$$

The scattered acoustic pressure field has been calculated and plotted in a similar way to Figure 6, as shown in Figure 7. Whilst the total acoustic pressure plots in Figure 6 show the strongest effect on the total field at the 548Hz mode, the scattered acoustic pressure plots in Figure 7 clearly shows acoustic scattering at all four frequencies, with the reflected wave propagating away from the cylinder (in the positive x direction) and an area of high scattering immediately behind the cylinder, where its presence creates a shadowing effect.

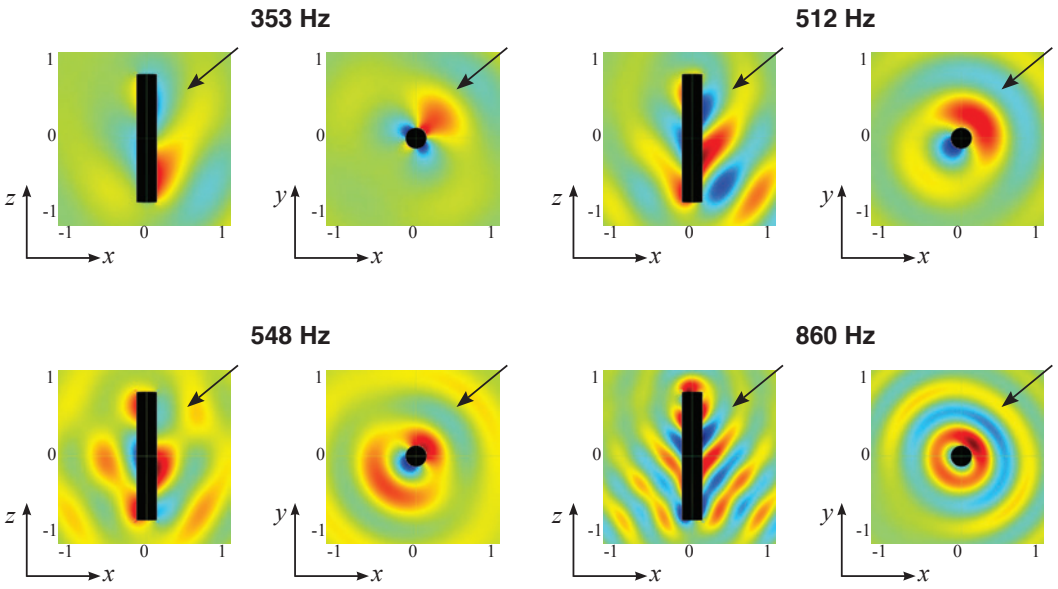


Figure 7: Predicted acoustic scattering when the cylinder is excited by an incident plane wave at 353Hz, 512Hz, 548Hz and 860Hz. The angle of incidence of the plane wave is marked.

To accurately assess how the acoustic scattering is affected by resonances within the cylinder, and to further benchmark the performance once active vibration control is implemented, the acoustic scattered power W_{scat} is calculated as an integral of the scattered sound pressure over a far-field sphere enclosing the cylinder:

$$W_{scat} = \int_S \frac{|p_s^2|}{2\rho_0 c_0}. \tag{2}$$

As in Figure 5, this was computed and plotted over a range of frequencies. A similar process was carried out on a rigid cylinder model to provide a comparison. The resulting scattered power for the rigid and flexible cylinder models is shown in Figure 8, along with zoomed in plots that focus on the two main resonances of interest. It can be seen from Figure 8 that the acoustic scattering behaviour of both the rigid and flexible cylindrical shells are almost identical except for when the cylinder is excited at the 548Hz or 860Hz modes, at which points there are clear resonances in the scattered acoustic field, as shown in the two lower subplots.

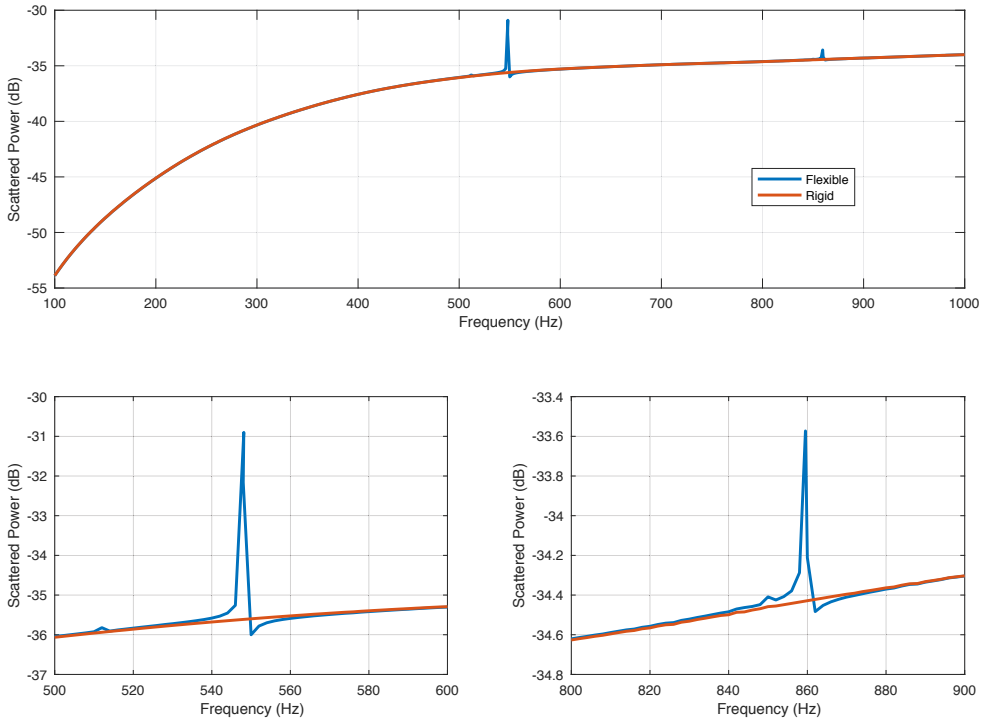


Figure 8: Total acoustic scattered power as a function of frequency, when excited by a plane wave from $\theta = 45$ $\phi = 45$. The bottom plots are zoomed in on two different frequency ranges to display the resonances of interest.

The results presented in Figure 8 are consistent with the analytical results shown by Bobrovnitskii [10], where the rigid cylinder behaves similarly to the flexible cylinder except at specific resonance peaks. Although the peak in the graph presented in [10] is at approximately $ka = 0.4$ whereas the peak presented in Figure 8 is at $ka \approx 1.1$, it should be noted that Bobrovnitskii's model was based on an external fluid of water rather than air. The effect of fluid loading on the cylinder will decrease the frequency of the structural resonances, therefore these results are still consistent.

3 Active Vibration Control

Figure 8 shows the scattered sound power spectra from the numerical model discussed above, for both a rigid and flexible scatterer. It has been discussed previously how the key difference is the presence of peaks in the scattered field of the flexible scatterer, caused by structural resonances within the cylindrical shell. This is further supported by the presentation of rigid scattering results by Williams [11] and Scandrett [13], both of which show consistently smooth scattering plots without the presence of sharp peaks. For many applications, it is likely to be these sharp peaks that cause the most coloration to the measured sound, rather than the smooth scattering curve caused by a rigid scatterer. Active vibration control can be used with accelerometers providing the error signal and structural actuators acting as control sources, in order to minimise the structural vibration of the cylinder. An Active Vibration Control system has thus been simulated within the framework of the numerical model, using accelerometers and control actuators attached to the surface of the cylinder.

3.1 Force-Sensor Configuration

An array of 97 velocity sensors and an array of 23 control forces have been defined over the surface of the cylinder, as shown in Figure 9. The response from each control force to every velocity sensor was firstly

calculated, leading to the construction of the plant matrix of complex transfer impedances $\mathbf{G}$.

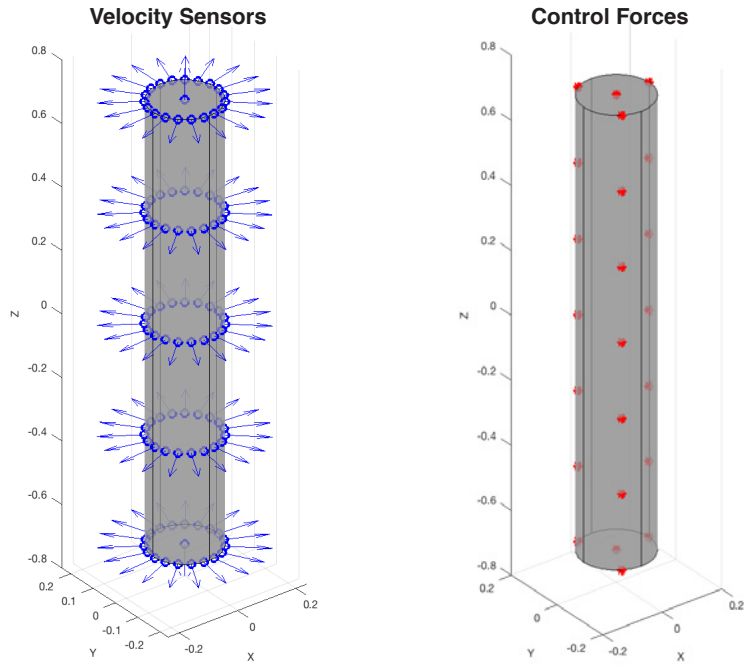


Figure 9: Location of the control forces and error sensors on the surface of the cylinder. Each control force acts inwards in the normal direction, whilst arrows mark the normal direction of each velocity sensor.

3.2 Active Vibration Control Formulation

The vector of velocities at the structural error sensors, $\mathbf{e}$, can be expressed as the linear superposition of the velocities due to the incident acoustic field, $\mathbf{d}$, and those due to the control actuators, which can be expressed as $\mathbf{Gf}$ where $\mathbf{f}$ is the vector of control forces. This gives the vector of error signals as

$$\mathbf{e} = \mathbf{d} + \mathbf{Gf}. \tag{3}$$

The vector of forces that minimises the sum of the squared error signals is then given by [14]

$$\mathbf{f_{opt}} = -\left(\mathbf{G}^H\mathbf{G} + \beta\mathbf{I}\right)^{-1}\mathbf{G}^H\mathbf{d}. \tag{4}$$

The suitable selection of the regularisation parameter β facilitates a trade-off between performance and robustness; this will be considered below.

3.3 AVC Tuning & Performance

Using the equations and source/sensor positions discussed above, single tone active vibration control has been simulated for a range of frequencies between 100Hz and 1kHz. The effect of regularisation will first be investigated and optimised, before the predicted structural performance of the AVC system is presented. Finally, the effect that this has on the scattered field will be discussed.

3.3.1 Selection of the Regularisation Parameter

To investigate the effect of regularisation, the AVC model has been solved with increasing values of regularisation from $\beta = 1 \times 10^{-10}$ to $\beta = 1 \times 10^{10}$. In each case, the condition number of the matrix inversion $\left(\mathbf{G}^H\mathbf{G} + \beta\mathbf{I}\right)^{-1}$ has been calculated, which relates to the robustness of the system, and the achieved attenuation in structural velocity of the cylindrical shell has also been calculated. These are shown in Figure 10. As expected, it can be seen that high levels of regularisation result in a well conditioned inversion, however achieve limited attenuation. A value of $\beta = 1 \times 10^{-2}$ has been marked with a vertical red line, and provides a low condition number whilst maintaining reasonable attenuation performance of the AVC system, thus reaching a reasonable tradeoff between performance and robustness.

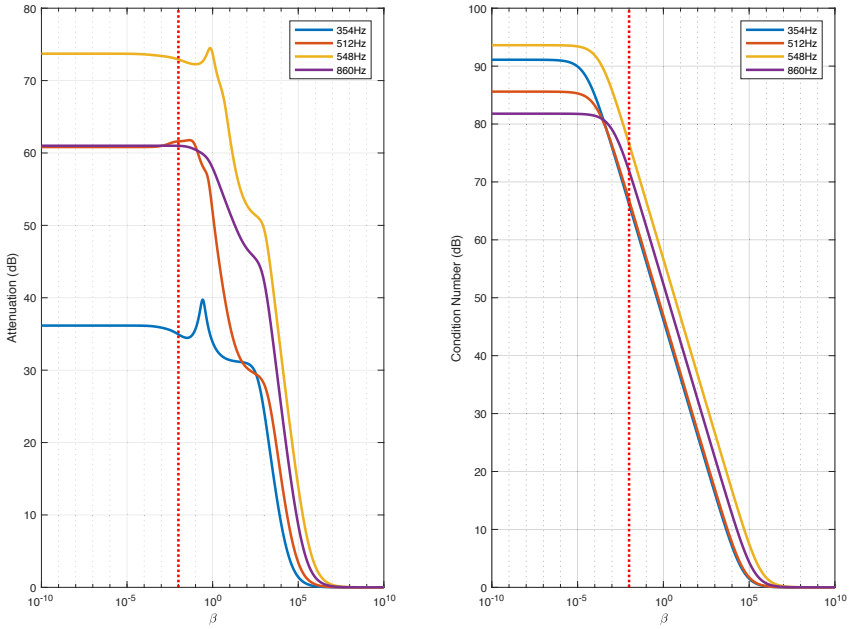


Figure 10: Condition number of matrix inverse, and achieved attenuation in structural acceleration, with varying amounts of regularisation at 354Hz, 512Hz, 548Hz and 860Hz. $\beta = 1 \times 10^{-2}$ is marked with a vertical red line.

3.3.2 Active Vibration Control Performance

Using Equations 3 and 4, as well as the matrix $\mathbf{G}$, the vector $\mathbf{d}$ and a value of $\beta = 1 \times 10^{-2}$, optimal control forces were calculated at each frequency. The resulting structural response before and after control is then shown in Figure 11. From these results it can be seen that a significant reduction in the structural velocity across the entire frequency range has been achieved. The structural velocity is reduced at every frequency, with the active vibration control effectively eliminating the resonance peaks completely. Although the structure is still vibrating, the magnitude of vibration is reduced sufficiently that it can be compared to a rigid body - that is, the velocity is close to zero.

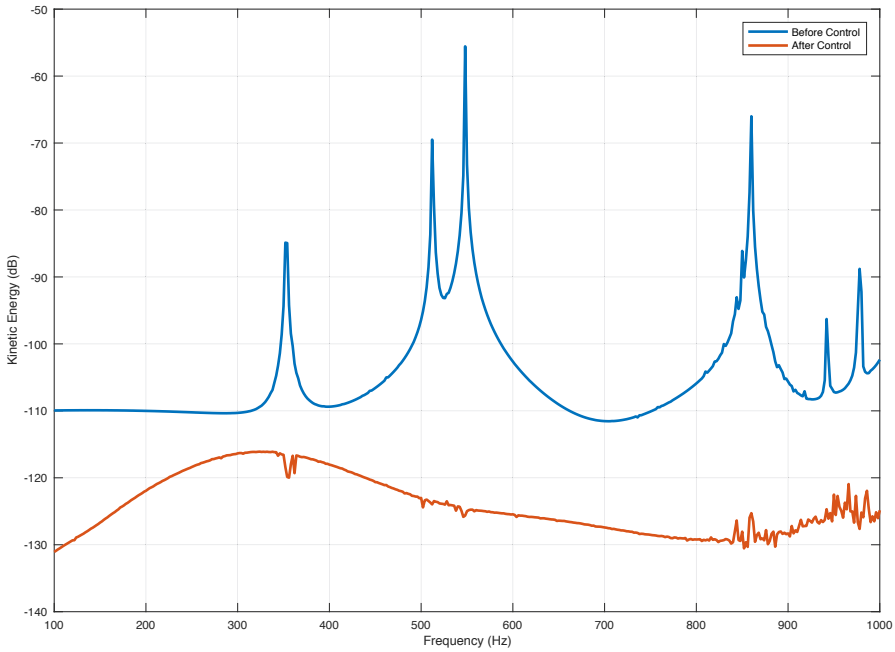


Figure 11: Kinetic energy before and after active vibration control

Using Equation 2, the acoustic scattered power has been computed before and after active vibration control, and these results are presented in Figure 12, along with the scattered sound power due to a rigid cylinder. From these results it can be seen that the scattered sound power for the flexible body before control shows significant peaks in the response, however these are attenuated by the AVC system and after control are consistent with a rigid cylinder.

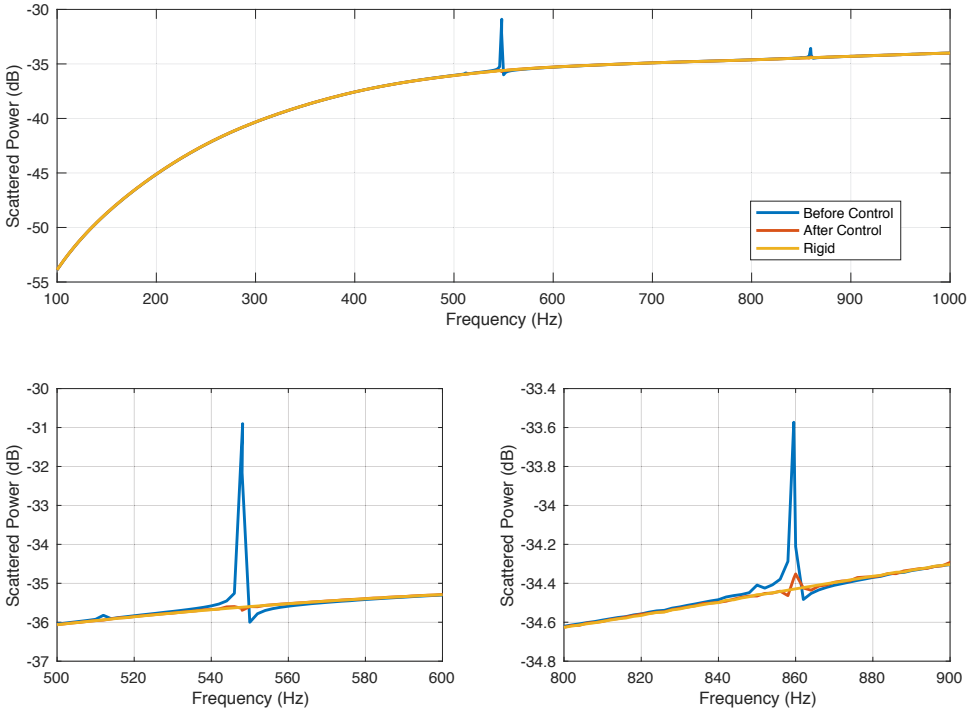


Figure 12: Acoustic scattered power before and after active vibration control, and for a rigid scatterer. The bottom plots are zoomed in on two different frequency ranges to display the resonances of interest.

4 Conclusions

This paper has investigated the effect of AVC on the acoustic scattering from a cylindrical scattering body. A numerical model of a flexible hollow cylindrical shell has been implemented and an eigenfrequency analysis has been carried out to identify the resonance frequencies of the cylinder, and to plot the corresponding mode shapes. Subsequently, the modelled cylinder was excited by an acoustic plane wave, and the resulting structural and acoustic responses were investigated.

Active vibration control was implemented on the cylindrical surface, reducing the structural velocity of the cylinder over a wide frequency band, but having significant effect when the cylinder is excited at resonance. The effect of this on the acoustic scattered field was investigated, and it was found that by implementing AVC the behaviour of the flexible cylinder converged to that of a rigid cylinder. The total acoustic scattered power was reduced by over 5dB when the cylinder was excited at its first bending mode. The amount of regularisation used in the calculation of optimal filters was investigated.

Although the structure has not been acoustically cloaked as it is still causing acoustic scattering, it no longer has resonances in the scattered field and therefore the detectability of the scattered field has been significantly reduced. For many applications (measurement microphones attached to a solid body, for example), full acoustic cloaking may not be necessary, and this reduction in sharp peaks in the scattered field may be sufficient.

5 Acknowledgements

The authors acknowledge the use of the IRIDIS High Performance Computing Facility, and associated support services at the University of Southampton, in the completion of this work. The first author is supported by an EPSRC iCASE studentship.

References

[1] D. Eggler, H. Chung, F. Montiel, J. Pan, and N. Kessissoglou, "Active cloaking of rigid and elastic cylindrical scatterers," *Acoustics 2017*, no. 1, pp. 2–7, 2017.

[2] J. Cheer, "Active control of scattered acoustic fields: Cancellation, reproduction and cloaking," *The Journal of the Acoustical Society of America*, vol. 140, no. 3, pp. 1502–1512, 2016. [Online]. Available: http://dx.doi.org/10.1121/1.4962284

[3] E. Friot and C. Bordier, "Real-time active suppression of scattered acoustic radiation," *Journal of Sound and Vibration*, vol. 278, no. 3, pp. 563–580, 2004.

[4] E. Friot, R. Guillermin, and M. Winninger, "Active control of scattered acoustic radiation: A real-time implementation for a three-dimensional object," *Acta Acustica united with Acustica*, vol. 92, no. 2, pp. 278–288, 2006.

[5] N. Han, X. Qiu, and S. Feng, "Active control of three-dimension impulsive scattered radiation based on a prediction method," *Mechanical Systems and Signal Processing*, vol. 30, pp. 267–273, 2012. [Online]. Available: http://dx.doi.org/10.1016/j.ymssp.2012.01.023

[6] G. Caruso, S. Galeani, and L. Menini, "Active vibration control of an elastic plate using multiple piezoelectric sensors and actuators," *Simulation Modelling Practice and Theory*, vol. 11, no. 5-6, pp. 403–419, 2003.

[7] S. Daley, F. A. Johnson, J. B. Pearson, and R. Dixon, "Active vibration control for marine applications," *Control Engineering Practice*, vol. 12, no. 4, pp. 465–474, 2004.

[8] I. Bruant, L. Gallimard, and S. Nikoukar, "Optimal piezoelectric actuator and sensor location for active vibration control, using genetic algorithm," *Journal of Sound and Vibration*, vol. 329, no. 10, pp. 1615–1635, 2010. [Online]. Available: http://dx.doi.org/10.1016/j.jsv.2009.12.001

[9] C. R. Fuller, S. J. Elliott, and P. A. Nelson, "Active Control of Vibration," in *Academic Press*. Academic Press, 1997.

[10] Y. I. Bobrovnitskii, "A new impedance-based approach to analysis and control of sound scattering," *Journal of Sound and Vibration*, vol. 297, no. 3-5, pp. 743–760, 2006.

[11] E. G. Williams, *Fourier Acoustics - Sound Radiation and Nearfield Acoustical Holography*. Elsevier, 1999.

[12] A. Rona, "The acoustic resonance of rectangular and cylindrical cavities," *Proceedings of the 13th CEAS/AIAA Aeroacoustics Conference*, vol. 1, no. 3, pp. 1–12, 2007. [Online]. Available: http://hdl.handle.net/2381/1986

[13] C. Scandrett, "Scattering and active acoustic control from a submerged spherical shell," *The Journal of the Acoustical Society of America*, vol. 111, no. 2, p. 893, 2002. [Online]. Available: http://link.aip.org/link/JASMAN/v111/i2/p893/s1{&}Agg=doi

[14] S. J. Elliott, *Signal Processing for Active Control*. Academic Press, 2001.

An investigation on a semi-active damping of forced structural vibrations by means of controllable structural nodes

G. Mikułowski [1], **B. Popławski** [1], **R. Wiszowaty** [1], **A. Mróz** [2], **Ł. Jankowski** [1]
[1] Institute of Fundamental Technological Research, Polish Academy of Sciences
ul. Pawińskiego 5 B, 02-106 Warsaw, Poland
e-mail: **ljank@ippt.pan.pl**

[2] Adaptronica Sp. z o. o.,
ul. Szpitalna 32, 05-092 Łomianki, Poland

Abstract
Vibration mitigation in space structures creates a unique class of a technical problem where resistant for outgassing and non-fluidic solutions are preferable. Additionaly, a vibration induced by time-varying excitations needs to be effectively reduced. The vibration mitigation task is speciffically difficult in the case of light, slender and inherently flexible structures of various types, such as supporting structures, deployable structures, modular structures or wide-span skeletal roofing structures. This study presents a concept of a vibration attenuation method based on semi-active joints and dedicated to frame structures under forced vibration excitation. The presented investigation contains an analysis of the problem of the optimal control of a structure fitted with semi-active structural members. Furthermore, an adequate model of the semi-active joints is developed and a numerical example is presented. Finally, the research provides an experimental verification of the developed control algorithms, which is conducted on a test stand in a laboratory environment.

1 Introduction

The concept of semi-active vibration damping systems was designed to bridge the gap between active and passive systems. Such systems should have a very high damping efficiency under varying external conditions (resemblance to active systems) and a high operational reliability (resemblance to passive systems). This combination of properties makes them perceived to be much more advanced and difficult to design than the active and passive damping systems to which they are compared. As a result, scientific activities devoted to this issue are relatively limited. However, their great advantages make it worthwhile to take up this research topic.

In applications where efficient vibration damping is required, active damping systems are considered as a first choice option. This is mainly due to the fact that they are characterized by a very high vibration damping performance and are relatively easy to design and implement in real structures. These features have attracted the interest of scientists for many years and therefore the active systems have been thoroughly researched in various applications. The literature on the subject is very extensive and covers a wide range of areas. They can be successfully applied as vibration dampers in vehicle suspensions [1], machine tools [2], drilling machines [3], hard disk drives [4], cable-stayed bridges [5], high-rise buildings [6] and many other fields of engineering. Active control strategy is usually applied by means of tendons [7, 8], hydraulic actuators [9] or tuned mass dampers [10]. There can also be found some unconventional concepts such as adaptive inerters [11]. Such solutions rely on an active generation of forces that affect the controlled structure. Active control techniques can therefore be very dangerous, because large external forces can lead, contrary to the original assumption, to destabilization and destruction of the controlled structure. Additional problems are the high

energy demand and the possible weakening of the structure if the power supply fails.

A semi-active system is the solution to maintain the effectiveness of vibration damping at a similar level, as well as to increase safety and reduce the energy demand. As in the case of active systems, semi-active ones can be used in many types of engineering structures and applications. Potential, practically important application areas include damping of vibrations of lightweight skeletal structures of various types, including deployable structures [12, 13], modular structures [14], wide-span skeletal roofing structures [15, 16], supporting structures subjected to moving loads [17] etc. They are also used in vibration damping in drive-train systems [18], damping of ground resonance in helicopters [19], adaptive suspensions [20, 21], vibration control of vehicle seat suspensions [25] and in many other fields of engineering.

A semi-active vibration damping system must be designed in conjunction with the design of the structure itself, since the basis of its operation lies in the local reconfiguration of the system in a certain way. Therefore, the design of the structure must take into account the introduction of this possibility. Local reconfiguration means that in a certain area of the structure its mechanical properties are modified, usually its stiffness or damping capabilities, causing the dissipation of the vibration energy to be increased. The local nature of introduced modifications allows for the use of local, decentralised control strategys as well. Decentralization of the control system is desirable because it allows for the use of such damping system in cases where the centralised one would require too large computational effort [24]. Another advantage of a decentralised approach is that the number of sensors required for its implementation can be significantly reduced in comparison to a centralised, global control strategy. It is also possible to use individual components of the structure as independent vibration damping devices, which can further improve the efficiency of the energy dissipation.

We have developed a comprehensive damping system, consisting of a semi-active control algorithm and some special rotational nodes that allow for the implementation of this algorithm to control planar frame structures. This system allows for achieving very good results in free vibration damping [26, 27] and in reducing the amplitude of forced vibrations.

2 Definition of the problem

The aim of the conducted research is to effectively damp free and forced vibrations in planar frame structures using a semi-active approach. Potential mechanical systems that could benefit from the use of such vibration damping systems are slender, lightweight space frame structures. This solution uses dry friction, without any fluid, which is very desirable in such applications.

2.1 Semi-active nodes

Especially designed semi-active nodes are used in the created damping system, allowing for a quick transition between the levels of the transmitted bending moment. They use a dry friction mechanism between two conical friction surfaces to transfer the bending moment. When these surfaces are pressed against each other by an external device (e.g., a spring) the node is in a state of maximum transfer of the bending moment. The piezoelectric stack located inside the node allows the friction surfaces to be separated and, consequently, the amount of transmitted moment to be reduced. Due to the fact that the interaction occurs through dry friction, the continuity of the moment level control is limited. The control technique that works best here is the step switching between the maximum and minimum moment values that a node can achieve. This approach is known as a bang-bang control.

2.2 Considered structure

Considered frame structure is presented in Fig. 1. It is built of box profile steel beams with the dimensions shown in the figure. Its slender structure corresponds with the frame structures used in the space industry. The

relatively low resonance frequencies allow the high efficiency of vibration reduction system to be observed visually.

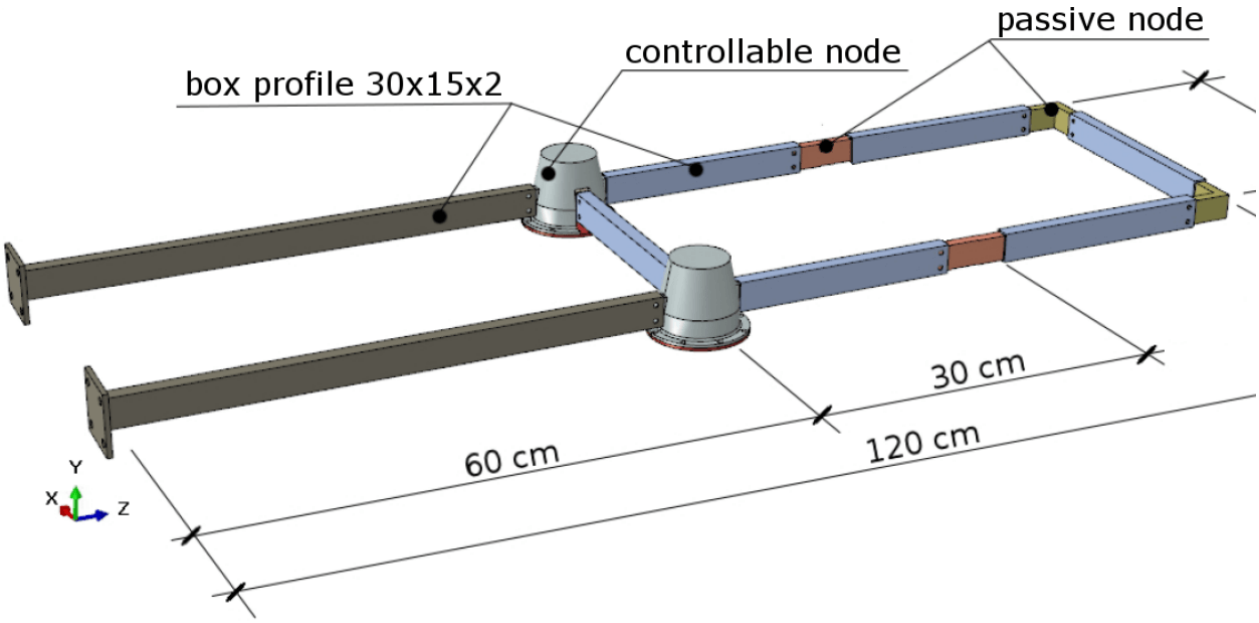


Figure 1: Considered frame structure

2.3 Numerical model

The model prepared for the needs of numerical simulations imitates the semi-active nodes described above using rotational viscous dampers with a freely controllable damping coefficient. Two overlapping rotational degrees of freedom can be coupled by means of such a damper and, in dynamic simulations, efficiently implement a frame node (transferring bending moments). Switching the damping coefficient to a minimal value (e.g., to zero) changes the state of operation of the node to a truss one (no transfer of moments). The general equation of motion of any structure equipped with the described nodes can be expressed as follows:

$$\mathbf{M}\ddot{\mathbf{x}}(t) + \left(\mathbf{C} + \sum_{i=1}^{N} \gamma_i(t)\mathbf{C_i}\right)\dot{\mathbf{x}}(t) + \mathbf{K}\mathbf{x}(t) = \mathbf{F}(t) \tag{1}$$

where $\mathbf{M}$ and $\mathbf{K}$ represent the mass and stiffness matrices, $\mathbf{C}$ is the damping matrix of the structure without any rotational dampers (truss-like state), γ_i is the variable damping coefficient of the ith rotational damper. $\mathbf{C}_i$ is the coefficient matrix of the ith rotational damper and $\mathbf{F}$ is the external force. This model of nodes does not introduce nonlinearities to the numerical model, and at the same time it allows for approximating the frame-like state of nodes operation with a satisfactory accuracy.

The developed heuristic control algorithm puts the bang-bang control concept into practice. Its mathematical definition looks as follows:

$$\gamma_i = \begin{cases} \gamma_{\min} & \text{if } E_i^{\text{el}} \text{ reaches maximum} \\ \gamma_{\max} & \text{otherwise,} \end{cases} \tag{2}$$

where E_i^{el} is the local strain energy in the vicinity of the ith controllable node (see [26] for details). The period during which the semi-active node remains in the truss state can be determined in couple of ways; the simplest is to define a constant time window, after which it returns to its original (frame) state of operation.

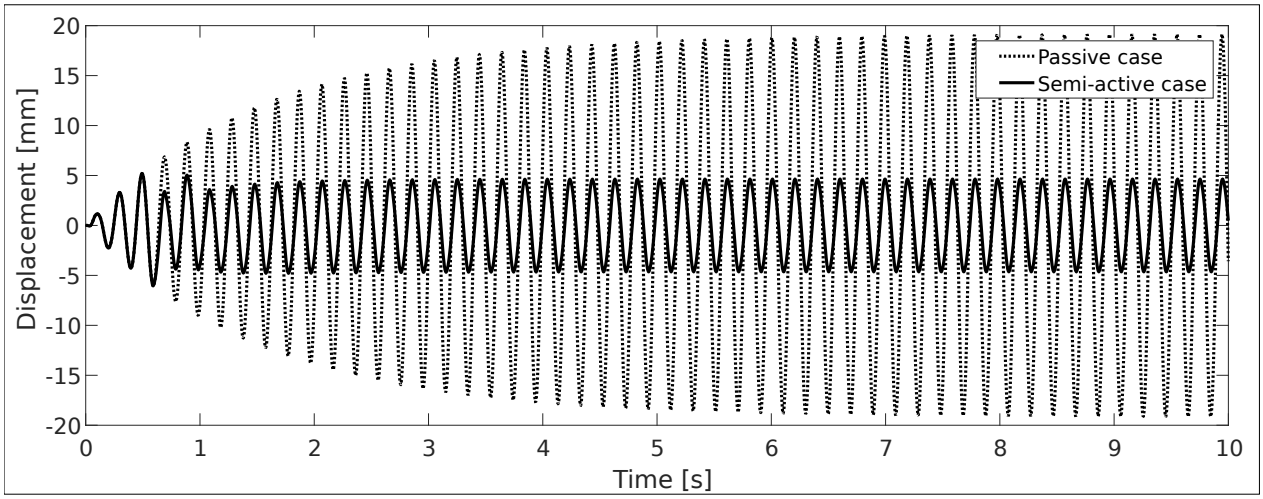


Figure 2: Comparison of lateral displacements of the tip for the first natural frequency

2.4 Exemplary numerical results

The achieved results of the reduction of vibrations excited by a harmonic external force are presented in Fig. 2. It compares the in-plane lateral displacements of the tip of a frame structure similar to the one presented in Fig. 1. The external excitation is a harmonic force applied to a selected point of the structure. Its frequency is equal to the first natural frequency of the considered frame. The high damping performance can be clearly seen. In this case, the amplitude reduction of the induced vibrations is about 75%.

3 Experimental investigation

Laboratory investigation aims to demonstrate the effectiveness of the localised control algorithm developed in course of the conducted optimization and numerical analyses. The objective is accomplished by means of reflecting three types of experimental tests: 1. modal analysis for examination of structural dynamics, 2. verification of the decentralised control approach dedicated to damping of free vibration, 3. verification of the decentralised control approach dedicated to damping of forced vibration.

The subject of the experiment is a steel, slender frame fixed in a cantilever configuration and equipped with semi-active joints, as depicted in Fig 1. The investigation is conducted in 2D configuration, therefore a set of geometrical points on OXY plane is defined on the structure (P1 – P22) as the measurement positioning system (Fig. 3). The semi-active joints are mounted in points P4 and P12 and allow the system to carry out the operation of a controllable reduction of the bending moments transmission in the beam between the joints.

The experimental vibration excitation is of two types: for inducing free vibration – an initial condition of a displacement type (introduced at point P20 in direction OX); for inducing forced vibration – a modal shaker (fixed at point PF in direction OX) (Fig. 3).

Sensing system has been configured in order to provide a relevant input in dependence on the particular experimental task. Sixteen accelerometers of 6 kHz bandwidth are used for modal analysis, whereas a setup for monitoring of the internal vibration energy comprises twelve strain gauges configured for bending measurements. The positioning of the utilised strain gauges is relevant to a selected control algorithm and is one of the tasks of the examination. The vibration amplitude monitoring task is accomplished by measuring velocity in the point P16 on the frame. In the case of the forced vibration, the excitation force level is acquired with a piezoelectric force sensor positioned at the tip of the modal shaker.

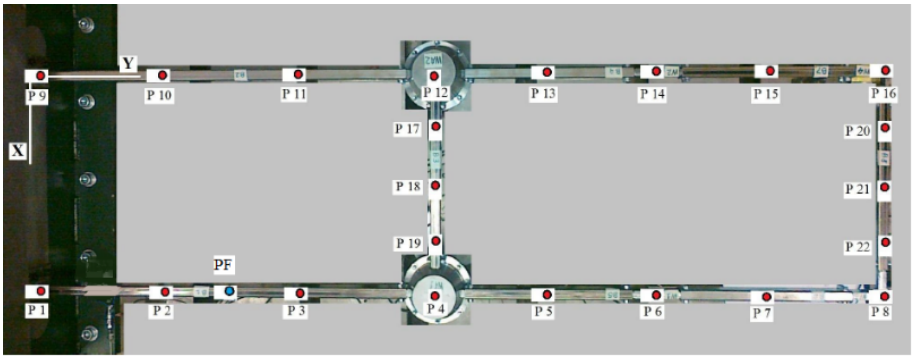


Figure 3: Experimental frame in the laboratory configuration

Laboratory controller is based on an FPGA processor unit (40MHz cRIO NI), which accomplishes two variants of the developed control law, where the strain energy in the structure is continuously monitored. The algorithms are programmed for detecting the time instant related to maximum values of the strain energy of the frame and initialising a short lasting switch operation in the semi-active joints. The duration of the switching process is anticipated to be relevant to the rate of a bending wave propagation in a steel structure. Particularly in this experimental setup the switching period is 2.3 ms, which results from a limitation of the piezoelectric actuation system.

A reference parameter for the effectiveness comparison is unified for all experiments and defined as an amplitude of velocity of the frame tip in the lateral plane.

3.1 Modal analysis

An operational modal analysis of the structure is performed on the basis of acceleration measurements in the twenty two measuring points distributed on the frame. The analysis is accomplished in the in-plane configuration with PolyMax algorithm (LMS TestLab 9B). Determination of changes in dynamics of the frame in the two basic passive operational configurations is the main objective of the analysis. The first configuration is the frame with the joints, transferring the bending moments (frame-like state) and the second configuration is with the transfer of the moments switched off (truss-like state).

3.1.1 Modal analysis results

A significant difference is demonstrated in the eigenfrequencies related to the particular modal shapes. The corresponding values of frequencies are given in Tab. 1. The in-plane modal shapes for the two configurations appear not to differ between each other. The first four modal shapes are depicted in Fig. 4 – 7.

$Mode\,No$	$Configuration\ I$ $Frequency\,[Hz]$	$Configuration\ II$ $Frequency\,[Hz]$	$Shift\,[\%]$
1	14.5	11.3	-22.0
2	40.1	39.4	-1.7
3	125.3	121.7	-2.8
4	166.3	152.8	-8.1

Table 1: Frequencies corresponding to in-plane modal shapes

An in-depth examination of the modal shapes represented by the beam between the semi-active joints shows that it takes a form with two extrema (S-shape) for the first, second and fourth mode. The S-shape form is characterised by high strain energy, which intensively influences the bending stiffness of the structure as



Figure 4: Modal shape for the first eigenfrequency

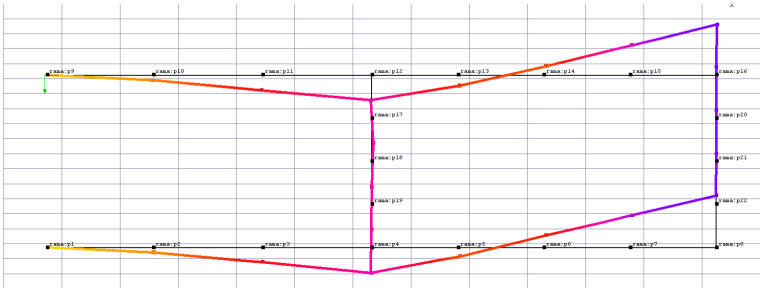


Figure 5: Modal shape for the second eigenfrequency

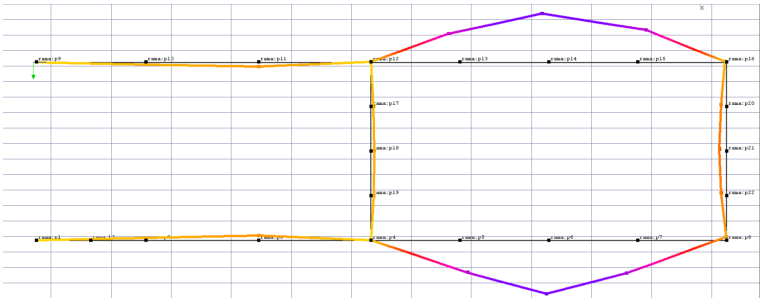


Figure 6: Modal shape for the third eigenfrequency



Figure 7: Modal shape for the fourth eigenfrequency

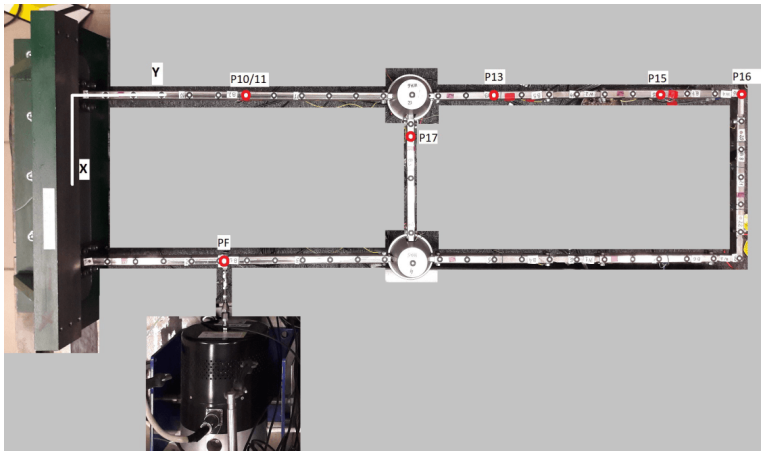


Figure 8: Experimental frame in the laboratory configuration

a whole. The third modal shape of the beam reveals one extremum (U-shape) and therefore it allows for accumulating a lower amount of the strain energy in the element. Furthermore, a relative angular distortion of the joints has a significant influence on the strain energy accumulation process. The S-shape deflection of the beam between the semi-active joints is associated with angular deflection of the joints carried out with the same turn. On the other hand, the U-shape is associated with counter rotation of the joints. The second modal shape demonstrates a configuration, in which the joints do not exhibit an angular distortion, since the localization of them is close to an extremum of the modal shape. The above described effects are visible in the eigenfrequencies shifts (Tab. 1), which directly represent modifications of the bending stiffness of the complete frame. The eigenfrequencies referenced to the first and fourth modal shapes are shifted most significantly, as they both represent the S-shape deflection modes with significant torsional deflections. The third modal shape introduces a moderate shift of 2.8% related to counter torsional deflection of the joints (U-shape case). The least influence is associated with the second modal shape, as the relative torsional deflections of the joints are minimal.

The analysis provided above reveals some preliminary, heuristic conclusions regarding the proper localisation of the semi-active joints in a larger frame structure. The favourable localisations are those which are characterised by torsional distorsions of a common turn, present in the majority of the modal shapes or in the modes of the most concern.

3.2 Decentralised vibration control

In the decentralised control approach, the feedback input signal is acquired in the direct neighbourhood of the semi-active joint (see Fig. 8). Therefore, a local response of the structure is monitored and an adequate interference of the electronic system is adopted. The thesis in this part of the study can be formulated as follows: it is feasible to control the vibration of a structure exclusively on the basis of the strain energy measured locally. The principle objective of this part of the investigation is to provide a survey of decentralised control configurations aiming at assessment of the system performance. The common feature of the tested configurations is an on-off feedback controller, which switches the state of the semi-active joints. The input signal is velocity of the vibration. The algorithm assumes short-duration switches of the joints at the time instants when the velocity of vibration is equal to zero, which corresponds to maximum accumulated strain energy. The control objective is minimisation of vibration velocity amplitudes at the tip of the frame along the direction OX (P16 in Fig. 8).

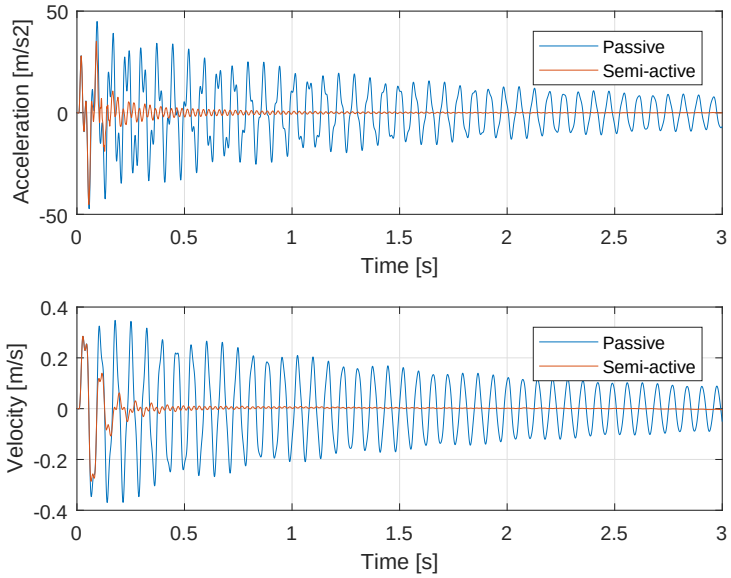


Figure 9: Free vibration response of the frame in passive and controlled modes in accordance with decentralised control approach

3.2.1 Decentralised control approach applied for free vibration

Experimental program dedicated to free vibration comprises acquiring a passive and a controlled response of the frame in accordance with the decentralised control approach. The input for the controller is provided by a strain gauge positioned at the point P17 on the frame. The consequent acceleration and velocity of the frame tip is depicted in Fig. 9, in which the passive response is compared to the controlled one. As demonstrated, the applied algorithm is able to recognize the correct time instants to release the accumulated strain energy efficiently. The vibration of the frame is damped after three periods of oscillation. The decentralised control approach can be assumed to be effective in accordance with the previous research findings [24].

3.2.2 Decentralised control approach applied for forced vibration

Primarily, the presented research of the forced vibration control aims to evaluate the system controllability in dependence on position of the input signal sensor on the frame under a continuous excitation. Furthermore, the switching phase shift influence on the system response is examined.

At the presented stage of the investigation, the setup is configured for parallel examination of the strain levels in four localisations. For accomplishment of the synchronous strain examination a dedicated experiment is proposed, i.e. generation of the input signal for the controller is referenced to the vibration excitation signal. This approach allows for examination of responses from the several sensor localisations under the same vibration conditions.

The vibration of the frame is induced with a modal shaker positioned in point PF exciting the frame along OX axis and the examined input sensor positions are depicted as P10/11, P13, P15, P17 (Fig. 8).

The testing instances are defined for two frequencies associated with the first and second mode of the in-plane vibration (14.5 Hz and 40.1 Hz) as well as a frequency sweep at 0.1 – 200 Hz bandwidth, which covers four in-plane vibrational modes of the object.

3.2.3 Results discussion of forced vibration control

Time histories of the strain response in P15 for passive and controlled instances are depicted in Fig. 10. The graphs depict responses of the structure to a harmonic excitation of the 1st and 2nd eigenfrequencies. The time instants for the switching signal are determined in reference to the excitation signal history.

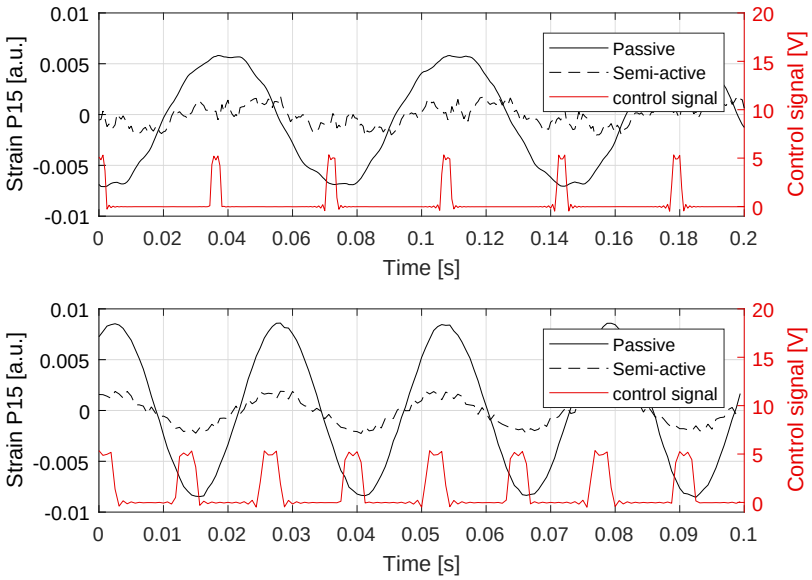


Figure 10: Strain in P15 in passive and controlled structure under the 1st and 2nd eigenfrequency harmonic excitation

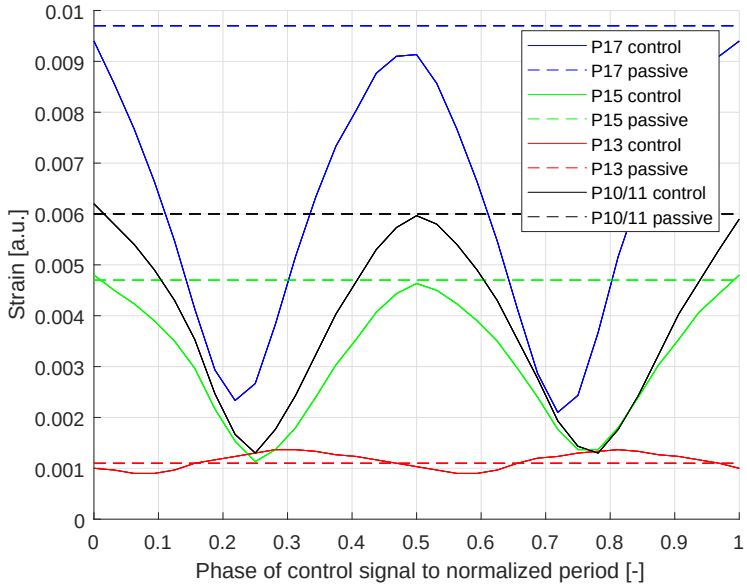


Figure 11: Forced vibration response of the frame in passive and controlled modes under 14 Hz

The first test of the frame is designed to determine the system controllability in reference to the phase shift of the control signal with regard to the structural response of the object. The result of the experiment is

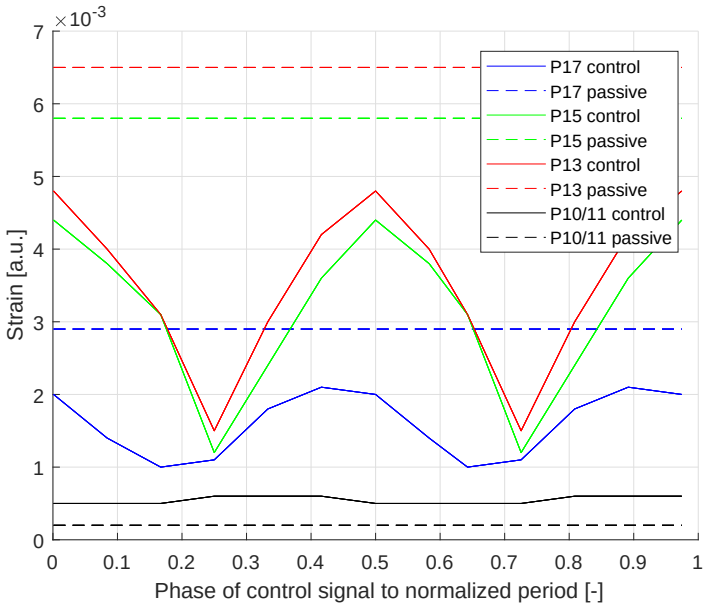


Figure 12: Forced vibration response of the frame in passive and controlled modes under 39 Hz

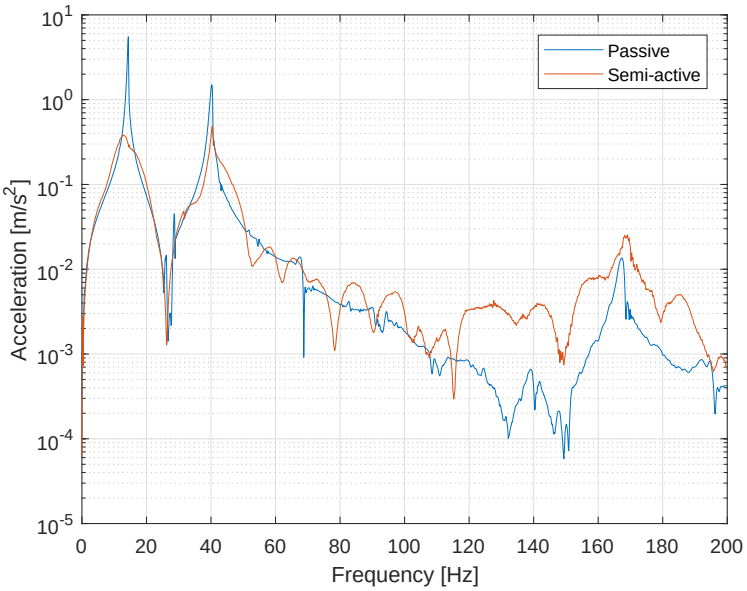


Figure 13: FFT of accelaration in P16 in passive and controlled modes

a reduction of strain amplitudes at 14.5 Hz and 40.1 Hz, as depicted in Figs. 11 and 12. The amplitudes of strains in the previously defined positions are presented in the domain of a time instants of the control signal generation. The time instants are referenced to the normalized period of the vibration. As a reference case for each time instant, the amplitudes of passive vibrations are provided. The data confirm that the effectiveness of the control algorithm is the highest (the amplitudes are reduced the most intensively) when the switching is provided at 0.25 and 0.75 of the period. Those time instants are associated with the extrema of the strain, and therefore with the maximum of the strain energy of the system. Furthermore, the results reveal that the implementation of the control routine decreases the amplitudes in the complete periods

duration. Consequently, the system does not deteriorate or destabilise performance of the original structure and confirms a dissipative character of the system. A consequent finding from the presented examination is that the vibration of the controlled beam between the semi-active joints is shifted in phase in reference to the vibration of the remaining beams of the structure. This may inherently influence the operation of the control algorithm. Further study is required for determination of the actual influence of the phase shift on the system performance. The decentralised and essentially nonparametric character of the investigated approach might require the employment of substructural nonparametric models [22] and facilitate applications in substructural-level monitoring methods [23].

The second group of tests is focused on frequency response of the system and assessment of the system's performance in the frequency domain. As depicted in Fig. 13, the first and second mode responses are effectively reduced. The presented results also confirm the results of the theoretical analysis of the problem as regards to the transfer of the vibrational energy from the lower modes to the higher modes. The graph in Fig. 13 presents two curves, where passive response has higher amplitudes in the range of lower frequencies (first and second modes) and lower amplitudes in the range of higher frequencies. It suggests that the control system mitigates the amplitudes in the low frequency range and induces the vibration of the system in the high frequency range. The higher frequency modes are better damped in structure because of naturally higher values of material damping.

4 Conclussions

An experimental survey dedicated to a decentralised control of vibration in a frame structure is presented. The demonstration for the Prestress Accumulation and Release control law is verified and examined. The control method reveals a significant potential in mitigation of the vibration in free vibration as well as forced vibration instances. The obtained results encourage to make effort directed to implementation of the method for more complex 2D as well as 3D structures. Furthermore, the obtained results encourage to perform studies on optimal localisation of the semi-active joints as well on optimisation of the position with regard to excitation localisation.

Acknowledgements

The authors gratefully acknowledge the support of the National Science Centre, Poland, granted through the project Re-Con (DEC-2017/25/B/ST8/01800), and of the National Centre for Research and Development, Poland, granted in the framework of the TANGO2 programme (TANGO2/341494/NCBR/2017).

References

[1] D. Karnopp, *Active Damping in Road Vehicle Suspension Systems*, Vehicle System Dynamics, Vol. 12, No. 6, 1983, pp. 291-311.

[2] C. Brecher, A. Schulz, M. Weck, *Electrohydraulic Active Damping System*, CIRP Annals, Vol. 54, No. 1, 2005, pp. 389-392.

[3] J. D. Jansen, L. van den Steen, *Active damping of self-excited torsional vibrations in oil well drillstrings*, Journal of Sound and Vibration, Vol. 179, No. 4, 1995, pp. 647-668.

[4] F. Huang, T. Semba, W. Imaino, F. Lee, *Active damping in HDD actuator*, IEEE Transactions on Magnetics, Vol. 37, No. 2, 2001, pp. 847-849.

[5] Y. Achkire, F. Bossens, A. Preumont, *Active damping and flutter control of cable-stayed bridges*, Journal of Wind Engineering and Industrial Aerodynamics, Vol. 74-76, 1998, pp. 913-921.

[6] M. Asano, Y. Yamano, K. Yoshie, Y. Koike, K. Nakagawa, T. Murata, *Development of Active-Damping Bridges and Its Application to Triple High-Rise Buildings*, JSME International Journal Series C: Mechanical Systems, Machine Elements and Manufacturing, Vol. 46, No. 3, 2003, pp. 854-860.

[7] M. Abdel-Rohman, H. H. Leipholz, *Active control of tall buildings*, Journal of Structural Engineering, Vol. 109, No. 3, 1983, pp. 628-645.

[8] A. Preumont, Y. Achkire, F. Bossens, *Active Tendon Control of Large Trusses*, AIAA Journal, Vol. 38, No. 3, 2000, pp. 493-498.

[9] A. M. Reinhorn, T. T. Soong, M. A. Riley, R. C. Lin, S. Aizawa, M. Higashino, *Full-scale implementation of active control. II: installation and performance*, Journal of Structural Engineering, Vol. 119, No. 6, 1993, pp. 1935-1960.

[10] C. C. Chang, H. T. Y. Yang, *Control of buildings using active tuned mass dampers*, Journal of Engineering Mechanics, Vol. 121, No. 3, 1995, pp. 355-366.

[11] R. Faraj, J. Holnicki-Szulc, L. Knap, J. Seńko, *Adaptive inertial shock-absorber*, Smart Materials and Structures, Vol. 25, 2016, pp. 035031-1-9.

[12] Y. Chikahiro, I. Ario, M. Nakazawa, S. Ono, J. Holnicki-Szulc, P. Pawłowski, C. Graczykowski, A. Watson, *Experimental and numerical study of full-scale scissor type bridge*, Automation in Construction, Vol. 71, 2016, pp. 171-180.

[13] A. Mróz, J. Holnicki-Szulc, J. Biczyk, *Prestress Accumulation–Release technique for damping of impact-born vibrations: Application to self-deployable structures*, Mathematical Problems in Engineering, Vol. 2015, 720236.

[14] M. Zawidzki, L. Jankowski, *Optimization of modular Truss-Z by minimum-mass design under equivalent stress constraint*, Smart Structures and Systems, Vol. 21, No. 6, 2018, pp. 715-725.

[15] W. Kaminski, K. Makowska, M. Miskiewicz, J. Szulwic, K. Wilde, *System of monitoring of the Forest Opera in Sopot structure and roofing*, 15th Int'l Multidisciplinary Scientific GeoConference (SGEM), Vol. 2, No. 2, 2015, pp. 471-482.

[16] K. Wilde, M. Miskiewicz, J. Chroscielewski, *SHM System of the Roof Structure of Sports Arena "Olivia"*, Structural Health Monitoring 2013: A Roadmap to Intelligent Structures, Procs. of the 9th Int'l Workshop on Structural Health Monitoring (IWSHM), Vol. 2, 2013, pp. 1745-1752.

[17] D. Pisarski, *Optimal control of structures subjected to traveling load*, Journal of Vibration and Control, Vol. 24, No. 7, 2018, pp. 1283-1299.

[18] M. Michajłow, L. Jankowski, T. Szolc, R. Konowrocki, *Semi-active reduction of vibrations in the mechanical system driven by an electric motor*, Optimal Control Applications & Methods, Vol. 38, No. 6, 2017, pp. 922-933.

[19] Y. Zhao, Y. T. Choi, N. M. Wereley, *Semi-Active Damping of Ground Resonance in Helicopters Using Magnetorheological Dampers*, Journal of the American Helicopter Society, Vol. 49, No. 4, 2004, pp. 468-482.

[20] G. Mikułowski, R. LeLetty, *Advanced Landing Gears for Improved Impact Absorption*, Proceedings of 11th International Conference on New Actuators, June 9-11, Bremen, 2008.

[21] G. Mikułowski, R. Wiszowaty, *Pneumatic Adaptive Absorber: Mathematical modelling with experimental verification*, Mathematical Problems in Engineering, Article No 7074206, 2016.

[22] G. Suwała, Ł. Jankowski, *Nonparametric identification of structural modifications in Laplace domain*, Mechanical Systems and Signal Processing, Vol. 85, 2017, pp. 867-878.

[23] J. Hou, L. Jankowski, J. Ou, *Frequency-Domain Substructure Isolation for Local Damage Identification*, Advances in Structural Engineering, Vol. 18, No. 1, 2015, pp. 137-153.

[24] D. Pisarski, *Decentralized stabilization of semi-active vibrating structures*, Mechanical Systems and Signal Processing, Vol. 100, 2018, pp. 694-705.

[25] H. Du, W. Li, N. Zhang, *Semi-active variable stiffness vibration control of vehicle seat suspension using an MR elastomer isolator*, Smart Materials and Structures, Vol. 20, No. 10, 2011.

[26] B. Poplawski, G. Mikułowski, A. Mróz, Ł. Jankowski, *Decentralized semi-active damping of free structural vibrations by means of structural nodes with an on/off ability to transmit moments*, Mechanical Systems and Signal Processing, Vol. 100, 2018, pp. 926-939.

[27] B. Poplawski, G. Mikułowski, A. Mróz, K. Sekuła, Ł. Jankowski, *A decentralized strategy of structural reconfiguration in mitigation of vibrations*, Procedia Engineering, Vol. 199, 2017, pp. 1683-1688.

Design of an inertial mass actuator for active vibration control of a planetary gearbox using piezoelectric shear actuator

P. Zech [1], **D. F. Plöger** [1], **T. Bartel** [2], **T. Röglin** [2], **S. Rinderknecht** [1]
[1] Technische Universtät Darmstadt, Mechatronic Systems in Mechanical Engineering,
Otto-Berndt-Str. 2, 64287, Darmstadt, Germany
e-mail: **zech@ims.tu-darmstadt.de**

[2] Fraunhofer LBF, Research Division Smart Structures,
Bartningstraße 47, 64289, Darmstadt, Germany

Abstract
To achieve higher bypass ratios and thus increase efficiency, high-speed planetary gearboxes are applied to geared turbofan engines. The gear meshing inside the gearbox causes high-frequency vibration that can potentially be uncomfortable for passengers in terms of airborne noise. In this work, a system for active vibration control using inertial mass actuators is proposed. One of the key challenges in the design of the system is the high frequency range around 5 kHz of the gear mesh vibration. The system requirements regarding frequency range and force are identified experimentally using a planetary gearbox test rig. The choice, design and development of the inertial mass actuator is presented. Piezoelectric shear actuators are selected due to their comparatively small electric capacitance, which is advantageous for the power amplifier. A simulation allows the optimization of actuator and amplifier properties. Parameters of the used models are identified experimentally. The performance of the final actuator-amplifier-unit is tested using the test-rig. The achievable vibration reduction is presented and results are discussed.

1 Introduction

High-speed and high-power lightweight planetary gearboxes are under development for use in future geared turbofan engines. In contrast to current engines the rotation speeds of fan and turbine can be chosen independently. More efficient engine designs are expected with planetary gearbox technology. The gearbox however causes additional high-frequency vibration and noise resulting from gear meshing. This noise can potentially be uncomfortable for passengers, especially as the gear mesh frequency will be in the range of 3 kHz to 5 kHz where the human ear is very sensitive.

The goal of the presented research is to develop a system for active vibration control (AVC) that can be applied to high speed planetary gearboxes. The objective of the projected system is twofold: To reduce the gear mesh noise as well as to allow more efficient gearbox designs. The idea is that using an AVC system, louder but more efficient gearbox design variants can be selected. That is because initially louder designs can be actively quietened down.

This contribution presents the development of an inertial mass actuator with a piezoelectric shear actuator that can be used for active vibration control in the desired frequency range. First the current state of research is analyzed and requirements are defined. Subsequently the design of the actuator using simulations is presented. Finally the performance of the actuator is characterized experimentally. Using a sub-scale planetary gearbox test rig the feasibility of active vibration control of high-frequency gear mesh vibration is demonstrated using adaptive feedforward control.

2 Requirements and current state of research

Requirements for the projected AVC system for planetary gearboxes have been defined using a sub-scale test rig which is described later in this paper. Table 1 summarizes the requirements for the actuators. A differentiation between two scenarios is given. One in which only the dominant vibration order is to be canceled and another where the overall force shall be reduced. Especially the very high mechanical frequencies are challenging to be canceled. With a given maximum mass of 0.1 kg it is possible to calculate the required specific forces of the actuator.

Table 1: Requirements for actuators of projected AVC system for two scenarios.

Scenario	Frequency in Hz	Force in N	Mass in kg	Spec. Force in N/kg
Dominant order 85	4723	55	< 0.1	> 550
Overall force	4200-5150	158	< 0.1	> 1580

Inertial mass actuators, also known as proof mass actuators, are widely used in research concerning active vibration control. In contrast to active mounts [1] where actuators are applied directly between structure to be controlled and the environment, inertial mass actuators can be mounted in a more flexible way. These kind of actuators can be used as add-on devices for AVC applications for existing machine designs. This flexibility makes them very attractive.

This type of actuator consist of a spring-mass-system with an integrated active element and can be considered as a point force generator when driven above its resonance frequency [2]. As shown in Fig. 1, inertial mass actuators can be represented by a spring-mass system with the stiffness k and the inertial mass m, enhanced by a damping d and a force actuator A [3]. At low frequencies up to the resonance frequency of the system,

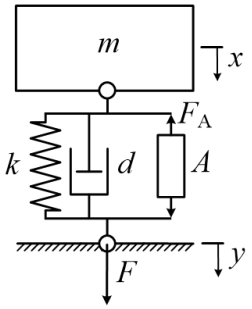


Figure 1: Model of an inertial mass actuator with stiffness k, inertial mass m, damping d, force actuator A, actuator force F_A and force of the inertial mass actuator F.

the force actuator exerts a force F_A onto the inertial mass which reacts with an in-phase acceleration. Above the resonance frequency the force actuator works in counter-phase to the inertial mass, inducing a force F into the mounting point and the connected structure.

In many cases, electrodynamic actuation is used to drive the inertial mass. For instance, inertial mass actuators of this type were successfully used for prototyping of vibration control in car suspensions [4], train bogies [5], or even for building floors [6]. Smaller units were deployed to lightweight panels [7, 8]. Restrictions in their use can be caused by ultrahigh frequency applications, the use of rare earth magnets, geometry restriction of electrodynamic actuators and the magnetic field of the permanent magnet. As an alternative, the integration of piezoelectric elements into inertial mass actuators has been studied. Since those solid state actuators possess an inherent high stiffness they can carry the inertial mass while providing high dynamic forces. Therefore they are especially suitable for high frequency applications. In [9] several concepts are proposed, and a piezoelectric disc actuator is used in a prototype set up. Also bending beam configurations were studied, either with integrated stack actuators [3] or foils [10].

The mentioned studies on piezoelectric inertial mass actuators pointed out their main advantages: If carefully designed, the actuator system contains a low number of parts with no movables. In a collocated control loop configuration together with an accelerometer, simple stable systems for active damping can be implemented [2]. This approach has been successfully studied for lightly damped structures with high resonance peaks, e.g. [8].

Table 2: Overview publications concerning inertial mass actuators for AVC after [11]. Principles are electrodynamic (ED), magnetostrictive (MS), dielectric elastomers (DE), electromagnetic (EM) and piezoelectric (PE).

Publication	Inertial mass in kg	Frequency range in Hz	Principle	Force in N	Spec. Force in N/kg
[7]	0.022	70-1000	ED	2.5	114
[12]	0.23	70-200	ED	n.s.	n.s.
[13]	n.s.	20-60	ED	1000	n.s.
[14]	0.022	80-250	ED	n.s.	n.s.
[15]	0.5	20-200	ED	50	100
[16]	0.22	167-1260	MS	40	182
[17]	0.32	150-350	MS	n.s.	n.s.
[18]	0.75	300-1200	MS	n.s.	n.s.
[19]	6.7	4-20	MS	1500	224
[20]	0.2	100-500	DE	4	20
[21]	1.2	40-200	EM	50	42
[22]	0.55	100-400	PE	200	364
[9]	0.15	260-1250	PE	n.s.	n.s.
[23]	n.s.	500-4000	PE	n.s.	n.s.
[24]	1.08	50-200	PE	n.s.	n.s.
Zech et al. [11]	0.115	4700-9300	PE	117	1020

The authors have investigated the vibration excitation of small high-speed planetary gearboxes in [25]. Due to modulation effects the vibration spectrum exhibits multiple sideband frequencies around the nominal gear mesh frequency. Different approaches for order tracking in this context have been compared in [26]. An overview of research concerning inertial mass actuators for AVC is given in Table 2 where characteristic values of each developed actuator are depicted. Different working principles have been investigated from which piezoelectric actuators seem best suited for the desired high frequency range. The authors have examined the use of prestressed piezoelectric low-voltage stack actuators in [11]. As given in Table 2 this type of actuator is well suited for the high frequency range. However as the used stack actuators have high capacitances of 1.5 µF high-performance switching power amplifiers are required to drive them at high frequencies. High currents need to be driven by the power electronics for high frequencies and capacitances [27] as described by

$$I_{\max} = V_{pp} \pi f C_a \tag{1}$$

where $I_{\max}$ denotes the maximum current, V_{pp} the peak-to-peak Voltage, f the frequency and C_a the capacitance of the actuator.

To circumvent the need for expensive high-performance power amplifiers this work investigates the use of piezoelectric shear actuators. Compared to stack actuators they have the advantage of lower capacitances. The shear actuator used in this work has capacitance of 90 nF which is smaller than the one of the stack actuator used in [11] by a factor of 16. As consequence also the required driving current would be reduced by this factor. Piezoelectric shear actuators have not been investigated in this context so far. This paper investigates advantages and drawbacks of this type of actuator when compared with stack actuators.

3 Simulation of shear actuator and amplifier

Supporting the design phase of the inertial mass actuator system, a simulation model is set up. The simulation model enables the estimation of actuator system effect and the dimensioning of the single components. The inertial mass actuator system consists of piezoelectric transducer, inertial mass and amplifier. For its simulation a modular model approach for active vibration systems on base of impedances and admittances is used [2]. An advantage of this approach is the compatibility of mechanical and electrical system components as well as the modular exchangeability of single components. Furthermore the required data for the derivation of the models can be achieved by analytical calculation, numerical simulation or experimental analysis. The impedance-admittance model structure of the inertial mass actuator is depicted in Fig. 2 indicating the exchange of power by the transmission of forces F, velocities v, differential velocity Δv, input voltage U_i, output voltage U_o and output current I_o between the single system components. The model of the inertial mass actuator can simply be enhanced by the models of the controller as well as the models of mass and elasticity of the base structure. Thus the single components can be modeled independently and combined by its defined

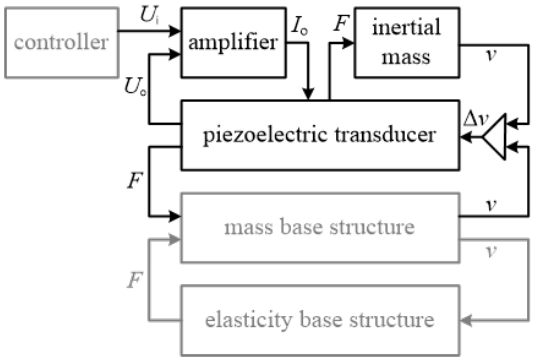


Figure 2: Impedance-admittance model structure of the inertial mass actuator system consisting of piezoelectric transducer, inertial mass and amplifier with forces F, velocities v, differential velocity Δv, input voltage U_i, output voltage U_o and output current I_o.

power interfaces. In the case of the inertial mass actuator, the amplifier is modeled by an analytic-empiric description based on experimental characterization results. Model inputs and outputs are input and output voltage of the amplifier as well as output current of the amplifier according to Fig. 2. Inertial mass and the piezoelectric transducer are analytically modeled. Their parameters are estimated through experimental characterization. Model inputs and outputs are forces and velocities.

In this work, two voltage amplifiers for piezoelectric transducers, one analog and one switching amplifier (Table 3) are investigated. Analog amplifiers regulate the power flow via power transistors, operating as resistors. Although these resistors provoke an energy drain, analog amplifiers are characterized by high signal quality at the amplifier output and robustness, which is independent of the load. In contrast to analog amplifiers, switching amplifiers recuperate mechanical energy during unloading. The minimized loss of energy into heat, enable compact design. Switching amplifiers also use transistors. In contrast to analog amplifiers, they discretely switch between conductive and blocking state. The capacitive behavior of the transducer and the limited switching frequency cause step-like changes at the output which can degrade signal quality. For the derivation of the required model data, the amplifiers are experimentally characterized. The amplifiers are loaded with film capacitors of different capacity in the range of typical, suitable piezoelectric actuators. In contrast to piezoelectric actuators, the used capacitors can be considered as linear. The results of the experimental characterization are depicted in Fig. 3. The switching power amplifier achieves unexpected high signal quality, probably related to its very high switching frequency.

The derived most characteristic properties of the amplifiers as results of the shown experimental characterization are described in Table 3. The analog amplifier is better suited for the shear actuator as it is able to drive

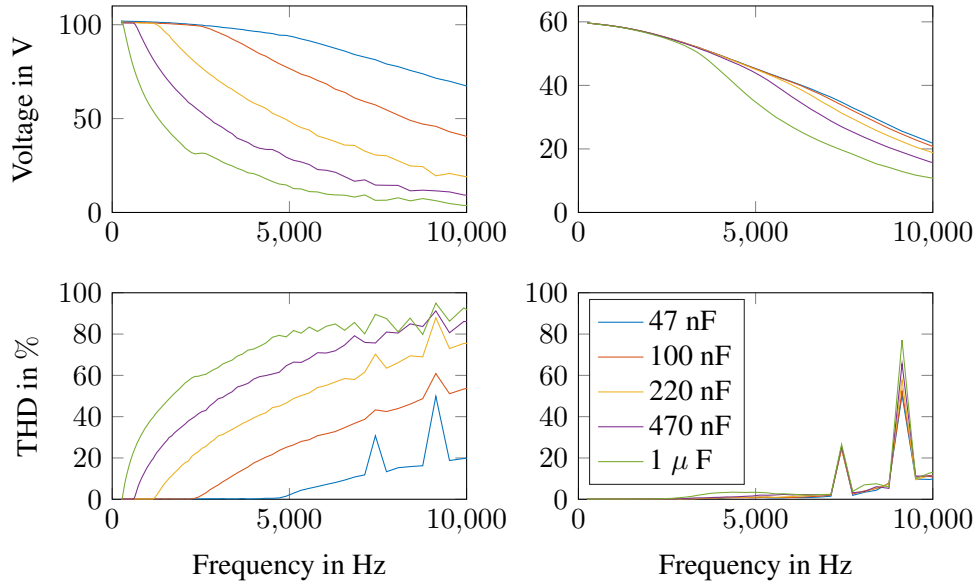


Figure 3: Experimental characterization of an analog and a switching voltage amplifier: Peak to peak voltage and total harmonic distortion (THD) for different capacitors. Left: Analog amplifier PIA-1115-2020. Right: Switching amplifier PI-E617.

Table 3: Characteristic properties of the amplifier, according to the experimental characterization.

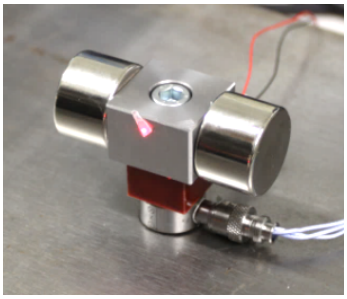
Image		
Model	PIA-1115-2020	PI-E617
Type	Class AB	Class D (100 kHz)
Voltage @ 5 kHz and 0.1 µF	76 V	45 V
Voltage @ 5 kHz and 1 µF	13 V	35 V
Total harmonic distortion @ 5 kHz	25 % (0.1 µF)	3.3 % (1 µF)

the 0.1 µF capacitance at higher voltages than the switching amplifier. The switching amplifier in turn is better suited for stack actuators as it is able to drive the 1 µF capacitance at higher voltages than the analog amplifier.

For this reason the analog power amplifier PIA-1115-2020 is chosen and numerically identified. The identification follows the methodology proposed by [28]. A high order behavior of the amplifier is taken into account to achieve good phase correlation.

As piezoelectric actuator, several transducer topologies can be used. Due to its very low capacitance, shear actuator make lowest demands on power electronics. Due to the required high frequency range of operation, the shear actuator concept is chosen and evaluated in this work.

At high frequencies, the output voltage of the amplifier is limited in dependence to the capacitance of the piezoelectric actuator. In order to derive low amplifier output voltage, the inertial mass actuator is designed in such way, that its dynamic resonance f_r meets its operating frequency at approx. 4 kHz. Doing so, the amplification of the voltage to force ratio by the dynamic resonance can be used. Since the stiffness k is predefined by the chosen actuator, the mass m has to be calculated via $f_r = \sqrt{(k/m)}/2\pi$. In order to



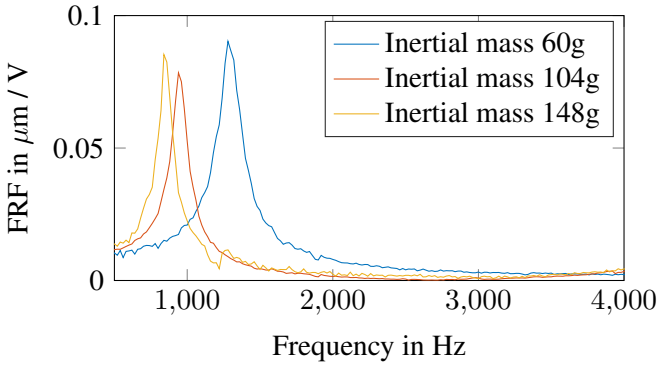


Figure 4: Left: Experimental characterization of the shear actuator. Right: Resulting frequency responses from actuator voltage to tip displacement with different inertial masses.

estimate the stiffness of the actuator, the actuator is excited with a broad band signal with three different masses attached to it.

The measurement setup and the measurement results are depicted in Fig. 4. On base of the experimental characterization, the actuator stiffness could be identified to 3.97 $\mathrm{N\mu m^{-1}}$ using a linear regression. The moving mass of the actuator (without additional mass) is calculated to be approx. 3 g. The identified actuator parameters as well as the identified power amplifier parameters were integrated into the system simulation (Figure 2). The additional mass is numerically estimated to be 8 g in order to tune the resonance frequency of the inertial mass actuator to the frequency range at approx. 4 kHz. Fig 5 (left) depicts the results of the numerical simulation for an input voltage sweep from 0 Hz to 6 kHz with 1 kHz per second. As numerically predicted, the result of the experimental characterization (Fig 5 (right)) show that the resonance frequency of the finally realized inertial mass actuator system lies in the expected frequency range.

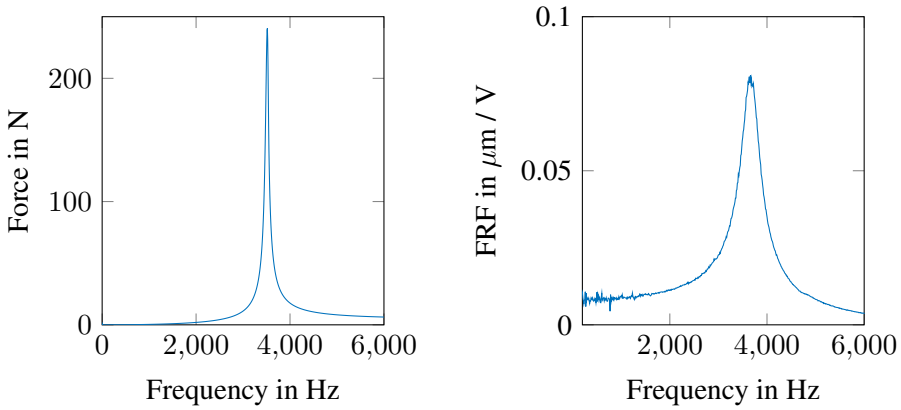


Figure 5: Left: Producible forces in simulation. Right: Measurement of resonance frequency of piezoelectric shear actuator with 8g of additional inertial mass and an analog voltage amplifier.

4 Adaptive feedforward control

The well known Filtered-x Least-Mean-Square (FxLMS) Algorithm is used in this work. However some modifications are used. It belongs to the class of adaptive feedforward control algorithms and requires a so called secondary path model. Figure 6 depicts the block diagram of the control algorithm. Reference signals are generated using a measurement of the actual planet carrier angle $\varphi_{\mathrm{carrier}}(n)$. This type of reference signals is often called synthetic as no real vibration sensor are involved. The reference oscillators for the k-th planet

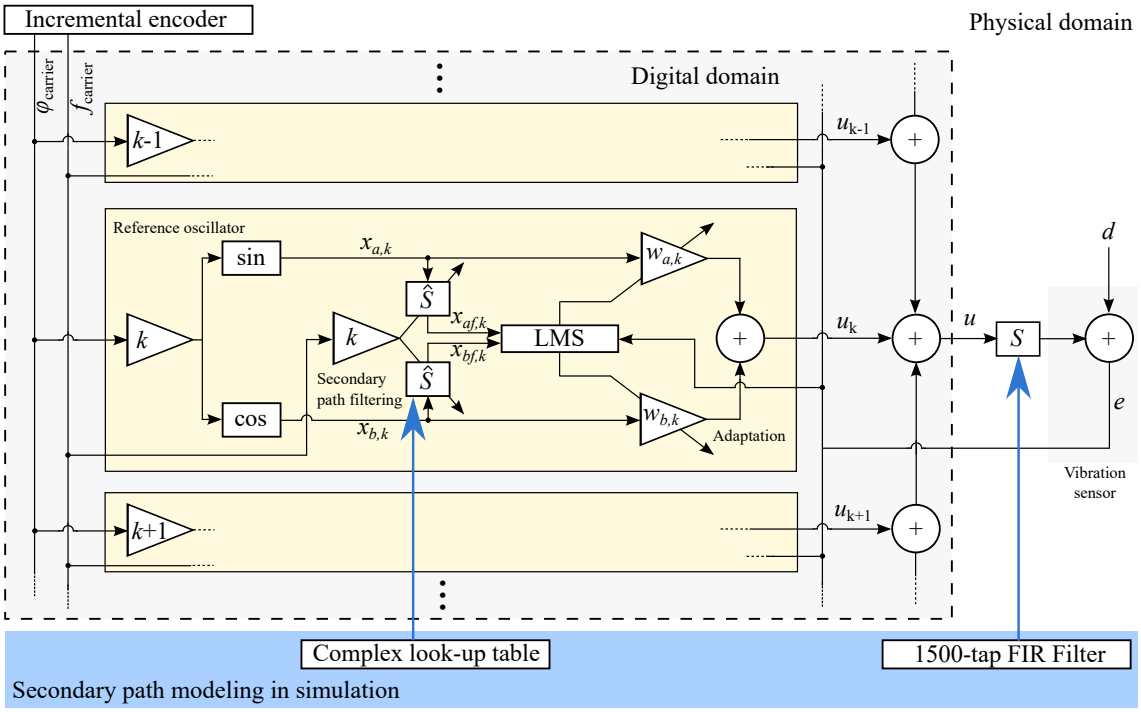


Figure 6: Narrowband FxLMS algorithm for multiple vibration orders with phase-exact reference oscillators.

carrier order is calculated using

$$x_a(n) = \sin(k\varphi_{\text{carrier}}(n)) \tag{2}$$
$$x_b(n) = \cos(k\varphi_{\text{carrier}}(n)) \tag{3}$$

where n denotes the current time step. For each frequency to be canceled two output weights are calculated with standard normalized update equations

$$w_{a,k}(n+1) = (1 - \alpha_{\text{FxLMS}}\gamma_{\text{FxLMS}})w_{a,k}(n) + \mu(n)x_{af,k}(n)e(n) \tag{4}$$
$$w_{b,k}(n+1) = (1 - \alpha_{\text{FxLMS}}\gamma_{\text{FxLMS}})w_{b,k}(n) + \mu(n)x_{bf,k}(n)e(n) \tag{5}$$

where α_{FxLMS} and γ_{FxLMS} denote step-size and forgetting factor, μ denotes the normalized step size, e the residual error signal and $x_{a,f}$ and $x_{b,f}$ the reference oscillator signals after filtering with the secondary path model $\hat{S}$. The filtering with the secondary path model is done using one complex multiplication

$$x_{f,k}(n) = \hat{S}(n) \cdot (x_{a,k}(n) + \mathrm{i}x_{b,k}(n)) \tag{6}$$

where $\hat{S}$ is the interpolated supporting point of the narrowband secondary path model and $x_{af,k}(n) = \text{Re}(x_{f,k}(n))$ and $x_{bf,k}(n) = \text{Im}(x_{f,k}(n))$. The normalized step-size μ is calculated in each time step using

$$\mu(n) = \frac{\alpha_{\text{FxLMS}}}{x_{af,k}^2(n) + x_{bf,k}^2(n)}. \tag{7}$$

The output of the k-th subsystem of the algorithm is

$$u_k(n) = w_{a,k}(n)x_{a,k}(n) + w_{b,k}(n)x_{b,k}(n). \tag{8}$$

Finally the overall output is the sum of the outputs for all carrier orders which can be described by

$$u(n) = \sum_{k=Z-N}^{Z+N} u_k(n) \tag{9}$$

where N carrier orders around the nominal gear mesh frequency $f_{\text{mesh}} = Z f_{\text{carrier}}$ are to be canceled. Z denotes the number of teeth of the ring gear. For the high desired frequency range a computational efficient implementation of the control algorithm is required. Two strategies are used in this work to achieve a 50 kHz closed-loop sampling frequency. Computational expensive convolution as needed when using FIR-filters can be replaced by complex multiplication when using complex lookup tables as secondary path model. Furthermore the update frequency of this complex lookup table can be chosen much lower than the update frequency of the output weights. These two measures significantly reduce computational complexity and therefore allow for the very high closed loop sampling frequency.

Figure 6 also shows that two kind of secondary path models are used in the simulation of the control algorithm. The internal model in the control algorithm is a complex look-up table while the real secondary path is modeled using a 1500-tap FIR filter.

5 Experiments

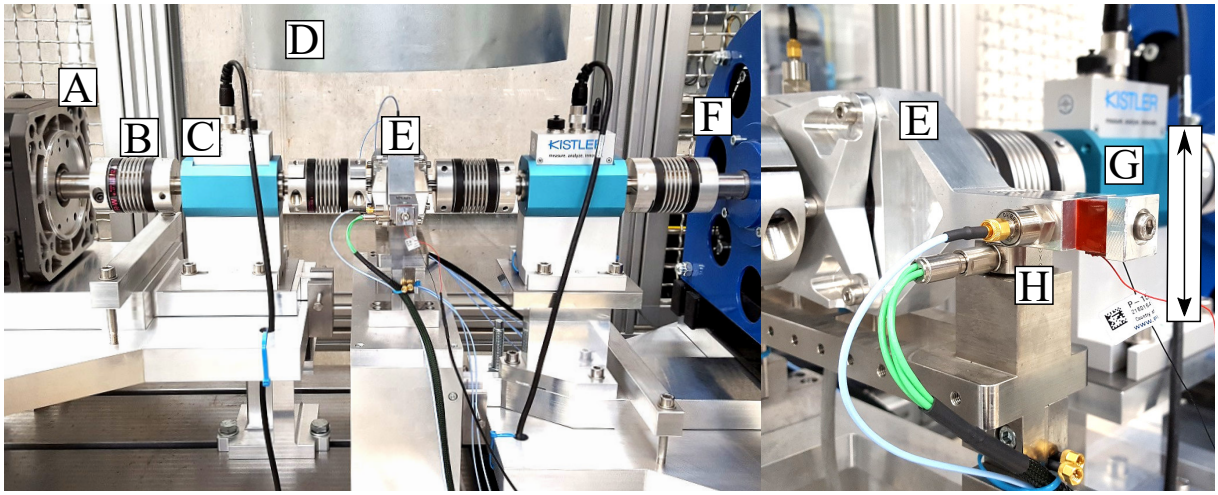


Figure 7: Test rig with asynchronous motor (A), couplings (B), torque sensors (C), planetary gearbox (E), eddy-current brake (F), shear actuator (G) and force sensor (H). Depicted is also the effective direction of the actuator.

Figure 7 depicts the test rig which is used for experiments. An asynchronous motor drives the planetary gearbox at a maximum speed of 10 000 min^{-1}. An eddy-current brake generates torques up to 50 Nm. A small spur-toothed planetary gearbox with a diameter of 60 mm, a gear ratio of 3 and 84 teeth on the ring gear is used. The test rig is equipped with multiple vibration sensors from which only one force sensor is used in this study as marked in Fig. 7 on the right side. The force sensor measures the force that is transmitted from the gearbox vibration into the surrounding structure. The piezoelectric shear actuator is mounted such that its effective direction conforms with the measurement direction of the force sensor. Signals are sampled at a frequency of 50 kHz. A speedgoat performance real-time target machine featuring an Intel Core i7 3770K 3.5 GHz quadcore CPU is used for signal processing and implementation of the control algorithm.

For the experiments an operating point with a gearbox input speed of 10 000 min^{-1} and a braking torque of 20 Nm is selected. The nominal gear mesh frequency at this operating point is 4666 Hz. However the planet carrier vibration order 85 (85 times the rotation frequency of the planet carrier) shows the highest vibration amplitude at a frequency of 4722 Hz as depicted in Fig. 9 for the situation with deactivated control. This vibration order 85 is selected for cancellation.

Figure 8 depicts the experimentally identified secondary path transfer function from actuator input voltage to measured force. The transfer function is rather complex with many structure resonances that are visible in the

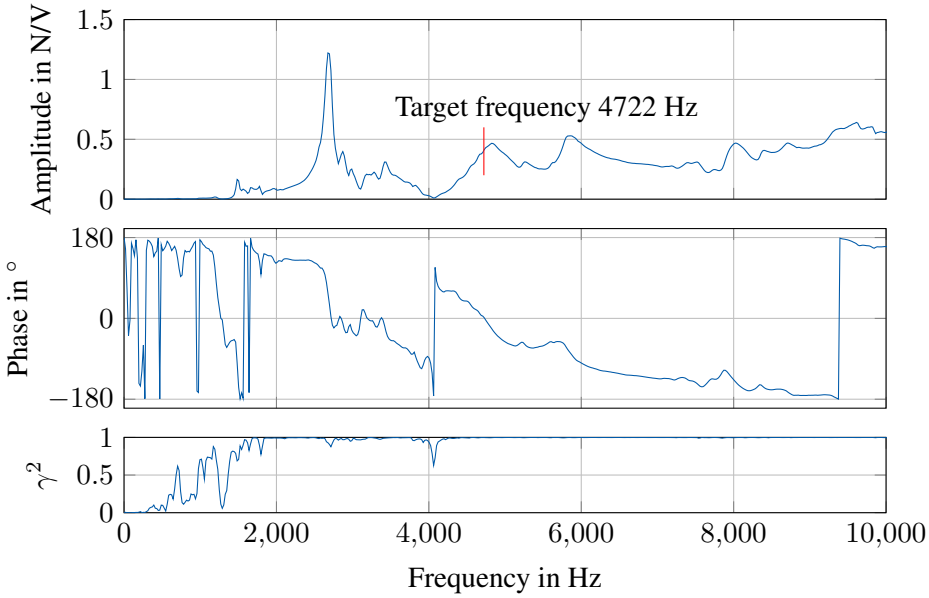


Figure 8: Identified secondary path transfer function from actuator input voltage to force sensor. Given at the bottom is the coherence (γ^2).

frequency range up to 10 kHz. The first eigenfrequency of the actuator is located at 2676 Hz. A specific force of 0.41 NV^{-1} can be generated using the actuator at the desired frequency.

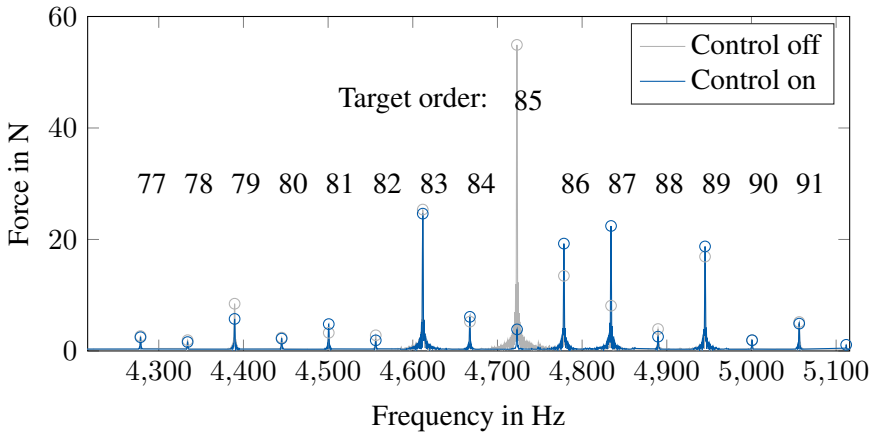


Figure 9: Frequency spectrum of force signal without and with activated control algorithm.

Figure 9 depicts the results of the experiment with activated control algorithm. The control algorithm is parameterized with $\alpha_{\text{FxLMS}} = 3.8e^{-4}$ and $\gamma_{\text{FxLMS}} = 2e^{-5}$. Using the piezoelectric shear actuator the target order can be significantly reduced from 54.9 N to 3.9 N which corresponds to a reduction of 93 %. To achieve this reduction an input peak-to-peak voltage of 120 V is required. This corresponds to 71 % of the maximum output voltage of the power amplifier. The vibration orders 86 and 87 are worsened when order 85 is controlled in Fig. 9. This phenomenon is investigated more in detail. For this purpose a simulation is conducted with a setting according to Fig. 6 where a measured force signal is used and the secondary path model as shown in Fig. 8 is represented by a 1500-tap FIR filter. In simulation and experiment the control algorithm is parameterized identically. Figure 10 depicts the simulation results and a comparison with a measurement from the experiment. Ordertracking based on least-mean-square algorithm is used to extract the amplitude of single vibration orders from the overall force signal. This allows a more detailed analysis. The amplitudes of all orders are slightly higher in simulation than in the experiment. That is because the vibration excitation shows

variations when the same operating point is measured multiple times at the test rig. At a time of 0.5 s the

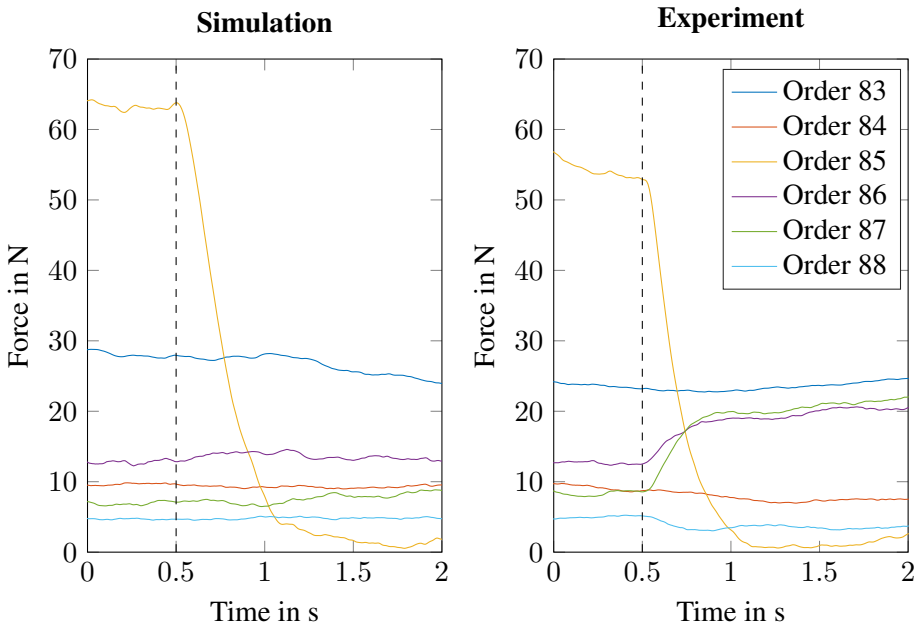


Figure 10: Comparison of simulation and experiment. Depicted are the amplitudes of the individual orders. Control is activated after 0.5 s (dashed line).

control algorithm is activated. Both simulation and experiment exhibit good agreement concerning reduction speed and residual force for the target order 85. However while in simulation the other orders remain constant this is not the case for the experiment where the amplitude of orders 86 and 87 are increased and order 88 is decreased. It is thus assumed that a coupling process between individual vibration orders exists in the planetary gearbox which cannot be represented by a simple FIR model of the secondary path.

Table 4: Comparison of the investigated actuator amplifier combinations.

Investigation	This contribution	Zech et al. [11]
Actuator Type	Piezo Shear	Piezo Stack
Amplifier Type	Analog	Switching
Weight Actuator in kg	0.0269	0.115
Capacitance in µF	0.09	1.5
Measured Force in N (at 4.7 kHz)	49.2	117
Utilization Output Voltage	71%	33%
Theoretic max. Force in N	69.3	354.6
Theoretic specific Force per Weight in $\mathrm{Nkg^{-1}}$	2576	3083
Theoretic specific Force per Capacitance in $\mathrm{N\mu F^{-1}}$	770	236

Finally the performance of the investigated actuator amplifier combination is compared with another which was examined by the authors in [11]. While the present work investigates the combination of piezoelectric shear actuator and analog power amplifier in [11] a piezoelectric stack actuator combined with a switching amplifier was used. Table 4 shows a comparison of both setups with their characteristics. It is interesting that the combination with piezo stack actuator exhibits slightly higher forces per weight of about $3000\,\mathrm{Nkg^{-1}}$. However the combination with shear actuator shows a force per capacitance that is more than three times higher. This indicates that forces can be generated more efficiently regarding driving current using piezo shear actuators than with piezo stack actuators. The reason for this is that less current is needed to drive an actuator with lower capacitance after Eq. 1. This results in lower current requirements for the power electronics. It has to be mentioned that the actuator amplifier combination investigated in this work operates

at maximum voltages of 175 V while the combination in [11] has a maximum voltage of 120 V. Nevertheless the combination investigated in [11] is better suited for AVC of the planetary gearbox as it is able to produce more than five times higher total forces in the desired frequency range.

6 Conclusion

A combination of a piezoelectric shear actuator and an analog power amplifier was investigated for use in an active vibration control system for planetary gearboxes. Power amplifiers were characterized experimentally and a model was used to tune the inertial mass shear actuator to the desired frequency range. The work revealed that the shear actuator is capable of actively reducing the most dominant vibration order of the gearbox. Related to electric capacitance forces can be generated more efficiently using piezoelectric shear actuators than with piezoelectric stack actuators. A coupling between amplitudes of individual vibration orders was observed in the experiment. This phenomenon could be examined further in detail in future studies. Furthermore the shear actuator should be scaled-up in order to be able to suppress multiple planetary gearbox vibration orders in parallel.

References

[1] R. Kraus, S. Herold, J. Millitzer, and T. Jungblut, *"Entwicklung aktiver Motorlagerungen auf Basis von Piezoaktoren,"* Automobiltechnische Zeitschrift, Vol. 116, Jan. 2014.

[2] A. Preumont, *Vibration Control of Active Structures: An Introduction*. Solid Mechanics and Its Applications, Springer Netherlands, 3 ed., 2011.

[3] P. Konstanzer, P. Jänker, and S. Storm, *"A piezo inertial force generator optimized for high force and low frequency,"* Smart Materials and Structures, Vol. 16, No. 4, p. 1260, 2007.

[4] W. Belgacem, A. Berry, and P. Masson, *"Active vibration control on a quarter-car for cancellation of road noise disturbance,"* Journal of Sound and Vibration, Vol. 331, pp. 3240–3254, July 2012.

[5] P. Persson, T. Lagö, and A. Norberg, *"Active Control of Sleeper-induced Sound in a High Speed Train,"* Proceedings of the Sixth International Congress on Sound and Vibration, pp. 1747–1752, 2018.

[6] I. Díaz and P. Reynolds, *"Robust saturated control of human-induced floor vibrations via a proof-mass actuator,"* Smart Materials and Structures, Vol. 18, 2009.

[7] C. Paulitsch, P. Gardonio, S. J. Elliott, P. Sas, and R. Boonen, *"Design of a lightweight, electrodynamic, inertial actuator with integrated velocity sensor for active vibration control of a thin lightly-damped panel,"* in *PROCEEDINGS OF ISMA -CD-ROM EDITION-*, (Leuven), 2004.

[8] P. Gardonio and C. G. Díaz, *"Downscaling of proof mass electrodynamic actuators for decentralized velocity feedback control on a panel,"* Smart Materials and Structures, Vol. 19, No. 2, p. 025004, 2010.

[9] G. A. Lesieutre, R. Rusovici, G. H. Koopmann, and J. J. Dosch, *"Modelling and characterization of a piezoceramic inertial actuator,"* Journal of Sound and Vibration, Vol. 261, pp. 93–107, Mar. 2003.

[10] J. Bös, E. Janssen, M. Kauba, and D. Mayer, *"Active vibration reduction applied to the compressor of an air-conditioning unit for trams,"* The Journal of the Acoustical Society of America, Vol. 123, pp. 3873–3873, May 2008.

[11] P. Zech, D. F. Plöger, R. Kraus, and S. Rinderknecht, "Piezoelektrische Inertialmassenaktoren zur aktiven Schwingungsreduktion von Zahneingriffsschwingungen im Kilohertzbereich," in *Smarte Strukturen und Systeme - Tagungsband des 4SMARTS-Symposiums 21.-22. Juni 2017*, Shaker Verlag, 2017.

[12] R. A. Burdisso and J. D. Heilmann, *"A new dual-reaction mass dynamic vibration absorber actuator for active vibration control,"* Journal of Sound and Vibration, Vol. 214, pp. 817–831, July 1998.

[13] A. Bilbao-Guillerna, I. Azpeitia, S. Luyckx, N. Loix, and J. Munoa, *"Low Frequency Chatter Suppression using an Inertial Actuator,"* in *International Conference on High Speed Machining*, (San Sebastian, Spain), pp. 1–6, Mar. 2012.

[14] C. González Díaz, C. Paulitsch, and P. Gardonio, *"Active damping control unit using a small scale proof mass electrodynamic actuator,"* Acoustical Society of America Journal, Vol. 124, p. 886, 2008.

[15] R. Kraus, J. Millitzer, J. Hansmann, and e. al, *"Experimental study on active noise- and active vibration-control for a passenger car using novel piezoelectric engine mounts and electrodynamic inertial mass actuators,"* in *25th International Conference on Adaptive Structures and Technologies, ICAST 2014*, pp. 307–319, 2014.

[16] F. Braghin, S. Cinquemani, and F. Resta, *"A low frequency magnetostrictive inertial actuator for vibration control,"* Sensors and Actuators A: Physical, Vol. 180, pp. 67–74, June 2012.

[17] M. H. Chen and M. J. Brennan, *"Active control of gear vibration using specially configured sensors and actuators,"* Smart Materials and Structures, Vol. 9, No. 3, p. 342, 2000.

[18] T. J. Sutton, S. J. Elliott, M. J. Brennan, K. H. Heron, and D. A. C. Jessop, *"Active isolation of multiple structural waves on a helicopter gearbox support strut,"* Journal of Sound and Vibration, Vol. 205, pp. 81–101, Aug. 1997.

[19] F. Claeyssen, F. Barillot, N. Lhermet, C. May, C. Natale, and A. Pages, *"Tunable Proof Mass Actuator Based on a Pendulum Structure,"* pp. 287–290, 2008.

[20] R. Karsten, M. Ibis, P. Groche, and H. F. Schlaak, *"Investigation of an Applicability of Dielectric Elastomer Actuators (DEA) for Active Vibration Attenuation on Planar Structures,"* (Merano), Mar. 2013.

[21] G. Loussert, D. Angleviel, and M. Delbaere, *"Moving Magnet Linear Actuator for Active Vibration Control,"* MTZ worldwide, Vol. 77, pp. 54–59, Jan. 2016.

[22] S.-B. Choi, M.-S. Seong, S. H. Ha, J. Jeon, and J. W. Sohn, *"Design of a piezostack-based inertial actuator and application to vibration control: experimental investigation,"* Proceedings of the Institution of Mechanical Engineers, Part I: Journal of Systems and Control Engineering, Vol. 225, pp. 1115–1124, Dec. 2011.

[23] C. Asckler, G. A. Lesieutre, G. H. Koopmann, and C. L. Davis, *"Inertial piezoceramic actuators for smart structures,"* in *SPIE Proceedings Vol. 2447*, Vol. 2447, pp. 14–25, 1995.

[24] S. Herold, D. Mayer, T. Melz, and T. Röglin, "Design and Test of a Piezoelectric Inertial Mass Actuator for Active Vibration Control," in *Vibration Engineering and Technology of Machinery*, pp. 587–597, Springer, Cham, 2015.

[25] D. F. Plöger, P. Zech, and S. Rinderknecht, "Experimental identification of high-frequency gear mesh vibrations in a planetary gearbox," in *Proceedings of ISMA2016 International Conference on Noise and Vibration Engineering*, pp. 911–924, Sept. 2016.

[26] D. F. Plöger, P. Zech, and S. Rinderknecht, *"Real-Time Order Tracking of Gear Mesh Vibration in High Speed Planetary Gearboxes,"* MATEC Web of Conferences, Vol. Volume 148, 2018, Feb. 2018.

[27] A. J. Fleming, *"Techniques and considerations for driving piezoelectric actuators at high speed,"* in *Modeling, Signal Processing, and Control for Smart Structures 2008*, Vol. 6926, p. 69260E, International Society for Optics and Photonics, 2008.

[28] T. Jungblut, *Ein Beitrag zur modellbasierten, hybriden Entwicklung elektromechanischer Systeme zur Schwingungsminderung*. Dissertation, Shaker Verlag, Aachen, Feb. 2016.

Self-adaptive fluid-based absorbers for impact mitigation and vibration damping

C. Graczykowski[1], R. Faraj[1]
[1] Institute of Fundamental Technological Research of the Polish Academy of Sciences
Pawinskiego 5B, 02-106, Warsaw, Poland
e-mail: **cezary.graczykowski@ippt.pan.pl**

Abstract
The paper presents development of innovative, self-adaptive, fluid-based absorbers and investigation of their application for mitigation of impacts and forced vibrations. The considered absorbers are composed of two chambers filled with fluid and separated by a piston equipped with a controllable valve. The valve enables control of the fluid flow between the chambers and adjustment of the actual value of force generated by the absorber. The aim of the research is to develop the strategy of valve control providing self-adaptive operation of the absorber ensuring dissipation of submitted energy by using minimal value of generated force. The paper includes description of self-adaptive impact absorber, presentation of the control system and numerical simulation of its effectiveness in the case of impact excitation and harmonic loading. It is concluded that self-adaptive system provides optimal mitigation of impact excitation, but its response in the case of harmonic loading is not always optimal and requires further improvement.

1. Introduction

Mitigation of impact loads and damping of vibrations remain challenging engineering problems. In case of impact excitation the main challenge is short period of the process (several to tens of milliseconds). In turn, in the case of harmonic excitation the main challenge is continuous supply of the external energy to the system and the requirement of its repetitive operation. Nowadays, the recent fast progress in technologies of sensors and actuators enables replacing classical passive systems by more efficient semi-active or active devices. It can be observed that the research efforts are dedicated separately to mitigation of impact excitation and damping of vibrations. The most important lines of research in these disciplines are briefly discussed below.

The important research area in the field of semi-active impact mitigation is the so-called Adaptive Impact Absorption (AIA) [1, 2]. The concept assumes that optimal shock absorbing system is composed of embedded system of sensors, the hardware controller and adaptive elements (so called structural fuses), which control the process of energy dissipation in semi-active way. The system constructed according to the principle of AIA utilizes data measured by sensors to identify the actual impact loading and performs adaptation providing optimal mitigation of impact. Typically, the objective of adaptation is to dissipate the entire impact energy with the lowest value of deceleration of the impacting object or the lowest overload of the impacted structure. The most popular AIA problems concern design of adaptive fluid based absorbers. The research in this field was focused on hydraulic [3, 4, 5, 6] or pneumatic [7, 8, 9] dampers equipped with fast controllable valves, as well as dampers based on magneto-rheological [10, 11, 12, 13] or electro-rheological fluids [14]. Nevertheless, other innovative types of absorbers e.g. based on inertial effects were also analyzed [15]. The motivation for development of these systems was a number of practical applications such as mitigation of frontal collisions of cars, high performance landing gears or seismic isolation of structures.

The research concerning semi-active vibration damping is nowadays very extensive and relates to various types of problems and applications. In general, the problems of vibration damping can be divided into two separate groups: damping of free vibrations and mitigation of forced vibrations. In the former case the

objective is to dissipate the energy introduced to the structure and to decrease of its oscillatory motion possibly fast. In turn, in the latter case the objective is to dissipate submitted energy and to obtain desired response of the structure. In both groups of problems various types of dissipaters and control techniques are applied. Among the most innovative solutions we can distinguish application of tuned mass damper with inerter of changeable inertance [16], controllable structural nodes with an on/off ability to transmit moments [17] and pneumatically controlled granular structure [18], to mention just a few. The practical applications of the vibration techniques encompass damping of flexible space structures [19, 20], vehicle-track/span systems [21, 22], design of suspension and seismic isolation systems [23, 24], damping of torsional vibrations in electro-mechanical systems [25, 26].

The review of the above mentioned systems for semi-active impact mitigation and vibration damping reveals that most of these systems require the knowledge about applied excitation and they do not operate optimally when variations of system parameters or harsh disturbances occur. Moreover, there are no universal control strategies which can be applied both the problem of impact mitigation and vibration damping. This paper attempts to fill this gap in the subject literature by proposing application of self-adaptive system to both mitigation of impact and damping of vibrations. The concept of such system was introduced by authors in [27] and developed in [28]. Herein its application will be extended to the problem of mitigation of forced vibrations, which was not analyzed before.

2. Basic concept of self-adaptive absorber

The proposed absorber serving for impact mitigation and vibration damping is composed of rigid compartment and two fluid chambers, Fig. 1. The chambers are separated by the piston equipped with valve, which enables control the actual mass flow rate of the fluid in order to adjust the actual value of reaction force generated by the absorber. In general, the chambers can be filled with either hydraulic or pneumatic fluid, however further discussion will be illustrated on the example of pneumatic absorber. The mathematical model of the absorber is described in previous paper of the authors [28]. The absorber will be subjected to two types of dynamic excitation:

- impact loading modeled by mass of the impacting object and its initial velocity (Fig. 1a),
- harmonic excitation modeled by time-dependent harmonic force (Fig. 1b).

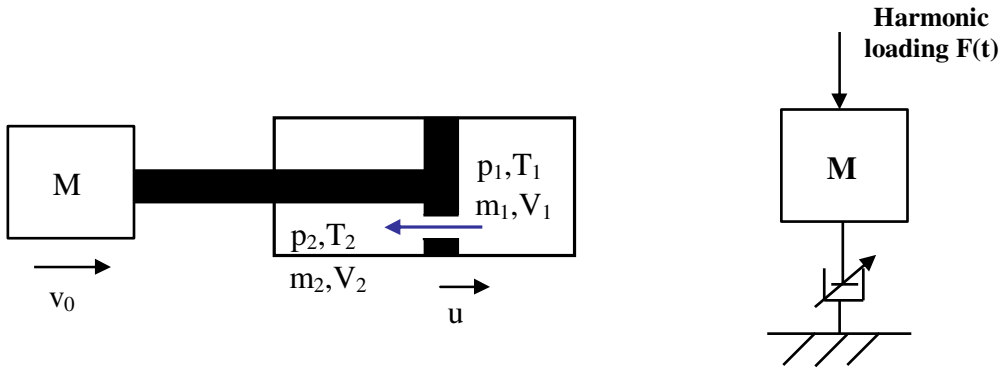


Figure 1: The considered problems: a) adaptive pneumatic absorber subjected to impact excitation, b) the same absorber (shown schematically) under harmonic loading

In the first case the objective of the adaptive absorber is to dissipate initial kinetic energy of the impacting object and decrease its velocity to zero with minimal level of deceleration. In the second case the considered object does not have initial kinetic energy, however the energy is continuously submitted to the system by the action of the external harmonic force. As a result, at the beginning of the process the considered object is accelerated by external force and its velocity increases. Therefore, the objective of the adaptive absorber is to counteract the external force and to stop the object with minimal level of generated reaction force and minimal level of corresponding deceleration. In addition, the proposed self-adaptive absorber has to fulfill three following requirements:

- automatic, online adjustment to actual dynamic loading with neither prior knowledge of the external load nor application of load identification system,
- robust operation in case of disturbances such as occurrence of additional damping or friction forces generated by the absorber,
- robust operation in case of unexpected change of system parameters such as sudden leakage of the fluid from one of the chambers.

In order to fulfill the above stated strict requirements three innovative elements of the control strategy are introduced. At first, the Automatic Path Finding (APF) algorithm is applied to determine optimal system path during the initial stage of operation by using complete information about actual system kinematics and the condition of kinematic optimality for the remaining part of the process. Secondly, the dedicated Hybrid Path Tracking (HPT) algorithm, which utilizes both continuous and bang-bang control, is used for robust tracking of determined system path. The former control law is based on mathematical model of the absorber and it is applied during typical operational conditions, whereas the latter one is used during short periods of system disturbance. Thirdly, the Automatic Path Update (APU) algorithm based on full kinematic feedback is triggered after the occurrence of harsh disturbances or changes of system parameters in order to properly modify previously determined system path. Each of these processes is performed in fully automatic way during operation of the self-adaptive system.

In order to make operation of the system easily understandable we will precisely describe each algorithm included in the proposed control strategy together with corresponding fundamental mathematical formulae.

Automatic Path Finding (APF) – the algorithm performed during first stage of impact absorption (pure energy accumulation – valve closed) until actual value of piston deceleration allows to decrease velocity of the impacting object to zero within remaining stroke of the absorber. The APF is terminated at the moment t_x when the following kinematic condition is satisfied:

$$|a(t_x)| \geq |a_{opt}| \tag{1}$$

The optimal piston deceleration $|a_{opt}|$ ensures dissipation of entire impact energy within absorber stoke d and can be described by the formula:

$$|a_{opt}| = \frac{v(t_x)^2}{2(d-u(t_x))} \tag{2}$$

The finite frequency of state measurements and data processing causes that deceleration of the piston at time instant t_x usually differs from the value $|a_{opt}|$. In such situation we cannot obtain exact realization of the optimal system path and thus we introduce the tolerance interval defining acceptable range of deceleration of the impacting object.

Hybrid Path Tracking (HPT) – the algorithm performed after termination of APF, aimed at possibly best following of the optimal system path ensuring dissipation of entire impact energy within available absorber stroke. The control law applied by HPT is determined for time period $\langle t_i, t_{i+1}\rangle$ and takes the form:

$$A_v^i(t) = \begin{cases} A_v^{min} & if \quad |a(t_i)| < |a_{opt}| \\ A_v^{max} & if \quad |a(t_i)| > |a_{opt}^+| \\ A_v^{opt}(t) & if \quad |a_{opt}| \leq |a(t_i)| \leq |a_{opt}^+| \end{cases} \tag{3}$$

The bang-bang control is performed when absorber operates outside the tolerance interval and it is aimed at the fastest possible return of the system to the optimal path. The upper limit of deceleration tolerance interval is designated by $|a_{opt}^+|$ and it corresponds to assumed maximum shortening of the admissible stroke of the absorber Δu_{tol}:

$$|a_{opt}^+| = \frac{v(t_x)^2}{2(d-\Delta u_{tol}-u(t_x))} \tag{4a}$$

Alternatively, the value $\left|a_{opt}^{+}\right|$ can be defined with the use of surplus of acceleration Δa_{tol} or the surplus of velocity Δv_{tol}:

$$\left|a_{opt}^{+}\right| = \left(\frac{v(t_x)^2}{2(d-u(t_x))} + \Delta a_{tol}\right), \quad \left|a_{opt}^{+}\right| = \left(\frac{(v(t_x)+\Delta v_{tol})^2}{2(d-u(t_x))}\right) \tag{4b,c}$$

The continuous change of the valve opening providing generation of constant reaction force can be calculated by using the model of thermodynamic and flow processes taking place in the absorber, see [27]:

$$A_v^{opt}(t) = f(u_x, v_x, a_x, p_{1x}, p_{2x}, t) \tag{5}$$

Automatic Path Update (APU) – the algorithm ensuring successful operation of the impact absorbing system in case of harsh disturbances, changes of system parameters or need of system re-adaption (e.g. series of unknown impact excitations). The APU algorithm sequentially updates the optimal value of system deceleration $\left|a_{opt}\right|$ determined with the use of APF algorithm. It operates after each control period and calculates the actual optimal value of deceleration at time instant t_i by using the formula:

$$\left|a_{opt}\right| = \frac{v(t_i)^2}{2(d-u(t_i))} \tag{6}$$

Let us note that proper operation of the self-adaptive system requires also sequential update of the upper limit of deceleration tolerance interval $\left|a_{opt}^{+}\right|$.

Let us note that in the proposed control method the tolerance interval for deceleration of the impacting object $\langle a_{opt}, a_{opt}^{+}\rangle$ is asymmetric, which directly results from the assumption that admissible displacement of the piston is in the range $\langle d - \Delta u^{tol}, d\rangle$. Such assumption ensures successful operation of the absorber – the piston will never hit absorber's bottom if the tolerance value is appropriately selected for the available frequency of measurements and data processing. In order to reduce effort and possible mistakes appearing during system tuning we can apply the automatic adaptation of the tolerance levels at time instant t_x which terminates operation of the APF algorithm; it will be discussed in further section.

As mentioned above, the definition of upper limit of deceleration tolerance interval $\left|a_{opt}^{+}\right|$ can be based on maximum shortening of the absorber stroke Δu_{tol} (displacement tolerance), velocity surplus $\Delta \mathrm{v_{tol}}$ or acceleration surplus Δa_{tol}. Selection of different definitions leads to differences in system behavior. In particular, assumption of acceptable level of absorber stroke shortening (Eq. 4a) results in increasing in time upper limit of deceleration tolerance interval. In such case, when no disturbances are present, the control system will not change the level of generated reaction force. In contrast, application of definition based on acceleration surplus (Eq. 4a) and velocity surplus (Eq. 4b) may result in often automatic corrections of the preliminary determined level of generated force. Such behavior is beneficial when extremely fast measurement and data processing system can be implemented. Nevertheless, in case of relatively low frequency of system operation, it is better to define the deceleration tolerance interval based on maximum shortening of the absorber's stroke. As a result, temporary system destabilization will be avoided and system efficiency maintained.

3. Control system architecture

According to introduced definitions of algorithms discussed in previous section they can be considered as processes appearing during system operation. Graphical representation of the processes conducted during unknown impact mitigation is shown in Fig. 2. The APF is performed until deceleration of the piston and impacting object is insufficient and maintaining its constant value would result in hitting the absorber bottom (the case of impact energy not entirely absorbed). When kinematic condition (Eq. 2) is met, "Scenario 2" is valid and the APF process terminates. In further operation the HPT has to be performed to ensure successful operation of the system. Realization of the actually optimal control path with acceptable tolerance indicates that absorber still operates according to "Scenario 2" so that continuous control of valve opening is applied. If unexpected disturbances occur and cause the reaction force jumps out the tolerance interval, the control system has to react immediately. Otherwise, too low value of reaction force ("Scenario 1") will result in the piston hitting the absorber bottom or too high value of reaction force

("Scenario 3") will cause that deceleration will not be optimally minimized and small rebound before the end of the absorber stroke will occur. In order to reduce influence of disturbances and to maintain high efficiency of the absorber the HPT will close the valve for "Scenario 1" or fully open it for "Scenario 3". The fact that system deceleration remains outside the optimal path for certain period of time causes the automatic path recalculation is required and it is performed by the APU algorithm.

Similarly, if next impact excitation occurs before the end of the first impact absorption process, the system will determine new actually optimal path by applying APU and will track this path with the use of HPT. It should be highlighted that determination of actually optimal path of the system is based on the kinematic condition describing optimality of the remaining part of the impact absorption process. This indicates that if there are no changes of impact conditions, the system will follow (with acceptable tolerance) the globally optimal solution. In turn, when the process includes unpredicted disturbances or several unknown impact excitations, the system will operate in robust, suboptimal way.

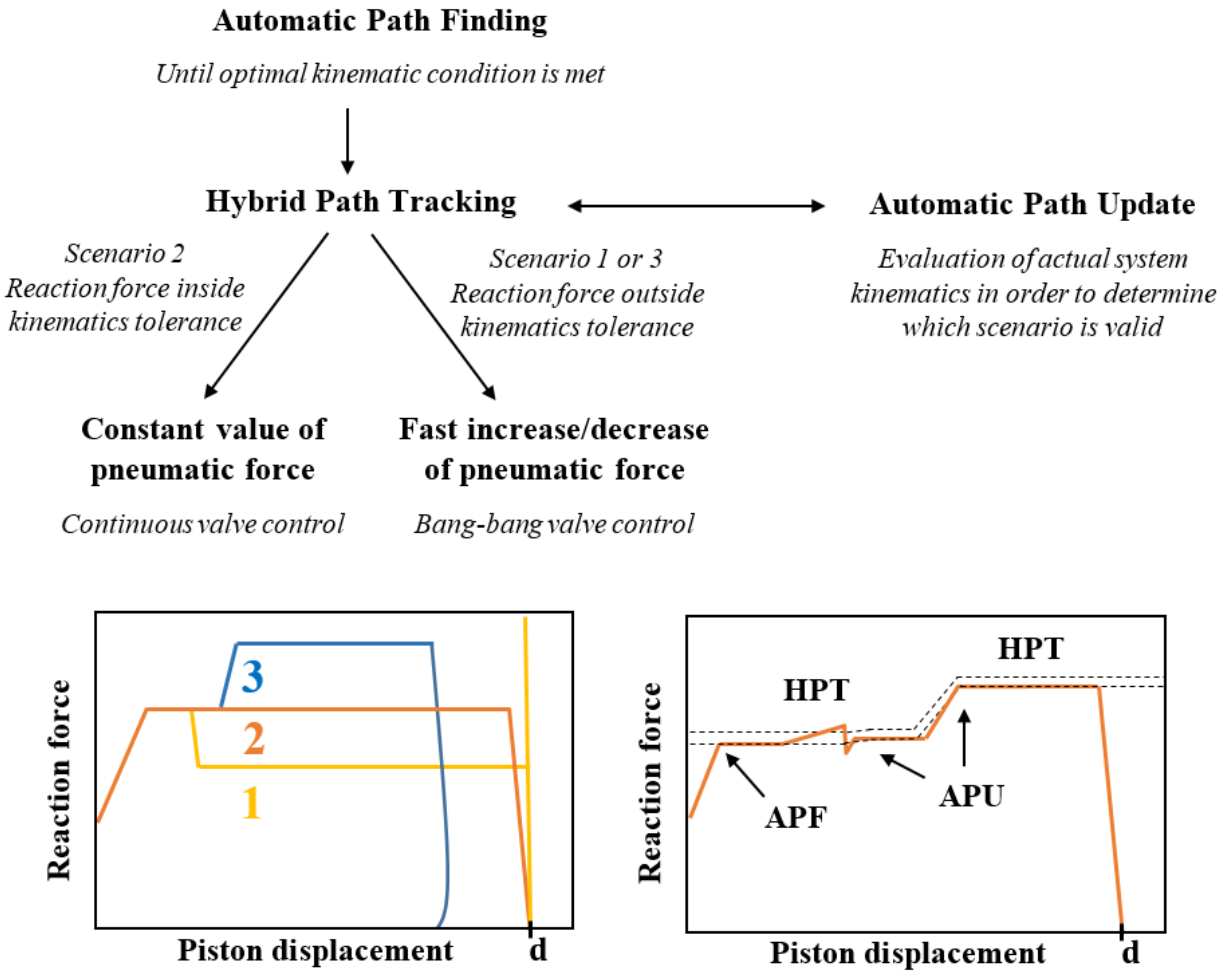


Figure 2: Scheme of self-adaptive system operation

Following the general idea of discussed self-adaptive impact absorbing system, we will introduce a block diagram of the control system ensuring desired system operation (Fig. 3). The considered system is subjected to dynamic excitation. The system response is measured by kinematic sensors (e.g. accelerometers, linear encoders) and pressure sensors (internal pressure in both absorber chambers). Path control system based on actual piston kinematics determines which scenario of system operation is valid at the moment. In case of too low or too high value of piston deceleration the bang-bang control of the valve is applied. Otherwise, the piston deceleration is optimal with acceptable tolerance and the reaction force has to be maintained constant. Therefore, measured values of internal pressure in absorber chambers and measured kinematic quantities are used to determine the optimal continuous valve control by applying mathematical model of the absorber.

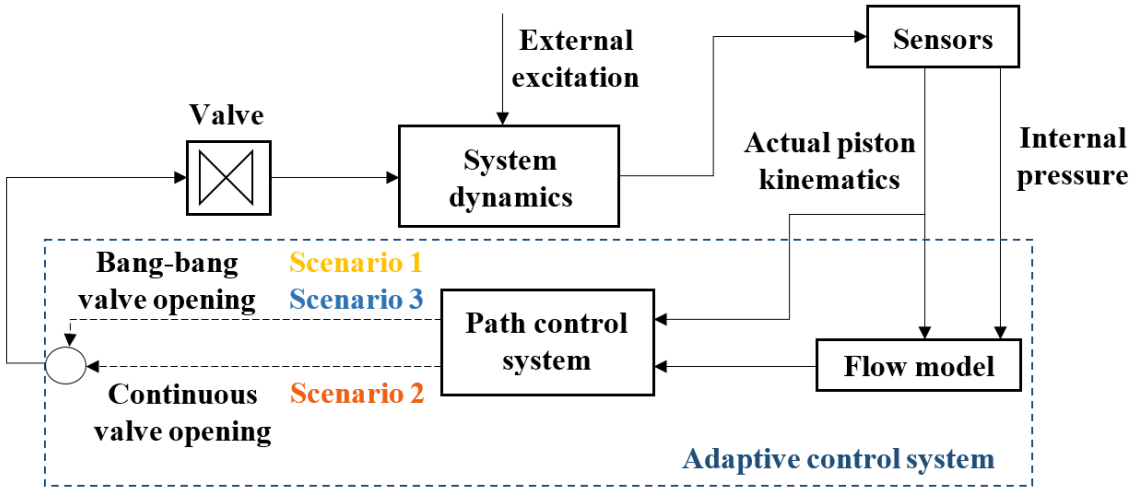


Figure 3: Block diagram of proposed self-adaptive control system

It should be indicated that the proposed control system does not have typical tuning parameters as in e.g. PID or LQR controllers. Nevertheless, two system parameters have a significant influence on the system operation and they have to be considered when control system is designed: i) frequency of kinematics and internal pressure measurements and ii) time of data processing. In further discussion we will use the term Frequency of Control Recalculation (FCR) resulting from speed of measurements gathering and data processing. The finite value of FCR results in small inaccuracy of the system operation and tracking of actually optimal system response with certain delay. In practice, the maximum achievable value of FCR is imposed in advance because of technological limitations. Because of that the tolerance imposed on optimal value of piston deceleration should be adjusted to the frequency of system operation and can be treated as tuning parameter of the control system.

4. System operation under impact excitation

The present section is aimed at investigation on the response of self-adaptive system under impact loading with a special attention to influence of the displacement tolerance determining the interval of acceptable piston decelerations, which can be treated as nearly optimal values. The influence of under- and overestimation of the upper limit of displacement tolerance is shown in Fig. 4

According to the graph in Fig. 4a, which presents response of the system operating with high value of FCR, overestimated value of the tolerance can result in lack of dissipation of the entire impact energy. This effect results from the fact that high frequency system finds the optimal value of absorber reaction force with high precision. In this situation assumption of high tolerance for maximum piston displacement is in contradiction to achieved accuracy of finding the optimal value of pneumatic force. When assumed final displacement of the piston $d - \Delta u_{tol}$ is exceeded, the valve is automatically opened resulting in light impact of piston against absorber bottom. This indicates that for system with high values of FCR the displacement tolerance should be selected at appropriately small level or some adjustment of proposed control method should be made.

If the tolerance is decreased to the proper value, the entire impact energy will be dissipated within assumed available stroke, simultaneously ensuring successful minimization of absorber reaction force. On the other hand, if displacement tolerance is decreased excessively, some overshoots of reaction force may appear (Fig. 4b), despite this the entire absorber stroke is finally utilized with better precision. In contrast, Fig. 4c presents behavior of the system operating with low values of FCR. It can be noticed that increase of displacement tolerance reduces force overshoot but also results in shortening of the utilized stroke. It can be concluded that value of displacement tolerance for optimal deceleration interval should be selected carefully. Depending on the operational requirements, the system without overshoots in the reaction force or system with higher stroke utilization can be a preferred option.

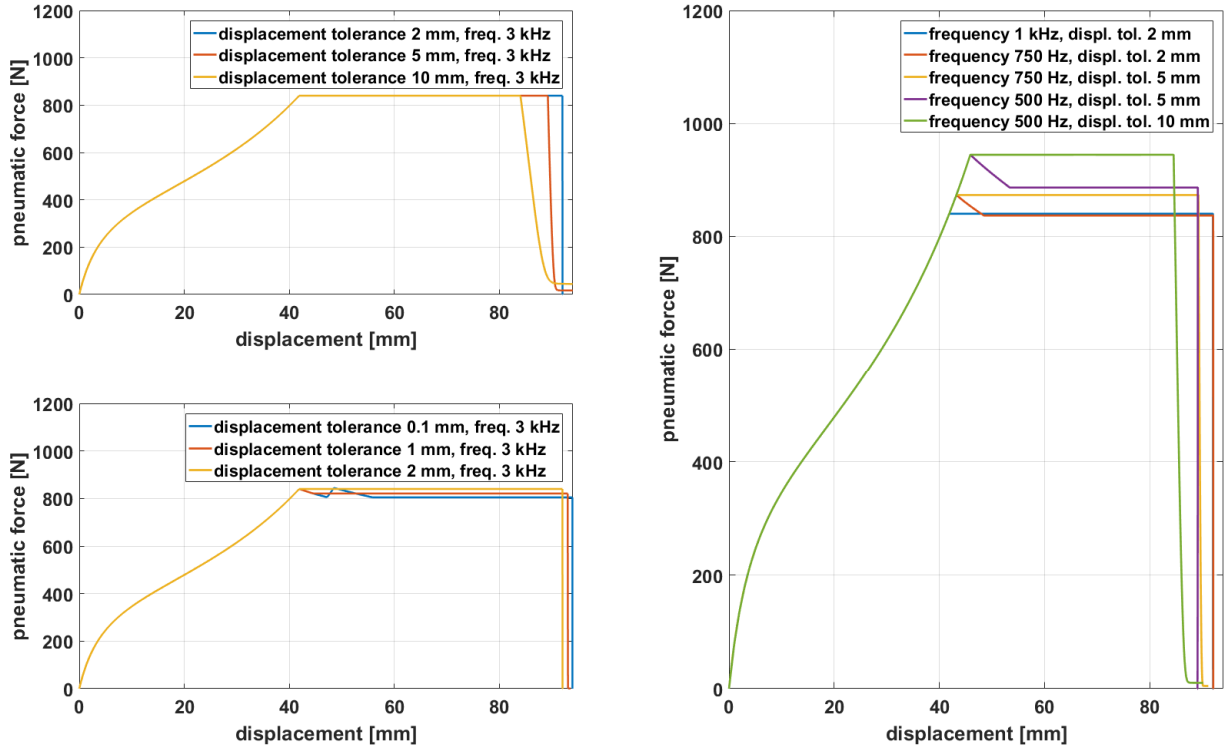


Figure 4: Influence of control recalculation frequency and optimality condition tolerance on the system response under single impact excitation

Automatic adjustment of displacement tolerance

Presented above analyses of the influence of displacement tolerance revealed difficulties in appropriate selection of tolerance for given value of FCR. In order to avoid this problem a simple automatic adjustment of the tolerance value can be introduced. At the beginning of impact absorption process we assume a certain value of the piston displacement tolerance Δu_{tol}, as it had been done before. When the reaction force reaches the value within the range corresponding to the optimal deceleration interval $\langle |a_{opt}|, |a_{opt}^{+}| \rangle$ and thus HPT is activated, the displacement tolerance is recalculated to ensure that entire impact energy will be dissipated within absorber stroke according to the equation:

$$\Delta u_{tol}^{adapted} = d - u(t_i) - \frac{v(t_i)^2}{2|a(t_i)|} \tag{7}$$

Thanks to tolerance adjustment made when the HPT is activated, the impact energy will be entirely dissipated for both low and high values of FCR independently on the initially assumed value of displacement tolerance. In Fig. 5 the response of systems operating with different values of FCR and initial displacement tolerance $\Delta u_{tol} = 5\ mm$ are shown. In case of low level of FCR the system may need to correct the path before initially assumed value of displacement tolerance and corresponding deceleration interval are met. Nevertheless, when the optimal deceleration interval is reached the displacement tolerance is recalculated to the value of actual deceleration $|a(t_i)|$ being in the range $\langle |a_{opt}|, |a_{opt}^{+}| \rangle$. As a result, maintaining the pneumatic force on the corresponding constant level results in stopping the impacting object on the distance $\left(d - \Delta u_{tol}^{adapted}\right)$ without any rebound and without hitting the end of absorber stroke. Proposed adjustment of the control principle provides also successful operation of the system working with high value of FCR and low value of displacement tolerance. The proposed control system with automatic adjustment of displacement tolerance will always ensure dissipation of entire impact energy within absorbers stroke.

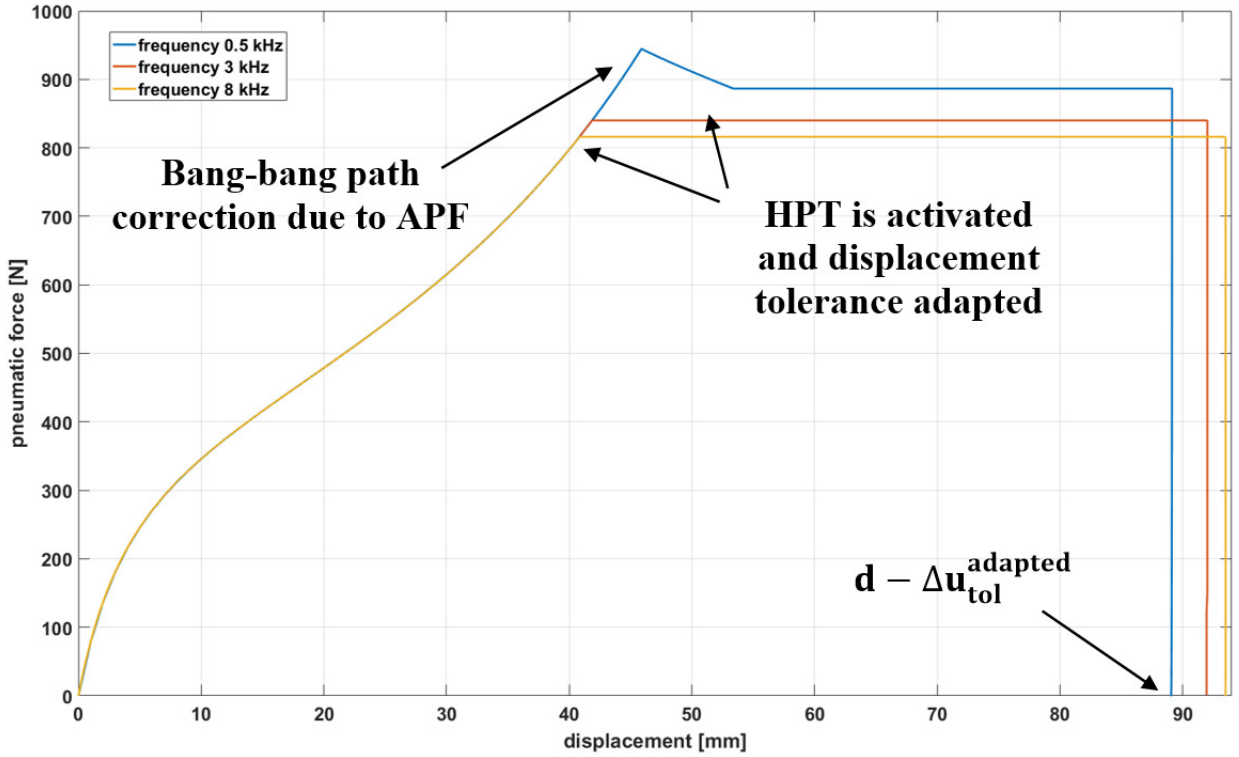
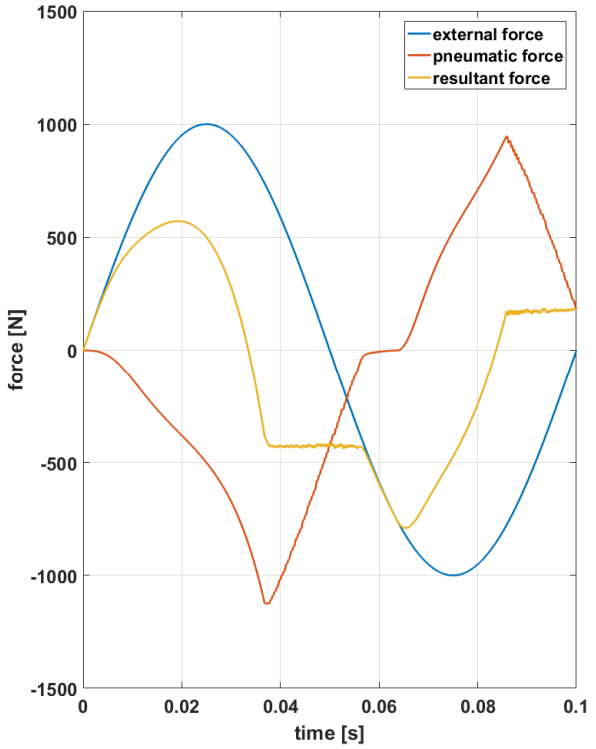


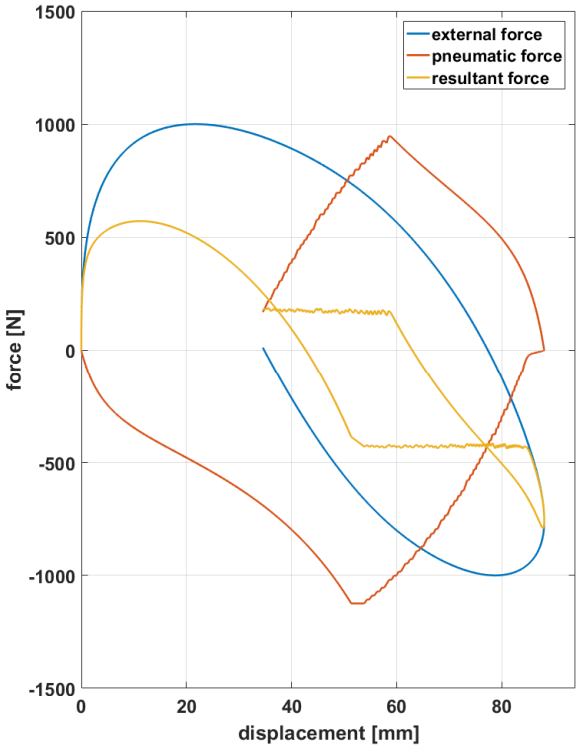
Figure 5: Operation of the system with automatic adaptation of displacement tolerance

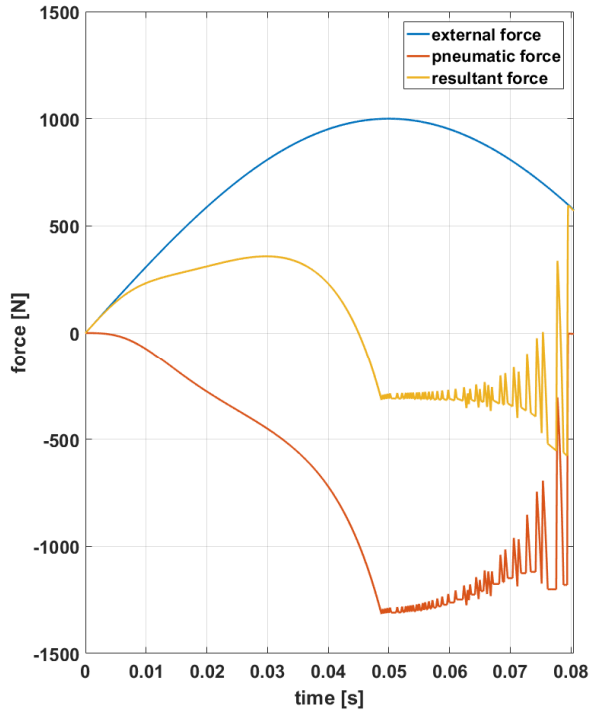
5. System operation under harmonic loading

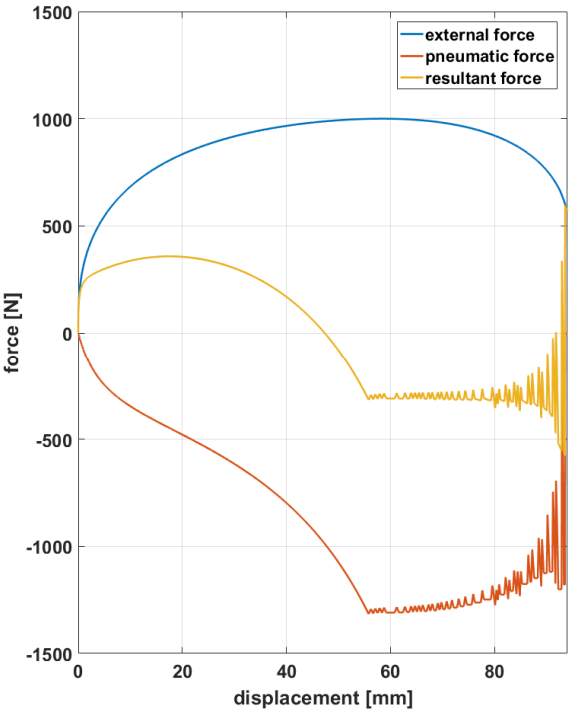
In this section the proposed self-adaptive control system is applied for mitigation of the harmonic excitation. Three different frequencies of excitation are investigated, whereas the control is always performed with frequency of 5 kHz. The conducted numerical simulations indicate that response of self-adaptive system in three considered cases is substantially different. In case of the lowest frequency of harmonic excitation equal to 5Hz the impacting object is stopped at the end of cylinder stroke before the cycle of harmonic excitation is accomplished. This indicates unfavorable situation when energy is still submitted to the system but there is no remaining stroke left to dissipate this energy (Fig. 6a). In contrast, in case of the largest frequency of impact excitation equal to 10 Hz the excitation drops below zero before the impacting object is stopped. This indicates non-optimal situation in which deceleration of the object suddenly rises and the entire stroke of the absorber is not utilized (Fig. 6b). Therefore, we can expect that there exists the frequency of excitation for which the object is stopped exactly at time instant when single excitation cycle is accomplished. Indeed, the numerical simulation shows that such situation occurs for the excitation frequency of 6.7 Hz. In this case the entire impact energy is dissipated and the object is stopped almost at the end of cylinder's stroke.

We conclude that proposed self-adaptive system does not provide optimal mitigation of the excitation of various frequencies. In order to improve the operation of the system the level of deceleration, which is maintained constant should take into account compatibility with time when single cycle of the harmonic excitation finishes. Development and testing of such system is the objective of current research.


external force
pneumatic force
resultant force
force [N]
time [s]
1500
1000
500
0
-500
-1000
-1500
0
0.02
0.04
0.06
0.08
0.1


external force
pneumatic force
resultant force
force [N]
displacement [mm]
1500
1000
500
0
-500
-1000
-1500
0
20
40
60
80


external force
pneumatic force
resultant force
force [N]
time [s]
1500
1000
500
0
-500
-1000
-1500
0
0.01
0.02
0.03
0.04
0.05
0.06
0.07
0.08


external force
pneumatic force
resultant force
force [N]
displacement [mm]
1500
1000
500
0
-500
-1000
-1500
0
20
40
60
80

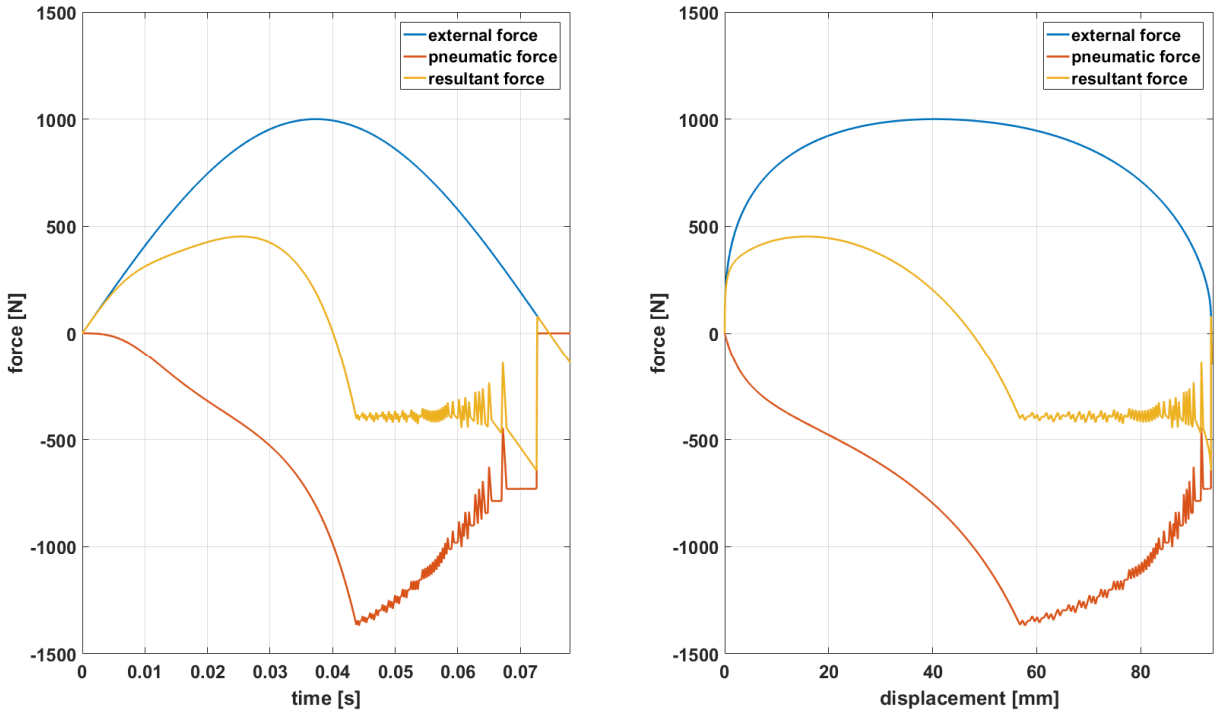


Figure 6: Response of self-adaptive system to harmonic excitation of various frequencies: a) 5 Hz (unacceptable response), b) 10 Hz (non-optimal response), c) 6.7 Hz (optimal response)

6. Conclusions

Performance of the innovative self-adaptive control system was thoroughly tested by using double-chamber pneumatic absorber subjected to impact excitation and harmonic loading. It was proved that the control system equipped based on APF, HPT and APU has the ability of automatic determination of the optimal system path, its robust realization and appropriate on-line modification as a response to disturbance. In the case of impact loading the requirements of energy dissipation and force minimization are always successfully fulfilled so it can be concluded that proposed control system is fully self-adaptive and it is superior to standard passive and typical adaptive absorbers used for impact and vibration mitigation. However, in case of harmonic excitation the current self-adaptive operation does not lead to optimal energy dissipation and some improvements of the control strategy have to be introduced.

Acknowledgements

The scientific work was funded from the budget for education in the years 2015–2019 as a research project within the program under the name ‘Diamond Grant’. Support of the National Science Centre, Poland, granted through the project Ad-DAMP (DEC-2014/15/B/ST8/04363), is gratefully acknowledged.

References

[1] J. Holnicki-Szulc, C. Graczykowski, G. Mikułowski, A. Mróz, P. Pawłowski, *Smart Technologies for Adaptive Impact Absorption,* Solid State Phenomena, Vol. 154, (2009), pp. 187-194.

[2] J. Holnicki-Szulc, C. Graczykowski, G. Mikułowski, A. Mróz, P. Pawłowski, R. Wiszowaty, *Adaptive Impact Absorption - the Concept and Potential Applications*, International Journal of Protective Structures, Vol. 6, No. 2, (2015), pp. 357-377.

[3] S.A.W. Jawad, *Intelligent hydraulic bumper for frontal collision mitigation,* ASME Applied Mechanics Division, Vol. 218, (1996), pp. 181-189.

[4] G.L. Ghiringhelli, *Testing of semi-active landing gear control for a general aviation aircraft*, AIAA Journal of Aircraft, Vol. 37, No. 4, (2000), pp. 606-616.

[5] R.L. Teixeira, F.P. Neto, J.F. Ribeiro, *Modelling and experimental investigation of an active damper*, Shock and Vibration, Vol. 13, No 4-5, (2006)

[6] Mikułowski G., Jankowski Ł., Adaptive Landing Gear: optimum control strategy and potential for improvement, *Shock and Vibration* 16(2), 2009, pp. 175-194.

[7] R.N. Khamitov, G.S. Aver'yanov, A.B. Korchagin, *Pneumatic Shock Absorber with an Active Damping System*, Russian Engineering Research, Vol. 29, No. 9, (2009), pp. 871–873.

[8] C. Graczykowski, *Mathematical models and numerical methods for the simulation of adaptive inflatable structures for impact absorption*, Computers and Structures, Vol. 174, (2016), pp. 3-20

[9] G. Mikułowski, R. Wiszowaty, *Pneumatic Adaptive Absorber: Mathematical Modelling with Experimental Verification*, Mathematical Problems in Engineering, Vol. 2016, (2016), pp. 7074206-1-14

[10] H. Gavin, J. Hoagg, M. Dobossy, *Optimal design of MR dampers,* in: *Proceedings of U.S.-Japan Workshop on Smart Structures for Improved Seismic Performance*, Seattle WA, (2001).

[11] D. Woo, S.B. Choi, Y.T. Choi, N.M. Wereley, *Frontal Crash Mitigation using MR Impact Damper for Controllable Bumper*, Journal of Intelligent Material Systems and Structures, Vol. 18, (2007), pp. 1211-1215.

[12] G. Mikułowski, J. Holnicki-Szulc, *Adaptive landing gear concept-feedback control validation*, Smart Matererials and Structures, Vol. 16, (2007), pp. 2146–2158.

[13] C. Graczykowski, P. Pawłowski, *Exact physical model of magneto-rheological damper*, Applied Mathematical Modelling, Vol. 47, (2017), pp. 400-424

[14] Z. Lou, R.D. Erwin R.D., C.B. Winkler, F.E. Filisko, *An electro-rheologically controlled semi-active landing gear*, SAE paper 931403, Langley Research Centre, (1993).

[15] R. Faraj, J. Holnicki-Szulc, L. Knap, J. Senko, *Adaptive inertial shock-absorber*, Smart Mater. Struct. Vol. 25, No.3, (2016), pp. 035031-1-9.

[16] M. Lazarek, P. Brzeski and P. Perlikowski, *Design and identification of parameters of tuned mass damper with inerter which enables changes of inertance*, Mechanism and Machine Theory, Vol. 119, (2018), pp. 161-173

[17] B. Popławski, G. Mikułowski, A. Mróz, Ł. Jankowski, *Decentralized semi-active damping of free structural vibrations by means of structural nodes with an on/off ability to transmit moments*, Mechanical Systems and Signal Processing, Vol.100, (2018), pp. 926-939.

[18] J.M. Bajkowski, B. Dyniewicz, C.I. Bajer, *Semi-active damping strategy for beams system with pneumatically controlled granular structure*, Mechanical Systems and Signal Processing, Vol.70-71, (2016), pp. 387-396

[19] L. Gaul, J. Lenz, D. Sachau, *Active damping of space structures by contact pressure control in joints*, Mech.Struct. Mach., Vol. 26, No.1, (1998), pp. 81–100.

[20] A. Mróz, J. Holnicki-Szulc, J. Biczyk, *Prestress accumulation–release technique for damping of impact-born vibrations: application to self-deployable structures*, Math. Probl. Eng., 720236, (2015), pp. 371–378.

[21] B. Dyniewicz, R. Konowrocki, C.I. Bajer, *Intelligent adaptive control of the vehicle-span/track system*, Mechanical Systems and Signal Processing Vol. 58–59, (2015), pp. 1–14.

[22] D. Pisarski, *Distributed control design for structures subjected to traveling loads*, Mathematical Problems in Engineering, 206870, (2015).

[23] J.N. Potter, S.A. Neild, D.J. Wagg, *Generalisation and optimisation of semi-active, on-off switching controllers for single degree-of-freedom systems*, J.Sound Vib., Vol. 329, No. 13, (2010), pp. 2450–2462.

[24] R. Ceravolo, M.L. Pecorelli, L.Z. Fragonara, *Comparison of semi-active control strategies for rocking objects under pulse and harmonic excitations*, Mechanical Systems and Signal Processing, Vol. 90, (2017), pp. 175-188.

[25] B. Dyniewicz, A. Pregowska, C.I. Bajer, *Adaptive control of a rotating system*, Mechanical Systems and Signal Processing, Vol. 43, (2014), pp. 90–102.

[26] A. Pręgowska, R. Konowrocki, T. Szolc, *On the semi-active control method for torsional vibrations in electro-mechanical systems by means of rotary actuators with a magneto-rheological fluid*, J. Theor. Appl. Mech., Vol. 51 (2013), pp. 979–99.

[27] C. Graczykowski, R. Faraj, *Development of control systems for fluid-based adaptive impact absorbers*, Mechanical Systems and Signal Processing, in review, (2018)

[28] R. Faraj, C. Graczykowski, *Hybrid Prediction Control for self-adaptive fluid-based shock absorbers*, Journal of Sound and Vibration, in review, (2018)

Simulation of active control systems considering different levels of detail in the signal processing chain

J. Millitzer [1], **J. Rohlfing** [2], **V. Mees** [1], **A. Döring** [1]
[1] Fraunhofer Institute for Structural Durability and System Reliability LBF
Bartningstr. 47, 64289 Darmstadt, Germany
e-mail: **jonathan.millitzer@lbf.fraunhofer.de**

[2] Fraunhofer Institute for Building Physics IBP
Nobelstr. 12, 70569 Stuttgart, Germany

Abstract
The continuing trend towards model-based design requires increasingly detailed numerical models. Active vibration control systems are characterized by a high interaction over several physical domains. Hence, early stage numerical investigation requires the set-up of holistic models which include structural components, actuators, sensors, power electronics and digital signal processing. Furthermore, these models need to be adaptable to represent subsystems with the varying level of detail available throughout the development process. This work focuses on the modeling of the digital signal processing chain for active vibration control systems. The goal is to evaluate the control performance and to assess the influence of practical component characteristic from early on in the development phase. Starting with an idealized signal processing chain, the component models are modified to reflect more realistic characteristics. It is shown that control performance is quite sensitive to parasitic effects caused by different elements in the signal processing chain.

1 Introduction

Adaptronics as a smart structure technology offers the possibility to compensate unwanted forced or resonant broadband and narrowband disturbances by means of – not necessarily structurally integrated – actuators, sensors and suitable adaptive control algorithms. One focal point of the current research is the application of active engine mount systems in an active vibration control (AVC) scenario [1, 2, 3]. Here, active systems are applied to reduce harmonic disturbances that are mainly correlated with the rotational speed of the engine.

Beside noise caused by rough road excitation and wind noise, engine noise makes a large contribution to the vehicle interior noise. This also applies to the measurable acceleration at relevant comfort points like the driver's seat and the steering wheel [4, 5]. Engine noise is primarily transmitted via the engine mounting points. The application of an active engine mount system represents a primary measure concerning comfort enhancement whereas an improved vibration reduction is achieved by means of enhanced source insulation. By reducing the accelerations at the mounting points of the engine, a global improvement of noise, vibration, and harshness (NVH) can be expected. The added value provided by an active engine mount system is an increased system performance compared to conventional elastomer or hydraulic engine mounts. Furthermore, active systems offer some future potential for light weight construction due to an enhanced source insulation and the possible omission of acoustic insulating material which particularly applies for the low frequency range.

In previous investigations at the Fraunhofer Institute LBF in Darmstadt, a test vehicle was equipped with an active engine mount system [6, 7] and the performance of the active control system was evaluated successfully during practical driving tests on public street. In the course of these studies, an adaptive control algorithm was implemented on an extensive rapid control prototyping (RCP) system and high-precision laboratory sensor equipment was utilized. However, the performance of the active engine mount system might deteriorate if laboratory equipment is successively replaced by low-cost hardware. The ongoing BMWi project LeichtFahr focuses on early stage development and validation of AVC technology in vehicles. By making use of holistic numerical simulations and sensitivity analyses in an early stage of the design process, requirements and important design criteria for low-cost sensors and tailored embedded signal

processing units can be investigated in detail. This procedure provides the analysis of the overall system performance and robustness of the system in the case the control algorithm is applied under non-ideal conditions.

Within the scope of this work, the performance of an active engine mount system and especially the performance and robustness of the narrowband feed-forward control algorithm under non-ideal conditions are examined in detail. Non-ideal operating conditions might be caused by low-cost acceleration sensors, a reduced resolution of analog-to-digital converters (ADC) and digital-to-analog converters (DAC), a reduced sampling frequency of the signal processing unit or non-ideal rotational speed measurement. After an overview on the engine mount under consideration and the applied principle of AVC, the modeling of the signal processing chain including acceleration sensor and rotational speed measurement are presented. Each model includes suitable error sources, e.g., colored noise in piezoelectric acceleration sensors. The influence of each of these error sources on the overall system performance is analyzed using Simulink simulations.

2 Active engine mount and active vibration control

The application of an active engine mount system represents a primary measure concerning comfort enhancement. For the generation of a counteracting force, different actuator concepts are available. E.g., AUDI uses an electrodynamic actuator [2]. Piezoelectric actuators are applied in [1, 3] where [3] makes use of a stroke amplified piezoelectric actuator. Beside the integration of an active engine mount system, also additional proof mass actuators can be attached to the car body or relevant comfort points and serve the reduction of unwanted vibrations or vehicle interior noise [4, 5].

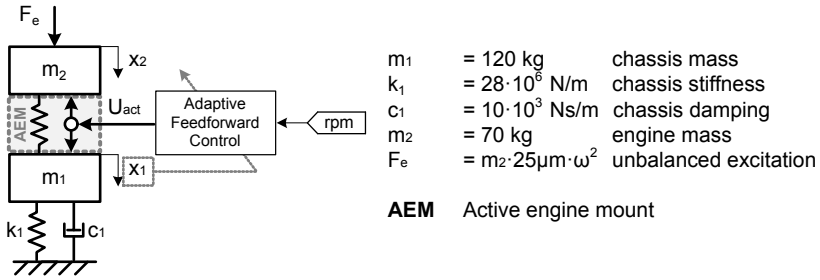


Figure 1: Active engine mount control scenario incorporating an AEM model derived by Hausberg et al. [8].

Figure 1 summarizes the considered AVC scenario within the scope of this work. The engine's mass m_2 is excited by a multi-order harmonic disturbance F_e which is mainly caused by the combustion process and which can be modeled by means of an unbalanced mass excitation with regard to the most significant engine order of interest (i.e. the second engine order for a four cylinder engine). The active engine mount (AEM) isolates the engine from the chassis given by m_1, k_1 and c_1. For simplification, the chassis dynamics are approximated by a single degree of freedom system whose parameters have been adapted to reasonably match a measurement of the dynamic stiffness of the actual mounting point of the AEM in the target vehicle. As the target vehicle will be equipped with an AEM based on a hydraulic engine mount implementing an electrodynamic actuator, the model of the AEM is based on the numerical model derived by Hausberg et al. [8].

AVC concepts based on adaptive digital filters are commonly used to reduce unwanted vibrations in AEM applications. Adaptive control concepts offer the advantage to readjust the applied control filter in case the excitation and/or the transfer behavior of the controlled system changes [9]. For the cancellation of periodic, engine induced vibrations or noise, adaptive narrowband feed-forward concepts are commonly used.

Figure 2 illustrates the conventional implementation of a single frequency filtered reference leaky normalized least mean squares (leaky FxNLMS) algorithm [9]. The primary waveform $d(n)$ is inducted via the primary path, i.e., the engine vibration transmitted through the passive characteristics of the AEM on the engine mount point. An additional secondary path $S(z)$ is used to cancel the primary waveform $d(n)$ by means of the secondary waveform $y'(n)$. The residual waveform $e(n)$ is measured and serves the adaptation of the control filter coefficients. Two orthogonal reference signals $x_i(n)$ serve the calculation of the actuator control signal $y(n)$ whereas the reference signals $x_i(n)$ are generated synthetically by measuring the current rotational speed and making use of a discrete time harmonic oscillator [10].

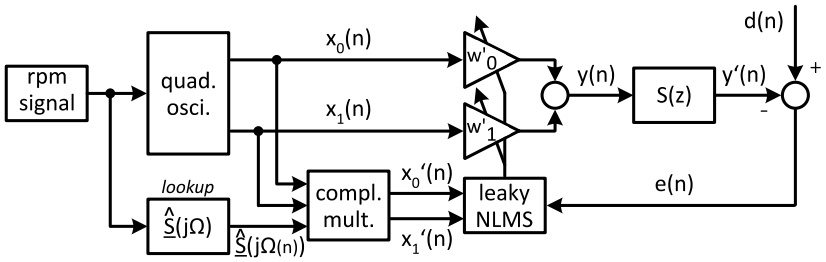


Figure 2: Narrowband adaptive feed-forward control algorithm applying a leaky normalized LMS algorithm, an optimized secondary path model and a quadrature oscillator for the generation of the quadrature reference signals.

$$w_i(n+1) = (1-\gamma\alpha)w_i(n) + \mu(n)x_i'(n)e(n) \text{ with } \mu(n) = \frac{\alpha}{\max\left(P_{x_i'}(n), P_{min}\right)} \tag{1}$$

Two adaptive filter coefficients $w_0(n)$ and $w_1(n)$ are used to adjust amplitude and phase of the actuator control signal $y(n)$. An optimal linear combination of the adaptive weights is determined iteratively by means of the leaky normalized filtered-x LMS algorithm as shown in Eq. (1). The update equation makes use of the measured remaining acceleration $e(n)$ at the mounting point of the AEM and the filtered reference signals $x_0'(n)$ and $x_1'(n)$. The speed of convergence can be adjusted by means of a user-defined normalized adaptation step size α whereas the resulting power-dependent adaptation step size $\mu(n)$ is bounded for a low reference signal power by means of an additional lower bound $P_{\min}$ [9]. In order to avoid divergence and to improve stability, the LMS adaptation equation can be extended by means of a leaking mechanism [9, 11]. For this purpose, a leakage factor is added to the update equation. This measure will increase the robustness of the control algorithm and avoid effects of longtime divergence [9]. A decreased control performance has to be accepted as the utilization of the leakage mechanism increases the attainable minimal mean-squared error in the performance surface due to a bias of the long-term coefficient estimate [12]. Further, as stated in [9, 12], the leakage factor has to be kept smaller than the normalized adaptation step size α. The leakage weighting factor $0 \leq \gamma \leq 1$ is introduced for this purpose.

The actual cancellation signal $y'(n)$ is generated by applying the control signal $y(n)$ to the secondary path. Due to this, the control filter coefficients w_i have to be adapted with regard to the secondary path's dynamics $S(z)$. Assuming the control algorithm to be utilized in an active engine mount scenario, the secondary path will equal the combined transfer behavior of the digital-to-analog converter, the reconstruction filter, the power amplifier, the active engine mount, the mechanical structure, the acceleration sensor, the anti-aliasing filter and the analog-to-digital converter.

The filtered reference signals $x_i'(n)$ can be computed as in Eq. (2) using a look-up table for the complex frequency response of the secondary path $\underline{\hat{S}}(j\Omega(n))$ that is determined experimentally.

$$x_0'(n) + jx_1'(n) = \underline{\hat{x}}'(n) = \underline{\hat{S}}(j\Omega(n))\underline{x}(n) \text{ with } \underline{x}(n) = x_0(n) + jx_1(n) \tag{2}$$

3 Modeling of the signal processing chain

Nowadays, digital signal processing is often preferred over analog signal processing due to the easy implementation and changeability of even complex control concepts. Furthermore, control parameters can be adjusted very precisely and digital control is not prone to electrical drifts or environmental conditions. By making use of model-based design, rapid control prototyping and hardware-in-the-loop testing, there is a consistent toolchain available to engineers and developers. Precise modeling is therefore even more important in order to take the full advantage during concept phases and early-stage system development.

Figure 3 shows the proposed modeling of the signal processing chain which has been implemented in Matlab/SIMULINK. Beside the adaptive narrowband feed-forward control algorithm, the signal processing model includes an anti-aliasing filter (AAF) for preventing aliasing effects and a reconstruction filter (RCF) to remove spectral artifacts caused by the holding mechanism of the digital-to-analog converter and the following rate transition. Parasitic quantization effects are modeled by means of analog-to-digital converter (ADC) and digital-to-analog converters (DAC) respectively. Additional delay times caused by the ADC and DAC as well as the computation time of the controller are taken into account by means of a conflating dead time element. Two zero-order hold blocks are used to sample the continuous input signals given by both the rotational speed sensor as well as the error sensor. As a continuous time solver is chosen

for the simulation of the AEM scenario both the zero-order hold model and the rate-transition block ensure discrete time calculation of the control algorithm itself as well as deterministic data transfers between systems of different sample times. This allows a constantly high simulation sampling rate for numerical stability while varying the sampling frequency of the controller block.

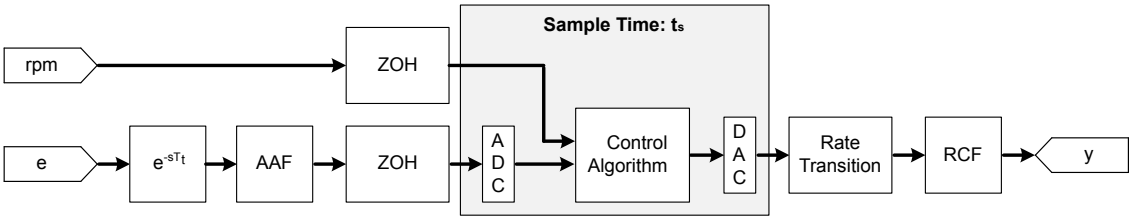


Figure 3: Modeling of the digital signal processing chain.

3.1 Digital signal processing

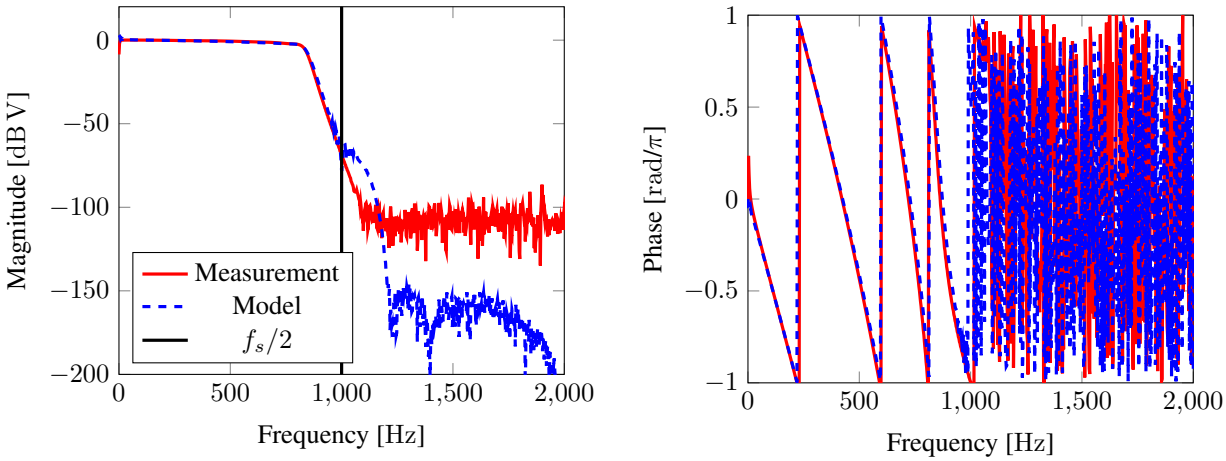
Two major effects have to be considered while modeling digital signal processing. Firstly, dead times caused by the sample and hold element and the dynamic characteristics of the anti-aliasing and reconstruction filters introduce a significant additional phase delay in the open-loop transfer function. Design guidelines for the design of anti-aliasing and reconstruction filters can be found in [13]. Secondly, quantization noise is introduced by the ADC and DAC respectively. As additional noise represents a loss in coherence which directly affects the control performance [9], quantization noise has to be considered during system design. This can also be seen in the fact that up to a resolution of approx. 12 bit, analog quantizing is the main error source compared to the errors contributed from multiplexers, signal amplification and sample-and-hold circuits [14]. The ADC and DAC model is realized by a quantizer with an interval of Δu as given in Equation (3), which depends on the difference between the maximum $U_{\max}$ and minimum output voltage $U_{\min}$ as well as the associated bit resolution n of the ADC/DAC.

$$\Delta u = \frac{U_{\max} - U_{\min}}{2^n - 1} \tag{3}$$

In addition to quantization noise, the ADC system adds noise in form of thermal and clock noise, which can be approximated as white noise and jointly described by noise power P_N. The signal-to-quantization-noise ratio (SQNR) is given by Equation (4) for a sinusoidal signal which spans the full range from $U_{\min}$ to $U_{\max}$. System measurements for the dSpace DS2003 ADC converter board show a signal-to-noise ratio (SNR) of $80\,\mathrm{dB}$ for an ADC resolution of 16 bit instead of the theoretically possible $96\,\mathrm{dB}$. This is in good agreement to the datasheet value of $78\,\mathrm{dB}$. This means, that for a resolution of 16 bit other noise sources dominate the quantization noise by a factor of 40 and the effective number of bits (ENOB) is 13 bit.

$$\mathrm{SQNR} = 1.76\,\mathrm{dB} + 20 \cdot \log_{10} 2^n \tag{4}$$

Figure 4 shows a comparison between the conflated transfer behavior (i.e. anti-aliasing and reconstruction filter, ADC and DAC as well as digital signal processing) of the measured and modeled digital signal processing chain. The measurement is conducted with an OnoSokki CF-7200A. For anti-aliasing a Kemo Cardmaster 255g Type 01 filter is set to $800\,\mathrm{Hz}$. The dSpace system's sampling frequency is $2\,\mathrm{kHz}$ and the sampling frequency of the spectrum analyzer is $100\,\mathrm{kHz}$. The system is excited by a sine sweep from 0 to $4\,\mathrm{kHz}$, allowing aliasing to occur. The anti-aliasing and reconstruction filter responses are modeled by an elliptical filter with the characteristics given in the data sheet [15]. To optimally match the measured response, the edge frequencies for pass- and stop-band are slightly perturbed. The ADC has a resolution of 16 bit and the DAC has a resolution of only 14 bit. A transport delay block accounts for additional dead times not covered by the filter responses and the domain conversions. These are $30\,\mu\mathrm{s}$ per Kemo filter and $6.3\,\mu\mathrm{s}$ for the ADC running on one channel and 16 bit resolution. The dependency of dead time on the number of bits and channels used in the DS2003 ADC board has been measured before in [16]. The model matches the measurements very well in magnitude as well as in phase. Only nearby the Nyquist frequency of $1\,\mathrm{kHz}$ the model simulation diverges from the measurements due to the finite frequency resolution of the test signal. Above $1\,\mathrm{kHz}$ the finite resolution of the spectrum analyzer's ADC limits the estimated transfer function to approximately $-100\,\mathrm{dB}$.



(a) Amplitude

(b) Phase

Figure 4: Conflated transfers function of the digital signal processing chain.

3.2 Acceleration sensors

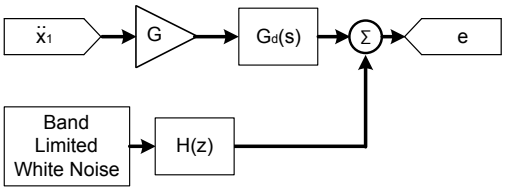
The input to the signal processing chain e is the error signal of the adaptive control algorithm and depends on the measured acceleration $\ddot{x}_1$ at the mounting point of the AEM. The acceleration is converted to a voltage signal by an acceleration sensor depending on the sensor's sensitivity and is perturbed by sensor noise.

Basically, there are two measurement principles to obtain the acceleration of a mechanical system. The first principle makes use of the piezoelectric effect. Here, the reaction force of a seismic mass is proportional to the resulting charge difference between the two compressed sides of a piezoelectric substrate. The resulting charge difference is measured by means of a charge amplifier and serves the estimation of the acceleration. This measurement principle is often utilized in high-precision laboratory sensor equipment. The second principle is applied in microelectromechanical systems (MEMS). Here, the displacement of a seismic mass is measured by means of a capacitive sensor. The measured displacement is proportional to the actual acceleration. MEMS acceleration sensors can be mass-produced economically and offer significant cost advantages compared to the high-precision laboratory sensor equipment. Both sensor types have a limited bandwidth resulting from the resonance frequency of the seismic mass. However, MEMS acceleration sensors usually show significant higher sensor noise compared to laboratory sensor equipment.

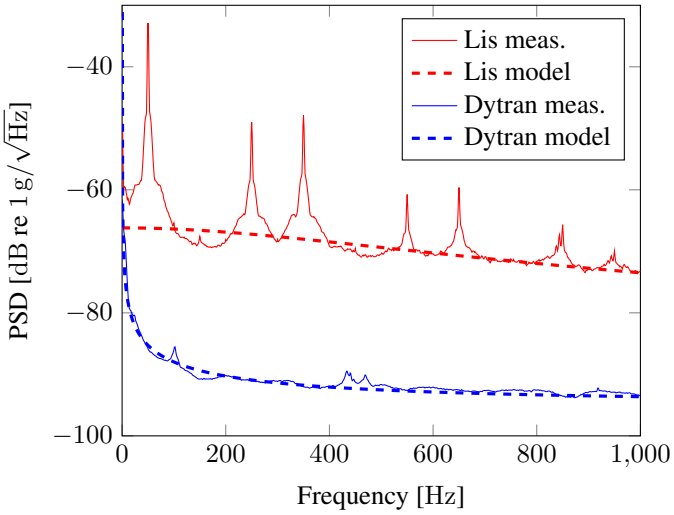
Acceleration sensor noise consists of white thermal noise and – especially in case of piezoelectric sensors – of pink noise, which is dominant in the lower frequency range. While a white noise characteristic can simply be modeled by a band-limited random number generator, colored noise requires additional information about the spectral content which can be used to design a weighting FIR filter. Colored noise is wide-sense stationary (WSS), that is the correlation depends (only) on the time difference τ and the PSD is in turn not constant. In the case of pink noise, the PSD decreases with $1/f$ or $10\,\mathrm{dB}$ per decade. For red noise, it decreases with $1/f^2$ or $20\,\mathrm{dB}$ per decade. The pink noise in piezoelectric sensors is due to an effect of the JFET used in the integrated charge amplifier [17].

Figure 5a illustrates the modeling of the acceleration sensor. The sensor's sensitivity is given by the scalar factor G. An additional FIR filter $H(z)$ serves the spectral weighting of the sensor noise and additional dynamic behavior (e.g. limited measurement range in MEMS sensors or dynamic response of the sensor) is taken into account by the transfer function $G_d(s)$.

Two acceleration sensors are compared, one for each construction principle. The class of piezoelectric IEPE sensors is represented by the Dytran 3049E3, a $100\,\mathrm{mV/g}$ sensor with a measurement range of $\pm 50\,\mathrm{g}$. The data sheet gives an equivalent noise floor in Grms, which is stated in Equation (5). This level matches the measured noise density very well at low frequencies but a single value does not model the colored nature of the sensor noise as shown in Figure 5b. To account for that, the total noise power has been distributed to a constant part, a pink and a red part. Numerical fitting shows, that white noise has a share of $0.05\,\%$ of the total noise power while the rest is distributed $80\,\%$ in red noise and $20\,\%$ in pink noise. The class of MEMS sensors is represented by STMicroelectronics LIS 344ALH, a $660\,\mathrm{mV/g}$ sensor with a measurement range of $\pm 2g$. The MEMS sensor shows purely white noise, which is only slightly colored by the sensor output filter. The measured noise level lies approximately $5\,\mathrm{dB}$ below the data sheet value of $1.09 \times 10^{-9}\,\mathrm{V^2/Hz}$ (Equation (6)). Therefore, for the comparison in Fig. 5b, the measured sensitivity of $500\,\mathrm{mV/g}$ was used instead of the data sheet value. In terms of measured acceleration, i.e., omitting the different sensitivities



(a) Acceleration sensor model



(b) Spectral noise density

Figure 5: Acceleration sensor modeling.

of the sensors, the noise level of both sensors is very similar at low frequencies. Towards higher frequencies, the laboratory sensor shows approximately 20 dB less noise due to its colored characteristic.

$$P_{\text{Dytran}} = \left(\frac{0.008\,\text{g} \cdot 100\,\text{mV/g}}{\sqrt{10\,\text{kHz}}} \right)^2 = 6.4 \times 10^{-11}\,\text{V}^2/\text{Hz} \tag{5}$$

$$P_{\text{LIS}} = \left(50\,\mu\text{g}/\sqrt{\text{Hz}} \cdot 0.66\,\text{V/g} \right)^2 = 1.09 \times 10^{-9}\,\text{V}^2/\text{Hz} \tag{6}$$

Figure 5b shows a power spectral density (PSD) estimate of the measured acceleration and the modeled acceleration as no excitation signal is applied to the acceleration sensor. The models match the measured behavior quite well. It should be noted, that the MEMS acceleration sensor's PSD shows an increased noise level at the multiple of the mains frequency of 50 Hz. Thus, special attention should be given to the design of the ripple of the sensor's supply voltage.

3.3 Rotational speed measurement

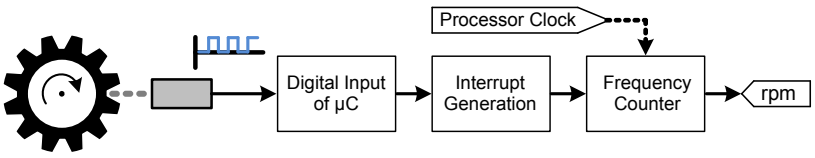


Figure 6: RPM measurement principle.

As indicated in Section 2 and verified in Section 4.3, the performance of the control algorithm strongly depends on precise frequency measurements [18, 19]. Within the system simulation, the acquisition of the rotational speed by means of scanning a toothed wheel is considered. An exemplary system is illustrated in Figure 6. Scanning of a toothed wheel by means of a suitable inductive, capacitive or optical sensor generates an impulse train. This measurement method has an inherent dead time dependent on the current rotational speed due to the angular difference between two cogs $\delta\phi$. The speed measurement can only be updated after the next tooth reaches the sensor. Therefore the error depends on the rotational speed as well as on its derivative. Fast changing velocity induces a higher error and the sign of the error is equal to the sign of the acceleration. The sampling frequency of a revolution counter is usually much higher than the frequency with which the teeth pass by the detector (usually 1 to 100 MHz). Therefore, it is not possible that a tooth transition will be missed and estimation error due to late detection of the transition is relatively low. For

example, a system with 60 tooths on the cog wheel rotating constantly with $1000\,\mathrm{min}^{-1}$ has a tooth-to-gap transition every $1\,\mathrm{ms}$. With the detection processor running at $100\,\mathrm{MHz}$, the maximum error of the estimation is

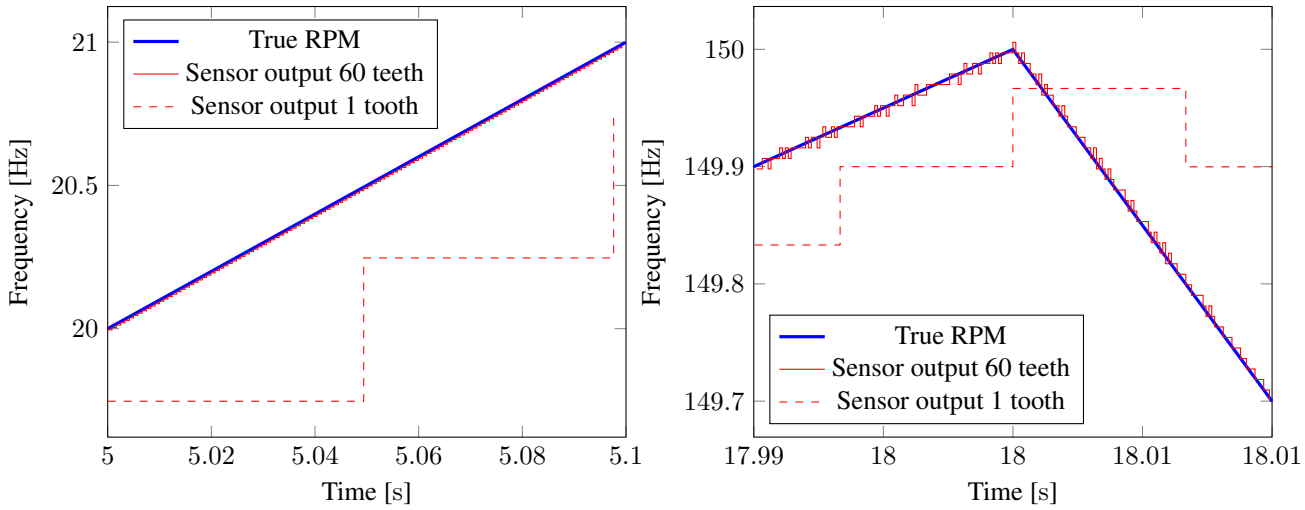
$$\frac{1/60}{(1\,\mathrm{ms} \pm 10\,\mathrm{ns})} - \frac{1/60}{1\,\mathrm{ms}} = \pm 1.67 \times 10^{-4}\,\mathrm{Hz} \tag{7}$$

This maximum instantaneous error is equally distributed with zero mean and therefore has no repercussion on the sensor performance, as long as the frequency is lower than the Nyquist frequency given by Eq. (9).

$$\frac{1/N_T}{\frac{1}{N_T f(t)} \pm \frac{1}{f_s}} - f(t) = f(t)\left(\frac{f_s}{f_s - N_T f(t)} - 1\right) \tag{8}$$

$$f_{ny} = \frac{f_s}{2N_T} \tag{9}$$

When the frequency is changing – in addition to the tooth detection error – a tracking error occurs, which is usually much larger. This is because the current frequency is estimated from the time between the last tooth detection and the current, i.e., the average frequency from this interval is returned. For rising frequencies this leads to a systematic underestimation and for falling frequencies to an overestimation of the same magnitude. The tracking error is shown in Fig.7 for low and high frequencies and two different cogwheel configurations. The tracking error depends linearly on the number of teeth on the cogwheel.



(a) At low frequency

(b) At high frequency

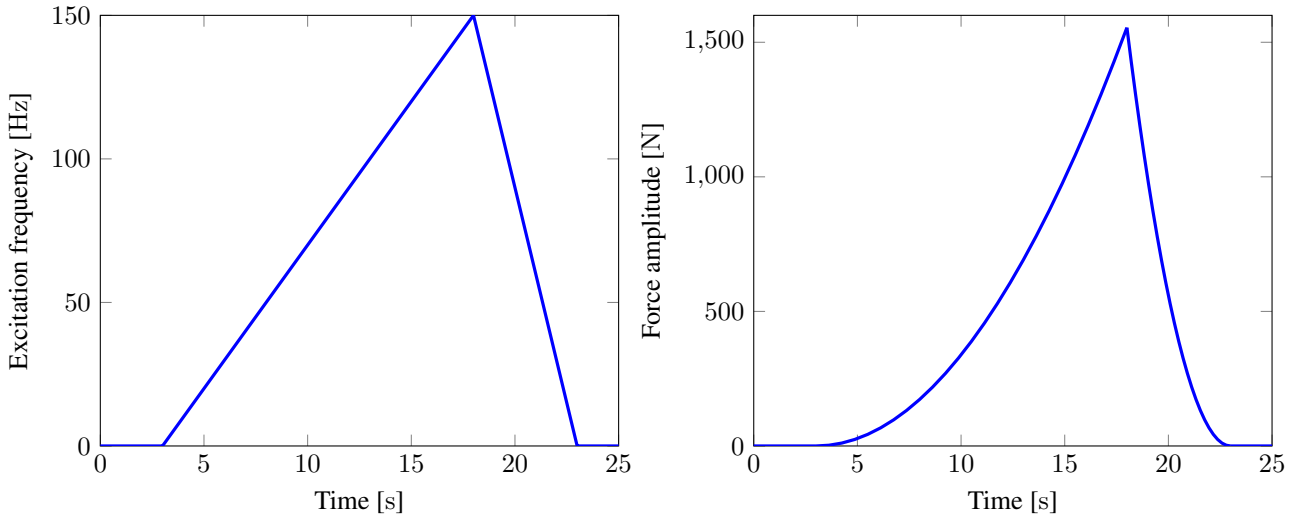
Figure 7: Detail of measurement error due to restricted sampling.

4 Sensitivity analysis

The performance of an active vibration control system depends on a multitude of different input parameters, many of which are subject to technical choices or can be freely selected. As there is a strong dependency between the selected control parameters and the properties of the respective signal processing elements [20], the derived simulation framework allows for an early-stage investigation of the control performance by means of a sensitivity analysis. For the scope of the simulations, a second engine order excitation is considered as shown in Figure 8a. It consists of a slow acceleration phase followed by a fast deceleration phase, which are framed by two phases of constant rotational speed. The engine's mass $m_2 = 70\,\mathrm{kg}$, see Fig. 1, is excited by an unbalanced mass excitation ($r = 25\,\mu\mathrm{m}$) with varying intensity depending on the excitation frequency. Figure 8b shows the resulting unbalance force amplitude, which depends on the current rotational frequency as:

$$F_e(t) = \hat{F}_e(t) \cdot \sin\left(\int_0^t 2\pi f(\tau) d\tau\right) \quad \text{with} \quad \hat{F}_e(t) = m_2 \cdot r \cdot (2\pi f(t))^2 . \tag{10}$$

The following sections are organized as follows: First, the control parameters of the narrowband feedforward control algorithm (i.e. the user defined adaptation step size α and the leakage weighting factor γ) are varied over a wide range in order investigate the maximum attainable control performance. Next, parasitic effects caused by sensor and quantization noise are considered and finally different rotational speed measurement scenarios are investigated.



(a) Second engine order frequency $f(t)$

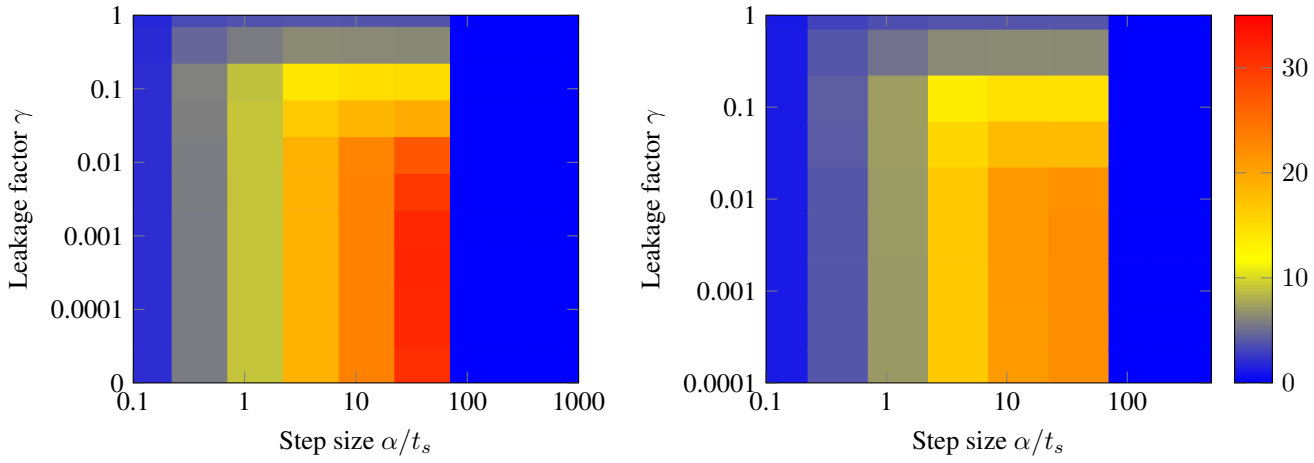
(b) Unbalance force amplitude $\hat{F}_e(t)$

Figure 8: Excitation modeling.

4.1 Variation of control parameters

The overall system behavior is investigated in the first part of the sensitivity analysis. Here, the controller's sampling frequency and relevant control parameters (i.e. the normalized adaptation step size α and the leakage weighting factor γ) are varied over a wide range allowing a close observation of the control performance. The upper and lower bound of the control parameters were previously determined in additional analysis. Logarithmically spaced vectors are chosen for an initial variation of the control parameters. A bit resolution of 16 bit is chosen for both the ADC and DAC respectively and no additional sensor noise was being applied to the acceleration sensor. Also, a decent rpm signal is selected featuring 60 pulses per revolution. The measure of interest is the acceleration of the chassis at the engine mount point $\ddot{x}_1$. Its average achievable reduction is shown within the α-γ-plane in Figure 9. Increasing the adaptation step size α allows for better reduction until the system becomes unstable for $\alpha \approx 100/t_s$. Also a high leakage weighting factor γ of approx. 0.01 decreases the control performance. However, a positive side-effect arises, if the control filter weights have to be adjusted rapidly, e.g., in a fast run-up scenario. Here, the leakage factor assists the fast adaptation of the control filter weights as a previously found linear combination is not retained. This effect doesn't get too obvious, as a relatively moderate rate of change in the excitation frequency was chosen for the sensitivity analysis. Furthermore, the control performance has been set to $0\,\mathrm{dB}$ in the case of an unstable control behavior. Decreasing the controller's sampling frequency from 2 to $1\,\mathrm{kHz}$ reduces the maximum attainable control performance from 34 to $26\,\mathrm{dB}$. This, however, has to be accepted if the computational burden on an embedded signal processing unit is critical.

For an in-detail analysis of the active vibration control system's behavior, the second engine order order-cuts are illustrated in Figure 10 whereas the controller's sampling frequency is $2\,\mathrm{kHz}$. Considering the uncontrolled scenario in the first case, the second engine order strikes the two resonances of the mechanical system. The fundamental frequency of the engine's mass m_2 is located at approx. $20\,\mathrm{Hz}$ and the chassis' resonance frequency (i.e. m_1) is set to a value of approx. $80\,\mathrm{Hz}$. It should be noted, that the actual dynamic behavior of the car's chassis shows a variety of different resonance frequencies which have not be considered within the scope of this investigation. The best configuration with $\alpha = 0.025$ and $\gamma = 0.0001$ achieves an average reduction of $34\,\mathrm{dB}$. But since this configuration acts on the verge of



(a) 2kHz sampling frequency

(b) 1kHz sampling frequency

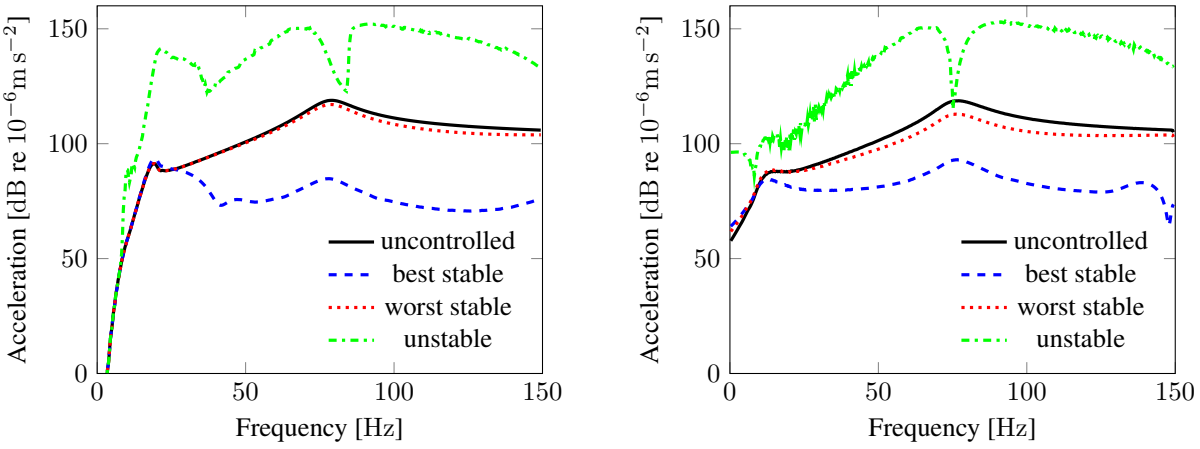
Figure 9: Control performance as a function of the control parameters.

instability, for the comparison the more conservative configuration with $\alpha = 0.005$ and $\gamma = 0.005$ has been chosen, which achieves a reduction of 26 dB. This configuration with $\alpha \cdot f_s = 10$ is kept throughout the following sections, giving $\alpha = 0.01$ for $f_s = 1$ kHz later on.

Figure 10 also shows a comparison between the run-up ranging from 3 to 18 s and the run-down ranging from 18 to 23 s. Due to the faster changing excitation frequency $f(t)$, the overall performance slightly decreases. Also, with this relatively large step size, the algorithm shows a slight deterioration of the control performance at around $t = 5$ s (i.e. passing the engine's mass resonance frequency), which is handled more graciously during the run-up by the overall worst stable configuration with $\alpha = 5 \times 10^{-5}$, $\gamma = 1$. In consequence, as the control performance deteriorates due to the phase change in the secondary path's frequency response, an adaptation of the control parameters with regard to the secondary path's phase change in accordance with the change in rotational speed seems advisable.

4.2 Effects of sensor and quantization noise

As depicted before, the control performance strongly depends on the coherence between the actuator's control signal $y(n)$ and the controller's error signal $e(n)$. The coherence will deteriorate as the secondary path shows non-linear behavior or if the secondary path includes noise sources that either can be given by additive sensor noise or quantization noise caused by the ADC and DAC respectively. For a comparative investigation, Figure 11a shows the second engine order order-cuts for the previous set-up (i.e. 2 kHz, 16 bit ADC/DAC resolution and no additional sensor noise) and



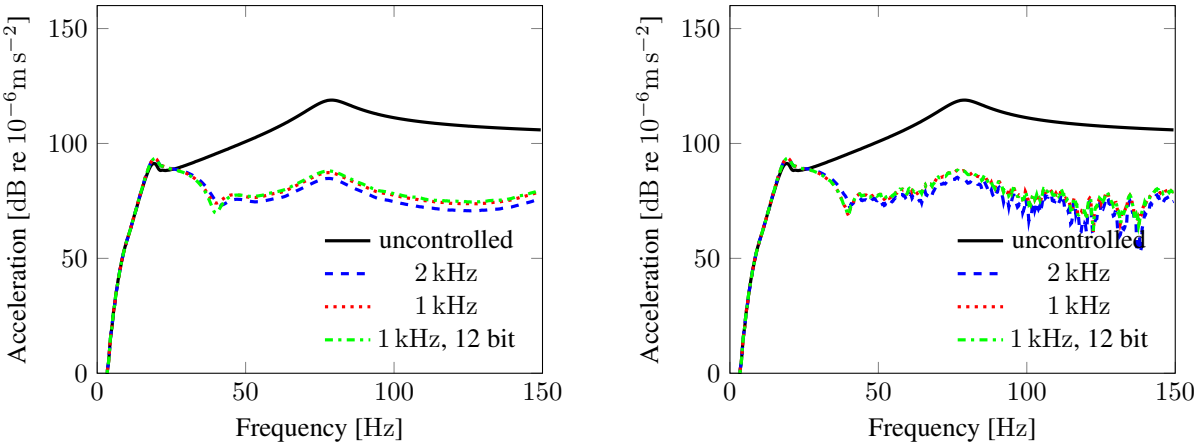
(a) Run-up

(b) Run-down.

Figure 10: Second engine order order-cuts (2 kHz sampling frequency, 16 bit ADC/DAC resolution).

a set-up where the sampling frequency is reduced to 1 kHz. As discussed before, reducing the sampling frequency slightly decreases the overall control performance over the whole frequency range of interest. Decreasing the bit resolution of the ADC and DAC to 12 bit, no significant deterioration of the controller's performance can be observed. This depicts a promising result, as embedded signal processors often feature a bit resolution of 12 bit for both the ADC and the DAC as well.

Next, additional sensor noise caused by the acceleration sensors (c.f. Section 3.2) is added in the overall system simulation. Figure 11b briefly recapitulates the results of the simulation by means of the second engine order order-cut. The previously introduced MEMS sensor (i.e. STMicroelectronics LIS 344ALH) is used for the simulations. Even though the order-cuts show a noisy behavior, the overall system performance remains the same compared to the simulations without any sensor noise (c.f Figure 11a). This again depicts a positive result with regard to system integration and the application of low-cost hardware. However, compared to other MEMS acceleration sensor types (e.g. the ADXL335) the LIS 344ALH MEMS sensor has significant less sensor noise which has to be taken into account, if another sensor type is desired during system design.



(a) Without sensor noise

(b) With sensor noise

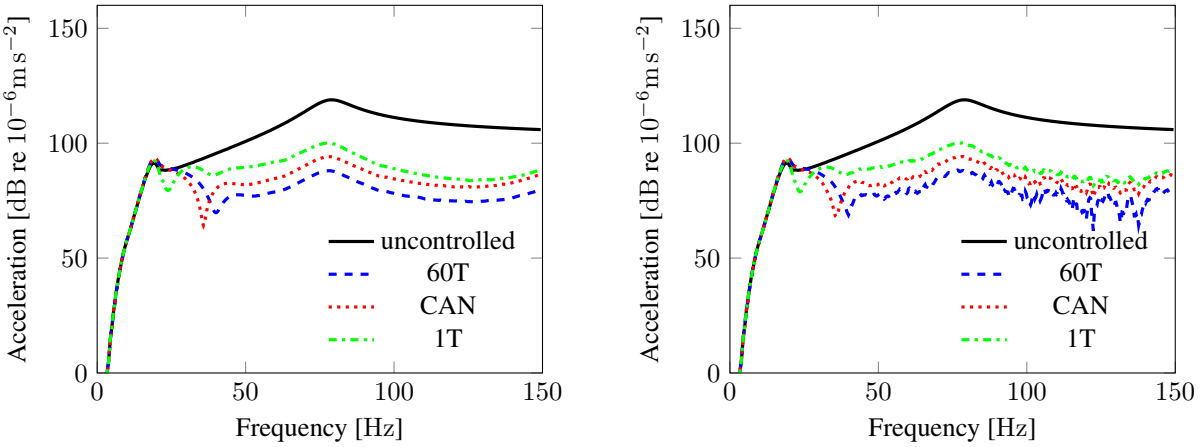
Figure 11: Second engine order order-cuts for reduced sampling frequency of 1 kHz, reduced ADC/DAC resolution and sensor noise.

4.3 Rotational speed measurement

Besides the coherence of the actuator's control signal $y(n)$ and the controller's error signal $e(n)$, the control performance also strongly depends on the correlation between the controller's error signal $e(n)$ and the synthetically generated reference signals $x_i(n)$. In a narrowband feed-forward control this falls down to precise frequency measurement which was already part of the investigations carried out in [18, 19, 20]. As introduced in Section 3.3, the quality of the rpm signal strongly depends on the number of teeth sampled by the microcontroller's digital input. Three different scenarios are investigated within the scope of the system simulation. First, a total of 60 samples over one revolution is assumed which remarks a usual measure in the automotive industry as such an rpm measurement signal can often be found in engine control applications. Next, the rpm measurement involves only one measurement (i.e. one tooth) per revolution. In the last scenario, still 60 measurements per revolution are considered but in addition the signal is sampled and held at an update rate of only 10 ms which corresponds to the distribution of the rpm measurement value over a CAN network. Other influences on the rpm signal quality which were not further taken into account include delayed transmission of the estimated rpm signal and missing teeth on the cog, which would allow to detect the absolute position of the crank shaft but introduce a higher estimation error once per revolution.

Again, the simulations are carried out without sensor noise (Figure 12a) and with sensor noise caused by the MEMS acceleration sensor LIS 344ALH (Figure 12b). As before, the sampling frequency is chosen to be 1 kHz with a bit resolution of 12 bit for the ADC and DAC respectively. As shown in Fig. 12 the 60 teeth rpm signal results in the best control results. The control performance shows a significant deterioration, if only one sample (i.e. one tooth) per revolution is used for rotational speed measurement. The order-cut results in being constantly 12 dB worse. The CAN network based control performance is located in between the formerly discussed simulation results. However, if the target application also involves the control of higher engine orders the errors introduced by both the one sample per revolution signal as well as the CAN network signal the errors in frequency measurement are also becoming more

obvious. Thus, making use of the best available rpm measurement signal (i.e. 60 samples per revolution without any additional delay) seems to be advisable. However, also additional frequency tracking algorithms [20, 21] may improve control performance whenever high-precision rpm signals are not available.



(a) Without sensor noise

(b) With sensor noise

Figure 12: Second engine order order-cuts for different rpm measurement scenarios also incorporating sensor noise.

5 Conclusion

Within the scope of the work presented, a highly accurate model of the digital signal processing chain for the early-stage numerical investigation of a narrowband feed-forward active vibration control system has been set up. Even tough the overall system's behavior has not yet been evaluated experimentally in vehicle tests, the numerical models of each component show a good accordance to actual measurements on component level which allows for an initial assessment of the control performance as low-cost digital signal processing components are successively integrated into the active vibration control system. As further investigations regarding high-accuracy and high-bandwidth simulation as well as experimental validation are planned within the scope of the ongoing research project LeichtFahr, the achieved results will lay the foundation for the design of several active vibration control systems.

Acknowledgments

This work was supported by the research project LeichtFahr (19|16004F) funded by the German Federal Ministry for Economic Affairs and Energy (BMWi). The support is greatly acknowledged. Special thanks go to Timo Potrafke, who set up an initial simulation framework during his master thesis at TU Darmstadt.

References

[1] H. J. Karkosch and P. M. Marienfeld. "Use of active engine mounts to optimize comfort in cars with innovative drives". In: *12th International Conference on New Actuators - ACTUATOR*. 2010.

[2] S. Römling, S. Vollmann, and T. Kolkhorst. "Active engine mount system in the new Audi S8". In: *MTZ worldwide* 74 (2013), pp. 34–38.

[3] R. Kraus et al. "Development of active engine mounts based on piezo actuators". In: *ATZ worldwide* 116 (2014), pp. 50–55.

[4] N. Müller. "Entwicklung eines multi-direktionalen aktiven Lenkradtilgers". In: *Fraunhofer-Allianz Adaptronik Workshop*. 2013.

[5] E. Kruse. "Interior noise effects of active vibration cancellation for a 4-cylinder engine". In: *8. Symposium für Motoren- und Aggregate Akustik*. 2014.

[6] S. Herold et al. “Vibration control of a medium-sized vehicle by a novel active engine mount”. In: *4. Wissenschaftliches Symposium PT-PIESA, Nürnberg*. 2013.

[7] Jonathan Millitzer et al. “Experimental Studies on Different Actuator-Sensor Configurations of Active Control Systems for the Reduction of Noise and Vibration in Vehicles”. In: *SAE Int. J. Passeng. Cars - Mech. Syst.* 9 (June 2016), pp. 1100–1110. DOI: 10.4271/2016-01-1844. URL: https://doi.org/10.4271/2016-01-1844.

[8] Fabian Hausberg et al. “Experimental and analytical study of secondary path variations in active engine mounts”. In: *Journal of Sound and Vibration* 340 (2015), pp. 22–38.

[9] S. M. Kuo and D. R. Morgan. *Active noise control systems - algorithms and DSP implementations*. Wiley, New York, 1996.

[10] C. S. Turner. “Recursive discrete-time sinusoidal oscillators”. In: *IEEE Signal Processing Magazine* 20(3) (2003), pp. 103–111.

[11] R. D. Gitlin, H. C. Meadors, and S. B. Weinstein. “The tap-leakage algorithm: an algorithm for the stable operation of a digitally implemented, fractionally spaced adaptive equalizer”. In: *Bell System Technical Journal* 61(8) (1982), pp. 1817–1839.

[12] Maurice G. Bellanger. *Adaptive digital filters and signal analysis*. M. Dekker, Denver, Colorado, 1987.

[13] Stephen Elliott. *Signal processing for active control*. Academic Press, Amsterdam, Boston, 2000.

[14] *Principles of data acquisition and conversion*. Application Bulletin SBAA051. Burr-Brown Corporation. May 1994. URL: http://www.ti.com/lit/an/sbaa051a/sbaa051a.pdf.

[15] *Filter response 01*. Kemo Limited. Unit 1, Dene Yard Green Street Green Road Dartford Kent DA2 8DH, 2017. URL: http://www.kemo.com/images/datasheets/fr_01.pdf.

[16] Timo Potrafke. “Modeling of dynamic systems for signal level hardware-in-the-loop applications”. MA thesis. TU Darmstadt, 2017.

[17] Yutian Wang et al. “Analysis of circuit noise in integral electronics piezoelectric accelerometer”. In: *Journal of applied science and engineering* 18.3 (2015), pp. 295–302.

[18] S.P. Nallabolu and S.M. Kuo. “Analysis of Frequency Synthesis Error in Narrowband Feedforward Active Noise Control Systems”. In: *Industrial Electronics Society, 2007. IECON 2007. 33rd Annual Conference of the IEEE*. Nov. 2007, pp. 851–856. DOI: 10.1109/IECON.2007.4460114.

[19] Hyeon-Jin Jeon, Tae-Gyu Chang, and S.M. Kuo. “Analysis of Frequency Mismatch in Narrowband Active Noise Control”. In: *Audio, Speech, and Language Processing, IEEE Transactions on* 18.6 (Aug. 2010), pp. 1632–1642. ISSN: 1558-7916. DOI: 10.1109/TASL.2009.2038815.

[20] Jonathan Millitzer. “Sensitivity analysis and robustness improvement of an adaptive control algorithm for an active engine mount application”. MA thesis. FernUniversität in Hagen, Sept. 2014.

[21] Yegui Xiao et al. “A filtered-X RLS based narrowband active noise control system in the presence of frequency mismatch”. In: *Circuits and Systems, 2005. ISCAS 2005. IEEE International Symposium on*. May 2005, 260–263 Vol. 1. DOI: 10.1109/ISCAS.2005.1464574.

Control of fluctuations of a tethered unmanned-underwater-vehicle

E. Paifelman [1,2], **G. Pepe** [1], **F. La Gala** [2], **A. Carcaterra** [1]
[1] Department of Mechanical and Aerospace engineering, Sapienza University of Rome

[2]Insitute of Marine Engineering, INM (ex CNR-INSEAN), Rome, Italy
e-mail: **elena.paifelman@uniroma1.it**

Abstract
The analysis of oscillating systems controlled by mechatronic devices, relies classically on differential equations, and the problem is frequently attacked in the frequency domain, for linear systems based on more conventional controls, or in the time space-state formulation to include also nonlinearities. In this paper we are faced with a system that exhibits memory effects. These are borne because of the presence of added mass and damping that are due to the rigid body motion coupling with the surrounding water. Memory effects are also generated by the presence of lifting surfaces (control wings) due to vortex shedding and transport along the wake. The mathematical formulation of the system dynamics, relies in these cases on an integral-differential equation. This paper introduces a novel formulation for the control of the vehicle that can include in the optimal control integral terms besides the more conventional differential ones.

1 Introduction

The goal of this paper is to develop a new optimal control strategy for oscillating systems affected by memory effects and described by integral-differential equations. Memory effects are induced by the fluid-structure interaction. In this paper two main phenomena claim for these effects in the model: vortex shedding and added mass and damping due to the presence of a free surface in the fluid. Underwater autonomous or remotely operated vehicles are examples [1, 2]. Vorticity is generated by the motion of the vehicle as well as by the presence of cables (ROV-Sonar array), [3, 4]. Also a vehicle moving close to the water free surface presents memory effects [5, 6].
Memory effects are represented, in time domain, by convolution integral between kernel functions and the vehicle state [7]. Control techniques are often used to control underwater vehicle [8] but they involve differential equations of motion. In fact, the underwater vehicles are normally represented by rigid body model [9] not involving integral memory effects. The control method presented in this paper, is an extension of the Pontryagin optimal solution, normally applied to differential equations. The novel approach is based on the variational feedback control.

This control logic has been applied in recent investigations of car mechatronics [10]. Moreover the same approach has been applied to optimal control problems of damping in structural dynamics as well [11, 12]. In this paper, a feedback formulation via model predictive control is also presented for integral-differential dynamic systems.

2 Modelling of the controlled underwater vehicle

2.1 The engineering problem

A classical towed mechanical system used in ocean exploration and military applications, is composed by a towed vehicle V and a towed line array (TLA) sonar [13]. The two subsystems

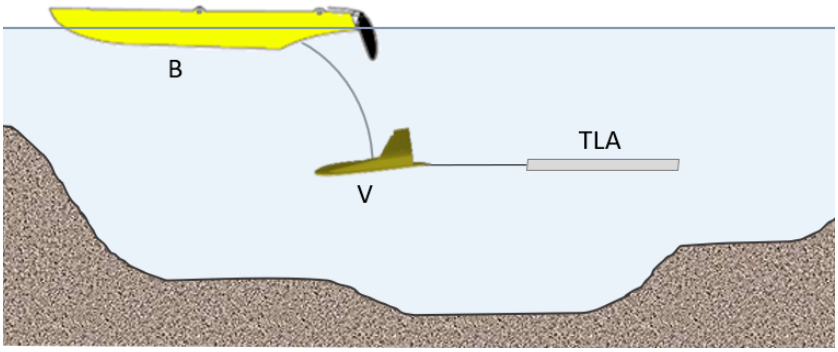


Figure 1: Underwater towed system

are towed by the towing cable attached to the moving boat, B (Figure 1). The goal of the vehicle V is to guarantee a TLA's depth of navigation and the reduction of the TLA's oscillations [14]. V is called "depressor" [15] and its heave motion generates memory effects which influence the proper operation of the TLA [16]. As already explained, if the depressor moves near to the free surface, memory effects called added mass and added damping respectively, are borne. The mathematical formulation of the underwater vehicle, implies the use of integral-differential equations in the time domain, that requires a nonstandard optimal control strategy.

2.2 Modelling

A fluctuations control method which presents a single degree of freedom is here investigated (Figure 2).
The x-axis is chord-wise and the z-axis is the heave direction. The equation of motion of the

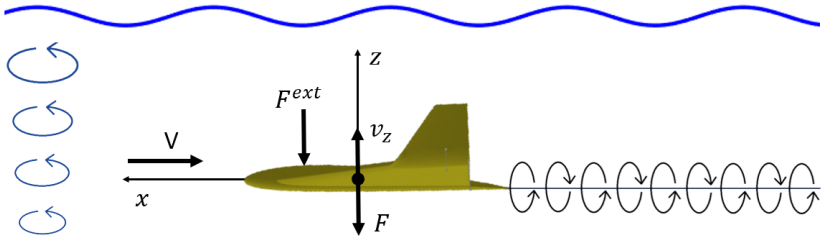


Figure 2: Force balance on finned vehicle

vehicle is [17]:

$$\left(m+\frac{1}{\mu}\right)\dot{v}_z+\int_{-\infty}^{t}K_W(t-\tau)\dot{v}_z(\tau)\,d\tau+ \\ +\int_{-\infty}^{t}K_M(t-\tau)\dot{v}_z(\tau)\,d\tau+\int_{-\infty}^{t}K_D(t-\tau)v_z(\tau)\,d\tau+F=0 \tag{1}$$

where m is the mass of the vehicle, v_z the heave velocity, $\mu=\pi\rho b^2/m$ the mass ratio and F the control force along the z-axis. The external forces F^{ext} are represented by the three integral terms. The first integral represents the circulatory part of the lift, due to the wake where $K_W(t)$ is the Wagner function [18]. The others convolution terms are the added mass contribution and the added damping to which $K_M(t)$ and $K_D(t)$ remain associated [17]. Using the property of the convolution, the final equation of motion is

$$M\dot{v}_z+\int_{-\infty}^{t}K(t-\tau)v_z(\tau)\,d\tau+F=0 \tag{2}$$

where $M=m+\frac{1}{\mu}$ and $K(t)=K_W(t)+\dot{K}_M(t)+K_D(t)$.

3 An indirect variational approach of the controlled vehicle

Using standard notation in control theory, eq. (2) becames:

$$\dot{v_z}=bu+b\int_{-\infty}^{t}K(t-\tau)v_z(\tau)\,d\tau \tag{3}$$

where *F=bu*, which $b=-\frac{1}{M}$ and *u* is the control variable. Equation (3) is completed with the initial conditions $v_z(\tau)$=$v_{z_0}(\tau)$, $\tau\in(-\infty,t]$. The cost function of the variational optimal control problem is described by the quadratic functional $\widetilde{J}$, the optimal control problem is stated as:

$$min\ \widetilde{J}=\int_{-\infty}^{T}\frac{1}{2}q{v_z}^2+\frac{1}{2}ru^2\,dt \\ \text{subjected to} \\ \dot{v_z}=bu+bK*v_z \tag{4}$$

where $*$ is the convolution product. When, introducing the Lagrange multiplier λ, the cost function becomes:

$$J = \int_{-\infty}^{T} \frac{1}{2} q {v_z}^2 + \frac{1}{2} r u^2 + \lambda(\dot{v_z} - bu - bK * v_z)\, dt \tag{5}$$

where *q* and *r* are gain parameters. The minimization of the functional *J* implies:

$$\delta J = \delta \int_{-\infty}^{T} L(v_z, \dot{v_z}, \lambda, u)\, dt - \delta \int_{-\infty}^{T} \lambda b K * v_z\, dt \tag{6}$$

and when it is expressed in terms of the variations δv_z, $\delta \dot{v_z}$, $\delta\lambda$, δu, produces the associated Euler-Lagrange equations:

$$\begin{cases} \dot{\lambda} = q v_z - b \displaystyle\int_{t}^{T} \lambda(\tau) K(\tau - t)\, d\tau \\ \dot{v_z} = \lambda \dfrac{b^2}{r} + b \displaystyle\int_{-\infty}^{t} K(t-\tau) v_z(\tau)\, dt \\ v_z(\tau) = v_{z_0}(\tau),\ \tau \in (-\infty, t] \\ \lambda(T) = 0 \end{cases} \tag{7}$$

Where the variations of the last term of equation (6) are:

$$\int_{-\infty}^{T} \lambda(t) \left[\delta \int_{-\infty}^{t} bK(t-\tau) v_z(\tau)\, d\tau \right]\, dt = \int_{-\infty}^{T} b \int_{t}^{T} \lambda(\tau) K(\tau - t)\, d\tau\, \delta v_z(t)\, dt \tag{8}$$

The system (7) consists of two integral-differential equations and one linear algebraic equation, which $u = \frac{b}{r}\lambda$.

4 Implicit solution of the variational problem

Equations (7) can be solved by numerical techniques, for example based on forward finite differences formulation:

$$\begin{cases} q v_{z_i} - \dfrac{\lambda_{i+1}}{\Delta T} + \dfrac{\lambda_i}{\Delta T} - b \displaystyle\sum_{j=i}^{N} \lambda_j K_{j-i} \Delta t = 0 \\ \dfrac{v_{z_{i+1}}}{\Delta T} - \dfrac{v_{z_i}}{\Delta T} - \lambda_i \dfrac{b^2}{r} - b \displaystyle\sum_{j=-\infty}^{i} v_{z_j} K_{i-j} \Delta t = 0 \\ v_{z_j} = v_{z_0},\ j \in (-\infty, i] \\ \lambda_T = 0 \end{cases} \tag{9}$$

with $N = \frac{T}{\Delta t}$ and Δt the discretization time interval.
We start with the vector of unknowns as $\{\boldsymbol{\eta}_{\boldsymbol{v_z}}^{\boldsymbol{(1,N)}}, \boldsymbol{\eta}_{\boldsymbol{\lambda}}^{\boldsymbol{(0,N-1)}}\}^T$, $\boldsymbol{\eta}_{\boldsymbol{v_z}}^{\boldsymbol{(1,N)}}$=$\{v_{z_1}, ..., v_{z_i}, ..., v_{z_N}\}^T$, $\boldsymbol{\eta}_{\boldsymbol{\lambda}}^{\boldsymbol{(0,N-1)}}$=$\{\lambda_0, \lambda_1, ..., \lambda_i, ..., \lambda_{N-1}\}^T$, where the *(N,M)* indicates dependence on the time values of t_i for $i \in [N, M]$. Analogously, $\{\boldsymbol{\xi}_{\boldsymbol{v_z}}^{\boldsymbol{(0)}}, 0\}^T$ where $\boldsymbol{\xi}_{\boldsymbol{v_z}}^{\boldsymbol{(0)}}$=$\{x_0\}$. Equation (9) in matrix form becomes:

$$\chi^{(0,N-2)} \left\{ \begin{array}{c} \boldsymbol{\eta}_{\boldsymbol{v_z}}^{\boldsymbol{(1,N)}} \\ \boldsymbol{\eta}_{\boldsymbol{\lambda}}^{\boldsymbol{(0,N-1)}} \end{array} \right\} = \Psi^{(0,N-1)} \left\{ \begin{array}{c} \boldsymbol{\xi}_{\boldsymbol{v_z}}^{\boldsymbol{(0)}} \\ 0 \end{array} \right\} \tag{10}$$

with obvious solution:

$$\left\{ \begin{array}{c} \boldsymbol{\eta}_{\boldsymbol{v_z}}^{\boldsymbol{(1,N)}} \\ \boldsymbol{\eta}_{\boldsymbol{\lambda}}^{\boldsymbol{(0,N-1)}} \end{array} \right\} = \chi^{(0,N-2)^{-1}} \Psi^{(0,N-1)} \left\{ \begin{array}{c} \boldsymbol{\xi}_{\boldsymbol{v_z}}^{\boldsymbol{(0)}} \\ 0 \end{array} \right\} \tag{11}$$

5 Feedback via model predictive control

The key strategy does not implies the use of the complete solution $\{\boldsymbol{\eta}_{\boldsymbol{v_z}}^{\boldsymbol{(1,N)}}, \boldsymbol{\eta}_{\boldsymbol{\lambda}}^{\boldsymbol{(0,N-1)}}\}^T$ and $u = \frac{b}{r}\boldsymbol{\eta}_{\boldsymbol{\lambda}}^{\boldsymbol{(0,N-1)}}$ along the time interval $[0, T]$ determined in the previous section, as for equation (11). We use only the first output for *u*, associated at the time $t = t_0$, to which is associated the first output for the state at the time $t = t_1$. Therefore, at the time $t = t_1$ we know v_{z_0}, v_{z_1}, λ_0 (and u_0). This terms are collected into the vector $\{\boldsymbol{\xi}_{\boldsymbol{v_z}}^{\boldsymbol{(0,1)}}, \boldsymbol{\xi}_{\boldsymbol{\lambda}}^{\boldsymbol{(0)}}\}^T$ and the unknowns are reduced to $\{\boldsymbol{\eta}_{\boldsymbol{v_z}}^{\boldsymbol{(2,N)}}, \boldsymbol{\eta}_{\boldsymbol{\lambda}}^{\boldsymbol{(1,N-1)}}\}^T$=$\{v_{z_2}, v_{z_2}..., v_{z_N}, \lambda_1, ..., \lambda_{N-1}\}^T$. The matrix $\chi^{(1,N-2)}$ reduces obviously its dimensions, following the reduction of the number of the unknowns. The matrix $\Psi^{(1,N-1)}$ increases its dimension, following the increase of the known term $\{\boldsymbol{\xi}_{\boldsymbol{v_z}}^{\boldsymbol{(0,1)}}, \boldsymbol{\xi}_{\boldsymbol{\lambda}}^{\boldsymbol{(0)}}\}^T$. Iterating this process at the generic *k-th* step one obtains:

$$\left\{ \begin{array}{c} \boldsymbol{\eta}_{\boldsymbol{v_z}}^{\boldsymbol{(k,N)}} \\ \boldsymbol{\eta}_{\boldsymbol{\lambda}}^{\boldsymbol{(k-1,N-1)}} \end{array} \right\} = \chi^{(k-1,N-2)^{-1}} \Psi^{(k-1,N-1)} \left\{ \begin{array}{c} \boldsymbol{\xi}_{\boldsymbol{v_z}}^{\boldsymbol{(0,k-1)}} \\ \boldsymbol{\xi}_{\boldsymbol{\lambda}}^{\boldsymbol{(0,k-2)}} \\ 0 \end{array} \right\} \tag{12}$$

In equation (7) an external disturbance $n_{v_z}(t)$ is now introduced which models an error in the theoretical modelling of the system or/and an external not controllable force. In fact, the solution of the two boundary problem in (7) precludes the knowledge of these external disturbances along the entire time domain $[0, T]$, that would imply the knowledge of the future values for $n_{v_z}(t)$. Introducing $n_{v_z}(t)$ equation (3) becomes:

$$\dot{v_z} = bu + b \int_{-\infty}^{t} K(t - \tau) v_z(\tau)\, dt + n_{v_z}(t) \tag{13}$$

with the initial condition $v_z(\tau) = v_{z_0}(\tau),\ \tau \in (-\infty, t]$. Equation (13) corresponds to the model of the system that includes the noise, while equation (7), the best representation of the system, is used to determine the control law to be applied to equation (13).

6 Numerical results

The integral MPC method, which includes memory effects, is applied to the control of the heave motion of the vehicle. This optimal control starting from an initial known value of the vehicle velocity, is finalized to minimize the vehicle fluctuations. The external noise $n_{v_z}(\mu, \sigma)$ is a random variable described by Gaussian normal distribution, μ its mean value, σ its standard deviation. The values of the parameters which characterize the dynamic of the model are shown in Table 1. Different kind of external disturbances are considered. Table 2 shows the expression of the disturbances inserted into the simulated dynamic system.

Table 1: Parameters values

Parameter	**Value**	**Unit**
M	10	kg
$v_{z_0}(\tau)$	1	$\frac{m}{s}$
ΔT	0.1	s
T	15	s

Table 2: External modeled disturbances

Disturbances	**Expression**
Zero	$n_{v_z} = 0$
Gaussian random $\sigma = 0.2$	$n_{v_z} = N(0, 0.2)$
Gaussian random $\sigma = 0.5$	$n_{v_z} = N(0, 0.5)$
Gaussian random $\sigma = 0.8$	$n_{v_z} = N(0, 0.8)$

The performances of the integral MPC is measured by the merit parameter:

$$Q_{MPC,\alpha} = \frac{J_{MPC} - J_\alpha}{J_\alpha} \cdot 100 \tag{14}$$

where J_{MPC} and J_α represent the cost function of the integral MPC and that of the method α, the LQR or Pontryagin solution. Figures 3 show the heave velocity and the control force when $n_{v_z} = 0$. In this case the integral MPC matches with the Pontryagin solution and presents best performaces than the LQR control method.

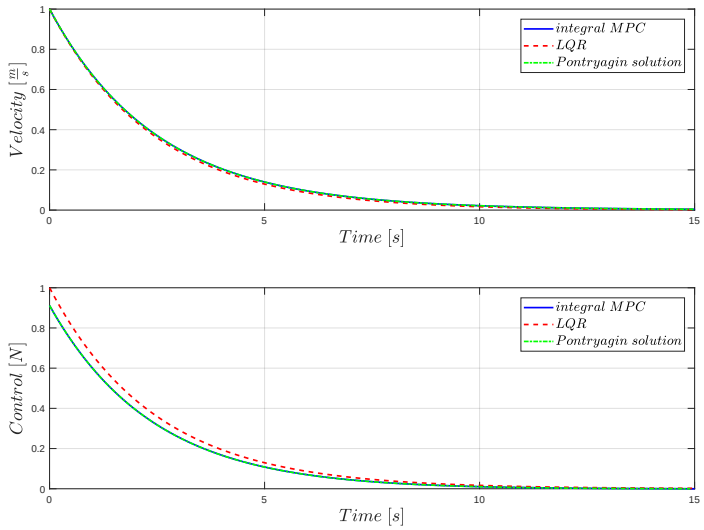


Figure 3: Zero external disturbances

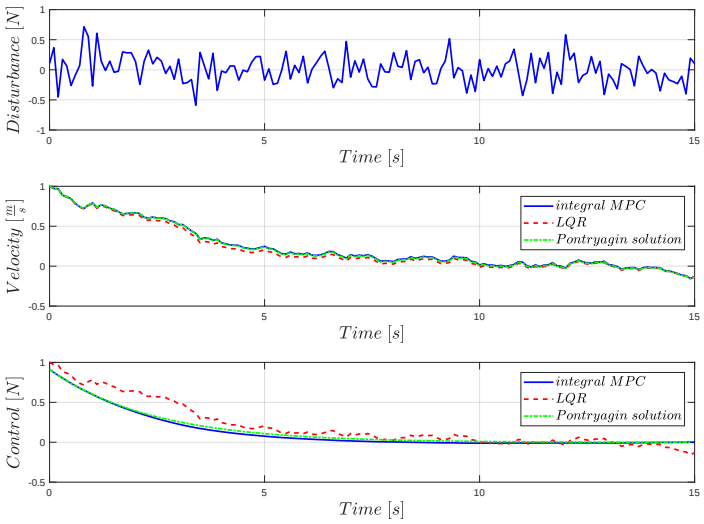


Figure 4: Gaussian random disturbances $\sigma = 0.2$

The performance of the integral MPC are compared with the LQR and the Pontryagin solution. Different levels of the disturbance in terms of standard deviation σ are considered: $\sigma = 0.2$ (fig. 4), $\sigma = 0.5$ (fig. 5) and $\sigma = 0.8$ (fig. 6). It appears the integral MPC shows better performances with respect to the benchmark LQR method for any type of numerical test. Table 3 shows the comparison between the Q's, defined by eq. (14).

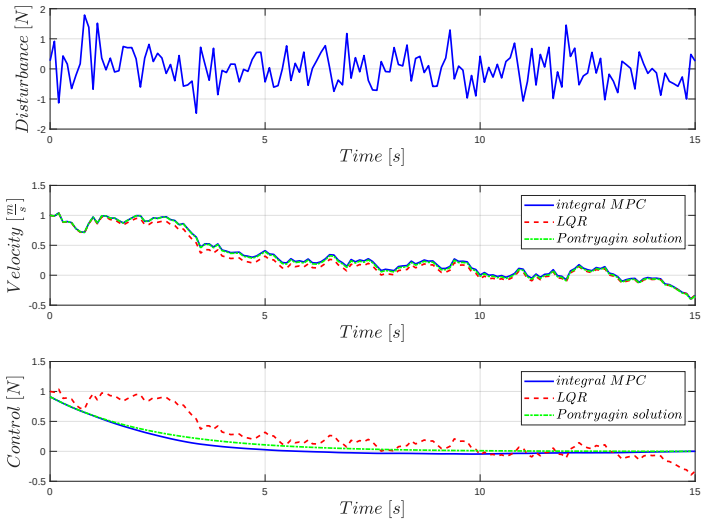


Figure 5: Gaussian random disturbances $\sigma = 0.5$

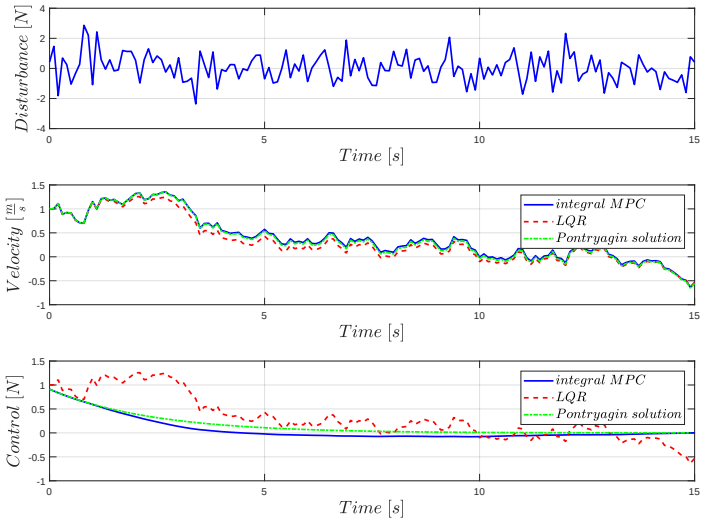


Figure 6: Gaussian random disturbances $\sigma = 0.8$

Figure 7 shows the cost function values J for each solution method for increasing random noise levels. A random external disturbance is applied on the system $n_v(\mu, \sigma)$ which has zero mean value μ and a standard deviation, σ, from zero value up to 1. The results show higher performaces in term of minimization of cost function of the integral MPC method respect to the LQR one and also to the Pontryagin solution when $0 < \sigma < 0.7$. For $0.7 < \sigma < 1$ values Pontryagin

Table 3: Merit parameter $[\%]$

Simulation	$Q_{MPC,LQR}$	$Q_{MPC,P}$
Zero disturbances	9	0
Gaussian random $\sigma = 0.2$	28	1.4
Gaussian random $\sigma = 0.5$	67.5	1.5
Gaussian random $\sigma = 0.8$	118.4	1

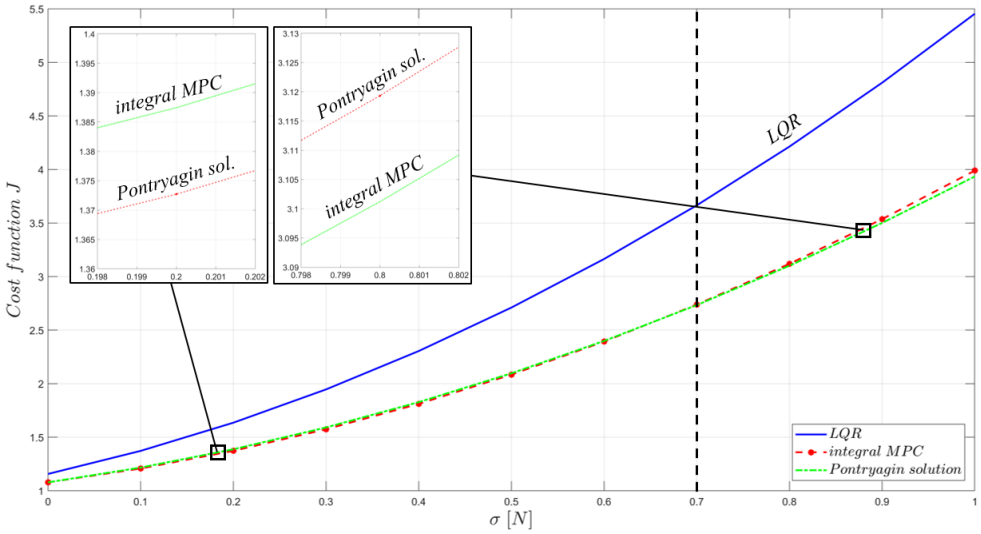


Figure 7: Cost function J at different disturbance levels

solution shows a better behaviour respect to the integral MPC.

7 Final comments

In this paper we examine a problem related to the control of fluctuations of small vehicles in a marine environment. The mathematical model of this engineering problem is an integral-differential equation that describes vortex shedding, added damping and mass effects. The optimal control literature does not include such mathematical model in standard control, that normally refers to differential equations. In the present work we describe a prototype equation that is integral-differential, such that a suitable method of optimal control is presented. Technically, the equations are solved by a direct discretization approach and through the use of a MPC model predictive control scheme. This allows the inclusion of external disturbances that are not known a priori. The method shows very good results, and comparisons are made with respect to the LQR analysis and the exact Pontryagin optimality solution.

References

[1] H. Ben-Gida, A. Liberzon, and R. Gurka, "A stratified wake of a hydrofoil accelerating from rest," *Experimental Thermal and Fluid Science*, vol. 70, pp. 366–380, jan 2016.

[2] J. Wang, P. Han, X. Deng, H. Dong, E. Akoz, and K. Moored, "Effects of flapping waveforms on the performance of intermittent swimming in viscous flows," in *2018 AIAA Aerospace Sciences Meeting*. American Institute of Aeronautics and Astronautics, jan 2018.

[3] Y. Jin and P. Dong, "A novel wake oscillator model for simulation of cross-flow vortex induced vibrations of a circular cylinder close to a plane boundary," *Ocean Engineering*, vol. 117, pp. 57–62, may 2016.

[4] B. Huynh and T. Tjahjowidodo, "Experimental chaotic quantification in bistable vortex induced vibration systems," *Mechanical Systems and Signal Processing*, vol. 85, pp. 1005–1019, feb 2017.

[5] T. Battista, C. Woolsey, T. Perez, and F. Valentinis, "A dynamic model for underwater vehicle maneuvering near a free surface," *IFAC-PapersOnLine*, vol. 49, no. 23, pp. 68–73, 2016.

[6] S. K. Shariati and S. H. Mousavizadegan, "The effect of appendages on the hydrodynamic characteristics of an underwater vehicle near the free surface," *Applied Ocean Research*, vol. 67, pp. 31–43, sep 2017.

[7] T. Theodorsen, *General theory of aerodynamic instabilities and the meccanism of flutter*. Naca report, 1935, vol. 496, no. 413-433.

[8] M. Kim, H. Joe, J. Kim, and S. cheol Yu, "Integral sliding mode controller for precise manoeuvring of autonomous underwater vehicle in the presence of unknown environmental disturbances," *International Journal of Control*, vol. 88, no. 10, pp. 2055–2065, jul 2015.

[9] S. Sedaghati, F. Abdollahi, and K. Khorasani, "Model predictive and non-cooperative dynamic game fault recovery control strategies for a network of unmanned underwater vehicles," *International Journal of Control*, pp. 1–29, aug 2017.

[10] G. Pepe and A. Carcaterra, "VFC – variational feedback controller and its application to semi-active suspensions," *Mechanical Systems and Signal Processing*, vol. 76-77, pp. 72–92, aug 2016.

[11] G. Pepe, A. Carcaterra, I. Giorgio, and D. D. Vescovo, "Variational feedback control for a nonlinear beam under an earthquake excitation," *Mathematics and Mechanics of Solids*, vol. 21, no. 10, pp. 1234–1246, aug 2016.

[12] G. Pepe and A. Carcaterra, "A new semi-active variational based damping control," in *2014 IEEE/ASME 10th International Conference on Mechatronic and Embedded Systems and Applications (MESA)*. IEEE, sep 2014.

[13] F. Arrichiello, G. Antonelli, and E. Kelholt, "Shape estimate of a streamer of hydrophones towed by an autonomous underwater vehicle," *IFAC - PaperOnLine*, vol. 49, no. 23, pp. 181–186, 2016.

[14] E. Paifelman, "A comparison between mathematical models of stationary configuration of an underwater towed system with experimental validations," in *OCEANS 2017 - Aberdeen*. IEEE, jun 2017.

[15] P. Vinod, R. Francis, P. Prabhasuthan, and O. Nandagopan, "Depth enhancement of an underwater towed system using hydrodynamic depressor," *Defence Science Journal*, vol. 66, no. 5, p. 546, sep 2016.

[16] Z. Feng and R. Allen, "Evaluation of the effects of the communication cable on the dynamics of an underwater flight vehicle," *Ocean Engineering*, vol. 31, no. 8-9, pp. 1019–1035, jun 2004.

[17] J. Newmann, *Marine hydrodynamics*. MIT Press, Cambridge, 1978.

[18] R. Jones, *The unsteady lift of a wing of finite aspect ratio*. Naca report, 1940, vol. 681, no. 31-36.

Optimization of skyhook control strategies and an alternative approach for the operational conditions

G. Papaioannou [1], **D. Koulocheris** [1]
[1] NTU of Athens, Mechanical Engineering, Department of Mechanical Design & Automatic Control, Vehicles Laboratory
Zografou Campus, Iroon Polytechniou 9, 15780, Athens, Greece
e-mail: **gdpapaioan@gmail.com**

Abstract
The aim of this work is to present a comparison of the main semi-active suspension systems for a passenger car using Logical Control. Their comparison will be conducted after having optimized them in respect with ride comfort and road holding. In this work, the semi active suspensions studied are comfort oriented and consist of (a) two versions of Skyhook control (SH-2 and SH-L, two states and linear approximation damper respectively), (b) the acceleration driven damper (ADD), (d) one version of the combination of Skyhook and ADD (SH-ADD) and (e) a second version implemented with the use of a sensor. Thus, a half car model, with a passenger and a seat, was excited by a random road profile of class C. The model was optimized using genetic algorithms (GA). This study, firstly, aims to highlight how the optimization of the vehicle model could lead to the best compromise between ride comfort and road holding, and secondly, the test of an alternative approach in the operational conditions of the control algorithms.

1 Introduction

Ride comfort is related to the passenger's perception of the moving vehicle's environment, while road holding is the degree to which a car maintains contact with the road surface in various types of directional changes. The aforementioned characteristics are related to the main conflict in the automotive industry [1, 2], where a good design of a suspension system can combine to some extent ride and stability. Thus, the optimization of them has been discussed extensively in the literature [3]. Suspension systems are classified by the way they are controlled in three categories : passive [4], semi-active [5] and active. From 1970s, semi-active suspensions have received much more attention and the research in their field follows two mainstreams. The first one consists of the study of new technologies of semi-active actuation of damping [6, 7]. While, the second mainstream studies the design of semi-active control strategies. In our work, the attention is turned on the optimum damping ratios and the control strategy.

Changing the damping ratio is a very interesting opportunity for a suspension designer so as to try and compromise more successfully the trade-off between road holding and ride comfort. Therefore, there exists a large number of researches where the development of modern optimization methods opened new perspectives in the field. In order to address the conflicting targets of ride comfort and road holding, single (SOO) and multi-objective (MOO) methods have been formed. The SOO offers a limited insight in the suspension optimization problem but due to its simplicity it is often selected. On contrary, MOO is offering an insight of the conflicted targets through the Pareto front. A simple multi-objective dealing strategy, known as pseudo-MOO technique, suggests the combination of multiple objective functions using weighting factors, so as to convert the MOO problem into a SOO one. Koulocheris et al. [3] compared the efficiency of various objective functions in SOO and pseudo-MOO approaches in the optimization of suspension systems of a heavy vehicle with three different optimization methods conducting conclusions regarding the optimum solutions in terms

of the results and the convergence of the problem.

In order to avoid the need to prespecify arbitrary weighting coefficients various methodologies have already been applied successfully. The Pareto Front approach is popular among optimization problems with conflicting targets. Nariman et al. [8] investigated the use of a uniform-diversity Genetic Algorithm in the Pareto optimization method, selecting five targets concentrating mainly in the handling and the road holding of the vehicle. Crews et al. [9] demonstrated a method for determining the optimality of control algorithms based on two performance objectives, the ride quality, as measured by absorbed power, and thermal performance, as measured by power dissipated in the suspension damper. Whereas, Gadhvi et al. [10] also dealt with the use of different optimization techniques in order to minimize the root mean square values of (i) the vertical acceleration experienced by the passenger's seat, (ii) the front tire deflection and (iii) the rear tire deflection, selecting objective functions depicting the ride comfort and the road holding. The selection of objective functions in the work of Gadhvi et al. [10] followed the work of Koulocheris et al. [3] regarding the importance of the objective functions where the variance of the vertical acceleration as well as the one of the tire deflections were highlighted as the most important ones. Similarly, Koulocheris et al. [11] compared the optimal solutions for various semi-active control laws providing conclusions regarding their behavior and an initial suggestion regarding their operational conditions, which will be extended and used in this work.

This work concentrates on the MO optimization using the Pareto Fronts of the most common ride-comfort oriented control algorithms of semi-active suspension systems. The main aim is to compare the optimum solutions of the algorithms and apply to three of them an alternative control strategy in order to improve the vehicle's dynamic behavior. The proposed control strategy, on contrary with the traditional SH ones, quantifies the severity of the operational conditions and control the damper's state based on their magnitude and not based on their sign. This value of the threshold depends on the class of the road profile that the vehicle drives through and it is evaluated with the use of the cumulative distribution function (CDF) of the algorithm's operational conditions. The modified algorithms will be compared with the traditional ones through the Pareto Fronts.

The organization of this paper is as follows: in Chapter 2 a brief description of the vehicle model and the passenger model used are presented along with important performance indexes used in this work, in Chapter 3 the control algorithms are presented and a proposed approach regarding the operational conditions is displayed, while in Chapter 4 the random road excitation applied in our vehicle model is is illustrated, whilst in Chapter 4 the optimization procedure is outlined, and finally, in Chapter 6 conclusions are presented.

2 Simulation Models

In the current study, the dynamic behavior of a passenger vehicle is investigated, as far as the vertical vibrations induced by the road surface are concerned. Different semi active suspension systems are applied to the vehicle model, so as to compare them and extract conclusion regarding their behavior. Moreover, a passenger model is added on the vehicle in order to study the human response in different riding conditions.

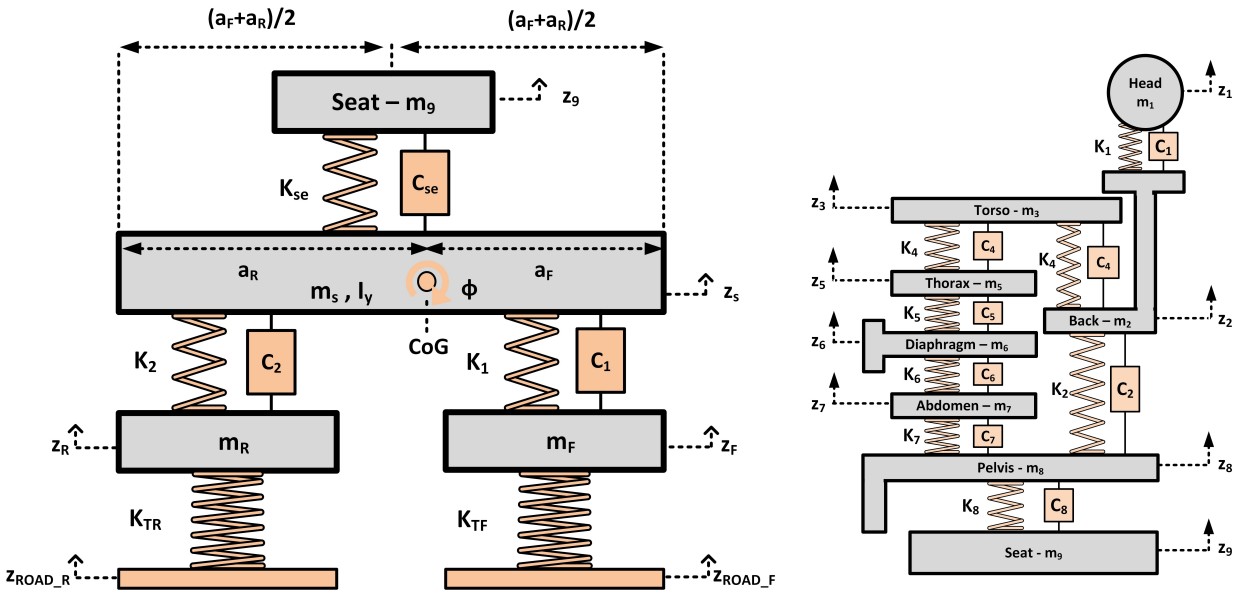
Parameters		**Subscripts**	
z:	Vertical motion coordinate	S:	Body
θ :	Pitch motion coordinate	F:	Front
m:	Mass	R:	Rear
a:	Distance of the GG of the vehicle	T:	Tire
C:	Damper's Coefficient	ROAD	Road Excitation
K:	Spring's Stiffness Coefficient		

Table 1: Nomenclature of vehicle parameters

2.1 Vehicle Model

A half car model, equipped with a seat and a 7-DOF human-body model is considered for analysis. The model includes the front and rear axle allowing the observation of the pitch phenomena. As shown in Fig. 1a, the vehicle model consists of three basic subsystems: the tires, the suspension systems and the body of the vehicle. The latter is considered as a rigid body of mass m, equal to the half of the total mass of the vehicle. The distance of the front and rear unsprung masses (m_F and m_R) from the center of mass is equal to a_F and a_R, respectively. The front and rear tires are modelled as linear springs, which receive as input the irregularities of the road profile.

Ideally, a suspension system should adjust its characteristics in order to function properly under different road conditions, ensuring the comfort of the travel and the safety of the vehicle. This adjustment is achieved through the use of semi active suspensions.



(a) • (b) •

Figure 1: (a) Half Car Model, (b) Seat-Passenger Model

Parameters	Values	Parameters	Values
m_s [kg]	520	a_F[m]	0.91
I_z [kg m^2]	473	a_R[m]	1.55
m_R, m_F [kg]	25	K_{TR}, K_{TF}[N/m]	2.00 10^5
e [m]	0.4		

Table 2: Parameters of half car model

The governing equations of the vehicle model are the following:

Body Bounce:

$$m \bullet \ddot{z}_s + C_F \bullet (\dot{z}_s - \dot{z}_F - a_F \bullet \dot{\theta}) + C_R \bullet (\dot{z}_s - \dot{z}_R + a_R \bullet \dot{\theta}) + K_{l_F} \bullet (z_s - z_F - a_F \bullet \theta + K_{l_R} \bullet (z_s - z_R + a_R \bullet \theta) = \quad (1)$$

Front Wheel Bounce:

$$m_F \bullet \ddot{z}_F - K_{l_F} \bullet (z_s - z_F - a_F \bullet \theta) - C_F \bullet (\dot{z}_s - \dot{z}_F - a_F \bullet \dot{\theta}) + K_{T_F} \bullet (z_F - z_{RoadF}) = 0 \quad (2)$$

Description	m [kg]	C [N.s/m]	K [N/m]
Seat(9)	15	2000	20000
Pelvis(8)	27.7	378	25500
Abdomen(7)	6.20	298	8941
Diaphragm(6)	0.46	298	8941
Thorax(5)	1.38	298	8941
Torso(3-4)	33.33	298	8941
Back(2)	6.94	3651	53460
Head(1)	6.20	3651	53460

Table 3: Parameters of seat and human body parameters

Rear Wheel Bounce:

$$m_R \bullet \ddot{z}_R - K_{l_R} \bullet (z_s - z_R + a_R \bullet \theta) - C_R \bullet (\dot{z}_s - \dot{z}_R + a_R \bullet \dot{\theta}) + K_{T_R} \bullet (z_R - z_{RoadR}) = 0 \quad (3)$$

Additionally, the seat and the passenger are modeled in order to investigate in depth the ride comfort of the passenger, as depicted in Fig. 1b. Different parts of the human body such as the pelvis, the diaphragm, the thorax etc. are described via several m−c−k subsystems and the parameters of each body part are presented in Table 3. The equations of the model as well as the parameters were retrieved from the literature [11]. The seat is excited by the vibration of the sprung mass without the coupling of any torques studying exclusively the vertical dynamics.

2.2 Performance Metrics

Important quantities or metrics indicating the dynamical behavior of the vehicle through the used model are the suspension travel and the tire deflection. The suspension travel (ST) depicts the ability of the suspension system to support the vehicle static weight. The vehicle static weight is well supported if the rattle space requirements of the vehicle are kept small. In the case of quarter car model, it can be quantified in terms of maximum suspension deflection undergone by the suspension or by its RMS value of ST (Eq. 4).

Whereas the tire deflection (TD) of the system and thus the normal tire forces illustrate the good road holding of the vehicle (Eq. 5). This performance can be characterized in terms of vehicle's cornering, braking and traction abilities and these abilities can be improved by minimizing the variations in normal tire loads, and thus its tire deflection considering that a tire roughly behaves like a spring. Therefore, the RMS value of tire deflection (Eq. 5) could be o good index for vehicle's road holding.

$$SuspensionTravel = \begin{cases} ST_F = z_s - z_F - a_F \bullet \theta, \text{ Front Suspension} \\ ST_R = z_s - z_R + a_R \bullet \theta, \text{ Rear Suspension} \end{cases} \quad (4)$$

$$TireDeflection = \begin{cases} TD_F = z_F - z_{RoadF}, \text{ Front Tires} \\ TD_R = z_R - z_{RoadR}, \text{ Rear Tires} \end{cases} \quad (5)$$

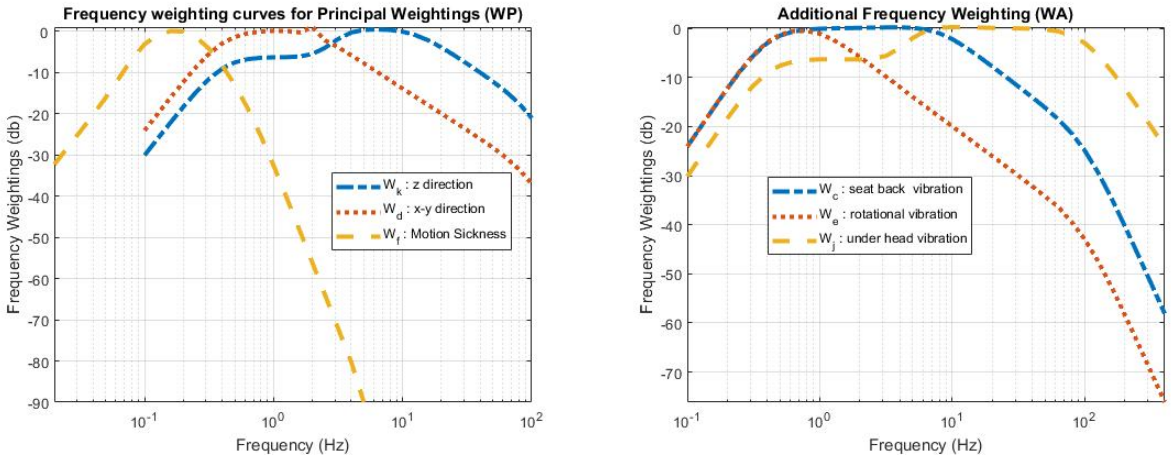
Moreover, a suspension system should be able to isolate a car body from road disturbances to provide good ride quality by reducing the vibratory forces transmitted from the axle to the vehicle body. This reduces vehicle body acceleration. In our case, through the results of the passenger model, the ride comfort could be measured via the Weighted RMS acceleration (RMS(a_w), Vibration Dose Value (VDV) and the Crest Factor (CF) of various subsystems. These characteristics are proposed by the ISO-2631 standard which evaluates the human exposure to whole-body vibration [12]. More specifically, the Weighted RMS acceleration is calculated through Eq. 6:

$$RC_i = RMS(\ddot{z}_{w_i}) = \left[\frac{1}{T}\left(\int_0^T \ddot{z}_{w_i}(t)^2 dt\right)\right]^{\frac{1}{2}} \tag{6}$$

where T is the duration of the measurement in seconds, $\ddot{z}_{w_i}$ is the weighted acceleration (translational or rotational) as a function of time (m/s^2) and i is the selected subsystem of the driver or the vehicle model so as to evaluate the $RMS(\ddot{z}_{w_i})$. The frequency weighting curves used based on ISO-2631 [12], are presented on the Fig. 2 and are used based on Eq. 7.

$$Z_{w_i} = WP_{i_1} * WA_{i_2} * Z_i \tag{7}$$

where Z_i is the measured acceleration z_i in the frequency domain, WP is the principal frequency weightings related to health, comfort and perception depicting the weighting frequency either for the z direction and for vertical recumbent direction except the head (i_1=k) or for the x-y direction and for horizontal recumbent position (i_1=d) and finally WS is the additional frequency weightings related (a) seat back measurements (i_2=c), (b) measurements for rotational vibrations (i_2=e), (c) measurement of vibration under the head of recumbent person (i_2=j). In case there is no need for additional weighting of the measurement WA is equal to 1.



(a) • (b) •

Figure 2: (a) Principal Frequency Weightings-WP, (b) Additional Frequency Weightings-WA

3 Semi active control laws

As it was mentioned before, the most classical control laws that have been implemented for semi-active suspension systems are the Logical Control Strategies. As far as they are concerned, the two most common types are the ”on-off” and the continuous ones. For the on-off logical dampers the damping is switched between the minimum and maximum level based on conditions that define the damper. While for the continuous logical dampers, the damping is adjusted in the whole range between the minimum and maximum levels. The most common types of logical semi active dampers are the 2-States Skyhook Control (SH-2), Skyhook Linear Control (SH-L), Acceleration Driven Damper Control (ADD), and two different versions of the combination of Skyhook and ADD Control (SH-ADD-1 and SH-ADD-2). All the above are comfort oriented, improving the ride comfort of the passengers by adjusting the damping coefficient of the suspension system according to the dynamic behavior of the vehicle and its response to the applied road excitation. Many different versions of these algorithms have been presented in the past, by changing slightly their operational conditions.

3.1 Proposed Control Algorithm

In the past, the operational condition was mainly checking the sign of a product in order to change the damper's state. In an attempt to minimize the chattering and improve significantly other aspects of the vehicle's performance, the proposed modified algorithm uses an appropriate threshold in the algorithms' operational conditions, as shown in Eq. 9, on contrary with the various versions of Skyhook (SH) algorithms that exist in the literature and use the logical control of Eq. 8.

The alternative control strategy lies upon the fact that the proposed algorithm quantifies the severity of the operational conditions with the use of this threshold and controls the damper's state based on their magnitude and not based on their sign. The values used (A, B) in this work as thresholds of different operational conditions are not selected randomly, but they depend on the class of the road profile, that the vehicle drives through. They are evaluated after fitting the values of the algorithm's operational conditions to a distribution, and then using their cumulative distribution function (CDF) so as to reduce the times that the damper was working with C_{max}. For example in the case of SH-2, fitting the operational conditions in the normal distribution, the times that its value are larger than zero -i.e. the damper works with the C_{max} -belong to the 55% of the sample. Whereas, with applying the CDF approach in this work, the damper operates with C_{max} for 20% less points of the sample, as it is illustrated in Fig. 3. This avoids the stiffening of the damping coefficient when there is no need without risking the road holding of the vehicle. This is achieved because the conditions are checked based on their magnitude and not their sign and the direction of the vibration of the sprung or the unsprung mass.

$$C = \begin{cases} C_{min} & ,if\ condition \leq 0 \\ f(C_{max}) & ,if\ condition > 0 \end{cases} \tag{8}$$

$$C = \begin{cases} C_{min} & ,if\ condition \leq A \\ f(C_{max}) & ,if\ condition > A \end{cases} \tag{9}$$

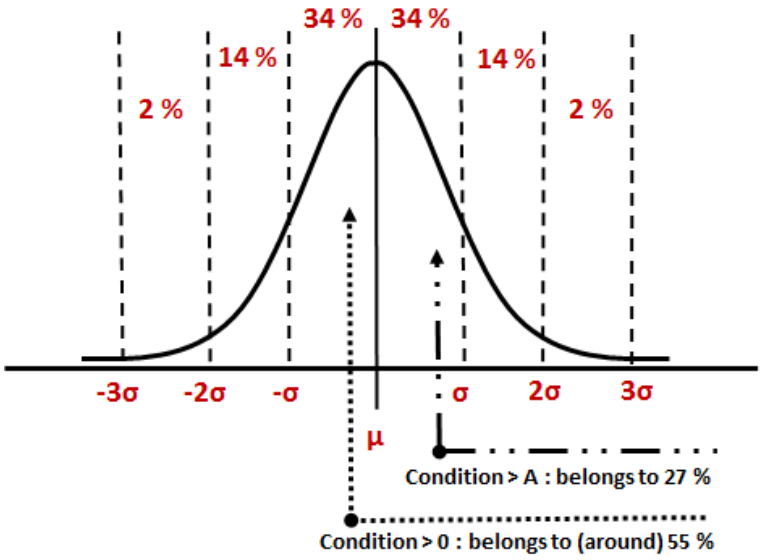


Figure 3: Cumulative Distibution Function on Normal Distribution

In this work, the operational conditions of five SH control strategies (SH-2, SH-L, ADD, SH-ADD-1 and SH-ADD-2) were optimized in order to be compared while in the three (SH-2, SH-L and SH-ADD-1) of them the proposed approach is adopted in an attempt to improve the vehicle's performance.

3.2 Modified Skyhook two states damper control (SH-2-CDF).

The 2-states control is an on-off strategy that switches between soft and stiff damping coefficient. This control law in literature consists of two states in which the damping factor C_u changes according to the sign of the product $\dot{ST}$ and $\dot{z}_s$. When the upper mass is moving up, and the two masses are getting closer, the damping constant should ideally be zero. Due to the physical limitations of a practical damper, a damping constant of zero is not practical and a low damping constant is used. When the upper mass is moving down and the two masses are getting closer, the Skyhook control policy ideally calls for an infinite damping constant. An infinite damping constant is not physically attainable, so in practice, the adjustable damping constant is set to a maximum. The effect of the Skyhook control scheme is to minimize the absolute velocity of the upper mass.

As it was described before, the CDF approach premises the use of a small threshold in the operational conditions. More specifically, in the SH-2, with the use of this threshold the control algorithm does not consider the direction of the movement of upper mass or if it is getting close with the unsprung or not. However, it quantifies the severity of this movement and it considers how fast they are going to get close or away. Then, based on the above, it selects to not change the damping coefficient in "less harmful and dangerous" situations, and continue using the soft value of the damper's state. The equation describing the control algorithm is presented in Eq. 10 .

$$C_i = \begin{cases} C_{min}, & if\ \dot{ST}_i\ \dot{z}_s < A \\ C_{max}, & if\ \dot{ST}_i\ \dot{z}_s > A \end{cases} \quad i = F, R \tag{10}$$

where $\dot{ST}_i$ is the stroke velocity of front or the rear damper, and C_{min} and C_{max} are the minimum and maximum damping factors achievable by the considered controlled damper, depicting the soft and the stiff damping coefficient respectively. The traditional SH-2 algorithm occurs by setting A equal to zero.

3.3 Skyhook linear approximation damper control (SH-L-CDF).

An improved version of Skyhook control has been used to achieve variable damping for additional energy saving. The linear approximation of the Skyhook control includes the change of the damping factor C_i according to the sign of the product of $\dot{ST}_i$ and $\dot{z}_s$:

$$C_i = \begin{cases} C_{min_i} & ,if\ \dot{ST}_i\ \dot{z}_s \leq A \\ \frac{\alpha C_{max_i} \dot{ST}_i + (1-\alpha) C_{max_i} \dot{z}_s}{\dot{ST}_i} & ,if\ \dot{ST}_i\ \dot{z}_s > A \end{cases} \quad i = F, R \tag{11}$$

where $\alpha \in [0,1]$ is a tuning parameter that modifies the closed-loop performances and enables the controller to adjust its stiff value (C_{max_i}) according to the needs of the application, saving more energy. More specifically, when a = 1, this control law is equivalent to the two-state Skyhook control. The traditional SH-L algorithm occurs by setting A equal to zero.

3.4 Acceleration driven damper control (ADD).

This strategy is shown to be optimal in the sense that it minimizes the vertical body acceleration when no road information is available (therefore, this control law is a comfort oriented one). The current control law is similar to the SH-2 approximation of the Skyhook algorithm, with the difference that the switching law depends on body acceleration $\ddot{z}_s$ instead of body speed $\dot{z}_s$.

While, the "switching dynamic" may influence the closed-loop performances, increasing the chatter effect significantly, due to the swift changing of values of the sprung acceleration which is involved in the operational conditions.

$$C_i = \begin{cases} C_{min,i} & ,if\ \dot{ST}_i \ddot{z}_s \leq 0 \\ C_{max,i} & ,if\ \dot{ST}_i \ddot{z}_s > 0 \end{cases} \quad i = F, R \tag{12}$$

The proposed approach of this work hasn't been adopted in this algorithm due to the fact that it is already using the $C_{min,i}$ for the 65 $\%$ of the samples.

3.5 Modified Mixed Skyhook-Acceleration driven damper control (SH-ADD-1).

As it was mentioned before, SH and ADD present complementary behaviors in terms of performance, with SH providing the best performance at low frequency (around the body resonance), and ADD ensuring optimality at mid and high frequency (beyond the body resonance). Therefore, a mixed control law has been proposed in the past using a very simple but effective frequency range selector.

$$C_i = \begin{cases} C_{SH-2} & ,if\ \ddot{z}_s^2 - a^2 \dot{z}_s^2 \leq 0 \\ C_{ADD} & ,otherwise \end{cases} \quad i = F, R \tag{13}$$

$$C_i = \begin{cases} C_{min,i}, & if \left(\ddot{z}_s^2 - a^2 \dot{z}_s^2 \leq 0\ and\ \dot{ST}_i \dot{z}_s \leq 0 \right) \\ & or \left(\ddot{z}_s^2 - a^2 \dot{z}_s^2 > 0\ and\ \dot{ST}_i \ddot{z}_s < 0 \right) \\ C_{max,i}, & otherwise \end{cases} \quad i = F, R \tag{14}$$

The parameter "α" represents the frequency limit between the low and the high frequency ranges. Specifically, the value of "α" is set at the crossover frequency (in rad/s) between SH and ADD. This law is almost optimal as it provides a mix of the best performance of the SH and ADD.

3.5.1 Modified Mixed Skyhook-Acceleration driven damper control with 1 sensor (SH-ADD-2-CDF).

The current law compromises the complementary performances of soft and stiff passive suspensions. Stiff suspension is able to damp optimally the body resonance, but without a desiring filtering at high frequencies. On the contrary, a soft suspension ensures the best filtering but with the drawback of a poorly damped body resonance. This law operates according to the current value of $\ddot{z}_s^2 - a^2 \dot{z}_s^2$, as shown in Eq. 15

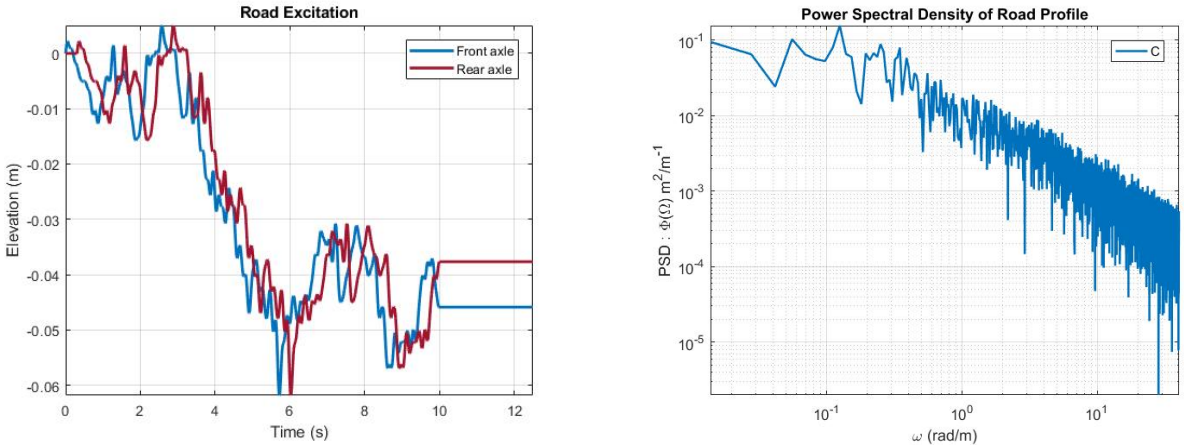
$$C_i = \begin{cases} C_{min,i}, & if\ \ddot{z}_s^2 - a^2 \dot{z}_s^2 \geq B \\ C_{max,i}, & if\ \ddot{z}_s^2 - a^2 \dot{z}_s^2 < B \end{cases} \quad i = F, R \tag{15}$$

In the previous versions, the soft damping condition is selected when it is positive, otherwise the hard-damping condition is used. In the modified version of CDF, the frequency selector is controller based on its value, if it is higher than a specific value (B). This specific value is evaluated again with the cumulative distribution function of the operational conditions. Similarly to the mixed SH-ADD-1, the amount $\ddot{z}_s^2 - a^2 \dot{z}_s^2$ can be considered as a simple "frequency-range selector", where the parameter "a" represents the limit between the ranges of low and high frequency. The traditional SH-ADD-2 algorithm occurs by setting B equal to zero.

4 Road Excitation

The irregularities on the road cause disturbances which are classified as shock or vibration. The first is related to discrete disturbances, usually associated with higher amplitudes, such as a bump or a pothole. The latter is related to continuous irregularities, such as an unpaved road. Both types have different requirements for the suspension system, but in order for the designer to design one has to fulfill both these applications. Thus, road profile generation is a strong asset for the researchers, as it enables them to test the vehicle under different road conditions. most common approach in the literature is the study of a vehicle under a road bump [3,4,8,13,14] or a random road profile [15–17]. In this research, a random road profile of Class C was generated as it is shown in 4, so as to optimize the controllable dampers under a severe road excitation.

4.1 Random Road Profile



(a) • (b) •

Figure 4: Road profiles in (a) Time Domain , (b) Frequency Domain

The excitation used in this work involves a random road profile, generated based on the ISO 8608 regulation [18]. ISO 8608 regulation classifies road profiles according to the quality of the road. The road profile can be represented by a PSD function as shown in Fig. 4b. The power spectral densities of roads show a characteristic drop in magnitude with the wave number. To determine the power spectral density function, or PSD, it is necessary to measure the surface profile with respect to a reference plane. Random road profiles can be approximated by a PSD in the form of:

$$\Phi(\Omega) = \Phi(\Omega_0)\left(\frac{\Omega}{\Omega_0}\right)^{-w} \tag{16}$$

where $\Omega = \frac{2\pi}{L}$ in rad/m denotes the angular spatial frequency, L is the wavelength, $\Phi(\Omega_0)$ in $m^2/(rad/m)$ describes the values of the psd at the reference wave number $\Omega_0 = 1\ rad/m$, $n = \frac{\Omega}{2\pi}$ is the spatial frequency, $n_0 = 0.1 cycle/m$ and w is the waviness, for most of the road surfaces equal to 2.

Based on the work of Tyan et al. [19], a random road profile C was generated using a sinusoidal approximation. If the vehicle is assumed to travel with a constant speed V over a given road segment with length (L_s), a random road profile can be approximated by a superposition of N($\rightarrow \infty$) sine waves then:

$$y(t) = \sum_{n=1}^{N} A_n sin(n\omega_0 t - \phi_n) \tag{17}$$

where the fundamental temporal frequency:

$$\omega_0 \triangleq V\Delta\Omega, \Delta\Omega \triangleq V\frac{2\pi}{L} \tag{18}$$

where s and the amplitude A_i are defined as:

$$A_i = \sqrt{\Phi(\Omega_i)\frac{\Delta\Omega}{\pi}},\ i = 1, ..., N \tag{19}$$

in which $\Delta\Omega = \frac{\Omega_N - \Omega_1}{N-1}(rad/sec)$, the phase angles ϕ_n, $n = 1, ..., N$ are treated as random variables following a uniform distribution in the interval of $[0, 2\pi)$ and V is the vehicle's velocity which is considered constant. The velocity of the vehicle in this case was set at 30 km/m for the road profile with L_s=1000m. The profile is illustrated in Fig. 4, displaying both the time domain (Fig. 4a) and the frequency domain (Fig. 4b) data of the road profiles.

5 Optimization Procedure

A multi objective optimization was applied to the model in respect to ride comfort and road holding using the Pareto front for several constraints. As design variables of the optimization, the damping ratios of the controllable dampers and the spring stiffness were selected, as shown in Eq. 20:

$$\text{design variables}=[K_F; C_{max,F}; C_{min,F}; K_R; C_{max,R}; C_{min,R}] \tag{20}$$

where $C_{min,F}$, $C_{max,F}$, $C_{min,R}$ and $C_{max,R}$ were the minimum and maximum achievable damping coefficient of the front and rear damper, respectively, according to the semi active control laws selected for optimization. Additionally, in semi active control laws SH-L, SH-ADD-1 and SH-ADD-2 the tuning coefficient "a" was added as a design variable.

The bounds of the design variables are illustrated in Table 4. Moreover, the optimization of the passive model was carried out for two different bounds for the damping coefficient of the front and rear suspension. At first, the bounds of the minimum damping coefficient of the semi active laws were used (PS-LP) and then the ones of the maximum damping coefficient were applied to the design variables (PS-UP). The bounds of the springs' stiffness were the same.

The objective functions of the optimization were selected so as to improve both the ride comfort and the road holding, using Eq. 6 and the average of the RMS values of Eq. 5. Therefore, two targets were chosen: the root mean square of the seat's acceleration (f_1), representing the ride comfort, and the average of the variances of both the front and rear tire deflections (f_2), representing the road holding, as shown in Table 4. The constraints used in the optimization problem were selected so as to incorporate the practical considerations into the design process, such as the working space of the suspension system, as well as to enhance the optimization targets, as shown in Table 4. Moreover, $f_3 \left(= \frac{RMS(ST_F)+RMS(ST_R)}{2} \right)$ was evaluated for all the solutions, so as to study the pareto fronts regarding the suspension travels.

After obtaining the optimum results, the CDF approach was implemented in SH-2, SH-L and SH-ADD-2 algorithms and by using the optimum design variables of Cases 1, 2 and 4, the vehicle model was simulated and the objectives (f_1,f_2 and f_3) were evaluated. In this way, the "pseudo" Pareto Fronts of SH-2-CDF, SH-L-CDF and SH-ADD-2-CDF were produced. All the results are presented in Fig. 5 and Fig. 6, where the Pareto Fronts of f_1 - f_2 and of f_1 - f_3 are illustrated respectively.

Design Variables	Bounds		Objectives	Constraints
	Lower	Upper		
$C_{min,F}, C_{min,R}$ [N.s/m]	500	2500	$f_1 = RC_9$	$ST_i \leq 0.127$m
$C_{max,F}, C_{max,R}$ [N.s/m]	2500	5000		$z_i \leq 0.07$ m
K_F, K_R [N.s/m]	15000	70000	$f_2 = \frac{RMS(TD_F)+RMS(TD_R)}{2}$	$max(\ddot{z}_9) \leq 4.5\frac{m}{s^2}$
a (SH-ADD) [rad/s]	10	60		

Table 4: Design Variables, Bounds, Objectives and Constraints

Cases	Description	Design Variables	Objectives (f)
1	SH-2	$[K_F; C_{max,F}; C_{min,F}; K_R; C_{max,R}; C_{min,R}]$	$[f_1; f_2]$
2	SH-L		
3	ADD		
4	SH-ADD-1	$[K_F; C_{max,F}; C_{min,F}; K_R; C_{max,R}; C_{min,R}, a]$	
5	SH-ADD-2		
6	PS-LB	$[K_F; C_F; K_R; C_R]$	
7	PS-UB		

Table 5: Optimization Scenarios

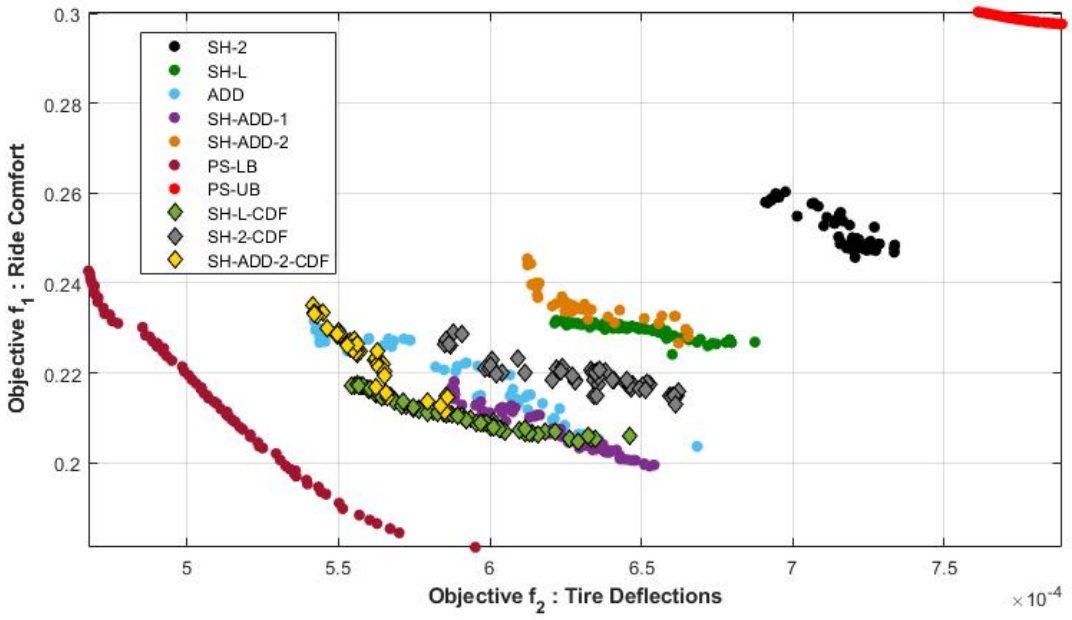


Figure 5: Comparison of the Pareto Fronts occured from the MO Optimization and the pseudo ones occured form simulation (SH-2-CDF, SH-L-CDF and SH-ADD-2-CDF)

6 Results

As it can be observed, in Fig. 5 and Fig. 6, all the Pareto fronts of the semi active suspension laws are within the area created by the Pareto Front of PS-LB and PS-UB, Cases 6 and 7 respectively, proving the main idea of semi active suspensions, which is the compromise of the advantages of a soft and a stiff suspension with a different control strategy. This difference in the ride comfort between Case 6 and 7 are depicted in Fig. 6, where the suspension travels are significantly increased in the PS-LB. Moreover, as it was expected the ADD(Case 3) and the SH-ADD-1(Case 4) improved the ride comfort of the vehicle more than all the other semi-active suspensions, while SH-2 produced the worst results.

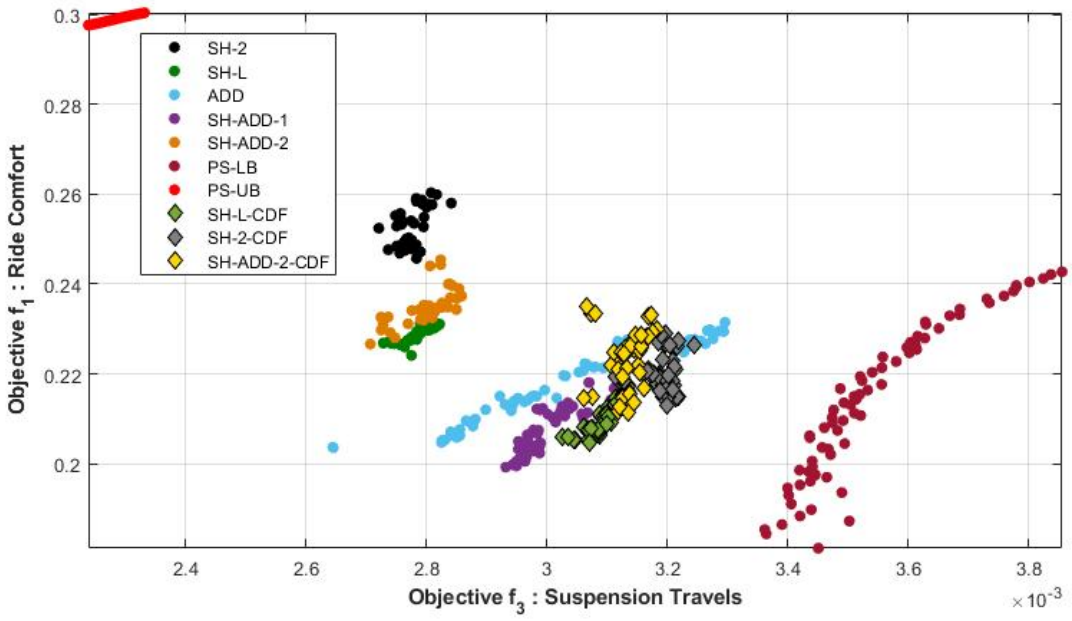


Figure 6: Comparison of the Pareto Fronts occured from the MO Optimization and the pseudo ones occured form simulation (SH-2-CDF, SH-L-CDF and SH-ADD-2-CDF)

Based on Fig. 6, it could be seen that the algorithms are divided to two groups considering the optimization cases only. The first group, consisting of SH-2, SH-L and SH-ADD-2, has reached to similar results regarding suspension travels, with SH-2 producing slightly lower ride comfort. However, they have important differences in the tire deflection, which depicts the handling of the vehicle, as it could be seen from Fig. 5. Where, the SH-ADD-1 seems to be better and having decreased the variations of the normal loads more than the other two. Additionally, SH-L algorithm managed to reach the performance of SH-ADD-2 algorithm, which considers to be one of best ride comfort oriented. Also, it managed to converge to solutions superior than SH-2 which is because of the value of the parameter "a" occuring around 0.5 for all the optimum solutions of the Pareto Front, significantly smaller than 1 where the SH-L algorithm operates as a SH-2. As far as the second group is concerned, it consists of SH-ADD-1 and ADD. Base on both Fig. 5 and Fig. 6, it could be seen that they have reached to almost the same solution, with SH-ADD-1 having less dispersion than ADD in its Pareto Fronts.

As far as the SH-ADD algorithms are concerned, it could be noticed that they delivered their purpose by combining the advantages of the SH and ADD algorithms by offering solutions between their Pareto Fronts (Cases 1 and 3), with SH-ADD-1 being slightly superior as far as the ride comfort is concerned. Also, it is important to mention that the frequency selector "a" of SH-ADD-1 converged to a different solution compared to SH-ADD-2, implying their different role on contrary with the literature. The tuning coefficient "a" of SH-ADD-2 reached to 11 rad/sec whereas for SH-ADD-1 to 39 rad/sec, in this case study.

Finally, as far as the CDF approach is concerned, this is an initial attempt to improve some of the logical control algorithms presented in this work, by implementing in them the CDF approach and benchmark them against the traditional ones. The "pseudo" Pareto Fronts of CDF (SH-2-CDF, SH-L-CDF and SH-ADD-2-CDF) were produced with the simulation of the vehicle model and the evaluation of the objectives (f_1, f_3 and f_2) for the optimum design variables of the tranditional algorithms (SH-2, SH-L and SH-ADD-2). As it can be noticed by 5, all the algorithms adopting the CDF approach managed to converge to a better solution compared to the corresponding tranditional one, improving significantly the ride comfort without risking the handling of the vehicle. Furthermore, the CDF cases managed to decrease the dispersion of the Pareto Fronts significantly compared to the traditional algorithms, regarding the suspesnion travels of the solutions, as it could be noticed in Fig. 6. Also, the CDF cases converged to a solution similar, as far as the performance is

concerned, to the algorithms of both SH-ADD-1 and ADD,which is the second group mentioned before.

7 Conclusions

To sum up, this work focused on the optimization of the most common comfort-oriented semi-active suspensions in order to compare them and exclude conclusions regarding their optimum solutions in terms of ride comfort and road holding. Moreover, an alternative approach was adopted to three algorithms in order to improve their results and these algorithms were benchmarked against the traditional ones by comparing the "pseudo" Pareto fronts of the CDF cases with the Pareto Fronts of the tranditional ones, occured from the optimization.

All the optimization results validated the theory of the semi-active suspension systems and the advantages of the studied algorithms. The impact of the use of each control algorithm in the vehicle performance is highlighted in this work with the use of the optimization results. Finally, the alternative approach regarding the operational conditions was proven successful improving the ride comfort of the passengers significantly. The modified algorithms managed to improve their efficiency to an important level compared to the traditional ones, by improving the handling of the vehicle through the tire deflections. Work is in progress to study the impact of this approach in depth and other possible improvements in the vehicle's performance or other aspects under the excitation of different road profiles.

References

[1] Cao D, Song X, Ahmadian M. Editors' perspectives: Road vehicle suspension design, dynamics, and control. Vehicle System Dynamics. 2011;.

[2] Faris WF, BenLahcene Z, Hasbullah F. Ride quality of passenger cars: an overview on the research trends. International Journal of Vehicle Noise and Vibration. 2012;8(3):185. Available from: http://www.inderscience.com/link.php?id=48169.

[3] Koulocheris DV, Papaioannou GD, Christodoulou DA. Assessment of the optimization procedure for the nonlinear suspension system of a heavy vehicle. International Journal for Vehicle Mechanics, Engines and Transportation Systems. 2016;42(2):19–35.

[4] Koulocheris D, Papaioannou G, Christodoulou D. An approach for multi-objective optimization of vehicle suspension system. IOP Conference Series: Materials Science and Engineering. 2017; 252. Available from: http://stacks.iop.org/1757-899X/252/i=1/a=012037?key=crossref.b5b8d118209e69517acffe2a3afe5a0a.

[5] Savaresi SM, Poussot-Vassal C, Spelta C, et al. Semi-Active Suspension Control Design for Vehicles. ; 2010.

[6] Prabakar RS, Sujatha C, Narayanan S. Response of a quarter car model with optimal magnetorheological damper parameters. Journal of Sound and Vibration. 2013;.

[7] Ahmadian M. Magneto-rheological suspensions for improving ground vehicle's ride comfort, stability, and handling. Vehicle System Dynamics. 2017;55(10):1618–1642. Available from: https://doi.org/10.1080/00423114.2017.1323106.

[8] Nariman-Zadeh N, Salehpour M, Jamali A, et al. Pareto optimization of a five-degree of freedom vehicle vibration model using a multi-objective uniform-diversity genetic algorithm (MUGA). Engineering Applications of Artificial Intelligence. 2010;23(4):543–551. Available from: http://dx.doi.org/10.1016/j.engappai.2009.08.008.

[9] Crews JH, Mattson MG, Buckner GD. Multi-objective control optimization for semi-active vehicle suspensions. Journal of Sound and Vibration. 2011;330(23):5502–5516. Available from: http://dx.doi.org/10.1016/j.jsv.2011.05.036.

[10] Gadhvi B, Savsani V, Patel V. Multi-Objective Optimization of Vehicle Passive Suspension System Using NSGA-II, SPEA2 and PESA-II. Procedia Technology. 2016;23:361–368. Available from: http://linkinghub.elsevier.com/retrieve/pii/S2212017316300391.

[11] Koulocheris D, Papaioannou G, Chrysos E. A comparison of optimal semi-active suspension systems regarding vehicle ride comfort. IOP Conference Series: Materials Science and Engineering. 2017; 252(1).

[12] International Organization for Standardization. Mechanical vibration and shock- Evaluation of human exposure to whole-body vibration - Part 1 : General requirements, ISO 2631-1 : 1997, 1997; 1997.

[13] Koulocheris DV, Papaioannou GD, Christodoulou DA. Optimal design solution among pareto alternatives for vehicle nonlinear suspension system. In: 26th JUMV International Automotive Conference "Science and Motor Vehicles"; Vol. 15; 2017. p. 174–188.

[14] Georgiou G, Verros G, Natsiavas S. Multi-objective optimization of quarter-car models with a passive or semi-active suspension system. Vehicle System Dynamics. 2007;45(1):77–92.

[15] Čorić M, Deur J, Kasać J, et al. Optimisation of active suspension control inputs for improved vehicle handling performance. Vehicle System Dynamics. 2016;54(11):1574–1600. Available from: https://doi.org/10.1080/00423114.2016.1177655.

[16] Čorić M, Deur J, Xu L, et al. Optimisation of active suspension control inputs for improved vehicle ride performance. Vehicle System Dynamics. 2016;54(7):1004–1030. Available from: http://www.tandfonline.com/action/journalInformation?journalCode=nvsd20.

[17] Hu Y, Chen MZ, Sun Y. Comfort-oriented vehicle suspension design with skyhook inerter configuration. Journal of Sound and Vibration. 2017;405:34–47. Available from: http://dx.doi.org/10.1016/j.jsv.2017.05.036.

[18] International Organization for Standardization. Mechanical vibration-Road surface profiles-Reporting of measured data; 1995. Available from: https://www.iso.org/standard/71202.html.

[19] Tyan F, Hong YF, Tu SH, et al. Generation of random road profiles. Journal of Advanced Engineering. 2009;4(2):151–156.

A compact and light acoustic transducer using dielectric elastomer films for low frequency active noise cancellation

A. Paradeisiotis [1], **C. Yiakopoulos** [1], **I. Antoniadis** [1]
[1] National Technical University of Athens, Department of Mechanical Engineering,
Heroon Polytechniou 9, 15780 Zografou Athens, Greece
e-mail: **aparadis@mail.ntua.gr**

Abstract
An acoustic transducer incorporating dielectric elastomer (DE) films, is proposed for active noise cancellation (ANC) setups inside the passenger compartment of ground and air vehicles, where compactness and lightness of the transducer along the effective generation of low frequency sound, are of primary concern. This transducer consists of two circular DE films in a push-pull configuration, fixed on a plastic frame. Application of electric field on a DE film, induces a change in thickness and surface area of the film, hence this configuration oscillates, generating sound. Meanwhile, the second film acts as a spring. In order to ensure effective generation of low frequency sound, the design of the transducer is based on its resonance frequency corresponding to the lower limit of the frequency range that it is able to generate. The total stiffness of the configuration depends in part on the pre-tension of the films, providing tuning ability of the resonance frequency. Simulations via finite element (FE) models confirm the accuracy of the analytical predictions.

1 Introduction

The concept of acoustic transducers incorporating piezoelectric/dielectric elastomer membranes as actuators has been around for some years. The advancements on the field of smart materials along with the constant drive to make speakers as compact and light as possible in order to serve a number of applications, from laptop and smartphone speakers to installations in air and ground vehicles, are pushing for alternatives to the traditional magnetic speakers. The concept of an extremely light push-pull acoustic transducer using DE elastomer films introduced in [1], is further examined in this paper. The trigger to revisit this concept, was to build an ANC configuration inside an aircraft cabin, where compactness and lightness of the components are of primary importance. The sound content inside an aircraft cabin mainly consists of low frequency noise coming from the rotation of the engines. Thus, the objective is to incorporate in the setup, a number of speakers with the aforementioned attributes in order to cancel this low frequency interference. Obviously, attributes such as the fidelity of the generated sound are secondary in this case. The theory and application of the ANC configuration as a whole, is beyond the scope of this paper, therefore the following analysis concerns specifically the study and parametrization of the required speakers/acoustic transducers. Specifically, the approach taken here stems mainly from the standpoint of structural dynamics while also focusing on the hyperelastic properties of the DE material and the ways of predicting and simulating its mechanical behaviour.

2 EAP Loudspeaker

2.1 Basic Principles of DE Films

A DE film acts as a capacitor and its electrical energy [2] is expressed as:

$$U_e = \frac{1}{2} C V^2 \tag{1}$$

where the capacitance is

$$C = \frac{\epsilon_0 \epsilon_r A}{z} \tag{2}$$

and

- ϵ_0 : dielectric constant of free space,
- ϵ_r : dielectric constant (relative permittivity) of elastomer,
- A: elastomer area,
- z: thickness of elastomer.

The infinitesimal mechanical work on the film come as

$$dW = -Ap\, dz \tag{3}$$

thus the Maxwell stress induced from the electrical field is

$$p = \epsilon_0 \epsilon_r \left(\frac{V}{z}\right)^2 \tag{4}$$

where the voltage to the membrane is of the form:

$$V = b + a(\sin \omega t)\ ,\ a, b : const \tag{5}$$

2.2 Design

Figure 1 demonstrates the transducer incorporating two DE films attached to the plexiglass frame and tie in the middle via the polystyrene joint. The top DE film is smeared with carbon conductive grease and is driven by voltage V, while the bottom one only acts as a spring.

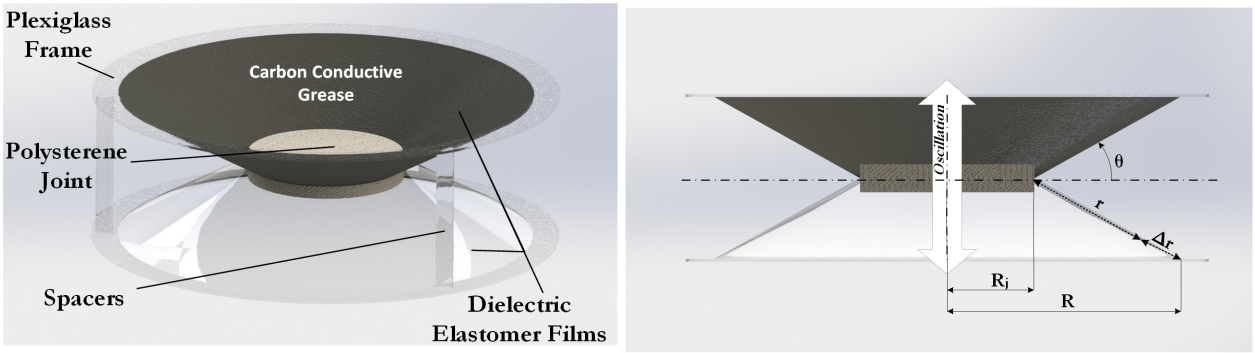


Figure 1: Loudspeaker incorporating dielectric elastomer films.

The notation of Fig.1:

- R_j: radius of the joint,
- R: internal radius of the frame,
- $r = R - R_j$: radius of the undeformed elastomer film minus the joint radius,
- Δr: stretch of the dielectric elastomer film in the radial direction of the diaphragm,
- θ: angle of the deformed elastomer film in the equilibrium position relative to the horizontal plane of symmetry.

2.3 Analytical Model

In order to establish a preliminary set of dimensions for the transducer, corresponding to a specific resonance frequency, a theoretical-analytical model is formulated [1, 3], to describe the relationship between the angle θ of a DE film -which essentially corresponds to certain pre-stress conditions- and the equivalent stiffness of the DE film in the direction of oscillation, as noted in Fig.1.

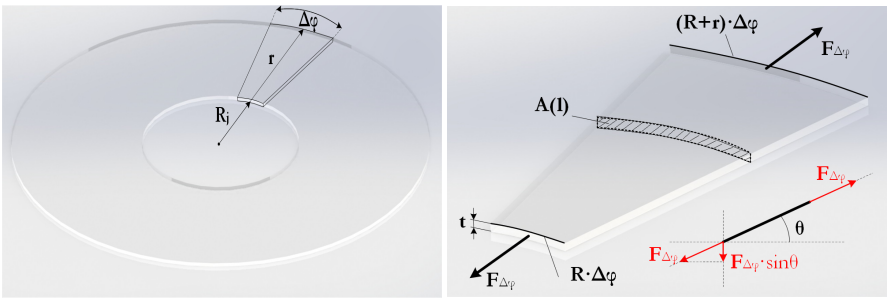


Figure 2: Elastomer film deformation model.

The notation of Fig.2, which shows the geometric parameters involved in the analytical deformation model of a DE film, is as follows:

- $\Delta\phi$: central angle of the infinitesimal strip measured at the centre of the diaphragm,
- t: thickness of the DE film,
- l: length in the radial direction of the diaphragm,
- $F_{\Delta\phi}$: tension between the joint and the frame,
- $A(l) = (R_j + l)(\Delta\phi)t$: cross area at length l.

The stretch of the dielectric elastomer film in the radial direction of the diaphragm is

$$\Delta r = r(1/cos\theta - 1) \tag{6}$$

The expansion per unit length $(\Delta r)'$ is

$$(\Delta r)' = \frac{F_{\Delta\phi}}{EA(l)}\Delta l \tag{7}$$

Therefore

$$\Delta r = \int_0^r (\Delta r)' = \int_0^r \frac{F_{\Delta\phi}}{EA(l)}dl = \frac{F_{\Delta\phi}}{E(\Delta\phi)t}\log_{10}\left(\frac{R_j + r}{R_j}\right) \tag{8}$$

which leads to

$$F_{\Delta\phi} = \frac{E(\Delta\phi)t\Delta r}{\log_{10}\left(\frac{R_j+r}{R_j}\right)} \tag{9}$$

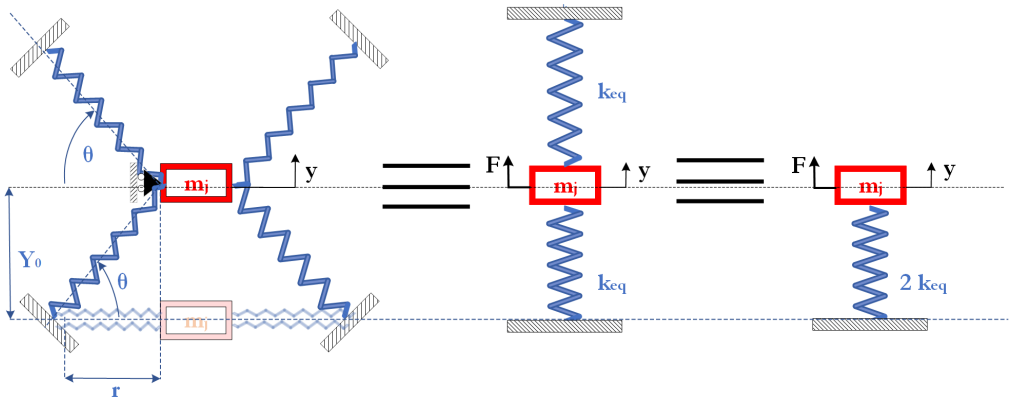


Figure 3: Mechanical equivalent model of the transducer.

The total tension $\overline{F}$ in the direction of the principal axis of the transducer, which is essentially the $\sin\theta$ component of the summation of $F_{\Delta\phi}$ for a circle, comes as

$$\overline{F} = \int_0^{2\pi} F_{\Delta\phi} \sin\theta d\phi = \frac{2\pi Et}{\log_{10}\left(\frac{R_j+r}{R_j}\right)} r(\tan\theta - \sin\theta) \tag{10}$$

Considering that the vertical displacement of the joint comes as

$$Y_0 = r\tan\theta \tag{11}$$

the expression of the vertical force $\overline{F}$ becomes:

$$\overline{F} = \frac{2\pi Et}{\log_{10}\left(\frac{R_j+r}{R_j}\right)}(1-\cos\theta)Y_0 \tag{12}$$

This vertical displacement Y_0, in the end is half of the total height of the full configuration. Therefore, the equivalent "vertical" stiffness of this DE film comes as:

$$k_{eq} = \frac{d\overline{F}}{dY_0} = \frac{2\pi Et}{\log_{10}\left(\frac{R_j+r}{R_j}\right)}(1-\cos\theta) \tag{13}$$

In order to formulate the final expression of the resonance frequency, the mechanical equivalent model of the transducer as in Fig.3 is considered.

The dynamic equation of motion of the equivalent mechanical model of Fig.3 is:

$$m\ddot{y} + k_{eq}y - k_{eq}(-y) = m\ddot{y} + 2k_{eq}y = F(t) \tag{14}$$

Meaning that the total stiffness of the push-pull configuration is essentially two springs in parallel, namely:

$$k_{tot} = k_{eq} + k_{eq} \Rightarrow k_{tot} = 2k_{eq} = k \tag{15}$$

therefore it is twice as large as the equivalent stiffness due to the symmetrical structure of the transducer, namely:

$$k = \frac{4\pi Et}{\log_{10}\left(\frac{R_j+r}{R_j}\right)}(1-\cos\theta) \tag{16}$$

Finally, the resonance frequency which signifies the lower limit of the reproduction frequency range of the transducer, is:

$$f_0 = \frac{1}{2\pi}\sqrt{\frac{k}{m_j + \frac{2}{3}m_f + 2M_s}} \tag{17}$$

where

- m_j : mass of the joint,
- m_f : mass of DE film,
- $M_s(f_0) \approx \frac{8}{3}\rho R_j^3$: additional mass derived from the reactance component of radiation impedance for one side of the diaphragm, where ρ is air density.

Therefore the final expression of the resonance frequency:

$$f_0 = \sqrt{\frac{Et_f(1-\cos\theta)}{\pi \log_{10}\left(\frac{R_j+r}{R_j}\right)\left(m_j + \frac{2}{3}m_f + 2M_s\right)}} \tag{18}$$

The term $2 \times m_f/3$ is added to take into account the effective mass of the oscillating DE films acting as springs. At last, using this analytic deformation model, allows the preliminary dimensioning of the transducer for a specific target resonance frequency.

2.4 Hyper-elastic Models

Hyper-elastic materials like silicon rubber, have the ability to experience large deformations under small loads and to retain their initial configuration, without considerable permanent deformation after removal of the load [4]. An example of such a material, specifically uniaxial stress data of a certain silicon rubber [7], is presented in Fig.4.a. Here is demonstrated a typical phenomenon in hyperelastic materials called "hysteresis" [8], where the unloading path of the stress-strain curve is different from the loading path due to reaching ultimate elongations. Figure 4.b shows the corresponding Young's Modulus $E = d\sigma/d\epsilon$ as a function of the material's strain during stretching up to 80%.

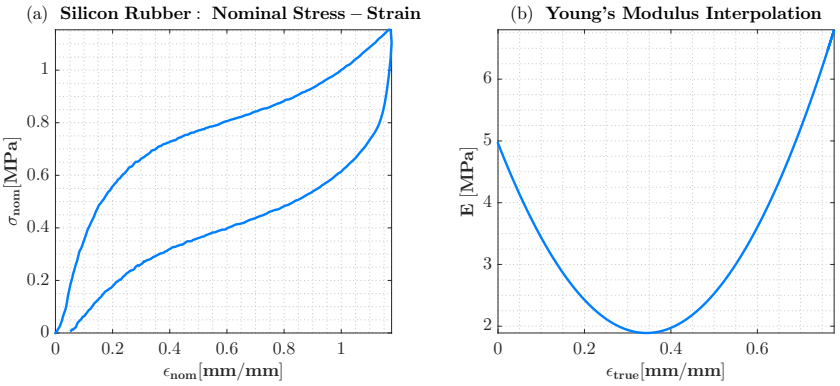


Figure 4: (a) Silicon rubber uniaxial test data. (b) Resulting Young's Modulus for $\epsilon = 0\ to\ 0.8$.

These materials demonstrate highly non-linear stress-strain behaviour [5], consequently a simple constant modulus of elasticity is not sufficient for its description. Therefore the aim of hyper-elastic models is to characterize hyper-elastic materials and to determine a suitable Strain Energy Function (SEF).

2.4.1 Strain Energy Function (SEF)

Generally, SEF is based on the three strain invariants I_1, I_2, I_3 and expresses the energy stored in material per unit of reference volume (initial configuration) as a function of strain at the certain point in the material [4, 6]. If $\lambda_1, \lambda_2, \lambda_3$ are the principal stretch ratios, then:

$$I_1 = \lambda_1^2 + \lambda_2^2 + \lambda_3^2 \tag{19}$$

$$I_2 = \lambda_1\lambda_2 + \lambda_2\lambda_3 + \lambda_3\lambda_1 \tag{20}$$

$$I_3 = \lambda_1^2\lambda_2^2\lambda_3^2 \tag{21}$$

In general, hyper-elastic materials are considered incompressible, thus, $I_3 = 1$. The suitable SEF depends on the specific application seeking to characterize.

2.4.2 Yeoh Model

The Yeoh model belongs in the category of the phenomenological models which are the most commonly used. The models in this category, are approaching hyper-elasticity from the viewpoint of continuum mechanics. They are stress-strain behaviour characterized without reference to the microscopic structure. Other models of this category are the Mooney-Rivlin, Neo-Hookean, Ogden etc. The Yeoh model has an advantage over other available models, exhibiting good matching with experimental data over large strain values for given rubber compositions. Essentially, the Yeoh model is a 3^{rd} order polynomial model, based only the first strain invariant I_1. The SEF of the Yeoh Model is defined as:

$$W = \sum_{i=1}^{3} C_{i0}(\bar{I}_1 - 3)^i + \sum_{i=1}^{3} \frac{1}{D_i}(J_{el} - 1)^{2i} \tag{22}$$

where

- C_{i0}: material constants controlling the shear behaviour. Can be determined from uni-axial, bi-axial and planar stress tests.
- D_i: material constants controlling bulk compressibility. Estimated from volumetric tests. For fully or nearly incompressible ($\nu \approx 0.5$) rubber materials are equal to 0.
- J_{el}: elastic volume ratio.

Therefore the coefficients $C_{10}, C_{20}, C_{30}, D_1, D_2, D_3$ are needed for the application of the Yeoh hyperelastic model, which may be introduced directly if known or be calculated via interpolation of given material stress-strain data. An example of such data is presented in Fig.4. Specifically, a set of uniaxial true stress- true strain data ($\sigma_{true}, \epsilon_{true}$) of a certain silicon rubber hyperelastic material (), is used. The curve in Figure 4.b is a 2nd order polynomial interpolation of the corresponding Young's Modulus $E = d\sigma/d\epsilon$ as a function of the material's strain. Figure 5.a demonstrates the fitting of various hyperelastic models, using the appropriate ABAQUS® module, to the given set of nominal stress-strain uniaxial data for a silicon rubber hyperelastic material. Furthermore, in Figs.5.b and 5.c, the corresponding biaxial and planar curves are constructed via the calculated coefficients of each model. Observation of all three curves leads to the conclusion that indeed, the Yeoh model provides the most realistic fitting in this case.

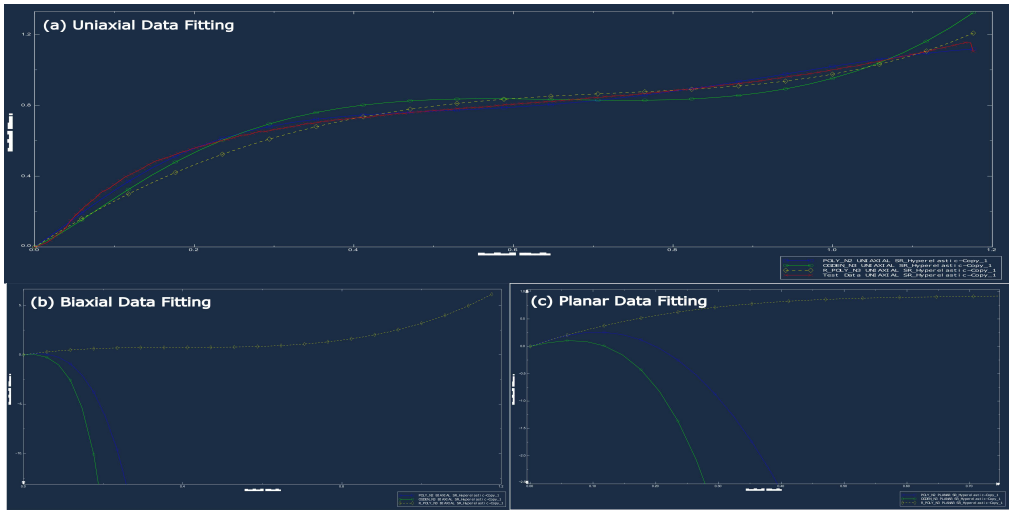


Figure 5: Nominal Stress-Strain curves. Fitting of hyperelastic models. (a) Uniaxial data (b) Biaxial data (c) Planar Data (Test Data: red $\times$, Ogden: green $\circ$, 2_{nd} order polynomial: blue $\square$, Yeoh: yellow $\diamond$)

For the fitting of the Yeoh model to these data, the nominal (engineering) stress and strain ($\sigma_{nom}, \epsilon_{nom}$) values were calculated as:

$$\epsilon_{nom} = e^{\epsilon_{true}} - 1 \tag{23}$$

$$\sigma_{nom} = \frac{\sigma_{true}}{e^{\epsilon_{true}}} \tag{24}$$

The resulting coefficients are presented in Table 1.

$C_{10}\ [MPa]$	$C_{20}\ [MPa]$	$C_{30}\ [MPa]$	D_1	D_2	D_3
0.481	-0.105	1.814×10^{-2}	4.189×10^{-2}	0	0

Table 1: Coefficients for the SEF of the hyperelastic Yeoh model.

2.5 Transducer Dimensioning

Considering the material of the DE films as the same silicon rubber demonstrated in Fig. 4, the equation of the 2_{nd} order interpolation in Fig. 4.b describing the Young's Modulus as a function of strain, is:

$$E(\epsilon) = 26.049\epsilon^2 - 17.893\epsilon + 4.963 \tag{25}$$

In order to approximate as best as possible the non-linear behaviour of the hyperelastic material for the purpose of the parametric examination of the resonant frequency, taking the strain as $\epsilon = \Delta r/r$, it can be expressed as a function of the angle θ:

$$\epsilon(\theta) = 1/cos\theta - 1 \tag{26}$$

Consequently, Young's Modulus may also be calculated for each angle θ. Table 2 summarizes the material properties of the DE film and joint along with other basic parameters.

$t_f\ [\mu m]$	ν	ϵ_r	$\epsilon_0\ [\frac{F}{m}]$	$\rho\ [\frac{kg}{m^3}]$	$\rho_f\ [\frac{kg}{m^3}]$	$\rho_j[\frac{kg}{m^3}]$
100	0.49	2.8	8.854×10^{-12}	1.225	1247	29

Table 2: Basic parameters and material properties

The geometric parameters of the loudspeaker have to be decided in order to achieve the target resonance frequency of $f_0 \approx 100\ Hz$. A starting set of geometric parameters is selected and summarized on Table 3.

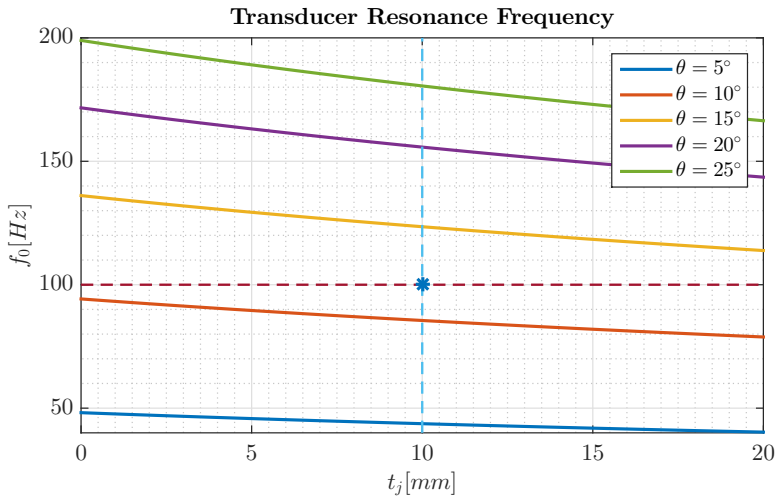


Figure 7: Resonant frequency of the transducer as a function of angle θ and thickness t_j of the joint.

$R\ [mm]$	$R_j\ [mm]$	$r\ [mm]$
40	10	30

Table 3: Geometrical parameters



Figure 6: Design of EAP loudspeaker - Initial State.

Therefore, the stiffness of the structure in the vertical direction, in the sense of the direction the films oscillate, and the mass of the joint which are the determining factors of the resonance frequency are now dependent only on the angle θ and the thickness of the joint t_j. The angle θ is essentially a direct marker of the pre-stress conditions on the DE films at the operating position of the loudspeaker and the thickness of the joint acts as a tuner of the mass. Considering the above joint and frame inner diameters constant, it is possible to examine the dependence of the resonance frequency from these parameters, which is demonstrated in Fig.7.

For practical reasons, a choice of $t_j \approx 10\ mm$ is indicated with the dotted light blue line along with the red dotted line for the target frequency, resulting to an angle of $\theta \approx 12°$.

3 FEM Models

For verification of the results from the analytic deformation model, a FEM based model is simulated. The goal is to confirm that the dimensioning of the loudspeaker based on the theoretical calculations, indeed leads to the target resonance frequency.

3.1 Stiffness Comparison

In order to check the validity of the analytical deformation model, a vertical static load is applied on the perimeter of the top frame, leading to the state shown in Fig.8.b, making it possible to calculate the stiffness

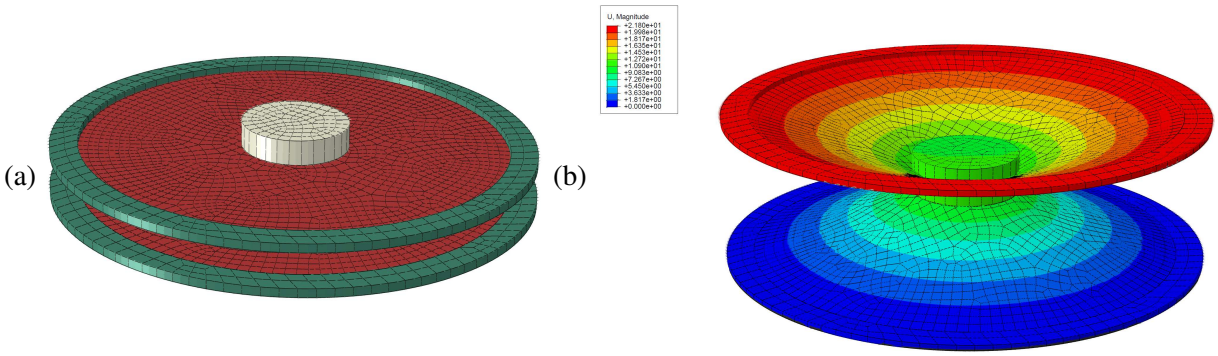


Figure 8: (a) Undeformed EAP loudspeaker. (b) EAP loudspeaker under vertical static load.

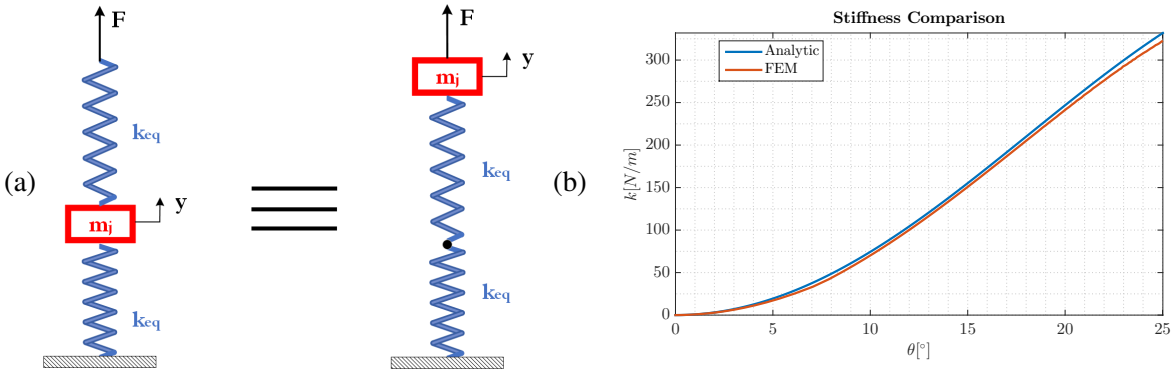


Figure 9: (a) Mechanical equivalent model of the static loading of the top frame. (b) Resulting stiffness as function of vertical displacement of the top frame. Comparison between FEM and analytical results.

of the configuration allowing direct comparison with the corresponding results acquired from the analytic deformation model.

It should be noted that in this stage, the DE films act as two springs in series because of the nature of the static loading. Meaning that the mechanical equivalent of this loading case has the form of Fig.9. Therefore the FEM results of the expression $d\overline{F}/dY_0$ are compared with the theoretical $k = k_{eq}/2$. The comparison between the analytic and FEM results is demonstrated in Fig.9.b. It is observed that the analytical and FEM models are almost in perfect agreement. Thus, it is expected that stiffness will not be a factor for any possible deviations from the resonance frequency estimated by the FEM model.

3.2 Modal Analysis

Using the full configuration FEM model, by importing pre-stress conditions on the transducer, namely vertical displacement of the top frame corresponding to the theoretically estimated angle $\theta = 12°$ of the DE films, the frequencies of the modes are calculated via modal analysis. The results are presented in the Table 4 for the first six modes.

$Mode$	1	2	3	4	5	6
$Frequency\ [Hz]$	95.79	117.57	117.70	133.07	133.70	134.16

Table 4: Eigenfrequencies

Therefore the frequency of the first mode from Table 4 shown in Fig.10, corresponds to the resonance frequency of the transducer $f_0 = 95.79\ [Hz]$, which compared to the theoretically estimated $f_0 = 101.27\ [Hz]$,

presents a deviation of 5.42%. The conclusion from these results, is that the slight deviation of the estimated resonance frequency between the FEM and analytical models comes down to the exact estimation of the effective mass of the transducer, especially considering Fig.9.b showing that the stiffness comparison is excellent. In general, the analytical deformation model, appears as a perfectly adept method to estimate the resonance frequency and thus act as the basis for the dimensioning of the transducer.

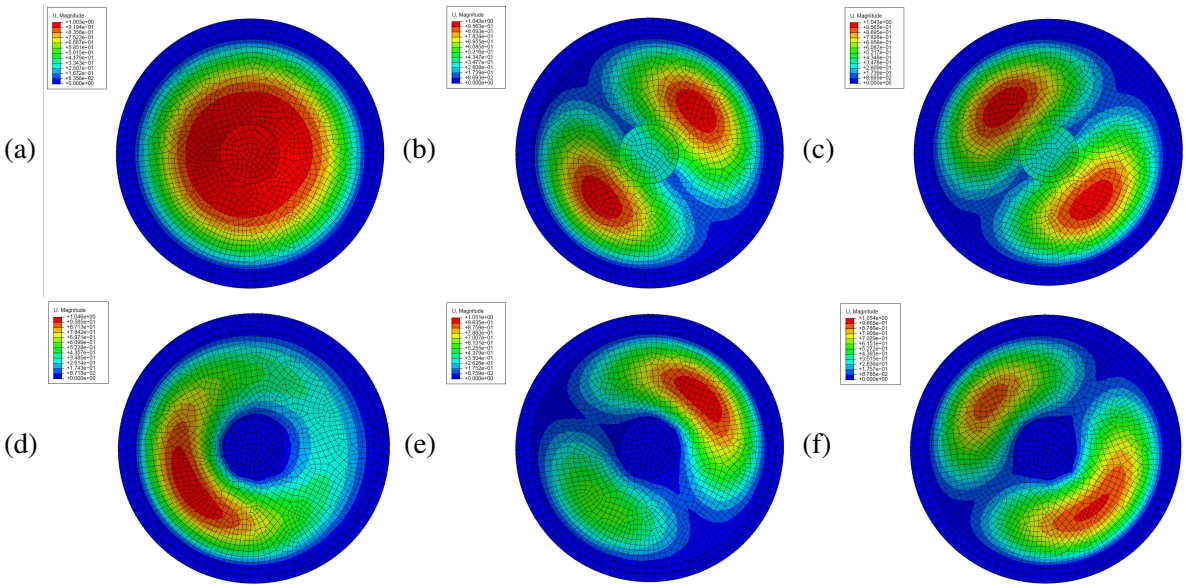


Figure 10: Graphical representation of the first 6 modes of the transducer (Deformation scale factor=1). (a) 1_{st}, (b) 2_{nd}, (c) 3_{rd}, (d) 4_{th}, (e) 5_{th}, (f) 6_{th}

.

4 Conclusions

The investigation of this concept for an acoustic transducer, mainly from the perspective of structural dynamics, demonstrated certain facts. Firstly, the theoretical model for the calculation of the resonant frequency and dimensioning of the transducer, was verified by the FEM simulations while also incorporating the hyperelastic properties of the material in the analysis. Also, it is clear that the construction of a compact and light transducer tuned for low frequency sound generation is possible through simple procedures and a cheap configuration overall. However, the exclusively acoustic aspects and performance of this speaker have to be examined in future research and experimental tests. Elements such as possible enclosures for the transducer and the required voltage levels to drive the DE films to achieve satisfactory sound levels or durability tests, are equally important and need to be investigated. Summarizing, this concept shows promise, especially considering how its main features line up to potential applications, market and technology trends.

5 Acknowledgements

Our occupation with this research subject was prompted by the project "Technologies for Active Vibration and Acoustic Comfort (TAVAC)" and funded by the European Commission under the framework of the "Clean Sky 2 LPA (Large Passenger Aircraft)" public-private partnership between the European Commission and the European aeronautics industry.

References

[1] T. Sugimoto, A. Ando, K. Ono, Y. Morita, K. Hosoda, D. Ishii, K. Nakamura, *A lightweight push-pull acoustic transducer composed of a pair of dielectric elastomer films*. The Journal of the Acoustical Society of America, 134(5) (2013) , EL432-EL437.

[2] F. Carpi, D. De Rossi, R. Kornbluh, R. E. Pelrine, P. (Eds.) Sommer-Larsen, *Dielectric elastomers as electromechanical transducers: Fundamentals, materials, devices, models and applications of an emerging electroactive polymer technology*, Elsevier, (2011).

[3] J. Zhu, S. Cai, Z. Suo, *Resonant behavior of a membrane of a dielectric elastomer*. International Journal of Solids and Structures, 47(24) (2010), 3254-3262.

[4] M. Shahzad, A. Kamran, M. Z. Siddiqui, M. Farhan, *Mechanical characterization and FE modelling of a hyperelastic material*, Materials Research, 18(5) (2015), 918-924.

[5] L.A. Wood, *Uniaxial Extension and Compression in Stress-Strain Relations of Rubber*, J. Res. Nat. Bur. Stand (1977), 57-63.

[6] D.S. Simulia, *Abaqus 6.11 theory manual*. Providence, RI, USA: DS SIMULIA Corp (2011).

[7] J. Bergstrom, (2004, January 25). *Experimental Data Files for Various Polymers*. Retrieved from https://polymerfem.com/articles/experimental-testing/25139-experimental-data-files-for-various-polymers.

[8] M. Wadham-Gagnon, *Hyperelastic Modelling of Rubber Behaviour in Finite Element Software*, Doctoral dissertation, McGill University Libraries (2006).

Simulink-PSpice co-simulation of Power Amplifier for driving piezoelectric actuators

Y. Park[1], T. Bartel[1], T. Röglin[1], G. M. Stoll[1], P. Zech[2], D. Plöger[2], S. Rinderknecht[2]
[1] Fraunhofer Institute for Structural Durability and System Reliability LBF, Darmstadt, Germany

[2]Institute for Mechatronic Systems IMS, Technical University of Darmstadt**,** Germany

Abstract
In most of active vibration control (AVC) applications piezoelectric transducers require appropriate power electronics to be driven with high electric voltage due to high capacitance [1]. Thus, circuit design of power amplifiers for driving piezoelectric transducers becomes a challenging task. Design problems need to be found in early design stage since prototyping the complete system can be time and cost intensive. Furthermore the electromechanical behaviour of the holistic system needs to be identified, since it determines requirements for electrical specifications of the power amplifier. As solution, the SLPS (SimuLinkPSpice) co-simulation environment of Cadence Design Systems is used as a new approach to embed electronic circuit simulation of the developed power amplifier in system model simulation in Simulink.

1 Introduction

Piezoelectric transducers are preferred actuators for AVC applications due to light weight and high stiffness which leads to high mechanical resonance frequencies. Furthermore, high precise motion and force control can be achieved [2]. To drive piezoelectric actuators, an adequate power amplifier is required. Limited in performance due to piezoelectric actuators which are considered as capacitive loads, piezo amplifiers typically have to provide an output voltage on order of 100 V to 200 V and constitute a challenging task in amplifier design processes. To simulate the performance of power amplifier, simulation of mathematical model is carried out in [3], but electromechanical relations between amplifier and actuator are often neglected in simulations. With regard to an AVC application on a planetary gearbox, analytical performance identification of an inertial mass actuator and class AB power amplifier are presented in this work. Based on the analytical identification, a Simulink model of actuator and amplifier are set up. Subsequently, the electronic design of the power amplifier is created in PSpice in order to embed the circuit design in Simulink environment and perform SLPS co-simulation.

A key technology for more efficient jet engines are high-speed and high-power lightweight planetary gearboxes. Using the gearbox both fan and turbine can be operated at their optimum speed. Engine manufacturers are currently developing planetary gearboxes for the next engine generation. During take-off the gearbox will have to transmit mechanical powers of more than 50 MW. The combination of a lightweight gearbox construction and high power transmission is prone to vibration excitation. Especially the gear meshing could result in noise that reduces the comfort of passengers as its frequency is in the range of 3 to 5 kHz where human ear is very sensitive. A research project is initiated to investigate feasibility of AVC in this application. One of the key challenges is the high frequency of gear meshing. Most commercially available active noise or vibration control systems such as active engine mounts or noise cancelling headphones work only for frequencies well below 1 kHz. An AVC system that is capable of producing anti-forces in the higher frequency range has thus to be developed.

A sub-scale test rig for small planetary gearboxes is used to experimentally identify requirements such as frequencies and forces for the projected actuator amplifier combination. The methodology of the research

project is to first scale the gearbox down to laboratory scale. However, the smaller gearbox is selected such that it can be operated at the same gear meshing frequency as the aerospace gearbox. An AVC system for the small gearbox shall be developed and later be scaled up to full-scale. The developed test rig is depicted with all components in Figure 1. The gearbox can be operated at input speeds up to 10000 rpm and output torques up to 30 Nm. The gearbox is spur-toothed has a diameter of 60 mm, three planets and a gear ratio of 3. When operated at maximum speed and load at the test rig it transmits a mechanical power of 10 kW. The gearbox assembly is equipped with seven accelerometers and two triaxial force sensors that measure forces which are transmitted from the gearbox into the surrounding structure.

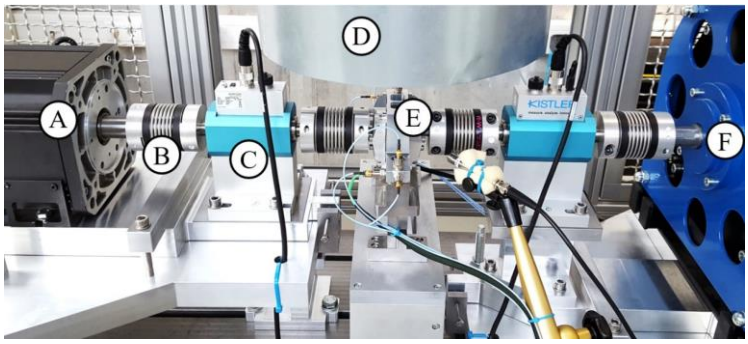


Figure 1: Test rig for measurement of vibration characteristics of small planetary gearboxes with asynchronous motor (A), couplings (B), torque sensors (C), air cooling (D), planetary gearbox (E) and eddy current break.

According to the frequency spectrum measurement of the gear mesh force excitation of the planetary gearbox, the nominal gear mesh frequency is not dominant, as common for planetary gearboxes. Instead the spectrum is full of neighbouring frequencies of varying amplitudes which is caused by amplitude and frequency modulation effects inside the gearbox. To actively reduce the most dominant single vibration at a frequency of approx. 4 kHz, an anti-force of approx. 55 N is required. If more frequencies shall be suppressed in parallel the anti-force requirements increase respectively.

2 Experimental characterization and analytical modelling of actuator and amplifier for AVC of planetary gearboxes

The most important challenge of system design is the high frequency range around 4 kHz of the gear mesh vibration. Consequently actuators have to be developed that are able to produce a significant amount of controlled force at this frequency as they go beyond the state of the art. Furthermore, an appropriate amplifier has to be selected which can provide the required power at high frequency. In the presented work, the problem is reduced to laboratory scale. Subsequently, the development of a solution at original scale is intended.

2.1 Analytical modelling of an Inertial mass actuator

In accordance to the demands, the principle of an inertial mass actuator utilizing a piezoelectric shear transducer is chosen for the investigated application. Inertial mass actuators consist of a spring-mass-system with an integrated active element and can be considered as a point force generator when driven above their resonance frequency [4]. As shown in Figure 2, inertial mass actuators can be represented by a spring-mass system with the stiffness k and the inertial mass m, enhanced by a damping d and a force actuator A [5].

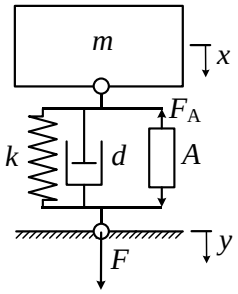


Figure 2: Model of an inertial mass actuator with stiffness *k*, inertial mass m, damping d, force actuator *A*, actuator force F_A and force of the inertial mass actuator *F*

Regarding ultra-high frequency applications, piezoelectric actuation is superior to electrodynamic actuation. Since those solid state actuators possess an inherent, quite high stiffness, they can carry the inertial mass while providing high dynamic forces. Therefore they are especially suitable for high frequency applications. The mentioned studies on piezoelectric inertial mass actuators pointed out their main advantages: If carefully designed, the actuator system contains a low number of parts with no movables. The inertial mass actuator can be considered as an ideal force generator when driven above its resonance frequency. It has been widely used in feedback control systems. In a collocated control loop configuration together with an accelerometer, simple stable systems for active damping can be implemented [4]. This approach has been successfully studied for lightly damped structures with high resonance peaks, e.g. [6].

In order to derive low amplifier output voltage, the inertial mass actuator is designed in such way, that its dynamic resonance f_r meets its operating frequency at approx. 4 kHz. Doing so, the amplification of the voltage to force ratio by the dynamic resonance can be used. Since the stiffness k is predefined by the chosen actuator, the mass m has to be calculated via $f_r = 1/2\pi\sqrt{(k/m)}$. In order to estimate the stiffness of the actuator, the actuator is excited with a broad band signal with three different masses attached to it. The measurement setup and the measurement results are depicted in Figure 3.

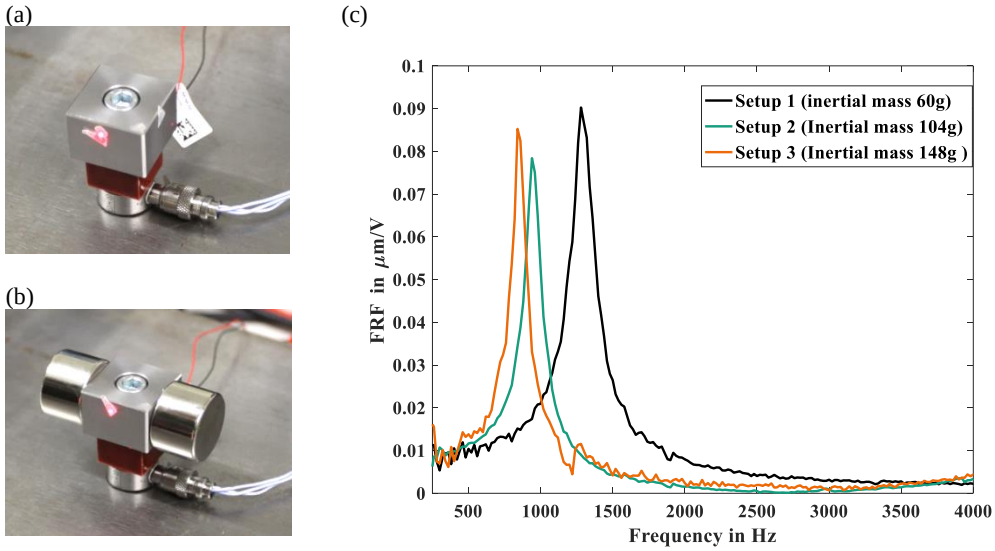


Figure 3: Experimental characterization of the stiffness estimation of the piezoelectric shear actuator.

(a) Experimental setup of the shear actuator with an additional mass of 60 g
(b) Experimental setup of the shear actuator with an additional mass of 144 g
(c) Resulting frequency response from actuator voltage to tip displacement of the different experimental setups

On base of the experimental characterization, the actuator stiffness could be identified to 3967 kN/m using a linear regression. The moving mass the actuator (without additional mass) is calculated to be approx. 3 g.

2.2 Analytical modelling of the power amplifier PIA-1115-2020

Considering the high signal quality of class AB amplifiers, the analogue amplifier PIA-1115-2020 is chosen for modelling. Analog amplifiers regulate the power flow via power transistors, operating as resistors. Although these resistors provoke an energy drain, analogue amplifiers are characterized by high signal quality at the amplifier output and robustness, which is independent of the load. For the derivation of the required model data, the amplifier is experimentally characterized while it is loaded with film capacitors of different capacity in the range of typical, suitable piezoelectric actuators. The experimental set up is depicted in Figure 4. According to the experiment results, PIA-1115-2020 is able to drive maximum capacitive load of 100 nF at 4 kHz (Figure 5).

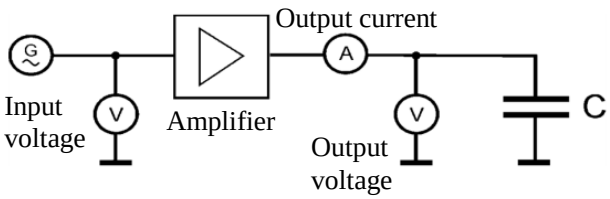


Figure 4: Scheme of the experimental setup for the characterization of amplifiers

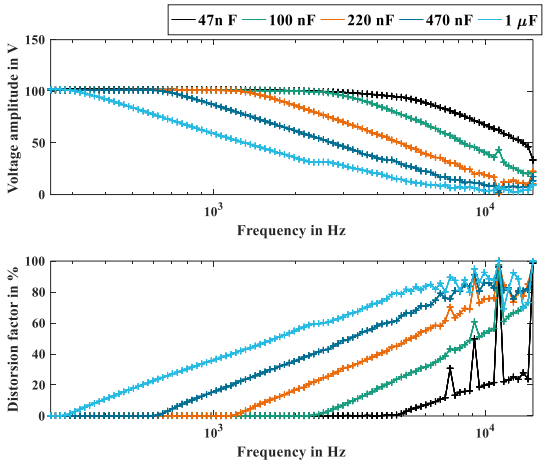


Figure 5: Results of the experimental characterization of an analogue voltage amplifier: voltage amplitude and distortion factor for different capacitors

For the integration into system simulation model, the numerical identification of the power amplifier carried out according to the methodology proposed by [7]. A modification of this method is described in this section. To replicate the measured phase behaviour of the transfer function, the higher order model shown in Figure 6 is used. The phase behaviour is modelled in such a way, that it allows convergence beyond $-180°$ phase angle for high frequencies, as depicted in Figure 7. This representation is based on the observation of the transfer behaviour and not motivated through the amplifier design. The parametrization proposed here thus cannot be done using amplifier specification making an experimental characterization necessary. Modelling the correct phase behaviour for a large frequency range is a prerequisite for the design of a high frequency control system.

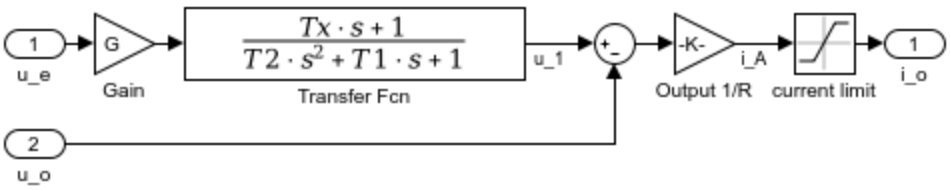


Figure 6: Amplifier model including extended transfer behaviour and current limitation for capacitive loads

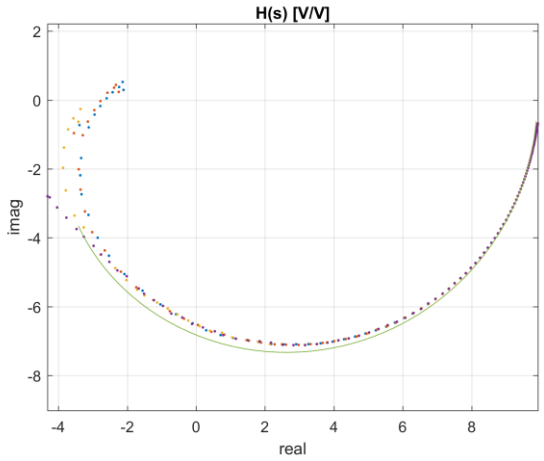


Figure 7: Measured (...) and estimated (-) phase curves of the amplifier transfer function *H(s)*.

$$U_1(S) = \frac{K(T_a s+1)}{T_2 s^2+T_1 s+1} \cdot U_i(s) \tag{1}$$

$$Y_{u_e,u_1}(s; K, T_a, T_1, T_2) = \frac{U_1(s)}{U_e(s)} \tag{2}$$

Based on measurements on an open circuit configuration the parameters for the load independent, frequency dependent voltage amplification are estimated using a least squares approach. Therefore the voltage amplification $\tilde{Y}_{uu}(s)$ is measured for a set of frequencies s_i with no electric load connected to the amplifier output and the model function Y_{uu} is factorized for the free parameters K, T_a, T_1 and T_2 where the solution for T_a is obvious:

$$\tilde{Y}_{uu}(s) = (K, KT_a, T_1, T_2) \cdot \begin{pmatrix} 1 \\ s \\ -s^2\tilde{Y}_{uu} \\ -s\tilde{Y}_{uu} \end{pmatrix} \tag{3}$$

The overdetermined system of linear equations can be solved using a least squares approach. Additionally a weighting of the values is implemented based on the harmonic distortion $k(s_i)$ measured for each frequency s_i to consider only those frequencies where dominantly linear system behaviour was observed:

$$W(s_i) = \begin{Bmatrix} k(s_i) < 0.01 : 1 \\ k(s_i) \geq 0.01 : 0 \end{Bmatrix}$$

$$\rightarrow \min_{K,KT_a,T_1,T_2} \sqrt{\sum_i \left(\left((K, KT_a, T_1, T_2) \cdot \begin{pmatrix} \vec{1}^{\mathsf{T}} \\ s \\ -s_i^2\tilde{Y}(s_i) \\ -s_i\tilde{Y}(s_i) \end{pmatrix} - \tilde{Y}(s_i)_{uu} \right) \cdot W(s_i) \right)^2} \tag{4}$$

The identification of the load dependent output resistance R and current limitation is done using measurements with different capacitive loads attached to the amplifier output. The transfer function for the output current of the amplifier under capacitive load is derived from the system equation:

$$i_A = U_e \cdot \frac{\left(\frac{K(T_a s+1)}{T_2 s^2+T_1 s+1}\right)}{\left(R+\frac{1}{sC}\right)} = U_e \cdot Y_{uu}(s) \cdot \left(R+\frac{1}{sC}\right)^{-1} \tag{5}$$

$$Y_{iu}(s) = \frac{i_A(s)}{U_i} \tag{6}$$

Where the output resistance R is expected to be a function of the capacitive load C. The identification of the capacitive loads and output resistances is performed similar to the method shown above through a least

squares approximation of the parameters of a factorized linear system Y_{iu} using the transfer function Y_{uu} of the open circuit configuration that has already been identified:

$$Y_{uu}(s) = \left(\tilde{Y}_{iu}(s), \frac{\tilde{Y}_{iu}(s)}{s}\right) \cdot \begin{pmatrix} R \\ \frac{1}{C} \end{pmatrix} \tag{7}$$

The problem is solved for different capacitors separately to observe the dependency of output resistance and capacitive load as shown in Figure 8. It appears that the output resistance can be modelled as a function of C of the following form, where the parameters R_0 and R_1 can be estimated using least squares regression.

$$R(C; R_0, R_1) = R_0 + \frac{R1}{C} \tag{8}$$

To model the current limitation, for different capacitive loads the maximum current amplitude is measured for which the harmonic distortion k is not bigger than 1% as proposed in [7]. The relation between capacitive load and current limitation is assumed to be of the form where the parameters can be estimated through least squares regression from measurement data.

$$i_{max}(C) = K_i \cdot \frac{C}{T_i + C} \tag{9}$$

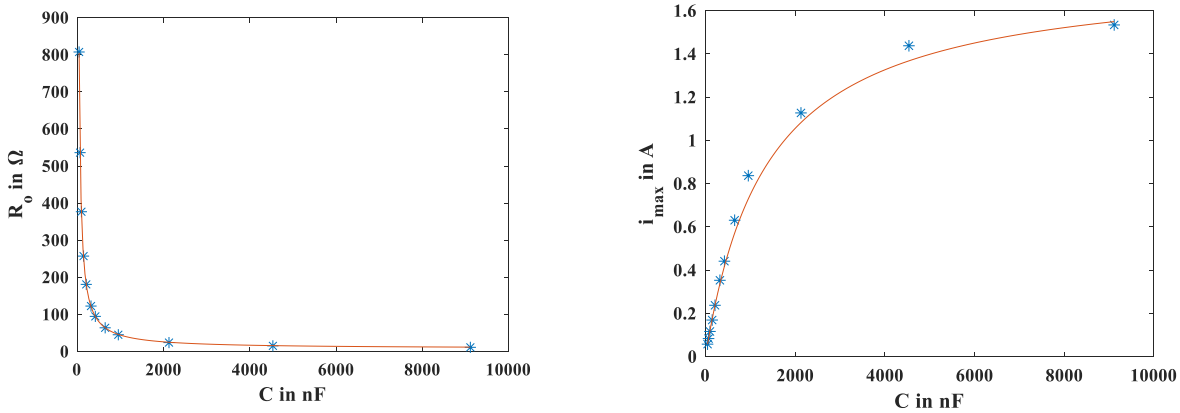


Figure 8: Estimates (-) and observations (*) of the output resistance and current limitation depending on capacitive load.

The estimated parameter values are listed up in Table 1.

Parameter	Unit	Value
G_0	V/V	24.37
T_x	s	$-0.9742 \cdot 10^{-5}$
T_2	s^2	$-0.7873 \cdot 10^{-10}$
T_1	s	$1.053 \cdot 10^{-5}$
R_0	Ω	0.54
R_1	ΩF	$2.085 \cdot 10^{-5}$
K_i	A	0.3232
T_i	C	$8.374 \cdot 10^{-8}$

Table 1: Analytical parameter Values estimated for PIA-1115-2020

2.3 Modelling of inertial mass actuator and power amplifier in Simulink

For the simulation of inertial mass actuator system, including piezoelectric transducer, inertial mass and amplifier, a modular model approach for active vibration systems on base of impedances and admittances is used [4]. The impedance-admittance model structure of the inertial mass actuator is depicted in Figure 9 indicating the exchange of power by the transmission of forces *F*, velocities *v*, differential velocity Δ*v*,

input voltage U_i, output voltage U_o and output current I_o between the single system components. The model of the inertial mass actuator can simply be enhanced by the models of the controller as well as the models of mass and elasticity of the base structure. The identified actuator parameters as well as the identified power amplifier parameters were integrated into the system simulation.

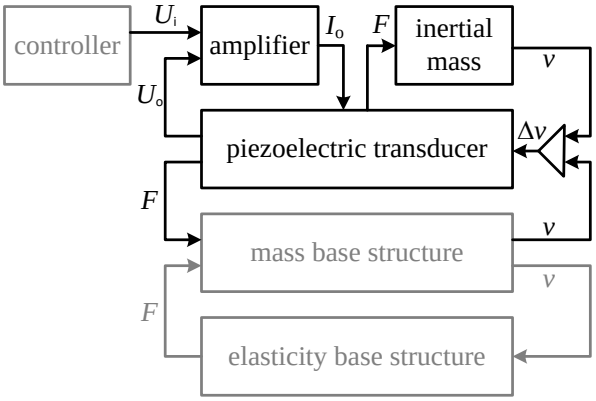


Figure 9: Impedance-admittance model structure of the inertial mass actuator system consisting of piezoelectric transducer, inertial mass and amplifier with forces F, velocities v, differential velocity Δv, input voltage U_i, output voltage U_o and output current I_o

The additional mass is numerically estimated to be 8 g in order to tune the resonance frequency of the inertial mass actuator to the frequency range at approx. 4 kHz. Figure 10 (a) shows the results of the numerical simulation for an input voltage sweep from 0 Hz to 6 kHz with 1 kHz per second. The x-axis represents both the time of the sweep in seconds and the frequency in kHz. As numerically predicted, the result of the experimental characterization (Figure 10 (b)) shows that the resonance frequency of the finally realized inertial mass actuator system lies in the expected frequency range at approx. 4 kHz.

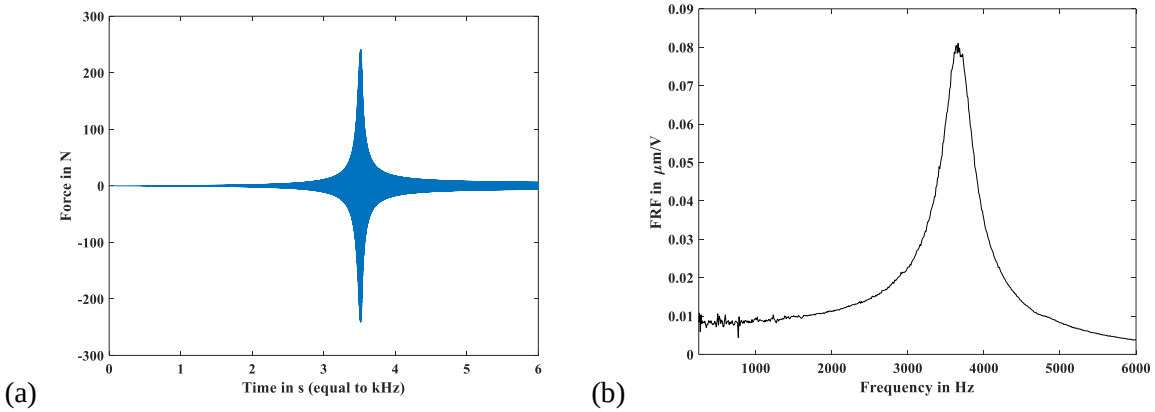


Figure 10: Results of the experimental characterization of the numerically investigated configuration of piezoelectric shear actuator with 8 of additional inertial mass and an analogue voltage amplifier

3 Modelling of the power amplifier in PSpice and Simulink

The experimentally investigated and numerically identified transfer function show good correlation. But the amplifier model solely relies on the observation of the transfer behaviour *H(s)*. Its real physical setup is not considered. A drawback of the methodology proposed by [7] is that hardware assemblies need to be available in order to carry out experimental characterizations. Regarding this aspect, the process of amplifier assessment and selection can be costly and time intensive due to the complexity of power electronic circuits. For instance, the power amplifier PIA-1115-2020 consists of two units, whereby the

first unit includes power supply components as a 200 W DC/DC-converter which has a nominal input voltage of +12 V and maximum output voltage of +200 V.

The second unit contains a pre-stage for input signal conditioning and power output stage to drive piezoelectric transducers. The signal conditioning comprises electrical impedance transformation, non-inverting integrator and pre-amplification. The main component of the output stage is the integrated circuit (IC) LT1166 from Linear Technology which is a bias generating system for controlling output current in high powered amplifiers and keeps the deadbeat distortions low.

The data flow from PSpice to Simulink for performing SLPS co-simulation is depicted in Figure 11. First, a project file has to be created in Capture. This project file includes the electronic circuit design which consists of electric models of actual components. Referring to the specifications of the component models, the PSpice simulation is carried out. In order to embed the electronic simulation in PSpice in Simulink model, the user has to select an input and output port of PSpice simulation model to define the interface to Simulink model.

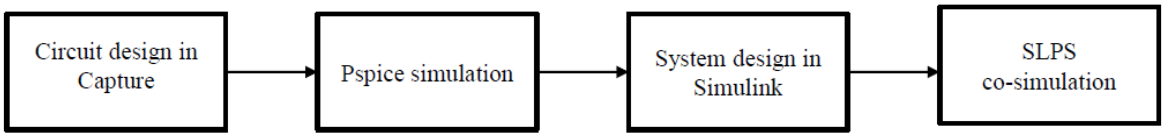


Figure 11: Simplified data flow from PSpice to Simulink for SLPS co-simulation

3.1 PSpice model of the power amplifier PIA-1115-2020

According to the diagram in Figure 11, the electronic circuit of the power amplifier PIA-1115-2020 has to be modelled in Capture first. Therefore, an adequate component model of the IC LT1166 is necessary. Although an extensive electronic model library is provided by PSpice, in some cases models have to be obtained from manufacturers of integrated circuits. Since LT1166 model is not available in PSpice model library, the LT1166 model from LTSpice, is used after adjustments. To verify the model functionality, application circuit diagrams from the datasheet of LT1166 [8] are created and tested in PSpice. For instance, Figure 12 depicts the simulation result of the LT1166 unity gain buffer circuit. Besides LT1166, the circuit consists of bipolar junction transistors MPS2907, MPS2222, 2N2907 and 2N2222 and MOSFETs IRF530 and IRF9350. All the components are available in PSpice library except 2N2907. For this component, the PSpice model is obtained from the website of the manufacturer. An ideal unity gain buffer should exhibit an output signal which is identical to the input signal. With regard to the output signal in Figure 12, it is noticeable that the slew-rate of LT1166 the output signal is divergent from the ideal input signal due to non-ideal specifications of the corresponding model. Furthermore the supply currents are not symmetrical. According to the datasheet, both entering and exiting current should be 15 mA. But the simulation result exposes that the supply current entering the IC is 15.21 mA and the supply current exiting the IC is -15.44 mA. The offset voltage of the simulated output is approximately -38.736 mV and is also not in accordance with the given offset value in the datasheet. After the functionality of the adjusted LT1166 model is verified, the electronic circuit diagram of the power amplifier PIA-1115-2020 with its main component LT1166 is created in PSpice.

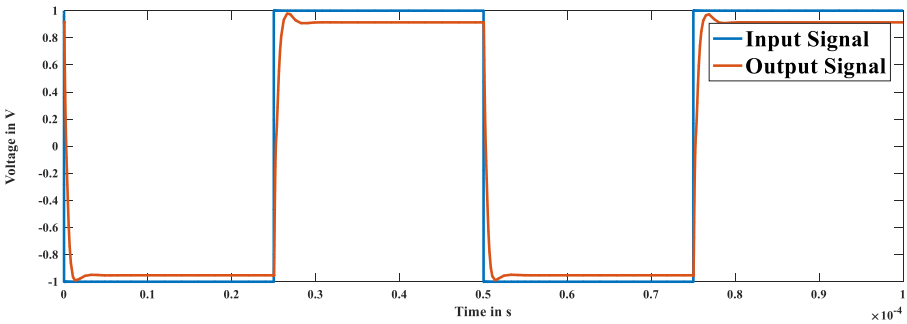


Figure 12: PSpice simulation result of LT1166 unity gain buffer circuit

By giving sine wave signal with amplitude of ±1V as input signal, an output signal of ±100 V should be obtained ideally. With regard to the simulation result (Figure 13) which considers non-ideal component parameters, it is noticeable that the positive amplitude is +99.98 V and the negative amplitude -98.80 V. This indicates that rail-to-rail operation is not provided by the chosen electronic components. Furthermore, time delay of output signal and offset voltage are existent. The offset voltage of negative sine wave is approximately +1 V. To identify the components which are responsible for this effect, every active component model of the pre-stage as well as output stage needs to be verified separately. Errors as offset voltage propagate along the amplifier signal chain and affect the output voltage.

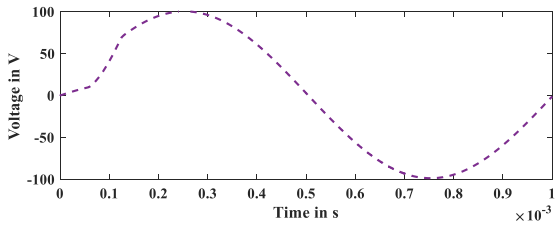


Figure 13: Simulated output voltage of power amplifier PIA-1115-2020 in PSpice

3.2 Simulink model of the power amplifier PIA-1115-2020

To constitute the ideal amplifier performance, an amplifier system model is set up in Simulink (Figure 14). Subsequently, the PSpice power amplifier model from Section 3.2 is embedded in the system model in Simulink in Section 4.

Parameters which are interesting for driving inertial mass actuators in the investigated application are output voltage, output current and impedance of the power amplifier. The amplifier system model implements following functionalities: I. Generation of amplifier excitation signal, II. Excitation signal amplification and offset adjustment, III. Impedance calculation and IV. Output current calculation. In particular, functionality II represents the power amplifier PIA-1115-2020 by means of “Gain”-block and “Constant”-block and exhibits the signal amplification and offset adjustment.

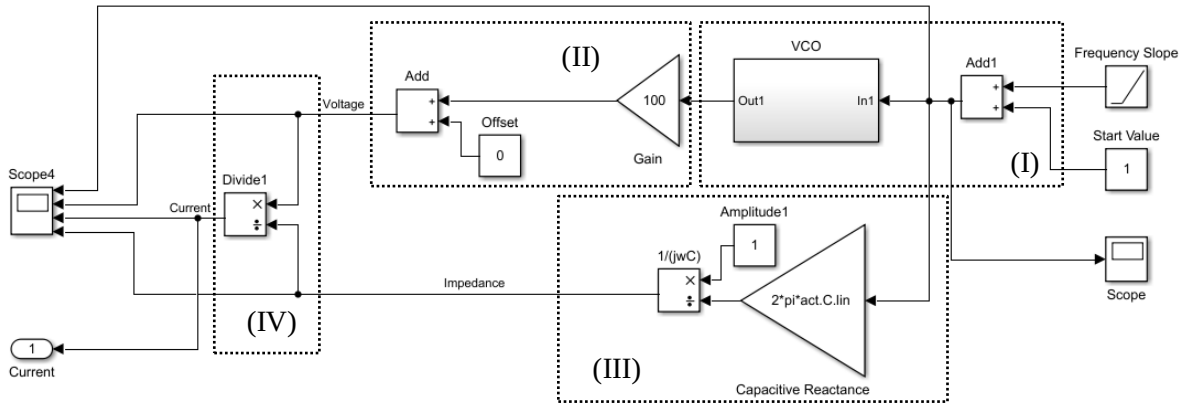


Figure 14: Simulink model with ideal power amplifier: I. Generation of amplifier excitation signal, II. Excitation signal amplification and offset adjustment, III. Impedance calculation, IV. Output current calculation

The simulation results are depicted in Figure 15. The excitation signal is a sine sweep signal from 1 kHz to 5 kHz with amplitude of ±1 V. The signal is amplified by a gain factor of 100. The current is calculated by dividing the voltage by impedance. While the amplitude of the voltage is constant over the whole frequency range, the amplitude of the current increases since the impedance is dependent from the impedance which is a function of frequency.

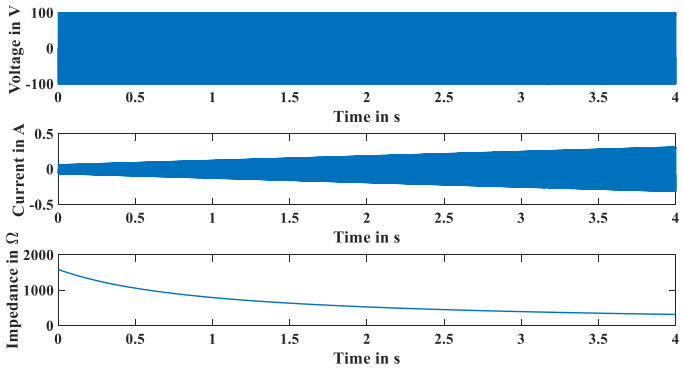


Figure 15: Simulation result of ideal power amplifier system model in Simulink

Parameter	Unit	Value
Amplitude	V	± 1
Frequency	kHz	1 to 5
Signal type	-	Sine Sweep
Step size	s	$10 \cdot 10^{-6}$
Run time	s	4

Table 2: Simulink simulation parameters of amplifier system model

4 Simulink-PSpice co-simulation of the power amplifier

The ideal amplification and offset adjustment blocks in Simulink system model from Section 3.2 are substituted by the PSpice power amplifier model by means of “PSpiceBlock” (Figure 16). The “PSpiceBlock” creates an interface between PSpice model and Simulink model and is provided by SLPS co-simulation environment. Only one “PSpiceBlock” can be placed in a single Simulink model [9]. In order to perform SLPS co-simulation, the block parameters have to be specified regarding the PSpice project file, input sources and outputs for the “PSpiceBlock” as well as PSpice data saving options. After selecting the project file (.OPJ) in parameter setting window, the corresponding simulation file (.SIM) is chosen automatically and available sources and outputs are visible. For this work, the constant sine wave input source and the output of the class AB stage of PSpice power amplier model are chosen as input source and output respectively. The SLPS co- simulation environment uses input source of PSpice model for initialization and replaces it by Simulink input source for further simulation. Simulation setting parameters in Table 3 are used for SLPS co-simulation.

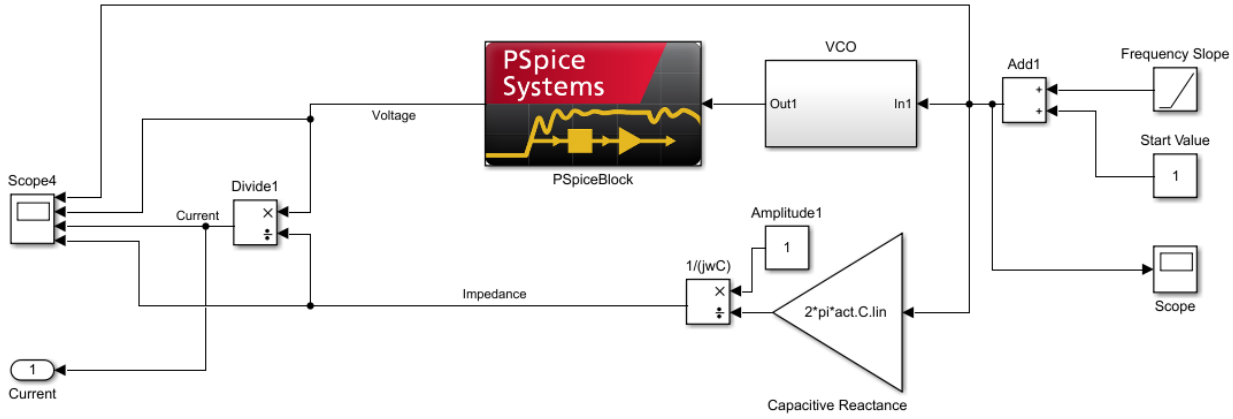


Figure 16: Simulink model with embedded PSpice power amplifier model in "PSpiceBlock"

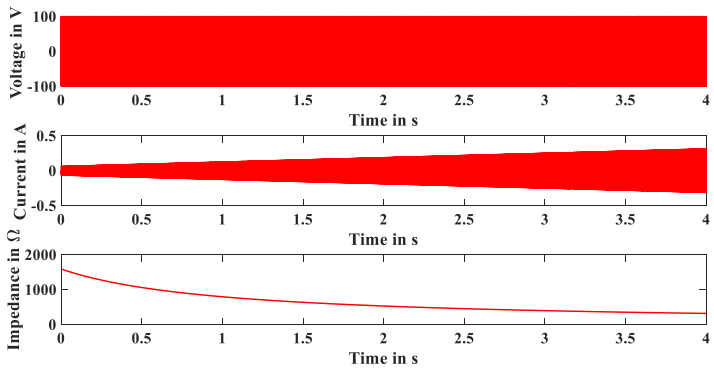


Figure 17: Simulation result of SLPS co-simulation

Parameter	Unit	PSpice	Simulink
Amplitude	V	± 1	± 1
Frequency	kHz	1	1 to 5
Signal type	-	Sine	Sine Sweep
Step size	s	$10 \cdot 10^{-6}$	$10 \cdot 10^{-6}$
Run time	s	4	4

Table 3: Simulation parameters for SLPS co-simulation

The general course of the output signal of SLPS co-simulation is identical to the ideal output signal of the Simulink amplifier model. But regarding slew-rate and offset voltage, marginal divergences between PSpice, Simulink and SLPS co-simulation can be noticed. The comparison of these simulations in Figure 18 shows the first amplitude of simulation result. While the sine wave of the Simulink model is ideal, the sine wave of PSpice and Simulink have a delay of around 0.1 ms. In addition, the amplitude of the SLPS simulation has a notch at 0.3 ms which is not caused by PSpice simulation and could be an error of initialization. Furthermore, due to the offset voltage of PSpice simulation which is caused by non-ideal parameters of components, the offset voltage of SLPS simulation is also affected. The maximum and minimum amplitude of PSpice and SLPS co-simulation are +99.98 V and -98.80 V as well as +99.98 V and -98.84 V respectively.

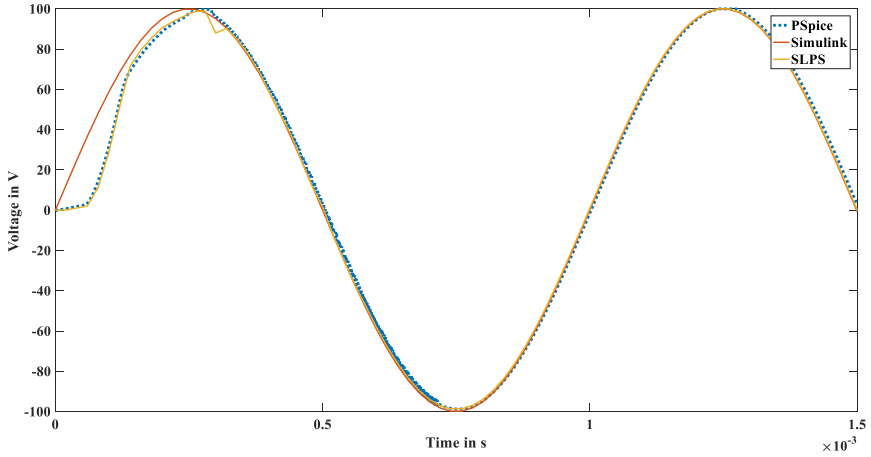


Figure 18: Comparison of PSpice, Simulink and SLPS co-simulation of the power amplifier

4.1 SLPS co-simulation setting conditions

In order to get proper co-simulation results, the simulation profiles of PSpice and Simulink have to fulfill setting conditions of step-size, run time and input source as following.

Step-size

In Figure 19 SLPS co-simulation results for different Simulink step-sizes but same run times are depicted. While the step-size of PSpice simulation is set to 10 µs for each simulation, the step-size of Simulink simulation is varied. By setting the same step-size of 10 µs for both PSpice and Simulink simulation, the correct simulation result can be obtained. Also the decrease of step-size by a factor of 10 in Simulink, which corresponds to a step-size of 1 µs in the given example, yields correct results. The increase of the Simulink step-size to 100 µs leads to an overlooking phenomena.

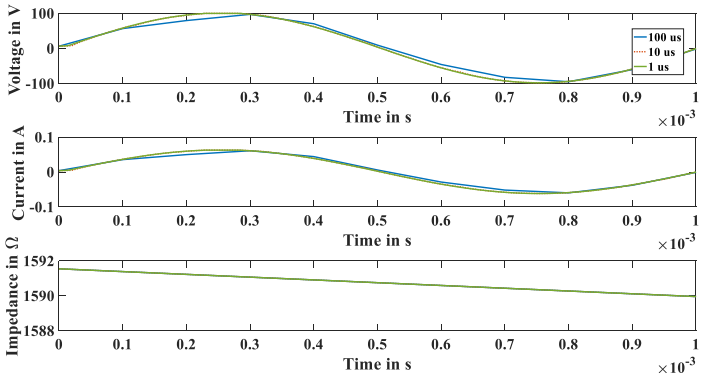


Figure 19: SLPS co-simulation for different-step sizes but same run time (4 s): The x-axis is scaled to 1ms to show the overlooking phenomena.

Run Time

Beside of step-size, the different run time of PSpice and Simulink simulation can cause errors. The Simulink simulation runtime of 4 s is determined by the sine sweep excitation signal which increases its frequency linearly and generates maximum frequency of 5 kHz at 4 s. If the run time of PSpice simulation is shorter than the run time of Simulink simulation, errors as in Figure 20 occur. The step-size is set to 10 µs for both simulations.

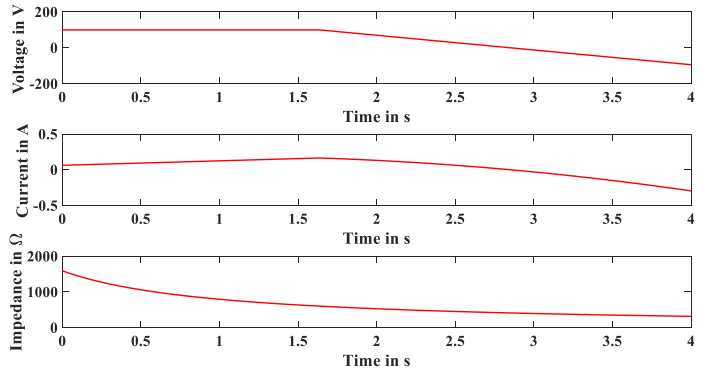


Figure 20: SLPS co-simulation error caused by different run time of PSpice (1 s) and Simulink (4 s)

Input Source

In the presented work, sine wave signal of 1 kHz is used as input source for PSpice model while the input source in Simulink model corresponds to sine sweep from 1 kHz to 5 kHz. For initialization of SLPS co-simulation the input source of PSpice model is used whereby it is replaced by the input source of Simulink model. Thus, simulation error occurs if the input source in PSpice simulation does not support the identification of the electronic circuit behaviour for Co-simulation. Errors occur if different types of input sources are used in PSpice model, e.g. DC voltage source.

4.2 Co-simulation linked to electromechanical actuator model

The Simulink inertial mass actuator model with embedded PSpice power amplifier model from Section 4 are used to perform SLPS co-simulation. The co-simulation result in Figure 21 demonstrates that electronic circuit design of the chosen power amplifier can be modelled in PSpice and the ideal power amplifier can be substituted, in order to perform electromechanical simulation with non-ideal parameters. In comparison to the analytical simulation from Section 2.3, it can be noticed that non-ideal parameters which are identified for the chosen power amplifier do not affect the electromechanical behaviour of the holistic system.

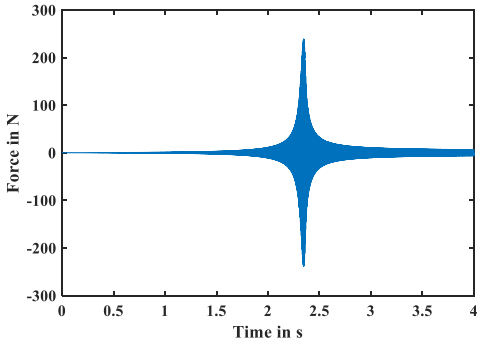


Figure 21: Co-simulation of Simulink actuator model system with PSpice power amplifier model

5 Summary and conclusion

The framework of the presented investigation is the active vibration control of planetary gearboxes. In order to simulate the inertial mass actuator and power amplifier of the AVC system, experimental characterization of actuator and amplifier are carried out. Based on this characterization, a Simulink system model, which includes components of inertial mass actuator and power amplifier, is set up. Since the model does not consider the physical set up of the power amplifier and non-ideal parameters are neglected, SLPS co-simulation is presented as a new approach to simulate power amplifier in Simulink simulation environment. SLPS co-simulation allows integration of electrical designs in system level designs since PSpice models which takes non-ideal parameters as non-linearity, delays and parasitic effects into account can be embedded in Simulink models. The power amplifier PIA-1115-2020 is simulated in PSpice first whereby the model of the main component LT1166 is not available in PSpice component library. Thus, the LTSpice model of LT1166 is adjusted and verified. The results of PSpice, Simulink and SLPS co-simulation are compared. Only marginal divergences in amplitude, offset voltage and delay time can be noticed. To carry out a proper SLPS co-simulation, the simulation parameters in PSpice as well as in Simulink have to be set correctly. Although electronic component models can be obtained from websites of IC manufacturers, they can be inaccurate and lead to false simulation results. Another drawback is the convergence problem of PSpice simulation which takes long calculation time into account. SLPS co-simulation environment can support design processes of power amplifier at simulation level but the co-simulation result still has to be verified by the actual hardware set up.

References

[1] R. Schirmacher, *Piezo actuators for active vibration control and isolation-principles and practical experiences*, The Journal of the Acoustical Society of America, Vol. 25, Issue 2, ASA (1999).

[2] A. J. Fleming, *Techniques and Considerations for Driving Piezoelectric Actuators at High-Speed*, in D. K. Lindner, editor, *Proceedings of SPIE, Vol. 6926, 2008 March 10 – 12,* San Diego (2008), pp. 1 - 11.

[3] S. P. Yadav et al., *Modelling and Simulation of Solid State Amplifier for Mobile Communication*, in *Proceeding International conference on Recent Innovations in Signal Processing and Embedded Systems, 2017 October 27 – 29*, Bhopal (2017), pp. 16-22.

[4] A. Preumont, *Vibration control of active structures*, 2nd Edition, Solid Mechanics and its Applications, Vol. 96, Kluwer Academic Publisher, Dordrecht, Boston, London (2002).

[5] P. Konstanzer, P. Jänker, S. Storm, *A piezo inertial force generator optimized for high force and low frequency*, Journal Smart Materials and Structures, Vol. 16, No. 4, IOP publishing (2007), pp. 1260 - 1264.

[6] P. Gardonio, C. González Díaz, *Downscaling of proof mass electrodynamic actuators for decentralized velocity feedback control on a panel*, Journal Smart Materials and Structures, Vol. 19, No. 2, IOP publishing (2010), pp. 1 – 14.

[7] T. Jungblut, *Ein Beitrag zur modellbasierten, hybriden Entwicklung elektromechanischer Systeme zur Schwingungsminderung*, Dissertation, Shaker Verlag, Aachen (2015).

[8] Linear Technology, *Power Output Stage Automatic Bias System***,** LT1166 datasheet, Rev. A (1995)

[9] Cadence, *PSPice SLPS Interface User Guide*, Product Version 17.2.-2016 User Guide (2016).

A practical approach of active vibration control with the use of piezoelectric actuators

D. Williams[1], H. Haddad Khodaparast[1], C. Yang[1]
[1] College of Engineering, Swansea University, Bay Campus,
Fabian Way, Crymlyn Burrows, Skewen, Swansea, SA1 8EN.
e-mail: **708199@swansea.ac.uk**

Abstract
A large focus within robotics engineering, as with other fields, is the reduction of weight of a system. A solution within robot systems is to replace heavy rigid links with lightweight flexible counterparts, however these are more susceptible to unwanted vibrations. Current research proposes the use of piezoelectric patches as actuators as part of active vibration control (AVC) as being a very viable solution. This research aims to design a solution to the problem by using an analytical model and simulation software both including two piezoelectric patches, before conducting a physical experiment. A physical experiment was conducted to verify the models, before a Proportional Differential (PD) controller was then implemented within the models. The output of the models with the inclusion of the control was then compared, and is to be validated further within future work by conducting an experiment that includes the same control.

1 Introduction

Unwanted vibrations can cause a threat to the integrity of structures and systems, and whilst re-enforcing structures reduces these vibrations it often comes at the cost of the mass of the system. One of the main goals throughout the fields of engineering, although its priority may vary depending upon the structure/system is to minimise mass and so a more suitable solution for the attenuation of unwanted vibrations is required. Focussing on robot systems one of the main methods to reduce the mass is to use thinner and lighter links, which are, unfortunately, more likely to be subject to unwanted vibrations. It is this engineering conundrum regarding flexible robot links which inspires the research focussing on the attenuation of vibrations. Current research suggests a promising solution lies within the use of Active Vibration Control (AVC) where the actuators within the system are piezoelectric transducers. This actuator choice is prevalent as it is possible to either surface bond or embed the piezoelectric patches within the structure with little to no effect on the structures weight and functionality, and they have a relatively large force output compared to their sizing.

The paper written by *Crawley and Luis* [1] shows considerable attention on the use of piezoelectric actuators as elements within intelligent structures. An analytical model was created using Euler-Bernoulli theory (EBT) for long, thin beams, and was then authenticated through physical experimentation. Another relevant research paper by *Rahman and Naushad Alum* [2] comprised of experimentation using a proportional integral derivative (PID) controller in combination with two collocated surface bonded piezoelectric patches as part of AVC. One of the piezoelectric patches was used within a piezo-sensing system to measure the vibrations experienced by a flexible beam. The other patch was used as an actuator with an output that was controlled through a data acquisition system, a computer running LabVIEW with a PID controller within the software and a voltage amplifier.

Within this research an analytical model based upon EBT has been produced of a structure which consists of a flexible link and two collocated piezoelectric patches. The link is envisioned as part of a robot arm, but the motion has been simplified to a transverse base excitation. A model of the same geometric and

material properties has been created within the simulation software COMSOL Multiphysics® for the purposes of further validation. These two models are then employed to predict the response of the tip acceleration of the link and the voltage output from the piezoelectric patches, and the results are compared with those acquired from a physical experiment. A solution for controlling the system will also be tested using the analytical and simulation models, to obtain a prediction of the output for experimental validation within future research.

2 Modelling the structure

2.1 Description

The structure consisting of a flexible link, two collocated piezoelectric actuator patches, an accelerometer, a clamp, a bracket support and the exciter armature has been modelled mathematically as a beam with added masses based on the Euler-Bernoulli beam theory. This method was chosen as the link to be modelled has dimensions which conform to those required by the beam theory; a long, slender beam. A model of the structure has also been created within the simulation software COMSOL Multiphysics®. The base of the link, including the clamp and bracket will be subject to a base excitation, and the tip acceleration and voltage produced by the piezoelectric patches are to be predicted by the model as a result. Within both models the bond between the link and piezoelectric patches will be considered to be perfect, and the effect of gravity needs not to be included as it will be cancelled out with the reaction force in the fixed point.

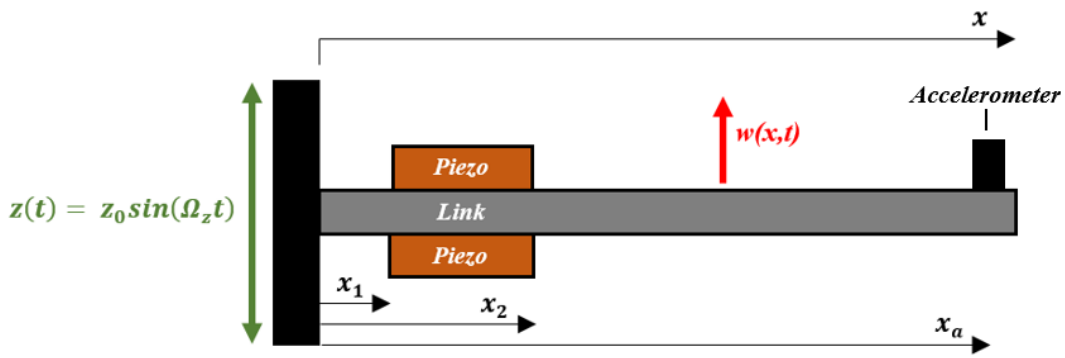


Figure 1. Visualisation of structure

The set-up of the model can be seen in Fig.1 above, where the view is as though looking from the top of the set-up. Where $z(t)$ is the base excitation, $w(x,t)$ is the transverse motion of the link, x_a is the location of the accelerometer and x_1 and $x_2$are the start and end positions of the piezoelectric patches along the length of the link, respectively.

2.2 Analytical model

The equation of motion for the structure can be written as [3]:

$$\frac{\partial^2}{\partial x^2}\left(EI(x)\frac{\partial^2 w(x,t)}{\partial x^2}\right)+\rho A(x)\frac{\partial^2 w(x,t)}{\partial t^2}+M_a\delta(x_a)\frac{d^2(x)}{dt^2}$$
$$+c_a\frac{\partial w(x,t)}{\partial t}+\rho A(x)M_{cba}\delta(x_{cba})Z_0\sin(\Omega_Z t) \quad (1)$$
$$=F_0\sin(\Omega_F t)\,\delta(x-L)+\vartheta V_{in}sin(\Omega_V t)\left(\frac{d\delta(x-x_1)}{dx}-\frac{d\delta(x-x_2)}{dx}\right)$$

where, $w(x,t)$ is the transverse motion of the beam, x is the position along the length of the beam, and t is time. The Dirac delta function is denoted as $\delta(x)$, and the viscous air damping coefficient as c_a. It is important to note that the mass of the clamp, bracket and exciter armature (M_{cba}) and the mass of the accelerometer (M_a) are both modelled as point masses on the structure at their respective positions (x_{cba} and x_a). The frequencies of the base excitation (Z_0), the applied force (F_0) and applied voltage (V_{in}) are represented by Ω_Z, Ω_F and Ω_V, respectively. The functions $EI(x)$ and $\rho A(x)$ have been included to account for the varying density and Young's modulus over the structure's length, and are as follows:

$$\rho A(x)=\rho A+\rho_p A_p[H(x-x_1)-H(x-x_2)] \quad (2)$$

$$EI(x)=EI_x+E_pI_{x_p}[H(x-x_1)-H(x-x_2)] \quad (3)$$

where $H(x)$ denotes the Heaviside function. The piezoelectric coupling term can be written as:

$$\vartheta=\frac{\bar{e}_{31}W_p}{20T_p}\left[\left(T_p+\frac{T}{2}\right)^2-\frac{T^2}{4}\right] \quad (4)$$

where, $\bar{e}_{31}$ is the effective transverse piezoelectric coefficient and W_p is the width of the piezoelectric patches. T and T_p are the thickness of the flexible link and piezoelectric patches, respectively. Employing the product rule and the Galerkin decomposition method to equation (1) yields [4]:

$$\ddot{T}_n(t)+2\zeta\omega_n\dot{T}_n(t)+\omega_n^2T_n(t)=F\sin(\Omega_F t)+\chi V_{in}sin(\Omega_V t)-Zsin(\Omega_Z t) \quad (5)$$

where $T_n(t)$ is the n^{th} generalised coordinate and,

$$\zeta=\frac{C}{2M\omega_n},\quad \omega_n=\sqrt{\frac{K}{M}},\quad F=\frac{F_b}{M},\quad \chi=\frac{\theta_p}{M},\quad Z=\frac{Z_b}{M}. \quad (6)$$

and,

$$M=\rho A(x)\int_0^L X_n^2(x)dx+M_aX_n^2(x) \quad (7)$$

$$C=c_a\int_0^L X_n^2(x)dx \quad (8)$$

$$K=\int_0^L\left[\frac{\partial^2 EI(x)}{\partial x^2}X_n''(x)+2\frac{\partial EI(x)}{\partial x}X_n'''(x)+EI(x)X_n^{iv}(x)\right]X_n(x)dx \quad (9)$$

$$F_b=F_0\int_0^L X_n(x)\delta(x-L)dx \quad (10)$$

$$\theta_p=\vartheta\left(\frac{dX_n(x_2)}{dx}-\frac{dX_n(x_1)}{dx}\right) \quad (11)$$

$$Z_b=Z_0\rho A(x)M_{cba}\int_0^L X_n(x)\delta(x_{cba})dx \quad (12)$$

2.3 Simulation model

A model was created within the software COMSOL Multiphysics® utilising its MEMS module to generate a Finite Element (FE) model of the structure. To reduce computational time and memory the clamp, bracket and exciter detail was minimised to a cube of the same mass and the mass of nuts and bolts which were used to hold the structure together. The accelerometer was included within the model as a point mass. A free tetrahedral mesh was used within the simulation with the predefined mesh size 'finer'. This mesh size option has a minimum element size of $0.00185m$, and has been proven to be sufficiently accurate whilst having a reasonable computational time.

3 Experiment, results and discussion

3.1 Description

The experiment was carried out to gain the FRFs of the structure both with and without two collocated piezoelectric patches (M5628-P2), as well as the natural frequencies of the first three modes of the structure. The structure was subject to the base excitation using an exciter (APS 113 ELECTRO-SEIS® Long Stroke Shaker), which was controlled using a data acquisition system (DAQs) (SignalCalc Abacus), requiring a power amplifier (APS 125 Power Amplifier) to power the exciter from the output voltage of the DAQs. Two accelerometers (PCB Piezotronics 352C03) were attached to the structure, one at the base of the structure to provide a reference acceleration, and one towards the free end of the link to measure the tip acceleration, and a FRF was created from the data collected. Once the two piezoelectric patches were attached, the experiment was repeated, however this time the voltage output from the piezoelectric patches was measured as well as the response from the tip of the beam. The Figures 2 and 3 show the illustration of the set up and an image taken of the experiment, respectively.

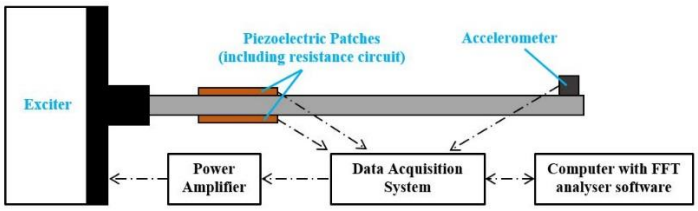


Figure 2. Illustration of FRF experiment

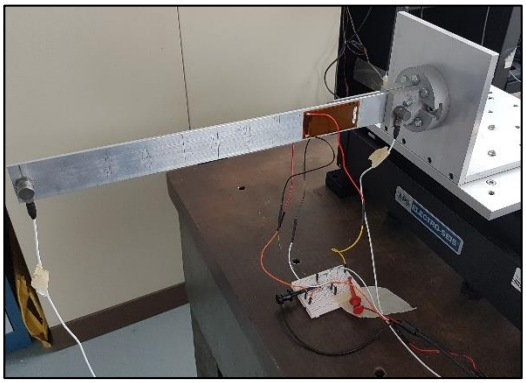


Figure 3. Image of FRF experiment

Table 1. Geometric, mechanical and electric properties of link and piezoelectric patches

Parameters	Link (Aluminium)	Piezoelectric Patch (PZT-5A)
Length (m)	0.36	0.056
Width (m)	0.035	0.028

Thickness (m)	0.003	0.0003
Density (kg/m^3)	2700	5440
Young's Modulus (GPa)	70	30.336
Piezoelectric coefficient, $\bar{e}_{31}$ (C/m^2)	N/A	-11

Table 1 contains the geometric and material properties of the link and the piezoelectric patches which were used within the experiment. The geometry and properties of these components were duplicated within both the COMSOL® and analytical models. Within the experiment a circuit was required in which a resistance of $300k\Omega$ was connected in parallel to the piezoelectric patches and the DAQs. This is due to the internal resistance of the DAQs affecting the readings from the piezoelectric patches, and a much greater resistance connected in parallel to the measured component would counteract this effect. The piezoelectric patches were bonded to the link using metal loaded epoxy (ensuring as thin of a layer as possible), at a distance from the start of the link of $x_1 = 0.036m$. This position was selected based upon previous analytical results, simulations and other research [5-6]. The accelerometer was attached to the beam temporarily using petro wax at a distance $x_a = 0.352m$, and was included as a point mass of $M_a = 0.012Kg$ in both the COMSOL® and analytical models. It should be noted that the data sheet for the accelerometers used states that they have a mass of $0.0058Kg$, however when weighed to include the petro wax and wires the mass of $M_a = 0.012Kg$ was found to be more accurate. The mass of the clamp, bracket and shaker armature was calculated to be $M_{cba} = 5.8825Kg$, which includes the mass of the attached accelerometer and any nuts and bolts used to secure the structure.

3.2 Results

The natural frequencies for the first three modes were obtained from the data collected from the experiment, from the COMSOL® simulation and from the analytical model. The percentage error was calculated for the simulation and analytical results, Tables 2 and 3 show the obtained results from the structure with and without the piezoelectric patches, respectively.

Table 2. Natural frequency comparison for link without piezoelectric patches

Natural Frequency Comparison (No Piezoelectric Patches)					
Mode	**Experiment (Hz)**	**COMSOL® (Hz)**	**Error (%)**	**Analytical (Hz)**	**Error (%)**
1	16	15.93	0.44	15.87	0.81
2	104.94	104.31	0.60	101.80	2.99
3	297.75	290.32	2.50	290.89	2.30

Table 3. Natural frequency comparison for link with piezoelectric patches

Natural Frequency Comparison (Two Piezoelectric Patches)					
Mode	**Experiment (Hz)**	**COMSOL® (Hz)**	**Error (%)**	**Analytical (Hz)**	**Error (%)**
1	16.69	16.96	1.62	17.09	2.40
2	104.03	104.77	0.71	101.27	2.65
3	288.3	287.04	0.44	295.31	2.43

The FRFs for the structure were obtained from the experiments, and plotted within the same graphs as the simulation and analytical results for comparison. Figures 4a and 4b show the FRFs of the structure without the piezoelectric patches bonded to the link, where the input is excitation of the base of the structure and the measured output is the acceleration of the tip of the link. Once the piezoelectric patches were bonded to the link, the resulting FRFs shown in Figures 5a to 6b were obtained, with the former two figures showing the tip acceleration output as a result of base excitation, and the latter two the voltage output from a piezoelectric patch as a result of the base excitation.

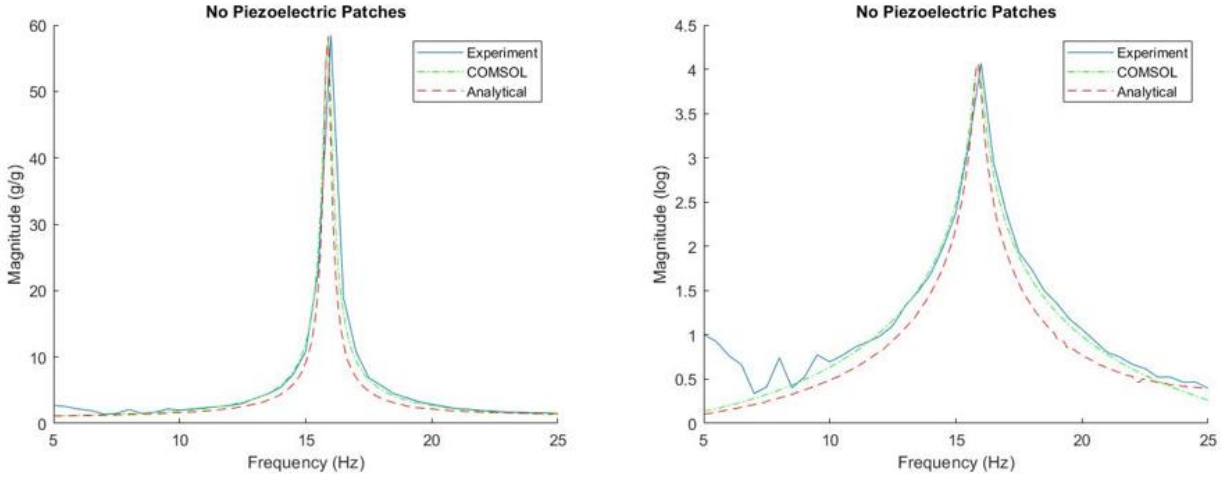


Figure 4 (a,b). FRF base excitation input, tip acceleration output with no piezoelectric patches.

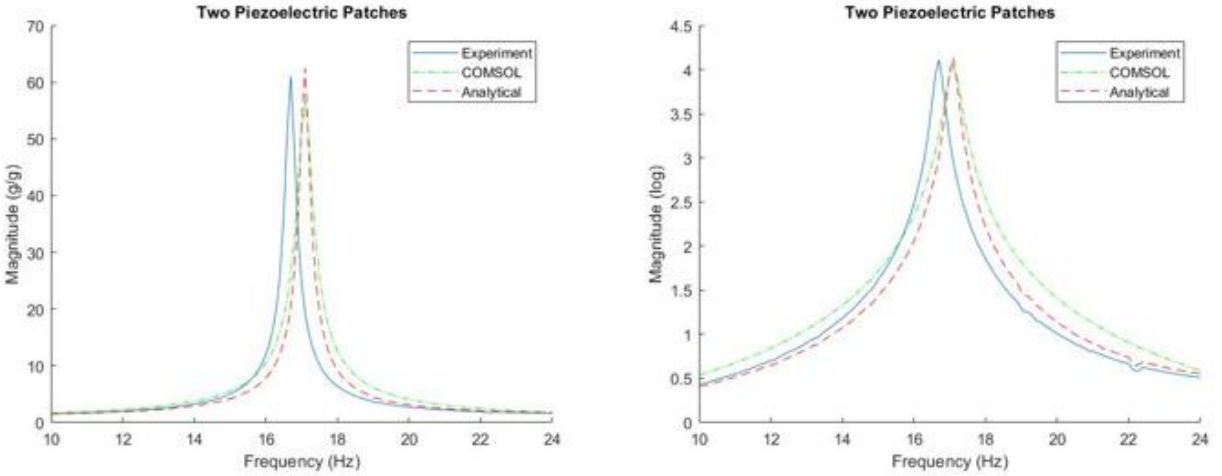


Figure 5 (a,b). FRF base excitation input, tip acceleration output with two piezoelectric patches.

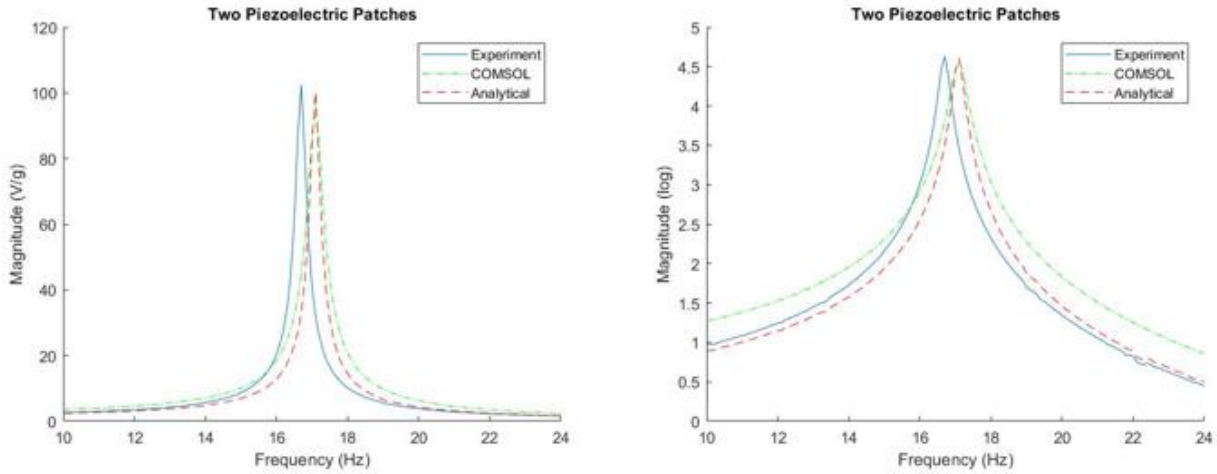


Figure 6 (a,b). FRF base excitation input, voltage output with two piezoelectric patches.

3.3 Discussion

The natural frequencies obtained from the analytical and simulation models were shown to have an error of less than 3% for the first three modes both with and without the piezoelectric patches (see Tables 2 and 3). With this low of a percentage error it can be confidently said that both models are a good prediction of the natural frequencies of the actual structures. From Figures 4a and 4b it can be seen that the FRFs produced by the analytical and simulation models (excluding the piezoelectric patches) are a very close match with those produced from the data of the experiment. Although, it should be noted that the damping ratio of the simulation model was set to $\zeta = 0.012$ whereas the analytical model was set to the same damping ratio as the experimental result ($\zeta = 0.008$). This was to accommodate for a factor of a property within COMSOL® which could not be readily altered. The damping ratio was also altered within the simulation when the piezoelectric patches were included such that the experimental and analytical damping was $\zeta = 0.0079$ and the simulation damping was $\zeta = 0.0104$.

With the simulation damping altered, the FRFs of the tip acceleration output as a result of base excitation for the structure that includes the piezoelectric patches also has a very good match between the experimental results and the analytical and simulation data (Figures 5a and 5b). A discrepancy between the resonance frequencies of the different results can be seen within the FRF, but as it is within 3% the models can be said to be accurate predictions of the experiment. The same can be said for the analytical and simulation FRF results for a base excitation input and measured voltage output; they would be considered as accurate prediction excusing the less than 3% error with the natural frequency. However, with regards to the COMSOL® results, they were also multiplied by a factor of 3.5 to counteract a difference within the material properties used within the software, as well as the original difference in the damping factor. Further studies are to be conducted in order to investigate the requirement of the multiplication factor and the slight difference in the damping ratios.

4 Active vibration control

To test the control theory a proportional differential (PD) controller was applied to the analytical model. Recalling equation (5), negating the applied force term as the control will just focus upon the base excitation as an input to the system, and equating to the controlled output (u) yields [7]:

$$\ddot{T}_n(t) + 2\zeta\omega_n\dot{T}_n(t) + \omega_n^2 T_n(t) = \chi V_{in} sin(\Omega_V t) - Z sin(\Omega_Z t) = u = -[k_p \quad k_d]\begin{bmatrix} T_n(t) \\ \dot{T}_n(t) \end{bmatrix} \qquad (13)$$

where k_p and k_d are the proportional and differential gains, respectively. From equation (13) the value of the controlled output u can be calculated using the proportional and differential gains and the generalised coordinate displacement and velocity values ($T_n(t)$ and $\dot{T}_n(t)$). From the same equation it is possible to obtain the input voltage required to obtain the controlled output u. As the application of $\pm 60V$ will not have a significant effect upon the structure compared to the maximum positive voltage, the usable range of voltage in this case will be 0V to 360V (as opposed to the actual range on the piezoelectric patches: -60V to 360V). This range is more suited to actual components to be used in future research. So, there will only ever be one piezoelectric patch being used to control the structure at one time, and which patch to be employed will be dependent upon the direction of the deflection of the link.

A parametric study was conducted to obtain the best combination of proportional and differential gains whilst adhering to the voltage limitations of the piezoelectric patches. The objective function of which was the percentage decrease of the tip acceleration when the control was applied to the model. It was concluded that the most suitable gain values for the PD controller are $k_p = 1$ and $k_d = 2.335\ s$, for a base excitation amplitude of $Z_0 = 0.2g$. All parameters are the same as those stated within section 3.1, with the exception of the damping ratio used, which was altered to $\zeta = 0.01$. The structure was excited at its resonance frequency.

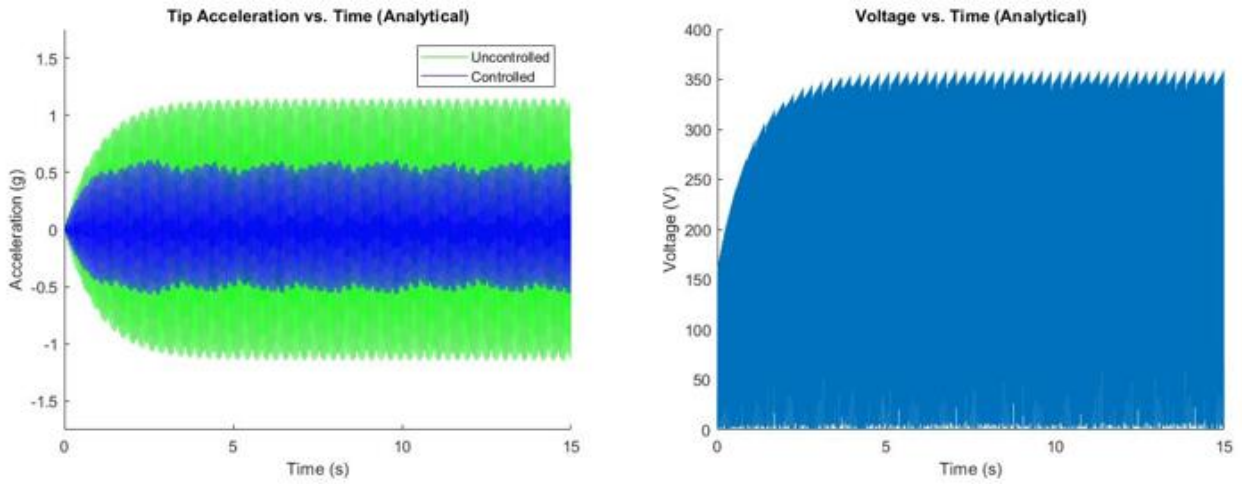


Figure 7 (a,b). Comparison of the analytical results of the controlled tip acceleration against uncontrolled, and the voltage to be applied each piezoelectric patch.

From the comparison of the tip acceleration of the structure with and without the control system (Figure 7a) it can be seen that when the PD controller is utilised the amplitude of the tip acceleration is reduced by approximately 50%. Figure 7b shows the voltage required to be applied across each piezo patch, where the maximum voltage required is within the limits set by the piezoelectric patch at a value of 359.81V.

The control system was then applied to the simulation model in a similar manner as it was the analytical model for the purpose of validation. The slight difference was that the controlled output was obtained by applying the voltage to the piezoelectric patches as a sin wave with the amplitude obtained through the analytical result (359.81V). This was opposed to the applying voltage calculated for each moment in time as within the analytical models, hence why the required voltage graphs (Figures 7b and 8b) have a difference in the shape initially. As with the previous simulation models, the damping ratio was increased in comparison to the ratio within the analytical model. The simulation model with the inclusion of a PD controller reduces the unwanted tip acceleration by approximately 50% (see Figure 8a), a very close match to the output from the analytical model hence validating the result. However, with some discrepancies with the input parameters of the models, further investigation will be carried out to resolve the differences before the results are compared with those from future experimentation.

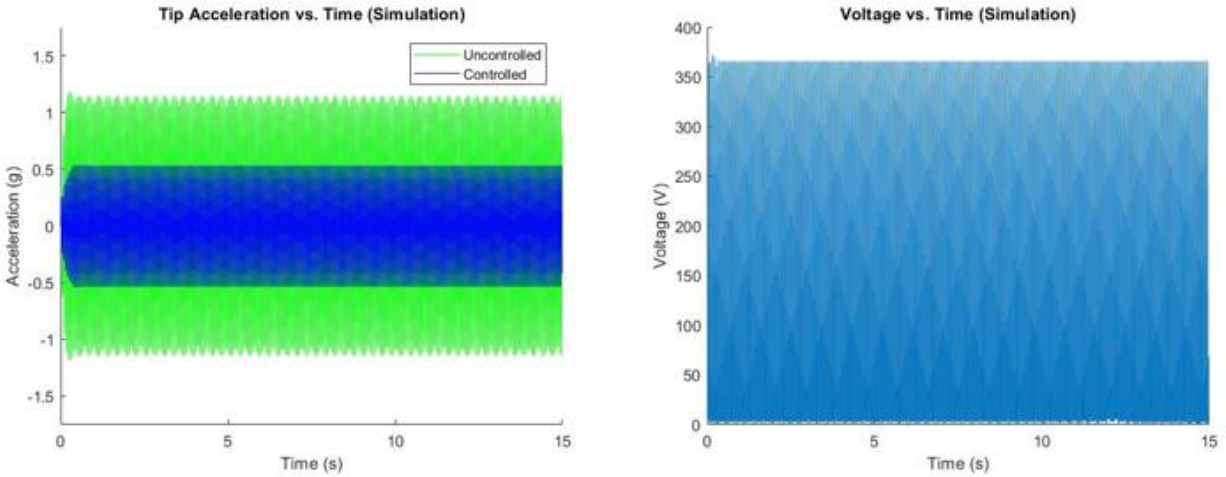


Figure 8 (a,b). Comparison of the simulation results of the controlled tip acceleration against uncontrolled, and the voltage to be applied each piezoelectric patch.

5 Conclusion

From the experimental data the accuracy of the analytically produced model and the finite element model created using COMSOL® has been proven. Therefore, the theory used to create the analytical model (EBT) has also been proven as an excellent choice for this structure in particular. This then means that using the same models with the control system included will have given an acceptably accurate prediction. As can been seen from the results presented within section four (Figures 7a to 8b), the inclusion of a PD controller to alter the voltage applied to the piezoelectric patches is predicted to be an effective solution for the attenuation of the vibrations experienced by the flexible link. A physical experiment is to be conducted to confirm the results of the two sets of predictions, and further validate the use of a PD controller and piezoelectric patches as part of AVC.

This experiment is to be part of future work, and will utilise an exciter to apply a base excitation to the structure to simulate the simplified motion of a robotic arm, as within this research. However, a Raspberry Pi module will employ PD control to alter the voltage across the piezoelectric patches via a high voltage driver in accordance with the measured acceleration at the tip of the link. The components to be used are chosen based on the aim of creating a method of control which is as practical and as inexpensive as possible. Once the models including control have been proven to be accurate, then a model of a robot arm will be included to provide the base excitation to the base of the link. Ultimately testing the control system with a more complicated input to the structure.

Acknowledgements

This research has been funded and supported by EPSRC, grant number: EP/N509553/1.

References

[1] E.F.Crawley and J.Luis, *Use of Piezoelectric Actuators as Elements of Intelligent Structures,* AIAA Journal, Vol. 25, No.10, (1987), pp.1373-1385.

[2] N. Rahman and M. Naushad Alam, *Active Vibration Control of a piezoelectric beam using PID controller: Experimental Study*, LAJSS, Vol. 9, (2012), pp. 657-673.

[3] Inman, D. J., *Engineering vibration*, (2014).

[4] H.Madinei et al., *Design of MEMS piezoelectric harvesters with electrostatically adjustable resonance frequency,* MSSP Journal, Vol. 81, (2016), pp. 360-374.

[5] D.Williams et al., *Active vibration control of a flexible link robot with the use of piezoelectric actuators*, MATEC Web of Conferences, Vol. 148, No. 11005, (2018).

[6] Q.Wang and C.M.Wang, *Optimal placement and size of piezoelectric patches on beams from the controllability perspective*. IOPSCIENCE Journal, Vol. 9, (2000), pp. 558-567.

[7] Bolton, W, *Control systems*, Newnes, (2002).

Wave-based control of a planar mechanical structure by piezoelectric actuators

P. Beneš[1], Z. Neusser[1], Z. Šika[1], M. Valášek[1], J. Zavřel[1]
[1] CTU in Prague, Faculty of Mechanical Engineering, Department of Mechanics, Biomechanics and Mechatronics
Technická 4, 166 07, Praha 6, Czech Republic
e-mail: **petr.benes@fs.cvut.cz**

Abstract
The aim of this paper is the research of possible usage of the wave-based control approach when dealing with the smart structure. This smart structure is represented by the plate equipped with multiple piezoelectric patches serving as actuators and sensors. The main goal is to increase damping properties – suppress unwanted vibration.

1 Introduction

New projects e.g in automotive or aerospace industry are often based on a usage of a modern hi-tech materials. These are very usually of a lightweight nature, which brings a number of advantages, but on the other hand also disadvantages. The typical one is a low mechanical damping resulting in unwanted vibration and acoustic discomfort [1]. The passive solution in the form of the structure stiffening by additional masses conflicts with the lightweight demand. Therefore, the usage of a light active elements incorporated in the structure should be considered. From a technological point of view, it should be feasible in near future to have piezo or other active components integrated into the „mechatronic network“, constituting a regular and dense matrix of multiple sensors and actuators throughout the mechanical structure considered [2], [3]. Such an active smart mechatronic material enables not only the active vibration suppression but it is interesting from the point of view of motion or shape control as well. One can hope then that relatively simple and scalable control algorithms could be developed that shall work effectively for arbitrary considered shape or final product made of this structure. So there is clearly a strong motivation to investigate possibilities of scalable and easily deployable control solutions by considering large and dense matrices of sensors and actuators installed throughout the structure, and by means of dedicated decentralized or distributed simple and scalable control laws. The aim of this paper is to investigate the potential of the wave-based control approach when dealing with the 2D mechanical structure equipped with the multiple piezoelectric elements.

2 Wave-based control approach

The wave-based control [4], [5] is a relatively new control method, which primarily doesn’t need the mathematical model of the controlled system that could be crucial for other approaches, e.g. feedforward command shaping techniques [6], [7]. The precise of the model could be Instead it uses the feedback. At the same time, however, it is not a classical feedback control because it doesn’t monitor the state of the output member of the system. Instead the state of the first one is measured and the main idea is that the system being controlled is the natural model for the control. The flexible structure is modelled as a set of rigid bodies connected by springs and dampers. The description of interaction between these bodies using transfer function represents so called wave model. The input actuator initiates the wave that spread through the system, bounce back and returns to the initial point where it is sensed. The detection of a

reflected wave means that we can adjust the control signal for demanded purpose, e.g. vibration suppression. The wave based control enables the stabilization of the whole system just from the local knowledge of active actuator states and its closest neighbours. The stability of such systems is discussed in [8].

2.1 Wave model of lumped mass system

Artificially created wave model is represented as a loop containing transfer functions. There are two parts of the loop on the Figure 1, co called launched wave is in the upper part of the loop, so called reflected wave is in the lower part of the loop.

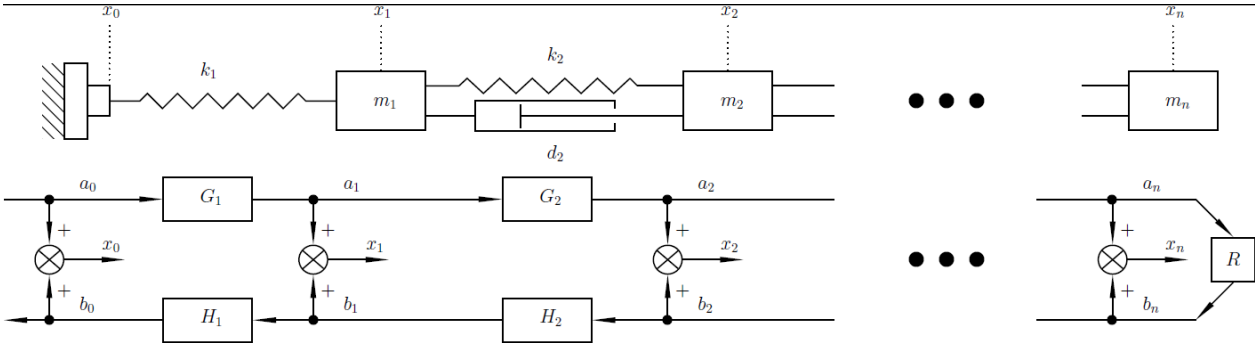


Figure 1: Wave model of lumped mass chain.

There are mechanical model parameters: masses m_i, spring constants (stiffness) k_i, damping ratios d_i and mass positions x_i. In the wave model are transfer functions G_i in the launched part and H_i in the reflected part, transfer function R is called reflection. Sum of two corresponding variables in the launched a_i and reflected b_i parts (waves) are equal to the corresponding mechanical model state x_i, see equation (1) which interconnects lumped masses model with the wave model.

$$x_i = a_i + b_i \tag{1}$$

The wave model transfer functions G_i, H_i and R are determined from the original model, the selection of particular transfer functions is not unique.

2.2 Wave-based control

The wave-based control cuts the wave model at the coordinate, where the measurement is performed, see Figure 2. The control uses the launched part of the control up to the variable a_i, then calculates reflected part b_1 using measurement at mass x_1 following the equation (1) with i = 1 and evaluates reflected part back to the beginning of model obtaining b_0 variable, which serves as a feedback.

The control input is now x_{0ref}, but control algorithm requires only launched wave variable a_0, reflected wave variable b_0 creates feedback used in the control algorithm to reflect the dynamic behavior of the whole system. Evaluation of a_0 from the desired coordinate x_{0ref} is performed at steady state using parameter $a_{0,ss}$, which is calculated in the equation (2) and it is evaluated as ratio between x_0 and a_0 at infinite time.

$$a_{0,ss} = \frac{x_{0ref}}{a_0} = \frac{x_0}{a_0} \tag{2}$$

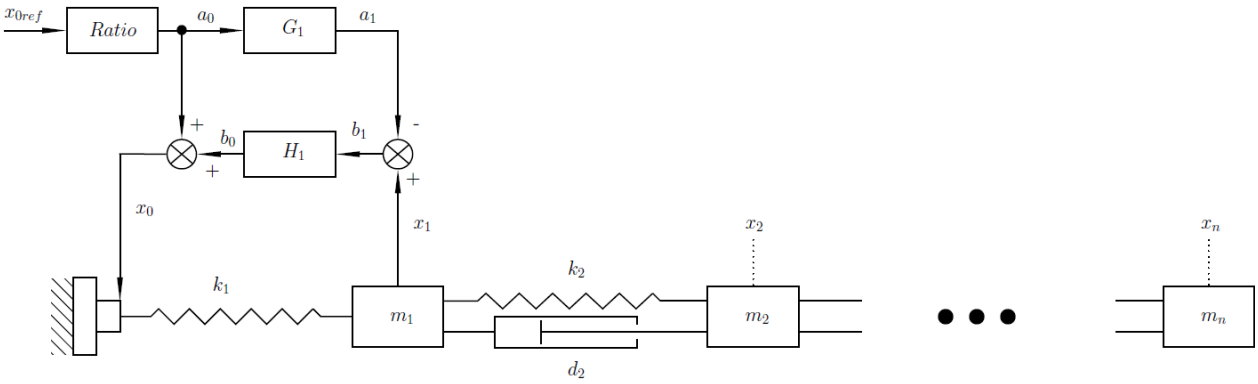


Figure 2: Wave based control scheme using first mass measurement.

3 Controlled smart structure

The steel plate with piezoelectric actuators/sensors was used as an example of a smart structure [9], Figure 3. The piezoelectric actuators and sensors are placed as a collocated pairs [10]. The term collocated pair in this case means that the actuator is on one side of the plate and the corresponding sensor is on the same place but on the other side of the plate. There is 25 of these pairs in the regular grid 5x5. The kinematic excitation of the system was used for experiments when the movement of the lower edge was prescribed.

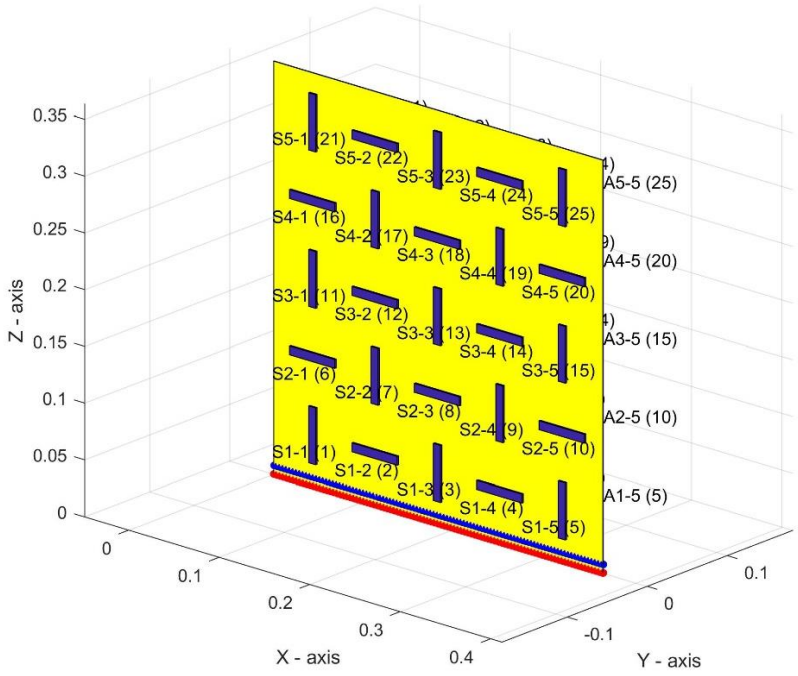


Figure 3: Plate with piezoelectric elements – Matlab visualisation

The system was modelled in ANSYS software and exported in matrix form - sparse matrices of the mass and stiffness. Then it was reduced [11] and transformed into the state space form

$$\dot{\boldsymbol{x}} = \boldsymbol{A}\boldsymbol{x} + \boldsymbol{B}\boldsymbol{u}, \tag{3}$$

$$\boldsymbol{y} = \boldsymbol{C}\boldsymbol{x} + \boldsymbol{D}\boldsymbol{u}, \tag{4}$$

where $\boldsymbol{A}$ is the system matrix, $\boldsymbol{x}$ is the state vector, $\boldsymbol{u}$ is the vector of inputs – voltage on the piezo patches and kinematic excitation, $\boldsymbol{y}$ is the output vector – voltage measured by the piezo sensors and Y-coordinates of nodes.

4 Experiments

The wave-based control was tuned to suppress the first natural frequency of the system. The following figures show the comparison of system response when no control is used vs. wave-based control. The output signal is the voltage measured on piezoelectric sensor no. 23 (in the middle of the free edge of the controlled plate). The excitation trajectory was a ramp signal - Figure 4 and the shifted cosine wave - Figure 5. The both experiments proved that the first natural frequency was suppressed. The settling time is significantly better as there is almost no residual vibration.

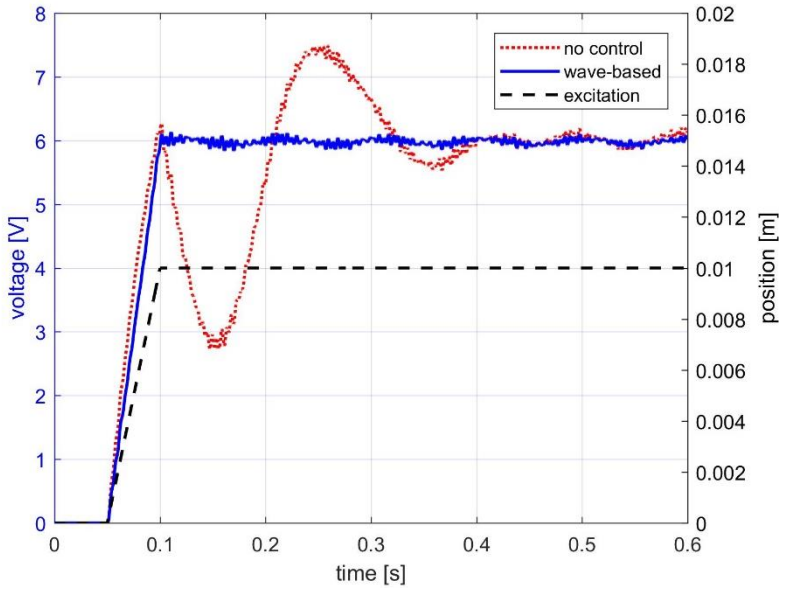


Figure 4: System response – ramp signal excitation

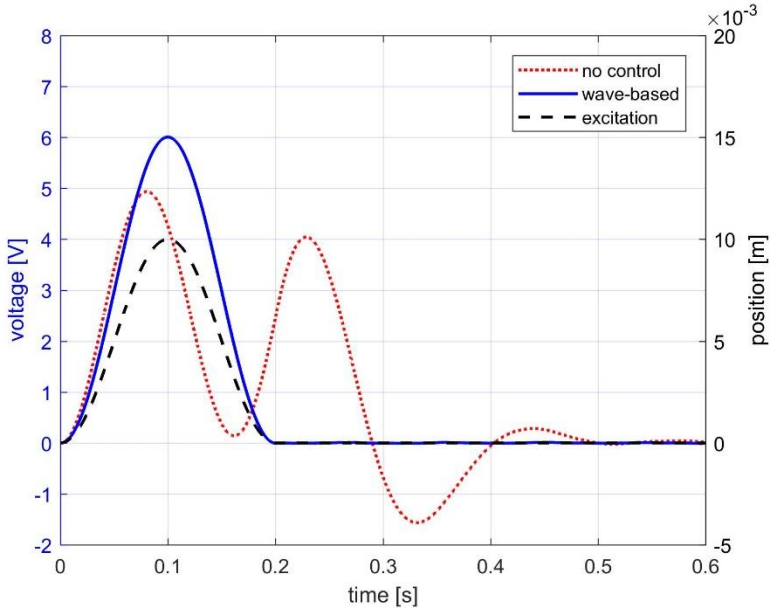


Figure 5: System response – wave signal excitation

5 Conclusions

It has been proven that this approach – wave-based control - is capable to significantly increase the damping properties of the so called smart structure. The experiments performed using a steel plate with regular grid of piezoelectric actuators and sensors were focused on suppression of the first natural frequency vibration and achieved a promising results for further research in this field. In the simple example presented in this paper the information from one sensor was sufficient to get demanded performance and active usage of more sensors wasn't neither necessary nor efficient. The future experiments will be focused on more complex types of excitation when information from more sensors would be beneficial.

Acknowledgements

This work is supported by the grant GA 16-21961S entitled „Mechatronic structures with heavily distributed actuators and sensors" of Czech Science Foundation.

References

[1] M. Kozek and A.Schirrer (Eds.), Modeling and Control for a Blended Wing Body Aircraft,Springer, 2015.

[2] M. Krommer, H. Irschik and M. Zellhofer, Design of Actuator Networks for DynamicDisplacement Tracking of Beams, Mechanics of Advanced Materials and Structures, vol. 15, pp.235–249, 2008.

[3] H. Irschik, M. Nader, Actuator placement in static bending of smart beams utilizing Mohr'sanalogy, Engineering Structures, vol. 31(8), pp. 1698-1706, 2009.

[4] W. J. O'Connor, Wave-based Modelling and Control of Lumped, Multibody Flexible Systems, Proc. of Multibody Dynamics 2005, Madrid, Spain, 2005 June 21-24.

[5] M. Valášek, Z. Neusser, T. Gordon, Wave-based control for intelligent longitudinal traffic column. In: 24th Symposium of the International Association for Vehicle System Dynamics (IAVSD 2015), 17 - 21 August 2016, Graz, Austria.

[6] W. E. Singhose, A. K. Banarjee and W. P. Seering, „Slewing Flexible Spacecraft with Deflection-Limiting Input Shaping," Journal of Guidance, Control and Dynamisc, vol. 20, no. 2, pp. 291-298, 1997.

[7] P. Benes and M. Valasek, "Optimized Re-entry Input Shapers", Journal of Theoretical and Applied Mechanics, Vol. 54, no. 2, pp. 353-368, 2016.

[8] M. Valasek, O. Marek, Stability analysis of wave-based control of flexible systems, The 1st Joint International Conference on Multibody System Dynamics: IMSD, Lappeenranta, Finland, 2010 May 25-27, pp. 1-8.

[9] H. Irschik, M. Krommer and Y. Vetyukov, "On the Use of Piezoelectric Sensors in Structural Mechanics: Some Novel Strategies," Sensors, vol. 10, no. 6, pp. 5626-5641, 2010.

[10] D. Halim and S. O. R. Moheimani, "Spatial resonant control of flexible structures-application to a piezoelectric laminate beam," IEEE Trans. Control Syst. Technol., vol. 9, no. 1, pp. 37-53, 2001.

[11] W.K. Gawronski, Advanced Structural Dynamics and Active Control of Structures, Springer-Verlag New York, Inc., 2004.

Decentralized and distributed MIMO H-infinity robust control of vibration suppression of planar structures

Z. Šika[1], M. Hromčík[2], F. Svoboda[2], J. Volech[1], J. Zavřel[1], J. Karlíček[1]
[1] Czech Technical University in Prague, Faculty of Mechanical Engineering
Technická 4, 166 07, Praha 6, Czech Republic
e-mail: **Zbynek.Sika@fs.cvut.cz**

[2] Czech Technical University in Prague, Faculty of Electrical Engineering,
Karlovo náměstí 13, 121 35, Praha 2 - Nové Město, Czech Republic

Abstract
Distributed control is nowadays a very active field of research, thanks to potential applications which require high scalability and reliability. The paper deals with the optimization of active vibration suppression of the planar flexible systems equipped by regular and dense matrix of multiple sensors and actuators. The H-infinity design with predefined controller structure has been chosen as an appropriate control method. At first, performance of H-infinity regulator was experimentally tested on simple beam demonstrator with piezoelectric patches as sensors and actuators. The simulation model of larger planar demonstrator has been firstly modelled by FEM and then exported into the state space form. Decentralized and distributed control laws have been investigated. The feasibility of attenuation of a large set of flexible modes has been demonstrated for the model of the demonstrator. The demonstrator itself has been prepared for the ongoing experiments. The possibility of alternative actuation by clusters of actuators has been also analyzed.

1 Introduction

Distributed control is nowadays a very active field of research, thanks to potential applications which require high scalability and reliability. The main advantage of using distributed control is the locality of the necessary measurement and actuation. The measurements are collected and processed in a distributed manner. This kind of control can be applied to many different systems including, for example, platoons of vehicles, the groups of mobile robots and others [1]. Important applications of distributed control are also in the branch of the vibration suppression or eventually motion control of light flexible structures. The established paradigm in past and current active damping and shape-control projects is as follows. The mechanical object is defined first. Systems detailed design and modelling phases follow [2], [3] giving rise to very accurate FEM models with many of thousands of degrees of freedom. Model order reduction [4], [3] then gives accurate-enough yet tractable models for optimal actuators and sensors placement [5], [6], [7]. Finally a very limited number of them is considered (say up to twenty) for the design of the control laws [3]. Alternatively for existing prototypes, the experimental identification approach can be applied to get the mathematical models directly via experimental modal analysis [8]. Finally, validation and verification of the solutions by high-fidelity simulations is performed, followed by laboratory experiments and final deployment of the product. From a technological point of view, it should be feasible in relatively near future to have piezo materials integrated to the primary structure in the form of network of multiple piezo patches, or even layers creating the „mechatronic material“. Such future mechatronic material will ideally contain not only a dense and regular matrix of actuators and sensors, but also attached embedded microcontrollers. One can hope that relatively simple and scalable control algorithms could be developed that shall work (after just minor modifications or tuning based e.g. on experimental identification) for arbitrary considered shape of final product made of this mechatronic material. The aim of the paper is the choice of the control concept appropriate for distributed active vibration suppression, the control and mechatronic structure optimization and the preparation of demonstrator suitable for the experimental testing

of distributed vibration suppression. The structure of the paper is as follows. Firstly in chapter 2 the H-infinity design method with predefined controller structure is shortly presented, secondly in chapter 3 this control design is primarily implemented to the cantilever beam with piezo patches including modelling, identification and experimental testing. The chapter 4 is devoted to the generation of the state space models of planar structures with piezo patch sensor/actuator network and their optimization. The prepared basic grid demonstrator is also shown. The subsequent chapter 5 presents the decentralized MIMO H-infinity optimal robust control design for the planar structures. The chapter 6 is a short conclusion.

2 H-infinity design with predefined controller structure

The H-infinity design methodology offers efficient algorithms how to obtain multivariable control laws by specifying closed-loop frequency response requirements. This approach was used e.g. in [9], where authors compare SISO, H-infinity and μ synthesis in termes of robustness and performance. Presented controllers can significantly increase damping and improve dynamic behavior of a flexible wing. The order of a control system is however equal to an augmented plant containing the model of a flexible wing and weighting filters, which are crucial for the design. This leads to excessively high order control laws typically, with strong negative impact on implementation and experimental fine-tuning. For this reason, in e.g. [10] there was a method presented for the controller order reduction which is one possible way how to get control laws with reasonable complexity. Nevertheless, loss or deterioration of closed-loop performance and/or stability is often an unwanted effect associated with this approach. Thanks to recent structured H-infinity control synthesis results, see e.g. in [11], [12], it is possible to receive the parameters of such reduced-order controllers directly, minimizing the H-infinity norm under the controller complexity constraints. More precisely, minimization of lower linear fractional transformation (LFT) of a system with augmented plant G and structured controller K. The general scheme of closed loop with the structured controller is in Figure 1. Such a system is described by generalize state space form according to equation (1). A great advantage is the possibility to design MIMO controllers of a really low-order proportional controllers as an example which can be crucial in some cases. One of the successful applications of fixed-order H-infinity synthesis in the aerospace context was within the ACFA project *www.acfa2020.eu*. See e.g. [13] where authors designed control laws of order up to five for system with dozens of states, meeting all control requirements and loosing literally only a few percent of performance (measured by the closed-loop H-infinity norm) compared to the full order designs. The structured H-infinity control could surpass existing solutions with controller order reduction [9], which can be infeasible for low-order controller requirement.

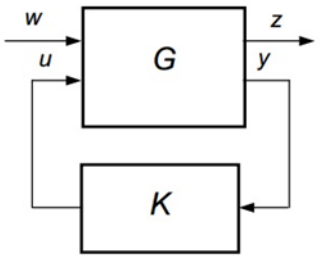


Figure 1. Closed-loop system configuration with H-infinity regulator [14]

$$\begin{bmatrix} \dot{\boldsymbol{X}} \\ \boldsymbol{z} \\ \boldsymbol{y} \end{bmatrix} = \begin{bmatrix} \boldsymbol{A} & \boldsymbol{B_1} & \boldsymbol{B_2} \\ \boldsymbol{C_1} & \boldsymbol{D_{11}} & \boldsymbol{D_{12}} \\ \boldsymbol{C_2} & \boldsymbol{D_{21}} & \boldsymbol{D_{22}} \end{bmatrix} \begin{bmatrix} \boldsymbol{X} \\ \boldsymbol{w} \\ \boldsymbol{u} \end{bmatrix}. \tag{1}$$

Such fixed-order designs can be practically executed thanks to availability of numerical solvers like *hinfstruct* in MATLAB described in [15] or the open-source alternative HIFOO [16]. A nice performance assessment of these software packages can be found in [17] where the benchmark problem of dual-stage inertial stabilization is considered. From the user's perspective, the structured H-infinity tools are very close to classical full-order H-infinity design procedures. We formulate our requirements through a proper

selection of weighting filters and assemble the augmented plant. In addition, the tunable parameters and the expected structure and order of the controller must be specified.

3 Active vibration suppression of beam system

At first, performance of H-infinity regulator was studied on simple steel cantilever beam with three piezoelectric patches. Detailed description of this issue could be seen in [18]. Steel plate with dimensions 250x28x0,55 mm is equipped with two piezoelectric actuators on top surface and one piezoelectric sensor on bottom surface collocated with actuator Act1 near the clamped end. Act1 is supposed to suppress the vibration generated by actuator Act2 further from clamped end.

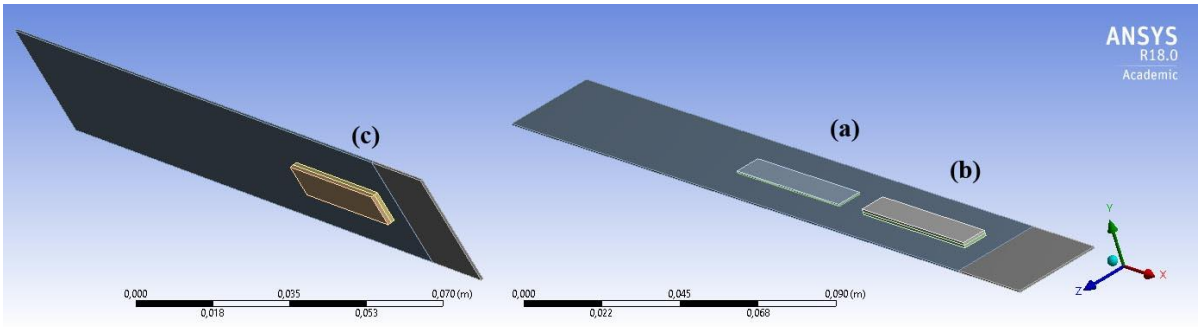


Figure 2. Model with three different piezo patches: (a), (b) – actuators, (c) – sensor. Bottom view is on the

Generated sensor voltage corresponding to deformation of the beam is send to controller, where appropriate control voltage to Act1 is computed. After creation of finite element model (Figure 2) experimental structure illustrated in Figure 3 was build.

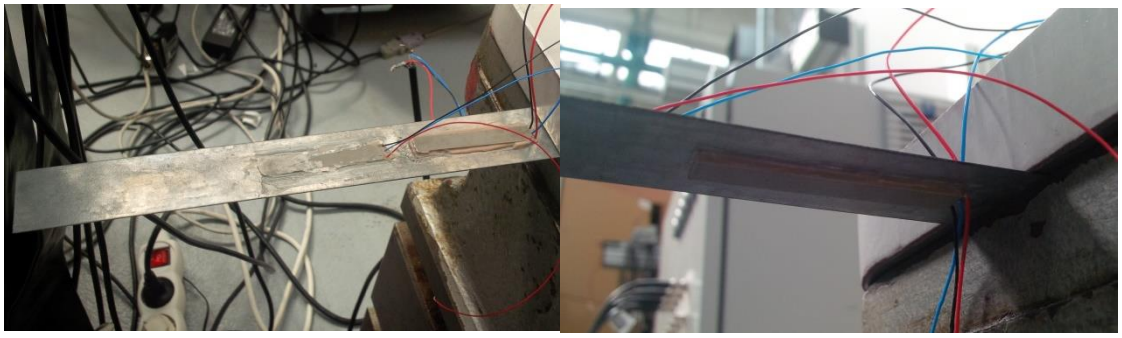


Figure 3. Cantilever beam. View from top (left) and detail of sensor (right)

Model of such a structure in state space form is acquired using system identification procedure. Based on measured input/output voltage, prediction error minimization (PEM) method in system identification toolbox in MATLAB is used and model of 14^{th} order obtained.

3.1 H-infinity controller design

For our needs HIFOO package [19] [12] for MATLAB is used to design the H-infinity regulator. This tool works in two phases. First, stabilization phase needs to find set of stabilizing regulators, which are the starting point for second, optimization phase. In this part of design chosen penalty function of stabilizing regulators is minimized.

Working principles of system with H-infinity regulator are described in chapter 2. Considering system according Figure 1, in our case inputs and outputs are chosen as follows: vector *w* represents reference signal

zero and disturbance from Act2; *z* corresponds to deviance from reference signal; *y* is sensor voltage and *u* is control voltage on Act1. Based on identified model H-infinity regulator of 5th order is designed.

3.2 Experimental results

Designed H-infinity regulator has been evaluated by means of experiment. Sinusoidal voltage with frequency 80 Hz is chosen as an input to disturbance generating Act2. Figure 4 shows voltage response of the sensor. Approximately 80% voltage and thus vibration reduction is achieved on this simple clamped beam.

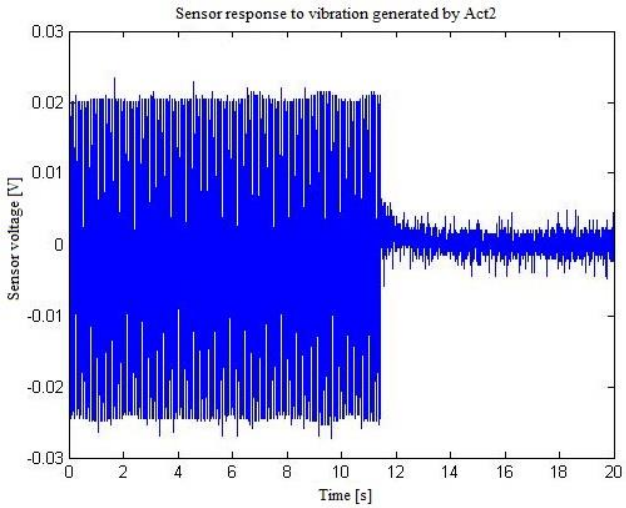


Figure 4. Sensor response to vibration generated by Act2 without control (until 11,5 sec) and with control (after 11,5 sec) in experiment

4 State space models of planar structures with piezo patch sensor/actuator network and their optimization

Experimental identification of the sheets with the glued piezo patches used as actuators and/or sensors brings the possibility of verification and tuning of the target state space models for control design and sensors/actuators positioning optimization. The careful attention has been paid to the mechanical, electrical and coupling parameters of the piezo actuators, modelling of coupling with primary structure, correct transformation of the electromechanical model to the state space form and to the appropriate model reduction. The tuned physical models transformed to the state space form proved to be more reliable for the control design than the black-box (input-output) identified models especially in the cases with many actuators and sensors. In order to design mechanical, electromechanical parameters and position of piezo actuators and piezo sensors it is necessary to create the mathematical simulation model. The main structure is modelled in the ANSYS environment and the final simulation model is the state space model in MATLAB-SIMULINK.

4.1 Modelling of the piezo actuator

The behavior of the one-dimensional piezoelectric material [20] is described by constitutive equations (2),(3)

$$D = \varepsilon^T + d_{33}T, \tag{2}$$

$$S = d_{33}E + s^E T, \tag{3}$$

where D is the electric displacement, E is the electric field, T is the stress, S is the strain and ε^T is the dielectric constant under constant stress, s^E is the compliance when the electric field is constant and d_{33} is the piezoelectric constant. The subscript 33 denotes, that it is always aligned to the poling direction of the material and the electric field is parallel to the poling direction. Various model configurations are used to analyze system behavior. The simulation electromechanical models are created in ANSYS environment. Every model consists of the steel plate and various number of piezo patches. Piezo patch is a very thin piezo element that consists of two layers (bimorf construction). There are two types of layers orientation, uniform and opposite. Piezo patches we are used have opposite oriented layers **(**Figure 5**).**

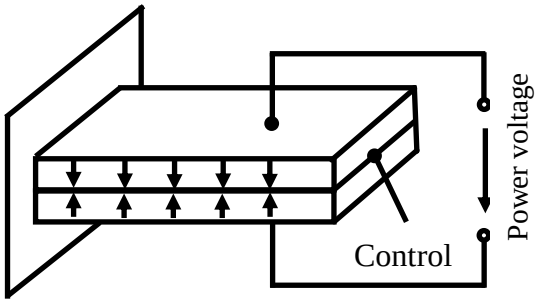


Figure 5. The piezo patch with layers oriented in the opposite direction

The basic model used to verifying the simulation model assembly algorithm is correct consists of simple steel sheet and three different piezo elements (piezo patches), see Figure 2. The same structure was used in experiments **(**Figure 3**).**

4.2 Getting the simulation model

The procedure how to become the simulation state-space model consists of following steps:

1. build an ANSYS model and use an analysis solution
2. export stiffness, mass and dumping matrices (usually in the text format)
3. import informations about mesh and nodes
4. import text files into MATLAB
5. create state-space model in MATLAB

The step one is easy and known. An example of such model can be structure with five times five actuators and the same number of sensors (Figure 6). They are arranged crosswise, but the orientation of the actuator and opposite sensor is the same. Actuators are placed at the top of the sheet and sensors at the bottom. Boundary condition can be changed operatively. In the model there is applied fixing to the frame.

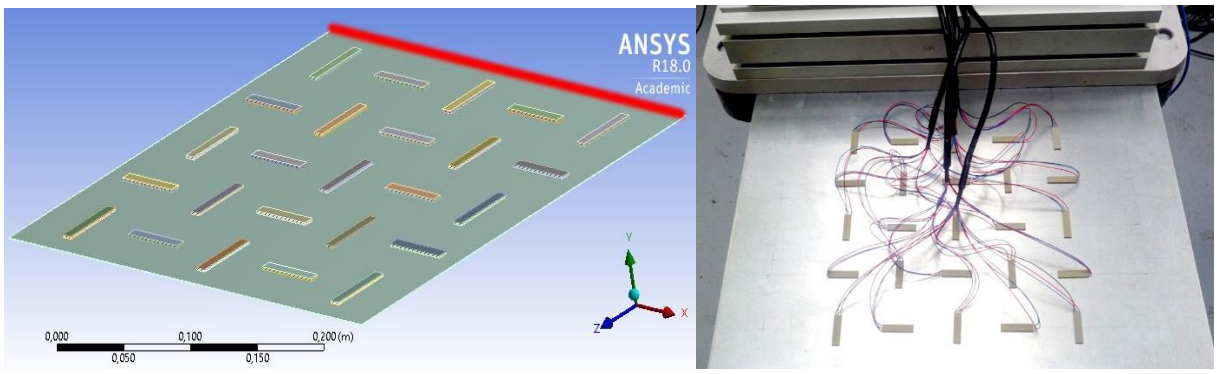


Figure 6. The top view of a model and demonstrator with a grid of 5x5 actuators and sensors placed on the bottom (not visible). The piezo patches are arranged crosswise. The boundary condition is highlighted by the red line.

The second step how to become structural matrices encounters some problems. The main problem is that it is impossible due to combined problem (structural and electricity) become matrices by usually way. It means to become matrices by usually sub structuring analysis. The only way how to obtain the mass, damping and stiffness matrices is through the Harwell-Boeing format. The matrix form of the whole system is

$$\begin{bmatrix} \boldsymbol{M_{uu}} & \boldsymbol{0} \\ \boldsymbol{0} & \boldsymbol{0} \end{bmatrix} \begin{bmatrix} \ddot{\boldsymbol{u}} \\ \ddot{\boldsymbol{v}} \end{bmatrix} + \begin{bmatrix} \boldsymbol{C_{uu}} & \boldsymbol{0} \\ \boldsymbol{0} & \boldsymbol{C_{vv}} \end{bmatrix} \begin{bmatrix} \dot{\boldsymbol{u}} \\ \dot{\boldsymbol{v}} \end{bmatrix} + \begin{bmatrix} \boldsymbol{K_{uu}} & \boldsymbol{K_{uv}} \\ \boldsymbol{K_{vu}} & \boldsymbol{K_{vv}} \end{bmatrix} \begin{bmatrix} \boldsymbol{u} \\ \boldsymbol{v} \end{bmatrix} = \begin{bmatrix} \boldsymbol{f} \\ \boldsymbol{q} \end{bmatrix}, \tag{4}$$

where $\boldsymbol{K_{uu}}$ is structural stiffness, $\boldsymbol{K_{vv}}$ is dielectric permittivity, $\boldsymbol{K_{uv}}$ is piezoelectric coupling ($\boldsymbol{K_{vu}} = \boldsymbol{K_{uv}^T}$), $\boldsymbol{C_{uu}}$ is structural damping, $\boldsymbol{C_{vv}}$ is dielectric dissipation and $\boldsymbol{M_{uu}}$ is the mass. On the right side the $\boldsymbol{f}$ means applied forces and $\boldsymbol{q}$ the electric charge. There are used two types of degrees of freedom. Symbol $\boldsymbol{u}$ denotes the physical coordinates like movements and rotations and $\boldsymbol{v}$ is used for velocity.

In order to become state space in agreement to the modelled system, it is necessary modify equation (4). The piezo patches can work in two modes, as actuators or sensors. Actuators are labelled by index i and sensors are labelled by index o. The $\boldsymbol{C}$ matrix is equal to zero matrix in this case. We will introduce dissipation (damping) later by the term (12).

The new matrix description is

$$\begin{bmatrix} \boldsymbol{M_{uu}} & \boldsymbol{0} & \boldsymbol{0} \\ \boldsymbol{0} & \boldsymbol{0} & \boldsymbol{0} \\ \boldsymbol{0} & \boldsymbol{0} & \boldsymbol{0} \end{bmatrix} \begin{bmatrix} \ddot{\boldsymbol{u}} \\ \ddot{\boldsymbol{v}}_{\boldsymbol{i}} \\ \ddot{\boldsymbol{v}}_{\boldsymbol{o}} \end{bmatrix} + \begin{bmatrix} \boldsymbol{K_{uu}} & \boldsymbol{K_{ui}} & \boldsymbol{K_{uo}} \\ \boldsymbol{K_{iu}} & \boldsymbol{K_{ii}} & \boldsymbol{K_{io}} \\ \boldsymbol{K_{ou}} & \boldsymbol{K_{oi}} & \boldsymbol{K_{oo}} \end{bmatrix} \begin{bmatrix} \boldsymbol{u} \\ \boldsymbol{v_i} \\ \boldsymbol{v_o} \end{bmatrix} = \begin{bmatrix} \boldsymbol{f} \\ \boldsymbol{q_i} \\ \boldsymbol{q_o} \end{bmatrix}. \tag{5}$$

We become three equations

$$\boldsymbol{M_{uu}\ddot{u} + K_{uu}u + K_{ui}v_i + K_{uo}v_o = f}\ , \tag{6}$$

$$\boldsymbol{K_{iu}u + K_{ii}v_i + K_{io}v_o = q_i}, \tag{7}$$

$$\boldsymbol{K_{ou}u + K_{oi}v_i + K_{oo}v_o = q_o}. \tag{8}$$

By completing the equation (8) in equation (6) we than obtain

$$\boldsymbol{M_{uu}\ddot{u} + [K_{uu} - K_{uo}K_{oo}^{-1}K_{ou}]u = [K_{uo}K_{oo}^{-1}K_{oi} - K_{ui}]v_i + f.} \tag{9}$$

The equation (9) describes a behaviour of the system composed of the structural part and electromechanical piezo system. In our case is the order of such system in the order of tens of thousands to hundreds of degrees of freedom for the whole model. Such simulation model isn't easy useful or optimization and real-time control algorithms. It is necessary to reduce the number of degrees of freedom before composing the state space model.

4.3 Model reduction

There is used the modal reduction in our case [21]. The modal reduction is based on the building the model from the selected eigenmodes $\boldsymbol{V}$.

Let's introduce the transform from physical coordinates u into modal coordinates $\boldsymbol{\xi}$ (10).

$$\boldsymbol{u = V\xi,\ \ddot{u} = V\ddot{\xi}.} \tag{10}$$

By substituting this transform, multiplying equation (9) from the left side by $\boldsymbol{V^T}$ we become expression

$$\boldsymbol{I\ddot{\xi} + \Delta\dot{\xi} + \Lambda\xi = V^T[K_{uo}K_{oo}^{-1}K_{oi} - K_{ui}]v_i + V^Tf}, \tag{11}$$

where $\boldsymbol{I}$ is the identity matrix, $\boldsymbol{\Lambda}$ the spectral matrix and $\boldsymbol{\Delta}$ the dumping matrix.

The dumping matrix $\boldsymbol{\Delta}$ is the diagonal matrix filled by the expression $2b_{r_i}\Omega_i$ at the main diagonal, where b_{r_i} is the relative attenuation on the given frequency Ω_i.

$$\boldsymbol{\Delta} = diag(2b_{r_i}\Omega_{\mathrm{i}}). \tag{12}$$

We will finally get the state-space description with states $\boldsymbol{z}$ in the form

$$\begin{bmatrix} \dot{z}_1 \\ \dot{z}_2 \end{bmatrix} = \begin{bmatrix} 0 & I \\ -\Lambda & -\Delta \end{bmatrix} \begin{bmatrix} z_1 \\ z_2 \end{bmatrix} + \begin{bmatrix} 0 & 0 \\ V^T & V^T[K_{uo}K_{oo}^{-1}K_{oi} - K_{ui}] \end{bmatrix} \begin{bmatrix} f \\ v_i \end{bmatrix}, \tag{13}$$

and the corresponding outputs y are

$$[y] = [-K_{oo}^{-1}K_{ou}V \quad 0] \begin{bmatrix} z_1 \\ z_2 \end{bmatrix} + [0 \quad -K_{oo}^{-1}K_{oi}] \begin{bmatrix} f \\ v_i \end{bmatrix}. \tag{14}$$

5 Decentralized MIMO H-infinity optimal robust control of planar structure

5.1 Description

Simulation model of the plate equipped with 25 actuators (control inputs u_i) and 25 collocated sensors (measured outputs y_i) is used in this section for design and validation of selected decentralized and distributed control laws. They are designed using the H infinity structured optimization methodology to attenuate resonant modes of this flexible structure. More specifically, local controllers were considered in the first place,

$$U_i = -k_i Y_i = -p_i \frac{s}{s+f_c} Y_i \tag{15}$$

where u_i is input voltage to i-th piezo patch. In the second case, we deal with distributed control law where the control action applied to each node depends on measured outputs at the neighboring nodes,

$$U_i = -p_{i1} \frac{s}{s+f_c} Y_i - \sum_{j \in E} p_{i2} \frac{s}{s+f_c} Y_j \,, \tag{16}$$

E is set of neighboring nodes. For both cases, the scenarios with constant gains throughout the structure, as well as controllers without this constraint, are studied.

5.2 H-infinity design

H-infinity synthesis with predefined controller structure is frequency-domain optimization method for controller tuning. HIFOO solver or *hinfstruct* function in robust control toolbox in MATLAB can be used for solving this task.

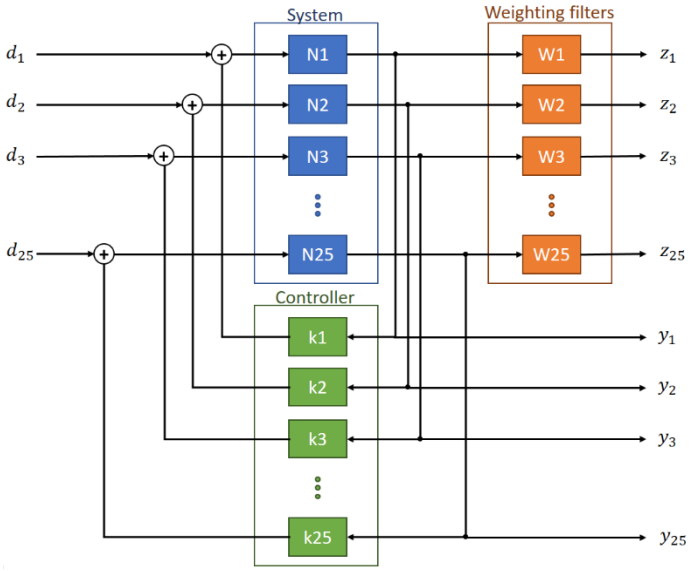


Figure 7. Design of the controller with weighting filters

5.3 Problem formulation

The control system is described as a generalized LTI system with tunable components and weighting filters, see Figure 7 (the generalized plant). The *hinfstruct* function tunes those components by minimizing the closed-loop H infinity gain from the system inputs $(d_1, d_2, \dots, d_i)$ to outputs $(z_1, z_2, \dots, z_i)$.

Weighting filters $(W_1, W_2, \dots, W_i)$ are included for resonant frequencies penalization. Those frequencies are clearly visible from the Bode magnitude graph below. The first peak corresponds to the first bending mode with frequency $\omega_1 = 22.5$ rad/s. To penalize resonant frequencies, the weighting functions can be stated as

$$W_i = \frac{k_i(s+1)^3}{(s+8)^3}, \tag{17}$$

where k_i is the gain for each channel. Tuning suitable parameters of such filters set is however complicated and time expensive, and for systems with more outputs it appears effectively infeasible. A possible solution to mitigate this problem is to select one or few representative channels only and penalize them. The figure below shows the modification of the generalized plant for the last node output penalization only (Figure 8).

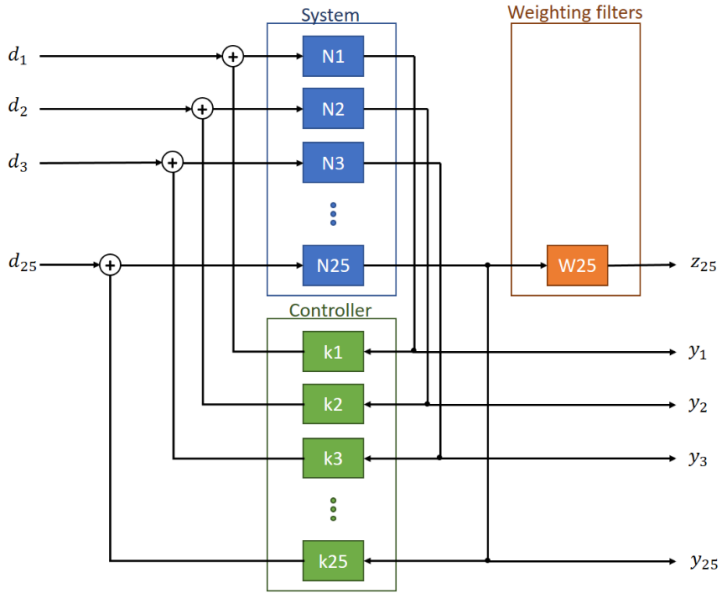


Figure 8. Design of the controller with the specific configuration of weighting filters

6 Results

For all results presented below the weighting filter (18) has been used

$$W_p = \frac{512(s+1)^3}{(s+8)^3} \tag{18}$$

This filter penalizes output voltage from piezo patch situated in the center of the plate. Singular value plot of the system and augmented system (system with filter W_p) is depicted below. The goal of W_p tuning is to amplify the red curve above the zero decibels (or penalize the peaks of the singular value plot, respectively (Figure 9.)).

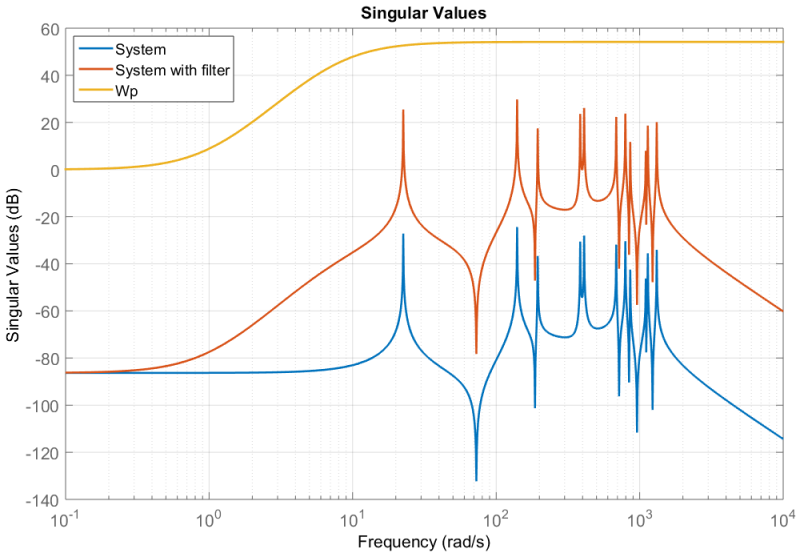


Figure 9. Frequency responses of weighting filters and the generalized plant

In the first case, only one controller

$$k_i = k = p\frac{s}{s+f_c},\ i = 1,2,\dots,25 \tag{19}$$

with parameters p, f_c for the local decentralized feedbacks was tuned. All modes are well suppressed. Achievable results are presented below in terms of the bode diagram (Figure 10.) and impulse response plots (Figure 11.) of the plate center without control and with the local proportional controllers.

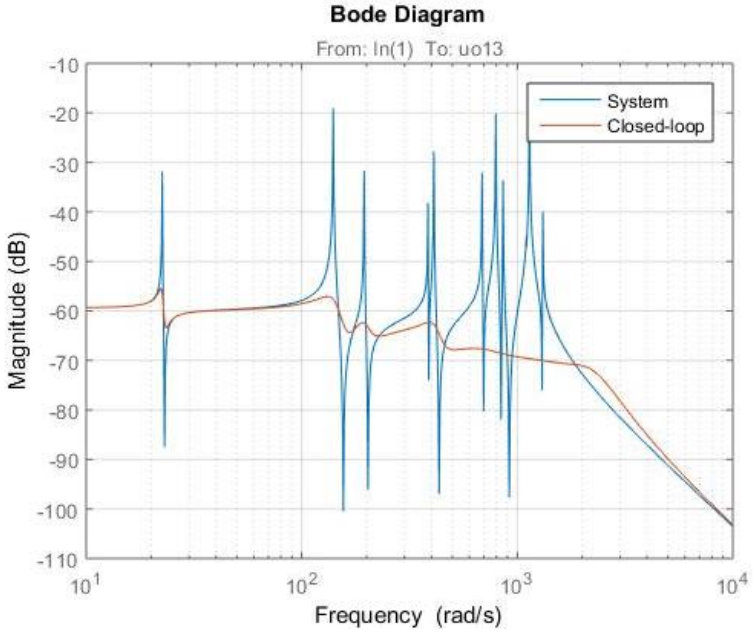


Figure 10. Bode diagram for the decentralized feedback, uniform gains

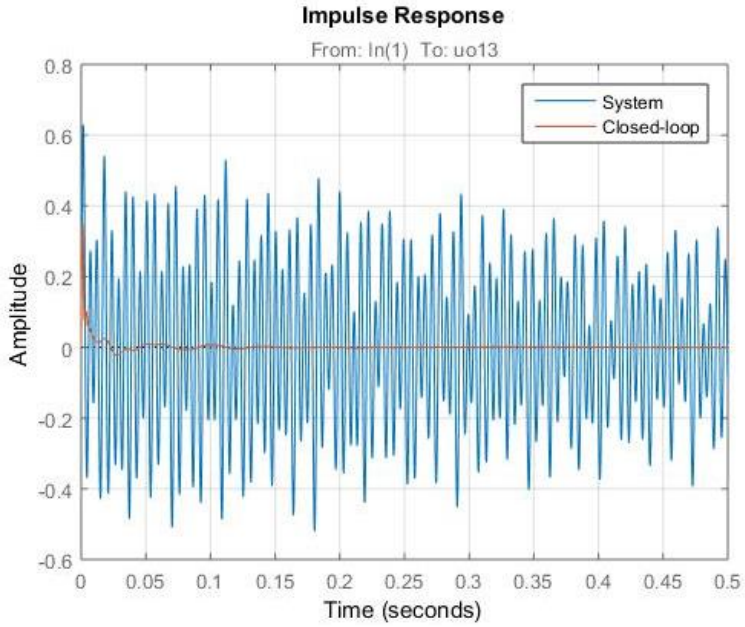


Figure 11. Impulse response for the decentralized feedback, uniform gains

In the second case, we examined the possibility to use distributed controllers, again with the same gains throughout the smart structure,

$$U_i = -p_{i1}\frac{s}{s+f_c}Y_i - \sum_{j\in E} p_{i2}\frac{s}{s+f_c}Y_j\,, \tag{20}$$

E is set of neighboring nodes. Subsequently, the constraint on equal control gains for all nodes was relaxed for both cases studied so far (decentralized and distributed, respectively). The first case then reads $k_i\,,\ i = 1,2,\ldots,25$ could have now different gains p_i. With this additional "degree of freedom", this decentralized control law is able to suppress all system resonant frequencies which is clearly visible in the Bode diagram and impulse response below (Figure 12. And Figure 13). In the last case studied in this paper, we relaxed the distributed-control structure and tuned all the $k_i's\,,\ i = 1,2,\ldots,25$ throughout the flexible structure. The resulting achievable damping is again significantly improved, as well as the range of frequencies covered (However, some frequency peaks are shifted significantly which is certainly not power-efficient way for the active damping systems.

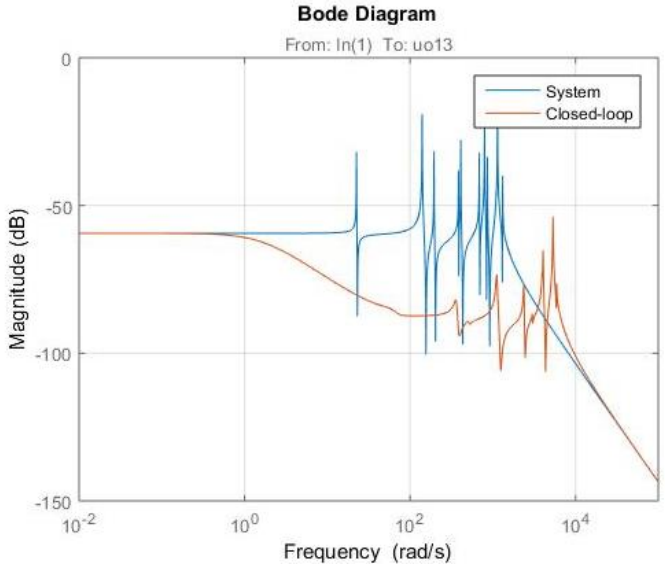


Figure 12. Bode diagram for the distributed feedback, relaxed gains

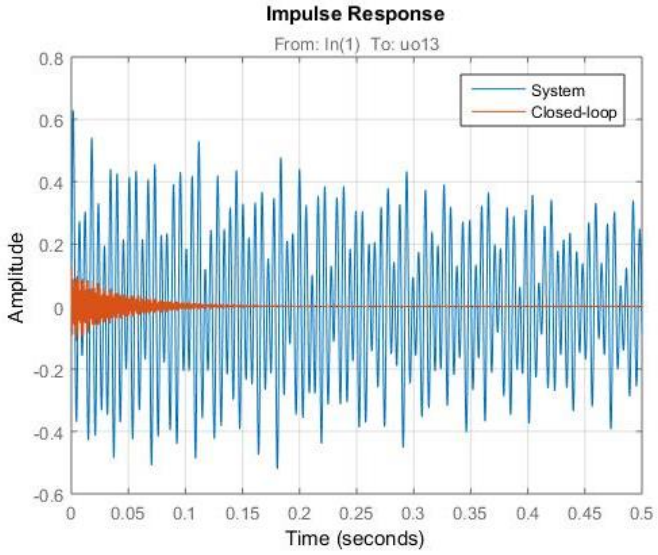


Figure 13. Impulse response for the distributed feedback, relaxed gains

7 Analysis of alternative actuation by clusters of piezo patches

The actuation can be also realized alternatively by the clusters of actuators with one common control signal for all patches in the particular cluster. Basic properties of the system state space system (***A, B, C, D***) include observability and controllability. Fundamental expression of controllability is, that the system is completely controllable if **N** *x* ***s*N** matrix (where ***s*** is the systems inputs)

$$\boldsymbol{C} = [\boldsymbol{B}\ \boldsymbol{AB}\ \boldsymbol{A^2}\ \ldots\ \boldsymbol{A^{N-1}B}] \tag{21}$$

has a rank N**.** And completely observable, when system ***rN*** *x* ***N*** with ***r*** outputs

$$\boldsymbol{O} = [\boldsymbol{C}\quad \boldsymbol{CA}\quad \boldsymbol{CA^2}\cdots\quad \boldsymbol{CA^{N-1}}\ ]^T, \tag{22}$$

has rank N. These criteria are very simple, but has a two main drawbacks. Firstly, the main disadvantage is that the criteria is yes and no answer based and tell us nothing about systems behaviour. And the second is that, for large system it's very demanding for computational power due to the rising exponent up to N-1.

For better understanding of the system is the qualitatively representation of controllability and observability desirable. For this purpose, the grammians were used.

$$W_c(t) = \int_0^t \exp(\boldsymbol{A}\tau)\,\boldsymbol{B}\boldsymbol{B}^T \exp(\boldsymbol{A}^T\tau)\,d\tau, \tag{23}$$

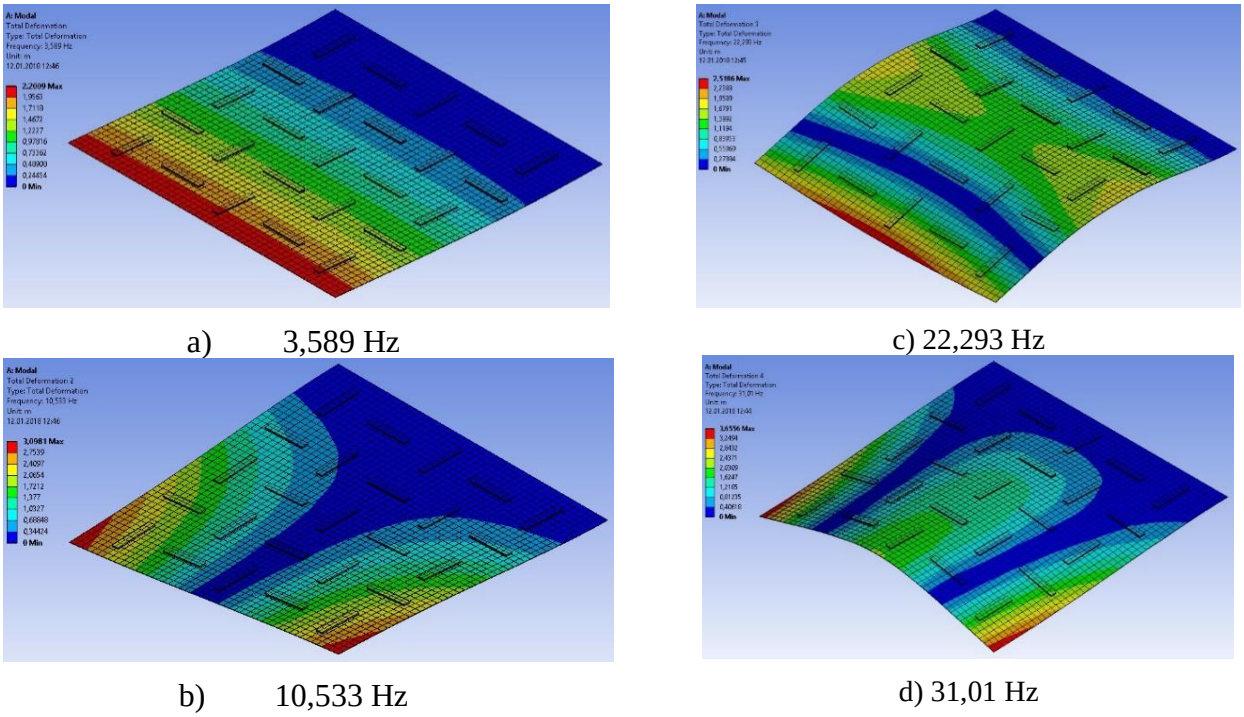
$$W_o(t) = \int_0^t \exp(\boldsymbol{A}^T\tau)\,\boldsymbol{C}^T\boldsymbol{C} \exp(\boldsymbol{A}\tau)\,d\tau, \tag{24}$$

Our case is stable and we can obtain stationary solution of the above expression assuming $W_c(t) - W_o(t) - 0$. Then the above equation can be written in following algebraic equations, called Lyapunov equations

$$\boldsymbol{A}\boldsymbol{W_c} + \boldsymbol{W_c}\boldsymbol{A}^T + \boldsymbol{B}\boldsymbol{B}^T = 0 \tag{25}$$

$$\boldsymbol{A}^T\boldsymbol{W_o} + \boldsymbol{W_o}\boldsymbol{A} + \boldsymbol{C}^T\boldsymbol{C} = 0. \tag{26}$$

For stable **A**, the obtained grammians $\boldsymbol{W_c}$ and $\boldsymbol{W_o}$ are positive definite and for our case even diagonal. This results can be transformed into balanced representation [22]. And the new grammians of controllability and observability is computed as usual. The eigenvalues of the grammians product are invariant and can be denoted γ_i These coefficients are called Hankel singular values of the system and represent a measure of energy for each mode (first four modes in Figure 7.).



a) 3,589 Hz

c) 22,293 Hz

b) 10,533 Hz

d) 31,01 Hz

Figure 14. First four eigenmodes of the system

The balanced grammians of controllability and observability are satisfying and the balanced system was tested on the experimental step trajectory applied on the 13th piezo patch and the system response is the same. Also the eigenfrequencies of both state-space system varying less than 0.09e^{-11}. Therefore, this was used as criterion for the further model response evaluation. This large system consist of the 25 actuators and 25 sensors (Figure 6)

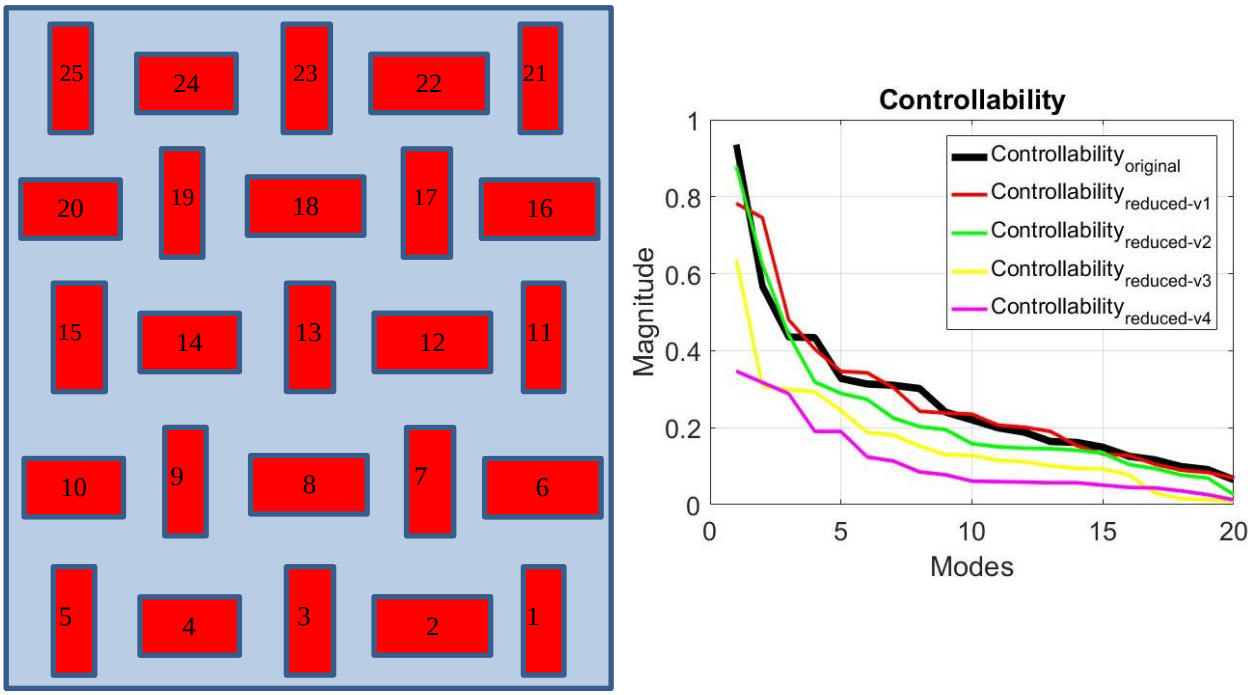


Figure 15. Scheme of the piezo patches and comparison of the individual input groups (actuator clusters)

For better impression of the individual input groups the Figure15. is presented along with the Table 1. Using fully collocated control leads to high demands on the control strategy, the high initial cost of the equipment and the large scale optimization of the piezo placement. There are possibilities for saving the energy consumption and the saving initial cost. The following subject of investigation is, if similar results can be achieved with less control units. Normally there need to be one control unit for one piezo patch. For this reason, four more concepts were proposed, where are formed several clusters of piezo patches which are powered with a single control unit and single control voltage.

Concept	Input U1	Input U2	Input U3	Input U4	Input U5	Input U6	Input U7	Input U8	Input U9	Input U10
Ver. 1	1,2,6,7	3,4,8,9	5,10	11,16	12,13, 17,18	14,15, 19,20	21,22	23,24	25	
Ver. 2	1,7,11	2,8,4	5,9,15	3	6,12, 16	13,17, 19,23	10,14, 20	21	25	18,22, 24
Ver. 3	1,5,7,9 ,13,17, 19,21, 25	3,11, 15,23								
Ver. 4	7,9,	17,19	2,4	12,14	22,24					

Table 1: Input groups (actuator clusters)

After balancing using Hankel's matrix the Observability and Controllability are almost equal, therefore for the evaluation was used only the Controllability. It is clear from Figure 15. that the control of the system is possible with minimum loss of the energy for each mode with configuration ver. 1. This means the similar results with only nine control units and nine different inputs voltages. That leads to saving the 16 control units with minimal loss of energy. The ongoing research is focused on the optimization of the piezo patches placements.

8 Conclusion

Distributed control is nowadays a very active field of research, thanks to potential applications which require high scalability and reliability. The paper deals with the optimization of active vibration suppression of the planar flexible systems equipped by regular and dense matrix of multiple sensors and actuators. The H-infinity design with predefined controller structure has been chosen as an appropriate control method. At first, performance of H-infinity regulator was experimentally tested on simple beam demonstrator with piezoelectric patches as sensors and actuators. The main larger demonstrator system consists of the 25 actuators and 25 sensors collocated with them. The tuned physical models transformed to the state space form proved to be more reliable for the control design than the black-box identified models especially in the case with many actuators and sensors. The simulation model was firstly modelled in ANSYS and then exported into MATLAB into the state space form. Decentralized and distributed control laws have been developed using the H-infinity design with predefined controller structure. The feasibility of attenuation of a large set of flexible modes has been demonstrated for the model of the main demonstrator. The demonstrator itself has been prepared for the ongoing evaluation experiments. The possibility of alternative actuation by clusters of actuators with one common control signal for all patches in the particular cluster has been also analyzed. This version allows to decrease the number of control units.

Acknowledgements

The work has been supported by the Czech Science Foundation project 16-21961S „Mechatronic structures with heavily distributed actuators and sensors”.

References

[1] N. Chopra and M. Spong, "Passivity-based control of multi-agent systems," in *Advances in robot control*, Berlin Heidelberg, Springer, 2006.

[2] R. R. Craig, "Coupling of Substructures for Dynamic Analyses: An Overview," *American Institute of Aeronautics and Astronautics,* pp. 1573-1593, 2000.

[3] M. Kozek, A. Schirrer and (Eds.), Modeling and Control for a Blended Wing Body Aircraft, Springer,, 2015.

[4] W. Gawronski, Advanced Structural Dynamics and Active Control of Structures, New York: Springer-Verlag New York, 2004.

[5] T. Haniš and M. Hromčík, "Optimal sensors placement and spillover suppression," *Mech. Syst. Mech. Syst.,* vol. 28, pp. 367-378, 2012.

[6] W. Liu, Z. Hou and A. A. Demetriou, "A computational scheme for the optimal sensor/actuator placement of flexible structures using spatial H2 measures," *Mech. Syst. Signal Process,* vol. 20, p. 881–895, 2006.

[7] T. Haniš, Active control for high capacity flexible aircraft, PhD dissertation, Czech Technical University in Prague, 2012.

[8] P. Verboven, Frequency-domain system identification for modal analysis, Ph. D. Thesis, Mechanical Engineering Department (WERK), Brussels: Vrije Universiteit Brussel, 2002.

[9] M. R. Waszak, "Robust Multivariable Flutter Suppression for Banchmark Active Control Technology Wind-Tunnel Model," *Journal of Guidance, Control, and Dynamics,* pp. 147-153, 2001.

[10] A. Varga, "Balancing Free Square-root Algorithm for Computing Singular Perturbation Approximations," in *30th Conference on Decision and Control*, Brighton, UK, 1991.

[11] P. Apkarian and D. Noll, "Nonsmooth H-infinity Synthesis," *IEEE Transactions on Automatic Control*, pp. 71-86, 2006.

[12] S. Gumussoy, D. Henrion, M. Millstone and M. L. Overton, "Multiobjective Robust Control with HIFOO 2.0," in *Proceedings of the IFAC Symposium on Robust Control Design*, Haifa, 2009.

[13] T. Haniš, V. Kučera and M. Hromčík, "Low Order H-infinity Optimal Control for ACFA Blending Wing Body Aircraft," *Progress in Flight Dynamics, GNC, and Avionics,* pp. 671-684, 2013.

[14] W. GAWRONSKI, Advanced Structural Dynamics and Active Control of Structures, New York: Springer-Verlag New York, 2004.

[15] P. Gahinet and P. Apkarian, "Structured H-infinity Synthesis in MATLAB," in *18th IFAC World Congress*, 2011.

[16] J. V. Burke, D. Henrion, A. S. Lewis and M. L. Overton, "HIFOO - A MATLAB Package for Fixed-order Controller Design and H-infinity Optimization," in *IFAC Symposium on Robust Control Design*, Toulouse, 2006.

[17] M. Řezáč and Z. Hurák, "Structured MIMO design for dual-stage inertial stabilization: Case study for HIFOO and Hinfstruct solvers," *Mechatronics,* pp. 1084-1093, 2013.

[18] J. Karlíček, Z. Šika, J. Volech, F. Svoboda and M. Hromčík, "Vibration suppression of cantilever beam using collocated piezoelectric," *Bulletin of Applied Mechanics,* vol. 13, no. 42, pp. 1-6, 2017.

[19] D. Aryelier, G. Deaconu, S. Gumussoz and D. Henrion, "H2 for HIFOO," in *International Conferenceon control and Optimization with Industrial Applications*, Ankara, Turkey, August, 2011.

[20] A. Preumont, Mechatronics. Dynamics of Electromechanical and Piezoelectric Systems, Springer, 2006.

[21] Z. Šika, J. Zavřel and M. Valášek, "Residual Modes for Structure Reduction and Efficient Coupling of Substructures," *Bulletin of Applied Mechanics,* vol. 5, no. 19, pp. 54-59, 2009.

[22] W. Gawronski and J. N. Juang, "Model Reduction for Flexible Structures," *Control and Dynamics Systems,* no. 36, pp. 143-222, 1990.

Virtual sensing of wheel center loads on a McPherson suspension

E. Risaliti [1,2], **T. Tamarozzi** [1], **B. Cornelis** [1], **W. Desmet** [2,3]
[1] Siemens Industry Software NV,
Interleuvenlaan 68, B-3001 Leuven, Belgium
e-mail: **enrico.risaliti@siemens.com**

[2] KU Leuven, Department of Mechanical Engineering,
Celestijnenlaan 300 B, B-3001, Heverlee, Belgium

[3] DMMS core lab, Flanders Make, Belgium

Abstract
This paper proposes a method for the indirect measurement of wheel center loads which makes use of a suspension flexible multibody model and strain measurements on the suspension components. Wheel center loads are the loads acting at the center of the vehicle wheels and due to the interaction with the road. Those loads are the principal cause of damage to the vehicle structural integrity and hence are very important for durability analyses, but their direct measurement requires the use of expensive and intrusive dedicated measurement devices. By reusing available design simulation models and common sensors, the proposed method thus represents an appealing alternative to the direct measurement approach. After the presentation of the method, which is based on an augmented extended Kalman filter to perform the information fusion, validation results on a McPherson suspension test rig are reported.

1 Introduction

When designing a new vehicle, the knowledge of so-called Wheel Center Loads (WCLs), i.e. the loads acting on the center of the vehicle wheels and due to the interaction with the road, is needed as an input quantity to assess durability performances [1]. In the current practice OEMs perform direct measurements of these loads during so-called Road Load Data Acquisition (RLDA) testing campaigns in which a prototype vehicle is heavily instrumented and then driven on proving grounds or public roads. The instrumentation includes so-called Wheel Force Transducers (WFTs) which directly measure WCLs, but which turn out to be expensive, intrusive and time-consuming to install. Therefore it would be appealing to find an alternative way of measuring WCLs which does not make use of such measurement devices.
During RLDA up to hundreds of other sensor channels including strain gauges, accelerometers and displacement sensors are acquired along with WFTs channels. On the other hand, virtual prototypes, i.e. system simulation models, are more and more used to assess the vehicle performances already before the first real prototype is built and tested. Therefore an appealing alternative is to re-use the readily available system simulation models in combination with these other sensors, in order to virtually measure the WCLs. This would imply a cost reduction and hence a tangible increase of the overall process efficiency.

A state estimation framework is developed in this work to perform the information fusion between the available measurements and a flexible multibody model of the vehicle suspension system. Such type of system simulation model is needed to accurately reconstruct the time domain signal for all six WCLs. In addition, this also allows to virtually measure the full strain field on the suspension flexible components.

Kalman filters (KFs) are the most successfully used state estimators. These have been first introduced to estimate the states of linear systems for which the inputs are known in [2]. However several methods have been later on introduced which represent extensions of the traditional KF to concurrently estimate both system states and unknown inputs, i.e. the so-called Augmented Kalman Filter (AKF) [3], [4], the so-called Dual Kalman Filter (DKF) [5] and the herewith referred to Joint Input-State Estimator (JISE) [6].
Extensions to non-linear dynamic systems have also been proposed over the years. The most popular one is the Extended Kalman Filter (EKF) [7], which derives from the application of a linear KF to a linearization of the non-linear system equations. A more sophisticated approach, i.e. the Unscented Kalman Filter (UKF) introduced in [8] makes use of so-called sigma points to estimate the state statistical moments. It results to be more computationally expensive than the EKF but it can outperform the latter in cases in which the system exhibits strong non-linearities. Augmented and Dual forms of such non-linear filters can be easily obtained in order to estimates the unknown inputs of the system along with its states. Extensions of the JISE to non-linear systems is instead more complicated and a first step in this sense has been made in [9], but only for systems with direct feedthrough.
In many of the aforementioned works about estimation for structural dynamics problems, finite element models were used. However a number of works related to estimation with multibody systems have also been proposed including [10], [11], [12], [13] and [14]. In all these works, examples related to simple mechanisms composed of rigid bodies have been given.

In this work a methodology is derived to perform input-state estimation for flexible multibody systems. The procedure is based on an Augmented EKF in order to be computationally efficient as it is assumed that linearizations of the system are analytically available. Furthermore implicit time-discretization schemes can be naturally employed in the approach, which can be needed to cope with the numerical stiffness arising in the resolution in time of the equations of motion of the system. The methodology is then validated on a real test-rig based on a vehicle suspension system, in which six so-called Wheel Center Loads (WCLs) are estimated along with the full strain field on the suspension components.

The paper is organized as follows. In section 2 the proposed methodology is presented. In section 3 the system under investigation for the experimental validation is described. In section 4 the system modeling is described along with a sensors selection strategy. Section 5 shows the validation results, while the conclusions of the work are exposed in section 6.

2 Model based virtual sensing

The system under investigation is described as a flexible muldibody system, i.e. a system of interconnected rigid or flexible bodies. The Equations of Motions (EOMs) of such a type of mechanical system can be written in the following general form, assuming that a penalty formulation is used to enforce the constraints between the several bodies [15]

$$\mathbf{M}(\mathbf{q})\ddot{\mathbf{q}} + \mathbf{f}_{nl}(\mathbf{q}, \dot{\mathbf{q}}, \mathbf{u}) = \mathbf{0} \tag{1}$$

where $\mathbf{M}$ is the mass matrix, while $\mathbf{f}_{nl}$ is a generic non-linear term including in general gyroscopic actions, constraint actions, as well as external actions. $\mathbf{q} \in \mathbb{R}^{n_{DOF}}$ is then the vector of the generalized coordinates, which is a set of coordinates used to describe the configuration of the system, while $\mathbf{u} \in \mathbb{R}^{n_I}$ is the vector of the external inputs to the system.
The explicit dependency with respect to time of the variables in Eq.1 is omitted as it will be omitted from the equations appearing in the rest of the chapter. In general all the variables are functions of time, unless they are related to a specific point in time.
By introducing the vector of generalized velocities $\mathbf{v}$ and by writing the relationship between the latter and the generalized coordinate vector $\mathbf{q}$ along with Eq.(1), the following system of equations is obtained

$$\begin{cases} \mathbf{v} - \dot{\mathbf{q}} = \mathbf{0} \\ \mathbf{M}(\mathbf{q})\dot{\mathbf{v}} + \mathbf{f}_{nl}(\mathbf{q}, \mathbf{v}, \mathbf{u}) = \mathbf{0} \end{cases} \tag{2}$$

In case the inverse of the mass matrix $\mathbf{M}^{-1}$ exists, then a continuous-time explicit state space equation for the system of Eq.(2) can be written as

$$\dot{\mathbf{x}} = \mathbf{f}(\mathbf{x}, \mathbf{u}) \tag{3}$$

where the state vector $\mathbf{x} \in \mathbb{R}^{n_S}$ has been defined as

$$\mathbf{x} = \begin{bmatrix} \mathbf{q} \\ \mathbf{v} \end{bmatrix} \tag{4}$$

and the real-valued non-linear function $\mathbf{f}$ has also been introduced. However, for particular choices of the generalized coordinates, as in [16] or in [17], the mass matrix $\mathbf{M}$ is instead not invertible and hence only a continuous-time implicit state space equation of the following form can be written as

$$\mathbf{g}(\dot{\mathbf{x}}, \mathbf{x}, \mathbf{u}) = \mathbf{0} \tag{5}$$

where the real-valued non-linear function $\mathbf{g}$ has been introduced. This happens also in this work as the same set of generalized coordinates as in [17], i.e. the set of so-called flexible natural coordinates, is used. Anyway a general notation will be kept in order to derive a general procedure, while further details about such set of general coordinates can be found in [17]. It is only added here that, as in many other generalized coordinates choice in flexible multibody dynamics, $\mathbf{q}$ is composed by stacking the vectors of generalized coordinates $\mathbf{q}^i$ of each body i. Each of the vectors $\mathbf{q}^i$ is then composed as $\mathbf{q}^i = \left[\mathbf{q}_r^i, \mathbf{q}_f^i\right]^T$ where $\mathbf{q}_r^i$ contains the rigid coordinates used to describe the global rigid motion of each body, while $\mathbf{q}_f^i$ contains the flexible coordinates used to describe the part of the motion related to each body's flexibility. This distinction will be useful in Section 4 to describe the modeling of the flexible bodies.

It is important to mention that the choice of using a penalty formulation to obtain the EOMs in Eq.(1) is crucial here. On the one hand, such choice implies having to introduce so-called penalty factors [15] which are arbitrary numbers defined in order to find a balance between computational efficiency and accuracy depending on the application. On the other hand, this choice offers the following decisive advantages over other possible formulations. It implies the EOMs of the system being a set of Ordinary Differential Equations (ODEs) in contrast with the set of Differential-Algebraic Equations (DAEs) which instead results from formulations based on Lagrange multipliers for the constraints enforcement, simplifying the estimation problem which remains unconstrained. Furthermore it also offers advantages with respect to formulations based on independent coordinates which equally lead to sets of ODEs. For those formulations the additional steps of expressing dependent states in function of independent ones and managing the possible change of set of independent states are required [10], which might become a hurdle during estimation and are not required when a penalty formulation is adopted. Different formulations of the EOMs would then lead to different estimation problem definitions and resolutions, but a more comprehensive and detailed comparison of all the different possibilities is out of the scope of this work.

Eqs.(3) and (5) can then be time-discretized by choosing an appropriate time-discretization scheme. If an explicit time-discretization scheme is used for Eq.(3), then an explicit discrete-time state space equation can be obtained in the following form

$$\mathbf{x}_{k+1} = \mathbf{f}_d(\mathbf{x}_k, \mathbf{u}_{k+1}) \tag{6}$$

where k and $k+1$ represent the current and next time step respectively. An implicit discrete-time state space equation is instead obtained in the cases in which an implicit time-discretization scheme is applied on Eq.(3) or either an implicit or an explicit time-discretization schemes are applied on Eq.(5), which reads

$$\mathbf{g}_d(\mathbf{x}_{k+1}, \mathbf{x}_k, \mathbf{u}_{k+1}) = \mathbf{0} \tag{7}$$

$\mathbf{x}_{k+1}$ can be explicitly computed with Eq.(6) if $\mathbf{x}_k$ and $\mathbf{u}_{k+1}$ are given, while an iterative Newton-Raphson scheme for the resolution of non-linear equations has to be adopted in the case of Eq.(7).
In this work an implicit integration scheme, namely backward Euler, is used in order to cope with the numerical stiffness which normally arises in the numerical resolution of flexible multibody equations and to be able to obtain a stable solution with a relatively large time step size.

In order to provide a full state space description of the system, a measurement equation is also introduced

$$\mathbf{y} = \mathbf{h}(\mathbf{x}) \tag{8}$$

where $\mathbf{y} \in \mathbb{R}^{n_O}$ is the system outputs vector.

Furthermore, in optimal estimation, a stochastic contribution to the equations is also introduced in order to model uncertainties on the system. The full combined deterministic-stochastic state space description of the system then reads

$$\begin{cases} \mathbf{x}_{k+1} = \mathbf{f}_d(\mathbf{x}_k, \mathbf{u}_{k+1}) + \mathbf{w}_k \\ \mathbf{y}_{k+1} = \mathbf{h}(\mathbf{x}_{k+1}) + \mathbf{v}_{k+1} \end{cases} \tag{9}$$

for the case of the explicit state space equation or

$$\begin{cases} \mathbf{g}_d(\mathbf{x}_{k+1}, \mathbf{x}_k, \mathbf{u}_{k+1}) = \mathbf{w}_k \\ \mathbf{y}_{k+1} = \mathbf{h}(\mathbf{x}_{k+1}) + \mathbf{v}_{k+1} \end{cases} \tag{10}$$

for the case of the implicit state space equation, where the so-called process noise vector and measurement noise vector, $\mathbf{w}_k$ and $\mathbf{v}_k$ respectively, have been introduced. It is assumed that both $\mathbf{w}_k$ and $\mathbf{v}_k$ are white, zero-mean, uncorrelated random processes with known covariance matrices $\mathbf{Q}_k$ and $\mathbf{R}_k$ respectively. As it can be seen from Eqs.(9) or (10), both the process noise and the measurement noise are considered to be additive in this work, but the procedure described can easily be adapted if a more general noise type is to be used.

As the aim of this work is then to estimate both states and inputs of the system, the following so-called random walk model is introduced for the vector of unknown inputs $\mathbf{u}^{UK}$

$$\mathbf{u}_{k+1}^{UK} = \mathbf{u}_k^{UK} + \mathbf{w}_k^{UK} \tag{11}$$

in which $\mathbf{w}_k^{UK}$ is assumed to be a white, zero-mean, uncorrelated random processes with known covariance matrix $\mathbf{Q}_k^{UK}$. The vector of unknown inputs $\mathbf{u}^{UK}$ is a subset of the input vector $\mathbf{u}$ such that

$$\mathbf{u} = \begin{bmatrix} \mathbf{u}^K \\ \mathbf{u}^{UK} \end{bmatrix} \tag{12}$$

where $\mathbf{u}^K$ represents instead the subset of the known inputs. The discrete-time state space representation of the so-called augmented system can then be obtained by combining Eq.(9) and Eq.(11) for the explicit case or Eq.(10) and Eq.(11) for the implicit case, i.e.

$$\begin{cases} \mathbf{x}_{k+1} = \mathbf{f}_d(\mathbf{x}_k, \mathbf{u}_{k+1}) + \mathbf{w}_k \\ \mathbf{u}_{k+1}^{UK} = \mathbf{u}_k^{UK} + \mathbf{w}_k^{UK} \\ \mathbf{y}_{k+1} = \mathbf{h}(\mathbf{x}_{k+1}) + \mathbf{v}_{k+1} \end{cases} \tag{13}$$

or

$$\begin{cases} \mathbf{g}_d(\mathbf{x}_{k+1}, \mathbf{x}_k, \mathbf{u}_{k+1}) = \mathbf{w}_k \\ \mathbf{u}_{k+1}^{UK} = \mathbf{u}_k^{UK} + \mathbf{w}_k^{UK} \\ \mathbf{y}_{k+1} = \mathbf{h}(\mathbf{x}_{k+1}) + \mathbf{v}_{k+1} \end{cases} \tag{14}$$

for which a new augmented state vector as well as a new augmented process noise covariance matrix are introduced as

$$\mathbf{x}^a = \begin{bmatrix} \mathbf{x} \\ \mathbf{u}^{UK} \end{bmatrix}, \quad \mathbf{Q}_k^a = \begin{bmatrix} \mathbf{Q}_k & \mathbf{0} \\ \mathbf{0} & \mathbf{Q}_k^{UK} \end{bmatrix} \tag{15}$$

As an EKF estimation scheme is to be applied, linearizations of the systems of Eq.(13) have to be determined to which the following so-called state Jacobian matrices for the state equation are associated

$$\mathbf{A} = \frac{\partial \mathbf{f}_d}{\partial \mathbf{x}_k}, \quad \mathbf{B} = \frac{\partial \mathbf{f}_d}{\partial \mathbf{u}_{k+1}} \tag{16}$$

Similarly for the system of Eq.(14) the following state Jacobian matrices can be obtained

$$\mathbf{A} = \frac{\partial \mathbf{f}_d^{\mathbf{g}}}{\partial \mathbf{x}_k}, \quad \mathbf{B} = \frac{\partial \mathbf{f}_d^{\mathbf{g}}}{\partial \mathbf{u}_{k+1}} \tag{17}$$

in which $\mathbf{f}_d^{\mathbf{g}}$ is the explicit non-linear function associated with $\mathbf{g}_d$, such that $\mathbf{x}_{k+1} = \mathbf{f}_d^{\mathbf{g}}(\mathbf{x}_k, \mathbf{u}_{k+1})$, which locally exists if $\mathbf{g}_d$ is continuously differentiable for the theorem of the implicit function. The measurement Jacobian matrix instead is the same for both Eq.(13) and (14) and reads

$$\mathbf{H} = \frac{\partial \mathbf{h}}{\partial \mathbf{x}_k} \tag{18}$$

The Jacobian matrices of the augmented systems then read

$$\mathbf{A}^a = \frac{\partial \mathbf{f}_d^a}{\partial \mathbf{x}^a} = \begin{bmatrix} \mathbf{A} & \mathbf{B}^{UK} \\ \mathbf{0} & \mathbf{I} \end{bmatrix}, \quad \mathbf{H}^a = \frac{\partial \mathbf{h}}{\partial \mathbf{x}_k^a} \tag{19}$$

where $\mathbf{B}^{UK}$ is the matrix obtained by keeping the columns of the Jacobian matrix $\mathbf{B}$ related to the unknown inputs.

It appears clear from all Eqs.(9), (10), (13) and (14) that both the state vector $\mathbf{x}$ and the augmented state vector $\mathbf{x}^a$ are now modeled as random processes. The aim of the estimation will be to provide the estimate of the first two statistical moments of the augmented state vector $\mathbf{x}^a$ given the sequence of measurements $\{\mathbf{y}_k\}$ and known inputs $\{\mathbf{u}_k^K\}$. The first moment corresponds to the mean value and the estimate of such quantity for the augmented state vector, the state vector and the unknown input vector will be indicated with $\hat{\mathbf{x}}^a$, $\hat{\mathbf{x}}$ and $\hat{\mathbf{u}}^{UK}$ respectively. The second moment corresponds instead to the augmented state error covariance matrix $\mathbf{P}^a$ defined as

$$\mathbf{P}_k^a = \mathbf{E}\left[\left(\mathbf{x}_k^a - \hat{\mathbf{x}}_k^a\right)\left(\mathbf{x}_k^a - \hat{\mathbf{x}}_k^a\right)^T\right] \tag{20}$$

where $\mathbf{E}$ represents the expected value operator. Furthermore in the following the superscript $\square^-$ will be used to indicate quantities that are estimated by making use of measurements up to time step k, i.e. to indicate so-called *a-priori* estimates. The superscript $\square^+$ will be instead used to indicate quantities that are estimated by making use of measurements up to time step $k+1$, i.e. to indicate so-called *a-posteriori* estimates.
It is now possible to illustrate the full estimation procedure which is obtained by applying a linear KF to the linearized version of system of Eqs.(13) or (14). The estimation is recursive and proceeds for each time step as indicated below.

AEKF based estimation procedure

Compute the a-priori estimate of the unknown input vector mean as

$$\hat{\mathbf{u}}_{k+1}^{UK-} = \hat{\mathbf{u}}_k^{UK+} \tag{21}$$

Compose the input vector as

$$\mathbf{u}_{k+1} = \begin{bmatrix} \mathbf{u}_{k+1}^K \\ \hat{\mathbf{u}}_{k+1}^{UK-} \end{bmatrix} \tag{22}$$

Compute the a-priori estimate of the state vector mean by solving

$$\mathbf{g}_d(\hat{\mathbf{x}}_{k+1}^-, \hat{\mathbf{x}}_k^+, \mathbf{u}_{k+1}) = \mathbf{0} \quad \text{or} \quad \hat{\mathbf{x}}_{k+1}^- = \mathbf{f}_d(\hat{\mathbf{x}}_k^+, \mathbf{u}_{k+1}) \tag{23}$$

Propagate the augmented state error covariance matrix by means of

$$\mathbf{P}_{k+1}^{a-} = \mathbf{A}_k^a \, \mathbf{P}_k^{a+} \mathbf{A}_k^{aT} + \mathbf{Q}_k^a \tag{24}$$

Compute the Kalman gain as

$$\mathbf{K}_{k+1} = \mathbf{P}_{k+1}^{a-} \mathbf{H}_k^{aT} (\mathbf{H}_k^a \, \mathbf{P}_{k+1}^{a-} \mathbf{H}_k^{aT} + \mathbf{R}_{k+1})^{-1} \tag{25}$$

Compute the a-posteriori estimate of the state vector and of the unknown input vector as

$$\hat{\mathbf{x}}_{k+1}^{a+} = \begin{bmatrix} \hat{\mathbf{x}}_{k+1}^{+} \\ \hat{\mathbf{u}}_{k+1}^{UK+} \end{bmatrix} = \begin{bmatrix} \hat{\mathbf{x}}_{k+1}^{-} \\ \hat{\mathbf{u}}_{k+1}^{UK-} \end{bmatrix} + \mathbf{K}_{k+1} (\mathbf{y}_{k+1} - \mathbf{h}(\hat{\mathbf{x}}_{k+1}^{-})) \tag{26}$$

Compute the a-posteriori augmented state error covariance matrix as

$$\mathbf{P}_{k+1}^{a+} = (\mathbf{I} - \mathbf{K}_{k+1} \mathbf{H}_k^a) \mathbf{P}_{k+1}^{a-} \tag{27}$$

Note that by carrying out only the steps in Eqs. from (23) to (27) for each time step and by replacing the augmented matrices $\mathbf{A}_k^a$, $\mathbf{P}_k^a$, $\mathbf{Q}_k^a$, $\mathbf{H}_k^a$ and $\mathbf{R}_k^a$ with their non-augmented counterparts $\mathbf{A}_k$, $\mathbf{P}_k$, $\mathbf{Q}_k$, $\mathbf{H}_k$ and $\mathbf{R}_k$, the states estimation only can be performed in case all the inputs are known.

3 Validation test rig

The estimation procedure presented in section 2 has been validated on the suspension test-rig shown in Figure 1. The latter is based on a McPherson suspension system which is attached to a fixed frame in correspondence of the regular connections-to-body locations and loaded at the tire contact patch by a six DOF hydraulic shaker capable of reproducing operational road loads. This is closely related to the case of operational vibration measurement campaigns performed on prototype vehicles driven on proving grounds useful to gather data for fatigue assessments.

Figure 2 better shows the McPherson suspension architecture. The suspension system includes a control arm, a lower strut, an upper strut and a tierod all connected to a steering knuckle. The four connection-to-body locations are indicated with the red dots.
A load cell is interposed between the knuckle and the tire rim as shown in Figure 3a. While being rigidly screwed on the knuckle side, the load cell includes bearings as well as a rotating spindle on the tire rim side such that the rolling motion of the tire is allowed. Such device directly measures the WCLs and provides validation signals for these quantities, which consist of three forces and three moments along and about the three global vehicle axes.
Sensors have been distributed over knuckle and control arm for 34 strain gauges channels in total as shown in Figure 3a and Figure 3b. This represents the main part of the test-rig instrumentation along with the load cell. Subsets of those sensor channels will make up the sensor sets used in the estimation procedure as explained in Section 4, while the other will be used as validation channels.
Additionally the signal from the internal lvdt sensor of the hydraulic shaker which measures the vertical position of the latter has been acquired. This sensor signal has been used to define the experimental runs.
An optical displacement sensor is also installed in order to measure the suspension deflection, i.e. the relative displacement between upper strut and lower strut along the strut axis, as it is visible in Figure 2. Such displacement sensor, along with several accelerometers distributed over knuckle, control arm and frame as well as a pair of additional strain gauges on the tierod, completes the full instrumentation. Even though those sensors are not relevant for this work, they have been listed here for completeness.
Table 1 lists the executed experimental runs that are relevant for this work. In all of them a purely vertical motion of the hydraulic shaker has been imposed. More in detail, sinusoidal motions of 5 mm of amplitude at 1 Hz, 4 Hz and 8 Hz have been imposed in the three runs.

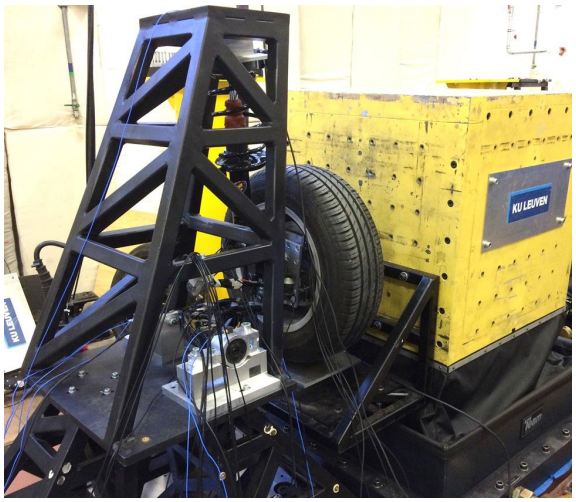


Figure 1: The validation test-rig is based on a McPherson suspension attached to a frame on one side and loaded by a six DOF hydraulics shaker capable of reproducing road loads on the other side.

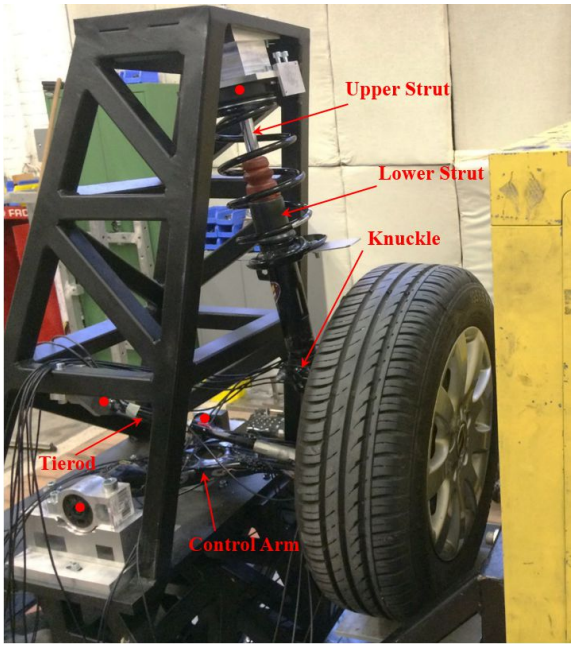
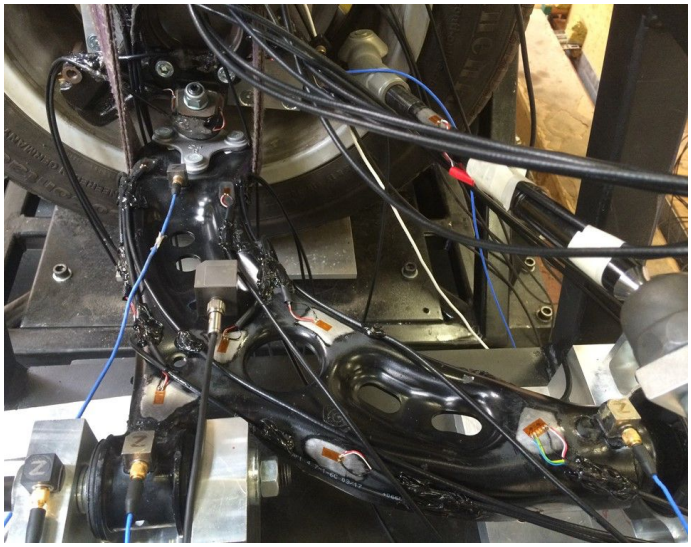


Figure 2: The McPherson suspension is composed of a control arm, a tierod, a lower strut and an upper strut all connected to a steering knuckle.



(a) A load cell is interposed between knuckle and tire rim in order to measure the WCLs and provides the validation signals for such quantities.



(b) Several strain gauges have been distributed over the steering knuckle and the control arm. Some of them are used in the estimation procedure, while the others are used for validation.

Figure 3: The instrumentation includes sensors usually employed in RLDA testing campaigns.

4 System modeling and sensors selection

4.1 The flexible multibody model

The system is modeled as a flexible multibody model as illustrated in Figure 4. The control arm and the steering knuckle are considered to be flexible bodies, while the tierod, the lower strut and the upper strut

ID	Signal type	Frequency (Hz)	Amplitude (mm)
1	Sine	1	5
2	Sine	4	5
3	Sine	8	5

Table 1: In the three experimental runs relevant for this work sinusoidal motions of the hydraulic shaker have been imposed

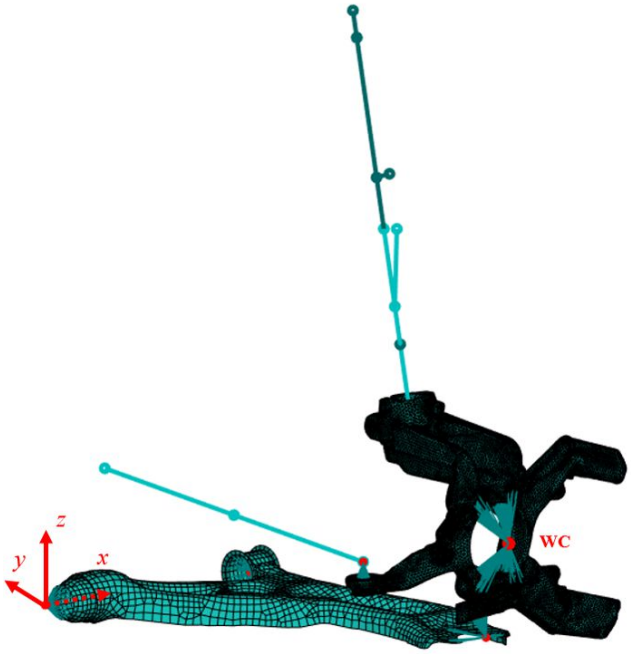


Figure 4: The system has been modeled as a flexible multibody system. The control arm and the knuckle are modeled as flexible bodies, while the tierod, the upper strut and the lower strut are modeled as rigid bodies. The external loads, i.e. the WCLs, are applied to the WC which is a point rigidly connected to the knuckle.

are described as rigid bodies. The frame is considered to be rigid and fixed to the ground. Spherical joints connect the control arm, the tierod and the upper strut to the frame. The steering knuckle is then connected to the lower strut by a rigid joint and to both the tierod and the control arm by two additional spherical joints. Finally, the lower strut and upper strut are connected to each other by a cylindrical joint.
The system has hence one global degree of freedom corresponding to the global vertical motion, in addition to the flexible degrees of freedom related to the two flexible components.
The global reference frame of the model is centered in one of the connection-to-chassis locations of the control arm. The x, y and z axes correspond to the longitudinal, lateral and vertical directions of the vehicle respectively, as visible in Figure 4.
The external loads are considered to be applied at the Wheel Center (WC) which is a point rigidly attached to the knuckle and is also highlighted in Figure 4. These external loads correspond to the WCLs for the suspension system and consist of three forces and three moments along and about the three global axes and are indicated with $WCFx$, $WCFy$, $WCFz$, $WCMx$, $WCMy$ and $WCMz$. The WC is located at the central location of the load cell shown in Figure 3a.
It is assumed that the two flexible bodies, i.e. the steering knuckle and the control arm, undergo only small deformations and are modeled as reduced order linear finite element models. The steering knuckle is mainly composed of quadratic tetrahedron elements while the control arm is mainly composed of bi-linear quadrilateral shell elements with a minority of linear triangular shell elements. Rigid elements are then used

in correspondance of the connections to the adjacent bodies. Such rigid elements connect all the nodes close to the connection to central independent nodes, as visible in Figure 4. The independent nodes are then used for the multibody joints definitions. The reduction of each finite element model is performed by modal truncation augmentation method as explained in [18]. The reduction basis for each body is composed of all the constraint modes [19] related to the interface of the body in order to ensure static completeness. The first normal mode of the control arm is then added to the reduction basis of the latter, while no additional normal mode is used for the normal modes set of the steering knuckle which results to be a pretty stiff component with first eigen-frequency at 951 Hz. The flexible generalized coordinates vector $\mathbf{q}_f^i$ of each body i hence contains the modal participation factors related to each vector of the reduction basis.
A linear spring force element is used to model the suspension main spring, while a non linear friction force element is used to model the viscous friction as well as the contact friction between the lower and upper damper. The parameters related to such force elements have been obtained by optimization procedures in order match the real system response in terms of global response over a set of relevant experimental runs.

4.2 Observability

In order to successfully build a virtual sensor, observability requirements have to be satisfied. Namely, the systems of Eqs.(6) or (7) has to be observable, which means that the augmented state vector $\mathbf{x}^a$ can be observed from the output measurements in $\mathbf{y}$. In this work the PBH observability test [20] is considered to cope with this aspect, which states that the linearized version of the system in point k is observable if and only if

$$\text{rank}\left(\mathbf{PBH}_k(s)\right) = \text{rank}\left(\begin{bmatrix}\mathbf{A}_k^a - s\mathbf{I} \\ \mathbf{H}_k^a\end{bmatrix}\right) = n_s + n_{UK}, \quad \text{for all } s \in \mathbb{C} \tag{28}$$

where n_s is the number of states already introduced in Section 2 and n_{UK} is the number of the unknown inputs. As most of the difficulties come from the estimation of the unknown inputs [4], here only the value $s = 1\ Hz$ is considered, which corresponds to the eigenvalue of the random walk model for the unknown inputs of Eq.(11). This leads to a theoretical condition for the minimal number of sensors, that is at least a number of position level sensors equal to the number of unknown inputs have to be employed in the estimation. As in this work strain gauges are to be used to estimate the six WCLs, then at least six of such sensors have to be used.

4.3 Sensors selection

This subsection explains how the sensor subset to be used in the estimation procedure has been composed, starting from the 34 strain gauges channel instrumented on the test-rig described in Section 3.

Figure 5 shows a comparison of strain amplitudes of response between simulated and measured signals for experimental run 2 of Table 1. The measured signals have been directly measured with the strain gauges, while the simulated ones have been obtained by applying the WCLs measured with the load cell to the flexible multibody model of the system. The strain locations have been ordered on the x-axis from the least to the most excited according to the measured values. A first sensor selection step has been applied, discarding sensors which exhibit an amplitude of response lower than 1 $\mu\epsilon$ in the reported experimental run. This to be sure that sensors with a minimal signal-to-noise ratio will be employed. In this way the five sensors S5:+X, S7:+X, S8:+Y, S27+X and S20:+Y have been discarded.

A second selection step has been applied to make sure that sensors that exhibit a minimal matching between simulation and experiments will be employed. Figure 6 shows the Root Mean Square Error (RMSE) between simulated and measured signals for the first 5 seconds of experimental run 2 of Table 1. Sensors with RMSE lower than 0.5 have been discarded, implying the exclusion of additional 6 of the 29 strain gauges channels remained, i.e. S17:+Y, S9:+X, S24:+Y, S18:+Y, S25:+Y and S19:+Y.

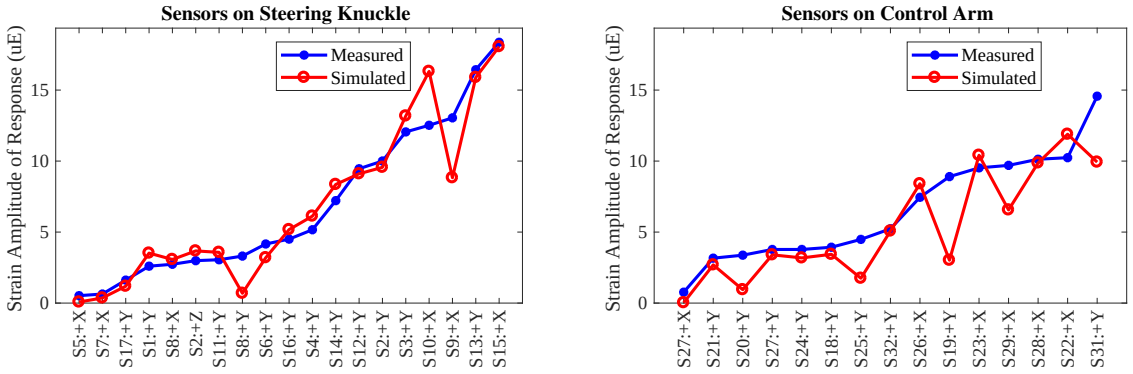


Figure 5: Sensors with amplitude of response lower than 1 $\mu\epsilon$ in a simulation resulting from the application of the measured WCLs of experimental run 2 of Table 1 have been discarded from the sensor selection

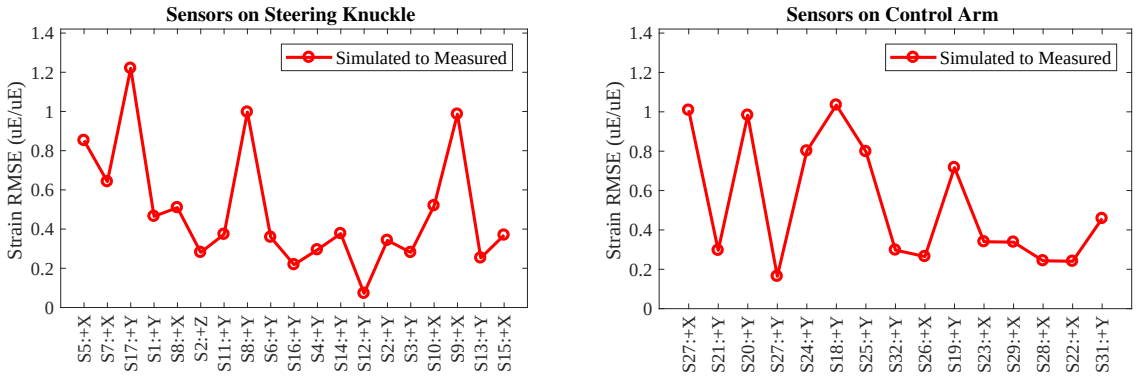


Figure 6: Sensors for which the RMSE between simulated and measured signal is higher than 0.5 have been discarded from the sensors selection according to step 3 of Table 2

Finally, a selection step which maximizes the observability of the system has been applied to retrieve the actual sensors set. An observability metric based on the observability test exposed in Subsection 4.2 has been introduced. More in detail, it is based on the condition number of matrix $\mathbf{PBH}$ as

$$\mathcal{O}_k = \left(\text{cond}\left(\mathbf{PBH}_k(1)\right)\right)^{-1} \tag{29}$$

Similarly to the procedure reported in [21] and [22], the selection has been done in order to maximize such observability metric. As the system of this work is non-linear, several linearizations over simulations of training scenarios corresponding to the three experimental runs of Table 1 have been considered and an averaged value of the observability metric has been maximized by means of an ad hoc optimization procedure. A minimal number of six sensors has been selected, which resulted in the sensors set composed of S2:+Z, S10:+X, S11:+Y, S14:+Y, S21:+Y and S22:+X and showed in Figure 7.

The sensor selection procedure is summarized in Table 2.

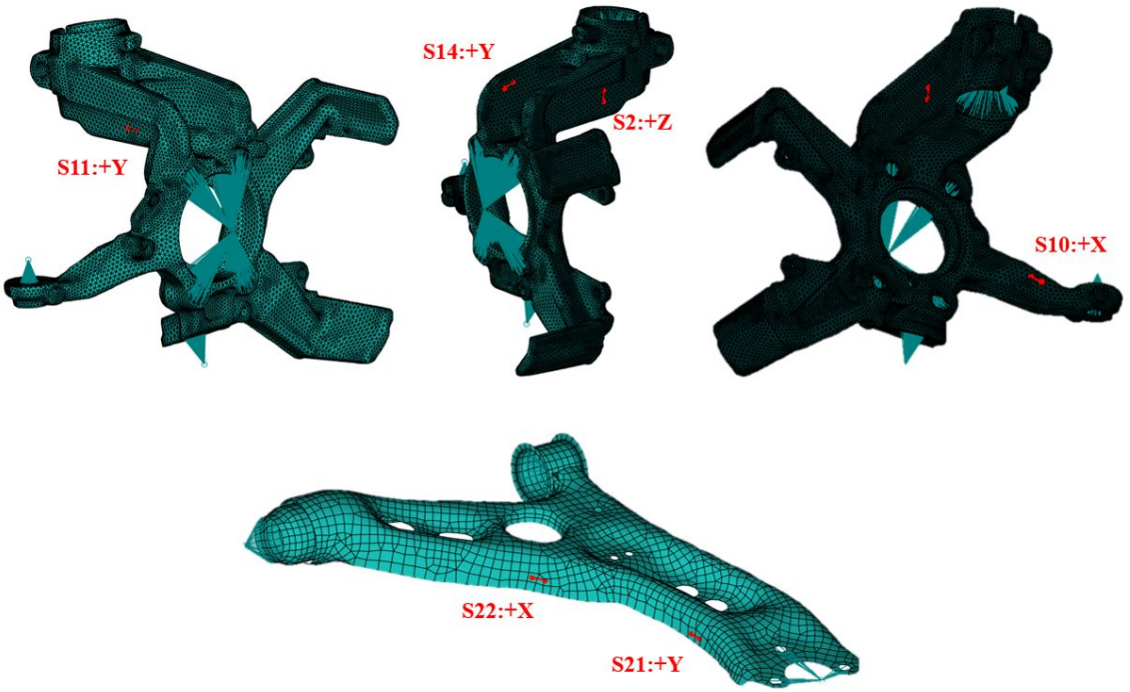


Figure 7: The six sensors shown maximize a predefined observability metric

Sensors selection procedure
1. Consider the initial pool of sensors composed of the 34 strain gauges channels distributed over Steering Knuckle and Control Arm
2. Remove sensors for which the simulated response of the model under specific training scenarios, namely experimental run 2 of Table 1, does not reach a certain threshold in amplitude
3. Remove sensors that do not exhibit a sufficient matching between the simulated response of the model and the correspondent measured response for experimental run 2 of Table 1
4. Keep the 6 sensors (minimal set) that maximize a certain observability metric based on the Popov-Belovich-Hautus (PBH) observability criteria

Table 2: The sensors to be used in the estimation have been selected in order to maximize signal-to-noise ratios, simulated response matching with experiments and observabiltiy

5 Results

In this section the results of the application of the estimation procedure presented in Section 2 to the experimental setup described in Section 3 are exposed. The objective of the estimation is to reconstruct the six WCLs and the full strain field on the suspension components.

5.1 Estimator parameters selection

The main parameters that have to be set for the estimator are the covariance matrices for the noise processes $\mathbf{w}_k$, $\mathbf{w}_k^{UK}$ and $\mathbf{v}_k$. Matrix $\mathbf{R}_k$ relative to the measurement noise $\mathbf{v}_k$ is set to be a diagonal matrix with diagonal non-zero entries estimated from the measured channels. Matrix $\mathbf{Q}_k$ related to $\mathbf{w}_k$ is set to zero as it is assumed that all the uncertainty in the system model is coming from the random walk model for the

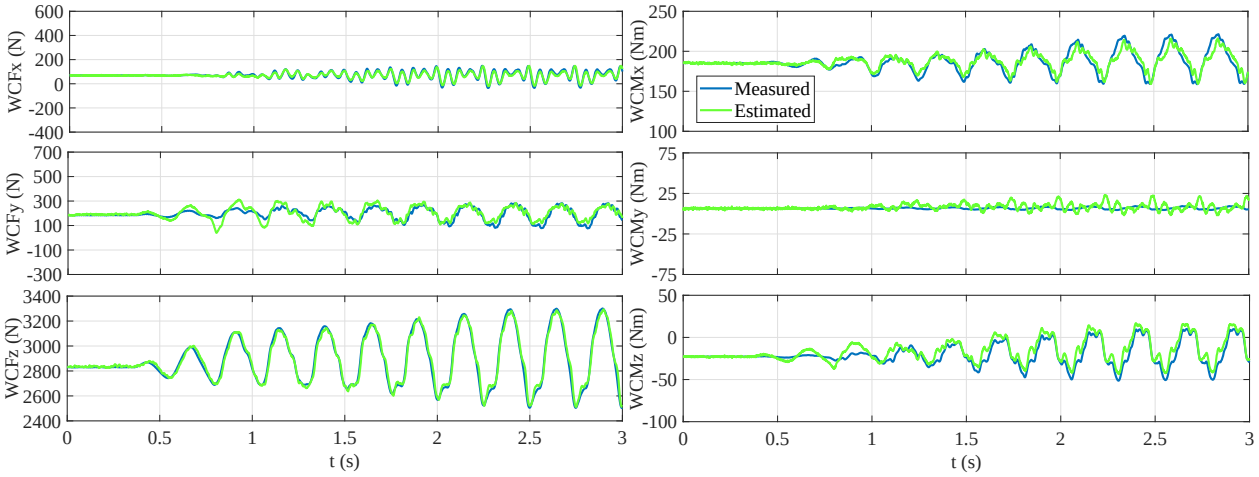


Figure 8: All six WCLs can be accurately estimated for experimental run 2 of Table 1

unknown inputs $\mathbf{u}_k^{UK}$. For the latter indeed the relative covariance matrix $\mathbf{Q}_k^{UK}$ is set to a non-zero value. More in detail, this matrix is set to be a diagonal matrix with diagonal entries all equal to the non-zero value Q_u. The latter hence turns out to be the only arbitrary parameter of the estimator. As already pointed out in other works, including [3] and [23], Q_u has the role of a regularization parameter for the estimation procedure. A value for this parameter can be found in the example of this work, above which all the estimation results converge to the same result with in addition a small noise increase. This corresponds to 10 and such value is used to retrieve the estimation results shown in the following subsection. The measurement units have been omitted for Q_u but they correspond to N^2 in case the related input is a force and to $(Nm)^2$ in case the related input is a moment.

5.2 Estimation of the six Wheel Center Loads and of the strain field on the suspension components

Figure 8 shows the input estimation results for the WCLs relative to experimental run 2 of Table 1. The estimated signals are compared with the ones directly measured with the load cell.
The results show an excellent matching between estimated and measured signals for all the six WCLs. Only $WCMy$ shows a little discrepancy. This is probably due to the fact that this load has a very small amplitude as the rolling movement of the tire is allowed as explained in Section 3. For this reason the information related to this quantity in the sensors is in the order of magnitude of the noise. Anyway the estimated amplitude for this load is the smallest with respect to the other moments, which is the same condition which holds for the measured data as well.
The excellent loads reconstruction quality is possible thanks to the accuracy of the sensors employed in the estimator. Figure 9 reports on the top two example representative of all these sensors, i.e. S10:+X and S14:+Y. As visible the matching between simulated and measured signals is high. Then the corrective action of the estimator results in signals which are even closer to the measured ones.
Figure 9 then shows on the center two examples, i.e. S16:+Y and S15:+X, of the high quality of reconstruction achieved for strains not employed in the estimator. Those two examples are representative of most of the locations. At the bottom of the same figure instead two example of points among the ones that exhibit the worst reconstruction quality, i.e. S9:+X and S31:+Y, are reported.
Figure 10 shows instead an overview of the accuracy of the strain estimation over steering knuckle and control arm in terms of RMSE and compares it with the accuracy of the simulation also reported in terms of RMSE. The measured signals are taken as reference for the RMSE calculations. The sensors are ordered on the x-axis according to the measured amplitude of response as in Figure 5. It can be observed how the overall accuracy of the strains estimation is similar to accuracy of the strains simulation. Five of the loca-

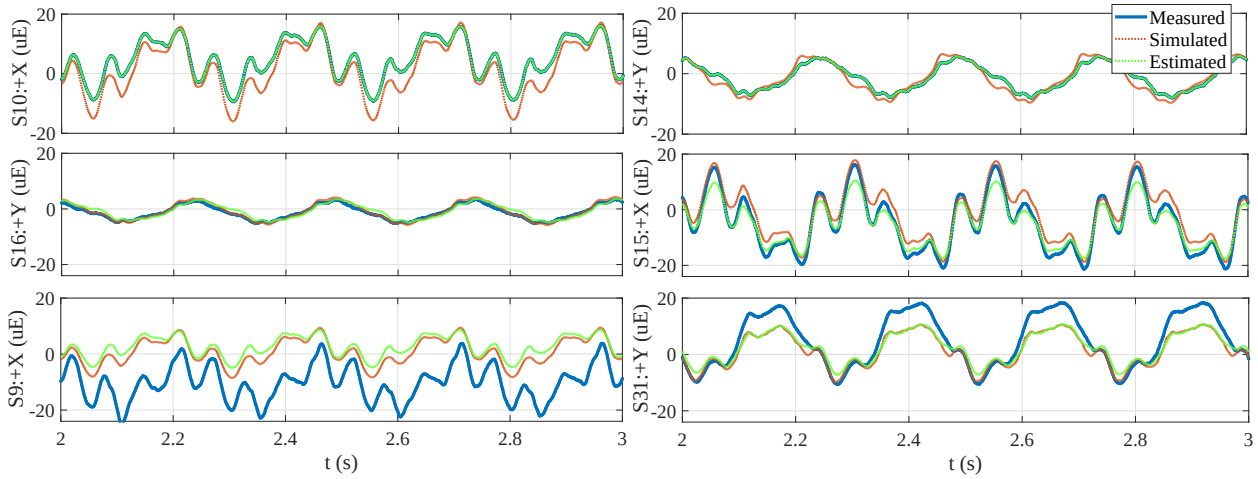


Figure 9: All six sensors employed in the estimation exhibit a very good matching between simulation and experiments as the one of S10:+X and S14:+Y. This is a necessary conditions to obtain an accurate input reconstruction. S16:+Y and S15:+X are then representative of most of the other sensors not employed in the estimator. S9:+X is an example of sensor located close to a connection between components. S31:+Y is an example where a good tracking is achieved but the amplitude is not correctly estimated

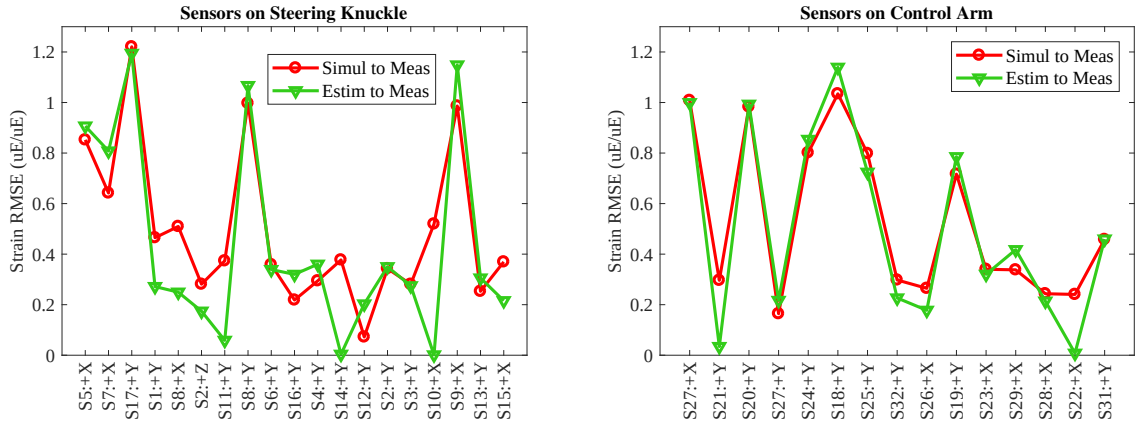


Figure 10: The overall quality of the strain estimation is similar to the one of the strain simulation. Higher RMSE values mainly correspond to locations that are weakly excited or close to connections where local effects not properly modeled might have an impact

tions with higher RMSE values correspond to very weakly excited points, i.e. S5:+X, S7:+X, S8+Y, S20:+Y and S27:+X. Most of the remaining ones are then located close to connection points between the different components where the influence of not properly modeled local effects might be strong. This is the case for instance of sensor S9:+X reported in 9

Concluding, an accurate estimation can be achieved for all the six WCLs and also for the strain field over control arm and knuckle when the sensors employed in the estimator are accurate, meaning that the matching between simulated and measured signals is above a certain threshold as explained in Subsection 4.3.

6 Conclusions

In this work, a general procedure has been presented to perform input-state estimation for flexible multibody systems. The procedure is based on an augmented extended Kalman filter in order to be computationally efficient as it is assumed that linearizations of the system are analytically available. Furthermore implicit

time-discretization schemes can be naturally employed in the approach, which can be needed to cope with the numerical stiffness arising in the resolution in time of the equations of motion of the system.
The methodology has been then validated on a real test-rig based on a vehicle suspension system, in which the six wheel center loads have been estimated along with the full strain field on the suspension components. The results showed that all estimated quantities could be accurately reconstructed, as a consequence of the high accuracy exhibited by the employed model.

Acknowledgements

The authors gratefully acknowledge the European Commission for its support of the Marie Sklodowska Curie program through the ITN ANTARES project (GA 606817), the support of VLAIO (Flemish Innovation & Entrepreneurship) through the O&O project ENDURANCE (IWT 150958) and through the Innovation Mandate project VIRTUAL MATES (IWT 140778), and the support of the Research Fund KU Leuven. The authors also acknowledge Daniele Brandolisio for his support in the execution of the experimental activity.

References

[1] P. Johannesson and M. Speckert. *Guide to Load Analysis for Durability in Vehicle Engineering*. John Wiley and Sons, Ltd., Chichester, West Sussex, United Kingdom, 2014.

[2] R.E. Kalman. A new approach to linear filtering and prediction problems. *Journal of Basic Engineering*, 82(1):35–45, 1960.

[3] E. Lourens, E. Reynders, G. De Roeck, G. Degrande, and G. Lombaert. An augmented Kalman filter for force identification in structural dynamics. *Mechanical Systems and Signal Processing*, 27:446–460, February 2012.

[4] F. Naets, J. Croes, and W. Desmet. An online coupled state/input/parameter estimation approach for structural dynamics. *Computer Methods in Applied Mechanics and Engineering*, 283:1167–1188, January 2015.

[5] E.A. Wan, A.T. Nelson. Dual extended Kalman filter methods. in: S. Haykin (Ed.), *Kalman Filtering and Neural Networks*, Wiley, New York, 2001, pp. 123-173.

[6] S. Gillijns and B. De Moor. Unbiased minimum-variance input and state estimation for linear discrete-time systems. *Automatica*, 43(1):111–116, January 2007.

[7] D. Simon. *Optimal state estimation: Kalman, H_∞ and nonlinear approaches*. Wiley-Interscience, Hoboken, NJ, 2006.

[8] S. Julier, J. Uhlmann, and H. F. Durrant-Whyte. A new method for the nonlinear transformation of means and covariances in filters and estimators. *IEEE Transactions on automatic control*, 45(3):477–482, 2000.

[9] W. Song. Generalized minimum variance unbiased joint input-state estimation and its unscented scheme for dynamic systems with direct feedthrough. *Mechanical Systems and Signal Processing*, 99:886–920, January 2018.

[10] J. Cuadrado, D. Dopico, A. Barreiro, and E. Delgado. Real-time state observers based on multibody models and the extended Kalman filter. *Journal of mechanical science and technology*, 23(4):894–900, 2009.

[11] F. Naets, R. Pastorino, J. Cuadrado, and W. Desmet. Online state and input force estimation for multibody models employing extended Kalman filtering. *Multibody System Dynamics*, 32(3):317–336, October 2014.

[12] I. Palomba, D. Richiedei, and A. Trevisani. Two-stage approach to state and force estimation in rigid-link multibody systems. *Multibody System Dynamics*, 39(1-2):115–134, January 2017.

[13] E. Risaliti, M. Vermaut, J. Croes, B. Cornelis, and W. Desmet. Force estimation on a McPherson system by means of a state estimator and a multibody model. in: proc. of *ECCOMAS Thematic Conference on Multibody Dynamics*, Prague, Czech Republic, 2017.

[14] E. Sanjurjo, D. Dopico, A. Luaces, and M. A. Naya. State and force observers based on multibody models and the indirect Kalman filter. *Mechanical Systems and Signal Processing*, 106:210–228, June 2018.

[15] J. G. De Jalon and E. Bayo. *Kinematic and dynamic simulation of multibody systems: the real-time challenge*. Springer Science & Business Media, 2012.

[16] A. A. Shabana. Euler parameters kinetic singularity. *Proceedings of the Institution of Mechanical Engineers, Part K: Journal of Multi-body Dynamics*, 228(3):307–313, June 2014.

[17] M Vermaut, F Naets, and W. Desmet. A flexible natural coordinates formulation (FNCF) for the efficient simulation of small-deformation multibody systems. *International Journal for Numerical Methods in Engineering*, June 2018.

[18] B. Besselink, U. Tabak, A. Lutowska, N. van de Wouw, H. Nijmeijer, D.J. Rixen, M.E. Hochstenbach, and W.H.A. Schilders. A comparison of model reduction techniques from structural dynamics, numerical mathematics and systems and control. *Journal of Sound and Vibration*, 332(19):4403–4422, September 2013.

[19] R. R. Craig. A review of time-domain and frequency domain component mode synthesis methods. *Journal of Modal Analysis*, 2(2):59–72, 1987.

[20] B. K. Ghosh and J. Rosenthal. A generalized Popov-Belevitch-Hautus test of observability. *IEEE transactions on automatic control*, 40(1):176–180, 1995.

[21] W. Rottiers, F. Naets, B. Forrier, M. Sarrazin, H. Van Der Auweraer, and W. Desmet. Mechatronic powertrain virtual sensor: system-level model and sensor selection. in: proc. of *the International Conference on Structural Engineering Dynamics* Ericeira, Portugal, July 2017.

[22] T. Tamarozzi, E. Risaliti, W. Rottiers, K. Janssens, and W. Desmet. Noise, ill-conditioning and sensor placement analysis for force estimation through virtual sensing. in: proc. of *International Conference on Noise and Vibration Engineering (ISMA2016),*, Leuven, Belgium, September 2016.

[23] E. Risaliti, J. Van Cauteren, T. Tamarozzi, B. Cornelis, and W. Desmet. Virtual sensing of wheel center forces by means of a linear state estimator. in: proc. of *International Conference on Noise and Vibration Engineering (ISMA2016),*, Leuven, Belgium, 2016.

Nonlinear feedback control of a stroke limited inertial actuator using a state estimation approach

M. Dal Borgo [1], **M. Ghandchi Tehrani** [1], **S.J. Elliott** [1]
[1] University of Southampton, Institute of Sound and Vibration Research,
Highfield, SO17 1BJ, Southampton, United Kingdom
e-mail: **m.dal-borgo@soton.ac.uk**

Abstract

Inertial actuators can be used with velocity feedback controllers to reduce structural vibration, but the finite stroke length can affect the behaviour and the stability of the control system. Stroke saturation results in impulse-like excitation, which is transmitted to the structure and may result in damage. Moreover, the shocks produced by the impacts reduce the overall damping and eventually leads to instability and limit cycle oscillations. This paper examines the implementation of a nonlinear feedback controller in order to avoid collisions of the proof mass with the actuator's end stops, thus preventing this instability. Firstly, the nonlinear model of a stroke limited inertial actuator is identified experimentally. Secondly, a nonlinear control strategy is presented, which actively increases the internal damping of the actuator, and its experimental implementation is discussed. Finally, the estimation of the relative proof mass velocity is presented using the nonlinear model of the actuator and an extended Kalman filter algorithm.

1 Introduction

Active solutions, using inertial actuators driven from sensors via feedback controllers, are important in the control of vibration in lightweight and flexible structures [1]. A velocity feedback controller (VFC) consists of an inertial actuator attached to a structure, a collocated vibration sensor on the structure and a controller, which feeds back the velocity of the structure to the actuator. Velocity feedback controllers are capable of increasing the effective damping in the structure, hence reducing its level of resonant vibration [2]. The main components of an inertial actuator as illustrated in figure 1 are: a magnetic proof mass, a coil and a suspension, which connects the proof mass to an outer casing or a base mass. The operating principle of an inertial actuator is that an input current to the coil generates a control force on the structure by reacting against the proof mass, which starts to accelerate [2].

One concern using inertial actuators in velocity feedback loops is that their internal, linear, dynamics will affect the behaviour of the control system, which then becomes only conditionally stable [3]. Moreover, mechanical nonlinearities of inertial actuators can further affect the stability of VFC. Stroke saturation is a nonlinear effect that is due to the proof mass hitting the actuator end stops, potentially imparting large shocks to the structure, which may be damaged. It has been observed experimentally that stroke saturation is also undesirable in terms of the stability of the closed loop control system, because it can reduce the stability margin, and in fact, enhance the level of vibration [4, 5]. This motivates for having accurate models of proof mass actuators and in particular of the nonlinearities that may affect the dynamics of these devices at low frequency or large excitation signals [6]. Several attempts have been made to overcome the issue of stroke saturation in inertial actuators [7, 8, 9, 10].

This research sets out a theoretical and experimental study of a nonlinear control strategy (NLFC) to prevent stroke saturation of inertial actuators. The control strategy acts as a second loop alongside the linear VFC and implements a simple nonlinear control law using the proof mass relative velocity signal [11, 12]. The

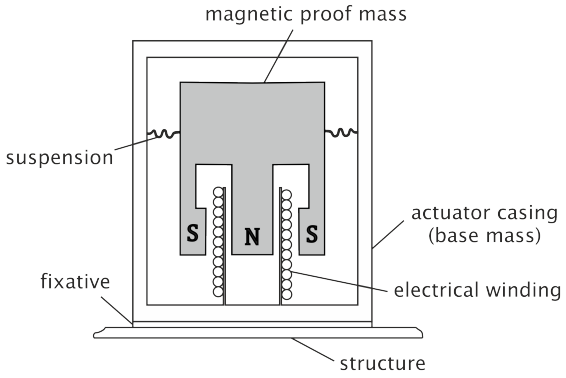


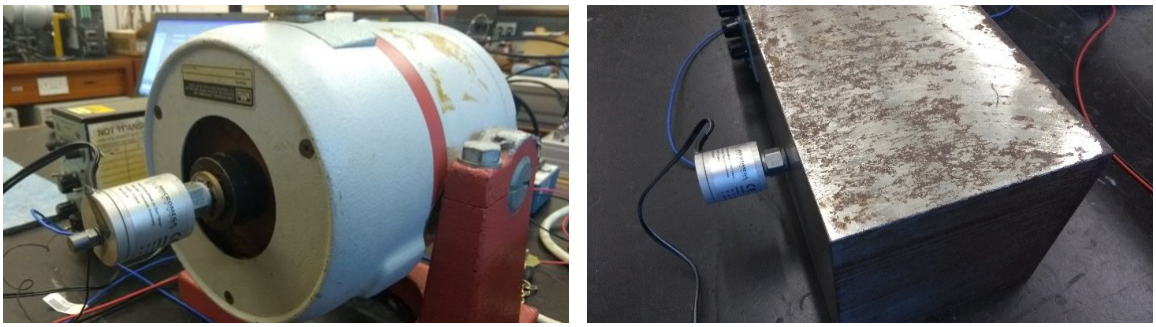
Figure 1: Schematic of an inertial actuator in cross-section

NLFC presented in this paper increases the internal damping of the actuator as the proof mass approaches the end stops, whilst not affecting it when the proof mass is clear from the constraints. A drawback of this control strategy is that it needs the relative proof mass velocity signal. In most cases it is impossible to directly instrument the proof mass, hence a virtual sensing approach using the other available measurements would be an interesting solution. Two different approaches are presented in this paper. The first one uses the underlying linear deterministic model of the actuator to calculate the coefficients of a digital filter to be applied on the current and base velocity signals. The second approach considers an extended Kalman filter algorithm and the nonlinear model of the actuator to predict and update the estimation of the relative proof mass velocity at each time step [13].

This paper is organised in three main sections. Section 2 investigates the nonlinear dynamics of the inertial actuator through an experimental identification using base excitation and direct excitation experiments. Section 3 presents the nonlinear feedback law and its experimental implementation on a control unit attached to the free end of a cantilever beam. Section 4 introduces a state estimation approach for the relative proof mass velocity using only the measurements of the electrical port of the actuator and the base velocity. The conclusions are summarised in section 5.

2 Identification and modelling of nonlinearities

A large amount of literature has shown that the internal dynamics of inertial actuators affect the stability and performance of VFCs [3]. This motivates for having an accurate models of inertial actuators and in particular to look for nonlinearities that may affect the dynamics of such devices for large excitation signals. This section briefly describes the methodology for the identification of mechanical nonlinearities of inertial actuators, which has been described in detail in [6]. The electrical nonlinearities are neglected since they mainly affect the behaviour at high frequencies. The inertial actuator considered in this study is a Micromega Dynamics IA-01 [14]. The characterisation of the inertial actuator is performed using two experiments. The first experimental set-up is called base excitation and is shown in figure 2(a). The actuator is mounted on a force sensor, which is rigidly connected to an electrodynamic shaker. An accelerometer is attached to the actuator casing in order to measure the acceleration of the base mass. The actuator's coil terminals are initially left open to measure the voltage due to the back-electromotive force (back-emf). The output force, acceleration and voltage signals are acquired by a dSpace 1103 control board. The second experimental set-up is called base blocked, or current excitation and is shown in figure 2(b). The actuator is fixed to a rigid clamped mass and the force at the base is measured by a force cell positioned between the actuator and the blocked mass. In this experiment, the signal generated by the dSpace is amplified by a voltage driven current amplifier before entering the actuator leads. The amplifier also has an output monitoring port for measuring the current of the load. Again, the current and voltage signals are acquired by the dSpace



(a) (b)

Figure 2: (a) picture of the set-up for the base excitation experiment; (b) picture of the set-up for the blocked base experiment

board. The underlying linear parameters for both tests have been measured by applying a broadband white noise with small amplitude excitation and recording the measurements for 60 seconds and taking averages. The actuator's coil terminals are firstly left open and then shunted in order to see the additional damping introduced by the electromechanical coupling. To identify the nonlinear behaviour, the base excitation test has been used with large amplitude signals. The actuator's coil terminals are left open circuit in order to measure the back-emf and a sine-sweep excitation has been used, in order to catch all the information about the instantaneous frequencies in the response. In this case the experiment is 60 seconds long for linearly sweeping up (down) from 5 Hz (25 Hz) to 25 Hz (5 Hz) at a rate of 40 Hz/min (-40 Hz/min). In order to understand the dynamic behaviour of the electrodynamic proof mass actuator, a two-port network is built for such a system. The equivalent electromechanical nonlinear lumped parameter model of the inertial actuator is shown in figure 3, where m_b represents the base mass of the actuator and m_p represents the proof mass. The base mass and proof mass displacements are x_b and x_p, respectively. The actuator's suspension is represented by a nonlinear restoring force $f_{RF}(\dot{x}_r, x_r)$, which for the underlying linear model is given by the stiffness and damping coefficients k_p and c_p. The external force applied to the base for the equilibrium is denoted by f. The variable i_a is the current flowing through the coil, while e_a is the voltage across the coil terminals. The electromechanical coupling factor, which in general is a nonlinear function of the displacement is $\phi(x_r) = Bl(x_r)$, where B is the magnetic flux generated by the permanent magnet and $l(x_r)$ is the length of the winding exposed to the magnetic flux B. In the underlying linear model the coupling factor is given by a constant. The voice coil is typically modelled as a series ideal inductance L_e and resistor R_e. The underlying linear parameters of the inertial actuator have been identified by matching the experimental driving-point electric and mechanical impedances and the transmissibility with the ones calculated from the linearised lumped parameter model of figure 3 [6]. The identified parameters are summarised in table 1.

Parameter	Symbol	Value	Units
Base mass	m_b	0.054	kg
Proof mass	m_p	0.031	kg
Transduction coefficient	ϕ	1.55	N/A
Natural frequency	ω_p	9.7	Hz
Damping ratio	ζ_p	30%	$-$
Coil resistance	R_e	3.2	Ω
Coil inductance	L_e	211	μH

Table 1: Identified actuator linear model parameters

In general, the assumption of linearity in the model holds only for small amplitude signals. For large ampli-

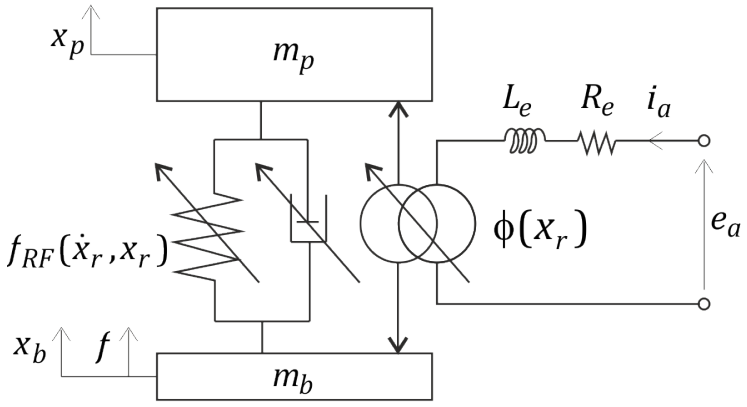


Figure 3: Nonlinear lumped parameter model of the proof mass actuator

tude signals, a nonlinear model of the inertial actuator is required. This is crucial in case of instabilities or large amplitude of motions. The governing equations of the nonlinear system in figure 3 can be written as,

$$\begin{cases} m_p\ddot{x}_p(t) = -f_{RF}(\dot{x}_r(t), x_r(t)) + \phi(x_r(t))i_a(t) \\ f(t) = \phi(x_r(t))i_a(t) - f_{RF}(\dot{x}_r(t), x_r(t)) + m_b\ddot{x}_b(t) \\ e_a(t) = \phi(x_r(t))\dot{x}_r(t) + R_e i_a(t) + L_e\dfrac{\mathrm{d}}{\mathrm{d}t}i_a(t) \end{cases}. \tag{1}$$

The nonlinearity of the inertial actuator is identified following three steps, namely detection, characterisation and parameter identification, as proposed in [15, 16]. The inertial actuator is tested using the base excitation experiment with a harmonic signal for detecting the nonlinearities. Then a linear sine sweep up and down excitation is used and a formulation can be chosen for the nonlinear model. Finally, the nonlinear model parameters can be identified using the restoring force surface method [15, 16, 17] and the back-emf signal for the transduction factor. Fig. 4(a) shows the experimental data points of the restoring force in the phase space for the largest amplitude of excitation. It can be seen that the restoring force measurements are close to a linear behaviour until the actuator reaches the end stops. The restoring force suddenly steepens if the proof mass collides with the end stops. In order to identify the nonlinear parameters of the nonlinear function, an assumption is made, which is

$$f_{RF}(\dot{x}_r, x_r) = f_{RF,v}(\dot{x}_r) + f_{RF,d}(x_r), \tag{2}$$

hence, the contribution of the damping and elastic restoring forces can be separated. The scattered data plot of the measured elastic restoring force is shown in figure 4(b) with the black dots. It can be seen that the behaviour of the elastic restoring force is piecewise linear, where the stroke saturation can be modelled as a non-smooth function with a very large stiffness. From this scattered data plot a nonlinear model can be fitted, which is shown in figure 4(b) with the red solid line. The elastic restoring force of the fitted polynomial model shown in Figure 13 with the red solid line can be written as,

$$f_{RF,d}(x_r) = \begin{cases} k_{sat}(x_r + x_0) - p_1 x_0 + p_2 & x_r \leq -x_0 \\ p_1 x_r + p_2 & |x_r| < x_0 \\ k_{sat}(x_r - x_0) + p_1 x_0 + p_2 & x_r \geq x_0 \end{cases}, \tag{3}$$

where the parameters appearing in equation (3) are $p_1 = 230N/m$, $p_2 = 0N$, $k_{sat} = 2 \cdot 10^4 N/m$ and $x_0 = 1.25mm$. The scattered data plot of the damping restoring force is shown in figure 4(c). It is observed that the experimental data points of the damping restoring force are well fitted by a linear model, which is shown with a red solid line and can be written as,

$$f_{RF,v}(\dot{x}_r) = p_1\dot{x}_r + p_2, \tag{4}$$

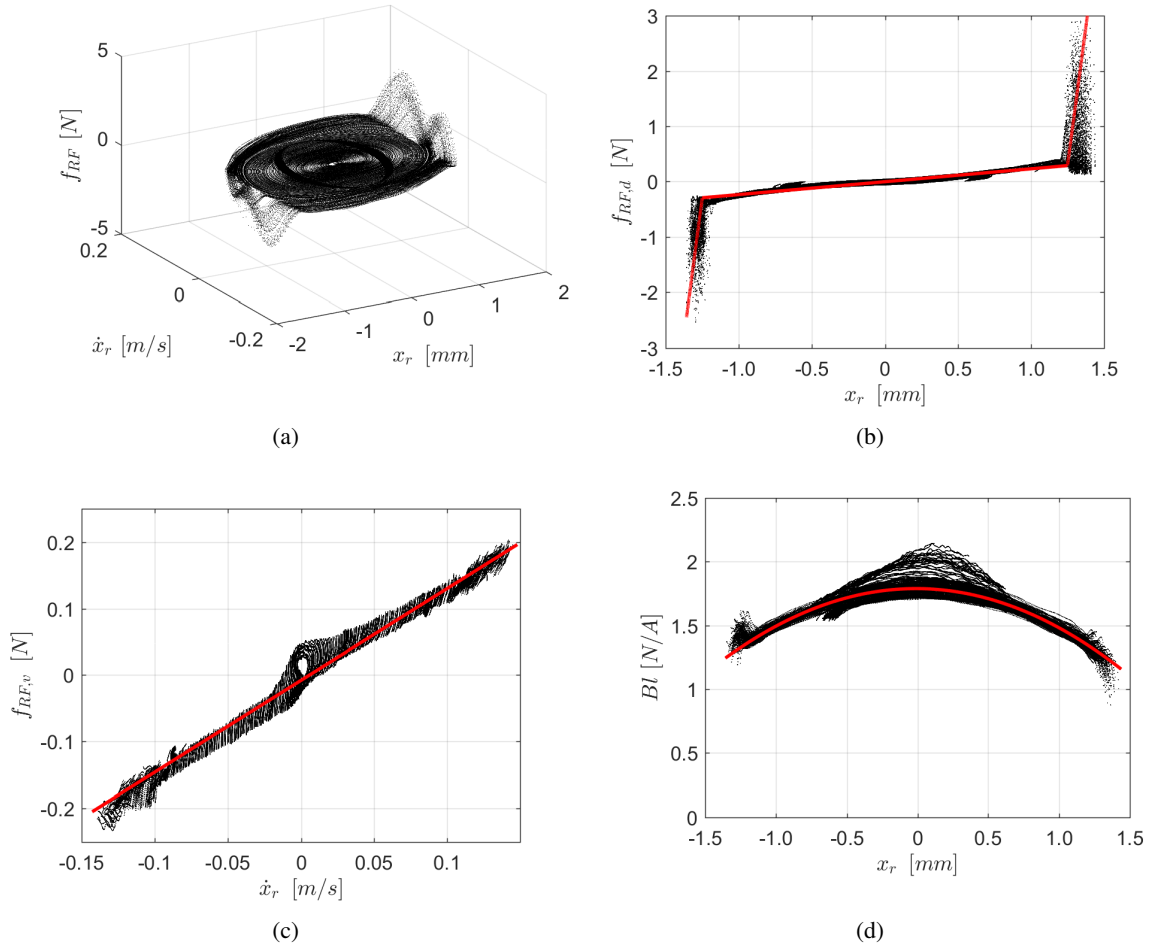


Figure 4: (a) 3D restoring force data points; (b) model identification of the elastic restoring force; (c) model identification of the damping restoring force; (d) model identification of the transduction factor.Experimental data (black dots), fitted curves (red solid line)

where the parameters appearing in equation (4) are $p_1 = 1.4N/ms^{-1}$ and $p_2 = 0N$. The scattered data plot of the transduction factor versus the displacement is shown in figure 4(d). The transduction factor behaviour is polynomial and symmetric. In fact, the peak in the transduction coupling is reached for the proof mass in centred position. From this scattered data plot a nonlinear model can be fitted, which is polynomial of the 2^{nd} order and can be then written as,

$$\phi(x_r) = p_1 x_r^2 + p_2 x_r + p_3, \tag{5}$$

where the parameters appearing in equation (5) are $p_1 = -300kN/Am^2$, $p_2 = -6.5N/Am$ and $p_3 = 1.8N/A$.

3 Experimental implementation of a nonlinear feedback controller

This section examines the experimental implementation of the VFC and NLFC loops for the vibration reduction of the first mode of a cantilever beam using the stroke limited inertial actuator presented in section 2. The experimental set-up is shown in figure 5. It consists of an aluminium cantilever beam and a control unit attached at the nodal point of the second mode of the beam. The control unit comprises the inertial actuator, a collocated accelerometer and a force sensor. The external excitation is given by an instrumented hammer,

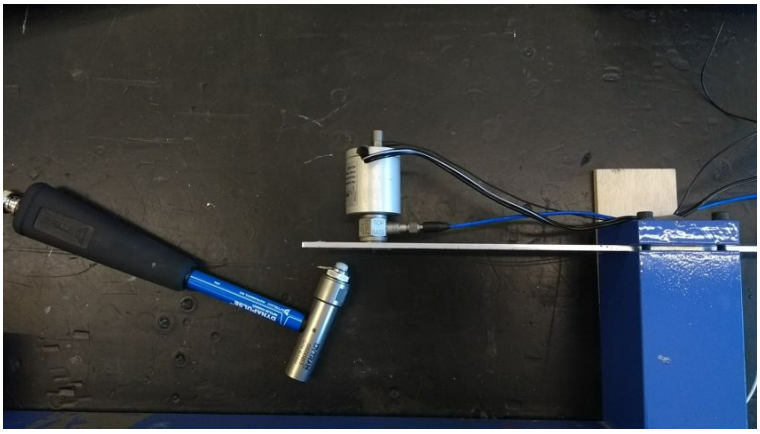


Figure 5: Experimental test rig for the active vibration control of the beam

whereas the acquisition and control system are performed by the dSPACE control board, where the sampling rate of has been set to $f_s = 10kHz$. The parameters of the test rig are given in Tab. 2 for the beam and control unit, and in section 2 for the nonlinear model of the inertial actuator.

Property	Value
l_{beam}	$175 \quad mm$
b_{beam}	$25 \quad mm$
h_{beam}	$3 \quad mm$
m_{acc}	$0.005 \quad kg$
m_{base}	$0.053 \quad kg$
m_{gauge}	$0.023 \quad kg$

Table 2: Parameters of the cantilever beam and the control unit

3.1 Velocity feedback control (VFC)

The stability of the VFC is analysed using the Nyquist criterion for the open loop FRF $L(j\omega) = h_s Y_{cc}(j\omega)$, where h_s is the velocity feedback gain and $Y_{cc}(j\omega)$ is the driving point mobility [18]. The VFC gain is set to unity and the actuator is driven by a broadband white noise current at small level, in order the actuator operates within its linear range. This results in the open loop FRF shown by the polar plot in figure 6. It can be seen that the locus of the Nyquist intersects the negative real axis at a distance $\delta = 0.068$, which corresponds to a gain margin $g_m = 1/\delta = 14.7$ and the closed loop system being only conditionally stable. As a result, the maximum velocity feedback gain that can be applied to the system without driving it unstable is $h_{s,max} = 14.7$. However, it has been noted that the VFC becomes unstable for feedback gains much lower than $h_{s,max}$ and this has to be attributed to the stroke saturation nonlinearity [19, 20]. In fact, this instability is caused by the proof mass leaving one end stop and quickly moving through the stroke, hitting the opposite end stop and imparting an impulse, which is in phase with the velocity of the structure. This reduces the overall damping of the system until the controller becomes unstable and limit cycle oscillations are observed.

3.2 Nonlinear feedback control (NLFC)

The study of the previous section motivates for the development of a nonlinear controller, whose aim is to prevent the destabilisation of the feedback loop due to stroke saturation yet maintaining the vibration suppression performance of the VFC. The author of [11] proposed to use a combination of relative velocity

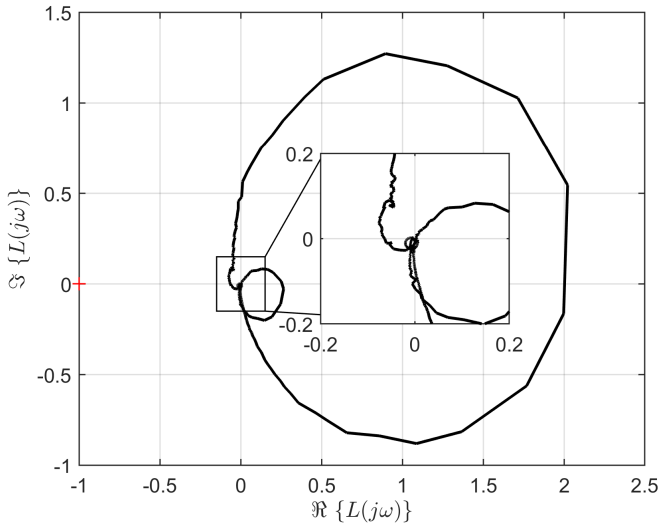


Figure 6: Nyquist of the measured open loop FRF with a control gain $h_s = 1$

feedback and VFC, where the tuning of the two feedback gains is a trade off between the stability and performance of the control system. Later on, other researchers dealt with the stroke saturation phenomenon using a nonlinear feedback controller, which is function of the relative proof mass displacement [21]. In this paper we merge these two ideas into a nonlinear feedback controller (NLFC) that acts as a second loop alongside the VFC and is implemented as illustrated in the schematic of figure 7. The acceleration signal from the accelerometer is high pass filtered and integrated to obtain the velocity at the control point $\dot{x}_c$. The velocity of the structure at the control point is then amplified by a fixed VFC gain. The amplified signal is then fed to the actuator for the VFC. The signal of the force cell, which corresponds to the control force f_c and the acceleration signal $\ddot{x}_c$ are high pass filter and the relative proof mass acceleration is calculated as,

$$\ddot{x}_r = \frac{f_c - m_c \ddot{x}_c}{m_p}, \tag{6}$$

where $m_c = m_{acc} + m_{base} + m_{gauge} + m_p$ is the total attached mass at the control point. The relative proof mass velocity and displacement are then calculated by high pass filtering and integrating the acceleration signal. Then, the NLFC input signal to the inertial actuator is calculated in real time using the following control law,

$$\psi(x_r, \dot{x}_r) = \frac{n_r \dot{x}_r}{(x_0 - |x_r|)^{2p} + b}, \tag{7}$$

where n_r is the feedback gain of the nonlinear controller, b is a limitation parameter and p is an exponent parameter. The control law of equation (7) increases the active damping of the inertial actuator as the proof mass approaches the end stops. As the relative displacement of the proof mass gets close to the stroke limit, the denominator term of equation (7) reduces, hence the current proportional to the relative velocity increases. In such a configuration, if b is set to zero, the input current for displacements close to the stroke length can take large values, with dangerous and impractical implications. Hence, a saturation limit on the maximum control action has to be set. The active damping added to the actuator can be derived from equation (7) as,

$$c_{active}(x_r) = \frac{\phi\psi(x_r, \dot{x}_r)}{\dot{x}_r} = \frac{n_r \dot{x}_r}{(x_0 - |x_r|)^{2p} + b}. \tag{8}$$

The control action is bounded between a minimum active damping $c_{active}(0) = c_{min}$, that is reached when the proof mass is centred within the casing, and a maximum active damping $c_{active}(x_0) = c_{max}$ that is

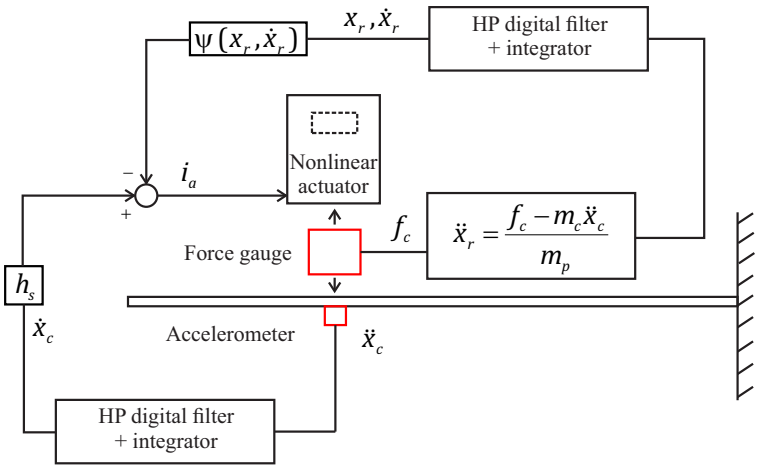
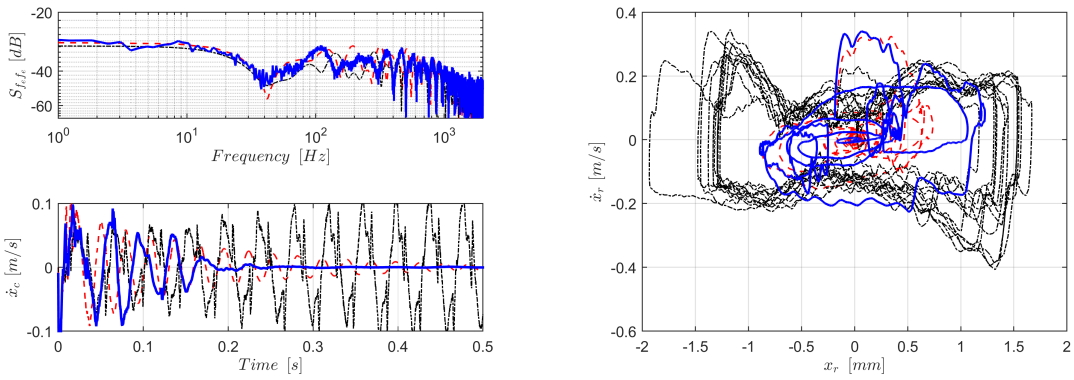


Figure 7: Schematic of the experimental implementation of the VFC and NLFC

reached when the proof mass saturates in stroke. From this consideration, the parameters b and n_r can be calculated. For this experiment the NLFC has been designed according to equation (7) to have $c_{min} = 0.5\ N/ms^{-1}$, $c_{max} = 100\ N/ms^{-1}$ and $p = 1$.

Figure 8 shows a comparison between the uncontrolled scenario (passive system, red dashed lines), the VFC case using $h_s = 42\% h_{s,max}$ (black dash-dotted lines) and the VFC plus NLFC case also with $h_s = 42\% h_{s,max}$ (blue solid lines). Figure 8(a) shows the spectrum of the excitation force and the time history of the velocity at the control point. Figure 8(b) instead shows the phase plane of the relative proof mass displacement and velocity. It can be seen that in the uncontrolled case, the vibration of the structure dies out,



(a) (b)

Figure 8: (a) Spectrum of the excitation force and time history of the velocity signal at the control point; (b) phase portrait of the relative proof mass displacement and velocity. Red dashed lines represent the response for the uncontrolled scenario; black dash-dotted lines represent the response with the NLFC switched off and $h_s = 42\% h_{s,max}$; blue solid lines represent the response with the NLFC switched on and $h_s = 42\% h_{s,max}$

but only after a certain period of time. Also, the trajectory of the proof mass starts to orbit until it eventually decays to zero. Implementing the VFC and assuming a feedback gain $h_s = 42\% h_{s,max}$ leads to instability for the same level of excitation of the uncontrolled case. In fact, the trajectory of the proof mass is fixed on a limit cycle. If the NLFC is also implemented, under the same conditions of level of excitation and velocity feedback gain, the system remains stable. This can be observed in both the time history of the structural

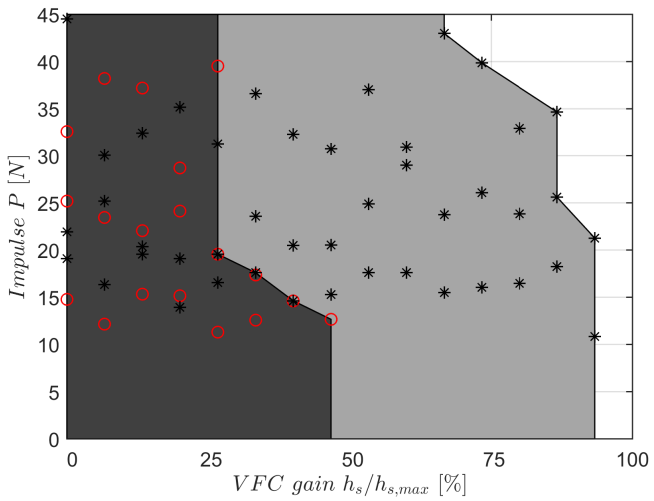


Figure 9: Comparison of the stability range for the feedback laws with the experimental inertial actuator. Red circles in the dark grey area show the experimental data points in which the VFC is stable; Black asterisks in the light grey area show the experimental data points in which the VFC plus NLFC is stable

velocity and in the trajectory of the proof mass. Of course, the stability of the nonlinear system does not depend only on the value of the VFC gain h_s, but also on the magnitude of the excitation P. Therefore, a parametric study has been carried out in order to investigate the potential benefits of the NLFC over different scenarios. In particular, the stability of the system has been evaluated for each value of P and h_s, and in two different testing conditions: the VFC loop is implemented with the NLFC switched off, and when both the VFC and NLFC are implemented. For each scenario, the operating region of the inertial actuator is defined as,

$$\mathcal{OR}(P, h_s) = \{(P, h_s) \ \max_{t\to\infty} |x_r(t)| < x_0\}, \tag{9}$$

where the sets of (P, h_s) inside the operating region are those in which the system is stable and the inertial actuator is adding damping to the structure. In this case the beam has been excited with three different levels of excitation, namely: low (below 20 N), medium (between 20 N and 30 N) and high (above 30 N). For each level of excitation, the test has been repeated increasing the velocity feedback gain from the uncontrolled case to $h_{s,max}$. The parametric study has been conducted firstly with the VFC loop only and secondly with both the VFC and NLFC in order to compare the operating regions of the inertial actuator with the two different control strategies. The results are shown in Fig. 9, where the red circles are the experimental data points in which the VFC is stable, and the black asterisks are the experimental data points in which the VFC plus NLFC is stable. The data points of the two control strategies defines the operating region of the inertial actuator that is highlighted by the light grey area for the VFC strategy and by the dark grey area for the VFC plus NLFC strategy. Hence, the main finding of the experimental study is that the added NLFC loop is able to increase the safe operating region of the inertial actuator.

4 State estimation

This section investigates two approaches for the estimation of the proof mass velocity from the available measurements. Often inertial actuators are surrounded by protective casings, thus preventing the proof mass to be directly instrumented with an accelerometer or a strain gauge. In fact, the previous section dealt with the problem of measuring the proof mass velocity by using a force gauge to measure the control force and then

retrieving the proof mass velocity considering the dynamic equation (6). However, a force gauge adds mass to the structure and is an expensive device. A better idea is to use a virtual sensor that calculates the proof mass velocity using the available measurements and the mathematical model of the actuator. Section 4.1 presents an open loop algorithm that calculates the proof mass velocity applying a digital filter to the current and base velocity signals, where the digital filter coefficients are calculated from the actuator underlying linear dynamics. Section 4.2 instead presents an extended Kalman filter algorithm that calculates the optimal estimate of the proof mass velocity using the nonlinear model of the actuator and the voltage, current and base acceleration signals.

4.1 Linear deterministic model

Considering an underlying linear model of the inertial actuator in figure 3 and that the control force $f_c = -f$, the equation of motion of the proof mass and the control force can be written as,

$$\begin{cases} j\omega m_p \dot{X}_p(j\omega) = \phi I_a(j\omega) - [c_p + \dfrac{k_p}{j\omega}]\dot{X}_r(j\omega) \\ F_c(j\omega) = -j\omega m_p \dot{X}_p(j\omega) - j\omega m_b \dot{X}_b(j\omega) \end{cases}, \tag{10}$$

where $\dot{X}_b(j\omega)$ is the base mass velocity in frequency domain. From the set of equations (10) the control force results,

$$\begin{cases} F_c(j\omega) = -\phi I_a(j\omega) + [c_p + \dfrac{k_p}{j\omega}]\dot{X}_r(j\omega) - j\omega m_b \dot{X}_b(j\omega) \\ F_c(j\omega) = -j\omega m_p \dot{X}_r(j\omega) - j\omega(m_p + m_b)\dot{X}_b(j\omega) \end{cases}. \tag{11}$$

Equalling the right hand side terms of the set of equations (11) leads to the equation of motion of the relative coordinate, which can be solved for the relative velocity as,

$$\dot{X}_r(j\omega) = \frac{\phi I_a(j\omega) - j\omega m_p \dot{X}_b}{j\omega m_p + c_p + \frac{k_p}{j\omega}}. \tag{12}$$

Equation 12 can be divided into two transfer functions: one for the current and one for the base velocity. These transfer functions are then translated in the digital domain using the bilinear transformation considering a pre-warping coefficient μ given by,

$$\mu = \frac{\omega_p}{\tan(\frac{\omega_p}{2f_s})}, \tag{13}$$

where f_s is the sampling rate. Thus, the digital filter applied to the current becomes,

$$H_{1d}(z) = \frac{\dot{X}_r(z)}{I_a(z)} = \frac{\phi\mu - \phi\mu z^{-2}}{(m_p\mu^2 + c_p\mu + k_p) + (2k_p - 2m_p\mu^2)z^{-1} + (m_p\mu^2 - c_p\mu + k_p)z^{-2}}, \tag{14}$$

and the digital filter applied to the base velocity becomes,

$$H_{2d}(z) = \frac{\dot{X}_r(z)}{\dot{X}_b(z)} = \frac{-m_p\mu^2 - 2m_p\mu^2 z^{-1} - m_p\mu^2 z^{-2}}{(m_p\mu^2 + c_p\mu + k_p) + (2k_p - 2m_p\mu^2)z^{-1} + (m_p\mu^2 - c_p\mu + k_p)z^{-2}}. \tag{15}$$

Finally, combining the filtered signals using equation (14) and equation (15) gives the estimation of the relative proof mass velocity. However, this is an open loop approach, thus a change in the system that is not considered in the model gives a poor estimation of the proof mass velocity.

4.2 Extended Kalman filter (EKF)

An approach that considers the nonlinearities in the model and gives a correction term to the estimate based on some measurements is given by the extended Kalman filter (EKF) [13]. The dynamic equations of the system in figure 3 can be written as,

$$\begin{cases} m_p\ddot{x}_r + c_p\dot{x}_r + \kappa(x_r)x_r = \phi i_a - m_p\ddot{x}_b \\ e_a = \phi\dot{x}_r + R_e i_a \end{cases}, \tag{16}$$

where the inductive term $L_e\frac{\mathrm{d}}{\mathrm{d}t}i_a$ has been neglected and the nonlinear stiffness $\kappa(x_r)$ is given by,

$$\kappa(x_r) = \begin{cases} k_p & |x_r| < x_0 \\ k_p + k_c(1 - \dfrac{x_0}{|x_r|}) & |x_r| \geq x_0 \end{cases}, \tag{17}$$

according to equation (3), where $k_c = k_{sat} - k_p$ is the impact stiffness. Considering the current signal and the base acceleration signal as inputs to the system and the voltage signal being the output measurement, the set of equations (16) can be written in state space form as,

$$\begin{cases} \dot{\mathbf{x}} = \mathbf{A}(\mathbf{x})\mathbf{x} + \mathbf{B}\mathbf{u} + \mathbf{W} \\ y = \mathbf{C}\mathbf{x} + \mathbf{D}\mathbf{u} + \mathbf{V} \end{cases}, \tag{18}$$

where the state vector is $\mathbf{x} = [x_r\ \dot{x}_r]^T$ and the input vector is $\mathbf{u} = [i_a\ \ddot{x}_b]^T$. The system matrix is given by,

$$\mathbf{A} = \begin{bmatrix} 0 & 1 \\ -\frac{\kappa(x_1)}{m_p} & -\frac{c_p}{m_p} \end{bmatrix}, \tag{19}$$

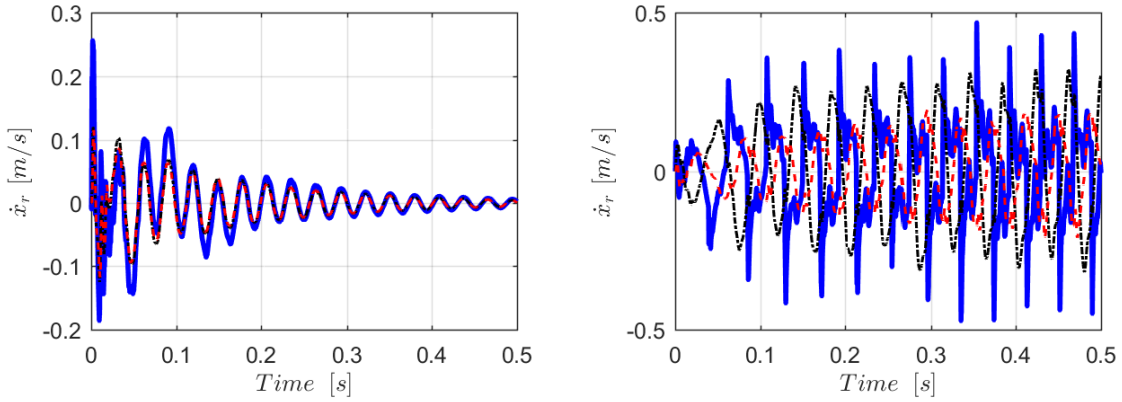
where the nonlinear stiffness is given by equation (17). The input matrix $\mathbf{B}$ is given by,

$$\mathbf{B} = \begin{bmatrix} 0 & 0 \\ \frac{\phi}{m_p} & -1 \end{bmatrix}, \tag{20}$$

the output is $y = e_a$ and the output matrices are $\mathbf{C} = [0\ \phi]$ and $\mathbf{D} = [R_e\ 0]$. $\mathbf{W}$ is the covariance matrix for the process noise, whereas $\mathbf{V}$ is the covariance matrix for the measurement noise. The observability matrix of the system of equation (18) is given by [13],

$$\mathbf{Ob} = \begin{bmatrix} \mathbf{C} \\ \mathbf{CA} \end{bmatrix} = \begin{bmatrix} 0 & \phi \\ -\frac{\phi\kappa(x_1)}{m_p} & -\frac{\phi c_p}{m_p} \end{bmatrix}, \tag{21}$$

which has rank 2, hence the system is observable [13]. The EKF algorithm linearises the system at each time step, it predicts the state values using the inputs to the system, then it updates the state estimation using the output measurement value. The EKF approach presented in this section and the linear digital filter discussed in section 4.1 are compared to the case where the proof mass velocity was calculated from the force gauge measurement. Figure 10(a) shows the proof mass velocity when the actuator operates within its linear range. The blue solid line represents the proof mass velocity derived from the force gauge measurement, the black dash-dotted line shows the virtual measurement using the linear deterministic model and the red dashed line represents the estimation using the EKF algorithm. Since the actuator is operating within its linear range the two virtual sensing approaches can reliably predict the proof mass velocity signal. However, this no longer apply when the actuator enters its nonlinear regime of motion. Figure 10(b) shows the response to the system when the actuator is subject to a limit cycle oscillation. In this scenario, the linear digital filter no longer describes correctly the proof mass velocity, whereas a better estimation is given by the EKF. The time history of the proof mass velocity given by the EKF almost matches the one measured with the force gauge except for a time delay, as shown in figure 10(b).



(a) (b)

Figure 10: Time histories of the relative proof mass velocity measured by using the force gauge (blue solid line), linear deterministic digital filter (black dash-dotted line) and EKF (red dashed line). (a) Linear response; (b) nonlinear response

5 Conclusions

This paper presented a nonlinear feedback controller that aims to prevent stroke saturation instability and its implementation using a virtual sensor is discussed.

Firstly, an experimental investigation on the nonlinear behaviour of the inertial actuator has been presented. Base excitation and direct excitation experiments have been performed in order to characterise and to identify the linear and nonlinear parameters of the actuator. in particular, the nonlinear parameters have been identified using the restoring force method and the back-electromotive force signal. Secondly, the nonlinear feedback control strategy has been presented and its real-time experimental implementation on a control unit attached to a cantilever beam has been discussed. The nonlinear controller operates as a second loop alongside the classical velocity feedback and it increases the internal damping of the actuator as the proof mass approaches the end stops. It has been shown that the nonlinear feedback controller is able to increase the safe operating region of the actuator. Hence, larger feedback gains can be used, or larger impulse excitations can be withstood, without the system becoming unstable if this nonlinear controller is used. Finally, the estimation of the proof mass velocity from the available measurements and the actuator model has been discussed. Preliminary results showed that an extended Kalman filter algorithm that uses the current signal and the base acceleration signal as inputs and the voltage signal across the actuator terminals as output measurement can accurately predict the proof mass velocity, hence it can be used as a virtual sensor algorithm. Future work may be related to the experimental implementation of such virtual sensor algorithm.

Acknowledgements

The authors gratefully acknowledge the European Commission for its support of the Marie Curie program through the ITN ANTARES project (GA606817).

References

[1] C.C. Fuller, S.J. Elliott, P.A. Nelson, *Active control of vibration*, Academic press, (1996).

[2] F. Fahy, P. Gardonio, *Sound and structural vibration: radiation, transmission and response*, Elsevier Science (2007).

[3] S.J. Elliott, M. Serrand, P. Gardonio, *Feedback stability limits for active isolation systems with reactive and inertial actuators*, Journal of Vibration and Acoustics-Transactions of the Asme, Vol. 123, No. 2, (2001), pp. 250-261.

[4] O.N. Baumann, S.J. Elliott, *The stability of decentralized multichannel velocity feedback controllers using inertial actuators*, The Journal of the Acoustical Society of America, Vol. 121, No. 1, (2007), pp. 188-196.

[5] M. Dal Borgo, M. Ghandchi Tehrani, S.J. Elliott, *Experimental implementation of a nonlinear feedback controller for a stroke limited inertial actuator*, *36th International Modal Analysis Conference (IMAC-XXXVI), Orlando, FL, USA, 2018 February 12-15*, Orlando (2018), pp. 1-17.

[6] M. Dal Borgo, M. Ghandchi Tehrani, S.J. Elliott, *Identification and analysis of nonlinear dynamics of inertial actuators*, Mechanical Systems and Signal Processing, (2018), https://doi.org/10.1016/j.ymssp.2018.05.044 .

[7] H. Politansky, W.D. Pilkey, *Suboptimal feedback vibration control of a beam with a proof-mass actuator*, Journal of Guidance Control and Dynamics, Vol. 12, No. 5, (1989), pp. 691-697.

[8] D.K. Lindner, G.A. Zvonar, D. Borojevic, *Nonlinear control of a proof-mass actuator*, Journal of Guidance Control and Dynamics, Vol. 20, No. 3, (1997), pp. 464-470.

[9] L.I. Wilmshurst, M. Ghandchi Tehrani, S.J. Elliott, *Active control and stability analysis of flexible structures using nonlinear proof-mass actuators*, *IX International Conference on Structural Dynamics (Eurodyn 2014), Porto, Portugal, 2014 June 30- July 02*, Porto (2014), pp. 1571-1578.

[10] J. Rohlfing, T. May, L. Walter, J. Millitzer, *Self-tuning velocity feedback control for a time varying structure using a voltage driven electrodynamic inertial mass actuator*, *27th International Conference on Noise and Vibration Engineering (ISMA2016), Leuven, Belgium, 2016 September 19-21*, Leuven (2016), pp. 1-16.

[11] D.J. Inman, *Control/structure interaction: effects of actuator dynamics*, *Dynamics Specialists Conference, Structures, Structural Dynamics, and Materials, Long Beach, CA, USA, 1990 April 05-06*, Long Beach (1990), pp. 507-533.

[12] C. Paulitsch, P. Gardonio, S.J. Elliott, *Active vibration control using an inertial actuator with internal damping*, The Journal of the Acoustical Society of America, Vol. 119, No. 4, (2006), pp. 2131-2140.

[13] D. Simon, *Optimal state estimation: Kalman, H infinity, and nonlinear approaches*, John Wiley & Sons, (2006).

[14] Micromega Dynamics, *Active damping devices and inertial actuators*, Web Page, http://www.micromega-dynamics.com/download/category/4-active-damping-device.html, Last accessed: 10 Jun 2017.

[15] G. Kerschen, K. Worden, A.F. Vakakis, J.-C. Golinval, *Past, present and future of nonlinear system identification in structural dynamics*, Mechanical Systems and Signal Processing, Vol. 20, No. 3, (2006), pp. 505-592.

[16] J.-P. Noël, G. Kerschen, *Nonlinear system identification in structural dynamics: 10 more years of progress*, Mechanical Systems and Signal Processing, Vol. 83, (2017), pp. 2-35.

[17] K. Worden, G.R. Tomlinson, *Nonlinearity in structural dynamics: detection, identification and modelling*, Institute of Physics, Bristol, UK (2000).

[18] P. Gardonio, M.J. Brennan, *Mobility and impedance methods in structural dynamics*, Advanced Applications in Acoustics, Noise and Vibration, Taylor and Francis, F. Fahy, London (2004), pp. 389-447.

[19] O.N. Baumann, S.J.Elliott, *Destabilization of velocity feedback controllers with stroke limited inertial actuators*, The Journal of the Acoustical Society of America, Vol. 121, No. 5, (2007), pp. EL211-EL217.

[20] M. Dal Borgo, M. Ghandchi Tehrani, S.J. Elliott, *Nonlinear control and stability analysis of a stroke limited inertial actuator in velocity feedback*, *9th European Nonlinear Dynamics Conference (ENOC2017), Budapest, Hungary, 2017 June 25-30*, Budapest (2017), pp. 1-10.

[21] G.A. Zvonar, D.K. Lindner, D. Borojevic, *Nonlinear control of a proof-mass actuator to prevent stroke saturation*, in L. Meirovitch, editor, *Dynamics and control of large structures; Proceedings of the 8th VPI&SU Symposium, Blacksburg, VA, USA, 1991 May 06-08*, Blacksburg (1991), pp. 37-48.

Piezoelectric patches with multi-resonant shunts for multiple frequency band vibration control

M. Zientek, P. Gardonio, Loris Dal Bo
Università degli Studi di Udine, DPIA
208 Via delle Scienze, 33100, Udine, Italy
e-mail: **michal.zientek@uniud.it**

Abstract
This paper presents a simulation and experimental study on the flexural response of rectangular thin panels equipped with shunted piezoelectric patches for multiple frequency band vibration control. The piezoelectric patches are connected to electrical multi-resonant shunt circuits, composed of several parallel RLC branches. Each branch is adjusted in such a way as to control the plate flexural response in a given frequency band. A practical methodology based on the maximisation of the electrical power absorption is proposed to set RLC branch components in such a way as to reduce the flexural response of the panel. The vibration control effects are investigated with reference to the PSD of the total flexural kinetic energy of the panel and the PSD of the total electrical power absorbed by the shunt circuits. The study shows that the proposed tuning procedure can be effectively used to set the RLC components of the shunts in such a way as to reduce low-frequency resonance peaks of the plate flexural response.

1 Introduction

This paper proposes a novel practical tuning method for current flowing multi-resonant shunts connected to piezoelectric patches that are bonded on thin structures to reduce the effects of flexural vibrations in a wide frequency band. The multi-resonant shunts are formed by multiple RLC branches connected in parallel. The proposed method sequentially sets the RLC elements of the branches in each shunt in such a way as to maximise the vibration energy absorption from a progressively larger number of resonant flexural modes of the hosting structure. In practical applications, the vibration energy absorption is estimated from the measured electric power absorbed by each shunt. In this way, the on-line tuning algorithm can be conveniently implemented in the electronic board of the shunts. To make the proposed tuning approach more readily comprehensible, a simple problem is first considered in Section 2, which is composed by a thin rectangular plate equipped with two piezoelectric patches connected to multi-resonant current-flowing shunts and excited by a rain on the roof space and time stochastic disturbance. The flexural response of the plate is derived by combining the classical modal formulation for the coupled electromechanical response of the plate and piezoelectric patches with an original modal formulation for the electric response of the multi-resonant shunts described in [1]. The proposed tuning approach of the RLC components in the branches of the shunts is then introduced and discussed. Finally, experimental validation of the proposed tuning method of multi-resonant is presented in Section 3.

2 Simulation studies

2.1 Description of the system

Figure 1 presents the system considered in this study, which comprises a simply supported rectangular thin plate with two piezoelectric patches bonded to its surface and connected to multi-resonant shunt circuits. The geometry and physical properties of the plate and piezoelectric patches are summarised in Table 1. As shown in Figure 1(a) the plate is excited by a white noise, rain-on-the-roof stochastic process, which is modelled as an 4×4 array of uncorrelated point forces distributed over the surface of the plate. The piezoelectric patches are connected to the multi-resonant shunts which are formed by cascades of parallel RLC branches as depicted in Figure 1(b). Each branch possesses a band pass filter composed by a inductor L_{fij} and a capacitor C_{fij} connected in series, which produces a current flowing effect with centre frequency $\omega_{fi} = 1/\sqrt{L_{fij}C_{fij}}$. The remaining inductances L_{sij} and resistances R_{sij} also connected in series constitute a shunting part of the circuit and generate the vibration energy absorption effects at the frequencies $\omega_{si} = 1/\sqrt{L_{sij}C_{pej}}$. In practice, by combining the series inductors together $L_{fij} - L_{sij}$, the multi-resonant shunt can be further simplified as shown in Figure 1(c).

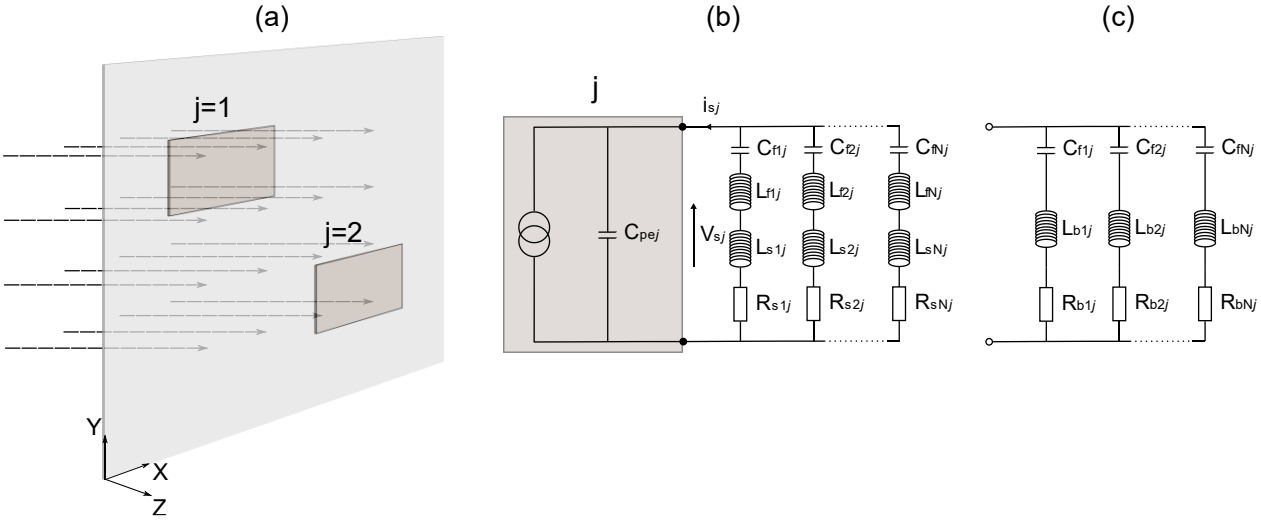


Figure 1: Plate equipped with two piezoelectric patch transducers and subjected to a rain on the roof excitation modelled as an 4×4 array of uncorrelated point forces (a), electrical model of the piezoelectric patch connected to the current-flowing shunt (b), simplification of the current-flowing shunt circuit (c).

Parameter	Plate	Piezoelectric patches
dimensions	$l_{xp} \times l_{yp} = 414 \times 314\ mm$	$l_{xpe} \times l_{ype} = 85 \times 85\ mm$
thickness	$h_p = 1\ mm$	$h_{pe} = 1\ mm$
density	$\rho_p = 2700\ kg/m^3$	$\rho_{pe} = 7600\ kg/m^3$
Young's modulus	$E_p = 7 \times 10^{10}\ N/m^2$	$E_{pe} = 2.7 \times 10^{10}\ N/m^2$
Poisson ratio	$\upsilon_p = 0.33$	$\upsilon_{pe} = 0.275$
modal damping ratio	$\zeta_p = 0.02$	$\zeta_{pe} = 0.02$
strain/charge constants		$d_{31}^0 = 150 \times 10^{-12}\ m/V$
		$d_{32}^0 = 150 \times 10^{-12}\ m/V$
		$d_{36}^0 = 0$
permittivity for constant stress		$\varepsilon_{pe}^T = 84 \times 10^{-9}\ F/m$
capacitance		$C_{pe} = 2.113 \times 10^{-7}\ F$
centre position patch j=1		$x_{pe1} = 166\ mm$, $y_{pe1} = 266\ mm$
centre position patch j=2		$x_{pe2} = 333\ mm$, $y_{pe2} = 133\ mm$

Table 1: Dimensions and physical properties of the panel and piezoelectric patches

2.2 Mathematical model

The mathematical formulation for the coupled flexural response of the panel and piezoelectric patches is based on Refs. [1,2] and considers the classical theory of out of plane flexural vibrations in plates that refers to Kirchhoff hypothesis [3]. In-plane vibrations are not taken into account, which is a reasonable assumption within the considered frequency range (20 Hz – 1 kHz). The response of the system is derived from the generalised form of Hamilton's principle for electromechanical systems [4-7]. Two matrix equations are derived for the flexural response of the panel, which is expressed in terms of R modal coordinates for the flexural modes of the plain panel [8], and for the electric response of the shunts [1]:

$$\mathbf{M}_t\ddot{\mathbf{d}}(t) + \mathbf{C}_p\dot{\mathbf{d}}(t) + \mathbf{K}_t\mathbf{d}(t) + \boldsymbol{\theta}_{pe}\mathbf{v}_s(t) = \boldsymbol{\Phi}_p\mathbf{f}_p(t)\,, \tag{1}$$

$$-\boldsymbol{\theta}_{pe}^T\mathbf{d}(t) + \mathbf{C}_{pe}\mathbf{v}_s(t) = \mathbf{q}_s(t)\,. \tag{2}$$

Here $\mathbf{d} = \lfloor d_1 \quad \cdots \quad d_R \rfloor^T$ is the vector with the modal coordinates, $\mathbf{f}_p = \lfloor f_{p1} \quad \cdots \quad f_{p16} \rfloor^T$ is the vector with the amplitudes of the 4×4 array of forces acting on the plate. As shown in Refs. [1,2], $\mathbf{M}_t = \mathbf{M}_p + \mathbf{M}_{pe}$ and $\mathbf{K}_t = \mathbf{K}_p + \mathbf{K}_{pe}$ are the $R \times R$ modal mass and stiffness matrices, which are given by the sum of a diagonal matrix for the plate effect and a fully populated matrix for the piezoelectric patches effects. Also, $\mathbf{C}_p$ is the $R \times R$ modal damping matrix of the plate and $\boldsymbol{\Phi}_p$ is a $R \times 16$ matrix with the modal amplitudes at the excitation points. The vectors $\mathbf{q}_s$ and $\mathbf{v}_s$ contain the charges and voltages of the shunts. Also, $\mathbf{C}_{pe}$ is the diagonal matrix with capacitances of the piezoelectric patches $C_{pej} = \varepsilon_{pe}^S A_{pe}/h_{pe}$. Finally, $\boldsymbol{\theta}_{pe}$ is the $R \times 2$ piezoelectric coupling matrix. The details of all these matrices, as well as the formulation for the system response in terms of the total time averaged flexural kinetic energy of the plate and total time averaged power absorbed by the shunt circuits can be found in [1].

2.3 The current flowing multi-resonant shunt

Figure 1(b) presents the current flowing shunt circuit introduced by Behrens et al. [9] as a mean to simplify the implementation of multi-resonant shunt circuits. In contrast to other multi-resonant shunts, the current-flowing shunt requires one RLC branch per one resonance frequency of the target flexural mode of the hosting structure. Assuming the capacitances $C_{f1j}, \ldots, C_{fNj}$ are fixed a priory, the filtering parts of the branches $L_{fij} - C_{fij}$ produce the current-flowing effects by approximating short circuits at frequencies of the target flexural modes: $\omega_{r1}, \omega_{r2}, \cdots, \omega_{rN}$, while approximating open circuits at frequencies of the neighbouring branches. This is achievable by setting the inductance values $L_{f1j}, \ldots, L_{fNj}$ to $L_{f1j} = \frac{1}{\omega_{r1}^2 C_{f1j}}$, $L_{f2j} = \frac{1}{\omega_{r1}^2 C_{f2j}}, \ldots, L_{fNj} = \frac{1}{\omega_{rN}^2 C_{fNj}}$. Then, for the given capacitance C_{pej} of the piezoelectric patch, the remaining inductances $L_{sij}, \ldots, L_{sNj}$ from the shunting part of the circuit can be tuned to obtain the vibration absorption effects at the frequencies of the target flexural modes i.e. $L_{s1j} = \frac{1}{\omega_{r1}^2 C_{pej}}$, $L_{s2j} = \frac{1}{\omega_{r2}^2 C_{pej}}, \ldots, L_{sNj} = \frac{1}{\omega_{rN}^2 C_{pej}}$. Also the resistances $R_{s1j} - R_{sNj}$ can be optimised in such a way as to maximize the vibration absorption effects. Moreover, as depicted in Figure 1(c), the two inductors from each branch: L_{fij}, L_{sij} can be combined together to form the simplified circuit, whose branch inductances are given by the following formula:

$$L_{bij} = L_{fij} + L_{sij} = \frac{1}{\omega_{ri}^2 C_{fij}} + \frac{1}{\omega_{ri}^2 C_{pej}} = \frac{C_{fij} + C_{pej}}{\omega_{ri}^2 C_{fij} C_{pej}} \tag{3}$$

This approach not only reduces the number of required passive components, but also delivers an approximate formula for the tuning of the resultant branch inductances.

In this study, each branch of the simplified current flowing shunt (i.e. L_{bij} and R_{sij}) is tuned in such a way as to maximise the vibration energy absorption from a specific resonant flexural mode of the plate structure.

2.4 Single resonance RL vs single resonance current flowing shunt

In this section the vibration absorption effect generated by a single piezoelectric patch connected to a classical RL shunt is contrasted with the effects produced by a single branch current flowing shunt. Here, the assumption is made that piezoelectric patch *N*.1 is connected to a classical RL shunt, whereas piezoelectric patch *N*.2 is left in open loop. Figure 2 shows the time averaged total flexural kinetic energy of the plate K, and total time averaged total power absorbed by the shunt P when the shunt inductance L_{s11} is iteratively increased in the range $2-300$ H and the shunt resistance R_{s11} is varied from $100\ \Omega$ to $2\ k\Omega$. Assuming constant piezoelectric patch capacitance $C_{pe1}=2.113\times10^{-7}$ F an inevitable increase of the inductance causes a gradual decrease of the resonance frequency of the circuit in accordance to the formula.

$$\omega_{s11}=\frac{1}{\sqrt{L_{s11}C_{pe1}}}. \tag{3}$$

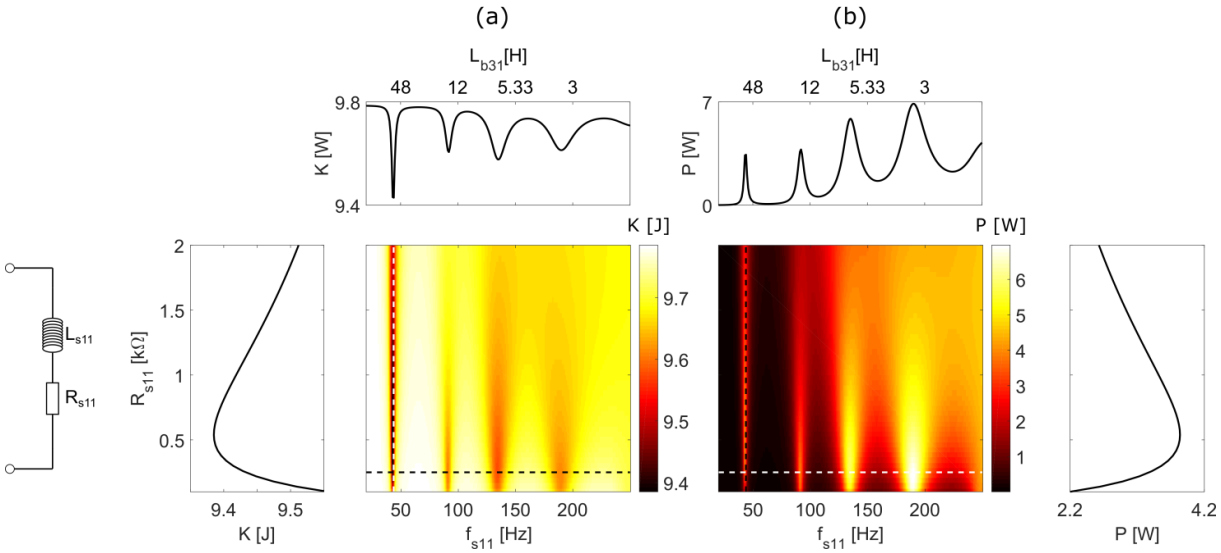


Figure 2: Time averaged total flexural kinetic energy of the smart plate structure (a) and time averaged electrical power absorbed (b) by the RL shunt circuit connected to the piezoelectric patch *N*.1.

Left-hand side plots (a) of figure 2 show that, when the shunt implements low resistance, the time averaged total flexural kinetic energy of the plate is characterised by multiple subsequent troughs aligned in parallel to the inductance axis. These troughs indicate the local minima of the time averaged total flexural kinetic energy and occur when the resonance frequency of the shunt f_{s11} is equal to one of the four resonance frequencies of the low order flexural natural modes of the plate, that is $f_{r1}=44$ Hz, $f_{r2}=92$ Hz, $f_{r3}=135$ Hz $f_{r4}=190$ Hz. Right-hand side plots (b) of figure 2 show the corresponding responses of the shunt in terms of the time averaged total electric power absorbed, which in this case, show a sequence of crests aligned in parallel to the inductance axis. One can note that the troughs depicted in plots (a) coincide with crests depicted in plot (b), which indicate that the minima of the kinetic energy and maxima of the electric power absorbed occur for the same shunt inductance and resistance (L_{s11}, R_{s11}). This means that when shunt minimises the kinetic energy of the vibrating plate, the absorption of the electric power is in fact maximised. Indeed the maxima of the crests for the absorbed electric power, and thus the minima of the troughs for the plate flexural kinetic energy occur when the
resonance frequency of the shunt f_{s11} is close to one of the four aforementioned resonance frequencies of the flexural natural modes of the plate. Such result suggests that the RL components of the shunt can be tuned to locally minimise the response of a flexural resonant mode of the plate by locally maximising the total power absorbed in correspondence to this mode.

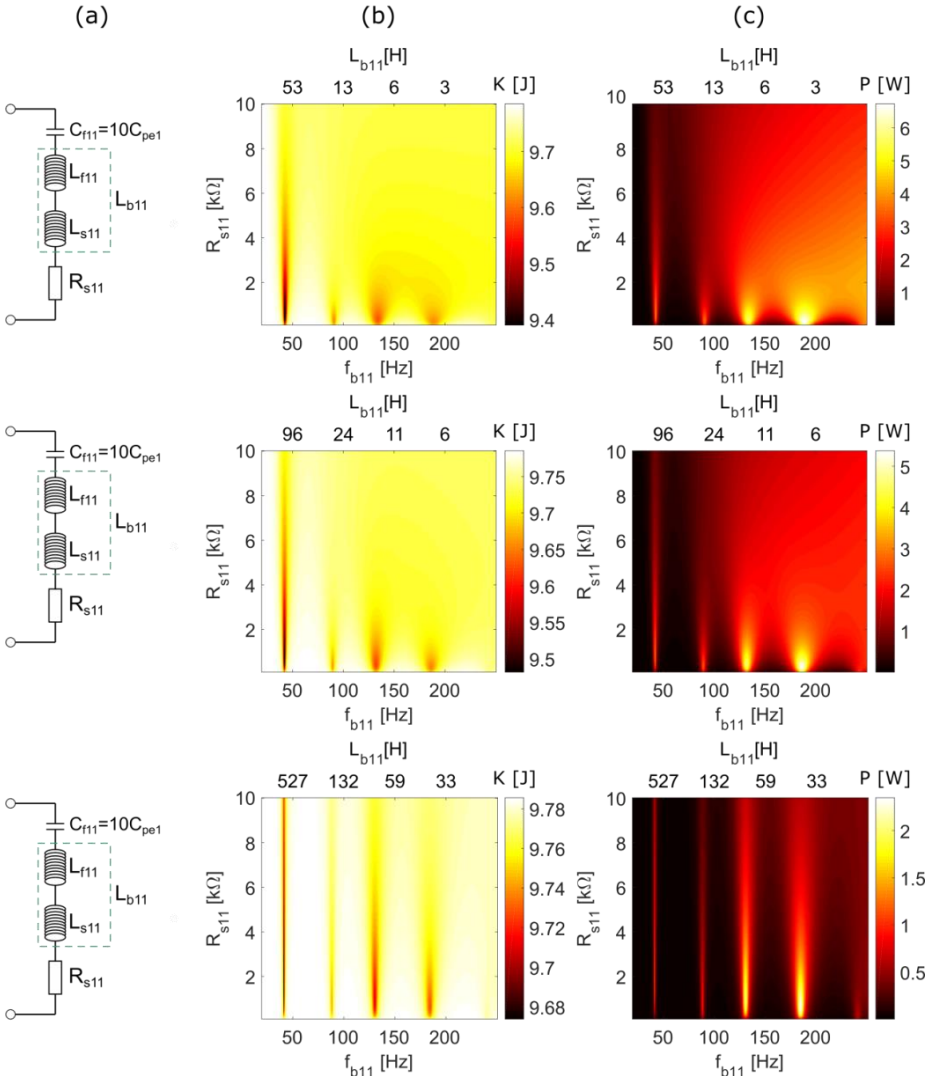


Figure 3: (a) RLC Shunt circuit configurations having $C_{f11} = 10C_{pe1}$ (first row), $C_{f11} = C_{pe1}$ (second row), $C_{f11} = 0.1C_{pe1}$ (third row); Time averaged total flexural kinetic energy of the smart plate structure (b) and time averaged electrical power absorbed (c) by the RLC shunt circuits connected to the piezoelectric patch *N*.1.

The effects produced by the single branch current flowing shunt are now investigated. As described in the previous section, a single branch of the current flowing shunt can be assembled by adding in series to a classical RL shunt an inductor and a capacitor (L_{f11}, C_{f11}), which together form a bandpass filter. The filter itself produces the current flowing effect, which limits the bandwidth of the current signal being passed to the shunting part of the circuit (R_{s11}, L_{s11}) to a narrow band with a centre frequency at $\omega_{f1} = \frac{1}{\sqrt{L_{f11}C_{f11}}}$. The shunting inductance L_{s11} is then set up to trigger the vibration absorption effect at the centre frequency of the filtered current signal, such that $\omega_{s11} = \frac{1}{\sqrt{L_{s11}C_{pe}}} = \omega_{f1}$. Since, both frequencies are adjusted to be the same, combining two inductances $L_{b11} = L_{s11} + L_{f11}$, leads to electrical resonance frequency given by

$$\omega_{b1} = \omega_{f1} = \omega_{s11} = \sqrt{\frac{C_{pe1}+C_{f11}}{L_{b11}C_{pe11}}}. \tag{3}$$

The subsequent plots in figure 3 show the time averaged total flexural kinetic energy of the plate (a), and the time averaged total electric power absorbed by the shunt (b), with respect to the combined inductance

of the shunt L_{b11} (upper horizontal axes) and resistance R_{s1} when the capacitance of the shunt C_{f11} is set to three different values equal to $C_{f11} = 10C_{pe1}$, $C_{f11} = C_{pe1}$, $C_{f11} = 0.1C_{pe1}$. Additional reference is made to the electrical resonance frequency of the shunt f_{b1} presented as the bottom horizontal axes.

The sequential plots in Figure 3 show that, when the combined inductance L_{b11} is varied within designated ranges, the electrical resonance frequency ω_{b1} is swept between 20 and 250 Hz. Also in this case, the graphs indicate the existence of the kinetic energy troughs and corresponding electrical power crests associated with four resonance frequencies of the plate. As the value of the shunts filter capacitance C_{f11} is gradually decreased with respect to the capacitance of the piezoelectric patch C_{f11}, the troughs and crests become progressively more narrow. Thus, to obtain a narrow band resonance effect for the vibration absorption from low order natural modes, a relatively small capacitances $C_{f11}$with respect to the internal capacitance of the piezoelectric patch C_{pe} is required. On the other hand, a low filtering capacitances C_{f11} enforces the application of a high aggregate inductance $L_{b11} = L_{s11} + L_{f11}$, which are necessary to obtain the assumed filtered vibration absorption effect. This leads to common practical implementation problems, where large inductance components have to be synthetized from active circuits comprising operational amplifiers [10].

2.5 Sequential tuning of the multi-resonant current flowing shunt

In this section a vibration control method based on sequential tuning of the multi-resonant RLC branches connected to the two piezoelectric patches is proposed. The procedure starts with piezoelectric patch *N*.1 connected to a single branch of the current flowing shunt, whereas the piezoelectric patch *N*.2 remains in open loop. Throughout this example, the number of branches connected to piezoelectric patch *N*.1 is iteratively increased up to four. The simulation results of this operation are summarized in Figure 4, which is divided into four rows each with three plots that show (a) the shunt circuit configuration used at this step of the procedure, (b) the time averaged total kinetic energy of the plate and (c) the time averaged total power absorbed by the shunt. The first row of Figure 4 depicts the case described before, when one of the piezoelectric patches is connected to a single branch of the current flowing shunt. Again, the two surface plots indicate sequences of parallel troughs and crests that occur for the shunt inductance L_{b11} such that the branch resonates in correspondence to one of the four resonances of the flexural natural modes of the plate. When the common inductance L_{b11} and resistance R_{s11} of this branch are set to the values indicated by black dots on the surface plots: L_{opt1}, R_{opt1}, the power absorbed in correspondence to the fourth crest would be maximised and thus the flexural kinetic energy associated with fourth trough minimised. Next, when the second RLC branch is added in parallel to the shunt circuit as depicted in plot (a) in the second row of Figure 4, the corresponding surface plots (b) and (c) are characterised by only three troughs and three crests, such that the second branch can resonate in correspondence to one of the three resonance frequencies of the plate. Note, that there is no fourth trough and fourth crest since the first branch of the shunt is already tuned. If now the components of the second branch are fixed such as $L_{b21} = L_{opt2}$, $R_{s21} = R_{opt2}$, the power absorbed in correspondence to the third crest would be maximised and the flexural kinetic energy with respect to the third through minimised. At this point the third branch can be added to the shunt circuit as shown in plot (a) of the third row. In this case, the corresponding plots (b) and (c) show only two troughs and two crests as the shunt is already tuned according to the third and fourth ones. The inductance L_{b31} and resistance R_{s31} can be now set to the values that would maximise the power and minimise the kinetic energy related to the second trough and second crest. In the last row of Figure 4, plots (b) and (c) show only one remaining trough and crest, thus the branch components: L_{b41}, R_{s41} can be set according to the optimal values indicated by the black dots (L_{opt4}, R_{opt4}) to maximise the absorbed electric power and minimise the flexural kinetic energy of the last crest and trough. This procedure can also be illustrated in terms of the Power Spectral Density functions of the plate flexural kinetic energy and electric power absorbed by the shunt circuit. Figure 5 shows how the aforementioned energy functions are incrementally modified by successively adding optimally tuned RLC branches.

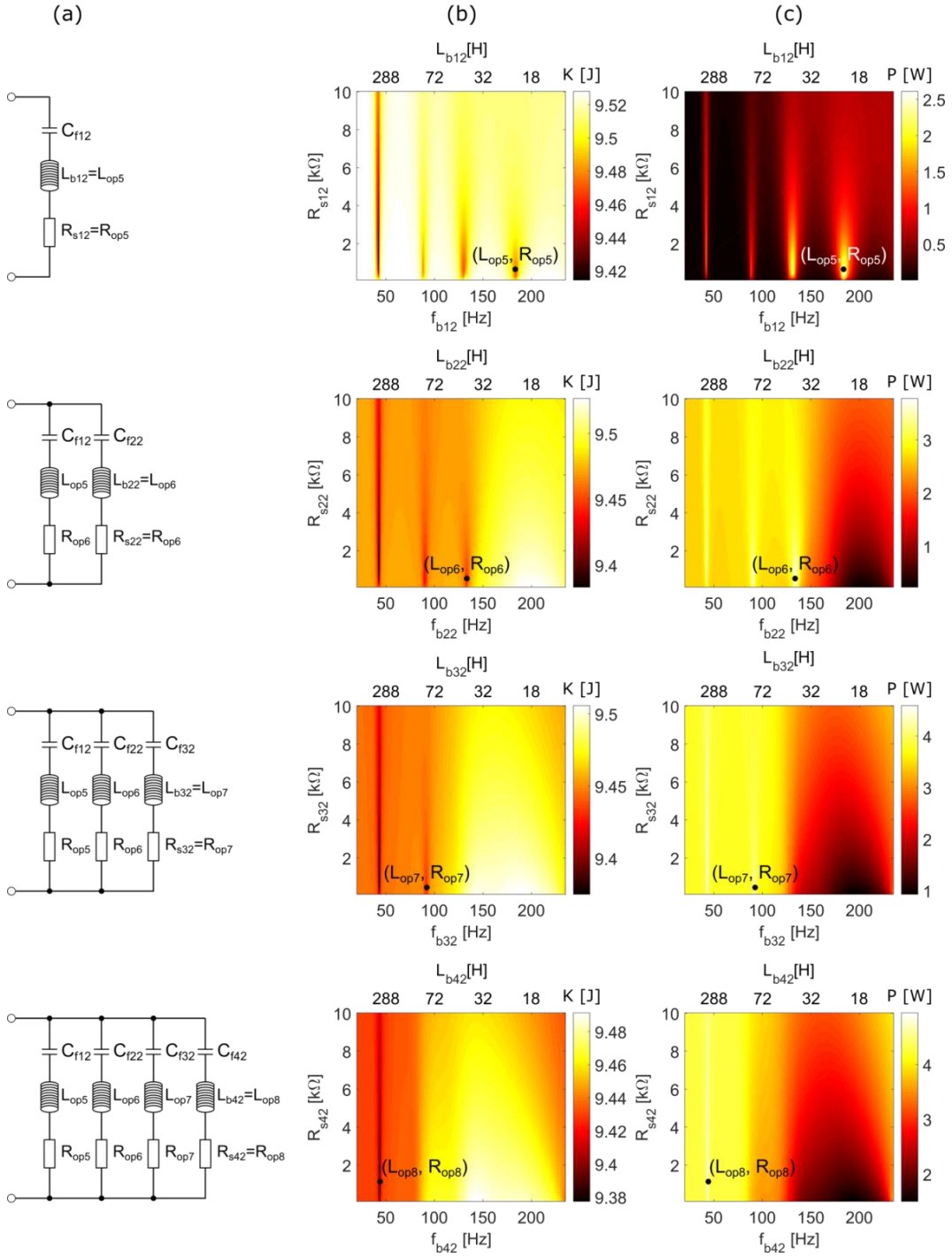


Figure 4: (a) Configuration of the multi-resonant shunt circuit; (b) Time averaged total flexural kinetic energy of the smart plate structure, (c) time averaged electrical power absorbed and (c) by the RLC multi-resonant shunt circuits connected to the piezoelectric patch N.1, while the piezoelectric patch N.1 implements a four branches multi-resonant shunt.

The simulation results depicted in Figure 5 are divided into 4 rows, where plots (b) in each row capture power spectral density functions associated to the shunt configuration depicted in plot (a). Starting from the first row, when the piezoelectric patch *N.*1 is connected to the optimally tuned ($L_{b11} = L_{opt1}, R_{s11} = R_{opt1}$) single branch RLC shunt, the PSD of the flexural kinetic energy is minimised in correspondence to the fifth resonance frequency of the plate, whereas the PSD of the absorbed electric power (dotted black line) is characterised by a dominant peak at the fifth resonance frequency of the plate. Note, that plots (b) and (c)

in the first row of Figure 4 are characterised respectively by four troughs and four crest, while the PSD function from Figure 5 comprises five resonance peaks. Indeed, plots in Figure 4 do not show through and crest in correspondence to the fourth resonance frequency of the plate. This is due to the fact that the piezoelectric patch *N*.1 is positioned in the vicinity of a nodal line of the fourth flexural mode of the smart plate so that the patch is weakly coupled with this mode. As a result, the shunt cannot extract vibration energy and thus minimise the flexural response of this resonant mode. When the second branch is connected and tuned in correspondence to the third crest and trough i.e. $L_{b21} = L_{opt2}$, $R_{s21} = R_{opt2}$, the PSD of the flexural kinetic energy would be effectively minimised in correspondence of the third and fifth resonance frequencies of the plate, whereas the PSD of the absorbed electric power (dotted black line) would be characterised by two dominant peaks at these two resonance frequencies. Application of the third branch optimised with respect to the second trough and crest, such as $L_{b31} = L_{opt3}$ and $R_{s31} = R_{opt3}$ results in the PSD of the flexural kinetic energy (solid black line and green line) being brought down in correspondence of the second, third and fifth resonance frequencies of the plate. Finally, addition of the fourth branch tuned to the first trough and crest ($L_{b41} = L_{opt4}$, $R_{s41} = R_{opt4}$) completes the tuning sequence for the piezoelectric patch *N*.1. In this case the PSD of the flexural kinetic energy (black solid line and green solid line) is brought down in correspondence of the first, second, third and fifth resonance frequencies of the plate, whereas the PSD of the absorbed electric power (dotted black line) is characterised by four peaks at the first, second, third and fifth resonance frequencies of the plate.

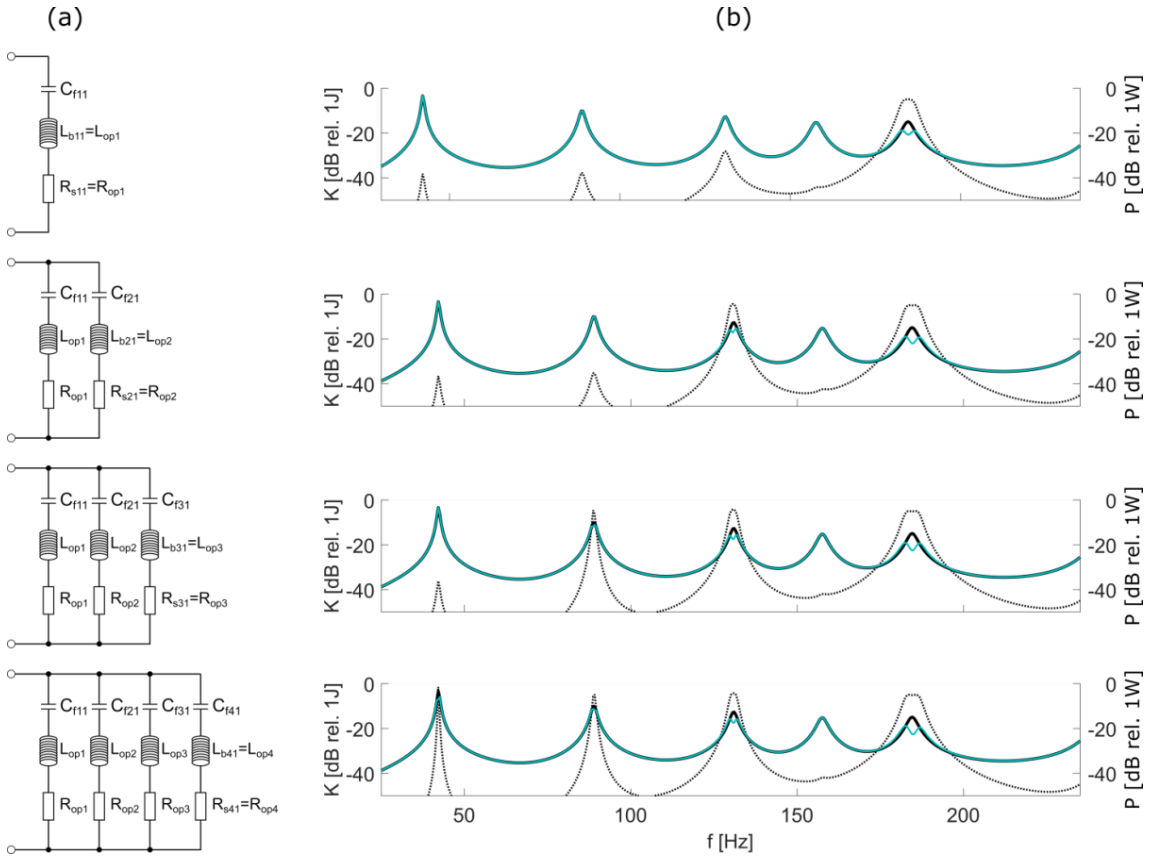


Figure 5: (a) Configuration of the multi-resonant shunt circuit; (b) PSD of the plate flexural kinetic energy (solid black line no shunt; solid green line with shunt) and electric power absorbed by the shunt (dotted black line) by the RLC multi-resonant shunt circuits connected to the piezoelectric patch N.1.

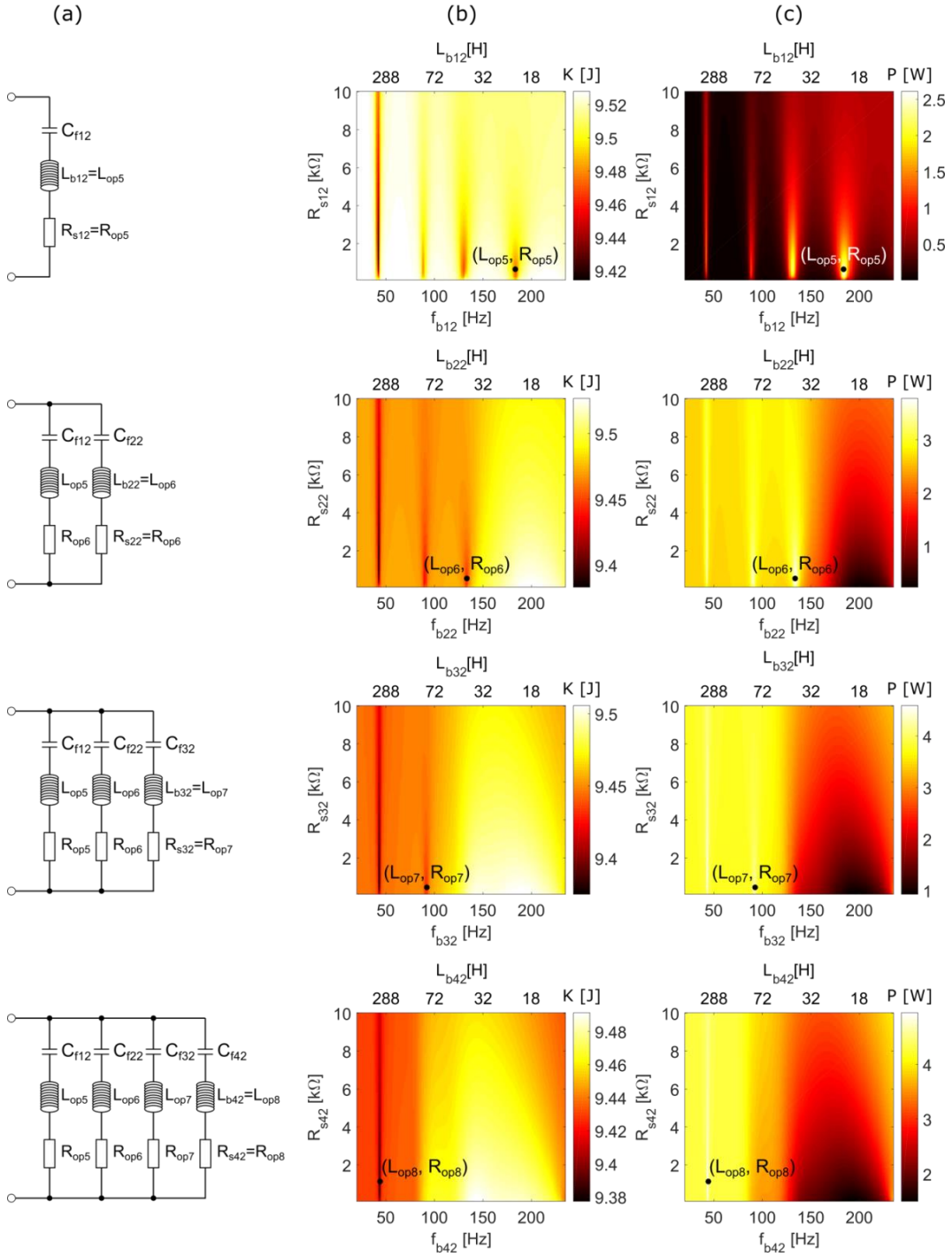


Figure 6: (a) Configuration of the multi-resonant shunt circuit; (b) Time averaged total flexural kinetic energy of the smart plate structure, (c) time averaged electrical power absorbed and (c) by the RLC multi-resonant shunt circuits connected to the piezoelectric patch N.2, while the piezoelectric patch N.2 implements a four branches multi-resonant shunt.

The same procedure can now be implemented for the piezoelectric patch *N.*2 assuming that the piezoelectric patch *N.*1 is already connected to the four branches multi-resonant shunt set to control the flexural response of the first, second, third and fifth resonances of the plate. Figure 6 shows the analogous sequence of plots as Figure 4, which is once more organised in four rows, each with three plots that show (a) the shunt circuit configuration, (b) the plate time averaged flexural kinetic energy, (c) the shunt time-averaged absorbed electric power. These plots present a very similar story to that depicted in Figure 4 for the piezoelectric patch *N.*1. Therefore, the same procedure is carried on to find the optimal values of the

inductance and resistance elements in the four branches connected to the piezoelectric patch *N.*2, such that: ($L_{b12} = L_{opt5}$, $R_{s12} = R_{opt5}$), ($L_{b22} = L_{opt6}$, $R_{s22} = R_{opt6}$), ($L_{b32} = L_{opt7}$, $R_{s32} = R_{opt7}$) and ($L_{b42} = L_{opt8}$, $R_{s42} = R_{opt8}$). Figure 7 shows how the PSD functions of the plate flexural kinetic energy and electric power absorbed by the shunt vary when the multiresonant shunt connected to the second patch is incrementally tuned. As one would expect a similar result to that presented in Figure 5 is obtained with an incremental effect of power absorption and decremental effect of plate flexural energy in correspondence to the 5th, 3rd, 2nd, and 1st resonance frequencies.

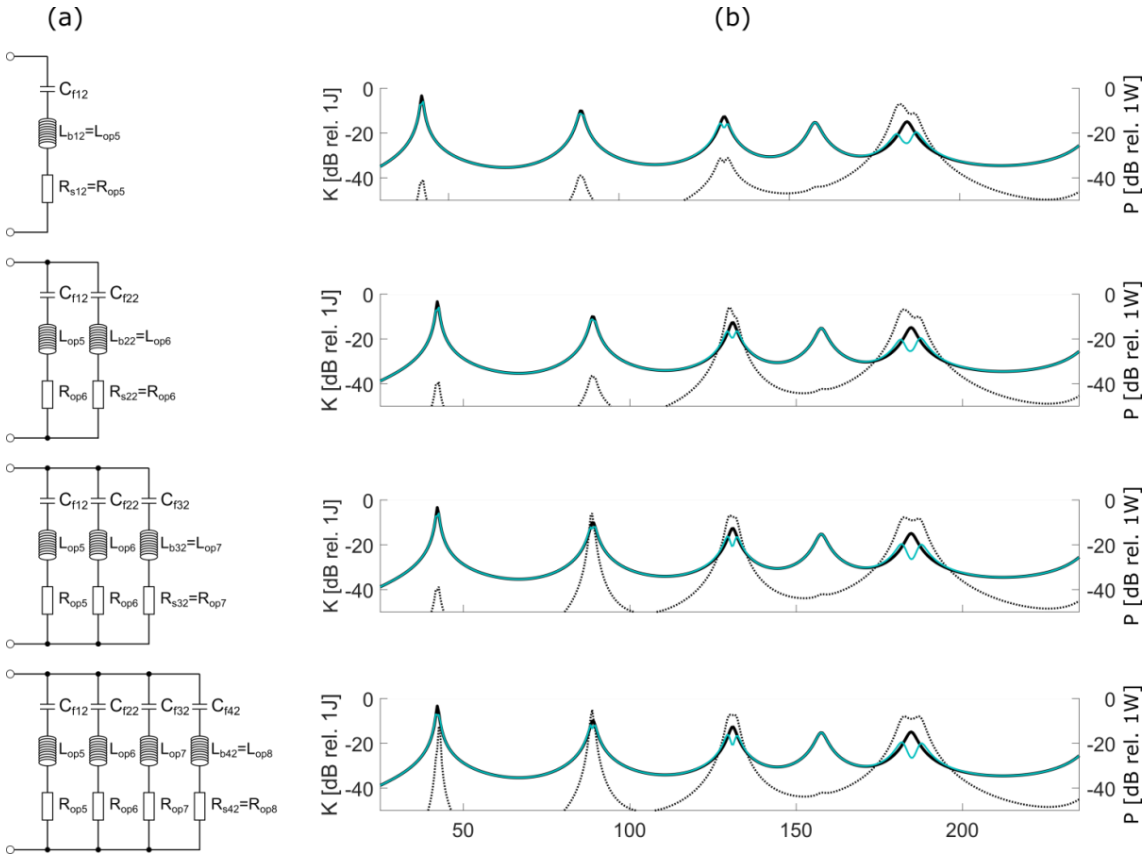


Figure 7: (a) Configuration of the multi-resonant shunt circuit; (b) PSD of the plate flexural kinetic energy (solid black line no shunt; solid green line with shunt) and electric power absorbed by the shunt (dotted black line) by the RLC multi-resonant shunt circuits connected to the piezoelectric patch N.2 (d).

The results presented in this section lead to the concept of a practical tuning of RL components in multi-resonant shunts. For instance, a gradient base algorithm, that iteratively searches for the maxima of the filtered power absorption in the close vicinity of resonance frequencies of the low order natural modes of the plate could be effectively used to implement locally on the shunts the proposed tuning approach. This process could be repeated sequentially in the shunts of all piezos to continuously track changes in the dynamic response of the hosting structure due for example to temperature changes or tensioning effects generated by operation conditions.

3 Experimental validation

This section presents experimental validation tests on the feasibility of the tuning approach proposed in the previous sections for multi-resonant RLC shunts connected to piezoelectric patches to form electromechanical vibration absorbers, that can be used to control the flexural vibrations of thin structures. A test rig is used, which is composed by a clamped aluminium plate equipped with five piezoelectric hexagonal patches connected to identical shunts, synthesised digitally in a multi-channel dSPACE platform.

The tuning approach presented in the previous section has been applied to find optimal RL branch parameters such that the shunted piezoelectric patches form multi-resonant vibration absorbers that control three flexural modes of the plate in the low frequency regime 40-150 Hz. Two set of measurements were carried out in order to evaluate the proposed method. In the first, the total kinetic energy of the vibrating plate was estimated with reference to the inductance and resistance values of the branches of the shunts. In the second, voltage drops across the piezoelectric patches and current flows through the shunt circuits were measured with respect to the inductance and the resistance values of the branches. With the help of these measurements, the evolution of both total flexural kinetic energy and absorbed electrical power with respect to the inductance and resistance implemented in the branches of the shunts was visualized on surface plots as in the previous section. In this way the flexural kinetic energy minimisation and shunt electric power maximisation was demonstrated experimentally.

3.1 Description of the experimental setup

Figure 8 shows the experimental setup used in this study, which is composed by a thin rectangular panel clamped on Perspex box. The panel is made of aluminum and has thickness of $1\ mm$ and dimensions of $414 \times 314\ mm$. Five hexagonal piezoelectric patches are bonded on the bottom side of the panel as depicted Figure 8 (b). The dimensions, positions and physical properties of the panel and piezoelectric patches are summarised in Table 2 panel is excited at position $x_p = 85\ mm$, $y_p = 110\ mm$ by a point random disturbance generated by the shaker located in the Perspex box. The flexural response of the panel was measured with a scanning laser vibrometer, while the electrical response of the shunt circuits was acquired with the ABACUS Data Physics acquisition system.

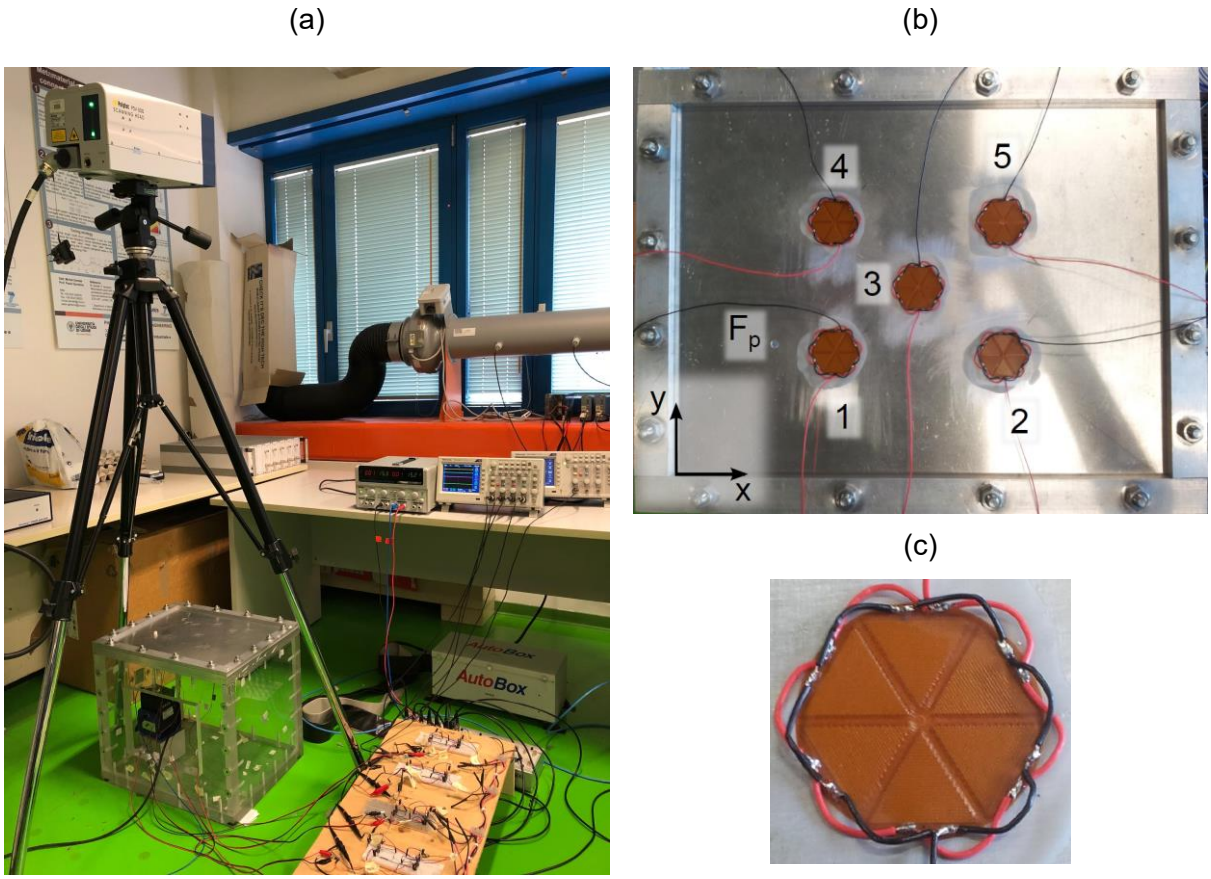


Figure 8 (a) Experimental setup. (b) Perspex box showing the five patches. (c) Hexagonal piezoelectric patch.

Parameter	Plate	Piezoelectric patches
Dimensions	$l_{xp} \times l_{yp} = 414 \times 314\ mm$	$l_{xpe} \times l_{ype} = 80 \times 80\ mm$
Thickness	$h_p = 1\ mm$	$h_{pe} = 1\ mm$
Density	$\rho_p = 2700\ kg/m^3$	$\rho_{pe} = 7600\ kg/m^3$
Young's modulus	$Y_p = 7 \times 10^{10}\ N/m^2$	$Y_{pe} = 5 \times 10^{10}\ N/m^2$
Poisson ratio	$\upsilon_p = 0.33$	$\nu_{pe} = 0.275$
Modal damping ratio	$\zeta_p = 0.02$	$\zeta_{pe} = 0.02$
Strain / charge constants		$d_{31}^0 = -190 \times 10^{-12}\ m/V$
		$d_{32}^0 = -190 \times 10^{-12}\ m/V$
Capacitances		$C_{pe1-5} = 5.3 \times 10^{-8}\ F$
Centre position patch j=3		$x_{pe3} = l_{xp}/2\ ,\ y_{pe3} = l_{yp}/2$
Centre position patches: j=1,2,4,5		$x_{pej} = \frac{l_{xp}}{2} \pm 60\ mm,\ y_{pej} = \frac{l_{xp}}{2} \pm 60\ mm$
Excitation force position	$x_f = y_f = 85.11mm$	

Table 2. Dimensions and physical properties of the panel and piezoelectric patches.

To facilitate the implementation of the multi-resonant shunts and thus to overcome a possible issue due to excessive values of RLC branch components, the multi-resonant shunts were synthesised digitally in a multi-channel dSPACE digital platform. To obtain the designed analogue multi-resonant shunt effect, the dSPACE platform was connected to the piezoelectric patches via ad hoc interface circuits specifically designed to produce the multi-resonant impedance load digitally programed in the platform. Considering a single piezoelectric patch, the circuitry used to implement the desired shunt impedance load is illustrated in Figure 9a. In this figure, a piezoelectric transducer is connected to the dSPACE platform through an operational amplifier characterized by high input impedance. This amplifier is used to deliver a voltage signal from the piezo to the platform, without affecting the current flow. Also, the output signal from dSPACE platform is connected to an operational amplifier such that there is no current flow. In this way the ratio between the voltage and current at the patch terminals is indeed the desired impedance load.

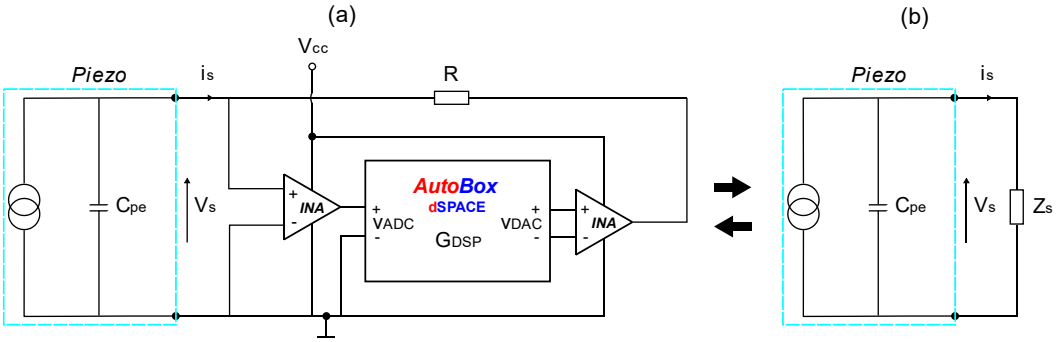


Figure 9 Electrical implementation of the shunts in dSPACE.



Figure 10 (a) Multi-resonant, current flowing shunt circuit and its simplification (b).

The synthesis of the multi-resonating shunt circuits is carried out digitally in the dSPACE system according to the following formulation for the electric response of the interface circuit.

Considering the electrical scheme depicted in Figure 9, the following relations can be written:

$$v_{ADC} = v_s \,. \tag{6}$$

$$v_{DAC} = G_{DSP} v_{ADC} \,, \tag{7}$$

$$v_s - v_{DAC} = R i_s \,. \tag{8}$$

In Eqs. (6)-(8), v_{ADC} is the potential difference at the terminals of the piezoelectric patch, v_{DAC} is the voltage at the output of the control system, G_{DSP} is the transfer function to be implemented in the dSPACE platform, R is the reference resistor and i_s is the current flowing through the piezoelectric patch terminal.

Also, according to the electrical scheme in Figure 10(b)

$$v_s = Z_s i_s \,, \tag{9}$$

where Z_s is the desired shunt impedance. Combining Eqs. (6)-(9)gives the following expressions for the impedance and the digital platform transfer function

$$Z_s = \frac{v_s}{i_s} = \frac{R}{1 - G_{DSP}} \,, \tag{10}$$

$$G_{DSP} = \frac{v_{DAC}}{v_{ADC}} = 1 - Z_s R \tag{11}$$

The complex admittance of the simplified multi-resonant shunt depicted in Figure 10(b) is given by the following summation of second order terms

$$Y_s = \sum_{i=1}^{N} \frac{1}{L_{bi}} \frac{j\omega}{-\omega^2 + j\omega\left(\frac{R_{bi}}{L_{bi}}\right) + \frac{1}{C_{fi} L_{bi}}} \,. \tag{12}$$

Substituting Eq. (12) into Eq. (11) gives the transfer function, that should be implemented in the dSPACE platform to generate the desired multi-resonance impedance load:

$$G_{DSP} = \frac{v_{DAC}}{v_{ADC}} = 1 - Y_s^{-1} R \,. \tag{42}$$

Indeed, implementing this transfer function in the digital platform connected to the piezoelectric patch via the interface circuit shown in Figure 9 produces indirectly the desired multi-resonant shunt load presented in Figure 10 on the piezoelectric patch.

3.2 Experimental results

This section discusses the effects produced when the incremental method of multi-resonant shunt tuning presented in the above simulation study is applied in practice. First of all, it is important to note, that in this practical investigation all the patches are tuned jointly, i.e. at every step of the incremental procedure all transducers are connected to identical RLC shunts. Although this approach differs from the one described in Section 2, which considers individual tuning of each piezoelectric patch, it constitutes a reasonable way to simplify the optimization process and shorten the otherwise lengthy measurements of the kinetic energy and electrical power cost functions. Second, the branch capacitances were chosen to be $C_{fi} = 0.1 C_{pe}$ and the investigated frequency range was set between 40 and 150 Hz. For the purpose of this study, the inductances of the shunts were varied using the formula $L_{bi} = \frac{C_{fi} + C_{pe}}{\omega_b^2 C_{fi} C_{pe}}$ to provide incremental changers of the branches resonance frequencies of 5 Hz starting from 40 Hz up to 150 Hz. Also, the shunt resistances were progressively raised in the range of $3.5\ \text{k}\Omega - 8\ \text{k}\Omega$ with increments of $500\ \Omega$ For each combination of branch parameters i.e. (f_{bi}, R_{si}), and for the given three branches, a set of measurements was taken including: velocity-excitation force transfer functions measurements at a 3×3 grid points located on the

surface of the plate, performed with the laser scanning vibrometer and current-excitation force and voltage-excitation force transfer functions measurements of at the terminals of the five piezoelectric patches. The total flexural kinetic energy per unit force and total electrical power absorbed by five shunts per unit force were obtained from the measurements for each combination of branch parameters (f_{bi}, R_{si}). Based on these results, two-dimensional maps with the evolution of the flexural kinetic energy and electric power absorption with reference to the shunt inductance and resistance parameters were created to experimentally validate the method proposed in Section 2. The experimental results for the incremental effects produced by the three branches in the five shunts are summarized in Figure 11 and Figure 12. Figure 11 is structured in the following way: sketches (a) show shunt circuits configurations, plots (b) show the smart plate kinetic energy per unit force, plots (c) show the electric power absorbed per unit force by five shunts. In turn Figure 12 shows the shunt circuits configurations in sketches (a) and the spectra of the smart plate kinetic energy per unit force (solid black line – shunts in open-loop, solid green line – with optimal shunts) and electric power absorbed per unit force by five shunts (dotted black line) in plots (b).

Considering the first row of Figure 11, when all five piezoelectric patches are connected to the first branches of the shunts (a), plots (b) and (c) are characterized respectively by a sequence of four local troughs and crests. In line with the simulation study findings presented in Section 2, the minima of the kinetic energy troughs and the maxima of the electric power crests occur for very similar values of the first branch components (L_{b1}, R_{s1}) of the shunts. Thus setting $L_{b1} = L_{opt1}$ and $R_{s1} = R_{opt1}$, where L_{opt1}, R_{opt1} are the optimal shunt parameters for the minimum of the third through and the maximum of the third crest of the kinetic energy and electric power measured cost functions respectively. Plot (b) of Figure 12 shows that the spectrum of the kinetic energy is lowered (green line) at the third resonance frequency of the plate, while at the same frequency the spectrum of the absorbed electric power is characterized by a rather wide and high peak. When the second RLC branch is added to the shunts, plot (b) of Figure 11 show three troughs of the measured kinetic energy in correspondence of the first, second and forth resonance frequencies of the plate, which are generated by the inductance L_{b2} and resistance R_{s2}. There is no third trough, since the first branch of the shunts is indeed tuned at the third resonance and thus the kinetic energy of the plate in correspondence to the third resonance frequency is already minimised. In contrast to plot (b), plot (c) of Figure 11 highlights four maxima for the measured power that can be obtain for the inductance value L_{b2}, which are due to the first, second, third and fourth resonances of the plate. The presence of the third crest at around 120 Hz is indicting that the tuning of the first branches could be improved, since the adopted values $L_{b1} = L_{opt1}$, $R_{s1} = R_{opt1}$ are now slightly offset. Continuing the procedure by setting $L_{b2} = L_{opt2}$ and $R_{s2} = R_{opt2}$, where L_{opt2} and R_{opt2} are the optimal shunt parameters for the minimum of the second through and the maximum of the second crest of the kinetic energy and electric power measured cost functions, the shunts resonate in correspondence to the second, and third resonances of the smart plate. This is particularly visible in plot (b) of Figure 12, where the flexural kinetic energy is effectively minimised and the power absorption maximised in correspondence of the second resonance peak of the plate, whereas the branch parameters associated with the third mode of the plate: $L_{b1} = L_{opt1}$, $R_{s1} = R_{opt1}$ are indeed not optimal due to the small shift of the vibration absorption effect towards higher frequencies.

When the third RLC branch is implemented into the shunts, plots (b) and (c) of Figure 11 show only two minima and two maxima respectively in correspondence to the first and forth resonance frequencies of the plate. As for the previous cases the inductances L_{b3} and resistances R_{s3} of third branch can be set to maximise the absorbed electric power and minimise the flexural response in correspondence to the first resonance frequency of the plate, i.e. $L_{b3} = L_{opt3}$ and $R_{s3} = R_{opt3}$. As a result of this iterative procedure, the spectra in plot (b) of Figure 12 shows that the flexural kinetic energy (green line), is brought down at the three target resonance frequencies of the plate. Similarly, the absorbed electric power (dotted black line) characterised by three peaks at these frequencies. These results indicate that the resonating shunts are effectively absorbing power at these three frequencies.

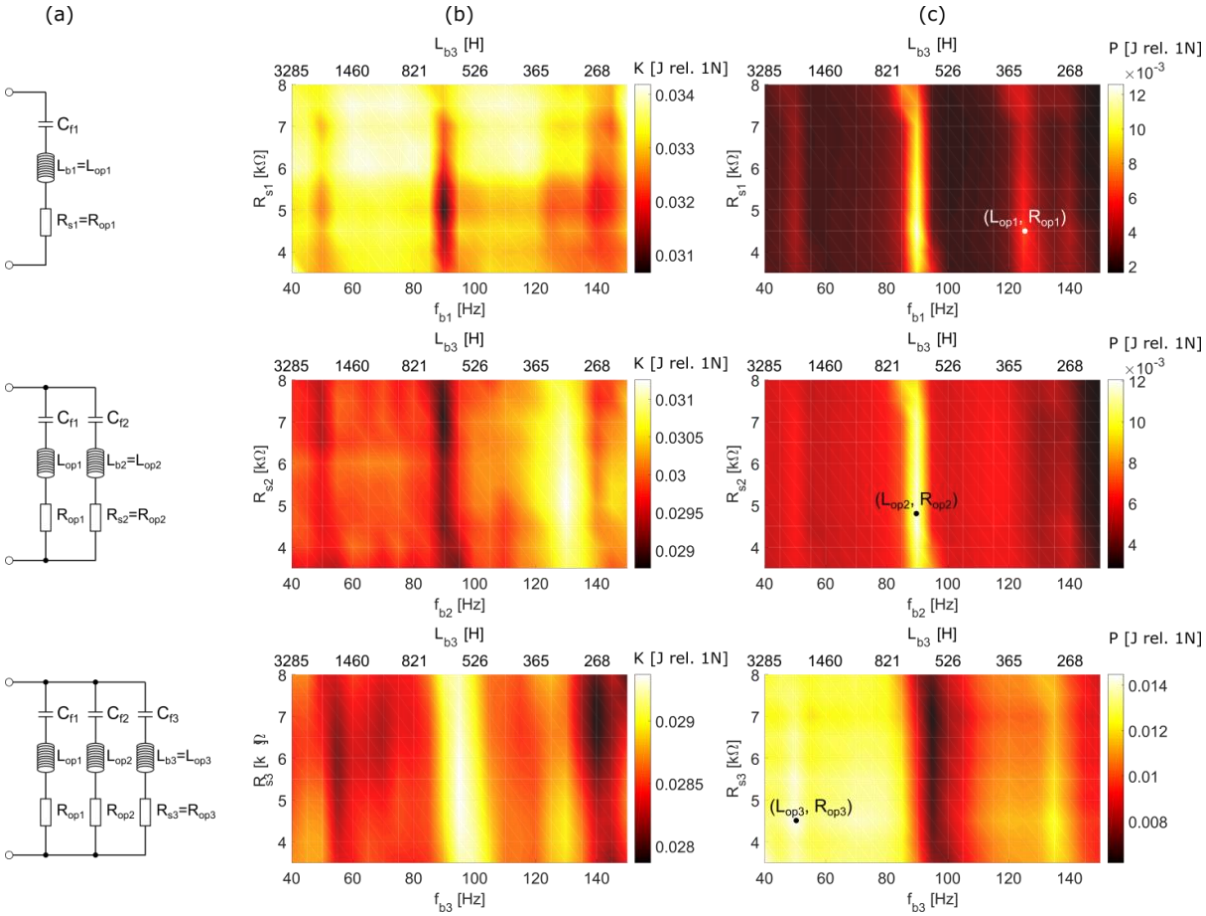


Figure 11: (a) Configuration of the multi-resonant shunt circuits (b); Time averaged total flexural kinetic energy of the smart plate structure, (c) time averaged electrical power absorbed by the RLC multi-resonant shunt circuits connected to the five piezoelectric patches.

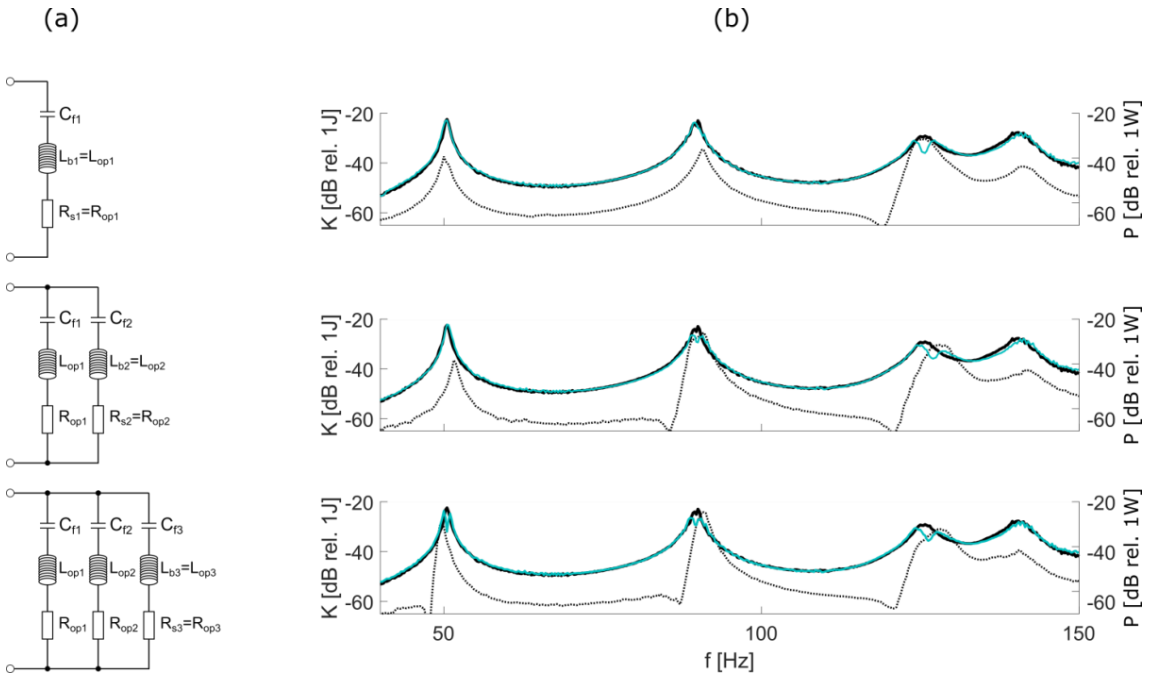


Figure 12: (a) Configuration of the multi-resonant shunt circuits; (b) PSD of the plate flexural kinetic energy (solid black line no shunt; solid green line with shunt) and electric power absorbed by the shunt (dotted black line) by the RLC multi-resonant shunt circuits connected to the five piezoelectric patches.

4 Conclusions

This paper has first presented a simulation study on the implementation of multi-resonant shunts connected to piezoelectric patches bonded on a plate, which produce multi-resonant vibration absorption effects. The study has shown that the RLC branches that form the shunts can be tuned to globally minimise the resonant response of given modes of the structure by locally maximising the electric power absorbed by each shunt. A simple tuning algorithm can be therefore implemented to tune on-line the branches in each shunt. The multi-resonant shunts composed by three RLC current flowing branches on five piezoelectric patches was then studied experimentally by utilising shunt impedances synthetized in a dSPACE paltform. The experimental study confirmed simulation predictions, that is the reduction of the total flexural kinetic energy of the plate and electrical power absorbed by the multi-resonant shunts with reference to the resistance and inductance parameters in a branch of the shunt is characterised by a sequence of minima and sequence of maxima. The corresponding minima and maxima coincide. This indicate that the branch RL components that would minimise the resonant response of low order flexural modes of the smart plate also maximise the electric power absorbed by the shunts. This effect of the RLC branch gives the opportunity to sequentially tune three branches in such a way as to maximise the electric power absorbed by five shunts, and thus to minimise the smart plate flexural kinetic energy in correspondence to given resonance frequencies. Although the simulation studies have shown that there is no need for a tuning update every time a branch is added to a shunt, the practical implementation showed that small adjustments may be required to track changes in the dynamic response due to the environmental changes during the long periods of operation.

Acknowledgements

The authors gratefully acknowledge the European Commission for its support of the Marie Skłodowska-Curie program through the ITN ANTARES project (GA 606817).

References

[1] P. Gardonio, M. Zientek, *On-line tuning of multi-resonant shunts connected to piezoelectric patches*, Journal of Sound and Vibration, 2018.

[2] D. Casagrande, P. Gardonio, M. Zilletti, *Smart panel with time varying shunted piezoelectric patch absorbers for broadband vibration control*, Journal of Sound and Vibration, Vol. 400, 2017.

[3] J.N. Reddy, *Mechanics of Laminated Composite Plates and Shells: Theory and Analysis*, CRC Press, Boca Raton, 2004.

[4] A. von Flotow, N.W. Hagood, W.H. Chung, *Damping of structural vibrations with piezoelectric materials and passive electrical network*, Journal of Sound and Vibration, Vol. 146, 1991.

[5] A. Preumont, Mechatronics, Springer, Dordrecht, 2006.

[6] A.F. Kurtz, S.H. Crandall, D.C. Karnopp, *Dynamics of Mechanical and Electromechanical Systems*, R.E. Krieger Pub. Co., Malabar, 1982.

[7] L. Meirovitch, *Principles and Techniques of Vibration*, Prentice Hall, New York, 1997.

[8] D. Casagrande, P. Gardonio, *Shunted piezoelectric patch vibration absorber on two-dimensional thin structures: Tuning considerations*, Journal of Sound and Vibration Vol. 295, 2017.

[9] A.J. Fleming, S. Behrens, S.O.R. Moheimani, *Multiple mode current flowing passive piezoelectric shunt controller*, Journal of Sound and Vibration, Vol. 266, 2003.

[10] D. Mayer, V. Krajenski, C. Linz, *Synthetic inductor for passive damping of structural vibrations*, ADAMES Abschlusskolloquium, 2001.

Experimental decentralised control of vibration on a plate with inertial actuators

S. Camperi, **M. Ghandchi-Tehrani**, **S. J. Elliott**
Institute of Sound and Vibration Research, University of Southampton, UK
e-mail: **s.camperi@soton.ac.uk**

Abstract

This paper presents the decentralised active control of vibration on a plate subjected to broadband excitation, by means of two velocity feedback control units, consisting of a velocity sensor and a collocated inertial actuator. The proposed multi-channel solution outperforms the single control unit both in terms of reduction of vibration and efficiency. The performance of the control system is first investigated with respect to the two feedback gains, in terms of total kinetic energy, mechanical power absorbed by the control units from the structure, and electrical power supplied. Secondly, the single powers absorbed and required by each single unit are analysed, in order to explore a local tuning solution. Finally, the efficiency of the different solutions is compared in terms of reduction of vibration with respect to the electrical power supplied. It is found that the multi-channel solution is more efficient than the single-channel one, since it provides a larger reduction of vibration with the same amount of electrical power provided.

1 Introduction

Active damping is an effective solution to reduce low-frequency flexural vibration of thin panels subjected to unknown broadband disturbance, which may lead to fatigue problems [1] as well as comfort issues [2, 3, 4] and noise radiation [5].
Active control systems often provides a larger reduction of vibration with less added mass to the structure, when compared to classic passive solutions. Furthermore, different factors can be easily included and tuned in the design of the controller, such as human sensitivity and changes into the structure dynamics.

Early studies [6, 7] showed that the optimal control of a fully centralised control system, by solving the Linear Quadratic Gaussian (LQG) problem associated, can be well approximated by a set of independent control units implementing a local velocity feedback, in a decentralised fashion.
A decentralised control system with local velocity feedback greatly simplifies the implementation of the control system, both in terms of cabling and scalability. Moreover, the design of an optimal controller reduces to the tuning of the velocity feedback gains. A preliminary study by Elliott *et al.* [8] showed that, when a decentralised control system consisting of local velocity feedback loops with the same feedback gain is considered, the global level of vibration of the plate, estimated through its kinetic energy, has a minimum. By increasing the feedback gain above the optimal value, the control system approaches a pinning condition, in which a new set of lightly damped resonances occurs at higher frequencies, and the global level of vibration is magnified.

Although the minimisation of the kinetic energy as cost function guarantees the convergence of the feedback gain tuning to a globally optimal solution, a set of monitoring sensors are required. An appealing alternative consists of defining a local cost function, which enables the tuning to be performed locally by the control unit, without any prior knowledge of the dynamic behaviour of the structure to be controlled. Following-up on this idea, the power absorbed by the control system from the structure has been investigated as alternative cost function [9, 10]. It was found [10, 11] that, when reactive actuators are used, the mechanical power

absorbed has a maximum, which almost corresponds to the optimal solution obtained by minimising the kinetic energy. This is because the mechanical power absorbed is the product of the control force and the plate velocity at the control position. Therefore, for small values of feedback gains, the power tends to zero because the control force is almost null; and similarly, for large values of feedback gains, the velocity at the control position tends to zero because of the pinning condition.

In this paper, the tuning of a two-channel control system with inertial actuators is investigated experimentally, with respect to the two independent feedback gains, in terms of kinetic energy and power flow. The power absorbed by each unit is measured with respect to the feedback gain pair implemented, and compared with the reduction of global level of vibration, estimated through nine sensors scattered on the plate.

In contrast with previous studies, inertial actuators are used in this work, as they do not need any external support and are suitable for the design of a self-contained control unit, which can be easily mounted on the structure.
Furthermore, the electrical power required by the control system is measured. This enables to overcome some limitations related to the analysis of the vibration reduction as function of the feedback gains only, such as the assessment of the control effort of a certain configuration, and the comparison of the results with other arrangements. Examples of these arrangements are control systems with different control positions, actuators, number of control units, or control laws.
The proposed solution consists of analysing the vibration reduction with respect to the control effort, expressed as electrical power. Through this approach, the two-channel control system is found to outperform the a single control unit system not only in terms of vibration reduction, but also in terms of required power. In particular, it is shown that the optimally tuned two-channel control system requires an amount of electrical power which almost corresponds to the one required by a less effective single unit.

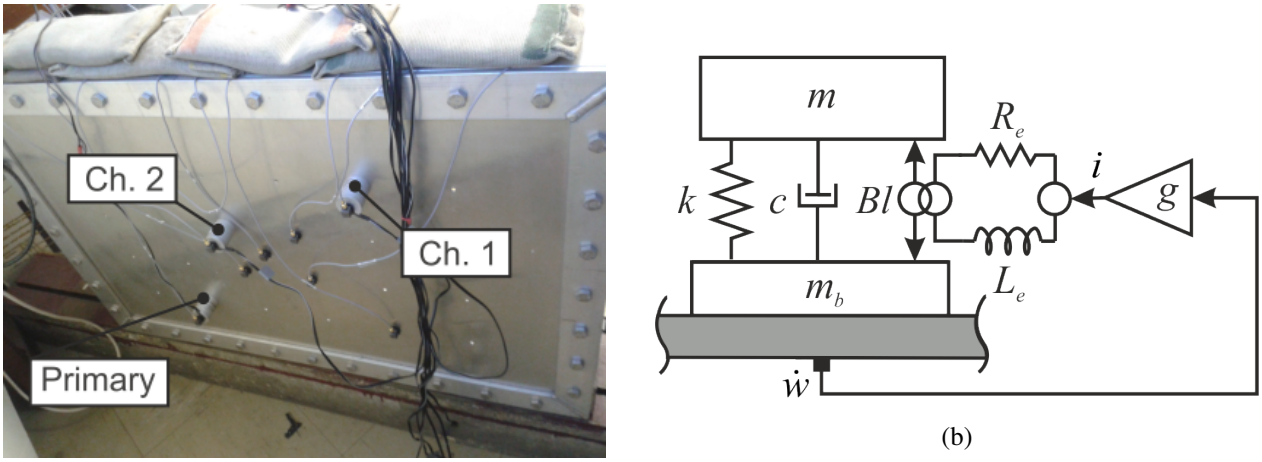
The paper is organised in three sections. In the first section the experimental setup is presented, and the estimation of the power flow by mean of a digital twin of the inertial actuators is introduced, which enables the power flow to be estimated directly from the velocity signals used in the feedback loops. In the second section, the experimental results obtained for more than 400 pairs of feedback gains are shown. The tuning of the control units by maximising the mechanical power absorbed is discussed, and the reduction of kinetic energy is analysed as function of the control effort. Finally, in the last section, the main results obtained are summarised and discussed.

2 Experimental setup

The objective of the experiment is to implement and analyse a decentralised velocity feedback control system on a plate with inertial actuators. The experimental setup for this study consists of a fully clamped, 2 mm thick, aluminium plate with two independent control units, as shown in Fig. 1.
The decentralised feedback control system can be described as two independent control units, consisting of an accelerometer and a current driven inertial actuator. The velocity feedback law for a two-channel decentralised feedback control system is

$$\begin{Bmatrix} i_1 \\ i_2 \end{Bmatrix} = \begin{bmatrix} g_1 & 0 \\ 0 & g_2 \end{bmatrix} \begin{Bmatrix} \dot{w}_1 \\ \dot{w}_2 \end{Bmatrix}, \tag{1}$$

in which the current i_n in the $n-$th control unit is proportional to the local velocity of the plate $\dot{w}_n$.
In this experiment, the kinetic energy and the power flow are investigated with respect to 441 different pairs of feedback gains (g_1, g_2), generated by 21 different values of g_1 and g_2.
The primary disturbance is generated by an additional inertial actuator, which is driven with a white noise up to 1 kHz. In addition, an array of seven additional accelerometers is mounted on the plate to monitor the global level of vibration up to 1 kHz, through an estimation of the kinetic energy as sum of the squared velocities measured at nine accelerometers positions, i.e. the seven monitoring accelerometers and the two used for the feedback control by the control units. The physical and geometric properties of the experimental



(a) (b)

Figure 1: (a) Experimental setup and (b) schematic representation of a velocity feedback control unit with inertial actuator.

setup are summarised in Table 1.
Although the experimental setup considered may represent a too academic example for vibration control, the positions of the primary and the control unit has been chosen without any particular criterion, except that of avoiding nodal lines. In this way, the results obtained do not depend on the particular configuration adopted, and they are more significant to general applications for vibration reduction on thin panels.

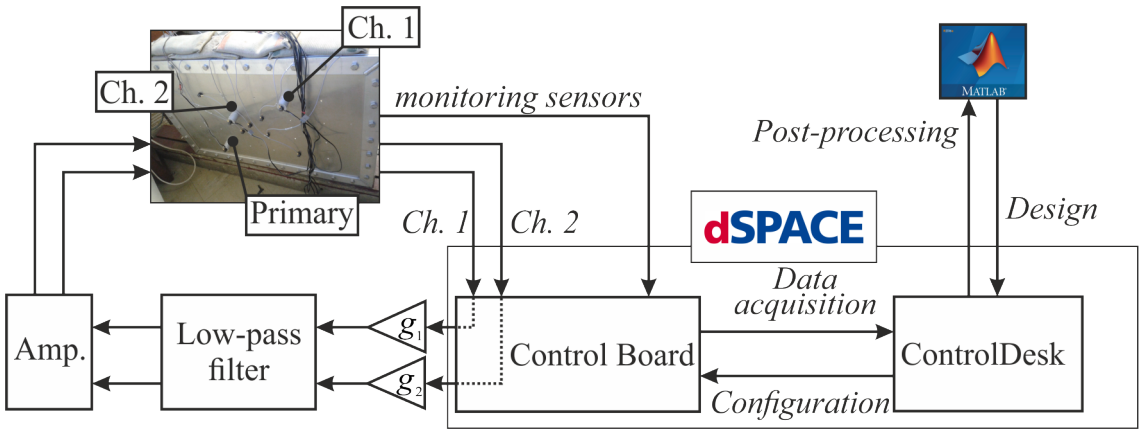


Figure 2: Schematic representation of the digital control and acquisition system.

The digital control system is an extension to the two-channel case of the single-channel control system presented in [12, 13], in which the measure of the kinetic energy, and of the power flow, is performed with a dSPACE® DS1103 PPC Control Board, running with a sampling frequency f_s of 16 kHz, which is configured through the dSPACE ControlDesk® and Matlab Simulink® software, and summarised in Fig. 2. In each control unit, the measured local acceleration of the structure is read by the dSPACE® Control Board, and digitally integrated to obtain the local velocity. Two independent current signals are then generated, proportional to the respective velocities by means of two feedback gains. The current signals are then filtered with a low-pass filter KEMO VBF/8 to avoid aliasing, and sent to a custom designed 4-channel Micromega current amplifier, which drives the Micromega IA01 inertial actuator.
The stability margin of each unit can be assessed, according to the Nyquist Criterion, measuring the open-loop transfer function between an independent input signal of the actuator and the collocated measured

velocity. The gain margin for both units is equivalent to 220 As/m, when the other unit is switched off. It is important to notice that the gain margin of each unit reduces as the feedback gain of the other unit increases [14], and this can be observed if a sequential loop closing approach is adopted, in which the stability of a control unit is determined with respect to the gain implemented in the other unit.
The power flow into the control system is measured in terms of power absorbed by the control units from the structure, and electrical power required by the control units to generate the control action. On each unit, the mechanical power absorbed can be written, for a stationary and ergodic process, as the product between the control force f_c and the local plate velocity $\dot{w}$ as [13, 12]

$$\bar{P}_m = -E\left[\Re\{f_c^H \dot{w}\}\right], \tag{2}$$

where E is the expectation operator, H indicates the complex conjugated, and $\Re$ the real part.
Similarly, the electrical power is the product of the voltage e and the current i

$$\bar{P}_{el} = -E\left[\Re\{e^H i\}\right]. \tag{3}$$

These powers can be directly estimated from the velocity signal used for the feedback control, if the dynamic behaviour of the actuator is known. The actuator dynamics can be identified independently from the structure to control [15], and expressed as a two-port network model [16]

$$\begin{cases} f_c = T_i i - Z_{mo}\dot{w} \\ e = Z_{eb} i - T_i \dot{w} \end{cases}, \tag{4}$$

where Z_{mo} is the open-loop mechanical impedance of the inertial actuator for a base excitation, Z_{eb} is the blocked electrical impedance seen by the electrical system when a current excitation is present, and T_i is the transduction coefficient of the force transmitted to the ground generated by a current flowing, or, equivalently, an induced voltage generated by the base movement.
Substituting the two-port model from Eq. (4) into Eq. (2) and Eq. (3), the power flow on each unit can be rewritten as

$$\bar{P}_m = \lim_{T\to\infty} E\left[\Re\{Z_{mo} + gT_i\}|\dot{w}|^2\right], \tag{5}$$

$$\bar{P}_{el} = \lim_{T\to\infty} E\left[\Re\{Z_{eb}g^2 + gT_i\}|\dot{w}|^2\right]. \tag{6}$$

3 Results

In this section, the effect of the two control units acting simultaneously on a decentralised arrangement is investigated, with respect to the two feedback gains g_1 and g_2.
The analysis is divided into three parts:

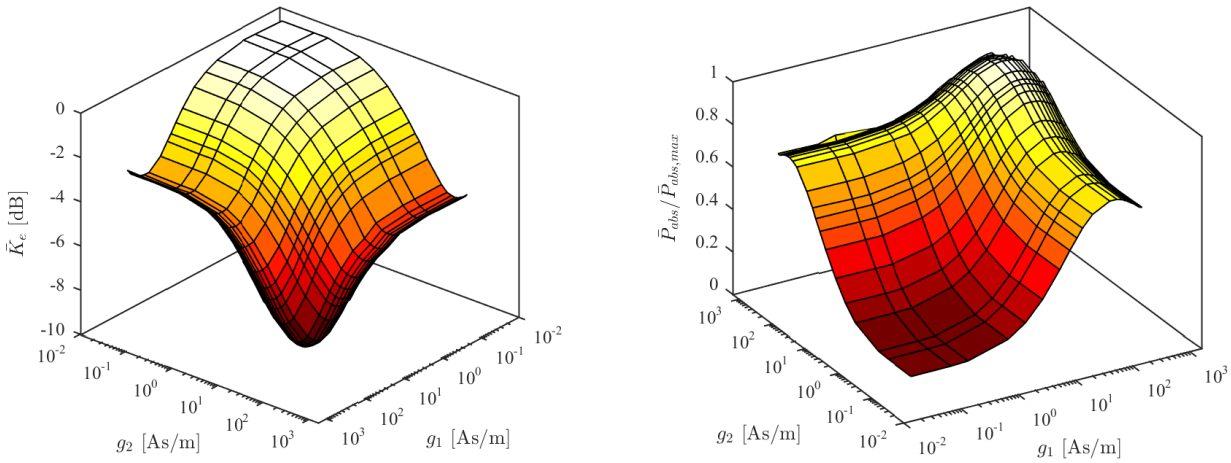
- *Global performance.* The reduction of kinetic energy and the total mechanical power absorbed by the two control units from the plate.
- *Local performance.* The local mechanical power absorbed by each control unit from the plate and the electrical power.
- *Control effort.* The reduction of kinetic energy with respect to the total electrical power.

The objective of the first part is to validate the maximisation of the mechanical power absorbed for the tuning of the control units, as an alternative solution to the kinetic energy minimisation for the two-channel control system. In the second part, the local power flow on each unit is investigated to assess the cross-interaction between different control units. Finally, in the third part, the performance of the two-channel decentralised control system is assessed with respect to the control effort required.
The results are obtained implementing 441 different pairs of feedback gains (g_1, g_2), in which 21 different values of g_1 and g_2 are considered ranging from 0 to 220 As/m.

	Parameter	Value
Aluminium plate	Dimensions (mm^2)	800 x 500
	Thickness (mm)	2
	Density (kg/m^3)	2720
	Young's modulus (N/m^2)	7×10^{10}
	Poisson ratio	0.33
	Internal damping ratio	1%
Sensors positions	Pos. #1 (x, y)(mm) - primary	(229,100)
	Pos. #2 (x, y)(mm)	(571,100)
	Pos. #3 (x, y)(mm)	(343,200)
	Pos. #4 (x, y)(mm)	(457,200)
	Pos. #5 (x, y)(mm)	(400,250)
	Pos. #6 (x, y)(mm)	(457,300)
	Pos. #7 (x, y)(mm) - channel 2	(343,300)
	Pos. #8 (x, y)(mm)	(229,400)
	Pos. #9 (x, y)(mm) - channel 1	(571,400)
Micromega IA01	Moving mass (g)	36
	Base mass (g)	53
	Natural frequency (Hz)	8.7
	Damping ratio	0.3
	Voice coil coefficient (N/A)	1.6
	Electrical resistance (Ω)	3
	Electrical inductance (μH)	100

Table 1: Geometry and physical properties of the experimental setup shown in Fig. 1.

3.1 Global performance



(a) (b)

Figure 3: Measured (a) kinetic energy of the plate and (b) total mechanical power absorbed by the control units from the structure, with respect to the feedback gains g_1 and g_2.

The measured reduction of kinetic energy and the total mechanical power absorbed by the two control units

from the plate with respect to two feedback gains, g_1 and g_2, are shown respectively in Fig. 3a and Fig. 3b. The kinetic energy has a global minimum, where a reduction of vibration of more than 8 dB is achieved. The optimal gain pair (g_1, g_2), minimising the kinetic energy, consists of two optimal gains, g_1 and g_2, which do not depend on each other, as shown in Fig. 3a. This means that when the optimal feedback gain on channel 1, for instance, is implemented, the optimal gain does not depend on the feedback gain implemented on channel 2, and vice-versa. Therefore, this system is proven to be robust against possible unit failures, since the other unit would still be optimally tuned, and its stability enhanced. Moreover, feedback gains values larger than the optimal ones increase the global level of vibration, since they do not introduce active damping but progressively generate new boundary conditions, approaching a pinning configuration with a new set of lightly damped structural resonances.
Secondly, the total mechanical power absorbed by the two control units from the plate has a global maximum, which corresponds to the minimum in the kinetic energy. This is a rather important result, as it shows that not only the control system can be tuned through the power absorption maximisation, but also that a sequential loop closing can be implemented, in which the global synchronisation between different units suggested by Zilletti *et al.* [17, 11] is greatly simplified. In a sequential loop closing arrangement, the tuning of each channel can be performed in series since the tuning of one channel does not detune other channels, and the convergence of the algorithm to the global minimum is guaranteed.

3.2 Local performance

The sequential loop closing discussed in the previous subsection requires the measure of the total mechanical power absorbed by both control units, which means that communication between the single units has to occur. In this subsection, the local power of each control unit is considered independently to investigate the tuning of a fully decentralised control system.
The local powers absorbed by the first and second unit, with respect to the feedback gains g_1 and g_2, are shown respectively in Fig. 4a and Fig. 4c. The powers are normalised with respect to the maximum total mechanical power absorbed, and their sum corresponds to the total mechanical power absorbed previously shown in Fig. 3b.
In order to analyse the effect of the two feedback gains, the mechanical power absorbed by the first unit is first investigated, from Fig. 4a. For each value of g_2, the mechanical power absorbed by the first channel with respect to g_1 has a maximum, which correspond to the optimal gain minimising the kinetic energy, and for further increase of the feedback gain, the mechanical power absorbed reduces, since a pinning condition is approached.
Nevertheless, if the feedback gain on the second unit, g_2, increases, the mechanical power absorbed by the first unit reduces, as part of the damping action is now performed by the second unit. Similarly, the mechanical power absorbed by the second unit shows a dual trend with respect to g_2. This shows that the tuning of each control unit can be performed locally in a sequential loop closing arrangement.

The electrical power required by the first and second control unit is shown, respectively, in Fig.4b and Fig. 4d. In this case, the electrical power required by each unit depends almost completely on the respective feedback gain, and it is quite insensitive to the changes in the other feedback gain. However, it can be noticed that the electrical power required by one unit slightly decreases as the feedback gain of the other unit increases. This depends on the cross-interaction between the two units, in which the control effort of a single unit decreases as the one on the other unit increases.

3.3 Control effort

The tuning of the control system can be carried out maximising the local mechanical powers absorbed on each unit. However, in an active control system, the control effort required to perform the control needs to

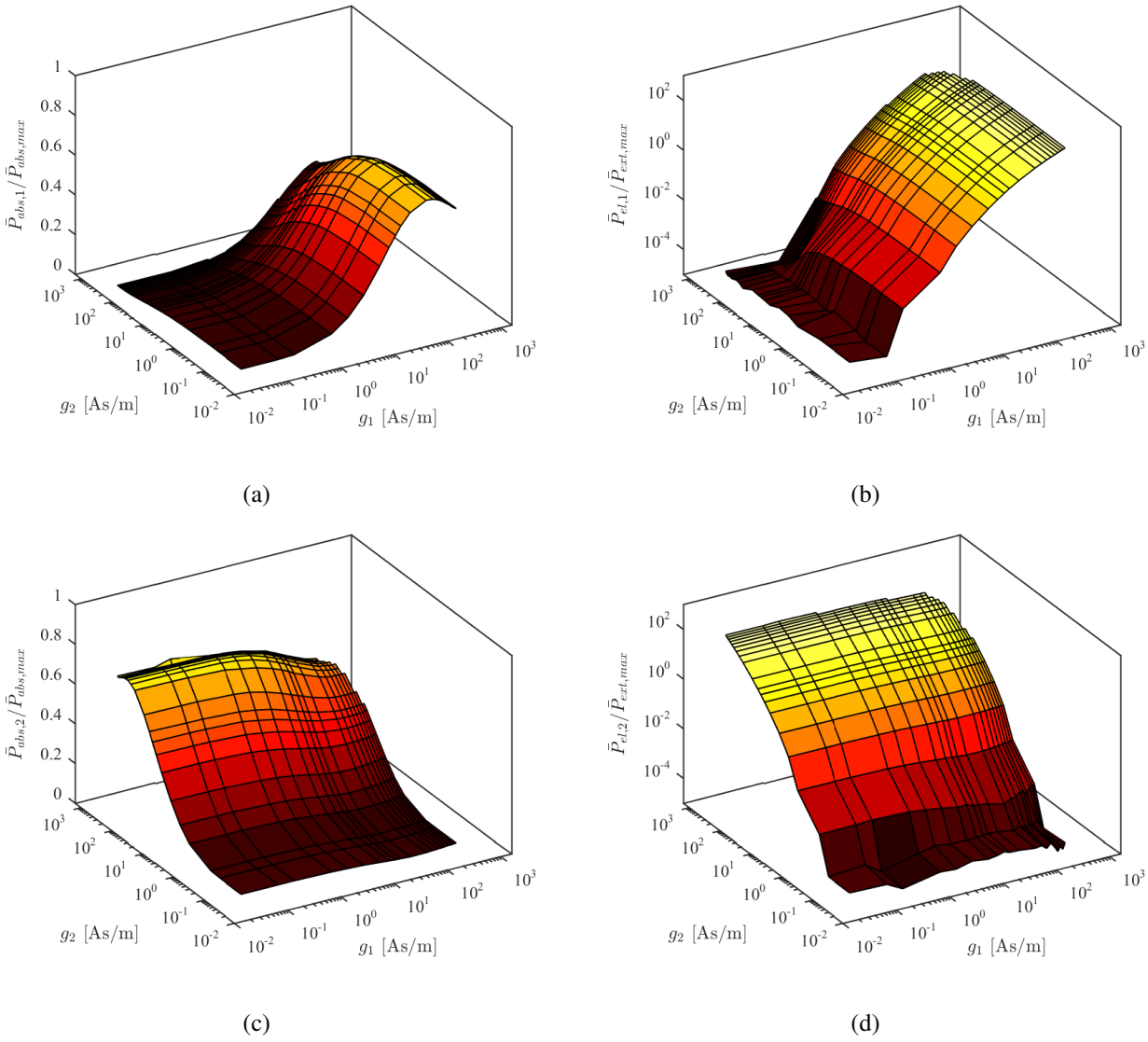


Figure 4: Measured mechanical and electrical power absorbed by each unit as function of the feedback gains g_1 and g_2: (a) mechanical power absorbed by the first unit; (b) electrical power of the first unit; (c) mechanical power absorbed by the second unit; (d) electrical power of the second unit.

be taken into account for a number of reasons. First, it gives an overview on the service costs of the control system. Secondly, it provides a general way of assessing the performance of the control system, which can be extended and transferred to other control systems enabling a quick and meaningful comparison. Examples of different control systems are those with a different number of control units, different type of actuators or different control laws and strategies.

The solution proposed here, is to re-map the reduction of kinetic energy shown in Fig. 3a to the total electrical power required by the two control units, which corresponds to the sum of the single electrical powers show in Fig.4b and Fig. 4d. The result is shown in Fig. 5, where each point has a size and colour proportional to the percentage of electrical power required by the first channel: this enables to analyse the distribution of the electrical power between the two different units.

It is significant to compare the results with the performance of the two single-channel arrangements from the first channel (solid blue) and the second channel (dashed blue), i.e. when only one channel is active and the feedback gain on the other unit is zero. Although the two-channel arrangement outperforms the single-channel ones in terms of reduction of the kinetic energy, the control effort does not increases. This means

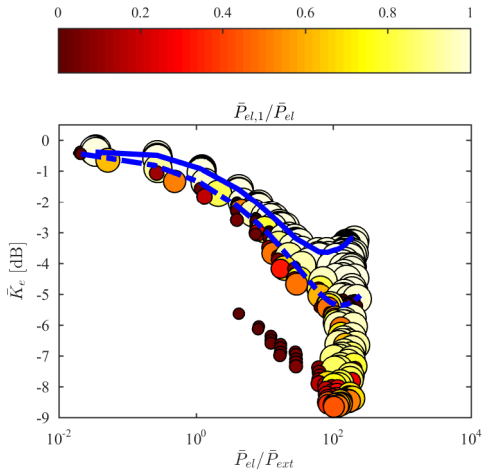


Figure 5: Measured kinetic energy of the plate as function of the total electrical power supplied to the control system, normalised with respect to the external power. The size and color of each point is proportional to the percentage of electrical power provided to the channel 1.

that the two-channel control system reduces the vibration on the plate more efficiently, requiring the same electrical power to operate, but simply redistributed on two different units.

4 Conclusions

This paper presents the experimental tuning of a decentralised velocity feedback control system with inertial actuators for plate vibration. The study is enriched with an analysis on the power requirements of the active control, with respect to the reduction of vibration.
A straightforward formulation of the mechanical power absorbed from the structure and of the electrical power is provided, which depends exclusively on the dynamic properties of the inertial actuator and the local velocity of the structure, which is also used for the feedback control. This enables the design of a smart and self-contained control unit, which can be tuned without identifying the structure to be controlled.
The tuning of each control unit can be performed locally with respect to the mechanical power absorbed by the single unit, for one channel at the time, in a sequential loop closing fashion. The maximisation of the single powers absorbed by each unit converges to the global maximum of the total mechanical power absorbed by the control system from the structure, which corresponds to the minimum in the kinetic energy of the plate.
In addition, the electrical power required by the inertial actuator to perform the control is introduced as a measure of the control effort. This enables to overcome some limitations of the analysis of the feedback control system just in terms of feedback gains. First, the electrical power provides a meaningful tool for a feasibility analysis of an active control system, as it enables to estimate the service costs. Second, it provides a valuable measure of comparison between different solutions in terms of number of control units used, type of actuators, control locations and control laws.
With reference to the study presented in this paper, the two-channel control system is proved not only to outperform the single-channel case providing more than 8 dB of global reduction of vibration, but is also competitive in terms of electrical power required. It is shown, indeed, that the optimal tuning corresponds to a configuration in which the amount of electrical power is comparable with the one of a single-channel case, but having a better distribution among the control units.

Acknowledgements

The authors gratefully acknowledge the European Commission for its support of the Marie Skłodowska-Curie program through the ITN ANTARES Project (GA 606817).

References

[1] R. A. Canfield, S. D. Morgenstern, and D. L. Kunz, "Alleviation of buffet-induced vibration using piezoelectric actuators," *Computers & structures*, vol. 86, no. 3-5, pp. 281–291, 2008.

[2] T. T. Soong and B. F. Spencer Jr, "Active, semi-active and hybrid control of structures," in *Proceedings of the 12WCEE 12th 12th World Conference on Earthquake Engineering, Auckland, New Zealand*, 2000.

[3] P. Reynolds, I. M. Díaz, and D. S. Nyawako, "Vibration testing and active control of an office floor," in *Proceedings of the 27th International Modal Analysis Conference, Orlando, Florida, USA*, 2009.

[4] P. Gardonio, "Review of active techniques for aerospace vibro-acoustic control," *Journal of aircraft*, vol. 39, no. 2, pp. 206–214, 2002.

[5] B. Petitjean, I. Legrain, F. Simon, and S. Pauzin, "Active control experiments for acoustic radiation reduction of a sandwich panel: Feedback and feedforward investigations," *Journal of sound and vibration*, vol. 252, no. 1, pp. 19–36, 2002.

[6] B. Petitjean and I. Legrain, "Feedback controllers for active vibration suppression," *Structural Control and Health Monitoring*, vol. 3, no. 1-2, pp. 111–127, 1996.

[7] W. P. Engels, O. N. Baumann, S. J. Elliott, and R. Fraanje, "Centralized and decentralized control of structural vibration and sound radiation," *The journal of the Acoustical Society of America*, vol. 119, no. 3, pp. 1487–1495, 2006.

[8] S. J. Elliott, P. Gardonio, T. C. Sors, and M. J. Brennan, "Active vibroacoustic control with multiple local feedback loops," *The Journal of the Acoustical Society of America*, vol. 111, no. 2, pp. 908–915, 2002.

[9] N. Hirami, "An active maximum power absorber for the reduction of noise and vibration," *Journal of sound and vibration*, vol. 200, no. 3, pp. 261–279, 1997.

[10] S. J. Elliott, M. Zilletti, and P. Gardonio, "Self-tuning of local velocity feedback controllers to maximise power absorption," in *Recent Advances Structural Dynamics: Proceedings of the X International Conference*, p. 12pp, University of Southampton, 2010.

[11] M. Zilletti, S. J. Elliott, P. Gardonio, and E. Rustighi, "Experimental implementation of a self-tuning control system for decentralised velocity feedback," *Journal of Sound and Vibration*, vol. 331, no. 1, pp. 1–14, 2012.

[12] S. Camperi, M. Ghandchi-Tehrani, and S. J. Elliott, "Experimental maximisation of the power absorbed by an inertial actuator for structural vibration control," in *Proceedings of the ICSV24 24th International Congress on Sound and Vibration, London, United Kingdom*, 2017.

[13] S. Camperi, M. Ghandchi-Tehrani, and S. J. Elliott, "Investigation on the performance of a velocity feedback control unit for structural vibration control: Theory and experiments," in *Proceedings of the IMACXXXVI Conference, Orlando, Florida (USA)*, 2018.

[14] S. Camperi, M. Ghandchi-Tehrani, and S. J. Elliott, "Multichannel decentralised feedback control using inertial actuators," in *Proceedings of the ISMA2016 27th International Conference on Noise and Vibration Engineering, Leuven, Belgium*, 2016.

[15] J. Rohlfing, P. Gardonio, and S. J. Elliott, "Base impedance of velocity feedback control units with proof-mass electrodynamic actuators," *Journal of Sound and Vibration*, vol. 330, no. 20, pp. 4661 – 4675, 2011.

[16] S. J. Elliott and M. Zilletti, "Scaling of electromagnetic transducers for shunt damping and energy harvesting," *Journal of Sound and Vibration*, vol. 333, no. 8, pp. 2185–2195, 2014.

[17] M. Zilletti, S. J. Elliott, and P. Gardonio, "Self-tuning control systems of decentralised velocity feedback," *Journal of Sound and Vibration*, vol. 329, no. 14, pp. 2738–2750, 2010.

Experimental tests of a flywheel proof mass actuator for velocity feedback control

A. Kras[1], P. Gardonio[1]
[1] Università di Udine, DPIA
Via delle Scienze 208, 33100 Udine, Italy
e-mail: **aleksander.kras@uniud.it**

Abstract
This paper presents the experimental tests carried out on a flywheel proof mass actuator used for the implementation of velocity feedback control loops to reduce the flexural vibration of a plate structure. Classical proof mass actuator is formed with a coil armature-magnet system connected via soft springs. At frequencies above its fundamental resonance frequency, it generates a constant force effect, which is in phase with the driving signal. However, the internal dynamics of the springs-coil armature system limits the stability, and thus control performance of the feedback loop. Moreover, when exposed to shocks, the soft springs may cause undesired stroke saturation effects, which can lead to instability of the feedback loops. The electromagnetic proof mass actuator presented in this paper includes an additional flywheel element that increases the inertia effect of the coil armature and improves the stability of velocity feedback loops, both by increasing the feedback gain margin and by improving the robustness to shocks.

1 Introduction

This paper presents experimental tests carried with a prototype flywheel proof mass actuator [1-3], to implement velocity feedback control loops to reduce the flexural vibration of a thin rectangular plate. The experimental results obtained with the prototype actuator are contrasted with simulation results obtained from a simplified mathematical model and compared with those of classical inertial actuator.

Active vibration control with a collocated velocity sensor - point force actuator can be used to reduce flexural vibrations in correspondence of resonance frequencies of the hosting structure [1-15]. In practice, a localised control point force can be generated with an inertial actuator. Classical inertial actuators used in velocity feedback control loops are typically based on electromagnetic linear motors where the heavier magnet or coil armature is suspended on soft springs [16-18]. Thus, when the inertial actuator is used to implement a negative velocity feedback to reduce the flexural vibrations of a thin structure, the dynamic response and the static deflection of the proof mass cause stability and control performance limitations [19]. If fact, at frequencies below the fundamental resonance frequency of the actuator, the produced net force at the actuator base, grows proportionally with frequency and has opposite phase with the driving signal. Thus, the feedback loop essentially produces a positive velocity feedback effect that is a negative damping effect, which leads to instability. Only above the fundamental resonance frequency of the actuator, the force produced at the base is constant and in phase with the driving current such that the feedback loop produces a damping force effect that guarantees stability. Therefore, when the inertial actuator is used to implement a velocity feedback loop, it is important that its fundamental resonance frequency is as low as possible. The design of a device with low internal resonance is rather challenging, since, for a given proof mass, it requires a comparatively soft suspension system, which makes the actuator more venerable to stroke saturation effects when it is exposed to shocks or high accelerations of the hosting structure [20-23].

Several solutions have been proposed to improve the robustness of inertial actuators used to implement negative velocity feedback control. A series of studies has been performed to implement within the actuator either a relative displacement, a relative velocity or a force feedback loop [24-26]. Alternatively, it was proposed to implement a compensator in the feedback controller that counteracts the dynamics of the

springs-mass assembly [27]. The electromagnetic inertial actuator presented in this paper includes an additional flywheel element that increases the inertia effect of the proof mass and is used to improve the stability of velocity feedback loops, both by reducing actuator fundamental resonance frequency and by reducing static deflection of the proof mass-spring system [28,29].

This paper is organized in five parts. Section two describes the classical proof mass actuator, which is used as a reference system, classical configuration with the same inertial mass as that of the flywheel prototype and the proposed flywheel proof mass actuator. Section three describes the mathematical formulation used to both analyse the stability and the control performance of the velocity feedback loops. Section four presents the stability and the control performance analyses of the velocity feedback loops implemented on a thin rectangular panel. The control performance of the velocity feedback loops is assessed by plotting the spectra of the error velocity reductions generated at the control position and the spectra of the total flexural kinetic energy of the rectangular plate. Also the frequency averaged plate kinetic energy reduction is used to assess the overall control effect with reference to the feedback control gain implemented in the loop. The static deflection study, presented in section five, demonstrates that the flywheel element can improve stability and robustness to shocks of the velocity feedback loop by reducing the static displacement of the suspended mass.

2 Flywheel proof mass actuator

Classical inertial actuators for velocity feedback control loops applications are based on linear electromagnetic actuators. In this study the actuator shown in Fig. 1a,d is used as a reference actuator. As depicted schematically in Fig. 1a this actuator is formed by a magnetic inner element, which is attached to the structure and acts as a base mass m_b. Instead, the external coil armature acts as a proof mass M_a, which is suspended to the inner element via two flexural springs of stiffness k and damping c. The two flexural springs that are attached on both sides of the coil armature, are characterised by soft axial stiffness and comparatively much higher transverse stiffness. The damping effect in this actuator is principally due to the eddy currents and the viscous damping effect due to the air gap between magnet and external metal coil armature. The electromagnetic effect of the actuator, modelled in terms of transduction coefficient ψ_a, produces a pair of forces F_a proportional to the voltage u_a applied at the electrical terminals and current i_a flowing in coil, which is characterised by inductance L and resistance R effects. The same transduction coefficient produces the back electromotive force u_{bmf} proportional to the relative velocity $\dot{w}_m - \dot{w}_b$ between the proof mass (coil armature) and the base (magnet) of the actuator. Design studies of similar electromagnetic actuators can be found in following references [30,31].

Fig. 1b,e presents the classical configuration which is characterised by the same inertial mass as that of the flywheel prototype. This configuration was used to compare the properties and performance of the classical inertial actuator with the fabricated prototype. To obtain the best similarity to the fabricated prototype the classical configuration with the same inertial mass was based on the flywheel inertial actuator. The flywheel and its supporting bracket was attached to the inertial mass. However, the pushing pin was disconnected from the base mass to deactivate the axial inertia effect produced by the flywheel element as schematically depicted in Fig. 1b and shown in Fig. 1e. The flywheel element was firmly attached to the supporting bracket to prevent any undesired rotational motion that could induce additional dynamics during measurements. The lumped parameter model for this configuration is characterised by the same elements as for the classical configuration. The total inertial mass is equal to the sum of proof mass M_a and flywheel mass m_w.

The third actuator presented in this study is equipped with an additional round flywheel element with dimensions optimised in such a way as to minimise weight m_w and to maximise the polar moment of inertia I_w. The flywheel element is attached via two flexural bearings of stiffness k_w to the bracket fixed to the external coil armature. The linear motion of the actuator is converted into a rotation of the flywheel by a pushing pin link attached to the inner magnet and the third pivot bearing that was mounted on one of the flywheel arms with an offset radius r_w from the flywheel horizontal axis of rotation.

The geometry and physical properties of the thin rectangular plate hosting structure considered in this study are summarized in Table 1. The physical properties of the classical and flywheel actuators with the flywheel element are summarized in Table 2.

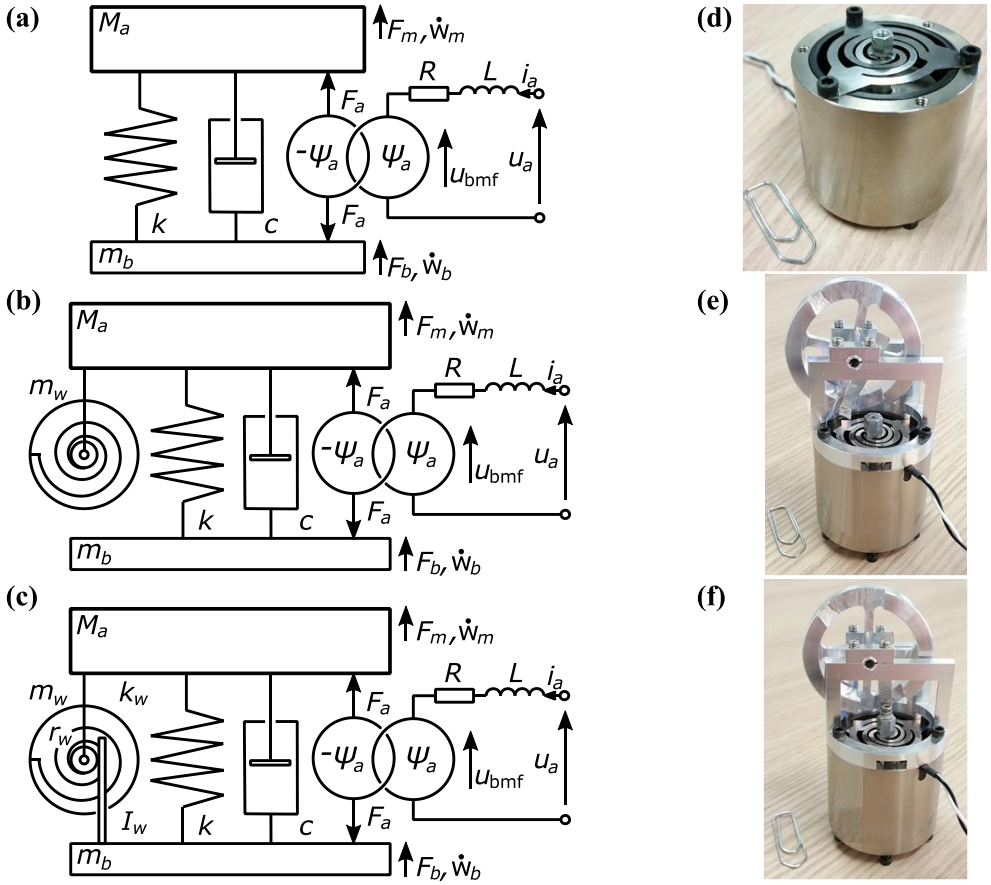


Figure 1: Schemes (a, b, c) and pictures (d, e, f) of the classical proof mass actuator (a, d), the classical proof mass actuator with the same inertial mass as the flywheel configuration (b, e) and the flywheel proof mass actuator (c, f).

Parameter	Value
Length	$l_x = 0.668$ m
Width	$l_y = 0.444$ m
Thickness	$h = 0.00137$ m
Mass density	$\rho = 8200$ kgm^{-3}
Elastic modulus	$E = 210 \times 10^9$ Nm^{-2}
Poisson ratio	$\nu = 0.31$
Damping ratio	$\zeta_p = 0.0035$
Position of the actuators	$(x_c, y_c) = (0.234\text{ m}, 0.178\text{ m})$
Position of the base	$(x_b, y_b) = (0.234\text{ m}, 0.178\text{ m})$
Excitation force location	$(x_p, y_p) = (0.433\text{ m}, 0.157\text{ m})$

Table 1: Mechanical parameters of the thin rectangular plate.

Parameter	Value
Proof mass	$M_a = 0.185$ kg
Flywheel mass	$m_w = 0.045$ kg
Base mass	$m_b = 0.115$ kg
Axial stiffness	$k = 2950$ Nm^{-1}
Torsional stiffness	$k_w = 0.009$ Nmrad^{-1}
Damping ratio	$\zeta = 0.2$
Flywheel inertia	$I_w = 6.8 \times 10^{-6}$ kgm^2
Flywheel offset radius	$r_w = 0.0064$ m
Transduction coefficient	$\psi_a = 22.5$ NA^{-1}
Coil resistance	$R = 22.5\ \Omega$
Coil inductance	$L = 4.35 \times 10^{-3}$H

Table 2: Mechanical parameters of the proof mass actuators.

3 Plate with flywheel proof mass actuators mathematical model

This section presents the mathematical formulation used to assess stability and control performance of velocity feedback loops using the classical, classical with the same inertial mass as the flywheel configuration and the proposed flywheel proof mass actuators. The schematic model and the picture of the velocity feedback loop system implemented on the plate are shown respectively in Fig. 2a and Fig. 2b. The tested inertial actuator was attached on one side of the panel while the small accelerometer sensor that measured error signal was attached on the other side at the base footprint of the actuator, as shown schematically in Fig. 2a. The panel was excited with a point force produced by a shaker as shown in Fig. 2b. A mobility–impedance model [32] was employed to derive the response of the plate with the velocity feedback loop using the inertial actuators. All frequency domain formulations presented in this paper consider the complex amplitudes $x(\omega)$ of time–harmonic phasors given in the form $x(\omega)\exp(j\omega t)$, where ω is the circular frequency and $j^2 = -1$. As shown in Fig. 2c, the system has been divided in four parts: the base mass, the flexible plate, the flexible suspension system with in parallel the electromagnetic actuator, and the proof mass of the actuator. The mechanical properties of the rectangular panel and location of the collocated sensor-actuator pair and the primary force are specified in Table 1.



Figure 2: Scheme (a), picture (b) and mobility-impedance model (c) of a velocity feedback control loop using the flywheel inertial actuator on a rectangular plate. The accelerometer sensor was installed on the other side of the plate at the base footprint of the actuator as shown in the scheme (a).

Considering the lumped parameter model shown in Fig. 2c, the complex velocities at the connecting points between these elements have been expressed with the following mobility relations:

$$\dot{w}_c = Y_{cc}F_c + Y_{cb}F_b + Y_{cp}p \,, \tag{1}$$

$$\dot{w}_m = Y_m F_m \,, \tag{2}$$

$$\dot{w}_b = Y_{bc}F_c + Y_{bb}F_b + Y_{bp}p \,, \tag{3}$$

where $\dot{w}_c$ is the complex velocity at the control position, $\dot{w}_m$ is the complex velocity of the proof mass, and $\dot{w}_b$ is the complex velocity at the base position. Mobilities of actuators proof masses Y_m are given by:

$$Y_m = \frac{1}{j\omega M_a} \quad \text{or} \quad Y_m = \frac{1}{j\omega(M_a+m_w)} \quad \text{or} \quad Y_m = \frac{1}{j\omega(M_a+m_w)} \tag{4}$$

respectively for the classical proof mass actuator (a), for the classical proof mass actuator with the same inertial mass as that of the flywheel configuration (b) and for the flywheel actuator (c) shown in Fig. 1. Also, $Y_{cc}, Y_{cb}, Y_{bc}, Y_{bb}, Y_{cp}, Y_{bp}$ are transfer mobilities between the locations *c*, *b* and *p* for the actuator, for the actuators case and for the primary force excitation. Considering two generic points *r* and *s* of the plate, these mobility functions can be calculated with following matrix expression:

$$Y_{rs}(\omega) = \frac{\dot{w}_r(\omega)}{f_s(\omega)} = \boldsymbol{\phi}^{\mathrm{T}}(x_r, y_r)\boldsymbol{\Omega}(\omega)\boldsymbol{\phi}(x_s, y_s) \,, \tag{5}$$

where $\dot{w}_r(\omega)$ and $f_s(\omega)$ are the complex transverse velocity and the complex transverse force acting at positions (x_r, y_r) and (x_s, y_s) respectively. Also $\boldsymbol{\Omega}(\omega)$ is a diagonal matrix of second order terms given by:

$$\Omega_n(\omega) = j\omega/\left[M_p\left(\omega_{\mathrm{n}}^2 + 2j\zeta_p\omega_{\mathrm{n}}\omega - \omega^2\right)\right], \tag{6}$$

where ζ_p is the damping ratio and ω_{n} is the *n*-th flexural natural frequency, which for a plate considered in this study is given:

$$\omega_{\mathrm{n}} = \left(\frac{D}{\rho h}\right)^{\frac{1}{2}}\left(\frac{\pi}{l_x}\right)^2\sqrt{G_{xn}^4 + G_{yn}^4\left(\frac{l_x}{l_y}\right)^4 + 2\left(\frac{l_x}{l_y}\right)^2\left[\nu H_{xn}H_{yn} + (1-\nu)J_{xn}J_{yn}\right]}, \tag{7}$$

where for first flexural natural frequency $G_1 = 1.506$, $H_1 = 1.248$ and $J_1 = 1.248$, while for the *n*-th mode the constants were obtained with the following expressions $G_n = n + 1/2$, $H_n = (n + 1/2)^2(1 - 4/(2n+1)\pi)$ and $J_n = (n + 1/2)^2(1 - 4/(2n+1)\pi)$. Here $D = Eh^3/[12(1-\nu^2)]$, ρ, E and ν are respectively the flexural rigidity, the density, the Young's modulus of elasticity and the Poisson ratio of the plate material. Also l_x, l_y, h, are the dimensions and thickness of the plate. Finally $\boldsymbol{\phi}$ is a column vector with the flexural modal amplitudes at a given point, which, for the plate considered in this study have been taken equal to $\phi_{\mathrm{n}}(x,y) = 2\sin(n_1\pi x/l_x)\sin\left(n_2\pi y/l_y\right)$. In this study all natural frequencies up to 1.3 kHz and the respective natural modes have been used in the plate mobility expressions. The p is the amplitude of the harmonic primary force.

Considering the lumped parameter model shown in Fig. 2c, the complex forces at the connecting points between the elements forming the system have been expressed with the following mobility relations:

$$F_c = -Z_a\dot{w}_c + Z_a\dot{w}_m + \psi_a i_a\,, \tag{8}$$

where F_c is the complex force acting at the control position,

$$F_m = Z_a\dot{w}_c - Z_a\dot{w}_m - \psi_a i_a\,, \tag{9}$$

where F_m is the complex force acting on the proof mass,

$$F_b = -Z_b\dot{w}_b\,, \tag{10}$$

where F_b is the complex force acting at the base position. The impedance Z_a of actuators suspension system are given by:

$$Z_a = c + \frac{k}{j\omega} \quad \text{or} \quad Z_a = c + \frac{k}{j\omega} \quad \text{or} \quad Z_a = c + \frac{k}{j\omega} + j\omega\frac{\mathrm{I_w}}{\mathrm{r_w^2}} + \frac{k_w}{j\omega r_w^2} \tag{11}$$

respectively for the classical proof mass actuator (a), for the classical proof mass actuator with the same inertial mass as that of the flywheel configuration (b) and for the pinned flywheel actuator (c) shown in Fig. 1. In these expressions k and c are the axial stiffness and damping coefficient of the proof mass suspension. The damping coefficient of the proof mass suspension is calculated with the following formula $c = 2\zeta\sqrt{kM_a}$ for the classical actuators, while for the flywheel configuration with the following formula $c = 2\zeta\sqrt{(k + k_w/r_w^2)(M_a + m_w)}$. The k_w is the torsional stiffness of the flexural bearings, I_w is the flywheel inertia, r_w is the flywheel offset radius, while ψ_a is transduction coefficient of the coil–magnet as specified in Table 1. The impedance of the actuators case masses is given by:

$$Z_b = \mathrm{j}\omega m_b\,, \tag{12}$$

where m_b is case mass as specified in Table 1. The complex voltage at the terminals of the coil shown in Fig. 2c, have been expressed with the following impedance relation:

$$u_a = Z_e i_a + \psi_a\dot{w}_c - \psi_a\dot{w}_m\,, \tag{13}$$

where Z_e is the coil electrical impedance given by:

$$Z_e = j\omega L + R\,. \tag{14}$$

Substituting Eq. (10) into Eq. (3), the velocity at the base position is given by:

$$\dot{w}_b = Q_{bc}F_c + Q_{bp}p\,, \tag{15}$$

where $Q_{bc} = (1 + Y_{bb}Z_b)^{-1}Y_{bc}$ and $Q_{bp} = (1 + Y_{bb}Z_b)^{-1}Y_{bp}$. Substituting Eq. (15) into Eq. (10) and then the resulting equation into Eq. (1), the velocity at the control positions is given by:

$$\dot{w}_c = Q_{cc}F_c + Q_{cp}p \,, \tag{16}$$

where $Q_{cc} = Y_{cc} - Y_{cb}Z_bQ_{bc}$ and $Q_{cp} = Y_{cp} - Y_{cb}Z_bQ_{bp}$. Substituting Eq. (9) into Eq. (2) the velocity at the proof masses is given by:

$$\dot{w}_m = Q_{am}\dot{w}_c + Q_a i_a \,, \tag{17}$$

where $Q_{am} = (1 + Y_mZ_a)^{-1}Y_mZ_a$ and $Q_a = -(1 + Y_mZ_a)^{-1}Y_m\psi_a$. Substituting Eq. (17) into Eq. (13) the complex voltage at the terminals of the coil is given by:

$$u_a = Q_e i_a + Q_w\dot{w}_c \,, \tag{18}$$

where $Q_e = Z_e - \psi_aQ_a$ and $Q_w = \psi_a - \psi_aQ_{am}$. Also, rewriting Eq. (18) and substituting into Eq. (17) and then the resulting equation into Eq. (8) the force acting at the control positions is given by:

$$F_c = Z_c\dot{w}_c + Z_f u_a \,, \tag{19}$$

where $Z_c = Z_aQ_aQ_w/Q_e - Z_a + Z_aQ_{am} - Q_w\psi_a/Q_e$ and $Z_f = Z_aQ_a/Q_e + \psi_a/Q_e$. Substituting Eq. (19) into Eq. (16) the velocities at the control positions can be expressed in terms of the primary force and control voltages with the following matrix expression:

$$\dot{w}_c = G_{ca}u_a + G_{cp}p \,, \tag{20}$$

where $G_{ca} = (1 - Q_{cc}Z_c)^{-1}Q_{cc}Z_f$ and $G_{cp} = (1 - Q_{cc}Z_c)^{-1}Q_{cp}$. Here G_{ca} is open loop sensor–actuator FRF for the voltage driven proof mass actuator, which is used later on to assess the stability of the feedback loops using the Nyquist criterion [1,3,5,6,28].

When the velocity feedback loops are closed with the gain g_c, the control voltage signal is given by:

$$u_a = -g_c\dot{w}_c \,, \tag{21}$$

Thus, substituting Eq. (21) into Eq. (20), the closed loop response at the control positions is given by the following expression:

$$\dot{w}_c = G_{clu}p \,. \tag{22}$$

where $G_{clu} = (1 + G_{ca}g_c)^{-1}G_{cp}$. The force $F_c(\omega)$ at the control position can be derived with the following steps: first, Eq. (21) is substituted into Eq. (19); second, Eq. (22) is substituted into the resulting equation, so that:

$$F_c = F_{cp}p \,, \tag{23}$$

where $F_{cp} = \left(Z_c - Z_fg_c\right)(1 + G_{ca}g_c)^{-1}G_{cp}$. Also, the forces $F_b(\omega)$ generated at the case masses positions can be derived by substituting Eq. (23) into Eq. (15) and then the resulting equation into Eq. (10) so that:

$$F_b = F_{bp}p \,, \tag{24}$$

where $F_{bp} = -Z_b\left(Q_{bc}F_{cp} + Q_{bp}\right)$.

The time–averaged total flexural kinetic energy is used to evaluate the flexural response of the plate without and with feedback loops. For time–harmonic vibrations, the time–averaged kinetic energy is given by the following formula:

$$KE(t) = \lim_{T\to\infty}\frac{1}{T}\frac{1}{2}\int_T \int_A \rho h\dot{w}^2(x,y,t)\mathrm{dA}\,dt = \frac{1}{4}\int_A \rho h|\dot{w}(x,y,\omega)|^2\mathrm{dA} \,, \tag{25}$$

where A is the area of the plate. Also, the complex velocity of the plate $\dot{w}(x,y,t)$ can be derived from the following expression:

$$\dot{w}(x,y,\omega) = \boldsymbol{\phi}^T(x_r,y_r)\left[\mathbf{a}_\mathrm{c}(\omega)F_c(\omega) + \mathbf{a}_\mathrm{b}(\omega)F_b(\omega) + \mathbf{a}_\mathrm{p}(\omega)p(\omega)\right] \,, \tag{26}$$

where

$$\mathbf{a}_{\mathrm{c}}(\omega) = \mathbf{\Omega}(\omega)\boldsymbol{\phi}(x_c, y_c) \quad , \quad \mathbf{a}_{\mathrm{b}}(\omega) = \mathbf{\Omega}(\omega)\boldsymbol{\phi}(x_b, y_b) \quad , \quad \mathbf{a}_{\mathrm{p}}(\omega) = \mathbf{\Omega}(\omega)\boldsymbol{\phi}(x_p, y_p)\,. \tag{27}$$

Thus, substituting Eq. (23) and Eq. (24) into Eq. (26) gives:

$$\dot{w}(x,y) = \boldsymbol{\phi}^T\left[\mathbf{a}_{\mathrm{c}}F_{cp} + \mathbf{a}_{\mathrm{b}}F_{bp} + \mathbf{a}_{\mathrm{p}}\right]p\,. \tag{28}$$

Recalling that for the flexural natural modes given above the following orthogonality properties holds, $\int_A \phi_n^2\, dA = A$ and $\int_A \phi_n \phi_{m\neq n}\, dA = 0$, the kinetic energy of the plate with the passive effects of the proof mass actuators and the active effects of the velocity feedback loop is given by:

$$KE(\omega) = \tfrac{1}{4}M_p\left[\mathbf{a}_{\mathrm{p}} + \mathbf{a}_{\mathrm{c}}F_{cp} + \mathbf{a}_{\mathrm{b}}F_{bp}\right]^H\left[\mathbf{a}_{\mathrm{p}} + \mathbf{a}_{\mathrm{c}}F_{cp} + \mathbf{a}_{\mathrm{b}}F_{bp}\right]|p|^2. \tag{29}$$

The kinetic energy for the plain plate without proof mass actuator can be derived by setting $F_{cp} = 0$ and $F_{bp} = 0$.

4 Stability and control performance analysis

The following subsections assess the stability and control performance of the velocity feedback loops implemented on thin rectangular plate using inertial actuators. The stability and control performance of the control system was assessed for the feedback loops using the classical, classical with the same inertial mass as the flywheel configuration and flywheel inertial actuators. The experimental results carried out on a rectangular panel have been contrasted with simulations. The stability of the velocity feedback loops has been assessed using the Nyquist stability criterion [1,3,5,6,12,28,33]. The control performance of the velocity feedback loops has been assessed by plotting the maximum velocity reductions generated at the control position and the total flexural kinetic energy of the rectangular plate. The effectiveness of the proposed control systems has been assessed considering the 10 Hz to 1 kHz frequency averaged plate kinetic energy reduction presented in the last subsection.

4.1 Stability

The stability of the velocity feedback loops implemented on thin rectangular plate have been assessed with reference to the open loop sensor – actuator frequency response functions for the voltage driven proof mass actuators. Fig. 3 shows the Bode plots while Fig. 4 shows the Nyquist plots of the open loop sensor–actuator frequency response functions specified in Eq. (20) in the previous section. Fig. 3 shows Bode plots of the open loop sensor – actuator frequency response functions considering the plate equipped with classical inertial actuator (Fig. 3a), with the classical configuration with the same inertial mass as that of the flywheel configuration (Fig. 3b) and with the flywheel inertial actuator (Fig. 3c). The experimental results (solid lines) are contrasted with the numerical simulations (dotted brown lines).

Considering first the classical inertial actuator shown in Fig. 3a, the modulus plot is characterized by a heavily damped resonance peak at the fundamental resonance of the inertial actuator and then a sequence of rounded resonance peaks and antiresonance lows pairs. The phase plot is characterized by a -180° phase lag at the fundamental resonance frequency of the actuator and then a sequence of -180° phase lag and +180° phase lead for each resonance peak and antiresonance low pair of the plate. The experimental results (solid blue lines) for the classical configuration of the inertial actuator align well with the numerical results (dotted brown lines). The mathematical model predicts well the resonance peak with the phase shift of the inertial actuator and most of the resonance peaks and antiresonance lows pairs of the plate. A small difference in amplitude and frequency between the numerical and measurement results can be observed between 400 Hz and 600 Hz. The simulated phase plot of the open loop sensor–actuator FRF for the voltage driven classical actuator also aligns well with measurement. The measured phase starts to decay at higher frequencies due to the electrical inductance of actuator coil, as found with measurements.

The Bode diagram shown in Fig. 3b presents the open loop sensor–actuator frequency response function for the voltage driven classical actuator with the same inertial mass as the flywheel configuration. The modulus and phase diagrams present almost identical characteristics to the phase diagram of the classical configuration. However, the slightly heavier inertial mass shift the fundamental resonance of the inertial actuator to a hardly noticeable lower frequency. The sequence of rounded off resonance peaks and narrow antiresonance lows pairs in the modulus diagram with the sequence of -180° phase lag and +180° phase lead in the phase diagram is almost identical as for the classical configuration. The experimental results (solid black lines) align well with the numerical results (dotted brown lines). The classical actuator with the same inertial mass as that of the flywheel configuration presents a small difference in the amplitude and frequency between 400 Hz and 600 Hz. The simulated phase spectrum of the open loop sensor–actuator frequency response function also aligns well with measurement.

Fig. 3c shows the Bode diagram for the flywheel inertial actuator. The plot shows that the axial inertia effect produced by the flywheel element shifts the resonance peak at the fundamental resonance of the inertial actuator to lower frequency. The experimental results (solid red lines) for the flywheel inertial actuator align well with the numerical results (dotted brown lines) mainly at lower frequencies. An additional resonance effect of the actuator at about 210 Hz causes the phase to shift from 70° to about 170°. However, this additional dynamics produces lower amplitude compared to the peak at the fundamental resonance of the flywheel inertial actuator. Compared to the experimental results, the resonance peaks and antiresonance lows in simulation results are rapidly smoothen above 300 Hz, as can be noticed in the modulus and the phase diagrams. Considering the phase diagram, the measured phase starts to decay at higher frequencies due to the electrical properties of the actuator coil that were predicted with simulations.

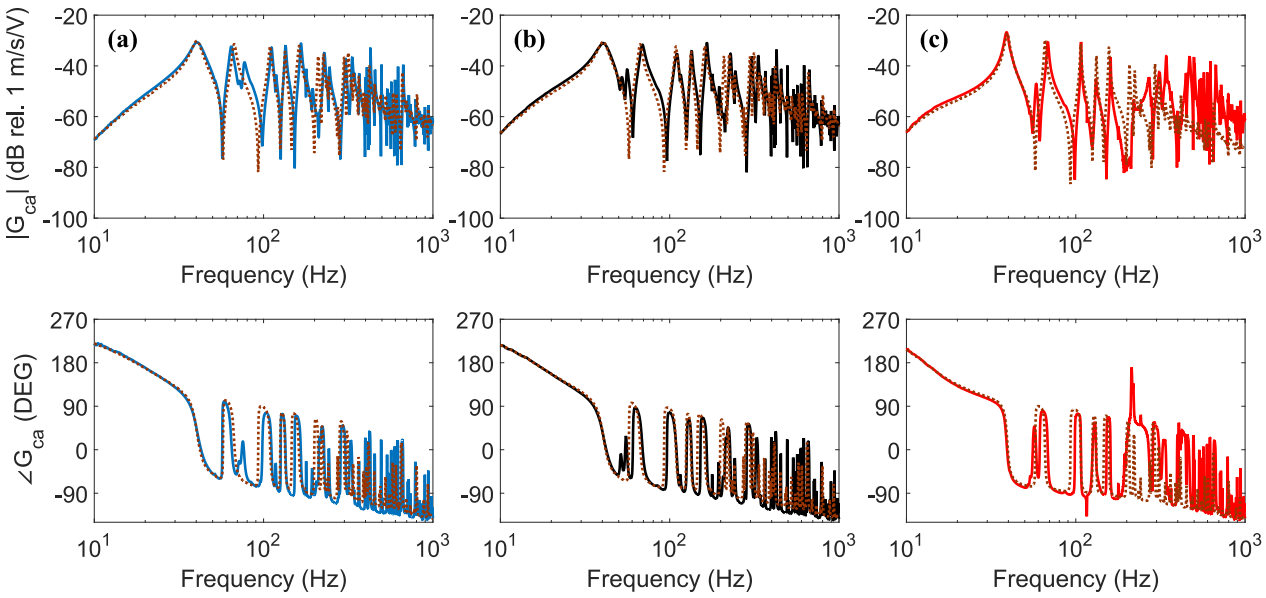


Figure 3: Bode plots of the open loop sensor – actuator frequency response functions for the voltage driven actuators. (a) Classical configuration (solid blue lines), (b) classical configuration with the same inertial mass as the flywheel configuration (solid black lines), (c) flywheel inertial actuator (solid red lines). Experimental results are contrasted with numerical simulations (dotted brown lines).

The stability of the velocity feedback loops using the classical configuration, classical with the same inertial mass as the flywheel configuration and the flywheel inertial actuator is assessed using the Nyquist criterion. Fig. 4 shows the Nyquist plots of the open loop sensor–actuator frequency response functions specified in Eq. (20) in the previous section. Fig. 4 shows the Nyquist plots of the open loop sensor – actuator frequency response functions considering the plate equipped with classical inertial actuator (Fig. 4a), with the classical with the same inertial mass as the flywheel configuration (Fig. 4b) and with the flywheel inertial actuator (Fig. 4c). The solid lines in the plots present the measurement results, while the dotted brown lines present the simulation results.

The Nyquist diagram for the open loop sensor - actuator frequency response function for the voltage driven classical inertial actuator (Fig. 4a) is characterised by a circle in the real negative quadrants, which is linked to the resonance effect generated by the fundamental resonance effect of the actuator. In contrast the series of progressively smaller circles in the real positive quadrants are linked to the resonance effects produced by the flexural natural modes of the plate. The circles are not centred along the axis due to high damping ratio of the inertial actuator that slightly rotates the pattern. The circle in the left hand quadrants indicates that the feedback loop is only conditionally stable with maximum signal gain margin of about 54 dB. The experimental results (solid blue lines) align well with the numerical results (dotted brown lines). The performance of the velocity feedback loops with the voltage driven inertial actuator can be assessed with the approximated equation $20\log_{10}(1+\delta_n/\delta_a)$ [33-35], where δ_n and δ_a are the real values of the open loop sensor-actuator frequency response function respectively for the nth resonance peak of the plate and resonance peak at the fundamental resonance of the inertial actuator as shown Fig. 4a. Therefore, the maximum reduction of the first resonance peak of the plate with the classical inertial actuator can reach 23.8 dB.

The Nyquist plot for the classical actuator with the same inertial mass as the flywheel configuration shown in Fig. 4b presents similar characteristics to the classical configuration. The circle in the left hand quadrants indicates that the stability gain margin is about 55 dB. The experimental results (solid black lines) align well with the numerical results (dotted brown lines) also for this configuration of the inertial actuator. The assessed performance shows that the maximum reduction of the first resonance peak of the plate with this configuration of the inertial actuator can reach 24.3 dB.

The Nyquist plot for the flywheel inertial actuator shown in Fig. 4c presents similar characteristic to the previous two configurations. However, the inertia effect produced by the flywheel element has significantly increased the stability of the feedback loops. Indeed, the stability gain margin is now about 59 dB. The experimental results for the flywheel inertial actuator (solid red lines) align well with the numerical results (dotted brown lines). As shown in Fig. 3c of the open loop sensor – actuator frequency response function, an additional resonance of the actuator creates a second circle in the left hand quadrants. The second circle is much smaller compared to the one of the inertial actuator fundamental resonance frequency and does not threaten the stability of the velocity feedback loop. The assessed performance for the flywheel inertial actuator shows that the maximum reduction of the first resonance peak of the plate can reach up to 32.8 dB.

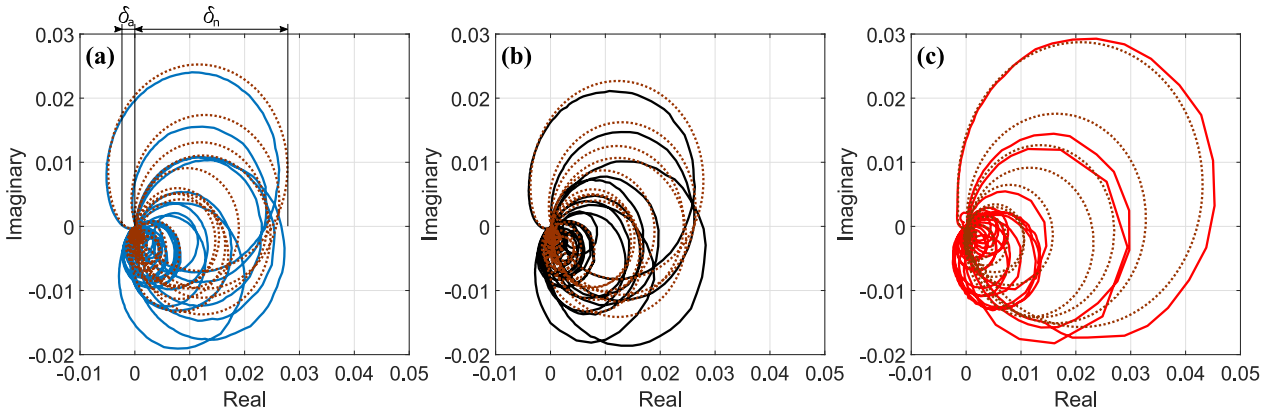


Figure 4: Nyquist plots of the open loop sensor – actuator frequency response functions for the voltage driven actuators. (a) Classical configuration (solid blue lines), (b) classical configuration with the same inertial mass as the flywheel configuration (solid black lines), (c) flywheel inertial actuator (solid red lines). Experimental results are contrasted with numerical simulations (dotted brown lines).

4.2 Control performance at control location

The control performance of the velocity feedback loops with the classical configuration, the classical configuration with the same inertial mass as the flywheel configuration and the flywheel inertial actuator is

first assessed by plotting the maximum velocity reductions of the rectangular plate at the control position. Fig. 5 shows the control performance of the velocity feedback loops implemented with maximum signal gains that guarantee stability, as defined in previous section. Fig. 5 shows the control velocity signal per unit force excitation specified in Eq. (22) considering the plane plate (dotted green line) and the plate with the velocity feedback loop using classical actuator (solid blue line), the classical actuator with the same inertial mass as the flywheel configuration (dashed black lines) and the flywheel inertial actuator (dashed-dotted red lines). The simulation results (Fig. 5a) are compared with the measurements taken on the experimental rig (Fig. 5b).

The spectrum of the plane plate flexural response at the control position (dotted green lines) is characterised by a fundamental resonance peak at about 43Hz and then a sequence of progressively smaller in amplitude sharp resonance peaks. The numerical results for the plate shown in Fig. 5a correspond well to the experimental results shown in Fig. 5b. However, the amplitude of the plate resonance peak starts to diminish with the increase of the frequency with numerical results, while in the experimental results, the amplitude of the plate resonance peaks stay relatively equal in entire measured band.

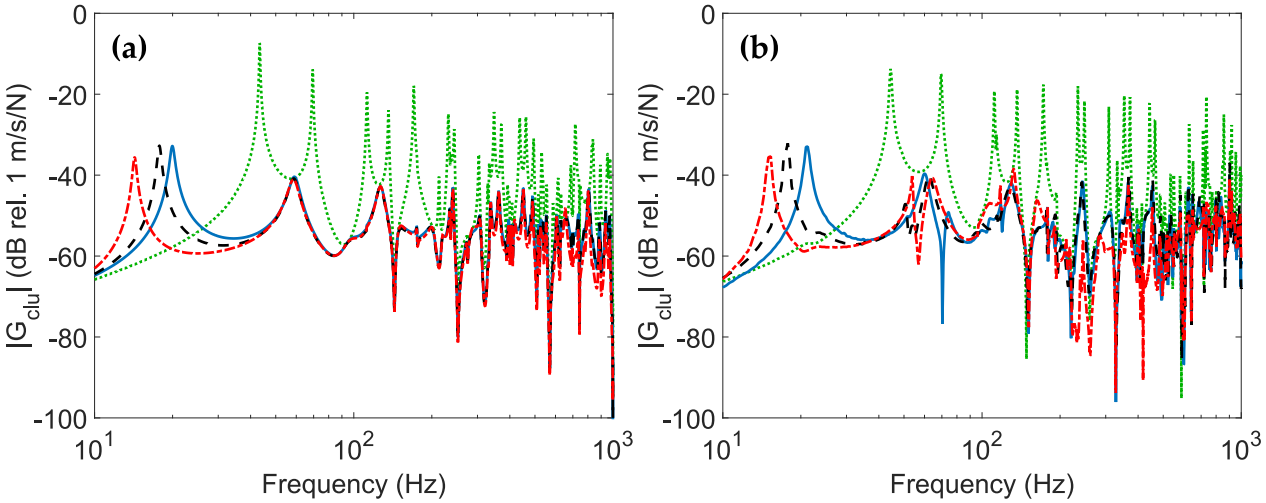


Figure 5: Velocity at the control position per unit force excitation of the plate with maximum signal gain applied to the control actuators that guarantee stability. Plate without inertial actuator (dotted green lines) and for the plate with the feedback control systems using voltage driven classical inertial actuator (solid blue lines), classical configuration with the same inertial mass as the flywheel configurations (dashed black lines) and with the flywheel inertial actuator (dashed-dotted red lines). Simulation results (plot a) compared with measurements (plot b).

When the velocity feedback loops are implemented with maximum control gains that ensure stability using the inertial actuators the response at the control position is characterised mainly by rounded off plate resonance peaks. However, both plots show that the velocity feedback loops also generate quite high control spillover effect around the fundamental resonance frequency of the actuators. Thus, for the classical configuration of the inertial actuator the spillover appears at about 20 Hz, for the classical configuration with the same inertial mass as the flywheel configuration at about 18 Hz, while for the pinned flywheel inertial actuator at about 15 Hz. The spillover effect produced by the flywheel configuration has lower amplitude of about 3 dB compared to the other two configurations. The simulation results show that all three configurations produce similar vibration control performance at low frequencies and round off the resonance peak at the fundamental mode of the plate by about 48 dB. However, the flywheel configuration produces higher reductions compared to the other two configurations above around 500 Hz. The measurement results present similar characteristics to the numerical results. The resonance peak of the plate fundamental mode is rounded off by about 40 dB by all three configurations. Measurement results also show that the flywheel configuration produces much smaller control effect at lower frequencies compared to other two configurations. However, between 200 Hz and 800 Hz the control performance of the flywheel configuration is much greater compared to the other two configurations. Additionally, both plots clearly show the pinning

effect of the plate at the control position due to the high feedback gains applied to the actuators. The first pinning effect appears at about 60 Hz, while the second at about 130 Hz.

4.3 Global control performance

The performance of the feedback loops with the proposed flywheel actuators has been assessed considering the total flexural kinetic energy of the hosting plate as defined in Eq. (29). The two plots in Fig. 6 show the 10 Hz – 1 kHz spectra of the total flexural kinetic energy of the panel per unit force excitation for the plate without actuators and when the velocity feedback loop using the three inertial actuators are implemented with maximum control gains that guarantee stability. Both figures show the total flexural kinetic energy per unit force excitation for the plain plate (dotted green lines) and for the plate with the classical proof mass actuator (solid blue lines), with the classical configuration with the same inertial mass as the flywheel configuration (dashed black lines) and with flywheel proof mass actuator (dashed-dotted red lines). The simulation results in Fig. 6a are compared with measurement results shown in Fig. 6b.

The spectrum of the kinetic energy for the plain plate (dotted green lines) is characterized by a sharp resonance peak at about 44 Hz, which is due to the fundamental natural mode of the plate followed by other peaks due to flexural modes of the plate [10]. The numerical results for the plate shown in Fig. 6a correspond well with the experimental results shown in Fig. 6b. However, the measurement results show that up to 200 Hz the amplitude of the plate resonance peaks stay relatively equal.

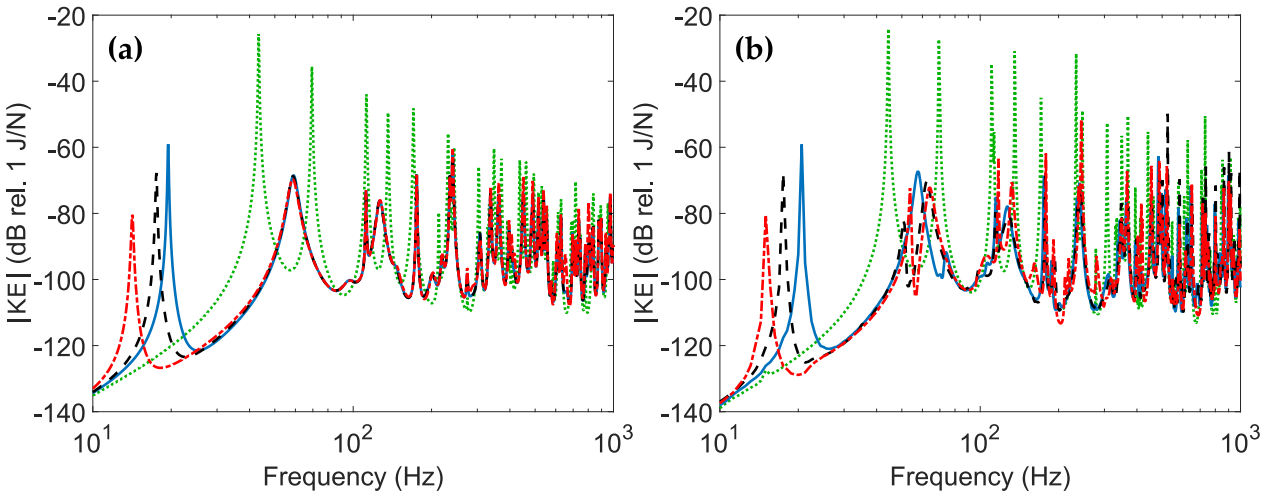


Figure 6: Total flexural kinetic energy per unit force excitation of the plate with maximum signal gain. Without inertial actuator (dotted green lines) and for the plate with the closed loop feedback control systems using voltage driven classical inertial actuator without flywheel (solid blue lines), classical configuration with the same inertial mass as the flywheel configurations (dashed black lines) and with the flywheel inertial actuator (dashed-dotted red lines). Simulation results (plot a) compared with measurements (plot b).

When the feedback loop with the inertial actuators are implemented with maximum control gains that ensure stability, the spectra of the kinetic energy are characterised by rounded off plate resonance peaks. The spectra also show that the velocity feedback loops generate a rather high control spillover peak in correspondence to the fundamental resonance frequency of the actuators. In contrast, the feedback loops using the flywheel inertial actuator produce much smaller control spillover effects, even though the maximum control gain is implemented in the feedback loop. This is due to the fact that, when the actuators are equipped with the flywheel, the spillover occurs at much lower frequency in correspondence to the fundamental resonance. Thus, when the feedback loop with the flywheel inertial actuator is implemented the spillover effect is about 20 dB lower compared to classical configuration and about 13 dB lower compared to the classical configuration with the same inertial mass as the flywheel actuator. The simulation results show that all three velocity feedback loops produce similar vibration control performance in the

entire frequency band. The feedback loops round off the first two resonance peaks of plate by about 77 dB and by about 57 dB (Fig. 6a). The measured spectra of the kinetic energy present slightly different characteristics to the simulated results. For instance, the first two resonance peaks are round off by about 79 dB and by about 60 dB (Fig. 6b). The measured performance of the velocity feedback loops with the flywheel inertial actuator is worse at lower frequencies compared to the other two configurations. However, the control performance of the flywheel configuration is much greater compared to the other two configurations above 500 Hz. The measured and simulated spectra of the kinetic energy also show the pinning effect of the plate at about 60 Hz.

4.4 Frequency averaged performance

The plate flexural kinetic energy vibration control effects presented in the previous section were derived when the velocity feedback loops are implemented only with maximum control gains that ensure stability. To better asses the effectiveness of the proposed control systems, the 10 Hz to 1 kHz frequency averaged plate kinetic energy reduction is considered with reference to increasingly higher feedback control gains. The reductions of the frequency averaged flexural kinetic energy of the plate equipped with the feedback control are normalised with reference to the frequency averaged kinetic energy of the plain rectangular plate. Fig. 7 shows reduction of the frequency average energy when the feedback loops are implemented using the classical (solid blue line), classical configuration that has the same inertial mass as the flywheel configuration (dashed black line) and the flywheel inertial actuator (dashed-dotted red line). The results show the frequency averaged plate kinetic energy reduction with increasing feedback control gains up to maximum control gain that guarantees stability.

Considering first the classical configuration (solid blue line), the feedback loop the inertial actuator produces up to 15.4 dB reduction of the frequency averaged kinetic energy with maximum control gain of 54 dB. The performance of the velocity feedback loop is slightly better when the classical configuration that has the same inertial mass as the flywheel configurations is used. Considering the dashed black line, when the velocity feedback loop is implemented the inertial actuator produces up to 15.6 dB reduction with maximum control gain of 55 dB. Finally, the feedback loop with the flywheel inertial actuator (dashed-dotted red lines) can implement much larger feedback control gains (up to 59dB) such that the frequency averaged kinetic energy of the plate is reduced by up to 15.9 dB. The improved control performance are obtained thanks to the possibility of implementing about higher control gains.

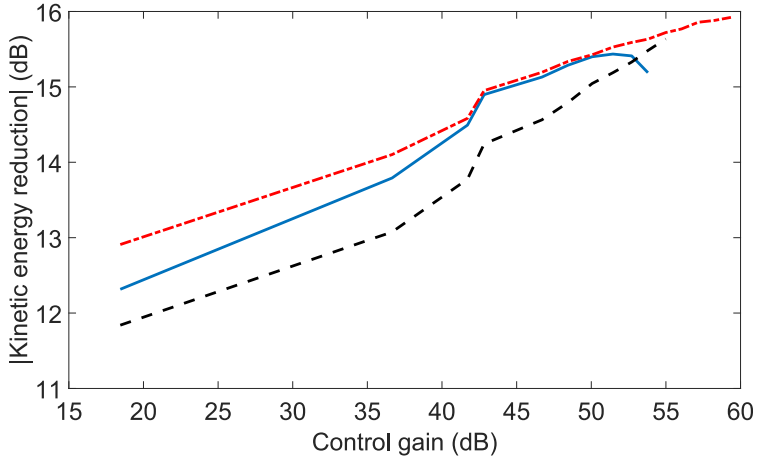


Figure 7: Reductions of the 10 Hz – 1 kHz frequency averaged kinetic energy produced by the feedback loops using either the voltage driven classical inertial actuator without flywheel (solid blue lines), classical configuration with the same inertial mass as the flywheel configurations (dashed black lines) and with the flywheel inertial actuator (dashed-dotted red lines).

5 Static deflection

One of the key parameters that characterise an inertial actuator for active vibration control is the static deflection [3]. The static displacement of the springs-proof mass assembly defines the robustness of the actuator to shocks that may cause stability and control performance limitations. Thus, considering physical properties of the inertial actuators summarized in Table 2, the static deflection for the classical configuration of the inertial actuator shown in Fig. 1a is given by:

$$\delta = \frac{M_a g}{k} = 615 \text{ μm} , \tag{30}$$

where $g = 9.81 \text{ m/s}^2$ is the gravitational acceleration. The static deflections for the classical configuration with the same inertial mass as the flywheel configuration shown in Fig. 1b given by:

$$\delta = \frac{(M_a + m_w) g}{k} = 765 \text{ μm} , \tag{31}$$

Comparing to the classical configuration, the static deflection of the classical configuration with the same inertial mass as that of the flywheel configuration increased by 24%. Finally, the static deflections for the flywheel inertial actuator shown in Fig. 1c is given by:

$$\delta = \frac{(M_w + m_w) g}{k + k_w / r_w^2} = 711 \text{ μm} . \tag{32}$$

Comparing to the classical configuration, the static deflection of the flywheel inertial actuator has increased only by 16%. Whereas, comparing to the classical configuration with the same inertial mass as that of the flywheel configuration, the static deflection of the flywheel inertial actuator has decreased by 7%. Although, the decrees of the static deflection for the flywheel configuration is due to additional flexural bearing, the result shown in Eqs. (30-32) clearly demonstrate that the static deflection of the flywheel inertial actuator does not depend on the axial inertia effect I_w / r_w^2 produced by the flywheel element. Also, it shows that the flywheel configurations can increase the robustness to shocks of the active vibration control systems by reducing the static deflection of the inertial actuator.

6 Conclusions

This paper has presented a new proof mass electromagnetic actuator with a flywheel element that can be effectively used in velocity feedback control loops to reduce the flexural vibrations of a thin rectangular panel. A mobility–impedance model has been introduced to assess the stability and control performance of a velocity feedback control loop with the voltage driven inertial actuator. Three different configurations of the inertial actuator have been considered and compared between each other. The stability and control performance of velocity feedback loops were considered using a classical inertial actuator, a classical actuator with the same inertial mass as the flywheel configuration and a flywheel inertial actuator. Experimental test results carried out on a rectangular panel test rig have been contrasted with simulations.

The stability analysis has shown that the addition of the flywheel element increases the gain margin of the feedback loops. Moreover, compared to the classical configuration with the same inertial mass as that of the flywheel configuration, the flywheel prototype has increased the gain margin without any increase of the actuator proof mass. More precisely, when the inertial actuators were driven with the voltage signal the maximum signal gain margin of 54 dB have been reached with the classical configuration, 55 dB with the classical configuration with the same inertial mass as that of the flywheel configuration and 59 dB with the flywheel prototype.

The experimental results presented in this paper confirmed the theoretical study results that the flywheel inertial actuators can improve the control performance of the velocity feedback loops to reduce the broadband vibration of thin plate. The improved control performance were obtained thanks to the possibility of implementing higher control gains. Both in stability and control performance study, the experimental testes matched well the numerical results.

Finally, the static deflection study has demonstrated that the flywheel element can be used to reduce the fundamental resonance frequency of the transducer without increasing the inertial mass. Thus, the flywheel element can improve stability and robustness to shocks of the implemented velocity feedback loops both by lowering the feedback control spillover effect at the fundamental resonance frequency of the actuator and without increasing the static deflection of the transducer.

Acknowledgements

The authors gratefully acknowledge the European Commission for its support of the Marie Skłodowska Curie program through the ITN ANTARES project (GA 606817).

References

[1] A. Kras, P. Gardonio, *Velocity feedback control with a flywheel proof mass actuator*, J. Sound Vib. Vol. 402 (2017) pp. 31–50.

[2] A. Kras, P. Gardonio, *Flywheel proof mass actuator for velocity feedback control, Proc. of the ICSV24 Int. Con. Sound Vib.*, (2017) pp. 1-8.

[3] A. Kras, P. Gardonio, *Flywheel inertial actuator for velocity feedback control: parametric study, Proc. of the ISMA2016 Int. Conf.* (2016) pp. 1217-1231.

[4] S. J. Elliott, P. Gardonio, T. J. Sors, M. J. Brennan, *Active vibroacoustic control with multiple local feedback loops*, J. Acoust. Soc. Am. Vol. 111 (2002) pp. 908–15.

[5] C. G. Diaz, P. Gardonio, *Feedback control laws for proof-mass electro-dynamic actuators*, J. Smart Mater. Struct. Vol. 16 (2007) pp. 1766–83.

[6] C. G. Diaz, C. Paulitsch, P. Gardonio, *Smart panel with active damping units. Implementation of decentralized control*, J. Acoust. Soc. Am. Vol. 124 (2008) pp. 898–910.

[7] H. Politansky W. D. Pilkey, *Suboptimal feedback vibration control of a beam with a proof-mass actuators*, J. Guid. Control Dynam. Vol. 12 (1989) pp. 691–7.

[8] D. K. Lindner, T. P. Celano, E. N. Ide, *Vibration suppression using a proofmass actuator operating in stroke/force saturation*, J. Vib. Acoust. Vol. 113 (1991) pp. 423–33.

[9] D. K. Lindner, G. A. Zvonar, D. Borojevic, *Performance and control of proof-mass actuators accounting for stroke saturation*, J. Guid. Control Dynam. Vol. 17 (1994) pp. 1103–08.

[10] E. Garcia, C. S. Webb, M. J. Duke, *Passive and active control of a complex flexible structure using reaction mass actuators*, J. Vib. Acoust. Vol. 117 (1995) pp. 116–22.

[11] D. K. Lindner, G. A. Zvonar, D. Borojevic, *Nonlinear control of a proof mass actuator, AIAA J.* Guid. Control Dynam. Vol. 20 (1997) pp. 464–70.

[12] F. Fahy, P. Gardonio, *Sound and structural vibration. Radiation, Transmission and Response 2nd ed.* Academic Press, London (2007).

[13] A. Preumont, *Vibration Control of Active Structures*, Kluwer Academic, Dordrecht (2002).

[14] C. Paulitsch, *Vibration control with electrodynamic actuators*, VDI Verlag, Düsseldorf (2005).

[15] L. Benassi, S. J. Elliott, *Global control of a vibrating plate using feedback-controlled inertial actuators*, J. Sound Vib. Vol. 283 (2005) pp. 69–90.

[16] A. Preumont, *Mechatronic dynamics of electromechanical and piezoelectric systems*, Springer, Dordrecht (2006).

[17] S. H. Crandall, D. C. Karnopp, J. E. F. Kurtz, D. C. Pridmore-Brown, *Dynamics of Mechanical and Electromechanical Systems*, Krieger Pub Co. Malabar (1982).

[18] C. Paulitsch, P. Gardonio, S. J. Elliott, P. Sas, R. Boonen, *Design of a lightweight, electrodynamic, inertial actuator with integrated velocity sensor for active vibration control of a thin lightly-damped panel*, *Proc. of the ISMA 2004 Int. Conf. Leuven* (2004). pp. 239–53.

[19] S. J. Elliott, M. Serrand, P. Gardonio, *Feedback stability limits for active isolation systems with reactive and inertial actuators*, J. Vib. Acoust. Vol. 123 (2001) pp. 250–61.

[20] O. N. Baumann S. J. Elliott, *Destabilization of velocity feedback controllers with stroke limited inertial actuators*, J. Acoust. Soc. Am. Vol. 121, (2007) pp. 211-217.

[21] O. N. Baumann, S. J. Elliott, *The stability of decentralized multichannel velocity feedback controllers using inetial actuators*, J. Acoust. Soc. Am. Vol. 121 (2007) pp. 188–96.

[22] L. I. Wilmshurst, M. Ghandchi-Tehrani, S. J. Elliott, *Nonlinear vibrations of a stroke-saturated inertial actuator*, Int. Conf. RASD Pisa (2013).

[23] M. Dal Borgo, M. Ghandchi Tehrani, S. J. Elliott, *Dynamic analysis of two nonlinear inertial actuators in active vibration control*, *Proc. of the ISMA2016* (2016) pp. 1179–1190.

[24] L. Benassi, S. J. Elliott, *Active vibration isolation using an inertial actuator with local displacement feedback control*, J. Sound Vib. Vol. 278 (2004) pp. 705–724.

[25] L. Benassi, S. J. Elliott, P. Gardonio, *Active vibration isolation using an inertial actuator with local force feedback control*, J. Sound Vib. Vol. 276 (2004) pp. 157–79.

[26] C.P. Paulitsch, P. Gardonio, S.J. Elliott, *Active Vibration Control Using an Inertial Actuator with Variable Internal Damping*, J. Acoust. Soc. Am. Vol. 119 (2006) pp 2131-2140.

[27] J. Rohlfing, P. Gardonio, S. Elliott, *Feedback compensator for control units with proof-mass electrodynamic actuators*, J. Sound Vib. Vol. 331 (2012) pp. 3437–50.

[28] A. Kras, P. Gardonio, *Flywheel proof mass actuator for velocity feedback control*, *Proc. of the MoViC–RASD 2016 Int. Conf. Southampton*, UK (2016) pp. 1–14.

[29] M. Zilletti, *Feedback control unit with an inerter proof-mass electrodynamic actuator*, J. Sound Vib. Vol. 369 (2016) pp. 16–28.

[30] G. Parmar, D. B. Hiemstra, Y. Chen, S. Awtar, *A Moving Magnet Actuator for Large Range Nanopositioning*, *Proc. of the ASME Conf.* (2011) pp. 41–48.

[31] D. B. Hiemstra, G. Parmar, S. Awtar, *Performance tradeoffs posed by moving magnet actuators in flexure-based nanopositioning*, *IEEE/ASME Trans. on Mechatro.* vol. 19, (2014) pp. 201–212.

[32] P. Gardonio, M. J. Brennan, *Mobility and impedance methods in structural dynamics*, in F. Fahy, J. Walker, editors, *Advanced Applications in Acoustics, Noise and Vibration*, Spon Press London (2004) pp. 387–447.

[33] C. G. Diaz, C. Paulitsch, P. Gardonio, *Active damping control unit using a small scale proof mass electrodynamic actuator*, J. Acoust. Soc. Am. Vol. 124 (2008) pp. 886–97.

[34] Y. Aoki, P. Gardonio, M. Gavagni, C. Galassi, S. J. Elliott, *Parametric Study of a Piezoceramic Patch Actuator for Proportional Velocity Feedback Control Loop*, J. Vib. Acoust. Vol. 132 (2010) pp. 1–10.

[35] Y. Aoki, P. Gardonio, D. Emo, S. J. Elliott, *Stability and controllability of velocity feedback loops with triangularly shaped piezoelectric actuators*, *Proc. of the Active 2006 Int. Symp.* (2006).

Numerical modeling of a flexural displacement-converter mechanism to excite a flat acoustic source driven by piezoelectric stack actuators

F. Tajdari [1], **A. P. Berkhoff** [1,2], **A. de Boer** [1]
[1] University of Twente, Faculty of Engineering Technology,
Drienerlolaan 5, 7500 AE Enschede, The Netherlands
e-mail: **f.tajdari@utwente.nl**

[2] TNO Technical Sciences, Acoustics and Sonar,
Oude Waalsdorperweg 63, 2597AK Den Haag, The Netherlands

Abstract
This paper studies an acoustic source with a relatively small thickness and high bending stiffness. The acoustic source operates in the low frequency, quasi-static regime. The focus of the current study is on the actuation part in order to design an appropriate excitation mechanism. A flexural mechanism is modeled in combination with piezoelectric actuators to convert an in-plane displacement of the actuators to a perpendicular out-of-plane direction. First, an optimization simulation is used to determine the size of the required piezoelectric actuator. Then an equivalent electrical circuit of the lumped acoustic source is developed. This equivalent circuit can directly be connected to the electrical model of a switching amplifier. Finally, a coupled numerical finite element analysis is carried out by using COMSOL Multiphysics software package to model the combination of both flexural mechanism and piezoelectric device. The suggested flexural mechanism is sufficiently narrow to overcome the space limitation challenge in the design.

1 Introduction

Thin acoustic sources operating at low frequencies can be useful in active noise control as sources with severe space constraints. In the current research, a thin acoustic source is studied. This acoustic source is introduced in Refs. [1] and [2]. In this acoustic source, a high bending stiffness is obtained by attaching the source to a sandwich structure. In another research [3], a lumped model is used to investigate the possibility of using piezoelectric stack actuators as the excitation parts of this acoustic source.

In the present work, the same acoustic source that is introduced in Ref. [1], is studied. The main focus in the current research is on the design of an excitation mechanism for the acoustic source. Due to the limited available space in the thin acoustic source, piezoelectric stack actuators cannot directly be used. Therefore, the design of a displacement-converter mechanism is crucial. With the aid of a displacement-converter mechanism, piezoelectric stack actuators can be used while their displacement in one direction is converted to a displacement in a desired direction.

Commercial amplified actuators are widely used in industry [4, 5]. Thanks to compact size, straightforward design, manufacturability, and wide range of output motion and output force, these integrated amplified piezoelectric actuators offer a larger stroke than single piezoelectric multilayer actuators. However, they are only manufactured in specific dimensions and in limited aspect ratios. Among all the commercial designs, on the one hand, there is no suitable amplified actuator available that has the small dimensions compatible with the dimensions of our acoustic source. On the other hand, the available small commercial designs are not capable of delivering the required stroke and force to our acoustic source.

Integrated mechanisms are investigated in several studies to amplify the displacement of stacked piezoelectric elements. Some suggested integrated designs that use piezoelectric devices are shown in Fig. 1. Reference [6] studies a design named bridge-type amplifier shown in Fig. 1(a), in which the input and the output displacements are in the same direction. In another model called flexure hinge [7], four similar piezoelectric stack actuators are located in a symmetric in-plane configuration and are connected through a central flexural hinge. According to Fig. 1(b), the resulting displacement is, however, in-plane. A honey-comb flexural design in Fig. 1(c) is proposed in Ref. [8]. This design can translate an input displacement into an out-of-plane displacement. The suggested oval-shaped design in Ref. [9] can generate an out-of-plane output displacement according to Fig. 1(d). However, these two out-of-plane designs only perform at high frequencies and require high applied voltages. Therefore, the suggested designs deliver either an in-plane output displacement or in the case of an out-of-plane displacement, the operating frequency range is not applicable to our acoustic source.

This motivated the authors to investigate a new design for the actuators. In the current research, a flexural mechanism is proposed and is numerically studied. Due to the lack of sufficient space for the actuators in the structure of the thin acoustic source, the input and output displacements are not in the same plane. In the suggested configuration, an output displacement of the flexural mechanism is obtained by using piezoelectric stack actuators in the horizontal plane. The suggested mechanism is able to convert the displacement of the actuators to a perpendicular out-of-plane displacement to drive our acoustic source.

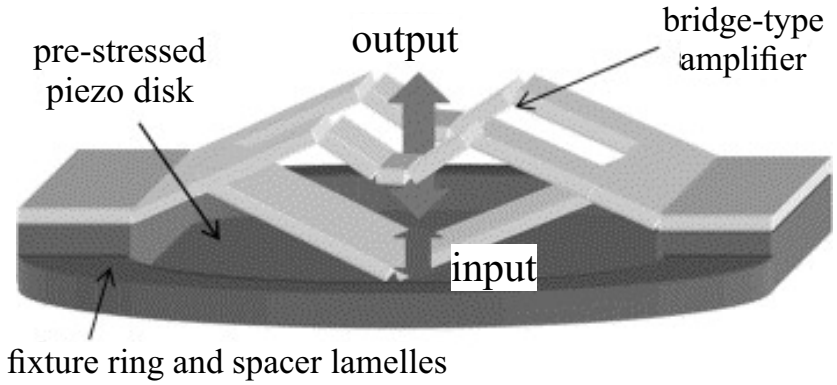
2 Methodology

2.1 Acoustic source

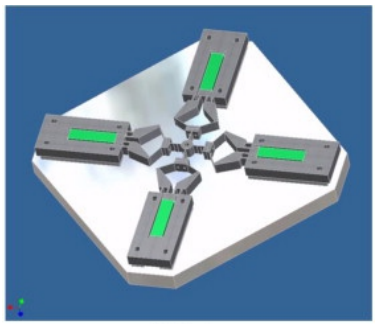
In our acoustic source, a high bending stiffness is obtained by attaching the source to a sandwich structure. The structure of the acoustic source is shown in Fig. 2. It consists of a radiating surface, a honey-comb structure, a perforated surface, an air cavity, and piezoelectric actuators. The face of the sandwich structure internal to the source is perforated to increase the acoustic compliance. The details of this acoustic source are described in Ref. [3].

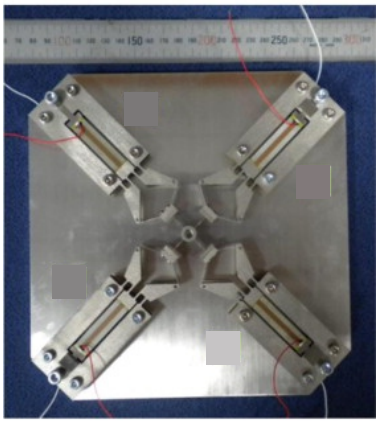
2.2 Equivalent electrical circuit

A fully-lumped model of the flat acoustic source is considered in this study. To simplify the computation, an equivalent electrical circuit of the lumped acoustic source is used in combination with the equivalent electrical circuit of piezoelectric stack actuators. The resulting circuit is represented in Fig. 3, where i_t and V_t are the total current and voltage, respectively, that are supplied to the electrical connected amplifier (*Amp.*). The current along and voltage across the piezoelectric element are respectively shown by i_{piezo} and V_{piezo}. Parameters i and e represent the output current and voltage of the electrical domain, respectively. Correspondingly, u and F_{in} show the input velocity and force to the mechanical domain, while F_{out} is the output force of the mechanical domain. In the acoustical domain, the input volume velocity and pressure are represented by U_d and P_{in}. In the electrical domain, C_0 shows the capacitance of the piezoelectric device. In the mechanical domain, Z_T and Z_S are the compliance and effective mass of the piezoelectric actuator, respectively. M_s, C_s and R_s are correspondingly the mass, compliance and mechanical damping of the acoustic source. Parameters Z_{cavity}, Z_{hollow}, Z_{screen} and Z_{rad} represent the equivalent acoustical impedances of air in the cavity, air in the hollows of the honeycomb structure, the perforated plate, and the radiation impedance of the acoustic source. U_1 and U_2 are the volume velocity along the cavity and hollows of the honeycomb panel, respectively. The parameters α and A are the conversion coefficients between domains, where the later is the surface area of the acoustic source. All the parameters in this fully-lumped model are described in detail in Ref. [3].

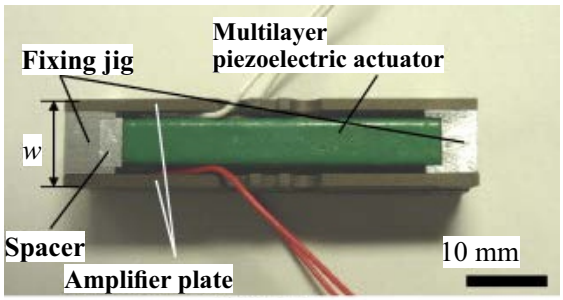


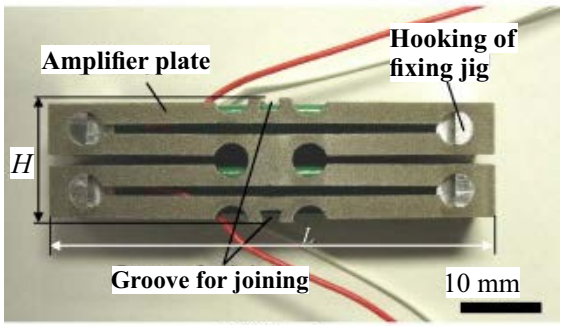
(a) Bridge-type model [6]



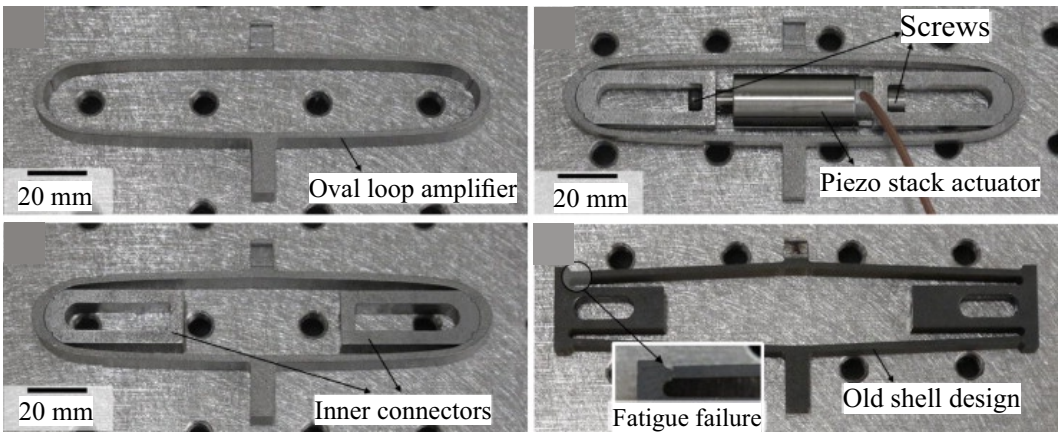


(b) Flexure hinge model [7]





(c) Honey-comb model [8]



(d) Ovel-shape model [9]

Figure 1: Available designs of the piezoelectric actuator amplified displacement models in the literature.

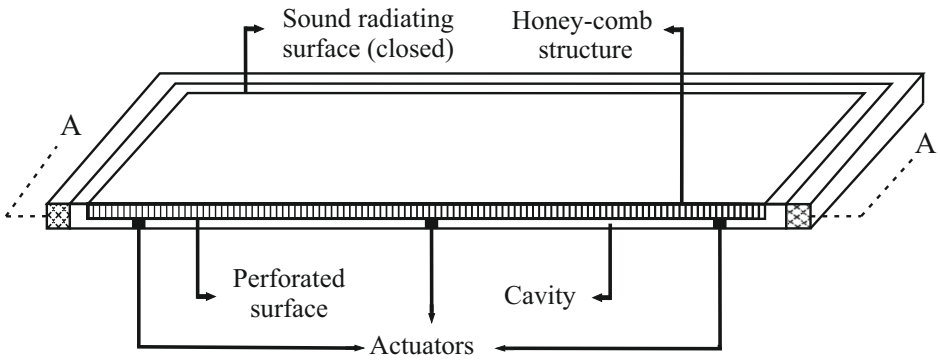


Figure 2: Cross section of the thin acoustic source.

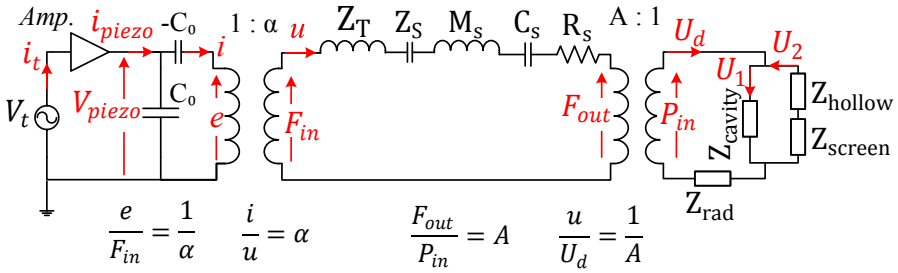


Figure 3: Complete equivalent electrical circuit of the acoustic source and piezoelectric actuators that can be connected to a switching amplifier.

According to the electrical analogy in Fig. 3, the radiation power of the lumped acoustic source is defined as the dissipated power in element Z_{rad}. This power dissipation occurs when U_d passes through the radiation impedance, Z_{rad}, in the circuit. One can evaluate P_{rad} by using the following equation:

$$P_{rad} = 0.5\Re(U_d^2 \cdot Z_{rad}^*) \tag{1}$$

Since the current in the acoustical domain, U_d, is a function of all the electrical elements in the circuit, the resulting radiation power is also a function of those elements. Therefore, P_{rad} is a function of i_{piezo} and V_{piezo}. That implies that P_{rad} is a function of the characteristics of the piezoelectric device, i.e. the dimensions of the piezoelectric element.

2.3 Optimization

The equivalent lumped electrical circuit, which is introduced in Ref. [3], is used in combination with MATLAB R2015b optimization toolbox to obtain optimum dimensions of the piezoelectric stack actuator. The following optimization problem is defined:

$$\begin{aligned} &\underset{r_p, l_p}{\text{maximize}} \quad P_{rad}(r_p, l_p) \\ &\text{subject to} \quad m_{piezo} = constant \end{aligned} \tag{2}$$

where r_p and l_p are the radius and length of the piezoelectric stack actuator, respectively. According to Eq. (2), the only constraint is the mass of the piezoelectric stack actuator (m_{piezo}). The objective is maximizing the radiation power (P_{rad}) of the acoustic source at a low frequency below 1000Hz (for instance, at 200Hz) when it is excited by a piezoelectric stack actuator. The radiation power in Eq. (2) is calculated according to Eq. (1).

The result of optimization is shown in Fig. 4. According to the figure, the maximum radiation power for

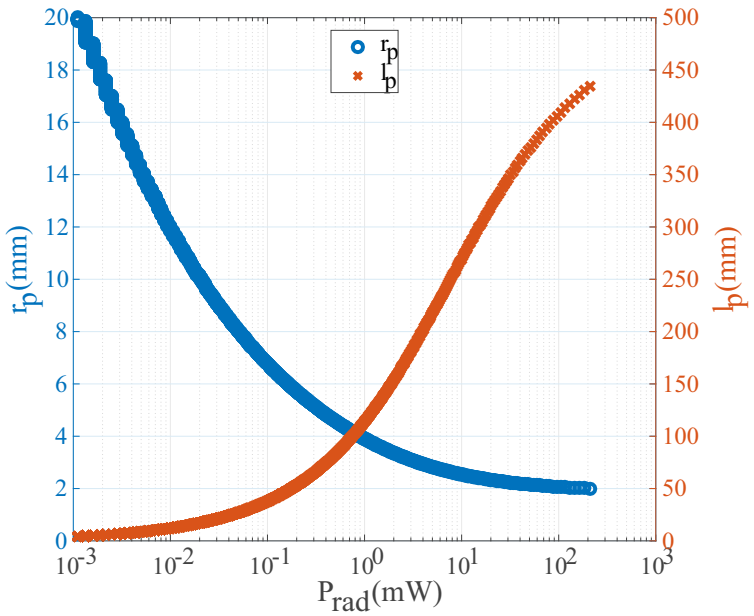


Figure 4: Optimization result showing the optimum radius and length of the piezoelectric actuator that results in a maximum radiation power of the acoustic source.

the acoustic source corresponds to the optimum radius and length of $4\mathrm{mm}$ and $100\mathrm{mm}$, respectively, for the piezoelectric stack actuator.

2.4 Requirements and limitations

According to the outcome of the optimization, a piezoelectric stack actuator with the length of $100\mathrm{mm}$ is needed. However, the available space for the actuator in the structure of the acoustic source is limited to the cavity gap with the thickness of $10\mathrm{mm}$. Since the defined piezoelectric element is not fitted in the available gap, the existence of a displacement-translator mechanism is crucial. With the aid of a displacement-converter mechanism, displacement of a piezoelectric device in a direction without any space constraint can be converted to the desired vertical displacement.

3 Numerical modeling

Flexures are elastically deforming parts that provide a precise range of motion in the desired degrees of freedom. The produced motion is predictable and repeatable [10]. These compliant mechanisms have a relatively high stiffness in the constrained directions [11]. Due to the fact that flexures are both frictionless and maintenance-free [11], they can be used in the design of the required converter mechanism in the current research.

Using a flexural displacement-converter, it is possible to use piezoelectric devices in a horizontal plane and obtain the converted displacement in a vertical out-of-plane direction. In the present paper, a 3D numerical finite element simulation in COMSOL Multiphysics software package is performed. The designed mechanism has only one degree of freedom for the displacement in the vertical direction.

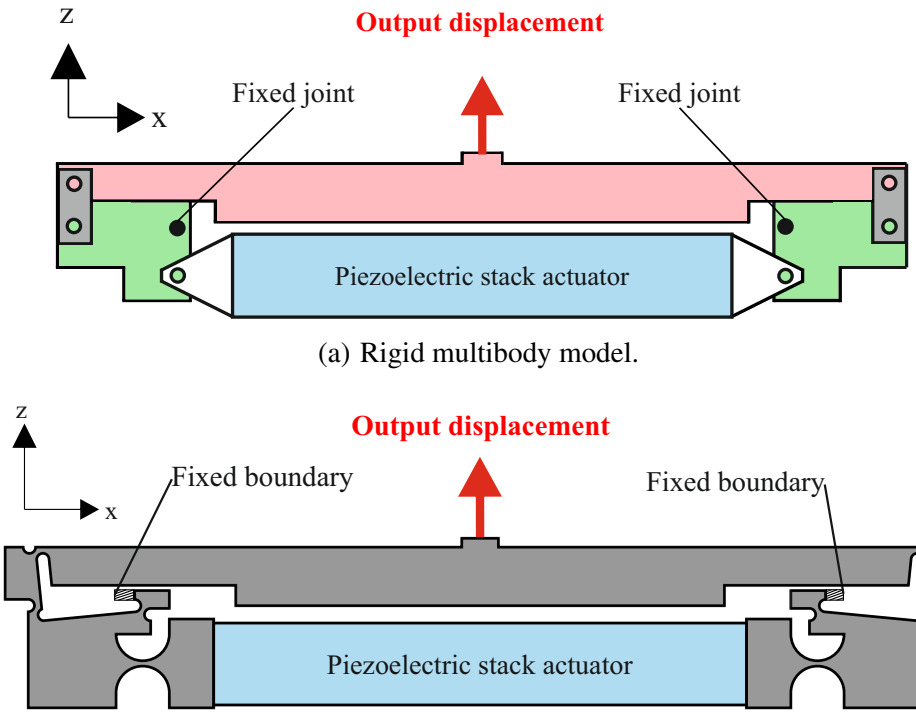
To design the flexural mechanism, first, a rigid multibody dynamics model is studied that fulfills the following requirements:

- The suggested structure has to be very small in order to be fitted in a ten-millimeter air cavity gap,
- Since a smooth vertical displacement is desired that has no parasitic motion in other directions, a symmetric design is crucial to ensure bending modes are not transmitted to the output.

In the next step, the rigid multibody dynamics model is converted to an equivalent flexure-based mechanism. Therefore, all hinge joints used in the multibody dynamics model are replaced by flexural notch hinges.

4 Results and discussion

The suggested 3D design is schematically shown in Fig. 5. First, a rigid multibody model is designed that is



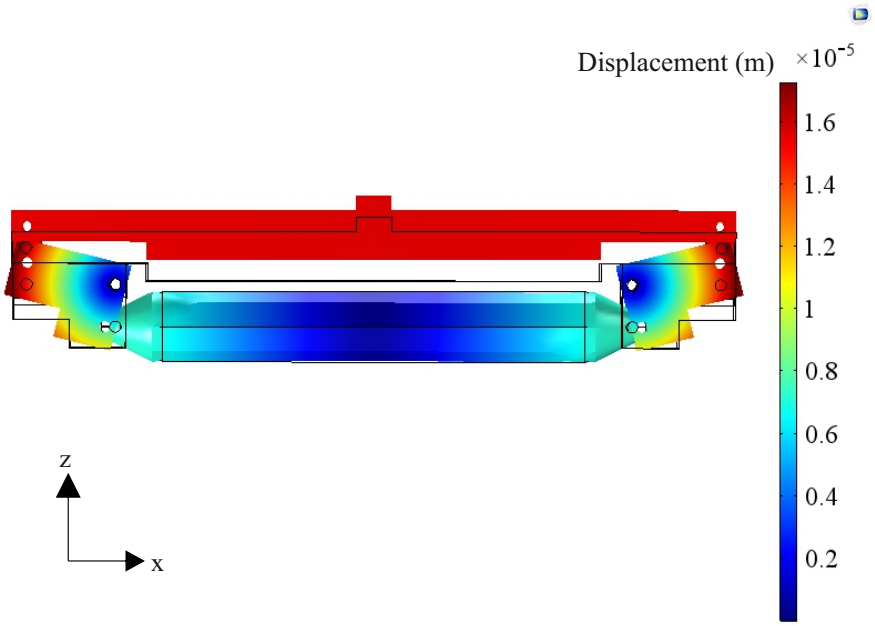
(a) Rigid multibody model.

(b) Flexural design.

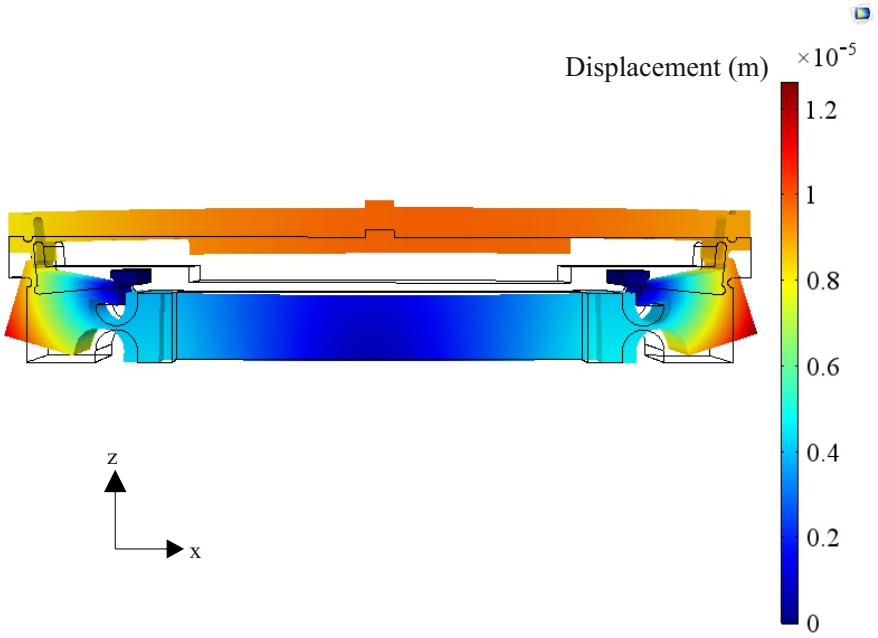
Figure 5: The suggested displacement-converter mechanism.

shown in Fig. 5(a). Then, the joints and hinges in the rigid multibody design is converted to the equivalent flexural notch hinges. According to Fig. 5(b), by using flexural notch hinges, the entire mechanism becomes a single piece. As it can be seen in the figure, both ends of the flexural mechanism are fixed to resemble the fixed joints in the multibody counterpart model. Therefore, the horizontal deformation of the piezoelectric stack actuator is translated to the output. Due to the symmetric design, the central part of the mechanism only experiences a vertical displacement. The thickness of the designed mechanism in the direction of z-axis is only $10\mathrm{mm}$ similar to the thickness of the air cavity. The out-of-plane thickness of the flexural mechanism in the direction of y-axis is $20\mathrm{mm}$ to ensure that the mechanism is stiff enough in the out-of-plane direction.

The results of a numerical simulation of the suggested mechanism in COMSOL Multiphysics is shown in Fig. 6. According to the figure, a vertical output displacement with the order of magnitude $1.5 \times 10^{-5}\mathrm{m}$ and



(a) Rigid multibody model.



(b) Flexural design.

Figure 6: Displacement of the suggested displacement-converter mechanism simulated in COMSOL.

$1.2 \times 10^{-5}\mathrm{m}$ is obtained using the rigid multibody model and the flexural design, respectively. The input displacement to both mechanisms is supplied by a piezoelectric stack actuator that is located in the horizontal plane (see Fig. 5) and deforms in the direction of x-axis. The deformation of the piezoelectric element is approximately $4.5 \times 10^{-6}\mathrm{m}$.

Thanks to the proposed flexural mechanism in the structure of our acoustic source, it is possible to use a piezoelectric stack actuator larger than the available cavity gap. The numerical results reveal that the proposed design is able to achieve the required force and displacement for the acoustic source, while the

small thickness of the thin acoustic source is preserved. The combination of the flexural mechanism and a horizontal piezoelectric element is an alternative for a vertical single piezoelectric multilayer actuator.

5 Summary

In the present research, the optimization study shows that the required length for the piezoelectric multilayer element as the excitation part of our acoustic source is approximately $100\mathrm{mm}$. However, due to space limitation in our thin acoustic source, it is not possible to use a piezoelectric stack actuator with a length larger than $10\mathrm{mm}$. Therefore, a flexural mechanism is designed to be used as a displacement-converter mechanism. The flexural mechanism is simulated numerically using COMSOL Multiphysics software package. The mechanism aims to translate an in-plane input displacement to an out-of-plane vertical output displacement. With the aid of the suggested displacement-converter mechanism, deformation of a piezoelectric stack actuator, which is located in the horizontal plane, is translated into a vertical direction. The configuration of the suggested flexural mechanism and the piezoelectric device can be used as the actuation part of the thin acoustic source. The thickness of the suggested flexural mechanism is small enough to be fitted in the air gap of the thin acoustic source.

Acknowledgements

The authors gratefully acknowledge the European Commission for its support of the Marie Curie program through the ITN ANTARES project (GA 606817).

References

[1] A. P. Berkhoff, *Sound generator*, US Patent, US20 100 111 351 A2 (2010).

[2] J. Ho, A. P. Berkhoff, *Flat acoustic sources with frequency response correction based on feedback and feed-forward distributed control*, Journal of Acoustical Society of America, Vol. 137, No. 4 (2015), pp. 2080-2088.

[3] F. Tajdari, A. P. Berkhoff, A. de Boer, *Numerical modeling of electrical-mechanical-acoustical behavior of a lumped acoustic source driven by a piezoelectric stack actuator*, in *Proceedings ISMA 2016, Leuven, Belgium, 2016 September 19-21*, Leuven (2016), pp. 1261-1276.

[4] F. Claeyssen, R. Le Letty, F. Barillot, O. Sosnicki, *Amplified Piezoelectric Actuators: Static & Dynamic Applications*, Ferroelectrics, Vol. 351, No. 1 (2007), pp. 3-14.

[5] R. Lucinskis, C. Mangeot, *Dynamic characterization of an amplified piezoelectric actuator*, in *Proceedings ACTUATOR 2016, Bremen, Germany, 2016 June 13-15*, Bremen (2016), pp. 73-76.

[6] J. Juuti, K. Kordas, R. Lonnakko, V. P. Moilanen, S. Leppavuori, *Mechanically amplified large displacement piezoelectric actuators*, The Journal of Sensors and Actuators, Vol. 120, No. A (2005), pp. 225-231.

[7] J. Guo, S. Keat Chee, T. Yano, T. Higuchi, *Micro–vibration stage using piezo actuators*, The Journal of Sensors and Actuators, Vol. 194, No. A (2013), pp. 119-127.

[8] M. Muraoka, S. Sanada, *Displacement amplifier for piezoelectric actuator based on honeycomb link mechanism*, The Journal of Sensors and Actuators, Vol. 157, No. A (2010), pp. 84-90.

[9] T. Yeom, T. W. Simon, M. Zhang, M. T. North, T. Cui, *High frequency, large displacement, and low power consumption piezoelectric translational actuator based on an oval loop shell*, The Journal of Sensors and Actuators, Vol. 176, No. A (2012), pp. 99-109.

[10] S. T. Smith, *Flexures, Elements of Elastic Mechanisms*, University of North Carolina, USA, CRC Press (2000).

[11] H. Soemers, *Design Principles for precision mechanisms*, University of Twente, The Netherlands, T-Pointprint (2011).

Active vibration control of a system subject to random excitation using impulsive parametric damping

M. Ghandchi Tehrani[1], T. Pumhoessel[2]
[1] Institute of Sound and Vibration Research, University of Southampton, UK
e-mail: **m.ghandchi-tehrani@soton.ac.uk**

[2] Institute of Mechatronic Design and Production, Johannes Kepler University Linz, Austria

Abstract
In this paper, active vibration control of a mechanical oscillator subjected to random excitation is considered using parametric impulsive damping. First, the theory of active vibration control is provided. Impulsive damping force is used as a secondary force to control the vibration. The instantaneous kinetic energy, potential energy and the dissipated energy in the passive damper are obtained. Using the energy balance, the equivalent linear damping of the impulsive damping is derived analytically. Numerical simulations are carried out to obtain the response of the system with and without impulsive damping using white noise. A parametric study is carried out and the effect of different intensities and impulse frequencies is investigated on the closed-loop response. The energy absorbed by the controller and the energy dissipated by the passive damper are also calculated for different feedback gains. The results from numerical simulation are compared with the results obtained analytically from the equivalent linear damping.

1 Introduction

Parametrically excited systems exhibit interesting dynamic behaviour and have been investigated extensively in the past [1, 2]. Parametric excitation occurs when a parameter of the system varies with time. Periodic, parametric stiffness excitation at anti-resonance frequencies, discovered by A. Tondl [3], leads to a coupling of the respective modes of vibration and allows to suppress self-excited vibrations. Due to this interaction between the modes, energy is transferred in a periodic manner from one mode to another [4, 5] and vice versa. This characteristic is of potential interest for energy harvesting, since the energy can be transferred to a mode with high amplitude of vibration. An interesting example of a parametrically excited system is a tuning fork gyroscope, in which the energy is transferred from vertical to horizontal motion due to coupling between the modes [6].

Pumhoessel et al. [7], for example, has recently investigated the effect of applying parametric stiffness excitation of impulsive type in a controlled manner. It turned out that an appropriate choice of the impulsive strength, as well as of the instants of time between adjacent impulses exists, which allows to control the amplitude of vibration by transferring energy from a weakly damped mode to a mode with higher damping, resulting in a much faster decrease of vibration amplitudes than without impulsive stiffness excitation.

Most attention has been paid to systems with stiffness modulation. However, parametric excitation with periodic time-varying damping has also been considered. Recently, the free response of a system with parametric impulsive damping subject to initial velocity has been investigated using analytical methods [8]. The dynamic response of a single degree-of-freedom mechanical oscillator with an impulsive damping subject to harmonic base excitation has been presented [9]. In this paper, the application of impulsive damping is extended to active vibration control. First, the theory of active control using impulsive damping is presented. Then, numerical simulations are carried out. It is demonstrated that parametric damping can significantly reduce the amplitude of vibration. The dissipated and the extracted energy is also calculated.

2 Theory

Consider a single degree-of-freedom mechanical oscillator as shown in Fig. 1 with feedback control. The equation of motion can be written as,

$$m\ddot{x}(t) + c\dot{x}(t) + kx(t) = f(t) + f_s(t). \tag{1}$$

where, m, c and k represent the mass, damping and stiffness of the system. A controller produces a secondary force $f_s(t)$ in the form of negative impulsive damping force to control the vibration.

$$f_s(t) = -c_p \sum_{k=1}^{N} \varepsilon_k \delta(t - t_k)\dot{x}(t), \tag{2}$$

The feedback force consists of a time-varying impulsive damping, which is made of a series of N Direct delta functions $\delta(t - t_k)$ having the strength of $c_p \varepsilon_k$. Each Dirac delta function can be seen as the simplest representative of e.g. a rectangular shaped impulse. The factor ε_k allows to scale the impulsive strength for each impulse. A sequence of periodic impulses is shown in Fig.2.

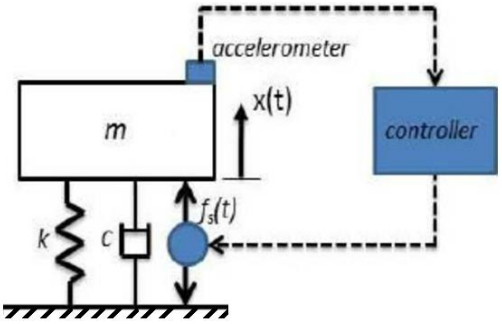


Figure 1: A single DOF system with feedback control

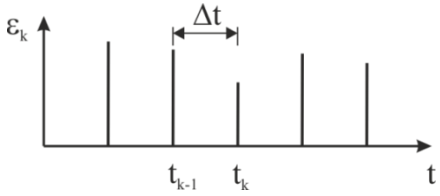


Figure 2: Periodic impulsive damping with the strength ε_k

The equivalent time-invariant linear damping of the parametric impulsive damping can be obtained from the power dissipation rates under linear and parametric damping.

$$P_L = c_{eqe}\dot{x}^2, \quad P_{NL} = f_s\dot{x}, \tag{3, 4}$$

If the constant c_{eqe} is chosen to equate the ensemble average of the two powers, $\mathrm{E}[P_L] = \mathrm{E}[P_{NL}]$, then the result is

$$c_{eqe} = \mathrm{E}[f_s(\dot{x})\dot{x}] / \mathrm{E}[\dot{x}^2] \tag{5}$$

In the expression for c_{eqe}, $\mathrm{E}[f_s(\dot{x})\dot{x}]$ and $\mathrm{E}[\dot{x}^2]$ can be interpreted as the cross-correlation between the impulsive damping force and the velocity and the auto-correlation function of the squared velocity, both at zero lag, in agreement with Nuttall's approach [10].

An iterative technique can also be used to obtain the power spectrum of the response, and hence c_{eqe}. For the first iteration $(j=1)$, it is assumed that $c_{eqe(1)} = 0$, and the auto power spectrum of the velocity is obtained from,

$$S_{\dot{x}\dot{x}(j)}(\omega) = \left|G_{(j)}(\omega)\right|^2 S_{ff}, \tag{6}$$

and the cross power spectrum of the velocity and force can be obtained from,

$$S_{\dot{x}f(j)}(\omega) = G_{(j)}(\omega) S_{ff}, \tag{7}$$

where, in general,

$$G_{(j)} = \frac{i\omega}{-\omega^2 m + i\omega\left(c + c_{eqe(j)}\right) + k} \tag{8}$$

and $c_{eqe(j)}$ is the equivalent time-invariant linear damping at the j-th iteration. The variance of the velocity can then be obtained from,

$$\sigma^2{}_{\dot{x}\dot{x}(j)} = \int_{-\infty}^{\infty} S_{\dot{x}\dot{x}(j)}(\omega) d\omega. \tag{9}$$

The next iteration of the equivalent time-invarient linear damping $c_{eqe(2)}$ for the impulsive function can then be calculated from,

$$c_{eqe(j+1)} = \frac{\mathrm{E}\left(f_s(\dot{x})\dot{x}(t)\right)}{\mathrm{E}\left(\dot{x}(t)\dot{x}(t)\right)} = \frac{1}{\sigma^2_{\dot{x}\dot{x}}} \int_{-\infty}^{\infty} \dot{x} f_s(\dot{x}) p(\dot{x}) d\dot{x} \tag{10}$$

where it is assumed that $p(\dot{x})$ is Gaussian at every iteration. This value is then used to obtain the next power spectrum and the variance of the velocity. This iteration continues until the convergence is achieved. The power spectral density of the velocity at resonance, $\left(\omega_n = \sqrt{k/m}\right)$, can also be obtained from,

$$S_{\dot{x}\dot{x}}(\omega_0) = \left|G(\omega_0)\right|^2 S_{ff} = \frac{S_{ff}}{\left(c + c_{eqe}\right)^2} \tag{11}$$

An analytical expression for c_{eqe} can be obtained by substituting for $f_s(\dot{x})$ into Eq. (5).

The "total equivalent" damping consists of the linear damping, c, and the "equivalent time-invariant linear damping" c_{eqe} for the feedback damping force .

$$c_e = c + c_{eqe} = c + c_p \sum_{k=1}^{N} \varepsilon_k \delta(t - t_k) \tag{12}$$

If we take average from the instantaneous feedback damping, for equal intensity impulses, we can obtain the equivalent time-invariant linear damping as,

$$c_{eqe} = \frac{1}{T}\int_0^T c_p \sum_{k=1}^{N} \varepsilon_k \delta(t - t_k)dt = \frac{c_p \varepsilon N}{T} \tag{13}$$

Here, N is the number of impulses per T sec. Therefore, the total damping becomes,

$$c_e = c + c_{eqe} = c + \frac{c_p \varepsilon N}{T} \tag{14}$$

3 Numerical simulation

For numerical simulation, a single DOF system with the following parameters is considered.

$$m = 1kg, \quad k = 1N/m, \quad c = 0.1Ns/m \tag{15}$$

The feedback control is the sequence of Dirac delta impulses $f_s(t) = -c_p \sum_{k=1}^{N} \varepsilon_k \delta(t - t_k)\dot{x}(t)$, in which the impulses are replaced by an equidistant series of rectangular shaped impulses shown in Fig.3, such that,

$$p(t) = \sum_{k=1}^{N} p_k(t) \tag{16}$$

Where

$$p(t) = \begin{cases} p = const & \text{if } t_k \le t \le t_k + \Delta t_p \\ 0 & \text{otherwise} \end{cases} \tag{17}$$

The intensity of the impulse κ is referred to the control parameter or the feedback gain, which is obtained from the area under the impulse.

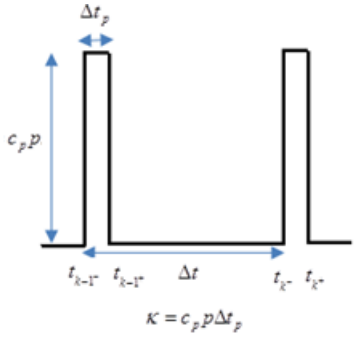
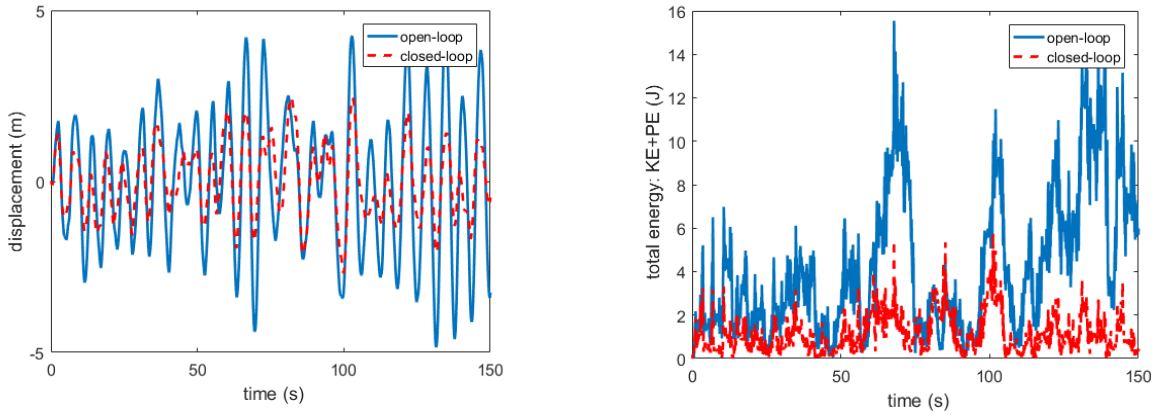


Figure 3: Feedback control with the intensity of impulses κ, period of impulses Δt and duration of impulse Δt_p

4 Results

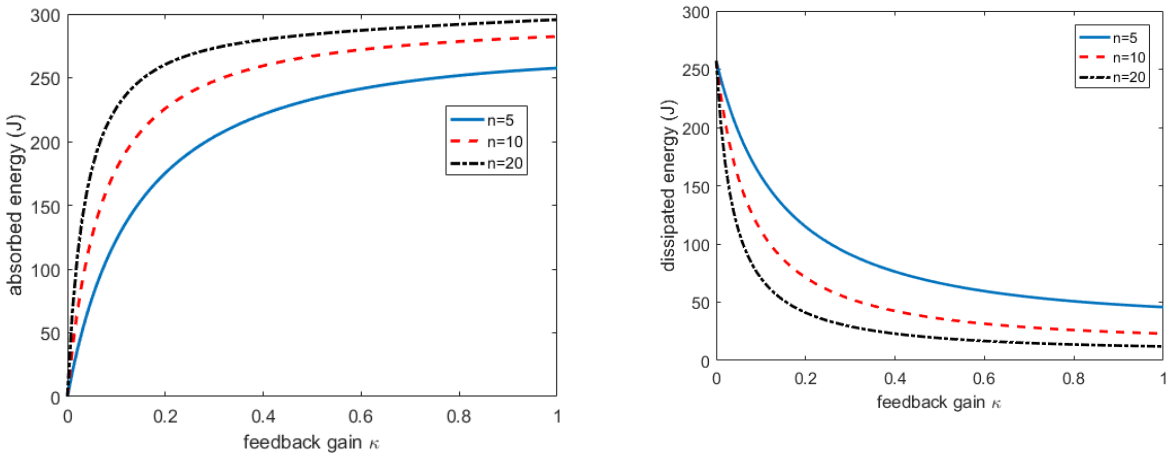
Random excitation with intensity of $S_{ff} = 1N^2$ is considered. The displacement and the total energy are shown in Fig. 4 for the open-loop (blue solid line) and closed-loop (red dashed line) system.



(a) (b)

Figure4: Random excitation: (a) displacement response (b) kinetic and potential energy for the open-loop system marked with blue solid line and closed-loop system marked with red dashed line

The absorbed energy and the dissipated energy are also obtained from integrating the instantaneous powers over the simulated time and varying the feedback gain from 0 to 1, as shown in Fig. 5 for three different numbers of impulses per period of natural vibration. The absorbed energy by the actuator increases when the feedback gain increases. Also, increasing the number of impulses increases the absorbed energy by active damping and reduces the dissipated energy in the passive damping.



(a) (b)

Figure 5: Random excitation: (a) absorbed energy by active control, (b) dissipated energy by the damper for three different number of impulses per period of external excitation as a function of the feedback gain

The equivalent linear damping for the feedback impulsive damping is found to be $c_{eqe} = \dfrac{0.1(20)}{2\pi} = 0.3183$. This is also obtained from the iterative approach described previously. The results are shown in Figure 6.

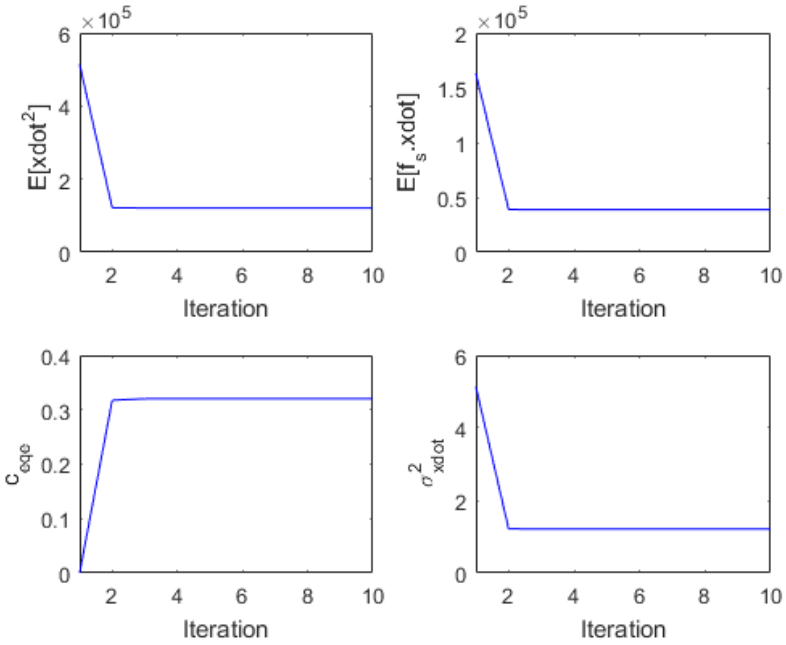
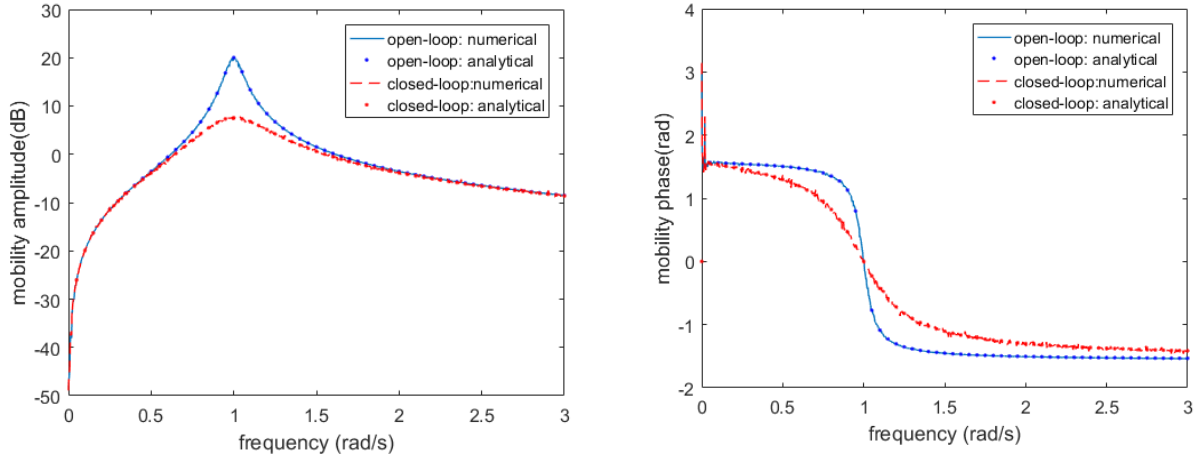


Figure 6: Random excitation: iterative approach to obtain the equivalent damping using Eq. (10)

The mobilities are obtained from time domain simulation as well as analytical formulation using Eq. (14) for open-loop and closed-loop systems. Time-domain simulation is carried out with a Gaussian random signal of 2×10^{4} points, having a sampling frequency of 318 Hz, divided into 128 blocks for averaging, and using a Hanning window with 50% overlap between each segment. The results are shown in Fig.7 There is a very good agreement between the numerical and analytical results for the open-loop and closed-loop systems, shown in Figure 7 with 20 number of impulses per 2π sec and the impulse intensity of 0.1.



(a) (b)

Figure 7: Random excitation: (a) mobility amplitude, (b) phase for the open-loop and closed-loop systems using numerical time-domain simulation and analytical formulation

The mobilities are also obtained for different feedback gains and three different numbers of impulses per natural frequency using time-domain simulation, as illustrated in Figure 8.

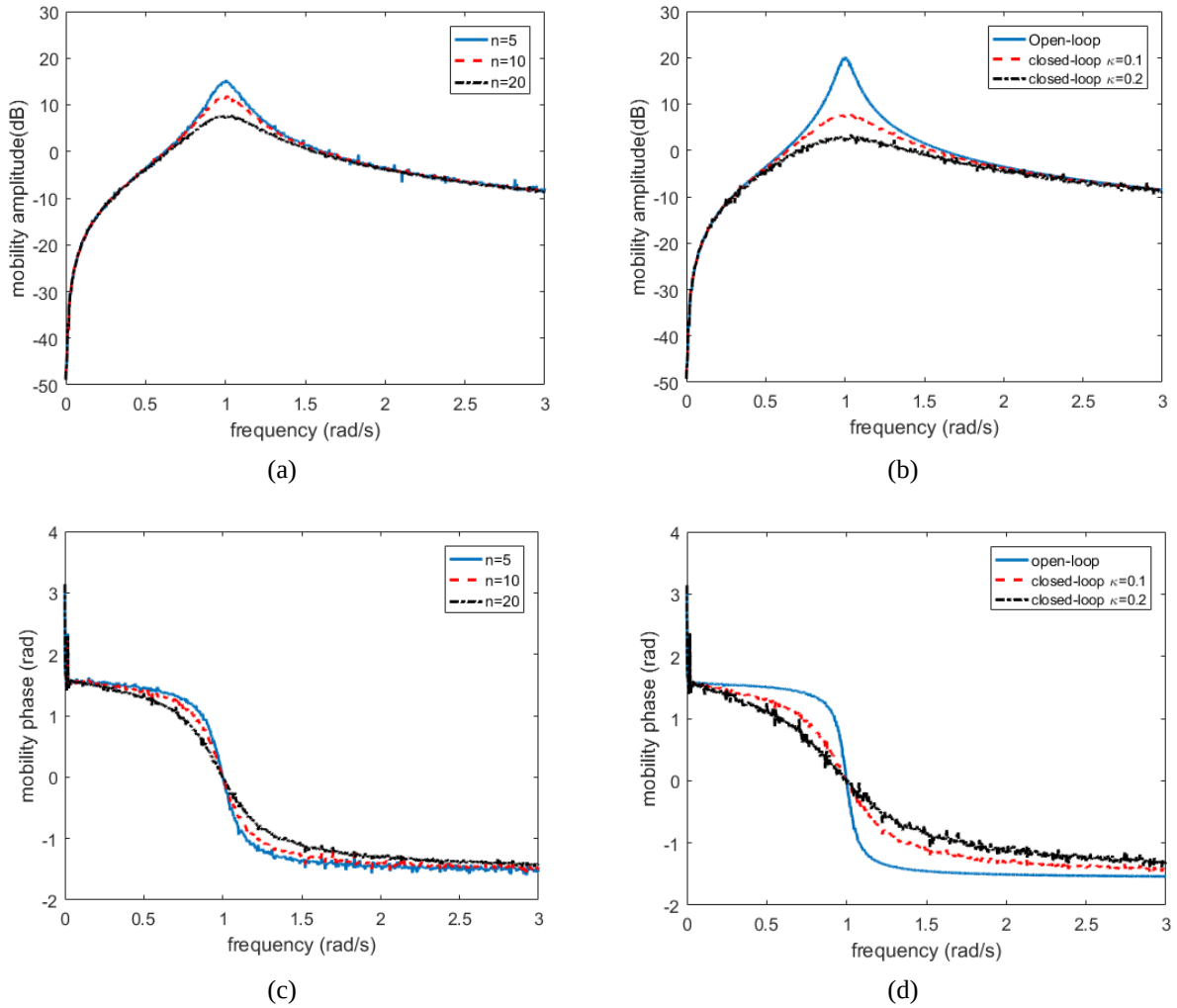


Figure 8: Random excitation: (a, b) mobility amplitudes, (c, d) phases for different number of impulses and feedback gains

5 Conclusions

In this paper, active control using impulsive feedback damping is presented. The closed-loop response of a single DOF system is obtained when the system is subjected to random excitation and the performance of active control is discussed using numerical simulations.

References

[1] M. Cartmell, , *Introduction to Linear, Parametric and Nonlinear Vibrations*, London: Chapman & Hall, (1990).

[2] A.H. Nayfeh , P.F. Pai,, *Linear and Nonlinear Structural Mechanics*, Wiley, New York, (2004).

[3] A. Tondl.., *To the problem of quenching self-excited vibrations,* Acta Technica CSAV, 43,109-116, (1998).

[4] F. Dohnal, Damping by Parametric Stiffness Excitation: Resonance and Anti-Resonance, *Journal of Vibration and Control*, 14 669-688, (2008).

[5] H. Ecker, T. Pumhoessel, *Vibration suppression and energy transfer by parametric excitation in drive systems, Proc. IMechE PartC: J. Mechanical Engineering Science*, 226(8) 2000-2014, (2012).

[6] M. Ghandchi Tehrani,.M Balthazar, M. Silveira,, *Parametric study of a macro-scale tuning fork gyroscope, ICOEV 2015*, Slovenia, (2015).

[7] T. Pumhössel, , *Energy-neutral transfer of vibration energy across modes by using active nonlinear stiffness variation of impulsive type*, ASME Journal of Computational and Nonlinear Dynamics, doi:10.1115/1.4034264, 12(1), pp. 011001–011001–11, (2016).

[8] M. Ghandchi Tehrani, and T. Pumhössel, , I*mpulsive parametric damping in energy harvesting, Recent Advances in Structural Dynamics RASD2016 Conference*, 3-6 July 2016, Southampton , UK.

[9] M. Ghandchi Tehrani., and T. Pumhoessel, , *Dynamic response of a system with impulsive parametric damping, In, Conference on Noise and Vibration Engineering, (ISMA2016)*, Leuven, BE, September 2016.

[10] A H. Nuttal, *Theory and application of the separable class of random processes*. Technical report no.343, Massachusetts Institute of Technology, Cambridge, MA.

A study on important criteria for the effectiveness of piezoelectric energy harvesters under a constant volume

N. Aboulfotoh[1, 2], J. Twiefel[1]
[1] Leibniz Universität Hannover, Institute of Dynamics and Vibration Research
Appelstr. 11, 30167 Hannover, Germany
e-mail: **naboulfotoh@aucegypt.edu**

[2] Cairo University, Institute of Statistical Studies and Research, Operations Research Department
Ahmed Zewail Str. 5, Orman, Giza 12613, Egypt

Abstract
This contribution introduces the full derivation of the applied load resistance and the excitation frequency that provides the maximum power capability of a bimorph piezoelectric cantilever. The derived formulas show capability to predict the applied load resistances and the corresponding excitation frequencies of the maximum power capability. The derived formulas can be further utilized to investigate the optimized operating conditions of the bimorph piezoelectric cantilever under volume constraints. The electrical damping is derived as a function of the system parameters and the applied load resistance.

1 Introduction

Piezoelectric energy harvesters (PEHs) have attracted the interest of many researchers over the last decades. Different geometrical shapes have been proposed for the transducers of PEHs in order to increase the power output. Goldschmidtboeing & Woias [1] studied three different beam shapes: rectangular, triangular and truncated-triangular. They found that the triangular-shaped beams outperformed the rectangular ones in terms of the maximum excitation amplitude and the maximum power output. The triangular-shaped beams were more effective in terms of curvature homogeneity independent of the proof mass. This effect was opposed by the adverse mass distribution and the increased stiffness of triangular-shaped beams. Therefore, the overall efficiency was found to be weakly influenced by the beam shape (the efficiency was calculated at the corresponding resonant mode for each beam shape). Iqbal & Mohd-yasin [2] investigated the performance of seven different cantilever designs (straight beam, straight-tapered beam, T beam, U beam, V beam, V-T beam and Y beam). All the cantilevers were made out of the same material. The thickness of the layers was considered to be the same for all the structures. It was reported that the maximum displacement was very similar for all beams. The Y-beam and the T-V beam generated the highest open-circuit voltages. The influence of the beam shape on the power output or the efficiency was not studied.

The energy harvester generates high power within a narrow band around its resonance frequency. A slight deviation between the excitation frequency and the resonance frequency will result in a significant drop in the harvested power of the tuned transducer. Broadband techniques have been proposed to overcome this limitation as reviewed in [3]. The broadband techniques include a structure to widen the bandwidth or a mechanism to tune the resonance frequency of the transducer. Energy harvesters in the form of an array of multiple elements instead of using only one element have been proposed to enlarge the bandwidth of PEHs. Eigenfrequencies of the elements in the array are tuned to the desired resonance frequencies by adapting the dimensions of the elements as in [4] or straining the elements by different axial forces as in [5]. In [6], the performance of the array energy harvester was investigated in comparison with a single reference harvester of the same volume as the entire array. It was found that the advantage of using the

array over the reference harvester was very limited to a small additional bandwidth to the detriment of a large drop in the power output.

The combined-eigenmodes strategy has been proposed for the energy harvesters to have two or more eigenfrequencies close to each other, and hence, enlarge the bandwidth of the generators. Yang and Yang [7] investigated the coupled flexural vibration of two piezoelectric beams either electrically-connected with a circuit or elastically-connected with a spring. It was reported that the two piezoelectric beams connected either electrically or elastically achieved wideband output. Some structures that have two or more eigenfrequencies close to each other have been proposed for the transducers, such as the M-shaped transducer in [8], the zigzag-shaped in [9], the V-shaped in [10], and the T-shaped in [11].

Vibration energy harvesters with two or more stable equilibrium positions have been proposed to enlarge the bandwidth, as investigated in [12]. Multistable systems with a snap-through action that transfer from one stable position to the other have a large amplitude motion and hence, improve the power output. For example, the construction consists of a beam holding a magnet at the end which is in repulsion with another auxiliary magnet. The nonlinear repulsion force between the magnets causes the beam to have two stable equilibrium positions. Under the ambient excitation, the system jumps back and forth between these positions and settles at its natural frequency as presented by Tang et al. [13].A bi-stable clamped-clamped beam was presented by Andoe et al. [14] utilizing the snap-through buckling phenomena. It was reported that the bistable nature of this conversion methodology allowed for rapid switching between the two stable states and large displacements. Scarselli et al. [15] applied the lever effect to add a bi-stable property to a clamped simply supported plate. They demonstrated that the activation force needed for the transition from a stable state to another was significantly lowered by this technique and strongly dependent on the boundary conditions.

The active tuning of the resonance frequency of the transducer has been proposed to increase the operation frequency range. Tuning the resonance frequency to match the excitation frequency was carried out either manually as in [16] or automatically as in [17] . The manual tuning does not consume electrical power, but requires the presence of an operator in the working environment. This conflicts with the idea central to the energy harvesting namely that they replace temporary batteries in applications where it is costly and inconvenient to frequently replace the batteries. On the other hand, the automatic tuning consumes electrical power. The broadband techniques have been proposed with a variety of sizes, boundary and operating conditions which makes it difficult to evaluate the differences between two techniques. In [18], a parametric study on piezoelectric energy harvesters considering a constant volume was introduced. In order to optimize the power output, the geometrical parameters (length, width, thickness, and tip mass) were recommended to be maximized within the available volume.

In order to study the optimized operating conditions of PEHs under volume constraints, the optimal load resistance and the corresponding excitation frequencies that provide the maximum power capability will be derived in this contribution. The major proposed geometry for PEHs is the uniform cross-sectional rectangular-shaped beam, especially in the studies which conducted experimental investigations, see the reviewed studies in [19][20][21]. The uniform rectangular-shaped geometry is easy to model and to manufacture, in addition to being easy to apply. Thus, the uniform rectangular-shaped geometry is considered for the study.

2 Rectangular-shaped bimorph piezoelectric cantilevers

The energy harvester under investigation is in the form of a cantilever, consisting of two piezoelectric layers and a middle non-piezoelectric layer as shown in figure 1. The considered piezoelectric cantilever has a free length of l, a total thickness of h and a width of b. Each piezoelectric layer has a thickness of h_p, a density of ρ_p and a modulus of elasticity of E_p. The total length of the piezoelectric layer is l_c. The middle layer has a thickness of h_s, a density of ρ_s and a modulus of elasticity of E_s. A tip mass of m_t is attached at the end of the cantilever. The mass ratio of the tip mass to the mass of the whole beam is β. The fixation is assumed to be rigid. An input excitation of a displacement $u(t)$ is provided to the fixation. The transversal displacement at the tip of the cantilever at any time t is given as $x(t)$.

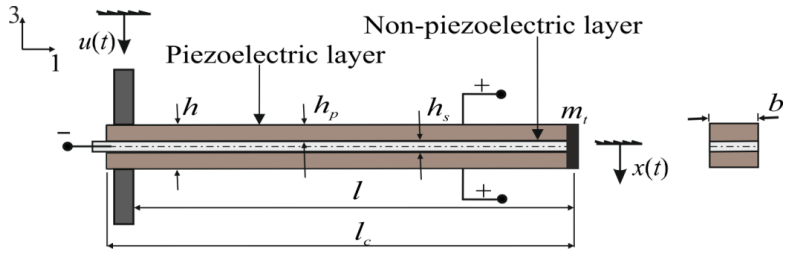


Figure 1: A bimorph piezoelectric cantilever (piezoelectric layers in parallel connection)

The power output of bimorph piezoelectric cantilevers is derived in [18], as expressed by equation 1, where m_{eq} is the equivalent mass of the beam and the tip mass, ζ_m is the mechanical damping ratio, Ω is the excitation frequency, ω_n is the resonance frequency and R is the applied load resistance, v_p is the output voltage, α is the equivalent coupling factor [N/V or C/m] and C_p is the capacitance of the two piezoelectric layers.

$$P = \frac{\alpha^2\Omega^2u^2\left(\frac{0.375+\beta}{0.2357+\beta}\right)^2}{\left(\frac{1}{R}+C_p^2\Omega^2R\right)\left(\left(1-\left(\frac{\omega_n}{\Omega}\right)^2-\frac{\alpha^2C_p}{m_{eq}(\frac{1}{R^2}+C_p^2\Omega^2)}\right)^2+\left(2\zeta_m\left(\frac{\omega_n}{\Omega}\right)+\frac{\alpha^2}{m_{eq}\Omega R(\frac{1}{R^2}+C_p^2\Omega^2)}\right)^2\right)} \quad (1)$$

3 Derivation of optimal load resistances

One method to obtain the load resistance that maximizes the power output is by equating the derivative of the power with respect to the load resistance with zero. In equation 1 of the power output, the solution to dP/dR=0 is very complicated. Thus, in order to reach the maximum power capability, another method of equating the denominator of the power formula with zero is utilized. The denominator has two multiplied parts. Both of them are equated by zero.

Part 1: Impedance matching

The first part of the denominator in equation 1 is equated by zero. The following equation is obtained:

$$\frac{1}{R}+C_p^2\Omega^2R=0 \quad (2)$$

The solution to equation 2 is a complex number ($j/C_p\Omega$). Since the applied load is assumed to be a pure load resistor, the first optimal load resistance equals the magnitude of ($j/C_p\Omega$) and is referred to as R_d (R_d =$1/C_p\Omega$).

To obtain the frequency ω_d which provides the maximum power when R_d is applied, the second part of the denominator in equation 1 is equated by zero. The following equation is obtained:

$$\left(1-\left(\frac{\omega_n}{\omega_d}\right)^2-\frac{\alpha^2C_p}{m_{eq}(\frac{1}{R_d^2}+C_p^2\omega_d^2)}\right)^2+\left(2\zeta\left(\frac{\omega_n}{\omega_d}\right)+\frac{\alpha^2}{m_{eq}\omega_dR_d(\frac{1}{R_d^2}+C_p^2\omega_d^2)}\right)^2=0 \quad (3a)$$

R_d is replaced by $1/C_p\omega_d$ and the equation is reduced as following:

$$\left(1-\left(\frac{\omega_n}{\omega_d}\right)^2-\frac{\alpha^2 C_p}{m_{eq}\left(2C_p^2\omega_d^2\right)}\right)^2=j^2\left(2\zeta_m\left(\frac{\omega_n}{\omega_d}\right)+\frac{\alpha^2}{m_{eq}\omega_d\frac{1}{C_p\omega_d}\left(2C_p^2\omega_d^2\right)}\right)^2 \tag{3b}$$

which can be reordered to:

$$1-\left(\frac{\omega_n}{\omega_d}\right)^2-\frac{\alpha^2 C_p}{m_{eq}\left(2C_p^2\omega_d^2\right)}=2\zeta_m\left(\frac{\omega_n}{\omega_d}\right)j+\frac{\alpha^2}{m_{eq}\omega_d\frac{1}{C_p\omega_d}\left(2C_p^2\omega_d^2\right)}j \tag{3c}$$

which can be reduced to:

$$\omega_d^2-\omega_n^2-\frac{\alpha^2}{2m_{eq}C_p}=2\zeta_m\omega_n\omega_d j+\frac{\alpha^2}{2m_{eq}C_p}j \tag{3d}$$

which can be reordered to:

$$\omega_d^2-2\zeta_m\omega_n j\omega_d-\left(\omega_n^2+\frac{\alpha^2}{2m_{eq}C_p}+\frac{\alpha^2}{2m_{eq}C_p}j\right)=0 \tag{3e}$$

The solution to equation 3e is:

$$\omega_d=\frac{2\zeta_m\omega_n j\pm\sqrt{-4\zeta_m^2\omega_n^2+4\left(\omega_n^2+\frac{\alpha^2}{2m_{eq}C_p}+\frac{\alpha^2}{2m_{eq}C_p}j\right)}}{2} \tag{3f}$$

which can be reduced to:

$$\omega_d=\zeta_m\omega_n j\pm\sqrt{\omega_n^2+\frac{\alpha^2}{2m_{eq}C_p}-\zeta_m^2\omega_n^2+\frac{\alpha^2}{2m_{eq}C_p}j} \tag{3g}$$

By taking the absolute value to Equation 3g, the frequency ω_d is obtained as:

$$\omega_d=\sqrt{\omega_n^2+\frac{\alpha^2}{2m_{eq}C_p}} \tag{4}$$

Hence, the formula of R_d can be expressed as:

$$R_d=\frac{1}{C_p\omega_d} \tag{5}$$

Part 2: Resonance and anti-resonance

The second part of the denominator in equation 1 is equated by zero. The following equation is obtained:

$$\left(1-\left(\frac{\omega_n}{\Omega}\right)^2-\frac{\alpha^2 C_p}{m_{eq}(\frac{1}{R^2}+C_p^2\Omega^2)}\right)^2+\left(2\zeta_m\left(\frac{\omega_n}{\Omega}\right)+\frac{\alpha^2}{m_{eq}\Omega R(\frac{1}{R^2}+C_p^2\Omega^2)}\right)^2=0 \tag{6}$$

In order to simplify the solution to equation 6, two operating conditions are assumed: the resonance operation condition and the anti-resonance operation condition.

a. Resonance operation condition

By substituting with $\Omega=\omega_n$ in Equation 6, and reducing the equation, the following equation is obtained:

$$\left(\frac{\alpha^2 C_p}{m_{eq}(\frac{1}{R^2}+C_p^2\omega_n^2)}\right)^2+\left(2\zeta_m+\frac{\alpha^2}{m_{eq}\omega_n R(\frac{1}{R^2}+C_p^2\omega_n^2)}\right)^2=0 \tag{7a}$$

which can be reordered to the following equation:

$$\left(\frac{\alpha^2 C_p}{m_{eq}(\frac{1}{R^2}+C_p^2\omega_n^2)}\right)^2=j^2\left(2\zeta_m+\frac{\alpha^2}{m_{eq}\omega_n R(\frac{1}{R^2}+C_p^2\omega_n^2)}\right)^2 \tag{7b}$$

By taking the square root of equation 7b and reordering it, the following equation is obtained:

$$\frac{\alpha^2 C_p}{m_{eq}(\frac{1}{R^2}+C_p^2\omega_n^2)}=2\zeta_m j+\frac{\alpha^2 j}{m_{eq}\omega_n R(\frac{1}{R^2}+C_p^2\omega_n^2)} \tag{7c}$$

which can be reordered to the following equation:

$$\alpha^2 C_p\omega_n R^2-\alpha^2 jR-2\zeta_m m_{eq}\omega_n j-2\zeta_m m_{eq}\omega_n^3 C_p^2 jR^2=0 \tag{7d}$$

which can be reordered to the following equation:

$$(\alpha^2 C_p\omega_n-2\zeta_m m_{eq}\omega_n^3 C_p^2 j)R^2-\alpha^2 jR-2\zeta_m m_{eq}\omega_n j=0 \tag{7e}$$

By solving equation 7e, the following equation is obtained:

$$R=\frac{\alpha^2 j\pm\sqrt{-\alpha^4-4(-2\zeta_m m_{eq}\omega_n j)(\alpha^2 C_p\omega_n-2\zeta_m m_{eq}\omega_n^3 C_p^2 j)}}{2(\alpha^2 C_p\omega_n-2\zeta_m m_{eq}\omega_n^3 C_p^2 j)} \tag{8a}$$

which can be reordered to the following equation:

$$R=\frac{\alpha^2 j\pm j\sqrt{\alpha^4+(-8\zeta_m m_{eq}\omega_n j)(\alpha^2 C_p\omega_n-2\zeta_m m_{eq}\omega_n^3 C_p^2 j)}}{2(\alpha^2 C_p\omega_n-2\zeta_m m_{eq}\omega_n^3 C_p^2 j)} \tag{8b}$$

which can be reordered to the following equation:

$$R=\frac{\alpha^2 j\pm j\sqrt{\alpha^4-8\zeta_m m_{eq}\alpha^2\omega_n^2 C_p j+16\zeta_m^2 m_{eq}^2\omega_n^4 C_p^2 j^2)}}{2(\alpha^2 C_p\omega_n-2\zeta_m m_{eq}\omega_n^3 C_p^2 j)} \tag{8c}$$

which can be reduced to the following equation:

$$R = \frac{\alpha^2 j \pm j\sqrt{\left(\alpha^2 - 4\zeta_m m_{eq}\alpha^2\omega_n^2 C_p j\right)^2}}{2C_p\omega_n(\alpha^2 - 2\zeta_m m_{eq}\omega_n^2 C_p j)} \tag{8d}$$

which can be reduced to the following equation:

$$R = \frac{\alpha^2 j \pm j(\alpha^2 - 4\zeta_m m_{eq}\alpha^2\omega_n^2 C_p j)}{2C_p\omega_n(\alpha^2 - 2\zeta_m m_{eq}\omega_n^2 C_p j)} \tag{8e}$$

By solving equation 8e, the value of R equals either

$$R_1 = \frac{\alpha^2 j + j(\alpha^2 - 4\zeta_m m_{eq}\alpha^2\omega_n^2 C_p j)}{2C_p\omega_n(\alpha^2 - 2\zeta_m m_{eq}\omega_n^2 C_p j)} = \frac{2j(\alpha^2 - 2\zeta_m m_{eq}\alpha^2\omega_n^2 C_p j)}{2C_p\omega_n(\alpha^2 - 2\zeta_m m_{eq}\omega_n^2 C_p j)} = \frac{j}{C_p\omega_n} \tag{8f}$$

or

$$R_2 = \frac{\alpha^2 j - j(\alpha^2 - 4\zeta_m m_{eq}\alpha^2\omega_n^2 C_p j)}{2C_p\omega_n(\alpha^2 - 2\zeta_m m_{eq}\omega_n^2 C_p j)} = \frac{2\zeta_m m_{eq}\alpha^2\omega_n^2 C_p j}{C_p\omega_n(\alpha^2 - 2\zeta_m m_{eq}\omega_n^2 C_p j)} \tag{8g}$$

The optimal load resistance can be obtained by the magnitude of equation 8g and is expressed as:

$$R_{op} = |R_2| = \frac{2\zeta_m m_{eq}\alpha^2\omega_n}{\sqrt{\alpha^4 + 4\zeta_m^2 m_{eq}^2\omega_n^4 C_p^2}} \tag{9}$$

b. Anti-resonance operation condition

First, a formula for the anti-resonance frequency is derived. The applied load is assumed to be very high (open circuit condition). The reciprocal of R approximately equals zero. By using this information, equation 6 can be reduced to Equation 10a.

$$\left(1 - \left(\frac{\omega_n}{\omega_{anti}}\right)^2 - \frac{\alpha^2 C_p}{m_{eq}(C_p^2\omega_{anti}^2)}\right)^2 + \left(2\zeta_m\frac{\omega_n}{\omega_{anti}}\right)^2 = 0 \tag{10a}$$

By reordering, the following equation is obtained:

$$\left(1 - \left(\frac{\omega_n}{\omega_{anti}}\right)^2 - \frac{\alpha^2 C_p}{m_{eq}(C_p^2\omega_{anti}^2)}\right)^2 = j^2\left(2\zeta_m\frac{\omega_n}{\omega_{anti}}\right)^2 \tag{10b}$$

By taking the square root, the following equation is obtained:

$$1 - \left(\frac{\omega_n}{\omega_{anti}}\right)^2 - \frac{\alpha^2 C_p}{m_{eq}(C_p^2\omega_{anti}^2)} = 2\zeta_m\frac{\omega_n}{\omega_{anti}}j \tag{10c}$$

By reordering, the following equation is obtained:

$$\omega_{anti}^2 - \left(2\zeta_m \omega_n j\right)\omega_{anti} - \left(\frac{\alpha^2}{m_{eq}C_p} + \omega_n^2\right) = 0 \tag{10d}$$

By solving equation 10d, the anti-resonance is obtained as:

$$\omega_{anti} = \frac{2\zeta_m \omega_n j \pm \sqrt{-4\zeta^2\omega_n^2 + 4\left(\frac{\alpha^2}{m_{eq}C_p} + \omega_n^2\right)}}{2} \tag{11a}$$

which can be reduced to the following equation:

$$\omega_{anti} = \zeta_m \omega_n j \pm \sqrt{-\zeta^2\omega_n^2 + \left(\frac{\alpha^2}{m_{eq}C_p} + \omega_n^2\right)} \tag{11b}$$

By getting the magnitude of equation 11b, and reducing the equation, the anti-resonance frequency is obtained as:

$$\omega_{anti} = \sqrt{\omega_n^2 + \frac{\alpha^2}{m_{eq}C_p}} \tag{12}$$

In order to derive the optimal load resistance (R_{op_anti}) at anti-resonance frequency, equation 6 is solved at $\Omega=\omega_{anti}$. The following equation is obtained:

$$\left(1 - \left(\frac{\omega_n}{\omega_{anti}}\right)^2 - \frac{\alpha^2 C_p}{m_{eq}\left(\frac{1}{R_{op_anti}^2} + C_p^2\omega_{anti}^2\right)}\right)^2 + \left(2\zeta_m\left(\frac{\omega_n}{\omega_{anti}}\right) + \frac{\alpha^2}{m_{eq}\omega_{anti}R_{op_anti}\left(\frac{1}{R_{op_anti}^2} + C_p^2\omega_{anti}^2\right)}\right)^2 = 0 \tag{13}$$

By taking the square root of equation 13 and reordering it, the following equation is obtained:

$$1 - \left(\frac{\omega_n}{\omega_{anti}}\right)^2 - \frac{\alpha^2 C_p}{m_{eq}\left(\frac{1}{R_{op_anti}^2} + C_p^2\omega_{anti}^2\right)} = 2\zeta_m\frac{\omega_n}{\omega_{anti}}j + \frac{\alpha^2 j}{m_{eq}\omega_{anti}R_{op_anti}\left(\frac{1}{R_{op_anti}^2} + C_p^2\omega_{anti}^2\right)} \tag{14a}$$

By reordering, the following equation is obtained:

$$\left(1 - \left(\frac{\omega_n}{\omega_{anti}}\right)^2 - 2\zeta_m\frac{\omega_n}{\omega_{anti}}j\right)m_{eq} = \frac{\alpha^2 C_p}{\left(\frac{1}{R_{op_anti}^2} + C_p^2\omega_{anti}^2\right)} + \frac{\alpha^2 j}{\omega_{anti}R_{op_anti}\left(\frac{1}{R_{op_anti}^2} + C_p^2\omega_{anti}^2\right)} \tag{14b}$$

By assuming a constant c_1, the following equation is obtained:

$$c_1 = \frac{\alpha^2 C_p}{\left(\frac{1}{R_{op_anti}^2} + C_p^2\omega_{anti}^2\right)} + \frac{\alpha^2 j}{\omega_{anti}R_{op_anti}\left(\frac{1}{R_{op_anti}^2} + C_p^2\omega_{anti}^2\right)} \tag{14c}$$

where

$$c_1 = \left(1 - \left(\frac{\omega_n}{\omega_{anti}}\right)^2 - 2\zeta_m \frac{\omega_n}{\omega_{anti}} j\right) m_{eq} \tag{14d}$$

By reordering equation 14c, the following equation is obtained:

$$c_1 = \frac{\alpha^2 C_p \omega_{anti} R_{op_anti} + \alpha^2 j}{\omega_{anti} R_{op_anti} (\frac{1}{R_{op_anti}^2} + C_p^2 \omega_{anti}^2)} = \frac{\alpha^2 (C_p \omega_{anti} R_{op_anti} + j)}{\omega_{anti} R_{op_anti} \frac{1}{R_{op_anti}^2} (1 + C_p^2 \omega_{anti}^2 R_{op_anti}^2)} \tag{15a}$$

By reordering, the following equation is obtained:

$$c_1 = \frac{\alpha^2 (C_p \omega_{anti} R_{op_anti} + j)}{\omega_{anti} R_{op_anti} \frac{1}{R_{op_anti}^2} (C_p \omega_{anti} R_{op_anti} + j)(C_p \omega_{anti} R_{op_anti} - j)} \tag{15b}$$

By reducing and reordering, the following equation is obtained:

$$c_1 = \frac{\alpha^2 R_{op_anti}}{\omega_{anti} (C_p \omega_{anti} R_{op_anti} - j)} = \frac{\alpha^2 / \omega_{anti}}{(C_p \omega_{anti} - j / R_{op_anti})} \tag{16a}$$

which can be reordered to the following equation:

$$\frac{j}{R_{op_anti}} = \frac{\alpha^2 / \omega_{anti}}{c_1} + C_p \omega_{anti} \tag{16b}$$

From the formula of the anti-resonance frequency (equation 12), the following equation can be obtained:

$$\omega_{anti}^2 \left(1 - \frac{\omega_n^2}{\omega_{anti}^2}\right) = \frac{\alpha^2}{m_{eq} C_p} \tag{17}$$

By substituting equation 17 in equation 14d of the constant c_1, the following equation is obtained:

$$c_1 = \left(\frac{\alpha^2}{C_p \omega_{anti}^2} - 2\zeta_m \frac{\omega_n}{\omega_{anti}} m_{eq} j\right) \tag{18}$$

By substituting equation 18 in equation 16b of the constant c_1, the following equation is obtained:

$$\frac{j}{R_{op_anti}} = \frac{-\alpha^2 / \omega_{anti}}{\left(\frac{\alpha^2}{C_p \omega_{anti}^2} - 2\zeta_m \frac{\omega_n}{\omega_{anti}} m_{eq} j\right)} + C_p \omega_{anti} = \frac{-\alpha^2 C_p \omega_{anti}}{\left(\alpha^2 - 2\zeta_m \omega_{anti} m_{eq} C_p j\right)} + C_p \omega_{anti} \tag{19}$$

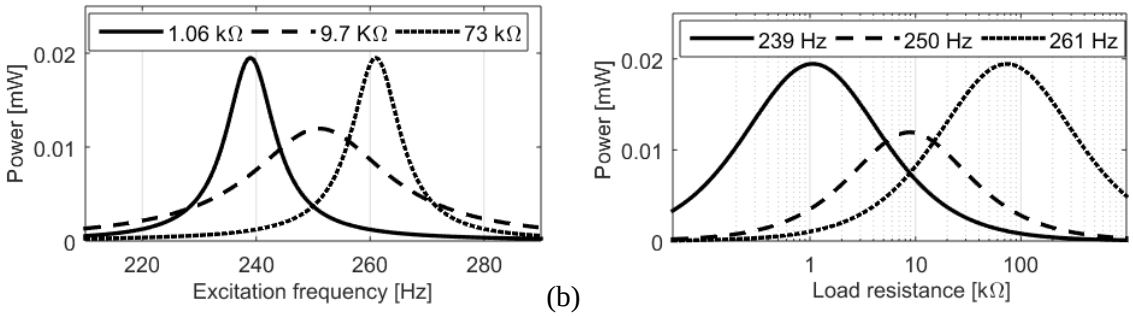
From equation 19, the magnitude optimal load resistance at anti-resonance frequency is obtained as following:

$$R_{op_anti} = \frac{\sqrt{\alpha^4 + 4\zeta_m^2 m_{eq}^2 \omega_n^2 C_p^2 \omega_{anti}^2}}{2\zeta_m m_{eq} \omega_n C_p^2 \omega_{anti}^2} \tag{20}$$

The capability of the derived formulas of the optimal load resistance is investigated. All investigations in this contribution consider the bimorph piezoelectric cantilever of the properties displayed in table 1. figure 2a displays the power output versus the excitation frequency at the three derived load resistances R_{op} of 1.06 kΩ, R_d of 9.7 kΩ and R_{op_anti} of 73 kΩ. figure 2b displays the power output versus the applied load resistance at three excitation frequencies (ω_n of 239 Hz, ω_d of 250 Hz and ω_{anti} of 261 Hz). The maximum possible power is obtained at the resonance frequency and the anti-resonance frequency for an applied load resistance of R_{op} and R_{op_anti}, respectively. It is shown also that the derived formulas show capability to predict the load resistances of the maximum power output. The applied load resistance of R_d causes the maximum electrical damping to the circuit. The maximum power output at an applied load resistance of R_d occurs at the excitation frequency of ω_d.

	Piezoelectric	Non-piezoelectric
Mechanical data	s_{11}^E = 14.2e-12 m²/N, ρ_p= 8100 kg/m³	E_s = 1.25e11 N/m², ρ_s = 1800 kg/m³
Piezoelectric data	d_{31} = 315e-12 C/N, ε_{33}^T = 3.98e-08 F/m	
Dimensions	h = 0.78 mm, h_p = 0.27 mm, h_s = 0.24 mm, l_c = 45 mm, b =7.25 mm, l=39mm	

Table 1: Properties of the bimorph type "VIBRIT 1100" Johnson Matthey (data sheet)



(a) (b)

Figure 2: (a) The power output versus the excitation frequency (b) The power output versus the applied load resistance

4 Derivation of electrical damping ratio

The piezoelectric energy harvester is governed by two coupled electromechanical equations as presented in [22]. The governing equations are expressed as following:

$$m_{eq}\ddot{x}(l,t) + d_m\dot{x}(l,t) + c_{eq}x(l,t) + \alpha v_p(t) = F_{eq} \tag{21a}$$

$$\alpha\dot{x}(l,t) - C_p\dot{v}_p(t) = \frac{v_p(t)}{R} \tag{21b}$$

where c_{eq} is the equivalent stiffness and d_m is the mechanical damping coefficient.

From Equation 21a, the transfer function between the output displacement and the input displacement is obtained as described in [18] as:

$$H_{xu}=\left(\frac{0.375+\beta}{0.2357+\beta}\right)\frac{1}{1-\left(\frac{\omega_n}{\Omega}\right)^2-\frac{\alpha^2 C_p}{m_{eq}(\frac{1}{R^2}+C_p^2\Omega^2)}-2\zeta_m\left(\frac{\omega_n}{\Omega}\right)j-\frac{\alpha^2}{m_{eq}\Omega R(\frac{1}{R^2}+C_p^2\Omega^2)}j} \tag{22a}$$

At resonance where $\Omega=\omega_n$, the equation of the transfer function can be reduced to:

$$H_{xu}\big|_{\Omega=\omega_n}=\left(\frac{0.375+\beta}{0.2357+\beta}\right)\frac{-1}{\frac{-\alpha^2 C_p}{m_{eq}(\frac{1}{R^2}+C_p^2\omega_n^2)}+2\zeta_m j+\frac{\alpha^2}{m_{eq}\omega_n R(\frac{1}{R^2}+C_p^2\omega_n^2)}j} \tag{22b}$$

The electrical damping as a function of the applied load resistance is an important factor to be investigated. In order to obtain a formula for the electrical damping ratio, the influence of the piezoelectric effect is represented by electrical damping of coefficient d_e where $d_e= 2\zeta_e m_{eq}\omega_n$ (ζ_e is the electrical damping ratio). The equation of motion of the beam can be expressed as:

$$m_{eq}\ddot{x}(t)+(d_m+d_e)\dot{x}(t)+c_{eq}x(t)=F_{eq} \tag{23a}$$

By taking the Laplace transform of equation 23a, the following equation is obtained:

$$-m_{eq}\Omega^2 x(\Omega j)+(d_m+d_e)\Omega x(\Omega j)+c_{eq}x(\Omega j)=m_f\Omega^2 u(\Omega j) \tag{23b}$$

As in [18], the equivalent mass is $m_{eq}=bl(0.2357+\beta)\ (\rho_s h_s+2\rho_p h_p)$ and the equivalent driving force is $F_{eq}=bl(0.375+\beta)\ (\rho_s h_s+2\rho_p h_p)\ddot{u}$. By substituting in Equation 23b, the transfer function between the tip displacement and the input displacement is obtained as:

$$H_{xu}=\frac{-(0.375+\beta)(\rho_s h_s+2\rho_p h_p)lb\Omega^2}{-m_{eq}\Omega^2+(d_m+d_e)\Omega+c_{eq}} \tag{24a}$$

At $\Omega=\omega_n$, the transfer function at resonance is as following:

$$H_{xu}\big|_{\Omega=\omega_n}=\frac{-(0.375+\beta)(\rho_s h_s+2\rho_p h_p)lb\omega_n^2}{(d_m+d_e)\omega_n}=\frac{-(0.375+\beta)(\rho_s h_s+2\rho_p h_p)lb\omega_n^2}{(2\zeta_m m_{eq}+2\zeta_e m_{eq})\omega_n^2} \tag{24b}$$

which can be reduced to:

$$H_{xu}\big|_{\Omega=\omega_n}=\left(\frac{0.375+\beta}{0.2357+\beta}\right)\frac{-1}{2(\zeta_m+\zeta_e)j} \tag{24c}$$

By equating equation 24c to equation 22b and reducing, the following equation is obtained:

$$\frac{-1}{2(\zeta_m+\zeta_e)j}=\frac{-1}{\frac{-\alpha^2 C_p}{m_{eq}(\frac{1}{R^2}+C_p^2\omega_n^2)}+2\zeta_m j+\frac{\alpha^2}{m_{eq}\omega_n R(\frac{1}{R^2}+C_p^2\omega_n^2)}j} \tag{25a}$$

From which, the following equation can be obtained:

$$2(\zeta_m+\zeta_e)j=\frac{-\alpha^2 C_p}{m_{eq}(\frac{1}{R^2}+C_p^2\omega_n^2)}+2\zeta_m j+\frac{\alpha^2}{m_{eq}\omega_n R(\frac{1}{R^2}+C_p^2\omega_n^2)}j \tag{25b}$$

By eliminating $2\zeta mj$ from both sides in Equation C.5b, the following equation is obtained:

$$2(\zeta_e)j=\frac{-\alpha^2 C_p}{m_{eq}(\frac{1}{R^2}+C_p^2\omega_n^2)}+\frac{\alpha^2}{m_{eq}\omega_n R(\frac{1}{R^2}+C_p^2\omega_n^2)}j \tag{25c}$$

By taking the magnitude of both sides in equation 25c, the electrical damping ratio can be obtained as following:

$$\zeta_e = \sqrt{\frac{\alpha^4 C_p^2}{4m_{eq}^2(\frac{1}{R^2}+C_p^2\omega_n^2)^2} + \frac{\alpha^4}{4m_{eq}^2\omega_n^2R^2(\frac{1}{R^2}+C_p^2\omega_n^2)^2}} = \sqrt{\frac{\alpha^4(C_p^2\omega_n^2+\frac{1}{R^2})}{4m_{eq}^2\omega_n^2(\frac{1}{R^2}+C_p^2\omega_n^2)^2}} \tag{26}$$

At an excitation frequency around the first eigenfrequency, the electrical damping is expressed as:

$$\zeta_e = \frac{\alpha^2}{2m_{eq}\omega_n\sqrt{(\frac{1}{R^2}+C_p^2\omega_n^2)}} = \frac{\alpha^2}{2m_{eq}\omega_n(\frac{1}{R}+C_p\omega_n j)} \tag{27}$$

In equation 27, if the applied load R is replaced by R_d (which equals $1/C_p\omega_d$), the electrical damping ratio will be maximized. The impact of the applied load resistance normalized to the resistance R_d on the electrical damping ratio is displayed by figure 3. The electrical damping is maximum at $R = R_d$.

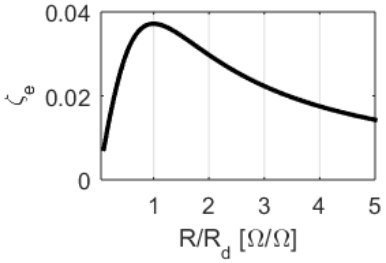


Figure 3: Impact of (R/R_d) on the electrical damping ratio

In equation 27, if the applied load R is replaced by the optimal load resistance at resoance, the magnitude of the electrical damping ratio will equal the magnitude of the mechanical damping ratio ($\zeta_e = \zeta_m$). Figure 4a displays the impact of the applied load resistance on the electrical damping ratio. At low applied load resistances much less than ($1/C_p\omega_d$), the electrical damping ratio is proportional to the applied load resistance. An increase in the applied load resistance results in an increase in the electrical damping. For load resistances much higher than ($1/C_p\omega_d$), the electrical damping ratio increases very slightly for a large increase in the applied load resistance. Figure 4b displays the impact of the mechanical damping ratio (ζ_m) on the optimal load resistance (R_{op}). At very low mechanical damping ratios, the optimal load resistance is proportional to ζ_m. After the optimal load resistance equals ($1/C_p\omega_d$), a large increase in the mechanical damping ratio causes a slight increase in the optimal load. The electrical damping ratio from figure 4a equals the mechanical damping ratio from figure 5b at the corresponding optimal load resistance. For example (follow the red dashed line), the optimal load resistance is 1 kΩ when the mechanical damping ratio is 0.01. Applying the optimal load resistance of 1 kΩ results in an electrical damping of ratio 0.01.

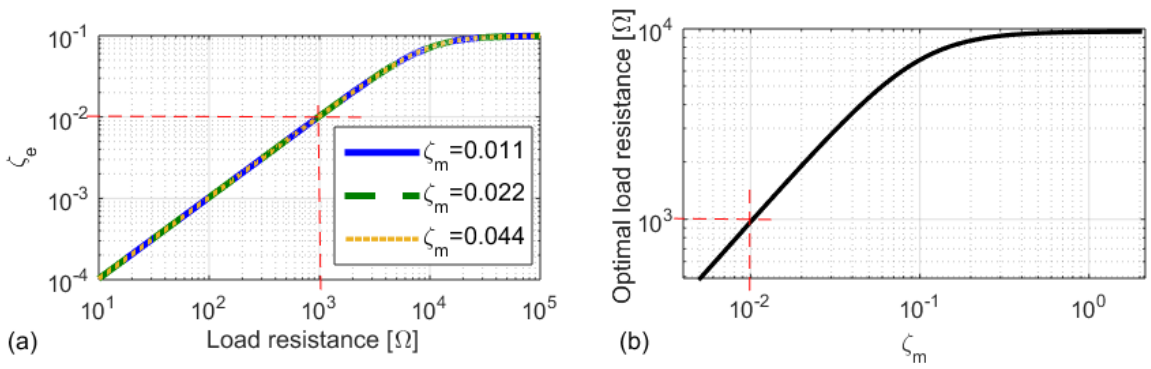


Figure 4: (a) Impact of applied load resistance on electrical damping ratio (b) Impact of mechanical damping ratio on optimal load resistance

5 Derivation of maximum power output

The maximum power is generated at resonance and at an applied load resistance which is equal to the magnitude of the internal impedance of the transducer as investigated in [18]. Formulas for the maximum power at R_{op} and ω_n as well as at R_d and ω_d are derived.

a. Maximum power at R_{op} and ω_n

At resonance, equation 1 of the power output can be reduced to:

$$P\big|_{\Omega=\omega_n} = \frac{\alpha^2\omega_n^2 u^2\left(\frac{0.375+\beta}{0.2357+\beta}\right)^2}{\left(\frac{1}{R}+C_p^2\omega_n^2 R\right)\left(\left(\frac{\alpha^2 C_p}{m_{eq}(\frac{1}{R^2}+C_p^2\omega_n^2)}\right)^2+\left(2\zeta_m+\frac{\alpha^2}{m_{eq}\omega_n R(\frac{1}{R^2}+C_p^2\omega_n^2)}\right)^2\right)} \tag{28}$$

From equation 27 of the electrical damping ratio, the following equation can be obtained:

$$-2\zeta_e\omega_n = \frac{-\alpha^2(\frac{1}{R}-C_p\Omega j)}{m_{eq}(\frac{1}{R^2}+C_p^2\Omega^2)} \tag{29a}$$

which can be reordered to the following equation:

$$\frac{-2\zeta_e\omega_n}{R(\frac{1}{R}-C_p\Omega j)} = \frac{-\alpha^2}{m_{eq}R(\frac{1}{R^2}+C_p^2\Omega^2)} \tag{29b}$$

By substituting in the equation 28, the equation can be reduced to the following equation:

$$P\big|_{\Omega=\omega_n} = \frac{\alpha^2\omega_n^2 u^2\left(\frac{0.375+\beta}{0.2357+\beta}\right)^2}{\left(\frac{1}{R}+C_p^2\omega_n^2 R\right)\left(\frac{-2\zeta_e\omega_n C_p R}{R(\frac{1}{R}-C_p\omega_n j)}-2\zeta_m j-\frac{2\zeta_e j}{R(\frac{1}{R}-C_p\omega_n j)}\right)^2} \tag{30a}$$

By reordering, the following equation is obtained:

$$P\big|_{\Omega=\omega_n} = \frac{\alpha^2\omega_n^2 u^2\left(\frac{0.375+\beta}{0.2357+\beta}\right)^2}{\left(\frac{1}{R}+C_p^2\omega_n^2 R\right)\left(-2\zeta_e\left(\frac{\omega_n C_p R+j}{R(\frac{1}{R}-C_p\omega_n j)}\right)-2\zeta_m j\right)^2} = \frac{\alpha^2\omega_n^2 u^2\left(\frac{0.375+\beta}{0.2357+\beta}\right)^2}{\left(\frac{1}{R}+C_p^2\omega_n^2 R\right)\left(-2\zeta_e j-2\zeta_m j\right)^2} \tag{30b}$$

which can be reduced to:

$$P\big|_{\Omega=\omega_n} = \frac{\alpha^2\omega_n^2 u^2\left(\frac{0.375+\beta}{0.2357+\beta}\right)^2}{4\left(\zeta_e+\zeta_m\right)^2\left(\frac{1}{R}+C_p^2\omega_n^2 R\right)} \tag{31}$$

A formula for the maximum power at ω_n and R_{op} is obtained. At these conditions, the electrical damping ratio equals the mechanical damping ratio as investigated in figure 3. In Equation 31, at $R=R_{op}$, the following equation is obtained:

$$P\big|_{\Omega=\omega_n,R_{op}} = \frac{\alpha^2\omega_n^2u^2\left(\frac{0.375+\beta}{0.2357+\beta}\right)^2}{4\left(2\zeta_e\right)^2\left(\frac{1}{R_{op}}+C_p\omega_n j\right)^2R_{op}} \tag{32a}$$

By utilizing Equation 27 of the electrical damping ratio, equation 32a can be reduced to

$$P\big|_{\Omega=\omega_n,R_{op}} = \frac{\alpha^2\omega_n^2u^2\left(\frac{0.375+\beta}{0.2357+\beta}\right)^2}{4\left(2\zeta_e\right)^2\left(\frac{\alpha^2}{2m_{eq}\omega_n\zeta_e}\right)^2R_{op}} \tag{32b}$$

The power output at an applied load resistance of R_{op} and an excitation frequency of ω_n is obtained as:

$$P\big|_{\Omega=\omega_n,R_{op}} \frac{\omega_n^4u^2m_{eq}^2\left(\frac{0.375+\beta}{0.2357+\beta}\right)^2}{4\alpha^4R_{op}} \tag{33}$$

It is observed in equation 33 that the maximum power is independent of the mechanical damping ratio (ζ_m), where ζ_m is implicitly included in the formula of the optimal load resistance $R_{op}=f(\zeta_m)$.

b. Maximum power at R_d and ω_d

An equation for the power output at excitation frequency of ω_d and an applied load resistance of R_d will be derived. At $\Omega=\omega_d$ and $R=R_d$, equation 1 of the power output is as following:

$$P\big|_{\omega_d,R_d} = \frac{\alpha^2\omega_d^2u^2\left(\frac{0.375+\beta}{0.2357+\beta}\right)^2}{\left(C_p\omega_d+C_p\omega_d\right)\left(\left(1-\left(\frac{\omega_n}{\omega_d}\right)^2-\frac{\alpha^2C_p}{m_{eq}(2C_p^2\omega_d^2)}\right)^2+\left(2\zeta_m\left(\frac{\omega_n}{\omega_d}\right)+\frac{\alpha^2}{m_{eq}\omega_d\frac{1}{C_p\omega_d}(2C_p^2\omega_d^2)}\right)^2\right)} \tag{34a}$$

which can be reduced to the following equation:

$$P\big|_{\omega_d,R_d} = \frac{\alpha^2\omega_d^6u^2\left(\frac{0.375+\beta}{0.2357+\beta}\right)^2}{\left(2C_p\omega_d\right)\left(\omega_d^2-\omega_n^2-\frac{\alpha^2}{m_{eq}(2C_p)}+2\zeta_m\omega_n\omega_d j+\frac{\alpha^2 j}{m_{eq}(2C_p)}\right)^2} \tag{34b}$$

From equation 4 of ω_d, it can be obtained that $(\omega_d)^2-(\omega_n)^2=\alpha^2/(2m_{eq}C_p)$ which is substituted in equation 34b to obtain the following equation:

$$P\big|_{\omega_d,R_d} = \frac{\alpha^2\omega_d^6u^2\left(\frac{0.375+\beta}{0.2357+\beta}\right)^2}{\left(2C_p\omega_d\right)\left(\frac{4\zeta_m\omega_n\omega_dC_pm_{eq}+\alpha^2}{2C_pm_{eq}}\right)^2} = \frac{\alpha^2\omega_d^6u^2\left(\frac{0.375+\beta}{0.2357+\beta}\right)^2}{\frac{2C_p\omega_d}{4C_p^2m_{eq}^2}\left(4\zeta_m\omega_n\omega_dC_pm_{eq}+\alpha^2\right)^2} \tag{35}$$

By reducing equation 36, the power output at $\Omega=\omega_d$ and $R=R_d$ is obtained as:

$$P\big|_{\omega_d,R_d} = \frac{2\alpha^2\omega_d^5 u^2 C_p m_{eq}^2 \left(\frac{0.375+\beta}{0.2357+\beta}\right)^2}{\left(4\zeta_m\omega_n\omega_d C_p m_{eq}+\alpha^2\right)^2} \tag{36}$$

6 Conclusion

The broadband techniques have been proposed with a variety of sizes, boundary and operating conditions. They mostly require a complicated setup, volume and mass and are costlier than a single piezoelectric energy harvester (PEH) with the transducer only. Due to the importance of volume in PEHs, one possible way to appraise the proposed PEHs is to evaluate their performance in comparison with a single reference harvester of the same volume. The rectangular-cross section bimorph piezoelectric cantilever is chosen as the reference. The optimal load resistance and the corresponding excitation frequencies that provide the maximum power capability were derived. They are found to be functions of the geometrical and material parameters. Formulas were derived for the maximum power output at the derived optimal load resistances. It is found that the maximum power output at resonance is dependent on the geometrical and material properties and independent of the mechanical damping at an applied load resistance of the corresponding optimal load resistance.

Acknowledgements

The authors gratefully acknowledge the European Commission for its support of the Marie Curie program through the ITN ANTARES project (GA 606817).

References

[1] F. Goldschmidtboeing and P. Woias, “Characterization of different beam shapes for piezoelectric energy harvesting,” *J. micromechanics microengineering*, vol. 18, no. 10, p. 104013 (7pp), 2008.

[2] A. Iqbal and F. Mohd-yasin, “Comparison of seven cantilever designs for piezoelectric energy harvester based on Mo / AlN / 3C-SiC,” *RSM2015 Proc. 2015*, no. 1, pp. 1–4, 2015.

[3] J. Twiefel and H. Westermann, “Survey on broadband techniques for vibration energy harvesting,” *J. Intell. Mater. Syst. Struct.*, vol. 24, no. 11, pp. 1291–1302, 2013.

[4] K. Swee-Leong, N. Mohamad, Y. David Fook Weng, C. Soo Kien, and D. Chang Fu, “Multi-frequency energy harvesting using thick-film piezoelectric cantilever,” *InECCE - Int. Conf. Electr. Control Comput. Eng.*, pp. 420–423, 2011.

[5] W. Al-Ashtari, M. Hunstig, T. Hemsel, and W. Sextro, “Physical Enhanced energy harvesting using multiple piezoelectric elements : Theory and experiments,” *Sensors Actuators A. Phys.*, vol. 200, pp. 138–146, 2013.

[6] N. Aboulfotoh and J. Twiefel, “A Study on Bandwidth and Performance Limitations of Array Vibration Harvester Configurations,” *Energy Harvest. Syst.*, vol. 4, no. 1, pp. 47–56, 2017.

[7] Zengtao Yang and Jiashi Yang, “Connected Vibrating Piezoelectric Bimorph Beams as a Wide-band Piezoelectric Power Harvester,” *J. Intell. Mater. Syst. Struct.*, vol. 20, no. 5, pp. 569–574, 2009.

[8] S. Leadenham and A. Erturk, “M-shaped asymmetric nonlinear oscillator for broadband vibration energy harvesting: Harmonic balance analysis and experimental validation,” *J. Sound Vib.*, vol. 333, no. 23, pp. 6209–6223, 2014.

[9] M. A. Karami and D. J. Inman, "Analytical Modeling and Experimental Verification of the Vibrations of the Zigzag Microstructure for Energy Harvesting," *J. Vib. Acoust.*, vol. 133, no. 1, p. 11002, 2011.

[10] M. M. R. El-Hebeary, M. H. Arafa, and S. M. Megahed, "Modeling and experimental verification of multi-modal vibration energy harvesting from plate structures," *Sensors Actuators, A Phys.*, vol. 193, pp. 35–47, 2013.

[11] A. R. M. Siddique, S. Mahmud, and B. Van Heyst, "Energy conversion by 'T-shaped' cantilever type electromagnetic vibration based micro power generator from low frequency vibration sources," *Energy Convers. Manag.*, vol. 133, pp. 399–410, 2017.

[12] T. Kumar, R. Kumar, V. S. Chauhan, and J. Twiefel, "Finite-Element Analysis of a Varying-Width Bistable Piezoelectric Energy Harvester," *Energy Technol.*, vol. 3, no. 12, pp. 1243–1249, 2015.

[13] L. Tang, Y. Yang, and C.-K. Soh, "Improving functionality of vibration energy harvesters using magnets," *J. Intell. Mater. Syst. Struct.*, vol. 23, no. 13, pp. 1433–1449, 2012.

[14] B. Andoe, S. Baglio, A. R. Bulsara, and V. Marletta, "A bistable buckled beam based approach for vibrational energy harvesting," *Sensors Actuators, A Phys.*, vol. 211, pp. 153–161, 2014.

[15] G. Scarselli, F. Nicassio, F. Pinto, F. Ciampa, O. Iervolino, and M. Meo, "A novel bistable energy harvesting concept," *Smart Mater. Struct.*, vol. 25, no. 5, p. 55001, 2016.

[16] M. O. Mansour, M. H. Arafa, and S. M. Megahed, "Resonator with magnetically adjustable natural frequency for vibration energy harvesting," *Sensors Actuators A Phys.*, vol. 163, no. 1, p. Pages 297–303, Jan. 2010.

[17] D. Zhu, S. Roberts, M. J. Tudor, and S. P. Beeby, "Physical Design and experimental characterization of a tunable vibration-based electromagnetic micro-generator," *Sensors Actuators A. Phys.*, vol. 158, no. 2, pp. 284–293, 2010.

[18] N. Aboulfotoh and J. Twiefel, "On developing an optimal design procedure for a bimorph piezoelectric cantilever energy harvester under a predefined volume," *Mech. Syst. Signal Process.*, vol. 106, pp. 1–12, 2018.

[19] H. S. Kim, J. J. Kim, and J. J. Kim, "A Review of Piezoelectric Energy Harvesting Based on Vibration," *Int. J. Precis. Eng. Manuf.*, vol. 12, no. 6, pp. 1129–1141, 2011.

[20] N. Elvin and A. Erturk, *Advances in energy harvesting methods*. Springer Science&Business Media New York, 2013.

[21] C. R. Bowen, V. Y. Topolov, and H. A. Kim, *Modern Piezoelectric Energy-Harvesting Materials*. Springer International Publishing Switzerland, 2016.

[22] N. W. Hagood and W. H. Chung, "Modelling of Piezoelectric Actuator Dynamics for Active Structural Control," no. July, pp. 327–354, 1990.

Stability, performance and power consumption of a centralised and decentralised active vibration control system

G. Lapiccirella[1], J. Rohlfing[2]
[1] Fraunhofer Institute for Structural Durability and System Reliability LBF, Darmstadt, Germany
e-mail: **giovanni.lapiccirella@lbf.fraunhofer.de**

[2] Fraunhofer Institute for Building Physics IPB, Stuttgart, Germany

Abstract
This paper presents simulations and experimental results on the stability, performance and power consumption of a Multiple Input Multiple Output (MIMO) Active Vibration Control (AVC) system comprising six inertial mass actuators (IMAs), when centralised and decentralised velocity feedback control architectures are implemented. The open-loop (OL) matrices for the centralised and decentralised systems are calculated and the AVC stability is assessed using the generalised Nyquist criterion for both control architectures. The control performance and the apparent power consumption of the AVC system IMAs are compared and discussed. Additionally, the percentage of reactive power is evaluated. Initial results show that both control architectures achieve similar control performances for simulations and measurements. However, the measured total apparent power as well as the reactive power consumption is higher than in simulations. Measurements show higher reactive power for the decentralised AVC.

1 Introduction

Structural vibrations represent a problem in lightly damped constructions. In vehicle and transportations industries (e.g. aerospace, automotive, naval etc.), lightweight design is increasingly important, due to the strict requirements on CO_2 emissions and fuel consumption. This may lead to lightly damped lightweight structures and hence to vibration problems. Passive measures are generally a first choice to cope with those problems. However, in order to be effective in the low frequency range, they tend to be heavy and bulky. For this reason, Active Vibration Control (AVC) systems are a promising approach for vibration attenuation whenever passive approaches are inadequate [1]. AVC systems exploit active elements (actuators) which apply forces to the structure under control in order to obtain stiffening, damping or isolation effects, depending on the implemented control strategy [2].

A notable control strategy for the attenuation of structural resonant peaks is to implement velocity feedback control (VFB) using AVC system comprising Inertial Mass Actuators (IMAs). VFB control is a linear time invariant control strategy which allows implementing active viscous damping into the structure under control [1, 3]. In this control strategy, a velocity signal taken from the structure is amplified and fed back via force transducers. The resulting effect is the addition of viscous damping into the structure [4, 5] which results in a broadband attenuation of the resonant response peaks. VFB has been intensively investigated for implementing active damping for vibro-acoustic applications [6, 7].

For the application of AVC systems on large structures, multiple actuators might be needed. In this case, the AVC system is composed of several actuators and sensors distributed on the controlled structure, resulting in a Multiple-Input-Mulitple-Output (MIMO) system [8]. MIMO AVC systems can be implemented with a centralised or decentralised control architectures. In centralised control systems all

sensor signals are fed into a single processor controller which evaluates all control signals for the actuators [3]. The centralised MIMO AVC system can be composed of a different number of actuators and sensors. The actuators and sensors can be selectively used to control different vibrational modes [1, 5]. However, centralised controllers may be difficult to implement, when a large number of actuators and sensors are used. The computational burden of centralised controllers scales drastically up with the number of sensors and actuators involved, limiting their applications. Alternatively, decentralised control consists of an equal number of sensors and actuators arranged in closely collocated pairs. Each actuator-sensor pair works independently in order to achieve a common result (e.g. kinetic energy reduction) [3]. This kind of control architecture is easier to be implemented since each controller deals with a single actuator-sensor pair.

Several studies compared the performance of VFB implemented on MIMO AVC systems with centralised and decentralised architectures. These studies show that VFB implemented on centralised AVC systems allow slightly higher performance than decentralised AVC systems [9, 10, 11]. However, in many cases the relatively low expected improvement in performance may not justify the implementation of centralised controllers.

One aspect that has generally not received much attention in previous studies is the electrical power consumption of AVC systems. In particular, thus far the difference in the power consumption between different MIMO VFB AVC system architectures has not been investigated in any greater detail. Most studies focus on performance achieved by the two control architectures rather than the power consumption. However, due to the strict requirements on power consumption for some applications, an additional discriminant aspect between the two control architectures may be the amount of electrical power required by the actuators.

In the following sections, a simulation and experimental studies on the stability, performance and power consumption of MIMO centralised and decentralised AVC systems is presented. In section two, the laboratory test rig and the simulation model is introduced. The studied AVC system is composed of six electrodynamic IMAs and six acceleration sensors. It is implemented to a laboratory six cells truss structure. In the third section, the stability analysis of the MIMO AVC system for the centralised and decentralised architectures is presented. In the fourth section, the simulation and experimental results for the performance and power consumption of the systems are presented and discussed. In the fifth section, the results and conclusions are summarised and an outlook on future work is given.

2 The laboratory test rig and the simulation model

This section presents the experimental test rig and the simulation model considered in this study. Figure 1a shows the laboratory test rig composed of a six cells truss structure with a MIMO AVC system with six IMAs attached. The disturbance force is induced using a ‘primary’ shaker, which is suspended from an external frame using elastic rubber bands and coupled to the truss structure via a stinger and a force gauge.

a) b)

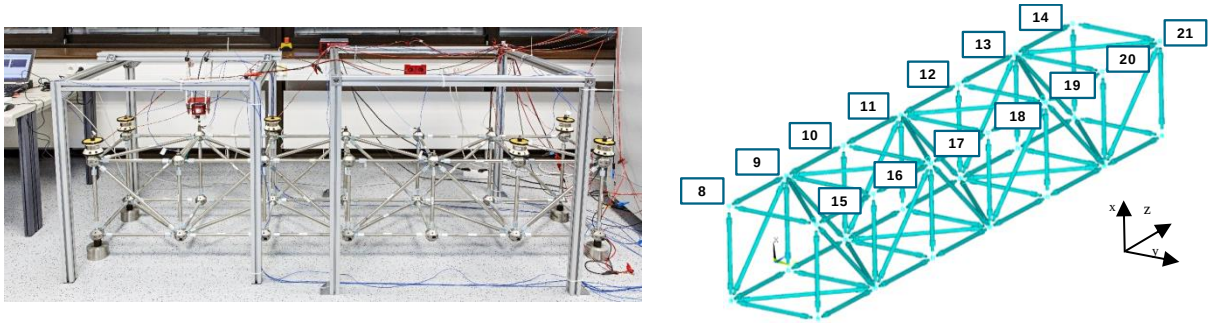


Figure 1– a) Laboratory six cells truss structure b) FEM model of the six cells truss structure, with the fourteen possible selected control positions

The six cells truss structure is composed of 28 nodes, connecting 52 short and 24 long struts. The short struts are used as vertical and horizontal elements, while the long struts are used as diagonal elements. The structure is mounted on four low stiffness rubber mounts at the four principal corners. The low stiffness of the rubber mounts guarantees that all the rigid body modes of the structure lie below 16 Hz. Six global modes occur within the frequency range from 50 Hz to 162 Hz. Three rhombic modes occur at 52.7 Hz, 54.2 Hz and 130.2 Hz. The first two bending modes occur at 143.5 Hz and 144.2 Hz and the first torsional mode occurs at 161.5 Hz. The modes occurring above 161.5 Hz are mostly local modes of the struts. The results from preliminary studies on the truss structure are presented in Ref. [12]. The results from experimental modal analysis on the six cells truss structure are given in Ref. [13].

Figure 1b shows the finite element method (FEM) model of the truss structure. The model consists of individual strut models of different lengths. These struts are modularly built up consisting of two connection bolts, two coupling nuts and the beam. The connections between the beams, the connection bolts and the two connecting nuts are defined by elastic element connections, for which the values were determined experimentally. The FEM model of the truss structure consists of more than 33000 degrees of freedom (DOF). The high number of degrees of freedom makes this model unpractical for numerical investigations on AVC systems. Hence, for the purpose of this study, the FEM model is reduced to the first 60 modes, which occur in the frequency range between 0 and 250 Hz. The input (forces) and output (velocities) points of the reduced order model are selected to be the fourteen connecting nodes on the top of the truss structure numbered as in Figure 1b. The degrees of freedom are constrained to translation in x-direction only. The reduced model is then converted to a state space model with 120 states using the AdaptroSim™ toolbox developed at the Fraunhofer LBF [14] and imported in Matlab® Simulink® for numerical simulations.

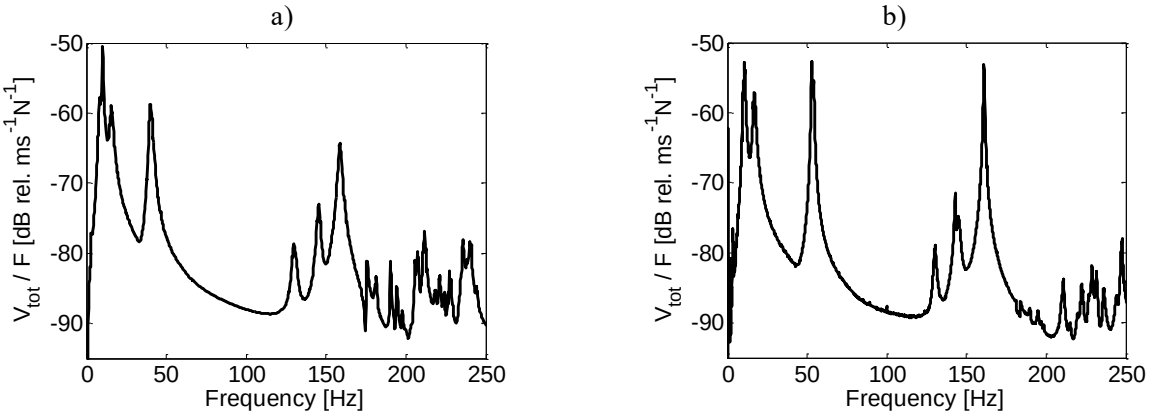


Figure 2 – FRFs of the mean total velocity normalised by the input force at node 9 – a) Simulations; b) Measurements

Figure 2 shows the frequency response functions (FRFs) of the total mean velocity of the truss structure normalised to the external primary disturbance force introduced at node 9 in x-direction. Figure 2 shows the simulation results obtained with the reduced order model. Figure 2 b shows the experimental results obtained from measurements on the truss structure on the fourteen output nodes. In both the simulation and the laboratory experiment, the peak responses of the rigid body modes occur between 0 Hz and 15 Hz and the peak responses of the first six global modes occur between 39 Hz and 162 Hz. The frequencies of the individual response peaks of the rigid and global modes in the simulated FRF match well with those in the measured FRF. A higher difference can be noted for the frequency of the response peak of the first rhombic mode, which occurs around 39 Hz in the simulation and around 52.7 Hz in the laboratory experiment (see Figure 2). The peak amplitudes in the simulated FRF are slightly lower than the amplitudes of the response peaks in the measured FRF. The results in Figure 2 show good general agreement for both rigid body and global modes occurring in the considered frequency range from 0 Hz to 250 Hz, which is sufficient since this study focuses to the AVC performance achieved on the global modes of the truss structure.

The six IMAs composing the AVC system (also visible in Figure 1a) are Fraunhofer LBF in house designs. The IMAs are constructed from a linear electrodynamic voice coil motor, where the coil is rigidly

mounted on the base. An aluminium beam, which is also rigidly mounted to the base, goes through the centre hole of the magnet. The magnet is suspended from the base via two membrane springs. If a current flows through the coil, a force is generated between the base and magnet which acts an inertial mass. Figure 3 shows the IMA used for the AVC system. In particular, Figure 3b shows the lumped parameter model used to describe the dynamic behaviour of the IMAs in the simulations. The moving mass corresponds to the mass of the magnet, while the static mass corresponds to the coil and the other structural elements rigidly connected to the base of the IMA. The mechanical characteristics of the membrane springs have been modelled as simple stiffness and damping elements. The electrical characteristics of the coil are modelled using inductive and resistive elements in an LR-2 model, which takes into account the divergence with the pure inductive behaviour of the theoretical electrical impedance. This model describes more precisely the behaviour of the electrical impedance at higher frequencies, where the effects of the inductance losses due to the eddy currents in the conductive magnetic pole are increasingly important. A comparison between the experimentally evaluated electrical impedance and the LR-2 model of the IMAs is given in Ref. [15]. The linear parameters of the six IMAs have been experimentally identified and are listed in Table 1.

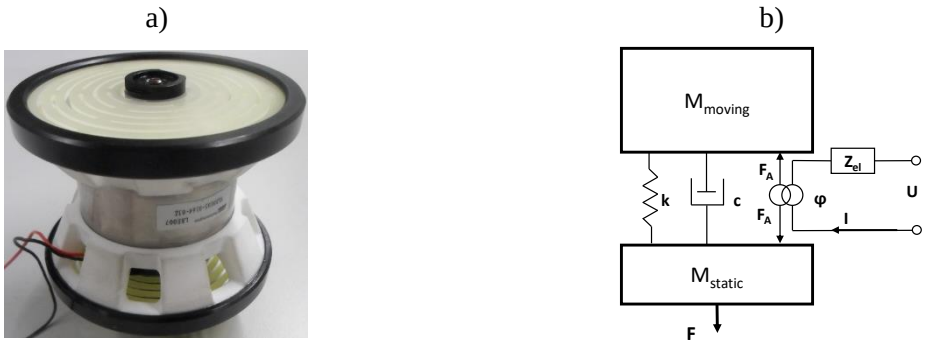


Figure 3 – a) Picture of an IMA used in the AVC system b) Lumped parameter model of the IMAs

The positioning of the IMAs on the truss structure is the result of previous research work [16, 17], where the scalar controllability measure, proposed by Hàc and Liu [18], has been applied to all possible combinations of positioning for six ideal forces on the fourteen input points on the truss structure. The results have shown that the positioning with the highest controllability degrees allow higher performance with lower electrical power consumption than the positioning with the lower controllability degrees. For this study, the IMAs positioning with the highest controllability degree have been selected. According to the node numbering convention used in Figure 1b, the IMAs are applied to nodes 8, 10, 14, 15, 20 and 21.

Parameters	**M_{moving} [kg]**	**M_{static} [kg]**	**ω_n [Hz]**	**c [Ns/m]**	**k [N/m]**	**L [mH]**	**R [Ω]**	**φ [N/A]**
IMA 1 – Node 8	0.65	0.35	25.5	7.9	16660	4.5	2.4	10
IMA 2 – Node 10	0.65	0.35	26.5	7.5	17993	4.5	2.4	10
IMA 3 – Node 14	0.65	0.35	27.25	7.1	19026	4.5	2.4	10
IMA 4 – Node 15	0.65	0.35	27	7.5	18886	4.5	2.4	10
IMA 5 – Node 20	0.65	0.35	26.25	7.3	17655	4.5	2.4	10
IMA 6 – Node 21	0.65	0.35	27.5	7.2	19376	4.5	2.4	10

Table 1. Electro – mechanical parameters of the IMAs 1 to 6

3 Stability analysis of centralised and decentralised AVC system

This section presents the stability analysis for the VFB implemented using centralised and decentralised AVC system architecture. Firstly, an open loop compensator and the gain matrix calculation for

simulations and experiments are presented. Secondly, the gain matrices used for the simulation and measurements are presented. Thirdly, the stability of the two AVC system architectures is discussed.

3.1 Open loop compensator

Due to the interaction between the rigid body modes of the truss structure and the IMAs own dynamics at low frequencies, the AVC system is only conditionally stable. The electrodynamic IMAs are typically driven by a controlled voltage source. In this case, above the electrodynamic cut-off frequency of the IMAs the amplitude of the IMAs blocked force FRF drop with increasing frequency and the phase converges to -90°. This can cause unwanted spillover effects that compromise the performance of the VFB loops for frequencies above the IMAs electrodynamic cut-off frequency.

In order to improve the stability and performance of the feedback loops an open-loop (OL) compensator has been designed. The compensator is designed to cope with the above mentioned effects in order to improve the stability and the performance of the system. The stability and performance of the feedback loops can be assessed by studying the OL FRF with the Nyquist criterion. Figure 4 shows the Nyquist and the equivalent Bode plots of the measured OL FRF of an IMA applied at node 20 for the uncompensated and compensated cases. According to the Nyquist criterion, the system is stable if the OL-FRF does not encircle the Nyquist point [-1 0j], which corresponds to the phase of the OL-FRF crossing 180° and the amplitude being larger than one at the same frequency. If the phase of the OL FRF crosses 180° at a frequency which its magnitude is lower than one, then the feedback loop is conditionally stable. The grey coloured regions in Figure 4 correspond to the spillover areas. At the frequencies corresponding to the OL FRF points lying inside these regions, spillover effects are produced by the closed feedback loops, i.e. the response of the structure under control is amplified. The uncompensated OL FRF shown in Figure 4 crosses the real negative axis in several points in the frequency range between 0 to 55 Hz. This frequency range includes the response peak of the first rhombic mode around 52.7 Hz, which hence cannot be controlled efficiently. The results for the compensated case of Figure 4a and b show that the sizes of the circles on the left hand side of the Nyquist plot are significantly reduced compared to the uncompensated case. The circle corresponding to the first rhombic mode of the truss structure is rotated clockwise out of the spillover region. Hence, the compensator significantly improves the stability and performance of the feedback control loop. A more detailed analysis of the compensator design can be found in Ref. [17].

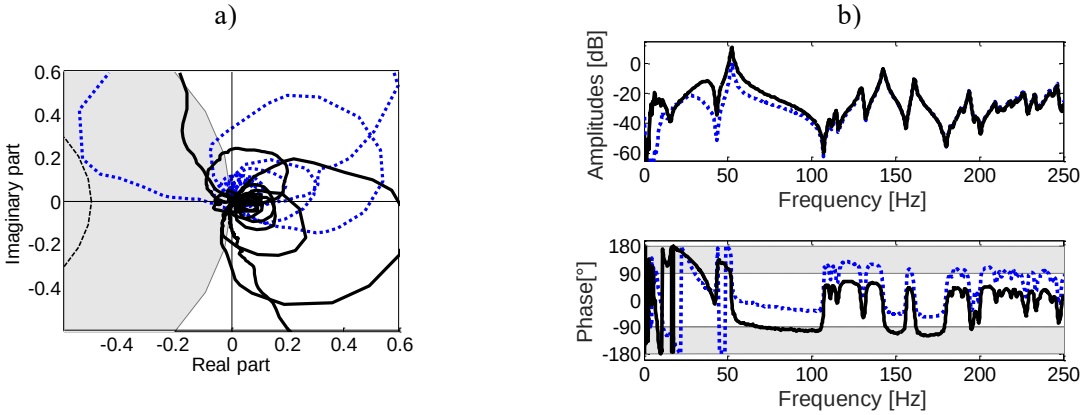


Figure 4 – Experimentally evaluated OL FRF for the IMA mounted at node 20 – a) Nyquist plot; b) Bode diagram. (Uncompensated – dotted blue line; Compensated – continuous black line)

3.2 Gain matrix calculation

In this section, the evaluation of the gain matrices for the simulations and the experimental analysis is presented. The AVC system is composed of six IMAs and six co-located acceleration sensors. Each IMA can be closed in feedback looped with any of the sensors composing the AVC system. Hence, in this case,

the AVC system is composed of thirty-six feedback loops and the full gain matrix is a six by six matrix where each gain refers to each of the loops of the system.

Thirty-six OL-FRFs are used to determine the gains of the matrix. The OL-FRFs are evaluated between the inputs to the power amplifiers driving the IMAs and the acceleration sensor signals at each considered node position, filtered by the controller function. The gains that guarantee stability and satisfying performance of each individual loop are evaluated. Usually in literature, half of the maximum stable gain is known as 6 dB gain margin and is used as criterion for a sufficient feedback stability. However, gains which guarantee 6 dB stability margin may cause excessive spillover which compromise the performance of the system. For this reason, a more conservative gain is represented by the 6 dB spillover gain. This gain value insures that each of the individual loops is stable and the spillover of each individual loop is limited to 6 dB at a single frequency. The 6 dB spillover gains corresponds to the gain values which give OL FRFs that tangent a circle of radius 0.5 around the Nyquist stability point [-1 0j].

Table 2 lists the 6 dB spillover gain matrices for the simulated and measured thirty-six OL-FRFs. The gains refer to the OL-FRFs between the input voltages sorted in the rows and the output signals sorted in the columns for each of the six node positions considered. The signs of the gains are chosen according to the phase relation between the input voltages and the output signals, in order to guarantee maximal performance on the frequency range of interest. Table 2a lists the gain values for the simulated OL-FRFs. The simulated gain matrix is dominated by gains along the main diagonal which are an order of magnitude higher than the off diagonal values, except for the gains referring to the loop between IMA at node 20 and the sensor signal at node 21 and the loop between IMA at node 21 and the sensor signal at node 20. Table 2b lists the gain values for the measured OL-FRFs. The diagonal values of the measured gain matrix are generally higher than the off-diagonal values, however the off diagonal terms are relatively larger than in the simulation.

a)

IMA positions \ Sensor positions	**8**	**10**	**14**	**15**	**20**	**21**
8	+3.10	+0.24	+0.22	+0.12	+0.28	+0.21
10	+0.24	+5.71	+0.24	-0.17	-0.61	-0.37
14	+0.22	+0.24	+3.10	+0.2	+0.15	+0.12
15	+0.12	-0.17	+0.20	+3.19	-0.31	+0.23
20	-0.27	-0.61	+0.16	-0.32	+4.98	+4.65
21	+0.19	-0.37	+0.12	+0.23	+5.10	+3.26

b)

IMAs positions \ Sensor positions	**8**	**10**	**14**	**15**	**20**	**21**
8	+3.32	+1.35	+1.09	-0.59	-2.87	+1.17
10	+1.25	+10.0	-1.37	-1.16	-4.08	-3.87
14	+1.11	+1.37	+2.72	+1.13	-0.71	-0.49
15	-0.55	-1.11	+1.33	+3.47	-3.97	+0.93
20	+3.12	-3.68	-0.72	-3.08	+5.36	+3.11
21	+1.27	-3.87	-0.60	+1.07	+4.23	+3.20

Table 2 – a) Simulated 6 dB spillover gain matrix b) Measured 6 dB spillover gain matrix

3.3 Stability analysis

The gain values evaluated in the previous sections guarantee that each individual loop is stable and does not produce spillover higher than 6 dB. However, for MIMO systems, the stability of the individual feedback loops is not sufficient to guarantee the stability of the entire system with centralised or decentralised architectures. The robustness of MIMO systems decreases with increasing number of IMAs, due to the cross excitation [19]. The MIMO AVC system stability can be assessed using the Generalised Nyquist criterion [20]. According to the generalised Nyquist criterion, the MIMO feedback system is stable if none of the frequency dependent eigenvalues of the fully populated OL system matrix encircles the Nyquist instability point [-1 0j]. For the application of this criterion, the Feedback system needs to be composed of an equal number of sensors and actuators.

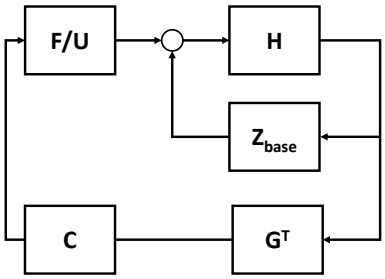


Figure 5 – AVC MIMO Feedback loop

Figure 5 shows a schematic block diagram representation of a generic MIMO AVC feedback loop. Let´s consider the systems with equal numbers of sensors and actuators. The block **H** represents the matrix describing the system dynamics, **G** represents the gain matrix, **C** represents a diagonal matrix where the diagonal elements describe the Compensators functions, **F/U** represents a diagonal matrix where the diagonal elements describes the IMAs dynamics and the $\mathbf{Z_{base}}$ represents a diagonal matrix corresponding to the static masses of the IMAs attached to the structure. From this representation, the fully populated OL system matrix can be evaluated as the result of the following matrix operation:

$$\mathbf{[G]^T\,[C][F/U]\,[H] + [Z_{base}]\,[H]}. \quad (1)$$

In this case, **G** and **H** matrices are both square matrices since the AVC system is composed of six IMAs and six acceleration sensors. The simulated fully populated matrices for the MIMO centralised and decentralised AVC system are calculated considering the gain matrices in Table 2a, where for the decentralised case the gain matrix the off-diagonal elements are set to 0.

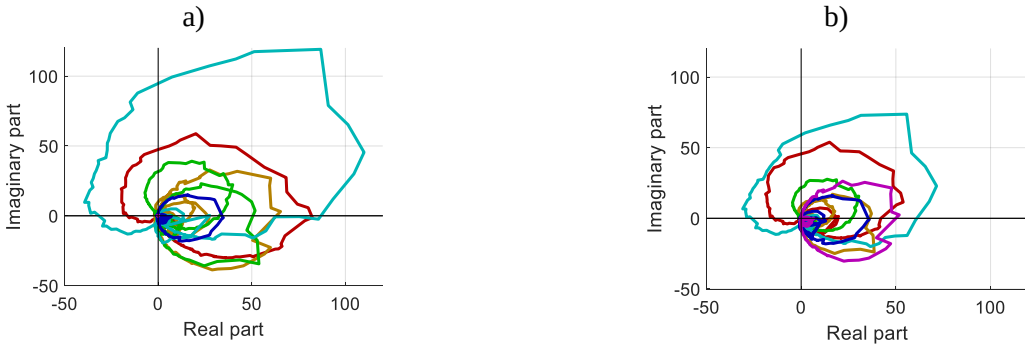


Figure 6 – Nyquist plots of the eigenvalues of the simulated OL system matrix for a) centralised and b) decentralised AVC system

Figure 6 shows the simulated eigenvalues of the OL system matrix for the centralised and decentralised AVC system. According to the generalized Nyquist criterion, the gain matrix resulting from the individual 6 dB spillover gains lead to an unstable AVC system, for both centralised and decentralised control architectures. In fact, two of the six frequency dependent eigenvalues of the OL system matrix encircle the Nyquist instability point at [-1 0j]. The eigenvalues of the centralised AVC system are larger than the eigenvalues those for the decentralised architecture. The values of both gain matrices need to be reduced in order to obtain stable AVC systems. In this form, the generalized Nyquist criterion can be analysed similarly to the classical Nyquist criterion. The eigenvalue analysis can be used to calculate a single value scaling factor $\boldsymbol{\lambda_{max}}$ that scales all gains of the OL system matrix uniformly in order to achieve a stable system.

$$\mathbf{G_{max} = \lambda_{max} \cdot [G]^T}. \quad (2)$$

The gain setting resulting from equation 2 corresponds to the maximum stable gain setting, while maintaining the relative proportions among the gain values of the original matrix. In this study, the scaling factor $\boldsymbol{\lambda_{max}}$ has been evaluated for both the centralised and the decentralised architectures with values of 0.03 and 0.037, respectively.

Figure 7 shows the measured eigenvalues of the OL system matrix for centralised and decentralised AVC system architectures. As in the simulations, the gain settings that satisfy the 6 dB spillover criterion for the

individual feedback loops yield unstable MIMO VFB AVC systems. Two of the eigenvalues encircle the Nyquist instability point at [-1 0j] for both the centralised and the decentralised system architectures. Similarly to the simulation results, the eigenvalues for the centralised AVC system are larger than the eigenvalues of the decentralised AVC system. However, the eigenvalues of the measured OL system matrix are significantly smaller than those from simulation. Differently than simulations, the Generalised Nyquist could not be used to determine the scaling factor $\boldsymbol{\lambda_{max}}$. The scaling factors resulting with the Generalised Nyquist were beyond the stability of the systems. Hence, the values have been determined experimentally by increasing the scaling factors $\boldsymbol{\lambda_{max}}$ until the systems resulted unstable. The scaling factor $\boldsymbol{\lambda_{max}}$ for the centralised and decentralised architectures, are evaluated to 0.1 and 0.14, respectively. As in the simulations, the scaling factor for the decentralised architecture is larger than that for the centralised architecture.

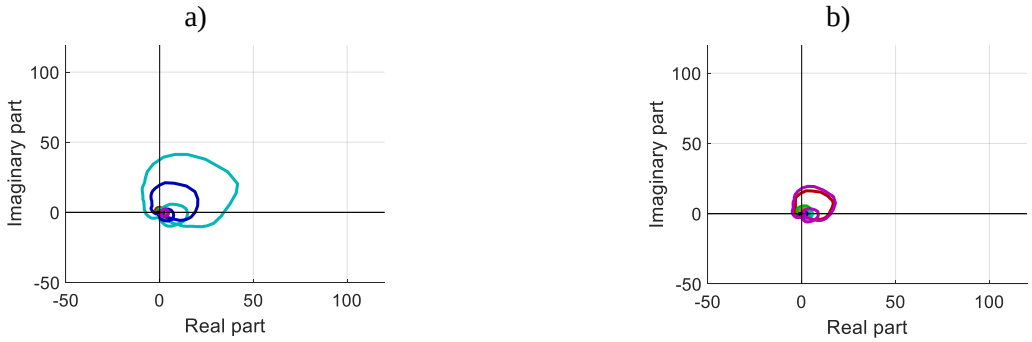


Figure 7– Nyquist plots of the eigenvalues of the measured OL system matrix for a) centralised and b) decentralised AVC system

4 Performance and Power consumption analysis

In this section, simulations and experiments on the performance and power consumption of the centralised and decentralised AVC system are analysed and compared. The control performances are evaluated in terms of changes in the kinetic energy of the truss structure R and R_{active} evaluated as follows:

$$R = \frac{\bar{E}_k}{\bar{E}_{k_0}} \text{ and } R_{active} = \frac{\bar{E}_k}{\bar{E}_{k_1}} \text{ where } \bar{E}_{k,k_0,k_1} = \int \left(\frac{\sum_{n=8}^{21} \left| \frac{v_n}{F} \right|}{14} \right)^2 (\omega) d\omega \tag{3}$$

where $\bar{E}_k$ refers to the actively controlled total mean kinetic energy and $\bar{E}_{k_0}$ refers to the mean kinetic energy of the uncontrolled truss structure without IMAs and $\bar{E}_{k_1}$ refers to the mean kinetic energy of the uncontrolled truss structure with IMAs. The total mean kinetic energy of the truss structure is estimated using the x- direction velocities v_n on locations from 8 to 21, see Figure 1b. The total mean kinetic energy has been evaluated in the frequency range of the global structural modes of the truss structure from 30 Hz to 200 Hz. The primary disturbance force F is applied at node 9. The truss structure is excited using a Low-pass filtered white noise signal. The cut-off frequency of the low pass filter is set to 500 Hz. The root mean square (RMS) value of the primary force excitation is 3.3 [N] for both, the simulations and the measurements. Both the time domain simulations and measurements were conducted using a sampling frequency of 16384 Hz.

The total apparent electrical power required by the IMAs is evaluated by summing the apparent power consumption of the six individual IMAs. The apparent power corresponds to the actual electrical power required by the IMAs to operate and represents the most conservative estimation for the power consumption. However, only a part of the apparent power is used to do work. This component is referred to as active electrical power. The remaining part of the power provided to the IMAs is oscillating between the IMAs and the power amplifier due to the phase shift between current and voltage. This part of the electric power is referred to as reactive power, which may be recovered using suitable power amplifiers which are able to store and regenerate the oscillating power. Hence additionally to the apparent electrical power, the percentage of reactive power involved in driven the IMAs is also evaluated.

The performance and the power consumption of the AVC system with centralised and decentralised architectures are estimated for eleven different gain settings. Each gain setting uses the gain matrices presented in Table 2, which are uniformly scaled by a factor $\boldsymbol{\lambda}$, as proposed in the previous section. The eleven values of scaling factor $\boldsymbol{\lambda}$ have been linearly spaced in the range from 0 to $\boldsymbol{\lambda}_{\mathbf{max}}$ evaluated for the corresponding control system architecture investigated in the simulations and the experiments. At each gain settings, the change in the kinetic energy, the total apparent electrical power consumption and the percentage of reactive power has been evaluated.

4.1 Simulation results

Figure 8 shows the simulation results for the changes in the kinetic energy over the total apparent electrical power consumption of the IMAs normalized by to the primary disturbance force for both the centralised and decentralised AVC system architectures. The results shown in Figure 8a are evaluated with reference to the truss structure without the IMAs mounted (total passive and active control effects) and the results in Figure 8b are evaluated with respect to the truss structure with passive IMAs mounted (active control effects). The results in Figure 8a show that mounting the IMAs onto the truss structure already results in a passive reduction of the truss structure kinetic energy of 2.4 dB. Increasing the scaling of the gain matrix of the AVC systems a maximum total kinetic energy reduction of about 6 dB for a total apparent electrical energy consumption of 2 10^{-3}VA/N is achieved for both the centralised and decentralised AVC system architectures. Increasing the gain scaling further until the maximum stable values are reached, the performance of the AVC systems decreases due to the increasing control spillover. The results in Figure 8b show that the maximum active control reduction in the kinetic energy is 3.6 dB for both AVC system architectures. The results for the control performance over apparent power electric power consumption are very similar. However, this can be explained by the dominance of the diagonal terms in the OL system matrix given in Table 2a. This corresponds well to the findings of Frampton et al. [10].

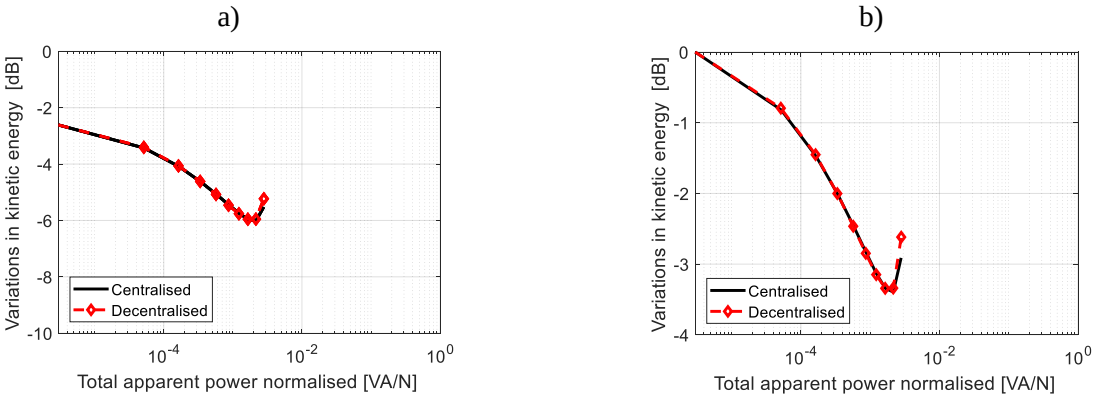


Figure 8 – Simulated variations of the kinetic energy for total apparent power consumption normalized - a) with respect to the uncontrolled structure and b) with respect the truss structure with the IMAs

Figure 9a and b show the simulated FRFs of the velocity spectra in the x-direction averaged over all 14 selected nodes of the truss structure normalized to the excitation force, for centralised and decentralised AVC systems architectures. The simulated FRFs of the uncontrolled truss structure without the IMAs is compared to the structure with passive IMAs and with the AVC system with the gain matrix scaling corresponding to the optimal performance point found from the results shown in Figure 8 and the maximum stable gain matrix scaling factor given in Section 3.3. As discussed above the response of the truss structure is considerably reduced by attaching the passive IMAs. The added mass shifts the response peaks of low order global modes towards lower frequencies. The passive IMAs also efficiently reduce the response peak of the first rhombic mode around 39 Hz by approximately 4 dB leading to the overall reduction of 2.4 dB reported above. Applying the optimal gain scaling, the response peaks of all global modes are efficiently reduced for both AVC system architectures. Control spillover occurs around 30 Hz, however its amplitude is low enough to not significantly affect the overall control performance. For the

maximum stable gain scaling, there are very little further reductions in the response peaks of the global structural modes of the truss structure. However, the magnitude of the spillover around 30 Hz is increased significantly, which affects the overall performance of the AVC systems (compare to Figure 8).

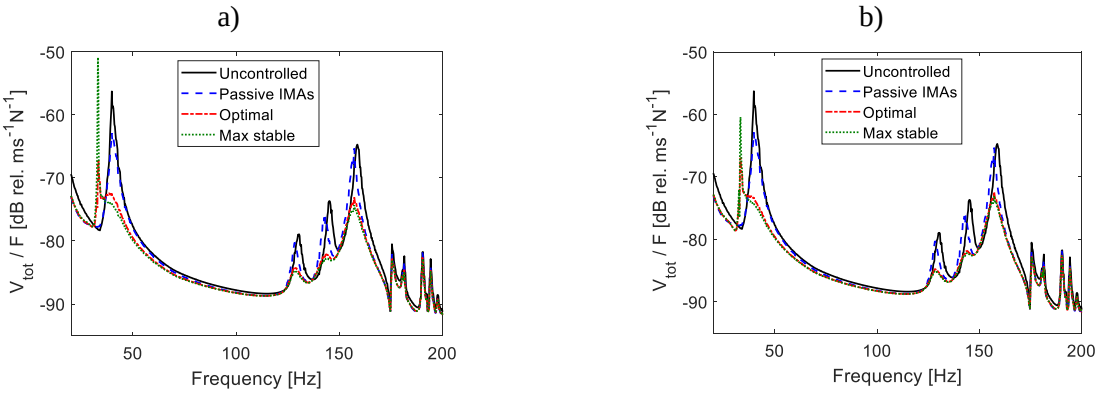


Figure 9 – Simulated FRF of the mean velocity normalized to the excitation force in the frequency range from 20 to 200 Hz – a) Centralised and b) Decentralised AVC system

Figure 10 shows the percentage of reactive compared to the apparent power consumed by the IMAs for the centralised and decentralised architectures evaluated from the simulations. As for the performance and the total power consumption, the amount of reactive power involved for the centralised and decentralised AVC systems are very similar. At the lowest gain matrix scaling analysed, the reactive power is assessed to be around 38 % of the total apparent power. The percentage of reactive power decreases continuously with increasing total apparent power consumption, reaching a minimum of about 17 % for the maximum stable gain matrix scaling.

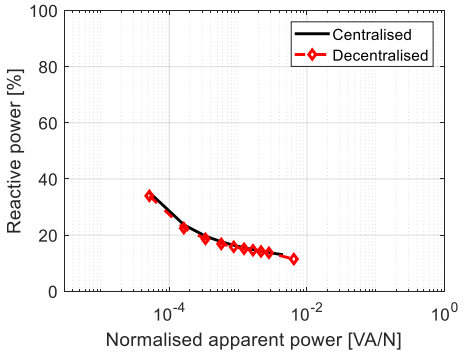


Figure 10 – Percentage of reactive power with respect to the total apparent power evaluated from simulations

4.2 Experimental results

This section presents the experimental results for the centralised and decentralised velocity feedback implemented on the AVC system composed of six IMAs. Figure 11 shows the measured changes in the kinetic energy over the total apparent power consumption of the IMAs. As in the simulations, the results in Figure 11a are evaluated with respect the uncontrolled structure without the IMAs mounted, and the results in Figure 11b are evaluated with respect to the uncontrolled structure with the IMAs installed. Figure 11a shows that the passive effect of the IMAs yields a reduction of 4.8 dB in the kinetic energy of the truss structure. Increasing scaling factor of the feedback gain matrix of the AVC systems a maximum reduction of 8.3 dB for a total apparent electrical energy consumption of 2.6 10^{-2} VA/N is achieved for the centralised AVC system and a maximum global reduction of 8.1 dB for a total apparent electrical energy consumption of 2.1 10^{-2} VA/N for the decentralised AVC system is achieved. Increasing the gain scaling further until the maximum stable values are reached, the performance of the AVC systems decreases due to the increasing control spillover. The results in Figure 11b show that the maximum active control

reduction in the kinetic energy is 3.5 dB for the case of the centralised AVC system and 3.3 dB in the case of decentralised AVC system. The centralised AVC system slightly outperforms the decentralised AVC system. However, the performances are generally comparable.

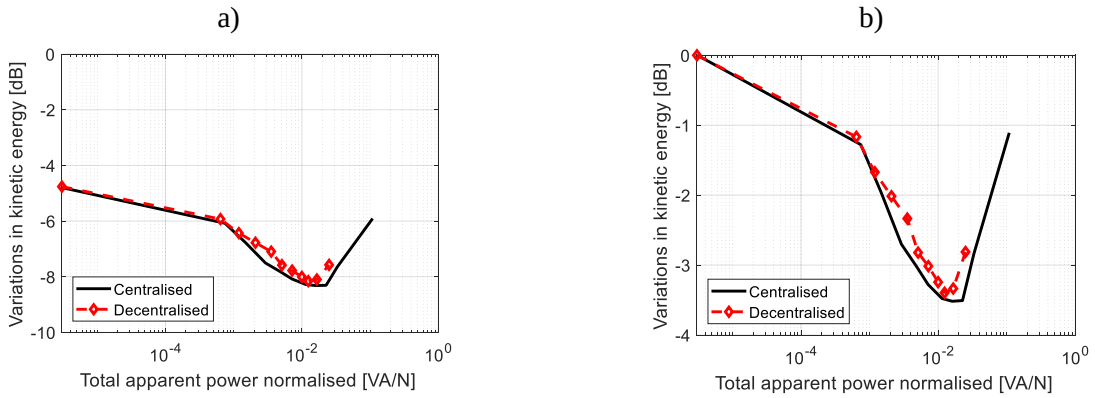


Figure 11– Measured variations of the kinetic energy per total apparent power consumption normalized - a) with respect to the uncontrolled structure and b) with respect the truss structure with the IMAs

Figure 12a and b show the experimentally evaluated velocity spectra averaged over all 14 nodes normalized to the primary excitation force for the truss structure without IMAs installed, with six passive IMAs installed and with six IMAs installed with optimal and maximum stable gain matrix scaling for the centralised and decentralised AVC systems. The optimal gain matrix scaling corresponds to the optimal performance point found from the results shown in Figure 11 and the maximum stable gain matrix scaling factor is that given in Section 3.3. It can be observed that the passive IMAs cause a shift of the peak response of the third rhombic mode from around 129 Hz to approximately 137 Hz and a shift of the response peak of the first torsional mode from around 161,8 Hz to 171 Hz. A new response peak arises around 118 Hz. These shifts and the reductions of the response peaks due to the installation of the passive IMAs in the measurements are higher than the passive effects seen in the simulations in Figure 9. This could be due to the reduction of the DOFs of the selected input/output position nodes of the truss structure to translation in the x-direction only. Hence, in simulations, the IMA forces and masses cannot affect the response of the truss model in other DOFs. However, in practice there will be such effects.

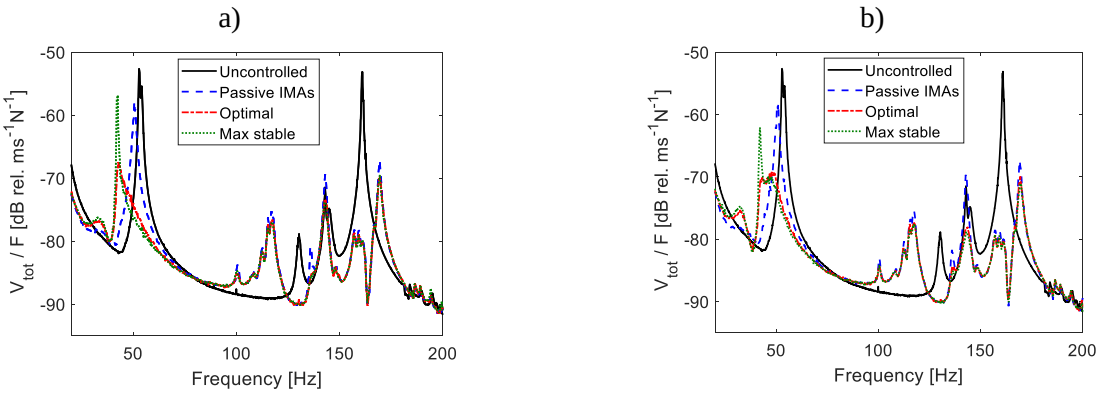


Figure 12– Measured FRF of the mean velocity normalized to the excitation force in the frequency range from 20 to 200 Hz – a) Centralised and b) Decentralised AVC system

However, the results in Figure 12 show that with the ‘optimal’ scaling of the gain matrices both AVC systems efficiently reduce the response peaks corresponding to the global modes of the truss structure in the entire observed frequency range. However, control spillover occurs around 40 Hz. For the maximum stable scaling of the gain matrices, minor further reductions are achieved around the response peaks of all global modes. However, there is a significant increase in the spillover peak around 40 Hz, which

outweighs the additional reductions and results in a reduced overall performance (compare to Figure 11). As for the simulations the results for the centralised and decentralised AVC systems are generally similar. Some differences between the results for the two control architectures can be observed for the response peak of the rhombic mode around 54 Hz, which is more efficiently damped by the centralised AVC system, and for the response peak around 137 Hz, which is more efficiently damped by the decentralised AVC system.

Figure 13 shows the percentage of reactive power per total normalized apparent power evaluated from the measurements. As in the simulations, the percentages of reactive power decrease as the total apparent power provided to the IMAs increases. However, the percentages of the reactive power evaluated from the measurements are significantly higher than those evaluated from simulations. Also the percentages of reactive power for the decentralised AVC system for all values of total apparent power are significantly higher than those evaluated for the centralised AVC system. For lower amounts of apparent power provided to the IMAs, the percentage of the reactive power for the decentralised AVC system is close to the 80%. With increasing total apparent power, the percentage of reactive power reaches a minimum of reaching of 45% for the maximum stable gain matrix scaling. For the centralised AVC system, the percentage of reactive power ranges from 65% for the minimum total apparent electrical power provided to the IMAs to 14% for the maximum stable gain matrix scaling.

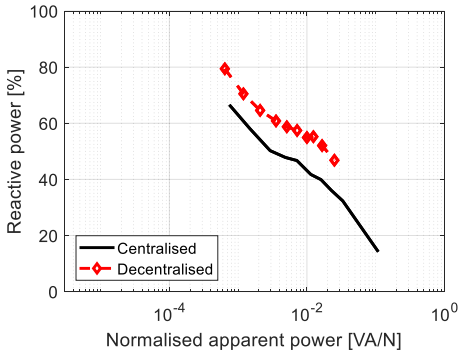


Figure 13 – Percentage of reactive power with respect to the total apparent power evaluated from measurements

5 Summary, Conclusions and Outlook

This paper presents the results of simulation and experimental studies on the stability, performance and power consumption of a VFB AVC system comprising six IMAs and six acceleration sensors installed on a six cells truss structure considering both centralised and decentralised system architectures. The gain matrices are initially evaluated for gain values which limit the control spillover for each of individual feedback loop of a fully populated AVC system matrices to a maximum of 6 dB. The resulting matrices show that the gain values on the diagonal are considerably larger than the off-diagonal ones, in particular in the simulation. However the stability analysis via the generalised Nyquist criterion shows that these gain matrix settings result in unstable MIMO control systems for both the centralised and the decentralised AVC system architectures, in the simulations as well as in the measurements. Hence, a uniform scaling factor is introduced, which allows to scale the gain matrices in order to satisfy the desired stability and maximum spillover criterion for the MIMO control systems. Finally, the simulation and measurement results of the performance and power consumption are presented for different gain matrix scaling factors. In the simulations, centralised and decentralised AVC systems achieve very similar results for both the control performance and the electrical power consumption. This is because the fully populated gain matrix is dominated by the terms on the diagonal, hence centralised and decentralised systems are bound to perform similarly. In the experimental study the centralised AVC system slightly outperforms the decentralised AVC system. The percentages of reactive power of the total apparent power consumption evaluated from measurements are generally higher than those evaluated from simulations. Also the evaluation of the measurements for the

decentralised AVC system yield considerably higher percentages of reactive power than those for the centralised AVC system. Hence, using power amplifiers that can recuperate reactive electric power may give the decentralised AVC system an edge over the centralised AVC system in terms of energy efficiency. However, these results are not yet fully conclusive and are part of ongoing research work. In future studies, it is intended to investigate AVC systems composed of six inertial mass actuators applying different control strategies (e.g. feedforward or internal model control) on the laboratory truss structure described in this paper.

Acknowledgements

The authors gratefully acknowledge the European Commission for its support of the Marie Sklodowska-Curie program through the ITN ANTARES project (GA 606817).

References

[1] A. Preumont and K. Seto, Active control of structures, Brussels: John Wiley and Sons, 2008.

[2] C. González Díaz and P. Gardonio, „Feedback control laws for proof-mass actuators electrodynaimc actuators," *Smart materials and structures,* Bd. 16, pp. 1766-1783, 2007.

[3] F. Fahy and P. Gardonio, Sound and structural vibrations, El Sevier, 2007.

[4] C. G. Diaz, C. Paulitsch und P. Gardonio, „Active damping control unit using a small scale proof mass electrodynamic actuator," Bd. 124, Nr. 2, 2008.

[5] C. R. Fuller and A. H. von Flotow, „Active control of sound and vibration," *IEEE Control System,* Bd. 15, pp. 9-19, 1995.

[6] C. González Díaz, C. Paulitsch and P. Gardonio, „Smart panel with active damping units. Implementation of decentralised control," *Journal of Acoustic Society of America,* Bd. 124, Nr. 2, p. 898–910, 2008.

[7] S. Elliott, M. Zilletti and P. Gardonio, „Self-Tuning of Local Velocity Feedback controllers to maximise power absorption," in *RASD 2010,* Southampton (UK), 2010.

[8] K. Ogata, Modern control of Engineering, Teheran: Aeeizh, 2002.

[9] W. P. Engels and S. J. Elliott, „Optimal centralised and decentralised velocity feedback on a beam," *Journal of Smart materials and Structures,* Nr. 17, pp. 1-10, 2008.

[10] K. Frampton, O. Baumann and P. Gardonio, „A comparison of decentralised, distributed and centralised vibro-acoustic control," *Journal of Acoustic society of America,* pp. 2798-2806, 2008.

[11] O. Baumann and S. Elliott, „An experiment comparing centralised and decentralised control using inertial actuators," in *ForumAcusticum,* Budapest, 2005.

[12] D. Flaschenträger, J. Thiel, J. Rausch, H. Atzrodt, S. Herold, T. Melz and R. Wethschützky, „Implementation and Characterisation of the Dynamic Behaviour of a Three - Dimensional Truss Structure for Evaluatiing Smart Devices," Leuven, 2010.

[13] D. Mayer, H. Stoffregen, O. Heuss, J. Pöllmann, E. Abele and T. Melz, „Additive Manufacturing of Active Struts for Piezoelectric Shunt Damping," *Journal of Intelligent Material Systems and*

Structures, pp. 1 -12, 2015.

[14] F. LBF, „Mechanical Simulation Toolbox," Fraunhofer LBF, 2017. [Online]. Available: http://www.mechanical-simulation.de/joomla/index.php/de. [Zugriff am 1 2017].

[15] M. Dal Borgo, G. Lapiccirella, M. Ghandchi Tehrani, J. Rohlfing and S. J. Elliott, „Experimental identification of mechanical nonlinearities in a proof mass actuator," in *ICSV 25*, Hirohima, 2018.

[16] G. Lapiccirella, J. Rohnlfing and M. Ghandchi Tehrani, „Optimal Placement of six inertial mass actuators for MIMO active vibration control on laboratory truss structure," in *ICSV 24*, London, 2017.

[17] G. Lapiccirella and J. Rohlfing, „Performance and power consumption of decentralised velocity feedback control system with six inertial mass actuators on a laboratory truss structure," in *Internoise*, Hong Kong, 2017.

[18] A. Hàc and L. Liu, „Sensor and Actuator Location in Motion Control of Flexible Structures," *Journal of Sound and Vibrations,* Bd. 167, Nr. 2, pp. 239-261, 1993.

[19] O. N. Baumann and S. J. Elliott, „The stability of dencetralised multi channel velocity feedback controllers using inertial actuators," *Journal of the Acoustic Society of America,* Bd. 1, Nr. 121, pp. 188-196, 2007.

[20] J. M. Maciejowski, Multivariable feedback design, Cambridge: Addison-Wesley, 1989.

[21] C. González Díaz, C. Paulitsch and P. Gardonio, „Active damping control unit using a small scale proof mass electrodynamic actuator," *Journal of acoustic society of America,* Bd. 12, Nr. 2, p. 886–897, 2008.

Efficient assembly of unit cells with Krylov based model order reduction

S. van Ophem [1,2], **E. Deckers** [1,2], **W. Desmet** [1,2]
[1] KU Leuven, Department of Mechanical Engineering,
Celestijnenlaan 300 B, B-3001, Heverlee, Belgium
e-mail: **sjoerd.vanophem@kuleuven.be**

[2] DMMS lab, Flanders Make, Belgium

Abstract
Recent developments indicate the possibility to obtain compact reduced order models for systems with many inputs by Krylov subspace techniques. Therefore, this paper looks into the possibility of applying these reduced order models for the numerical assembly of a structure consisting of unit cells with dynamic substructuring methods. The proposed strategy consists of two steps: First the unit cell is reduced by using the aforementioned Krylov subspace technique, where the inputs are defined as the interface degrees of freedom. Then, these reduced unit cells are combined by a dual assembly technique to arrive at the numerical model of the full structure. This model is then reduced for a second time with Krylov based model order reduction. Several strategies for the assembly of the reduced basis on unit cell level are shown. The performance of the several reduction strategies are compared, and show that the resulting reduced order models are very accurate and compact.

1 Introduction

Structures that are based on Unit Cells (UCs), such as meta-materials [1, 2], are commonly modeled with the assumption that the UCs are extended to infinity, by using Bloch's theorem [3]. However, in real applications the amount of UCs is always limited and therefore it is necessary to perform additional simulations with only a limited amount of UCs and realistic boundary conditions to evaluate the real performance of the structure. Depending on the complexity of the problem, these additional calculations can be quite expensive.

The dynamic analysis of finite structures based on a repetition of UCs can be done efficiently with substructuring methods [4]. When substructuring methods are used in a Finite Element (FE) model, they allow both for a straightforward assembly that can be specified by the end user and they can lead to a gain in computational efficiency when they are combined with Model Order Reduction (MOR) techniques, since the UC is reduced in size before assembly. Furthermore, by using parametric MOR (pMOR) [5], the end user can even retain parametric dependencies in the Reduced Order Model (ROM), thus providing a powerful design tool for periodic structures with fluctuations in the UC properties.

The most commonly used MOR techniques in a substructuring context are modal based methods, also known as Component Mode Synthesis (CMS). In particular, the Craig-Bampton method is well known and widely used [6]. When no damping is present, modal analysis leads to a set of decoupled equations that can be reduced by truncating the eigenvalues and corresponding eigenvectors at a user set threshold. The combination of decoupled equations and small system sizes can make it possible to solve the resulting system effectively, even when a large amount of substructures are present. A known disadvantage of using modal analysis to reduce the system is that the method lacks accuracy, because it does not take into account input/output

information.

Recently, other MOR methods are gaining popularity, namely Balanced Truncation [7], Proper Orthogonal Decomposition [8, 9] and Krylov based MOR [10]. In contrast to modal reduction methods, these schemes are based on preserving the input/output behavior of the system. This naturally leads to the question of their performance in a substructuring context. In [11] it has been shown that the reduced basis resulting from these newer MOR techniques can effectively act as an replacement of the eigenmodes in the Craig-Bampton scheme, although they mention that Krylov based methods might not be the most effective, due the growth in model size as function of the amount of inputs. In fact, in the worst case the model size increases linearly with the amount of inputs, meaning that for a large amount of inputs, there would be no reduction [11, 12].

Recently, it has been shown that in most cases this increase in system size is not necessary to obtain a good ROM and can be kept moderate by either tangential interpolation techniques [13] or by combining block second order Krylov techniques with an a-posteriori Singular Value Decomposition (SVD) [14, 15]. Therefore, in this paper it is opted to use the algorithm presented in [14] for MOR on a unit cell. Several methods to effectively reduce the UC are detailed in Sec. 2. Since the assembly of unit cells again leads to an increase in model size, a second MOR step is done to reduce the assembled system of reduced unit cells. Therefore, different procedures to assemble the reduction basis are compared in Sec. 3. Due to the specific shape of the assembled system matrices, the Arnoldi procedure can be calculated by mainly performing operations on UC level and on the coupling matrices, leading to a very efficient reduction procedure, as has been shown in Sec. 4.1. The paper concludes with a numerical example that shows the effectiveness of the chosen strategy in Sec. 5.

2 Model order reduction of the UCs

The first step of the proposed strategy for efficient but accurate MOR of combined UCs is the reduction of the UC itself. With most existing methods, like Craig-Bampton, the boundaries and inner nodes are treated separately when the reduction step is performed. We will show several strategies, of which some of them also explicitly split the boundary nodes and the inner nodes in the reduction step, while others do not separate them. Firstly, a strategy is proposed that does not require the separation between internal and external nodes. This strategy is straightforward to implement and leads to the smallest reduction basis of all the methods that are shown in this section. However, it leads to fully populated coupling matrices when the substructures are coupled. Secondly, a Krylov/Craig-Bampton hybrid, as proposed in [11] is evaluated. The explicit inclusion of the interface DOFs leads to a larger ROM, but also leads to sparsely populated coupling matrices. The final strategy is based on a split basis approach: The resulting reduced basis is shown to be the same as the combined Krylov/Craig-Bampton basis, but without the coupling matrix. This leads to a more memory efficient implementation, while the accuracy is retained.

2.1 Krylov based model order reduction

The Krylov based MOR techniques are based on a concept called moment matching. They aim to match the transfer function of the Full Order Model (FOM) around an expansion point (or shift) σ by applying a power series of the following form:

$$h(s) = \mu_0 + \mu_1(s-\sigma) + \mu_2(\sigma - s)^2 + \cdots = \sum_{j=1}^{\infty}(s-\sigma)^{j-1}\mu_{j-1}, \tag{1}$$

in which μ_i is the i-th moment. The explicit calculation of these moments is known to have numerical issues [16]. It can be shown however, that the reduced order model resulting from a Krylov subspace implicitly matches these moments [10]. For a second order system of the following form

$$\mathbf{M}\ddot{x}(t) + \mathbf{C}\dot{x}(t) + \mathbf{K}x(t) = \mathbf{F}u(t), \tag{2}$$

the input second order Krylov subspace is defined as follows:

$$\mathcal{K}_r = (\mathbf{A}_1, \mathbf{A}_2, \boldsymbol{b}) = \text{span}\left\{\boldsymbol{p}_0, \boldsymbol{p}_1, \cdots, \boldsymbol{p}_r\right\}, \tag{3}$$

with

$$\mathbf{A}_1 = -(\mathbf{K} + s\mathbf{C} + s^2\mathbf{M})^{-1}(\mathbf{C} + 2s\mathbf{M}), \tag{4}$$
$$\mathbf{A}_2 = -(\mathbf{K} + s\mathbf{C} + s^2\mathbf{M})^{-1}\mathbf{M}, \tag{5}$$
$$\boldsymbol{b} = -(\mathbf{K} + s\mathbf{C} + s^2\mathbf{M})^{-1}\boldsymbol{F}. \tag{6}$$

The reduced bases $\mathbf{V}$ that span these Krylov subspaces can be calculated with an efficient numerical procedure, called the Second Order Arnoldi SOAR algorithm [17]. The resulting ROM for a reduced basis $\mathbf{V} \in \mathbb{C}^{n\times r}$ is then calculated as follows:

$$\mathbf{M}_r = \mathbf{V}^H\mathbf{M}\mathbf{V},\ \mathbf{K}_r = \mathbf{V}^H\mathbf{K}\mathbf{V}, \tag{7}$$
$$\mathbf{C}_r = \mathbf{V}^H\mathbf{C}\mathbf{V},\ \mathbf{F}_r = \mathbf{V}^H\mathbf{F}, \tag{8}$$
$$\mathbf{L}_r = \mathbf{L}\mathbf{V},\ \boldsymbol{x} = \mathbf{V}\boldsymbol{x}_r, \tag{9}$$

resulting in

$$\mathbf{M}_r\ddot{\boldsymbol{x}}_r(t) + \mathbf{C}_r\dot{\boldsymbol{x}}_r(t) + \mathbf{K}\boldsymbol{x}_r(t) = \boldsymbol{F}_r u(t), \tag{10}$$
$$y_r = \mathbf{L}_r\boldsymbol{x}_r. \tag{11}$$

Several strategies for calculating $\mathbf{V}$ are compared in the following sections.

2.2 Strategy I: MIMO Krylov

The first strategy builds up a reduction basis by running a MIMO reduction scheme on the full UC, and considers all the interface DOFs as extra inputs. The system that is reduced by the scheme proposed in [14] is defined as follows (shown here in the time domain, but also valid in the frequency domain. assuming that all the matrices are frequency independent):

$$\underbrace{\begin{bmatrix}\mathbf{M}_{ii} & \mathbf{M}_{ib}\\ \mathbf{M}_{bi} & \mathbf{M}_{bb}\end{bmatrix}}_{\mathbf{M}_{UC}}\underbrace{\begin{bmatrix}\ddot{\boldsymbol{x}}_i\\ \ddot{\boldsymbol{x}}_b\end{bmatrix}}_{\ddot{\boldsymbol{x}}_{UC}} + \underbrace{\begin{bmatrix}\mathbf{C}_{ii} & \mathbf{C}_{ib}\\ \mathbf{C}_{bi} & \mathbf{C}_{bb}\end{bmatrix}}_{\mathbf{C}_{UC}}\underbrace{\begin{bmatrix}\dot{\boldsymbol{x}}_i\\ \dot{\boldsymbol{x}}_b\end{bmatrix}}_{\dot{\boldsymbol{x}}_{UC}} + \underbrace{\begin{bmatrix}\mathbf{K}_{ii} & \mathbf{K}_{ib}\\ \mathbf{K}_{bi} & \mathbf{K}_{bb}\end{bmatrix}}_{\mathbf{K}_{UC}}\underbrace{\begin{bmatrix}\boldsymbol{x}_i\\ \boldsymbol{x}_b\end{bmatrix}}_{\boldsymbol{x}_{UC}} = \underbrace{\begin{bmatrix}\mathbf{F}_i\\ \mathbf{G}_i\end{bmatrix}}_{\mathbf{F}_{UC}}. \tag{12}$$

The subscript $()_{ii}$ defines the interior DOFs, $()_{bb}$ are the boundary DOFs, and $()_{ib},\ ()_{bi}$ describe the coupling between the two. The reduction is performed on the full system matrices $\mathbf{M}_{UC},\ \mathbf{C}_{UC}$ and $\mathbf{K}_{UC}$, using the algorithm in [14], but with a slightly different error estimate: To take into account the relative importance of the interfaces, the estimated relative error is calculated by summing contributions of all the inputs at a few output locations. Thus, if an input does not contribute significantly to the output, it is seen as less important. The resulting reduced basis $\mathbf{V}_{kr,UC}$ is directly used in the substructuring approach in Sec. 3. As stated before, this approach leads to the smallest ROMs, but a disadvantage of this strategy is that the coupling matrices of the substructures are not sparse anymore after reduction, leading to an increase in memory usage and computational effort when many interfaces are present.

2.3 strategy II: Craig-Bampton like basis with Krylov vectors

The second strategy uses a Craig-Bampton inspired method to calculate the reduction basis, with the difference that no modes are considered, but Krylov vectors. This approach has been previously described in [11]. Consider a partioning of the system matrices, as shown in Eq. (12). Then, the reduction basis according to Craig-Bampton has the following form:

$$\mathbf{V}_{CB,UC} = \begin{bmatrix} \mathbf{V}_i & \mathbf{K}_{ii}^{-1}\mathbf{K}_{ib} \\ \mathbf{0} & \mathbf{I} \end{bmatrix}. \tag{13}$$

The basis consists of a part resulting from static condensation $\mathbf{K}_{ii}^{-1}\mathbf{K}_{ib}$ and a dynamic part ($\mathbf{V}_i$). As is shown in [18] the reduction basis for the dynamic part can be calculated by using the following system (the damping is neglected):

$$\mathbf{M}_{ii}\ddot{\boldsymbol{x}}_i + \mathbf{K}_{ii}\boldsymbol{x}_i = \underbrace{\begin{bmatrix}\mathbf{F}_i & -(\mathbf{M}_{ib} + \mathbf{M}_{ii}\mathbf{K}_{ii}^{-1}\mathbf{K}_{ib})\end{bmatrix}}_{\tilde{\mathbf{F}}_i} \begin{bmatrix} \boldsymbol{u} \\ \ddot{\boldsymbol{x}}_b \end{bmatrix} \tag{14}$$

making it possible to perform Krylov subspace reduction, even when no inputs are present. This equation is derived by applying the Craig-Bampton based reduced basis in Eq. (13) to Eq. (12), and noting that the terms related to the stiffness coupling forces are zero. The disadvantage of the reduction basis in Eq. (13) as compared to strategy I is that the size of the ROMs is almost doubled. Since the inputs due to the interface connections are still present on the right hand side, the size of $\mathbf{V}_i$ will be almost the same as $\mathbf{V}$, while the explicit addition of the boundary DOFs will lead to an increase of DOFs proportional to the boundary DOFs. On the other hand, the sparsity pattern of the coupling matrices is retained, while the previous strategy leads to fully populated coupling matrices.

2.4 strategy III: Split Krylov reduction basis

Another possibility to split the interior DOFs and the exterior DOFs is to use a split basis approach. Starting from the reduced basis given in Sec. 2.2, the reduced basis is rewritten as follows:

$$\mathbf{V}_{UC} = \begin{bmatrix} \mathbf{V}_i \\ \mathbf{V}_b \end{bmatrix}. \tag{15}$$

Then, the reduced basis is split as follows:

$$\mathbf{V}_{split,UC} = \begin{bmatrix} \mathrm{orth}(\mathbf{V}_i) & \mathbf{0} \\ \mathbf{0} & \mathrm{orth}(\mathbf{V}_b) \end{bmatrix}. \tag{16}$$

In practice, the matrix $\mathrm{orth}(\mathbf{V}_b)$ rarely contains less columns that rows, meaning that the subdomain relating to the boundary DOFs is not reduced. This means that this matrix can be replaced by an identity matrix, without any loss of accuracy. Thus, the resulting reduced basis is given by

$$\mathbf{V}_{split,UC} = \begin{bmatrix} \mathrm{orth}(\mathbf{V}_i) & \mathbf{0} \\ \mathbf{0} & \mathbf{I} \end{bmatrix}. \tag{17}$$

Comparison to the reduced basis in Eq. (13) leads to the conclusion that the addition of the static condensation information is not necessary in the context of Krylov based MOR. This statement will be further validated in Sec. 5.

2.5 Interface reduction

When a large amount of inputs are considered, it might be interesting to reduce the amount of DOFs that represent the interface. This corresponds to the case that the matrix $\mathrm{orth}(\mathbf{V}_b)$ in Eq. (16) has less columns than rows. This could be achieved by applying an SVD on the reduced basis corresponding to the interface, and only retaining the most significant left-singular vectors as new projection basis, which is a similar strategy to [14]. Another possibility is to already reduce the inputs a-priori, as is suggested by [18]. In the rest of the paper interface reduction will not be considered.

3 Substructuring approach

The substructuring approach that we follow is based on a dual formulation and is described in [4]. This formulation is chosen, because it preserves the sparsity of the system matrices, making an efficient second reduction step possible. The technique will be explained shortly in the following section. Assume that we have n substructures of which we know the reduced basis $\mathbf{V}^{(i)},\ i = 1 : n$, for example by the methods described in the previous section. The reduced bases are put on the diagonals of an assembled reduced basis $\mathbf{V}$:

$$\mathbf{V} = \mathrm{diag}\left(\mathbf{V}^{(1)}, \ldots, \mathbf{V}^{(n)}\right). \tag{18}$$

This leads to a reduced state vector $\hat{\boldsymbol{x}}$, with $\boldsymbol{x} \approx \mathbf{V}\hat{\boldsymbol{x}}$. The UCs are coupled by a connecting force matrix $\boldsymbol{G}$ on the interfaces between the domains. Additionally, the external forces that are not related to the interfaces are captured in matrix $\boldsymbol{F}$. The system matrices then are

$$\mathbf{M} = \mathrm{diag}\left(\mathbf{M}^{(1)}, \ldots, \mathbf{M}^{(n)}\right), \tag{19}$$

$$\mathbf{C} = \mathrm{diag}\left(\mathbf{C}^{(1)}, \ldots, \mathbf{C}^{(n)}\right), \tag{20}$$

$$\mathbf{K} = \mathrm{diag}\left(\mathbf{K}^{(1)}, \ldots, \mathbf{K}^{(n)}\right). \tag{21}$$

The fully assembled system can be written as

$$\hat{\mathbf{M}}\hat{\boldsymbol{x}} + \hat{\mathbf{C}}\hat{\boldsymbol{x}} + \hat{\mathbf{K}}\hat{\boldsymbol{x}} = \hat{\mathbf{F}} + \hat{\mathbf{G}}, \tag{22}$$

with

$$\begin{aligned}
\hat{\mathbf{M}} &= \mathbf{V}^H\mathbf{M}\mathbf{V}, \\
\hat{\mathbf{C}} &= \mathbf{V}^H\mathbf{C}\mathbf{V}, \\
\hat{\mathbf{K}} &= \mathbf{V}^H\mathbf{K}\mathbf{V}, \\
\hat{\boldsymbol{F}} &= \mathbf{V}^H\boldsymbol{F}, \\
\hat{\mathbf{G}} &= \mathbf{V}^H\mathbf{G}.
\end{aligned} \tag{23}$$

To couple the substructures, compatibility conditions are introduced in matrix $\mathbf{B}$ that conform to the following condition

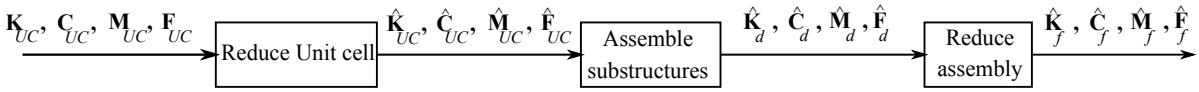


Figure 1: MOR strategy.

$$\mathbf{B}\boldsymbol{u} = \mathbf{0} \tag{24}$$

$$\hat{\mathbf{B}}\hat{\boldsymbol{u}} = \mathbf{0}. \tag{25}$$

The matrix $\mathbf{B}$ is a Boolean matrix that describes the matching of the interface DOFs such that the displacements in the coupled DOFs is the same. A dual assembly is considered, thus the interface forces are described as follows

$$\mathbf{G} = -\mathbf{B}^T\boldsymbol{\lambda}, \tag{26}$$

where $\boldsymbol{\lambda}$ is the vector of Lagrange multipliers that represent the intensity of the interface forces. This allows us to write the assembled system in the following form:

$$\underbrace{\begin{bmatrix}\hat{\mathbf{M}} & \mathbf{0}\\ \mathbf{0} & \mathbf{0}\end{bmatrix}}_{\hat{\mathbf{M}}_d}\underbrace{\begin{bmatrix}\ddot{\hat{\boldsymbol{x}}}\\ \boldsymbol{\lambda}\end{bmatrix}}_{\ddot{\boldsymbol{x}}_d} + \underbrace{\begin{bmatrix}\hat{\mathbf{C}} & \mathbf{0}\\ \mathbf{0} & \mathbf{0}\end{bmatrix}}_{\hat{\mathbf{C}}_d}\underbrace{\begin{bmatrix}\dot{\hat{\boldsymbol{x}}}\\ \boldsymbol{\lambda}\end{bmatrix}}_{\dot{\boldsymbol{x}}_d} + \underbrace{\begin{bmatrix}\hat{\mathbf{K}} & \hat{\mathbf{B}}\\ \hat{\mathbf{B}}^T & \mathbf{0}\end{bmatrix}}_{\hat{\mathbf{K}}_d}\underbrace{\begin{bmatrix}\hat{\boldsymbol{x}}\\ \boldsymbol{\lambda}\end{bmatrix}}_{\hat{\boldsymbol{x}}_d} = \underbrace{\begin{bmatrix}\hat{\boldsymbol{F}}\\ \mathbf{0}\end{bmatrix}}_{\hat{\mathbf{F}}_d}, \tag{27}$$

which is then reduced in the second MOR step.

4 Resulting MOR strategy

The resulting algorithm has been shown schematically in Fig. 1. It can be seen that two MOR steps are performed: One on the UC before assembly and one on the fully assembled structure. The second step is performed with an automatic Krylov reduction algorithm for single inputs, as shown in [19].

4.1 Efficient implementation of the Arnoldi step in the second ROM

When a large amount of substructures are coupled, it is straightforward to see that the system matrices in Eq. (27) can still become quite large. Since an LU-decomposition is performed at the beginning of the Arnoldi procedure to calculate the starting vector on which moment matching is applied, this step could use a large amount of memory. Fortunately, the specific structure allows to rewrite the system in blocks following the strategy in [20]. Considering that the dynamic system matrix for a certain frequency $\omega = 2\pi f$ is of the following form:

$$\hat{\mathbf{K}}_{dyn,d} = \begin{bmatrix}\mathbf{K_{dyn}} & \hat{\mathbf{B}}\\ \hat{\mathbf{B}}^T & \mathbf{0}\end{bmatrix}, \tag{28}$$

with

$$\mathbf{K}_{dyn} = -\omega^2\hat{\mathbf{M}} + j\omega\hat{\mathbf{C}} + \hat{\mathbf{K}}. \tag{29}$$

Properties	Symbol	Value
Young's modulus shell	E_1	$69e9$ Pa
Density shell	ρ_1	2700 kg/m^3
Poisson's ratio shell	ν_1	0.33
Thickness shell	t_1	0.001 m
Young's modulus solid	E_2	$4.85e9$ Pa
Density solid	ρ_2	1185 kg/m^3
Poisson's ratio solid	ν_2	0.31

Table 1: Physical properties of the UC.

It is then possible to solve Eq. (27) in two steps, namely

$$\hat{\boldsymbol{x}} = \hat{\mathbf{K}}_{dyn}^{-1}(\mathbf{F} - \hat{\mathbf{B}}\boldsymbol{\lambda}), \tag{30}$$

and

$$(-\hat{\mathbf{B}}^T\hat{\mathbf{K}}^{-1}\hat{\mathbf{B}})\boldsymbol{\lambda} = -\hat{\mathbf{B}}^T\hat{\mathbf{K}}_{dyn}^{-1}\mathbf{F}. \tag{31}$$

Since the matrix $\hat{\mathbf{K}}_{dyn}$ consists of blocks that are uncoupled, the inverse or LU-decomposition of this matrix can be calculated block-wise. This not only leads to a reduction in the used memory, but also gives the option to calculate $\hat{\boldsymbol{x}}$ for the several UCs in parallel. As can be seen in Eqs. (30), (31), the full coupling matrices $\hat{\mathbf{B}}$ are still present. This shows the importance of choosing the correct reduced basis on UC level to have the proper balance between memory usage on one hand and small system size on the other hand.

4.2 Obtaining the Frequency Response Function

After the second MOR step is performed, the system response is calculated. Since the system has been reduced in two steps, also two steps have to be performed to return to the Full Order Model (FOM) response. Firstly, the system is solved for $\hat{\boldsymbol{x}}_d(\omega)$ and the response is calculated at every generalized output point $\hat{\boldsymbol{y}}_d(\omega)$ by

$$\hat{\boldsymbol{y}}_d(\omega) = \mathbf{I}_d\mathbf{V}_d\hat{\boldsymbol{x}}_d(\omega), \tag{32}$$

in which $\mathbf{I}_d$ is an identity matrix. Then, the response of the FOM is obtained by using the reduced basis in Eq. (18), as follows

$$y(\omega) = \boldsymbol{l}\mathbf{V}\hat{\boldsymbol{y}}_d(\omega), \tag{33}$$

in which $\boldsymbol{l}$ is a vector that indicates the position of the desired output point. Since $\mathbf{V}$ is a block diagonal matrix, Eq. (33) only has to be calculated for the relevant UC, thus the explicit construction of $\mathbf{V}$ is not necessary.

5 Numerical results

To validate the numerical accuracy of the given methodology, a metamaterial assembly of 5 by 3 UCs is considered, see Fig. 2. The size of the assembly is kept moderate, since it allows for a comparison of the solution to the full order model in a relatively short time frame. The UC consists of shell elements on the base and a resonator modeled with solid elements, both with linear shape functions. The material properties

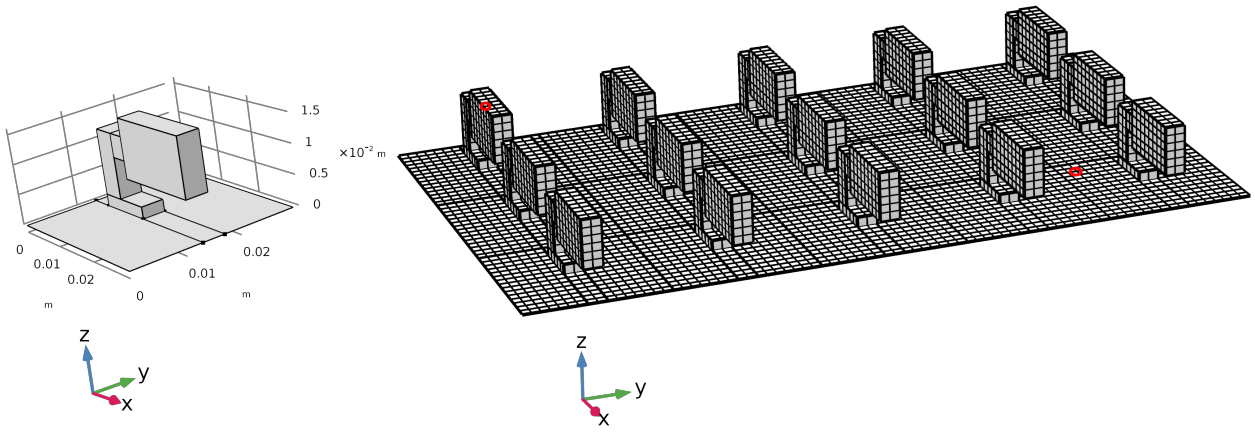


Figure 2: Dimensions of the UC in m (left hand side) and the assembly of the UCs (right hand side). Also the locations of the force and the output for the FRF comparison are indicated in red.

of both are shown in Table 1. The assembly is excited by a point force of 1 N on the top left UC, and the Frequency Response Function (FRF) is evaluated on the bottom right UC: Both points are indicated in Fig. 2. The initial UC is reduced with the algorithm explained in [14] such that the relative error on the sum of FRFs is below $1e-3$ from 1 to 1500 Hz. The inclusion of all the interface DOFs as input forces leads to a total of 311 inputs. As a comparison, also the model was reduced by skipping reduction step 1, thus directly assembling the full UC matrices and reducing it once. This leads to the following ROM sizes: $\mathbf{V}_{kr,UC} \in \mathbb{C}^{2178\times396}$, $\mathbf{V}_{CB,UC} \in \mathbb{C}^{2178\times815}$, and $\mathbf{V}_{split,UC} \in \mathbb{C}^{2178\times706}$. Thus, as stated before, strategy I gives the smallest reduced basis, and the Craig-Bampton inspired reduced basis is the largest. The second reduction step is performed with a relative error estimate that should be below $1e-5$. After the second reduction step, the ROMs are compared in accuracy and size by using the FOM as reference.

In Fig. 3 the FRFs and the relative error are plotted for the reduced models, resulting from the proposed reduced bases. It can be seen that they all give a very accurate result over the full desired frequency range. The second reduced basis has the following sizes for the different strategies: $\mathbf{V}_{d,kr} \in \mathbb{C}^{7750\times55}$, $\mathbf{V}_{d,CB} \in \mathbb{C}^{18645\times67}$ and $\mathbf{V}_{d,split} \in \mathbb{C}^{12360\times78}$, and $\mathbf{V}_{d,one} \in \mathbb{C}^{34440\times51}$ (which is the reduced basis resulting from skipping the first reduction step). Furthermore, the sparsity $\mathbf{K}_d$ for the different formulations are shown in Fig. 4. It has to be noted here that the block matrices on the diagonals of the ROM resulting from step one can be diagonalized by eigenvalue decomposition, under the assumption that the matrices are symmetric and no (or proportional) damping is applied. This has been demonstrated as a special case in Fig. 4. It can be seen that the split basis strategy, in combination with diagonalization, leads to a matrix that is relatively sparse, while the direct application of Krylov reduction on the UC leads to a less sparse matrix, which on the other hand is of smaller size.

Since the resulting assembled matrices are quite large, the most efficient method for this specific problem, both from a memory standpoint, speed of reduction and final model size, is the one step Krylov reduction method. It is expected that the proposed two step strategy will be more successful when the amount of DOFs on the edge is significantly less in comparison to the rest of the model, due to the dependence of the Krylov reduction bases on the amount of inputs. This would happen when the UC has a more complex shape, thus more inner DOFs. Furthermore, this can be achieved by re-meshing the problem, so that there are less DOFs at the edge, or by applying an interface reduction technique that reduces the inputs, such as SVDMOR [18]. Another observation that can be made is that the addition of the static condensation term in the reduced basis is not required to arrive at an efficient ROM.

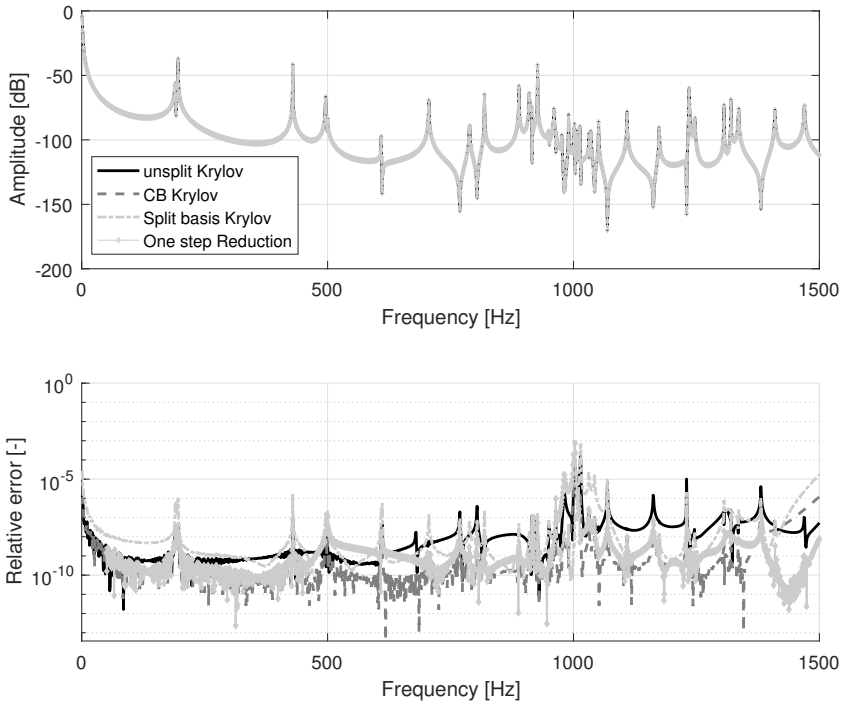


Figure 3: Reduction error with the several reduced bases.

6 Conclusions

Recent developments have demonstrated how to build a compact reduced basis for dynamic systems with many inputs, by using Krylov subspace projection. This paves the way to new applications, such as reduced order modeling of structures resulting from the substructuring of unit cells, which are traditionally done by techniques with a modal basis, such as Craig-Bampton. The advantage of Krylov methods over methods such as Craig-Bampton, is that the resulting ROM has more accurate input/output behavior. Also, the addition of damping to the system is quite straightforward.

A two stage reduction method is described, that first reduces the size of the UC, and then applies MOR on the fully assembled system with the reduced order system matrices of step I. Several ways to formulate the reduced basis are shown and compared from both a performance and computational perspective. It is shown that the static condensation term in the reduction basis, such as is done with Craig-Bampton, is not required to arrive at an accurate ROM. Furthermore, it is shown that, although the splitting of the basis leads to larger ROMs, the sparsity in the coupling matrices is preserved, which might be desirable from a memory perspective.

Further steps are devoted to a more in-depth analysis of the efficiency of the several implementations. Also, the need of the first MOR step will be investigated, since it was observed that the preservation of sparsity might be more important than the reduction of the UCs for both memory efficiency and calculation complexity. Due to the dependency of the Krylov subspace on the input size, also interface reduction techniques will be investigated. Another interesting future research topic is the addition of parametric model order reduction for the modeling of fluctuations in the UCs, such as they often occur in the assembly/production process.

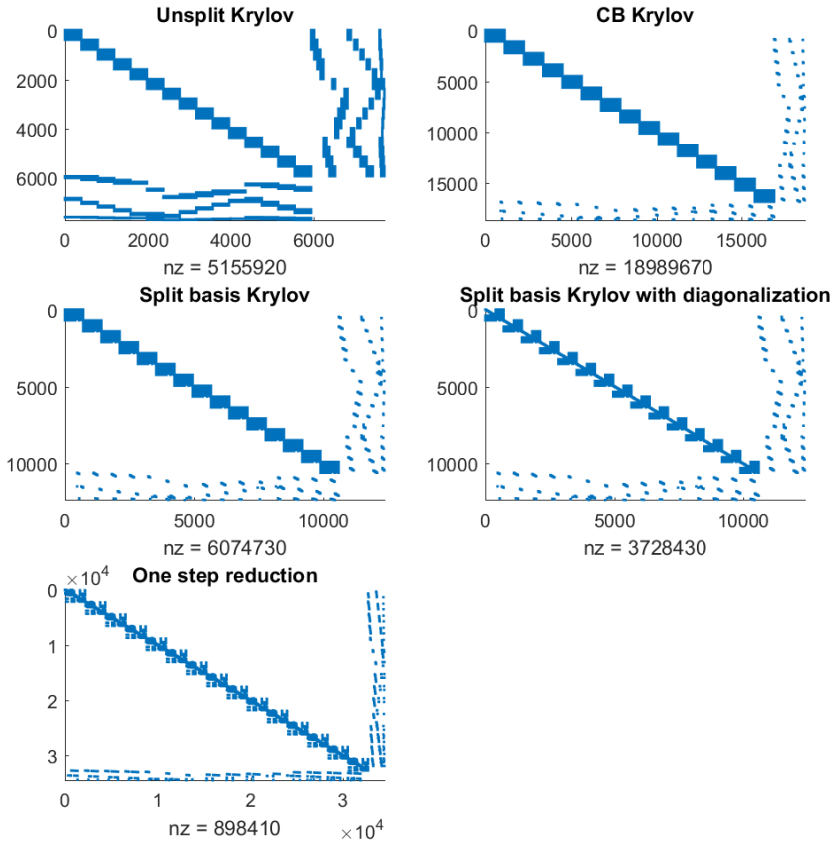


Figure 4: Sparsity of $\mathbf{K}_d$ before second reduction step. The number of non-zero terms is indicated with nz.

Acknowledgements

The European Commission is gratefully acknowledged for their support of the ANTARES research project (GA 606817). The research of E. Deckers is funded by a grant from the Research Foundation Flanders (FWO). The Research Fund KU Leuven is gratefully acknowledged for its support. This research was partially supported by Flanders Make, the strategic research centre for the manufacturing industry.

References

[1] C. Claeys, E. Deckers, B. Pluymers, W. Desmet, *A lightweight vibro-acoustic metamaterial demonstrator: Numerical and experimental investigation*, Mechanical Systems and Signal Processing, Vol. 70-71, (2016), pp. 853–880.

[2] L. Van Belle, C. Claeys, E. Deckers, W. Desmet, *On the impact of damping on the dispersion curves of a locally resonant metamaterial: Modelling and experimental validation*, Journal of Sound and Vibration, Vol. 409, (2017), pp. 1–23.

[3] F. Bloch, *Über die quantenmechanik der elektronen in kristallgittern*, Zeitschrift fr Physik, Vol. 52, No. 7-8, (1929), pp. 555–600.

[4] D. de Klerk, D. J. Rixen, S. N. Voormeeren, *General framework for dynamic substructuring: History, review, and classification of techniques*, AIAA Journal, Vol. 46, No. 5, (2008), pp. 1169–1181.

[5] P. Benner, S. Gugercin, K. Willcox, *A Survey of Projection-Based Model Reduction Methods for Parametric Dynamical Systems*, SIAM Review, Vol. 57, No. 4, (2015), pp. 483–531.

[6] R. Craig, M. Bampton, *Coupling of substructures for dynamic analysis*, AIAA Journal, Vol. 6, No. 7, (1968), pp. 1313–1319.

[7] B. Moore, *Principal component analysis in linear systems: Controllability, observability, and model reduction*, IEEE Transactions on Automatic Control, Vol. 26, No. 1, (1981), pp. 17–32.

[8] Y. C. Liang, H. P. Lee, S. P. Lim, W. Z. Lin, K. H. Lee, C. G. Wu, *Proper orthogonal decomposition and its applicationsPart I: Theory*, Journal of Sound and Vibration, Vol. 252, No. 3, (2002), pp. 527–544.

[9] Y. C. Liang, W. Z. Lin, H. P. Lee, S. P. Lim, K. H. Lee, H. Sun, *Proper orthogonal decomposition and its applications Part II: Model reduction for MEMS dynamical analysis*, Journal of Sound and Vibration, Vol. 256, No. 3, (2002), pp. 515–532.

[10] E. J. Grimme, *Krylov Projection Methods for Model Reduction*, Ph.D. thesis, University of Illinois, Illinois (1997).

[11] P. Holzwarth, P. Eberhard, *SVD-based improvements for component mode synthesis in elastic multibody systems*, European Journal of Mechanics - A/Solids, Vol. 49, (2015), pp. 408–418.

[12] B. Salimbahrami, B. Lohmann, *Order reduction of large scale second-order systems using Krylov subspace methods*, Linear Algebra and its Applications, Vol. 415, No. 2, (2006), pp. 385–405.

[13] K. Gallivan, A. Vandendorpe, P. Van Dooren, *Model Reduction of MIMO Systems via Tangential Interpolation*, SIAM Journal on Matrix Analysis and Applications, Vol. 26, No. 2, (2004), pp. 328–349.

[14] S. van Ophem, A. van de Walle, E. Deckers, W. Desmet, *Efficient MIMO Krylov subspace model order reduction for vibro-acoustic systems*, *ANTARES - Advanced Training and Research in Energy Efficient Smart Structures*, KU Leuven - Faculty of Engineering, Heverlee (2018), 27–45.

[15] Z. Bai, Y. Su, *Dimension Reduction of Large-Scale Second-Order Dynamical Systems via a Second-Order Arnoldi Method*, SIAM Journal on Scientific Computing, Vol. 26, No. 5, (2005), pp. 1692–1709.

[16] K. Gallivan, E. Grimme, P. Van Dooren, *Asymptotic waveform evaluation via a Lanczos method*, Applied Mathematics Letters, Vol. 7, No. 5, (1994), pp. 75–80.

[17] Z. Bai, Y. Su, *SOAR: A Second-order Arnoldi Method for the Solution of the Quadratic Eigenvalue Problem*, SIAM Journal on Matrix Analysis and Applications, Vol. 26, No. 3, (2005), pp. 640–659.

[18] P. Holzwarth, P. Eberhard, *Interface Reduction for CMS Methods and Alternative Model Order Reduction*, IFAC-PapersOnLine, Vol. 48, No. 1, (2015), pp. 254–259.

[19] A. van de Walle, *The power of model order reduction in vibroacoustics*, PhD thesis, KU Leuven, Leuven, Belgium (2018).

[20] Y. Saad, *Domain decomposition methods*, *Iterative Methods for Sparse Linear Systems*, Pws Pub Co, 2nd Ed. (2003), 469–478.

Nonlinearity assessment of MIMO electroacoustic systems on Direct Field Environmental Acoustic Testing

M. Alvarez Blanco [1,2], **P. Z. Csurcsia** [1,3], **B. Peeters** [1], **K. Janssens** [1], **W. Desmet** [2,4]
[1] Siemens Industry Software NV
Researchpark 1237, Interleuvenlaan 68, B-3001 Leuven, Belgium
e-mail: **mariano.alvarez_blanco@siemens.com**

[2] KU Leuven, Department of Mechanical Engineering
Celestijnenlaan 300 B, B-3001, Heverlee, Belgium

[3] Vrije Universiteit Brussel, Department of Engineering Technology
Pleinlaan 2, B-1050, Elsene, Belgium

[4] Member of DMMS core lab Flanders Make

Abstract
Direct Field Environmental Acoustic testing consists in reproducing the sound field inside a spacecraft vehicle's fairing using an array of loudspeakers. In order to ensure the accurate reproduction of the sound pressure field, the actuators need to be actively controlled. The performance of state-of-the-art Multiple-Input Multiple-Output (MIMO) random controllers is strongly dependent on the control strategy. The system identification, methodology applied at low power level excitation before the test, is one of the most sensitive aspects of such strategy. This is because it provides a linear nonparametric model of the electroacoustic system, which is used to design the signals to drive the loudspeakers. In this work novel system identification strategy is explored. The proposed method is a MIMO Best Linear Approximation (BLA). In this technique, instead of using classical excitation signals and the H1 estimate, a BLA model is estimated, and the coherence function is split into noise level and nonlinear contribution estimates.

1 Introduction

Environmental testing is required in the space industry to evaluate the survivability of space hardware to the launch environment. In particular, environmental acoustic testing consists in reproducing the acoustic field of a Launch Vehicle (LV) with acoustic power distribution comparable to the operating conditions.

Direct Field Acoustic eXcitation (DFAX) is a testing method which consists in reproducing this acoustic field with an array of loudspeakers (i.e. actuators). In order to ensure uniform spatial distribution of sound pressure level, such electroacoustic system needs to be controlled. Then, microphones are necessary to provide pressure error signals to compare measured outputs against references, or the so-called test targets.

State-of-the-art control strategy relies, among other factors, on an experimental model of the electroacoustic system used to design the signals feeding the loudspeakers. Furthermore, closed-loop grants adaptive features to the control procedure, allowing to track and compensate model uncertainties due to: noise, nonlinearities and/or time variant characteristics of the electroacoustic system. Through Multiple-Input Multiple-

Output (MIMO) closed-loop control strategies, state-of-the-art random controllers have shown good performance in achieving the test requirement at the discrete controlled locations of the test volume [1][2][3]. Although such a good performance encourages the use of DFAX for space hardware qualification, it has been shown that the controllability of the electroacoustic system is strongly dependent on the control strategy [4]. Where control strategy is a wide concept comprehending several aspects of the test setup, namely: control algorithm principle, system overdetermination, system identification strategy, MIMO test references definition, acoustic sources and control sensors placement, test specimen placement and orientation, drive signals processing and randomization, drive signals amplification, among others.

One of the most sensitive aspects is the system identification strategy, since it determines the quality of the experimental and nonparametric model of the electroacoustic system used for the computation of the signals driving the loudspeakers array. Poor models turn into inaccurate driving signals and, consequently, may lead to large sound pressure errors. Although, in principle, MIMO random controllers are able to tackle such error (i.e. mismatch between outputs and references), it is clear that starting from a model which is (highly) representative of the dynamics shown by the physical electroacoustic system would increase the efficiency of the test campaign. This is because the time taken by the controller to reach the reference would be shorter. In practice, this means that the device under test would be exposed to the test specifications, strictly, the required test time. While, on the other hand, inefficient control strategies may expose the device under test more time than necessary to under-testing (although very high) sound pressure levels, which may over-stress the structure by accumulated fatigue.

In his work it is studied if the efficiency of a DFAX environmental acoustic test can be improved by novel system identification strategy in a test campaign. The proposed method is a MIMO Best Linear Approximation (BLA). Similar methodology has been widely used in the last decades to efficiently estimate FRFs of single-input single-output systems [5]. In this technique, instead of using the classical H1 estimate and its coherence function [6], a BLA model is estimated, and the coherence function is split into (i) noise level and (ii) nonlinear contribution estimates. The proposed BLA technique makes use of the knowledge that the excitation signal has both stochastic and deterministic properties.

This paper is organised as follows, Section 2 introduces MIMO random control to understand the context and practical importance of the system identification process. Section 3 describes the expected dynamics of the electroacoustic systems used for DFAX testing. It is followed by an explanation of state-of-the-art system identification strategies, which derives in the MIMO Best Linear Approximation methodology proposed in this paper. The results section shows the improvement provided by MIMO BLA through the analysis of experimental data acquired at a system level environmental acoustic tests.

2 MIMO random control for DFAX testing

This section introduces the analytical concepts to understand the role and importance of the system identification procedure in the context of MIMO random control for DFAX testing. The minimum equipment necessary to perform an environmental acoustic test with DFAX method comprehends a data-acquisition/control system and an electroacoustic system, where the latter comprises a set of transducers, amplifiers and filters. As shown in figure 1, the transducers consist of an array of loudspeakers surrounding the test specimen, and a set of microphones. MIMO control strategies for DFAX imply that such electroacoustic system is driven by multiple independent signals, while multiple pressure responses are acquired at different locations in the acoustic field.

The dynamics of a linear MIMO electroacoustic system consisting of d inputs and l outputs can be nonparametrically characterised by the Frequency Response Matrix (FRM), $\boldsymbol{G}(k) \, \epsilon \, \mathbb{C}^{lxd}$, which relates the inputs $\boldsymbol{U}(k) \, \epsilon \, \mathbb{C}^{dx1}$ to outputs $\boldsymbol{Y}(k) \, \epsilon \, \mathbb{C}^{lx1}$ at frequency index k, as shown by equation (1). In this work, the nomenclature of the signals involved in the control process takes as reference the physical electroacoustic system. Therefore, inputs are called the electrical signals driving the loudspeakers, while outputs are called

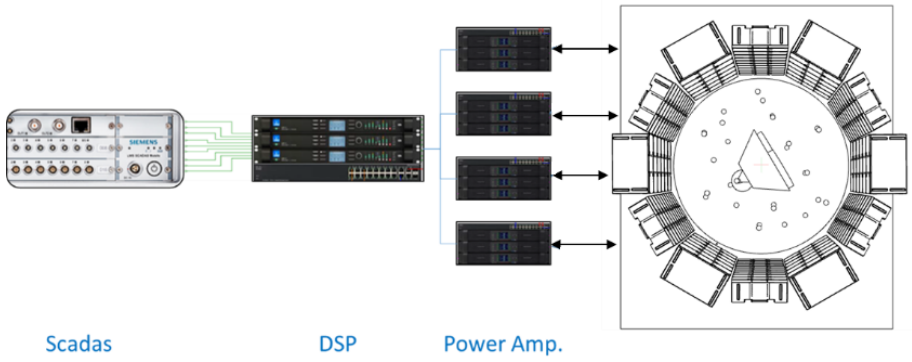


Figure 1: Simcenter SCADAS and top-view of electroacoustic system for DFAX

the acoustic pressure signals acquired by the microphones.

$$\boldsymbol{Y}(k) = \boldsymbol{G}(k)\boldsymbol{U}(k) \tag{1}$$

The electroacoustic system represented by $\boldsymbol{G}(k)$ is linear when the superposition principle is satisfied. This means that:

$$\boldsymbol{Y}(k) = \boldsymbol{G}(k)(a+b)\boldsymbol{U}(k) = a\,\boldsymbol{G}(k)\boldsymbol{U}(k) + b\,\boldsymbol{G}(k)\boldsymbol{U}(k) = (a+b)\boldsymbol{G}(k)\boldsymbol{U}(k) \tag{2}$$

where a and b are scalar values. If $\boldsymbol{G}(k)$ is constant, then, the system is called linear-time invariant (LTI). On the other hand, when $\boldsymbol{G}(k)$ varies over time, then, the system is called linear time-varying (LTV).

State-of-the-art random controllers operate under the assumption that above conditions are satisfied. Given the stochastic, stationary and ergodic nature of the dynamic loading in environmental acoustic testing [7][8], it is convenient to represent the input-output relation for the electroacoustic system in terms of (power) Spectral Density Matrices (SDM) as:

$$\boldsymbol{S}_{yy}(k) = \boldsymbol{G}(k)\boldsymbol{S}_{uu}(k)\boldsymbol{G}^{H}(k) \tag{3}$$

where $\boldsymbol{S}_{uu}(k)\ \epsilon\ \mathbb{C}^{dxd}$ is the input SDM, $\boldsymbol{S}_{yy}(k)\ \epsilon\ \mathbb{C}^{lxl}$ the output SDM, and $\bullet^{H}$ is the complex-conjugate transpose operator.

The purpose of a MIMO random control algorithm for DFAX is the automatic computation of the d random electrical signals (i.e. drives) required to feed the loudspeakers in order to achieve certain test references at multiple points in the acoustic field. Currently, this computation is done based on a model of the MIMO electroacoustic system assuming LTI behaviour. In environmental testing it is a standard off-line practice to perform nonparametric, experimental system identification to estimate this model. In active acoustic control the same method is known as nonblind multi-channel identification and leads to an estimate of the physical system [9]. From such estimate and certain user-defined test references, the random controller automatically generates the first set of drives following equation:

$$\boldsymbol{S}_{uu}(k) = \hat{\boldsymbol{G}}^{\dagger}(k)\boldsymbol{S}_{yy}^{REF}(k)(\hat{\boldsymbol{G}}^{\dagger}(k))^{H} \tag{4}$$

where $\bullet^{\dagger}$ is the (pseudo-)inverse operator, $\hat{\bullet}$ indicates estimate and $\boldsymbol{S}_{yy}^{REF}(k)\ \epsilon\ \mathbb{C}^{lxl}$ are the test references, arranged in a SDM.

Initially, the physical electroacoustic system is driven by time domain signals with power and cross-correlation derived from equation (4). Next, adaptive feedback control allows correcting such drives. This becomes necessary due to noise in the measurements, and in case the electroacoustic system does not behave linearly

and time invariantly. The correction is performed sequentially, based on the average of a fixed amount of measured pressure response windows, which determines a loop time. The generation of the updated drive signals for subsequent loops, depends on the difference between the test reference SDM and the measured output SDM. This difference represents the error on the reproduction of the targeted sound field.

High control performance translates into accurate drives generation. On this subject, equation (4) shows how the computation of the spectral density matrix of the initial drives depends on the (i) validity of the electroacoustic system dynamics assumptions, (ii) the electroacoustic system estimate, (iii) (pseudo-)inversion of the FRM, (vi) and compatibility between test references and the electroacoustic system estimate.

In this work (i) and (ii) are studied by assessing how the electroacoustic system estimate depends on the excitation signal, how can a MIMO BLA model be efficiently estimated, and how it is possible to separate noise and nonlinearity information from a measurement.

3 Dynamics of DFAX electroacoustic system

Figure 1 shows an example of the acquisition and electroacoustic systems used for DFAX. The electroacoustic system consists of a digital audio processor and a set of electroacoustic transducers arranged in, typically, an acoustically ordinary room [10]. The digital audio processor includes a digital signal processor (DSP) providing equalization, delay, dynamic processing, crossover filtering capabilities and power amplification. On the other hand, the transducers consist of an array of electrodynamic loudspeakers and a set of pre-polarized condenser microphones.

Figure 2 shows a conceptual block diagram of the electroacoustic system. It corresponds to the signal flow of an independent drive feeding a set of loudspeakers. The blocks represent the processing and power amplification stages of the electroacoustic system. As it can be observed, each drive can be equalized and independently delayed in time. Afterwards the drive signal is filtered to split it up, typically, into four frequency ranges: sub-low, low, mid and high frequency bands. These bands cover the frequency range specified as test requirement for the qualification. Each band can be independently delayed in order to correct the phase-alignment between drivers of the loudspeaker. Furthermore, according to its voltage waveform, the audio signal feeding each band can be RMS/peak limited through a dynamic processor. The purpose of such a processor is to avoid overloading the input of the amplifiers, because this could lead to unwanted nonlinearities. However, as dynamic processors are nonlinear subsystems *per-se*, limiting threshold parameter must be set in such a way that they do not introduce unwanted nonlinearity at working operating conditions.

As shown in Figure 2 the electroacoustic system can be split and studied component by component. Theoretically, for *small amplitude signals* each of these components can be treated as a LTI subsystem. However, the assumption holds in between certain frequency and dynamic ranges. Outside these ranges, the system may not satisfy the superposition principle and the behaviour of the observed system is nonlinear.

3.1 Expected nonlinearities in DFAX testing

The most common loudspeakers used for DFAX exploit the electrodynamic transduction principle. This principle comprises a driving part (i.e. the motor), which is a moving coil into a static magnetic field. The driving signal (V in Figure 2) goes through the coil and creates a variable magnetic field that interact with a fixed magnet and generates a mechanical force that is roughly proportional to the electrical current. The acoustic radiation is then provided by a lightweight diaphragm attached to the coil, ideally moving as a rigid piston. This driving part is attached to a frame by elastic suspensions, which in turn is fixed to the loudspeaker cabinet (a vented-box in case of the low frequency sources used for the experiments).

A simplified linear model based on lumped parameters describes the loudspeaker mechanism in a vented-box at low frequencies and small amplitudes [11]. However, it has been shown that even at not so high driving amplitudes, the force factor determined by the product of magnet field strength in the voice coil gap and the

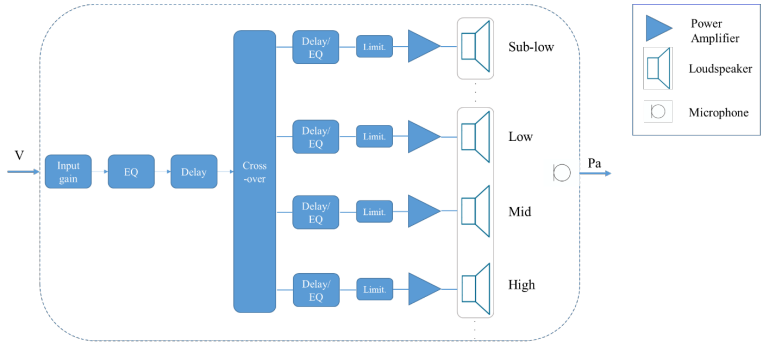


Figure 2: Conceptual block diagram of the electroacoustic system

length of wire in the magnetic field, the voice coil inductance, and the stiffness of the suspension can behave nonlinearly [12]. The contribution of such nonlinearities (among others [13][14]) to the radiated acoustic field as harmonic distortion is traditionally quantified by standardized sinusoidal signal measurement techiniques [14].

4 System identification strategies

Several approaches exist for building a model of an electroacoustic system as used in DFAX. Numerical modelling tools can be used to analyse and build such system model. While simulations (may) provide clear insight in the underlying physical processes and generate full field information, they often only approximately describe the real operating conditions of the system. This is especially the case for simulation of complex electroacoustic scenarios with electrodynamic loudspeakers, where oversimplification of the involved multi-physics may lead to poor quality models.

Alternatively, experimental data gathered during the DFAX test campaign can be used to build the electroacoustic model in-situ. Ideally, the objective would be to fully characterise the acoustic field. However, due to industrial feasibility constraints (i.e. costs and time) not all locations of interest may be measured, or even accessible, to build such model. Moreover, the gathered data can be corrupted by measurement noise, process noise, disturbing transients and other disturbances. Despite these drawbacks, the experimental modelling approach has the advantage of reflecting the performance of the real system in operating conditions, which in the space industry is considered a critical attribute of the model to ensure a safety environmental testing procedure. Hence, in this work the system identification process for modelling the MIMO electroacoustic system relies on an experimental nonparametric estimate.

4.1 Experimental system identification strategy

Experimental identification of the MIMO electroacoustic system consists in performing a low-level random test for the estimation of the FRFs. During this procedure the loudspeakers are driven by uncorrelated low power level signals, ensuring a riskless environment for the test specimen. Observed input-output data allows to build a nonparametric model of the dynamic system, an estimate of the physical system concerning the path between inputs and outputs, capturing signal processing (e.g. filtering), loudspeaker dynamics, acoustic wave propagation phenomena and microphone dynamics.

4.2 Multisine excitation

In modern system identification special excitation signals are available to assess the underlying systems in a user-friendly, time efficient way [15]. In order to avoid any spectrum leakage, to reach full nonparametric

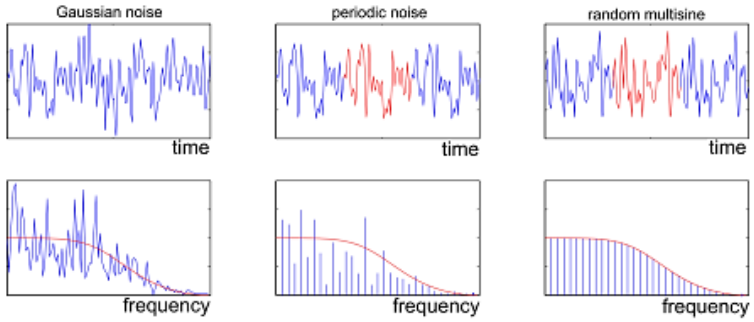


Figure 3: Different excitation signals in time and in frequency domain

characterization of the noise, and to be able to detect nonlinearities, a periodic signal is needed. Many users prefer noise excitations, because they are simple to implement (see Figure 3), but in this case nonlinearities are not identifiable, and there is a possible leakage error. The best signal that satisfies the desired properties is the user-friendly multisine signal (see Figure 3) which looks like Gaussian white noise, behaves like it, but it is not a noise.

In this work, random phase multisines are used and generated in the frequency domain such that the magnitude characteristic is set by the user, and the phases of the cosines are chosen randomly from a uniformly distribution [16]. The random phase (uniformly distributed) multisine is, therefore, a sum of harmonically related sinusoids as shown in the following equation:

$$u(t)_m = \sum_{m=1}^{F} A_m \cos(\omega_0 m t + \varphi_m), \quad \varphi_m \sim \mathcal{U}(0, 2\pi) \tag{5}$$

where ω_0 is the fundamental angular frequency, A_m is the amplitude of the m^{th} harmonic and F is the highest harmonic component. The amplitude distribution of a random phase multisine is approximately normal (it approaches a Gaussian distribution as the number of harmonics tend to infinity). If the multisine contains all/only odd or even harmonics, then, it is full/odd or even multisine.

4.2.1 Detecting even and odd nonlinearities with multisines

In general, when exciting a physical system with low power excitation level, the effects of nonlinearities can be hidden in the noise. If the excitation level is higher, the nonlinearities will appear. Figure 4 shows, for example, how a system response may consist of a linear and a nonlinear part.

If a full multisine excitation is used, then the details of nonlinear behaviour are not separable from the linear part. On the other hand, with an excitation set of only even harmonics, the odd nonlinearities are not detectable. The solution to detect both kinds (even/odd) of nonlinearities is to use an excitation set only with odd harmonics, i.e. odd random phase multisine. In order to examine the odd frequencies, it is needed to skip several odd harmonics in the multisine. The experiences show that the odd, random phase multisine with randomly skipped harmonics is the best approach to study the nonlinearities [16].

4.3 Best Linear Approximation approach

The Best Linear Approximation (BLA) has been widely used in the last decades to efficiently estimate FRFs [17][5]. The BLA of a nonlinear system is an approach of modelling that minimizes the mean square error between the true output of a nonlinear system and the output of the linear model. In this technique, instead of using the classical H1estimate (cross-power spectral density estimate [18]) and its coherence function, a

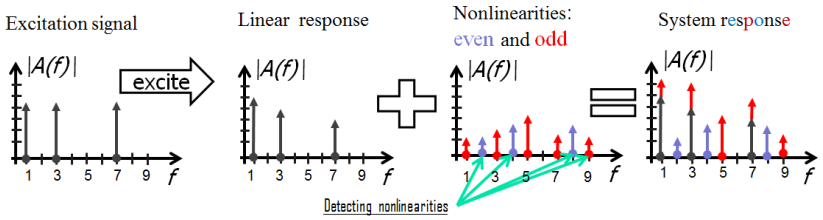


Figure 4: System response originating from linear and nonlinear part of excited system

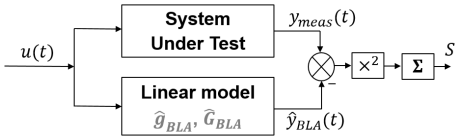


Figure 5: The baseline model for best linear approximation framework

BLA model is estimated, and the coherence function is split into (i) noise level and (ii) nonlinear contribution estimates. The proposed BLA technique makes use of random phase multisine signals with known excited frequency lines. Furthermore, this technique exploits the knowledge that such excitation signal has both stochastic and deterministic properties.

4.3.1 Differences with respect to H1

A significant difference between BLA and H1 estimate, as applied in this work, is that the latter makes use of *periodic random* excitation [19].

Another fundamental difference is that a partial BLA estimate is calculated for each period of the random phase multisine excitation signal. Then, a BLA FRF estimate for a given signal is calculated via the average of different BLAs. On the other hand, the H1 estimation directly uses the averaged input and output data.

4.3.2 Theoretical structure and the basic assumptions

In Figure 5 the BLA of a nonlinear system is represented by an impulse response function $\hat{g}_{BLA}(t)$, or a frequency response function $\hat{G}_{BLA}(k)$ estimate [16]. This approach of modelling minimizes the mean square error between the true output of a nonlinear system $y_{meas}(t)$ and the output of the linear model $\hat{y}_{BLA}(t)$.

Figure 6 shows the theoretical structure of BLA, where several component can be identified [15]:

- G_E corresponds to the the ordinary measurement noise, which in this work is assumed to be additive i.i.d. normal distributed with zero mean and with a finite variance σ^2, (i.e. $e \sim \mathcal{N}(0, \sigma^2)$).
- G_{Linear} represents the true underlying linear system (if it exists). Its response is independent of the excitation power spectrum and it is a smooth frequency function. For this linear component of BLA we make use of the fact that each random phase rotation in the input excitation would result in a proportional phase rotation at the output (i.e. phase coherence), when the underlying system is linear.
- G_{Bias} denotes a bias error of the BLA, the systematic nonlinear contribution whose spectrum is smooth. This is the result of the coherent nonlinearities remaining after multiple realizations of excitation signal. Its value is fixed in the same excitation set (a realization of the excitation signal).

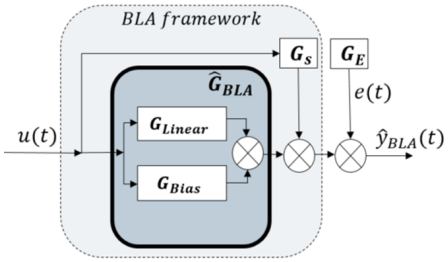


Figure 6: The theoretical structure of the best linear approximation

- $\hat{G}_{BLA}$, as sum of G_{Linear} and G_{Bias}, it has also smooth FRF, which is fixed for a realization of the excitation signal.
- G_S can be seen as an additional (nonlinear) noise source generator. As mentioned for G_{Linear}, in the proposed robust BLA framework, multiple realizations of random phase multisine excitation are needed. In case of noncoherent nonlinearities, the input phase rotation would result in a random phase rotation at the output. Therefore, G_S can be modelled as a half-stochastic nonlinear noise generator with zero mean circular complex normal distribution.

The output of a nonlinear system strongly depends on (i) the energy level of each excited frequency, (ii) the probability density function of the input, (iii) even and odd nonlinear distortions of the system, (iv) type of the disturbing noise and its impinge point. Assuming that there is no transient, measurement or round-off error, the BLA FRF is given by:

$$\hat{G}_{BLA}(k) = G_{Bias}(k) + G_{Linear}(k) \tag{6}$$

and the measured FRF is:

$$\hat{G}_{measured}(k) = \hat{G}_{BLA}(k) + G_S(k) + G_E(k) \tag{7}$$

The next section discusses a possibility to reduce the effects of the measurement noise (G_E) and the nonlinearities (G_S).

4.3.3 The effects of two dimensional averaging

In order to estimate the underlying system one has to average over p periods of repeated excitation signal, and over the m different realizations of the excitation signal [16] (see Figure 7). The considered model in frequency domain at frequency index k is given by:

$$\hat{G}^{[m,p]}_{measured}(k) = \frac{\hat{Y}^{[m,p]}_{measured}(k)}{U^{[m]}(k)} = \hat{G}_{BLA}(k) + G^{[m]}_S(k) + G^{[m,p]}_E(k) \tag{8}$$

First, let us average over the p periods in the same excitation set. If p is sufficiently large, then (originated from the law of large numbers and the distribution properties the observation noise), the expected value of the observed system will boil down to:

$$\begin{aligned} E\{\hat{G}^{[m]}_{measured}(k)\} = \frac{1}{p}\sum_{i=1}^{p} \hat{G}^{[m],i}_{measured}(k) &= \frac{1}{p}\sum_{i=1}^{p}(\hat{G}_{BLA}(k) + G^{[m]}_S(k) + G^{[m],i}_E(k)) \\ &= \hat{G}_{BLA}(k) + G^{[m]}_S(k) + 0 = \hat{G}_{BLA}(k) + G^{[m]}_S(k) \end{aligned} \tag{9}$$

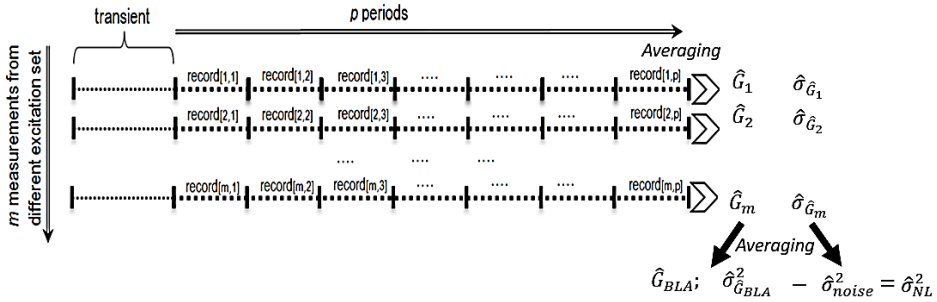


Figure 7: Evaluation of BLA estimate with the help of two dimensional averaging

and its sample variance:

$$Var\{\hat{G}^{[m]}_{measured}(k)\} = \sum_{i=1}^{p} \frac{|\hat{G}^{[m],i}_{measured}(k) - \hat{G}^{[m]}_{measured}(k)|^2}{p(p-1)} \tag{10}$$

Second, let us average over the m realizations. If m is sufficiently large, then:

$$E\{\hat{G}_{measured}(k)\} = \frac{1}{m}\sum_{i=1}^{m} \hat{G}^{i}_{measured}(k) = \frac{1}{m}\sum_{i=1}^{m}(\hat{G}_{BLA}(k) + G^{i}_{S}(k)) = \hat{G}_{BLA}(k) + 0 = \hat{G}_{BLA}(k) \tag{11}$$

and its sample variance is given by:

$$Var\{\hat{G}_{BLA}(k)\} = \sum_{i=1}^{m} \frac{|\hat{G}^{i}_{measured}(k) - \hat{G}_{BLA}(k)|^2}{m(m-1)} \tag{12}$$

The estimate of the noise sample variance is given by:

$$Var\{G_E(k)\} = \frac{1}{m^2}\sum_{i=1}^{m} Var\{\hat{G}^{[m]}_{measured}(k)\} \tag{13}$$

The difference between the total variance and the noise variance is an estimate of the variance of the stochastic nonlinear contributions. For one experiment it is given by:

$$Var\{G_S(k)\} \approx m(Var\{\hat{G}_{BLA}(k)\} - Var\{G_E(k)\}) \tag{14}$$

This means that the influence of the noise and nonlinear contribution can be decreased with this special 2D averaging. As a final result the measured and post-processed FRF will be BLA. In [15] it has been shown that the above statements are completely correct with the condition and assumptions declared in Section 4.3.2, when the number of periods is greater or equal than two ($p \geq 2$) and the different realizations are more than six ($m \geq 7$). Note that in the experiments reported in Section 6, seven realizations were designed for the BLA estimate. However, due to technical difficulties one realization is lost. Although convergence is actually guaranteed as from $m \geq 4$ [17], this results in a less accurate BLA estimate of the FRM.

5 MIMO Best Linear Approximation

In this section the measurement of the FRM for MIMO systems is explained as a straightforward extension of the SISO methodology presented above. For the sake of simplicity but without loss of generality, we will focus on systems with 6 inputs and outputs.

5.1 Estimating the Frequency Response Matrix

The straightforward extension of the SISO excitation case can be formulated in the frequency domain at frequency index k as follows:

$$\begin{bmatrix} Y_1(k) \\ \vdots \\ Y_6(k) \end{bmatrix} = \begin{bmatrix} G_{11}(k) & \dots & G_{16}(k) \\ \dots & \dots & \dots \\ G_{61}(k) & \dots & G_{66}(k) \end{bmatrix} \begin{bmatrix} U_1(k) \\ \vdots \\ U_6(k) \end{bmatrix} \tag{15}$$

where the indices of the input and output data refer to channel number. Even when there are multiple periods of excitation applied, the above-mentioned set of linear equations suffers from the degrees of freedom: there are 36 unknown parameters and 6 independent equations. In order to overcome the issue with the degrees of freedom, the number of equations has to be increased. In this work this has been done by increasing the number of experiments such that the new base-line equation is defined as follows:

$$\begin{bmatrix} Y_{11}(k) & \dots & Y_{16}(k) \\ \dots & \dots & \dots \\ Y_{61}(k) & \dots & Y_{66}(k) \end{bmatrix} = \begin{bmatrix} G_{11}(k) & \dots & G_{16}(k) \\ \dots & \dots & \dots \\ G_{61}(k) & \dots & G_{66}(k) \end{bmatrix} \begin{bmatrix} U_{11}(k) & \dots & U_{16}(k) \\ \dots & \dots & \dots \\ U_{61}(k) & \dots & U_{66}(k) \end{bmatrix} \tag{16}$$

where the first digit of the indices refer to channel and the second digit refers to the number of experiment. To obtain the FRM estimate, at each frequency index k, equations (16) must be solved.

5.2 Conditioning of the input matrix

The solvability of the linear algebraic equations (16) strongly depends on the condition number (i.e. the randomness) of the excitation matrix. Highly correlated elements in $\boldsymbol{U}(k)$ matrix will result in singularity and therefore no solution can be obtained.

In classical MIMO identification, one of the most often applied solution to this problem is the use of Hadamard decorrelation technique. A Hadamard matrix is a square matrix whose entries are either +1 or 1, and whose rows are mutually orthogonal. In this technique there is one realization of the excitation signal which is multiplied with such Hadamard matrix resulting in a well-conditioned matrix (for certain linear cases [20]). The problem here lies in the fact that the Hadamard matrix only exist for certain dimensionalities: the order of a Hadamard matrix must be 1, 2, or multiples of 4. For input dimensions where the Hadamard matrices cannot be defined, the most often used solution is to take the Hadamard matrix with highest closer order, and truncate it to the desired size.

For certain dimensions this solution might not be adequate or rich enough to identify the nonlinearities because only one realization of the input signal and its conjugate are applied. For detecting the nonlinearities richer signals are required. Therefore, in order to overcome the issue and to improve the estimation properties, in [21] and [22], it is proposed to use orthogonal random multisines, extending the idea of the orthogonal inputs proposed for linear MIMO measurements in [23]. In this work the proposed procedure is to generate independent random excitations for every input channel for the first experiment in a block of experiments, and to shift them orthogonally for the subsequent experiments with the following weighting-shifting matrix (W):

$$\boldsymbol{W}(m,n) = e^{-j2\pi(m-1)(n-1)/d} \tag{17}$$

where l refers to channel number, n refers to the experiment number, and d stands for the number of independent inputs.

6 Results

This section concerns the classification and characterization of the measurement obtained at Thales Alenia Space facilities in Toulouse, France, where subsystem and system level industrial DFAX tests were performed. Further, this section shows a validation study case of the proposed MIMO BLA methodology.

The analysis below intends, ultimately, to explain the capability of MIMO BLA to predict measured responses more accurately than done by standard estimator. From such capability, it is inferred that MIMO BLA model would derive in more efficient closed-loop control tests. On top of that, it is highlighted that MIMO BLA allows to split the coherence function into noise and nonlinear components. Further, the nonlinearity and noise analysis of the waveform generator is performed as well, intending to understand the influence it may have on the model accuracy.

The BLA measurement has been executed at three different levels. Figure 8 shows the lowest and highest level excitation signals in the frequency domain. The arbitrary waveform generator (Simcenter SCADAS) has a very low noise level (around -90 dB in mid frequencies) resulting in a good measurement quality of the excitation signal. With the help of Figure 8, the estimated value of the SNR is around 70 dB at mid frequencies. Despite the good SNR, there are some even nonlinearities presented in a magnitude of 25 dB w.r.t. noise level.

The microphone output displayed on the left of Figure 9 is measured with a significant lower SNR value: around 45 dB at low, and around 30 dB at high frequencies. The microphone output is governed by even nonlinearities, which become especially dominant at mid and higher frequencies, and their levels are even more dominant at the higher excitation profile.

The FRF shown in Figure 10 is measured with high noise level due to transient and nonlinearities. However, the noise level and the nonlinearities can be clearly distinguished (with a relative difference of 20 dB) on the arbitrary chosen FRF.

Observing the level and type of nonlinearities in the estimates (Figure 9 and 10) confirms that a LTI random controller may be adequate to conduct DFAX tests. This is because the relatively low level even nonlinearities can be considered as process noise in the LTI control framework [15]. Furthermore, since the odd nonlinearities are not dominating even at much higher excitation power levels, no extreme dynamic changes are to be expected.

Despite the high level of nonlinearities shown in Figure 9 and 10, the best linear approximation resulted in an acceptable linear model. This model is cross validated on an independent dataset and is compared to the traditional H1 estimate in Figure 11 to 13. In the cross validation the estimated outputs (i.e. forward simulation) are compared to the measured output from qualification test, where the BLA estimate results in around 6 times smaller relative Root-Mean-Square (RMS) error, as shown by the dots in Figure 11. This is meaningful taking into account that, due to test campaign constraints, H1 estimate was done based on excitations with much higher power level than in case of the BLA. Since the level of nonlinearities at low frequency is not as significant (and therefore the system seems to be less sensitive to the excitation power level) Figure 12 shows through the magnified cross validation results how BLA clearly outperforms H1 estimate.

Figure 13 shows the same output signals than the previous two figures, but in a $1/3rd$ octave band plot. This is how qualification test results are reported to the launching authorities in order to certify that the required sound pressure levels were achieved during the test. Therefore, the plot is useful to assess relative differences in the cross validation w.r.t. to typically specified test tolerances per band ($-1/+3$ dB [24]). Note that H1 based prediction is at least 6 dB below the measured output in the band centered at 31.5 Hz. At the other extreme of the spectrum, cross validation shows that BLA over-estimates the output, specially over 3150 Hz. This is due to the high level of even nonlinearity in high frequencies, as displayed in Figure 9 to 11. Such results may justify future research efforts to model even nonlinearities of the electroacoustic system contributing to the acoustical responses observed in environmental acoustic testing.

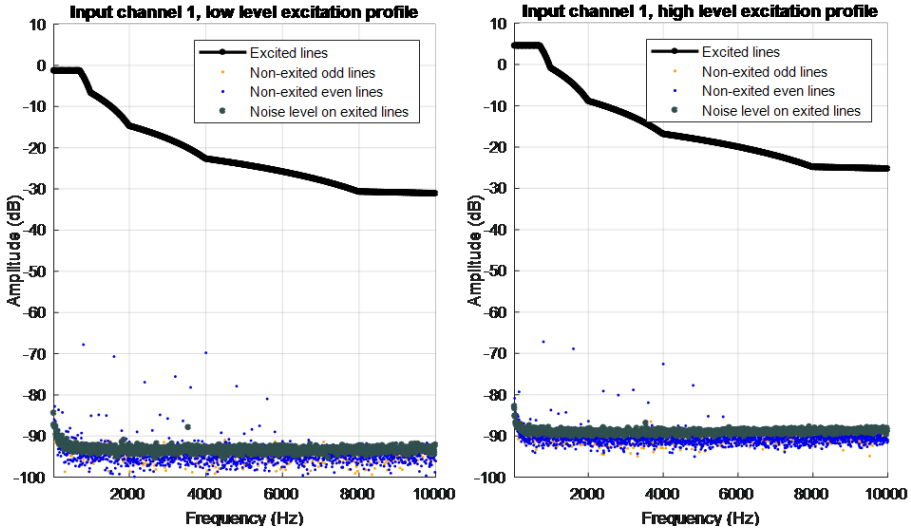


Figure 8: Magnitude of electrical input to the DSP in frequency domain

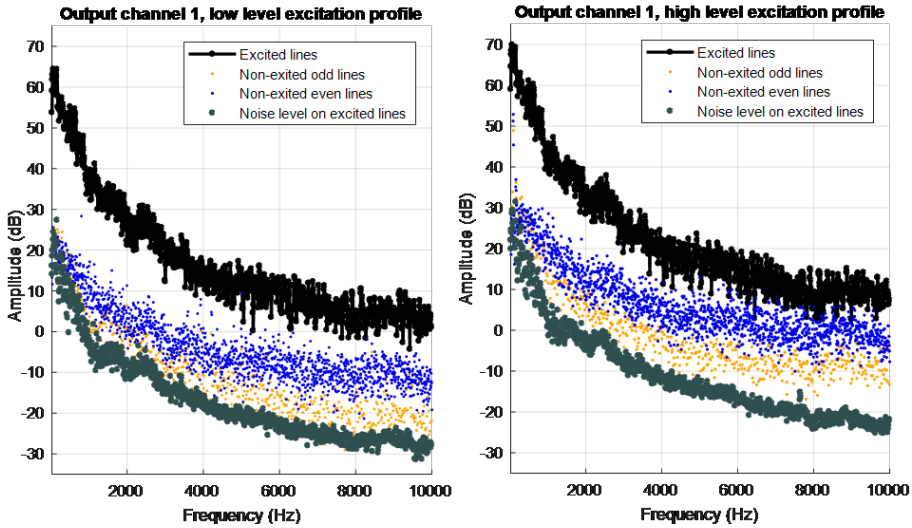


Figure 9: Magnitude of acoustic output in frequency domain

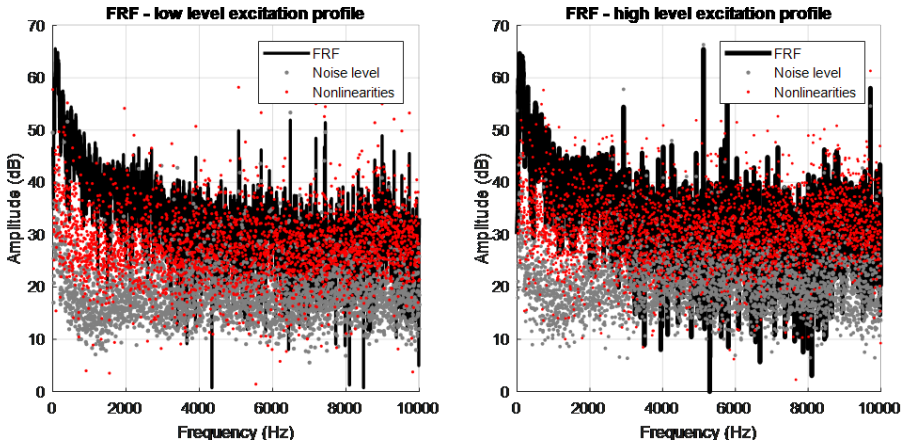


Figure 10: Electroacoustic FRF $[Pa/V]$

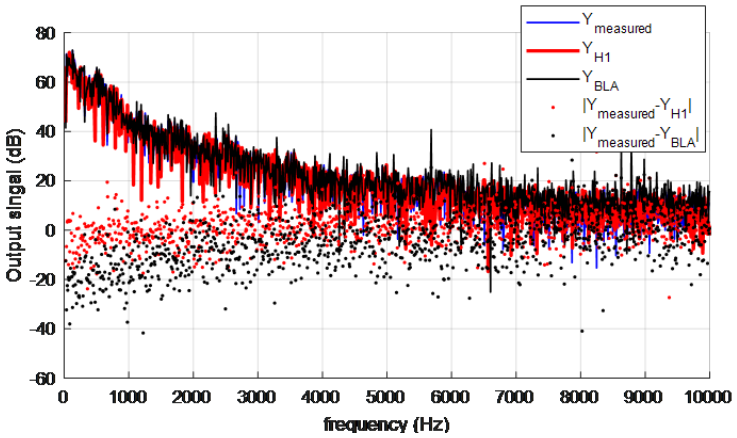


Figure 11: Comparison between estimated and measured magnitudes of acoustic output signals

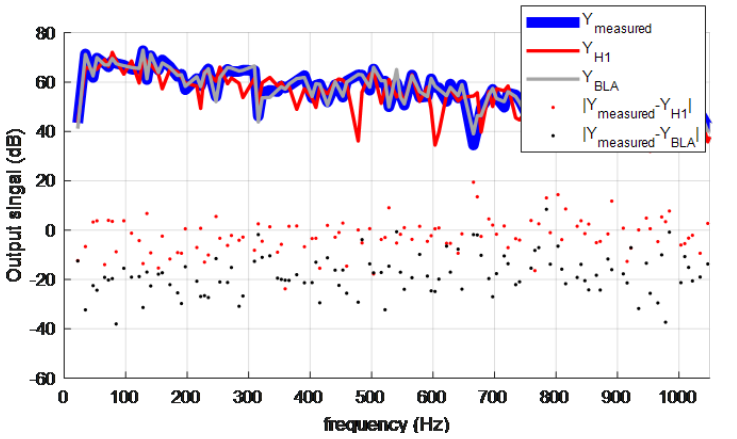


Figure 12: Comparison between estimated and measured magnitudes of acoustic output signals

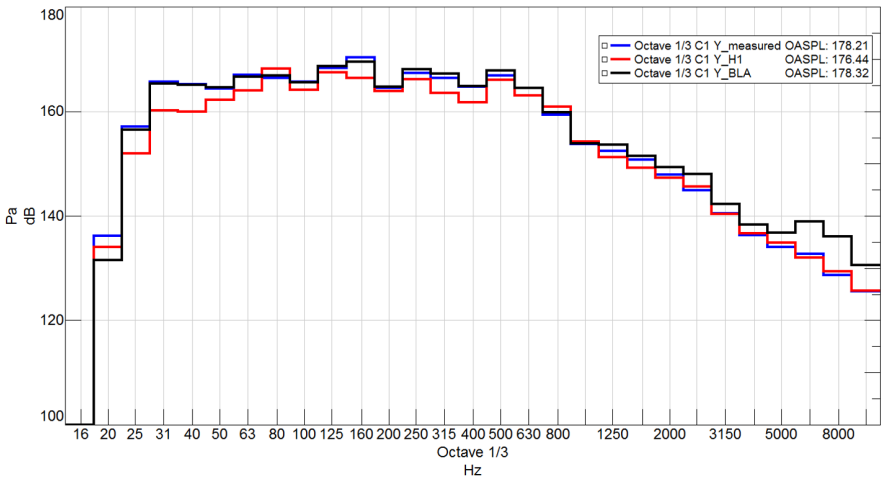


Figure 13: Comparison between estimated and measured magnitudes of acoustic output signals in 1/3 octave bands

7 Conclusions

Electroacoustic systems can be nonlinear and there is no unique solution for modelling such nonlinear behaviour. Although theoretical frameworks and analytical tools may be available, in the industrial context of environmental acoustic testing, the cost-benefit analysis of nonlinear dynamics modelling is still not completely assessed. Perhaps, due to the current unavailability of universal design tools for this kind of models.

In this work a MIMO Best Linear Approximation framework was developed to provide a user-friendly interpretation of the nonlinear behaviour of MIMO measurement data by extracting user relevant information. The proposed framework turned to be useful for modelling an electroacoustic system in a Direct Field Environmental Acoustic Testing setup, because:

- the input excitation system was characterized, and it was verified that the nonlinearities are not originated by the signal generation setup,
- the output measurement was characterized, and it was verified that (i) the higher the level of excitation, the more nonlinearities are present, (ii) the dominant nonlinearities are *even*, which supports the belief that a linear controller framework would suffice for such kind of electroacoustic system,
- the frequency response matrix was characterized, and the coherence function was splitted into noise and nonlinearity level information. Despite the unideal measurement circumstances, the proposed framework was able to provide reliable output prediction,
- the estimated nonlinearities (in other words, the gap between the BLA errors and the noise floor of the data) provided an indication of the potential gain by using an advanced nonlinear modelling technique instead of a linear framework.

Acknowledgements

The authors gratefully acknowledge the European Commission for its support of the Marie Skłodowska-Curie program through the ITN ANTARES project (GA 606817) in collaboration with Siemens Industry Software NV and KU Leuven. A special thank you also to Thales Alenia Space (Italy and France) for their collaboration during the test campaign.

This work was partially funded by the VLAIO Innovation Mandate project number HBC.2016.0235 in a collaboration between Siemens Industry Software NV and Vrije Universiteit Brussel.

References

[1] P. A. Larkin, M. Whalen, Direct, near field acoustic testing, in *Proceedings of SAE World Aviation Conf.* (1999).

[2] A. Merrick, B. Markowicz, Direct field acoustic testing at SSL, in *Proceedings of 29th Aerospace Testing Seminar* (2015).

[3] B. Brevart, C. Fabries, A. Carrella, K. Janssens, J. Debille, Direct field acoustic experiment on satellite subsystem, in *Proceedings of 29th Aerospace Testing Seminar* (2015).

[4] M. Alvarez Blanco, K. Janssens, F. Bianciardi, Experimental verification of projection algorithms and optimization routines for acoustic field uniformity enhancement in MIMO direct field acoustic control, in *Proceedings of ISMA Int. Conf. on Noise and Vibration Engineering* (2016).

[5] P. Gil-Cacho, T. van Waterschoot, M. Moonen, S. H. Jensen, Study and characterization of odd and even nonlinearities in electrodynamic loudspeakers, in *Proceedings of 127th AES* (2009).

[6] A. Brandt, *Noise and vibration analysis: signal analysis and experimental procedures*, John Wiley & Sons (2011).

[7] ECSS-E-HB-32-26A, *Space engineering. Spacecraft mechanical loads analysis handbook*, European Cooperation for Space Standardization (2013).

[8] I. Yunis, The standard deviation of launch vehicle environments, in *Proceedings of 46th Structures, Structural Dynamics and Materials Conf.*, Austin, Texas (2005).

[9] Y. Huang, J. Benesty, J. Chen, Identification of acoustic mimo systems: Challenges and opportunities, *Signal Processing*, Vol. 86, (2005).

[10] M. Alvarez Blanco, A. Carrella, K. Janssens, B. Peeters, Pre-test analysis for design of MIMO control strategies on DFAX, in *Proceedings of ECSSMET* (2018).

[11] N. Thiele, Loudspeakers in vented boxes: Part 1, *Journal of the AES*, Vol. 19, (1971).

[12] P. Brunet, *Nonlinear System Modeling and Identification of Loudspeakers (PhD dissertation)*, Northeastern University, Boston, Massachusetts (2014).

[13] W. Klippel, Tutorial: Loudspeaker nonlinearitiescauses, parameters, symptoms, *Journal of the AES*, Vol. 54, (2006).

[14] B. R. Pedersen, *Error Correction of Loudspeakers: A study of Loudspeaker Design supported by Digital Signal Processing (PhD dissertation)*, Aalborg University, Esbjerg, Denmark (2008).

[15] R. Pintelon, J. Schoukens, *System Identification: A Frequency Domain Approach*, Wiley-IEEE Press, New Jersey (2012).

[16] P. Z. Csurcsia, Static nonlinearity handling using best linear approximation: An introduction, *Pollack Periodica*, Vol. 8, (2013).

[17] J. Schoukens, R. Pintelon, Y. Rolain, *Mastering System Identification in 100 exercises*, John Wiley & Sons, New Jersey (2012).

[18] R. Priemer, *Introductory Signal Processing*, World Scientific, New Jersey (1991).

[19] W. Heylen, S. Lammens, P. Sas, *Modal Analysis Theory and Testing*, Department of Mechanical Engineering, Katholieke Universiteit Leuven (2013).

[20] T. Dobrowiecki, J. Schoukens, P. Guillaume, Optimized excitation signals for MIMO frequency function measurements, *IEEE Transactions on Instrumentation and Measurements*, Vol. 55, (2006).

[21] M. Solomou, D. Rees, Measuring the best linear approximation of systems suffering nonlinear distortions: An alternative method, *IEEE Transactions on Instrumentation and Measurements*, Vol. 52, (2003).

[22] T. Dobrowiecki, J. Schoukens, Linear approximation of weakly nonlinear MIMO systems, *Proceedings of IEEE Int. Instrumentation and Measurement Technology Conf.* (2004).

[23] P. Guillaume, R. Pintelon, J. Schoukens, Accurate estimation of multivariable frequency response functions, in *Proceedings of 13th World Congress of IFAC* (1996).

[24] Arianespace, Vega user's manual, Technical report, (2014).

Efficiently assessing changes in boundary conditions using vibro-acoustic information

P. Becht [1,2], **S. van Ophem** [1,2], **E. Deckers** [1,2], **C. Claeys** [1,2], **B. Pluymers** [1,2], **W. Desmet** [1,2]
[1] KU Leuven, Department of Mechanical Engineering,
Celestijnenlaan 300 B, B-3001, Heverlee, Belgium
e-mail: **philip.becht@kuleuven.be**

[2] DMMS lab, Flanders Make,
3001 Leuven (Heverlee), Belgium

Abstract
The challenge addressed in this paper is the detection of changed boundary conditions at boundaries, which are either partially or entirely not accessible and possibly also not visible. One possible field in which such a strategy could be applied is nondestructive testing and structural health monitoring. In contrast to conventional methods targeting the same challenge, it is proposed to test the structure in a mid-frequency range, where both the required sensitivity is reached and the desired robustness to geometrical features or changes in the environment is still present. Furthermore it is proposed to exploit a numerical model of the healthy test object in order to predict damage in areas, which are not accessible for manual inspection. Therefore, a two-step algorithm is proposed, where the first step consists of a Time-Reversal Multiple Signal Classification to narrow down the defect location. In the second step, the damage location is further concretised and the defect extent is estimated based on a model updating scheme using a parametrically reduced order model.

1 Introduction

In many cases changes of boundary conditions can be linked to the appearance of damage. In order to detect such damage, detection strategies often make use of mechanical vibrations - whether induced by ambient excitation (e.g. wind) or explicitly excited waves. These strategies can be categorised according to the frequency range used for the detection. This leads to basically two groups: The low-frequency methods [1], which work in a frequency range where the vibration is driven by single modes and the high-frequency methods, relying on the physics of one or more propagating wavemodes, which requires significantly higher test-frequencies.

Since high-frequency techniques naturally use small wavelengths, they show a good sensitivity to small defects. On the other hand this advantage comes at the price of a potentially equally high sensitivity to non-damage related features, as e.g. small changes in the environment or due to re-assembling parts of a complex setup, which will never be perfectly the same as the initial condition. Therefore these techniques are either limited to a very small local inspection range or to simple geometries.

The most prominent high-frequency technique for long-range detection is the guided wave method. The basic concept of guided waves is to excite a specific wave, typically in the high kHz range, which then propagates along a wave-guide and scatters at a defect. From there the reflected and converted waves propagate to the sensor array, where they are recorded. Based on the time of flight the location of the defect can be determined. The intensity of the reflection, as well as the mode-conversion [2] can give insight to the type or size of the defect. The main disadvantage of this method is that it is only applicable to simple structures [3], where it can be guaranteed that the reflected and converted waves are caused by the scattering at a defect

and not by the scattering at a geometrical feature of the test-structure, such as a flange in a pipe [4].

Low-frequency techniques on the other hand often rely on the detection of a change in modal features, such as modal damping, mode-shapes or natural frequencies [1]. These techniques are applicable to very complex structures, but suffer from a low sensitivity to small defects, since these do not significantly influence the global features, which are observed by this kind of techniques.

Both low- and high-frequency techniques cannot be used to observe changing boundary conditions, related to a defect in real-life structures. While guided waves cannot be used for the detection of such damage, due to the complexity of these structures, low-frequency methods cannot be applied either, since they often do not show the desired sensitivity in order to indicate a defect in time. A proposal to overcome this problem is to move the inspection into a mid-frequency range in order to combine the advantages of both strategies [5, 6].

The proposed procedure for damage detection in the mid-frequency range is the excitation of the entire structure, without the ambition to excite exclusively specific wavemodes, which is similar to the low-frequency methods, and to measure the structural response with an array of sensors. Knowing the structural response of a healthy structure it is possible to calculate the scattered wave-field, which is what is used in high-frequency methods. This is in essence what is proposed and explained in more detail in the bulk of this paper.

An additional challenge in the discipline of nondestructive testing and evaluation (NDT&E) is the detection of inaccessible or invisible defects. An example for such applications is beyond others the inspection of bolted connections in a framework, which is covered by a revetment. In particular as a solution for this case, in this paper the use of model based inspection strategies is proposed, where the vibration at the hidden or inaccessible inspection location is predicted using a vibro-acoustic model (digital twin) of the test object.

It is proposed to proceed in two-steps, where in the first step the location of the changed boundary (damage) is predicted using a Time-Reversal MUltiple Signal Classification (TR-MUSIC) algorithm. This process is described in section 2.1. In the second step, the information on the damage location from step 1 is refined and the size of the damage is estimated making use of a model updating procedure based on a parametric reduced order model of the test object. More detail on this step is provided in section 2.2. In section 3 the derived strategy is applied to a numerical example and in section 4 it is validated on a physical experiment. Concluding remarks are given in section 5.

2 Sequential TR-MUSIC / pMOR model updating algorithm

In this section a two-step strategy for defect detection in complex geometries is explained. The first step consists of the localisation of the damaged area using a TR-MUSIC algorithm, which is described in section 2.1. In step 2, the prediction of the defect location is refined and the size of the defect is determined based on a model updating algorithm, which is explained in section 2.2. As this step is highly expensive for large scale numerical models, it is only possible in a reasonable time by applying model order reduction techniques and pre-defining the potential zone of unknown parameters making use of the knowledge gained in step 1.

2.1 Time-Reversal based defect detection

In this section the fundamental principles and algorithms forming the foundation of step 1 of the proposed defect detection strategy are introduced, starting with the TR principle, followed by the TR-MUSIC algorithm, which is an algorithm based on the TR principle but increasing the performance of classical TR.

2.1.1 Time-Reversal principle

A TR experiment consists of 3 steps. First, a source is emitting a signal, which propagates to an array of sensors. In the second step the received signal is recorded by the sensor array of N sensors. Then, in step

3, the recorded signal at each sensor n is reversed in time and re-emitted (what was recorded last is emitted first) at the sensor locations. According to the TR principle, the re-emitted signal will focus on the original source location due to a constructive superposition of the re-emitted signals of all sensors.

Since a scatterer can be regarded as the source of the scattered wave field, applying the TR theory to the scattered wave field Ψ_s only leads to a superposition of the re-emitted signals at the scatterer location.

In the general case depicted in figure 1, where a wave field excited by an excitation at x_m in D_t and scattered at D_0 is recorded at an arbitrary point x_n in D_r, the recorded signal at one rotational frequency ω

$$\Psi_{tot}(\omega, x_n, x_m) = \Psi_{init}(\omega, x_n, x_m) + \Psi_s(\omega, x_n, x_m) \tag{1}$$

can be seen as the superposition of the signal that would be observed without scatterer $\Psi_{init}(\omega, x_n, x_m)$ superimposed with the pure scattered signal $\Psi_s(\omega, x_n, x_m)$, which is the one of interest for the TR process applied to the detection of a scatterer. In consequence, $\Psi_s(\omega, x_n, x_m)$ can be calculated based on the measured vibration $\Psi_{tot}(\omega, x_n, x_m)$, provided that the vibration at the initial condition without scatterer $\Psi_{init}(\omega, x_n, x_m)$ is known.

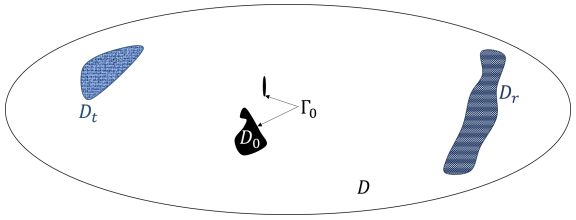


Figure 1: Sketch of the domains in the test object, with D_t being the transmitter domain (excitation), D_r the receiver domain (sensors), D the image domain and D_0 the damage domain. Γ_0 indicates the boundary between D_0 and D.

2.1.2 TR-MUSIC algorithm

In the following frequency-dependency will be assumed, but not specifically indicated by ω as done in the previous section in order to facilitate readability.

In order to improve the focusing of a TR signal on a scatterer, Prada et al. [8] showed that by repeating the experiment multiple times (ideally infinitely often), it is possible to focus each time more energy on the largest scatterer due to the focusing property of the TR principle. Furthermore, the experiment can be repeated with different excitation locations, potentially resulting in different incident waves at the scatterer and thus additional information in the scattered wave field. The same authors proved that each eigenvector of the TR matrix (also called TR Operator):

$$\boldsymbol{TRO} = \boldsymbol{K}^{\mathrm{H}}\boldsymbol{K} \tag{2}$$

is equal to the TR array with the best possible focusing on one scatterer, respectively, where $\boldsymbol{K}$ is a matrix with element

$$K_{m,n} = \Psi_s(x_n, x_m), \tag{3}$$

being the scattered wave field due to an excitation at x_m and measured at location x_n. Superscript H indicates the complex conjugate transpose of a matrix. This procedure, referred to as 'decomposition of the time-reversal operator' (DORT) allows for obtaining the perfect focusing without the need to repeat the experiment

multiple times. Later Lehmann et al. [9] showed that the same result can be achieved applying a singular value decomposition on the matrix $\boldsymbol{K}$.

An algorithm providing even superior detection results is the so called TR-MUSIC algorithm [10]. Similar to the DORT algorithm, TR-MUSIC relies on the decomposition of $\boldsymbol{K}$ into its singular values and vectors, but in contrast to DORT, the time-reversal and back-propagation is performed in an alternative manner, as explained below in detail.

Properties of the scattered wave field

A necessary requirement for the application of the TR-MUSIC algorithm is the square integrability of the transfer function $H(x_n, x_m)$ in the image domain or observed domain D ($\int_D \|H(x_n, x_m)\|^2 dx_m < \infty$), which holds for linear damped mechanical systems and the square integrability of the excitation signal. Under this assumption the scattered wave field can be re-written according to the Lippmann Schwinger formulation as [9]:

$$\Psi_s(x_n, x_m) = \int_{\Gamma_0} H(x_n, r)\Theta(r)\Psi_{tot}(r, x_m)dr, \tag{4}$$

with r being a point on the boundary Γ_0 between scatterer D_0 and image domain D ($\Gamma_0 \subset D$), $H(x_n, r)$ the transfer function between r and the sensor location x_n, $\Theta(r)$ the scattering potential at r and $\Psi_{tot}(r, x_m)$ the total wave field at r due to excitation at x_m. Due to the square integrability properties of $\Psi_s(x_n, x_m)$, it can be re-formulated in a product of linear operators [11]:

$$\Psi_s(x_n, x_m) = P_r(x_n, r)\Theta(r)P_t(r, x_m)\rho(x_m). \tag{5}$$

The excitation $\rho(x_m)$ is applied in D_t, while the sensor is placed in the domain D_r. The propagators $P_r(x_n, r)$ and $P_t(r, x_m)$ describe the propagation from r to x_n and from x_m to r, respectively.

Decomposition of the system with arbitrary scatterers

In this sub-section, it is assumed that there are scatterers at arbitrary locations in the image domain D. The receiver propagator $P_r(x_n, r)$

$$P_r(x_n, r)J(r) = \sum_{n=1}^{\infty} \lambda_n^D \Phi_n^D J(r) \tag{6}$$

can be decomposed in its singular values λ_n^D and singular functions Φ_n^D describing the propagation from r to x_n and the secondary source $J(r)$ describing the excitation of waves due to the scattering of incident waves at an arbitrary scatterer at r.

Equation (6) can be truncated by keeping only the N most relevant singular values:

$$P_r(x_n, r)J(r) \simeq \sum_{n=1}^{N} \lambda_n^D \Phi_n^D J(r), \tag{7}$$

which is an approximation if a continuous receiver domain or a very high number of sensors is considered. In the case of a rather small finite array, N is automatically given by the number of sensors.

In a similar fashion, the transmitter propagator $P_t(r, x_m)$ can be decomposed the same way as shown for the receiver propagator in equation (6) resulting in a set of singular vectors Ψ_m^D.

As the final objective is to find the boundary of the scattering domain Γ_0 in the observed domain D, the aim is to be able to assess for all points $z \in D$ if it is on Γ_0.

If the information provided by the N sensors and M excitations is sufficiently large, the dynamics in the entire observation domain D can be described by the truncated set of singular functions Φ_n^D and Ψ_m^D.

Decomposition of the system with known scatterers

As the searched-after scatterer location Γ_0 is logically a subset of all possible scatterer locations, which was considered in equation (6), the decomposition of the receiver propagator for the case of a known scatterer domain writes as:

$$P_r(x_n, r)^{D_0} J(r) \simeq \sum_{n=1}^{N} \lambda_n^{D_0} \Phi_n^{D_0} J(r), \tag{8}$$

and the number of meaningful singular values in $P_r(x_n, r)^{D_0}$ is $\leq N$, due to $\Gamma_0 \subset D$. Applying the same logic to the decomposition of the transmitter operator of the searched-after scattering domain, one finds that the number of meaningful singular values in $P_t(r, x_m)$ can maximally reach M.

Decomposition of the measured wave field $\boldsymbol{K}$

Replacing $P_r(x_n, r)$ and $P_t(r, x_m)$ in equation (5) with equation (8) and its equivalent for the transmitter side leads to

$$\Psi_s(x_n, x_m) = \sum_{n=1}^{N} \sum_{m=1}^{M} \Phi_n^{D_0} \Lambda_{n,m}^{D_0} \Psi_m^{D_0} \rho(x_m), \tag{9}$$

where $\Lambda_{n,m}^{D_0}$ is composed of the singular vectors $\lambda_n^{D_0}$ and $\lambda_m^{D_0}$ and the scattering potential Θ and describes the actual scattering at the defect surface. $\Psi_m^{D_0}$ and $\Phi_n^{D_0}$ are singular functions describing the wave propagation from the excitation to the defect and from the defect to the sensor array, respectively. The largest number of meaningful singular values in (9) is $\min(M, N)$.

Writing equation (9) in matrix notation, according to equation (3), it follows for a unit excitation that the singular value decomposition of the matrix $\boldsymbol{K}$ leads to the singular system:

$$\boldsymbol{K} = \boldsymbol{\Phi} \boldsymbol{\Lambda} \boldsymbol{\Psi}^{\mathrm{H}}, \tag{10}$$

where $\boldsymbol{\Phi}$ is a matrix containing the N singular vectors $\boldsymbol{\Phi}_n$ related to the propagation from scatterer to sensor array, $\boldsymbol{\Psi}$ contains the M singular vectors $\boldsymbol{\Psi}_m$ related to the propagation from excitation to scatterer and $\boldsymbol{\Lambda}$ is the diagonal matrix of singular values. Due to the dimensions of $\boldsymbol{K}$, its rank cannot be greater than $\min(M, N)$.

Assuming a sufficiently large number of excitations M and sensors N, to illuminate the entire inspection domain D and a defect that is small as compared to D, it is likely that $\boldsymbol{K}$ is rank deficient, meaning the rank of $\boldsymbol{K}$, $R_0 < \min(M, N)$. In this case one obtains from equation (10) a set of R_0 singular vectors $\boldsymbol{\Phi}_n$ and $\boldsymbol{\Psi}_m$ related to the non-negligible singular values. Those vectors describe the physical vibration due to the scattering and will be referred to in the following as the vectors spanning the signal space S_Φ and S_Ψ, respectively. Furthermore, there are $N - R_0$ vectors $\boldsymbol{\Phi}_n$ and $M - R_0$ vectors $\boldsymbol{\Psi}_m$ related to the negligible or zero singular values. These vectors spanning the noise spaces N_Φ and N_Ψ, respectively have no physical interpretation, but the mathematical property of being orthogonal to the signal space:

$$\begin{aligned} S_\Phi \oplus N_\Phi, \\ S_\Psi \oplus N_\Psi. \end{aligned} \tag{11}$$

Assembling TR-MUSIC pseudospectrum

In this sub-section, only the TR-MUSIC algorithm for sensor-side imaging is explained, as in the upcoming sections only this one will be used. However, the necessary equations for excitation-side imaging can be derived following the same line of thoughts explained here below for sensor-side imaging.

Due to the orthogonality between signal and noise space (equation (11)), vectors from the signal space cannot share information with vectors from the noise space, which results mathematically in:

$$\boldsymbol{\Phi}_{n_1}^{\mathrm{H}} \boldsymbol{\Phi}_{n_2} = 0, \text{ for } n_1 \leq R_0 \text{ and } n_2 > R_0. \tag{12}$$

As all physical propagation paths relate to the propagation from the surface of the scatterer Γ_0 to the sensor array, this information is completely captured in the signal space singular vectors. As a consequence of this property and equation (12), it follows for a vector $\boldsymbol{g}_z$ with each element containing the transfer function from a random point $z \in D$ to one sensor in the sensor array, that

$$\boldsymbol{g}_z^{\mathrm{H}} \boldsymbol{\Phi}_n = 0, \text{ for } R_0 < n \leq N, \tag{13}$$

if $z \in \Gamma_0$. On the other hand, if $z \notin \Gamma_0$,

$$\boldsymbol{g}_z^{\mathrm{H}} \boldsymbol{\Phi}_n \neq 0, \text{ for } R_0 < n \leq N, \tag{14}$$

since in this case the test vector $\boldsymbol{g}_z$ also contains components relating to the noise space N_Φ.

The TR-MUSIC algorithm makes use of the relations of equation (13) and (14), by calculating a pseudospectrum

$$I(z) = \left(\mid \boldsymbol{g}_z^{\mathrm{H}} \boldsymbol{\Phi}_n \mid \right)^{-1}, \text{ for } R_0 < n \leq N, \tag{15}$$

for each point of interest $z \in D$, which reaches a maximum for $z \in \Gamma_0$ and has a smaller value for $z \notin \Gamma_0$.

In order to improve the robustness of the method, a summation over the entire noise space is commonly applied. Furthermore, recent publications suggest a multiplication of the pseudospectra over a large frequency range (N_f discrete frequency lines), often called interferometric MUSIC. The advantage of this is that random measurement errors, as well as small errors in the model contribute differently to the pseudospectrum at different frequencies, while the contribution of the scatterer is always the same. As a result the contributions of the scatterer interfere constructively, while other influences do not [12, 13]. This leads to the TR-MUSIC algorithm as it is used in this paper:

$$I(z) = \left(\prod_{f=1}^{N_f} \sum_{n=R_o+1}^{N} \mid \boldsymbol{g}_{z,f}^{\mathrm{H}} \boldsymbol{\Phi}_{n,f} \mid \right)^{-1}, \tag{16}$$

where in addition the vectors $\boldsymbol{g}_z$ are normalised in order to account for the modal behaviour [5], which is still not negligible in the mid-frequency range.

2.2 Model updating

The model updating algorithm applied in the framework of this investigation is extensively described in [14]. In this section, only a short summary is given. For more details, the reader is referred to [14].

In order to update parameters of models, typically the model is evaluated at multiple frequency lines and the results are compared to a measurement. Based on the difference between the two, a cost function is defined.

The objective of the model updating is to minimise this cost function by gradually changing the unknown parameters until the model represents the measurement with a satisfying accuracy. For model with a large number of degrees of freedom (DOFs) this procedure becomes extremely time consuming. Therefore, for this work, the models are reduced using a Krylov subspace projection, so that the simulation can be run with a reduced number of DOFs, which results in a reduced simulation time.

Furthermore, the parameter dependency of the original model, resulting from the unknown and to be updated parameters, is kept in the reduction scheme used in this publication in order to avoid that a new reduced order model has to be constructed for each parameter change. The consequence is an additional speed up of the model updating procedure.

In [14], the number of parameters to be updated needs to be limited to guarantee convergence, as can be seen by the assumed pre-knowledge of the defected edge. This is why the two-step strategy is necessary to narrow down the number of DOFs to be updated.

3 Numerical validation

The algorithm of section 2 is numerically validated at the example of an acoustic cavity covered by an A3 aluminium plate of 3mm thickness, as shown in figure 2. The boundaries of the plate are modelled as hinged. However, the nodal rotational stiffness along the boundary in the intact state is chosen sufficiently high (10^4 Nm/rad) in order to be seen as a quasi clamped connection. Following the longest edge in each direction, the acoustic cavity has a dimension of 0.82m x 0.98m x 1.15m. More details to the exact dimensions of the acoustic cavity can be found in [14]. The mesh is chosen such that the model is accurate up to 400Hz using 10 elements per acoustic wavelength.

Inside the acoustic cavity there are $N = 10$ virtual microphones at which the acoustic pressure is recorded. A structural excitation acting in z-direction and thus exciting the out-of-plane motion of the plate is applied to the aluminium plate at x = 0.2735m, y = 0.3440m, z = -0.35m (yellow point in figure 2). As there is only one excitation, it follows that there is also one singular vector of the signal space. The leftover 9 singular values are attributed to the noise space.

Defects in this example are modelled as reduced rotational stiffness values at 7 adjacent nodes along a boundary of the aluminium plate closing the acoustic cavity. The case of 1 defect at the centre and 1 defect at the top of the right boundary (case 1), of 1 defect at the top of the right boundary (case 2) and of 1 defect at the centre of the top boundary (case 3) are investigated. Additional cases studied at the same experimental setup can be found in [7].

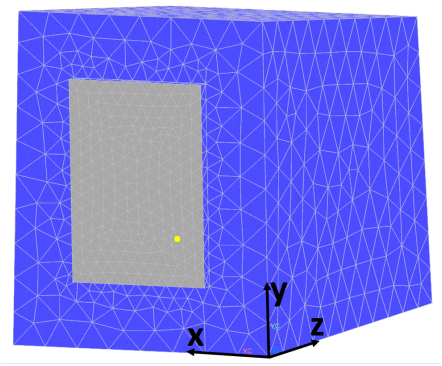


Figure 2: Numerical model of the acoustic cavity (blue) closed at one side by an aluminium plate (grey). The yellow point indicates the excitation location.

Even in an experimental setup, in both cases, the vectors $\boldsymbol{g}_z$ must be simulated and cannot be measured. In the first case this is because a rotational DOF at a hinged plate would have to be excited, which would require a complicated excitation mechanism. In the second case an excitation in z-direction would need to be applied very close to the boundary, where the z DOF is constrained. This would result in the best case in a very noisy measurement.

The edge-detection results of the TR-MUISC algorithm are presented in figure 3. The bars represent a damage index per edge of the plate which is calculated by summing the pseudospectrum of all nodes at one edge, dividing this sum by the number of nodes at this edge and normalising the values for all edges by the damage index corresponding to the largest value obtained for one edge.

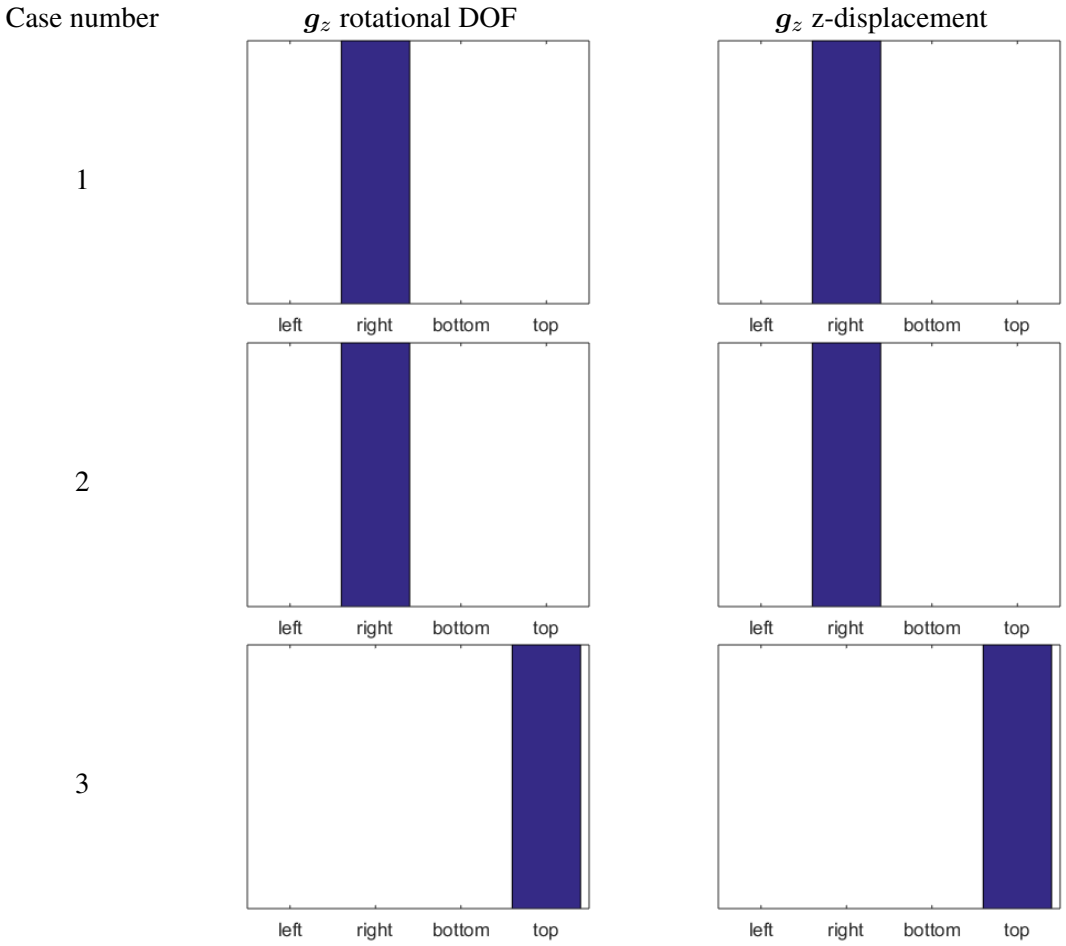


Figure 3: Edge detection results for the 3 defect scenarios listed previously. The bar for each edge represents the damage index corresponding to the respective edge.

For the first step of the detection procedure, the calculation of the pseudospectrum based on the TR-MUSIC algorithm as described in section 2.1.2, the noise space vectors $\boldsymbol{\Phi}_n$ will be orthogonal to a vector characterising the propagation from the defect to each microphone location. Since, in this example, it is known that the rotational stiffness along the edge has been changed in order to simulate a defect, it is obvious to choose $\boldsymbol{g}_z$ so that it contains the propagation path from a node z on the boundary of the aluminium plate, excited by a torque to the microphone array. However, in a real defect detection example, typically a defect changes more than only one property. In order to verify, that the TR-MUSIC algorithm can also provide good results in this case, a second set of vectors $\boldsymbol{g}_z$ is investigated. In this second attempt, $\boldsymbol{g}_z$ contains the acoustic pressure at the microphone array due an out-of-plane (z-direction) excitation on the plate at a node located at z, very near the boundary.

As can be seen from figure 3, the defected edge is indicated correctly in all cases studied, independent,

whether there are 2 or 1 defects per edge.

Furthermore, it can be seen that the image based on the force-excitation generated $\boldsymbol{g}_z$ shows as good results as the image based on the torque-excitation generated $\boldsymbol{g}_z$. From this observation it can be concluded that the TR-MUSIC algorithm can indicate accurately the location of a defect, although not the correct quantity (here $\boldsymbol{g}_z$ based on z-displacement, not based on rotational DOF) is used.

Starting from the correctly detected defected edge, the model updating procedure introduced in section 2.2 is applied to all cases listed previously. In figure 4, central column, the rotational stiffness after the model updating along the detected edge is plotted. A node on the edge is considered to be defected as soon as the logarithm of the rotational stiffness at this location drops below 2.

Based on this criterion, the model updating provides the correct defected zone in the case that the defect is located in the centre of the top edge (case 3).

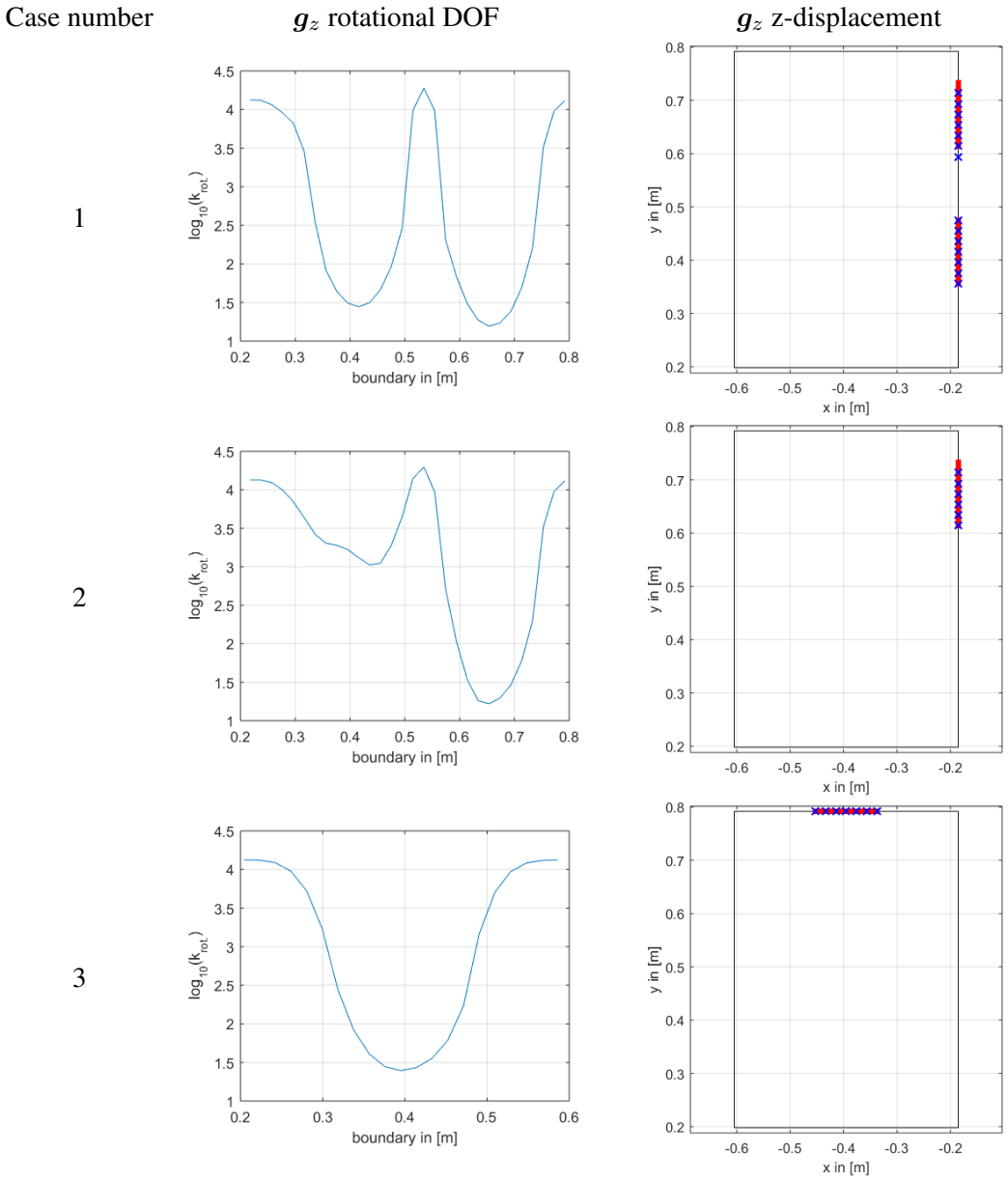


Figure 4: Prediction of the defected zone based on the edge detection results presented in figure 3 for the 3 studied defect scenarios. In the central column, the rotational stiffness after the model updating is shown on a logarithmic scale. In the right column, the edges of the plate are shown as a black rectangle. The truly defected area is highlighted by a bold red line and the predicted defected area is indicated with blue crosses.

If the defect is close to a corner (case 2), size and location of the defect are still predicted approximately correctly. However, the defect's extent towards the corner is slightly underestimated. This can be explained since a change of the rotational stiffness close to a corner has less effect on the plate's dynamics, since the corner is also supported by the stiffness of the adjacent edge.

If there are 2 defects at the same edge, one close to the centre, one close to a corner (case 1), 2 defects are detected with approximately the right extent and location. The observations of the previously discussed cases, where those defects were investigated separately, can be applied to the combination of the two.

Thinking of the application of the proposed method to a real detection scenario, it is important that the result is provided within a reasonable time, so that by applying this two-step approach, time is saved as compared to manually inspecting the test object. Therefore, the computation time (Dell laptop, core i7, physical memory: 8GB) for all cases is listed in table 1.

As can be seen from table 1, processing the data for the edge detection can be performed within 3s (1st step, TR-MUSIC) in this example. The calculation time is independent of the application case, since in all cases, the pseudospectrum needs to be calculated for the same amount of nodes on the boundary. The total calculation time for the refinement of the defect size and location spreads between 415s and 1013s, depending on the case. This is due to the different number of nodes per edge, and thus different number of unknowns in the updating procedure and the building of the parametrised reduced order model. Furthermore, the simulation time is influenced by the time the algorithm needs to converge. For example 1 defect at the top of the right boundary (case 2) is found faster than 2 defects at the same boundary (case 1).

4 Experimental validation

The numerical results presented in section 3 are verified in this section using the same numerical model (material properties updated with experimental data), but real measurements. The measurement data used here was acquired by van Ophem et al. and sets the basis for the results presented in [14]. A picture of the test setup can be found in figure 5. As can be seen, the plate is mounted to the box enclosing the acoustic cavity with bolts.

Defects are simulated by successively removing bolts at the right edge, starting from the centre. Frequency response functions due to a hammer excitation at the same location as indicated in figure 2 are measured at the microphone locations every time a new bolt is removed. As the bolts are not explicitly modelled in the numerical model, only the influence of a removed bolt on a related property, e.g. rotational stiffness at the modelled boundary of the plate or z-displacement close to the edge can be used for the detection algorithm. That this is in principle possible for the TR-MUSIC based edge detection is shown in the previous section, where a reduced rotational stiffness can be detected based on the z-displacement close to that edge. For the second step, the refinement of the defect location and size, it is assumed that a removed bolt can be best represented in the numerical model by a locally reduced rotational stiffness.

The TR-MUSIC results for the detection of the edge at which there is a removed bolt are presented in figure 6. In all cases, the left edge is correctly and uniquely indicated as defected. As both, the damage index

Case number	time MUSIC [s]	time model updating		
		model order reduction [s]	model updating [s]	total [s]
1	3	304	709	1013
2	3	329	455	784
3	3	225	190	415

Table 1: Simulation time to obtain results based on numerical simulations.

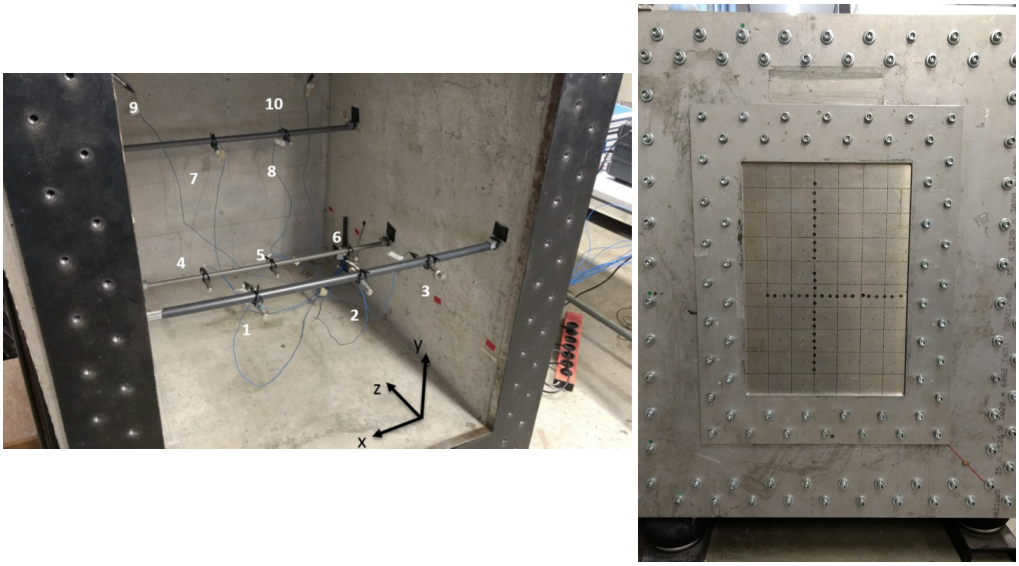


Figure 5: Test setup: Acoustic cavity with microphones installed (left) and cavity closed by an aluminium plate bolted to the structure (right) [14].

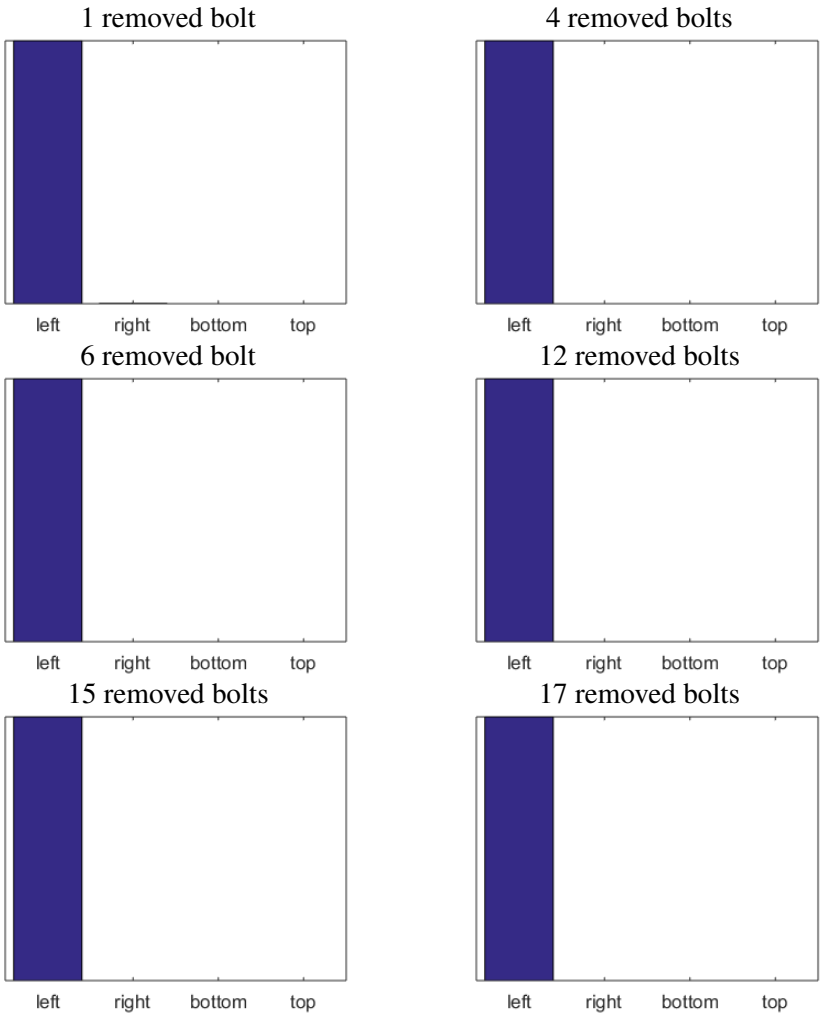


Figure 6: Edge detection results for different numbers of removed bolts along the left edge. The bar for each edge represents the damage index corresponding to the respective edge.

using $\boldsymbol{g}_z$ containing the response to an excitation in z-direction and the damage index using $\boldsymbol{g}_z$ containing the response to an excitation of a rotational DOF show the same result, only the first of the two is shown in figure 6.

In figure 7, the final results of the second step, the model updating, are presented. These base on the detection of the correct edge by the TR-MUSIC algorithm. For completeness, the stiffness values after the model updating can be found in [14]. As in figure 4, the edges of the plate are sketched by a black rectangle and the zone on the edge that is predicted to be defected is indicated by blue crosses. Furthermore, the positions of the bolts used to clamp the plate are indicated by black crosses. The removed bolts are highlighted with a red circle.

The results demonstrate that for 1 loose bolt at the centre of the left hand side, the rotational stiffness value

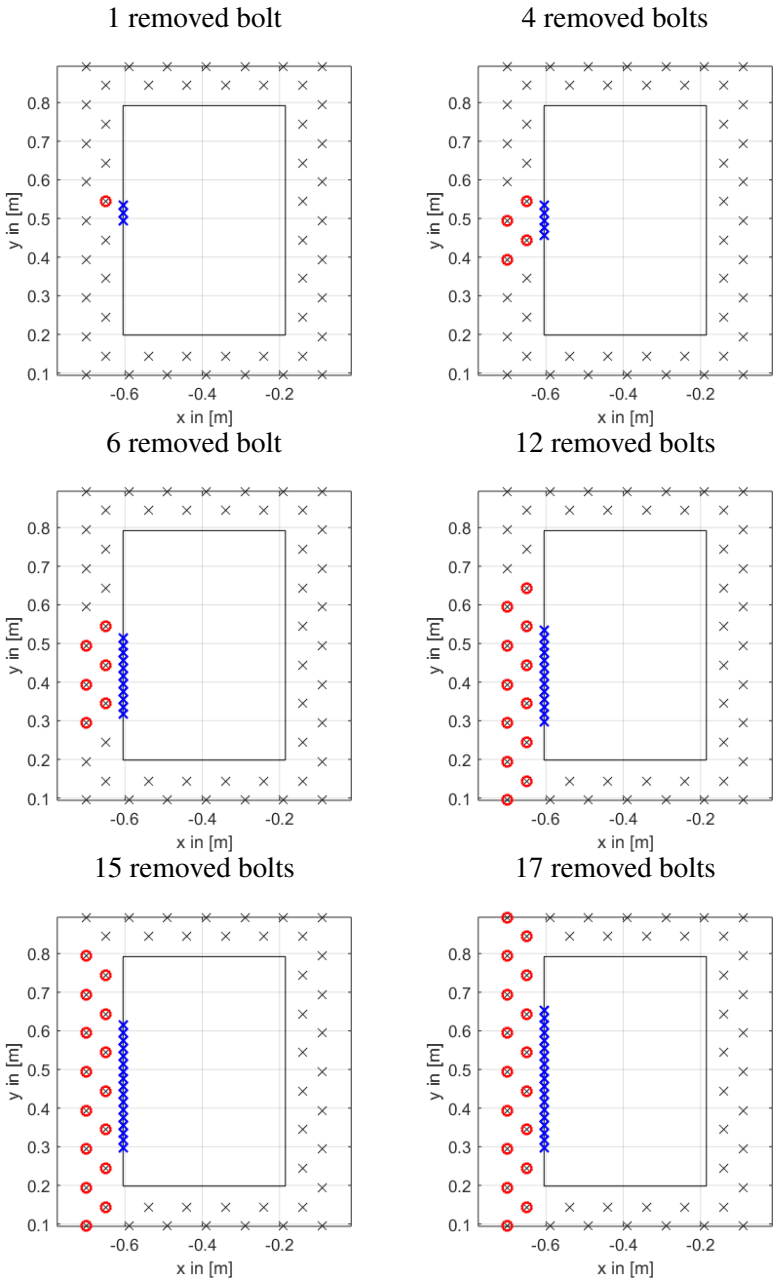


Figure 7: Prediction of the defected zone based on the results presented in figure 6. The plate's boundary is drawn as a black square and the bolts clamping the plate are indicated as black crosses. The removed bolt is highlighted with a red circle and the predicted defected zone on the edge is marked with blue crosses.

after the model updating drops in the region of the edge nearby this bolt. When increasing the number of removed bolts to 4, 6 and 10 in negative y-direction, the zone of reduced rotational stiffness and thus the area along the plate boundary predicted to be defected increases in the same direction. However, there seems to be a certain saturation, so that the predicted defect zone never ranges to the corner of the boundary. This phenomenon was already observed and explained in the numerical part in section 3 by the increasing influence of the stiffness of the adjacent edge on the stiffness of the edge under investigation, which gains importance the closer one gets towards the corner.

If in addition bolts are successively removed in positive y-direction, which is the case for the examples of 12, 15 and 17 removed bolts, the zone marked as defected increases step by step in this direction, while the lower end of the predicted defect does not change. This shows that the method is able to detect in which direction bolts are removed. However, if the number of removed bolts is initially already very high, the sensitivity towards an additionally removed bolt decreases, as can be seen e.g. by the comparison of the evolvement of the predicted defect from 1 to 4 removed bolts. The observation that the predicted defect does not range until the corner of the left edge, although all bolts along this boundary are removed also holds for the upper corner, for the same reason as explained previously.

One can conclude that the prediction of the defected edge based on the TR-MUSIC algorithm works reliably for all cases under investigation. Although the subsequent model updating cannot point out removed bolts directly, it can be used to refine the information about the defect, since as expected, the updated rotational stiffness along the boundary of the edge under investigation correlates well with the number of removed bolts.

As already mentioned in the section covering the numerical examples, the simulation time is important, since the objective of the developed method is to provide insights into the health status of a test object within a reasonable time, so that it can be used e.g. directly during a measurement campaign. Therefore, the calculation time for each number of removed bolts is listed in table 2. The time needed by the TR-MUSIC algorithm constitutes 2s to 3s and thus did not change as compared to the numerical examples (the small difference is due to the different sorting of the matrices used as input for the TR-MUSIC algorithm applied to the simulations and the measurements). This is to be expected, since the same numerical model is used in both, the numerical and the experimental applications and therefore the number of nodes along the boundary at which the pseudospectrum needs to be evaluated remains constant. For a real user this fast calculation time would mean that a result for the edge detection could be expected almost immediately after obtaining the necessary input data.

The total calculation time for the model updating step ranges between 500s and 1048s and is comparable to that of the numerical examples. Also the fact that the simulation time increases in tendency with the number of removed bolts goes in line with the observations previously made. It can be explained by the larger difference between the frequency response of the healthy and the defected system, which results in a larger number of optimisation steps until convergence. Since the model order reduction step is independent of the actual defect, this step could be taken offline, as proposed by van Ophem [14]. As can be seen from

Removed bolts	time MUSIC [s]	time model updating		
		model order reduction [s]	model updating [s]	total [s]
1	2	350	150	500
4	2	351	370	721
6	2	349	569	918
12	3	350	469	819
15	3	348	491	839
17	3	350	698	1048

Table 2: Simulation time to obtain results based on measurements.

table 2, this would reduce the total simulation time in all cases by 350s.

5 Conclusion

A two step strategy is developed in order to rapidly and reliably predict zones of a test object where boundary conditions have changed (defect). The first step consists in locating this area of the test object using a Time-Reversal MUltiple Signal Classification (TR-MUSIC) algorithm. In the second step dimension and location of the area predicted in the previous step are updated making use of a parametrised reduced order model.

The strategy is first explained and then applied to a numerical example and a physical experiment. As numerical example an acoustic cavity covered by an aluminium plate is selected. The plate is modelled as hinged, defects are modelled by changing the rotational stiffness at the edges. The experimental setup uses the same acoustic cavity, covered by the same plate. In contrast to the numerical example, the plate is mounted to the acoustic cavity with 52 bolts along the edges. In order to simulate a defect 1, 4, 6, 12, 15 and 17 bolts are removed successively along one edge.

Based on the numerical simulation and experimental validation the following conclusions can be made:

The TR-MUSIC algorithm allows a very fast prediction of the defected zone, which is independent on the actual defect size and severity, but depends solely on the inspected area and the desired resolution. In all cases studied the correct edge is reliably indicated after a calculation time of maximum 3s.

The model updating based on a parametrised reduced order model is a valuable tool to gain further insight on the defect zone detected previously by the TR-MUSIC algorithm. In the numerical examples studied, the size and location of the defect can be predicted correctly, if there are only defects (one or multiple defects are possible) at one edge. In the physical experiment it can be observed that the number and locations of removed bolts corresponds well with the zone along the edge of the plate, which is indicated as defected by the algorithm.

The simulation time needed for the model updating is below 12min (if the reduced order model is built offline) in all cases, with the tendency to decrease for smaller defects.

The necessity and advantage of a model based defect detection strategy is pointed out, since the necessary quantities for the MUSIC algorithm (frequency response due to the excitation of a rotational degree of freedom at a clamped edge of a plate or out-of plane displacement very close to a clamped edge) cannot or only with huge difficulties be determined experimentally. The need of a numerical model for the model updating algorithm is obvious. The successful application shows that it is possible to combine both, physical measurements with numerical models.

Acknowledgements

The European Commission is gratefully acknowledged for their support of the ANTARES project (GA606817). Elke Deckers is a postdoctoral fellow of the Research Foundation - Flanders (FWO). Also the Research Fund KU Leuven is gratefully acknowledged for its support. Furthermore, the authors gratefully acknowledge SIM (Strategic Initiative Materials in Flanders) and VLAIO (Flemish government agency Flanders Innovation & Entrepreneurship) for their support of the SBO project DETECT-IV, which is part of the research program MacroModelMat (M3).

References

[1] Y. ZOU, L. TONG, AND G. STEVEN, *Vibration-based model-dependent damage (delamination) identification and health monitoring for composite structuresa review*, Journal of Sound and vibration, 230 (2000), pp. 357–378.

[2] A. DEMMA, P. CAWLEY, M. LOWE, A. ROOSENBRAND, AND B. PAVLAKOVIC, *The reflection of guided waves from notches in pipes: a guide for interpreting corrosion measurements*, Ndt & E International, 37 (2004), pp. 167–180.

[3] Z. SU, L. YE, AND Y. LU, *Guided lamb waves for identification of damage in composite structures: A review*, Journal of sound and vibration, 295 (2006), pp. 753–780.

[4] D. ALLEYNE AND P. CAWLEY, *The long range detection of corrosion in pipes using lamb waves*, in Review of progress in quantitative nondestructive evaluation, vol. 14B, Springer, 1995, ch. Chapter 7: Materials' Degradation and Specific Applications, pp. 2073–2080.

[5] P. BECHT, E. DECKERS, C. CLAEYS, B. PLUYMERS, AND W. DESMET, *Time reversal MUSIC imaging for non-destructive testing of complex materials and geometries*, Journal of Nondestructive Evaluation (under review), (2018).

[6] P. BECHT, E. DECKERS, C. CLAEYS, B. PLUYMERS, AND W. DESMET, *Non-destructive testing based on vibrations in the low to mid–frequency range, Proceedings of VETOMAC 2018, Lisbon, Portugal, 2018*, Lisbon (2018).

[7] P. BECHT, S. VAN OPHEM, E. DECKERS, C. CLAEYS, B. PLUYMERS, AND W. DESMET, *Model based vibro-acoustic defect detection*, in W. Desmet, B. Pluymers, S. van Ophem, P. Becht, editors, *ANTARES - Advanced Training and Research in Energy Efficient Smart Structures*, Leuven (2018), pp. 1–26.

[8] C. PRADA, S. MANNEVILLE, D. SPOLIANSKY, AND M. FINK, *Decomposition of the time reversal operator: Detection and selective focusing on two scatterers*, The Journal of the Acoustical Society of America, 99 (1996), pp. 2067–2076.

[9] S. K. LEHMAN AND A. J. DEVANEY, *Transmission mode time-reversal super-resolution imaging*, The Journal of the Acoustical Society of America, 113 (2003), pp. 2742–2753.

[10] M. E. YAVUZ AND F. L. TEIXEIRA, *On the sensitivity of time-reversal imaging techniques to model perturbations*, IEEE transactions on antennas and propagation, 56 (2008), pp. 834–843.

[11] E. A. MARENGO, F. K. GRUBER, AND F. SIMONETTI, *Time-reversal music imaging of extended targets*, IEEE Transactions on image processing, 16 (2007), pp. 1967–1984.

[12] G. RUVIO, R. SOLIMENE, A. CUCCARO, AND M. J. AMMANN, *Comparison of noncoherent linear breast cancer detection algorithms applied to a 2-d numerical model*, IEEE Antennas and Wireless Propagation Letters, 12 (2013), pp. 853–856.

[13] R. SOLIMENE, A. DELL'AVERSANO, AND G. LEONE, *Interferometric time reversal music for small scatterer localization*, Progress In Electromagnetics Research, 131 (2012), pp. 243–258.

[14] S. VAN OPHEM, A. VAN DE WALLE, E. DECKERS, AND W. DESMET, *Efficient vibro-acoustic identification of boundary conditions by low-rank parametric model order reduction*, Mechanical Systems and Signal Processing, 111 (2018), pp. 23–35.

Object-oriented model-based condition monitoring

M. Gonzalez[1,2], **O. Salgado**[1], **J. Croes**[2,3], **B. Pluymers**[2,3], **W. Desmet**[2,3]
[1] IK4-Ikerlan Technology Research Center, Control and Monitoring Area,
J.M. Arizmendiarrieta 2, 20500 Mondragón, Spain,
e-mail: **mgonzalez@ikerlan.es**

[2] KU Leuven, Department of Mechanical Engineering,
Celestijnenlaan 300 B, B-3001, Heverlee, Belgium

[3] DMMS lab, Flanders Make, Belgium

Abstract
In systems with a reduced number of sensors, the observability requirements of state-parameter estimation schemes may lead to over simplified models, limiting the use of the estimation for condition monitoring. To overcome this limitation, this paper presents a framework where a high-fidelity model is used in combination with reduced estimation models. The estimation models are used to estimate variables related to the system's current condition, and the high-fidelity model provides the best guess on the non-observable phenomena. Thus, the high-fidelity model may aid the estimation by providing virtual inputs and a first benchmark for the estimation. In particular, this paper focuses on how to obtain estimation models from the high-fidelity model, and how to select the right sensor sets. The framework is finally applied to an scaled test bench of a vertical transportation system, showing the potential of this approach in the condition monitoring of complex industrial systems.

1 Introduction

Condition monitoring strategies rely on the measurement of variables of interest that reflect the system's condition. Obtaining these measurements, however, is not always straightforward. Certain quantities require sensors which are either too costly or too intrusive to be used in a continuous monitoring approach. In such situations, a model-based monitoring scheme is a useful solution to estimate the required variables [1].

Model-based methods use a first principles model to monitor the system [2]. By running a high-fidelity model of the system under the same operational conditions as the real system, immeasurable quantities can be derived from the model in the form of virtual sensors. Furthermore, if the model is combined with the available measurements, it can be continuously corrected, adapting its output to the current condition of the system and improving the accuracy of the derived virtual sensors. Bayesian state/parameter estimation techniques, such as Kalman Filtering, are a powerful tool to combine models and measurements, correcting both model discrepancies and sensor noise [3].

State/parameter estimation is a useful tool to obtain accurate virtual sensors updated to the current condition of the system. However, obtaining models suitable for state estimation is not a trivial task. To ensure the convergence of state estimation methods, the physical phenomena described in the model has to be represented in the measurements used [4]. Consequently, if the number of sensors is very limited, several approximations have to be assumed in the system models. Hence, common industrial models are generally too large to be

directly used in an state estimation framework. Therefore, estimation models are often developed ad-hoc for a particular monitoring task, neglecting other physics that could be of interest. As an example, consider the case where the underlying physics describing the evolution of a certain force are neglected, and this force is estimated as an unknown input, such as in [5]. This approach may require less sensors, and thus help making this monitoring scenario observable. However, there is no knowledge on why that force is changing. In a condition monitoring scheme, this could mislead the assessment, as changes in that force due to current operational conditions could not be isolated from changes due to faulty conditions.

As a workaround, a framework is proposed where a high-fidelity model of the system is used in combination with estimation models. The estimation models are used to track different features of the system in combination with the measurements available, resulting in more updated virtual sensors. On the other hand, the high-fidelity model is used to provide the best information possible on the non-observable quantities. This way, the high-fidelity model can provide information to the estimation models in the form of virtual inputs, or can provide a first benchmark, to track the system's degradation by comparing its output with the estimation.

Additionally, the estimation models may update the high-fidelity model with the estimated parameters. For instance, in phases where additional sensors are available, such as commissioning or during maintenance, more advanced estimation models may be activated to estimate parameters and update other subsystems of the high-fidelity model. Furthermore, using industrial model ex-change standards, estimation models aimed at different monitoring scenarios may be automatically obtained from the high-fidelity model. This provides a cost efficient way to adapt the high-fidelity model to other monitoring scenarios as new necessities arise.

In particular, this paper studies how new estimation models can be obtained from the high-fidelity model, presenting an approach to select the right model approximation and sensors sets. As an application case, the approach is used to select the best model approximation and sensor sets to monitor the condition of the guiding system of vertical transportation systems.

The rest of the paper is organized as follows. In section 2, the state/parameter estimation algorithm used is explained, including the observability requirements. Section 3 describes the proposed framework for the model-based condition monitoring of large systems. Next, section 4 presents the application case, and shows the results of applying the presented framework to an scaled test bench of the case study. Finally, conclusions and future steps are drawn in section 5.

2 Model-based state and parameter estimation

Model-based state estimation filters combine available sensors with a first-principles model to estimate variables that could not be measured otherwise. The well known Kalman Filter (KF) is the most widely used and the optimal state estimator, but it is limited to linear systems. Several extensions of KF may be found in [3]. In this paper, the Extended Kalman Filter (EKF) is used due to its simple implementation and relatively low computational cost.

The EKF uses a nonlinear model defined in state space form as shown in equation 1. Both the process and measurement equations of this model are assumed to be disturbed by zero mean white Gaussian noise (w and v in equation 1) of covariance $\mathbf{Q}$ and $\mathbf{R}$ respectively. Similarly, the system's states (x) are assumed to be Gaussian variables with a covariance $\mathbf{P}$: ($\widehat{x} \sim \mathbf{N}(\widehat{x}, \mathbf{P})$).

$$\begin{aligned} \dot{x} &= f(x, u, t) + w \\ y &= h(x, u, t) + v \end{aligned} \tag{1}$$

The EKF is described in the pseudo-algorithm 1. In each k-time step the system model is simulated and compared with measured data. Additionally, the EKF linearizes the model around the estimation point and propagates a linear approximation of the covariance [3]. This is done recursively in two steps: prediction and update. In the prediction step, an a-priori estimation of the states mean and covariance is obtained. In the update step, this estimation is corrected using the available measurements. The simple implementation and

reduced computational cost of the EKF make it an attractive option for the estimation of states in nonlinear systems.

Algorithm 1 Extended Kalman Filter

Initialize:
$\widehat{\mathbf{x}}_{\mathbf{0}}^{+}, \mathbf{P}_{\mathbf{0}}^{+}$
for $each\ k$ **do**
    State and Covariance prediction
    $\widehat{x}_{k+1}^{-} = f_k(\widehat{x}_k^{+}, u_k, k) + w_k$
    $y_{k+1} = h_{k+1}(\widehat{x}_{k+1}, u_{k+1}, k) + v_k$
    $P_{k+1}^{-} = F_k P_k^{+} F_k^T + Q_k$ with $F_k = e^{\frac{\partial f_k}{\partial x_k} T_s}$
    Update
    $K_{k+1} = P_{k+1}^{-} H_{k+1}^T (H_{k+1} P_{k+1}^{-} H_{k+1}^T + R)^{-1}$ with $H_{k+1} = \frac{\partial h_{k+1}}{\partial x_{k+1}}$
    $\widehat{x}_{k+1}^{+} = \widehat{x}_{k+1}^{-} + K_{k+1}(z_{k+1} - y_{k+1})$ with z_{k+1} the measurement at step $k+1$
    $P_{k+1}^{+} = (I - K_{k+1}.H_{k+1}) P_{k+1}^{-}$
end for

Where: x is the states vector, y is the model output,u is the input, z is the system output, w is the process noise, v is the measurement noise, $\mathbf{P}$ is the initial covariance of the states, $\mathbf{Q}$ is the covariance of w, $\mathbf{R}$ is the covariance of v, $\mathbf{F}$ is the discretized system matrix, $\mathbf{H}$ is the output matrix, and T_s is the sampling frequency.

2.0.1 Unknown Input Estimation

In addition to estimating states, the EKF can be augmented to also estimate unknown inputs [6], [7]. The system's states vector is augmented with the unknown inputs, and the directional derivatives of the inputs are included in the system matrices (equation 2). These unknown inputs are assumed to change according to a random walk model (equation 3).

$$\mathbf{x}^{aug} = \begin{bmatrix} \mathbf{x} \\ \mathbf{u} \end{bmatrix} \qquad \mathbf{A}^{*} = \begin{bmatrix} \frac{\partial \mathbf{f}}{\partial \mathbf{x}} & \frac{\partial \mathbf{f}}{\partial \mathbf{u}} \\ \mathbf{0} & \mathbf{0} \end{bmatrix} \tag{2}$$

$$\dot{\mathbf{u}}(t) = \mathbf{0} + \mathbf{w}_u(t) \tag{3}$$

2.0.2 Observability

The observability is the property of the system that determines if the outputs have enough information to estimate the states of the model. A discrete-time system is observable if its initial state can be reconstructed at any time k with the measurements available [3]. If a model is not observable for the selected measurements, either additional sensors have to be included in the estimation or the model has to be reduced. There are several methods to assess the observability of the system, with one of the most common ones being the Popov-Belevitch-Hautus (PBH) criterion [8]. This method states that the corresponding linear system is observable if the PBH matrix (eq.4) is full rank for each $s \in \mathbb{C}$. In practice, the PBH matrix could only be low rank if s is an eigenvalue of $\mathbf{A}$ or for $s = 0$. Therefore, it is enough to check the PBH matrix for the eigenvalues of $\mathbf{A}$. Furthermore, by checking which modes of the system are actually not observable, one can draw conclusions on what extra measurements should be included.

$$PBH = \begin{bmatrix} s\mathbf{I} - \mathbf{A} \\ \mathbf{C} \end{bmatrix} \tag{4}$$

Where $s \in \mathbb{C}$, $\mathbf{A}$ is the system's process matrix and $\mathbf{C}$ is the system's output matrix.

This method is meant for linear systems, and extending it to nonlinear systems is not straightforward. For nonlinear systems, a good option is to assess the observability along the states' trajectory, linearizing the system at each time step and computing the observability matrix locally. In addition, since comparing the matrix rank only gives a 'true'-'false' observability assessment, to assess different sensors sets, it is more interesting to compare the matrix condition number[9].

It should be noted, that these methods do not take into account the accuracy of the measurements used. When adding a sensor with significant noise in its output, the observability will improve due to the additional sensor, but due to the measurement's high noise covariance, the estimation will not improve [10]. A work around is to use the observability criteria to understand the effect of certain sensors, and then check these sensor's effect in the estimation's accuracy by running subsequent estimations with synthetic measurements from a high-fidelity model. Since all the estimated variables are available in the high-fidelity model, the performance of the estimation using different sensor sets may be evaluated, and the best sensor set chosen.

3 Condition monitoring using state estimation and detailed system models

As explained in section 2.0.2, to accurately estimate the physics of interest with an state estimation framework, the observability of the system has to be ensured. If the system is not observable, either more sensors have to be included or the model has to be reduced. This implies neglecting non-observable physics and potentially limiting the possibilities of using the estimation to assess the system's condition. To address this problem, a high-fidelity model of the system could be used in combination with reduced models suitable for state/parameter estimation. In this work, this high-fidelity model will be referred to as *Digital Twin* (DT).

The DT is a detailed model of the system, which takes into account all the physics of interest and is simulated parallel to the real system, with the same input and known operational conditions. As stated above, such a model will probably not be suitable for state estimation, as it may not be observable. Therefore, this model runs in open-loop (i.e. without being corrected by current measurements), predicting the outcome of the system. Since no correction is done, the output of this model will be subjected to model inaccuracies. Furthermore, it will represent the condition of the system when the model was last updated, rather than the current one.

In order to have an estimation of the system's current condition, reduced models of the DT are used in an state estimation framework. These estimation models, are adapted from the DT to suit the requirements of a particular monitoring scenario. For instance, during maintenance or commissioning, as more sensors are available, more detailed estimation models will be used. In such phases, the estimation models will be used to estimate parameters of the installation that can be used to update the DT, ensuring that it will always provide the most updated prediction possible.

On the other hand, during normal operation the system sensors are more limited, and therefore smaller models will be required to ensure observability. In such phases, the estimation is mainly aimed at obtaining accurate virtual sensors to be used for condition monitoring. As stated above, the main limitation of these models is that the neglected phenomena may influence the estimation. In such cases, the DT may be used to enhance the estimation in two ways. Firstly, by comparing the estimation and the DT, system changes not related to operational conditions may be isolated, and thus faulty conditions and early degradation may be detected and quantified. Secondly, the DT could provide equivalent parameters and non-measurable variables to fit the phenomena neglected in the estimation model. These variables would enter the model as virtual inputs, and will result in more realistic virtual sensors and parameters. The flowchart of this framework is shown in Figure 1.

By using the right modeling approach, the DT can be automatically adapted to generate estimation models. Therefore, the model-based monitoring framework may be extended in a cost efficient way to tackle new necessities as they arise (e.g. to understand the underlying cause behind an unexpected behavior of the

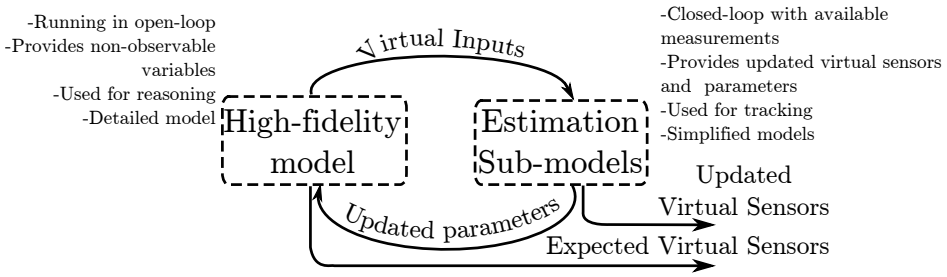


Figure 1: Combination of estimation sub-models with a high-fidelity *Digital Twin* of the model

system). However, there is still the question on how should a certain estimation model be approximated (i.e. which dynamics of the DT to keep, and how the removed ones affect the estimation). The next sections describe how to obtain reduced models in a cost efficient way and how to select of the best model-sensor combination.

3.1 Modeling Strategies

Models are mainly used in the system's early design and virtual commissioning phases. These models are usually developed using advanced modeling tools, which reduce errors and speed up the modeling process. Furthermore, sub-systems of the same plant may be modeled using different modeling tools, taking advantage of the expertise of each tool to model a particular engineering domain. This approach results in cost efficiency and model reliability in a sub-system level, but it hinders the re-usability of design models in a model-based monitoring framework. As a consequence, it is common to hand-code estimation models in less efficient languages, resulting in overly simplified models or increased modeling complexity (either in modeling the system or in developing an ad-hoc interface).

The Functional Mock-up Interface (FMI) is a tool independent standard for model exchange and co-simulation of dynamic systems, which could effectively address this problem. According to the FMI standard, the model is exported (either for exchange or co-simulation) as a so called Functional Mock-up Unit (FMU). The FMU is a compressed file containing an XML-file with the model description, a set of C-functions to execute model equations and further data required by the model (including tables, icons and documentation). Simulation programs or software packages that implement the FMI standard can import FMUs, access their resources, and run simulations [11]. Unlike other model exchange tools, its implementation is open-source and does not depend on the exchanging software version. Thus, as shown in Figure 2, it allows the combination of simulation tools otherwise incompatible, settling a general approach that reduces errors and speeds up the modeling process. This allows a simple model exchange between suppliers and OEMs but also a seamless combination of models with custom applications, allowing the user to manipulate the solution at each time step, as required by certain algorithms.

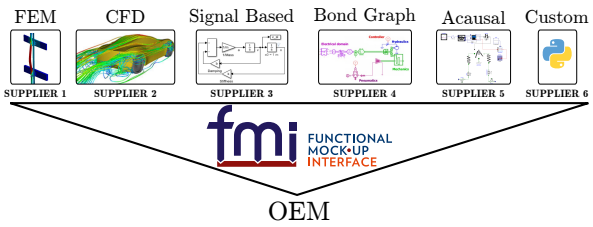


Figure 2: FMI for model exchange

The FMI is a promising candidate to become the industry standard for model exchange [12], and is being supported by an increasing number of modeling tools. In particular, port-based modeling tools, such as the *Modelica* modeling language, are an interesting option for the development of model-based monitoring strategies. Such modeling languages enhance the re-usability of different models. For instance, some of the model's constitutive equations may be activated/deactivated by assigning boolean parameters to these equations, as shown in Figure 3. Alternatively, the number of subsystems (or constitutive equations) could be defined through an integer and a for loop. This way, it is straightforward to include or exclude certain dynamic states from the model, easily adapting to the complexity level required by the monitoring scheme. Thus, starting from large high-fidelity model of the system, new models could be compiled automatically to address particular monitoring scenarios. Furthermore, open source alternatives are available for Modelica software (e.g. OpenModelica, JModelica.org), resulting in a highly cost efficient and less version dependent approach.

```
model BooleanMass
  parameter Boolean UseTwoMasses = true;
  Components.Fixed fixed (s0=0.0);
  Components.Mass Mass1(m = 20);
  Components.Mass Mass2(m = 20) if UseTwoMasses;
  Components.SpringDamper springDamper1(c = 1000, d = 10);
  Components.SpringDamper springDamper2(c = 1000, d = 10)
  if UseTwoMasses;
  Sources.Force InputForce;
equation
  if UseTwoMasses then
    connect(Mass2.flangeb, InputForce.flange);
  else
    connect(Mass1.flangeb, InputForce.flange));
  end if;
  connect(springDamper2.flangeb, Mass2.flangea);
  connect(Mass1.flangeb, springDamper2.flangea);
  connect(springDamper1.flangeb, Mass1.flangea);
  connect(fixed.flange, springDamper1.flangea);
end BooleanMass;
```

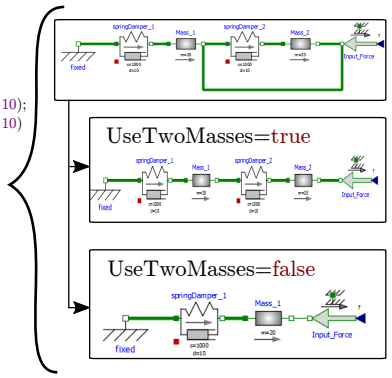


Figure 3: Example of a Boolean activation of sub-systems within the same model

3.2 Model-Sensor selection

Following the framework explained in section 3.1, it is straightforward to create and/or reuse detailed models of complex systems and connect them to state estimation algorithms. However, not every model is directly suitable for state estimation. As explained in section 2.0.2, the measurements used in the estimation should capture the physical phenomena represented in the model. Consequently, as models increase in size a greater number of sensors is usually required. Given the commonly limited number of sensors, it is highly important to select a sensor-model combination that minimizes the number of sensors while still being able to capture he relevant physics of the system.

In this section, a method is proposed to aid in the selection of the required sensor set and system model. Firstly, the possible sensor sets and model approximations are defined. Following the approach described in section 3.1, the detailed model of the system could be reduced automatically, directly compiling reduced models with the defined states' sets. Secondly, the PBH criterion (see section 2.0.2) is used to determine which model-sensor combinations are not observable (i.e. PBH matrix is not full rank for at least one of the eigenvalues of the system matrix). These model-sensor combinations are then excluded from the selection. In addition, the combinations where a certain sensor is not relevant in the model are also excluded (e.g. if the vibration of a certain element is neglected, the acceleration of that element wont be included as a sensor). For the sensor set-model combinations which are observable, the condition number of the PBH matrix is compared. This allows having a first quantitative evaluation of the observability of the different sensor set-model combinations.

As explained in section 2.0.2, the PBH criterion does not provide a metric on the accuracy of the estimation. Thus, to also take the expected estimation accuracy into account, the observable sensor-model combinations are used to estimate the variables of interest using synthetic data from the high-fidelity model. As the

estimated variables are known (since this process is done using synthetic data from the model), the accuracy of each sensor-model combination can be evaluated to add to the outcome of the PBH criterion. Additionally, it is also worth considering the estimated steady state covariance, since an increasing covariance will also indicate non-observability. By checking these three metrics (i.e. condition number of the PBH matrix, root mean square error (RMSE) of the estimation and covariance of the estimation), the most suitable sensor-model combinaton may be selected.

Possibly, different model abstraction levels will require different filter tuning (i.e. different assumptions of the model's noise covariance matrix, $\mathbf{Q}$, as $\mathbf{R}$ will only depend on the sensors). To compare different estimations equivalently, the automatic tuning procedure shown in Figure 4 is used. Firstly, an initial assumption on the filter's $\mathbf{Q}$ matrix is obtained based on the state's trajectory ($\mathbf{Q_0}$). Namely, a diagonal $\mathbf{Q}$ is used, where the covariance associated to each state is computed as a 1% of the magnitude of that state. Next, subsequent estimations are run where the filter $\mathbf{Q}$ is $\mathbf{Q_0}$ multiplied by a factor ϵ. The final $\mathbf{Q}$ is selected using the ϵ which minimizes the difference between the estimated state covariance and the real covariance (i.e. covariance of the difference between the estimated state and the actual state). In the real installation, the filter design will need further tuning, as the high-fidelity model is more similar to the estimation model than the real system. Thus, this tuning may be used as a starting point, but the final tuning is done manually with the aid of the filter performance statistics shown in [13].

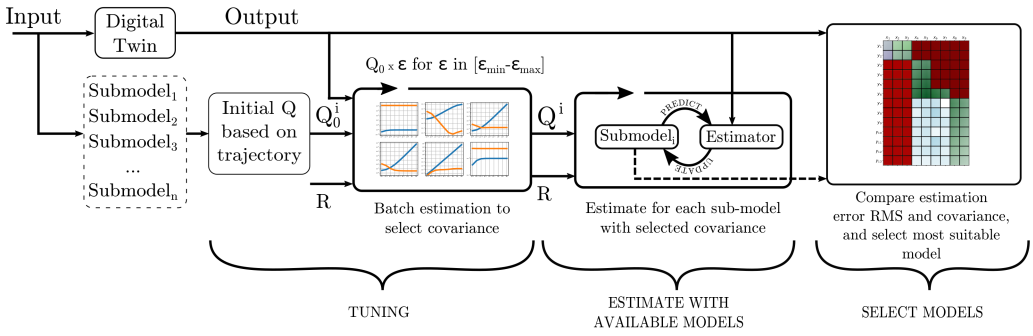


Figure 4: Tuning process to compare different models under similar conditions

4 Case study

The proposed framework is applied to the condition monitoring of a vertical transportation system (VTS), particularly on an electric traction lift with a 1:1 suspension. In particular, this paper focuses on the condition of the guiding system, as it significantly affects the energy efficiency and ride quality of the installation [14]. This is the most common type of vertical transportation system, and it is usually composed of the following components [15]:

- **Lift Cabin**: It is the component carrying the payload.
- **Counterweight (cw)**: balances the lift cabin's weight, making the lifting more efficient.
- **Electric Machine**: Commonly a gearless Permanent Magnet Synchronous Machine (PMSM) is used due to its high energy density.
- **Control System**: A Field Oriented Control (FOC) strategy is used, which aims at maximizing the active power and minimizing the reactive power of the machine, by controlling the direct and quadrature axis currents independently.

- **Guiding System**: ensures an homogeneous vertical movement of the cabin. It normally consists of two T-shaped rails mounted on the walls of the elevator shaft. Defects such as narrowing of the rails due to misalignment, bumps at the rail joints, or rail deflections, have a significant influence in the efficiency, comfort and useful life of vertical transportation systems.
- **Sliding shoe:** U-shaped polymeric pads located in the corners of the cabin and counterweight frames, which grab the guiding rails. It is does the interface between the guiding system and the cabin/counterweight.
- **Suspension Rope and Driving Pulley:** A steel rope is used to connect the car and the counterweight. In the simplest rope arrangement (1:1 suspension), the rope passes once over the traction sheave. The pulley transmits the traction from the electric machine.

4.1 Model of a VTS

Since faults in the guiding system tend to increase friction forces, estimating these friction forces provides a valuable indicator of the guiding rails condition. These friction forces depend mainly in four parameters: 1) friction coefficient, 2) condition of the guides, 3) geometry of the cabin, and 4) operational conditions (load, acceleration profile). Therefore, in order to isolate the condition of the guides from other operational conditions, a first approach may be to use a detailed model of the system, including the lateral and rotational movement of the cabin and a contact and friction model. To account for the condition of the guides, the model is updated as described in [16]: using an equivalent friction coefficient which takes into account both the coulomb friction coefficient and the condition of the guides. This model, can effectively account for the phenomena affecting the friction in the guides, but as shown in Table 1, it has a large number of states.

Table 1: Description of the dynamic states of a VTS model with all the relevant subsystems

System	States	Description
Cabin	x, y,z, $\dot{x}$,$\dot{y}$,$\dot{z}$	Cabin's translation movement
	α, β, γ, $\dot{\alpha}$, $\dot{\beta}$, $\dot{\gamma}$	Cabin's rotation movement
Counterweight	x, y,z, $\dot{x}$,$\dot{y}$,$\dot{z}$	CW's translation movement
	α, β, γ, $\dot{\alpha}$, $\dot{\beta}$, $\dot{\gamma}$	CW's rotation movement
Pulley	φ_P,ω_P	Pulley's rotation
Pulley/Machine Set	z_m,$\dot{z}_m$	Pulley/machine set's vertical vibration
	α_m,$\dot{\alpha}_m$	Pulley/machine set's off-axis inclination
PMSM	i_d,i_q	Currents in the electric machine
Controller	x_s,x_q,x_d	Derivative of the input error in each of the controller's PI loops

Therefore, although this model is useful to understand the effect of faults and different operational conditions, it may not be suitable for an estimation framework due to the large number of states. Particularly, due to the inherent uncertainty in the contact between the guides and the cabin, the states related to the lateral and rotational movement would have to be measured, with the consequent additional sensor cost. Therefore, a better approach may be to neglect the physics related to the unobservable states, i.e the rotation and lateral translation of the cabin, and don't make any assumptions on the underlying physics of the forces acting on the cabin. Instead, all the contact and friction forces are summarized in a single resultant force acting on the cabin and counterweight center, as shown in Figure 5. This forces may then be estimated together with the states as unknown inputs. However, the direct estimation of forces may lead to False Positives in the condition monitoring scheme, as there is no knowledge on the underlying physics of these forces. To aid in the assessment, the framework described in section 3 is used. This detailed model may then be used to predict the expected friction forces, and the estimation model may be used to obtain the actual ones.

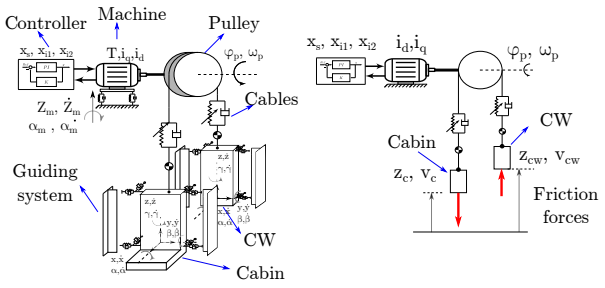


Figure 5: Detailed model of the system and equivalent reduced estimation model

In addition to summarizing the friction force in a single resultant force, there is still the question of which sensors should be used, and if other states should be neglected as well. Next, the approach shown in section 3.2 is followed to evaluate the optimal model and set of sensors.

4.2 Model-Sensor selection

In this section, the approach described in section 3.2 is used to select the best possible sensor set and model abstraction to monitor the friction forces in a vertical transportation system. In addition to removing the lateral and rotational dynamics of the cabin, there is still the question on what other states of the system will affect the estimation. As more states are included in the model, the computational cost increases and the observability tends to decrease. In addition, if the parameters associated to these states are uncertain, including them may reduce the estimation accuracy. In particular, the effect of the following states is studied:

- **Controller states:** The PI loops of the FOC introduce three states. Removing them leads a steady state error in the simulation, that can be assumed as another model disturbance and corrected with the estimation.
- **Machine direct axis:** The FOC keeps the direct axis current at zero. Thus, it is studied whether this state can be neglected.
- **Unknown inputs:** It is studied whether the forces acting on the guiding system of cabin and counterweight may be estimated together with the states, or if a different approach is required.
- **Split mechanical and electrical models:** It is studied whether splitting the electrical and mechanical sub-systems is better than including both together in the model. Splitting the model in two leads to smaller models, which may be better conditioned and thus improve the estimation.

The models and sensor sets studied are described in Tables 2 and 3 respectively. Figure 6 shows the observability results for the studied model-sensor set combinations. As explained in section 2.0.2, the following indicators are used to check the observability of each sensor-model combination: 1) PBH matrix condition number (shown for the eigenvalue of $\mathbf{A}$ leading to the largest PBH condition number), 2) Accuracy of the estimation, as the rmse of the estimation with respect to the actual variable taken from the high-fidelity model and 3) Estimated covariance (not shown due to size limitations). Next, these results are discussed in detail. This model-sensor selection strategy can be directly extended to other estimation scenarios.

Joint estimation of $\mathbf{F}_{\mathbf{fric}}^{\mathbf{cabin}}$ and $\mathbf{F}_{\mathbf{fric}}^{\mathbf{cw}}$ (models $\mathbf{x_1}$ to $\mathbf{x_4}$): Taking a look at models x_1-x_4, it is clear that the joint estimation of friction forces both in cabin and counterweight sides is only possible by measuring the cabin side's cable tension. This is because both friction forces have the same overall influence on the other measurements:

Table 2: Model approximations studied

Tag	Model group	Description	States
a	Control	Controller states	x_s, x_q, x_d
b	Machine 1	Quad. and Direct current	i_q, i_d,
c	Machine 2	Quad. current	i_q
d	Pulley Vib.	Pulley/Machine vertical vibration	z_p, v_p
e	Vertical Dynamics	Cabin and CW move	z_c, v_c z_{cw}, v_{cw}
f	Pulley Rot.	Pulley move	φ, ω
g	FricCabin	Cabin friction	F^c_{fric}
h	FricCw	CW friction	F^{cw}_{fric}
i	Torque	Machine generated torque	τ

Model	Groups used	Model	Groups used
x1	a,b,d,e,f,g,h	x8	c,e,f,g
x2	b,d,e,f,g,h	x9	a,b,f,i
x3	b,e,f,g,h	x10	b,f,i
x4	c,e,f,g,h	x11	c,f,i
x5	a,b,d,e,f,g	x12	d,e,f,g
x6	b,d,e,f,g	x13	e,f,g
x7	b,e,f,g		

Table 3: Sets of sensors studied

Tag	Sensor group	Description	Name
A	Force 1	Force in the machine support	F_s
B	Force 2	Cabin side cable tension	F_c
C	Cabin 1	Cabin acc. and position	A_c, Z_c
D	Cabin 2	Cabin acc.	A_c
E	Cabin 3	Cabin position	Z_c
F	Encoder	Rotor acc. and position	α, φ
G	Machine 1	Quad. and Direct current and voltage	i_q, i_d, V_q, V_d
H	Machine 2	Quad. current and voltage	i_q, V_q

Sensor set	Groups used	Sensor set	Groups used
y1	A, C, F, G	y10	C, F, H
y2	B, C, F, G	y11	D, F, H
y3	C, F, G	y12	E, F, H
y4	D, F, G	y13	F, H
y5	E, F, G	y14	C, H
y6	F, G	y15	C,F
y7	C, G	y16	D,F
y8	A, C, F, H	y17	E,F
y9	B, C, F, H	y18	F

- The cable couples the dynamics of the cabin, pulley and counterweight. Consequently, the vertical movement of cabin and counterweight are described mainly by two modes: a rigid-body mode which couples their movement to the rotation of the pulley, and the first vertical vibration mode of the cable (10-30Hz in the current case). Therefore, the acceleration of cabin and counterweight follow closely the angular acceleration of the pulley. Increments on the guides' friction (e.g. due to misalignment in the guides), will lead to a small increment in the cable's elongation and tension force. If this friction force decreases again, the cable will go back to its former elongation, and will behave as spring, affecting the vertical vibration related to the first mode. However, the movement related to the rigid-body mode will generally not be affected, as that would require a significantly high friction force that makes the cable slip in the pulley, uncoupling their movement. Thus, increments in friction force are not directly seen in the acceleration measurements.

- The friction forces in cabin and counterweight will lead to increased tension in both cable sides, both of them resulting in a torque opposed to the movement of the pulley. Consequently, both friction forces have the same overall effect on the measurements of the electric machine and the pulley. These measurements are thus not enough for the evaluation of friction forces in both sides.

- A theoretical (rather than practical) alternative to the tension in the cable would be to use the resultant

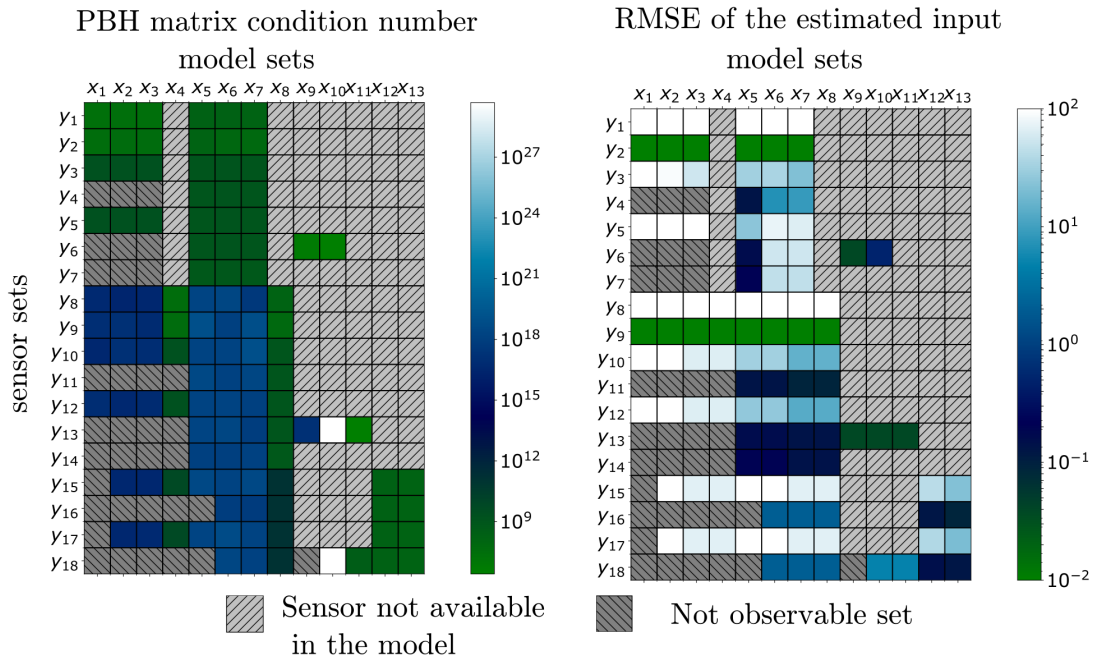


Figure 6: PBH matrix condition number (left) and rmse of the estimated input (right) for all the studied sensor-model combinations

force in the support of the electric machine. This could be a suitable measurement, as the friction forces affect this resultant force in an opposite way (as they have opposite directions). However, the estimation using this measurement leads to very high error, suggesting that the system is not observable with this measurement. Possibly, as F_s is significantly larger than the friction forces, the effect of F_{fric}^{cabin} is blurred out with other estimation errors (e.g. differences in cabin/counterweight acceleration). Thus, even though this sensor set has a good observability index according to the PBH criterion, it is deemed as not observable.

Joint estimation of $\mathbf{F_{fric}^{cabin}}$ (models $\mathbf{x_5}$ to $\mathbf{x_8}$): As explained in 3, a possible alternative when some physics of the system are required but not observable, is to use a Digital Twin of the system to provide the missing information. In this case, the F_{fric}^{cw} is a virtual input coming from the DT (i.e. an updated high-fidelity model of the system) and only the F_{fric}^{cabin} is estimated with the states. Next, the effect of different sensor sets on this estimation are explained.

- The combination of the measurements Z_c with φ (sets $y_3,\ y_5,\ y_{10},\ y_{12},\ y_{15},\ y_{17}$) leads to larger estimation errors than those which do not combine these two measurements. Although increasing the number of sensors tends to improve system's observability, in this case it occurs otherwise. The reason for this is that both Z_c and φ are essentially the same measurement (as explained earlier, the cabin moves mainly with a rigid-body motion, Z_c, coupled with the pulley's motion,φ). Errors in one of these measurements could thus make the estimator over-correct some states and yield unrealistic estimations of the augmented states. In this particular case, due to differences in the estimation model and the simulation model, the estimator over-corrects the position of the cabin, which leads to a larger elongation in the cable and wrong friction force estimations. This issue could be solved by improving the tuning of the filter. In particular, increasing the covariance of the position sensor. However, then it may not influence the estimation at all. Therefore, it is preferred not to use the position (Z_c) sensor in this case.

- Looking at measurements y_{16} and y_{18}, it seems that not using current and voltage measurements will

lead to higher errors than if those measurements are used. As the error is not significantly high, one could argue that this is a suitable measurement set. However, taking a closer look at those estimations, the covariance of the estimated augmented states grows continuously, suggesting that the system is not observable with this measurement sets. In fact, the value of the estimated F_{fric}^{cabin} is constant along the estimation, and the small RMSE is only due to the initial value of F_{fric}^{cabin} being close to the actual one. Thus, this matrix has to be interpreted with caution, and is better to check it together with another matrix showing the estimated covariance (not shown here due to size limitations).

- Including the vibration of the pulley in the estimation models worsens the estimation slightly, and therefore it is preferred to remove the related states.

Joint estimation of τ (models $\mathbf{x_9}$ to $\mathbf{x_{11}}$): In this models, no assumption is made on the friction forces affecting on the system. Instead, the mechanical sub-system is neglected and only the torque (τ) generated in the electric machine is estimated. Assessing the effect of different sensor sets on models x_9 to x_{11} yields similar conclusions as in the precious cases. The assessment suggests that both the controller states and the direct current axis may be neglected, and that the measurement sets required are the encoder and the machine current and voltage.

Joint estimation of $\mathbf{F_{fric}^{cabin}}$ with τ as model input (models $\mathbf{x_{12}}$ and $\mathbf{x_{13}}$): In this models, only the mechanical sub-system is taken into account. The torque generated by the electric machine is used as input to the model, and the friction in the counterweight is assumed known (e.g. coming from a Digital Twin of the system). As in the previous cases, the combination of Z_c and φ in the same measurement set provides worst estimation results.

Continuously measuring the tension in the cable is a costly solution and may limit the operational range of the system (in certain cases the sensor may clash with the driving pulley). Consequently, it may be used during certain operations, such as maintenance or commissioning, but is not suitable to continuously monitor the system. As a consequence, based on the previous assessment, the most suitable model-based monitoring solution is to use the model x_5 without the states in the pulley, together with the measurement set y_6. In this model, friction in the counterweight is introduced as a virtual input coming from the DT, as explained in section 3. For that, the high-fidelity model has to be properly updated (for example, estimating an equivalent friction coefficient as shown in [16]). In addition, this implies that the condition of the counterweight's guiding system will remain the same as when the high-fidelity model was updated. In this particular case, this assumption is deemed valid because: 1) the counterweight is usually well balanced, leading to smaller friction forces and less wear and 2) it is not subjected to varying loads as the cabin.

4.3 Estimation of friction forces using the selected sensors and models

This section shows the results of estimating friction forces in a VTS, using the framework presented in section 1. The proposed methodology is tested in the scaled test bench of a vertical transportation system presented in [17], which has a height of 2.5 meters and allows a travel length of circa 1.8 meters. This test bench allows studying defects and using sensors that could not be tested in real installations. The guiding system consists of two guiding rails for the counterweight and two for the cabin. Each of these rails is made up of four rail segments (I to VI).

As explained in section 3, in this problem a high-fidelity model of the system (DT) is used in combination with estimation sub-models. The DT for this application is summarized in section 4.1. Prior to using this model, it has to be calibrated to accurately represent the system, for which additional sensors are required. In this particular case, the DT is updated by estimating an equivalent friction coefficient as shown in [16]). For that, the additional measurements required are the cable's tension, acceleration in the cabin and cabin's position. The estimation sub-model used to continuously monitor the friction forces in the system is obtained from the analysis done in section 4.2. This estimation model is a reduced version of the DT, where mainly the lateral and rotational movement of the cabin is neglected. The states of this model and the sensors used

Table 4: Summary of the states, sensors and tuning of the estimation model

States	Q matrix	Measurements	R matrix	Input
z_{cw},$\dot{z_c}$,z_{cw},$\dot{z_{cw}}$, ϕ_P,ω_P,i_q,i_d, x_q,x_i,x_s, F_{fric}^{cabin}	$diag(1^{-9}, 1^{-9}, 1^{-9}, 1^{-9}$ $1^{-6}, 1^{-1}, 1^{-1}, 1^{-1}$ $, 1^{-7}, 1^{-7}, 1^{-7}, 10)$	V_q, i_q, V_d, i_d, $, \phi$,α	diag(1^{-3},1^{-6} ,1^{-3}, 1^{-7})	W_{ref}, $\widehat{F}_{fric}^{cw}$

in the estimation are shown in Table 4. By following this approach, friction force in the cabin side may be estimated, improving the accuracy of other virtual sensors. Additionally, the estimated friction may be compared to the one predicted by the DT. As the later one is not updated to the current condition of the system, differences in the estimated and the predicted friction forces may be used as damage indicators. This is shown in Figure 7, which compares the friction virtual sensor of the estimation model, the friction virtual sensor of the detailed model and the measured friction (obtained from the difference between the measured tension and cabin acceleration). In the counterweight side, the friction is introduced as a virtual input in the estimation model. Thus, only the friction virtual sensor of the detailed model and the measured friction are shown. This estimation was done after introducing a fault in the guiding system. In particular, the position of the joint between cabin's rail's segments 3 and 4 (h=1.25m) of the guide is modified, changing the condition of the guide. The current condition of the guide, differs thus from the condition for which the DT was calibrated.

Consequently, in the counterweight side, the friction virtual sensor of the DT still follows closely the measured friction. On the cabin side, however, the detailed model differs significantly from the measurement in the region near the defect. On the other hand, the virtual sensor of the estimation model adapts to this change, and has a value closer to the actual measurement.

By continuously comparing the estimation and the output of the detailed model, a Key Performance Indicator (KPI) of the guiding system's condition can be defined. Although the estimation adapts better to changes in the actual system, there is still a significant deviation between heights $1.01m$ and $1.55m$. This is due to the error in the virtual input of the counterweight's friction, which directly affects the estimation. This reflects the main limitation of this framework: errors in the virtual inputs obtained with the DT directly affect the estimation. Consequently, when following the presented approach it should be ensured that the virtual inputs are as accurate as possible, and do not change in the system's life cycle. In order to validate the estimation,

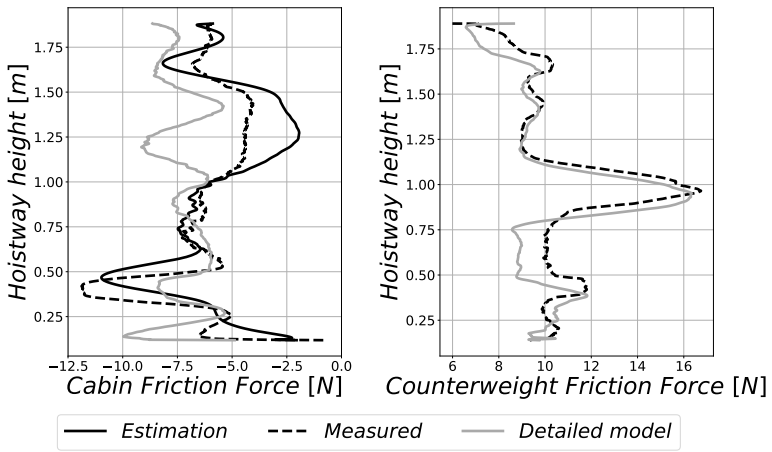


Figure 7: Friction forces estimated and measured

the tension in the cable and vertical accelerations both in cabin and counterweight sides are used used. The cable tension depends directly on the friction in the guides and the acceleration of the cabin, and therefore it

reflects the accuracy of the friction estimation. In Figure 8, the estimated tension forces and accelerations are compered to the ones measured in the test bench. The estimation remains bellow a 5%, showing the potential of these techniques.

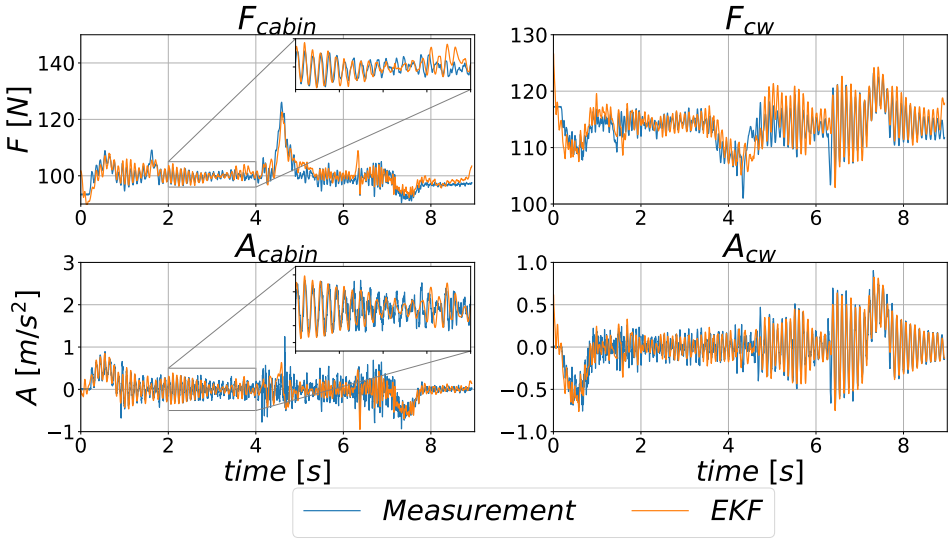


Figure 8: Comparison of the estimated and measured cable tension forces and cabin and counterweight accelerations

5 Conclusions

State estimation techniques combine available sensors with a system's model, correcting both sensor noise and model inaccuracies to obtain virtual sensors. Thus, they can virtually measure variables of interest that could not be measured otherwise. To ensure the convergence of these methods, the physical phenomena described in the model has to be included in the measurements used. Consequently, if the number of sensors is very limited, a number of approximations have to be assumed in the system models. This poses mainly two limitations: First, the neglected physics could mislead the assessment of the system's condition. Second, adapting to new monitoring scenarios as they are required requires new modeling effort.

In this paper, a high-fidelity model (Digital Twin, DT) of the system was used to overcome these limitations. In particular, the paper was focused on how to select the required model and sensor sets. A main limitation of this method, is that if the virtual inputs are not accurate enough, they may have a significant influence on the estimation's accuracy.

In future steps, the framework will be extended to assess other sub-systems. Similarly, the DT will provide virtual inputs to the estimation models, but in addition it will be updated with the outcome of the estimation models. Thus, in case additional sensors are available (e.g. during maintenance or commissioning), the DT can be updated with the estimated parameters in order to represent always the most updated system's condition. This DT will then be used to obtain KPIs on the system's condition, and to run *what-if* analyses, by simulating the results of setting a maintenance action.

Acknowledgements

The authors gratefully acknowledge the European Commission for its support of the Marie-Sklodowska Curie program through the ITN ANTARES project (GA 606817) and the support from the KU Leuven

research fund.

References

[1] R. Isermann. Integration of fault detection and diagnosis methods. In *Issues of Fault Diagnosis for Dynamic Systems*, pages 15–49. Springer, 2000.

[2] V. Venkatasubramanian, R. Rengaswamy, K. Yin, and S. N. Kavuri. A review of process fault detection and diagnosis: Part i: Quantitative model-based methods. *Computers & chemical engineering*, 27(3):293–311, 2003.

[3] D. Simon. *Optimal state estimation: Kalman, H infinity, and nonlinear approaches*. John Wiley & Sons, 2006.

[4] M. N. Chatzis, E. N. Chatzi, and A. W. Smyth. On the observability and identifiability of nonlinear structural and mechanical systems. *Structural Control and Health Monitoring*, 22(3):574–593, 2015.

[5] L. R. Ray. Nonlinear Tire Force Estimation and Road Friction Identification: Simulation and Experiments,. *Automatica*, 33(10):1819–1833, 1997.

[6] R. Isermann and M. Munchhof. *Identification of Dynamic Systems: An Introduction with Applications*. Springer Berlin Heidelberg, 2011.

[7] F. Naets, J. Croes, and W. Desmet. An online coupled state / input / parameter estimation approach for structural dynamics . 283:1167–1188, 2014.

[8] B. Ghosh and J. Rosenthal. A generalized popov-belevitch-hautus test of observability. *IEEE Transactions on Automatic Control*, 40(1):176–180, 1995. cited By 14.

[9] M. Nakhaeinejad and M. D. Bryant. Observability analysis for model-based fault detection and sensor selection in induction motors. *Measurement Science and Technology*, 22(7), 2011.

[10] J. Croes. *Virtual sensing in mechatronic systems State estimation using system level models*. PhD thesis, 2017.

[11] T. Blochwitz, M. Otter, J. Akesson, M. Arnold, C. Clauss, H. Elmqvist, M. Friedrich, A. Junghanns, J. Mauss, and D. Neumerkel. Functional mockup interface 2.0: The standard for tool independent exchange of simulation models. In *Proceedings of the 9th International MODELICA Conference; September 3-5; 2012; Munich; Germany*, number 076, pages 173–184. Linköping University Electronic Press, 2012.

[12] C. Bertsch, E. Ahle, and U. Schulmeister. The functional mockup interface-seen from an industrial perspective. In *10th International Modelica Conference, Lund, Sweden*, 2014.

[13] J. V. Candy. *Bayesian signal processing: classical, modern, and particle filtering methods*, volume 54. John Wiley & Sons, 2016.

[14] J. Andrew and S. Kaczmarczyk. *Systems engineering of elevators*. Elevator World, 2011.

[15] G. Strakosch. *The Vertical Transportation Handbook*. Wiley, 1998.

[16] M. Gonzalez Cocho, O. Salgado, J. Croes, B. Pluymers, and W. Desmet. Model-based virtual sensors by means of Modelica and FMI. pages 337–344, 2017.

[17] E. Esteban, O. Salgado, A. Iturrospe, and I. Isasa. Design methodology of a reduced-scale test bench for fault detection and diagnosis. *Mechatronics*, 47:14–23, 2017.

Metamodel-based optimization of an energy harvester from stall-induced pitching oscillations of airfoils

C. R. dos Santos [1], **M. M. da Silva** [1], **F. D. Marques** [1]
[1] University of São Paulo, São Carlos School of Engineering, Department of Mechanical Engineering, Avenida Trabalhador São-Carlense, 400, São Carlos, SP, Brazil
e-mail: **carlos.renan.santos@usp.br**

Abstract

Aeroelastic vibrations have been investigated as a way to convert the energy from airflows into electric energy. In the case of stall-induced oscillations, previous works have demonstrated that structural parameters affect the amount of energy extracted from the airfoil motion. In this sense, the present work proposes the optimization of such structural parameters to increase the power harvested from an airfoil undergoing pitching oscillations at high angles of attack. The optimization process utilizes a metamodel to approximate the cost function in the interval of interest for the variables to be optimized. The metamodel considers the four-dimensional Kriging interpolation, which models the results obtained from different simulations previously set by the Design of Experiments (DOE). Results show that the absence of torsional springs and the reduction of the airfoil mass and moment of inertia, as well the position of the elastic axis around 0.336 of the chord length characterizes the optimal harvester.

1 Introduction

Optimization process are frequent in any engineer field given the search for optimal conditions of some system or component. When aeroelastic problems are taken into account, optimization can be developed to increase the flutter velocity or to generate the best composite structure by considering its weight and aeroelastic responses [1]. However, fluid-structure interactions are also relevant in the analyses of civil structures such like bridges and, as consequence, optimization problems can be set looking for the improvement of dynamic characteristics of such structures subjected to loads imposed by the airflow [2].

The optimization was also applied for the design of flexible wings operating beyond the flutter onset velocity. Under this condition, the aeroelastic behavior is driven by limit cycle oscillations due to structural and aerodynamic nonlinearities [3, 4]. Here, the objective relied on the optimal weight distribution of the wing constrained by the maximum amplitude allowed for the oscillations.

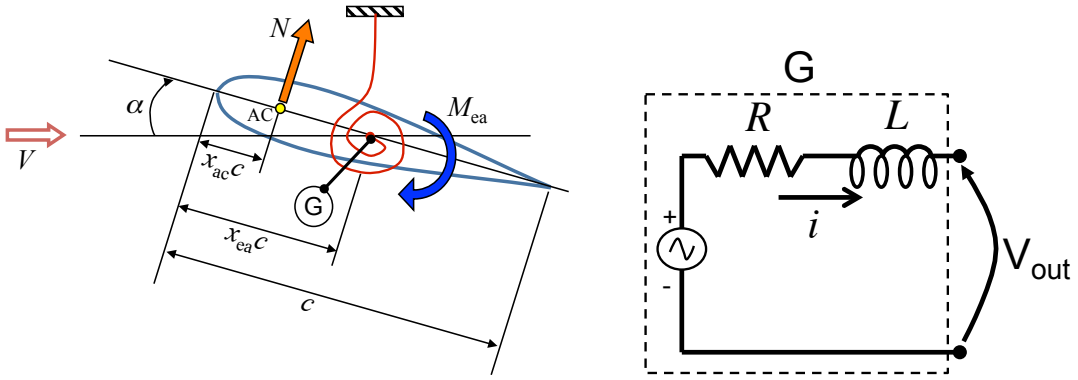
If limit cycle oscillations reach high angle of attack, dynamic stall effects become relevant and stall-induced oscillations are observed [5]. Some experimental efforts have considered the nonlinear behavior of such oscillations to harvest energy [6, 7]. On the other hand, dos Santos, Marques and Hajj (2018) [8] presented a model to the harvesting process and have indicated that structural parameters of the harvester affect the amount of extracted power. Such conclusion suggests the needing of an optimization to find the parameters that can increase the harvesting process.

In this sense, the present work proposes the optimization of a harvester from stall-induced oscillations. Three parameters are considered during the optimization process: the position of the elastic axis of the airfoil; inertial features summarized by the product of the squared radius of gyration and the mass ratio of the airfoil; and the natural frequency of pitching.

2 Methodology

The optimization problem is going to be solved with the sequential quadratic programming (SQP) solver. The cost function is evaluated from the metamodel based on the Kriging interpolation of the cost function calculated at some points set by the design of experiments (DOE). The evaluation of the cost function at these points depends on the time integration of a system of differential equations that describes the electroaeroelastic model, which results on time histories for the angle of attack of the pitching airfoil and the current output of the generator. Then, the root mean squared power is assessed for each wind speed in the range of interest and the negative integer of this curve is defined as the cost function to be minimized.

2.1 Electroaeroelastic model



(a) Typical aeroelastic section (b) Detail of the electric generator circuit

Figure 1: Schematic representation of the electroaeroelastic model.

As illustrated in Figure 1, the electroaeroelastic model considers a typical aeroelastic section with chord c undergoing pitching oscillations. One electric generator with internal resistance R and inductance L is attached to the elastic axis of the airfoil. Then, the system of differential equations that models the variation of the angle of attack of the airfoil, α, and the current generated in the electric circuit, i, is given by:

$$\begin{cases} \ddot{\alpha} + \omega_\alpha^2 \alpha = \frac{8V^2}{r_\alpha^2 \mu \pi c^2} C_{m_{ea}} - \frac{16\kappa}{\pi \rho c^4 r_\alpha^2 \mu} i \\ \frac{di}{dt} = \frac{\kappa}{L}\dot{\alpha} - \frac{R}{L} i \end{cases} , \tag{1}$$

where ω_α is the natural pitching frequency of the typical aeroelastic section, r_α is the radius of gyration of the airfoil and $\mu = (4m)/(\pi \rho c^2)$ is its mass ratio, being m the mass of the airfoil and ρ the air density. The dimensionless $r_\alpha^2 \mu$ summarizes inertial parameters. Moreover, κ is the electro-mechanical couple factor, V is the airspeed and $C_{m_{ea}}$ is the pitching moment coefficient with respect to the elastic axis, that is given by:

$$C_{m_{ea}}(t) = C_m(t) + C_n(t)(x_{ea} - x_{ac}) , \tag{2}$$

where x_{ea} and x_{ac} are, respectively, the position of the elastic axis and of the aerodynamic center of the airfoil as a fraction of the chord length. $C_m(t)$ is the aerodynamic moment coefficient at the quarter chord and $C_n(t)$ is the normal force coefficient. Because the airfoil can reach high angles of attack during its motion, dynamic stall effects become relevant. Thus, aerodynamics will be modeled by the Beddoes-Leishman method in state-space representation, which is able to capture nonlinear loads during unsteady motions. Such approach for the unsteady aerodynamic behavior of an airfoil, computes components of aerodynamic loads related to important events of the flow. By doing so:

$$\begin{cases} C_n(t) = C_n^p(t) - C_n^c(t) + C_n^f(t) + C_n^v(t) \\ C_m(t) = C_m^p(t) + C_m^f(t) + C_m^v(t) \end{cases} , \tag{3}$$

where superscripts p denote components related to the attached flow condition, c indicates the circulatory component, f is associated with the separation of the flow from the trailing edge and v denotes components due to the shedding of vortices from the airfoil leading edge.

The loads related to the attached flow condition are given through eight aerodynamic states such that:

$$\{\dot{x}\} = [A]\{x\} + [B]\begin{Bmatrix}\alpha \\ q\end{Bmatrix} , \tag{4}$$

$$\begin{Bmatrix}C_n^p \\ C_m^p\end{Bmatrix} = [C]\{x\} + [D]\begin{Bmatrix}\alpha \\ q\end{Bmatrix} , \tag{5}$$

where the input $q = \dot{\alpha}c/V$ is the dimensionless variation of the angle of attack, $\{x\}$ is the vector that represents the 8 states and $[A]$, $[B]$, $[C]$ and $[D]$ are matrix extensively discussed in the literature [9, 10].

The normal force coefficient due to the attached flow can be divided into a circulatory and a non-circulatory components, i.e., $C_n^p = C_n^c + C_n^i$, and the circulatory component is defined as:

$$C_n^c(t) = C_{n_\alpha}\beta^2\left(\frac{2V}{c}\right)(A_1 b_1 x_1 + A_2 b_2 x_2) , \tag{6}$$

being C_{n_α} the slope of the curve of the normal force coefficient as function of the angle of attack in the linear range and $\beta = \sqrt{1-M^2}$, where M is the Mach number of the flow.

Dynamically, some delay is observed in the normal force coefficient. State x_9 models this delay as a first order system dependent on a empirical time constant T_p:

$$\dot{x}_9 = \left(\frac{2V}{c}\right)\frac{-x_9 + C_n^p(t)}{T_P} , \tag{7}$$

$$C_n'(t) = x_9 . \tag{8}$$

The separation of the flow also contributes for the aerodynamic loads and impose them nonlinear characteristics. If f_d is the fraction of the airfoil where the flow is attached, the aerodynamic coefficients are given by:

$$\begin{cases} C_n^f(t) = C_n^c\left(\frac{1+\sqrt{f_d}}{2}\right)^2 \\ C_m^f(t) = \left\{K_0 + K_1(1-\hat{f}) + K_2\sin[\pi(\hat{f})^m]\right\}C_n^c(t) + C_{m_0} \end{cases} , \tag{9}$$

where typically $m = 2$, K_0, K_1 and K_2 are empirical constants that match the curve for static moment coefficient per angle of attack. C_{m_0} is the zero-lift moment coefficient, $\hat{f} = \max[f_d(t), f_m(t)]$ and $f_d(t)$ and $f_m(t)$ are given by two aerodynamic states as systems of first order with dependence on a time constant T_f, which has a standard value T_{f_0} that can be modified during the vortex shedding phase:

$$\dot{x}_{10} = \left(\frac{2V}{c}\right)\frac{-x_{10} + f(\frac{C_n'(t)}{C_{n_\alpha}})}{T_f} , \tag{10}$$

$$f_d(t) = x_{10} , \tag{11}$$

and:

$$\dot{x}_{11} = \left(\frac{2V}{c}\right)\frac{-2x_{11} + 2f(\alpha)}{T_{f_0}} , \tag{12}$$

$$f_m(t) = x_{11} , \tag{13}$$

where $f(\hat{\alpha})$ is a function that models the flow separation from the airfoil trailing edge in static conditions and is empirically given for NACA airfoils as [11]:

$$f(\hat{\alpha}) = \begin{cases} 1 - 0.3e^{\frac{|\hat{\alpha}|-\alpha_1}{s_1}} & \text{if } |\hat{\alpha}| \le \alpha_1 \\ 0.04 - 0.66e^{\frac{\alpha_1-|\hat{\alpha}|}{s_2}} & \text{if } |\hat{\alpha}| > \alpha_1 \end{cases} , \tag{14}$$

where α_1 is an angle defined when $f = 0.7$, and s_1 and s_2 are constants defined empirically to match the function $f(\hat{\alpha})$ with experimental data.

The contribution of the vortex shedding phase is also taken into account by the Beddoes-Leishman model. This phase is triggered when the absolute value of C_n' is increasing and becomes larger than C_{n_1}, which is the value of C_n at the stall imminence in static conditions. When $|C_n'| \geq C_{n_1}$, a dimensionless counter τ_v is established and marches according to the dimensionless time $2Vt/c$. Then, the normal force coefficient associated with the vortex shedding phase is modeled by a first order system dependent on a empirical time constant T_v:

$$\dot{x}_{12} = \left(\frac{2V}{c}\right) \frac{-x_{12} + \dot{C}_v}{T_v} \ , \tag{15}$$

$$C_n^v(t) = x_{12} \ , \tag{16}$$

where:

$$C_v = \begin{cases} C_n^c[1 - 0.25(1 + \sqrt{f_d})^2] & \text{, if } \tau_v \leq 2T_{vl} \\ 0 & \text{, if } \tau_v > 2T_{vl} \ , \end{cases} \tag{17}$$

in which T_{vl} is an empirical time constant defined as the dimensionless time needed by the vortex shed from the leading edge to reach the airfoil trailing edge. As consequence of the vortex shedding, the pressure center varies along the airfoil chord length, thereby contributing with an additional term to the moment coefficient, which can be written as:

$$C_m^v(t) = -0.25 \left[1 - \cos\left(\frac{\pi \tau_v}{T_{vl}}\right)\right] C_n^v \ . \tag{18}$$

The optimization of an energy harvester from the oscillatory behavior of the airfoil, looks for the high power extraction. For one given wind speed, the harvested power is given by $P(t) = \kappa \dot{\alpha}(t) i(t)$. Time histories for $\dot{\alpha}(t)$ and $i(t)$ are given by the time integration of Equation (1) by using a forth-order Runge Kutta. Then, considering the range of wind speeds between 0 and 10m/s, the cost function to be minimized can be written as:

$$g(x_{ea}, r_\alpha^2 \mu, \omega_\alpha) = -\int_0^{10} P_{RMS}(x_{ea}, r_\alpha^2 \mu, \omega_\alpha) \mathrm{d}V = -\int_0^{10} \sqrt{\overline{[\kappa \dot{\alpha}(t) i(t)]^2}} \mathrm{d}V \ . \tag{19}$$

2.2 Design of experiments

The simulations will be conducted by varying $x_{ea} \in [0.25, 0.4]$, $r_\alpha^2 \mu \in [1, 5]$ and $\omega_\alpha \in [0, 1]$Hz. The factorial designs is adopted, by considering 512 experiments organized in a cube with 8 points $\mathbf{x} = [x_{ea}, r_\alpha^2 \mu, \omega_\alpha]$ in its edges [12]. Such organization allows a better control of the results and the identification of regions where the cost function $g(x_{ea}, r_\alpha^2 \mu, \omega_\alpha) = 0$.

2.3 Four-dimensional Kriging

Let $g_0 = g(\mathbf{y}_0)$ be the unknown value of the cost function g when the function is applied in the point $\mathbf{y}_0 = [x_{ea}, r_\alpha^2 \mu, \omega_\alpha]_0$. If $\mathbf{G} = g(\mathbf{y}_i)$ is the vector with known values of g at $i = 1, 2, ..., m$ points, the interpolated value $\hat{g}_0$ can be determined by using the Kriging method [13]. Following this methodology, firstly, $\mathbf{G}$ is used to create a linear approximation of the function g, such that:

$$\bar{g}(\mathbf{y}) = C_0 + C_1 x_{ea} + C_2 r_\alpha^2 \mu + C_3 \omega_\alpha \ , \tag{20}$$

with C_j being constants defined by least-squares solution of the system $\mathbf{AC} = \mathbf{G}$, where $\mathbf{A}$ is a $m \times 4$ matrix in which each row has the values of $\mathbf{y}_i$.

Let $\bar{\mathbf{G}} = \bar{g}(\mathbf{y}_i)$, which is supposed to differ from $\mathbf{G}$ since the values of $\bar{\mathbf{G}}$ are given by a linear approximation of the function g. Let $\mathbf{E} = \mathbf{G} - \bar{\mathbf{G}}$ be the vector which store the differences between both values. Then, for

the point $\mathbf{y}_0$, $\hat{g}_0 = E_0 + \bar{g}(\mathbf{y}_0)$, where E_0 is the difference between the value of the linear function $\bar{g}$ in the point $\mathbf{y}_0$ and the actual value of g in this point. Thus, by determining E_0 the value of $\hat{g}_0$ is also known.

The Kriging method considers that the value of the function at some point is a weighted average of the neighbor values of the function. So, the value E_0 is determined by $E_0 = \mathbf{E}^T\mathbf{W}$, where $\mathbf{W}$ is the vector with the weights which prioritize points closer to the unknown point. Mathematically:

$$\mathbf{W} = \begin{Bmatrix} W_1 \\ W_2 \\ \vdots \\ W_m \end{Bmatrix} = \begin{bmatrix} l(\mathbf{y}_1,\mathbf{y}_1) & l(\mathbf{y}_1,\mathbf{y}_2) & \dots & l(\mathbf{y}_1,\mathbf{y}_m) \\ l(\mathbf{y}_2,\mathbf{y}_1) & l(\mathbf{y}_2,\mathbf{y}_2) & \dots & l(\mathbf{y}_2,\mathbf{y}_m) \\ \vdots & \vdots & \ddots & \vdots \\ l(\mathbf{y}_m,\mathbf{y}_1) & l(\mathbf{y}_m,\mathbf{y}_2) & \dots & l(\mathbf{y}_m,\mathbf{y}_m) \end{bmatrix}^{-1} \begin{Bmatrix} l(\mathbf{y}_1,\mathbf{y}_0) \\ l(\mathbf{y}_2,\mathbf{y}_0) \\ \vdots \\ l(\mathbf{y}_m,\mathbf{y}_0) \end{Bmatrix}, \tag{21}$$

where $l(\mathbf{y}_j,\mathbf{y}_k)$ is a function of the distance between points $\mathbf{y}_j$ and $\mathbf{y}_k$, $d(\mathbf{y}_j,\mathbf{y}_k)$. Some functions can be applied for this purpose: the linear function, $l(\mathbf{y}_j,\mathbf{y}_k) = sd(\mathbf{y}_j,\mathbf{y}_k)$, the spherical function $l(\mathbf{y}_j,\mathbf{y}_k) = 1.5sd(\mathbf{y}_j,\mathbf{y}_k)/r - 0.5s[d(\mathbf{y}_j,\mathbf{y}_k)/r]^3$, or the exponential function $l(\mathbf{y}_j,\mathbf{y}_k) = s - se^{[-d(\mathbf{y}_j,\mathbf{y}_k)/r]}$, being r the range of the functions and s their sill value.

2.4 Optimization

The nonlinear optimization problem can be written as:

$$\min_{[x_{ea},r_\alpha^2\mu,\omega_\alpha]} \hat{g}(x_{ea}, r_\alpha^2\mu, \omega_\alpha) \,, \tag{22}$$

subject to:

$$\begin{cases} 0.25 \leqslant x_{ea} \leqslant 0.40 \\ 1 \leqslant r_\alpha^2\mu \leqslant 5 \\ 0 \leqslant \omega_\alpha \leqslant 1 \end{cases} \tag{23}$$

The optimization problem must be constrained due to the limits adopted for the database and, as consequence, the limits where the Kriging interpolation is valid. Sequential Quadratic Programming (SQP) [14] was adopted to the optimization process. The start point was set in the inferior limit of the variables: $[x_{ea}, r_\alpha^2\mu, \omega_\alpha]$ = [0.25, 1, 0].

3 Results and discussion

The electroaeroelastic model was used to calculate the cost function $g(x_{ea}, r_\alpha^2\mu, \omega_\alpha)$ at the points indicated by the DOE. The analyses were made by considering an NACA 0012 airfoil with chord 0.4m. The electric generator had the parameters fixed: internal resistance $R = 30\Omega$/m, inductance $L = 0.1$H/m and electrical mechanical coupling factor $\kappa = 5 \times 10^{-4}$Vs/(rad m). Parameters for the Beddoes-Leishman model were extracted from Leishman and Beddoes (1986) [15]. Figure 2 shows the original data and the Kriging interpolation for calculations of the cost function for the points indicated by the DOE process. The cost function is equal to zero in many points within the range of analyses, which indicates one of the following situations:

1) The dynamic behavior of the harvester is damped for all the range of wind speeds from 0 to 10m/s (the flutter velocity is higher than 10m/s);

2) The dynamic behavior of the harvester is unstable within all the range of wind speeds (limit cycle oscillations are not observed);

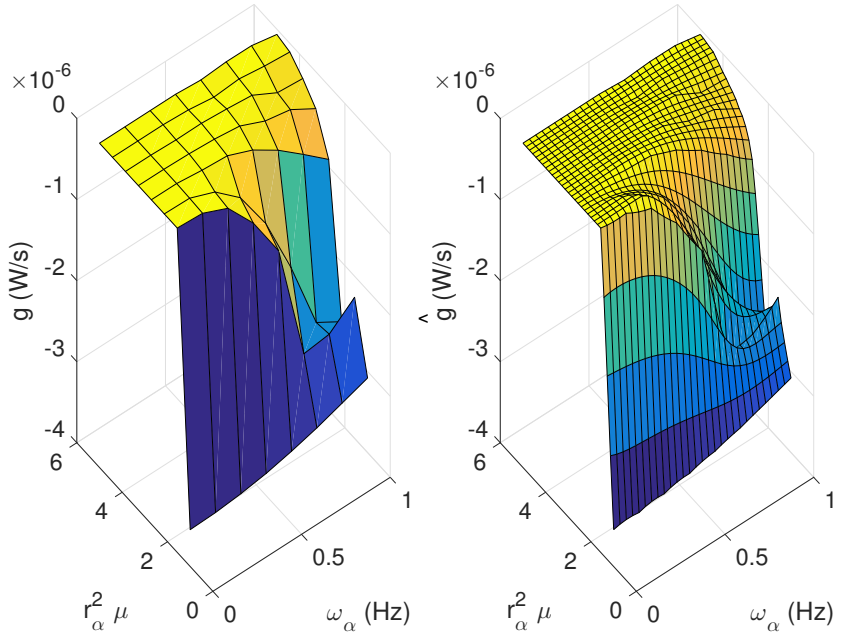


Figure 2: Original data from the electroaeroelastic model and values interpolated by the Kriging method for $x_{ea} = 0.336$.

3) Limit cycle oscillations have amplitude higher than 60deg. within all the range of wind speeds (the limit of 60deg. is adopted as the valid range of application for the Beddoes-Leishman method. If limit cycle oscillations are observed with an higher amplitude, the power harvested from such oscillations is imposed to be zero, such as when the oscillatory behavior is unstable).

The first situation occurs in systems with high natural frequencies or high values for inertial parameters ($r_\alpha^2\mu$). The second and the third situations are usually observed for systems with small values for inertial parameters or natural frequencies. Furthermore, when the elastic axis is shifted in direction of the trailing edge, the system tends to have more situations of unstable dynamics. Such tendency can be observed in Figure 2 with the increasing of zero values at low natural frequencies and inertial parameters for $x_{ea} > 0.35$. On the other hand, when x_{ea} is closer to the aerodynamic center of the airfoil at the quarter chord, damped situations are more common, which can be observed in Figure 2 by the presence of many zeros for the cost function at higher values of ω_α and $r_\alpha^2\mu$. In fact, such tendencies indicates the existence of an optimal point in the range of analyses where the harvested power is higher.

The proposal of a metamodel to fit the simulated data and to be used during the optimization process reduces the time demanded by all the simulations required by a conventional optimization. However, due to the high non-linearity associated with the analyzed cost function, the response surface methodology (RSM) and the use of radial base functions (RBF) have failed to interpolate the simulated data. Despite of the complexity of the problem, the Kriging methodology was able to capture the fluctuations in the values of the cost function with great fidelity.

Seven points were selected to validated the Kriging interpolation. The value of the cost function given by the Kriging method and the value from the simulation at each point as well as the difference between both quantities are presented in Table 1.

As observed in Table 1, the Kriging method was able to approximate the values of the cost function. Large differences between interpolated and simulated data can be observed when the cost function is one order of magnitude lower than typical values (in the order of 10^{-6}). However, this difference does not affect the minimization of the cost function because negatives values in the order of 10^{-7} are higher than other values observed in the order of 10^{-6}.

x_{ea}	$r_\alpha^2\mu$	ω_α (Hz)	Simulated value (W/s)	Interpolated value (W/s)	Difference (%)
0.290	3.00	0.70	-1.05$\times10^{-6}$	-1.06$\times10^{-6}$	1.62
0.295	2.50	0.15	-1.46$\times10^{-6}$	-1.44$\times10^{-6}$	-1.59
0.300	1.60	0.50	-1.26$\times10^{-6}$	-1.45$\times10^{-6}$	14.8
0.305	1.90	0.30	-1.54$\times10^{-6}$	-1.73$\times10^{-6}$	12.3
0.310	2.25	0.05	-2.06$\times10^{-6}$	-2.26$\times10^{-6}$	10.1
0.315	4.50	0.85	-3.45$\times10^{-7}$	-4.37$\times10^{-7}$	26.8
0.320	1.10	0.90	-2.14$\times10^{-6}$	-2.32$\times10^{-6}$	8.38

Table 1: Validation of the Kriging method for interpolation of the cost function.

Then, by considering the Kriging interpolation, the optimization process was evaluated. The optimal condition was indicated to be $x_{ea} = 0.336$, $r_\alpha^2\mu = 1$ and $\omega_\alpha = 0$Hz, which indicates a condition without structural stiffness. Moreover, the value for inertial parameters in the inferior limit imposed for the optimization process indicates that the energy harvesting from stall-induced pitching oscillations is improved in airfoils with low mass and moment of inertia. In such conditions, limit cycle oscillations are kept due to dynamic stall effects, as indicated by Figure 3 with the variation of the aerodynamic moment coefficient with the angle of attack. At high angles of attack, the strong pitching down moment which is a typical feature of dynamic stall effects tends to rotate the airfoil on the other direction and limit cycle oscillations can be observed.

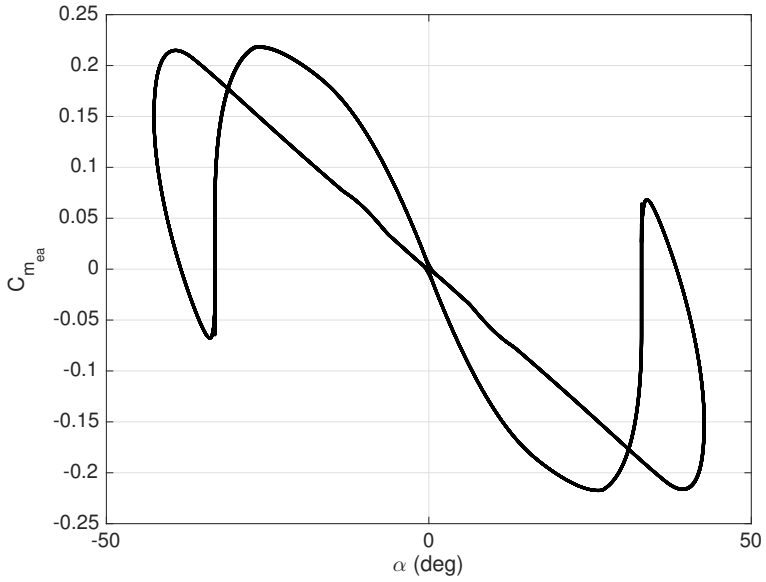


Figure 3: Aerodynamic moment coefficient at the elastic axis as function of the angle of attack for the optimal harvester at $V = 9.8$m/s.

Figure 4 indicates the Hopf diagram with the maximum amplitudes of oscillation for the optimal harvester as the wind speed varies. The amplitudes of oscillations are kept almost constant. In fact, the curve for the aerodynamic moment coefficient shown in Figure 3 is valid not only at $V = 9.8$m/s but also is characteristic for all the analyzed wind speeds with slight modifications in the maximum and minimum angles of attack.

However, aerodynamic loads during dynamic stall are supposed to vary with the reduced frequency of oscillation. Then, one can infer that the reduced frequency assumes constant values throughout the range of analyzed wind speeds. To investigate this hypothesis, Figure 5 shows the variation of the frequency of oscillation of the optimal harvester, i.e., the inverse of the period for a complete oscillation, as function of the wind speed. The frequency of oscillation varies linearly with the wind speed, which indicates that the reduced frequency, in fact, is almost constant to 0.29 in all the cases.

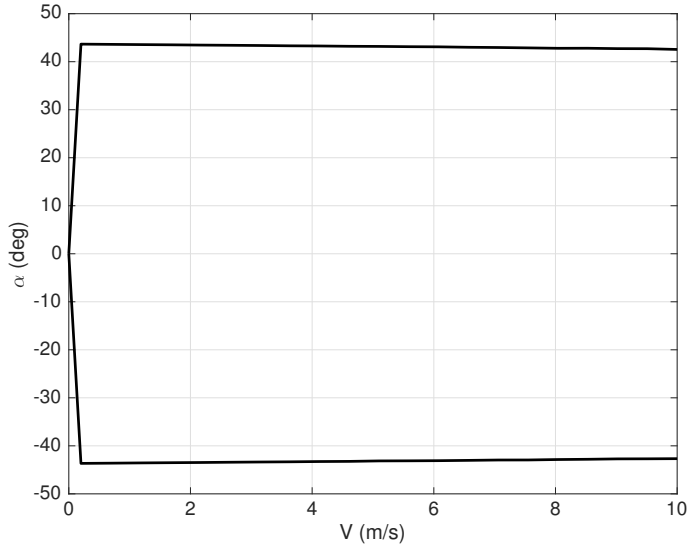


Figure 4: Hopf bifurcation diagram for the optimal harvester.

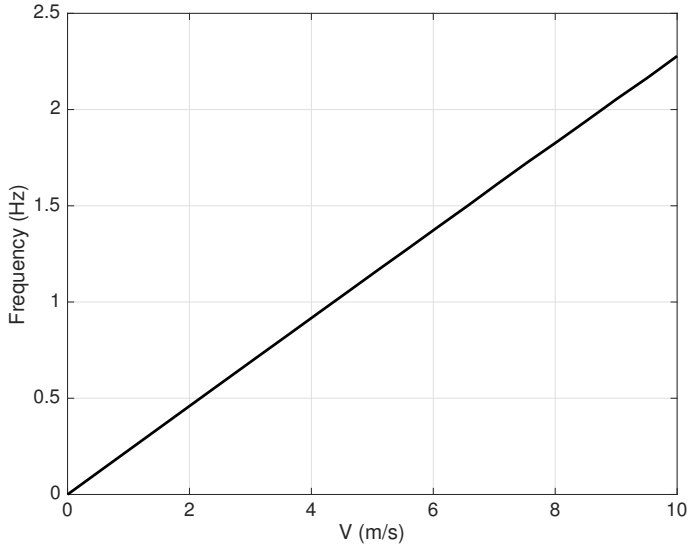


Figure 5: Variation of the frequency of oscillation with the wind speed for the optimal harvester.

The conditions indicated by the optimization process allow the harvester to oscillate even at small wind speeds due to absence of torsional stiffness or damping effects (which are not considered in this work). Such behavior increases the range of wind speeds where the harvester extracts energy from the oscillations, which minimizes the cost function. For the optimal harvester, the cost function is $\hat{g} = -3.545 \times 10^{-6}$W/s. The variation of the power RMS with the wind speed is showed in Figure 6.

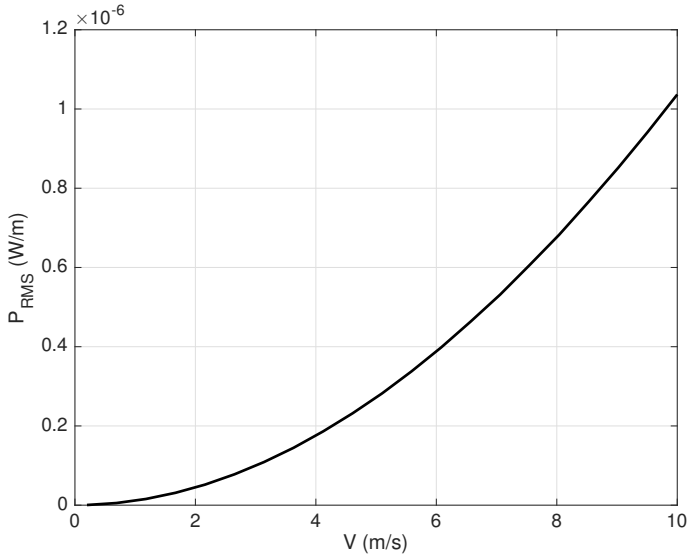


Figure 6: Variation of P_{RMS} with the wind speed for the optimal harvester.

4 Conclusions

The present work presented optimal values for an energy harvester from stall-induced oscillations by considering a NACA 0012 with chord 0.4m and an electric generator attached to the elastic axis of the structure. The optimization process was based on the Kriging interpolation of numerical data for the cost function given by simulations of an electroaeroelastic model. The Kriging approximation was validated to be applied to the problem. Results from the optimization process indicates that an optimal harvester from stall-induced oscillations has the elastic axis positioned at $x_{ea} = 0.336$. Furthermore, the optimal harvester is supposed to have no torsional stiffness and moment of inertia and mass of the airfoil as low as possible. In such conditions, oscillations are driven by dynamic stall effects at high angles of attack even at low wind speeds.

Acknowledgements

The authors acknowledge the financial support of: grants #2017/09468-6 and #2017/02926-9, São Paulo Research Foundation (FAPESP) and grant #307658/2016-3, National Council for Scientific and Technological Development (CNPq).

References

[1] A. Manan, G. A. Vio, M. Y. Harmin, J. E. Cooper, *Optimization of aeroelastic composite structures using evolutionary algorithms*, Engineering Optimization, Vol. 42, No. 2, Taylor & Francis (2010), pp. 171-184.

[2] M. C. Montoya, J. P. C. King, L. Kong, F. Nieto, S. Hernndez, *A method for improving the dynamic response of full bridge reduced-scale models in aeroelastic wind tunnel tests by using optimization algorithms*, Journal of Wind Engineering and Industrial Aerodynamics, Vol. 167, Elsevier (2017), pp. 198-216.

[3] B. Stanford, P. Beran, *Computational strategies for reliability-based structural optimization of aeroelastic limit cycle oscillations*, Structural and Multidisciplinary Optimization, Vol. 45, No. 1, Springer-Verlag (2012), pp. 83-99.

[4] B. Stanford, P. Beran, *Direct flutter and limit cycle computations of highly flexible wings for efficient analysis and optimization*, Journal of Fluids and Structures, Vol. 36, Elsevier (2013), pp. 111-123.

[5] S. Sarkar, H. Bijl, *Nonlinear aeroelastic behavior of an oscillating airfoil during stall-induced vibration*, Journal of Fluids and Structures, Vol. 24, No. 6, Elsevier (2008), pp. 757-777.

[6] J. Chen, A. Dhanushkodi, C. L. Lee, *Energy harvesting measurements from stall flutter limit cycle oscillations*, in *Proceedings of the SPIE Smart Structures and Materials + Nondestructive Evaluation and Health Monitoring, San Diego, United States, 2014 March 913*, Bellingham (2014), pp. G90570-1G90570-9.

[7] F. D. Marques, D. A. Pereira, M. Y. Zakaria, M. R. Hajj, *Power extraction from stall-induced oscillations of an airfoil*, Journal of Intelligent Material Systems and Structures.

[8] C. R. dos Santos, F. D. Marques, M. R. Hajj, *Structural nonlinearities influence on the energy harvesting from stall-induced oscillations*, in *2018 AIAA/ASCE/AHS/ASC Structures, Structural Dynamics, and Materials Conference, AIAA SciTech Forum, Kissimmee, United States, 2018 January 8-12*.

[9] J. G. Leishman, G. L. Crouse, *State-space model for unsteady airfoil behavior and dynamic stall*, in *Proceedings of the 30^{th} Structures, Structural Dynamics and Materials Conference, Mobile, United States 1989 April 3-5*, Mobile (1989), pp. 1372-1383.

[10] C. Chantharasenawong, *Nonlinear aeroelastic behaviour of aerofoils under dynamic stall*, Ph.D. Thesis, University of London, London (2007).

[11] J. G. Leishman, T. S. Beddoes, *A semi-empirical model for dynamic stall*, Journal of the American Helicopter Society, Vol. 34, No. 3, American Helicopter Society (1989), pp. 3-17.

[12] T. W. Simpson, J. D. Peplinski, P. N. Koch, J. K. Allen, *Metamodels for computer-based engineering design: survey and recommendations*, Engineering with Computers, Vol. 17, No. 2, Springer-Verlag (2001), pp. 129-150.

[13] G. Matheron, *Principles of geostatistics*, Economic Geology, Vol. 58, No. 8, Society of Economic Geologists (1963), pp. 1246-1266.

[14] S. S. Rao, *Engineering Optimization: Theory and Practice*, Forth edition, John Wiley & Sons, Hoboken, United States (2009).

[15] J. G. Leishman, T. S. Beddoes, *A generalised model for airfoil unsteady aerodynamic behaviour and dynamic stall using the indicial method*, in *Proceedings of the 42^{nd} Annual forum of the American Helicopter Society*, Washington (1986), pp. 243265.

On-line tracking of aircraft aeroelastic modes during flutter flight tests

B. Jacquier [1], **F. Ayme** [2]
[1] ONERA - The French Aerospace Lab - Department of Information Processing and Systems
2, avenue Edouard Belin - BP 74025 - 31055 TOULOUSE CEDEX, France
e-mail: **beatrice.jacquier@onera.fr**

[2] AIRBUS OPERATION SAS,
316, route de Bayonne - 31060 TOULOUSE CEDEX 9, France

Abstract
In the context of flutter flight tests, the paper describes the overall fully automatic process devised to perform a continuous tracking of the aeroelastic modes for an aircraft with a slowly time-varying structural behavior observed during the acceleration phases. On-line monitoring is realized through a sliding fixed-length time-window applied to time response of the aircraft to a persistent and periodic excitation signal. The identification algorithm dedicated to flutter flight tests is based on output-error formulation of the problem in the frequency domain. Parameters of a continuous time model are estimated iteratively. Tracking of modes for each new identified model is achieved using the MACXP criterion (mode association criterion based on modes shapes and poles). The process is applied to simulated data representative of the real aeroelastic behavior of a transport aircraft during an acceleration phase, including the simulation of the background noise.

1 Introduction

Among the various phenomenons that can affect the flight of an aircraft, flutter is one of the most feared one since this dynamic instability can lead to a sudden destruction of the airplane. Flutter flight tests represent a major stage in the certification procedure of a new aircraft. The objectives are to demonstrate the absence of instability throughout the flight envelop and to check the compliance of the aircraft actual behavior with predicted aeroelastic models.

The typical approach to flight flutter testing is to fly the aircraft at several stabilized test points arranged in increasing order of speed. Excitations are applied to the aircraft through the control surfaces and the measurements of the structure response are used to estimate aeroelastic modes. The damping ratio estimates obtained at each stabilized test point establish a trend as a function of airspeed which is used to evaluate the stability of the next higher airspeed test point and to clear the airplane to this point.

In the framework of a research program in collaboration with Airbus Operation SAS and Dassault aviation, a new approach was devised in order to reduce the duration of the flutter tests and consequently their cost. The idea is to replace some stabilized test points by a uniformly accelerated phase where the evolution of the modal parameters would be monitored continuously. This procedure would lead to a substantial reduction of the overall duration of the flutter tests. Moreover, security of the flight would be improved during all flight phases.

The paper describes the process devised to perform a continuous tracking of the aeroelastic modes for an aircraft with a slowly time-varying structural behavior observed during the acceleration phases. This modal

analysis problem is particularly challenging as it applies to time-varying systems and has to deal with highly noisy measurements.

Research efforts in this area have resulted in the development of recursive time-domain methods as recursive algorithms based on subspace [1] or auto regressive and moving average (ARMA) model [2]. Nevertheless, as we deal with slowly time-varying behavior, the use of frequency domain methods coupled with moving window over time is prefered as frequency domain methods permits to reduce the amount of data to process [3].

In the case of severe air turbulence, the effect of the excitation might be dominated by turbulence. In such situations, stochastic output-only identification approaches have been applied to the monitoring of flight test data [4, 5]. These methods are built upon the assumption that the system is excited by unknown inputs supposed to be white gaussian noises. But at the flight altitude of commercial aircraft, turbulent conditions are quite occasional. The data are only affected by a persistent background noise. So the proposed monitoring process is based on a deterministic identification method and on an efficient excitation of the structure.

The paper is organized as follows. The second section is devoted to the description of the context of flutter flight tests. The overall monitoring process is presented in the third section. Finally, the fourth section presents results on a simulation environment representative of the real aeroelastic behavior of a transport aircraft during an acceleration phase, including the simulation of the background noise.

2 Flutter flight tests context

2.1 Current flutter testing approach

Current flight tests are composed of several series of tests carried out when the aircraft is stabilized at a constant speed and constant altitude. Each series of tests is performed at a constant Mach number. As flutter likelihood increases with airspeed, these points are explored in increasing order of speed. Several hundred of test points are analyzed for a new aircraft.

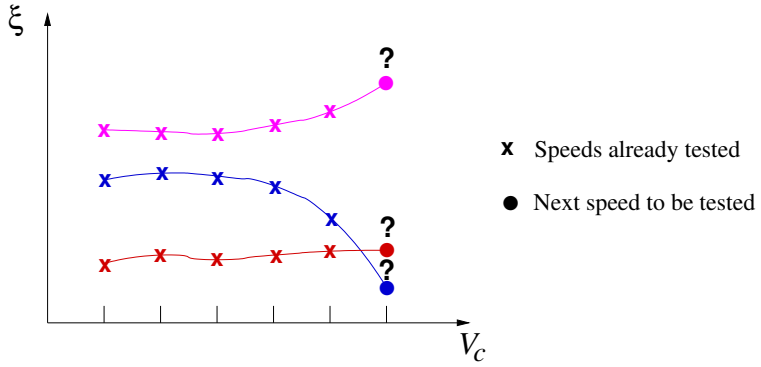


Figure 1: Extrapolation of damping ratios ξ

At each of these points, several tests are performed by applying excitations through the control surfaces to the aircraft structure. The measurements of the aircraft response are transmitted in real time by telemetry to the ground test center where parameters of a modal model are identified. As illustrated in figure 1, the damping estimates obtained at each stabilized test point establish a trend as a function of airspeed which is used to evaluate the stability of the next higher airspeed test point and to clear the airplane to this point. Measurements are provided by accelerometers distributed all over the structure. They give the structure movements along three directions. More than 100 sensors can be used.

2.2 New testing approach

The current test approach has two main drawbacks. First it is extremely time consuming since the aircraft has to be stabilized at specific test points, the tests have to be performed, the data processed and the results analyzed by the operator. The other weakness of this procedure is that flutter can appear in the acceleration phase between two test points where no monitoring of the aircraft stability is performed.

The idea of the new testing procedure is to replace some stabilized test points by a uniformly accelerated phase where the stability of the aircraft would be monitored continuously. This procedure eliminates the most hazardous part of flight flutter testing. It will also lead to a substantial reduction of the overall duration of flight tests.

For a precise and timely detection of any impending instability, the aircraft structure must be excited continuously during the acceleration phase.

2.3 Requirements for monitoring methods

The flight test conditions are not quite favorable to an accurate identification. Firstly, as the aircraft operates in operational conditions, the measurements are affected by the ambient noise due to the airflow around the aircraft. Sometimes, the data are also corrupted by air turbulence when the aircraft encounters wind gusts. Secondly, the excitations by the control surfaces are limited in amplitude, frequency and position. Therefore some of the structural modes are not excited efficiently. Then the algorithms should operate in rather adverse conditions.

Another demanding requirement is that the processing algorithms operate in a near real-time manner and produce results at a specified rate (at least every second) in the course of the acceleration phase. Moreover these results should have as little delay as possible compared to the actual system evolution. So it implies that the monitoring process should be fully automatic.

The results of the identification should also be reliable so that the monitoring underway should not be stopped unduly by incorrectly low damping estimates. On the other hand, the flutter onset should of course not happened unnoticed.

Though aeroelastic models of the aircraft structural dynamics are available before the first flight, the identification of the structural modes of the aircraft cannot make use of this a priori information. The reason is to prevent that any inaccuracies or errors in these aeroelastic models should affect the results of the modal analysis.

3 The monitoring process

3.1 The overall process

The procedure considered in this paper consists in a continuous automatic monitoring of the modal parameters during a uniformly slowly acceleration phase. The objectives are then to collect data, identify the aeroelastic modes and to follow the evolution of their modal parameters.

As the acceleration is slow, evolution of the modal parameters are supposed to be slow as well, then the approach chosen consists in applying a sliding fixed-length time window to the collected data. On this window the aeroelastic behavior of the aircraft is supposed to be linear and stationary. Linear time invariant identification methods can then be used to identify aeroelastic modes.

The identification method considered is in the frequency domain. The modal analysis can be focused on a frequency band were the excitation is effective. The direct consequence of that is a sheer decrease of the amount of data to process. This diminution has an immediate and favorable impact on the computation time.

The identification tool developed is based on a parametric approach. A common denominator polynomial transfer function has been chosen to model the system, since it is very convenient for modal modeling. The model is chosen in continuous-time.
A deterministic approach is preferred to a stochastic one because stochastic approaches require long data sequence to estimate the modal parameters with a sufficient statistical confidence level [6, 7, 8] which is conflicting with the necessity of the sliding window to be small enough for the aircraft behavior to be assumed time-invariant. Then excitation is one of the key point of the procedure, it will be detailed in paragraph 3.2. The modal analysis procedure is detailed in paragraph 3.3.

Monitoring of modal parameters, and so identification of a new model, are performed at a specified rate. Then another key point of the procedure is the mode tracking process; in order to monitor modal parameters evolutions, each aeroelastic mode has to be recognized from one identified model to another. In order to offer a good initialization to the modes tracking process, a first identification is performed during a stabilized phase. The tracking procedure is detailed in paragraph 3.4.

3.2 Excitation

Excitation of the structure is a key feature in the identification process. It is essential to excite all the modes of interest with a sufficient energy level in order to assess their stability correctly. In the case of continuous monitoring, this excitation has to be persistent.

We have chosen a PRBS (Pseudo Random Binary Sequence) type excitation signal. PRBS is a deterministic periodic sequence that switches between -1 and $+1$. The switches occur on a discrete-time grid at multiples of the clock period T_c and are chosen such that the autocorrelation approaches a Dirac [9]. This signal offers many advantages. Firstly, this is a periodic signal then, provided that the identification is performed in a finite number of periods of the signal, the leakage phenomenon is minimized. Secondly, its spectrum is relatively flat and the choice of the clock frequency permits to concentrate the power on a frequency band. According to [9], the optimal choice of the clock frequency is $f_c = 2.5\, f_{max}$ with f_{max} the maximum frequency of interest.

The excitation signal is applied simultaneously through a set of control surfaces with appropriate signs for the deflections. Compared to excitation through a single pair of control surfaces, the use of control surfaces combinations enables to maximize the energy transferred to the aircraft and to evenly distribute this energy over the different components of the structure. As explained in [10, 11], a single control surfaces symmetrical combination is enough to identify all the symmetrical modes of interest while a single control surfaces antisymmetrical combination is enough to identify all the antisymmetrical modes of interest.

3.3 Modal analysis tool

This paragraph details the modal analysis tool used to identify the aeroelastic modes for each position of the sliding window.

The general organization of the tool is depicted in figure 2. The procedure is composed of four main modules detailed in the next paragraphs. The inputs to this routine are the raw time-domain measurements from the sliding window and the frequency band for the modal analysis which depends on the excitation signals. The outputs are those of the identified modes which presumably correspond to structural modes.

Since the aircraft is excited by a unique excitation signal, the model chosen to describe its behavior in frequency domain is a transfer function $\mathsf{H}(s,\, \theta)$ between the excitation signal and the outputs, modeled as the ratio of a numerator (vector of polynomials) by a scalar denominator (polynomial). Thus

$$\mathsf{H}(s,\, \theta) = \frac{\mathsf{N}(s,\, \theta)}{\mathsf{d}(s,\, \theta)} \qquad \text{with} \quad \dim\, \mathsf{N}(s,\, \theta) = n_y \times 1 \quad \text{and} \quad \dim\, \mathsf{d}(s,\, \theta) = 1 \times 1 \tag{1}$$

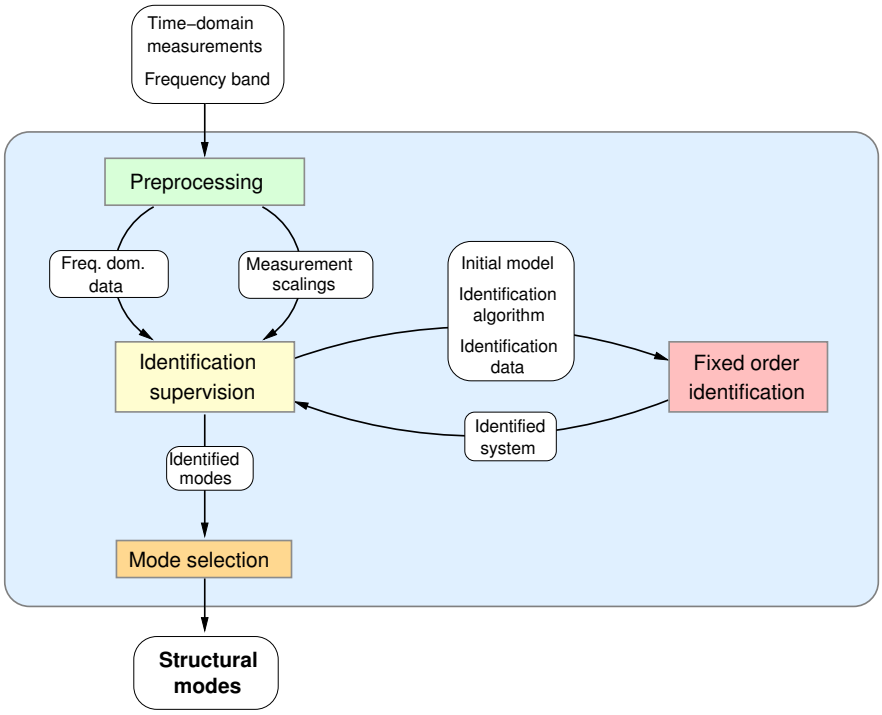


Figure 2: General organization of the identification procedure

where n_y denotes the number of outputs. The vector θ gathers the coefficients of the numerator and of the denominator. It is thus composed of $(n_y + 1)\ (n_x + 1)$ parameters. The excitation signal is not disturbed. So only measurement noise is considered and it is supposed to be Gaussian.

The identification problem is expressed as an output-error method in the frequency domain: the goal is to find the best parametric model such that the difference between the preprocessed measured outputs and the outputs calculated with the parametric model is minimized.

3.3.1 Pre-processing module

Computation of estimated inputs and outputs in the frequency domain is realized in the pre-processing module (pale green box in figure 2). As the excitation signal is periodic and provided that the length of the window corresponds to a finite number M of periods of the excitation signal, the frequency response function (FRF) may be estimated using averaging techniques. Let $u(n)$ and $Y(n)$ respectively the samples of the excitation signal and of the outputs on the sliding time window, Δt the sampling period of those signals and N_p the number of samples in one period of the excitation signal. The number of samples in the window is then MN_p. The FRF estimate at frequency $f = \dfrac{k}{N_p\,\Delta t} \quad (k = 0, \ldots, N_p - 1)$ is:

$$\hat{H}(j\,2\,\pi\,f) = \frac{\hat{Y}_f}{\hat{u}_f} \tag{2}$$

with $\hat{u}_f$ and $\hat{Y}_f$ the average of the Discrete Fourier Transforms (DFT) of respectively the excitation and the outputs on the M periods (which is the same as the DFT of the average of the time samples on the M periods), at frequency f.

$$\hat{u}_f \;=\; \frac{1}{M}\sum_{m=0}^{M-1} u_f^{[m]} = u_f \quad \text{and} \quad \hat{Y}_f \;=\; \frac{1}{M}\sum_{m=0}^{M-1} Y_f^{[m]} \tag{3}$$

with $u_f^{[m]}$ and $U_f^{[m]}$ the DFT of respectively the excitation and the outputs on the m^{th} period

$$u_f^{[m]} = \frac{1}{\sqrt{N_p}} \sum_{n=0}^{N_p-1} u(n+lN_p)e^{-j2\pi fn\,\Delta t} \quad \text{and} \quad Y_f^{[m]} = \frac{1}{\sqrt{N_p}} \sum_{n=0}^{N_p-1} Y(n+lN_p)e^{-j2\pi fn\,\Delta t} \tag{4}$$

As the excitation signal is not disturbed its average DFT equals the DFT in one period.
An estimate of the noise covariance matrix at frequency f is also given by

$$\hat{\Sigma}_f = \frac{1}{M-1} \sum_{m=1}^{M} \left| Y_f^{[m]} - \hat{Y}_f \right|^2 \tag{5}$$

The pre-processing module also carries out the selection of the good quality measurements and the computation of measurement scalings for the identification algorithms. These quantities are based on an estimation of a signal-to-noise $(\mathrm{S/N})_l$ ratio computed in the frequency domain from each measurement l.

$$(\mathrm{S/N})_l = \frac{\sigma_{s_l}}{\sigma_{n_l}} \tag{6}$$

with σ_{s_l} and σ_{n_l} the standard deviations of, respectively of the estimated output l and the estimated noise on the output l, on the frequency band of interest $\mathcal{F} = [f_{\min}\ f_{\max}]$. They are given by

$$\sigma_{s_l} = \sqrt{\frac{2}{N_p} \sum_{f\in\mathcal{F}} |\hat{y}_{l,f}|^2} \quad \text{and} \quad \sigma_{n_l} = \sqrt{\frac{2}{N_p} \sum_{f\in\mathcal{F}} \hat{\Sigma}_f(l,\, l)} \tag{7}$$

where $\hat{y}_{l,f}$ is the l^{th} component of $\hat{Y}_f$.
The selection of the measurements is then performed by discarding the measurements with an estimated $(\mathrm{S/N})_l$ ratio below a certain threshold.

As detailed below, the identification routines are based on a non-linear least-square fitting in the frequency domain. It is necessary to apply scalings on the measurements in order to account for the various magnitudes and levels of quality.
In conventional output-error approaches, the noise on the measurements is assumed to be white and Gaussian. The measurements are weighted by the inverse of the noise covariance matrix $\hat{\Sigma}_f$ [9]. The approach adopted departs from these theoretical precepts for several reasons.
In the first place, the nature of the noise on the measurements does not comply with the white Gaussian hypothesis. This conventional weighting might also lead to attribute similar weights to measurements with various levels of quality. The fitting of poor quality measurements would lead to the identification of spurious modes and to a wider scatter of the estimated damping ratios. It is then essential to account for the quality of the data in the scalings of the measurements. The measurement magnitudes also vary largely depending on the location of the sensors on the aircraft. For instance, the sensors on the wing tips yield much greater values that those on the fuselage. The scalings should compensate for this variability in order that the modes associated to the different components of the structure be identified precisely.
For each measurement l, the associate scaling ρ_l was defined in the following manner

$$\rho_l = \frac{\delta_l}{\sigma_{s_l}} \tag{8}$$

where σ_{s_l} is the average magnitude of this signal defined in equation (7). The objective of this coefficient is to equalize the magnitude of the aircraft responses for all the measurements. The factor δ_l reflects the quality of each measurement. It is defined as a quantity bounded by 0 and 1. The value 0 is the minimum level of quality which implies that the measurement is not taken into account in the identification. This factor was chosen equal to

$$\delta_l = \frac{(\mathrm{S/N})_l^2}{1 + (\mathrm{S/N})_l^2} \tag{9}$$

3.3.2 Identification module

The identification module (pink box in figure 2) carries out the identification of a model of a given order. The identification objective, in the frequency domain, is to find the best fit between the outputs calculated with the parametric model $\mathsf{H}(s,\,\theta)$ and the estimated outputs in frequency domain $\hat{Y}_f$. Only data for the frequencies f of interest in the set $\mathcal{F}$ are considered. The output-error identification problem boils down to finding the set of parameters θ that minimizes the following criterion

$$J(\theta) \;=\; \sum_{f\,\in\,\mathcal{F}} \left\| (\hat{Y}_f - \mathsf{H}(j2\pi f,\,\theta)\,u_f) \right\|_W^2 \;=\; \sum_{f\,\in\,\mathcal{F}} (\hat{Y}_f - \mathsf{H}(j2\pi f,\,\theta)\,u_f)^H\, W^2\, (\hat{Y}_f - \mathsf{H}(j2\pi f,\,\theta)\,u_f) \tag{10}$$

where $W = \mathrm{diag}(\rho_l)$ and ρ_l are the scalings defined in equation (8). As the vector θ is composed of the polynomial coefficients of the numerator and the denominator, the quantities $\mathsf{N}(j2\pi f,\,\theta)$ and $\mathsf{d}(j2\pi f,\,\theta)$ depend linearly on θ. However, $\mathsf{H}(j2\pi f,\,\theta)$ does not. So the optimization problem defined by equation (10) is non-linear.

During the development of the modal analysis procedure, it was found that a thorough optimization significantly improve the quality of the results. This precise optimization of the identification criterion implies the use of iterative algorithms. The procedure is based on two algorithms:

- the Sanathanan-Koerner method [12]: this algorithm is an iterative method where, in order to circumvent the non-linearity induced by the denominator, one utilizes the frequency values of the denominator $\mathsf{d}(j2\pi f,\,\tilde{\theta})$ computed with the vector $\tilde{\theta}$ estimated at the previous iteration.
- the Whitfield formulation of the Gauss-Newton algorithm [13]: the basic principle of this method is to replace $\mathsf{H}(j2\pi f,\,\theta)$ in equation (10) by its first-order development about $\tilde{\theta}$, values of the parameters of the previous iteration.

The Sanathanan-Koerner method offers two main advantages. First, it does not require any initial model. Second, it is known for its robustness to provide a fair estimation of the model parameters. However, no general proof of convergence was established. The evaluation of this method revealed that it does not converge to a local minimum of the identification criterion of equation (10). On the contrary, the Gauss-Newton algorithm requires a sufficiently precise initialization. But this method is very efficient to converge to a local optimum of the identification criterion if properly initialized. As detailed in paragraph 3.3.3 and similarly to the approach adopted in [14], one could benefit from the complementary of these two approaches by using them in combination.

The details of the implementation of these algorithms are not presented in this paper. Anyhow, it is worth mentioning that it is based on orthogonal polynomials [15, 16, 17] in order to improve the numerical stability and the execution speed of the codes.

3.3.3 Supervision module

The goal of the supervision module (yellow box in figure 2) is to control the execution of the identification so that the modal analysis operates entirely automatically. It first manages the use of the two identification algorithms. It also determines the best model order.

A first model with a deliberately oversized order $n_{x_{\max}}$ is identified using the Sanathanan-Koerner algorithm in conjunction with the Gauss-Newton algorithm as in [14]. The philosophy is to use the Sanathanan-Koerner method as an "explorer" in order to find out a good initial guess for the identified model. For this reason, this method does not include any monitoring to ensure the decrease of the identification criterion between successive iterations. During the first identification from the initial stabilized phase, the Sanathanan-Koerner algorithm is initialized from scratch. Whereas during the acceleration phase, in order to minimize

the iterations number, the previous identified model is used to initialize the algorithm. The best model obtained with the Sanathanan-Koerner algorithm, i.e. the one with the smallest value of $J(\theta)$, is then refined by the Gauss-Newton algorithm. A line-search technique was implemented in this method to force the minimization of $J(\theta)$.
The selection of the order $n_{x_{\max}}$ of the initial model is rather crucial. It should be chosen high enough in order to encompass all the modes excited in the test. However a too large value will lead to a longer and more complex mode elimination process. Thus, the selection of an appropriate value for $n_{x_{\max}}$ requires a slight preliminary experience to have a clue of the number of modes that can be identified for the type of test under analysis.

Once this initial model of order $n_{x_{\max}}$ is obtained, the supervision module will scrutinize the relevance of each identified mode so as to decide whether to keep it or discard it from the identified model. The general idea is to test each mode of this model by analyzing whether, without this mode, the identification model still fits suitably to the data. The quality of the fit is evaluated by the two following adequacy criteria

$$\mathcal{C}(\theta) = \left(\frac{\sum\limits_{f \in \mathcal{F}} \left\| (\hat{Y}_f - \mathsf{H}(j2\pi f,\, \theta)\, u_f) \right\|_W^2}{\sum\limits_{f \in \mathcal{F}} \left\| \hat{Y}_f \right\|_W^2} \right)^{1/2} = \left(\frac{J(\theta)}{\sum\limits_{f \in \mathcal{F}} \left\| \hat{Y}_f \right\|_W^2} \right)^{1/2} \tag{11}$$

and

$$c_l(\theta) = \left(\frac{\sum\limits_{f \in \mathcal{F}} |\hat{y}_{l,f} - \mathsf{h}_l(j2\pi f,\, \theta)\, u_f|^2}{\sum\limits_{f \in \mathcal{F}} |\hat{y}_{l,f}|^2} \right)^{1/2} \tag{12}$$

where $\hat{y}_{l,f}$ and $\mathsf{h}_l(j2\pi f,\, \theta)$ are the l^{th} components of $\hat{Y}_f$ and $\mathsf{H}(j2\pi f,\, \theta)$. The measurement criteria $c_l(\theta)$ are used because some modes may have a local effect on the structure. So their contribution could be significant but limited to a small number of measurements. In this situation, the consideration of the sole global criterion $\mathcal{C}(\theta)$ may result in the improper exclusion of such modes. The significance of the modes of the initial model are evaluated in a three-stage process. Let θ designates the identified parameters of the initial model of order $n_{x_{\max}}$. First, for each mode i, a reduced transfer function is computed by discarding the mode from the identified model. The associated parameters of this reduced model are denoted $\widetilde{\theta}_i$. In a second stage, the *a priori* quality of fit of these models is evaluated by computing the criteria $\mathcal{C}(\widetilde{\theta}_i)$ and $c_l(\widetilde{\theta}_i)$. The mode for which these values remain close to the corresponding criteria $\mathcal{C}(\theta)$ and $c_l(\theta)$ of the full model are selected as potential candidates for elimination. Finally, for each candidate, an identification is launched based on the sole Gauss-Newton algorithm initialized by $\widetilde{\theta}_i$. This identification yields an optimized set parameters denoted $\widehat{\theta}_i$. The elimination of the mode is confirmed if the criteria $\mathcal{C}(\widehat{\theta}_i)$ and $c_l(\widehat{\theta}_i)$ associated with these parameters remain close to the corresponding criteria $\mathcal{C}(\theta)$ and $c_l(\theta)$ of the full model.

3.3.4 Selection module

At this stage, the identified model reflects the overall behavior of the aircraft in the frequency band of interest. However this model might include modes that are not associated with the structural dynamics of the aircraft such as actuators modes, aerodynamic delays, ... It is then necessary to select amongst the identified modes the sole modes which are presumably connected with the structural dynamics. This selection is performed in the final phase of the procedure (orange box in figure 2).

3.4 Tracking tool

In order to follow modes characteristics evolutions, each time a new model is identified, its modes are compared to the modes of the previous identified one in order to pair them.

This mode association is based on a criterion that is a pole weighted version of an extension of the classical MAC criterion [18] (Modal Assurance Criterion) to complex modes. This dedicated criterion called MACXP is described in [19]. Compared to this criterion we have added the use of the measurement scalings to scale the modes shapes in order to be consistent with the identification process. The criterion which compares two modes whose poles are respectively λ_1 and λ_2 and mode shapes μ_1 and μ_2 is:

$$\text{MACXP}(\mu_1,\, \mu_2) = \frac{\left(\frac{|\mu_1^*\, W^2\, \mu_2|}{|\overline{\lambda}_1+\lambda_2|} + \frac{|\mu_1^\top\, W^2\, \mu_2|}{|\lambda_1+\lambda_2|} \right)^2}{\left(\frac{\mu_1^*\, W^2\, \mu_1}{2\,|\text{Re}\,\lambda_1|} + \frac{|\mu_1^\top\, W^2\, \mu_1|}{2\,|\lambda_1|} \right) \left(\frac{\mu_2^*\, W^2\, \mu_2}{2\,|\text{Re}\,\lambda_2|} + \frac{|\mu_2^\top\, W^2\, \mu_2|}{2\,|\lambda_2|} \right)} \tag{13}$$

Two modes are considered associated if the value of their MACXP criterion is greater than 0.6.

The tracking process is initialized storing the modal characteristics of the modes identified during the initial stabilized phase in a reference structure. Then, for each new position of the sliding window (iteration i), a new model is identified and modal characteristics of its modes are compared to those stored in the reference structure with the MACXP criterion. When a mode of this new model is paired, its characteristics are updated in the reference structure. For the non paired modes, they are compared with modes of iteration $i-2$ which are stored as well in another structure. This second comparison allows to reduce the number of mode chains breaks. For modes which are still non paired, their characteristics are stored behind the others in the structure in order to be compared with modes of next identified models. Hence apparition of a new mode would not be missed.

4 Results on simulated data

4.1 Description of the benchmark

The simulation environment used in this study has been developed in the framework of the TRAMPOLINE working group of the FLITE2 project [20].

The simulation is based of an elaborate aeroelastic model provided by Airbus. This is a linear model derived for a given Mach number from a finite element modeling of the aircraft. It is parametrized by the conventional speed V_c. Its inputs are the deflections of the control surfaces and the components of the turbulence wind. Its 13 outputs are accelerometric measurements at different locations on the structure. The original model was modified for industrial confidentiality reasons and also for presenting an evolution towards flutter.
Expressed in a parametrized state-space form, the size of its state vector is 328. It includes 42 structural modes ranging between 1 and 11 Hz and 244 delay modes. The frequency band $\mathcal{F}$ retained for modal analysis is 1 to 6 Hz. 27 aeroelastic modes lie in the frequency band.

Aircraft response to the stimulations applied on the control surfaces takes into account the actuators dynamics, modeled as a second-order linear model.

Turbulence inputs of the model are used to simulate aircraft response to the background noise. This one is modeled as a low intensity turbulence. Parameters of the noise model are tuned by the spectral analysis of real flight test data.

A sampling rate of $f_e = 128$ Hz is chosen for the simulated measurements as it corresponds to the rate used for flight data recording. Simulation of this high order, parameter varying system is performed using a Runge-Kutta method to integrate the evolution of the state vector.

As explained in paragraph 3.2, we have chosen a PRBS type excitation signal. We choose a period of $N_p = 2040$ points (≈ 16 s). The maximum frequency of interest is $f_{max} = 6$ Hz then the optimal choice of the clock frequency of the signal is $f_c = 2.5\ f_{max} = 15\ Hz \approx f_e/8$. Then a period of the signal is obtained from a PRBS of length $N = 255$, each value of the signal being held during 8 sampling periods.
Excitation signal is applied simultaneously and antisymmetricaly to ailerons, elevators and rudder.

The simulated scenario is made up of two phases: the initial phase where the conventional speed is fixed and the acceleration phase which consists in a slow acceleration.

4.2 Identification of the initial model

A first identification process in launched during a phase of duration 4 periods of the excitation signal (64 s) where the airspeed is stabilized at 330 kts. The response of the aircraft to the periodic excitation signal is supposed to be in steady-state. The aim is to provide a good initialization to the monitoring process.

Results of a Monte Carlo type analysis of this process are presented in figure 3 for a set of 100 simulated tests generated with different noise sequences but with the same response to the excitation signal. Statistics are computed from the series of 100 identification results. The computation of these statistics requires the pairing between the identified modes and the simulated ones. This mode association is based on the MACXP criterion presented in paragraph 3.3.3.

The values of the signal-to-noise ratios defined in paragraph 3.3.1 vary from one measurement to another form 9 dB up to 28 dB. The threshold below which measurements are discarded is fixed to 12 dB. On average, 11 measurements are selected out of the 13 available.

An order $n_{x_{\max}} = 32$ is chosen for the initial model (initialization of the supervision module described in paragraph 3.3.3).

The upper part of the figure depicts the location of the identified modes for the 100 Monte Carlo runs. These modes are plotted in the frequency–damping ratio plane together with the 27 modes of the simulation model which are indicated by the encircled numbers. The mode 8 does not appear because of the high value of its damping ratio. The identified modes that can be paired based on the value of the MACXP criterion with a simulation mode are plotted with red dots.

The identification rates of the 27 aeroelastic modes are presented on the bar diagram on the middle part of the figure. The identification rate of a mode is simply the ratio between the number of times this mode is identified and the number of runs of the Montecarlo test.

Finally, the relative RMS (Root Mean Square) errors on the damping ratios are depicted on the bar diagram of the lower part of the figure. RMS error is only computed for the modes with an identification rate superior to 0.6.

12 modes are identified with an identification rate superior to 0.6 and 7 modes with an identification rate superior to 0.95 and the relative RMS error an damping ratio of this 7 modes is inferior to 26%.

4.3 Monitoring during the accelerated phase

At the end of this stabilized phase, aircraft response behavior to the excitation signal during a continuous acceleration has been simulated. This acceleration phase consists in a slow acceleration of 30 kts on the conventional speed from 330 to 360 kts performed in 5 min which corresponds to 1 kts every 10 seconds.

The length of the sliding window is chosen at 2 periods of the excitation signal (32 s) and the monitoring rate is fixed at 1 s. A new model then is identified each second and its modes are compared and paired with the previously identified ones. The tracking process is initialized with the modes identified during the initial phase. At the end of this process, we get “chains” of modes. We choose to retain chains composed of at least 50% of identification points.

Unlike identification of the initial model results presented in the previous paragraph, monitoring results during the accelerated phase are presented for a single simulated test. They are presented in figures 4 and 5. The upper part of figure 4 shows the evolution with time of the frequency of each retained modes chains whereas the lower part presents the evolution of their damping ratio with time. Figure 5 contains the same

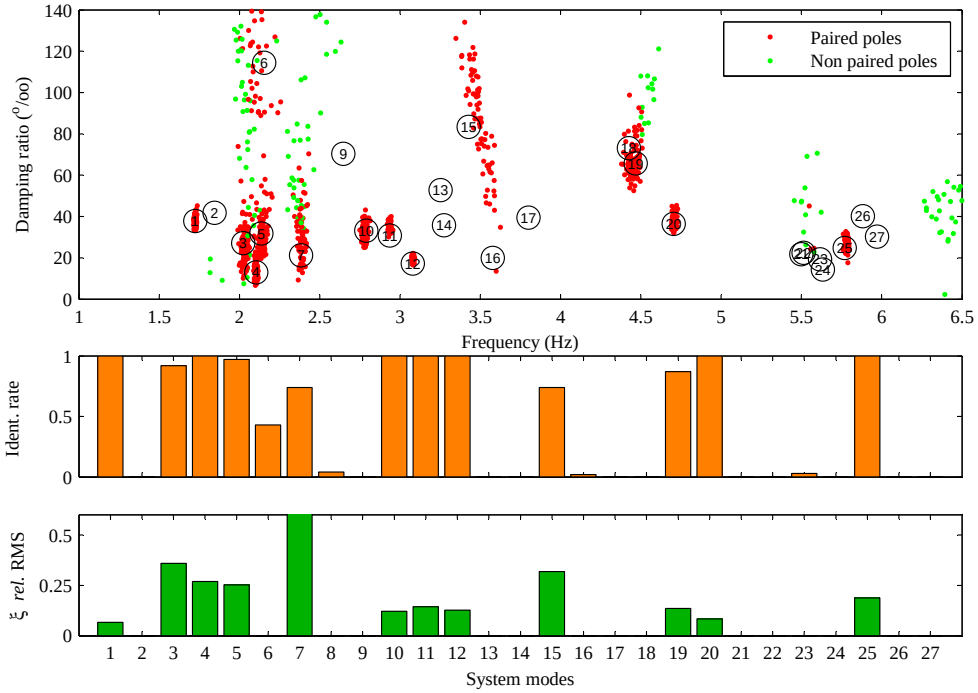


Figure 3: Identification on stabilized flight point at Vc=330kts - Monte Carlo analysis

results but with a detailed mode by mode presentation. Evolution with time of frequency and damping ratio of simulated modes are also plotted on those figures.

The monitoring tool manages to track 7 modes for a long time. Those modes correspond to modes 1, 4, 5, 10, 11 12 20, 25 of the simulated model. Compared to Monte Carlo results of the initial identification on stabilized phase of figure 3, we notice that in this case those modes are identified with an identification rate up to 0.95. So results of the monitoring process are in accordance with the Monte Carlo analysis.
Identified modal frequencies are very precise whereas identified modal damping ratios are scattered. This is again in accordance with the results of the Monte Carlo analysis of figure 3 which shows the scattering in damping ratio caused by the background noise acting in the aircraft.
Damping ratio of mode 4 of the simulated model decreases until instability. This decrease is also observed on the evolution of the damping ratio of the corresponding identified mode (mode 2 on figure 5).

The overall process was fully implemented in MATLAB computing environment. The procedure was run a computer equipped with an Intel Core I5 processing unit with 2 cores and a 2.6 Ghz clock rate. The mean duration of the monitoring process, i.e. the duration to perform 280 runs of identification and tracking tools, is 54 s. Analysis of one flight point takes on average 0.19 second.

5 Conclusion

A fully automatic process to perform continuous tracking of aeroelastic modes during a slow acceleration phase has been presented. It is based on the use of a persistent and periodic excitation signal, applied to the structure through a combination of control surfaces, to efficiently excite the modes on the frequency band of interest.
On-line monitoring is realized through a sliding fixed-length time-window in which the system behavior can be assumed time-invariant.
One of the key features of the process is the identification algorithm dedicated to flutter flight tests. It is

based on a parametric approach in the frequency domain. Parameters of a SIMO continuous time model are estimated by minimizing iteratively the error between the preprocessed measured outputs and the outputs calculated with the model. This algorithm is fully automatic, numerically robust and operating in quasi-real time. Another essential feature of the process is the tracking of modes for each new identified model. Comparison and pairing of modes are achieved using the MACXP criterion.

Application of this process to a realistic simulation of the aircraft response during an acceleration phase, proved that the performance of the procedure is quite satisfactory taking into account the very noisy environment. We have shown that all the modes which have been efficiently identified during an initial stabilized phase are successfully identified and tracked during the acceleration phase. Moreover, evolution of their frequency and damping ratio are consistent with the simulated ones, particularly, the ability of the procedure to follow the decrease in damping ratio of a mode has been proved.
Finally, the execution times are completely compatible with an operational use.

In the framework of this research project, dedicated flight tests are planned in order to evaluate the procedure on real data.

Acknowledgements

The procedure was developed in the framework of the SEFA-IKKY project in cooperation with Airbus Operation SAS and Dassault Aviation and funded by the French civil aviation board (DGAC). The authors would like to thank Claire Meyer at Dassault Aviation, Jean Roubertier and Adrien Pavie at Airbus Operation SAS for their technical support and expertise on the aeroelastic models and flutter tests.

References

[1] K. De Cock, G. Mercère, B. De Moor, *Recursive subspace identification for in-flight modal analysis of airplanes*, in *Proceedings of International Conference on Noise and Vibration Engineering (ISMA), Leuven, Belgium, 2006 Sep. 18-20*, pp. 1563–1577.

[2] T. Uhl, M. Petko, G. Karpiel, A. Klepka, *Real time estimation of modal parameters and their quality assessment*, Shock and Vibration, vol. 15, no. 3-4, IOS Press (2008), pp. 299–306.

[3] R. Pintelon, P. Guillaume, Y. Rolain, J. Schoukens, H. Van Hamme, *Parametric identification of transfer functions in the frequency domain - a survey*, IEEE Transactions on Automatic Control, vol. 39, IEEE (1994) pp. 2245–2260.

[4] J. Schwochow, G. Jelicic, *Automatic operational modal analysis for aeroelastic applications*, in *Proceedings of the International Operational Modal Analysis Conference (IOMAC), Gijón, Spain, 2015 May 12-14*.

[5] G. Jelicic, J. Schwochow, Y. Govers, J. Sinske, R. Buchbach, J. Springer, Böswald, *Online monitoring of aircraft modal parameters during flight test based on permanent output-only modal analysis*, in *Proceedings of the 58th AIAA/ASCE/AHS/ASC Structures, Structural Dynamics and Materials Conference, Grapevine, Texas, USA, 2017 3–13 jan.*.

[6] M. Kehoe, *A historical overview of flight flutter testing*, tech. rep., NASA, Dryden Flight Research Center, Edwards, California (1995).

[7] E. Parloo, *Application of frequency-domain system identification techniques in the field of operational modal analysis*, PhD thesis, Vrije Universiteit Brussel, Brussels (2003).

[8] B. Peeters, P. Karkle, M. Pronin, R. Van der Vorst, *Operational modal analysis for in-line flutter assessement during wind tunnel testing*, in *Proceedings of the International Conference on Noise and Vibration Engineering (ISMA), Leuven, Belgium, 2011 September*.

[9] R. Pintelon and J. Schoukens, *System identification: A frequency domain approach*, John Wiley & Sons, Inc., 2^{nd} ed., (2012).

[10] B. Jacquier, P. Vacher, A. Bucharles, A. Cordeau, and S. Leroy, *Improved flutter testing by coordinated excitations of several control surfaces*, in *Proceedings of the Society of Flight Test Engineers European Chapter (SFTE-EC) symposium, Toulouse, France, 2011 14 - 16 June*.

[11] P. Vacher, B. Jacquier, and A. Bucharles, *Design of linear input combinations for improved modal analysis of mimo systems*, Journal Européens des Systèmes Automatisés (JESA), vol. 46, no. 6-7, Lavoisier (2012), pp. 741–761.

[12] C. Sanathanan and J. Koerner, *Transfer function synthesis as a ratio of two complex polynomials*, IEEE Transactions on Automatic Control, vol. 9, IEEE (1963), pp. 56–58.

[13] A. Whitfield, *Asymptotic behaviour of transfer function synthesis methods*, International Journal of Control, vol. 45, no. 3, Taylor and Francis (1987), pp. 1093–1101.

[14] D. S. Bayard, *High-order multivariable transfer function curve fitting: algorithms, sparse matrix methods and experimental results*, Automatica, vol. 30, IFAC (1994), pp. 1439–1444.

[15] Y. Rolain, R. Pintelon, K. Xu, and H. Vold, *Best conditioned parametric identification of transfer function models in the frequency domain*, IEEE Transactions on Automatic Control, vol. 40, IEEE (1995), pp. 1954–1960.

[16] G. E. Forsythe, *Generation and use of orthogonal polynomials for data–fitting with a digital computer*, Journal of the Society for Industrial and Applied Mathematics, vol. 5, SIAM (1957), pp. 74–88.

[17] P. Vacher and A. Bucharles, *A multi-sensor parametric identification procedure in the frequency domain for the real-time surveillance of flutter*, in *Proceedings of IFAC Symposium on System Identification (SYSID), Newcastle, Australia, 2006 March*.

[18] R. Allemang, *The modal assurance criterion - twenty years of use and abuse*, Sound and Vibration Magazine, vol. 37, no. 8, (2003), pp. 14 – 21.

[19] P. Vacher, B. Jacquier, and A. Bucharles, *Extensions of the MAC criterion to complex modes*, in *Proceedings of International Conference on Noise and Vibration Engineering (ISMA), Leuven, Belgium, 2010 september 20-22*.

[20] P. Vacher and A. Bucharles, *Realistic simulation of flutter flights tests*, in *Proceedings of International Conference on Noise and Vibration Engineering (ISMA) - Invited session Flite 2 EUREKA, Leuven, Belgium, 2008 September*.

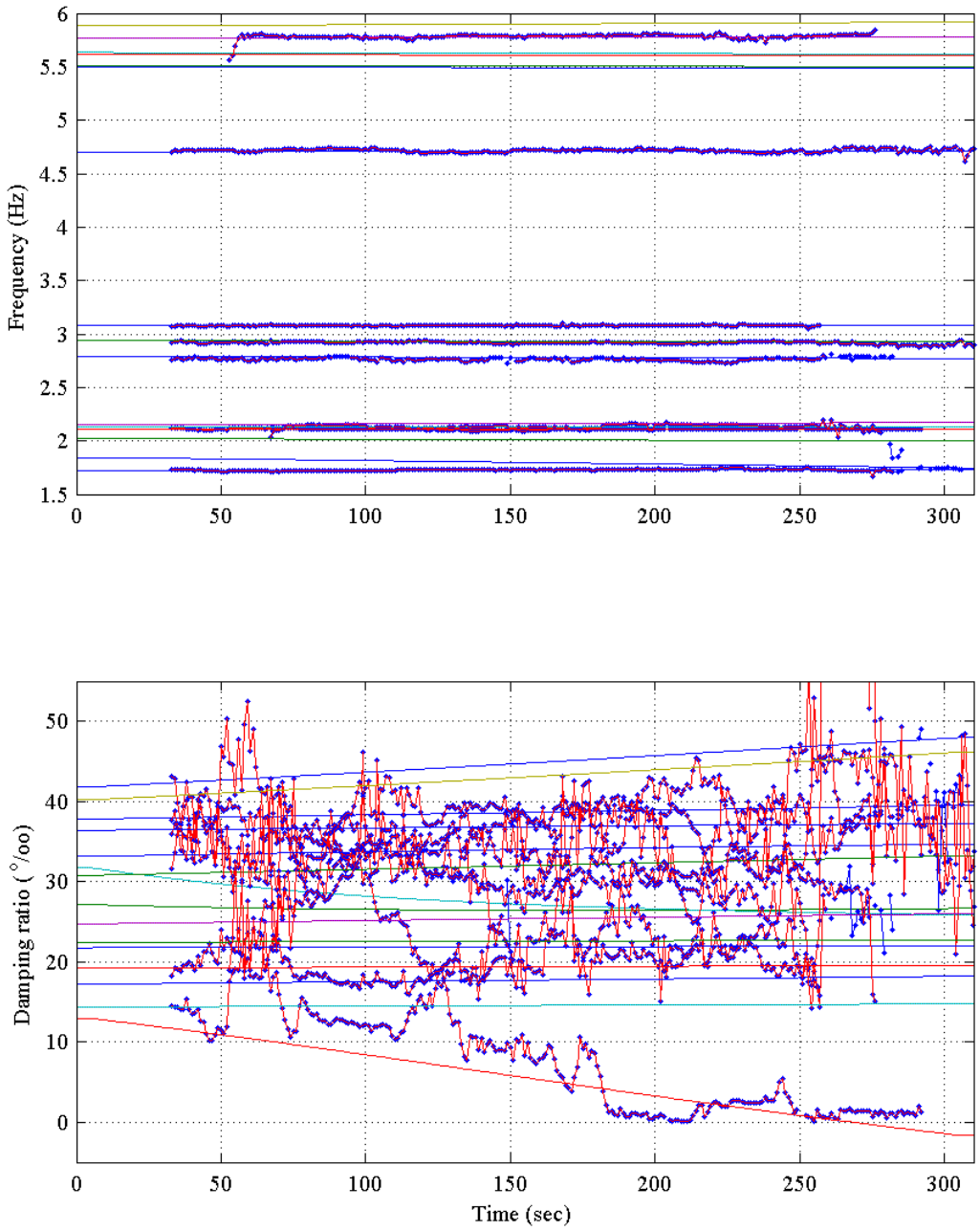


Figure 4: Monitoring during the acceleration phase from 330kts to 360kts

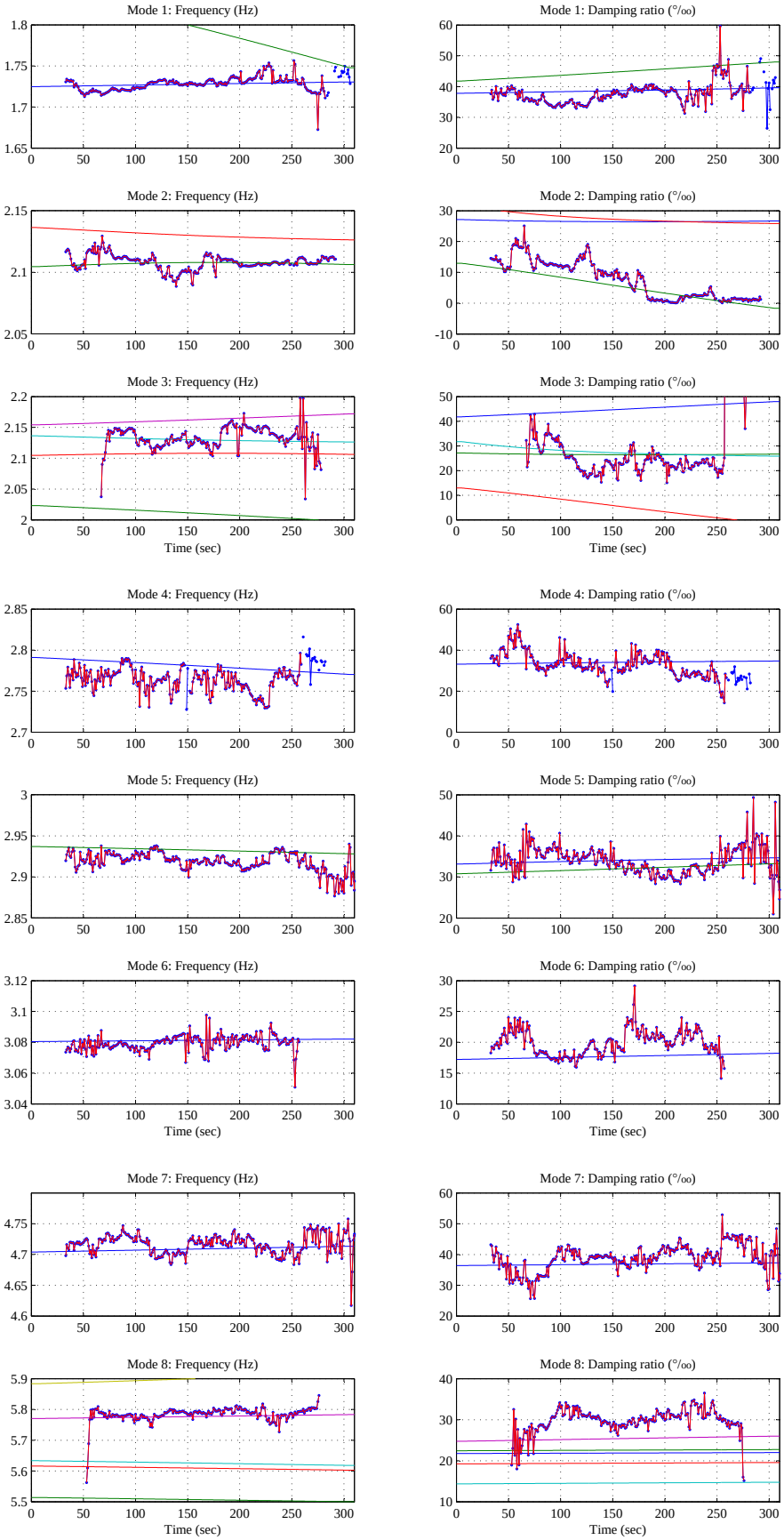


Figure 5: Monitoring during the acceleration phase from 330kts to 360kts (detail mode by mode)

On the effect of control surface deflections on the aeroelastic response of an aerofoil at transonic buffet conditions

N.F. Giannelis [1] **& G.A. Vio** [1]
[1] School of Aerospace, Mechanical and Mechatronic Engineering,
The University of Sydney, NSW, 2006, Australia
e-mail: **nicholas.giannelis@sydney.edu.au**

Abstract
At certain conditions in the transonic flight regime, interactions between oscillating shock waves and a forced or freely oscillating structure may incite frequency lock-in between the aerodynamic and structural modes, resulting in large amplitude limit cycle oscillations. This study investigates the influence of both static and dynamic control surface deflections on this aerodynamic instability. A static trailing edge flap deflection is found to reduce the buffet onset incidence, while simultaneously increasing the mean lift coefficient. This is advantageous for extending the flight envelope. Static leading edge deflections are less promising, reducing the mean lift at buffet onset. Forced harmonic excitation of the trailing edge flap induces synchronisation of the buffet response with the control surface motion. With large amplitude deflections, at driving frequencies above the buffet, the root mean square buffet loads are significantly attenuated. This, however, does not extend to an elastically-suspended aerofoil, where harmonic flap excitation exacerbates the buffet response.

1 Introduction

For certain flight conditions in a transonic flow, interactions between shock-waves and thin/separated shear-layers may give rise to large amplitude, self-sustained shock oscillations. This transonic buffet phenomenon is a limiting factor in aircraft performance. The low-frequency shock motions are typically on the order of the structural natural frequencies, leaving the aircraft susceptible to Limit Cycle Oscillation (LCO), and consequently, diminished handling qualities and fatigue life [1].

Although the phenomenon of transonic shock buffet was first identified over six decades ago, shock buffet alleviation remains an active area of research. A range of potential mitigation techniques are evident in the literature, including mechanical and fluid vortex generators [2], trailing edge deflector tabs [3], shock control bumps [4] and plasma-based actuators [5], however, a robust buffet suppression technology has proven elusive. Early research in the field by Lee [6] has shown a significant dependency of buffet onset boundaries and intensities to static trailing edge flap deflections. Additionally, the ability of static leading and trailing edge flap settings to delay buffet onset was found to be sensitive to aerofoil geometry. Studying the influence of harmonic flap excitation in the vicinity of shock buffet onset, Iovnovich & Raveh [7] showed that low-amplitude control surface excitation can significantly influence the oscillatory flowfield characteristic of the buffet phenomenon, with aerodynamic frequencies synchronising with the imposed driving frequency. Recent research by Gao et. al. [8, 9] has also found that a simple closed-loop linear delay control law based on the unstable lift response can effectively quench transonic shock oscillations for a rigid aerofoil, with a marginal effect on the flight condition.

Although recent literature has shown that, at least for simple rigid aerofoil sections, the transonic buffet instability can be effectively mitigated, little consideration has been given to aeroelastic systems, which

better represent the in-flight behaviour of a true aircraft. The aim of the present work is to explore the potential for static and dynamic control surface deflections to alleviate shock buffet for elastically-suspended wing sections. The NACA 0012 aerofoil will be investigated owing to the experimental data available in open literature for validation. The paper will begin with a description of the numerical method employed in the static aerofoil simulations. This will be supported by the main results of the static simulations, including validation of the buffet response against experimental data and the nature of the buffeting flow for a nominal flight condition with a rigid wing section. The influence of static leading and trailing edge deflections on the buffet boundary will then be presented and discussed with reference to the experimental findings of Lee [6] as a means of validating the method of geometry and mesh deformation. A parametric study on the influence of flap oscillation amplitude, frequency and phasing for a rigid section will then be provided and validated against the experimental findings of Braza [10]. This will be extended to an elastically-suspended aerofoil free to rotate in pitch, so that relationships between the various control parameters and their influence on the buffet response in both rigid and aeroelastic systems can be developed. A summary of the principal findings and suggestions for future work will then be presented.

2 Numerical method

2.1 Test case

The test case considered in this study is the transonic flowfield around the symmetrical NACA 0012 aerofoil. Early experiments were conducted on this section by McDevitt & Okuno [11] at NASA Ames High Reynolds Number Facility. The HRC-2 test section, in which the investigation was performed, is equipped with perforated sidewall vents and contoured upper and lower walls to minimise tunnel interference effects, resulting is data that has remained popular even in contemporary literature for validation of buffet simulations [12, 13, 14]. A 203.2 mm chord wind tunnel model was manufactured with a 0.4 mm thick trailing edge, and instrumented with 40 static pressure orifices and six embedded dynamic pressure transducers. Static and dynamic pressure readings were recorded for freestream Mach numbers between 0.7 and 0.8, with Reynolds numbers ranging from 1×10^6 to 14×10^6. The experiments were performed with free transition over the aerofoil surface, and due to the erratic pressure wave form responses at low Reynolds numbers, McDevitt & Okuno [11] recommend the data set at $Re = 10 \times 10^6$ be used for validation of buffet simulations. At these conditions, analysis of the unsteady pressure data yields buffet frequencies for conditions deep within the buffet envelope.

Additionally, to validate the influence of trailing edge flap deflections on the buffeting flowfield of the NACA 0012, simulations are compared to the experimental data provided by Braza[10]. Experiments on a 180 mm chord NACA 0012 were performed at the Institute of Aerodynamics (IoA) N3 trisonic wind tunnel. The model was instrumented with 48 static pressure orifices and two unsteady pressure transducers, with Schlieren imaging also employed to qualitatively observe the flowfield. The model was equipped with a 20% chord aileron and a slider-crank mechanism, capable of driving the aileron with deflection amplitudes $\Delta\delta_f = \pm 2^\circ$ at frequencies in the range $f_f = 0 - 35$ Hz. Static pressure distributions and buffet onset were captured at several Mach numbers with varying static flap deflection, in addition to spectral data for forced flap actuation at $\Delta\delta_f = \pm 2^\circ$ and $f_f = 35$ Hz.

2.2 Flow solver

Simulations are performed using the commercial, cell-centred finite volume code ANSYS Fluent R18.0 [15]. The two-dimensional pressure-based implicit solver is used to formulate the coupled set of momentum and pressure-based continuity equations, which are solved segregated from the energy equation. Second-order upwind differencing is used for all convective variables. All diffusive fluxes are treated with a second-order accurate central-difference scheme. Gradients of the convective and diffusive terms are computed at the

cell faces through a Green-Gauss reconstruction scheme, with a differentiable gradient limiter employed to mitigate spurious shock oscillations.

The Stress-Omega Reynolds Stress Model (SORSM), a stress-transport model developed from the omega equations and the Launder-Reece-Rodi (LRR) model [16], is employed for closure of the Navier-Stokes equations. The SORSM is derived by taking the second-moments of the exact momentum equations, yielding (in a two-dimensional flow) an additional four transport equations for the Reynolds stresses, together with an equation for the dissipation rate. All turbulent transport equations are solved segregated from the coupled set of continuity, momentum and energy equations, with second-order accurate upwind discretisation of the turbulent quantities.

2.3 Spatial & temporal discretisation

Simulations in this investigation are performed on a two-dimensional CH-type structured grid, with an upstream boundary of 40 chords and downstream boundary of 60 chords. The grids are constructed through hyperbolic extrusion of nodes in the wall normal direction, allowing for high orthogonality throughout the domain. To ensure mesh independent solutions of the unsteady flowfield, three levels of grid refinement are considered. Refinement is primarily concentrated in the shock region and at the aerofoil trailing edge, to ensure sufficient resolution in regions of significant pressure fluctuation. The node count for each of the grids, along with the corresponding resolution through the mean shock location are provided in Table 1, where i indicates the streamwise direction and j the wall-normal direction.

Grid	Size ($i \times j$)	Shock Resolution (c)
G1	230×112	0.0075
G2	410×126	0.005
G3	570×138	0.0025

Table 1: Computational grid properties.

To assess mesh independence, simulations are performed at the established buffet condition from McDevitt & Okuno [11] ($M = 0.72$, $Re = 10 \times 10^6$ and $\alpha = 6^\circ$). Mesh independence is achieved at the medium resolution grid, where the peak root mean square pressure coefficient and buffet reduced frequency are within 2% of the fine grid. To assess temporal convergence, the baseline McDevitt & Okuno [11] condition was again employed on the medium density grid for three levels of temporal resolution. The root mean square pressure fluctuations indicate convergence of the pressure field with a nondimensional time-step (with respect to the speed of sound) of 0.002. The lift coefficient frequency responses (not shown) display consistent predictions of the fundamental and first harmonic frequency for $\tau = 0.001$ and $\tau = 0.002$, with marginally lower reduced frequencies at the coarsest resolution. Owing to this, all subsequent simulations are performed with a nondimensional time-step of 0.002.

3 Results

3.1 Static aerofoil

Employing the developed solution procedure, the buffet onset boundary for the NACA 0012 at $Re = 10 \times 10^6$ is computed by angle of attack sweeps at Mach numbers corresponding to the nominal conditions investigated by McDevitt & Okuno [11]. The resulting stability boundary is shown in Figure 1. The computed onset is in excellent agreement with the experiments for data sets 1, 5 and 6. At each of these conditions, onset is characterised by the emergence of Tijdeman Type A[17] periodic shock oscillations over the suction surface of the aerofoil.

The higher Mach number condition corresponding to data set 4 is anomalous. The onset incidence at this condition is overpredicted by approximately $0.5°$. This result is, however, consistent with a number of studies investigating this test case, including Barakos & Drikakis [12] and Iovnovich & Raveh [18]. The difficulty in accurately capturing onset at this condition is related to a shift in the nature of shock dynamics at low incidence. At lower Mach numbers and moderate incidence, the NACA 0012 exhibits Type II shock oscillations constrained to the suction surface. The low incidence onset condition at $M = 0.8$ consists of oscillations of both a strong upper surface shock and weaker lower shock. This shock motion is akin to Type I shock oscillations typically observed on biconvex and symmetric aerofoils at zero incidence [19, 20]. Relative to onset at lower Mach numbers, the emergence of Type I shock-induced oscillations is subtle, with comparatively smaller shock travel and lower levels of pressure fluctuations.

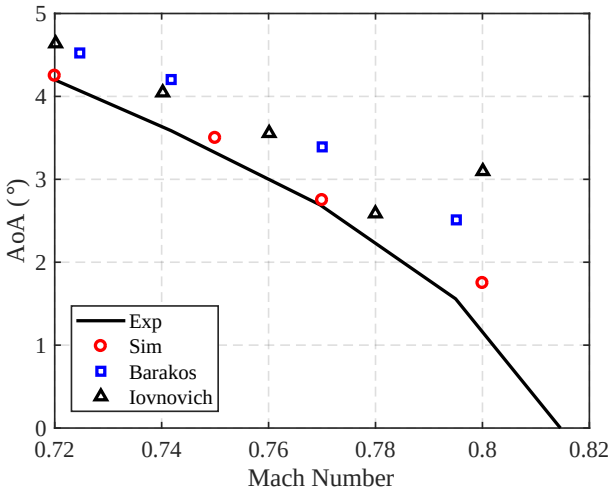


Figure 1: NACA 0012 buffet onset boundary.

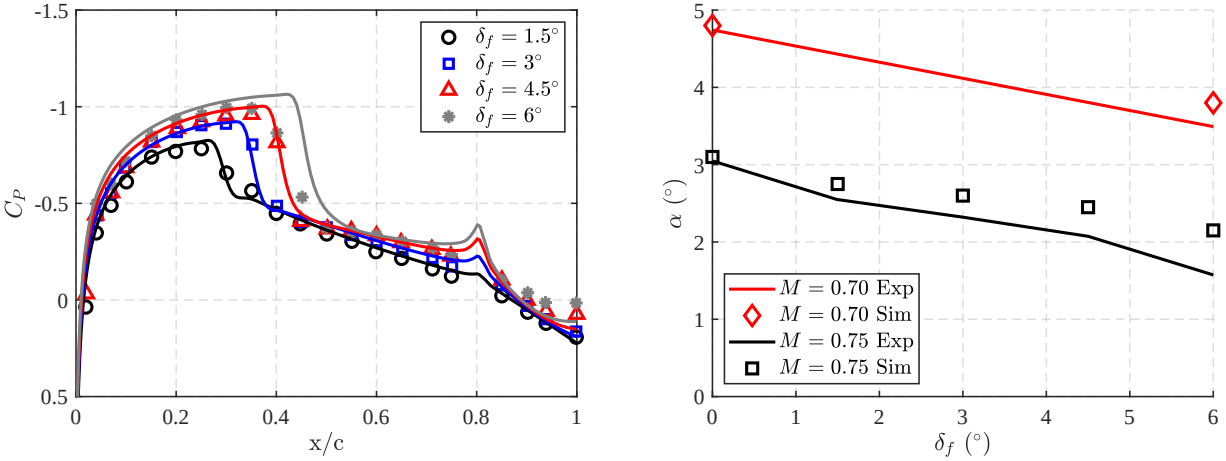
The reduced aerodynamics frequencies at developed buffet conditions for each of the data sets are provided in Table 2. While the buffet frequency is accurately captured at $M = 0.72$, discrepancies arise at higher Mach numbers. At $M = 0.75$ and $M = 0.77$, the computed buffet frequencies are underpredicted and overpredicted, respectively. The values are however within reasonable deviations from the experiments and are consistent with URANS results reported by several authors[13, 18]. The result at $M = 0.8$ is somewhat less convincing. The simulations yield a steady solution where the experiments predict sustained shock oscillations. Repeating this condition at various levels of spatial and temporal resolution consistently produced a steady flowfield. As previously noted, the buffet magnitudes at $M = 0.8$ are significantly smaller than those observed at the lower Mach numbers. It is possible that this condition lies toward the upper Mach number bound of the buffet envelope. In a similar light to the delay in onset prediction to higher incidence, the simulations appear to predict offset at a lower Mach number. While further investigation is necessary to confirm this, the solution method presented herein correlates well with the experiments of McDevitt & Okuno [11] across the majority of conditions considered and will be employed to examine the influence of control surface deflections on the aerodynamic and elastic response of the NACA 0012 at buffet conditions.

M	$\alpha(°)$	k_{sim}	k_{exp}
0.72	6	0.55	0.55
0.75	4	0.43	0.47
0.77	4	0.47	0.44
0.80	4	Steady	0.38

Table 2: Comparison of computed NACA 0012 buffet frequencies with McDevitt & Okuno [11].

3.2 Static trailing edge deflections

The influence of static trailing edge deflections on the buffet response of the NACA 0012 aerofoil is investigated by means of a blended flap configuration. The aft 20% of the section is statically deformed by the flap deflection angle δ_f, with diffusion-based smoothing applied to the baseline grid. The study of Braza [10] has shown that inclusion of a slotted flap may have an appreciable effect on the trailing edge flowfield, and in some instances, the shock location. Nonetheless, the grid densities required to sufficiently resolve the flow through the slot are not amenable to the parametric study of dynamic control surface deflections intended in this study. To this effect, the data from Braza [10] are employed to validate the present method of incorporating control surface deflections.



(a) Pressure coefficients ($M = 0.75$, $\alpha = 0°$, $Re = 3 \times 10^6$)

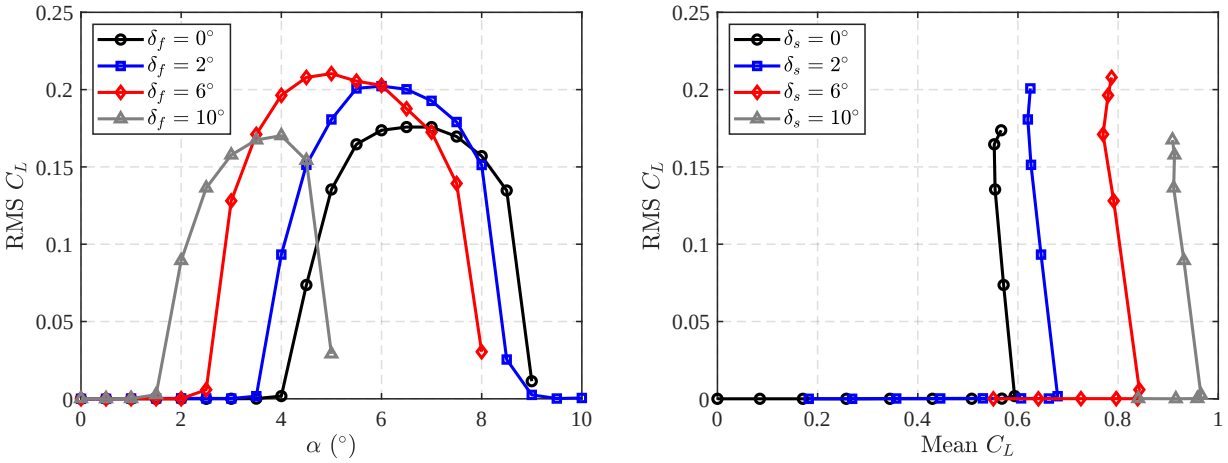
(b) Buffet boundary ($Re = 3 \times 10^6$)

Figure 2: Validation of static trailing edge flap deflection.

In Figure 2(a), the computed suction surface mean pressure coefficients for a range of flap deflection angles are compared to those found in the experiments of Braza [10]. At small deflections, the simulations accurately reproduce the pressure distribution over the entire section. As the flap deflection angle increases, discrepancies in the pressure distribution aft of the hinge axis begin to emerge, with the computations overestimating the pressure recovery through to the trailing edge. The shock location is generally well predicted, with the exception of $\delta_f = 6°$, where the computed shock location lies approximately 5% chord upstream of the experiment. While these discrepancies could potentially be addressed through resolution of the slotted flap flow, the results are in sufficient agreement with the experiment to warrant the continued use of the blended flap. This is further demonstrated by the excellent correlation in buffet onset prediction relative to the experiment evident in Figure 2(b). While the onset prediction degrades, expectantly, at larger flap deflection, the reduction in onset incidence is apparent. Further, at the developed buffet condition of $M = 0.70$, $\alpha = 6.8°$ and $Re = 3 \times 10^6$, the computations yield a buffet frequency within 5% of the experiment. Owing to the fair agreement presented, the blended flap configuration is employed through the remainder of this study.

To further probe the effect of static trailing edge deflections on the aerodynamic response of the NACA 0012 at buffet conditions, conditions corresponding to data set 6 of McDevitt & Okuno are considered ($M = 0.72$ and $Re = 10 \times 10^6$). In Figure 3, the root mean square (RMS) lift coefficient is shown for angle of attack sweeps at various static deflection amplitudes. Figure 3(a) plots the RMS lift against angle of attack. It is immediately apparent that an increase in control surface deflection reduces the onset incidence. This reduction is significant; falling from $\alpha = 4°$ in the baseline configuration to $\alpha = 1.5°$ at $\delta_f = 10°$. Peak RMS loading through the centre of the buffet envelope also increases with control surface deflection - growing 20% from the baseline to $\delta_f = 6°$. At $\delta_f = 10°$, the peak RMS loading is again equivalent to

the baseline, however, the extent of the buffet region has narrowed by 30%. While positive deflection of the trailing edge control surface reduces the buffet onset incidence, Figure 3(b) indicates that this is accompanied by an increase in the mean lift coefficient at onset. Similar behaviour has been identified experimentally by Lee [21], where it was noted that the rapid increase in RMS loads at onset (as shown in Figure 3(b)) is characteristic of onset at lower Mach number conditions. The tendency of trailing edge flap deflections to delay the onset of large-scale unsteadiness to higher lift coefficient is a favourable outcome. At a given Mach number, the buffet-free envelope of an aircraft may be extended through a small-amplitude static deflection of an aft control surface. Large amplitude deflections ($\delta_f > 6°$) should be avoided; although the mean lift at onset is significantly higher and a comparatively narrow region of shock unsteadiness exists, complete stall of the aerofoil occurs at relatively low incidence ($\alpha = 5.5°$ for the NACA 0012 at conditions considered herein).



(a) RMS C_L variation with incidence

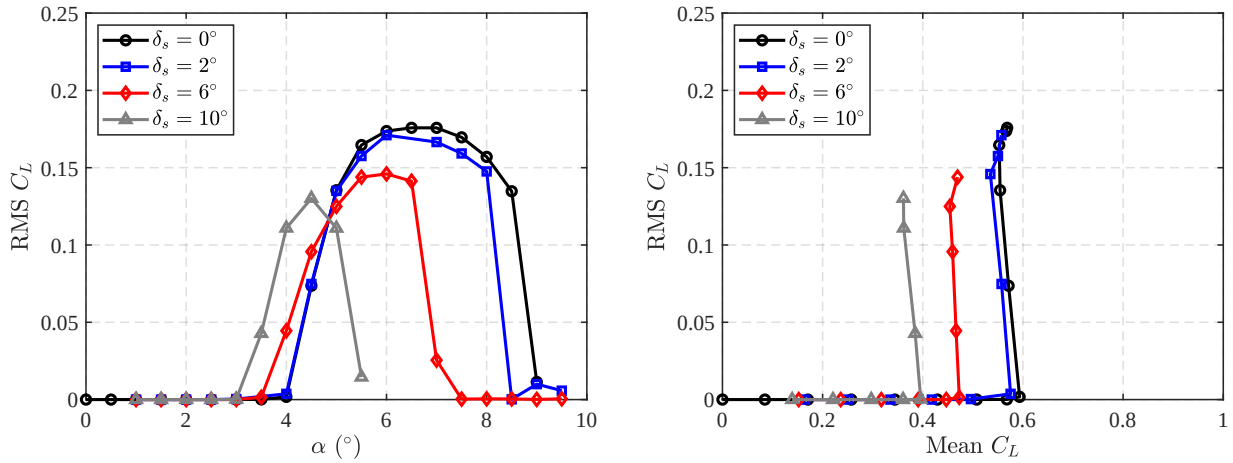
(b) RMS C_L variation with mean C_L

Figure 3: RMS lift variation with changes in incidence at various trailing edge flap deflections.

3.3 Static leading edge deflections

While the effects of static trailing edge control surface deflections have been investigated in the past [6, 22], no studies on the influence of leading edge slat deflections are available in the literature. These effects are investigated herein, with the baseline condition again corresponding to data set 6 from McDevitt & Okuno [11] ($M = 0.72$ and $Re = 10 \times 10^6$). Angle of attack sweeps are performed at this condition to capture the extent of incidence for which buffet persists with static leading edge slat deflections (δ_s) between 2° and 10°. A blended slat geometry with hinge line at 15% chord of the NACA 0012 is considered.

Analogous to the preceding Section, Figure 4 shows the variation in RMS lift coefficient with both angle of attack and mean lift coefficient at various leading edge slat settings. Clear trends are apparent in the effects of slat deflection on the buffet envelope. An increase in slat deflection imparts similar influence to the buffet boundary as is observed with an increase in Mach number. This is to be expected, as the increase in flow acceleration around the leading edge is analogous to an increase in freestream Mach number. From Figure 4(a), an increase in slat deflection is accompanied by both a reduction in buffet amplitudes and a narrowing of the incidence region for which buffet persists. In a similar fashion to the influence of trailing edge flap deflections, increasing the leading edge slat setting acts to reduce the onset incidence. However, from Figure 4(b) this reduction in onset incidence is also accompanied by a reduction in mean lift coefficient at onset. Ultimately, while deflection of a leading edge slat may alleviate the severity of autonomous shock oscillations, it inhibits the maximum lift coefficient at onset, and may thus be ineffective as a means of extending the buffet-free flight envelope.



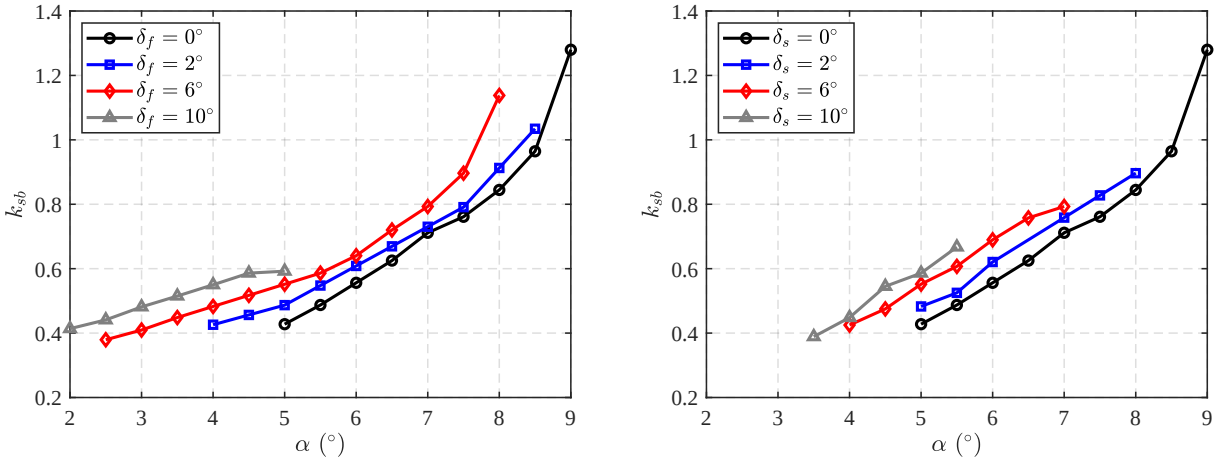
(a) RMS C_L variation with incidence

(b) RMS C_L variation with mean C_L

Figure 4: RMS lift variation with changes in incidence at various leading edge slat deflections.

3.4 Influence of static control surface deflection on buffet frequency

Figure 5 shows the influence of static control surface deflections on the reduced buffet frequencies of the NACA 0012 throughout the buffet region at $M = 0.72$ and $Re = 10 \times 10^6$. In both instances, and increase in control surface deflection appears to have a marginal effect on the reduced buffet frequencies. At onset, a reduced buffet frequency of $k_{sb} \approx 0.4$ persists, growing approximately linearly with an increase in incidence. For lower δ_f and δ_s, where the instability region is larger in extent, the gradient $\partial k_{sb}/\partial\alpha$ steepens at higher incidence, adopting a quadratic character. Ultimately, the control surface setting predominately acts to reduce the onset incidence, however, from this point the reduced buffet frequency evolves with incidence in a consistent manner with the baseline configuration [23].



(a) Trailing edge flap

(b) Leading edge slat

Figure 5: Effect of control surface deflection on reduced buffet frequency.

3.5 Dynamic trailing edge deflections

In recent studies of transonic shock buffet, numerous authors [24, 25, 13, 7] have noted the emergence of a frequency synchronisation phenomena occurring when an aerofoil experiencing buffet is harmonically excited at a frequency close to the fundamental flow frequency. When this excitation is in the pitch or heave degrees-of-freedom, this can lead to amplification in the unsteady loads experienced by the section. However, Iovnovich & Raveh [7] have shown that for a harmonic excitation in the flap degree of freedom, attenuation of loads may emerge for certain driving frequencies. In this study, the trailing edge flap of the NACA 0012 is driven at frequencies $0.5 \leq k_f/k_{sb} \leq 1.5$, where k_f is the flap excitation frequency and k_{sb} the rigid aerofoil buffet frequency.

In Figure 6, a map of the lock-in region across various excitation amplitudes and frequencies is shown. At conditions marked with response at the driving frequency, the aerodynamic coefficients exhibit frequency content concentrated at the driving frequency, and potentially, the sub- and superharmonics of this excitation frequency. The extent of the lock-in frequency band is seen to grow as the excitation amplitude increases. This growth with driving amplitude is approximately symmetric about the buffet frequency. This is contrary to the synchronisation behaviour observed for harmonic pitch excitation, where the lock-in region is concentrated at driving frequencies above the buffet (where the pitching moment coefficient leads the structure) [7, 24]. Additionally, the amplitude of flap excitation necessary to incite lock-in is significant if the driving frequency is far from the buffet. A flap amplitude of $\delta_f = 8°$ is required for the lock-in region to span a 50% deviation from the rigid buffet frequency. While the control effort necessary maintain such large amplitude flap deflections is likely prohibitive, synchronisation can be promoted by smaller amplitude oscillations if the flow frequency is known.

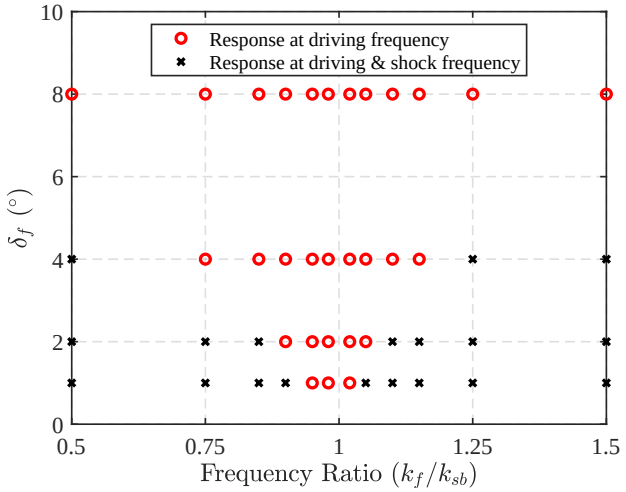
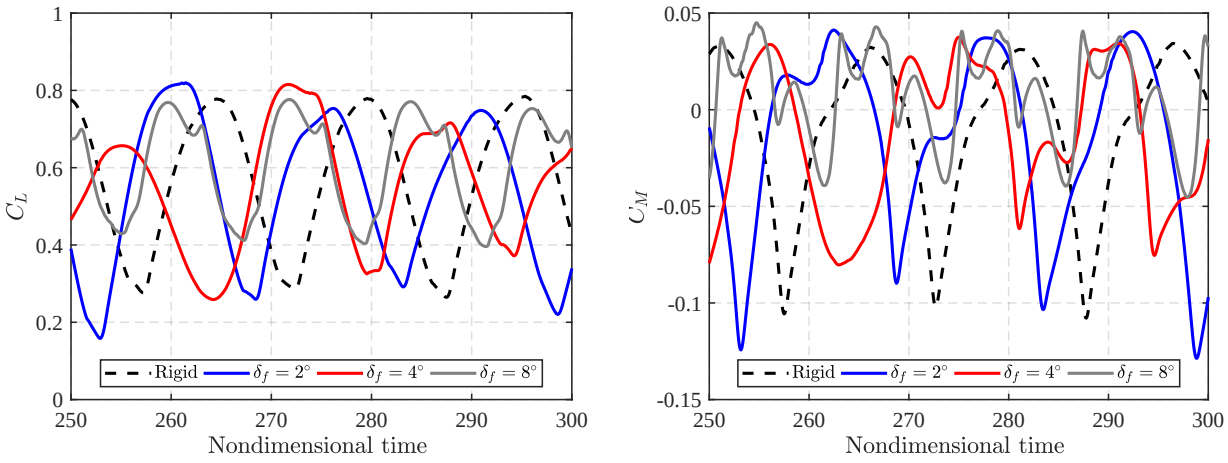


Figure 6: Map of lock-in region with trailing edge flap excitation.

To gauge the influence of forced trailing edge oscillations on the unsteady aerodynamic response, Figure 7 presents the lift and pitching moment response across various excitation amplitudes and an excitation frequency of $k_f = 1.25k_{sb}$. At low driving amplitude ($\delta_f = 2°$), the buffet frequency dominates the response in both aerodynamic coefficients, with the secondary presence of the excitation frequency producing a mild beating response that amplifies the fluctuations relative to the rigid section. As the excitation amplitude increases, the buffet frequency continues to dominate the frequency content of the aerodynamic coefficients. The first subharmonic of the buffet frequency also becomes prominent in this instance, and the interaction with the driving frequency yields aperiodic responses in both the lift and pitching moment coefficients. For $\delta_f = 8°$, The buffet frequency has vanished and frequency content is concentrated at the excitation frequency and its first superharmonic. At these conditions, attenuation in the unsteady response of both aerodynamic coefficients is apparent.

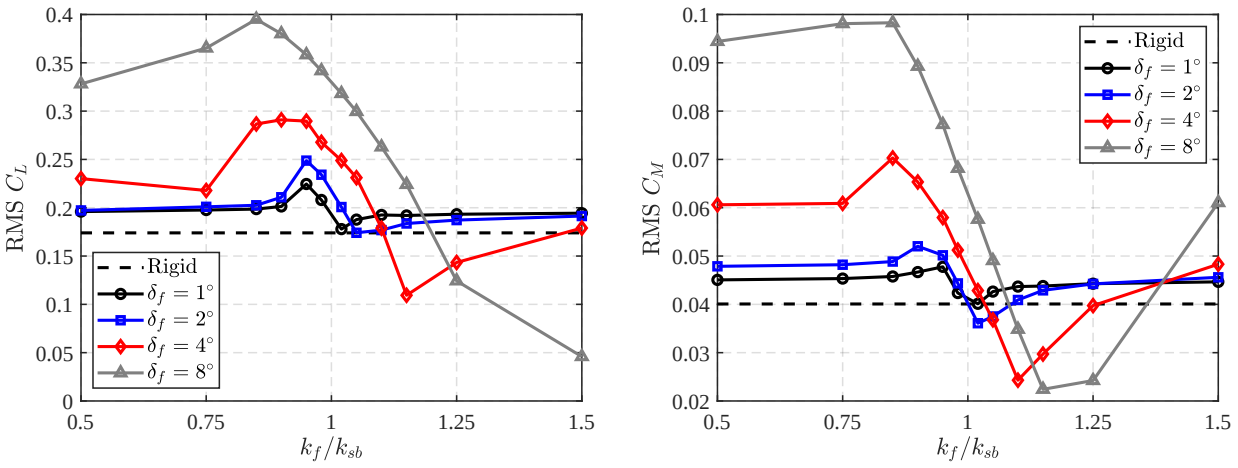


(a) Lift coefficient

(b) Pitching moment coefficient

Figure 7: Aerodynamic coefficient time histories at various excitation amplitudes ($k_f/k_{sb} = 1.25$).

To better understand the effect of driving frequency on the unsteady load fluctuations, Figure 8 shows the root mean square lift and pitching moment coefficients for the range of excitation amplitudes and frequencies investigated. For each driving amplitude, in the absence of frequency sychronisation the excitation frequency imparts a negligible influence on the RMS of the aerodynamic coefficients and the aerofoil under dynamic trailing edge oscillations experiences nominally larger fluctuation in loads relative to the rigid section. Within the lock-in region, excitation frequencies below the buffet exacerbate the unsteady aerodynamic response; an effect that becomes more pronounced at larger excitation amplitudes. Attenuation in both lift and pitching moment fluctuations is observed within the lock-in region for driving frequencies above the buffet. The most favourable response is evident at $\delta_f = 8°$ and $k_f/k_{sb} = 1.25$, where a 30% and 40% reduction in RMS lift and pitching moment coefficients is found, respectively. Again, the control effect necessary to achieve significant unsteady load attenuation in both the lift and pitching moment coefficients is inordinate for a true aircraft system. From this parameter study it would appear that robust buffet alleviation through open-loop trailing edge flap oscillations is not achievable.

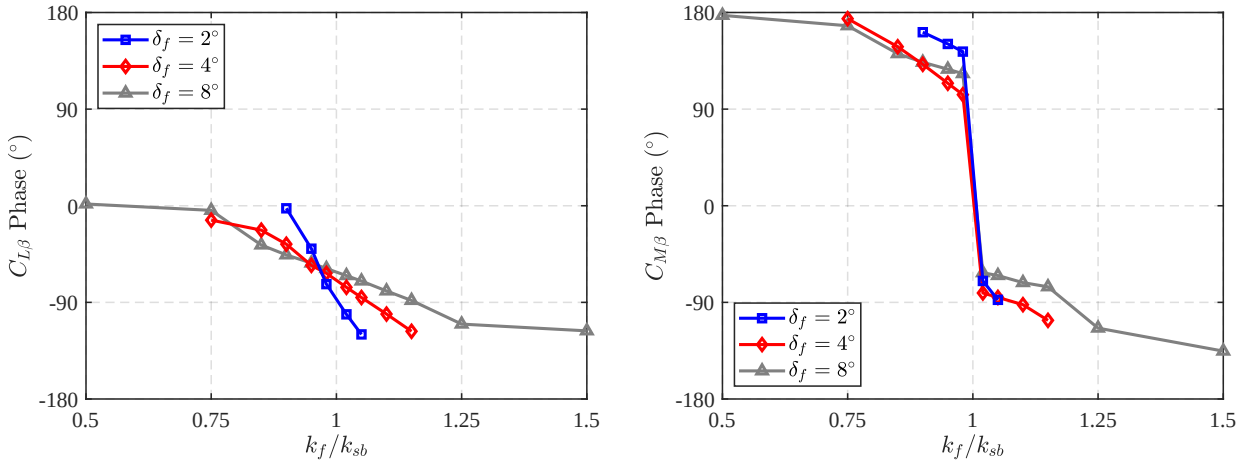


(a) Lift coefficient

(b) Pitching moment coefficient

Figure 8: RMS variation in aerodynamic coefficients at various excitation amplitudes and frequencies.

The preceding discussion demonstrates that shock buffet lock-in to the trailing edge flap excitation occurs for a range of driving frequencies in the vicinity of the buffet. The extent of the lock-in frequency band grows with excitation amplitude. Although shock buffet and the associated lock-in phenomenon is inherently non-linear, under synchronisation conditions the aerodynamic response consists primarily of a single frequency (and its harmonics), permitting analysis of the response through a frequency sweep study. The amplitude response behaves in an analogous manner to the RMS coefficients present in Figure 8 and so this is not repeated here. Figure 9 shows the phase of the lift and quarter-chord pitching moment to trailing edge excitation at lock-in conditions. At all excitation amplitudes the lift coefficient lags the control surface motion, with a steeper phase gradient through the buffet frequency encountered at lower δ_f. The pitching moment coefficient yields a more interesting response. At all amplitudes the aerodynamics lead the motion for excitation frequencies below the buffet, indicating the possibility of an aerodynamic instability at these conditions. At the buffet frequency, the pitching moment response experiences a 180° phase lag, which persists for driving frequencies above the buffet. In conjunction with the attenuation in RMS loads in this frequency band (as shown in Figure 8), it appears mitigation of autonomous shock oscillations through harmonic trailing edge oscillation is most receptive to large amplitude deflections at driving frequencies above the buffet. This analysis has been repeated at a driving amplitude of $\delta_f = 4°$ and with phase shifts ϕ of 90°, 180° and 270°. The influence of excitation phase is negligible. Once frequency lock-in occurs, the aerodynamic response becomes phase locked with the excitation and the response is identical to that presented in this section.



(a) Lift coefficient

(b) Pitching moment coefficient

Figure 9: Phase of lift and moment coefficients at lock-in conditions.

3.6 Aeroelastic pitching

The shock buffet lock-in phenomenon briefly described in Section 3.5 for harmonic excitation of an aerofoil further extends to elastically suspended aerofoils, so long as the structural eigenfrequency is sufficiently close the buffet [26, 27, 28, 14, 29, 9]. In this section, the aeroelastic response of the NACA 0012, free to rotate in pitch, is examined at the nominal buffet condition of $M = 0.72$, $Re = 10 \times 10^6$ and $\alpha = 6°$. A fourth-order Runge-Kutta time-marching integration is employed to solve for the structural displacement, as given by:

$$I_\alpha(\ddot{\bar{\alpha}} + 2\zeta\omega_\alpha\dot{\bar{\alpha}} + \omega_\alpha^2\bar{\alpha}) = M_{1/4c} \tag{1}$$

where $\bar{\alpha}$, $\dot{\bar{\alpha}}$ and $\ddot{\bar{\alpha}}$ are the pitch displacement, velocity and acceleration respectively, ω_α is the pitch natural frequency, ζ is the structural damping and $M_{1/4c}$ is the pitching moment about the quarter-chord point. The elastic axis and centre of gravity are enforced at the quarter-chord point such that all moments in Equation 1

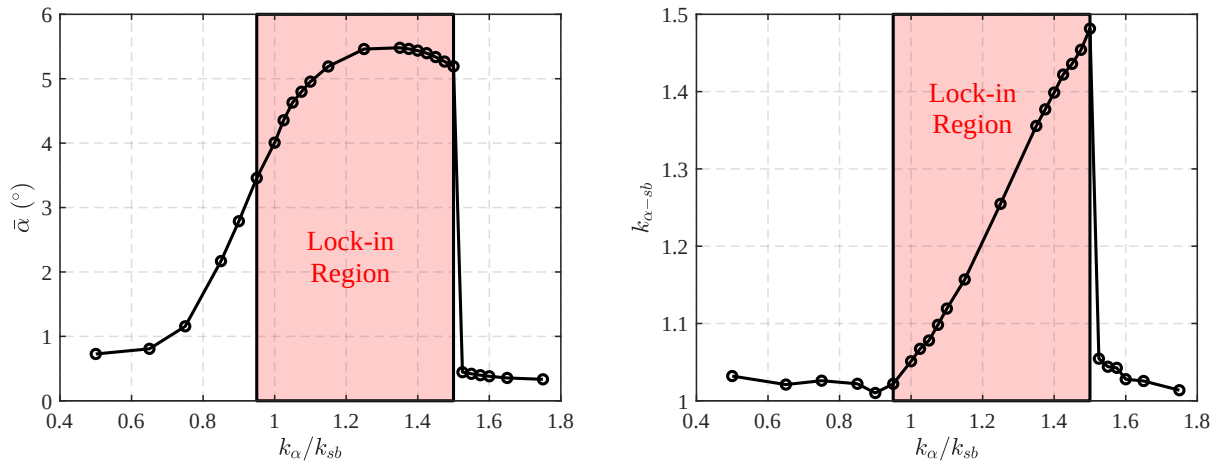
are taken about this point. The pitch moment of inertia I_α is computed by:

$$I_\alpha = \mu\pi\rho_\infty b^3 r_\alpha^2 \tag{2}$$

where ρ_∞ is the freestream density, b is the aerofoil semi-chord and $r_\alpha^2 = 0.5$ is the radius of gyration, which is held constant across all simulations. The parameter μ is the sectional mass ratio, given by:

$$\mu = \frac{m}{\pi\rho_\infty b^2} \tag{3}$$

Nominal structural parameters of $\mu = 100$ and $\zeta = 0.02$ are employed and the wind-off pitch natural frequency is varied between $0.5 \leq k_\alpha/k_{sb} < 1.75$. In Figure 10, the variation of pitch displacement amplitude and response frequency are plotted against the ratio of wind-off structural eigenfrequency and rigid aerofoil buffet frequency. The parameter $k_{\alpha-sb}$ represents the dominant pitch response frequency once a steady state LCO is achieved. The plots are divided into three distinct regions, where qualitatively dissimilar behaviour is observed.



(a) Pitch amplitude

(b) Pitch frequency ratio

Figure 10: Effect of frequency ratio on pitch response amplitude and frequency.

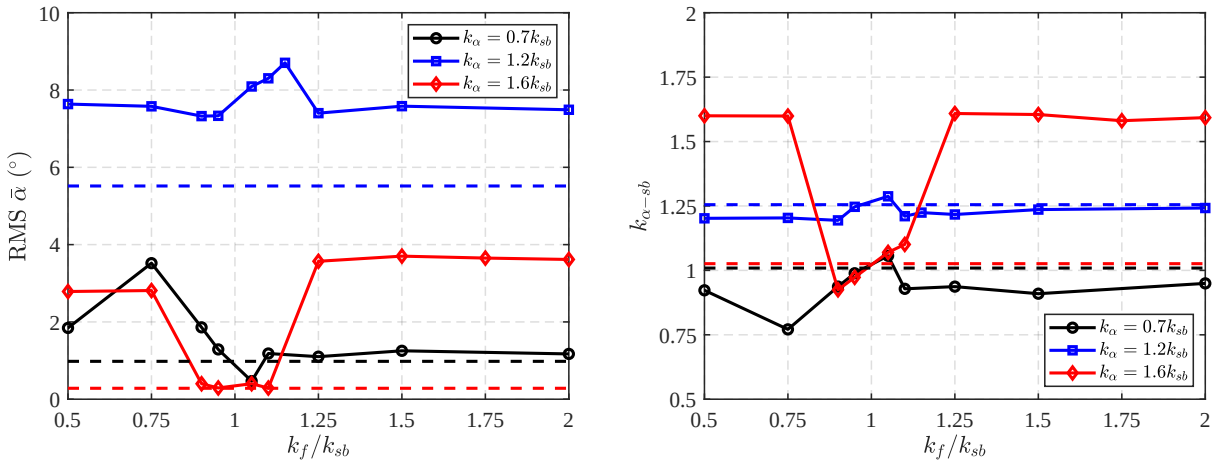
From Figure 10(b) at frequency ratios below 0.95, the coupled pitch response frequency follows approximately the rigid aerofoil buffet frequency. In this region, the oscillating shock acts as an external forcing to the aeroelastic system. The pitching motion is driven at the buffet frequency, and a gradual increase in LCO amplitude is evident as the structural natural frequency approaches the buffet. From approximately $k_\alpha/f_{sb} = 0.95$, lock-in of the shock oscillation frequency to the pitching mode is observed. This is in accordance with previous studies on both the NACA 0012 [30] and the OAT15A [27], where the onset of lock-in occurs at the rigid aerofoil buffet frequency. In Figure 10(b), the structural response is shown to be concentrated at the modal frequency through to $k_\alpha \approx 1.5 f_{sb}$. Throughout this region a distinct resonance is present in the pitch amplitude, with the maximum amplitude LCO response occurring at $k_\alpha \approx 1.25 k_{sb}$. This shift in the maximum amplitude aeroelastic response to higher frequencies relative to the dominant aerodynamic mode is supported by similar findings for forced harmonic motions [31, 13, 25]. At $k_\alpha \approx 1.5 f_{sb}$ offset of the shock buffet lock-in phenomenon occurs. The pitch response settles to a low amplitude LCO driven at the frequency of shock oscillation, essentially behaving as a single degree-of-freedom harmonic oscillator.

3.7 Aeroelastic pitching with dynamic trailing edge deflections

To access the influence of harmonic trialing edge excitation on the aeroelastic response of the NACA 0012, this section considers three aeroelastic configurations; $k_\alpha = 0.7 k_{sb}$, $k_\alpha = 1.2 k_{sb}$ and $k_\alpha = 1.6 k_{sb}$. These

configurations are representative of the three distinct aeroelastic behaviours observed for an aerofoil at shock buffet conditions in Figure 10. The mass and damping ratio of the elastically-suspended section are once more $\mu = 100$ and $\zeta = 0.02$, with a mean flow condition of $M = 0.72$, $Re = 10 \times 10^6$ and $\alpha = 6°$. For each configuration the trailing edge is driven at an amplitude of $\delta_f = 4°$ with excitation frequencies in the range $0.5 \leq k_f/k_{sb} \leq 2$.

In Figure 11, the root mean square pitch displacement and response frequency are shown for the three configurations described across the excitation frequencies considered. Dashed lines represent the RMS and response frequency of the corresponding aeroelastic response in the absence of trailing edge oscillations. With both the pitch and flap excitation frequencies below the buffet, the aerofoil experiences amplification in the pitch response. For the particular case of $k_\alpha = 0.7k_{sb}$, Figure 11(b) shows that lock-in of the pitch mode to the flap excitation frequency occurs through $0.75 \leq k_f/k_{sb} \leq 1.05$. In this region the pitch amplitude attenuates up to the offset of lock-in, from which the pitch response amplitude and frequency approximately follow that of the fixed trailing edge, with the response concentrated at the rigid aerofoil buffet frequency.



(a) Pitch amplitude

(b) Pitch frequency ratio

Figure 11: Effect of frequency ratio on pitch response amplitude and frequency.

Considering the structural configuration for which lock-in to the pitch mode was observed in Section 3.6 ($k_\alpha = 1.2k_{sb}$), harmonic trailing edge excitation has a negligible effect on the response frequency. From Figure 11(b) it is evident that the pitch response remains synchronised with the pitch natural frequency regardless of the flap excitation frequency. This is accompanied by an approximately 35% increase in RMS pitch displacement across all driving frequencies. At flap excitation frequencies in the vicinity of the buffet a mild resonance effect is noted. While the dominant pitch response frequency is concentrated at the pitch mode, for these conditions frequency content is also evident at k_f, which exacerbates the response amplitude.

In the case for which the pitch natural frequency exceeds the offset of pitch-mode lock-in, the inclusion of trailing edge oscillations is generally detrimental to the response. With the frequency band $0.9 \leq k_f/k_{sb} \leq 1.1$, the pitch response synchronises with the flap excitation, yielding pitch displacements analogous to the rigid trailing edge. Outside of this region, the perturbations induced by the control surface act to expand the bounds of the pitch-mode lock-in region, resulting in a response frequency that follows the pitch eigenfrequency and a significant amplification in the pitch response. From the combination of parameters considered herein it appears that open-loop control surface actuation of an elastically-suspended aerofoil at shock buffet conditions is globally detrimental to the system's aeroelastic response. It is possible that larger amplitude control surface deflections may have a more appreciable influence on the response, however, as previously noted, the necessary control effect becomes prohibitive for implementation in a true aircraft system. Ultimately, feedback control actuation could provide a remedy, so long as a physically observable state of the system that is directly correlated with the buffet response can be identified. Gao et. al. [8] have employed the

balanced lift coefficient as a parameter in their control law for buffet alleviation of a rigid aerofoil. Regarding the observable in an aeroelastic system, the pitch displacement is the logical selection, and future work will investigate the efficacy of a number of control laws for suppression of the buffet instability in an aeroelastic system.

4 Conclusion

This paper has investigated the transonic shock buffet phenomenon on the NACA 0012 aerofoil through URANS simulation. The test case has been validated against available experimental data and has accurately captured the buffeting response in the vicinity of onset. The influence of both static leading and trailing edge control surfaces on the buffet response has also been considered. Static deflection of a trailing edge flap is found to decrease the incidence at which onset occurs. This is, however, accompanied by a significant increase in the mean lift at onset, and may provide a viable means of extending the flight envelope of an aircraft operating near the buffet envelope. The contrary is observed for static leading edge flap deflections, where a narrowing of the buffet region is accompanied by a reduction in the mean lift coefficient at onset. Static deflection of either control surface is seen to have a negligible effect on the buffet frequency.

Dynamic trailing edge flap excitation has also been found to have a pronounced influence of the buffet response. Synchronisation of the shock oscillation to the trailing edge excitation occurs at driving frequencies in the vicinity of the buffet. This lock-in region extends to frequencies farther from the buffet as the excitation amplitude increases. At driving frequencies below the buffet, amplification in the RMS aerodynamic coefficients has been observed. In this frequency band, the pitching moment coefficient also exhibits a phase lead relative to the control surface motion; an indicator of a potential aeroelastic instability. Single degree-of-freedom simulations of an elastically-suspended NACA 0012 free to rotate in pitch also display have also shown the presence of a frequency lock-in phenomena, with the aerodynamic response synchronising with the pitch mode for wind-off pitch natural frequencies above the buffet. Forced harmonic trailing edge oscillations in the elastically-suspended system tend to exacerbate the aeroelastic response, extending the lock-in frequency range and amplifying pitch displacements. To effectively mitigate the large amplitude displacements associated with this lock-in phenomenon, a feedback control system is required. This is currently being investigated by the authors.

Acknowledgements

The authors would like to thank Dr Oleg Levinski from DST Group and Dr Robert Carrese from RMIT University for their comprehensive insight into transonic buffet phenomenon and for assisting in the development of the preliminary test matrix from which the present work was derived. This research is supported by the Defence Science and Technology Group, Australia.

References

[1] N. F. Giannelis, G. A. Vio, and O. Levinski. A review of recent developments in the understanding of transonic shock buffet. *Progress in Aerospace Sciences*, 92:39–84, 2017.

[2] J. Dandois, A. Lepage, J. B. Dor, P. Molton, F. Ternoy, A. Geeraert, V. Brunet, and E. Coustols. Open and closed-loop control of transonic buffet on 3d turbulent wings using fluidic devices. *Comptes Rendus Mécanique*, 342(6):425–436, 2014.

[3] D Caruana, A Mignosi, M Corrège, A Le Pourhiet, and AM Rodde. Buffet and buffeting control in transonic flow. *Aerospace Science and Technology*, 9(7):605–616, 2005.

[4] S. Bogdanski, P. Gansel, T. Lutz, and E. Krämer. Impact of 3D shock control bumps on transonic buffet. In *High Performance Computing in Science and Engineering '14*, pages 447–461. Springer, 2015.

[5] O.I. Vishnyakov, P.A. Polivanov, A.D. Budovskiy, A.A. Sidorenko, and A.A. Maslov. Control of buffet onset by plasma-based actuators. In *Proceedings of the 18th International Conference on the methods of Aerophysical Research, Perm, Russia*, 2016.

[6] B. H. K. Lee. Effects of trailing-edge flap on buffet characteristics of a supercritical airfoil. *Journal of Aircraft*, 29(1):93–100, 1992.

[7] M. Iovnovich and D. E. Raveh. Transonic unsteady aerodynamics in the vicinity of shock-buffet instability. *Journal of Fluids & Structures*, 29:131–142, 2012.

[8] C. Gao, W. Zhang, and Z. Ye. Numerical study on closed-loop control of transonic buffet suppression by trailing edge flap. *Computers & Fluids*, 132:32–45, 2016.

[9] Chuanqiang Gao, Weiwei Zhang, Jiaqing Kou, Yilang Liu, and Zhengyin Ye. Active control of transonic buffet flow. *Journal of Fluid Mechanics*, 824:312–351, 2017.

[10] M. Braza. NACA0012 with Aileron. In P. Doerffer, C. Hirsch, J. P. Dussauge, H. Babinsky, and G. N. Barakos, editors, *Unsteady Effects of Shock Wave Induced Separation*, pages 101–131. Springer, 2010.

[11] J. B. McDevitt and A. F. Okuno. Static and dynamic pressure measurements on a NACA 0012 airfoil in the Ames high Reynolds number facility. NASA TP-2485, National Aeronautics and Space Administration, Scientific and Technical Information Branch, 1985.

[12] G. Barakos and D. Drikakis. Numerical simulation of transonic buffet flows using various turbulence closures. *International Journal of Heat and Fluid Flow*, 21(5):620–626, 2000.

[13] D. E. Raveh. Numerical study of an oscillating airfoil in transonic buffeting flows. *AIAA Journal*, 47(3):505–515, 2009.

[14] C. Gao, W. Zhang, X. Li, Y. Liu, J. Quan, Z. Ye, and Y. Jiang. Mechanism of frequency lock-in in transonic buffeting flow. *Journal of Fluid Mechanics*, 818:528–561, 2017.

[15] ANSYS. *Fluent 12. 1 User Manual*. ANSYS Inc, 2011.

[16] B. E. Launder, G. Reece Jr, and W. Rodi. Progress in the development of a Reynolds-stress turbulence closure. *Journal of Fluid Mechanics*, 68(03):537–566, 1975.

[17] H. Tijdeman. *Investigations of the transonic flow around oscillating airfoils*. PhD Thesis, TU Delft, Delft University of Technology, 1977.

[18] M. Iovnovich and D. E. Raveh. Reynolds-averaged Navier-Stokes study of the shock-buffet instability mechanism. *AIAA Journal*, 50(4):880–890, 2012.

[19] J. B. McDevitt, L. L. Levy Jr, and G. S. Deiwert. Transonic flow about a thick circular-arc airfoil. *AIAA Journal*, 14(5):606–613, 1976.

[20] D. G. Mabey, B. L. Welsh, and B. E. Cripps. Periodic flows on a rigid 14% thick biconvex wing at transonic speeds. RAE-TR-81059, British Royal Aircraft Establishment, 1981.

[21] B. H. K. Lee and F. C. Tang. Transonic buffet of a supercritical airfoil. *Journal of Aircraft*, 26(5):459–464, 1989.

[22] B. H. K. Lee and F. C. Tang. Transonic buffet of a supercritical airfoil with trailing-edge flap. *Journal of Aircraft*, 26(5):459–464, 1989.

[23] N. F. Giannelis, O. Levinski, and G. A. Vio. Influence of Mach number and angle of attack on the two-dimensional transonic buffet phenomenon. *Aerospace Science and Technology*, 78:89–101, 2018.

[24] N. F. Giannelis and G. A. Vio. Investigation of frequency lock-in phenomena on a supercritical aerofoil in the presence of transonic shock oscillations. In *Proceedings of the 17th International Forum on Aeroelasticity and Structural Dynamics, Como, Italy*, 2017.

[25] D. E. Raveh and E. H. Dowell. Frequency lock-in phenomenon for oscillating airfoils in buffeting flows. *Journal of Fluids and Structures*, 27(1):89–104, 2011.

[26] N. F. Giannelis and G. A. Vio. Aeroelastic interactions of a supercritical aerofoil in the presence of transonic shock buffet. In *Proceedings of the 54th AIAA Aerospace Sciences Meeting, San Diego, CA*, 2016.

[27] N. F. Giannelis, G. A. Vio, and G. Dimitriadis. Dynamic interactions of a supercritical aerofoil in the presence of transonic shock buffet. In *Proceedings of the 27th International Conference on Noise and Vibration Engineering, Leuven, Belgium*, 2016.

[28] D. E. Raveh and E. H. Dowell. Aeroelastic responses of elastically suspended airfoil systems in transonic buffeting flows. *AIAA Journal*, 52(5):926–934, 2014.

[29] N. F. Giannelis, J. A. Geoghegan, and G. A. Vio. Gust response of a supercritical aerofoil in the vicinity of transonic shock buffet. In *Proceedings of the 20th Australasian Fluid Mechanics Conference, Perth, Western Australia*, 2016.

[30] J. Quan, W. Zhang, C. Gao, and Z. Ye. Characteristic analysis of lock-in for an elastically suspended airfoil in transonic buffet flow. *Chinese Journal of Aeronautics*, 29(1):129–143, 2016.

[31] S. S. Davis and G. N. Malcolm. Transonic shock-wave/boundary-layer interactions on an oscillating airfoil. *AIAA Journal*, 18(11):1306–1312, 1980.

Development of a nonlinear state space model of the forces acting on an aerofoil oscillating in pitch

M. F. Siddiqui [1,*], **J. Ertveldt** [2], **J. Decuyper** [1], **T. De Troyer** [1], **J. Schoukens** [1], **M. C. Runacres** [1]
[1] Vrije Universiteit Brussels, Department of Engineering Technology
Pleinlaan 2, 1050 Brussels, Belgium
[*]e-mail: **muhammad.faheem.siddiqui@vub.be**

[2] Vrije Universiteit Brussels, Department of Mechanical Engineering
Pleinlaan 2, 1050 Brussels, Belgium

Abstract
In this article, we develop a nonlinear data-driven model of the aerodynamic force on an aerofoil made to oscillate in pitch in a wind tunnel under constant flow conditions. The proposed model structure is a polynomial nonlinear state-space model (PNLSS) which is an extension of the classical linear state-space model with nonlinear functions. In this work, we use experimental data of an aerofoil onto which a pitching motion is imposed, using a dedicated cyber-physical fluid dynamic (CPFD) setup. The pitch angle is considered as the input to the system, while the aerodynamic force is considered as the output of the system. Different input signals (single sines, multisines) are considered at different amplitudes and offset angles for the pitching aerofoil. Results show that the PNLSS model is three times more accurate than the linear model in minimising the least squares cost function. To the author's knowledge, this constitutes the first instance of a fully nonlinear state space model of an oscillating aerofoil developed from experimental measurements.

1 Introduction

Reducing the weight of aircraft is an important factor in improving their performance. In order to ensure that light-weight aircraft operate under an acceptable factor of safety, accurate identification of the nonlinear dynamic response of the aircrafts becomes very important. Modelling unsteady aerodynamics is quite a challenging task and even for 2D incompressible flows, closed form unsteady aerodynamic theories are not trivial. Analytical models by Theodorsen [20] and the semi-empirical model of Leishman and Beddoes [12] are still used today to gauge the performance of different unsteady aerodynamic models. The Theodorsen model calculates lift and pitching moment of an aerofoil undergoing harmonic motion and Leishman et al. presented a dynamic stall model for an aerofoil in pitch/heave motion. Comparison of different unsteady aerodynamic models using potential flow theory can be found in [10].

In most cases, the analytical representation of the physical system is complex and sometimes even impossible. Another approach to model nonlinear phenomena is by using data-driven (black-box) models constructed from input and output data. One such class of black-box models is the polynomial nonlinear state space model (PNLSS). The PNLSS framework allows to model nonlinear phenomena in an efficient manner which is suitable for computer implementation [15].

Decuyper et al. [4] modelled the kinematics of oscillating cylinder using the PNLSS technique. They used Computational Fluid Dynamics (CFD) simulations to calculate forces acting on the cylinder for different oscillating frequencies. Using the CFD data, they identified a PNLSS model. This model was able to capture the dynamic features of oscillating cylinders such as the lock-in phenomenon and vortex shedding. In this work, a similar strategy is adopted but instead of CFD data, experimental data of a pitching aerofoil is used

to develop the PNLSS model. The experimental data is obtained from the Cyber-Physical Fluid Dynamic (CPFD) setup developed by Ertveldt et al. [9].

2 Experimental Setup

Most of the recently developed experimental setups, such as Babbar et al. [1, 2], which allows for forced motion of the wind tunnel model, are capable of exciting the wind tunnel model with harmonic excitation signals only, whereas the CPFD setup allows to excite the wind tunnel model through arbitrary excitation in both plunge and pitch. In case of the nonlinear systems, the choice of the excitation signal becomes very important. The CPFD setup has the ability to excite the wind tunnel model with a variety of input signals, e.g. single sines, swept sines and multisines, at different pitch amplitudes and offset angles [7, 8]. The CPFD setup, shown in Figure 1, imposes pitching/plunging motion on a wing using four linear actuators, two on each side of the wing. The resulting unsteady aerodynamic forces are measured by four load cells that are placed between the linear actuator and the pitch beam. The pitch beam converts the linear motion of the actuators to a rotary motion of the wing. The pitch beam is restricted by a linear mechanism to move only in the plunge direction i.e. perpendicular to the wind. The setup is symmetric, i.e. the support and actuation mechanism at both side of the wing are identical. The complete CPFD mechanism is installed in the wind tunnel section with a test area 1.3 m $\times$ 0.45 m (width $\times$ height). A rectangular wing of profile NACA 0018 was used for its high thickness and therefore stiffness. The wing span is 1.22 m, which is almost equal to the width of the test section. A modal analysis revealed that the first resonance frequency of the system is at 83 Hz.

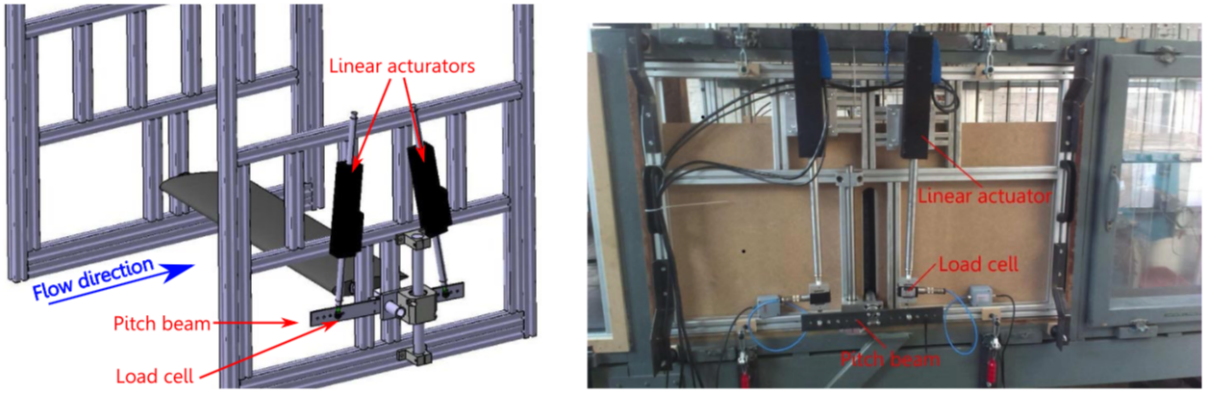


Figure 1: The Active Aeroelastic Test Bench. CAD model illustrating the leading- and trailing-edge linear actuators, the pitch beam, and the wing (left). One side of the CPFD mounted to the wind tunnel (right) [7]

In this work, single sine and multisine excitation signals are used as the input and the resulting forces are measured on the aerofoil undergoing pitch oscillation at different offset angles. Forces on the trailing and leading edge of the wing are measured separately by two load cells each. The total force is calculated by adding the forces on each actuator. The contribution of the aerodynamic forces in the total force is estimated by subtracting the inertial forces exerted by the wing. Details about the aerodynamic force calculation are given in [6].

3 PNLSS modelling strategy

Polynomial nonlinear state-space (PNLSS) models are an extension of the linear state-space models where the state and output equations are extended with nonlinear functions f and g, as shown in Equation (1). The

PNLSS model is built in discrete time which is more suitable for control applications. The output of the system, which is the lift force in our case, is denoted by c_l and the input, which is pitching angle, is denoted by α. The set of internal variables, called the states, are given by *x*.

$$x(k+1) = \mathbf{A}x(k) + \mathbf{B}\alpha(k) + f(x(k), \alpha(k)) \tag{1a}$$
$$c_l(k) = \mathbf{C}x(k) + \mathbf{D}\alpha(k) + g(x(k), \alpha(k)) \tag{1b}$$

where $x(k) \in \mathbb{R}^{n_x}$ is the state vector with n_x being the order of the linear part. The input vector $\alpha(k) \in \mathbb{R}^{n_\alpha}$ with n_α equal to the number of inputs and $c_l(k) \in \mathbb{R}^{n_{c_l}}$, which is a vector of all the n_{c_l} outputs. As mentioned earlier, forces at trailing and leading edge of the aerofoil are measured separately. Thus we have a single input (pitch oscillation) and multiple output (trailing and leading edge forces) **SIMO** system. In this work, we have identified a nonlinear model for the trailing edge forces only, thus making it a Single Input Single Output **SISO** system, where $n_{c_l} = n_\alpha = 1$. A nonlinear model for the leading edge forces can be identified in the same way and the two nonlinear models can be used to calculate the aerodynamic force on the complete wing as discussed in section Section 2. Using the SISO implementation, the dimensions of the matrices of the state and the output equations become: $\mathbf{A} \in \mathbb{R}^{n_x \times n_x}$, $\mathbf{B} \in \mathbb{R}^{n_x \times 1}$, $\mathbf{C} \in \mathbb{R}^{1 \times n_x}$ and $\mathbf{D} \in \mathbb{R}^{1 \times 1}$.

In the PNLSS case, the nonlinear functions *f* and *g* are expanded in monomial basis functions. This can be written as a product of a matrix of monomial basis functions and a vector of coefficients for the selected terms of the monomials. Hence Equations (1a) and (1b) can be rewritten as:

$$x(k+1) = \mathbf{A}x(k) + \mathbf{B}\alpha(k) + \mathbf{E}\zeta(k) \tag{2a}$$
$$c_l(k) = \mathbf{C}x(k) + \mathbf{D}\alpha(k) + \mathbf{F}\eta(k) \tag{2b}$$

where $\zeta(k) \in \mathbb{R}^{n_\zeta}$ and $\eta(k) \in \mathbb{R}^{n_\eta}$ contain the nonlinear monomials in the state and output equation respectively. The monomials $\zeta(k)$ and $\eta(k)$ are formed as cross products between the input and the state variables raised to a degree *p* for the state equation (Equation (2a)) and *q* for the output equation (Equation (2b)). Generally, the first degree is omitted since these contributions are already covered by the linear part of the structure. An example of an element in $\zeta(k)$ is given by :

$$\zeta_{g,h_1,\ldots,h_{n_x}}(k) = \alpha^g(k) \prod_{i=1}^{n_x} x_i^{h_i}(k) \tag{3}$$

with the total degree of the monomial satisfying the condition: $g + \Sigma_{i=1}^{n_x} h_i \in \{0, 2, 3, ..., p\}$ with $[g, h_i] \in \mathbb{N}$. Therefore, $\mathbf{E} \in \mathbb{R}^{n_x \times n_\zeta}$ and $\mathbf{F} \in \mathbb{R}^{n_x \times n_\eta}$, with n_ζ and n_η the number of combinatorial products between the states and the input, satisfying the condition on the total degree of the monomial [3].

3.1 Cost function

The choice of the cost function depends upon the features of the training data that the user wants to incorporate in the resulting PNLSS model. Since we wanted the PNLSS model to be more accurate in the frequency band of interest (0-25 Hz), we used a frequency-domain weighted least squares cost function to minimise the error on the selected frequencies as given in Equations (4a) and (4b).

$$V_{WLS}(\theta) = \sum_{k=1}^{N_f} |e(\omega_k, \theta)|^2 \tag{4a}$$
$$e(\omega_k, \theta) = W(\omega_k)(C_L(\omega_k) - C_{L_{mod}}(\omega_k)) \tag{4b}$$

Here $W \in \mathbb{R}^{n_{C_L} \times n_{C_L}}$ is a frequency domain weighting matrix specified by the user. C_L and $C_{L_{mod}}$ are the discrete Fourier transform (DFT) of the training data and the simulated output of the nonlinear model respectively and N_f is the total number of frequency lines. θ is a vector of parameters to be optimised. These parameters are all the coefficients in the **A, B, C, D, E,** and **F** matrices:

$$\theta = [vec(\mathbf{A}); vec(\mathbf{B}); vec(\mathbf{C}); vec(\mathbf{D}); vec(\mathbf{E}); vec(\mathbf{F})] \tag{5}$$

where *vec* denotes the operator which stacks all the elements of a matrix in a single column vector.

The PNLSS model identification consists of four main steps:

1. First a linear nonparametric estimate ($\hat{G}$) of the system is obtained from data. The linear nonparametric estimate is a frequency response function (FRF).
2. Secondly a linear parametric estimate $\hat{G}_{par}(\theta_{lin})$ of the FRF is obtained using linear identification techniques.
3. Next, all coefficients are further tuned to the data via nonlinear optimisation of the cost function given in Equation (4). As initial values for the **A, B, C** and **D** matrices the parametric estimate $\hat{G}_{par}(\theta)$ is used, **E** and **F** are initially set to zero. The data used in this step is called the training data.
4. Finally, the model is validated by assessing its performance of simulating the output to a new (not used during the tuning of the model) data sequence. This new data is called the validation data.

3.2 Optimisation

As discussed previously, the parametric PNLSS model is tuned to training data using a nonlinear optimisation of the cost function given in Equation (4). The optimisation is performed using the Levenberg-Marquardt (LM) algorithm [13], which is a gradient descent based method. The LM algorithm falls under the category of local optimisation techniques, thus it strongly depends on the choice of the initial values. Given the starting values, the optimisation can be seen as a descending path along the cost function. Unfortunately, the optimisation may easily end up in a local minimum, close to the starting point. It is in fact unlikely that the global minimum is obtained. To increase the chances of ending up in a sufficiently good local minimum, one would like to descend the cost function over multiple paths, in different descending directions. A way to come to different descending paths, from a certain starting point, is by calculating the gradient based on a subset of the parameters, as opposed to all parameters simultaneously. Keeping a number of parameters constant during the optimisation reduces the degrees of freedom, resulting in different paths. This is a valid approach considering that generally not all monomials and hence degrees of freedom are required.
We have used the same optimisation strategy as described in [4]. In each iteration run, a number of possible subsets are individually tested and the resulting models for each subset are compared on the basis of their Root Mean Square (RMS) error. The model with the lowest RMS error is selected to proceed to the next iteration step and this iterative process is continued untill no subset can be found for which the optimisation yields a better estimate. The details on the optimisation strategy are given in [3, 4].

4 PNLSS model identification

In this section the PNLSS model identification technique is used to estimate a nonlinear model for the training data. The identification process starts with calculating the linear nonparametric estimate of the training data. The nonparametric estimate is used to obtain a parametric model, which is subsequently used as the initial model for the optimisation algorithm to identify the best nonlinear PNLSS model.

4.1 Training data

The training data used for the PNLSS model identification is the experimental data of forces acting on the pitching aerofoil. Making a model which captures the dynamical features of the system requires a training data which covers the desired region of the solution space. This results in the fact that the nonlinear model will be strongly conditioned on the training data which was used. An efficient way of covering the solution space of nonlinear systems is by exciting it using a multisine excitation signals [16]. A multisine signal is composed out of *N* harmonically related sines, which are integral multiple of a base frequency f_0.

$$\alpha(t) = \sum_{k=1}^{N} A_k \sin(2\pi k f_0 t + \phi_k) \tag{6}$$

The amplitude A_k of each harmonic can be explicitly selected by the user. We have used an odd random phase multisine signals in which only the odd harmonics are excited and some of the odd harmonics are randomly omitted. The omitted frequency lines allow for the estimation of nonlinear distortions [22]. The phases ϕ_k are randomly chosen between [0-2π). Choosing random phases for the multisine signal has a number of advantages. Random phases avoid the energy accumulation at the start of frequency band, thus improving the crest factor [17]. Random signals are more suitable for estimating nonlinear distortions and random phase multisine resembles a random signal as it attains a gaussian distribution for a sufficiently large number of data samples [18].

4.2 Non parametric linear approximation

The local polynomial method (LPM) developed by Schoukens et al. [19] is used to obtain a non-parametric linear approximation of the system. The noise and the nonlinear distortions in the training data are also estimated. The noise on the training data is estimated by calculating the variance over multiple periods of the data. Generally, the nonlinear distortions are estimated by calculating the variance over multiple realisations of the data, but the odd random phase multisine signals allow for the calculation of the nonlinearities from a single realisation.

4.2.1 Quantification of nonlinearity

The experimental data from the CPFD setup is in the low-speed subsonic regime. In this flow regime, the major source of aerodynamic nonlinearity are the boundary layer and the separated flow regions, as compressibility effects are negligible. The experiments were performed below the stall angle of attack of the aerofoil. The NACA 0018 aerofoil has a very gentle stall behaviour and its stall angle of attack is around 21° [21]. At lower angles of attack, the boundary layer remains attached at all times and the resulting aerodynamic nonlinearity is weak. Strong aerodynamic nonlinearity generally occurs only when part of the flow is separated either permanently or instantaneously. Separated flow occurs around bluff bodies and streamlined bodies at high angles of attack or motion rates [5]. As we were interested in modelling the aerodynamic nonlinearity, the experiments with high offset angles were considered for the PNLSS model identification.

The noise and nonlinear distortion estimates obtained are very useful in comparing the available experimental datasets. The estimated FRF, noise and nonlinear distortion for the experimental data of 35 m/s at 12° offset angle and 4° pitch oscillation are shown in Figure 2.

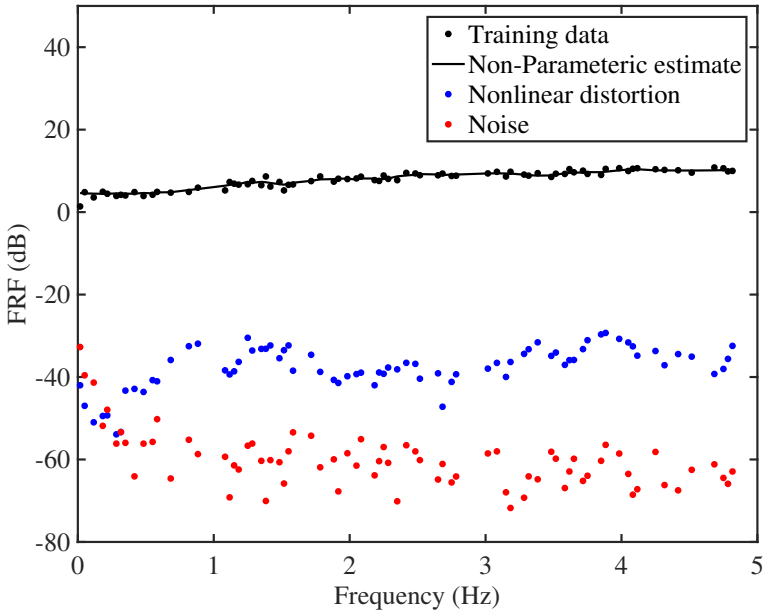


Figure 2: FRF measurement of the force at one load cell of trailing edge actuator of the CPFD setup with quantification of the level of nonlinear distortions and the noise in the measurement.

The level of nonlinearity for the available experimental datasets are compared by computing the average of the FRF, the noise and the nonlinear (NL) distortion as shown in Table 1. The pitch oscillation for experiments at 35 m/s and 30 m/s are 4° and 2° respectively. The gap between the magnitude of the FRF, which is the linear response of the system, and the nonlinear distortion is around 20-40 dB. This shows that the nonlinear distortions are less than 10 $\%$ of the linear response of the system. The level of the nonlinear distortion increases with the increase of the offset angle but the level of noise on the data also increases. A good nonlinear model should capture the nonlinearities above the noise floor. In terms of difference between the nonlinear distortion and the noise level, data for 35 m/s and 12° offset angle has the largest gap. This data was used as the training data for the PNLSS model identification.

Table 1: Average of the FRF, nonlinear distortion and noise in the experimental datasets at different velocities and offset angles

Velocity (m/s)	Offset angle (deg)	FRF_{avg} (db)	Noise_{avg} (db)	NL_{avg} (db)	FRF_{avg} - NL_{avg} (db)	NL_{avg} - Noise_{avg} (db)
35	8	9.71	-33.30	-26.71	36.41	6.60
35	10	8.09	-30.76	-25.03	33.12	5.74
35	12	7.90	-30.09	-18.86	26.77	11.22
30	12	7.55	-22.86	-16.16	23.71	6.70
30	14	7.64	-21.24	-14.34	21.98	6.90
30	16	8.64	-19.30	-17.05	25.69	2.24
30	18	9.37	-15.97	-13.02	22.39	2.96

4.3 Parametric linear approximation

Linear parametric models were identified using both the frequency domain subspace module [14] and the frequency domain identification **FDIDENT** [11] tool box for the selected training data. Models with order

1-5 were scanned and the model order with the best fit in the excited band was selected. It may be noted that a high order model does not ensure a better fit. Increasing the model order also increases the number of states which leads to a combinatorial growth of the parameters to be estimated and may result in over-fitting. Models with too low order, on the other hand, may not be able to capture the dynamics of the system appropriately. The third order model estimated by FDIDENT toolbox gave the best fit and was therefore used as the initialisation for the PNLSS model.

4.4 Optimising the PNLSS model

The selected parametric model is used as an initial model for the PNLSS iterative optimisation routine. The excitation signal used for the training data is the odd random phase multisine excited in the frequency range of 0-5 Hz. The training data consists of 90 000 samples and has a sampling frequency of 5 kHz. A uniform frequency weighting from 0-25 Hz is used during the PNLSS optimisation step. The output of the third order linear model, which was used for initialisation of the PNLSS optimisation, is compared with the PNLSS model output at only the excited lines in Figure 3. The relative RMS error on the excited lines for the PNLSS output is only 3% compared to the relative RMS error of 11.5% for the linear model output. The outputs of the linear model and the PNLSS model are shown in Figure 4 along with the error of the PNLSS output and the noise level in the training data. The PNLSS output has a good agreement with the training data in excited as well as unexcited frequency range. It can be observed that the error is almost at the noise level, indicating that the nonlinear model was able to capture almost all the nonlinear behaviour of the system.

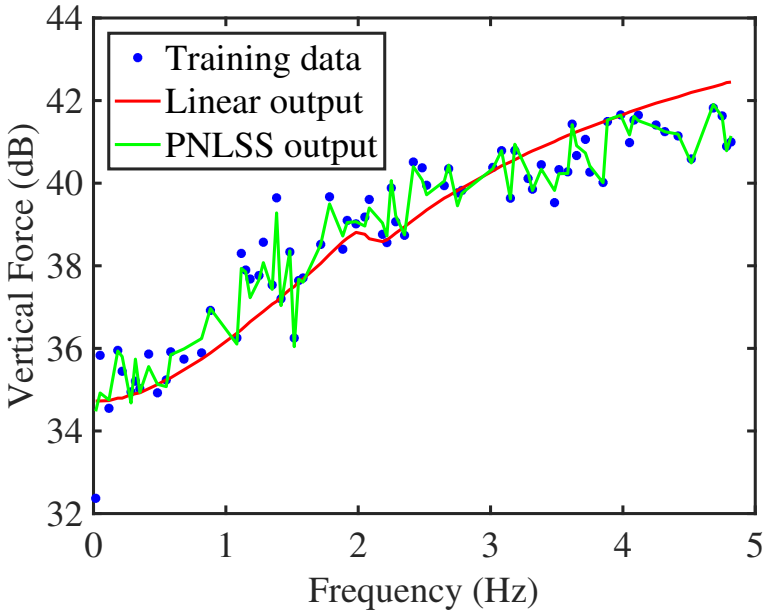


Figure 3: Comparison of the output of the Linear model and the PNLSS model at the excited frequencies

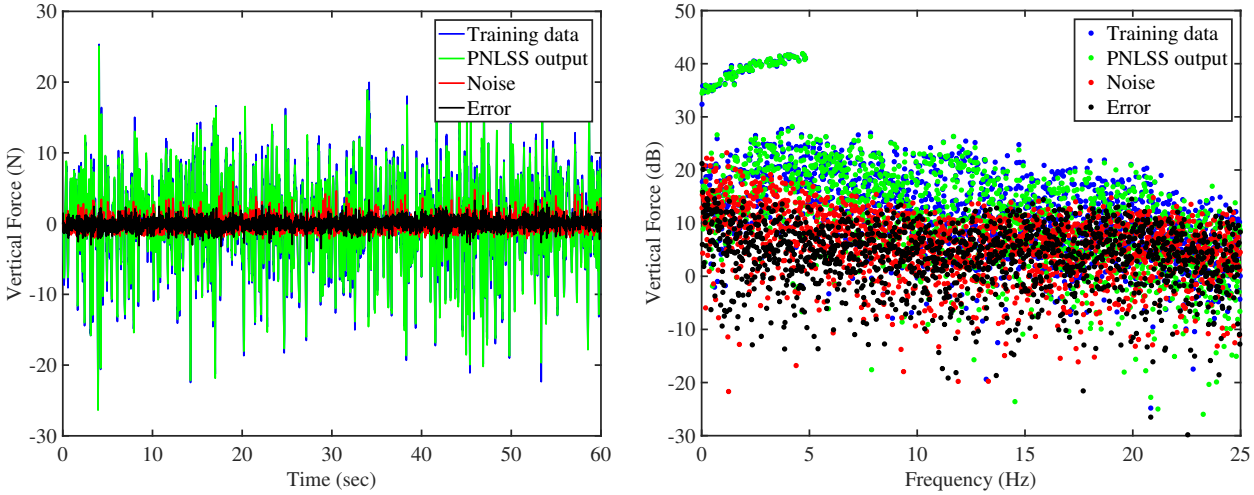


Figure 4: Comparison of the DFT of the measured output (training data), the PNLSS output along with the error on the outputs and the noise on the measured output in the time domain (left) and frequency-domain (right)

The relative RMS error of the linear model and the PNLSS model for the output on excited lines, excitation band and the weighted band are shown in Table 2. The PNLSS model is three times more accurate than the linear model.

Table 2: Comparison of the relative RMS error of the linear model with the PNLSS model at the excited harmonics, the excitation band and the weighted band.

Models	Relative RMS error %		
	Excited harmonics	Excitation band (0-5Hz)	Weighted band (0-25Hz)
Linear	11.5	22	33
PNLSS	3	6	10

5 Validation

To assess the performance of the estimated model, validation is performed on a dataset which was not used for model estimation. The validation datasets are chosen so to resemble the operating conditions of the model. It is not necessarily so that the model which gave the least RMS error during the estimation will also perform best in the validation step as well. It may happen that due to overfitting of the estimation model, it performs poorly on the validation data. Therefore, all models obtained during the optimisation procedure (where every iteration yields a new model) were saved and validated.

The estimated model is validated on a single sine experiment at 2 Hz for the same velocity and offset angle as that of the training data but with 1° pitch oscillation. The relative RMS error of the on the validation data is 21% while the error of the linear model is 32%. The output of both models is compared with the validation data in Figure 5. The linear model was not able to accurately estimate the maximum amplitude. The DFT of the output reveals the limitation of the linear model, as linear models cannot estimate the higher harmonics of the excited frequencies. The PNLSS model, on the other hand, estimates the amplitude of the excited harmonic as well as the higher harmonics.

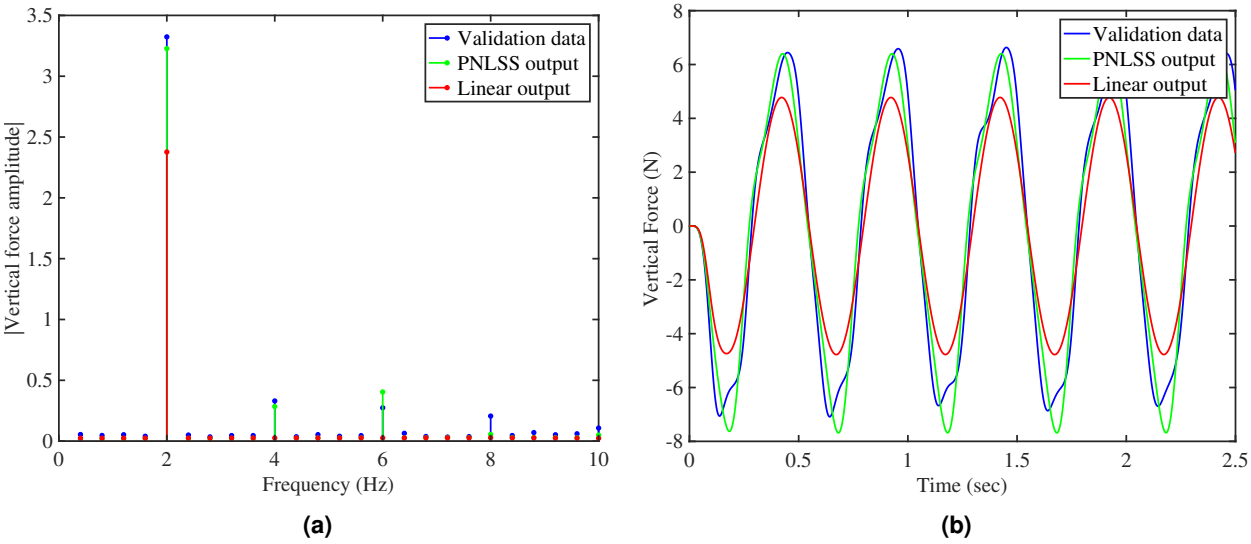


Figure 5: Comparison of the output of the PNLSS validation model with the linear output and the validation data in frequency domain (Left) and time domain (Right)

The model was additionally used to simulate the output of two single sines experiments at 1 Hz and 5 Hz for the same speed, offset angle and pitch oscillation as that of the validation data. The error of the PNLSS model is high but it is still three times lower than the error of the linear model. The reason for the high error on the validation data is that the estimation model was tuned on limited training data as only a single realisation was used. The accuracy of the model can be improved on the validation data by using data for multiple realisations as the training data. The high error on the single sine validation might indicate that single sines induce a considerable different flow regime than multisine at the same wind speed and angle of attack. If single sines are the intended operating signals then training to swept sines might be more appropriate.

Table 3: Comparison of the relative RMS error on the output of the PNLSS model and the linear model for single sines at 1, 2 and 5 Hz.

Frequency	Relative RMS error %	
(Hz)	PNLSS	Linear
1	78	240
2	21	32
5	38	170

6 Conclusion

This work presents a first polynomial nonlinear state space (PNLSS) model able to simulate the aerodynamic force on a pitching aerofoil. The experimental data used to estimate the model is obtained from the Cyber Physical Fluid Dynamic (CPFD) setup. Initially a non-parametric model is obtained using the Local Polynomial Method (LPM) which was then used to obtain a linear parametric model. The parametric model was used as initialisation for the PNLSS model, which was optimised using the Levenberg-Marquardt algorithm. To improve the optimisation, an iterative procedure was adopted in which subsets of parameters were optimised instead of all the parameters at once. The estimated PNLSS model performed significantly better than the linear approximation yielding an error of 6% on the training data in the excitation band. Thus, we show that a reliable model can be constructed from wind tunnel data that correctly captures the nonlinearity of the aerodynamic force. Higher error were observed for the single sine validation. It was suggested that single

sine experiments induce a flow regime which may be considerably different from the one obtained using multisines.

References

[1] Y. Babbar, V. S. Suryakumar, A. Mangalam, and T. W. Strganac. An approach for prescribed experiments for aerodynamic-structural dynamic interaction. In *51st AIAA Aerospace Science Meeting Including the New Horizons Forum and Aerospace Exposition, number January, Grapevine (Dallas/Ft. Worth Region), Texas*, pages 07–10, 2013.

[2] Y. Babbar, V. S. Suryakumar, and T. W. Strganac. Experiments in aeroelastic response and control under gust. In *54th AIAA/ASME/ASCE/AHS/ASC Structures, Structural Dynamics, and Materials Conference*, page 1637, 2013.

[3] J. Decuyper. *Nonlinear State-Space Modelling of the Kinematics of an Oscillating Cylinder in a Fluid Flow*. PhD thesis, VUB, November 2017.

[4] J. Decuyper, T. De Troyer, M. Runacres, K. Tiels, and J. Schoukens. Nonlinear state-space modelling of the kinematics of an oscillating circular cylinder in a fluid flow. *Mechanical Systems and Signal Processing*, 98:209–230, 2018.

[5] G. Dimitriadis. *Introduction to Nonlinear Aeroelasticity*. John Wiley & Sons, 2017.

[6] J. Ertveldt. *Application of frequency-domain system identification to wind tunnel experiments on the Active Aeroelastic Test Bench*. PhD thesis, VUB, Belgium, Jan. 2017.

[7] J. Ertveldt, J. Schoukens, R. Pintelon, and S. Vanlanduit. Experiments on the Active Aeroelastic Test Bench (AATB) for the identification of unsteady aerodynamics. In *International Forum on Aeroelasticity and Structural Dynamics*, June 2015.

[8] J. Ertveldt, J. Schoukens, R. Pintelon, S. Vanlanduit, B. De Pauw, and A. Rezayat. Design and testing of an active aeroelastic test bench AATB for unsteady aerodynamic and aeroelastic experiments. In *56th AIAA/ASCE/AHS/ASC Structures, Structural Dynamics, and Materials Conference*, page 1857, 2015.

[9] J. Ertveldt, R. Pintelon, and S. Vanlanduit. Identification of unsteady aerodynamic forces from forced motion wind tunnel experiments. *AIAA Journal*, pages 3265–3273, 2016.

[10] T. Kier. Comparison of unsteady aerodynamic modelling methodologies with respect to flight loads analysis. In *AIAA Atmospheric Flight Mechanics Conference and Exhibit*, page 6027, 2005.

[11] I. Kollár, R. Pintelon, and J. Schoukens. Frequency domain system identification toolbox. *The MathWorks*, pages 8–12, 1994.

[12] J. G. Leishman and T. S. Beddoes. A Semi-Empirical Model for Dynamic Stall. *Journal of the American Helicopter Society*, 34(3):3–17, July 1989. doi: 10.4050/JAHS.34.3.

[13] K. Levenberg. A method for the solution of certain non-linear problems in least squares. *Quarterly of applied mathematics*, 2(2):164–168, 1944.

[14] P. V. Overschee and B. D. Moor. *Subspace Identificaqtion for Linear Systems*. Kluwer Academic Publishers, 1996.

[15] J. Paduart, L. Lauwers, J. Swevers, K. Smolders, J. Schoukens, and R. Pintelon. Identification of nonlinear systems using polynomial nonlinear state space models. *Automatica*, 46(4):647–656, 2010.

[16] R. Pintelon and J. Schoukens. Measurement and modelling of linear systems in the presence of non-linear distortions. *Mechanical systems and signal processing*, 16(5):785–801, 2002.

[17] J. Schoukens, R. Pintelon, Y. Rolain, and T. Dobrowiecki. Frequency response function measurements in the presence of nonlinear distortions. *Automatica*, 37(6):939–946, 2001.

[18] J. Schoukens, J. Swevers, R. Pintelon, and H. Van Der Auweraer. Excitation design for FRF measurements in the presence of non-linear distortions. *Mechanical Systems and Signal Processing*, 18(4): 727–738, 2004.

[19] J. Schoukens, Y. Rolain, and R. Pintelon. Leakage Reduction in Frequency-Response Function Measurements. *IEEE Transactions on Instrumentation and Measurement*, 55(6):2286–2291, Dec. 2006. ISSN 0018-9456. doi: 10.1109/TIM.2006.887034.

[20] T. Theodorsen. General theory of aerodynamic instability and the mechanism of flutter. Technical report, National Advisory Committee for Aeronautics; Washington, DC, United States, 1979.

[21] W. Timmer. Two-dimensional low-reynolds number wind tunnel results for airfoil NACA 0018. *Wind engineering*, 32(6):525–537, 2008.

[22] Y. Van Ingelgem, E. Tourwé, O. Blajiev, R. Pintelon, and A. Hubin. Advantages of odd random phase multisine electrochemical impedance measurements. *Electroanalysis*, 21(6):730–739, 2009.

Computationally-efficient aeroelastic analysis tool for short-wing / propeller configuration on compound helicopters

Z. Wang [1], **A. A. Popov** [1]
[1] Department of Mechanical, Materials and Manufacturing Engineering,
University Park, University of Nottingham, Nottingham, United Kingdom
e-mail: **Zi.Wang@nottingham.ac.uk**

Abstract
A time-domain aeroelastic analysis for short-wing/propeller configuration in compound helicopters is presented in this paper. A linear Timoshenko beam is used in conjunction with analytical aerodynamic theories, while propeller effects are simplified as defined velocity profiles in the advancing and vertical directions. A numerical modal analysis approach is used to incorporate the coupling between bending and torsion. The paper focuses on the application of coupled mode shapes and Timoshenko beam in an aeroelasticity context. A Eurocopter X3-liked short-wing/propeller configuration is studied. Differences introduced by coupled mode shapes and Timoshenko beam theory are discussed. The results show that coupled modal analysis gives a better representation of the modal behaviour with less computational power required. While rotary inertia and shear deformation effects result in a higher mean deflection and a smaller amplitude in the steady state, revealing a different energy distribution mechanism compare to Euler-Bernoulli beam in the system studied.

1 Introduction

A major and still open issue in rotorcraft design is the high level of vibration resulting from the complex interaction between the main rotor and other structures. This interaction strongly affects the fatigue life of structures, maintenance costs, on-board instrumentation efficiency, and comfort. In the cases of compound helicopters and tilt-rotor aircraft, the vibrational behaviour is further complicated by the presence of fixed wings with propellers, or lateral rotors attached to the wing main structure. Another distinctive feature of these types of rotorcraft is the necessity to deliver rotational power to all rotors by the transmission systems which further influences the overall structural behaviour with their own dynamics.

The initiative of this paper is to disclose the scientific background of such complex aeroelastic behaviour using simple and numerically efficient models, which can be further implemented into design and optimisation stages for compound helicopter wing structures. The paper focuses on the application of coupled modal analysis and Timoshenko beam theory for aeroelastic response of short-wing/propeller configuration on compound helicopters.

The aeroelastic behaviour is governed by the structural dynamics and aerodynamic loadings of the wing-propeller system. To achieve the aim, the wing semi-span is simplified as a cantilever beam with a tip loaded propeller. Having to provide lift, secure tractor propellers in place and still maintain the compatibility of existing helicopter facilities, the wing needs to be a stiff and short one. Effects of shear deformations need to be taken into account in this case. Hence, a linear model based on the Timoshenko beam theory is used for characterising the wing's structural behaviour.

Studies using Euler-Bernoulli beam theory is a much more common topic in the area of aeroelasticity. As classic fixed-wing aircraft features a much slender wing, Euler-Bernoulli beam theory is usually sufficient enough [1–6]. For rotorcrafts, rotor blades are also slender structures that can be characterised by Euler-Bernoulli beam theory [7, 8]. There are some, however, limited cases featuring other beam theories when

studying aeroelastic systems. Application of a quasi-slender Rayleigh beam into a semi-analytical model was carried out by Berci et al. in [9]. Kämpchen et al. studied the aeroelastic response of a very elastic wing [10]. In his case, Timoshenko beam was used to avoid any energy dispersion by coupling between bending and translational motions. For short wings on compound helicopters, Timoshenko beam incorporating shear deformation effects is much more suitable.

For the aerodynamic loadings, predictions are made based on time-domain analytical sectional theories, such as the Wagner's and Küssner's models. In this particular case, the propeller slipstream effects on the wing are modelled as additional velocity components in the vertical and axial directions. Finally, by integrating the structural and aerodynamic models, the governing equations of motion for the short-wing and propeller system can be obtained. At this stage, only flapping and torsional motion are taken into account.

A numerical modal analysis approach is used to incorporate coupling between bending and torsion. Cantilever beam with coupled bending-torsion motion has been studied by Banerjee et al. [11–13]. They developed the analytical coupled modal frequencies and shapes for Euler-Bernoulli and Timoshenko beams, also stating that the application of coupled modes can be further used for aeroelasticity problems for better accuracy with less computational efforts. In the current paper, a numerical model based on transfer matrix method will be introduced and applied in an aeroelasticity context.

Based on the coupled mode shapes, the complete aeroelastic model can be discretised by Galerkin's method and solved numerically by Newmark-beta algorithm. An approach described in [14, 15] is used. The capability of the complete model is shown through a case study in similar configuration to Eurocopter X3. The aeroelastic responses will be compared to the ones obtained by uncoupled mode shapes and Euler-Bernoulli beam theory, respectively.

2 Mathematical model

2.1 Timoshenko beam theory

In the early 20th century, Timoshenko derived a beam theory that considers shear deformation and rotary inertia effects for thick/short beams [16, 17]. While an Euler-Bernoulli beam assumed slenderness and cross-section being planar and normal to the neutral axis, a Timoshenko beam allows shear deformation between beam cross-section and the neutral axis. For compound helicopters having fixed-wing features and tip-mounted propellers, the wing is a short one for the purpose of providing lift, securing propellers in place while still maintaining the compatibility with existing helicopter facilities. Therefore, the Euler-Bernoulli beam assumption for being slender is not valid. Instead a linear Timoshenko beam, in this case, can give a much more accurate representation for short and stiff wings in compound helicopters.

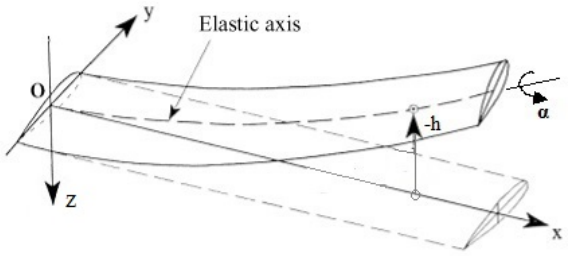


Figure 1: Beam model xyz coordinate

For a Timoshenko beam considering flapping (h) and torsional (α) motion as illustrated in Figure 1, its

governing equations can be written as

$$\begin{aligned} &m\frac{\partial^2 h}{\partial t^2} - mx_\alpha \frac{d^2\alpha}{dt^2} - \frac{\partial}{\partial x}[\kappa_h GA(\frac{\partial h}{\partial x} - \varphi_h)] = L_h \\ &\rho_w I_y \frac{\partial^2 \varphi_h}{\partial t^2} - \frac{\partial}{\partial x}(EI_y \frac{\partial \varphi_h}{\partial x}) - \kappa_h GA(\frac{\partial h}{\partial x} - \varphi_h) = 0 \\ &I_\alpha \frac{\partial^2 \alpha}{\partial t^2} - mx_\alpha \frac{\partial^2 h}{\partial t^2} - \frac{\partial}{\partial x}(GJ\frac{\partial \alpha}{\partial x}) = M_\alpha \end{aligned} \tag{1}$$

Where m is the mass per span, x_α is the distance between gravitational and shear centres, κ_h is the shear coefficient, E and G are the Young's and shear moduli, respectively, A is the cross-sectional area, φ_h is the sectional rotation allowing shear deformations, ρ_w is the wing's material density, I_y is the second moment of area, I_α is the mass moment of inertia per span, J is the torsional coefficient and L_h, M_α are the loadings in flapping and torsional coordinates.

Dimensionless time ($\tau = U_\infty t/b$) domain is used for this simulation by modifying the real time with the aircraft advancing speed U_∞ and half chord length b. Therefore, Equation (1) can be rewritten considering dimensionless bending displacement ($\xi = h/b$) as

$$\begin{aligned} &m\frac{U_\infty^2}{b}\ddot{\xi} - mx_\alpha \frac{U_\infty^2}{b^2}\ddot{\alpha} - [\kappa_h GA(b\xi' - \varphi_h)]' = L_h \\ &\rho_w I_y \frac{U_\infty^2}{b^2}\ddot{\varphi}_h - (EI_y\varphi_h')' - \kappa_h GA(b\xi' - \varphi_h) = 0 \\ &I_\alpha \frac{U_\infty^2}{b^2}\ddot{\alpha} - mx_\alpha \frac{U_\infty^2}{b}\ddot{\xi} - (GJ\alpha')' = M_\alpha \end{aligned} \tag{2}$$

Note that $\ddot{\xi}$, $\ddot{\alpha}$ and $\ddot{\varphi}_h$ are derivatives with respect to dimensionless time τ, while ξ', φ_h' and α' are derivatives with respect to wing span coordinate x.

Using modal analysis techniques, displacements in flapping and torsion can be rewritten as Equation (3). In the case studied, coupling between these two motions are involved. Therefore, coupled mode shapes are characterised through the transfer matrix method. Hence, they share the same time-dependent function $q_j(\tau)$.

$$\xi = \sum_{j=0}^{\infty} \theta_j(x) q_j(\tau); \qquad \varphi_h = \sum_{j=0}^{\infty} \phi_j(x) q_j(\tau); \qquad \alpha = \sum_{j=0}^{\infty} \eta_j(x) q_j(\tau); \tag{3}$$

2.1.1 Numerical modal analysis

To perform modal analysis, a numerical approach is introduced here. Comparing to theoretical expressions, this is a much more versatile way to obtain natural frequencies and mode shapes for structures with coupled motions. Simple harmonic motions for bending and torsion are assumed as

$$\xi = \sum_{j=0}^{\infty} \theta_j(x) e^{i\omega_j t}; \qquad \varphi_h = \sum_{j=0}^{\infty} \phi_j(x) e^{i\omega_j t}; \qquad \alpha = \sum_{j=0}^{\infty} \eta_j(x) e^{i\omega_j t}; \tag{4}$$

Therefore, with uniform beam properties, the governing equations of motion can be written as

$$\begin{aligned} &- mb\omega_j^2\theta_j + mx_\alpha\omega_j^2\eta_j - \kappa_h GA(b\theta_j'' - \phi_j') = 0 \\ &- \rho_w I_y\omega_j^2\phi_j - EI_y\phi_j'' - \kappa_h GA(b\theta_j' - \phi_j) = 0 \\ &- I_\alpha\omega_j^2\eta_j + mbx_\alpha\omega_j^2\theta_j - GJ\eta_j'' = 0 \end{aligned} \tag{5}$$

In general matrix form, Equation (5) can be rearranged as

$$\begin{Bmatrix} \theta_j' \\ \theta_j'' \\ \phi_j' \\ \phi_j'' \\ \eta_j' \\ \eta_j'' \end{Bmatrix} = \begin{bmatrix} 0 & 1 & 0 & 0 & 0 & 0 \\ -\frac{m\omega_j^2}{\kappa_h GA} & 0 & 0 & \frac{1}{b} & \frac{mx_\alpha\omega_j^2}{\kappa_h GAb} & 0 \\ 0 & 0 & 0 & 1 & 0 & 0 \\ 0 & -\frac{\kappa_h GAb}{EI_y} & \frac{\kappa_h GA - \rho_w I_y \omega_j^2}{EI_y} & 0 & 0 & 0 \\ 0 & 0 & 0 & 0 & 0 & 1 \\ \frac{mx_\alpha\omega_j^2}{GJ} & 0 & 0 & 0 & -\frac{I_\alpha\omega_j^2}{GJ} & 0 \end{bmatrix} \begin{Bmatrix} \theta_j \\ \theta_j' \\ \phi_j \\ \phi_j' \\ \eta_j \\ \eta_j' \end{Bmatrix} = \mathbf{A} \begin{Bmatrix} \theta_j \\ \theta_j' \\ \phi_j \\ \phi_j' \\ \eta_j \\ \eta_j' \end{Bmatrix} \tag{6}$$

Therefore,

$$\left\{\theta_j(x)\ \theta_j'(x)\ \phi_j(x)\ \phi_j'(x)\ \eta_j(x)\ \eta_j'(x)\right\}^{\mathrm{T}} = e^{\mathbf{A}x} \left\{\theta_j(0)\ \theta_j'(0)\ \phi_j(0)\ \phi_j'(0)\ \eta_j(0)\ \eta_j'(0)\right\}^{\mathrm{T}} \tag{7}$$

To implement boundary conditions, the displacement parameters can be corrected into loading/displacement parameters as

$$\begin{Bmatrix} \theta_j(x) \\ S(x) \\ \phi_j(x) \\ M(x) \\ \eta_j(x) \\ T(x) \end{Bmatrix} = \begin{bmatrix} 1 & 0 & 0 & 0 & 0 & 0 \\ 0 & \kappa_h GAb & -\kappa_h GA & 0 & 0 & 0 \\ 0 & 0 & 1 & 0 & 0 & 0 \\ 0 & 0 & 0 & -EI_y & 0 & 0 \\ 0 & 0 & 0 & 0 & 1 & 0 \\ 0 & 0 & 0 & 0 & 0 & GJ \end{bmatrix} \begin{Bmatrix} \theta_j(x) \\ \theta_j'(x) \\ \phi_j(x) \\ \phi_j'(x) \\ \eta_j(x) \\ \eta_j'(x) \end{Bmatrix} = \mathbf{D} \begin{Bmatrix} \theta_j(x) \\ \theta_j'(x) \\ \phi_j(x) \\ \phi_j'(x) \\ \eta_j(x) \\ \eta_j'(x) \end{Bmatrix} \tag{8}$$

For cantilever beams, boundary conditions write as

Table 1: Cantilever beam boundary conditions

Root condition	$\theta_j(0) = 0$	$\phi_j(0) = 0$	$\eta_j = 0$
Tip condition	$S(l) = 0$	$M(l) = 0$	$T(l) = 0$

With boundary conditions applied to both ends of the beam, Equation (8) becomes

$$\begin{Bmatrix} S(l) = 0 \\ M(l) = 0 \\ T(l) = 0 \end{Bmatrix} = \mathbf{T}\mathbf{D}e^{\mathbf{A}l}\mathbf{D}^{-1}\mathbf{R} \begin{Bmatrix} S(0) \\ M(0) \\ T(0) \end{Bmatrix} \quad \text{where} \quad \mathbf{T} = \begin{bmatrix} 0 & 1 & 0 & 0 & 0 & 0 \\ 0 & 0 & 0 & 1 & 0 & 0 \\ 0 & 0 & 0 & 0 & 0 & 1 \end{bmatrix} \ ; \ \mathbf{R} = \mathbf{T}' \tag{9}$$

By solving the zero determinant of $\det(\mathbf{T}\mathbf{D}e^{\mathbf{A}l}\mathbf{D}^{-1}\mathbf{R})$, coupled natural frequencies and mode shapes can be obtained.

2.2 Aerodynamic Loadings

The unsteady aerodynamic loadings are characterised through analytical theories. The same approach was developed and used in [14, 15], featuring the Wagner's and Küssner's functions. As illustrated in Figure 2, the aerodynamic loadings consist of circulatory terms (L_C, M_C) and non-circulatory terms (L_{NC}, M_{NC}).

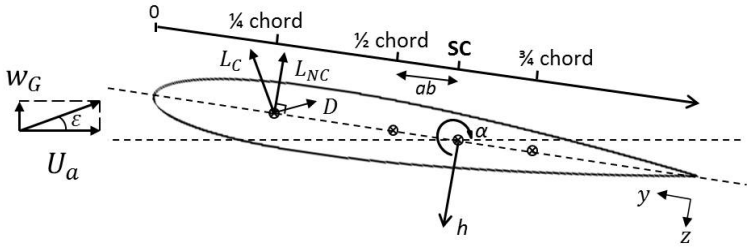


Figure 2: Aerofoil notation

Wagner discovered that the circulatory lift can be formulated in dimensionless time domain as a function of downwash induced at 3/4 chord $w_{3/4}$ [18]. Therefore, it writes

$$\begin{aligned} L_C =& -2\pi b\rho U_a\phi(\tau)w_{3/4}(0) - 2\pi b\rho U_a\int_0^\tau \phi(\tau-\tau_0)w_{3/4}(\tau_0)d\tau_0 \quad ; \quad M_C = -(\frac{1}{2}+a)bL_C\cos(\varepsilon+\alpha) \\ &\text{Where } w_{3/4} = U_a\alpha + \frac{dh}{dt} + (\frac{1}{2}-a)b\frac{d\alpha}{dt} = U_a\alpha + U_\infty\dot{\xi} + U_\infty(\frac{1}{2}-a)\dot{\alpha} \end{aligned} \tag{10}$$

Where ρ is the air density, U_a is the flow approaching velocity, $\phi(\tau)$ is the Wagner's function approximated by R.T. Jones [19,20]. As propeller effects are defined as velocity distributions, U_a is not the same with U_∞.

For non-circulatory lift, they are arised from apparent mass ($\pi\rho b^2$) and can be formulated in dimensionless time domain as

$$\begin{aligned} L_{NC} &= -\pi\rho bU_\infty^2(\ddot{\xi} - a\ddot{\alpha}) - \pi\rho bU_aU_\infty\dot{\alpha} \\ M_{NC} &= \pi\rho ab^2U_\infty^2(\ddot{\xi} - a\ddot{\alpha}) - (1/2-a)\pi\rho b^2U_aU_\infty\dot{\alpha} - \frac{1}{8}\pi\rho b^2U_\infty^2\ddot{\alpha} \end{aligned} \tag{11}$$

Propellers mounted on the wing not only add weights G_{prop} on wing tips, but also complicate the flow characteristics. As shown in Figure 3, for the propeller-covered area, there are additional velocity in the y-direction, additional velocity in the z-direction and sinusoidal velocity variation in the z-direction.

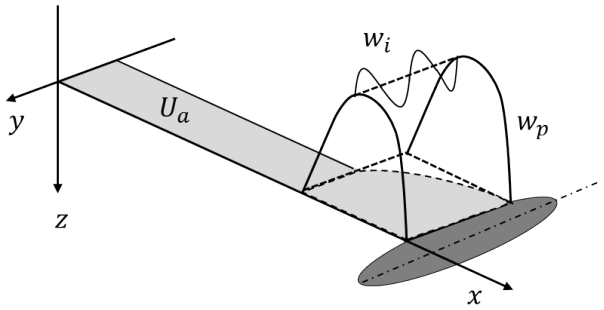


Figure 3: Propeller vertical and axial effects on fixed wing

In the vertical direction, there are several velocity components needed to be taken into consideration for the present study. Firstly, to reproduce effects of the wing's built-in angle (ε_0), a equivalent step-gust ($w_0 = U_a\tan\varepsilon_0$) going through horizontally-placed wing can be used along full length of the wing span. As for the propellers, in the propeller-covered area, a parabolic velocity profile w_p was assumed with sinusoidal variation w_i. Therefore, the total vertical velocity component can be written as Equation (12).

$$w_G(x,\tau) = \begin{cases} w_0(x,\tau) & \text{without propeller} \\ w_0(x,\tau) + w_p(x,\tau) + w_i(x,\tau) & \text{with propeller} \end{cases} \tag{12}$$

Due to the periodical nature of a propeller, the sinusoidal variation w_i regarding to the shear centre can be expressed in dimensionless domain as

$$w_i(x,t) = w_i(x)\sin\omega_p(t - b(1+a)/U_a) \Longrightarrow w_i(x,\tau) = w_i(x)\sin k_p(\tau - U_\infty(1+a)/U_a)$$

Where ω_p is the blade-passing frequency relative to the wing, $k_p = \omega_p b/U_\infty$ is the reduced frequency in the dimensionless time domain.

As Küssner developed a theory characterising aerodynamic loadings exerted in any arbitrary velocity field [21], the lift and moment components can be written as Equation (13). Due to its circulatory nature, L_g shares the same direction with L_C, while M_g shares a similar formulation with M_C.

$$L_g(\tau) = -2\pi\rho b U_a \int_0^\tau w_G(\tau)\frac{\partial\psi(\tau-\tau_0)}{\partial\tau}d\tau_0 \quad ; \quad M_g(\tau) = -(1/2+a)bL_g\cos(\varepsilon+\alpha) \tag{13}$$

Where $\psi(\tau)$ is the Küssner's function approximated by Sears and Sparks [22].

Overall, loadings in the flapping and torsional directions can be written as

$$L_h = (L_C{+}L_g)\cos(\varepsilon{+}\alpha){+}L_{NC}{+}D\sin(\varepsilon{+}\alpha){+}G_{prop}\cos\alpha\,;\; M_\alpha = M_C{+}M_{NC}{+}M_g{-}(\frac{1}{2}{+}a)bD\sin(\varepsilon{+}\alpha) \tag{14}$$

2.3 Aeroelastic Model

A general matrix form of the governing equation can be obtained by combining the Timoshenko beam model and aerodynamic loadings and then lead to an solution by applying Galerkin's method. Note that there is no added damping for the structure. Any damping effect is originated from aerodynamic loading formulations.

$$\mathbf{M}\ddot{\boldsymbol{u}} + \mathbf{K}\boldsymbol{u} = \boldsymbol{F}$$

$$\text{where} \quad \mathbf{M} = [\mathbf{M_{ij}}]_{N\times N} = \begin{bmatrix} m\int_0^l \theta_i\theta_j dx & 0 & -mx_\alpha\int_0^l \theta_i\eta_j dx \\ 0 & \rho I_y\int_0^l \phi_i\phi_j dx & 0 \\ -mx_\alpha\int_0^l \eta_i\theta_j dx & 0 & I_\alpha\int_0^l \eta_i\eta_j dx \end{bmatrix}_{N\times N}$$

$$\mathbf{K} = [\mathbf{K_{ij}}]_{N\times N} = \begin{bmatrix} -\kappa_h GAb\int_0^l \theta_i\theta_j''dx & \kappa_h GA\int_0^l \theta_i\phi_j'dx & 0 \\ -\kappa_h GAb\int_0^l \phi_i\theta_j'dx & -EI_y\int_0^l \phi_i\phi_j''dx + \kappa_h GA\int_0^l \phi_i\phi_j dx & 0 \\ 0 & 0 & -GJ\int_0^l \eta_i\eta_j dx \end{bmatrix}_{N\times N}$$

$$\ddot{\boldsymbol{u}} = [\ddot{\boldsymbol{u}}_j]_{N\times 1} = \begin{bmatrix} \frac{U_\infty^2}{b}\ddot{q}_j \\ \frac{U_\infty^2}{b^2}\ddot{q}_j \\ \frac{U_\infty^2}{b^2}\ddot{q}_j \end{bmatrix}_{N\times 1} \qquad \boldsymbol{u} = [\boldsymbol{u}_j]_{N\times 1} = \begin{bmatrix} q_j \\ q_j \\ q_j \end{bmatrix}_{N\times 1} \qquad \boldsymbol{F} = [\boldsymbol{F}_i]_{N\times 1} = \begin{bmatrix} \int_0^l \theta_i L_h dx \\ 0 \\ \int_0^l \eta_i M_\alpha dx \end{bmatrix}_{N\times 1} \tag{15}$$

Recursive optimisation was carried out on convolution integral to improve model efficiency, with a linear Newmark-beta integration method implemented, as discussed in [14].

3 Case study parameters

A case resembling a similar short-wing configuration with Eurocopter X3 is studied to investigate the tool's capability. The parameters are presented as Table 2. The propeller velocity distribution are shown in Figure 4.

Table 2: Structural parameters of short wing

Mass m	22.3040 kg/m	Wing built-in angle ε_0	2 deg
Mass moment of inertia I_α	0.4714 kgm^2/m	Aircraft cruising speed U_∞	120 m/s
Bending stiffness EI_y	3.2146×10^5 Nm^2	Max. advancing speed addition	8 m/s
Torsional stiffness GJ	4.1276×10^5 Nm^2	Max. vertical velocity addition	7 m/s
Rotary inertia $\rho_w I_y$	0.0127 kgm^2/m	Sinusoidal variation	10%
Shear stiffness $\kappa_h GA$	9.7416×10^7 N	Blade-passing frequency ω_p	136.5 Hz
Aerofoil chord $c = 2b$	0.6 m	Propeller weight	490.5 N
Wing semi-span l	2.5 m	Lift/drag ratio	1/10
Shear centre offset x_α	0.09 m	Air density	1.225 kg/m^3

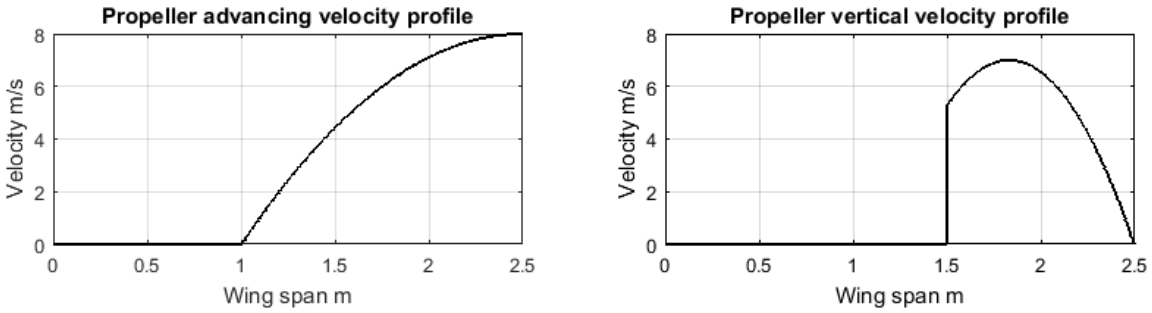


Figure 4: Propeller velocity addition in the y (advancing) and z (vertical) directions

3.1 Shear coefficient determination

For Timoshenko beam, shear coefficient is an important parameter. The shear coefficient κ_h is dependent on the shape of beam cross-section. In many studies, shear coefficients for various of cross-sectional types were approximated or validated. Although most beams have an arbitrary cross-section, simplification can be made in many cases. Standard cross-sections, such as rectangular, circular and hollow, etc. are used. In this case, the wing is simplified as a wing-box section, therefore a thin-wall box section was assigned. According to Cowper's study in [23], shear coefficient for box section is 0.44. This value is implemented in the presented Timoshenko beam model.

3.2 Modal analysis

Based on structural parameters given in Table 2, natural frequencies and their corresponding mode shapes can be investigated . Using modal analysis techniques introduced in Section 2.1.1, modal properties of the given system can be obtained. In Table 3, natural frequencies obtained by uncoupled and coupled approaches are listed and compared. Great differences can be observed from the third mode, especially when torsion is involved.

Uncoupled mode shapes for beam bending and torsion are well established and used for vibration problems. Their analytical expression can be found in many standard books. The coupled mode shapes obtained by transfer matrix method are shown in Figure 5. As illustrated, the first two modes are bending governed

Table 3: Natural Frequency comparisons

Uncoupled approach	Coupled approach	% Difference
10.73 Hz (Bending)	10.71 Hz	0.19%
66.70 Hz (Bending)	65.43 Hz	1.94%
93.57 Hz (Torsion)	120.31 Hz	22.23%
184.27 Hz (Bending)	177.49 Hz	3.82%
280.71 Hz (Torsion)	329.02 Hz	14.68%
354.38 Hz (Bending)	365.40 Hz	3.02%

with little torsion involvement. From the 3rd mode onwards, coupled behaviour in bending and torsion starts to show. The third and forth modes are torsion governed with considerable amount of bending and sectional rotation involved. While for the fifth and sixth modes, they are governed by sectional rotation, with considerable bending and torsion behaviour.

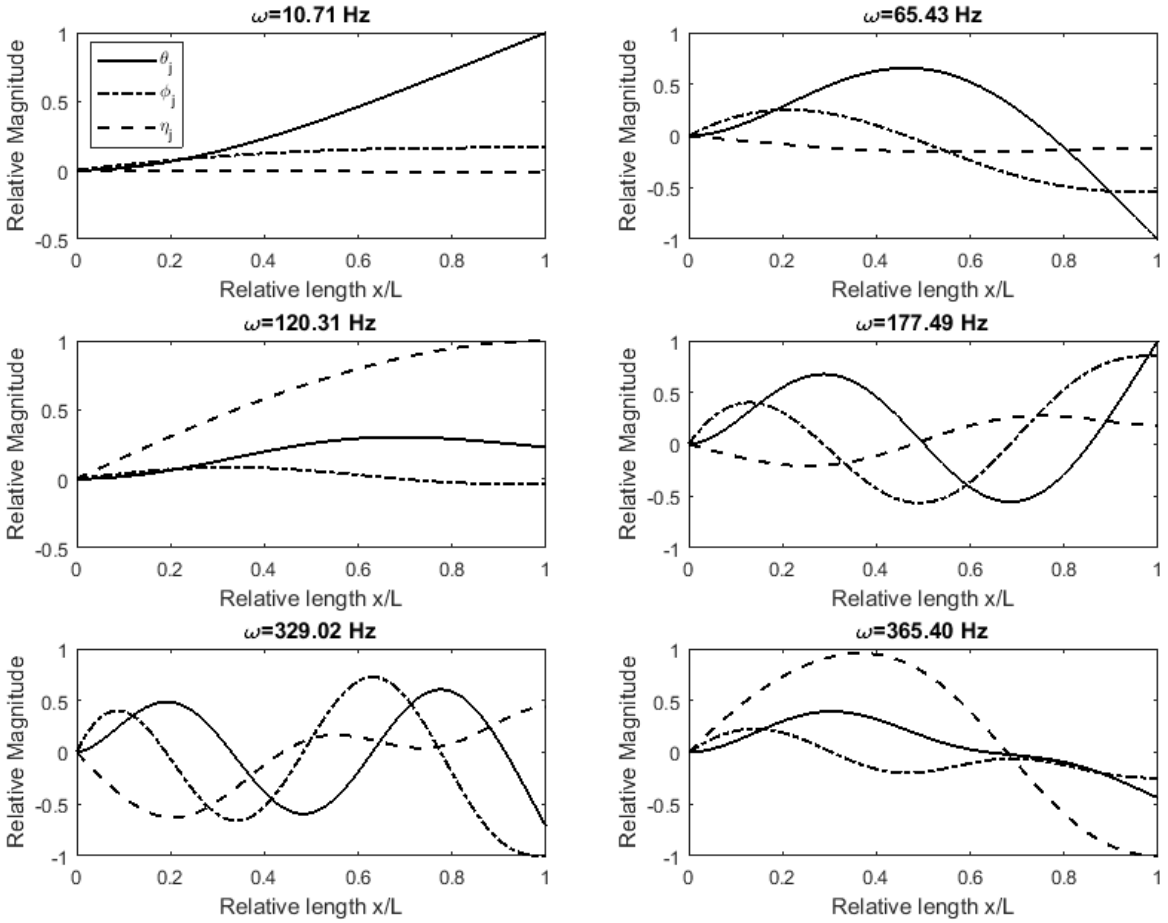


Figure 5: Coupled modal frequencies and shapes

3.3 Convergence study

A convergence study is carried out to determine the minimum number of modes to include and the maximum iterative time step. Steady-state vibrating amplitudes are compared with different number of modes and time step sizes. A 5% difference is considered as convergence. Detailed convergence study procedures can be found in [14]. In the case studied, five coupled modes is considered and iterative time step is taken as 1/8 of the smallest natural period involved.

4 Results and discussions

Aeroelastic responses of a short wing undergoing constant cruising velocity and an operating propeller is simulated to demonstrate capabilities of the numerical model. Transient and steady-state responses are shown and compared with the ones obtained by uncoupled modes, also with results based on the Euler-Bernoulli beam theory.

Comparing aeroelastic responses captured via coupled and uncoupled analytical mode shapes, an illustration is shown in Figure 6. For both methods, a similar transient response is shown. For the steady states, again, these two approaches gave very similar responses. However, differences can be observed for the transient and steady-state amplitudes. In the transient regime, coupled modes gave a slightly larger deflection compared to results from uncoupled modes. As for the steady states, 2.5% and 6.8% differences in amplitude are found between coupled and uncoupled mode shapes for bending and torsion respectively. However, vibrating amplitudes are less than 1% of the overall deflections. Therefore, they are insignificant for the overall steady-state behaviours. More importantly, by using coupled mode shapes, computational time is reduced. For uncoupled mode shapes, each vibration mode shape has one time-dependent function. While for coupled modes, one time-dependent function is shared between three mode shape functions. This reduces the number of variables by three, hence reduces the computational power needed. For solving the presented case with a standard desktop PC, using coupled modes can reduce the program operation time by 30%.

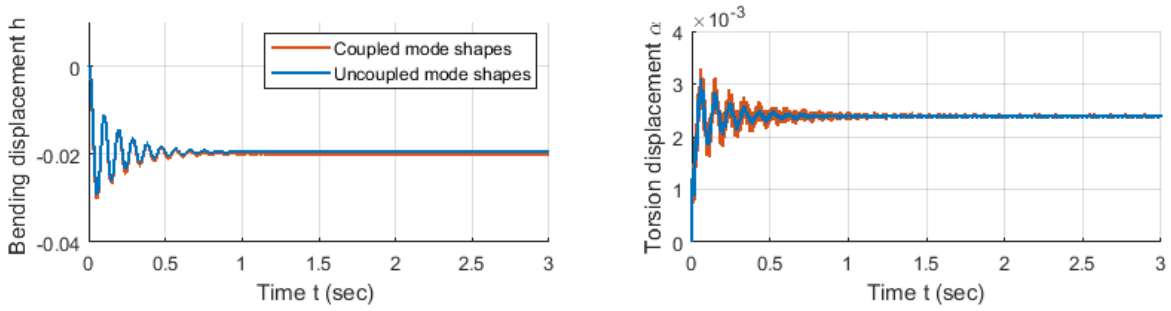


Figure 6: Coupled/Uncoupled transient response comparison (left: bending, right: torsion)

Table 4: Uncoupled/coupled mode shape steady-state response comparison

	Uncoupled	Coupled	% Difference
Bending mean deflection	0.01946 m	0.0.01995 m	2.5%
Bending amplitude	1.981e-06 m	1.952e-06m	1.5%
Torsional mean deflection	0.002387 rad	0.002390 rad	0.1%
Torsional amplitude	2.550e-5 rad	2.735e-5 rad	6.8%

Figure 7 shows the aeroelastic responses given by Euler-Bernoulli and Timoshenko beam theories. Two methods showed an extremely similar transient response and a very close steady state, according to Table 4. Therefore, for this case, the rotational and shear deformation effects are not significant. When use Euler-Bernoulli beam theory, sectional rotation is constrained to be perpendicular to the neutral axis. This coupling stiffens the structure [10]. While for the Timoshenko beam, bending and rotational coupling can be avoided, making the beam more flexible and resulting in a greater steady-state bending deflection. However, due to energy conservation, while having a smaller mean deflection, Euler-Bernoulli beam model has a greater vibration amplitude in bending. As for torsion, stiffness remains the same for Timoshenko and Euler-Bernoulli beams, therefore, the steady-state mean deflection is nearly identical. The amplitude differences in bending, however, propagated into its torsional behaviour, resulting in a difference of just below 10%. This revealed a different energy distribution mechanism when rotary inertia and shear deformations are considered in the presented aeroelastic system.

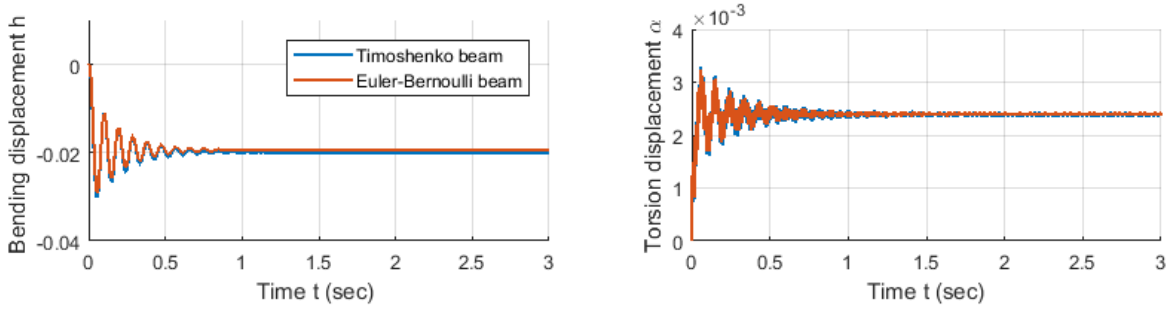


Figure 7: Timoshenko / Euler-Bernoulli response comparison

Table 5: Steady-state response comparison

	Euler-Bernoulli	Timoshenko	% Difference
Bending mean deflection	0.019402 m	0.019947 m	2.7%
Bending amplitude	2.146e-6 m	1.952e-6 m	9.9%
Torsional mean deflection	0.002398 rad	0.002390 rad	0.3%
Torsional amplitude	2.487e-5 rad	2.735e-5 rad	9.1%

5 Conclusion

This paper has presented a simplified numerical model based on a short and bending-torsion coupled structure in cruising and propeller inflow. Focusing on the application of coupled modal analysis and Timoshenko beam theory in an aeroelaticity context, a case similar to the Eurocopter X3 short-wing/propeller configuration has been studied for its time-domain response. Differences in aeroelastic response introduced by coupled mode shapes and Timoshenko beam theory are analysed and discussed. In general, the steady-state response given by uncoupled and coupled approach are similar. However, with the coupled modal analysis approach, a more realistic modal behaviour can be captured with less computational power. Also, it is compatible with complex structural models, allowing stiffness, material, geometry or any other cross-sectional property variations along the wing span to be considered. Hence, its advantages over uncoupled modal analysis approach will appear further as complex structures and more modes are included. As for the implementation of Timoshenko beam, its response is not significantly different compared to Euler-Bernoulli beam. However, Timoshenko beam showed that the rotary inertia and shear deformations affect how energy is distributed in the steady state, giving a larger mean deflection and a smaller vibration amplitude in the flapping coordinate, revealing a different energy distribution mechanism in the aeroelastic system studied.

Acknowledgements

The work of ZW is partially supported by EU Clean Sky 2 Joint Undertaking ASTRAL project.

References

[1] A. Mazidi, H. Kalantari, and S. A. Fazelzadeh, “Aeroelastic response of an aircraft wing with mounted engine subjected to time-dependent thrust,” *Journal of Fluids and Structures*, vol. 39, pp. 292–305, 2013.

[2] S. Shams, M. H. Sadr Lahidjani, and H. Haddadpour, “Nonlinear aeroelastic response of slender wings based on Wagner function,” *Thin-Walled Structures*, vol. 46, no. 11, pp. 1192–1203, 2008.

[3] M. J. Patil and D. H. Hogdes, "Limit-Cycle Oscillations in High-Aspect-Ratio Wings," *Journal of Fluids and Structures*, vol. 16, no. 15, pp. 107–132, 2001.

[4] S. Preidikman, "Numerical Simulations of Interactions Among Aerodynamics, Structural Dynamics, and Control Systems," Ph.D. dissertation, Virginia Polytechnic Institute and State University, USA, 1998.

[5] T. W. Strganac, "A Numerical Model of Unsteady, Subsonic Aeroelastic Behavior," Ph.D. dissertation, Virginia Polytechnic Institute and State University, USA, 1987.

[6] M. Gennaretti, M. Molica Colella, and G. Bernardini, "Prediction of tiltrotor vibratory loads with inclusion of wing-proprotor aerodynamic interaction," *Journal of Aircraft*, vol. 47, no. 1, pp. 71–79, 2010.

[7] D. H. Hodges and R. A. Ormiston, "Stability of elastic bending and torsion of uniform cantilever rotor blades in hover with variable structural coupling," NASA, Tech. Rep. D-8192, 1976.

[8] D. H. Hodges and E. H. Dowell, "Nonlinear equations of motion for the elastic bending and torsion of twisted nonuniform rotor blades," NASA, Tech. Rep. D-7818, 1974.

[9] M. Berci, P. H. Gaskell, R. W. Hewson, and V. V. Toropov, "A semi-analytical model for the combined aeroelastic behaviour and gust response of a flexible aerofoil," *Journal of Fluids and Structures*, vol. 38, pp. 3–21, 2013.

[10] M. Kämpchen, A. Dafnis, H. G. Reimerdes, G. Britten, and J. Ballmann, "Dynamic aero-structural response of an elastic wing model," *Journal of Fluids and Structures*, vol. 18, no. 1, pp. 63–77, 2003.

[11] J. R. Banerjee, "Explicit Frequency Equation and mode shapes of a centilever beam coupled in bending and torsion," *Journal of Sound and Vibration*, vol. 224, no. 2, pp. 267–281, 1999.

[12] ——, "Explicit modal analysis of an axially loaded timoshenko beam with bending-torsion coupling," *Journal of Applied Mechanics*, vol. 67, no. 2, pp. 307–313, 2000.

[13] J. R. Banerjee and H. Su, "Free transverse and lateral vibration of beams with torsional coupling," *Journal of Aerospace Engineering*, vol. 19, no. 1, pp. 13–20, 2006.

[14] Z. Wang, A. Anobile, and A. A. Popov, "Efficient numerical methods for aeroelastic analysis of wing-propeller configuration compound helicopters," in *XXIV A.I.D.A.A. Conference*, Palermo, Italy, 2017.

[15] ——, "Time-domain aeroelastic model for compound helicopter propeller-wing configuration," in *Aerospace Europe 6th CEAS Conference*, Bucharest, Romania, 2017.

[16] S. Timoshenko, "On the correction factor for shear of the differential equation for transverse vibrations of bars of uniform cross-section," *Philosophical Magazine*, vol. 41, pp. 744–746, 1921.

[17] ——, "On the transverse vibrations of bars of uniform cross-section," *Philosophical Magazine*, vol. 43, pp. 125–131, 1922.

[18] H. Wagner, "Über die Entstehung des dynamischen Auftriebes von Tragflügeln," *Zeitschrift für angewandte Mathematik and Mechanik*, vol. 5, no. 1, pp. 17–35, 1925.

[19] R. T. Jones, "Operational treatment of the nonuniform-lift theory in airplane dynamics," NACA, Tech. Rep. 667, 1938.

[20] ——, "The unsteady lift of a wing of finite aspect ratio," NACA, Tech. Rep. 681, 1940.

[21] H. G. Küssner, "Zusammenfassender Bericht über den instationären Auftrieb von Flügeln," *Luftfahrtforschung*, vol. 13, no. 12, pp. 410–424, 1935.

[22] W. Sears and B. Sparks, "On the reaction of an elastic wing to vertical gusts," *Journal of the Aeronautical Sciences*, vol. 9, no. 2, pp. 64–67, 1941.

[23] R. G. Cowper, "The Shear Coefficient in Timoshenko's Beam Theory," *Journal of Applied Mechanics*, vol. 33, pp. 335–340, 1966.

A recursive transfer admittance formulation in time domain

H. Denayer [1,2], **W. De Roeck** [1], **W. Desmet** [1,2]
[1] KU Leuven, Department of Mechanical Engineering,
Celestijnenlaan 300, B-3001, Leuven, Belgium
e-mail: **herve.denayer@kuleuven.be**

[2] Flanders Make, DMMS Lab

Abstract

A transfer admittance relation is commonly used in frequency domain linear acoustics to represent elements, characterized by a geometrical length scale which is much smaller than the acoustic wavelength, in an efficient way. However, the equivalent time domain formulation involves costly convolution integrals. This paper presents an efficient time domain formulation: using a rational approximation of the transfer admittance coefficients, formulated in frequency domain, a recursive formulation is obtained with significantly reduced memory and CPU requirements. This formulation has been implemented in a time domain solver for the linearized Euler equations, using a discontinuous Galerkin spatial discretization and a Runge-Kutta time integration scheme. The methodology is successfully validated on two benchmark cases: a lined duct with a grazing flow and a simplified automotive muffler with a perforated duct.

1 Introduction

In many applications, elements are present with a length scale that is much smaller than the acoustic wavelength. Typical examples are perforated plates, filters, heat exchangers, etc. where acoustic damping is generated by the forcing of the acoustic waves through small openings. Simulating such elements with all their details results in a prohibitive computational cost. In linear frequency domain acoustics, this type of elements is therefore commonly represented in an averaged way by specifying an admittance boundary condition or a transfer admittance relation. These formulations relate the surface-averaged acoustic pressure and acoustic normal velocity by a linear relation in frequency domain. Using such a formulation relaxes the grid requirements near the element and results in a computationally efficient formulation. Time domain formulations, on the other hand, offer a clear advantage for broadband cases and allow for a more natural description of aeroacoustic noise sources. In this context, the need for a time domain admittance and transfer admittance formulations emerges.

The development of efficient time domain admittance or impedance formulations has been a key topic in aeroacoustics research for many years, mainly driven by the importance of liners for the sound propagation through aircraft engine nacelles. It is therefore no surprise that many different approaches are available in literature, among others in references [1–7]. Transfer admittance relations on the other hand are commonly used in frequency domain models for representing perforated pipes in automotive exhaust mufflers or heat exchangers and filters in ventilation systems. Although many impedance models can be extended to a transfer admittance relation, the use of such formulation in time domain has not been studied so far. This paper therefore presents a time domain transfer admittance formulation, based on the recursive time domain impedance formulation of reference [5]. This formulation relies on a rational approximation of the transfer admittance coefficients in frequency domain, which is ideally suited for representing typical transfer admittance ap-

plications such as perforated panels. The recursive method is first extended to cope with multi-stage time marching schemes, as commonly used for acoustic propagation solvers and the obtained transfer relation is implemented in a time domain solver for the linearized Euler equations [8, 9], relying on a discontinuous Galerkin spatial discretization [10] and an explicit Runge-Kutta time-integration scheme [11]. This solver is used to illustrate the potential of the transfer admittance formulation for modeling the aeroacoustic behavior of complex elements, such as perforated panels, in the presence of grazing or bias flow .

This paper is structured as follows. The following section first introduces the recursive transfer admittance formulation and its implementation in the acoustic propagation solver. In section 3, the transfer admittance is used to represent a perforated panel in two validation cases: a lined duct with a uniform grazing flow and a through flow muffler, representative for automotive applications. Finally, section 4 concludes this paper with a summary of the main results and conclusions.

2 Acoustic transfer admittance in time domain

At any angular frequency ω, a transfer admittance relation prescribes a matrix relation in frequency domain between the normal component of the acoustic velocity $v_n(\omega)$ at two points x_1 and x_2 on each side of a surface and the acoustic pressure $p(\omega)$ at these positions:

$$\begin{Bmatrix} v_n(x_1,\omega) \\ v_n(x_2,\omega) \end{Bmatrix} = \begin{bmatrix} A_{11}(\omega) & A_{12}(\omega) \\ A_{21}(\omega) & A_{22}(\omega) \end{bmatrix} \begin{Bmatrix} p(x_1,\omega) \\ p(x_2,\omega) \end{Bmatrix} \tag{1}$$

Applying the inverse Fourier transform to this matrix relation leads to a set of convolution integrals in time domain:

$$\begin{aligned} v_n(x_1,t) &= \int_{-\infty}^{\infty} a_{11}(\tau)\, p(x_1, t-\tau)\, \mathrm{d}\tau + \int_{-\infty}^{\infty} a_{12}(\tau)\, p(x_2, t-\tau)\, \mathrm{d}\tau \\ v_n(x_2,t) &= \int_{-\infty}^{\infty} a_{21}(\tau)\, p(x_1, t-\tau)\, \mathrm{d}\tau + \int_{-\infty}^{\infty} a_{22}(\tau)\, p(x_2, t-\tau)\, \mathrm{d}\tau \end{aligned} \tag{2}$$

These convolutions are typically costly operations, that additionally require the storage of the full time history of the acoustic pressure $p(t)$. The time domain equivalent of the transfer admittance coefficients $a_{\mu\nu}(t)$ in equations (2) is defined as:

$$a_{\mu\nu}(t) = \int_{-\infty}^{\infty} A_{\mu\nu}(\omega)\, \mathrm{e}^{\mathrm{j}\omega t}\, \mathrm{d}\omega. \tag{3}$$

Hence, to obtain this time domain coefficient, the transfer admittance coefficient needs to be known for the complete frequency axis. Since, transfer admittance coefficients are typically measured for a discrete set of frequencies within the frequency range of interest, an interpolating model is required. This model has to be causal and real to yield a physical time domain equivalent.

2.1 Broadband model for the transfer admittance coefficients

Any causal and real transfer admittance model can be used to generate a time domain formulation. However, the convolution integral typically results in a memory-intensive formulation. By wisely choosing the model for the coefficients, it is possible to overcome this issue. By analogy to the time domain impedance model proposed by Reymen et al. [5], each of the coefficients $A_{\mu\nu}(\omega)$ of the transfer admittance matrix $\underline{\underline{\mathbf{A}}}(\omega)$ is written as a partial fraction expansion:

$$A_{\mu\nu}(\omega) = \sum_{k=1}^{S+2T} \frac{B_k}{\mathrm{j}\omega + \lambda_k} \tag{4}$$

As will be shown in section 3, this form is ideally suited for representing perforated panels, one of the most important applications of transfer admittance relations.

The time domain equivalent of the model (4) is real when the poles λ_k are real or occur as a pair of complex conjugates. For convenience, the summation in equation (4) can be split in a sum over S first-order systems with real poles λ_k and T second-order systems with complex conjugate poles $\alpha_l \pm \mathrm{j}\beta_l$:

$$A_{\mu\nu}(\omega) = \sum_{k=1}^{S} \frac{B_k}{\mathrm{j}\omega + \lambda_k} + \sum_{l=1}^{T} \frac{\mathrm{j}\omega C_l + D_l}{(\mathrm{j}\omega + \alpha_l)^2 + \beta_l^2} \tag{5}$$

The time domain equivalent of this rational model can be written as:

$$a_{\mu\nu}(t) = \sum_{k=1}^{S} B_k \, \mathrm{e}^{-\lambda_k t} \, H(t) + \sum_{l=1}^{T} \left(K_{1l} \, \cos(\beta_l t) + K_{2l} \sin(\beta_l t)\right) \mathrm{e}^{-\alpha_l t} H(t) \tag{6}$$

where $H(t)$ is the Heaviside function, $K_{1l} = C_l$ and $K_{2l} = (D_l - \alpha_l C_l)/\beta_l$. This time domain model is causal when the real part of the poles λ_k in equation (4) is positive. The residuals B_k, C_l and D_l can be freely chosen to obtain an accurate interpolating model. When modeling a passive system, the choice of the coefficients has to be such to ensure the passivity of the transfer admittance relation. This can be verified using the scattering matrix equivalent of the transfer relation and the procedure of reference [12].

For a conventional impedance boundary condition, finding a rational approximation of the liner impedance is often a challenging task. Several approaches to obtain a real and causal model of the form (5) have therefore been presented in literature [6, 13–15]. Any of these methods can also be applied to transfer admittance coefficients if a rational model is not readily available. In this work, the following approaches are considered [8]:

Single frequency model: if only the value at a single frequency is of interest, a rational model can be obtained using the three parameter model of references [6, 13]. The resulting model consists of only one second-order system and represents the exact value of the transfer admittance coefficient at the design frequency.

Multiple discrete frequencies: when a set of N discrete frequencies is of interest, an interpolating model can be obtained with the "ad-hoc broadband model" described in reference [14]. The resulting model consists of N second-order systems and represents the exact value of the transfer admittance coefficient at the design frequencies. In between these frequencies, the rational approximation oscillates and can deviate substantially from the exact values.

Broadband model: an approximate broadband model can be computed using the "vector fitting" algorithm [15]. This model iteratively fits a predefined number of first-order systems through the complex data set. Since the algorithm only returns real or complex conjugated pairs of poles, the outcome is always a real and causal model. The resulting model is an approximation over a broad frequency range, but does not ensure an exact representation of the transfer admittance coefficient at any frequency.

A complete transfer admittance description requires a rational model for the four admittance matrix coefficients $A_{\mu\nu}(\omega)$. It is not required that the model for each of the coefficients is identical, although there are often physical reasons, such as reciprocity or symmetry, to use the same model for more than one coefficient [16]. If the same model is used for all coefficients, it is straightforward to show that a passive model ensures the passivity of the transfer admittance relation.

2.2 Time domain formulation

Equation (2) indicates that a time domain transfer admittance formulation requires the computation of convolution integrals of the type:

$$a_{\mu\nu}(t) * p(x_\nu, t) = \int_{-\infty}^{\infty} a_{\mu\nu}(\tau)\, p(x_\nu, t-\tau)\, \mathrm{d}\tau \tag{7}$$

for each of the matrix coefficients $a_{\mu\nu}(t)$. In what follows, the subscripts μ and ν are omitted for clarity. For a causal system the acoustic velocity at time t can't depend on the acoustic pressure at later instances of time. The lower limit of the convolution integral is therefore set to zero without loss of generality.

It is assumed that the time-axis is discretized using a multi-stage explicit time-integration scheme, with a constant timestep Δt, subdivided in a number of stages which length is not necessarily equal (figure 1). Hence, the convolution integral will be evaluated at discrete times $t^{n,s} = n\Delta t + \delta t^s$, with δt^s the length of the current stage s. With this assumption, the convolution integral equation (7) can be split in an integral over the current timestep, up to the current stage, and a sum of integrals over the previous timesteps:

$$\int_0^{t^{n,s}} a(\tau)\, p(t^{n,s}-\tau)\, \mathrm{d}\tau = \int_0^{\delta t^s} a(\tau)\, p(n\Delta t + \delta t^s - \tau)\, \mathrm{d}\tau + \sum_{m=0}^{n-1} \int_{m\Delta t}^{(m+1)\Delta t} a(\tau + \delta t^s)\, p(n\Delta t - \tau)\, \mathrm{d}\tau \tag{8}$$

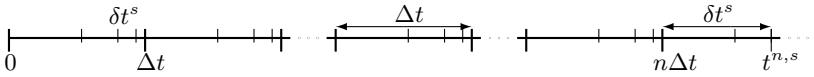


Figure 1: Discretized time axis

To compute these integrals, an assumption is needed regarding the behavior of the pressure in between two timesteps. By analogy to the time domain impedance model by Reymen et al. [5], a piecewise linear behavior is assumed within each timestep:

$$p(t) = p^m + \frac{p^{m+1} - p^m}{\Delta t}\,(t - m\Delta t) \qquad\qquad t \in [m\Delta t, (m+1)\Delta t] \tag{9}$$

Here, the subscripts refer to the value of the pressure at a certain timestep: $p^m = p\,(m\Delta t)$. Introducing this assumption and the model for the transfer admittance coefficients (equation (6)) in the second part of equation (8) yields, after some algebra, the result obtained by Reymen et al. [5]:

$$\begin{aligned}\sum_{m=0}^{n-1} \int_{m\Delta t}^{(m+1)\Delta t} a(\tau + \delta t^s)\, p(n\Delta t - \tau)\, \mathrm{d}\tau = &\sum_{k=0}^{S} B_k\, \mathrm{e}^{-\lambda_k \delta t^s}\, \psi_k^n \\ &+ \sum_{l=0}^{T} \left(K_{1l}\, \Re\left\{ \mathrm{e}^{(-\alpha_l + \mathrm{j}\beta_l)\delta t^s}\, \hat{\psi}_l^n \right\} + K_{2l}\, \Im\left\{ \mathrm{e}^{(-\alpha_l + \mathrm{j}\beta_l)\delta t^s}\, \hat{\psi}_l^n \right\} \right)\end{aligned} \tag{10}$$

In this equation, the variables ψ_k^n and $\hat{\psi}_l^n$ are accumulator functions that can be computed recursively, using only the pressure at the current timestep p^n and the previous timestep p^{n-1} [5]:

$$\begin{aligned}\psi_k^n &= p^n \chi_k^0 + \left(p^{n-1} - p^n\right) \xi_k^0 + \mathrm{e}^{-\lambda_k \Delta t}\, \psi_k^{n-1} \\ \hat{\psi}_l^n &= p^n \hat{\chi}_l^0 + \left(p^{n-1} - p^n\right) \hat{\xi}_l^0 + \mathrm{e}^{(-\alpha_l + \mathrm{j}\beta_l)\Delta t}\, \hat{\psi}_l^{n-1}\end{aligned} \tag{11}$$

Also the variables χ_k^m, ξ_k^m can be computed recursively [5]:

$$\chi_k^{m+1} = \mathrm{e}^{-\lambda_k \Delta t}\, \chi_k^m \qquad \chi_k^0 = (\lambda_k)^{-1} \left(1 - \mathrm{e}^{-\lambda_k \Delta t}\right)$$
$$\xi_k^{m+1} = \mathrm{e}^{-\lambda_k \Delta t}\, \xi_k^m \qquad \xi_k^0 = (\lambda_k)^{-2} \left(1 + \lambda_k \Delta t\right) \mathrm{e}^{-\lambda_k \Delta t}$$

Identical equations hold for $\hat{\chi}_l^m$ and $\hat{\xi}_l^m$, where the real poles λ_k are replaced by the complex poles $\alpha_l + \mathrm{j}\beta_l$.

For the computation of the first part of the integral in equation (8), assumption (9) would result in an implicit formulation. To keep the time integration scheme explicit, the slope of the linear behavior of the pressure within the current timestep is estimated using the pressure at the current substage:

$$p(t) = p^n + \frac{p^{n,s} - p^n}{\delta t^s} \left(t - n\Delta t\right) \qquad t \in [n\Delta t, n\Delta t + \delta t^s] \tag{12}$$

where $p^{n,s} = p\left(n\Delta t + \delta t^s\right)$. Introducing this assumption, together with the model equation (6) for the transfer admittance coefficients into the first integral of equation (8) yields:

$$\begin{aligned} \int_0^{\delta t^s} a(\tau)\, p(n\Delta t + \delta t^s - \tau)\, \mathrm{d}\tau = \sum_{k=1}^{S} B_k \left(p^{n,s} I_k^s + \left(p^n - p^{n,s}\right) J_k^s\right) \\ + \sum_{l=1}^{T} \left(K_{1l}\, \Re\left\{ p^{n,s} \hat{I}_l^s + \left(p^n - p^{n,s}\right) \hat{J}_l^s \right\} + K_{2l}\, \Im\left\{ p^{n,s} \hat{I}_l^s + \left(p^n - p^{n,s}\right) \hat{J}_l^s \right\} \right) \end{aligned} \tag{13}$$

The constants I_k^s, $\hat{I}_l^s$, J_k and $\hat{J}_l^s$ in this equation are recurring at stage s in every timestep. It is hence sufficient to compute these constants once, at the beginning of the simulation, for all stage lengths and to use their pre-computed values during the time marching:

$$\begin{aligned} I_k^s &= \frac{1 - \mathrm{e}^{-\lambda_k \delta t^s}}{\lambda_k} & J_k^s &= \frac{1 - \mathrm{e}^{-\lambda_k \delta t^s} \left(\lambda_k \delta t^s + 1\right)}{\lambda_k^2 \delta t^s} \\ \hat{I}_l^s &= \frac{1 - \mathrm{e}^{(-\alpha_l + \mathrm{j}\beta_l)\delta t^s}}{\alpha_l - \mathrm{j}\beta_l} & \hat{J}_l^s &= \frac{1 - \mathrm{e}^{(-\alpha_l + \mathrm{j}\beta_l)\delta t^s} \left(\left(\alpha_l - \mathrm{j}\beta_l\right) \delta t^s + 1\right)}{\left(-\alpha_l + \mathrm{j}\beta_l\right)^2 \delta t^s} \end{aligned} \tag{14}$$

Recombining equations (10) and (13) shows that the convolution integral (equation (8)) can be computed as the sum of a recursively computed integral, accounting for the previous timesteps, and a term depending on the current timestep only:

$$\begin{aligned} a(n\Delta t + \delta t^s) * p(n\Delta t + \delta t^s) = \sum_{k=1}^{S} B_k \left(\mathrm{e}^{-\lambda_k \delta t^s}\, \psi_k^n + p^{n,s} I_k^s + \left(p^n - p^{n,s}\right) J_k^s \right) \\ + \sum_{l=1}^{T} K_{1l}\, \Re\left\{ \mathrm{e}^{(-\alpha_l + \mathrm{j}\beta_l)\delta t^s}\, \hat{\psi}_l^n + p^{n,s} \hat{I}_l^s + \left(p^n - p^{n,s}\right) \hat{J}_l^s \right\} \\ + \sum_{l=1}^{T} K_{2l}\, \Im\left\{ \mathrm{e}^{(-\alpha_l + \mathrm{j}\beta_l)\delta t^s}\, \hat{\psi}_l^n + p^{n,s} \hat{I}_l^s + \left(p^n - p^{n,s}\right) \hat{J}_l^s \right\} \end{aligned} \tag{15}$$

When evaluating this equation at the beginning of a timestep ($\delta t^s = 0$), all constants I and J are zero and only the terms depending on the accumulator functions ψ remain. These accumulators are updated using equation (11). When evaluating the transfer admittance relation at any other stage ($\delta t^s \neq 0$), the value of the accumulator functions remains unchanged. In this case, the constants I and J are nonzero and the summation is complemented with the terms depending on the current stage. As a result, an efficient scheme is obtained where only a small set of summations and multiplications is carried out at every stage of the time-marching scheme and where only the pressure at the current stage and at the beginning of the timestep needs to be stored.

2.3 Implementation

The time domain transfer admittance formulation is implemented in a high-order discontinuous Galerkin method with low-storage Runge-Kutta time integration scheme [11] for the linearized Euler equations (LEE) [9]. The transfer admittance relation is included in this solver via the inter-element fluxes at the transfer admittance surface and is supported for linear and curved [10] surfaces. The LEE can take into account the effect of a steady non-uniform mean flow, as encountered in many engineering applications.

3 Validation of the time domain transfer admittance formulation

The time domain transfer admittance formulation is validated using two benchmark cases: a duct with a locally reacting liner (figure 2) and a through flow muffler (figure 7). In both cases, the transfer admittance formulation is used to represent a thin perforated plate. This section therefore first elaborates on the modeling of a perforated plate using a transfer admittance relation, before presenting the results of the benchmark problems.

3.1 Modeling of perforated plates

A perforated panel is typically characterized by its acoustic impedance $Z(\omega)$, defined in frequency domain as the ratio between the acoustic pressure drop over the panel $\Delta p(\omega) = p(x_1, \omega) - p(x_2, \omega)$ and the acoustic velocity through the surface u_w:

$$Z(\omega) = \frac{\Delta p(\omega)}{u_w(\omega)} \tag{16}$$

In a quiescent medium, continuity of acoustic velocity over the plate thickness is typically assumed, i.e. $v_n(x_1, \omega) = v_n(x_2, \omega) = u_w(\omega)$. This allows writing the transfer admittance relation (equation (1)) as a function of the panel impedance:

$$\begin{bmatrix} A_{11}(\omega) & A_{12}(\omega) \\ A_{21}(\omega) & A_{22}(\omega) \end{bmatrix} = \frac{1}{Z(\omega)} \begin{bmatrix} 1 & -1 \\ 1 & -1 \end{bmatrix} \tag{17}$$

Hence, only a single rational approximation of the panel impedance $Z(\omega)$ is needed to represent the four transfer admittance matrix coefficients. Additionally, such rational approximation is often straightforward to derive for a perforated panel. This will be illustrated in the validation cases of the following sections, where impedance models from literature [17, 18] are used to describe the exact panel impedance.

In the presence of a grazing flow over the panel, this assumption of continuity of acoustic velocity does not account for the influence of the boundary layer and is therefore questionable. In this case, continuity of particle displacement [19] or an intermediate assumption [20] is more appropriate. A detailed discussion on the validity of the different assumptions lies outside the scope of the current paper and, for simplicity, continuity of particle velocity is assumed in the following examples.

3.2 Modeling of a locally-reacting liner in a two-dimensional duct

3.2.1 Problem description

A first validation case considers a two-dimensional duct with a height of 50 mm, lined on the lower wall with a honeycomb liner over a distance of 2 m, as shown in figure 2. The honeycomb structure on the lower wall consists of 300 cells of 6.67 mm by 25 mm, connected to the duct by a perforated plate. A uniform axial flow with a Mach number of $M_0 = 0.3$ is present in the duct and the air in the honeycomb cavities

is assumed at rest. This type of wall treatments is typically modeled more efficiently using an impedance boundary condition, but for validation purposes, a different approach is followed in this paper: the facing sheet is represented by the transfer admittance boundary condition and the liner cells are meshed explicitly. For a plane wave propagating through such a lined duct, an analytical solution for the decay of the acoustic pressure exists which assumes that edge effects are negligible and that the sound pressure field is dominated by the least attenuated mode [21].

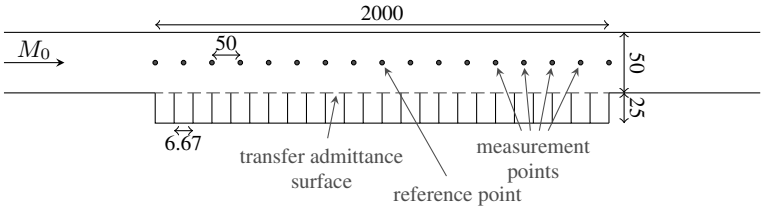


Figure 2: Schematic overview of the numerical configuration for the lined duct (all dimensions in mm).

It is assumed that the exact impedance of the panel $Z(\omega)$ is described by the semi-analytical model of Elnady et al. (equations (6) and (7) in reference [17]). The parameters of the impedance model are chosen to represent a typical liner. The facing sheet is a panel with a thickness of $t = 1$ mm, with circular perforations with a diameter of $d_h = 1.5$ mm and a porosity of $\sigma = 4\%$. The discharge coefficient is set to $C_D = 0.6$ and the dynamic and adiabatic dynamic viscosity of air are, respectively, $\mu = 1.77625 \cdot 10^{-5}$ Pa s and $\mu' = 2.179\mu$. The resulting panel impedance is shown in figure 3.

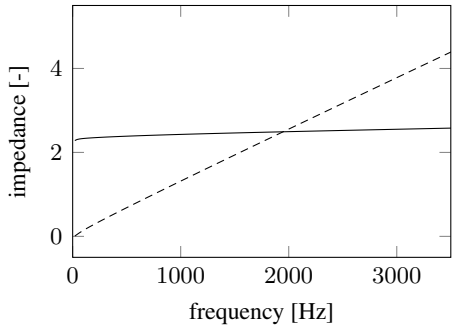


Figure 3: Exact non-dimensional resistance (——), i.e. the real part of the impedance, and reactance (- - - -), i.e. the imaginary part of the impedance, of the perforate sheet according to the model of reference [17].

3.2.2 Numerical setup

An unstructured triangular grid, consisting of 21255 elements, is generated with gmsh [22]. For the spatial discontinuous Galerkin discretization, a seventh order polynomial basis is used within each element and the inter-element communication is realized by Lax-Friedrich fluxes. An optimized 8 stage fourth-order Runge-Kutta time integration scheme [11] is used for the time marching. The inlet and outlet of the duct are represented by characteristic non-reflecting boundary conditions and slip conditions are imposed at all rigid walls. The perforated plate is represented by the transfer admittance relation, given by equation (17).

Three different types of excitation are considered: a single frequency harmonic excitation at 1360 Hz, a multiple frequency harmonic excitation from 340 Hz to 2720 Hz with a step of 340 Hz and a pulse excitation. All excitations are applied as plane waves in the rigid inlet section of the duct, at an upstream distance of 200 mm from the liner leading edge. For each excitation, the most suited approach is followed to obtain a rational approximation of the transfer admittance coefficients. For the single frequency harmonic excitation, the three-parameter model of references [6, 13] is used to generate a rational model representing the exact panel admittance at the excitation frequency. For the multiple sine excitation, an ad-hoc broadband model

with 8 second-order systems is designed to obtain an exact impedance value at the excitation frequencies, using the procedure of reference [14]. Finally, for the pulse excitation, a broadband rational approximation is generated using the vector fitting algorithm [15]. This rational approximation consists of 8 first-order systems. Figure 4 visualizes the error of the different rational impedance models, with respect to the exact impedance of figure 3. Because of the similarity between the exact impedance model and a first-order system, the broadband rational model is an excellent approximation of the exact panel impedance, with nearly zero error within the frequency range of interest. On the other hand, the ad-hoc broadband model and single frequency model are only exact at their respective design frequencies.

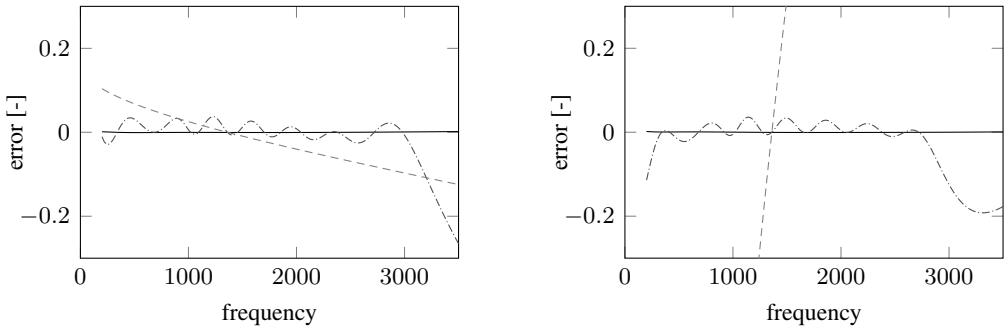


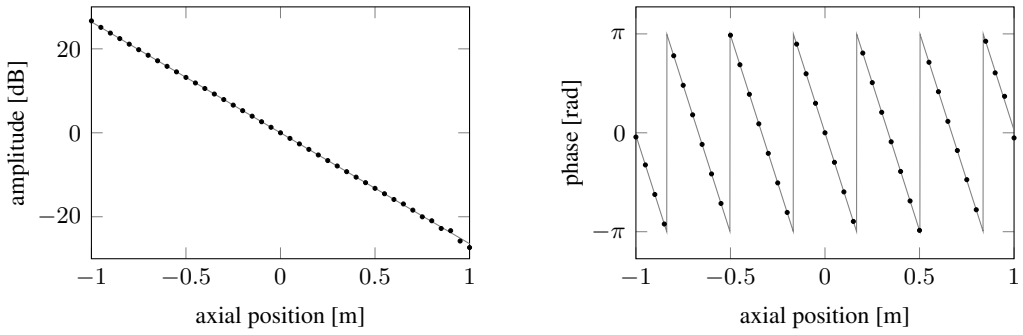
Figure 4: Absolute error on the (a) non-dimensional resistance and (b) non-dimensional reactance of the perforated plate, using the approximate broadband model obtained with the vector fitting algorithm (——), the ad-hoc broadband model (- - - -) and the single-frequency model (- - - -).

For all simulations, the acoustic pressure is stored at 41 points, with an equal spacing of 50 mm, along the center-line of the duct. For the harmonic excitations, the simulation is run for 30 ms and only the last 15 ms are used for further processing. For the pulse excitation, all energy has left the system and the simulation is considered converged after a simulated time of 30 ms. In all cases, the results are transformed to the frequency domain using an FFT algorithm and normalized with the pressure at a reference point p_{ref}, located in the center of the lined section.

3.2.3 Discussion of the results

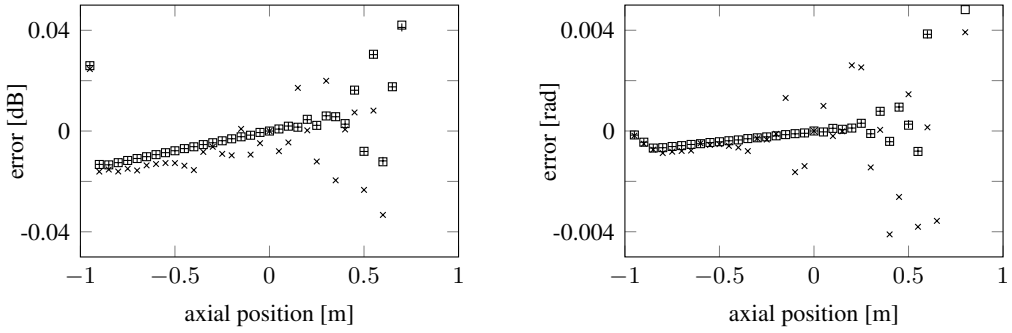
Figure 5 shows the evolution of the normalized pressure at 1360 Hz as a function of the axial distance from the reference point, in comparison to the analytical solution, for the simulation with a pulse excitation and the broadband impedance approximation. Excellent agreement is obtained for both the amplitude and the phase of the pressure along the duct, besides some small oscillations at the extremities. These originate from the scattering at the hard wall – soft wall transition, which is not included in the analytical solution. Similar results are obtained for the simulations with the other excitation signals and impedance approximations.

Figure 6 presents the amplitude and phase error on the normalized pressure along the axis of the duct, computed using the different excitation signals and rational impedance models. By definition, the error equals zero at the center of the duct due to the normalization of the computed pressure and the analytical solution. Besides the expected errors caused by the reflections at the liner leading and trailing edge, the results of all simulations are in excellent agreement with the analytical solution. As expected, the largest errors are obtained for the simulation with a pulse excitation. The broadband impedance model used for this case is a good approximation of the panel impedance, but it is not exact. The other simulations use a model that is exact at the excitation frequency and therefore yield lower errors. As expected for a linear system, no difference can be observed between the result of the single frequency harmonic excitation and the multiple frequency harmonic excitation.



(a) (b)

Figure 5: Analytical reference solution (——) and numerical results (•) for the normalized pressure along the duct axis at 1360Hz: (a) amplitude and (b) phase obtained using a broadband model with a pulse excitation.



(a) (b)

Figure 6: Absolute error on the (a) amplitude and (b) phase of the pressure along the axis of the duct for the simulation with the broadband impedance model and a pulse excitation (×), the simulation with the ad-hoc broadband impedance model and a multiple frequency excitation (▫) and the simulation with the single frequency model and a harmonic excitation (+).

3.3 Transmission loss of a through-flow muffler

3.3.1 Problem description

The second validation case considers the trough-flow muffler of figure 7 in a medium at rest. It consists of a central perforated pipe with a diameter of 42 mm, surrounded by an expansion chamber with a diameter of 158 mm and a length of 225 mm. The exact impedance of the perforated tube is modeled using the model of Sullivan and Crocker [18]:

$$\frac{Z(\omega)}{\rho_0 c_0} = \frac{6 \cdot 10^{-3} + \mathrm{j} k_0 \left(t + 0.75 d_h\right)}{\sigma} \tag{18}$$

where $k_0 = \omega / c_0$ is the acoustic wavenumber, $c_0 = 340$ m/s is the speed of sound and $\rho_0 = 1.225$ kg/m^3 is the density of the medium. The perforated pipe has a thickness of $t = 1$ mm and a porosity of $\sigma = 19.7\%$. The perforations have a diameter of $d_h = 3.5$ mm.

The transmission loss of the trough-flow muffler is computed from the simulated pressure spectra $p'(\omega)$ at two points in the inlet and the outlet duct, located at $z_1 = 100$ mm and $z_2 = 130$ mm from the inlet or outlet of the perforated pipe. Below the cut-off frequency (approximately 4750 Hz), only plane waves are propagating in the inlet and outlet duct and the complex amplitude of the right-running (p^+) and left-running

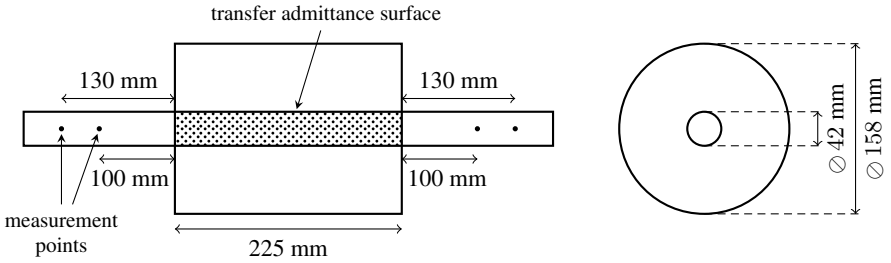


Figure 7: Geometry of the through-flow muffler.

(p^-) wave can be computed from these pressure spectra [23]:

$$\begin{Bmatrix} p^+(\omega) \\ p^-(\omega) \end{Bmatrix} = \begin{bmatrix} \exp(-\mathrm{j}k_0 z_1) & \exp(\mathrm{j}k_0 z_1) \\ \exp(-\mathrm{j}k_0 z_2) & \exp(\mathrm{j}k_0 z_2) \end{bmatrix}^{-1} \begin{Bmatrix} p'(\omega, z_1) \\ p'(\omega, z_2) \end{Bmatrix} \tag{19}$$

The transmission loss (TL) of the muffler is computed from the result of this plane wave decomposition as [23]:

$$\mathrm{TL} = 20 \log_{10} \left| \frac{p_i^+}{p_o^+} \right| \tag{20}$$

where p_i^+ and p_o^+ refer to the right-running plane waves in, respectively, the inlet and the outlet duct.

3.3.2 Numerical setup

Two unstructured tetrahedral meshes are generated with gmsh [22]: a fine mesh with 7760 linear elements and a coarser mesh with 1717 second-order elements using the curved boundary treatment from reference [10]. A seventh-order polynomial basis is used within each element and the inter-element communication is realized by Lax-Friedrich fluxes. Characteristic non-reflective boundary conditions are applied at the inlet and outlet of the duct, while a slip wall condition is imposed at the other outer boundaries of the domain. The perforated duct is represented by the time domain transfer admittance formulation of equation (17). For the impedance model of equation (18), the transfer admittance matrix coefficients can be written exactly as a first-order system with:

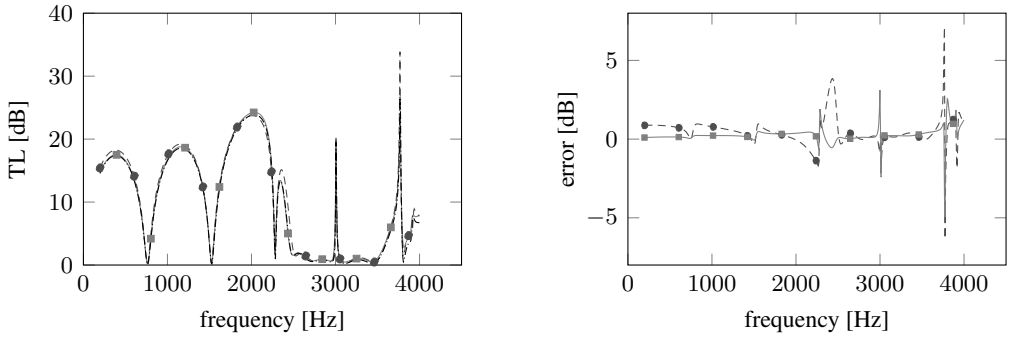
$$\lambda_1 = \frac{6 \cdot 10^{-3} c_0}{t + 0.75 d_h} \qquad B_1 = \frac{\sigma c_0}{t + 0.75 d_h} \tag{21}$$

As a result, an exact rational model for the transfer admittance coefficients is readily available and no approximate models need to be derived. Since equation (21) is an exact broadband model, a computationally efficient approach with a broadband excitation can be adopted. Therefore, a plane pulse excitation is applied in the inlet duct and a time history of approximately 88 ms is simulated. At the end of the simulation, most of the energy has left the system through the inlet and outlet or via dissipation in the transfer admittance. The pressure signal is stored at two points in the inlet and outlet duct, as shown in figure 7, and transformed to the frequency domain using an FFT algorithm. The transmission loss is computed from these spectra using equations (19) and (20).

A reference solution is obtained using a commercial high-order FEM solver (LMS Virtual.Lab Rev.13.2) for the Helmholtz equation in frequency domain. A fine mesh, consisting of 95420 prismatic elements, is used for this simulation. A velocity boundary condition is imposed at the inlet and the characteristic impedance of air is imposed at the outlet. The perforated duct is represented using the exact impedance model equation (18) and the transfer admittance formulation of equation (17). Similar to the time domain simulations, the transmission loss is computed from the simulated pressure spectra at two points in the inlet and outlet duct, as indicated in figure 7, using equations (19) and (20).

3.3.3 Discussion of the results

Figure 8 shows the results of the time domain simulation, together with the reference FEM solution. For frequencies up to approximately 2400 Hz, the plane waves in the muffler dominate the acoustic behavior of the muffler and the perforated duct has only a small influence on the transmission loss. Therefore, the agreement between time domain simulations and the reference solution mainly depends on the geometrical accuracy of the model. This results in a slightly lower error for the simulation using curved elements at the boundaries.



(a) (b)

Figure 8: (a) Transmission loss of the muffler, obtained with the RKDG solver using a linear mesh (-•-) and a locally second-order mesh (—▪—) and the reference FEM solution (-·-·-) and (b) error between the RKDG solutions and the reference solution.

For higher frequencies, the radial modes in the cavity gain importance and the transmission loss of the muffler is highly dependent on the transfer admittance. Also in this frequency region, excellent agreement is obtained between the different numerical solutions. As expected, slightly larger errors between the time domain simulations and the reference solution are observed at the resonance frequencies of the expansion chamber around 2300 Hz, 3000 Hz and 3800 Hz. Therefore, it can be concluded that the transfer admittance relation performs properly for both linear and curved surfaces in a three-dimensional context.

4 Conclusion

This paper presents a recursive transfer admittance formulation in time domain. The formulation is an extension of a time domain impedance boundary condition, allowing to model the acoustic transfer through a component characterized by small-scale geometrical features. Because of the recursive formulation, the storage needs and the computational cost are kept to a minimum, requiring only the storage of the pressure at the previous timestep and no more than a few algebraic operations at every stage of the time marching scheme.

The method is implemented in a high-order acoustic propagation solver and validated using two benchmark cases, where the transfer admittance is used to model a perforated plate. It is shown that the rational model for the transfer admittance matrix coefficients is ideally suited for this type of applications and that an accurate approximation of the panel impedance is straightforward to obtain. In the first validation case, the transfer admittance is used to model the facing sheet of a two-dimensional honeycomb liner in the presence of a grazing flow. Excellent agreement with the analytical solution is obtained for different harmonic and broadband excitations. In the second example, the transfer admittance relation is applied to represent a perforated tube in a through flow muffler. The excellent agreement with a reference solution, obtained with a commercial finite element solver for the Helmholtz equation, validated the formulation for three-dimensional cases with linear and curved boundary formulations.

The developed time domain transfer admittance formulation provides a powerful approach for the broadband characterization of complex structures. It allows modeling the acoustic propagation through small-scale geometrical features, much smaller than the acoustic wavelength, in a computationally efficient way. Implemented in a solver for the linearized Euler or Navier-Stokes equations, it can account for the influence of a mean flow over or through the transfer admittance surface by using a proper model for the coefficients. The recursive time domain transfer admittance formulation is therefore ideally suited for modeling the aeroacoustic behavior of applications involving heat exchangers, filters and in particular (micro-)perforated plates.

Acknowledgements

The Flanders Innovation & Entrepreneurship Agency within the TUMULT project and the Research Fund KU Leuven are gratefully acknowledged for their support.

References

[1] K.-Y. Fung, H. Ju, *Time-domain impedance boundary conditions for computational acoustics and aeroacoustics*, International Journal of Computational Fluid Dynamics, Vol. 18, No. 6, (2004), pp. 503–511.

[2] X. D. Li, C. Richter, F. Thiele, *Time-domain impedance boundary conditions for surfaces with subsonic mean flows*, The Journal of the Acoustical Society of America, Vol. 119, (2006), pp. 2665–2676.

[3] X. Y. Li, X. D. Li, C. K. W. Tam, *Improved multipole broadband time-domain impedance boundary condition*, AIAA Journal, Vol. 50, No. 4, (2012), pp. 980–984.

[4] Y. Özyörük, L. N. Long, M. G. Jones, *Time-domain numerical simulation of a flow-impedance tube*, Journal of Computational Physics, Vol. 146, No. 1, (1998), pp. 29–57.

[5] Y. Reymen, M. Baelmans, W. Desmet, *Efficient implementation of Tam and Auriault's time-domain impedance boundary condition*, AIAA Journal, Vol. 46, No. 9, (2008), pp. 2368–2376.

[6] C. K. W. Tam, L. Auriault, *Time-domain impedance boundary conditions for computational aeroacoustics*, AIAA Journal, Vol. 34, No. 5, (1996), pp. 917–923.

[7] S. Zhong, X. Zhang, X. Huang, *A controllable canonical form implementation of time domain impedance boundary conditions for broadband aeroacoustic computation*, Journal of Computational Physics, Vol. 313, (2016), pp. 713–725.

[8] Y. Reymen, *3D high-order discontinuous Galerkin methods for time-domain simulation of flow noise propagation*, Ph.D. thesis, K.U. Leuven (2008).

[9] T. Toulorge, *Efficient runge-kutta discontinuous Galerkin methods applied to aeroacoustics*, Ph.D. thesis, KU Leuven (2012).

[10] T. Toulorge, W. Desmet, *Curved boundary treatments for the discontinuous Galerkin method applied to aeroacoustic propagation*, AIAA Journal, Vol. 48, No. 2, (2010), pp. 479–489.

[11] T. Toulorge, W. Desmet, *Optimal Runge-Kutta schemes for discontinuous Galerkin space discretizations applied to wave propagation problems*, Journal of Computational Physics, Vol. 231, No. 4, (2012), pp. 2067–2091.

[12] Y. Aurégan, R. Starobinski, *Determination of acoustical energy dissipation/production potentiality from the acoustical transfer functions of a multiport*, Acta Acustica united with Acustica, Vol. 85, No. 6, (1999), pp. 788–792.

[13] D. Botteldooren, *Finite-difference time-domain simulation of low-frequency room acoustic problems*, The Journal of the Acoustical Society of America, Vol. 98, No. 6, (1995), pp. 3302–3308.

[14] Y. Reymen, M. Baelmans, W. Desmet, *Time-domain impedance formulation based on recursive convolution*, *12th AIAA/CEAS Aeroacoustics Conference (27th AIAA Aeroacoustics Conference)*, American Institute of Aeronautics and Astronautics, AIAA 2006-2685.

[15] B. Gustavsen, A. Semlyen, *Rational approximation of frequency domain responses by vector fitting*, IEEE Transactions on Power Delivery, Vol. 14, No. 3, (1999), pp. 1052–1061.

[16] V. Easwaran, V. Gupta, M. Munjal, *Relationship between the impedance matrix and the transfer matrix with specific reference to symmetrical, reciprocal and conservative systems*, Journal of Sound and Vibration, Vol. 161, No. 3, (1993), pp. 515–525.

[17] T. Elnady, M. Åbom, S. Allam, *Modeling perforates in mufflers using two-ports*, Journal of Vibration and Acoustics, Vol. 132, (2010), pp. 061010.

[18] J. W. Sullivan, M. J. Crocker, *Analysis of concentric-tube resonators having unpartitioned cavities*, The Journal of the Acoustical Society of America, Vol. 64, (1978), pp. 207–215.

[19] R. Kirby, F. D. Denia, *Analytic mode matching for a circular dissipative silencer containing mean flow and a perforated pipe*, The Journal of the Acoustical Society of America, Vol. 122, No. 6, (2007), pp. 3471–3482.

[20] Y. Aurégan, M. Leroux, *Failures in the discrete models for flow duct with perforations: an experimental investigation*, Journal of Sound and Vibration, Vol. 265, No. 1, (2003), pp. 109–121.

[21] F. Mechel, *Duct acoustics*, F. Mechel, Editor, *Formulas of Acoustics*, Springer-Verlag GmbH (2008).

[22] C. Geuzaine, J.-F. Remacle, *Gmsh: A 3-D finite element mesh generator with built-in pre- and post-processing facilities*, International Journal for Numerical Methods in Engineering, Vol. 79, No. 11, (2009), pp. 1309–1331.

[23] B. Vanelderen, W. De Roeck, W. Desmet, *Numerical two-port characterization of the aeroacoustic propagation effects in exhaust mufflers including non-uniform mean flow effects*, *6th International Styrian Noise, Vibration and Harshness Congress*, 2010-01-1428.

Monte-carlo computation of wall-pressure spectra under turbulent boundary layers for trailing-edge noise prediction.

G. Grasso [1,2]**, P. Jaiswal** [1]**, S. Moreau** [1]
[1] Université de Sherbrooke, Département de Génie Mécanique,
2500 Bd. de l'Université, J1H4X2 Sherbrooke, QC, Canada

[2] Currently affiliated with École Centrale de Lyon, Laboratoire de Mécanique des Fluides et d'Acoustique
36 Avenue Guy de Collongue, 69134 Écully Cedex, France
e-mail: **gabriele.grasso@ec-lyon.fr**

Abstract
The quantification of the spectrum of wall-pressure fluctuations under a turbulent boundary layer has a fundamental role in problems of aerodynamic noise generation and structural vibration. Advanced analytic formulations of the wall-pressure spectrum involve multi-dimensional integrals. The computation of these integral formulations with quadrature methods proves computationally expensive, especially if many flow configurations are taken into account. For this reason, Monte-Carlo methods are used to distribute a predefined number of samples of the integrand function in the integration space and obtain a rapid and accurate estimate of the integral value. This work reviews the expression of the wall-pressure spectrum based on the Poisson equation for pressure fluctuations in a turbulent field and then applies three different Monte-Carlo methods to its computation: the quasi-uniform sampling, the recursive stratified sampling and the importance sampling. The criteria for the choice of the most appropriate Monte-Carlo method are finally discussed.

1 Introduction

The problem of estimating of the spectrum of wall-pressure fluctuations under a turbulent boundary layer arises in the description of aeroacoustic and structural phenomena. From the aeroacoustic point of view, Amiet's model and its extension [1, 30] state that the spectrum of trailing-edge noise emitted by a stationary airfoil is directly proportional to the spectrum of wall-pressure fluctuations generated by the turbulent boundary layer that develops over the airfoil surface. This model is extended to the prediction of noise from low-speed fans [31, 33]. The scattering of the wall-pressure fluctuations at the trailing edge of a blade is one of the main contributions to the broadband noise emitted by subsonic fans [21] and it represents the minimum level of noise emitted by a fan when all leading-edge and tip interactions are removed. Also, the turbulent boundary layer that develops on the external surfaces of air, ground and marine transportation vehicles generates unsteady loads that can excite the underlying structure and propagate towards the interior of the vehicle as sound and vibration [4]. These facts justify the introduction of a fast and accurate prediction of the wall-pressure spectrum in the design process of many different industrial applications. Empirical models of the wall-pressure spectrum scaled with boundary layer variables have been developed most notably by Corcos [9], Chase [6], Schlinker and Amiet [34], Efimtsov [10], Goody [13], Rozenberg *et al.* [32] and Caiazzo *et al.* [4], among others. The advantage of these models consists in their easy mathematical formulation, which poses no problems of numerical implementation. However, they do not provide an explicit correlation between the statistics of the wall pressure and those of the overlying turbulent field. This correlation is formulated in the models based on the Poisson equation of the pressure fluctuations in a turbulent field. The

disadvantage, in this case, is that the formulations of the wall-pressure spectrum resulting from the Poisson equation involve multi-dimensional integrals that require a high computational time when solved with traditional quadrature techniques. This problem was circumvented in the TNO-Blake family of models by making simplifying assumptions on the turbulence statistics that allowed to reduce the dimensionality of the integral formulation (see e.g. Kamruzzaman *et al.* [15] and Bertagnolio *et al.* [2]). However, these assumptions have recently been dismissed as non-physical by Fischer *et al.* [11]. In other works, such as those of Panton and Linebarger [22], Remmler *et al.* [28], Peltier and Hambric [23] and Slama *et al.* [35], the multi-dimensional integral formulations are computed in a reasonable time with different numerical techniques, particularly Monte-Carlo methods and Kriging. This work explores the application of different Monte-Carlo methods to a possible solution of the wall-pressure spectrum based on the Poisson equation considering especially the efficiency and the ease of implementation of these methods.

2 Analytic formulation of the wall-pressure spectrum

2.1 Solution of the Poisson equation

The Poisson equation governing the pressure fluctuations in a turbulent boundary layer derives from the divergence of the incompressible momentum equation, introducing Reynolds decomposition into mean and fluctuating quantities, then subtracting the time-averaged equation. As a result,

$$\frac{1}{\rho}\frac{\partial^2 p}{\partial x_i^2} = \underbrace{-2\frac{\partial u_j}{\partial x_i}\frac{\partial U_i}{\partial x_j}}_{\text{turbulence-mean shear}} \underbrace{-\frac{\partial^2}{\partial x_i \partial x_j}\left(u_i u_j - \overline{u_i u_j}\right)}_{\text{turbulence-turbulence}} \tag{1}$$

where lowercase letters indicate fluctuating quantities and uppercase letters indicate mean quantities. The Laplacian of the unsteady pressure field is equal to the sum of two source terms: the turbulence-mean shear and the turbulence-turbulence interaction. In this work, it is assumed for mathematical simplicity that the main contribution to the wall-pressure spectrum is that of the turbulence-mean shear interaction, according to the estimation made by Kraichnan [16]. However, recent research has highlighted the importance of turbulence-turbulence interaction term on the lower frequency range of the spectrum (see e.g. [35]). Equation (1) is solved for the fluctuating pressure in the domain represented in Fig. 1 using the Neumann boundary condition at the wall and assuming that p vanishes at infinity. The mean flow speed is aligned with the x_1 coordinate and is uniform with respect to x_1 and x_3 As a result, the only significant mean-velocity gradient is in the normal-to-wall direction and the source term of the Poisson equation is reduced to $-2\frac{\partial u_2}{\partial x_1}\frac{\partial U_1}{\partial x_2}$. The turbulent field is considered homogeneous in planes parallel to the wall (having constant x_2 coordinate). Therefore, Eq. (1) can be Fourier-transformed in the x_1 and x_3 directions, yielding the following modified Helmholtz equation:

$$\frac{\partial^2 \hat{p}(\kappa, x_2)}{\partial x_2^2} - \kappa^2\, \hat{p}(\kappa, x_2) = -2\,\rho\,\mathrm{i}\,k_1\,\frac{\partial U_1}{\partial x_2}\hat{u}_2(\kappa, x_2) \tag{2}$$

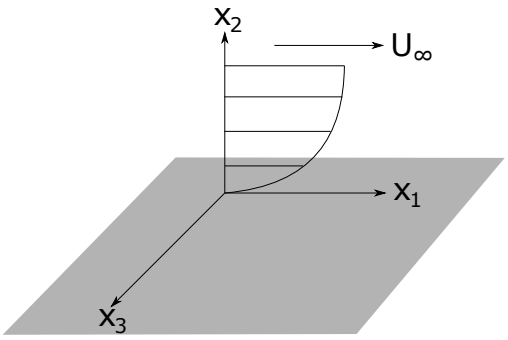


Figure 1: Turbulent boundary layer over an infinite flat plate.

where $(\hat{\cdot})$ represents the double spatial Fourier transform and $\kappa = \sqrt{k_1^2 + k_3^2}$. The solution of Eq. (2) is obtained with the following Green's function (see Gerolymos *et al.* [12] for a complete derivation):

$$G\left(x_2, X_2; \kappa \neq 0\right) = -\frac{\mathrm{e}^{-\kappa|x_2 - X_2|}}{2\kappa} - \frac{\mathrm{e}^{-\kappa(x_2 + X_2)}}{2\kappa} \tag{3}$$

hence the wall pressure is

$$\hat{p}(\kappa, x_2 = 0) = 2\,\mathrm{i}\,\rho \frac{k_1}{\kappa} \int_0^\infty \frac{\partial U_1(X_2)}{\partial x_2} \hat{u}_2(\kappa, X_2) \mathrm{e}^{-\kappa\, X_2} dX_2. \tag{4}$$

The spectrum of wall-pressure fluctuations is obtained by multiplying Eq. (4) by its complex conjugate and taking the ensemble average. The result is integrated over the transverse wavenumber k_3, yielding the streamwise-wavenumber wall-pressure spectrum:

$$\varphi_{pp}(k_1) = 8\rho_0^2 \iiint_0^\infty \frac{k_1^2}{\kappa^2} \mathrm{e}^{-(X_2 + X_2')\kappa} \frac{\partial U_1(X_2)}{\partial x_2} \frac{\partial U_1(X_2')}{\partial x_2} \langle \hat{u}_2(\kappa, X_2) \cdot \hat{u}_2(\kappa, X_2') \rangle dX_2\, dX_2'\, dk_3. \tag{5}$$

According to the hypothesis of 'frozen' convection of the turbulence (see e.g. [22, 11]), the frequency spectrum, $\varphi_{pp}(\omega)$, is a function of the streamwise wavenumber spectrum, $\varphi_{pp}(k_1)$, as $\varphi_{pp}(\omega) = \varphi_{pp}(k_1 \rightarrow \omega/U_c)/U_c$.

2.2 Cross-spectrum of vertical velocity fluctuations

The vertical velocity fluctuation statistics that appear in Eq. (5) is modeled with the following relationship:

$$\langle \hat{u}_2(\kappa, X_2) \cdot \hat{u}_2(\kappa, X_2') \rangle = \sqrt{\overline{u_2^2(X_2)}\, \overline{u_2^2(X_2')}}\, S_{22}(\kappa, X_2, X_2') \tag{6}$$

where S_{22} is the normalized cross-spectrum of u_2. The analytic expression of S_{22} is derived as follows.

The normalized vertical velocity correlation coefficient is defined for a homogeneous turbulent field as

$$R_{22}\left(r_1, r_2, r_3\right) = F\left(r\right) + \frac{r_1^2 + r_3^2}{2r} F'\left(r\right) \tag{7}$$

where $r = \sqrt{r1^2 + r_2^2 + r_3^2}$ and $F(r)$ is the longitudinal correlation function. For the present calculations, the correlation function is assumed to be a Gaussian:

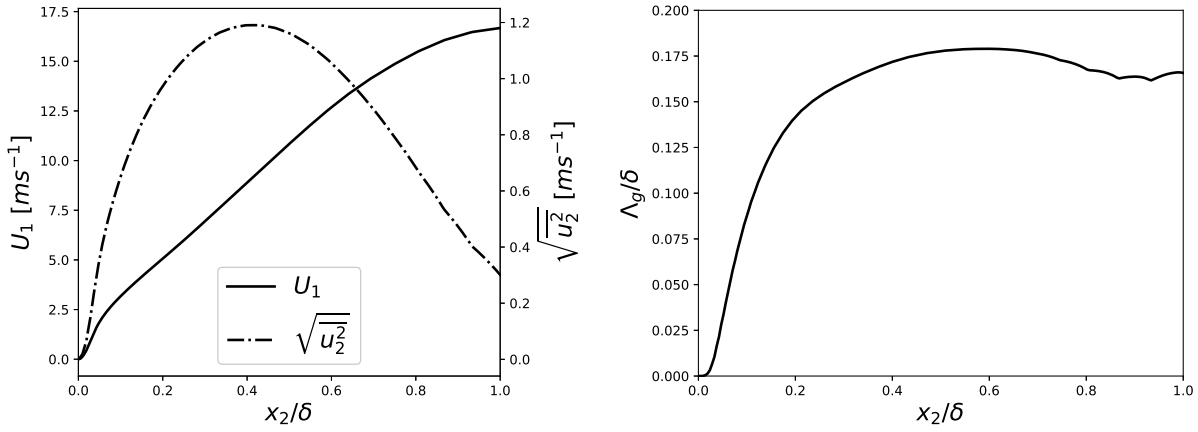
$$F\left(r\right) = \exp\left(-\frac{r^2}{\Lambda_g^2}\right). \tag{8}$$

where Λ_g is an integral length scale. Other functions can be chosen to represent $F(r)$ (see [36] for an extensive discussion) but the Gaussian has the advantage of providing a simple closed-form solution of the cross-spectrum, S_{22}, and is therefore well-suited for numerical validation. The cross-spectrum of vertical velocity fluctuations is defined as the real part of the double spatial Fourier transform of R_{22} in the streamwise and transverse directions:

$$S_{22}(\kappa, X_2, X_2') = \frac{1}{4\pi^2} \int_0^\infty \int_0^{2\pi} R_{22} \cos(k_1\, r_{1,3} \cos(\theta)) \cos(k_3\, r_{1,3} \sin(\theta)) d\theta dr_{1,3} \tag{9}$$

where the polar coordinates $r_{1,3} = \sqrt{r_1^2 + r_3^2}$ and $\theta = \arcsin(r_3/r_1)$ have been used. It can be shown that the integral in $d\theta$ of Eq. (9) has an analytic solution, which yields

$$S_{22}(\kappa, X_2, X_2') = \frac{1}{2\pi} \int_0^\infty R_{22} J_0\left(r_{1,3}\, \kappa\right) r_{1,3} dr_{1,3} \tag{10}$$



(a) Mean velocity and turbulence intensity

(b) Integral length scale

Figure 2: Boundary layer profiles of the CD airfoil used as input to the wall-pressure spectrum calculation.

where J_0 is the Bessel function of the first kind of order 0. The last equation states that the cross-spectrum of u_2 is the Hankel transform of R_{22} in the $r_{1,3}$ direction. Finally, the solution of the integral of Eq. (10) yields

$$S_{22}(\kappa, X_2, X_2') = \frac{1}{2\pi} \mathrm{e}^{-\frac{(X_2 - X_2')^2}{\Lambda_g^2}} \frac{\kappa^2 \Lambda_g^4}{8} \mathrm{e}^{-\frac{\kappa^2 \Lambda_g^2}{4}} \tag{11}$$

where the X_2 and X_2' coordinates are written explicitly due to the inhomogeneity of the turbulence in the normal-to-wall direction. The introduction of Eqs. (9), (10) or (11) in Eq. (5), although formally indifferent, yields a five-dimensional, a four-dimensional or a three-dimensional integral formulation of the wall-pressure spectrum, respectively. The computation of the wall-pressure spectrum with classical quadrature techniques requires an amount of computational time that increases with the number of dimensions in the integral formulation. However, this mathematical model provides a useful test case to assess the efficiency of Monte-Carlo methods working with a pre-defined number of samples of integrand functions of increasing complexity.

3 Test Case

The application case for the computation of wall-pressure spectra is a controlled-diffusion (CD) airfoil for which it exists a large experimental and numerical database [19, 33]. The present profile corresponds to the mid-span section of the H380EC1 fan blade [18]. It has a 4% relative thickness and a camber angle of 12^o. The airfoil chord length is $c = 0.1356$ m. It is set at a geometrical angle of attack of $\alpha_w = 8^o$. The reference velocity is $U_0 = 30$ m/s, defining a Reynolds number based on the airfoil chord length $Re_c = 2.8 \cdot 10^5$. A LES and a RANS simulation of the flow over the CD airfoil have been performed with OpenFOAM [7]. The turbulence model selected for the RANS simulation was the k-ω SST. The boundary-layer quantities necessary for the wall-pressure spectrum prediction have been extracted from the RANS simulation using BATMAN, the VKI in-house code for noise prediction. The results of the extraction are depicted in Fig. 3, where the x_2 coordinate is normalized by the boundary layer thickness, δ. Details of the computation of $\sqrt{\overline{u_2^2}}$ and Λ_g from a RANS simulation are given in the paper of Remmler *et al.* [28]. The wall-pressure spectrum directly computed from the LES simulation is retained throughout this study for comparison with the predicted spectra.

The frequency wall-pressure spectra presented in the following figures are computed from the corresponding wavenumber spectra given by Eq. (5). The convective speed of pressure fluctuations over the blade surface, U_c, is supposed to be independent of the wavenumber and equal to 70% of the reference velocity U_0. This is a common value for turbulent boundary layer convection velocity (see [29, p. 50] and [20, Tab. 1]). The

treatment of length scale anisotropy in the turbulent field and of its effect on S_{22} is described in detail by Remmler [28].

4 Monte-Carlo methods

Various numerical schemes have been devised in the past for the numerical calculation of multi-dimensional integral, and the reader is referred to [26] for a brief overview. However most of the classical quadrature schemes can be computationally demanding if the dimension of the integral is high [17]. As an estimate if 100 points are required for calculation of a single independent variable, then the required cost for N dimensional integral using a classical quadrature technique would be 100^N. Furthermore this would be the cost for a single streamwise-wavenumber calculation, in principle then if one wants to calculate the pressure spectra at M different streamwise wavenumber this cost will go upto $M \times 100^N$. This can be computationally heavy if N is large, even by current state of the art computer. Whereas as noted if we want to estimate wall pressure spectra from a pre-design perspective where a hundred of test cases are to be tested and as such a large computational cost for a single case can prove to be detrimental. With this in mind the Monte-Carlo method for numerical integration has been used, which is computationally much cheaper and can converge with just a moderate $3000 - 5000$ iterations per streamwise wavenumber as noted previously by [22], [17] and [28] using a similar formulation for the calculation of wall-pressure spectra.

4.1 Quasi uniform sampling

The simplest way to integrate a generic function $f : \mathbb{R}^n \to \mathbb{R}$ with Monte-Carlo schemes is to generate N random vectors, $\mathbf{x}_i$, over the integration domain. Following the review made by Press and Farrar [25], we can define the estimator of f, which is obtained by calculating the mean of the N randomly sampled function values:

$$\langle \tilde{f} \rangle = \frac{1}{N} \sum_{i=1}^{N} f(\mathbf{x}_i). \tag{12}$$

An indication of the error of the Monte-Carlo integration is given by the square root of the variance of the estimator, $\mathrm{Var}(\langle \tilde{f} \rangle)$. The variance of the estimator, in its turn, is related to the variance of the function as

$$\mathrm{Var}(\langle \tilde{f} \rangle) = \frac{\mathrm{Var}(f)}{N} \tag{13}$$

so that the following asymptotic relation holds for the error of the estimation:

$$\epsilon = \mathcal{O}\left(\frac{\sigma}{\sqrt{N}}\right) \tag{14}$$

where $\sigma = \sqrt{\mathrm{Var}(f)}$. However it is a known fact that generating random numbers using a deterministic computer is not possible, since a deterministic computer will always generate the same output if the starting conditions and inputs are the same. On the other hand one can generate so called pseudo random numbers using built-in libraries. However such random number generators are based on recurrence relations, and as such they would repeat afterwards. Although, there exists a random number generators which can take care of this problem of short-periods [26], nevertheless variance reduction obtained by generating pseudo-random sequence is quite slow and it converges with a rate of $N^{-1/2}$ [26], where N is the number of samples. To avoid this [22] and [17] used quasi-random sequences to sample the integral, this can improve the rate of convergence of the integral to N^{-1} under certain boundary conditions [26]. Thus for our test cases we use the Sobol sequence for generating Quasi-Random (QR) numbers using the function $sobseq$ taken directly from [27].

4.2 Recursive stratified sampling/Miser algorithm

A different technique, the recursive stratified sampling, has been developed by Press and Farrar and implemented in the MISER algorithm [25]. The fundamental idea is to divide the integration region V into two equal and disjoint subvolumes, a and b, and sample them with N_a and $N_b = N - N_a$ uniformly distributed points, respectively. Then, a new estimator of $\langle f \rangle$ is defined as

$$\langle \tilde{f} \rangle' = \frac{1}{2}\left(\langle \tilde{f} \rangle_a + \langle \tilde{f} \rangle_b\right) \tag{15}$$

where the $\langle \tilde{f} \rangle_{a,b}$ terms are computed according to Eq. (12). The variance of the newly defined estimator is

$$\text{Var}\left(\langle \tilde{f} \rangle'\right) = \frac{1}{4}\left(\frac{\text{Var}_a(f)}{N_a} + \frac{\text{Var}_b(f)}{N - N_a}\right) \tag{16}$$

which is minimized when

$$\frac{N_a}{N} = \frac{\sigma_a}{\sigma_a + \sigma_b}. \tag{17}$$

In case N_a satisfies the previous equation, the variance of the function mean estimator is

$$\text{Var}\left(\langle \tilde{f} \rangle'\right) = \frac{(\sigma_a + \sigma_b)^2}{4N}. \tag{18}$$

The advantage of this method is that Var $\left(\langle \tilde{f} \rangle'\right)$ is never larger than the variance of the estimator computed in the general Monte-Carlo method, defined in Eq. (13). The stratified sampling can be applied recursively to solve high-dimensional problems; the details of this procedure are given in [25]. The MISER algorithm is available in the `Scikit-Monaco` package for Python [3].

4.3 Importance sampling

Another way to accelerate the convergence by reducing variance the technique of Importance Sampling (IS) method can be used as done previously by [22], [17] and [28]. The method of importance sampling is based on the simple idea that by introducing a change in variable the function could be made flatter in the new co-ordinate system and hence fewer samples would be required to reach convergence. In fact if the function is flat just a single sample would be required.

Mathematically importance sampling can be defined as

$$E_f[h(X)] = \int_X h(x)g(x)dx \tag{19}$$

In the above equation we seek to determine the expectation E of function $h(x)$ under the Probability Density Function (PDF) $g(x)$.

Generally we need to either find the PDF $g(x)$ that mimics the function $h(x)$ in case if such a function is not present intrinsically in the integral. Then from there on samples could be drawn from the function $g(x)$ using the technique known as Inverse transform sampling.

The algorithm for inverse transform sampling can be summarized as-

1) Determine the PDF function $g(x)$ which "resembles" $h(x)$.

2) Determine its Cumulative Distribution Function (CDF) $u(x)$.

3) Find its inverse $u^{-1}(x)$ either numerically or analytically.

4) Generate uniformly distributed random numbers using Sobol sequence and plug it to $u^{-1}(x)$, this would generate random number based on the PDF $g(x)$.

5) Solve Eq. (19).

Before importance sampling was realised, the Quintuple Integrals was further simplified in order to facilitate its numerical implementation. Firstly all the length scales in the equation were normalised using δ (the boundary layer thickness) as follows : $k = k\delta$, $x_2 = x_2/\delta$, $\lambda_g = \lambda_g/\delta$ and $r = r/\delta$. Secondly the integral is split in two different terms $\varphi(K_1) = I_1 - I_2$ as was done by [22],with I_1 :

$$\left\{ \begin{array}{l} I_1 = \dfrac{2\alpha {k_1}^2 \rho^2}{\pi^2} \displaystyle\int_0^{2\pi} \int_0^{\infty} \int_0^1 \int_0^1 \int_0^{\infty} \frac{1}{\kappa^2} \times \mathrm{e}^{(-\kappa(X_2{}' + X_2))} \ldots \\ \sqrt{\overline{u_2^2(X_2)}\,\overline{u_2^2(X_2')}}\,\delta^3 \times \left[(r) \times \exp\left(- \left(\dfrac{r^2 + (X_2 - X_2{}')^2}{{\Lambda_g}^2} \right) \right) \right] \\ \dfrac{\partial U}{\partial x_2} \dfrac{\partial U}{\partial x_2{}'} \cos(k_1 \alpha r \cos\theta) \cos(k_3 r \sin\theta) d\theta dr dX_2 dX_2{}' dk_3 \end{array} \right\} \tag{20}$$

and I_2 :

$$\left\{ \begin{array}{l} I_2 = \dfrac{2\alpha {k_1}^2 \rho^2}{\pi^2} \displaystyle\int_0^{2\pi} \int_0^{\infty} \int_0^1 \int_0^1 \int_0^{\infty} \frac{1}{\kappa^2} \times \mathrm{e}^{(-\kappa(X_2{}' + X_2))} \ldots \\ \sqrt{\overline{u_2^2(X_2)}\,\overline{u_2^2(X_2')}}\,\delta^3 \times \left[\left(\dfrac{r^3}{{\Lambda_g}^2} \right) \times \exp\left(- \left(\dfrac{r^2 + (X_2 - X_2{}')^2}{{\Lambda_g}^2} \right) \right) \right] \\ \dfrac{\partial U}{\partial x_2} \dfrac{\partial U}{\partial x_2{}'} \cos(k_1 \alpha r \cos\theta) \cos(k_3 r \sin\theta) d\theta dr dX_2 dX_2{}' dk_3 \end{array} \right\} \tag{21}$$

For the variance reduction for the variables x_2 and $x_2{}'$ a normal distribution is used,while tailored design of the PDF's used for these variables are driven from previous observations on wall-pressure spectra. In particular the design is motivated by the fact that high frequency and high wave-number contributions comes from the inner part of boundary layer, while at low wavenumber contributions are usually due to external parts of the boundary layer [5]. Secondly the higher frequency contributions are much more localised or stratified, while low frequency contributions are more spread out [22]. Lastly the inner most part of viscous sub-layer part of the boundary layer will have very low contribution towards overall spectra due to the fact that vertical velocity fluctuations tend to zero. By taking these considerations into account, the Eq. (22) is devised :

$$g(x) = 2 * \sqrt{(b * k_1)} \times \left[\frac{\left[\exp[-(b * k_1 * (x - \frac{ah}{k_1})^2)] \right]}{\left[\sqrt{\pi} [\mathrm{erf}(\frac{a * \sqrt{b} * h}{\sqrt{k_1}}) + \mathrm{erf}(\frac{\sqrt{b}(-a*h+k_1)}{\sqrt{k_1}})] \right]} \right] \tag{22}$$

where erf is the Error function. Here K_1, corresponds to the streamwise wavenumber, while b, a and h are empirical constants, to accomplish the above mentioned objectives. The CDF of Eq. (22) turns out to be fairly complicated such that it cannot be analytically inverted. To do this Brent's method of finding the root was used [27]. Brent's method of finding root is a hybrid method [26], and it uses a combination of bisection method, the secant method and inverse quadratic interpolation root , to find roots. An advantage is that, such a method compared to other classical root finding method such as the method of false position used by [17], it performs better even when the function is not smooth near the root [26].

The variance reduction for the variable $\tilde{k}_3$ was realised by using the following PDF:

$$g(x) = (a \times \exp(-(x^2 \times a^2/4)))/(\sqrt{(\pi)} * \mathrm{erf} * (ad/2)) \tag{23}$$

where d is the upper limit of integration for the variable $\tilde{k}_3$. Finally a in Eq.(23) is meant to emulate the behaviour of λ_g. The PDF used for variance reduction for the variable r in the integral I_1 Eq. (20) and I_2 Eq. (21), have following form respectively.

$$g(x) = \left[2 * x \frac{\left[\exp(-[\frac{x^2+c^2}{L^2}])\right]}{L^2 \exp[-(\frac{c^2}{L^2})]}\right] \tag{24}$$

$$g(x) = \left[2 * x^3 \frac{\left[\exp(-[\frac{x^2+c^2}{L^2}])\right]}{L^2\left[L^2 \times \exp[-\frac{c^2}{L^2}]\right]}\right] \tag{25}$$

Here the variable c is meant to emulate $[x_2 - x_2{}']$. L mimics Λ_g.

Lastly for the variable θ, the variable selection turns out to be quite tricky; this was the reason why [22], [17] used a uniform distribution to sample it. However, we know that the variable θ behaves like a Bessel function of the first kind of order 1. But due to its oscillatory behaviour we cannot construct a PDF directly. Although there is an option to take the absolute value of the function and then create the PDF in a piecewise fashion. However this would be a complicated step to implement numerically. A more realistic way is then to note that a Bessel function decreases with a rate of $1/\sqrt{x}$. And since this function is simple enough, it is more amenable to mathematical and programming procedure involved. Hence the PDF chosen for variance reduction for the variable θ is :

$$g(x) = \frac{1}{2 \times \sqrt{(x * 2 * \pi)}} \tag{26}$$

5 Adaptive Quadrature method

The techniques described in section 6 have already been used in the past by numerous other authors e.g. [22], [17] and more recently by [28] to calculate the wall-pressure spectra. However due to mathematical complexities and high computational cost associated with performing a numerical quadrature scheme, a direct one to one comparison between MC integration scheme and a quadrature scheme has not been realized yet in the context of wall-pressure spectra calculations. This is important since while performing such a stochastic integration scheme a notion of absolute or relative accuracy cannot be devised. Rather only the variance of the integral can be controlled. Hence the notion of variance reduction exists which was discussed in the sections before. Be it as it may, this does not let one to determine the accuracy of results. Hence although [22] have extensively tested reduction in variance while using such a stochastic scheme, it is unknown if there solution did or did not converge to the right answer. Also as discussed in section 6 that variance reduction while using importance sampling scheme (as was employed by all the previous authors [22], [17] and [28]) is very sensitive to the choice of distribution function. A wrong choice of distribution function while may lead to an efficient reduction in variance it can nevertheless certainly make the solution digress from the correct solution. In order to quantify the relative accuracy of the calculated wall-pressure spectra using various Monte-Carlo schemes we employ an adaptive quadrature schemes wherein relative errors can be set a-priori, which then can be considered as the reference. This indirect method provides an alternative way of quantifying errors, in a relative sense. The method used for adaptive quadrature integration scheme was tplquad, which can be simply imported from the Python inbuilt scipy.integrate library [14]. For the case where limits of integration are finite, this package uses Clenshaw-Curtis method of cubature [24]. The way it is implemented in Python, user has a choice of either specifying absolute or relative accuracy or both. Since the value of the integral being calculated is below the default absolute accuracy limit, this value was modified and ascribed an arbitrary low value that cannot be achieved numerically, and the relative accuracy was set as 0.9×10^{-3}. This forces the integral to converge within the prescribed limits of relative accuracy.

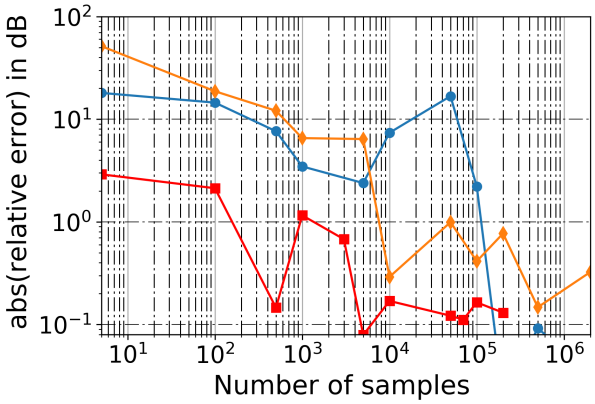
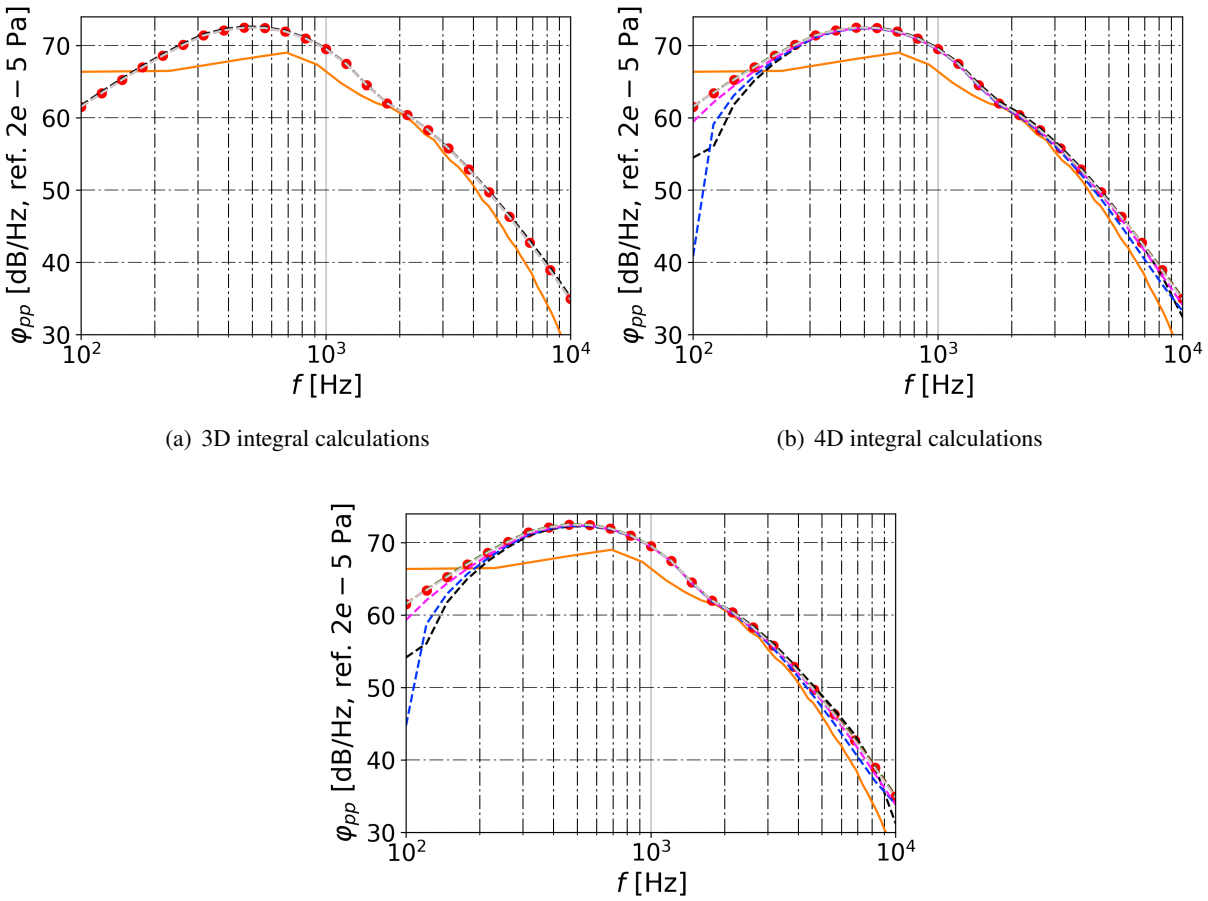


Figure 3: Convergence of different integration schemes Legends: MC MISER sampling error calculated at lowest frequency ; MC QR sampling error calculated at lowest frequency; MC IS sampling error calculated at highest frequency

6 Compare the convergence of the three algorithms against the quadrature scheme

Methods discussed above for the calculation of wall pressure spectra were tested and comparisons are presented in this section. All the cases were run on a Intel(R) Xeon(R) CPU $E3-1270$ v5 Linux workstation with memory base frequency of 3.60GHz and 8 processors with a total of 32 Gb of ram and 8 Mb cache memory. It is worth noting that while both the Monte-Carlo schemes (the importance sampling and the Quasi-random sampling) were written in $Fortran90$, the MISER algorithm and adaptive quadrature scheme-$tplquad$ are both standard Python libraries. Moreover the $Fortran90$ codes were not parallelized while MISER algorithm is. Therefore the differences in time taken for calculation of wall pressure spectra do not necessarily correlate with efficiency of the scheme. Nevertheless time taken for calculation remains an important metric especially, if this method for wall-pressure calculations has to be used in conjunction with pre-design. For the 3 dimensional Quasi-random sampling the rate of calculation per sample was found to be around 2.9×10^{-5} seconds. 2 million samples were calculated under 1 minute. For 4 and 5 dimensional Quasi-random sampling the calculation rate was found to be around 4.4×10^{-5} seconds and 1.4×10^{-4} seconds respectively. Whereas due to inherent complexity involved in coding and number of supplementary operations required in the case of importance sampling meant that the solver takes longer to calculate integral for a single sample. For example in case of 5D integral using importance sampling scheme takes 0.9×10^{-3} seconds to calculate a single sample. For a 4 dimensional integral the cost of calculating integral is about 0.84×10^{-3} seconds, while for a 3 dimensional integral it costs about 1.02×10^{-3} seconds for a single sample. The differences in the latter results are most probably caused by an optimization issue with the code. In any case, it is an order of magnitude higher compared with the time taken by Quasi-random sampling technique for an integral of 5 dimensions. Lastly the [MISER or the Recursive stratified sampling] [25], as implemented in Python [3] is parallelized, hence the time taken per sample is no longer linear as function of sample. The rate is now a function of number of Monte-Carlo samples. For comparison purposes we only report that it takes about 7 minutes to perform Recursive stratified sampling technique on 2 million samples, irrespective of the dimension of the integral. Finally, one should now compare the time taken by these stochastic integration techniques against deterministic quadrature technique. The time taken for the $tplquad$ solution is about 1 hour and 15 minutes with the errors specified. This then clearly shows that Monte-Carlo schemes are several orders of magnitude faster then adaptive quadrature method for integration and it also gives reasonable estimate on a dB scale. Also the Monte-Carlo Quasi-random sampling scheme for integration converges very quickly at higher frequencies while the variance at low frequency is relatively high, this has also been reported in a previous study by Christophe *et al.* [8]. Figure 3 compares the convergence of

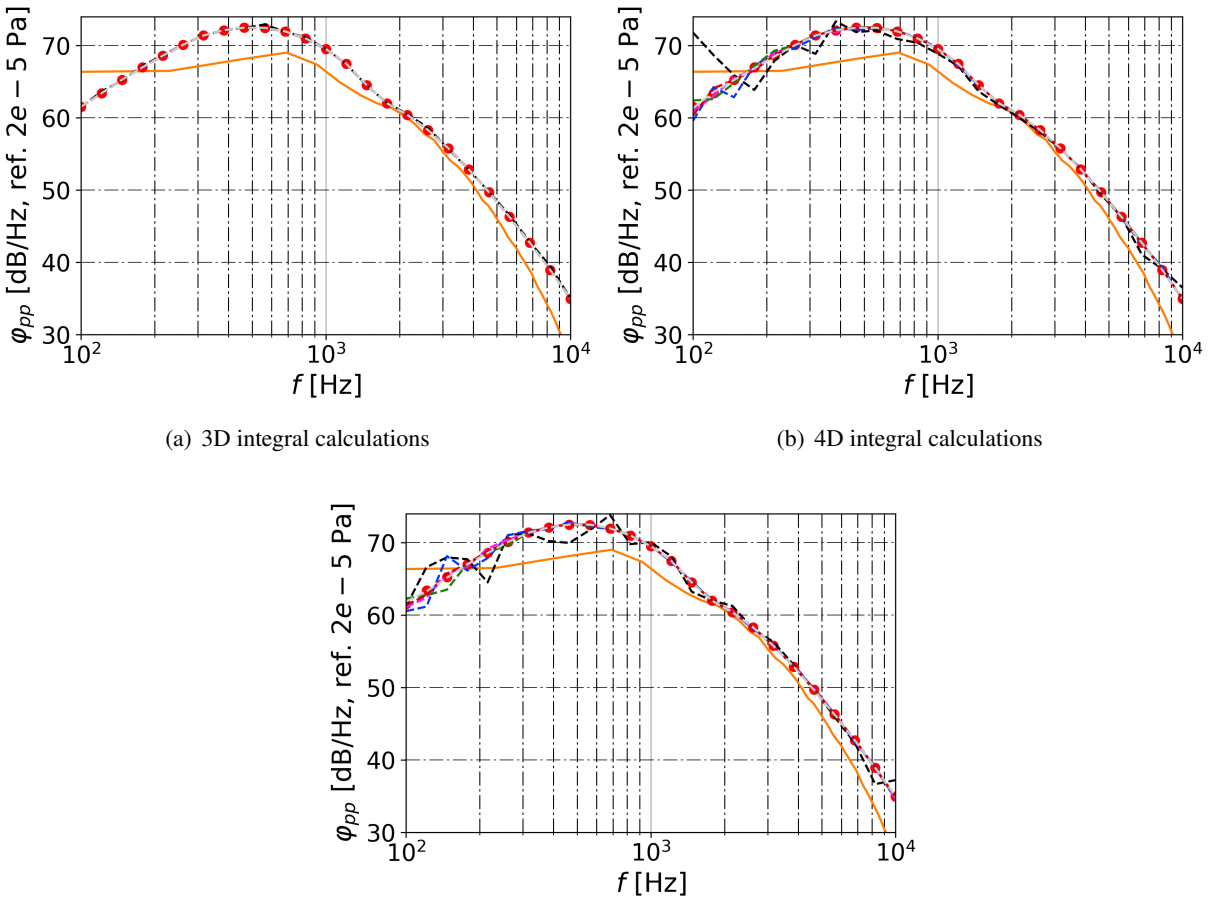


(a) 3D integral calculations

(b) 4D integral calculations

(c) 5D integral calculations

Figure 4: Wall pressure spectra at $x_1/chord = 0.98$ for MC QR sampling. Legends: ● Quadrature solution using tplquad ; —— Reference LES ; - - - With 10k samples; - - - With 50k samples ; - - - With 100k samples ; - - - With 200 k samples ; - - - With 500k samples ; - - - With 2M samples

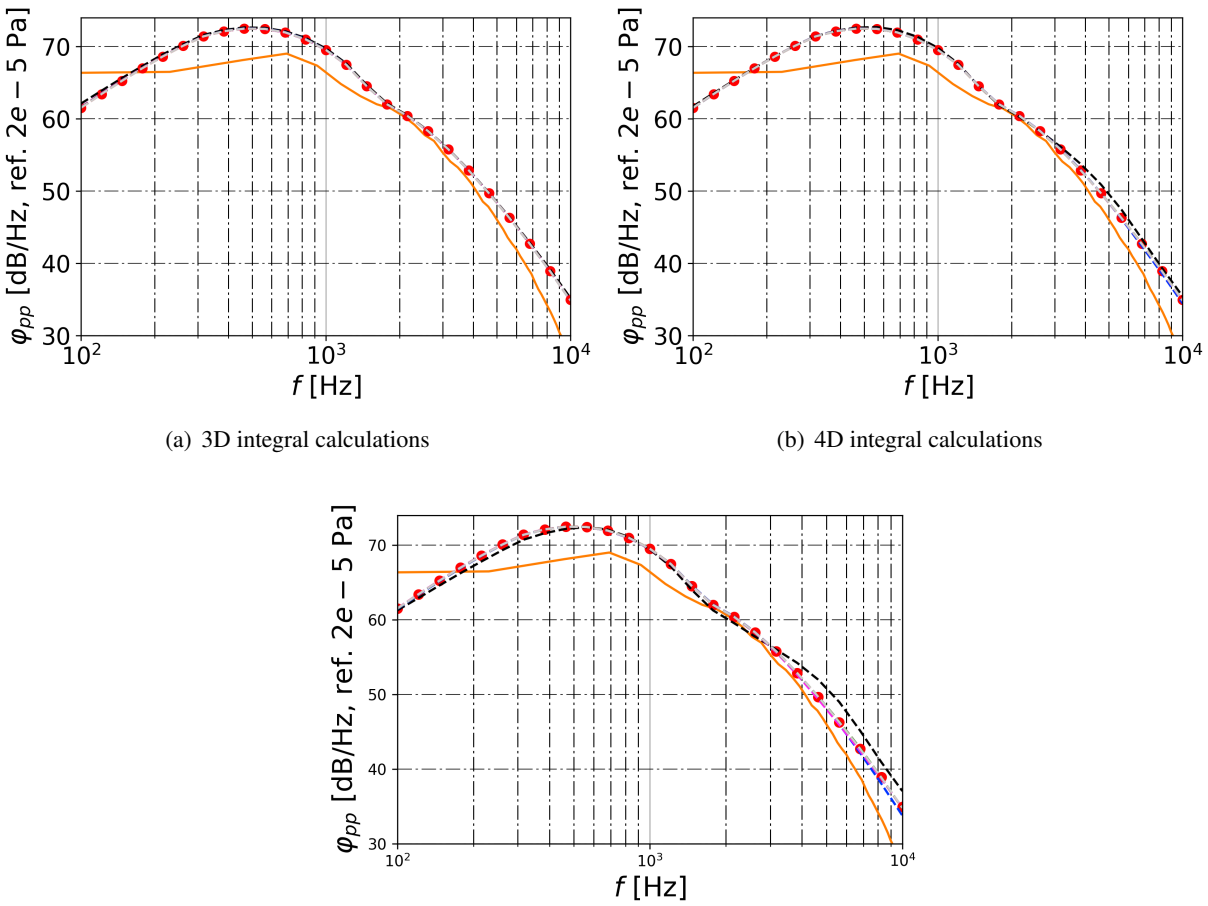


(a) 3D integral calculations

(b) 4D integral calculations

(c) 5D integral calculations

Figure 5: Wall pressure spectra at $x_1/chord = 0.98$ for MC MISER. Legends: ● Quadrature solution using tplquad ; —— Reference LES ; - - - With 10k samples; - - - With 50k samples ; - - - With 100k samples ; - - - With 200k samples ; - - - With 500k samples ; - - - With 2 M samples



(a) 3D integral calculations

(b) 4D integral calculations

(c) 5D integral calculations

Figure 6: Wall pressure spectra at $x_1/chord = 0.98$ for MC IS. Legends: ● Quadrature solution using tplquad ; — Reference LES ; - - - With 100 samples; - - - With 1k samples ; - - - With 5k samples ; - - - With 10k samples ; - - - With 100k samples ; - - - With 200 k samples

the three Monte-Carlo methods to the adaptive quadratures solution with the number of samples for a given frequency. In this case, the advantage of importance sampling appears clearly.

The wall-pressure spectra computed with the three Monte-Carlo methods are presented in Figs. 4 to 6. First, it can be noticed that the Quasi-Random sampling (Fig. 4) and the MISER algorithm (Fig. 5) exhibit a similar behavior. In fact, for the 3D integration test both algorithms provide a solution consistent with that of the adaptive quadratures already at the lowest number of samples of the integrand function. When the dimensions of the integral formulation are increased to 4 and 5, both methods require a larger number of samples (the order of 10^5) to converge to the reference solution in the lower frequency range. The slow statistical convergence at low frequencies of a Monte-Carlo method for the computation of the wall-pressure spectrum based on the Poisson equation was already noticed by Christophe *et al.* [8]. In their work, a slightly different formulation of the turbulence cross-spectrum was used, assuming an exponential longitudinal correlation function instead of a Gaussian, following [17] and [22]. Figure 6 presents the results of the application of the Importance sampling method to the three integral formulations. These plots demonstrate the advantage of using a variance-reduction method tailored to the integrand function: a converged solution can be obtained with a lower number of samples than the previous Monte-Carlo methods irrespective of the number of dimensions of the integral.

7 Conclusions and future work

This work has presented the application of three different Monte-Carlo techniques to integrand functions of increasing complexity that are of great interest in the study of sound and vibration generated by turbulent boundary layers. The methods taken into account range from the simplest application of Monte-Carlo integration, in which the samples of the function are selected quasi-randomly, to a technique tailored to the specific problem, such as Importance sampling. The results of the convergence tests presented in Sec. 6 show that the Importance sampling technique requires a significantly lower amount of computational resources to obtain the same result as the Quasi-random sampling or the MISER algorithm. However, the drawback of the Importance sampling technique is the necessity of developing an algorithm tailored to every given problem of integration. The MISER algorithm, on the contrary, can be applied to a very wide range of functions of any dimension and is efficiently parallelized in Python and therefore it constitutes a valid alternative.

The analytic modeling of wall-pressure spectra under turbulent boundary layers will be extended in future works to the use of different longitudinal correlation functions of the turbulent field, which are possibly not as mathematically convenient as the Gaussian (see [36]). Furthermore, the effect of the turbulence-turbulence interaction source term in the Poisson equation can be taken into account, leading to six-dimensional integral formulations, as shown in [23] and [35]. In light of these analytic developments, the use of efficient integration techniques illustrated in this paper will be all the more necessary.

Acknowledgements

The Authors gratefully acknowledge the support of the European Union under the project SCONE (grant agreement no. 755543) and the Canadian NSERC Discovery Grant (no: RGPIN-2014-04111).

References

[1] R. K. Amiet, *Noise due to turbulent flow past a trailing edge*, Journal of Sound and Vibration **4** (1976), no. 3.

[2] F. Bertagnolio, A. Fischer, and W. J. Zhu, *Tuning of turbulent boundary layer anisotropy for improved surface pressure and trailing-edge noise modeling*, Journal of Sound and Vibration **333** (2014), 991–1010.

[3] P. Buignon, *Scikit-monaco documentation*, `http://scikit-monaco.readthedocs.io/en/latest/`, 2013.

[4] A. Caiazzo, D'Amico R., and W. Desmet, *A generalized corcos model for modelling turbulent boundary layer wall pressure fluctuations*, Journal of Sound and Vibration **372** (2016), 192–210.

[5] Peter A Chang III, *Relationships between turbulent wall pressure and velocity field sources*, Ph.D. thesis, 1998.

[6] D. M. Chase, *Modeling the wavevector-frequency spectrum of turbulent boundary layer wall pressure*, Journal of Sound and Vibration **70** (1980), no. 1, 29–67.

[7] J. Christophe, *Private communication*.

[8] J Christophe, S Moreau, CW Hamman, JAS Witteveen, and G Iaccarino, *Uncertainty quantification for the trailing-edge noise of a controlled-diffusion airfoil*, AIAA Journal **53** (2014), no. 1, 42–54.

[9] G. M. Corcos, *The structure of the turbulent pressure field in boundary-layer flows*, Journal of Fluid Mechanics **18** (1964), 353–379.

[10] B. M. Efimtsov, *Characteristics of the field of turbulent wall pressure fluctuations at large reynolds numbers*, Soviet Physics Acoustical **28** (1982), no. 4, 289–292.

[11] A. Fischer, F. Bertagnolio, and H. Aa. Madsen, *Improvement of tno type trailing edge noise models*, European Journal of Mechanics B/Fluids (2017), no. 61, 255–262.

[12] G. A. Gerolymos, D. Sénéchal, and I. Vallet, *Wall effects on pressure fluctuations in turbulent channel flow*, Journal of Fluid Mechanics **720** (2013), 15–65.

[13] M. Goody, *Empirical spectral model of surface pressure fluctuations*, AIAA Journal **42** (2004), no. 9, 1788–1794.

[14] Eric Jones, Travis Oliphant, Pearu Peterson, et al., *SciPy: Open source scientific tools for Python*, 2001–, [Online; accessed May 27th 2018].

[15] M. Kamruzzaman, Th. Lutz, W. Würz, W. Z. Shen, W. J. Zhu, M O. L. Hansen, F. Bertagnolio, and H. Aa. Madsen, *Validations and improvements of airfoil trailing-edge noise prediction models using detailed experimental data*, Wind Energy **15** (2012), 45–61.

[16] R. C. Kraichnan, *Pressure fluctuations in turbulent flow over a flat plate*, Journal of the Acoustical Society of America **28** (1956), no. 3, 378–390.

[17] J. H. Linebarger, *Computation of the spectra of turbulent boundary layer surface-pressure fluctuations*, Ph.D. thesis, Oklahoma State University, 1972.

[18] S. Magne, S. Moreau, and A. Berry, *Subharmonic tonal noise from backflow vortices radiated by a low-speed ring fan in uniform inlet flow*, Journal of the Acoustical Society of America **137** (2015), no. 1, 228–237.

[19] S. Moreau, *Symposium on the cd airfoil - introduction*, `https://www.researchgate.net/publication/304582435_CD-day_S-Moreau`, 2016.

[20] S. Moreau and M. Roger, *Effect of airfoil aerodynamic load on trailing edge noise*, AIAA Journal **43** (2005), no. 1, 41–52.

[21] Stephane Moreau and Michel Roger, *Competing broadband noise mechanisms in low-speed axial fans*, AIAA journal **45** (2007), no. 1, 48–57.

[22] R. L. Panton and J. H. Linebarger, *Wall Pressure Spectra Calculations for Equilibrium Boundary Layers*, J. Fluid Mech. **65** (1974), no. 02, 261–287.

[23] L. J. Peltier and S. A. Hambric, *Estimating turbulent-boundary-layer wall-pressure spectra from cfd rans solutions*, Journal of Fluids and Structures **23** (2007), 920–937.

[24] Robert Piessens, Elise de Doncker-Kapenga, Christoph W Überhuber, and David K Kahaner, *Quadpack: a subroutine package for automatic integration*, vol. 1, Springer Science & Business Media, 2012.

[25] W. H. Press and G. R. Farrar, *Recursive stratified sampling for multidimensional monte carlo integration*, Computers in Physics **190** (1990), no. 4.

[26] W. H. Press, S. A. Teukolsky, W. T. Vetterling, and B. P. Flannery, *Numerical recipes in fortran 77. vol. 1*, Press Syndicate of the University of Cambridge, New York, NY, 1992.

[27] William H Press, Saul A Teukolsky, William T Vetterling, Brian P Flannery, and M Metcalf, *Numerical recipes in fortran 90: Volume 2, volume 2 of fortran numerical recipes: The art of parallel scientific computing*, Cambridge University Press, 1996.

[28] S. Remmler, J. Christophe, J. Anthoine, and S. Moreau, *Computation of wall-pressure spectra from steady flow data for noise prediction*, AIAA Journal **48** (2010), no. 9, 1997–2007.

[29] M. Roger and S. Moreau, *Broadband self noise from loaded fan blades*, AIAA Journal **42** (2004), no. 3, 536–544.

[30] M. Roger and S. Moreau, *Back-scattering correction and further extensions of Amiet's trailing-edge noise model. Part 1: Theory*, Journal of Sound and Vibration **286** (2005), no. 3, 477–506.

[31] M. Roger, S. Moreau, and A. Guédel, *Broadband fan noise prediction using single-airfoil theory*, Noise Control Engineering Journal **54** (2006), no. 1, 5–14.

[32] Y. Rozenberg, G. Robert, and S. Moreau, *Wall-pressure spectral model including the adverse pressure gradient effects*, AIAA Journal **50** (2012), no. 10, 2168–2179.

[33] M. Sanjosé and S. Moreau, *Fast and accurate analytical modeling of broadband noise for a low-speed fan*, Accepted for publication in the Journal of the Acoustical Society of America, 2018.

[34] R. Schlinker and R. K. Amiet, *Helicopter trailing edge noise.*, Tech. report, NASA, 1981.

[35] M. Slama, C. Leblond, and P. Sagaut, *A kriging-based elliptic extended anisotropic model for the turbulent boundary layer wall pressure spectrum*, Journal of Fluid Mechanics **840** (2018), 25–55.

[36] D. K. Wilson, *Three-dimensional correlation and spectral functions for turbulent velocities in homogeneous and surface-blocked boundary layers*, Tech. report, Army Research Laboratory, July 1997.

Experimental analysis of aeroacoustic instabilities in Helmholtz resonators

L. Criscuolo [1,2] **, H. Denayer** [1,2]**, W. De Roeck** [1]**, W. Desmet**[1,2]
[1] KU Leuven, Department of Mechanical Engineering,
Celestijnenlaan 300 B, B-3001, Heverlee, Belgium
e-mail: **luigi.criscuolo@kuleuven.be**

[2] Flanders Make, DMMS Lab

Abstract
This paper presents an experimental study of the aeroacoustic characteristics of Helmholtz resonators. The two-port characterization technique is applied to compute the scattering properties of the resonators from measured pressure spectra. The onset of aeroacoustic instabilities is investigated using an acoustic power balance based on the linear scattering matrix formulation. The influence of the grazing flow velocity on the aeroacoustic instability onset is discussed. Additionally, the effect of the orifice dimensions is analyzed with two different configurations. The results offer a valuable database for the validation of computational techniques for the prediction of whistling onset in duct systems.

1 Introduction

Helmholtz resonators and perforated plates are passive acoustic devices typically used in flow duct systems to suppress or control tonal noise propagation. Those devices are commonly integrated into many industrial applications such as aircraft engine liners, automotive mufflers, ventilation and exhaust systems for vehicles or buildings. To improve the acoustic performance of such products it is important to consider the potential interaction between the aerodynamic flow and sound waves, which can lead to high levels of vibrations and unacceptable noise emissions. Such aeroacoustic coupling phenomena have gained a marked interest due to their relevance for many engineering applications, such as pipe networks with an open or closed side branches [1, 2, 3, 4], T-junctions [5, 6, 7, 8] or orifice plates [9, 10, 11, 12], and cars with an open window or sunroof [13, 14]. Several numerical and experimental studies also discuss the modeling of the fluid-mechanics of flow-excited Helmholtz resonators [15, 16, 17, 18, 19, 20, 21, 22, 23]. Under certain conditions, the vortical flow disturbances, generated in the detached shear layer over the orifice, can interact with the acoustic field, resulting in an energy transfer between the flow and the acoustic oscillations. The constructive reinforcement of the unstable vortical structures, due to the coupling with the resonator cavity modes, can lead to aeroacoustic instabilities and whistling. As argued in [9] and [12], these phenomena develop from a linear state and their onset can be efficiently predicted using linear aeroacoustic theory.

This paper presents an experimental study of the aeroacoustic instabilities in Helmholtz resonators under a low Mach number grazing flow. The experiments are carried out on the open circuit aeroacoustic test facility at KU Leuven [24, 25]. A two-port technique is applied to characterize acoustically the test objects [26, 27, 28]. The frequency ranges for the onset of the instability phenomena are detected via an acoustic energy analysis of the resonators scattering properties [12]. The paper is organized as follows. Section 2 discusses the theory of the two-port characterization technique and the acoustic energy criterion. Section 3 introduces the test object and the experimental set-up. In Section 4 the results are presented and discussed. Concluding remarks are given in Section 5.

2 Theory

2.1 Acoustic two-port modeling

A two-port model is an efficient method to characterize the acoustic properties of a duct component, mounted between an inlet and outlet duct with rigid walls (Fig.1). It makes abstraction of the complex physics inside the acoustic element and describes the transmission and the reflection of the propagating sound using a linear matrix relation in frequency domain [26, 29, 28]. Analytical models of many simple duct geometries can be found in literature [26, 30, 31], while experimental and numerical approaches are typically adopted for more complex geometries.

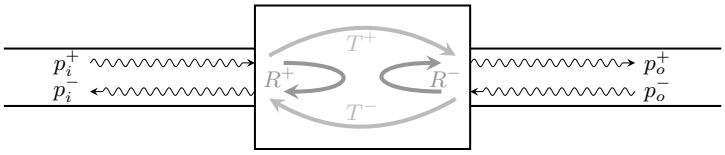


Figure 1: Two-port model of the acoustic element [32].

The two-port model assumes that only plane waves propagate in the ducts and all high-order modes are evanescent. This assumption allows describing the acoustic field in a duct using only two independent variables, such as the acoustic pressure and velocity or the complex amplitudes of the upstream and downstream propagating wave. The linear acoustic properties of a duct component are therefore determined by the relation between these variables at the inlet and at the outlet of the two-port element. Using the scattering matrix formulation, the acoustic behavior at an angular velocity ω is described by a linear matrix relation between the complex amplitudes of the downstream (p^+) and upstream (p^-) propagating pressure wave at the inlet ($\bullet_i$) and outlet ($\bullet_o$) of the acoustic element:

$$\underline{\boldsymbol{p}}_{\text{out}} = \underline{\underline{\boldsymbol{S}}}\,\underline{\boldsymbol{p}}_{\text{in}} \tag{1}$$

$$\underline{\boldsymbol{p}}_{\text{in}} = \begin{Bmatrix} p_i^+(\omega) \\ p_o^-(\omega) \end{Bmatrix}, \qquad \underline{\boldsymbol{p}}_{\text{out}} = \begin{Bmatrix} p_o^+(\omega) \\ p_i^-(\omega) \end{Bmatrix}, \qquad \underline{\underline{\boldsymbol{S}}} = \begin{bmatrix} T^+(\omega) & R^-(\omega) \\ R^+(\omega) & T^-(\omega) \end{bmatrix}. \tag{2}$$

The scattering matrix $\underline{\underline{\boldsymbol{S}}}$ contains the coefficients T^+, T^-, R^+ and R^-, which represent, respectively, the transmission and reflection coefficients for the downstream ($\bullet^+$) and upstream ($\bullet^-$) propagating waves. Given the assumption of plane wave propagation, the validity of the model is restricted to frequencies below the cut-off frequency of the first transversal mode.

The scattering matrix determination requires at least two independent states of the system. This can be achieved by varying the position of the excitation [33] (*two-source* method), by modifying the downstream impedance [34] (*two-load* method) or by a combination of both [35]. The scattering matrix is then computed as:

$$\underline{\underline{\boldsymbol{S}}} = \begin{bmatrix} T^+(\omega) & R^-(\omega) \\ R^+(\omega) & T^-(\omega) \end{bmatrix} = \begin{bmatrix} p_{o,\mathrm{I}}^+(\omega) & p_{o,\mathrm{II}}^+(\omega) \\ p_{i,\mathrm{I}}^-(\omega) & p_{i,\mathrm{II}}^-(\omega) \end{bmatrix} \begin{bmatrix} p_{i,\mathrm{I}}^+(\omega) & p_{i,\mathrm{II}}^+(\omega) \\ p_{o,\mathrm{I}}^-(\omega) & p_{o,\mathrm{II}}^-(\omega) \end{bmatrix}^{-1} \tag{3}$$

where the Roman number refers to the two independent states. The use of more than two states, using a Moore-Penrose pseudoinverse for the matrix inversion, can improve the accuracy of the solution by suppressing the influence of randomly distributed errors.

The complex amplitudes $p^\pm$ are computed by mapping the measured pressure spectra p' at $n \geq 2$ distinct positions in the duct on the analytical expression for the acoustic pressure field [36]:

$$\begin{Bmatrix} p^+(\omega) \\ p^-(\omega) \end{Bmatrix} = \begin{bmatrix} e^{-jk^+z_1} & e^{jk^-z_1} \\ \vdots & \vdots \\ e^{-jk^+z_n} & e^{jk^-z_n} \end{bmatrix}^{\otimes} \begin{Bmatrix} p'(\omega, z_1) \\ \vdots \\ p'(\omega, z_n) \end{Bmatrix} \tag{4}$$

where z is the axial position of the measurement points and the symbol $\bullet^{\otimes}$ denotes the Moore-Penrose pseudoinverse. The axial wavenumber $k^{\pm}$ is computed from the expression derived by Weng and Bake [37], accounting the visco-thermal attenuation at the walls:

$$k^{\pm} = \frac{k_0}{(1 \pm \mathrm{M}_0)} \left(1 + \frac{1-j}{R} \sqrt{\frac{\nu}{2\,\omega\,(1 \pm \mathrm{M}_0)}} \left(1 + \frac{\gamma - 1}{\sqrt{\mathrm{Pr}}}\right)\right) \tag{5}$$

The term $k_0 = \omega / c_0$ is the wavenumber in a quiescent medium, depending on angular velocity ω and the speed of sound c_0. M_0 is the steady flow Mach number, Pr the Prandtl number, ν is the kinematic viscosity, γ is the ratio of specific heat constants and R is the hydraulic radius of the duct. The accuracy of the plane wave decomposition is directly affected by measurement errors on these parameters. These uncertainties can be reduced using an iterative optimization method [38, 32], which exploits the overdetermination of equation (4) to compute better estimates of selected parameters. In this paper, the speed of sound and the mean flow Mach number are optimized using this iterative method.

2.2 Acoustic energy criterion based on scattering matrix

Assuming the flow-acoustic interaction effects are included in the linear scattering matrix relation, the modulation of incident acoustic waves and the potential onset of aeroacoustic instabilities can be determined by analyzing the scattering properties of the acoustic element. A theoretical criterion for the prediction of the fluid-driven whistling potentiality of a duct component, based on an acoustic energy balance, has been proposed by Auregan and Starobinski [12]. This criterion is formulated in terms of exergy wave contributions $w^{\pm}$, which can easily be derived from the complex amplitude of the corresponding pressure waves using a scaling factor:

$$w^{\pm} = (1 \pm \mathrm{M}_0)\, p^{\pm} \tag{6}$$

Introducing the exergy wave vectors $\underline{\boldsymbol{w}}_{\mathrm{in}}$ and $\underline{\boldsymbol{w}}_{\mathrm{out}}$, it is possible to define the power scattering matrix $\underline{\underline{\boldsymbol{S}}}_w$ according to the following relation:

$$\underline{\boldsymbol{w}}_{\mathrm{out}} = \underline{\underline{\boldsymbol{S}}}_w\, \underline{\boldsymbol{w}}_{\mathrm{in}}. \tag{7}$$

$$\underline{\boldsymbol{w}}_{\mathrm{in}} = \begin{Bmatrix} w_i^+(\omega) \\ w_o^-(\omega) \end{Bmatrix} \qquad \underline{\boldsymbol{w}}_{\mathrm{out}} = \begin{Bmatrix} w_o^+(\omega) \\ w_i^-(\omega) \end{Bmatrix} \tag{8}$$

This power scattering matrix $\underline{\underline{\boldsymbol{S}}}_w$ is computed in a similar way as the scattering matrix, using equation (3) formulated in terms of exergy waves $w^{\pm}$ instead of pressure waves $p^{\pm}$.

The acoustic power entering (W_{in}) and leaving (W_{out}) the two-port element is determined by the exergy waves:

$$W_{\mathrm{in}} = \underline{\boldsymbol{w}}_{\mathrm{in}}^*\, \underline{\boldsymbol{w}}_{\mathrm{in}} \qquad W_{\mathrm{out}} = \underline{\boldsymbol{w}}_{\mathrm{out}}^*\, \underline{\boldsymbol{w}}_{\mathrm{out}} \tag{9}$$

Hence, the acoustic power W_{diss} dissipated inside the element can be expressed as a function of the power scattering matrix:

$$W_{\mathrm{diss}} = W_{\mathrm{in}} - W_{\mathrm{out}} = \underline{\boldsymbol{w}}_{\mathrm{in}}^* \left(\underline{\underline{\boldsymbol{I}}} - \underline{\underline{\boldsymbol{S}}}_w^*\, \underline{\underline{\boldsymbol{S}}}_w\right) \underline{\boldsymbol{w}}_{\mathrm{in}} \tag{10}$$

where $\underline{\underline{\boldsymbol{I}}}$ is the identity matrix, and the superscript $\bullet^*$ represents the Hermitian transpose. According to this formula, an amplification of the incident sound power due to a flow-acoustic interaction results in a negative W_{diss}. Following the formalism proposed in [12], this power balance can be reformulated as:

$$W_{\mathrm{diss}} = \underline{\boldsymbol{d}}^* \left(\underline{\underline{\boldsymbol{I}}} - \underline{\underline{\boldsymbol{\Lambda}}}\right) \underline{\boldsymbol{d}} \tag{11}$$

The diagonal matrix $\underline{\underline{\boldsymbol{\Lambda}}}$ contains the real and positive eigenvalues λ_i of the product of the power scattering matrix with its Hermitian transpose $\underline{\underline{\boldsymbol{S}}}_w^*\, \underline{\underline{\boldsymbol{S}}}_w$. The vector $\underline{\boldsymbol{d}}$ is obtained from $\underline{\boldsymbol{d}} = \underline{\underline{\boldsymbol{V}}}^*\, \underline{\boldsymbol{p}}_{\mathrm{in}}$, which corresponds

to an orthogonal change of variables defined by the matrix $\underline{\underline{\boldsymbol{V}}}$ which columns are the eigenvectors of $\underline{\underline{\boldsymbol{S}}}_w^* \, \underline{\underline{\boldsymbol{S}}}_w$. As a result, the quadratic form of the dissipated power can be expressed as:

$$W_{diss} = \sum_i (1 - \lambda_i) \, |d_i|^2 = \sum_i \xi_i \, |d_i|^2 \tag{12}$$

where $\xi_i = 1 - \lambda_i$ are the so-called dissipation potentials. These potentials represent the minimum and maximum sound power dissipated by the two-port element, considering all possible incident acoustic fields. A positive dissipation potential indicates a net dissipation of acoustic energy inside the two-port element, whereas a negative potential implies a net amplification of the incident power. The whistling potential can hence be determined by considering the values of $\xi_{\min} = 1 - \lambda_{\max}$. In particular, $\xi_{\min} < 0$ indicates that the acoustic element can amplify the incident acoustic power, which can lead to whistling. Therefore, although the intrinsic non-linearity of aeroacoustic instabilities, their onset can be predicted using a linear two-port formulation and the acoustic power balance approach.

3 Experimental set-up

The experimental campaign for the analysis of the aeroacoustic instabilities in Helmholtz resonators has been carried out on the open circuit aeroacoustic test facility at KU Leuven. The resonators are designed considering a quasi-two-dimensional geometry shown in figure 2. It consist of a rectangular cavity with a length $\mathrm{l_x} = 40$ mm, a depth $\mathrm{l_y} = 55$ mm connected to a duct by an orifice. Two different neck geometries are manufactured in order to study the orifice length effect. The resonator A is characterized by a neck with an orifice length of $\mathrm{L_A} = 5$ mm and a depth of $\mathrm{d_A} = 5$ mm; while the resonator B has a length of $\mathrm{L_B} = 10$ mm with the same depth $\mathrm{d_B} = 5$ mm. In both cases the main duct has an height of $\mathrm{H} = 40$ mm. This 2D geometry is extruded over $\mathrm{W} = 90$ mm in the third dimension. Figure 3 shows the test object mounted between an inlet and an outlet duct with a rectangular cross-section of 90 by 40 mm. Each of these ducts is equipped with 4 flush-mounted 1/4" microphones (type PCB 378C10), located respectively at 425 mm, 506 mm, 637 mm and 849 mm from the center of the orifice. An in-line loudspeaker is installed at the extremities of the measurement ducts to provide the acoustic excitation. At the exhaust of the downstream duct, various types of termination can be mounted to change the acoustic load. The upstream duct is connected to a flow generating unit, consisting of a frequency-regulated roots blower and an after-cooler. Measurements have been carried out imposing different inlet flow velocities. Besides the reference case in a quiescent medium, three different mean flow cases are tested, imposing an inlet velocity of $u_0 = 10\,\mathrm{m/s}$, $15\,\mathrm{m/s}$, $20\,\mathrm{m/s}$; corresponding respectively to a Reynolds number of $\mathrm{Re} = 2\,\rho\,u_0\,R/\mu = 37218$, $\mathrm{Re} = 55868$ and $\mathrm{Re} = 74646$. For the resonator B an additional test cases is studied, imposing an inlet velocity of $u_0 = 35\,\mathrm{m/s}$ corresponding to a Reynolds number of $\mathrm{Re} = 130631$. The temperature and the volume flow rate are continuously monitored using a vortex-flow meter.

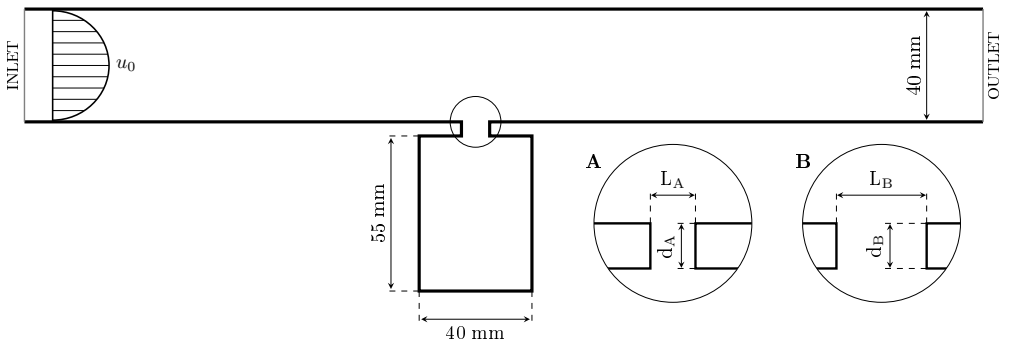


Figure 2: Schematic description of the Helmholtz resonator with two different neck geometries.

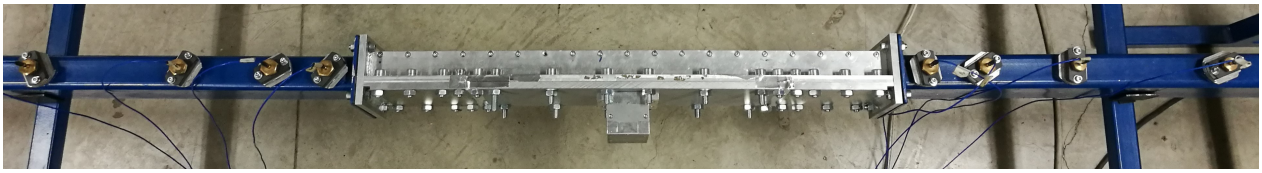


Figure 3: Test object mounted in the experimental set-up.

The two-port characterization has been carried out following a combined multiple source and multiple load approach obtaining 4 independent dataset for each case. The data acquisition has been done using a a LMS SCADAS III system, in combination with LMS Test.Lab rev.15. All the experiments have been performed with a stepped sine excitation in a frequency range from 100 Hz to 1880 Hz. This upper limit corresponds to the cut-off frequency of the first transversal mode of the duct. The frequency resolution is set to 20 Hz around the expected resonance frequency, and to 50 Hz in the remainder of the frequency range. All autopower and crosspower spectra are computed using Welch's averaging technique with 60 averages and 25% overlap [39]. In-house processing routines have been applied to the measurement data to carry out the iterative plane decomposition, to compute the power scattering matrices and to obtain the dissipation potentials [32].

4 Discussion of results

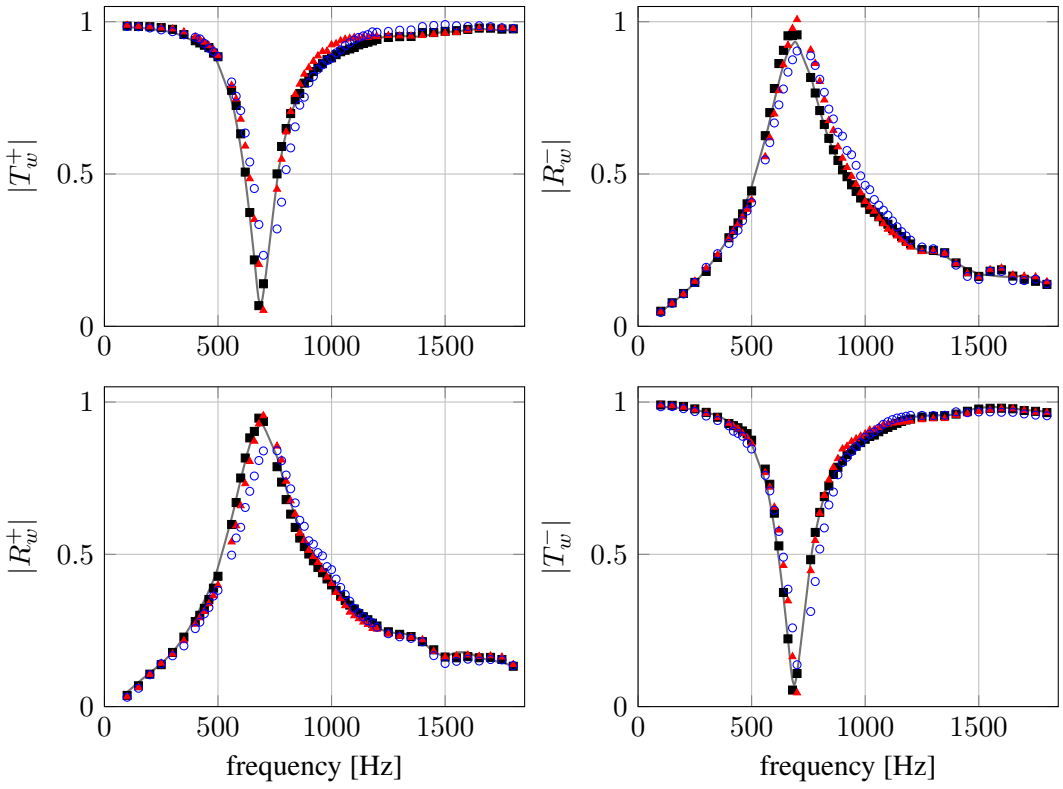


Figure 4: Amplitude of the power scattering matrix coefficients for the Helmholtz resonator A at different mean flow velocities: $u_0 = 0\,\mathrm{m/s}$ (——), $u_0 = 10\,\mathrm{m/s}$ (■), $u_0 = 15\,\mathrm{m/s}$ (▲), $u_0 = 20\,\mathrm{m/s}$ (○).

Figures 4 and 5 report the amplitude of the power scattering matrix coefficients for the resonator A and B. The results for a quiescent medium and for different inlet flow velocities are presented. In quiescent fluid conditions, both Helmholtz resonators passively act as effective sound absorbers around their resonance frequency f_{res}. In figure 4, the transmission coefficients show a minimum around the natural frequency of

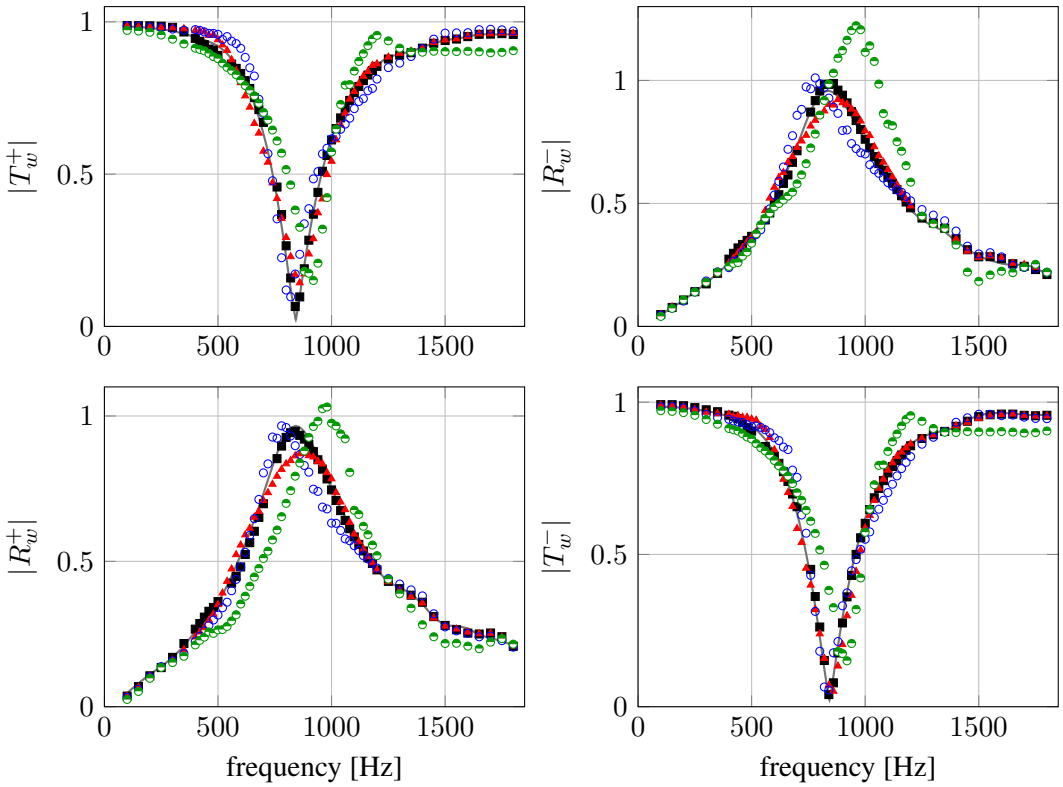


Figure 5: Amplitude of the power scattering matrix coefficients for the Helmholtz resonator B at different mean flow velocities: $u_0 = 0\,\mathrm{m/s}$ (——), $u_0 = 10\,\mathrm{m/s}$ (■), $u_0 = 15\,\mathrm{m/s}$ (▲), $u_0 = 20\,\mathrm{m/s}$ (○), $u_0 = 35\,\mathrm{m/s}$ (●).

the resonator $f_{\mathrm{res}} = 690\,\mathrm{Hz}$, where the reflection coefficients have their maximum. In agreement with the mechanical system analogy [27], whereby the angular resonance frequency of the resonator $\omega_{\mathrm{res}} = 2\pi f_{\mathrm{res}}$ is proportional to the square root of the orifice length $\sqrt{\mathrm{L}}$, the natural frequency of the resonator B at zero flow occurs at a higher frequency of about $f_{\mathrm{res}} = 850$ Hz (figure 5). The results of resonator A at the flow velocities of $u_0 = 10\,\mathrm{m/s}$ reveal an increase of a resonant peak in the reflection coefficient $|R_w^-|$ above the reference case without mean flow. This effect becomes more pronounced when the inlet velocity is increased to $u_0 = 15\,\mathrm{m/s}$, for which $|R_w^-|$ exceeds the value of 1 in the proximity of the resonance frequency. A further increase of the flow velocity results in a decrease of the resonant peak of the reflection coefficients, with a shift towards higher frequencies and a lower quality factor. A similar trend has already been observed in experimental results with smaller orifice length resonators under grazing flow [40], and suggest an increased damping caused by the flow-acoustic interaction.

For the resonator B in figure 5, the decrease of the quality factor and the shift of the resonant peak towards higher frequencies are already observed at the inlet velocity of $u_0 = 15\,\mathrm{m/s}$. At higher flow velocities, the resonator behavior changes appreciably. At $u_0 = 35\,\mathrm{m/s}$ the mean flow effect is more pronounced, and it leads to an increase of the power reflection property of the two-port element. According to the previous arguments, this indicates that the resonator are not working properly as a sound absorber. In addition, for this case, a peak shift towards higher frequencies is identified.

Figures 6 and 7 report the minimum dissipation potential, ξ_{min} for resonators A and B, computed from the measured power scattering matrix. The results are plotted versus the Strouhal number $St = f\mathrm{L}/u_c$, based on the orifice length L and the convection velocity of vorticity across the orifice u_c. The correction factor $u_c/u_0 = 0.45$ refers to numerical and experimental studies of similar cases [16, 1, 5, 41, 42]. Given the different orifice lengths, the Strouhal number St_B for resonator B is scaled with a factor 2 with respect to the Strouhal number St_A of resonator A. For both resonators distinct frequency ranges for the onset of

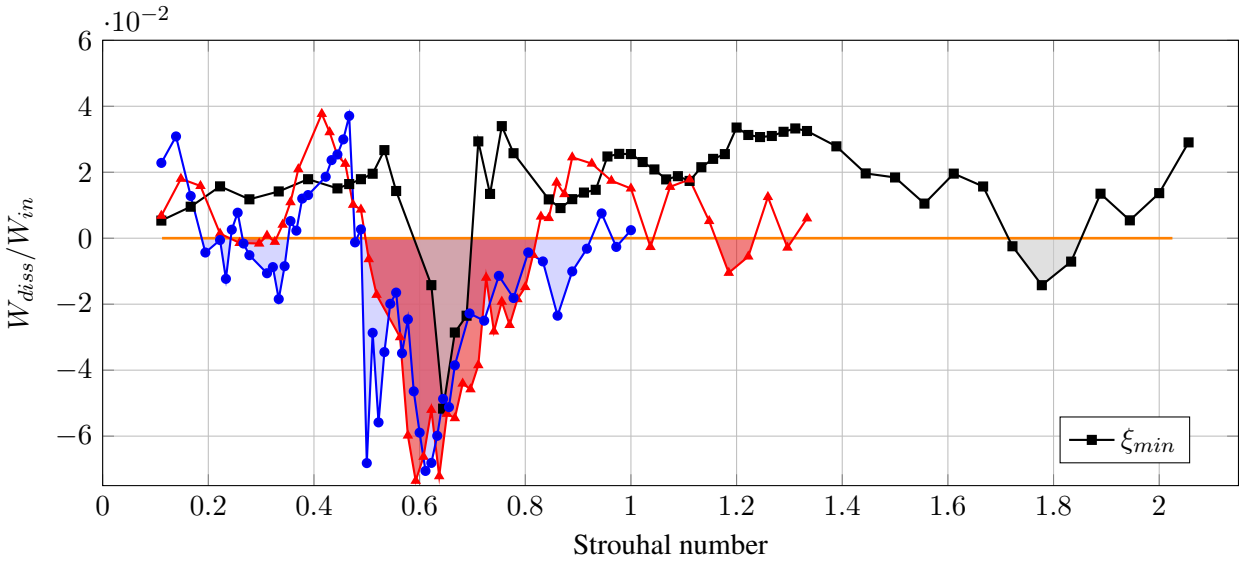


Figure 6: Acoustic power balance of the Helmholtz resonator A at different mean flow velocities. Minimum dissipation potential at $u_0 = 10\,\mathrm{m/s}$ (ξ_{min}), $u_0 = 15\,\mathrm{m/s}$ (ξ_{min}), $u_0 = 20\,\mathrm{m/s}$ (ξ_{min}).

aeroacoustic instabilities are identified for different mean flow velocities.

Figure 6 shows the minimum dissipation potential for resonator A. At the inlet velocity of $u_0 = 10\,\mathrm{m/s}$, the minimum dissipation potential ξ_{min} is negative in the ranges corresponding to $0.62 < St_{A_1} < 0.69$ and $1.72 < St_{A_2} < 1.825$. Increasing the grazing flow velocity to $u_0 = 15\,\mathrm{m/s}$, we observe the onset of a whistling mode in a lower frequency region, corresponding to $0.25 < St_{A_0} < 0.32$. While, the second whistling mode, corresponding to $0.5 < St_{A_1} < 0.81$, is centred around the first unstable region detected at $u_0 = 10\,\mathrm{m/s}$. At the inlet velocity of $u_0 = 20\,\mathrm{m/s}$ the first unstable range widens to $0.19 < St_{A_0} < 0.35$, while the second whistling range is enlarged and shifted to higher Strouhal numbers, occurring in the region of $0.47 < St_{A_1} < 0.97$.

A similar pattern is observed for the resonator B in figure7. At the lower velocity, $u_0 = 10\,\mathrm{m/s}$, two whistling modes are detected, the first around $St_{B_1} = 1.822$ and the second between $3.40 < St_{B_2} < 3.60$. Increasing the grazing flow velocity to $u_0 = 15\,\mathrm{m/s}$, two main whistling modes are identified, in the frequency ranges corresponding to $0.43 < St_{B_0} < 0.93$ and $1.5 < St_{B_1} < 1.77$. At higher velocities those ranges widen, and, in addition, the first region of instability onset is shifted to lower Strouhal number. At the same time, the second unstable region is translated to higher Strouhal numbers: at $u_0 = 20\,\mathrm{m/s}$ a negative dissipation potential is observed in the range corresponding to $0.37 < St_{B_0} < 0.93$ and $1.48 < St_{B_1} < 2$. For the mean flow velocity of $u_0 = 35\,\mathrm{m/s}$ the potential onset of aeroacoustic instabilities is detected in the range of $0.33 < St_{B_0} < 0.93$.

As supported by the previous results, the effects of fluid-dynamic and resonant phenomena are identified for both resonators. The different orifice lengths influence the natural frequency of the resonators, according to [27], and leads to a frequency shift of f_{res}. A similar trend is also observed for the Strouhal number ranges of aeroacoustic instability onset, confirming that the instabilities originate from the interaction between the unstable shear layer and the Helmholtz resonance. In addition, the increased mean flow velocity results in wider frequency ranges of aeroacoustic instability onset. Analyzing the results for both resonators, the minimum dissipation potential shows a clear periodic pattern that require further investigations. For this purpose, the two-port assumption seems to be restrictive, and a multi-port model [32] is required to extend the framework to higher frequencies.

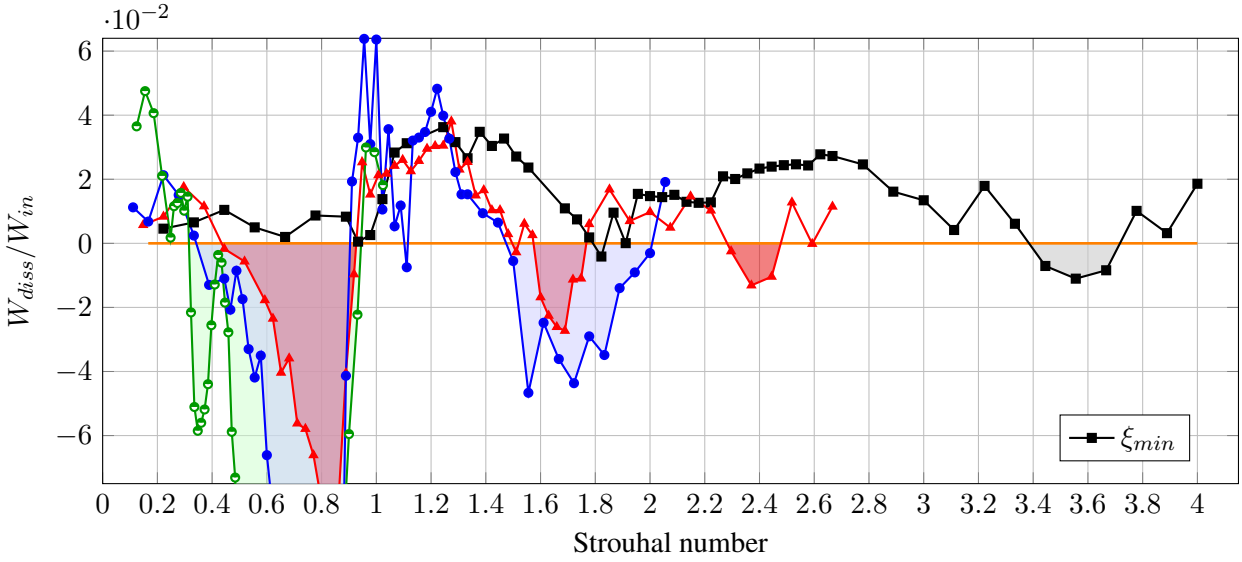


Figure 7: Acoustic power balance of the Helmholtz resonator B at different mean flow velocities. Minimum dissipation potential at $u_0 = 10\,\mathrm{m/s}$ (ξ_{min}), $u_0 = 15\,\mathrm{m/s}$ (ξ_{min}), $u_0 = 20\,\mathrm{m/s}$ (ξ_{min}), $u_0 = 35\,\mathrm{m/s}$ (ξ_{min}).

5 Conclusion

In this paper, the onset of aeroacoustic instabilities in Helmholtz resonators is analyzed experimentally. A measurement campaign has been carried out on the open circuit aeroacoustic test facility at KU Leuven, considering two resonator geometries and various mean flow conditions. An acoustic power balance, computed from the scattering matrix of the resonator, is used to detect the frequency ranges where aeroacoustic instabilities could initiate, and to study the influence of grazing flow velocity and the orifice length. For each resonator geometry and mean flow condition, several frequency ranges are detected where the onset of aeroacoustic instabilities could take place. As also observed in numerical studies [41], increasing the grazing flow velocity results in a stronger interaction between the unstable shear layer and the resonance of the cavity. This interaction leads to wider frequency regions of potential aeroacoustic instabilities and a slight shift in terms of Strouhal number. The effect of the orifice length on the onset of aeroacoustic instabilities can be explained predominantly by its influence on the resonance frequency of the Helmholtz resonator. The presented results are a first contribution to a valuable experimental database, which will be used to gain a deeper understanding of the flow-acoustic phenomena in flow-excited Helmholtz resonators. Additional measurements, extending the database to higher Strouhal numbers by adopting a multi-port based formalism [**?**], are foreseen to further investigate the periodic pattern of unstable frequency ranges.

Acknowledgements

The research of L. Criscuolo is funded by an Early Stage Researcher grant within the European Project SSeMID Marie Curie Initial Training Network (GA 675008). The Flanders Innovation & Entrepreneurship Agency within the SILENCEVENT project and the Research Fund KU Leuven are also gratefully acknowledged for their support.

References

[1] J. C. Bruggeman, A. Hirschberg, M. E. H. van Dongen, A. P. J. Wijnands, J. Gorter, *Self-sustained aero-acoustic pulsations in gas transport systems: Experimental study of the influence of closed side branches*, Journal of Sound and Vibration, Vol. 150, No. 3, (1991), pp. 371–393.

[2] S. Föller, W. Polifke, D. Tonon, *Aeroacoustic characterization of T-junctions based on large eddy simulation and system identification*, *16th AIAA/CEAS Aeroacoustics Conference*, American Institute of Aeronautics and Astronautics.

[3] D. Tonon, E. Moers, J. Golliard, A. Hirschberg, *Aeroacoustics of a wall perforation in the pure grazing flow regime: effect of the perforation geometry*, *18th AIAA/CEAS Aeroacoustics Conference (33rd AIAA Aeroacoustics Conference)*, American Institute of Aeronautics and Astronautics, AIAA 2012-2054.

[4] D. Tonon, *Aeroacoustics of shear layers in internal flows: closed branches and wall perforations*, Ph.D. thesis, Technische Universiteit Eindhoven (2011).

[5] M. Karlsson, M. Åbom, *Aeroacoustics of T-junctions - An experimental investigation*, Journal of Sound and Vibration, Vol. 329, No. 10, (2010), pp. 1793–1808.

[6] M. Karlsson, M. Åbom, *On the use of linear acoustic multiports to predict whistling in confined flows*, Acta Acustica united with Acustica, Vol. 97, (2011), pp. 24–33.

[7] L. Du, A. Holmberg, M. Karlsson, M. Åbom, *Sound amplification at a rectangular T-junction with merging mean flows*, Journal of Sound and Vibration, Vol. 367, (2016), pp. 69–83.

[8] A. Holmberg, M. Karlsson, M. Åbom, *Aeroacoustics of rectangular T-junctions subject to combined grazing and bias flows An experimental investigation*, Journal of Sound and Vibration, Vol. 340, No. Supplement C, (2015), pp. 152 – 166.

[9] A. Kierkegaard, S. Allam, G. Efraimsson, M. Åbom, *Simulations of whistling and the whistling potentiality of an in-duct orifice with linear aeroacoustics*, Journal of Sound and Vibration, Vol. 331, No. 5, (2012), pp. 1084–1096.

[10] A. Kierkegaard, S. Boij, G. Efraimsson, *A frequency domain linearized Navier-Stokes equations approach to acoustic propagation in flow ducts with sharp edges*, The Journal of the Acoustical Society of America, Vol. 127, No. 2, (2010), pp. 710–719.

[11] P. Testud, Y. Aurégan, P. Moussou, A. Hirschberg, *The whistling potentiality of an orifice in a confined flow using an energy criterion*, Journal of Sound and Vibration, Vol. 325, (2009), pp. 769–780.

[12] Y. Aurégan, R. Starobinski, *Determination of acoustical energy dissipation/production potentiality from the acoustical transfer functions of a multiport*, Acta Acustica united with Acustica, Vol. 85, No. 6, (1999), pp. 788–792.

[13] P. Hmon, F. Santi, X. Amandolse, *On the pressure oscillations inside a deep cavity excited by a grazing airflow*, European Journal of Mechanics - B/Fluids, Vol. 23, No. 4, (2004), pp. 617 – 632.

[14] F. Ghanadi, M. Arjomandi, B. Cazzolato, A. Zander, *Interaction of a flow-excited helmholtz resonator with a grazing turbulent boundary layer*, Experimental Thermal and Fluid Science, Vol. 58, (2014), pp. 80 – 92.

[15] P. A. Nelson, N. Halliwell, P. Doak, *Fluid dynamics of a flow excited resonance, part I: Experiment*, Journal of Sound and Vibration, Vol. 78, No. 1, (1981), pp. 15 – 38.

[16] P. A. Nelson, N. A. Halliwell, P. E. Doak, *Fluid dynamics of a flow excited resonance, part II: Flow acoustic interaction*, Journal of Sound and Vibration, Vol. 91, (1983), pp. 375–402.

[17] R. Ma, P. E. Slaboch, S. C. Morris, *Fluid mechanics of the flow-excited Helmholtz resonator*, Journal of Fluid Mechanics, Vol. 623, (2009), pp. 126.

[18] S. K. Tang, *On sound transmission loss across a Helmholtz resonator in a low mach number flow duct*, The Journal of the Acoustical Society of America, Vol. 127, No. 6, (2010), pp. 3519–3525.

[19] M. Massenzio, A. Blaise, C. Lesueur, *Mechanisms of Self-Sustained Oscillations Induced by a Flow Over a Cavity*, Journal of Vibration and Acoustics, Vol. 130, No. 5, (2008), pp. 051001.

[20] L. Stein, J. Reiss, J. Sesterhenn, *Numerical simulation of a resonant cavity: Acoustical response under grazing turbulent flow*, *New Results in Numerical and Experimental Fluid Mechanics XI*, Springer International Publishing, Cham, 671–681.

[21] M. Howe, *On the helmholtz resonator*, Journal of Sound and Vibration, Vol. 45, No. 3, (1976), pp. 427–440.

[22] M. S. Howe, *Edge, cavity and aperture tones at very low mach numbers*, Journal of Fluid Mechanics, Vol. 330, (1997), pp. 61–84.

[23] M. S. Howe, *The influence of mean shear on unsteady aperture flow, with application to acoustical diffraction and self-sustained cavity oscillations*, Journal of Fluid Mechanics, Vol. 109, (1981), pp. 125–146.

[24] H. Denayer, W. De Roeck, W. Desmet, T. Toulorge, *Acoustic characterization of a Helmholtz resonator under grazing flow conditions using a hybrid methodology*, *19th AIAA/CEAS Aeroacoustics Conference*, American Institute of Aeronautics and Astronautics, AIAA 2013-2076.

[25] W. De Roeck, W. Desmet, *Experimental analysis of the aerodynamic noise generating mechanisms in a simple expansion chamber*, *14th AIAA/CEAS Aeroacoustics Conference (29th AIAA Aeroacoustics Conference)*, American Institute of Aeronautics and Astronautics, AIAA 2008-3055.

[26] M. Munjal, *Acoustics of Ducts and Mufflers with Application to Exhaust and Ventilation System Design*, John Wiley & Sons (1987).

[27] A. D. Pierce, *Basic linear acoustics*, T. D. Rossing, Editor, *Springer Handbook of Acoustics*, Springer Science+Business Media (2007).

[28] M. Åbom, *Measurement of the scattering-matrix of acoustical two-ports*, Mechanical Systems and Signal Processing, Vol. 5, No. 2, (1991), pp. 89–104.

[29] A. D. Pierce, *Acoustics: An Introduction to Its Physical Principles and Applications*, Acoustical Society of America (1989).

[30] T. Elnady, M. Åbom, S. Allam, *Modeling perforates in mufflers using two-ports*, Journal of Vibration and Acoustics, Vol. 132, (2010), pp. 061010.

[31] C. To, *The acoustic simulation and analysis of complicated reciprocating compressor piping systems, i: Analysis technique and parameter matrices of acoustic elements*, Journal of Sound and Vibration, Vol. 96, No. 2, (1984), pp. 175–194.

[32] H. Denayer, *Flow-acoustic characterization of duct components using multi-port techniques*, Ph.D. thesis, KU Leuven (2017).

[33] M. Munjal, A. Doige, *Theory of a two source-location method for direct experimental evaluation of the four-pole parameters of an aeroacoustic element*, Journal of Sound and Vibration, Vol. 141, No. 2, (1990), pp. 323–333.

[34] T. Y. Lung, A. Doige, *A time-averaging transient testing method for acoustic properties of piping systems and mufflers with flow*, The Journal of the Acoustical Society of America, Vol. 73, No. 3, (1983), pp. 867–876.

[35] M. Åbom, *A note on the experimental determination of acoustical two-port matrices*, Journal of Sound and Vibration, Vol. 155, No. 1, (1992), pp. 185–188.

[36] T. Fujimori, S. Sato, H. Miura, *An automated measurement system of complex sound pressure reflection coefficients*, *Proceedings of Inter Noise*, Vol. 84, Vol. 84, 1009–1014.

[37] C. Weng, F. Bake, *An analytical model for boundary layer attenuation of acoustic modes in rigid circular ducts with uniform flow*, Acta Acustica united with Acustica, Vol. 102, No. 6, (2016), pp. 1138–1141.

[38] H. Denayer, W. De Roeck, W. Desmet, *Iterative procedure for accurate plane wave decomposition in flow ducts*, *Proceedings of the International Conference on Noise and Vibration Engineering ISMA 2014*, 279–288.

[39] P. Welch, *The use of fast Fourier transform for the estimation of power spectra: A method based on time averaging over short, modified periodograms*, IEEE Transactions on Audio and Electroacoustics, Vol. 15, No. 2, (1967), pp. 70–73.

[40] H. Denayer, J. Tournadre, W. De Roeck, W. Desmet, P. Martínez-Lera, *Combined numerical and experimental study of a slit resonator under grazing flow*, *20th AIAA/CEAS Aeroacoustics Conference*, American Institute of Aeronautics and Astronautics, AIAA 2014-2959.

[41] L. Criscuolo, H. Denayer, W. De Roeck, W. Desmet, *Analysis of aeroacoustic instabilities in helmholtz resonators using linear scattering-transfer matrices*, *2018 AIAA/CEAS Aeroacoustics Conference*, American Institute of Aeronautics and Astronautics, AIAA 2018-3785.

[42] E. Moers, D. Tonon, A. Hirschberg, *Strouhal number dependency of the aero-acoustic response of wall perforations under combined grazing-bias flow*, Journal of Sound and Vibration, Vol. 389, (2017), pp. 292 – 308.

Broadband noise from serrated UAS propellers: validation of a lattice Boltzmann approach

B.G. Marinus [1], **D. Bontea** [2], **A. Halimi** [3], **A. Pire** [1]
[1] Royal Military Academy, Department of Mechanical Engineering,
Renaissancelaan 30, B-1000, Brussels, Belgium
e-mail: **benoit.marinus@rma.ac.be**

[2] Military Technical Academy, Department of Mechanical Engineering,
Bulevardul George Coşbuc 81-83, Bucharest 050141, Romania

[3] National Polytechnic School of Algiers, Laboratory of Mechanical Engineering and Development,
Rue des Frères OUDEK 10, El-Harrach 16200, Algeria

Abstract
With the increased use on Unmanned Aerial Systems equipped with propellers and rotors, serrated edges are considered to reduce broadband noise emissions without affecting the aerodynamic performance. In this context, a full sensitivity study is performed to assess the independence of the solution to the space (voxel resolution) and time discretization (time step, sampling rate and number of revolutions). This way, the computational tools are validated for the prediction of both the aerodynamic and aeroacoustic performance. The results show there is enough confidence in such models for them to be used to optimize serrated propeller geometries and achieve a reduction of the noise emissions by 3$\sim$10dB in the 1000Hz to 10.000Hz range.

1 Introduction

With the increased presence of mini-RPA (Remotely Piloted Aircraft) buzzing around, aural detection has become a commonplace experience and underline the need for reduced noise emissions. The dominant noise is radiated by the rotating blades of propellers and or rotors and is composed, given the low tip-speed, of broadband noise with a few tones at the blade passing frequency and harmonics. Broadband noise includes self noise generated by the scattering of the boundary layer turbulence at the trailing edge, and turbulence ingestion noise due to the interaction of the oncoming gust at the leading edge of the blade. This is the leading contribution. Tonal components arise from the action of forces on the blade surface, the kinematics of the blade, the eddies around the blade, and potentially the interaction with upstream turbulence.

The work of Amiet [3] and later Roger and Moreau [22, 20, 21, 23, 5] lead to analytical formulations for trailing edge noise and turbulence ingestion noise that can conveiently be applied to slightly cambered thick airfoils or rotating blades with lightly cambered edges . Howe [14] derived an analytical model revealing the potential of serrations on a flat plate in low Mach number flow to reduce the broadband self-noise. The final solution shows that the use of sharp sawtooth serration leads to significant noise reduction. Gruber, Joseph, Azerpeyvand and co-workers made several contributions [10, 11, 4] investigating analytically the effects of serrations geometry on the trailing edge noise reduction. Recently, Lyu, Sinayoko, and Azerpayvand [16, 18, 17] studied the effect of different trailing or leading edge serrations geometries in the case of rotating blades, using an analytical model combining Howe's low Mach number isolated airfoil theory with Amiet's rotating airfoil technique. According to these analytical models, the potential sound reduction of sharp sawtooth serrations could be of 5-10 dB for a wide bandwidth. Fischer et al. confirmed lower reductions for wind turbines[9].

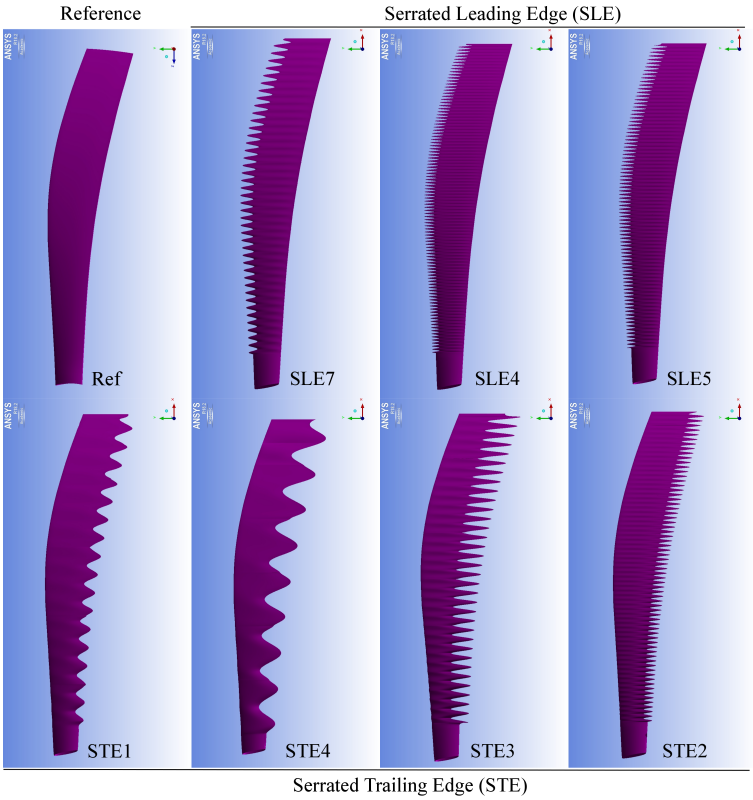


Figure 1: Blade geometries under investigation.

For the purpose of exploring the potential of serrations to reduce the acoustic signature of a mini-RPA propeller in forward flight, a Lattice Boltzmann Model (LBM) solver [1] computes unsteady time-domain high-fidelity simulations from which the pressure fluctuations at several probe locations are extracted. A full sensitivity study is performed to assess the independence of the solution to the space (voxel resolution) and time discretization (time step, sampling rate and number of revolutions). The broadband noise spectra obtained from the LBM are compared to those obtained from frequency-domain analytical models [12, 13].

The paper is organized as follows. After a brief description of the propeller blade's geometry and operating conditions, the numerical (LBM) and analytical models are shortly introduced with emphasis on the space and time discretization. Next, we present, discuss and analyse the results before drawing conclusions.

2 Blade Geometry and Operating Conditions

The blades under investigation for the four bladed single-rotation propeller are illustrated in Fig. 1. The reference blade is identical to the blade described in described in [19]. The serrations extend from 20% to 98% radius such that the structural integrity of the blade's base is not impacted. The NACA-16 airfoil family [2] is used along the entire span.

The propeller, with a diameter D of 1m operates at an altitude of 1000m in cruise conditions (zero incidence) with a flight Mach number M_∞ of 0.2 so that the Reynolds number based on the chord of the reference blade at 75% radius is of $8.28e5$ since the reference advance ratio $J = v/(n.D)$ is of 1.4 with n the rotational velocity in rps. This corresponds to a subsonic tip Mach number of 0.49 obtained from the vector sum of the rotational and flight velocities. The blade angle at 75%-radius β_{ref} is of $40°$ with respect to the plane of rotation.

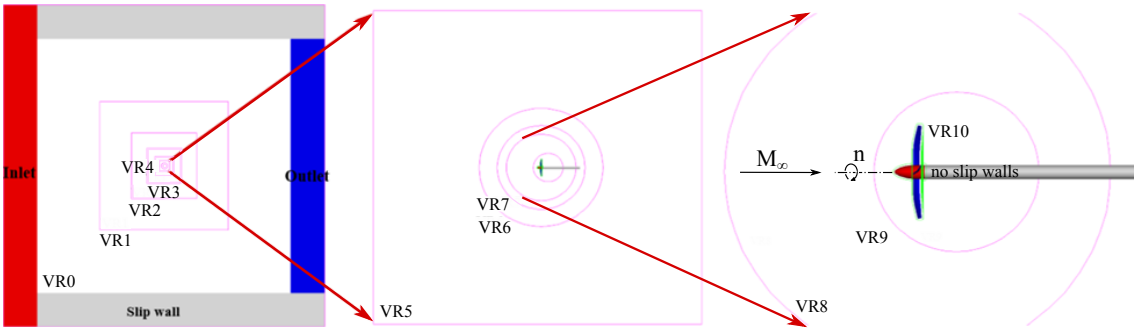


Figure 2: Voxel Refinement (VR) regions and boundary conditions.

3 Numerical and Analytical Models

3.1 Lattice Boltzmann High-Fidelity Time-Dependent Simulations

The Very Large Eddy Simulations (VLES) were performed by leveraging the inherently transient capabilities of the PowerFLOW solver [1] based on the three-dimensional 19 discrete particle velocities (D3Q19) lattice Boltzmann model (referred to as LBM in this paper). The Boltzmann equation governs the dynamics of particle distribution-functions representing the probability to find a number of particles having a velocity in a given interval in an elementary volume during an infinitesimal time interval. The model constructs a simplified form of the mesoscopic dynamics which includes sufficient physics so that the desired macroscopic behavior is recovered. Macroscopic flow quantities such as density and momentum are calculated by discrete integration of the distribution functions. According to turbulence theory, the unresolved universal scales in the dissipative and inertial ranges are modeled by introducing a local effective relaxation time in the collision operator governing the Boltzmann equation. This can be compared to the concept of eddy viscosity in a Navier-Stokes solver. The sub-grid scale turbulence dynamics is represented by two additional equations which complete the LBM. These equations are derived from an extended Renormalization Group theory. More details about the mathematical foundations of the mesoscopic flow model behind the LBM-solver can be found in [6, 15].

3.2 Space and Time Discretization

The cubic Cartesian lattice (voxels) for the LBM-solver[1] is generated automatically from the CAD-file of the propeller which is enclosed in a sliding-mesh region. As visible in fig. 2, the blades (blue) and the rotating spinner (red) are enclosed by a volume that denes the rotating mesh region (green) and the spinner is extended with a solid non rotating cylinder (grey). All these surfaces have a no-slip wall-boundary condition. A series of variable resolution or Voxel Refinement (VR) regions are set around the propeller from the coarsest one (VR0) to the nest one (VR13) with the mesh resolution varying by a factor 2 between two adjacent VR levels. VR10 corresponds to the rotating mesh region (green). VR levels from 12 onwards are generated by offsetting the geometry parts in the wall normal direction. Solid surfaces are covered automatically by intersecting the mesh with the wall geometry using planar surface elements (surfels).

In the standard configuration (here after referred to as v8), for aeroacoustic calculations, 600 voxels are generated along the blade chord at 75% radius for VR13 as shown in fig. 3 resulting in about 114 million voxels in total.

All unsteady simulations are conducted for three full rotations of the propeller after a transient period of three rotations to yield satisfactory periodic convergence. The computations are started using the seeding technique from previous converged cases. With the maximum acoustic frequency of interest set at 11kHz and taking an anti-aliasing factor of 2 into account and at least 7 time steps per wave, this results in $6.5e6$ time steps of the order of $5.5e-7$s each.

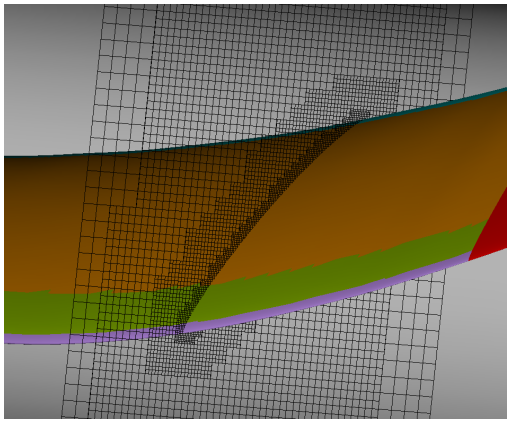


Figure 3: Highest refinement in VR12 and VR13 (blocks of 2x2 voxels shown for clarity).

3.3 Analytical Model

The analytical models for the prediction of noise from a serrated trailing edge or a serrated leading edge were recently developed by Lyu et al. [16, 18, 17] by generalizing Amiet's theories. Both models yield the Power Spectral Density (PSD) and follow similar steps. The airfoil broadband noise models are extended to a rotating blade using the strip theory [25, 24] and by introducing a Doppler factor before integrating over all possible angular locations of the blade segment. Given the dependency of the flow conditions and boundary layer statistics on the spanwise location [8], the blade is divided in six segments. The present implementation of these models have been validated for airfoils and rotating blades in [12].

4 Results and Analysis

4.1 Influence of Model Parameters on the Prediction of Aerodynamic Performance

The influence of several model parameters is first assessed according to table 1 in order to yield adequate grid independence. The thrust coefficient is

$$C_T = \frac{T}{\rho n^2 D^4} \tag{1}$$

with T the net propeller thrust, ρ the freestream volumic mass and D the propeller diameter. The power coefficient is given by

$$C_P = \frac{P}{\rho n^3 D^5} \tag{2}$$

where P is the net power. And the resulting efficiency is

$$\eta = \frac{J C_T}{C_P} \tag{3}$$

As can be seen from table 1, the v8 settings offers an accurate solution for a moderate cost since the computational time scales roughly with the number of voxels whenever the number of CPUs is kept constant. From a purely aerodynamic point of view, this setting satisfies the requirement on accuracy of the solutions as can be seen from table 2 which shows the results from a grid dependency study performed according to Celik et al. [7]. The computed order of the extrapolation polynomial is of 3.3 for C_T and 0.3 for C_P.

Using the v8 set-up, different geometries are being analyzed under constant flow conditions. The aerodynamic performance of some of the geometries from Fig. 1 is shown in Fig. 4 where it appears that although differences exist in terms of net thrust and power, the penalty from trailing-edge serrations is limited in terms of efficiency. Leading-edge serrations lead to a larger efficiency.

Version		VR region of the blade	#vovels per chord	frequency of interest	C_T	C_P	η
v2		12	450	11kHz	0.158	0.289	0.76
v3		13	450	11kHz	0.163	0.309	0.74
v4	raw	13	450	12kHz	0.162	0.309	0.73
v5		12	600	11kHz	0.160	0.299	0.75
v6	fine	13	700	11kHz	0.167	0.314	0.74
v8	standard	13	600	11kHz	0.166	0.313	0.74

Table 1: Influence of model parameters on the aerodynamic performance (STE4 at J =1.4).

ϕ	C_T	C_P
$\phi^{\text{ext}}_{\text{fine,std}}$	0.1685	0.3155
$e^{\text{a}}_{\text{fine,std}}$	0.60%	0.32%
$e^{\text{ext}}_{\text{fine,std}}$	0.89%	0.47%
GCI_{fine}	1.12%	0.59%

Table 2: Grid convergence study according to Celik et al. [7] with the refinement factors $r_{\text{fine,std}} = 1.17$ and $r_{\text{raw,std}} = 1.33$.

4.2 Aeroacoustic Prediction Capability

The influence of the different settings (see table 1) onto the aeroacoustic predictions is shown in Fig. 5 where it is compared to the spectrum obtained from the analytical model. The v8 set-up delivers valuable results.

Using the v8 set-up, the spectra from the reference and STE4 blades are compared in Fig. 6 from the analytical and LBM approach. This figure illustrates the potential of the analytical method since it accurately captures the trend and relative differences between two geometries without the need for the intricate set-up of a numerical model. The required resources and its computational time are at least one order of magnitude less than for the LBM approach. Nevertheless, one should be careful not to miss some of the physics going on around the blades. Therefore, several samples should be analyzed using both approaches.

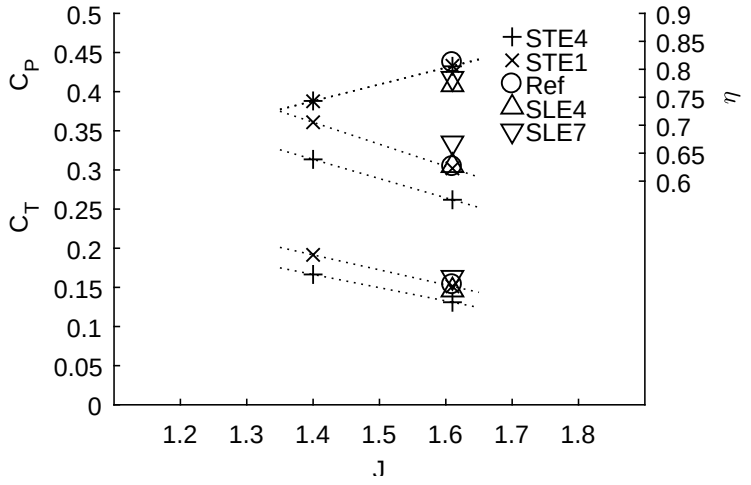


Figure 4: Aerodynamic performance in terms of C_T, C_P, and eta fro different individuals.

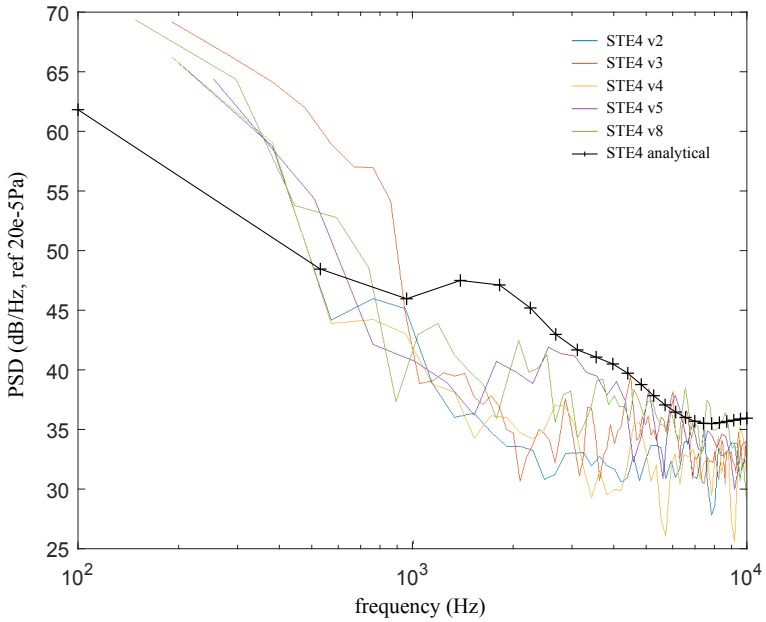


Figure 5: Influence of model parameters on the predicted power spectral density.

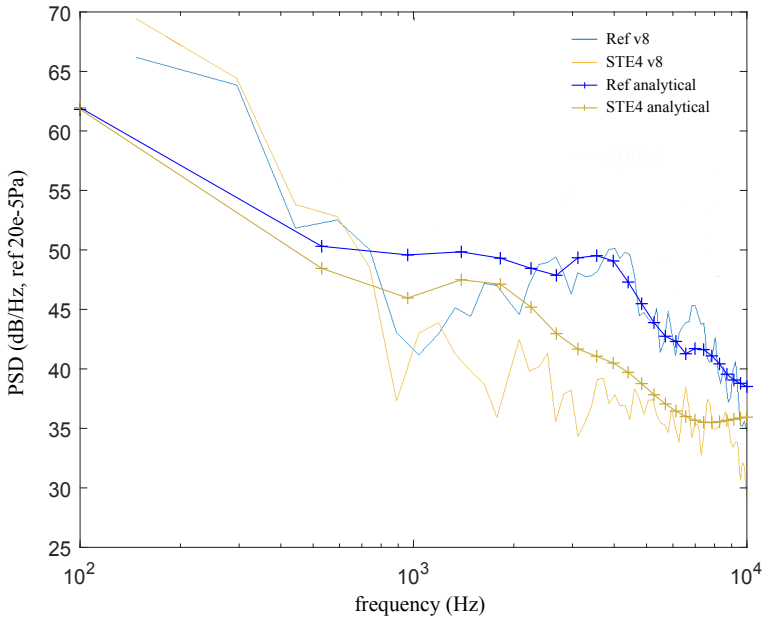


Figure 6: Power Spectral Density for different geometries compared to the results from the analytical model.

5 Conclusions

Simulations have been performed with a time-domain Lattice Boltzmann Solver to compute the flow around propeller blades with a straight or a serrated trailing or leading edge. The grid dependency study of the simulations revealed the best set-up for aerodynamic computations. This set-up is also able to accurately model the broadband sound spectrum of the rotating blades.

The STE4 blade, although it features large serrations ($h/\delta = 4$, $h/\lambda = 1$), has interesting properties since it effectively reduces the noise emissions typically by $-5dB$ in the rotational plane. The good correspondence between analytical and LBM results allows to use the analytical tool in the search for interesting geometries.

Acknowledgments

The authors wish to acknowledge the Belgian Defense Scientific and Technological Research initiative for its funding of the present study under grant MSP-16/07.

References

[1] Powerflow. www.exa.com/product/powerflow, 2016. ExaCorp.

[2] I.H. Abbott, A.E. von Doenhoff, and L.S. Stivers Jr. Summary of airfoil data. Report R-824, NACA, NACA-Langley aeronautical laboratory (USA), 1945.

[3] R.K. Amiet. Acoustic radiation from an airfoil in a turbulent stream. 41(4):407–420, 1975.

[4] Mahdi Azarpeyvand, Mathieu Gruber, and Phillip Joseph. An analytical investigation of trailing edge noise reduction using novel serrations. In *19th AIAA/CEAS Aeroacoustics Conference*, number AIAA 2013-2009, Berlin (Germany), may 2013. American Institute of Aeronautics and Astronautics.

[5] Arnulfo Carazo, Michel Roger, and Magdi Omais. Analytical prediction of wake-interaction noise in counter-rotating open rotors. In *17th AIAA/CEAS Aeroacoustics Conference*, number AIAA 2011-2758, Portland (USA), jun 2011. American Institute of Aeronautics and Astronautics.

[6] D. Casalino, S. Noelting, E. Fares, T. Van de Ven, F. Perot, and G. Bres. Towards numerical aircraft noise certification: Analysis of a full-scale landing gear in fly-over configuration. In *18th AIAA/CEAS Aeroacoustics Conference*, number AIAA 2012-2235, Colorado Springs (USA), June 4-6 2012.

[7] I.B. Celik, U. Ghia, P.J. Roache, C.J. Freitas, H. Coleman, and P.E. Raad. Procedure for estimation and reporting of uncertainty due to discretization in CFD applications. *Journal of Fluids Engineering*, 130(7):1–4, July 2008.

[8] J. Christophe, J. Anthoine, and S. Moreau. Amiets theory in spanwise-varying flow conditions. *AIAA Journal*, 47(3):788–790, March 2009.

[9] Andreas Fischer, Franck Bertagnolio, Wen Zhong Shen, and Jesper Madsen. Noise model for serrated trailing edges compared to wind tunnel measurements. *Journal of Physics: Conference Series*, 753:022053, 2016.

[10] M. Gruber, P. Joseph, and Tze Pei Chong. Experimental investigation of airfoil self noise and turbulent wake reduction by the use of trailing edge serrations. In *16th AIAA/CEAS Aeroacoustics Conference*, number AIAA 2010-3803, Stockholm (Sweden), June 7-9 2010. American Institute of Aeronautics and Astronautics (AIAA).

[11] Mathieu Gruber. *Airfoil noise reduction by edge treatments*. PhD thesis, University Of Southampton, February 2012.

[12] A. Halimi, B.G. Marinus, and S. Larbi. Characterization of the broadband noise of mini rpa propeller blades. In *23rd AIAA/CEAS Aeroacoustics Conference*, number AIAA 2017-4053, Denver (USA), 2017.

[13] A. Halimi, B.G. Marinus, and S. Larbi. Trailing edge noise of innovative mini-rpa propeller blade geometry. In *accepted for the 24th AIAA/CEAS Aeroacoustics Conference*, Atlanta (USA), 6 2018.

[14] M.S. Howe. Aerodynamic noise of a serrated trailing edge. *Journal of Fluid and Structures*, 5(1):33–45, 1991.

[15] D.P. Lockard, L.-S. Luo, and B.A. Singer. Evaluation of the Lattice-Boltzmann equation solver PowerFLOW for aerodynamic applications. Contractor Report CR 2000-210550, NASA-ICASE, Langley Research Center, October 2000.

[16] B. Lyu, M. Azarpeyvand, and S. Sinayoko. A trailing-edge noise model for serrated edges. In *21st AIAA/CEAS Aeroacoustics Conference*, number AIAA 2015-2362. American Institute of Aeronautics and Astronautics (AIAA), jun 2015.

[17] B. Lyu, M. Azarpeyvand, and S. Sinayoko. Prediction of noise from serrated trailing edges. *Journal of Fluid Mechanics*, 793:556–588, 2016.

[18] Benshuai Lyu, Mahdi Azarpeyvand, and Samuel Sinayoko. Noise prediction for serrated leading-edges. In *22nd AIAA/CEAS Aeroacoustics Conference*, number AIAA 2016-2740, Lyon (France), May 29 - June 1 2016.

[19] B.G. Marinus and J. Poppe. Data and design models for military turbo-propeller aircraft. *Aerospace Science and Technology*, 41:63–80, February 2015.

[20] S. Moreau and M. Roger. Effect of airfoil aerodynamic loading on trailing-edge noise sources. *AIAA Journal*, 43(1):41–52, January 2005.

[21] M. Roger. Noise from lifting surfaces: analytical modelling. In *Lecture Series on Aerodynamic Noise from Wall-Bounded Flows*, number LS 2009-03, Sint-Genesius-Rode (Belgium), March 9-13 2009. von Karman Institute for Fluid Dynamics.

[22] M. Roger and S. Moreau. Back-scattering correction and further extensions of amiets trailing-edge noise model. part i: Theory. *Journal of Sound and Vibration*, 286(3):477–506, 2005.

[23] M. Roger and S. Moreau. Extension and limitations of analytical airfoil broadband noise models. *International Journal of Aeroacoustics*, 9(3):273–305, 2010.

[24] Y. Rozenberg, M. Roger, A. Gudel, and S. Moreau. Rotating blade self noise: Experimental validation of analytical models. In *13th AIAA/CEAS Aeroacoustics Conference*, number AIAA 2007-3709, 2007.

[25] Paterson R.W. and Amiet R.K. Noise a model helicopter rotor due to ingestion of turbulence. Technical Report Contractor Report 3213, NASA, Langley Research Center, 1979.

Inverse methods in aeroacoustic three-dimensional volumetric noise source localization

G. Battista [1], **P. Chiariotti** [1], **M. Martarelli** [2], **P. Castellini** [1]
[1] Università Politecnica delle Marche, DIISM,
Via Brecce Bianche, 60131, Ancona, Italy
e-mail: **g.battista@pm.univpm.it**

[2] Università degli studi e-Campus, Novedrate (CO), Italy

Abstract
Acoustic source mapping with microphone arrays usually involves the implicit assumption that sources are situated on the surface where the calculation points are located. However, in some application, such as aeroacoustic source localization, this assumption may produce misleading results. This paper describes the use of inverse methods in the context of aeroacoustic volumetric source imaging. A comparative investigation in exploiting a single planar array or multiple planar arrays, observing noise sources from different directions, is performed. Moreover, since aeroacoustic data are often spoiled by noise and different sources of quite different strengths are present, a novel use of CLEAN-SC as pre-processing step for inverse methods is discussed. The simulated and experimental results presented in the paper refer to a Counter Rotating Open Rotor installed on a 1/7th scale aircraft model placed in a large Low Speed Wind Tunnel.

1 Introduction

Aeroacoustic measurements are usually performed using phased-microphone array techniques to ease the noisy source identification task. Despite their simplicity and robustness, simple beamforming algorithms, like Conventional Beamforming (CB), suffer of poor dynamics and poor spatial resolution at low frequencies, which lead to difficult interpretation of maps in case of multiple sources having different levels. In three-dimensional acoustic mapping, i.e. when a three-dimensional calculation grid is used, these limitations become even more evident. Indeed, beamformers have poor spatial resolution along the focusing direction when a single array is used, while the sidelobe level dramatically increases when multiple arrays are combined, even in presence of a single monopole. These characteristics make direct beamformers not appropriate for three-dimensional source mapping. Over the years, deconvolution techniques (e.g. DAMAS [3], CLEAN-SC [9]) of beamforming maps have been developed in order to improve results accuracy in terms of spatial resolution and quantification of source strengths. The goal of these methods is to remove the effect of array spatial response, i.e. the Point Spread Function (PSF), from the map and return the real source distribution that has generated the original map and hence pressure data measured at microphone locations. Deconvolution algorithms are the only possibility to effectively use CB for volumetric mapping [14]. On the other hand, inverse methods start from a discretization of the region of interest using a cloud of elementary sources (e.g. monopoles and dipoles) and aim to return the whole source distribution which optimally approximates pressure data at microphone locations, hence having the possibility to deal with correlated and spatially-distributed sources. In [2] Battista et al. described and compared different inverse methods for three-dimensional acoustic mapping using a single planar array, while Padois et al. [10] compared the behaviour of different acoustic mapping methods using one or two planar arrays. The aim of this work is to describe some strategies to successfully perform volumetric noise source localization in aeroacoustic appli-

cations. In particular, advantages and drawbacks in using one or two planar arrays are discussed. Moreover, a novel use of CLEAN-SC as pre-processing step to inverse approaches is presented to ease the localization task when source of different strength are present (as it might be the case, in an aeroacoustic application, when considering engine and wing noises). These aspects are discussed on data recorded on a Counter Rotating Open Rotor (CROR) installed on a 1/7th scale aircraft model. The model was tested in a large Low Speed Wind Tunnel (WT) at The Pininfarina Aerodynamic and Aeroacoustic Research Center in Turin, Italy, within the framework of the FP7 EU Clean-Sky WENEMOR (Wind tunnel tests for the Evaluation of the installation effects of Noise EMissions of an Open Rotor advanced regional aircraft) project.

2 Inverse acoustic problem and solution strategies

2.1 Acoustic direct and inverse problem formulations

In frequency domain the discrete acoustic direct problem can be described, for each frequency, by the following linear relationship:

$$\mathbf{G}\mathbf{q} = \mathbf{p} \tag{1}$$

where $\mathbf{q}$ is the vector of complex source strengths of S elementary sources in assumed positions, $\mathbf{p}$ is the vector containing the complex pressures on M receiver locations and the complex matrix $\mathbf{G}$ represents the acoustic propagation matrix. The *direct acoustic problem* identifies the problem of calculating $\mathbf{p}$ for given $\mathbf{q}$ and $\mathbf{G}$. This is a well-determined problem having a unique solution. Conversely, the calculation of $\mathbf{q}$ for given $\mathbf{G}$ and $\mathbf{p}$ describes the *inverse acoustic problem*, which results to be ill-posed in Hadamard sense, i.e. existence, uniqueness and stability of solution are not guaranteed [5]. Also the inverse problem can be expressed as linear transformation

$$\hat{\mathbf{q}} = \mathbf{T}\mathbf{p}\,. \tag{2}$$

While the direct operator $\mathbf{G}$ is well-defined, the inverse operator $\mathbf{T}$ can assume different forms depending on the approach adopted. For this reason, the estimated source coefficients $\hat{\mathbf{q}}(\mathbf{T})$ depend on the assumptions and a priori information about the source distribution. A detailed review about different inverse operators is provided by Leclere et al. in [7]. Inverse problems are generally under-determined because the number of microphones is limited by practical aspects, while the number of potential sources is often larger, in particular when dealing with three-dimensional volumetric acoustic mapping. In addition, the inversion step can be very sensitive to noise present in measurements and inaccuracy in the direct operator, therefore, a regularization procedure is required. Several strategies for finding a solution to inverse acoustic problem are present in literature. For example Generalized Inverse Beamforming (GIBF) [15] or Equivalent Source Method (ESM) [13] provide methods to obtain the source coefficient distribution solving the linear formulation.

2.2 Three-dimensional acoustic inverse problem solution strategies

In the context of volumetric mapping a good spatial resolution is requested in all directions and only few potential sources in the volume of interest contributes significantly to the sound field. For these reasons a *sparse solution* is assumed. Sparsity can be enforced by minimizing the generic L_p-norm of solution, thus having the following problem:

$$\hat{\mathbf{q}}(\eta^2, p) = \arg\min_{\mathbf{q}} \left(\|\mathbf{G}\mathbf{q} - \mathbf{p}\|_2^2 + \eta^2 \|\mathbf{q}\|_p^p \right) \tag{3}$$

where $\eta^2 \geq 0$ is the *Regularization parameter*. Sparsity is enforced minimizing for $p < 2$. This problem has no analytic solution but can be solved iteratively using the following strategy:

$$\|\mathbf{q}\|_p^p = \sum_{n=1}^{N} |q_n|^p = \sum_{n=1}^{N} w_{sp,n}^2 |q_n|^2 = \|\mathbf{W}_{sp}\mathbf{q}\|_2^2\,. \tag{4}$$

This leads to the *Iteratively Reweighted Least Squares* (IRLS) [4] algorithm, which makes use of a diagonal weighting matrix $\mathbf{W}_{sp}$ to converge to a sparse solution. Weights depend on the result of the previous iteration according to the following expression:

$$w_{sp,n}^{(it+1)} = \left| \hat{q}_n^{(it)} \right|^{\frac{p-2}{2}} \tag{5}$$

where it is the current iteration and $w_{sp,n}$ is the n-th generic diagonal element. Each iteration is a regularized least-square problem solved using the general form of *Tikhonov regularization* [16]

$$\hat{\mathbf{q}}(\eta^2, \mathbf{W}) = \arg\min_{\mathbf{q}} \left(\|\mathbf{G}\mathbf{q} - \mathbf{p}\|_2^2 + \eta^2 \|\mathbf{W}\mathbf{q}\|_2^2 \right) . \tag{6}$$

As the exponent of weights is negative for $p < 2$, division by null elements must be somehow avoided to have an invertible weighting matrix. This algorithm boils down to an iterative procedure that is a fixed-point for Eq. 3 and converges to global minimum for convex problems ($p \geq 1$) or to a global or local minimum for non-convex problem ($0 \leq p < 1$).

Tikhonov regularized solution results a particular case of a more general approach to inverse acoustic problems which has been proposed by Antoni [1]. He exploited Bayesian inference for developing a method which is able to

- identify the optimal basis functions which minimize the reconstruction error, given the topology of the specific acoustic problem;
- include *a priori* information on source distribution to better condition the problem and ease the localization task;
- provide a robust regularization criterion.

The *Bayesian Approach* (BA) encodes measurement errors in the *likelihood function* which describes the direct probability to measure certain pressures values, given the propagation model and the probability density function of measurement noise. If complex normal *prior probability density function* (pdf) for source coefficients is assumed, the Bayesian framework "mechanically" produces a regularized solution similar to the Tikhonov one. Instead, assuming a p-generalized normal distribution as prior pdf, cost function of Eq. 3 appears from BA [6]. In addition BA explicitly identifies the regularization parameter η^2 in the Noise-to-Signal Ratio and provides its estimation as *Maximum A Posteriori* estimation (MAP), selecting the value with the maximum probability of occurrence, given the measurements. The cost function to estimate η^2 provided by BA has a unique global minimum and outperform many other regularization strategies. For this reason, the regularization task in this work is fulfilled by empirical Bayesian regularization. The interested reader might refer to [12] for a deeper insight into BA.

The IRLS procedure to solve the inverse acoustic problem can be formalized with the following expression:

$$\hat{\mathbf{q}}^{(it+1)} = F\left(\hat{\mathbf{q}}^{(it)}, \mathbf{W}^{(it)}, \eta^{2\,(it)}, \mathbf{G}, \mathbf{p}, p \right) . \tag{7}$$

where the function F is given by Eq. 6. From a Bayesian point of view this method can be seen as an Expectation-Maximization algorithm which converges to MAP solution. The following algorithm is used:

1. Set the weighting matrix for the current iteration $\mathbf{W}^{(it)} = \mathbf{W}_0\, \mathbf{W}_{sp}^{(it)}$, where $\mathbf{W}_{sp}^{(1)} = \mathbf{I}$ and $\mathbf{W}_0$ is used to introduce a priori information on source distribution. Both matrices are normalized such that $\|\mathbf{W}_0\|_\infty = \|\mathbf{W}_{sp}^{(it)}\|_\infty = 1$.
2. Estimate the regularization parameter $\eta^{2\,(it)}$ for the current iteration.

3. Calculate the solution $\hat{\mathbf{q}}^{(it+1)}$ and apply a threshold to discard potential sources that do not contribute significantly to the acoustic field using the following criterion

$$10\log_{10}\left(\frac{\hat{\mathbf{q}}^{(it+1)}}{\|\hat{\mathbf{q}}^{(it+1)}\|_\infty}\right) < THR_{dB}\,. \tag{8}$$

4. Calculate $\mathbf{W}_{sp}^{(it+1)}$ using Eq. 5.

5. Evaluate a convergence criterion; if not fulfilled go back to step 1, otherwise stop the iterative procedure.

This approach returns a sparse solution for the inverse acoustic problem. A priori information can be used to penalize region where is less likely to find sources. For example Padois et al. [11] proposed to use CB map for similar purposes. In fact, CB map is rough and smooth but it provides robust estimation of source location. The discard of sources is done both for avoiding the division by zero in calculation of weights and for speeding up the algorithm. The threshold used in this work is $THR_{dB} = -100$ dB. In [2] a convergence criterion is proposed:

$$\varepsilon^{(it)} = 10\log 10\left(MSR - \left|\frac{\mathrm{d}(MSR)}{\mathrm{d}(it)}\right| - \left|\frac{\mathrm{d}^2(MSR)}{\mathrm{d}(it)^2}\right|\right) \quad , \quad MSR = \left\langle\left|\hat{q}_n^{(it)}/\hat{q}_n^{(it-1)}\right|\right\rangle \tag{9}$$

where MSR stands for *Mean Source Ratio* and the operator $\langle\cdot\rangle$ refers to the spatial average. This criterion can be evaluated only for $it > 2$ (given the second derivative term) and requires solution variation to be small over three last iterations. The algorithm stops when $\varepsilon^{(it)} \geq -0.1$ dB. Elements of the $\mathbf{G}$ matrix are calculated using the following pressure-to-pressure acoustic transfer function formulation

$$G_{mn} = \frac{r_{0n}}{r_{mn}} e^{-\mathrm{j}k(r_{mn}-r_{0n})} \tag{10}$$

which returns the acoustic pressure at microphone location m depending on sound pressure at reference point "0" caused by the monopole source at location n. The terms r_{mn} correspond to geometric distances in case of free-field propagation. Instead, in presence of flow, these terms are calculated as virtual distances corresponding to the actual travelling time for a given flow field and speed of sound. In this paper, the assumption of an uniform flow in wind tunnel is made, thus leading to the following expression for r_{mn}:

$$r_{mn} = \frac{\|\mathbf{r}_n - \mathbf{r}_m\|_2}{-C_{mn} + \sqrt{C_{mn}^2 - M_a^2 + 1}} \quad , \quad C_{mn} = (\mathbf{r}_n - \mathbf{r}_m)\cdot\hat{\mathbf{f}}\, M_a \tag{11}$$

where $\hat{\mathbf{f}}$ is the flow direction and M_a is the Mach number. A critical aspect for three-dimensional inverse acoustic mapping is to balance the energy needed by sources to induce a certain pressure on microphone locations, otherwise the farthest sources would be easily excluded in the norm minimization process. The acoustic propagator in Eq. 10 manages to achieve this task without any weighting strategy required.

2.3 Pressure data

In aeroacoustic measurements, pressure data is generally processed in frequency domain to obtain the CSM $\mathbf{P}$, given the random nature of aeroacoustic noise. Since the CSM is Hermitian and non-negative definite, it can be decomposed as

$$\mathbf{P} = \mathbf{E}_{vec}\,\mathbf{E}_{val}\,\mathbf{E}_{vec}^H\,, \tag{12}$$

where $\mathbf{E}_{vec}$ is a unitary matrix of M orthonormal eigenvectors and $\mathbf{E}_{val}$ is a diagonal matrix containing the corresponding eigenvalues (the superscript ^{H} stands for the conjugate transpose). It is possible to define the eigenmode $\mathbf{e}_i$ as the eigenvector including its amplitude

$$\mathbf{e}_i = \sqrt{e_{val,i}}\,\mathbf{e}_{vec,i} \qquad i = 1,\ldots,M \tag{13}$$

where $\mathbf{e}_{vec,i}$ is the $i\text{-}th$ eigenvector and $e_{val,i}$ is the corresponding eigenvalue. Under the constraint of orthogonality, each eigenvector represents a coherent signal across the microphones. For this reason Suzuki proposes to solve an inverse problem for each eigenmode [15]:

$$\mathbf{G}\mathbf{q}_i = \mathbf{e}_i \qquad i = 1, \ldots, M_0 \tag{14}$$

where M_0 is the number of relevant eigenmodes. When dealing with aeroacoustic measurements, the trend of eigenvalues of CSM is typically smooth, thus making difficult to properly set M_0 for each frequency.

A different method to extract source components from CSM is to exploit the CLEAN-SC procedure described by Sijtsma [9]. This iterative procedure extracts the coherent source components exploiting the fact that side lobes of a single source CB map are spatially coherent with their main lobe. The concept of spatial source coherence is described in [8]. At the end of CLEAN-SC procedure, where a loop gain $\varphi = 1$ is used, the source components $\mathbf{c}_i$ are calculated similarly to the eigenmodes as

$$\mathbf{c}_i = \sqrt{P_{max}^{(i-1)}}\, \mathbf{h}^{(i)} \qquad i = 1, \ldots, IT \tag{15}$$

where IT is the number of iterations for each frequency. Indeed, if the source components are considered as in an eigenmode decomposition approach, the inverse problem can be modelled as

$$\mathbf{G}\mathbf{q}_i = \mathbf{c}_i \qquad i = 1, \ldots, M_0\,. \tag{16}$$

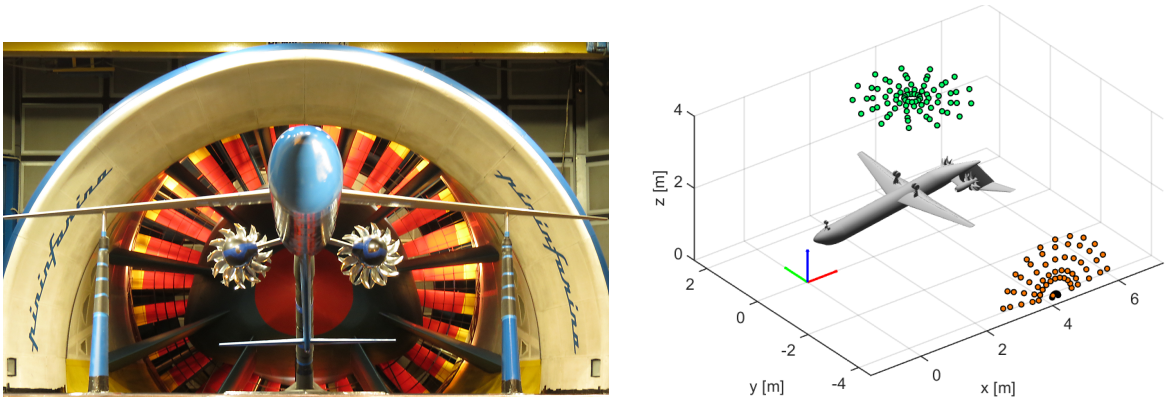
In this case the number of relevant components M_0 for each frequency is given directly by the number of iterations IT, which corresponds to the number of extracted components. Independently of decomposition used, a full map can be obtained summing all contributes. This approach can therefore be used as a preprocessing step to the inverse calculation phase, thus giving the possibility to spatially separate sources of very different strengths. To the authors' knowledge, this is the first time CLEAN-SC is used for such a purpose.

3 Application results

3.1 Reference set-up

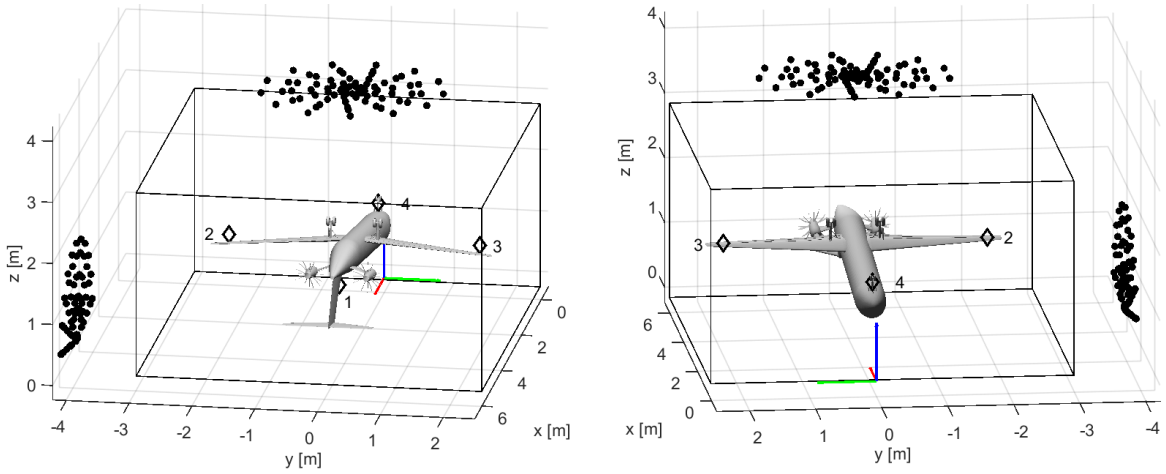
The test program was conducted at the Pininfarina Aerodynamic and Aeroacoustic Research Center in Turin, Italy within the EU WENEMOR project. Pininfarina's facility contains a test section of 8 m $\times$ 9.6 m $\times$ 4.2 m (see Figure 1(a)). The wind tunnel was specifically acoustically treated in order to reduce reverberation and background noise. Two planar microphone arrays were installed at Pininfarina Wind Tunnel (WT), as depicted in Figure 1(b): a 78 microphone wheel array (3 m diameter) placed at the ceiling of the WT at a distance of 2.5 m from the model axis and a 66 microphone half-wheel array (3 m diameter) located broadside, parallel to the axis of the open rotor and 4.2 m far from the longitudinal axis of the model. Signals were synchronously sampled at a sample rate of 32,768 Hz for a total observation length of 10 s. Time data has been processed to estimate the CSM using Welch's method (block size: 1024 samples, overlap: 50%, window: Hanning).

The CROR tested featured two rotors of 12 blades each. Both left and right engines of the aircraft model were driven from a single power supply and controlled by dedicated control systems (one per motor). Strouhal number scaling was performed to represent flight conditions of the full scale aircraft. Different design configurations of the model were tested during the whole test campaign (different tails, CROR in pusher and tractor configuration, different distances of the CRORs with respect to the model fuselage, etc.) at different flow speeds and angles of attack. Angle of attacks (AoA) differed also with respect to the take-off or approach model configuration. However, all the results discussed in this paper refer to the T-tailed model, in approach condition with CRORs in pusher configuration for AoA = 8 deg and flow speed of 28 m/s. The flow direction is considered to be the X positive axis of the coordinate system represented in Figure 1(b).



(a) (b)

Figure 1: (a) Test set-up in Pininfarina WT (front view of the aircraft model). (b) Microphone array layout with respect to WT and aircraft model (green dots: top wheel array, orange dots: side half-wheel array)



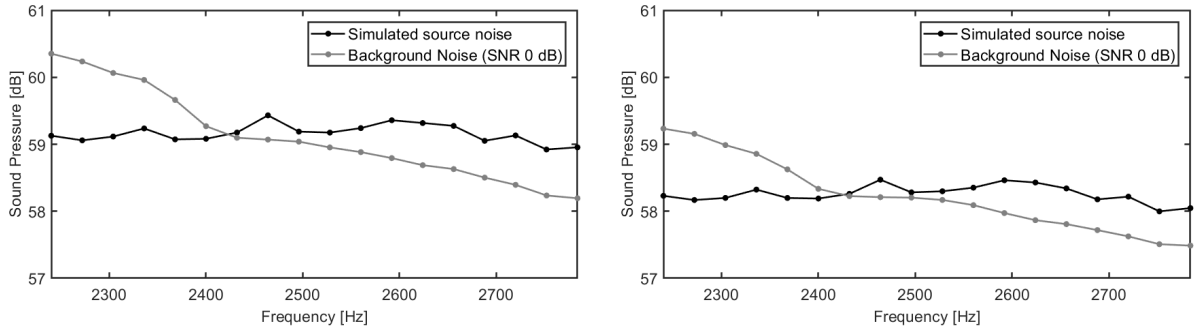
(a) (b)

Figure 2: Position of simulated sources (black diamonds) with respect to the aircraft model. The black dots represent microphone locations of the two arrays - (a) Rear view. (b) Front view.

3.2 Simulated data

Before analysing the experimental data recorded, some simulated test cases are presented to better understand performance of methods in terms of source separation capability, dynamics and robustness in case of different level of background noise. Each simulated test case consists of four monopoles emitting uncorrelated white noise and located in the four spots depicted in Figure 2. Monopoles level and coordinates are chosen in order to simulate typical sources of noise expected in a real setup. Source 1 is the loudest (1 Pa rms at 1 m distance) and represents the CROR noise, sources 2 and 3 represent the wing tip noise and are 10 dB weaker than source 1, source 4 is positioned on the front landing gear and is 20 dB weaker than source 1. During measurement campaign, time signals of real WT noise were acquired by the arrays without the model in the test section at flow speed of 28 m/s. These signals have been used as background noise (BGN), in the synthesis of simulated signals, to obtain more realistic simulations. The simulated total pressure $p_{tot,m}(t)$ on each microphone is obtained as follows

$$p_{tot,m}(t) = p_{sig,m}(t) + G \cdot p_{bgn,m}(t) \qquad m = 1, \ldots, M \tag{17}$$



(a) (b)

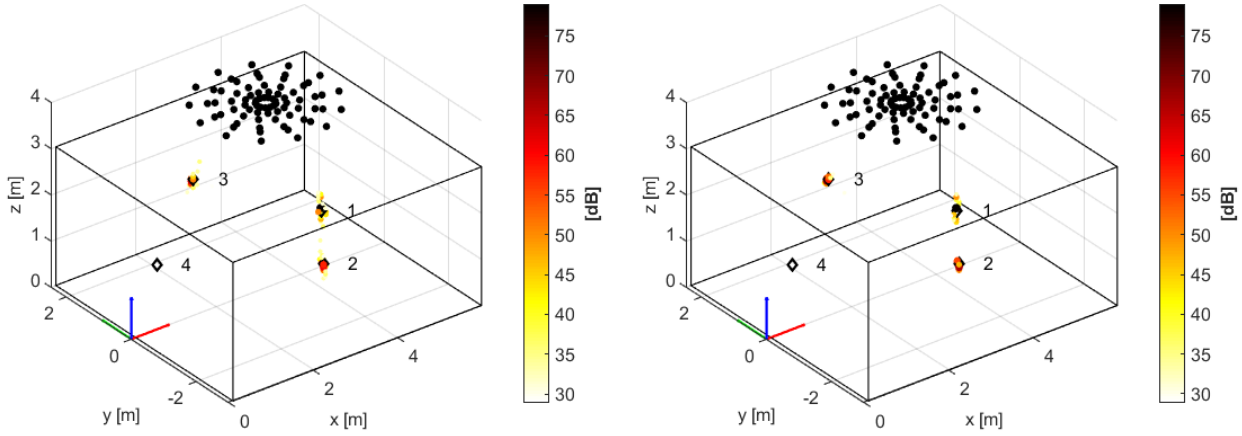
Figure 3: Average microphone auto-spectra - (a) Top array, (b) Side and top arrays

where $p_{sig,m}(t)$ is the contribution of all simulated sources on each microphone and $p_{bgn,m}(t)$ is the real WT noise recorded by each m-th microphone. The desired Signal-to-Noise Ratio (SNR) is obtained by setting the proper gain G and has been calculated using microphone auto-spectra, averaged over all microphones, respectively of simulated and real WT noise signals. Once selected the band of interest, the overall band power P_{sig} and P_{bgn} are estimated and G is calculated as

$$G = \sqrt{\frac{P_{sig}}{P_{bgn}}} 10^{(-\mathrm{SNR}_{dB}/20)} \tag{18}$$

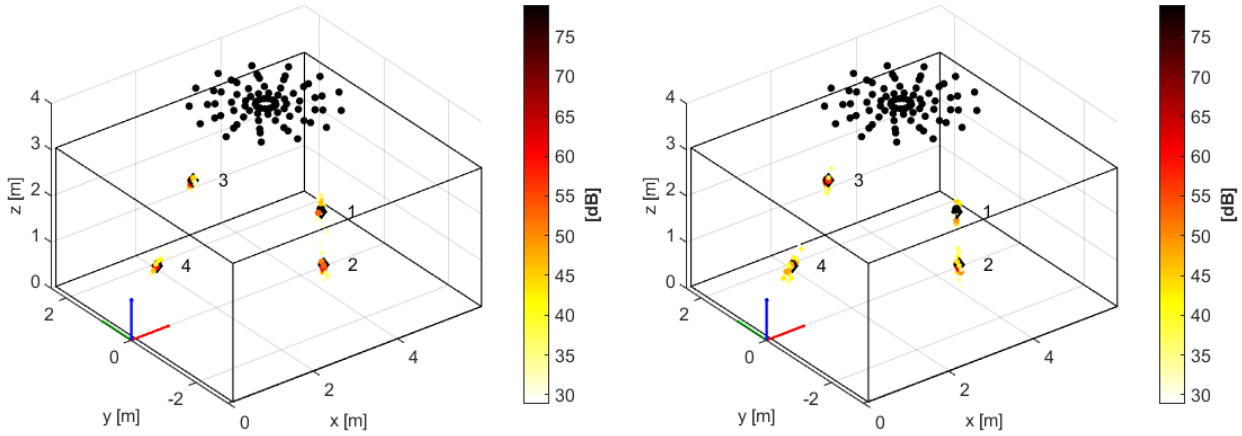
where SNR_{dB} is the target SNR, expressed in dB. In this way data produced have an overall SNR $= P_{sig}/P_{bgn}$ for the whole band of interest. Two different test cases are shown in this section: noise-free and SNR $= 0$ dB. Figure 3 shows the average microphone auto-spectrum induced by simulated source noise compared with average microphone auto-spectrum of background noise added for the noisy test case. All acoustic maps reported refers to one-third octave band at 2500 Hz.

The volume of interest, depicted in Figure 2, contains the whole model and it is discretized with a regular grid of monopoles using a step of 0.06 m, thus having 464,508 potential sources in the volume. Maximum solution sparsity is obtained by setting $p = 0$. Both eigenmodes and CLEAN-SC decomposition of CSM are used to map noise sources and then compared in terms of localization and robustness to noise. All CLEAN-SC extracted components are analysed while the number of relevant eigenmodes is set to $M_0 = 20$. The inverse method described in the previous section is applied without any change when single or multiple array are utilized. In addition, it is also tested if the use of CB map of single components as a priori information $\mathbf{W}_0$ can improve results. All maps report the sound pressure level at the reference point, that is the origin of the coordinate system and are represented using a dynamic range of 50 dB.



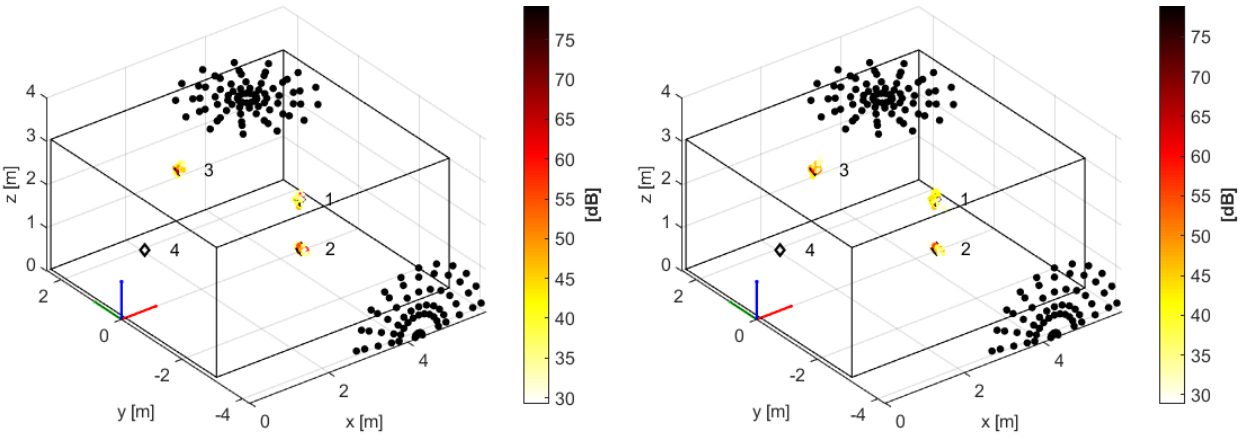
(a) (b)

Figure 4: Noise-free simulation, top array - (a) CLEAN-SC Components, (b) Eigenmodes



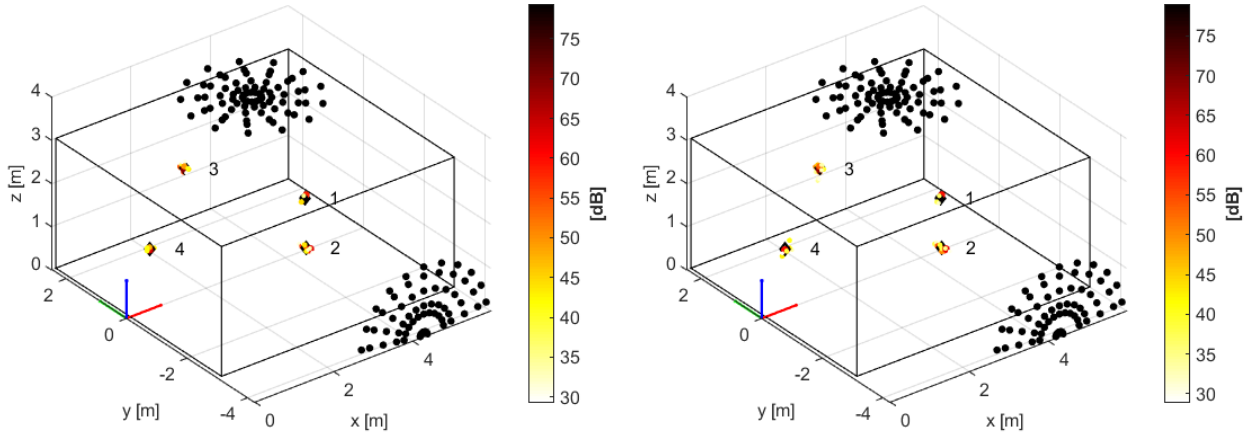
(a) (b)

Figure 5: Noise-free simulation, top array with CB map as a priori information - (a) CLEAN-SC Components, (b) Eigenmodes



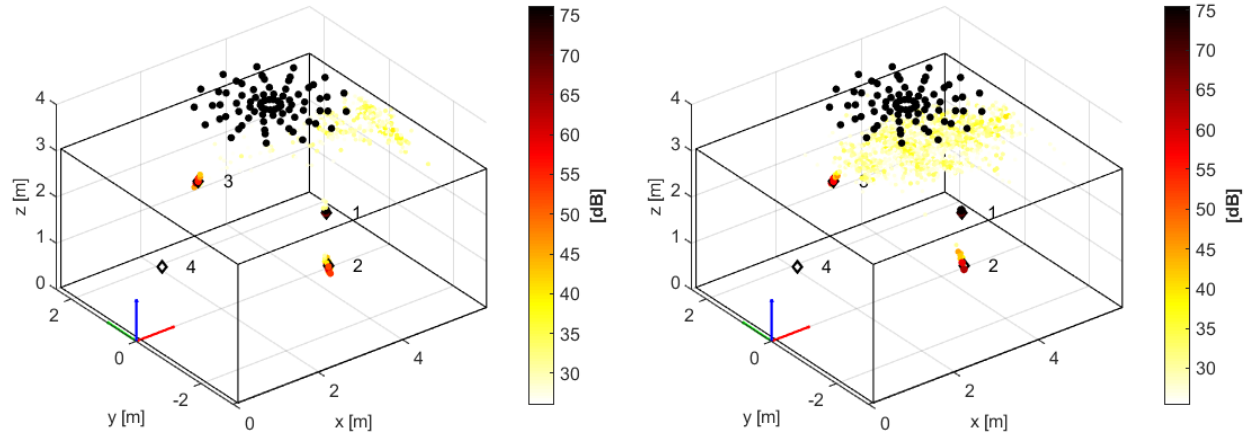
(a) (b)

Figure 6: Noise-free simulation, side and top arrays - (a) CLEAN-SC Components, (b) Eigenmodes



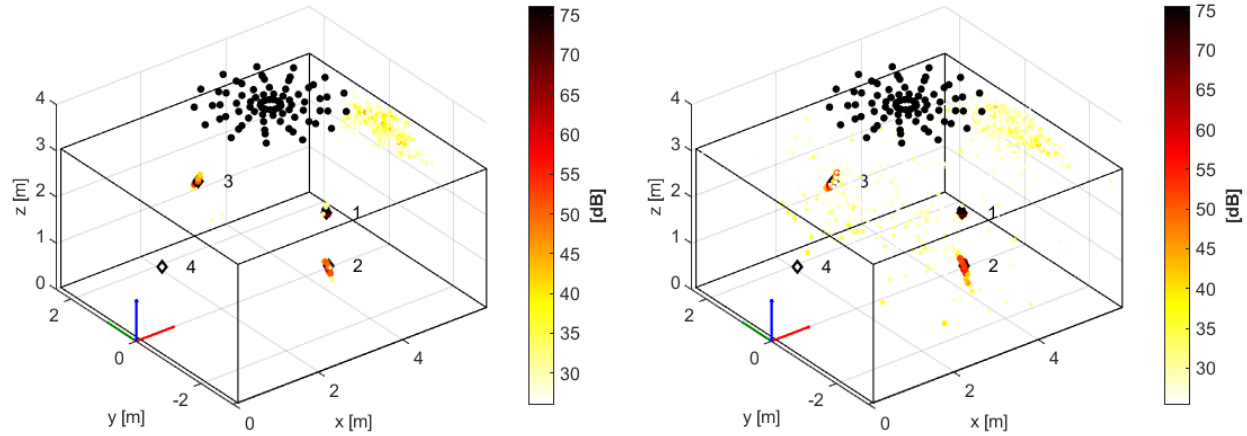
(a) (b)

Figure 7: Noise-free simulation, side and top arrays with CB map as a priori information - (a) CLEAN-SC Components, (b) Eigenmodes



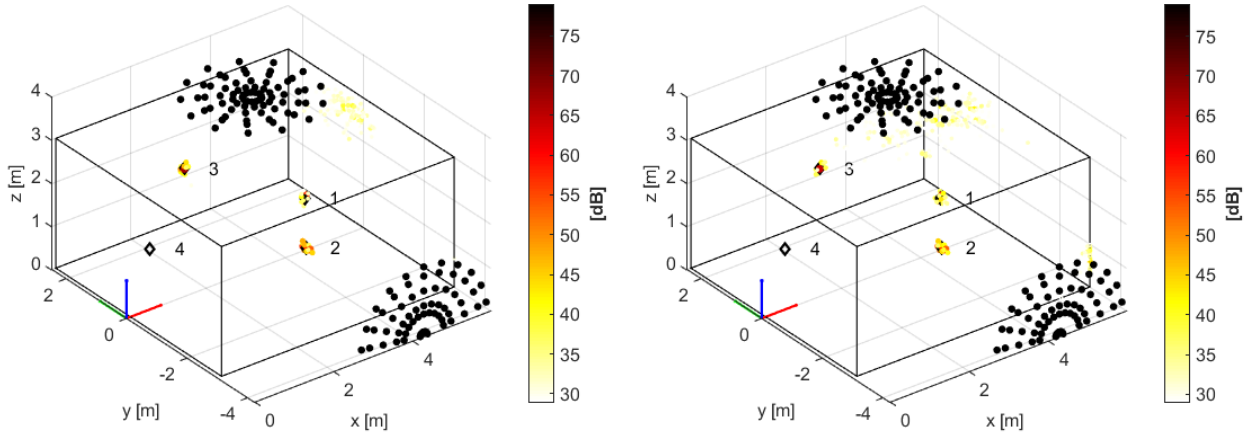
(a) (b)

Figure 8: Simulation with SNR $= 0$ dB, top array - (a) CLEAN-SC Components, (b) Eigenmodes



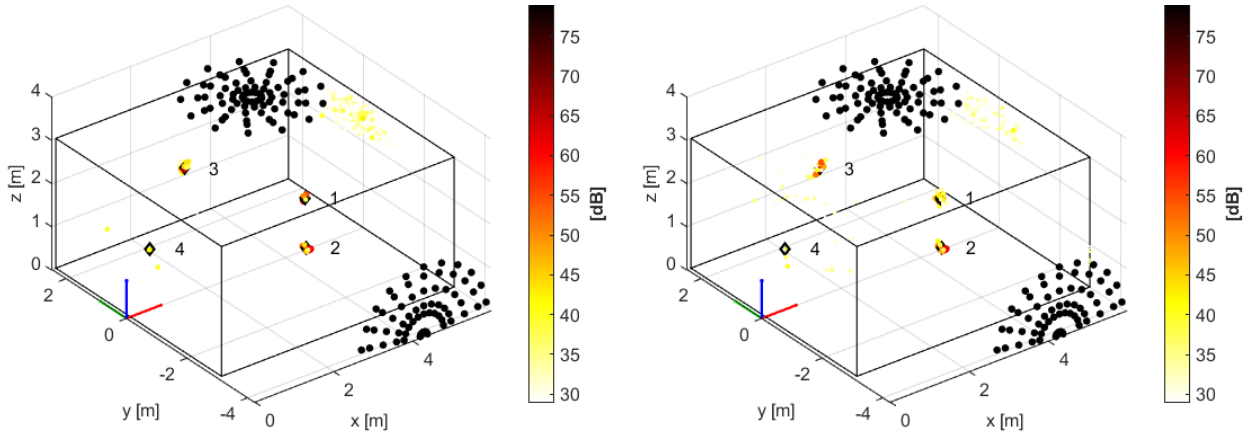
(a) (b)

Figure 9: Simulation with SNR $= 0$ dB, top array with CB map as a priori information - (a) CLEAN-SC Components, (b) Eigenmodes



(a) (b)

Figure 10: Simulation with SNR = 0 dB, side and top arrays - (a) CLEAN-SC Components, (b) Eigenmodes



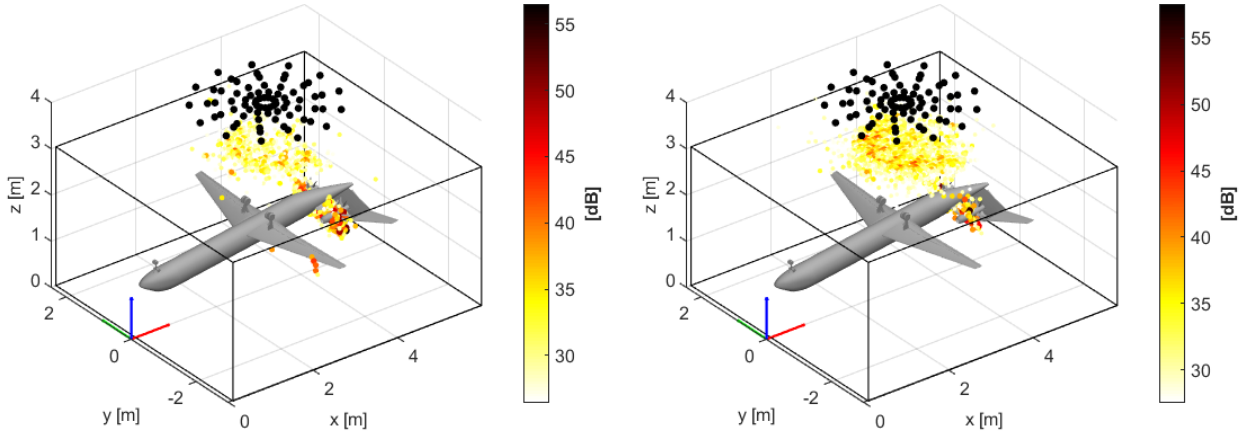
(a) (b)

Figure 11: Simulation with SNR = 0 dB, side and top arrays with CB map as a priori information - (a) CLEAN-SC Components, (b) Eigenmodes

These results show how it is possible to properly combine different strategies and arrays to have maps with high accuracy and dynamics even in presence of strong noise. Indeed, a priori information introduced make possible to reconstruct even the weakest source, while the use of the second array increases localization accuracy and the capability of suppressing noise and artefacts.

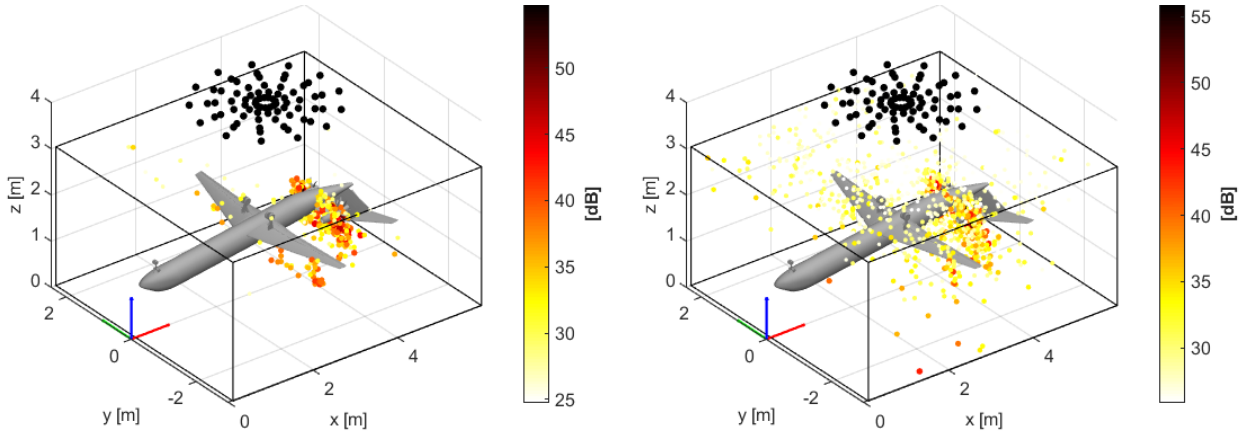
3.3 Experimental data

The band analysed is the same of simulated test cases. The number of relevant eigenmodes is empirically set to $M_0 = 30$ because otherwise noise spoils excessively the components. All CLEAN-SC components are processed resulting to be $M_0 < 30$ for each frequency within the band analysed. The volume of interest and its discretization are the same of the simulated test cases. Figures from 12 to 15 show results for the test case with the CRORs switched-on. Figures from 16 to 19 show the acoustic maps with the CRORs switched-off. All data are represented using a dynamic range of 30 dB.



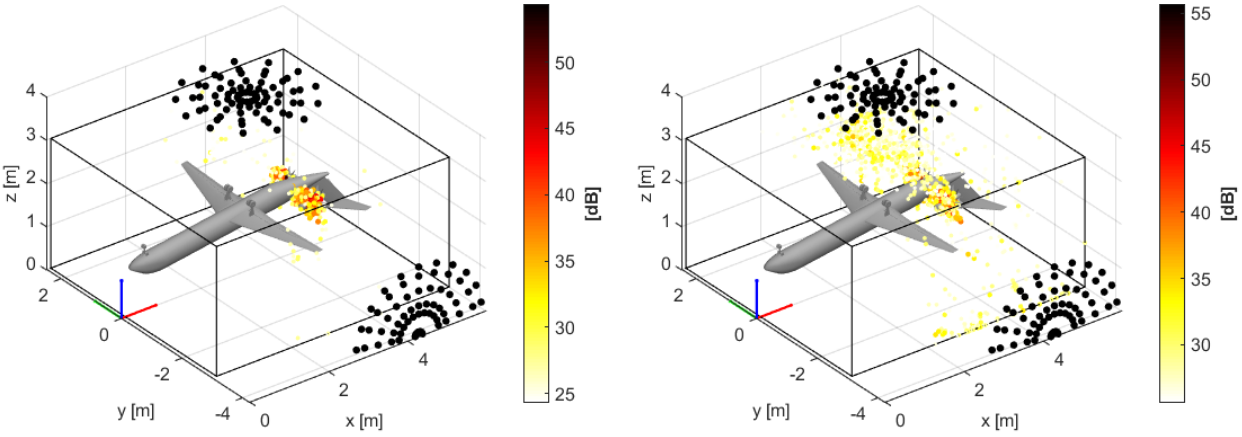
(a) (b)

Figure 12: CROR turned-on, top array - (a) CLEAN-SC Components, (b) Eigenmodes



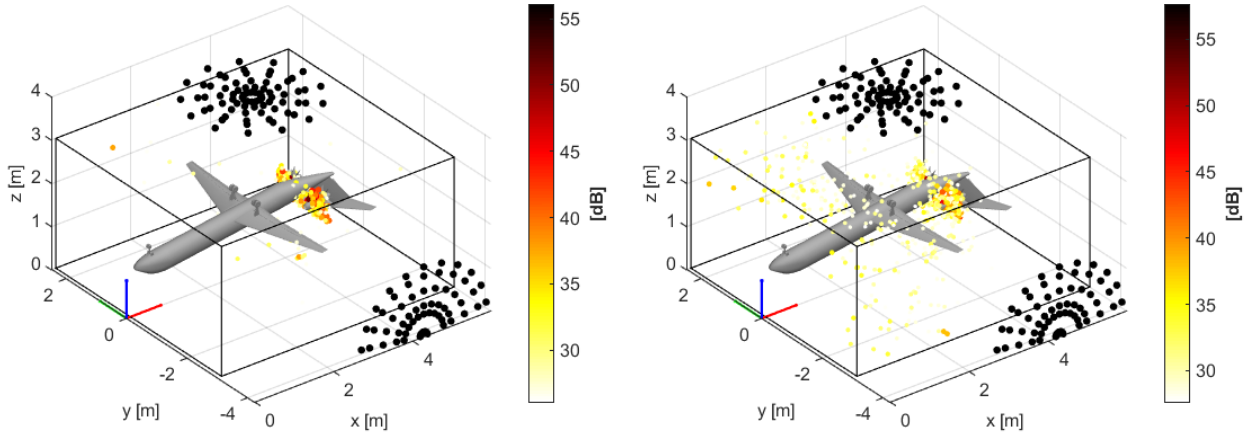
(a) (b)

Figure 13: CROR turned-on, top array with CB map as a priori information - (a) CLEAN-SC Components, (b) Eigenmodes



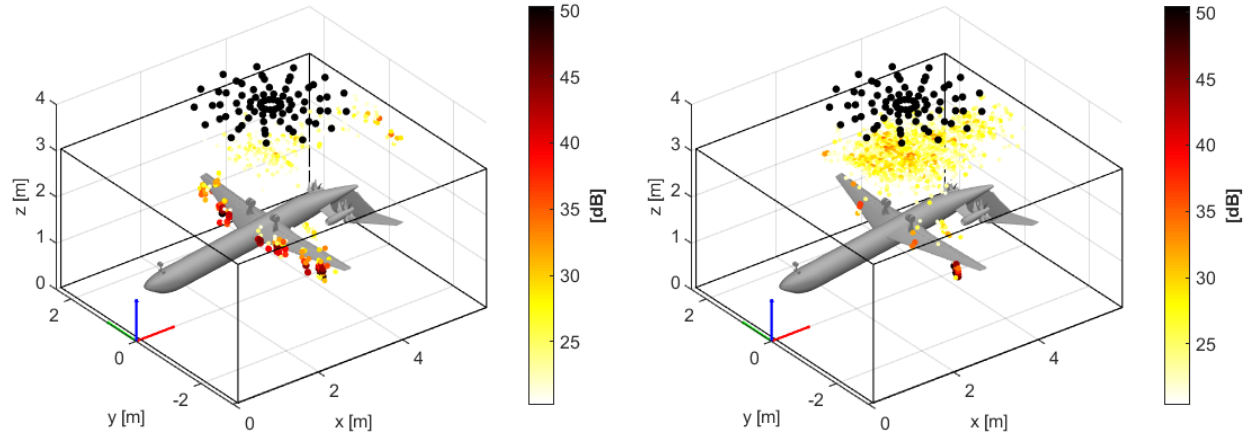
(a) (b)

Figure 14: CROR turned-on, side and top array - (a) CLEAN-SC Components, (b) Eigenmodes



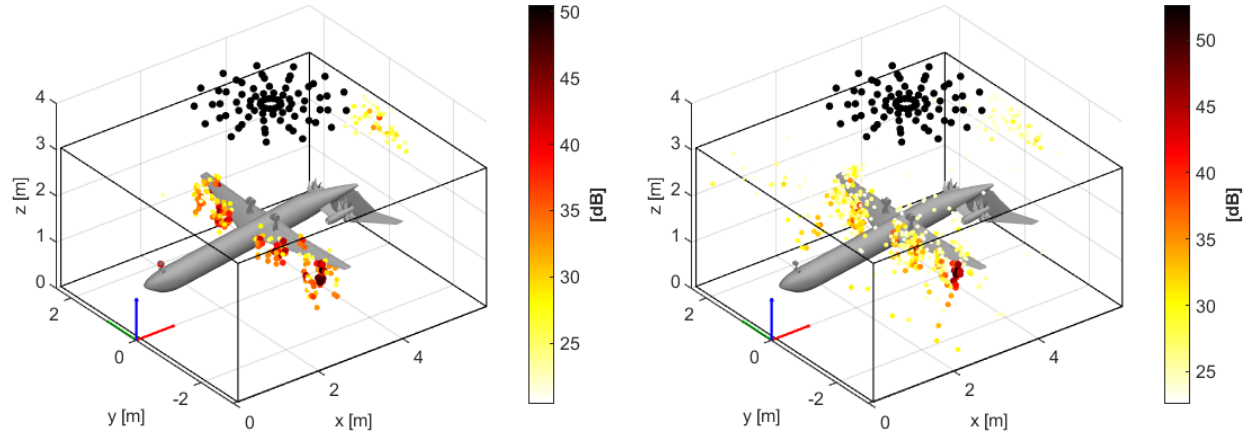
(a) (b)

Figure 15: CROR turned-on, side and top array with CB map as a priori information - (a) CLEAN-SC Components, (b) Eigenmodes



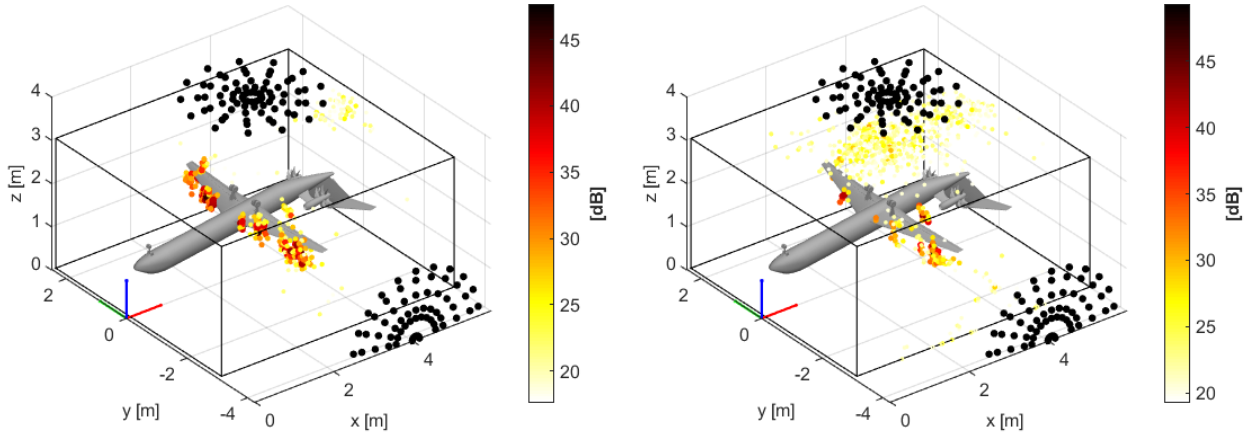
(a) (b)

Figure 16: CROR turned-off, top array - (a) CLEAN-SC Components, (b) Eigenmodes



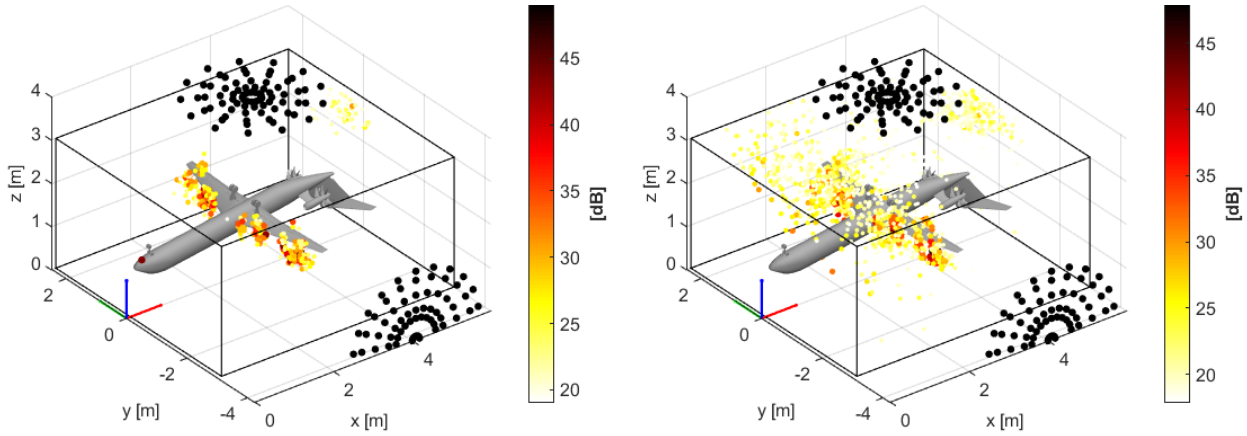
(a) (b)

Figure 17: CROR turned-off, top array with CB map as a priori information - (a) CLEAN-SC Components, (b) Eigenmodes



(a) (b)

Figure 18: CROR turned-off, side and top array - (a) CLEAN-SC Components, (b) Eigenmodes



(a) (b)

Figure 19: CROR turned-off, side and top array with CB map as a priori information - (a) CLEAN-SC Components, (b) Eigenmodes

The presence of CRORs noise makes difficult the task of locating weaker noise sources. The use of two arrays gives an improvement in the localization of rotors noise, while it brings no advantage in the aeroacoustic source localization. Indeed, only in Figure 13(a), some aeroacoustic sources are clearly visible in addition to the CROR sources. When CRORs are turned-off, some sources close to the wings, that might hint to wing tip noise, starts to appear on the maps, even if the background noise remains the same. In some of the results presented for the single-array case, it is clearly visible that a lot of energy is located close to the array. When this phenomenon occurs, it means that the regularization process fails due to the high level of noise and the severe under-determination of the problem. Moreover, these results remark the difference between CLEAN-SC components and eigenmodes. Indeed the former usually give less artefacts in the maps due to lower level of noise in the CSM components.

4 Conclusions

This work described how to exploit inverse methods in the context of volumetric mapping targeted to aeroacoustic applications. The problem has been faced both from the point of view of the algorithm and from the possible choice to use multiple planar arrays on orthogonal planes. The main issues that have been faced are:

- severely under-determined inverse problems due to the great number of potential sources in volumes,
- high level of noise present in aeroacoustic data,
- sources having large difference in terms of strengths.

The first issue entails the ill-posedness and ill-conditioning of the problem. These two characteristics are addressed by using an IRLS algorithm that enforces sparsity of solution and exploits BA as regularization strategy. The other two issues have been faced, in this paper, by performing a decomposition of the microphone CSM, which makes it possible to separate source components from noise, and by exploiting the a priori information on source distribution provided by CB. With this in mind, a novel approach that uses CLEAN-SC as pre-processing step to inverse method has been presented. The novel approach generally outperforms the classic eigenmodes decomposition typically adopted, with the further advantage of providing the number of relevant components in the pressure CSM. Moreover, the introduction of CB map for each component as a priori information in the inverse problem makes possible to correctly reconstruct even sources 20 dB weaker than the principal one.

Results from both simulated and experimental data demonstrated that is possible to use a single planar array to map aeroacoustic noise sources with fair accuracy. The use of a second array is suggested when localization accuracy is crucial. However, the downside of combining multiple arrays looking at the acoustic scene from different point of view, is that one of them may not detect enough signal from some sources acting in the scenario (e.g. due to masking effect of the target or excessive source directivity) thus deteriorating the reconstruction of these sources.

Independently on the use of one or two arrays, results showed that the algorithm and the strategies described in this work can lead to accurate volumetric source localization even in presence of strong background noise.

Acknowledgements

The research leading to these experimental data has received funding from the European Unions Seventh Framework Programme (FP7/2007-2013) for the Clean Sky Joint Technology Initiative under grant agreements n^{o} 278419 (WENEMOR). Authors kindly acknowledge all the partners.

References

[1] Jérôme Antoni. A bayesian approach to sound source reconstruction: Optimal basis, regularization, and focusing. *The Journal of the Acoustical Society of America*, 131(4):2873–2890, apr 2012.

[2] Gianmarco Battista, Paolo Chiariotti, Gert Herold, Ennes Sarradj, and Paolo Castellini. Inverse methods for three-dimensional acoustic mapping with a single planar array. In *Proceedings of the 7th Berlin Beamforming Conference*, 2018.

[3] T. F. Brooks and W. M. Humphreys, Jr. A Deconvolution Approach for the Mapping of Acoustic Sources (DAMAS) Determined from Phased Microphone Arrays. In *10th AIAA/CEAS Aeroacoustics Conference*, 2004.

[4] Rick Chartrand and Wotao Yin. Iteratively reweighted algorithms for compressive sensing. In *2008 IEEE International Conference on Acoustics, Speech and Signal Processing*. IEEE, mar 2008.

[5] Jacques Hadamard. Sur les problèmes aux dérivés partielles et leur signification physique. *Princeton University Bulletin*, 13:49–52, 1902.

[6] Q. Leclere, Antonio A. Pereira, and Jérôme Antoni. Une approche bayésienne de la parcimonie pour l'identification de sources acoustiques. In *Congrès Français d'Acoustique*, pages –, Poitiers, France, 2014.

[7] Quentin Leclère, Antonio Pereira, Christophe Bailly, Jerome Antoni, and Christophe Picard. A unified formalism for acoustic imaging techniques: illustrations in the frame of a didactic numerical benchmark. In *Proceedings on CD of the 6th Berlin Beamforming Conference, 29 February-1 March 2016*, February 2016.

[8] S. Oerlemans and P. Sijtsma. Determination of Absolute Levels from Phased Array Measurements Using Spatial Source Coherence. In *8th AIAA/CEAS Aeroacoustics Conference and Exhibit, Breckenridge, Colorado, June 17-19, 2002*, 2002.

[9] Sijtsma P. Clean based on spatial source coherence. *International Journal of Aeroacoustics*, 6(4):357–374, December 2007.

[10] Thomas Padois and Alain Berry. Two and three-dimensional sound source localization with beamforming and several deconvolution techniques. *Acta Acustica united with Acustica*, 103(3):392–400, may 2017.

[11] Thomas Padois, Philippe-Aubert Gauthier, and Alain Berry. Inverse problem with beamforming regularization matrix applied to sound source localization in closed wind-tunnel using microphone array. *Journal of Sound and Vibration*, 333(25):6858–6868, 2014.

[12] A. Pereira, J. Antoni, and Q. Leclère. Empirical bayesian regularization of the inverse acoustic problem. *Applied Acoustics*, 97:11–29, oct 2015.

[13] Antonio Pereira. *Acoustic imaging in enclosed spaces*. PhD thesis, INSA de Lyon, 2014.

[14] E. Sarradj. Three-dimensional acoustic source mapping with different beamforming steering vector formulations. *Advances in Acoustics and Vibration*, 2012(292695):1–12, 2012.

[15] Takao Suzuki. L1 generalized inverse beam-forming algorithm resolving coherent/incoherent, distributed and multipole sources. *Journal of Sound and Vibration*, 330:5835–5851, 2011.

[16] A. N. Tikhonov. Solution of incorrectly formulated problems and the regularization method. *Soviet Math. Dokl.*, 4:1035–1038, 1963.

Prediction of outdoor sound propagation from firearms shooting ranges: a comparison

B.G. Marinus [1], **K. Harri** [1]
[1] Royal Military Academy, Department of Mechanical Engineering,
Renaissancelaan 30, B-1000, Brussels, Belgium
e-mail: **benoit.marinus@rma.ac.be**

Abstract

The short-duration large-amplitude impulsive noise from firearms and howitzers is characterized by a wide-band frequency content that distinguishes it from industrial noise sources. Therefore, the ISO 9613 standard which is based on the concepts of sound power and sound intensity, does not apply as such. The NordTest ACOU-099 standard based on sound pressure level, has been developed specifically for this purpose. Both approaches differ from ISO 17201 which is purposely developed for firearms and in which one considers the energy of the event and the energy density. The predicted sound attenuation during propagation through these standards is compared to on-site measurements to reveal the shortcomings stemming from neglection of the non-linear effects in the far-field of such potent noise sources.

1 Introduction

In densely populated areas surrounding military training facilities, environmental noise from shooting ranges remains an issue. Even if exceptions are raised to the Environmental Noise Directive 2002/49/EC for the noise emissions due to military activities, especially in operational context, the annoyance to communities caused by daily training activities requires ad hoc assessment and management.

The short-duration large-amplitude impulsive noise from firearms and howitzers results in a wide-band frequency content that distinguishes it from industrial noise sources. Existing noise propagation software used by experts are based on predefined sources (spectrum and magnitude) often with no directional characteristics other than point/line/volume sources. A standards-based propagation model with fixed, frequency-dependent attenuation levels corrects for local conditions (wind, humidity, temperature, obstacles and soil type) in addition to that due to spherical divergence and atmospheric absorption. These standards have been developed for 'industrial' (civil) noise sources, frequently from a national perspective, and are at present often used for military noise (firearms, guns, detonation & explosions) with little or no account for the spectral and directional characteristics of those military sources and the non-linear propagation occurring in their immediate and extended vicinity.

In the present paper, we compare three standards to compute the propagation of machine gun and howitzer shots taking place in a free field around the muzzle. The ISO 9613 standard [**?**] is based on the concept of sound power i.e. energy per time period (Watt), and sound intensity i.e. power per unit surface. The NordTest ACOU-099 standard [**?**] is based on sound pressure level. These approach differs from ISO 17201 [**?**] which consider the energy of the event (Joule) and the energy density i.e. the energy per unit surface. The predicted sound propagation through these standards is compared to on-site measurements.

The comparison yields precious information on which propagation model is best suited for this type of sound and which attenuation levels need to be addressed first to take the particular propagation properties better

into account in future prediction codes. Next, this assessment delivers hints on how to better address specific propagation issues in measurement campaigns.

2 Methodology

2.1 Standards

2.1.1 ISO 9613

The ISO 9613 standard [**?**] is intended to calculate the attenuation of industrial sound propagating outdoors so that the level of environmental noise from various sources of known characteristics can be predicted at some distant location. Therefore, the standard accounts for most of the dominant noise attenuation mechanisms that can occur along the propagation path. However, ISO 9613 is not intended for and does not apply for impulsive sound from firearms since it does not apply for time-weighted metrics [**?**]. Moreover, changes in the pressure-time history occurring during propagation by non-linear effects are not accounted for.

This standard applies to octave-band levels originating from a point source (or an assembly of point sources). It expresses the octave-band sound pressure level at a receiver location (r_r, θ)

$$L_p(r_r, \theta) \; = \; L_w + D_{c,\theta} - A_e \tag{1}$$

where L_w is the octave-band sound power level produced by the point sound source (ref. 1pW), $D_{c,\theta}$ is the directivity correction giving the deviation from the level of an omnidirectional point source of level L_w in the direction θ, and A_e is the excess attenuation due to environmental conditions. The excess attenuation is composed according to

$$A_e \; = \; A_{div} + A_{atm} + A_{gr} + A_{bar} + A_{misc} \tag{2}$$

with A_{div} accounting for geometrical divergence, A_{atm} for the attenuation due to atmospheric absorption, A_{gr} for the ground effects, A_{bar} for noise barriers, and A_{misc} for miscellaneous other effects. Doing so, this standard provides terms account for the major physical effects such as geometrical divergence, atmospheric absorption, ground effects, as well as reflection from surfaces and potentially screening by obstacles, buildings or foliage.

The overall accuracy of the method is $\pm$3dB according to table 5 in [**?**].

2.1.2 ISO 17201

ISO 17201 [**?**] is intended to modify where necessary the ISO 9613 standard so that the propagation of shooting sound from firearms (with a caliber $\leq$20mm) can be modeled at a reception point. The ISO 17201 standard takes the source energy, its directivity, and its spectrum as inputs. The source energy is essentially produced by the muzzle blast —the often supersonic expulsion of the propellant gas from the barrel— which yields very high levels in excess of 154dB peak sound pressure level in the immediate vicinity of the muzzle. The standard defines the 154dB level as the limit of the region where non-linear propagation occurs and does not apply within that region. Away from that region, the standard assumes propagation according to linear acoustics.

The angular source energy distribution octave-band levels $L_q(\theta)$ are obtained from the sound exposure level $L_E(r_m, \theta)$ measured at a distance r_m and angle θ after corrections are applied for the rotation around the line of fire. Once $L_q(\theta)$ is known, the octave-band sound exposure level at a receiver is calculated according to:

$$L_E(r_r, \theta) \; = \; L_q(\theta) - A_e + 11dB - A_z \tag{3}$$

where A_e is obtained by eq. 2, A_z accounts for non-standard meteorological conditions, the $+11$dB correction for the conversion of sound energy into a pressure-level. The attenuation terms are essentially computed according to ISO 9613 with some minor modifications for specific situations.

In terms of uncertainty, ISO 17201 states that the actual sound pressure levels at the receiver's location could be $\pm$20dB than the values obtained with the propagation model behind ISO 17201 and ISO 9613. The reason behind such high uncertainties lie with the short duration of shot sound. The averaged quantities used in the propagation model to account for atmospheric refraction, reflection, absorption, and the effect of atmospheric turbulence —which all increase with distance from the source— are obtained over a much larger period than the actual shot duration.

2.1.3 NORDTEST ACOU 099

This NORDTEST standard aims at modelling the sound propagation in downwind summer conditions of single shots from small arms (calibre$\leq$20mm). It is based on the measured octave-band source sound pressure levels $L_{p,s}(10m, \theta)$, corrected to free field conditions, at 10m distance from the muzzle. At the receiver's location (r_r, θ), the octave-band sound pressure levels $L_{p,r}$ are given by

$$L_{p,r}(r_r, \theta) \;=\; L_{p,s}(10m, \theta) + \underbrace{\Delta L_d + \Delta L_a + \Delta L_g + \Delta L_s + \Delta L_v}_{\approx -A_e} \tag{4}$$

as shooting halls or reflections are not taken into account in the present work. The attenuation terms are similar, though not equal, to the excess attenuation A_e from eq. 2 and follow a similar approach.

The method is accurate to within $\pm$3dB for the present set-up.

2.2 Measurements

Measurements were made on soft ground with a GRAS 46AM 1/2"-microphone placed 1.5m above the surface. The GRAS 46AM pre-polarized free-field microphone is assembled with a GRAS 26CA preamplifier. This assembly has a 25dB to 149dB dynamic range for a frequency range of 3.15 Hz to 31.5 kHz. The signal is digitized using a National Instruments NI PXI-4462 module in a PXIe chassis and controller. The signal is sampled at 70kHz in order to avoid aliasing. The measurements are triggered by the command and control sequence preceding each shot.

Each individual measurement is later post-processed through in-house analysis and propagation codes written in Matlab.

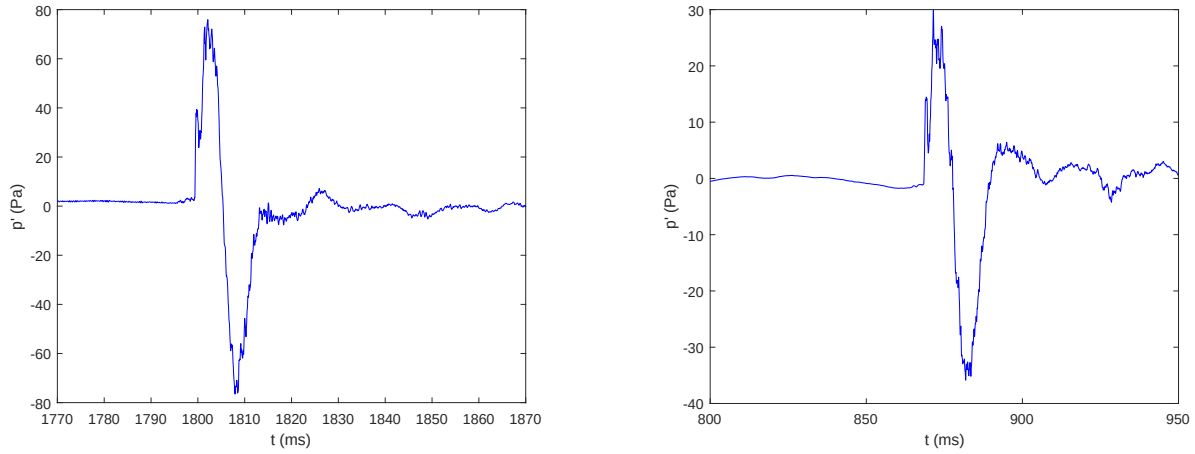
As can be seen from fig. 3, the background noise levels are at least 10dB below the signal of interest so that no corrections should be applied [**?**, **?**].

3 Results and Discussion

3.1 Howitzer 105mm

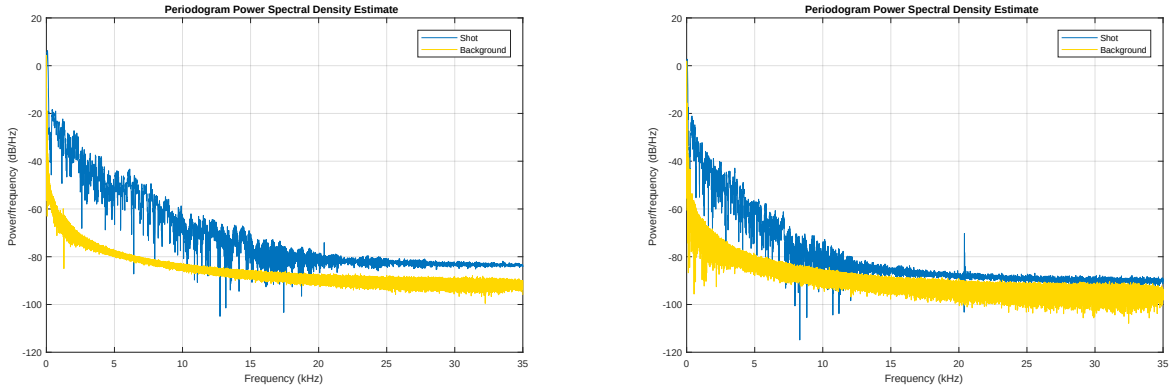
As a preliminary to this section, it should be noted that strictly speaking none of the standards apply for this caliber. The section is intended to identify and quantify the shortcomings of such standard for this type of weapon.

A typical pressure-time signal for the two measurement locations is shown in fig. 1. The locations are respectively at 117m and 200m from the muzzle in the 225°$\pm$5° direction. These pressure-time signatures are archetypal of impulsive noise from firearms and howitzers. They exhibit the same characteristics as those reported in [**?**] including the dip between the initial acoustic pressure rise when the projectile exits the barrel



(a) 117m. (b) 200m.

Figure 1: Time signal for a howitzer 105mm shot at 225° directivity.



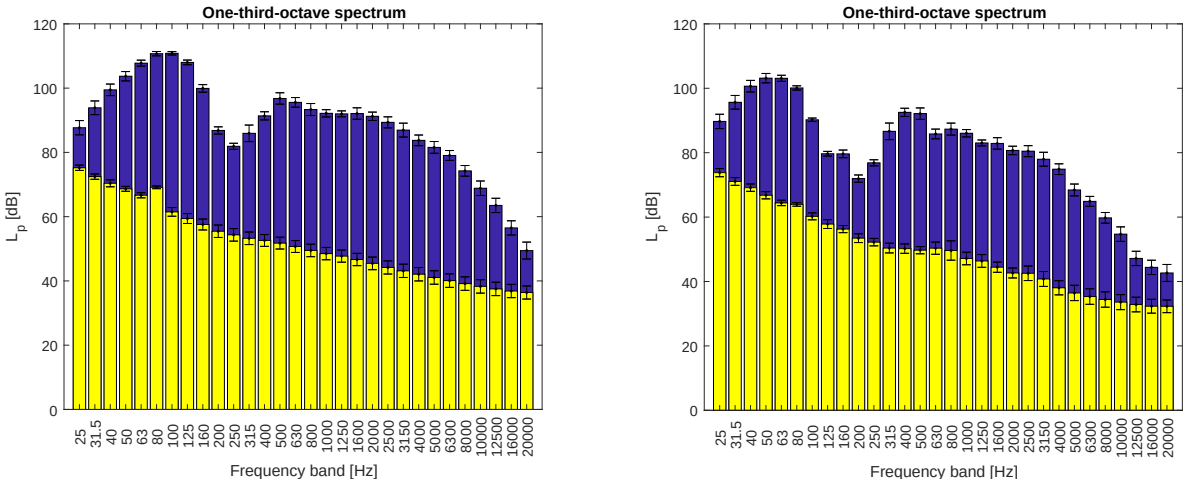
(a) 117m. (b) 200m.

Figure 2: Power spectral density for a howitzer 105mm shot at 225° directivity.

and the rise to peak pressure when the hot gases exhaust violently the barrel. The consequent underpressure has a significant amplitude as can be expected for measurement locations that far from the muzzle. The corresponding periodograms are shown in fig. 2. These reveal that most of the acoustic power in contained in frequencies lower than 15kHz and that there is considerable attenuation for the frequency bands above 15kHz which vanish between the two measurement locations.

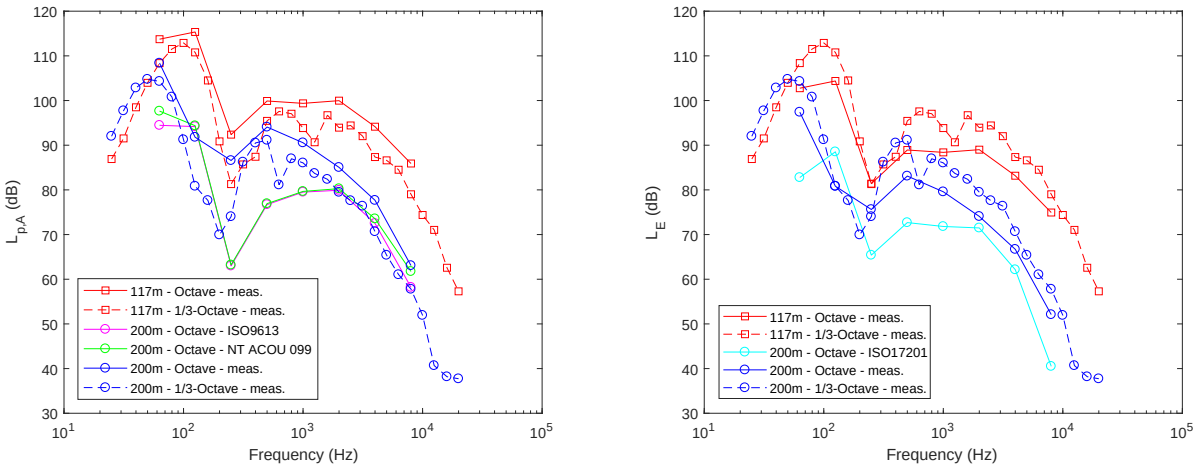
The spectra shown in fig. 3 for both measurement locations are averaged over five shots or five samples of 4s each for the background noise. The errorbars indicate for each frequency-band the standard error which is $\pm$2dB. SHot impulses feature two distinct peaks: one in the low-bass to bass frequency range around 80Hz, and one in the low mid-range around 400Hz. These are superimposed on a signal with large high-frequency contributions.

Figures 4 and 5 compare the frequency spectra and the attenuation between the values predicted by the standards and the measured ones. As can be seen, both ISO9613 and NORDTEST NT ACOU 099 yield values that are very similar but generally overpredict the attenuation typically by 10dB below 2kHz though the overprediction is frequency dependent (see fig. 5(a)). Both underpredict the attenuation at 125Hz so that the nearby peak is well represented in the predicted signal. Above 2kHz, the results of both standards fall within 5dB from the measurements. These are the reasons ISO9613 is considered as not applicable to such signals [**?**]. Despite being intended for propagation of noise from small arms, NORDTEST NT ACOU 099



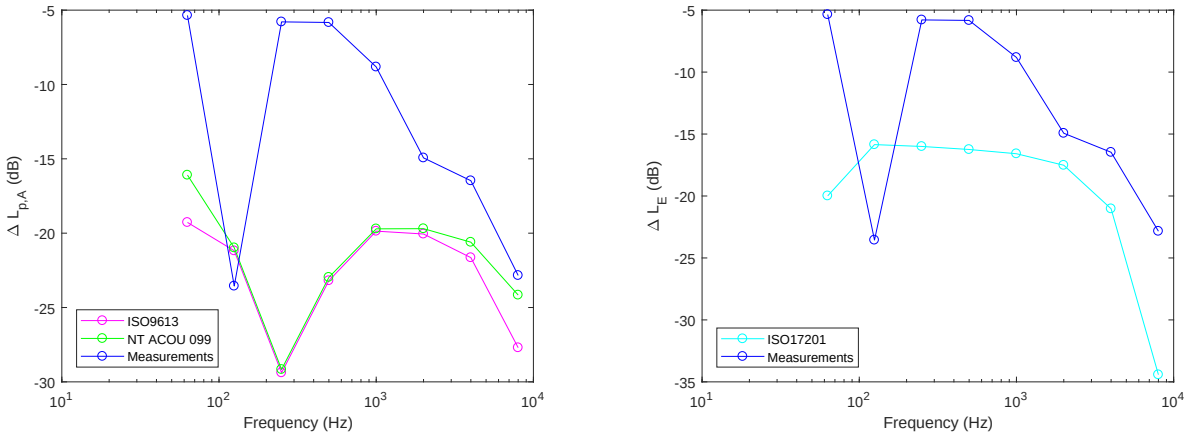
(a) 117m. (b) 200m.

Figure 3: 1/3-octave band spectra for a howitzer 105mm shot at 225° directivity and the background noise. (BLUE: shot — YELLOW: background)



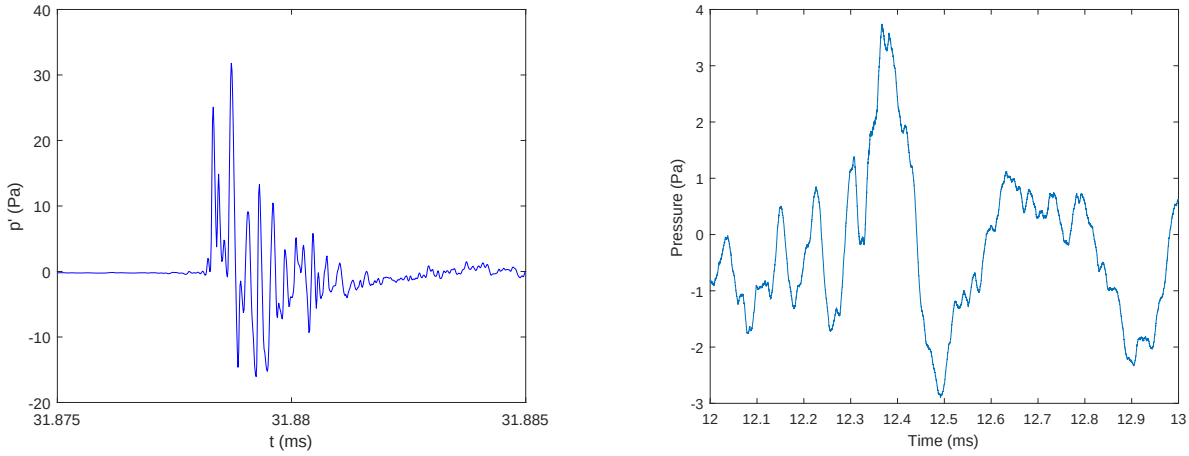
(a) ISO9613 & NT ACOU 099 (b) ISO17201

Figure 4: Octave band and 1/3-octave band spectra obtained through standards and compared to the corresponding spectra for a howitzer 105mm shot at 225° directivity.



(a) ISO9613 & NT ACOU 099 (b) ISO17201

Figure 5: Predicted and measured octave band attenuation for a howitzer 105mm shot at 225° directivity.



(a) 10m. (b) 100m.

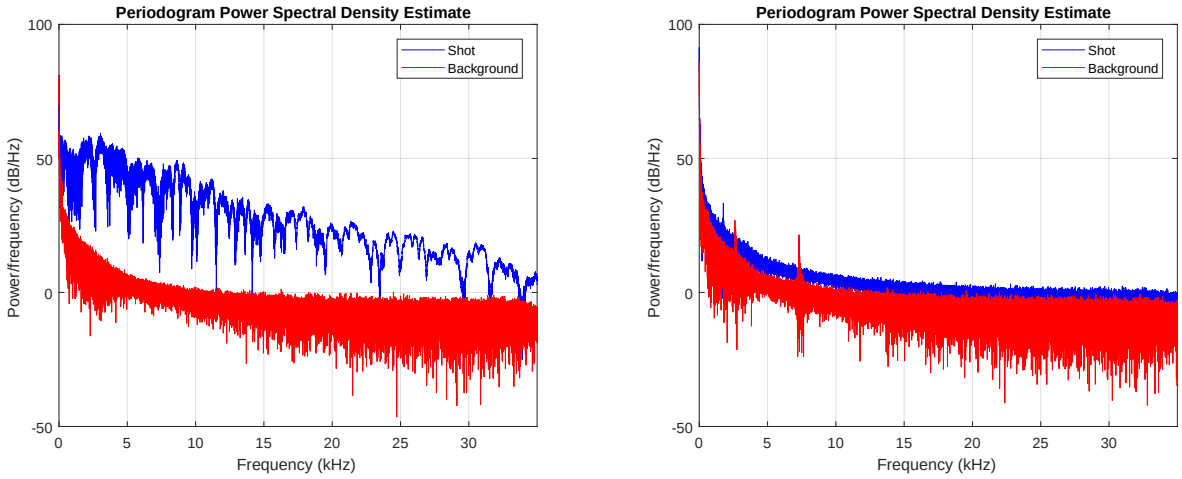
Figure 6: Time signal for a carabine 5.7mm shot at 180° directivity.

does not perform any better and predicts attenuations close to those encountered in ISO 9613.

It can also be seen from figs. 4 and 5 that ISO17201 performs globally better. The attenuation levels are more consistent with the measured ones as the typical difference is of the order of 7dB. The comparison of fig. 5(b) with fig. 5(a) reveals this improvement. The reason behind it is that ISO 17201 is written in terms of sound energy so next to the acoustic pressure, the sound velocity is also taken into account. These two concepts are intertwined in reality as the pressure wave cannot propagate without velocity [**?**]. Since acoustic energy is conserved, in contrary to sound pressure or intensity, the formulation of ISO 17201 is better matched to those situations where pressure and velocity play a significant role.

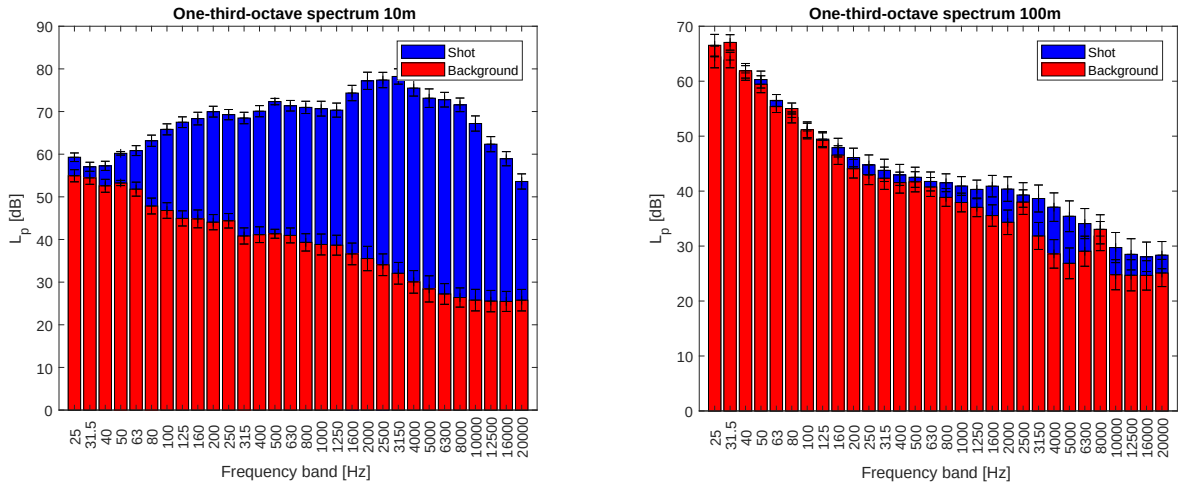
3.2 Carabine 5.7mm

The time signal for two locations, respectively at 10m and 100m from the muzzle in the 180°±5° direction, are shown in Fig. 6. As apparent from Fig. 6, the shooting range is bordered by wooden walls for security purposes so that significant reflections occur. It is therefore required to perform these measurements again



(a) 117m. (b) 200m.

Figure 7: Power spectral density for a carabine 5.7mm shot at 180° directivity.

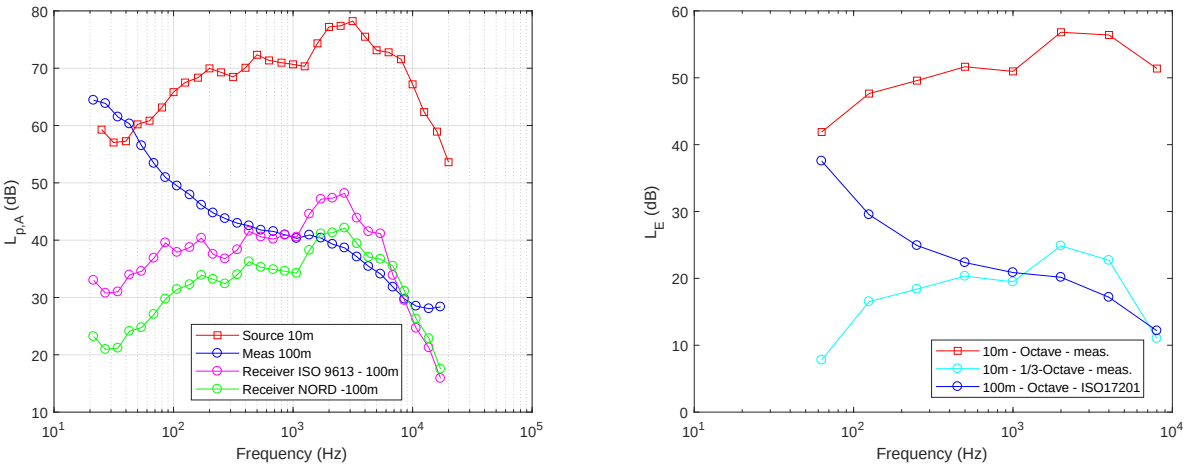


(a) 10m. (b) 100m.

Figure 8: 1/3-octave band spectra for a carabine 5.7mm shot at 180° directivity and the background noise.

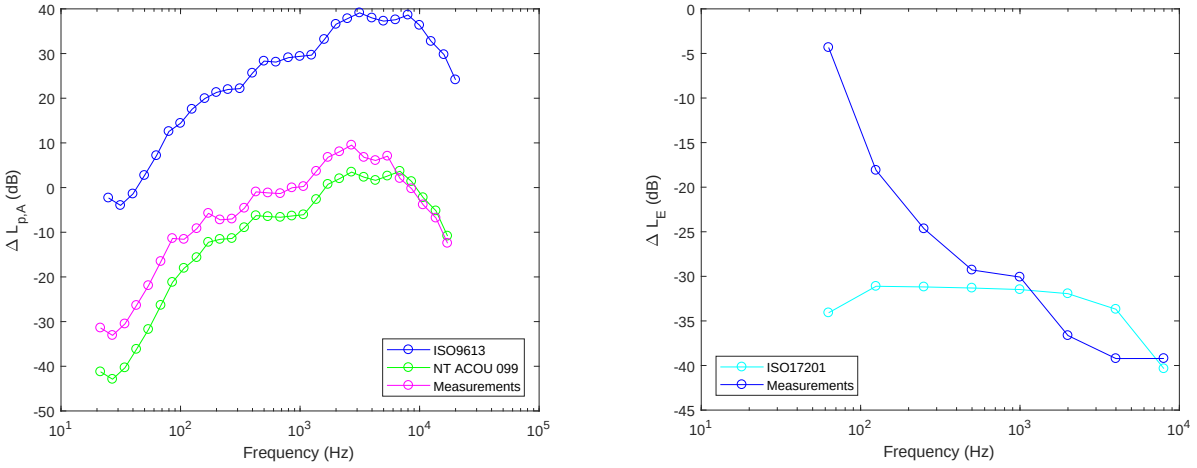
within an open field at the same range. The corresponding PSD is shown in Fig. 7. These graphs reveal that at long distance, the background noise can not be effectively differentiated ($\Delta > 10$dB) from the muzzle signal. This is especially true at low frequency. Fortunately, this effect is not present at 10m from the nozzle. This is even more apparent from Fig. 8, since the standard error at 100m is of the same order of magnitude as the difference between the shot and background noise.

Despite these shortcomings, and in awaiting of new measurements campaigns, the following discussion focuses on the 1000Hz to 5000Hz range where the muzzle signal is dominant. In this frequency range, Figs. 9 and 10(b) the NORDTEST standard predicts attenuation to within $-3dB$ of the measured value. ISO9613 is underpredicting the attenuation by $-10dB$ whereas ISO17201 falls within $-7dB$.



(a) ISO9613 & NT ACOU 099 (b) ISO17201

Figure 9: Octave band and 1/3-octave band spectra obtained through standards and compared to the corresponding spectra for a carabine 5.7mm shot at 180° directivity.



(a) ISO9613 & NT ACOU 099 (b) ISO17201

Figure 10: Predicted and measured octave band attenuation for a carabine 5.7mm shot at 180° directivity.

4 Conclusions

The discrepancies between predicted and measured sound levels reveal the peculiarity of military sources of impulsive noise. As pointed out by Hirsch [**?**], their coherence, strong directivity, high energy, and intense non-linear effects occurring far from the source, should be better taken into account if one wishes to accurately predict the noise signature from firearms wheter from a small or large caliber. Of all three standards tested, the ISO 17201 standard yields the best results even for large calibers since it is written in terms of acoustic energy. This makes the situation even more complicated since most attenuation terms, in particular all the attenuation terms accounted for in this study, are computed from ISO 9613. These results confirm that ISO 9613 is not well suited for the prediction of noise propagation from firearms, particularly below 2kHz. The NORDTEST NT ACOU 099 standard yields very similar results as ISO 9613. Since it is formulated purely in terms of pressure levels, it cannot account for the contribution of sound velocity in large impulsive noise from firearms.

Acknowledgements

The authors wish to acknowledge the contributions from D. Cathebras of the Ecole Spéciale Militaire of Saint-Cyr Coëtquidan (France) and H. Topal of the Military Technical Academy of Bucharest (Romania) for the measurements as well as the acquisition and post-processing software. The help from J. Vercauteren from the Royal Military Academy of Brussels is also acknowledged. Next, thanks go to the Artillery Battalion and Center for Testing of Material of the Belgian Defence for allowing us to plug-in during exercises on the firing range.

References

Axial propagation of flow-induced vibrations in thick walled pipes and hoses

I. F. Rodrigues [1], **I. Lopez Arteaga** [1]
[1] Technische Universiteit Eindhoven (TU/e), Department of Mechanical Engineering,
P.O box 513 5600 MB Eindhoven, Netherlands
e-mail: **i.f.rodrigues@tue.nl**

Abstract

This paper presents a numerical study in which the thick-wall assumption in a fluid-structure interaction analysis of liquid-filled pipes subjected to axial vibration is adopted. The influence of wall thickness on the dynamic characteristics of the system in the frequency domain is investigated and the validity of the thin-wall assumption is assessed for different scenarios. The analytical expressions are derived from the equations of motion in cylindrical coordinates and the mathematical model is compared with a 3D numerical model, developed via the finite element method. It is shown that a great range of industrial applications of pipe systems can be analyzed using a thin-wall assumption. However, for small pipe diameters such as those used in high precision machines, the wall thickness of a pipe becomes larger compared to its radius. For these scenarios, thin-walled pipe equations no longer hold since they are not able to predict stresses variation within the cross section of the pipe. Furthermore, this difference amplifies for soft wall materials.

1 Introduction

Flow-induced vibrations in high precision machines

One of the challenges in high precision equipment industry is to fulfill the requirement of high accuracy thermal specifications while keeping vibration levels to a minimum. In order to control the temperature, the provision of water cooling for sensitive components is required, while avoiding unacceptable levels of flow-induced vibrations (FIV). Discontinuities in the flowing water system, such as diameter changes, bends, branches and restrictions, give rise to disturbances in the fluid that propagate along the circuit. Due to acoustic pressure waves traveling through the water, FIV can be transmitted far from their source through the cooling system into the (mechanically) isolated structure. In order to predict the system behavior, an accurate model is necessary. For this reason, understanding the effect of flow disturbances in producing vibration forces in system, due to fluid-structure interaction (FSI), is a matter of great interest.

2 Governing equations

The axial motion of a liquid-filled pipe system can be described by a four equation model (similar as used by [1], [2], [3]), assuming four generalized coordinates: $V(z,t)$ and $P(z,t)$, the axial velocity and pressure of the fluid, respectively; $\dot{u}_z(z,t)$ and $\sigma_z(z,t)$ the velocity and stress of the pipe wall, respectively. This system of equations is obtained by combining the equations of motion and continuity equations for both the pipe

and the fluid, which results:

$$\begin{aligned}
\frac{\partial V}{\partial t} + \frac{1}{\rho_f}\frac{\partial P}{\partial z} + V_0\frac{\partial V}{\partial z} &= 0 \\
\frac{1}{K^*}\frac{\partial P}{\partial t} - \frac{2\nu}{E}\frac{\partial \sigma_z}{\partial t} + \frac{\partial V}{\partial z} &= 0 \\
\frac{\partial \dot{u}_z}{\partial t} - \frac{1}{\rho_p}\frac{\partial \sigma_z}{\partial z} &= 0 \\
\frac{1}{E}\frac{\partial \sigma_z}{\partial t} - \frac{\partial \dot{u}_z}{\partial z} - \gamma\frac{\nu}{E}\frac{R}{e}\frac{\partial P}{\partial t} &= 0,
\end{aligned} \tag{1}$$

where ρ_f and V_o are the density and the initial velocity of the fluid, ν, E and ρ_p are the Poisson's ratio, the Young's modulus of elasticity and density of the pipe wall, respectively. The cross-section of the pipe is defined by the inner radius of the pipe (R) and the wall thickness (e). K^* arises from interface conditions between the fluid and the pipe and accounts for the effect of the compliance of the pipe wall on the bulk modulus of the fluid (K). It is given by

$$K^* = (\frac{1}{K} + \varphi\frac{2R}{Ee})^{-1}. \tag{2}$$

The dimensionless variables φ and γ are introduced in this approach and represent the correction terms that appear in the equations of motion due to the thick-wall assumption. These terms are given by

$$\begin{aligned}
\varphi &= 1 + \frac{e}{R}\left(\frac{1+\frac{e}{R}}{2+\frac{e}{R}} + \nu\right), \\
\gamma &= \frac{1}{1+\frac{1}{2}\frac{e}{R}}.
\end{aligned} \tag{3}$$

Thin-wall assumption implies that if $e \ll R$, $\frac{e}{R}$ can be neglected respect to the unity and so $\varphi = \gamma = 1$. The errors associated with such assumption are discussed in sections 2.1 and 3.1.
Is it possible to rewrite this set of equations by grouping the variables into a vector of physical quantities ($\mathbf{y}(z,t)^T = \{P(z,t), V(z,t), \sigma_z(z,t), \dot{u}_z(z,t)\}$) and its coefficients into matrices:

$$\mathbf{A}\frac{\partial \mathbf{y}(z,t)}{\partial t} + \mathbf{B}\frac{\partial \mathbf{y}(z,t)}{\partial z} + \mathbf{C}\mathbf{y}(z,t) = \bar{\mathbf{r}}(z,t), \tag{4}$$

where $\bar{\mathbf{r}}(z,t)$ represent the environmental sources of excitation and the matrices $\mathbf{A}$ and $\mathbf{B}$ defined by the coefficients of the governing equations:

$$\mathbf{A} = \begin{bmatrix} 1 & 0 & 0 & 0 \\ 0 & \frac{1}{K^*} & 0 & -\frac{2\nu}{E} \\ 0 & 0 & 1 & 0 \\ 0 & -\frac{\gamma\nu R}{Ee} & 0 & \frac{1}{E} \end{bmatrix}, \qquad \mathbf{B} = \begin{bmatrix} V_0 & \frac{1}{\rho_f} & 0 & 0 \\ 1 & 0 & 0 & 0 \\ 0 & 0 & 0 & -\frac{1}{\rho_p} \\ 0 & 0 & -1 & 0 \end{bmatrix}.$$

Assuming $\mathbf{C}$ is null, that lead to the eigenvalue problem:

$$[\mathbf{B}\mathbf{A}^{-1} - \Lambda\mathbf{I}]\mathbf{\Phi} = \Lambda\mathbf{\Phi} \quad \rightarrow \det(\mathbf{B}\mathbf{A}^{-1} - \lambda\mathbf{I}) = 0, \tag{5}$$

where Λ is composed by the eigenvalues of the characteristic equation, and $\mathbf{\Phi}$ by their respectively eigenvectors. Here, $\mathbf{B}\mathbf{A}^{-1}$ can be computed as

$$\mathbf{B}\mathbf{A}^{-1} = \begin{bmatrix} V_0 & c_f^2 & 0 & 2\nu c_f^2 \\ 1 & 0 & 0 & 0 \\ 0 & -\gamma\nu\frac{R}{e}(c_f^2)\frac{\rho_f}{\rho_p} & 0 & -\frac{E}{K}\frac{\rho_f}{\rho_p}(c_f^2\rho_f) \\ 0 & 0 & -1 & 0 \end{bmatrix},$$

where

$$c_f^2 = \left(\rho_f \left(\frac{1}{K^*} - \gamma \frac{2\nu^2}{E}\frac{R}{e}\right)\right)^{-1},$$
$$c_s^2 = \frac{E}{\rho_p}, \tag{6}$$

are the square of the classical pressure wave speed (without FSI) for thick pipes and the square of the classical bar velocity, respectively. Considering $V_0 = 0$, the characteristic equation can be expressed in therms of a bi-quadratic dispersion relation:

$$\lambda^4 - \Pi^2\lambda^2 + c_f^2 c_s^2, \tag{7}$$

where $\Pi^2 = \left(1 + c_s^2 \frac{\rho_f}{K^*}\right) c_f^2$.
Once this parameters are part of the hyperbolic system of PDE's, each eigenvalue λ_i represent a modified (as a consequence of FSI) wave propagation speed (in both positive and negative direction) of axial waves in straight pipes, associated with a mode of vibration (ϕ_i). The solution for Eq. 7 is given by:

$$\lambda_1 = -\sqrt{\frac{1}{2}\left[\Pi^2 - \sqrt{(\Pi^4 - 4c_f^2c_s^2)}\right]}$$
$$\lambda_2 = +\sqrt{\frac{1}{2}\left[\Pi^2 - \sqrt{(\Pi^4 - 4c_f^2c_s^2)}\right]}$$
$$\lambda_3 = -\sqrt{\frac{1}{2}\left[\Pi^2 + \sqrt{(\Pi^4 - 4c_f^2c_s^2)}\right]}$$
$$\lambda_4 = +\sqrt{\frac{1}{2}\left[\Pi^2 + \sqrt{(\Pi^4 - 4c_f^2c_s^2)}\right]}, \tag{8}$$

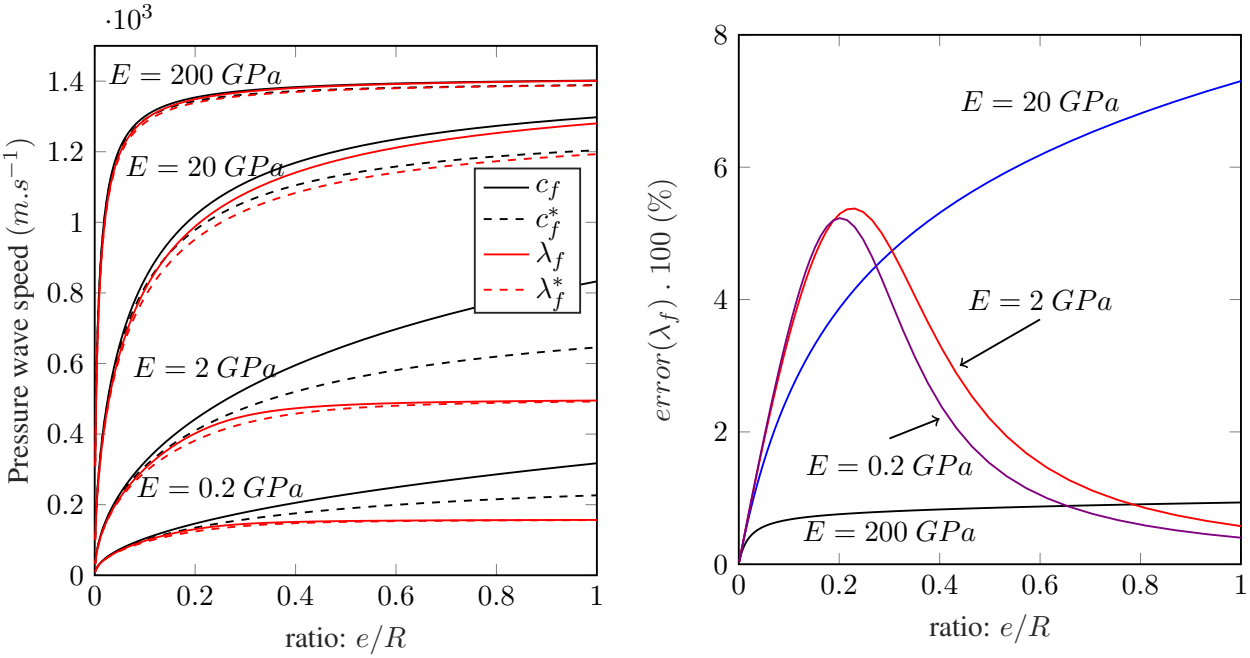
where $|\lambda_{1,2}| = \lambda_f$ stands for pressure wave speeds and $|\lambda_{3,4}| = \lambda_s$ for the the structural wave speeds. The outer sign on the right side of Eq. 8 indicate the direction in which the wave propagates (positive or negative).

2.1 Application 1: Effect of wall compliance on the wave speeds

The circuits of interest in cooling systems contain combinations of rigid, elastic and viscoelastic pipes (hoses), leading to subtle and complex behavior as pressure waves are generated, reflected and damped. A previous study [2] indicates that the use of thin-wall assumption - ratio of thickness to radius (e/R) $\ll 1$ - is valid for long waves in thick metal pipes, where E is typically in the order of 200 GPa. This can be seen in Eq. 2, which shows that the effect of φ is minimized when $E \gg K$. However, when the elastic modulus of the pipe wall is in the same order of magnitude as the bulk modulus of the water or lower, both correction terms γ and φ are amplified considerably and so is the error introduced by the different assumptions.
Figure 1a shows the classical (c_f) and the modified (λ_f) - as a consequence of FSI - pressure wave speeds, with ($c_f^*,\ \lambda_f^*$) and without ($c_f,\ \lambda_f$) thick-wall assumption. Figure 1b shows the error between different ways of estimating the modified wave speeds, defined as

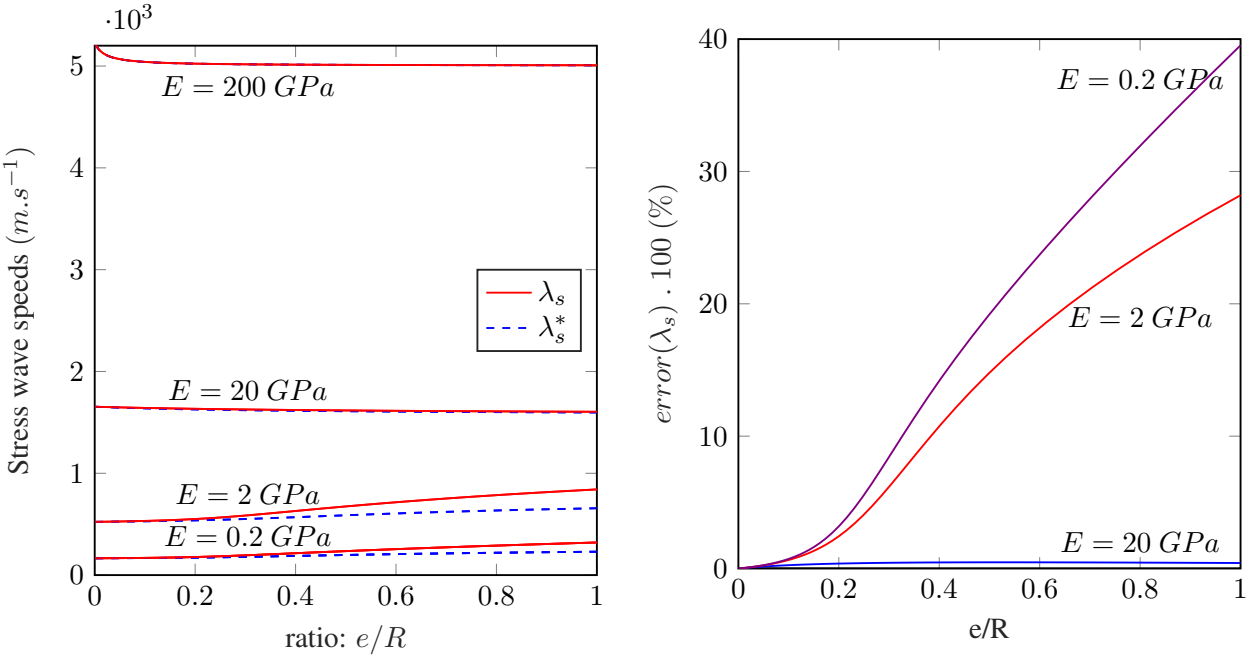
$$error = \frac{\lambda}{\lambda^*} - 1. \tag{9}$$

It is clear that the error between the classical approach and λ_f^* continuously increases with the ratio e/R and also with lower values of E. Furthermore, for higher values of E, thick-wall assumption (c_f^*) provides a better approximation of λ_f^*, while for lower values of E, the assumption of FSI (λ_f) provides a better approximation.
Figure 2a shows the modified stress wave speeds with (λ_s^*) and without (λ_s) thick-wall assumption. Figure 2b shows the error of the structural wave speeds as defined by Eq. 9. While for metal pipes the error associated with thin-wall assumption is negligible for λ_s and is less than 1% for λ_f even for very thick pipes, soft materials such as hoses used in industrial applications (where typical values are: $E \leq 0.2\ GPa$ and $0.1 \leq e/R \leq 0.4$) can lead to an error of about 5% for the pressure wave speeds and around 10% for structural wave speeds.



(a) (b)

Figure 1: (a) classical and modified pressure wave speeds as a function of e/R and E, (—) thin-wall assumption, (- - -) thick-wall assumption. (b) error between λ_f and λ_f^* as a function of e/R and E.



(a) (b)

Figure 2: (a) modified stress wave speeds as a function of e/R and E, (—) thin-wall assumption, (- - -) thick-wall assumption. (b) error between λ_f and λ_f^* as a function of e/R and E.

3 Frequency domain approach

It is possible to use the method of characteristics to solve the set of partial differential equations in time domain (Eq. 1). An analogous approach can be used in the analysis of the frequency domain solution for

this PDE, as presented by [3], by applying the Laplace transform to Eq. (4), which results

$$s\mathbf{A}\mathbf{Y}(z,s) + \mathbf{B}\frac{\partial}{\partial z}\mathbf{Y}(z,s) + \mathbf{C}\mathbf{Y}(z,s) = \mathbf{R}(z,s) + \mathbf{A}\mathbf{Y}(z,0), \tag{10}$$

where $\mathbf{Y}(z,s) = \mathscr{L}\{\mathbf{y}(z,t)\}$; $\mathbf{R}(z,s) = \mathscr{L}\{\mathbf{r}(z,t)\}$, and the last term on the right side appears as a property of the Laplace transform . In a more general approach on the frequency domain, the matrices $\mathbf{A}$, $\mathbf{B}$ and $\mathbf{C}$ may be complex, indicating damping.
Equation 10 can be reorganized by introducing the matrix $\tilde{\mathbf{A}}$ as

$$\tilde{\mathbf{A}}(s) = \mathbf{A} + \frac{1}{s}\mathbf{C}. \tag{11}$$

Then, the solution for Eq. 10 by using the method of characteristics is given by:

$$\mathbf{Y}\left(z,s\right) = \mathbf{\Phi}\left(s\right)\mathbf{E}\left(z,s\right)\eta_0\left(s\right) + \mathbf{\Phi}\left(s\right)\tilde{\eta}_r\left(z,s\right), \tag{12}$$

where the matrix $\mathbf{E}(z,s)$ is composed by the exponential part of the solution:

$$\mathbf{E}\left(z,s\right) = \mathrm{diag}\left(e^{-sz/\lambda_i(s)}\right) \qquad i = 1,2,3,4. \tag{13}$$

The vector $\tilde{\eta}_r\left(z,s\right)$ indicates a particular form of the solution and is given by

$$\bar{\eta}_r(z,s) = \frac{se^{-sz/\lambda_i(s)}}{\lambda_{i(s)}}\int^z n_{ri}(\tau)e^{s\tau/\lambda_i(s)}d\tau, \tag{14}$$

where τ is an auxiliary variable used for integration and n_{ri} are the elements of

$$\eta_{\mathbf{r}}\left(z,s\right) = \mathbf{\Phi}{-}1\tilde{\mathbf{A}}^{\mathbf{-1}}\mathbf{R}\left(z,s\right) + I\eta\left(z,0\right). \tag{15}$$

One can notice that if n_{ri} is not a function of z, then $\bar{\eta}_{ri}(z,s) = n_{ri}$. The vector $\eta_0\left(s,\right)$ is determined from the boundary conditions and is given by

$$\eta_0\left(s\right) = \tilde{\mathbf{D}}_{\mathbf{z}^*}^{-1}\tilde{\mathbf{F}}\left(z^*,s\right), \tag{16}$$

where $z = z^*$ denotes a known boundary location,

$$\begin{aligned}\tilde{\mathbf{F}}\left(z^*,s\right) &= \mathbf{F}\left(z^*,s\right) - \mathbf{D}_{\mathbf{z}^*}\mathbf{\Phi}\left(s\right)\tilde{\eta}_r\left(z^*,s\right)\\ \tilde{\mathbf{D}}_{\mathbf{z}^*} &= \mathbf{D}_{\mathbf{z}^*}\mathbf{\Phi}\left(s\right)\mathbf{E}\left(z^*,s\right)\end{aligned} \tag{17}$$

and $\mathbf{D}_{\mathbf{z}^*}$ contains the coefficients of the relation between $\mathbf{Y}(z^*,s)$ and the Laplace transformed boundary excitation $\mathbf{F}\left(z^*,s\right)$ at that location:

$$\mathbf{D}_{\mathbf{z}^*}\mathbf{Y}\left(z^*,s\right) = \mathbf{F}\left(z^*,s\right). \tag{18}$$

3.1 Application 2: Effect of wall compliance on the FRF

Four different configurations, as described in Tab. 1, are used in a straight pipe with closed ends as numerical test cases in order to compare both approaches (thin/thick-wall) in frequency domain using the methodology describe above. A 3D finite element model, which can simulate moderately thick-walled pipes, is used for comparison.
The chosen parameters are those that affect the most the compliance of the wall (assuming a constant radius): the thickness (e) and the Young's modulus of elasticity (E). Two geometries with different thickness-to-radius ratio were chosen to demonstrate the difference between thin-wall and thick-wall approaches. The first geometry has a thickness-to-radius ratio close to the theoretical limit for thin-wall assumption, while the second has a thickness-to-radius ratio similar to that used in many industrial hoses. Two different elastic

moduli are used to evaluate the effect for hard (metal pipes) and soft (hoses) materials.
An harmonic analysis is performed by applying an unitary axial force at $z = 0\ m$ and evaluating the pressure response at $z = 4\ m$. The results are shown in Fig. 3. A normalized frequency is used such as $f = \frac{\omega}{\omega_1}$, where ω_1 is the first resonant frequency obtained by the FEM model of the respective case of study.

	ratio: e/R	$E\ [GPa]$
Case 1	0.1	200
Case 2	0.3	200
Case 3	0.1	0.2
Case 4	0.3	0.2

Table 1: Cases of study.

Property	**Value**
Bulk modulus	$K = 2\ [GPa]$
Density	$\rho_f = 1000\ [Kg/m^3]$
Length	$L = 5\ [m]$
Inner radius	$R = 0.1\ [m]$

Table 2: Material and geometrical properties.

For a closed-closed pipe, the boundary conditions are obtained from the fact that the axial velocity of both the pipe and the fluid are the same in each of the ends and by performing the equilibrium of forces between the pipe (assuming a massless end) and the fluid:

$$\begin{aligned} V(z^*,t) - \dot{u}_z(z^*,s) &= 0 \\ A_f P(z^*,s) - A_p \sigma_z(z^*,s) &= F_{z^*}. \end{aligned} \tag{19}$$

Assuming the ends of the pipe are located at $z^* = 0$ and $z^* = L$, respectively, the matrices from Eq. 18 can be written as:

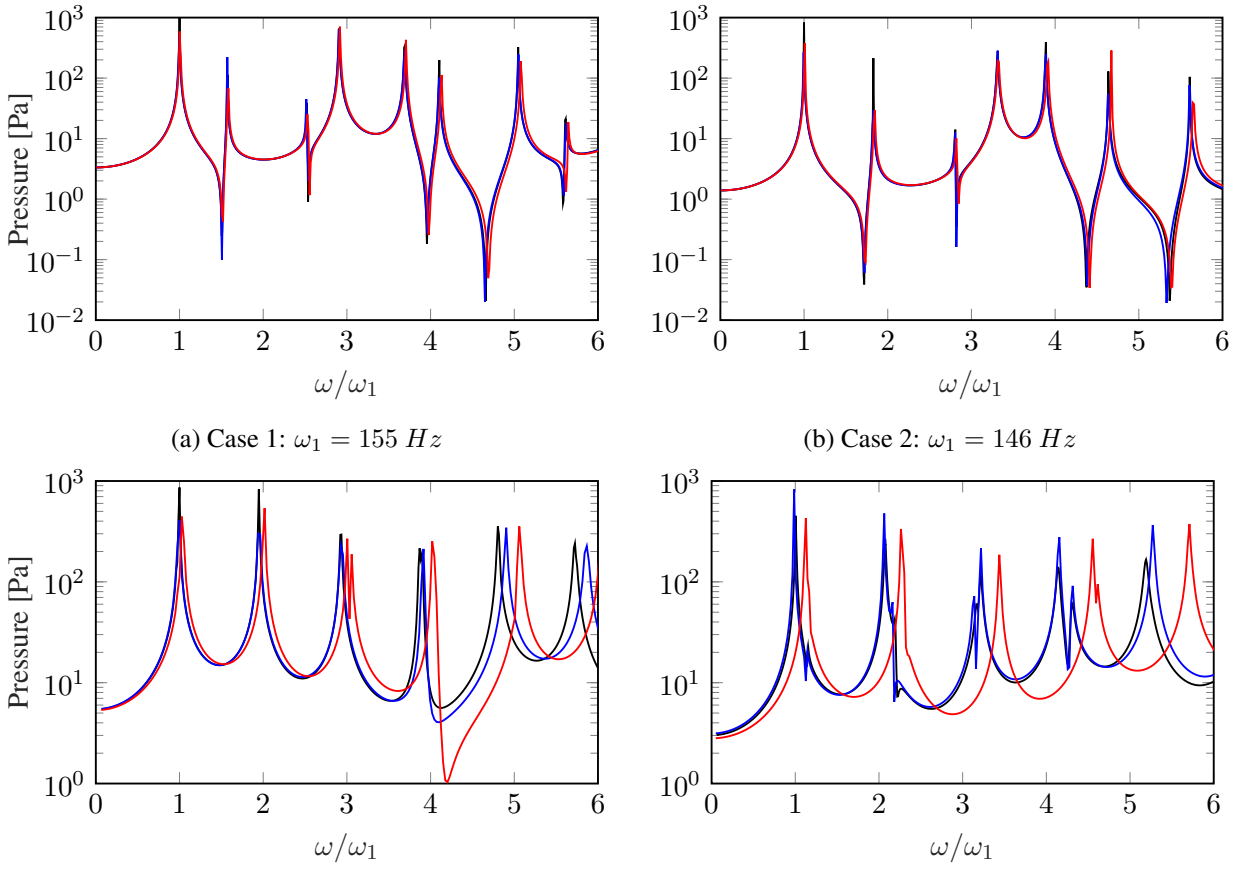
$$\mathbf{D}_{\mathbf{z}^*} = \begin{bmatrix} \mathbf{D_0} \\ \mathbf{D_L} \end{bmatrix} = \left[\begin{array}{cccc} 1 & 0 & -1 & 0 \\ 0 & A_f & 0 & -A_p \\ \hline 1 & 0 & -1 & 0 \\ 0 & A_f & 0 & -A_p \end{array}\right] \quad \text{and} \quad \mathbf{F} = \begin{bmatrix} \mathbf{F_0} \\ \mathbf{F_L} \end{bmatrix} = \left[\begin{array}{c} 0 \\ 1 \\ \hline 0 \\ 0 \end{array}\right], \tag{20}$$

where A_f and A_p are the cross-sectional area of the fluid and pipe wall, respectively.

Figures 3a and 3b shows that, for metal pipes, both assumptions provides a suitable match for the FRF obtained by FEM, even for relatively thick pipes (Case 2). For higher modes, resonant frequencies obtained by thin-wall assumption slightly deviates from the correct values.
In the case of soft materials, one can see in Figs. 3c and 3d that the thin wall assumption is not able to fully represent the behaviour of the system, even for the lower modes. The error on the resonant frequencies is in the order of 5% for Case 3 and 10% for Case 4. For these cases, the 1D thick wall assumption provides a better match. However, for higher modes where the wavelength is comparable with the diameter of the pipe, this assumption also present some discrepancies when compared to the FEM model, with errors on the resonant frequencies in the order of 2%, as shown in Tables 3 and 4.

Mode	**FEM**	**Thick-wall**	Error (%)	**Thin-wall**	Error (%)
1st	15.33	15.36	0.2	15.76	2.8
2nd	29.86	29.71	-0.5	30.91	3.5
3rd	44.98	44.87	-0.25	46.06	2.4
4th	59.31	60.02	1.2	61.62	3.9
5th	73.64	75.18	2.1	77.57	5.35
6th	87.76	89.93	2.5	92.32	5.2

Table 3: Case 3: resonant frequencies obtained by different approaches.



(a) Case 1: $\omega_1 = 155\ Hz$

(b) Case 2: $\omega_1 = 146\ Hz$

(c) Case 3: $\omega_1 = 15.3\ Hz$

(d) Case 4: $\omega_1 = 20.1\ Hz$

Figure 3: Frequency response of the pipe due to axial vibration. (—) FEM; (—) thick-wall assumption; (—) thin-wall assumption.

Mode	**FEM**	**Thick-wall**	Error (%)	**Thin-wall**	Error (%)
1st	20.1	19.74	-1.8	22.54	12.1
2nd	41.6	41.28	-0.75	45.27	8.8
3rd	63.29	62.81	-0.75	68.8	8.7
4th	82.79	83.15	0.45	91.13	10
5th	103.9	105.5	1.55	114.3	10
6th	125.4	128.2	2.25	137.8	9.9

Table 4: Case 4: resonant frequencies obtained by different approaches.

Conclusions

The present paper describes a numerical study on the acoustic behaviour of pipes conveying fluid, with focus on the comparison between thin-wall and thick-wall assumptions. First, pressure and structural wave speeds are obtained and compared using the different approaches for several thickness-to-radius ratio and Young's modulus of elasticity. Then, a FRF is used to compare the deviation on the pressure responses for a metal pipe (high density and Young's modulus of elasticity) and a hose (low density and Young's modulus of elasticity). Results shows that, as expected, the difference between thin/thick-wall assumptions increases with the thickness-to-radius ratio. Furthermore, the compliance introduced by the use of hoses with low Young's modulus enhances the difference between thin/thick-wall assumptions. For metal pipes, both assumptions can satisfactorily predict the behaviour of the system, even for relatively thick walls. However,

when the elastic modulus of the pipe is in the same order of magnitude as the bulk modulus of water or lower, the hypothesis made for thin-walls no longer hold to analyze thick pipes. For this cases, stresses variation within the cross section of the pipe due to wall thickness cannot be neglected in the governing equations.

Acknowledgements

This work is supported by the High-tech Systems Center (HTSC) at Eindhoven University of Technology.

References

[1] A. S. Tijsseling, *Exact solution of linear hyperbolic four-equation system in axial liquid-pipe vibration*, Journal of Fluids and Structures, Vol. 18, Elsevier (2003), pp. 179-196.

[2] A. S. Tijsseling, *Water hammer with fluid-structure interaction in thick-walled pipes*, Computers and Structures, Vol. 85, Elsevier (2007), pp. 844-851.

[3] L. Zhang, A. S. Tijsseling, A. E. Vardy, *FSI analysis of liquid-filled pipes*, Journal of Sound and Vibration, Vol. 224, No. 1, Academic Press (1999), pp. 69-99.

[4] Q. S. Li, K. Yang, L. Zhang, N. Zhang, *Frequency domain analysis of fluid structure interaction in liquid-filled pipe systems by transfer matrix method*, International Journal of Mechanical Sciences, Vol. 44, Elsevier (2002), pp. 2067-2087.

Predicting the sound insulation of finite double-leaf walls with a flexible frame

J. C.E. Van den Wyngaert[1], **M. Schevenels**[2] **and E. P.B. Reynders**[1]
[1] KU Leuven Faculty of engineering science,
Department of Civil Engineering, Kasteelpark Arenberg 40, B-3001 Leuven, Belgium.
e-mail: **jan.vandenwyngaert@kuleuven.be**

[2] KU Leuven Faculty of engineering science,
Department of Architecture, Kasteelpark Arenberg 1, B-3001 Leuven, Belgium.

Abstract
Double-leaf wall systems such as plasterboard walls can potentially achieve a high sound insulation with a relatively low weight. The accurate sound transmission analysis of this type of wall is challenging since the leafs are usually coupled to a common frame for reasons of cost and lateral stability, and since the finite dimensions play a role at lower frequencies. In this work, a sound transmission prediction model that achieves a high prediction accuracy at a low computational cost is developed. The wall components that display low geometrical complexity are modeled in a analytic way while the metal studs are modeled in full detail with finite elements. The wall is coupled to the diffuse sound fields in the sending and receiving rooms by employing a hybrid deterministic-statistical energy analysis framework. The sound insulation is predicted for a range of different double-leaf plasterboard walls. The obtained transmission losses are validated against the results of an extensive set of experimental tests.

1 Introduction

Double leaf wall systems are often used because of their light weight and potentially high sound insulation the construction, aerospace, railway, and other industries. The leafs are usually coupled to a common frame for reasons of cost and lateral stability, even when the walls are not load bearing, Double-leaf plasterboard walls with a common metal frame are very often employed in the construction industry for partitioning large open spaces into smaller rooms. However, the common frame introduces a structural transmission path between both leafs in addition to the airborne path through the cavity. The airborne sound insulation of a decoupled double wall depends mainly on the individual plate thicknesses, the number of plates, the combination of different thicknesses and plate materials, the cavity depth, and the wall dimensions. The stud geometry, the number of studs and the number of screws per stud are additional parameters influencing the sound insulation when the leafs are coupled. The mass-spring-mass resonance is both defined by the total weight of the leafs and the cavity depth. The coincidence frequency, at which the wavelength of the incident wave and the bending wavelength of a leaf are equal, depends on the material parameters of the leaf and its thickness. All these different phenomena and input parameters make it hard to accurately predict the airborne sound insulation using a simplified model.

Existing models for the prediction of the airborne sound insulation of double-leaf walls can be subdivided into analytical and numerical models. Analytical models are often used to gain insight into the main physical phenomena. A low computational cost is achieved by assuming diffuse conditions in the transmission rooms and by using simplified models for the vibrational behavior of the leafs and the cavity. The prediction of

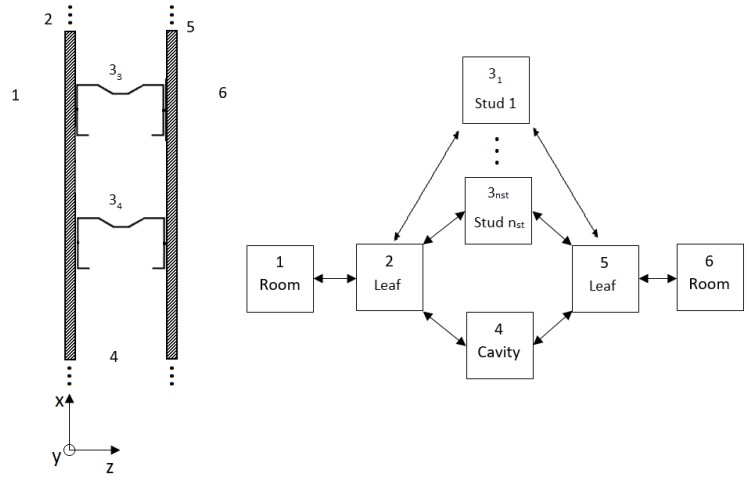


Figure 1: Components of a double wall with a flexible stud frame.

the sound insulation is often inaccurate due to this simplified representation. Numerical models, e.g finite element models, give a more accurate representation of the vibratory behavior of both the wall and the transmission rooms. This makes it possible to accurately predict the single number rating at a high computational cost at high frequencies.

A prediction model for the airborne sound insulation of double walls is developed with both a high prediction accuracy and a low computational cost. Due to this low computational cost and high prediction accuracy, the model can be used as a design tool for the sound insulation of double walls.

The present paper is an abbreviated version of a more detailed analysis to be found in reference [1].

2 Prediction model

The wall is modelled deterministically while the sound fields in the sending and receiving rooms are modelled as diffuse. The components of the model are represented in Fig. 1. The metal studs, shown as part 3_1 till $3_{\mathrm{n_{st}}}$ in Fig. 1, are modelled in full detail with finite elements due to their highly deformable cross-section and complex geometrical shape. To reduce the computational cost, the wall leafs and the cavity, represented as components 2, 4 and 5 in Fig. 1, are modelled in an analytical way. The hybrid DET-SEA modelling framework is used to rigorously couple the diffuse sound fields in the transmission rooms, represented as components 1 and 6 in Fig. 1, to the deterministic wall model by employing the diffuse field reciprocity relationship [2]. In what follows, the deterministic model of the wall system is elaborated first. Subsequently, the interaction between the wall and the sound fields in the adjoining rooms is described.

2.1 Deterministic model

The double wall consists of two thin leafs coupled to a common stud frame and separated by an air cavity. In the first instance, the leafs, the cavity and the individual studs are decoupled from each other. The out-of-plane vibration field of the two wall leafs, $\mathrm{u_{l1}}$ and $\mathrm{u_{l2}}$, the pressure field within cavity, $\mathrm{p_{cav}}$, and the vibration field of the stud number l, $\mathrm{u_{st},}_l$, at spatial location $\mathbf{x}$ and frequency ω, are approximated using a finite set of basis functions ϕ, that satisfy the boundary conditions. The choice of the basis functions ϕ of the decoupled components will be discussed in detail below. Subsequently, the interaction between the components will be achieved by introducing coupling loads between the cavity and the leafs and by constraining the leaf and stud displacements to be equal at the connection locations. This will result in a system of equations in which the generalized coordinates of the wall components are coupled:

$$\begin{bmatrix} \mathbf{D}_{\mathrm{l1}} & \mathbf{0} & \mathbf{L}_{\mathrm{f1}} & \mathbf{0} & \dots & \mathbf{0} & \mathbf{C}_{\mathrm{l1}}^T \\ \mathbf{0} & \mathbf{D}_{\mathrm{l2}} & \mathbf{L}_{\mathrm{f2}} & \mathbf{0} & \dots & \mathbf{0} & \mathbf{C}_{\mathrm{l2}}^T \\ \mathbf{L}_{\mathrm{s1}} & \mathbf{L}_{\mathrm{s2}} & \mathbf{D}_{\mathrm{cav}} & \mathbf{0} & \dots & \mathbf{0} & \mathbf{0} \\ \mathbf{0} & \mathbf{0} & \mathbf{0} & \mathbf{D}_{\mathrm{st},1} & \dots & \mathbf{0} & \mathbf{C}_1^T \\ \vdots & \vdots & \vdots & \vdots & \ddots & \vdots & \vdots \\ \mathbf{0} & \mathbf{0} & \mathbf{0} & \mathbf{0} & \dots & \mathbf{D}_{\mathrm{st},n_{\mathrm{st}}} & \mathbf{C}_{\mathrm{n_{st}}}^T \\ \mathbf{C}_{\mathrm{l1}} & \mathbf{C}_{\mathrm{l2}} & \mathbf{0} & \mathbf{C}_1 & \dots & \mathbf{C}_{\mathrm{n_{st}}} & \mathbf{0} \end{bmatrix} \begin{bmatrix} \mathbf{q}_{\mathrm{l1}} \\ \mathbf{q}_{\mathrm{l2}} \\ \mathbf{q}_{\mathrm{cav}} \\ \mathbf{q}_{\mathrm{st},1} \\ \vdots \\ \mathbf{q}_{\mathrm{st},n_{\mathrm{st}}} \\ \boldsymbol{\lambda} \end{bmatrix} = \begin{bmatrix} \mathbf{f}_{\mathrm{l1}} \\ \mathbf{f}_{\mathrm{l2}} \\ \mathbf{0} \\ \mathbf{0} \\ \vdots \\ \mathbf{0} \\ \mathbf{0} \end{bmatrix} \tag{1}$$

or shortly,

$$\mathbf{D}_{\mathrm{d}}\mathbf{q} = \mathbf{f} \tag{2}$$

In Eq. (1), $\mathbf{D}_{\mathrm{l1}}$, $\mathbf{D}_{\mathrm{l2}}$, $\mathbf{D}_{\mathrm{cav}}$ and $\mathbf{D}_{\mathrm{st},l}$ represent the dynamic stiffness matrices the first wall leaf, the second wall leaf, the cavity and stud number l, respectively; $\mathbf{L}_{\mathrm{f1}}$ and $\mathbf{L}_{\mathrm{f2}}$ account for the fluid loading (acoustic pressure) of the cavity onto the first and the second wall leaf, respectively; $\mathbf{L}_{\mathrm{s1}}$ and $\mathbf{L}_{\mathrm{s2}}$ account for the structural vibration loading by the first and second wall leaf, respectively, onto the cavity fluid; the $\mathbf{C}$ matrices are matrices that are employed for constraining the stud and wall displacements at their connection locations, and $\boldsymbol{\lambda}$ collects the corresponding Lagrange multipliers; and finally $\mathbf{f}_{\mathrm{l1}}$ and $\mathbf{f}_{\mathrm{l2}}$ represent the external fluid loading, by the acoustic pressure in the adjoining rooms, onto respectively wall leafs 1 and 2. All matrices introduced above will be discussed in detail in the following sections.

2.1.1 Analytical model of the wall leafs

The dynamic behavior of the leafs is modelled as a simply supported plate using Kirchoff-Love thin plate theory as in [3]. When decoupled from all other wall components, the vibrational behavior of the leaf can be modelled analytically. This is presented here for the first wall leaf; the same can be followed for the second leaf. The mass-normalized mode shapes of the decoupled, thin, rectangular, simply supported wall leaf, with the corresponding angular natural frequency $\omega_{l1,k}$, are used to approximate the vibrational behavior of the leaf:

$$\phi_{\mathrm{l1},k}(\mathbf{x}) = \frac{2}{\sqrt{m_{\mathrm{l1}}}} \sin\left(\frac{q_k \pi x}{L_{\mathrm{x}}}\right) \sin\left(\frac{r_k \pi y}{L_{\mathrm{y}}}\right) \qquad \text{and} \qquad \omega_{\mathrm{l1},k} = \sqrt{\frac{D_{\mathrm{l1}}}{m''_{\mathrm{l1}}}} \left(\left(\frac{q_k \pi}{L_{\mathrm{x}}}\right)^2 + \left(\frac{r_k \pi}{L_{\mathrm{y}}}\right)^2 \right), \tag{3}$$

where m_{l1} denotes the total mass of the leaf, L_{x} and L_{y} denote its planar dimensions in the x and y coordinate directions, respectively, and $q_k \in \mathbb{N}_0$ and $r_k \in \mathbb{N}_0$ denote the number of half wavelengths in those directions, specific for mode number k; D_{l1} denotes the bending stiffness of the leaf, and m''_{l1} its mass per unit surface area. The modes are numbered according to increasing natural frequency.

The leaf may consist of a single thin plate, or of multiple plates on top of each other. In the latter case, it will be assumed that there are no shear connections between the plate, such that perfect slip conditions exist at the plate-plate interfaces. In this way the bending stiffness of the leaf is slightly underestimated since in reality the plates are jointly screwed into the flexible studs at discrete points. However, Davidsson and Brunskog [3] have shown that the perfect slip assumption is fairly accurate, so the bending stiffness of the entire leaf can be obtained from

$$D_{\mathrm{l1}} = \sum_{s=1}^{n_{\mathrm{pl1}}} D_{\mathrm{pl},s} \tag{4}$$

where n_{pl1} denotes the total number of plates from which the considered leaf is composed, and $D_{\mathrm{pl},s}$ denotes the dynamic bending stiffness of plate number s:

$$D_{\mathrm{pl},s} = \frac{E_s {\mathrm{t_s}}^3}{12(1-\nu_s^2)}, \tag{5}$$

In this equation, E_s denotes the Young's modulus of plate s, ν_s its Poisson's ratio, and t_s its thickness.

Since the basis functions have been chosen to be the mass-normalized mode shapes of the leaf, the corresponding generalized coordinates are the modal amplitudes of the leaf. Its equation of motion therefore reads

$$\mathbf{D}_{\mathrm{l1}}\mathbf{q}_{\mathrm{l1}} = \tilde{\mathbf{f}}_{\mathrm{l1}} \tag{6}$$

where $\mathbf{D}_{\mathrm{l1}}$ is a diagonal matrix with entries

$$D_{\mathrm{l1},kk} = -\omega^2 + \omega_{\mathrm{l1},k}^2(1 + \mathrm{i}\eta_{\mathrm{l1},k}), \tag{7}$$

$\mathrm{i} := \sqrt{-1}$ is the imaginary unit and $\eta_{\mathrm{l1},k}$ denotes the damping loss factor of mode k.

2.1.2 Analytical model of the cavity

The conventional linear acoustic theory is adopted for the sound field within the cavity. Since there are no sound sources within the cavity itself, the acoustic pressure within the cavity $\mathrm{p}_{\mathrm{cav}}(\mathbf{x}, \omega)$ satisfies the homogeneous Helmholtz equation. The interaction between the sound field in the cavity and the studs is neglected, i.e., the studs are assumed to be acoustically transparent, such that the cavity has a rectangular cuboid shape. Since the particle velocity at the boundaries is small, hard-walled boundary conditions are assumed. The interaction between the wall leafs and the cavity is not modeled by imposing continuity of the velocity fields, but by taking the displacement fields of the wall leafs as external loads onto the cavity pressure field, and vice versa. These interactions will be detailed further on.

The normalized mode shapes of the decoupled, hard-walled, rectangular cuboid cavity, with corresponding angular natural frequencies $\omega_{\mathrm{cav},k}$, are used to approximate the behavior of the cavity [4]:

$$\phi_{\mathrm{cav},k}(\mathbf{x}) = a_k \cos\left(\frac{m_k\pi x}{L_{\mathrm{x}}}\right)\cos\left(\frac{n_k\pi y}{L_{\mathrm{y}}}\right)\cos\left(\frac{p_k\pi z}{L_{\mathrm{z}}}\right) \quad \text{and} \quad \omega_{\mathrm{cav},k} = \mathrm{c}\sqrt{\left(\frac{m_k\pi}{L_{\mathrm{x}}}\right)^2 + \left(\frac{n_k\pi}{L_{\mathrm{y}}}\right)^2 + \left(\frac{p_k\pi}{L_{\mathrm{z}}}\right)^2}, \tag{8}$$

where L_{z} denotes the cavity depth, $m_k \in \mathbb{N}$, $n_k \in \mathbb{N}$ and $p_k \in \mathbb{N}$ denote the number of half wavelengths in the x, y and z coordinate directions. The modes are numbered according to increasing natural frequency. The normalization constant satisfies

$$a_k = \frac{\mathrm{c}\gamma(m_k)\gamma(n_k)\gamma(p_k)}{\sqrt{L_{\mathrm{x}}L_{\mathrm{y}}L_{\mathrm{z}}}} \quad \text{where} \qquad \gamma(s) = \begin{cases} \sqrt{2} & \text{if } s = 0 \\ 1 & \text{if } s \neq 0 \end{cases} \tag{9}$$

and c denotes the sound speed.

Since the basis functions have been chosen to be the normalized mode shapes of the cavity, the corresponding generalized coordinates are the modal amplitudes of the cavity. Its equation of motion therefore reads

$$\mathbf{D}_{\mathrm{cav}}\mathbf{q}_{\mathrm{cav}} = \tilde{\mathbf{f}}_{\mathrm{cav}} \tag{10}$$

where $\mathbf{D}_{\mathrm{cav}}$ is a diagonal matrix with entries

$$D_{\mathrm{cav},kk} = -\omega^2 + \omega_{\mathrm{cav},k}^2(1 + \mathrm{i}\eta_{\mathrm{cav},k}), \tag{11}$$

and $\eta_{\mathrm{cav},k}$ denotes the damping loss factor of mode k. When the cavity is empty, the damping inside the cavity is prescribed in terms of a reverberation time T_{cav}, the modal loss factors can be determined from [5, Ch 2.4.1]

$$\eta_{\mathrm{cav},k} = \frac{4.4\pi}{\omega_{\mathrm{cav},k}T_{\mathrm{cav}}}. \tag{12}$$

To increase thermal and acoustic performance, soft porous materials such as mineral wool are often placed inside the cavity. Since the deformation of the solid skeleton of the porous material is negligible, the presented cavity fluid model can still be employed yet with modified, complex material properties. Several of

these so-called equivalent fluid models have been proposed in the literature on an empirical basis. In the present work, the Delany-Bazley-Miki equivalent fluid model (DBM) is used. The DBM-model depends only on the flow resistivity σ of the porous material and the frequency. When reformulated in terms of a complex sound speed c_c and complex fluid density ρ_c, this model reads

$$c_\mathrm{c} = \frac{c}{1 + 7.81a - \mathrm{i}11.41a} \qquad \text{and} \qquad \rho_\mathrm{c} = \frac{c\rho_\mathrm{a}}{c_\mathrm{c}} \left[1 + 5.50b - \mathrm{i}8.43b\right], \tag{13}$$

$$a = \left(10^3 \frac{f'}{\sigma'}\right)^{-0.618} \qquad \text{and} \qquad b = \left(10^3 \frac{f'}{\sigma'}\right)^{-0.632}, \tag{14}$$

where $f' := \frac{f}{1\,\mathrm{Hz}}$ denotes a dimensionless frequency, $\sigma' := \frac{\sigma}{1\,\mathrm{Ns/m^4}}$ a dimensionless flow resistivity and ρ_a the air density. Note that, when cavity damping is modelled with complex material properties, $\eta_{\mathrm{cav},k}$ is taken to be zero in (11).

2.1.3 Fluid-structure interaction at the cavity boundaries

In the following the interaction between the velocity of the decoupled wall leafs and the pressure inside the hard-walled cavity is considered. Let us now consider the part of the modal load onto the first wall leaf, $\tilde{\mathbf{f}}_{\mathrm{l}1}$, which is due to the cavity pressure $p_\mathrm{cav}(\mathbf{x}, \omega)$. Note that the same line can be followed to obtain the fluid-structure coupling matrices between the cavity and wall leaf 2. When a particular mode k of the leaf is considered, this load equals

$$f_{\mathrm{l}1,k,\mathrm{cav}}(\omega) = -\int_{\Gamma_{\mathrm{l}1}} \phi_{\mathrm{l}1,k}(\mathbf{x}) p_\mathrm{cav}(\mathbf{x}, \omega) d\mathbf{x} \tag{15}$$

where $\Gamma_{\mathrm{l}1}$ denotes the interface surface area between the leaf and the cavity. The minus sign results from the fact that for a positive cavity pressure, the force exerted onto the first wall leaf points in the negative z direction (see Fig. 1). With the chosen set of basis functions for the cavity pressure, the above expression can be elaborated as

$$f_{\mathrm{l}1,k,\mathrm{cav}}(\omega) \approx -\sum_{l=1}^{n_\mathrm{cav}} L_{\mathrm{f}1,kl} q_{\mathrm{cav},l}(\omega) \quad \text{where} \quad L_{\mathrm{f}1,kl} := \int_{\Gamma_{\mathrm{l}1}} \phi_{\mathrm{l}1,k}(\mathbf{x}) \phi_{\mathrm{cav},l}(\mathbf{x}) d\mathbf{x} \tag{16}$$

Substitution of (3) and (8) into (16) and evaluating the integral yields

$$L_{\mathrm{f}1,kl} = \frac{-2a_l \mathrm{L_x L_y}}{\pi^2 \sqrt{m_{\mathrm{l}1}}} \cos\left(\frac{p\pi z}{\mathrm{L_z}}\right) \mathrm{b}\left(q_k, m_l\right) \mathrm{b}\left(r_k, n_l\right) \tag{17}$$

where

$$\mathrm{b}\left(\alpha, \beta\right) := \begin{cases} \frac{\beta \cos(\alpha\pi)\cos(\beta\pi) - \beta + \alpha \sin(\alpha\pi)\sin(\beta\pi)}{\alpha^2 - \beta^2} & \text{for } k \neq l \\ \frac{\sin(\alpha\pi)^2}{2\alpha} & \text{for } k = l \end{cases} \tag{18}$$

Subsequently, let us consider the part of the modal load onto the cavity, $\tilde{\mathbf{f}}_\mathrm{cav}$, which is due to displacement of the first wall leaf, $u_{\mathrm{l}1}(\mathbf{x}, \omega)$. When a particular mode k of the cavity is considered and with the chosen set of basis functions for the leaf displacement, this load equals

$$f_{\mathrm{cav},k,\mathrm{l}1}(\omega) \approx -\sum_{l=1}^{n_1} L_{\mathrm{s}1,kl} q_{\mathrm{l}1,l}(\omega) \quad \text{where} \quad L_{\mathrm{s}1,kl} := \rho_\mathrm{a} \omega^2 L_{\mathrm{f}1,lk} \tag{19}$$

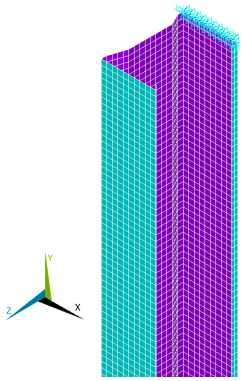


Figure 2: Finite element mesh of a single decoupled metal C-stud for a cavity depth of 75 mm. Structural shell elements are used. As indicated on the top right part of the figure, the boundary displacements are restrained at one of the flange edges and at the opposite flange at the bottom.

2.1.4 Finite element model of the studs

The dynamic behavior of the studs has a large influence on the overall sound insulation when both wall leafs are connected to a common frame. Two types of stud are commonly employed in the construction industry: wooden studs with a solid rectangular cross-section, and metal studs with a thin-walled open cross section, such as metal C-studs. The dynamic mechanical behavior of both types of stud is fundamentally different. The cross section of rectangular studs is relatively rigid, and therefore they can be taken to satisfy Euler-Bernouilli or Timoshenko beam theory. The studs that are usually employed in the construction industry are very flexible; it typically concerns metal C-studs with a wall thickness of $0.6\,\mathrm{mm}$ and a web height of up to $100\,\mathrm{mm}$ and more. It is this type of stud that is considered here, and it has been confirmed in the present study that such studs show, next to a beam-like behavior, also substantial cross-sectional deformation, even at low frequencies.

The studs can be adequately modelled numerically with structural shell elements as they are thin-walled profiles. In this model, the Shell181 element from the Ansys finite element software is used; it is a four-node element with six degrees of freedom - three displacements and three rotations - at each node. An element edge length of $5\,\mathrm{mm}$ is employed (Fig. 2), as the wavelength of deformation at high frequencies of the flexible studs is small. 'Hinged' boundary conditions are assumed at the ends of each stud; they are implemented by restraining all nodal displacements (but not the rotations) at one flange at the bottom and at the opposite flange at the top (Fig. 2). This is a simplification, as the metal studs of a double-leaf wall are usually placed in flexible rails that are mounted on the floor and the ceiling. These rails are not considered in the present model.

This finite element model represents a single stud that is decoupled from the leafs and from the cavity, since any interaction between the cavity and the leafs is neglected. The interaction with the wall leafs will be detailed further on. The model is employed for computing the natural frequencies and mass-normalized displacement mode shapes of the decoupled stud. These numerically computed mode shapes are taken to be the basis functions to approximate their vibrational behavior. The corresponding generalized coordinates are then the modal amplitudes of the stud. The equation of motion of a particular stud l therefore reads

$$\mathbf{D}_{\mathrm{st},l}\mathbf{q}_{\mathrm{st},l} = \tilde{\mathbf{f}}_{\mathrm{st},l} \qquad \text{and} \qquad D_{\mathrm{st},l,kk} = -\omega^2 + \omega^2_{\mathrm{st},l,k}(1 + i\eta_{\mathrm{st},l,k}) \tag{20}$$

where $\mathbf{D}_{\mathrm{st},l}$ is a diagonal matrix with entries $D_{\mathrm{st},l,kk}$. $\omega_{\mathrm{st},l,k}$ is the numerically computed angular natural frequency of mode k of stud l, and $\eta_{\mathrm{st},l,k}$ the corresponding structural damping loss factor. When the loading onto the stud is coupled within the modal load vector $\tilde{\mathbf{f}}_{\mathrm{st},l}$, (20) is fully consistent with block row $3+l$ of the equation of motion of the entire wall system, Eq. (1). Note that, when all studs are identical, the numerical modal analysis needs to be performed only once, i.e., for a single decoupled stud.

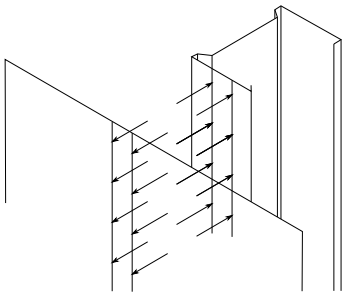


Figure 3: Coupling of the out-of-plane displacements of a metal C-stud and the leaf at four pairs of discrete screw positions. The screws constituting a pair have the same height and they have a horizontal distance of 1 cm.

2.1.5 Stud-leaf interaction

A stud is loaded only through the connections with the wall leafs, i.e there is no interaction between the studs and the cavity. For the walls that are considered in the present work, the plates constituting the leafs are screwed directly into the studs at a few points over the height of the stud. Typically, the vertical joints between the plates (not modelled here) coincide with the center of the flange of a stud. Since both plates are screwed into the same common stud, the screws connecting stud and leaf occur in pairs of two. The screws constituting a pair have the same height and a relatively small horizontal distance between them; a distance of $1\,\mathrm{cm}$ is taken in the present paper. The stud-leaf connections are modelled by rigidly coupling the out of plane displacements at the screw locations (Fig. 3). This implies that in the model, the finite stiffness of the screws is neglected, and the studs and leafs can deform independently everywhere except at the screw locations. This connection model was found to result in a good prediction accuracy as discussed further. Alternative connection models, where the stud and the leaf are connected along the entire centerline of the stud flange, or even at the entire stud-leaf interface area, were also considered but they result in a wall system that is too stiff.

The interaction between the stud and the wall leaf can be modelled by means of constraint equations on the displacements rather than through explicitly accounting for the interface forces because rigid point couplings are considered. Let us take the interaction between leaf 1 and stud l. Note that the same line can be followed for all other studs and their interaction with the second wall leaf. This results in the following set of constraint equations:

$$\forall s : u_{\mathrm{st},l}(\mathbf{x}_{l1s}) = u_{\mathrm{l1}}(\mathbf{x}_{l1s}) \tag{21}$$

where $\mathbf{x}_{l1s}$ denotes the location at which screw number s connects stud number l to the first wall leaf. Using the basis functions to describe the vibrational behavior of the stud and the wall leaf, the constraints can be expressed in terms of the generalized coordinates:

$$\forall s : \boldsymbol{\phi}_{\mathrm{st},l}(\mathbf{x}_{l1s})\mathbf{q}_{\mathrm{st},l} = \boldsymbol{\phi}_{\mathrm{l1}}(\mathbf{x}_{l1s})\mathbf{q}_{\mathrm{l1}} \tag{22}$$

or in matrix form:

$$\tilde{\mathbf{C}}_l\mathbf{q}_{\mathrm{st},l} + \tilde{\mathbf{C}}_{\mathrm{l1},l}\mathbf{q}_{\mathrm{l1}} = \mathbf{0} \tag{23}$$

where $\boldsymbol{\phi}_{\mathrm{st},l}(\mathbf{x}_{l1s})$ equals row number s of $\tilde{\mathbf{C}}_l$, and $-\boldsymbol{\phi}_{\mathrm{l1}}(\mathbf{x}_{l1s})$ equals row number s of $\tilde{\mathbf{C}}_{\mathrm{l1},l}$.

Consider for a moment the equations of motion of leaf 1 (6) and of stud l (20) without any external loading:

$$\begin{bmatrix} \mathbf{D}_{\mathrm{l1}} & \mathbf{0} \\ \mathbf{0} & \mathbf{D}_{\mathrm{st},l} \end{bmatrix} \begin{bmatrix} \mathbf{q}_{\mathrm{l1}} \\ \mathbf{q}_{\mathrm{st},l} \end{bmatrix} = \mathbf{0} \tag{24}$$

The constraints of Eq. (23) can be incorporated into the equations of motion of Eq. (24) with the technique of Lagrange multipliers [6, Sec. 13.2]. Suppose for a moment that the loading by the first wall leaf is the

only loading acting on stud l, and vice versa. This results in

$$\begin{bmatrix} \mathbf{D}_{\mathrm{l1}} & \mathbf{0} & \tilde{\mathbf{C}}_{\mathrm{l1},l}^{\mathrm{T}} \\ \mathbf{0} & \mathbf{D}_{\mathrm{st},l} & \tilde{\mathbf{C}}_{l}^{\mathrm{T}} \\ \tilde{\mathbf{C}}_{\mathrm{l1},l} & \tilde{\mathbf{C}}_{l} & \mathbf{0} \end{bmatrix} \begin{bmatrix} \mathbf{q}_{\mathrm{l1}} \\ \mathbf{q}_{\mathrm{st},l} \\ \boldsymbol{\lambda}_{\mathrm{l1},l} \end{bmatrix} = \mathbf{0}, \tag{25}$$

where the Lagrange multipliers have been collected into the vector $\boldsymbol{\lambda}_{\mathrm{l1},l}$.

More generally, the system of equations (23) can be extended to include all stud-leaf interactions:

$$\mathbf{C}_{\mathrm{l1}}\mathbf{q}_{\mathrm{l1}} + \mathbf{C}_{\mathrm{l1}}\mathbf{q}_{\mathrm{l2}} + \sum_{l=1}^{\mathrm{n_{st}}} \mathbf{C}_{l}\mathbf{q}_{\mathrm{st},l} = \mathbf{0}. \tag{26}$$

Application of the Lagrange multiplier technique to the entire wall system then leads to the overall system of equations, (1).

2.1.6 Reduction of the dynamic stiffness matrix

Since the only external loading by the sound pressure in the adjoining rooms is applied at the leafs, all interior degrees of freedom can be eliminated from (1). The resulting reduced system of equations is denoted as

$$\mathbf{D}'_{\mathrm{d}}\mathbf{q}' = \mathbf{f}' \tag{27}$$

where

$$\mathbf{D}'_{\mathrm{d}} := \begin{bmatrix} \mathbf{D}_{\mathrm{l1}} & \mathbf{0} \\ \mathbf{0} & \mathbf{D}_{\mathrm{l2}} \end{bmatrix} + \mathbf{D}'_{\mathrm{fsi}} + \mathbf{D}'_{\mathrm{st}} \quad \text{and} \quad \mathbf{q}' := \begin{bmatrix} \mathbf{q}_{\mathrm{l1}} \\ \mathbf{q}_{\mathrm{l2}} \end{bmatrix} \tag{28}$$

In this equation, $\mathbf{D}'_{\mathrm{fsi}}$ is a fluid-structure interaction matrix resulting from the elimination of the cavity pressure degrees of freedom from (1),

$$\mathbf{D}'_{\mathrm{fsi}} = \omega^2 \begin{bmatrix} \mathbf{L}_{\mathrm{f},1} \\ \mathbf{L}_{\mathrm{f},2} \end{bmatrix} \mathbf{D}_{\mathrm{cav}}^{-1} \begin{bmatrix} \mathbf{L}_{\mathrm{s},1} & \mathbf{L}_{\mathrm{s},2} \end{bmatrix}, \tag{29}$$

and $\mathbf{D}'_{\mathrm{st}}$ is a matrix resulting from the elimination of the stud displacement degrees of freedom and the Lagrange multipliers from (1),

$$\mathbf{D}'_{\mathrm{st,cp}} = \begin{bmatrix} \mathbf{C}_{\mathrm{l1}}^{T} \\ \mathbf{C}_{\mathrm{l2}}^{T} \end{bmatrix} \left(\sum_{l=1}^{\mathrm{n_{st}}} \mathbf{C}_{l}\mathbf{D}_{\mathrm{st},l}^{-1}\mathbf{C}_{l}^{T} \right) \begin{bmatrix} \mathbf{C}_{\mathrm{l1}} & \mathbf{C}_{\mathrm{l2}} \end{bmatrix} \tag{30}$$

2.2 Transmission suite model

In the previous section, the deterministic model of the double-leaf wall was described in full detail. In the present section, this wall model is coupled to models for the sound fields in the adjoining rooms.

The hybrid model contains two diffuse (SEA) subsystems - the sending and receiving rooms - and in the context of a sound transmission analysis, the quantity of interest is the so-called coupling loss factor between both rooms. If in a stationary situation, the sound power flow from room 1 to room 2 (so through the wall) is denoted as P_{12}, the total acoustic energy of room k is denoted as E_k and its modal density (i.e., the expected number of modes per unit radial bandwidth) as n_k, then the coupling loss factor η_{12} is defined as [7]

$$\eta_{12} := \frac{\omega n_1}{P_{12}} \left(\frac{E_1}{n_1} - \frac{E_2}{n_2} \right) \tag{31}$$

Although the coupling loss factor is a random quantity (because the sound fields in the rooms are random, diffuse fields), only its mean value will be of interest in the present analysis as the intention is to predict the mean sound transmission loss of the wall. The coupling loss factor relates directly to the sound transmission coefficient, τ, which is defined as the ratio between the power flow P_{12} from room 1 to room 2 through the wall, and the incident sound power on the wall in room 1. The relationship reads [8]

$$\tau = \frac{4V_1\omega}{L_\mathrm{x}L_\mathrm{y}c}\eta_{12} \tag{32}$$

where V_1 denotes the volume of the sending room. The sound transmission loss (or airborne sound insulation) of the wall then immediately follows from

$$R := 10\log\frac{1}{\tau} = 10\log\frac{L_\mathrm{x}L_\mathrm{y}c}{4V_1\omega\eta_{12}} \tag{33}$$

Within the hybrid DET-SEA framework, the coupling loss factor η_{12} can be rigorously evaluated by considering the interaction between the wall and the direct field response of the rooms at their interfaces [9, 10, 11]. The direct field response of a room is the sound field that would occur if the room would be of infinite extent, in other words, if the room would behave as an acoustic half-space as seen from the room-wall interface when that interface is embedded in an infinite planar baffle. The related acoustic dynamic stiffness matrix is then termed the direct field dynamic stiffness matrix of the room. For room 1 for example, this matrix describes the relationship between the displacements and forces at the interface with the first wall leaf:

$$\mathbf{D}_{\mathrm{dir1}}\mathbf{q}_{\mathrm{l1}} = \tilde{\mathbf{f}}_{\mathrm{dir1}} \tag{34}$$

The components of $\tilde{\mathbf{f}}_{\mathrm{dir1}}$ denote the forces acting on the (generalized) degrees of freedom of the first wall leaf $\mathbf{q}_{\mathrm{l1}}$ due to the pressure field in the acoustic half-space The direct field dynamic stiffness matrix $\mathbf{D}_{\mathrm{dir1}}$ can be numerically computed via evaluation of the Rayleigh integral, e.g. using a wavelet discretization of the baffled interface; details of this approach are provided by Langley [12].

Once the direct field acoustic dynamic stiffness matrices of both rooms have been computed, the coupling loss factor is obtained from [9]

$$\eta_{12} = \frac{2}{\pi\omega n_1}\sum_{rs}\mathrm{Im}\left(\mathbf{D}'_{\mathrm{dir2},rs}\right)\left(\mathbf{D}_{\mathrm{tot}}^{-1}\mathrm{Im}\left(\mathbf{D}'_{\mathrm{dir1}}\right)\mathbf{D}_{\mathrm{tot}}^{-\mathrm{H}}\right)_{rs} \tag{35}$$

where

$$\mathbf{D}_{\mathrm{tot}} := \mathbf{D}'_{\mathrm{d}} + \mathbf{D}'_{\mathrm{dir1}} + \mathbf{D}'_{\mathrm{dir2}}, \tag{36}$$

$\mathbf{D}'_{\mathrm{d}}$ denotes the reduced dynamic stiffness matrix of the wall as defined in (28), and $\mathbf{D}'_{\mathrm{dir1}}$ and $\mathbf{D}'_{\mathrm{dir2}}$ are the direct field acoustic dynamic stiffness matrices expressed in terms of the reduced wall coordinate vector $\mathbf{q}'$.

The computational efficiency can be further increased by exploiting the block structure of the direct field acoustic dynamic stiffness matrices:

$$\mathbf{D}'_{\mathrm{dir1}} = \begin{bmatrix}\mathbf{D}_{\mathrm{dir1}} & \mathbf{0}\\ \mathbf{0} & \mathbf{0}\end{bmatrix} \quad \text{and} \quad \mathbf{D}'_{\mathrm{dir2}} = \begin{bmatrix}\mathbf{0} & \mathbf{0}\\ \mathbf{0} & \mathbf{D}_{\mathrm{dir2}}\end{bmatrix}. \tag{37}$$

Equation (35) can be elaborated as

$$\eta_{12} = \frac{2}{\pi\omega n_1} \sum_{rs} \mathrm{Im}\left(\mathbf{D}_{\mathrm{dir2},rs}\right) \left(\left(\mathbf{D}_{\mathrm{tot}}^{-1}\right)_{2,1} \mathrm{Im}\left(\mathbf{D}_{\mathrm{dir1}}\right) \left(\mathbf{D}_{\mathrm{tot}}^{-1}\right)_{2,1}^{\mathrm{H}} \right)_{rs} \tag{38}$$

where $\left(\mathbf{D}_{\mathrm{tot}}^{-1}\right)_{2,1}$ denotes the left bottom block matrix of $\mathbf{D}_{\mathrm{tot}}^{-1}$ which can be computed using the following property of block-matrices.

$$\left(\mathbf{A}^{-1}\right)_{2,1} = -\left(\mathbf{A}_{2,2} - \mathbf{A}_{2,1}\mathbf{A}_{1,1}^{-1}\mathbf{A}_{1,2}\right)^{-1} \mathbf{A}_{2,1}\mathbf{A}_{1,1}^{-1} \tag{39}$$

where $\mathbf{A}_{i,j}$ represents the block matrix with index (i,j) of the matrix $\mathbf{A}$.

3 Validation

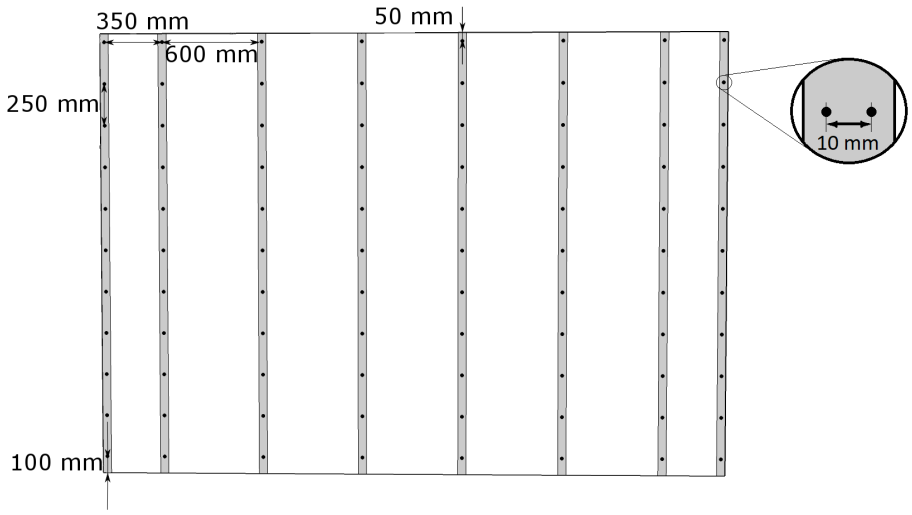


Figure 4: Positioning of studs and screw pairs within a wall. Eleven screw pairs are situated on each side of the stud with a vertical distance of 250 mm starting 100 mm from the bottom. Center to center spacing of the studs is 600 mm for the middle studs and 350 mm at the sides.

The airborne sound insulation of 14 different double-leaf plasterboard walls that each have a common flexible metal stud frame is predicted using the model as described above. The walls have different the cavity depths (40, 45, 50 or 100 mm), different material inside the cavity (air or mineral wool) and a different number of plasterboard layers comprising the leafs (single, double or triple plating). The results are compared to an extensive measurement campaign [13] to assess the accuracy of the predictions.

3.1 Wall and room properties

The transmission suite at the TNO TPD Delft Acoustics Laboratory is modelled in this validation study. The transmission rooms have a volume of 100 m^3 each and are separated by an opening with a width of 3.75 m and a height of 2.65 m where the test samples are mounted. The walls are constructed using a frame consisting of steel C-studs with a flange width of $50\,\mathrm{mm}$ and a wall thickness of $0.6\,\mathrm{mm}$. The web height of the studs equals the cavity depth, i.e. 40, 45, 50 or 100 mm. All walls contain eight studs in total, two of which are placed against the vertical edges of the test opening, and six in between. The center to center distance between two adjoining studs equals 350 mm at the vertical edges of the test opening and 600 mm in between. In order to connect a plasterboard plate to a metal stud, eleven screws are used along the vertical

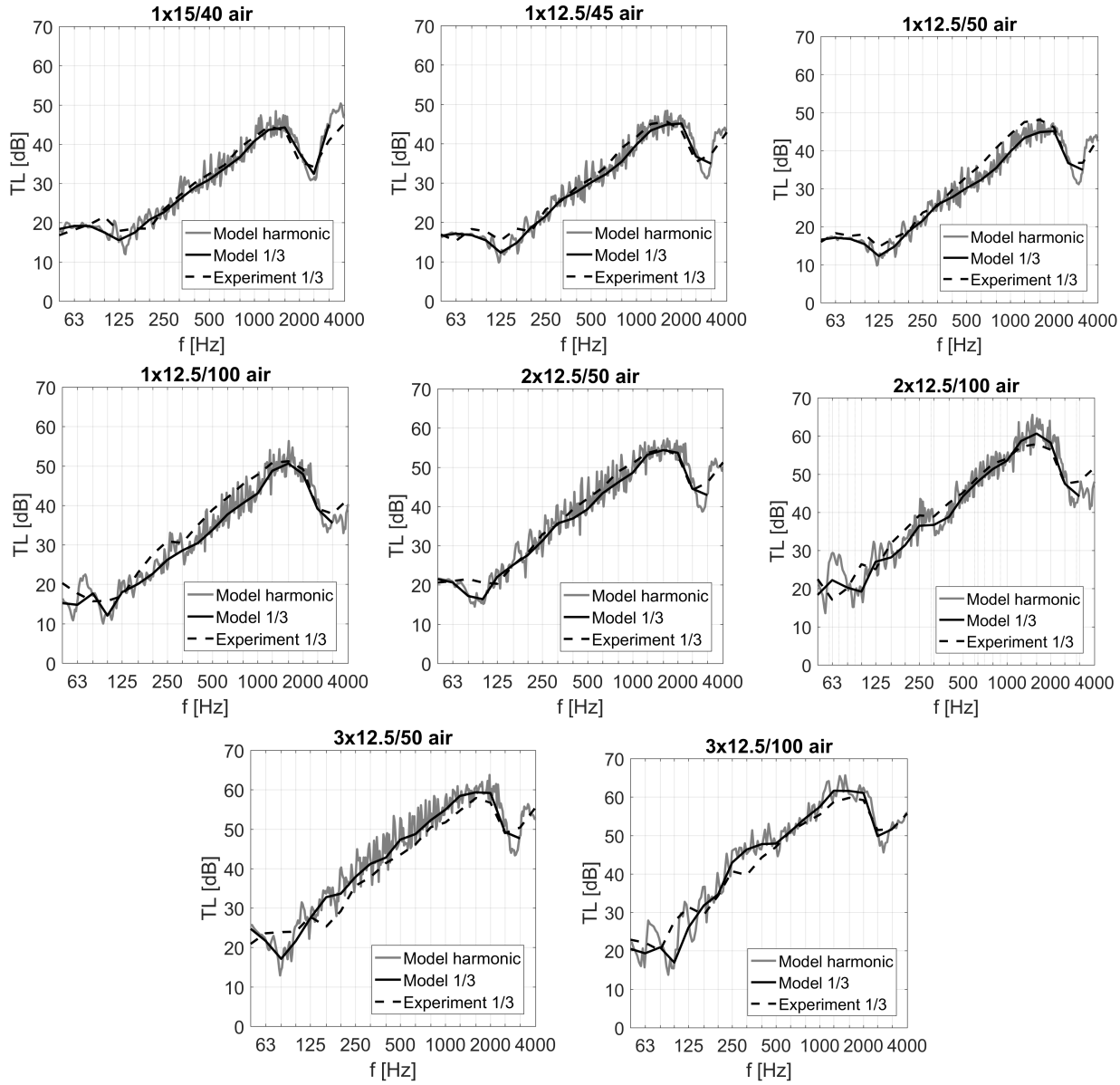


Figure 5: Predicted versus measured airborne sound insulation of a set of studded double-leaf plasterboard walls. Cavity filled with air.

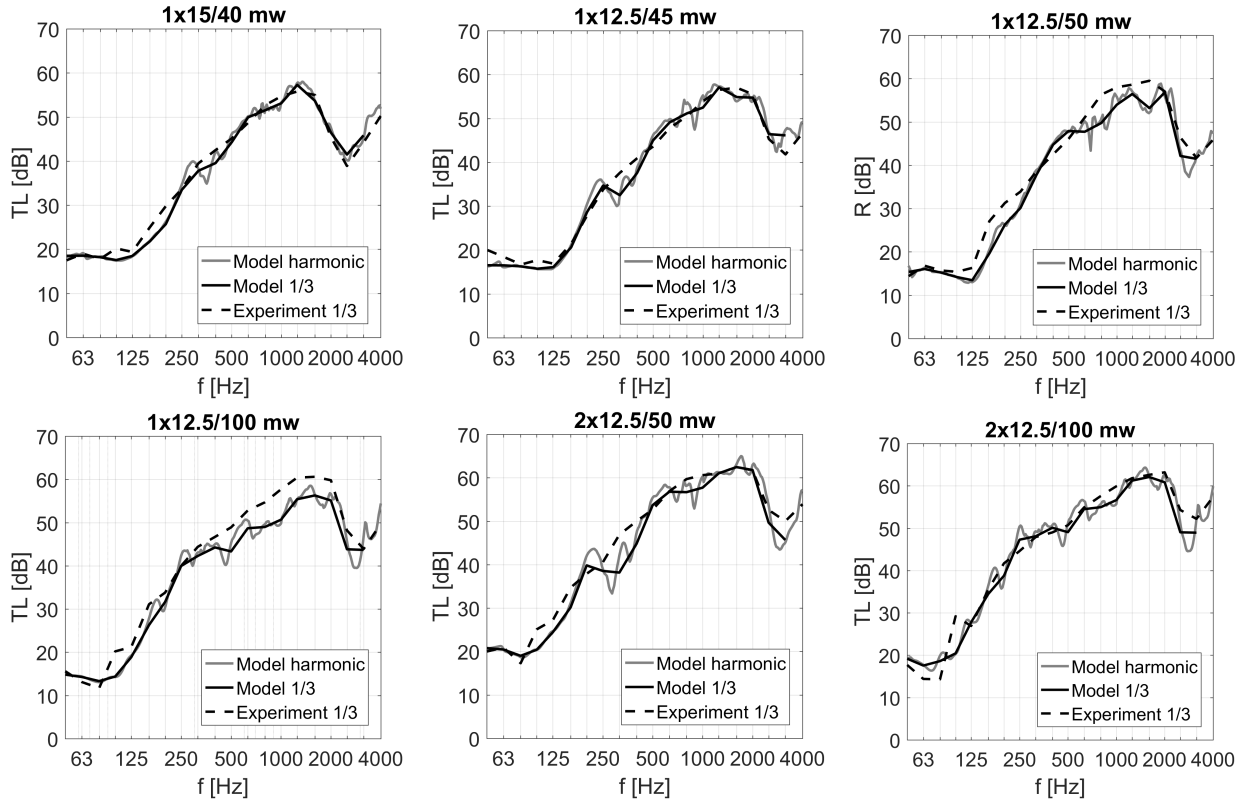


Figure 6: Predicted versus measured airborne sound insulation of a set of studded double-leaf plasterboard walls. Cavity filled with mineral wool.

plate edge. Screws start at 100 mm from the bottom edge and end at 50 mm from the top edge of a plate. The vertical distance between two screws is 250 mm. The horizontal distance between two screws in a pair is 10 mm in the model. The stud and screw positions are depicted in Fig. 4.

The plasterboard plates have a nominal density of 720 $\mathrm{kg/m^3}$ [13]. The Young's modulus and the Poisson ratio of the plasterboard plates are chosen to match the experimental coincidence frequencies in two of the sound transmission tests, since no experimental values are available. This results in a Young's modulus of 2.5 GPa and a Poisson's ratio of 0.3 [14]. A constant damping loss factor of 0.03 is assumed for the plasterboard, as in [14]. The assumed material properties for the galvanized steel studs are: a Young's modulus of 210 GPa, a density of 7800 $\mathrm{kg/m^3}$, a Poisson's ratio of 0.25 and a damping loss factor of 0.02. For air the following material properties are assumed: a density of 1.21 $\mathrm{kg/m^3}$ and a sound speed of 340 m/s. The flow resistivity of the mineral wool, used as sound absorbent in the cavity, was measured to be 5000 $\mathrm{N/sm^4}$ [13].

3.2 Sound insulation predictions

The airborne sound transmission loss is computed at 320 frequency lines with center frequencies between 50 and 4000 Hz. These frequency lines coincide with the 1/48-octave band center frequencies. The harmonic transmission losses are subsequently averaged over each 1/3 octave band for comparison with the experimental results. The calculations have been performed on a single personal computer with a 2.7 GHz Intel Core i7 processor and 16 GB RAM. The time needed to compute the transmission loss at all 320 frequency lines ranged from 45 minutes to 1 hour, depending on the specific wall configuration.

The 14 walls that are considered in this study are labeled by the combination of the number of platings constituting one leaf, the thickness of a single plating in mm, the cavity depth in mm and the type of cavity filling (air or mineral wool). For example, the wall labeled as 2x12.5/50 mw has leafs with double plasterboard

plating, an individual plating thickness of 12.5 mm and, a cavity with a depth of 50 mm and mineral wool as filling. In Table 1, the sound insulation predictions are summarized in terms of the single-number ratings according to the ISO 717 - 1 : 1996 standard [15]. The transmission loss curves as a function of frequency are displayed in Figs. 5 and 6.

Wall type	$\mathrm{R_W(C;C_{tr})_{exp}}$ dB	$\mathrm{R_W(C;C_{tr})_{model}}$ dB
1x15/40 air	34(-1;-5)	33(-1;-5)
1x12.5/45 air	34(-2;-6)	33(-2;-6)
1x12.5/50 air	34(-2;-6)	33(-2;-6)
1x12.5/100 air	38(-1;-6)	36(-2;-7)
2x12.5/50 air	42(-2;-7)	41(-2;-8)
2x12.5/100 air	47(-2;-6)	44(-1;-7)
3x12.5/50 air	45(-2;-7)	47(-2;-8)
3x12.5/100 air	49(-2;-7)	49(-2;-7)
1x15/40 mw	42(-2;-7)	40(-3;-8)
1x12.5/45 mw	41(-3;-9)	41(-4;-10)
1x12.5/50 mw	42(-3;-10)	40(-3;-9)
1x12.5/100 mw	46(-3;-9)	43(-1;-11)
2x12.5/50 mw	50(-2;-8)	46(-2;-8)
2x12.5/100 mw	52(-3;-8)	50(-4;-11)

Table 1: Wall type with corresponding experimental results and predictions of the single number ratings.

3.3 Physical interpretation and comparison with experiments

In Table 1 and Figs. 5 and 6, the prediction results are also compared with data from the extensive experimental study as reported by Vermeir and Gerretsen [13].

In general, a very good agreement between the model predictions and the experimental results can be observed. This is also the case at low frequencies, although the sound fields in the rooms are modelled as diffuse while in a single experiment, the modal behavior of the rooms will be important. The ISO 12999 - 1 : 2014 standard [16] defines an average experimental reproducibility for the single number ratings $\mathrm{R_w}$, $\mathrm{R_w + C}$ and $\mathrm{R_w + C_{tr}}$ as respectively 2.0, 2.1 and 2.4 dB for a 95 $\%$ confidence interval. From Table 1 it can be concluded that for nearly all walls, the predicted single-number ratings differ from the experimental values by 0 to 2 dB which is close to the average reproducibility with a coverage probability of 95 $\%$ for experiments.

An important resonance phenomenon for double-leaf walls is the so-called mass-spring-mass resonance. For an infinite wall without studs, the leafs then vibrate as rigid masses and compress the cavity fluid. For a finite studded wall, the mass-spring-mass resonance cannot fully develop due to restrained motion at the leaf edges and the presence of the studs. Nevertheless, a dip in the airborne sound insulation is usually observed around the theoretical mass-spring-mass resonance frequency, especially when there is no absorbent present in the cavity. This is also the case for the walls considered here. As can be observed in Figs. 5 and 6, the mass-spring-mass resonance dip is situated between 71 Hz (for wall 3x12.5/100 air) and 182 Hz (for wall 1x12.5/45 air). From these figures, it can also be observed that the predicted sound insulation around the mass-spring-mass resonance frequency agrees very will with the experimental findings.

At high frequencies, a pronounced dip can be observed in all transmission loss curves. This is the so-called coincidence dip. It occurs at the critical frequency of a single plasterboard plating, i.e., the lowest frequency at which the free bending wavelength on an infinite leaf matches the projected free wavelength in air. The theoretical value of the critical frequency is 2274 Hz for a plasterboard plate with thickness of $15\,\mathrm{mm}$, and 2728 Hz for a plate of $12.5\,\mathrm{mm}$ thickness. The predicted and observed coincidence dips match well. For

walls 1x15/40 air and 1x12.5/45 air, this comes as no surprise, since the Young's modulus and Poisson ratio of the plasterboard material were determined from the coincidence dips that are observed for these two walls. More important is that in the experimental results, the critical frequency remains unchanged when the number of platings is increased from one to two or three: this proofs that the assumption of perfect slip conditions at the plate-plate interfaces is valid.

4 Conclusions

In this paper, an accurate and computationally efficient model is presented for the prediction of the airborne sound insulation of studded double walls. In this model, the parts of the wall that display a low geometrical complexity, i.e. the leafs and the cavity, are modelled analytically to reduce computational cost. The studs are modelled in detail with the shell finite elements, since flexible studs display a large cross-sectional deformation that cannot be captured with an analytical model. The sound fields in the rooms are modeled as diffuse, and a rigorous coupling with the deterministic wall model is achieved within the hybrid DET-SEA framework. The computation cost of this model was verified to be more than three orders of magnitude lower than that of a recently proposed detailed finite element model of the transmission suite with frequency-dependent mesh, while the prediction accuracy remains the same.

The model was extensively validated against measured transmission loss data of 14 different plasterboard walls with metal C-studs. An absolute accuracy between 0 and 2 dB on the single number ratings was achieved for nearly all wall types. This is within the average reproducibility of the experiments. Thanks to its prediction accuracy and computational efficiency, the model can be employed as a high-fidelity tool for the design of double-leaf wall systems.

Acknowledgments The research presented in this paper has been performed within the framework of the research project G0A7717N AcOpt: Numerical optimization of the airborne sound insulation of single and double walls, funded by the Research Foundation - Flanders (FWO), Belgium. The financial support by FWO is gratefully acknowledged.

References

[1] J. C. E. Van den Wyngaert, M. Schevenels, and E. P. B. Reynders. Predicting the sound insulation of finite double-leaf walls with a flexible frame. *Applied Acoustics*, 2018.

[2] P.J. Shorter and R.S. Langley. On the reciprocity relationship between direct field radiation and diffuse reverberant loading. *Journal of the Acoustical Society of America*, 117(1):85–95, 2005.

[3] J. Brunskog and P. Davidsson. Sound transmission of structures. A finite element approach with simplified room description. *Acta Acustica united with Acustica*, 90(5):847–857, 2004.

[4] H. Kuttruff. *Room Acoustics*. Spon Press, Oxon, UK, 5th edition, 2009.

[5] T.E. Vigran. *Building Acoustics*. Taylor & Francis, Oxon, UK, 2008.

[6] R.D. Cook, D.S. Malkus, M.E. Plesha, and R.J. Witt. *Concepts and applications of finite element analysis*. John Wiley and Sons, fourth edition, 2002.

[7] R.H. Lyon and R.G. DeJong. *Theory and application of statistical energy analysis*. Butterworth-Heinemann, Newton, MA, second edition, 1995.

[8] M.J. Crocker and A.J. Price. Sound transmission using statistical energy analysis. *Journal of Sound and Vibration*, 9(3):469–486, 1969.

[9] P.J. Shorter and R.S. Langley. Vibro-acoustic analysis of complex systems. *Journal of Sound and Vibration*, 288(3):669–699, 2005.

[10] E. Reynders, R.S. Langley, A. Dijckmans, and G. Vermeir. A hybrid finite element - statistical energy analysis approach to robust sound transmission modelling. *Journal of Sound and Vibration*, 333(19):4621–4636, 2014.

[11] R.S. Langley and J.A. Cordioli. Hybrid deterministic-statistic analysis of vibro-acoustic systems with domain couplings on statistical components. *Journal of Sound and Vibration*, 321(3–5):893–912, 2009.

[12] R.S. Langley. Numerical evaluation of the acoustic radiation from planar structures with general baffle conditions using wavelets. *Journal of the Acoustical Society of America*, 121(2):766–777, 2007.

[13] G. Vermeir and E. Gerretsen. Onderzoek van de luchtgeluidisolatie van lichte scheidingswanden met gipskartonplaten. Technical Report PV4335/DGT-RPT-020028, K.U.Leuven and TNO, Leuven / Delft, 2002.

[14] E. Reynders and C. Van hoorickx. An investigation into the sound insulation of finite-sized rib-stiffened plates. In *Proceedings of 7th Forum Acusticum*, Kraków, Poland, September 2014. CD-ROM.

[15] International Organization for Standardization. *ISO 717-1:1996: Acoustics – Rating of sound insulation in buildings and of building elements – Part 1: Airborne sound insulation*, 1996.

[16] International Organization for Standardization. *ISO 12999-1:2014: Acoustics – Determination and application of measurement uncertainties in building acoustics – Part 1: Sound insulation*, 2014.

Finite element analysis of the acoustic behavior of poroelastic materials based on experimentally determined frequency-dependent material properties

P. Schrader[1], F. Duvigneau[2], M. Gavila-Lloret[3], H. Rottengruber[1], U. Gabbert[2]
[1]Otto von Guericke University Magdeburg, Department of Mechanical Engineering, Chair of Energy Conversion Systems of Mobile Applications, Universitätsplatz 2, D-39106, Magdeburg, Germany
e-mail: **peter.schrader@ovgu.de**

[2] Otto von Guericke University Magdeburg, Department Mechanical Engineering, Chair of Numerical Mechanics, Universitätsplatz 2, D-39106, Magdeburg, Germany
e-mail: **fabian.duvigneau@ovgu.de**

[3]BMW Group, Department of Air-Borne-Acoustics, Knorrstraße 147, D-80788, Munich, Germany
e-mail: **maria.gavila-lloret@bmw.de**

Abstract
The paper examines the possibility to predict the noise absorption behavior of poroelastic materials with a simple modeling approach which avoids the extensive experimental efforts of advanced modeling based upon the Biot theory of poroelastic media. It is assumed that experimental data of the dynamic stiffness and damping characteristics captures all dissipative influences, which are estimated by extended Biot models. The results of the approach show high compliance with the numerical results of synchronous Biot modeling. The application is limited by the highest reliable frequency of the experimental measurement of the dynamic Young's modulus and damping ratio, which actually reaches 2 kHz if no extrapolation is desired. Parallel, acoustic measurements with 19 different poroelastic materials were conducted to validate the simulation results and to get an overview the acoustic behavior of different plastic foams. The results show coincidence with the experimentally determined dynamic Young's modulus, pore size and density of the material.

1 State of the art in numerical modeling of poroelastic media

The theory of poroelasticity by Biot-Allard [1–3] is the most extended approach to describe the sound propagation in elastic porous media. Its main underlying assumption is the homogenization. This means that, provided that the wavelengths of the waves propagating inside the material are much larger than the pores size, the biphasic aggregate can be considered as a homogenous medium in which the two phases are simultaneously present. Consequently, the resolution of the pores on the microscale is avoided. The two governing equations have the form of a fluid-structure interaction problem with the particularity that the mechanical coupling between the elastic frame deformation and the fluid behavior is not limited to the fluid structure interfaces, but is of a volume nature.

The parameters defining the equations coefficients can be grouped into three classes: fluid, elastic and poro-mechanical. The first set includes the material properties of the filling fluid, namely its density ρ_0, its viscosity η_0 and the speed of sound c_0. The elastic parameters characterize the response of the frame in vacuum and are typically the Young's modulus E, the Poisson's ratio ν, the structural damping coefficient η and the density of the drained material ρ_1. The poro-mechanical parameters help to link the microscopic thermal and viscous effects at a local level with the changes in the macroscopic effective bulk modulus and effective dynamic density. This requires a constitutive model as, for example, the one proposed by Johnson-Champoux-Allard (JCA,[4], [5]), which is employed as reference in this paper.

Some of the procedures to determine the values of these mentioned material parameters can be found in [6-8]. The characterization of poroelastic materials is associated with inaccuracies of different kind. First, the tested samples often include inhomogeneities as a result of the manufacturing processes. Second, the measurement equipment and techniques employed suffer from reproducibility issues as highlighted in [9]. Lastly, the use of elastic properties obtained from quasi-static tests is a common practice, but their value may differ significantly at higher frequencies [10]. Thus, a frequency-dependent testing of the elastic properties may be considered as a proper modeling approach. In Section 2 below, a measurement technique for this purpose is introduced.

The key for a correct prediction of the acoustic effects in poroelastic material is the proper modeling of its dissipation effects. They are subdivided into structural damping losses W_{str}, viscous losses W_{visc} and thermal effects W_{th}. For the displacement-pressure (u, p)-formulation of the Biot theory [8] explicit relations for these losses are derived in [11]. The total losses are obtained by integration over the material domain Ω. The structural damping loss W_{str} is determined as the Frobenius inner product of the imaginary part of the complex stress tensor of the elastic solid in vacuum $\Im\left(\hat{\underline{\underline{\sigma}}}^s(\mathbf{u})\right)$ and of the strain tensor $\varepsilon(\mathbf{u}^*)$ of the complex conjugate deformations $\mathbf{u}^*$ of the solid phase

$$W_{str} = \int_\Omega \Im\left(\hat{\underline{\underline{\sigma}}}^s(\mathbf{u})\right) : \varepsilon(\mathbf{u}^*) d\Omega . \tag{1}$$

The viscous losses W_{visc} consist of the losses in the solid phase W_{visc}^s, the fluid phase W_{visc}^f and due to the coupling between solid and fluid phase W_{visc}^{sf} as

$$W_{visc} = W_{visc}^s + W_{visc}^f + W_{visc}^{sf} . \tag{2}$$

They are calculated as

$$W_{visc}^s = -\pi\omega^2 \int_\Omega \Im(\tilde{\rho}) \cdot |\mathbf{u}|^2 d\Omega \tag{3}$$

and

$$W_{visc}^f = \pi \int_\Omega \Im\left(\frac{\phi^2}{\tilde{\rho}_{22}\omega^2}\right) \cdot |\nabla \mathbf{p}|^2 d\Omega \tag{4}$$

and

$$W_{visc}^{sf} = -2\pi \int_\Omega \Im\left(\frac{\phi}{\tilde{\alpha}}\right) \cdot \Re\left(\mathbf{u}^* \nabla p\right) d\Omega . \tag{5}$$

In these equations ϕ denotes the open porosity. The tilde symbol indicates that the corresponding material coefficient is complex and frequency-dependent, namely the effective density $\tilde{\rho}$, the mass coefficient for the fluid phase $\tilde{\rho}_{22}$ and the dynamic tortuosity $\tilde{\alpha}$. Their calculation in the context of the theory developed by Johnson [4] requires the experimentally determined open porosity ϕ, the airflow resistivity σ, the tortuosity α_∞ and the viscous characteristic length Λ. Finally, the thermal dissipation losses are given by the relation

$$W_{th} = \frac{\phi \cdot \pi \cdot \Re\left(\tilde{R}\right)}{\left|\tilde{R}\right|^2} \int_\Omega |p|^2 d\Omega \tag{6}$$

that furthermore requires the real part of the complex elastic coefficient of the fluid phase $\Re\left(\tilde{R}\right)$. If the stiffness of the solid phase is much larger than that of the bulk material and of the filling fluid, its value can be approximated by $\tilde{R} = \phi \cdot \tilde{K}_f$ using the open porosity and the dynamic bulk modulus of the air in the pores $\tilde{K}_f$. The dynamic bulk modulus has to be calculated from the experimental parameters mentioned above as well as from the thermal characteristic length Λ', the adiabatic index, the static pressure and the Prandtl number. Their relation is derived by Champoux and Allard in [5].

The model briefly sketched above is the state of the art in the modeling of poroelastic materials. It is based upon extensive and highly advanced measurements for each poroelastic material specimen that have to be

carried out by specialized institutions. The advantage of the model is its ability to estimate the contributions of the different dissipation mechanisms. Since the losses described in Eqs. (1-6) cannot or can only partially be separated in experiments (e. g. by avoiding fluid damping, solid-fluid interaction and thermal dissipation by evacuation of the open-cell porous material) such modeling enables to gain more knowledge about the partition of each mechanism in overall damping. The model allows a separate investigation of a rigid frame model and a limp frame model of the porous structure and thus the separation of fluid and solid-fluid interaction effects (stiff frame) from solid effects (elastic frame).

2 Simplified approach using experimentally determined damping parameters

The assumption is that the sum of the effects of all poro-mechanical parameters of a given material can effectively be measured and summarized by the frequency-dependent complex Young's modulus in the frequency range of interest. This avoids the experimental efforts and the error sources described in the section above. This approach will not allow an estimation of the contribution of each damping mechanism to the overall dissipation, but a frequency-dependent characterization of the overall dissipation whose single contributions are summarized in a simple expression as Eq. (1). This leads to a numerical solution based on the principle of virtual displacements for homogenous materials with linear elastic material behavior using only one damping term. Transformed in the frequency range, it results in the following linear differential equation system

$$(-\omega^2\mathbf{M} + i\omega\mathbf{C} + \mathbf{K})\tilde{\mathbf{u}} = \tilde{\mathbf{f}}\ , \tag{7}$$

wherein $\mathbf{M}$, $\mathbf{C}$, and $\mathbf{K}$ represent the system mass matrix, the system damping matrix and the stiffness matrix. The vector of the complex external forces $\tilde{\mathbf{f}}$ is derived from a force signal in the time domain by discrete or fast Fourier transform (DFT / FFT) and thus depends on the system's angular excitation frequency ω. The displacements $\tilde{\mathbf{u}}$ are thus complex and frequency-dependent as well. In the approach that is pursued in this paper the damping matrix $\mathbf{C}$ and the stiffness matrix $\mathbf{K}$ are frequency-dependent and contain expressions of the experimentally determined, frequency-dependent dynamic Young's modulus E and the dynamic damping ratio D. The Poisson's ratio ν is assumed to be constant. Hence, the approach results in a significant reduction of material parameters to be measured or estimated in advance. In this approach a successful prediction mainly depends on the appropriate measurement of the complex Young's modulus in the frequency range of interest. The coupled vibroacoustic models introduced in the fourth section will be used for the acoustical prediction based on the proposed simplified elastic approach. The required material characterization is described in the following Section.

2.1 Experimental damping measurements

The experimental setup used for the characterization of the frequency-dependent stiffness and damping properties of the investigated foam materials is shown in Figure 1. A material sample of a thickness of 20 mm and a diameter of 30 mm was placed between an electrodynamic shaker and a seismic mass. The shaker excited the material sample with an harmonic oscillation.

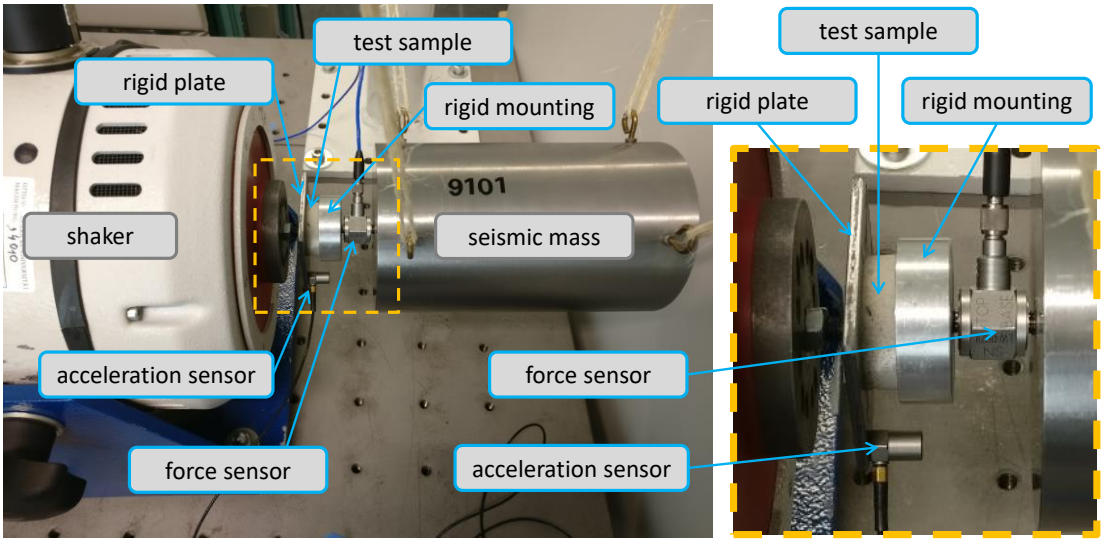


Figure 1: Experimental setup for determining the frequency-dependent properties of damping materials

Except for the material sample of interest, the whole setup is assumed to be rigid. Hence, the system can be treated as a single degree of freedom spring-mass-damper system. The mounting on a seismic mass under free-free boundary conditions (eigenfrequencies almost zero) was used to avoid resonances of the mounting part within the frequency range of interest. Each frequency was excited by a monofrequent harmonic force with the help of an electrodynamic shaker and measured separately. The measured data include the excitation force (force sensor) and the displacement (acceleration sensor). The retrieved acceleration has to be transformed to obtain the displacement. To avoid errors caused by numerical integration the relation

$$x(t) = \hat{x}e^{-i\omega t} \rightarrow a(t) = \ddot{x}(t) = -\omega^2 \hat{x}e^{-i\omega t} \rightarrow a(t) = -\omega^2 x(t) \tag{8}$$

was used, which holds for harmonic states. The resulting Young's modulus was determined out of the spring stiffness under consideration of the dimensions of the test sample. The spring stiffness was calculated with the help of the measured force and displacement. Moreover, the damping properties, either expressed as the loss modulus E'', the loss factor $\eta = E''/E'$ or the damping ratio D, were obtained from the hysteresis loss in the force-displacement diagram. These calculations were repeated at each measured frequency in the investigated range beginning at 0.1 kHz and increased with a constant step size of 0.1 kHz. The maximum operable frequency was limited by the power of the shaker. Furthermore, it is important that the signal to noise ratio is feasible and that resonance effects as well as other perturbations were avoided. With the presented setup it was possible to reliably determine the material parameters up to 2 kHz. Several characterization methods and influence parameters and how they affect the resulting frequency-dependent material properties were investigated in advance. Additionally, numerous numerical studies were also conducted to gain a better understanding of the working principle of the setup and all important influence parameters. More detailed information is given in [12].

Figure 2 shows different foams whose dynamic parameters were determined with the test method described above. The equally scaled images display the macroscopic pore structure of different foam materials sorted by their density. Most of the foams are polyesters (PES) and polyethers (PETH). The polyester foams have a very regular porosity, with a small pore size variation within each material and a decreasing pore size with increasing density. The PES 1 foam haptically shows a higher rigidity than the other polyesters with higher density. In comparison to the PES foams, each of the polyether materials show a bigger variance of the pore size and a more irregular, stochastic structure. The pore size decreases with increasing density as well. There are no samples with palpable high rigidity. The melamine resin sample (MR) also has a high variance of the pore sizes and seems to be stiff analogously to the polyethylene foam (PE), which presents very small pores and a regular pore size. The relatively stiff polyurethane foam (PUR) has a small pore size and shows a medium pore size variance. The EPDM foams of high density have a smooth surface and very small, regular pores.

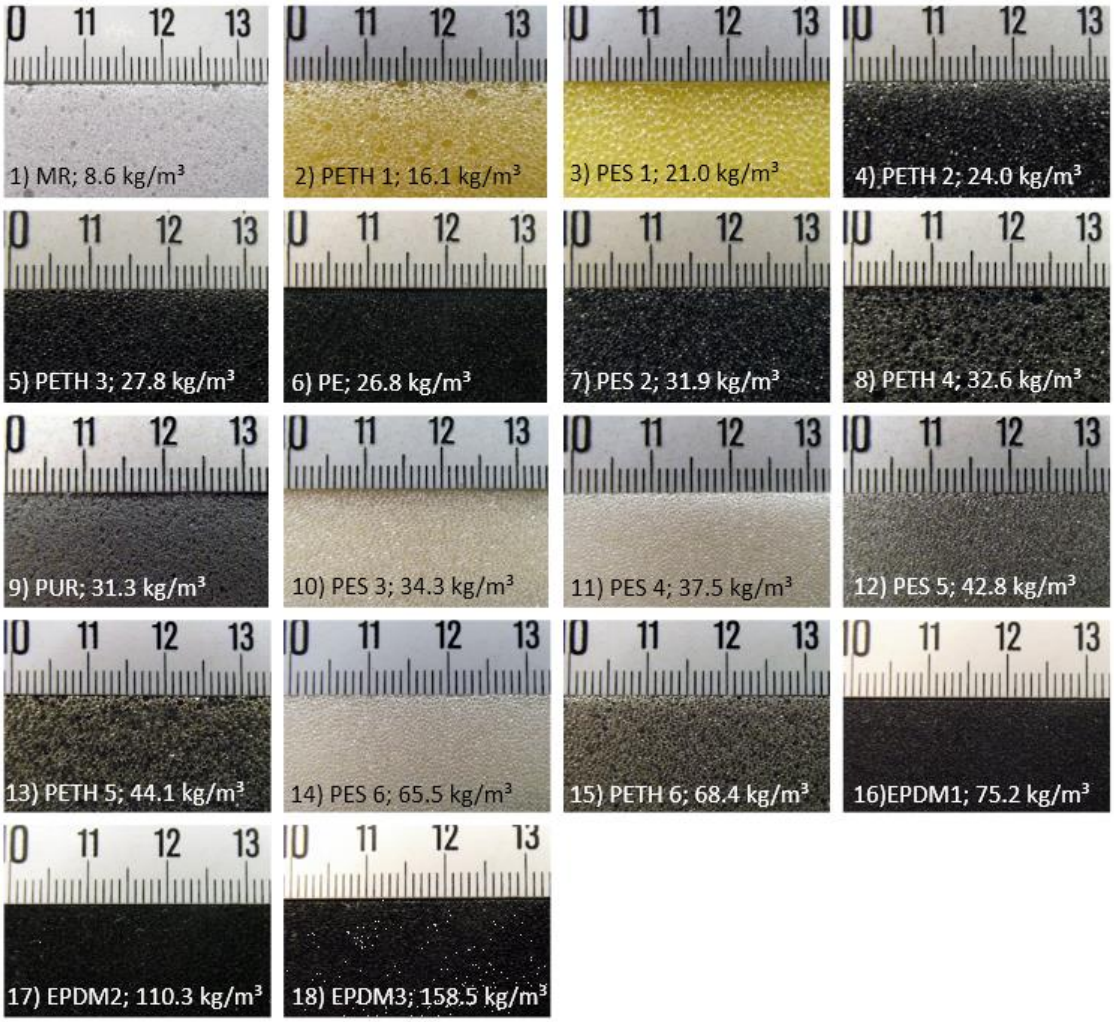


Figure 2: Investigated foams. The abbreviations stand for: EPDM – ethylene propylene diene monomer; MR – melamine resin; PE – polyethylene; PES – polyester; PETH – polyether

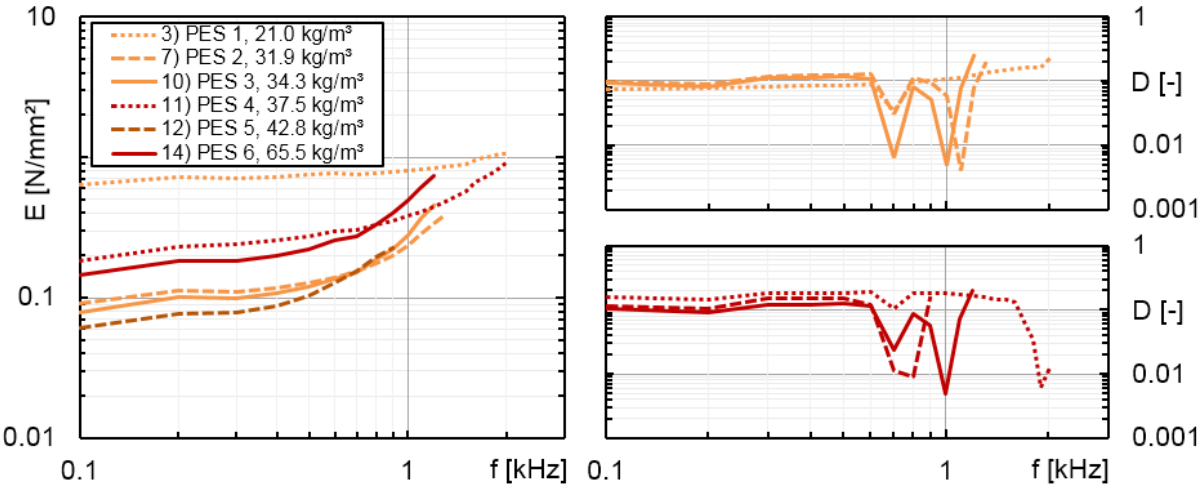


Figure 3: Young's modulus E (left diagram) and damping ratio D (right diagrams) of polyester foams with a thickness of 20 mm

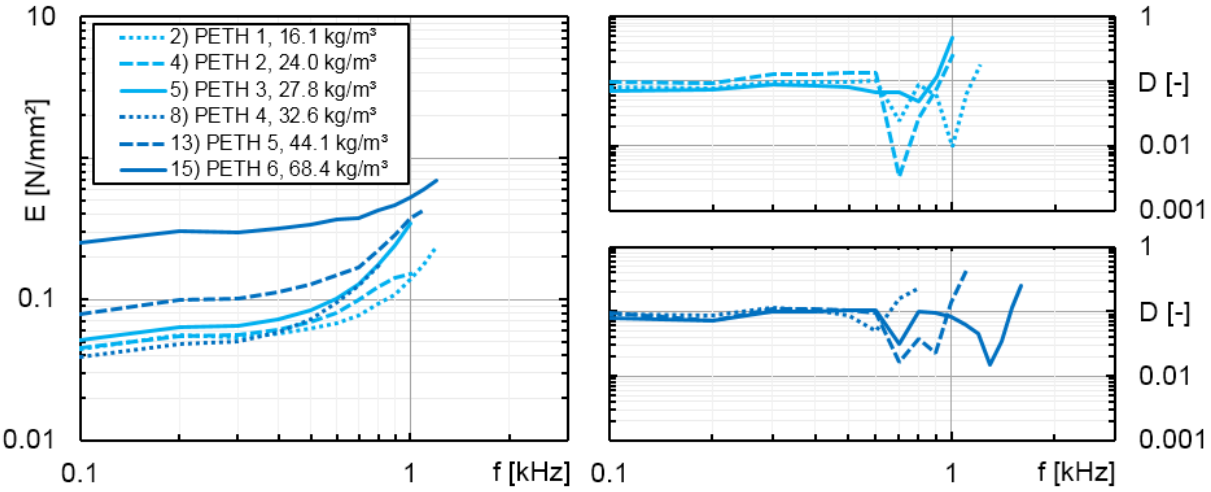


Figure 4: Young's modulus E (left diagram) and damping ratio D (right diagrams) of polyether foams with a thickness of 20 mm

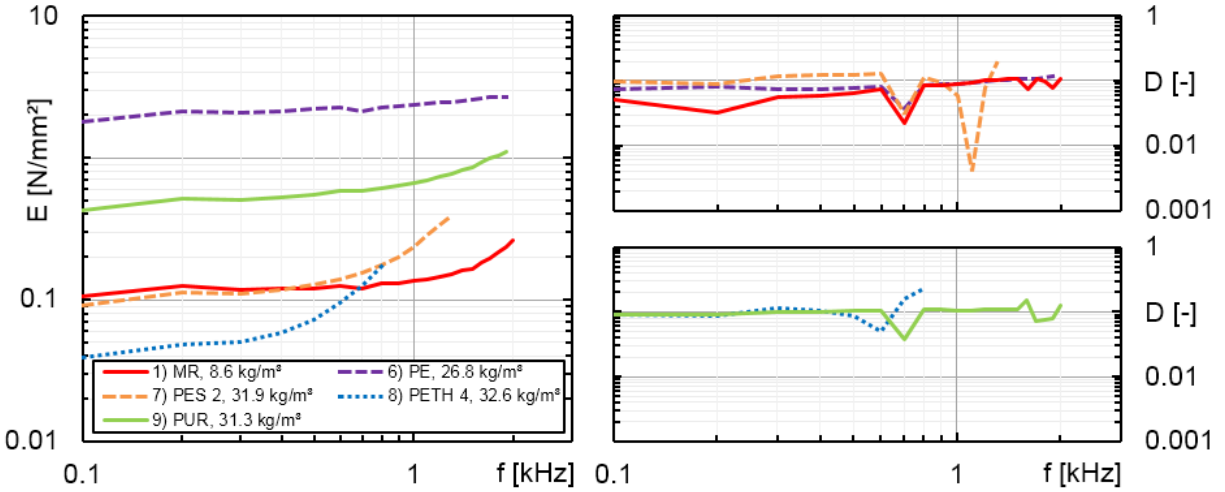


Figure 5: Young's modulus E (left diagram) and damping ratio D (right diagrams) of plastic foams of different materials with a thickness of 20 mm

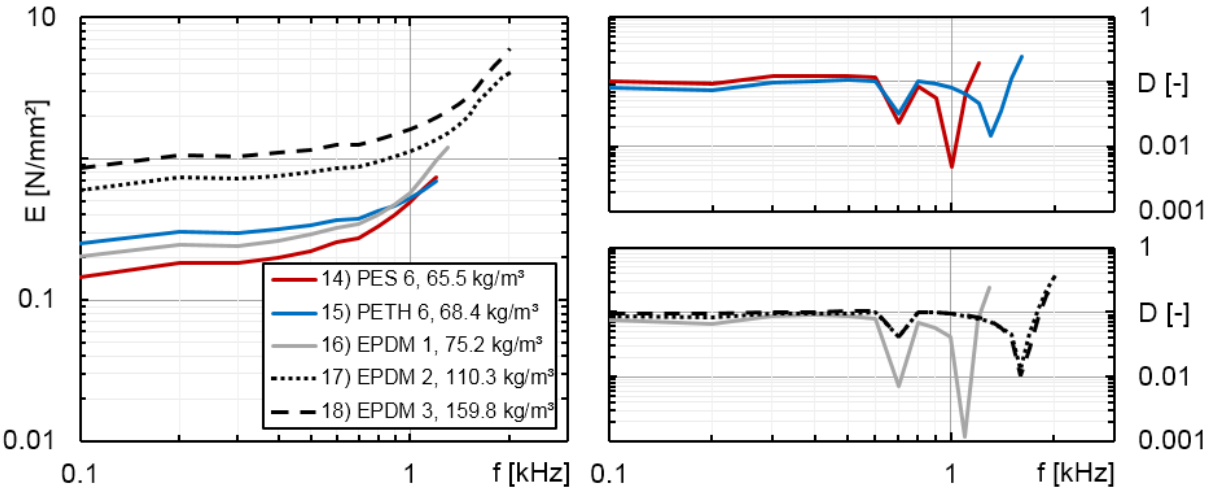


Figure 6: Young's modulus E (left diagram) and damping ratio D (right diagrams) of heavy and EPDM plastic foams with a thickness of 20 mm

The Figures 3-6 show the experimentally determined dynamic Young's modulus E and the dynamic damping ratio D measured with the test setup displayed in Figure 1. The Young's modulus steadily increases with the frequency. The foams with a stiff appearance as MR, PES 1, PE and PUR present, in comparison to the softer foams as PETH 1-5, just a slight increase of the Young's modulus throughout the frequency range. Moreover, their results show small irregularities in the damping ratio. In the case of the PUR foam (Figure 5) the damping could even be assumed to be frequency-independent up to 2 kHz, where it is not determinable anymore. Up to 0.6 kHz all investigated materials show an almost constant damping ratio close to 0.1. Here, a higher Young's modulus causes a higher absolute loss modulus E'' under a constant damping ratio. Above this frequency, many of the investigated materials show a higher slope of the Young's modulus and this increase corresponds with a characteristic local decrease of the damping ratio and of the loss modulus. At this point it cannot be excluded that these local minima are no intrinsic material properties of the specific samples but result from resonant interactions between the experimental setup and the probes. Actually, it must furthermore be stated that the current experimental configuration does not allow to determine the elastic material data for higher audible frequencies.

3 Acoustic measurements

The materials were investigated in an anechoic room with full absorption above 100 Hz at all walls. Figure 7 shows the experimental setup. Each material probe was fixed with a steel frame at the surface of an aluminum plate with the dimensions 400 x 200 x 18 mm. The frame was fixed as shown in the lower right image with screw nuts at thread rods that were screwed into the plate. The screw nuts were tightened at each prototype until the small gap between foam and plate had disappeared at each side. Furthermore, the samples were tested at a steel sheet with identical dimensions but a thickness of 1 mm. Here, the materials were fixed with a double-sided tape. The plate was coupled to an electrodynamic shaker by a rod that was tightly connected with the backside of the plate (lower left image of Figure 7). The shaker was excited with a white noise current generated and amplified with a constant magnitude by a signal

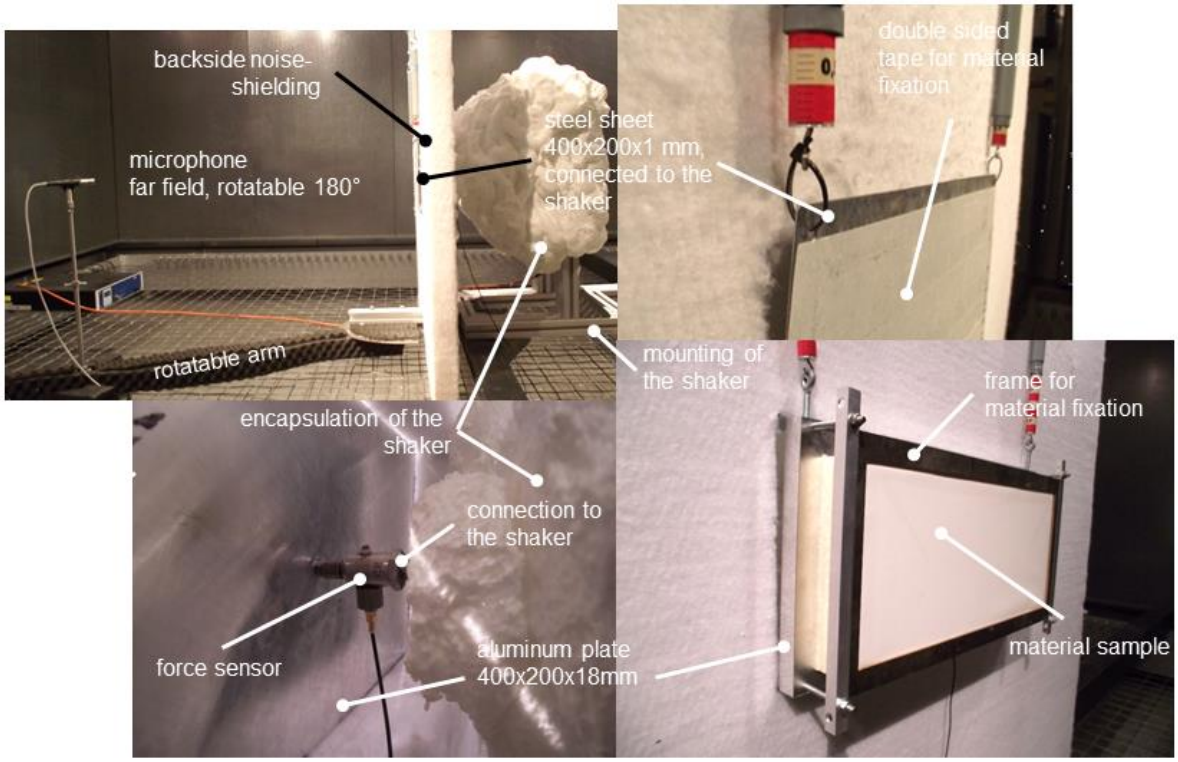


Figure 7: Test setup for acoustic measurements in an anechoic chamber

generator and an amplifier. The transduced force between shaker and plate was measured with a force sensor mounted in line with the connection rod. The radiated noise of the plate was recorded by a single microphone

positioned in a distance of 0.9 m from the plate and in the height of the plate's center. The microphone was rotated horizontally around the plate between 0° and 180° in steps of 10° to obtain a directional characteristic of the sound pressure level (SPL) in the frequency range 0.1-12.8 kHz. This directional characteristic was averaged arithmetically so that the overall SPL characteristic contains all frequency lobes of the sound radiating structure. Within the anechoic room, the averaged SPL represents the radiated power of the plate in the far field. The results are shown below as third octave band levels of the SPL characteristics. The insertion loss (IL) of the foam mounted at the plate was calculated by subtraction of its third octave band SPL from the third octave band SPL of the uncovered plate, which is possible due to the identity of the sound pressure level and the sound power level under free-field-conditions in the far field.

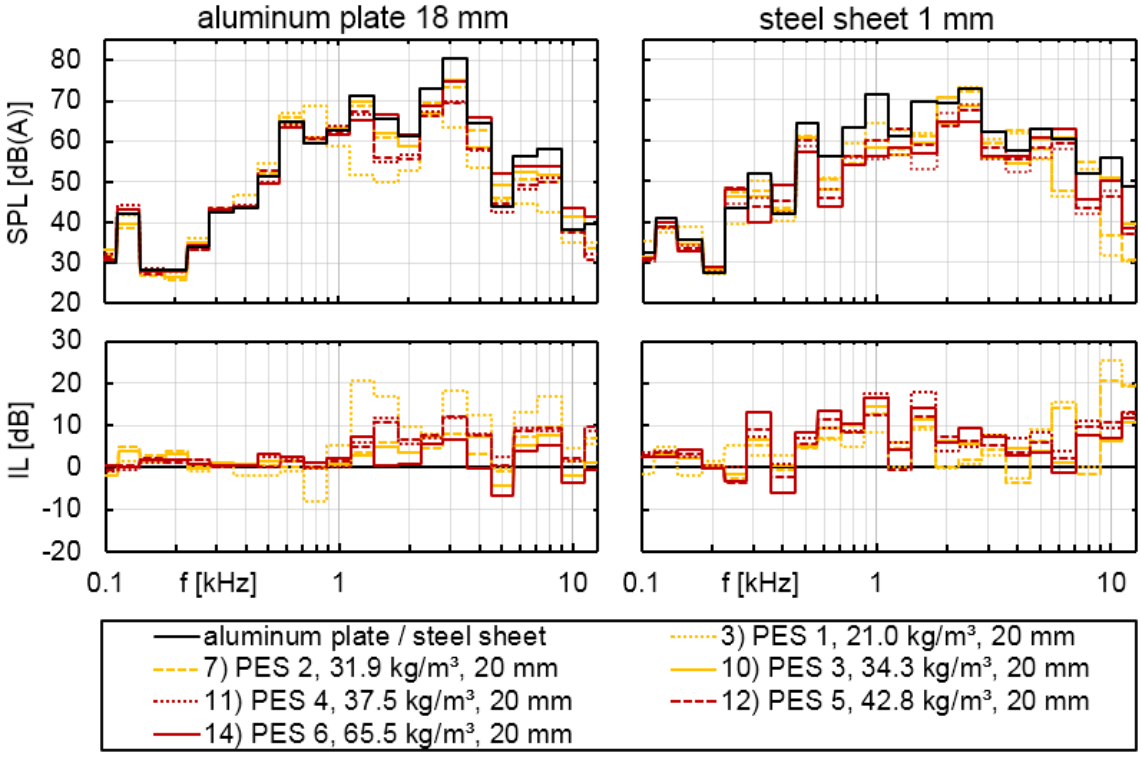


Figure 8: Sound pressure level and insertion loss (IL) of polyester foams of different density

The Figure 8-12 show the sound pressure level and the IL that were measured in the test bench for all of the investigated foams fixed on a 18 mm aluminum plate and on a 1 mm steel sheet. The materials and their appearing order in the Figure 8-11 are identical to the ones shown in the Figure 3-6. The left and right diagrams compare the noise reducing effect measured at the stiff aluminum plate where each foam's influence on the system's stiffness was negligible small, in comparison to the effect on the 1 mm steel sheet, where it was not. The lower stiffness of the steel sheet results in a first structural resonance below 0.3 kHz and in significant noise reductions below 1 kHz for all foams. However, for the thick aluminum plate no significant noise reductions were detected below 1 kHz in any measurement. On the other hand, the effect of a noise reduction due to a stiffening of the structure by a foam is most apparent in the right diagrams of Figure 10. Here, at the 1 mm steel sheet the foam with the highest dynamic Young's modulus at low frequencies, the PE-Foam (violet curve), leads to significant reductions in the low frequency range. For the aluminum plate a comparable effect is not visible.

The acoustic measurements do not show a coincidence with the characteristic damping ratio decrease of soft foams at certain frequencies shown in the Figure 3-6. The specific materials do not show a generally reduced insertion loss in the third octave bands for these frequencies. The foams with the biggest pore size, PES 1 and PETH 1, show a significantly higher noise reduction above 1 kHz on the aluminum plate. The comparison of the IL in the diagrams of Figure 8 and Figure 9 shows a high degree of similarity. It is obvious that the effects of the PES and PETH materials are similar. The changes in the acoustic behavior due to an increase of the material density are complex, but occur in a synchronous pattern for both materials.

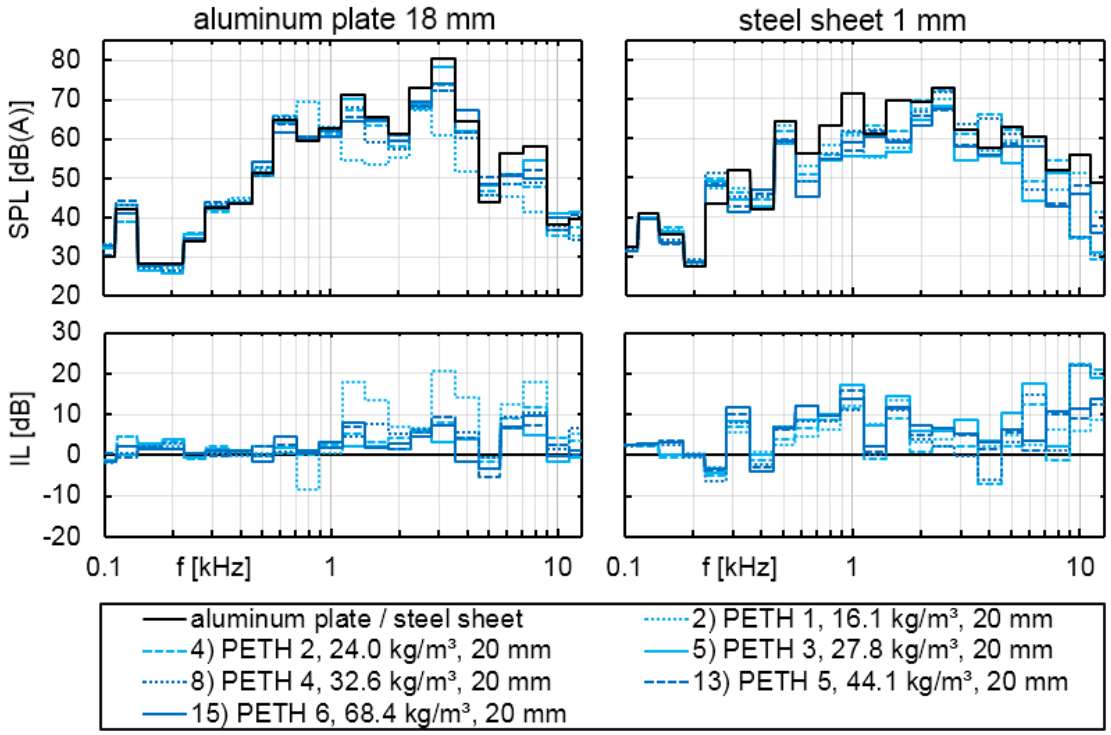


Figure 9: Sound pressure level and insertion loss of polyether foams of different density

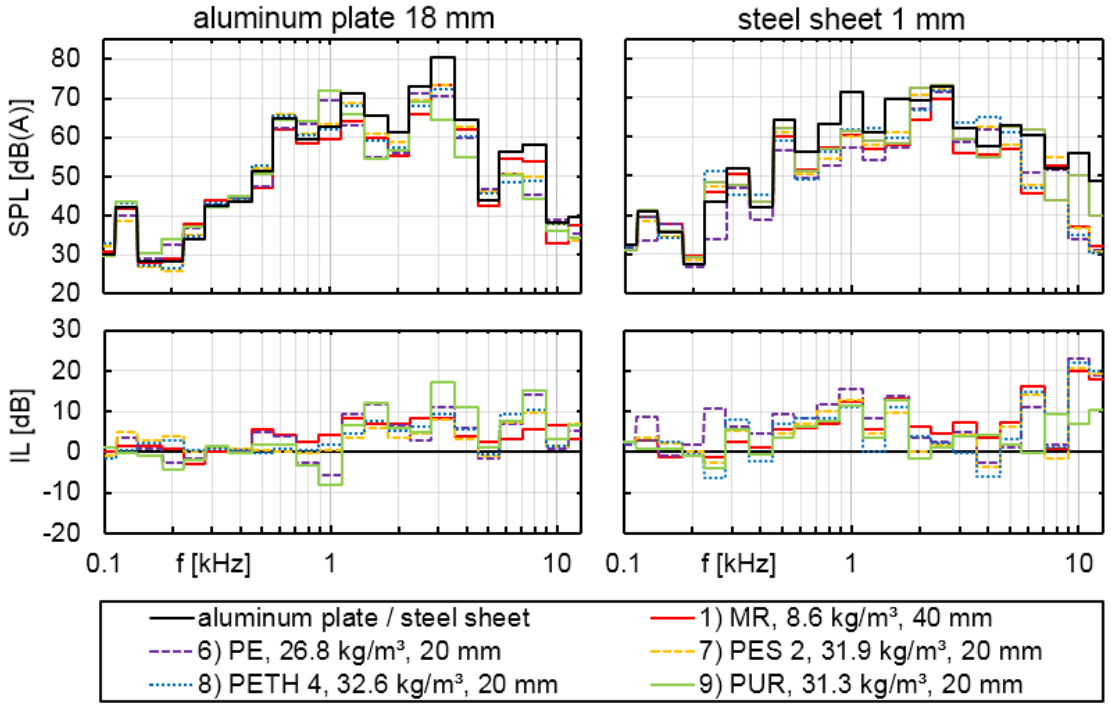


Figure 10: Sound pressure level and insertion loss of foams of different materials

In Figure 10, the effects of different foam materials with various dynamic Young's modulus are presented. The low frequency effect of the PE foam on the steel sheet due to the foam high dynamic stiffness has already been mentioned above. In comparison, the PETH 4 foam with a low dynamic Young's modulus at low frequencies as well as the MR and the PES 2 foam have no significant influence on the steel sheets noise radiation in the low frequency range. The good results of the very light MR foam at medium and low

frequencies at the aluminum plate cannot be derived from a high dynamic Young's modulus or damping ratio. It is supposed to be the result of the higher thickness of the probe (40 mm instead of 20 mm).

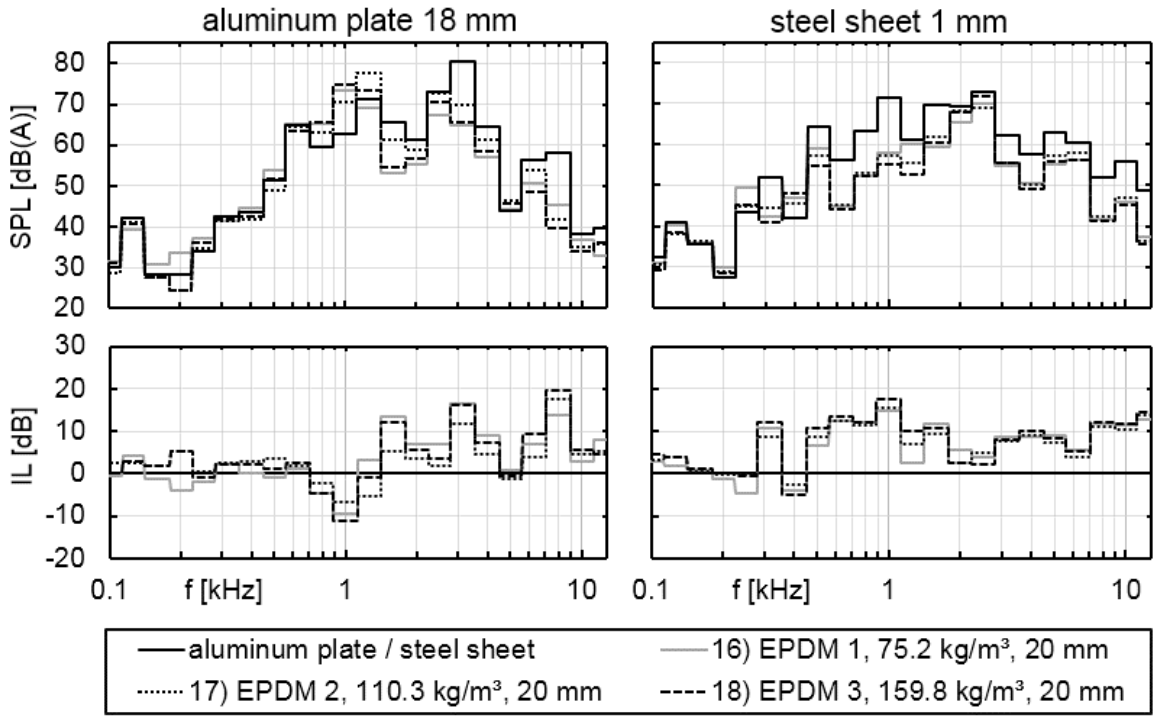


Figure 11: Sound pressure level and insertion loss of EPDM foams of different density

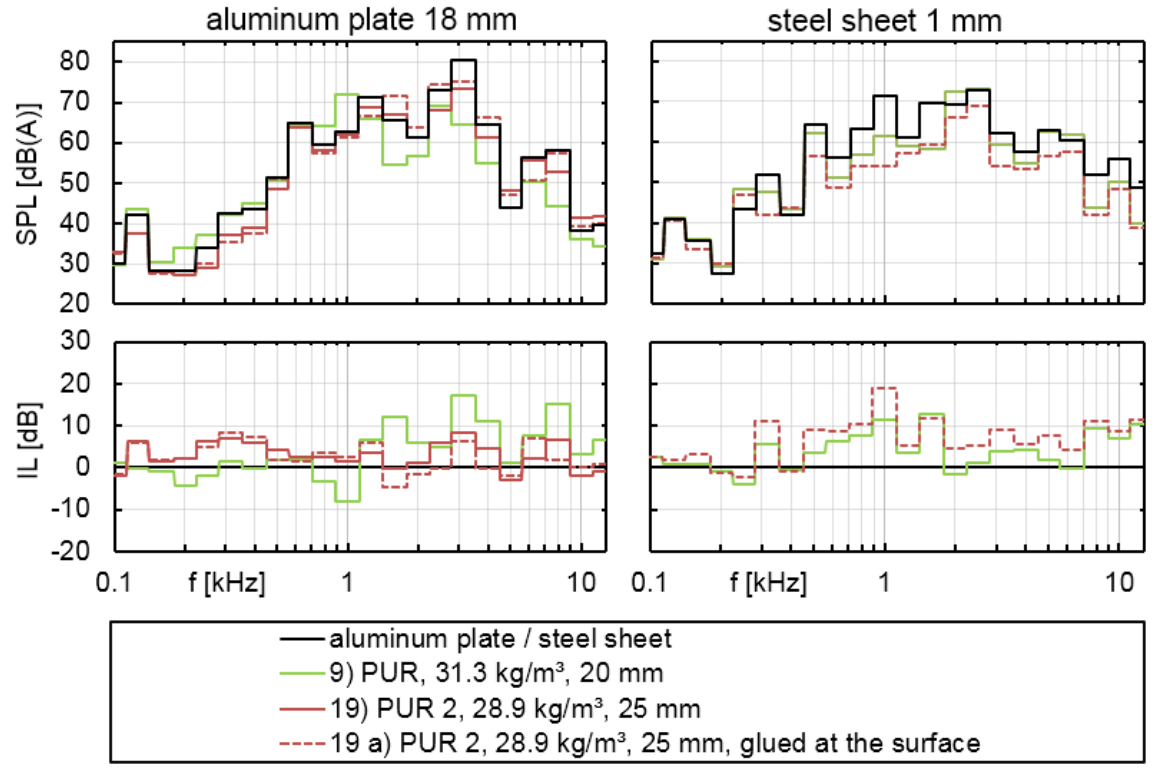


Figure 12: Sound pressure level and insertion loss IL of PUR foams with different mounting conditions

In Figure 11, as well as in Figure 8 and Figure 9, an increase of the density improves the noise reduction at the steel sheet below 1 kHz. Above that frequency, lighter and softer foams show better effects. In contrast,

a higher density in the EPDM materials on the aluminum plate leads to an improvement of the damping behavior at the dominating octave bands above 1 kHz.

For the comparison with the simulations presented in the next section another PUR foam ("PUR 2") was examined experimentally, whose Biot parameters are known. This additional material allows a modeling with the complex approach described in the first section. To ensure the comparability of the finite element model and the experimental setup the foam was not only fixed with the frame to the aluminum plate but additionally with double-sided tape. So, a planar coupling between plate and foam was ensured and later adopted for the simulation. Figure 12 shows the acoustic effect of the foam for its two different mounting configurations on the aluminum plate in comparison to the effect of the PUR foam examined above. The results for the surface glued PUR 2 foam are used as a reference for the numerical investigations.

4 Numerical investigation

Two numerical models of the aluminum plate used in the experimental investigation above were examined. The models differ in their complexity. For all numerical simulations in this paper the Finite Element Method (FEM) is used. The simpler model (Variant 1) is shown in Figure 13, the more complex (Variant 2) in Figure 14. Variant 1 includes the rectangular aluminum plate and the material sample. All boundary conditions are applied directly on the aluminum plate (see the red dots in Figure 13). In each highlighted node all three degrees of freedom (displacement) are pinned. The excitation load is also applied directly to the aluminum plate, in the middle of the backside. In the simple model exclusively hexahedral elements with quadratic shape functions are used.

The results of the simple model with constant and frequency-dependent stiffness and damping can be seen exemplarily for one investigated damping material in Figure 18 in comparison to the measurement in the acoustic test bench. The results are shown in terms of insertion loss curves as the difference of the calculated sound power of the aluminum plate with and without applied damping material. Obviously, the simple model is not sufficient to represent the real setup. For this reason a more complex simulation model was built (Variant 2), which is displayed in Figure 14. The Variant 2 additionally contains the steel hooks on which the whole system is suspended as well as a part of the connection rod to the shaker by which the load is applied and which represents an additional boundary condition. Due to the more complex geometry this model requires also tetrahedral elements for modeling, for which quadratic shape functions were used as well. To ensure the model's quality, a validation is conducted.

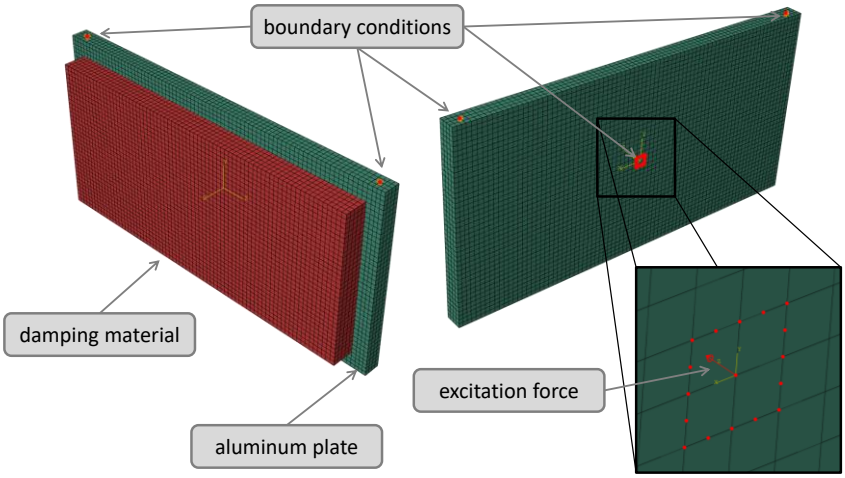


Figure 13: Simple numerical model (Variant 1) of the aluminum plate in the acoustic test bench

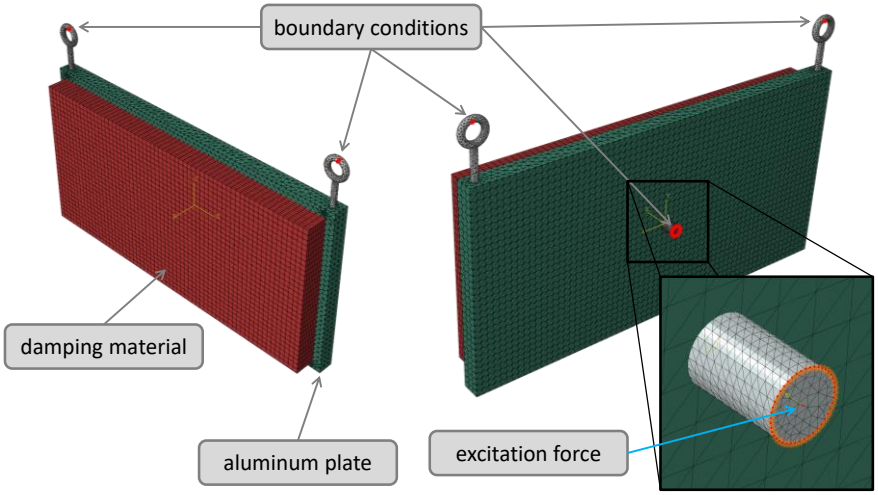


Figure 14: Complex numerical model (Variant 2) of the aluminum plate in the acoustic test bench

For this purpose, a one dimensional Laser-Scanning-Doppler-Vibrometer was used to measure the vibration behavior of the plate without damping material. The aim was to validate the model itself including all loads and boundary conditions, without additional uncertainties caused by the damping material. The experimental setup is shown in Figure 15 both as schematic sketch and as a photograph.

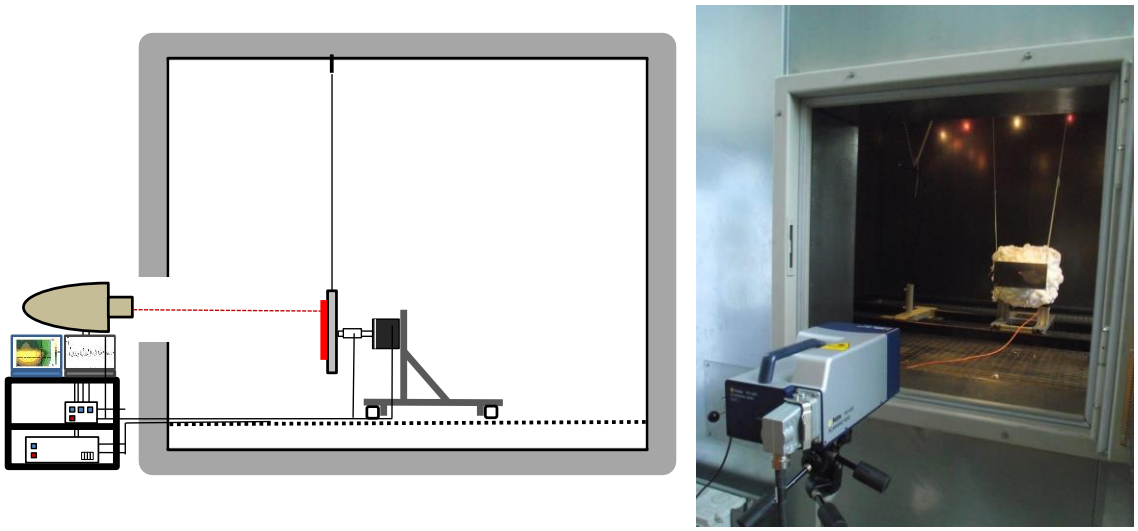


Figure 15: Experimental vibration analysis on the acoustic test bench via Laser-Scanning-Vibrometer

The comparison of the experimental and the numerical vibration analysis of the aluminum plate without additional damping material in Figure 16 makes clear that the complex model (Variant 2) can capture the vibration behavior of the acoustic test bench very well. In Figure 16, three arbitrary eigenfrequencies and their corresponding eigenmodes are shown. It has to be noted that even in the high frequency regime the model prediction is close to the measured data, even if the difference in the eigenfrequencies becomes larger. In contrast, the agreement of the eigenmodes is very good in the whole frequency range.

For the calculation of the radiated sound power of the different configurations a vibroacoustic simulation was necessary. For this purpose, the vibrating structure is fully coupled to a fluid domain. The surrounding fluid volume was modeled as a half sphere and meshed with quadratic tetrahedral elements, which only have the acoustic pressure as a single degree of freedom. The size of the elements has to ensure that all wavelengths of interest can be approximated with sufficient accuracy. The resulting mesh is displayed in Figure 17. To avoid reflections on the borders of the discretized region and, thus, to fulfill the free field radiation condition, an absorbing boundary condition was applied on the outer surface of the fluid volume.

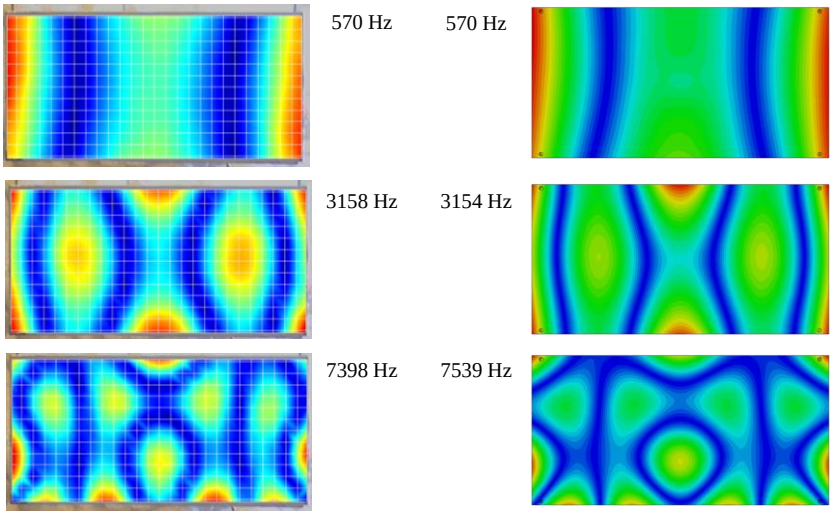


Figure 16: Comparison of the experimental (left) and the numerical (right) vibration analysis of the aluminum plate without additional damping material

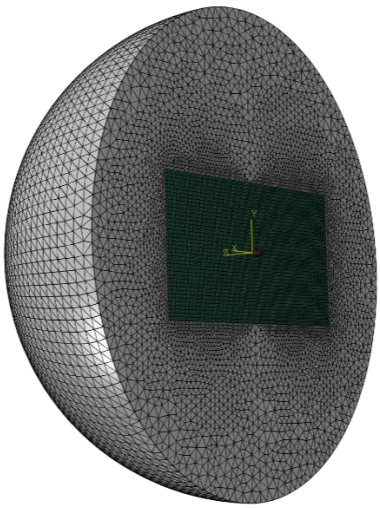


Figure 17: Discretization of the fluid domain in the surrounding of the emitting structure

In Figure 18 the calculated insertion loss (IL) curves of the two different models are contrasted to the experimental results of the PUR 2 foam glued to the surface of the aluminum plate and the steel sheet. The experimental results are shown in Figure 12. As expected, it can be seen that the more complex model of the test configuration leads to results that are closer to the experimental ones. Especially the conspicuous peaks in the IL curves calculated with the simple model are not observable in the experimental results. For the stiff aluminum plate a frequency-dependent modeling of the damping and the elasticity delivers more accurate results than a classical model with constant material parameters. This observation can be made for both the simple model (Variant 1) and the complex model (Variant 2).

Nevertheless, even the prediction quality of the complex model with frequency-dependent material parameters is not yet satisfactory in comparison with the measured data. Consequently, further investigations and improvements have to be made. The calculated IL curve of the corresponding poroelastic material formulation is given with the yellow graph in the upper diagram of Figure 18. For this calculation the JCA-approach was applied. The poroelastic model also shows some peaks that are not visible in the measurement results, and the overall agreement is not sufficient either. At least, it can be stated that the presented approach which uses frequency-dependent determined stiffness and damping values has for the given test case an accuracy that is comparable to the common Biot model.

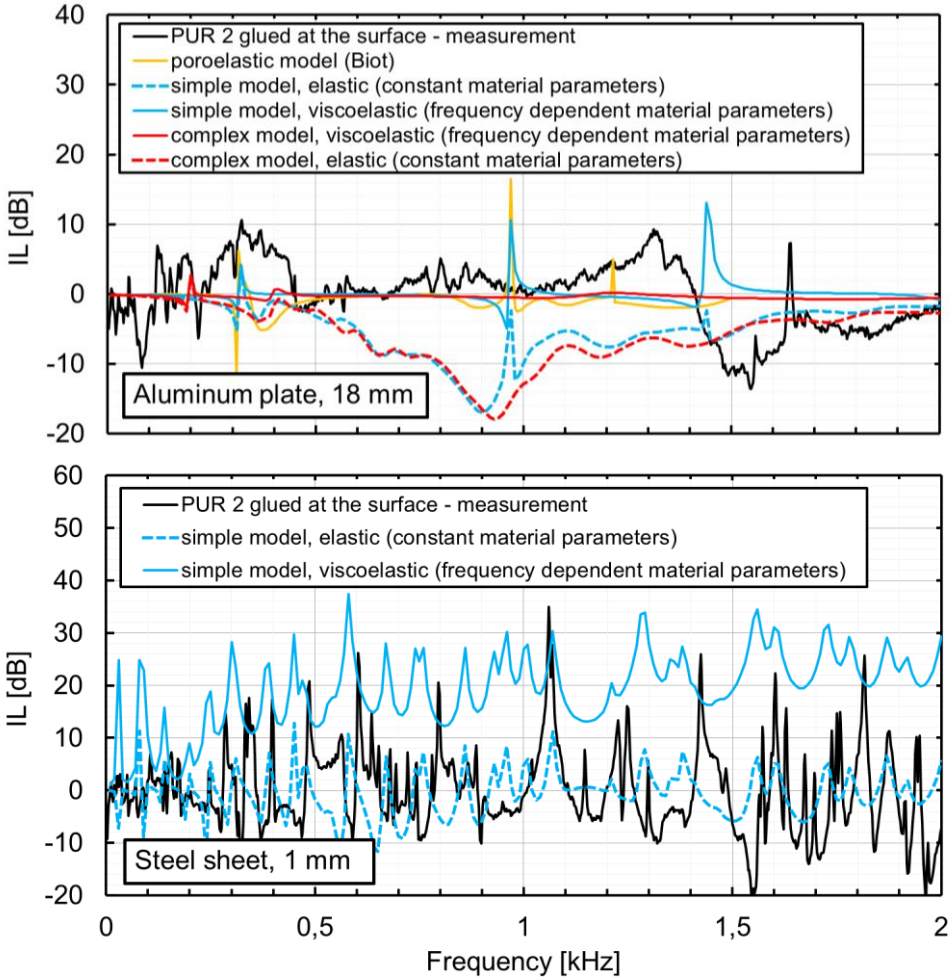


Figure 18: Calculated insertion loss (IL) compared with experimental data from the 18 mm aluminum plate and the 1 mm steel sheet. The yellow curve represents JCA-calculation for this application case; the red curves show the results of Variant 2 of the aluminum plate model.

In contrast, it becomes clear that the usage of frequency-dependent material parameters to represent a viscoelastic material behavior overestimates the IL in the case of the thin steel plate. For this example, the constant material parameters show a better agreement with the experimental results. However, it has to be noted again that all tested simulation approaches lead to insufficient results for the examined test cases. Possible reasons for this have been already mentioned in the text above. Other causes may emerge in further studies that will focus both on the experimental determination of dynamic material properties on the one hand, and on an adequate, simplified and generalizable damping modeling for acoustical predictions on the other hand.

5 Summary and outlook

The aim of this study was to examine a simplified modeling method for poroelastic materials that avoids the experimental and simulative efforts of the complex modeling of such materials based on the Biot formulation. The proposed method considers the frequency dependency of the stiffness and damping as sufficient parameters to numerically predict the dissipation behavior of poroelastic materials in different application cases. This can be derived without knowledge of the open porosity, the viscous and thermal characteristic length, the tortuosity and other specific properties of poroelastic materials. The effects of these poro-mechanical parameters, so the made assumption, can effectively be measured and summarized by the frequency-dependent complex Young's modulus. For this purpose different experimental setups were constructed and tested in advance. The best variant was used in this investigation to measure the parameters

for 19 different material samples. These measurements were reliable only up to a frequency of 2 kHz. The acoustical effects of the tested materials on the noise radiation of a stiff aluminum plate and a more flexible steel sheet were investigated in an anechoic chamber as well.

The test setup of the acoustical experiment was approximated by two finite element models that differed in their complexity. The accuracy of the structural models was verified by laser vibrometer measurements of the aluminum plate in the acoustic test setup. The results of the complex model showed the best agreement with the vibration characteristics of the test setup.

All calculated insertion losses differed significantly from the experimental results. The best fitting was obtained with the frequency-dependent modeling in the complex model of the aluminum plate. For the steel sheet, the simple solution with frequency independent material parameters reached the best agreement while the frequency-dependent overestimated the IL of the plastic foam.

The results of this study show that the proposed simplified approach with frequency-dependent stiffness and damping values is able to approximate the results of an advanced poroelastic formulation and deliver better results than a simple elastic formulation, depending on the application case. To obtain a higher agreement and achieve a better prediction further investigations are necessary. On the one hand, the experimental measurement of the material parameters should be extended to higher frequencies, and influences of the experiment setup on the measured parameters have to be identified to be reduced, if existent. On the other hand, the test setup could be preliminary simplified to gain more knowledge and accuracy in modeling the damping behavior of the porous materials. The poroelastic material could be regarded in its structural behavior alone without acoustic coupling and calculation of the surrounding fluid domain. The experimental reference would be Laser-Scanning-Vibrometer measurements of the vibrating structure with and without poroelastic material. Additionally, a reverse optimization) could deliver the best fitting dynamic Young's modulus and damping coefficient curves. Their comparison with real measured data would improve the knowledge of the physical appropriateness of the approach.

6 References

[1] BIOT, M.A.: Theory of Propagation of Elastic Waves in a Fluid-Saturated Porous Solid. I. Low-Frequency Range. The Journal of the Acoustical Society of America, Vol. 28 (1956) Nr. 2, pp. 168–178.

[2] BIOT, M.A.: Theory of Propagation of Elastic Waves in a Fluid-Saturated Porous Solid. II. Higher Frequency Range. The Journal of the Acoustical Society of America, Vol. 28 (1956) Nr. 2, pp. 179–191.

[3] ALLARD, J.-F.; DAIGLE, G.: Propagation of Sound in Porous Media. Modeling Sound Absorbing Materials. The Journal of the Acoustical Society of America, Vol. 95 (1994) Nr. 5, pp. 2785.

[4] JOHNSON, D.L.; KOPLIK, J.; DASHEN, R.: Theory of dynamic permeability and tortuosity in fluid-saturated porous media. Journal of Fluid Mechanics, Vol. 176 (1987) Nr. 1, p. 379.

[5] CHAMPOUX, Y.; ALLARD, J.-F.: Dynamic tortuosity and bulk modulus in air-saturated porous media. Journal of Applied Physics, Vol. 70 (1991) Nr. 4, pp. 1975–1979.

[6] JAOUEN, L.; RENAULT, A.; DEVERGE, M.: Elastic and damping characterizations of acoustical porous materials. Available experimental methods and applications to a melamine foam. Applied Acoustics, Vol. 69 (2008) Nr. 12, pp. 1129–1140.

[7] SALISSOU, Y.; PANNETON, R.: Pressure/mass method to measure open porosity of porous solids. Journal of Applied Physics, Vol. 101 (2007) Nr. 12, p. 124913.

[8] ATALLA, Y.; PANNETON, R.: Inverse acoustical characterization of open cell porous media using impedance tube measurements. Canadian Acoustics, Vol. 33 (2005) Nr. 1, pp. 11–24.

[9] POMPOLI, F., et al.: How reproducible is the acoustical characterization of porous media? The Journal of the Acoustical Society of America, Vol. 141 (2017) Nr. 2, p. 945.

[10] VAN DER KELEN, C., et al.: On the influence of frequency-dependent elastic properties in vibro-acoustic modeling of porous materials under structural excitation. Journal of Sound and Vibration, Vol. 333 (2014) Nr. 24, pp. 6560–6571.

[11] DAZEL, O., et al.: Expressions of dissipated powers and stored energies in poroelastic media modeled by {u,U} and {u,P} formulations. The Journal of the Acoustical Society of America, Vol. 123 (2008) Nr. 4, p. 2054–2063.

[12] SPANNAN L., et al.: On the characterization of damping materials for acoustic simulations, in preparation, (2018).

Experimental-numerical methods for inverse characterization of the anisotropic-anelastic properties of porous materials, based on dynamic Digital Image Correlation.

L. Manzari[1], **H. Mao**[1], **P. Göransson**[1], **J. Cuenca**[1,2], **I. Lopez Arteaga**[1]
[1] KTH Royal Institute of Technology, Aeronautical and Vehicle Engineering, Teknikringen 8, SE-10044 Stockholm, Sweden
[2] Siemens Industry Software, Interleuvenlaan 68, B-3001 Leuven, Belgium
e-mail: **manzari@kth.se**

Abstract
One of the major challenges in accurately modeling poroelastic materials is the choice of the parameters required for their modeling, immediately followed by the practical difficulty in obtaining them. The directional dependencies of the physical properties further complicate the task of designing experimental setups capable of providing the macroscopic properties. In the work presented here, the focus has been set on the acquisition of high quality displacement data by means of two high-speed cameras and 3D Digital Image Correlation. The obtained displacement field, is fed into a general inverse formulation which is guided by an optimization tool that minimizes the difference between the predicted and the measured data. As a minimum is found, the corresponding parameters are interpreted as material properties for a certain physical model. The solutions for each iteration are calculated with numerical prediction tools, in the cases discussed here the finite element method, where it must be ascertained that the numerical errors are kept to a minimal level.

1 Introduction

Diverse experimental non-contact methods are as of today available to measure the dynamic viscoelastic properties of porous media with an elastic frame. Many of these methods take advantage of laser Doppler vibrometers to measure the velocity of a vibrating poroelastic sample [1, 2]. Still, the characteristic strut thickness of an open cell foam is many times smaller than the typical beam spot diameter of a laser Doppler vibrometer [3, 4, 5]. This results in the measured velocity being the average velocity of all the points that happen to be in the region of focus of the laser – an unknown that becomes even more relevant for high-porosity foams, and may contribute to the poor reproducibility observed in previous inter-laboratory tests [1, 2].

With the aim of estimating the dynamic properties of anisotropic poroelastic materials, the team of the authors has previously model-fit a series of transfer functions measured on a melamine foam sample, exploiting the fact that many porous materials can be modeled as anisotropic viscoelastic solids when placed in vacuum [6, 7]. The setup used for such experiments is shown in Figure 1: the material sample is mounted on a stiff foundation connected to a shaker emitting a monochromatic signal, and transfer functions are computed between the reference point r_0, where a uniaxial accelerometer is mounted, and the points $r_{i,j}$ $(i, j = 1, 2)$ on top of the seismic mass, where the velocity is measured with a laser Doppler vibrometer.

While insightful, such a measurement gives limited information regarding the shear-compression and shear-shear coupling between stresses and strains in the material. The setup is then revisited, with the new arrangement shown in Figure 2: the amount of input data is extended from four points on top of the seismic mass to a full, three-dimensional vector field spanning the four exposed sides of the sample and the foundation.

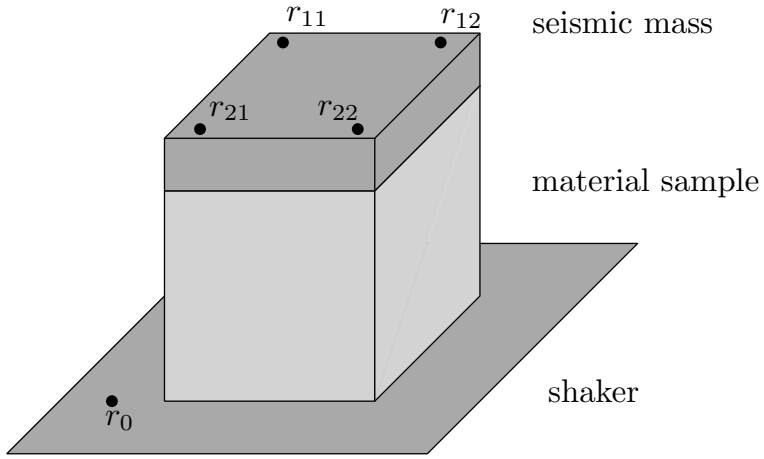


Figure 1: Original setup as used in [7]. The foam sample (in light gray) is placed between a shaker and a seismic mass. An accelerometer measures at point r_0, and a laser vibrometer at points $r_{i,j}$ $(i, j = 1, 2)$.

To the knowledge of the authors, such an approach has not been attempted to date. Such experimental setup is described in Section 2. The measured transfer functions are compared to the output of a model, based on an augmented Hooke's law and described in Section 3, whose parameters are varied by an optimization routine, presented in Section 4, until convergence is reached. Three transfer functions, representative of the frequency-dependent behavior of the material, are shown in Section 5.

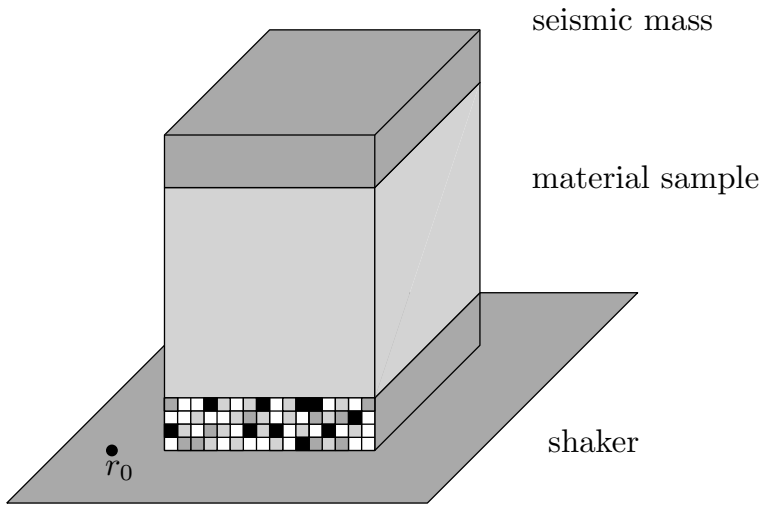


Figure 2: Proposed setup for the present approach. The displacement of the foam sample is computed over its whole external surface using an optical system. The displacement of the base (marked with a speckle pattern) is computed by the same optical system.

2 Data acquisition

The experimental setup, whose components are thoroughly described in [8], is here briefly presented for the sake of self-containedness. Similarly, refer to [9] for a much more detailed description of the post-processing undergone by the displacement fields in order to get usable transfer functions.

2.1 Experimental setup

A pair of high-speed cameras records the sample and the foundation, mounted on an electrodynamic shaker excited with a monochromatic signal. The whole shaker assembly is placed in a vacuum chamber, along with a rotation stage that allows for the rotation of the sample without having to open the vacuum chamber. The high-speed cameras are situated outside the vacuum chamber, and look at the sample through a transparent poly(methyl methacrylate) window. A laser vibrometer is used to perform a preliminary auto-ranging and to try to ensure that the sample has reached steady state conditions. All the frequencies of interest are spanned randomly, in order to decouple frequency-induced trends from trends that might be due to changes in environmental conditions while the measurement is ongoing. The pressure in the vacuum chamber is automatically kept below a set threshold by a microcontroller, also responsible for turning on the lighting unit only for the time the cameras are actually filming. Such a short exposure time is necessary to avoid motion blur and acquire at a high enough frame rate. The data acquisition process is completely automatic, allowing for high repeatability and reproducibility of the results.

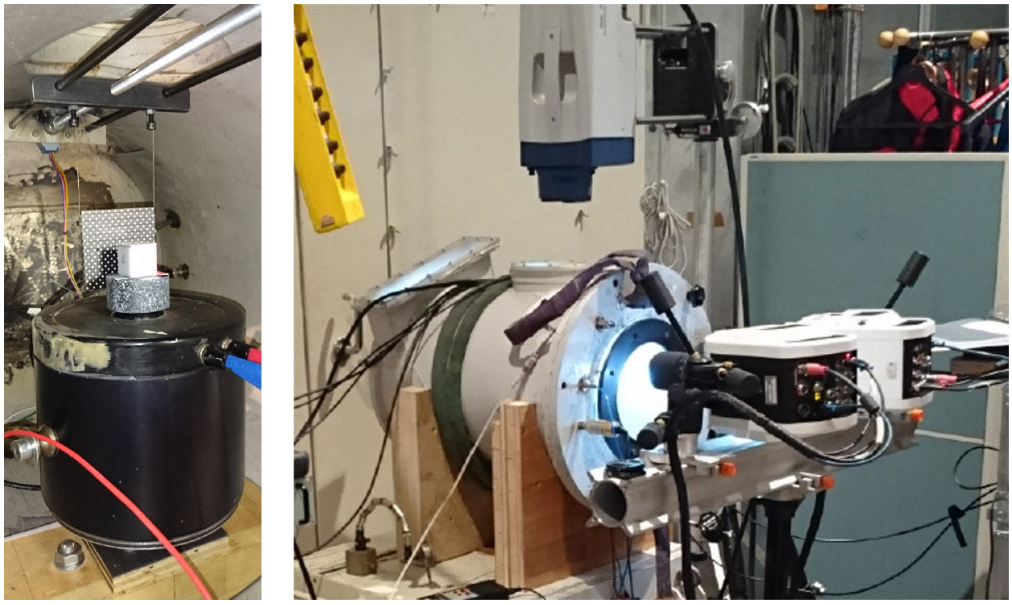


Figure 3: A sample mounted on the shaker in the vacuum chamber (left), and the whole setup during a measurement with the light on and both the high-speed cameras and the laser vibrometer visible (right). The shaker sits on a stepper motor (non visible, inside the wooden block), while the stepper motor responsible for the translation of the calibration plate used by the cameras is clearly visible along with the whole linear actuator assembly.

2.2 Data analysis

The displacement fields produced by the Digital Image Correlation are not polished enough to be directly used: the algorithm may locally fail due to specular reflections in the open cells of the foam, and the coordinate system in which the data is obtained is not relative to the sample but to the initial view of the calibration plate. For every frame then, principal component analysis is performed on the height map of the foundation, assumed non-deformable, and the data is transformed in a coordinate system that is at all times referred to the foundation. Interpolation is used whenever information is missing, and data points that are deemed of low quality (i.e. data points where the Digital Image Correlation has failed for most of the frames) are discarded. A pure sinusoid is fit to every displacement time series, as the solution of a non-linear optimization problem where the parameters to be found are its amplitude, frequency, phase and offset – see Figure 4 for an example. As a consequence, computing transfer functions reduces to a complex division of the phasors

expressing the motion of the sample with the phasors representing the motion of the foundation.

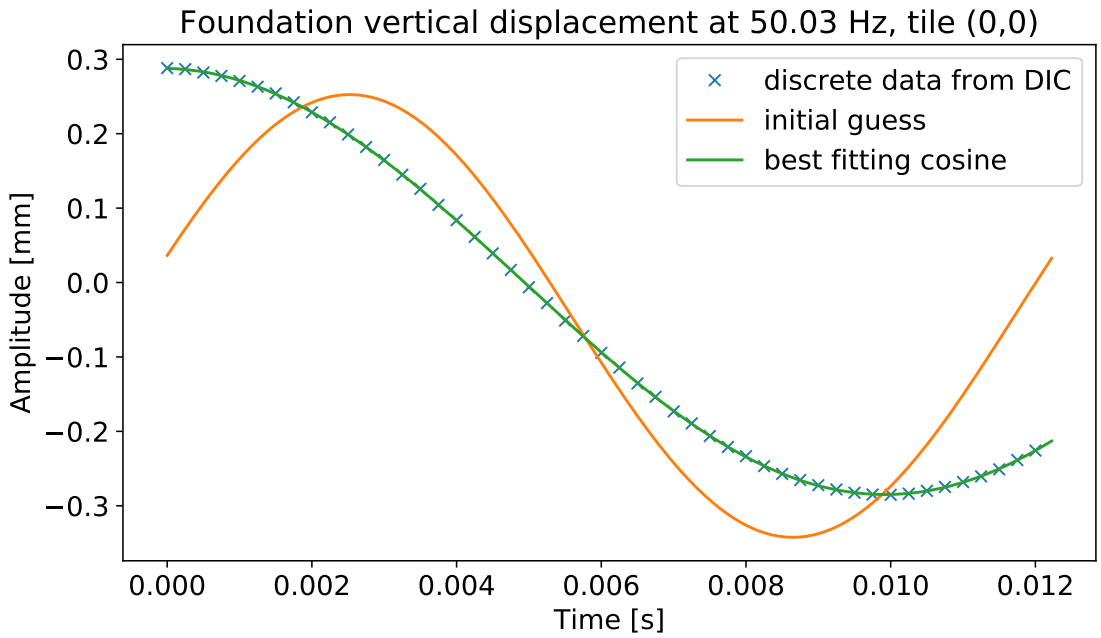


Figure 4: Vertical displacement of a subset of the foundation, as computed by the DIC algorithm using 50 frames. An initial guess for a best fitting cosine is performed using a Fast Fourier Transform to estimate frequency and phase, the standard deviation as an estimator of the amplitude and the mean value as an estimator of the offset. Such guess is fed to a non-linear optimization algorithm, and the best fitting cosine is found.

3 Model of the material

3.1 Constitutive equation

The constitutive laws for fluid-saturated porous materials may be derived as a special case of Biot's equations for anisotropic porous materials including a solid and a fluid phase [10]. The solid and fluid phases are assumed independent and spatially homogeneous at scales of wavelengths much larger than the pore size. For a porous material under vacuum conditions with zero pressure, a Hooke's law can be used to provide a causal representation of the stiffness matrix of the materials with a linear superposition of an elastic part, accounting for the frequency-independent fully relaxed state of the material, and an anelastic part, accounting for frequency-dependent reversible viscoelastic deformation. This has been used in the past in order to estimate various properties of the frame of porous materials without the influence of air [11, 12, 13, 7]. The simplified fractional derivative approach in [7] is used here. The constitutive equation of the anisotropic materials in the frequency domain is thus given by

$$\sigma_i(\omega) = H_{ij}(\omega)\varepsilon_j(\omega), \tag{1}$$

with

$$\sigma = [\sigma_{11}\ \sigma_{11}\ \sigma_{22}\ \sigma_{33}\ \sigma_{12}\ \sigma_{13}\ \sigma_{23}]^T, \tag{2a}$$

$$\varepsilon = [\varepsilon_{11}\ \varepsilon_{11}\ \varepsilon_{22}\ \varepsilon_{33}\ 2\varepsilon_{12}\ 2\varepsilon_{13}\ 2\varepsilon_{23}]^T, \tag{2b}$$

where $\omega = 2\pi f$ is the circular frequency. The components of the frequency-dependent stiffness matrix are given by

$$H_{ij}(\omega) = C_{ij} + \frac{B_{ij}\,(i\omega/\beta)^{\alpha}}{1 + (i\omega/\beta)^{\alpha}}, \tag{3}$$

where C_{ij} denotes the components of the fully relaxed stiffness matrix, α is the fractional derivative order, β is the relaxation frequency in rad·s^{-1}. The stiffness matrix provides a model of the deformation of the material as a superposition of its fully relaxed state and a complex frequency-dependent relaxation phenomenon. In general, a given material may present different types of anisotropy in the elastic and anelastic phenomena. However, both phenomena share the same microstructural geometry and therefore it is here assumed that the elastic and anelastic parts of the stiffness matrix are collinear,

$$B_{ij} = b\,C_{ij}, \tag{4}$$

where b is a real scalar constant. Then the final form of the stiffness matrix is [7]

$$H_{ij}(\omega) = C_{ij}\left(1 + \frac{b\,(i\omega/\beta)^{\alpha}}{1 + (i\omega/\beta)^{\alpha}}\right), \tag{5a}$$

$$H_{ij}(\omega) = H_{ij}^{(R)} + iH_{ij}^{(I)}, \tag{5b}$$

where $H_{ij}^{(R)}$ and $H_{ij}^{(I)}$ are respectively the real and imaginary parts of the complex Hooke's matrix $\mathbf{H}(\omega)$.

3.2 Constraints

The Hooke's matrix must be positive definite according to the second law of thermodynamics, thus the real part of the Hooke's matrix must satisfy the following constraints [14],

$$H_{ii}^{(R)} > 0, \quad i = 1, ..., 6, \tag{6a}$$

$$g_j(\mathbf{H}^{(R)}) - 1 < 0, \quad j = 1, ..., 4, \tag{6b}$$

$$det(\mathbf{H}^{(R)}) > 0, \tag{6c}$$

$$b > 0, \quad \alpha > 0, \quad \beta > 0. \tag{6d}$$

with

$$g_1 = \frac{(H_{23}^{(R)})^2}{H_{22}^{(R)} H_{33}},\ g_2 = \frac{(H_{13}^{(R)})^2}{H_{11}^{(R)} H_{33}},\ g_3 = \frac{(H_{12}^{(R)})^2}{H_{11}^{(R)} H_{22}} \tag{7a}$$

$$g_4 = g_1 + g_2 + g_3 - 2\frac{H_{12}^{(R)} H_{23}^{(R)} H_{31}^{(R)}}{H_{11}^{(R)} H_{22}^{(R)} H_{33}^{(R)}}. \tag{7b}$$

4 Inverse Estimation

The anisotropic model has 21 material properties and 3 anelastic parameters to be inversely estimated, assuming material symmetries in Eq. 3, which are gathered in the form

$$\mathbf{x} = [C_{11}\, C_{12}\, C_{22}\, C_{13}\, C_{23}\, C_{33}\, C_{14}\, C_{24}\, C_{34}\, C_{44}\, C_{15}\, C_{25}\, C_{35}\, C_{45}\, C_{55}\, C_{16}\, C_{26}\, C_{36}\, C_{46}\, C_{56}\, C_{66}\, b\, \alpha\, \beta] \tag{8}$$

Hence, the model has a 24-dimensional space parameter $\mathbf{x}$. The material properties of a given material are defined as a set $\mathbf{x}$ that minimizes a distance in such space between the model and the experiment. The objective function is defined by minimizing the distance as

$$d(\mathbf{x}) = \sum_{m=1}^{M}\sum_{n=1}^{N} \frac{\left\| u_m(\omega_n, \mathbf{x}) - u_m^{(\exp)}(\omega_n) \right\|^2}{\left\| u_m^{(\exp)}(\omega_n) \right\|^2}, \tag{9}$$

where M transfer functions are extracted from the measurement and replicated using the model, N is the number of frequency points of each transfer function, and $u_m^{(\text{exp})}$ and u_m respectively denote the experimental and simulated transfer functions of the displacement deformations in x, y, and z direction including real and imaginary parts. The objective function, formulated in terms of a relative difference, gives equal importance to all frequency samples in the transfer functions.

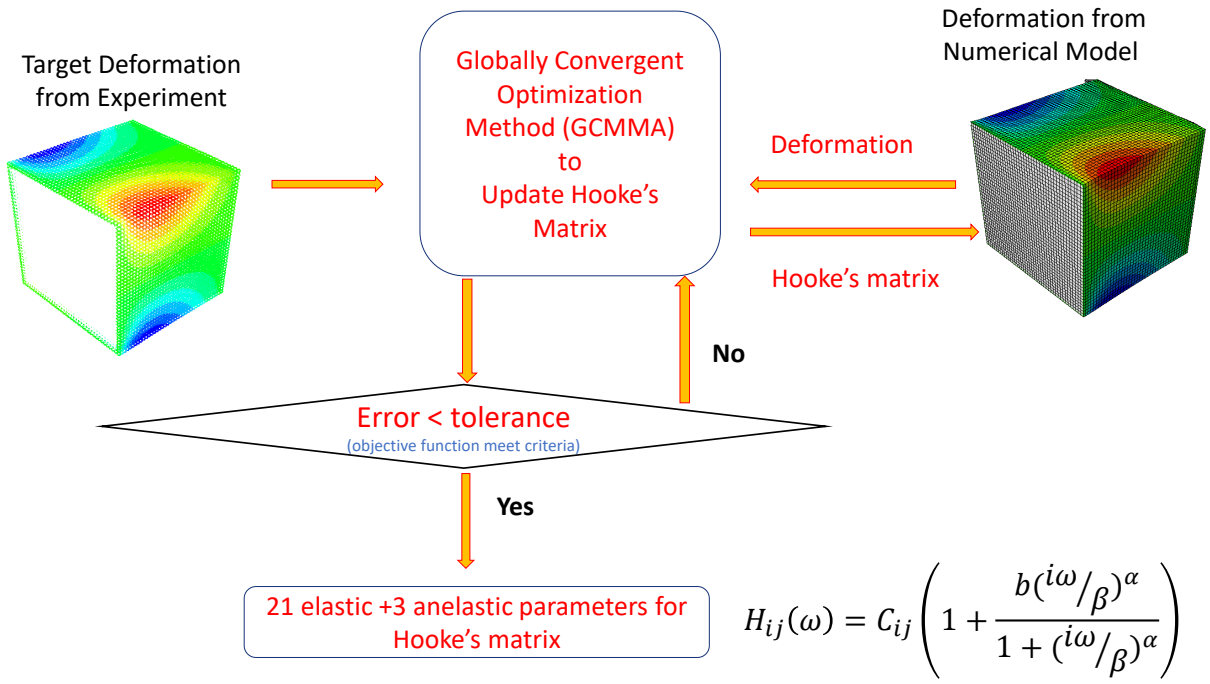


Figure 5: A flowchart illustrating the inverse estimation framework.

Figure 5 shows a flowchart of the inverse estimation framework. The globally convergent method of moving asymptotes (GCMMA) has already been successfully used for the optimization [15, 16, 17]. The finite element model that numerically simulates the experiment is included within the optimization as a subroutine providing the transfer functions, where the stiffness matrix of the material is updated at each iteration. A set of displacements on four observed surfaces (x_-, x_+, y_-, and y_+) extracted from the experimental setup are used as the target transfer functions. The deformations of the numerical model are extracted at the same position as they are measured in the experiment, in order to build the objective function that minimizes the distance in between them. The algorithm is considered to have converged to an optimal solution if both the objective function and the optimization variables vary less than 10^{-3} in 3 successive iterations.

5 Preliminary results

The measurement system is able to resolve displacements in three dimensions both for the foundation and the sample, giving rise to 9 transfer functions to be computed for each subset of pixels on each face of the sample.

For the illustrative purpose of this work, the direction in which the shaker operates defines the vertical Y axis, and the face of the sample that is observed by the cameras defines the XY plane.

After having checked that the foundation effectively moves mainly along one direction (i.e. the vertical, Y direction), the phasor describing the vertical displacement of each pixel subset on the sample is divided by the average of the phasors describing the vertical displacement of the foundation. The result of this operation is close to what would be ideally obtained by a completely resolved material model where a unit displacement is imposed on the foundation.

The excitation frequency is determined as the frequency of the best fitting cosine on the excitation signal that is fed to the power amplifier driving the shaker. The aperture of the normalized displacement field resolved by the data processing routine measures less than the nominal $20\,\mathrm{mm}$, which is the original dimension of the side of the cubic sample. This is due to the fact that the data processing routine excluded the points near the edges of the samples, where the Digital Image Correlation gave inconsistent results. Decreasing the dimension of the subsets on which to run the Digital Image Correlation leads the aperture of the displacement field to better approximate the actual sample size. A bigger subset size has been chosen for its reduced computational time, given the purely illustrative purpose of these results.

Three distinct behaviors of the sample can be observed.

At 50 Hz the face of the sample under observation does not deform to any quantifiable extent, and moves perfectly in phase with the foundation exactly as much as the foundation. The amplitude of the transfer function is 1 for every subset, and there is no phase lag.

At $\approx$ 200 Hz the phase lag is constant and the observed face of the sample stretches so much that its topmost edge moves ≈ 8 times as much as the foundation. The normalized amplitude at the edge that is closest to the foundation is 1, as it should be because of the continuity of displacement.

At 280 Hz the behavior of the observed face is more complex: while the edge closest to the foundation keeps obeying the continuity of displacement, the central part of the sample does not move at all. Its top part instead displaces vertically twice as much in opposite phase.

6 Conclusions

The basis have been set for a framework potentially able to fully characterize the anisotropic-anelastic properties of porous materials, building on a less complex version of the same framework successfully employed in the past by the team of the authors. The increased resolving power of full-field measurements based on Digital Image Correlation, along with the automation implemented in the test rig and the subsequent data processing, effectively produces transfer functions that well fit into the aforementioned framework.

Acknowledgments

Part of the funding for this work is received under the Swedish Research Council, Grant No. 2015-04258. The authors also acknowledge the funding provided by the Knut and Alice Wallenberg Foundation, in the form of the the MUSCLE project awarded to the Odqvist Laboratory in which the equipment used in the current research has been funded.

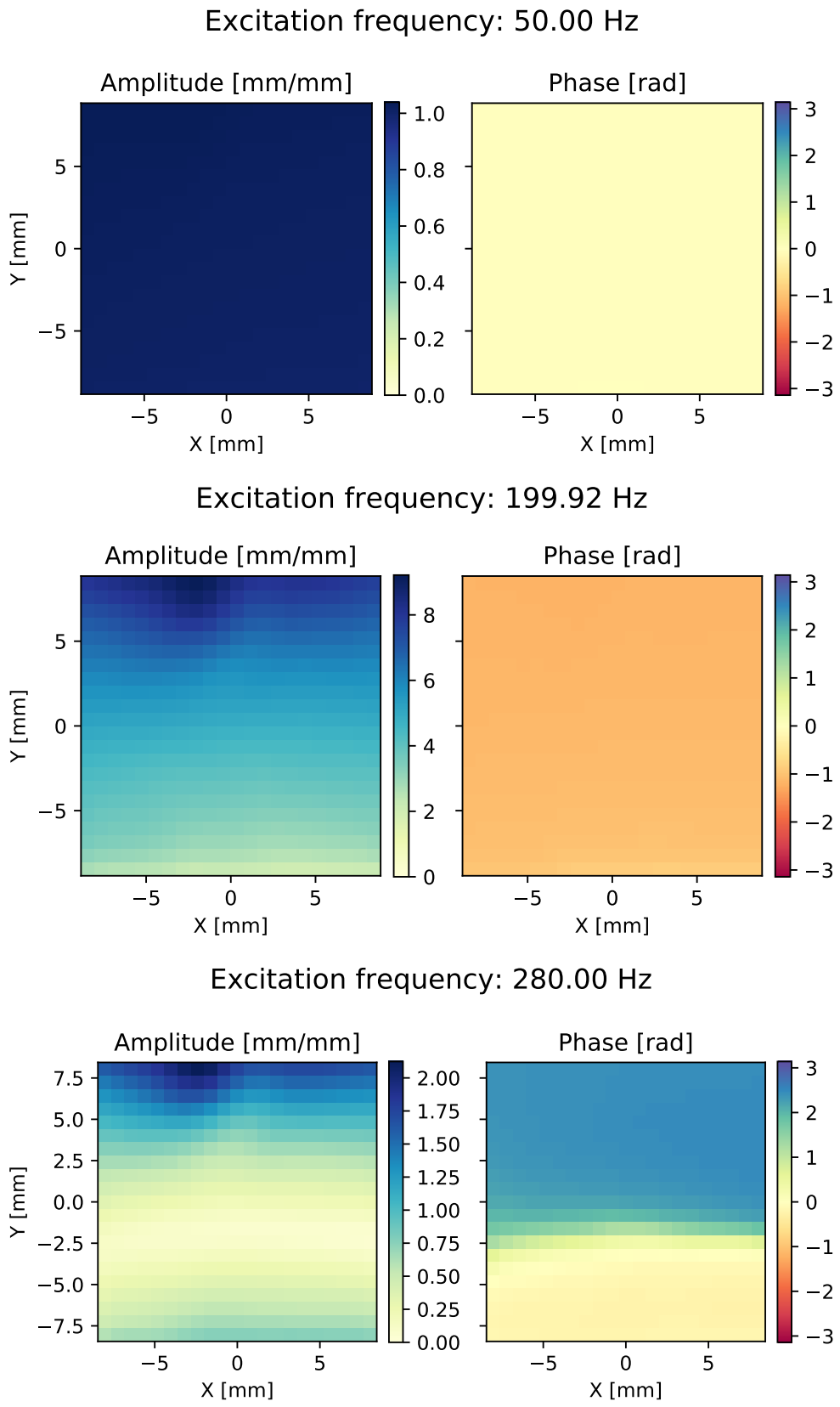


Figure 6: Transfer functions relating the vertical displacement of each subset of one face of the sample with the average vertical displacement of the foundation.

References

[1] Bonfiglio, P., Pompoli, F., Horoshenkov, K. V., Rahim, M. I. B. A., Jaouen, L., Rodenas, J., Bécot, F.-X., Gourdon, E., Jaeger, D., Kursch, V., Tarello, M., Roozen, N. B., Glorieux, C., Ferrian, F., Leroy, P., Vangosa, F. B., Dauchez, N., Foucart, F., Lei, L., Carillo, K., Doutres, O., Sgard, F., Panneton, R., Verdiere, K., Bertolini, C., Bär, R., Groby, J.-P., Geslain, A., Poulain, N., Rouleau, L., Guinault, A., Ahmadi, H., and Forge, C., "How reproducible are methods to measure the dynamic viscoelastic properties of poroelastic media?" *Journal of Sound and Vibration*, Vol. 428, August 2018, pp. 26–43.

[2] Jaouen, L., Renault, A., and Deverge, M., "Elastic and damping characterizations of acoustical porous materials: Available experimental methods and applications to a melamine foam," *Applied Acoustics*, Vol. 69, No. 12, Dec. 2008, pp. 1129–1140.

[3] Lundberg, E., "Micro-Structure Modelling of Acoustics of Open Porous Material," 2016.

[4] Kino, N. and Ueno, T., "Comparisons between characteristic lengths and fibre equivalent diameters in glass fibre and melamine foam materials of similar flow resistivity," *Applied Acoustics*, Vol. 69, No. 4, 2008, pp. 325 – 331.

[5] Martin, P. and Rothberg, S., "Laser vibrometry and the secret life of speckle patterns," Vol. 7098, 2008.

[6] Cuenca, J. and Göransson, P., "Inverse estimation of the elastic and anelastic properties of the porous frame of anisotropic open-cell foams," *The Journal of the Acoustical Society of America*, Vol. 132, No. 2, Aug. 2012, pp. 621–629.

[7] Cuenca, J., Van der Kelen, C., and Göransson, P., "A general methodology for inverse estimation of the elastic and anelastic properties of anisotropic open-cell porous materials—with application to a melamine foam," *Journal of Applied Physics*, Vol. 115, No. 8, Feb. 2014, pp. 084904.

[8] Manzari, L., Göransson, P., Cuenca, J., and Lopez Arteaga, I., "A fully automated high-speed optical rig for in vacuo, full field, non-contact vibration measurements for viscoelastic, anisotropic materials," *NOVEM 2018 Proceedings – Noise and vibration emerging methods – The* 6^{th} *conference*, 2018, pp. 91–102.

[9] Manzari, L., Göransson, P., Cuenca, J., and Lopez Arteaga, I., "A fully automated high-speed optical rig for in vacuo, full field, non-contact vibration measurements for viscoelastic, anisotropic materials," *AIVELA 13th International Conference on Vibration Measurements by Laser and Noncontact Techniques*, 2018.

[10] Biot, M. A., "Theory of Propagation of Elastic Waves in a Fluid-Saturated Porous Solid. I. Low-Frequency Range," *The Journal of the Acoustical Society of America*, Vol. 28, No. 2, 1956, pp. 168–178.

[11] Pritz, T., "Frequency dependence of frame dynamic characteristics of mineral and glass wool materials," *Journal of Sound and Vibration*, Vol. 106, No. 1, 1986, pp. 161–169.

[12] Sfaoui, A., "On the viscoelasticity of the polyurethane foam," *The Journal of the Acoustical Society of America*, Vol. 97, No. 2, 1995, pp. 1046–1052.

[13] Rice, H. and Göransson, P., "A dynamical model of light fibrous materials," *International journal of mechanical sciences*, Vol. 41, No. 4-5, 1999, pp. 561–579.

[14] Jones, R. M., *Mechanics of composite materials*, Taylor & Francis, Philadelphia, 1999.

[15] Svanberg, K., "A class of globally convergent optimization methods based on conservative convex separable approximations," *SIAM journal on optimization*, Vol. 12, No. 2, 2002, pp. 555–573.

Microstructure based modelling of the thermal and viscous dissipation of a transversely isotropic porous fibrous insulation material.

B.P. Semeniuk[1], **P. Göransson**[1], **O. Dazel**[2]
[1] KTH Royal Institute of Technology, Aeronautical & Vehicle Engineering,
100 44 Stockholm, Sweden,
e-mail: **semeniuk@kth.se**

[2] University of Le Mans,
LAUM UMR CNRS 6613, Le Mans, 72000, France.

Abstract
This paper focusses on the modelling and prediction of two of the main mechanisms of acoustic attenuation, the dynamic drag and thermal heat transfer, of a bundle of fibres typical of lightweight fibrous porous materials. The methodology uses geometrical properties derived from microscopy, and is based on the assumption that the interaction between the shear stress fields as well as the thermal fields of neighbouring fibres, may be neglected in the predicted dynamic impedances of an individual fibre. Analytical procedures are discussed which provide an estimation of the impedances acting on infinite longitudinal and transversely orientated cylinders. The frequency-dependent viscous and thermal contributions may be scaled in terms of statistical fibre diameter distributions and orientation angles. Using these analytical models, a three-dimensional poroelastic model of coupled acoustic and structural wave propagation through a transversely isotropic, fibrous, highly porous thermal insulation material is presented.

Introduction

Recent work into the modelling of fibrous porous materials has strongly focussed on microstructural aspects, i.e. the fibre diameter distributions, fibre orientation angles, and the distributions of fibre lengths [1], [2] and [3] in order to predict the transport properties of the material. In practice, this means that a combination of numerical and experimental techniques are used to estimate the macroscopic transport properties of the fibrous material, such as static viscous and thermal permeabilities, viscous characteristic lengths, and high frequency tortuosity. Using this information, the vibroacoustic performance may then be simulated using established Biot-based poroelastic models [4], and [5]. This approach is now improving the relationship between the physical modelling of these materials and parameters which are controllable in manufacturing processes, thus allowing more efficient virtual material development. Unfortunately, this approach often requires a series of intermediate steps: either complex fluid flow and thermal diffusion simulations, and existing material samples for laboratory measurements.

It would be much more convenient if the microstructural aspects of the fibrous material were taken into account specifically in the formulation of the governing poroelastic equations, meaning direct relationships between physical properties such as fibre diameter distributions and orientation angles, and resulting acoustic performance could be made in an efficient way using analytical expressions.

In order to achieve this goal, we have taken the coupled fluid and elastic solid fibre momentum equations for a transversely isotropic fibrous material [6], [7] and [8] as a starting point, and have utilised analytical

expressions to describe the dynamic viscous drag forces resulting from relative motion between the assumed array of longitudinal and transverse cylindrical fibres and the surrounding viscous fluid [9]. Analytical expressions describing heat flow from the cylindrical fibres to the surrounding fluid [10], [11] have also been introduced through a modified fluid dilatation term which is valid for non-equilibrium conditions, thus allowing oscillatory heat transfer from the solid to the fluid phases to be considered. Viscous and thermal field interactions between neighbouring fibres are neglected, meaning the formulation is targeted at higher porosity materials having large spacings between fibres.

In a second step, equations describing coupled acoustic and structural wave propagation through the material have been derived in terms of a new set of Biot coupling coefficients, allowing a Transfer Matrix of the transversely isotropic fibrous material to be defined in terms of constitutive material parameters, and fibre microstructure parameters only. The model is then validated in comparison against impedance tube absorption coefficient measurements. Lastly, we have carried out thermoviscous acoustic fluid finite element modelling in order to investigate the viscous and thermal boundary layer interaction within a regular array of fibres as a means of confirming the underlying assumptions that viscous and thermal field interactions between neighbouring fibres can be neglected.

Table 1: Fibre Microstructure Model Material Properties

Mean fibre diameter	$2\bar{a}$	1.28×10^{-6} m
Mean fibre spacing	b	18.052×10^{-6} m
Bulk density	ρ_b	10.88 kg/m^3
Fluid density	ρ_f	1.2044 kg/m^3
Fibre density	ρ_s	2450 kg/m^3
Fluid dynamic viscosity	μ_f	1.8140×10^{-5} kg/ms
Fluid bulk modulus	K_f	101325 Pa
Fibre bulk modulus	K_s	35 GPa
Fluid thermal conductivity	κ_f	0.02577 W/mK
Fibre thermal conductivity	κ_s	775 W/mK
Fluid specific heat	C_{pf}	1005 J/kgK
Fibre specific heat	C_{ps}	775 J/kgK
Fluid expansion coeff.	η	3.411×10^{-3} 1/K
Young's modulus, z	E_1	135 Pa
Young's modulus, x, y	E_2	10300 Pa
Shear modulus, z	G_1	700 Pa
Shear modulus, x, y	G_2	8200 Pa
Poisson ratio, z	ν_1	0
Poisson ratio, x, y	ν_2	0
Loss factor, z	η_1	0.1
Loss factor, x, y	η_2	0.1
Porosity	Ω	0.9961

Material Definition

The fibrous material considered is a lightweight and flexible aircraft fuselage acoustical and thermal insulation from the Johns Manville Company [9]. The solid fibre skeleton consists of a distribution of glassfibres, having diameters ranging from 0.125 to 5.0 micrometres, with a mean fibre diameter d_m of 1.28 micrometres. The orientation of the fibres is assumed to be primarily transversely isotropic, with some fibres being orientated through the thickness of the material. The transversely isotropic elastic properties for this material have been previously determined from *in-vacuo* static measurements [12]. A complete list of the fluid properties (air at 20 deg. C.), the assumed glass fibre properties, and the measured transversely isotropic macroscopic elastic properties are provided in Table. 1.

Solid Fibre and Fluid Momentum Equations

The governing coupled fluid-solid equations are formulated using the Biot assumption that the volume fraction is uniform throughout the solid, interconnected fibre skeleton; every plane cuts through a fraction ϕ of solid fibre per unit total area. For any realistic choice of control volumes, on average the so-called infinite fibres will extend beyond the boundaries of the volume. Thus we do not have any pressure gradient forces at the fluid-fibre interfaces inside the control volume boundary. It is recognised that if we hold the contents of the control volume constant, pressurising the fluid applies a compressive stress or dilatation of the solid fibre. Alternatively, if the control volume is held constant, applying a stress to the solid applies a pressure stress or dilatation to the fluid. This coupling between the solid fibres and surrounding fluid results in a set of stress-strain relations for the porous composite following the work of Biot [7], [8] and [13].

Momentum Equations for the Solid Fibre Skeleton

If we assume a continuous porous-solid model for the thermal insulation control volume and apply a momentum balance, the equation of motion for the fibre skeleton in Cartesian coordinates is, no summation on indices implied,

$$\phi\rho_s\ddot{u}_i = \left(\frac{\partial\sigma_{ii}}{\partial x_i} + \frac{\partial\sigma_{ij}}{\partial x_j} + \frac{\partial\sigma_{ik}}{\partial x_k}\right) - F_{D_i}, \tag{1}$$

where i, j, k are component ordinal numbers in Cartesian co-ordinate system, e.g. $i = 1, 2, 3$, $(.)_{,i} = \frac{\partial(.)}{\partial x_i}$ is the partial derivative with respect to Cartesian co-ordinate x_i, x_i is the Cartesian co-ordinate component in direction i, and where F_{D_i} are the components of the dynamic viscous drag force vector $\mathbf{F}_D$, which the skeleton exerts on the fluid per unit volume of composite material. This viscous drag force is a linear function of the skeleton strains and fluid displacements, given in the frequency domain in matrix form in terms of the relative motion between the solid fibre skeleton and surrounding viscous fluid

$$\{\mathbf{F}_D\} = \left[\bar{Z}\right]\left\{\dot{\mathbf{u}} - \dot{\mathbf{U}}\right\}, \tag{2}$$

where $\left[\bar{Z}\right]$ represents the spatially-averaged dynamic viscous drag force impedance matrix, per unit volume, for a transversely isotropic insulation material

$$\left[\bar{Z}\right] = \frac{\phi}{A}\begin{bmatrix} J & 0 & 0 \\ 0 & J & 0 \\ 0 & 0 & K \end{bmatrix}. \tag{3}$$

Here, the coefficients J, K, are defined in terms of the axial, Z_l, and transverse, Z_t, viscous drag force impedances, per unit fibre length, for an individual fibre

$$Z_l = 2\pi a k_\beta \mu_f \frac{H_1^{(2)}(k_\beta a)}{H_0^{(2)}(k_\beta a)}, \tag{4}$$

$$Z_t = j\pi\rho_f\omega a^2\left[1 - \frac{4H_1^{(2)}(k_\beta a)}{k_\beta a H_0^{(2)}(k_\beta a)}\right], \tag{5}$$

and ϕ/A is the total fibre length per unit volume of the thermal insulation material. The shear wavenumber of the infinite viscous fluid medium surrounding the fibre is given by $k_\beta = [-(j\omega\rho_f)/\mu_f\,]^{1/2}$.

A more complete description of the formulation of the terms of the viscous drag force impedance matrix is provided in [9]. Note that it is also possible to average the viscous drag force impedance matrix for the distribution of fibre diameters, and also for a distribution of fibre orientation angles, allowing a completely anisotropic fibre microstructure to be considered. The viscous drag force impedance matrix $\left[\bar{Z}\right]$ defined by Eq. (3), is also directly comparable to Biot's permeability tensor [7].

Momentum Equations for the Fluid

Similarly, upon performing a momentum balance on the fluid phase of the composite porous medium control volume, the equation of motion for the fluid in Cartesian coordinates is

$$(1-\phi)\,\rho_f \ddot{U}_i = \frac{\partial \sigma}{\partial x_i} + F_{D_i}, i = 1,2,3, \tag{6}$$

Constitutive Relations for Equilibrium

Under equilibrium conditions, $\{\sigma\}$ and $\{\varepsilon\}$ are related for any porous material by constitutive stress-strain relations of the form [7]

$$\{\sigma\} = [D]\,\{\varepsilon\}\,, or\,\{\varepsilon\} = [D]^{-1}\,\{\sigma\}\,. \tag{7}$$

The matrix $[D]$ is referred to as the stiffness matrix while its inverse $[D]^{-1}$ is referred to as the compliance matrix; these matrices possess symmetry properties by virtue of $\{\sigma\}$ and $\{\varepsilon\}$ being conjugate variables. These symmetry properties are assumed to not extend to non-equilibrium conditions. Therefore, the equilibrium relations given by Eq. (7) need to be modified to describe solid skeleton and fluid stresses in terms of strains (or displacements) away from equilibrium, for instance when heat transfer from the solid fibres to the surrounding fluid phase results in a corresponding thermal expansion of the fluid.

For a transversely isotropic material, the relations represented by Eq. (7) are specified in terms of strains by:

$$e_{xx} = a\sigma_{xx} + d\sigma_{yy} + g\sigma_{zz} + h\sigma, \tag{8}$$

$$e_{yy} = d\sigma_{xx} + a\sigma_{yy} + g\sigma_{zz} + h\sigma, \tag{9}$$

$$e_{zz} = g\sigma_{xx} + g\sigma_{yy} + b\sigma_{zz} + m\sigma, \tag{10}$$

$$e_{yz} = t\sigma_{yz}, \tag{11}$$

$$e_{zx} = t\sigma_{zx}, \tag{12}$$

$$e_{xy} = 2\,(a-d)\,\sigma_{xy}, \tag{13}$$

$$\varepsilon = h\,(\sigma_{xx} + \sigma_{yy}) + m\sigma_{zz} + n\sigma. \tag{14}$$

These relations are invariant under rotation about the z-axis. Here, σ_{xx}, σ_{yy}, etc., are the skeleton contributions to the forces on the faces of a unit cube of porous material, and σ is the fluid force contribution. The coefficients of Eqs. (8 - 14) can be written in terms of the *in-vacuo* elastic material constants E_1, E_2, ν_1, ν_2, G_2 as follows [8]:

$$a = \frac{1}{E_1}, b = \frac{1}{E_2}, d = -\frac{\nu_1}{E_1}, g = -\frac{\nu_2}{E_2}, t = \frac{1}{G_2}, \tag{15}$$

$$h = \frac{1}{3\,(1-\phi)\,K_s} - \frac{\phi}{(1-\phi)}\,(a+d+g)\,, \tag{16}$$

$$m = \frac{1}{3\,(1-\phi)\,K_s} - \frac{\phi}{(1-\phi)}\,(b+2g)\,, \tag{17}$$

$$n = \frac{1}{(1-\phi)^2}\left(\frac{(1-\phi)}{K_f} - \frac{\phi}{K_s}\right) + \frac{\phi^2}{(1-\phi)^2}\,(2a+b+2d+4g)\,. \tag{18}$$

In the above, K_f and K_s are the bulk moduli of the fluid and solid phases respectively. These coefficients are identical to those given by Biot, assuming that K_s is the same in all directions within the porous insulation. Internal structural damping may be allowed for in the transversely isotropic skeleton by giving complex, frequency-dependent, values to the 5 material constants which describe the skeleton deformation under constant pore pressure, or through the use of frequency-dependent thermodynamic relaxation functions, [12].

These relations now allow us to express the compliance matrix explicitly in symmetric form as

$$[D]^{-1} = \begin{bmatrix} a & d & g & 0 & 0 & 0 & h \\ d & a & g & 0 & 0 & 0 & h \\ g & g & b & 0 & 0 & 0 & m \\ 0 & 0 & 0 & t & 0 & 0 & 0 \\ 0 & 0 & 0 & 0 & t & 0 & 0 \\ 0 & 0 & 0 & 0 & 0 & 2(a-d) & 0 \\ h & h & m & 0 & 0 & 0 & n \end{bmatrix}, \tag{19}$$

for a transversely isotropic porous material. Notice that this matrix is of 7×7 order, reflecting coupling between the fluid and elastic solid phases of the composite porous material.

Non-Equilibrium Constitutive Relations

It is now possible to express the skeleton stresses and fluid dilatation as functions of the skeleton strains and fluid stress, i.e.

$$\{\sigma_s\} = f(\{\varepsilon_s\}, \sigma), \tag{20}$$

$$\varepsilon = g(\{\varepsilon_s\}, \sigma). \tag{21}$$

Physically, departures from the equilibrium constitutive relations arise for two reasons:

(i) assumed one-way heat transfer between the solid and fluid phases leads to thermal expansion of the fluid, which is reflected in an altered fluid dilatation term, ε;

(ii) internal damping in the skeleton also causes the coefficients in $[D]^{-1}$ to differ, under loading dynamic conditions, from their equilibrium values.

Mechanism (i) is represented by introducing the following set of hypotheses:

(A) Thermoelastic coefficients may be neglected. This means that the solid phase is treated as having zero coefficient of thermal expansion (or negligible as compared with the thermal expansion of the fluid phase);

(B) Thermal expansion of the fluid does not alter Eq. (20) for the skeleton stresses. In other words the skeleton stresses are determined uniquely, at a given frequency, by the skeleton strains and the fluid pressure.

Note that this is different from assuming a relationship like

$$\{\sigma_s\} = F(\{\varepsilon_s\}, \varepsilon), \tag{22}$$

(i.e. one involving the fluid dilatation in place of σ) which remains unaffected by heat transfer. It seems physically reasonable to assume that the effect of the fluid phase on $\{\sigma_s\}$ is mediated by the fluid pressure, rather than by the fluid dilatation ε.

Modified Skeleton Stress Equation

Inversion of $[D]^{-1}$ gives the 7×7 stiffness matrix $[D]$, which is specified in the notation of Biot [8] as

$$\begin{Bmatrix} \sigma_{xx} \\ \sigma_{yy} \\ \sigma_{zz} \\ \sigma_{yz} \\ \sigma_{zx} \\ \sigma_{xy} \\ \sigma \end{Bmatrix} = \begin{bmatrix} P & A & F & 0 & 0 & 0 & M \\ A & P & F & 0 & 0 & 0 & M \\ F & F & C & 0 & 0 & 0 & Q \\ 0 & 0 & 0 & L & 0 & 0 & 0 \\ 0 & 0 & 0 & 0 & L & 0 & 0 \\ 0 & 0 & 0 & 0 & 0 & N & 0 \\ M & M & Q & 0 & 0 & 0 & R \end{bmatrix} \begin{Bmatrix} e_{xx} \\ e_{yy} \\ e_{zz} \\ e_{yz} \\ e_{zx} \\ e_{xy} \\ \varepsilon \end{Bmatrix}, \tag{23}$$

which allows us to write the usual fluid dilatation in terms of the coefficients of the stiffness matrix

$$\varepsilon = \frac{1}{R}\sigma - \left(\frac{M}{R} e_{xx} + \frac{M}{R} e_{yy} + \frac{Q}{R} e_{zz} \right). \tag{24}$$

If this is now substituted into the fluid momentum expressions given by Eqs. (6), we are able to eliminate ε in favour of σ, and the result is a modified set of stress-strain relations for the skeleton stresses. These are expressed in matrix form as

$$\left\{ \overset{*}{\sigma} \right\} = [B] \left\{ \begin{matrix} e \\ \varepsilon \end{matrix} \right\}, \tag{25}$$

where

$$\begin{Bmatrix} \sigma^*_{xx} \\ \sigma^*_{yy} \\ \sigma^*_{zz} \\ \sigma^*_{yz} \\ \sigma^*_{zx} \\ \sigma^*_{xy} \end{Bmatrix} = \begin{bmatrix} P - \frac{M^2}{R} & A - \frac{M^2}{R} & F - \frac{MQ}{R} & 0 & 0 & 0 & \frac{M}{R} \\ A - \frac{M^2}{R} & P - \frac{M^2}{R} & F - \frac{MQ}{R} & 0 & 0 & 0 & \frac{M}{R} \\ F - \frac{MQ}{R} & F - \frac{MQ}{R} & C - \frac{Q^2}{R} & 0 & 0 & 0 & \frac{Q}{R} \\ 0 & 0 & 0 & \frac{1}{L} & 0 & 0 & 0 \\ 0 & 0 & 0 & 0 & \frac{1}{L} & 0 & 0 \\ 0 & 0 & 0 & 0 & 0 & N & 0 \end{bmatrix} \begin{Bmatrix} e_{xx} \\ e_{yy} \\ e_{zz} \\ e_{yz} \\ e_{zx} \\ e_{xy} \\ \sigma \end{Bmatrix}. \tag{26}$$

Note that the coefficients of the modified stiffness matrix $[B]$ of order 6×7 consist of components of the stiffness matrix $[D]$.

Fluid Dilatation With Heat Transfer

In this section, we derive a fluid dilatation equation in the form of Eq. (24), which is valid under non-equilibrium conditions, i.e. when waves propagate through the porous material. Its extension away from equilibrium involves the linearised entropy equation for the two-phase porous material.

Let Υ be the rate of heat input to the fluid from the solid fibre skeleton, per unit total volume. Then the rate of entropy input, per unit total volume, is

$$\dot{S} = \frac{\Upsilon}{T_f}, \tag{27}$$

where T_f is the absolute temperature of the fluid. The macroscopic entropy balance equation relates the rate of entropy change within a fixed region to the entropy input from the solid fibre skeleton and the net in-flow across the fluid boundaries. Per unit total volume, the entropy of the fluid then is

$$\rho_s s \left(1 - \phi\right), \tag{28}$$

where s is the specific entropy. The entropy input from the fibre skeleton is $\dot{S}$ and the entropy in-flow across the boundary of the region is

$$-\nabla \cdot \left[\rho_f s \left(1 - \phi\right) \dot{\mathbf{U}} \right]. \tag{29}$$

The rate of entropy production within the fluid region is second-order and therefore neglected in a linearised approximation; we then have

$$\frac{\partial}{\partial t}\left[\rho_f s\left(1-\phi\right)\right] = \dot{S} - \nabla\cdot\left[\rho_f s\left(1-\phi\right)\dot{\mathbf{U}}\right]. \tag{30}$$

Subtracting s times ($\sigma = -\left(1-\phi\right)p$) from Eq. (30) gives

$$\rho_f\left(1-\phi\right)\frac{\partial s}{\partial t} = \dot{S} - \rho_f\left(1-\phi\right)\left(\dot{\mathbf{U}}\cdot\nabla\right)s, \tag{31}$$

$$\frac{Ds}{Dt} = \frac{\dot{S}}{\rho_f\left(1-\phi\right)}. \tag{32}$$

Combining Eqs. (27) and (32) results in

$$\frac{Ds}{Dt} = \frac{\Upsilon}{T_f\rho_f\left(1-\phi\right)}. \tag{33}$$

For oscillations at a single frequency, Υ is written in terms of the fluid temperature perturbation T_f' as

$$\Upsilon = -\bar{Y}_e T_f', \tag{34}$$

where $\bar{Y}_e = \left(1/Y_f + 1/Y_s\ \right)^{-1}$ is called the unit volume effective thermal impedance function, written in terms of the respective fluid and fibre thermal impedances [10, 11], since it relates the heat transfer rate to the fluctuating fluid temperature. From Eqs. (33) and (34), the following relation between Υ and the fluid stress is defined as

$$\Upsilon = \alpha\sigma = -\alpha\left(1-\phi\right)p, \tag{35}$$

where

$$\alpha = \eta T_f'\left\{\frac{\rho_f C_{pf}\left(1-\phi\right)}{\bar{Y}_e} + \frac{1}{j\omega}\right\}^{-1}. \tag{36}$$

Combining Eqs. (33) and (35) with the general relationship for fluid density in terms of pressure and specific entropy

$$d\rho_f = \frac{1}{c^2}dp - \frac{\rho_f\eta T_f'}{C_{pf}}ds, \tag{37}$$

we arrive at a pressure-density relation for the fluid medium which allows interphase heat transfer

$$\frac{1}{\rho_f}\frac{\partial\rho_f}{\partial t} = \frac{1}{\rho_f c^2}\frac{\partial p}{\partial t} + \frac{\alpha\eta}{\rho_f C_{pf}}p. \tag{38}$$

General Continuity Equation

The general continuity equation for a two-phase composite, in which both the fluid and solid fibre skeleton phases are regarded as compressible, may be written as

$$\left(1-\phi\right)\dot{\varepsilon} + \phi\dot{e} = \left(1-\phi\right)\frac{1}{\rho_f}\frac{\partial\rho_f}{\partial t} + \phi\frac{1}{\rho_s}\frac{\partial\rho_s}{\partial t}. \tag{39}$$

This is a kinematic relation and is not affected by heat transfer or other departures from equilibrium. For given values of $\{\varepsilon_s\}$ and σ, we can use Eqs. (38, 39) to determine how the fluid dilatation ε now departs from its equilibrium value. Note that by hypothesis (B) posed earlier, $\{\sigma_s\}$ is the same function of $\{\varepsilon_s\}$ and σ, whether or not heat transfer is present; the same therefore applies to the density of the solid phase ρ_s. The skeleton dilatation e is then determined by $\{\varepsilon_s\}$ alone without regard to non-equilibrium effects. Therefore Eq. (39) gives

$$\dot{\varepsilon} - \left(\dot{\varepsilon}\right)_{eq} = \frac{1}{\rho_f}\frac{\partial\rho_f}{\partial t} - \left(\frac{1}{\rho_f}\frac{\partial\rho_f}{\partial t}\right)_{eq}, \tag{40}$$

where the subscript eq refers to equilibrium, i.e. without heat transfer.

Continuity Equation with Heat Transfer

The non-equilibrium term in $(1/\rho_f)(\partial\rho_f/\partial t)$ is identified in Eq. (38) as $\{(\alpha\eta)/(\rho_f C_{pf})\}p$. Substituting this value in Eq. (40), and combining with Eq. (21), gives

$$\varepsilon = g_{eq}(\{\varepsilon_s\}, \sigma) + \left(\frac{1}{j\omega}\frac{\alpha\eta}{\rho_f C p_f}\right) p, \tag{41}$$

where $g_{eq}(\{\varepsilon_s\}, \sigma)$ is the equilibrium fluid dilatation expression as defined by Eq. (24). The substitution of Eq. (24) then allows the fluid dilatation expression to be re-written for non-equilibrium conditions as

$$\chi\sigma = R\varepsilon + (Me_{xx} + Me_{yy} + Qe_{zz}), \tag{42}$$

where χ is defined by

$$\chi = \left[1 - \frac{\alpha\eta R}{j\omega\rho_f C p_f (1-\phi)}\right]. \tag{43}$$

Poroelastic Equation Summary

The entire set of three-dimensional, microstructure-based, dynamic equations defining wave propagation through a transversely isotropic fibrous, porous thermal insulation are now presented together here in vector component form in terms of fluid stress, and the fluid and fibre skeleton displacements, as given by Eq. (42), and Eqs. (1), Eqs. (6), and the modified relations for the fibre skeleton stress, Eq. (26).

It is important to highlight that these relations are valid for single temperatures only; the dynamic viscous drag force and heat transfer terms are presented here as being uncoupled, i.e. an increase of viscous forces does not increase the fluid temperature, which would be a non-linear effect. This means that the long-term increase of temperature in the porous material due to the continued presence of dynamic viscous forces is not accounted for.

Plane Wave Propagation Through a Layer of Insulation Material

As a means of verification of the theory presented here, the absorption coefficient of a prescribed thickness of rigidly-backed insulation material is calculated and compared with standard impedance tube experimental results. In this case, the fibrous insulation sample considered is assumed to be composed of stacked layers of fibres having a normalised diameter and are distributed at random orientations within an isotropic plane (transversely isotropic). Alternatively, a material composed of a distribution of fibre diameters at completely random spatial orientations (fully anisotropic) can be considered as well.

Wave Equations

Assuming harmonic plane wave propagation in the transverse z direction through the thickness of the material, the fluid and fibre skeleton displacement quantities U_x, U_y, u_x, u_y are all zero and only dilatational waves are propagated through the porous insulation layer. Following these assumptions, the fluid dilatation equation, and the fluid and solid phase momentum equations reduce to

$$R\varepsilon + Qe_z - \chi\sigma = 0, \tag{44}$$

$$\nabla\sigma + \left[\omega^2(1-\phi)\rho_f - j\omega\bar{Z}_z\right]U_z + j\omega\bar{Z}_z u_z = 0, \tag{45}$$

$$\frac{Q}{R}\nabla\sigma + j\omega\bar{Z}_z U_z + \left(C - \frac{Q^2}{R}\right)\nabla^2 u_z + \left(\omega^2\phi\rho_s - j\omega\bar{Z}_z\right)u_z = 0. \tag{46}$$

Substitution for σ then allows the fluid and solid skeleton momentum equations to be rewritten in terms of strains and displacements

$$\nabla\left(Qe_z + R\varepsilon\right) = \chi\left[-\omega^2\left(1-\phi\right)\rho_f + j\omega\bar{Z}_z\right]U_z - j\omega\chi\bar{Z}_z u_z, \tag{47}$$

$$\nabla\left(\hat{C}e_z + Q\varepsilon\right) = -j\omega\chi\bar{Z}_z U_z - \chi\left(\omega^2\phi\rho_s - j\omega\bar{Z}_z\right)u_z \tag{48}$$

where the coefficient $\hat{C}$ is defined as, $\hat{C} = \chi C + \frac{Q^2}{R}\left(1-\chi\right)$.

Biot also writes these momentum equations in terms of the ρ^* coupling coefficients

$$\nabla\left(Qe_z + R\varepsilon\right) = -\omega^2\left({\rho^*}_{12}u_z + {\rho^*}_{22}U_z\right), \tag{49}$$

$$\nabla\left(\hat{C}e_z + Q\varepsilon\right) = -\omega^2\left({\rho^*}_{11}u_z + {\rho^*}_{12}U_z\right). \tag{50}$$

Comparison of Eqs. (47, 48) and Eqs. (49, 50) then allows us to define a new set of Biot coupling coefficients [13] which are specified in terms of the microstructural heat transfer from the fibres of the solid skeleton to the surrounding viscous fluid, and in terms of the microstructural dynamic viscous drag forces present due to the relative motion between the solid and fluid phases

$${\rho^*}_{11} = \chi\left(\phi\rho_s - j\frac{\bar{Z}_z}{\omega}\right), {\rho^*}_{12} = j\frac{\chi\bar{Z}_z}{\omega}, {\rho^*}_{22} = \chi\left[\left(1-\phi\right)\rho_f - j\frac{\bar{Z}_z}{\omega}\right]. \tag{51}$$

Taking the divergence of Eqs. (49, 50) then gives

$$\nabla^2\left(Qe_z + R\varepsilon\right) = -\omega^2\left({\rho^*}_{12}e + {\rho^*}_{22}\varepsilon\right), \tag{52}$$

$$\nabla^2\left(\hat{C}e_z + Q\varepsilon\right) = -\omega^2\left({\rho^*}_{11}e + {\rho^*}_{12}\varepsilon\right), \tag{53}$$

and solving for $\nabla^2\varepsilon$ and ε results in

$$\varepsilon = \frac{\left(\hat{C}R - Q^2\right)\nabla^2 e + \omega^2\left({\rho^*}_{11}R - {\rho^*}_{12}Q\right)e}{\omega^2\left({\rho^*}_{22}Q - {\rho^*}_{12}R\right)}, \tag{54}$$

$$\nabla^2\varepsilon = \frac{\left({\rho^*}_{12}Q - {\rho^*}_{22}\hat{C}\right)\nabla^2 e + \omega^2\left(\left({\rho^*}_{12}\right)^2 - {\rho^*}_{11}{\rho^*}_{22}\right)e}{\left({\rho^*}_{22}Q - {\rho^*}_{12}R\right)}, \tag{55}$$

which is of the same form as Bolton's expressions [4] for $\nabla^2\varepsilon$ and ε. Taking the Laplacian of ε and combining the equations results in

$$\nabla^4 e_z + A_1\nabla^2 e_z + A_2 e_z = 0, \tag{56}$$

$$A_1 = \omega^2\frac{\left({\rho^*}_{11}R - 2{\rho^*}_{12}Q + {\rho^*}_{22}\hat{C}\right)}{\left(\hat{C}R - Q^2\right)}, A_2 = \omega^4\frac{\left[{\rho^*}_{11}{\rho^*}_{22} - \left({\rho^*}_{12}\right)^2\right]}{\left(\hat{C}R - Q^2\right)}, \tag{57}$$

where Eq. (56) governs the propagation of dilatational waves through the solid skeleton. The plane wave harmonic solution of Eq. (56) yields two wave numbers given by

$${k^2}_{1,\,2} = \left(A_1 \pm \sqrt{{A_1}^2 - 4A_2}\right)/2\,, \tag{58}$$

representing a dilatational *slow wave*, and the dilatational *fast wave* propagating through the solid and fluid phases of the elastic porous material. Application of the curl operation to the fluid and fibre skeleton momentum equations Eqs. (49, 50) results in

$$-\omega^2\left({\rho^*}_{11}\bar{\omega} + {\rho^*}_{12}\bar{\Omega}\right) = L\nabla^2\bar{\omega}, \tag{59}$$

$$-\omega^2\left(\rho^*{}_{12}\bar{\omega}+\rho^*{}_{22}\bar{\Omega}\right)=0, \tag{60}$$

where the rotational wave in the fibre skeleton is defined as

$$\nabla^2\bar{\omega}+{k_t}^2\bar{\omega}=0, \tag{61}$$

with corresponding rotational wavenumber

$${k_t}^2=\left(\omega^2/L\right)\left[\rho^*{}_{11}-\left(\rho^*{}_{12}\right)^2/\rho^*{}_{22}\right]. \tag{62}$$

These dilatational and rotational wavenumbers, the fluid and fibre skeleton momentum equations, along with the modified stress-strain relations, then allow a poroelastic transfer matrix to be defined according to the methods presented by [4] and [5]. With the application of appropriate boundary conditions, the acoustic performance of a finite layer of the glassfibre thermalinsulation material, as mounted in an impedance tube, can be predicted.

Transfer Matrix Model Validation and Results

The dynamic equations of motion of a transversely isotropic porous fibrous insulation material developed in this work are assumed to represent an array of axial and transverse fibres, having measured fibre diameter distributions, orientations and spacing between fibres. They have been formulated entirely based on microstructure-derived viscous and thermal dissipation mechanism assumptions which are suitable for high-porosity lightweight fibrous porous materials. For validation purposes, the aforementioned model has been applied in transfer matrix form to calculate the normal incidence absorption coefficient of a 50 mm thickness of rigidly-backed sample of fibrous thermalinsulation material, refer to Table. 1, and is compared to impedance tube measurements. A mean fibre diameter of 1.28 micrometres was used in this analysis, and a representative fibre inclination angle of 50 degrees (from the xy plane) was chosen, which was sufficient for the validation shown here. We will present results using an expanded set of fibre distributions and orientation angles in future work.

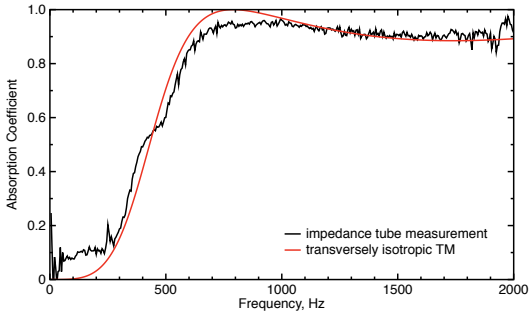


Figure 1: Comparison of the normal-incidence absorption measurement and transversely isotropic microstructure TM simulation. 50mm thickness fibrous insulation sample, mounted in an impedance tube with rigid backing, with plane wave acoustic excitation to 2000 Hz.

Good agreement exists in the comparison between the numerical simulation and measured absorption coefficient across the entire frequency range, as shown in Fig. 1. Material inertial and dissipative effects have been correctly represented in the simulation through the modified stress-strain relations, and the analytical expressions used to describe microstructural viscous and thermal dissipation and coupling in the model. Further improvements in the results are expected as more detailed fibre diameter and orientation distributions are considered.

In addition, the analytical expressions for dynamic viscous drag impedance $\bar{Z}_z$ through the thickness of the material sample, as defined by Eq. (3), may also be scaled according to fibre diameter distributions and orientations to provide an estimate of the airflow resistance of the material. This is shown in Fig. 2, in the form of the low frequency asymptote of the dissipative (real part) of $\bar{Z}_z$.

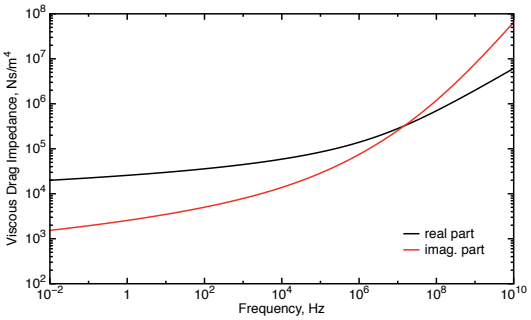


Figure 2: Dynamic viscous drag force impedance function, assuming a mean fibre diameter of 1.28 micrometres, and a vertical fibre inclination angle of 50 degrees.

Thermoviscous Acoustic Fluid Finite Element Modelling

In the formulation of the microstructure-based equations for acoustic-structural wave propagation through a fibrous porous material presented here, the underlying assumption is that the dynamic viscous and thermal fields surrounding individual fibres do not interact significantly with the fields of neighbouring fibres. For a given frequency, the boundary layer thicknesses for these fields are $l_{vor} = (2\mu/\omega\rho)^{1/2}$ and $l_{ent} = (2\kappa/\omega\rho C_p)^{1/2}$, such that for the case of having air as the fluid surrounding the cylindrical glassfibres, the typical viscous and thermal boundary layer thicknesses are $l_{vor} \approx 2.2\times10^{-3}m$, and $l_{ent} \approx 2.6\times10^{-3}m$ for a fibre excitation frequency of $1Hz$. As frequencies increase, the depth of the respective boundary layers decrease, and become $l_{vor} \approx 6.9 \times 10^{-5}m$, and $l_{ent} \approx 8.2 \times 10^{-5}m$ for a fibre excitation frequency of $1000Hz$. In the low frequency range, these boundary layer thicknesses are very much greater than the average spacing between fibres (18.052 micrometres), and become significantly less than the spacing between fibres at the highest frequencies.

In our finite element modelling approach, we consider the fluid surrounding the glass fibres as being a thermoviscous acoustic one, allowing the coupled acoustic, vorticity and entropy modal fields in the fluid surrounding an array of cylindrical glassfibres, as described by [14], to be investigated.

Viscous and Thermal Boundary Layers of a Single Cylindrical Fibre

The first case of a sinusoidally oscillating elastic cylinder, embedded in an infinite thermoviscous acoustic fluid was considered in order to establish a modelling criteria for the FE numerical procedure, using as a reference the analytical formulation for transverse dynamic drag force as defined by Eq. (5). The main challenges with this approach are realising an exact representation of the viscous and thermal boundary layers in the vicinity of the fibre surface, and of the definition of non-reflecting outer boundary conditions to allow sufficient decay of the boundary layers with increasing radial distance from the fibre surface.

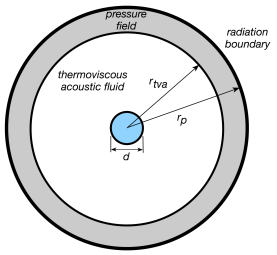


Figure 3: Sinusoidally oscillating rigid cylinder of mean fibre diameter embedded in a thermoviscous acoustic fluid. The radius of the surrounding thermoviscous acoustic fluid region is 15 mm, and the depth of the surrounding pressure field is 5 mm.

The fluid region surrounding the fibre of mean diameter was divided into two separate domains, an inner

thermoviscous acoustic fluid one having a radius of 15 mm, which was then encased by a 5 mm thickness acoustic pressure field having a non-reflecting radiation boundary on the outer surface, as shown in Fig. 3. The combined depth of the fluid surrounding the fibre is then 20 mm. The excitation frequency was $1Hz$, and the fibre oscillation amplitude was chosen to be 0.01 micrometres in order to ensure linearity.

For the FE modelling, the COMSOL Multiphysics simulation package [15] was chosen, for the possibility of modelling the air surrounding the cylindrical fibres as a thermoviscous acoustic fluid. In the single fibre model, a combination of linear pressure, and quartic velocity and thermal elements were used for the thermoviscous fluid and acoustic pressure regions, respectively. Quartic elastic stress elements were used for the stress field internal to the fibre, which was then coupled to the surrounding fluid regions. The combined single-fibre model contained a total of approximately 12 million degrees-of-freedom. Integrating over the fibre surface to estimate the reaction forces, then allows the transverse dynamic viscous drag impedance per unit length values to be estimated. From the single fibre FE model a value of 87642 Nsm^{-4} was found, which is within 0.2 percent of the analytical result of 87449 Nsm^{-4}, refer to [9]. These results should then be considered as a very satisfactory validation of the numerical FE modelling procedure.

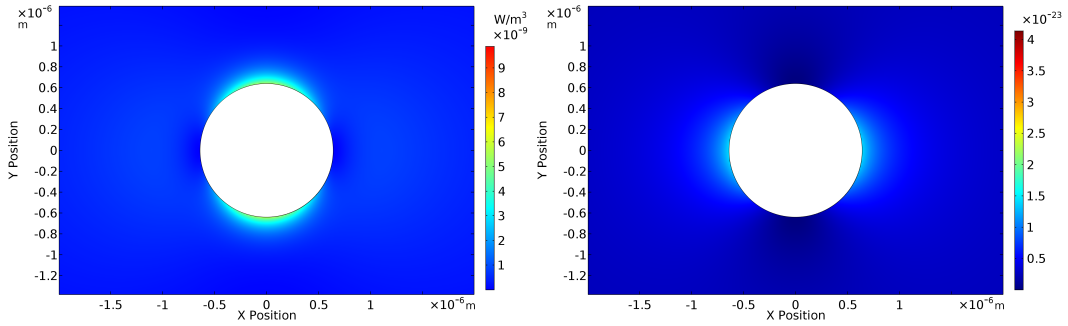


Figure 4: Single fibre viscous and thermal power dissipation density fields $\left(W/m^3\right)$ for 1 Hz excitation frequency assuming a linear excitation amplitude of 0.01 micrometres in the x-dir. for all fibres in the array.

Examination of the viscous and thermal power dissipation density fields, as shown in Figs. 4a and 4b, indicates the concentration of the viscous and thermal boundary layers in the vicinity of the fibre surface, at micro and nano-scale levels. Considering these fields radially in the x direction from the fibre surface, as shown in Figs. 5a and 5b, further demonstrates that even for the very low excitation frequency of $1Hz$, there is a concentration of the boundary layers to the immediate vicinity of the fibre surface. The viscous boundary layer, which is responsible for most of the dissipation losses in the analytical model, has decayed approximately 98 percent at the position of the next neighbouring fibre, according to the known fibre spacing parameter b.

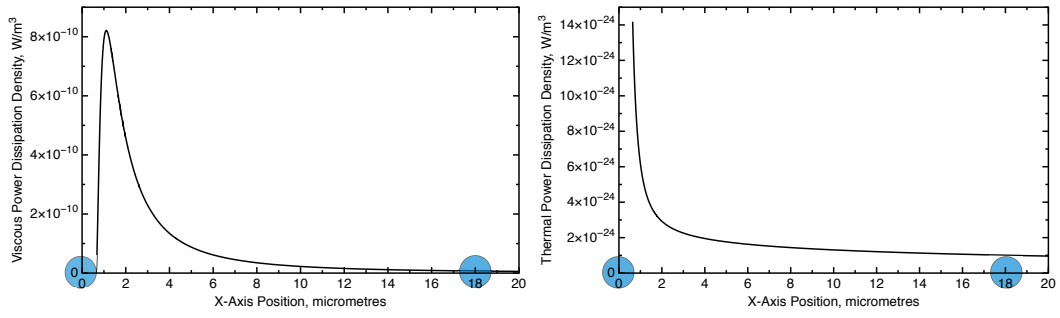


Figure 5: Single fibre viscous and thermal power dissipation along the x-dir. of the fibre array for 1 Hz excitation frequency assuming a linear excitation amplitude of 0.01 micrometres in the x-dir.

Boundary Layer Interaction Within a Multi-Fibre Array

To investigate the significance of viscous and thermal boundary layer interaction between fibres, a more realistic case with a large array of 225 fibre diameters based on the known diameter distribution was modelled, using the mean fibre spacing b of 18.052 micrometres, as schematically shown in Fig. 6. This model adds not only increased complexity due to a larger number of interacting fibres, it also incorporates the effects related to a variation of the fibre diameters in the array. The array was centered around a fibre with the mean diameter. Using the verified single-fibre modelling procedure, the resulting FE model consisted of approximately 130 million degrees-of-freedom.

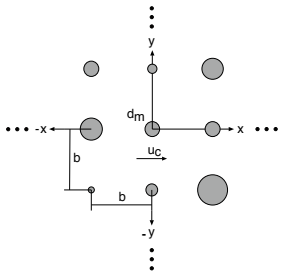
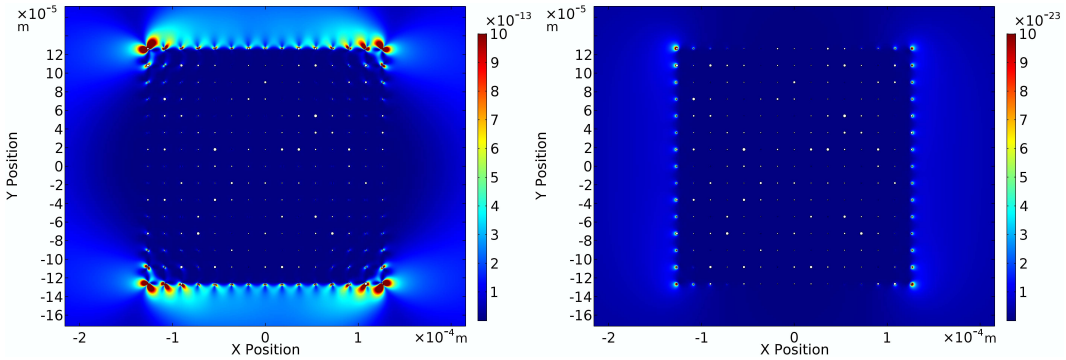


Figure 6: 225 fibre array, with diameters according to the measured distribution, and the estimated fibre spacing b. The center fibre in the array has the mean fibre diameter of 1.28 micrometres.

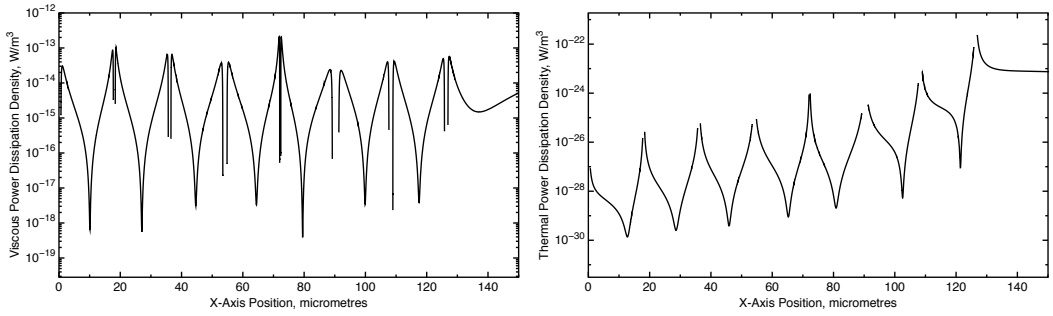


(a) viscous (b) thermal

Figure 7: 225 random fibre distribution viscous and thermal power dissipation density field (W/m^3) for 1 Hz excitation frequency assuming a linear excitation amplitude of 0.01 micrometres in the x-dir. for all fibres in the array.

All fibres in the array were excited in-phase at a frequency of $1Hz$, and the fibre oscillation amplitude was chosen to be 0.01 micrometres in order to ensure linearity. The resulting viscous and thermal power dissipation density fields are shown in Figs. 7a and 7b, zoomed to the immediate vicinity of the fibres. As a comparison, the arithmetic mean of the viscous drag force impedance function, using the measured statistical distribution of fibre diameters [9], gives a value of 79527 Nsm^{-4}. Integrating over the surfaces of all 225 fibres, the simulated fibre reaction forces allowed the dynamic drag impedance to be estimated to within 5.1 percent. Computational limits did not allow a denser mesh required for even improved accuracy.

Considering these fields radially in the x direction from the fibre surface, as shown in Figs. 8a and 8b, demonstrates that the viscous boundary layers maintain a uniqueness in amplitude around individual fibres as one moves across the fibre array. This suggests that for the glassfibre thermalinsulation material, there is not a significant level of boundary layer interaction between the fibres. The thermal boundary layers trend upwards in amplitude with each subsequent fibre, indicating a certain level of interaction between the fibres. This significance of this will be investigated further in future work.



(a) viscous (b) thermal

Figure 8: Viscous and thermal power dissipation density along the x-dir. of the fibre array, assuming a 1 Hz linear excitation amplitude of 0.01 micrometres for all fibres in the array.

Conclusions

We have developed a new set of dynamic equations of motion for transversely isotropic, highly-porous fibrous insulation materials based entirely on physical microstructure considerations. Viscous losses are included in the model through analytical expressions for the dynamic drag impedance of cylindrical fibres, in a form similar to Biot's permeability tensor. Non-equilibrium conditions are included in the fluid dilatation expressions to characterise heat transfer effects between the fibre skeleton and surrounding fluid. A new set of Biot coupling parameters have been derived to reflect the interaction of the fluid and solid phases of the material. Fibre spacing (i.e. porosity), and distributions of diameter and fibre orientation angles are easily considered. A transfer matrix representation of the model has been developed, with the subsequent simulation of an impedance tube experiment providing very good agreement with measurements. In addition, thermoviscous acoustic fluid finite element simulations have been used to demonstrate the interaction of viscous shear and thermal boundaries between neighbouring fibres in the material.

The approach eliminates the need for experimental or numerical determination of traditional porous material transport parameters. As such, the model presented here has a direct relationship to parameters which are controllable in fibrous material manufacturing processes, and lends itself well to the physically-based numerical optimisation of lightweight fibrous porous materials for acoustics.

Acknowledgements

The authors would like to express their appreciation to Professors C.L. Morfey and M. Petyt of the Institute of Sound and Vibration Research, Southampton, UK for their support in the initial theoretical development. The second author gratefully acknowledges the funding from the Swedish Research Council, grant nr 2015-04258, which has partially contributed to this work.

References

[1] He, M., Perrot, C., Guilleminot, J., Leroy, P., and Jacqus, G., "Multiscale prediction of acoustic properties for glass wools: Computational study and experimental validation," *The Journal of the Acoustical Society of America*, Vol. 143, No. 6, 2018, pp. 3283–3299.

[2] Xue, Y., Bolton, J. S., Gerdes, R., Lee, S., and Herdtle, T., "Prediction of airflow resistivity of fibrous acoustical media having two fiber components and a distribution of fiber radii," *Applied Acoustics*, Vol. 134, 2018, pp. 145–153.

[3] Zielinski, T. G., "Microstructure representations for sound absorbing fibrous media: 3D and 2D multiscale modelling and experiments," *Journal of Sound and Vibration*, Vol. 409, 2017, pp. 112 – 130.

[4] Bolton, J., Shiau, N., and Kang, Y., "Sound transmission through multi-panel structures lined with elastic porous materials," *Journal of Sound and Vibration*, Vol. 191, No. 3, 1996, pp. 317–347.

[5] Allard, J. F. and Atalla, N., *Propagation of sound in porous media. Modelling sound absorbing materials*, John Wiley & Sons, 2nd ed., 2009.

[6] Semeniuk, B. P., Morfey, C. L., and Petyt, M., "Acoustic and structural wave propagation through a fibrous, highly porous thermal insulation material," *Proceedings of ISMA 21, the International Conference on Noise and Vibration Engineering, Leuven, Belgium, 18- 20 September 1996*.

[7] Biot, M. A., "Theory of Elasticity and Consolidation for a Porous Anisotropic Solid," *J. Appl. Phys.*, Vol. 26, No. 2, 1955, pp. 182–185.

[8] Biot, M. A. and Willis, D. G., "The elastic coefficients of the theory of consolidation," *Journal of Applied Mechanics*, Vol. 24, 1957, pp. 594–601.

[9] Semeniuk, B. P. and Göransson, P., "Microstructure based estimation of the dynamic drag impedance of lightweight fibrous materials," *The Journal of the Acoustical Society of America*, Vol. 141, No. 3, 2017, pp. 1360–1370.

[10] Kuntz, H. L., "High-intensity sound in air saturated fibrous bulk porous materials," *NASA-CR-167979*, 1982.

[11] Kuntz, H. L. and Perreira, N. D., "Oscillatory Conductive Heat Transfer for a Fiber in an Ideal Gas," *Journal of Heat Transfer*, Vol. 107, No. 1, 1985, pp. 52–56.

[12] Rice, H. and Göransson, P., "A dynamical model of light fibrous materials," *Int. J. Mech. Sci.*, Vol. 41, 1999, pp. 561–579.

[13] Biot, M. A., "Theory of Propagation of Elastic Waves in a Fluid-Saturated Porous Solid. I. Low-Frequency Range," *The Journal of the Acoustical Society of America*, Vol. 28, No. 2, 1956, pp. 168–178.

[14] Pierce, A., *Acoustics: An Introduction to Its Physical Principles and Applications*, Acoustical Society of America, 1989.

[15] "COMSOL Multiphysics v. 5.3a. www.comsol.com. COMSOL AB, Stockholm, Sweden," .

Modelling of nonlinear prestrain effects on the dynamic properties of viscoelastic materials

L. Rouleau [1], **J.-F. Deü** [1]
[1] Laboratoire de Mécanique des Structures et des Systèmes Couplés,
Conservatoire national des arts et métiers,
292 Rue Saint-Martin, 75003, Paris, France
e-mail: **lucie.rouleau@cnam.fr**

Abstract
In some enginerring applications, viscoelastic materials are applied at the interface between components and subjected to important prestrains during the assembly which may modify the vibration damping performance. Some studies have evidenced: i) an increase of the modulus and a decrease of the loss factor with increasing static prestrain ; ii) a variation of the frequency-dependency of the loss factor due to static prestrains. To better understand this nonlinear prestrain effect, virtual DMA experiments based on a finite element model of a constrained viscoelastic film under several static prestrain levels are carried out. A static prestrain is taken into account through a nonlinear static calculation; then calculations in the linear frequency domain are based on a frequency-dependent (and prestrain-independent) viscoelastic model. Results are compared to the frequency- and prestrain-dependent viscoelastic model derived from DMA measurements by Martinez-Agirre et al (2014).

1 Introduction

Structural vibration reduction is an issue of concern in many industrial applications, and can be passively achieved by using constrained viscoelastic layers. For design purposes, the dynamic properties of viscoelastic materials, which depend on several environmental parameters such as temperature, frequency or static prestrain [1], should be properly modelled. In some enginerring applications, viscoelastic materials are applied at the interface between components and subjected to important prestrains during the assembly which may modify the vibration damping performance. However, while various modelling strategies have be developed to take into account the temperature- and the frequency-dependency of such materials, few studies focus on the nonlinear static prestrain effects on viscoelastic properties.
In the past few years, the characterization and modelling of the influence of static prestrain on the elastic and dissipative properties of viscoelastic materials have gained increased interest [1, 2, 3, 4, 5]. Some authors have carried out experiments consisting in applying a static load (or displacement) to specimen before realizing a frequency sweep. Results indicate an increase of the modulus and a decrease of the loss factor with increasing static prestrain. Moreover, the static prestrain level was found to affect the frequency-dependency of the loss factor. This nonlinear prestrain effect is generally taken into account through additional parameters in a classical viscoelastic model. In [3, 5], a modified generalised Maxwell model is proposed, introducing prestrain dependent viscosities. In [4], prestrain- and frequency-dependent coefficients are applied to the real and the imaginary part of the complex modulus which is described by a fractional derivative model. In both cases, the parameters introduced in the viscoelastic model are phenomenological and identified from experiments using curve fitting techniques. The goal of this work is to investigate whether this experimentally evidenced nonlinear behavior could be due, at least in part, to geometric nonlinearities, and explained through nonlinear static calculations. This would encourage the development of hyper-viscoelastic models.

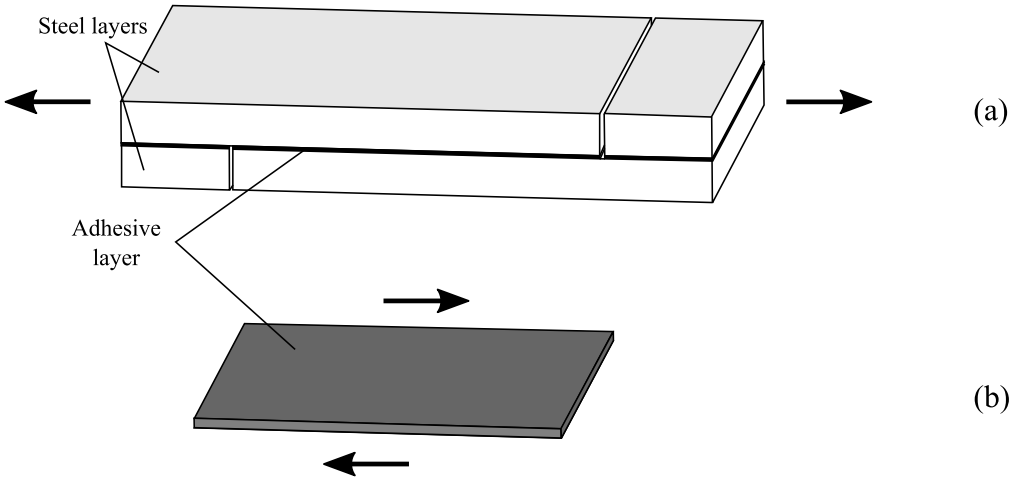


Figure 1: Geometry and loading of the specimen (a) in the DMA tests carried out in [4], (b) in the present study.

To this end, virtual DMA (Dynamic Mechanical Analysis) experiments based on a finite element model of a constrained viscoelastic film under several static prestrain levels are carried out. A static prestrain is taken into account through a nonlinear static calculation; then calculations in the linear frequency domain are based on a frequency-dependent (and prestrain-independent) viscoelastic model. Results are compared to the frequency- and prestrain-dependent viscoelastic model derived from DMA measurements by Martinez-Agirre et al (2014). This comparisons will shed light on the source of the nonlinear behavior observed in previous experiments (material and/or geometric nonlinearities).

2 Numerical tests

In [4], DMA tests are performed on a three-layer specimen to characterise the static prestrain dependence of a viscoelastic adhesive. The specimen are composed of two steel layers of equal thickness joined by an EPDM adhesive, and are tested in tension configuration (see Figure 1.(a)). Due to the cuts in the elastic faces, pure shear deformation is induced in the viscoelastic layer. Therefore, only the viscoelastic adhesive layer subjected to a pure shear stress is modelled in the present study (see Figure 1.(b)). The dimensions of the adhesive layer are 5 mm $\times$ 5 mm $\times$ 25 μm.

The specimen is meshed by 20-node hexahedra, with two elements in the thickness and 20 elements in both lateral directions. The load is applied in two steps (Figure 2):

1. A static shear prestress τ_s is imposed,
2. A harmonic stress of constant amplitude τ_d is applied around the prestressed equilibrium position $\tau(t) = \tau_s + \tau_d \sin(\omega t)$.

The first step of the load is carried out through nonlinear static calculations since the levels of static prestress applied generates large deformations. In this step, the properties of the adhesive are modeled by a Yeoh hyperelastic model [6], whose parameters are given in Table 1. The corresponding stress/stretch curve is shown in Figure 5.
The second step is to compute the linear harmonic response of the specimen around its prestressed state. The frequency dependency of the material properties are described by a fractional derivative viscoelastic model whose parameters are taken from [4] and given in Table 1. The corresponding master curves at 30^oC are given in Figure 4.

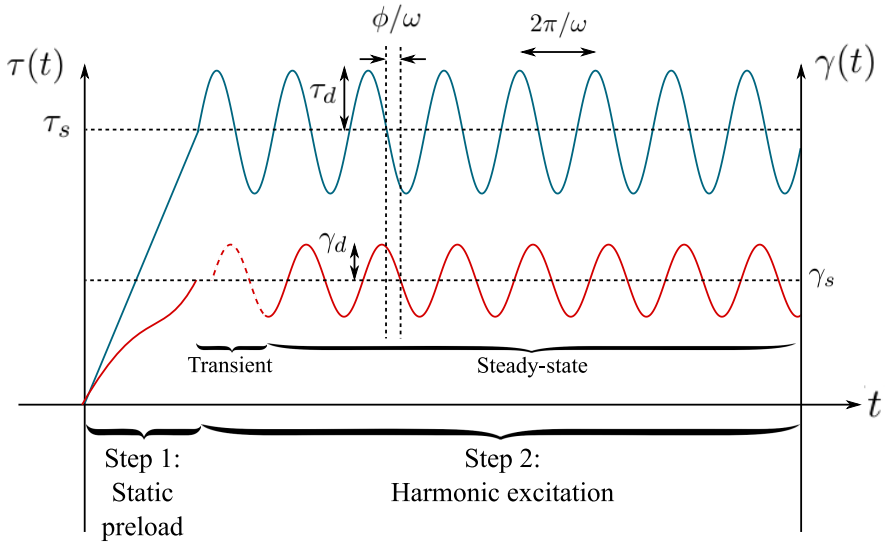


Figure 2: Description of the loadcase.

Yeoh hyperelastic model			
$c_{10} = 1.55\ 10^6$ Pa	$c_{20} = -1.0333\ 10^3$ Pa	$c_{30} = 3.781\ 10^2$ Pa	$k_0 = 1.5397\ 10^9$ Pa
Fractional derivative viscoelastic model			
$G_0 = 3.10\ 10^5$ Pa	$G_\infty = 3.14\ 10^8$ Pa	$\tau = 2.15\ 10^{-8}$ s	$\alpha = 0.6$

Table 1: Parameters of the Yeoh hyperelastic model and the fractional derivative viscoelastic model considered in this numerical study.

In both steps, the stress is imposed by applying a distributed load F to the top surface while clamping the bottom one:

$$\tau = \frac{F}{A} \tag{1}$$

where $A = 2.5\ 10^{-5}$ m^2 is the area of the top surface. Since a constant strain distribution is observed along the joint (Figure 3), the resulting shear strain γ is computed from the maximum displacement u_{max}:

$$\gamma = \frac{u_{max}}{h} \tag{2}$$

where $h = 25$ μm is the thickness of the viscoelastic layer. In the case of harmonic excitation, the response is induced with a phase lag ϕ, as schematically represented in Figure 2. The complex shear modulus is computed from the ratio between the imposed stress and the induced strain [7]:

$$G^* = \frac{\tau(t)}{\gamma(t)} = \frac{\tau_d}{\gamma_d}(\cos(\phi) + \mathrm{i}\sin(\phi)) \tag{3}$$

The complex shear modulus is evaluated for various static preloads, from 0.04 to 2.04 MPa (which corresponds to shear strains varying from 0.13 to 4, as shown in Figure 5), on the frequency range $[0 - 200]$ Hz:

$$G^*(\tau_s, \omega) = G'(\tau_s, \omega)\,(1 + \mathrm{i}\eta(\tau_s, \omega)) \tag{4}$$

where G' is the storage modulus and η is the loss factor.

3 Results and discussion

The results of the numerical simulations are presented in Figures 6 and 7. Figure 6 shows how the prestress influences the shear storage modulus and the loss factor at various frequencies, while Figure 7 shows the

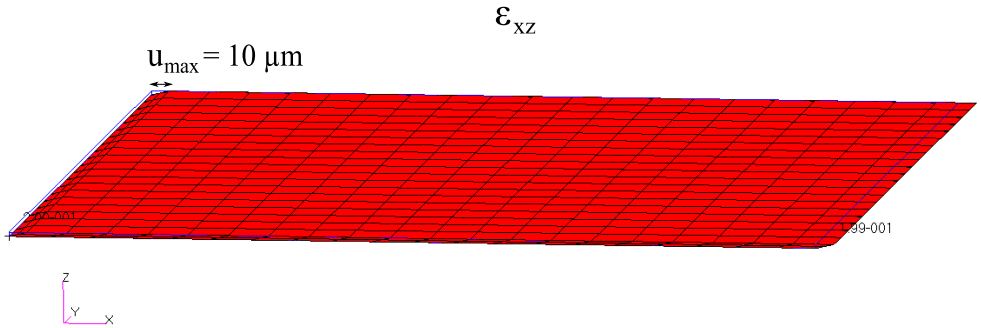


Figure 3: Shear strain field $\epsilon_{xz} = \gamma/2 = 0.2$ in response to a distributed static load of 30 N applied on the top surface (corresponding to a shear stress $\tau = 1.2$ MPa).

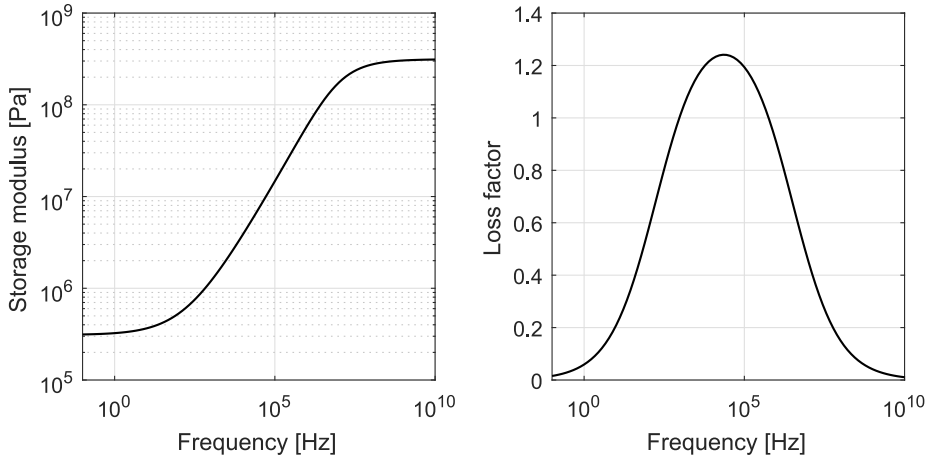


Figure 4: Shear storage modulus and loss factor from the viscoelastic model (at the reference temperature of 30^o).

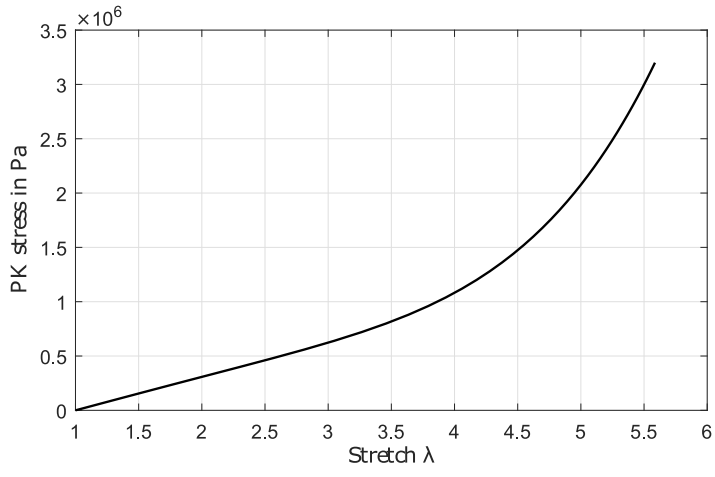


Figure 5: Piola-Kirchhoff stress-stretch curve of the Yeoh hyperelastic model.

$c_{r1} = 2.226\ 10^{-2}$	$c_{r2} = 1.397\ 10^{-2}$	$c_{r3} = 1.485\ 10^{-3}$	$n_r = 2.754$
$c_{i1} = 5.918\ 10^{-3}$	$c_{i2} = 1.913\ 10^{-2}$	$c_{i3} = 3.621\ 10^{-3}$	$n_i = 2.761$

Table 2: Parameters of the functions $f_R(\omega, \gamma_s)$ and $f_I(\omega, \gamma_s)$.

shear storage modulus and the loss factor as a function of frequency under different prestress levels. As expected, since nonlinearities are taken into account only in the static calculation, prestress does not have any influence on the the loss factor. However, it can be observed that it has a significant influence on the storage modulus as prestress levels increase.
To allow for a comparison with the results presented in [4], the modified viscoelastic model proposed by the authors to describe the prestrain-dependency of the viscoelastic properties of the adhesive is implemented:

$$G^*(\omega, \gamma_s) = f_R(\omega, \gamma_s) G'(\omega) + \mathrm{i} f_I(\omega, \gamma_s) G''(\omega) \tag{5}$$

where G' and G'' are the real part and the imaginary part of the complex shear modulus described by a fractional derivative model (whose parameters are those given in Table 1):

$$G^*(\omega) = \frac{G_0 + G_\infty (\mathrm{i}\omega\tau)^\alpha}{1 + (\mathrm{i}\omega\tau)^\alpha} \tag{6}$$

The prestrain-dependency of the viscoelastic properties is taken into account through the functions f_R and f_I, whose expression are:

$$\begin{cases} f_R(\omega, \gamma_s) = 1 + \left(c_{r1} + c_{r2} e^{-\omega c_{r3}}\right) \gamma_s^{n_r} \\ f_I(\omega, \gamma_s) = 1 + \left(c_{i1} + c_{i2} e^{-\omega c_{i3}}\right) \gamma_s^{n_i} \end{cases} \tag{7}$$

where the coefficients c_{rj}, c_{ij}, n_r and n_i are identified by curve fitting to experimental data in [4], and given in Table 2.
Results from this modified fractional derivative model are presented in Figures 8 and 9. In both figures 7 and 9, prestress/prestrain is found to have little influence on the storage modulus for low values of prestress/prestrain. In this region, the values of storage modulus obtained from the numerical study and those predicted by the modified fractional derivative model are very similar. As the prestress/prestrain increases, the storage modulus increases, and some discrepancies are observed between the two approaches (see figures 6 and 8). This can be related to the parameters of the hyperelastic Yeoh model. Coefficient c_{10} is computed as $c_{10} = G_0/2$, which ensures consistency of the results at low values of prestress. However, coefficients c_{20} and c_{30} were chosen arbitrarily since no experimental stress-stretch data is available for curve fitting. With the chosen parameters, the material properties become too strongly nonlinear for prestress above 1 MPa to match the results from [4].
Nevertheless, this numerical study clearly indicates that part of the prestrain effect on the dynamic properties of viscoelastic material can be taken into account by considering geometric and material nonlinearities in the model. Morevoer, Figure 10 indicates that the application of prestress results in a shift of the storage modulus curve along the log plot of the y-axis, as suggested by the modified fractional derivative model [4].

4 Conclusion

The goal of this numerical study was to better understand the nonlinear effect of prestrain on the dynamic properties of viscoelastic materials. Results show that by considering large deformations in a nonlinear static calculation, the trend in the variation of the storage modulus with prestrain can be captured. Therefore the shift of the storage modulus curve observed along the log plot may be predicted by the hyperelastic model. Stress/stretch experiments should be carried out on this material to validate the conclusions of the numerical study and realise not only a qualitative comparison but also a quantitive one.

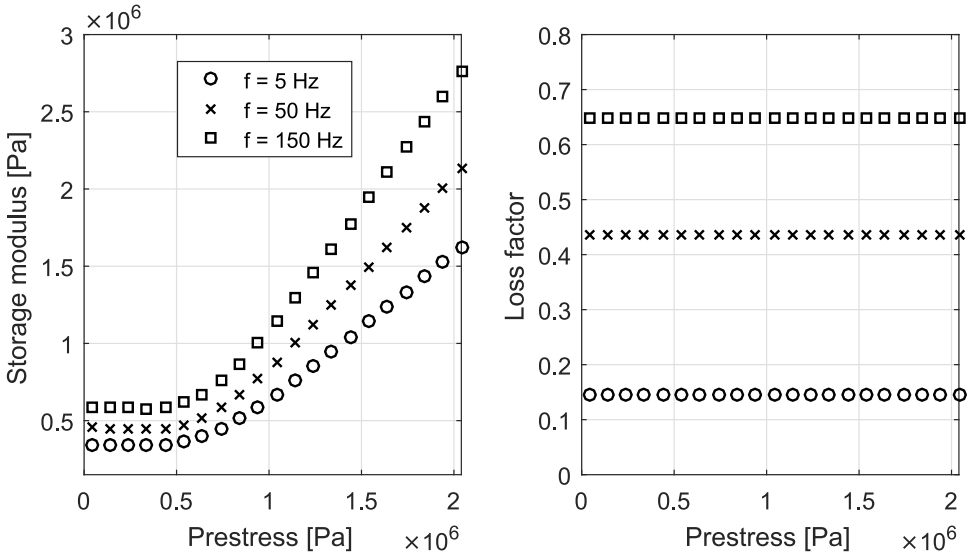


Figure 6: Prestrain dependency of the storage shear modulus and loss factor at different frequencies.

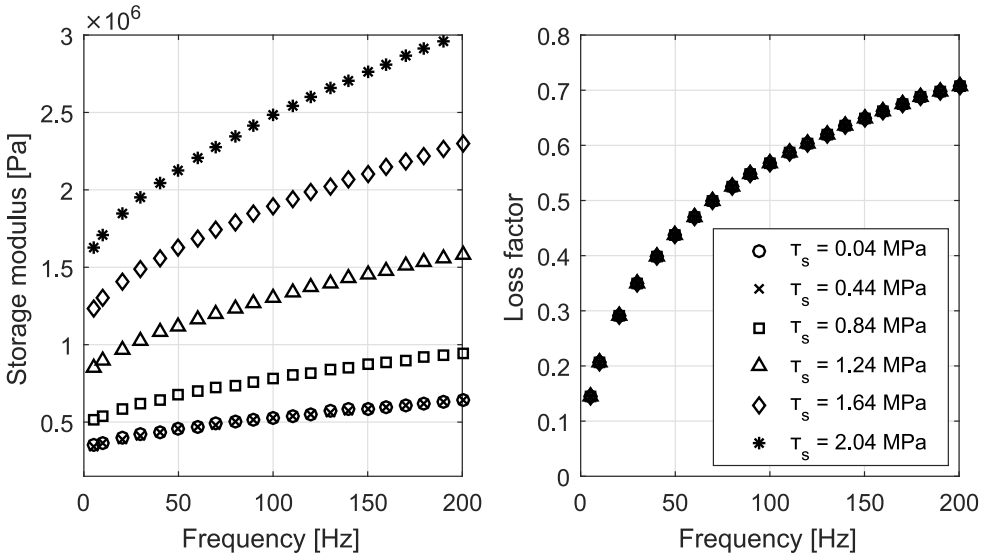


Figure 7: Frequency dependency of the storage shear modulus and loss factor at different prestress levels.

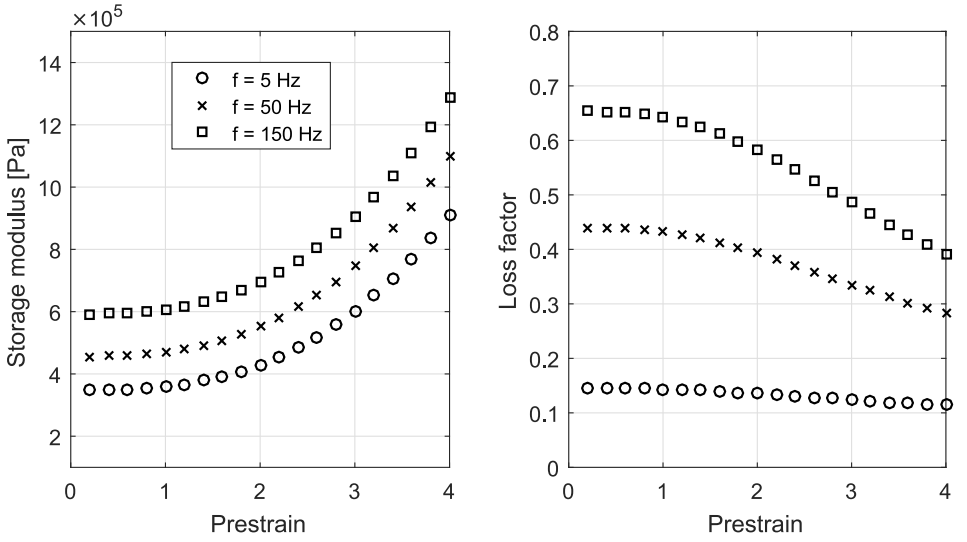


Figure 8: Prestrain dependency of the storage shear modulus and loss factor at different frequencies, predicted by the modified fractional derivative model from [4].

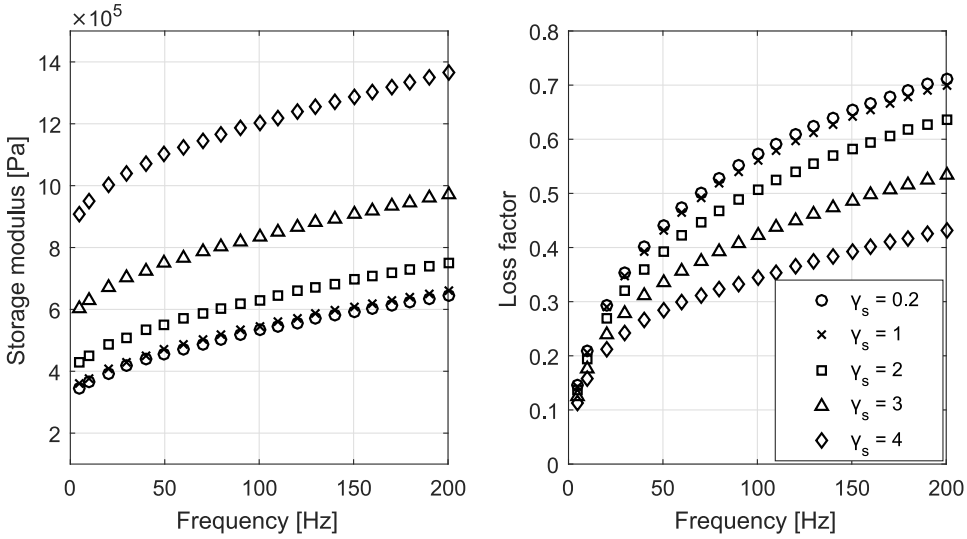


Figure 9: Frequency dependency of the storage shear modulus and loss factor at different prestrain levels, predicted by the modified fractional derivative model from [4].

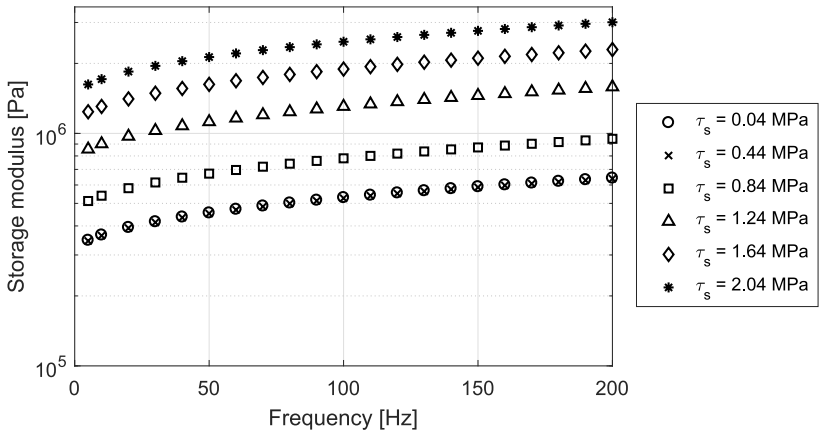


Figure 10: Frequency dependency of the storage shear modulus and loss factor at different prestress levels in log scale.

In the present study, the influence of prestrain on the loss factor of the material was not evidenced. Further numerical study will aim at identifying the origin of the nonlinear effects of prestrain on the loss factor. It is most likely related to the mobility of polymer chains. Prestraining the material restricts the mobility of the polymer chains resulting in a reduction of its damping capabilities.
Finally, a long-term perspectives is to implement a hyper-viscoelastic model wich would enable to consider vibrations of large amplitudes of viscoelastic materials.

Acknowledgements

Many thanks to Christophe Hoareau for his help and his PELICAN (Program with finite ELements for fluid-structure Interactions and Coupled vibration Analysis with Non-linearities).

References

[1] G. Kergoulay, E. Balmès, G. Legal, *A characterization of frequency-temperature-prestress effects in viscoelastic films*, Journal of Sound and Vibration, Vol. 297 (2006), pp. 391-407.

[2] J.-H. Lee, K.-J. Kim, *Characterization of complex modulus of viscoelastic materials subject to static compression*, Mechanics of Time-Dependent Materials, Vol. 5, No. 3 (2001), pp. 255-271.

[3] A. Thorin, A. Azoug, A. Constantinescu, *Influence of prestrain on mechanical properties of highly-filled elastomers: measurements and modeling*, Polymer Testing, Vol. 31, No. 8 (2012), pp. 978-986.

[4] M. Martinez-Agirre, S. Illescas, M.J. Elejabarrieta, *Characterisation and modelling of prestrained viscoelastic films*, International Journal of Adhesion and Adhesives, Vol. 50 (2014), pp. 183-190.

[5] D. Jalocha, A. Constantinescu,R. Neviere, *Prestrain-dependent viscosity of a highly filled elastomer: experiments and modeling*, Mechanics of Time-Dependent Materials, Vol. 19, No. 3 (2018), pp. 243-262.

[6] O.H. Yeoh., *Some forms of the strain energy function for rubber*, Rubber Chemistry Technology, Vol. 66, (1993), pp. 745–771.

[7] L. Rouleau, J.-F. Deü, A. Legay, F. Le Lay, *Applications of Kramers-Kronig relations to time-temperature superposition for viscoelastic materials*, Mechanics of Materials, Vol. 65, (2013), pp. 66-75.

Installation effects on sound absorption and flow resistivity of glass wool fibres

G. Petrone[1], A. Sorrentino[1], E. De Bono[1], T. Polito[1], F. Marulo[1]
[1] University of Naples Federico II, Department of Industrial Engineering – Aerospace section
via Claudio 21, 80125, Naples, Italy
e-mail: **giuseppe.petrone@unina.it**

Abstract
Fibrous materials, such as mineral wool or glass wool, are commonly used for thermal insulation and sound absorption, because of their low cost and high performance (sound absorption coefficient very high at mid-high frequencies). However these performances worsen when a fibrous layer is compressed and hence its thickness is reduced. In this paper installation effects on acoustic properties for a commercial soundproofing material have been studied in the low frequency region. Acoustical properties of glass wool fibres blankets have been experimentally evaluated, in terms of sound absorption coefficient and flow resistance by means of a Kundt's and a piston-tube apparatus (as proposed by Uno Ingard) respectively. The two measurements have been then efficiently correlated thanks to the Delany-Bazley and Miki empirical models. The results are very interesting indicating that increases in compression ratio usually decrease the absorption coefficient in the low and medium frequency range.

1 Introduction

Modern air transportation has benefitted from technological advances to increase flight safety and reliability. However, airlines are also competing to attract more passengers by means of offering various levels of design, services and prices. A number of studies [1,2] have shown that improving the sense of comfort associated with a trip results in an increase in the proportion of passengers who wish to use the same vehicle (aircraft) on future occasions. For this reason, in the past twenty years human comfort plays an important role in their acceptance and airliners have paid great attention to noise and vibration, as well as the air quality aspects, all addressing the human sensations of comfort [3].
Aircraft noise is generally divided into two sources: external and internal noise sources. Internal noise field, affecting passenger comfort and crew performance, is mainly due to intense Boundary Layer Noise, high engine noise levels transmitted into the aircraft via the structure and/or air as well as very annoying noise of the internal systems due to air-conditioning, ventilation and ducts. For what concern the external sources, indeed, the main components contributions are the propellers, the wings and the Low Pressure Compressors (LPCs) [4, 5].
Noise attenuation methods involve active and passive controls. The main purpose of the active sound control is to provide higher noise reduction at low frequencies by installing many microphones and speakers within the room to cancel the noise. At higher frequencies standard solutions are applied, and they are based on the application of absorbing properties of the materials, such as: porous, foams, wood fibres, vibrating and perforated resonant absorbing panels which are chosen in terms of material types and dimension and also based on the frequency of sound to be controlled [6].
The addition of trim materials is one of the most common solutions, usually introduced in the latest phases of a design project in order to guarantee satisfactory noise reduction performance. Most of the porous sound-absorbing materials commercially available are fibrous and they have been used increasingly in the construction of aircraft, spacecraft and ships because of their low weight and effectiveness when used correctly. A not adequate/good installation of this material affects its performances [7-9]. For instance, the seat padding in the vehicle is subjected to compression/expansion cycles due to the passenger's weight

which results in squeezing down the porous materials with negative effects on acoustic performances. Under compression the various fibres in the mat are brought nearer to each other without any deformation (without any change in fibres size) resulting in a decrease of thickness. Numerous studies, that dealt with sound absorption in porous materials, have concluded that low frequency sound absorption has direct relationship with thickness: the effective sound absorption of a porous absorber is achieved when the material thickness is about one tenth of the wavelength of the incident sound. The increase of sound absorption with thickness is valid only at low frequencies. At higher frequencies thickness has insignificant effect on sound absorption. Above reduction in thickness the compression of a material leads to the variation of other important physical parameters. Castagnede et al. [7] found that compression resulted in an increase in tortuosity and airflow resistively, and a decrease of porosity and thermal characteristic length (shape factor).
In the present work, the installation effect of the traditional soundproofing material (glass wool fibres) on different acoustic parameters is experimentally and numerically investigated. An overview of the theoretical basis and of the measurements is provided in Section 2. Hence, the analytical model is described in section 3 while the effect of compression on sound absorption coefficient and flow resistivity is reported in section 4. Finally, in section 5, some concluding remarks are given.

2 Flow resistivity and absorption coefficient measurements

Sound absorption coefficients of a glass wool fibres were measured by means of an impedance tube at different compression conditions. These results have been used as reference to validate, by means of analytical equations, a piston-tube device for flow resistivity measurements.

2.1 Experimental setup for Sound Absorption Coefficient

An impedance tube (Fig. 1) is used to measure the normal incidence sound absorption coefficient of the samples according to regulations [10-11]. The tube has been designed and produced by the Department of Industrial Engineering at University of Naples Federico II. The two-microphone transfer-function method in used to determine the acoustical impedance of the glasswool fibres and evaluate the sound absorption coefficient. The loudspeaker generates random sound waves which propagate as plane waves in the tube and are partially reflected off by the sample surface.

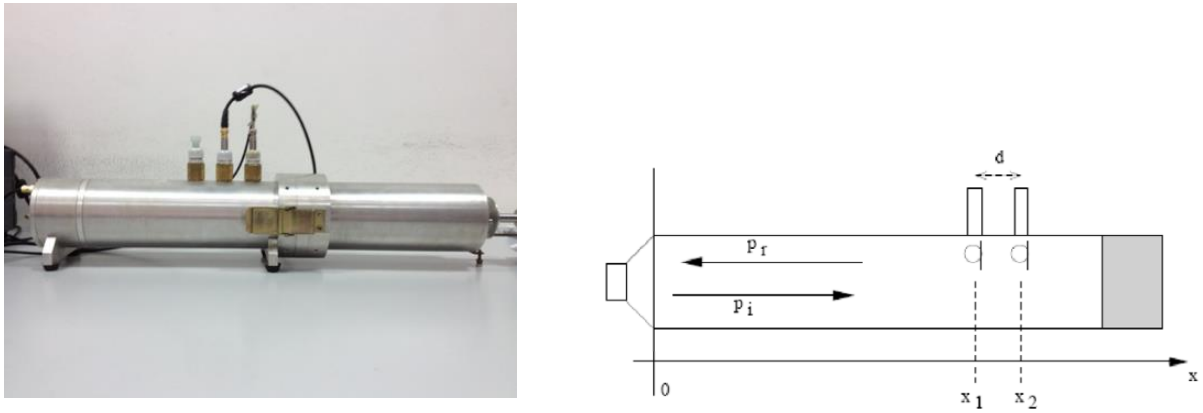


Figure 1: Impedance tube

This leads to a standing-wave interference pattern resulting from forward and backward travelling waves inside the tube.

$$p_1(x_1, f) = p_i(f)e^{-jkx_1} + p_r(f)e^{jkx_1}$$
$$p_2(x_2, f) = p_i(f)e^{-jkx_2} + p_r(f)e^{jkx_2} \quad (1)$$

From the sound pressure measured at two microphone locations, the transfer function is calculated:

$$H = \frac{p_2(f)}{p_1(f)} = \frac{e^{jkx_2} + R(f)e^{-jkx_2}}{e^{jkx_1} + R(f)e^{-jkx_1}} \tag{2}$$

The Transfer Function (H) needs to be corrected for any mismatch (in amplitude and phase) present between the two microphones. This is done by repeating the measurements with the microphone locations interchanged and calculating a correction factor:

$$H_c = |H_C|e^{j\varphi c} = (H_A H_B)^{1/2} \tag{3}$$

$$|H| = \frac{|H_T|}{|H_C|} \tag{4}$$

From the Transfer Function (H), the reflection coefficient (R) and therefore the normal sound absorption coefficient (α) are calculated:

$$R(f) = \frac{H(f) - e^{jkd}}{e^{-jkd} - H(f)} e^{2jkx_1} \tag{5}$$

$$\alpha = 1 - |R|^2 \tag{6}$$

2.2 Experimental setup for Flow Resistivity

The Piston-Tube apparatus is a simple device for the evaluation of the steady flow resistivity as proposed by Uno Ingard [12] **Errore. L'origine riferimento non è stata trovata.**. A prototype of this instrument has been designed and produced by the Department of Industrial Engineering at the University of Naples Federico II (Figure 2).

Uno Ingard has proposed an apparatus for estimating the flow resistance of a specimen simply by means of a stop watch and does not require any flow moving device, flow rate meter, or pressure gauge. The flow is indeed produced by a piston of known weight, which falls under the influence of gravity through a vertical tube covered at one end with the porous sample to be tested [12].

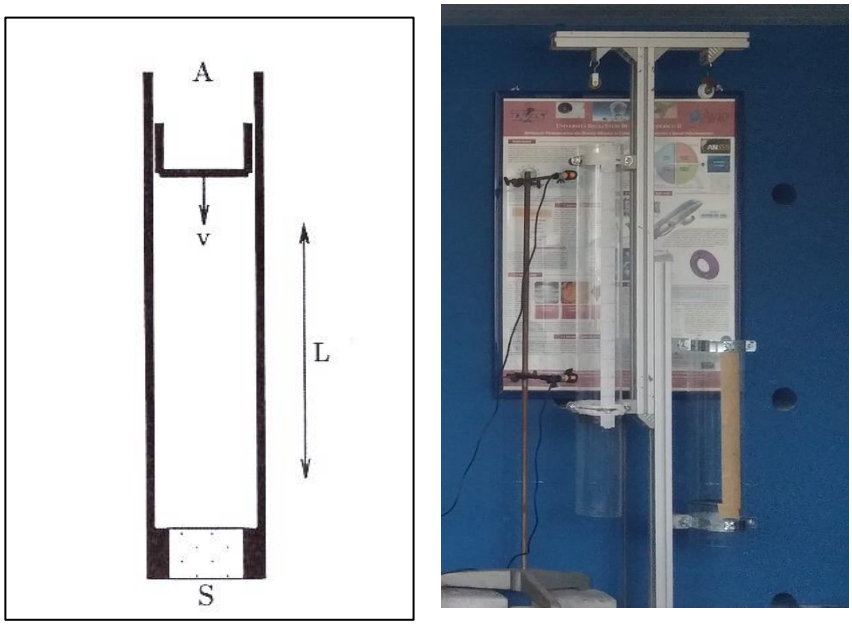


Figure 2: Impedance tube

The air inside the volume, enclosed between the tube walls, the falling piston and the porous specimen, will be compressed by the falling piston, forcing the flow through the sample. The piston will therefore be subjected to the following forces: the gravity force, the friction between the piston and the tube and the pressure gradient between the volume under the piston, and the external environment. This pressure gradient is directly linked to the flow resistivity, and the momentum equation reduces to an algebraic balance of forces in the hypothesis that the piston has reached a constant speed.

$$Mg = (P - P_0)A + \alpha v \tag{7}$$

where P is the pressure between the piston and the sample and P_0 outside the tube and on the top of the piston, v is the velocity of the piston. The term αv represents the friction force between the piston and the tube wall and is not known a priori. However, it can be readily determined from the travel time t_0 in the case of open tube. If it is the case indeed, then $P = P_0$ and v is simply given by L/t_0.

$$\alpha = \frac{Mg}{v_0} = \frac{Mgt_0}{L} \tag{8}$$

The other equation to take into account is the conservation of mass applied to the air volume between the sample and the piston.

$$\rho A v = \rho S v + \rho S_{av_a} \pi r^2 \tag{9}$$

or in terms of flow resistances:

$$\rho A v = \rho S \frac{\Delta P}{r} + \rho S_a \frac{\Delta P}{r_a} \tag{10}$$

where:

- ΔP is the pressure gradient $P - P_0$;
- $r = \Delta P / v$ is the Flow Resistance of the specimen;

- $r_a = \Delta P / v_a$ is the Flow Resistance relative to the leakage through the gaps between the piston and the tube;
- S is the area of the specimen;
- S_a is the area of the annular gap between piston and tube;
- $(S\rho / r)\Delta P$ is the mass flow rate through the specimen:
- $(S_a\rho / r_a)\Delta P$ is the mass flow rate leaking through the annular gap.

S_a / r_a is not known a priori but can be determined from the measurement of the travel time t_∞ of the piston when the tube is closed (corresponding to the case where $r = \infty$), therefore:

$$\rho A v_\infty = \rho S_a \frac{\Delta P}{r_a} \tag{11}$$

Neglecting the friction force between piston and tube, the delta pressure can be substituted by Mg/A, therefore:

$$\frac{S_a}{r_a} = \frac{A^2 v_\infty}{Mg} = \frac{A^2 L}{Mgt_\infty} \tag{12}$$

Combining these equations, neglecting a term $t_0/t_{inf} << 1$, and substituting v with L/t_s Uno Ingard obtained an algebraic expression for the flow resistance (r) in terms of the only measurable variable t_s = time needed for the piston to travel the distance at its terminal (constant) speed.

$$r = \frac{CMgS}{LA^2} ts \tag{13}$$

where,

r = flow resistance, in (N·s)/m^3
C = (1-t0/ts)/(1-ts/tinf) = correction factor for the loss of pressure estimation
M = piston mass, in kg
g = gravitational acceleration, in m/s^2
S = airflow exposed surface, in m^2
A = piston section, in m^2
L = piston covered distance, in m
ts = falling time, in s

It is important to specify that this discussion is based on the assumption that the terminal speed has been reached when the measurement of *ts* starts. If the time *ts* is measured by starting the clock when the piston is released, then the velocity will not have yet reached its terminal value, and therefore the governing equation of motion of the piston will be a differential equation which must be solved numerically [12].

3 Validation of the Piston-Tube apparatus measurements

In order to assess the reliability of the Piston-Tube apparatus for the flow resistivity measurements a first trial test has been set. The flow resistivity of a specimen of glass wool fiber of thickness 30 mm and mass 6.6 grams has been retrieved by in-house piston-tube apparatus. The very low deviation percentage from the average value (1.45 %) certifies the repeatability of the measurements (Table 1). It has been found out that the main factor affecting the measurement variations is the mechanism of piston release. By perfecting this

aspect, lower values of measurement deviations have been achieved which can still be improved by better design of the whole apparatus.

sample	mass	thickness	Flow resistivity [Ns/m^4]										Average value	Standard deviation
#	[grams]	[mm]	Test 1	Test 2	Test 3	Test 4	Test 5	Test 6	Test 7	Test 8	Test 9	Test 10		%
Unpressed	6,6	30	23318	22533	23115	22929	22168	22867	22667	22532	22980	22781	22789	

Table 1: Flow Resistivity values corresponding to 10 different tests.

Once known the flow resistivity value, the sound absorption coefficient of the investigated glass wool fibre sample can be evaluated analytically by means of the empirical models of Delany-Bazley [13] and Miki [14] for fibrous porous materials. We report here the empirical power laws found by Delany-Bazley and Miki in Equations (14) and (15) respectively, thanks to which it is possible to retrieve the characteristic impedance Z_c and the characteristic wave number k_c of the equivalent fluid model of the rigid porous material [14]. Based on Z_c and k_c it is possible to calculate the normal impedance of the rigid porous material [14], from which the absorption coefficient computation is straightforward (see Equations (16)).

$$Z_c = \rho_0 c_0 \left[1 + 9.08\left(10^3 \frac{f}{\sigma}\right)^{-0.75} - j11.9\left(10^3 \frac{f}{\sigma}\right)^{-0.73}\right]$$
$$k_c = \frac{\omega}{c_0}\left[1 + 10.8\left(10^3 \frac{f}{\sigma}\right)^{-0.70} - j10.3\left(10^3 \frac{f}{\sigma}\right)^{-0.59}\right] \quad (14)$$

$$Z_c = \rho_0 c_0 \left[1 + 5.50\left(10^3 \frac{f}{\sigma}\right)^{-0.632} - j8.43\left(10^3 \frac{f}{\sigma}\right)^{-0.632}\right]$$
$$k_c = \frac{\omega}{c_0}\left[1 + 7.81\left(10^3 \frac{f}{\sigma}\right)^{-0.618} - j11.41\left(10^3 \frac{f}{\sigma}\right)^{-0.618}\right] \quad (15)$$

$$Z_n = -jZ_m cotg(k_c d)$$
$$\alpha = 1 - |R|^2 = 1 - \left(\frac{Z_n - \rho c_0}{Z_n + \rho c_0}\right)^2 \quad (16)$$

The sound absorption coefficient thus determined, has finally been compared to the measurement of an impedance tube (Figure 3).

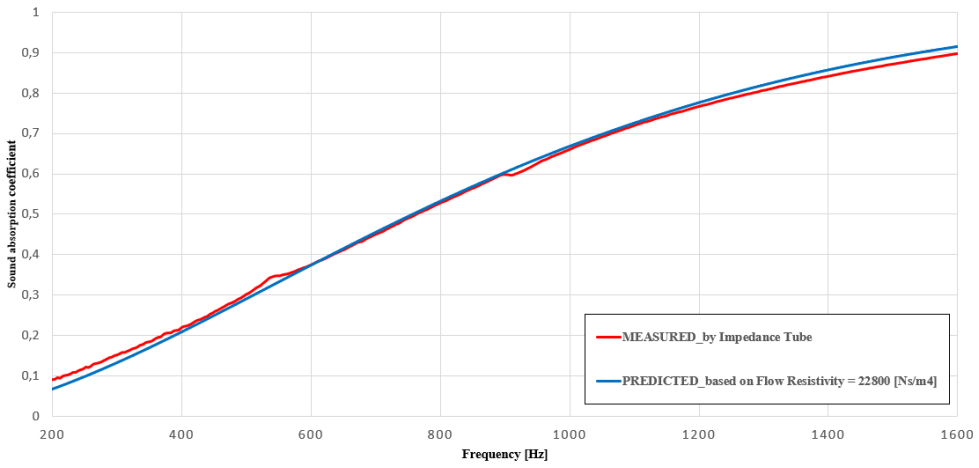


Figure 3: Absorption coefficient for a glass wool fiber specimen of 6.6 grams and 30 mm of thickness: measured and predicted curve.

The good agreement between the measured values of sound absorption coefficient (α) and the analytical curve resulted from the application of the Delany-Bazley model to the flow resistivity, allows for confidently operating the prototype of Piston-Tube apparatus, following the Ingard's guidelines.

4 Effect of compression on sound absorption coefficient and flow resistivity

The installation effect upon the acoustic properties of porous materials is investigated by applying three different levels of compression on a sample of glass wool fiber of mass 14.2 grams and thickness 65 mm. The compression levels have been accomplished by placing three different weights on the specimen, each one applied for 60 seconds resulting in final thicknesses pairs to 51 mm and 40 mm.
The absorption coefficient and the flow resistivity of the compressed samples have been measured with the impedance tube and the Piston-Tube prototype respectively. The two measurements have been then correlated as described in Section 3. The different levels of compression result in different thicknesses of the samples. Castagnède et al. [7,8] have provided simple formulas to predict the changes of the poro-mechanical parameters due to compression. Based upon ultrasonic techniques, they found that the measured flow resistivity followed the law reported in Equation (14) for a 1D compression.

$$\sigma_{(n)} = n\,\sigma_{(0)} \tag{14}$$

where $\sigma_{(n)}$ and $\sigma_{(0)}$ are the flow resistivity of the specimen before and after the compression respectively, and n is the compression rate factor given by the ratio of the initial thickness to the final thickness.
The values of the flow resistivity corresponding to the three different levels of compression (*uncompressed, compressed 1, compressed 2*) are reported in Table 2, together with the values corresponding to Castagnède's law. As can be noted the higher the compression, the higher is the deviation of the empirical value of flow resistivity from the predicted one by Equation (14).

sample	**mass**	**thickness**	**empirical flow resistivity, σ**	**Compression rate**	$\sigma_{(n)}=n*\sigma_{(0)}$
#	[*grams*]	[*m*]	[Ns/m^4]	$n=th_i/th_f$	[Ns/m^4]
Uncompressed	14.2	0.065	15777.07	-	-
Compressed 1	14.2	0.051	21750.47	1.24	20108.03
Compressed 2	14.2	0.040	28751.19	1.27	25637.74

Table 2: Empirical values of flow resistivity relative to different level of compressions and Castagnède predictions.

The higher compression and the lower thickness of the sample increase the values of flow resistivity. The curves of the absorption coefficient at different levels of compression (and relative thickness), measured by an impedance tube, are reported in Figure 4.

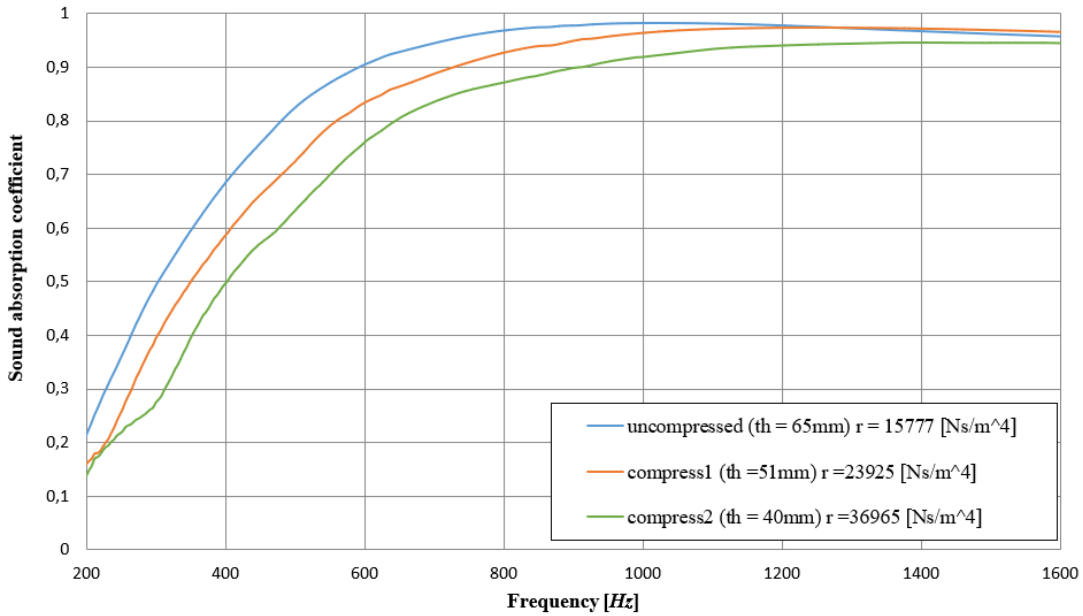


Figure 4: Absorption coefficients corresponding to three compressions of glass wool fiber of mass 14.2 grams.

As can be noticed, by compressing the specimen the sound absorption coefficient decreases especially in the lower frequency range and, as noticed by Castagnède et al [7], the thickness reduction is the main responsible of the decreasing of the absorption properties, rather than the augmentation of flow resistivity.

As done for the previous test, a comparison of the experimental value carried out by means of the piston tube apparatus and the analytical values obtained by using Miki and Delany-Bazley models, for the three different levels of compression of the glasswool fibres are reported in the Figures 5,7 and 9 with respectively absolute error in Figures 6,8 and 10.

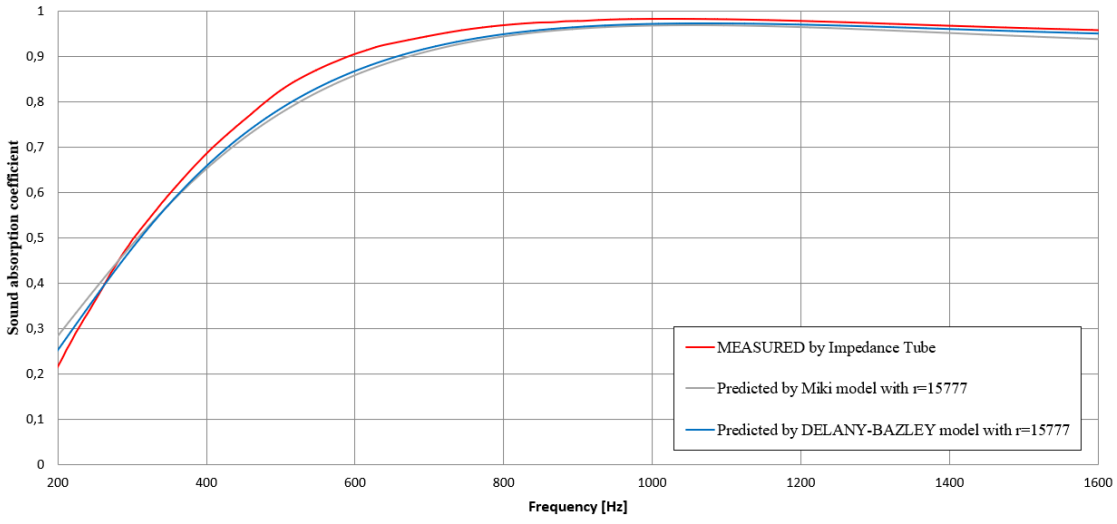


Figure 5: Absorption coefficient curves for uncompressed glass wool fiber of 14.2 grams (thickness 0.065 m, flow resistivity=15777 [Ns/m^4]).

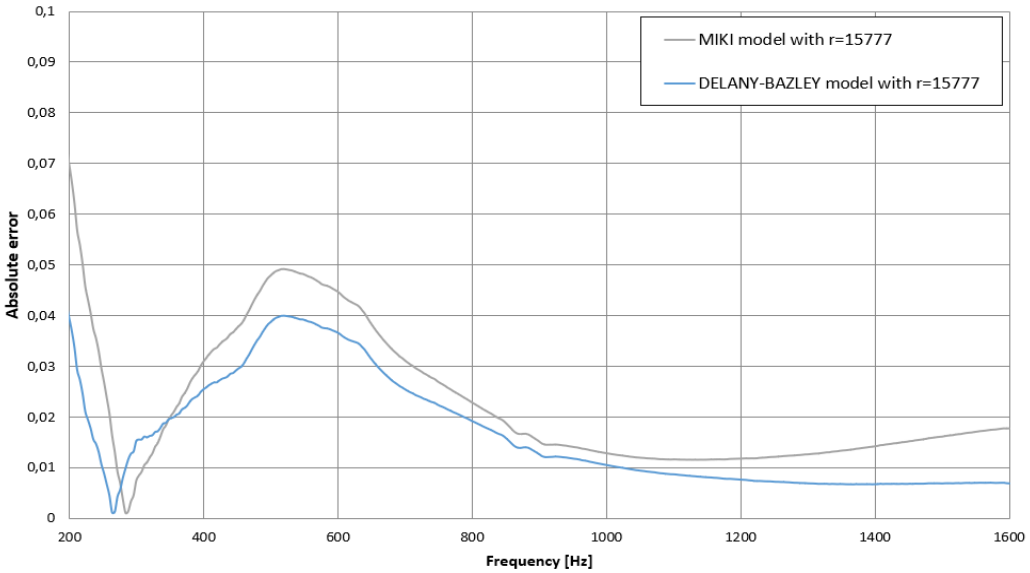


Figure 6: Predicted and measured error values of absorption coefficient of the uncompressed specimen (thickness 0.065 m, flow resistivity=15777 [Ns/m^4]).

As can be seen from Figure 6, and especially from Figure 7, the values of absorption coefficient obtained through our empirical flow resistivity is always lower than 5%, except in the lower frequency region, where the error grows up to 7%. Specifically, there is a pick of error in the frequency band 500 – 600 Hz. From Figure 5 it can be noted that the Delany-Bazley model provides, in overall, a better approximation of the experimental values, than the Miki model. Same conclusions apply for the specimen subjected to the first compression level (see Figure 7 and Figure 8). In particular, the error increases in the frequency range of 300-800 Hz up to 8.5% around 500 Hz. Same trend is confirmed by Figure 9 and Figure 10, where the error rises to 16% at 600 Hz. The errors between the α predicted through the Delany-Bazley/Miki models based upon the Flow Resistivity, and the measurements obtained by the impedance tube, should not surprise us, as both the Delany-Bazley and Miki power laws are retrieved from measurements relative to fibrous porous materials with a porosity almost equal to 1 [14] and [15]. The compression of the specimen, on the contrary, evidently reduces the value of the porosity. Although we do not know the exact value of porosity for our specimen, the variation with the thickness can be estimated thanks to the formula provided by Castagnède [7] in Equation (17):

$$\phi_n = 1 - n(1 - \phi_0) \tag{17}$$

where ϕ_n and ϕ_0 are the porosities before and after the compression respectively. By giving as input the value of the compression rate n (realized during our compressions), the value of ϕ_n will drop well below 1. Therefore, the reason of non-correspondence between the curves of α in Fig. 6 must be sought in a consistent reduction of the porosity and the consequent inapplicability of the prediction models of both Delany-Bazley and Miki. Moreover, it is worth reminding the frequency range of applicability of these models:

$$0.01 < \frac{f}{\sigma} < 1 \tag{17}$$

The frequency limit reported in Equation (17) depends upon the flow resistivity. In our cases, it provides an additional restraint on the lower frequency of applicability of the above models.

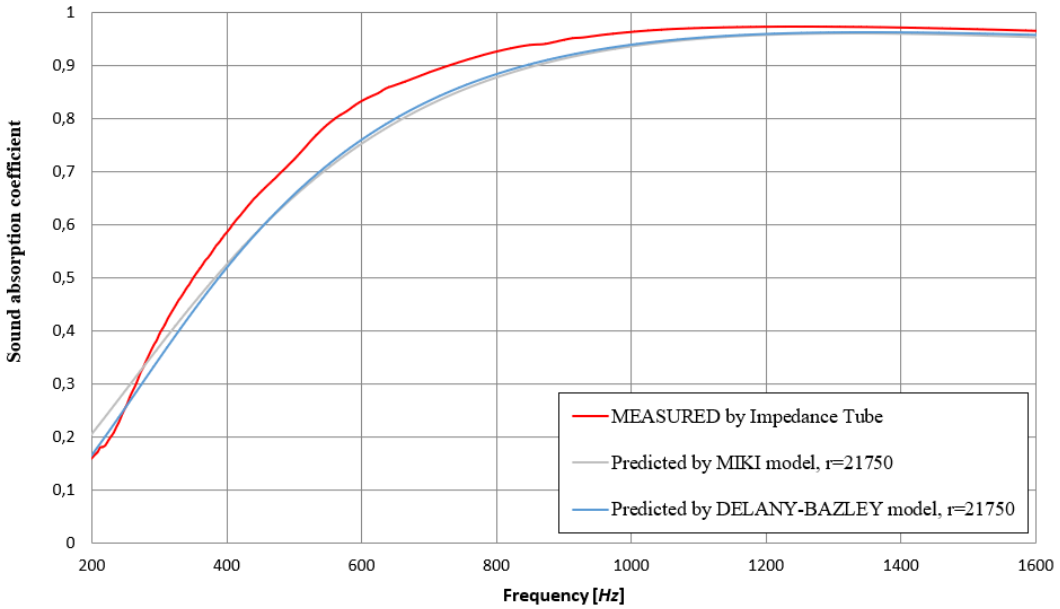


Figure 7: Absorption coefficient curves for glass wool fiber of 14.2 grams subjected to first compression (thickness 0.051 m, flow resistivity=21750 [Ns/m^4]).

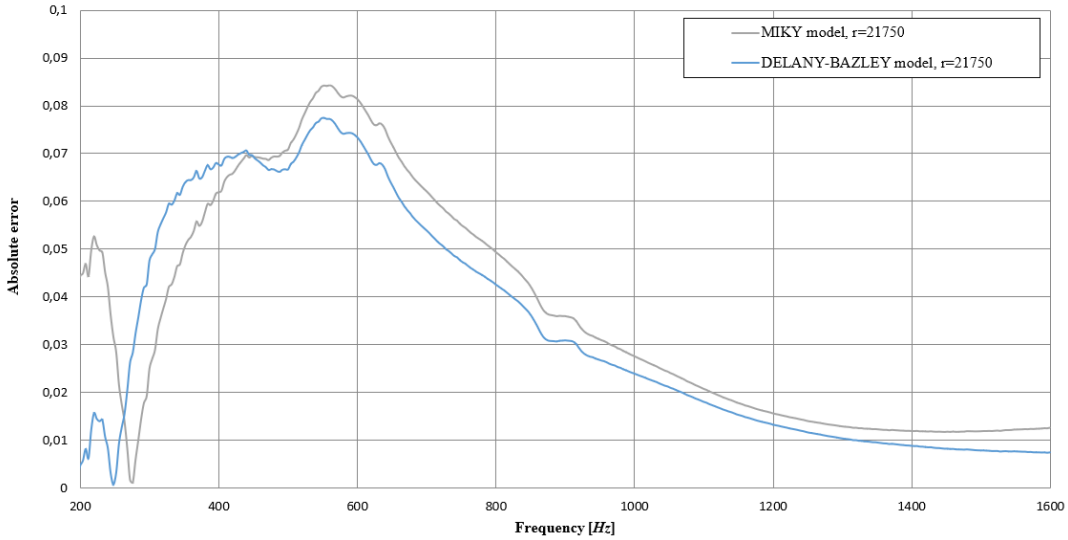


Figure 8: Predicted and measured error values of absorption coefficient of the specimen subjected to first compression (thickness 0.051 m, flow resistivity=21750 [Ns/m^4]).

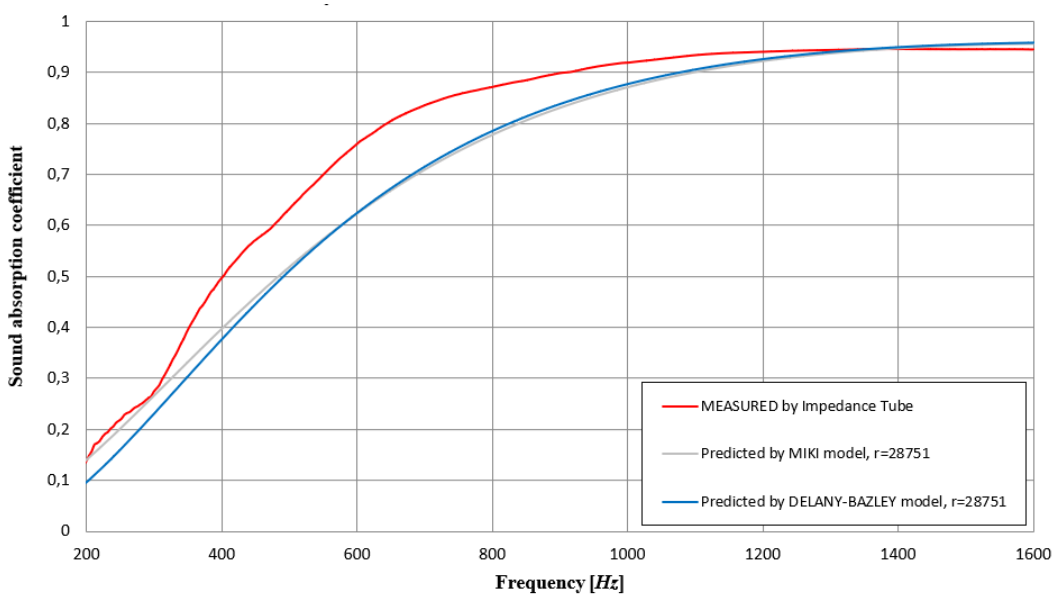


Figure 9: Absorption coefficient curves for glass wool fiber of 14.2 grams, subjected to second compression (thickness 0.040 m, flow resistivity=28751 [Ns/m^4]).

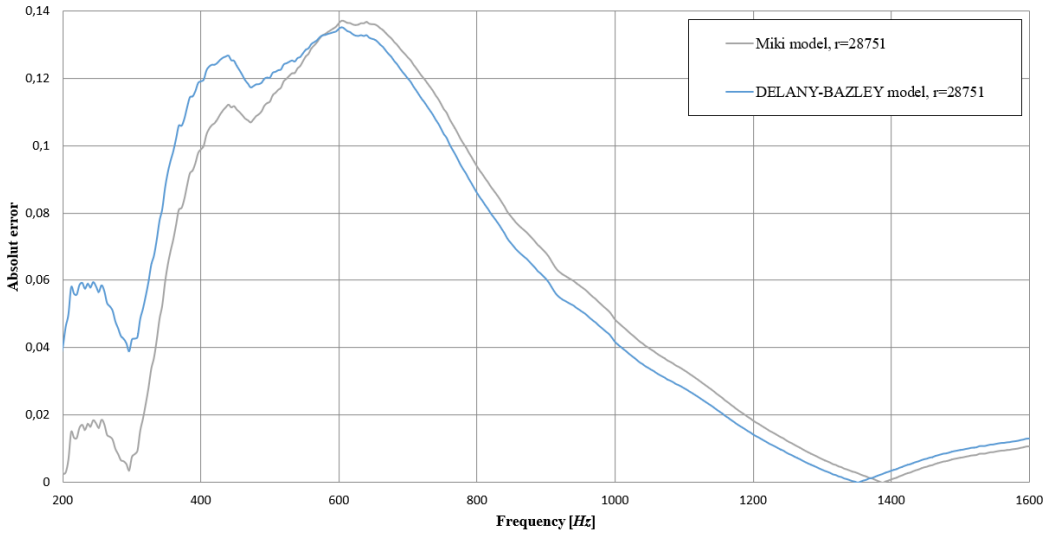


Figure 10: Predicted and measured error values of absorption coefficient of the specimen subjected to second compression (thickness 0.040 m, flow resistivity=28751 [Ns/m^4]).

4.1 Effect of compression on transmission loss

Additional analyses were performed to evaluate the impact on the transmission loss of an aluminium panel with attached multilayer Noise Control Treatment (NCT) for different configurations (uncompressed and compressed). The studies have been performed by using the Hybrid tool FE/SEA of the commercial software Va-One and results are reported in Figure 11. It can be noted that the presence of a NCT increase the TL performances of the investigated plate in overall the frequency range and, at same time, it is possible to highlight that this increase is strongly related to the NCT compression. In fact, the highest value of TL is reached for the uncompressed configuration of NCT; the lowest value for the compressed configuration.

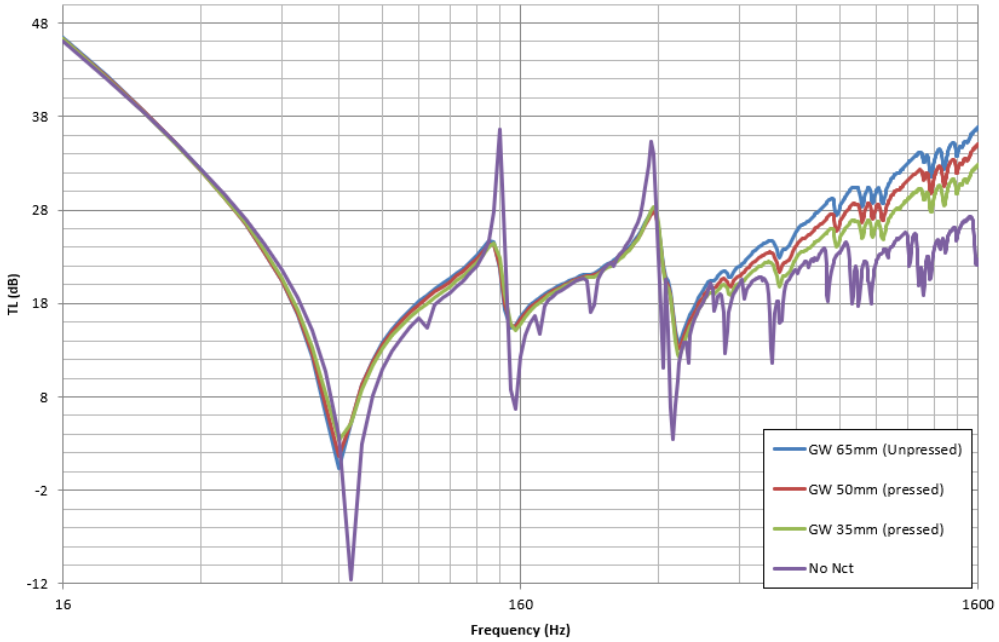


Figure 11: Effect of compression on transmission loss of an aluminum flat plate with attached NCT.

5 Conclusions

The effect of compressing porous materials on their acoustic performance was investigated in this paper. First an impedance tube was used to measure the sound absorption coefficient of a glasswool fibre which has been used as reference for validate, indirectly, an in-house piston tube apparatus, developed at University of Napoli Federico II, for flow resistivity measurements. In fact, once known the flow resistivity value, the sound absorption coefficient of the investigated glass wool fiber sample was evaluated also analytically by means of the empirical models of Delany-Bazley and Miki for fibrous porous materials. A good correlation was found between the experimental and the analytical results. This validates the piston-tube apparatus.
Then, the investigated glass wool fibre has been compressed for two different conditions and the sound absorption coefficient was seen to reduce in certain frequency regions. At same time, the air-flow-resistivity values of the porous materials increase when the materials were compressed. In this case the correlation between analytical and experimental results presents an error due to the reduction of porosity and the consequent non-validity of the Delany-Bazley and Miki prediction laws. Finally, the effect of the compression on Transmission Loss of a flat aluminium plate with NCT attached has been investigated numerically and results confirm the reduction of performances in case of compressed NCT.

References

[1] Richards, L.G. (1980). On the psychology of passenger comfort. In: D.J. Oborne and J.A. Levis (Eds.), Human factors in Transport Research vol. 2 (pp.15-23). London, UK: Academic press.

[2] Vink, P., Bazley, C., Kamp, I., Blok, M. (2012a). Possibilities to improve the aircraft interior comfort experience. Applied Ergonomics, 43(2), 354-359

[3] J.S. Mixson, CA. Powell, “A review of recent research on interior noise of propeller aircraft”, AIAA/NASA 9th Aeroacoustics Conference, Williamsburg, Virginia; 1984.

[4] C.M. Harris, “Handbook of Noise Control”, McGraw-Hill, New York 1991.

[5] J. Depriest, “Aircraft Engine Attachment and Vibration Control”, Lord Corporation, 2000.

[6] Francisco Simon and Jaime Pfretzschner, "Guidelines For The Acoustic Design Of Absorptive Devices, Noise and Vibration worldwide, 2004
[7] B. Castagnède, A. Aknine, B. Brouard, V. Tarnow, "Effects of compression on the sound absorption of fibrous materials", Appl. Acoust., 61, 3-7 (2000).
[8] B. Castagnède, J. Tizianel, A. Moussatov, A. Aknine, B. Brouard, "Acoustique, ondes, vibrations/Acoustics, waves, vibrations Parametric study of the influence of compression on the acoustical absorption coefficient of automotive felts", C. R. Acad. Sci. Paris, t. 329, Série II b, 125-130 (2001).
[9] G. Iannace, E. Ianniello, S. Basturk, "An experimental study of effects of concentrated compressions on sound absorption of polyester fibre panels", Proceedings of Euronoise 2009, Edinburgh, Scotland, 2009.
[10] ASTM E1050, *Standard Test Method for Impedance and Absorption of Acoustical Materials Using A Tube,* Two Microphones and A Digital Frequency Analysis System.
[11] ISO 10534-2, *Determination of sound absorption coefficient and impedance in an impedance tube* - Part II: Transfer function method.
[12] Ingard K. U., "Sound Absorption Technology", Noise Control Foundation, 1994.
[13] M.E. Delany, E.N. Bazley, *Acoustical properties of fibrous absorbent materials,* Applied Acoustics, Volume 3, Issue 2, 1970.
[14] Y. Miki, *Acoustical properties of porous materials-Modifications of Delany-Bazley models-,* Journal of the Acoustical Society of Japan (E), 2011.
[15] J. F. Allard and N. Atalla, *Sound Propagation in Porous Materials Having a Rigid Frame*, 2nd ed., Wiley and Sons, Chichester, UK, 2009.

Simulations and experiments for vibro-acoustical behaviours of circular multi-layered plates

T. Deng[1], X. Sheng[1], Y. Ma[2], J. Li[2]
[1] Southwest Jiaotong University, State Key Laboratory of Traction Power
No. 111, the First Northern Section of the Second Ring road, Chengdu, Sichuan, China
e-mail: **dengtiesong1988420@163.com**

[2] Sichuan University, State Key Laboratory of Polymer Materials Engineering
No. 24, the First Southern Section of the First Ring Road, Chengdu, Sichuan, China

Abstract
In order to study the vibro-acoustical behaviours of a circular multi-layered plate and compare it with impedance tube measurement, the axisymmetric Lamé functions of each layer are established and solved using appropriate scalar and vector potentials. Modal and wave superposition methods are used to simulate sound transmission loss of the plate. It is shown that, modal number, modal frequency and sound transmission loss become invariant with the number of layers if the number is large enough. Around the cut-on frequency, a multi-layered plate consisting of a softer material (A) and a stiffer material (B) and repeated a number of times exhibit a better sound insulation performance than that of a single-layered one. It is observed that layer aligning sequence has almost no effect on the vibro-acoustical characteristics of a layered plate. When the total thickness increases, although combined flexural-radial longitudinal and flexural-thickness shear modes may appear, the sound transmission loss is enhanced.

1 Introduction

Multi-layered plates are widely used in many engineering applications for their excellent vibro-acoustical performances and high strengths. For example, on high speed trains, the floors and walls are mostly constructed with composite plates laminated by polymers and aluminium panels for high sound insulation and vibration damping to achieve a good acoustical comfort. Therefore, many researchers have focused on the vibro-acoustical behaviours of multi-layered plates.

Vibration characteristics of a layered plate are prerequisite to understand the acoustical behaviour. In the determination of a layered plate's vibration, some researchers regarded the composites as several plates or shells coupled together by interface conditions. Reddy discussed and compared the mechanics of laminated composites using classical plate theory (CLPT), first-order shear deformation theory (FSDT), third-order shear deformation theory (TSDT) and layer-wise theory (LW or equivalent single layer theory, ESL), respectively [1-3]. The higher order shear deformation theory in reference [1] was also applied to analyse the modal behaviours and vibration responses of laminated plates subjected to different loads and different boundary conditions [4-7]. Altenbach [8] used the LW or ESL concepts to establish the theory of sandwich panels. However, if a multi-layered plate is so thick that the shear deformation could not be approximated by the high order deformation plate theory, the structure should be treated as a 3D solid. Therefore, for circular laminated plates, Bottega [9] established an axisymmetric solution of multi-layered thick plates with isotropic elastic theory and transfer matrix method. Modal orthogonality of modal shapes was also proved [10]. Based on Bottega, Lange [11] studied the dynamic behaviour of multi-layered plates under impact loads. El-Raheb and Wagner [12] investigated transient axisymmetric elastic waves in a periodic layered finite media. For rectangular multi-layered plates, Srinivas etc. [13] exactly investigated the vibration behaviour of simply supported homogeneous and laminated thick rectangular plates by

providing analytical solutions. Based on a differential quadrature method, Liew and Teo [14] built a three dimensional model to analyse the vibration characteristics for thick rectangular plates.

In addition to the analytical solutions discussed above, researchers also used finite element method to study the multi-layered structure based on different plate/ shell theories, or more generally, the 3D solid elastic theory [15-18]. Salvatore Brischetto et al. [19] compared the characteristic frequencies of plates, cylinders, cylindrical panels and spherical panels calculated by 2D FE model and 3D FE model, showing that the FE model meshed by SHELL QUAD4 elements agree well with the exact 3D model.

Based on the multi-layered plate models mentioned above, the acoustical performance of the plates has also been investigated by many researchers. Researches on acoustical behaviours for multi-layered plates can be grouped into three types, (1) functionally graded plates (FGP), in which the material properties vary continuously from one surface to the other; (2) sandwich panels, the middle layer of which is aluminium panels or fiber reinforced material; and (3) normal laminates, in which each layer is formed with homogeneous and isotropic material.

For FGP, Chandra et al. [20] presented an investigation using a simple first-order shear deformation theory. Huang et al. [21] proposed an analytical model for sound transmission through unbounded panels of FGP materials. Daneshjou [22] established a theoretical model of relatively thick FGM cylindrical shells with third order shear deformation theory to investigate the vibro-acoustical behaviour of the shells.

For sandwich panels, Wen-chao et al. [23] showed that application of facings on a honeycomb would have significant impact on sound insulation. A new core design was recommended to achieve high sound transmission loss at frequencies between 100 and 200 Hz by Ng et al. [24]. With the statistical energy method, Zhou et al. [25] analytically and experimentally investigated the sound transmission loss of two sandwich panels filled with different cores. Arunkumar et al. [26] numerically studied the sound radiation and transmission loss of two types of honeycomb sandwich panels with finite element method.

However, the vibro-acoustical behaviour of normal laminates has rarely been researched. A kind of multi-layered plates, laminated alternatively with only two polymers and consisting of 2^n layers is just a periodic normal laminate [27]. It is experimentally observed that this kind of composite plates has a higher sound transmission loss than a single-layered one of the same thickness. This observation is yet to be investigated more rigorously. So this paper is aimed at studying the vibro-acoustical behaviours of such a multi-layered plate analytically and experimentally.

2 The model and method

In order to compare simulations with impedance tube measurements, the plate is modelled as a multi-layered circular structure and the solution is simplified as an axisymmetric problem shown in Figure 1.

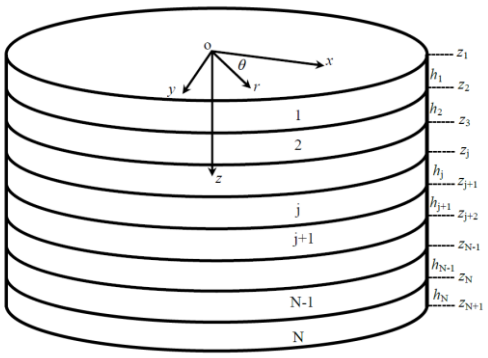


Figure 1: The model and Coordinate system

2.1 Solution for a single layer

Each layer is treated as a 3D solid. With the geometric equation, constitutive equation and motion equation, the governing equation expressed in terms of displacements and the Cartesian coordinate system, is given by (which is called the Lamé-Navier's equation),

$$(\lambda+\mu)\nabla\nabla\cdot\mathbf{u}+\mu\nabla^2\mathbf{u}=\rho\frac{\partial^2\mathbf{u}}{\partial t^2}, \tag{1}$$

where λ and μ are the Lame constants determined by

$$\lambda=\frac{\nu E\left(1+i\eta\,\mathrm{sgn}(\omega)\right)}{(1+\nu)(1-2\nu)} \qquad \mu=\frac{E\left(1+i\eta\,\mathrm{sgn}(\omega)\right)}{2(1+\nu)}. \tag{2}$$

$\mathbf{u}=(u_x,u_y,u_z)$ is the displacement vector in the Cartesian form and $\mathbf{u}=(u_r,u_\theta,u_z)$ in the Cylindrical form, $\nabla=\frac{\partial}{\partial x}\mathbf{i}+\frac{\partial}{\partial y}\mathbf{j}+\frac{\partial}{\partial z}\mathbf{k}$ is the gradient and $\nabla^2=\frac{\partial^2}{\partial x^2}+\frac{\partial^2}{\partial y^2}+\frac{\partial^2}{\partial z^2}$ is the Laplace operator.

To solve equation (1), the displacement vector $\mathbf{u}$ is decomposed in terms of a dilatational scalar potential ϕ and a rotational vector potential $\boldsymbol{\Psi}$, i.e.

$$\mathbf{u}=\nabla\phi+\nabla\times\boldsymbol{\Psi}, \tag{3}$$

where $\nabla\phi$ is the dilatational displacement vector since $\nabla\times\nabla\phi=0$ and $\nabla\times\boldsymbol{\Psi}$ is the rotational displacement vector since $\nabla\cdot\nabla\times\boldsymbol{\Psi}=0$.

With equation (3), equation (1) becomes

$$\nabla\left((\lambda+2\mu)\nabla^2\phi-\rho\frac{\partial^2\phi}{\partial t^2}\right)+\nabla\times\left(\mu\nabla^2\boldsymbol{\Psi}-\rho\frac{\partial^2\boldsymbol{\Psi}}{\partial t^2}\right)=0. \tag{4}$$

Equation (4) is satisfied if the potentials ϕ and $\boldsymbol{\Psi}$ meet the following equations

$$(\lambda+2\mu)\nabla^2\phi-\rho\frac{\partial^2\phi}{\partial t^2}=0 \tag{5}$$

and

$$\mu\nabla^2\boldsymbol{\Psi}-\rho\frac{\partial^2\boldsymbol{\Psi}}{\partial t^2}=0. \tag{6}$$

Under harmonic loads, the potentials ϕ and $\boldsymbol{\Psi}$ could be expressed as $\phi=\bar{\phi}e^{i\omega t}$ and $\boldsymbol{\Psi}=\bar{\boldsymbol{\Psi}}e^{i\omega t}$. Then equations (5) and (6) yield,

$$c_p^2\nabla^2\bar{\phi}+\omega^2\bar{\phi}=0 \tag{7}$$

and

$$c_s^2\nabla^2\bar{\boldsymbol{\Psi}}+\omega^2\bar{\boldsymbol{\Psi}}=0, \tag{8}$$

where $c_p=\sqrt{\frac{\lambda+2\mu}{\rho}}$ and $c_s=\sqrt{\frac{\mu}{\rho}}$ are the compression and shear wave speeds respectively.

$\bar{\boldsymbol{\Psi}}$ can be decomposed into $\bar{\Psi}_r$, $\bar{\Psi}_\theta$ and $\bar{\Psi}_z$, which are related to $\bar{\Psi}_x$, $\bar{\Psi}_y$ and $\bar{\Psi}_z$ by

$$\bar{\Psi}_x=\bar{\Psi}_r\cos\theta-\bar{\Psi}_\theta\sin\theta \tag{9}$$

and

$$\overline{\Psi}_y = \overline{\Psi}_r \sin\theta + \overline{\Psi}_\theta \cos\theta, \tag{10}$$

If the solution is simplified as axisymmetric problem with $\overline{\Psi}_z = 0$ and $\overline{\Psi}_r = 0$ are set to be zeros, the solutions of equations (7) and (8) are that

$$\bar{\phi}(r,z) = \left(A_1 e^{\alpha z} + A_2 e^{-\alpha z}\right) J_0(kr) \tag{11}$$

and

$$\overline{\Psi}_\theta(r,z) = \left(A_3 e^{\beta z} + A_4 e^{-\beta z}\right) J_1(kr), \tag{12}$$

where k are the radial wave number, $J_0(kr)$ and $J_1(kr)$ are the first kind Bessel functions of 1st and 2nd order respectively, $\alpha^2 = k^2 - \dfrac{\omega^2}{c_p^2}$ and $\beta^2 = k^2 - \dfrac{\omega^2}{c_s^2}$.

With the transformation relationships between Cartesian coordinates and cylindrical coordinates, the harmonic displacements $\mathbf{u} = \bar{\mathbf{u}} e^{i\omega t}$ in cylindrical coordinates yields that

$$\bar{\mathbf{u}} = \left(\bar{u}_r, \bar{u}_\theta, \bar{u}_z\right)^T = \left(\frac{\partial \bar{\phi}}{\partial r} - \frac{\partial \overline{\Psi}_\theta}{\partial z}, 0, \frac{\partial \bar{\phi}}{\partial z} + \frac{\partial \overline{\Psi}_\theta}{\partial r} + \frac{\overline{\Psi}_\theta}{r}\right)^T, \tag{13}$$

where

$$\bar{u}_r = \left(-A_1 k e^{\alpha z} - A_2 k e^{-\alpha z} - A_3 \beta e^{\beta z} + A_4 \beta e^{-\beta z}\right) J_1(kr) \tag{14}$$

and

$$\bar{u}_z = \left(A_1 \alpha e^{\alpha z} - A_2 \alpha e^{-\alpha z} + A_3 k e^{\beta z} + A_4 k e^{-\beta z}\right) J_0(kr). \tag{15}$$

With the axisymmetric problem and the deviating process discussed above, the displacement $\left(\bar{u}_r, \bar{u}_\theta, \bar{u}_z\right)^T$ are independent of θ, particularly, $\bar{u}_\theta = 0$. So in the cylindrical coordinates, the harmonic stresses on one plane $\bar{\sigma}_{zz} e^{i\omega t}$, $\bar{\sigma}_{zr} e^{i\omega t}$ and $\bar{\sigma}_{z\theta} e^{i\omega t}$ can be expressed as

$$\bar{\sigma}_{zz} = \left\{\left[\left(\lambda + 2\mu\right)\alpha^2 - \lambda k^2\right] e^{\alpha z} A_1 + \left[\left(\lambda + 2\mu\right)\alpha^2 - \lambda k^2\right] e^{-\alpha z} A_2 + 2\mu k \beta e^{\beta z} A_3 - 2\mu k \beta e^{-\beta z} A_4\right\} J_0(kr), \tag{16}$$

$$\bar{\sigma}_{zr} = \left[-2\mu k \alpha e^{\alpha z} A_1 + 2\mu k \alpha e^{-\alpha z} A_2 - \left(\beta^2 + k^2\right)\mu e^{\beta z} A_3 - \left(\beta^2 + k^2\right)\mu e^{-\beta z} A_4\right] J_1(kr), \tag{17}$$

and $\bar{\sigma}_{z\theta} = 0$.

When let $\bar{\mathbf{S}} = \left(\bar{u}_r, \bar{u}_z, \bar{\sigma}_{zr}, \bar{\sigma}_{zz}\right)^T$, then equations (14), (15), (16) and (17) can be expressed in matrix form as

$$\bar{\mathbf{S}} = \left(\bar{u}_r, \bar{u}_z, \bar{\sigma}_{zr}, \bar{\sigma}_{zz}\right)^T = \mathbf{J} \cdot \mathbf{R} \cdot \mathbf{H} \cdot \mathbf{A}, \tag{18}$$

where

$$\mathbf{J} = \begin{bmatrix} J_1(kr) & 0 & 0 & 0 \\ 0 & J_0(kr) & & 0 \\ 0 & 0 & J_1(kr) & 0 \\ 0 & 0 & 0 & J_0(kr) \end{bmatrix}, \tag{19}$$

$$\mathbf{R}^T = \begin{bmatrix} -k & \alpha & -2\mu k\alpha & \left[\left(\lambda+2\mu\right)\alpha^2 - \lambda k^2\right] \\ -k & -\alpha & 2\mu k\alpha & \left[\left(\lambda+2\mu\right)\alpha^2 - \lambda k^2\right] \\ -\beta & k & -\left(\beta^2 + k^2\right)\mu & 2\mu k\beta \\ \beta & k & -\left(\beta^2 + k^2\right)\mu & -2\mu k\beta \end{bmatrix}, \tag{20}$$

$$\mathbf{H}=\begin{bmatrix} e^{\alpha z} & 0 & 0 & 0 \\ 0 & e^{-\alpha z} & & 0 \\ 0 & 0 & e^{\beta z} & 0 \\ 0 & 0 & 0 & e^{-\beta z} \end{bmatrix}, \tag{21}$$

and

$$\mathbf{A}=\left(A_1, A_2, A_3, A_4\right)^T. \tag{22}$$

2.2 Solution for the multi-layered plates

2.2.1 The transfer matrix

The layered structure contains *N* layers, numbered from 1 to *N*. The Cartesian and cylindrical coordinates lie on the top surface of the 1st layer. The thickness of each layer is $h_j\left(j=1,2\cdots,N\right)$. The vertical position of the top side of the j^{th} is $z_j\left(j=1,2\cdots,N\right)$ and that of the bottom side is $z_{j+1}\left(j=1,2\cdots,N\right)$. The young's modulus, Poisson's ratio, loss factor and density are defined as E_j, ν_j, η_j and ρ_j respectively.

Then the displacements and stresses vector of the j^{th} layer is

$$\bar{\mathbf{S}}_j=\left(\bar{u}_{rj},\bar{u}_{zj},\bar{\sigma}_{zrj},\bar{\sigma}_{zzj}\right)^T=\mathbf{J}\cdot\mathbf{R}_j\cdot\mathbf{H}_j\cdot\mathbf{A}_j\ , \tag{23}$$

The displacements and stresses vector of the top side on j^{th} layer is

$$\bar{\mathbf{S}}_{j,1}=\left(\bar{u}_{rj},\bar{u}_{zj},\bar{\sigma}_{zrj},\bar{\sigma}_{zzj}\right)^T_{z=z_j}=\mathbf{J}\cdot\mathbf{R}_{j,1}\cdot\mathbf{H}_{j,1}\cdot\mathbf{A}_j, \tag{24}$$

where $\mathbf{R}_{j,1}=\mathbf{R}_{j,z=z_j}$ and $\mathbf{H}_{j,1}=\mathbf{H}_{j,z=z_j}$. The displacements and stresses vector of the bottom side on j^{th} is

$$\bar{\mathbf{S}}_{j,2}=\left(\bar{u}_{rj},\bar{u}_{zj},\bar{\sigma}_{zrj},\bar{\sigma}_{zzj}\right)^T_{z=z_{j+1}}=\mathbf{J}\cdot\mathbf{R}_{j,2}\cdot\mathbf{H}_{j,2}\cdot\mathbf{A}_j, \tag{25}$$

where $\mathbf{R}_{j,2}=\mathbf{R}_{j,z=z_{j+1}}$ and $\mathbf{H}_{j,2}=\mathbf{H}_{j,z=z_{j+1}}$.

By requiring the continuity of the displacements and balance of the stresses on the interface, from equation (24) and (25) the relationship of constants between the j^{th} layer and the j+1th layer could be obtained, i.e.

$$\mathbf{A}_{j+1}=\mathbf{T}_j\cdot\mathbf{A}_j \qquad \left(j=1,2,\cdots,N-1\right), \tag{26}$$

where $\mathbf{T}_j=\left(\mathbf{R}_{j+1,1}\cdot\mathbf{H}_{j+1,1}\right)^{-1}\cdot\left(\mathbf{R}_{j,2}\cdot\mathbf{H}_{j,2}\right)\left(j=1,2,\cdots,N-1\right)$.

Using the recurrence, the constants between the j^{th} layer and the j+k^{th} layer yields

$$\mathbf{A}_{j+k}=\mathbf{I}_{j+k-1,j}\mathbf{A}_j, \tag{27}$$

where $\mathbf{I}_{j+k-1,j}=\mathbf{T}_{j+k-1}\mathbf{T}_{j+k-2}\cdots\mathbf{T}_{j+1}\mathbf{T}_j$ is called the Transfer Matrix between the j^{th} layer and the j+k^{th} layer.

2.2.2 Modal Analysis

The displacements and stresses vector of the top side on the 1st layer is

$$\bar{\mathbf{S}}_{1,1} = \mathbf{J} \cdot \mathbf{R}_{1,1} \cdot \mathbf{H}_{1,1} \cdot \mathbf{A}_1 . \tag{28}$$

The displacements and stresses vector of the bottom side on the Nth layer is

$$\bar{\mathbf{S}}_{N,2} = \mathbf{J} \cdot \mathbf{R}_{N,2} \cdot \mathbf{H}_{N,2} \cdot \mathbf{A}_N . \tag{29}$$

From equation (27), equation (29) yields

$$\bar{\mathbf{S}}_{N,2} = \mathbf{J} \cdot \mathbf{R}_{N,2} \cdot \mathbf{H}_{N,2} \cdot \mathbf{I}_{N-1,1} \mathbf{A}_1 , \tag{30}$$

where $\mathbf{I}_{N-1,1} = \mathbf{T}_{N-1}\mathbf{T}_{N-2}\cdots\mathbf{T}_2\mathbf{T}_1$.

For the free vibration, the stresses $\bar{\sigma}_{zr}$ and $\bar{\sigma}_{zz}$ on the top side of the 1st layer and the bottom side of the Nth layer must equal to zeros. With this condition and equation (28) and (30), the following relation can be obtained

$$\begin{bmatrix} \mathbf{R}_2 \\ \mathbf{R}_3 \end{bmatrix} \mathbf{A}_1 = \mathbf{0} , \tag{31}$$

where $\mathbf{R}_2$ represents the last 2 rows of $\mathbf{R}_{1,1}$ and $\mathbf{R}_3$ represents the last 2 rows of $\mathbf{R}_{N,2} \cdot \mathbf{H}_{N,2} \cdot \mathbf{I}_{N-1,1}$. To get a nontrivial solution,

$$\det \begin{bmatrix} \mathbf{R}_2 \\ \mathbf{R}_3 \end{bmatrix} = 0 , \tag{32}$$

from which, the dispersion relation (modal characteristics) can be obtained. The dispersive curve looks like the dispersive curve of infinite plates, but not is that because the dispersive curves of infinite plates and finites plates are continuous and discrete respectively. For each $k = k_n$, several discrete modal frequencies ω_{nm} exist, satisfying equation (32) and k_n is determined by the boundary conditions on the cylindrical surface.

In this model, the radial displacement $\bar{u}_r$ and transverse displacement $\bar{u}_z$ on the cylindrical surface can't be zeros at the same time shown in equation (23). So it is assumed that $\bar{u}_z = 0$, meaning the wavenumber k should be the values that satisfy $J_0(kR) = 0$. From the dispersion equation (32), each wavenumber k_n will produce several ω_{nm}.

From equation (32), the constant vector $\mathbf{A}_1^{(nm)} = \left(A_1^{(nm)}, A_2^{(nm)}, A_3^{(nm)}, A_4^{(nm)}\right)^T$ corresponding to k_n and ω_{nm} will be obtained. So under the harmonic excitation of the radian frequency ω_{nm}, the free vibration response of the jth layer can be expressed as modal superposition form

$$\mathbf{S}_j = \left(u_{rj}, u_{zj}, \sigma_{zrj}, \sigma_{zzj}\right)^T = \sum_{n=1}^{+\infty}\sum_{m=1}^{+\infty} B_{nm}\mathbf{J}(k_n r)\cdot\mathbf{R}_j(k_n,\omega_{nm})\cdot\mathbf{H}_j(k_n,\omega_{nm})\cdot\mathbf{I}_{j-1,1}(k_n,\omega_{nm})\mathbf{A}_1^{(nm)} e^{i\omega_{nm}t}$$

$$(j = 2,3,\cdots,N) . \tag{33}$$

where let $\mathbf{I}_{j-1,1}(k_n,\omega_{nm}) = \mathbf{e}$ (unit matrix) when $j = 1$.

2.2.3 Forced vibration

From equation (33), the displacements u_r and u_z are expressed as

$$\mathbf{u}=\begin{pmatrix}u_r\\u_z\end{pmatrix}=\sum_{n=1}^{+\infty}\sum_{m=1}^{+\infty}B_{nm}\bar{\mathbf{u}}_{nm}e^{i\omega_{nm}t}\,, \tag{34}$$

where $\bar{\mathbf{u}}_{nm}$ is the first two components of $\mathbf{J}(k_n r)\cdot\mathbf{R}_j(k_n,\omega_{nm})\cdot\mathbf{H}_j(k_n,\omega_{nm})\cdot\mathbf{I}_{j-1,1}(k_n,\omega_{nm})\mathbf{A}_1^{(nm)}$, called the modal shape. In particular, $\bar{\mathbf{u}}_{nm}$ satisfies the equation $\int_V\rho\bar{\mathbf{u}}_{nm}^T\cdot\bar{\mathbf{u}}_{lp}=\delta_{nm,lp}$ which means the orthogonality between two different modes.

For the axisymmetric load $\mathbf{F}(r,t)$ applied on the top surface of the 1st layer, a solution is assumed to be in the form of an expansion of the normal modes *i.e.*

$$\mathbf{u}=\begin{pmatrix}u_r\\u_z\end{pmatrix}=\sum_{n=1}^{+\infty}\sum_{m=1}^{+\infty}\bar{\mathbf{u}}_{nm}q_{nm}(t)\,. \tag{35}$$

Considering the load $\mathbf{F}(r,t)$, the Lamé-Navier equation becomes

$$(\lambda+\mu)\nabla\nabla\cdot\mathbf{u}+\mu\nabla^2\mathbf{u}=\rho\frac{\partial^2\mathbf{u}}{\partial t^2}-\mathbf{F}(r,t)\,. \tag{36}$$

Substituting $\mathbf{u}$ in equation (36) with equation (35), inner producting $\bar{\mathbf{u}}_{lp}^T$ on both sides, integrating within the volume of the entire multilayered plates and considering the modes orthogonality, the expression of equation (36) becomes

$$\int_V\bar{\mathbf{u}}_{lp}^T\cdot\left[(\lambda+\mu)\nabla\nabla\cdot\bar{\mathbf{u}}_{lp}+\mu\nabla^2\bar{\mathbf{u}}_{lp}\right]dvq(t)=\int_V\rho\bar{\mathbf{u}}_{lp}^T\cdot\bar{\mathbf{u}}_{lp}dv\ddot{q}(t)-\int_V\bar{\mathbf{u}}_{lp}^T\cdot\mathbf{F}(r,t)dv\,. \tag{37}$$

Letting

$$K_{lp}=-\int_V\bar{\mathbf{u}}_{lp}^T\cdot\left[(\lambda+\mu)\nabla\nabla\cdot\bar{\mathbf{u}}_{lp}+\mu\nabla^2\bar{\mathbf{u}}_{lp}\right]dv\,, \tag{38}$$

$$M_{lp}=\int_V\rho\bar{\mathbf{u}}_{lp}^T\cdot\bar{\mathbf{u}}_{lp}dv\,, \tag{39}$$

and

$$Q_{lp}(t)=\int_V\bar{\mathbf{u}}_{lp}^T\cdot\mathbf{F}(r,t)dv\,, \tag{40}$$

equation (37) becomes

$$M_{lp}\ddot{q}(t)+K_{lp}q(t)=Q_{lp}(t)\,, \tag{41}$$

where M_{lp}, K_{lp} and $Q_{lp}(t)$ is called the modal mass, modal stiffness and modal force and $\omega_{lp}^2=\dfrac{K_{lp}}{M_{lp}}$.

2.3 Vibro-acoustical analysis

The solution of the circular multi-layered plate for axisymmetric problem could be used to model the clamped plate in an impedance tube. In order to investigate the sound transmission loss in the impedance tube (see Figure 2), it's necessary to couple the sound and vibration.

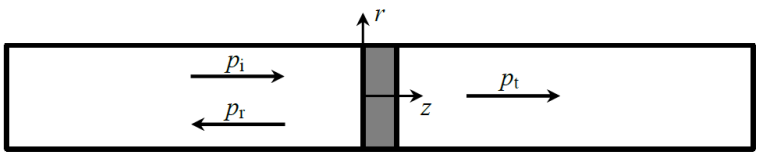


Figure 2: The impedance tube for sound transmission loss

In Figure 2, p_i is the incident wave, assumed to be a plane wave, i.e.

$$p_i = p_{ai} e^{i(\omega t - k_i z)}, \tag{42}$$

where $k_i = \omega / c$. p_r is the reflected wave, which can be expressed to be the sum of a number of modal waves in the tube for the axisymmetric problem, i.e.

$$p_r = \sum_{n=0}^{+\infty} A_{0n} J_0\left(k_{0n} r\right) e^{i(\omega t + k_{zr} z)}, \tag{43}$$

where n is the radius modal index and $k_{zr} = \sqrt{\frac{\omega^2}{c^2} - k_{0n}^2}$ and k_{0n} is obtained by the equation $J_1\left(k_{0n} R\right) = 0$.

p_t is the transmitted wave, which can be written to be

$$p_t = \sum_{q=0}^{+\infty} C_{0q} J_0\left(k_{0q} r\right) e^{i(\omega t - k_{zt} z)}, \tag{44}$$

where q is the radius modal index and $k_{zt} = \sqrt{\frac{\omega^2}{c^2} - k_{0q}^2}$ and k_{0q} is obtained by the equation $J_1\left(k_{0q} R\right) = 0$.

Then the applied body force $\mathbf{F}(r,t)$ becomes

$$\begin{aligned} \mathbf{F}(r,t) &= \left(0, p_i \delta(z) + p_r \delta(z) - p_t \delta(z-H)\right) \\ &= \left(0, p_{ai} e^{i(\omega t - kz)} \delta(x) + \sum_{n=0}^{+\infty} A_{0n} J_0\left(k_{0n} r\right) e^{i(\omega t + k_z z)} \delta(x) - \sum_{q=0}^{+\infty} C_{0q} J_0\left(k_{0q} r\right) e^{i(\omega t - k_z z)} \delta(x-H)\right), \end{aligned} \tag{45}$$

where H is the total thickness of the multi-layered plates.

Therefore, with equation (35), (41) and (45), the displacements vector $\mathbf{u}$ yields that

$$\mathbf{u} = \begin{pmatrix} u_r \\ u_z \end{pmatrix} = \sum_{l=1}^{+\infty} \sum_{p=1}^{+\infty} \bar{\mathbf{u}}_{lp} \frac{G_{lp}}{K_{lp} - \omega^2 M_{lp}} e^{i\omega t}. \tag{46}$$

where G_{lp} is a function of A_{0n} and C_{0q}.

The coupling conditions, i.e. the air velocity on two sides of the plates are equal to the velocity of the plates in the direction vertical to the plates, are shown as

$$\begin{cases} v_{iz=0} + v_{rz=0} = v_{pz=0} \\ v_{tz=H} = v_{pz=H} \end{cases}, \tag{47}$$

where $v_{iz=0}$ and $v_{rz=0}$ are the incident and reflected sound wave velocities at $z = 0$. $v_{tz=H}$ is the transmitted sound wave velocity at $z = H$. $v_{pz=0}$ and $v_{pz=H}$ are the plate's velocities of two sides. If the modes of the reflected wave and transmitted wave are truncated to be *N* and *Q* respectively, there are *N*+*Q*+2 unknown numbers in (47) for a given frequency ω. For a given frequency ω, the plate should be discretized along the radius direction and at least (*N*+*Q*+2)/2 nodes along the radius direction should be considered in order to achieve the *N*+*Q*+2 unknown constants.

3 Validation

Modal frequency/shape and sound transmission loss are validated for two materials. The material parameters are shown in Table 1. The radius of the circular plate is 30 mm, corresponding to the inner radius of the impedance tube, and the total thickness (*H*) is 4 mm. The frequency ranges from 0 to 10000 Hz and wave number ranges from 0 to $1000 \times 2\pi$ rad/m.

Material ID	Material Name	Young's Modulus (MPa)	Poisson's Ratio	Density (kg/m^3)	Loss Factor
A	PP(T30s)	1837	0.41	905	0.064
B	POE(8150)	29.90	0.45	868	0.039

Table 1: Material Parameters

Notes: The material parameters are measured at 25 ℃.

3.1 Comparison in modal parameters between the methods in this paper and Ansys

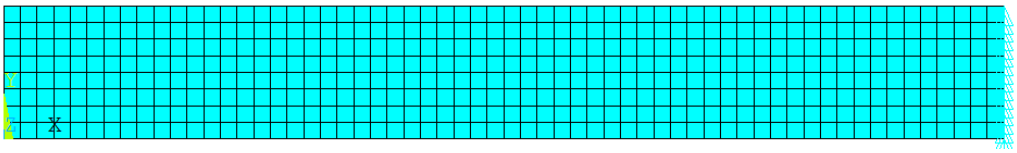


Figure 3: FE models of this axisymmetric problem

Modal No.	1 layer of B		1 layer of A		2 layers of B-A		4 layers of B-A		8 layers of B-A	
	FE	Paper	FE	Paper	FE	Paper	FE	Paper	FE	Paper
1	240	241	1803	1806	721	720	948	949	1032	1031
2	1172	1171	8836	8835	3668	3667	3323	3324	3445	3444
3	2573	2574	—	—	8598	8599	6388	6387	6043	6043
4	2640	2643	—	—	—	—	—	—	8849	8850
5	4232	4231	—	—	—	—	—	—	—	—
6	5991	5993	—	—	—	—	—	—	—	—
7	6012	6011	—	—	—	—	—	—	—	—
8	7846	7845	—	—	—	—	—	—	—	—
9	9179	9180	—	—	—	—	—	—	—	—
10	9701	9702	—	—	—	—	—	—	—	—

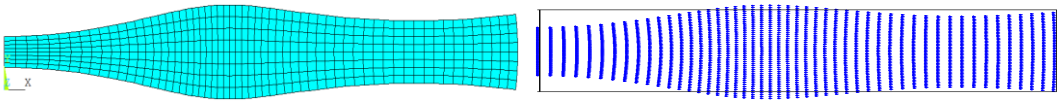
Modal No.	16 Layers of B-A		32 Layers of B-A		64 Layers of B-A		128 Layers of B-A	
	FE	Paper	FE	Paper	FE	Paper	FE	Paper
1	—	1053	—	1059	—	1060	—	1061
2	—	3510	—	3530	—	3535	—	3537
3	—	6057	—	6076	—	6082	—	6084
4	—	8637	—	8620	—	8619	—	8619

Table 2: Comparison in modal frequencies between FE and this paper (Hz)

The derivations and the related Matlab program are checked for modal parameters by comparing results with Ansys FE calculation. The axisymmetric 8-node quadrilateral element is used in FE models and the transverse (in z-direction) displacements of nodes at R = 30 mm are fixed, as shown in Figure 3.

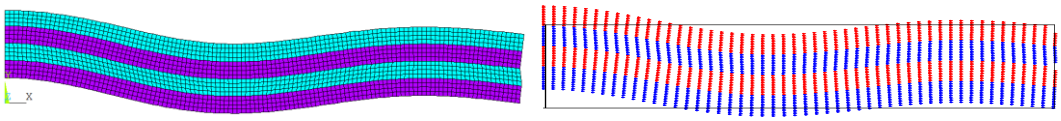
The comparisons in modal frequencies are listed in Table 2. It shows that the modal frequencies from the method developed in this paper agree well with Ansys, with a maximum difference of only 3 Hz. It can also be seen that the composite plates of two materials has a modal behaviour which is quite different from that of a single layer. The composite plates with different number of layers exhibit different values and numbers of modal frequencies. When the number of layers exceeds 16, the number of modes and values of modal frequencies become invariant.

The modal shapes at 9180 Hz (the 9th mode of 1 layer B) and 6387 Hz (the 3rd mode of 4 layers) in Table 2, calculated by FE method and by the method in this paper, are compared in Figure 4. It shows that the modal shapes produced by the two methods are almost the same.



FE model This paper

(a) The 7th modal shape of 1 layer B (at 9180 Hz)



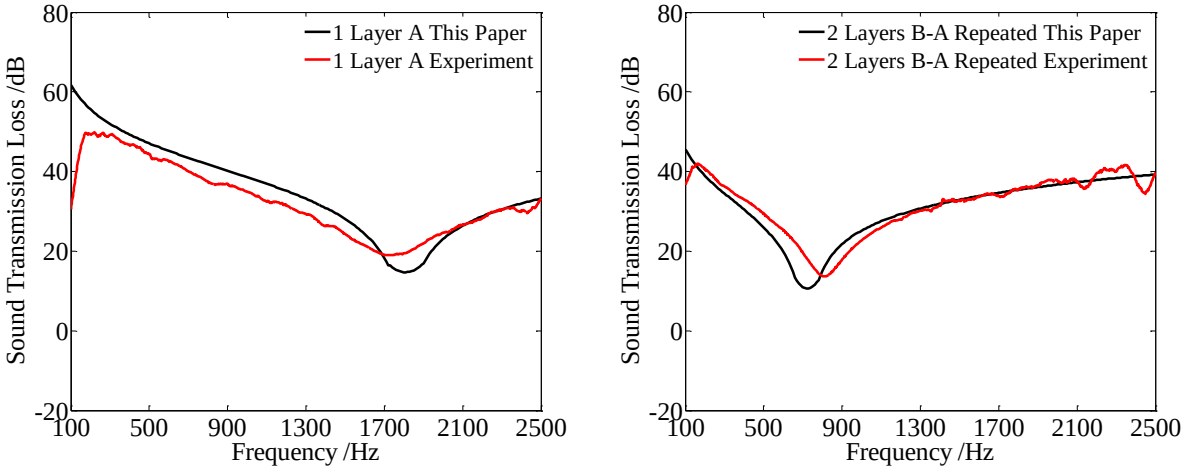
FE model This paper

(b) The 3rd modal shape of 4 layer B-A-B-A (at 6387 Hz)

Figure 4: Comparison of modal shapes calculated by Ansys and the method in this paper

3.2 Validation of sound transmission loss

The sound transmission loss predicted using the method of this paper is compared with the impedance tube measurement and the comparison is shown in Figure 5. The results show that the sound transmission loss of this paper agrees well with the impedance tube experiments. However, the predicted dip and the measured dip occur at different frequencies. This may be caused by differences in boundary condition. For the model in this paper, the transverse displacements on the cylindrical surface are fixed, i.e.



(a) 1 layer A (b) 2 layers B-A

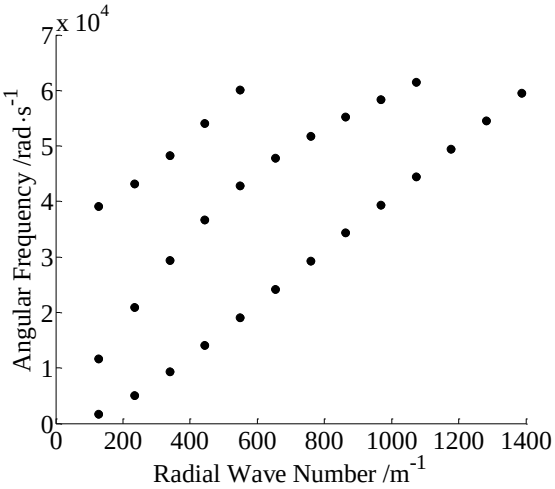
Figure 5: Sound transmission comparison between experiments and this paper

$u_z = 0$. However for the experiments, the plates are placed tightly between two tubes, indicating that both the transverse and radial displacements should be fixed, i.e. $u_r = 0$ and $u_z = 0$.

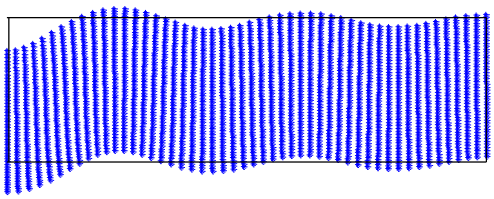
4 Results

4.1 Classification of modal types

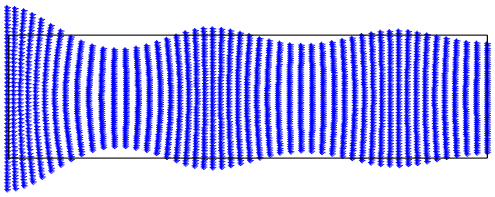
In FE model, the modal frequencies are aligned and numbered in the ascending order, but the exact modal shape information is unknown and cannot be classified. However, the analytical method of this paper for modal calculation can distinguish different types of modal shapes by making use of the dispersive curves. In order to illustrate this characteristic, a softer material TPU with 1 layer (The young's modulus is 8 Mpa, Poisson ratio is 0.47, loss factor is 0.09 and density is 1210 kg/m^3, radius is 30 mm, total thickness is 4 mm) is adopted. Figure 6 is the dispersive curve formed by modal frequencies and modal shapes of 1 layer TPU. The modal frequencies lie in three lines and each line represents different modal shapes. The lowest line is the flexural mode, the middle line is the radial-longitudinal mode and the highest line is the thickness shear mode.



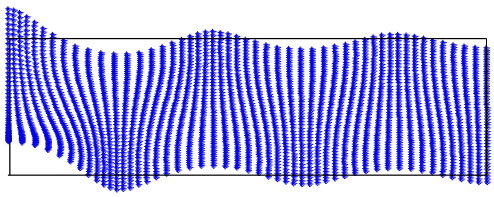
(a) Dispersive curve(modal frequencies)



(b) The 5th modal shape in the lowest line



(c) The 5th modal shape in the middle line

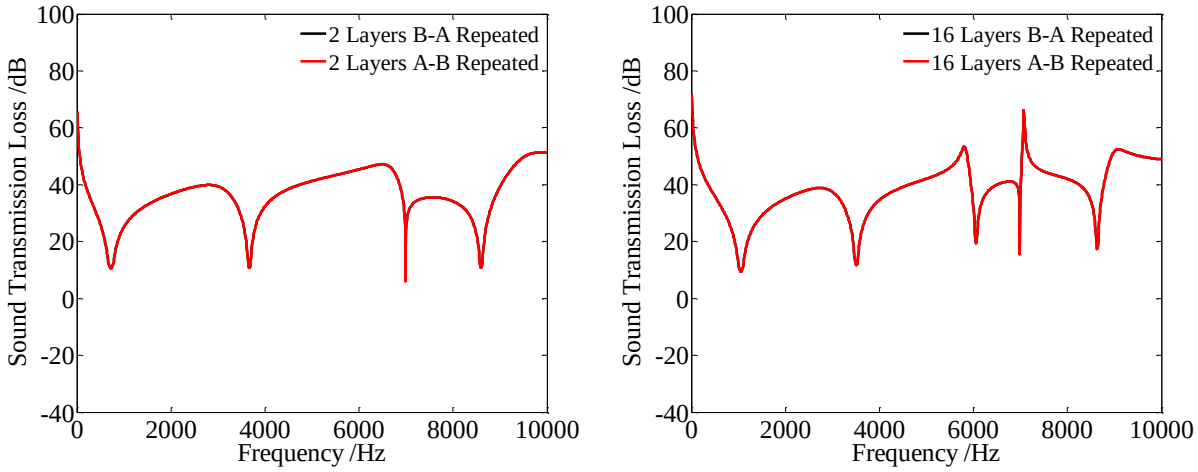


(d) The 5th modal shape in the highest line

Figure 6: Dispersive curve and modal shapes of 1 layer TPU

4.2 Influence of layer aligning sequences on vibro-acoustical behaviours

The sound transmission loss of sequence A-B and B-A with total thickness of 4 mm are compared in Figure 7. Since the modal characteristics tend to be invariant with layer increasing, the results of 16 layers are chosen to represent the cases when the plates are more than 16 layers. It shows that the sound transmission losses of the two sequences are almost the same. This is because the vibro-acoustical behaviours of the layered plate are mainly determined by bending modes of the plate rather than by modes in which displacement in the axial direction is important.



(a) 2 layers (b) 16 layers

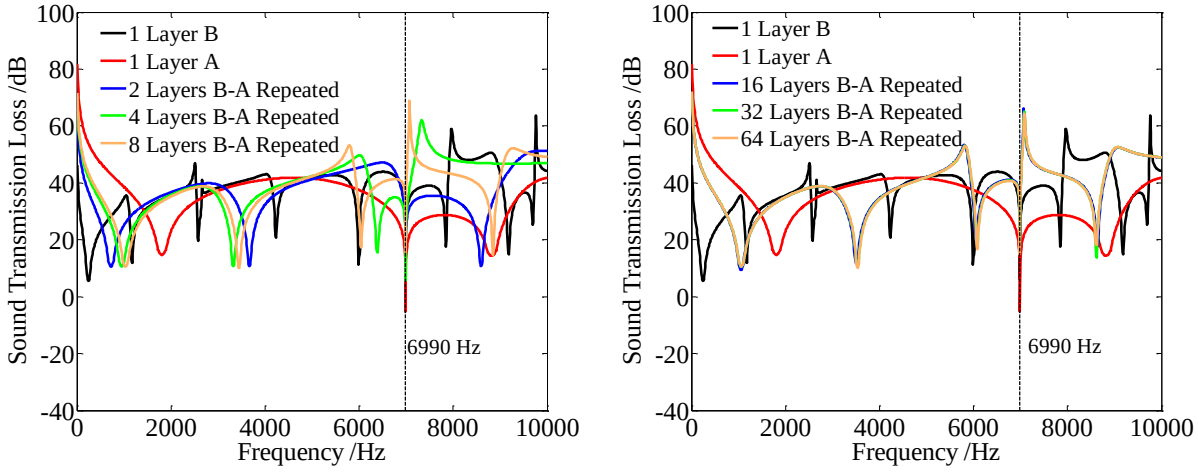
Figure 7: Sound transmission loss comparison between sequence A-B and B-A

4.3 Influence of layer numbers on vibro-acoustical behaviours

Figure 8 is the sound transmission loss comparison between different layers for sequence B-A with total thickness of 4 mm. It can be seen that:

(1) All the dips but the one at around 6990 Hz of each layer structure are in accordance with the plates modes listed in table 2. The dip at around 6990 Hz is not one of the modal frequencies in Table 2, rather, it is one of the cut-on frequencies of the circular tube, which can be approximated by $a\frac{c_0}{2\pi R}$ for axisymmetric modal waves in the circular tube, where $a = 3.832$ is the second zero of first kind Bessel Function of 1st order.

(2) At low frequency ranges, the sound transmission losses of 1 layer A, multi-layered plates with B-A repeated and 1 layer B are reduced successively for their decreasing stiffness in turn and with number of layers increasing, the sound transmission loss is enhanced for the multi-layered plates.



(a) 1-8 layers (b) 16-64 layers

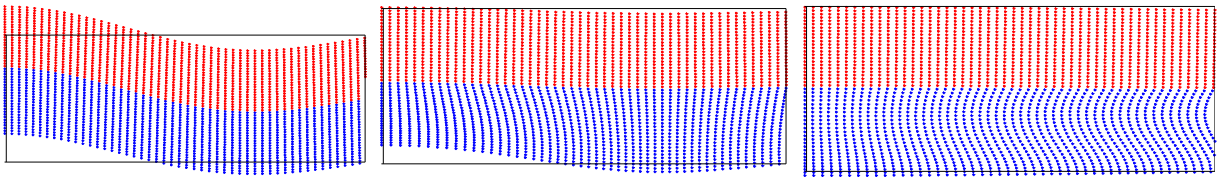
Figure 8: Sound transmission loss comparison between different layers for sequence B-A

(3) At frequency ranges around the cut-on frequency, the multi-layered plates show a higher sound transmission loss performance than a single-layered one.

(4) The sound transmission loss becomes invariant with layer increasing, which is because that the modal performance is almost the same seen in Table 2. Therefore, based on the asymptotic vibro-acoustical behaviours with layer increasing, the multi-layered plates can be regarded as an equivalent plate or it evolves to another plate with new material properties. However, it should be noticed that the properties of the direction vertical to the plate are different than other two directions.

4.4 Influence of layer thicknesses on vibro-acoustical behaviours

The vibro-acoustical behaviours of total 4 mm thickness, 8 mm thickness and 16 mm thickness are compared. When the total thickness is thin (thinner than 4 mm), the layers of the multi-layered plates only exhibit flexural mode. However, combined flexural-radial longitudinal modes and combined flexural-thickness shear modes occur for 8 mm thickness and 16 mm thickness, respectively, shown in Figure 9. It's obvious that softer layer (blue area) performs radial longitudinal or thickness shear modes and stiffer layer (red area) performs flexural modes.



(a) 4 mm thickness (b) 8 mm thickness (c) 16 mm thickness

Figure 9: Combined modal shapes of the 2nd mode for 2 layers B-A

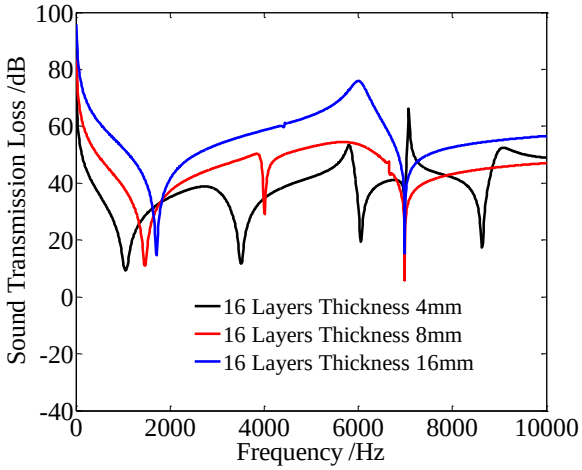


Figure 10: Comparison of sound transmission loss with 16 layers for different thicknesses

Figure 10 is the sound transmission loss comparison for different thicknesses and only 16 layers are chosen to represent other cases. It can be got that the sound transmission losses are improved with total thickness increasing for the mass increased with thickness doubled.

5 Conclusions

The axisymmetric problem of circular multi-layered plates is established theoretically. The vibro-acoustical performances of composites PP/POE with different layer numbers, layer aligning sequences and total thickness are investigated in this paper. The results show that

(1) The vibro-acoustical behaviours tend to an asymptotic phenomenon with number of layers increasing indicating that the modal number, each modal frequency and sound transmission loss tend to become invariant if the number of layers is large enough.

(2) The sound transmission loss performances of 1 layer A, multi-layered plates of B-A repeated and 1 layer B are reduced successively for their decreasing stiffness in turn at low frequency ranges. At frequencies around the cut-on frequency, the multi-layered plates exhibit a better sound insulation performance than the single-layered one.

(3) Layer aligning sequence (A-B or B-A) has almost no influence on the vibro-acoustical behaviour.

(4) The vibro-acoustical behaviours are largely determined by total thickness of the plates. With total thickness increasing, the combined flexural-radial longitudinal and combined flexural-thickness shear modal shapes will occur and the sound transmission losses are enhanced.

Acknowledgements

This work was supported by the Ministry of Science and Technology of China (2016YFE0205200) and the Opening Project of State Key Laboratory of Polymer Materials Engineering (Sichuan University) (Grant No. sklpme2017-4-01).

References

[1] J. N. Reddy, *Mechanics of laminated composite plates and shells: Theory and Analysis*, CRC Press, Boca Raton, Florida, America (2003).

[2] J. N. Reddy, N. D. Phan, *Stability and natural vibration of isotropic, orthotropic and laminated plates according to higher order shear deformation theory*, Journal of Sound and Vibration, Vol. 98, (1985), pp. 157-170.

[3] J. N. Reddy, T. Kuppusamy, *Natural vibration of laminated anisotropic plates*, Journal of Sound and Vibration, Vol. 94, (1984), pp. 63-69.

[4] C.C. Chao, T. P. Tung, C. C. Sheu, J. H. Tseng, *A constant higher order theory of laminated plates with nonlinear impact modal analysis*, ASME Journal of Vibration and Acoustics, Vol. 116, (1994) pp. 371-378.

[5] A. Noiser, R. K. Kapania, J. N. Reddy, *Low velocity impact of laminated composites using a layerwise theory*, Computational Mechanics, Vol. 13, (1994), pp. 360-379.

[6] N. F. Hanna, A. W. Leissa, *A higher order shear deformation theory for the vibration of thick plates*, Journal of Sound and Vibration, Vol. 170, (1994), pp. 545-555.

[7] T. Kant, K. Swaminathan, *Free vibration of isotropic, orthotropic and multilayered plates based on higher order refined theory*, Journal of Sound and Vibration, Vol. 241, No. 2, (2001), pp. 319-327.

[8] H. Altenbach, *Theories for laminated and sandwich plates*, Mechanics of Composite Materials, Vol. 34, No. 3, (1998), pp. 243-252.

[9] W. J. Bottega, *An axisymmetric solution for the transient problem of a multilayered elastic solid of finite extent*, Mechanics Research Communications, Vol. 15, No. 1, (1988), pp. 11-20.

[10] W. J. Bottega, *On the orthogonality of the normal modes for multilayered elastic solids*, Mechanics Research Communications, Vol. 15, No. 4, (1988), pp. 237-241.

[11] K. A. Lange, W. J. Bottega, *On the elastodynamic response of thick multilayered plates subjected to impact loads*, Journal of Sound and Vibration, Vol. 211, No. 1, (1998), pp. 39-93.

[12] M. El-Raheb, P. Wagner, *Transient elastic waves in a finite layered media*, Journal of the Acoustical Society of America, Vol. 99, (1996), pp. 3513-3527.

[13] S. Srinicas, C. V. Joga Rao, A. K. Rao, *An exact analysis for vibration of simply supported homogeneous and laminated thick rectangular plates*, Journal of Sound and Transmission, Vol. 12, (1970), pp. 187-199.

[14] K. M. Liew, T. M. Teo, *Three-dimensional vibration analysis of rectangular plates based on differential quadrature method*, Journal of Sound and Vibration, Vol. 220, (1999), pp. 577-599.

[15] S. Ahmad, B. Irons, O. C. Ziekiewicz, *Analysis of thick and thin shell structures by curved finite elements*, International Journal for Numerical Methods in Engineering, Vol. 2, (1970), pp. 419-451.

[16] A. K. Ghosh, S. S. Dey, *Free vibration of laminated composite plates-a simple finite element based on higher order theory*, Computers and Structures, Vol. 52, No. 3, (1994), pp. 397-404.

[17] M. C. Manna, *Free vibration analysis of isotropic rectangular plates using a high-order triangular finite element method*, Journal of Sound and Vibration, Vol. 281, (2005), pp. 235-259.

[18] V. N. Burlayenko, H. Altenbach, T. Sadowski, *An evaluation of displacement-based finite element models used for free vibration analysi of homogeneous and composite plates*, Journal of Sound and Vibration, Vol. 358, (2015), pp. 152-175.

[19] S. Brischetto, Roberto Torre, *Exact 3D solutions and finite element 2D models for free vibration analysis of plates and cylinders*, Curved and Layer, Vol. 1, (2014), pp. 59-92.

[20] N. Chandra, S. Raja, K. V. Nagendra Gopal, *Vibro-acoustic response and sound transmission loss analysis of functionally graded plates*, Journal of Sound and Vibration, Vol. 333, (2014), pp. 5786-5802.

[21] C. Huang, S. Nutt, *Analytical study of sound transmission through unbounded panels of functionally graded materials*, Journal of Sound and Vibration, Vol. 330, (2011), pp. 1153–1165.

[22] K. Daneshjou, M. M. Shokrieh, M. G. Moghaddam, R. Talebitooti, *Analytical model of sound transmission through relatively thick FGM cylindrical shells considering third order shear deformation theory*, Composite Structures, Vol. 93, (2010), pp. 67–78.

[23] H. Wen-chao, N. Chung-Fai, *Sound insulation improvement using honeycomb sandwich panels*, Applied Acoustics, Vol. 53, No. 1, (1998), pp. 163–177.

[24] C. Ng, C. Hui, *Low frequency sound insulation using stiffness control with honeycomb panels*, Applied Acoustics, Vol. 69, No. 4, (2008), pp. 293–301.

[25] R. Zhou, M. J. Crocker, *Sound transmission loss of foam-filled honeycomb sandwich panels using statistical energy analysis and theoretical and measured dynamic properties*, Journal of Sound and Vibration, Vol. 329, No. 6, (2010), pp. 673–686.

[26] M. P. Arunkumar, M. Jagadeesh, J. Pitchaimani, K. V. Gangadharan, M. C. L. Babu, *Sound radiation and transmission loss characteristics of a honeycomb sandwich panel with composite facings: Effect of inherent material damping*, Journal of Sound and Vibration, Vol. 383, (2016), pp. 221-232.

[27] J. Zhu, J. Shen, S. Guo, H-J. Sue, *Confined distribution of conductive particles in polyvinylidene fluoride-based multilayered dielectrics: toward high permittivity and breakdown strength*, Carbon, Vol. 84, (2015), pp. 355–64.

Optimization and testing of periodic and locally resonant dead-end pores for sound absorption in frequencies below 1000 Hz

A. Carvalho de Sousa [1,2,a], **M. Camargo** [3], **A. Lenzi** [3], **C. Claeys** [1,2], **E. Deckers** [1,2]
[1] KU Leuven, Department of Mechanical Engineering, Celestijnenlaan 300 B, B-3001, Heverlee, Belgium
[a] e-mail: **augusto.carvalho@kuleuven.be**

[2] DMMS lab, Flanders Make, Belgium

[3] Federal University of Santa Catarina, Laboratory of Acoustic and Vibration, Florianpolis, Brazil

Abstract
The design and application of periodic structures and geometries as a strategy to overcome sound absorption problems in the lower frequency range has increased, making subwavelength absorption feasible. In this work we use a differential evolution algorithm to optimize a design already available in literature, which consists of a cylindrical pore with smaller cylinders periodically spaced along its axis. Two samples were optimized to achieve unit and thus perfect absorption in a narrow band between 500 Hz and 600 Hz. These were further 3D-printed and tested in an impedance tube. For the first sample, a unit absorption coefficient was found at 562 Hz for a thickness of $\lambda/13.3$, reaching a good agreement between theory and experiment. The second sample was optimized for maximum absorption at 1000 Hz. Results for both samples show good agreement between theory, experiment and numerical simulation.

1 Introduction

Foams are a classic solution for achieving absorption of sound energy. These foams are vastly used in the form of acoustic panels for many applications such as enhancing the acoustic environment of a recording studio or lowering the transmission of sound in between two partitions in the same building [1]. The main issue with this approach is that the foams are required to have a thickness of $\lambda/4$ to be effective, λ being the acoustic wavelength. As such, the typical frequency range in which they are effective is typically above 1000 Hz.

In recent years many strategies have been used and developed to enhance the acoustic behaviour of materials for lower frequencies [2, 3, 4]. The approaches used may be coiling up space [5, 6], using dead-end pores [7, 8, 9], membranes [10, 11] or achieving a negative density [12]. These strategies fall in the class of metamaterials, most of which rely on the repetition of a periodic structure, namely a unit cell, to achieve desired physical properties that one cannot find in nature itself [13]. However, most of these designs do not work in a broad frequency range, meaning that one needs to match the dimensions of the different parts of the geometry in order to target a certain frequency band and this process can be very time-consuming [14].

In this work we optimize a design of a periodic resonant structure already existing in literature [9] through a Differential Evolution Algorithm [15, 16], in order to achieve a unit absorption coefficient in frequencies below 1000 Hz. The design is based on an array of small cylinders periodically-spaced along the axis of another cylinder. This assembly was tested for sound absorption in the original paper but did not achieve sound absorption for $f < 1000$ Hz nor was it optimized. A similar design from the same authors [17] was

optimized through a transfer matrix model, but not through an algorithm dedicated to optimization. This is the main contribution of this work.

The work is organized as follows: section 2 describes the theory for the wave propagation in the geometry and its formulation, section 3 presents the optimization and 3D printing process and section 4 presents and discusses the results obtained.

2 Problem setting

This section highlights the theory for the geometry that is the focus of this paper, as taken from ref. [9]. Such geometry relies on the assembly of small cylinders (dead-end pores) periodically spaced along the axis of a bigger cylinder (main pore), as depicted in Fig. 1 a).

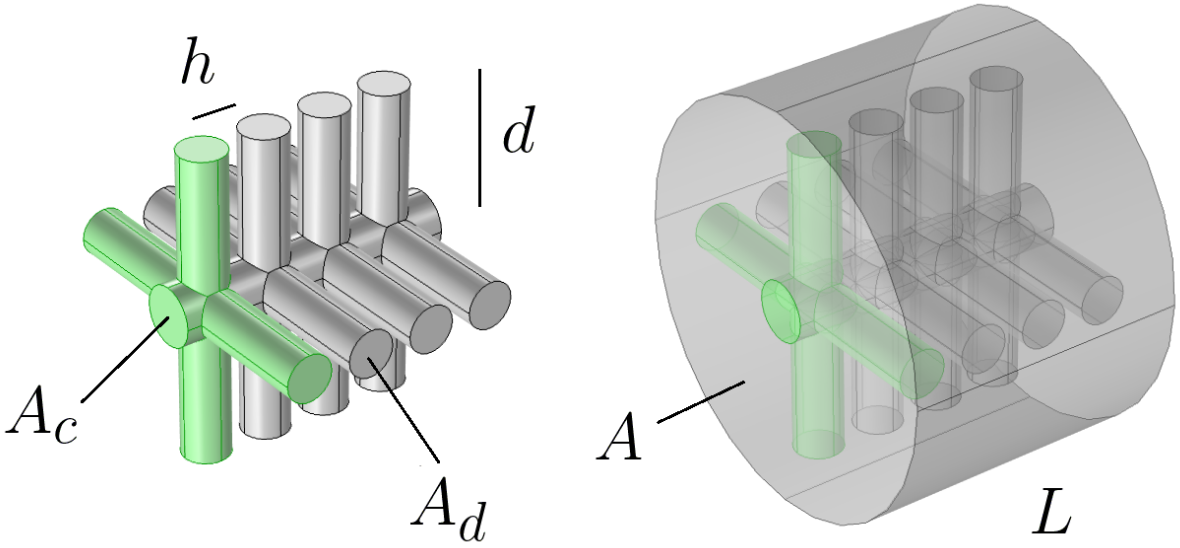


Figure 1: Unit cell (green highlight), array of unit cells (left) and array of unit cells embedded in a cylinder to be 3D-printed (right), where A_c and L are the cross sectional area and length of the main pore, respectively, and A_d and d are the same quantities but for the dead-end pores, h is the period in between unit cells and A is the cross sectional area of the sample to be 3D-printed.

The acoustic impedance for the array of unit cells is given by [9]

$$Z = -i\frac{N}{2}\frac{A_s}{A_c}\frac{Z_c}{Z_s}tan(k_s d), \tag{1}$$

where N is the number of side branches per period ($N = 4$ in the Fig. 1), Z_c is the impedance of the main cylinder and Z_s, k_s and d are the impedance, wavenumber and length of the side branches, respectively, which are given by

$$Z_i = \sqrt{\rho_i / C_i}, \tag{2}$$

$$k_i = \omega\sqrt{\rho_i C_i}, \tag{3}$$

with $i = c$ for the main cylinder or s for the side branches, $\omega = 2\pi f$, and C_i and ρ_i are the equivalent compressibility and equivalent density of the fluid within the cylinder, respectively.

Table 1: Expressions for the assessing of the impedance Z as seen in ref. [9]

Parameter		Expression
c_0	Speed of sound in ar	343 m/s
P_0	Atmospheric pressure	101325 Pa
ρ_0	Air density	1.204 g/cm^3
Z_0	Impedance of the air	$\rho_0 c_0$
μ	Absolute viscosity	1.511e-5 Pa.s
γ	Constant for ideal gases	1.42
Pr	Prandtl's Number (for current model)	0.6282
A_i	Cross section area	a_i^2
σ_i	Flux resistivity	$8\mu/a_i^2$
κ_i	Thermal permeability	$a_i^2/8$
Λ_i	Viscous characteristic length	a_i
$\Lambda_i^{'}$	Viscous characteristic length	a_i
$\omega_i^{'}$	-	$\omega\sqrt{Pr}$
$\omega_{b,i}$	-	$\sigma_i^2\Lambda_i^2/4\rho_0\mu$
$\omega_{b,i}^{'}$	-	$\Lambda_i^{'2}/4\rho_0\kappa_i^2$
ρ_i	Equivalent density	$\rho_0(1+(\sigma_i/-i\omega\rho_0))\sqrt{1+(-i\omega/\omega_{b,i})}$
C_i	Equivalent compressibility	$\xi(\gamma-(\xi^{'}/(1+(\mu/(-i\omega_i^{'}\rho_0\kappa_i)\sqrt{(1+(-i\omega_i^{'}/\omega_{b,i}^{'}))}))))$
ξ	-	$1/\rho_0 c_0^2$
$\xi^{'}$	-	$\gamma-1$

For the sake of clarification and reproducibility of this work, all the other equations and constants needed for the assessing of the impedance Z in Eq. (1) are presented in Table 1.

In Table 1 the items whose descriptions are marked with "-" are simply a re-writing strategy to make the equations look more elegant and decrease their number of terms, having no physical meaning on their own. Once more, the index i can be c for the main pore or s for the side branches.

To assess the sound absorption, the geometry is then embedded into a cylindrical shape such as the one shown in Fig. 1 (right) to form a sample. The shape of the sample could be any other than cylindrical as long as a relation between A_c and A can be maintained. Here it was chosen to be cylindrical for 3D-printing purposes, as the geometry is supposed to be tested in an impedance tube whose cross section is also circular. A relation between the area of the main cylinder and the area of the sample can be obtained as being $\phi = A_c/A$, which corresponds to the surface perforation rate (or surface porosity).

The period h in which the unit cells are spaced will cause a phase shift of $y = e^{ik_c h}$ in a plane wave directed towards the sample. If the number of periods is $n = L/h$, from the transfer matrix method [18] it is possible to relate the waves propagating in the sample and relate them to a matrix $\mathbf{M}$ as follows:

$$\mathbf{M} = \begin{pmatrix} (1+Z)y & Z \\ -Z & \dfrac{(1-Z)}{y} \end{pmatrix}^{\mathbf{n}} = \begin{pmatrix} M_{11} & M_{12} \\ M_{21} & M_{22} \end{pmatrix}, \tag{4}$$

k_c being the wavenumber in the main cylinder as taken from Eq. (3).

For a sample with surface porosity ϕ, there is a matrix

$$\mathbf{T} = \begin{pmatrix} \dfrac{1+\phi'}{2\phi} & -\dfrac{1-\phi'}{2\phi} \\ -\dfrac{1-\phi'}{2\phi'} & \dfrac{1+\phi'}{2\phi'} \end{pmatrix} \tag{5}$$

that correlates the waves propagating forwards and backwards in the given geometry, with $\phi' = \phi(Z_0/Z_c)$.

The reflection coefficient is then

$$r = \frac{M'_{11} - M'_{21}}{M'_{22} - M'_{12}}, \tag{6}$$

with M'_{ij} being the element in the i-esimal line and j-esimal column of a matrix $\mathbf{M'} = \mathbf{MT}$. The absorption coefficient can then be found as $\alpha = 1 - |r|^2$.

3 Optimization and further validation

In the previous section the outline of the geometry and its theory was given. The reader can then see that many parameters influence the final result of the absorption coefficient. As such, in order to obtain a perfect absorption for a certain frequency, the most timely effective approach is to use some sort of optimization. This section highlights the optimization method used and the two validation methods, namely a numerical validation through COMSOL software and an experimental validation by impedance tube testing.

3.1 Optimization

Given the number of variables to be optimized, the approach chosen is the differential evolution [19]. It is based on the theory of evolution as seen in biological studies, where one individual crosses with another and the best features keep passing to future individuals. An algorithm already available elsewhere [20] is used to perform such optimization. For each geometrical parameter a boundary condition is established, based on the dimensions of the impedance tube available for testing (diameter = 27 mm), as shown in Table 2.

Table 2: Boundary conditions used in the optimization process

Parameter	Inferior limit	Superior limit	Increase rate
N	1	8	1
L [cm]	1	5	0,5
d [cm]	1	6	0,5
a_c [mm]	0,5	3	0,1
a_s [mm]	0,5	3	0,1
h [mm]	0,5	4,5	0,5
ϕ [%]	0	11	0,1

where a_c and a_s are the radius of the cross section of the main cylinder and the side branches, respectively.

Another condition imposed to the algorithm is that $h \geq a_s$. The initial population is of 100 individuals, with a crossover factor of 0.7 and a mutation factor of 0.93. A maximum of 20 iterations is imposed to the algorithm and the objective function used was

$$F_{obj} = \sum(1 - \alpha(f_{min} : f_{max})^2), \tag{7}$$

with f_{min} = 500 Hz and f_{max} = 600 Hz. No further changes were made to the algorithm.

For this first sample, final dimensions after optimization were $L = 45$ mm, $N = 8$, $d = 8.5$ mm, $a_c = 2$ mm, $a_s = 1.6$ mm, $h = 4.5$ mm, and $\phi' = 2.19\%$. The expected frequency for the absorption peak to occur with these dimensions is 562 Hz. The lower limit of d was extrapolated to achieve a better result in the absorption curve.

The 3D-printed sample is shown in Fig. 2. Pores were closed for testing with plastic tape (Fig. 2, right) and by the walls of the sample holder of the impedance tube itself.

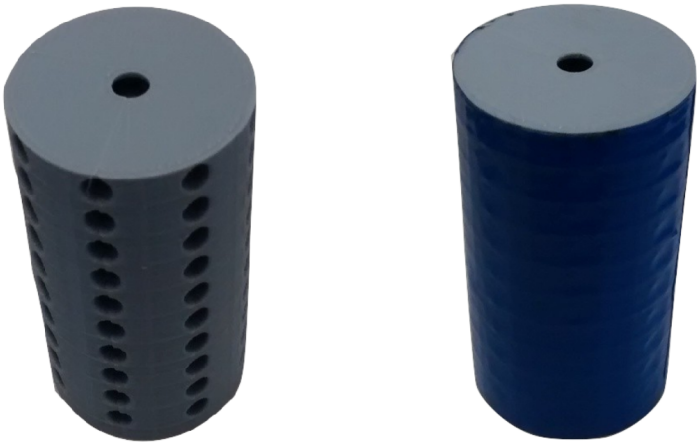


Figure 2: 3D-printed sample with open pores (left) and closed pores with plastic tape (right). Dimensions are $L = 45$ mm, $N = 8$, $d = 8.5$ mm, $a_c = 2$ mm, $a_s = 1.6$ mm, $h = 4.5$ mm, and $\phi = 2.19\%$.

3.2 Numerical simulation

To validate the theory proposed in Section 2, the optimized model shown in Section 3.1 is implemented in COMSOL. The idea is to simulate a full impedance tube experiment, and, as such, the model consists of the sample itself and the impedance tube, as shown in Fig. 3.

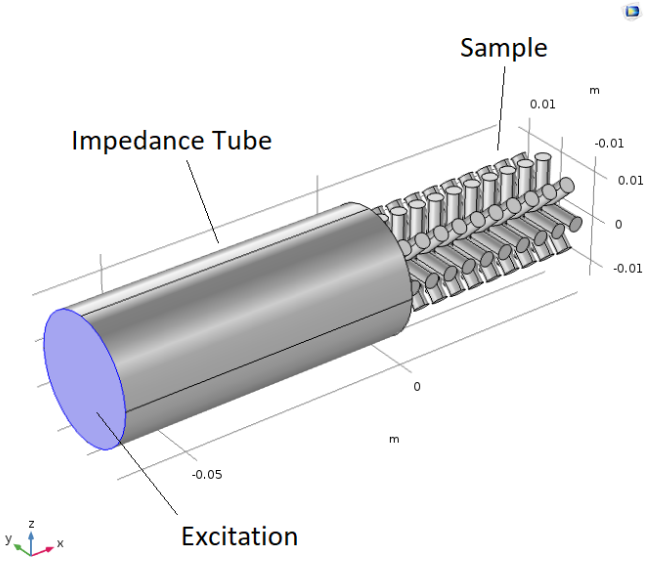


Figure 3: COMSOL Simulation

The model uses the *Pressure Acoustics* module with viscous and thermal losses accounted for and also with the *Narrow Acoustic Region* (NRA) in both main cylinder and side branches. The NRA is set to use the *circular duct* approximation. Such approximation for ducts with constant cross-section gives exactly the same results as if one was using the full *Thermoviscous Acoustics* module but with way less computation

time [21]. For the excitation, a unit pressure is applied at the extremity of the tube. As for the mesh, *Free Tetrahedral* elements are used, with the embedded *Extra Fine* element size, which obeys the rule of thumb of 6 elements per wavelength in the selected frequency range for this simulation, i.e. between 1 Hz and 850 Hz.

4 Results and Discussion

Results for the optimized geometry, which are shown in Fig. 4, are presented and discussed in this section. The difference in the peak of the experimental and theory results is 11 Hz (peak is in 562 Hz for the theory and 573 Hz for the experiment), with an error of 1.96% and showing good agreement between both outcomes. The total length of the sample is $\lambda/13.3$ at 562 Hz, which beats three times the $\lambda/4$ of regular acoustic absorbing materials.

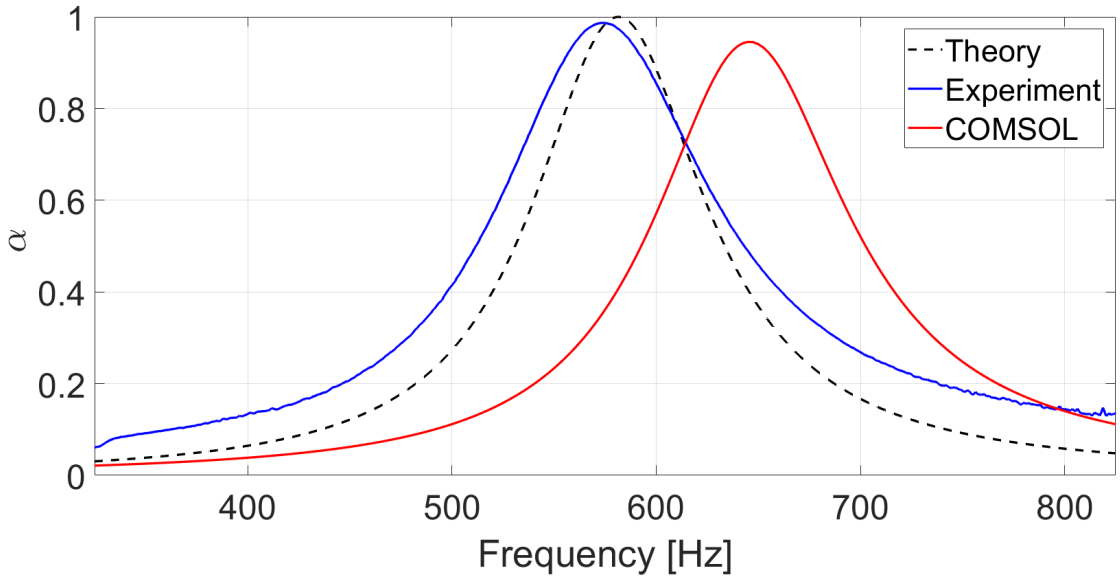


Figure 4: 3D-printed sample 1 absorption curves.

Moreover, the curve is not so narrow, as between 522 Hz and 630 Hz more than 60% of the sound energy is absorbed. The difference in the peak of the theory and experiment curves might be due to the fact that the 3D printing process is not necessarily exact and that deviations in the dimensions of the 3D model can happen during such process. In addition, the final sample has rugosity to some extent, which is not foreseen neither in the theory nor in the numerical model.

However, the results from the numerical simulations do not match the theory nor do they match the experiment. Due to their diameter and period, the side branches overlap with each other, which causes a considerable loss of volume in the dead-end pores and, mainly, do not evaluate each pore as a single structure. The 3D-printed sample did not present such overlapping as the 3D-model considers each pore separately but with a smaller length. This overlapping can be seen in Fig. 5.

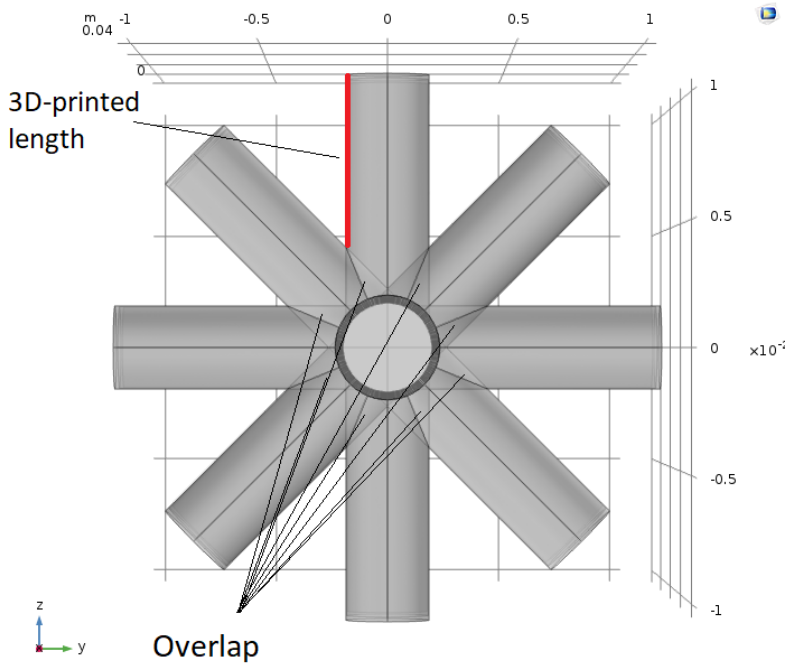


Figure 5: Overlap of the side branches.

To test this idea of the overlapping, a new sample was 3D-printed and implemented in COMSOL, whose inner geometry is shown in Fig. 6. It has $N = 4$ and the ratio between the main cylinder's and side branches' diameters was such that there was no overlapping. The dimensions of this new sample were then $a_c = 2.5$ mm, $a_s = 1.5$ mm and $\phi = 3.43\%$. All the other parameters were the same of the sample in Fig. 2.

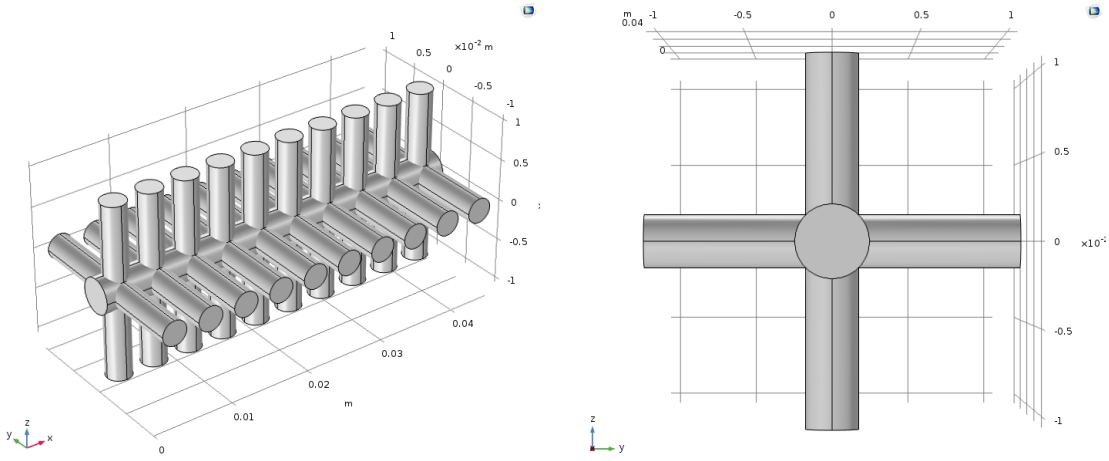


Figure 6: Inner geometry of new sample without overlapping.

As for the numerical simulation, it followed exactly the procedures discussed in Section 3.2, whereas the theory is the same described in Section 2. The experiments in the impedance tube also followed the same standard. Results are presented in Fig. 7

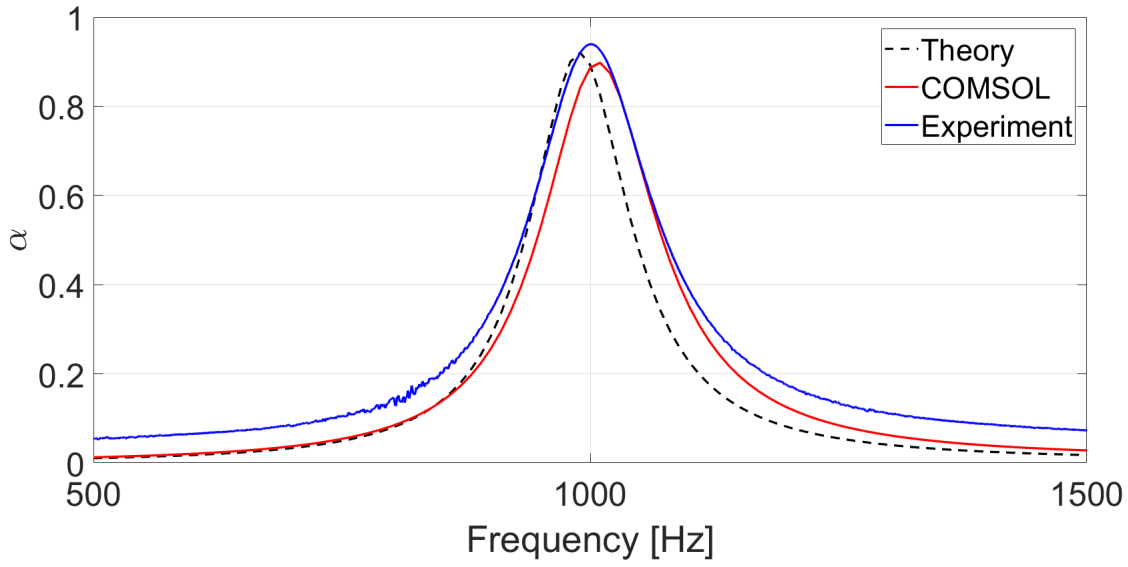


Figure 7: 3D-printed sample 2 absorption curves.

The difference between theory and experiment and experiment and virtual simulation is 10 Hz (peaks are at 990 Hz, 1000 Hz and 1010 Hz for the theory, experimental and virtual simulation results, respectively). As for the peak in the experimental curve, 94% of the sound energy is absorbed at 1000 Hz. The goal with this second sample was to validate the theory from virtual and real measurements, which can be considered to be done successfully. Shift in the peaks between the approaches might be, again, related to the imperfections in the cylinders resultant of the printing process, which might have influenced the small difference in the results.

5 Conclusion

In this paper a periodic structure design available in literature[9] is optimized through a differential evolution algorithm [20]. Experimental results for the final geometries from two different optimization runs are presented. Results for both theory and experiments showed good agreement with simulations using COMSOL.

As for the first sample, optimization is in the range of 500 Hz and 600 Hz. The absorption peak is at 562 Hz and is not so narrow, having a bandwidth of approximately 108 Hz (between 522 Hz and 630 Hz), in which a sound absorption coefficient higher than 60% is found. The second sample is optimized for unit absorption at 1000 Hz and results from theory, experiment and simulation are in good agreement.

6 Acknowledgements

This research was funded by the Education and Engineering Foundation of the State of Santa Catarina - FEESC.

E. Deckers is a post-doctoral fellow of the research foundation - Flanders.

References

[1] F. Dunn, W. Hartmann, D. Campbell, N. Fletcher, and T. Rossing, *Springer handbook of acoustics*. Springer, 2015.

[2] M. A. Biot, "Theory of propagation of elastic waves in a fluid-saturated porous solid. i. low-frequency range," *The Journal of the acoustical Society of america*, vol. 28, no. 2, pp. 168–178, 1956.

[3] M. A. Biot, "Theory of propagation of elastic waves in a fluid-saturated porous solid. ii. higher frequency range," *the Journal of the Acoustical Society of America*, vol. 28, no. 2, pp. 179–191, 1956.

[4] J. Allard and N. Atalla, *Propagation of sound in porous media: modelling sound absorbing materials 2e*. John Wiley & Sons, 2009.

[5] X. Cai, Q. Guo, G. Hu, and J. Yang, "Ultrathin low-frequency sound absorbing panels based on coplanar spiral tubes or coplanar helmholtz resonators," *Applied Physics Letters*, vol. 105, no. 12, p. 121901, 2014.

[6] Y. Li and B. M. Assouar, "Acoustic metasurface-based perfect absorber with deep subwavelength thickness," *Applied Physics Letters*, vol. 108, no. 6, p. 063502, 2016.

[7] T. Dupont, P. Leclaire, O. Sicot, X. L. Gong, and R. Panneton, "Acoustic properties of air-saturated porous materials containing dead-end porosity," *Journal of applied physics*, vol. 110, no. 9, p. 094903, 2011.

[8] T. Dupont, P. Leclaire, and R. Panneton, "Acoustic methods for measuring the porosities of porous materials incorporating dead-end pores," *The Journal of the Acoustical Society of America*, vol. 133, no. 4, pp. 2136–2145, 2013.

[9] P. Leclaire, O. Umnova, T. Dupont, and R. Panneton, "Acoustical properties of air-saturated porous material with periodically distributed dead-end poresa)," *The Journal of the Acoustical Society of America*, vol. 137, no. 4, pp. 1772–1782, 2015.

[10] J. Mei, G. Ma, M. Yang, Z. Yang, W. Wen, and P. Sheng, "Dark acoustic metamaterials as super absorbers for low-frequency sound," *Nature communications*, vol. 3, p. 756, 2012.

[11] Z. Yang, H. Dai, N. Chan, G. Ma, and P. Sheng, "Acoustic metamaterial panels for sound attenuation in the 50–1000 hz regime," *Applied Physics Letters*, vol. 96, no. 4, p. 041906, 2010.

[12] S. H. Lee, C. M. Park, Y. M. Seo, Z. G. Wang, and C. K. Kim, "Acoustic metamaterial with negative density," *Physics letters A*, vol. 373, no. 48, pp. 4464–4469, 2009.

[13] M. Yang and P. Sheng, "Sound absorption structures: From porous media to acoustic metamaterials," *Annual Review of Materials Research*, vol. 47, pp. 83–114, 2017.

[14] A. Carvalho de Sousa, "Modelagem de metamaterial acústico para absorção sonora em baixas frequências," master's thesis, Federal University of Santa Catarina, 2017. 143 p.

[15] R. Storn, "On the usage of differential evolution for function optimization," in *Fuzzy Information Processing Society, 1996. NAFIPS., 1996 Biennial Conference of the North American*, pp. 519–523, IEEE, 1996.

[16] M. Snellen, D. G. Simons, and C. Van Moll, "Application of differential evolution as an optimisation method for geo-acoustic inversion," in *Proceedings of the 7th European Conference on Underwater Acoust.(Delft, The Netherlands, 2004)*, pp. 721–726, 2004.

[17] T. Dupont, P. Leclaire, R. Panneton, and O. Umnova, "A microstructure material design for low frequency sound absorption," *Applied Acoustics*, vol. 136, pp. 86–93, 2018.

[18] E. Pestel and F. A. Leckie, *Matrix methods in elastomechanics*. McGraw-Hill, 1963.

[19] R. Storn and K. Price, "Differential evolution–a simple and efficient heuristic for global optimization over continuous spaces," *Journal of global optimization*, vol. 11, no. 4, pp. 341–359, 1997.

[20] M. Buehren, “Differential evolution algorithm,” 2008.

[21] M. H. Jensen, *How to Model Thermoviscous Acoustics in COMSOL Multiphysics*, 2014 (accessed June 29, 2018). https://br.comsol.com/blogs/how-to-model-thermoviscous-acoustics-in-comsol-multiphysics/.

Detection of faulty accelerometer mounting

R.B. Randall[1], W.A. Smith[1]
[1] UNSW Sydney, School of Mechanical and Manufacturing Engineering
Sydney 2052, Australia
e-mail: **b.randall@unsw.edu.au**

Abstract
Data integrity has become more critical with the growth in remote semi-automated machine health monitoring. The mounted resonance frequency of an accelerometer, if correctly mounted on a flat surface, is normally quite repeatable, for example at different locations on the same object. A method has recently been developed which largely separates forcing and transfer functions in response signals, by applying an exponential window in the cepstrum. This technique can show the resonance peaks in response spectra at all measurement points. Changes in the natural frequencies of the structure should show up equally in all measurements, but deterioration in the mounting condition of an individual accelerometer would only affect the mounted resonance frequency for that transducer. This paper demonstrates these principles using measurements on a gear test rig, operating with a range of different speed profiles, with two similar accelerometers, one having correct and then faulty mounting.

1 Introduction

With the increase in remote online monitoring of machines, it has become critical to have a means of checking the integrity and repeatability of vibration measurements, as made by accelerometers. When mounted correctly, usually using a screwed stud to attach the transducer on a smooth flat surface, these can give repeatable measurements up to very high frequencies, often in the range of 10-20 kHz or more. This is limited by the mounted resonance frequency, which is maximised by having a solid contact over the entire base of the accelerometer, which gives a much higher stiffness than that of the screw stud alone. Response will be linear up to 1/3 of the mounted resonance frequency, but the signals are often analysed up to 2/3 of the latter, as long as the mounting is repeatable, since it is usually changes in response levels, rather than the levels themselves, which indicate developing faults, so the frequency response does not have to be completely uniform, just repeatable. If the contact pressure is not maintained across the whole base, the stiffness, and mounted resonance frequency, will drop, compromising the validity of the measurements.

We have recently developed a method to separate measured responses into the components from the forcing functions and transfer functions (ie modal properties) by applying an exponential window to the response cepstrum. This has for example been used to pre-process response signals to greatly reduce problems associated with operational modal analysis of rotating machines, where forcing functions can be very complicated [1]. In this paper we use that technique to identify the accelerometer mounting frequencies, along with other structural resonances, in the high frequency range of the responses. As long as several measurements are being made with different transducers, it should be possible to distinguish between actual changes in the measurement object, which should be the same for all transducers, and changes in the mounted resonance of an individual transducer. Even if the accelerometer resonance frequency is outside the normal measurement range, it is likely that the frequency range could be extended to cover it for occasional periodic measurements, or when there is some suspicion of the integrity of the measurements.

2 Separation of forcing and transfer functions

2.1 Application of the real cepstrum to response measurements

The cepstrum is defined as the inverse Fourier (or z-) transform of a log spectrum [2]. Thus:

$$C_c(\tau) = \Im^{-1}\left\{ \log\left(F(f)\right)\right\} = \Im^{-1}\left\{ \ln\left(A(f)\right) + j\phi(f)\right\} \tag{1}$$

where

$$F(f) = \Im\left\{ f(t)\right\} = A(f)e^{j\phi(f)} \tag{2}$$

in terms of the amplitude and phase of the spectrum. $C_c(\tau)$ is called the "complex cepstrum", since it retains the phase information from the spectrum. However, it can only be applied to transient signals, such as impulse responses, since in requires the phase to be unwrapped to a continuous function of frequency. If the phase in Eq. (1) is set to zero, the so-called "real cepstrum" is obtained, as in Eq. (3):

$$C_r(\tau) = \Im^{-1}\left\{\ln\left(A(f)\right)\right\} \tag{3}$$

This can be applied to (sections of) continuous stationary or non-stationary signals, and if the cepstrum is edited ("liftered", from "filtered") the modified log amplitude spectrum can be obtained by a forward transform. As shown in Refs. [1, 2], the modified log amplitude spectrum can be combined with the original phase spectrum to form edited time signals, but in this paper, only the modified log spectrum is used.

The complex cepstrum of a transfer function can be expressed in terms of its poles and zeros in the z-plane, as shown by Oppenheim and Schafer [3], and in [2] it is shown that for a single degree-of-freedom (SDOF) system, with one complex conjugate pair of poles inside the unit circle, and no zeros, it can be expressed as:

$$\begin{aligned} C_{sdof}(n) = \frac{c^n}{n} + \frac{c^{*n}}{n} \quad &= \frac{|c|^n}{n}\left[\exp\left(jn\arg\left(c\right)\right) + \exp\left(-jn\arg\left(c\right)\right)\right] \\ &= 2\frac{e^{-\sigma n\Delta t}}{n}\cos\left(n\arg(c)\right) \qquad , \; n > 0 \end{aligned} \tag{4}$$

where c and c^* are the poles, n is quefrency (time) sample number, Δt is time sample spacing (so that $t = n\Delta t$), and σ is the damping constant corresponding to the exponential decay $|c|^n$. The cepstrum is thus seen to have the same form as the impulse response function (complex exponential), but additionally weighted by 2/*n*. Zeros have the same form as (4), but with negative sign, since they are negative poles on a log amplitude scale, and the cepstrum of the whole transfer function can be obtained by adding those of the individual conjugate pole and zero pairs.

2.2 Identification of resonances by exponential liftering

Thus, it can be seen that if the response cepstrum is multiplied by the exponential window $e^{-\sigma_0 t}$, it adds σ_0 to the damping of every mode of the system, but this can in principle be compensated for after analysis (as for an exponential window used in impact testing). σ equals half the 3 dB bandwidth (in rad/s) of the corresponding resonance. Such a weighting in the cepstrum is called a "lifter", from filter by analogy with cepstrum-spectrum and quefrency-frequency. As will be seen in later results, most of the modal information is at low quefrency (ie slowly varying with frequency) while most forcing functions are at high quefrency (eg closely spaced harmonics and sidebands in gear response spectra). This is seen to apply even when the harmonics/sidebands are not separated but smeared as a result of speed variations [1].

In [1] it is shown that the cepstra of multiple responses to a single force (ie a single input/multiple output or SIMO system) are the sum of the cepstra of the forcing function and of the transfer functions to the response measurement points, and this allows them to be curve-fitted for the poles and zeros of each transfer function,

and ultimately to the reconstruction of the latter. However, even in the case of a multiple input (MIMO) system, all the poles are the same, even if the zeros differ, and the cepstra can be curve-fitted for the poles. In the current paper, use is only made of the fact that the poles (resonances) of a MIMO system can be recognised in the log amplitude spectrum of a response signal, after removal of most forcing function effects by applying an exponential lifter to the cepstrum.

3 Test object, measurements, and analysis techniques

3.1 Test object and measurements

Measurements were made on a gearbox test rig as shown in Figure 1(a). This is a single stage parallel gear reducer with ratio 19:52, driven by an induction motor with variable frequency drive, and driving a brake with controllable torque load. The actual accelerometer types and positions used in this study are shown in Fig. 1(b). All were attached with screw studs to mounting pads cemented onto the casing rim with epoxy cement. The accelerometer type whose mounting integrity was to be tested is the Brüel & Kjær (B&K) type 4370, which has a nominal mounted resonance frequency of 15 kHz. One of them (denoted R for "Ref") was always mounted tightly, while the other (denoted T for "Test") was mounted tightly in one set of measurements, but was loosened by a quarter turn on the thread (denoted as "faulty") in other tests. A B&K

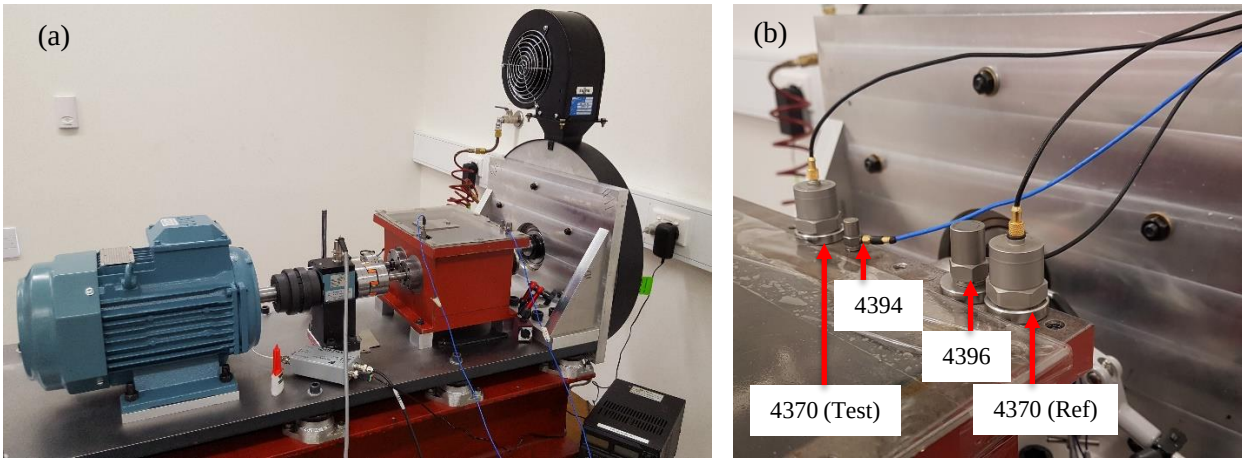


Figure 1: Gear test rig (a) Overall view (b) detail of accelerometer positions

type 4394 accelerometer, with nominal mounted resonance frequency close to 50 kHz, was mounted close to the 4370T, and a B&K type 4396, with nominal mounted resonance frequency close to 26 kHz was mounted close to the 4370R.

Figure 2 compares PSD spectra for the different accelerometers for different recordings, representing different speed profiles, as follows, with the test accelerometer (4370T) tight for Record 1, but loose for the other records. Note that the dB scales are not properly calibrated here, but are arranged to be comparable.

A number of recordings were made, but those in the following list are used in this paper:

Record 1 – 20 s constant at 10 Hz (input), followed by 80 s harmonic profile – 10 Hz mean, +/-5%, 60 s modulation period – Accelerometer 4370T tightened.

Record 5 – As for Record 1, but Accelerometer 4370T loose.

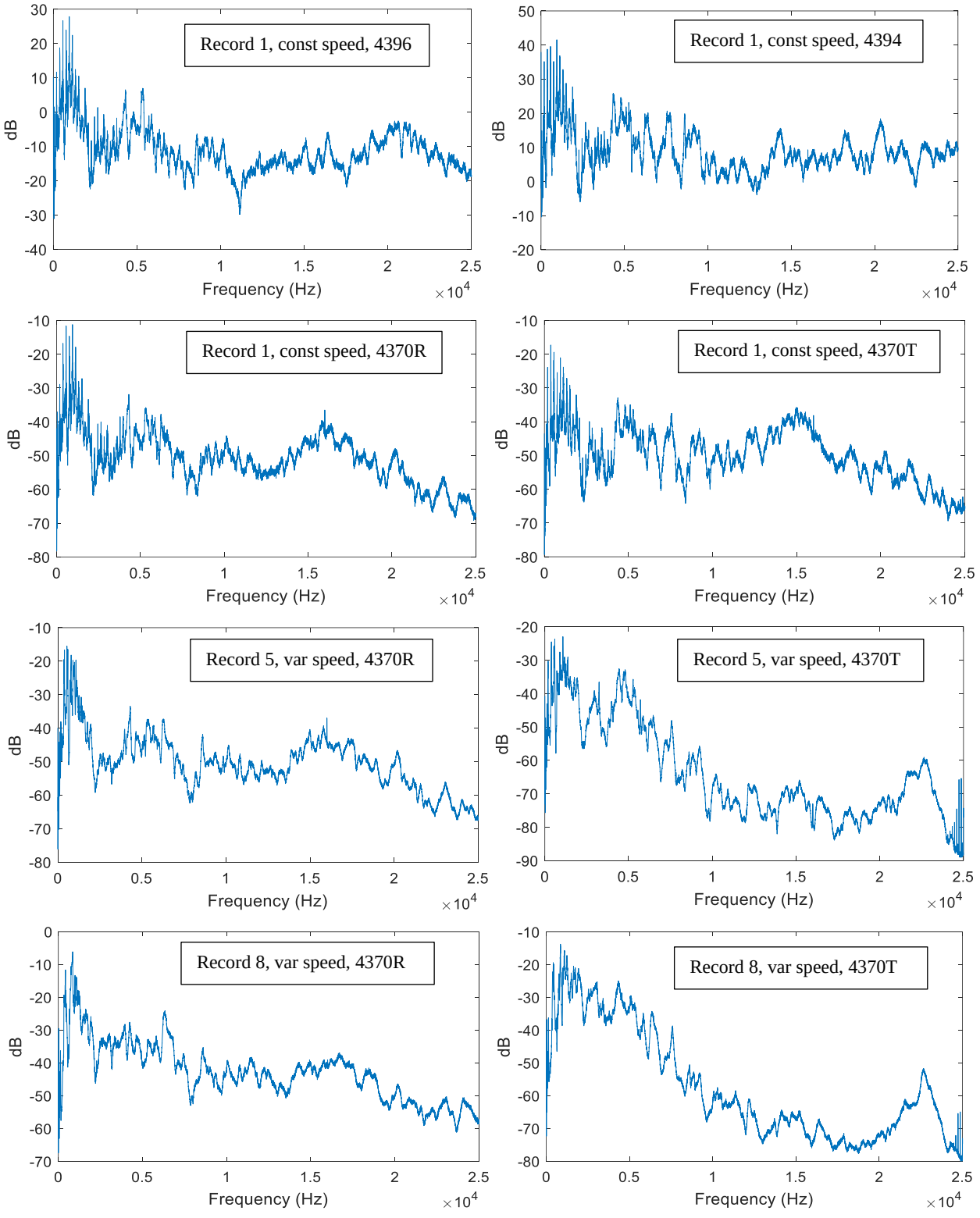


Figure 2: Comparison of PSD spectra for different accelerometers and speed profiles

Record 8 – 20 s constant at 20 Hz, followed by 80 s harmonic profile - 20 Hz mean, +/-20%, 2 s modulation period – Accelerometer 4370T loose.

Record 11 – The last 250s of the speed profile from a wind turbine, originally of total length 550s, around a mean speed of 25 Hz, scaled to a length of 60s with +/-20% variation around the mean speed 20 Hz. This speed profile is described in detail in Ref. [4].

A nominally constant input torque of 15 Nm was maintained for all the recordings. The signals were sampled at 100 kHz, but while the valid linear frequency range would be 40 kHz, the results presented here are limited to 25 kHz.

3.2 Discussion of PSD spectra

Even though the dB scales have not been adjusted correctly here (they are for the later results in Section 4), the figures have been arranged so as to be roughly comparable in terms of amplitude. The comparison here is mainly about the spectrum shape. For Record 1 with constant speed 10 Hz, the gearmesh frequency is 190 Hz, and a number of harmonics of this can be seen in the first four figures corresponding to this condition. Up to about 10 kHz, the spectra are very similar for the 4396 and 4370R, mounted adjacent to each other, and similarly for the 4394 and 4370T. A peak appears at about 16 kHz for accelerometer 4370R and at about 15 kHz for 4370T, and these are assumed to be the mounted resonance frequencies for these two accelerometers, since these peaks are not apparent for the 4396 and 4394 accelerometers. On the other hand, a peak appears just above 20 kHz for the 4396 (not apparent for the 4394) and this could be its mounted resonance, despite the theoretical value being 26 kHz. The reduction could be caused by the cement attaching the mounting base. The expected mounting resonance of the 4394 is not within the displayed frequency range.

The spectrum levels are about 10 dB higher for the 20 Hz speed compared with the 10 Hz speed for the same accelerometer, and this is thought to be explained by higher forces at the higher speed. Otherwise, the shape of equivalent spectra appears very similar for the different speed profiles.

It is seen that for the loose accelerometer 4370T, the response falls away above about 6 kHz, and the resonance peak at 15 kHz is no longer evident.

3.3 Analysis techniques

An exponential lifter was applied to all signals to separate the modal information (theoretically the same) from the very different forcing functions of the different speed regimes. The damping constant σ_0 was set to 800π rad/s, corresponding to 400 Hz and a time constant of 0.4 ms. Figure 3 shows a comparison of the original and liftered spectra for the specific case of 4370R from Record 5, variable speed. This confirms the accelerometer mounted resonance frequency of 16 kHz. The damping constant was chosen to be less than the apparent modal damping in this frequency range (measured 3 dB bandwidth 3000 Hz compared with 800 Hz added damping from the lifter), but would most likely be too great for the lower resonances below 1 kHz. It could be adjusted if modal analysis were to be done in the lower frequency bands.

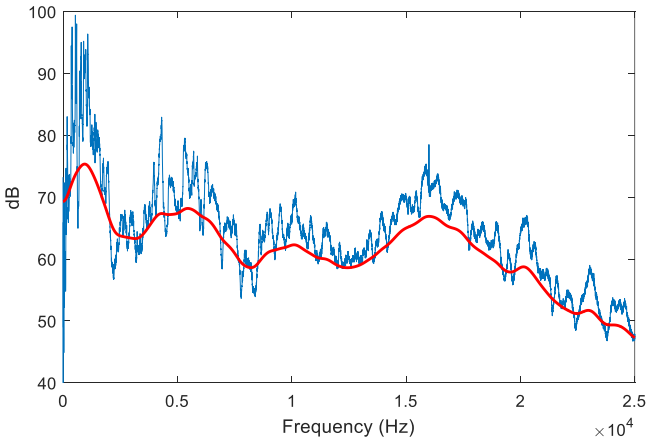


Figure 3: Comparison of original and liftered spectra

4 Discussion of results

Figure 4 compares the liftered spectra, now correctly scaled, for each of the records (with variable speed). At low frequencies, up to 5 kHz, the spectra for the 4370R and 4396 (mounted adjacent to each other) are very close, but diverge as the 4370R approaches its mounted resonance of 16 kHz. The 4370T follows a similar pattern to the 4370R for Record 1, but differs by up to 5 dB, mainly because its resonance is slightly lower at 15 kHz, but also because of the different mounting position. For Records 5, 8 and 11, the 4370R and 4396 spectra are very similar to those for Record 1, but the spectrum for the 4370T, with loose mounting, diverges greatly from the 4370R above about 6 kHz, with differences well over 20 dB over a wide frequency range. A lower resonance frequency is not detectable, but this could be explained by much higher damping resulting from the looseness.

It is therefore quite obvious that the loose mounting of this one accelerometer could be detected quite easily by the disappearance of the mounted resonance frequency of 15 kHz, at the same time as the other apparent resonance peaks, including those for the 4370R accelerometer (16 kHz) and 4396 accelerometer (21 kHz) remain unchanged. It would not be difficult to devise an automated procedure for detecting changes in the response of a single accelerometer, even if the response levels do change somewhat because of different operating conditions, such as speed and load. This will be the subject of future work.

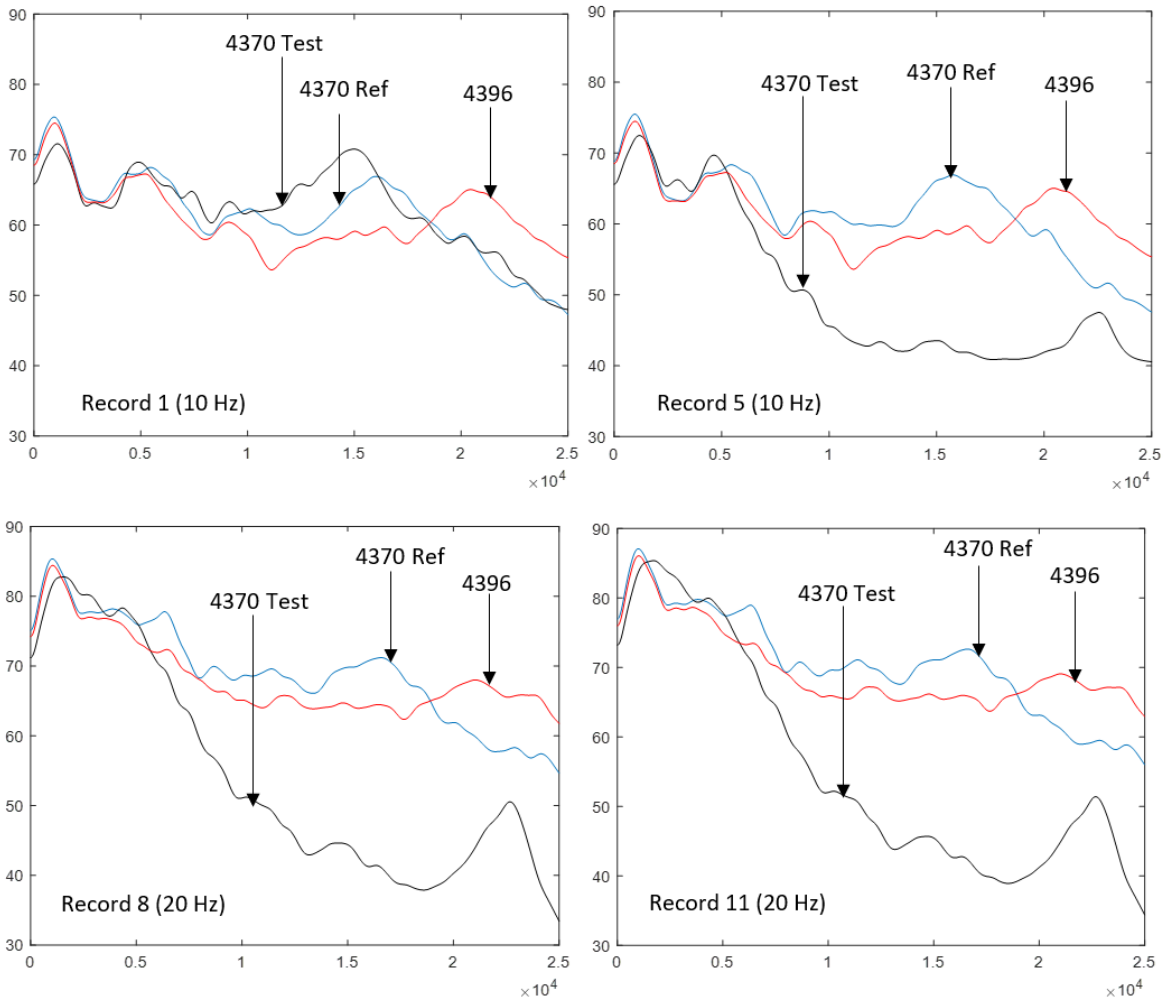


Figure 4: Comparison of liftered spectra for different records (varying speed).

5 Conclusion

This paper demonstrates that the mounted resonance frequency of an individual accelerometer can be detected in the response spectra at that point, and compared with that of nominally identical accelerometers mounted elsewhere on the machine. Even if these frequencies do vary slightly with position, they should remain constant with time, and for different operating conditions, even if the response levels change for these conditions. A method is proposed, using exponential liftering in the real cepstra corresponding to the various response spectra, to expose the various resonances, not only of the transducers, but also of the structure itself. If the latter change, this should be apparent at most measurement points, but if a change in the resonance of a single accelerometer is detected, that would indicate a faulty mounting.

The results presented in this paper confirm these conclusions, but further work is required to automate the detection of faulty mounting.

References

[1] R.B. Randall, W.A. Smith, *New cepstral techniques for operational modal analysis*, *First World Congress on Condition Monitoring*, BINDT, London, UK, (2017).

[2] R.B. Randall, *A history of cepstrum analysis and its application to mechanical problems*, Mechanical Systems and Signal Processing, Vol. 97, Elsevier (2017) pp. 3-19.

[3] A.V. Oppenheim, R.W. Schafer, *Digital signal processing*, Prentice-Hall, Englewood Cliffs, N.J. (1975).

[4] Q. Leclère, H. André, J. Antoni, *A multi-order probabilistic approach for Instantaneous Angular Speed tracking debriefing of the CMMNO14′ diagnosis contest*, Mechanical Systems and Signal Processing, Vol. 81, Elsevier (2016), pp. 375-386.

Aircraft braking dynamics and brake system modeling for fault detection and isolation

L. C. Navarro [1], **L. C. S. Goes** [1]
[1] ITA, Department of Electrical Engineering,
São José dos Campos, Brazil
e-mail: **lucas_sertao@hotmail.com;**

Abstract

Due to the increasing complexity of aeronautical systems, it became more and more important to detect possible failures, avoiding costs with maintenance and time out of operation. Modeling techniques and computational softwares made possible to analyze systems behaviour under normal and failure conditions, helping to prevent these problems. In this work, an aircraft anti-skid brake system is considered as a study case. Therefore, the aircraft brake dynamics and the brake system are modeled using Simulink. In the brake model, some common faults are introduced in order to observe its impacts on the braking performance. A model based fault detection and isolation (FDI) method using analytical redundancy relations (ARRs) is proposed. ARRs are equations relating the system constraints. The numerical evaluation of these equations generates residuals indicating the system deviation from its normal operation. The coupling of the Simulink behavior model with the ARRs is presented, permitting the residuals analyses for each failure mode.

1 Introduction

Modeling has become a powerful engineering tool, making possible to study and evaluate complex systems, preview systems projects behaviors without spend money on expensive prototypes and prevent systems failures through model based fault detection and isolation (FDI) methods. FDI methods can be divided into qualitative and quantitative approaches. Qualitative FDI methods are used when the studied system model is too hard to be obtained, or it cannot be analyzed in order to obtain a faithful model. To analyze the systems, these methods are based on artificial intelligence techniques [1]. Quantitative methods compare the real system behavior with a system ideal model behavior. In this work, the aircraft brake dynamics and its hydraulic brake system will be modeled and simulated in order to preview some failure modes effects on the aircraft brake performance. After that, an FDI method based on analytical redundancy relations (ARRs) will be proposed in order to detect and isolate these faults.

2 Modeling methodology

Physical modeling is a simplified system representation through idealized elements with the intention of representing the dynamics phenomena of real systems. These elements simulate supply sources, as well as the storage, dissipation and transformation of the system energy. In this work, the concept of effort and flow was used. This concept is common to all energy domains. The Table 1 lists for each domain what effort and flow represents.

	Variable types			
System	**Flow (f)**	**Accumulated Flow (q)**	**Effort (e)**	**Accumulated Effort (p)**
Translational Mechanical	Velocity	Displacement	Force	*Momentum*
Rotational Mechanical	Angular Velocity	Displacement	Torque	Angular Momentum
Electrical	Current	Electric Charge	Voltage	Magnetic Flux
Hydraulic	Flow rate	Volume	Pressure	Pressure *Momentum*
Thermal	Heat Flow	Energy/Enthalpie	Temperature	--

Table 1: Flow and effort concept for each energy domain.

Based on this concept it is possible to represent the system in an unified way, taking into account only the elements energy interactions. Thus, in this work, electrical equivalents were used to perform mathematical modeling, representing the entire system. From the electrical equivalents, the state equations that reflects the system behavior can be derived. The Figure 1 summarizes what was used to represent, in its electrical equivalent, the system parameters in all covered domains. More details about hidromechanic modeling can be found in [4].

MECHANICAL SYSTEMS

Classical analogy (Voltage-Force / Current-Velocity):

$$F = K\int vel \Longleftrightarrow V = \frac{1}{C}\int I \longrightarrow C = \frac{1}{K}$$

$$F = B.vel \Longleftrightarrow V = R.I \longrightarrow R = B$$

$$F = M.\dot{vel} \Longleftrightarrow V = L.\frac{\partial I}{\partial t} \longrightarrow L = M$$

HYDRAULIC SYSTEMS

Flow Through Control Orifices:
(No. Reynolds, R>2000)

$$Q = C_d.A_0.\sqrt{\frac{2}{\rho}.(\Delta P)}$$

Flow Through pipes:

$$R_{hid} = \frac{128.\mu.L}{\pi.D^4}$$

Hydraulic Capacitance (Control Volumes):

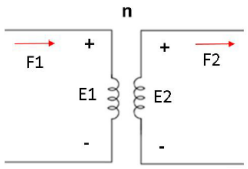
$$C_f = \frac{V_0}{\beta}$$

Fluid Inertance:

$$L_f = \frac{L.\rho}{A}$$

POWER TRANSFER

Transformer:

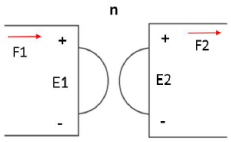


$$E_1.F_1 = E_2.F_2$$

$$E_2 = E_1.n$$

$$F_2 = \frac{F_1}{n}$$

Gyrator:



$$E_1.F_1 = E_2.F_2$$

$$E_2 = F_1.n$$

$$F_2 = \frac{E_1}{n}$$

Figure 1: Representation of hidromechanics parameters on its electrical equivalent.

2.1 State equations from the electric equivalent

To obtain the set of differential equations that describe the systems dynamics from its electrical equivalent, it is necessary to write the equations for the flow and effort storage elements. In other words, write the voltage equations for the inductors and current for the capacitors.

Making it this way, for the inductor, it is possible to obtain the current from the voltage integration and, for

the capacitor, the voltage is obtained from the current integration. Simulating through integrations makes it possible to define an initial condition and prevents spurious results from noise.

In this work, the capacitors currents were represented as the electric charge variation $\dot{q}$ and the inductors voltages, as the magnetic flux variation $\dot{p}$.

3 Fault detection and isolation method

FDI methods are based the comparison between a system real behavior and its theoretical behavior given by a model [1].The method proposed by this work is a model based FDI, also called quantitative FDI method. Model based fault detection and isolation applications can be found in [1],[2] and [3].The first step is to create a behavior model where the state equations describing the dynamic behavior of a given system, can be derived. In this model, some sensors are introduced in order to monitor the states. The second step is to create a diagnostic model. Instead of measuring the states, this model will receive from the behavior model the sensor measurement as a source. This way, the equations describing the system dynamics (the system constraints) will be written in terms of the real system sources, parameters and sensor measurements. Thus, these equations will have a redundance, creating a real test from the actual system. This equations are called analytical redundancy relations (ARRs). If the real system works in normal operation, theoretically the ARR equation value must be around zero, also called as residual value. If the residual value of an ARR differs significantly from zero, it can indicate a fault in some system component. The Figure 2 ilustrates the FDI method proposed.

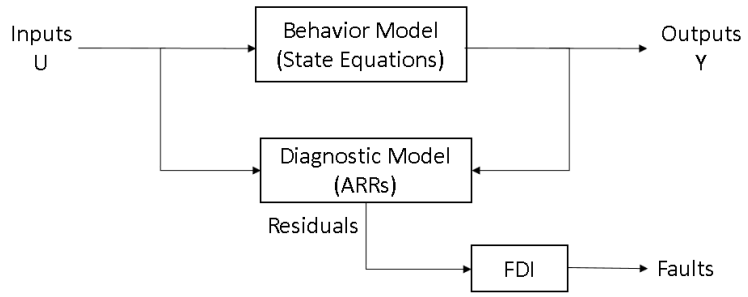


Figure 2: FDI method based on residual generation. Adapted from [2].

The Figure 2 shows that the diagnostic model works in parallel with the behavior model, monitoring the outputs results and generating constantly the residuals. Thus, the FDI method will evaluate the residual generation and be able to determine the fault origin. The Figure 1 a), b) and c) shows a mass, damper and spring system, its electrical equivalent behavior model with a flow sensor (mass velocity sensor) and the diagnostic model with the sensor measurement source, respectively.

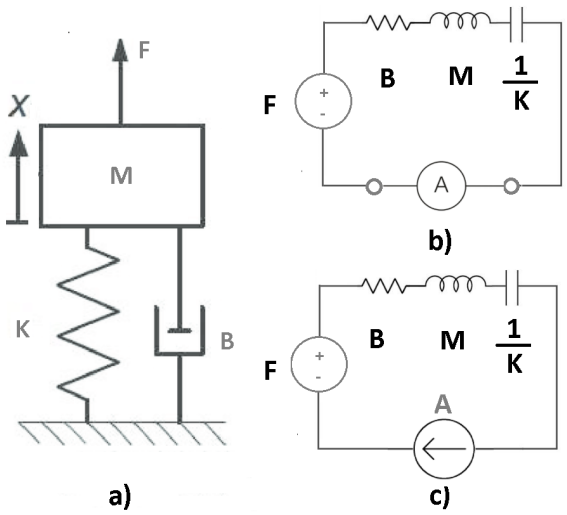


Figure 3: a) Mass, Spring and Dumper system. b) Electrical equivalent behavior model. c) Electrical equivalent diagnostic model.

From the behavior model, the state equations describing the system dynamics are:

$$\dot{p} = F - \frac{q}{(1/k)} + B.\frac{p}{M} \tag{1}$$

$$\dot{q} = \frac{p}{M} \tag{2}$$

From the diagnostic model, the ARR equation can be generated.

$$ARR: \quad F - M.\ddot{A} - K.A - B.\dot{A} = r \tag{3}$$

If the sensor measurement comes from the orginal system, without faults, the residual value (r) must be around zero. however, if the sensor measurement comes from the same system, but with some spring or damper malfunction, the residual value will differs from zero, indicating the fault. The system FDI application in the section 6 shows more details about this method.

4 System modeling

4.1 Aircraft and wheel dynamics

The main part of the aircraft kinectics energy is dissipated by the brake system when landing. The brake force is derived from the counter torque to the wheels movement, which is generated from the brake system actuators. The Figure 4 shows the forces acting on the aircraft and the wheels during braking time and its electrical equivalent. The equations derived from the electrical equivalent circuit are represented by 4 and 5.

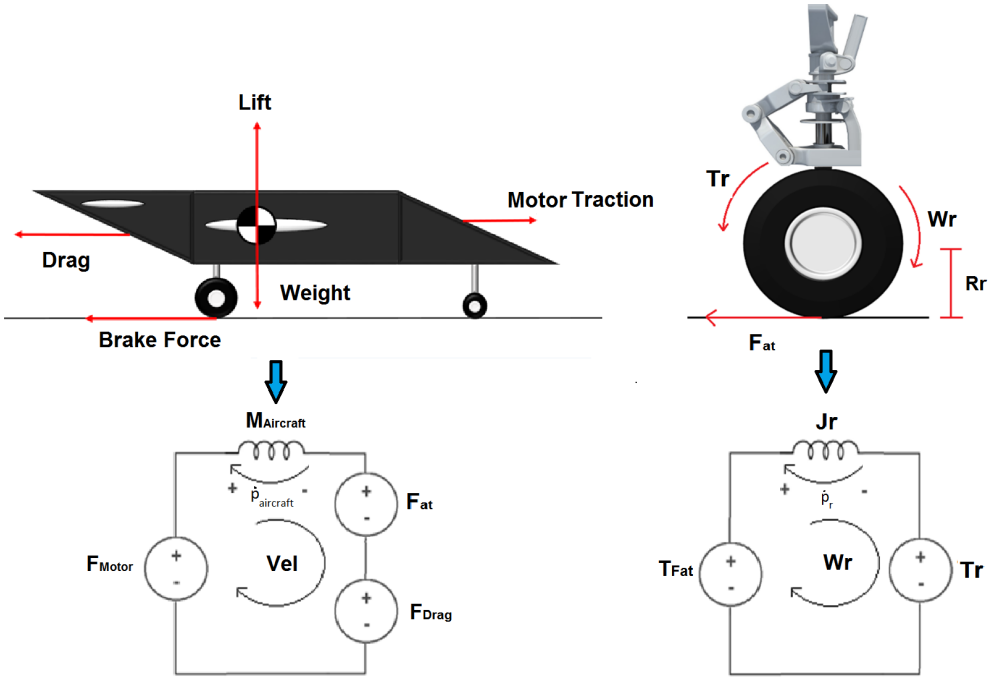


Figure 4: Forces acting on the aircraft and wheels during braking and the corresponding electrical equivalent.

$$\dot{p_{aircraft}} = F_{Motor} - F_{at} - F_{Drag} \tag{4}$$

$$\dot{p_r} = T_{fat} - T_r \tag{5}$$

Where:

$$F_{at} = N.\mu_{at}(S) \tag{6}$$

$$T_{at} = N.u_{at}(S).R_r \tag{7}$$

$$F_{drag} = \frac{1}{2}.\rho.V^2.C_d.S \tag{8}$$

The normal force on the aircraft depends on its weight and lift acting on the braking moment. The normal force corresponding to each wheel, cosidering that each wheel receives one third of the resulting force is described as follows:

$$N = \frac{W - L}{3} \tag{9}$$

Where:

$$L = \frac{1}{2}.\rho.V^2.C_l.S \tag{10}$$

T_r is the counter torque generated by the brake actuator and F_{Motor} is the motor traction. The wheel and aircraft equations are related by the wheel slip. The slips relates the aircraft speed and the wheel speed, as described by the equation 11.

$$S = 1 - \frac{W_r}{W_t} \tag{11}$$

Where:

$$W_r = \frac{1}{J_{roda}} . \int (\dot{p_r}) \tag{12}$$

$$W_t = \frac{Vel}{R_r} \tag{13}$$

$$Vel = \frac{1}{M_{aircraft}} . \int (\dot{p_{aircraft}}) \tag{14}$$

4.2 Brake system

The Figure 5 a) shows the servo valve schematic and 5 b), its corresponding electrical equivalent circuit. This valve controls the brake pressure. The torque motor has the function of moving the flapper coupled to its axis. The flapper moves in the longitudinal direction. The flapper displacement is proportional to the voltage applied to the torque motor terminal.

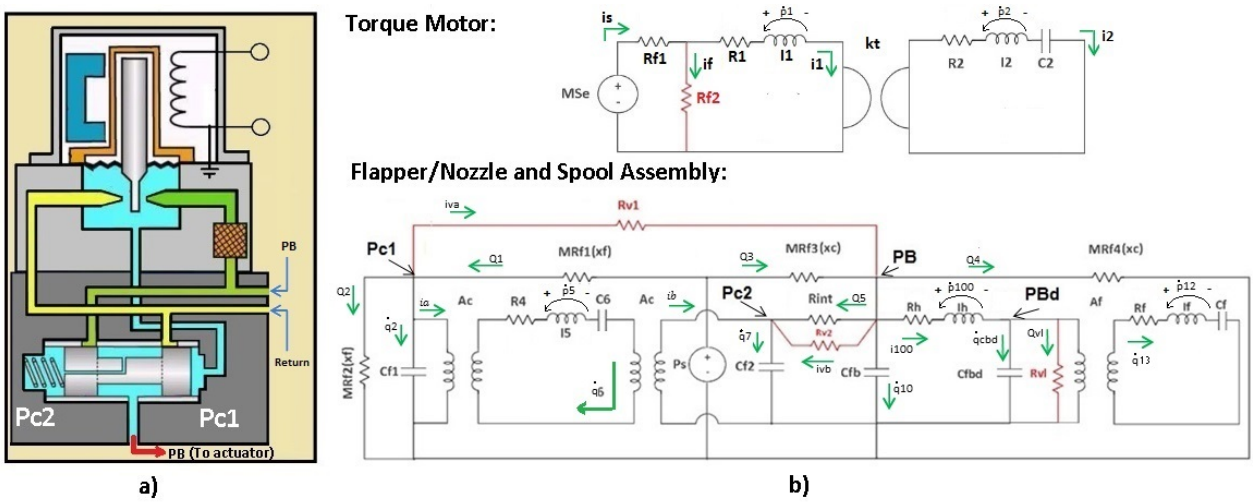


Figure 5: a) Servo-valve schematic. b) Servo-valve electrical equivalent

The torque motor modeling can be simplified considering that it is a DC motor. In the Figure 5 b) the electrical equivalent of a DC motor is presented, where Rf1 and R1 represents the motor wiring resistances before and after a possible current leak (if) represented by Rf2. I1 represents the motor windings resistance, inductance and the voltage applied to the motor respectively. The gyrator is the representation of the energy transformation, where the motor current (flow) turns into torque (effort), in a Kt ratio proportion. R2, I2 and C2 represents respetively the viscous friction, flapper mass and flapper return spring. When the flapper moves, the pressure nozzle is released, generating a fluid flow toward the spool side called Pc1. This will generate a pressure proportional to the flapper movement. At this point, the spool will move, releasing another orifice that leads to a pressure port linked to the spool camara. When this happens, a flow is generated toward the volume that goes until the pressure actuator and the volume at the other spool side (Pc2), via a feedback orifice. When the Pc2 side reaches the same pressure rate as the Pc1 side, the spool will stop moving. at this time, the return spring at the Pc2 side will make the spool returns to the original position,

closing the pressure port. This will make the brake actuator pressure be equal to the control pressure (Pc1 pressure). When the flapper comeback to the idle position, the pressure at the Pc1 side returns to zero, as the flow goes trough the return nozzle. This will make the spool moves to the other direction, releasing the return port of the spool camara, making the brake pressure decrease until zero. This way, the brake pressure is controlled.

In the electrical equivalent, Ps is the pressure supply, MRf1(xf) and MRf2(xf) are the fluid resistances modulated by the flapper movement, where the flow trough them are represented by the flows Q1 and Q2.

$$Q_1 = C_d.\pi.dn.xf.\sqrt{\frac{2}{\rho}.(P_s - P_{c1})}; \quad Q_2 = C_d.\pi.dn.(L - xf).\sqrt{\frac{2}{\rho}.(P_{c1})} \tag{15}$$

Where L is the distance between the nozzles, dn is the nozzle diameter and xf is the flapper position. The capacitances Cf1 and Cf2 represent the volumes in both side of the spool.

$$C_{f1} = \frac{V_{flapper}}{\beta}; \quad C_{f2} = \frac{V_{feedback}}{\beta} \tag{16}$$

The spool dynamics is represented in the circuit by the RLC circuit, where R4 is the viscous friction, I5 is the spool mass and C6 represents the spring rigidity. The transformers represent the spool head cross section area, where pressure is transformed into force, moving the spool.

$$R_4 = b_{spool}; \quad I_5 = M_{spool}; \quad C_6 = \frac{1}{K_{spool}} \tag{17}$$

MRf3(xc) and MRf4(xc) are the fluid resistances modulated by the spool movement. The flow trough MRf3(xc) happens when the spool moviment is positive, whereas for MRf4(xc), when it is negative.

$$Q_3 = C_d.w.xc.\sqrt{\frac{2}{\rho}.(P_s - PB_{bl})}; \quad Q_4 = C_d.w.xc.\sqrt{\frac{2}{\rho}.(PB_{bl})} \tag{18}$$

Cfb is the hydraulic line volume and Cfbd is the volume referring to the brake actuator.

$$C_{fb} = \frac{V_{bl}}{\rho} \quad C_{fbd} = \frac{V_{brake}}{\rho} \tag{19}$$

Rint is the fluid resistance between the control volumes represented by Cf2 and Cfb.

$$R_{int} = \frac{128.\mu.L_{int}}{\pi.D_{int}^4} \tag{20}$$

Rh represents the fluid resistance offered by the hydraulic line until the brake actuator and lh represents the fluid inertance to move inside the pipe.

$$I_h = \frac{L_h.\rho}{A_h} \quad R_h = \frac{128.\mu.L_h}{\pi.D_h^4} \tag{21}$$

Where Ah, lh and Dh are the cross section area, length and the pipe cross section diameter respectively.

The transformer followed by a RLC circuit represent the actuator assembly where Af, Rf, Cf and If represents respectively the brake actuator efective area, brake viscous friction, brake rigidty and brake piston mass.

The resistances Rv1 and Rv2 represented in the Figure 5 b) in red are the leakage in the spool walls. The resistance Rvl, also in red, in parallel with the capacitance Cbd, represents a possible leakage in the hydralic line.

$$R_{v1} = R_{v2} = \frac{128.\mu.Ls_h}{\pi.Dvs_h^4}; \quad Q_{vl} = C_d.Dvl.\sqrt{\frac{2}{\rho}.(PB)} \tag{22}$$

Where Dvs and Dvl are respectively the leakages diameters of the spool and the hydraulic line.

In accordance with the 2.1 section, the state equations describing the servo valve dynamics are as follows, where the states are ilustrated in the Figure 5 b) :

$$\dot{p}_1 = \frac{M_{SE} - R_{f1}.\frac{p_1}{I_1} - (\frac{R_{f1}}{R_{f2}} + 1).(R_1.\frac{p_1}{I_1} + \frac{p_2}{I_2}.K_t)}{(\frac{R_{f1}}{R_{f2}} + 1)} \tag{23}$$

$$\dot{p}_2 = V_2 - R_2.\frac{p_2}{I_2} - \frac{q_{C2}}{C_2} \tag{24}$$

$$\dot{q}_{C2} = \frac{p_2}{I_2} \tag{25}$$

$$\dot{q}_2 = Q_1 - Q_2 - i_{va} - i_b \quad \begin{cases} Q_1 = C_d.\pi.dn.xf.\sqrt{\frac{2}{\rho}.(P_s - P_{c1})} \\ Q_2 = C_d.\pi.dn.(L - xf).\sqrt{\frac{2}{\rho}.(P_{c1})} \\ i_{va} = \frac{P_{c1} - P_B}{Rv1} \\ i_a = Ac.\frac{p_5}{I5} \end{cases} \tag{26}$$

$$\dot{p}_5 = V_1 - V_{R4} - V_{C6} - V_2 \quad \begin{cases} V_1 = Ac.P_{c1} \\ V_{R4} = \frac{p_5}{I5}.R4 \\ V_{C6} = \frac{q_6}{C6} \\ V_2 = Ac.\frac{q_7}{C7} \end{cases} \tag{27}$$

$$\dot{q}_{cbd} = i_{100} - Q_{vl} - i_e \quad \begin{cases} i_{100} = Ac.if \\ Q_{vl} = C_d.Avl.\sqrt{\frac{2}{\rho}.(PB_d)} \\ i_e = Af.\frac{p_{12}}{Cf} \end{cases} \tag{28}$$

$$\dot{p}_{100} = V_{Cfb} - V_{Rh} - V_{Cfbd} \quad \begin{cases} V_{Cfb} = PB \\ V_{Rh} = Rh.\frac{p_{100}}{I100} \\ V_{Cfbd} = PBd \end{cases} \tag{29}$$

$$\dot{q}_7 = Q_5 + i_b + i_{vb} \quad \begin{cases} Q_5 = \frac{PB - Pc2}{Rint} \\ i_b = Ac.\frac{p_5}{I5} \\ i_{vb} = \frac{PB - Pc2}{Rv2} \end{cases} \tag{30}$$

$$\dot{q}_{10} = Q_3 - Q_4 - Q_5 - i_{vb} + i_{va} - i_{100} \quad \begin{cases} Q_3 = C_d.w.xc.\sqrt{\frac{2}{\rho}.(P_s - PB_{bd})} \\ Q_4 = C_d.w.xc.\sqrt{\frac{2}{\rho}.(PB_{bd})} \\ Q_5 = \frac{PB - Pc2}{Rint} \\ i_{vb} = \frac{PB - Pc2}{Rv2} \\ i_{va} = \frac{P_{c1} - P_B}{Rv1} \\ i_{100} = \frac{p_{100}}{I_{100}} \end{cases} \tag{31}$$

$$\dot{p}_{12} = V_f - V_{Rf} - V_{Cf} \quad \begin{cases} V_f = Ac.PBd \\ V_{Rf} = Rf.\frac{p_{12}}{I_{12}} \\ V_{Cf} = \frac{q_{13}}{Cf} \end{cases} ; \tag{32}$$

$$\dot{q}_{13} = \frac{p_{12}}{I_f} \tag{33}$$

$$\dot{q}_6 = \frac{p_5}{I_5} \tag{34}$$

$$P_{c1} = \frac{q_2}{C_{f1}} \tag{35}$$

$$P_{c2} = \frac{q_7}{C_{f2}} \tag{36}$$

$$P_B = \frac{q_{10}}{C_{fb}} \tag{37}$$

$$P_{Bd} = \frac{q_{cbd}}{C_{cbd}} \tag{38}$$

4.3 Anti-skid system

The anti-skid system model is based on the differential equations that describe the wheel and aircraft dynamics, deduced in 5 and 4. The figure 6 illustrates the anti-skid system control loop diagram.

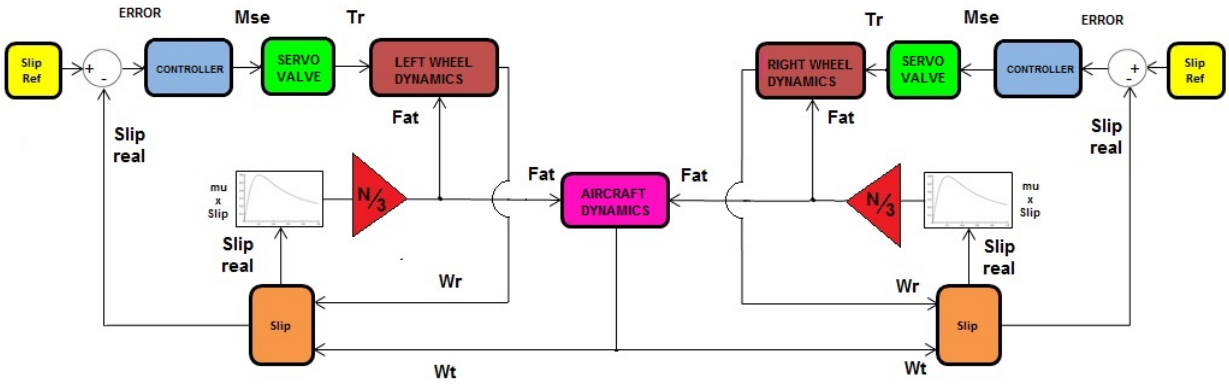


Figure 6: Anti-skid system control loop diagram.

During braking time, the servo valve applies a pressure to the brake actuators, generating a torque (T_r), causing the wheel to decrease its angular velocity (W_r). At that time, the wheel speed is slower than aircraft's speed (W_t). This difference causes a wheel slip with the ground. In Figure 6 the slip is calculated by the Slip block. With the calculated slip, the friction coefficient is obtained through the curve m μ x slip. Thus, with the friction coefficient value for that instant and with the information of the aircraft normal force, it is possible to obtain the frictional force (F_{at}) that acts on the wheels at that instant of time. With the wheel slip information, it is possible to calculate the reference error (error = Slip - Slip ref). From this error, a PI controller modulates the voltage acting on the servo valve, modulating the pressure that drives the brakes, closing the control loop.

5 System simulation

The servo valve is the main brake system component. Thus, in order to reproduce the aircraft braking dynamics as faithful as possible, the servo valve parameters were adjusted in order to validate the model with the real system behaviour. To perform the simulations, $Simulink^{®}$ software was used. The Figure 7 shows the adjusted model response for a step voltage and the comparison between the real and simulated servo valve brake pressure, in response to a current increase in the torque motor. The flapper and spool displacements and brake pressure evolution are in accordance with what was mentioned in section 4.2.

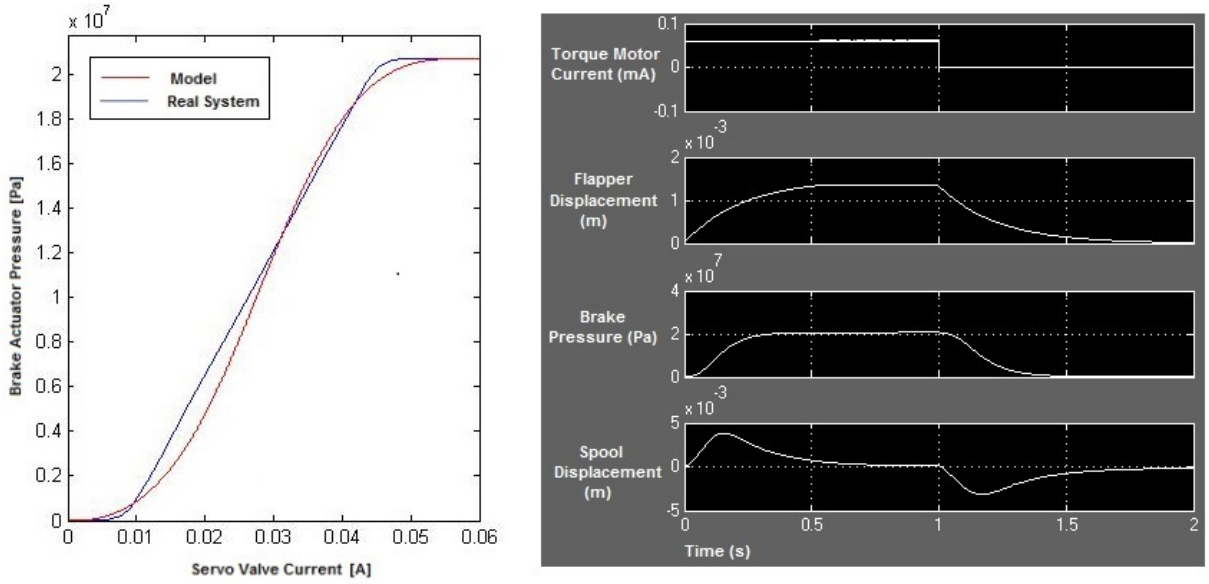


Figure 7: Current curve versus brake actuator pressure on the actual and simulated servo valve.

With the servo valve model validated, it is possible to simulate the aircraft braking performance, comparing the results for the healthy and faulty servo valve. The Figure 8 shows the anti-skid system control loop Simulink model for one wheel.

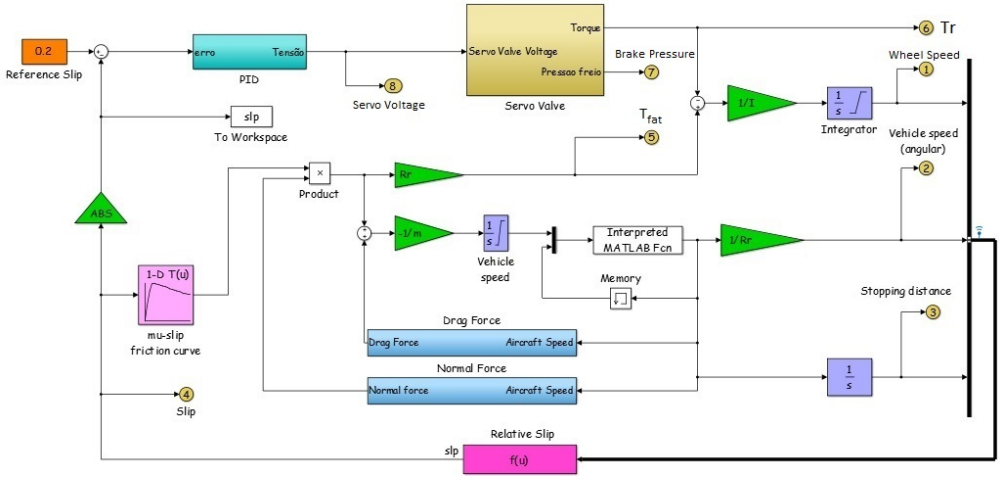


Figure 8: System's Simulink Model.

The wheel slip is one of the most important model output to monitor because it reflects the system performance in a brake event. The Figure 9 shows how the slip varies when a fault is introduced in the servo valve.

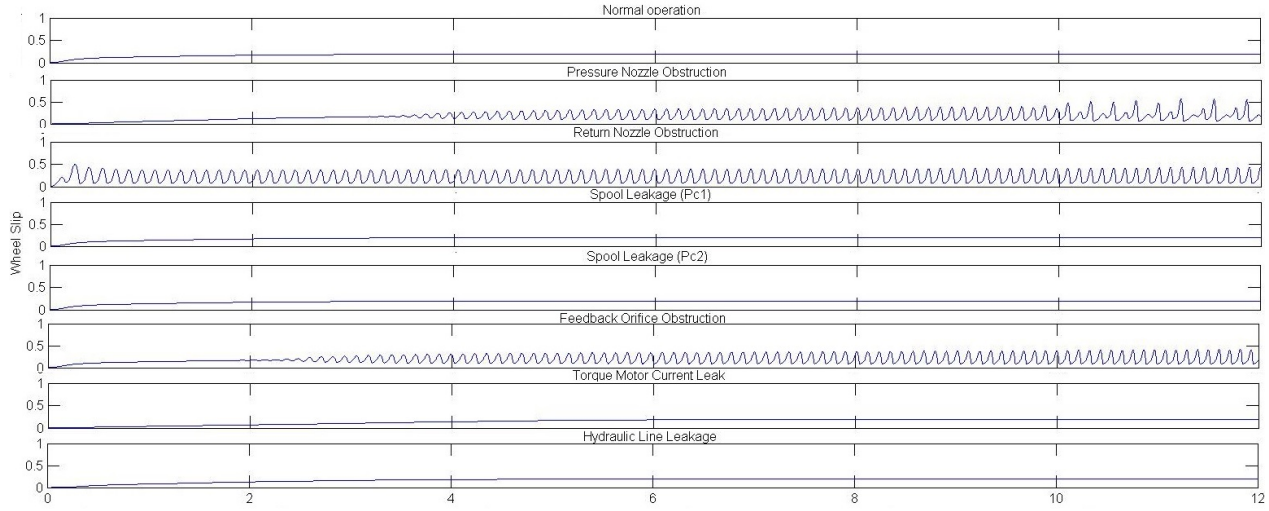


Figure 9: Wheel slip for different fault modes.

It is possible to notice that the slip is largely affected when the servo valve is not healthy. Depending on the fault level, the aircraft may also be subject to damage when not being able to stop in the track distance and due to lurch problems, which may compromise the physical integrity of the occupants.

6 Fault detection method

As shown on the previous section, a single fault on the servo-valve can total affect the brake performance. Thus the FDI method was applied, using the servo-valve model. The first step on this FDI method is to create the diagnostic model. For this, it is necessary to define where and how many sensors will be placed in the behavior model, in order to be able to extract the ARRs and monitor as much parameters as possible. The Figure 10 a) shows the behavior model with the sensor placement and the Figure 10 b) shows the diagnostic model, with mesured sources from behavior model.

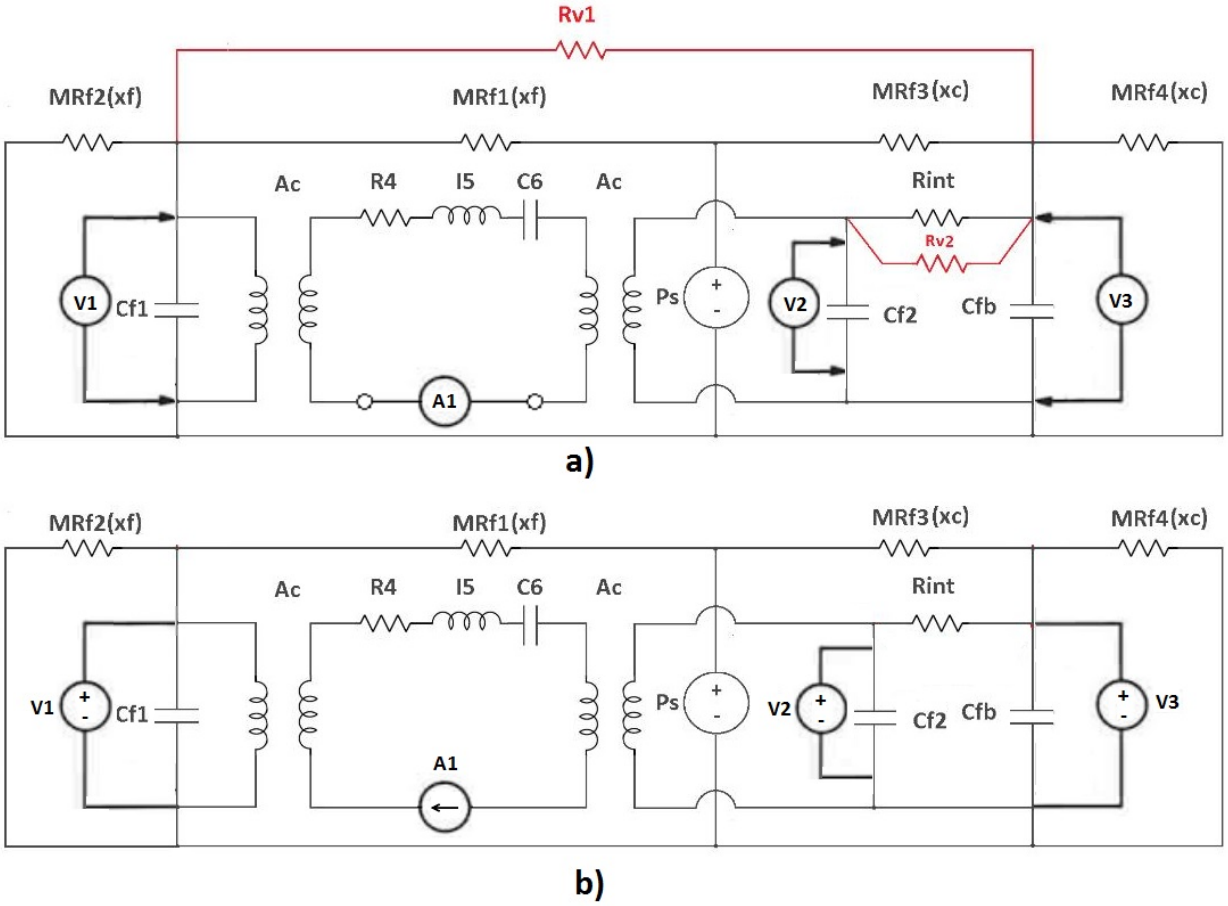


Figure 10: a) Sensor placement in the behavior model. b) Diagnostic model and measured sources from behavior model.

With this sensor placement configuration, it is possible to extract the ARRs. Thus, from each measured source, there will be an ARR. The current measurement with the sensor A1 in the behaviour model shown in Figure 10 is the spool velocity. However, its usual to have the spool posistion instead of the spool velocity. Thus, the ARRs will be derived for this constraint, considering the spool position (xc), that is the A1 sensor measurement integration.

$$ARR\,1: \quad Q_1 - Q_2 - i_1 - i_{V1} - i_{Cf1} = r_1 \qquad \begin{cases} Q_1 = C_d.\pi.dn.xf.\sqrt{\frac{2}{\rho}.(P_s - V_1)} \\ Q_2 = C_d.\pi.dn.(L - xf).\sqrt{\frac{2}{\rho}.(V_1)} \\ i_1 = Ac.\dot{x}_c \\ i_{V1} = 0 \\ i_{cf1} = \dot{V}1.C_{f1} \end{cases} \tag{39}$$

$$ARR\,2: \quad Ac.V_1 - R4.\dot{x}_c - I5.\ddot{x}_c - \frac{1}{C_{f1}}.x_c - Ac.V_2 = r_2 \tag{40}$$

$$ARR\,3: \quad i_2 - i_{cf2} + i_{Rint} + i_{V2} = r_3 \qquad \begin{cases} i_2 = Ac.V_1 \\ i_{cf2} = Cf2.\dot{V}_2 \\ i_{Rint} = \frac{V3 - V2}{R_{int}} \\ i_{V2} = 0 \end{cases} \tag{41}$$

$$ARR\,4: \quad Q_3 - Q_4 - i_{Rint} - i_{cfb} - i_{V3} = r_4 \qquad \begin{cases} Q_3 = C_d.w.xc.\sqrt{\frac{2}{\rho}.(P_s - V3)} \\ Q_4 = C_d.w.xc.\sqrt{\frac{2}{\rho}.V3} \\ i_{Rint} = \frac{V3-V2}{R_{int}} \\ i_{cfb} = Cfb.\dot{V}_3 \\ i_{V3} = 0 \end{cases} \tag{42}$$

From the ARRs it is possible to obtain the fault signature matrix, shown in Table 2. The fault signature matrix makes the relationship of the residuals sensibility for each parameter in the model. Taking as an example the residual 1 (r1), the parameters that most affect its value are Q1, Q2, Ac, and the Pc1 measurement V1. So, thinking about failure modes, if there is a pressure nozzle obstruction (the nozzle that controls the flow Q1), the flow Q1 will be smaller and, depending on the obstruction level, the pressure Pc1 will be significantly smaller than it would be without the nozzle obstruction, thus, the residual r1 will not be zero anymore, if there is a pressure nozzle obstruction. The two last matrix rows relate the detectability and the isolation of the parameter fault. So, if at least in one residual row the true value appears, then it is detectable. For example, the parameter Q1 is detectable because, if it has a disturbance from the original value, the residue 1 would be affected. For one parameter fault isolation, the pattern of the residual appearance must be unique. For example, the parameter xc (spool position) is isolable because, if there is an abnormal condition and the spool position differs from its normal movement (in a hydraulic line leakage or increased spool friction), the residuals r2 and r3 would be modified and this residual appearance pattern is unique for the xc failure mode.

	Q1	Q2	xc	Ac	Ps	V1	R4	I5	C6	V2	V3	Rint	Q3	Q4
r1	1	1	0	1	1	1	0	0	0	0	0	0	0	0
r2	0	0	1	1	0	1	1	1	1	1	0	0	0	0
r3	0	0	0	1	0	1	0	0	0	1	1	1	0	0
r4	0	0	1	0	1	0	0	0	0	1	1	1	1	1
D	1	1	1	1	1	1	1	1	1	1	1	1	1	1
I	0	0	1	0	1	0	0	0	0	1	0	0	0	0

Table 2: Servo valve fault signature matrix.

The Simulink model linking the behavior model and the diagnostic model, generating the states and the residuals is shown in Figure 11. The simulations were made introducing some failure modes in the behavior system, making it possible to observe the residual response. The Figure 12 shows the simulation results for 4 different faults. Pressure source fault, spool internal leakage, hydraulic line leakage, and position sensor measurement fault.

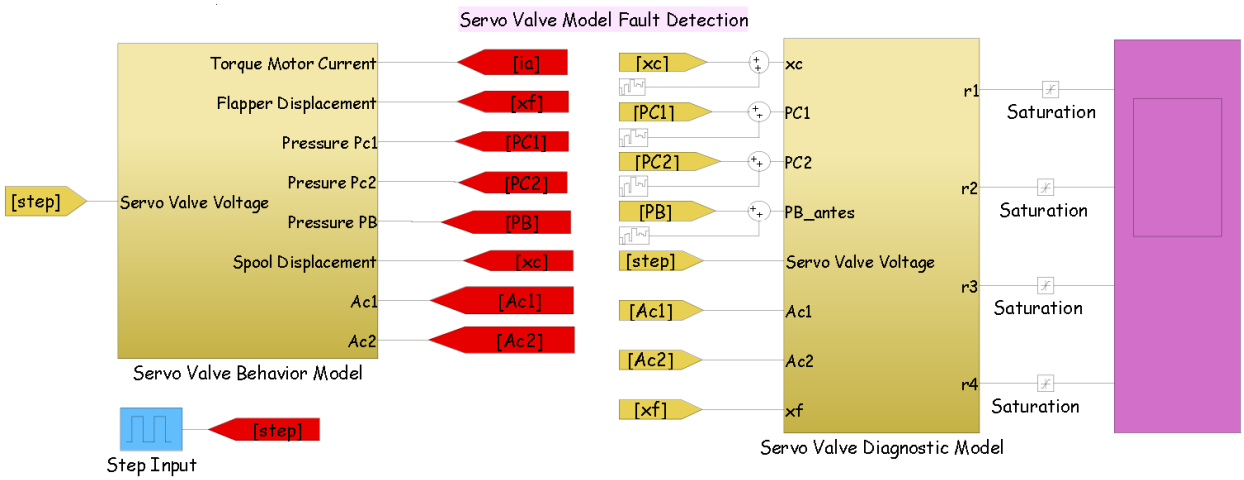


Figure 11: Simulink for residual analyses.

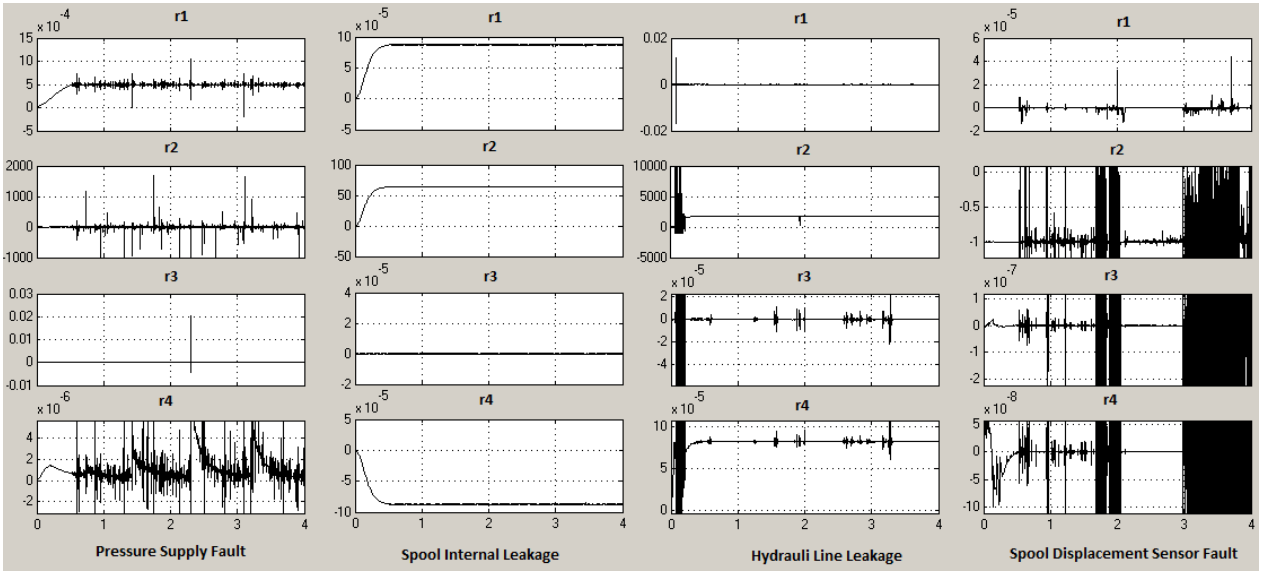


Figure 12: Residual response for different failure modes.

With the simulations results, it is possible to see that the residual response reflects the fault signature matrix. For the pressure supply fault, the matrix indicates that the most sensitive residuals are r1 and r4. The Figure 12 indicates variation on these two residuals, as expected. Analysing the spool internal leakage fault, the deviation occurs in more then one parameter. In this case, the most affected parameters are the spool displacement and the flows Q1, Q2 and Q3. Thus, based on the matrix, the residuals sensible to these faults are r1, r2 and r4 as confirmed by the simulation results in Figure 12. The hydraulic line leakage directly affects the spool displacement and the flows Q3 and Q4. This parameters affects the residuals r2 and r4 as confirmed by the simulation. Introducing a measure fault in the displacement sensor, caused a deviation in the residue r2, as expected according to the matrix.

7 Conclusion

The objective of this work was to develop a model for the aircraft braking dynamics and its hydraulic brake system, demonstrating, besides its normal operation behavior, what some common failure modes could cause

on the system performance. The FDI method proposed presented good results, being able to detect all the faults indroduced on the system, showing coherence with the fault signature matrix. Thus, this methodology is a viable solution, helping to support early failure identification.

References

[1] K. Medjaher, *A bond graph model-based fault detection and isolation.*, Brenguer and L. Jackson. Maintenance Modelling and Applications. Chapter 6 : Fault Diagnostics.,Det Norske Veritas (DNV), pp.503-512, 2011. hal-00635549

[2] W. Borutzky, *Bond Graph Model-based Fault Diagnosis of Hybrid Systems*, (2016). Springer Verlag

[3] A.K. Samantaray, K. Medjaher, B. Ould Bouamama, M. Staroswiecki, Dauphin-Tanguy *Diagnostic bond graphs for online fault detection and isolation*, Department of Mechanical Engineering, Indian Institute of Technology, 721 302 Kharagpur, India

[4] Merritt, H. E., *Hydraulic Control Systems*, (1967). New York - London - Sydney: John Wiley and Sons

Employment of an auto regressive moving average model for on-board knock detection of a spark ignited engine

D. Siano[1], M. A. Panza[1]
[1] Istituto Motori, National Research Council (CNR)
Via G. Marconi 4,80125 Napoli, Italy
e-mail: **d.siano@im.cnr.it**

Abstract
Knock control is still considered one of the main issues of spark ignition (SI) engines. In this paper, a proper mathematical procedure for knock detection is presented. More precisely, an Auto Regressive Moving Average (ARMA) algorithm is implemented on vibrational signals acquired by an accelerometer placed on the cylinder block of a SI engine. In order to demonstrate the effectiveness of the methodology, the same analysis is carried out by using the traditional IMPO (Integral of Modulus of Pressure Oscillations) based method, relying on the frequency domain processing of the in-cylinder pressure data.
Results demonstrate the high sensitivity and reliability of the proposed mathematical technique in accurately identifying knock events by using the engine block vibrational signals. The comparison with a standard processing of the knock sensor output definitely proves the potential of the model for developing more sensitive on-board control strategies for knock diagnostics and prevention.

1 Introduction

In automotive, modern engine control systems are designed to minimize exhaust emissions while maximizing power and fuel economy. The potential to maximize engine efficiency, through the optimization of the spark timing for a given air/fuel ratio is limited by engine knock [1][2]. An accurate knock detection is thus required in order to choose the right knock-limited spark advance for providing the best power and fuel economy. In spark ignition (SI) engines normal combustion occurs when a gaseous mixture of air and fuel is ignited by the spark plug and burns smoothly from the point of ignition to the cylinder walls. Engine knock, or detonation, occurs when the excess level of temperature or pressure in the unburned air/fuel mixture (end gases) cause auto-ignition of the end gases. This produces a sudden energy release that generates a rapid increase in cylinder pressure, with typical oscillations whose amplitudes gradually attenuate. The induced shock wave impulse excites resonances in the cylinder at characteristic frequencies which depend primarily on cylinder bore diameter and combustion chamber temperature [3]. Other structural resonances in the engine can be excited by the shock wave as it hits the cylinder wall. Serious damage to pistons, rings, and valves can result if uncontrolled heavy knock occurs.

The best signal to analyze to detect engine knock is the pressure directly measured inside the combustion chamber of a running engine by proper transducers [4]. Due to the still high sensor costs, pressure sensors are not usually installed in production engines, they are used primarily for research purposes.
The most common approach for implementing knock detection and control strategies in series production vehicles consists in the monitoring of the knock sensor's signal [5]. This sensor uses vibrations transmitted through the structure of the engine to detect knock in the combustion chamber. The vibration signal is typically processed in the frequency domain, to derive a knock intensity index which strongly depends on the engine operating conditions. The signal can be contaminated by other sources than engine knock, which increases the difficulty of signal detection. This is especially true at higher engine speeds in which background mechanical vibrations are much higher, effectively reducing the signal-to-noise ratio. A sophisticated treatment of the signal is thus required, usually based on the amplification of the signal magnitude in the frequency range of the knock-excited resonance.

In this paper, a novel methodology is proposed, based on an Auto Regressive Moving Average (ARMA) algorithm which is implemented on the vibrational signals acquired by an accelerometer placed on the cylinder block of a SI engine [6][7]. The technique, suitable for time series analysis, allows to build-up a model which reconstructs each sample of the signal as a linear combination of a specified number (model order) of previous samples (AR property), adding a prediction error in the form of a Moving Average (MA). The error of the reconstructed signal is then utilized to define an appropriate knock index. In order to verify the model, an accurate knock detection method based on cylinder pressure analysis is carried out, by using the traditional IMPO (Integral of Modulus of Pressure Oscillations) based method [8]. For this purpose, vibrational and in-cylinder pressure signals were collected for different engine speeds, load conditions and spark advances.

Results of the comparison with the reference cylinder pressure based method, demonstrate the effectiveness of the presented model in properly detecting knock phenomena. The high correlation with a standard processing of the knock sensor output definitely proves the potential of the algorithm to develop more sensitive knock control strategies for enabling the setting of optimum spark timing so that the engine can run at the knock threshold.

2 Experimental tests

Experimental data were acquired on a four-stroke, multi-cylinder SI engine, installed at the test-bench. The engine was equipped with a piezo-quartz pressure transducer to detect pressure signal within cylinder #1. Moreover, a single axis high frequency accelerometer was adhesively mounted on the engine block in proximity of the head of cylinder #1, in order to detect combustion-induced cylinder vibration along its axis. The engine block vibration signals provided by a commercial knock sensor in proximity of cylinder #1 were also measured. In-cylinder pressure and vibrational data were simultaneously acquired by a multi-channel acquisition system. They were properly triggered with the tachometer signal coming from the optical encoder connected to the engine crankshaft. Moreover, a high sampling resolution of 0.1 crank angle degrees was selected for an accurate combustion analysis.
Engine control was realized by switching from the reference commercial ECU to external mode. In this way, main engine parameters, such as spark advance and start of injection, were handled. Tests were carried out at variable speed (1100, 1300 and 1500 rpm) in high and part load conditions. A spark advance variation was imposed at each speed and load condition. The most retarded spark time was set in order to ensure a knock-free condition, while the most advanced spark was chosen in order to favor knock onset in each instantaneous cycle. A list of the 12 analyzed operating conditions is reported in Table 1. Spark advance values are expressed as delta values referred to the most retarded spark time of each engine operating point or EOP (no knock condition).

EOP	Speed, rpm	SA, deg BTDC	Load
1	1200	0/9	Part
2	1200	0/6	High
3	1400	0/7	Part
4	1400	0/5	High
5	1600	0/5	Part
6	1600	0/5	High

Table 1: Test conditions.

Due to cycle-by-cycle variations occurring during the combustion process of a SI engine, it is expected that faster-than-average cycles are most likely to knock. Therefore, knock detection procedures need to be applied on a statistical basis, taking into account the current percentage of knocking cycles. To this aim,

acquisition time was set to 60s for each test point, which allowed to collect more than 500 consecutive engine cycles for each operating condition.
Figure 1 shows an example of the acquired data with reference to the 133rd engine cycle at 1300 rpm, part load, in knock (SA=10.5 deg BTDC) and no knock (SA=3.5 deg BTDC) conditions. It can be observed that in knock condition the high vibration amplitudes are phased with the knock signature clearly evident in the pressure cycle, meaning that the accelerometer was correctly positioned so as to locate knock event in time reducing any possible time delay related to the propagation of pressure oscillations through the engine block.

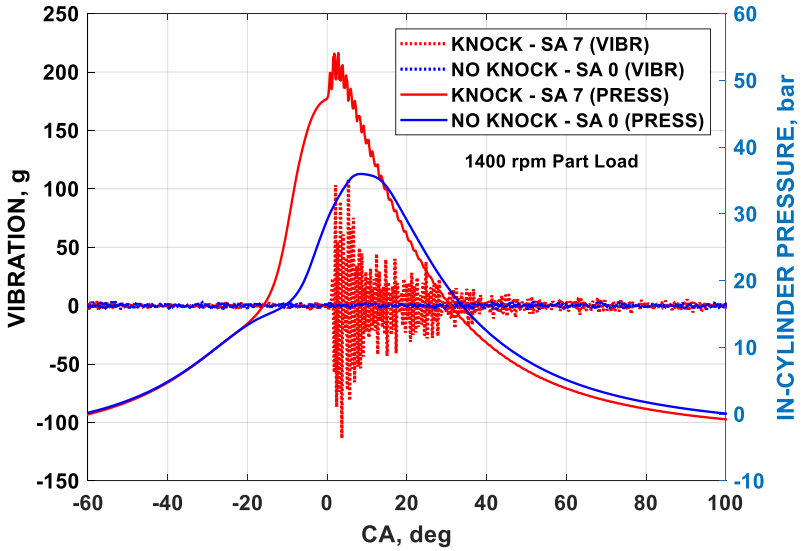


Figure 1: In-cylinder pressure and vibrational signals for to the 133rd cycle acquired at 1400 rpm, part load, SA=7 deg BTDC (knock condition) and SA=0 deg BTDC (no knock condition).

3 Vibration-based methodology

3.1 ARMA model

The Auto Regressive and Moving Average (ARMA) model is recognized as one of the most important polynomial models, widely used in system identification and in fault diagnosis problems. It represents a simple form of the generalized notion of transfer functions used to express the relationship between the input, the output and the noise of a system [9]. The methodology allows to model with reasonable accuracy a time series, representing it as a linear combination of a specified number (model order) of previous samples (AR property) adding a disturbance term in the form of a Moving Average (MA) of white noise.
The ARMA model structure is given by:

$$y(t) + a_1 y(t-1) + \cdots + a_n y(t-n) = b_1 e(t-1) + \cdots + b_m e(t-m) + e(t) \quad (1)$$

where

- *y(t)* is the output at time *t*,
- *n* is the model order (the number of poles),
- *m* is the number of disturbance coefficients,
- *y(t-1)…y(t-n)* are the previous outputs on which the current output depends,
- *e(t-1)…e(t-m)* are the white-noise disturbance values.

In order to build-up an accurate ARMA model, the number of coefficients and their value need to be proper estimated. For specified AR and MA orders, the a_n and b_m coefficients have to be selected in order to minimize the prediction error *e(t)*. The reliability level of the ARMA model is then synthesized in terms of variance of the disturbance function (noise variance, σ^2). The smaller the variance, the better the estimated model fits the time series. On the contrary, changes in the variance of the prediction error identify the presence of physical phenomena altering the characteristics of the time series. This peculiarity can be used to identify the onset of knock phenomena during engine operation. Hence, in the paper the ARMA modelling technique was used to reconstruct the engine block vibration data which in this case can be considered as the time series *y(t)* directly affected by an external disturbance *e(t)*, i.e. knocking. Changes in the time series will cause some deviations of the noise variance from its mean value. By monitoring the noise variance level, identifiable as a knock index, it is thus possible to detect the knock occurrence even in the case of low knock intensity.
The correct number of ARMA model coefficients was chosen, so as to yield a model with the simplest structure and the smallest number of adjustable parameters that can achieve the desired accuracy. To this aim, the measure of model quality provided by the Akaike's Information Criterion (AIC) was assessed [7]. Therefore, different models of the vibration time series in a knock-free operation were computed by varying the AR and MA orders from 1 to 5, and then compared using this criterion. Figure 2 shows the AIC surface resulting from the application of the algorithm in the knock-free test condition #2 (see Table 1). Taking into account that, according to Akaike's theory the most accurate model has the smallest AIC, the fit initially improves and AIC rapidly reduces by increasing both AR and MA orders and thus the flexibility of the model structure. Negligible AIC variations are progressively obtained by further increasing the orders value. The minimum AIC value is obtained with n=4, m=1.

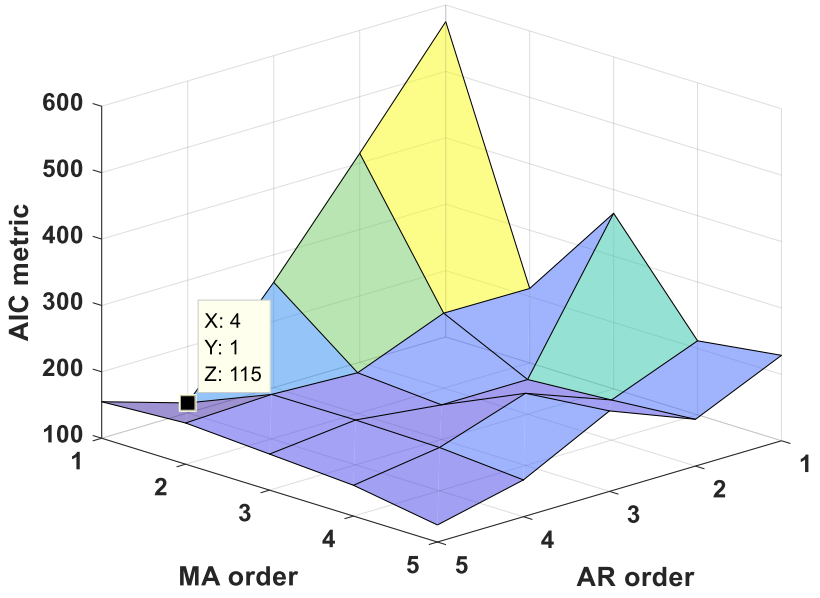


Figure 2: AIC surface with n_{max}=m_{max}=5. Optimal orders: n=4, m=1.

Figure 3 shows the comparison plot between the measured and the model-reconstructed vibration signals in EOP #2 over the CA window [0,40] deg. It definitely validates the identified ARMA model, indicating high confidence in the estimation. Similar results were also obtained for the other no-knock conditions.

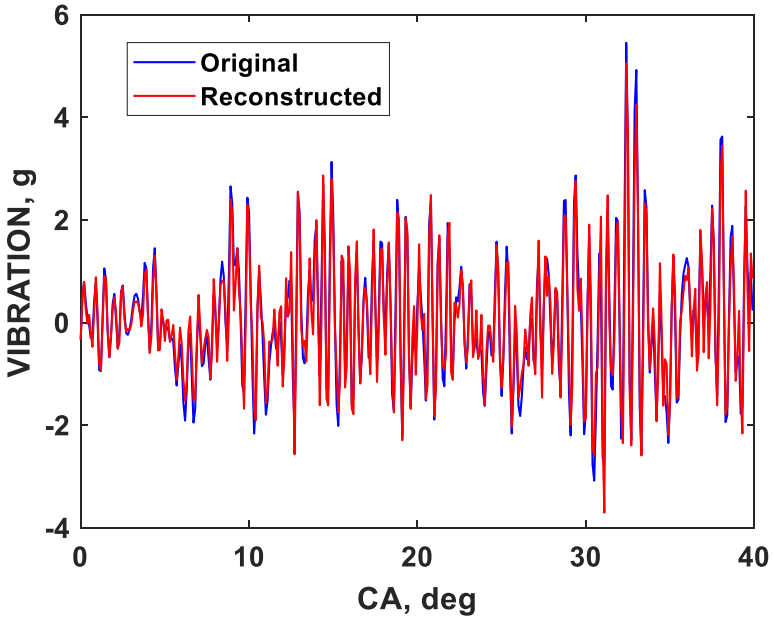


Figure 3: Comparison between the measured and the model reconstructed accelerometer signals (EOP #2).

Once the ARMA model was set up as described, it was applied all over the investigated operating conditions. Results will be presented in Section 5.

4 Pressure-based methodology

In order to verify the ARMA model outcomes, an accurate knock detection method based on in-cylinder pressure analysis was also performed. In many direct methods, knock occurrence is identified through a proper analysis of in-cylinder pressure signals in frequency domain. After a band-pass filtering, the pressure signals are rectified and processed to give proper knock indices. In the paper, the Integral of Modulus of Pressure Oscillations (IMPO) index was derived for all engine operating conditions.

IMPO is an integral index which derives from the integration of a signal portion. Specifically, it is defined as the integral of the filtered pressure signal absolute value, calculated in a proper crank angle window including the combustion [8]:

$$IMPO = \frac{1}{N}\sum_{1}^{N}\int_{\theta_0}^{\theta_0+\delta}|\hat{p}|d\theta \tag{2}$$

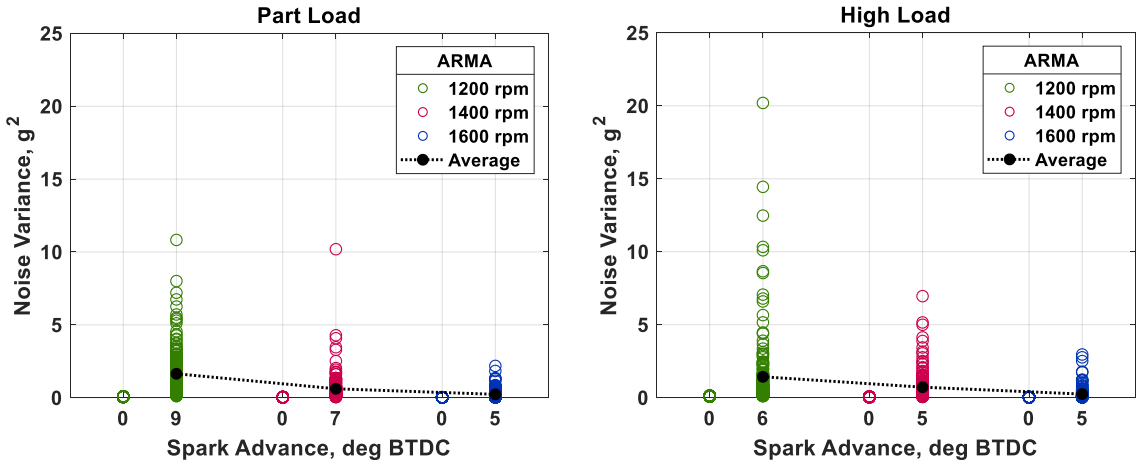
In the definition N is the number of samples in the calculation window, θ_0 is the first crank angle value of the window; δ is the window width, $\hat{p}$ is the filtered in-cylinder pressure.

In this case in-cylinder pressure signals, calculated in the knock CA window [0,40] deg, were filtered using a band-pass filter with cut frequencies 4-60 kHz.

5 Results analysis and discussion

The previously described methodologies were applied for analyzing 200 consecutive engine operating cycles for each investigated operating condition.
An overview of the ARMA model results obtained for each of the 200 experimentally acquired vibration cycle (vertical dots), in all engine operating conditions, is shown in Figure 4. Thanks to a proper tuning of the ARMA model, no cycle-by-cycle variations of the noise variance are visible for the knock-free

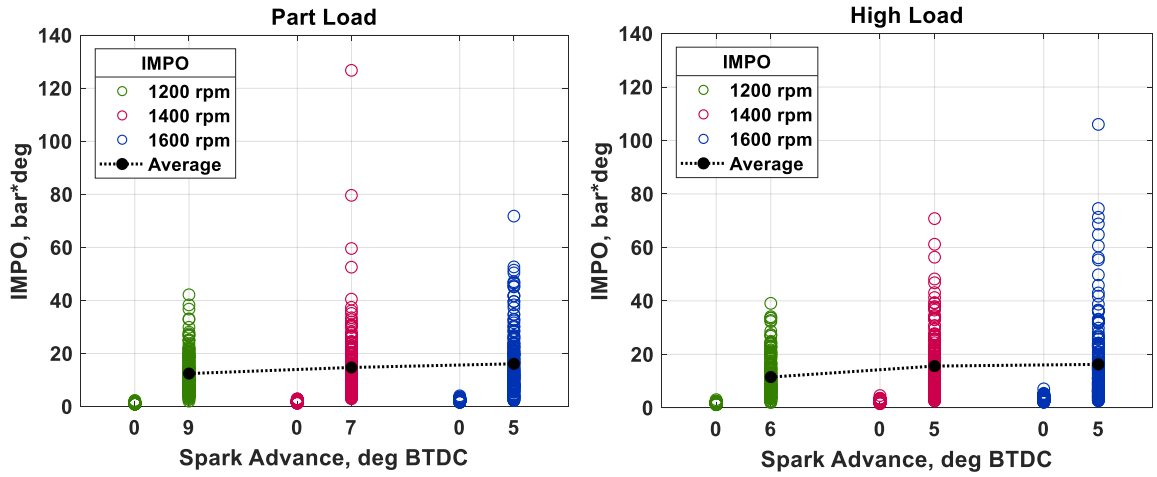
conditions. As expected, significant variations are found in the conditions characterized by the most advanced spark time.



(a) (b)

Figure 4: Noise Variance values at all investigated engine conditions, (a) part load and (b) high load.

In a similar way, results in terms of IMPO knock index are plotted in Figure 5. Due to the extremely different processing techniques, results in terms of raw indices cannot be adequately compared.

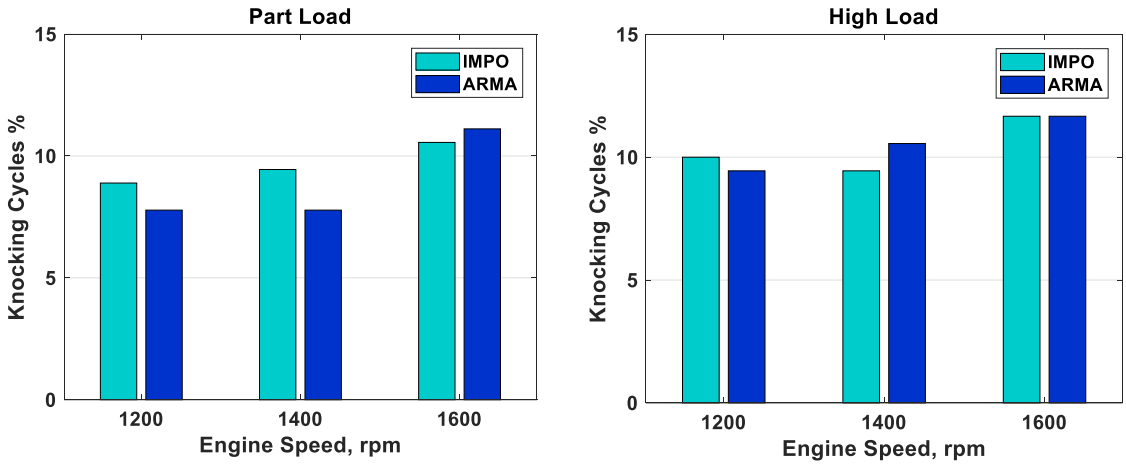


(a) (b)

Figure 5: IMPO values at all investigated engine conditions, (a) part load and (b) high load.

In order the establish an accurate comparison between the two approaches proving the effectiveness of the ARMA model, a limit threshold level for both knock indices was properly set. A unique procedure able to compare results obtained from such different methodologies is needed. Taking into account that, due to cycle-by-cycle variations, knock detection procedures are applied on a statistical basis, a possible way to define a knock threshold consists in normalizing the current knock index value with respect to the average of a certain number of previous values. A constant limit threshold of the normalized index can be then set, on the basis of the safety level to ensure. In this case, the relative indices were calculated over 20 past values of the knock indexes (Noise Variance and IMPO) and the limit threshold of the relative indices was set to 2 for IMPO-based approach and to 2.5 for ARMA-based one. The choice was supported by a deep analysis of the acquired in-cylinder pressure signals. The percentages of knocking cycles detected by the

two methodologies are compared in Figure 6. A good agreement is achieved with differences lower than 2%. Thanks to the optimal choice of the threshold levels, it is thus possible to obtain vibration-based percentages very close to those computed by the pressure-based approach.



(a) (b)

Figure 6: ARMA- and IMPO-based knocking cycles percentage in knock conditions, (a) part load and (b) high load.

For a further check of ARMA model sensitivity, the cycle-by-cycle variation of the two relative knock indexes for one of the knocking condition at part load (1400 rpm SA=7 deg BTDC), is compared in Figure 7. Despite some local differences, a substantial agreement on the cycle-by-cycle trend can be observed.

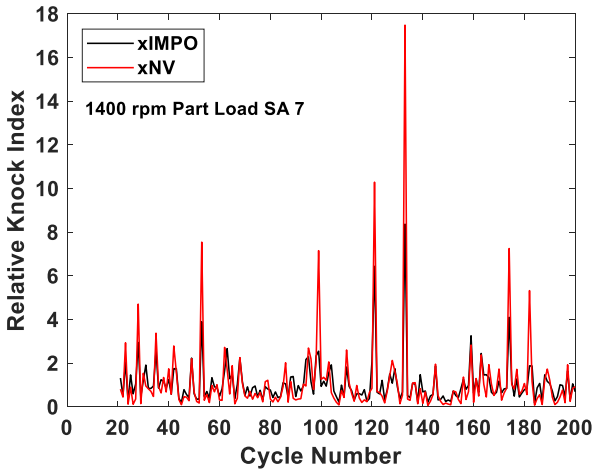
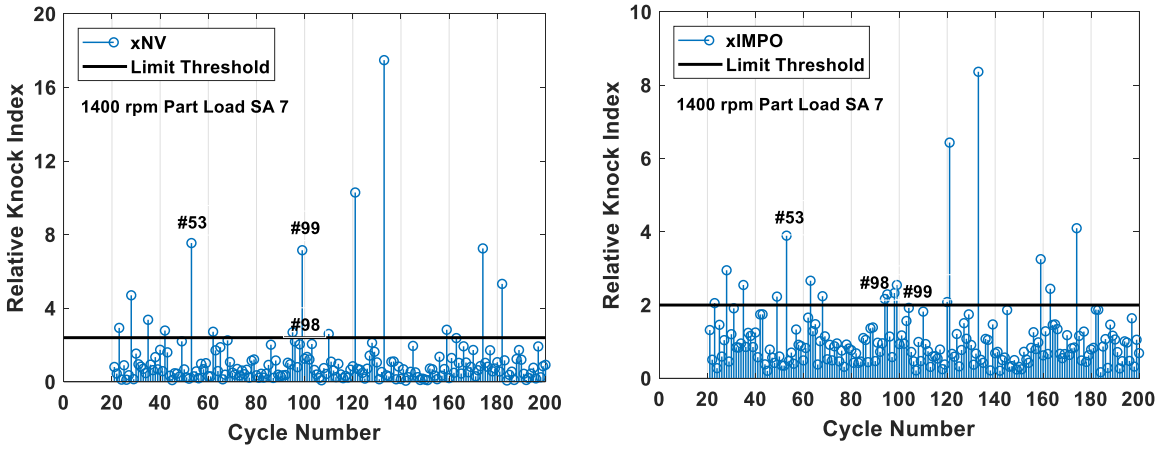


Figure 7: ARMA and IMPO derived relative knock indices at 1400 rpm, part load, SA=7 deg BTDC.

A higher accuracy of ARMA model in measuring knock intensity with respect to pressure-based method also emerged. In Figure 8(a,b) three different in-cylinder pressure cycles are identified, in terms of both Noise Variance and IMPO relative knock indices. A direct check of the related in-cylinder and vibration data is performed in Figure 9(a,b). The plot in Figure 9(b) confirms that cycles #53 and #99 present almost comparable knock intensity levels, as properly highlighted by ARMA-based values in Figure 8(a). The same result is not attained by IMPO analysis, which levels the knock intensity of cycles #98 and #99. Figure 9(a) demonstrates indeed that lower-amplitude pressure oscillations characterize cycle #98, as also shown by the substantial difference in the vibration signature of the two cycles.



(a) (b)

Figure 8: Relative knock indices and thresholds at 1400 rpm, part load, SA=7 deg BTDC.

A careful analysis of all obtained results finally led to conclude that, if properly tuned, ARMA model is able to correctly detect knock occurrence and to measure its intensity with high accuracy. Moreover, the methodology turned out to be more sensitive even to small knock intensity differences, if compared to a typical pressure-based approach.

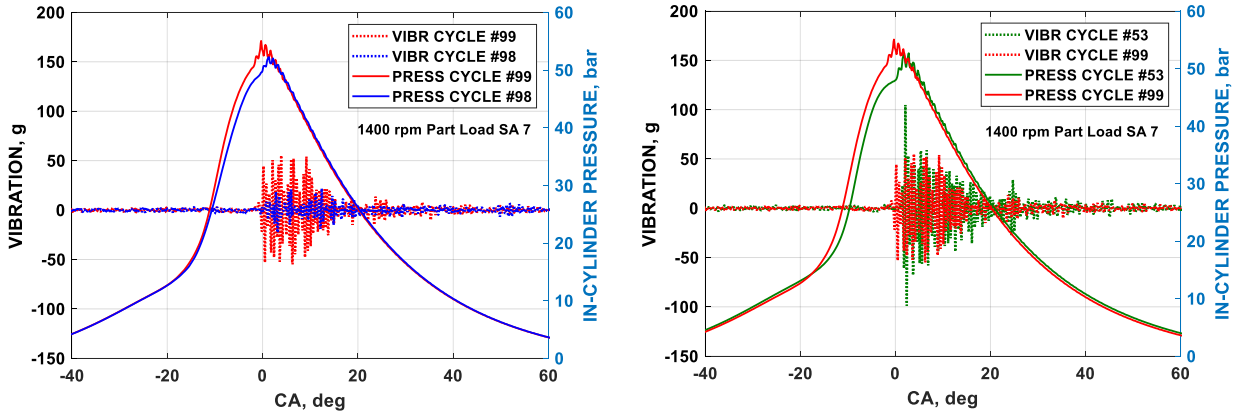


Figure 9: In-cylinder pressure and vibrational signals acquired at 1400 rpm, part load and SA=7 deg BTDC, (a) cycles #98 and #99, (b) cycles #53 and #99.

To prove the potential of ARMA technique for on-board knock control purposes, the model results were also compared to the outputs of a standard processing of the knock sensor signal. This latter relies on a frequency domain analysis. Similarly to IMPO, filtration, rectification, and integration in a defined knock sensitive window are the main steps of the procedure, which allows to yield the so-called Integral of Modulus of Accelerometer Oscillations (IMAO) [7]. To compute the index, the same windowing and band-pass filter than previous IMPO analysis were utlized. For the comparison, also IMAO values were expressed as relative values. Results were analyzed in terms of correlation plots, reported in Figure 10 for the EOPs in knocking conditions. As can be easily seen, a good linear correlation exists between the two relative indices, whose coefficient of determination in each condition is never below 0.69.

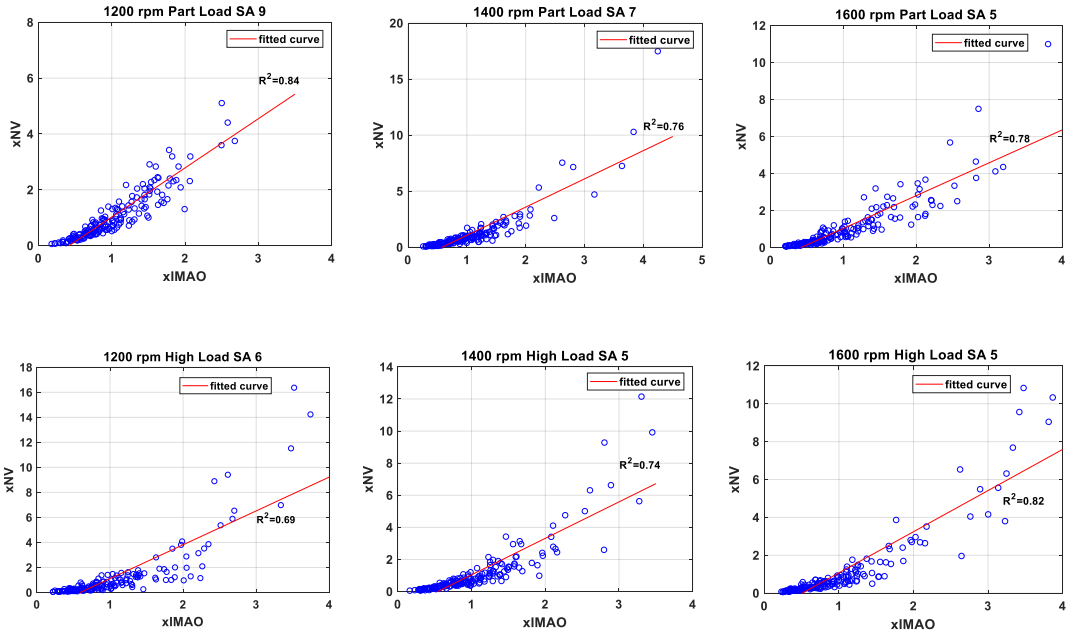


Figure 10: Correlation plots between the relative Noise Variance and IMAO knock indices.

Knock occurrence is hence detected by ARMA model similarly to a frequency domain processing of a conventional knock sensor. Deviations may be due to the different characteristics and mounting positions of the two acceleration sensors.

6 Conclusion and future developments

In this paper a proper engine-knock detection algorithm is presented. The methodology relies on the implementation of an Auto Regressive Moving Average (ARMA) model of the vibrational signal acquired by an accelerometer placed on the engine cylinder block. Results proved the effectiveness of the model, which is able to correctly detect knock occurrence and to measure its intensity with high accuracy. The approach turned out to be more sensitive even to small knock intensity differences, if compared to a typical pressure-based approach. The high correlation with a standard frequency processing of the knock sensor output definitely led to consider the possibility to use the model as a valid and effective alternative for developing more sophisticated knock control strategies in SI engines. Even though the methodology requires a careful preliminary set-up and tuning of the model, it would allow to overcome one of the limitations of the standard processing of the knock sensor signal, represented by the requirement of a different sensor tuning for each engine type due to variations in the characteristic frequency.

Further analyses will be carried out in order to test the methodology on other engines, assessing the impact of the sensor mounting position on the model performance as well.

References

[1] Wang, Z., Liu, H., & Reitz, R. D. (2017). Knocking combustion in spark-ignition engines. *Progress in Energy and Combustion Science*, *61*, 78-112.

[2] Günther, M., & Sens, M. (Eds.). (2017). *Knocking in Gasoline Engines: 5th International Conference, December 12-13, 2017, Berlin, Germany*. Springer.

[3] Horner, T. G. (1996). *Knock detection using spectral analysis techniques on a Texas Instruments TMS320 DSP* (No. 960614). SAE Technical Paper.

[4] Galloni, E. (2012). Dynamic knock detection and quantification in a spark ignition engine by means of a pressure based method. *Energy Conversion and Management*, *64*, 256-262.

[5] Movahed, M. M., Tabrizi, H. B., & Mirsalim, S. M. A. (2016). Normalized knock intensity determination based on the knock sensor analysis to have a fixed detection threshold at different operating conditions. *Journal of Engineering for Gas Turbines and Power*, *138*(6), 061501.

[6] Siano, D., Panza, M. A., & D'Agostino, D. (2015). Knock detection based on MAPO analysis, AR model and discrete wavelet transform applied to the in-cylinder pressure data: results and comparison. *SAE International Journal of Engines*, *8*(1), 1-13.

[7] Siano, D., Bozza, F., D'Agostino, D., & Panza, M. A. (2014). *The use of vibrational signals for on-board knock diagnostics supported by in-cylinder pressure analyses* (No. 2014-32-0063). SAE Technical Paper.

[8] D. Siano, M.A. Panza, *Sensitivity Analysis of Knock Indices and Combustion Noise Evaluation for a S.I. Engine*, International Review on Modelling and Simulations (I.RE.MO.S.), Vol. 7, N. 6, ISSN 1974-9821, December 2014, pp. 1003-1010.

[9] Ljung, L. (1999). *System Identification, Theory for the User. Upper Saddle River, NJ 07458, USA, Prentice-Hall*. ISBN 0-13-656695-2.

Speed-dependent wet road surface detection using acoustic measurements, octave-band frequency analysis and Support Vector Machines

S. Kanarachos[1], M. Kalliris[1], M. Blundell[1], R. Kotsakis[2]
[1] School of Mechanical, Aerospace, and Automotive Engineering,
Coventry University, Coventry CV1 5FB, UK;
e-mail: **ab8522@coventry.ac.uk**

[2] School of Journalism and Mass Communications, Lab of Electronic Media,
Aristotle University of Thessaloniki, Thessaloniki 541 24, Greece

Abstract
Rain, even shortfall rain, can adversely influence road safety. Currently, most methods for the detection of slippery road conditions require considerable excitation – by braking or steering – of the tyre forces. Thus, the safety margin between detection and reaction is minimal and dangerous situations can occur, for example hydroplaning. In this study, we explore the detection of wet road conditions by utilising a relatively inexpensive technology, acoustic measurements. A vehicle instrumented with a microphone, GPS and CAN bus data logger was driven at a wide range of speeds and for different road wetness conditions. A wet road surface detector for high and low speeds was developed and evaluated. The detector included a ground-truth database that was constructed by combining speed, road surface condition and audio features. The classification results by testing the performances of different machine learning algorithms on the database are discussed. The best results were obtained with Support Vector Machines.

1 Introduction

Weather conditions adversely affect road safety. Wet or otherwise slippery roads influence the road grip capacity of vehicles, as most road users probably know from experience. Slippery roads may be caused by rainfall, snow or ice, or by wet leaves in the autumn. In the USA, on average, there are over 5.7 million vehicle crashes each year. Approximately a quarter of these crashes are weather-related. On average, nearly 6,000 people are killed, and over 445,000 people are injured in weather-related crashes each year[i].

Weather-related crashes are defined as those crashes that occur in adverse weather for example rain, sleet, snow, fog, severe crosswinds, blowing snow/sand/debris or on the slippery pavement (wet pavement, snowy/slushy pavement, or icy pavement). The vast majority of most weather-related accidents happen on wet pavement and during rainfall: 73% on wet pavement and 46% during rainfall. A much smaller percentage of weather-related crashes occur during winter conditions: 17% during snow or sleet, 13% occur on icy pavement, and 14% of weather-related crashes take place on snowy or slushy pavement. Only 3% happen in the presence of fog. Omranian et al. (2018) recently reported that rainfall increases crash risk by about 57%. Regarding EU, the total cost of weather-related road deaths in Europe is over £15bn per year. 10% of the fatal road accidents happen during rainfall and only 1% due to snow, sleet or hail[2]. Approximately 43% of those who die are pedestrians, motorcyclists and cyclists who are Vulnerable Road Users. Motorcycle fatalities are highly dependent on weather and account for 15% of the total deaths[3].

The condition of the road surface is also important for vehicle's Active Safety Systems, including Advanced Driver Assistance Systems (ADAS) and Autonomous Driving (AD). The decision logic of Adaptive Cruise Control (ACC) and Collision Avoidance System (CAS) is heavily dependent on the Time-To-Collision metric, which is a direct function of the road friction value. Ghandour et al. (2010) discussed the importance

of road condition adaptable ADAS and the need to estimate the tyre-road friction value under any driving condition. Singh and Taheri (2014) studied how much Anti-lock Braking System (ABS) and Collison Avoidance Systems (CAS) can benefit, if the road friction value is known beforehand. It was found that substantial performance improvements can be achieved, for example the braking distance using ABS can be shortened by over 2 m and the relative impact speed using a CAS can be reduced by 9.5 m/s. Gordon and Lidberg (2015) pointed out the importance of friction knowledge for Autonomous Driving, including the one for vehicle control at the limits of handling. As highlighted by Olofsson *et al.* (2013), the optimal vehicle path at the limits of handling is invariant to the road conditions; therefore there is only one way for optimally controlling the vehicle: by knowing the road grip and taking action before the vehicle maneuverability is lost (Acosta, 2017).

Acosta, Kanarachos and Blundell (2018) provide a comprehensive review of the available road-friction estimation methods, based on "cause and effect". Most of the "cause and effect" methods require considerable excitation – by braking or steering – of the tyre forces. The main disadvantage of these methods is that the safety margin between detection and reaction is minimal. Thus, a dangerous situation may occur, for example hydroplaning. Furthermore, it is not possible to adapt pro-actively the operation of ADAS and AD systems, for example in platooning or Autonomous Emergency Braking (AEB). To this end, several methods for detecting the road friction, without requiring considerable excitation force have been explored. Panhuber *et al*. (2016) investigated the use of an onboard camera and various classifiers. Jonsson *et al*. (2015) have explored the use of a near-infrared camera. Bystrov et al. (2017) employed a 24 GHz radar and 40 kHz ultrasonic sensor. Tuononen et al. (2009) used an optical sensor for detecting aquaplaning. Matlainen et al. (2011) used tie-rod force measurements for estimating the road friction, while Niskanen (2015) employed accelerometers embedded on the inner liner of a tyre.

This paper contributes to the field of wet road detection by introducing a speed dependent detector using Support Vector Machines. For this, we used acoustic measurements near the tyre, octave-band frequency analysis and compared several machine learning algorithms. Our focus was at very low excitation levels, for example when driving at steady speed. For this, an experimental investigation took place at Coventry, UK. A vehicle instrumented with a microphone, GPS and CAN bus data logger was driven at a wide range of speeds and for different road wetness conditions. The potential of the developed road wetness detector is significant from a road safety and ADAS development point of view. First, the proposed solution is based on a relatively inexpensive technology and are expected to be widely used in AD; thus wide-scale implementation is possible[4]. Second, they can improve the reliability of road wetness detection by supporting detections in scenarios where other detectors do not perform well or serve as a second voter.

The rest of the paper is structured as follows. The second chapter focuses on related work in acoustic measurements and road wetness detection. The third chapter details the experimental set-up and the data generation. The fourth chapter presents the machine learning algorithms used and the results. Finally, conclusions and future research directions are given.

2 Related work

Rain influences road friction in different ways. As tyres move over a wet surface, the water fills in the tiny pits in the road surface, effectively smoothing out the surface (Ressel, 2017). There are also substances on roads that can lead to a loss of friction when water is added. For example, most dry roads contain a layer of tar, rubber, and oil. When it starts to rain, these substances can mix with the water, creating a greasy layer that can be very slippery. Another case is that of third bodies sticking on the road surface, like wet leaves. Eventually, on wet road surfaces, the adhesive forces (direct contact between the tyre and road) and part of the tyre forces due to hysteresis (road surface micro-roughness) is lost. The actual friction loss also depends on the speed of the vehicle, as the force generation mechanism is different at low and high velocities (Al-Assi, 2017). In the worst case, if there is a lot of water on the road, including standing water in puddles, the vehicle is moving at least with a moderate speed (> 13.88 m/s) and there is insufficient tyre tread depth then the tyre cannot remove the complete volume of water between the tyre and road. In these cases, tyres can completely lose contact with the road surface and start sliding (Li *et al*., 2015). When this occurs, it is called hydroplaning or aquaplaning, and it can be hazardous.

Tyre-road noise depends on a number of parameters that characterize either the tyre, the road or the interface between them. Bezemer-Krijnen et al. (2016) studied the influence of two key tyre tread parameters, the air-ratio and pattern-continuity. For this, a range of tests was conducted in a controlled environment for a set of road surfaces and tyres. The tyre tread type heavily influenced the generated noise levels and different sensitivities for the frequencies 500, 1000 and 2000 Hz were recorded for each road surface type. The tyre tread was more influential for frequencies close to 1000 Hz, while the road porosity for frequencies close to 2000 Hz. Kindt, De Coninck, Sas, and Desmet (2007) investigated the influence of road undulations on tyre-road noise. Tests were conducted in a laboratory environment and speeds up to 8.33 m/s (30 km/h) were achieved. The sound pressure was measured at a radial distance of 100 mm from the tyre surface. The sound pressure spectrum showed a dominant peak at 80,8 Hz, which corresponded to the 1st vertical tyre resonance. Smaller peaks appeared at other resonance frequencies of the tyre, in the range 49-230 Hz. The spectral content of the radiated noise showed no important components at frequencies above 500 Hz. Therefore, it was concluded that the whole tyre vibrations were causing the radiated noise. The radiated noise in the frequency range up to 500 Hz is not influenced by the tread pattern, but only on the tyre construction. Mioduszeski measured the influence of speed on tyre/road noise spectra and illustrated that the exterior tyre/road noise was proportional to the logarithm of the speed[5].

The presence of water on the road is also an important factor of tyre-road noise but has not been studied in the same depth as other parameters. Cai *et al*. (2017) measured traffic noise on wet and dry road surfaces and found that the noise level increases by up to 10.09 dB due to road wetness. Furthermore, the results showed that for the wet road asphalt the sound pressure level is high at high frequency and low at low frequency, which was completely different from the response on a dry asphalt road. In addition, for a wet asphalt road the noise energy percentage changes little with speed, while for dry asphalt road, the vehicle's noise energy percentage at low frequency decreases as the speed increases, whereas at high frequency, the percentage increases as the speed grows. Boyraz [46,131] presented an acoustic-based approach for automatically distinguishing different road surface types (asphalt, gravel, snowed and stone). Neural Networks were used for this purpose and a 91% accuracy was achieved in the worst case. The acoustic data were collected using a cardioid microphone. The microphone was installed on the suspension strut of a small electric vehicle. Data were collected at low constant vehicle speeds 2.77–8.33 m/s (10–30 km/h). Boyraz *et al*. processed the audio signals and extracted features such as linear predictive coefficients (LPC), mel-frequency cepstrum coefficients (MFCC) and power spectrum coefficients (PSC) for the classification task. The features were extracted using time windows of 0.02, 0.05 and 0.1 s to facilitate real-time application. Alonso et al. (2014) presented a method for wet road surface conditions using Support Vector Machines. Trials in a controlled environment were conducted using an instrumented passenger vehicle, on the chassis of which an electret microphone was installed. Measurements took place on dry and then on wet asphalt. The method was validated for vehicle speeds between 8.33–19.44 m/s (30–70 km/h). The audio samples were processed in chunks by a 1/3 octave filter band, in the frequency range from 20 Hz to 20 kHz. Two different methods were applied for selecting the most informative features, which were then used to train a Support Vector Machine (SVM). The experimental results showed that when the vehicle was driven on the wet asphalt, the noise level increased. The level increase was noticeably higher in the 500 Hz to 8 kHz range. The proposed classifier had no misses for the wet asphalt status detection, and less than 12% misses for the wet to dry transition. Abdic *et al*. (2017) employed a deep learning approach for detecting road wetness using audio signals. For this they acquired approximately 800000 bins of audio, recorded while driving in a range of road surfaces, traffic conditions, precipitation levels, and speeds. A Long-Short-Term-Memory Recurrent Neural Network (LSTM-RNN) was developed using as inputs spectral features (0- 8000 Hz) computed using the short-time Fourier Transform. Each spectrogram had been converted to the Mel-Frequency scale. Detection of road wetness was achieved with a 93.2 % accuracy in the worst case.

3 Methods and tools

We employed a portable experimental setup and simultaneously recorded the sound generated by the tyres, the vehicle GPS position and speed. Six experiments took place at a wide range of speeds and for different road surface and wetness conditions. Each test had a length of approximately 25 minutes. A ground-truth annotated database for the different labelled classes of road wetness was constructed. Various machine

learning classification algorithms were trialled to obtain the discrimination accuracy of the different algorithms. Furthermore, we analysed and identified the most significant audio features (principal components).

3.1 Experimental set up and data acquisition

The tyre-road noise was recorded with a microphone, mounted at a close distance to the tyre-road interface. Figure 1 shows the position of the microphone. Since sound waves travel almost omnidirectional, the side that is affected less by water spraying when the vehicle is moving on a wet surface was preferred. Furthermore, we selected to place the microphone close to the rear left tyre, as this tyre was the most distant from the engine and exhaust system. We covered the microphone with a waterproof film and a windshield to protect it from the water spray. For consistency, we kept the protection even during the experiments on the dry road surfaces. The microphone used (Vivanco EM35) was an electret condenser type powered by an AA 1.5-volt battery. It is a low cost but good quality clip-on microphone with a wide frequency response for the entyre audible spectrum.

A digital audio recorder (Zoom H1), manually controlled from the inside of the vehicle, was used to record the audio signals in uncompressed PCM *.wav. We selected a sampling rate of 44.1 kHz, because a higher sample-rate would result in larger data sizes, however without offering more information. A 24-bit depth was set for the digital coding of the samples so that the dynamic range was high enough and there was no need to adjust and change the input gain and the recording level throughout the entyre experimental process. In fact, the input gain was initially set during pilot experimental routes to obtain appropriate recording levels so that no clipping occurs and after that, it remained unchanged for all experiments.

The vehicle GPS position and speed were acquired using Racelogic's Videobox data logging system. Figure 2 illustrates a log of vehicle speed during one of the experiments conducted. A wide range of speeds was achieved. Simultaneously with the GPS position and speed we video recorded the road in front of the vehicle using a forward-facing camera. Furthermore, CAN-bus signals, including the wheel speed, braking pedal position, acceleration pedal position, accelerometer and yaw rate, were retrieved from the vehicle's On-Board-Diagnostics (OBD) interface. The retrieved data were used to establish the ground truth database.

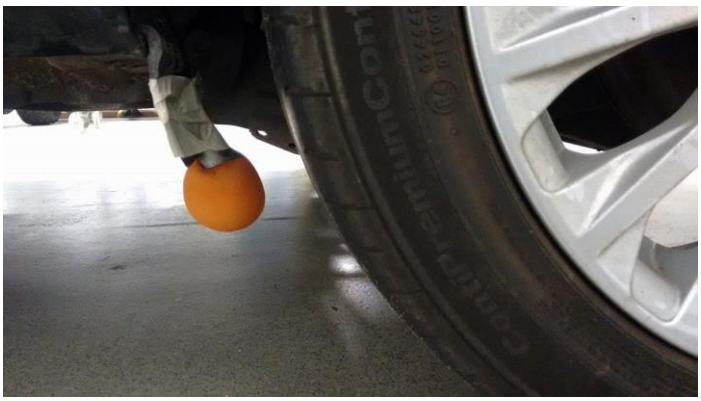


Figure 1: Microphone position during the field trials

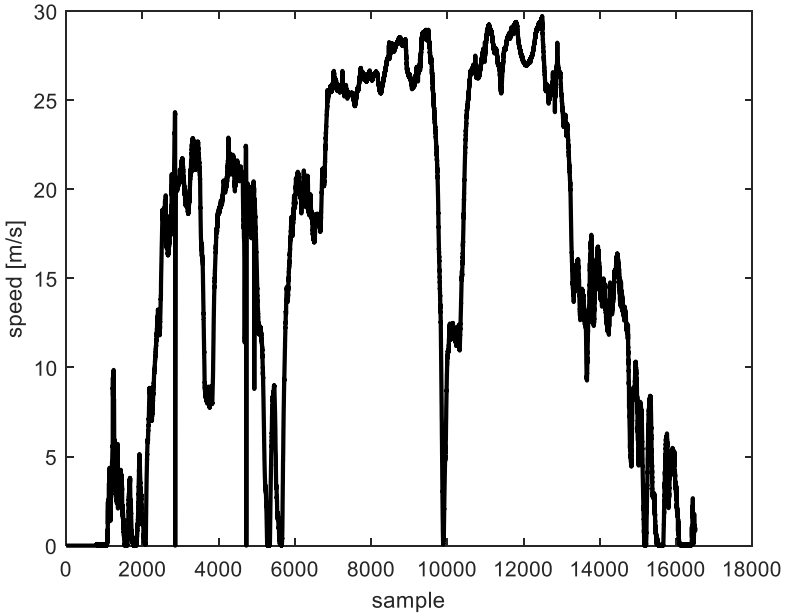


Figure 2: Vehicle speed during one of the naturalistic field trials.

First, we executed two pilot trials to calibrate the equipment. Then six field trials took place on public roads and under real traffic conditions. We collected data on dry road, wet road while raining and wet road following a shortfall rain.

From the whole set of experimental data, we selected three experiments for constructing the ground-truth database. The criteria for choosing the three routes were on the one hand the similarity of the vehicle route and on the other hand the differences in weather and road surface conditions (i.e. wet, slightly wet, dry). In some cases, it was difficult to retain all parameters needed to be constant because the experiments were conducted in a non-controlled environment. For example, the vehicle speed on the highway varied because of the different traffic situations.

An illustration of the three routes that were finally selected for further analysis is provided in Figure 3.

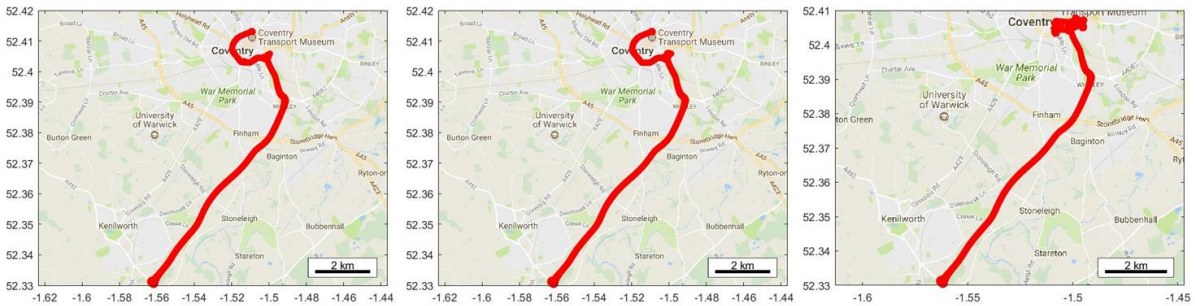


Figure 3: The vehicle trajectory in the three field experiments at Coventry, U.K.

3.2 Data processing and labelling

Before proceeding with the classification experiments, a preprocessing step was involved in which we removed redundant data such as start-stop pauses, and preparation intervals. Furthermore, to avoid extra data load the audio recordings were transcoded into a PCM *.wav format with a sampling rate of 44.1 kHz and a 16-bit depth dynamic range.

As already mentioned, the present study presents the classification results for three different road wetness conditions, for which the following 3-class annotation scheme was selected:

- 3.*15wet1*: A recording that was conducted on 15 March 2018 on wet road surface conditions during light rain.
- *4.13wet2*: A recording that took place on 13 April 1018 on damp road surface conditions. In particular, the experiments were conducted following a shortfall rain.
- *5.15dry*: A recording that was captured on 15 May 2018 on a completely dry road surface.

Since the feature extraction procedure demands a proper segmentation of the prolonged recordings, we decided to use a segmentation time window of 100 ms. The main reason for choosing this window length is that the tyre sounds are quasi-stationary signals and since the current research is focused on changes of the frequency distribution of the tyre sounds as the road surface wetness or dryness change, a time window offering a proper frequency resolution (10 Hz) should be selected. The selected segmentation window is also aligned with the GPS and vehicle speed sampling rates. Finally yet importantly, a segmentation length of 100 ms it is adequate from a road safety point of view, under the condition that the task is to identify the condition of the road wetness for low levels of tyre excitation.

3.3 Feature extraction

A variety of distinctive properties can be extracted from audio samples, from either the time or spectral domain signal representation. Since the interest lies in the detection of dry or wet road surface conditions, the investigation of changes in the quasi-stationary form of the signal is more appropriate. Time-domain properties such as zero-crossing rate, number of signal peaks, statistics etc. are not suitable for the classification task in this work (Lartillot *et al*., 2007, Kotsakis *et al*., 2012a, Kotsakis *et al*., 2012b).

We decided to perform the classification task via the spectral analysis of the captured audio content, in particular by exploiting the frequency-domain properties for each audio sample (with duration 100ms). The feature vector included the energy-related parameters of the audio signals in predefined spectral bands. Several experiments were conducted while testing the efficiency of linearly-spaced versus octave spectrum representation for the computation of frequency bands energies (Lartillot *et al*., 2007). The comparisons revealed that octave-band features presented a better performance, since the linear audio signal brightness properties were strongly correlated to the octave-band ones without any additive value (Lartillot *et al*., 2007, Kotsakis *et al*., 2012a, Kotsakis *et al*., 2012b).

Specifically, the audio spectrum of each audio sample was divided into 11 octave bands with central frequencies as shown in Table 1, while the range of each octave band has an upper frequency that is twice that of the lower one (ANSI S1.11). Based on the defined octave bands, an Infinite Impulse Response (IIR) bandpass Butterworth filter (order 4) was imposed on each audio sample, which returns each audio sample withholding only the corresponding frequencies (Bianchi, G. and Sorrentino, R, 2007). Finally, a Fast Fourier Transform (FFT) was applied into the processed samples for each octave band, in order to calculate the FFT coefficients, from which the RMS (Root Mean Square) energy was computed for each octave band as the square root of the average of the sum of the squared values of the FFT coefficients. The aforementioned vector of RMS energies for each octave band was extracted, using MATLAB 2017a and the Machine Learning Toolbox, with the following notation:

Band	Nominal Centre Frequency	Calculated Centre Frequency	Lower Band Limit	Upper Band Limit
1	16 Hz	15.625 Hz	11 Hz	22 Hz
2	31.5 Hz	31.25 Hz	22 Hz	44 Hz
3	63 Hz	62.5 Hz	44 Hz	88 Hz

4	125 Hz	125 Hz	88 Hz	177 Hz
5	250 Hz	250 Hz	177 Hz	355 Hz
6	500 Hz	500 Hz	355 Hz	710 Hz
7	1000 Hz	1000 Hz	710 Hz	1420 Hz
8	2000 Hz	2000 Hz	1420 Hz	2840 Hz
9	4000 Hz	4000 Hz	2840 Hz	5680 Hz
10	8000 Hz	8000 Hz	5680 Hz	11360 Hz
11	16000 Hz	16000 Hz	11360 Hz	22720 Hz

Table 1: Octave bands for extracting the energy features of the audio signal

The ground-truth database for the machine learning experiments was constructed using the octave-band features of the audio signals obtained in the field trials "3.15wet1", "4.13wet2" and "5.15dry".

4 Results and discussion

The first classification attempt included all sound segments that corresponded to speeds ranging from 10km/h up to the maximum recorded speed (i.e. 108.2km/h). The classification scheme included the three classes *3-15wet1*, *4-13wet2*, 5-*15dry*, presented in Section 3. In total, 22 classification algorithms were trialed using as inputs the 11 octave band filtering energies. The classification was performed using Matlab 2017a Classification Learner App.

For the classification we employed the *%-split* training method. We preferred this method rather than the *k-fold* training method, because of the large dataset size. The *%-split* method splits the data in two separate subsets. One part of the data is used for the training of the algorithm (i.e. training data) and the rest of the data is used for prediction and evaluation of the classification accuracy (i.e. control data). An efficient ratio of 75% training data to 25% control data split was therefore selected and used for each one of the 22 classification algorithms that were checked. It is highlighted that the same 75-25% split ratio was used in all tests for all classification attempts and all classification schemes.

In the first classification attempt the Quadratic SVM algorithm performed with the best accuracy of 81% (Joachims, 1999; González-Mendoza, 2005). From the confusion matrix results shown in Figure 4 it is clear the class *3-15wet1* is better categorized than class *5-15dry*, and class *4-13wet2* but less than class *5-15dry*. This seems reasonable since for the *3-15wet1* experiment the road surface was much wet than for the *4-13wet2* experiment.

We further investigated the above observation, by utilising binary classification schemes in the second classification attempt. The three classes were checked in pairs for the same speed range (10km/h to maximum) and the Quadratic SVM again performed best with an accuracy of 92.3% giving the best discrimination for the pair of flooded versus dry surfaces and the worst discrimination for the pair of slightly wet versus dry surfaces as was expected. The results of the second classification attempt are shown in Figure 5.

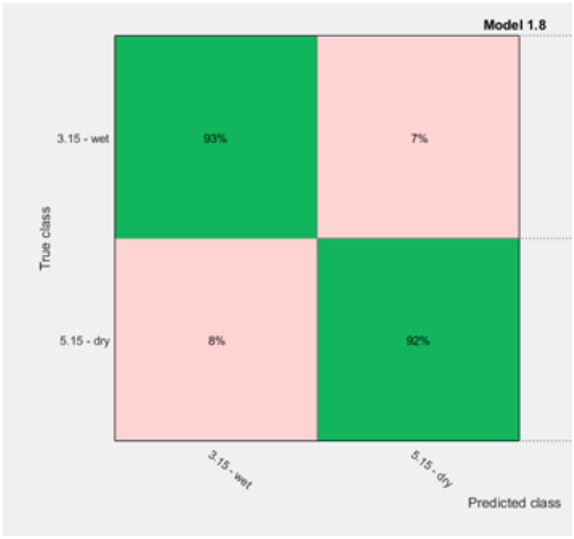
In the next classification attempts, the data were classified in "highway" and "city" driving, taking into account the vehicle speed and GPS location. For the highway driving condition, speeds ranging from 80 km/h up to 108.2 km/h and for the city driving condition speeds ranging from 10 to 40 km/h were considered respectively. The two conditions were separately checked with the classification algorithms for the same as before three schemes first and the binary schemes after. In Figure 6 speed data selected for the highway driving condition are plotted.

The Quadratic SVM algorithm again performed best for the 3-class scheme with an overall accuracy of 86.3%. The resulted confusion matrix is shown in Figure 7. For the binary 2-class schemes the best

performance was observed for the pair *3-15wet* versus 5-*15dry* i.e. wet versus dry with an accuracy of 98.4%. The resulted confusion matrix is shown in Figure 8. It is worth noting that for this binary 2-class scheme that had the best performance three algorithms i.e. Logistic Regression, Quadratic SVM and Cubic SVM resulted to this same overall accuracy of 98% as shown in Figure 9.



Figure 4: Confusion matrix of the SVM classification for the three experiments (3-class scheme) and speeds from 10km/h to maximum



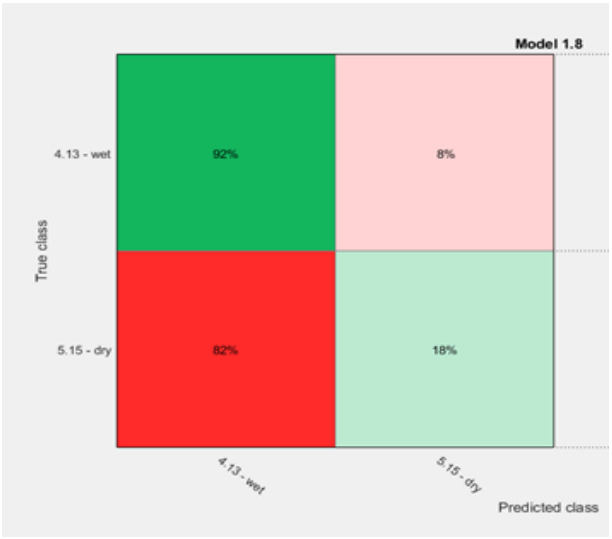


Figure 5: Confusion matrix of the SVM classification in pairs (binary 2-class scheme) for speeds from 10 km/h to the maximum achieved (a) best prediction *3-15wet1* versus , (b) worst prediction *4-13wet2* versus *5-15dry*

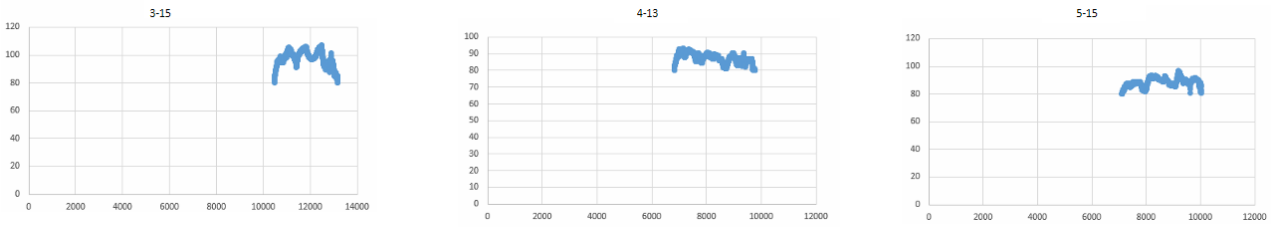


Figure 6: Data selected for the highway driving condition for speeds ranging from 80 km/h up to the maximum achieved for each experiment

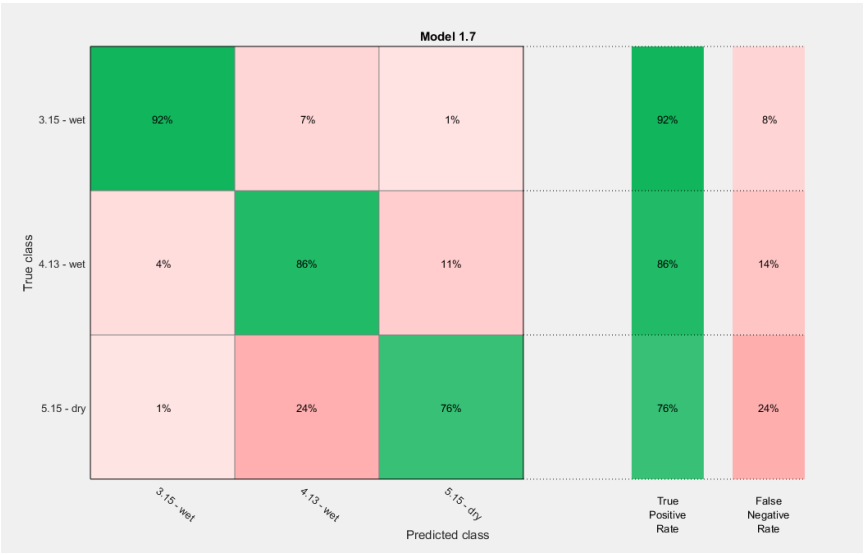


Figure 7: Confusion matrix of the SVM classification for the three experiments (3-class scheme) at the highway driving condition for speeds ranging from 80km/h up to the maximum

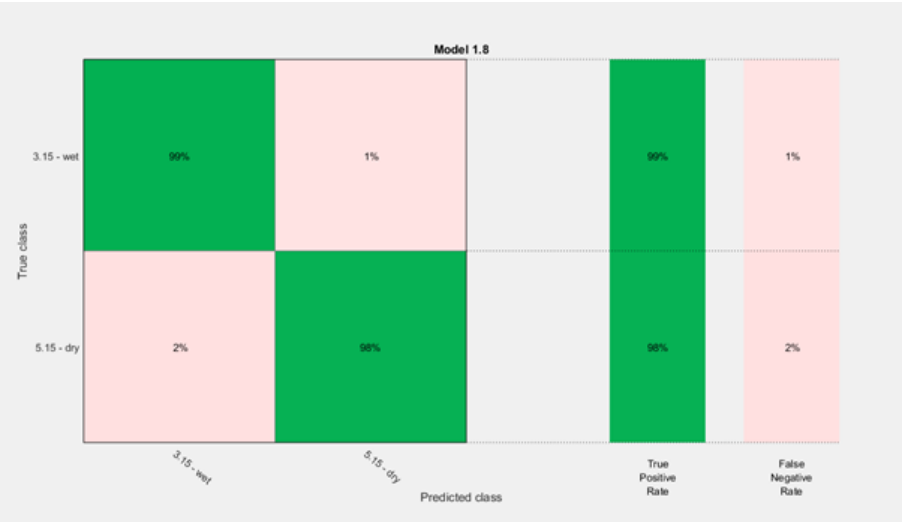


Figure 8: Best prediction *3-15wet1* versus *5-15dry* confusion matrix of the *SVM* classification in pairs (binary 2-class scheme) at the highway driving condition for speeds ranging from 80 km/h up to the maximum

For the city driving cases, speeds ranging from 10 to 40 km/h, similar in classification performance results were obtained. Quadratic SVM performed best with an accuracy of 84.4% for the 3-class scheme in the city driving condition, Figure 9. For the binary 2-class scheme the best prediction was again for the same pair *3-15wet* versus *5-15dry* i.e. flooded versus dry. In this case the Cubic SVM algorithm performed best with an

accuracy of 93.7%, in Figure 10 slightly better than that of Quadratic SVM algorithm with an accuracy of 93%.



Figure 9: Confusion matrix of the SVM classification for the three experiments (3-class scheme) at the city driving condition for speeds ranging from 10 to 40 km/h

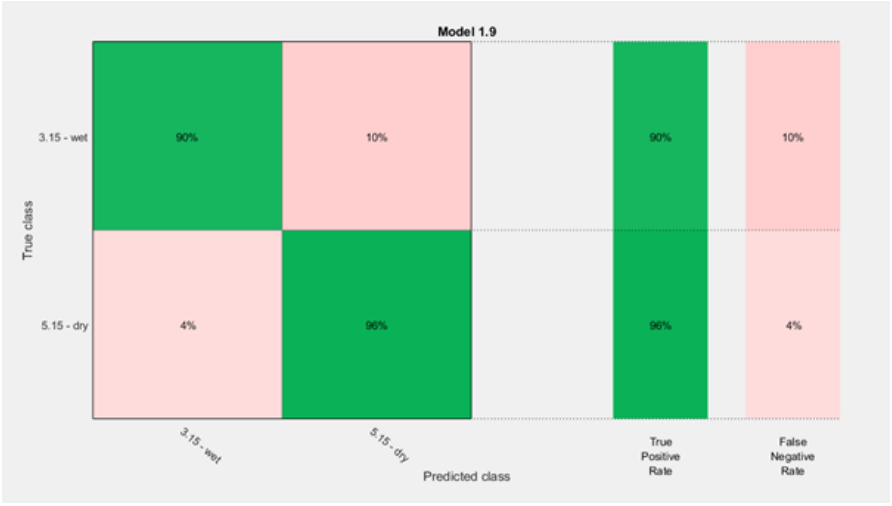


Figure 10: Best prediction (3-15wet1 versus 5-15dry) confusion matrix of the SVM classification in pairs (binary 2-class scheme) at the city driving condition for speeds ranging from 10 to 40 km/h

4.1 Feature ranking

In order to get further insight regarding the classification accuracy and the features that enable the discrimination between the classes *3-15wet1*, *4-13wet2*, and 5-*15dry*, a feature significance analysis was conducted. For this reason, the specialized evaluation algorithm "OneR Attribute Evaluation" in WEKA 3.7 Data Mining Software was implemented that functions as follows (Witten *et al.*, 2016):

1:	For each input variable/ feature:
2:	For each value of audio property:

3:	The number of appearances of each output class is counted
4:	The most frequent class is detected
5:	The current feature value is assigned to this class
6:	The total error of the above rule is computed for each feature
7:	The ranking is executed from the features with smallest to higher total errors

Table 2: Pseudocode for feature ranking

	City 10-40km/h	Highway 80km/h-max	Overall 10km/h-max
1	Oct125Hz	Oct500Hz	Oct2kHz
2	Oct250Hz	Oct250Hz	Oct62.5
3	Oct62.5	Oct125Hz	Oct4kHz
4	Oct500Hz	Oct62.5	Oct31.25
5	Oct31.25	Oct31.25	Oct125Hz
6	Oct1kHz	Oct1kHz	Oct15.625
7	Oct16kHz	Oct16kHz	Oct1kHz
8	Oct2kHz	Oct4kHz	Oct250Hz
9	Oct8kHz	Oct8kHz	Oct500Hz
10	Oct15.625	Oct2kHz	Oct8kHz
11	Oct4kHz	Oct15.625	Oct16kHz

Table 3: Feature ranking for different speed ranges via the OneR Attribute Evaluation algorithm

5 Conclusions and future work

In this study, the feasibility of acoustic measurements and machine learning algorithms for discriminating between dry, wet and damp road surfaces was investigated. The results show that the classification can be performed with relatively high accuracy, comparable to results presented elsewhere in the literature. Furthermore, we presented for the first time a speed-dependent classifier, which increases the classification accuracy and robustness of the classification task. The equipment required for obtaining the acoustic measurements and processing is relatively low-cost, which can be an enabler for its wide-scale implementation. The audio signal was processed in sliding windows of 100ms lengths which fitted well with the sampling rate of GPS data.

There are certain weaknesses or limitations of the adopted procedure that need to be addressed in future work. As already mentioned, the route experiments were carried out on public roads and not in controlled environments. For this reason, experiments at specific conditions were difficult to obtain. Speed was one parameter that was heavily influenced. For example, the highway *3-15wet1* route was conducted with an average speed of approximately 100 *km/h*, while the other two highway routes had average speeds of 90 *km/h*. More experiments are required that will allow us to increase the information richness of our database. This includes experiments with other vehicles and tyres, as well as road wetness conditions.

Another research direction is the utilization of more audio channels, by using more microphones, with the purpose to apply noise cancellation techniques to reduce the effect of other noises for example the engine noise. The use of microphones with higher directivities or microphone arrays, where practically possible, could also be assessed as a mean to increase the classification accuracy.

References

[1] Abdic, I., Fridman, L., Brown, D.E., Angell, W., Reimer, B., Marchi, E. & Schuller, B. 2017, "Detecting road surface wetness from audio: A deep learning approach", Proceedings - International Conference on Pattern Recognition, pp. 3458.

[2] Acosta, M., Kanarachos, S. & Blundell, M. 2017, "Vehicle agile maneuvering: From rally drivers to a finite state machine approach", 2016 IEEE Symposium Series on Computational Intelligence, SSCI 2016.

[3] Acosta, M., Kanarachos, S. and Blundell, M. (2017). Road Friction Virtual Sensing: A Review of Estimation Techniques with Emphasis on Low Excitation Approaches. Applied Sciences, 7(12), p.1230.

[4] Al-Assi, M. & Kassem, E. 2017, "Evaluation of adhesion and hysteresis friction of rubber-pavement system", Applied Sciences (Switzerland), vol. 7, no. 10.

[5] Alonso, J., López, J.M., Pavón, I., Recuero, M., Asensio, C., Arcas, G. & Bravo, A. 2014, "On-board wet road surface identification using tyre/road noise and Support Vector Machines", Applied Acoustics, vol. 76, pp. 407-415., J.; Lopez, J.M.; Pavon, I.; Recuero, M.; Asensio, C.; Arcas, G.; Bravo, A. On-board wet road surface identification using tyre/road noise and Support Vector Machines. Appl. Acoust. 2014, 76, 407–415.

[6] ANSI S1.11: Specification for Octave, Half-Octave, and Third Octave Band Filter Sets

[7] Bezemer-Krijnen, M., Wijnant, Y. & De Boer, A. 2016, "Tyre-road noise measurements: Influence of tyre tread and road characteristics", Proceedings of the INTER-NOISE 2016 - 45th International Congress and Exposition on Noise Control Engineering: Towards a Quieter Future, pp. 2242.

[8] Bianchi, G. and Sorrentino, R. 2007, Electronic filter simulation & design, McGraw-Hill Professional, 2007, pp. 17–20. ISBN 978-0-07-149467-0

[9] Boyraz, P. & Dogan, D. 2013, "Intelligent traction control in electric vehicles using an acoustic approach for online estimation of road-tyre friction", IEEE Intelligent Vehicles Symposium, Proceedings, pp. 1336.

[10] Boyraz, P. 2014, "Acoustic road-type estimation for intelligent vehicle safety applications", International Journal of Vehicle Safety, vol. 7, no. 2, pp. 209-222.

[11] Boyraz, P.; Dogan, D. Intelligent Traction Control in Electric Vehicles Using an Acoustic Approach for Online Estimation of Road-Tyre Friction. In Proceedings of the IEEE Intelligent Vehicles

[12] Bystrov, A., Hoare, E., Tran, T., Clarke, N., Gashinova, M. and Cherniakov, M. (2017). Automotive System for Remote Surface Classification. Sensors, 17(4), p.745.

[13] Cai, M., Zhong, S., Wang, H., Chen, Y. and Zeng, W. (2017). Study of the traffic noise source intensity emission model and the frequency characteristics for a wet asphalt road. Applied Acoustics, 123, pp.55-63.

[14] Ghandour, R., Victorino, A., Doumiati, M. & Charara, A. 2010, "Tyre/road friction coefficient estimation applied to road safety", 18th Mediterranean Conference on Control and Automation, MED'10 - Conference Proceedings, pp. 1485.

[15] González-Mendoza, M., Ibarra Orozco, R.E., García Gamboa, A.L., Hernández-Gress, N., Mora-Vargas, J. & López-Pimentel, J.C. 2014, "Quadratic optimization fine tuning for the Support Vector Machines learning phase", Expert Systems with Applications, vol. 41, no. 3, pp. 886-892.

[16] Gordon, T. and Lidberg, M. (2015). Automated driving and autonomous functions on road vehicles. Vehicle System Dynamics, 53(7), pp.958-994.

[17] Johnson, S.G. & Frigo, M. 2007, "A modified split-radix FFT with fewer arithmetic operations", IEEE Transactions on Signal Processing, vol. 55, no. 1, pp. 111-119.

[18] Jonsson, P., Casselgren, J. & Thornberg, B. 2015, "Road surface status classification using spectral analysis of NIR camera images", IEEE Sensors Journal, vol. 15, no. 3, pp. 1641-1656.

[19] Kindt, P., De Coninck, F., Sas, P., and Desmet, W., "Analysis of Tyre/Road Noise Caused by Road Impact Excitations," SAE Technical Paper 2007-01-2248, 2007, https://doi.org/10.4271/2007-01-2248.

[20] Kotsakis, R., Kalliris, G. & Dimoulas, C. 2012, "Investigation of broadcast-audio semantic analysis scenarios employing radio-programme-adaptive pattern classification", Speech Communication, vol. 54, no. 6, pp. 743-762.

[21] Kotsakis, R., Kalliris, G., Dimoulas C. 2012, Investigation of salient audio-features for pattern-based semantic content analysis of radio productions, Proceedings of the 132nd Audio Engineering Society (AES) Convention, Budapest, Hungary, April 26-29, 2012, paper no. 8663.
[22] Lartillot, O., Toiviainen, P., Mir in matlab (ii): A toolbox for musical feature extraction from audio, Proceedings of the 8th International Conference on Music Information Retrieval (ISMIR 2007), Vienna, Austria, 2007 September 23-27, pp. 127-130.
[23] Li, Z., Leduc, J., Nunez-Ramirez, J., Combescure, A. & Marongiu, J.-. 2015, "A non-intrusive partitioned approach to couple smoothed particle hydrodynamics and finite element methods for transient fluid-structure interaction problems with large interface motion", Computational Mechanics, vol. 55, no. 4, pp. 697-718.
[24] Matilainen, M.J. & Tuononen, A.J. 2011, "Tyre friction potential estimation from measured tie rod forces", IEEE Intelligent Vehicles Symposium, Proceedings, pp. 320.
[25] Matlab R2017a and Classification Learner (Machine Learning Toolbox), The MathWorks, Inc., Natick, Massachusetts, United States.
[26] Niskanen, A. and Tuononen, A. (2015). Three Three-Axis IEPE Accelerometers on the Inner Liner of a Tyre for Finding the Tyre-Road Friction Potential Indicators. Sensors, 15(8), pp.19251-19263.
[27] Olofsson, B., Lundahl, K., Berntorp, K. & Nielsen, L. 2013, "An investigation of optimal vehicle maneuvers for different road conditions", IFAC Proceedings Volumes (IFAC-PapersOnline), pp. 66.
[28] Omranian, E., Sharif, H., Dessouky, S. and Weissmann, J. (2018). Exploring rainfall impacts on the crash risk on Texas roadways: A crash-based matched-pairs analysis approach. Accident Analysis & Prevention, 117, pp.10-20.
[29] Panhuber, C., Liu, B., Scheickl, O., Wies, R. & Isert, C. 2016, Recognition of road surface condition through an on-vehicle camera using multiple classifiers.
[30] Ressel, W., Wolff, A., Alber, S. & Rucker, I. 2017, "Modelling and simulation of pavement drainage", International Journal of Pavement Engineering, , pp. 1-10.
[31] Singh, K. and Taheri, S. (2014). Estimation of tyre–road friction coefficient and its application in chassis control systems. Systems Science & Control Engineering, 3(1), pp.39-61.
[32] Thorsten Joachims. 1999. Making large-scale support vector machine learning practical. In Advances in kernel methods, Bernhard Schölkopf, Christopher J. C. Burges, and Alexander J. Smola (Eds.). MIT Press, Cambridge, MA, USA 169-184.
[33] Tuononen, A. and Matilainen, M. (2009). Real-time estimation of aquaplaning with an optical tyre sensor. Proceedings of the Institution of Mechanical Engineers, Part D: Journal of Automobile Engineering, 223(10), pp.1263-1272.
[34] Witten, I., Frank, E., Hall, M. and Pal, C. (2017). Data mining. Amsterdam: Morgan Kaufmann.
[35] Yi, K., Moon, S., Lee, I., Um, J. and Moon, I. (2007). DESIGN OF A FULL-RANGE ACC WITH COLLISION AVOIDACNE/MITIGATION BRAKING. IFAC Proceedings Volumes, 40(10), pp.127-134.

[i] https://ops.fhwa.dot.gov/weather/q1_roadimpact.htm
[2] https://ec.europa.eu/transport/road_safety/sites/roadsafety/files/pdf/statistics/dacota/asr2016.pdf
[3] https://ec.europa.eu/transport/sites/transport/files/road_safety/pdf/vademecum_2015.pdf
[4] https://www.wired.com/story/driverless-cars-need-ears-as-well-as-eyes/
[5] http://www.conforg.fr/internoise2000/cdrom/data/articles/000306.pdf

A diagnostic protocol for the monitoring of bearing fault evolution based on blind deconvolution algorithms

M. Buzzoni [1], **E. Soave** [1], **G. D'Elia** [1], **E. Mucchi** [1], **G. Dalpiaz** [1]
[1] University of Ferrara, Department of Mechanical Engineering,
via Saragat 1, 44122 Ferrara, Italy
e-mail: **marco.buzzoni1@unife.it**

Abstract

The vibration contributions due to early stage bearing faults are usually weak and masked by strong background noise and mechanical interferences. In this scenario, blind deconvolution algorithms, such as Maximum Correlated Kurtosis Deconvolution (MCKD) and Multipoint Optimal Minimum Entropy Deconvolution Adjusted (MOMEDA), can be exploited for extracting impulsive patterns in rotating machines. However, their effectiveness on monitoring the progressive degradation of rolling element bearings has not yet been exhaustively studied. In this paper, the experimental data from an endurance test are investigated by means of MCKD and MOMEDA. The results in terms of incipient fault detection and fault identification accuracy are discussed from different perspectives, highlighting advantages and limits of these blind deconvolution methods. Furthermore, this research proposes an original diagnostic protocol based on a condition indicator and a non-parametric statistical threshold.

1 Introduction

One of the most frequently failures in rotating machines is represented by bearing faults. The early detection and identification of bearing faults through vibration analysis is a powerful strategy in order to prevent catastrophic failures and to reduce machine downtimes as well. However, the bearing fault identification may be very challenging since the impulsive pattern generated by periodic impacts due to localized faults is often masked by strong background noise, the dynamic response of the structure and other mechanical interferences.

Over the years, several strategies have been proposed for the detection and identification of bearing faults. The most popular signal processing technique for bearing fault identification is the envelope analysis. The envelope analysis is based on extracting the diagnostic information carried by the amplitude modulations caused by the bearing faults after filtering around a resonance frequency band in order to maximize the Signal-to-Noise Ratio (SNR) [1]. Furthermore, many other signal processing techniques have been proposed such as: second-order cyclostationary analysis [2], the (fast) kurtogram [3], Blind Deconvolution methods (BD) [4] and a number of other approaches well summarized in Ref. [5].

The proposed research work is focused on BD algorithms which can be exploited in order to extract a source exhibiting a specific statistical property only from a noisy observation (response), under the hypotheses that the system is unknown and linear time-invariant. The first BD algorithm was introduced by Wiggins [6] in the field of seismic. Its methodology, called Minimum Entropy Deconvolution (MED), blindly estimates an inverse filter which maximizes the kurtosis of the source. It should be noted that even if the name recalls the minimization of the entropy, MED is actually based on the maximization of the kurtosis. In other words, the MED extracts the source having the highest kurtosis. The main limit of this method in rotating machine diagnosis is that it tends to extract the most impulsive source rather than a pattern of periodic impulses, that is how the local faults of rotating machines appear in vibration signals.

McDonald et al. [9] improved the MED proposing a novel BD method, named Maximum Correlated Kurtosis Deconvolution (MCKD), that is rooted on a novel criterion called Correlated Kurtosis (CK). The CK is a criterion sensitive to the impulsiveness related with a certain repetition rate.

Recently, McDonald and Zao [10] proposed another BD method, called Multi-point Optimal Minimum Entropy Deconvolution (MOMEDA) that is an improvement of the BD method proposed in Ref. [11] by Cabrelli. The MOMEDA is based on a criterion called Multipoint Kurtosis (MK) and estimates an inverse filter which minimizes the least square error between the response and the target source that is assumed as a Dirac comb. The MED and the most recent methods, i.e. MCKD and MOMEDA, proved to be effective for the fault identification in rotating machines, with particular reference to gears and bearings.

In particular, the final values of the BD criteria can be exploited for assessing the bearing condition. In this direction, Sawalhi et al. [4] used the kurtosis values after performing MED in order to improve the sensitivity of kurtosis to the bearing faults. Analogously, McDonald et al. [9] exploited the CK after performing MCKD together with a threshold for surveying the condition of a multi-stage gearbox. Despite these promising applications [4, 9], the use of BD methods for monitoring the progressive damage of the system has not yet been exhaustively studied. For instance, the kurtosis is not sensitive to the bearing fault type or the indicator variance can make their interpretation difficult. Thus, these aspects should be investigated in more detail.

This research proposes a diagnostic protocol based on MCKD and MOMEDA exploiting the criteria maximized by the BD algorithms combined with a non-parametric threshold based on the Tukey's test. The core of the proposed methodology is rooted on two novel indicators, called Cumulative Correlated Kurtosis (CCK) and Cumulative Multipoint Kurtosis (CMK) that are derived from CK and MK, respectively.

These indicators overcomes the kurtosis since they allow for identifying the bearing fault being dependent on the fault frequency. Moreover, the CCK and the CMK have two valuable properties for diagnostic purposes: (i) as the sample size increases their variance decreases and (ii) being cumulative quantities, they can keep track of the progressive damage of the bearing. This methodology is then particularly fit for industrial applications which require clear data interpretation and early fault detection capability.

The proposed procedure is validated by using the run-to-failure test provided by the Center of Intelligent Maintenance System (IMS) of the University of Cincinnati [12]. The results show that the CCK and the CMK overcome the performance of the raw values of CK and MK in terms of early fault detection and identification as well as bearing damage assessment. The results are presented and discussed in order to enlighten the improvements introduced by the proposed method.

Section 2 reviews the application of BD algorithms for bearing fault identification, with a specific focus on MCKD and MOMEDA. Section 3 addresses the new diagnostic method for the detection and identification of rolling elements bearing faults through the definition of a novel condition indicator. Section 4 concerns the experimental validation by using the IMS dataset. Finally Section 5 summarizes the final remarks.

2 Bearing fault identification through Blind Deconvolution algorithms

In general, the response due to a localized bearing fault occurring in a rotating machine can be modeled as a train of impulses convolved with an Impulse Response Function (IRF) that depends on the vibration transfer path between source and excitation. A scheme about how BD works on a simplified signal model is depicted in Figure 1. The term "simplified" refers to the fact that the bearing fault signatures consist of a blend of random (cyclostationary) and periodic contributions [13] but, for the sake of simplicity, we consider only the contribution of the transfer path and the background Gaussian noise. More details about the principle of model bearing fault signatures and how to model them can be found in [14]. Figure 1 is a Single-Input-Single-Output (SISO) model that considers response x as a convolutive mixture of two contributions: (i) a repetitive train of impulses s_0 which refers to the excitation due to the local fault and (ii) a Gaussian background noise n. Note that all these quantities are a function of time. Both are convolved with

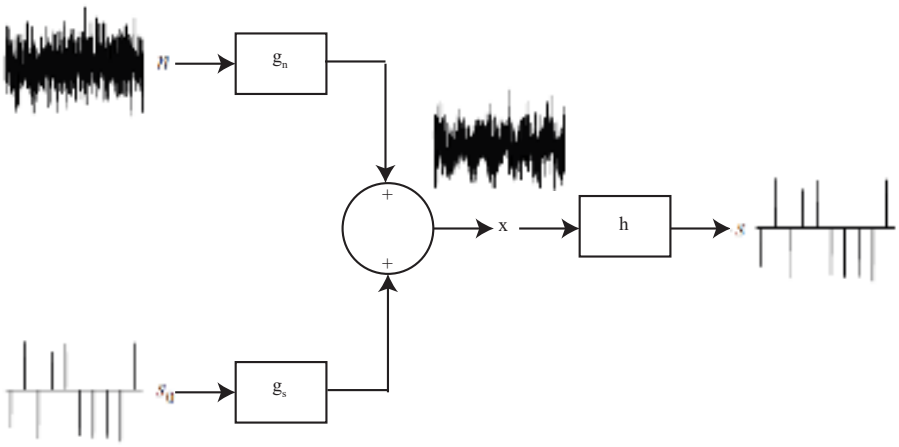


Figure 1: General scheme of blind deconvolution.

their respective impulse response functions depending on the system properties (transmission path, natural frequencies and damping). The schematic in Figure 1 can be then formalized as follows:

$$x = s_0 * g_s + n * g_n \tag{1}$$

where g_s and g_n are the IRFs related to s_0 and n, respectively and $*$ is the convolution operator.

Frequently, g_s and g_n are unknown and the goal of BD methods is to estimate the inverse filter h, assumed to be a FIR filter, that enables the extraction of s_0 just through a noisy observation x. The estimation of the source of interest, s_0, can be achieved considering an arbitrary criterion based on a prior assumption, e.g. assuming that a certain statistical property is strictly related to the target source. Therefore, the BD finds h such that:

$$s = x * h \approx s_0 \tag{2}$$

where s is the estimation of s_0 by means of h. It is important to underline that the approximation symbol refers to the fact that BD methods are not designed for the system identification but for estimating an inverse filter which extracts the source that exhibits the maximum value of a given (statistical) criterion. This research work focuses on two recent BD methods specifically designed for the diagnosis of rotating machines: the MCKD and the MOMEDA. Both criteria have been proposed considering the fact that a criterion which describes the degree of impulsiveness of a vibration signal, e.g. the kurtosis, is often inadequate to deal with mechanical fault signatures. For instance, the vibration signature of a developed bearing fault is typically described by an impulsive contribution which is characterized by a series of impulsive components repeated according to the rotational frequency and the bearing kinematics. Thus, these criteria do not consider only the impulsiveness of the vibration signature but also the repetition rate of the impulses. Thus, they are particularly fit to detect bearing faults.

2.1 Maximum Correlated Kurtosis Deconvolution

The MCKD is an iterative BD algorithm that aims to estimate the source having maximum CK. Unlike the kurtosis which measures the tailedness of a probability distribution and reaches its maximum with signals having a dominant peak, the MCKD is sensitive to signal peakedness according to a given periodicity. The

definition of CK is given in the following:

$$CK_M = \frac{\sum_{n=1}^{N}\left(\prod_{m=0}^{M} s_{n-mT}\right)^2}{\left(\sum_{n=1}^{N} s_n^2\right)^{M+1}} \tag{3}$$

where T is the impulse period and M the number of shifts. The CK combines two features typical of the localized fault signatures, i.e. high kurtosis and repetitive occurrence of the fault. It should be noticed also that the CK is a cyclostationary criterion. Indeed, the numerator of Equation (3) with $M = 1$ is nothing but the autocorrelation function of the instantaneous power of the signal. In this particular case, the CK is a measure of the degree of autocorrelation referenced to a given lag T. Therefore, the CK with $M = 1$ quantifies if the autocorrelation function exhibits periodicities at the fundamental cyclic frequency $1/T$. For this reason, the CK can be considered a cyclostationary criterion since a process which exhibits periodicities in its autocorrelation function is defined as a cyclostationary process.

It should be remarked that the CK [9] has been introduced empirically without explicit mention of its cyclostationary nature. By definition, the parameters of CK (i.e. the FIR filter length L and the number of shifts M) must be properly set in order to achieve satisfying results. In particular M has to be carefully set if MCKD is applied to mechanical vibration signals. In fact, low values of M may not encourage enough the deconvolution of sequential impulses while high values of M, from experience more than 8, could lead to numerical precision issues since the CK can assume very low values.

2.2 Multipoint Optimal Minimum Entropy Deconvolution Adjusted

The MOMEDA is a non-iterative BD method and it is an improvement of the OMEDA. In brief, the MOMEDA estimates a optimal inverse filter (in the Least Square sense) for recovering a source that approximates a target vector t, represented by a Dirac comb. The definition of the MOMEDA criterion is the following:

$$MK = \frac{1}{||t||}\frac{t^T s}{||s||}. \tag{4}$$

Target vector t drives the deconvolution by imposing both spacing and weights of the impulses to be recovered. Since t is defined as a train of equispaced impulses having unit amplitude, this criterion can be considered as a periodic one as opposed to the CK that is a cyclostationary criterion.

Since it is a periodic criterion, it naturally fits with the diagnosis of gears or in any case of periodic fault signature. Indeed, its first application regards the identification of a chipped tooth in a 2-stage gearbox [10]. As said before, bearing fault signatures exhibit second-order cyclostationarity and thus MCKD appears to be more suitable than MOMEDA for the fault detection and identification. However, a recent research [15] proved the effectiveness of MOMEDA for extracting bearing fault signatures taking into account the Case Western database.

3 Proposed diagnostic protocol

3.1 Theoretical formulation

The proposed method is based on condition indicators, namely CK and MK, capable to both detect and identify bearing faults at their early stage. Specifically, this research investigates how the final values of the criteria of MCKD and MOMEDA can be exploited as bearing condition indicators. Particular attention is devoted to verify how these indicators can be used for the real-time monitoring of bearings and for detecting trends related to the progressive degradation of the bearings.

Let $\psi[k]$ be the final value of the BD criterion evaluated from a vibration signal in the time window k. Let us assume that $\psi[k]$ is constituted of three different contributions: a constant (trend) part, a variable part and a Gaussian noise. This model can be formalized as:

$$\psi[k] = \overline{\psi}[k] + \widehat{\psi}[k] + n[k] \tag{5}$$

$\overline{\psi}$ is the constant part of ψ, $\widehat{\psi}$ is the variable part of ψ, n is the additive Gaussian noise.

Hypothesizing that the diagnostic information is retained into $\widehat{\psi}$, $\overline{\psi}$ and n de facto represent masking contributions. Furthermore, variable part $\widehat{\psi}$ is not supposed to be necessarily a monotonically increasing function. This latter property is particularly useful for the design of robust indicators due to the fact that it allows for keeping trace of the "degree of damage" taking into account the whole time history of the component under investigation.

In order to reduce the effects of $\overline{\psi}$ and n, a possible strategy is to consider the cumulative of ψ:

$$c[j] = \frac{1}{j}\sum_{k=1}^{j}\left(\bar{\psi}[k] + \hat{\psi}[k] + n[k]\right). \tag{6}$$

Equation (6) is nothing but the sum of the expected values of all the contributions of ψ. After some simple manipulations, it can be noted that (under the hypothesis of large j) the estimated expected value of n converges to zero while the estimated expected value of $\overline{\psi}$ converges to its true (constant) value. Thus, Equation (6) can be rewritten as follows:

$$c[j] = E\left[\bar{\psi}\right] + \frac{1}{j}\sum_{k=1}^{j}\hat{\psi}[k]. \tag{7}$$

where $E[\bullet]$ stands for the expected value of $\bullet$. From the physical standpoint, the constant part of ψ, $\overline{\psi}$, describes the healthy condition of the system and the variable one, $\widehat{\psi}$, reflects the occurrence of the bearing fault. At this point, after reducing the Gaussian noise contribution through the cumulative, the constant part $\overline{\psi}$ can be minimized as well by subtracting the expected value of $\overline{\psi}$ which is called $E[\bar{\psi}]^*$:

$$\beta[j] = c[j] - E[\bar{\psi}]^* = \frac{1}{j}\sum_{k=1}^{j}\hat{\psi}[k] \tag{8}$$

where $E[\bar{\psi}]^*$ is the expected value of data referenced to the healthy condition. $E[\bar{\psi}]^*$ is theoretically unknown but a reasonable estimation can be done by estimating the mean value of $\overline{\psi}$ in the very first part of the acquisition when the component is supposed to be healthy.

Indicator β describes the evolution of the bearing condition and has two important properties: (i) it is monotonically increasing – so it retains all the variations in its whole time history – and (ii) it is consistent in the sense that the random noise is reduced according to the considered number of samples. This indicator can be therefore exploited for defining a diagnostic protocol in order to monitor bearings. Specifically, when β is close to 0 it means that the variable part of ψ is negligible and thus the system is healthy. When β changes, it means that the bearing condition is changing as well and an incipient bearing fault may be occurring. For this purpose, a non-parametric statistical threshold can be used, such as the thresholds evaluated through the Tukey's method [16]: mild outlier threshold $T_{H,1}$ can be used for establishing when the bearing degradation process starts; outlier threshold $T_{H,2}$ can be used for establishing when the fault is manifest. Such thresholds are called also Tukey's fences and can be calculated by means of the following formula:

$$T_H = Q_3 + k\left(Q_3 - Q_1\right) \tag{9}$$

where Q_3 and Q_1 are the lower and upper quartiles while k is a constant that defines $T_{H,1}$ if $k = 1.5$ and $T_{H,2}$ if $k = 3$. These thresholds are computed taking account the values of β referenced to the first day

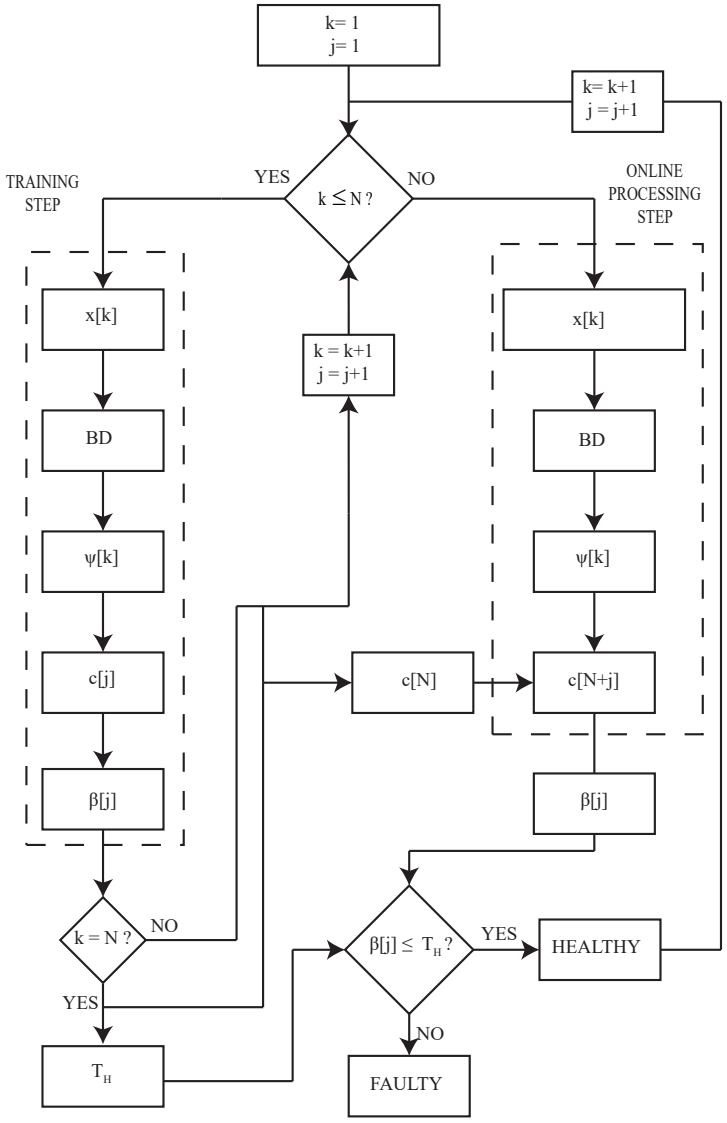


Figure 2: Flow chart of the proposed diagnostic protocol.

of test, under the hypothesis that in this time span the bearings are healthy. Note that the first hours have been discarded since the vibration signature may affected by the contribution of running-in phenomena so the values of β obtained in this time period can be biased and consequently the related thresholds can be overestimated.

The proposed diagnostic protocol is reported schematically in Figure 2 and can be summarized as follows:

1. Training step: perform the BD algorithm on $x[k]$, take the final value of the BD criterion ($\psi[k]$), compute the cumulative function $c[j]$ and then subtract the expected value in order to obtain $\beta[j]$. Repeat this step for the N time spans referenced to the healthy condition in order to compute the thresholds T_H.

2. On-line processing step: perform the BD algorithm on $x[k]$, take the criterion after maximization $\psi[k]$ and compute the cumulative function reduced by the expected value $\beta[j]$.

3. Compare the cumulative function $\beta[j]$ obtained in step 2 and the thresholds T_H calculated in step 1. If $\beta[j] < T_H$, the bearing is healthy and the procedure starts again from step 2. Otherwise, the bearing fault is detected and identified.

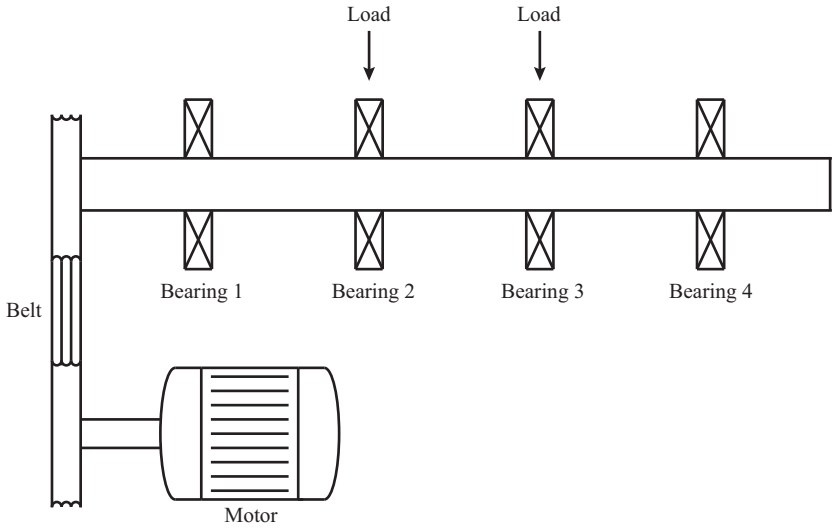


Figure 3: Experimental setup.

Note that in this paper, the novel indicator β will be called in two different ways: Cumulative Correlated Kurtosis (CCK) and Cumulative Multipoint Kurtosis (CMK). The former refers to the diagnostic procedure that exploits the MCKD while the latter refers to the diagnostic procedure that exploits the MOMEDA.

4 Experimental verification

4.1 Setup

The data used in this experimental verification have been provided by the Center of Intelligent Maintenance System (IMS) of the University of Cincinnati [12]. The test rig is composed of four bearings type Rexnord ZA-115 tied on the same shaft, as shown in Figure 3.

This test has been performed at constant speed of 2000 rpm with a load of 27.7 kN applied on bearings 2 and 3. The vibration signals have been collected by four accelerometers type $PCB\ 253B33$ mounted in radial direction. The vibration signals have been recorded with a sampling frequency of 20.48 kHz with a rate of 1 s of acquisition each 10 minutes. After 7 days, corresponding to 16.4 minutes of actual acquisition, the test has been stopped and an outer race fault, occurred in Bearing 1, has been detected.

4.2 Results and discussion

The experimental data have been investigated by means of the BD algorithms described in Section 2, specifically MCKD and MOMEDA. The final values of the BD criteria, respectively CK and MK, have been computed for signal segments of duration 1 s in order to monitor the progressive damage of the bearings during the endurance test. According to the technical report provided by the experimenters, an outer race fault has been occurred in Bearing 1. Hence, only the accelerometer placed on bearing 1 have been considered.

Figure 4 and Figure 5 depict the application of the proposed diagnostic protocol on the IMS dataset, respectively starting from MCKD and MOMEDA analysis: (a) represents the CK and MK values estimated for each signal segments of the endurance test, (b) shows the smoothed values of the previous CK and MK values, called for simplicity Smoothed Correlated Kurtosis (SMK) and Smoothed Multipoint Kurtosis (SMK) while (c) reports the values of the proposed indicator, namely CCK and CMK. All these figures include the non-parametric statistical thresholds, calculated as described in Section 3, in order to compare the time

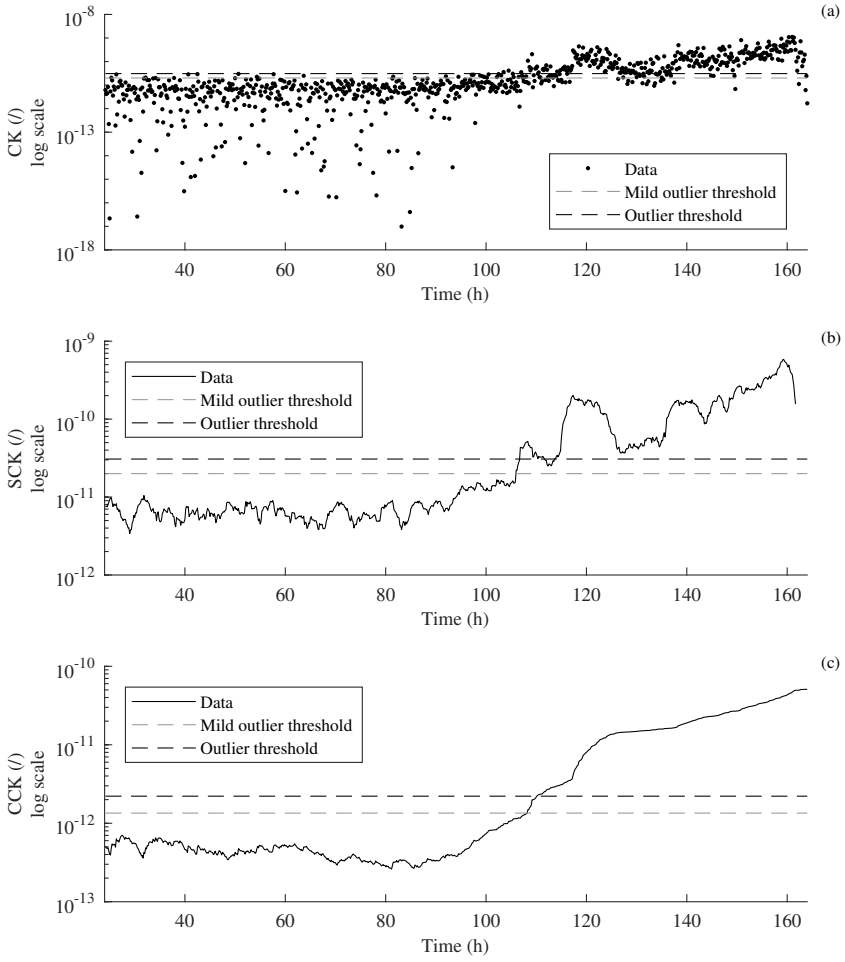


Figure 4: Application of proposed method with MCKD: (a) CK values, (b) smoothed CK values (moving average), (c) cumulative CK values. The considered prior period is referenced to the outer race bearing fault.

instant of appearance of the bearing fault. Note that the SCK and the SMK have been computed by means of moving average and that these results are referenced to the prior period related to the outer race bearing fault.

Figure 4(a) and Figure 5(a) clearly show that the trend of CK and MK is substantially constant taking into account the first hundred hours of test. Reasonably, this behavior means that the bearings can be considered healthy in this time span. Then, the values change, according to the model given in Equation (5): the variable part $\widehat{\psi}$ is no longer negligible with respect to the other contributions. Therefore, it can be noticed a time-dependent deviation with respect to the constant trend exhibited in the first part of test. From the physical point of view, it can be deduced that this variation is directly related to the appearance of a bearing fault. Moreover, the time-dependent variation of the indicators are not monotonically increasing but oscillatory. This fluctuating trend reflects the different stages of the bearing fault development and propagation which can be briefly summarized as consecutive phases of damaging and healing until the complete breakdown, as explained in Ref. [17],

In order to estimate the time instants associated to the fault appearance, the indicators must be compared with the thresholds calculated through the Tukey's method. Considering Figure 4(a) and Figure 5(a), one

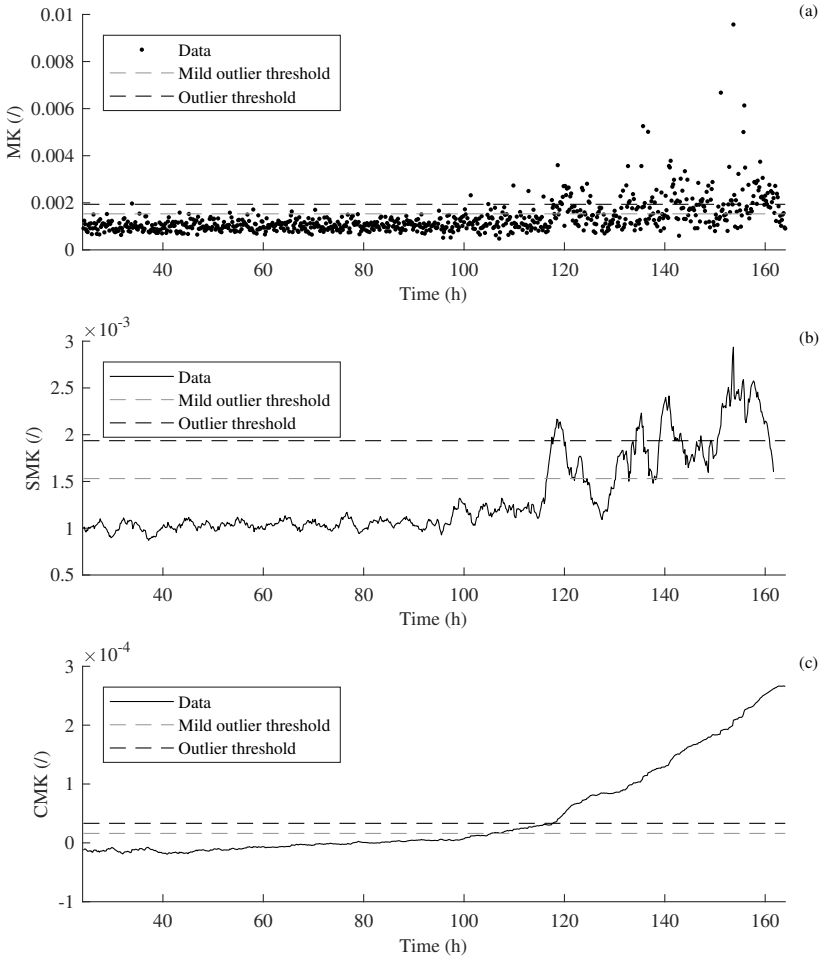


Figure 5: Application of proposed method with MOMEDA: (a) MK values, (b) smoothed MK values (moving average), (c) cumulative MK values. The considered prior period is referenced to the outer race bearing fault.

can immediately find two drawbacks on the use of the raw BD criteria, hereafter called ψ in general terms but referenced to CK and MK. The first one is related to the dispersion of the values of ψ: although the major part of the values remains below the thresholds during the early stage of the test, some values cross the threshold although no fault has occurred. The second one regards the behavior of the variable part, $\widehat{\psi}$, during the last stage of test: this variable contribution does not appear as a monotonically increasing function and thus the raw indicator ψ is not a good candidate for describing the bearing damage level since the bearing damage is irreversible.

The first issue, i.e. the variance of ψ, can be mitigated by using a smoothing technique, such as the moving average. This approach improves the results by reducing the dispersion of the indicators, as reported in Figure 4(b) and Figure 5(b). Indeed, the indicators (SCK and SMK) lie below the thresholds in the healthy stage but, during the faulty stage, is not able to represent the evolution of the fault with a strictly growing trend.

At this point, let us consider β defined in Equation (8) as the absolute error between the expected value $E[\bar{\psi}]^*$ and the actual cumulative indicator c. By definition, β has two important properties: (i) its variance

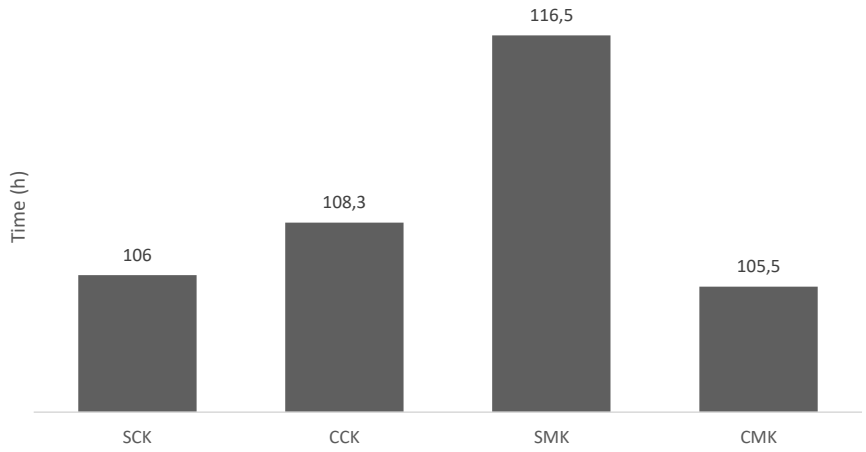


Figure 6: Time associated to the appearance of the outer race bearing fault.

decreases when the number of observation increases and (ii) it is a strictly growing function in presence of non-nil values of $\widehat{\psi}$. Figure 4(c) and Figure 5(c) show the values of CCK and CMK estimated through the procedure depicted in Figure 2. As expected, CCK and CMK return a smoother trend with respect to the raw values of CK and MK (see Figure 4(a) and Figure 5(a)). At the same time, the dispersion is reduced as well with respect to the smoothed values of CK and MK (see Figure 4(b) and Figure 5(b)). CCK and SMK show a strictly growing trend that makes the monitoring of the bearing conditions and the fault detection easier and returns also a consistent information about the overall damage level of the bearing. Therefore, this experimental verification demonstrates that β has a lower dispersion with respect to the raw indicator and that β is actually a monotonically growing function. These properties open to different scenarios concerning the industrial applications, in particular on the use of β as an indicator for the overall damage level of the bearing. Furthermore, the use of thresholds for the bearing fault detection is strongly improved thanks to the reduction of the data dispersion.

Figure 6 reports the time instants when the indicators cross threshold $T_{H,1}$ with reference to the results reported in Figure 4 and Figure 5. Considering the results related to the MCKD (first and second column of Figure 6), both SMK and CMK provide approximatively the same time, specifically 108 and 106 hours, respectively. This slight difference can be explained since MCKD is based on a cyclostationary criterion and thus is particularly fit for the early fault detection of bearings. Considering the results related to the MOMEDA (third and fourth column of Figure 6), SMK and CMK provide values that are significantly different, i.e. 116 and 105 hours, respectively. Comparing the times related to the CK and the MK (first and third column of Figure 6), it can be noticed a significant difference in favor of the CK, due to the fact that the CK is a cyclostationary indicator – thus sensitive to cyclostationary signals as the bearing fault signatures – while MK is a periodic indicator. This difference is reduced if we consider the times referenced to the CCK and the CMK (second and fourth column of Figure 6). This demonstrates that the proposed method is able to improve the effectiveness of the MK for the bearing fault detection in addition to its desired properties for the definition of a robust bearing damage indicator.

Until now, the analyses have been performed by using as a prior period the one referenced to the outer race fault. A further and necessary investigation is how the method behaves taking into account also the other possible prior fault periods, i.e. the one related to the inner race fault and the one related to the ball bearing. The results of this other analysis, in terms of CMK and CCK trend, is summarized and shown in Figure 7. According to the previous considerations, the expectation is that the estimated trends should remain below the thresholds throughout the test. It is possible to note that all the trends, after a first stage, are decreasing so we can deduce that the only fault occurred on bearing is the one on the outer race, according to what has been detected experimentally on the physical system. It is worth noting also that the CCK estimated by using

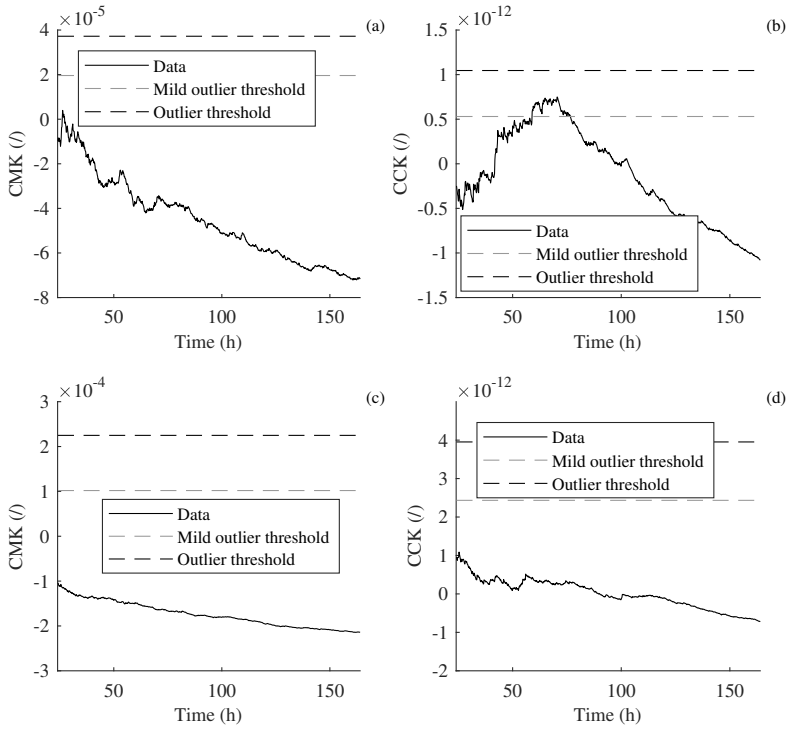


Figure 7: Application of the proposed method considering (a-b) the inner race fault frequency and (c-d) rolling element fault frequency.

the inner race fault frequency as a reference prior period (see Figure 7(b)) actually crosses the mild-outlier threshold but just for a short time span and, above all, never crosses the outlier threshold.

5 Final remarks

BD methods proved to be effective for the diagnosis of bearings. In particular, the final values of the BD criterion can represent a convenient strategy for the assessment of the bearing condition. Despite some promising applications [4, 9], the use of BD methods for monitoring the progressive damage of the system has not yet been exhaustively studied.

In order to partially fill this gap, this research focuses on the development of a diagnostic protocol based on a novel condition indicator derived from the cumulative of the criterion maximized by the BD algorithm. The fault detection is assessed by using Tukey's statistic thresholds. Specifically, the proposed indicators, i.e. CCK and CMK that are derived form the CK and MK, are sensitive to the fault frequency and keeps track of the progressive damage of the bearing. Moreover, by definition, as the sample size increases their variance decreases. This aspect represents an improvement with respect to the other similar applications reported in [4, 9].

The proposed methodology has been verified on the IMS run-to-failure test by comparing the diagnostics performance of the proposed indicator with respect to the raw values of the BD criteria. The results show that the proposed methodology improve the effectiveness of the criteria of MCKD and MOMEDA for the bearing fault detection in terms of early fault diagnosis and clarity of data interpretation.

Acknowledgements

This research work has made use of data provided by the Center for Intelligent Maintenance Systems (IMS), University of Cincinnati. The analyses have been performed through the Matlab code within the Minimum Entropy Deconvolution Multipack kindly coded and provided by Geoff McDonald.

References

[1] P. Borghesani, P. Pennacchi, S. Chatterton *The relationship between kurtosis- and envelope-based indexes for the diagnostic of rolling element bearings* Mechanical Systems and Signal Processing. Vol. 43, No. 1-2, (2014), pp. 25-43.

[2] G. D'Elia, M. Cocconcelli, E. Mucchi, and G. Dalpiaz *Combining blind separation and cyclostationary techniques for monitoring distributed wear in gearbox rolling bearings*, Proceedings of the Institution of Mechanical Engineers, Part C: Journal of Mechanical Engineering Science, Vol. 231, No. 6, (2001), pp. 1113-1128. doi:10.1006/mssp.2001.1418.

[3] J. Antoni *Fast computation of the kurtogram for the detection of transient faults* Mechanical Systems and Signal Processing. Vol. 21, No. 1, (2007), pp. 108-124.

[4] N. Sawalhi, R.B. Randall, H. Endo *The enhancement of fault detection and diagnosis in rolling element bearings using minimum entropy deconvolution combined with spectral kurtosis* Mechanical Systems and Signal Processing. Vol. 21, No. 6, (2007), pp. 26162633.

[5] R.B. Randall, J. Antoni *Rolling element bearing diagnostics-A tutorial* Mechanical Systems and Signal Processing. Vol. 25, No. 2, (2011), pp. 485520.

[6] R. A. Wiggins, *Minimum entropy deconvolution*, Geoexploration. Vol. 16, No. 1-2, (1978), pp. 2135.

[7] J Antoni and R. B. Randall, *A Stochastic Model for Simulation and Diagnostics of Rolling Element Bearings With Localized Faults*, Journal of Vibration and Acoustics. Vol. 125, No. 3, (2003), p. 282.

[8] J. Antoni, F. Bonnardot, A. Raad, and M. El Badaoui, *Cyclostationary modelling of rotating machine vibration signals*, Mechanical Systems and Signal Processing. Vol. 18, No. 6, (2004), pp. 12851314.

[9] G. L. McDonald, Q. Zhao, and M. J. Zuo, *Maximum correlated Kurtosis deconvolution and application on gear tooth chip fault detection*, Mechanical Systems and Signal Processing. Vol. 33, (Nov. 2012), pp. 237255.

[10] G. L. McDonald and Q. Zhao, *Multipoint Optimal Minimum Entropy Deconvolution and Convolution Fix: Application to vibration fault detection*, Mechanical Systems and Signal Processing. Vol. 82, (2017), pp. 461477.

[11] Carlos A. Cabrelli, *Minimum entropy deconvolution and simplicity: A noniterative algorithm*, GEOPHYSICS. Vol. 50, No. 3, (1985), pp. 393-413.

[12] J. Lee, H. Qiu, G. Yu, J.Lin, *Rexnord Technical Services, Bearing Data Set, IMS, University of Cincinnati, NASA Ames Prognostics Data Repository.*, 2007. url: http://ti.arc.nasa.gov/project/prognostic-data-repository.

[13] J. Antoni., *Cyclic spectral analysis of rolling-element bearing signals: Facts and fictions* Journal of Sound and Vibration, Vol. 304, No. 3-5, (2017), pp. 497-529.

[14] G. DElia, M. Cocconcelli, E. Mucchi *An algorithm for the simulation of faulted bearings in non-stationary conditions* Meccanica. Vol. 53, No. 4, (2017), pp. 1-20.

[15] Y. Wang, N. Hu, L. Hu, Z. Cheng, *Rolling bearing fault diagnosis based on multipoint optimal minimum entropy deconvolution adjusted technique and direct spectral analysis*, *Proceedings of The 2017 Prognostics and System Health Management Conference, Harbin, China, 2017 9-12 July*, Harbin (2017).

[16] J. W. Tukey, *Exploratory data analysis* Addison-Wesley Publishing Company, (1977).

[17] T. Williams, X. Ribandeira, S. Billington, T. Kurfess, *Rolling element bearing diagnostics in run-to-failure lifetime testing*, Mechanical Systems and Signal Processing. Vol. 15, No. 5, (2016), pp. 979-993.

Fleet-wide condition monitoring combining vibration signal processing and machine learning rolled out in a cloud-computing environment

J. Helsen[1], **C. Peeters**[1], **T. Verstraeten**[1 2], **J. Verbeke**[1], **N. Gioia**[1], **A. Nowé**[2]
[1] Vrije Universiteit Brussel, Acoustics and Vibrations Research Group (AVRG)/OWI-lab,
Pleinlaan 2, B-1050, Brussel, Belgium
e-mail: **jan.helsen@vub.be**

[2] Vrije Universiteit Brussel, Artificial Intelligence Lab (AI-lab),
Pleinlaan 2, B-1050, Brussel, Belgium

Abstract
Today, we are at the beginning of Industry 4.0. Machines are becoming increasingly sensorized and connected to the internet. Streaming data will thus be sent continuously to cloud computing data-centers. Condition monitoring techniques can leverage these huge volumes of available data to increase detection potential and insights in system behavior by long-term trending, anomaly detection and learning approaches. Additionally, the fact that data of similar machines of a fleet is collected allows for exploiting system similarity. This paper illustrates an integrated monitoring approach for the Industry 4.0 context. Our cloud processing approach is shown. Furthermore, we show an integrated failure detection and severity assessment approach. Asset performance in the fleet is used as a proxy for potential failure. Health assessment and fault localization combines state-of-the-art vibration signal processing on high frequency data ($> 10kHz$) with machine learning models trained on low frequency (1Hz) bearing temperature data to create a health score.

1 Introduction

The wide implementation of the internet all over the world has made continuous data-connectivity possible for a wide range of systems: machines, vehicles, OEMs and end-users of machines have taken this opportunity to instrument their machines for condition monitoring purposes. Today, common practice is to perform condition assessment intermittently on the different machines in a process chain. Typically, an engineer goes around in the factory and acquires measurements manually using a hand-held device. Acquisition is done from time to time for those machines that are important but non-critical. Today, permanent monitoring systems only target plant critical machines. Those monitoring systems take measurements automatically at intermittent moments in time. These measurements are then processed automatically on the monitoring device or sent to a central location for interpretation. However, these practices are changing. With the rise of Industry 4.0 and correspondingly the Industrial Internet of Things (IIoT), more and more instrumentation will be available in machines, either directly mounted by the OEM or installed during lifetime by owner-operators[1, 2, 3]. Particularly, the IIoT context brings sensors that are directly connected to the internet. As such, measurements can be transferred continuously to a cloud data-center. These can be raw measurements or data preprocessed at the edge.

These large amounts of sensor data can be used for condition monitoring purposes. In contrast to current practices using intermittent data, it will be possible to collect continuous streams of data. Such streams have both a finer granularity and longer signal length. These aspects allow to get a more detailed analysis and get a better grasp on the normal system characteristics and behavior changes a healthy machine experiences. This

is particularly interesting for modern machines designed for operation in a wide speed and load range. For these machines the range of normal operation is widening and thus also the difficulty for anomaly detection to distinguish between normal and abnormal behavior.

Nonetheless, only increasing data-amounts brings no added value. Processed data needs to be directly actionable for machine operators. As such integrated condition monitoring techniques are necessary to automatically process the data and combine the health indicators in conclusions about system condition. Long-term data allows long-term trending and anomaly detection on features extracted using signal processing techniques or from machine learning models. To get good insights in system health it is suggested to use a combination of the methods mentioned above and fuse the results into a limited number of health scores.

To grasp this Industry 4.0 facilitated opportunity offered by continuous data streams, several challenges need to be overcome. First, a balance needs to be found between data transfer to a cloud data-center and local processing on the acquisition device. Second, given that continuous streaming results in large data quantities, there is a need for automated condition monitoring approaches able to autonomously process these large amounts of monitoring data. Third, the IIoT trend makes that a wider variety of sensor data types is available for analysis. Each of these data sources requires a dedicated approach. Moreover, the resulting multitude of indicators from all these analyses need to be fused into a joint conclusion about system health by applying sensor fusion approaches.

2 Methodology

This paper addresses the opportunities and challenges linked to the Industry 4.0 monitoring trend by proposing an integrated automatic multi-level monitoring approach specifically designed for continuous data from IIoT sensors. This way of working is applicable for a multitude of systems. In this paper, we focus on rotating mechatronic machines. Moreover, the approach is structured such that it is applicable to prognosis by linking the properties of each monitoring workflow to the specifics of the failure modes. A schematic representation of the methodology is shown in Figure 1. The goal of this paper is to introduce the different techniques that are used and link them together into a single approach. For a detailed description of the different sub-aspects the reader is referred to targeted references.

The suggested monitoring approach has the following sub-aspects:

- First, the important failure modes of the system are extracted from a historical failure database. Ranking the failure modes has the advantage that the monitoring system targets the most relevant failure modes of that specific machine family. Moreover, it allows to adapt the monitoring tools specifically for each failure mode.

- Second, we exploit the fleet context for machine monitoring. Highly similar machines are combined into a fleet. System similarity is learned based on historical data. We assume these similar systems to be comparable in behavior and thus that it is possible to pinpoint underperforming machines based on machine comparison. Such underperformance is linked to either control setting problems or potential degradation of the system itself. If no control problems are known, the performance indication is used as a proxy for machines with potential health problems.

- Third, we determine features using vibration signal processing algorithms. Complex pipelines of signal processing algorithms are combined in order to extract characteristic health features. In this paper an approach for bearing fault detection is illustrated.

- Fourth, operational machine parameters, such as temperatures, pressures, are modeled using machine learning approaches combined with anomaly detection to detect abnormal behavior. The latter is captured in health indicators. Again a bearing failure detection is illustrated.

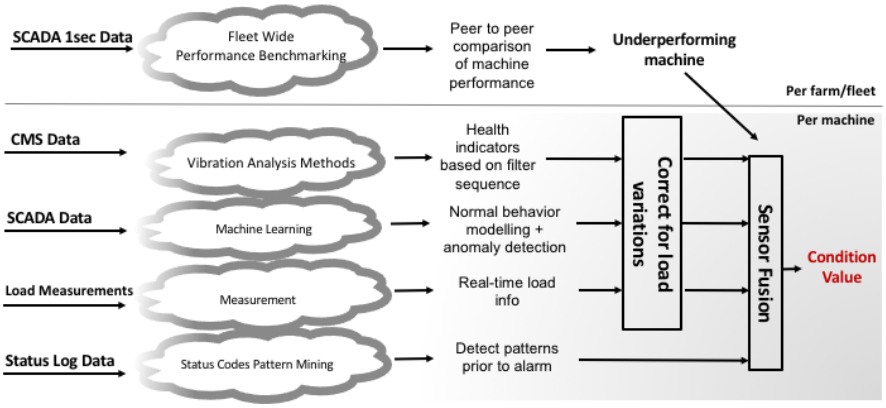


Figure 1: Monitoring approach overview

- Fifth, to take changing environmental conditions into account, loading information is used to normalize the extracted features of step three and four. In case loads are measured directly these values are used as input for machine learning models that describe and predict the variation of health features based on operational parameters. If no direct load measurements are available loading information is extracted from operational parameters originating from SCADA or other supervisory systems. Particularly for mechatronic systems the use of torque loading calculated based on motor power and RPM is a good approach to have an indication of load without the need for complex additional instrumentation.

- Sixth, status logs are used to gain additional information in the loading sequences a machine is exposed to and particularly to better understand how the controller deals with these events. Each action that a modern machine undertakes, is captured in logs. Extracting which events occur prior to machine alarms helps in better understanding what actions machines do in response to triggers from the environment, such as alarms linked to machine protection activation (e.g. converter shutdown due to overcurrent) or actions taken by external actors (e.g. emergency stop of a wind turbine after a technician pushes a stop button).

- Seven, the information and health indicators originating from the previous steps need to be integrated into a single assessment of machine health using sensor fusion approaches. A single health indicator is defined using a fusion of the different calculated indicators by model ensemble. For the machine, an overall health indicator is defined by cascading the individual failure mode alarms.

- Finally, since the availability of data for training and optimizing is a challenge for most methods, the use of virtual training data is suggested. Acceleration signal simulations containing representative faults are created in order for machine learning models to have accurate training data and to allow the configuration parameters of the physics-based signal processing methods to be optimized. This allows to maximally optimize monitoring approaches prior to usage.

3 Cloud implementation

The following subsections illustrate the integrated approach by means of several real-life examples from onshore and offshore wind turbines. The wind application is used, since it is a challenging case due to the continuously varying speed and changing loading conditions because of the variability of the wind.

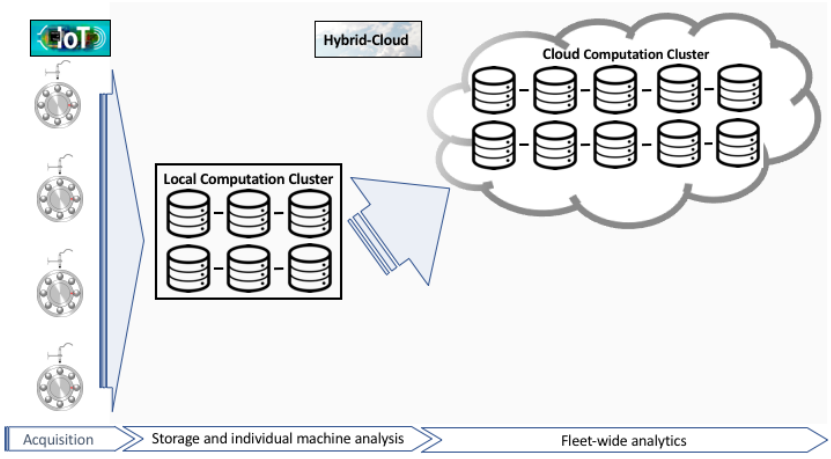


Figure 2: Cloud approach overview

3.1 Data collection

Different data sources are used in this research, ranging from vibration data, over embedded SCADA sensors, to status logs. Today, the latter two sources are collected on a wider variety of machines. However, detailed vibration measurements are typically only acquired for high-cost critical machines. In the near future, also less critical machines will be instrumented with this type of vibration sensors due to the rise of IoT. Low-cost accelerometers combined with dedicated acquisition systems will make instrumentation to be more cost-efficient allowing to monitor also lower cost machines. We anticipate this evolution. However, in this paper we focus on existing higher-cost monitoring systems and corresponding applications such as wind turbine gearboxes.

3.2 Data storage and cloud processing

In order to be able to integrate the different monitoring approaches their data needs to be made available in a central data-storage location. Figure 2 illustrates the approach that we are currently using. Sensor data is being collected by a number of sensors. These can be embedded SCADA system sensors or additionally mounted vibration sensors. Sensor data is typically collected by a data-acquisition system and then made available to external data-clients by means of standardized ODBC or OPC servers[4].

Typically, this sensor data is stored at a local centralized data-cluster. Recently, there has been a trend to move from traditional historian and SQL databases towards big data storage approaches such as Hadoop or no-sql databases [5]. In case of the offshore wind turbines, the following data-sources are combined into a single data-cluster: SCADA sensors sampled at 10-minutes internal, SCADA sensors sampled at 1 second interval, status logs, and vibration time data from the condition monitoring system [6].

In addition to storage, also dedicated data-processing is necessary. Dedicated data-processing pipelines need to be defined to transform raw sensor data into failure indicators. We opt to define dedicated pipelines for each type of failure mode. In order to keep the cost of the infrastructure under control we use a hybrid-cloud solution. Raw sensor data is processed locally at a local computation cluster close to the machines. Data-processing pipelines convert the raw sensor data into machine specific health indicators for each individual machine. The memory, CPU, and storage characteristics of the local cluster are optimized such that all standardly running analyses on the data-streams can be handled. To facilitate multi-machine analytics in the fleet context, a cloud computation cluster is used. The main goal of the cloud calculations is to combine the health features extracted for the different individual machines to compare fleet wide behavior. Additionally, Memory and CPU intensive calculations are performed in the cloud to maximally leverage these resources

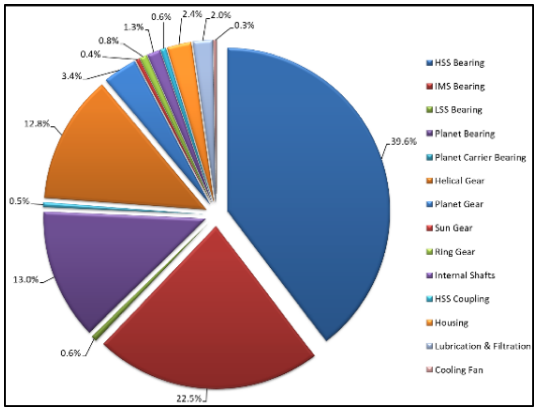


Figure 3: Failure statistics from GRC failure database [7, 8]

and minimize cost. In our case, we opt to work with the infrastructure of the Flemish Supercomputing center. Data is transferred to the cloud, used in calculations and then discarded to keep resource utilization as optimal as possible.

4 Failure database

Different failure modes for bearings and gears are illustrated in this paper. These failure modes were extracted from the Gearbox Reliability Collaborative (GRC) failure database of the National Renewable Energy Laboratory (NREL) [7, 8]. This failure database contains information about the drivetrain failure rates and specifics of the failure modes for the majority of the US wind turbine fleet. This makes it a world unique collection of data. The main US owner-operators take part in this initiative and document the failures they experience in a structured way to allow extraction of failure statistics for each failure mode. From these statistics, it was found that the most important failure modes are high speed stage (HSS) bearing axial cracking due to white etching cracks; and planet bearing failures, as shown in FIgure 3. Based on the failure mode statistics from this database, our method development focus was targeted towards the planetary stage and high speed stage (HSS) bearing and gear problems. In addition, converter switch faults are added, since these power electronic components have been substantially scaled-up and are increasingly responsible for turbine stand-still [9].

5 Fleet-wide benchmarking

To get a global overview of asset performance, fleet-wide operational monitoring is done to compare the performance of systems that are alike. Different monitoring parameters can be used. In our case, we illustrate this approach by means of an offshore wind farm example. We opt to monitor the power curve determining parameters power and rpm. Underperformance is detected by means of turbine to turbine comparison of turbines that are closely spaced and where it can be assumed that they are subjected to similar wind loading conditions. Wake effects should therefore be taken into account, as well as the influence of sensor noise should be considered. Comparison of behavior is done at each time block. If turbines start to deviate from their neighbors for long periods of time, deeper investigations are done to unveil the cause of this deviation. In general, the deviation can be related to problems with the control settings or malfunctioning of subcomponents of the turbine. In order to have sufficient insights into the dynamics of the wind turbine, we use SCADA signals sampled at 1 second time intervals.

In case of the offshore wind farm example, illustrated in Figure 4, underperformance was detected for the

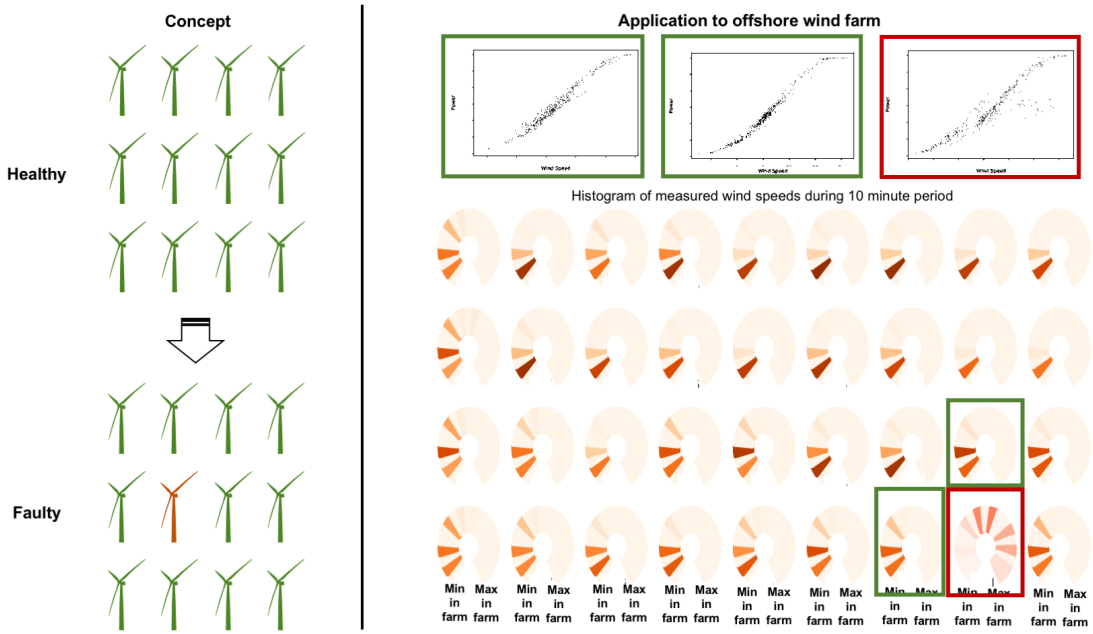


Figure 4: Fleet-wide benchmarking. Wind farm layout and exact values masked due to confidentiality.

red turbine. Prior to this time segment, the turbine was behaving similarly to its peers. The power curves for three neighboring turbines are shown (two green and one red box). These power curves were constructed using the operational data of one day. Based on the comparison of the three power curves (two green and one red) of the neighboring turbines, it can be seen that the red turbine shows significantly different behavior than the green turbines. Particularly for none-full load conditions the red turbine is underperforming, since a significant amount of operational points (dots in the power curve) is below the expected power curve.

This underperformance could be due to many factors. Further failure mode analysis unveiled that the controller was behaving strangely due to unreliable wind speed measurements. In Figure 4, the histogram of the wind speed is shown for each turbine in the farm. For most turbines, the wind speeds measured by the anemometers on the nacelle of the turbine show consistent results. For the red turbine on the other hand the wind speed measurements show high variability. In other words, the turbine controller assumes the wind speeds to be higher than is the case in reality. Thus, it will use other control settings. In this case the turbine was using a control scheme tailored for higher wind speeds (pitch control), which resulted in the turbine underperformance. Fleet-wide comparison was able to unveil this in a straightforward way.

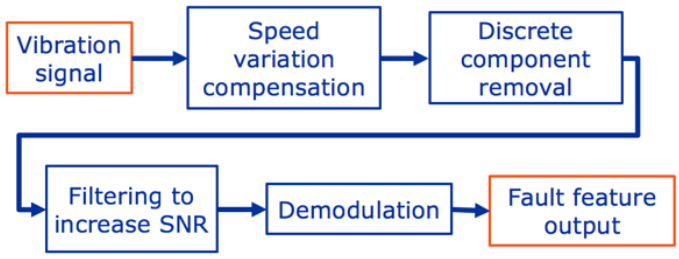


Figure 5: Schematic representation of the processing procedure for bearing failure detection

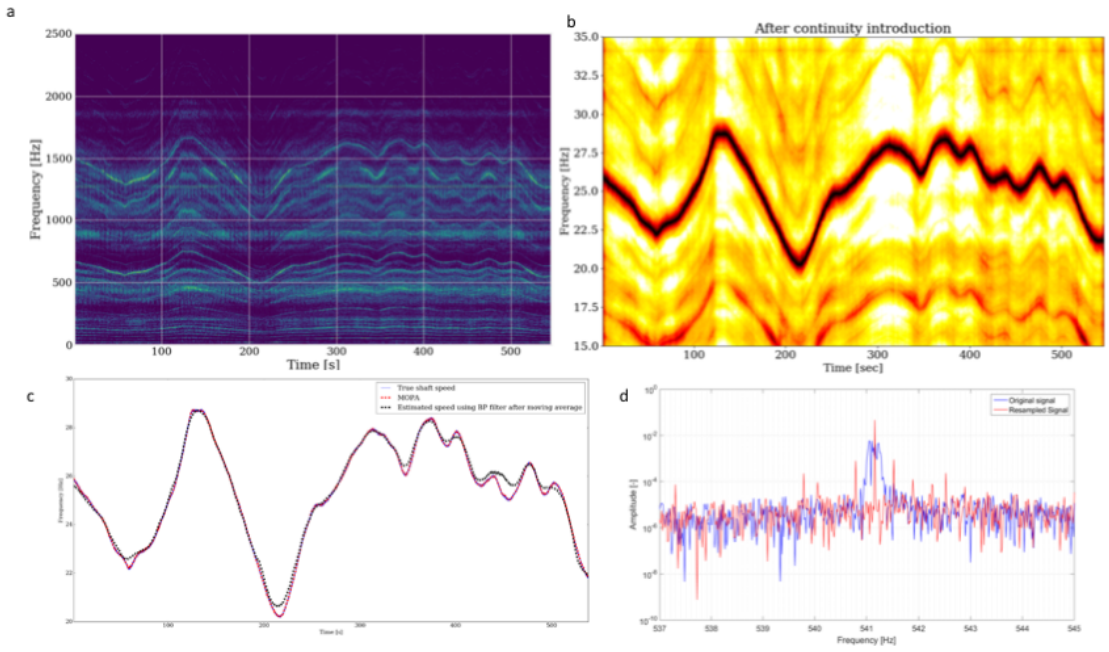


Figure 6: Speed estimation using MOPA, a) Spectrogram of CMMNO data, b) PDF map, c) estimated speed profile, d) before and after angular resampling spectra

6 Data processing for condition indicator extraction

6.1 Vibration analysis

Vibration signal processing allows for extracting complex health features from raw data[10]. Signals are processed by a sequence of data-cleaning and filtering steps. A typical flow is shown in Figure 5.
In case of wind turbine vibration signals, specific care should be given to compensation of speed fluctuations. Due to the variability of the wind, the operational speed will continuously change in the vicinity of the target value set by the controller[11]. To overcome this, the signal is transferred to the angular domain. In this domain, signals are sampled at predefined angular rotation steps instead of time periods. A such the influence of speed variation disappears. In order to be able to perform this correction, detailed knowledge of the instantaneous speed is necessary. Detailed encoders can provide this information, however, on most commercial machines only limited detail speed information is available. To tackle this problem, instantaneous speed estimation techniques, so-called virtual tacho methods, are used.

Different virtual tacho methods are available. In our monitoring approach, we opt to use the Multi-Order Probabilistic Approach (MOPA) originally developed by Leclère [12, 13]. This method makes use of multiple harmonic orders typically present in a gearbox, and assumes them to be probability density functions that can be integrated in a single probability density function describing the speed profile. It is possible to take all orders into account or choose optimal orders based on a least square optimization method. Figure 6 illustrates the use of the method on wind turbine data. The dataset originates from the International Conference on Condition Monitoring of Machinery in Non-Stationary Operations (CMMNO) condition monitoring contest in 2014 [12]. The vibration signal was measured on a gearbox housing of a wind turbine near the epicyclic gear train and sampled at 20kHz. Figure 6.a shows the spectrogram of the raw signal. Based on the spectrogram, a probability density function is constructed that combines contributions of all harmonics. Considering longer temporal periods ensures time stability in the probability density functions. The probability density function for the considered signal is shown in Figure 6.b. Extracting the most probable estimate of the speed based on this results in the speed signal illustrated in Figure 6.c. Comparison to the true speed

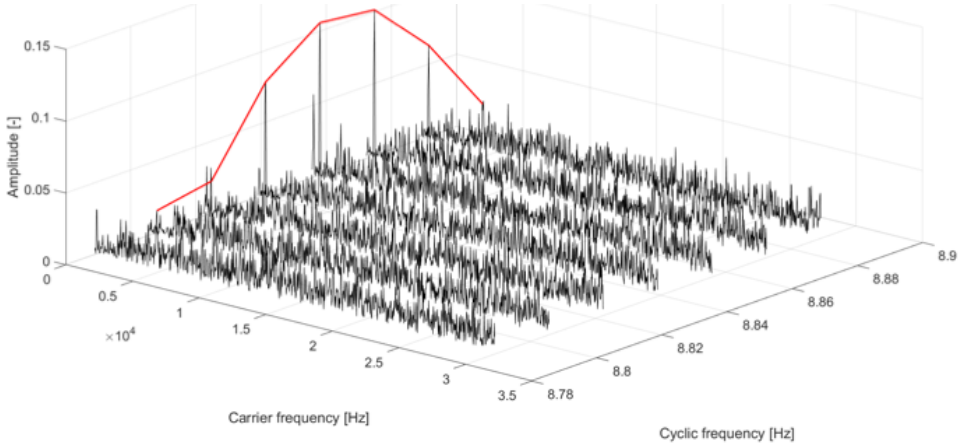


Figure 7: 2D-map of the cyclic spectral coherence applied on the vibration data of the NREL test turbine gearbox data set. An outer race fault of the planet carrier bearing is detected at its characteristic frequency of 8.84Hz around a carrier frequency of 4.6 kHz (red line)[14].

shows the high accuracy of the MOPA method, when compared to a more classical approach, such as band pass filtering. Figure 6.d. illustrates the effect of using the extracted speed to resample the signal in the angular domain. It can be seen that the smearing effect is substantially reduced.

For bearing failure detection it is necessary to remove the disturbances of the harmonic components originating from gears. Cepstrum based techniques proved to be highly effective for achieving this removal [15]. Both targeted discrete component removal as well as cepstral pre-whitening are used [16, 17]. Once the harmonic components are removed, envelope analysis allows to extract bearing failure related signal modulations [18].

Detecting bearing faults is a challenge, since the signatures linked to the bearing fault impulsive excitations are small compared to the other disturbances, particularly in the case of a multi-stage gearbox being part of a complex machine. Thus, it is necessary to perform enveloping at the optimal frequency band, where the signature is best visible. As such the use of cyclic spectral coherence is a powerful approach [19]. Determining the cyclic spectral coherence map allows to determine in which frequency band the bearing signature is optimally amplified by the structural resonances of the system. Selectively performing the envelope analysis on the strongest band can optimize the detection potential substantially. An example of such a cyclic spectral coherence map for the GRC gearbox is shown in Figure 7. In this particular case the outer race planet carrier bearing fault was clearly visible using the cyclic spectral coherence at its characteristic frequency 8.84Hz [14].

6.2 Bearing temperature analysis

Time series machine sensor data (e.g. from SCADA systems) supports the extraction of information about systems health. Depending on signal sampling rates, the corresponding granularity of this information allows to perform a finer or more rough analysis. The data streams of embedded sensors are used in an anomaly detection framework. A good example for which this can be used, is HSS bearing temperature modeling to predict bearing problems by detecting abnormal heat conditions.

Machine learning approaches (e.g. regression techniques) are used to model healthy system behavior [20]. A training data set is created. To validate the created models the training data is split in a sub-dataset used for training the machine learning model and a sub-dataset used for validation of the created model. System variability due to e.g. non-steady-state operating conditions, seasonal effects on temperature, need to be accounted for in the model. Therefore, the measured operational parameters linked to these influences, e.g.

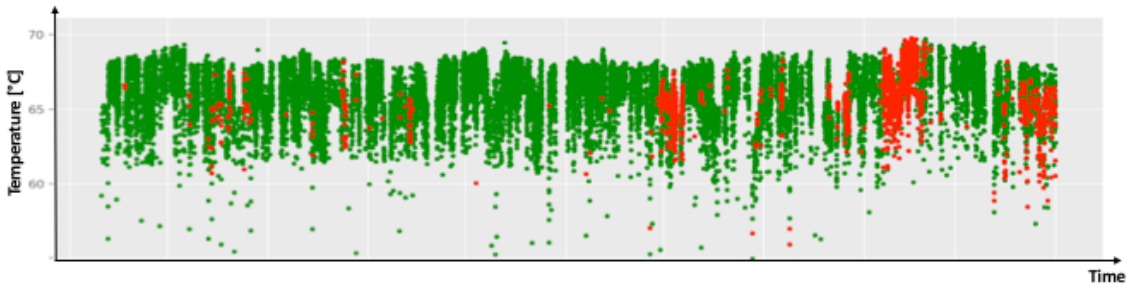


Figure 8: HSS bearing temperature signal (10 months sampled at 10-minutes intervals) classified using instantaneous alarm levels.

rpm, power, should be taken into account as inputs for the model.

To avoid overfitting of the training data and increase the robustness of the detection approach an ensemble of models is used. A variety of machine learning models is fitted to the training data. Each specific model is allocated a particular subset of the training data. Random distribution of this data is done amongst the different models. Once the training phase is over, the machine learning models are used to predict system behavior, e.g. bearing temperature. The time series for the model input parameters are provided to the model, which predicts the model output (e.g. bearing temperature). Determining the difference between this predicted output parameter and the measured values of the output parameter allow to define a residual. As long as these residual values remain small the system behaves normally. Once the residues exceed a predefined threshold an anomaly is noted. This anomaly detection approach is done for each of the machine learning models. As mentioned above, to avoid overfitting of the data an ensemble of models is used each using different parts of the data. In the final step these models vote on anomalous state. A majority determines whether the state at each timestamp is labeled as anomalous or not.

To illustrate this approach the failure of an HSS bearing is detected by means of 10 minute sampled SCADA signals. Based on the failure database this type of failure is important for wind turbine gearboxes. Given that there is an active cooling system to control the gearbox oil temperature, it is not straightforward to detect the subtle temperature changes linked to the fault. Figure 8 shows the resulting classified temperature signal for a period of 10 months. Three machine learning models are used in the ensemble. Only if all models indicate anomalous behavior, the classification is set to anomaly (red), otherwise the indication is green. Based on the colors it can be seen that there are clear time periods for which the bearing has increased temperature. During those periods the bearings were showing high anomalous behavior. These were linked to high wind loading periods that were probably enhancing the fault. At the end the temperature was consistently anomalous for several weeks before turbine shutdown. It is expected that a failure was initiated in the first long anomalous period (early winter period), worsened significantly (end winter period), started to become consistently present (early spring) and was then detected by the vibration condition monitoring system.

7 Influence of varying loading conditions

In addition to the speed fluctuation, the load is continuously changing. Particularly for the absolute comparison of feature values between different time instances this is posing problems. To overcome this issue, several approaches can be used: features can be classified based on predefined loading bins, features can be chosen that are unsusceptible to the variation in load [21], or the load information can be included after feature values were calculated. The first is often used in commercial condition monitoring systems. The last, -modeling of features and load together-, is used in the context of this paper.

A machine learning model, e.g. regression technique, is used to interlink the features with the operational parameters of the machine. The approach used, is similar to the one discussed in Section 6.2. In our case,

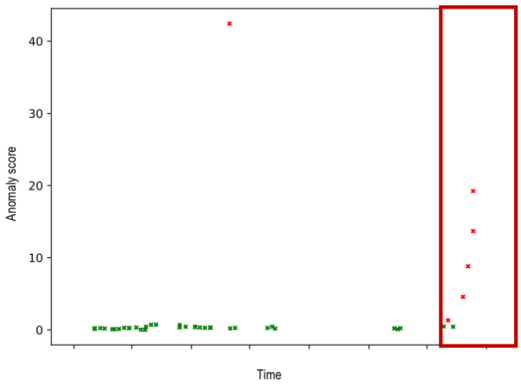


Figure 9: Modeled feature for the gearbox problem.

we use the torque load and speed of the machine under investigation. These parameters are extracted from the SCADA system. The model is trained during a period for which we know the machine has healthy conditions. Using this approach offers two advantages; one, it becomes possible to continuously compare feature values, even while machine operation is changing; second, anomaly detection is possible. Anomaly detection allows to indicate in a more objective way if feature values are changing too much and thus to indicate erroneous state.

To illustrate this concept, Figure 9 shows the resulting anomaly score for an example on real-life data. A vibration feature similar to the ones illustrated in Section 6.1 was calculated based on the vibration signals on the gearbox. Each dot indicates one sample point. It can be seen that the modeling approach succeeds in taking abstraction of the normal load and speed fluctuations and thus avoid false alarms (all dots are marked green). Towards the failure, a drastic change can be seen in the modeled feature and the anomaly is clearly marked by the red color.

8 Status log analysis

Unfavorable loading conditions play a key role in the development of failures in rotating machines. It is seen in the field that the same machine type can experience failures in one wind farm, while not at other farms. This is not solely linked to variability in the production process or material properties. In order to understand which machines are more susceptible to problems than others, we aim to gain insights in the loading each specific machine is subjected to and how this differs from machine to machine in the fleet. Linking this loading information to failure data can help in pinpointing where the designs might have flaws. To achieve this goal it is possible to use time series data of load. However, load sensing is often not present in the machine. To overcome this, torque loads can be estimated by combining power and speed information together with the inertia properties of the machine. These loading time series need to have sufficient granularity to be able to detect the specifics of the dynamic event: e.g. start-up. Often this forms a problem, since time series data is only available through SCADA data sampled at 10-minutes rates. Status log information on the other hand is stored continuously for most wind turbines. Each time the turbine performs a control action, e.g. start-up, a log of this action is stored. As such the logs are not susceptible to the loss of information due to data aggregation. These logs are often underexploited, but contain significant information with regard to system behavior and to understand loading conditions leading to failure.

The most straightforward method to benchmark turbines is a direct comparison between the occurrence rates of their status codes. This allows to pinpoint to the machine that is experiencing the most events of a certain type. Figure 10 illustrates this for the example of the frequency converter alarm. It can be seen that there is a clear outlier turbine. This turbine should be targeted for more detailed monitoring investigations. As such

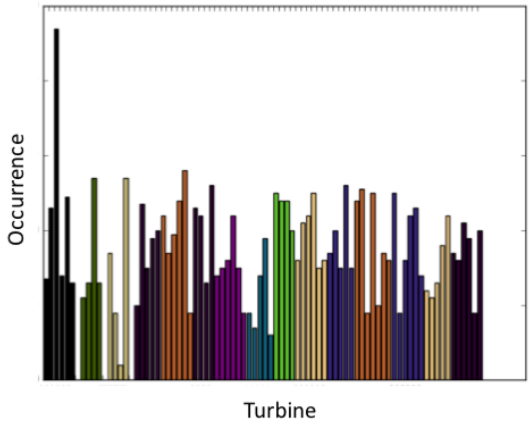


Figure 10: Converter alarm status code across the fleet.

this approach is useful to keep a global overview of the fleet and complementary to the approach discussed in Section 5. However, there is more potential for the use of status logs.

In addition to the benchmarking of machines, status log analysis can play an important role in unveiling the links between the different events that have led to an alarm or failure. Turbine controller behavior is expected to be consistent and repetitive. We assume that the machine is expected to respond consistently to similar external triggers. Thus, by extracting the status log sequences from historical data it is possible to capture this behavior. Using this approach to learn the typical sequence of events that will lead to an alarm or failure, can help in understanding which actions to take to change controller settings or modify controller design.

We suggest a pattern mining approach based on market basket analysis to extract these typical sequences. In order to strategically target certain events and to avoid an overload of unmeaningful patterns the approach uses an alarm trigger, e.g. occurrence of an alarm. Around this specific trigger, a period of data is extracted and pattern mining using the eclat algorithm is performed on this window of data [22]. Typically, we opt for a period of one day prior to or after the detection of the alarm. The extraction of these windows is done for all turbines in the fleet in order to have a sufficiently big database of events. For details on the specifics of our approach the reader is referred to [23]. We have shown that this approach was capable of detecting the typical sequence of wind turbine shutdown due to very high wind speed alarms by comparing the episodes resulting from the pattern mining approach to the expected sequences a domain expert was defining. This showed the potential of the approach in detecting and understanding normal operating events of the machine.

However, still a high number of potential patterns was produced using the approach. Thus, in order to maximize the detection potential of the approach, the data was pre-conditioned by embedding expert knowledge in the approach, so-called expert data-cleaning. Data is filtered taking into account the physical meaning of the status logs and the inherent links there are between the occurrence of certain events, e.g. electricity grid problems and changes in the voltages of the grid phases. As such, it is possible to remove all unnecessary logs and focus is put on those logs contributing to the physical understanding of the investigated failure.

To illustrate the approach, the frequency converter alarm again serves as the case. The status logs for a fleet of more than 50 turbines for more than two years serve as data-pool for the analysis. The data-set was optimized using expert data-cleaning. Windows were extracted around the status log linked to converter alarm and the remaining logs investigated. Based on the analysis we found that in some cases the wind turbine initiated a converter alarm and linked shutdown action when there was high wind instability at the site, combined with an alarm linked to the grid behavior after changing the turbine set point. This meant that the rotor speed would (briefly) increase above the expected values. Based on these events the turbine detects that there is a grid loss and responds to this by fast shutdown. This can pose high loads on the bearings and other subcomponents of the wind turbine drivetrain.

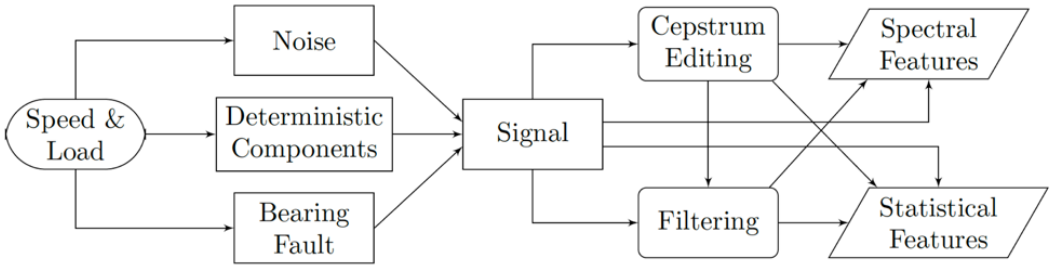


Figure 11: Overview of the proposed framework. Left side represents acceleration signal generation. Right side shows integrated automatic processing.

9 Health indicator fusion

Based on the previous sections, it is clear that detecting a failure and assessing its progression requires a combination of different approaches. Particularly to avoid false alarms and increase confidence in anomalies it is advisable to have multiple indicators. Automatic monitoring frameworks require these indicators to be converted autonomously into a single health conclusion. Different fusion approaches are available to achieve this, e.g. principal component analysis and neural networks. We opt for an approach that is more physics based and still human interpretable: the model ensemble. Indicator processing pipelines are fed with different subsets of the data. Each of the pipelines performs feature calculation and anomaly assessment. Finally, a majority vote amongst the features decides on the anomalous state of the machine. More complex voting algorithms are possible and part of future work. A health indicator is defined for each subcomponent of the machine. These are propagated to machine level to indicate the total health of the machine.

10 Detection pipeline optimization based on simulation data (digital twin)

Given that high quality failure data is rare, particularly if the machine is of a new design, usage of data-driven techniques requiring a lot of high-quality training data is a challenge. On the other hand, the physics-based signal processing techniques also have configuration parameters to be set. Based on the exact values set for these parameters the monitoring techniques can be faster or slower in detecting problems. In order to maximize the detection potential, we suggest tuning the configuration settings by calculating an optimization problem on virtual training data. These virtual simulation data are generated for the most important failure cases and allow to optimize the physics-based signal processing methods for each of these cases. As such, optimized configuration parameters can be defined for the different failure modes that we are monitoring. These configuration parameters form the basis for setting up the monitoring data-processing pipeline for each specific failure mode.

To illustrate this approach a case is illustrated that links to the failure modes investigated prior in this paper: a progressively growing bearing fault in the gearbox HSS. The fault is modeled using an acceleration signal model containing the addition of the following components: deterministic harmonic components d(t), random contributions of gears q(t), noise n(t), and the bearing fault signal b(t).

$$x(t) = d(t) + q(t) + n(t) + b(t) \tag{1}$$

These bearing signals are built up based on expertise from analysing experimental data in the past. For the case illustrated in this paper, the geometric characteristics of the NREL Gearbox Reliability Collaborative

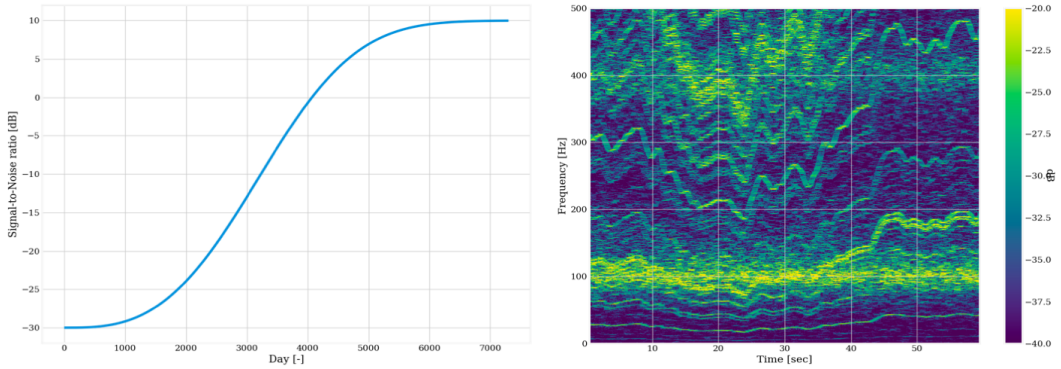


Figure 12: Left: Weibull cumulative distribution for Signal-to-Noise ratio evolution trend. Right: Spectrogram of a 60 second simulated vibration signal.

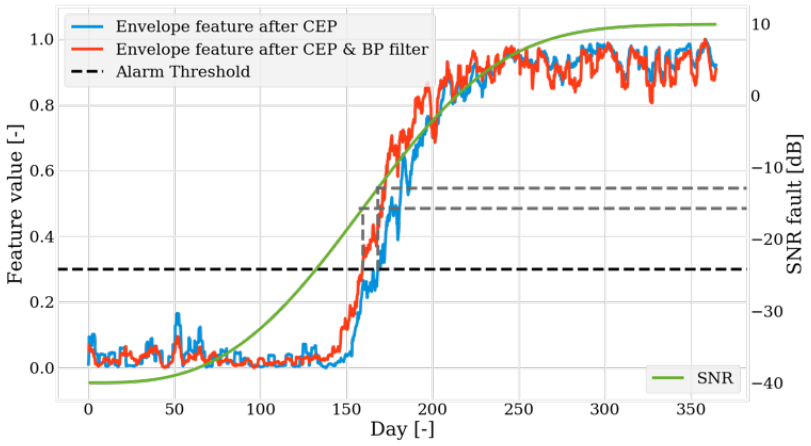


Figure 13: Envelope feature on CEP processed data before and after filtering.

(GRC) gearbox from the GRC condition monitoring round robin are used. We analysed experimental data of this gearbox in the past and its properties are public domain. For details on the approach to simulate the gearbox acceleration signals the reader is referred to [24].

In order to account for the changes in operating conditions the gearbox is subjected to, we simulate a year of measurements. We assume that several one-minute datasets are collected each day. Power level effects on the vibration signal are accounted for making the vibration signals and their modulations speed dependent. The latter allows for the signals to be binned according to overall speed and RMS values, as is the case in most wind turbine condition monitoring systems. We use an automated processing scheme on the generated data consisting of a combination of techniques as described in [14, 15, 13]. The overall schema of the approach is shown in Figure 11.

In our current example, an HSS bearing fault is simulated. Figure 12 Left shows the signal-to-noise ratio (SNR) evolution (dB) of the introduced bearing fault represented by the in reliability engineering often used degradation trend described by the Weibull distribution. The spectrogram of a representative simulated signal is shown in Figure 12 Right.

Figure 13 illustrates examples of processing pipelines and their detection potential for the bearing fault. Two envelope features trends are compared. One with and one without bandpass filtering after the cepstrum filtering (CEP). A small improvement of (approximately 3dB) is seen. Based on the simulations and experimental experience, we find it to be good practice to determine an optimal demodulation band after CEP even for

bearing faults. For further details on the analysis the reader is referred to [24].

11 Conclusions

This paper illustrated an integrated fleet-wide approach for condition monitoring. The fleet level was used to pinpoint underperforming machines. On machine level, different health indicators were defined. Both signal processing and machine learning approaches were used. To account for variations in loading and speed conditions, features were modeled using data-driven techniques. Finally, these features were fused to global health indicators with higher confidence level. To overcome the challenge of minimal training data a virtual simulation approach was suggested to optimize the settings of the different approaches and find the optimal combination of methods to form the data processing pipeline for each specific failure mode.

Acknowledgement

The authors would like to acknowledge the financial support of VLAIO (Flemish Agency for Innovation & Entrepreneurship) through the SBO project HYMOP and the SIM project MaSiWEC. Furthermore, the authors would like to acknowledge FWO for their support through the SB grant of N.Gioia and T.Verstraeten. The authors also thank support of OWI-lab and their partners for delivering the monitoring data.

References

[1] J. Lee, H.-A. Kao, S. Yang, *Service innovation and smart analytics for industry 4.0 and big data environment*, Procedia Cirp, 16:pp. 3–8, 2014.

[2] S. Jeschke, C. Brecher, T. Meisen, D. Özdemir, T. Eschert, *Industrial internet of things and cyber manufacturing systems*, in *Industrial Internet of Things*, (pp. 3–19) (Springer), 2017.

[3] M. N. Sadiku, Y. Wang, S. Cui, S. M. Musa, *Industrial internet of things*, IJASRE, 3, 2017.

[4] M. Schleipen, *Opc ua supporting the automated engineering of production monitoring and control systems*, in *Emerging Technologies and Factory Automation, 2008. ETFA 2008. IEEE International Conference on*, (pp. 640–647) (IEEE), 2008.

[5] K. Shvachko, H. Kuang, S. Radia, R. Chansler, *The hadoop distributed file system*, in *2010 IEEE 26th Symposium on Mass Storage Systems and Technologies (MSST)*, (pp. 1–10), 2010, ISSN 2160-195X, doi:10.1109/MSST.2010.5496972.

[6] J. Helsen, G. De Sitter, P. J. Jordaens, *Long-term monitoring of wind farms using big data approach*, in *Big Data Computing Service and Applications (BigDataService), 2016 IEEE Second International Conference on*, (pp. 265–268) (IEEE), 2016.

[7] S. Sheng, *Report on wind turbine subsystem reliability-a survey of various databases (presentation)*, *Tech. rep.*, National Renewable Energy Lab.(NREL), Golden, CO (United States), 2013.

[8] S. Sheng, *Gearbox reliability database: Yesterday, today, and tomorrow (presentation)*, *Tech. rep.*, National Renewable Energy Laboratory (NREL), Golden, CO., 2014.

[9] Z. Daneshi-Far, G.-A. Capolino, H. Henao, *Review of failures and condition monitoring in wind turbine generators*, in *Electrical Machines (ICEM), 2010 XIX International Conference on*, (pp. 1–6) (IEEE), 2010.

[10] E. P. Carden, P. Fanning, *Vibration based condition monitoring: a review*, Structural health monitoring, 3:pp. 355–377, 2004.

[11] W. Yang, P. J. Tavner, C. J. Crabtree, Y. Feng, Y. Qiu, *Wind turbine condition monitoring: technical and commercial challenges*, Wind Energy, 17:pp. 673–693, 2014.

[12] Q. Leclère, H. André, J. Antoni, *A multi-order probabilistic approach for instantaneous angular speed tracking debriefing of the cmmno 14 diagnosis contest*, Mechanical Systems and Signal Processing, 81:pp. 375–386, 2016.

[13] C. Peeters, Q. Leclere, J. Antoni, P. Guillaume, J. Helsen, *Vibration-based angular speed estimation for multi-stage wind turbine gearboxes*, in *Journal of Physics: Conference Series*, vol. 842, (p. 012053) (IOP Publishing), 2017.

[14] C. Peeters, P. Guillaume, J. Helsen, *Vibration-based bearing fault detection for operations and maintenance cost reduction in wind energy*, Renewable Energy, 116:pp. 74–87, 2018.

[15] C. Peeters, P. Guillaume, J. Helsen, *A comparison of cepstral editing methods as signal pre-processing techniques for vibration-based bearing fault detection*, Mechanical Systems and Signal Processing, 91:pp. 354–381, 2017.

[16] P. Borghesani, P. Pennacchi, R. Randall, N. Sawalhi, R. Ricci, *Application of cepstrum pre-whitening for the diagnosis of bearing faults under variable speed conditions*, Mechanical Systems and Signal Processing, 36:pp. 370–384, 2013.

[17] L. Barbini, M. Eltabach, J. du Bois, *Application of cepstrum prewhitening on non-stationary signals*, in *Advances in Condition Monitoring of Machinery in Non-Stationary Operations*, (pp. 275–283) (Springer), 2018.

[18] R. B. Randall, *Vibration-based condition monitoring: industrial, aerospace and automotive applications* (John Wiley & Sons), 2011.

[19] J. Antoni, *Cyclic spectral analysis of rolling-element bearing signals: Facts and fictions*, Journal of Sound and vibration, 304:pp. 497–529, 2007.

[20] J. Helsen, C. Devriendt, W. Weijtjens, P. Guillaume, *Condition monitoring by means of scada analysis*, in *Proceedings of European Wind Energy Association International Conference Paris*, 2015.

[21] K. Gryllias, S. Moschini, J. Antoni, *Application of cyclo-nonstationary indicators for bearing monitoring under varying operating conditions*, Journal of Engineering for Gas Turbines and Power, 140:p. 012501, 2018.

[22] B. Goethals, *Survey on frequent pattern mining*, Univ. of Helsinki, 19:pp. 840–852, 2003.

[23] L. Feremans, B. Cule, C. Devriendt, B. Goethals, J. Helsen, *Pattern mining for learning typical turbine response during dynamic wind turbine events*, in *ASME 2017 International Design Engineering Technical Conferences and Computers and Information in Engineering Conference*, (pp. V001T02A018–V001T02A018) (American Society of Mechanical Engineers), 2017.

[24] C. Peeters, N. Gioia, J. Helsen, *Stochastic simulation assessment of an automated vibration-based condition monitoring framework for wind turbine gearbox faults*, in *Journal of Physics: Conference Series*, vol. 1037, (p. 032044) (IOP Publishing), 2018.

Development and testing of health monitoring of the bearings of traction system of a regional train locomotive during commercial service

P. Pennacchi[1], S. Chatterton[1], A. Vania[1]
[1] Politecnico di Milano, Department of Mechanical Engineering
Via La Masa,1 – 20156 Milan, Italy
e-mail: **paolo.pennacchi@polimi.it**

Abstract

This paper presents the results of a research project in which special methods were developed and successfully applied for the health monitoring of the bearings of the traction system of rolling stocks. A prototype monitoring system was developed by the authors and installed on an Italian E464 locomotive. This regional train locomotive class is not equipped by any monitoring system for the bearings of the traction system. The locomotive has been monitored for about three years of service, during which it has undergone to a major maintenance and all the bearings of the traction system has been replaced. This allowed to examine them and to assess if damage indexes corresponded to actual faults.

A huge amount of data, in commercial service, has been collected and it was possible to assess that the overall system cannot be considered as in stationary operation, neither when the train speed is constant nor when the same track is travelled.

1 Introduction

Condition monitoring offers new opportunities to increase reliability and availability of the traction system by detecting incipient damage and preventing mechanical damages and failures.

There is a lot of literature regarding the monitoring of bearings, axles and gearboxes in industrial machinery [1]-[7]. Furthermore, experimental and theoretical studies conducted to understand and model the process of degradation of roller bearing due to wear and rolling contact fatigue [8],[9], with the aim of performing the prognosis of these components, i.e. once identified the amount of damage in the bearing, quantify the remaining useful life [10],[11] of the component.

However, the application in the railway field of health monitoring and prognostics for roller bearings and gearboxes has been limited so far [12]. Some pilot studies are available for the condition monitoring of mechanical parts in the traction equipment of Electric Multiple Units [13] and Locos [14], including the testing on suitable test rigs of intentionally damaged bearings. Therefore, there is a need to transfer to the railway sector the conspicuous body of knowledge available in other fields of industrial engineering. At the same time, it is necessary to evaluate the advantages of the use of health monitoring and prognostics techniques in the traction equipment of railway vehicles, and especially to identify the most suitable sensors for this application and to define a complete set of specifications for these devices.

The main components in the traction system for which monitoring of mechanical quantities is feasible including traction motor, gearbox and bearings.

The traction motor is a converter driven 4-pole asynchronous motor, whose rotor is mounted on two different types of bearings: a single row, deep groove ball bearing and a cylindrical roller bearing on the driven end side.

The gearbox follows the typical layout with single or double stages, with helical gearing. A coupling capable to allow the relative movements between motor and gearbox connects the helical pinion (input

shaft) of the gearbox to the electrical motor. In a single stage gearbox, there are two tapered rolling bearings for the output shaft, which can be mounted directly on the wheelset or on a hollow shaft fitted on the wheelset, two cylindrical roller bearings, and one split inner ball (four-point) bearing for the input shaft. The split inner ring ball bearing supports the axial thrust of the input shaft.

Other components of the traction equipment, particularly shafts, toothed wheels and couplings, can also be the object of health monitoring to improve the reliability of the entire system. The physical quantities of interest to be monitored for these components include vibration, speed, pressure, misalignment, shaft deflection and lubricant temperature depending on the specific needs of the health monitoring application.

The most common mechanical quantities worth of being monitored are mechanical vibrations. These can be measured on the outer surface of the casing of the motor and gearbox, at selected positions that are suitable to provide diagnostic information concerning vibrations originated by damaged bearings and/or gears. These vibration signals are then processed according to different data processing techniques [1] that are suitable to identify the signature of typical damages and possibly to quantify the degree of severity of the damage.

Other sensors maybe used for this application, such as temperature sensor, subject to similar procedure in selection. The temperature sensors extract heat from the bearings to establish any indication of failure.

Considering the feasibility in real application, the positions of interest for the sensors are both the flanges of bearings (only one side is shown in the figure) and the top on the motor case. The type and number of sensors will be determined after the characteristic analysis of the operating conditions of the traction system based on the comparisons of available sensors for this purpose in the market.

2 Monitoring for the traction system of a regional train locomotive

The E464 model (see Figure1) is an electric locomotive manufactured by Bombardier Transportation Italy at the Vado Ligure site since 1999 and intended primarily for regional and also interregional programs.

The locomotive can develop a continuous power of 3000 kW at the wheels, up to a speed of 160 km/h. The car-body rests on two bogies with two axles, each with 2 three-phase synchronous motors of 800 kW. Between the motor and the wheel axle there is a two-stage gearbox with ratios 27/55 and 26/64. The connection between these two elements is achieved through a coupling joint on which is also keyed the disc brake system.

The locomotive used for the installation of the monitoring system was built in 2008, and was close the first *"2nd level"* maintenance, scheduled to 1.2x10^{6} km.

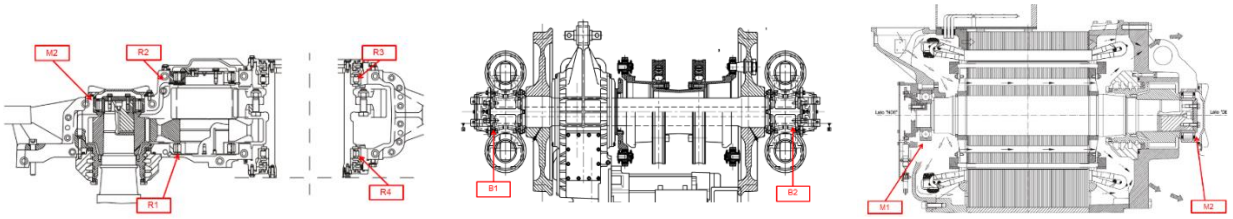
The bearings monitored are those belonging to the powertrain motor (see Figure 2c) and gearbox (see Figure 2a) and those installed on the axle (bushings) as shown in Figure 2b.

The vibrations of the bearings are measured by IEPE industrial accelerometers. A tachometer sensor is installed in correspondence of each motor for the detection of the number of revolutions. The accelerometers installed on the gearbox-motor assembly have sensitivity of 100 mV/g range up to 50 g. On the bushings, accelerometers range up to 500 g are installed, due to the higher acceleration level available on the axle. All the used sensors are dual-sensors, namely also capable of providing a temperature signal.

For each of the 4 drive units, on each gearbox-motor assembly, 5 accelerometers are placed, and 2 are located on the bushings of the axle.



Figure1: E464 regional train locomotive



a) b) c)

Figure 2: Gearbox a), axle b) and motor c) bearings.

All the signals are acquired by two data acquisition systems, one per bogie that also have the task of data logging. Acquired data are sent for processing to a central system (industrial PC) that manages the entire apparatus. The data acquisition system for the leading bogie is positioned under the car-body and the other for the trailing bogie is placed on board the car-body. The connection between the PC and the on-board system is via Ethernet cable, while wireless connection is adopted for to the device of the leading bogie (see Figure 3).

The industrial PC is placed on board the car-body, in the tail of the locomotive at the rear cargo area. It is connected to a GPRS module which allows a remote connection, and a Wi/Fi module ensures the local connection with the leading bogie acquisition system.

The function of the PC is to manage the acquisition and connectivity, to perform data storage and then to process them. Locomotive's BUS is also connected to the same network.

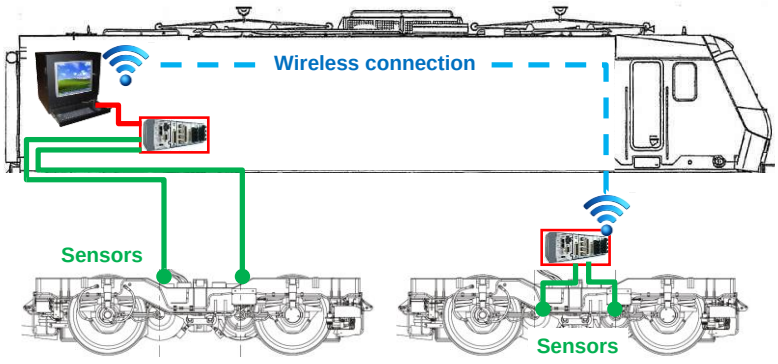


Figure 3: Connection of electronic devices.

2.1 Amplitude-based fault indicators

The fault indicators must be able to be proportional to the severity of the fault but, at the same time, they should not be very reactive to instantaneous phenomena, which are not representative of a real problem. Several indicators have been developed during the project, but for the sake of brevity, only amplitude-based ones are considered in this paper.

Amplitude-based indicators are mainly based on the Square Envelope Spectrum (SES2) diagram [[14]]. The reason why the SES2 was used instead of the simple Square Envelope Spectrum resides in the fact that, the noise affecting the diagram was smoothed, allowing thus a better and simpler identification of the peaks in correspondence of the Characteristic Faults Frequencies (CFF). Theoretical CFF can be evaluated by means of the bearing geometry.

The investigation of the faults starts from the identification of the peaks close to the CFF, paying attention to not detecting false peaks that could compromise the whole analysis. The automatic identification algorithm works in the following way: in correspondence of the CFF, with a range interval of ±5% of the value of theoretical Fundamental Train Frequency (FTF), it detects the maximum peak of the diagram, only if this peak is higher than a certain statistical threshold, which will be explained later. It should be noticed that this algorithm scans also to the 2X and 3X components, and this is a fundamental step in order to have a significant indication of fault.

The reason of the choice of that particular range amplitude, equal for each kind of damage (corresponding to Ball Pass Frequency Outer race - BPFO, Ball Pass Frequency Inner race - BPFI, FTF or Ball/roller Spin Frequency - BSF), lies in the characteristic of the interval itself: it is indeed known that FTF is generally the smallest one. For this reason, a range of ±5% of FTF represents a good compromise between the necessity of identifying the real peak frequency (that can be slightly different from the theoretical one) and of avoiding peaks detection, which are not corresponding to effective damage, but are coming from other phenomena (for example, the harmonic component of the motor or of the gearbox). It is important to note that the 1X and 2X components of the motor have been researched singularly and a specific control algorithm has been implemented in order to avoid the superposition with the CFF.

It is important to notice that if it was assumed to search the peaks in an interval range equal to ±5% of each CFF, absolutely inappropriate range length would be obtained, because they would be too large and the risk of identifying a false peak would become too high.

The statistical threshold which was previously mentioned is used in order to be sure that the detected peak is significant and that it does not come from noise contamination.

Borghesani et al. in [16] has defined this statistical threshold that allows to define a statistical limit on the amplitude of each spectral frequency. If the detected peak is higher than the punctual statistical threshold, it is possible to say that there is a probability equal to p that the considered peak represents a real damage on the bearing.

This threshold is evaluated starting from the same analytic signal of the SES2, and so it is comparable to the harmonic amplitudes relative to the fault, because they have the same uncertainty sources coming from the environmental conditions and the filtering process. Thus, it is reasonable to state that the ratio between the peak amplitude and its corresponding threshold value is not affected by these uncertainties.

The threshold is defined by the following formula:

$$Thr_{SES2} = \chi^{-1}(p,2)\left\{\frac{1}{2}\left|R_x\left(\left|\mathcal{F}(x_a^2)\right|^2\right)\right|\right\} \tag{1}$$

where R_x stands for the autocorrelation function, $\mathcal{F}(x_a)$ is the Fourier Transform of the analytic signal and $\chi^{-1}(p,2)$ is the inverse of the cumulative "chi-square" statistical distribution, with probability p with two degrees of freedom.

The coupling of Kurtosis based-indexes and envelope analysis represents one of the most successful and widespread procedure for the diagnostics of incipient faults on rolling element bearings [16].

The Band Kurtosis (BK) indicator has been defined as the ratio between the SES2 and its RMS4 on the filtered analytic signal; in formula, it can be expressed as:

$$BK = \frac{\sum SES2_{filt}}{RMS_{filt}^4} \tag{2}$$

In the previous expression, the ratio is performed on the filtered signal. The expected behaviour of the BK indicator can be described by four different phases:

- phase 1: no damage, stable indicator at its nominal value;
- phase 2: incipient fault, indicator starts to arise because of the increasing values of CFF;
- phase 3: growth of the damage, indicator stays stable due to the increase of the value of the RMS, elevated at the fourth power;
- phase 4: rapid decrease and increase of the value due to the total damage of the bearing.

On the other hand, if a simply RMS-based indicator was developed, the value of this indicator would not increase until the total seizing of the mechanical element; this cannot be accepted because the aim of the research is the detection of the fault in its incipient state and not when it has already happened, with its catastrophic effects consequences.

Since the energy component of the CFF is not focused only in its characteristic frequency, the RCC parameter has been defined to overcome this problem. The reason of the smearing of the energy component of the harmonics is mainly due to the leakage effect: this causes an error on the Fourier Transform, that considers the signal as periodic.

The RCC indicator has been defined by Borghesani et al. in [16], and it is:

$$RCC = \frac{\sum_{k=q}^{r} SES2_{filt}[k]}{\sum SES2_{filt}} \tag{3}$$

This indicator performs the ratio between the sum of each component near the considered CFF and the sum of the totality of the signal; q and r are respectively the lower and upper limit in which the CFF have to be searched.

The characteristic property of this indicator is its readiness: it is indeed able to detect a problem even before the BK indicator, thus allowing a better and earlier detection of the possible faults and allowing in this way a correct scheduling of the maintenance interventions.

2.2 Condition monitoring results

In this section the results of the whole analysis will be presented. Afterwards, a critical analysis on the state of the bearings will be performed, comparing the results of the previously presented indicators with the actual state of health of the bearings evaluated during the visual inspection after the maintenance operation in November 2015 in which all the bearings have been removed and replaced with new ones.
Moreover, the comparison between the results of the analysis performed on the 2015 data with the results of the analysis of the 2016 data will be proposed.

For the sake of brevity, only the results of the NDE bearing of the motor unit 4 (sensor SM41A) will be shown.

The trends assumed by the indicators for each type of damage are shown in Figure 4, where 2015 data and 2016 data are separated by a black line. It is necessary to remember that the reported diagrams are the moving averages of the indicators; this has been done in order to reduce the negative effects of some outlier values and to obtain more significant results.

The windows length of the moving average has been set as 50 samples for the 2015 data and 40 samples for the 2016 ones. The total number of the analyzed files is 605 for 2015 and 553 for 2016.

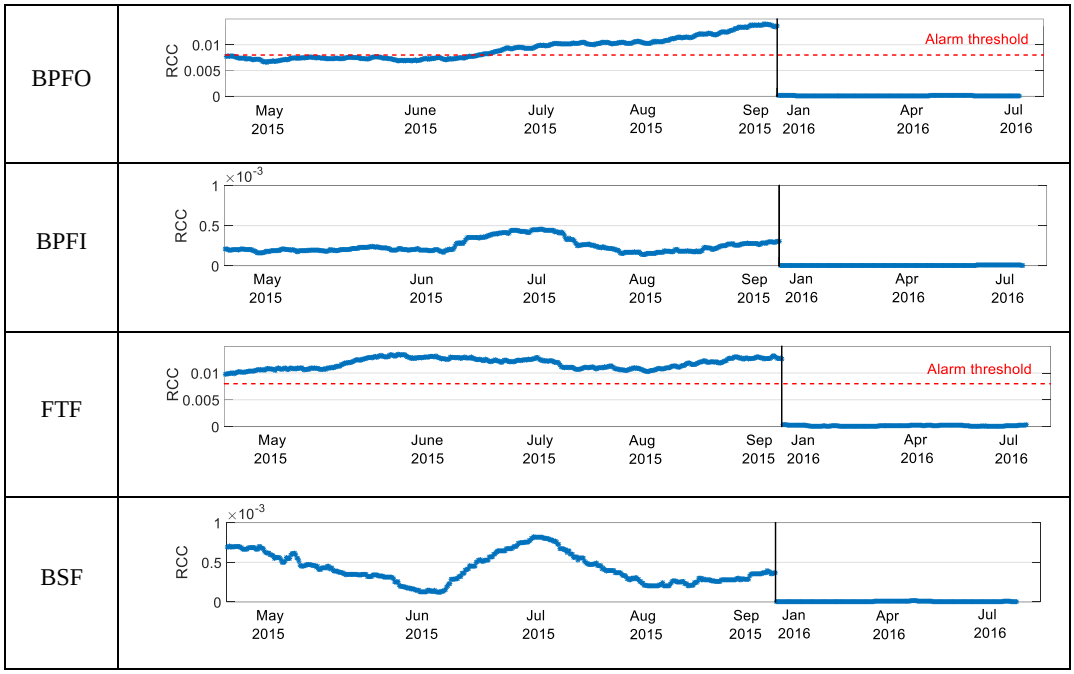


Figure 4: Fault indicator results from sensor SM41A.

By looking at the RCC diagrams shown in Figure 4, it is possible to observe:

- the presence of a serious damage on the outer race (BPFO diagram) of the bearing in the year 2015 with an evident upward trend. This means that this indicator was able to detect the increase of the fault over the time, and this can be useful for prognostics considerations.
- it is reasonable to think that no serious damage of the inner race (BPFI diagram) was present in the 2015; no threshold alarm was reported since it would have a excessive high magnitude respect to the data values;
- the presence of a serious damage on the cage (FTF diagram) of the bearing for the year 2015. Even if no trends can be clearly found, RCC was extremely higher than the threshold limit; this allows to say without doubt that a non-negligible problem of the FTF type was present, as it has been confirmed by the observation of the bearings performed during the maintenance operation of November 2015 and shown in Figure 5.



Figure 5: Outer ring and cage damages as resulted from the inspection perfomed during the maintenance operations in November 2015.

As for the outer race, no significant damages could be found by the inspection of the RCC related to BSF diagram, as reported in Figure 4; the not-null value can be attributed to the normal wear of their lifecycle. The only thing that can be noticed is a slight periodic trend. One can notice that no threshold alarm was reported since it would have excessive high magnitude respect to the data values.

3 Conclusions

This paper shows the preliminary results of a long-lasting campaign of experimental tests, which aimed to apply a condition monitoring system for the traction system of locomotives for regional passenger service.

Firstly, the monitoring system, which has been designed and developed specifically for this locomotive class is described. After the system was built and installed on the locomotive, it continued its commercial service until the second level maintenance, when the bearings of the traction system were disassembled and inspected.

Some damage indexes, which are independent of the operating conditions of the system, have been developed on purpose and have been tested on the vibration measurements acquired during the operation of the locomotive. By analyzing the behavior of these indexes, and the definition of suitable threshold indexes, it was possible to diagnose some damages that were then actually found during the inspection of the bearings

References

[1] Randall, R.B., Antoni, J.: Rolling element bearing diagnostics-A tutorial. Mechanical Systems and Signal Processing 25(2), 485-520 (2011).
[2] Borghesani, P., Ricci, R., Chatterton, S., Pennacchi, P.: A new procedure for using envelope analysis for rolling element bearing diagnostics in variable operating conditions. Mechanical Systems and Signal Processing 38 (1), 23-35 (2013).
[3] Borghesani, P., Pennacchi, P., Randall, R.B., Sawalhi, N., Ricci, R.: Application of cepstrum pre-whitening for the diagnosis of bearing faults under variable speed conditions. Mechanical Systems and Signal Processing 36 (2), 370-384 (2013).
[4] Pennacchi, P., Ricci, R., Chatterton, S., Borghesani, P.: Effectiveness of MED for fault diagnosis in roller bearings. Springer Proceedings in Physics 139, 637-642 (2011).
[5] Pennacchi, P., Chatterton, S., Vania, A., Ricci, R., Borghesani, P.: Experimental evidences in bearing diagnostics for traction system of high speed trains. Chemical Engineering Transactions 33, 739-744 (2013).
[6] Borghesani, P., Ricci, R., Chatterton, S., Pennacchi, P.: Fault symptoms of rolling element bearings under variable operating conditions: A multi domain analysis. In: Proc. of the ASME Design Engineering Technical Conference (PARTS A AND B), vol. 1, pp. 177-183. Chicago (2012).
[7] Ricci, R., Borghesani, P., Chatterton, S., Pennacchi, P.: The combination of empirical mode decomposition and minimum entropy deconvolution for roller bearing diagnostics in non-stationary operation. In: Proceedings of the ASME Design Engineering Technical Conference 1 (PARTS A AND B), Vol. 1, pp. 723-730. Chicago (2012).
[8] El-Thalji, I., Jantunen, E.: A descriptive model of wear evolution in rolling bearings. Engineering Failure Analysis, 45, 204-224 (2014).
[9] Waldron, W.D.: Railcar roller-bearing failure-progression tests. Lubrication Engineering 36(9), 534-540 (1980).
[10] Ben Ali, J., Chebel-Morello, B., Saidi, L., Malinowski, S., Fnaiech, F.: Accurate bearing remaining useful life prediction based on Weibull distribution and artificial neural network. Mechanical Systems and Signal Processing 56, 150-172 (2015).
[11] Loutas, T.H., Roulias, D., Georgoulas, G.: Remaining useful life estimation in rolling bearings utilizing data-driven probabilistic E-support vectors regression. IEEE Transactions on Reliability 62(4), 821-832 (2013).

[12] Ferreira, J.L.A., Balthazar, J.C., Araujo, A.P.N.: An investigation of rail bearing reliability under real conditions of use. Engineering Failure Analysis 10(6), 745-758 (2003).
[13] Pennacchi, P., Bruni, S., Chatterton, S., Borghesani, P., Ricci, R., Marinis, D., Didonato, A., Unger-Weber, F.: A Test Rig for the Condition-Based Maintenance Application on the Traction Chain of Very High Speed Trains. In: Proc. of 9th World Congress on Railway Research - WCRR, pp. 1-11, Lille, France (2011).
[14] Chatterton, S., Pennacchi, P., Vania, A., Borghesani, P.: Architecture of the Monitoring System for Traction System Bearings of a Regional Locomotive. Mechanisms and Machine Science 21, 455-464 (2015).
[15] Randall, R.B., Antoni, J., Chobsaard, S.: The relationship between spectral correlation and envelope analysis in the diagnostics of bearing faults and other cyclostationary machine signals. Mechanical Systems and Signal Processing 15(5), 945-962 (2001).
[16] Borghesani, P., Pennacchi, P., Ricci, R., Chatterton, S.: Testing second order cyclostationarity in the squared envelope spectrum of non-white vibration signals. Mechanical Systems and Signal Processing 40, 38-55 (2013).
[17] Borghesani, P., Pennacchi, P., Chatterton, S.: The relationship between kurtosis – and envelope – based indexes for the diagnostic of rolling element bearings. Mechanical Systems and Signal Processing 43, 25-43 (2014).

A novel multi-harmonic demodulation technique for instantaneous speed estimation

C. Peeters[1,*], **J. Antoni**[2], **N. Gioia**[1], **P. Guillaume**[1], **J. Helsen**[1]
[1] Vrije Universiteit Brussel, Department of Mechanical Engineering,
Pleinlaan 2, 1050, Elsene, Belgium
[2] Univ Lyon, INSA-Lyon, Laboratoire Vibrations Acoustique, F-69621 Villeurbanne, France
[*]e-mail: **cedric.peeters@vub.be**

Abstract
Perhaps the most used approach for vibration-based instantaneous angular speed estimation is based on phase demodulation of a shaft-speed related harmonic. While this approach can deliver very accurate IAS estimations in cases where such a single, constantly present, and dominant harmonic is existing, there are ample cases where this approach has its limitations regarding applicability. In complex rotating systems, the harmonics are not necessarily all harmonically related, causing crossing orders and skewing the extracted instantaneous phase. Additionally, such systems often operate in strongly varying conditions which can cause harmonics to fade into the noise. In order to more adequately utilize the amount of information contained within the vibration signal, this paper proposes the use of a demodulation method that jointly exploits multiple harmonics instead of only one. The proposed approach takes advantage of the multitude of harmonics typically present in physical systems and promises to be more robust to changing operating conditions.

1 Introduction

Nowadays, vibration analysis has become one of the primary tools in condition monitoring of rotating machinery. While the implementation of monitoring and diagnosis schemes is advancing [1, 2], there are still major scientific improvements to be made for it to evolve into a fully mature technology. Many analyses are currently still being done manually by a domain expert and often the available knowledge with which decisions regarding maintenance are made, is far from complete. Therefore, understanding the machine and component behavior is essential to advance the signal processing and data analysis methodologies used in condition monitoring. One of the problems that has received a lot of attention over the past two decades is the presence of speed variation in measured vibration signals. The importance of an accurate speed estimation scheme is underlined by the existence of a special issue on Instantaneous Angular Speed processing and angular applications in MSSP [3] and of a conference dedicated solely to condition monitoring in non-stationary operations. This paper focuses on estimating the IAS based on the information contained within the vibration signal. While it is possible to utilize the IAS itself as a form of indicator for the condition of the machine, this typically involves installing a high-frequency encoder [4, 5, 6] in order to reach the required accuracy of the IAS to be able to detect small faults. Analyzing signals in the angular domain is one of the main reasons why most condition monitoring procedures include speed estimation.
The two techniques that are compared in this paper are based on phase demodulation of the harmonic orders in the vibration signal. Speed estimation through phase demodulation has proven itself already multiple times in the past to be a fairly reliable way to obtain accurate instantaneous angular speed estimations [7, 8, 9, 10, 11]. It only requires a single well-excited and speed related harmonic order with preferably no crossing orders and it is also very easy to implement. Despite its popularity, the possibility to employ more than one harmonic simultaneously in the demodulation has not yet been investigated. This paper investigates

the potential advantages of using a multi-harmonic demodulation approach compared to the single harmonic approach.

2 Methodology

The method proposed in this paper is based on the idea of extending phase demodulation of just a single harmonic to multiple harmonics. The name of the technique is therefore coined as the Multi-Harmonic Demodulation method (MHD). The method does require an a-priori rough estimate of the speed (and is partly inspired by Ref.[10]).

2.1 Multi-harmonic demodulation

To find an expression of the speed that takes into account multiple harmonics, the signal is considered to be a sum of a set of K complex harmonic signals $x_k(n)$ with noise:

$$x(n) = \sum_{k=1}^{K} A_k(n) e^{j(\alpha_k \theta(n) + \phi_k)} + \nu_k(n) \tag{1}$$

with n being the sample number, k the harmonic number, K the total number of harmonics, A the amplitude, α the harmonic order, ϕ the constant phase, θ the instantaneous angle of rotation. For one harmonic k this becomes:

$$x_k(n) = A_k(n) e^{j(\alpha_k \theta(n) + \phi_k)} + \nu_k(n) \tag{2}$$

Calculating the corresponding derivatives $\dot{x}_k(n)$ (the notation means a sample of the time derivative) gives:

$$\dot{x}_k(n) = \dot{A}_k(n) e^{j(\alpha_k \theta(n) + \phi_k)} + A_k(n)(e^{j(\alpha_k \theta(n) + \phi_k)} j \alpha_k \dot{\theta}(n)) \tag{3}$$

Multiplying with the conjugate of $x_k(n)$ removes the unwanted exponentials:

$$x_k^*(n) = A_k(n) e^{-j(\alpha_k \theta(n) + \phi_k)} \tag{4}$$

$$\dot{x}_k(n) x_k^*(n) = \dot{A}_k(n) A_k(n) + A_k^2(n) j \alpha_k \dot{\theta}(n)) \tag{5}$$

Restructuring of the equation to find $\dot{\theta}(n))$:

$$\dot{\theta}(n)) = (\frac{\dot{x}_k(n) x_k^*(n)}{\alpha_k A_k^2(n)} - \frac{\dot{A}_k(n)}{\alpha_k A_k(n)}) j \tag{6}$$

It can be assumed that usually the rate of amplitude variation $\dot{A}_k(n)$ is quite slow compared to the amplitude values themselves, therefore the second term within the brackets becomes very small compared to the first one so Eq.6 can be simplified to:

$$\dot{\theta}(n)) = \frac{\Im\{\dot{x}_k(n) x_k^*(n)\}}{\alpha_k |x_k(n)|^2} \tag{7}$$

Eq. 7 can also be obtained by directly taking the imaginary part of Eq. 5.

Doing the same derivation but for all harmonics is not difficult and can be achieved by adding again the summation over all harmonics K in the signal:

$$\sum_{k=1}^{K} x_k(n) = \sum_{k=1}^{K} A_k(n) e^{j(\alpha_k \theta(n) + \phi_k)} + \nu_k(n) \tag{8}$$

This results in almost the exact same equation as for one harmonic but simply summed for all harmonics:

$$\dot{\theta}(n)) = \frac{\sum_{k=1}^{K} \Im\{\dot{x}_k(n) x_k^*(n)\}}{\sum_{k=1}^{K} \alpha_k |x_k(n)|^2} \tag{9}$$

The advantage of this formulation is to embody several harmonics in the demodulation and, as compared to classical demodulation based on the analytic signal, to guarantee a finite variance because the denominator has a low probability of approaching zero. This reduces the need to do an a-posteriori smoothing of the resulting speed profile (which is often necessary for standard single harmonic demodulation). For a single harmonic, a band-pass filter is typically defined based on the minimum and maximum expected frequency of that harmonic. Due to overlapping harmonic content, this approach limits the maximum bandwidth of such a band-pass filter and thus the maximum amount of speed fluctuation. This can be mitigated by using a windowed band-pass filtering approach. For the multi-harmonic demodulation method as proposed above, this overlap issue can be avoided. In practice, the complex harmonic signals $x_k(n)$ can be obtained by complex demodulation using a rough speed estimation. This way the harmonics get shifted towards zero frequency (DC) and one can employ a simple and more narrow low-pass filter for every harmonic. The required a-priori rough speed can be obtained in multiple ways that require little input, e.g. using maximum tracking in the spectrogram. Using the rough speed for the complex demodulation does mean that when calculating $\dot{\theta}$ as specified in Eq.7, the result is the deviation of the instantaneous frequency of the estimated speed compared to the rough speed. Another reason to do complex demodulation plus low-pass filtering prior to using the formula in Eq.7 is because of the differentiation involved. Differentiating filters usually increase high-frequency noise as can be seen from their transfer function. Close to zero frequency they have a linear response and the influence of the multiplication with the frequency in the spectral domain is reduced when combined with low-pass filtering. An example of the transfer function magnitude responses for four differentiation schemes are shown in Fig.1. In this paper a simple first order difference is employed since it has the lowest computation time and the produced results do not depend significantly on the type of differentiation.

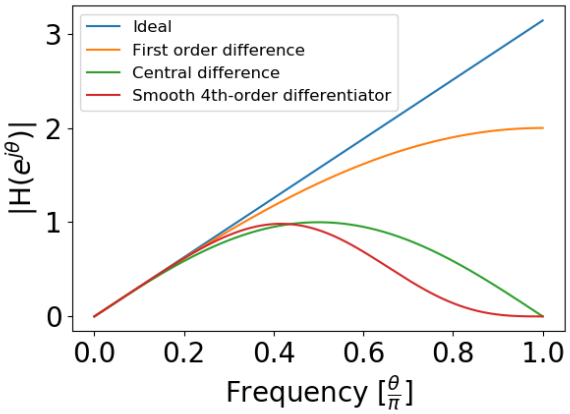


Figure 1: Magnitude responses of four differentiators.

2.2 Single harmonic instantaneous phase demodulation

The method that is used for comparison of the MHD method on the experimental data is straightforward and is based on using an ideal band-pass filter around a well-separated, high SNR harmonic of the rotation speed. After defining the optimal lower and upper cutoff frequencies for the band-pass filter, the harmonic is filtered out of the complex spectrum and translated around zero frequency. Next, the complex band-pass filtered spectrum is inverse Fourier transformed to the time domain. The angle is then unwrapped of the

complex signal after addition of the demodulation frequency to obtain the instantaneous phase. Finally, the instantaneous angular speed is estimated based on the phase variation.

3 Experimental application

To illustrate the performance of the proposed multi-harmonic demodulation method, a comparison is made with the conventional single harmonic demodulation (SHD) method on experimental wind turbine gearbox vibration data. This data set originates from the diagnosis contest held in light of the International Conference on Condition Monitoring of Machinery in Non-Stationary Operations (CMMNO) in 2014 [12].

The vibration signal used for this analysis was measured on the gearbox housing of a wind turbine near the epicyclic gear train and sampled at 20 kHz. The goal was to estimate the IAS of the high-speed shaft (carrying gear #7 in Fig.2). This estimate was then compared with a reference speed signal measured by an angle encoder. The length of the measurement was approximately 550 seconds at a sample rate of 5 kHz. The spectrogram of the measurement can be seen in Fig.3 (generated using a Hanning window of 1 second and 50% overlap).

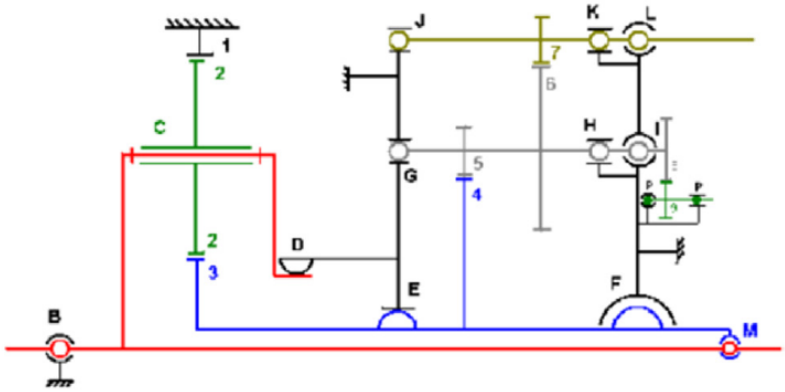


Figure 2: Visualization of the wind turbine gearbox used in the CMMNO 2014 diagnosis contest.

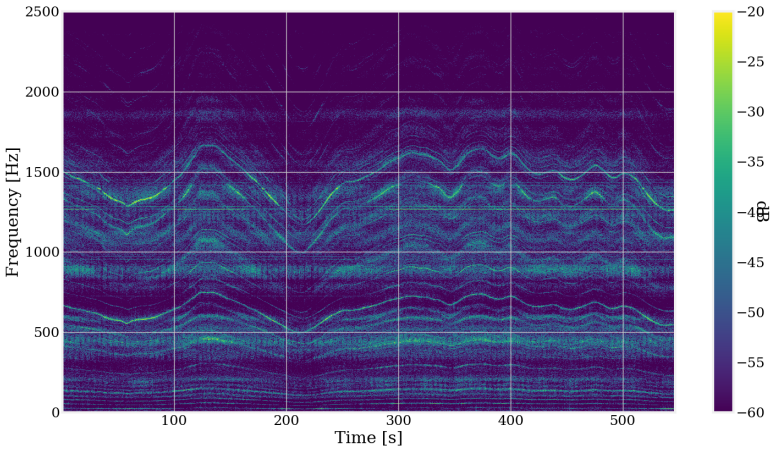


Figure 3: Spectrogram of the CMMNO 2014 diagnosis contest data.

Table 1: Fundamental orders related to high-speed shaft.

Gear pair	Order value
1	1
2/3,1/2	1.025459229
4/5	5.316666667
6/7	29
8/9	15.225
10/11	6.619565217

4 Results & Discussion

Since the measured signal is so long and contains strong speed fluctuations, the single harmonic demodulation (SHD) is performed on windowed parts of the vibration signal. The signal is split up into windows of 20 seconds with an overlap of 50%. The obtained speed profiles of overlapping sections are averaged together using a weighted average based on a Hanning window with its center in the middle of the window. This is done to reduce the influence of the end effects associated with using an ideal FFT band-pass filter. The second harmonic of the high-speed shaft is chosen for the demodulation since it has a high SNR and no crossing orders. Also other teams in the CMMNO contest chose this harmonic due to the good results they obtained using it [12]. The second harmonic is also utilized for the rough speed estimation required by the multi-harmonic demodulation method. A simple maximum tracking is employed in this case. The harmonics used as input for the multi-harmonic demodulation method (MHD) are based on the fundamental orders that can be observed in the system and are summarized in Table. 1.

All of the orders in Table. 1 are used as input for the MHD method together with 20 harmonics of each order (if they are below the Nyquist frequency). Figure 4 shows the resulting profiles of the estimated speeds together with the provided encoder speed. Small deviations from the encoder can be observed for the single harmonic demodulation. Figure 5 provides a zoom of the estimated speed profiles between 55 and 90 seconds (illustrated by the black rectangle in Fig. 4). The main observation here is that the MHD approach is able to accurately track very small speed fluctuations as indicated by the encoder speed. This can be expected because the MHD allows to take into account higher order harmonics that emphasize those small speed fluctuations. Figure 6 displays the relative error in percentage of the two estimated speeds compared to the encoder. The error of the MHD speed is clearly smaller on average as is corroborated by the mean and median absolute errors shown in Fig. 7.

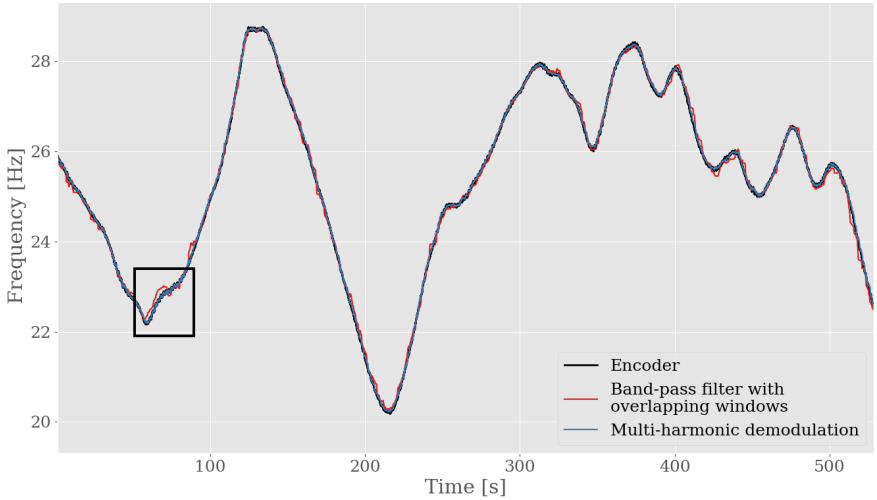


Figure 4: Speed profiles of single and multi-harmonic demodulation methods compared to the encoder speed.

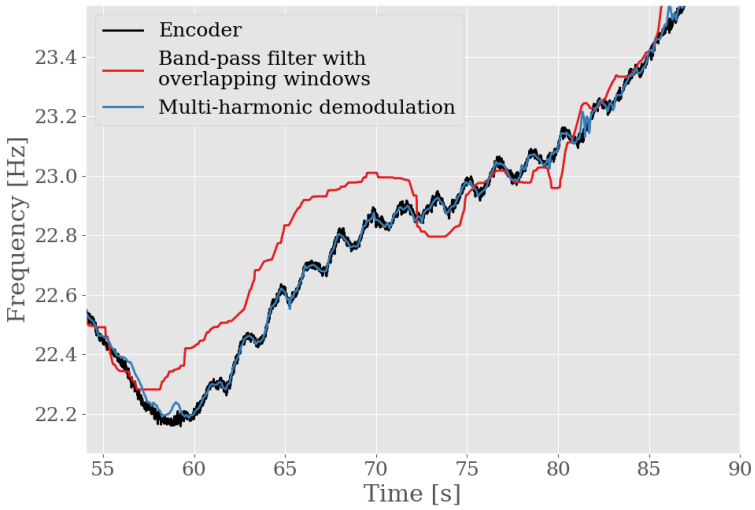


Figure 5: Zoom of the estimated speed profiles between 55 and 90 seconds.

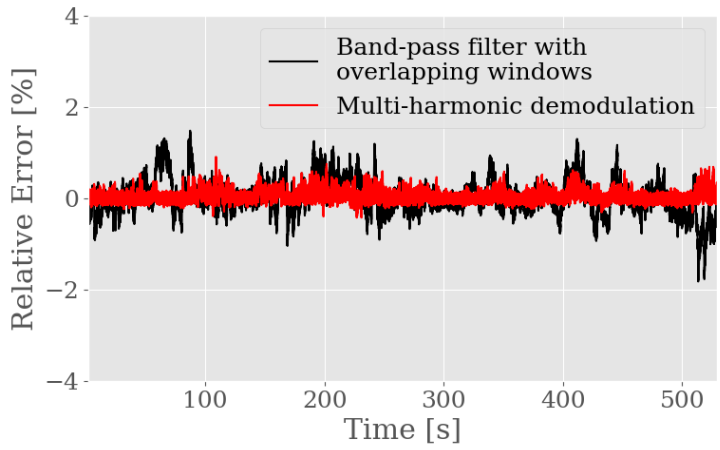


Figure 6: Relative error of the estimated speed to the encoder speed.

The results obtained by the single harmonic demodulation method are of course dependent on the window size used and on the bandwidth setting of the moving band-pass filter. It would also be possible to improve the result of the SHD method by optimizing the window lengths and bandwidths manually for every signal part. However, manual optimization is not the focus of this paper nor is it a desirable practice in industry nowadays. The MHD method on the other hand does not require any windowing or critical choice of a bandwidth of a band-pass filter. The most important inputs are the harmonic orders to take into account. For the case presented in this paper, this choice is not that critical since good results are obtained even without paying close attention to which harmonics are well separated and with a high SNR. It is plausible however that some data sets might contain low SNR harmonics with crossing orders. Therefore future work will focus on finding a potential automatic weighting of the different harmonics since currently all the demodulated harmonics are weighted equally. Such a solution would take away even the possible manual investigation of the harmonic structure of a vibration signal in order to define a set of harmonics to demodulate. It would also broaden again the automated application of the MHD method, due to the fact that then only design information of the gearbox would be required, which a manufacturer naturally possesses.

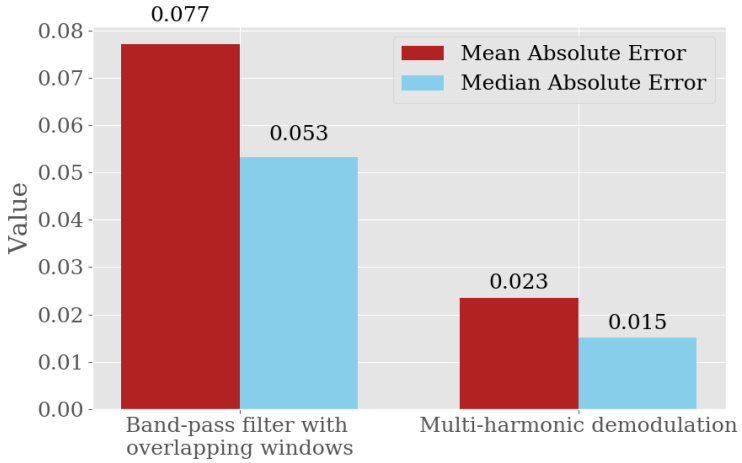


Figure 7: Mean and median absolute errors of the single and multi-harmonic demodulation estimated speeds.

5 Conclusion

This paper proposes a novel vibration-based speed estimation method based on the demodulation of multiple harmonics as compared to the conventional way of only utilizing a single harmonic. The multi-harmonic demodulation (MHD) method is used after an a-priori rough speed estimation and takes a set of speed-related harmonic orders as input. Taking into account multiple harmonics increases the robustness and the accuracy of the speed estimation at the same time, since the result is a type of average of the demodulation of multiple harmonics. Lower order harmonics often have a good signal-to-noise ratio but are not sensitive enough for small speed fluctuations, while the opposite is often true for the higher order harmonics. Another major advantage of the MHD method compared to the single harmonic demodulation (SHD) method is the finite variance of the resulting estimated speed. This reduces the need to do an a posteriori smoothing of the resulting speed profile. The performance of the method is validated on experimental wind turbine gearbox vibration data originating from the CMMNO 2014 contest. The results clearly indicate the improvement in speed estimation accuracy. The average errors have decreased by a factor of three approximately, without the need for windowing the signal. Since the MHD method relies on the input set of harmonics, the method could be adapted such that it uses a particular set of harmonics based on the operating regime the system is in. Another approach that will be investigated in future work is the automatic calculation of optimized weights per harmonic order. This would allow for easy integration in an automated processing scheme which is often required or at least desirable in industrial applications.

6 Acknowledgment

The authors of VUB would like to thank FWO for their support with an SB Ph.D. fellow grant and the agency for Innovation by Science and Technology in Belgium for supporting the SBO HYMOP project.

References

[1] A. K. Jardine, D. Lin, D. Banjevic, *A review on machinery diagnostics and prognostics implementing condition-based maintenance*, Mechanical systems and signal processing, 20:pp. 1483–1510, 2006.

[2] P. Tchakoua, R. Wamkeue, M. Ouhrouche, F. Slaoui-Hasnaoui, T. A. Tameghe, G. Ekemb, *Wind turbine condition monitoring: State-of-the-art review, new trends, and future challenges*, Energies, 7:pp. 2595–2630, 2014.

[3] D. Rémond, J. Antoni, R. Randall, *Editorial for the special issue on instantaneous angular speed (ias) processing and angular applications*, Mechanical Systems and Signal Processing, 1:pp. 1–4, 2014.

[4] Q. L. Hugo Andre, Ilyes Khelf, *Harmonic product spectrum revisited and adapted for rotating machine monitoring based on ias*, in *Surveillance9*, 2017.

[5] L. Renaudin, F. Bonnardot, O. Musy, J. Doray, D. Rémond, *Natural roller bearing fault detection by angular measurement of true instantaneous angular speed*, Mechanical Systems and Signal Processing, 24:pp. 1998–2011, 2010.

[6] A. Yousef Ben Sasi, F. Gu, B. Payne, A. Ball, *Instantaneous angular speed monitoring of electric motors*, Journal of Quality in Maintenance Engineering, 10:pp. 123–135, 2004.

[7] J. Urbanek, T. Barszcz, N. Sawalhi, R. Randall, *Comparison of amplitude-based and phase-based methods for speed tracking in application to wind turbines*, Metrology and measurement systems, 18:pp. 295–304, 2011.

[8] A.-O. Boudraa, J.-C. Cexus, F. Salzenstein, L. Guillon, *If estimation using empirical mode decomposition and nonlinear teager energy operator*, in *Control, Communications and Signal Processing, 2004. First International Symposium on*, (pp. 45–48) (IEEE), 2004.

[9] F. Bonnardot, M. El Badaoui, R. Randall, J. Daniere, F. Guillet, *Use of the acceleration signal of a gearbox in order to perform angular resampling (with limited speed fluctuation)*, Mechanical Systems and Signal Processing, 19:pp. 766–785, 2005.

[10] J. Urbanek, T. Barszcz, J. Antoni, *A two-step procedure for estimation of instantaneous rotational speed with large fluctuations*, Mechanical Systems and Signal Processing, 38:pp. 96–102, 2013.

[11] F. Combet, L. Gelman, *An automated methodology for performing time synchronous averaging of a gearbox signal without speed sensor*, Mechanical systems and signal processing, 21:pp. 2590–2606, 2007.

[12] Q. Leclere, H. André, J. Antoni, *A multi-order probabilistic approach for instantaneous angular speed tracking debriefing of the cmmno 14 diagnosis contest*, Mechanical Systems and Signal Processing, 2016.

A comparison of different features for discrepancy analysis-based bearing diagnostics

S. Schmidt[1,*], P.S. Heyns[1], K.C. Gryllias[2,3]
[1]Centre for Asset Integrity Management, Department Mechanical and Aeronautical Engineering, University of Pretoria
cnr Lynnwood Road and Roper Street, Hatfield, Pretoria, South Africa
[*]e-mail: **stephanschmidt@zoho.com (Stephan Schmidt)**

[2]KU Leuven, Department of Mechanical Engineering
Celestijnenlaan 300 B, B-3001, Heverlee, Belgium

[3]Dynamics of Mechanical and Mechatronic Systems, Flanders Make, Belgium

Abstract
Discrepancy analysis is a novelty detection technique which can be used for bearing diagnostics under varying speed conditions. In discrepancy analysis, features are extracted from the vibration signal and used with a model of the healthy features to generate a discrepancy signal which is subsequently analysed for bearing damage. However, the feature extraction process that is used affects the fault diagnosis capabilities of discrepancy analysis. It is therefore important to ensure that the extracted features result in a discrepancy signal that is not only sensitive to damage, but also robust to varying speed conditions. In this paper, the suitability of different features is compared for performing bearing diagnostics with discrepancy analysis under varying speed conditions. Investigations are performed on data generated with a phenomenological gearbox model and on experimental data, with the results indicating that wavelet packet features and cyclostationary features are well-suited for discrepancy analysis.

1 Introduction

Rolling element bearings are used as critical components in many rotating machines and therefore it is imperative that they operate as intended. However, rolling element bearings are prone to failure which makes it very important to use condition monitoring techniques capable of inferring the condition of the bearing. Additionally, many rotating machines operate under unavoidable varying conditions which impede the condition monitoring process and therefore it is also very important for the condition monitoring techniques to be robust to varying operating conditions.

Signal processing and analysis techniques can be used to extract or enhance diagnostic information in the signal [1,2] but can be difficult to implement and to infer the condition of the machine correctly by a non-expert. It is therefore useful to combine the extracted diagnostic information with machine learning techniques for automatic condition inference when historical fault data of all the damage modes are available. However, the historical fault data are difficult or impractical to acquire which makes it challenging to apply supervised machine learning techniques. This makes novelty detection approaches, requiring only historical healthy data, attractive for condition monitoring applications [3].

Discrepancy analysis is a novelty detection technique that assigns a localised novelty detection score or a localised discrepancy measure to different portions of a signal based on a healthy data model [4-6]. This localised discrepancy measure is used to construct a discrepancy signal which is processed and used to infer the condition of the machine. The localised discrepancy measure is usually assigned to diagnostic features extracted from the vibration signal to improve the performance of discrepancy analysis. Hence, it is important to use features that are rich with diagnostic information. In the work of Schmidt et al. [6], the

wavelet packet transform is used in the feature extraction process. However, cyclostationary analysis techniques and the empirical mode decomposition can also be used as potential alternatives for extracting features and have not been investigated for discrepancy analysis yet.

The objective of this work is therefore to investigate and compare the performance of different features in the discrepancy analysis process to perform bearing diagnostics under varying speed conditions. The investigations are performed on numerical and experimental data in this paper. In the next section, an overview of discrepancy analysis and the features investigated in this work are given, whereafter numerical and experimental investigations are performed in Section 3 and Section 4, respectively.

2 Discrepancy analysis

2.1 Overview

A discrepancy analysis methodology for bearing diagnostics presented by Schmidt et al. [6] is followed in this paper. The general steps for discrepancy analysis are as follows:

1) Process the vibration signal (e.g. filtering) and extract localised diagnostic information in the form of features from the processed vibration signal.
2) Model the features of the healthy data with models such as Gaussian models, Gaussian mixture models or hidden Markov models.
3) Calculate the discrepancy between the features extracted from the vibration signal and the features of a healthy machine with the discrepancy measure associated with the healthy model. Construct a discrepancy signal from the calculated localised discrepancies.
4) Process the discrepancy signal to attenuate the influence of operating conditions [6] or to enhance the damage components [5] for example.
5) Analyse the processed discrepancy signals to infer the condition of the machine.

It is very important to have information related to the phase or rotational speed of the shaft when performing discrepancy analysis. This is attributed to the vibration signals generated by damaged mechanical components, being angle-dependent and therefore the features need to be described in terms of shaft angle as opposed to time. This speed or phase information can be obtained with a tachometer or it can be estimated from the vibration signal using tacholess rotational speed estimation approaches.

2.2 Feature extraction

It is necessary to extract diagnostic information from the measured vibration signal to improve the condition inference capabilities of discrepancy analysis. In discrepancy analysis, the multi-dimensional features should present information pertaining to the condition of the machine over angle. Another important consideration of potential discrepancy features is that even though the modulation due to bearing damage is angle-dependent, the carrier component is time-invariant [7,8]. The implication of this is that the signal is approximately angle-time cyclostationary as opposed to time- or angle-cyclostationary under varying speed conditions [7,8] and therefore the feature extraction methods should be carefully designed.

The following signal analysis and processing tools are considered to perform feature extraction in this investigation:

1. Wavelet packet transform
2. Spectrogram
3. Instantaneous power spectrum

4. Empirical mode decomposition

The D-dimensional features extracted at angular instant *n* is denoted by a *D* × *1 vector* $\mathbf{b}_n$ in this section.

2.2.1 Wavelet Packet Transform (WPT)

The Wavelet Packet Transform (WPT) forms part of wavelet analysis where a signal is recursively decomposed into approximation (i.e. low-frequency content) and detail (i.e. high-frequency content) coefficients by using a filter bank of quadrature mirror filters [9]. A two-level wavelet packet decomposition of the signal *x(m)* is shown in Figure 1 with the Wavelet Coefficients (WCs) of each level presented as well.

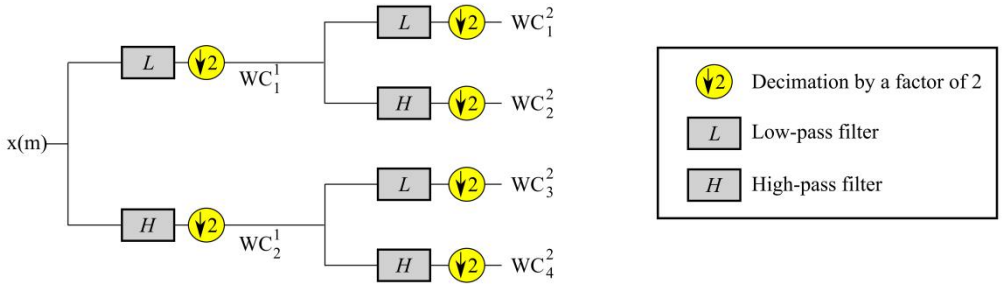


Figure 1: Two-level wavelet packet decomposition of a discrete temporal signal *x(m)* with a filterbank of low-pass (L) and high-pass (H) quadrature mirror filters. WC_i^j indicates the *i*th coefficients of the *j*th level.

The impulse response function of the low-pass filter h_L and of the high-pass filter h_H are determined by the specific wavelet basis function that is used [9]. For example, the filters are used to obtain filtered versions of the original signal *x(m)*

$$x_L(m) = x(m) \otimes h_L \,, \tag{1}$$

and

$$x_H(m) = x(m) \otimes h_H \,, \tag{2}$$

where x_L and x_H denote the low-pass and high-pass filtered signals. The low-pass and high-pass filtered signals are decimated with a factor of two to obtain the wavelet coefficients at the first level. This is performed repeatedly on the wavelet coefficients as shown in Figure 1 to obtain a set of wavelet coefficients.

The effectiveness of the WPT for diagnostics depends on the level of the decomposition as well as the wavelet function that is used and therefore a few common wavelet basis functions are investigated.

In the paper by Schmidt et al. [6], the WPT is used in the feature extraction process for discrepancy analysis with a similar procedure being used in this investigation. The WPT is performed on the temporal vibration signal to decompose the signal into a set of narrowband WCs. The WCs of the final level are order tracked to obtain an angle domain representation of the specific WCs which are subsequently used as features in the discrepancy analysis process. The resulting features are given by

$$\mathbf{b}_n = \left[WC_1^N(n), WC_2^N(n) \ldots WC_{2^N}^N(n)\right]^T \tag{3}$$

where $WC_i^N(n)$ is the *n*-sample of the *i*th order tracked wavelet coefficients at level *N* and the superscript *T* indicates the vector is transposed.

In the feature extraction procedure, the WCs are order tracked as opposed to the vibration signal to preserve the angle-time cyclostationary properties of the bearing damage. In the feature extraction procedure by Schmidt et al. [6], the WCs are windowed to extract localised statistics as features to enhance the discrepancy signal. However, this is not performed on the wavelet packet features, because this can be applied to all investigated features and does not convey their actual performance.

2.2.2 Spectrogram

The spectrogram is the squared magnitude of the Short-Time Fourier Transform (STFT) and can show how the time-frequency components of the vibration signal evolve over time. However, there is a trade-off between the time and frequency resolution of the STFT and therefore the STFT is ill-suited for representing the time-frequency information of non-stationary signals in general. Despite its limitations, some diagnostic information may still be contained within the spectrogram and it has the benefit that it is relatively computationally efficient to calculate due to the Fast Fourier Transform (FFT) being an essential part of the calculation process. The fact that the signal has a relatively poor time (or angle) resolution is not problematic for discrepancy analysis where the sampling frequency of the signal is usually reduced by windowing the signal [4,5]. The feature extraction procedure is as follows:

1. Order track the vibration signal
2. Calculate the STFT of the order tracked vibration signal.
3. Calculate the spectrogram, as the squared magnitude of the STFT, and use as features. The number of frequency bins is equal to the number of features that is extracted. The discrete spectrogram of the order-tracked vibration signal *x(m)* is given by

$$S(l,k)=\left|\sum_{m=0}^{L_w-1} x\left(m+R_w l\right)w(m)e^{\frac{-2j\pi mk}{L_w}}\right|^2 \tag{4}$$

and calculated for a windowing function $w(m)$ of length L_w and an overlap between consecutive windows O_w, where $R_w = L_w - O_w$. The D-dimensional features extracted from the spectrogram is denoted by

$$\mathbf{b}_n = \left[S(n,0), S(n,1), \ldots, S(n, L_w - 1)\right]^T \tag{5}$$

where *n* relates to the shaft angle with $n\Delta\varphi/2$ rad, where $\Delta\varphi$ is the angular resolution of the spectrogram in radians. Due to the fact that the angle-time cyclostationary properties of the bearing damage are not preserved in the calculation of the features, it is expected that the features will be sensitive to varying speeds, which is non-ideal under varying speed conditions.

2.2.3 Instantaneous Power Spectrum (IPS)

The interactions of rotating components (e.g. gear meshing, impacts due to bearing damage) of machines operating under stationary conditions result in the generation of time-cyclostationary signals i.e. stochastic vibration signals with periodic statistical properties in terms of time. This makes cyclostationary analysis very powerful for performing rotating machine diagnostics [2]. However, for bearings operating under varying speed conditions, the time-cyclostationary properties of the signal are lost and the signals are rather cyclo-non-stationary. Abboud et al. [7] showed that the signals from damaged bearings can be approximated as angle-time second-order cyclostationary under varying speed conditions and gave angle-time cyclostationary estimators for classical second-order cyclostationary tools such as the spectral coherence and the Instantaneous Power Spectrum (IPS). The IPS is very powerful for rotating machine diagnostics [10,11] and is used as discrepancy analysis features in this work. The time-frequency IPS (TF-IPS)

$$I_{TF}(t,f)=\int_{-\infty}^{\infty}\Re_{2X}(t,\tau)\cdot e^{-j2\pi tf}d\tau\,, \tag{6}$$

describes how the energy of the signal manifest in its frequency bands over time where $\Re_{2X}$ is the time-autocorrelation function. The Welch-based estimator of the TF-IPS [7]

$$\hat{I}_{TF}(l,k)=\frac{1}{f_s L\sum_{a=0}^{N_w-1}w(a)^2}\left|\sum_{m=0}^{L_w}x(m+R_w l)w(m)e^{\frac{-2j\pi mk}{L_w}}\right|^2, \tag{7}$$

has a very similar form to Equation (4) and is used in this work with the same notation. Under varying speed conditions, the Angle-Frequency IPS (AF-IPS) is more appropriate and obtained by order-tracking each frequency band of the TF-IPS separately [7]

$$\hat{I}_{AF}(n,k)=OT_{t\to\varphi}\left(\hat{I}_{TF}(l,k)\right), \tag{8}$$

where $OT_{t\to\varphi}$ indicates that the time index l is converted to an angle index n with Order Tracking (OT). The features at angle index n is obtained by concatenating the values of the AF-IPS at all frequency bands for angle increment n and given by

$$\mathbf{b}_n=\left[\hat{I}_{AF}(n,0),\hat{I}_{AF}(n,1),\ldots,\hat{I}_{AF}(n,L_w-1)\right]^T. \tag{9}$$

It is evident from Equation (5) and Equation (9) that the dimensionality of the feature space is governed by the length of the window that is used, while Equation (4) and Equation (7) indicate the time resolution is dependent on the length of the window as well as the overlap between consecutive windows. In all subsequent investigations the AF-IPS as opposed to the TF-IPS is used for feature extraction and is shortened to IPS in the figures and when it is being referred to.

2.2.4 Empirical Mode Decomposition (EMD)

The Empirical Mode Decomposition (EMD) is a powerful self-adaptive time-frequency analysis technique that decomposes a signal into a set of orthogonal Intrinsic Mode Functions (IMFs). The EMD is capable of analysing non-stationary signals in contrast to the STFT and it does not rely on a priori assumptions on the form of the signal components compared to the WPT [12]. However, the EMD has a few problems such as the IMFs not being orthogonal and the occurrence of mode mixing, a phenomenon where a signal component manifest within a few IMFs. The ensemble EMD and other techniques have been proposed in literature aiming to circumvent the aforementioned problems of the EMD [12].

In this paper, the standard EMD without any improvements is used in spite of the aforementioned problems, because this is an initial investigation of the EMD. The EMD is performed on the temporal vibration signal to extract N temporal IMFs. The temporal IMFs are order tracked to obtain the angular IMFs which are subsequently used as features in the discrepancy analysis process, with the features given by

$$\mathbf{b}_n=\left[IMF_1(n),IMF_2(n),\ldots,IMF_N(n)\right]^T. \tag{10}$$

In discrepancy analysis, localised features are converted to a discrepancy measure. This means that phenomena which result in spurious changes in features such as mode mixing will result in corresponding spurious discrepancies. These spurious discrepancies may dominate the discrepancy signal which will cause erroneous inferences to be made.

In the next section, the feature modelling and discrepancy signal generation processes are discussed.

2.3 Feature modelling and discrepancy signal generation

The features extracted from a healthy machine are used to optimise a healthy model which is subsequently used to generate a discrepancy measure or localised novelty detection score for new features. The features can for example be modelled with a Gaussian mixture model [4], a hidden Markov model [5] or a Gaussian model [6]. Gaussian models have closed form solutions for their parameters, which means that convergence issues do not influence the results when comparing different features. Gaussian models also do not have any data dependent hyperparameters, are sensitive to damage, and relatively robust to varying speed conditions [13]. Therefore, Gaussian models are used in this work.

The negative log-likelihood of the Gaussian model is used as a discrepancy measure for the features extracted from the angle index *i* and given by

$$\eta(i) = -\log \mathrm{N}(\mathbf{b}_i \mid \boldsymbol{\mu}, \boldsymbol{\Sigma}) \tag{11}$$

where $N(\mathbf{b}_i \mid \boldsymbol{\mu}, \boldsymbol{\Sigma})$ is a Gaussian probability density function with its mean $\boldsymbol{\mu}$ and covariance $\boldsymbol{\Sigma}$ obtained by maximising the likelihood function of the model with the features of a healthy gearbox.

The robustness of the discrepancy signal could be improved by compensating for the varying speed conditions [6], however, this is not investigated in this work. Instead, the discrepancy signal's sensitivity to varying speed conditions is compared for the investigated features.

2.4 Analysing the discrepancy signals

The synchronous average of the discrepancy signal is a useful tool for investigating the presence of gear damage [4,5]. However, the synchronous average of the discrepancy signal is ill-suited for bearing damage due to potential slip of the rolling elements in the bearing. Instead, the spectrum of the discrepancy signal is used with the analytical defect frequencies to infer the presence of damage in the signal [6]. The power spectral density using the Welch estimator is used in this work.

3 Numerical investigation

3.1 Overview of the phenomenological gearbox model

The phenomenological gearbox model presented by Abboud et al. [14] and used by Schmidt et al. [6] is used in this work. The casing vibration signal consist of a deterministic gear component attributed to the gear mesh component x_{dg}, a random gear component attributed to distributed gear damage x_{rg}, an outer race bearing damage component x_b and noise x_n. The casing vibration signal is given by

$$x_c(t) = x_{dg}(t) + x_{rg}(t) + FS \cdot x_b(t) + x_n(t) \tag{12}$$

where a Fault Severity (FS) factor is explicitly included to alter the magnitude of the baseline bearing damage component and to simulate a deteriorating bearing. The deterministic gear component is given by

$$x_{dg}(t) = M(\omega) \cdot h_{dg}(t) \otimes \left(\sum_{k=1}^{N} A_k^{dg} \sin(k \cdot N_{teeth} \cdot \varphi(t) + \phi_k^{dg}) \right) \tag{13}$$

where $M(\omega)$ simulates the sensitivity of the signal to changes in rotational speed ω rad/s, $h_{dg}(t)$ is a single degree-of-freedom impulse response function, A_k^{dg} and ϕ_k^{dg} are the magnitude and phase of the *k*th

harmonic component. The phase of the shaft is given by $\varphi(t) = \int_0^t \omega(\tau) d\tau$ and the number of teeth of the gear connected to the shaft is denoted by N_{teeth} and is 40. The distributed damage component

$$x_{rg}(t) = M(\omega) \cdot h_{rg}(t) \otimes \left(\varepsilon(t) \sum_{k=1}^{N} A_k^{rg} \sin(k \cdot \varphi(t) + \phi_k^{rg}) \right) \tag{14}$$

has a similar form as the deterministic gear component, except for the zero-mean Gaussian noise component with unit standard deviation $\varepsilon(t) \sim N(0,1)$. The outer race bearing damage component

$$x_b(t) = M(\omega) \cdot h_b(t) \otimes \left(\sum_{i=1}^{N_b} A_i^b \delta(t - T_i) \right) \tag{15}$$

consist of a Dirac comb convolved with the single degree-of-freedom transfer function. The coefficient controlling the magnitude of the *i*th bearing impulse A_i^b is a sample from a uniform distribution with a mean of unity and a range of 0.2. The time-of-arrival of the *i*th bearing impulse is calculated from the instantaneous speed of the shaft and the ball-pass outer race order of the bearing. Slip is also introduced in the model by adding noise to the angle-of-arrival.

Finally, the noise is given by

$$x_n(t) = M(\omega) \cdot \sigma_n \cdot \varepsilon(t) \tag{16}$$

where σ_n is the standard deviation of the noise signal if $M(\omega)$ =1. A more detailed overview of the model can be found in Ref. [14] with a similar notation and implementation to this paper used in Ref. [6].

The impulse response function of the deterministic gear component, the random gear component and the bearing damage have the same damping ratio of 0.05 and natural frequencies of 1.5kHz, 2.5kHz and 5.0kHz respectively. For all models, $M(\omega) = \omega$ and the ball-pass outer race order of the bearing is 8.14 shaft orders.

Five operating condition profiles are separately used to generate the vibration data with the phenomenological gearbox model and are presented in Figure 2.

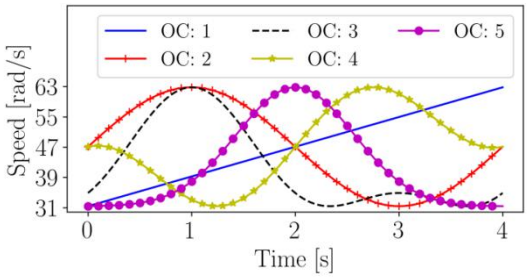


Figure 2: Rotational speed profiles for the phenomenological gearbox model.

The vibration components that correspond to operating condition profile four is presented in Figure 3, with the influence of the speed on the envelope of the signal components clearly being seen.

Six bearing conditions are investigated with the model namely FS = [0.0, 0.02, 0.04, 0.08, 0.12, 0.16] which is separately used in Equation (12). Two damaged bearing signals corresponding to the vibration signal components in Figure 3 are presented in Figure 4.

It is evident from the results that the gear mesh frequency component dominates the casing vibration signal with the bearing damage component being small in comparison. Deterministic-random separation methods [15] are not used to remove the gear mesh components in this investigation. This is to investigate the ability of the features to detect the bearing damage without any pre-processing techniques being used. However, it can certainly increase the robustness of discrepancy analysis and should be investigated in future work.

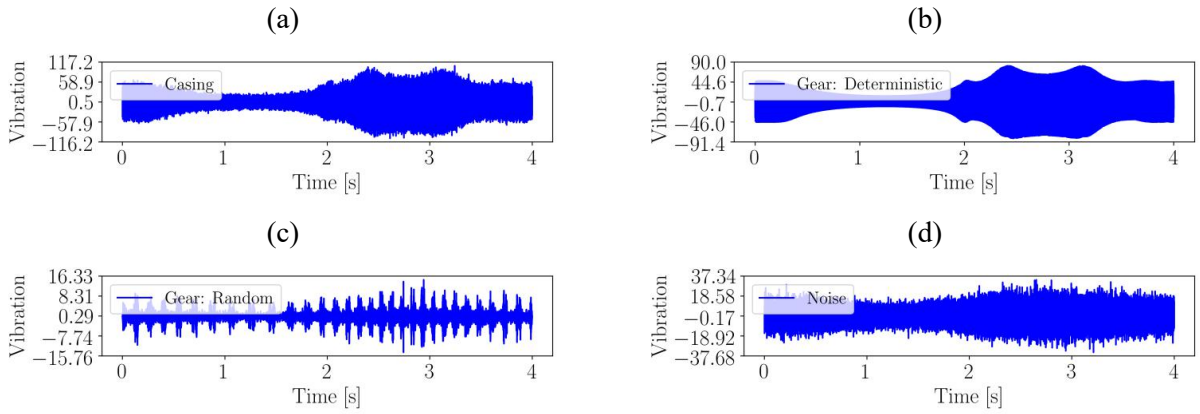


Figure 3: Vibration components generated by the phenomenological gearbox model corresponding to operating condition four.



Figure 4: Bearing components for two different fault severities are presented, with operating condition profile four being used.

3.2 Results

3.2.1 Implementation of discrepancy analysis

The first step of the discrepancy analysis procedure used in this work is to extract diagnostic features from the vibration signal. The dimensionality of the features should be approximately the same to ensure that a fair comparison between the different features can be given. The dimensionality of the features in this paper is set to 16 unless it is not practically possible. The WPT decomposition level is set to four, which results in 16 wavelet coefficients to be extracted from the vibration signal. Many wavelet basis functions can be used to perform the decomposition, with the focus placed on Daubechies wavelets which is very popular for bearing diagnostics. The following Daubechies wavelet basis functions are investigated in this section: db1, db2, db4, db8, db10, db16, db20, and db44.

The spectrogram features are calculated by using a Hann windowing function with a window length of 16 and an overlap of 75% between consecutive windows. The TF-IPS is implemented with the same characteristics as the spectrogram features, whereafter the TF-IPS is order tracked to obtain the AF-IPS. The window length is selected to have the same dimensionality as the WPT features.

The EMD is a self-adaptive signal processing technique to extract multiple IMFs which are used to obtain features as discussed in Section 2.2.4. It was found that a different number of IMFs is extracted for different signals and to ensure that all measurements have the same dimensionality, the number of IMFs that is extracted is set to 12. If more IMFs are used in the training phase, there is a risk that some datasets in the testing phase may be unusable due to an insufficient number of IMFs being extracted.

The features of a system with a healthy bearing (i.e. FS = 0.0 in Equation (12)) for the first four operating conditions are used to obtain the healthy model as discussed in Section 2.3. The negative log-likelihood, given by Equation (11), is used to generate the discrepancy signals for the different datasets, whereafter the spectra of the discrepancy signals are calculated. The spectra are presented in the next section.

3.2.2 Discrepancy signal spectra

The spectra of the discrepancy signals are presented in Figure 5, where the bearing damage component at 8.14 shaft orders and its harmonics are clearly seen for the AF-IPS, spectrogram and most WPT features. The spectra associated with the spectrogram features contain a relatively large gear mesh component at 20 shaft orders when compared to the other features. While only the fundamental bearing component can clearly be seen in the spectra of the discrepancy signal associated with the WPT db44. In contrast to the other results, the EMD features do not contain any clear diagnostic information in its spectra.

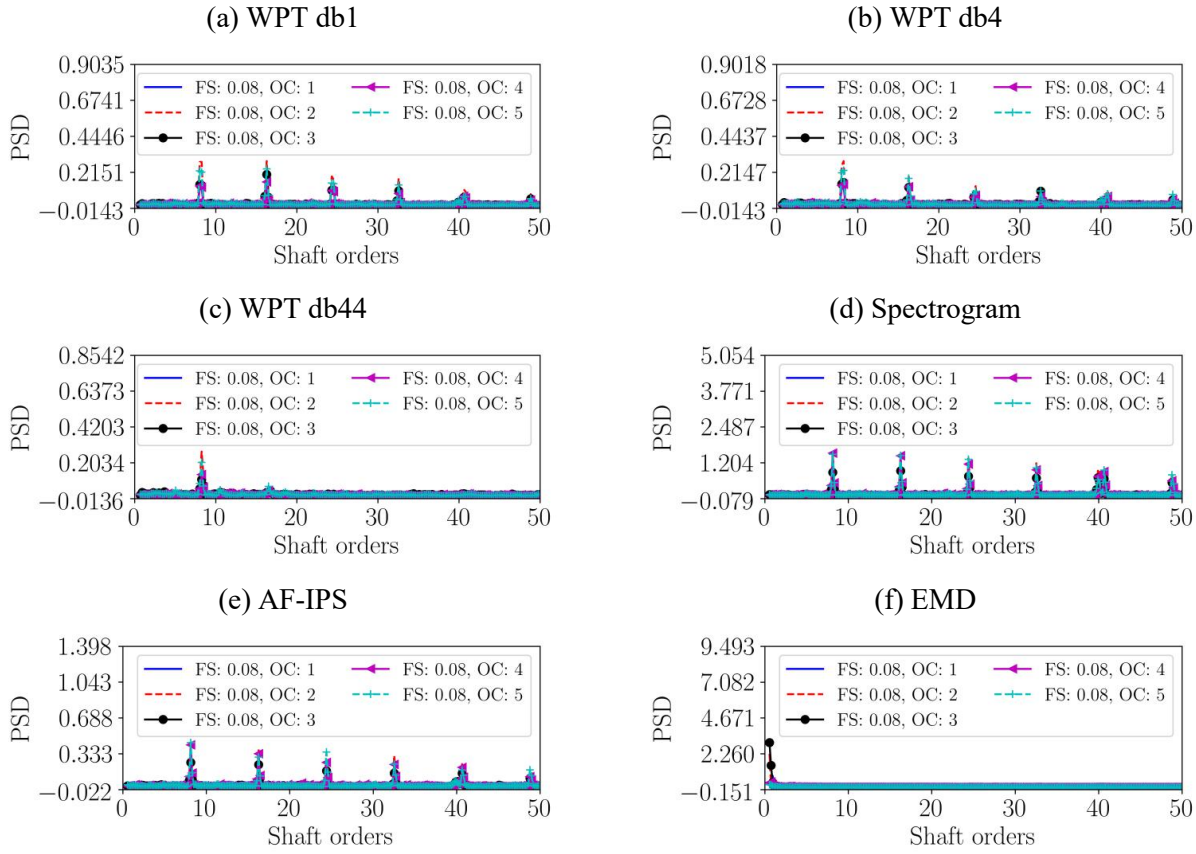


Figure 5: Discrepancy spectra for the different features used for the phenomenological gearbox model with a fault severity of 0.08.

It is difficult to compare the performance of the features from the spectra in Figure 5 and therefore their performance is quantified and compared in the next section.

3.2.3 Quantifying the performance of the features

The amplitude of the fundamental ball-pass outer race component contains diagnostic information as seen in Figure 5 and is investigated over fault severity to quantify the sensitivity of the features to damage. The raw amplitude is presented in Figure 6(a) and the normalised amplitude is presented in Figure 6(b). The normalised amplitude, calculated by dividing the amplitude of the different fault severities by the amplitude of the healthy bearing component (FS = 0.0), is used to quantify the relative change of the amplitude over fault severity.

The mean of the normalised amplitude presented in Figure 6(a) is presented Table 1. Surprisingly, the spectrogram features are the most sensitive to the damage, with the AF-IPS being second most sensitive.

The discrepancy signal associated with the EMD features are the least sensitive to damage. This is attributed to mode mixing, which result in spurious discrepancies to be detected.

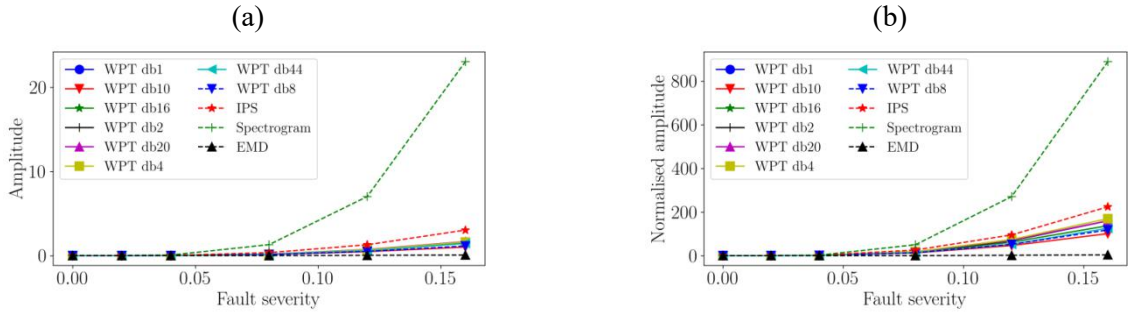


Figure 6: The sensitivity of the amplitude of the fundamental bearing component versus fault severity.

EMD	WPT db10	WPT db8	WPT db44	WPT db16	WPT db1	WPT db2	WPT db20	WPT db4	AF-IPS	Spectrogram
1.84	27.68	31.56	32.92	36.73	42.06	42.14	42.36	44.79	58.53	202.77

Table 1: The mean normalised amplitude of the fundamental bearing component for the different features.

It is not only important to quantify the sensitivity of the features to damage, but also their robustness to varying speed conditions. The amplitude of the fundamental outer race component is presented over rotational speed in Figure 7(a) and the normalised amplitude is presented in Figure 7(b). The normalised amplitude is obtained by dividing the mean amplitude of the fundamental component at different speeds by the amplitude of the component corresponding to the minimum rotational speed. The results of the EMD features are not included in Figure 7; the EMD features are relatively insensitive to changes in operating conditions and distorted the results in the figure. In Table 2, the mean normalised amplitude over rotational speed is presented for all investigated features.

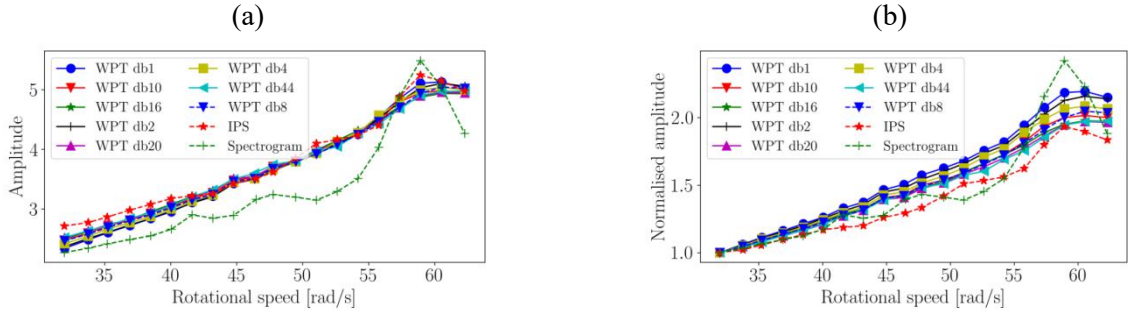


Figure 7: The sensitivity of the amplitude of the fundamental bearing component for different rotational speeds.

EMD	WPT db10	WPT db8	WPT db44	WPT db16	WPT db1	WPT db2	WPT db20	WPT db4	AF-IPS	Spectrogram
1.36	1.50	1.50	1.47	1.49	1.58	1.55	1.47	1.53	1.39	1.47

Table 2: The mean normalised amplitude of the fundamental bearing component for the different features over rotational speed.

The EMD features were the least sensitive to changes in speed, while the AF-IPS performed second best. Even though the Spectrogram features' average normalised amplitude was not the most, the variation of

the features in Figure 7 was the most. This indicates that it is relatively sensitive to varying speed conditions with fairly large fluctuations with respect to rotational speed.

3.2.4 Discussion

The spectrogram features performed the best of the features in terms of its sensitivity to damage, however, the features were fairly sensitive to speed changes as seen in Figure 7(b). The spectrogram features and the AF-IPS features are presented for the phenomenological gearbox model with operating condition profile three being present in Figure 8. It is clear that the spectrogram features are very sensitive to rotational speed changes because the bearing damage resides in different features as the speed varies which is in contrast to the AF-IPS features. The characteristics of the features depend on the rotational speed which makes feature selection approaches difficult to apply. This also means that a healthy Gaussian model, which is likely non-isotropic, may be more sensitive to bearing damage for specific features than others which is an undesirable characteristic.

(a) Spectrogram (b) AF-IPS

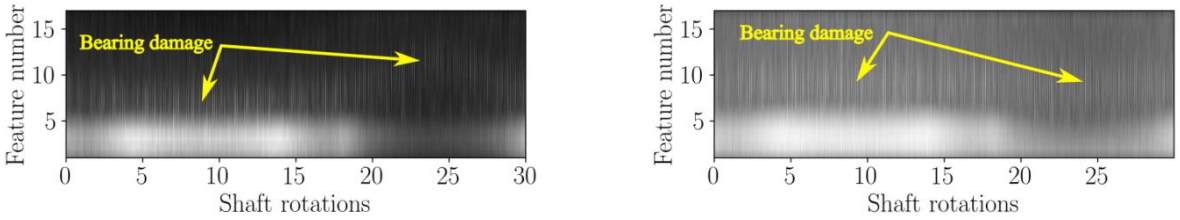


Figure 8: A comparison of the spectrogram features and the AF-IPS features over shaft rotations for the phenomenological gearbox model with bearing damage. Operating condition profile three was used to generate the results.

The WPT features also performed very well compared to the AF-IPS. The db4 features performed the best, while the db10 features performed the worst. The db44 wavelet basis function, which has performed very well in the literature [16], does not perform well in this numerical investigation. Hence, it is clear that the performance of the WPT features is sensitive to the choice of wavelet basis functions and therefore care should be taken when using it in a novelty detection framework. This also highlights the benefits of using the AF-IPS; the basis function is fixed and does not have to be altered for different applications.

In contrast to the other feature extraction approaches, the EMD was time-consuming to apply and also did not perform very well for discrepancy analysis due to mode mixing. However, there are many improvements to the EMD such as the ensemble EMD that is not investigated in this work but can potentially result in better features for discrepancy analysis.

In conclusion, the AF-IPS performed the best on the numerical data and is investigated with the spectrogram features and the WPT features on experimental data in the next section. The EMD features are not investigated in the next section due to their poor performance in the numerical investigation.

4 Experimental investigation

4.1 Overview of the dataset

A SpectraQuest, Inc. Machinery Fault Simulator dataset that contains vibration data for a healthy bearing, a bearing with inner race damage, outer race damage and rolling element damage, is investigated in this section. A more detailed description of the experimental data is given in Ref. [6]. The test bench was

operated under constant loads, but varying speed conditions with the rotational speeds of the shaft presented against time in Figure 9 for the different experiments.

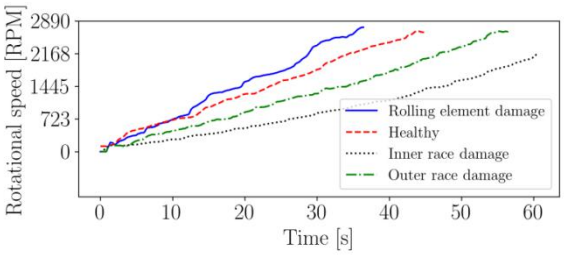


Figure 9: Rotational speed profiles for the different datasets of the experimental data.

The y-direction vibration data of the testing bearing, sampled at 25.6 kHz, are used with the measured rotational speed in Figure 9 for the discrepancy analysis investigation. In the next section, the performance of the different feature extraction procedures is investigated for the vibration data.

4.2 Discrepancy analysis results

The discrepancy analysis procedure investigated in this section has the same properties compared to the investigation in Section 3. The spectrogram features and the IPS features are compared to the wavelet packet features with db4 (the best performing wavelet basis function), db1 (a robust wavelet basis function), db44 (a wavelet basis function that has performed well in literature) being used. The Gaussian model, optimised on the healthy vibration data, is used to generate discrepancy signals for the vibration data with the corresponding spectra shown in Figure 11. The analytical characteristic frequency of the bearing damage is presented for the different conditions as well.

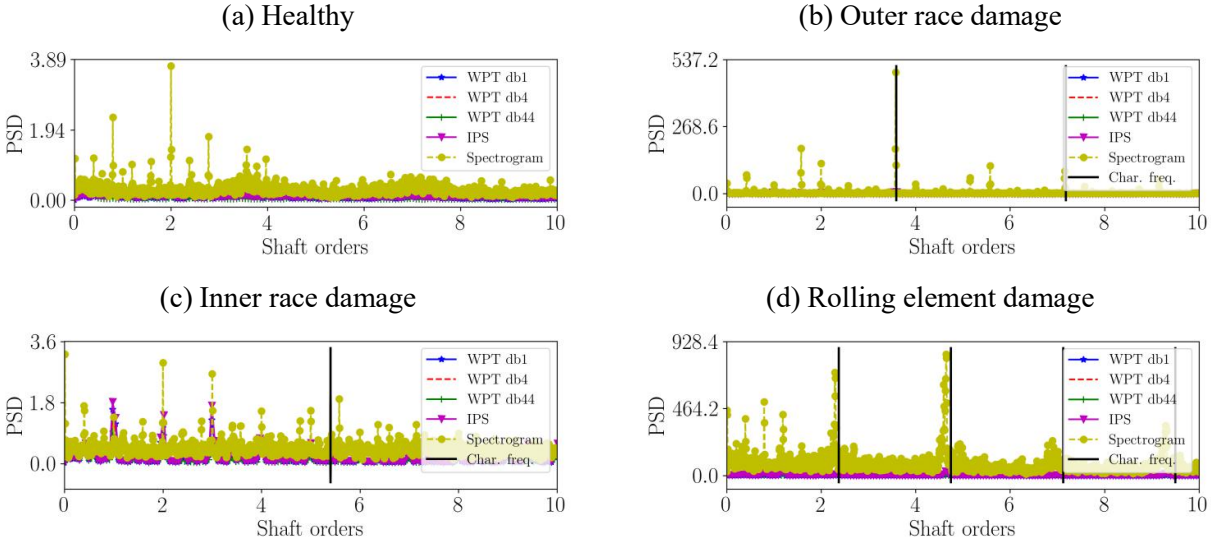


Figure 10: The discrepancy spectra for the different experimental bearing conditions and the different features.

The spectra associated with the spectrogram features dominate the results in Figure 11; not only are the characteristic frequency amplitudes larger, there is significant noise content in the spectra as well.

Therefore, the spectra without the spectrogram features' results are presented in Figure 12 to show the characteristics of the IPS and wavelet features.

In Figure 11 and Figure 12, the outer race damage and the rolling element damage can clearly be seen for all features. The inner race damage is small compared to contaminating components attributed to the bearing being improperly installed and cannot be clearly seen in the spectra. It is difficult to compare the performance of the features with Figure 11 and Figure 12 and therefore a similar process is followed as the numerical investigation to quantify the performance of the features. In Table 3, the fundamental amplitude of the characteristic component is divided by the average value of the healthy spectrum to indicate the sensitivity of the features to damage. Hence, the features with a larger value are more sensitive to damage than the features with a smaller value.

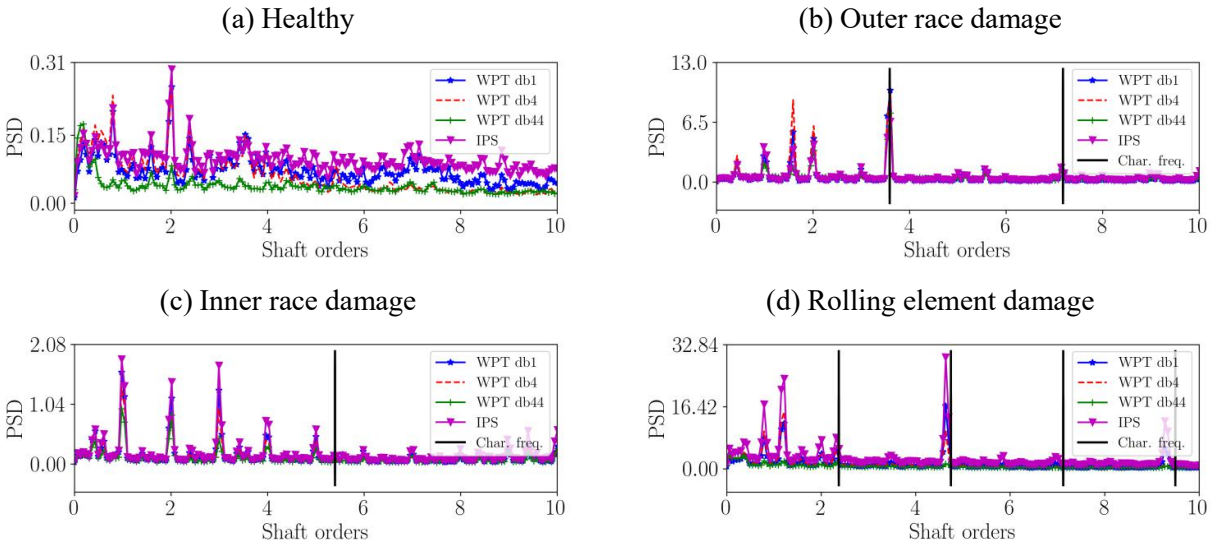


Figure 11: The discrepancy signal spectra in Figure 11 are presented without the results obtained with the spectrogram features.

	Outer race damage	Inner race damage	Rolling element damage
WPT db1	152.95	7.27	76.07
WPT db4	205.16	2.57	96.43
WPT db44	233.04	2.42	48.99
Spectrogram	1737.04	6.83	2550.54
AF-IPS	73.04	1.64	91.58

Table 3: The fundamental amplitude of the characteristic component divided by the average value of the health spectrum for the different damage modes.

The results indicate that the spectrogram features are the most sensitive to damage. Even though the WPT db44, has very small amplitudes for its characteristic components in Figure 12, it is the second most sensitive to damage according to the results in Table 3. This is because the amplitude of the healthy signal is significantly smaller than the amplitudes of the other features as seen in Figure 12(a). The IPS and WPT db1 features have the smallest values which indicate that they are the least sensitive to damage from this investigation, however, the results obtained from the features are still very good.

5 Conclusion

In this investigation, the suitability of the spectrogram, the angle-frequency instantaneous power spectrum, the wavelet packet transform and the empirical mode decomposition are investigated for bearing diagnostics under varying speed conditions with discrepancy analysis. The results indicate that the angle-frequency instantaneous power spectrum, the spectrogram and the wavelet packet features are well suited for discrepancy analysis-based bearing diagnostics. However, the performance of the wavelet packet features are very sensitive to the choice of wavelet basis function and the spectrogram features are inherently sensitive to varying speed conditions, which is undesirable. The angle-frequency instantaneous power spectrum is based on the theory of cyclostationarity, it respects the angle-time second-order cyclostationary properties of bearing damage and is relatively robust to varying speeds and sensitive to damage. Therefore, the angle-frequency instantaneous power spectrum features are suggested as a first choice for applying discrepancy analysis. The results indicated that the empirical mode decomposition is ill-suited for discrepancy analysis due to mode mixing problems which result in spurious discrepancies to be detected.

In future research, it is suggested that more elaborate performance quantification indicators need to be investigated for the different feature extraction approaches. It is also suggested that the extensions and improvements of the empirical mode decomposition need to be investigated for discrepancy analysis. It is expected that better results will be obtained by reducing the mode mixing problem. Pre-processing techniques on the vibration signal can also be investigated to improve the robustness of discrepancy analysis and to remove spurious frequency components. Lastly, it is suggested that more potential feature extraction methods and datasets need to be used for a more complete discrepancy analysis investigation to find optimal features.

Acknowledgements

The authors gratefully acknowledge the support that was received from the Eskom Power Plant Engineering Institute (EPPEI) in the execution of the research. The authors would also like to acknowledge Siemens Industry Software and Dr. ir. Karl Janssens for allowing the use of the SpectraQuest experimental data. K.C. Gryllias gratefully acknowledges the Research Fund KU Leuven.

References

[1] R. B. Randall and J. Antoni, *Rolling element bearing diagnostics - A tutorial,* Mechanical Systems and Signal Processing, Vol. 25, No. 2, (2011), pp. 485–520.

[2] J. Antoni, *Cyclostationarity by examples*, Mechanical Systems and Signal Processing, Vol. 23, No. 4, (2009), pp. 987–1036.

[3] M. Timusk, M. Lipsett, and C. K. Mechefske, *Fault detection using transient machine signals*, Mechanical Systems and Signal Processing, vol. 22, (2008) ,pp. 1724–1749.

[4] T. Heyns, P. S. Heyns, and J. P. De Villiers, *Combining synchronous averaging with a Gaussian mixture model novelty detection scheme for vibration-based condition monitoring of a gearbox*, Mechanical Systems and Signal Processing, Vol. 32, (2012), pp. 200–215.

[5] S. Schmidt, P. S. Heyns, and J. P. de Villiers, *A novelty detection diagnostic methodology for gearboxes operating under fluctuating operating conditions using probabilistic techniques*, Mechanical Systems and Signal Processing, Vol. 100, (2018) ,pp. 152–166.

[6] S. Schmidt, P. S. Heyns, and K.C. Gryllias, *A discrepancy analysis methodology for rolling element bearing diagnostics under variable speed conditions*, Mechanical Systems and Signal Processing, Vol. 116, (2019), pp. 40-61.

[7] D. Abboud and J. Antoni, *Order-frequency analysis of machine signals*, Mechanical Systems and Signal Processing, Vol. 87, (2017), pp. 229–258.

[8] D. Abboud, S. Baudin, J. Antoni, D. Rémond, M. Eltabach, and O. Sauvage, *The spectral analysis of cyclo-non-stationary signals*, Mechanical Systems and Signal Processing, Vol. 75, (2016) ,pp. 280–300.

[9] G. G. Yen, S. Member, and K. Lin, *Wavelet packet feature extraction for vibration monitoring*, IEEE Transactions on Industrial Electronics, Vol. 47, No. 3, (2000),pp. 650–667.

[10] J. Urbanek, T. Barszcz, R. Zimroz, and J. Antoni, *Application of averaged instantaneous power spectrum for diagnostics of machinery operating under non-stationary operational conditions*, Measurement, Vol. 45, No. 7, (2012), pp. 1782–1791.

[11] N. Baydar and A. Ball, *Detection of gear deterioration under varying load conditions by using the instantaneous power spectrum*, Mechanical Systems and Signal Processing, Vol. 14, No. 6, (2000), pp. 907–921.

[12] Y. Lei, J. Lin, Z. He, and M. J. Zuo, *A review on empirical mode decomposition in fault diagnosis of rotating machinery*, Mechanical Systems and Signal Processing, Vol. 35, No. 1–2, (2013),pp. 108–126.

[13] S. Schmidt, P. S. Heyns, K.C. Gryllias, *Discrepancy analysis for gearbox condition monitoring: A comparison of different healthy data models*, *31st International Congress and Exhibition on Condition Monitoring and Diagnostic Engineering Management*, North-West, South Africa, 2018 July 2-5, North West (2018).

[14] D. Abboud, J. Antoni, S. Sieg-Zieba, and M. Eltabach, *Envelope analysis of rotating machine vibrations in variable speed conditions: A comprehensive treatment*, Mechanical Systems and Signal Processing, Vol. 84, (2017), pp. 200–226.

[15] D. Abboud, J. Antoni, S. Sieg-Zieba, and M. Eltabach, *Deterministic-random separation in nonstationary regime*, Journal of Sound and Vibration, Vol. 362, (2016), pp. 305–326,.

[16] X. Qi, Z. Yuan, and X. Han, *Diagnosis of misalignment faults by tacholess order tracking analysis and RBF networks*, Neurocomputing, Vol. 169, (2015), pp. 439–448.

Experimental validation of a bearing fault model for an independent cart conveyor

M. Cocconcelli [1], **J. Cavalaglio Camargo Molano** [1], **R. Rubini** [1], **L. Capelli** [2]
[1] University of Modena and Reggio Emilia, Department of Sciences and Methods of Engineering,
Via G. Amendola 2 - Pad. Morselli, 42122, Reggio Emilia, Italy
e-mail: **jacopo.cavalagliocamargomolano@unimore.it**

[2] Tetra Pak Packaging Solutions spa,
Via Delfini 1, 41123, Modena, Italy

Abstract
One of the most promising technology in industries is undoubtedly the independent cart conveyor system. It tries to replace induction motors and kinematic chains in several applications, especially in the field of automatic packaging machines. The independent cart conveyor system is made up of several induction linear motors. The carts are connected to the frame through a series of rollers, the bearings of which are subject to wear. In a previous paper the authors developed a theoretical model of the expected vibration signal from a faulted bearing, taking into account several design parameters. In this paper, the model is updated thanks to a new formulation of amplitude modulation effect and it is validated on the basis of an experimental campaign on a specific test-rig, where a bearing was artificially damaged on the external ring (the moving one). Finally, experiments have been used to validate the model in different configurations, proving the effectiveness of the proposed model and paving the way for future diagnostics of the independent cart conveyor.

1 Introduction

Independent Cart Conveyor System is an emerging technology in the automation field. It is an intelligent transport system based on modular linear motors [1], which mainly consists of two components: modular stators and several carts containing permanent magnets. The modular stators contain coils and in some cases also drives, they have different length and different shapes (linear and curved with different angles). They can be connected in different ways in order to develop machines with different shapes and functionalities. The carts are placed along the motors and they are connected, through rolling bearings, to a rail set on the motors themselves. They are directly moved through variable magnetic fields produced by the stators. Each cart contains an encoder flag that can be a Hall sensor or a tag, which allows the position and velocity feedback. The carts can be freely moved since they do not depend on one another, thanks to this function it is possible to change the distance and the velocity among the carts during the execution of the tasks; moreover, they can be moved back and forth. The carts can have high dynamics (e.g. they can reach a speed of 4 m/s) and they can have different shapes depending on the function they must execute. They can be used in CNC and robotic applications since the positioning of each mover is accurate.
The most important automation companies [2, 3, 4] produce this system in versions that differ from one another in maximum payload, maximum current, drivers architecture, programmable environment etc.

This technology can be used for the most typical functions of automatic machines, such as pick and place, cutting, stripping, screwing etc. The advantages in the use of Independent Cart Conveyor System are multiple [5]: high flexibility in the layout of the machine and in the functionality of the system, reduction of cycle

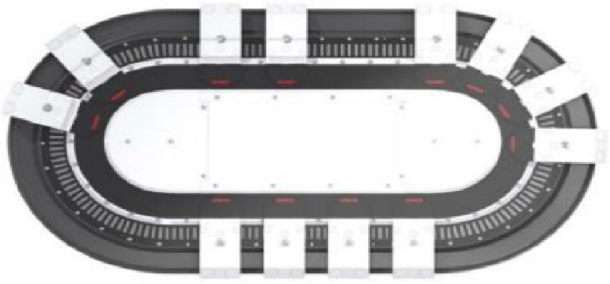


Figure 1: Beckhoff XTS independent cart system with 12 carts.

time and downtime.
The flexibility of the layout is obtained thanks to the modular stators, which allow the optimization of the machine and the reduction of the footprint of the system. The functional flexibility is ensured by the independent control of each cart. De facto, it is possible to dynamically adapt the functionality of the system to the process only by means of the software implementation and without any mechanical changes. For example, it is possible to work with products that have different shapes by defining a different motion profile for each cart or the independent cart system can dynamically change its velocity with respect to the change of the production rate.
This is not possible with the traditional motor-driven chains, belts and gears because in order to change the functionality of the machine it is necessary to design different mechanical links for every type of product and rate of production.
The reduction of cycle time is due to the possibility of defining an optimized motion profile for every single product, while in chain, belt and gear drivers the possible motion profiles are reduced by the high number of physical constraints of mechanics.
The other important advantage lies in the reduction of the downtime of the machine. De facto, with the Independent Cart Conveyor System it is not necessary to stop the machine for mechanical changes when there is a variation in the product because the end-effector is fixed to each cart and so it is only necessary to change the motion profiles of the carts. On the contrary, with the chain, belt and gear system it is necessary to stop the machine for the change of the mechanical parts so the downtime of the system increases.
Independent Cart Conveyor System can present the following problem: a high number of carts require a high number of rolling bearings. Consequently, the possibility of a bearing fault due to the infant mortality and wear of the components increases significantly.
Condition monitoring strategies are necessary to overcome this problem and increase the reliability of the system. Several condition monitoring methods are capable of monitoring the health state of the bearings and the future conditions of the system while it is working [6, 7, 8, 9]. The most used strategies in the bearing diagnostics are based on the vibration analysis of the system [10]. There are several vibration analysis techniques, such as statistical analyses [11], frequency domain analyses [10], time-frequency analyses [12, 13] and machine learning algorithms [14].
All these techniques need historical data in order to define the standard condition vibration signature of the system necessary to identify the possible changes due to a fault development [15, 16, 17, 18] or to define learning patterns for machine learning algorithms.
With the Independent Cart Conveyor System it is difficult to have historical data of the machine because of the high number of the possible configurations of the system. De facto, systems can have different length and shapes of the track, different geometry of the carts, different motion and load profiles and different types and positions of the bearings. In order to overcome this problem, a model of the vibration signal produced by a definite fault for a definite system configuration can be carried out. It allows to model all the possible configurations of the system and with the simulated data it is possible to analyze fault vibration signature and develop vibration thresholds and learning patterns even without any historical data.
This paper defines a generic flexible model of the expected vibration signals produced by different types of

damages on bearings and tracks for different configurations of the Independent Cart System. Thanks to this model, all geometric and dynamic variations in the possible system configurations are parametrized in order to reduce the modelling time. By simulating only some components of the vibration signal, this model helps to reduce the complexity of the analysis since it focuses only on certain types of fault. This is not directly possible with experimental data in particular in the presence of strong masking signals caused by other machine components.
The disadvantage in the use of a simulated vibration signal lays on the fact that too simple model cannot represent the main effects of the phenomena taken into consideration.
Several authors propose different models for the expected fault signals of bearings, especially as regards rotary motors. McFadden and Smith [19, 20, 21, 22] have proposed to model the faulted bearing as an epicycle gear where the outer ring is the annular gear, the cage is the planet carrier, the rolling elements are the planet gears and the inner ring is the sun gear. The modulation of the vibration signal due to the loading cycle of the elements is taken into account by Su et alt. [22]. Ho and Randall [23] have modelled the bearing fault vibration as a single-degree-of-freedom system.
The model proposed in this paper is an extension of the theoretic one [24] based on the work of D'Elia [25]. The model has been extended to the signal of multiple bearings for localized and distributed faults. Moreover a more accurate load modulation based on Tomovic [26], slipping effects and lubricant effect have been taken into consideration and the model has been tuned and validated with experimental data.
This paper is organized as follows: Section 2 describes the analytic models for bearing faults on linear motors; Section 3 is focused on the algorithm for the model implementation; Section 4 deals with experimental results and model tuning in case of constant speed and variable velocity motion profile; Section 5 explains the conclusions of the research.

2 Vibration model

The vibration signal produced by a fault in a rolling bearing can be modelled as the repetition of impact forces due to the collisions between the faulted part and the other components of the bearing or of the machine. The collisions excite resonance in the bearing and in the whole machine. The repetition of the impacts is due to the geometry and the velocity of the bearing, while the amplitude of the vibration signal depends on the load of the bearing, the position of its internal components and the wear state of the faulted part.
As shown below, the vibration signal of a localized fault is modelled on the basis of the reading of a sensor placed on the bearing [25].

$$x(t) = \sum_{i=-\infty}^{\infty} h(t - iT - \tau_i)q(iT) + n(t) \tag{1}$$

Where $h(t)$ is the impulse response to an impact on the damage point, T is the interval between two consecutive impacts, $q(t)$ represents the modulation due to the load distribution, τ represents the uncertainties due to the random slipping of the rolling elements and $n(t)$ is the system noise. The T interval between two consecutive impacts depends on the type of damage. De facto, each type of fault produces a unique frequency component that depends on the geometry and rotational frequency of the bearing [9].
Through the fault frequency of each type of damage it is possible to determine the T interval between two consecutive damages. In case of fixed inner race, the fault frequencies are the following:

$$f_{outer} = \frac{n}{2} f_r (1 - \lambda cos\beta) \tag{2}$$

$$f_{inner} = \frac{n}{2} f_r (1 + \lambda cos\beta) \tag{3}$$

$$f_{ball} = \frac{f_r}{2} \frac{1 - (\lambda cos\beta)^2}{\lambda} \tag{4}$$

$$f_{cage} = \frac{f_r}{2}(1 + \lambda cos\beta) \tag{5}$$

where n is the number of rolling elements, d is the ball diameter, D is the pitch diameter, β is the ball contact angle and f_r is the rolling frequency of the outer ring. In case of linear motors, there are other two types of possible fault: - the damage on the fixed rail, the characteristic frequency of which is equal to:

- the damage on the fixed rail, the characteristic frequency of which is equal to:

$$f_{rail} = \frac{v}{l} \tag{6}$$

  where l is the distance between the damages along the rail and v is the linear velocity of the bearing. If multiple bearings are installed on the same rail, the signal will be repeated according to the number of moving components and the distance among them.

- the damage on the external surface of the bearing, the characteristic frequency of which is equal to:

$$f_{surface} = \frac{v}{\pi D_{out}} \tag{7}$$

  where v is the linear velocity and D_{out} is the external surface diameter.

3 Model implementation

The motion profile of the cart moving along the track (constant or variable velocity profile), the characteristics of the cart (center of gravity (COG) of the cart, position of the bearings, mass, etc.) and of the track (length, shape) are the inputs of the model. The implementation of the expected vibration signal is based on (Eq. 1). where the T interval between two consecutive impacts is considered as the distance of two fault points along the motion profile of the cart.
In order to perform these operations, all the fault frequencies have been rewritten as the projection of two consecutive fault points along the external surface of the bearing. This formulation allows to transpose the fault frequency as a position variation of the bearing. In this way the damage of an element of the bearing is directly correlated with the position of the bearing itself along the motion profile. For example, in the case of a fault on the outer ring, it is possible to write (Eq. 4) as the projection of the fault on the external surface of the bearing as follows:

$$\Delta p_e = \frac{2\pi}{n} D_{out} \frac{1}{1 - \frac{dcos\beta}{D}} \tag{8}$$

where Δp_e is the distance between two damages projected on the external surface of the bearing. In this way each fault is defined as a series of equispaced impulses, but fault signals are not actually equispaced because of the slipping of the mechanical components on the rail. In order to simulate the random slipping of the mechanical elements of the bearing, for each Δp_e a random slipping factor $r(t)$ with a mean equal to zero and a standard deviation equal to 1/100 of the Δp_e is summed. This factor is represented as the τ element of the uncertainties in Eq. 1. The load modulation $q(t)$ on the bearings consists of two elements. The former represents the variation of the load on the whole cart computed on the contact point of each bearing. This modulation is due to the inertia of the cart, the variation of acceleration during the process, the mechanical cams that are used in order to move the end-effector placed on the cart. This contribution is calculated for each bearing with respect to the position of the cart along the motion profile.
The latter represents the load variation on the rolling elements of the bearing due to the rotation of the bearing itself. It depends on the azimuth position of the rolling element and it can be computed by analyzing the geometry and the contact deflection of the bearing. Like in Sjovall [27], this phenomenon is modelled as a

modulating factor multiplied by the radial load on the bearing. The modulating factor is computed through the Sjovall integrals $J_r(t)$ and $J_a(t)$, the computation of the load zone parameter ϵ , the axial load F_a and radial load F_r as follows:

$$W(\Psi) = W_{max}\left[1 - \frac{1}{2\epsilon}(1 - \cos(\Psi))\right]^t \tag{9}$$

where $W(\Psi)$ is the load distribution, $t = 3/2$ for ball bearings ($t = 40/37$ or $10/9$ for roll bearings) and Ψ is the half load-zone angle and it is equal to:

$$\Psi(\epsilon)\begin{cases} \cos^{-1}(1-2\epsilon) & \epsilon \leq 1 \\ \pi & \epsilon \geq 1 \end{cases} \tag{10}$$

While the maximum load of a rolling element W_{max} is equal to:

$$W_{max} = \frac{1}{Z}\sqrt{\left(\frac{F_r}{j_r}\right)^2 + \left(\frac{F_a}{j_a}\right)^2} \tag{11}$$

where Z is the spare number. In this way for each angle it is possible to compute the load on the rolling element.

The implementation of the model can be divided into 5 steps:

1. Define a vector S filled with zeros. It represents the expected vibration signal recorded by a sensor placed on the moving cart. Each cell of the vector corresponds to a period of time equal to $t = 1/f_s$ where f_s is the sampling frequency of the sensor in Hz and t is the time period between two data read by the sensor.

2. Resample the defined motion profile $M(t)$ and the load vector $q(t)$ at the same sampling frequency f_s of the sensor.

3. . Place 1 in the cells of vector S with index values defined by dividing $M(t)$ by $\Delta p_e + r(t_i) + R_{sum(t)}$. $R_{sum(t)}$ is the sum of all the previous random factors $r(t_i)$. In this way the phenomenon of slipping is taken into account along the whole motion profile.
   The factor $\Delta p_e + r(t_i) + R_{sum(t)}$ is a rational number and its value may be between two samples of the motion profile. Therefore an error is introduced and it depends on the sampling frequency f_s (the greater is f_s, the lower is the error), but it is possible to compute for each division the correlate error as below:

$$E(t_i) = |M(t_i) - \Delta p_{e,i}| \tag{12}$$

4. Weight the vector S with the vector of the load $q(t)$ computed on the contact point between the bearing and the rail. In the case of a fault on a rolling element $q(t)$, it also includes the modulation of the internal dynamics of the bearing.

5. . Filter vector S with the FFT-based model with overlap-add method by choosing the acceleration of the impulse response of a SDOF system as filter coefficients. The generated response of the SDOF system to a unit impulse in the time domain is:

$$x_{SDOF}(t) = \frac{F/m}{\omega_d} e^{-\zeta\omega_n t} sin(\omega_d t) \tag{13}$$

   where F is the amplitude of the external excitation, m is the system mass, ζ is the damping coefficient, ω_n is the natural frequency in [rad/s] and $\omega_d = \omega_n\sqrt{1-\zeta^2}$.

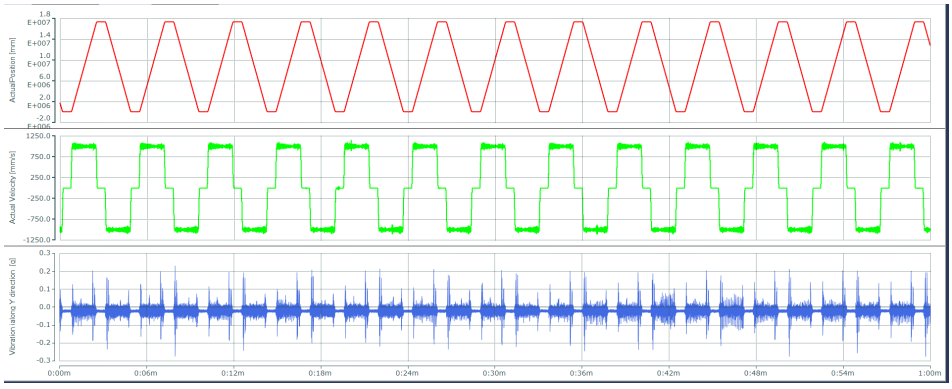


Figure 2: Motion profile and vibration signal of the cart

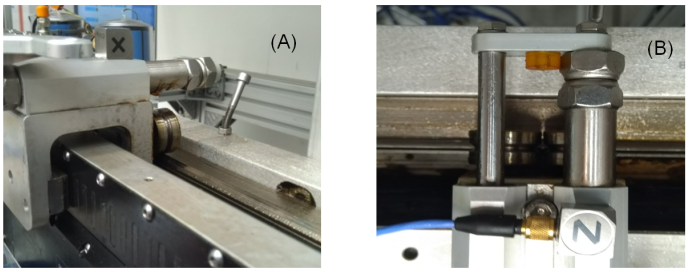


Figure 3: Test rig: A) lateral picture of the mover along the straight motor B) Top picture of the mover on the rail .

In the case of simulation of multiple faults on the same bearings, Step 3 has to be repeated for each fault. The model takes into consideration multiple bearings, for this reason the five steps listed above have to be repeated for each bearing. If a bearing has not any fault, the model considers the vibration signal produced by the healthy bearing to be equal to the rotational frequency of the bearing itself.

4 Experimental Validation

This section describes the experiments carried out with an XTS, a type of Independent Cart Conveyor System produced by Beckhoff Automation (Fig.1), in order to verify and validate the proposed model. The system taken into account consists in seven straight motors, each of which is 250 mm long; they are connected to each other in order to develop a straight path that is 1750 mm in length. A cart, connected to a lubricated straight rail as in Fig.3 and Fig.4 by means of three rolling bearings, moves along the motors. An accelerometer placed on the top of the cart measures all the vibrations along the vertical direction. For the tests the cart follows a trapezoidal motion profile consisting of three zones: an acceleration zone, a constant velocity zone and a deceleration zone. First the motion profile is executed by cart from the right to the left side and then from the left to the right side (Fig2).

The test has been run with three different velocity of the cart along the constant velocity zone:

- 500 mm/s,
- 1000 mm/s,
- 1500 mm/s,
- 2000 mm.

Table 1: Bearings dynamic parameters and dimensions

Model parameters	
Bearing A/B D_{out} (mm)	21.2
Bearing A/B d (mm)	17.7
Bearing A/B D (mm)	5
Bearing C D_{out} (mm)	31.1
Bearing C d (mm)	4.30
Bearing C D (mm)	20
Bearing A/B/C number of spheres	7
Bearing A/B/C Sample frequency f_s (Hz)	$20E3$
Bearing A/B/C SDOF spring stiffness k (N/m)	$2E13$
Bearing A/B/C SDOF damping coefficient ζ	5%
Bearing A/B/C SDOF natural frequency f_n (Hz)	300

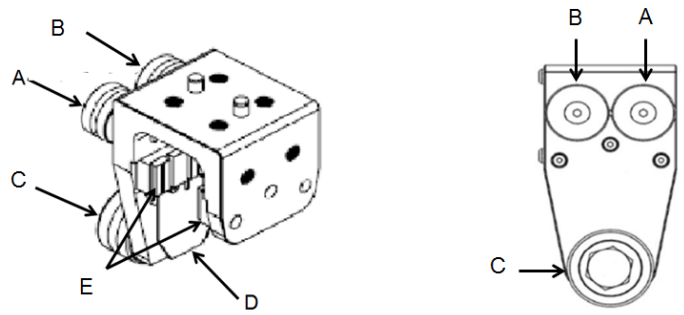


Figure 4: Cart architecture: A) Right bearing , B) Left bearing, C) bottom bearing E) Permanent magnets, D) Encoder flag.

The tests have been carried out at the aforementioned velocities with two different configurations of the mover (Fig.4). In the former all the bearings of the mover are healthy, in the latter bearing B is damaged on the outer ring surface. Bearing dimensions are listed in Table 1.

The actual position of the mover and the vibration signal recorded along the vertical direction have been used for the verification and validation of the model.

4.1 Healthy bearings

For the sake of brevity, Fig.5 shows the raw vibration data in the case of healthy bearings at the speed of 500mm/s with respect to the position of the mover along the rail. The vibrations recorded show that there are some vibration hits along the rail. The vibration hits are in the same positions even at different velocities. Some of them depend on the transition between two different motors, while the other ones depend on the configuration of the rail that presents some discontinuities due to the assembly of the mechanical system. The positions correlated to the vibration hits are shown in Fig.6 and the following ones are the most important:

- Rail discontinuity : 122 mm, 1500mm, 1624 mm ,
- Motor-to-motor transition : 700 mm.

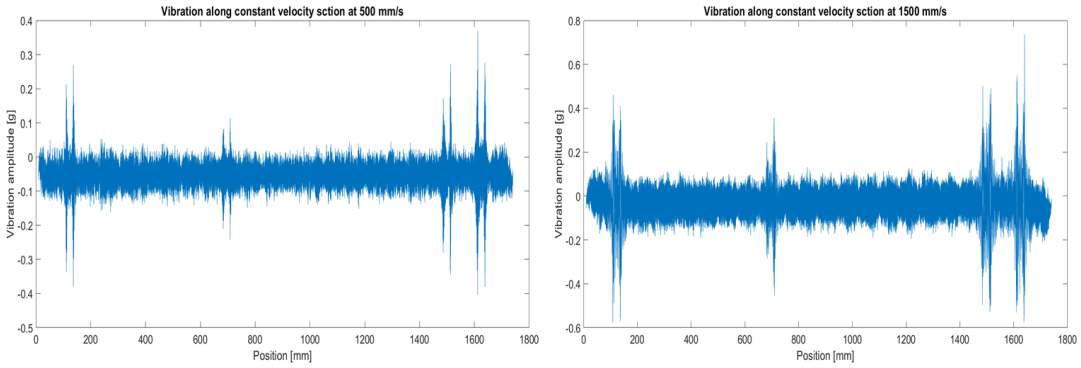


Figure 5: Vibration signal along constant velocity section at 500mm/s and 1500 mm/s

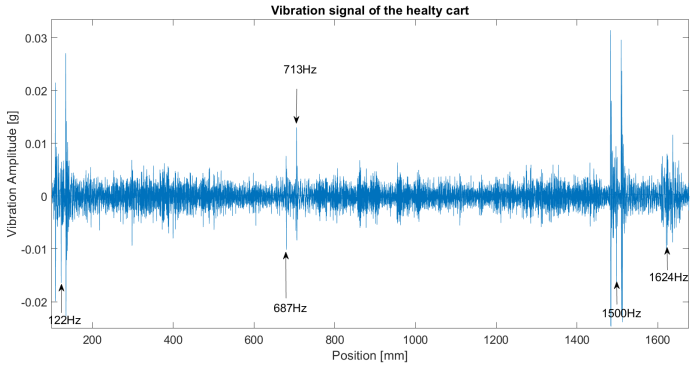


Figure 6: Vibration correlated to rail discontinuity and motor-to-motor transition

For each position of the rail discontinuity there are three vibration peaks: the highest two are due to the two bearings mover (A and B) placed on the upper part of the mover, while the other one is due to the bearing (C) placed on the lower part of the mover. The time distance between the highest peaks is correlated to the distance between bearing A and bearing B that is equal to 26 mm, while the time distance between the first highest peak and the low peak is correlated to the distance between bearing A and bearing C that is equal to 13 mm. The different amplitude depends on the position of the accelerometer placed on the top of the cart. Fig.7 shows the simulated signal produced by the model with the computation of the three rail discontinuities and the motor-to-motor transition in the same positions as the real ones.

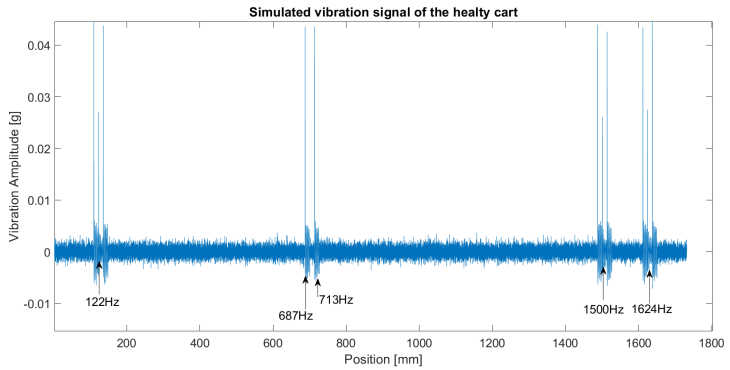


Figure 7: Simulated vibration signal with rail discontinuity and motor-to-motor transition

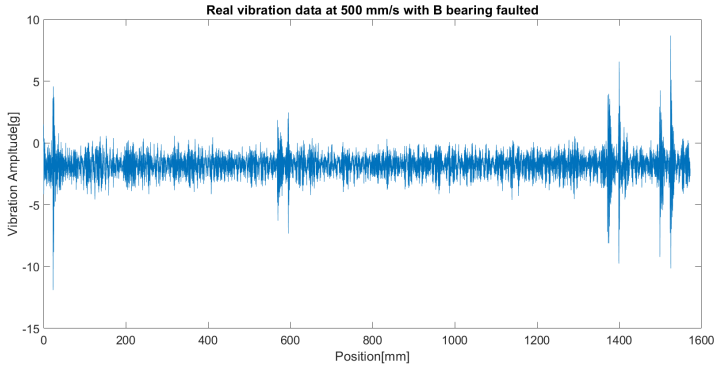


Figure 8: Real vibration signal at 500 mm/s with B bearing faulted

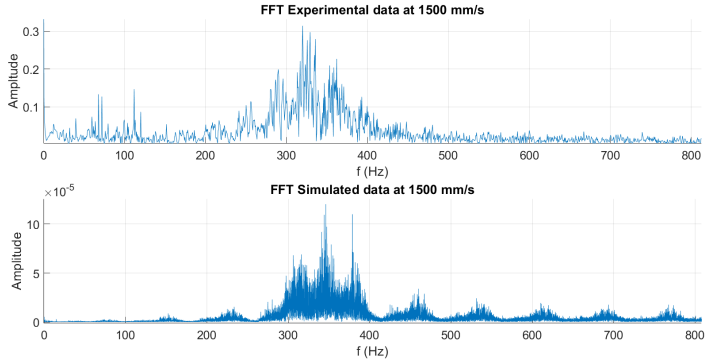


Figure 9: Comparison between the FFT of real and simulated data

4.2 Faulted bearing

Fig.8 shows the raw vibration data in the case in which the mover has a velocity of 1500 mm/s and the bearing B has a fault on the outer ring. Even in this case the vibrations due to the rail variation and the motor-to-motor transition are evident. Through Hilbert transform of the signal along the constant velocity zone of the motion profile it is possible to find the frequency of the fault of the outer ring of the bearing at different velocities.

The model considers the rail variation, the motor-to-motor transition, the fault frequency of bearing B and it uses the real motion profile and the load profile of the cart as inputs. The FFT of the simulated vibration are compared withe the real ones in Fig.9. In the time domain the two signals have a very similar signal periodicity while there is a difference in the amplitude of the signal. However, the principal goal of the model is to simulate the frequency components of the experimental signal correctly. Fig.10 compares the Hilbert transform of the experimental data and the simulated data in which the theoretical fault frequency of outer ring is equal to 64.18 Hz.In the simulated data the spectrum components of the controller position loop, velocity loop, current loop and the duty cycle of the transistors are not present in the frequency spectrum since the model is focused on the fault frequency of the system; however, they can be added.

5 Conclusions

The paper details a flexible model for the simulation of the expected fault vibration signal for the Independent Cart Conveyor System.

The model allows to:

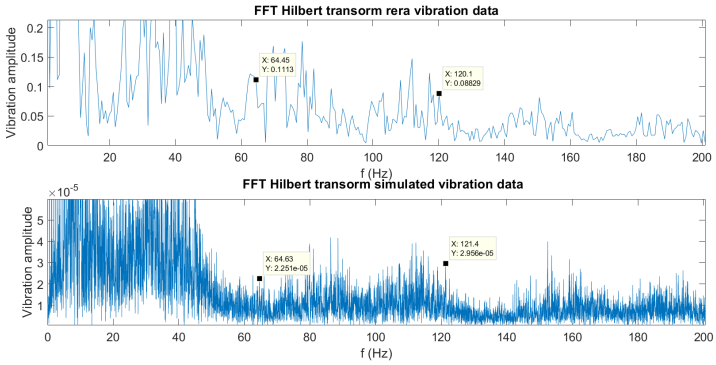


Figure 10: Comparison between the Hilbert transform of real and simulated data

- Choose any shape of the rail track
- Use variable velocity and constant velocity profiles
- Use variable load profiles
- Simulate several bearings of different dimensions
- Simulate the most common damage of a rolling bearing along a linear rail
- Consider the resonance of the system
- Consider random contributions
- Consider the modulation of the load on the bearings.

The model has been validated through several experimental tests carried out with a Beckhoff XTS system for a cart moving along a path made up of 7 straight motors. The simulated vibration signal has the same fault frequency components and the same resonance frequency as the experimental data. The model could be used to simulate a model of the vibration signal produced by a definite fault for a definite system configuration. With the simulated data it will be possible to analyze fault vibration signature and develop vibration thresholds and learning patterns even without any historical data.

Acknowledgements

The authors are grateful for the National University Research Fund (FAR 2016) of the University of Modena and Reggio Emilia - Departmental and Interdisciplinary Projects (DR. 73/2017, Prot. n. 37510-27/02/2017) and the support from Tetra Pak Packaging Solutions.

References

[1] B&R, *The fast track to flexible packaging*, https://tinyurl.com/yb4mv4qy (2017).

[2] Rockwell Automation, *iTRAK The Intelligent Track System Increase machine exibility and throughput to enhance overall productivity*, https://tinyurl.com/ydh9nade (2015).

[3] Beckhoff Automation, *XTS. The eXtended Transport System*,https://tinyurl.com/yc9v3wzq (2012).

[4] B&R, *ACOPOStrak Ultimate Production Effectiveness*, https://tinyurl.com/y9kvesk9 (2017).

[5] J. Cavalaglio Camargo Molano, S. Rossi, M. Cocconcelli, R. Rubini, *Dynamic model of an independent carts system*, Adv. Ita. Mech. Sc. Mech. and Machines Sc., Vol. 47, Springer (2017), pp. 379-387.

[6] A. Bellini, F. Filippetti, C. Tassoni, G.A. Capolino, *Advances in diagnostic techniques for induction machines*, IEEE Trans. Ind. Electron., Vol. 55, No. 12, IEEE (2008), pp. 4109-4126.

[7] S. Poyhonen, P. Jover, H. Hyotyniemi, *Signal processing of vibrations for condition monitoring of an induction motor*, in *Proc. 1st Int. symp. Control, Commun. Signal Process.*, (2004), pp. 499-502.

[8] S. Nandi, H. Toliyat, X. Li, *Condition monitoring and fault diagnosis of electrical motors-A review*, IEEE Trans. Energy Convers., Vol. 20, No. 4, IEEE (2005), pp. 719-729.

[9] R.B. Randall, *Vibration-based Condition Monitoring:Industrial,Aerospace and Automotive Application*, John Wiley & Sons Inc. (2011).

[10] R.B. Randall, J. Antoni, *Rolling element bearing diagnostics A tutorial*, Mech. Syst. Signal Process., Vol. 25, No. 2, Elsevier (2011), pp. 485-520.

[11] M. Delgado Prieto, G. Cirrincione, A.G. Espinosa, J.A. Ortega, H. Henao, *Bearing Fault Detection by a Novel Condition-Monitoring Scheme Based on Statistical-Time Features and Neural Networks*, IEEE Trans. Ind. Electron., Vol. 60, No. 8, IEEE (2013), pp. 3398-3407.

[12] W. Wang, P.D. McFadden, *Early detection of gear failure by vibration analysis I. Calculation of the time-frequency distribution*, Mech. Syst. Signal Process., Vol. 7, No. 3, Elsevier (1993), pp. 193-203.

[13] W. Wang, P.D. McFadden, *Application of wavelets to gearbox vibration signals for fault detection*, J. Sound Vib., Vol. 192, No. 5, Elsevier (1996), pp. 927-939.

[14] M. Gan, C. Wang, C. Zhu, *Construction of hierarchical diagnosis network based on deep learning and its application in the fault pattern recognition of rolling element bearings*, Mech. Syst. Signal Process., Vol. 72-73, Elsevier (2016), pp. 92-104.

[15] S. Braun, *Mechanical Signature Analysis*, Academic Press, London (1986).

[16] G. Curcurú, M. Cocconcelli, F. Immovilli, R. Rubini, *On the detection of distributed roughness on ball bearings via stator current energy: Experimental results*, Diagnostyka, Vol. 51, No. 3, (2001), pp. 17-21.

[17] F. Immovilli, M. Cocconcelli, A. Bellini, R. Rubini, *Detection of generalized roughness bearing fault by spectral-kurtosis energy of vibration or current signals*, IEEE Trans. Ind. Electron., Vol. 56, No. 11, IEEE (2009), pp. 4710-4717.

[18] M. Hayes, *Statistical Digital Signal Processing and Modelling*, John Wiley & Sons (1996).

[19] P.D. McFadden, J.D. Smith, *Vibration monitoring of rolling element bearings by the high frequency resonance technique a review*, Tribol. Int., Vol. 117, Elsevier (1984), pp. 3-10.

[20] P.D. McFadden, J.D. Smith, *Model for the vibration produced by a single point defect*, J. Sound Vib., Vol. 96, Elsevier (1984), pp. 69-82.

[21] P.D. McFadden, J.D. Smith, *The vibration produced by multiple point defects in a rolling element bearing*, J. Sound Vib., Vol. 98, Elsevier (1984), pp. 263-273.

[22] Y.T. Su, S.J. Lin, *On initial detection of a tapered roller bearing frequency domain analysis*, J. Sound Vib., Vol. 155, Elsevier (1992), pp. 75-84.

[23] D. Ho, R.B. Randall, *Optimization of bearing diagnostic techniques using simulated and actual bearing fault signals*, Mech. Syst. Signal Process., Vol. 14, Elsevier (2000), pp. 763-788.

[24] M. Cocconcelli, J. Cavalaglio Camargo Molano, R. Rubini, L. Capelli, D. Borghi, *Bearing fault model for an independent cart Conveyor*, in *Proc. 6th Int. Conf. Cond. Monit. Machinery Non-Stat. Condit.*, (2018), in press.

[25] G. D'Elia, M. Cocconcelli, E. Mucchi, *An algorithm for the simulation of faulted bearings in non-stationary conditions*, Meccanica, Vol. 53, No. 45, Springer (2018), pp. 1147-1166.

[26] R. Tomović, *Calculation of the boundary values of rolling bearing deflection in relation to the number of active rolling elements*, Mech. Mach. Theory, Vol. 47, Elsevier (2012), pp. 74-88.

[27] H. Sjovall, *The Load Distribution within Ball and Roller Bearings under Given External Radial and Axial Load*, TekniskTidskrift Mek., Vol. 9, (1933).

Methodologies for designing new condition indicators

J. Antoni [1], **P. Borghesani** [2], **S. Kass** [3], **A. Raad** [3], **K. Gryllias** [4]
[1] Laboratoire Vibrations Acoustique, Univ Lyon, INSA-Lyon, LVA EA677, F-69621 Villeurbanne, France
e-mail: **jerome.antoni@insa-lyon.fr**

[2] School of Mechanical and Manufacturing Engineering, UNSW Sydney, Kensington, NSW 2052, Australia

[3] Engineering faculty, Lebanese University, Tripoli, Lebanon

[4] KU Leuven, Faculty of Engineering, Department of Mechanical Engineering, Division PMA, Member of

Flanders Make

Abstract
The current practice of machines health monitoring strongly relies on the use of condition indicators. They ideally measure a certain property in the signal, whose occurrence is correlated with the symptom of a fault. Despite their importance, the corpus of popular condition indicators is surprisingly narrow. In a recent publication, the first two authors introduced as statistical methodology to design new indicators from the time domain which, among all possible indicators attached to a specific symptom, maximize the probability of detection of the fault. The aim of this paper is to investigate the extension of this methodology to the frequency domain. Cyclostationary symptoms only are of concern, due to their practical importance. Advantage is taken of a recently proposed fast algorithm to compute the spectral coherence, on which all the proposed condition indicators happen to be rooted. It is shown that different condition indicators can thus be designed in a rather general setting, whether the fault frequency is known, partially known or even unknown.

1 Introduction

From its beginning, condition monitoring has strongly relied on the use of scalar indicators which aim at summarizing the information contained in signals into single values [**?**]. The so-called "condition" or "health" indicators are now routinely used, not only for monitoring, but also for fault detection, in machine diagnostics and in prognostics. They also serve as the main inputs fed to statistical models for classification (e.g. in diagnostics) and for regression (e.g. in prognostics). Typical examples are measures of non-Gaussianity (e.g. kurtosis, crest-factor, power means [**?**]) and, to a lesser extent, measures of non-stationarity (e.g. indices of cyclostationarity [**?**]). Surprisingly, the state-of-the-art on condition indicators has evolved slowly as compared to new techniques that make heavy use of them, such as machine learning. The aim of this paper is to contribute to bridging this gap.

In a recent publication, the first two authors introduced a statistical methodology to design new indicators based on a probabilistic formulation of the symptoms to be tracked [**?**]. The resulting indicators are optimal in the sense that they maximize the probability of detection of the symptoms for a given risk of false alarm. It was shown that several known indicators could be recovered as particular cases of or as approximations to this approach. Several new indicators were also discovered. At the same time, the proposed statistical methodology has the benefit to provide a threshold against which the indicators can be compared, which is crucial in applications and rarely available from other approaches.

The goal of this paper is to investigate the possibility to extend the condition indicators of Ref. [**?**], which were derived in the time domain, to the frequency domain. Since Gaussianity is generally preserved when moving to the frequency domain, only condition indicators dedicated to the detection of cyclostationary Gaussian signatures are investigated in this paper. They are indeed of prime importance in the condition monitoring of rotating machines. Proceeding from the frequency domain may be advantageous for at least two reasons. The first one is that it easily allows the consideration of non-harmonically related cyclic frequencies (e.g. in the case of a sum of multiple cyclostationary signals, also called poly-cyclostationary signals). The second one is that it allows the insertion of weights in the computation of the indicator, so as to emphasize or reduce certain carrier and modulation frequencies. For the sake of simplicity, generalization to cyclo-non-stationary configurations (e.g. non-constant rotating speed [**?**]) is not addressed in this work.

The description of Gaussian cyclostationary signals being completely contained in the spectral correlation, it will appear without surprise that the proposed indicators are all rooted on this bi-spectral quantity; they will try to resume its information into a single scalar value. At this stage, advantage will be taken of the recently proposed fast algorithm to compute the spectral correlation [**?**].

The paper is organized as follows. First, a brief review is given in section **??** as how to design optimal indicators from the methodology introduced in Ref. [**?**]. Next, the principle is extended to the frequency domain in section **??**. Two cases are investigated, whether the fault frequency is known or not. These results are then used in section **??** to propose three plausible condition indicators: the first one is based on known or partially known fault frequency, the second one applies when the fault frequency is unknown and shows interesting similarity with a measure of roughness, and the last one is specifically designed to measure accumulated fatigue damage.

2 Design of optimal indicators

This section briefly resumes the statistical methodology proposed in Ref. [**?**] to design condition indicators. The starting point is two describe the health of the system under investigation by two alternative hypotheses, H_0 and H_1, which correspond to the healthy and the faulty states, respectively. Let $\mathbf{x} = \{x(n); n = 0, ..., L-1\}$ be the measured signal from which a decision is to be taken, as whether the system is in state H_0 or in state H_1. The next step is to describe the expected statistical properties of the signal states by means of the probability density functions $f_X(\mathbf{x}|H_0)$ and $f_X(\mathbf{x}|H_1)$. A typical choice often found in the literature is to assume that $f_X(\mathbf{x}|H_0)$ is Gaussian stationary in the healthy state and that $f_X(\mathbf{x}|H_1)$ reflects some departure from this point of equilibrium, for instance through a non-Gaussian or a nonstationary behavior. Yet many other scenarios are conceivable, as long as H_1 includes H_0 as a particular case (for instance a more general scenario is to assume $f_X(\mathbf{x}|H_0)$ non-Gaussian stationary and $f_X(\mathbf{x}|H_1)$ non-Gaussian nonstationary). In general, the probability density functions will depend on some vectors of unknown parameters θ_0 and θ_1 (with the dimension of θ_1, say d_1, greater than the dimension of θ_0, say d_0). The proposed condition indicator is then defined as the time average of the logarithm of the "generalized likelihood ratio" (GLR)

$$I_X = \left\langle \ln \left(\frac{\max_{\theta_1} f_X(\mathbf{x}|H_1, \theta_1)}{\max_{\theta_0} f_X(\mathbf{x}|H_0, \theta_0)} \right) \right\rangle \tag{1}$$

where symbol $\langle \cdots \rangle$ stands for the time average operator (the adjective "generalized" refers to the fact that the unknown parameters θ_0 and θ_1 are replaced by their maximum likelihood estimates in the likelihood ratio). The so defined indicator has several properties:

- it is positive and theoretically nil (in the large sample limit) when H_0 is true,
- it is optimal as it maximizes the probability of detection of state H_1 given a probability of false alarm p_F under state H_0,
- it comes with a statistical threshold – returned by Wilk's theorem and equal to $\chi^2_{d_1-d_0,1-p_F}/L$ under H_0 – to be used in statistical tests.

In the special case where H_0 is Gaussian stationary and H_1 is Gaussian cyclostationary with cyclic period M, the corresponding indicator reads

$$I_X = -\left\langle \ln\left(\frac{s^2(n)}{\langle s^2(n)\rangle}\right)\right\rangle \tag{2}$$

where

$$s^2(n) = \frac{1}{K}\sum_{k=0}^{K-1} |x(n+kM)|^2,\ K=[L/M] \tag{3}$$

is the synchronous average of the squared signal (the signal being assumed zero-mean). The associated threshold under H_0 and risk p_F is $\chi^2_{N-1,1-p_F}/L$.

It is noteworthy that, unless interpolation is used, the above formula applies only to cyclostationary signals whose fundamental frequency is equal to $\alpha = 1/M$ with $M \in \mathbb{N}$. This evidences one limitation of the time domain approach.

3 Extension to the frequency domain

The aim of this section is to extend the previous methodology to the frequency domain. This is essentially motivated by the needs to return indicators in frequency bands and to allow the weighting of frequency components in the definition of indicators. There are several possible scenarios to be considered, essentially divided into two families depending on whether the cyclic frequency of the signature to be detected is known or not. From now on, signal x is assumed Gaussian (poly)cyclostationary with a set of cyclic frequencies $\alpha_p \in \mathcal{A}$, $\alpha_p \neq 0$, which are not necessarily harmonically related.

3.1 Known cyclic frequency

3.1.1 Strategy 1

In the case of a known cyclic frequency, an immediate extension of the GLR-based indicators to the frequency domain is obtained after filtering the signal filtered in subbands. This is in principle quite trivial and should not pose any practical problem, as long as the bandwidth of the subbands is set greater than the highest cyclic frequency (i.e. $\Delta f > \max_p \alpha_p$) in virtue of the uncertainty principle. The resulting indicator, say $I_X(f_k, \Delta f)$, then depends on both the frequency f_k (the center of the k-th subband) and on the frequency resolution Δf (the bandwidth).

3.1.2 Strategy 2

A second approach is to proceed from an estimate of the spectral correlation $S_X(\alpha, f)$ of the underlying stochastic process, which in theory is not subjected to the uncertainty principle [**?**]. The spectral correlation is defined as the covariance function between two short-time Fourier transforms (STFT) when the integration time grows to infinity (or equivalently the spectral resolution tends to zero): $S_X(\alpha, f) = \lim_{N\to\infty} \mathbb{E}\{X_N(i,f)X_N(i,f-\alpha)^*\}$ with $X_N(f) = \sum_{n\in\mathbb{Z}} w(n-iR)x(n)e^{-j2\pi fn}$, $w(n)$ a data window (e.g. a Hann window) of length N centered on time instant iR and R the time step (it is noteworthy that $S_X(\alpha, f)$ ultimately does not depend on i). Therefore, it appears that under H_1 the set of STFTs $\{X_N(i, f_k); i = 1, ..., I, k = 0, ..., F-1\}$ (assumed independent with respect to index i) arranged in column vectors $\mathbf{X}_i = (X_N(i, f_0), ..., X_N(i, f_{F-1}))^T$, $i = 1, ..., I$ is distributed like a multivariate complex Gaussian with covariance matrix $\mathbf{C}_{H_1}(\mathcal{A})$,

$$f(\mathbf{X}_1, ..., \mathbf{X}_I) = \frac{e^{-\sum_{i=1}^{I} \mathbf{X}_i^H \mathbf{C}_{H_1}(\mathcal{A})^{-1}\mathbf{X}_i}}{\pi^I |\mathbf{C}_{H_1}(\mathcal{A})|^I}, \tag{4}$$

where $[\mathbf{C}_{H_1}(\mathcal{A})]_{kl} = S_X(f_k - f_l, f_k)$ for any combination $f_k - f_l = \alpha_p \in \mathcal{A}$ and is zero otherwise (the notation $\mathbf{C}_{H_1}(\mathcal{A})$ is to emphasize that the covariance matrix depends on the cyclic frequencies $\alpha_p \in \mathcal{A}$). This is now to be compared to the null hypothesis where the covariance matrix C_{H_0} is diagonal with k-th diagonal element equal to the power spectral density (PSD) $S_X(0, f_k)$. After replacing in the LR the covariance matrices $\mathbf{C}_{H_1}(\mathcal{A})$ and $\mathbf{C}_{H_0}$ by their maximum likelihood estimates $[\hat{\mathbf{C}}_{H_1}(\mathcal{A})]_{kl} = I^{-1}\sum_{i=1}^{I} X_N(i, f_k)X_N(i, f_l)^* = \hat{S}_X(f_k - f_l, f_k)$ and $[\hat{\mathbf{C}}_{H_0}]_{kl} = \delta_{kl}[\hat{\mathbf{C}}_{H_1}(\mathcal{A})]_{kl} = \hat{S}_X(0, f_k)\delta_{kl}$, respectively, the following indicator is found

$$I_X(\mathcal{A}) = \ln \frac{|\hat{\mathbf{C}}_{H_1}(\mathcal{A})|}{|\hat{\mathbf{C}}_{H_0}|} = \ln \left| \hat{\mathbf{C}}_{H_0}^{-\frac{1}{2}} \hat{\mathbf{C}}_{H_1}(\mathcal{A}) \hat{\mathbf{C}}_{H_0}^{-\frac{H}{2}} \right|. \tag{5}$$

Note that $I_X(\alpha) = 0$ when $\hat{\mathbf{C}}_{H_1}(\mathcal{A}) = \hat{\mathbf{C}}_{H_0}$. The associated threshold at risk p_F is $\chi^2_{F(F-1),1-p_F}/(2I)$. Unfortunately, at first sight, this result is rather impractical as it involves the computation of a potentially very large determinant. It has however a theoretical value since it establishes that the quantity of interest in the GLR is actually the (empirical) spectral coherence, i.e. the normalized estimate of the spectral correlation, $\hat{\gamma}_X(\alpha, f) = \hat{S}_X(\alpha, f)/(\hat{S}_X(0, f - \alpha)\hat{S}_X(0, f))^{-1/2}$.

From here on, several suboptimal indicators can be devised. The simplest one is probably to replace the log-determinant measure in Eq. (**??**) by the Frobenious norm of the off-diagonal elements. This simply reads

$$I_X^{(1)}(\mathcal{A}) = \frac{1}{FP} \sum_{\alpha_p \in \mathcal{A}} \sum_{k=0}^{F-1} w_{k,p} \cdot |\hat{\gamma}_X(\alpha_p, f_k)|^2 \tag{6}$$

where the sum is taken over $P = |\mathcal{A}|$ cyclic harmonics of interest and $w_{k,p} \geq 0$ is an optional weight used to emphasize or reduce some frequency components. Another possibility is to replace the log-determinant by its upper bound given in Hadamard theorem, that is

$$I_X^{(2)}(\mathcal{A}) = \frac{1}{2F} \sum_{k=0}^{F-1} \cdot \log \left(1 + \sum_{\alpha_p \in \mathcal{A}} w_{k,p} \cdot |\hat{\gamma}_X(\alpha_p, f_k)|^2 \right) \tag{7}$$

These quantities are eligible candidates to define indicators, as long as $\hat{\gamma}_X(\alpha_p, f_k)$ is a valid estimator. In particular, $I_X^{(1)} = I_X^{(2)} = 0$ when $\hat{\gamma}_X(\alpha_p, f_k) = 0, \forall p$. In order to keep their variance low, it is recommended to limit the number P of cyclic frequencies. A major drawback of the approximations (**??**) and (**??**) as compared to definition (**??**) is that their associated statistical thresholds are no longer given in a systematic way by Wilk's theorem.

3.2 Unknown cyclic frequency

The case with unknown cyclic frequency is of practical importance, especially in the context of diagnosis where the fault frequency is not always known to an arbitrary degree of precision or is sometimes completely unknown. It can be approached in several ways, some of which which are described hereafter.

3.2.1 Strategy 1: tuned cyclic frequencies

The first approach is to include the cyclic frequencies as unknown variables in the GLR and then to maximize the latter with respect to them. This leads to the indicator

$$I_X^{(3)}(\mathcal{A}) = \text{Arg} \max_{\alpha_p \in \mathcal{A}} \ln \left| \hat{\mathbf{C}}_{H_0}^{-\frac{1}{2}} \hat{\mathbf{C}}_{H_1}(\mathcal{A}) \hat{\mathbf{C}}_{H_0}^{-\frac{H}{2}} \right|. \tag{8}$$

and its related approximations given by Eqs. (**??**) and (**??**). The computation of $I_X^{(3)}$ might become troublesome if the number of unknown cyclic frequencies is high. An easier situation arises when the cyclic frequencies are harmonically related, i.e. $\alpha_p = p\alpha$, in which case the maximization in Eq. (**??**) is carried out only over the fundamental frequency α.

3.2.2 Strategy 2: full-scan

The second approach is to include in the indicator all possible cyclic frequencies, that is to replace the covariance matrix $\hat{\mathbf{C}}_{H_1}(\mathcal{A})$ in (**??**) by its counterpart $\hat{\mathbf{C}}_{H_1}$ computed for all frequency differences $f_k - f_l$ and not only those satisfying $f_k - f_l = \alpha_p \in \mathcal{A}$. The "full-scan" indicator then reads

$$I_X^{(4)} = \frac{1}{F_1 F_2} \sum_{l=1}^{F_1-1} \sum_{k=0}^{F_2-1} w_{k,p} \cdot |\hat{\gamma}_X(\nu_k, f_k)|^2, \tag{9}$$

where the notation ν is used instead of α to emphasize the fact that ν is now a free variable and where care is taken to not include the zero cyclic frequency $\nu_0 = 0$ in the sum.

If the approximation given in Eq. (**??**) is considered with unit weights $w_{k,p} = 1$, $F_1 = F_2 = L$, it can be shown that the full-scan indicator boils down to

$$I_X^{(4)} = \frac{L}{I^2} \sum_p K(p)^2 \left(\langle |\tilde{x}(n)|^2 |\tilde{x}(n-p)|^2 \rangle - \frac{L}{N} \langle |\tilde{x}(n)\tilde{x}(n-p)|^2 \rangle^2 \right), \tag{10}$$

where $\tilde{x}(n)$ stands for the whitened signal as obtained form the inverse STFT of $X_w(i,f)/\sqrt{S_X(0,f)}$ and where the autocorrelation function of the data window, $K(p) = \sum_i w(n-iR)w(n-p-iR)$, is found almost independent of n and R when $R \ll N$. Interestingly, this is recognized as the total "mass" of the autocorrelation of the squared envelope, which is therefore justified as a valid indicator within the present formalism. Incidentally, the relevance of the autocorrelation of the squared envelope to evidence diagnostic information has been recognized in a recent publication [**?**]. A remarkable case is when $N = 1$ and thus $R = 1$ – i.e. when no Fourier transformation is done – which then simply yields

$$I_X^{(4)} = \langle |\tilde{x}(n)|^4 \rangle - 1 = \frac{|x(n)|^4}{\langle |x(n)|^2 \rangle^2} - 1, \tag{11}$$

a result which connects the kurtosis with the sum of the squared envelope spectrum and first established in Ref. [**?**].

Here again, Wilk's theorem cannot be invoked since this is an approximation to the GLR. There is another drawback with indicator $I_X^{(4)}$. To see it, one should remark that the empirical matrix $\hat{\mathbf{C}}_{H_1}$ is generally different from $\hat{\mathbf{C}}_{H_1}(\mathcal{A})$: the former is a full matrix while the latter is sparse (made of a few non-zero elements aligned along parallel diagonals, i.e. such that $[\mathbf{C}_{H_1}(\mathcal{A})]_{kl} = [\mathbf{C}_{H_1}]_{kl} \cdot \mathbb{I}[f_k - f_l \in \mathcal{A}]$ with $\mathbb{I}$ the characteristic function of set $\mathcal{A}$). Consequently, when all frequencies are summed in the Frobenius norm, the estimation errors in the complimentary set $\bar{\mathcal{A}}$ are accumulated and might eventually mask the contribution from the set $\mathcal{A}$. This fact jeopardizes the capability of the indicator in terms of detection. This is equivalently seen in Eq. (**??**), where the autocorrelation of the squared envelope mixes all frequencies with the risk to hide the diagnostic information.

3.2.3 Strategy 3: measure of roughness

Based on the above observation, a different point of view is taken to design an indicator based on the spectral coherence. The principle is to consider the squared magnitude of the estimated spectral coherence as the random quantity of interest, rather than the signal. Note that a random field is now of concern, rather than a random process. Under the null hypothesis H_0, the random field $|\hat{\gamma}_X(\nu_l, f_k)|^2$, seen as a function of the two frequency variables ν_l and f_k, can be shown to have zero probability of being nil at any "position" (ν_l, f_k) even though having small values. Under the alternative hypothesis H_1, it will have higher magnitudes along parallel lines defined by $\nu_l = \alpha_p$, $\alpha_p \in \mathcal{A}$. The objective is to keep only these values and to zero all the other ones. The following empirical steps are proposed. The presence of a possible bias (as typically produced by transient disturbances in the signal or the presence of unexplained nonstationarities) in the

squared magnitude of the estimated spectral coherence is first removed by subtracting a running median. The results is then standardized by dividing it with a running median of the absolute deviation. This step is necessary to produce a pivotal statistics, i.e. whose variance does not depend on the location in the frequency plane (ν,f). These two steps can be though as a "normalization" of the H_1 statistics with respect to the H_0 statistics. The rationale for using a running median is to leave unaffected informative peaks in the spectral coherence (i.e. under H_1). Let $\tilde{\gamma}_X^2(\nu_l, f_k)$ denotes the resulting statistics. The next step is to zero all non-significant values in $\tilde{\gamma}_X^2(\nu_l, f_k)$ which are found below a given threshold. A reasonable choice is to define the threshold as a high percentile p_c (e.g. $p_c = 0.99$), which means that only the $100(1-p_c)\%$ highest values will be kept. Thanks to the standardization step, the threshold is constant over the full (ν, f) plane. The resulting indicator reads

$$I_X^{(5)} = \frac{1}{F_1 F_2} \sum_{l=1}^{F_1-1} \sum_{k=0}^{F_2-1} w_{k,p} \cdot \tilde{\gamma}_X^2(\nu_l, f_k) \cdot \mathbb{I}[\tilde{\gamma}_X^2(\nu_l, f_k) > p_c]. \tag{12}$$

By analogy with the result given in Eq. (**??**), the above indicator might be interpreted as a kurtosis, yet sensitive only to cyclostationary components. It is proposed to call it "roughness" indicator, for reasons to become clear in the next section.

4 Condition indicators

This section exploits the theoretical results that have been established so far to define condition indicators.

1. The approximation of indicator (**??**) by the Frobenius norm of Eq. (**??**) has been used by the authors to define a condition indicator dedicated to the diagnosis of rolling element bearings [**?**]. First, assuming that the bearing fault is localized in a certain frequency band (which may be identified from a pre-analysis with the kurtogram), the weights w_k are designed as a bandpass filter; second, assuming that the fault frequency is not exactly known but that it is contained in a band $\mathcal{B}$, the indicator becomes

$$I_X^{(6)} = \mathrm{Arg}\max_{\alpha \in \mathcal{B}} \frac{1}{FP} \sum_{p=1}^{P} \sum_{k=0}^{F-1} w_{k,p} \cdot |\hat{\gamma}_X(p\alpha, f_k)|^2 \tag{13}$$

   where P stands for the number of harmonics of interest. A slightly different version of this indicator, based on the post-processed spectral coherence $\tilde{\gamma}_X^2(\nu_l, f_k)$ introduced in subsection **??** instead of $|\hat{\gamma}_X(p\alpha, f_k)|^2$, has been proposed in Ref. [**?**].

2. A related condition indicator is directly obtained by specializing Eq. (**??**) in frequency bands where the fault is expected, that is

$$I_X^{(7)} = \frac{1}{F_1 F_2} \sum_{\nu_l \in \mathcal{B}_\mathcal{P}} \sum_{k=0}^{F_2-1} w_{k,p} \cdot \tilde{\gamma}_X^2(\nu_l, f_k) \cdot \mathbb{I}[\tilde{\gamma}_X^2(\nu_l, f_k) > p_c] \tag{14}$$

   where $\mathcal{A}_\mathcal{P}$ is the union of the bands that contain the P harmonics of interest and $F_1 = |\mathcal{B}_\mathcal{P}|$ is the number of frequency lines in this set.

3. Another condition indicator is obtained by noting that $I_X^{(5)}$ is very similar to Aures' roughness measure used in psychoacoustics [**?**]. The latter is well approached by setting the weights $w_{k,p}$ so as to select the audible frequency range from about 20 Hz to 20 kHz and the audible modulation range from about 15 Hz to 200 Hz. One difference is that Aures' roughness is based on a decomposition of the signal through a Bark filter bank whereas a narrow-band decomposition is used in this paper, yet this is more or less transparent after integration over the frequency plane (ν, f). Another difference is that Aures' roughness does not involve any time average and is therefore prone to significant estimation errors. On the contrary, the indicators introduced in this work are statistically "consistent" (i.e. their variances converge to zero when the signal length increases).

4. Finally, a condition indicator is proposed which intends to measure the fatigue damage sustained in a bearing. Let $p\alpha$, $p = 1, ...P$ be the bearing fault harmonics and m the exponent in the fatigue crack growth model provided by Paris' law. Then, using Miner's rule, the accumulated damage during a time duration T can be shown to be

$$I_X^{(8)} = CT\alpha \left(\sum_{p=1}^{P} \left| \sum_{k=0}^{F-1} \hat{S}_X(p\alpha, f_k) \right|^2 \right)^{\frac{m}{2}} \tag{15}$$

where C is a constant of proportionality which depends on the bearing. It must be emphasized that this formula theoretically applies to the stress history, which unfortunately is rarely observable. In order to remove the effects of the transfer function when the vibration signal is observed instead of the stress, it might be advantageous to substitute the spectral correlation for the spectral coherence $\hat{\gamma}_X(p\alpha, f_k)$ in Eq. (**??**).

5 Conclusion

This paper has investigated the possibility to define condition indicators directly from the frequency domain by following a statistical methodology recently introduced by the first two authors. As compared to the time-domain approach, the main advantages are that non-harmonic cyclic frequencies are easily handled and that weights in the form of filters can be inserted so as to emphasize or reduce the contribution of some carrier and modulation frequencies. The optimal indicator has been found to involve the determinant of a large matrix filled with the values of the spectral coherence, whose computation seems unfortunately quite impractical. Consequently, several suboptimal indicators have been proposed, all rooted on the spectral coherence for which a fast estimator has recently been proposed. A challenging configuration is when the cyclic frequencies of the signal are not known, which requires either to plug in estimates in the indicator or to compute the latter for all possible values. This second strategy has led to the proposal of an indicator that bears a strong similarity with a measure of roughness, as used in psychoacoustics.

Acknowledgements

This work was performed within the framework of the Labex CeLyA of Universit de Lyon, operated by the French National Research Agency (ANR-10-LABX-0060/ANR-11-IDEX-0007).

References

[1] R. B. Randall, *Vibration-based Condition Monitoring: Industrial, Aerospace and Automotive Applications*, Wiley (2011).

[2] P. Vecere, M. Kreidl, R. Smid, *Condition indicators for gearbox condition monitoring systems*, Acta Polytechnica, Vol. 45 (6) (2005) pp. 35-43.

[3] A. Raad, J. Antoni, M. Sidahmed, *Indicators of cyclostationarity: Theory and application to gear fault monitoring*, Mechanical Systems and Signal Processing, Vol. 22 (3) (2008) pp. 574-587.

[4] J. Antoni, P. Borghesani, *A statistical methodology for the design of condition indicators*, Mechanical Systems and Signal Processing, Vol. 114 (2019) pp. 290-327.

[5] K. Gryllias, S. Moschini, J. Antoni, *Application of Cyclo-Nonstationary Indicators for Bearing Monitoring Under Varying Operating Conditions*. ASME. J. Eng. Gas Turbines Power. Vol. 140(1), (2017), pp. 012501-012501-6

[6] J. Antoni, G. Xin, N. Hamzaoui, *Fast computation of the spectral correlation*, Mechanical Systems and Signal Processing, Vol. 92 (2017), pp. 248-277.

[7] P. Borghesani, P. Pennacchi, S. Chatterton, *The relationship between kurtosis- and envelope-based indexes for the diagnostic of rolling element bearings*, Mechanical Systems and Signal Processing, Vol. 43 (12) (2014), pp. 25-43.

[8] E. Cardenas Cabada, Q. Leclere, J. Antoni, N. Hamzaoui, *Fault detection in rotating machines with beamforming: Spatial visualization of diagnosis features*, Mechanical Systems and Signal Processing, Vol. 97 (2017), pp. 33-43.

[9] A. Moshrefzadeh, A. Fasana, *The Autogram: An effective approach for selecting the optimal demodulation band in rolling element bearings diagnosis*, Mechanical Systems and Signal Processing, Vol. 105, pp. 294-318.

[10] S. Kass, A. Raad, J. Antoni, *Self-running Fault Diagnosis Method for Rolling Element Bearing*, in Rizk, Rany and Awad, Mariette, editor, *Mechanism, Machine, Robotics and Mechatronics Sciences* (2019), Springer International Publishing, Cham, pp. 127-140.

[11] W. Aures, *Ein Berechnungsverfahren der Rauhigkeit.* Acustica, Vol. 58 (1985), pp. 268-281.

Online fault identification for rotating machinery

C. Ludwig [1,2], **U. Wever** [3]
[1] Siemens AG
Otto-Hahn-Ring 6, 81739 Munich, Germany
e-mail: **christoph.ludwig@siemens.com**

[2] Technical University of Munich,
Arcisstraße 21, 80333 Munich, Germany

[3] Siemens AG
Otto-Hahn-Ring 6, 81739 Munich, Germany

Abstract
Early detection of mechanical faults in large rotating machines is of crucial importance in today's industry. If not treated properly, such faults may lead to a deterioration of machine performance and eventually cause critical failures. One of the most frequently occurring examples and hence of special interest is the presence of unbalances in the shaft that have to be detected at an early stage. To this end, a model-based identification algorithm capable of reliably estimating magnitude and position of mechanical unbalances in shafts has been developed and is presented in this work. Based on the famous Extended Kalman Filter, the algorithm uses online vibration measurements as well as a supplementary mathematical model of the system to obtain an accurate estimation of the current vibrational state of the machine as well as its unbalance distribution.

1 Introduction

Large rotating machines such as electric motors and generators play a huge role in today's industry. One of the most prominent type are turbomachines that transfer energy between a rotor and a gas and that are used in the production, transmission and consumption of electrical energy [1] as well as jet engines, fans or pumps [2]. Due to their importance, it is clear that unexpected failures will not only lead to considerable revenue losses but may have serious impacts such as jeopardizing energy supply as replacements are usually not readily available due to the high acquisition cost. In addition to being costly, maintenance repairs can be very time-consuming if they involve on-site root cause analysis and ordering spare parts. This is especially critical for machines in remote locations that are not easily accessible. For those reasons, condition monitoring techniques for rotating machines have been a strong research focus in the past aiming at detecting and analyzing deviations from normal behavior during the operation of the machine. Assessing its health condition based on the corresponding results is then facilitating the adoption of appropriate measures to avoid system breakdown. This approach is best-known by the term *predictive maintenance*.

To this end, data-driven techniques are usually applied [3, 4]. Conclusions about the health state of the machine are drawn solely based on the characteristics of the sensor by comparing them to reference signals in order to detect anomalies. As faults in rotating machines are typically discernible in frequency domain, signal processing methods able to track changes in spectral characteristics over time are often used to identify such faults. Examples of the application of such time-frequency analysis to detect motor faults including cracks in rotor shafts, misalignment or rotor-stator rub were presented in [5, 6].

Model-based techniques form a contrast to those purely data-driven approaches. They use a mathematical de-

scription of the rotating machine which is running in parallel to the operation of the system and is frequently updated using measurements. These methods have received increasing attention in the past [7, 8, 9, 10, 11]. One of the most important algorithms in this class is the Kalman Filter [12] yielding optimal state estimates for linear system in the presence of Gaussian model and sensor noise. For nonlinear systems, multiple extensions have been proposed, including the Extended Kalman Filter (EKF) [13, 14] and the Unscented Kalman Filter (UKF) [15]. These extensions make it possible to apply the Kalman Filter to estimate system parameters by regarding them as additional state variables [16, 17, 18]. This approach can readily be applied to fault identification problems if an appropriate parametrized fault model is available.

In this work, the fault identification problem is presented in the context of large rotating machines. An online identification algorithm based on the Extended Kalman Filter is proposed that is able to estimate the magnitude and position of an imbalance in the rotor shaft. The algorithm uses vibration data, i.e. shaft displacements, that are measured at the bearings and continuously updates its underlying mathematical description of the system to estimate imbalance forces. This property makes the algorithm applicable for real-time fault identification. Its ability to accurately localize and quantify the shaft imbalance is demonstrated using a shaft model of a large industrial rotating machine.

In addition to presenting a model-based method for identification of a shaft imbalance, a frequency-based approach is presented that can readily be applied to detecting changes in system stiffness properties. It is shown that, by using a carefully chosen output function, changes in the system's eigenfrequencies can be detected reliably.

2 Problem Description

In this section we describe the mathematical model which is one of the key components of model-based condition monitoring. This model is augmented by introducing fault parameters that will contain the information on the health state of the machine. A zero fault parameter corresponds to a particular fault that is not present in the machine whereas a nonzero parameters indicates that the machine is affected by this fault. In order to correctly identify the parameters and their evolution in time during the machine operation, the system has to be reduced in size to make a simulation feasible in real-time. This goal is achieved via Model Order Reduction (MOR) which is also briefly described in this section.

2.1 Principles of Rotordynamics and Equations of Motion

The analysis of rotordynamical phenomena has been a field of research since the end of the 19th century. In 1919, Jeffcott presented a simplified model consisting of a disk that was mounted onto a massless shaft which, in turn, was supported by two bearings. This model, even though being an obvious oversimplification of real-life rotor systems, inhibits typical effects that play an important role in the analysis of rotating machinery and is therefore still used today.

Since we aim to analyze rotating systems, we briefly describe some of the most important phenomena appearing in rotordynamics. For additional information, confer [19, 20, 2].

- *Gyroscopic effects*
  If a rotor shaft is rotating, a sudden impact will not lead to unidirectional vibrations but rather cause a whirling motion. This *natural whirling* is caused by gyroscopic effects, similar to a top that is precessing around a fixed vertical axis. The whirling frequency is determined by the rotational speed and geometric and material properties.

- *Dependence on the rotational speed*
  Apart from the gyroscopic effects there are additional quantities depending on the rotational speed. Mechanical properties such as stiffness and damping values for fluid bearings generally vary with

rotating speed and oil temperature. Numerical software is usually used to calculate those values for certain speeds serving as interpolation for the remaining ones.

- *Critical speeds*
  As the model depends on the speed of rotation, the eigenfrequencies are likewise depending on the operating conditions. Unbalance forces as well as external harmonic input exciting the system with a frequency close to an eigenfrequency will cause resonance to appear in the system leading to increased and potentially unsafe vibration levels. A Campbell diagram is often created, showing the dependency of the critical speeds on the rotational speed and therefore providing insight into the machine behavior.

In order to obtain a discrete system of equations, a rotating shaft is usually discretized along its axis of rotation (which we assume to be the x-axis) into a finite number of nodes which are connected by beam elements with varying dimensions and material properties [20]. The degrees of freedom of the system correspond to the two lateral translations (in the direction of the y- and z-axis) and two additional rotational degrees of freedom around these axes.

The global mass, damping, gyroscopic and stiffness matrices are obtained by assembling the respective matrices of each beam segment. This assembly yields the equations of motion for the rotating shafts:

$$M_s\ddot{d}_s + (D_s + G_s(\omega))\dot{d}_s + K_s d_s = F_s(\omega). \tag{1}$$

where d_s is the vector of displacements of the shaft nodes and M_s, D_s, G_s, K_s are the global mass, damping, gyroscopic and stiffness matrices of the shaft. The right hand side $F_s(\omega)$ accounts for the ensemble of input forces acting upon the shaft including gravity, imbalance forces and electromagnetic excitation to name a few. Note that these forces may depend on the rotational speed ω.

Every shaft has to be supported by some kind of bearing. A variety of different bearing types exist for different applications and purposes. Large industrial rotating machines are usually supported by fluid bearings in which an oil film prevents direct contact between the rotating shaft and the bearing shell resulting in minimal wear and friction. Fluid bearings can exhibit high stiffness and damping depending on the rotational speed. The corresponding structural matrices may be obtained by modeling the fluid film inside the bearing using the so called Reynolds equations [20] or by performing experiments [21]. A surrogate mass-spring model of the bearings is constructed by calculating the oil stiffness and damping for various rotational speeds and applying linear interpolation. The bearing housing and foundation may be included into the model by linear springs and lumped masses. This way, a bearing model is obtained whose stiffness and damping values depend on the rotational speed ω. Taking into account this dependency, the model of the shaft (1) supported by fluid film bearings reads

$$M\ddot{d} + (D(\omega) + G(\omega))\dot{d} + K(\omega)d = F(\omega) \tag{2}$$

The omission of the subscript s indicates that not only the shaft nodes but also the bearing nodes are now considered in the system formulation.

2.2 Model Order Reduction

Detecting faults via simulation during machine operation requires the underlying algorithms and numerical integration schemes to be real-time capable. This can be achieved by reducing the size of the system of equations using Model Order Reduction (MOR) and hence the computational effort of the simulation. In the following, we briefly describe the MOR method used in this work.

A dynamic substructuring technique is applied to the supported rotor shaft [22] where the substructures have been chosen as the rotating shaft and the two bearings. Note that the shaft may be further divided into the drive-end, middle and non-drive-end part to conform to the interface nodes at the bearing positions.

Following [22], the state vector d is reordered to reflect the distinction between interface degrees of freedoms d_b and degrees of freedom in the interior of each substructure d_i:

$$d = \begin{pmatrix} d_b \\ d_i^{(1)} \\ \vdots \\ d_i^{(N_s)} \end{pmatrix} \approx T_{CB} \begin{pmatrix} d_b \\ \eta^{(1)} \\ \vdots \\ \eta^{(N_s)} \end{pmatrix} = T_{CB}\hat{d}$$

where N_s is the number of substructures and T_{CB} is the Craig-Bampton transformation matrix which is obtained by reducing each substructure individually using a modal approach and corresponding modal coordinates η [23].

Note that T_{CB} depends on the systems stiffness and damping matrix which in turn depend on the rotational speed. Therefore, if ω is not constant, the transformation matrix has to be recalculated in each time step which is computationally expensive. In order to mitigate the computational costs, parametrized model order reduction based on interpolation can be applied [16]. Note that, for the remainder of this work, we will refrain from indicating the reduced order model by mathematical accents for the sake of clarity.

2.3 Reduction to first order

System (1) is readily reduced to first order by writing

$$\dot{x} = Ax + Bu \tag{3}$$

where

$$x = \begin{pmatrix} d \\ \dot{d} \end{pmatrix}, \quad A = \begin{pmatrix} 0 & I \\ -M^{-1}K(\omega) & -M^{-1}\left(D(\omega) + G(\omega)\right) \end{pmatrix}, \quad Bu = \begin{pmatrix} 0 \\ F \end{pmatrix}.$$

This form is widely used and constitutes the basis for the application of the Kalman Filter. In the next section we will show how the system is augmented by introducing mechanical faults.

Sensors allow the operator to monitor the vibrational behavior of rotating machines. Vibration sensors include displacement probes, velocity transducers and accelerometers which are mounted at certain machine components. The measured values at time t can then be written as

$$y(t) = C(t)x(t) + D(t)u(t) + v(t) \tag{4}$$

where $C(t)$ is the system output matrix, $D(t)$ the feedthrough matrix and $v(t) \sim N(0, R)$ is white noise representing measurement errors. We will subsequently assume that we are able to measure the system displacements at certain nodes directly such that the output equation reduces to

$$y(t) = Cx(t) + v(t) \tag{5}$$

where C is a constant selection matrix. We let $x \in \mathbb{R}^n, y \in \mathbb{R}^{n_y}$.

2.4 Models of Mechanical Faults

In order to detect occurring faults an enriched system description is used incorporating information about typical fault patterns. Each fault is represented by one or more additional parameters that are introduced into the system equations. Two kinds of faults are generally distinguished [8, 10]. *Additive faults* affect the sensors and actuators which are not inherent to the system itself but can be seen as external effects while

multiplicative faults describe defects in the system's components. A faulty system is then generally described by a modified version of eq. (3) and (5):

$$\dot{x}(t) = (A + \Delta A)\, x(t) + (B + \Delta B)\, u(t) + f(t) \tag{6}$$

$$y(t) = Cx(t) + v(t) + g(t) \tag{7}$$

Here, $\Delta A, \Delta B$ represent component faults while f, g denote actuator and sensor faults, respectively. For the remainder of this work we will assume that $g = 0$, i.e. the measurements are only affected by measurement noise.

Unbalances in a rotor shaft's cross section appear if the center of rotation does not coincide with the center of mass. This deviation will cause centrifugal forces to act upon the shaft that depend on the eccentricity and the rotational speed. Consider the i-th node and denote by F_y^i, F_z^i the external forces acting upon this node and corresponding to translation in y- and z-axis, respectively. Assuming that the rotational speed ω is constant, an unbalance located at node i is introduced into the system via

$$\begin{pmatrix} F_y^i \\ F_z^i \end{pmatrix} = \begin{pmatrix} b_i\omega^2 \cos(\omega t + \psi_i) \\ b_i\omega^2 \sin(\omega t + \psi_i) \end{pmatrix} = b_i\omega^2 \begin{pmatrix} \cos(\psi_i) & -\sin(\psi_i) \\ \sin(\psi_i) & \cos(\psi_i) \end{pmatrix} \begin{pmatrix} \cos(\omega t) \\ \sin(\omega t) \end{pmatrix} \tag{8}$$

Here, the scalar b_i is the unbalance magnitude and ψ_i is the unbalance angle which is measured with respect to a fixed reference angle. The total force matrix is naturally assembled by considering unbalance forces at each shaft node.

3 Detection of Faults

In this section we describe how mechanical faults in rotating systems can be detected and identified using the enriched system model introduced in the previous section. We will restrict ourselves to the analysis of two particular mechanical fault types that appear frequently in large rotating machinery: the analysis of imbalanced shafts and localized changes in the stiffness properties of the shaft, e.g. due to broken rotor bars or wear.

In the following we will consider the system formulation introduced in the previous section. We apply a numerical scheme to obtain the discrete system

$$x_{k+1} = A_k x_k + B_k u_k \tag{9}$$

which will be the basis for the fault identification methods presented in this work.

3.1 The Kalman Filter

The well-known Kalman Filter first introduced in 1960 [12] is the basis for the fault identification process. In order to predict the state evolution, the Kalman Filter uses the mathematical model (9) of the system, assuming that it is subject to a process uncertainty $w_k \sim N(0, Q)$:

$$x_{k+1} = A_k x_k + B_k u_k + w_k \tag{10}$$

$$y_k = Cx_k + v_k \tag{11}$$

A correction of the estimated state vector is then performed taking into account the actual measurements y_{k+1} obtained via eq. (11) at the corresponding time step.

The optimal state estimation x_{k+1}^+ at time t_{k+1} is then obtained by application of the Kalman Filter equations:

Prediction

$$x_{k+1}^- = A_k x_k^+ + B_k u_k \tag{12}$$
$$P_{k+1}^- = A_k P_k^- A_k^\top + Q \tag{13}$$

Correction

$$K_{k+1} = P_{k+1}^- C^\top \left(C P_{k+1}^- C^\top + R \right)^{-1} \tag{14}$$
$$x_{k+1}^+ = x_{k+1}^- + K_{k+1} \left(y_{k+1} - C x_{k+1}^- \right) \tag{15}$$
$$P_{k+1}^+ = P_{k+1}^- - K_{k+1} C P_{k+1}^- \tag{16}$$

Note that the Kalman Filter incorporates the estimates for model and measurement noise. Additionally, it has to be initialized providing initial estimates for the state variables and corresponding error covariance matrix P_0.

3.2 Extended Kalman Filter

For nonlinear systems given by

$$x_{k+1} = f(x_k, u_k) + w_k \tag{17}$$
$$y_k = h(x_k, u_k) + v_k \tag{18}$$

the Extended Kalman Filter (EKF) again uses a two step process as before where the prediction is given by

$$x_{k+1}^- = f(x_k^+, u_k) \tag{19}$$

and linearizes eq. (17) in each time defining the Jacobian matrices

$$A_k = \frac{\partial f(x,u)}{\partial x}\Big|_{x=x_k^+}, \quad C_k = \frac{\partial h(x,u)}{\partial x}\Big|_{x=x_{k+1}^-} \tag{20}$$

With these definitions, the usual Kalman Filter eqs. (12) to (16) are used to obtain state estimates. Note that, in contrast to linear Kalman Filtering, optimality of the estimates might not be achieved.

3.3 Kalman Filter Augmentation

Kalman Filter based approaches for parameter identification have been under active research in the past. The basic idea is to add the fault parameter vector θ to the system state and apply the conventional Kalman Filter or EKF for state estimation. The augmented equations read

$$\begin{pmatrix} x \\ \theta \end{pmatrix}_{k+1} = \begin{pmatrix} A_k + \Delta A(\theta_k) & 0 \\ 0 & I \end{pmatrix} \begin{pmatrix} x \\ \theta \end{pmatrix}_k + \begin{pmatrix} B_k + \Delta B(\theta_k) \\ 0 \end{pmatrix} u_k + \begin{pmatrix} w \\ \eta \end{pmatrix}_k \tag{21}$$
$$y_k = [C, 0] \begin{pmatrix} x \\ \theta \end{pmatrix}_k + v_k. \tag{22}$$

Note that an additional parameter noise η_k is introduced into the system representing the assumption that the fault may develop over time. In the following section we will describe how the system augmentation is performed in order to identify the faults we are interested in. In this work we are concerned with the quantification and localization of shaft unbalances.

3.4 Unbalanced shaft

Unbalances in the rotor shaft can be modeled as a pure external force not affecting the system's properties. Therefore, considering eq. (21), one may set $\Delta A_k = 0$. Furthermore, the unbalance force vector in eq. (8) may be written as

$$\begin{pmatrix} F_y^i \\ F_z^i \end{pmatrix} = B(b_i, \psi_i)u(t). \tag{23}$$

Identifying the unbalance state of the machine now consists of determining the coefficients b_i, ψ_i for each node i of the shaft that are contained in the matrices B.

The complete set of equations in view of eq. (21) is now given as

$$\begin{pmatrix} x \\ \theta \end{pmatrix}_{k+1} = \begin{pmatrix} A_k & 0 \\ 0 & I \end{pmatrix} \begin{pmatrix} x \\ \theta \end{pmatrix}_k + \begin{pmatrix} B_k(\theta_k) \\ 0 \end{pmatrix} u_k \tag{24}$$

$$y_k = [C, 0] \begin{pmatrix} x \\ \theta \end{pmatrix}_k + v_k \tag{25}$$

where B_k is obtained via assembling the input matrix for every node i on the shaft and performing discretization.

Generally, the imbalance force is given by a right hand side vector $F(\theta)$, where θ is a collection of imbalance fault parameters. One possibility is to set $\theta = (b_i, \psi_i), i \in 1, \ldots, n_{nodes}$ where n_{nodes} is the total number of nodes in the shaft. Note that other parametrizations are possible.

In order to apply the Extended Kalman Filter, the Jacobian matrices of the state equation with respect to the physical state x_k as well as the parameters θ_k needs to be calculated. Note that it has the form

$$J_k = \begin{pmatrix} A_k & \frac{\partial B_k(\theta)}{\partial \theta}\Big|_{\theta=\theta_k} u_k \\ 0 & I \end{pmatrix} \tag{26}$$

and that $\frac{\partial B_k(\theta)}{\partial \theta}\Big|_{\theta=\theta_k}$ can be readily obtained using the formulation of the unbalance force.

3.5 Changes in the dynamic properties

Model-based parameter identification may also be applied to identify changes in the dynamic properties of the shaft. Consider wear or crack formation in a particular component of the shaft. This effect may be modeled as a change in the stiffness properties that has to be identified during the operation phase of the machine. In this case, the stiffness is given as $K(\omega, t) = K_0(\omega) + \Delta K(\omega, t)$ where K_0 represents the nominal stiffness matrix in the fault free case and ΔK describes the stiffness change due to component wear. The complete reduced and discretized system now reads

$$\begin{pmatrix} x \\ \theta \end{pmatrix}_{k+1} = \begin{pmatrix} A_k + \Delta A(\theta_k) & 0 \\ 0 & I \end{pmatrix} \begin{pmatrix} x \\ \theta \end{pmatrix}_k + \begin{pmatrix} f_k \\ 0 \end{pmatrix} \tag{27}$$

$$y_k = [C, 0] \begin{pmatrix} x \\ \theta \end{pmatrix}_k + v_k \tag{28}$$

where we assume that the system is excited by an external force f_k.

Note that those kind of faults can be considered as fundamentally different from pure imbalance faults since they affect system characteristics such as eigenfrequencies and corresponding modes. This motivates the usage of Discrete Fourier Transform (DFT) to identify such shifts in the frequency domain. An additional advantage of considering frequencies is the possibility to apply bandpass filtering effectively ignoring oscillating inputs which are usually present in rotating machines. Note that even unknown inputs that do not affect the eigenfrequencies can be ignored but might disturb identification in time domain.

In order to apply DFT, we have to consider vibrations recorded over a time interval of length T. An extended state X_k is introduced as

$$X_k = (x_k^\top, \dots, x_{k-T+1}^\top)^\top \in \mathbb{R}^{n \times T} \tag{29}$$

capturing a history of states with corresponding output

$$Y_k = (y_k^\top, \dots, y_{k-T+1}^\top)^\top \in \mathbb{R}^{n_y \times T} \tag{30}$$

The extension makes it possible to take into account past states and measurements and to observe frequency shifts on a time window. This approach was taken in [24] where a nonlinear output function h was used to observe the first moment of the power distribution in a frequency interval. For a vector $\hat{y} \in \mathbb{R}^T$ the function

$$h(\hat{y}) = \frac{\sum_{\ell \in I} \omega_\ell |\hat{a}_\ell|^2}{\sum_{\ell \in I} |\hat{a}_\ell|^2} \tag{31}$$

is defined, where ω_ℓ are the discrete frequency bands obtained by the DFT of $\hat{y}$ inside a chosen frequency band of interest I and $\hat{a}_\ell$ are the corresponding Fourier coefficients. The total output vector is obtained by applying h to the history of each observed component.

In the next section, the output function is applied to a model problem to illustrate how a change in stiffness influences the first moment of the power spectrum. This dependency motivates the use of this nonlinear output in the frequency domain for fault identification. Note that, in view of eq. (20), the formulation of the EKF now involves the derivative of h with respect to the state variables and fault parameters.

4 Examples

In this section, the previously presented unbalance identification approach is applied to a motor-generator system. Data is obtained by deliberately introducing a discrete unbalance at a particular node and numerically integrating the system of equations. It is shown that the identification algorithm is in fact able to accurately estimate the position and magnitude of the disturbance. Furthermore, a simple rotor system based on the famous Jeffcott rotor is considered. It is shown how a change in the stiffness properties affects the eigenfrequencies in a specific frequency band and how the nonlinear output function presented in the previous section develops in time.

4.1 Unbalance Identification

The setup that is considered as an example consists of a generator that is coupled to a motor with a total length of about 10m. The rotor was modeled by linear Timoshenkov beams and the supporting fluid bearings are represented by springs whose coefficients depend on the rotational speed. A visualization of the shaft is shown in fig. 1.

The system has 280 degrees of freedom. Using the substructuring method described in section 2.2 this number was reduced to 44, considerably lowering computational cost.

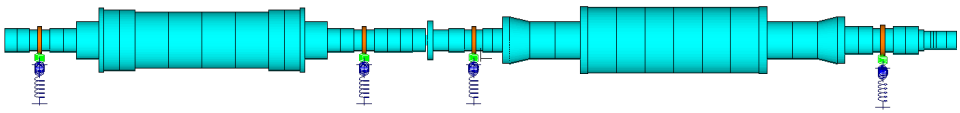


Figure 1: Visualization of the motor-generator setup that, in this work, is used as an example for the application of unbalance identification based on the EKF.

We assume that displacement probes are available at the bearings measuring the relative distance between the shaft and the bearing housing in horizontal and vertical direction. If the initial distance at rest is defined to be zero, the output matrix is then given as

$$C = L_B - L_S \in \mathbb{R}^{8\times 44} \tag{32}$$

where L_B, L_S are selection matrices selecting the displacements in horizontal and vertical direction of the Bearing housing and the shaft, respectively.

In order to validate the identification algorithm, data was created by numerically integrating system (2) using the Newmark method with a time step of $\Delta t = 5 \times 10^{-4}$ s. A discrete unbalance was placed near the non-drive-end of the generator at a shaft position of 7.8 m with a magnitude of $b = 0.1$ kg·m and an angle of $\psi = 120°$. The rotor setup is accelerated with a constant angular acceleration of 60 RPM/s until a rotational speed of 2400 RPM was reached. An input noise $w(t)$ with standard deviation 0.1 was introduced as well as a white measurement noise with standard deviation of 2×10^{-6}.

The unbalance identification algorithm presented in section 3 is applied to the motor-generator system given the data that was created as described previously.

As the exact noise parameters are generally unknown, an over-estimated input model noise standard deviation of 0.3 was prescribed. The exact measurement noise was provided during the identification process since an accurate estimation of the measurement is often available either by relying on sensor specifications or measuring fluctuations in the data while the machine is still at rest. The initial state was set to zero, representing the machine being at rest at $t_0 = 0s$. This assumption also justifies an initial zero error covariance for the displacements and velocities. For the fault parameters the initial state is obviously unknown but it is assumed that the unbalance configuration is not changing in time. This motivates the selection of nonzero initial uncertainty and small or even zero model noise in the equations for the fault parameters.

In order to assess the quality of the identification, an estimated position, magnitude, and angle was extracted from the model of the external force by considering its contribution at every single node. These three generalized parameters are compared to the exact values of the discretely placed unbalance. Figure 2 shows the temporal convergence of the parameters with respect to the actual position, magnitude and angle.

It can be seen that the identification algorithm quickly manages to identify magnitude and position quite accurately. This information can be used by the machine operator to assess the unbalance state of the shaft and detect the occurrence of a fault, localize the faulty component and assess the severity of the damage. Moreover, as the model is continuously being calibrated, the future development of faults can be predicted by numerical simulation.

4.2 Changes in dynamic properties due to a change in stiffness

In this section the motivation for using time-frequency based identification methods to track structural changes is illustrated using a model problem from a test case of the Finite Element software Code Aster [25] that is based on the famous Jeffcott rotor. Consider a rotating shaft of length L with an unbalanced disk mounted at $L/3$ that is supported by a bearing at position $2L/3$ (fig. 3).

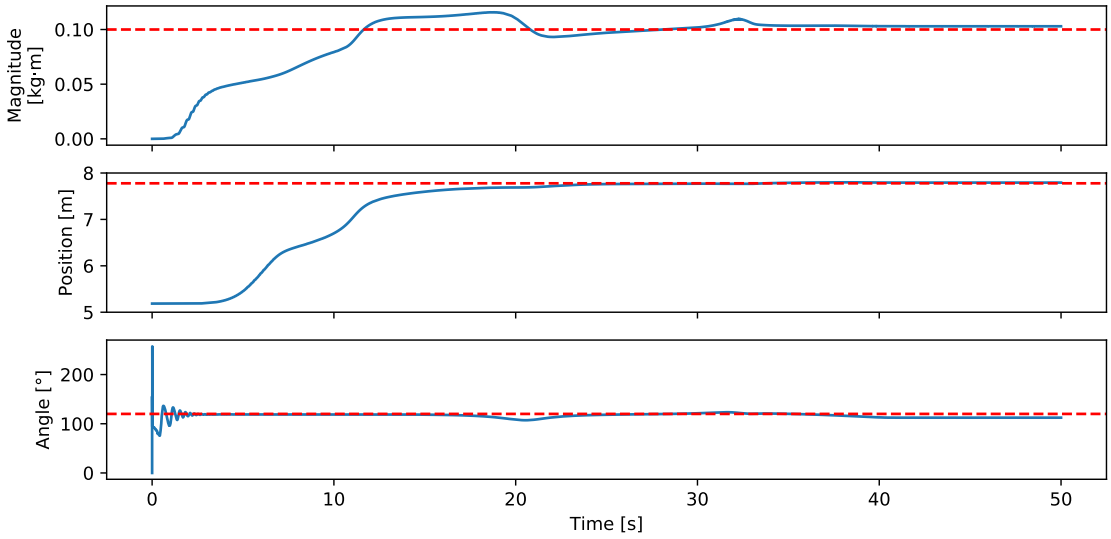


Figure 2: Convergence plots for unbalance position, magnitude and angle. Solid line: Estimated parameters for every time step. Dashed line: Exact parameters.

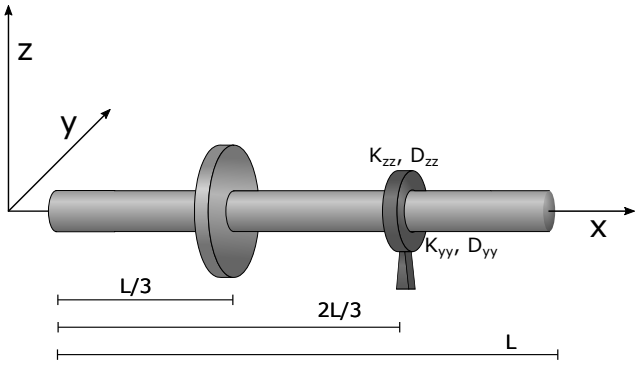


Figure 3: A simple example of a rotating shaft. Both ends of the shaft are fixed. Vibrations are introduced by an unbalanced disk mounted on the shaft.

We assume that the bearing is subject to wear resulting in an effective decrease of bearing stiffness and that the shaft dynamics are described by the system of equations

$$M\ddot{d} + (D(\omega) + G(\omega))\dot{d} + (K_0(\omega) + \theta(t)\Delta K)d = F(\omega) + w(t) \tag{33}$$

$$y(t) = Cd(t) + v(t). \tag{34}$$

Here, $F(\omega)$ accounts for the unbalance forces and the output matrix C selects the displacement measurements obtained at the bearing.

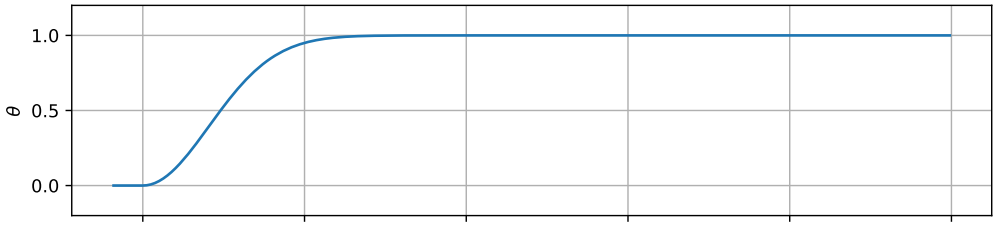
The matrix ΔK is a constant fault matrix and represents bearing wear affecting the stiffness of the system. The goal is to identify the fault parameter θ and its evolution in time using information on eigenfrequencies of the shaft.

In order to illustrate the expressiveness of the nonlinear output function from eq. (31), the dynamic system was integrated between 0s and 60s using a time step size of 10^{-3}s. The fault parameter θ was initially set to zero and was gradually increasing over time until reaching the value 1.0.

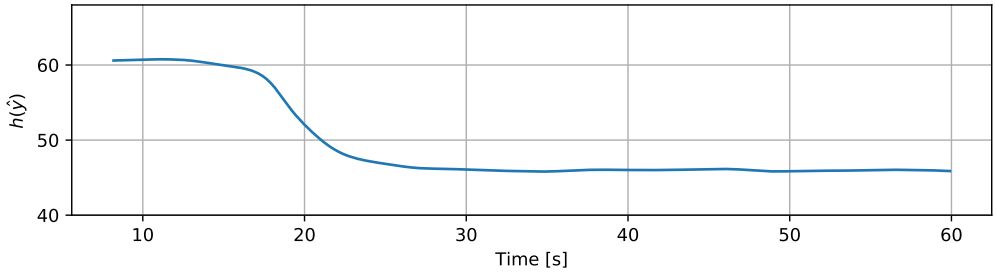
We assume that shaft displacements are observed at the bearing in horizontal direction. These measurements are obtained by extracting the respective components from the simulation results and disturbing them by

adding white noise.

For each output component, the output function h was calculated using eq. (31) with a window size of $T = 2^{13}$ corresponding to approximately 8s. The exact fault parameter used for the creation of the data and the output obtained from the measurements are shown in fig. 4. It can be seen that the output clearly indicates the change in the fault parameter. Note that, by definition of the extended state eq. (29), the output at time t_k is obtained from the *previous* T time steps explaining the lag between the exact parameter evolution and the estimated counterpart (fig. 4). For the same reason the output function is only calculated for $t \geq T$.



(a) Exact evolution of the fault parameter θ affecting the bearing stiffness.



(b) Output of the transformation eq. (31) applied to the measured displacements in y-direction.

Figure 4: Comparison of the exact evolution of the fault parameter and the observed first energy moment. It can be seen that the nonlinear output is strongly correlated to the actual fault parameter facilitating the identification of developing faults.

5 Conclusions

In this work, a model-based fault detection algorithm based on the Extended Kalman Filter was presented, that is capable of identifying magnitude and position of a single unbalance in a rotating shaft. It was shown that by using a mathematical model of the machine during the operation phase and calibrating it online with measurements important insight into the health state of the machine can be gained, offering new possibilities in diagnostics and predictive maintenance. Note that, as those models are usually created during the engineering phase, the approach that was adopted in this work bridges the gap between design and operation. The ability to localize and quantify unbalance faults was demonstrated on a motor-generator example where a single unbalance magnitude and position was identified in the presence of random inputs and measurement noise. In addition, a signal transformation was proposed that yields an accurate description of changes of an eigenfrequency residing in a preselected frequency interval. This method was used to detect wear in a bearing supporting a simple shaft. It was shown that the output of the transformation is strongly correlated to the evolution of model parameters related to the change in system stiffness caused by wear. This property motivates its usage in fault detection methods, e.g. by tracking the fault parameter based on the output of the signal transformation using a Kalman filter based method.

References

[1] S. Vukosavic, *Electrical Machines*, Springer (2013).

[2] O. Matsushita, M. Tanaka, H. Kanki, M. Kobayashi, P. Keogh, *Vibrations of Rotating Machinery*, Springer Japan (2017).

[3] S. Nandi, H.A. Toliyat, X. Li, *Condition monitoring and fault diagnosis of electrical motors - a review*, IEEE Transactions on Energy Conversion, Vol. 20 (2005), No. 4, pp. 719–729.

[4] Y. Lei, J. Lin, Z. He, M.J. Zuo, *A review on empirical mode decomposition in fault diagnosis of rotating machinery*, Mechanical Systems and Signal Processing, Vol. 35 (2013), No. 1, pp. 108–126.

[5] N.H. Chandra, A.S. Sekhar, *Fault detection in rotor bearing systems using time frequency techniques*, Mechanical Systems and Signal Processing, Vol. 72 (2016), pp. 105–133.

[6] Z. Feng, M. Liang, F. Chu, *Recent advances in time–frequency analysis methods for machinery fault diagnosis: A review with application examples*, Mechanical Systems and Signal Processing, Vol. 38 (2013), No. 1, pp. 165–205.

[7] A.S. Willsky, *A survey of design methods for failure detection in dynamic systems*, Automatica, Vol. 12 (1976), No. 6, pp. 601–611.

[8] R. Isermann, *Model-based fault-detection and diagnosis – status and applications*, Annual Reviews in Control, Vol. 29 (2005), No. 1, pp. 71–85.

[9] A.W. Lees, J.K. Sinha, M.I. Friswell, *Model-based identification of rotating machines*, Mechanical Systems and Signal Processing, Vol. 23 (2009), No. 6, pp. 1884–1893.

[10] I. Hwang, S. Kim, Y. Kim, C.E. Seah, *A survey of fault detection, isolation, and reconfiguration methods*, IEEE Transactions on Control Systems Technology, Vol. 18 (2010), No. 3, pp. 636–653.

[11] A. Jungiewicz, H. Brandtstädter, Lutz Hübner, C. Ludwig, E. Tsouchnika, U. Wever, *Digital twins for large electric drive trains*, in *2018 Petroleum and Chemical Industry Conference Europe (PCIC Europe)*, June (2018).

[12] R.E. Kalman, *A new approach to linear filtering and prediction problems*, Journal of Basic Engineering, Vol. 82 (1960), No. 1, pp 35–45.

[13] B.D.O. Anderson, J.B. Moore, *Optimal Filtering*, Prentice-Hall (1979).

[14] C.K. Chui, G. Chen, *Kalman Filtering*, Springer (1999).

[15] R. Kandepu, B. Foss, L. Imsland, *Applying the unscented kalman filter for nonlinear state estimation*, Journal of Process Control, Vol. 18 (2008), No. 7, pp. 753–768.

[16] F. Naets, J.Cuadrado, W. Desmet, *Stable force identification in structural dynamics using kalman filtering and dummy-measurements*, Mechanical Systems and Signal Processing, Vol. 50 (2015), pp. 235–248.

[17] F. Naets, J. Croes, W. Desmet, *An online coupled state/input/parameter estimation ap- proach for structural dynamics*, Computer Methods in Applied Mechanics and Engineering, Vol. 283 (2015), pp. 1167–1188.

[18] E. Lourens, E. Reynders, G. De Roeck, G. Degrande, G. Lombaert, *An augmented kalman filter for force identification in structural dynamics*, Mechanical Systems and Signal Processing, Vol. 27 (2012), pp. 446–460.

[19] J. Vance, F. Zeidan, B. Murphy, *Machinery Vibration and Rotordynamics*, John Wiley & Sons (2010).

[20] Y. Ishida, T. Yamamoto, *Linear and Nonlinear Rotordynamics: A Modern Treatment with Applications*, Wiley-VCH (2012).

[21] R. Tiwari, A.W. Lees, M.I. Friswell, *Identification of dynamic bearing parameters: a review*, Shock and Vibration Digest, Vol. 36 (2004), No. 2, pp. 99–124.

[22] D.J. Rixen, *A dual craig–bampton method for dynamic substructuring*, Journal of Computational and Applied Mathematics, Vol. 168 (2004), No. 1, pp. 383–391.

[23] B. Besselink, U. Tabak, A. Lutowska, N. Van De Wouw, H. Nijmeijer, D.J. Rixen, M.E. Hochstenbach, W.H.A. Schilders *A comparison of model reduction techniques from structural dynamics, numerical mathematics and systems and control*, Journal of Sound and Vibration, Vol. 332 (2013), No. 19, pp. 4403–4422.

[24] C. Ludwig, O. Junge, U. Wever, *Online parameter identification methods for oscillatory systems: Estimation of changes in stiffness properties*, (2017), *(Manuscript submitted for publication)*.

[25] Electricité de France, *Finite element code_aster, analysis of structures and thermomechanics for studies and research*, Open source on www.code-aster.org (1989-2017).

Cyclostationary-based tools for bearing diagnostics

A. Mauricio [1,2], **W. Smith** [3], **R. Randall** [3], **J. Antoni** [4], **K. Gryllias** [1,2]
[1] KU Leuven, Department of Mechanical Engineering,
Celestijnenlaan 300 B, B-3001, Heverlee, Belgium
e-mail: **alex.ricardomauricio@kuleuven.be**

[2] Dynamics of Mechanical and Mechatronic Systems, Flanders Make,,
Celestijnenlaan 300 B, B-3001, Heverlee, Belgium

[3] School of Mechanical and Manufacturing Engineering, University of New South Wales,
Sydney, Australia,

[4] Laboratoire Vibrations Acoustique, University of Lyon, INSA-Lyon,
Villeurbanne, France

Abstract
Rolling element bearings are among the most common components which lead to machinery breakdown. Lately, focus has been targeted to cyclostationary-based tools that show a good performance in describing and detecting the bearing vibration signatures and early damage diagnosis. The Cyclic Spectral Correlation (CSC) and Coherence (CSCoh) describe the signal in terms of frequency-frequency content, detecting the hidden modulations and their carriers. Their integration results in an equivalent band-pass filtering and demodulation of the signal. Angular resampling methods are also applicable on the CSC or CSCoh, resulting in the signature description in the order-frequency or order-order domain. In this paper different methodologies for bearing fault detection based on CSC tools are presented. An optimization criterion is proposed in order to select the optimum integration limits. The methodologies are evaluated and compared in terms of performance on a number of real data.
Keywords : Condition monitoring, Bearing diagnostics, Cyclostationarity, Cyclic spectral coherence

1 Introduction

Rolling element bearings are critical components of rotating machinery and their failure can cause sudden breakdown of the system, leading to time-loss and increased costs. Condition monitoring is the field where rotating machinery is analysed, including bearings and gears and damages that may be present on the structures can be detected. Therefore, maintenance and faulty component repair can be performed before breakdown. The diagnostics of bearings continues to be a challenge however, as their signatures are usually masked under noise and other stronger component signatures (e.g. gears). Recently the interest of the research community started focusing on condition monitoring of complex machinery due to their difficult analysis under many component signatures [1, 2]. Diagnostics under varying speed conditions has also attracted increased attention in the field, as they represent the real operating conditions of many structures on which widely accepted methods are yet to be provided [3, 4, 5, 6, 7, 8]. Typical examples including wind turbines, aircraft engines and helicopter gearboxes operate usually under varying load and speed conditions, which limit the detectability of damage present on these rotating structures.

One of the most well established methods is the Envelope Analysis, where the signal is demodulated after band-pass filtering around the resonant frequencies excited by the damage impulses, obtaining in the end a filtered Squared Envelope Spectrum (SES). The main idea is to obtain an optimal filter band which presents

a high Signal-to-Noise ratio (SNR) leading to a SES after demodulation where the fault harmonics are enhanced. The frequency band for demodulation is commonly extracted through the Fast Kurtogram (FK), which is an automated band selection tool based on the maximum kurtosis level [9]. Aside from this tool there are other band selection tools that have been developed to obtain the SES. Moshrefzadeh and Fasana [10] proposed the Autogram, a tool with the same representation and the same objective of selecting the optimal band for demodulation to obtain the SES. It is also based on the maximum kurtosis, but unlike the FK, it is calculated from the unbiased autocorrelation of the squared envelope of the demodulated signals. Randall *et. al.* [5] and Smith *et. al.* [6] proposed the ICSgram, where the optimal band selection is based on a feature that maximizes the cyclostationary value of a determined fault frequency. These and other band selection tools show improvement on selecting an optimal band, resulting in enhanced fault frequency harmonics in the SES when compared to classical FK.

The Cyclic Spectral Correlation (CSC) and the Cyclic Spectral Coherence (CSCoh) have been proposed recently as an alternative for the SES-based methods [11, 12]. The main advantage of this method falls on its ability to reveal hidden periodicities of second-order cyclostationarity, like bearing signals that are masked under stronger signals. They are represented in bi-variable maps in the frequency-frequency domain, from which its spectral axis can be integrated to obtain either the Enhanced Envelope Spectrum (EES) or the Improved Envelope Spectrum (IES). These spectra, the EES and IES, have been seen to improve the detection of cyclostationary faulty signals [13, 14]. However, to obtain the optimal band of demodulation for the CSC or CSCoh, its bi-variable map needs to be analysed in order to select the optimal band for integration along the spectral axis. The IESFOgram has been proposed as a band selection tool similar to the FK but for application on the CSC and CSCoh [3]. This displays a 1/3 binary tree like the FK and is seen to provide an optimal band of integration resulting in an IES allowing the detection of the fault frequency harmonics.

However, these cyclostationary-based tools are based on the notion that only small speed fluctuations occur and not on the notion of varying speed conditions. Under varying speed conditions, SES-based tools are usually re-sampled in the angular domain, resulting to the Order Tracked Squared Envelope Spectrum (OT-SES). The same Order Tracking method has also been applied to the CSC and CSCoh with success, providing robust diagnosis of bearings. The methods rely on the theory that bearing faults are dependent on the shaft angle and independent of time. Therefore, the hidden periodicities remain on the angular domain although the signal are non-stationary in the time domain. This fact generated the idea of classification of the bearing signals under varying speed conditions as cyclo-non-stationary signals and as long as they are analysed on the order domain, diagnosis is possible. Moreover the transformation of the signals into the angular domain before the calculation of the CSC-based methods in order to obtain the Order-Order Cyclic Spectral Correlation/Coherence (OO-CSC and OO-CSCoh) has been proposed [3]. The method has shown a robust detection of the hidden modulations under carrier of random frequency. On the other hand, re-sampling of the Time-Frequency domain on the angular domain, in order to obtain the Angular-Frequency domain map leading to the Order-Frequency Cyclic Modulation Spectrum has also been proposed as a tool to detect hidden modulations under varying speed conditions [7, 8]. These methods have shown good performance on bearing diagnosis under varying speed conditions.

Therefore, the objective of this paper is the description of two methodologies based on CSC-based tools for bearings diagnostics under varying speed conditions, by integration of the optimal band of frequencies selected in an automated manner. The Order-Order domain and Order-Frequency domain maps are calculated and the IESFOgram is applied to select the band that integrates the maps, in order to provide an enhanced diagnosis. The methodologies are validated on real signals of two datasets (one from a Safran aircraft engine and oned from a UNSW planetary gearbox). Furthermore, the performance of the methodologies is compared with the OT-SES, the OT-SES filtered by the ICSgram band selection, and EES-based methods. The rest of the paper is organised as follows. The state of the art for the cyclostationary spectral analysis is described in Section 2. The proposed methodologies and their order tracked versions are detailed in Section 3. The experimental setups used to capture the data are described in Section 4. The proposed methodologies are validated and their results are presented in Section 5. Finally some conclusions are provided in Section 6.

2 Overview of CSC based methods

The presence of cyclostationary (CS) based approaches is increasing in the research community. They have been used to analyse vibration signals in order to diagnose damage on rotating machinery. This increased attention is due to their good performance, as described in the recent published research. One of the main advantages is that they allow the description of (second-order) CS signatures, thus providing a good distinction between different signatures present in a single signal. For this reason, they have proven to be extremely useful when diagnosing rotating components that are not completely phase-locked with shaft speeds, such as the bearings, which show a second-order cyclostationary signature. Additionally, the bearing signals are commonly masked by other stronger components of the first-order cyclostationary, like gears and shafts. This results in a more difficult detection of damage unless an efficient differentiation of first-order cyclostationarity from the second-order cyclostationarity is obtained.

A signal is said to be cyclostationary (CS) of first-order if its first-order moment or mean R_{1x} is periodic with time:

$$R_{1x}(t) = R_{1x}(t+T) = \mathbb{E}\{x(t)\} \tag{1}$$

where $x(t)$ is the signal function of time t sampled at constant time intervals and $\mathbb{E}$ is the ensemble average.

Moreover a signal is said to be CS of second-order if the second-order moment (Autocorrelation function) is periodic of period T as described by Eq. 2 :

$$R_{2x}(\tau, t) = R_{2x}(\tau, t+T) = \mathbb{E}\{x(t)x(t-\tau)^*\} \tag{2}$$

where τ is the time-lag.

Randall *et. al.* [11] proposed the Cyclic Spectral Correlation (CSC) to detect first and second-order cyclostationarity patterns present in the signals. CSC is a bi-variable map of two frequency values, the *spectral frequency* f and the *cyclic frequency* α. The spectral frequency describes the carrier frequencies while the cyclic frequency describes the modulation frequencies. The CSC describes in fact the correlation value between these two frequency variables (f, α), justifying its name as Cyclic Spectral Correlation (CSC), and can be described as in Eq. 3 :

$$CSC_x(\alpha, f) = \lim_{T\to\infty} T^{-1}\, \mathbb{E}[\mathscr{F}^T\{x(t)\}^* \mathscr{F}^T\{x(t-\tau)\} \tag{3}$$

where $\mathscr{F}^T\{x(t)\}$ is the Fourier transform of the signal $x(t)$. The processing of the CSC reveals the hidden modulations as high correlation values at which the carrier frequency f is modulated by the cyclic frequency α.

In order to minimize uneven distributions, a whitening operation can be applied to the CSC. This extended tool, named the Cyclic Spectral Coherence (CSCoh), describes the spectral correlations in normalized values between 0 and 1, and is defined as in Eq. 4 :

$$CSCoh_x(\alpha, f) = \frac{CSC_x(\alpha, f)}{\sqrt{CSC_x(0, f) CSC_x(0, f-\alpha)}} \tag{4}$$

Both the CSC and the CSCoh bi-variable maps can be integrated along the spectral frequency axis in order to obtain a regular spectrum. The integration over the full band of frequencies results in a spectrum that exhibits all modulations present in the signal, in a similar manner to the Squared Envelope Spectrum (SES). This is useful for a simpler detection of the characteristic frequencies, as the analysis of a bi-variable map is certainly more complex than the analysis of a single variable spectrum. The integration can also be made on a specific band of frequencies instead of the full band. An optimal band of frequencies which can minimize

the effect of other components in the signal can be extracted. In this manner, the integration over a specific band on the frequency-frequency domain can improve the detection of the characteristic peak frequencies in the resulting envelope spectrum. This method is similar to the application of a band-pass filter on the signal. The resulting spectrum is then named Improved Envelope Spectrum (IES) and it is obtained from the frequency-frequency domain according to Eq. 5 :

$$IES(\alpha) = \frac{1}{F_2 - F_1} \int_{F_1}^{F_2} |CSCoh_x(\alpha, f)| df \tag{5}$$

where F_1 and F_2 are the lower and upper frequencies of the band of integration over the spectral frequency axis. It is interesting to note that EES can be described as a specific case of the IES obtained through the integration of its full available band, or in other words, F_1 is zero and F_2 is the Nyquist frequency ($Fs/2$), where Fs is teh sampling frequency. The IES has been described as an integration over the CSCoh but in analogy a corresponding IES can be estimated over the CSC as well.

3 Proposed methodologies

3.1 Improved Envelope Spectrum via Feature Optimisation - gram – IESFOgram

An automated selection of the integration band can be obtained through IESFOgram. In the same manner the Fast Kurtogram can be applied for an automated selection of the band-pass frequencies to be filtered on the signal [9], the IESFOgram can be applied to extract the band-pass frequencies to be integrated on the frequency-frequency domain [3].

The IESFOgram is a band selection tool based on an optimisation of a defined feature. The representation of the method is done in a 1/3 binary tree analogous with the Kurtogram. The integration of the resulting band with the maximum feature leads to the IES with the optimised feature, therefore explaining the acronym for the method as Improved Envelope Spectrum via Feature Optimisation- *gram* (IESFOgram). A series of bands following a 1/3 binary tree structure are integrated, with various bandwiths bw and center frequencies cf. Each applied band results in a spectrum from which a feature is extracted. The feature values are then represented as a function of the center frequency cf and bandwidths bw, in analogy to the Kurtogram. The band of frequencies (cf, bw) that corresponds to the maximum feature value is selected as the optimal band for integration on the frequency-frequency map.

The feature $feat(cf, bw)$ can be defined as the sum of the amplitude of $N-$harmonics of the characteristic fault frequency f_fault normalized by the background noise level around each harmonic ranging by 2 times a set bandwidth ($2 \times f_b$) and can be described by Eq. 6 :

$$feat(cf, bw) = \sum_{k=1}^{N} \frac{IES(k\ f_{fault})}{\frac{1}{2f_b}\left[\int_{kf_{fault}-f_b}^{kf_{fault}+f_b} IES(\alpha)d\alpha - IES(kf_{fault})\right]} \tag{6}$$

This feature is defined based on a specific fault frequency, meaning that the method is not blind and the feature value should be calculated for each characteristic frequency of interest. On the other hand it could be easily combined with an automated characteristic frequency identification tool. The background noise level bandwidth for normalization is defined here as the 1/4th of the shaft speed on which the specific bearing is mounted on. The band selection procedure is described in the diagram of Fig. 1.

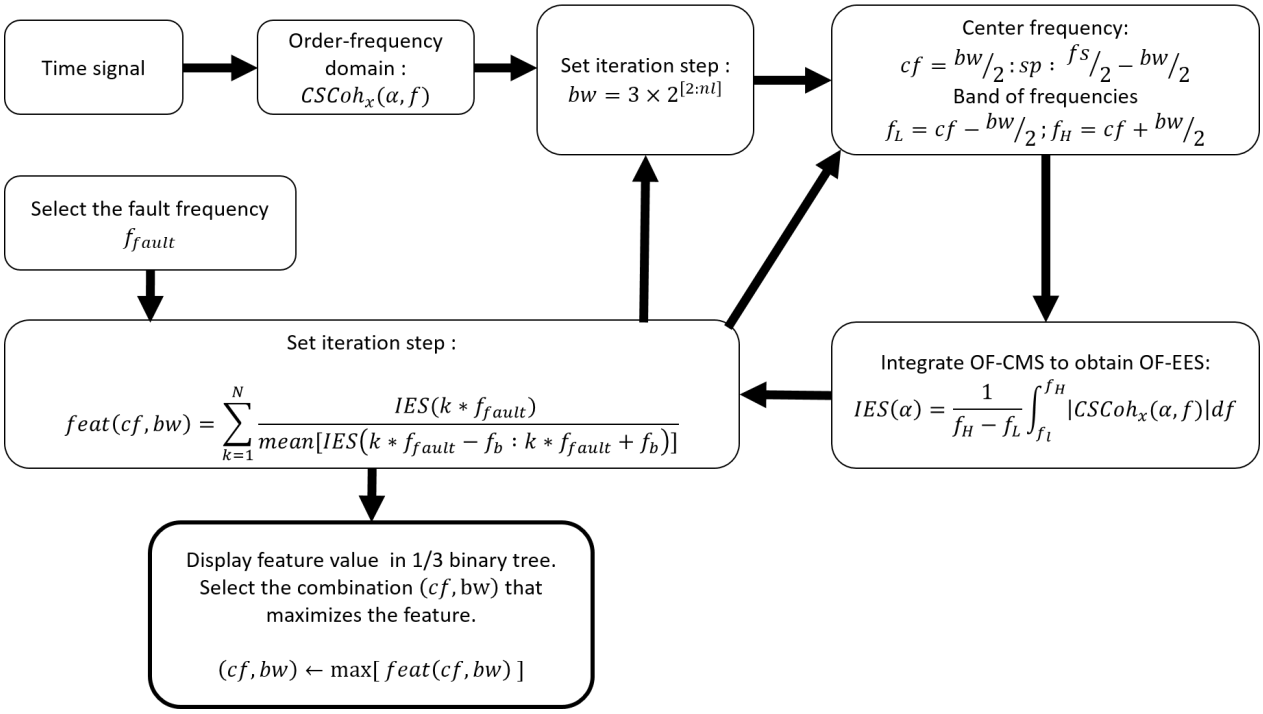


Figure 1: Procedure for the generation of IESFOgram.

3.2 Order-Order domain vs Order-Frequency domain

In the presence of a faulty bearing operating under constant speed condition, the bearing faults are described on the CSC (or CSCoh) as modulations on the cyclic frequency axis α and as resonant frequencies (carriers) excited by the impulses on the spectral frequency axis f.

However, under varying speed conditions, the impulses are no longer cyclostationary in time, thus becoming smeared over the α axis. This phenomenon is due to the fault impacts occurring as a function of the shaft angle position rather than time. In order to overcome this problem, two versions of order tracking can be applied to obtain the bi-variable map.

The signal can be resampled into constant angle intervals before the calculation of the CSC (or CSCoh). As the signal is no longer in the time domain but rather in the angular domain and providing the number of samples per revolution as the new sampling frequency, the result of the CSC and CSCoh is a bi-variable map in the **Order-Order** domain [3]. This causes smearing of the high frequencies on the spectral order variable f which are time-dependent (resonant frequencies) but enhances the components that are angle-dependent (harmonics). In other words, the carrier frequencies that are speed related (e.g. gearmesh frequencies) are therefore enhanced through Order-Order analysis. On the other hand, the Order-Order CSC (OO-CSC) and the Order-Order CSCoh (OO-CSCoh) can also identify the random carrier frequencies of semi-periodic modulation and finally the fault frequency can be detected on a bi-variable map at the corresponding cyclic order variable α. The OO-CSC values can be interpreted as the measure of spectral correlation of the transformed version of the signal related to its angle $x_\alpha(\theta)$ and itself, as described in Eq. 7 :

$$OOCSC(\alpha(\theta), f(\theta)) = \lim_{T \to \infty} T^{-1}\, \mathbb{E}[\mathscr{F}^T\{x_\alpha(\theta)\}^* \mathscr{F}^T\{x_\alpha(\theta)\}] \tag{7}$$

The second method allows the description of the bivariable map in the **Order-Frequency** domain. This overcomes the smearing of the resonant frequencies over the spectral f axis while at the same time describing the modulations in the order domain as being discrete over the cyclic α axis. Abboud *et. al.* [7] proposed a methodology to obtain the Order-Frequency CSC (OF-CSC) and Order-Frequency CSCoh (OF-CSCoh) and

later [8] proposed a method with less computational cost, the Order Frequency Cyclic Modulation Spectrum (OFCMS), analogous with the OF-CSC.

The OFCMS is based on the angle-frequency spectrogram, where the Angle-Time Domain estimates the impulses at a constant angle intervals correlated with the carriers in the frequency domain. This is obtained by applying angular resampling on the Time-Frequency Instantaneous Power Spectrum (TF-IPS) on the time axis alone. This results in the Angle-Frequency Instantaneous Power Spectrum (AF-IPS), on which the second Fourier transform can be applied with respect to angle, thus obtaining the OFCMS. The OFCMS can then be interpreted as the measure of the spectral correlation between the time signal $x(t)$ and its transformed version related to angle $x_\alpha(\theta)$, or in other words, equals to the Fourier transform of the angle/frequency spectrogram and can be formulated by Eq. 8 :

$$OFCMS(\alpha(\theta), f(t)) = \lim_{T\to\infty} T^{-1}\,\mathbb{E}[\mathscr{F}^T\{x(t)\}^*\mathscr{F}^T\{x_\alpha(\theta)\}] \tag{8}$$

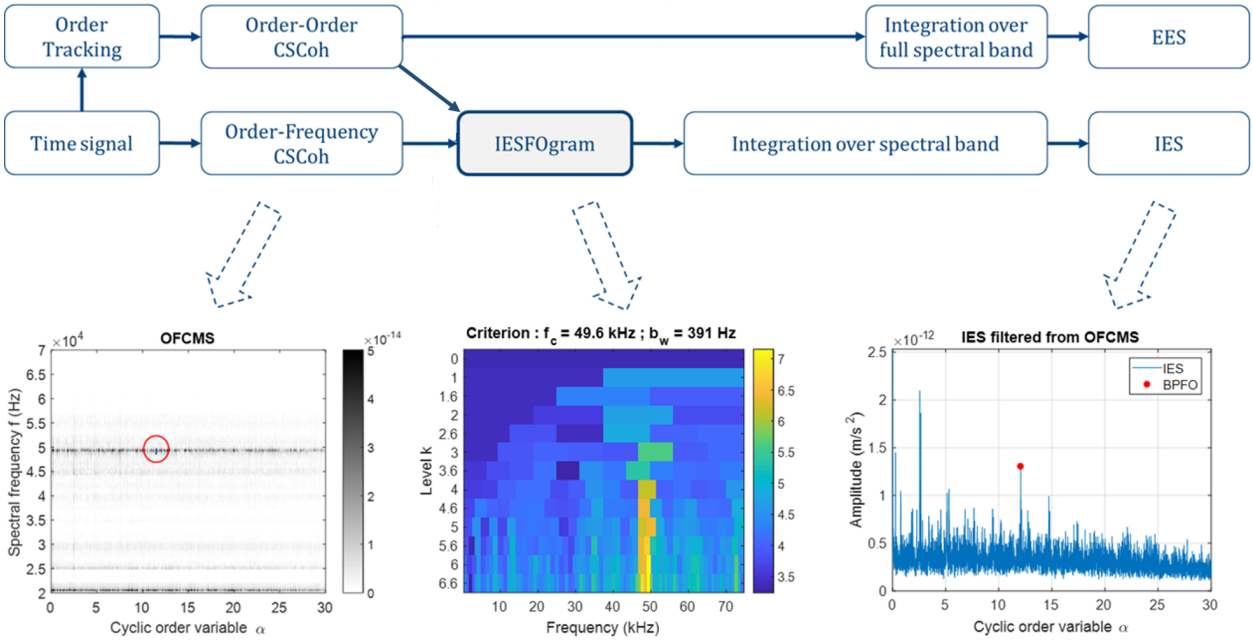


Figure 2: Methodologies diagram for analysis of cyclo-non-stationary signals.

Both methodologies result in bi-variable maps describing the cyclo-non-stationary time signals that show a cyclostationary behavior as a function of angle. Therefore, partial or full integration of the maps to obtain the EES or the IES remains applicable. Furthermore, the IESFOgram can be calculated in the same way for the selection of the optimal band.

The procedures for obtaining the EES or the IES through the IESFOgram, by either the Order-Order or the Order-Frequency bi-variable are described in the diagram of Fig. 2 .

4 Experimental Setups

In order to test and validate the proposed methodologies, vibration data have been captured from two separate test rigs. One dataset corresponds to an aircraft engine with two damaged bearings and the second dataset corresponds to a planetary gearbox with one damaged bearing.

4.1 SAFRAN aircraft engine

This dataset has been measured on a civil aircraft engine under varying speed conditions. The vibration dataset was provided by Safran and corresponds to the Safran contest which took place during the Conference Surveillance [4].

The engine has two main shafts and an accessory gearbox. The kinematics of the gearbox are described in Fig. 3.

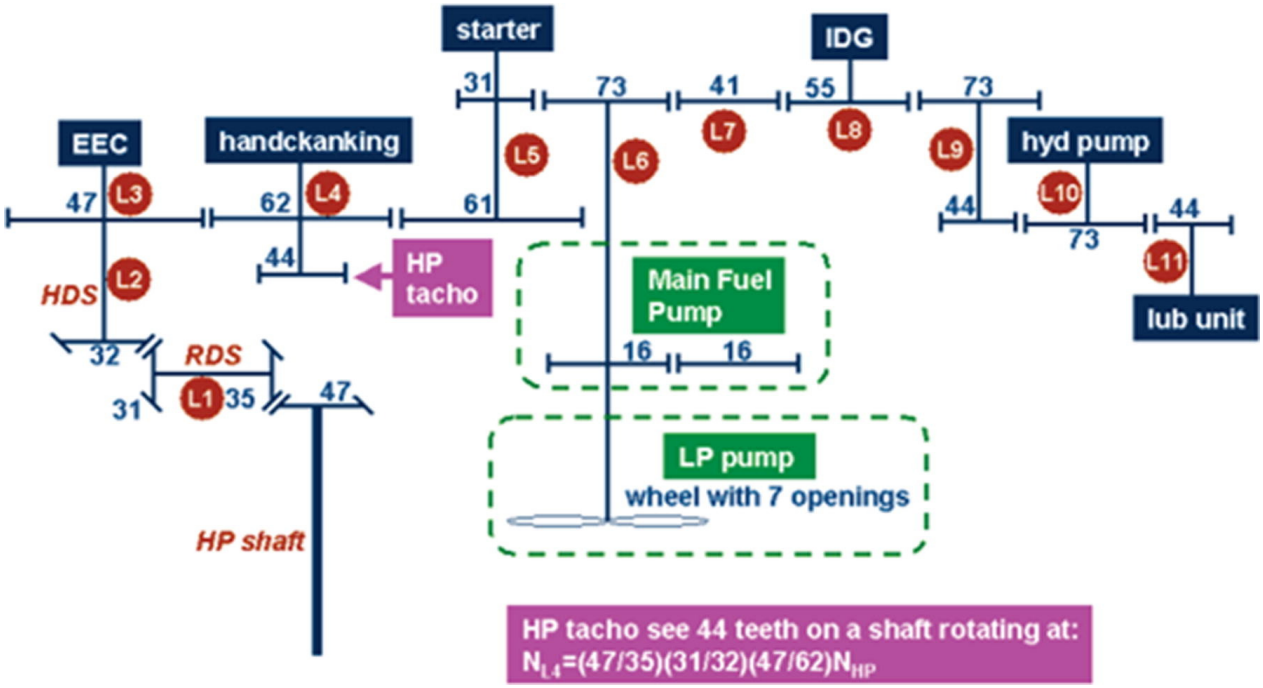


Figure 3: Kinematics of the gearbox of the Safran engine [4].

On the gearbox there are two damaged bearings: one on the radial drive shaft L1 and one on the shaft L5. The ball bearing on L1 is damaged on the outer race with a heavy scratch of 0.3 mm of depth and 1 mm of width. The roller bearing on shaft L5 is also damaged on the outer race but spalled on a wide area with a depth of 0.1 mm.

The signals were measured starting from idle to full power with a duration of 200 seconds at a sampling rate of 50 kHz. The speed reference is obtained from the tachometer mounted on shaft L4, with a resolution of 44 pulses per revolution. The vibration signals came from two accelerometers. One accelerometer (named 'Acc1') is mounted near the shaft L1 and second one (named 'Acc2') is mounted in the vicinity of shaft L5. The fault order for the ball bearing outer race damage on shaft L1 is 4.066 orders of the shaft L1 and the fault order for the roller bearing outer race damage is 7.759 orders of the shaft L5.

One claimed problem was that signal Acc1 apparently did not contain any signature of the bearing faults. Only signal Acc2 evidenced the presence of the outer-race fault in the bearing supporting shaft L5 [4].

4.2 UNSW Epicyclic gearbox

The second dataset has been provided by the University of New South Wales (UNSW) and has been measured on a planetary gearbox test rig. The planetary gearbox test rig comprises of one parallel spur stage and a planetary spur, as presented in Fig. 4 .

The planet carrier is the input of the planetary stage, while the sun gear is the output. The gear teeth are 80, 34 and 20 for the ring, the sun and the planets respectively. As the ring gear is fixed, the planet gears rotate

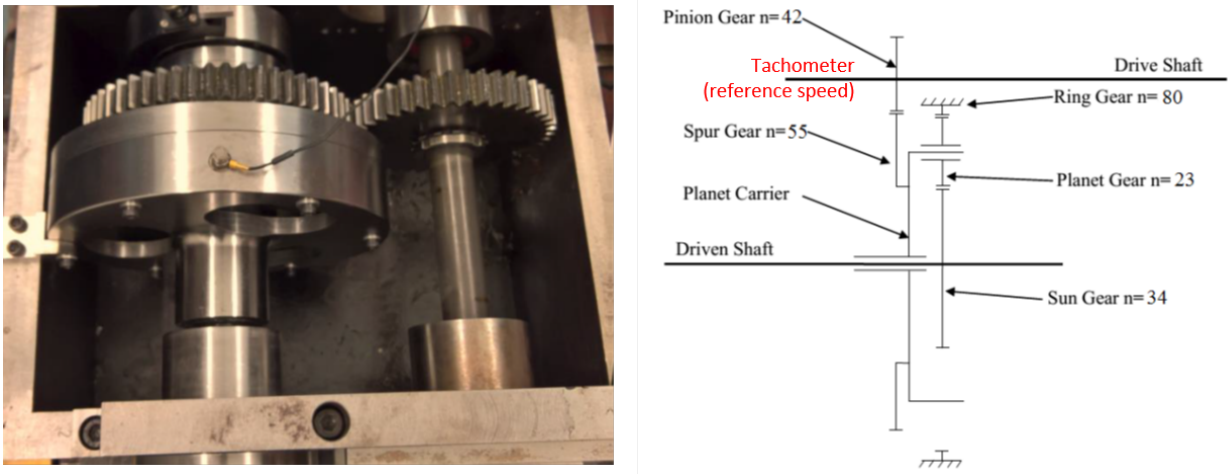


Figure 4: (left) UNSW planetary gearbox close up, (right) Gearbox kinematics [5].

with a ratio 2.66 times the drive shaft. The damaged bearing is a radial cylindrical roller bearing (IKO RNAF 162812) and is mounted on one of the planets. The damaged bearing has a fault on the outer race with a width of 1.6 mm, while its roller diameter is 3.0 mm. Thus the expected Ball Pass Order of the Outer Race fault (BPOO) is 12.3 orders of the drive shaft. Due to the fact that the tachometer measures the speed of the drive shaft, all characteristic orders of the mechanism are calculated and referenced in relation to the drive shaft speed.

In order to capture the vibration signal, one external accelerometer was mounted on the gearbox over the planet gears. The signals were acquired with a sampling frequency of 150 kHz and synchronised by a National Instrument data acquisition system. Two tests have been performed under different speed operating conditions: one at a constant rotational speed of 5.4 Hz and a second one at a varying speed between 2.8 Hz and 4.2 Hz.

5 Results and Discussion

5.1 SAFRAN aircraft engine

The signal from the SAFRAN engine captured by the accelerometer 'Acc2' is analysed in a first step. The signal corresponds to 100 seconds at a sampling frequency of $fs = 50$ kHz, under a run-up from 180 Hz to 210 Hz of the shaft rotation speed. The speed signal is captured by a tachometer and the corresponding raw signal can be seen in Fig. 5 .

Initially, order tracking using the speed reference has been applied to analyse the spectrum of the signal. The characteristic orders of the mechanism have been detected confirming that a correct angular sampling has been performed.

The Order-Order Cyclic Spectral Coherence (OO-CSCoh) is then estimated from the angular re-sampled signal and the Order-Order Enhanced Envelope Spectrum (OO-EES) is estimated based on the integration of the whole spectral order, as presented in Fig. 6 .

A vertical line at the cyclic order α corresponding to the Ball Pass Order of the Outer Race (BPOO) can be identified in the OO-CSCoh. The diagnosis of the damage through the analysis of the map usually requires some level of expertise but on the other hand, the OO-EES presents clearly the harmonics of the damage on the spectrum, allowing a confident diagnosis.

Then the IESFOgram is obtained and the Order-Order Improved Envelope Spectrum (OO-IES) is estimated based on the integration of the band returned by the IESFOgram, as presented in Fig. 7.

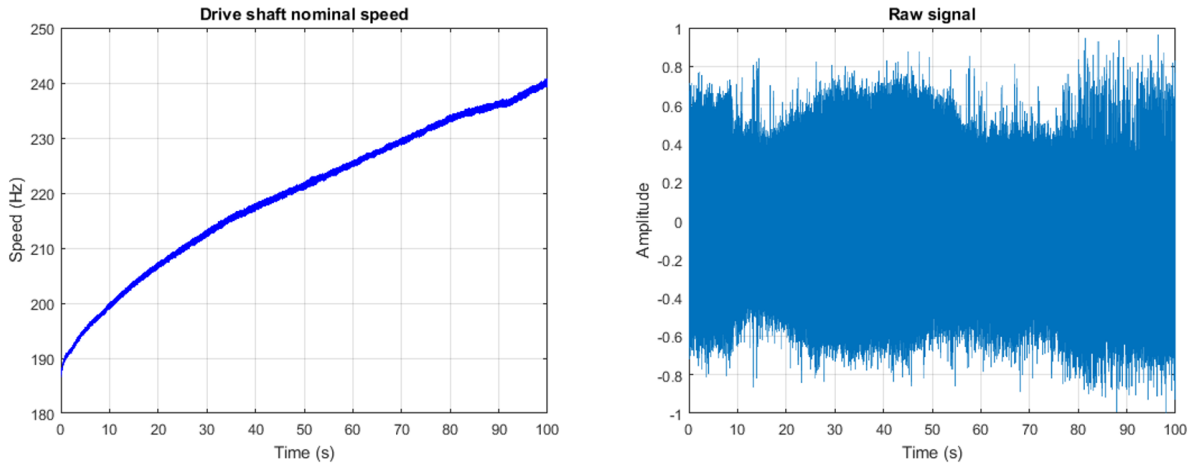


Figure 5: (left) Safran speed signal, (right) Vibration raw signal.

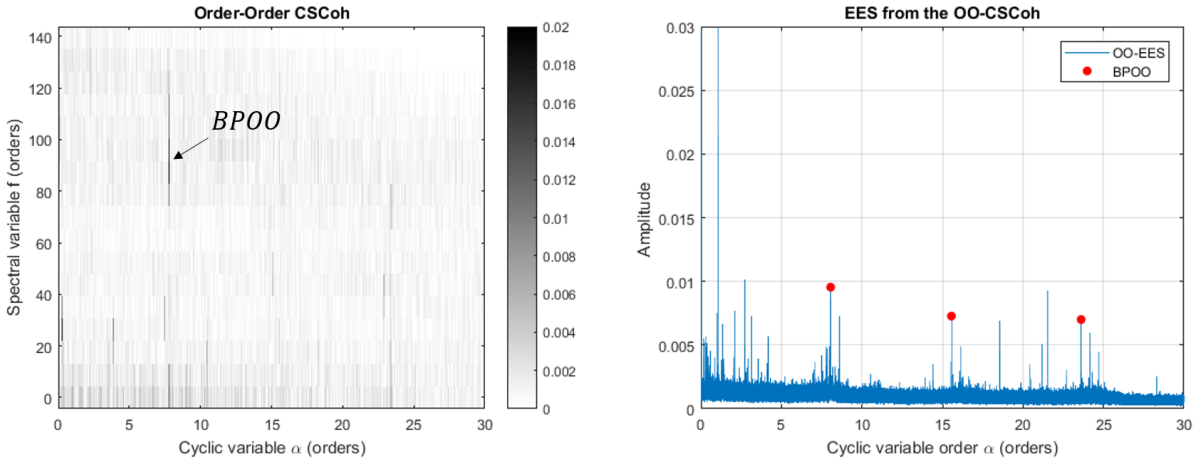


Figure 6: (left) Order-Order CSCoh, (right) OO-EES.

The selected band is seen to be the centred around 52 orders on the spectral band. The method seems to select an optimal band that maximizes the 2^{nd} harmonic of the BPOO. Upon closer analysis of the OO-CSCoh, it is noticed that the BPOO is excited across several bands over the spectral axis. The 1^{st} harmonic of the BPOO exhibits its carriers with high values centred around 30 orders, while the 2^{nd} harmonic exhibits around the 50 orders band.

Unlike the OO-CSCoh, which is obtained through the angular re-sampled signal, the Order-Frequency Cyclic Modulation Spectrum (OF-CMS) is obtained from the raw signal while providing the speed signal. The OFCMS map for the 'Acc2' signal and its OF-EES, from its full spectral band integration, can be seen in Fig. 8.

The OF-EES shows a similar result when compared to its order-order version, as the integration is realised over all the spectral content. However the bi-variable map shows the damage-related CS content to be more centralized on the lower frequency band of the spectral axis and the gears and shaft harmonics are reduced in the spectrum. This is most likely due to the nature of the OF-CSC theory, where the carrier information is kept as a function of time and thus not smearing the time-dependent carrier frequencies over the spectral axis.

When IESFOgram is applied on the OFCMS, the previous statement can be confirmed due to the selection of a narrow band, in the lower frequency spectrum, as the optimal band. The IESFogram and the resulting OF-IES can be seen in Fig. 9 .

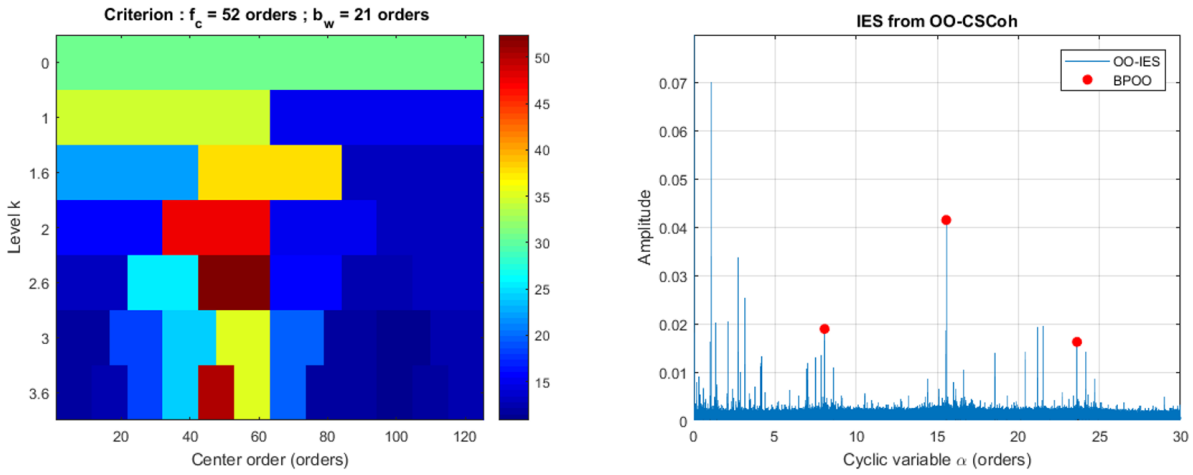


Figure 7: (left) IESFOgram for the OO-CSCoh, (right) OO-IES.

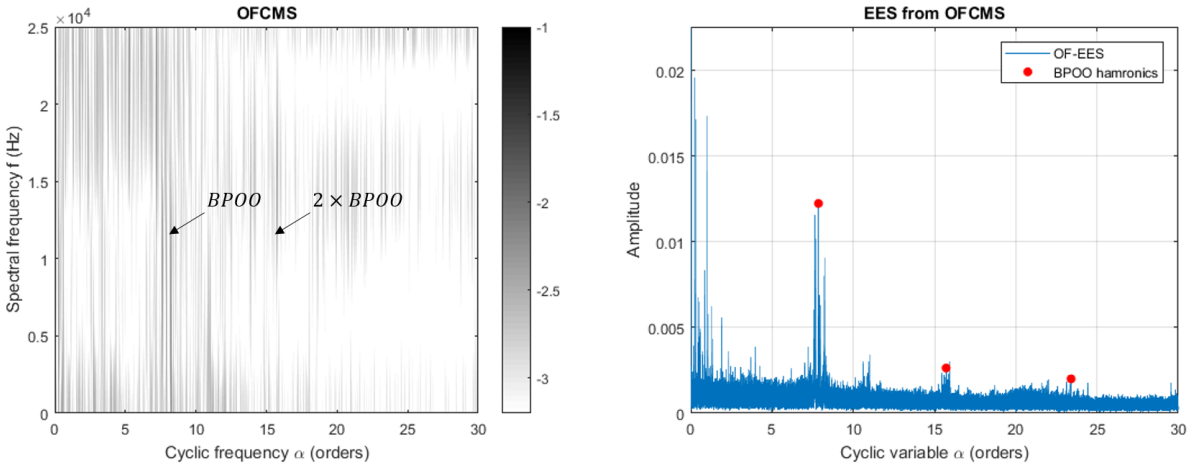


Figure 8: (left) OFCMS, (right) OF-EES from the OFCMS.

From the OF-IES the present fault frequencies are noticed to have been slightly enhanced when compared to the OF-EES. Some of the remaining speed-related harmonics were further reduced while integrating on the carrier band of the BPOO.

This dataset also provides a good example on the complexity of the analysis for bi-variable maps. While the detection of the bearing damage cannot be extracted in a straightforward manner from the analysis of the 2D maps, the analysis of the resulting envelope spectra provides a clear detection of the fault order.

5.2 UNSW Epicyclic gearbox

The methodologies are further applied to the UNSW measured vibration signal under varying speed operating conditions. The vibration signal was truncated to contain the varying speed conditions fluctuating between 2.8 Hz and 4.2 Hz, as described in Fig. 10.

Spectral analysis and Envelope Analysis have been performed in order to detect the characteristic frequencies of the system and to confirm that a correct order tracking has been performed. Despite confirming that the signal has been correctly re-sampled in the angular domain, no bearing fault frequencies were detected in the spectrum. However, filtering the signal with the band selected by ICSgram [5, 6] results in an Order-Tracked Squared Envelope Spectrum (OT-SES) from which the first harmonic of the damage can be extracted, as can be seen from Fig. 11 .

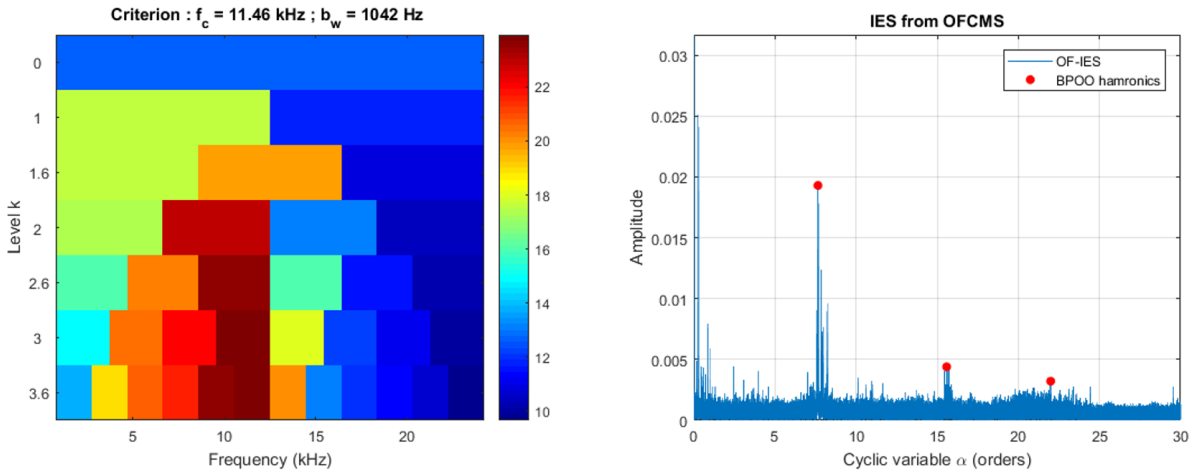


Figure 9: (left) IESFOgram for the OFCMS, (right) OF-IES.

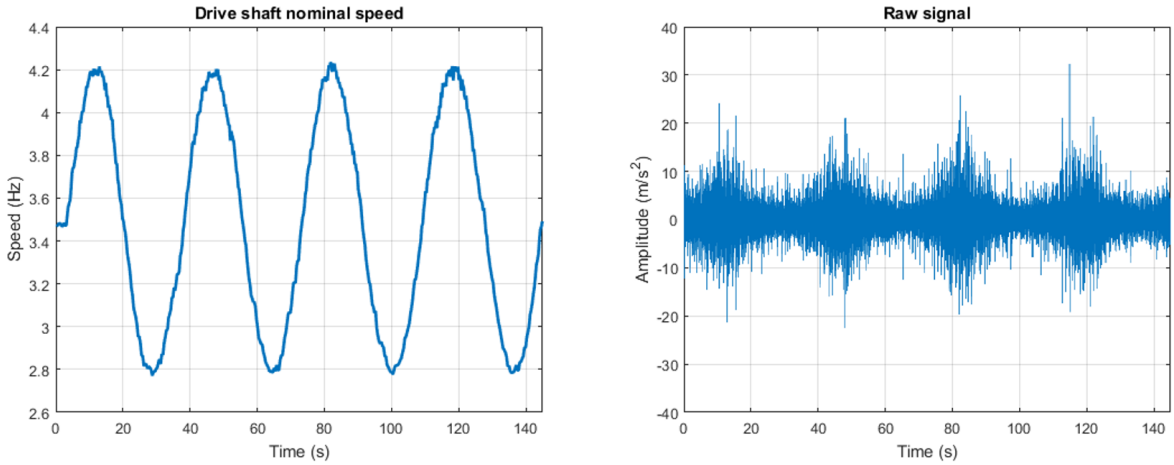


Figure 10: (left) UNSW speed signal, (right) Vibration raw signal.

The OO-CSCoh is then estimated and a weak component of the fault frequency can be detected on the 2D map. Integration on the full spectral axis results in the OO-EES where a small peak near the fourth harmonic of the shaft can be detected as the fault frequency. Once again, the analysis of the 2D map is not straightforward but obtaining the spectrum results in a simpler analysis. Furthermore, the IESFOgram is applied and the OO-CSCoh is integrated on its selected band. This results in a more clear fault diagnosis because two fault order harmonics can be detected from the spectrum as can be seen in Fig. 12 .

As for the OFCMS analysis, the fault order on the correspondent cyclic axis cannot be easily detected. Full spectral integration also does not provide a clear detection, due to the fault order being completely masked by the other components and noise level, as can be seen from Fig. 13.

On the other hand, when the IESFOgram is applied, a narrow band around 49 kHz is selected, where two harmonics of the fault order are clearly exhibited. In this particular case, the second harmonic is detected with more confidence than with the OO-IES case, due to its enhanced amplitude above the noise level.

For a performance analysis of the different methods explained on this paper for each dataset, Tab. 1 describes the total number of harmonics that can be extracted and detected in the resulting spectrum of each case.

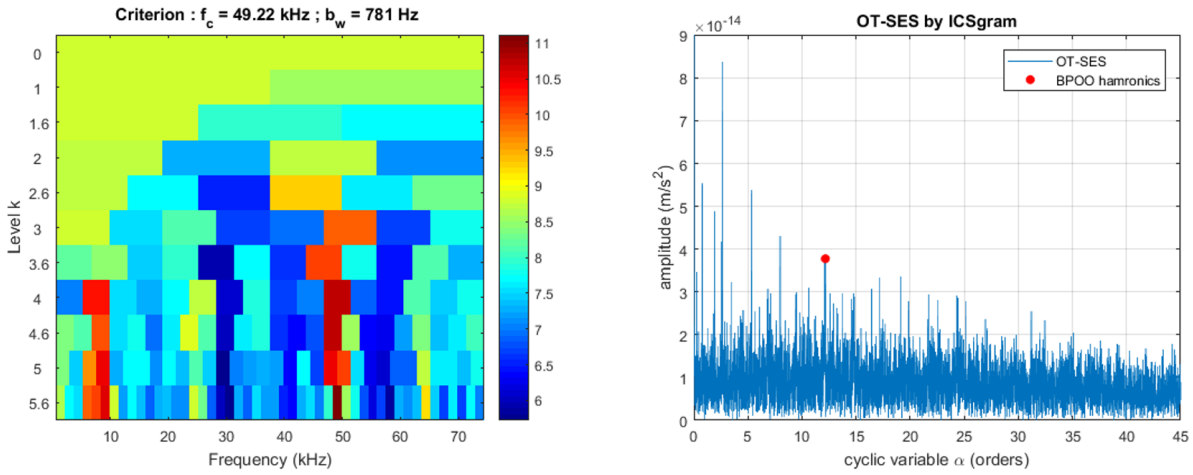


Figure 11: (left) ICSgram , (right) OT-SES by ICSgram filter selection.

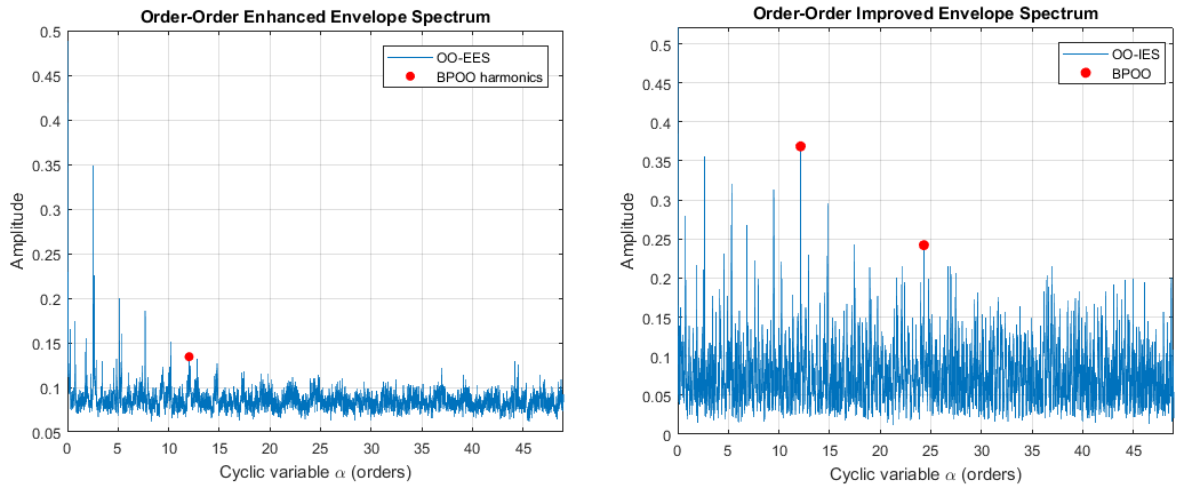


Figure 12: (left) OO-EES , (right) OO-IES .

6 Conclusion

In this paper, two novel spectral indicators, the OO-IES and OF-IES by IESFOgram, have been proposed for the fault detection of rolling element bearings under varying speed operating conditions. The IESFOgram is proposed as a band selection tool similar to the Kurtogram and is built as a binary tree in the same manner. Spectral analysis using cyclostationary based tools, such as the Cyclic Spectral Coherence (CSCoh), are seen to be powerful tools for bearing diagnostics. Furthermore, it has been demonstrated that the integration on a specific band of the spectral axis of the bi-variable maps results in more enhanced exhibition of the fault orders in the spectrum. The first procedure is based on the Order-Order Cyclic Spectral Coherence (OO-CSCoh), which results from the estimation of the CSCoh on the angular re-sampled signal. The second procedure is based on the Order-Frequency Cyclic Spectral Correlation (OF-CSC), where angular re-sampling is applied on the Time-Frequency domain and Fourier transformed, leading to the Order-Frequency

Table 1: Number of harmonics detected for each dataset and each method.

	OT-SES	**ICSgram**	**OO-EES**	**OO-IES**	**OF-EES**	**OF-IES**
SAFRAN	3	3	3	3	3	3
UNSW	0	1	1	2	0	2

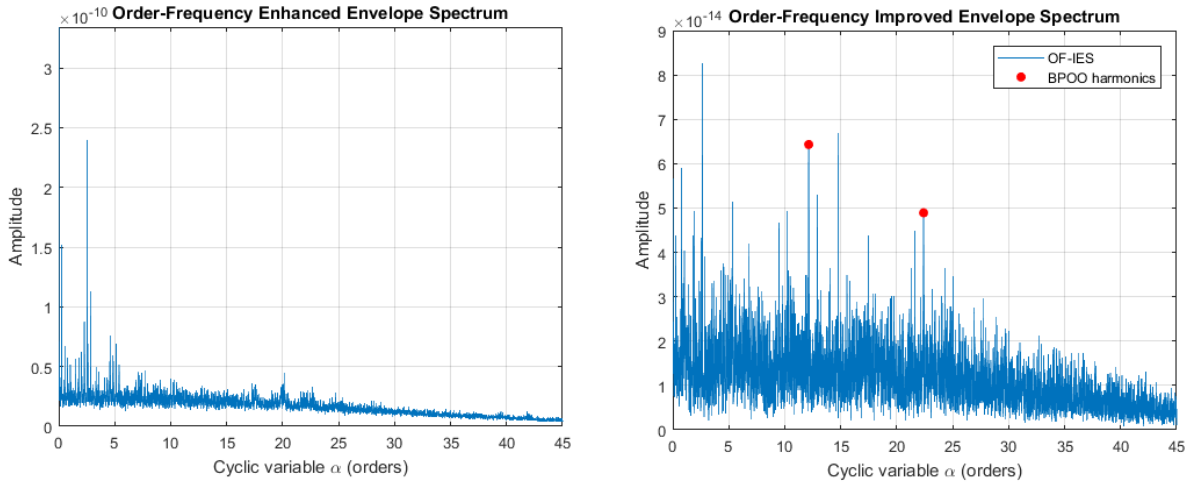


Figure 13: (left) OF-EES , (right) OF-IES.

domain. The Enhanced Envelope Spectrum (EES) is estimated based on both procedures, leading to the OO-EES and OF-EES. Both show good capabilities in the detection of damage. Furthermore, the Improved Envelope Spectrum (IES) is also estimated based on both procedures, leading respectively to the OO-IES and OF-IES and show consistently improved detection of the damage when compared to the EES based methods.

Acknowledgements

K. Gryllias would like to gratefully acknowledge the Research Fund KU Leuven.

References

[1] Sheng, S., Wind Turbine Gearbox Condition Monitoring Round Robin Study Vibration Analysis. In: *NREL/TP-5000-54530. Golden, CO: National Renewable Energy Laboratory*, July (2012).

[2] Mahvash, A., Lakis, A. A., Application of Cyclic Spectral Analysis in Diagnosis of Bearing Faults in Complex Machinery. In: *Tribology Transactions*, **58**, 1151-1158 (2015).

[3] Mauricio, A., Smith, W., Qi, J., Randall, R., Gryllias, K., Cyclo-non-stationary based bearing diagnostics of planetary gearboxes. In: Proceedings of CMMNO 2018, 20-22 June, Santander, Spain, (2018).

[4] Antoni, J., Griffaton, J., André, H., Avendaño-Valencia, L. D., Bonnardot, F., Cardona-Morales, O., Castellanos-Dominguez, G., Daga, A. P., Leclére, Q., Vicuña, C. M., Acuña, D. Q., Ompusunggu, A. P., Sierra-Alonso, E. F., Feedback on the Surveillance 8 challenge: Vibration-based diagnosis of a Safran aircraft engine. In: *Mechanical Systems and Signal Processing*, **97**, 112-144 (2017).

[5] Randall, R.B., Smith, W.,A., du Mée, X. C., Peng, P., Planet bearing diagnostics under variable speed operation, International Conference Surveillance 9, May 22-24, Fes, Morocco. (2017).

[6] Smith, W.,A., Randall, R.B., du Mée, X. C., Peng, P., Use of Cyclostationary properties to diagnose planet bearing faults in variable speed conditions. In: 10th DST Group International Conference on Health and Usage Monitoring Systems, 17th Australian Aerospace Congress,26-28 February, Melbourne, Australia (2017).

[7] Abboud, D., Baudin, S., Antoni, J., Rémond, D., Eltabach, M., Sauvage, O., The spectral analysis of cyclo-non-stationary signals. In: *Mechanical Systems and Signal Processing*, **75**, 280-300 (2016).

[8] Abboud, D., Antoni, J.,Order-frequency analysis of machine signals. In: *Mechanical Systems and Signal Processing*, **87**, 229-258 (2017).

[9] Antoni, J., Fast computation of the kurtogram for the detection of transient faults. In: *Mechanical Systems and Signal Processing*, **21**, 108-124 (2007).

[10] Moshrefzadeh, A., Fasana, A., The Autogram: An effective approach for selecting the optimal demodulation band in rolling element bearings diagnosis. . In: *Mechanical Systems and Signal Processing*, **105**, 294-318 (2018).

[11] Randall, R.B., Antoni, J., Chobsaard, S., The relationship between spectral correlation and envelope analysis in the diagnostics of bearing faults and other cyclostationary machine signals. In: *Mechanical Systems and Signal Processing*, **15**, 945-962 (2001).

[12] Antoni, J., Xin, G., Hamzaoui, N.,, Fast computation of the spectral correlation. In: *Mechanical Systems and Signal Processing*, **92**, 248-277 (2017).

[13] Antoni, J., Abboud, D., Xin, G., Cyclostationarity in Condition Monitoring: 10 years after. In: Proceedings of ISMA 2016 including USD 2016, Leuven, Belgium, (2016).

[14] Mauricio, A., Qi, J., Gryllias, K., Vibrationbased condition monitoring of wind turbine gearboxes based on cyclostationary analysis. In: Proceedings of the ASME 2018 Turbomachinery Technical Conference Exposition Turbo Expo 2018, 11-15 June, Oslo, Norway, (2018).

Optimal frequency band selection via stationarity testing in time frequency domain

A. Michalak [1], **A. Wyłomańska** [1], **J. Wodecki** [1], **R. Zimroz** [2], **K. Gryllias** [3, 4]
[1] Research and Development Centre, KGHM Cuprum Ltd,
Sikorskiego 2-8, 53-659 Wrocław, Poland

[2] Faculty of Geoengineering, Mining and Geology, Diagnostics and Vibro-Acoustic Science Laboratory, Wrocław University of Science and Technology,
Na Grobli 15, 50-421 Wrocław, Poland

[3] KU Leuven, Department of Mechanical Engineering,
Celestijnenlaan 300 - box 2420, 3001 Leuven, Belgium

[4] Dynamics of Mechanical and Mechatronic Systems, Flanders Make, Belgium

e-mail of Corresponding Author: **jwodecki@cuprum.wroc.pl**

Abstract
In the last decades a plethora of signal processing tools have been proposed for the analysis of vibration signals, focusing on fault detection and diagnosis of rotating machinery. Despite the existence of numerous methodologies, there is still a need to construct more specific diagnostic algorithms. The informative frequency band is a purely frequency-domain idea, so very often the approach of spectral selectors is pursued and those are digital filters prepared in a custom way. In this paper a novel signal processing approach is proposed based on the analysis of the time-frequency domain. The vibration signal is firstly transformed to the time-frequency domain. Moreover the stationarity of the time series vectors within the discrete frequency bins of the Time-Frequency (T-F) map is statistically tested by using the Augmented Dickey-Fuller (ADF) test. A frequency band filter selector is then constructed by the aggregation of the ADF statistic values of narrow frequency bins into a vector spanning over the whole Nyquist band of the given signal.

1 Introduction

The notion of introducing so-called *intelligent solutions* for maintenance of industrial machinery drives the need for development of specialized analytical methods for more and more demanding diagnostic scenarios. Machines with rotating components are in the center of research interest due to the high industrial relevance and the high diversity of possible fault cases regarding components interacting with each other. Mechanisms of signal generation by kinematic pairs (e.g. pair of gears) when one of the components is faulty have been studied by many researchers [1–4]. The fault signature of rolling element bearings may be described as impulsive [5], cyclic (or periodic) [6], nonlinear, non-Gaussian [7], amplitude/phase modulated [8], etc. Most of these descriptors have been already used as detection criteria - kurtosis was used as a measure of impulsiveness [9], cyclostationary analysis was developed to detect and identify cycles related to damage [10, 11] etc. However in this paper the authors propose to use testing of the signal stationarity for machine diagnostics. It is well known, that in case of healthy bearings, a vibration signal measured on the housing will be stationary and will closely follow a Gaussian distribution. In case of local damage, two surfaces in contact

will produce a disturbance. Effectively, a series of such impacts in the time domain will manifest itself as a cyclic (or periodic) additive impulsive component. It will definitely introduce disturbance in the signal, which will contribute to the degree of non-stationarity. This observation, made already also by other researchers [12] is the basis for this paper. The key idea here is to test whether the signal is stationary or not and more specifically, instead of evaluating the signal itself, a more structure-oriented approach is proposed. Due to the complexity of machinery and the number of potential sources of non-stationarity, including accidental disturbances [13, 14], the test of stationarity will be done in the time-frequency domain, for each frequency bin – similarly to the Spectral Kurtosis (SK) or to other methods developed for informative frequency band identification. A variety of techniques have been proposed for testing of stationarity of a signal [15–17]. In this paper the use of the Augmented Dickey-Fuller (ADF) test [15] is proposed. The distribution of the ADF statistical value along the frequency scale can be estimated and used as a spectral selector similar to SK, being the basis for digital filter characteristic for signal enhancement [18]. The approach is validated on real signals captured on pulley bearings. As a further validation step, the results are compared with the SK method in terms of the selector shape as well as of the quality of the obtained filtered signal. The rest of the paper is organised as follows. The methodology is first proposed in Section 2 and it is further applied on real signals and teh results are presented in Section 3. The paper closes with some conclusions in Section 4.

2 Methodology

In this section, the key aspects of the methodology are described. The main idea is to develop a frequency-domain selector based on the spectral stationarity of the signal. The proposed approach in some sense is an extension of the classical methodology based on the Spectral Kurtosis, which is a popular measure of impulsiveness. However the ADF statistic (calculated for each frequency band) is considered here which may indicate the nonstationarity of a subsignal corresponding to a given frequency band. The flowchart of the proposed algorithm is presented in Figure 1.

First, the spectrogram of the input data is calculated as a time-frequency representation allowing to access narrow frequency bands. Next, for each subsignal of the time-frequency representation the ADF statistic (see Equation (2)) is estimated. It should be mentioned that the ADF test, based on the ADF statistic, is a classical test often used to test the nonstationarity of real data. Finally the selector is smoothed and thresholded. In the following subsections the proposed procedure is described in more details.

2.1 Time-frequency representation

The procedure begins with the calculation of a spectrogram (see Equations (1) and (2)). The spectrogram parameters are selected based on empirical testing taking into account the length of the signal time series. For the specific analyzed real signal (see section 3) the parameters are presented in Table 1.

The Short-Time Fourier Transform (STFT) for the discrete signal $y_0, y_1, \ldots, y_{N-1}$ is defined as follows [19]:

$$\text{STFT}(t, f) = \sum_{m=0}^{L-1} y_{t+m} \omega_m e^{-j2\pi f m/N} \tag{1}$$

for $0 \leq f \leq f_{max}$ and $0 \leq t \leq t_{max}$. In the above equation ω is a shifted window of length L. Furthermore, the spectrogram is estimated as the squared absolute value of the STFT:

$$\text{Spec}(t, f) = |\text{STFT}(t, f)|^2. \tag{2}$$

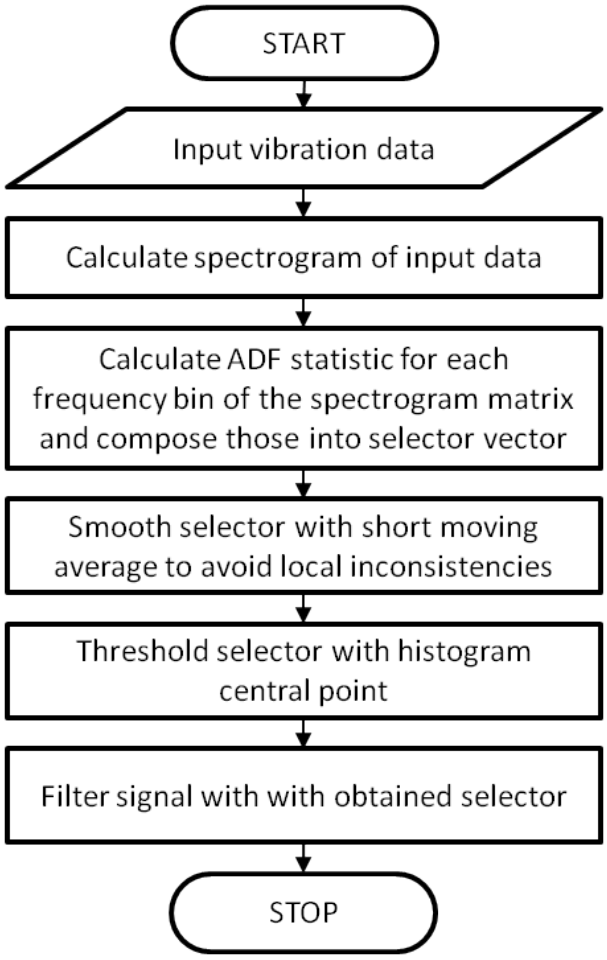


Figure 1: Flowchart of the proposed procedure.

2.2 Augmented Dickey-Fuller (ADF) selector

The problem of testing stationarity of real data has been widely discussed in the literature. Different approaches applied in this issue can be found. Classical tests are for instance the Dikey-Fuller (DF), the Kwiatkowski-Phillips-Schmidt-Shin (KPSS) and the Durbin-Watson [15–17]. However one of the most popular tests for stationarity is the augmented DickeyFuller test (ADF). The null hypothesis of the ADF test is that the unit root is present in the analyzed data, i.e. the data follow the model:

$$y_t = c + \delta t + \phi y_{t-1} + \beta_1 \Delta y_{t-1} + \ldots + \beta_p \Delta y_{t-p} + \epsilon_t, \tag{3}$$

where Δ is the differencing operator, p is the number of lagged difference terms and $\{\epsilon_t\}$ constitutes a sample of independent identically Gaussian distributed random variables with mean zero and variance σ^2 $\left(N(0, \sigma^2)\right)$. The unit root is found when $\phi = 1$, i.e. after differentiation, the signal corresponds to an autoregressive process of order p (AR(p)). In this paper, the authors take under consideration the simpler version with no drift ($c = 0$), no trend ($\delta = 0$) and (p=0). In this case the model (3) takes the form:

$$y_t = \phi y_{t-1} + \epsilon_t, \tag{4}$$

which is an autoregressive model of order 1 (AR(1)) in case $\phi \neq 1$. In the considered case, the ADF statistic used in ADF test with null hypothesis, defined as in (4), is given by:

$$ADF_{stats} = \frac{\hat{\phi}}{se(\hat{\phi})}, \tag{5}$$

where $\hat{\phi}$ is the AR(1) coefficient computed by using the Ordinary Least Squares method and se is the standard error of the estimated value. According to the scheme of this procedure, presented in Figure 1, ADF statistics are calculated for each frequency bin from the spectrogram. The ADF selector is set equal to the absolute value of the ADF statistic.

2.3 Spectral Kurtosis

The Spectral Kurtosis has been introduced by Antoni and Randall [20, 21] and it is considered as one of the most powerful and popular approaches to localize an Informative Frequency Band (IFB), especially for vibration signal analysis. The general principle of operation is to calculate the kurtosis value (see Equation (6)) for each frequency bin of the spectrogram:

$$\text{Kurt}[Spec(t,f)] = \frac{m_4}{{m_2}^2} = \frac{\frac{1}{n}\sum_{i=1}^{n}(y_i - \overline{y})^4}{\left(\frac{1}{n}\sum_{i=1}^{n}(y_i - \overline{y})^2\right)^2}, \tag{6}$$

where m_4 is the fourth central moment, m_2 is the second sample moment (sample variance), y is a single time-domain vector corresponding to the given frequency bin f and $0 \leq f \leq f_{max}$.

As a result, an indicator of impulsiveness across the signal spectrum can be obtained, allowing to determine which frequency bands carry the most visible information about the damage-related impulsive behavior. The indicator is named Spectral Kurtosis (SK) and a Vector of SK can be then used as a filter to extract the impulsive components from the signal.

2.4 Post-processing of ADF selector

After obtaining an ADF selector (as well as the SK selector), it is proposed to post-process it for further enhancement. First, it is smoothed using the moving average with a relatively small window (10 samples in this case) just to eliminate the local variance between the adjacent frequency bands. Afterwards a noise gate is applied by thresholding the smoothed selector with the central point of its histogram. The details of this procedure can be found in [22].

As a final step, after the calculation of the proposed ADF selector in function of f, which is just an absolute value of the ADF statistic obtained for each subsignal from the spectrogram, the signal can be further filtered. It is expected that the filtered signal in time domain is more impulsive than the original one. This is related to the fact that the filter characteristic emphasizes the frequency bands which contain the impulses related to the damage. One of the classical measure of impulsiveness is the kurtosis, therefore this statistic is finally calculated for the envelope of the filtered signal in order to prove the effectiveness of the proposed procedure. As a comparison, the SK selector is calculated also for the original signal and is considered as the filter characteristic. Finally, the kurtosis of the envelope of the SK filtered signal is calculated and is compared to the kurtosis of the envelope of the signal filtered by the ADF filter characteristic.

3 Real-life data analysis

Vibration data have been captured by a commercial measurement system on the rolling ball bearing of the drive pulley operating in a belt conveyor driving station, presented in Figure 2. The sensor for measuring the vibration signal was located in the horizontal direction. The sampling frequency is equal to 19 200 Hz. In Figure 3 are presented 2.5 seconds of raw vibration signals captured over a healthy bearing (top panel) and a faulty bearing (bottom panel).

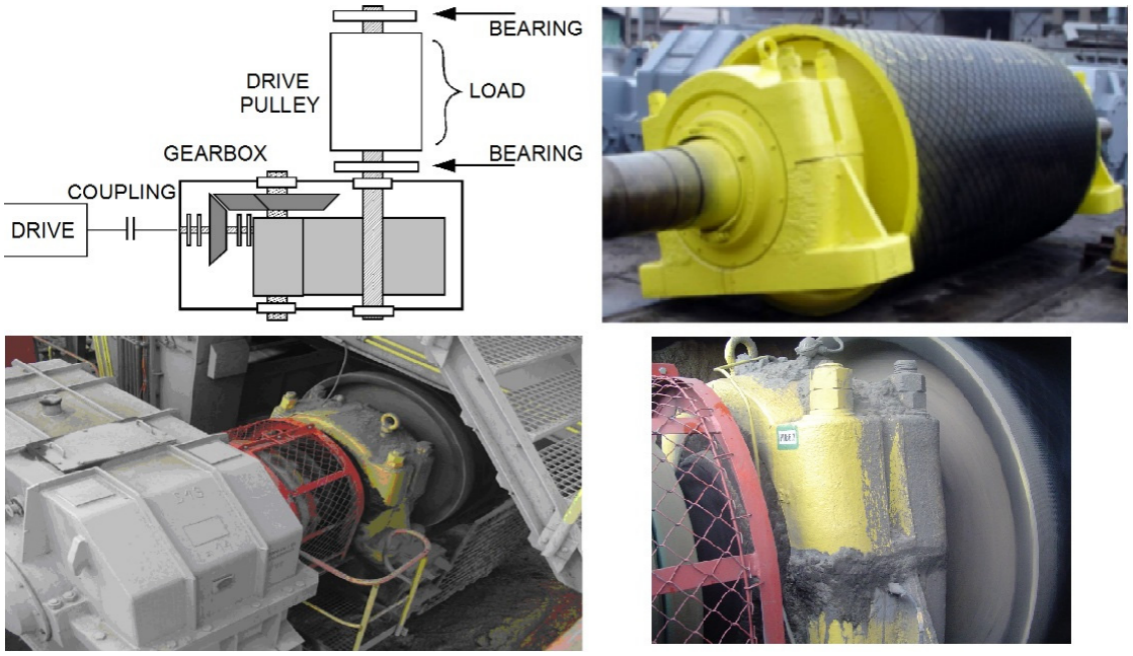


Figure 2: A drive pulley operating in a belt conveyor driving station

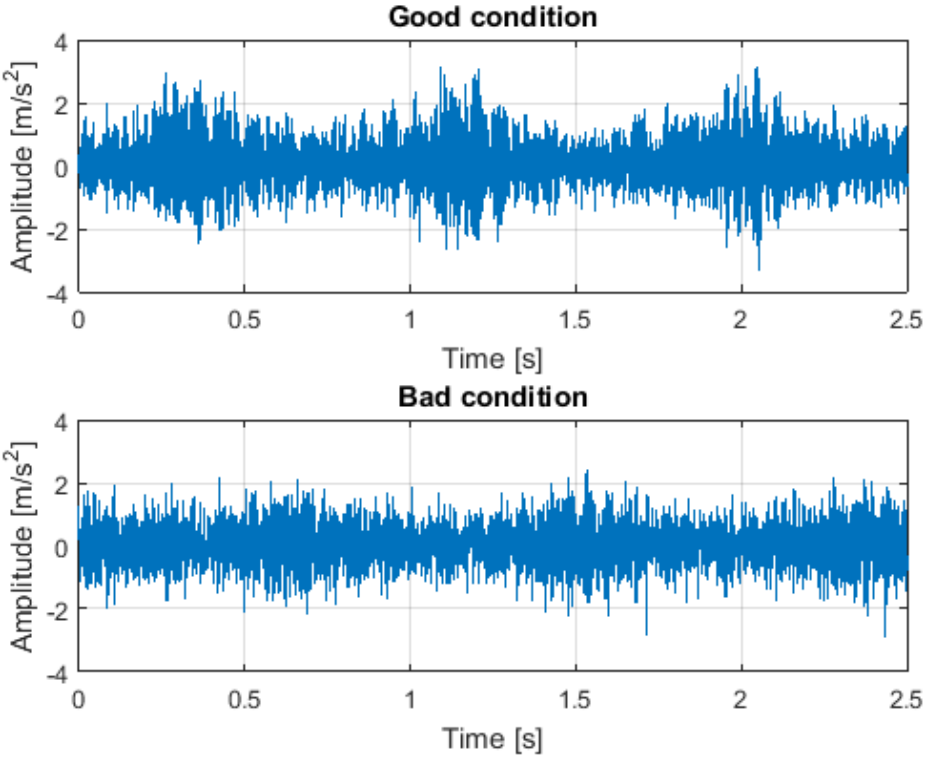


Figure 3: Raw vibration data

The envelop spectrum of both analysed signals are presented in Figure 4. It should be noted, that analysing the raw time signals, it is difficult to observe an impulsive behavior corresponding to the bad (faulty) condition. Moreover the envelope spectrum does not provide clear information about the damage.

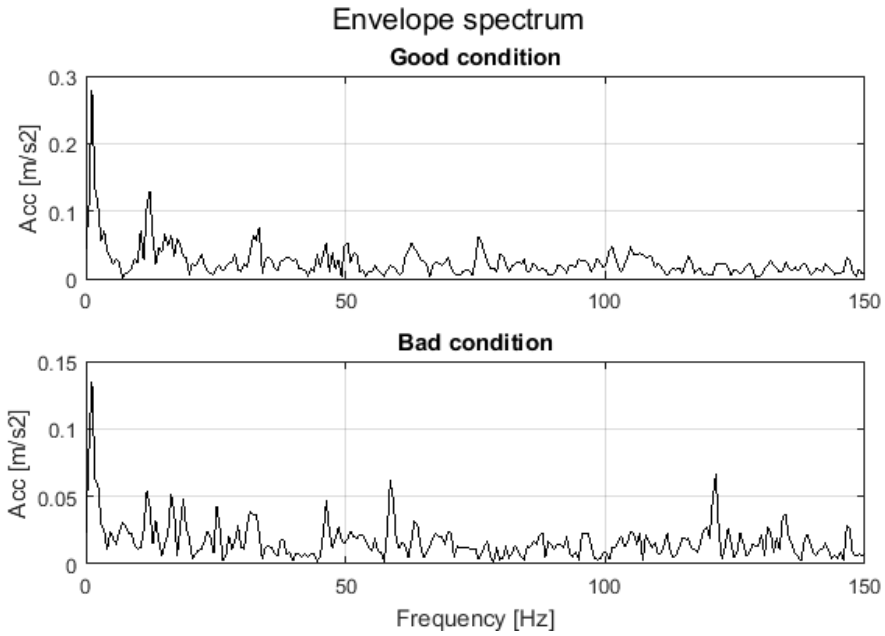


Figure 4: Envelope spectrum of raw vibration data.

Furthermore, the time-frequency representation (spectrogram) of the signals presented in Figure 3 are shown in Figure 5. They have been calculated according to the parameters presented in Table 1. Some peaks between 1 and 6 kHz are observed at the spectrogram corresponding to the signal from the machine in bad condition.

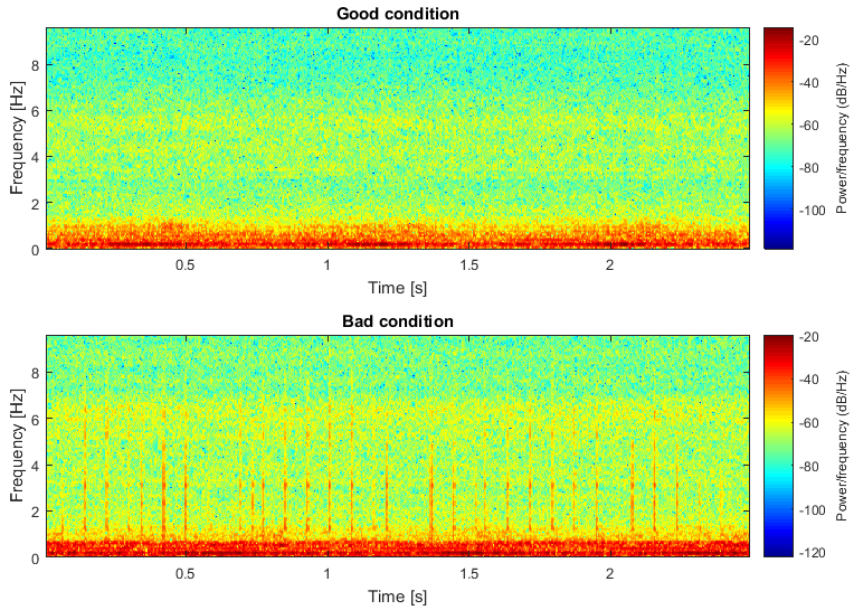


Figure 5: Time-frequency representation (spectrogram) of the input data.

Next, the ADF statistic for each frequency bin of the spectrogram is calculated. In Figure 6 the values of ADF statistic are presented.

The values of the statistic are lower for those frequencies for which an impulsive behavior is expected. This

Table 1: Parameters of compared results.

Parameter	**Value**
Sampling frequency	19200 Hz
Window	Hamming, 256 samples
Overlap	60% window
FFT points	512

indicates that the subsignals corresponding to those frequencies are ”more nonstationary” compared to other frequency bands.

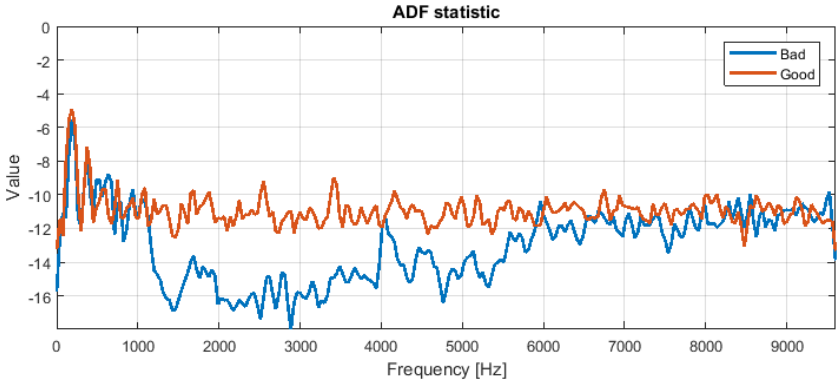


Figure 6: ADF statistic for signal of the machine in good and bad condition.

The ADF selector, i.e. the absolute value of the ADF statistic and the corresponding filter characteristic are presented in Figure 7.

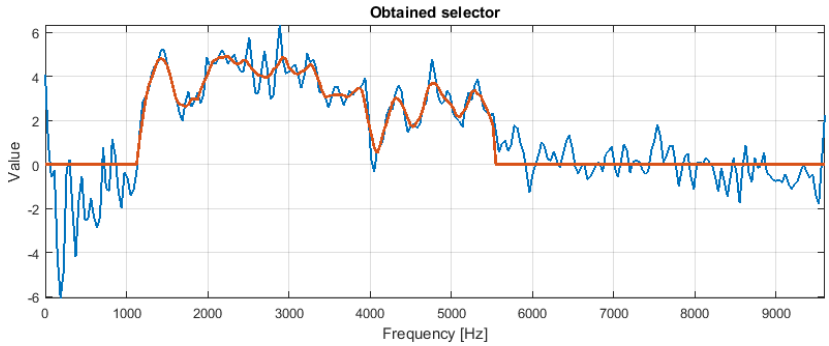
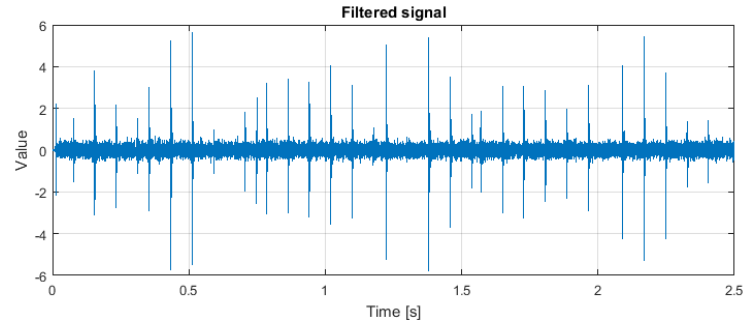


Figure 7: ADF selector and ADF filter characteristic.

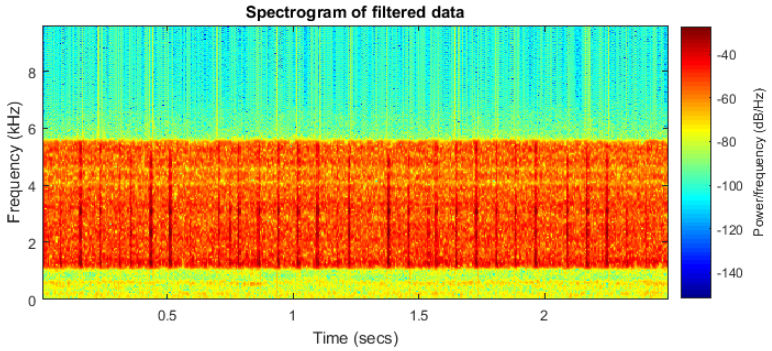
After its estimation, the filter function is applied over the signals. The filtered signal captured over the machine in a bad condition (using the obtained characteristics) is presented in Figure 8a while the corresponding spectrogram of the filtered signal is presented in Figure 8b.

Finally the envelope spectrum of the filtered signal is analysed. Comparing Figure 4 and Figure 8c, it can be observed that the impulsiveness can be easier detected at the filtered signal compared to the original signal. Moreover, in order to compare the SK- and the ADF- selector results, a similar methodology have been followed for the SK approach.

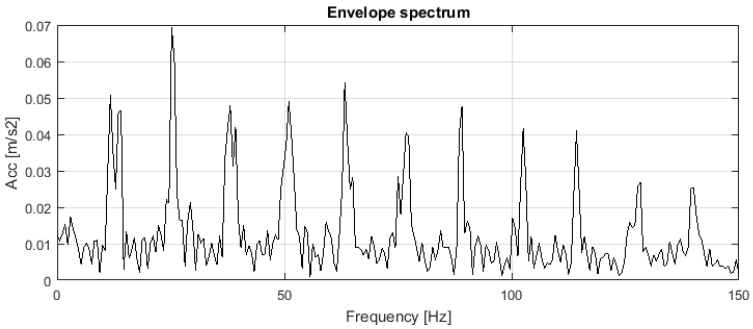
More precisely, the SK has been calculated for the raw signal corresponding to the machine in bad condition and the signal is further filtered according to SK characteristic.



(a) Signal after filtration using ADF filter characteristic.



(b) Spectrogram of filtered signal.



(c) Envelope spectrum of filtered signal.

Figure 8: Presentation of signal in various domains after filtration procedure using obtain selector.

Similar to the ADF statistic, the SK statistic has been also smoothed and thresholded (see the red line in Figure 9). Finally the kurtosis of the envelope of the filtered signals obtained after using the ADF and the SK approach are compared. The kurtosis of the envelope of the filtered data for the ADF selector has been calculated equal to 88.2290 while for the SK it was calculated equal to 66.7322.

4 Conclusions

In this paper, a novel method for fault detection in bearings, based on the Augmented Dickey-Fuller (ADF) test has been presented, as an alternative to the classical Spectral Kurtosis approach. The ADF statistic is used as a measure of nonstationarity which results from the impulsive behavior of a signal and further as an Informative Frequency Band selector. The methodology has been applied on a signal captured over a drive pulley operating in a belt conveyor driving station and has been compared to the classical SK approach. Based on this comparison, the new algorithm seems to be more effective compared to the classical SK.

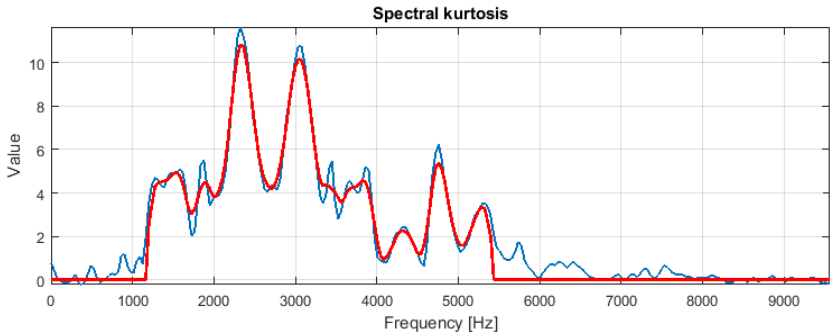


Figure 9: Spectral kurtosis and SK selector.

Acknowledgments

The work of R.Zimroz was supported by the statutory grant.

References

[1] R. Randall. A new method of modeling gear faults. In Journal of Mechanical Design, vol. 104, no. 2, (1982), pp. 259–267.

[2] F. Chaari, W. Baccar, M. S. Abbes, M. Haddar. Effect of spalling or tooth breakage on gearmesh stiffness and dynamic response of a one-stage spur gear transmission. In European Journal of Mechanics-A/Solids, vol. 27, no. 4, (2008), pp. 691–705.

[3] J. Antoni, R. Randall. Differential diagnosis of gear and bearing faults. In Journal of Vibration and Acoustics, vol. 124, no. 2, (2002), pp. 165–171.

[4] J. Antoni, R. Randall. A stochastic model for simulation and diagnostics of rolling element bearings with localized faults. In Journal of vibration and acoustics, vol. 125, no. 3, (2003), pp. 282–289.

[5] J. Antoni, R. Randall. The spectral kurtosis: application to the vibratory surveillance and diagnostics of rotating machines. In Mechanical Systems and Signal Processing, vol. 20, no. 2, (2006), pp. 308–331.

[6] A. Michalak, J. Wodecki, A. Wyłomańska, R. Zimroz. Application of cointegration to vibration signal for local damage detection in gearboxes. In Applied Acoustics. doi:10.1016/j.apacoust.2017.08.024.

[7] A. Wylomanska, G. Żak, P. Kruczek, R. Zimroz. Application of tempered stable distribution for selection of optimal frequency band in gearbox local damage detection. In Applied Acoustics, vol. 128, (2016), pp. 14–22.

[8] F. Chaari, W. Bartelmus, R. Zimroz, T. Fakhfakh, M. Haddar. Gearbox vibration signal amplitude and frequency modulation. In Shock and Vibration, vol. 19, no. 4, (2012), pp. 635–652.

[9] J. Wodecki, A. Michalak, R. Zimroz. Optimal filter design with progressive genetic algorithm for local damage detection in rolling bearings. In Mechanical Systems and Signal Processing, vol. 102, (2018), pp. 102–116.

[10] J. Wodecki, R. Zimroz, T. Barszcz. Informative frequency band identification for automatic extraction of impulsive components in vibration data from rotating machinery. vol. 13. JVE International Ltd., pp. 109–114.

[11] P. Kruczek, J. Obuchowski, A. Wylomanska, R. Zimroz. Multiple local damage detection in gearbox by novel coherent bi-frequency map and its spatial, cycle oriented enhancement. In Applied Acoustics. doi:10.1016/j.apacoust.2017.10.006.

[12] N. Martin. Advanced signal processing and condition monitoring. In Insight-Non-Destructive Testing and Condition Monitoring, vol. 49, no. 8, (2007), pp. 459–464.

[13] J. Wodecki, R. Zdunek, A. Wyłomańska, R. Zimroz. Local fault detection of rolling element bearing components by spectrogram clustering with semi-binary NMF. In Diagnostyka, vol. 18, no. 1, (2017), pp. 3–8.

[14] G. Żak, M. Teuerle, A. Wyłomańska, R. Zimroz. Measures of Dependence for-Stable Distributed Processes and Its Application to Diagnostics of Local Damage in Presence of Impulsive Noise. In Shock and Vibration, vol. 2017, no. 1963769.

[15] D. A. Dickey, W. A. Fuller. Distribution of the estimators for autoregressive time series with a unit root. In Journal of the American statistical association, vol. 74, no. 366a, (1979), pp. 427–431.

[16] J. Durbin, G. S. Watson. Testing for serial correlation in least squares regression. II. In Biometrika, vol. 38, no. 1/2, (1951), pp. 159–177.

[17] D. Kwiatkowski, P. C. Phillips, P. Schmidt, Y. Shin. Testing the null hypothesis of stationarity against the alternative of a unit root: How sure are we that economic time series have a unit root? In Journal of Econometrics, vol. 54, no. 1-3, (1992), pp. 159–178.

[18] J. Obuchowski, A. Wyłomańska, R. Zimroz. Selection of informative frequency band in local damage detection in rotating machinery. In Mechanical Systems and Signal Processing, vol. 48, no. 1-2, (2014), pp. 138–152.

[19] A. V. Oppenheim. Discrete-time signal processing. Pearson Education India (1999).

[20] J. Antoni, R. Randall. The spectral kurtosis: application to the vibratory surveillance and diagnostics of rotating machines. In Mechanical Systems and Signal Processing, vol. 20, no. 2, (2006), pp. 308 – 331. doi:https://doi.org/10.1016/j.ymssp.2004.09.002.

[21] J. Antoni. The spectral kurtosis: a useful tool for characterising non-stationary signals. In Mechanical Systems and Signal Processing, vol. 20, no. 2, (2006), pp. 282 – 307. doi:https://doi.org/10.1016/j.ymssp.2004.09.001.

[22] P. Daponte. IEEE standard on transitions, pulses, and related waveforms. In .

Semi-blind Wiener filtering of mechanical source vibrations: theory and application to aircraft gearbox surveillance

D. Abboud[1], Y. Marnissi[1], M. Elbadaoui[1,2]
[1] Safran Tech, Rue des Jeunes Bois – Châteaufort 78772 Magny–les–Hameaux, France
e-mail: **dany.abboud@safrangroup.com**

[2] Univ Lyon, UJM-St-Etienne, LASPI, EA3059, F-42023, Saint-Etienne, France

Abstract
Wiener filtering is an important operation in vibration analysis of mechanical systems. It consists on estimating the linear-time-invariant filter that, when convolved with the signal, gives an optimal estimate of a signal of interest in the least mean square sense. This paper addresses the estimation of the Wiener filter in the case where the signal of interest is a vibratory contribution generated by a mechanical source. For this purpose, the paper starts by proposing the concept of mono-source cyclostationarity, before establishing a valuable link between the Wiener filter and the cyclic power spectra of the signal associated with the cyclic frequency set of the source of interest. Based on this relation, two estimators are proposed and their performances are compared through simulations. Last, the efficiency of the proposed approach is demonstrated on a real vibration signal captured from a helicopter gearbox and compared with the classical spectral kurtosis. Results have asserted the superiority of the proposed approach over the classical one.

1 Introduction

Mechanical systems are often subjected to defects that alter their normal operating conditions causing performance degradation or, ultimately, a complete breakage. In order to ensure operation continuity, systems need to be monitored and defects, when occur, must be detected at their earlier stages. Several methods have been developed for rotating machine fault diagnostics in the literature. Among these techniques, vibration analysis is perhaps the most efficient as vibrations carry a lot of information about the health of the machine as well as potential existing anomalies. Shock-like defects (e.g., pitting, spalling), frequently encountered in rotating machines, typically produce consecutive and periodic impulses in the vibration signal caused at each contact between the faulty element and its mating surface [1]. However, the signature of the defect is very often masked by high level noise and other interfering components from other mechanical sources, thus hardens its characterization. Therefore, the enhancement of such component in the signal is required for vibration based health monitoring. This is mainly achieved through an optimal filtering that enables the detection of transients in the vibration signal.

The spectral Kurtosis (SK) is an efficient tool for characterizing non-stationarities in the signal. In [2], the theoretical foundations of the SK have been presented and a relationship between the SK and the noise-to-signal ratio has also been established. As a consequence, the SK has been widely used to design the Wiener filter that blindly estimates the presumed *non-stationary signal of interest* carrying information about the defect from the presumed *stationary noise* in the least mean square sense. Other extensions have been also explored such as the kurtogram [3], fast kurtogram [4], protugram [5], infogram [6]. However, as shown in [3], the efficiency of these techniques may be highly deteriorated when the stationary Gaussian assumption is not satisfied. Many researches have proposed solutions to these issues. A common one is the separation into deterministic and random components. Several methods have been proposed to perform this separation such as linear prediction, time synchronous average, adaptive filtering etc. Reference [7], provides a comparison of these techniques. However, the performance of the SK may still be affected by the presence of other non-stationary random components [8,9].

Beside this, cyclostationarity offers a rigorous framework to model and analysis mechanical signals [10,11]. This paper attempts to address the shortcoming of the aforementioned filtering techniques by reconsidering the problem in the CS framework. The main idea relies on the use of an a priori knowledge on the periodicity of the defect in order to design a linear-time-invariant deconvolution filter that is able to extract the signature of the mechanical component of interest from the signal. More specifically, two estimators of the Wiener filter are derived from the cyclic power spectra of the signal and their performances are discussed afterwards. This paper is organized as follows. Section 2 recalls the concepts and some useful properties of mono-source CS. Section 3 discusses the steps of the designed filters. Numerical simulations are presented in Section 4 and a real case fault detection in a helicopter gearbox is then discussed in Section 5. Finally, the paper is concluded in Section 6.

2 Cyclostationary modeling of mechanical source

This section opens with a brief introduction on cyclostationarity and its basic operators, then introduces the concept of mono-source cyclostationary signals which models mechanical signals (the responses) generated by a single mechanical source (the excitation).

2.1 Mechanical signals and cyclostationarity

Being generated by rotating or reciprocating machines, mechanical signals are likely to exhibit periodic statistics. This is principally due to the nature of their operation being based on repetitive motions. Therefore, when the machine operates under stationary condition (speed and load), the cyclostationary (CS) framework is effective to describe and process mechanical signals. CS signals enjoy an insightful representation in terms of a Fourier series

$$x(t) = \sum_{\alpha_i \in \mathcal{A}} x_{\alpha_i}(t) e^{j2\pi\alpha_i t} \tag{1}$$

whereof the Fourier coefficients $x_{\alpha_i}(t)$ are stochastic and jointly stationary signals, whereas the complex exponentials are parameterized by non-zero cyclic frequencies α_i that belong to a cyclic frequency set denoted as $\mathcal{A}$. This representation makes explicit the existence of hidden periodicities in the form of periodic modulations of the random carriers $x_{\alpha_i}(t)$. The statistical properties of $x(t)$ are completely described by the periodicity of the autocorrelation function $\Re_{2x}(\tau, t) \stackrel{\text{def}}{=} \mathbb{E}\{x(t)x(t-\tau)^*\}$, which also decomposes into a series of non-zero cyclic frequencies at the cyclic frequency order set:

$$\Re_{2x}(\tau, t) = \sum_{\alpha_i \in \mathcal{A}} \Re_{2x}^{\alpha_i}(\tau) e^{j2\pi\alpha_i t} \tag{2}$$

where τ denotes the time-lag, $\Re_{2z}^{\alpha_i}(\tau)$ is the (angle\time) cyclic correlation function. This function associates the cyclic evolution of the modulation signal to the time variable (via the exponential kernels) and the waveform characteristics of the carrier to the time-lag variable (via the Fourier coefficients). A more relevant quantity is the bi-spectral counterpart of the autocorrelation function– called the "spectral correlation (SC)"– being defined as the double Fourier transform of $\Re_{2x}(\tau, t)$:

$$\mathcal{S}_{2x}(f, \alpha) \stackrel{\text{def}}{=} \underset{\tau \to \mathrm{f}}{\mathcal{F}_{\mathrm{t} \to \alpha}}\{\Re_{2x}(\tau, t)\} \tag{3}$$

where α stands for cyclic frequency in Hertz which has for role to describe the modulations (the periodicity) in the signal, contrary to the spectral frequency f whose role is to describe the spectral content of the carrier. In the CS case, the SC returns the following characteristics:

$$\mathcal{S}_{2x}(f, \alpha) = \sum_{\alpha_i \in \mathcal{A}} \mathcal{S}_{2\mathrm{x}}^{\alpha_i}(\mathrm{f}) \delta(\alpha - \alpha_i) \tag{4}$$

where $\mathcal{S}_{2x}^{\alpha_i}(f) = \mathcal{F}_{\tau \to \mathrm{f}}\{\Re_{2\mathrm{x}}^{\alpha_i}(\tau)\}$ is the cyclic power spectrum (CPS) associated with the cyclic frequency α_i. The above equation means that, in the case of a CS signal, the SC exhibits a collection of continuous parallel lines discretely distributed over the α-axis at the cyclic orders $\alpha_i \in \mathcal{A}$. This symptomatic distribution is what makes the SC efficient to detect and identify CS components associated with distinctive mechanical sources.

2.2 The principle of mono-source cyclostationary signals

As this paper deals with the optimal filtering of a CS source contribution, it is thus useful to consider an accurate model of this latter. In fact, a CS source contribution can be often seen as the response of a CS white excitation to a linear-time-invariant (LTI) system. In this regard, the concept of mono-source cyclostationarity is proposed hereafter to describe mono-source signals. Specifically, it is proposed to model a mono-source CS signal with a fundamental cyclic frequency β as:

$$x(t) = h(t) * \sum_{k\in\mathbb{Z}^*} p_\beta^k(t) e^{j2\pi k\beta t} \tag{5}$$

where $\otimes$ denotes the convolution product, the coefficients $p_\beta^k(t)$ are jointly stationary and white— i.e $\mathbb{E}\left\{p_\beta^{k_1}(t_1)p_\beta^{k_2}(t_2)\right\} = \sigma^2_{p_\beta^{k_1},p_\beta^{k_2}}(t_1 - t_2)$. The corresponding SC takes this particular form:

$$S_{2x}(f,\alpha) = H(f)H(f+\alpha)^* \sum_{k\in\mathbb{Z}} S_{2p}^k \delta(\alpha - k\beta) \tag{6}$$

where $S_{2p}^k = \sum_{k'\in\mathbb{Z}} \sigma^2_{p_\beta^k, p_\beta^{k-k'}}$, $H(f)$ denotes the frequency response function of $h(t)$ and $\delta(\alpha)$ is the Kronecker delta function. Obviously, mono-source CS signals consist a subclass of CS signals with a special structure.

2.3 A signal/noise model

This section provides the signal/noise model used afterwards to derive an optimal LTI filter. A mechanical signal, say $y(t)$, measured by a given sensor (accelerometer, microphone, etc.) comprises (i) a signal of interest (SOI) being related to a source of interest (e.g. gear, rolling element bearing, fan, etc.) and (ii) a noise:

$$y(t) = x(t) + n(t). \tag{7}$$

The SOI $x(t)$ is modeled as a mono-source CS signal; its description was previously addressed in subsection 2.2. The noise $n(t)$ is modeled as a general CS with a cyclic frequency set $\mathcal{N}$. This latter is characterized through its SC which reads as:

$$S_{2n}(f,\alpha) = \sum_{\alpha_i\in\mathcal{N}} S_{2n}^{\alpha_i}(f)\delta(\alpha - \alpha_i). \tag{8}$$

Whereas the above model excludes potential non-CS noise components such as random impulses, it can enfold vibratory components generated by other rotating part in the system as well as stationary noise (e.g. measurement electric errors). For simplicity, it is assumed that the cyclic frequency set of $x(t)$ is known and does not intersect with that of $n(t)$, that is to say the periodicity of $x(t)$ is unique.

3 LTI filtering of mechanical signals

This section addresses the issue of LTI optimal filtering of a mechanical source contribution (i.e. a mono-source cyclostationary signal). It starts by reviewing the Wiener filtering theory, before establishing a valuable link with the SC via the cyclic power spectra associated with the SOI cyclic frequencies. Eventually, two estimators are proposed based on the established relationship.

3.1 The theory of Wiener filtering

The Wiener filter is widely used in many engineering applications. Theoretically, it is defined as being the optimal LTI filter, say $w(t)$, that finds the best estimate of the SOI (the target), $x(t)$, from the noisy measurement $y(t)$ in the least mean square sense:

$$w(t) = argmin\{|\hat{x}(t) - x(t)|^2\} \tag{9}$$

where $\hat{x}(t) = y(t) \otimes w(t)$ denotes the SOI estimate and $\otimes$ denotes the convolution product. The FRF of the WF has solution:

$$W(f) = \frac{1}{1 + \rho(f)} \tag{10}$$

where $\rho(f) = S_{2n}(f)/S_{2x}(f)$ stands for the NSR spectrum, $S_{2n}(f)$ and $S_{2x}(f)$ denotes the noise and SOI power spectral densities, respectively. Obviously, $W(f)$ is a real function of f which approaches the unity in the frequency zones dominated by the SOI and approaches to zero when the signal is dominated by the noise. Therefore, its structure shapes the spectral content of the signal in such a way that optimally estimates the SOI. Despite its apparent simplicity, the construction of the WF assumes an *a priori* knowledge of the SOI and noise spectra, which is very restrictive in practice. A common practice is to use a reference signal being coherent with the source of interest (the notion of coherence expresses the linear relationship between the reference and the SOI) to estimate the NSR spectrum. As anticipated in the introduction, Ref. [4] proposed a relevant way to blindly estimate the WF without the need of a reference signal. It uses the square root of the spectral kurtosis to estimate a scaled version $W(f)$, whereas it has been proposed to estimate the scale factor by minimizing the kurtosis of the estimated noise – i.e. minimizing the kurtosis of $y(t) - \hat{x}(t)$.

3.2 Relationship with the SC

The aim of this section is to establish a relationship between the FRF of the WF and the CS, using the models provided in section 2. Without loss of generality, it is assumed hereafter that the SOI and the noise don't share any cyclic frequency. Under this assumption and using Eq. (3), one can show that the cyclic power spectra of $y(t)$ associated with the SOI non-zero cyclic frequencies equals those of the SOI :

$$\begin{aligned} S_{2y}^{k\beta}(f) &\overset{\text{def}}{=} S_{2x}^{k\beta}(f) && \forall\, k \in \mathbb{Z}^* \\ &= H(f)H(f + k\,\beta)^* S_{2p}^{k} && \forall\, k \in \mathbb{Z}^* \\ &= \frac{S_{2x}(f)}{\lambda_k \xi_k(f)} && \forall\, k \in \mathbb{Z}^* \end{aligned} \tag{11}$$

where

- $S_{2x}(f) \overset{\text{def}}{=} \lim_{W\to\infty} \frac{1}{W} \mathbb{E}\{S_W(f) S_W(f)^*\} = |H(f)|^2 \sigma_p^2$ denotes the power spectrum
- $\xi_k(f) = H(f)^*/H(f + k\beta)^*$
- $\lambda_k = \frac{\sigma_p^2}{S_{2p}^k}$

From the above equation, the relationship between the FRF of the WF and the CPS $S_{2y}^{k\beta}(f)$ can be found as:

$$\begin{aligned} W(f) &\overset{\text{def}}{=} \frac{S_{2x}(f)}{S_{2y}(f)} \\ &= \lambda_k \xi_k(f) \frac{S_{2y}^{k\beta}(f)}{S_{2y}(f)} \quad \forall\, k \in \mathbb{Z}^* \end{aligned} \tag{12}$$

The above equation relates the WF with the ratio $S_{2y}^{k\beta}(f)/S_{2y}(f)$ (that can be seen as a normalized SC), through a scaling factor λ_k and an error function $\xi_k(f)$. While the ratio can be estimated through common estimators of the SC (e.g. averaged cyclic periodogram, fast-SC, etc.), the estimation of λ_k and $\xi_k(f)$ could be more delicate. The next subsection addresses two possible estimators to the WF.

3.3 Semi-blind estimation of the WF

Let's consider now the case where the SOI $x(t)$ is characterized through a finite number of cyclic power spectra and M denotes the cardinal of the cyclic frequency set of the SOI. The goal is to estimate the WF using the cyclic power spectra of the signal $y(t)$ at the non-negative cyclic frequency set associated with the SOI, namely $\left\{\hat{S}_{2y}^{1\beta}(f), \ldots \hat{S}_{2y}^{M\beta}(f)\right\}$. It is the knowledge of the cyclic frequency set what makes the method semi-blind, as opposed to spectral kurtosis based estimate of the WF which does not require any a priori knowledge on the SOI.

3.3.1 A simple estimator (est#1)

The simplest and most straightforward way to estimate a scaled version of the Wiener filter is by neglecting the effect of $\xi_k(f)$. A typical scenario in which this assumption is respected is in the case where the period of the SOI is largely greater than the correlation time of the system impulse response. As the deviation of $\xi_k(f)$ from one increases with the variability of the transfer function $H(f)$ between f and $f+\alpha$, the modulus of $\xi_k(f)$ can be approximated to the unity for low α-values.

increases with the variability of the transfer function $H(f)$ between the frequency f and $f+\alpha$, its effect is insignificant for the low α-values and, thus, its modulus can be approximated to the unity. Under this approximation, one can rewrite Eq. (11) as:

$$\lambda_k^{-1} W(f) \quad = \quad \frac{S_{2y}^{k\beta}(f)}{S_{2y}(f)} \quad \forall\, k \in \mathbb{Z}^* \qquad (13)$$

The above equation comprises an overdetermined system to estimate a scaled version of the $W(f)$ since the coefficients λ_k are unknown. By performing an empirical sum of both the equality side, one obtains the biased estimator of the WF as:

$$\widehat{W}(f) \quad = \quad \lambda \sum_{k\in\mathbb{Z}^*} \frac{S_{2y}^{k\beta}(f)}{S_{2y}(f)} \qquad (14)$$

where $\lambda = \sum_{k\in\mathbb{Z}^*} 1/\lambda_k^{-1}$. As the scaling factor λ is unknown, the above equation can only estimate a scaled factor of the WF. To estimate λ, the authors propose to optimize this latter in such a way that minimize the cyclostationarity of the estimated noise. A simple way to do this is to minimize the magnitude sum of the cyclic power associated with the SOI cyclic frequency set:

$$\lambda = argmin\left\{\left|S_{2\hat{n}}^{k\beta}\right|^2\right\} \qquad (15)$$

where $S_{2\hat{n}}^{k\beta}$ denotes the cyclic power of the estimated noise (i.e. $\hat{n}(t) = y(t) - y(t)\otimes\widehat{w}(t)$) associated with the cyclic frequency $k\beta$ and defined as:

$$S_{2\hat{n}}^{k\beta} = \lim_{W\to\infty} \int_W |\hat{n}(t)|^2 e^{-j2\pi k\beta t} dt \qquad (16)$$

3.3.2 An more accurate estimator (est#2)

An unbiased estimator of the WF can be derived from Eq. (12) by estimating first the error function $\xi_k(f)$ using the SOI cyclic power spectra. It can be shown from that

$$\xi_{j-i}(f) \quad \stackrel{\text{def}}{=} \quad \frac{\lambda_i}{\lambda_j} \frac{S_{2y}^{i\beta}(f-i\beta)}{S_{2y}^{j\beta}(f-i\beta)} \quad \forall \quad (i,j)_{i\neq j} \in \mathbb{Z}^{*2} \qquad (17)$$

By applying the variable change $k = j - i$, one can show that the following equation holds for any k

$$\frac{\lambda_{i+k}}{\lambda_i}\xi_k(f) \quad = \quad \frac{S_{2y}^{i\beta}(f - i\beta)}{S_{2y}^{(i+k)\beta}(f - i\beta)} \quad \forall \ (i,k) \in \mathbb{Z}^{*2} \qquad (18)$$

In order to estimate the function $\xi_k(f)$ from Eq. (7), one has $M - i$ estimation to estimate the function. A possible estimator boils down to an empirical average over the possible cyclic frequencies:

$$\hat{\xi}_k(f) \quad = \quad \gamma_k^{-1}\frac{1}{M-k}\sum_{i=1}^{M-k}\frac{S_{2y}^{i\beta}(f - i\beta)}{S_{2y}^{(i+k)\beta}(f - i\beta)} \quad k = 1 \dots M-1 \qquad (19)$$

where $\gamma_k = \left(\sum_{i=1}^{M-k}\lambda_{i+k}/\lambda_i\right)/(M-k)$. Then, from Eq. (12), an overdetermined system can be considered whereof a straightforward solution can be derived as:

$$\widehat{W}(f) = k\,\widehat{W}_n(f) \qquad (20)$$

where $\zeta = \frac{1}{M-1}\sum_{k=1}^{M-1}\lambda_k\gamma_k$ is a constant that can be determined in the same way as λ in subsection 3.3.1 appropriately and

$$\begin{aligned}\widehat{W}_n(f) \quad &= \quad \frac{1}{M-1}\sum_{k=1}^{M-1}\hat{\xi}_k(f)\ \frac{S_{2y}^{k\beta}(f)}{S_{2y}(f)} \\ &= \quad \frac{1}{M-1}\sum_{k=1}^{M-1}\frac{S_{2y}^{k\beta}(f)}{S_{2y}(f)}\frac{1}{M-k}\sum_{i=1}^{M-k}\frac{S_{2y}^{i\beta}(f - i\beta)}{S_{2y}^{(i+k)\beta}(f - i\beta)}\end{aligned} \qquad (21)$$

Let's try to arrange the above equation in a matrix form. To do so, let's first define the $(M-1)$-by-$(M-1)$ matrix $\mathbf{A}(f)$ having for elements

$$\alpha_{ik}(f) \quad = \quad \begin{cases}\dfrac{S_{2y}^{i\beta}(f - i\beta)}{S_{2y}^{(i+k)\beta}(f - i\beta)} & i \le M-k \\ 0 & elsewhere\end{cases} \qquad (22)$$

and the $(M-1)$-by-1 vector $\boldsymbol{b}(f)$ having for elements

$$b_k(f) \quad = \quad \frac{S_{2y}^{k\beta}(f)}{(M-k)S_{2y}(f)} \qquad (23)$$

With that being sad, one can rewrite Eq. (21) in a compact form:

$$\begin{aligned}\widehat{W}_n(f) \quad &= \quad \frac{1}{M-1}\sum_{i=1}^{M-1}\left(\mathbf{A}(f)\boldsymbol{b}(f)\right)_i \\ &= \quad \frac{1}{M-1}\left(\mathbf{A}(f)\boldsymbol{b}(f)\right)^T\mathbf{1} \\ &= \quad \frac{1}{M-1}\boldsymbol{b}(f)^T\mathbf{A}(f)^T\mathbf{1}\end{aligned} \qquad (24)$$

where $\underline{1}^T = [1 \dots 1]$ is a 1-by-$(M-1)$ vector.

4 Numerical evaluation of the performance

This section aims at evaluating the performance of the proposed WF estimation method on synthetic signals. The synthetic signal comprises four common types of machine signal components. The sampling frequency

is equal to 12 kHz. The reference frequency is constant and will be given hereafter. The simulated signal comprises the following components:

- A train of cyclic transients built from having a constant period equal to that of the reference (i.e. its order equals 1) and an impulse response equal to a single-degree-of-freedom (s.d.o.f) system with resonance frequency equal to 2 kHz and a bandwidth equal to 600 Hz.
- A smooth CS signal consisting of five speed-varying sinusoids synchronized modulating a white noise, and exciting a single degree of freedom system with resonance frequency equal to 4 kHz and a bandwidth equal to 800 Hz. The five sinusoids have a fundamental order equal to 1.1 times the reference frequency.
- An periodic signal consisting of five sinusoids with a fundamental frequency equal to 2.11 times the reference frequency.
- A stationary white Gaussian noise.

These components as well as the synthetic signal (i.e. their sum) are illustrated in Fig. 1 for a reference frequency equal to 80 Hz. The actual WF is calculated through Eq. (4) by calculating the power spectral densities of the signal and the noise. Then, the WF is estimated through estimators est#1 and est#2, previously proposed in subsections 3.3.1 and 3.3.2 respectively. The FRF of the actual and estimated WFs are normalized by their maxima and exposed in Fig. 2 for four different reference speeds, namely 25 Hz, 50 Hz, 75 Hz and 100 Hz. In the low speed case (i.e. 25 Hz), both of the estimators were accurate in estimating the FRF of the WF. As the speed gets higher, the estimation error of est#1 gets higher whereas that of est#2 remains consistent. This is caused by the fact that est#1 neglects the effect of $\xi_k(f) = H(f)^*/H(f+k\beta)^*$ which becomes significant for high speed (i.e. high β). On the contrary, est#2 does take into account this factor and thus the estimation performance remains consistent in the higher speeds. Eventually, another simulation is made and the WF is now estimated for 4 different SNR: 0 dB, -7.28 dB, -14.32 dB and -20.8 dB. The results are exposed in Fig. 3. In the first 3 cases, the performance of est#2 are better than those of est#1. However, in the last case, where the noise is extremely strong, the performance of est#2 is compromised owing to the high error encountered in the SC (even though the averaged cyclic periodogram, the most efficient estimator in terms of statistical performances, has been used) when estimating the factor $\xi_k(f)$.

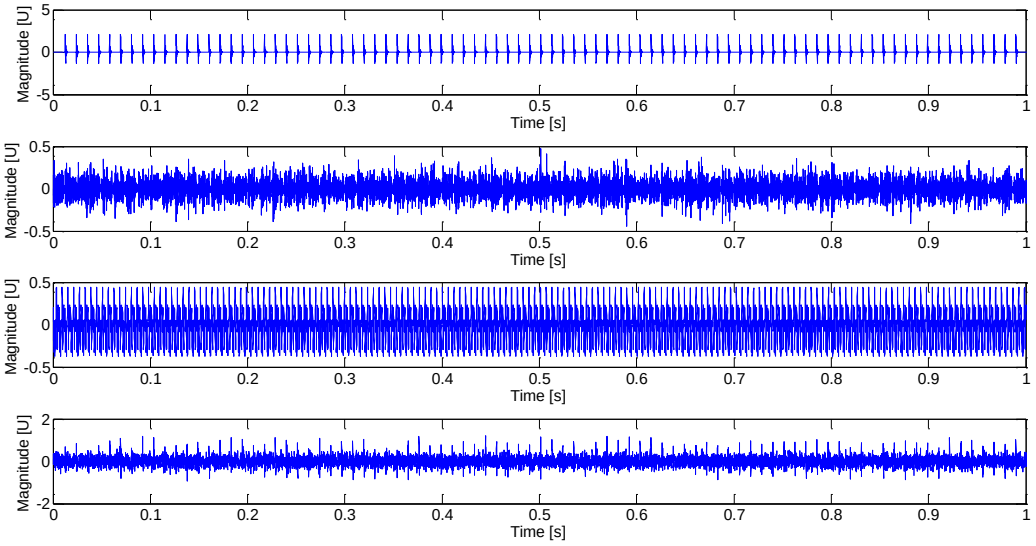


Fig. 1. (a) The SOI, (b) the smooth CS component, (c) deterministic sinusoidal component and (d) the total simulated signal.

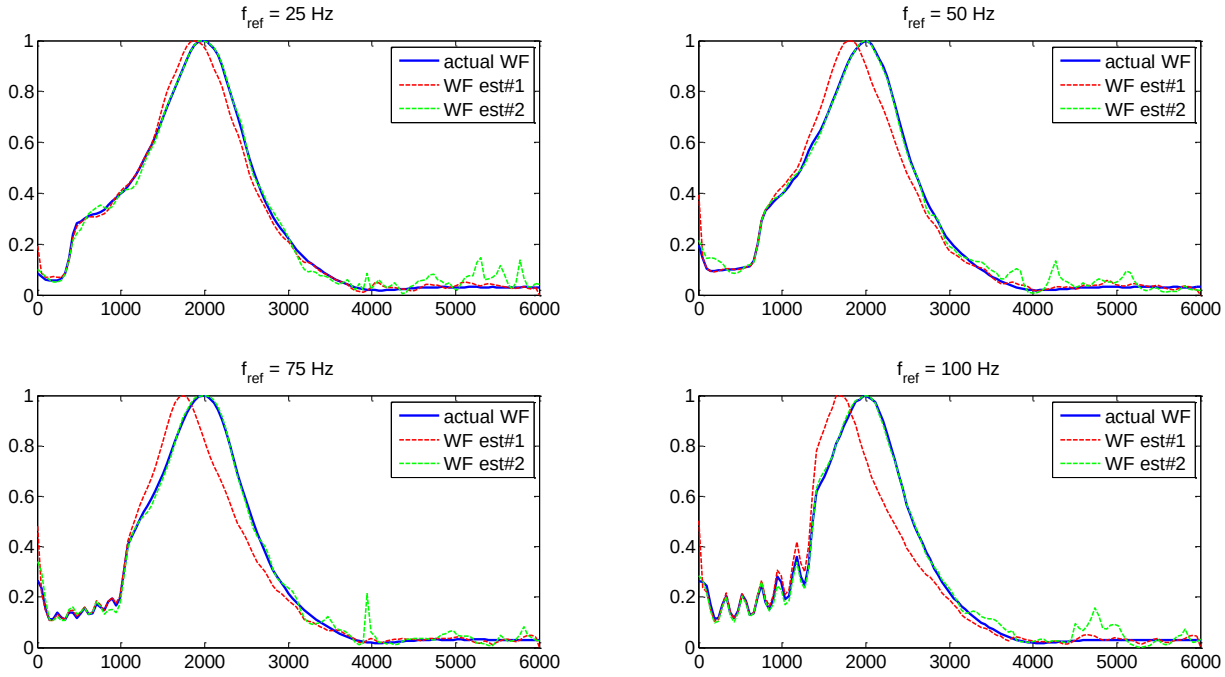


Fig. 2. The FRFs of the actual WF (black plot), the est#1 and est#2 the WF (red and green plots, respectively) calculated for 4 different reference speeds: 25 Hz, 50 Hz, 75 Hz and 100 Hz.

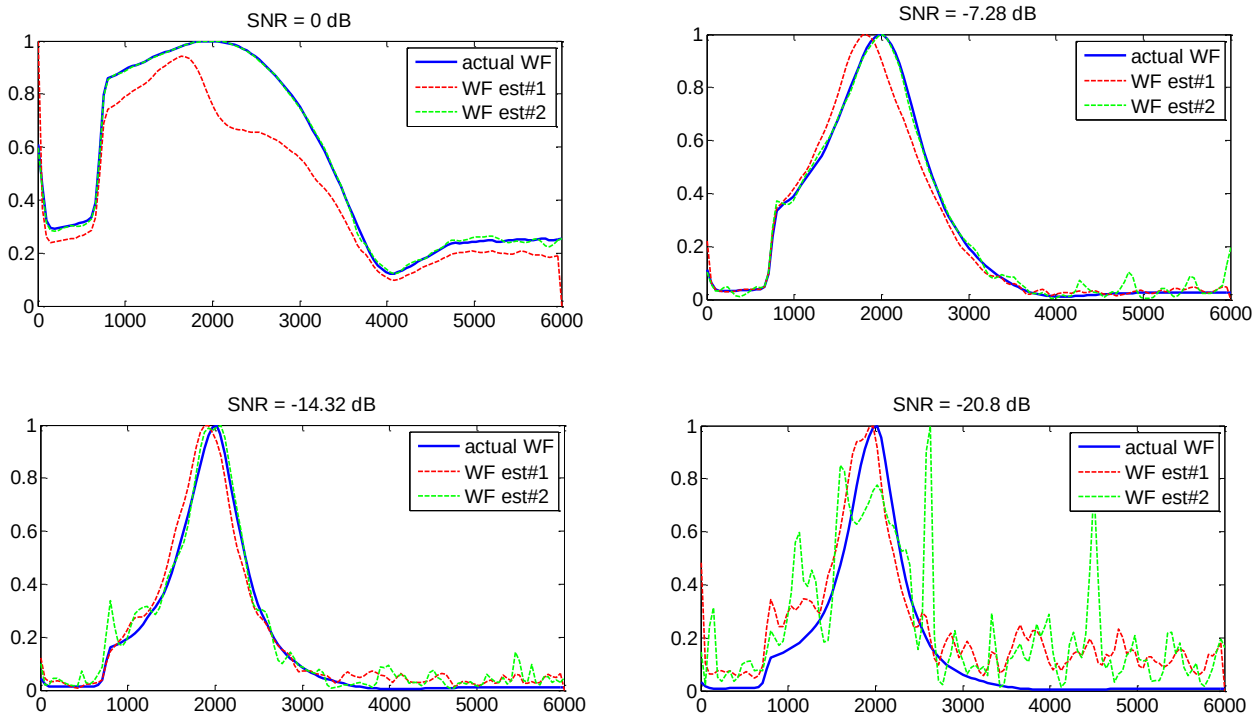


Fig. 3. The FRFs of the actual WF (black plot), the est#1 and est#2 the WF (red and green plots, respectively) calculated for 4 different SNR: 0 dB, -7.28 dB, -14.32 dB and -20.8 dB.

5 Application: Helicopter gearbox

In this section, the proposed WF is validated on vibration signals acquired on a helicopter gearbox under a quasi-constant speed with a constant sampling frequency. A shock-like anomaly is inspected in one of the gears. For confidential issues, the sampling frequency is set to one, the speed is normalized by the sampling frequencies and the acceleration signal is normalized by its standard deviation. In order to enhance the gear fault detection, an optimal filtering operation is required to promote cyclic transients with gear period. To do this, the WF is estimated using the two estimators est#2 and the spectral kurtosis for comparison. Fig. 4 shows the raw vibration signal and two FRFs of the estimated WFs. The SK-based estimate of the WF shows higher values in many— sometimes wide— spectral bands, while the proposed est#2 shows high values in a single narrow-band (around the normalized frequency 0.04) indicating the presence of a specific resonance probably triggered by a shock-like excitation. To make things clearer, the SOI estimates are then calculated by filtering the raw signal with both of these filters and the results are displayed in Fig. 5. Zooms between 20 and 25 ksamples are also provided in Fig. 6. The SK-based estimate comprises some repetitive impulses only seen at some specific regimes (e.g. between 20 and 25 ksamples), whereas est#2-based filtered signal reveals obvious repetitive transients. The results obtained by the SK techniques are obviously less convincing than the proposed estimator wherein the recovered SOI comprises clear fault symptoms. Results thus evidences the effectiveness of the proposed approach in promoting a mechanical SOI.

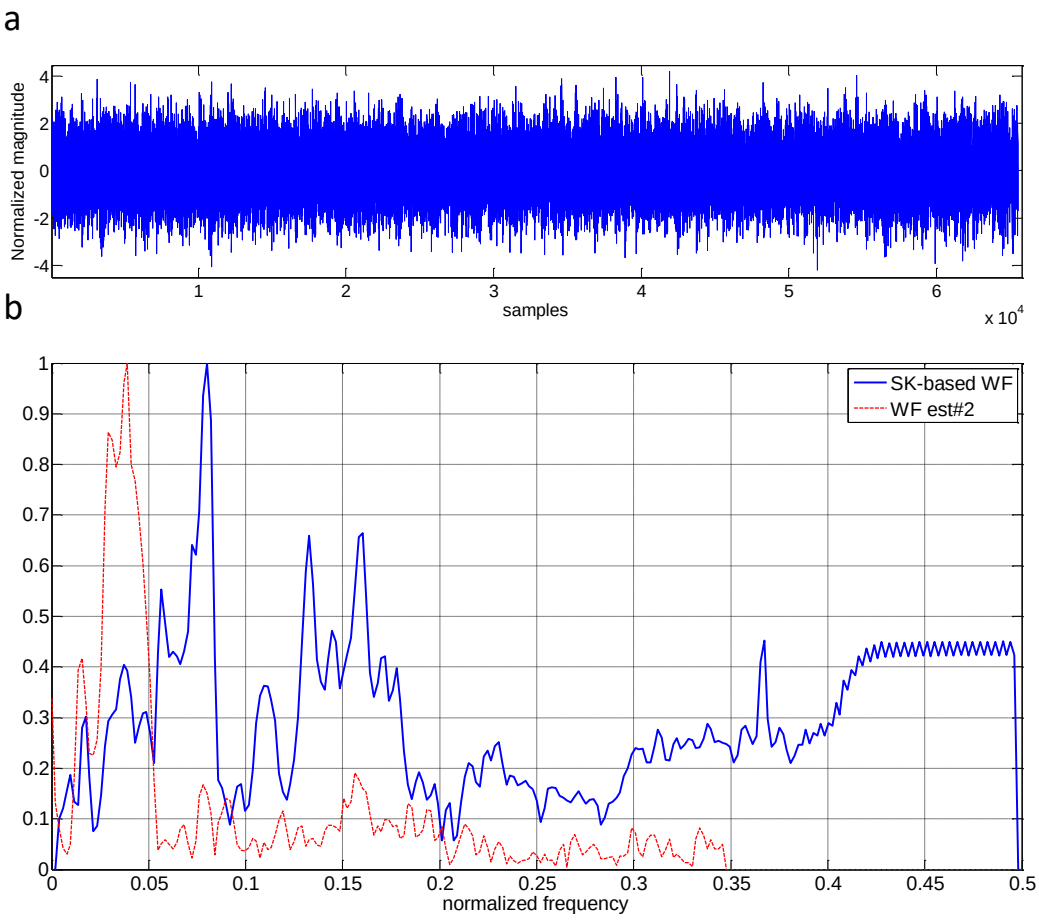


Fig. 4. (a) Raw vibration signal, (b) WF estimates using the SK (continuous blue line) and the CCoh (red dashed line).

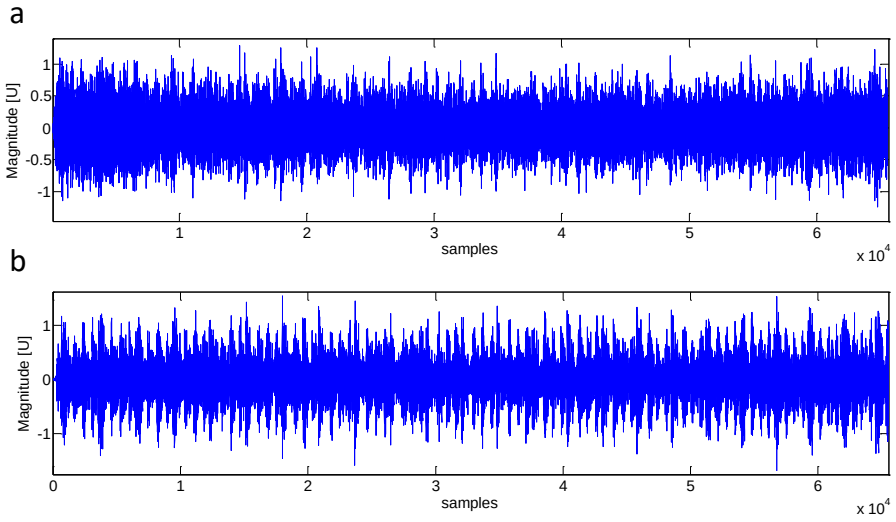


Fig. 5. (a) The filtered signal by the SK-based WF and (a) the filtered signal by the est#2-based WF.

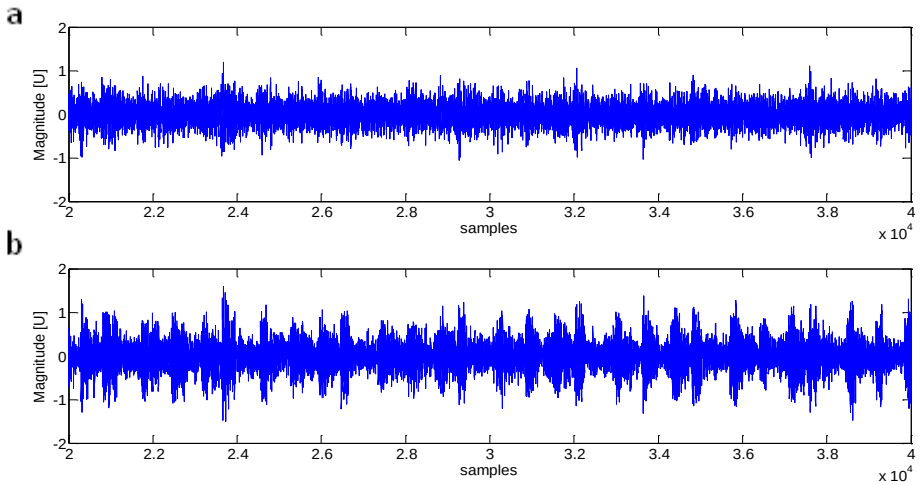


Fig. 6. (a) The filtered signal by the SK-based WF and (a) the filtered signal by the est#2-based WF.

6 Conclusion

This paper has addressed the optimal linear-time invariant filtering problem of a vibratory contribution generated by a mechanical source of interests. The concept of mono-source cyclostationarity is proposed to model a mechanical contribution in a vibration signal. A useful relationship between the spectral correlation and the Wiener filter is then established, offering the possibility of estimating the latter via the cyclic power spectra of the vibration signal using the a priori knowledge of the mechanical source cyclic frequencies. Two estimators are also proposed and their performances are evaluated through multiple simulations. The proposed approach is eventually validated on a real case of a helicopter engine and compared with the spectral kurtosis based estimate of the Wiener filter. Results have demonstrated the superiority of the proposed approach over the classical one.

References

[1] Vishwakarma, M., Purohit, R., Harshlata, V., Rajput, P.: Vibration Analysis & Condition Monitoring for Rotating Machines: A Review, Materials Today: Proceedings, Volume 4, Issue 2, Part A, 2017, Pages 2659-2664, ISSN 2214-7853.

[2] Antoni, J. 'The spectral kurtosis: a useful tool for characterising non-stationary signals'. Mechanical Systems and Signal Processing, 2006, vol. 20, no 2, p. 282-307.

[3] Antoni, J., Randall, R. B.: The spectral kurtosis: application to the vibratory surveillance and diagnostics of rotating machines, Mechanical Systems and Signal Processing (2006) 308–331

[4] Antoni, J.: Fast Computation of the Kurtogram for the Detection of Transient Faults, Mechanical Systems and Signal Processing, Volume 21, Issue 1, January 2007, Pages 108-124.

[5] Barszcz, T., JabŁoński, A. : A novel method for the optimal band selection for vibration signal demodulation and comparison with the kurtogram, Mech. Syst. Sig. Process., 25 (1) (2011), pp. 431-451

[6] Antoni, J.: The infogram: Entropic evidence of the signature of repetitive transients, Mechanical Systems and Signal Processing 74 (2016) 73-94.

[7] Randall, R. B., Sawalhi, N., and Coats, M. A comparison of methods for separation of deterministic and random signals. International Journal of Condition Monitoring 1.1 (2011): 11-19.

[8] Smith, W. A., Fan, Z., Peng, Z., Li, H., Randall, R. B.: Optimised Spectral Kurtosis for bearing diagnostics under electromagnetic interference, Mechanical Systems and Signal Processing, Vol. 75, pp. 371-394 (2016).

[9] Borghesani, P., Antoni, J.: CS2 analysis in presence of non-Gaussian background noise – Effect on traditional estimators and resilience of log-envelope indicators, Mechanical Systems and Signal Processing, Elsevier, 2017, 90, pp.378 – 398.

[10] Antoni, J., Bonnardot, F., Raad, A., ElBadaoui, M.: Cyclostationary modelling of rotating machine vibration signals, Mechanical Systems and Signal Processing 18 (2004) 1285–1314

[11] Antoni, J.: Cyclostationarity by examples. Mech. Syst. and Sign. Proc., 23 (2009) 987–1036.

Gearbox fault diagnosis based on Convolutional Neural Networks

Z. Chen [1,2], W. Li [1], K. Gryllias [2,3]
[1] School of Mechanical and Automotive Engineering,
South China University of Technology, Guangzhou 510640, China
e-mail: **whlee@scut.edu.cn**

[2] KU Leuven, Department of Mechanical Engineering,
Celestijnenlaan 300 B, B-3001, Heverlee, Belgium

[3] Dynamics of Mechanical and Mechatronic Systems, Flanders Make,
Celestijnenlaan 300 B, B-3001, Heverlee, Belgium

Abstract
A major challenge in mechanical intelligent diagnosis process lies in how to full exploit potential information and extract robust features to achieve more reliable diagnosis results. In real environment, machines are usually running under variable speed and load conditions and the measured signals present a complex amplitude and frequency signature, making fault identification a difficult task. In this paper, Wavelet transform is firstly utilized to convert the time signals into (2D) time-frequency images to obtain good representative features. Then a deep learning method based on CNN is constructed to automatically learn discriminative features from inputs, which obstacles the deficiencies of manual feature extraction and selection stage. The proposed method is evaluated on datasets with gear and bearing faults acquired under variable speed operating conditions. Experimental results show that the proposed method has improved the performance of gearbox fault classification and outperforms other methods.

1 Introduction

Monitoring defects and failures of key components such as gears and bearings of gearboxes is crucial in the running operation of machines. With the emerging of large amounts of industrial data, fault diagnosis based data-driven methods are increasingly receiving more attention from the research community since they require less expertise and provide relative fast and accurate decisions.

In the intelligent fault diagnosis field, a typical machine learning scheme involves two key steps including feature extraction and selection and fault recognition [1]. Feature extraction and selection methods are expected to extract and select a small set of informative features to describe the health condition of machines. Many different types of health indexes can be obtained by signal processing techniques such as the Fourier transform (FT), the Empirical Mode Decomposition (EMD) and the Wavelet Transform (WT) [2]. Additionally different data-driven techniques such as SVM and ANNs have been developed to built-up an intelligent decision-making system.

In [3], permutation entropy has been proposed to detect the malfunctions of bearings while the Ensemble Empirical Mode Decomposition (EEMD) and the optimized Support Vector Machines (SVM) have been further adopted for motor fault diagnosis. Liu [4] proposed a multi-fault classification method for rolling element bearings based on the Empirical Mode Decomposition (EMD), distance evaluation techniques and Wavelet Support Vector Machines (WSVM). In [5], statistic features such as the mean, the kurtosis and the skewness are extracted from vibration signals and a feature selection is carried out using a decision tree algorithm. Moreover SVM has been used for hydraulic brakes condition monitoring. Ali [6] integrated time-domain features and Intrinsic Mode Functions (IMFs) extracted by EMD to train an Artificial Neural

Network which achieved a good performance in automatic bearing fault diagnosis. In [7] features have been extracted from vibration signals using the Discrete Wavelet Transform (DWT) and a Genetic Algorithm (GA) has been further proposed to optimize the hyper-parameters of the neural network in order to improve the classification rates of gear faults.

Feature extraction and selection are effective methods to reflect the health condition of machines by fully exploiting prior knowledge based on signal processing techniques and fault diagnostic expertise. However, the feature extraction and selection techniques are sometimes time-consuming and present a low level generation ability compared to other diagnosis techniques [8]. In order to effectively process massive data generated from online rotating machine and to overcome the overhead of feature engineering for specific fault issues, some automatic feature learning methods using deep neural networks are explored to capture the useful fault features from measurement based on hierarchical architectures and powerful non-linear mapping capacity. Oh [9] proposed a scalable and unsupervised feature learning method for rotor system diagnosis by using a vibration image and deep belief network. Jia [10] constructed an improved Local Connect Network (LCN) with Normalized Sparse AE (NSAE) to extract dissimilar and meaningful features for bearing and gear diagnosis. In [11], raw amplitudes of the frequency spectrum are firstly extracted and then a 2D CNN with one convolutional layer is designed to learn useful features for bearing fault detection. In [12] a deep auto encoder network has been designed to learn discriminative features from raw vibration signals and an artificial fish swarm algorithm is further applied to optimize the key parameters of the deep model to achieve high diagnosis result in an application of electrical locomotive roller bearings. Zhang [13] used the Deep Neural Networks (DNN) for bearing fault which could effectively recognize the type of bearing faults by taking advantage of the temporal coherence of the raw data. In [14], a two-dimensional Spectral Energy Maps (SEM) of the Acoustic Emission (AE) signals are first proposed and Convolutional Neural Networks (CNNs) are trained via the Stochastic Diagonal Levenberg-Marquardt (S-DLM) algorithm in order to perform diagnosis both for single and compound defects at six different operating speeds. Especially in [15], a Cyclic Spectrum Map (CSM) that shows the distribution of cycle energy across different bands of raw vibration signal has been generated and Deep Convolutional Neural Network is used for bearing fault diagnosis.

As mentioned above, deep learning models seem to achieve satisfactory performance in many different fault diagnosis tasks. However, most of the models above have been validated on datasets collected at a steady working conditions. For rotating machines operating under variable speed operation conditions, time-series vibration signals are not able to directly reveal the inherent information of the running conditions of machines due to the variable frequency and amplitude. Additionally traditional spectral analysis techniques, based on Fourier transform lead to the frequency smearing phenomenon during speed and frequency transients [16]. Feature extraction based on EEMD used above also showed a limitation at the detection of impulses that are influenced by the presence of the mode mixing and the end effect [17]. Thus, it's relatively difficult to extract machinery health information discriminative features which are able to reveal the entire running health condition by the original signal or selected features based on their time-varying characteristics. In the field of signal processing, time-frequency analysis techniques like Short-Time Fourier Transform, Wavelet Transform and Wigner–Ville distribution, are applied for machinery nonstationary signal fault diagnosis [18]. They are effective tools to identify the signal variant components and extract health information contained in nonstationary signals. Wavelet transform has achieved great success in the analysis of non-stationary signals due to its advantage of multi-resolution analysis and many distinct merits [19]. Order tracking is also effective to remove speed fluctuations by transforming the measured signals from time-domain to the angular domain. On the other hand the actual rotating speed is sometimes unavailable. In this paper, a Deep Learning model based on Convolution Neural Networks (CNN) and the Wavelet Transform is proposed in order to perform diagnosis of gearbox faults. Rather than extracting different statistical feature indexes, the work focuses on exploring the learning capacity of Convolutional Neural Network from time-frequency representations constructed from raw time-series signals operating under variable operating conditions. Amplitude scalogram based on the wavelet transform is first applied on speed-up vibration signals in order to build up feature representations. After that, CNNs are applied in order to learn discriminative features focusing towards robust and fast identification of different defects. The rest of the paper is organized as follows. The basic theory background and the diagnosis procedure of the proposed method is described in Section 2. The experimental setup and the results are introduced in Section 3. Finally some conclusions are summarized in Section 4.

2 Proposed methods

This paper presents a fault diagnosis model based on CNN and wavelet transform to recognize gearbox faults. The method consists of two steps: the Wavelet transform for feature representation and the CNN training and diagnosis. In order to detect bearing and gear faults under variable speed conditions, it is rather difficult to design crafted features from vibration measurements. The scalogram of time-frequency transform could contain rich information by building the bridge between time domain and frequency domain which is more effective compared to the simple raw signals in varying speed operations. Therefore, in the proposed method, the scalogram obtained from wavelet transform is firstly used to represent different health conditions of gears and bearings. CNN is further applied in order to learn good discriminative representations. The Convolutional Neural Network being a variant of multi-layer feedforward neural networks is very suitable for two dimensional signal feature learning and classification. It has been proposed and used in hand-writing recognition [20] and then achieved a state-of-the-art performance in image classification of ImageNet large scale visual recognition challenge [21]. Due to its powerful capability to learn complex non-linear relationships from raw input, the Convolutional Neural Network model is chosen an efficient tool to learn distributed features from amplitude scalogram generated by the application of wavelet transform over the raw signals.

2.1 Wavelet transform

The Continuous Wavelet Transform (CWT) is used as a powerful tool for the detection and localization of signals in both the time and frequency domain. It decomposes the raw signal into localized components represented by scaling and translating operations. Compared to Short Time Fourier Transform (STFT), it can obtain good time-frequency features at various locations in space at different scales [22, 23]. The continuous wavelet transform of a signal x (t) is defined by the follow equation [23]:

$$W(a,b) = \frac{1}{\sqrt{a}} \int_{-\infty}^{+\infty} x(\mathrm{t}) \psi\left(\frac{t-b}{a}\right) \mathrm{dt} \tag{1}$$

Where the scale parameter *a* controls the frequency and the translation parameter *b*, provides the position of wavelet. $\psi(t)$ is the mother wavelet function, which can generate a family of local window basis functions. As such, the signal to be analyzed is matched and convolved with the set of basis functions and the original signal is expressed as a weighted integral of the wavelet basis function. In wavelets application, different types of basis functions have been developed and a number of mother wavelets have been proposed for fault detection and diagnosis include the Harr, the Mexican Hat and the Morlet wavelet function, depending on the application requirements. In this paper, the Morlet wavelet function is used to convert the raw time-series signals to time-frequency representations as it is especially applicable to impulse components extraction and has been successful used for fault diagnosis [23, 18].

2.2 Convolutional Neural Networks

The Convolutional Neural Network is composed of three basic operations: convolutional layer, pooling layer and fully-connected layer. Convolution and pooling layers are usually stacked alternately to combine a CNN, which can obtain distribution features from low-level to high-level layers. Convolution is a common technique which is used to create filters and extract useful features of each input. A convolution defined by a kernel is applied to the input by placing the kernel over the input to be convolved and sliding a window around every value in the original input. The size of the kernel corresponds to the length of the convolution window and the number of kernels is the number of the feature maps. In a CNN architecture, a set of *k* kernel matrices $\mathbf{w}(k, l)$, k= 1, 2, … , K are used and the output feature maps $\mathbf{z}^l$, l = 1, 2, …, L are represented as follows:

$$\mathbf{z}^l = f\left(\sum_{k=1}^{K} \mathbf{w}^{(k,l)} * \mathbf{x} + \mathbf{b}^l\right) \tag{2}$$

$$f(\mathbf{x}) = \mathrm{ReLU}(\mathbf{x}) = max(0, \mathbf{x}) \tag{3}$$

Where * represents the convolution operation. The matrix $\mathbf{w}(k, l)$ is the filter and $\mathbf{b}^l$ is the bias term for each feature map l. After the convolution with a valid operation, feature maps with reduced dimension are obtained. An activation function is then applied on the output of the convolutional kernels to acquire a non-linear expression of the input signal. The activation function $f(\cdot)$ is chosen to be a Rectified Linear Unit (ReLU) due to its good ability to accelerate the convergence of CNN. Max Pooling operation is employed to each feature map to reduce the spatial size of the convolutional features. This not only leads to less trainable parameters but also achieve robust feature representations with some degree of translation-invariant characteristics. According to the features achieved from the last pooling operation, softmax function which is a generalization of the logistic function is used to convert the input into a categorical probability output. The function is given by:

$$p(\mathrm{y} = i \mid \mathrm{x}) = \frac{e^{\mathbf{w}_i \mathbf{x}}}{\sum_{j=1}^{c} e^{\mathbf{w}_j \mathbf{x}}} \quad for\ i = \{1, 2, \cdots, c\} \tag{4}$$

Where the output value y is the predicted label, x is the input of the softmax, $\mathbf{w}$ is the weight of the classifier and c corresponds to the categories. In order to obtain an optimized set of parameters, the back-propagation algorithm is used to get each parameter's gradient and gradient-based optimization is used to update each layer parameters.

2.3 CNN based on Wavelet transform for fault diagnosis

The model architecture of the proposed CNN using scalogram generated from raw vibration data for gearbox fault diagnosis under variable operating speed is displayed in Figure 1. The details of different layer parameters are listed in Table 1. The input signal corresponds to a short window of time and is analyzed using the wavelet transform. Then the amplitude scalogram is obtained and fed into the CNN for diagnosis. In the proposed CNN, there are two convolutional layers, two pooling layers, two batch normalization layers and one softmax output layer. The fist convolutional layer extracts local features from raw pixel values of the input scalogram by convolutional operation. Max Pooling is used to reduce the feature map size and create position invariance over larger local regions. Then batch normalization [24] (Shorthand BN in Figure 1) is implemented to reduce the distribution of each layer's input by performing the normalization for each training mini-batch. There are two advantages: (1) Allows to use much higher learning rates and be less careful about initialization. (2) Reduces the internal covariate shift to accelerate the training of CNN. Afterwards feature learning is conducted layer-by-layer by forward propagation. In the last layer, the softmax is added to estimate the class probability.

The proposed approach for fault diagnosis involves four stages:

(1) The vibration signals of the gearbox are collected and the scalogram using wavelet transform (WT) are generated. The scalogram is rescaled to a dimension 64*64 and is converted into gray images to reduce the computations.

(2) Secondly, the samples are divided into training and testing samples and are further rescaled into [0, 1] as the input of network.

(3) The network parameters are randomly initialized and the training samples are fed into CNN model for updating parameters using stochastic optimization method.

(4) After the model is trained, the test instances are put into the CNN model for fault recognition. The predictions can be obtained by computing the softmax output probability of each category.

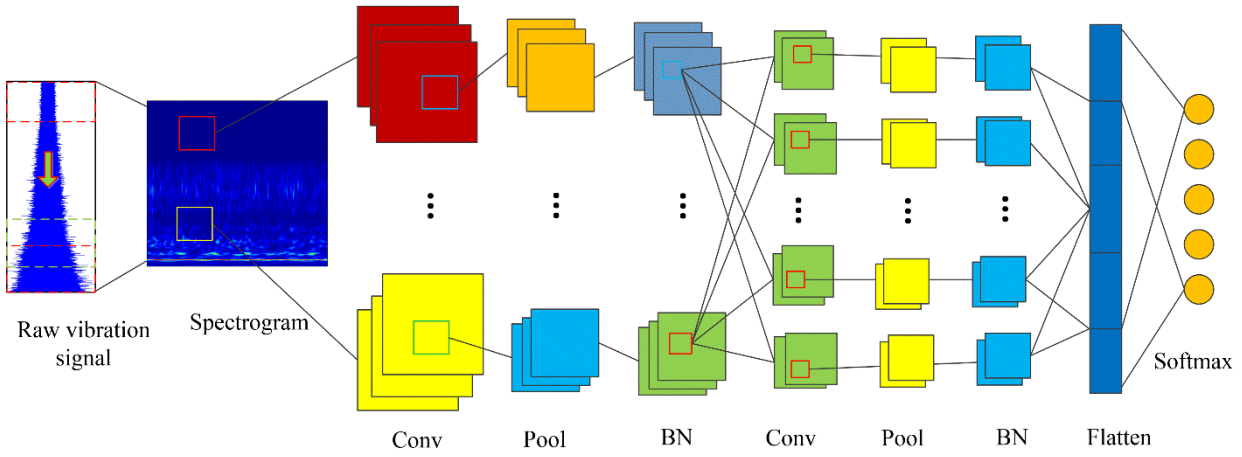


Figure 1: Model architecture of the proposed CNN

Layers	0	1	2	3	4	5	6
Name	Input	Conv	Max Pooling	Conv	Max pooling	Flatten	Softmax
Channel	1	6	6	12	12	/	5
Filter size	/	5*5	2*2	3*3	2*2	/	/
Output	64*64	60*60	30*30	28*28	14*14	2352	5

Table 1: Parameters of the proposed CNN

3 Experiment descriptions and Result analysis

3.1 Experiment descriptions

In order to validate the proposed method, gear and bearing fault experiments have been conducted on an automobile five-speed gearbox. Two levels of outer race faults, 0.2mm and 2mm are respectively introduced at the bearing of the output shaft. Moreover a chipped tooth fault has been introduced at the fifth-shift gear. Totally there are five types of health state conditions, including normal, outer race fault, gear chipped fault and two types of compound faults used for validation. In order to simulate the varying speed operation condition, the driving motor rotation speed is gradually increased from 500rpm to 1350rpm. Accelerometers are vertically installed on the bearing house of the output shaft and vibration signals are collected with a sampling rate of 12 KHz.

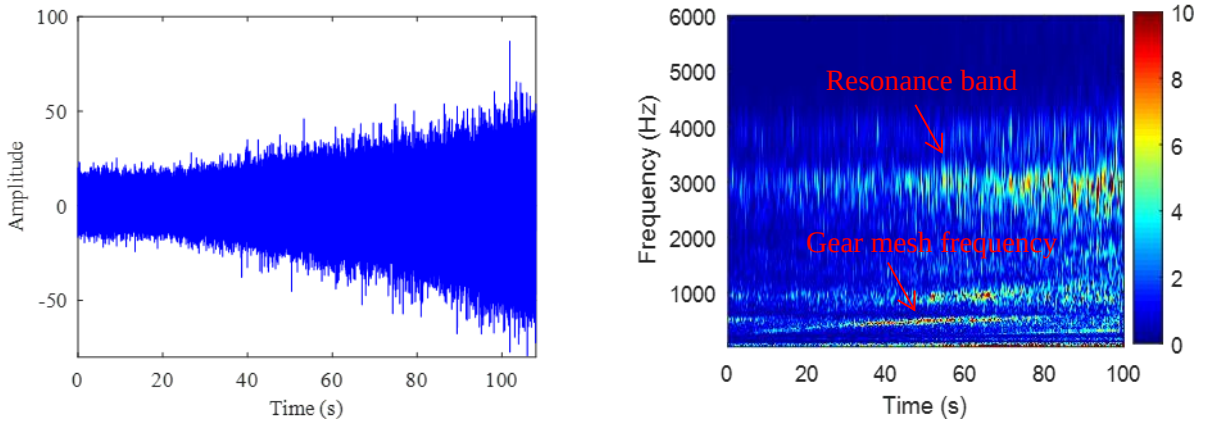
For each type of health condition, a long signal of 120000 points has been collected from the gearbox. In order to realistically include the information of at least one cycle of fault characteristics and achieve a better time-frequency representation, 6000 points are used to form one sample without overlap, allowing the capture of the local characteristics. Each sample is further transformed into a magnitude scalogram by the wavelet transform. Total there are 200 samples obtained for each health condition. The details of dataset can be found in Table 2. And the time-series of the vibration signal and the corresponding wavelet scalogram of the chipped gear case through all the testing time is presented in Figure 2.

From the time-series vibration signal, it can be seen clearly that as the operating speed increases with time, the amplitude of the signal rises gradually. The amplitude of signal at the next second is obviously larger than that of any amplitude at the begin. Additionally there is minor impulse information that can also be captured in time domain signal. The vibration signal responses of a chipped tooth fault in a gear can be considered as the repetition of impact forces when a defect gear meshes with another gear, which can also

excite resonances in the machine. For FFT, it is relative difficult to find the dominant frequency in a small time interval, so the scalogrom is given. As can be seen from the wavelet scalogram, there is an obvious resonance band in the range of 2000Hz to 4000Hz, which remains unchanged with the speed increases. Moreover there are some frequency components below 2000 Hz such as the gear mesh frequency and its harmonics which are related to the rotating speed and are changing with the time increases.

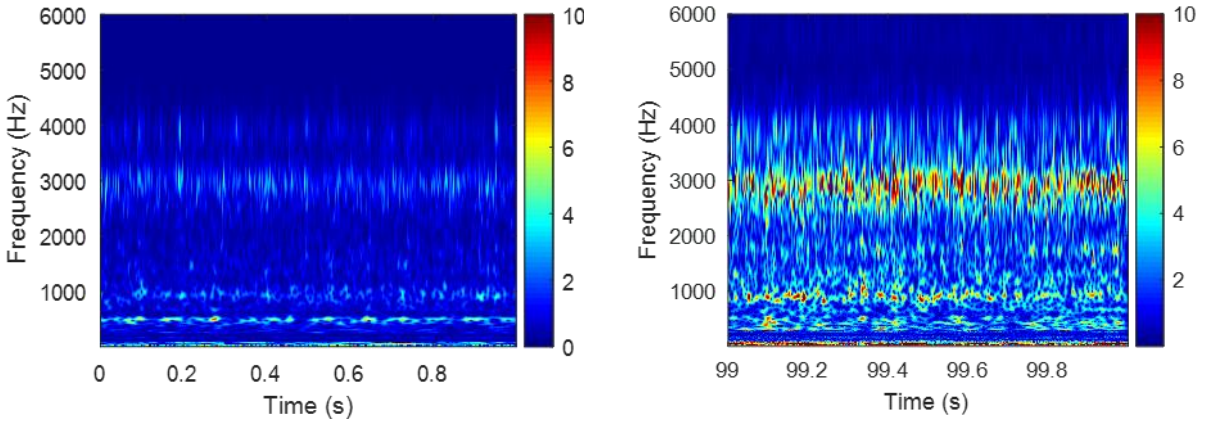
Dataset	Speed (rpm)	Fault Types		Number of Samples	Label
		The Fifth shift gear	Output bearing		
	500-1350	Normal	Normal	200	1
		Chipped tooth	Normal	200	2
		Normal	0.2mm outer race fault	200	3
		Chipped tooth	0.2mm outer race fault	200	4
		Chipped tooth	2mm outer race fault	200	5

Table 2: Description of dataset



(a) (b)

Figure 2: Time domain signal and scalogram in the case of a chipped gear: (a) Original vibration signal, (b) Scalogram



(a) (b)

Figure 3: Wavelet scalogram: (a) The first second, (b) The 100th seconds

In order to give more details in a short time interval, the scalogram using the vibration signal captured during the first second and the vibration signal captured at the 100th seconds are shown respectively in Figure 3. When the gearbox is operating on a constant speed, the scalogram of different time intervals should be nearly the same. In the variable load condition, the amplitude of different frequency component are changed. On the other hand, when the gearbox is working in speed-up conditions, the fault characteristic frequencies, the shaft rotation frequency, the gear meshing frequency and the corresponding harmonics and as well the amplitudes vary with the speed. It can be seen from Figure 3 that in the early stage, only the meshing frequency and the natural frequency are dominant components. However, when the speed increases to a large value, more frequency components are present. The two stage scalograms are not exactly the same though they share the same fault types. Therefore, in case the early stage samples are used for training and the last stage samples are used for testing, it would be challenging to recognize the fault. As CNN are capable of learning a small degree of translation-invariant representations to the common transformations such as translation, rotation and small deformations [25], it is used and is expected to improve the fault classification capability under variable speed condition.

The analyzed dataset consists of five health states and each health state has in total 200 samples. Therefore, in total 1000 samples have been obtained. All the samples for each class/state are divided into a training set and a testing set. In order to test different data input schemes, two cases are designed to estimate the proposed model.

(1) Case 1 (C1): The first half of the samples (corresponding to the former 50 seconds) are used as training set and the second half samples are regarded as testing instances.

(2) Case 2 (C2): The second half of the samples (corresponding to the 50-100 seconds) are used as training set and the rest is applied to test.

The two types of cases represent two different diagnosis issues. In C1, the training samples are acquired in a low speed condition, while the testing samples are selected in a high speed condition, which will allow the estimation of the CNN classification capability from low speed to high speed condition. On the other hand in C2, the capability of CNN to generalize from high speed to low speed condition will be estimated.

3.2 Evaluation metrics

		True label	
		Normal	Fault
Predicted label	Normal	TP	FP
	Fault	FN	TN

Table 3: Confusion matrix of a two class problem

To assess how well the proposed model is able to predict different fault types, the evaluation metrics accuracy, precision, recall and *f*1-score have been calculated for all categories individually. For illustration purposes, Table 3 give a simple description of the confusion matrix for a binary label classification with a normal and a fault class. True Positives (TP) are the amount of correctly identified normal samples. False Negative (FN) are the number of misclassified samples as normal. False Positive (FP) means the number of misclassified samples as normal. True Negative (TN) is the number of corrected classified samples as fault categories. In the real condition monitoring system, in order to achieve good decision performance, it's expected to detect as many of the fault cases as possible (high recall) and present a low false alarm rate (high precision). A good classifier is trying to optimize both [15]. The *f*1-score is the harmonic mean of precision and recall by taking both metrics into account. The accuracy is also used to reflect the mean correctly recognized samples rate from all samples. All metric computation equations are given in (5)-(8).

$$accuracy = (TP+TN)/ (TP+FN+FP+TN) \quad (5)$$

$$precision = TP/ (TP+FP) \quad (6)$$

$$recall = TP/ (TP+FN) \quad (7)$$

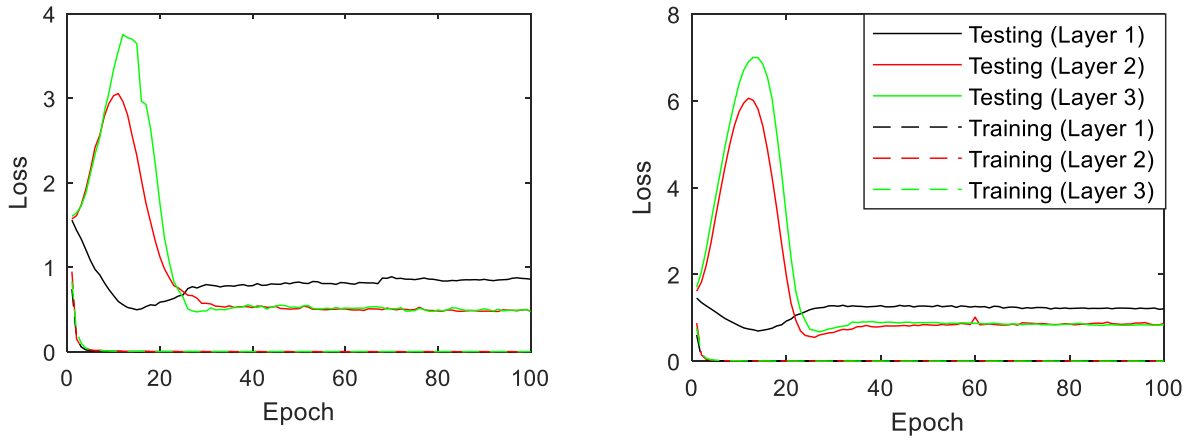
$$f1\text{-score} = 2*(precision*recall)/ (precision + recall) \quad (8)$$

3.3 Result analysis

3.3.1 CNN classification in different datasets

CNN with deep architectures usually can achieve better performance than the shallow ones. However, models with deeper architecture also lead to various hyper-parameters choice problems, over-fitting issues and to more computation time. For the CNN parameters, there is not a practically guild to choose. In order to get a relative good architecture, referred to [14, 15], small convolution kernel sizes are used in this paper and CNN with three architectures are studied: Layer 1: [Conv-Pool-BN-Softmax]; Layer 2: [Conv-Pool-BN-Conv-Pool-BN-softmax]; Layer 3: [Conv-Pool-BN-Conv-Pool-BN-Conv-Pool-BN-Softmax]. In the first layer, 5*5 convolutional kernels with 6 filters has been used. Moreover in the second layers, 3*3 convolutional kernels with 12 filters are set. Finally in the third layer, 3*3 convolution kernels with 24 filters are taken.

The results of the loss curve of CNN with three architectures that have been trained on training data and have been tested on testing data in C1 and C2 respectively are shown in Figure 5. It can be observed that the training loss declines rapidly within the first 5 epochs in all the architectures, while the testing loss gradual decreases and then reaches a steady value after 40 epochs. The CNN with layer 2 presents the best result in terms of testing loss, which is selected as the final model. In contrast, the CNN with just one layer achieves a good result, but not better than the CNN with Layer 2 and Layer 3. It should be also noted that in CNN adding more layers (Layer 3) does not contribute to low testing loss. It is possible that CNN with deeper architecture could provide more powerful learning capability, but the increase of parameters may also have negative influence on the testing performance of CNN.

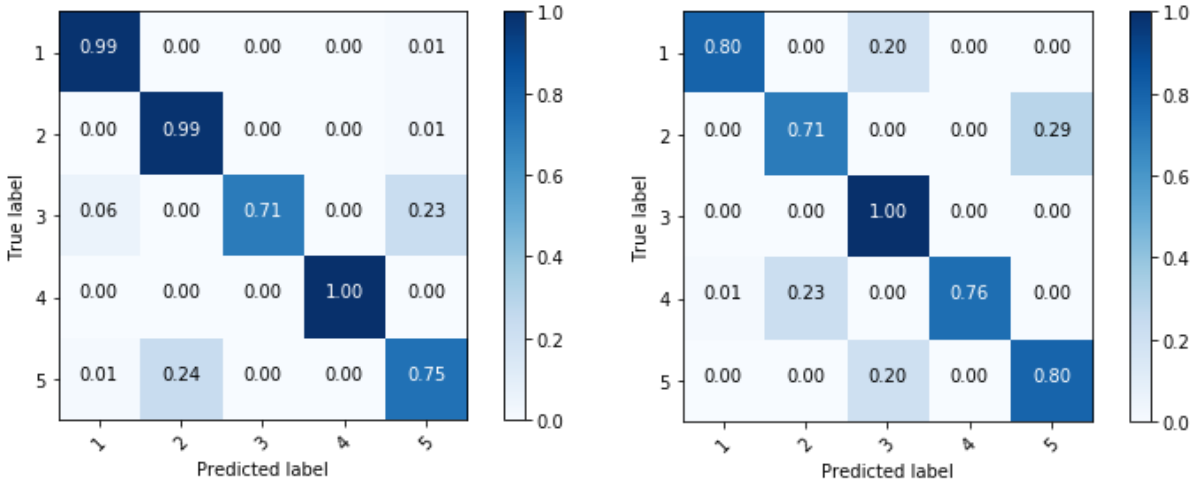


(a) (b)

Figure 4: Loss curve of training and testing samples with different architectures: (a) C1, (b) C2

The confusion matrices for selected CNN models in C1 and C2 are presented to visualize the performance of CNN, where the actual and misclassified cases can be observed. The diagonal elements of the confusion matrix represent the number of correctly classified data samples while the non-diagonal elements indicate the incorrectly classified samples. According to the results presented in Figure 5(a), class 1, class 2 and class 4 present high classification accuracy in C1. On the other hand there is also a large number of samples in class 5 and class 3 that are misclassified as class 2 and class 3, respectively. It is demonstrated that the testing samples in class 2, class 3 and class 5 present large similarity that make them hard to be

discriminated. In Figure 5 (b), a good accuracy is obtained in class 1, class 3 and class 5 but a number of samples are misclassified as class 2 and class 5.



(a) (b)

Figure 5: The Confusion matrices demonstrating the classification performance: (a) C1, (b) C2

The results of precision, recall and f1-score for each health types/states are listed in Tables 4. From the results, it can be seen that the fault 2, fault 3 and fault 5 achieve a relative low *f*1-scores in both C1 and C2, which means that the model does not perform very well for those three fault types. Class 1 and Class 4 are relative well discriminated as there are large differences among the health conditions. In Table 4, there is a high precision of 100% in class 3, but a low recall of 70.77%. It shows that model tends to well recognize class 3, but many samples from other classes are misclassified as class 3. In Table 5, it can be observed that there is a low precision of 73.53% and a high recall of 100 for class 3, which is totally different with the result in C1. It is possible that for class 3, there is only a minor outer race 0.2mm fault which probably is not so obvious in the low speed condition. Therefore, in C2 where a dataset acquired from high speed condition is used for training, it's difficult to diagnose class 3 instances acquired in low speed condition. This also demonstrates that for variable speed condition, it is relative difficult to achieve a good balance between precision and recall due to the similarity of different classes.

Class (C1)	Precision	Recall	*f*1-score
1	93.42	98.61	95.95
2	78.82	98.53	87.58
3	100	70.77	82.88
4	100	100	100
5	96.71	74.67	75.68
Average (%)	90.04	88.29	88.01

Table 4: Classification result in C1

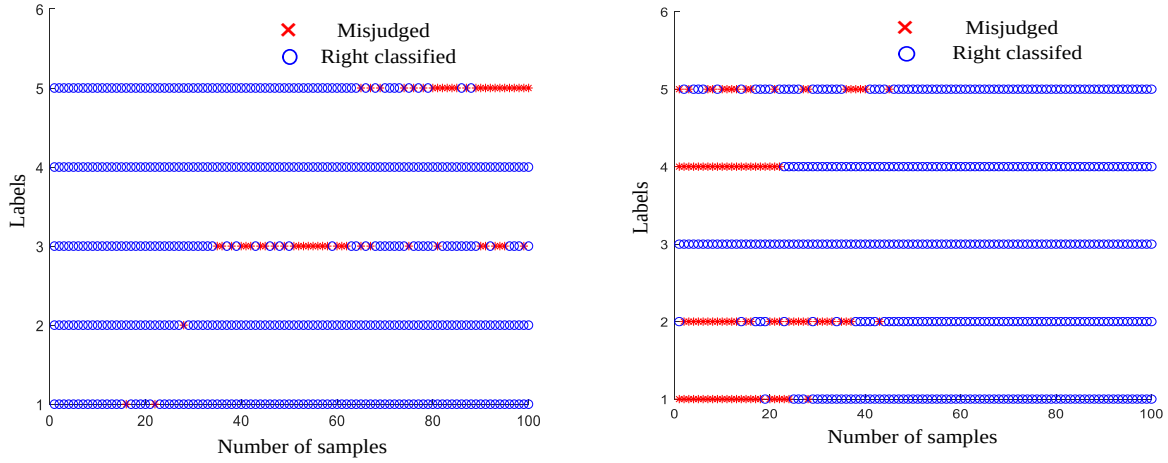
Class (C2)	Precision	Recall	*f*1-score
1	98.28	80.28	88.37
2	75.38	71.01	73.13
3	73.53	100	84.75
4	100	76.06	86.40
5	71.83	79.69	75.56
Average (%)	83.97	81.71	81.85

Table 5: Classification result in C2

In the real industrial application, it is meaningful to know which samples are correctly judged and which one is misclassified. It could provide an intuitively understanding and a practical guild to improve data pre-processing methods and model architectures. In order to reveal the distribution of the correctly classified and the misclassified testing samples for all the dataset, all testing samples class outputs are given and the misclassified samples and correctly classified samples are plotted based on the time sequence the testing samples are located.

From Figure 6 (a), it can be clearly seen that most of the misclassification samples are classified as class 3 and class 5. Additionally it can be noted that those misclassified samples are concentrated on the last part of the testing samples. In Figure 6 (b), a similar phenomenon can be found that most of misclassification samples are distributed in the former part of testing samples. This is in accordance with the fact that for C1,

training samples from the former 50 seconds are used, while testing samples from 50-100 seconds are used. Therefore, the misclassification testing instances acquired from a higher speed range presents more differences with training samples in amplitude and frequency components. Therefore, those samples are more difficult to be discriminated. This also demonstrates that the deep learning model could conduct a good decision when the testing samples are very similar to the training samples. When the testing samples present large differences with training samples, it is difficult to let the model to recognize those sample categories based on the knowledge trained from the training samples. Therefore, in order to improve the classification in the different tasks, it is necessary to collect more samples from different working conditions as soon as possible to reduce the distribution differences between training instances and real testing instances.



(a) (b)

Figure 6: Classification result distribution for different classes: (a) C1, (b) C2

3.3.2 Comparison with other methods

In order to show its advantages, Four methods are used for gearbox fault diagnosis, including the proposed method, Deep neural network (DNN), CNN-SVM, SVM listed as follows:

(1) DNN; Two hidden layers are used to construct the deep neural network (DNN); The number of units in the first and second hidden layer are 400 and 200, respectively. Rectified Linear Unit (ReLU) is defined as the activation function in neural network. The maximum iteration is 100. Additional, Adam optimization algorithm an extension to stochastic gradient descent is used to update the network parameters.

(2) CNN-SVM. In this method, a trained CNN is regarded as feature extractor to extract the last pooling layer output and then the features are fed into SVM for diagnosis and classification. That means that the top softmax layer of CNN is replaced by the SVM for the last diagnosis.

(3) SVM with a RBF kernel. The regularization parameter C is chosen from [0.1, 1, and 10,100] and kernel parameter gamma is chosen from [0.01, 0.001, and 0.0001] using grid search.

(4) SVM with linear kernel. The regularization parameter C is chosen from [0.1, 1, and 10,100] using grid search.

The classification results in C1 and C2 are shown on Table 6 and Table 7. It can be observed that CNN achieves *f*1-scores equal to 88.36% and 81.85% in C1 and C2, respectively. It achieved at least 25% higher accuracy and f1-score compared to SVM. DNN also obtained a high recognition accuracy in two cases, which is better than SVM，but a little bit lower than CNN. In contrast, SVM with RBF or Linear kernel yields relatively poor scores in all the metric indexes. This result conforms to the intuition that when the dataset becomes more complex, the shallow architecture may not be suitable to conduct a complex map and achieves a relative poor performance. It should be also noted that the CNN-SVM achieves *f*1-scores scores equal to 81.72% and 78.08% in all indexes that obvious outperform the SVM one. The features extracted

from the CNN, are much more separable compared to those extracted from scalogram enabling the SVM classifier to diagnose different fault categories more easily. The reason why deep features perform better than the raw input itself may be due to the non-linear expression conducted from CNN. In scalogram, the fault types are not easily distinguished. After mapping the scalogram into high level abstract features, the difference between the classes of data is enlarged. Among all the results, CNN outperforms the other algorithms. This is due to the fact that the parameters of softmax are jointly optimized with previous layers, which can be further optimized to reduce the classification error. Thus, the proposed method presents better adaptability and higher diagnosis precision. It also reveals that layers learned from CNN could improve the generalization ability of the model.

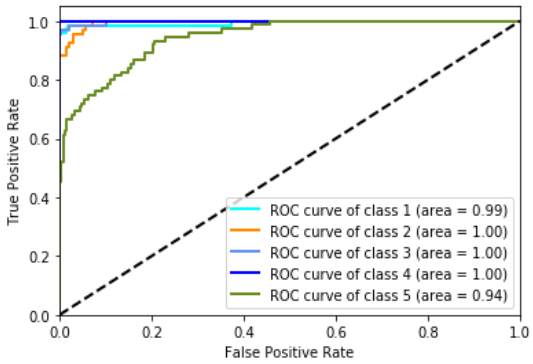
Classifiers (C1)	Accuracy	precision	Recall	*f*1-score
CNN	88.57	89.54	88.57	88.36
DNN	84.20	88.05	84.20	83.37
CNN-SVM	81.43	85.09	82.86	81.72
SVM (RBF)	53.71	72.50	62.00	58.03
SVM(Linear)	53.14	71.99	60.29	55.89

Table 6: Classification accuracy (%) of different algorithms in C1

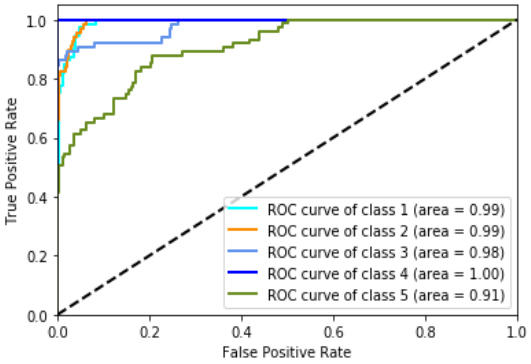
Classifiers (C2)	Accuracy	precision	Recall	*f*1-score
CNN	81.71	83.97	81.71	81.85
DNN	76.00	73.27	76.00	71.47
CNN-SVM	77.14	83.74	78.57	78.07
SVM (RBF)	56.57	66.56	56.29	57.84
SVM(Linear)	56.57	67.18	56.57	58.10

Table 7: Classification accuracy (%) of different algorithms in C2

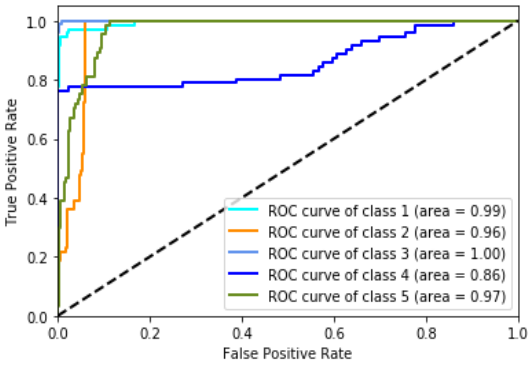
In order to further compare the diagnosis performance between CNN and CNN-SVM, the Receiver Operating Characteristic (ROC) curve and the Area Under the ROC Curve (AUC) are employed. ROC presents the confidence of CNN in decision for classifying different fault types. In the case of a good classifier, the area underneath the ROC should have a large value. Figure 7 shows the ROC area under ROC of CNN and CNN-SVM for each fault categories. From Figure 7 (a), it can be observed that for different methods almost all classes have a ROC curve near ideal in C1 and C2. In C1, the AUC has a low value of class 5, which means this type of fault (compound fault) is more difficult to separate than other health conditions. And in C2, the result of CNN in class 4 is worse than that of CNN-SVM. This means that classifying this type of category with CNN comes with a degree of uncertainty. It also can be seen that that CNN has a larger area under the curve than CNN-SVM in C1 and C2, which indicates a better performance.



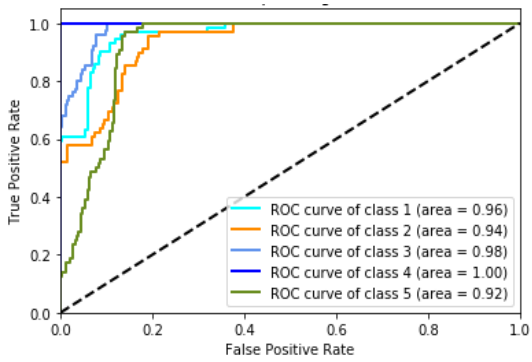
(a)



(b)



(c)



(d)

Figure 7: ROC of each category in C1 and C2: (a) CNN in C1, (b) CNN-SVM in C1, (c) CNN in C2, (d) CNN-SVM in C2

4 Conclusion

The paper proposes a deep learning approach based on CNN and wavelet transform for fault diagnosis of gearboxes operating under variable speed condition. A scalogram is constructed from raw vibration data to represent the raw input of classifiers. The DNN and SVM algorithms are trained with scalogram to conduct classification. Deep features extracted from a trained CNN model is also regarded as the input of SVM for comparison. The results show that the SVM using deep features extracted from the CNN without additional pre-processing can obviously improve the classification compared to the raw scalogram. Compared to DNN, SVM and CNN-SVM, CNN achieves the best results with amplitude scalogram input, which implies that CNN is able to learn features effectively to diagnose different classes under various speed conditions. Although mechanical fault diagnosis under variable speed is still a challenge problem, deep learning provide a potential tool to deal with it. In CNN, the selection of hyper-parameters by manual is sometimes time-consuming and low efficiency, therefore, it's meaningful to find some efficient methods to optimize those parameters and explore more different architectures, which will be conducted in the future.

References

[1] R. Liu, B. Yang, E. Zio, X. Chen, *Artificial intelligence for fault diagnosis of rotating machinery: A review*, Mechanical Systems and Signal Processing, Vol.108 (2018), pp.33-47.

[2]] A. Boudiaf, A. Moussaoui, A. Dahane, *A Comparative Study of Various Methods of Bearing Faults Diagnosis Using the Case Western Reserve University Data*. J. Fail. Anal. and Preven. Vol. 16, No.2 (2016), pp. 271–284.

[3] X. Zhang, Y. Liang, J. Zhou, J, *A novel bearing fault diagnosis model integrated permutation entropy, ensemble empirical mode decomposition and optimized SVM*, Measurement, Vol. 69 (2015), pp. 164-179.

[4] Z. Liu, H. Cao, X. Chen, Z. He, Z. Shen, Z. *Multi-fault classification based on wavelet SVM with PSO algorithm to analyze vibration signals from rolling element bearings*, Neurocomputing, Vol. 99 (2013), pp. 399-410.

[5] R. Jegadeeshwaran, V. Sugumaran, *Fault diagnosis of automobile hydraulic brake system using statistical features and support vector machines*, Mechanical Systems and Signal Processing, Vol. 52 (2015), pp. 436-446.

[6] J. B. Ali, N. Fnaiech, L. Saidi, B. Chebel-Morello, F. Fnaiech, *Application of empirical mode decomposition and artificial neural network for automatic bearing fault diagnosis based on vibration signals*, Applied Acoustics, Vol. 89 (2015), pp. 16-27.

[7] S. Tyagi, S. K. Panigrahi, *A Hybrid Genetic Algorithm and Back-Propagation Classifier for Gearbox Fault Diagnosis,* Applied Artificial Intelligence (2017), pp. 1-20.

[8] F. Jia, Y. Lei, J. Lin, X. Zhou, N. Lu, *Deep neural networks: A promising tool for fault characteristic mining and intelligent diagnosis of rotating machinery with massive data,* Mech. Syst. Signal Process, Vol. 72-73 (2016), pp. 303-315,.

[9] H. Oh, J. H. Jung, B. C. Jeon, B. D. Youn, *Scalable and Unsupervised Feature Engineering Using Vibration-Imaging and Deep Learning for Rotor System Diagnosis,* IEEE Trans. Ind. Electron, Vol. 65, No. 4 (2018), pp. 3539-3549.

[10] F. Jia, Y. Lei, J. Lin, X. Zhou, N. Lu, *Deep neural networks: A promising tool for fault characteristic mining and intelligent diagnosis of rotating machinery with massive data,* Mech. Syst. Signal Process., Vol.72-73 (2016), pp. 303-315.

[11] O. Janssens, V. Slavkovikj, B. Vervisch, K. Stockman, M. Loccufier, S. Verstockt, S., S. Van Hoecke, *Convolutional neural network based fault detection for rotating machinery,* Journal of Sound and Vibration, Vol. 377 (2016), , pp. 331-345.

[12] H. Shao, H. Jiang, H. Zhao, F. Wang, *A novel deep autoencoder feature learning method for rotating machinery fault diagnosis,* Mech. Syst. Signal Process., vol. 95 (2017), pp. 187-204.

[13] R. Zhang, Z. Peng, L.Wu, B. Yao, Y. Guan, *Fault diagnosis from raw sensor data using deep neural networks considering temporal coherence,* Sensors, Vol. 17, No. 3 (2017), pp. 549.

[14] V. Tra, J. Kim, S. A. Khan, J. M. Kim. *Bearing Fault Diagnosis under Variable Speed Using Convolutional Neural Networks and the Stochastic Diagonal Levenberg-Marquardt Algorithm,* Sensors, Vol. 17, No. 12 (2017), pp. 2834.

[15] M. M. Islam, J. M. Kim, J. M, *Motor Bearing Fault Diagnosis Using Deep Convolutional Neural Networks with 2D Analysis of Vibration Signal,* In Advances in Artificial Intelligence: 31st Canadian Conference on Artificial Intelligence, Canadian AI 2018, Toronto, ON, Canada, May 8–11, 2018, Springer International Publishing, Proceedings, Vol. 31, pp. 144-155

[16] M. Blodt, D. Bonacci, J. Regnier, M. Chabert, J. Faucher, *On-line monitoring of mechanical faults in variable-speed induction motor drives using the Wigner distribution,* IEEE Transactions on Industrial Electronics, Vol. 55, No. 2 (2008), pp. 522-533.

[17] H. Mahgoun, F. Chaari, A. Felkaoui, *Detection of gear faults in variable rotating speed using variational mode decomposition (VMD),* Mechanics & Industry, Vol.17, No. 2 (2016), pp. 207.

[18] Z. Feng, M. Liang, F. Chu, *Recent advances in time–frequency analysis methods for machinery fault diagnosis: A review with application examples,* Mechanical Systems and Signal Processing, Vol. 38, No.1 (2013), pp. 165-205.

[19] J. Chen, Z. Li, J. Pan, G. Chen, Y. Zi, J. Yuan, Z. He, Z. *Wavelet transform based on inner product in fault diagnosis of rotating machinery: A review,* Mechanical systems and signal processing, Vol. 70 (2016), pp. 1-35.

[20] Y. LeCun, L. Bottou, Y. Bengio, P. Haffner, *Gradient-based learning applied to document recognition, Proceedings of the IEEE,* Vol. 86, No. 11 (1998), pp. 2278-2324.

[21] A. Krizhevsky, I. Sutskever, G. E. Hinton, *Imagenet classification with deep convolutional neural networks,* In Advances in neural information processing systems (2012). pp. 1097-1105.

[22] Y. Meyer, *Wavelets-algorithms and applications,* Wavelets-Algorithms and applications Society for Industrial and Applied Mathematics Translation., (1993) , pp. 142

[23] G. Strang, T. Nguyen, *Wavelets and filter banks*, SIAM (1996).

[24] S. Ioffe, C. Szegedy, *Batch normalization: Accelerating deep network training by reducing internal covariate shift,* arXiv preprint arXiv:1502.03167 (2015).

[25] E. Kauderer-Abrams, *Quantifying translation-invariance in convolutional neural networks,* arXiv preprint arXiv:1801.01450 (2017).

Blade tip timing based condition monitoring of bladed disks in rotating machines

N. Jamia [1,*] **, M.I. Friswell** [1] **, S. El-Borgi** [2]**, P. Rajendran** [3]
[1] Swansea University, College of Engineering,
Bay Campus, Fabian Way, Crymlyn Burrows,
Swansea SA1 8EN, UK
*e-mail: **842543@swansea.ac.uk**

[2] Texas A&M University at Qatar, Mechanical Engineering Program,
Engineering Building, P.O. Box 23874,
Education City, Doha, Qatar

[3] School of Mechanical Engineering, SASTRA Deemed University,
Thanjavur - 613 401,
Tamil Nadu, India.

Abstract
Several researchers have considered non-contact methods to monitor blade vibration such as the blade tip timing method. This method uses contactless sensors mounted on the casing around the engine. Eddy current sensors are investigated in this work due to their efficacy for monitoring blade vibration in harsh environments compared to other type of sensors. Very little experience in the modelling of eddy current sensors is available in the literature; therefore, a detailed 3D finite element model to simulate a rotating bladed disk passing an eddy current sensor was performed. In addition, a laboratory scale test rig was designed and manufactured in order to validate the proposed model with experimental measurements. Numerical and experimental results are presented in this paper. The integrated measured output of the sensor was investigated to show the effect of the blade deformation and clearance on the accuracy of the Blade Tip Timing measurements. Finally, a demonstration of blade vibration based on measurements was performed.

1 Introduction

Vibratory loads are a main cause of blade failures in turbomachinery that can lead to total failure of the engine. Therefore the maintenance of a rotating machine is vital and has enormous impact on the life cycle cost of the engine. To realise efficient maintenance, an intelligent assessment is important for early damage diagnosis and condition based maintenance activities. Several monitoring techniques based on using stationary sensors mounted to the casing around the rotating blades have been developed to measure and analyse the Time of Arrival (ToA) of the blade tips passing by the sensors. In the 1960's a contact method was firstly used by Fragman et al. [1] to monitor and measure the rotating blade responses. They used strain gauges mounted on the blade. This method has several shortcomings such as time and cost, and the low resistance to the harsh environment found inside the machine. To overcome these shortcomings, many investigators considered contactless methods as an alternative. This method is based on monitoring blade vibrations in the rotating machinery due to the non-intrusive and easy installation of sensors which allows prompt detection of potential damage.

One of the well-known contactless method is the Blade Tip Timing (BTT) approach, which estimates the blade vibration that is crucial in the assessment of machine operation and the prediction of blade failure due to fatigue. The concept of this method relies on using a number of probes fixed to a casing of the machine to detect the blade tip as it passes by the probes. Then, the difference between the time of arrival (ToA) of non-vibrating and vibrating blades leads to the estimation of the vibration displacement utilized to identify vibration parameters [2]. During the early 1970s, Zablotsky and Korostelev [3, 4] introduced the first non-contact measurement based on their own device to measure vibration called ELURA. This technique was extended by Heath and Imregun [5] based on an improved formulation to extract the blade arrival times using optical laser probes. Dimitriadis et al. [2] simulated data from traditional BTT tests of rotating blades. They performed a qualitative analysis of different phenomena that can affect the identification of blade vibration parameters such as mistuning or coupling. A modal parameter identification of rotating machine blades was presented by Salhi et al. [6] using BTT data. Liu and Jiang [7] monitored the blade vibration of a rotating machinery test rig using the BTT method. They proposed a method to improve the accuracy of the measurements in the presence of torsional vibration. Similarly, Madhavan et al. [8] conducted an experiment to monitor vibration using the BTT technique.

The focus of previous research has been mainly on the experiment work to describe the BTT method. Several sensing technologies have been proposed to monitor blade positions in turbomachinery relying on capacitance, inductance, optics, microwaves and eddy-currents. The focus in this paper will be mainly on the eddy current sensor (ECS) due to its potential to assess the health of a machine without any need for direct access to the blade (e.g. the possibility to monitor through the casing) and therefore they are insensitive to the presence of any type of contaminant. Also, both tip timing and tip clearance of each blade could be measured by these sensors in real time and at high resolution. Dowell and Sylvester [9] described the physical principles of ECSs and the approach used to develop a health management program for turbomachinery. Lackner [10] assembled a test rig of three spinning test blades to test the ability of ECSs in a simulated gas turbine environment, and showed that ECSs could mitigate the drawbacks of other types of sensors, such as capacitive sensors. The arrival times of a rotor blade based on ECSs have been measured by Chana and Cardwell [11] in various machine trials to evaluate the ability of these sensors to detect pre-existing damage and to capture dynamic foreign object damage events. More recently, Mandache et al. [12] developed a pulsed eddy current technology to detect the blade and disk damage through the machine casing based on monitoring the blade tip displacement. In addition, Jamia et al. [13] developed a detailed 2D and 3D model of the use of ECS in blade tip timing. They investigated the accuracy of the timing measurement when the blades pass by the sensor in addition to the effect of the rotation speed and the tip clearance between the blade tip and the sensor on the sensor output.

The past investigations using eddy current testing in blade tip timing of rotating blades have been predominately experimental. Therefore there is a lack of modelling that can help to understand the error sources in the estimation of the blade time of arrival and hence its effect on the accuracy of the timing measurement, which depends on the blade deformation and clearance between the blade and the sensor. Further development of BTT systems therefore requires detailed models of both the sensor and the rotating bladed disk. Hence, for the first time, quasi-static 3-D finite element models of the electro-magnetic field have been developed to simulate the integrated measured outputs from an Active Eddy Current Sensor (AECS) and a Passive Eddy Current Sensor (PECS). An integrated test rig was designed and manufactured to generate BTT outputs in order to validate the models of the ECS. The effect of the rotation speed and the tip clearance between the blade tip and the sensor on the sensor output is investigated. Finally, a comparison between the data collected from different types of sensors was performed to investigate the effect of system parameters on the accuracy of Blade Tip Timing measurements of a vibrating blade.

2 Operation principle of ECS monitoring a moving target

2.1 Basic theory

In this section the approach of using passive and active ECSs to monitor a moving target is described. Starting with the operating concept of the AECS which is described as follows [14]. An alternating current in the coil of the ECS generates a time-varying magnetic field around the coil. This magnetic field penetrates the conductive target passing by the sensor to form a primary magnetic field that leads to variation of the magnetic flux through the target. Based on Faraday's law of induction, a flow of electric current is created in a perpendicular plane to the magnetic field within the target. This current is named the eddy current. Considering Lenz's law, these induced currents generate a secondary magnetic field that opposes the primary one and therefore the currents repel back on the primary magnetic field as shown in Figure 1.

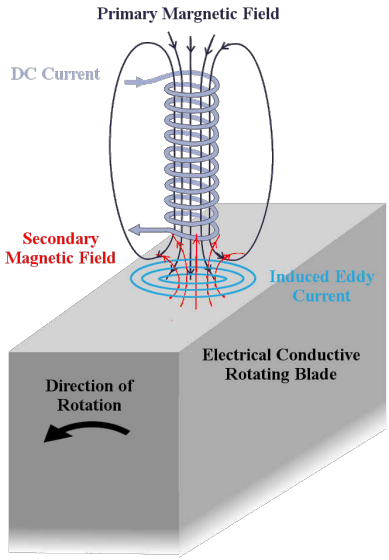


Figure 1: Mechanics of ECS monitoring moving target

This reaction leads to a variation of the coil impedance which is captured by the sensor and it is very sensitive to the distance between the target tip and the sensor. The commercial sensors are calibrated in order to convert this variation to the relative displacement.

Similarly, the operation of a PECS is almost the same, except that a permanent magnetic field is generated as a primary magnetic field, and the motion of the conductive target through the magnetic field generates the induced eddy currents. The secondary magnetic field generated by these eddy currents is measured by the sensor. The magnetic field needs to vary to generate an output in the sensor coil, and hence a PECS essentially measures velocity. Thus a PECS is not used as a displacement sensor, but does work well for blade tip timing where the blade is always moving past the sensor. A numerical model of a PECS and an AECS are considered in this paper.

2.2 Basic Physical background

In this section, the model of an ECS for a moving target is developed. Describing the material properties in relation to the electromagnetic fields and the corresponding flux densities, the following constitutive relations are considered [15]:

$$\mathbf{D} = \varepsilon \mathbf{E} \tag{1}$$

$$\mathbf{B} = \mu \mathbf{H} \tag{2}$$

where $\boldsymbol{E}$ is the electric field vector, $\boldsymbol{H}$ is the magnetic field strength vector, $\boldsymbol{D}$ is the displacement flux density vector, $\boldsymbol{B}$ is the magnetic flux density vector, $\boldsymbol{\varepsilon}$ is the electric permittivity and $\boldsymbol{\mu}$ is the magnetic permeability of the medium.

For a moving target, the general time-dependent Maxwell's equations (Eqs. (3)–(6)) are used to describe the electro-magnetic field in terms of sources as [16]. These equations are written in vector notation and in differential form as:

$$\nabla \times \mathbf{H} = \mathbf{J} + \frac{\partial \mathbf{D}}{\partial t} \tag{3}$$

$$\nabla \times \mathbf{E} = -\frac{\partial \mathbf{B}}{\partial t} \tag{4}$$

$$\nabla \cdot \mathbf{D} = \rho \tag{5}$$

$$\nabla \cdot \mathbf{B} = 0 \tag{6}$$

where $\boldsymbol{J}$ is the current density and $\boldsymbol{\rho}$ is the charge density. Satisfying the 4$^{\text{th}}$ Maxwell equation (Eq. (6)), a magnetic vector potential $\boldsymbol{A}$ can be defined as,

$$\mathbf{B} = \nabla \times \mathbf{A} \tag{7}$$

To define the electric field intensity, and satisfy the 2$^{\text{nd}}$ Maxwell equation (Eq. (4)), the field quantity can be derived from the potential as,

$$\mathbf{E} = -\nabla\varphi - \frac{\partial \mathbf{A}}{\partial \mathrm{t}} \tag{8}$$

where $\boldsymbol{\varphi}$ is the electric scalar potential. In the particular problem of an eddy current sensor, the electric current generated is composed of two parts and given by

$$\mathbf{J} = \mathbf{J_t} + \mathbf{J_s} \tag{9}$$

where $\boldsymbol{J_t}$ is the current density induced in the electro-conductive target close to the coil sensor and $\boldsymbol{J_s}$ is the current density in the coil region of the sensor generated by the voltage supply in this coil. Following Ohm's law for a moving conductor, along with the presence of the magnetic field, the eddy current generated in the target is defined as

$$\mathbf{J_t} = \sigma\left(\mathbf{E} + \nu \times \mathbf{B}\right) \tag{10}$$

where $\boldsymbol{\nu}$ is the velocity of the target and $\boldsymbol{\sigma}$ is the conductivity of the target's material.

Since the eddy current problem is a magneto-quasi-static problem [17], the displacement current can be ignored, i.e. $\frac{\partial \mathbf{D}}{\partial \mathrm{t}} \simeq 0$. Therefore, substituting Eqs. (7)–(10) and Eq. (2) into Eq. (3) yields

$$\nabla \times \mathbf{B} = \mu\,\mathbf{J} + \sigma\,\mu\,\left(\mathbf{E} + \nu \times \mathbf{B}\right) \tag{11}$$

By rearranging the terms in Eq. (11) and replacing the electric field and magnetic flux density by their expressions in Eqs. (7)–(8), we obtain, in terms of $\boldsymbol{A}$ and $\boldsymbol{\varphi}$, the following magnetic governing equation

$$\nabla \times (\nabla \times \mathbf{A}) - \sigma\,\mu\,\left(-\nabla\varphi - \frac{\partial \mathbf{A}}{\partial t} + \nu \times (\nabla \times \mathbf{A})\right) = \mu\,\mathbf{J_s} \tag{12}$$

3 Numerical model description of an ECS and rotating blade

3.1 Initial work and model geometry

The authors have performed an initial investigation where they proposed a 2D model of a PECS monitoring a moving target [13]. A simple rotating disk was composed of 4 rectangular blades and surrounded by a casing

onto which a PECS was attached. The aim was to simulate the measurement process used for blade tip timing using PECS. They investigated the sensitivity of the eddy current signal to different model geometry parameters which led to fix strategically these parameters in order to increase damage sensitivity and in terms of experimental work, the voltage picked can be chosen with no influence of the blade. Furthermore, this modelling approach was utilized to design and optimize the bladed disk model geometry presented in this paper.

Name	Value	Description
b	31 mm	Blade width
l	100 mm	Blade length
w	4 mm	Blade thickness
R_{out}	200 mm	Outer diameter of the disk
R_{inn}	60 mm	Inner diameter of the disk
W_{out}	30 mm	Outer thickness of the disk
W_{inn}	20 mm	Inner thickness of the disk

Table 1: Parameters of the bladed disk model geometry

Therefore, an integrated bladed disk composed of a rotating disk and 12 rectangular twisted blades was designed using SolidWorks. Based on the parametric study performed in [13], the bladed disk geometry is generated based on the parameters given in Table 1. The model geometry details are shown in Figure 2.

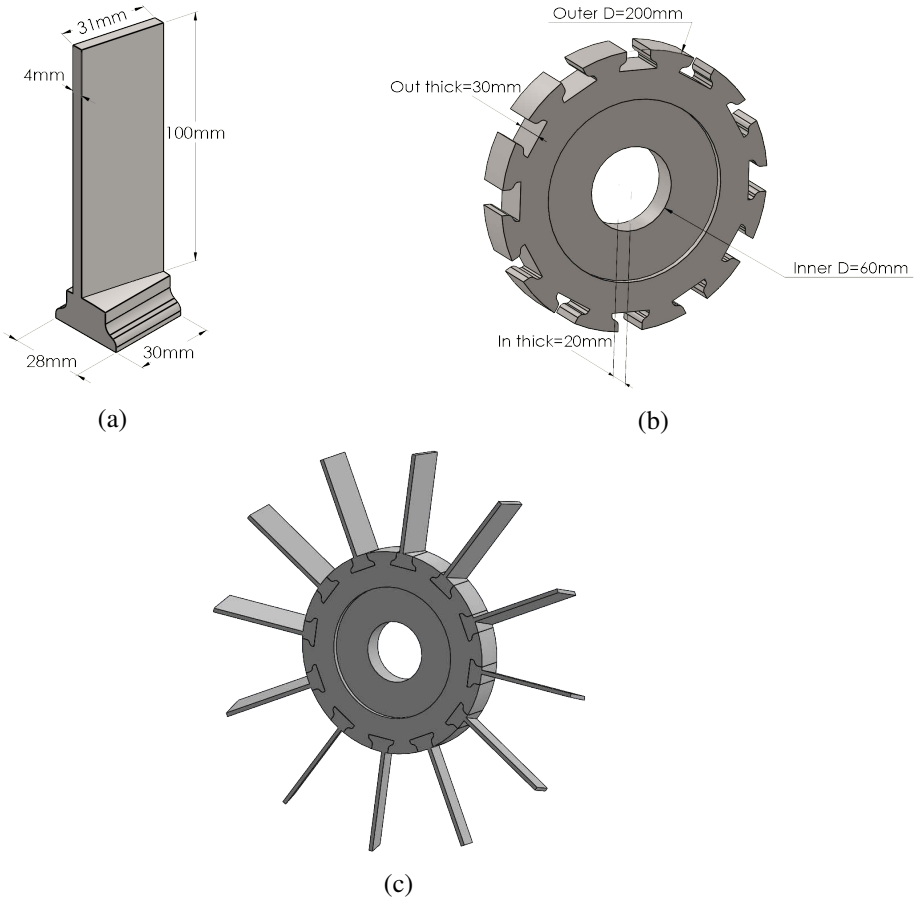


Figure 2: The test rig (a) Blade design (b) Disk design (c) Bladed disk design

3.2 PECS and AECS model description

In this section, the modelling of a PECS monitoring a rotating bladed disk is described. To achieve this task, a commercial FEA software package, COMSOL Multiphysics ®was used [18]. The model geometry is first uploaded as a 3D CAD object to the geometry interface of the software. A hollow cylindrical ECS with 3 mm inner diameter and 6 mm outer diameter is fixed at a distance δ which equals the gap between the blade tip and the sensor. This sensor is mounted to a cylindrical casing that surrounds the bladed disk at a distance of $\delta/2$. Structural steel was assigned as the material of the bladed disk and the casing, and copper was assigned to the core of the sensor. In order to have a reasonable time of computation, only two blades were considered in the model geometry as shown in Figure 3.

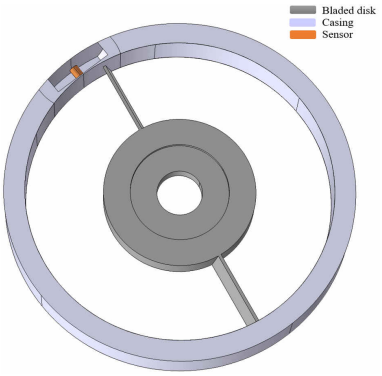
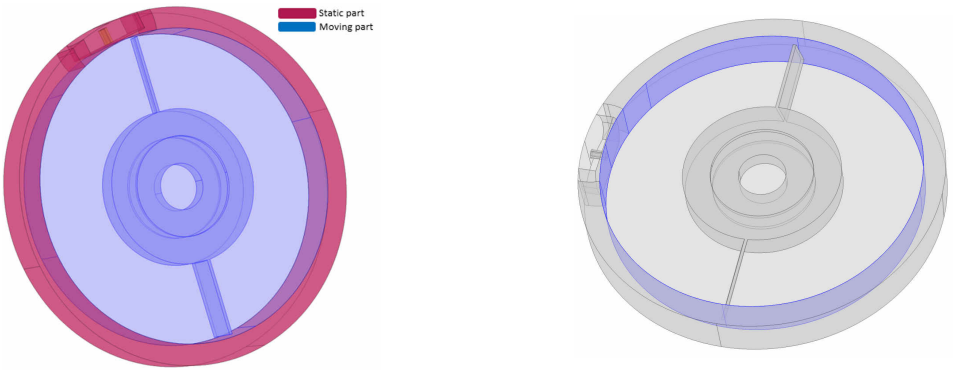


Figure 3: Model geometry of the PECS case

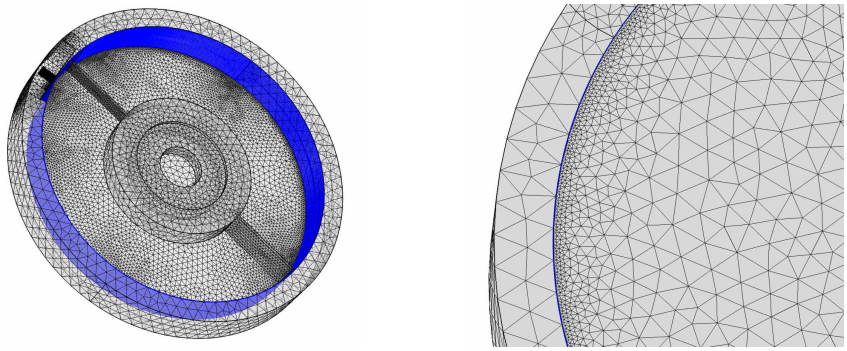
First, the geometry of the model was discretized by cutting the geometry along the air gap between the blade tip and the sensor into two parts: one containing the static part of the model (the sensor and casing), and the other containing the moving part (i.e. the disk, the blades and the surrounding air) as shown in Figure 4a. These two parts share the cut boundary as highlighted in Figure 4b.



(a) (b)

Figure 4: Bladed disk design with 2 blades

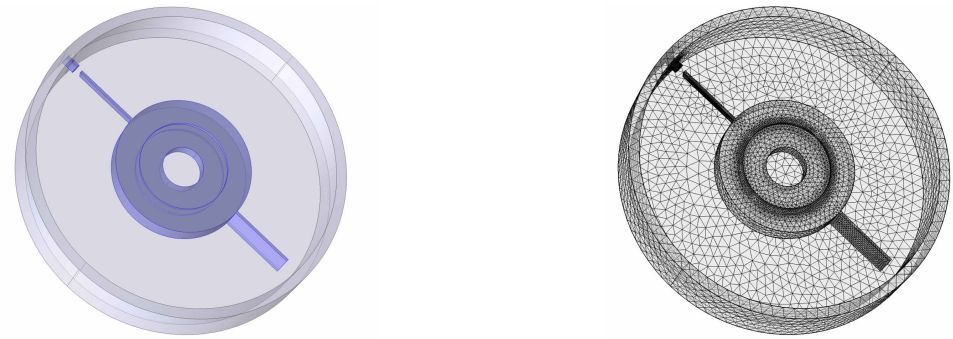
The model was meshed using tetrahedral elements for the different 3D parts and triangular element for the cut boundary surface. To overcome the difficulties of handling the rotating mesh in finite element method, the COMSOL interface uses a moving mesh approach to model the rotation. The static part remains stationary while the moving part rotates. The two parts are then meshed separately as shown in Figure 5b by the different positions of the mesh nodes on the two sides. Therefore, the meshes slide on each other, remaining always in contact at the cut boundary. Finally, 861810 tetrahedral elements were used for the model, as shown in Figure 5a.



(a) (b)

Figure 5: (a) Mesh details of PECS model (b) A close up of the model mesh

The dynamics of the system is defined using the rotating domain interface of COMSOL by applying a rotational velocity to the moving parts. Then, COMSOL enables the moving mesh for the rotating part and guarantees suitable transformations of the electromagnetic field. In time dependent analyses, the quasi-static approximation, which neglects the displacement current density, is applied by the software and therefore all of the currents in the system are induced in the conductive parts or applied externally through the sensor in this case. In order to compute the distribution of the electromagnetic field, COMSOL solves Maxwell's equations using mixed formulations. A vector potential formulation based on the magnetic vector potential A in such away to fulfill two of Maxwell's equations (Faraday's law and the magnetic Gauss's law). The second formulation is the scalar potential formulation based on a magnetic scalar potential which used to define the magnetic field such that Ampère's law is automatically fulfilled and the magnetic flux conservation law is solved. These two formulations are used together by combining the vector potential formulation for conductive domains (e.g. bladed disk and sensor) and the scalar potential formulation for the free-current domain, such as the surrounding air and air gap. In addition, due to convergence issues of the model, the current value in the coil is ramped from a low value using a smoothed step function. For the case of the AECS,



(a) (b)

Figure 6: (a) Model geometry of AECS (b) Mesh details of AECS

the model is based on measuring the change in the coil impedance which is related to the gap between the sensor and the target, and hence the sensor output gives the relative displacement. Therefore, compared to the PECS model, the continuous rotation approach is ignored and replaced with a series of blade positions using a sweep of geometry parameter defined as

$$rot_angle = t_para * \Omega * 2\,\pi \quad (rad) \tag{13}$$

where Ω is the rotational speed of the bladed disk, *t_para* is a parametric time and the blade will rotate with an angle equal to *rot_angle* with respect to this time. Then, the model is solved as a series of frequency domain

studies whilst rotating the blades in the geometry via a parametric sweep. A frequency domain study defines that an alternative current is used for the coil excitation oscillating at a parameter f_0. This excitation has been set to be 1000 times the rotational speed, to ensure that the quasi-static approximation is valid. A slightly simpler model geometry described in Figure 6a is used in the case of the AECS model. For the meshing of this model, a very fine mesh is used for the fan and the coil. The mesh in the blades has been heavily refined to resolve the currents well. Finally, 468634 tetrahedral elements have been used for the model as shown in Figure 6b. Due to the absence of rotation, the model is solved using the vector potential formulation in all domains.

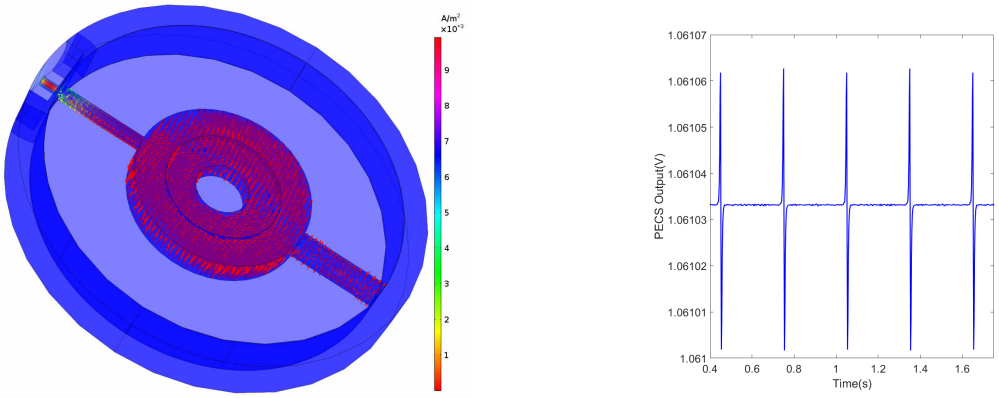
Finally, to simulate the sensor in the two models, a coil feature from the magnetic fields interface in COMSOL was assigned to the hollow cylinder in the model geometry to model the sensor as a conductor subject to an externally applied current or voltage. This feature transforms the applied excitation into local quantities (e.g. electric field and electric current density), and calculates the lumped parameters such as the impedance or voltage output.

3.3 Boundary Conditions

For both models, the tangential components of the magnetic potential is set to zero at the external boundary with magnetic vector potential. In addition, since the magnetic scalar potential is used in the PECS model, the normal component of the magnetic flux density is set to zero on external boundaries with magnetic scalar potential. Finally, an identity pair is created connecting the static and moving part in the PECS model in order to enforce the continuity for the magnetic scalar potential in the global coordinate system.

3.4 Model simulation results

A time-dependent analysis for an interval of time of 1.7 seconds and at a rotational speed of the rotor equal to 100 rev/min was performed for the PECS model. Figure 7a shows the surface plot of the magnetic flux

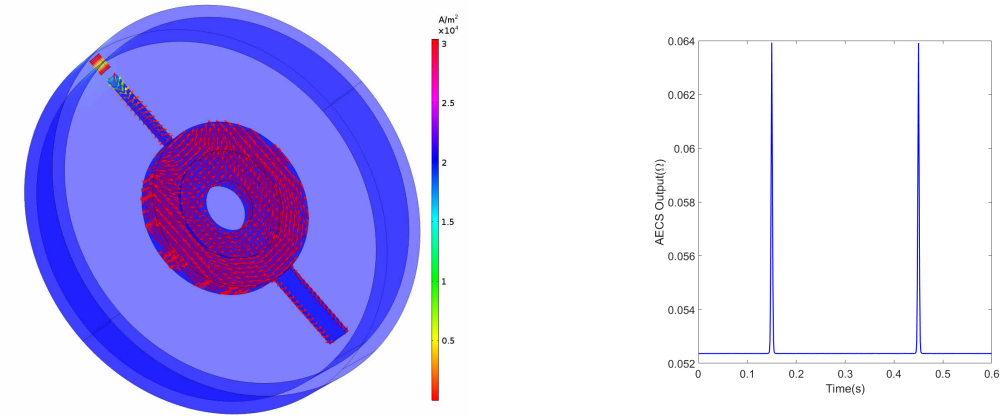


(a) (b)

Figure 7: (a) Magnetic flux density (surface) and current density (arrows) for PECS model when a single blade passes (b) PECS output when several blades pass

density at the instant when one of the blades passes by the PECS. The current density is also shown by volume arrows induced through the bladed disk. We can notice a variation in the induced current density at the blade tip. This variation is due to the interference between the primary magnetic field generated by the ECS and the secondary magnetic field generated by the moving blades past the sensor. This agrees with the concept of the PECS described in section 2. Figure 7b shows the corresponding coil voltage captured by the PECS when a blade passes by it. A signal peak is obtained every time a conducting blade enters the field of the sensor which alters the magnetic field through the induced eddy currents in the blades. This describes

clearly the behavior of the PECSs signal output; based on a reference voltage which will correspond to a known position on the blade, the time of blade passing can be determined. This gives information about the time of arrival of the blade at the sensor probe. In addition, the shape of a single peak corresponding to the PECS case, gives a reference to determine when the blade is positioned at the middle of the sensor which gives more detail about the exact blade position.



(a) (b)

Figure 8: (a) Magnetic flux density (surface) and current density (arrows) for AECS model when a single blade passes (b) AECS output when several blades pass

The AECS model is solved for a full period of rotation of the bladed disk, $T_0=\frac{1}{\Omega}$, for 1000 time steps within that time interval. Figure 8a shows the surface plot of the magnetic flux density at the instant when one of the blades passes by the AECS. The current density is also shown by arrows volume induced through the bladed disk. The induced eddy currents by the coil in the blades results in variation of the current resistance of the coil. This variation in the coil's impedance causes an electrical signal which is measured by the sensor and calibrated in order to be proportional to the distance between the blade tip and the sensor coil. This signal is showed in Figure 8b. The shape of the signal gives more detail about the gap between the blade and the sensor but is not that accurate as PECS regarding the exact position of the blade.

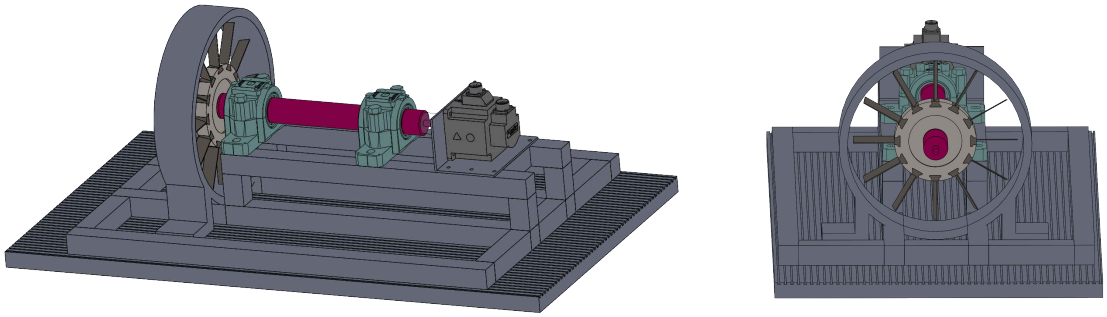
4 Experimental test rig

In order to increase the reliability of the models described in this paper, an integrated test rig is designed and manufactured in order to replicate a BTT application and generate BTT measurements using commercial AECS and PECS and therefore a validation of the model results can be performed.

4.1 Test rig design and fabrication

A test rig was designed using SolidWorks. The rig is composed of the bladed disk attached to a rotating shaft supported by two bearings. In order to avoid any vibration caused by the flexibility of the shaft and not the disk, a finite element analysis of the shaft was undertaken using ANSYS to ensure that the shaft is effectively rigid. Finally, a shaft of 60 mm diameter and 600mm length was designed. The design of the full test rig is shown in Figure 9.

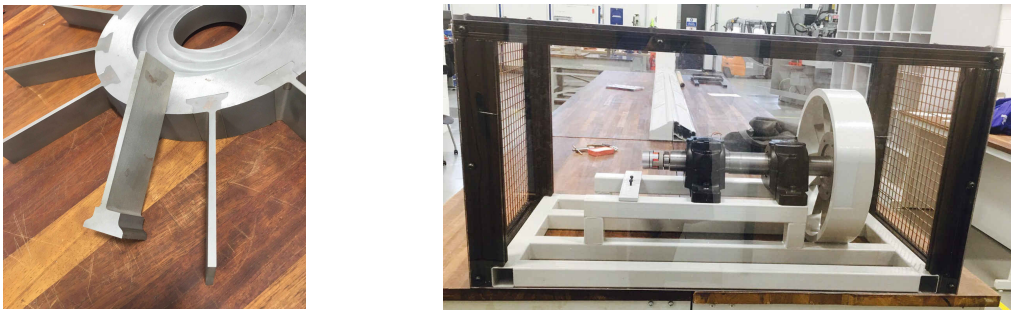
The test rig was fabricated in the machine shop at Swansea University using a CNC machine which uses a very thin wire cutter to provide an accurate joint between the blade and the disk and decrease the uncertainties that could be introduced through contact regions. To provide support for the rotating shaft, two split Plummer block housings are used with compatible ball bearings fitted in the housings. For safety, a plexiglass casing



(a) (b)

Figure 9: Test rig design: (a) Overall view (b) Side view

was used to cover the entire test rig while operating. Different manufactured parts of the test rig are shown in Figure 10.



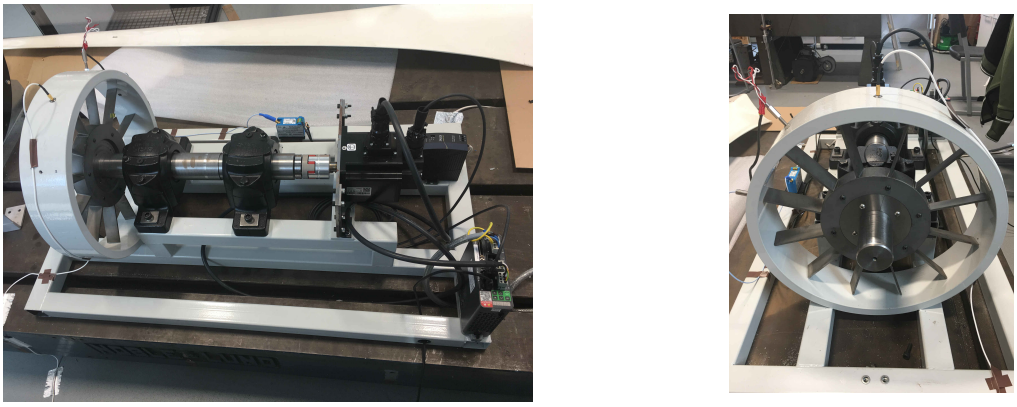
(a) (b)

Figure 10: (a) Manufactured blade and disk (b) Manufactured test rig

4.2 Test rig setup and validation of numerical models

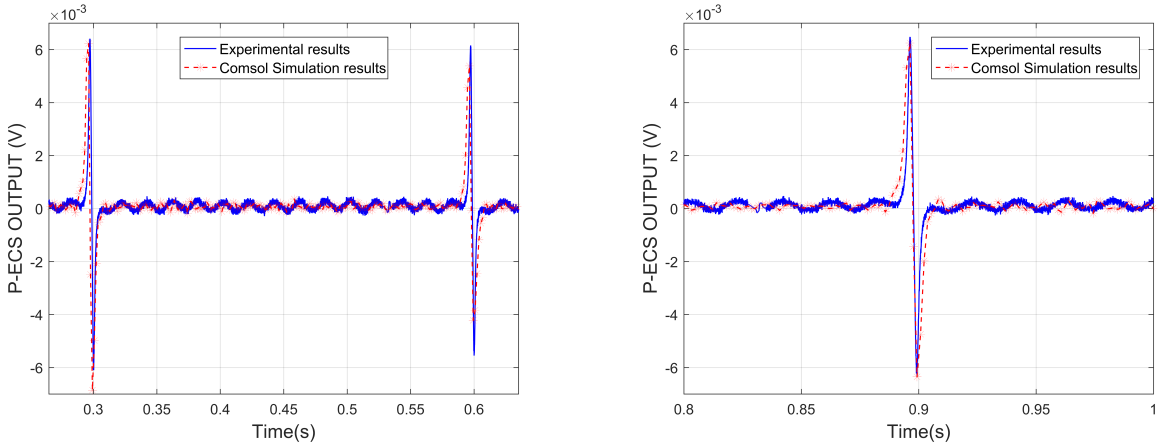
In order to replicate a BTT application, the shaft is driven by a Schneider Electric servo drive system composed of a BCH servo motor and a LXM28 (AC servo drive). Two commercial sensors, Active and Passive ECSs, were mounted on the casing around the bladed disk through holes as shown in Figure 11. These sensors were connected to a 4-channel Data Acquisition system (DAQ) in order to collect the sensor outputs. Because of the high computational cost of the 3-D models of the PECS and AECS, only a model composed of a disk with two blades was exported to COMSOL and analysed. Therefore, only two blades were kept on the bladed disk for the validation of the numerical models, since the blades were manufactured so that they can be easily removed from the disk.

At a rotational speed of 100 rpm and a gap of 3mm between the sensors and the blade tip, the BTT measurements were collected from the AECS and PECS for a period of 1.28s with a sampling rate of 13kHz. The comparison of measured outputs of the PECS and AECS and the numerical results from the models described above are shown in Figures 12 and 13, respectively. These figures show a good agreement between the simulated and measured data of BTT for a PECS and an AECS.



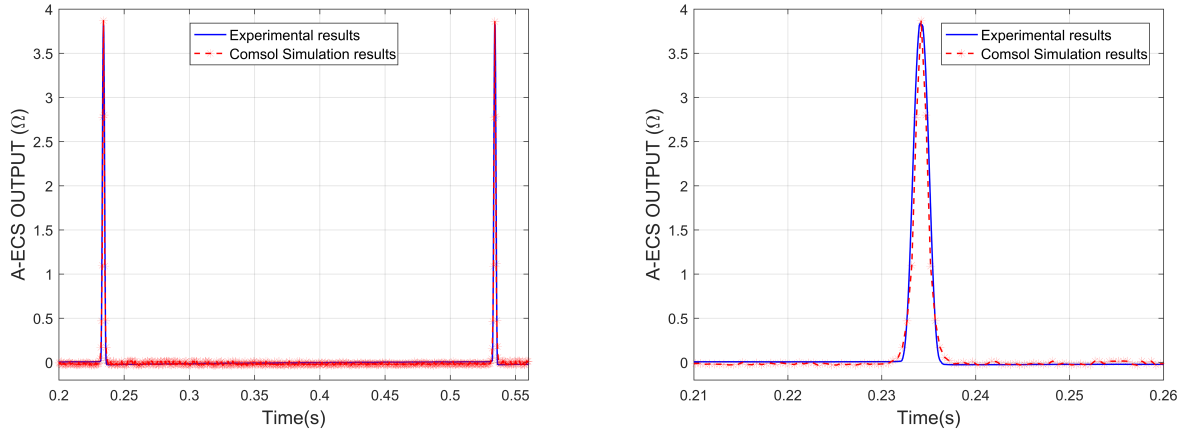
(a) (b)

Figure 11: (a) Test rig setup (b) Mounting of sensors on the casing



(a) (b)

Figure 12: (a) Comparison of numerical results with experimental measurements for the PECS (b) A locally enlarged graph of Fig. 12a

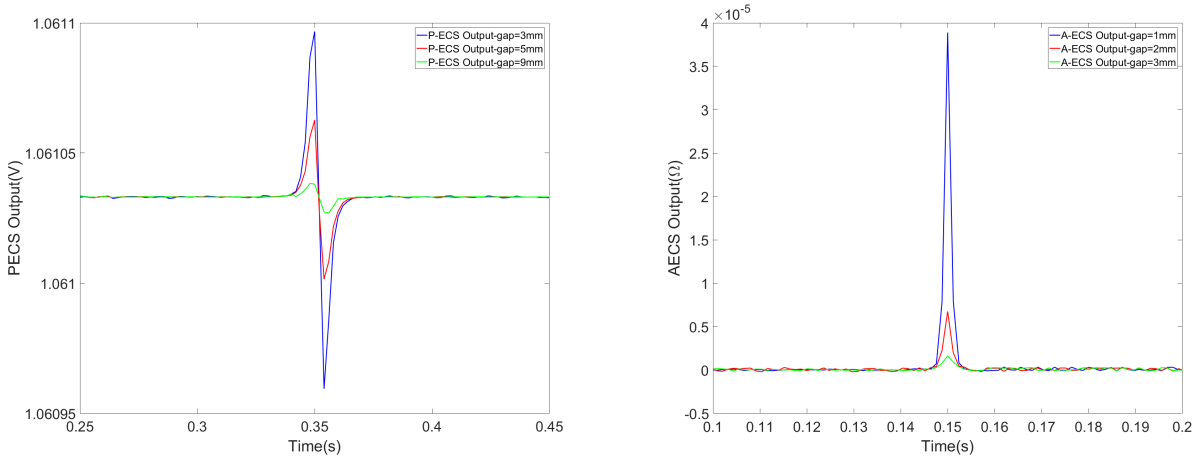


(a) (b)

Figure 13: (a) Comparison of numerical results with experimental measurements for the AECS (b) A locally enlarged graph of Fig. 13a

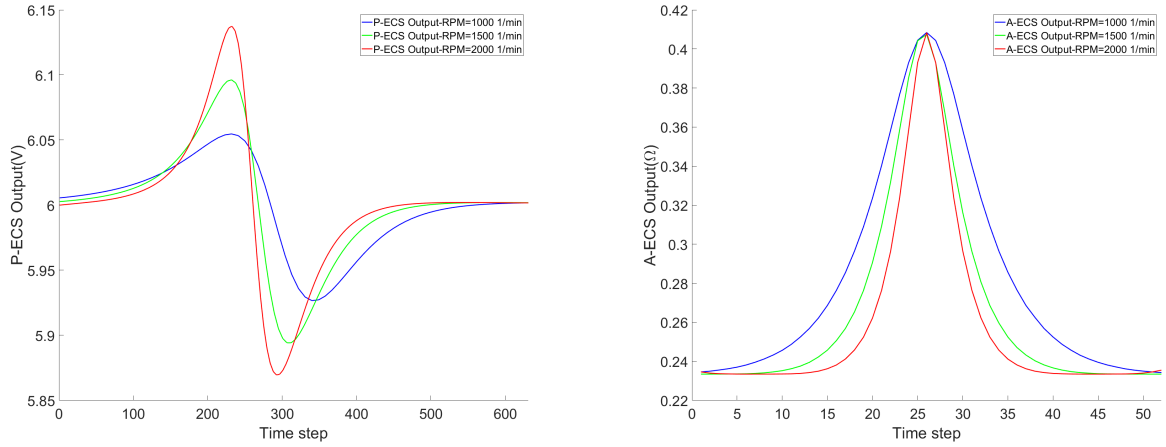
5 Effect of the gap and rotational speed on the sensor output

In this section, the effect of the variation of the gap (i.e. the distance separating the blade tip and the surface of the sensor during the rotation of the bladed disk) and the bladed disk rotational speed on the output of the AECS and PECS model was investigated. For the PECS model, Figure 14a shows that the amplitude of the signal decreases when the gap increases. These results show that the PECS can still detect the blade at a large gap (around 10 mm).



(a) (b)

Figure 14: The sensor output with time for different gaps (a) PECS model (b) AECS model



(a) (b)

Figure 15: The sensor output with time for different rotational speeds (curves shifted to a common point) (a) PECS model (b) AECS model

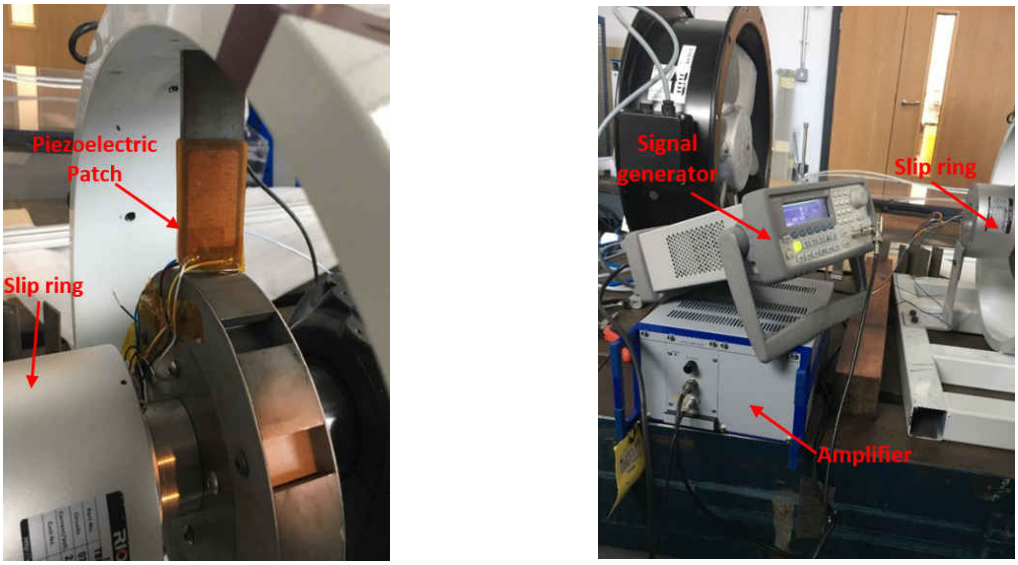
For the AECS, the effect of the variation of the gap on the sensor output is shown in Figure 14b. The results show a clear decrease in the signal amplitude when the gap increases from 1 mm to only 3 mm between the sensor and the blade tip. This shows the high sensitivity of the AECS to small distance variations which agrees with the fact that this type of sensor is considered as a displacement sensor but also shows that the performance of this type of sensor is limited for larger gaps.

Finally, Figure 15 shows the effect of the rotational speed of the bladed disk on the PECS and AECS output. Due to the difficulty in analysing the raw results in this case, the signal outputs have been shifted to a

common point so that the blade passes the sensor at the same time. For the PECS, in Figure 15a, we notice an increase of the signal amplitude with increasing rotational speed. This shows the sensitivity of this type of sensor to the speed variation, since the PECS is considered as a velocity sensor and not as a displacement sensor. However, Figure 15b shows the insensitivity of the AECS model output with speed variation which agrees with the fact that the AECS is behaving as a displacement sensor. This parametric study leads to the conclusion that the PECS could be more efficient for the BTT measurement due to its high sensitivity to the velocity of the blade which can be a source of error affecting the accuracy of the BTT measurement.

6 Blade Tip Timing measurements of a vibrating blade

In this section, the setup of the test rig to generate a BTT measurement of a rotating and vibrating blade is described and the identification of this vibration using the ToA of the blades is shown. In order to obtain a BTT measurement for a vibrating and rotating blade, the blade needs to be excited to obtain the vibrating behavior while it is rotating. Hence, a pair of piezoelectric patches was used as an actuator due to the inverse piezoelectric effect. If a voltage is applied to the patches, they will strain and generate vibration or deflection of the structure that they are bonded to. The piezo patches were bonded to the bottom surfaces of the host blade using an EPOXY optical adhesive as shown in Figure 16a.



(a) (b)

Figure 16: (a) Piezo patches bonded to the blade (b) Setup of the process of the blade excitation

In order to obtain the first natural frequency of the blade, a hammer test was performed on the blade with bonded patches. The first natural frequency was around 113Hz. Then, an excitation voltage was generated from a wave generator with a excitation frequency around 113Hz and an amplitude of 7V. This voltage was amplified by a piezo amplifier and then transmitted to the piezo patches through the slip ring as shown in Figure 16b. An optical sensor was mounted to the casing in order to collect the BTT measurements of all blades. To identify the vibration through the BTT measurement, the effect of vibration on the inter-blade distance was monitored. A reference blade was designated and blade number 8 was excited. The 12 inter-blade distances were calculated using the ToA of two successive blades multiplied by the speed of revolution of the corresponding cycle. Figure 17 shows 4 inter-blade distances calculated during 20 cycles for the non-vibrating and vibrating cases.

There is an important variation of the 8th and 9th inter-blade distances in the vibrating case compared to the 6th and 10th inter-blade distances. This corresponds to the neighborhood of blade 8 and therefore a demonstration of the blade vibration is realised based on the BTT measurement.

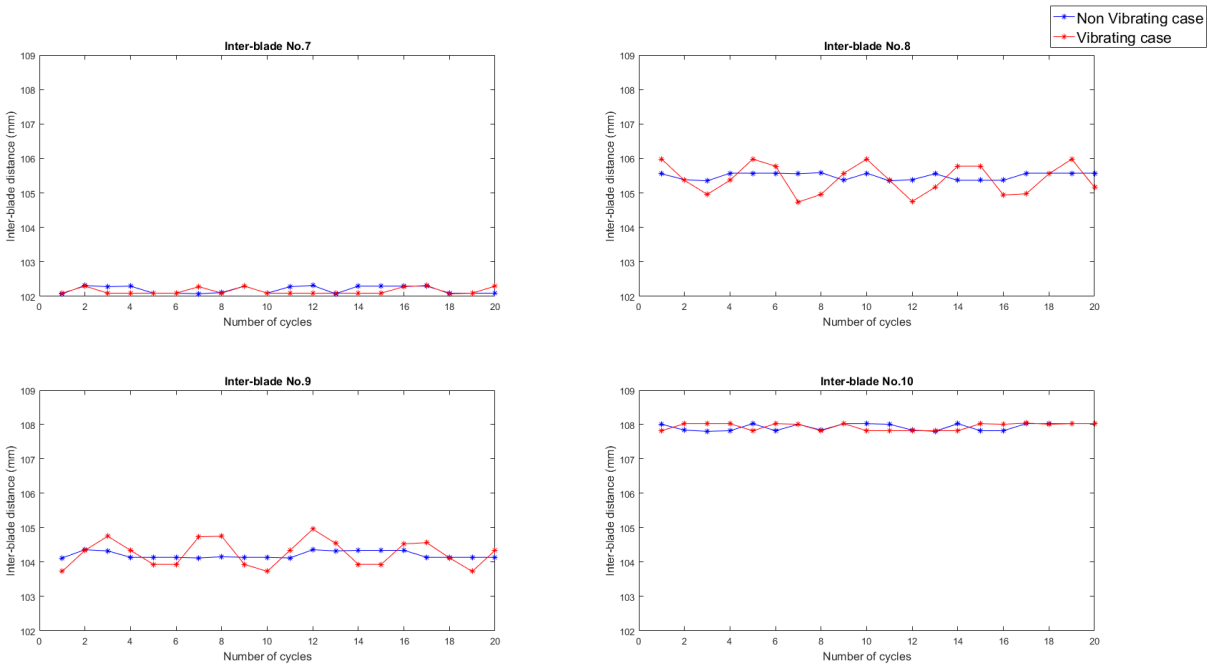


Figure 17: Inter-blade distance during 20 cycles for non-vibrating and vibrating cases using measurements from an optical sensor

7 Conclusion

A rotating bladed disk monitored by passive and active eddy current sensors on a casing surrounding the bladed disk is simulated in this paper. The goal was to simulate the signal output of the sensor used for blade tip timing using eddy current sensors. Due to their robustness in harsh environments, the eddy current sensors have been considered in this paper. The governing equations modelling the magneto electric field of a moving target have been described for a quasi-static problem. A detailed description of the 3-D models for a PECS and an AECS were presented, together with the rotating mesh details, and the physics of the electro-magnetic fields. An integrated test rig was designed and manufactured in order to generate BTT measurement for PECS and AECS. These measurements were used to validate the numerical models. This modelling approach can be utilized to design more complex BTT applications with multiple sensors and complex geometries. In addition, a demonstration of blade vibration based on the BTT measurements was performed. Finally, a BTT study to identify damage in vibrating blade while rotating will be the subject of future research.

Acknowledgements

The authors gratefully acknowledge the support of the Qatar National Research Fund through grant number NPRP 7-1153-2-432.

References

[1] C. Fangman, V. Zastrow, J. Bobeck. *High-speed-turbocharger blade-vibration mesurement*. Experimental Mechanics, vol. 7, no. 1 (1967), pp. 19A–21A.

[2] G. Dimitriadis, I. B. Carrington, J. R. Wright, J. E. Cooper. *Blade-tip timing measurement of synchronous vibrations of rotating bladed assemblies*. Mechanical Systems and Signal Processing, vol. 16, no. 4 (2002), pp. 599–622.

[3] I. Zablotskii, Y. A. Korostelev, L. Sviblov. *Contactless measuring of vibrations in the rotor blades of turbines*. Tech. rep., Foreign technology div Wright-Patterson AFB, OH (1974).

[4] I. Y. Zablotskiy, Y. A. Korostelev. *Measurement of resonance vibrations of turbine blades with the elura device*. Tech. rep., Foreign Technology Div Wright-Patterson AFB, OH (1978).

[5] S. Heath, M. Imregun. *An improved single-parameter tip-timing method for turbomachinery blade vibration measurements using optical laser probes*. International Journal of Mechanical Sciences, vol. 38, no. 10 (1996), pp. 1047–1058.

[6] B. Salhi, J. Lardies, M. Berthillier, P. Voinis, C. Bodel. *Modal parameter identification of mistuned bladed disks using tip timing data*. Journal of Sound and Vibration, vol. 314, no. 3-5 (2008), pp. 885–906.

[7] C. Liu, D. Jiang. *Improved blade tip timing in blade vibration monitoring with torsional vibration of the rotor*. In *Journal of Physics: Conference Series*, vol. 364. IOP Publishing (2012), p. 012136.

[8] S. Madhavan, R. Jain, C. Sujatha, A. Sekhar. *Vibration based damage detection of rotor blades in a gas turbine engine*. Engineering Failure Analysis, vol. 46 (2014), pp. 26–39.

[9] M. Dowell, G. Sylvester. *Turbomachinery prognostics and health management via eddy current sensing: current developments*. In *Aerospace Conference, 1999. Proceedings. 1999 IEEE*, vol. 3. IEEE (1999), pp. 1–9.

[10] M. Lackner. *Vibration and crack detection in gas turbine engine compressor blades using eddy current sensors*. Ph.D. thesis, Massachusetts Institute of Technology (2003).

[11] K. Chana, D. Cardwell. *The use of eddy current sensor based blade tip timing for fod detection*. In *ASME Turbo Expo 2008: Power for Land, Sea, and Air*. American Society of Mechanical Engineers (2008), pp. 169–178.

[12] C. Mandache, T. Mcelhinney, N. Mrad. *Aircraft engine blade tip monitoring using pulsed eddy current technology*. In *Proceedings of the 4th International Symposium on NDT in Aerospace, Augsburg, Germany* (2012), pp. 13–15.

[13] N. Jamia, M. I. Friswell, S. El-Borgi, R. Fernandes. *Simulating eddy current sensor outputs for blade tip timing*. Advances in Mechanical Engineering, vol. 10, no. 1 (2018), p. 1687814017748020.

[14] J. García-Martín, J. Gómez-Gil, E. Vázquez-Sánchez. *Non-destructive techniques based on eddy current testing*. Sensors, vol. 11, no. 3 (2011), pp. 2525–2565.

[15] A. Rosell, G. Persson. *Finite element modelling of closed cracks in eddy current testing*. International Journal of Fatigue, vol. 41 (2012), pp. 30–38.

[16] K. Karakoc, A. Suleman, E. J. Park. *Analytical modeling of eddy current brakes with the application of time varying magnetic fields*. Applied Mathematical Modelling, vol. 40, no. 2 (2016), pp. 1168–1179.

[17] R. Pohl, A. Erhard, H.-J. Montag, H.-M. Thomas, H. Wüstenberg. *Ndt techniques for railroad wheel and gauge corner inspection*. NDT & E International, vol. 37, no. 2 (2004), pp. 89–94.

[18] E. Weststrate, M. Steinback, N. M. Rensing, T. Tiernan. *Comsol multiphysics modeling for design optimization of eddy current crack detectors*. In *Proceedings of the COMSOL Conference, Boston* (2010).

A comparison of the prognostic approaches for rolling element bearings

P. Shakya [1], **A. K. Darpe** [2], **M. S. Kulkarni** [3]
[1] Department of Mechanical Engineering, Indian Institute of Technology Madras, Chennai-600036, India. e-mail: **pshakya@iitm.ac.in**

[2] Department of Mechanical Engineering, Indian Institute of Technology Delhi, New Delhi-110016, India.

[3] Department of Mechanical Engineering, Indian Institute of Technology Bombay, Mumbai-400076, India.

Abstract
The Artificial Neural Network (ANN) and curve fitting are traditionally prevalent for prognosis of bearing due to the simplicity of application. The fusion techniques are known to increase the diagnostic capabilities of the damage identification parameters (such as RMS, Peak etc.). However, the role of the fusion techniques in the prognosis of a bearing is still to be explored (attempted in this work). The Mahalanobis-Taguchi-Gram-Schmidt (MTGS) technique is used to fuse various damage identification parameters into a single fused parameter, Mahalanobis Distance (MD). The MD is used as a damage identification parameter for the ANN and the curve fitting. Three methods (i) ANN with damage identification parameters (ii) ANN with MD and (iii) Curve fitting with MD are compared for the effectiveness of the prognosis. The polynomial fit, the Gaussian fit, the sum of sinusoidal fits, and the sigmoid shape fit are attempted. The vibration data for these methods is acquired from a naturally induced and progressed defect through an accelerated life test.

1 Introduction

Rolling element bearing is a mechanical part with a wide application range. In the industry, the sudden failure of the bearings may have severe consequences both direct and indirect. The direct consequences may be in terms of the production loss and the indirect consequences may include the idle labor cost, the overtime payments to compensate the lost production, and the cost of the scrapped components due to incomplete manufacturing etc. [1]. In critical applications, such as the transportation industry, the failure of the bearing may cause accidents resulting in the loss of human lives [2]. Therefore, a robust prognosis of the rolling element bearing is required for remaining useful life (RUL) prediction.

Data fusion is an emerging field in the diagnosis of rolling element bearing. In the data fusion, the data obtained from different sources are fused to increase the efficiency of the diagnosis [3]. The Artificial Neural Network (ANN) and curve-fitting are the most commonly used techniques for the RUL prediction. In the present work, an attempt is made to assess the effect of integrating the data fusion technique (MD) with the commonly used RUL prediction techniques (ANN and curve-fitting) on the prediction of the RUL.

2 Experimental set-up

A life test has been performed to acquire the vibration data. Figure 1 shows the schematic of the test rig used to perform the life test. The shaft of the test rig may rotate up to a speed of 5000 rpm and the applied load

on the test bearings may go up to 50% of the bearing dynamic capacity. The RHP make 7917A5 angular contact bearing was run under accelerated operating conditions. The radial load was kept constant at 23% of rolling element bearing dynamic load capacity. The speed of the shaft was fixed at 2280 rpm. The vibration data was recorded at every 10 minutes for a duration of 10 seconds using a PCI4472 card (from NI). A sampling frequency of 50kHz is used for the vibration data acquisition. The first 9 second datasets are used for training the ANN or the curve-fitting, the 10^{th} second dataset has been used for prediction. The rolling element bearing lasted for 137 hours and 40 minutes.

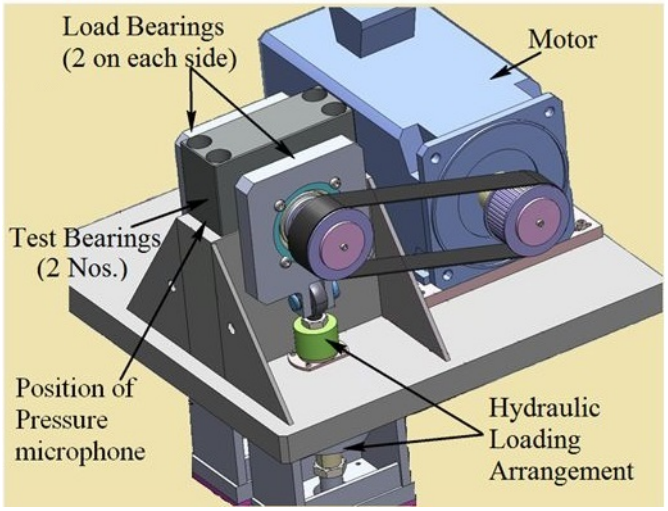


Figure 1: The schematic of the experimental set-up [1].

3 Data fusion technique

The vibration data acquired is processed in the time-domain, the frequency domain, and the time-frequency domain. The RMS, peak, Kurtosis, and Crest Factor are computed in the time domain. The outer race defect frequency amplitude (ORDFA), inner race defect frequency amplitude (IRDFA), and ball defect frequency amplitude (BDFA) are computed in the frequency domain and the HHT peak is computed in the time-frequency domain. These eight damage identification parameters (features) are fused together into Mahalanobis distance (introduced by Mahalanobis [4]) using a data fusion technique Mahalanobis-Taguchi-Gram-Schmidt method. The Mahalanobis distance is a distance between an observation (acquired vibration data, depicted by the corresponding eight damage identification parameters) and the considered distribution (vibration data from the healthy dataset).

3.1 Mahalanobis-Taguchi-Gram-Schmidt method

Using the Mahalanobis-Taguchi-Gram-Schmidt method [5], the eight features are fused into the Mahalanobis distance. Initially, all the features (from different observations) are converted into standardized vectors (Z_{ij}).

$$Z_{ij} = \frac{(X_{ij} - m_i)}{S_i} \tag{1}$$

where X_{ij}= value of the i^{th} feature in the j^{th} observation, m_i = mean of the i^{th} feature of the considered distribution (healthy group), S_i= standard deviation of the i^{th} feature of the considered distribution (healthy group).

The standardized vectors are converted into the orthogonal vectors of the same linear span using the following set of equations:

$$U_1 = Z_1 \tag{2}$$

$$U_2 = Z_2 - \frac{Z_2' U_1}{U_1' U_1} U_1 \tag{3}$$

$$\vdots$$

$$U_k = Z_k - \frac{Z_k' U_1}{U_1' U_1} U_1 - \ldots\ldots - \frac{Z_k' U_{k-1}}{U_{k-1}' U_{k-1}} U_{k-1} \tag{4}$$

Where $Z_k = (Z_{k1}, Z_{k2}, ..., Z_{kn})$ is the k^{th} set of the standardized vector obtained as per equation (1) and $U_k = (U_{k1}, U_{k2}, ..., U_{kn})$ is the k^{th} set of the mutually perpendicular vector with the same linear span.

The Mahalanobis distance corresponding to the j^{th} observation is given by the following equation:

$$MD_j = \frac{1}{k}\left(\frac{U_{1j}^2}{S_1^2} + \frac{U_{2j}^2}{S_2^2} + \ldots\ldots + \frac{U_{kj}^2}{S_k^2}\right) \tag{5}$$

where U_{kj} is the element of U_k, S_k is the standard deviation of the U_k and k is the total number of features.

4 Results and discussions

Three approaches (i) ANN with damage identification parameters (ii) ANN with the MD and (iii) Curve fitting with the MD are compared for the effectiveness of the prognosis. The details of these approaches are discussed in this section.

4.1 ANN with damage identification parameters (features)

In this approach, different sets of 8 damage identification parameters (features) are taken as inputs and the corresponding actual remaining useful life (RUL) values are taken as the targets. The datasets from the first 9 seconds are used for the training of the ANN. A two-layered ANN with one hidden layer is trained using Neural Network Fitting Tool in Matlab®. The Levenberg-Marquardt algorithm is used for the training and 70% of the training dataset is used for training, 15% for the validation, and 15% for the testing. The overall $R - squared$ value for the training came out to be 0.978.

For the prediction of the remaining useful life (RUL) at a given time, 3 consecutive vibration datasets are considered. The RUL is predicted at these 3 consecutive datasets using the ANN. The moving average of these three predictions is used to indicate the RUL at the given time. This is done to avoid the effect of the outliers. The RUL is predicted from the start of the life test, however, the importance of the prediction increases towards the end of the life of the bearing (as towards the end of the bearing life the decision to purchase a spare has to be made). Figure 2 shows the RUL prediction for the ANN with damage identification parameters approach. It may be seen in Figure 2 that after 100 hours onwards, the difference in the actual and the predicted RUL (error) is small, which indicates the robustness of the approach. However, it may be noted that for a few points, the predicted RUL is negative clearly indicating that the physics of the problem is not properly captured by the current approach.

Figure 3 shows the histogram of the RUL prediction error for the ANN with damage identification parameters approach, which is useful for qualitative analysis of the RUL prediction error. The root mean square error

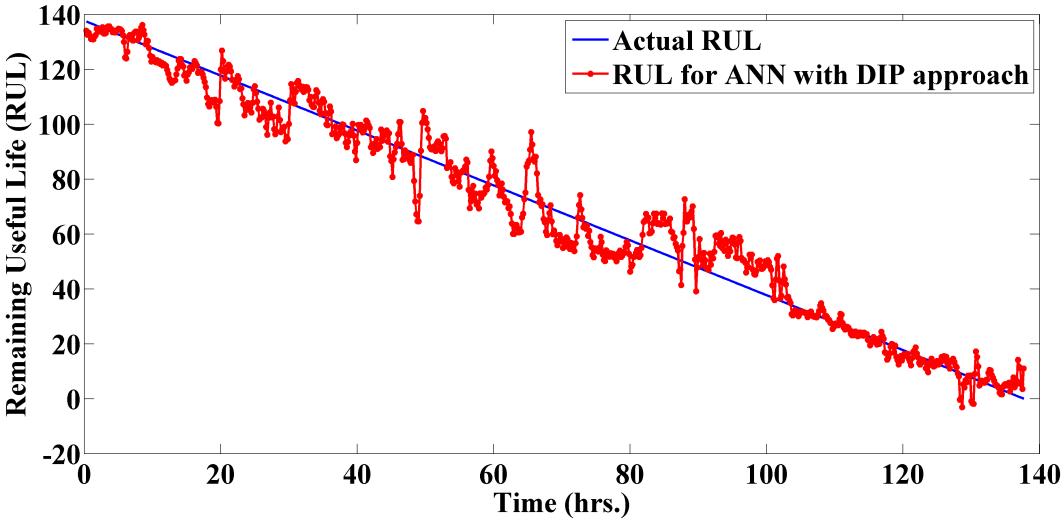


Figure 2: The RUL prediction from the ANN with damage identfication parameters.

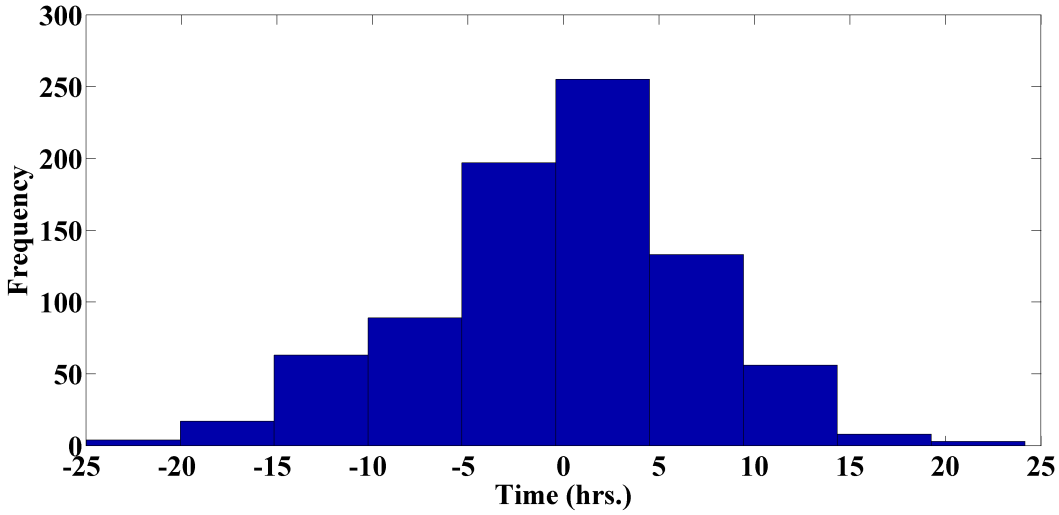


Figure 3: The histogram of the RUL prediction errors for the ANN with damage identfication parameters.

(RMSE) of the RUL prediction is computed to be 7.12 hours and the $R - squared$ is 0.968. In addition, the 56.2% of the RUL predictions are within $\pm$5 hours (3.6% of the bearing life) and the 82.3% of the RUL predictions are within $\pm$ 10 hours (7.2% of the bearing life).

4.2 ANN with the MD

As discussed in Section 3, using the MTGS method the 8 damage identification parameters are fused in the Mahalanobis distance (MD). The different sets of the MD values are taken as the inputs and the corresponding actual RUL values are taken as the targets and the ANN is trained. All the aspects of the ANN are kept same as in the previous approach. The overall $R - squared$ value for the training is computed to be 0.951.

Figure 4 shows the RUL for the ANN with the MD approach. A comparison with figure 2 clearly indicates that the performance of RUL prediction has degraded while the ANN is trained with the MD. Figure 5 shows the histogram of the RUL prediction error for the ANN with the MD approach. The RMSE of the RUL prediction is 11.67 hours and the $R - squared$ is 0.914. In addition, only 36.5% and 62.1% of RUL predictions are within $\pm$5 hours (3.6% of the bearing life) and $\pm$10 hours (7.2% of the bearing life) respectively. Therefore, the training of ANN with only MD results in poor performance of the RUL prediction in compar-

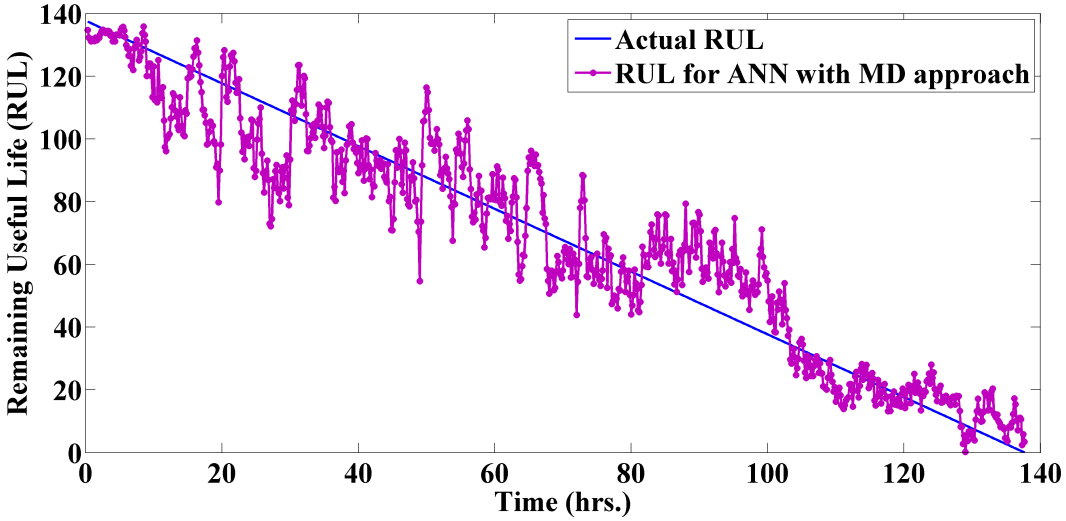


Figure 4: The RUL prediction from the ANN with the MD.

ison with the training of ANN with damage identification parameters (the previous approach). This is on the expected line as in the first approach, 8 features were used as input as opposed to only 1 feature (MD) in the second approach. Though the overall performance is worse than the first approach, it may be noted that all the predictions are non-negative (close to the physics of the problem).

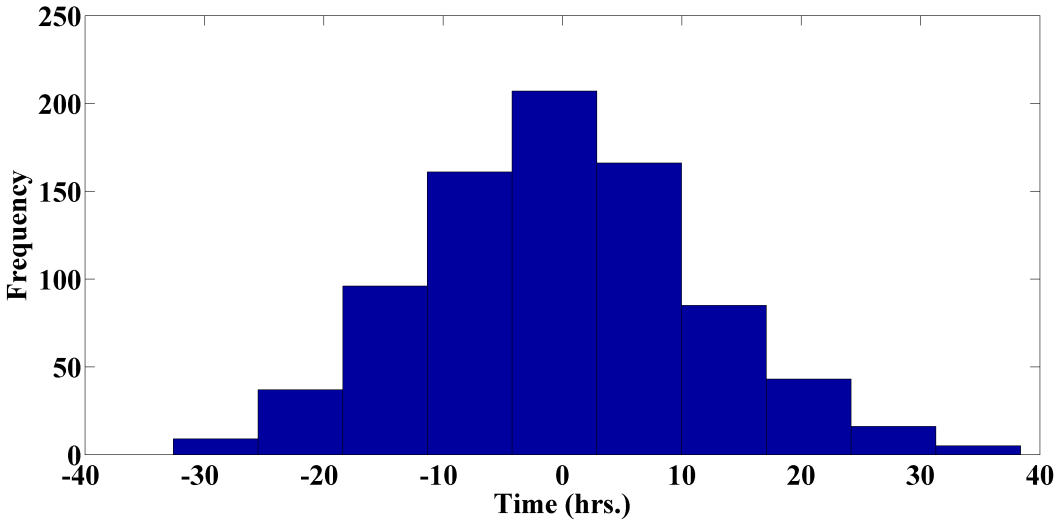


Figure 5: The histogram of the RUL prediction errors for the ANN with the MD.

4.3 Curve fitting with the MD

The last approach is curve fitting with the MD (more of trial and error type). Initially, multiple curve-fits such as polynomial fit, the Gaussian fit, the sum of sinusoidal fits, and the sigmoid shape fit are attempted. The curve fitting is done between the RUL and the $log_{10}MD$ (as the range of the MD is high up to 10^6). In addition, before curve fitting the values of the $log_{10}MD$ are smoothened using moving average method (of span 3). The fit with the maximum $R-squared$ value and practical suitability (the trend of the end of the curve; a curve stabilizing towards zero RUL toward the end is desirable) is used for RUL prediction for the 10^{th} dataset. In addition, it should be ensured that the RUL should not be negative and the 95% confidence bounds of the higher order coefficients should not cross zero, which means overfitting of data.

The following polynomial model is used for the curve fitting:

$$y = \sum_{i}^{n} p_i x^{n+1-i} \tag{6}$$

where n is the degree of the polynomial and $n+1$ is the number of the coefficients to be fitted for the model (denoted by p_i).

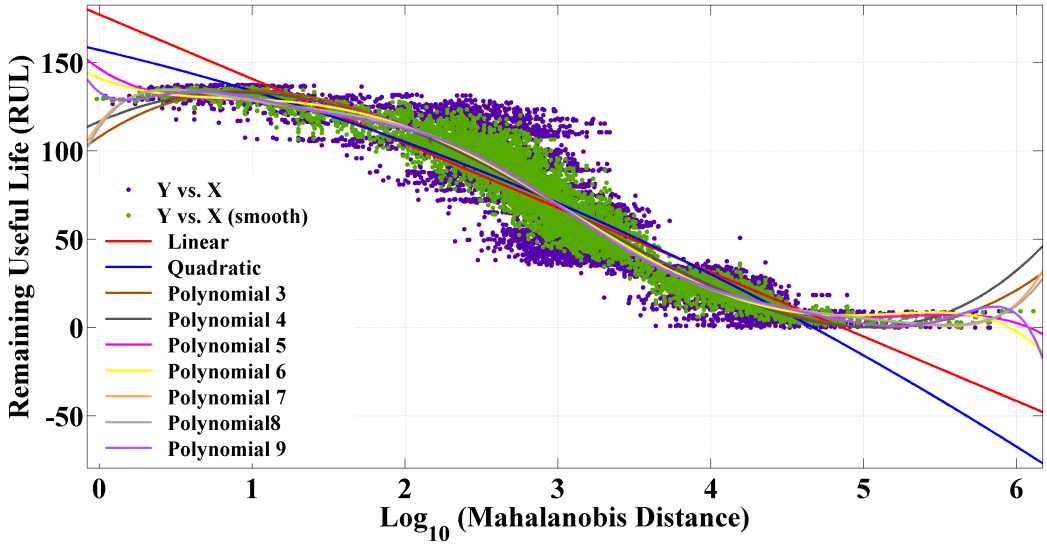


Figure 6: Curve fitting for the family of the polynomial fits.

Figure 6 shows the curve fitting for the family of the polynomial fits. It may be noted from the Figure 6 that towards the end of the curve (near the maximum value of the $log_{10}(MD)$), none of the curve-fits remains steady. Therefore, the prediction of the RUL is not accurate towards the end of the bearing life where it matters the most. However, it may be noted in the Figure 6 that the extent of the overfit is small for the family of the polynomial fits.

The following model is used for the sum of sinusoidal fits:

$$y = \sum_{i}^{n} a_i \sin(b_i x + c_i) \tag{7}$$

where n is the number of terms in the series. The a_i, b_i, and c_i are the amplitude, frequency, and phase constant for the i^{th} term of the series.

Figures 7 depicts the curve fitting for the fitting of the remaining useful life and the $log_{10}(MD)$. It may be noted that towards the end of the bearing life (corresponding to the high value of the Mahalanobis distance) the curve-fits do not stabilize (Figure 7). In addition, many of the fits from the family tend to overfit (multiple valley and crests are visible in the fits). Therefore, the family of the sum of sinusoidal fits is not suitable for the remaining useful life prediction of the bearings.

The following definition of the Gaussian fits is used for the curve fitting:

$$y = \sum_{i}^{n} a_i \exp[-(\frac{x - b_i}{c_i})^2] \tag{8}$$

where n is the number of the peaks to fit. The a_i, b_i, and c_i are the amplitude, centroid and a parameter related to the width of the peak respectively.

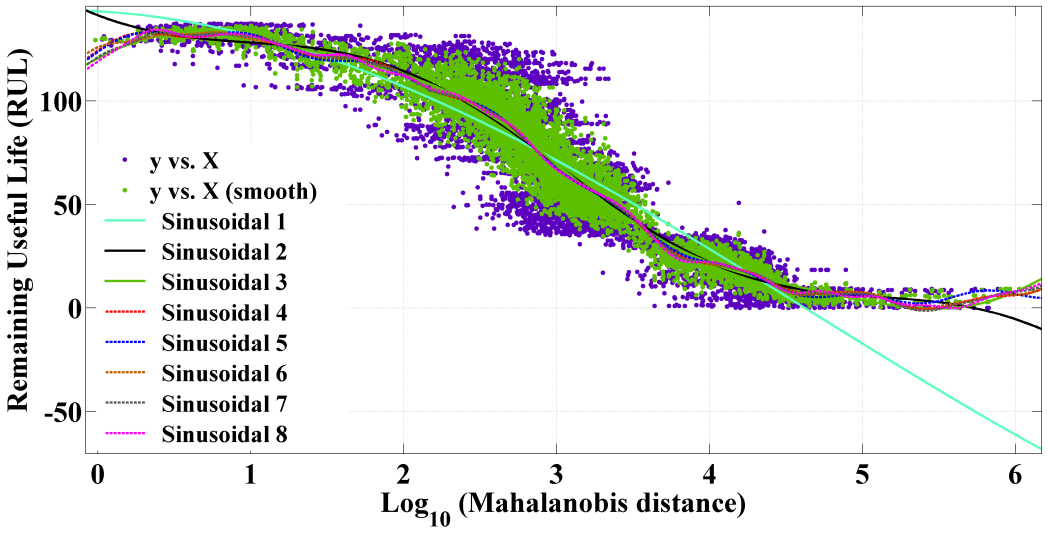


Figure 7: Curve fitting for the family of the sum of sinusoidal fits.

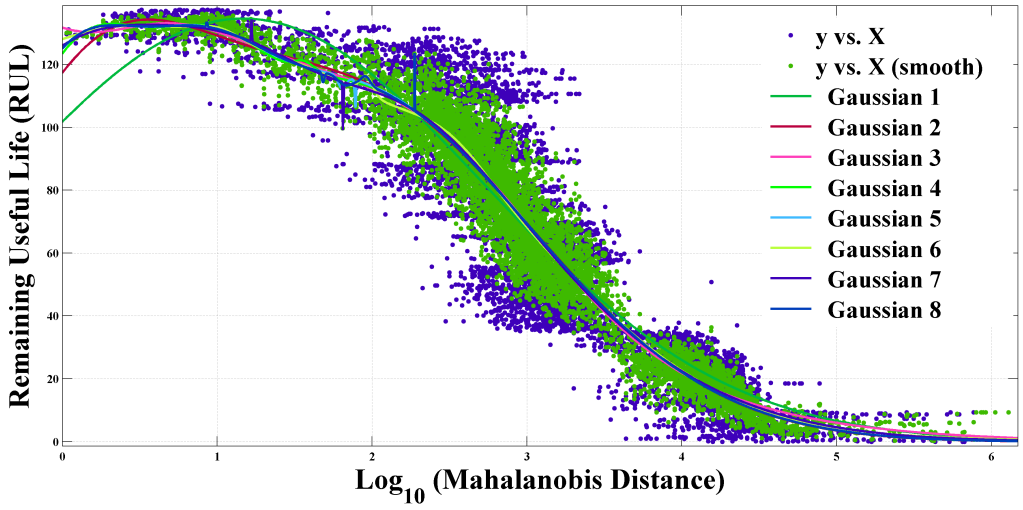


Figure 8: Curve fitting for the family of the Gaussian fits.

Figure 8, the curve-fits between the RUL and the $log_{10}(MD)$ for the Gaussian family, clearly shows that toward the end of the bearing life most of the fits stabilize. However, for a couple of fits (Gaussian 7 and Gaussian 8) tend to overfit is clearly visible. A comparison among the polynomial fits, sum of sinusoidal fits, and Gaussian fits shows that the Gaussian 3 is the best curve-fit. However, it tends to overfit the data as the 95% confidence bound for a parameter crosses zero.

As the RUL should stabilize towards the start and end of the bearing life, a scaled form of the sigmoid shape is a good choice. As many functions (hyperbolic tangent function, error function, inverse tangent function etc.) have a shape similar to the sigmoid shape, a linear combination of these is used for curve-fitting. This linear combination of functions having the shape closer to sigmoid is defined as follows:

$$y = a(\tanh(x-1)) + b\left[\frac{x}{\sqrt{1+(x-3)^2}}\right] + c\left[\text{erf}\left(\frac{\sqrt{\pi}}{2}(x-3)\right)\right] + d\left(\frac{2}{\pi}\tan^{-1}\frac{\pi}{2}(x-3)\right) + e \quad (9)$$

Figure 9 shows the curve-fitting by the considered combination of functions having the shape similar to sigmoid along with the previous best fit "Gaussian 3". The RMSE and $R-squared$ values are close for

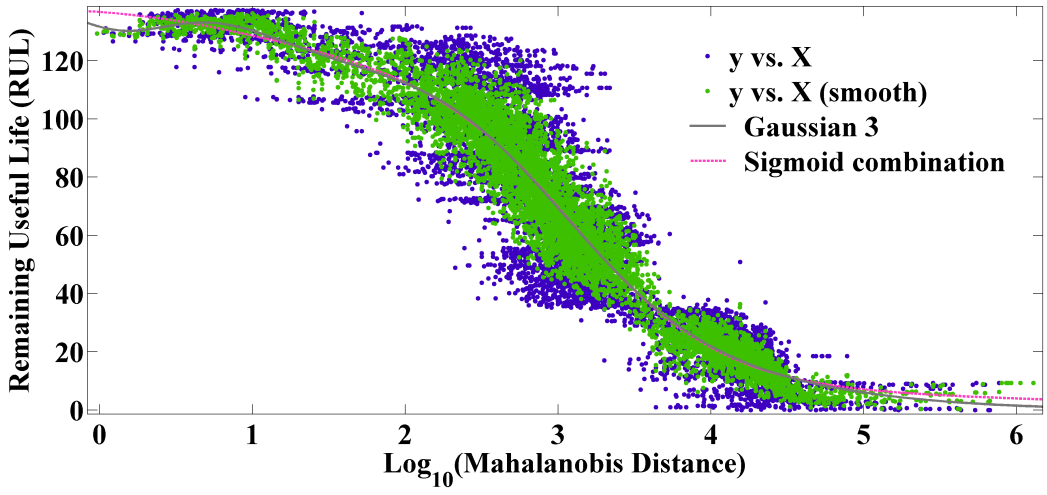


Figure 9: Curve fitting for the Gaussian3 and sigmoid combination fit.

Type of fit	RMSE	$R-squared$
Gaussian 3	8.689	0.9469
Sigmoid shape	8.724	0.9464

Table 1: Comparison of parameters for the Gaussian 3 and sigmoid shape curve-fits

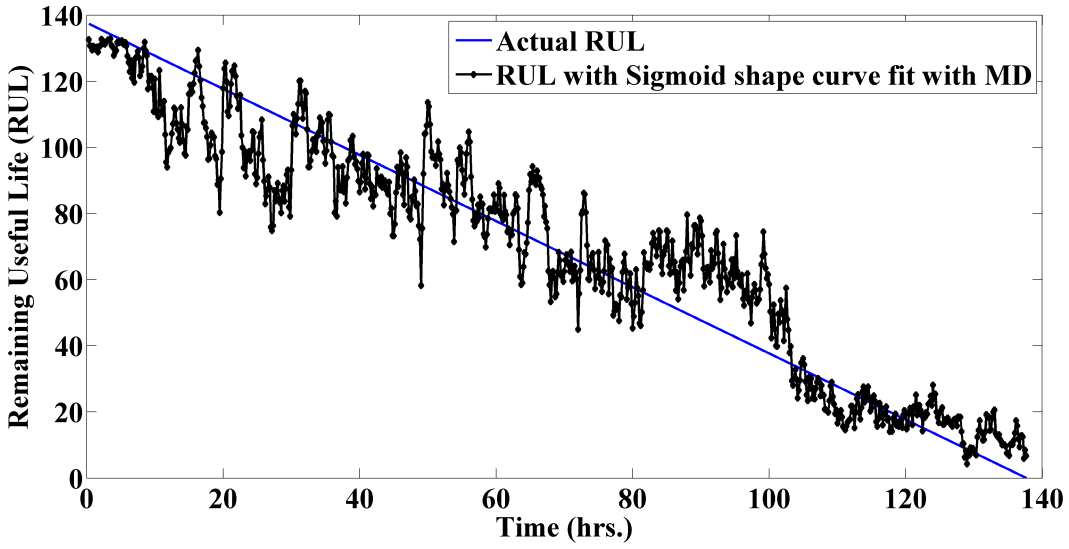


Figure 10: The RUL prediction from the sigmoid shape curve-fit with the MD.

Approach	RMSE	$R-squared$	within $\pm$ 5 hours	within $\pm$ 10 hours
ANN with DIP	7.12 hours	0.968	56.2%predictions	82.3% predictions
ANN with MD	11.67 hours	0.914	36.5% predictions	62.1% predictions
Curve fit with MD	12.16 hours	0.906	34.5% predictions	62.2% predictions

Table 2: Comparison of parameters for the Gaussian 3 and sigmoid shape curve-fits

both the fits, the Gaussian 3 being marginally better (see Table 1). However, as discussed earlier the Gaussian 3 tends to overfit (clearly seen towards the start of bearing life). The sigmoid shape fit does not overfit the data and the RUL prediction also stabilizes towards the end (from the definition of the sigmoid shape functions). Therefore, the sigmoid shape curve-fit is used for the RUL prediction for the 10^{th} second dataset.

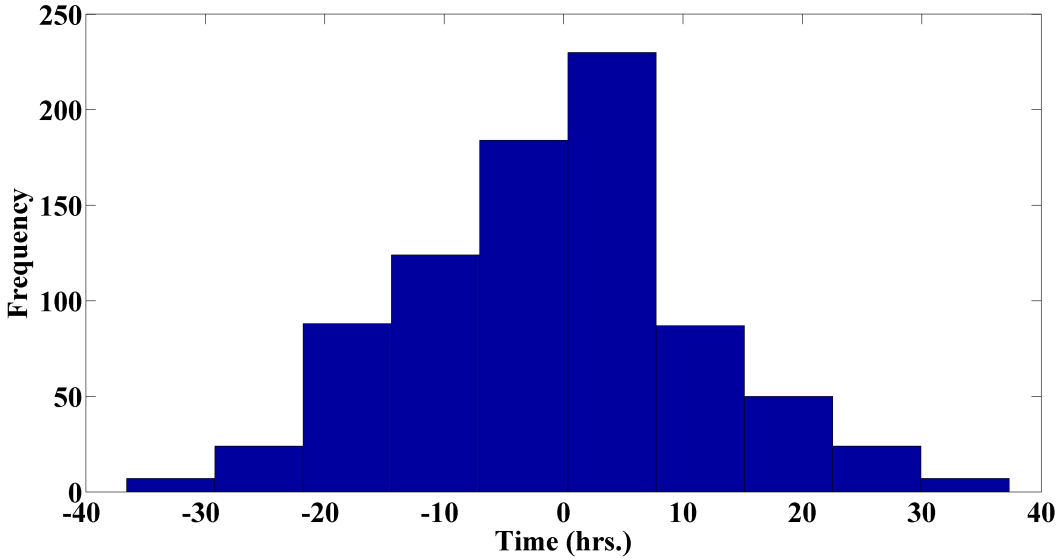


Figure 11: The histogram of the RUL prediction errors for the sigmoid shape curve-fit with the MD.

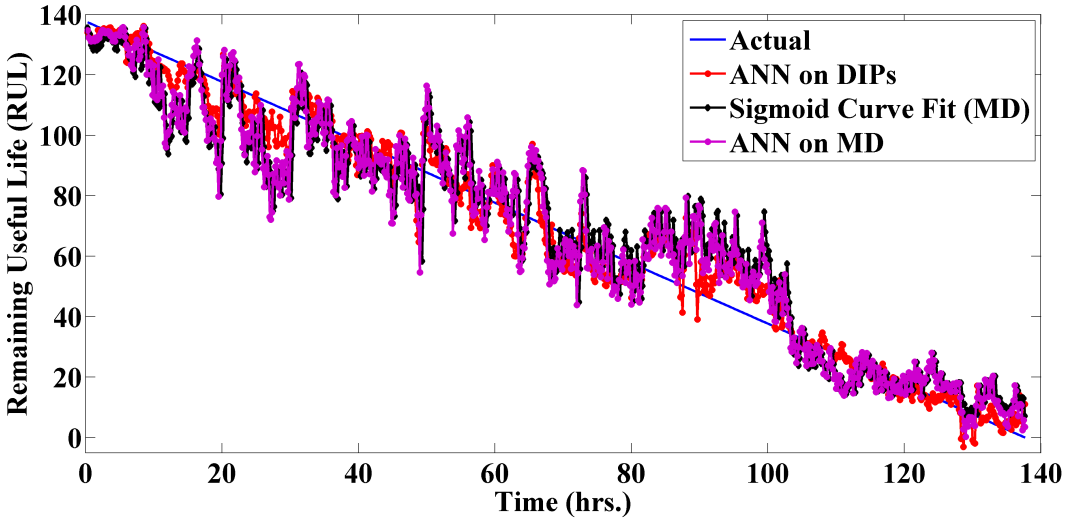


Figure 12: The comparison of RUL prediction from all approaches.

Figure 10 shows the RUL for the curve-fitting approach (with the sigmoid shape fit). Figure 11 shows the histogram of the RUL prediction error for the sigmoid shape fit on the MD. The RMSE of the RUL prediction is 12.16 hours and the $R - squared$ value is 0.906. In addition, only 34.5% and 62.2% of RUL predictions are within ± 5 hours (3.6% of the bearing life) and ± 10 hours (7.2% of the bearing life) respectively. The RUL prediction in the current approach is similar to the previous approach (ANN with MD) but worse in comparison to the first approach (ANN with DIP). It may be noted that all the predictions are non-negative.

The RUL predictions of all the approaches are compared in the Figure 12. It may be noted that performances of the second approach (ANN with MD) and the third approach (Sigmoid curve fit with MD) are comparable at many time instants. To provide a better insight, different parameters related to all approaches are compared in Table 2.

5 Conclusions

Three different approaches are compared for the RUL prediction for a set of common data originating from a naturally induced and progressed defect. In the first approach, the ANN is trained with the help of 8 damage identification parameters while in the second approach the ANN is trained with the help of the MD (a fused feature obtained by data fusing the 8 damage identification parameters by the MTGS method). The third approach is curve fitting a function of the MD and the RUL by a linear combination of the sigmoid shape function. The first approach, the ANN with DIP, performs the best. The data fusion of 8 damage identification parameters does not perform well as the ANN is trained by less amount of data in comparison with the first approach.

Acknowledgements

The financial support provided by the office of the Principal Scientific Adviser to the Government of India is gratefully acknowledged by the authors. We also acknowledge the support of Mr. K. N. Madhu and Virendra Singh at Vibration Research Laboratory, IIT Delhi and the technical inputs by Micromatic Grinding Technology Ltd., Ghaziabad, India for the experimental work.

References

[1] P. Shakya, M. S. Kulkarni, A. K. Darpe, *A novel methodology for online detection of bearing health status for naturally progressing defect*, Journal of Sound and Vibration, Vol. 333, No. 21, Elsevier (2014), pp. 5614-5629.

[2] I. Salam, A. Tauqir, A.U. Haq, A.Q. Khan, *An air crash due to fatigue failure of a ball bearing*, Eng. Fail. Anal., Vol. 5, (1998), pp. 261–269.

[3] D. L. Hall, J. Llinas, *An Introduction to multi-sensor data fusion*, Proceedings of the IEEE, Vol. 85, No. 1, 1997, pp. 6-23.

[4] P. C. Mahalanobis, *On the generalized distance in statistics*, Journal of the Asiatic Society of Bengal, Vol. 2, (1936), pp. 49-55.

[5] G. Taguchi, R. Jugulum, *The Mahalanobis Taguchi Strategy, A Pattern Technology System*, John Wiley & sons, USA (2002).

Multi-fault diagnosis based on bi-frequency cyclostationary maps clustering

P. Kruczek [1], **J. Wodecki** [2], **A. Wyłomańska** [1], **R. Zimroz** [2], **K. Gryllias** [3,4]
[1] KGHM Cuprum Ltd, R & D Centre,
Sikorskiego 2-8, 53-659 Wroclaw, Poland,
e-mail: **p.kruczek@cuprum.wroc.pl**

[2] Faculty of Geoengineering, Mining and Geology, Wrocław University of Science and Technology,
Na Grobli 15, 50-421 Wroclaw, Poland

[3] KU Leuven, Department of Mechanical Engineering,
Celestijnenlaan 300 B, B-3001, Leuven, Belgium

[4] Dynamics of Mechanical and Mechatronic Systems, Flanders Make, Belgium

Abstract
Condition monitoring of rotating machinery is a field of intensive research. One of the most powerful diagnostic tools are based on the cyclostationary properties of the signals. In this paper an advanced signal processing diagnostic tool is introduced based on Cyclic Spectral Coherence (CSC). The CSC is represented in a 3D bi-frequency map, which can be integrated on the carrier frequency leading to 2D vectors. Fault diagnosis is more challenging in the case of complex signals, which often contain many different sources of noise and more than one fault components. Therefore, a new methodology is proposed, which focuses on the separation of the information linked to different types of defects by applying tools for clustering on the CSC map. As a result, each cluster will contain the separated information of each fault. Moreover, a CSC map will be recreated based on each cluster and the integrated maps will include only one type of defect. The methodology is tested on real signals recorder on heavy duty machine located in an underground mine.

1 Introduction

Modern condition monitoring techniques are able to diagnose damages at early stage, in complex machines operating under varying speed/load conditions in presence of heavy impulsive noise [1–5]. In [6] a method for cyclic source extraction from complex vibration signals has been presented. Moreover the application of the Schur filter for local damage detection in machinery has been illustrated in [7]. However, in order to face such challenging tasks in an industrial context, researchers continuously develop and propose new advanced signal processing techniques and diagnostic procedures [8–10]. Often the methodologies are complex for use by the machinery operators and an expert is required in order to interpret the results. This is a typical obstacle for most 3-dimensional representations of signals, such as different Time-Frequency Maps, the Bi-Spectrum and the Cyclic Spectral Coherence map[11]. Obviously, the final result depends on the level of complexity of both the method and the analyzed signals. The real industrial signals are complex and usual contaminated by noise. Experts prefer to use methods which are easy to be interpreted. Therefore, there is a ever growing need for automatic damage detection methods [12]. To overcome the abovementioned limitations, an automatic procedure is proposed in this paper in order to facilitate the understanding of such 3D maps and to provide a simple picture commonly presented in textbooks. In some sense the proposed methodology can be consider as a source separation technique in the bi-frequency domain.

The Cyclic Spectral Coherence (CSC) is a 3D bi-frequency map, providing information about the modulation and the carrier frequencies, which are present in vibration signals. Moreover, characteristic fault frequencies related to the local damage can be observed in the CSC. Furthermore, these 3D maps can be integrated over the whole frequency band or on optimally selected bands leading to 2D vectors which are considered equivalent to the classical Squared Envelope Spectrum (SES). However, in case of heavy duty machines with multiple faults located at different shafts (rotating at different speeds) it might happen that the fault related patterns in a CSC map integrated to a 2D envelope spectrum are hard to be identified. On the other hand by applying a clustering technique of the map, the content related to a given fault could be separated and finally instead of one figure with multiple faults, several figures with a single fault could be obtained. In this way the analysis and the interpretation of the results might be easier.

In this paper a complete procedure is proposed in order to automatically process a 3D CSC map where two faults are present at different component (i.e. fault frequencies) and different carrier frequencies. The procedure is applied on a real signal from a two stage gearbox operating in a heavy duty drive unit used in mining applications. Based on the results, source separation in a bi-frequency domain is possible after the integration of the new map in order to calculate an Envelope Spectrum (ES) [13]. The structure of ES is much clearer and allows to easily identify the damage. The clustering algorithm used in this paper is based on the Expectation Maximization (EM) algorithm [14, 15].

The paper is organized as follows. The proposed methodology is first described in section **??**. The CSC and the EM methods are presented and the clustering of the map is explained. Moreover in section 3 the application of the method to real data is presented. The paper closes with some conclusions.

2 Methodology

The proposed procedure is a combination of three techniques, namely the CSC representation, the clustering based on the EM algorithm and the integration of the obtained new CSC maps (for each cluster separately). In fact all these techniques are well-known, however their combination is a novel approach in condition monitoring, focusing specifically on multiple fault cases and provides promising results. In this section the definitions and the main properties of the proposed methodology are briefly introduced. Furthermore, their fusion is illustrated and described.

2.1 Cyclic Spectral Coherence

The Cyclic Spectral Coherence is a function, which depends on the modulation and the carrier frequency. It has been introduced by Antoni in 2007 [16] and it has been proven as a powerful tool to indicate the cyclostationary property of signals. The Cyclic Power Spectrum (CPS) $S_X(f;\alpha)$ of a signal $\mathbf{x}$ can be estimated based on the equation:

$$S_X(f;\alpha) = \lim_{L\to\infty} \frac{1}{L}\mathbb{E}\left(\mathcal{F}_{\mathbf{x},L}(f+\frac{\alpha}{2})\overline{\mathcal{F}_{\mathbf{x},L}(f-\frac{\alpha}{2})}\right), \tag{1}$$

where $\mathcal{F}_{\mathbf{x},L}(f)$ is the Fourier transform of the signal $\mathbf{x}$ calculated on an interval of length L. CPS is used in order to measure the spectral dependency in the analyzed signal and it relies on the modulation (α) and the carrier (f) frequencies. It is expected that the CPS satisfy the equation $|S_X(f;\alpha)| > 0$ for a cyclostationary signal for some $\alpha \neq 0$. Furthermore, the definition of CSC can be formulated as: [16]:

$$CSC(f;\alpha) = |\gamma_X(f;\alpha)|^2 = \frac{|S_X(f;\alpha)|^2}{S_X(f+\frac{\alpha}{2};0)S_X(f-\frac{\alpha}{2};0)}. \tag{2}$$

The Cyclic Spectral Coherence is a normalized CPS and thus its value is bounded in the interval $(0,1)$. It is expected that the CSC describe the spectral cyclic autocorrelation of the signal. Therefore, it can be used

as a cyclostationary indicator. Once the $|\gamma_X(f;\alpha)|^2$ is significantly higher than 0, then the signal presents a cyclostationary property for a modulation frequency $T = 1/\alpha$ and a carrier frequency f.

The estimation of the CSC can be performed directly using the CPS estimator. Thus the following formula is obtained:

$$|\hat{\gamma}_X(f;\alpha)|^2 = \frac{\left|\hat{S}_X(f;\alpha)\right|^2}{\hat{S}_X(f+\frac{\alpha}{2};0)\hat{S}_X(f-\frac{\alpha}{2};0)}, \tag{3}$$

where $\hat{S}_X(f;\alpha)$ is an estimator of the CPS. It is worth mentioning that the CPS can be estimated based on different methods[17] but here the Welch method is used.

2.2 Expectation - Maximization clustering algorithm

In this section the Expectation-Maximization method, for clustering the data, is described [14, 18]. The Expectation Maximization (EM) is an iterative optimization method for the estimation of unknown parameters for given measurement data X. EM is particularly useful for separating mixtures of Gaussian distributions (or any other distribution) over the considered feature space. It consists of two main steps: the Expectation (E-step) and the Maximization (M-step), which are iterated until convergence.

Firstly, it is assumed that the following N data points are observed in a D-dimensional space

$X = \{\overrightarrow{x}_1, \overrightarrow{x}_2, \ldots \overrightarrow{x}_N\}$

Furthermore, N points are drawn from a D-dimensional Gaussian distribution. The l-th distribution is characterized by the parameters $\theta_l = \{\overrightarrow{\mu}_l, \Sigma_l\}$, where $\overrightarrow{\mu}_l$ is the D-dimensional mean and Σ_l is the covariance matrix. we assign Then a prior probability α_l is assigned to the l-th Gaussian, where $\sum_{l=1}^{N} \alpha_l = 1$.

In the first iteration, the algorithm has to be fed with some initial values of parameters Θ. This can be done by picking random means, covariances and distribution weights, but it is a good practice to pre-estimate the means $\overrightarrow{\mu}_l$ using a simpler algorithm like the k-means or the hierarchical clustering and then to compute the covariance matrices Σ_l based on the results of this pre-clustering as well as the set weights α_l in order to normalized the amount of points in each cluster.

- E-step

This step is responsible for the estimation of the probability that a data point $\overrightarrow{x}_i$ belongs to a cluster θ_l:

$$p(\theta_l|\overrightarrow{x}_i) = \alpha \frac{1}{(2\pi)^{\frac{D}{2}}|\Sigma_l|^{\frac{1}{2}}} \exp\left(-\frac{1}{2}(\overrightarrow{x}_i - \overrightarrow{\mu}_l)^T \Sigma_l^{-1}(\overrightarrow{x}_i - \overrightarrow{\mu}_l)\right). \tag{4}$$

- M-step

In this step the algorithm estimates the new parameters Θ of the probability distribution of each cluster for the next iteration. Firstly the mean for each cluster is computed by calculating the mean of all points in function of the relevance degree of each point:

$$\mu_l(t+1) = \frac{\sum_{i=1}^{N} p(\theta_l|\overrightarrow{x}_i)\overrightarrow{x}_i}{\sum_{i=1}^{N} p(\theta_l|\overrightarrow{x}_i)}. \tag{5}$$

Then the covariance matrices can be computed, based on the conditional probability of the cluster occurrence:

$$\Sigma_l(t+1) = \frac{\sum_{i=1}^{N} p(\theta_l|\overrightarrow{x}_i)(\overrightarrow{x}_i - \overrightarrow{\mu}_l(t))^T(\overrightarrow{x}_i - \overrightarrow{\mu}_l(t))}{\sum_{i=1}^{N} p(\theta_l|\overrightarrow{x}_i)}. \tag{6}$$

At the end of the M-step, the probability of occurrence of each class is computed through the mean of probabilities of each point from the cluster in function of the relevance degree:

$$\alpha_l(t+1) = \frac{1}{N}\sum_{i=1}^{N} p(\theta_l|\vec{x}_i), l = 1, \ldots, K. \tag{7}$$

It is very important to remember the limitations of the EM methodology. It only approximates the maximum likelihood estimate and do not find the theoretical value. If the likelihood function has multiple peaks (non-concavity case) EM will not necessarily find the global optimum of the likelihood. In practice, it should not been performed only once. It is very common to start EM multiple times with multiple random initial guesses and choose the one with the largest likelihood as the final estimate for Θ. In this work EM has been run 10 times.

2.3 Clustering of the map

In this section the clustering of the bi-frequency map is described. The CSC map defined in section 2 is analysed. The procedure of map clustering is shown in Fig. 1. In the first step, the CSC map is computed for

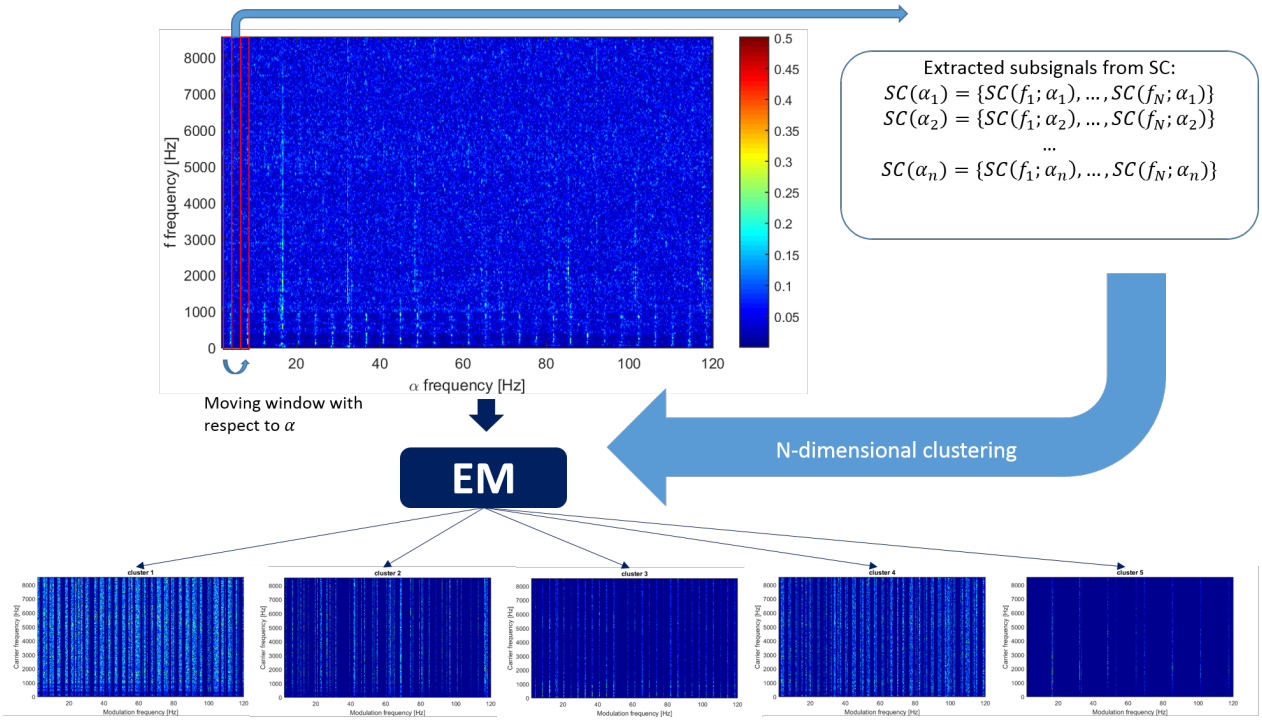


Figure 1: The schema of CSC map clustering.

the given signal. Therefore the two dimensional function of modulation and carrier frequencies is obtained having for example size $N \times n$. Then, the subsignals are extracted from the map. For example, for given i-th modulation frequency α_i the following one dimensional function $SC(\alpha_i) = \{SC(f_1; \alpha_i), \ldots, SC(f_1; \alpha_i)\}$ is considered. These N dimensional vectors are the inputs of EM. In the next step, the number of clusters should be selected. In order to determine the optimal number of clusters the Silhouette criterion can be used. Each of the subsignals is assigned to an appropriate group using the EM. Finally, the CSC can be plotted for each cluster separately. It is expected that each cluster will contain information about only one signal component.

2.4 CSC map integration

It can be observed that the CSC provides information about the excitation for given modulation and carrier frequencies. On the other hand, the total energy of a given frequency band is also interesting for diagnostic purposes. In such case, the CSC map can be integrated with respect to the carrier frequency and the given modulation frequency [13]. Therefore, the following formula for the integrated CSC in the frequency band $[f_1, f_2]$ can be introduced:

$$ISC(\alpha; f_1, f_2) = \sum_{f=f_1}^{f_2} |SC(\alpha, f)|\,, \tag{8}$$

where α is a modulation frequency bin. As a result, the one dimension function of modulation frequency is obtained. The integrated map present values which are significantly higher than zero for a cyclostationary signal and are related to the the well-known envelope spectrum.

3 Application

The proposed methodology is applied, tested and evaluated on a real data case. The processed signal has been captured using an accelerometer positioned on a belt conveyor's gearbox under operation. The gearbox consists of a bevel stage and a spur stage. The machine is located in an underground copper mine. The operational conditions are harsh and the signal is highly contaminated by external noise. The raw signal is presented in Fig. 2. Its length is equal to 10 seconds while the sampling frequency is 17066 Hz and the rotation frequency of the first shaft is equal to 16.5 Hz.

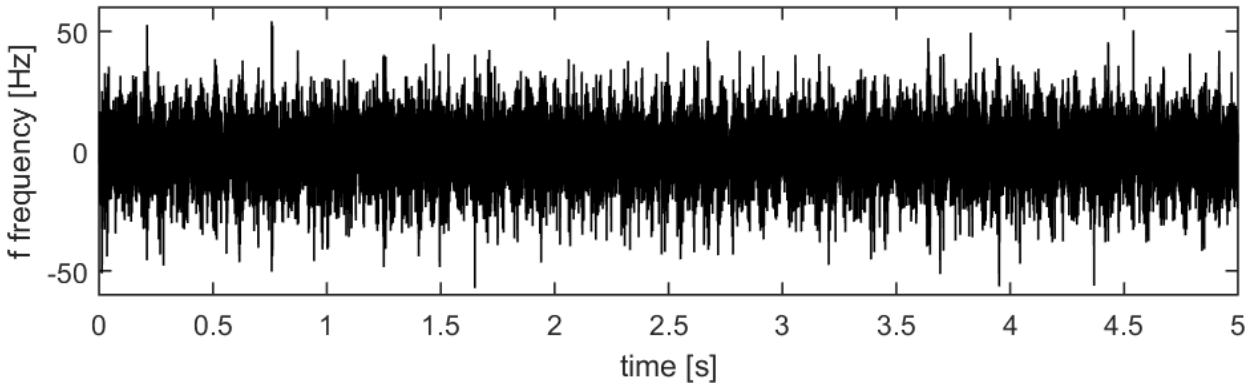


Figure 2: The raw vibration signal measured on a belt conveyor's gearbox.

The machine under monitoring contains two different local gear faults, one mounted on the first shaft and one on the second one. Their fault frequencies are equal to 16.5 Hz and 4.17 Hz respectively. Following the methodology described above, it is expected that two separate clusters, one for each fault will be created. In the first step, the Cyclic Spectral Coherence map is computed (Fig. 3). Analysing carefully the map, a cyclic excitation can be observed at low carrier frequencies with a modulation frequency equal approximately to 4.1 Hz. Furthermore a wide range excitation can be identified for modulation frequencies around 16.5 Hz and its multiples. Therefore, the SC contain the information about both local damages of the analyzed machine. In order to automatically separate the information for both damages, the SC map could be clustered using the EM method. In clustering methods, it is especially important to select a priori the appropriate number of clusters. Therefore the Silhouette criterion has been used in order to determine the cluster number which is selected equal to 5. The assigned clusters are presented in Fig. 3. Each cluster is marked with a specified color. It can be observed that each local damage has been assigned to a different cluster. The clusters

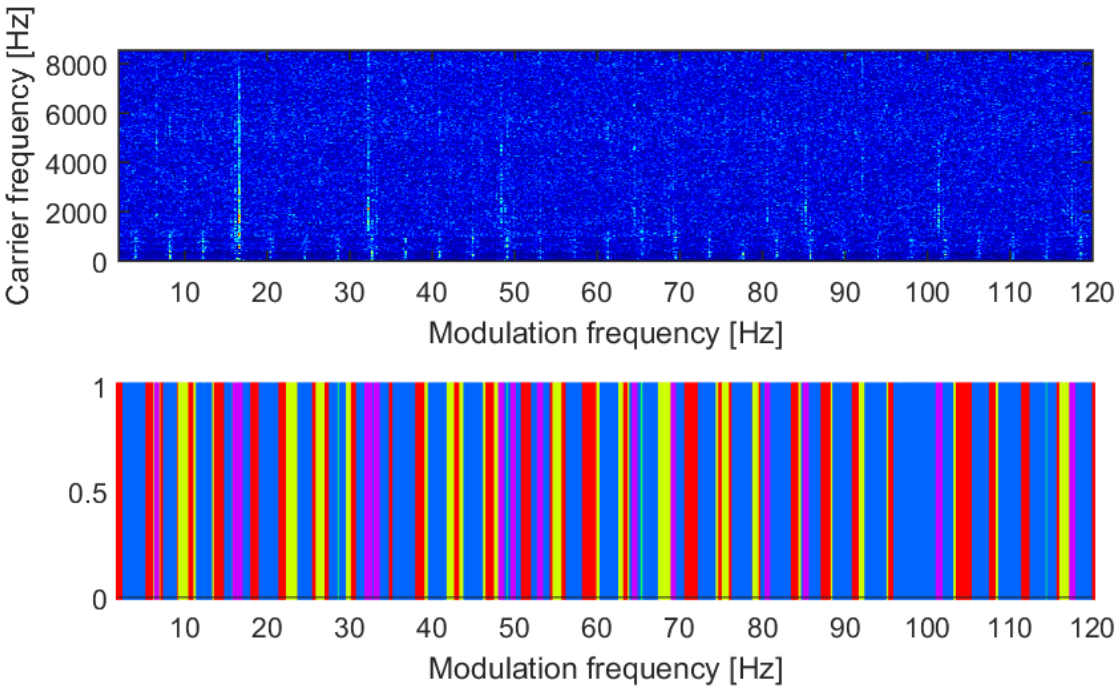


Figure 3: The Cyclic Spectral Coherence map (upper panel) and the assigned clusters from EM (bottom panel).

contain only the components related to the local faults. In further analysis, only clusters no. 3 and no. 5 are considered as they contain information about the two local damages. Moreover the SC maps are reconstructed based on the clusters and are presented separately. The map containing the information about the damage on the second shaft (4.1 Hz) is presented in Fig. 4. It can be noted that the energy of the reconstructed map is concentrated at a low carrier frequency band around to 1500 Hz. The SC map of the cluster which contains diagnostic information for the damage related to the first shaft (16.5 Hz) is presented in Fig. 5. In this case a wide band excitation can be identified. Finally the integrated maps for the clusters no 3 and no 5 are computed. In Fig. 6 the integrated SC for the cluster containing information about the damage related to the second shaft is presented. The excitation of 4.1 Hz and its multiples are clearly observed. In Fig. 7 the integrated map for the cluster no 5 is presented. In this case, the map contains information about the damage of the first shaft. The excitation of 16.5 Hz and its multiples can be clearly identified. Therefore, only the signal component related to the local damage of the gear mounted on the first shaft is present.

The presented results show that the SC map can be automatically clustered and information about several different faults can be extracted and separated.

It is worth mentioning that the usage of the appropriate number of clusters is crucial. Each of the signal components should be assigned to a different cluster. Indeed, in the analyzed signal two clusters are automatically created containing the components related to two different local damages.

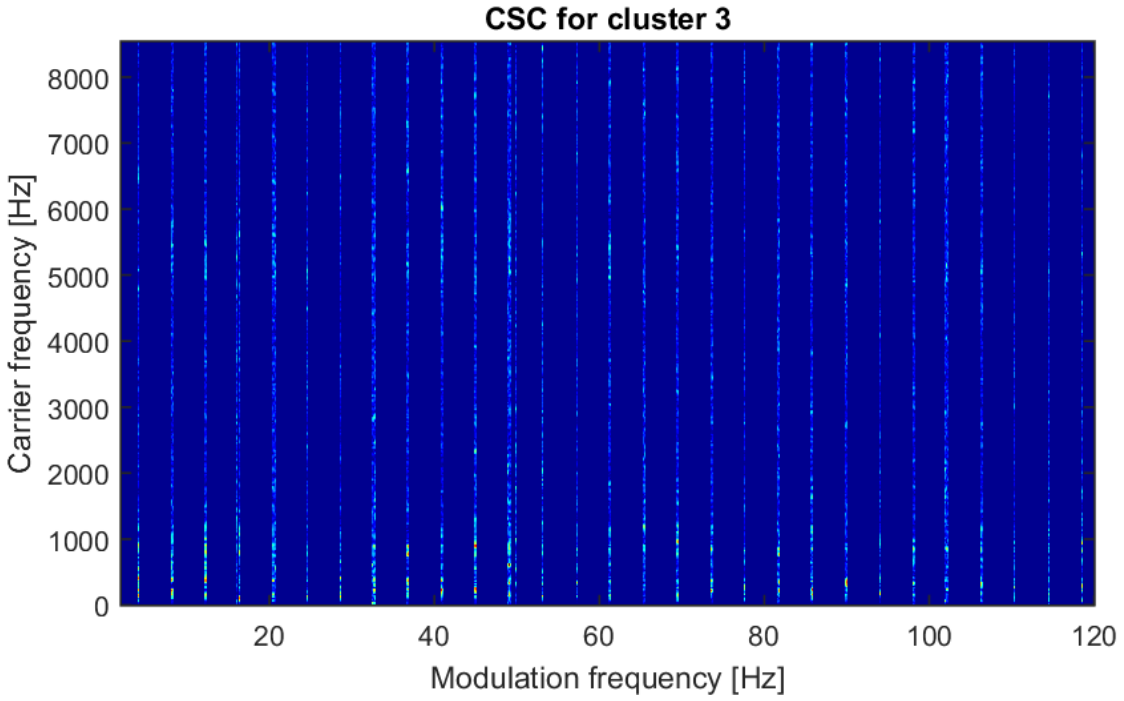


Figure 4: The Cyclic Spectral Coherence map for the cluster containing information about the damage on the second shaft.

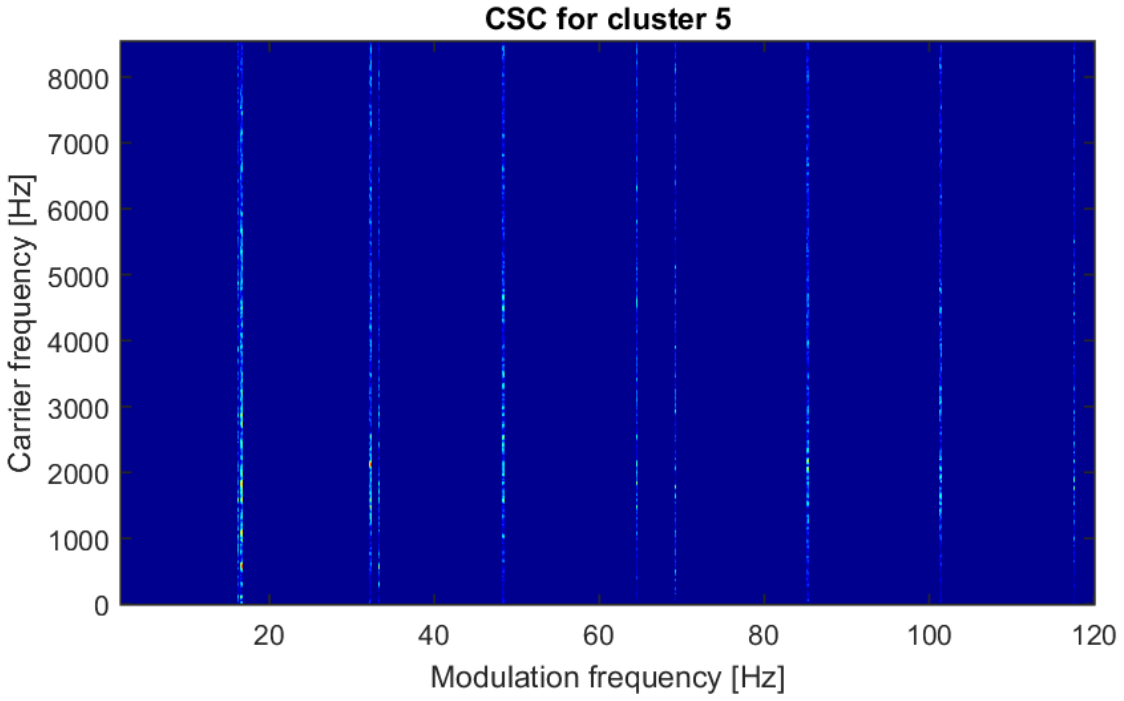


Figure 5: The Spectral Coherence map of the cluster containing information about the damage on the first shaft.

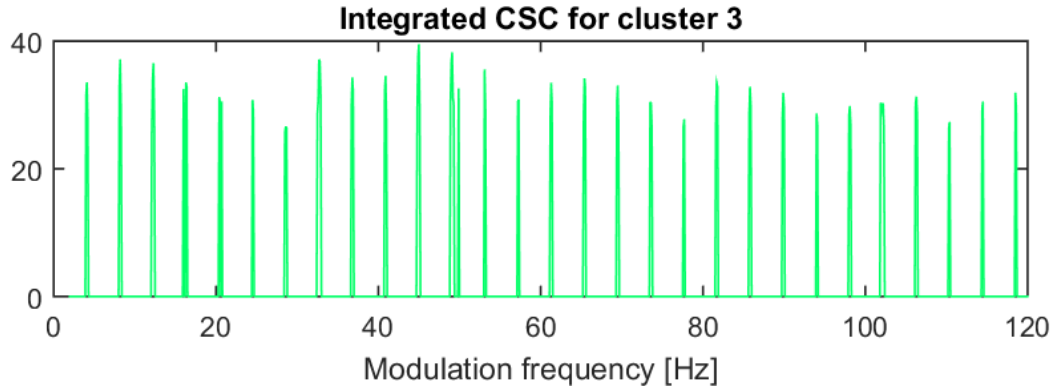


Figure 6: The Integrated Spectral Coherence map of the cluster containing information about the damage on the second shaft.

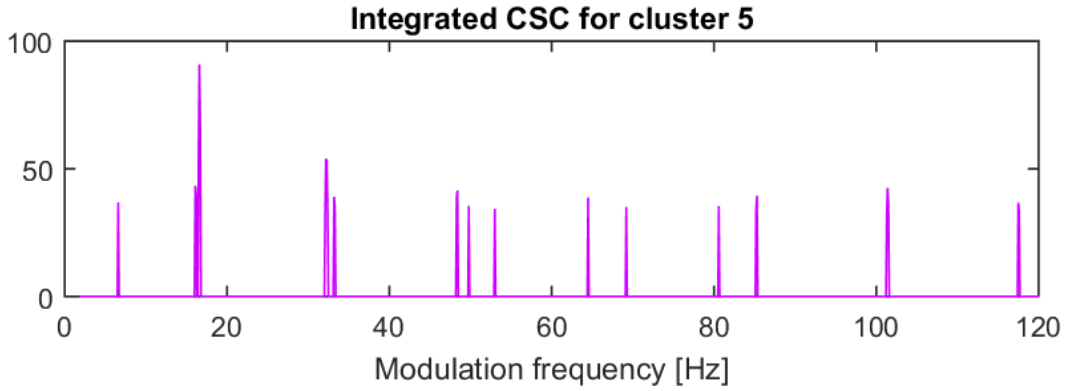


Figure 7: The Integrated Spectral Coherence map of the cluster containing information about the damage on the first shaft.

4 Conclusions

In this paper the bi-frequency cyclostationary map has been considered. The well known Cyclic Spectral Coherence has been computed in order to extract information about local damage on gears from a vibration signal. CSC has been proven as a powerful tool for condition monitoring of the rotating machinery. However, it is often analyzed only visually and in case of signals with many different cyclic components its interpretation can be challenging. Therefore in this paper an automatic method has been proposed applying a clustering approach on the CSC map. The EM method, applied on the SC, has been used in order to cluster the different subsignals. The proposed methodology was tested and evaluated on real vibration data capture on a belt conveyor operating in a harsh environment in an underground copper mine. The analyzed belt conveyor had two local gear faults (mounted on the first and the second shaft). Based on the results, it is shown that the proposed method is able to automatically assign the information about separate local damages to different clusters, facilitating the diagnostic procedure.

Acknowledgements

The work of R.Zimroz and J.Wodecki was supported by the statutory grant.

References

[1] A. Wyłomańska, G. Żak, P. Kruczek, R. Zimroz. Application of tempered stable distribution for selection of optimal frequency band in gearbox local damage detection. In Applied Acoustics, vol. 128, (2017), pp. 14–22.

[2] P. Borghesani, R. Ricci, S. Chatterton, P. Pennacchi. A new procedure for using envelope analysis for rolling element bearing diagnostics in variable operating conditions. In Mechanical Systems and Signal Processing, vol. 38, no. 1, (2013), pp. 23–35.

[3] S. Schmidt, P. S. Heyns, J. P. De Villiers. A novelty detection diagnostic methodology for gearboxes operating under fluctuating operating conditions using probabilistic techniques. In Mechanical Systems and Signal Processing, vol. 100, (2018), pp. 152–166.

[4] K. Gryllias, S. Moschini, J. Antoni. Application of Cyclo-Nonstationary Indicators for Bearing Monitoring Under Varying Operating Conditions. In Journal of Engineering for Gas Turbines and Power, vol. 140, no. 1, (2018), pp. 1–30.

[5] I. Javorskyj, I. Kravets, I. Matsko, R. Yuzefovych. Periodically correlated random processes: Application in early diagnostics of mechanical systems. In Mechanical Systems and Signal Processing, vol. 83, (2017), pp. 406–438.

[6] P. Kruczek, J. Obuchowski, A. Wylomanska, R. Zimroz. Cyclic sources extraction from complex multiple-component vibration signal via periodically time varying filter. In Applied Acoustics, vol. 126, (2017), pp. 170–181.

[7] R. Makowski, R. Zimroz. New techniques of local damage detection in machinery based on stochastic modelling using adaptive Schur filter. In Applied Acoustics, vol. 77, (2014), pp. 130–137.

[8] A. Wyłomańska, R. Zimroz, J. Janczura, J. Obuchowski. Impulsive noise cancellation method for copper ore crusher vibration signals enhancement. In IEEE Transactions on Industrial Electronics, vol. 63, no. 9, (2016), pp. 5612–5621.

[9] C. Hu, W. A. Smith, R. B. Randall, Z. Peng. Development of a gear vibration indicator and its application in gear wear monitoring. In Mechanical Systems and Signal Processing, vol. 76, (2016), pp. 319–336.

[10] A. Michalak, J. Wodecki, A. Wyłomańska, R. Zimroz. Application of cointegration to vibration signal for local damage detection in gearboxes. In Applied Acoustics. doi:10.1016/j.apacoust.2017.08.024.

[11] P. Kruczek, J. Obuchowski, A. Wylomanska, R. Zimroz. Multiple local damage detection in gearbox by novel coherent bi-frequency map and its spatial, cycle oriented enhancement. In Applied Acoustics. doi:10.1016/j.apacoust.2017.10.006.

[12] J. Wodecki, A. Michalak, R. Zimroz. Optimal filter design with progressive genetic algorithm for local damage detection in rolling bearings. In Mechanical Systems and Signal Processing, vol. 102, (2018), pp. 102–116.

[13] R. B. Randall, J. Antoni, S. Chobsaard. The relationship between spectral correlation and envelope analysis in the diagnostics of bearing faults and other cyclostationary machine signals. In Mechanical systems and signal processing, vol. 15, no. 5, (2001), pp. 945–962.

[14] A. P. Dempster, N. M. Laird, D. B. Rubin. Maximum likelihood from incomplete data via the EM algorithm. In Journal of the royal statistical society Series B (methodological), vol. 39, no. 1, (1977), pp. 1–38.

[15] L. Kaufman, P. J. Rousseeuw. Finding groups in data: an introduction to cluster analysis, vol. 344. John Wiley & Sons (2009).

[16] J. Antoni. Cyclic spectral analysis of rolling-element bearing signals: facts and fictions. In Journal of Sound and vibration, vol. 304, no. 3, (2007), pp. 497–529.

[17] J. Antoni. Cyclic spectral analysis in practice. In Mechanical Systems and Signal Processing, vol. 21, no. 2, (2007), pp. 597–630.

[18] R. Sundberg. Maximum likelihood theory for incomplete data from an exponential family. In Scandinavian Journal of Statistics, vol. 1, no. 2, (1974), pp. 49–58.

Stabilised Layer Method for linear and nonlinear spatial non classical damping identification

D. Lisitano[1], E. Bonisoli[2] and **J.E. Mottershead[3]**
[1] Politecnico di Torino, Department of Management and Production Engineering
Corso Duca degli Abruzzi 24, 10129, Torino, Italy
e-mail: **domenico.lisitano@polito.it**

[2] Politecnico di Torino, Department of Mechanical and Aerospace Engineering
Corso Duca degli Abruzzi 24, 10129, Torino, Italy

[3] University of Liverpool, School of Engineering
L69 3GH, Liverpool, United Kingdom

Abstract
In the Layer Method the damping matrix is written as a sum of several layers characterised by a semi-definite positive elementary matrix. Each layer is modulated by an unknown damping coefficient and finally expanded to the system total dimensions, using a localisation matrix based on the system topology. The linear and nonlinear spatial damping distribution most close to the real dissipations can be identified directly from experimental FRFs combining the Stabilised Layer Method approach with the inverse receptance method. In this paper the Stabilised Layer Method is experimentally applied to a simple non-classically viscous damping system and to a quite complex industrial example as a body in white chassis. Finally a nonlinear system with a localised magnetic eddy-current damping is numerically investigated. The nonlinear damping coefficients are identified from numerical nonlinear frequency response functions with additional random noise.

Keywords: experimental identification, non proportional damping, describing function approximation, air dashpot, magnetic damping.

1 Introduction

Damping identification, localisation and quantification in mechanical system is still a challenging topic. A lot of different methods are available in literature [1, 2], among all the inverse receptance method [3, 4] seems to be the most performing for non-classical viscous damping matrix identification. This approach is one of the most promising methods for spatial damping identification directly from experimental frequency domain responses of the system. The application of the inverse receptance method for damping matrix identification implies a least square problem inversion and usually leads to unphysical results such as dampers acting between nodes not physically linked or locally unstable dampers. This problem can be solved by combining the above least square approach with the Stabilised Layer Method (SLM), presented in [5, 6]. SLM lets to impose topological constraints, known the system geometry, and stability constraint, when the system is known to be stable (as usual in passive systems). The inversion problem is therefore transformed in an optimisation problem to find out the vector of the unknowns damping coefficients, guaranteeing all the constraints. Possible applications of SLM for nonlinear damping identification are investigated. Nonlinear damping can be modeled with equivalent linear viscous damping [7], but the equivalent linear damping should be identified for each level of oscillation. Damping identification method is extended to nonlinear damping identification for system with a localised damping nonlinearity. The nonlinearity is replaced with its amplitude dependent describing function approximation [8]. All the coefficients of the nonlinear damping equation in frequency domain are identified by SLM using the

modal responses of the system at few different levels of constant displacements across the system nonlinearity.

The robustness of the identified spatial damping distribution is checked through a stability diagram, introduced by the authors in [6], involving location and amount of spectral lines used in the identification process, to increase the robustness and correctness of the identification.

The paper is organized as follow: in § 2 the inverse receptance method for damping matrices identification is presented in the general case of non-proportional damping: viscous, hysteretic and localised nonlinear damping. In § 3 the Stabilised Layer Method is explained and combined to the inverse receptance method for spatial damping identification. In § 4 the SLM is applied for the experimental identification of the non-proportional viscous damping matrix of a simple test rig and in § 5 for the experimental identification of viscous and hysteretic damping in a body in white car chassis. In § 6 a numerical example of a nonlinear damped system is identified using the proposed method. Finally some conclusions are provided.

2 Inverse receptance method for general damping identification

The general equation of motion of multi degrees of freedom mechanical system with nonlinear amplitude dependent damping can be written as in Eq. (1):

$$\mathbf{M}\,\ddot{\mathbf{x}} + \mathbf{C}\,\dot{\mathbf{x}} + \left(\mathbf{K} + \mathrm{i}\mathbf{D}\right)\mathbf{x} + \mathbf{f}_{\mathbf{C,nl}}\left(\mathbf{x},\dot{\mathbf{x}}\right) = \mathbf{f}\left(t\right) \tag{1}$$

where $\mathbf{M}$, $\mathbf{C}$, $\mathbf{K}$ and $\mathbf{D}$ are respectively the mass, non-proportional viscous damping, stiffness and non-proportional hysteretic damping matrices, $\mathbf{f}_{\mathbf{C,nl}}\left(\mathbf{x},\dot{\mathbf{x}}\right)$ is the amplitude dependent nonlinear damping force, $\mathbf{f}\left(t\right)$ is the vector of the external forces and $\ddot{\mathbf{x}}$, $\dot{\mathbf{x}}$, $\mathbf{x}$ are respectively the acceleration, velocity and displacement vectors.

When the nonlinear force is localised on the structure, it acts on a single d^{th} DoF (absolute) or between two d^{th} and e^{th} DoFs (relative), Eq. (1) can be simplified in:

$$\mathbf{M}\,\ddot{\mathbf{x}} + \mathbf{C}\,\dot{\mathbf{x}} + \left(\mathbf{K} + \mathrm{i}\mathbf{D}\right)\,\mathbf{x} + \mathbf{g}f_{C,nl} = \mathbf{f}\left(t\right) \tag{2}$$

where $\mathbf{g}$ is a column null vector with a unitary entry in the d^{th} row in the case of absolute nonlinearity and also a negative unitary entry in the e^{th} row in the case of relative nonlinearity.

Eq. (2) can be written in frequency domain as:

$$\left[-\omega^2\mathbf{M} + \mathrm{i}\omega\mathbf{C} + \mathbf{K} + \mathrm{i}\mathbf{D} + F_{C,nl}\left(A,\omega\right)\mathbf{g}\mathbf{g}^{\mathrm{T}}\right]\mathbf{x}\left(\omega\right) = \mathbf{F}\left(\omega\right) \tag{3}$$

where $F_{C,nl}\left(A,\omega\right)$ is the constant amplitude describing function approximation of the nonlinear damping force. The location of only the nonlinear damping force has to be known. Since the nonlinear damping force $\mathbf{f}_{\mathbf{C,nl}}\left(\mathbf{x},\dot{\mathbf{x}}\right)$ is a pure dissipative force, its describing function $F_{C,nl}\left(A,\omega\right)$ results in the form:

$$F_{C,nl}\left(A,\omega\right) = \mathrm{i}\omega\left(c_0 + z_1 A c_1 + z_2 A^2 c_2 + \cdots + z_t A^t c_t\right) \tag{4}$$

where z_i are gain coefficients resulting from the describing function approximation, c_i are the unknown coefficients of the nonlinear damping force to be identified and t is the order of the nonlinear damping force. Both z_i and t depend on the type of nonlinear damping.

The nonlinear dynamic stiffness matrix of the system at constant amplitude across the nonlinearity can be written as:

$$\left[\mathbf{H}_{\mathbf{nl}}^{C}\left(A,\omega\right)\right]^{-1} = \left(\mathbf{K} - \omega^2\mathbf{M}\right) + \mathrm{i}\omega\left[\mathbf{C} + \frac{\mathbf{D}}{\omega} + \left(c_0 + z_1 A c_1 + \cdots z_t A^t c_t\right)\mathbf{g}\mathbf{g}^{\mathrm{T}}\right] \tag{5}$$

and its imaginary part contains all the dissipation terms:

$$\Im\left(\left[\mathbf{H}_{\mathbf{nl}}^{C}\left(A,\omega\right)\right]^{-1}\right)=\omega\left[\mathbf{C}+\frac{\mathbf{D}}{\omega}+\left(c_0+z_1Ac_1+\cdots z_tA^tc_t\right)\mathbf{g}\mathbf{g}^{\mathrm{T}}\right]. \tag{6}$$

Eq. (3) can also be written as:

$$\left[\mathbf{H}^{N}\left(\omega\right)\right]^{-1}\mathbf{x}\left(\omega\right)+\left[\mathrm{i}\omega\mathbf{C}+\mathrm{i}\mathbf{D}+F_{C,nl}\left(A,\omega\right)\mathbf{g}\mathbf{g}^{\mathrm{T}}\right]\mathbf{x}\left(\omega\right)=\mathbf{F}\left(\omega\right) \tag{7}$$

where $\mathbf{H}^{N}\left(\omega\right)$ is the real normal receptance matrix of the underlying undamped and linear system.

Premultiplying Eq. (7) by $\mathbf{H}^{N}\left(\omega\right)$ yields:

$$\mathbf{X}(\omega)=\left[\mathbf{I}+\mathrm{i}\,\mathbf{G}(\omega)\right]^{-1}\mathbf{H}^{N}(\omega)\mathbf{f}(\omega) \tag{8}$$

where $\mathbf{G}\left(\omega\right)$ is the real transformation matrix

$$\mathbf{G}\left(A,\omega\right)=\left[\mathbf{H}^{N}\left(\omega\right)\right]\left[\omega\mathbf{C}+\mathbf{D}+\omega\left(c_0+z_1Ac_1+\cdots z_tA^tc_t\right)\mathbf{g}\mathbf{g}^{\mathrm{T}}\right]. \tag{9}$$

Comparing Eq. (3) and Eq. (7), the relationship between complex $\mathbf{H}_{\mathbf{nl}}^{C}$ and normal receptance $\mathbf{H}^{N}\left(\omega\right)$ matrices is given by:

$$\mathbf{H}^{N}\left(\omega\right)=\left[\mathbf{I}+\mathrm{i}\,\mathbf{G}\left(A,\omega\right)\right]\mathbf{H}_{\mathbf{nl}}^{C}\left(A,\omega\right). \tag{10}$$

Since $\mathbf{G}\left(\omega\right)$ has to eliminate the imaginary part in Eq. (10), it results:

$$\mathbf{G}\left(A,\omega\right)=-\mathbf{H}_{\mathbf{nl},I}^{C}\left(A,\omega\right)\left[\mathbf{H}_{\mathbf{nl},R}^{C}\left(A,\omega\right)\right]^{-1} \tag{11}$$

where $\mathbf{H}_{\mathbf{nl},R}^{C}=\Re\left(\mathbf{H}_{\mathbf{nl}}^{C}\right)$ and $\mathbf{H}_{\mathbf{nl},I}^{C}=\Im\left(\mathbf{H}_{\mathbf{nl}}^{C}\right)$.

Finally $\mathbf{H}^{N}\left(\omega\right)$ can be obtained as:

$$\mathbf{H}^{N}\left(A,\omega\right)=\mathbf{H}_{\mathbf{nl},R}^{C}\left(A,\omega\right)+\mathbf{H}_{\mathbf{nl},\mathrm{I}}^{C}\left(A,\omega\right)\left[\mathbf{H}_{\mathbf{nl},R}^{C}\left(A,\omega\right)\right]^{-1}\mathbf{H}_{\mathbf{nl},\mathrm{I}}^{C}\left(A,\omega\right). \tag{12}$$

The normal receptance $\mathbf{H}^{N}\left(A,\omega\right)$ is also amplitude dependent, because it represents the equivalent linear and undamped system for each level of oscillation. All the damping coefficients can be estimate from Eq. (9) directly from experimental FRFs obtained at constant amplitude across nonlinearity:

$$\begin{bmatrix}\omega_1\mathbf{H}^{N}\left(A,\omega_1\right) & \mathbf{H}^{N}\left(A,\omega_1\right) & \omega_1z_1A\mathbf{H}^{N}\left(A,\omega_1\right) & \cdots & \omega_1z_tA^t\mathbf{H}^{N}\left(A,\omega_1\right)\\ \omega_2\mathbf{H}^{N}\left(A,\omega_2\right) & \mathbf{H}^{N}\left(A,\omega_2\right) & \omega_2z_1A\mathbf{H}^{N}\left(A,\omega_2\right) & & \omega_2z_tA^t\mathbf{H}^{N}\left(A,\omega_2\right)\\ \vdots & \vdots & & & \vdots\\ \omega_K\mathbf{H}^{N}\left(A,\omega_K\right) & \mathbf{H}^{N}\left(A,\omega_K\right) & \omega_Kz_1A\mathbf{H}^{N}\left(A,\omega_k\right) & \cdots & \omega_Kz_tA^t\mathbf{H}^{N}\left(A,\omega_K\right)\end{bmatrix}\begin{bmatrix}\mathbf{C}_{lin}\\ \mathbf{D}\\ c_1\mathbf{g}\mathbf{g}^{\mathrm{T}}\\ \vdots\\ c_t\mathbf{g}\mathbf{g}^{\mathrm{T}}\end{bmatrix}=\begin{bmatrix}\mathbf{G}\left(A,\omega_1\right)\\ \mathbf{G}\left(A,\omega_2\right)\\ \vdots\\ \mathbf{G}\left(A,\omega_K\right)\end{bmatrix} \tag{13}$$

where ω_i $1<i<K$ are selected spectral lines of the receptance matrix and $\mathbf{C}_{lin}=\mathbf{C}+c_0\mathbf{g}\mathbf{g}^{\mathrm{T}}$ is the total viscous damping matrix. The zero order coefficient of the nonlinear dissipative describing function and the linear viscous coefficient acting in parallel to nonlinear dampers cannot be identified separately, but only the sum of the two coefficients together can be identified. Eq. (13) has ∞^{t+1} solutions; to avoid the undetermination problem, the unknowns can be identified combining $t+1$ like-Eq. (13) systems, differing for the constant amplitude A values. Calling $\mathbf{A}$ the matrix on the l.h.s. in Eq. (13) and $\mathbf{B}$ the known terms matrix in Eq. (13), the final problem can be written as:

$$\mathbf{V}\begin{bmatrix}\mathbf{C}_{lin}\\ \mathbf{D}\\ c_1\mathbf{g}\mathbf{g}^{\mathrm{T}}\\ \vdots\\ c_t\mathbf{g}\mathbf{g}^{\mathrm{T}}\end{bmatrix}=\mathbf{Q},\ \mathbf{V}=\begin{bmatrix}\mathbf{A}_1\\ \vdots\\ \mathbf{A}_t\end{bmatrix},\ \mathbf{Q}=\begin{bmatrix}\mathbf{B}_1\\ \vdots\\ \mathbf{B}_t\end{bmatrix} \tag{14}$$

where $\mathbf{A}_i, \mathbf{B}_i$ with $1 < i < t+1$ are the matrix $\mathbf{A}$ and $\mathbf{B}$ when constant amplitude A assumes the i^{th} value.

3 Stabilised Layer Method

In the Stabilised Layer Method the damping matrices of a system are written as the sum of a finite number of element damping matrices $\mathbf{C}_j$ and $\mathbf{D}_j$, called "layers":

$$\mathbf{C}_{lin} = \sum_{j=1}^{NL} \mathbf{C}_j \,,\ \mathbf{D} = \sum_{j=1}^{NL} \mathbf{D}_j \tag{15}$$

where j^{th} is a generic layer and NL is the number of layers.

Each layer represents an elementary matrix expanded to the total system size,

$$\mathbf{C}_j = c_j \mathbf{T}_j^T \mathbf{C}_{el,j} \mathbf{T}_j \,,\ \mathbf{D}_j = d_j \mathbf{T}_j^T \mathbf{D}_{el,j} \mathbf{T}_j \tag{16}$$

where $c_j, d_j \geq 0$, $\mathbf{T}_j$, $\mathbf{C}_{el,j}$ and $\mathbf{D}_{el,j}$ are respectively the damping coefficient value, the localisation matrix and the elementary matrices of the j^{th} viscous or hysteretic damping element.

The elementary damping matrices can represent relative damping elements ($\mathbf{C}_{el}^R$, $\mathbf{D}_{el}^R$) or absolute damping elements (C_{el}^A, D_{el}^A):

$$\mathbf{C}_{el}^R = \mathbf{D}_{el}^R = \begin{bmatrix} +1 & -1 \\ -1 & +1 \end{bmatrix}, \quad C_{el}^A = D_{el}^A = 1 \,. \tag{17}$$

The elementary matrices are locally stable and symmetric; therefore also the global identified damping matrix will be globally stable and symmetric.

The localisation matrices $\mathbf{T}$ for an absolute and relative damper are defined as,

$$\mathbf{T}_j^A = \mathbf{0}_{(n\times 1)} \text{ and } \mathbf{T}_j^A\left(dof_m, 1\right) = 1 \,,\ \mathbf{T}_j^R = \mathbf{0}_{(n\times 2)} \text{ and } \begin{matrix} \mathbf{T}_j^R\left(dof_m, 1\right) = 1 \\ \mathbf{T}_j^R\left(dof_n, 2\right) = 1 \end{matrix} \tag{18}$$

where dof_m and dof_n are the DoF index in which the damper acts. Only layers involving physically linked DoFs should be used in the identification choosing coherently the localisation matrices, because dissipations can occurs only between physically linked DoFs.

Distinguishing the effects of absolute and relative dampers, the non-proportional viscous and hysteretic damping matrices may be written from Eq. (16) as

$$\begin{aligned} \mathbf{C}_{lin} &= \sum_{j=1}^{NL} \mathbf{C}_j = \sum_{p=1}^{NA} \sum_{t=1}^{N_p} c_p \mathbf{T}_{p,t}^{A\ T} C_{el}^A \mathbf{T}_{p,t}^A + \sum_{q=1}^{NR} \sum_{u=1}^{N_q} c_q \mathbf{T}_{q,u}^{R\ T} \mathbf{C}_{el}^R \mathbf{T}_{q,u}^R \\ \mathbf{D} &= \sum_{j=1}^{NL} \mathbf{D}_j = \sum_{p=1}^{NA} \sum_{t=1}^{N_p} d_p \mathbf{T}_{p,t}^{A\ T} D_{el}^A \mathbf{T}_{p,t}^A + \sum_{q=1}^{NR} \sum_{u=1}^{N_q} d_q \mathbf{T}_{q,u}^{R\ T} \mathbf{D}_{el}^R \mathbf{T}_{q,u}^R \end{aligned} \tag{19}$$

where NA and NR are respectively the number of absolute and relative damping coefficients, N_p and N_q are respectively the number of elementary absolute and relative dampers associated with damping coefficients c_p and c_q, when it is know that more elements have the same damping coefficient.

The nonlinear terms can be written as:

$$\mathbf{C}_f = c_f \mathbf{g}\mathbf{g}^{\mathrm{T}} \text{ with } 1 \leq f \leq t \,. \tag{20}$$

The vector of the unknown damping coefficients is defined as:

$$\overline{\mathbf{c}} = \left\{ \mathbf{c}_A^T \quad \mathbf{c}_R^T \quad \mathbf{d}_A^T \quad \mathbf{d}_R^T \quad c_1 \quad c_2 \quad \cdots \quad c_t \right\}^T \tag{21}$$

where $\mathbf{c}_A$, $\mathbf{c}_R$, $\mathbf{d}_A$ and $\mathbf{d}_R$ are four column vectors containing respectively the absolute and relative viscous and hysteretic damper coefficients. Eqs. (19-20) become,

$$\begin{aligned} \mathbf{C}_{lin} &= \sum_{j=1}^{NL} \mathbf{C}_j = \sum_{p=1}^{NA} \overline{c}_p \sum_{t=1}^{N_p} \mathbf{T}_{p,t}^{A\ T} C_{el}^A \mathbf{T}_{p,t}^A + \sum_{q=1+NA}^{NA+NR} \overline{c}_q \sum_{u=1}^{N_q} \mathbf{T}_{q,u}^{R\ T} \mathbf{C}_{el}^R \mathbf{T}_{q,u}^R \\ \mathbf{D} &= \sum_{j=1}^{NL} \mathbf{D}_j = \sum_{p=1+NA+NR}^{2NA+NR} \overline{c}_p \sum_{t=1}^{N_p} \mathbf{T}_{p,t}^{A\ T} D_{el}^A \mathbf{T}_{p,t}^A + \sum_{q=2NA+NR}^{2(NA+NR)} \overline{c}_q \sum_{u=1}^{N_q} \mathbf{T}_{q,u}^{R\ T} \mathbf{D}_{el}^R \mathbf{T}_{q,u}^R \end{aligned} \tag{22}$$

$$\mathbf{C}_f = \overline{c}_{2(NA+NR)+f} \mathbf{g}\mathbf{g}^{\mathrm{T}} C_{el}^A \text{ with } 1 \le f \le t\,. \tag{23}$$

Defining the absolute $\mathbf{P}_p^A$ and relative $\mathbf{P}_q^R$ patterns:

$$\mathbf{P}_p^A = \sum_{t=1}^{N_p} \mathbf{T}_{p,t}^{A\ T} C_{el}^A \mathbf{T}_{p,t}^A\,, \quad \mathbf{P}_q^R = \sum_{u=1}^{N_q} \mathbf{T}_{q,u}^{R\ T} \mathbf{C}_{el}^R \mathbf{T}_{q,u}^R \tag{24}$$

and the pattern of the nonlinear term as

$$\mathbf{P}_{nl} = \mathbf{g}\mathbf{g}^{\mathrm{T}} \tag{25}$$

then Eq. (8) may be re-arranged in the form:

$$\begin{aligned} \mathbf{C}_{lin} &= \left[\mathbf{P}_1^A \quad \cdots \quad \mathbf{P}_p^A \quad \cdots \quad \mathbf{P}_{NA}^A \quad \mathbf{P}_1^R \quad \cdots \quad \mathbf{P}_q^R \quad \cdots \quad \mathbf{P}_{NR}^R \right] \begin{bmatrix} \overline{c}_1 \mathbf{I} \\ \vdots \\ \overline{c}_{NA} \mathbf{I} \\ \overline{c}_{NA+1} \mathbf{I} \\ \\ \overline{c}_{NA+NR} \mathbf{I} \end{bmatrix} \\ \mathbf{D} &= \left[\mathbf{P}_1^A \quad \cdots \quad \mathbf{P}_p^A \quad \cdots \quad \mathbf{P}_{NA}^A \quad \mathbf{P}_1^R \quad \cdots \quad \mathbf{P}_q^R \quad \cdots \quad \mathbf{P}_{NR}^R \right] \begin{bmatrix} \overline{c}_{NA+NR+1} \mathbf{I} \\ \vdots \\ \overline{c}_{2NA+NR} \mathbf{I} \\ \overline{c}_{2NA+NR+1} \mathbf{I} \\ \\ \overline{c}_{2(NA+NR)} \mathbf{I} \end{bmatrix} \end{aligned} \tag{26}$$

$$\mathbf{C}_f = \mathbf{P}_{nl} \overline{c}_{2(NA+NR)+f} \text{ with } 1 \le f \le t \tag{27}$$

or more compactly as

$$\begin{aligned} \mathbf{C}_{lin} &= \overline{\mathbf{P}} \left[\overline{c}_1 \mathbf{I} \quad \cdots \quad \overline{c}_{NA} \mathbf{I} \quad \overline{c}_{NA+1} \mathbf{I} \quad \cdots \quad \overline{c}_{NA+NR} \mathbf{I} \right]^T \\ \mathbf{D} &= \overline{\mathbf{P}} \left[\overline{c}_{1+NA+NR} \mathbf{I} \quad \cdots \quad \overline{c}_{2NA+NR} \mathbf{I} \quad \overline{c}_{2NA+NR1} \mathbf{I} \quad \cdots \quad \overline{c}_{2(NA+NR)} \mathbf{I} \right]^T \end{aligned} \tag{28}$$

with the obvious definition of matrix $\overline{\mathbf{P}}$.

The stability of the elementary matrix are given from the condition $\overline{c}_j \ge 0$, the topological coherence of the damping matrix is ensured using layers involving only physically linked DoFs. The symmetry of the resulting damping matrix is guaranteed by the symmetry of the elementary matrices.

Substituting Eq. (28) in Eq. (14) and using matrices properties, it results:

$$\overline{\overline{\mathbf{Vc}}} = \overline{\overline{\mathbf{Q}}}, \overline{\overline{\mathbf{V}}} = \begin{bmatrix} \mathbf{V}\overline{\overline{\mathbf{P}}}\mathbf{Z}_1 \\ \mathbf{V}\overline{\overline{\mathbf{P}}}\mathbf{Z}_2 \\ \vdots \\ \mathbf{V}\overline{\overline{\mathbf{P}}}\mathbf{Z}_n \end{bmatrix}, \overline{\overline{\mathbf{Q}}} = \begin{bmatrix} \mathbf{QW}_1 \\ \mathbf{QW}_2 \\ \vdots \\ \mathbf{QW}_n \end{bmatrix} \tag{29}$$

where

$$\overline{\overline{\mathbf{P}}} = \mathrm{diag}\left[\overline{\mathbf{P}} \quad \overline{\mathbf{P}} \underbrace{\mathbf{P}_{nl}^A \quad \cdots \quad \mathbf{P}_{nl}^A}_{t} \right] \tag{30}$$

$$\mathbf{Z}_i = \mathbf{0}, \ \mathbf{Z}_i\left((T-1)n+i,t\right) = 1 \ \text{ with } 1 < T < 2\left(NA+NR\right)+t \tag{31}$$

$$\mathbf{W}_i = \mathbf{0}, \ \mathbf{W}_i\left(i,1\right) = 1 \tag{32}$$

The system can now be solved with a least square approach, guaranteeing the positive value of $c_i \geq 0$:

$$\min_{\bar{\mathbf{c}}}\left(\left|\overline{\overline{\mathbf{Vc}}} - \overline{\overline{\mathbf{V}}}\right|\right), \text{ with } \bar{\mathbf{c}} \geq 0 \tag{33}$$

The identification is performed several times changing the number K of spectral lines used in Eq. (13) and the range r in which the spectral lines are equally spaced around each natural frequency. A robust identification should give the same results also changing slightly the number of used spectral lines: when this happens, the identification is defined to be stable.

The stabilisation diagram can be developed for each element of the unknown vector, changing both the number of spectral lines K and amplitude of the range r around the system natural frequency where K spectral lines are spread:

$$\mathbf{S}_f\left(k,r\right) = 1 \quad \text{when} \ \frac{\left|c_{k,r} - c_{k+j,r+i}\right|}{c_{k,r}} < \varepsilon \quad \forall -1 < i,j < 1 \cap \left(i,j\right) \neq \left(0,0\right) \tag{34}$$

where $\mathbf{S}_i$ is a logical matrix related to the identified coefficient c_f with $1 < f < 2\left(NA+NR\right)+t$.

The identification is globally stable in the regions where the identification of all the coefficients is locally stable:

$$\bar{\mathbf{S}} = \bigcap_{f=1}^{2(NA+NR)+f} \mathbf{S} \tag{35}$$

Usually a region of stable solution is identified; the identification result is the one with lower inversion error $E_{\%}$ among all the stable points:

$$E_{\%} = 100\sqrt{\frac{\sum_i \left(\overline{\overline{\mathbf{Vc}}} - \overline{\overline{\mathbf{Q}}}\right)_i^2}{\sum_i \overline{\overline{\mathbf{Q}}}_i^2}} \tag{36}$$

4 Lumped system viscous damping experimental identification

A lumped 3 DoFs viscous damped system shown in Fig. 1 is identified using the SLM. Two air dashpots damp the system vibrations: D_{12} is a relative damper between the first and the second DoFs, while D_3 is an absolute damper acting on the third DoF. The reference viscous damping coefficients are: $c_{12} = 11.41$ Ns/m and $c_3 = 13.39$ Ns/m .

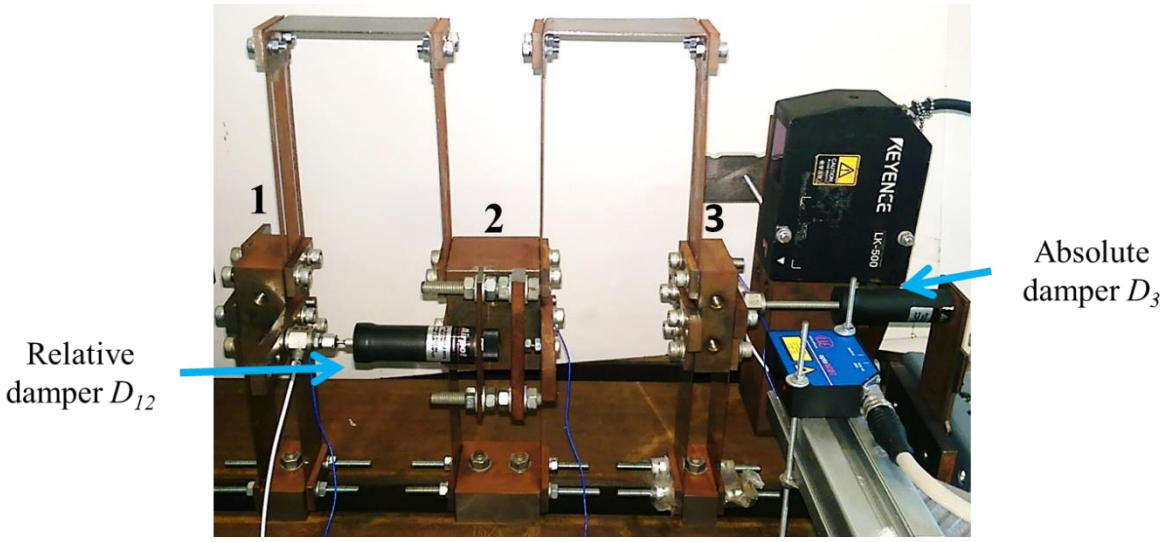


Figure 1: Non-proportional viscous damping system

The non-proportional viscous damping matrix of the system is a 3 by 3 matrix. It was identified using the SLM opportunely simplified to identify only the viscous damping matrix coefficients, therefore simplifying Eq. (14). The system is supposed linear, hence there is no necessity to control the oscillation amplitude and only viscous damping coefficients are identified. The simplified formulation becomes:

$$\mathbf{VC} = \mathbf{Q}\,,\ \mathbf{V} = \begin{bmatrix} \omega_1 \mathbf{H}^N(\omega_1) \\ \vdots \\ \omega_K \mathbf{H}^N(\omega_K) \end{bmatrix},\ \mathbf{Q} = \begin{bmatrix} \mathbf{G}(\omega_1) \\ \vdots \\ \mathbf{G}(\omega_k) \end{bmatrix} \tag{37}$$

and the unknown vector:

$$\overline{\mathbf{c}} = \left\{ \mathbf{c}_A^T \quad \mathbf{c}_R^T \right\}^T \tag{38}$$

Eq. (33) is used to identify the viscous damping matrix.

Five physical dampers must be identified: three absolute dampers acting on each mass, called c_1, c_2, c_3, and two relative dampers acting between two consecutive DoFs, called c_{12}, c_{23}. Thera are no directly links between the 1st and the 3rd DoFs, therefore the relative damper cannot be one of the damping matrix layers. The resulting identified viscous damping matrix is shown in Fig. 2 and the viscous damping coefficients values are listed in Table 1. The viscous damping coefficients identified for the dampers D_3 and D_{12} are really close to the reference values, while as expected all the other viscous coefficients are close to zero. The viscous damping matrix is the identified result with the lowest inversion error (blue cross of Fig. 3 left), corresponding to a point in the stable region, shown in Fig. 3 right. The global stabilisation, Fig. 3 right, presents a stable green region, and the relative inversion error, Fig. 3 left, is quite low in the same region. More details on this example can be found in [6].

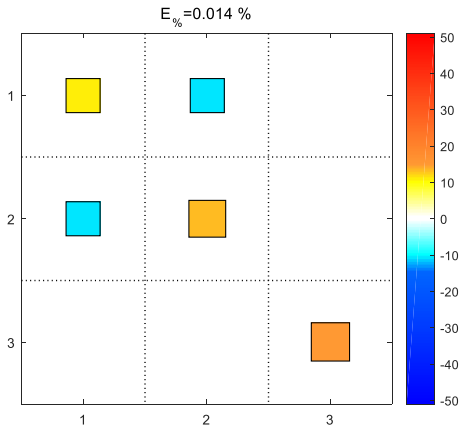


Figure 2: Identified damping matrix

Damper	Value
c_1	$5 \cdot 10^{-19}$
c_2	2.31
c_3	14.57
c_{12}	10.83
c_{23}	$8 \cdot 10^{-24}$

Table 1: Identified damping coefficients

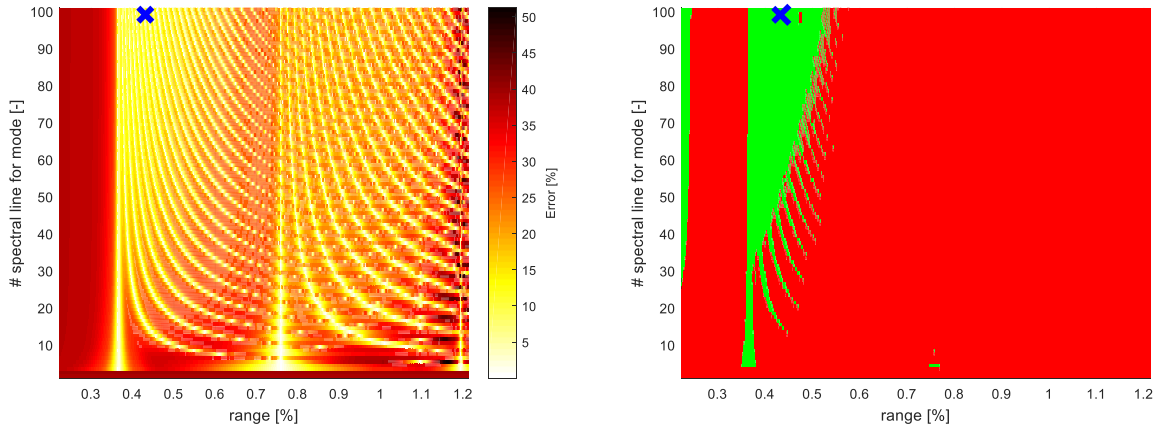


Figure 3: Identification error (left) and stabilisation (right) maps

5 Car chassis viscous and hysteretic matrix identification

The dynamics of a body in white car chassis with front and rear suspensions system has been experimentally studied through impact test modal analysis in free-free conditions, Fig. 4.



Figure 4: Body in white chassis test-rig

95 points, excited in 3 directions, are selected to have a good description of both mode shapes and structure geometry. The non-proportional viscous and hysteretic damping matrices of the system, reduced to 285 DoFs, were identified using Eq. 14 simplified to linear system with viscous and hysteretic dampers.

$$\mathbf{V}\begin{bmatrix}\mathbf{C}\\ \mathbf{D}\end{bmatrix}=\mathbf{Q}\,,\ \mathbf{V}=\begin{bmatrix}\omega_1\mathbf{H}^N(\omega_1) & \mathbf{H}^N(\omega_1)\\ \vdots & \vdots\\ \omega_K\mathbf{H}^N(\omega_K) & \mathbf{H}^N(\omega_K)\end{bmatrix},\ \mathbf{Q}=\begin{bmatrix}\mathbf{G}(\omega_1)\\ \vdots\\ \mathbf{G}(\omega_K)\end{bmatrix} \tag{39}$$

The unknowns vector becomes:

$$\overline{\mathbf{c}}=\left\{\mathbf{c}_A^T\quad \mathbf{c}_R^T\quad \mathbf{d}_A^T\quad \mathbf{d}_R^T\right\}^T \tag{40}$$

Eq. (33) is used to identify the viscous and hysteretic coefficients. The topology of the system requires 1818 relative patterns to be identified, corresponding to all the physical links between the tested points in all the possible directions ($c_{xx}, c_{xy}, c_{xz}, c_{yy}, c_{yz}, c_{zz}$) and 285 absolute dampers in the three directions to identify localised damping sources at each tested point. Due to computational cost the identification is performed directly in a point inside the stable region, estimated as explained in [6].

The identified matrices in all the directions are shown in Fig. 5. Some patterns are clearly visible: shock absorbers and tyres damping in vertical direction, seals between glass and structure, the viscoelastic material covering almost all the floor of the chassis and glass dissipation in the sunroof. The identified viscous damping coefficient of the front shock absorbers is compared with the reference values from datasheet (see Fig. 6). The identified values results to be the linearisation of the nonlinear characteristic of the front shock absorber viscous coefficient value. More details on this work can be found in [5].

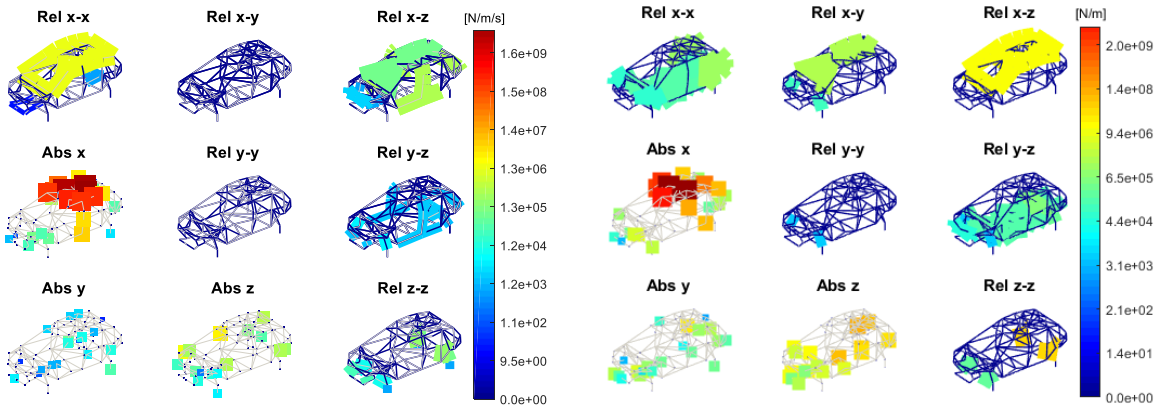


Figure 5: Body in white car chassis identified viscous damping matrix (left) and hysteretic matrix (right)

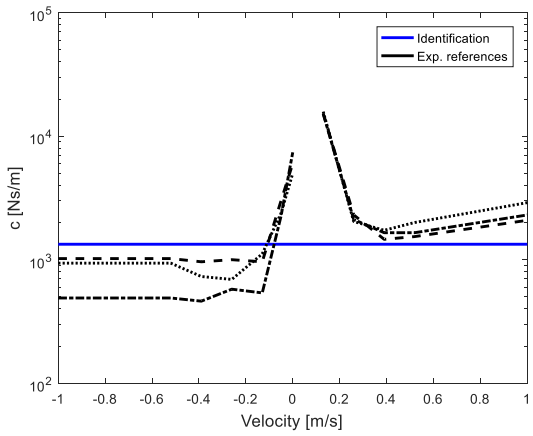


Figure 6: Identified front shock absorber viscous damping coefficient

6 Magnetic damping numerical identification

A five DoFs system with linear non-proportional viscous damping and nonlinear magnetic damping acting between the 4th and 5th DoFs is numerically studied. The magnetic damping represents two aluminium DoFs oscillating in the air gap between two permanent magnets. The dissipation force is due to the eddy currents induced by the magnetic field in the aluminium material; it is proportional to the frequency and presents elastic and dissipative components. The dissipative component of the force is amplitude dependent and can be written as a second order polynomial:

$$f_{c,nl_{4,5}} = \left(c_0 + c_1|z| + c_2 z^2\right)\dot{z}\,,\ z = x_4 - x_5 \tag{41}$$

The system equation of motion becomes:

$$\mathbf{M}\,\ddot{\mathbf{x}} + \mathbf{C}\,\dot{\mathbf{x}} + \mathbf{K}\,\mathbf{x} + f_{c,nl_{4,5}}\mathbf{g} = \mathbf{f}\left(t\right) \tag{42}$$

and in frequency domain:

$$\left[\left(\mathbf{K} - \omega^2\mathbf{M}\right) + F_{c,nl_{4,5}}\left(\omega, A\right)\mathbf{g}\,\mathbf{g}^T\right]\mathbf{X}\left(\omega\right) = \mathbf{f}\left(\omega\right) \tag{43}$$

where $F_{c,nl_{4,5}}\left(\omega, A\right)$ is the describing function of the nonlinear damping force of Eq. (41):

$$F_{c,nl_{4,5}}\left(\omega, A\right) = \mathrm{i}\omega\left(c_0 + c_1 z_1 A + c_2 z_2 A^2\right),\ z_1 = \frac{4}{3\pi},\ z_2 = \frac{1}{4}, \tag{44}$$

where A is the relative oscillation amplitude between 4th and 5th DoFs.

The nonlinear FRFs with constant amplitude A are necessary to apply the identification method presented in § 2. The nonlinear receptance matrix $\mathbf{H}_{nl}\left(\omega, A\right)$ can be numerically computed using the Sherman–Morrison formula [9, 10] from the linear receptance matrix $\mathbf{H}\left(\omega\right)$:

$$\mathbf{H}_{nl}\left(\omega, A\right) = \mathbf{H}\left(\omega\right) - \frac{F_{c,nl_{4,5}}\mathbf{H}\left(s\right)\left(\mathbf{e}_4 - \mathbf{e}_5\right)\left(\mathbf{e}_4 - \mathbf{e}_5\right)^T\mathbf{H}\left(\omega\right)}{1 + F_{c,nl_{4,5}}\left(\mathbf{e}_4 - \mathbf{e}_5\right)^T\mathbf{H}\left(\omega\right)\left(\mathbf{e}_4 - \mathbf{e}_5\right)} \tag{45}$$

where $\mathbf{e}_4$ and $\mathbf{e}_5$ are respectively the 4th and 5th column of the dimension 5 identity matrix.

The order of the nonlinear damping describing function is $t = 2$, therefore three nonlinear FRFs with different levels of the constant amplitude A are necessary.

The identification can be performed by simplifying Eq. (13) to remove the hysteretic damping component:

$$\begin{bmatrix} \omega_1\mathbf{H}^N\left(A,\omega_1\right) & \omega_1 z_1 A\mathbf{H}^N\left(A,\omega_1\right) & \omega_1 z_2 A^2\mathbf{H}^N\left(A,\omega_1\right) \\ \omega_2\mathbf{H}^N\left(A,\omega_2\right) & \omega_2 z_1 A\mathbf{H}^N\left(A,\omega_2\right) & \omega_2 z_2 A^2\mathbf{H}^N\left(A,\omega_2\right) \\ \vdots & \vdots & \vdots \\ \omega_K\mathbf{H}^N\left(A,\omega_K\right) & \omega_K z_1 A\mathbf{H}^N\left(A,\omega_K\right) & \omega_K z_2 A^2\mathbf{H}^N\left(A,\omega_K\right) \end{bmatrix}\begin{bmatrix} \mathbf{C}_{lin} \\ c_1\mathbf{g}\mathbf{g}^{\mathrm{T}} \\ c_2\mathbf{g}\mathbf{g}^{\mathrm{T}} \end{bmatrix} = \begin{bmatrix} \mathbf{G}\left(A,\omega_1\right) \\ \mathbf{G}\left(A,\omega_2\right) \\ \vdots \\ \mathbf{G}\left(A,\omega_K\right) \end{bmatrix} \tag{46}$$

The nonlinear numerical FRFs $\mathbf{H}_{nl}\left(\omega, A\right)$ are contaminated with a random noise of 10% of the amplitude, to check the identification method robustness against the noise effects.

The system matrices are:

$$\mathbf{M}=10^{-2}\,diag\left(\begin{bmatrix}1 & 2 & 3 & 4 & 5\end{bmatrix}\right)\text{kg},\quad c_0=1\text{ Ns/m},\quad c_1=100\text{ Ns/m}^2,\quad c_2=2\cdot10^7\text{ Ns/m}^3$$

$$\mathbf{K}=10^2\begin{bmatrix}15 & -5 & & & \\ -5 & 18 & -3 & & \\ & -3 & 21 & -8 & \\ & & -8 & 23 & -5 \\ & & & -5 & 15\end{bmatrix}\text{N/m}\quad \mathbf{C}=\begin{bmatrix}1 & & & & \\ & 0.5 & -0.5 & & \\ & -0.5 & 0.5 & & \\ & & & 0 & \\ & & & & 0\end{bmatrix}+10^{-6}\mathbf{M}+4\cdot10^{-5}\mathbf{K}\text{ Ns/m} \tag{47}$$

The nonlinear FRFs at constant amplitude across the nonlinearity, with an additional Gaussian random noise, are shown in Fig. 7. It is worth noting that the FRFs are not perfectly symmetric due to the added noise.

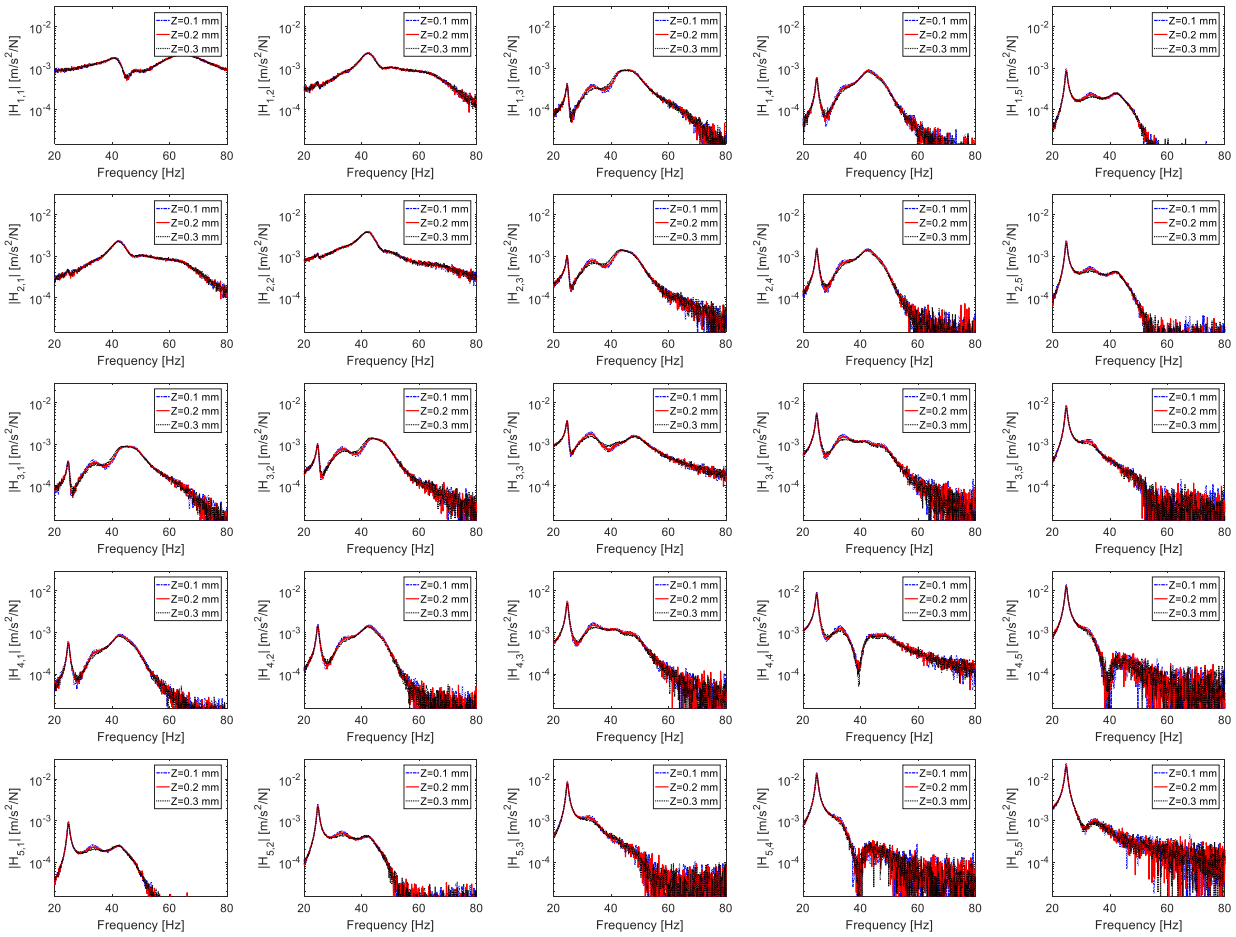


Figure 7: $\mathbf{H}_{nl}\left(\omega,A\right)$ matrix for 3 different excitation amplitudes

The system response in Fig. 7 is visibly nonlinear, in particular the second mode shape pick is affected by the damping nonlinearity. The results of the identification of linear viscous damping matrix and nonlinear coefficients are shown in Fig. 8 and in Table 2.

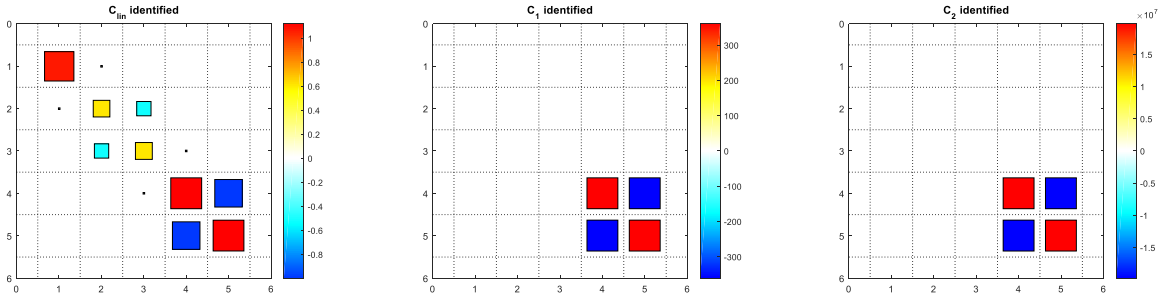


Figure 8: Identified linear and nonlinear damping matrix

The identification results are quite close to the systems parameters, except for c_1, because its influence is much lower with respect to the linear and quadratic terms. The stabilisation diagram of the nonlinear coefficients and the global stabilisation diagram together with the error map are shown in Fig. 9. The numerical test provides an interesting result for the nonlinear damping identification issue.

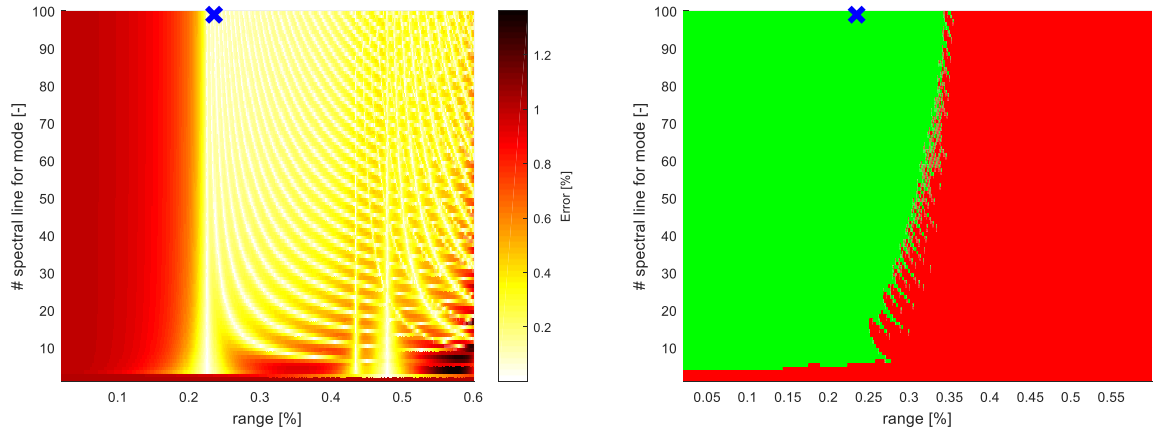


Figure 9: Error map (left) and stabilisation diagram (right) of the magnetic damped system.

Damper	Reference	Identified
$c_{l,1}$	1.04	1.045
$c_{l,2}$	0.04	0.064
$c_{l,3}$	0.04	0.045
$c_{l,4}$	0.04	0.074
$c_{l,5}$	0.04	0.118
$c_{l,12}$	0.012	0.02
$c_{l,23}$	0.52	0.519
$c_{l,34}$	0.032	0.048
$c_{l,45} + c_0$	1.02	0.999
c_1	100	361
c_2	$2 \cdot 10^7$	$1.97 \cdot 10^7$

Table 2: Identified linear and nonlinear viscous damping coefficients

7 Conclusion

Linear and nonlinear spatial damping identification through the Stabilised Layer Method is presented in the paper. The non-classical damping matrices (viscous, hysteretic and nonlinear damping) can be identified directly from common frequency domain responses of the system. Only the system topology and its dynamics response are necessary to identify the dissipation matrices of a linear system. Since the system is linear there is no need of controlling the response amplitude of the system and therefore it can be obtained with classical hammer test. When localised nonlinearity should be identified, also the location of the nonlinearity has to be known and the system response can be obtained with shaker test, controlling the oscillation amplitude across the nonlinearity. A stabilisation diagram is obtained for each linear and nonlinear identified damping coefficient to ensure a stable spatial damping identification. The SLM was applied experimentally to a simple three DoFs lumped system in order to validate the approach and to a quite complex system as a body in white car chassis. In both the examples the spatial identification is quite close to the expected results. The identification of a magnetic damping nonlinearity is then performed on a numerical system. The method seems to be quite robust in the linear and nonlinear damping identification also when the data are affected by noise. The future developments of the work are the application of the SLM for the experimental identification of an amplitude dependent nonlinear damping force and the extension to the identification of systems with multiple nonlinear forces.

References

[1] M. Prandina, J.E. Mottershead, E. Bonisoli, *An assessment of damping identification methods*, Journal of Sound and Vibration, Vol. 323, 2009, pp. 662-676.

[2] M. Brumat, J. Slavic, M. Boltezar, *Spatial damping identification in the frequency domain - A theoretical and experimental comparison*, Journal of Sound and Vibration, Vol. 376, 2016, pp. 182-193.

[3] S.Y. Chen, M.S. Ju, T.G. Tsuei, *Estimation of mass, stiffness and damping matrices from frequency response functions*, Transactions of the ASME, Vol. 118, 1996, pp. 78-82.

[4] J.H. Lee, J. Kim, *Identification of damping matrices from measured frequency response functions*, Journal of Sound and Vibration, Vol. 240, No. 3, 2001, pp. 545-565.

[5] E. Bonisoli, D. Lisitano, A. Vigliani, *Damping identification and localisation via layer method: experimental application to a vehicle chassis focused on shock absorbers effects*, submitted to Mechanical System and Signal Processing.

[6] D. Lisitano, E. Bonisoli, J.E. Mottershead, *Experimental direct spatial damping identification by the Stabilised Layer Method*, submitted to Journal of Sound and Vibration.

[7] S. J. Elliott , M. Ghandchi Tehrani, R. S. Langley, *Nonlinear damping and quasi-linear modelling*, Philosophical Transaction Royal Society A, Vol. 373, 2014, pp. 1-30.

[8] A. Gelb, W. E. Vander Velde, *Multiple-input describing functions and nonlinear system design*, McGraw-Hill, New York (1968).

[9] G. H. Golub, C. F. V. Loan, *Matrix computations*, Johns Hopkins University Press, Baltimore, MD (1983).

[10] J. E. Mottershead, Y. M. Ram, *Inverse eigenvalue problems in vibration absorption: Passive modification and active control*, Mechanical Systems and Signal Processing, Vol. 20, No. 1, 2006, pp. 5-44.

Analysis and simulation of structures with local visco-elastic damping from elastomers

M. Böswald[1], M. Gröhlich[1], J. Biedermann[1], R. Winter[1]
[1] Deutsches Zentrum für Luft- und Raumfahrt (DLR)
Institute of Aeroelasticity, Department for Structural Dynamics and System Identification
Bunsenstraße 10, D-37073 Göttingen, Germany
e-mail: **Marc.Boeswald@DLR.de**

Abstract
In the design of lightweight structures, the construction of damping still is an unused design freedom. While material inherent damping of aluminum or composite materials is generally low, the internal damping of elastomers is significant. The basic concept of including local elastomer dampers into aluminum or composite components of aeronautic structures is addressed with the objective to increase the damping of specific vibration modes. The modelling from 1D rheological models of visco-elastic material up to 2D and 3D modelling using finite elements is addressed. Using the finite element method, a global damping matrix can be generated which enables forecasts of modal damping levels. A parameter study on a simple dynamic oscillator has been performed to better understand the influence of the parameters of visco-elastic material models. The experience gained on simple oscillators has been transferred towards damping design of a simple aluminum structure subjected to forced harmonic vibrations.

1 Introduction

Lightweight design is mandatory in the construction of aeronautic structures. As a consequence, such structures are prone to vibration. While sophisticated mathematical models are generated for the representation of structural stiffness and mass distribution, the modelling of damping is still very basic and mostly pursued in terms of modal damping with rough estimates of damping ratios.

In general, damping can be attributed to distributed material damping or to local damping at joints. Since metallic materials or composites used in the design of aeronautic structures have little internal material damping, the overall damping ratios of such structures are rather low. Therefore, the design of damping e.g. by introduction of local dampers is considered as an objective, because it is a design degree of freedom that is currently not used. The design of damping e.g. for an aircraft fuselage or even for aircraft wings would be beneficial for the reduction of overall vibration levels and will lead to longer fatigue life and improved cabin comfort in terms of acoustics and vibrations. For example, local dampers on specific fuselage frames or fuselage stringers can help to dissipate vibration energy for the reduction of cabin interior noise levels. This is an attractive concept in particular in the vibro-acoustic domain e.g. when stationary excitation from turbulent boundary layer is considered in cruise flight or steady engine induced vibrations in the climb phase. In case of transient events, such as gust encounter or landing impact, rapid decay of vibrations achieved with proper placement of dampers would help to passively alleviate dynamic loads. Many more examples from aeronautics could be named where increase of damping is beneficial.

Since the material damping is rather low and the damping at joints of metallic components is related to strong non-linear friction effects influenced by lubrication and wear, another source of damping is discussed in this paper: the visco-elastic material properties of elastomers. First, the material behavior is reviewed in the time- and in the frequency-domain leading to the definition of the relaxation function and the complex shear modulus. Afterwards, a 3D material law is formulated which allows the generation of frequency-dependent element stiffness- and damping matrices of 1D, 2D, and 3D solid elements. The inclusion of local elastomer dampers based on Free-Layer-Damping and Constrained-Layer-Damping is

discussed. They contribute to the overall damping when shear deformation is activated. The challenges in the damping design based on supplemental elastomer dampers and the difficulties in the dynamic response simulation of assembled structures with local elastomer dampers will be addressed in the paper.

2 Theoretical background of visco-elastic material modelling

In this section, different idealized material properties are discussed. Afterwards, the specific visco-elastic properties are reviewed in more detail together with appropriate equivalent rheological models.

2.1 Hooke's law for linear elasticity

Linear elastic material deforms under external loads. After removing the load, the deformation will disappear and the material will return to its original geometric shape. When scaling the load by a certain factor, the deformation will appear with the same scale. When small strains and small stresses are considered, a linear-elastic material law can be formulated in matrix-vector-notation for a three-dimensional (3D) body relating all elements of the generalized 3D strain tensor with the corresponding elements of the 3D stress tensor [1]:

$$\{\sigma\} = [E]\{\varepsilon\} \tag{1}$$

This is referred to as Hooke's law for linear elasticity. When furthermore isotropic materials are addressed, e.g. metallic materials like steel and aluminum or elastomers like rubber, the number of independent parameters in the material law reduces significantly [1]:

$$\begin{Bmatrix} \sigma_{xx} \\ \sigma_{yy} \\ \sigma_{zz} \\ \tau_{xy} \\ \tau_{yz} \\ \tau_{zx} \end{Bmatrix} = \frac{E}{(1+\nu)(1-2\nu)} \begin{bmatrix} 1-\nu & \nu & \nu & 0 & 0 & 0 \\ \nu & 1-\nu & \nu & 0 & 0 & 0 \\ \nu & \nu & 1-\nu & 0 & 0 & 0 \\ 0 & 0 & 0 & \frac{1-2\nu}{2} & 0 & 0 \\ 0 & 0 & 0 & 0 & \frac{1-2\nu}{2} & 0 \\ 0 & 0 & 0 & 0 & 0 & \frac{1-2\nu}{2} \end{bmatrix} \begin{Bmatrix} \varepsilon_{xx} \\ \varepsilon_{yy} \\ \varepsilon_{zz} \\ \gamma_{xy} \\ \gamma_{yz} \\ \gamma_{zx} \end{Bmatrix} \tag{2}$$

The Young's modulus E relates the 1D stress with 1D strain. The Poisson's ratio ν is the ratio of transverse strain to longitudinal strain in the direction of loading in a 1D load case. The shear modulus G relates the shear stresses τ with the shear strains γ as follows [1]:

$$\tau_{xy} = G\gamma_{xy}\,,\ \tau_{yz} = G\gamma_{yz}\,,\ \tau_{zx} = G\gamma_{zx} \quad \rightarrow \quad G = \frac{E}{2(1+\nu)} \tag{3}$$

2.2 Viscosity of Newtonian fluids

Pure viscous material behavior can only be attributed to fluids. Viscosity is the resistance of a fluid against shear deformation [2]. When a fluid is subjected to a relative transverse motion in the gap between two surfaces of solid material as sketched in Figure 1, a shear stress will be induced in the fluid. Integration over the surface exposed to the fluid will resistance force proportional to the relative (shear) velocity. In case of a linear relation between shear velocity and shear stress, the fluid is referred to as a Newtonian fluid. The factor μ relating the shear stress with the relative shear velocity is the dynamic viscosity of the fluid.

$$\tau_{xy} \propto \frac{\dot{x}}{y} \quad \rightarrow \quad \tau_{xy} = \mu \frac{d\dot{x}}{dy} \tag{4}$$

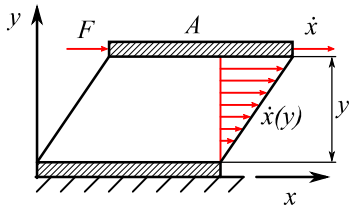


Figure 1: Shear deformation of a fluid

2.3 Linear visco-elasticity

Visco-elasticity is a combination of linear elasticity of solids and viscosity of fluids, [2]. It thus appears in materials that feature both properties at the same time. The essential difference to linear elasticity is that response of visco-elastic material to a given loading is time-dependent, see Figure 2.

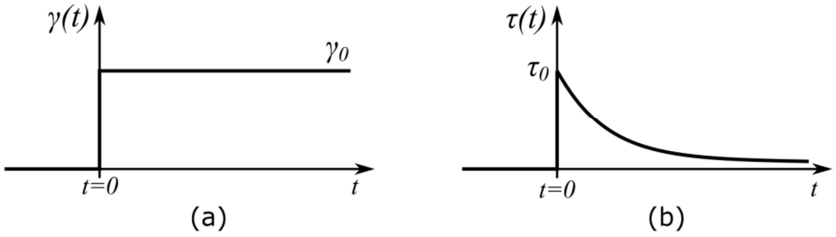


Figure 2: Time-dependent shear stress response of visco-elastic materials to step shear strain input

This requires time-dependent material parameters, or respectively, a time-dependent material law. The essential time-dependent function *G(t)* is referred to as relaxation function :

$$\tau(t) = G(t)\ \gamma_0 \tag{5}$$

The sketch of Figure 2 refers to a step function for the prescribed shear strain and the corresponding exponential decay of the shear stress with time.

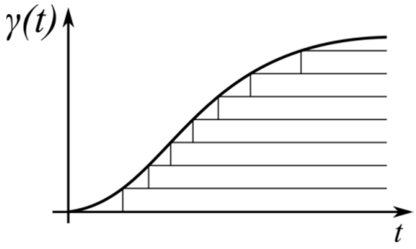


Figure 3: Arbitrary time-history of prescribed shear strain decomposed into a sequence of step functions according to [3]

In general, the time-history of the prescribed shear strain *γ(t)* can be arbitrary. Nonetheless, arbitrary time histories of the prescribed shear strain can be decomposed into a sequence of steps as shown in Figure 3.

The increment in shear strain $d\gamma$ to the total shear strain γ at the time $\tilde{t}$ of a particular step is:

$$d\gamma(\tilde{t}) = d\dot{\gamma}(\tilde{t})dt \tag{6}$$

Consequently, when taking into account the time-dependence of the material law, the increment $d\tau$ in the shear stress is [3]:

$$d\tau(\tilde{t}) = G\left(t-\tilde{t}\right) d\dot{\gamma}(\tilde{t}) dt \tag{7}$$

Summation of an infinite number of steps in the approximation of the $\gamma(t)$ will finally lead to the following convolution integral [3]:

$$\tau(t) = \int_{-\infty}^{t} G\left(t-\tilde{t}\right) d\dot{\gamma}(\tilde{t}) d\tilde{t} \tag{8}$$

As can be seen, the constitutive equation for linear visco-elastic material is rather complicated in the time-domain and will not lead to the desired global viscous damping model for damped multi-degree of freedom systems.

The time-dependent reduction of the stress as output to prescribed strain as input is referred to as relaxation. This is caused by internal viscous effects in the material, e.g. friction between the macromolecules. For completeness, the relation between prescribed stress as input and strain as output is referred to creep. These equations are not developed here and will not be used later on.

When harmonic motion is considered, e.g. in the circular frequency of excitation Ω, the equations for linear visco-elastic behavior can be simplified considerably.

$$\varepsilon(t) = \Re\left(\hat{\varepsilon} e^{j\Omega t}\right), \quad \hat{\varepsilon} = \varepsilon_{re} + j\varepsilon_{im} \quad \xrightarrow[system]{linear} \quad \tau(t) = \Re\left(\hat{\tau} e^{j\Omega t}\right), \quad \hat{\tau} = \tau_{re} + j\tau_{im} \tag{9}$$

$$\hat{\tau} = \hat{G}(j\Omega)\,\hat{\varepsilon} \tag{10}$$

When using complex notation for harmonic strain and harmonic stress, a frequency-dependent complex shear modulus can be derived:

$$\hat{G}(j\Omega) = G'(\Omega) + jG''(\Omega) \tag{11}$$

Its real part $G'(\Omega)$ is called the storage modulus and its imaginary part $G''(\Omega)$ is the loss modulus. The ratio of storage and loss modulus is the so-called loss factor η:

$$\eta(\Omega) = \frac{G''(\Omega)}{G'(\Omega)} \tag{12}$$

It should be noted that all material parameters are frequency-dependent and also temperature-dependent. The dependence on temperature is however neglected in the following and constant temperature is assumed.

For the development of a material law, an equivalent rheological model is required. Combinations of springs and Maxwell elements (i.e. an elastic spring and a viscous damper arranged in series) can be used to approximate the observed time-dependent behavior of visco-elastic material. In a so-called Prony-Series, a number of Maxwell elements are arranged in parallel with an elastic spring to approximate the material behavior, see Figure 4.

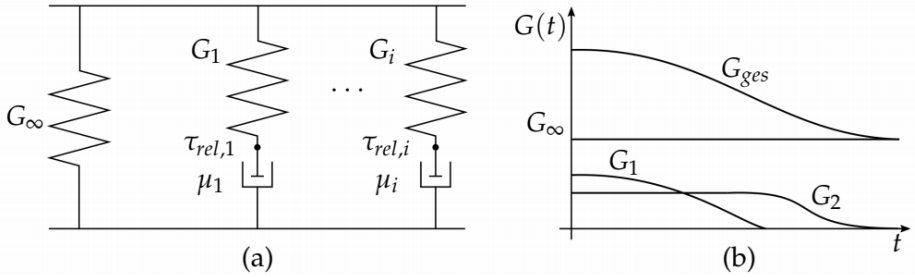


Figure 4: Setup of a Prony-Series (a) and typical time-dependent behavior (b) [4]

Each Maxwell element has a spring stiffness G_i and a damper constant μ_i. The damper constant and the spring stiffness of the Maxwell element are related with its relaxation time constant $\tau_{rel,i}$ [3]:

$$\tau_{rel,i} = \frac{\mu_i}{G_i} \tag{13}$$

With the Prony-Series as an equivalent rheological model at hand, the time dependent shear modulus in equation (5) can now be revisited [4]:

$$G(t) = G_\infty + \sum_{i=1}^{n} G_i \, e^{-\frac{t}{\tau_{rel,i}}} \tag{14}$$

In this equation, the stiffnesses (or storage moduli) G_i of the different Maxwell elements can be expressed as a fraction of the modulus G_0 [5]:

$$G(t) = G_0 \left(\alpha_\infty + \sum_{i=1}^{n} \alpha_i \, e^{-\frac{t}{\tau_{rel,i}}} \right) \tag{15}$$

It should be noted that G_∞ characterizes the storage modulus of the material for infinitely slow deformation, i.e. the static storage modulus at frequency of 0 Hz. At the same time, G_0 characterizes the storage modulus of the material for infinitely fast deformation, i.e. the storage modulus at infinite excitation frequency. The α_i are referred to as relative moduli for which the following relations exist [6]:

$$G_\infty = G_0 \alpha_\infty \quad , \quad \alpha_\infty + \sum_{i=1}^{n} \alpha_i = 1 \quad , \quad G_0 = G_\infty + \sum_{i=1}^{n} G_i \tag{16}$$

When assuming harmonic stress and harmonic strain, the Prony-Series can be transformed into the frequency-domain so that the storage and loss modulus of the visco-elastic material can be determined [5]:

$$G'(\Omega) = G_0 \left(1 - \sum_{i=1}^{n} \left(\alpha_i - \frac{\alpha_i \tau_{rel,i}^2 \Omega^2}{1 + \tau_{rel,i}^2 \Omega^2} \right) \right) \tag{17}$$

$$G''(\Omega) = G_0 \sum_{i=1}^{n} \left(\frac{\alpha_i \tau_{rel,i} \Omega}{1 + \tau_{rel,i}^2 \Omega^2} \right) \tag{18}$$

The typical evolution of storage modulus, loss modulus and loss factor with frequency is shown in Figure 5. Here, a Prony-Series consisting of an elastic spring G_∞ and a single Maxwell element with the modulus $G_1 = \alpha_1 G_0$ and the relaxation time constant $\tau_{rel,1} = \mu_1 / G_1$ has been used. It can be observed that the storage modulus starts at G_∞ and increases with frequency and finally converges towards G_0, which is the sum of all spring stiffnesses. The loss modulus starts at zero, increases significantly and reaches a maximum. Afterwards it decreases and seems to converge towards a lower value. The loss factor evolution with frequency is similar. However, the maximum of the loss factor is not at the same frequency than the loss modulus. This is caused by the frequency dependence of both, storage and loss modulus.

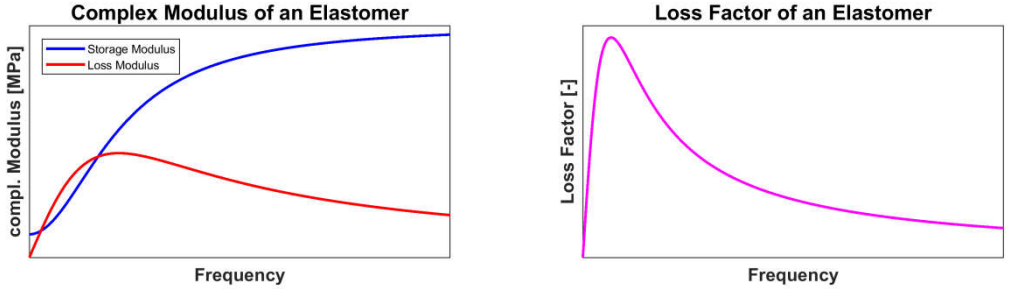


Figure 5: Typical variation of complex modulus and loss factor of an elastomer with frequency

The frequency dependent material behavior has been developed for the complex shear modulus. The same relations can also be derived for the complex Young's modulus for elongation of the material. When considering elastomers with visco-elastic behavior, it is justified to assume isotropy. In this case, the simple and well-known relation between shear modulus G and Young's modulus E as stated in equation (3) can be applied. It should be noted that elastomers can be considered as incompressible fluid, so that the Poisson ratio is close to 0.5:

$$G = \frac{E}{2(1+\nu)} \quad \rightarrow \quad E = 2G\left(1+\nu\right), \quad \nu \approx 0.499 \tag{19}$$

$$E'(\Omega) = 2G'(\Omega)\cdot\left(1+\nu\right) \quad , \quad E''(\Omega) = 2G''(\Omega)\cdot\left(1+\nu\right) \tag{20}$$

Using these relations, an extension to Hooke's law, see equations (1) and (2), can be derived for the generic 3D state for stress and strain. A frequency dependent material law is obtained with real part (i.e. matrix of storage modulus) and imaginary part (i.e. matrix of loss modulus):

$$\{\hat{\sigma}\} = \left(\left[E'(\Omega)\right] + j\left[E''(\Omega)\right]\right)\{\hat{\varepsilon}\} \tag{21}$$

2.4 Implementation of visco-elasticity into the finite element method

The availability of the 3D material law for visco-elastic materials has been derived in the previous section. It is a prerequisite for the modelling of local damping from visco-elastic materials using the Finite Element (FE) method. The FE method utilizes spatial discretization of continuous displacements fields. A continuous structure is virtually disassembled into a finite number of elements. Within each element, the continuous displacements u, v, w in x-, y- and z-direction are approximated by shape functions $h_i(x,y,z)$ and nodal point displacements U_i, V_i, W_i. for $i = 1,..,N$ with N being the number of nodes of the element [1], [7]:

$$u(x,y,z) = \sum_{i=1}^{N} h_i(x,y,z)U_i = \{h(x,y,z)\}^T\{U\} \tag{22}$$

$$v(x,y,z) = \sum_{i=1}^{N} h_i(x,y,z)V_i = \{h(x,y,z)\}^T\{V\} \tag{23}$$

$$w(x,y,z) = \sum_{i=1}^{N} h_i(x,y,z)W_i = \{h(x,y,z)\}^T\{W\} \tag{24}$$

$$\begin{Bmatrix} u(x,y,z) \\ v(x,y,z) \\ w(x,y,z) \end{Bmatrix} = \begin{bmatrix} \{h(x,y,z)\}^T & \{0\} & \{0\} \\ \{0\} & \{h(x,y,z)\}^T & \{0\} \\ \{0\} & \{0\} & \{h(x,y,z)\}^T \end{bmatrix} \begin{Bmatrix} U \\ V \\ W \end{Bmatrix} \tag{25}$$

$$\left\{u_g(x,y,z)\right\} = \left[h_g(x,y,z)\right]^T\left\{U_g\right\} \tag{26}$$

Inserting this approximation into the kinematic relation between displacements and strains yields [1], [7]:

$$\{\varepsilon(x,y,z)\} = [\partial]\left\{u_g(x,y,z)\right\} = [\partial]\left[h_g(x,y,z)\right]^T\left\{U_g\right\} \tag{27}$$

$$\left[\partial\right]^T = \begin{bmatrix} \frac{\partial}{\partial x} & 0 & 0 & \frac{\partial}{\partial y} & 0 & \frac{\partial}{\partial z} \\ 0 & \frac{\partial}{\partial y} & 0 & \frac{\partial}{\partial x} & \frac{\partial}{\partial z} & 0 \\ 0 & 0 & \frac{\partial}{\partial z} & 0 & \frac{\partial}{\partial y} & \frac{\partial}{\partial x} \end{bmatrix} \tag{28}$$

Finally, the equivalence of the virtual work of external loads with the virtual work of internal stress and strain yields an analytical expression for the stiffness matrix of a finite element:

$$\left[K_e\right] = \int_V \left(\left[\partial\right]\left[h_g\right]^T\right)^T \left[E\right]\left(\left[\partial\right]\left[h_g\right]^T\right) dV \tag{29}$$

Now, the frequency-dependent 3D visco-elastic material law can be inserted in this equation. The real part of the material law (i.e. matrix of storage modulus) will lead to a frequency dependent element stiffness matrix. The imaginary part of the material law (i.e. matrix of loss modulus) will lead to a frequency dependent element damping matrix.

$$\left[K_e(\Omega)\right] = \int_V \left(\left[\partial\right]\left[h_g\right]^T\right)^T \left[E'(\Omega)\right]\left(\left[\partial\right]\left[h_g\right]^T\right) dV \tag{30}$$

$$j\left[D_e(\Omega)\right] = j\int_V \left(\left[\partial\right]\left[h_g\right]^T\right)^T \left[E''(\Omega)\right]\left(\left[\partial\right]\left[h_g\right]^T\right) dV = j\eta(\Omega)\left[K_e(\Omega)\right] \tag{31}$$

As can be seen, the damping of visco-elastic material in case of harmonic excitation leads to a structural damping matrix (i.e. a hysteretic damping matrix) instead of a viscous damping matrix. The essential difference to classical structural damping is the frequency-dependence of the loss factor and the frequency-dependence of the stiffness matrix

As with other element stiffness matrices, they must be assembled to a global stiffness matrix. This is typically done with Boolean matrices relating the global degrees of freedom of the overall system with the local element degrees of freedom. Summation over all elements yields the global stiffness matrix. This approach can be applied here for the frequency dependent stiffness and damping matrices from elements with visco-elastic material as well:

$$\left\{U_e\right\} = \left[T_e\right]\left\{U_{global}\right\} \tag{32}$$

$$\left[K(\Omega)\right] = \sum_e \left[T_e\right]^T \left[K_e(\Omega)\right]\left[T_e\right] \tag{33}$$

$$j\left[D(\Omega)\right] = j\sum_e \left[T_e\right]^T \left[D_e(\Omega)\right]\left[T_e\right] \tag{34}$$

Finally, the equation of motion can be formulated only for harmonic excitation, or respectively, in the frequency domain.

$$\left(-\Omega^2\left[M\right] + j\left[D(\Omega)\right] + \left[K(\Omega)\right]\right)\left\{\hat{u}\right\} = \left\{\hat{f}\right\} \tag{35}$$

For each frequency of excitation, the system is linear. However, due to the material being frequency dependent, the global stiffness and damping matrix must be evaluated for each frequency of interest. It should be noted however, that significant benefit can be obtained from the isotropic material. In fact, the frequency dependence can be factored out as a frequency-dependent scalar multiplier in the 3D material law. To this end, also the frequency dependence can be factored out in the same way for the element stiffness and damping matrices, and finally, also for the global stiffness and damping matrix. It would be possible to evaluate the global stiffness and damping matrix for one specific frequency. In this case, the

relative size of all elements in this matrix is correct. Just a global scaling by a frequency-dependent factor is required. However, the stiffness matrix must be scaled with a different frequency dependent multiplier than the damping matrix, because the storage modulus has a different frequency-dependent behavior than the loss modulus.

When an overall assembled system is considered which has some components from standard linear elastic material and some other components from frequency-dependent visco-elastic material, the frequency-dependent scaling must be applied only to a subpart of the stiffness matrix. It is therefore good practice to separate the linear-elastic part in the model from the visco-elastic part:

$$\left[K(\Omega)\right]=\left[K_{el}\right]+\left[K_{vis}(\Omega)\right] \quad , \quad \left[D(\Omega)\right]=\left[D_{el}\right]+\left[D_{vis}(\Omega)\right] \tag{36}$$

3 Parameter study for linear visco-elastic materials

The modelling of frequency-dependent stiffness and (hysteretic) damping has been discussed in the previous section. In this section, a basic oscillator is modelled with visco-elastic material to investigate its response characteristics from harmonic excitation. The sensitivities of the parameters of the Prony-Series used to model the visco-elastic material law are investigated for their impact on frequency response curves.

3.1 Parameter study for one-dimensional state of stress

In this study, the influence of the parameters of a Prony-Series on the dynamic response characteristic of a simple mechanical oscillator shall be investigated. To this end, the example is kept rather simple, i.e. a simple rod clamped at one end and excited harmonically at the other end, see Figure 6. The visco-elastic material is represented by a Prony-Series with one spring and one Maxwell element in parallel. The parameters of the Prony-Series, the material parameters and geometric parameters of the example are given in Table 1. They do not refer to real existing material, but are modified from existing material.

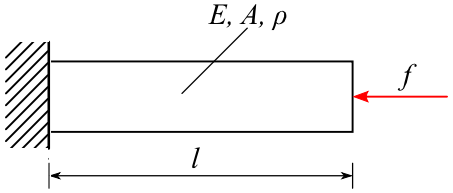


Figure 6: 1D rod with visco-elastic material properties

Table 1: Parameters of the 1D simulation example

Parameter	E_0 [N/m^2]	α [-]	τ_{rel} [s]	l [m]	A [m^2]	ρ [kg/m^3]
Value	$4\cdot10^5$	0.1	0.1	1.0	0.0625	1100

The Young's modulus in the equation for the stiffness of the rod is now replaced by the frequency dependent complex modulus leading to frequency dependent element stiffness and frequency-dependent hysteretic damping:

$$k=\frac{EA}{l} \xrightarrow[material]{visco-elastic} k(\Omega)=\frac{E'(\Omega)A}{l} \quad , \quad d(\Omega)=\frac{E''(\Omega)A}{l}=\eta(\Omega)k(\Omega) \tag{37}$$

Due to the frequency dependence of stiffness and damping properties, eigenvalue analysis is no longer possible. However, the frequency response can be obtained in the direct way from inversion of the dynamic stiffness matrix:

$$\left(-\Omega^2 m + jd(\Omega) + k(\Omega)\right)\hat{u} = \hat{f} \quad \rightarrow \quad \hat{u} = \frac{1}{-\Omega^2 m + jd(\Omega) + k(\Omega)}\hat{f} \tag{38}$$

The frequency response analysis has now been conducted under variation of the parameters of the Prony-Series, i.e. variation of E_0, the relaxation time constant τ_{rel} and the relative modulus α around their nominal values as given in Table 1. The effect of variation of E_0 on storage modulus and loss modulus can be found in the left diagram of Figure 7, whereas in the right diagram, the effect of E_0 on the frequency response of the rod is shown.

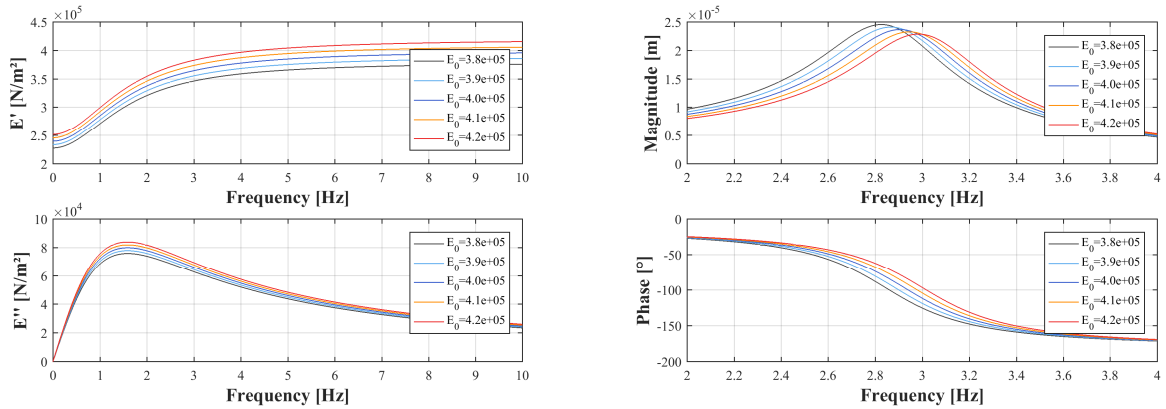


Figure 7: Influence of E_0 on storage modulus E' and loss modulus E'' (left) and influence of E_0 on magnitude displacement response and phase response (right)

The effect of variation of the relaxation time τ_{rel} on storage modulus and loss modulus can be found in the left diagram of Figure 8, whereas in the right diagram, the effect of the relaxation time τ_{rel} on the frequency response of the rod is shown.

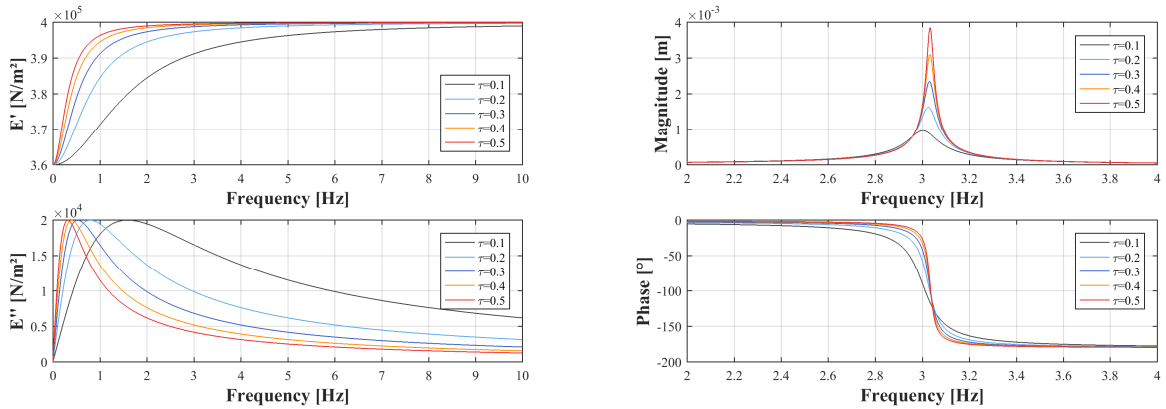


Figure 8: Influence of relaxation time τ_{rel} on storage modulus E' and loss modulus E'' (left) and influence of relaxation time τ_{rel} on magnitude displacement response and phase response (right)

Finally, the effect of variation of the relative modulus α on storage modulus and loss modulus can be found in the left diagram of Figure 9, whereas in the right diagram, the effect of the relative modulus α on the frequency response of the rod is shown.

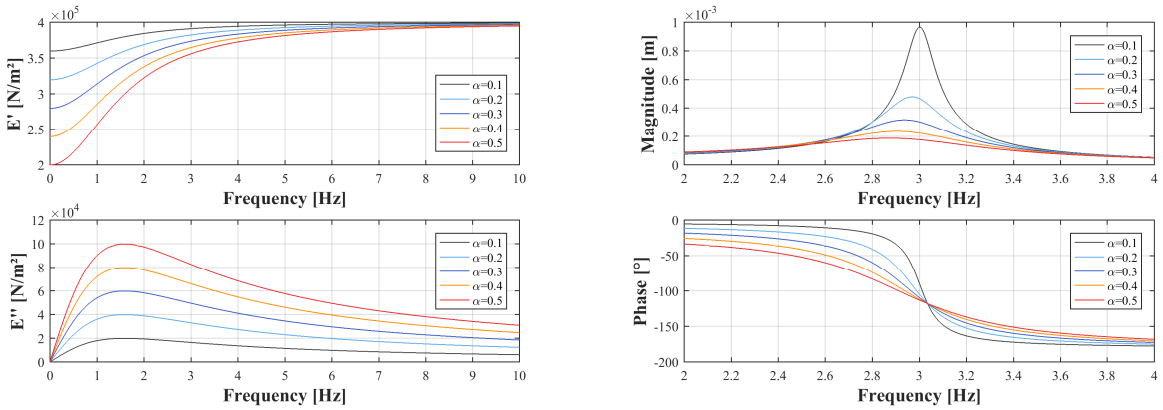


Figure 9: Influence of relative modulus α storage modulus E' and loss modulus E'' (left) and influence of relative modulus α on magnitude displacement response and phase response (right)

Next to the sensitivity of the parameters of the Prony-Series, also the sensitivities of the geometrical parameters of the oscillator have been investigated. The following relevant results quantities were considered for the sensitivity study: the storage modulus E', the maximum of the loss modulus E''_{max}, the frequency $f^{E''}_{max}$ under which the E''_{max} occurs, the maximum value of the loss factor η_{max}, the maximum amplitude $|\hat{u}|_{max}$ of the displacement response, the frequency $f^{|\hat{u}|}_{max}$ under which the maximum response occurs, and the modal viscous damping ratio D. The results of the sensitivity study are summarized in Table 2. An upwards pointing arrow means results quantity increases with increasing parameter. A downward pointing arrow means results quantity decreases with increasing parameter. The equal sign means no change. Finally, *'case dep.'* means that the observation is dependent on the case considered and cannot be generalized.

Table 2: Influence of Prony-Series parameters and geometrical parameters on characteristic features of the 1D oscillator

Parameter	E'	E''_{max}	$f^{E''}_{max}$	η_{max}	f^{η}_{max}	$\lvert\hat{u}\rvert_{max}$	$f^{\lvert\hat{u}\rvert}_{max}$	D
E_0	↑	↑	=	=	=	↓	↑	=
α	↓	↑	=	↑	↓	↓	↓	↑
τ	↑	=	↓	=	↓	*case dep.*	↑	*case dep.*
l	=	=	=	=	=	*case dep.*	↓	*case dep.*
A	=	=	=	=	=		=	=

3.2 Parameter study for two-dimensional state of stress

In a two dimensional study, the 1D rod has been exchanged by a 2D membrane element whose cross sectional properties are equivalent to those of the rod. Also the boundary conditions and loading conditions were retained. This example served to investigate the influence of the Poisson's ratio ν on the dynamic characteristics of the mechanical oscillator. Since there is little influence on the Poisson's ratio in the development of elastomeric materials, the results of this study are somehow academic and are not presented here.

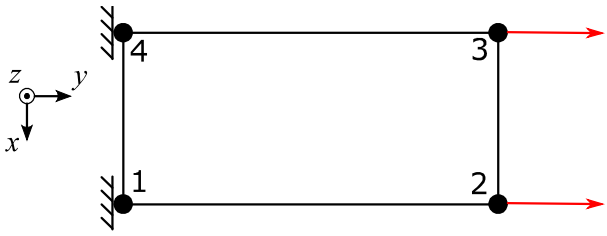


Figure 10: 2D membrane element with visco-elastic material properties

4 Parameter optimization for visco-elastic materials

It has been discovered during the literature research that material properties of elastomers are not available as for example those of metallic materials like different alloys of steel or aluminum. The reason is that an almost unlimited number of different mixtures and vulcanisates exist for a given polymer type. This has posed problems in the mathematical modelling of the visco-elastic material. In fact, this is the main reason why artificial material parameters from a modification of real existing elastomers had to be used.

Nonetheless, this opens up the possibility for material parameter optimization, because in case of the development of technical elastomers for specific applications, the material parameters like storage modulus, loss modulus, shore hardness, glass transition temperature, etc. can be influenced and adapted to a large extent - much more than e.g. the Young's modulus for steel or aluminum. Based on this, the idea of optimizing the Prony-Series parameters for a given technical application has been considered feasible.

The basic equations of finite element model updating can be applied here. A residual r must be defined between the desired dynamic properties a_{target} of an oscillator and the current dynamic properties $a(p)$ obtained with the current set of material parameters:

$$\{r(p)\} = \{a_{target}\} - \{a(p)\} \tag{39}$$

The objective of the parameter optimization is the minimization of the following objective function:

$$J = \{r(p)\}^T \{r(p)\} \quad \rightarrow \quad \min \tag{40}$$

A Taylor-Series approximation is introduced to linearize the non-linear relation between the current dynamic properties and the material parameters:

$$\{a(p)\} = \{a(p_0)\} + [S](\{p\} - \{p_0\}) = \{a_0\} + [S]\{\Delta p\} \tag{41}$$

The sensitivity matrix $[S]$ contains the partial derivatives of the dynamic properties a_i used as output features with respect to the parameters p_j of the Prony-Series. For example, the output features a_i can be the viscous damping ratio D of the oscillator and the frequency f_{max}^{η} under which the maximum of the loss factor occurs. On the other hand, the parameters of the Prony-Series can be the relaxation time τ_{rel} and relative modulus α:

$$[S] = \begin{bmatrix} \frac{\partial a_1}{\partial p_1} & \cdots & \frac{\partial a_1}{\partial p_j} \\ \vdots & \ddots & \vdots \\ \frac{\partial a_i}{\partial p_1} & \cdots & \frac{\partial a_i}{\partial p_j} \end{bmatrix} \quad \rightarrow \quad [S] = \begin{bmatrix} \frac{\partial D}{\partial \tau_{rel}} & \frac{\partial f_{\max}^{\eta}}{\partial \tau_{rel}} \\ \frac{\partial D}{\partial \alpha} & \frac{\partial f_{\max}^{\eta}}{\partial \alpha} \end{bmatrix} \tag{42}$$

Inserting this linearization into the residual and into the minimization problem finally leads to the following linear equation, from which an incremental change of the material parameters can be deduced:

$$\{\Delta p\} = \left([S]^T [S]\right)^{-1} [S]^T \{a_0\} = [S]^+ \{a_0\} \tag{43}$$

Due to the linearization of the non-linear parameter dependence, the parameter changes are only incremental and the determination of parameter changes must be performed iteratively until convergence is achieved.

Starting from given set of parameters of a Prony-Series, it is now possible to formulate target values for viscous damping ratio D and frequency of the loss factor maximum f_{max}^{η} for a given application. The elements of the sensitivity matrix must be determined from finite differences in this case.

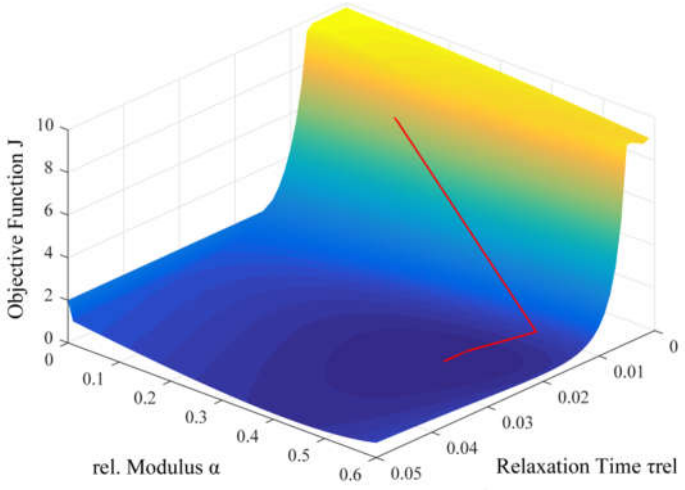


Figure 11: Objective function and path of iterative parameter optimization for Prony-Series parameters viscous damping ratio and relaxation time

It can be stated, that for a given application and for given initial values of a Prony-Series for a visco-elastic material, optimized parameters can be obtained from model updating by providing target values for dynamic response characteristics. This is shown in Figure 11, where the objective function is plotted over the two Prony-Series parameters relaxation time τ_{rel} and relative modulus α. These optimized Prony-Series parameters can now be provided for the development of an optimized elastomer vulcanisate.

5 Design of supplemental dampers based on visco-elastic materials

The experience gained from the parameter studies of chapter 3 shall be now applied to design the damping of a given dynamic structure. One of the targeted applications is to increase damping of aircraft fuselage structures to reduce cabin noise levels through distributed energy dissipation by visco-elastic dampers. All tools required to implement visco-elastic dampers in a finite element model were presented above in chapter 2.

5.1 Free-Layer-Damping

The example considered here is a cantilever beam made from aluminum. A beam is selected here, because the fuselage frames to be supplemented by local dampers are ring-shaped bending beams made from aluminum.

The setup is sketched in Figure 12. The beam is clamped at one end and a harmonic excitation force is introduced in vertical direction at the unconstrained beam tip. The aluminum material properties are listed

in Table 3. It should be noted that it also contains a structural damping coefficient. An additional damping layer is added onto the upper flange of the I-shaped cross section of the cantilever beam. This corresponds to the concept of Free-Layer-Damping (FLD). Butyl rubber has been identified as damping material and the frequency-dependent behavior is modelled by a Prony-Series with 10 parameters. The finite element software used is ANSYS Workbench. The resulting evolution of storage modulus and loss modulus of this material is shown in Figure 13. It must be noted, however, that these material properties are not from an existing material, but instead, they have been created from some other material because the required Prony-Series parameters for the targeted butyl rubber vulcanisate were not available when the numerical study has been conducted.

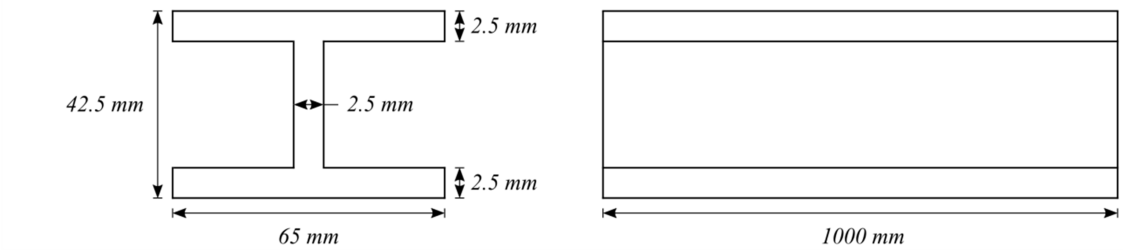


Figure 12: Geometry of the cantilever beam example

Table 3: Aluminum material properties used for the cantilever beam example

Material	ρ [kg/m^3]	E [N/m^2]	ν	η
Aluminum	2700	$7.1 \cdot 10^{10}$	0.3	0.005

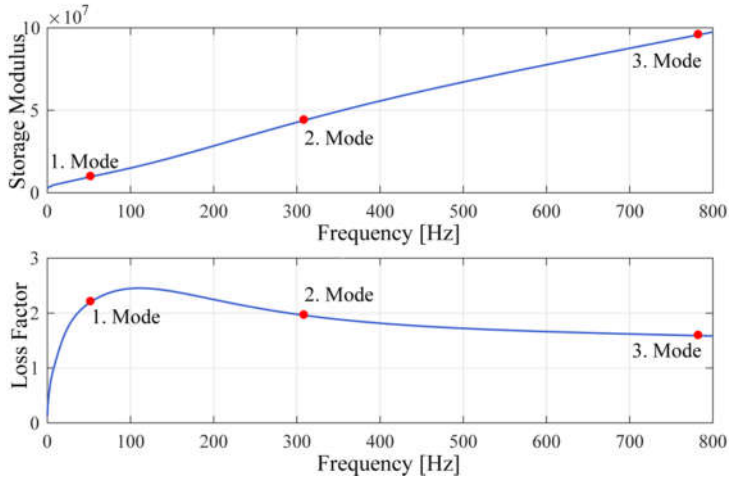


Figure 13: Storage modulus and loss factor of the butyl rubber as a function excitation frequency

Of course, the FLD concept has been verified for an additional layer of butyl rubber all along the beam and parameters like thickness of the layer have been varied. However, in order to keep the amount of additional material and the weight penalty at a minimum, the volume of supplemental damping material shall not exceed 5% of the volume of the original metallic structure. This corresponds roughly to 2.5% increase in the weight of the overall structure due to the supplemental elastomer damper.

This can be achieved by applying the damper not as a full layer, but instead as short segment placed onto the upper flange of the I-shaped beam. The placement of the segment along the beam largely influences the modal damping that can be achieved. In the FLD concept, the damping layer should be placed where the strain is significant. In Figure 14, the equivalent strain distribution is plotted for the 3rd mode and 5 different locations z_i, $i=1,...,5$, for the placement of the FLD damper segment are indicated.

For the evaluation of the effectiveness of the supplemental FLD damper segment, the parameter β_D is introduced. It represents the ratio of the relative difference in the viscous damping ratio ΔD and the added elastomer material volume ΔV (in percent):

$$\beta_D = \frac{\Delta D}{\Delta V} \tag{44}$$

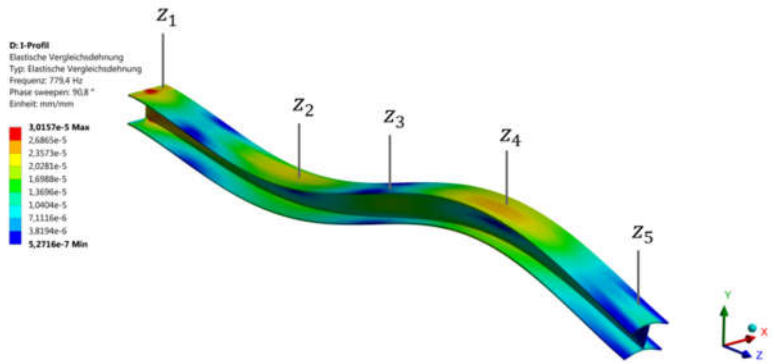


Figure 14: 3rd bending mode of the I-shaped beam and 5 locations for the application of damper segments

Based on this effectiveness parameter β_D, the results shown in the bar chart of Figure 15 have been obtained.

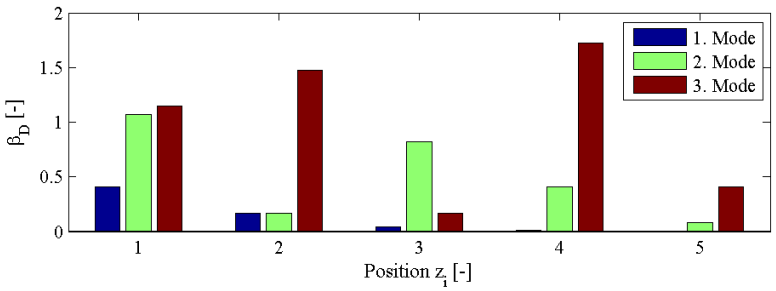


Figure 15: Effectiveness of supplemental FLD damper segment for different modes and different damper positions

It can be observed that the different modes can be damped with different effectiveness. This has basically two different reasons.

The first reason can be found in the location of the damper. In case of FLD, it should be placed at a position with significant strain. This explains why mode 1 can be damped most effectively when the damper is located at the clamping position z_1 and no damping can be achieved when located at the unconstrained beam tip z_5. The same applies to z_1 and z_5 for the second and the third mode. Best damping effectiveness can be achieved for mode 2 and 3 when the damper element is located at an antinode, or respectively, a local deflection maximum, e.g. z_4 in case of mode 3 and z_3 in case of mode 2.

The second reason for the different damping effectiveness can be found in the frequency dependence of the loss modulus and the storage modulus. In Figure 13, the variation of storage modulus and loss factor is shown for the butyl rubber used here. It can be seen in the lower diagram that the loss factor is higher for mode 1 than for mode 2 and the loss factor for mode 2 is higher than the one for mode 3. More important is, however, the strong linear increase in the storage modulus. When taking into account that the loss modulus is the product of loss factor and storage modulus, see equation (12), it is clear that the loss modulus also increases and is highest for mode 3 but almost a factor of 10 lower for mode 1.

As indicated in Figure 15, the concept of FLD yields an increase of the damping ratio of the aluminum beam. The beam material was simulated with a structural damping coefficient of 0.005, see Table 3. This

corresponds to an equivalent viscous damping ratio of 0.25%, i.e. a weakly damped system. The additional 5% (in volume) of elastomer can increase the damping of the aluminum beam by +172%, i.e. up to 0.43% damping ratio. This is still weakly damped. However, the material properties used are not from a realistic material. There is more potential of elastomer dampers e.g. when a specific damping material is designed for a specific application (i.e. defined in terms of frequency range, operating temperature, desired loss modulus, etc.).

5.2 Constrained-Layer-Damping

In the Constained-Layer-Damping concept, the damping can be introduced by a layer of visco-elastic material which undergoes shear deformation. In particular, the shear rate of this material shall be much higher than those of the material of the original structure for which damping shall be designed. Based on preliminary simulations, it can be anticipated that the Constraint Layer Damping concept is much more effective when applied to the aluminum beam example of chapter 5.1. It is based on the idea, that the damper segment can be activated significantly by an auxiliary mechanism. The concept studied is sketched in Figure 16. Unfortunately, the results from simulations with Prony-Series parameters were not complete at the time of compilation of this paper, so that this chapter is more like an outlook on future work.

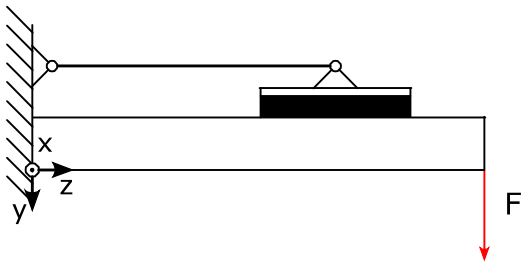


Figure 16: Constrained layer damping (CLD) concept applied to cantilever beam with auxiliary mechanism to increase shear strain in elastomer

6 Summary and Conclusions

The modelling of visco-elastic materials has been discussed, starting from rheological models like Prony-Series and going towards frequency-dependent 3D material law. The generation of frequency-dependent element stiffness and damping matrices can be pursued based on this approach. It leads to an equation of motion similar to the classical structural damping (or hysteretic damping) approach. The essential difference is, however, that the loss factor is frequency-dependent and also the stiffness matrix. Numerical eigenvalue analysis no longer possible when frequency-dependent stiffness and damping matrices are involved. Instead, the direct frequency response analysis has been applied to simulate frequency responses from which eigenfrequencies and damping ratios have been identified using the Peak-Fit modal parameter estimator, [8].

Parameter studies demonstrated the feasibility of finite element analysis using 1D, 2D and 3D elements with visco-elastic material modelled with a Prony-Series. In the course of these studies, the sensitivities of the material parameters of the Prony-Series have been investigated. The experience gained from these simple applications has been used afterwards for the damping design of an I-shaped cantilever beam. The potential of the Free-Layer-Damping concept has been presented. Unfortunately, the increase in damping ratio cannot be determined precisely, because no reliable material data for elastomers was available so that modified material behavior of other elastomers had to be used. Nonetheless, the preliminary results obtained with the Constrained-Layer-Concept already indicate that more damping effectiveness can be achieved using this concept.

Finally, the selection of the right material for a given application is crucial for the success. The variation in material properties like storage modulus and loss modulus is immense even for a given type of polymer. Therefore, well-defined requirement for the targeted application can help the polymer chemists to develop a vulcanisate for this application with high damping effectiveness and low impact on structural weight or dimensions. However, temperature dependence and compatibility with substances like oil, oxygen, water, etc. must be considered.

References

[1] Link, Michael: *Finite Elemente in der Statik und Dynamik*. Springer-Verlag, 2014

[2] Gross, D., Hauger, W., Schnell, W., Wriggers P.: *Technische Mechanik 4: Hydromechanik, Elemente der Höheren Mechanik, Numerische Methoden*. Springer-Verlag, 2007

[3] Popov, V.: *Kontaktmechanik und Reibung: von der Nanotribologie bis zur Erdbebendynamik*. Springer-Verlag, 2016

[4] Michaeli, W., Brandt, M., Brinkmann, M., Schmachtenberg, E.: *Simulation des nicht-linear viskoelastischen Werkstoffverhaltens von Kunststoffen mit dem 3D-Deformationsmodell*. In: Zeitschrift für Kunststofftechnik (2006)

[5] ANSYS, Inc.: *Theory Reference for the Mechanical APDL and Mechanical Applications*. Version 17.2. : ANSYS, Inc., 2017

[6] Imaoka, S.: *Analyzing Viscoelastic Materials*. In: Ansys Advantage 2 (2008), Nr. 4, S. 46–47

[7] Knothe, K., Wessels, H.: *Finite Elemente: Eine Einführung für Ingenieure*. Springer-Verlag, 2017

[8] Böswald, M.: *Analysis of the bias in modal parameters obtained with frequency-domain rational fraction polynomial estimators, Proc. of ISMA 2016, KU Leuven, Belgium, 2016*

The effect of friction damping on the dynamic response of vibrating structures: an insight into model validation

M. Umer [1], **C. Gastaldi** [1] **D. Botto** [1]
[1] Politecnico di Torino, Department of Mechanical and Aerospace Engineering,
Corso Duca degli Abruzzi 24, 10129 Torino, Italy
e-mail: **muhammad.umer@polito.it**

Abstract
Dry friction is widely used in turbomachinery in the form of under platform dampers to limit resonant vibration and avoid high-cycle fatigue failures of the blades. Most test rigs that are used to investigate the behavior of dampers aim to evaluate their performance by reduction in blade vibration amplitude. This approach is insufficient to understand local nonlinearities of the contact and influence of blade dynamics on UPDs behavior. A newly developed test rig provides the user with an unprecedented set of information: it measures contact forces and relative displacements between dampers and blade together with the overall blade response. This controlled environment, together with a state-of-the-art numerical model of the test rig, is used to provide an insight into the subject of model validation. The presented experimental and numerical study of the damper is used to highlight the relevance of an accurate representation of the constraints induced by friction contacts and to discuss the adequacy of state-of-the-art contact models.

1 Introduction

Dry friction damping is used, in the field of turbomachinery, to mitigate the structural vibrations caused by fluctuating stresses[1, 2]. Under platform-dampers (UPDs) are small metallic components placed between two consecutive blades of a turbine to minimize the blade vibration by dissipating the energy at contact interface. Highly nonlinear behavior of the frictional contacts makes it challenging for researchers and engineers to precisely model and predict the response of complete damper-blade structures at various load conditions. In this regard, explicit numerical models of under platform dampers (UPDs) are used with a multi-harmonic balance solver to predict its non-linear behavior. A detailed study on the modelling of UPDs is presented by several authors [3, 4, 5, 6, 7, 8, 9, 10] in which a routine is adopted to compute the damper contact forces as a function of given relative displacement between two contact surfaces. Such routines, also known as contact models, require calibration. This step is crucial as numerical results are strongly dependent on the chosen set of contact parameters [11, 12, 10]. Therefore, experimental measurements are necessary:

- to actually determine the performance of the damper in terms of blade amplitude reduction and frequency shift;
- to estimate the contact parameters used to calibrate contact models.

These two necessities are sometimes fulfilled with the same set of experimental evidence. Experimental evidences most commonly available are FRFs [7, 13, 14, 15]. Unfortunately fine tuning the contact parameters to obtain the desired frequency response is not a viable practice, as multiple combinations of contact parameters may produce the same frequency response (i.e. under-determined problem). Another way to obtain contact parameters is through the use of single-contact test arrangements[16, 17]. A test rig improved in [18] is capable of measuring friction coefficients and contact stiffness values of a flat-on-flat contact interface.

This test rig has a facility to control the relative displacement and high temperature of the contacting surfaces. However, the applied normal load is constant, which is not consistent with the real working conditions of UPDs. An upgrade first proposed in 2010 [19] has a single damper constrained between two dummy platforms. A feedback controlled displacement is provided with the help of piezoelectric actuator on one of the platform whereas, damper contact forces are measured on the other platform by using two load cells. Since then this test rig has been used to investigate the kinematics of several dampers [20, 21]. Nevertheless, as this test rig does not have a blade, the effect of blade dynamics on kinematics of the damper is not present. Therefore, a novel test bench [22, 23] has been designed and commissioned by the authors to overcome these limitation. This novel test rig has been developed with the purpose of investigating the kinematics of the dampers in the presence blade dynamics (a topic of recent interest in the community [10]). This test bench is composed of a single turbine blade with two UPDs and has a facility to measure damper contact forces and its relative displacement with respect to the blade. This allows a direct investigation of the variation in damper kinematics and overall structure dynamics at various loading conditions. This is achieved by recording:

- the FRFs of the blade with accelerometer to estimate damper performance (blade dynamics)
- Damper-blade contact behavior with the help of load cells and laser (contact forces and displacements)

These experimental measurements establish a base to study the behavior of dampers at their contact level. Moreover, a multi-step model validation is possible using this experimental evidence.

1. Measured contact forces applied as external forces on the FE model of the blade (comparison of numerical and experimental FRFs) - validation of the linear FE model of the blade constrained in the rig.
2. Measured platform displacements fed to the damper model already presented in[] (comparison of numerical and experimental contact forces) - validation of the damper model and of the contact model used to represent friction.

These two steps give the unprecedented opportunity to verify separately and independently the adequacy of the user-constrained blade FE model with the adequacy of the contact model. An endeavor which is simply not possible if a standard experimental-numerical comparison of FRFs is the sole benchmark.

A brief description of this test rig is present in section 2 (the reader is referred to [23] for a detailed design study). The numerical model of the blade and damper is addressed in Sect. 3. The first step of the validation procedure described above is recounted in Sect. 4. Section 4.1 carries out a careful analysis of the measurement error of contact forces, an indication the authors hope will be useful to other researchers. The second step of the validation procedure is recounted in Sect. 5 and the adequacy of the contact model is discussed.

2 Experimental Setup

Due to the complex and nonlinear behavior of friction, a test rig with a capability to directly measure parameters at the damper-blade contact level is required. The novel test rig used to obtain the experimental evidence presented in this article has several distinct features. However, the feature that best distinguishes the test rig used in this research from other experimental setups is the direct measurement of the contact forces when the damper is dynamically coupled with the blade. A top view of the test rig is shown in Fig.1 which presents a single turbine blade is visible, placed inside a cavity engraved in the blade-adapter according to the geometry of the blade root. This blade-adapter is a replaceable part thus allowing to accommodate a number of turbine blades in test on the rig, provided that the maximum length of the blade is not exceeded. A controllable and

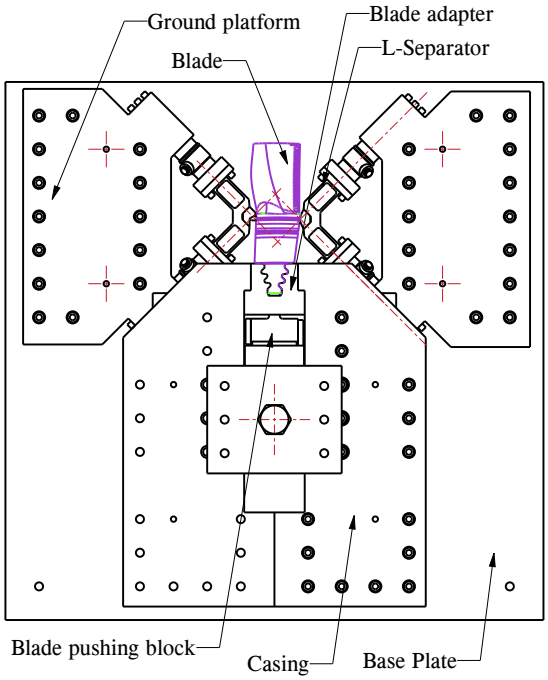


Figure 1: Top view of test rig

measurable pushing force F_P is applied on the root of the blade to simulate the actual centrifugal force which acts on the blade while the turbine runs. Two under platform dampers are placed against the blade platforms on each side of the blade. The dampers are in contact with the under-platform of the blade on one side and with a ground platform on the other side.
The ground platform is linked to a contact force measuring system. Two contact force measuring systems are used, one for each damper. A component named L-Separator, designed with two orthogonal limbs, separates the contact forces into two components acting along each limb axes. A piezoelectric load cell is placed at the end of each limb to measure the respective force component. The accuracy of the force measuring system depends upon several factors. Electronics involved in force measurement, misalignment introduced by the mechanical tolerances and contact angles are the major sources of uncertainty. A complete description of the force measuring accuracy is given in [23].
The contact forces at the blade side are obtained from the measured contact forces at the ground platform side through a simple force equilibrium, depicted in Fig. 2. In it, the damper inertia forces are neglected, a perfectly valid assumption at frequencies lower than 5 kHz (cite my thesis). Forces can also be decomposed into their normal (N) and tangential (T) components, as shown in Fig. 2 or along the blade axial-radial directions (XYZ reference system). This last reference system is the same used in the FE model of the blade and will be used throughout the paper.
The blade excitation is provided by means of an electromagnetic shaker. The shaker stinger is connected at a point near the blade root (low mobility point) to excite the structure at desired frequency and excitation level.

3 Damper and Blade Numerical Models

As stated in the introduction the experimental capabilities of the test rig allow for two separate and independent validations. As a result, the numerical models used in the validation process will separately represent the blade and damper environment. This section describes both models together with the chosen solution techniques.

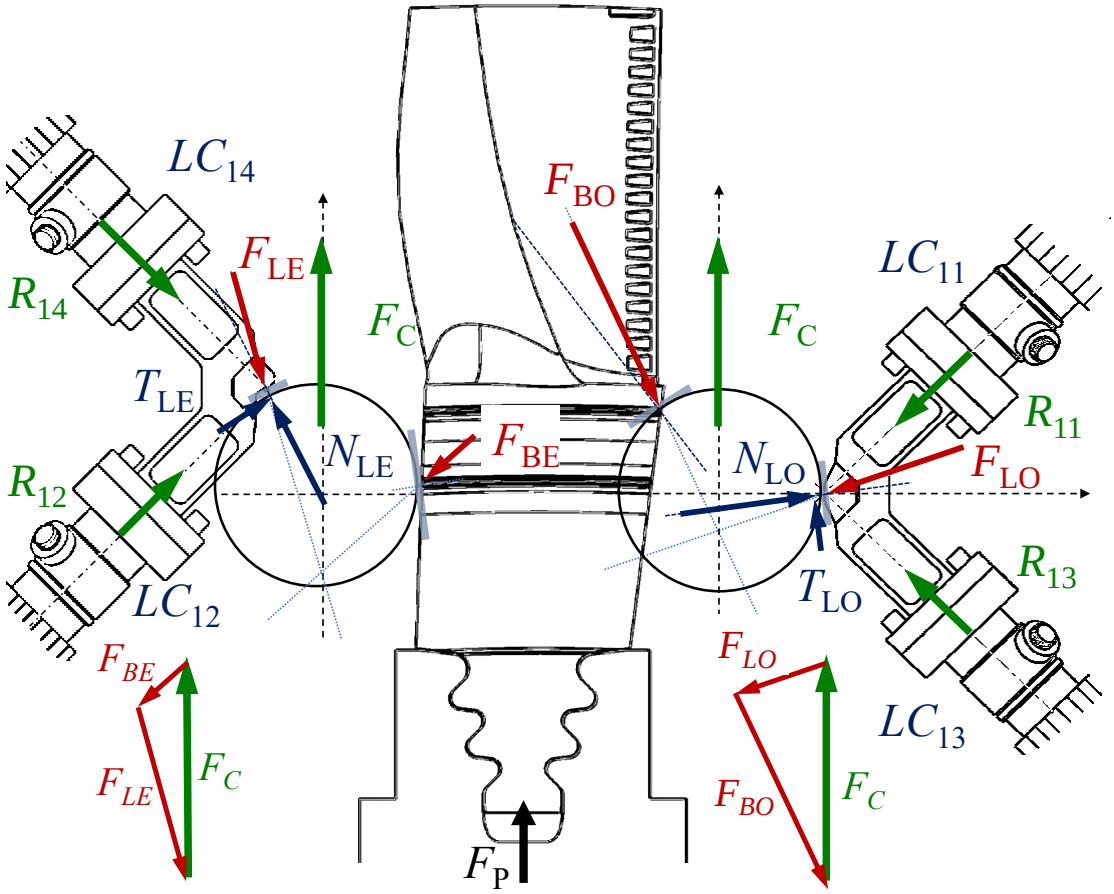


Figure 2: Damper static force equilibrium, both dampers at their nominal positions

3.1 The blade numerical model

The general forced response of any friction-damped structure can be written as follows:

$$M\ddot{Q} + C\dot{Q} + KQ = F_E + F_C \tag{1}$$

where M, C and K corresponds to mass, damping and stiffness matrices of the elastic structure respectively. Further details on the procedure used to obtain FE matrices representing the constrained blade are given in Sect. 3.1.1 and 3.1.2. The vector Q represents the displacement of all degrees of freedoms (DOFs) of the system. Vectors F_E and F_C correspond to external and contact forces respectively. In the present case, the external force is applied to the system with the help of external excitation source i.e electromagnetic shaker, at a given frequency and amplitude level. Whereas the contact forces F_C are nonlinear forces acting on the blade underplatform, i.e. at the blade-damper contact interface.

3.1.1 Craig-Bampton Reduction

The Craig-Bampton Reduction method, also known as CB-CMS, is a commonly used technique to reduce the size of a large finite element model by acquiring the fundamental frequency modes of the structure [24, 25]. In this method, only a subset of physical DOFs of the full model, corresponding to chosen nodes, are retained as master DOFs while the remaining DOFs are reduced in a set of orthogonal modes (slave DOFs). In the blade finite model presented in this paper and shown in Fig. 3, master nodes include contact nodes at the blade platforms and at the root attachment, one blade excitation node where the shaker is attached and a blade response node where the accelerometer is positioned. In Fig. 3 a, master nodes corresponding to the left platform and root are not visible due to given orientation of the blade.
It was here chosen to apply the CB-CMS technique to the free blade model, and to constrain the structure, i.e. to reproduce the clamping of the root, at a subsequent step. Section 3.1.2 gives further details on this matter.

3.1.2 Preliminary tuning of the clamped blade structure

A common method to tune a clamped blade is to fully constrain (i.e. impose zero displacement at all DOFs) of a few nodes belonging to the blade root. This approach may be convenient, but has several drawbacks:

- It does not reproduce real contact conditions: since the zero displacement hypothesis is very strong, only a subset of nodes must be constrained if the simulated and measured resonance frequencies have to match.
- The level of approximation is too rough, it is sometimes impossible to match at least 2-3 measured resonance frequencies with this method, thus producing a sub-optimal free model as input to the subsequent nonlinear calculations.

For these reasons the authors decided to improve the way blade clamping is modeled by introducing a 3D spring element at each node on the blade roots, as shown in Fig.3 b. The 3D spring element connects each selected blade root node element either to a corresponding node on the surrounding structure (if the blade or the disk is modeled) or simply to ground (if, as in this case, the bulkiness and stiffness of the blade adapter allows for this simplification.)
The use of a 3D spring element (which may be easily upgraded to an actual contact element capable of slip if deemed necessary) allows modeling the effect of compliance of the contact interface in all directions. The user will notice that the 3D spring element needs three calibration parameters: k_n, k_{t1} and k_{t2}. The values

of the springs are determined by imposing that the first three measured frequencies of the clamped free (i.e. no damper) blade match the simulated ones:

$$\begin{cases} f_{1,MEAS} = f_{1,SIM}(k_n, k_{t1}, t_{t2}) \\ f_{2,MEAS} = f_{2,SIM}(k_n, k_{t1}, t_{t2}) \\ f_{3,MEAS} = f_{3,SIM}(k_n, k_{t1}, t_{t2}) \end{cases} \tag{2}$$

Since the fist three modes see the root moving along three different directions, the resulting system produces a unique solution (i.e. set of contact springs) thus yielding a system with a unique solution (three conditions for three unknowns).
The experimental clamped free blade response is also used to tune the structural damping level (i.e. matrix C), see result in Fig. 3 c. The measured/simulated FRFs confirm that the clamping force applied to the blade produce a minimal contribution to the damping at the root.

3.1.3 Forced response calculation

This section gives further details on the method used to solve Eq. 1. Harmonic balance is used to compute the steady state solution of equations where an applied periodical excitation force of frequency ω results in the periodical response of the system [26, 27].
If the damper is not present (i.e. clamped free blade), then $F_C = 0$, the equilibrium is linear and can be solved, in the frequency domain, as a simple system of algebraic equations:

$$\overline{Q}^1 = \left(-\omega^2 \cdot M + i \cdot C + K\right)^{-1} \overline{F}_E^1 \tag{3}$$

where $\overline{Q}^1$ and $\overline{F}_E^1$ represent the first harmonic Fourier components of the displacement and external force vectors.
If, on the other hand, the damper is present, contact forces are non-zero $F_C(Q, \dot{Q})$. These forces are due to Coulomb friction nonlinearities and are typically determined as a function of relative displacements at the contact using a suitable contact model [28]. Given the dependence of contact forces on displacements, the equations are clearly nonlinear. As a result, iterative techniques such as Newton-Raphson or Continuation methods are applied [29].
At this first validation stage, the iterative procedure is avoided. Contact forces and external forces are directly measured, transformed in the frequency domain using FFT, and applied to the clamped free blade model.

$$\overline{Q}^1 = \left(-\omega^2 \cdot M + i \cdot C + K\right)^{-1} \left(\overline{F}_{E,MEAS}^1 + \overline{F}_{C,MEAS}^1\right) \tag{4}$$

The dependence of contact forces on relative displacements is still present, in fact different experimental conditions (different ω, different excitation levels F_E) yield different measured values of F_C. However, no assumption on the formulation of this displacement-contact force relation is needed at this stage. The authors are willingly separating the validation of the blade dynamic model (results in Sect. 4) from the assessment of the adequacy of the contact model formulation (addressed in Sect. 5).

3.2 The damper numerical model

The damper here is considered as a rigid body with six degrees of freedom at its centre of mass. The rigid body assumption is well justified by the bulkiness of solid-bar underplatform dampers, and has already been validated against specific experimental evidence on underplatform dampers [8, 23, 25]. The same conclusion has been reached for similar applications in [6].
A 2D view of the damper numerical model is shown in Fig. 4, together with the damper DOFs expressed in the same reference frame as the blade. Only the YZ plane is shown here because this investigation is focused on the first bending mode, which can be completely described in the YZ plane (i.e. no motion along the X

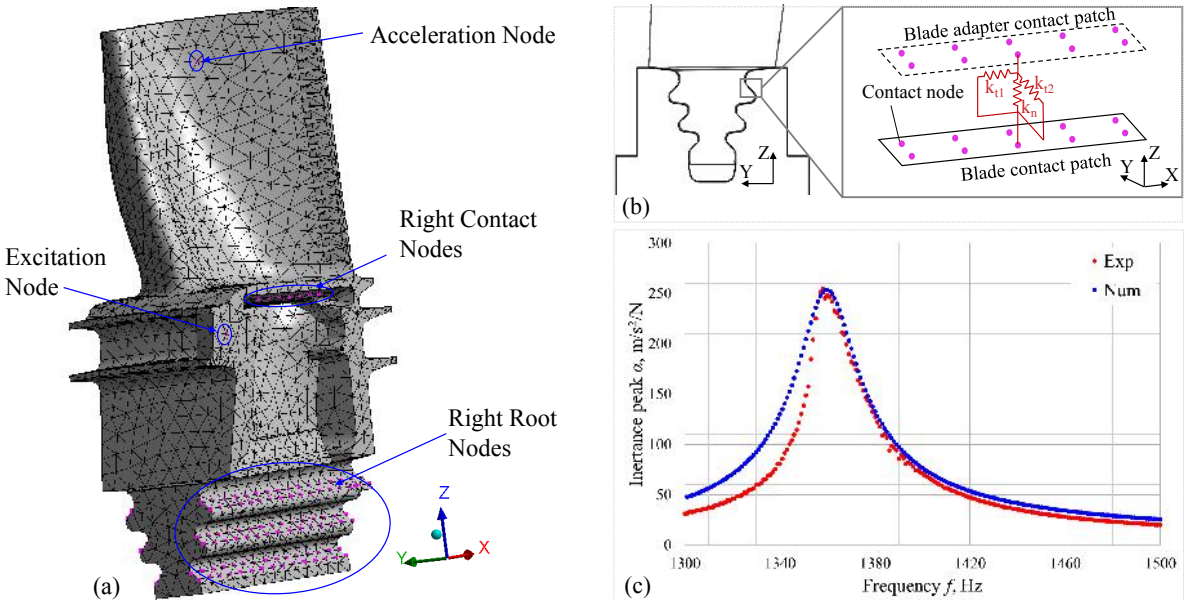


Figure 3: (a) Selected master nodes for CB-CMS reduction. (b) Comparison between experimentally measured Free FRF with the FRF of tuned numerical model. (c) A 3D spring compliance introduced to tune the free elastic blade structure

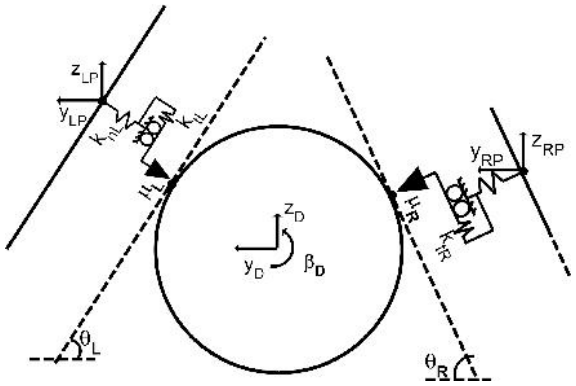


Figure 4: 2D view of the damper numerical model

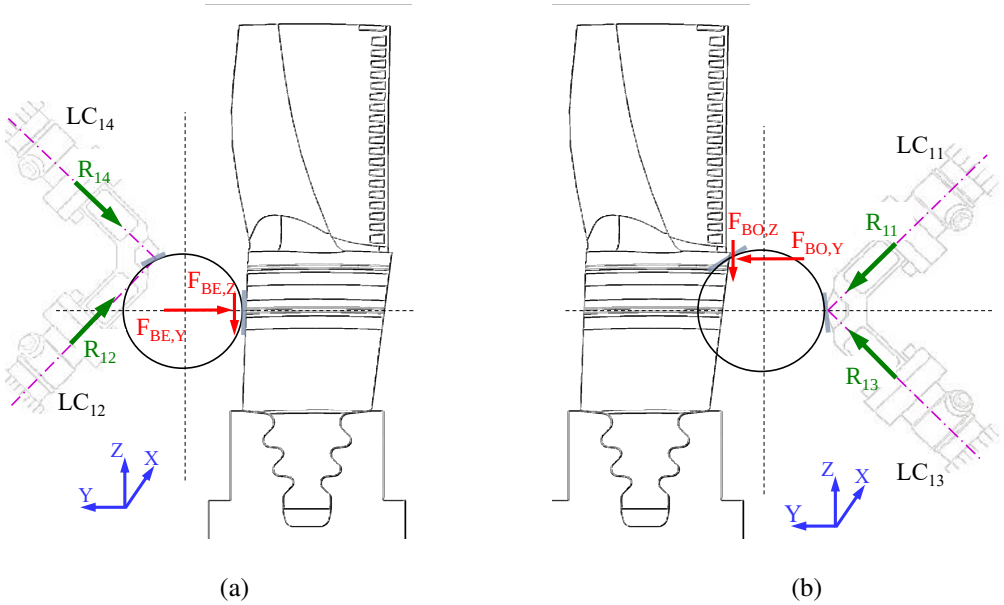


Figure 5: (a) Even side damper placed at its nominal position to measure contact forces. (b) Odd side damper placed at its nominal position to measure contact forces

direction). The inputs to the model are the displacement vectors, (y_{LP}, z_{LP}) and (y_{RP}, z_{RP}), at the retained contact nodes on the surface of the FE model of the blade.

Time discrete macroslip elements shown in the figure Fig. 4 and further analyzed in [28], are used to obtain the contact forces as a function of the relative damper-platform displacements. Their adequacy will be discussed in Sect. 5.

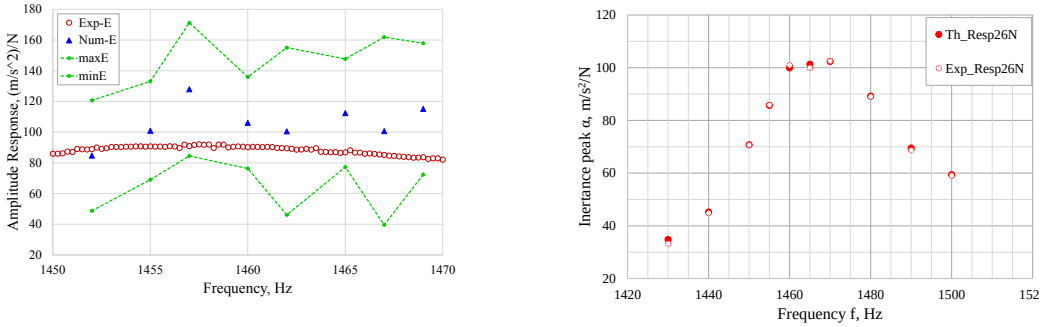
The damper equilibrium equations are solved using a time-marching method, whose complete description can be found in [30]. This novel quasi-static method can be applied to systems whose inertial effects are negligible (as in the damper-only case). Unlike Harmonic Balance, there is no risk of misrepresenting contact forces with insufficient number of harmonics, and is more than ten times faster than standard Direct Time integration.

4 Validation of the blade dynamic model

The purpose of this section is to verify whether the forced response computed using the clamped FE model of the blade, fed with the measured contact forces values (see Eq. 4), matches the measured FRF. The excitation level applied through the shaker (and mimicked in the numerical environment) is in all cases set at $\|\overline{F}_E^1\| = 1$ N.

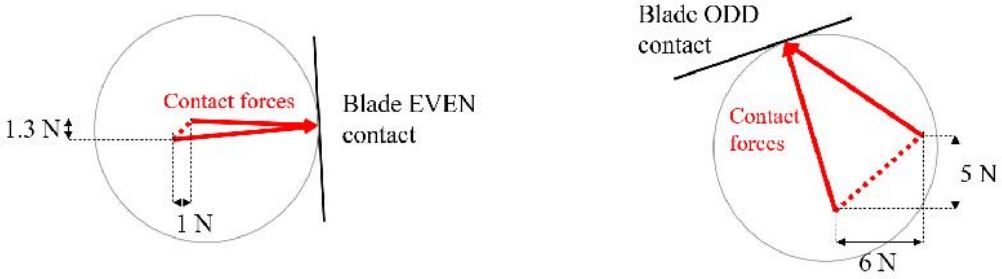
This validation procedure is attempted using two different configurations. As explained in Sect. 2 there are two dampers on either side of a single turbine blade. The validation is performed by mounting only one damper at a time (see Fig. 5).

Contact forces are measured at the ground platforms' side. Force components applied on the blade are obtained through the damper static force equilibrium as shown in Fig. 2. A detailed description and formulation of the force diagrams can be found in [23]. The uncertainty level of contact force measurements is in the [0.75-1] N range, and cannot be reduced further due to mechanical tolerances, electronics/signal noise and uncertainty involved in the estimation of platform angles. It will be shown that, depending on the magnitude of harmonic variation of the contact forces, the uncertainty level of the forces may hinder the validation procedure.



(a) (b)

Figure 6: (a) Error sensitivity of blade response amplitude due to even side contact forces measurement at F_C = 26 N. (b) Numerical vs Experimental results comparison for damper forces measured on Odd side at F_C = 26 N



(a) (b)

Figure 7: (a) Typical contact forces harmonic variation when only the ”even” side damper is present. (b) Typical contact forces harmonic variation when only the ”odd” side damper is present.

4.1 Noise effect on measured Contact Forces

At first, the left side of the blade is considered: contact forces measurements R_{12} and R_{14} from load cells LC_{12} and LC_{14} are used to compute the corresponding contact forces at the blade side ($F_{BE,Y}$ and $F_{BE,Z}$) which are finally applied as external forces on the numerical model as shown in Fig. 5 a. The experimental-numerical comparison is shown in Fig. 6 a. A large discrepancy between the measured FRF and the numerical ”prediction” can be observed. The cause of this difference does not reside in the model itself, rather in the measured contact force signals fed to the model.

It has been found that harmonic variation of the force components (i.e. then transformed in $\overline{F}^1_C$) measured by the even load cells (LC_{12} and LC_{14}) at an excitation force of 1 N, ranges between 1 to 2 N at most (see also Fig. 7 a). The magnitude of the harmonic variation of the force depends upon the contact angles and the platform kinematics (i.e. blade mode shape and experimental set-up). The level of uncertainty on the contact force signals ($\approx$ 0.75 N) is of the same order of magnitude as the signal itself and this easily explains the very large discrepancies between numerical and experimental results.

To evaluate further the effect of the force measurement error on the blade response amplitude, a sensitivity analysis has been performed. A sinusoidal error has been added ”numerically” to the measured force signals. The amplitude of this error is equal to the uncertainty level (0.75 N) with a phase shift with respect to the contact force signals varying from 0 to 15 degrees. This sensitivity analysis is performed for a single experimental condition, i.e. centrifugal load on the damper F_C=26 N and excitation force $\|\overline{F}^1_E\|$=1. The maximum and minimum values of the blade response produced by the perturbed contact force signals are shown in Fig. 6 a. It can be seen that even a seemingly small noise signal can have a significant impact on the blade

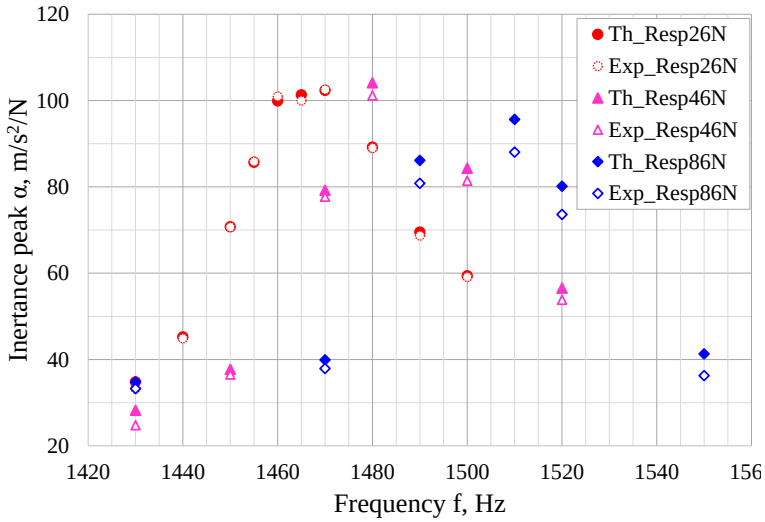


Figure 8: Comparison of numerical and experiment results for three different static damper centrifugal load values F_C = 26, 46 and 86 N

amplitude response. The following section addresses the second validation attempt, operated on the set up shown in Fig. 5 b.

4.2 Successful experimental-numerical comparison

The experimental set-up shown in Fig. 5 b, thanks to a different combination of choice of contact angles and platform kinematics, produces:

- higher harmonic variation of the measured contact forces (in this case recorded at the load cells LC_{11} and LC_{13}), now ranging between 5 and 8 N (see also Fig. 7 b);
- increased stiffening effect, as shown in Fig.6 b, the peak for F_C=26 N is now sharper and few Hz higher than that shown in Fig. 6 a.

Furthermore, in this case, the uncertainty level guaranteed by the load cell measurement is adequate (reasonably smaller than the force signals themselves). As a result, the validation procedure summarized in Eq. 4 can be safely applied. The experimental-numerical comparisons are shown, for different levels of centrifugal load on the damper, in Fig. 6 b and 8: numerical results match their experimental counterpart quite satisfactorily in all investigated cases.

5 Validation of the damper numerical model

This section seeks to assess the adequacy of the numerical model of the damper between a set of ideal platforms shown in Fig. 4. This task requires:

- estimating a set of contact parameters to calibrate the contact model (Sect. 5.1);

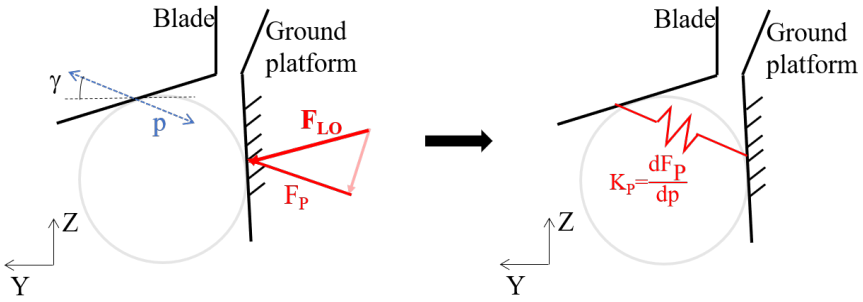


Figure 9: (Left) Relative platform kinematics p and reaction force F_P, component of the contact force F_{LO} parallel to p. (Right) definition of the effective platform-to-platform stiffness K_P starting from quantities p and F_P.

- comparing the result of the numerical model with that of the reference experimental evidence (Sect. 5.2).

This task is performed on the experimental configuration shown in Fig. 5 b where reliable contact force measurements are available.

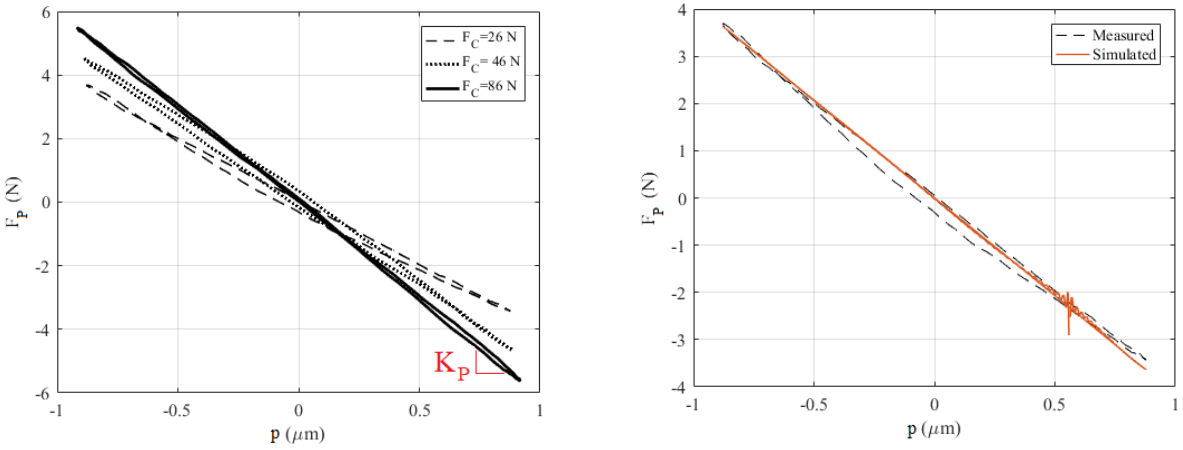
5.1 Contact parameter estimation

The contact model shown in Fig. 4 requires three calibration parameters: the friction coefficient μ and the normal and tangential contact stiffness values k_n and k_t. It is here assumed that all contact points share the same set of parameters, a reasonable assumption given to the identical geometry and material of the two damper-platform interfaces.
The analysis of the Tangential/Normal force ratio at the two interfaces reveals that the contacts never reach the gross slip condition (i.e. the force ratio never reaches a plateau [31]). Since the ratio is, in the investigated cases, always lower than 0.25, a lower limit for the friction coefficient can be set at $\mu > 0.25$.
The "odd" damper is "hidden" inside the blade cavity, therefore measuring the damper-platform relative displacement to estimate the contact stiffness in a straightforward manner is not possible. A different formulation, developed for In-Phase blade vibration in [32], is here extended to a more general case.
The damper acts as a constraint between two adjacent platforms, this effect is at its maximum during the full-stick condition. The platform-to-platform relative kinematics can be easily determined, either through the validated FE model or by direct measurement with a differential laser head. In Fig. 9 the relative platform displacement for the experimental set up shown in Fig. 5 b is represented by the vector $p = (p_y, p_z) = (y_{LP} - y_{RP}, z_{LP} - z_{RP})'$ oriented with an angle $\gamma = atan\left(\frac{z_{LP}-z_{RP}}{y_{LP}-y_{RP}}\right)$ with respect to the global reference system. In the present case the relative platform displacement has a simple linear trajectory with $\gamma = 22.5°$ for all investigated levels of excitation $\|F_C\|/\|F_E\|$.
It is worth noting that only the component of the contact forces oriented along the direction of motion will contribute to stiffening the structure, e.g. only the projection F_P of the force on the ground platform F_{LO} acts as an effective constraint. Starting from the relation, valid in full stick condition:

$$\begin{pmatrix} F_{LO,y} \\ F_{LO,z} \end{pmatrix} = \begin{bmatrix} K_{yy} & K_{zy} \\ K_{yz} & K_{zz} \end{bmatrix} \cdot \begin{pmatrix} p_y \\ p_z \end{pmatrix} \tag{5}$$

where K_{yy}, $K_{yz} = K_{zy}$ and K_{zz} are simple linear combinations of the contact springs k_n and k_t which depend on the position of the contact points and on the contact angles θ_R and θ_L.
If the direction of the relative platform kinematics γ is known, it is possible to isolate the corresponding force component:

$$F_P = \begin{pmatrix} \cos(\gamma) & \sin(\gamma) \end{pmatrix} \cdot \begin{bmatrix} K_{yy} & K_{zy} \\ K_{yz} & K_{zz} \end{bmatrix} \cdot \begin{pmatrix} \cos(\gamma) \\ \sin(\gamma) \end{pmatrix} \cdot \|p\| \tag{6}$$



(a) (b)

Figure 10: (a) Measured platform-to-platform hysteresis cycles at resonance for increasing values of centrifugal load on the damper (b) Measured vs. simulated platform-to-platform hysteresis cycle for $F_C = 26$ N.

Then, the effective platform-to-platform stiffness can be defined as:

$$K_P = \begin{pmatrix} \cos(\gamma) & \sin(\gamma) \end{pmatrix} \cdot \begin{bmatrix} K_{yy} & K_{zy} \\ K_{yz} & K_{zz} \end{bmatrix} \cdot \begin{pmatrix} \cos(\gamma) \\ \sin(\gamma) \end{pmatrix} \tag{7}$$

The platform-to-platform stiffness $K_P = f\left(k_n, k_t, \theta_L, \theta_R, \gamma\right)$ value can be easily determined experimentally, as shown in Fig. 10 a. Since parameters $\theta_L, \theta_R, \gamma$ are known the comparison between the "analytical" value of K_P and its measured counterpart can be used to estimate the k_n and k_t values.
The analytical-experimental comparison discussed above is not enough to uniquely estimate a k_n, k_t pair (one equation with two unknowns). Fortunately, a validated estimate of the k_n value can be found in Harris[33] which sets k_n in the $5 \cdot 10^7 - 10^8$ N/m range, depending on the effective length of contact (known with some uncertainty). As a result the comparison between analytical and experimental K_P values yields estimates for the tangential contact spring k_t, shown in Table 1. The uncertainty band on each k_t estimate is not due to the K_P measurement itself (remarkably repeatable), rather on the uncertainty of the k_n value. Fortunately the uncertainty band on k_t is reasonably limited and still allows the user to detect a clear dependence of k_t on the load at the contact.

Table 1: Tangential contact stiffness estimates as a function of the centrifugal load on the damper

F_C (N)	k_t (N/μm)
26	[3-6]
46	[6-8]
86	[9-11]

5.2 Results discussion

The proper estimates for k_n and k_t derived in Sect. 5.1 and the relative platform kinematics vector p are fed to the damper numerical model (see Fig. 4). The resulting platform-to-platform hysteresis cycle (i.e. F_P vs. p) is compared to its measured counterpart (one example for $F_C = 26$ N is shown in Fig. 10 b). The comparison is quite satisfactory however two main points which require improvement can be detected.

- The adopted contact model underestimates the (minor) damping contribution present in the microslip regime. In fact, the numerical platform-to-platform hysteresis cycle has zero area (i.e. proportional to dissipated energy), while the measured counterpart has a certain damping contribution which decreases as the ratio $\|F_C\|/\|F_E\|$ increases (see Fig. 10 a).
- The contact model has no built-in capability to catch changes in the contact conditions produced by increased contact pressure. As a result, it requires re-calibration if the centrifugal load on the damper increases (see different values of K_P in Fig. 10 a and resulting k_t estimates in Table 1).

6 Conclusions

The paper was successful in:

1. building an improved linear clamped blade model to faithfully reproduce the test rig condition and its root constraints;
2. validating said model by feeding it measured contact forces signals and comparing numerical vs. experimental FRFs;
3. providing unique estimates for the contact parameters values;
4. assessing the adequacy of the contact model by comparing numerical vs. experimental platform-to-platform hysteresys cycles.

Steps 2 and 4 can be thought of as two equally important validation steps.
Step 2 validates the dynamics of the "linear clamped FE model of the blade" in the nonlinear regime without assumptions on the contact model, i.e. it answers the question: "if the contact model was capable of producing correct estimates of the friction forces, would the constrained blade FE model predict the correct frequency response?".
Step 4 addresses separately and independently the adequacy of the contact model, i.e. it answers the question: "if the contact model is fed the correct input displacements, is it capable of predicting correct estimates of the friction forces?".
Thanks to the test rig capabilities these two validation steps can be performed independently using a complete set of experimental evidence: the blade response (FRF) and the corresponding set of contact forces. Limitations of this approach due to insufficient resolution of the contact force signals for given damper configurations are highlighted as an important warning for the experimenters.
Since the two validation steps have been achieved successfully, the authors are now working on the implementation of the validated damper model with the validated clamped FE model of the blade.

References

[1] J. H. Griffin, *Friction Damping of Resonant Stresses in Gas Turbine Engine Airfoils*, Journal of Engineering for Power, Vol. 102, No. 2, ASME International(1980), pp. 329-333.

[2] W. Sextro, K. Popp, I. Wolter, *Improved Reliability of Bladed Disks due to Friction Dampers*, *ASME. Turbo Expo: Power for Land, Sea, and Air, Orlando, Florida, USA, 1997 June 2-5*, The Orlando (1997), pp. V004T14A035.

[3] B. D. Yang, C. H. Menq, *Characterization of contact kinematics and application to the design of wedge dampers in turbomachinery blading: part 1stick-slip contact kinematics*, Journal of engineering for gas turbines and power, Vol. 120, No. 2, ASME(1998), pp. 410-417.

[4] B. D. Yang, C. H. Menq, *Characterization of Contact Kinematics and Application to the Design of Wedge Dampers in Turbomachinery Blading: Part 2Prediction of Forced Response and Experimental Verification*, Journal of engineering for gas turbines and power, Vol. 120, No. 2, ASME(1998), pp. 418-423.

[5] G. Csaba, *Modelling of a microslip friction damper subjected to translation and rotation*, *ASME 1999 International Gas Turbine and Aeroengine Congress and Exhibition, Indiana, USA, 1999 June 7-10*, The Indiana (1999), pp. V004T03A012-V004T03A012.

[6] K. Y. Sanliturk, D. J. Ewins, A. B. Stanbridge, *Underplatform dampers for turbine blades: theoretical , analysis and comparison with experimental data*, *ASME 1999 international gas turbine and aeroengine congress and exhibition, Indiana, USA, 1999 June 7-10*, The Indiana (1999), pp. V004T03A037-V004T03A037.

[7] L. Panning, K. Popp, W. Sextro, K. Popp, *Optimization of interblade friction damper design*, *ASME Turbo Expo 2000: Power for Land, Sea, and Air, Munich, Germany, 2000 May 8-11*, The Munich (2000), pp. V004T03A068-V004T03A068.

[8] E. P. Petrov, D. J. Ewins, *Analytical formulation of friction interface elements for analysis of nonlinear multi-harmonic vibrations of bladed discs*, *ASME Turbo Expo 2002: Power for Land, Sea, and Air, Amsterdam, The Netherlands, 2002 June 3-6*,

[9] S. Zucca, D. Botto, M. Gola, *Range of variability in the dynamics of semi-cylindrical friction dampers for turbine blades*, *ASME Turbo Expo 2008: Power for Land, Sea, and Air, Berlin, Germany, 2008 January 9-13*, The Berlin (2008), pp. 519-529.

[10] L. Pesaresi, L. Salles, A. Jones, J.S. Green, C.W. Schwingshackl, *Modelling the nonlinear behaviour of an underplatform damper test rig for turbine applications*, Mechanical Systems and Signal Processing, Vol. 85, Elsevier (2017), pp. 662-679.

[11] C.W. Schwingshackl ,E.P. Petrov, D. J. Ewins, *Effects of Contact Interface Parameters on Vibration of Turbine Bladed Disks With Underplatform Dampers*, Journal of Engineering for Gas Turbines and Power, Vol. 134, No. 3, ASME International (2012), pp. 032507.

[12] C. Gastaldi, *Modeling Friction for Turbomachinery Applications: Tuning Techniques and Adequacy Assessment of Heuristic Contact Models*, *Contact and Fracture Mechanics* InTech(2018).

[13] I. A. Sever, E. P. Petrov, D. J. Ewins, *Experimental and numerical investigation of rotating bladed disk forced response using underplatform friction dampers*, Journal of Engineering for Gas Turbines and Power, Vol. 130, No. 4, ASME(2008), pp. 042503.

[14] T. berruti, *A test rig for the investigation of the dynamic response of a bladed disk with underplatform dampers*, Mechanics Research Communications, Vol. 37, No. 6, Elsevier(2010), pp. 518-583.

[15] A. Bessone, F. Toso, T. Berruti, *Investigation on the dynamic response of blades with asymmetric under platform dampers*, *ASME Turbo Expo 2015: Turbine Technical Conference and Exposition, Montreal, Quebec, Canada, 2015 June 15-19*, The Montreal (2015), pp. V07BT33A003-V07BT33A003.

[16] C.W. Schwingshackl, E.P. Petrov, D.J. Ewins, *Validation of test rig measurements and prediction tools for friction interface modelling*, *ASME Turbo Expo 2010: Power for Land, Sea, and Air, Glasgow, UK, 2010 June 14-18*, The Glasgow (2010), pp. 1015-1024.

[17] D. Botto, M. Lavella, M. M. Gola, *Measurement of Contact Parameters of Flat on Flat Contact Surfaces at High Temperature*, *ASME Turbo Expo 2012: Power for Land, Sea, and Air, Copenhagen, Denmark, 2012 June 11-15*, The Copenhagen (2012), pp. 1325-1332.

[18] M. Lavella, D. Botto, M. Gola, *Design of a high-precision, flat-on-flat fretting test apparatus with high temperature capability*, Wear, Vol. 302, No. 1-2, Elsevier(2013), pp. 1073-1081.

[19] M. M. Gola, M. B. dos Santos, L. Tong, *Design of a new test rig to evaluate under-platform damper performance*, *ASME 2010 10th Biennial Conference on Engineering Systems Design and Analysis, Istanbul, Turkey, 2010 July 12-14*, The Turkey (2010), pp. 85-94.

[20] C. Gastaldi, M. M. Gola,, *A Random Sampling Strategy for Tuning Contact Parameters of Underplatform Dampers*, *ASME Turbo Expo 2015: Turbine Technical Conference and Exposition, Montreal, Quebec, Canada, 2015 June 15-19*, The Montreal (2015), pp. V07BT33A004.

[21] C. Gastaldi, M. M. Gola, *Pre-optimization of Asymmetrical Underplatform Dampers*, Journal of Engineering for Gas Turbines and Power, Vol. 139, No. 1, ASME International (2016), pp. 012504.

[22] D. Botto, C. Gastadi, M. M. Gola, M. Umer, *An Experimental Investigation of the Dynamics of a Blade With Two Under-Platform Dampers*, Journal of Engineering for Gas Turbines and Power, Vol. 140, No. 3, ASME International (2017), pp. 032504.

[23] D. Botto, M. Umer, *A novel test rig to investigate under-platform damper dynamics*, Mechanical Systems and Signal Processing, Vol. 100, Elsevier (2018), pp. 344-359.

[24] R. Craig, M. Bampton, *Coupling of substructures for dynamic analyses*, AIAA journal, Vol. 6, No. 7, (1968), pp. 1313-1319.

[25] Hurty, C. Walter, *Dynamic analysis of structural systems using component modes*, AIAA journal, Vol. 3, No. 4, (1965), pp. 678-685.

[26] T. H. Cameron, J. H. Griffin, *An alternating frequency/time domain method for calculating the steady-state response of nonlinear dynamic systems*, Journal of applied mechanics, Vol. 56, No. 1, ASME(1989), pp. 149-154.

[27] A. Cardona, T. Coune, A. Lerusse, M. Geradin, *A multiharmonic method for non-linear vibration analysis*, International Journal for Numerical Methods in Engineering, Vol. 37, No. 9, Wiley Online Library(1994), pp. 1593-1608.

[28] C. M. Firrone, S. Zucca, *friction contacts in structural dynamics and its application to turbine bladed disks*, InTech (2011).

[29] M. Krack, L. Salles, F. Thouverez, *Vibration Prediction of Bladed Disks Coupled by Friction Joints*, Archives of Computational Methods in Engineering, Vol. 24, No. 3, Springer(2017), pp. 589-636.

[30] C. Gastaldi, T. M. Berruti, *Competitive Time Marching Solution Methods for Systems with Friction-Induced Nonlinearities*, Applied Sciences, Vol. 8, No. 2, Multidisciplinary Digital Publishing Institute(2018), pp. 291.

[31] C. Gastaldi, M. M. Gola, *Testing, simulating and understanding under-platform damper dynamics*, *Proceedings of the VII European Congress on Computational Methods in Applied Sciences and Engineering, Crete, Greece, 2016 June*, The Crete (2016).

[32] C. Gastaldi, M. M. Gola, *Criteria for best performance of pre-optimized solid dampers*, *ASME Turbo Expo 2004: Power for Land, Sea, and Air, Oslo, Norway, 2018 June 11-15*, The Oslo(2018).

[33] T.A. Harris, M.N. Kotzalas, *Rolling Bearing Analysis*, edition 5th, CRC Press(2006).

Identification of hysteretic systems for damping modelling

V. Kehr-Candille[1]
[1] ONERA, Department of Materials and Structures,
29 avenue de la Division Leclerc, 92320 Châtillon, France
e-mail: **veronique.kehr-candille@onera.fr**

Abstract
We are interested in the modelling of the damping at the junction between two substructures. In previous works, we have represented the connection by a meta-model, which takes into account both dissipative and non-linear aspects: we used a Bouc-Wen model or a Dahl model, which are adapted to be inserted in a finite element system. The purpose of the present work is to identify the numerical values of the Bouc-Wen or Dahl model parameters. The identification is carried out from the hysteresis curve (nonlinear force in function of displacement). First, we present the method, and then its application to academic cases.

1 Introduction

In structural dynamics, vibratory levels depend directly on damping. So it is necessary to have, from the design phase, tools and models allowing to correctly represent the damping.

The origin of energy dissipation in the aeronautical structures is double: on one hand, materials intrinsic damping, and on the other hand, dissipation generated by the friction phenomena at the interfaces between the sub-structures. We are interested here in the representation of this second source of dissipation. For the metallic structures, the dissipation generated in the interfaces is the main damping source.

In a previous study [1], we have represented the connection between sub-structure by what we called a meta-model, that is to say a relatively simplified model, which allows to correctly represent dissipative and non-linear aspects of the junction, without leading to excessively long time in the calculations of dynamic response. This meta-model is a Bouc-Wen model or a Dahl model, which are adapted to be inserted in a finite element system. The purpose of the present work is to identify the numerical values of the Bouc-Wen or Dahl model parameters.

After a brief state of art in section 2, we present in section 3 the hysteretic models, and then, the identification methods, for the Dahl model in section 4, and for the Bouc-Wen model in section 5. We use these methods for identify parameters for academic cases in section 6.

2 State of art

As the Bouc-Wen model is widely used in various fields (earthquake dynamics, fluid dampers, seismic isolation, …), most of the papers deal with identification of the Bouc-Wen model.

Identification can be done either from the hysteresis curve [3, 7, 8], taking advantage of its properties, or from time response [4, 5, 6], sometimes with the harmonic balance method [2]. Some authors have investigated the time interval of the answer which is used for identification [9], others have used the limit

cycle [4]. In reference [6], the hysteresis curve is split in four domains, according to the sign of speed, and the sign of the force derivate.

As regards the identification itself, some approaches [2] use the Nelder-Mead optimisation algorithm or the least-square method [6, 11], and others [3, 5, 9, 10, 12, 13], more numerous, use genetic algorithm.

Several papers highlight the difficulty in identifying the parameter n (cf. equation (4)); the method of reference [6], using the logarithm function, allows to overcome this difficulty.

3 Hysteretic models

3.1 Hysteretic curve

We consider the dynamical equation for a one degree of freedom system, with a non-linear component $F_{nl} = z$:

$$m\,\ddot{x} + k\,x + z = f_e(t) \tag{1}$$

where x is the displacement, m is the mass, k the linear stiffness and $f_e(t)$ is the excitation force.

For a multi degrees of freedom, we consider a similar matrix equation (cf. [1]):

$$\boldsymbol{M}\,\ddot{\boldsymbol{X}} + \boldsymbol{K}\,\boldsymbol{X} + z\,\boldsymbol{F_f} = \boldsymbol{F_e}(t) \tag{2}$$

The non-linear component is $\boldsymbol{F_{nl}} = z\,\boldsymbol{F_f}$ where $\boldsymbol{F_f}$ is a constant vector.

So, in both cases (one or multi degrees of freedom), the non-linearity aspect is fully described by z.

We consider an input periodical excitation, for instance $f_e(t) = A\,\sin(\omega t)$. The output answer converges to a stabilized periodic solution, and we can consider only the hysteresis curve (x, z) on one period (cf. figure 1).

In the following, we assume that we know $x = x(t)$ and $z = z(t)$ on one period. From these data, we can estimate $\dot{x} = \frac{dx}{dt}$ and $\dot{z} = \frac{dz}{dt}$ if we need so. The data $x(t)$ and $z(t)$ can be obtained either by simulation (for instance a refined finite element calculation with friction) or by experience.

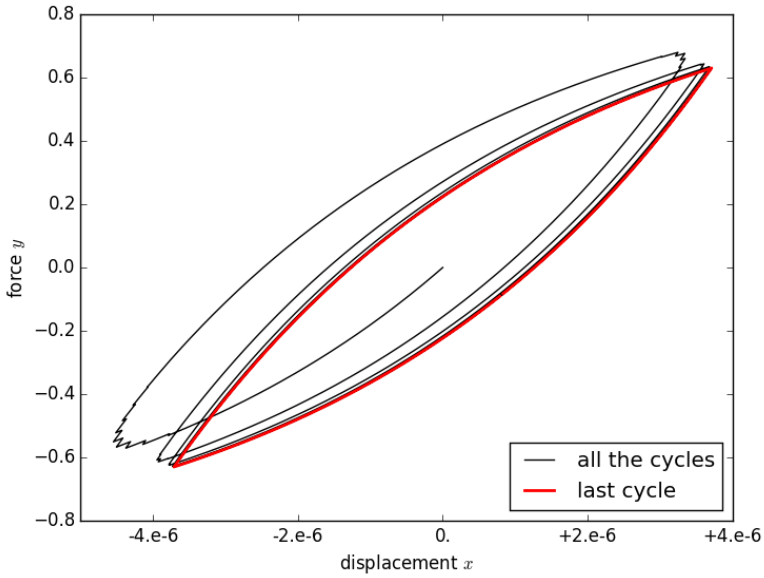


Figure 1 : Hysteresis cycles

3.2 Dahl model

The Dahl model is described by a differential equation which links the non-linear force $F_{nl} = z$ and the displacement:

$$\dot{z} = \sigma\, \dot{x} \left(1 - \frac{z}{F_C} \operatorname{sign} \dot{x}\right)^{\alpha} \tag{3}$$

The Dahl model is fully described by 3 parameters: σ, F_C and α. For physical reasons (cf. [19]), we have $F_C > 0$ and > 0 : F_C is the asymptotic force value, and σ is the quasi elastic stiffness when ${}^{F}/_{F_C} \ll 1$. We have also $\alpha > 0$.

3.3 Bouc-Wen model

The Bouc-Wen model (cf. [15] for instance) is described by a differential equation which links the non-linear force $F_{nl} = z$ and the displacement x:

$$\dot{z} = \alpha[A\, \dot{x} - \beta\, |\dot{x}||z|^{n-1}\, z - \gamma\, \dot{x}|z|^{n}] \tag{4}$$

Equation (4) is the usual writing for the Bouc-Wen model; it allows separating linear and non-linear components in the differential equation (1):

$$m\, \ddot{x} + (1 - \alpha) \underbrace{F_{\text{linear}}}_{k\, x} + \underbrace{\alpha\, F_{\text{non-linear}}}_{z} = f_e(t) \tag{5}$$

In our case, the distinction between linear and non-linear components is useless; the linear component (stiffness component k or stiffness matrix $\boldsymbol{K}$) is well-known, and we are only interested by the non-linear component which models the junction. In this context, some parameters of (4) are redundant. We can set $\alpha = 1$ and the Bouc-Wen equation becomes:

$$\dot{z} = A\, \dot{x} - \beta\, |\dot{x}||z|^{n-1}\, z - \gamma\, \dot{x}|z|^{n} \tag{6}$$

One can note that for $\gamma = 0$ and $n = 1$, the Bouc-Wen model is equivalent to a Dahl model with $\alpha = 1$.

The Bouc-Wen model is fully described by 4 parameters: A, β, γ and n (n is not necessarily an integer).

The Bouc-Wen model satisfies the laws of thermodynamic if we have $-\beta \leq \gamma \leq +\beta$ (cf. [15] and [18]). Otherwise, one can show that the model is stable and dissipative if $A > 0$, $\beta + \gamma > 0$ and $\beta - \gamma \geq 0$. These two last relations involve $\beta > 0$ and satisfy the laws of thermodynamic. As the parameter A can be considered as the quasi linear stiffness model, we also have the condition A>0.

4 Dahl model identification

We present in this part the identification method for the Dahl model.

First, the hysteresis cycle is divided in two parts: one part where $\dot{x} > 0$ and another one where $\dot{x} < 0$ (cf. figure 2). For each of these sub-cycles, we have $\operatorname{sign} \dot{x} = \text{constant} = \epsilon$ with $\epsilon = \pm 1$. If we express time derivatives as $\dot{x} = \frac{dx}{dt}$ and $\dot{z} = \frac{dz}{dt}$, equation (3) can be written:

$$\frac{dz}{dx} = \sigma \left(1 - \epsilon\, \frac{z}{F_C}\right)^{\alpha} \tag{7}$$

So the slope value $\frac{dz}{dx}$ in $z = 0$ allows to obtain the value of the parameter σ.

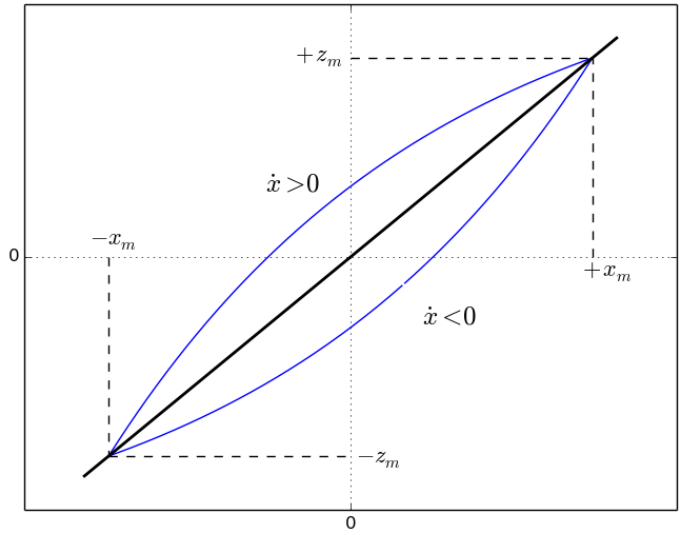


Figure 2 : Hysteresis curve

Then, we define the following quantities (cf. figure 2):

- $x_0 = x(z = 0)$,
- $z_0 = z(x = 0)$,
- $(+x_m, +z_m)$ and $(-x_m, -z_m)$ the extreme points of the hysteresis curve defined by $\dot{x} = 0$.

We assume now either $\alpha = 1$ or $\alpha \neq 1$.

● If we assume $\alpha = 1$, then equation (7) leads to:

$$-\epsilon F_C \ln\left(1 - \epsilon \frac{z_0}{F_C}\right) - \sigma\, x_0 = 0 \tag{8}$$

We can solve numerically equation (8) to obtain F_C value.

● If we assume $\alpha \neq 1$, first, directly from equation (7), we obtain, denoting p_0 the slope of $\ln\left(\frac{dz}{dx}\right)$ with respect to variable z, in $z = 0$:

$$\alpha = -p_0 \epsilon\, F_C \tag{9}$$

Then, integrating equation (7) between the two extreme points, with the help of equation (9), we obtain:

$$\frac{F_C}{1 + p_0 \epsilon F_C}\left\{\left(1 + \frac{z_m}{F_C}\right)^{1+p_0 \epsilon\, F_C} - \left(1 - \frac{z_m}{F_C}\right)^{1+p_0 \epsilon\, F_C}\right\} - 2\sigma x_m = 0 \tag{10}$$

We solve numerically equation (10) to obtain the value of F_C parameter, and then we deduce the value of parameter α with the help of equation (9).

We have two opportunities to identify the values of the Dahl model parameters: $\dot{x} > 0$ ou < 0 . For each parameter, we can choose for the final value the mean of the two values we have found. An important disparity between the sets of value means that the Dahl model is not suitable for the considered hysteretic curve.

5 Bouc-Wen model identification

The identification process presented in this paragraph is inspired by some aspects of the work presented in [17].

First, the hysteresis cycle is divided into four parts: $(\dot{x} > 0\,, z > 0)$, $(\dot{x} > 0\,, z < 0)$, $(\dot{x} < 0\,, z > 0)$ and $(\dot{x} < 0\,, z < 0)$ (cf. figure 2).

- For the case $(\dot{x} > 0\,, z > 0)$, equation (6) can be written:

$$\dot{z} = [A - (\beta + \gamma)\, z^n]\, \dot{x} \tag{11}$$

Writing time derivatives as $\dot{x} = \frac{dx}{dt}$ and $\dot{z} = \frac{dz}{dt}$, we obtain:

$$\frac{dz}{dx} = A - (\beta + \gamma) z^n \tag{12}$$

The value of the slope $\frac{dz}{dx}$ for $z = 0$ leads to the value of parameter A.

It has been shown in [15] that $\beta + \gamma > 0$. So, by taking the logarithm of equation (12), we obtain:

$$\ln\left(\frac{dz}{dx} - A\right) = \ln(\beta + \gamma) + n \ln z \tag{13}$$

So, the values of n and $\ln(\beta + \gamma)$ (and consequently the value of $\beta + \gamma$) can be identified from the curve $\left(\ln z\,, \ln\left(\frac{dz}{dx} - A\right)\right)$, for instance with a least-square method.

- For the case $(\dot{x} > 0\,, z < 0)$, if we note $z' = -z$, equation (6) can be written:

$$\frac{dz'}{dx} = A - (\beta - \gamma) z'^n \tag{14}$$

It has been shown [15] that $\beta - \gamma > 0$. So, by taking the logarithm of equation (14), we obtain:

$$\ln\left[-\left(\frac{dz'}{dx} + A\right)\right] = \ln(\beta - \gamma) + n \ln z' \tag{15}$$

So, the values of n and $\ln(\beta - \gamma)$ (and consequently the value of $-\gamma$) can be identified from the curve $\left(\ln z'\,, \ln\left[-\left(\frac{dz'}{dx} + A\right)\right]\right)$, for instance with a least-square method.

At the end, we can calculate the values of β and γ from the values of $\beta + \gamma$ and $\beta - \gamma$.

In the particular case $\beta = \gamma$, the expression $\ln(\beta - \gamma)$ doesn't make sense. But in this case $\beta + \gamma = 2\beta$ and equation (15) is useless.

We have four opportunities to identify the values of A: $(\dot{x} > \text{ou} < 0\,,\ z > \text{ou} < 0)$, and two opportunities to identify the value of β and γ $(\dot{x} > \text{ou} < 0)$. As for the Dahl model identification, we can choose for the final value the mean of the different values we have found. An important disparity between the sets of value means that the Bouc-Wen model is not suitable for the hysteretic curve.

6 Application

We have developed in Python language the methods we have presented in sections 4 and 5. In this section, the identification methods are applied to a single degree of freedom case. First, the hysteretic curve is computed solving the non-linear time equation (1), for a Dahl (resp. Bouc-Wen) model. Then, we identified from these curves the Dahl (resp. Bouc-Wen) parameters, and compare the results with initial values.

6.1 Dahl model

The parameters of equation (1) are $k = 10^5\ N/m$ and $m = 1\ kg$. The Dahl model parameters are $\sigma = 2\ 10^5$, $F_C = 1$ and α takes various values between 1 and 2.5. The excitation force is $f_e(t) = F\ \sin(2\pi f_0 t)$ with $F = 1\ N$ and $f_0 = 2\ Hz$. The dynamic response is computed for the interval $[0 - 8\ s]$ with a time step $\Delta t = 10^{-3}\ s$, using an explicit Runge-Kutta method of order 4(5) algorithm. The hysteretic loop is deduced from the dynamic response.

	$\alpha = 1$		$\alpha = 1.5$		$\alpha = 2.5$	
	hypothesis $\alpha = 1$	hypothesis $\alpha \neq 1$	hypothesis $\alpha = 1$	hypothesis $\alpha \neq 1$	hypothesis $\alpha = 1$	hypothesis $\alpha \neq 1$
σ	$1.99\ 10^5$	$1.99\ 10^5$	$2.00\ 10^5$	$1.99\ 10^5$	$2.00\ 10^5$	$2.01\ 10^5$
F_C	1.04	1.01	0.74	1.00	0.49	0.99
α		1.016		1.505		2.46

Table 1: Identified Dahl parameters for initial Dahl model ($\sigma = 2\ 10^5$, $F_C = 1$)

The identification results are presented in the table 1. The values of identified parameters are closed to the initial values when the hypothesis on α is in agreement with the initial values. When $\alpha = 1$, the hypothesis " $\alpha \neq 1$ " leads also to good results. Otherwise, when $\alpha \neq 1$, the hypothesis "$\alpha = 1$" leads to values for F_C parameter which are far from the initial value.

We compare on figures 4 and 5 the initial hysteresis loop with the hysteresis loop obtained with identified values. When initial and identified values are not in agreement, hysteresis loops are clearly different.

The identification process has been carried out on modified initial systems, with various values of the stiffness value k, various values of the intensity F or frequency f_0 of the excitation force, or various values of the initial Dahl models. The results are consistent with previous results; we generally observe good agreement between initial and identified values using the hypothesis "$\alpha \neq 1$".

However, when the energy dissipated by the Dahl model is low, we encounter numerical difficulties during the identification process, and the identified parameters are far from initial values. For instance, with the set of initial values($\sigma = 2\ 10^5$, $F_C = 10$, $\alpha = 1$), either the identification process fails or identified values on each sub cycle differ strongly (cf. table 2).

hypothesis $\alpha = 1$		hypothesis $\alpha \neq 1$	
sub cycle $\dot{x} > 0$	sub cycle $\dot{x} < 0$	sub cycle $\dot{x} > 0$	sub cycle $\dot{x} < 0$
no solution found for equation (9)	$F_C = 1.9e5$	$F_C = 4.32$ $\alpha = 0.43$	$F_C = 0.65$ $\alpha = 0.11$

Table 2: Identified Dahl parameters for initial Dahl model ($\sigma = 2\ 10^5$, $F_C = 10$, $\alpha = 1$)

The damping is estimated through the equivalent damping rate $\xi_{\text{eq}} = {}^1/_{4\pi}\ {}^{E_d}/_{E_e}$, where E_e is the elastic energy and E_d the dissipated energy (hatched area, see figure 3). For the previous systems ($\sigma = 2\ 10^5$, $\alpha = 1$), we have $\xi_{\text{eq}} = 0.15$ when $F_C = 1$ and $\xi_{\text{eq}} = 0.014$ when $F_C = 10$.

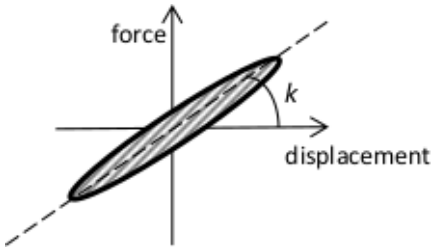


Figure 3 : Estimation of dissipated energy

Except for low damping case, this identification process leads to satisfactory results. Failures of the process can be identified either by strongly different values according each sub cycle or by numerical difficulties solving equation (8) or (10) or by noticeable differences between initial and identified hysteresis loop.

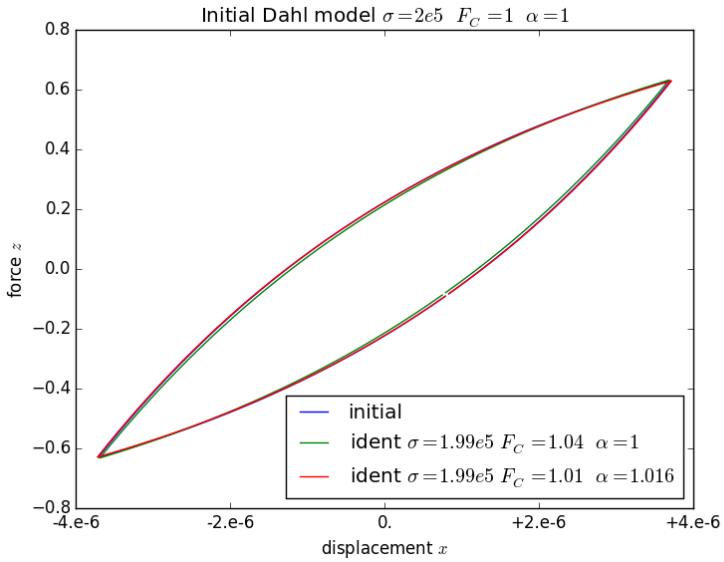


Figure 4 : Initial and identified Dahl model (1)

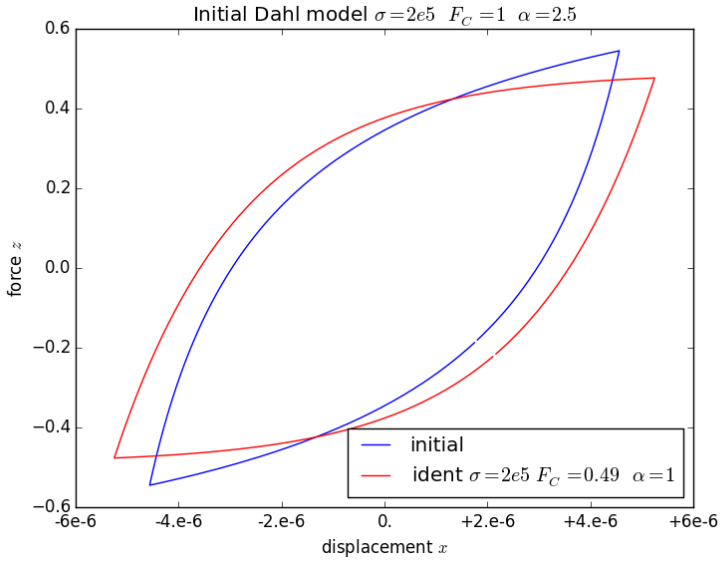


Figure 5 : Initial and identified Dahl model (2)

6.2 Bouc-Wen model

The parameters of equation (1) are $k = 200\ N/m$ and $m = 1\ kg$. The Bouc-Wen model parameters are $\alpha = 200$ and $A = 1$, and β, γ and n take various values between 1 and 2.5. The excitation force is $f_e(t) = F\ \sin(2\pi f_0 t)$ with $F = 10\ N$ and $f_0 = 5\ Hz$. The dynamic response is computed for the interval $[0 - 8\ s]$ with a time step $\Delta t = 10^{-3}\ s$, using the same Runge-Kutta algorithm. The hysteretic loop is deduced from the dynamic response.

	A	β	γ	n	
initial	1	0.5	0.2	1	
identified	0.99	0.50	0.15	1.09	
initial	1	0.5	0.2	3	
identified	1.00	0.48	0.17	3.18	
initial	1	0.5	-0.2	1	
identified	1.02	0.52	-0.22	0.98	
initial	1	0.2	0.2	1	
identified (1)	0.99	0.17	0.16	0.67	hyp. $\beta \neq \gamma$
identified (2)	0.99	0.17	0.17	1.33	hyp. $\beta = \gamma$

Table 3: Identified Bouc-Wen parameters for initial Bouc-Wen model ($\alpha = 200\ , A = 1$)

The identification results are presented in table 3, and we compare in figures 6 and 7 the initial hysteresis loop with the hysteresis loop obtained with identified values. The values of identified parameters are closed to the initial values, even in the particular case $\beta = \gamma$.

As for Dahl model, the identification process has been carried out on modified initial systems (various values of stiffness k, mass m, excitation intensity F or excitation frequency f_0). The results are consistent with previous results; we generally observe good agreement between initial and identified values.

However, when damping is very low, results are not so good. For instance, for the initial system ($A = 1, \beta = 0.005, \gamma = 0.001, n = 1$) for which $\xi_{\text{eq}} = 0.003$, the identification process leads to noticeable different identified values of n and $\beta + \gamma$ according to the considered sub-cycle ($\dot{x} > 0$ or $\dot{x} < 0$).

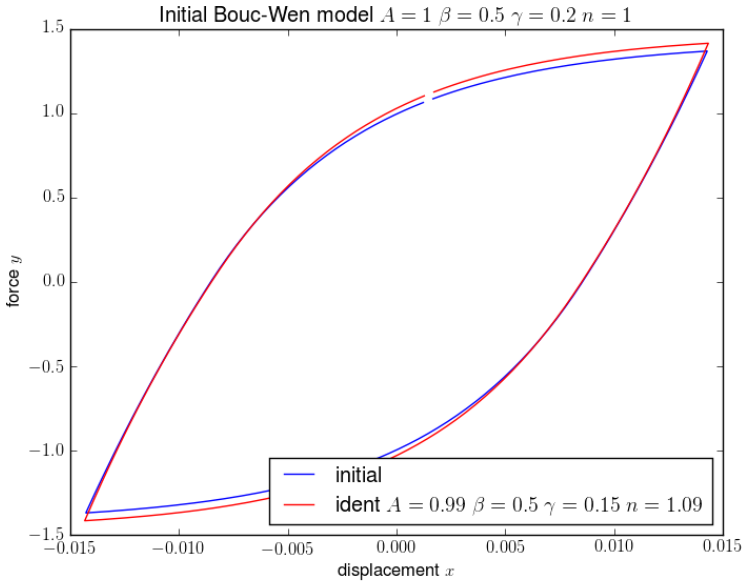


Figure 6 : Initial and identified Bouc-Wen model (1)

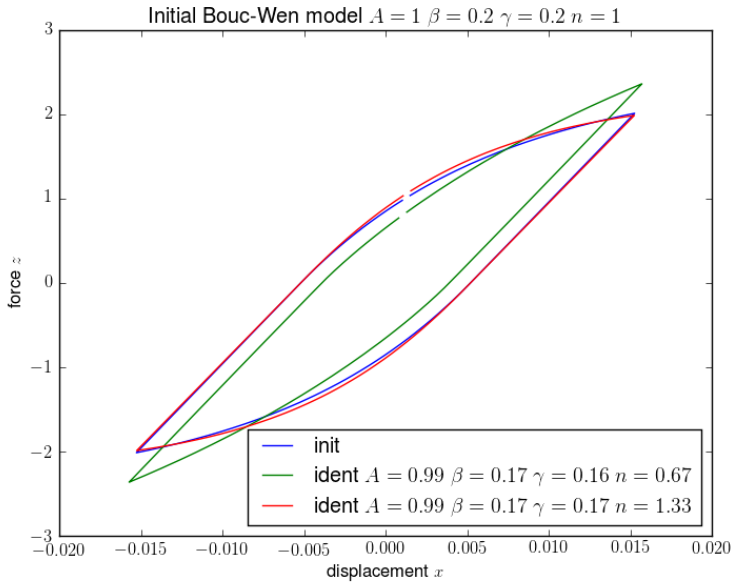


Figure 7: Initial and identified Bouc-Wen model (2)

7 Conclusion

We have presented semi-analytical methods to identify the parameters of two hysteretic models: the Dahl model and the Bouc-Wen model. The implementation is very easy. We have shown the efficiency of these methods, and also their limits, in particular when damping is low.

The next step of our research is to carry out identification from “real” hysteretic cycles, obtained either by simulation (refined finite element simulation with friction) or by experience. Such studies are presently in progress at Onera.

References

[1] V. Kehr-Candille, *Modelling the damping at the junctionbetween tawo substructures by non-linear meta-models*, Journal Aerospace Labs, Issue 14 (2018)

[2] Y.Q. Ni, J. M. Ko, C.W. Wong, *Identification of non-linear hysteretic isolators from periodic vibration tests*, Journal of Sound and Vibration Vol. 217, No. 4 (1998), pp.737-756

[3] T. Sireteanu, M. Giuclea, A.M. Mitu, *Identification of an extended BoucWen model with application to seismic protection through hysteretic devices*, Comput Mech., Vol.45 (2010), pp. 431-441

[4] F. Ikhouane, J. Rodellar, *On the Hysteretic BoucWen Model, Part I: Forced Limit Cycle Characterization, Part II: Robust Parametric Identification*, Non-linear Dynamics (2005) Vol. 42, pp. 63-95

[5] A. Kyprianou, K. Worden, *Identification of hysteretic systems using the differential evolution algorithm*, Journal of Sound and Vibration Vol. 248, No. 2 (2001), pp. 289-314

[6] Y. Rochdi, F. Giri, F. Ikhouane, F.Z. Chaoui, J. Rodellar, *Parametric identification of nonlinear hysteretic systems*, Nonlinear Dyn. Vol. 58 (2009), pp.393-404

[7] S. Kwag, S.Y. Ok, *Robust Design of Seismic Isolation System using Constrained Multi-objective Optimization Technique*, Journal of Civil Engineering Vol. 17, No. 5, (2013), pp. 1051-1063

[8] G.C. Marano, S. Sgobba, *Stochastic energy analysis of seismic isolated bridges*, Soil Dynamics and Earthquake Engineering Vol. 27 (2007), pp. 759-773

[9] S. Talatahari, A. Kaveh, N.Mohajer Rahbari, *Parameter identification of Bouc-Wen model for MR fluid dampers using adaptive charged system search optimization*, Journal of Mechanical Science and Technology Vol. 26, No. 8 (2012), pp. 2523-2534

[10] Y. Guo, J. Mao, *Modeling of Hysteresis Nonlinearity Based on Generalized Bouc-Wen Model for GMA*, ICIRA 2010, Part I, LNAI 6424, (2010), pp. 147-158

[11] K. Guo, X. Zhang, H. Li, G. Meng, *Non-reversible friction modeling and identification*, Arch Appl Mech Vol. 78 (2008), pp. 795-809

[12] Y. Qiang, Z. Li, W. Xinming, *Parameter identification of hysteretic model of rubber-bearing based. on sequential non-linear least square estimation*, Earthquake Engineering and Engineering Vibration, Vol. 9, No. 3 (2010), pp. 375-383

[13] M. Ye, X.Wang, *Parameter estimation of the BoucWen hysteresis model using particle swarm optimization*, Smart Mater. Struct. Vol. 16 (2007), pp. 2341-2349

[14] D. Capecchi, R.Masiani F.Vestroni, *Periodic and Non-Periodic Oscillations of a Class of Hysteretic Two Degree of Freedom Systems*, Nonlinear Dynamics Vol. 13(1997), pp. 309-325

[15] M. Ismail, F. Ikhouane, J. Rodellar, *The Hysteresis Bouc-Wen Model, a Survey*, Comput. Methods Eng. Vol. 16 (2009), pp.161-188

[16] A.E. Charalampakis, V.K. Koumousis, *On the response and dissipated energy of Bouc-Wen hysteretic model*, Journal of Sound and Vibration Vol. 309 (2009), pp. 887-895

[17] F. Ikhouane, V. Maosa, J. Rodellar, *Dynamic properties of the hysteretic Bouc-Wen model*, Systems , Systems and Control Letters Vol. 56 (2007), pp. 197-205

[18] S. Erlicher, N. Point, *Thermodynamic admissibility of Bouc-Wen type hysteresis models*, Compte rendus Mcanique Vol. 332 (2004), pp. 51-57

[19] A. AL Majid, *Dissipation de l'énergie en mécanique vibratoire*, doctoral thesis report, INSA Lyon France, (2002)

Semi-active damping of forced vibrations by means of pneumatic supports

G. Mikułowski [1]
[1] Institute of Fundamental Technological Research, Department of Intelligent Technologies,
ul. Pawinskiego 5 B, 02-106 Warszawa, Poland
e-mail: **gmikulow@ippt.pan.pl**

Abstract
Vibration mitigation and vibration isolation are problems existing in a variety of industry branches. Pneumatic suspensions and isolators are a widely utilized technology, and in many applications they need to adapt their properties to a varying mass of the supported object, e.g., loaded or unloaded lorries. However, the pneumatic solutions posses limitations in the field of adequate damping. The change in mass results in a change in the required level of damping. This contribution presents and verifies a concept of an enhanced damping pneumatic device using an example of a Pneumatic Adaptive Absorber (PAA) adapted to the task of mitigation of forced vibrations. The investigation presents a concise introduction to the concept, as well as analytical and numerical modelling of the conceptual device. The contribution proposes a control algorithm based on performed analysis of mechanical energy dissipation process. The concept is verified experimentally in a laboratory. The proposed modelling seems to be in agreement with the demonstrator response.

1 Introduction

Pneumatic vibration isolation is a well recognized and appreciated technique, which is utilized in many applications like precision measurements, fabrication, or suspensions in means of transport. The most widely implemented pneumatic systems dedicated to suppress the vibration transmission are passive ones due to their simplicity and maintainability. Much effort has been put into development of modelling, optimizing and design methods associated with the passive solutions. Many of dedicated to double chamber pneumatic suspensions are based on simplified linear models [1], and others are based on advanced non-linear approaches [2]. A comprehensive approach to the design of the passive pneumatic springs has been proposed by Lee et. al., in which the values of three design parameters are precisely determined: ratio of the pneumatic volumes, geometry of the capillary tube and dynamic stiffness of the rubber diaphragm [3]. The proposed method allows for designing a proper isolator for particular steady vibration instances. Furthermore, a thorough stability analysis and design procedures has been provided for multi point systems pneumatic vibration isolation supports [4].

The uncontested advantages of the passive pneumatic vibration isolation systems have one major limitation, which is demonstrated when the mass of the suspended object varies and also when the mechanical disturbances vary in the range of frequencies and amplitudes. The passive systems respond adequately in condition of steady vibration and the performance drops when the conditions change continuously. For such instances advanced systems of actively controlled pneumatic systems are developed, e.g. train suspensions [5, 6]. The effectiveness in reduction of transmissibility in the active pneumatic vibration isolation systems is obtained by utilization of external sources of energy for counter acting the vibrational forces. In comparison to the passive systems, the active ones are much more effective in a wide frequency spectrum of frequencies, but at the same time they are expensive and require a lot of space for packaging in applications. The active systems require to be supplied with pressured gas from external sources, which significantly influence the response

delays in the system [7, 8]. Recently, the performance improvement of the active pneumatic vibration isolation systems with utilization of proportional valves[9] and employment of PID controllers [10] is being investigated.

The extended requirements of the active systems in the area of energy supply and packaging drive researchers to search among unconventional solutions e.g. based on a negative stiffness concept [11], which allows for reducing of the required additional energy supply level. An investigation on this idea, on the example of a suspension system configured with self contracting pneumatic springs has been presented by Pesik et.al. [12]. Such solutions lead to savings in the pneumatic operational energy demands. The negative stiffness configuration of coil springs combined with an active pneumatic actuator allows for development of vibration isolation systems dedicated to the low frequency range (0.5 - 5 Hz), which is specifically difficult to stand with [13, 14].

The trend of minimization of the additional energy supply level is also demonstrated in concepts of semi-active [15, 16] and adaptive solutions [17], in which the elements of the isolation system posses a possibility of the mechanical parameters modification. In those solutions the required additional energy is lower, since it is only needed for setting of an operational state of actuators like valves or throttles. For example, the parametric modification aims to adapt the stiffness of the spring by switching between several pneumatic elements of various volumes [18, 19]. Another attempt has been carried out to tune the pneumatic vibration isolators by means of a controllable throttling valve positioned in between two gas chambers [20], which is reported as not an efficient method of the pneumatic springs tuning.

The common feature of the mentioned investigated systems is the desire of finding a method to tune adaptively the steady parameters of the isolation system adequately to the vibration conditions. In contrast, the concept presented in this study proposes a real-time adaptive method of updating the mechanical response of the isolating adaptive element to the recognized frequency and amplitude of the vibration. Therefore, the proposed system has a potential to adapt itself to a variety of the mechanical excitation conditions, since it monitors the kinematics of the object. Furthermore, the Pneumatic Adaptive Absorber allows for limiting the problem of response delays thanks to positioning of a controllable valve directly in the piston between the chambers. Additionally, it allows to receive short response delays due to the fact that the valve is based on a piezoelectric actuator. The presented results are an introductory attempt to provide a broader study of the concept.

2 Pneumatic Adaptive Absorber concept

PAA is considered as a piston-cylinder device with two sealed volumes divided by a piston equipped with a controllable valve. The valve enables a gas mass transfer between the volumes and therefore a regulation of the pressures difference between the volumes.

In principle, the device may be considered as a double chamber pneumatic spring, in which the reaction force can be regulated by controlling the pressure difference acting on the piston. Simultaneously, the induced spontaneous gas decompression results in dissipation of a mechanical energy supplied to the absorber. In that meaning the device is a dissipative element. Furthermore, the operation of the valve introduces a change of an instantaneous mechanical reaction of the absorber, which can be interpreted as modification of mechanical parameter of the system. This feature defines the PAA as a semi-active actuator.

3 Mathematical model

Mathematical model of the PAA is based on thermodynamic relations coupled with equations of motion. The objective is to reflect the response of the element to a kinematic excitation. The method of modelling is based on previous work described in [22]. The model comprises three elementary issues: dynamics of the

piston considered as a rigid body, thermodynamics of the gas in the absorber chambers and gas flow through the valve. Assumptions made for the purpose of the analysis are formulated as:

1. inertia of the piston and piston rod is negligible in the considered configuration,
2. gas in the control volumes fulfils demands to be modelled as an ideal gas,
3. gas is in a uniform state,
4. gas mixes instantaneously in the chambers.

The assumptions related to gas flow through the valve can be stated as:

1. state of the mass entering the valve is constant within the time steps and uniform over the volume of the valve where the flow occurs,
2. state of the mass within the control volumes can change with time, but at any instant of time the state is uniform over the entire control volume,
3. changes in the kinetic energy of the gas are negligible,
4. inertia and gravity forces of the gas are negligible.

The total force equilibrium of the piston can be stated as:

$$F_{p_1}(z, T_1, m_1) - F_{p_2}(z, T_2, m_2) - F_a + F_f(\dot{z}) = F_e(t) \tag{1}$$

where: F_e – external excitation, F_{p_1} – force resulting from pressure p_1 in the chamber 1, F_{p_2} – force resulting from pressure p_2 in the chamber 2, F_a – force resulting from ambient pressure, F_f – friction force, z – displacement of the piston, T_1, T_2 – gas temperatures in the corresponding volumes, m_1 – mass of the gas in volume 1, m_2 – mass of the gas in volume 2.

The forces acting on the piston can be formulated as:

$$F_{p_1} = p_1\left(T_1, \rho_1\right) \cdot A_1, \tag{2}$$

$$F_{p_2} = p_2\left(T_2, \rho_2\right) \cdot (A_1 - A_2), \tag{3}$$

$$F_a = p_a A_2, \tag{4}$$

$$F_f = f_f \, sgn(\dot{z}) \tag{5}$$

denoted as: ρ_1, ρ_2 – gas densities in chambers 1 and 2, A_1 – effective piston area, A_2 – area of piston rod radial cross section, p_a – ambient pressure, f_f – friction coefficient.

The thermodynamic model of the processes in the chambers can not be assumed as polytropic with constant value of the coefficient, as the heat through the cylinder walls is not stabilized. Therefore, a dedicated numerical algorithm is adopted in order to comprise that phenomenon. The calculation of the gas state in the consequent time steps of simulation is performed as:

1. determination of the gas state change due to the volume change on the basis of the adiabatic model,
2. determination of the internal energy of the gas,

3. determination of the heat exchange between the control volume and the surroundings (with the actual area of the cylinder walls interfacing the gas computed),
4. determination of the energy balance in the control volume with the mass and heat exchange taken into consideration,
5. recalculation of the gas state parameters on the basis of the energy balance equation.

The algorithm described above allows for reflecting the thermodynamic polytropic-like process in dependence on the operating conditions.

The main equation of the energy balance in the system of two volumes denoted as 1 and 2 can be stated as:

$$\dot{Q}_1 + \dot{m}_{1i} h_2 = \dot{W}_1 + \dot{m}_{1o} h_1 + \frac{d}{dt}(m_1 u_1), \tag{6}$$

$$\dot{Q}_2 + \dot{m}_{2i} h_1 = \dot{W}_2 + \dot{m}_{2o} h_2 + \frac{d}{dt}(m_2 u_2), \tag{7}$$

where $\dot{Q}$ is heat transfer, $\dot{W}$ is work done by the gas, h is specific enthalpy of the gas and m is mass of the gas in particular volumes. The subscripts 1 and 2 refer to the volumes in the cylinder divided by the piston, and subscripts i and o refer to inflow or outflow of the gas into or out of the volume.

The $\dot{Q}_1$ and $\dot{Q}_2$ depend on: (a) the difference between the temperatures of the gas in the control volume and the surroundings, (b) the area of cylinder walls that the gas is in contact with, and (c) the material constants and can be denoted as:

$$\dot{Q}_1 = A_1(z) \cdot \alpha \cdot (T_1(t) - T_a(t)), \tag{8}$$

$$\dot{Q}_2 = A_2(z) \cdot \alpha \cdot (T_2(t) - T_a(t)), \tag{9}$$

where: $A_1(z)$ – area of cylinder being in contact with gas in volume 1, α – heat transfer coefficient, $T_a(t)$ – ambient temperature. The quantities of index 2 describe the same values related to volume 2.

According to the continuity principle, the mass of gas leaving the control volume 1 is equal to the mass of gas entering the control volume 2 and vice versa. That leads to the property of mass transferred between the volumes as:

$$\dot{m}_{1t} = -\dot{m}_{2t} \tag{10}$$

where

$$\dot{m}_{1t} = \dot{m}_{1e} - \dot{m}_{1i} = \begin{cases} > 0 & when \quad p_1 > p_2 \\ < 0 & when \quad p_1 < p_2 \end{cases} \tag{11}$$

as well as

$$\dot{m}_{2t} = \dot{m}_{2e} - \dot{m}_{2i} = \begin{cases} > 0 & when \quad p_2 > p_1 \\ < 0 & when \quad p_2 < p_1 \end{cases} \tag{12}$$

Let us denote the transferred mass of gas as:

$$\dot{m}_t = \dot{m}_{1t} = -\dot{m}_{2t} \tag{13}$$

The specific enthalpies h_1 and h_2 of the gas in volumes 1 and 2 respectively are different in general. Therefore, when the assumption of isenthalpic flow through the valve holds true, the specific enthalpy of the gas transferred between the volumes depends on the flow direction, and is equal to:

$$h_1 = c_p T_1, \quad \text{when the gas leaves volume 1} \tag{14}$$

and

$$h_2 = c_p T_2, \quad \text{when the gas leaves volume 2} \tag{15}$$

where: c_p – specific heat of the gas by the constant pressure.

The work done by the gas is defined for the particular control volumes as:

$$\dot{W}_1 = p_1(z)\frac{dV_1}{dt}, \tag{16}$$

$$\dot{W}_2 = p_2(z)\frac{dV_2}{dt}. \tag{17}$$

In accordance with the throttled flow theory [21], the flow through the valve is modelled as one dimensional and is assumed to be choked when the Mach number Ma is close to 1. Thus, the gas flow through the valve is calculated as:

$$\dot{m}_t = \begin{cases} C_d \frac{Ma\, A\, p_0 \sqrt{\kappa/RT_0}}{[1+(\kappa-1)Ma^2/2]^{\kappa+1/2(\kappa-1)}}, & if Ma < 1 \\ C_d\, A\, p_0 \sqrt{\kappa/RT_0} \left(\frac{2}{\kappa+1}\right)^{\kappa+1/2(\kappa-1)}, & if Ma = 1 \end{cases} \tag{18}$$

where: A depicts cross-section of the flow duct, κ is isentropic coefficient, R is gas constant, Ma is Mach number, T_0 is initial temperature, p_0 is initial pressure. The flow losses are described by means of a discharge coefficient C_d treated as a characteristic design parameter of the valve [23].

4 Control algorithm

Control algorithm adopted to the considered instance of vibration isolation is based on a strategy called Prestress Accumulation Release (PAR) [24, 25]. In the strategy an internal energy of an object, e.g. strain energy, is monitored in real-time and managed by means of semi-active structural elements [26]. The principle of the PAR strategy is to detect time instants in which the maximum accumulated potential energy of the system is reached, and to release it in a controlled way by means of semi-active structural fuses. The algorithm, in the presented investigation utilizes a sensing system for monitoring of the piston kinematics and the piezoelectric valve positioned in the piston of the PAA for actuation.

Principle of the algorithm is based on referencing the instantaneous potential energy level with the kinematics of the object. An assumption here is adopted that the maximum potential energy appears at the time instants when the linear velocity of the piston in reference to the PAA cylinder equals to zero. Those time instants indicate the maxima of the piston's deflections, and therefore the maximum value of the energy accumulated in the compressed gas.

The optimized control algorithm [26] is an on-off feedback type and can be formulated as follows:

$$CTRL(t) = \begin{cases} C_{close}, & \text{if } \dot{u}(t) > 0 \\ C_{open}, & \text{if } \dot{u}(t) = 0 \\ C_{close}, & \text{if } \dot{u}(t) < 0, \end{cases} \tag{19}$$

where C_{open} and C_{close} refer to two opposed states of the valve.

The control algorithm introduces the velocity feedback signal to the pneumatic system, in which typically the reaction is inherently dependent on displacement. The velocity feedback creates an enhanced performance of the device.

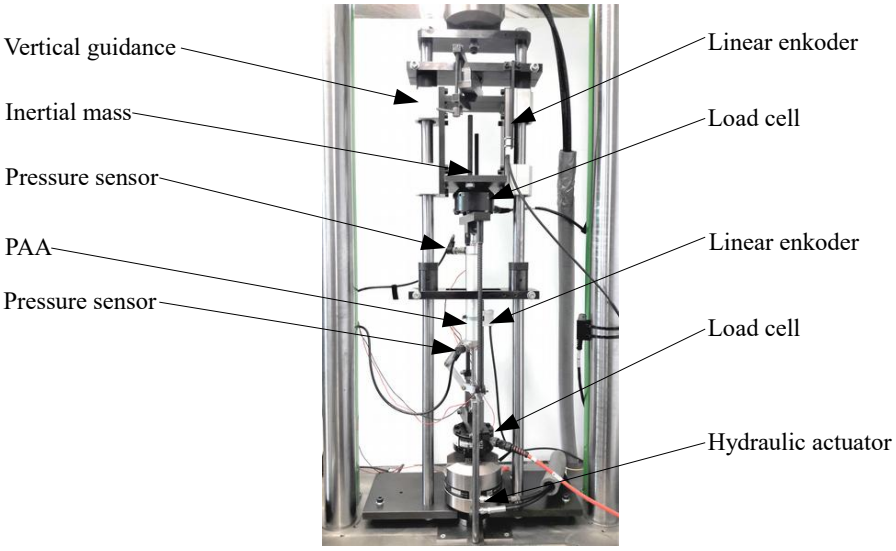


Figure 1: Experimental stand

5 Experimental investigation

Experimental investigation aims to demonstrate the principle of the PAR control algorithm applied to the PAA absorber and to assess its feasibility. The objective is accomplished within a set of experiments conducted on a dedicated setup designed for testing a PAA laboratory demonstrator.

5.1 Experimental stand and setup

The experimental setup is prepared to test vibration isolation systems in a uniaxial vertical configuration. The setup is based on a hydraulic actuator (manufacturer MTS Corporation) positioned in a vertical steel frame (Fig. 1). The PAA absorber is mounted on top of the hydraulic actuator, which provides mechanical excitation to the system and from top is loaded with an inertial mass guided along the frame. The setup allows for conducting tests in two configurations:

- the first for fixed configuration of the inertial element,
- the second for free vibration of the inertial element.

The configuration with the fixed inertial element allows for testing a mechanical response of the absorbers faced to a predefined mechanical excitation provided with the hydraulic actuator, whereas the configuration with the free inertial mass allows for testing an effectiveness of vibration isolation systems. The actuator is equipped with two parallel servohydraulic valves which allow for testing with maximum velocities up to 3 m/s. The setup is equipped with a set of sensors described in Fig. 1.

The Pneumatic Adaptive Absorber demonstrator is a 32 mm inner diameter cylinder of 200 mm length with a piston equipped with a built-in piezoelectric valve. The valve allows for transferring a predetermined mass of gas between the volumes. A mechanical response delay of the valve opening is equal to 1.2 ms.

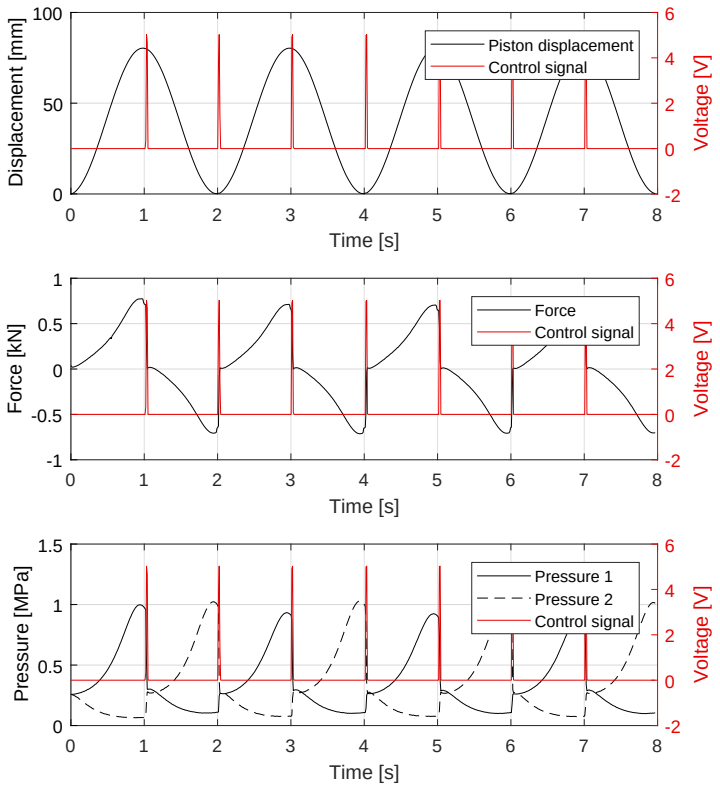


Figure 2: Mechanical response of the PAA absorber controlled in accordance with the PAR algorithm

5.2 Testing programme

The presented testing programme aims to determine the performance of the demonstrator and is conducted in the fixed mass configuration of the stand. The set of dedicated tests of the PAA is defined for determination of the following features of the experimental object:

- a response time of the PAA operation, which determines its operational bandwidth,
- verification of the numerical model proposed for modelling of the device,
- assessment of the energy absorption process carried out with the absorber.

The response time of the demonstrator is defined as the shortest period, in which the pressure difference generated by the PAA can be reduced. The delay depends on the gas transfer rate between the volumes and it is restricted by performance of the valve in the piston. The maximum mass flow rate through the valve depends on the gas pressure and temperature. The verification of the mathematical model is carried out by means of a referencing it against the experimental results. The energy absorption capability of the device is assessed on the basis of force-displacement curves that are generated.

5.3 Results and discussion

A mechanical response of the PAA to a sinusoidal excitation (amplitude 40 mm, frequency 0.5 Hz) in time domain is presented in Fig. 2. The first graph depicts the time history of the displacement excitation in reference to the generated control signal. The second graph depicts the axial force generated by the demonstrator.

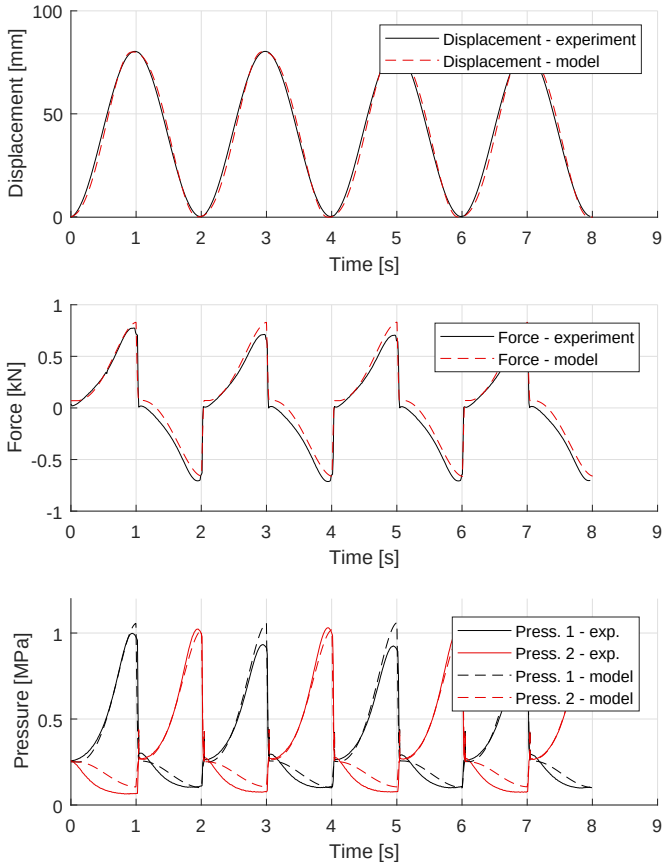


Figure 3: PAA response to the PAR control algorithm - experimental results vs. numerical modelling.

During each period the force increases to a maximum value associated with coexistent decompression and compression of the gas in the cylinder's volumes. At the time periods of control signal application, the force is reduced and therefore, dissipation of the accumulated mechanical energy takes place via the process of spontaneous gas decompression. The third graph depicts pressure courses in the first and second volumes of the cylinder. The switching of the valve results in a rapid reduction of the pressure difference between the two sides of the piston and consequent immediate drop of the reaction force transmitted by the piston rod, which represents the semi-active operation of the device. The opening period of the valve adopted for this particular setup is 10 ms, That period allows for obtaining the operating frequency up to 12.5 Hz, assuming that opening period should not exceed 12.5% of the period. In the presented results the axial force due to operation of the algorithm is reduced to very low value, which may be unfavourable in the instance of pneumatic supports. This is an inherent feature of this particular demonstrator and the kind of experiment which assumes the fixed mass configuration with the gravity reaction excluded. It is feasible to design a PAA in order to provide a relevant value of the supporting force by adjusting the diameter of the piston rod. The current design of the demonstrator allows for vibration testing with assistance of additional springs providing the required stiffness for a support.

Verification of the numerical results obtained with the proposed mathematical model versus experimental measurements is presented in Fig. 3. The graphs depict the excitation, force response and pressure time histories in the volumes of the absorber. As it is depicted, the proposed model allows to properly reflect the behaviour of the device under the analysed conditions. Additional validation of the model, which confirms

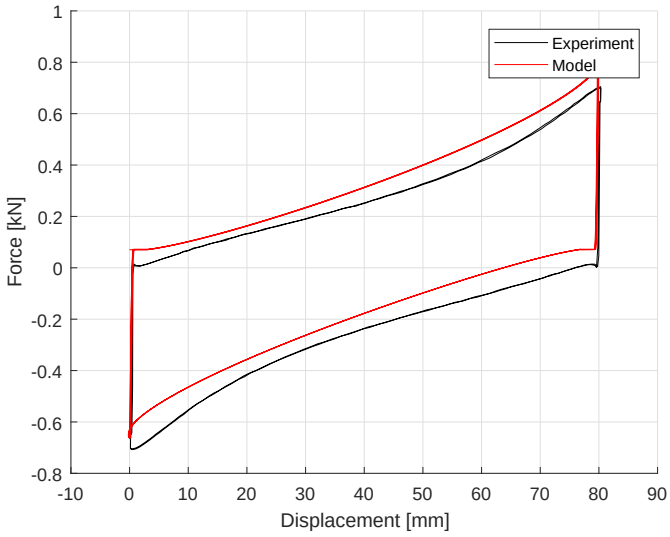


Figure 4: Force–displacement curve acquired under 0.5 Hz sinusoidal excitation

its proper response for a variety of operational conditions is published in [22].

An example of the PAA mechanical response in a force-displacement graph is depicted in Fig. 4. The excitation is sinusoidal with the analogical parameters to the test described previously. Initial pressure in the cylinder is 0.25 MPa. The plotted data represent an elementary energy dissipation process, which demonstrates the idea standing behind the concept. The mechanical energy accumulated in the compressed and decompressed gas in volumes 1 and 2 during a stroke is dissipated in a controllable way. An important feature of the system is that after reducing the pressure difference the process of the energy accumulation restarts instantaneously, which inherently increases the energy absorbing capability of the conceptual device. The presented curve depicts an instance of 40 mm amplitude and therefore the energy is accumulated on a stroke equal to a double amplitude. The control algorithm adapts the system for random amplitudes and frequencies within the previously described limits. The integration of the curve allows for obtaining energy dissipated per a single period by the device as well as for estimating its absorption efficiency. The energy absorbed by the device per a period is 47.2 J and the efficiency factor is 45%.

6 Conclusions

The presented study of the mechanical response of the PAA under harmonic excitation allows for enhancing pneumatic supports dissipative behaviour and a possibility of a fast modification of its properties. The proposed control algorithm, tested numerically and experimentally, appears to be effective. To conclude, the presented concept of the pneumatic adaptive device shows a significant potential for further studies, and the continuation of the investigation will be aimed at the development of a broader range of control methods and defining the applicability limits.

Acknowledgements

The author gratefully acknowledge the support of the National Science Centre, Poland, granted through the project Re-Con (DEC-2017/25/B/ST8/01800), and of the National Centre for Research and Development, Poland, granted in the framework of the TANGO2 programme (TANGO2/341494/NCBR/2017).

References

[1] X. Zeng, L. Zhang, Y. Yu, M. Shi, J. Zhou, *The stiffness and damping characteristics of a dual-chamber air spring device applied to motion suppression of marine structures*, Applied Sciences, Vol. 6, 74 (2016)

[2] J.-H. Moon, B.-G. Lee, *Modelling and sensitivity analysis of a pneumatic vibration isolation system with two air chambers*, Mechanisms and Machine Theory, Vol. 45 (2010), pp. 1828-1850

[3] J-H. Lee, K-J. Kim, *A method of transmissibility design for dual-chamber pneumatic vibration isolator*, Journal of Sound and Vibration, Vol. 323 (2009), pp. 67-92

[4] V.M. Ryaboy *Static and dynamic stability of pneumatic vibration isolators and systems of isolators*, Journal of Sound and Vibration, Vol. 333 (2014), pp. 31-51

[5] H. Kitada *History of air spring development for Shinkansen trains*, SEI Technical Review, No 84 (2017), pp. 114-119

[6] R. Bogacz, R. Konowrocki, *On new effects of wheel-rail interaction*, Archive of Applied Mechanics, Vol. 82, Issue 10-11 (2012), pp.1313-1323

[7] Y-H. Shin, K-J. Kim, *Performance enhancement of pneumatic vibration isolation tables in low frequency range by time delay control*, Journal of Sound and Vibration, Vol. 321 (2009), pp. 537-553

[8] P-H. Chang, D.K. Han, Y-H. Shin, K-J. Kim, *Effective suppression of pneumatic vibration isolators by using input-output linearization and time delay control*, Journal of Sound and Vibration, Vol. 329 (2010), pp. 1636-1652

[9] Y-H. Shin, S-J. Moon, *A mathematical model for a nonlinear pneumatic actuation system to control dynamic pressure*, Int. Journal of Precission Engineering and Manufacturing, Vol.19, No 3 (2018), pp. 325-337

[10] P.V. Kosenkov, G.M. Makaryants, *Control algorithm design of the active pneumatic vibration isolator*, Proceedia Engineering, Vol. 176 (2017), pp. 653-660

[11] M.I. Friswell, E.I. Saavedra Flores, Y. Xia, *Vibration isolation using nonlinear springs*, in Proceedings of ISMA2012 - USD2012 (2012), pp. 2333-2342

[12] L. Pesik, A. Skarolek, O. Kohl, *Vibration isolation system with a throttle valve*, The latest methods of construction design, V. Dynybyl ed., Springer International Publishing Switzerland (2016)

[13] T.D. Le, K.K. Ahn, *Fuzzy sliding mode controller of a pneumatic active isolating system using negative stiffnaess*, Journal of Mechanical Science and Technology, Vol. 26(12)(2012), pp. 3873-3884

[14] T.D. Le, K.K. Ahn, *Active pneumatic vibration isolation system using negative stiffness structures for a vehicle seat*, Journal of Sound and Vibration, Vol. 333 (2014), pp. 1245-1268

[15] M. Michajlow, L. Jankowski, T. Szolc, R. Konowrocki, *Semi-active reduction of vibrations in the mechanical system driven by an electric motor*, Optimal Control Applications and Methods, Vol. 38, Issue 6 (2017), pp. 922-933

[16] D. Pisarski, *Optimal control of structures subjected to travelling load*, Journal of Vibration and Control, Vol. 24, Issue 7 (2018), pp. 1283-1299

[17] R. Faraj, J. Holnicki-Szulc, L. Knap, J. Senko, *Adaptive inertial shock-absorber*, Smart Materials and Structures, Vol. 25, Issue 3 (2016), No 035031

[18] A.J. Nieto, A.L. Morales, J.M. Chicharro, P. Pintado *Unbalanced machinery vibration isolation with a semi-active pneumatic suspension*, Journal of Sound and Vibration, Vol. 329 (2010), pp. 3-12

[19] M.E. Shalabi, A.I. Abdel-Aziz, N.S. Elnahas, *Performance of automotive air suspension control system*, Int. Journal of Engineering Research & Technology, Vol. 4, Issue 9 (2015), pp. 80-83

[20] H. Pu, X. Luo, X. Chen, *Modelling and analysis of dual-chamber pneumatic spring with adjustable damping for precision vibration isolation*, Journal of Sound and Vibration, Vol. 330 (2011), pp. 3578-3590

[21] M. A. Boles and Y. A. Cengel, Thermodynamics, McGraw-Hill, 2nd edition (1994)

[22] G. Mikułowski, R. Wiszowaty, *Pneumatic Adaptive Absorber: Mathematical modelling with experimental verification*, Mathematical Problems in Engineering (2016), No. 7074206.

[23] G. Mikułowski, R. Wiszowaty, J. Holnicki-Szulc, *Characterisation of a piezoelectric valve for an adaptive pneumatic shock-absorber*, Smart Materials and Structures (2013), No. 125011.

[24] A. Mróz, A. Orłowska, J. Holnicki-Szulc, *Semi-active damping of vibrations. Prestress Accumulation-Release strategy development*, Shock and Vibration, Vol.17 (2010), pp.123-136.

[25] A. Mróz, J. Holnicki-Szulc, J. Biczyk, *Prestress Accumulation–Release technique for damping of impact-born vibrations: Application to self-deployable structures*, Mathematical Problems in Engineering (2015), No. 720236.

[26] B. Poplawski, G. Mikułowski, A. Mróz, Ł. Jankowski, *Decentralized semi-active damping of free structural vibrations by means of structural nodes with an on/off ability to transmit moments*, Mechanical Systems and Signal Processing, Vol. 100 (2018), pp. 926-939.

Implementation and comparison of advanced friction representations within finite element models

A. T. Mathis[1], **A. R. Brink**[2], **D. Dane Quinn**[1]
[1] The University of Akron, Department of Mechanical Engineering, Akron, OH 44325–3903, USA

[2] Sandia National Laboratories*, Albuquerque, NM 87185–0847, USA

Abstract
Advanced friction models are often mathematically defined as nonlinear differential equations or complicated algebraic operations acting in single degree-of-freedom systems; however, such simplified conditions are not relevant to most design applications. As a result, current designers of practical structures typically simplify friction modeling to classical, Coulomb-like descriptions. In order to be viable for design purposes, friction models must be applicable to realistic structures and available in standard commercial codes. The goal of this work is to implement several different friction models into the commercial code, Abaqus, as user-defined contact models and to explore their properties in a dynamic simulation. A verification problem of interest to the joints community is utilized to evaluate efficacy. Several output quantities of the model will be presented and discussed, including frictional energy dissipation, amplitude, and frequency. The selected results are comparable to commonly observed experimental phenomena in mechanics of jointed structures.

1 Introduction

Over the past century, many different mathematical descriptions of friction, or friction-like, behavior have been developed beyond the standard Coulomb model. Several of these are of particular interest to the joints community as whole-joint models, such as the famous Iwan-element [1], and their application can vary between modal models [2] or physical-domain models [3]. Regardless of their use however, these mathematical reduced-order models are generally constructed to represent hysteretic, frictional behavior. In this work, a set of models are used to represent tangential contact forces (friction) at each contact node in a continuum FEA model, in contrast to a reduced-order representation of the joint. Specifically, the following models are studied in this work,

- Coulomb
- Stribeck
- Jenkins/Mignolet Element
- 4 and 5 Parameter Iwan Element
- Bouc-Wen
- Dahl

*Sandia National Laboratories is a multimission laboratory operated by National Technology and Engineering Solutions of Sandia, LLC., a wholly owned subsidiary of Honeywell International, Inc., for the U.S. Department of Energy's National Nuclear Security Administration under contract DE–NA0003525.

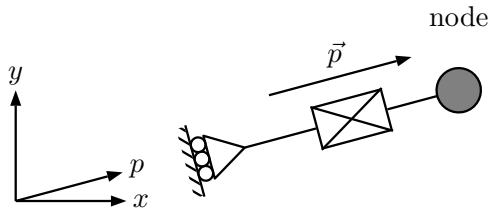


Figure 1: 2-D Implementation of Contact Models

- LuGre
- Elasto-Plastic

In this work, only 2D (planar) problems with contact are studied, and the contact models are implemented at each node, as shown in Figure 1.

All of these friction models can be grouped into two distinct categories, rate-independent and rate-dependent models. The friction force, F_f, for the rate-independent models: Coulomb, Jenkins/Mignolet, 4 and 5 Parameter Iwan, Bouc-Wen, and Dahl can all be characterized by the following form,

$$F_f = L(u, z), \tag{1}$$

$$\dot{z} = g\left(u, z, \operatorname{sgn}\left(\dot{u}\right)\right)\dot{u}, \tag{2}$$

where $L(\cdot)$ is an affine function, z is an internal state variable, and u is the curvilinear nodal displacement along to the contact line. The second requirement, that the evolution of z is dependent only on the sign, not magnitude, of $\dot{u}$, specifically implies that these models are rate-independent. Likewise, the rate-dependent models need not satisfy either Eq. (1) or Eq. (2). Individual descriptions of each of the models are provided in the following subsections where the force F_f is assumed to oppose the nodal velocity $\dot{u}$.

1.1 Coulomb

Coulomb friction is the defacto standard for FEA users that require fictional contact in their models. Mathematically, Coulomb friction can be stated as,

$$F_f = \mu_c N \operatorname{sgn}\left(\dot{u}\right), \tag{3}$$

where μ_c is the coefficient of friction and N is the normal force for that degree of freedom. This model does not involve any dependence on an internal state variable.

1.2 Stribeck

The Stribeck model is another standard tool for many engineers and offers a simple improvement on the standard Coulomb model by incorporating a difference between static and dynamic coefficients of friction. The model can take many forms, but here it is be described as,

$$F_f = \mu_s N \operatorname{sgn}\left(\dot{u}\right), \tag{4}$$

$$\mu_s = \mu_c + \gamma\left[\exp\left(\beta\left|\dot{u}\right|\right) - 1\right] + \alpha\left|\dot{u}\right|, \tag{5}$$

where μ_c has the interpretation of static friction, γ and β are parameters involved with the transition between static and dynamic friction, and α is a parameter that controls linear viscous damping [4] Again, this model does not require dependence on internal state variables.

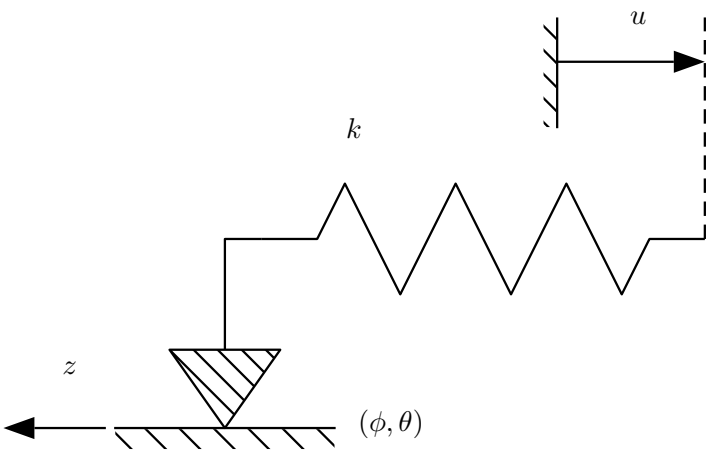


Figure 2: Schematic of a Jenkins/Mignolet Element

1.3 Jenkins/Mignolet

The classical Jenkins element is simply a Coulomb slider in series with an elastic element, as shown in Figure 2. Mathematically, the combined Jenkins/Mignolet element can be represented as,

$$F_f = z, \tag{6}$$

$$\dot{z} = \begin{cases} k\dot{u} & \text{during slip,} \\ 0 & \text{during stick,} \end{cases} \tag{7}$$

where k is the elastic stiffness. The onset of slip is dictated by,

$$\text{slip onset} \|u(t^-) - z(t^-)\| = \phi, \tag{8}$$

$$\text{after slip} \|u(t^+) - z(t^+)\| = \theta\phi, \tag{9}$$

where ϕ is interpreted as the stick-slip force for the internal variable, and $\theta \equiv \mu_D/\mu_S \leq 1$ is defined as the ratio of dynamic to static friction. Note that when $\theta = 1$, the Jenkins element is recovered, but $\theta \in (0, 1]$ is defined here as the broader class of Mignolet sliders [5, 6].

1.4 4 and 5 Parameter Iwan Models

Perhaps the most well-recognized whole-joint model in the joints community is the 4-Parameter Iwan element by Segalman [CITE]. This model consists of a parallel arrangement of Jenkins elements with a distribution of stick/slip parameters chosen such that the energy dissipation per cycle is linear with forcing amplitude on a log-log scale. An extension of this model is the 5-Parameter Iwan model by Mignolet, which is essentially identical to the 4-Parameter model but with the Jenkins elements generalized to Mignolet elements and θ being the 5th parameter. The 5-Parameter model technically encompasses the 4-Parameter model and can

be described as,

$$F_f = \sum_{i=1}^{N} z_i, \tag{10}$$

$$\dot{z}_i = \begin{cases} k_i \dot{u} & \text{during slip,} \\ 0 & \text{during stick,} \end{cases} \tag{11}$$

$$\tag{12}$$

$$\text{slip onset} \| u(t^-) - z_i(t^-) \| = \phi_i, \tag{13}$$

$$\text{after slip} \| u(t^+) - z_i(t^+) \| = \theta \phi_i, \tag{14}$$

In addition to θ, there are four other parameters needed to specify the model, (F_s, K_t, χ, β). Depending on the methodology of the user's application, it may be more useful to specify other parameters related to the derivation of these model; however this work relies on the traditional interpretation given by these four parameters. Please see the work of Segalman and/or Mignolet to clarify the proper parameter transformations [7, 1, 6].

1.5 Bouc-Wen

The Bouc-Wen model as derived by Y.K. Wen [8], based on prior work by Bouc [9], defines the output friction force as,

$$F_f = k_j \left[c \cdot u + (1 - c)\, z \right], \tag{15}$$

$$\dot{z} = \left\{ A - \left[\alpha \operatorname{sgn}\left(z \dot{u} \right) - \beta \right] |z|^n \right\} \dot{u}. \tag{16}$$

Note that in this case, slightly different definitions of this model are available dependent on the source. The Bouc model, from which Wen's work draws from, is actually a subset of the parameter-space of Bouc-Wen models when $(\beta, n) = (0, 1)$,

$$\dot{z} = \left(A - \alpha \operatorname{sgn}\left(\dot{u} \right) z \right) \dot{u}. \tag{17}$$

1.6 Dahl

Dahl's model can be defined as,

$$F_f = z \tag{18}$$

$$\dot{z} = \sigma_0 \left| 1 - \left(\frac{z}{z_c} \right) \operatorname{sgn}\left(\dot{u} \right) \right|^n \operatorname{sgn}\left(1 - \left(\frac{z}{z_c} \right) \operatorname{sgn}\left(\dot{u} \right) \right) \dot{u}, \tag{19}$$

where z_c has the interpretation of static friction, σ_0 is analogous to a linear stiffness, and n is given specified bounds in Dahl's work as,

$$n \in \begin{cases} [0, 1) & \text{for brittle materials,} \\ [1, \infty) & \text{for ductile materials.} \end{cases} \tag{20}$$

The interesting features of this model are that it can reduce to either the Jenkins element or Bouc model dependent on the parameter space. For the case of $(n, \sigma_0, z_c) = (0, k, \phi)$, Dahl's model yields identical results to the Jenkins element in a continuous-time sense. For the case of $(n, \sigma_0, z_c) = \left(1, A, \frac{\alpha}{A}\right)$, the model reduces the differential equation exactly to the Bouc model. Sometimes in the literature, this Bouc form of the Dahl model is what is colloquially referred to as the Dahl model, but Dahl's original work is given by Eq. (19). Dahl's model was specifically included in this work because of its historical relation between the Bouc-Wen and LuGre models, [10].

1.7 LuGre Model

From Dahl's model, the LuGre model was constructed as,

$$F = \sigma_0 z + \sigma_1 \dot{z} + f(\dot{u}), \tag{21}$$

$$\dot{z} = \left(1 - \operatorname{sgn}(\dot{u}) \left(\frac{1}{g(\dot{u})}\right) z\right) \dot{u}, \tag{22}$$

$$g(\dot{u}) \equiv \frac{1}{\sigma_0} \left(z_c + (z_s - z_c) e^{-\left(\frac{\dot{u}}{\dot{u}_s}\right)^2}\right), \tag{23}$$

where $f(\dot{u})$ is often defined as a linear function, i.e. linear damping, such that,

$$F = \sigma_0 z + \sigma_1 \dot{z} + \sigma_2 \dot{u}. \tag{24}$$

In terms of the mathematical structure, this model is similar to the Dahl model with $n = 1$, the Bouc model. The LuGre model deviates from that model by introducing a Stribeck-like term, $g(\dot{u})$. Additionally the damping term $f(\dot{u})$ gives additional flexibility to the model to capture viscous damping effects [11].

1.8 Elasto-Plastic Model

Using the LuGre model as a base, several other researchers have expanded on this work to incorporate different phenomena. One popular LuGre variant is the Elasto-Plastic Friction Model, which attempts to further reflect the original hypothesis of Dahl, that elasto-plastic deformation at the micro-scale, material failure of surface asperities, is the primary culprit of friction forces [12].

The general concept for the description of the restoring force remains the same; however, the evolution of the internal, hysteretic variable z changes,

$$F = \sigma z + \sigma_1 \dot{z} + \sigma_2 \dot{u}, \tag{25}$$

$$\dot{z} = \left(1 - \alpha(z, \dot{u}) \frac{z}{z_{ss}(\dot{u})}\right) \dot{u}, \tag{26}$$

where z_{ss} is the steady-state friction value with respect to velocity, given by,

$$z_{ss}(\dot{u}) = \frac{g(\dot{u})}{\sigma_0}. \tag{27}$$

The function $g(\dot{u})$ has the same connotation as from before in the LuGre model; however the form changes by adding an exponent,

$$g(\dot{u}) = z_c + (z_s - z_c) e^{-\left(\left|\frac{\dot{u}}{\dot{u}_s}\right|\right)^n}, \tag{28}$$

where the authors specify integer n, i.e. $n \in \mathbb{Z}$. The additional rate-dependent function $\alpha(z, \dot{u})$ is given by,

$$\alpha(z, \dot{u}) = \begin{cases} 0, & |z| \leq z_{ba} \wedge \operatorname{sgn}(\dot{u}) = \operatorname{sgn}(z), \\ \alpha_m(*), & z_{ba} < |z| < z_{ss} \wedge \operatorname{sgn}(\dot{u}) = \operatorname{sgn}(z), \\ 1, & z_{ss} \leq |z| \wedge \operatorname{sgn}(\dot{u}) = \operatorname{sgn}(z) \\ 0, & \operatorname{sgn}(\dot{u}) \neq \operatorname{sgn}(z), \end{cases} \tag{29}$$

where z_{ba} is the break-away displacement such that,

$$0 < z_{ba} \leq z_{ss}^{max}, \tag{30}$$

and

$$z_{ss}^{max} = \max(z_{ss}(\dot{u})) = \frac{z_s}{\sigma_0}. \tag{31}$$

The function $\alpha_m(*)$ is given by,

$$\alpha_m(*) = \frac{1}{2}\sin\left(\pi\left[\frac{z - \left(\frac{z_{ss}^{max}+z_{ba}}{2}\right)}{z_{ss}^{max} - z_{ba}}\right]\right) + \frac{1}{2}. \tag{32}$$

2 Numerical Implementation

In this work, the aforementioned advanced mathematical models for frictional contact forces are implemented into Simulia's commercial finite element code, Abaqus, through user-defined Fortran subroutines. The models of interest to this work can be generally classified as phenomenological models which accept a displacement input and give a force output. This is in contrast to stress/strain constitutive models. Because of this phenomenological structure, these models are only capable of being directly implemented into the Abaqus Explicit simulations using the VFRIC subroutine. In order to implement these models into Abaqus Implicit simulations would require that they be reformulated as stress/strain relationships, a non-trivial endeavor and outside the scope of this work.

Despite the VFRIC subroutine allowing for direct input of phenomenological models, user-defined subroutines in Abaqus are generally limited in the sense that Abaqus itself is still a black-box from the perspective of any subroutine. One of the primary consequences of this code structure is that the evolution equations for z in this study cannot be included in the set of coupled-nonlinear ODEs that Abaqus solves. Thus evolution of the internal variables was calculated within each subroutine. The calculation method varied for each model; however they can be grouped into three classes. The zero-dimensional models: Coulomb and Stribeck, did not involve internal variables and did not require additional work. The differential models: Bouc-Wen, Dahl, LuGre, and Elasto-Plastic, were all conceptually similar in that they merely required the solution of a nonlinear ODE, and in this case, the ODE was solved for these models using the standard RK4 method. Test problems were used to ensure that the calculation accuracy was sufficient. In contrast, the Iwan-type models: Jenkins/Mignolet and the 4 and 5 Parameter Iwan model are defined by complex algebraic relationships depending on the stick/slip state of the internal variables. Further, the incorporation of the difference between static and dynamic friction, through θ, creates solutions with discontinuities. A more sophisticated selection algorithm was developed to calculate the evolution of these models. For each node in contact and for each Jenkins/Mignolet-type element in that contact model, two state variables were assigned, z and $slip$. The variable z is the internal state variable as shown previously, but $slip$ is a binary variable that represents whether or not an individual slider is sticking or slipping. The algorithm can be concisely stated for each time-step, n, as,

1) if: A reversal has occurred, i.e. $\mathrm{sgn}(\dot{u}_n) \neq \mathrm{sgn}(\dot{u}_{n-1})$.
   - Slip state is automatically set to stuck, i.e. $slip_n = 0$
   - $\dot{z} = 0 \implies z_n = z_{n-1}$
   - $F_n = u_n - z_n$

2) else: No reversal has occurred, i.e. $\mathrm{sgn}(\dot{u}_n) = \mathrm{sgn}(\dot{u}_{n-1})$.

   Predict the friction force using the internal state-variable from the previous time-step by $F_{pre} = u_n - z_{n-1}$

   2a) if: The slider was stuck in the previous time-step, i.e. $slip_{n-1} = 0$; two possible sub cases:

      2ai) if: The slider is still stuck, i.e. $|F_{pre}| \leq \phi$.
      - slip state does not change, i.e $slip_n = slip_{n-1}$
      - $\dot{x} = 0 \implies z_n = z_{n-1}$
      - $F_n = F_{pre}$

2aii) else: the slider was stuck and is now slipping
- Slip state changes from stick to slip, i.e. $slip_n = 1$
- $F_n = \theta\phi$
- Use the jump discontinuity to calculate x, i.e. $z_n = u_n - F_n$

2b) else: The slider was and is sliding and nothing is changing, i.e. $slip_{n-1} = 1$
- slip state does not change
- $F_n = \theta\phi$
- $\dot{z} = \dot{u} \implies x_n = u_n - F_n$

Once the code evaluates the evolution of all of the Jenkins/Mignolet elements in the model at that node, the total force at that node is evaluated as a summation of the forces of all of the elements.

Furthermore, there are additional physical conditions that need to be accounted for. In a contact problem between two deformable bodies, one of the implicit requirements for a physically meaningful solution is that the strongest possible friction forces are those that enforce no-slip conditions. The force required to maintain no-slip conditions at a particular degree of freedom, F_{stick}, is problem-dependent, and solution state-dependent. Many of the models in this study mimic this behavior for the internal state variable, z, but only the Coulomb and Stribeck models are capable of enforcing this requirement in all cases. It is also commonly known to engineers that friction forces generally scale with the normal force; however again, only Coulomb and Stribeck account for this phenomena. In order to enforce these requirements in general for all of the models, a "Meta-Coulomb" concept was developed. Using this concept, the tangential frictional contact force in the FEA problem at a particular degree of freedom, F_t, can be mathematically be stated as,

$$F_t = \min\left[F_{stick}, \left(\mu_m N\right) F_f \operatorname{sgn}\left(\dot{u}\right)\right], \tag{33}$$

where μ_m is defined as the meta coefficient of friction, and N is the normal force for the degree of freedom. By convention, F_{stick} is assumed to be positive in this work, but it is also assumed that F_t is always in the direction opposing the slip direction. Multiplication of F_f by $\operatorname{sgn}\left(\dot{u}\right)$ reorients the friction force to be in the proper direction for this convention. These conventions are chosen to be consistent with Abaqus documentation. In addition to the physically-motivated reasons shown previously, another benefit of this approach is that because the normal load and meta coefficient of friction are used to provide appropriate scaling, the hysteretic friction force, F_f should generally be of $\mathcal{O}(1)$.

A final consideration is that of numerical stability. Hysteresis phenomena are numerically difficult to solve for a variety of reasons. At reversal points, the derivative of the internal state variables are discontinuous, leading to non-smooth, potentially numerically-stiff solutions. The solution of the state-variables themselves can also be discontinuous, as shown with the Mignolet-type models. Additionally, because many of these contact models incorporate elastic stiffness effects, there are limited regions of the hysteresis curve during which the friction force might not oppose the slip when the elastic element is releasing stored energy. In the context of Eq. (33), this would be the case of $F_t < 0$. Such situations can actually lead to unstable solutions, as stated in the Abaqus user-subroutine documentation. Interestingly, another scientific area where hysteresis shows up is the numerical/mathematical electromagnetics community [13]. While the application is different, the underlying differential equations are similar, and those hysteresis problems also suffer from numerical stability in time-dependent problems. In the case of continuum mechanics problems, the reason for this instability is that the time-marching algorithm used in Abaqus Explicit is of relatively low-order. Specifically, Abaqus Explicit uses central-difference integration with limited adaptability based on wave-propagation and damping through the structure. For this work, that algorithm was found to be insufficient for realistic problems and it is not currently possible to adjust the time-marching algorithm within Abaqus Explicit. To compensate for this difficulty, the absolute value of the friction force is taken to ensure the stability requirements dictated by the Abaqus documentation,

$$F_t = \min\left[F_{stick}, \left(\mu_m N\right) \left|F_f\right| \operatorname{sgn}\left(\dot{u}\right)\right]. \tag{34}$$

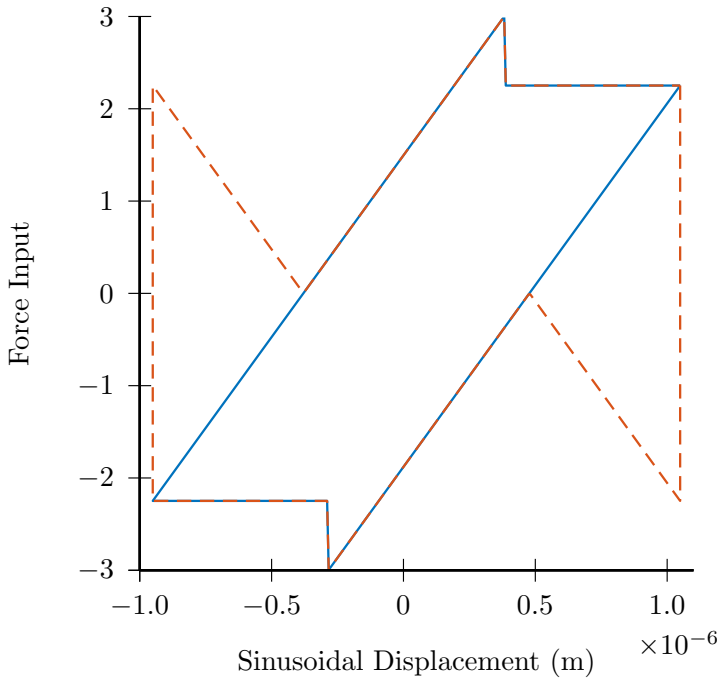


Figure 3: Stabilized Hysteresis Curve
Unstable Hysteresis Curve: ——, Stable Hysteresis Curve: - - -

This change can be thought of as a mapping to ensure stability. One interesting note regarding the mapping in Eq. (34) is that contact models involving only viscous and/or coulombic elements are mapped onto themselves. An example of the effect of this change is shown in Figure 3

3 Verification

In order to ensure the efficacy of the calculations presented in this work, a representative, realistic test problem was developed in order to verify that the advanced friction models are capable of representing commonly observed experimental phenomena in problems with lap joints. The problem is derived from the C-Beam used by the NOMAD Institute at Sandia National Laboratories.

3.1 Problem Setup

While nearly all lap-joints are three-dimensional problems by nature, the methods presented here are only capable of representing two-dimensional (planar) problems involving contact. A schematic of the test problem is shown in Figure 4. The test problem used in this study is essentially a two-dimensional cross section of the C-Beam with the shank of the bolt allowed to pass through the body of the beam. Tied contact was used to fix the washers to the upper and lower faces of the beam, and because no other interactions were prescribed between the bolt and beam, the shank of the bolt is allowed to move freely through the beam. While this is certainly not a realistic way to design a structure with bolted connections, it is a reasonable two-dimensional representation that captures a great deal of the physics of interest to this work.

Applying the bolt preload however was not nearly as simple. Abaqus Implicit has a built in subroutine specifically designed to apply preload to bolts; however this algorithm has not yet been implemented in

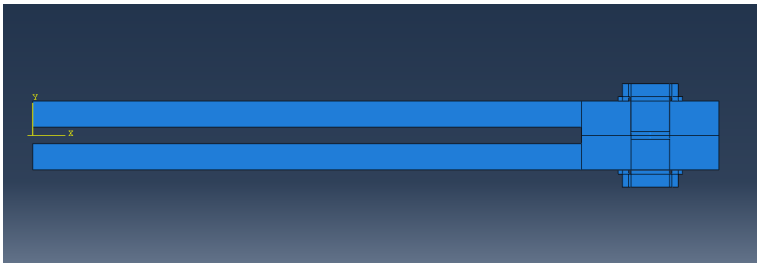


Figure 4: 2-D C-Beam Test Problem

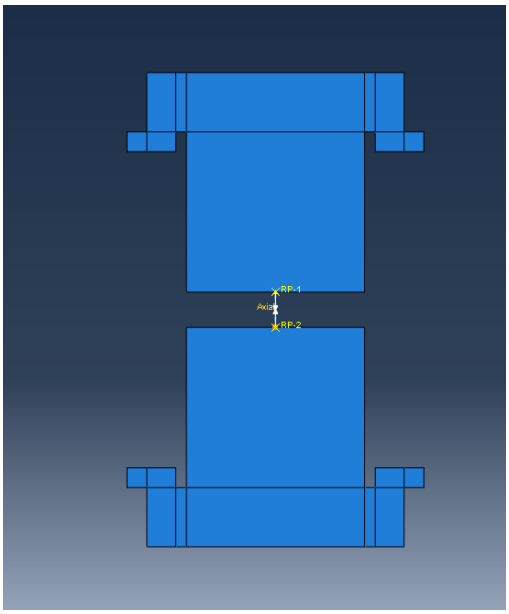


Figure 5: 2-D C-Beam Test Problem Bolt

Abaqus Explicit. To compensate, a custom method was used. A small portion of the bolt was cut away near the midpoint of the shank. The two revealed ends were each given a reference point and the revealed nodes were kinematically-coupled to their respective reference points, i.e. the edge nodes are rigidly connected to the reference point. The two reference points were then connected with an axial connector. This axial connector acts as a slotted connection. The two reference points may translate axially along the connector, but the connector does not allow for relative notation, only rigid rotation. A schematic of this connection is shown in Figure 5. A relatively small preload of $2000N$ was applied as a connector force to act as a preload. The actual magnitude of the preload is arbitrary in this situation, but it was found to be sufficient to uncover significant phenomena.

This method of applying the bolt preload is applicable to both Abaqus Explicit and Abaqus Implicit simulations. That fact is important because linearized mode shapes and natural frequencies can only be calculated after Abaqus Implicit static preloading steps. For this test problem, the lowest mode that participates in the joint occurs at 331 Hz and the corresponding mode shape is shown in Figure 6.

The beam was loaded in two steps. First, a quasi-static preloading step was used to load the bolt as previously described, and then a $1.0\,ms$ haversine impulse was applied to the midpoint of the upper branch of the C-Beam. This approach was symmetric about the y-axis and thus reduced the problem size greatly. Several different magnitudes of haversine impulse were applied to beams containing each of the different contact models. The impulse magnitudes were: $10\,N$, $50\,N$, $100\,N$, and $200\,N$. Notably, no significant difference was found between Abaqus' built-in penalty friction model and a strict Coulomb friction model, thus Abaqus' penalty, or default, friction was used as the baseline for this study. The transient response was calculated for $1.0\,sec$ of simulation time.

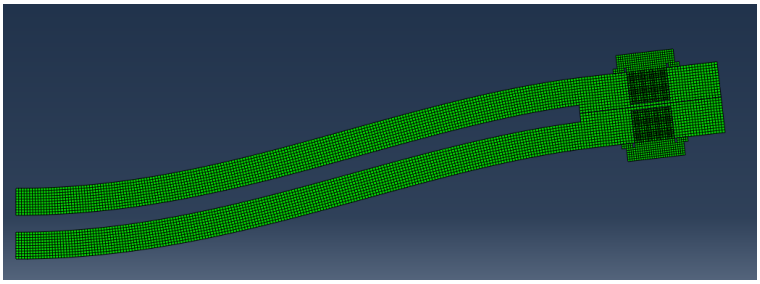


Figure 6: Dominant Mode of the Verification Problem

During the investigation of this work, it was found that the friction models were extremely sensitive to parameter tuning. In order to glean meaningful comparisons between the different friction models, a tuning scheme was used to ensure that the energy dissipation per cycle among the models was similar. A meta coefficient of friction of $\mu_m = 0.5$ was arbitrarily chosen. Additionally, because the Coulomb friction model's parameter, μ_c, is redundant within the meta coefficient of friction framework, it was set to unity, i.e. $\mu_c = 1$. The other friction models were then tuned in comparison to the Coulomb model by examining the response of a single degree of freedom excitation. The output forces, F_f, for each of the models were calculated assuming a sinusoidal input of,

$$u_{inp} = u_o \sin\left(\omega_{fd}\, t\right), \tag{35}$$

where u_o is a characteristic displacement and ω_{fd} is the fundamental natural frequency of the system. Examining the results for different loading impacts on the beam with the Coulomb model revealed that a reasonable characteristic displacement at the interface is approximately $u_o = 10^{-7}\, m$, and it is was shown previously that the relevant fundamental natural frequency is $\omega_{fd} = 331\, Hz$. Note that the forcing frequency is relevant only for the rate-dependent models. The tuned hysteresis curves are shown in Figure 7.

3.2 Results

Two metrics were primarily studied in this system, modal frequency response functions and frictional energy dissipation. For each of the transient simulations, the displacement data was decomposed by the modeshapes identified through Abaqus' linear perturbation analysis to uncover the modal response of the mode shown in Figure 8. In that figure, it can be seen that the tuning scheme is effective in calibrating the models somewhere between $50\, N$ and $100\, N$, but as the load changes, the response of the system can change considerably depending on the model.

In addition to comparing the models, another goal of this verification problem is to assure that the different models obey commonly observed experimental phenomena, particularly as the impact magnitude changes. Figure 9 shows the effect of changes the loading impact magnitude on the Coulomb model and the Iwan model. As the magnitude of the impact increases, the damped natural frequency decreases, and the damping increases in a nonlinear fashion.

Finally, the total energy dissipated through contact is examined in Figure 10. This output quantity, known as ALLFD in Abaqus, is able to shed light on the different regimes of the response. Note that this metric only measures the dissipation through frictional contact, not material damping. In this case, the material damping is extremely small, only large enough to mitigate numerical issues, such that microslip can be assumed to be the only significant source of damping in the system. In the early portion of the response, up to $0.5\, sec$ depending on the model, the energy dissipation is large, indicating that micro-slip is a dominant effect. In the later portions of the response however, the interface locks and only material damping is present. This can be see as the frictional energy dissipated asymptotically approaches a steady-state value. Each model approaches a slightly different value depending on its parameters and behavior.

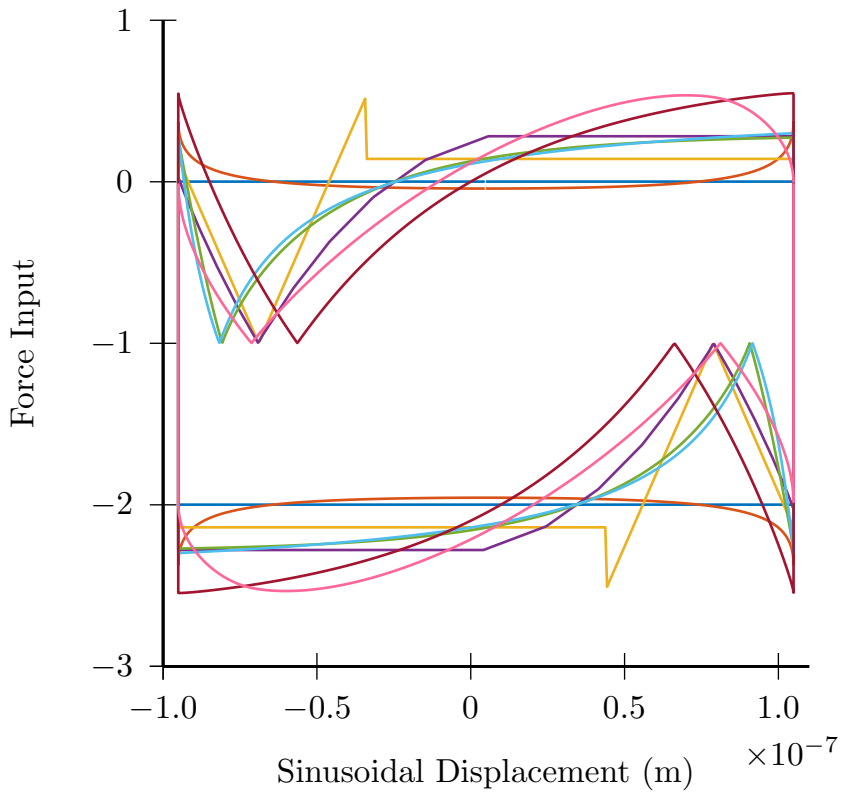
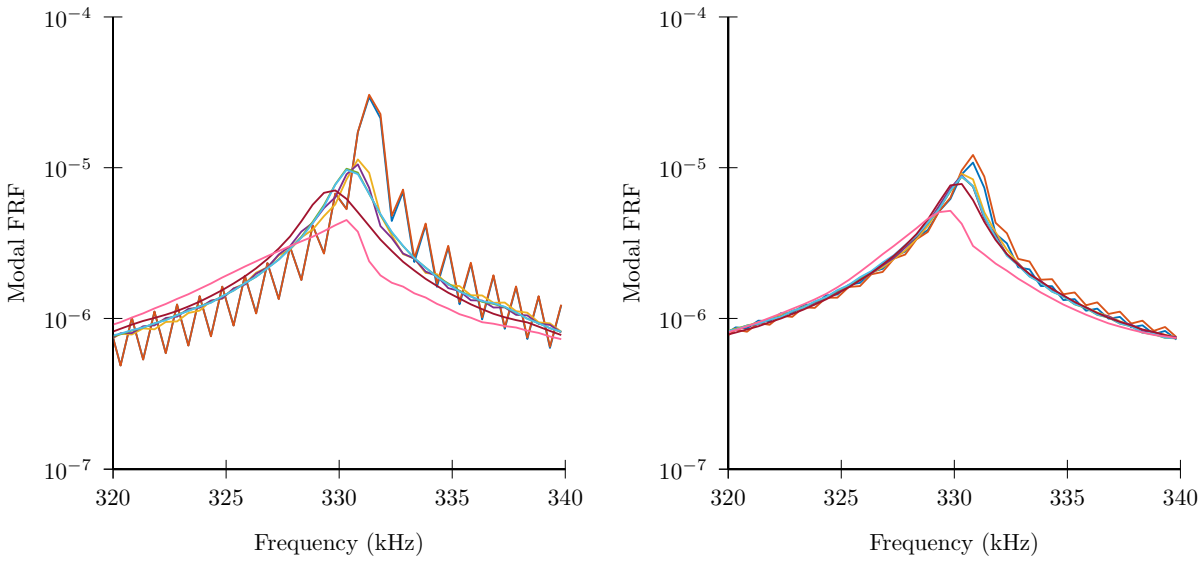


Figure 7: Tuned, Stabilized Hysteresis Curves
Coulomb: —, Stribeck: —, Jenkins/Mignolet: —, Iwan: —
Bouc-Wen: —, Dahl: —, LuGre: —, Elasto-Plastic: —

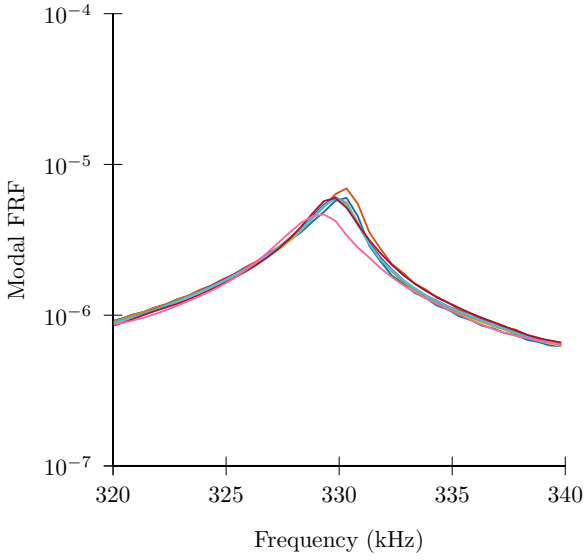
4 Conclusion

In this work, several of the best friction models available in academic literature have been combined with commercially available software to open up new possibilities for physical-domain analysis of jointed-structures. Using a representative verification problem, it was shown that standard experimentally observed nonlinear damping phenomena can be recovered, and differences between the different models can be observed. Future work in this research area will include extension of the methodology into three-dimensional contact problems, and analysis of the effects of parameter tuning on system response.

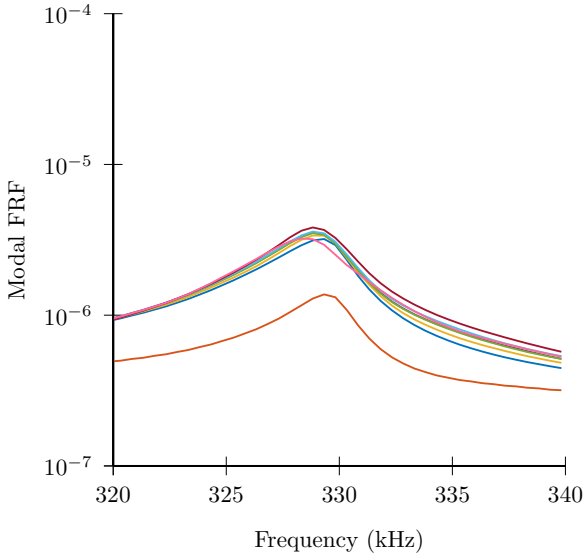


(a) 10 N Impact

(b) 50 N Impact

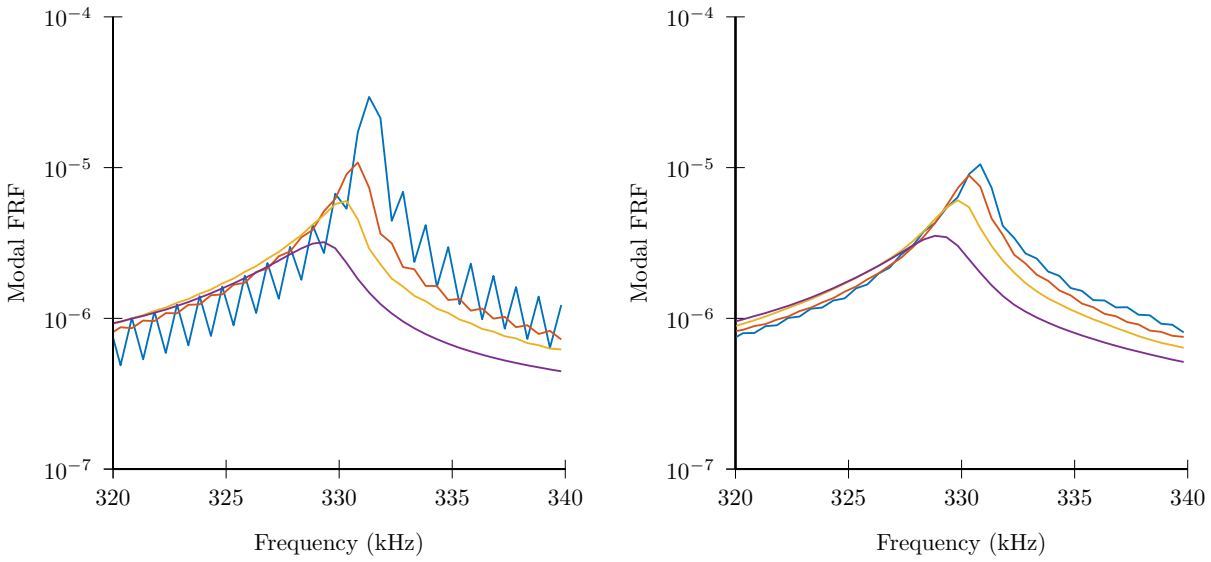


(c) 100 N Impact



(d) 200 N Impact

Figure 8: Frequency Response Functions Under Different Loading Conditions
Coulomb: —, Stribeck: —, Jenkins/Mignolet: —, Iwan: —
Bouc-Wen: —, Dahl: —, LuGre: —, Elasto-Plastic: —



(a) Coulomb Model (b) Iwan Model

Figure 9: Frequency Response Functions for Different Models
10 N: —, 50 N: —, 100 N: —, 200 N: —

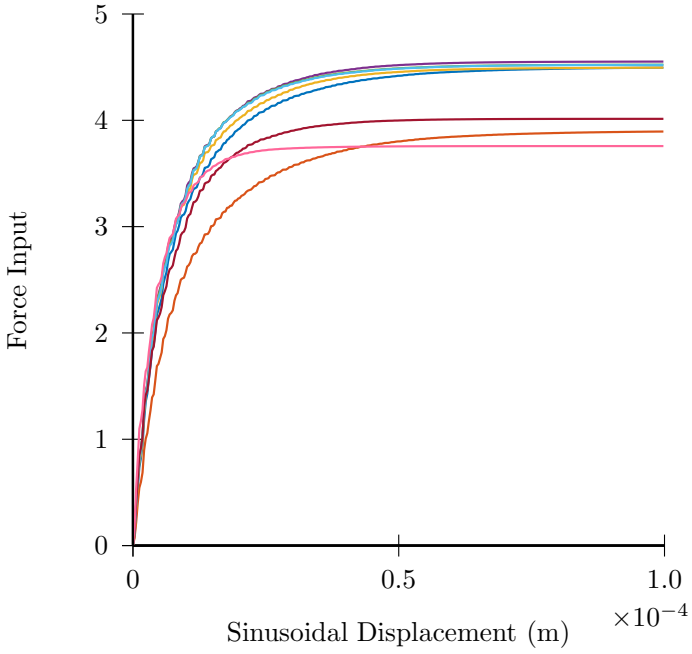


Figure 10: Frictional Energy Dissipation for the Whole Model
Coulomb: —, Stribeck: —, Jenkins/Mignolet: —, Iwan: —
Bouc-Wen: —, Dahl: —, LuGre: —, Elasto-Plastic: —

References

[1] D. J. Segalman. A four-parameter iwan model for lap-type joints. *Transactions of the ASME*, 72(5):752–760, 2005.

[2] D. R. Roettgen and M. S. Allen. Nonlinear characterization of a bolted, industrial structure using a modal framework. *Mechanical Systems and Signal Processing*, 84(B):152–170, 2015.

[3] M. Allen, R. M. Lacayo, and M. R. Brake. Quasi-static modal analysis based on implicit condensation for structures with nonlinear joints. In *ISMA 2016, International Conference on Noise and Vibration Engineering, Leuven, Belgium*, 2016.

[4] A. Harnoy, B. Friedland, and S. Cohn. Modeling and measuring friction effects. *IEEE Control Systems*, 28(6):82–91, 2008.

[5] Augusto Visintin. *Differential Models of Hysteresis*. Springer, 1991.

[6] M. P. Mignolet, P. Song, and X.Q. Wang. A stochastic iwan-type model for joint behavior variability modeling. *Journal of Sound and Vibration*, 349(4):289–298, 2015.

[7] W.D. Iwan. A distributed-element model for hysteresis and its steady-state dynamic response. *Journal of Applied Mechanics*, 33(4):893–900, 1966.

[8] Y.K. Wen. Method for random vibration of hysteretic systems. *Journal of the Engineering Mechanics Division*, 102(2):249–263, 1976.

[9] R. Bouc. Modèle mathématique d'hystérésis. *Acustica*, 24(1):16–25, 1971.

[10] P. R. Dahl. A solid friction damping of mechanical vibrations. *AIAA Journal*, 14(12):1675–1682, 1976.

[11] C. Canudas de Wit, H. Olsson, K. J. Astrom, and P. Lischinsky. A new model for control of systems with friction. *IEEE Transactions on Automatic Control*, 40(3):419–425, 1995.

[12] P. Dupont, B. Armstrong, and V. Hayward. Elasto-plastic friction model: Contact compliance and stiction. In *Proceedings of the American Control Conference, Chicago, Illinois*, volume 2, pages 1072–1077, 2000.

[13] L. Perkkio, B. Upadhaya, A. Hannukainen, and P. Rasilo. Stable adaptive method to solve fem coupled with jiles-atherton hysteresis model. *IEEE Transactions on Magnetics*, 54(2):1–8, 2018.

Sound transmission through checkerboard sandwich panels

B. Van Damme [1], **G. Hannema** [1], **A. Zemp** [1]
[1] Empa, Laboratory for Acoustics/Noise Control,
Ueberlandstrasse 129, CH-8600, Dübendorf, Switzerland
e-mail: **bart.vandamme@empa.ch**

Abstract

Resonant metamaterials and phononic crystals are popular ways to design the dynamic properties of materials. Especially sought-for are frequency ranges with high damping, so-called bandgaps. A possible approach to achieve forbidden frequency bands in plates is altering the bending stiffness in a regular pattern, e.g. by varying the thickness profile or the material stiffness. The destructive interference of incoming and reflected bending waves, due to impedance changes, results in a series of wide bandgaps. We investigate a two-dimensional phononic crystal sandwich plate consisting of a pattern of rectangular unit cells. Each cell's core has an area with higher stiffness and mass density, captured between two thin homogeneous faces. Unlike resonant metamaterials, such panels do not require expensive parts with a complex shape and are therefore more economical. The dispersion relation is modelled using periodic boundary conditions on a unit cell, which results in the prediction of highly anisotropic material properties.

1 Introduction

Lightweight panels are widely used for automotive and aerospace applications, but also as a flexible solution for separation walls between offices and meeting rooms. The economic and practical advantages are clear: a lower weight results in reduced fuel consumption and a higher flexibility due to easier handling. The acoustic performance of such materials, however, is negatively influenced by the low weight [2]. The sound transmission loss depends mainly on the mass in a large frequency range, and the general consensus is to achieve a compromise between weight and acoustic restrictions [10].

Elastic waves can be efficiently attenuated in wave guides with an engineered structure. Resonators added to a host structure absorb wave energy at their eigenfrequency [8]. Alternatively, a periodic alteration of elastic properties (Young's modulus, bending stiffness, mass, ...) leads to wave scattering and destructive interference in certain frequency ranges [6]. Such structured materials are called resonant metamaterials or phononic crystals, respectively [4, 5]. They are widely investigated for vibration and acoustic isolation applications, since the attenuation is no longer ruled by the material constants, but by directly altering the dynamic properties of the structure.

Several solutions for lightweight walls with high transmission loss based on the metamaterial approach exist. The goal is to reduce out-of-plane motion of the walls, for which mainly bending waves are responsible. Resonators can be added directly on a thin light plate [1], or two faces of a double-leaf wall can be decoupled by highly attenuated connectors [3]. In the first case, wave energy is absorbed by the resonators, thereby avoiding the host plate to vibrate at that particular frequency. In the second case, the vibration of one face is not transmitted to the second face, leading to a reduced sound radiation. These resonant solutions are highly efficient, but requires parts with a complicated geometry and is therefore not always cost effective.

In this paper, we investigate two-dimensional phononic crystals to achieve vibration attenuation in plates. It is known that beams with a periodically varying cross section exhibit forbidden frequency bands for bending waves [7, 12]. The width and efficiency of these band gaps depends on the geometry and material properties.

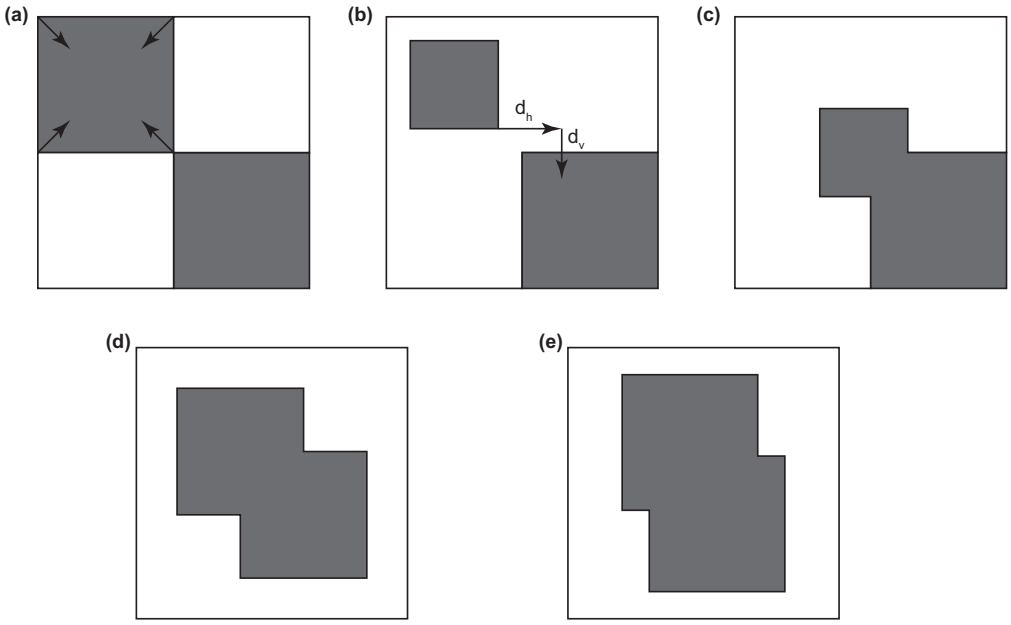


Figure 1: Unit cell of a pure checkerboard plate (a), the areas with different bending stiffness are shown in grey and white. Two transformations of the initial unit cell: scaling (b) and translation (c). Geometries investigated in this work: 35×35 mm translation (d) and 60×30 mm translation (e).

Despite the easy design, very high wave attenuation can be achieved. This idea can be expanded to plates, when filling a plane with rectangular tiles of alternating thickness. The band gaps depend on the wave propagation direction, since the periodicity a wave encounters varies with the propagation angle. Extending the attenuation efficiency of periodic beams to plates is therefore a non-trivial problem, and we will look into some possible designs.

We present a possible geometry for sandwich panels with periodically varying bending stiffness. The bending waves of a structure with a limited number of design parameters are modelled. Periodic boundary conditions can be applied to calculate the wave dispersion in an infinite plate based on a single unit cell. Using an inverse ($f \rightarrow k$) dispersion calculation scheme allows for the computation of the real and imaginary part of the wave numbers as a function of frequency. Thus, knowledge of spatial attenuation of waves in all directions can be addressed.

The geometry and modelling method are shown in Sec. 2. Numerical dispersion results, including direction dependent phase velocities, are shown in Sec. 3.

2 Modelling checkerboard phononic sandwich plates

2.1 Unit cell geometry

In order to realise a 2D phononic crystal for bending waves, the bending stiffness has to exhibit a periodic pattern. We propose a rectangular tiling of the plane to achieve periodicity. The bending stiffness can be altered by changing e.g. the thickness or material in each cell, but these possibilities are not very practical for production. Therefore, we propose sandwich plates of which the core consists of two materials in a chosen tiling. This results in a structure with flat outer faces but with a locally varying bending stiffness depending on the core.

A perfect checkerboard structure, with alternating square tiles having 2 different bending stiffnesses, is an ill-defined design due to the line contacts between individual tiles, leading to non-manifold edges (Fig. 1(a)). It

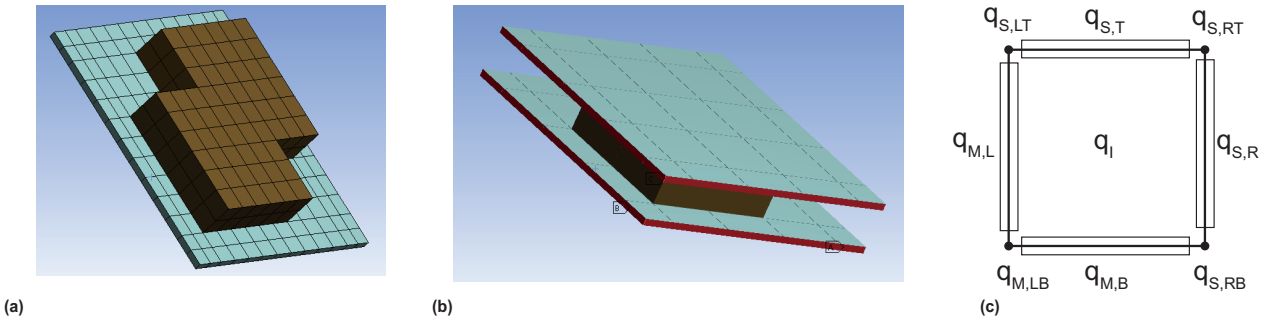


Figure 2: Steps in the preparation of the FE model with periodic boundary conditions. Mesh (a), selection of the master and slave surfaces in red (b), location of the master and slave nodes (c).

also lacks flexibility to change the overall dynamic behaviour of the sandwich plates. We introduce three additional design parameters by defining two operations on one quarter of the initial unit cell: scaling (Fig. 1(b)) and a horizontal (d_h) and vertical (d_v) translation (Fig. 1(c)). In this example, the white material is expanded so that the initial shape of the unit cell remains unchanged. After applying one or both transformations, there are no more non-manifold edges.

For the study in this paper, we limit ourselves to translations only. In the models, the resulting octagons are made out of aluminum ($E = 71$ GPa, $\rho = 2770$ kg/m^3) and have a thickness of 10 mm. The octagons are placed in a 150 mm$\times$150 mm pattern between two plexiglass plates ($E = 3.3$ GPa, $\rho = 1190$ kg/m^3) with a thickness of 3 mm. The rest of the space between the plexiglass faces is left open. The filled space has a considerably higher bending stiffness than the open parts, resulting in wave scattering. Two different translations are considered in the model: one along the diagonal with $d_h = d_v = 35$ mm, resulting in an octagon with point symmetry, and one asymmetric scenario with $d_h = 60$ mm and $d_v = 30$ mm.

2.2 Floquet boundary conditions for complex wave number calculation

Wave dispersion in an infinite, periodic assembly of plane unit cells can be calculated by applying Floquet boundary conditions in two dimensions. This calculation can be conveniently performed starting from a finite element model (FEM) of the unit cell. For this work, the FEM preparation and meshing is done in Ansys 18.2 (Fig. 2(a)), for clarity the upper face is omitted), after which the mass and stiffness matrices M and K are exported for further calculations. This offers the possibility to consider more complex geometries than the one presented here.

The equation of motion, considering a harmonic excitation, of the FEM unit cell is given by

$$\hat{D}\mathbf{q} = [K - \omega^2 M]\mathbf{q} = \mathbf{f},$$

where $\hat{D}$ is the dynamic stiffness matrix. Damping is included by adding an imaginary part to the stiffness matrix, in our case equal to 5% of the real values: $K_{damp} = (1 + 0.05i)K$. In the absence of external forces, the force vector on the internal DOFs $\mathbf{q_I}$ equals zero:

$$\hat{D}\begin{bmatrix} \mathbf{q}_\square \\ \mathbf{q_I} \end{bmatrix} = \begin{bmatrix} \mathbf{f} \\ \mathbf{0} \end{bmatrix},$$

where $\mathbf{q}_\square$ denotes the DOFs on the boundary of the unit cell. Therefore, these nodes can be eliminated out of the equation of motion in order to reduce the matrices and increase the calculation speed, according to [9, 11]:

$$D\mathbf{q}_\square = \mathbf{f}.$$

A harmonic wave with wave vector $\mathbf{k}$ travelling through an assembly of unit cells relates the (slave) degrees of freedom (DOFs) $q_{S,R}$ on the right side of the unit cell to the (master) DOFs $q_{M,L}$ on the left:

$$q_{S,R} = \exp(-ik_x D_x) q_{M,L},$$

where k_x is the x-component of the wave vector, and D_x the size of the unit cell in this direction. In the same way, the DOFs on the top side can be related to those of the bottom side. The relation between the diagonal corner DOFs is given by

$$q_{S,RT} = \exp(-ik_x D_x - ik_y D_y) q_{M,LB}.$$

The master sides of the unit cell under consideration are shown in (Fig. 2(b)).

In matrix form, the DOF vector can now be reduced to

$$\mathbf{q} = \Lambda_R \mathbf{q_M},$$

where $\mathbf{q_M}$ contains the master DOFs only. Due to force equilibrium between the boundary nodes, the force vector can be reduced using the relationship

$$\Lambda_L \mathbf{f} = \mathbf{0}.$$

The detailed structure of the reduction matrices Λ_L and Λ_R can be found in [9, 11].

Using these relations, the equation of motion can be rewritten as

$$\bar{D}(\omega; k_x, k_y)\mathbf{q_M} = [\bar{K}(k_x, k_y) - \omega^2 \bar{M}(k_x, k_y)]\mathbf{q_M} = 0,$$

with $\bar{K} = \Lambda_L K \Lambda_R$ and $\bar{M} = \Lambda_L M \Lambda_R$.

The direct dispersion calculation method, choosing a value for k_x and k_y, and calculating the eigenfrequencies ω is a straightforward eigenvalue problem. However, the result is only valid in pass bands, and the spatial attenuation of waves cannot be retrieved. It is also not a useful method if material damping is considered.

The inverse method, calculating the wave number for a chosen frequency, is more intricate but results in more complete information. It can be shown that the reduced equation of motion can be written as a polynomial eigenvalue problem in case $k_y D_y / k_x D_x = m_2/m_1$ is rational. The highest order of the eigenvalue is $p_{max} = 2(m1 + m2)$. Although relatively efficient to solve, the calculation time becomes exorbitant if $p_{max} > 20$.

We implemented the inverse method in Matlab, keeping for each frequency the 12 wave numbers with the lowest real part. The results for two geometries are shown in the next section.

3 Modelling results

3.1 Direction dependent dispersion

The result of the inverse calculation method described in the previous section is a set of complex wave numbers for the frequency range 0-5000 Hz. An example is given in Fig. 3(a). Since only out-of-plane waves play an important role for acoustic radiation, we filter out the in-plane wave modes, resulting in the dispersion curve in Fig. 3(b).

The colours represent the imaginary part of the wave number. It can be seen that band gaps can both occur on the edges of the first Brillouin zone, but there are also frequency bands with high damping at intermediate wave numbers. This happens where two or more branches cross. These frequency bands appear as veering if the direct calculation scheme is used: a certain branch of the dispersion curve bends back towards lower frequencies, and veers a neighbouring branch. However, using the indirect method, it can be seen that a single branch can be tracked continuously over the entire frequency range.

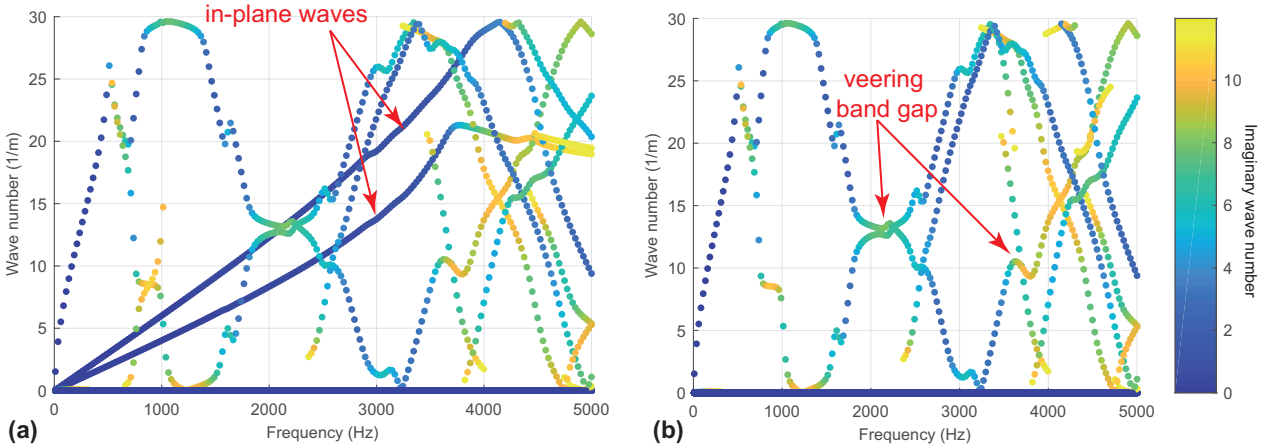


Figure 3: Full dispersion curve for the 35×35 geometry, in the $45°$-direction (a) and dispersion curve with out-of-plane modes only (b).

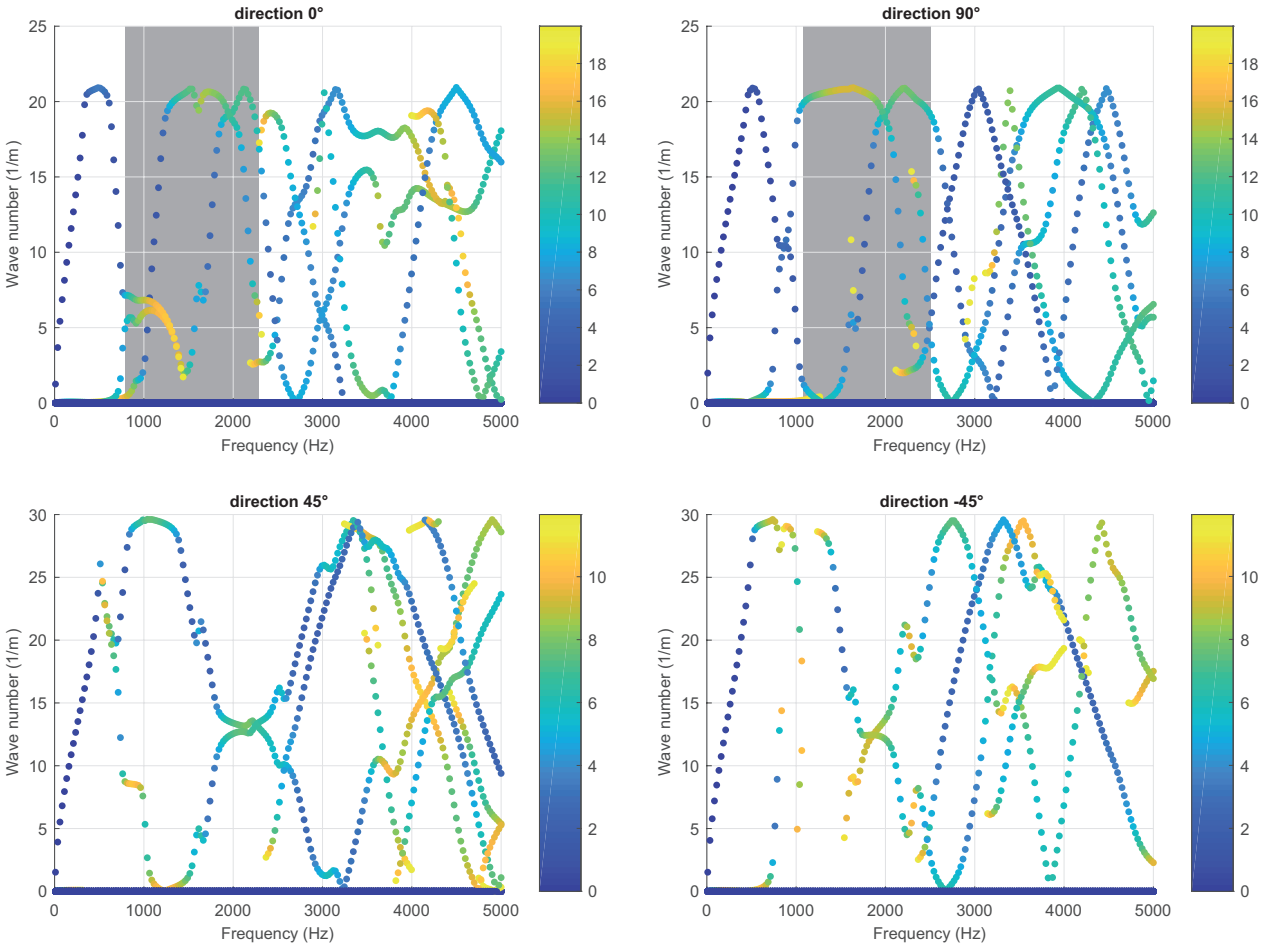


Figure 4: Out-of-plane-wave dispersion curve for the 35×35 geometry, in four different directions. The colour represents the imaginary part of the wave number, blue for low attenuation and yellow for high attenuation. (Partial) band gaps are highlighted in grey.

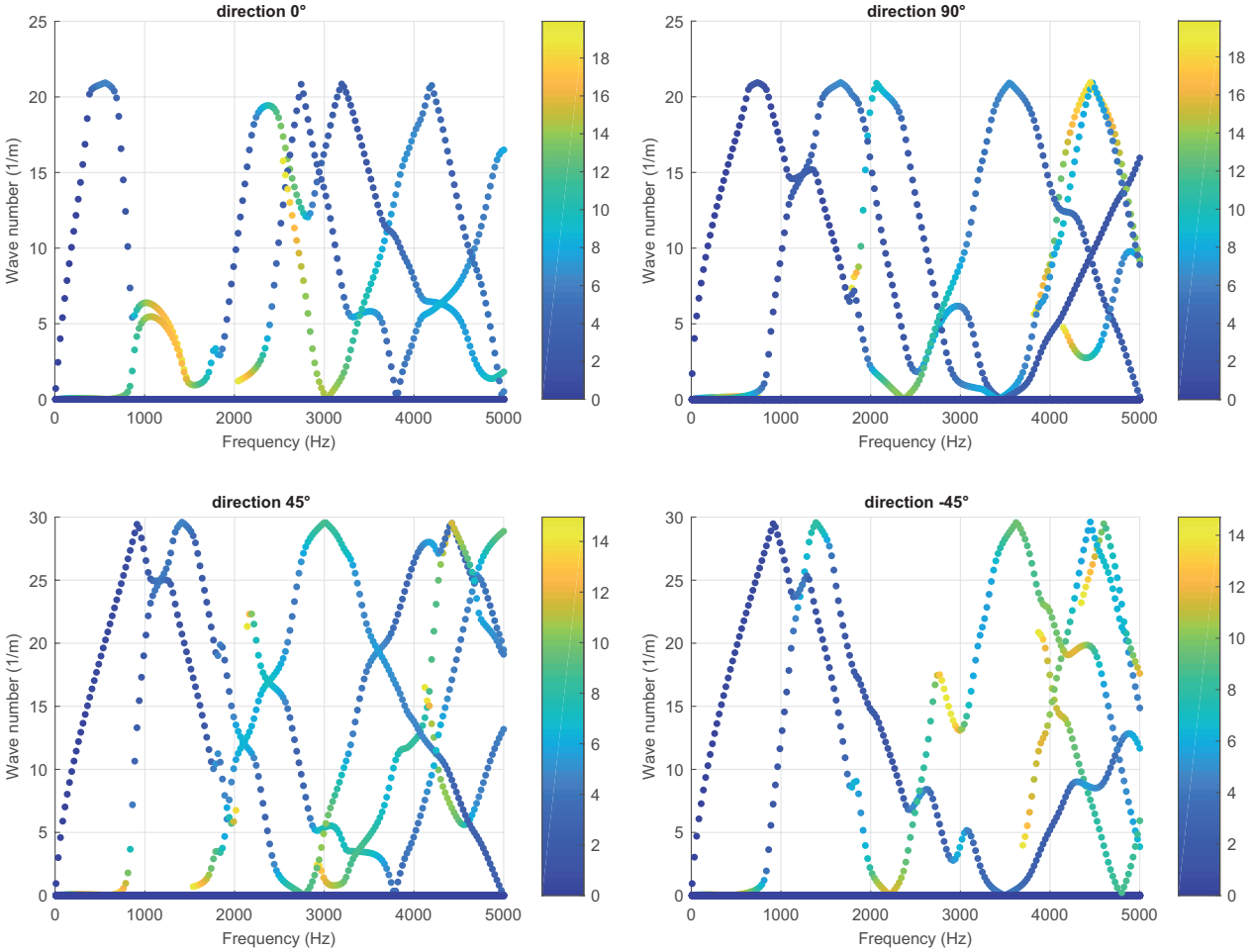


Figure 5: Out-of-plane-wave dispersion curve for the 60×30 geometry, in four different directions. The colour represents the imaginary part of the wave number, blue for low attenuation and yellow for high attenuation.

In the $45°$-direction, this geometry has very high damping ($\Im(k) > 20$) over almost the entire frequency range, except for the lowest frequencies up to 700 Hz, and some individual branches around 1500 and 3000 Hz.

Fig. 4 shows the dispersion curves in four different directions for the 35×35 geometry. The asymmetry is clearly noticeable. However, in the $0°$ and $90°$, no wide total band gaps are present. On the other hand, the areas in grey highlight zones with high damping for most waves. The steep dispersion branches with low attenuation result in sharp frequency bands where elastic wave motion is possible. It can be expected, however, that bending waves will be efficiently damped.

Fig. 5 shows the dispersion curves in four different directions for the 60×30 geometry. Once again, a relatively high damping is achieved above 2500 Hz for the $\pm 45°$-directions. On top of that, a full band gap is clearly noticeable in the $0°$-direction, between 1000 Hz and 2000 Hz.

3.2 Frequency dependent phase velocity

From the dispersion curves, the phase velocity of the waves can be calculated directly using the relation $v_{p,x} = \omega/\Re(k_x)$ and $v_{p,y} = \omega/\Re(k_y)$. We calculated the dispersion curve in 33 different directions in order to create a polar plot of the phase velocity as a function of frequency. This gives useful insight in the wave propagation behaviour and direction dependent wave attenuation.

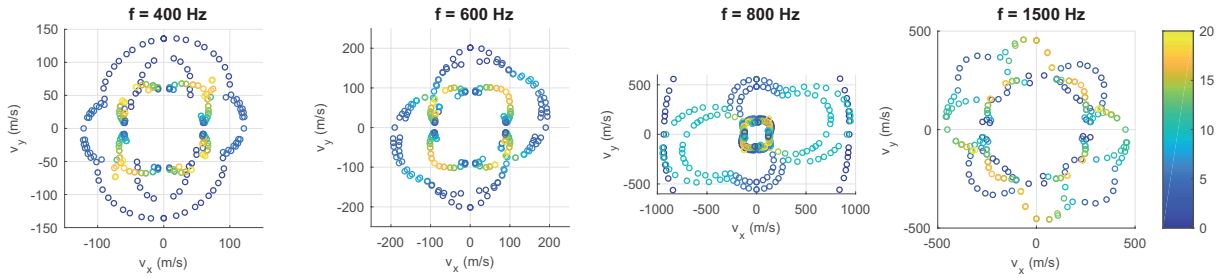


Figure 6: Phase velocity of out-of-plane waves for the 35×35 geometry at four different frequencies.

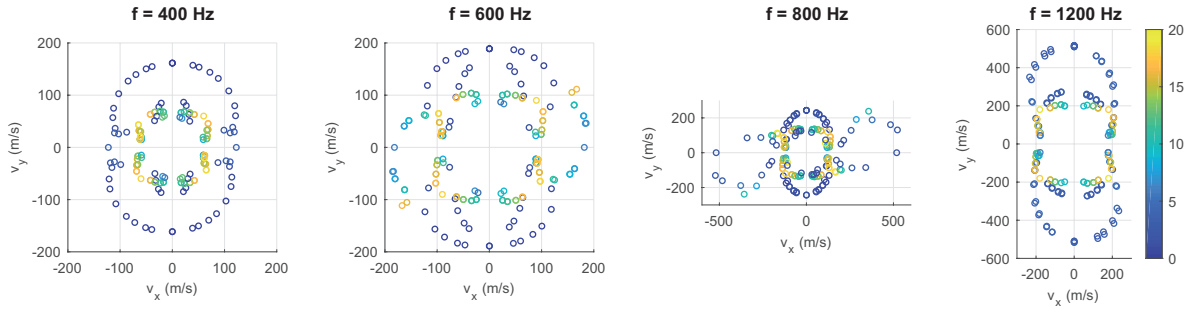


Figure 7: Phase velocity of out-of-plane waves for the 60×30 geometry at four different frequencies.

At first sight, intricate wave speed patterns can be noticed at every frequency. Even in the low frequency range, the typical circular/elliptical velocity which is expected in isotropic/orthotropic plates is absent. Eight-shaped patterns that occur at multiple frequencies are usually found in layered structures.

From these images, it is easy to read the direction dependent wave attenuation. In the 35×35 case (Fig. 6), waves are highly damped in the horizontal direction at 400 Hz, and almost omnidirectional at 600 Hz. The 60×30 scenario delivers an overall high damping at 1200 Hz (Fig. 7).

4 Conclusion

Despite the simple design, sandwich plates with a transformed checkerboard core results in intricate wave dispersion. As an example of phononic crystals, the wave numbers, phase velocities and band gaps are direction dependent. However, frequency areas with high omnidirectional attenuation can be created by choosing a suitable core geometry.

Using octagonal core stiffenings, band gaps can be created both on the edges of the Brillouin zone, and due to wave mode veering. The implementation of periodic boundary conditions with the inverse approach ($f \rightarrow k$) results in the prediction of broadband damping of bending waves. Since the out-of-plane waves are responsible for acoustic transmission, we expect that reduced vibration amplitudes will improve the acoustic transmission loss. For other applications, such as wave steering or lensing, the panels can be designed to attain desired phase and group velocities.

Based on these initial numerical results, future work will consist of (1) making a prototype and compare the predicted structural behaviour with measurements, (2) measure the sound transmission effects of a checkerboard sandwich core, and (3) implement an optimization scheme for attain predefined elastic and acoustic properties. The limited number of free parameters allows a feasible topological optimization.

References

[1] C. Claeys, K. Vergote, P. Sas, and W. Desmet. *On the potential of tuned resonators to obtain low-frequency vibrational stop bands in periodic panels*. Journal of Sound and Vibration, 332(6):1418–1436, 2013.

[2] L. Cremer and M. Heckl. *Structure-borne sound: structural vibrations and sound radiation at audio frequencies*. Springer Science & Business Media, 2013.

[3] T. Delpero, S. Schoenwald, A. Zemp, and A. Bergamini. *Structural engineering of three-dimensional phononic crystals*. Journal of Sound and Vibration, 363:156–165, 2016.

[4] P. A. Deymier. *Acoustic metamaterials and phononic crystals*. Springer, Berlin, Heidelberg, 2013.

[5] M. Haberman and M. Guild. *Acoustic metamaterials*. Physics Today, 69(6):42–48, 2016.

[6] M. I. Hussein, M. J. Leamy, and M. Ruzzene. *Dynamics of Phononic Materials and Structures: Historical Origins, Recent Progress, and Future Outlook*. Applied Mechanics Reviews, 66(4):040802, 2014.

[7] L. Liu and M. I. Hussein. *Wave Motion in Periodic Flexural Beams and Characterization of the Transition Between Bragg Scattering and Local Resonance*. Journal of Applied Mechanics, 79(1):011003, 2012.

[8] Z. Liu, X. Zhang, Y. Mao, Y. Zhu, Z. Yang, C. Chan, and P. Sheng. *Locally Resonant Sonic Materials*. Science, 289(5485):1734–1736, 2000.

[9] B. R. Mace and E. Manconi. *Modelling wave propagation in two-dimensional structures using finite element analysis*. Journal of Sound and Vibration, 318(4-5):884–902, 2008.

[10] S.Schoenwald, B. Zeitler, I. Sabourin, and F. King. *Sound insulation performance of cross laminated timber building systems.* In INTER-NOISE and NOISE-CON Congress and Conference Proceedings, volume 247, pages 4337–4346. Institute of Noise Control Engineering, 2013.

[11] L. Van Belle, C. Claeys, E. Deckers, and W. Desmet. *On the impact of damping on the dispersion curves of a locally resonant metamaterial: Modelling and experimental validation.* Journal of Sound and Vibration, 409:1–23, 2017.

[12] B. Van Damme and A. Zemp. *Measuring dispersion curves for bending waves in beams: A comparison of spatial fourier transform and inhomogeneous wave correlation.* Acta Acustica united with Acustica, 104(2):228–234, 2018.

Design of a Kelvin cell acoustic metamaterial

H. Rice[1], **J. Kennedy**[1], **P. Göransson**[2]
[1] Trinity College Dublin, Department of Mechanical engineering,
e-mail: **hrice@tcd.ie**

[2] KTH Royal Institute of Technology, Aeronautical & Vehicle engineering,
100 44 Stockholm, Sweden

Abstract
Advancements in 3D print technology now allows the printing of structured acoustic absorbent materials at appropriate microscopic scale and sample sizes. Optimisation of parameter sets associated with a Kelvin Cell structure have the potential to develop various metabehaviours in the associated acoustic responses. The repeatability of the fundamental cell unit also provide a route for the development of viable macro models to simulate built up structures based on detailed models of the individual cell units. This paper describes a process to model, print and test of such a sample. Manufacturing restraints will initially guide the optimised design. Micro to macro models based on a single cell structure which are cross checked against a full visco thermal acoustic finite element model of the individual cell. A macro model based on a reduced lossy helmholtz system is then used to predict the absorptive response response under normal incidence and checked against a manufactured sample under experimental test.

1 Introduction

It is generally accepted that viable working models of the acoustic behaviour of certain classes of of acoustically absorbent materials can be adequately predicted by empirical models calibrated by for example Delaney, Bazely, Miki [1]. By these models the absorptive parameters can be expressed as frequency (ω), flow resistivity (σ), density $\rho_0(\omega, \sigma)$ and bulk modulus $K(\omega, \sigma)$ with the acoustical modelling then proceeding using an equivalent fluid obeying a lossy Helmholtz equation. Due to the statistical nature of the solidifcation process it is usually necessary to supplement the modelling with some static flow tests to determine σ or alternatively to estimate this using reduced models in the case of fibrous materials at least to estimate σ from the individual fibre geometries themselves. A 3D meta structure, on the other hand, generates a regular repeated geometric structure which allows the modelling of the losses though the use of an equivalent hydraulic radius and a companion equivalent cylindrical tube model. Bezemer-Krijnen et al [2] successfully demonstrate this approach on a stacked sphere structure.

In this paper we analyse a single open kelvin cell using a full visco-thermal model and then determine the equivalent hydraulic radius by comparison woth a lossy helmholtz model of the the same structure. Once r is determined we can then build an efficient hardbacked model of a manufacturable system 10 cells deep and estimate the absorbency. This is finally compared with experimental test results.

1.1 Background models

The lossy acoustics in a fine absorptive medium can be modelled by linearised visco thermal fluid mechanical models. These are governed by the equation system given for example in Nijhof *et al.* [3]

$$\rho_0(\boldsymbol{\nabla}.\boldsymbol{v}) + j\omega\rho = 0 \tag{1}$$

$$j\omega\rho_0\boldsymbol{v} = -\boldsymbol{\nabla}p + \mu(\boldsymbol{\nabla}.\boldsymbol{\nabla}\boldsymbol{v} + \frac{1}{3}\boldsymbol{\nabla}\boldsymbol{\nabla}.\boldsymbol{v}) \tag{2}$$

$$j\omega\rho_0 C_p T = \kappa\Delta T + j\omega p \tag{3}$$

$$p = R(\rho_0 T + \rho T_0) \tag{4}$$

where $\boldsymbol{v}, p, \rho, T, \mu, R, \rho_0, T_0, \kappa, C_p$ and ω are the acoustic harmonic velocity, pressure, density, temperature, dynamic viscosity, gas constant, static density, static temperature, thermal conductivity, specific heat at constant pressure and angular frequency. In the above formulation the fluid is assumed to be Stoksian. A finite element model implementing the above was constructed using a mixed weak formulation following [3] and Zienkiewicz *et al.* [4] which can present the system in the matrix form

$$[\mathbf{K} + j\omega\mathbf{M}]\mathbf{a} = \mathbf{F} \tag{5}$$

As the density variable may be eliminated using the equation of state, Equation 4, each node will have five degrees of freedom including three velocity components, temperature and pressure stored in $\mathbf{a}$. The forcing vector $\mathbf{F}$ then models boundary pressure loads, material injection and heat flux. $\mathbf{K}$ and $\mathbf{M}$ were constructed following the procedures for mixed formulations outlined in [4]. In order to develop a stable mixed model it is critical to use shape functions of one order less for the pressure and its weighting functions, In this work quadratic 10 noded tetrahedal elements were used with linear functions for pressure and quadratic functions for the velocity and temperature. The redundant mid side nodal pressure degrees of freedom were decoupled from the formulation and 2nd order volumetric integrations were used.

The general equation system in Section 1.1 has also shown itself to be amenable over the frequency ranges of interest to efficient Padé type frequency sweeps such as the WCAWE method proposed by Slone *et al.* [5]. In the cell system equation needed only to be solved at a single frequency with extrapolation using derivatives up to order 25 being adequate to cover the frequency range,

1.2 From Micro to Macro visco thermal modelling

Solution of the full system equations is extremely expensive and precludes the solutions for structures of conjoined cell models of practical interest. Unfortunately the equation systems themselves are poorly conditioned and there does not seem to be a viable preconditioning method reported in the literature at this time to enable iterative solution approaches. Therefore full visco-thermal simulations of absorptive labrynthine structures of the scale needed for the application projects will not viable. Clearly a model reduction strategy such as, for example, the Low Reduced Frequency approaches whereby a simple Helmholtz model is formulated enabling the simulation of much more extensive structures with the lossy elements modelled as boundary loads. The losses themselves are modelled approximately using equivalent cylindrical duct losses following, for example, Allard and Atalla [6]. The link between more complex structures such as stacked spheres by Bezemer-Krijnen*et al* [2] is through the use of an "hydraulic radius" r. This is given by

$$r = \frac{2V}{A} \tag{6}$$

where V is the volume of a single acoustic cell entrapped by the spheres and A is the wetted surface area. Using the corrections for averaged density $\rho(\omega)$ and bulk modulus $K(\omega)$ in cylindrical bores provided for

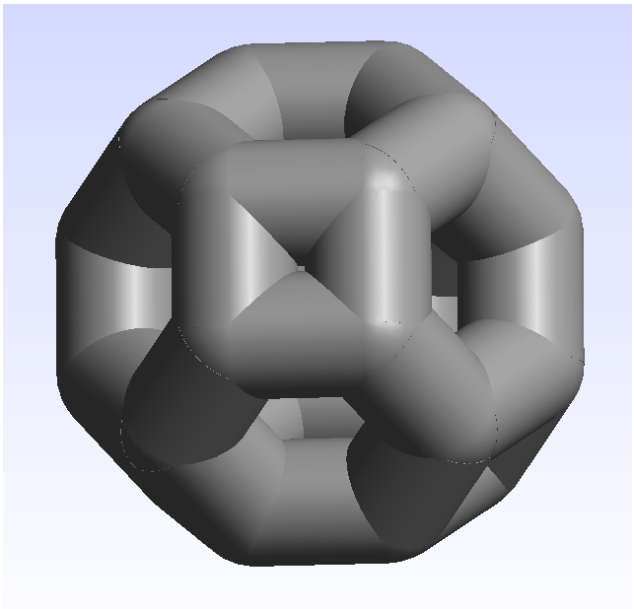


Figure 1: Kelvin Cell

example by [6] which can be summarised as

$$\rho(\omega) = \frac{\rho_0}{G(\omega)} \tag{7}$$

$$K(\omega) = \frac{K_0}{\Gamma(\omega)} \tag{8}$$

where

$$s = r\sqrt{\frac{\omega\rho_0}{\mu}} \tag{9}$$

$$B = \sqrt{\frac{\mu C_p}{\kappa}} \tag{10}$$

$$G(\omega) = 1 - \frac{2J_1(s\sqrt{-j})}{s\sqrt{-j}J_0(s\sqrt{-j})} \tag{11}$$

$$\Gamma(\omega) = 1 + \frac{2(\gamma-1)J_1(Bs\sqrt{-j})}{Bs\sqrt{-j}J_0(Bs\sqrt{-j})}. \tag{12}$$

The modelling strategy gives consistent results when compared with experiments also in [2]. The concept of a geometrically sensitive single parameter r which can be defined by a single (repeating) cell then defining the losses is in a sense consistent with Delaney-Bazely-Miki type models [1] where the flow resistivity defines the frequency dependent losses for more random fibrous type absorbent structures.

In this study we consider an absorbent layer 10 cells deep of the form shown in figure 1.2.

The lengths of the individual struts were 375 μm with diameters 250 μm. A one eight model of the complementary acoustic cavity was geometrically modelled and meshed using gmsh 3.06. This had an open outlet with a forced pressure inlet and a symmetry condition appiled to the side walls. No slip and zero acoustic temperature was applied to the curved wetted surface areas. The geometric hydraulic radius r for this structure using equation 6 yielded a value of 400 μm. The results for the temperature and axial velocity are shown in figure 1.2 and 1.2 for the system running at 1000 Hz.

The computer resources required to model of higher complexity become very expensive, as in addition to the high number of degree of freedom required per node (5) there is also clearly a requirement to locally refine the meshes at the boundaries particularly as the frequencies rise.

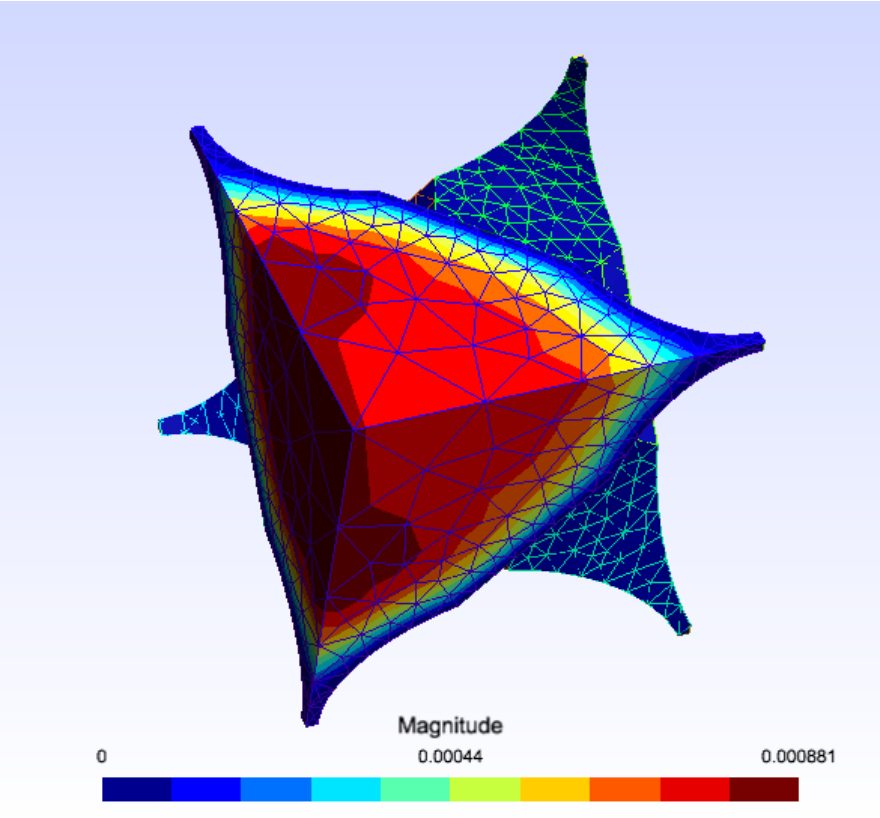


Figure 2: Acoustic Temperature

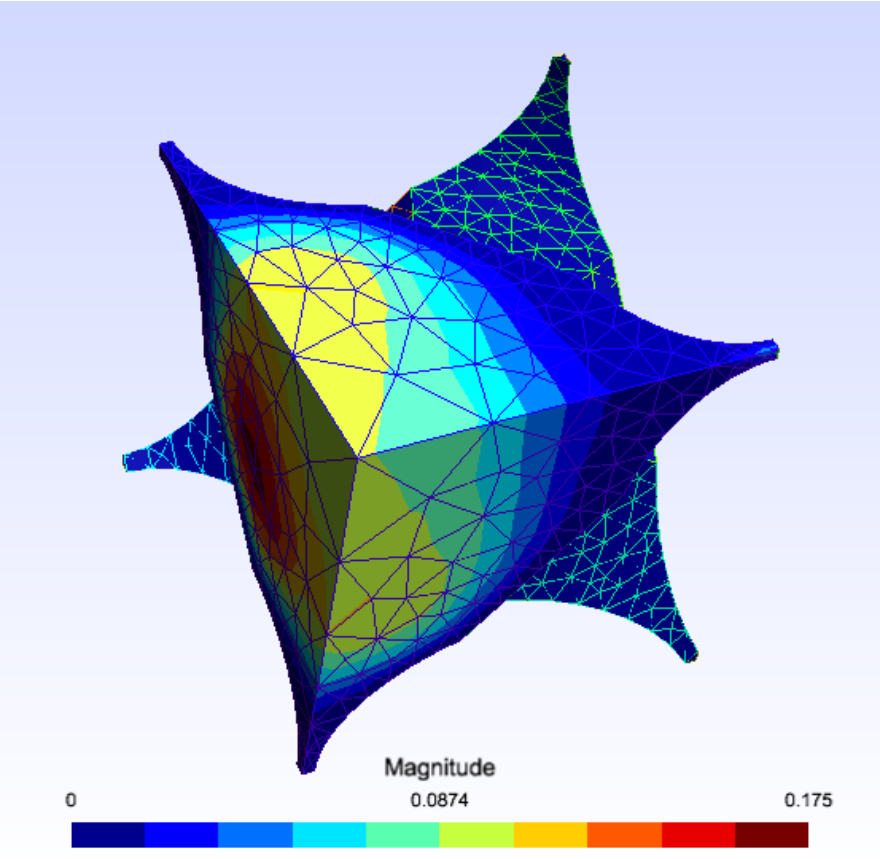


Figure 3: Axial Velocity

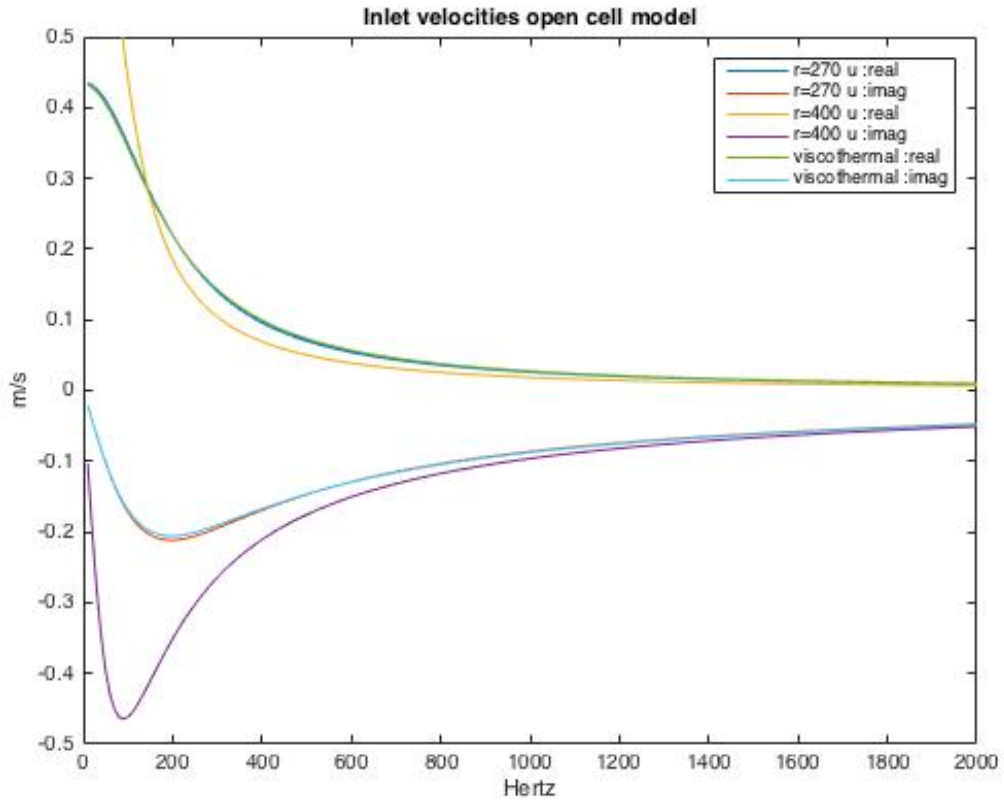


Figure 4: Comparison of Cell Models

2 Equivalent Helmholtz Model

A lossy Helmholtz model of the same subsystem was then constructed using an Finite Element model of the equation system following procedures described in [4] ...

$$\omega^2 \frac{\Gamma(\omega}{K_0} p + \frac{G(\omega)1}{\rho_0} \nabla^2 p = f \tag{13}$$

where the density and bulk modulus are given by 8 and 8. Comparative Padé WCAWE type [5] frequency sweeps of both the Helmoltz system and the full viscothermal model were then run as shown in figure 2.

Two values of r are used for the lossy Helmholtz model. The geometric value of 400 μm is shown to underestimate the loss, whilst a tuned value of 270 μm generates results which are indistinguishable from the full visco thermal model. The same mesh was used for both systems.

3 Multi-Cell Macro model

The next stage is then to model the full 10 cell structure using the efficient Helmholtz model with the two different values of r. The model is shown in figure 3 and can sustain a uniform mesh structure as there is no specific boundary layer action. A closed boundary condition (hard wall) was implemented on the model end.

This model was also suitable for a WCAWE frequency sweep and the calculated absorbency at inlet is shown in figure 3. Note that no inlet manifold has been included in this model so the blockage effect is directly modelled as a simple area based porosity $\phi = 0.4883$. Thus the inlet impedance was given by

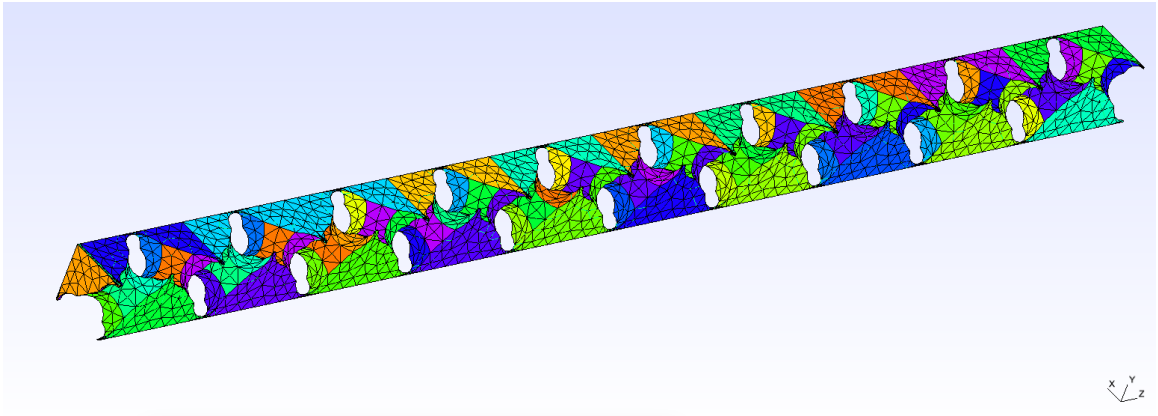


Figure 5: 10 Cell Lossy Helmholtz model

$$Z_i = \frac{p_{inlet}}{\phi \bar{u}_{inlet}} \tag{14}$$

The absorptivity a was then calculated according to ...

$$Ref = \frac{Z_i - \rho_0 c}{Z_i + \rho_0 c} \tag{15}$$

$$a = 1 - |Ref|^2 \tag{16}$$

The sensitivity to the choice of hydraulic radius r values is illustrated in the plot.

4 Experimental Measurements

The relevant ISO standard for the measurement of the acoustical properties of the material is ISO 10534-2:2001. This standard describes the test rig and procedures for estimating the complex acoustic impedance of a material under normal incidence using the "two-microphone" or "transfer function" method. This methodology is used to calculate the reflection and absorption coefficients which are the usual measures used to quantify the performance of an acoustic material.

4.1 Normal Incidence Impedance Tube Testing

In order to facilitate impedance tube testing samples were manufactured using additive techniques. Due to the high resolution and precision required for the material selective laser melting was chosen as the additive manufacturing technology. The 3D Systems Prox DMP 200 was used with the following capabilities:

- Resolution: x=100 μm ; y=100 μm ; z=20 μm
- Material: metals - Titanium, CoCr, Aluminium, SS
- Build Volume: x=140 mm ; y=140 mm ; z=125 mm
- Wall Thickness: 150 μm
- Surface Roughness: Up to 5 Ra μm

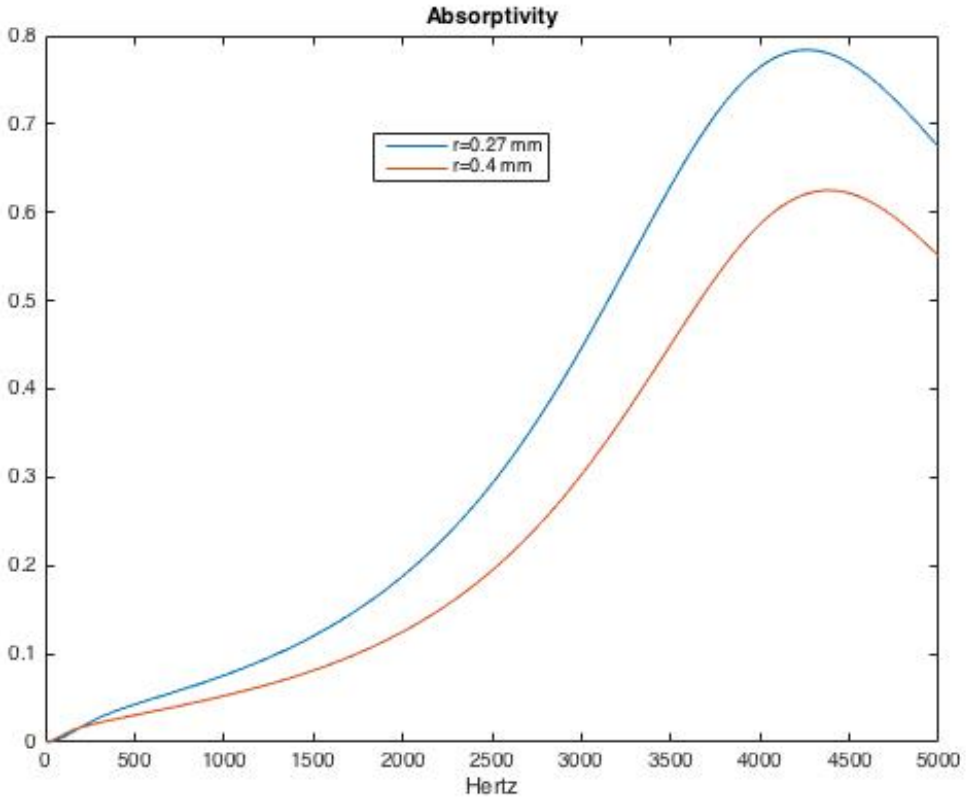


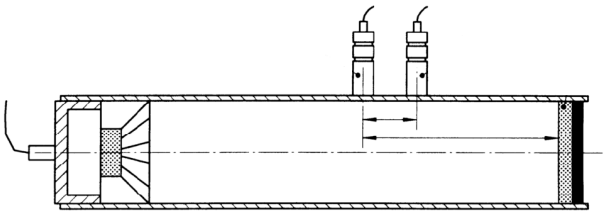
Figure 6: Absorbtivity of 10 Cell model

Normal incidence impedance tube tests are used to obtain the reflection factor R and absorption coefficient α, in accordance with the international standard ISO 10534-2:2001. In these tests, the sample is placed in an impedance tube as shown in figure 7 (a), which is taken from the ISO standard. The material is backed by a hard, reflective termination. The custom rig used for this work is also shown in figure 7 (b). In the experimental rig, the hard termination is provided by a 20 mm thick piece of aluminium which can be bolted on the end of the tube.

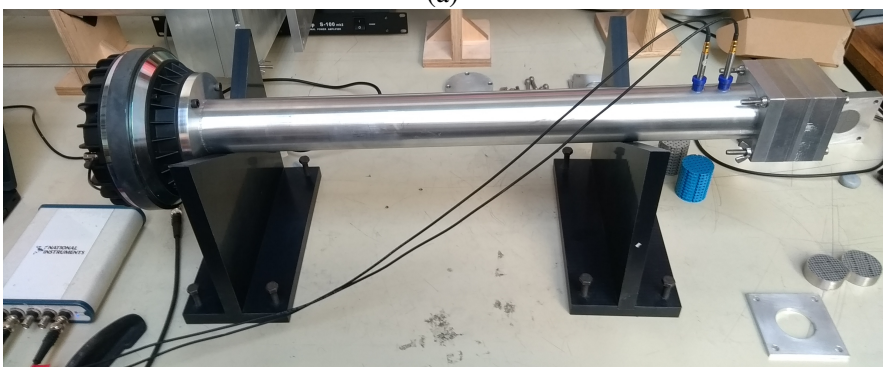
The cut-on frequency for this tube means that it is only possible to perform tests reliably up to 5050 Hz. The lower limit is determined by the speaker and is in the region of 300 Hz. On the left hand side of figure 7 (b) we can see the BMS 4591 speaker which is driven by the output signal of a National Instruments DAQ which has been amplified by a power amplifier. The box bolts on to the end of the tube to provide a tight seal with little leakage of sound. The square section on the right of figure 7 is the sample holder which opens to hold cylindrical samples of 40 mm diameter and up to 50 mm thick. The sample holder is held shut by four long bolts with wing nuts.

GRAS 40PH array microphones were chosen to instrument the rig as they have a frequency response of 10 Hz - 20 kHz and upper limit of the dynamic range of 135 dB re 20 μPa allowing for testing up to high pressure amplitudes. The microphones are connected to the National Instruments DAQ and the signals are recorded in Matlab. The microphones are calibrated using the switching methods described in the standards to achieve a calibration transfer function which corrects for any differences in the behaviour of the microphones.

The impedance tube requires samples of a 40 mm diameter but due to the periodic structure of the Kelvin cell material a disc of this material will include many partial cells at the edges. These partial cells are impossible to manufacture due to unsupported overhangs in the print so to avoid these the entire sample was printed within a hard wall supporting ring. This hard wall ring was designed to have an inner diameter of 40 mm so as to allow an exact flush fit with the walls of the impedance tube. Custom sample holders were designed to enable this flush fit with the walls of the tube. The sample and holder is shown in figures 8 to 9.



(a)



(b)

Figure 7: (a) Impedance tube design ISO 10535-2 (b) TCD Impedance tube rig

A comparison of the experimental and numerical results obtained for this test sample are shown in figure 10. Despite the excellent print quality achieved this type of material design pushes current additive manufacturing technologies to their limit. At the time of writing no detailed inspection of the manufactured

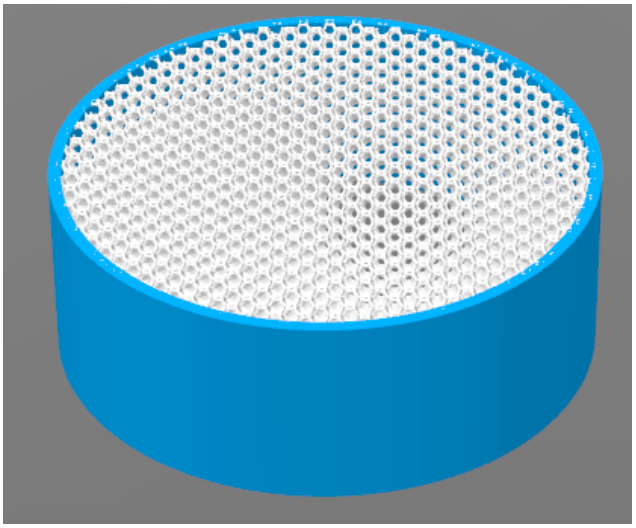


Figure 8: CAD of Impedance Tube Sample

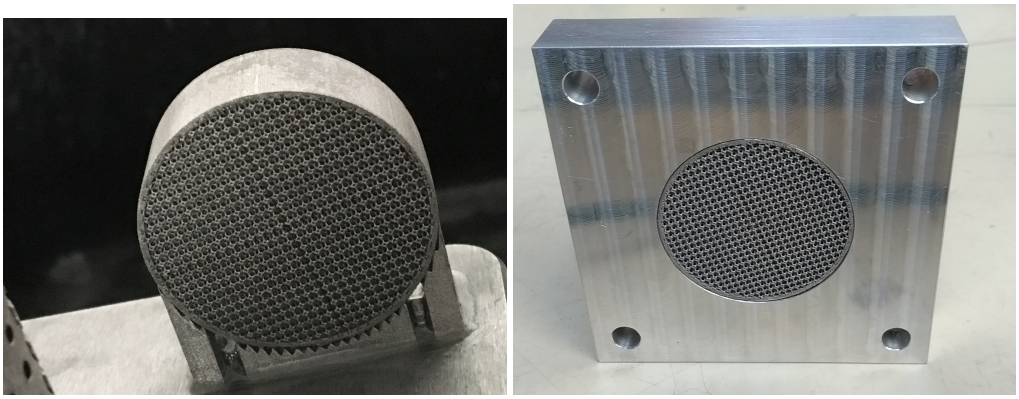


Figure 9: Sample attached to build plate manufactured with a 3D Systems Prox DMP 200 and sample in holder for impedance tube testing.

sample has been conducted. However there is promising agreement between the experimental measurement and the numerical simulation. Both sets of results identify a peak absorptivity in the region of 4-4.5 kHz. In general the numerical models have over predicted the achieved experimental absorptivity. Further work will continue to characterise the test sample and attempt to achieve closer agreement in the numerical simulations.

5 Conclusions

The use of a single parameter r to inform density and bulk modulus frequency variations in an efficient equivalent fluid model for the present class of kelvin type meta structure would appear to be a viable proposition to model acoustic losses. The lossy helmholtz model will still retain geometric detail and has thus the potential model gross metabehaviour under more complex loadings.

The use of visco thermal models at a cell level to tune the loss model is a critical part of the procedure and has the further potential to extend the modelling to more detailed local boundary behaviour which can then subsequently be removed from the model in the micro to macro process.

Design optimisation will be facilitated by use of a clearly identifiable geometric parameter. The proposed structure was realised using state of the art additive manufacturing technologies. Initial experimental results conform well the numerical simulations and demonstrate the potential of the approach taken in this work.

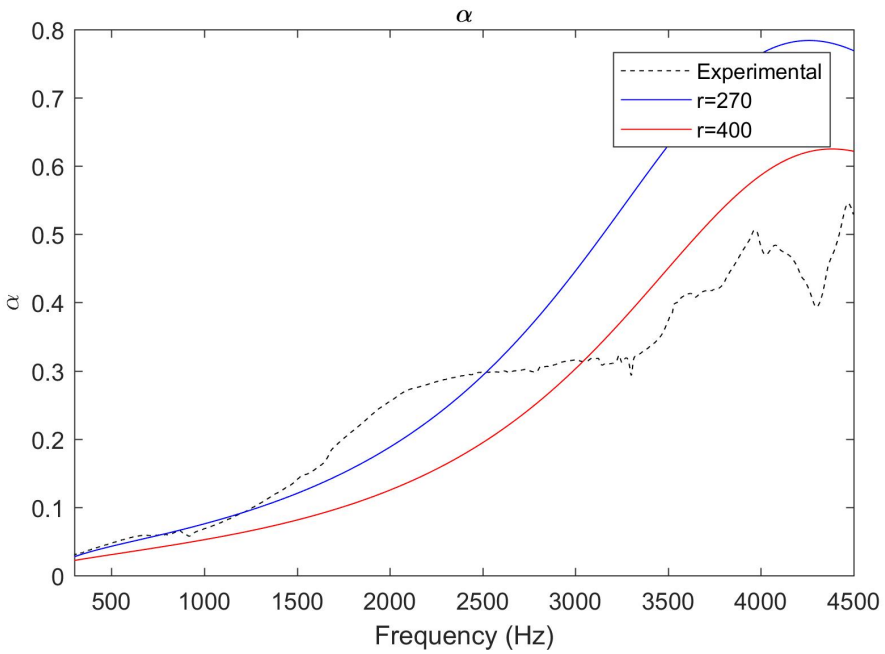


Figure 10: Comparison of experimental and numerical results.

Acknowledgements

This work was funded through the AERIALSIT project no: 723367 European Union H2020-EU.3.4. SOCIETAL CHALLENGES - Smart, Green And Integrated Transport.

The authors wish to acknowledge the AMBER Additive Research Lab in the facilitating of the manufacturing of our metal test specimens and the AR Lab staff on providing training and guidance on the manufacturing process. The AR-Lab has been enabled by a €3.3M award from Science Foundation Ireland as part of their Research Infrastructure program and an additional €1M investment from the European Research Council through our world leading investigators.

References

[1] Miki, Y., "Acoustical properties of porous materials—modifications of Delaney-Bazley models," *J. Acoust. Soc. Jpn*, Vol. 11, No. 94, 1990, pp. 19–24.

[2] Bezemer-Krijnen, M., Wijnant, Y., and de Boer, A., "Predicting sound absorption of stacked spheres: combining an analytical and numerical approach ," *Acta Acustica united with Acustica*, Vol. 102, No. 6, 2016, pp. 971–983.

[3] Nijhof, M., Wijnant, Y., and de Boer, A., "An acoustic finite element including viscothermal effects," *ICSV14, Cairns, Australia*, 9-12 July, 2007, pp. 1–8.

[4] Zienkiewicz, O., Taylor, R., and Zhu, J., "The finite element method : its basis and fundamentals 6th Edition," *Elsevier Butterworth Heinmann*, 2006.

[5] Slone, R., Lee, R., and Lee, J., "Well conditioned asymptotic waveform evaluation for finite elements," *IEEE Transactions on Antennas and Propagation*, Vol. 51, No. 9, 2003, pp. 2442–2447.

[6] Allard, J. and Atalla, N., "Propagation of sound in porous media," *Wiley*, 2009.

A concept demonstrator of adaptive sound absorber/insulator involving microstructure-based modelling and 3D-printing

K. C. Opiela[1,3], **M. Rak**[2,3], **T. G. Zieliński**[1,4]
[1] Institute of Fundamental Technological Research of the Polish Academy of Sciences,
ul. Pawińskiego 5B, 02-106 Warsaw, Poland

[2] Engineering Design Center,
al. Krakowska 110/114, 02-256 Warsaw, Poland

[3] PhD student at the Institute of Fundamental Technological Research

[4] Corresponding author
e-mail: **tzielins@ippt.pan.pl**

Abstract
The purpose of this work is to present and investigate the concept of adaptive sound absorbers, that is, periodic porous media with modifiable micro-geometry, so that their ability of sound absorption or insulation can be changed in various frequency ranges. To demonstrate this concept, a simple periodic porous micro-geometry with small bearing balls inside pores is proposed. By a simple positioning of the periodic porous sample the gravity force is used for the small balls to close some of the windows linking the pores, changing in that way the flow path inside pores, which entails significant modifications of the relevant parameters of permeability and tortuosity. Also the viscous characteristic length is changed, while the porosity as well as the thermal characteristic length remain unchanged. Nevertheless, such significant changes of some crucial transport parameters strongly affect the overall acoustic wave propagation in the porous medium. All this is studied using an advanced dual-scale modelling as well as experimental testing of 3D-printed specimens.

1 Introduction

Porous materials are widely recognized as effective acoustic insulators. They owe their acoustic damping properties to a specific internal structure and to the presence of voids (pores) in particular. Geometry of voids and their spatial distribution are considered to be one of the main determinants of the acoustic performance of porous materials. Such a correspondence between the internal constitution and the acoustic characteristics opens up the possibility of designing structure with a required acoustic behaviour. This observation in conjunction with the idea of controlling micro-flow paths inside porous medium led to the concept of an adaptive sound absorber demonstrated in this work. Since with the advent and development of the additive manufacturing technologies the issue of fabricating porous materials with a definite microstructure became technically feasible, a simple demonstrator could be fabricated to illustrate potential behind the idea of the aforementioned adaptive absorber.

In principle, the proposed adaptive demonstrator is 3D-printed, however, during fabrication, some large pores of its open-cell periodic microstructure are used to trap steel bearing balls which would play the role of adaptive valves controlling the character of airflow on the micro-scale inside the interconnected voids (and between the large pores, in particular). From the macroscopic perspective, the flow in porous media depends on the so-called transport parameters, which are also strongly related to the propagation and absorption of

acoustic waves. The steel balls can change their position inside pores thanks to the gravity or inertial forces, and modify – in that way – the flow and relevant transport parameters, and as a consequence – the sound absorption of porous medium. Thus, loading the 3D-printed pores with the steel balls was found to be a simple yet effective way to furnish the porous material with a rudimentary adaptation mechanism.

This kind of adaptive sound absorbers can be used, for example, in acoustic treatments of engines in aircraft or vehicles. Usually, the engine noise and its predominant frequencies are related to the speed and acceleration: typically, a higher frequency noise is produced during the acceleration and at higher speeds. The character of noise at various speed and acceleration conditions can be precisely determined during acoustical testing of engines by applying signal analyses to the measured data. In an adaptive sound insulator the acceleration forces may be used to switch the valve balls into the position which adapts the sound absorbing/insulating properties of material to better comply with the expected noise conditions. For the investigated demonstrator, the gravity is used for this purpose.

In this work, the adaptive sound absorbing porous material as well as its non-adaptive preceding version are modelled according to the so-called equivalent-fluid approach for porous media with rigid frame [1], and using an advanced model with 8 transport parameters related to the micro-geometry of solid and 5 additional parameters of visco-thermal pore-fluid. The latter are some well-known parameters of air, while the transport parameters are calculated for the designed materials from their periodic microstructure. Currently, this approach is well established and has been successfully applied for various sound absorbing media, namely: granular materials [2–4], open-cell aluminium foams [5, 6], perforated closed-cell metallic foams [7], ceramic foams with spherical pores [8], polymeric foams [9–13], double-porosity foams [14], syntactic hybrid foams (i.e., open cell polyurethane foams with embedded hollow microbeads) [15], 3D-printed foams [16], and fibrous materials [17–20]. For the proposed demonstrator of adaptive porous material, the transport parameters must be computed for for each case related to a particular adaptation position.

When the microstructre-based parameters of materials are found, the wave propagation in the investigated porous media (or rather, in the homogenised effective fluids equivalent to them) can be determined on the macro-scale level using the Helmholtz equation of time-harmonic acoustics. Relevant macroscopic finite element solutions and also some analytical predictions allow to evaluate the sound absorption for a few configurations, in particular, for the designed adaptive porous absorber in two extreme adaptation states.

The investigation scheme presented above is realised in the paper as follows. The designed periodic micro-geometry of the adaptive sound absorbing porous material is described in Section 2.1, whereas the manufacturing of adaptive demonstrator and other necessary samples is explained in Section 2.2. Section 3 presents the results of all microstructure-based calculations, while the macroscopic analyses are discussed in Section 4, where the final modelling results – in the form of acoustic absorption curves – are presented and confronted with the corresponding measurements of the adaptive demonstrator as well as other samples.

2 Design and manufacturing of an adaptive sound absorber

2.1 Design of periodic micro-geometry

Figure 1 shows the proposed periodic micro-geometry of an adaptive sound absorbing material. Notice that the fluid domain of pores is depicted here, instead of the solid skeleton. The periodic porosity of such an adaptive sound absorber can be represented by a single periodic cell visualised in Figure 1. The porous cell is cubic and its micro-geometry of voids contains:

- a single large pore in the cell centre,
- 8 one-eights of small pores in the cell corners,
- 6 wide cylindrical channels (2 vertical and 4 horizontal ones) to link the large pore with its counterparts in the neighbouring cells,

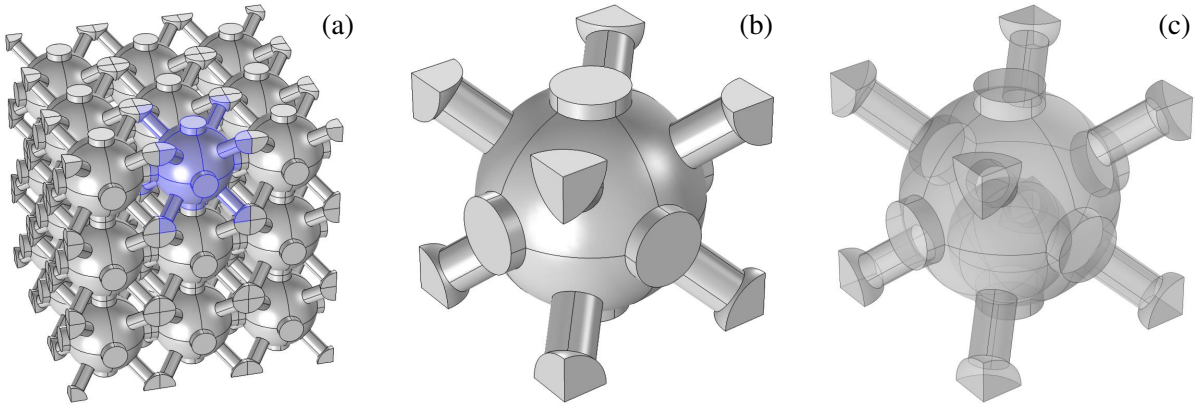


Figure 1: The geometry of porosity: (a) a fragment of periodic fluid domain (i.e., voids filled with air) with a single representative cubic cell distinguished in blue; (b) the designed (original) geometry of voids in a single cell, and (c) the transparent "actual" (updated) geometry of voids in the periodic cubic cell with a sphere (steel ball) inside the main pore

Void type	**Diameters** [mm] (designed)	("actual")
large pore	4.6	4.4
small pore	2.0	1.8
wide channel	1.6	1.4
narrow channel	1.0	0.8

Table 1: Diameters of pores and channels in the porous periodic cube of size 5 mm

- 8 oblique narrow cylindrical channels linking the large central pore with the small corner ones.

The porous cubic cell is obviously scalable. The budget 3D-printing technology used for this research permitted for fabrication of samples with rather large cells of 5 mm in size. Table 1 shows the diameter values for pores and channels in the cell of such a size. Two slightly different values are listed for each diameter:

1. the designed original value from the CAD model used for 3D-printing, see Figure 1(b),
2. the "actual" value valid for the updated model used for numerical calculations, see Figure 1(c) where a 2.5 mm steel ball inside the large pore is also visualised.

In the "actual" configuration, the steel ball centre is set 1 mm below the centre of large pore, which means that a narrow slit is left between the ball and the edge of the wide channel below. This thin regular aperture simulates the effect of tiny openings which exist in the contact between the smooth steel ball and the rough 3D-printed edge of the channel. As a matter of fact, because of the roughness, the channel can be blocked by the steel ball but not fully sealed.

2.2 Manufacturing of the adaptive sound-absorbing demonstrator

The sound-absorbing demonstrator was manufactured using a 3D-printing technology and steel bearing balls. The *FlashForge Creator Pro 3D Printer* was used to fabricate all samples and also other useful elements, see Figure 2, namely: a special tray device for precise placement of steel balls in a regular 6×6 array, see Figure 2(b), and a square-to-circular-shape threaded adapter to replace a part of the impedance tube, see Figure 2(d). Many 3D-printing tests had been conducted before fabricating the final sound-absorbing samples.

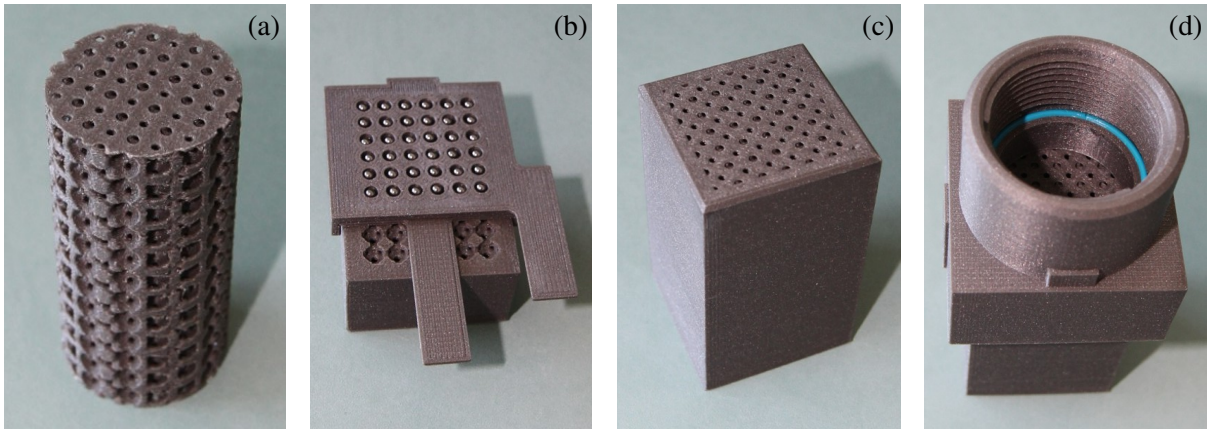


Figure 2: Porous samples and their manufacturing: (a) porous cylinder (with empty pores), (b) an original technique for the placement of steel balls into the large pores (during 3D-printing), (c) porous cuboid (with steel balls hidden inside large pores), (d) the porous cuboid sample inside the 3D-printed threaded adapter being a replacement for a part of the impedance tube

These tests allowed to choose a proper material and many important 3D-printing parameters (e.g., temperatures) suitable for the designed micro-geometry. It was found that the actual sizes (diameters) of voids in 3D-printed probationary specimens were smaller (roughly by 0.2 mm) than the corresponding original design values in the CAD model presented in Figure 1(b). Therefore, a corrected CAD micro-geometry was generated as shown in Figure 1(c), with the "actual" values of all diameters, see Table 1; this CAD model served in all numerical calculations.

Three final complete samples were 3D-printed based on the same porous micro-geometry: a cylinder with diameter 29 mm and height 60 mm – see Figure 2(a), and two cuboids with a 38 mm $\times$ 38 mm square base, and 65 mm in height – see Figure 2(c). These samples differ in two main features: the macroscopic shape, and the presence (or absence) of steel bearing balls inside the large pores.

The CAD geometry for the cylindrical sample was generated as a $6 \times 6 \times 12$ array of the cubic periodic cells shown in Figure 1, each cell 5 mm in size, and so the porous cylinder was virtually cut out from the 30 mm $\times$ 30 mm $\times$ 60 mm porous cuboid. The cylinder diameter of 29 mm was chosen so that the 3D-printed sample could be tightly fitted into the smooth metal impedance tube. The cylindrical shape means that all lateral cubic cells of the sample are to some extent not complete, i.e., cut (in fact, some of them are nearly gone), see Figure 2(a), and it is impossible to fit a full 2.5 mm steel ball in most of these partially 3D-printed cells. Therefore, the cylindrical sample was manufactured without steel balls.

The cuboid samples were 3D-printed as a $6 \times 6 \times 12$ array of the 5 mm cubic periodic cells surrounded with additional solid walls: 4 mm thick on lateral faces, and 5 mm thick at the bottom, while the top face was left open, see Figure 2(c). Therefore, the cuboid specimen is, in fact, composed of the 30 mm $\times$ 30 mm $\times$ 60 mm porous cuboid 3D-printed together with (and inside) the solid square tube closed at one end with a thick termination wall; now, the cuboid sample sizes can be explained as follows: the base edge-lengths equal 38 mm $=$ 6×5 mm (cell size) $+$ 2×4 mm (wall), while the height is 65 mm $=$ 12×5 mm (cell size) $+$ 5 mm (bottom). One of the cuboid samples was simply 3D-printed – with all empty pores, the other was manufactured so that each of its large pores contains a 2.5 mm steel ball. To this end, 12 pausing commands had been added to the 3D-printer code to pause the 3D-printing process successively at the specified heights when the large pores of the current layer are still wide open (unfinished) so that a 2.5 mm ball may be easily dropped into each of them, and then, stay below the currently 3D-printed surface. The special tray device, which was designed and 3D-printed for the purpose, see Figure 1(b), allowed for quick taking and precise placement of $6 \times 6 = 36$ steel balls into the array of (not yet completed) large pores. Finally, a square-to-circular-shape adapter was designed and 3D-printed, see Figure 2(d). The cylindrical part of the adapter has a well-fitted inner thread which permits to link it tightly with the set-up of impedance tube. The square

part matches the cuboid samples so that each of them can be very well fitted inside the adapter. In that way, the adapter with a cuboid sample inside forms a replacement for one end of the metal impedance tube. Of course, in this case, the plane waves propagating in the original metal impedance tube pass into the slightly larger cuboid porous absorber, where the propagation becomes a little bit more complex, that is, it is no longer ideally planar, and this effect must be taken into account during modelling.

3 Calculations of transport parameters from microstructure

Both sound-absorbing porous media, which were designed and fabricated as discussed above, that is, the one with empty pores and the adaptive one with valve balls inside large pores, can be modelled as homogenised equivalent fluids which means that the Helmholtz equation of time-harmonic acoustics is used to describe the acoustic wave propagation in such media. Their effective properties (i.e., the frequency-dependent complex-valued density, bulk modulus, and speed of sound) are computed from the Johnson-Champoux-Allard-Pride-Lafarge (JCAPL) model [1, 21–25] for rigid-frame sound-absorbing porous media. This model requires 8 transport parameters (listed in Table 2), which can be calculated from porous microstructure [2–4,6,17]. The porosity and thermal length are found directly from the micro-geometry, whereas the remaining parameters require solution of three static problems: (1) the Stokes flow, (2) the Laplace problem, and (3) the Poisson problem. The first problem describes a steady, viscous, incompressible flow through pores and channels of the periodic representative cell, with no-slip boundary conditions on solid surfaces. The Laplace problem simulates the electric conduction of a porous material with dielectric skeleton and conductive pore-fluid, whereas the Poisson problem simulates the thermal transport in the fluid inside pores with isothermal boundary conditions on solid surfaces. For all problems, the appropriate periodic boundary conditions are applied on fluid boundaries lying on the faces of the cubic representative cell. Their solutions serve to determine the relevant transport parameters using formulas involving averaging over the fluid domain.

The transport parameters were calculated for the updated (“actual”) micro-geometry of periodic cell with and without the valve ball, see Table 2. When the valve balls are present the material properties can be adapted, because the balls can be used to block some channels and, in that way, change the material (viscous) permeability and tortuosity, as well as the viscous characteristic length and static viscous tortuosity. This approach is very effective when the main transport direction is parallel to the blocked channels, since the flow is then directed through auxiliary channels which are oblique and narrow. Therefore, two cases were considered for the adaptive material with valve balls: (1) the horizontal direction, and (2) the vertical direction – referring to the direction of the pressure gradient driving the viscous flow, or the unit external electric field for the re-scaled conduction problem (i.e., the Laplace problem), assuming that the position of valve balls is at the bottom of large pores. Figure 3 compares the character of viscous flows for both cases, and also for the material without balls. In this latter case, however, adequately the same results are obtained for the horizontal directions, since the cell without ball has full cubic symmetry.

Transport parameter	Unit	Without valve balls	Horizontal direction	Vertical direction
(open) porosity	%	44.92	38.38	38.38
viscous permeability	$10^{-9}\,\mathrm{m}^2$	13.56	11.69	2.172
thermal permeability	$10^{-9}\,\mathrm{m}^2$	128.9	48.98	48.98
(inertial) tortuosity	–	1.981	1.856	2.483
static viscous tortuosity	–	3.255	3.092	5.289
static thermal tortuosity	–	1.607	1.649	1.649
viscous charact. length	mm	0.627	0.575	0.231
thermal charact. length	mm	1.227	0.863	0.863

Table 2: Transport parameters for the “actual” micro-geometry

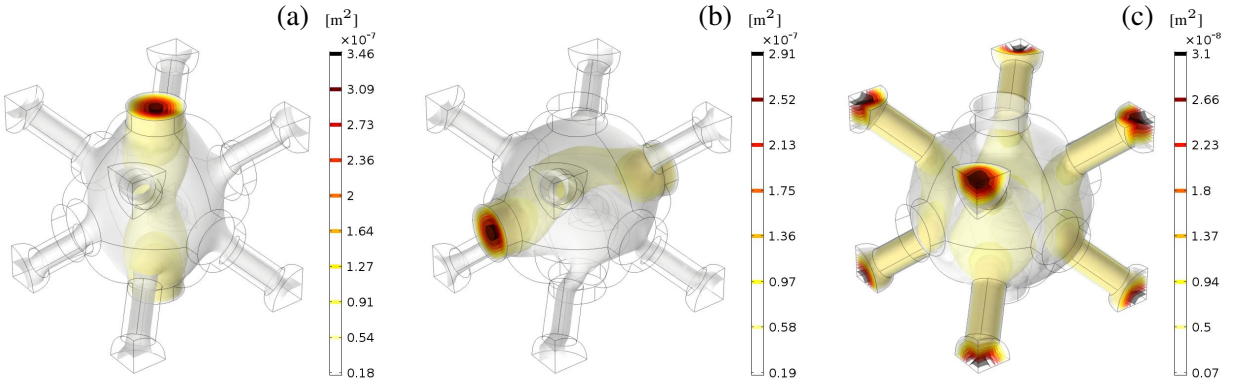


Figure 3: Viscous flow through the periodic cell: (a) with empty pores, and (b,c) with a sphere (valve ball) inside the main pore, at the bottom of it; the pressure gradient driving the flow is in the horizontal (b) or vertical (a,c) direction

The results presented in Table 2 confirm that the thermal parameters are non-directional (therefore, the same for both direction cases), as obviously is the porosity. For the horizontal direction case, that is, when the channel blocked by the valve ball is perpendicular to the main transport direction, the inertial tortusity and all viscous parameters tend to be quite similar to the corresponding values obtained for the material without valve balls (with differences in the range from 5% to 14%). For the vertical direction case, the viscous and inertial tortuosities are significantly larger, while the viscous permeability and characteristic length are much smaller than their counterparts computed for any of the two other cases.

4 Macroscopic analyses and experimental testing of the adaptive sound absorber

Nine macroscopic analyses of sound propagation were carried out for the porous media discussed in the previous Sections, that is, for the material without balls and for the adaptive material with valve balls in two different positions with respect to the direction of wave propagation. Therefore, one may speak here, in fact, about three porous media characterised by different sets of transport parameters (see Table 2), since from that perspective the adaptive material is treated as two different porous media. Consequently, three analyses were carried out for each of the three sets of transport parameters from Table 2, namely:

1. a one-dimensional analytical analysis of plane waves propagating in air and penetrating into a porous medium at normal incidence to its surface (see, for example, [26] for complete analytical formulas for single- and double-layer configurations),

2. a three-dimensional numerical analysis of a quarter of porous cylinder with an adjacent layer of air, see Figure 4(a) for the corresponding finite-element mesh,

3. a three-dimensional numerical analysis of a quarter of porous cuboid with an adjacent quarter of cylinder of air, see the corresponding finite-element mesh in Figure 4(b).

The adjacent air domain is added in these models only to ensure the *plane* waves at the top surface (i.e., at some distance above the porous cuboid), where the surface acoustic impedance is to be computed in order to determine sound absorption. The height of air domain is 20 mm, which equals to one-third of the height of porous domains which is 60 mm (that is, twelve 3D-printed periodic porous layers). The diameter of cylinders is 29 mm and the full width of cuboid is 30 mm (which means 15 mm for the quarter of cuboid).

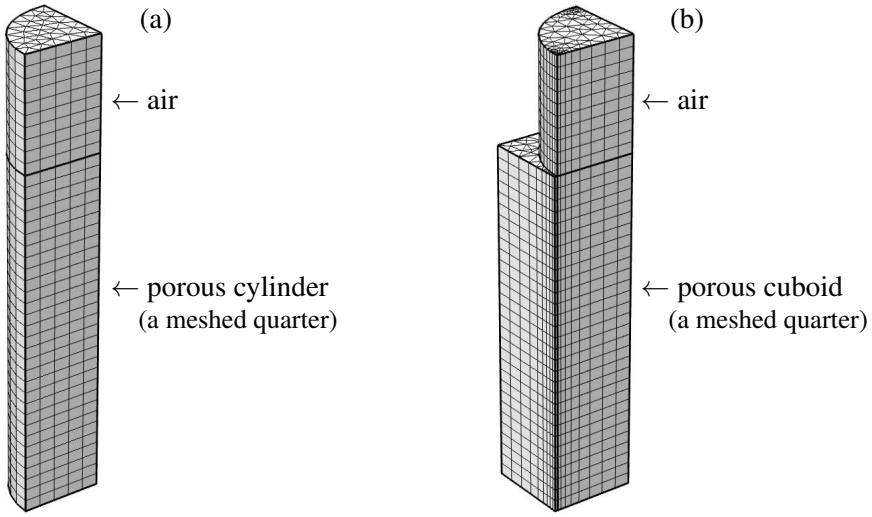


Figure 4: Finite-element meshes to model (a) cylindrical and (b) cuboid samples – only quarters of both macro-geometries are presented and meshed (taking advantage of symmetries)

The wave propagation in the porous domains and in air were modelled using the Helmholtz equation (for the porous media using also the JCAPL model). In the case of three-dimensional analyses the quarters of the porous and air domains could be modelled with finite elements because of symmetry, see Figure 4. The symmetry is realised by applying the sound-hard boundary conditions on the lateral surfaces of symmetry. On all other lateral surfaces and also on the bottom surfaces of porous domains in both macroscopic configurations presented in Figure 4, the sound-hard boundary conditions are also applied to simulate the rigid wall terminations. In the case of the porous cuboid this condition is also applied on the 'external' part of the top surface (the 'internal' part forms the interface with the cylindrical air domain). In reality, the rigid wall terminations are metal walls of the cylindrical impedance tube and its closing piston – in the case of the porous cylinder; or they are also 3D-printed as inherent parts of the cuboid samples or as the square-to-circular-shape adapter – in the case of the porous cuboid.

On the top surfaces of the cylindrical air domains in both macroscopic configurations shown in Figure 4, the pressure boundary condition is applied to simulate the plane acoustic wave propagating into these systems. In the case of the purely cylindrical system, i.e., the one with porous cylinder as in Figure 4(a), the wave propagation is planar everywhere and the problem and all results are in fact unidimensional, that is, they are constant on all quarter-circle cross-sections and their variations along the cylinder height should be the same as the corresponding results obtained analytically. In fact, the main purpose of this numerical analysis was to check the applied finite element modelling. The one-dimensional problem and the corresponding three-dimensional cylindrical configuration simulate the plane wave propagation in the impedance tube with the cylindrical porous sample (or, in a vast porous layer of the same thickness as the cylinder height) and their solutions are practically the same as confirmed by the results presented further in Figures 5–8.

In the configuration with porous cuboid, see Figure 4(b), the wave propagation is more complex and to some point three-dimensional (especially, close to the interface between the air and porous medium), although the waves are still planar in the air domain away from the porous cuboid and they become planar again inside the porous cuboid away from its top surface. This configuration serves to model the case where the plane acoustic waves propagate in the cylindrical metal impedance tube and pass into the 3D-printed thick-walled internally-porous cuboid absorber which terminates the tube.

When any of the harmonic wave propagation problems is solved, the surface acoustic impedance is computed on the top surface of air domain, where the waves are plane – as they are in reality, in the impedance tube (at least at some distance from the surface of porous cuboid absorber) and in particular at the two microphones measuring the acoustic pressure at two specified positions inside the tube, in accordance with

the Two-Microphone Transfer Function Method [27]. The frequency-dependent complex-valued surface acoustic impedance together with the known characteristic impedance of air allow to determine the real-valued acoustic absorption coefficient in the considered frequency range [1, 27]. The wave propagation in the air domain is lossless, so the sound absorption computed in that way for the meshed configurations depicted in Figure 4 comes only from the porous absorbers.

Figure 5 presents the sound absorption results for the porous material without valve balls. In that case, the cylindrical sample could be manufactured, so the predictions can be compared with the corresponding measurements obtained not only for the porous cuboid, but also for the porous cylinder. The analytical result and numerical calculations for the cylinder are similar with the experimental curve for the cylindrical sample when comparing the peaks in absorption, however, there is some underestimation at frequencies between the peaks, where the acoustic absorption is low, anyway. The same is observed when comparing the numerical predictions for porous cuboid with the corresponding experimental curve, although in that case the discrepancies are even larger, especially at frequencies exceeding $3.5\,\mathrm{kHz}$.

The results obtained for the adaptive material with valve balls are shown in Figures 6–8 for the two extreme cases, that is, when:

1. the valve balls block the channels *perpendicular* to the direction of wave propagation which means that the impedance tube with adaptive porous sample is set in the *horizontal* position;
2. the valve balls block the channels *parallel* to the direction of wave propagation which means that the impedance tube with adaptive porous sample is set in the *vertical* position.

Figure 6 presents the acoustic absorption of waves propagating in the horizontal directions in the adaptive material – with respect to the vertical gravity force. Generally speaking, the character of absorption curves in that case is quite similar to the absorption presented in Figure 5 for the material without valve balls, although the porosity and other transport parameters are rather different. As expected, the numerical predictions for the adaptive porous cuboid are closer to the measurements (possible only for the cuboid sample) than other calculations: in particular, a small relative shift of absorption peaks to slightly lower frequencies is well predicted. Nevertheless, the overall discrepancy of the experimental result from the numerical prediction tends to be larger than differences between two different numerical calculations.

The numerical predictions shown in Figure 7 for the adaptive porous cuboid in vertical position are quite correct under $3\,\mathrm{kHz}$, but with large discrepancies at higher frequencies, especially over $4.5\,\mathrm{kHz}$. However, the overall character and low-frequency absorption peaks are well predicted in general. Now, by comparing the corresponding absorption curves obtained for the two adaptive material states plotted in Figure 6 and in Figure 7, respectively, it can be observed that the absorption of sound waves propagating in the vertical direction in the adaptive porous material, (i.e., in the direction of gravity force, see Figure 7), is completely different than in the case of the horizontal propagation (i.e., across the direction of gravity force, see Figure 6). In order to better see that difference, all numerical and experimental results obtained for the cuboid adaptive sample are re-plotted together in Figure 8. It is clear that the overall absorption tends to be generally better for the vertical position, however, there are wideband frequency ranges where the horizontal position ensures the best absorption (for example, in the frequency range from $2.7\,\mathrm{kHz}$ to $3.3\,\mathrm{kHz}$ a local minimum in absorption of the adaptive porous material in the vertical position can be changed to a local maximum of the horizontal position). More precise and quantitative observations can be stated as follows:

- after changing the absorber from the horizontal to vertical position, the three absorption peaks are dramatically shifted in frequency from about $1\,\mathrm{kHz}$, $2.9\,\mathrm{kHz}$, and $4.4\,\mathrm{kHz}$ to lower values of about $0.7\,\mathrm{kHz}$, $2.2\,\mathrm{kHz}$, and $3.8\,\mathrm{kHz}$, respectively;
- in the vertical position the lowest-frequency absorption peak reaches 1.0, the next peak is 0.95, and higher frequency peaks are about 0.9, while in the horizontal position the lowest-frequency peak is about 0.85 and the maximal absorption value of 1.0 is gained by the third peak (of the highest frequency in the considered frequency range).

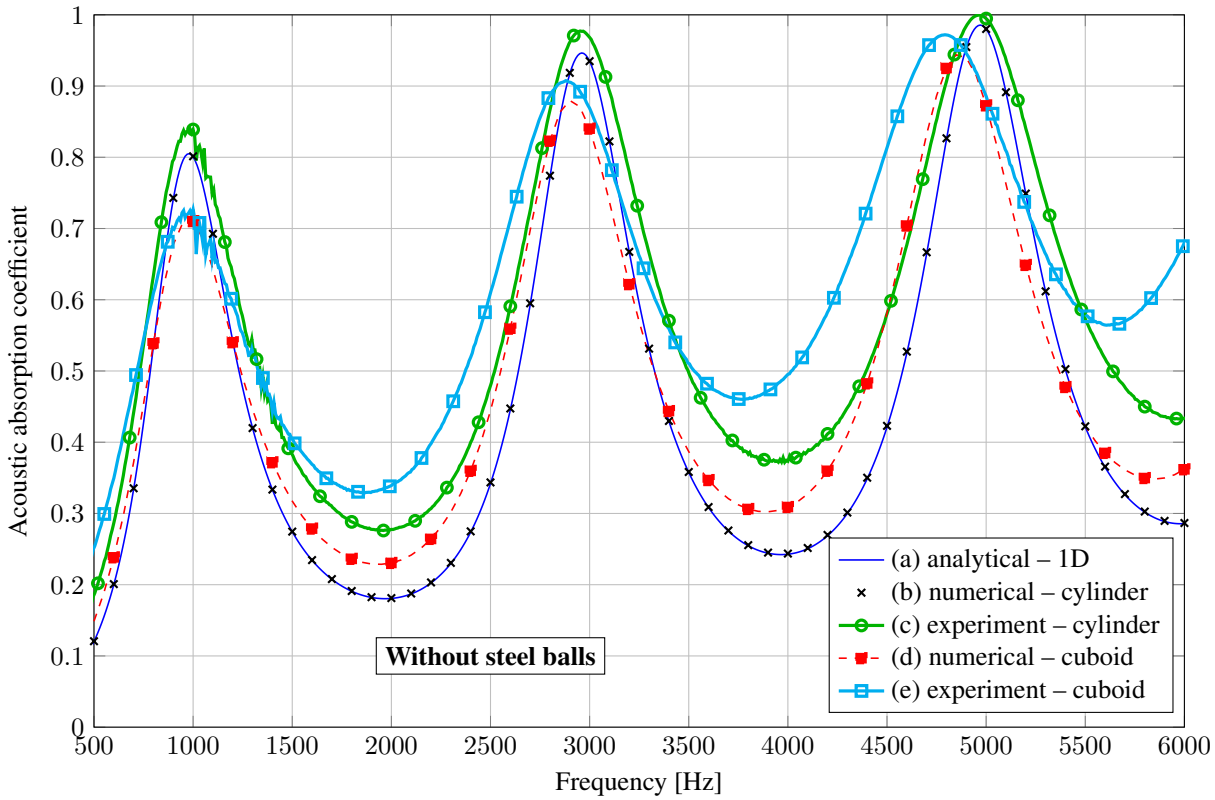


Figure 5: Predictions for the updated micro-geometry without steel balls (cylindrical and cuboid absorbers) and the corresponding experimental results

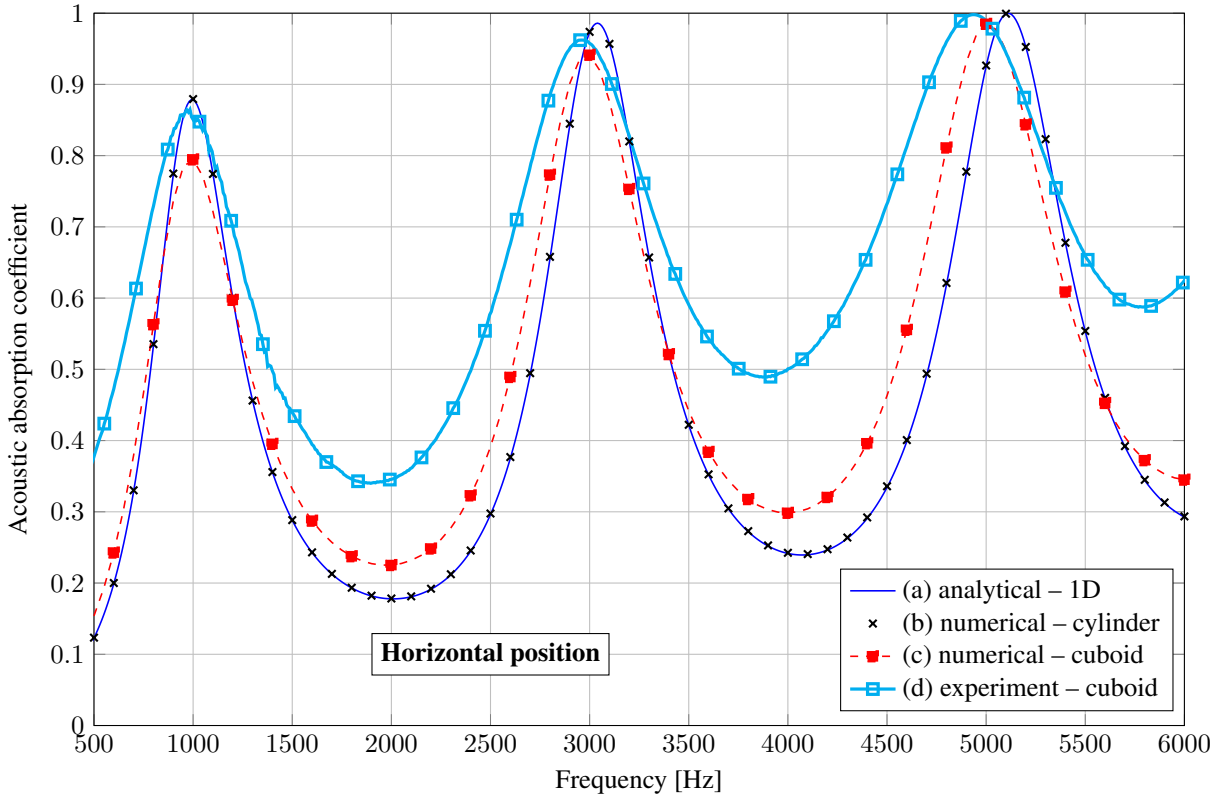


Figure 6: Predictions for the cylindrical and cuboid absorbers in the horizontal position, with steel balls (and the "actual" micro-geometry), and the corresponding experimental result for the cuboid sample

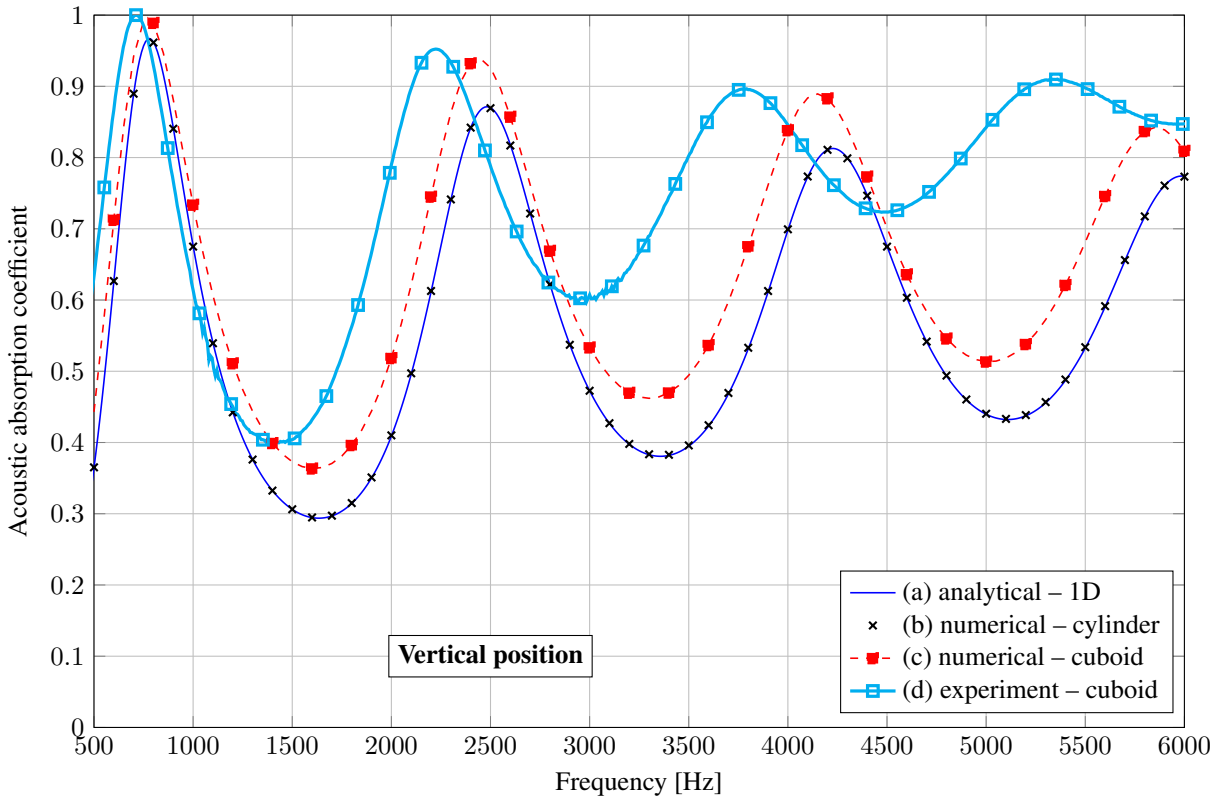


Figure 7: Predictions for the cylindrical and cuboid absorbers in the vertical position, with steel balls (and the "actual" micro-geometry), and the corresponding experimental result for the cuboid sample

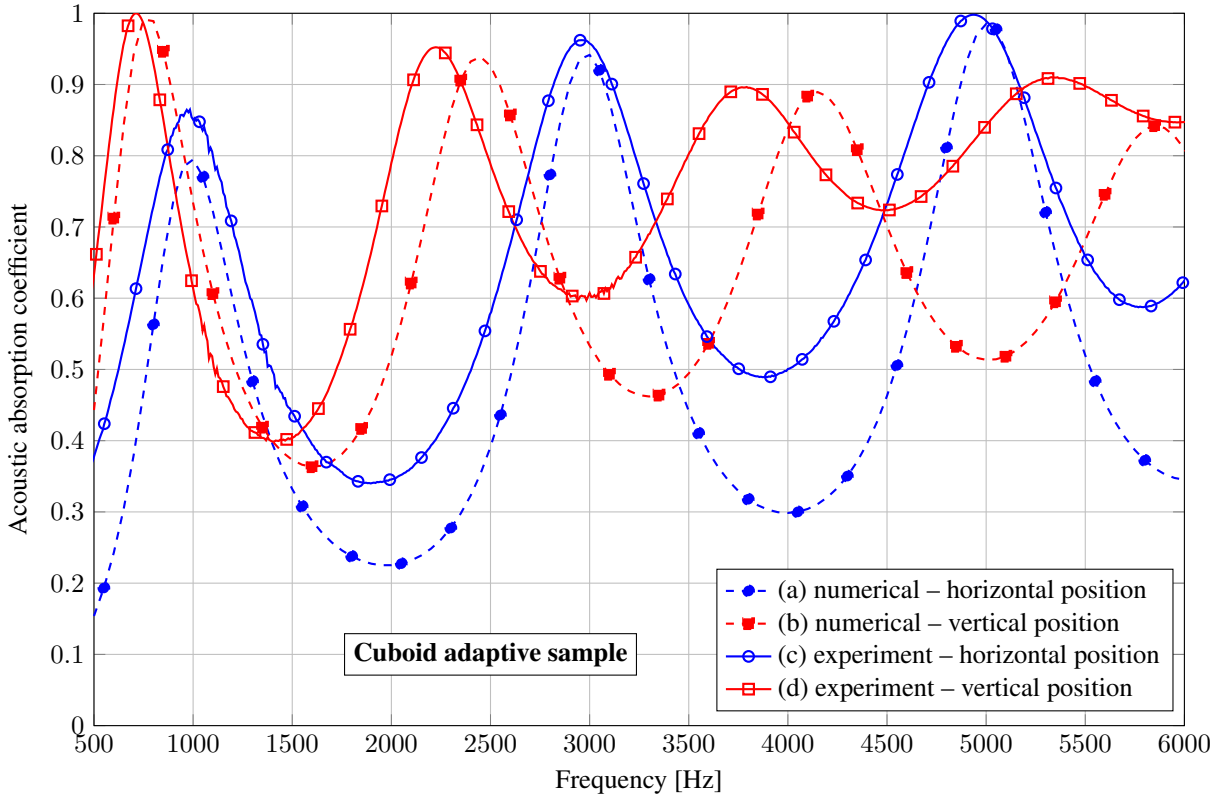


Figure 8: Predictions and experimental results for the cuboid sample of the adaptive absorber

5 Final remarks

The experimental investigations presented in this work demonstrated the feasibility and potential of the proposed concept of adaptive sound absorbing materials. The applied advanced, dual-scale modelling proved suitable, making possible the complex design process and allowing for correct (though not extremely precise) predictions. Moreover, it seems that poor quality of 3D-printing (a low-resolution budget 3D-printer was used) is responsible for most of the discrepancies between the measurements and predictions. These discrepancies should diminish or become quite negligible after using a fabrication technique or device of better quality. Moreover, larger discrepancies appeared at higher frequencies which can usually be neglected in most of the practical applications targeted here.

Nonetheless, new designs of adaptive sound absorbers should be developed and fabricated using techniques and/or instruments and devices of much better quality. Even further developments of the proposed concept should consider a semi-active approach, for example, using small switchable membranes (instead of valve balls positioned by the gravity), which should also lead to the investigation of some additional effects related to quick persistent membrane movements to and fro between the 'open' and 'closed' positions.

Acknowledgements

The financial support of Project No. 2015/19/B/ST8/03979: "*Relations between the micro-geometry and sound propagation and absorption in porous and poroelastic media*", financed by the Polish National Science Centre (NCN), is gratefully acknowledged. Dissemination of this work is also supported by European Cooperation in Science and Technology (COST) through the COST Action CA15125 – DENORMS: "Designs for Noise Reducing Materials and Structures".

References

[1] J. F. Allard, N. Atalla, *Propagation of Sound in Porous Media: Modelling Sound Absorbing Materials, Second Edition*, Wiley (2009).

[2] S. Gasser, F. Paun, Y. Bréchet, *Absorptive properties of rigid porous media: Application to face centered cubic sphere packing*, J. Acoust. Soc. Am., Vol. 117 (2005), pp. 2090–2099.

[3] Ch.-Y. Lee, M. J. Leamy, J. H. Nadler, *Acoustic absorption calculation in irreducible porous media: A unified computational approach*, J. Acoust. Soc. Am., Vol. 126 (2009), pp. 1862–1870.

[4] T. G. Zieliński, *Microstructure-based calculations and experimental results for sound absorbing porous layers of randomly packed rigid spherical beads*, J. Appl. Phys., Vol. 116 (2014), 034905.

[5] C. Perrot, R. Panneton, X. Olny, *Periodic unit cell reconstruction of porous media: Application to open-cell aluminum foams*, J. Appl. Phys., Vol. 101 (2007), 113538.

[6] C. Perrot, F. Chevillotte, R. Panneton, *Dynamic viscous permeability of an open-cell aluminum foam: Computations versus experiments*, J. Appl. Phys., Vol. 103 (2008), 024909.

[7] F. Chevillotte, C. Perrot, R. Panneton, *Microstructure based model for sound absorption predictions of perforated closed-cell metallic foams*, J. Acoust. Soc. Am., Vol. 128 (2010), pp. 1766–1776.

[8] T. G. Zieliński, *Generation of random microstructures and prediction of sound velocity and absorption for open foams with spherical pores*, J. Acoust. Soc. Am., Vol. 137 (2015), pp. 1790–1801.

[9] C. Perrot, F. Chevillotte, M. T. Hoang, G. Bonnet, F.-X. Bécot, L. Gautron, A. Duval, *Microstructure, transport, and acoustic properties of open-cell foam samples. Experiments and three-dimensional numerical simulations*, J. Appl. Phys., Vol. 111 (2012), 014911.

[10] O. Doutres, M. Ouisse, N. Atalla, M. Ichchou, *Impact of the irregular microgeometry of polyurethane foam on the macroscopic acoustic behavior predicted by a unit-cell model*, J. Acoust. Soc. Am., Vol. 136 (2014), pp. 1666–1681.

[11] Ju Hyuk Park, Sei Hyun Yang, Hyeong Rae Lee, Cheng Bin Yu, Seong Yeol Pak, Chi Sung Oh, Yeon June Kang, Jae Ryoun Youn, *Optimization of low frequency sound absorption by cell size control and multiscale poroacoustics modeling*, J. Sound Vib., Vol. 397 (2017), pp. 17–30.

[12] Ju Hyuk Park, Kyung Suh Minn, Hyeong Rae Lee, Sei Hyun Yang, Cheng Bin Yu, Seong Yeol Pak, Chi Sung Oh, Young Seok Song, Yeon June Kang, Jae Ryoun Youn, *Cell openness manipulation of low density polyurethane foam for efficient sound absorption*, J. Sound Vib., Vol. 406 (2017), pp. 224–236.

[13] K. Gao, J. A. W. van Dommelen, M. G. D. Geers, *Investigation of the effects of the microstructure on the sound absorption performance of polymer foams using a computational homogenization approach*, Eur. J. Mech. A Solids, Vol. 61 (2017), pp. 330–344.

[14] F. Chevillotte, C. Perrot, E. Guillon, *A direct link between microstructure and acoustical macrobehavior of real double porosity foams*, J. Acoust. Soc. Am., Vol. 134 (2013), pp. 4681–4690.

[15] Juhyuk Park, Sei Hyun Yang, Kyung Suh Minn, Cheng Bin Yu, Seong Yeol Pak, Young Seok Song, Jae Ryoun Youn, *Design and numerical analysis of syntactic hybrid foam for superior sound absorption*, Mater. Des., Vol. 142 (2018), pp. 212–220.

[16] T. G. Zieliński, *Pore-size effects in sound absorbing foams with periodic microstructure: modelling and experimental verification using 3D printed specimens*, in: P. Sas, D. Moens, A. van de Walle (Eds.), *Proceedings of ISMA2016 International Conference on Noise and Vibration Engineering and USD2016 International Conference on Uncertainty in Structural Dynamics*, Leuven (Belgium), KU Leuven (2016), pp. 95–104.

[17] C. Perrot, F. Chevillotte, R. Panneton, *Bottom-up approach for microstructure optimization of sound absorbing materials*, J. Acoust. Soc. Am., Vol. 124 (2008), pp. 940–948.

[18] T. G. Zieliński, *Microstructure representations for sound absorbing fibrous media: 3D and 2D multiscale modelling and experiments*, J. Sound Vib., Vol. 409 (2017), pp. 112–130.

[19] Shuwei Ren, Qingbo Ao, Han Meng, Fengxian Xin, Lixi Huang, Chuanzeng Zhang, Tian Jian Lu, *A semi-analytical model for sound propagation in sintered fiber metals*, Composites B, Vol. 126 (2017), pp. 17–26.

[20] H. T. Luu, C. Perrot, R. Panneton, *Influence of porosity, fiber radius and fiber orientation on the transport and acoustic properties of random fiber structures*, Acta Acust. united Ac., Vol. 103 (2017), pp. 1050–1063.

[21] D. L. Johnson, J. Koplik, R. Dashen, *Theory of dynamic permeability and tortuosity in fluid-saturated porous media*, J. Fluid Mech., Vol. 176 (1987), pp. 379–402.

[22] Y. Champoux, J.-F. Allard, *Dynamic tortuosity and bulk modulus in air-saturated porous media*, J. Appl. Phys., Vol. 70 (1991), pp. 1975–1979.

[23] S. R. Pride, A. F. Gangi, F. D. Morgan, *Deriving the equations of motion for porous isotropic media*, J. Acoust. Soc. Am., Vol. 92 (1992), pp. 32780–3290.

[24] S. R. Pride, F. D. Morgan, A. F. Gangi, *Drag forces of porous medium acoustics*, Phys. Rev. B, Vol. 47 (1993), pp. 4964–4978.

[25] D. Lafarge, P. Lemarinier, J. F. Allard, V. Tarnow, *Dynamic compressibility of air in porous structures at audible frequencies*, *J. Acoust. Soc. Am.*, Vol. 102 (1997), pp. 1995–2006.

[26] T. G. Zieliński, *Normalized inverse characterization of sound absorbing rigid porous media*, J. Acoust. Soc. Am., Vol. 137 (2015), pp. 3232–3243.

[27] ISO 10534-2: *Determination of sound absorption coefficient and impedance in impedance tubes*, International Organisation for Standardization (1998).

The use of a benchmark periodic metamaterial to inform numerical modelling and additive manufacturing approaches.

L. Dowling[1], **L. Flanagan**[1], **H. Rice**[1], **D. Trimble**[1], **J. Kennedy**[1],
[1] Trinity College Dublin, Department of Mechanical engineering,
e-mail: **kennedj@tcd.ie**

Abstract

The development of metamaterial modelling tools requires agreed benchmark designs which are suitable for manufacture and acoustic testing. A proposed design for a benchmark metamaterial consists of a periodic structure of cubes with a spherical internal cavity connected through cylindrical openings on each face of the cube. This design is highly amenable to both numerical modelling and manufacture through additive techniques. This work will report on the design, manufacture, modelling and validation of this benchmark metamaterial. The influence of manufacturing deviations on the predicted acoustic behaviour will be quantitatively assessed through acoustic testing. Furthermore, deliberate deviations from the basic design will be introduced during the manufacture to allow a systematic assessment of the impact of the manufacturing tolerances on the targeted meta-behaviour. Thereby this work will produce initial guidance on the impact of additive manufacturing approaches on the performance of acoustic metamaterials.

1 Introduction

The European COST action DENORMS (Designs for Noise Reducing Materials and Structures) has the stated goal of providing a framework for efficient information exchange, avoiding duplication of research efforts and channelling the work of groups involved towards the common goal of designing multifunctional, light and compact noise reducing treatments. As part of this effort there is a need for benchmark designs and materials which can be used to cross check and validate new numerical approaches as well as experimental measurements and manufacturing technologies. The group proposed a design for a benchmark periodic metamaterial which was amenable to numerical modelling, manufacture and experimental testing. This work reports on initial results for the proposed design where the entire process of simulation, manufacture, experimental testing and validation was attempted.

The recent surge in metamaterial research has been facilitated by a number of advances in enabling technologies. Advances in numerical modelling and processing power have enabled the simulation of meta-behaviours under realistic conditions. This has led to proposals for effective designs however, until recently, these were often unrealisable. Research into advanced additive manufacturing technologies has opened the door to complex geometries that are unsuited to traditional manufacturing techniques. At present there are a number of additive manufacturing technologies available and these include:

- Stereolithography
- Jetting systems
- Direct Light Processing
- Laser Metal Deposition

- Electron Beam Melting
- Lithography-based Ceramic Manufacturing
- Selective laser melting/sintering
- Fused Deposition Modelling

The various technologies provide different capabilities in terms of resolution and build volumes. These limit the scale and quantity of metamaterial that can be produced. The design and manufacturing processes from conception through to realization of a metamaterial is also of vital importance as is it currently unknown to what extent manufacturing tolerances or defects will impact the targeted meta-behaviour. Therefore the correct selection of manufacturing process and inspection of the produced material are topics which require research.

A survey of the state of the art in terms of additive manufacturing technologies reveals the capabilities currently available to metamaterial researchers. The key capabilities of build volume and minimum feature size have been graphed in figure 1. The graph shows a clear relationship between the build volume and minimum feature size and shows the overlap in the capabilities of the various technologies considered. As a general rule an increase in build volume is matched by a corresponding increase in the minimum feature size which can be achieved. There were three printing technologies used for this research which extend from low cost desktop printers to the state of the art machines. One of the most widely used low cost (approx. €3k) desktop printers is the Ultimaker series highlighted by a red $\bigtriangledown$ on the plot. The Formlabs Form 2 is a relatively low cost desktop printer (approx. €5k) highly suited to laboratory research of metamaterials as many prototype designs can be produced quickly and cost effectively and is highlighted with a red + on the plot. The 3D Systems Prox DMP 200, highlighted by the red $\triangleright$ symbol, can print in titanium, cobalt chrome, aluminium and stainless steel. This is a state of the art machine (approx. €450k) and in this work was used to manufacture in cobalt chrome at a cost of €200 per kilo of powder.

2 Design

The DENORMS benchmark design consists of a periodic structure of cubes with spherical internal cavities connected through cylindrical openings on each face of the cube. This design, while basic, has a number of features which can be varied to alter the acoustic performance of the periodic cellular material. It is also amenable to manufacture at different scales and with the parameters of sphere and cylinder diameter easily varied within a cell of a given size.

In this work a single 5mm cubed cell size was used with fixed interior spherical cavities of radius 2.25mm with interconnecting cylinders of radius 1mm from all faces of the cell. These parameters were chosen in the first instance to allow for a successful manufacture of the structure. Figures 2 and 3 show the dimension and design design of the periodic cell.

While the DENORMS cell does not correspond closely to many of the wide range of metamaterial designs currently published in literature the lessons learned for the manufacture, simulation and testing are still widely applicable to other materials. For example, recent papers on: optimal sound absorber design [1], ultra thin metasurfaces [2] and space coiling metamaterials [3, 4, 5] have all utilised periodic structures realised through additive manufacturing.

3 Manufacture

Most low cost commercial 3D printers make use of fused filament fabrication which is a 3D printing process that uses a continuous filament of a thermoplastic material, for example the Ultimaker desktop printers.

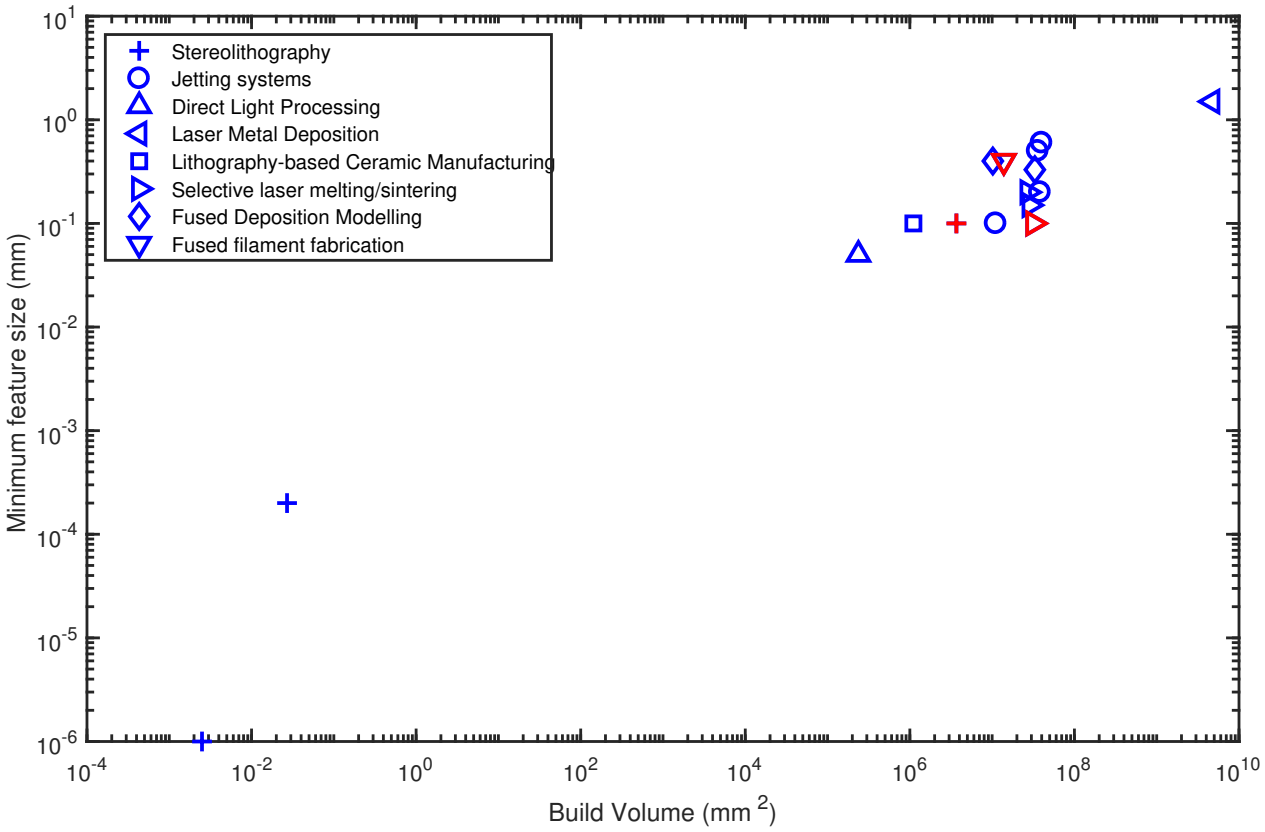


Figure 1: Build volume and minimum feature size for commercial additive manufacturing systems

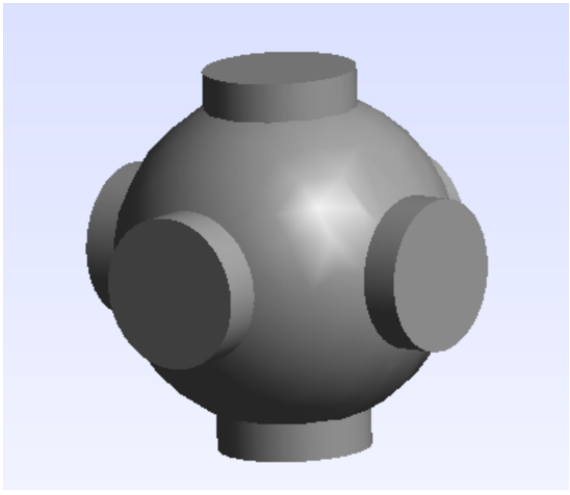


Figure 2: DENORMS benchmark design

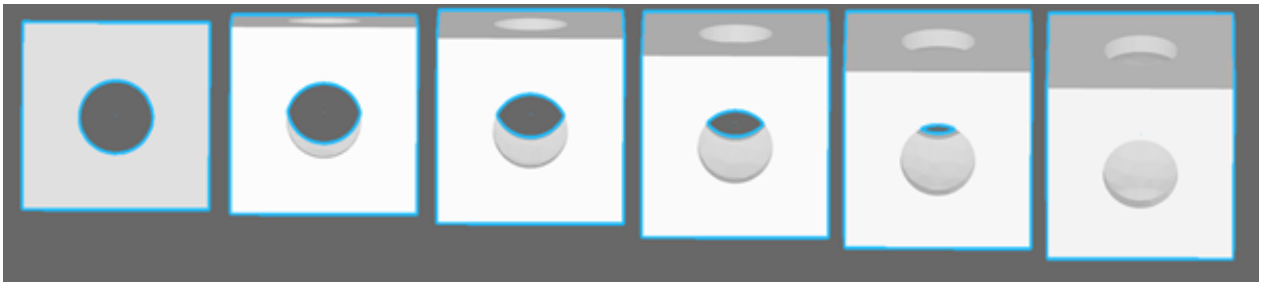


Figure 3: DENORMS benchmark design- rotation of individual cell from zero to twenty five degrees

The resolution of these machines is potentially insufficient to accurately manufacture the spherical internal cavities and circular openings of the connecting cylinders which are included in this material's design. Additionally these "fuzzy" internal surfaces may influence the achieved acoustic performance, potentially leading to an enhanced broadband performance [4] due to additional losses caused by the spurs. It is not possible to quantify the influence of these manufacturing defects on the achieved acoustic performance of the material therefore they may be unsuitable for a benchmark validation material. The Formlabs Form 2 printer which is based on stereolithography technology can achieve a resolution which is, conservatively, four times smaller than Ultimaker technology while still being a low cost desktop printer. It is hoped that more accurate manufacturing will lead to greater agreement with the numerical simulations of the acoustic behaviour. Finally the 3D Systems Prox DMP 200, based on selective laser melting/sintering, can achieve the smoothest surfaces with the best resolution and will be the closest to the ideal benchmark material sample. Manufacture with these three different technologies essentially introduces defects into the design which are inherent to the technology chosen.

There are however significant disadvantages to all of these technologies when considering a periodic cellular design. For the stereolithography based printers the entrainment of the resin material inside the cells leads to blockages which are more difficult to remove deeper in the material. This limits the number of layers of cells which can be manufactured in a single piece. This problem is not encountered in fused filament fabrication as there is no excess material to be entrained inside the cells. In this work attempts were made to remove the entrained resin material through compressed air cleaning, ultrasonic baths and manual evacuation. A decision was made to print the cells in high resolution single and dual layers which could be combined for testing. This introduces a new complication in that it is possible to have air gaps between layers of the cells, the effect of which may be very significant on the acoustic performance. A move to selective laser melting/sintering in metals avoids all of the above issues, however this technology can no longer be considered low cost. The additive manufacturing process is outlined in figure 4.

Stage one occurs in the Computer Aided Design Laboratory where the component CAD files are analysed and prepared for the additive manufacturing process. The following software packages are used at TCD for this purpose:

- CAD Software: SolidWorks, Creo
- Finite Element Analysis: Ansys Workbench
- 3D Printing Software: Materialise, 3D Builder, PreForm

The second stage is the additive manufacturing process where the appropriate technology is chosen based on consideration such as:

- Material: Polymer, ceramic, titanium, aluminium, cobalt chrome, stainless steel
- Build volume
- Resolution
- Manufacturing Time

In stage three the component must be extracted from the baseplate and support structure used in the additive manufacturing process. In addition to traditional manufacturing tools Wire Electrical Discharge Machine (EDM) is available to remove metals from AM baseplate with a cutting path as small as 21 μm .

In order to achieve the desired material properties the manufactured components must be post-processed. Certain polymers may respond to curing under UV light and the metals may require heat treatment. Two specialised industrial sintering furnaces designed for thermal processing of materials up to 1280 C are

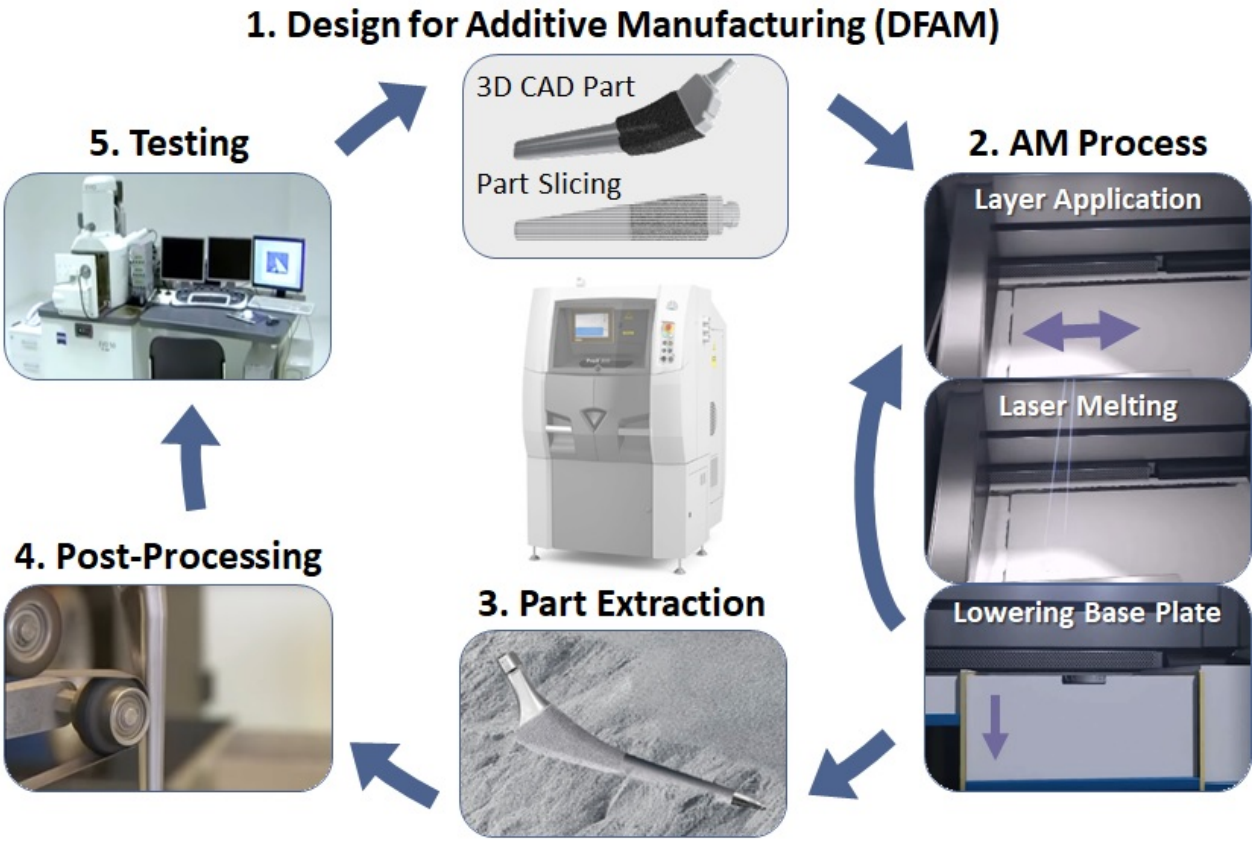


Figure 4: Additive manufacturing process

available as well as UV curing facilities. This process may be necessary to achieve required microstructure and removal residual stresses.

A number of inspection procedures are available in order to verify the dimensional accuracy of the manufactured metamaterials. The influence of manufacturing defects on the meta-behaviour is currently unknown and has not been reported in literature to date. The primary inspection procedures involve high resolution microscopy and CT scanning technology.

The initial DENORMS cell design was created in the open source GMSH software. GMSH can produce a mesh around the designed cell of varying levels of fineness depending on the needs of the design and export the mesh as .stl file. Key quality factors that need to be addressed and inspected at this stage of design are the quality of the feature mesh, the size of the files, any erroneous triangles added in meshing that deviate from the design requirements and any impinged features such as intersecting struts.

Once the design is finalised it can be taken into the 3D builder software as a .stl file. 3D Builder allows the cells to be propagated out in a regular pattern. Its inbuilt repair tools allows designs to be repaired at the joins between cells, remove extraneous triangles formed by the merging of several cells and fill any holes between cells in propagation.

A bottleneck in the production of the geometry relates to the file size and on board memory in the printers. This stage of design is important as the reduction in file size by converting to alternative supported file formats, such as .obj files, reduces the memory requirements by a factor of 5. An even greater reduction is possible by converting to .3mf format but this is not supported by the next stage in the process, namely the proprietary printer software, but might be a potential solution for even larger file sizes required in future.

The simplification tool can also be a strong means to reduce the file size by merging some of the finer features in the design that are not of a resolution available in the manufacturing process. The CAD files are then sliced to form the manufacturing code. Features that are significantly thinner than a single slice will not appear in regular operation but use memory to be stored. The danger in the simplification process is the potential for the simplification to join features across small gaps, thus altering the fundamental design of the cell. The effect of this is that smaller square openings can become rounded or sealed in extreme cases.

As the simplification can also lead to feature removal, a visual inspection of the CAD is conducted using a split tool to provide an internal view of the CAD file. This validation of the features allows errors or issues to be addressed before manufacturing occurs.

This final optimized .obj file can be provided as input to whichever proprietary slicing software is available for the desired printer. There are two main steps in the preparation of a design for print; orientation and support. The design is oriented to reduce overhangs, flat bridging surfaces and other potential causes for build failure such as cups. Overhangs are the most common cause for failure and these are produced by a model which has a long distance before another section or support which can cause the material to sag and no longer join correctly. Cups form in concave features and cause layer separation to occur producing a failed layer in the build which can cascade into total failure.

If at any point a print is not supported from below the laser will solidify the material but it will not be connected to the build. In the Form 2 printer, this cured resin remains in the resin tank and can cause issues during the rest of the build as it can impact other section of the design or become embedded into another feature. Care also has to be taken in the support placement as the support struts can be larger than gaps in the design or the design struts. This can cause issues as the design cannot be extracted intact from the support structure or the design can become compromised with extraneous features.

This problem is most frequently seen at the smaller scales where the support point is placed on the upper bound of a designed hole and completely seals it. A check should be made of support placement and a full visual inspection of the final sliced code should be carried out verifying the required support is present and that no part is filled by a support structure.

Following this the part is ready for manufacture in the printer. There are a few checks that need to be made in order to have a successful print. For example in the Form 2, the baseplate must be clean with no major

gauges or scuffs, these defects will develop over time through regular usage. The resin tank can also develop clouding or have partially cured resin that may interfere with the laser pass. Both of these possible errors are easily corrected but can lead to failed prints if not addressed in a timely manner. The resin tank and resin reservoir must sufficient material for a full print, if the material runs out the print will be paused and potentially cause failure as restarting the print can have poor layer cohesion where the pause occurred.

Following a successful print the part must be removed from the support structure and build plate. The first stage is removing the print from the build plate. The polymer prints include a solid resin base of 2mm attached to the aluminium build plate that keeps the print steady in manufacture however the build plate cannot be put through the material washing system or it will not be able to form a strong bond with subsequent prints. The metal build plates require specialist tools to successfully remove the parts. Once the print is removed from the base plate excess uncured resin or metal powder must be removed. In the resin case this is done using two absolute alcohol baths both for ten minutes. This removes the excess resin but needs to be controlled as alcohol can be absorbed by the resin making it swell and can degrade parts if left for a significant amount of time.

Completed prints undergo a rigorous inspection procedure. The initial inspection is a visual inspection after print removal. This stage of inspection checks for large scale defects such as support failures, missing or damaged cells and layer disconnects. These macro defects usually necessitate a new print or support redesign.

The first quantitative check is to verify that all faces are level. This ensures that the print is not warped or twisted it is possible that uneven curing causes the print to curl inwards on the more cured side, this is due to entrapped and entrained liquid leaving the material and causing a modest amount of shrinkage. To avoid this prints are rotated regularly over the curing period to achieve an even curing.

The next visual inspection is to check all corners are complete and undamaged. As the printing process includes a wiper passing over the print it is possible, at the exposed corners, for a wiper crash to cause damage. The corners are also where any damage in inserting the print into the test apparatus is likely to be noticed as they are the weakest points. This weakness is due to fewer neighbouring cells being available to dissipate force without deforming.

The final element of the visual inspection is to check that all designed channels are formed and clear. The DENORMS cell design has a series of cylindrical channels that air passes through. Any internal defects can usually be seen through these regular channels such as debris being embedded in the material or residue from the support spur failing into the channel. These blockages could potentially impact the effectiveness of the metamaterial.

4 Numerical Modelling

An initial 3D numerical model of the DENORMS cell was developed using a commercial finite element software COMSOL Multiphysics. The proposed DENORMS design was simulated using a fully thermoviscous acoustic model in the COMSOL acoustics module.

The structure of the proposed design as shown in Figure 2 consists of a sphere r=2.25mm enclosed by a box of sides a=5mm and three cylinders with r=1mm.

In order to effectively model the losses associated with propagation of sound waves in this problem, the thermal conductivity and viscosity effects which occur in the narrow regions were included. Due to the small size of the unit cell it was appropriate to simulate this problem as a full thermoviscous model. Near the walls, viscous and thermal boundary layers occur, a no-slip condition is applied to the velocity and an isothermal condition for the temperature.

The model in consideration solves for the linearised Navier-Stokes equation,

$$\jmath\omega\rho_0\mathbf{u} = -\nabla p + \nabla.(\mu[\nabla\mathbf{u} + (\nabla\mathbf{u})^T) - [\frac{2}{3}\mu - \mu_b][\nabla.\mathbf{u}]I) \tag{1}$$

the conservation equation,

$$\jmath\omega\rho + \rho_0\nabla\mathbf{u} = 0 \tag{2}$$

and the energy equation in the frequency domain.

$$\jmath\omega\rho_0 C_p T = \nabla.(k\nabla T) + \jmath\omega p T_0\alpha_0 \tag{3}$$

where ρ_0 , μ , μ_b , C_p, k and α_0 are the fluids density, dynamic viscosity, bulk viscosity, heat capacity at constant pressure, thermal conductivity and isobaric coefficient of thermal expansion, respectively and ω is the angular frequency. This model requires careful consideration to correctly resolve the acoustic boundary layer. Furthermore, while it is important to accurately capture the thermal and viscous losses by providing refinement towards the boundaries, it is important to keep the number of elements to an acceptable minimum. Far-away from the boundaries the size of the elements can be larger, this will avoid large computation time. The thermoviscous acoustics model is computationally expensive as it solves for the pressure, velocity field and temperature variations.

4.1 Numerical grid

The numerical grid used in the models of different numbers of layers of the DENORMS cell have the same mesh. The appropriate boundary layer thickness required is frequency dependent and can be determined from:

$$\delta = \sqrt{2\nu/\omega} \tag{4}$$

where ν is the kinematic viscosity of air.

Multiple numerical grids would have to be used for the frequency range of 0-4000 H_z. Due to significantly large computation time required for a fully thermoviscous model for an array of up to ten cells deep, it was decided to have a slightly thicker boundary layer to encapsulate the range of frequencies analysed. As with increasing frequency the boundary layer's thickness should become thinner, the boundary layer thickness was automatically set by COMSOL Multiphysics.

The mesh used for the analyses is shown in 5. A manifold was added to the inlet of the unit cell to capture the entry effects.

4.2 Boundary conditions

A quarter model of the unit cell was used for all models to reduce computation time. Therefore symmetry boundaries were used to model the adjacent cells. A first model with an open ended outlet was used to quantify the velocity entering the cell.

Air properties at $P = 101kP_a$ and $T = 293K$ are used in these analyses.

A harmonic adiabatic pressure condition of amplitude $p = 1P_a$ was set at inlet face of the manifold, and $p = 0P_a$ at the outlet face of the cell. The outer surface of the cells where set as walls. For the other models the outlet surface is closed with $u_t = 0$.

To reduce simulation time a Padé approximation was used in COMSOL so that the response is not calculated at each frequency.

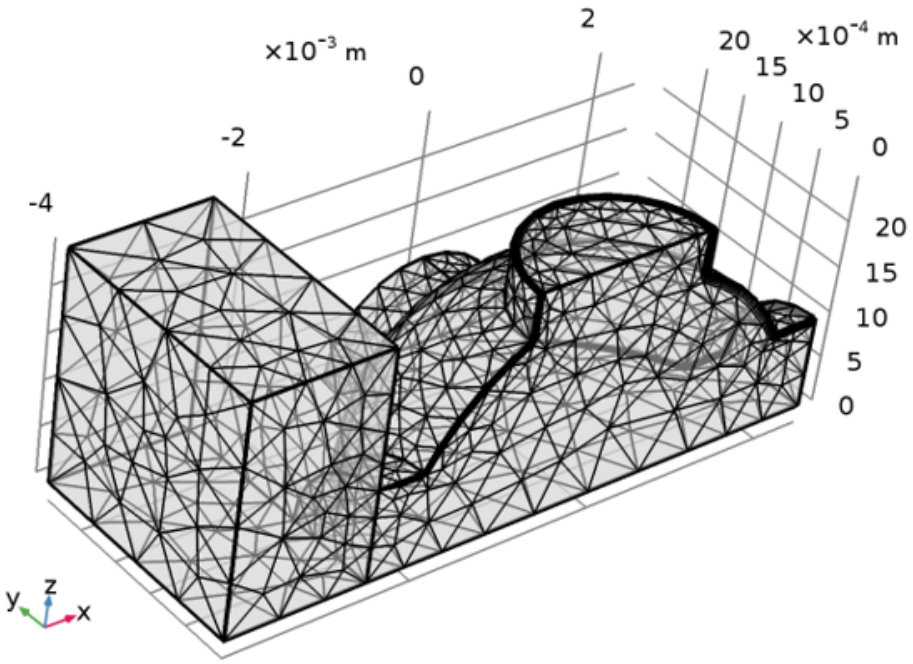


Figure 5: Numerical grid for DENORMS unit cell with inlet manifold

4.3 Results COMSOL

The impedance is calculated at the inlet of the manifold by the following,

$$Z = \frac{P_b}{\overline{u}} \tag{5}$$

Where P_b is the inlet boundary pressure and the average velocity $\overline{u}$ over the surface. The impedance is then translated by the width of the manifold to model the entry into the cell,

$$Z_t = Z_c[\frac{Z - Z_c\jmath \tan K_c h}{-Z\jmath \tan K_c h + Z_c}] \tag{6}$$

Where Z_c , K_c , h are the characteristic impedance of air, the wave number, and the distance from the inlet of the manifold and cell.

From this, the reflection coefficient R is obtained.

$$R = \frac{Z_t - Z_c}{Z_t + Z_c}] \tag{7}$$

$$\alpha = 1 - |R^2| \tag{8}$$

The velocity and temperature distributions are presented at $f = 1000 H_z$ for the unit cell in Figure 6 and Figure 7, and for 4 stacked cells in Figure 8 and Figure 9, respectively.

At the time of writing the modelling activity has not been finalised and absorption results as a function of layer depth are not available. The results reported here are outline the modelling approach taken.

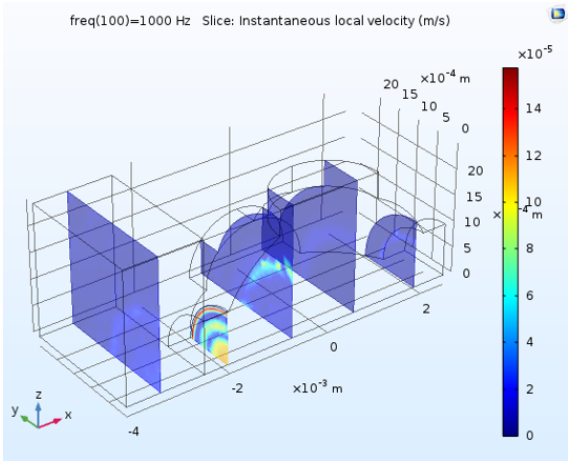


Figure 6: Instantaneous local velocity (m/s) unit cell, at f=1000 H_z

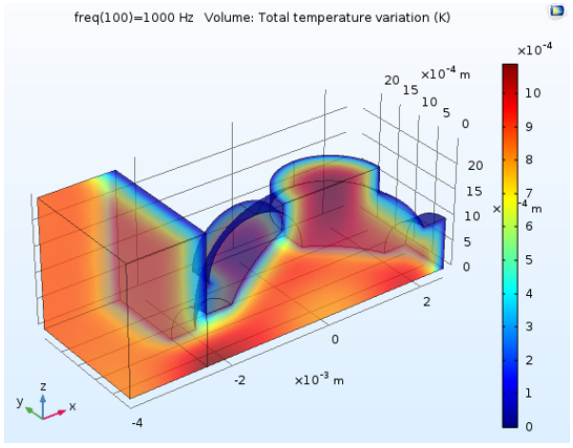


Figure 7: Total temperature variation(K) unit cell at f=1000 H_z

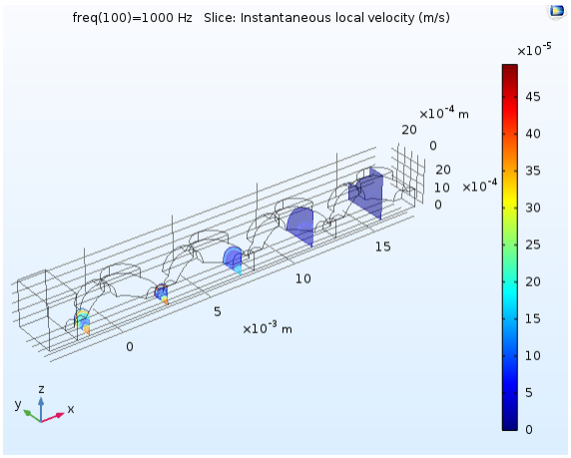


Figure 8: Instantaneous local velocity (m/s) 4 cells, at f=1000 H_z

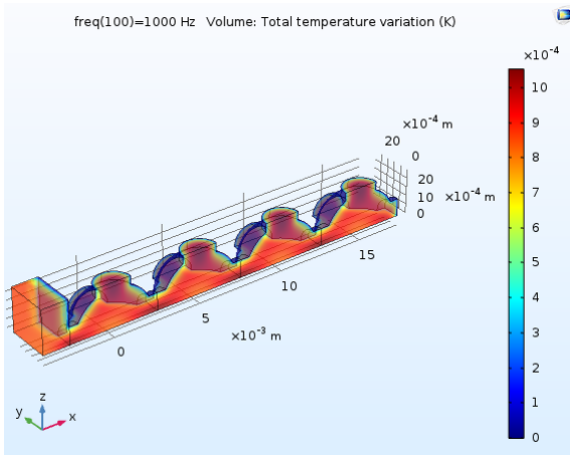


Figure 9: Total temperature variation(K) 4 cells, at f=1000 H_z

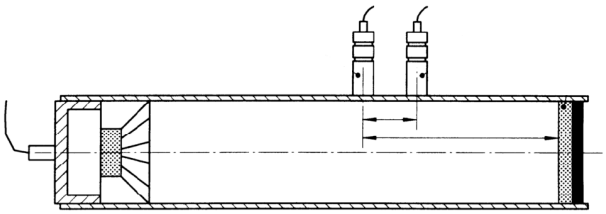
5 Results

The performance of the acoustic metamaterials is to be assessed against numerical predictions. Modelling work which considers the metamaterial behaviour as simply a surface boundary condition often requires the material behaviour to be expressed in terms of the complex acoustic impedance of the material. Microscale modelling of the interior structure of the material also attempts to predict the complex acoustic impedance of the material. Therefore the primary lab based acoustic validation of the material performance is the measurement of the complex acoustic impedance through impedance tube testing.

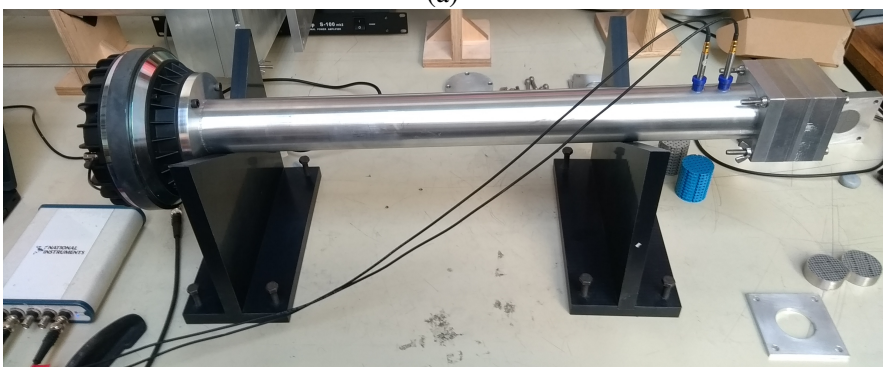
The relevant ISO standard for the measurement of the acoustical properties of the material is ISO 10534-2:2001. This standard describes the test rig and procedures for estimating the complex acoustic impedance of a material under normal incidence using the two-microphone or transfer function method. This methodology is used to calculate the reflection and absorption coefficients which are the usual measures used to quantify the performance of an acoustic material.

5.1 Normal Incidence Impedance Tube Testing

Normal incidence impedance tube tests are used to obtain the reflection factor R and absorption coefficient α, in accordance with the international standard ISO 10534-2:2001. In these tests, the sample is placed in an impedance tube as shown in figure 10 (a) which is taken from the ISO standard. The material is backed by a hard, reflective termination. The custom rig used for this work is shown in figure 10 (b).



(a)



(b)

Figure 10: (a) Impedance tube design ISO 10535-2 (b) TCD Impedance tube rig

In the experimental rig, the hard termination is provided by a 20 mm thick piece of aluminium which can be bolted on the end of the tube. The reflection coefficient is given by the ratio of the reflected wave amplitude (B) to the incident wave amplitude (A) i.e.

$$R = B/A \tag{9}$$

The absorption coefficient α is calculated from the reflection using:

$$\alpha = 1 - |R^2| \tag{10}$$

Values of the absorption coefficient vary with frequency and range between 0 and 1, with 1 being complete absorption.

The normalised acoustic impedance $(Z/\rho_0 c)$ may also be determined from:

$$Z/\rho_0 c = (1 + R)/(1 - R) \tag{11}$$

During the test procedure white noise is played through the speaker and the sound pressures p_1 and p_2 are measured by microphones 1 and 2. The complex sound pressures at the two microphones are given by the sum of the forward and backward travelling waves in the tube:

$$p_1 = Ae^{jkx_1} + Be^{-jkx_1} \tag{12}$$

$$p_2 = Ae^{jkx_2} + Be^{-jkx_2} \tag{13}$$

where x_1 and x_2 are the distances from the face of the sample to microphone 1 and 2 respectively. These two complex pressures can then be used to find the transfer function H_{12}

$$H_{12} = p_1/p_2 = (Ae^{jkx_1} + Be^{-jkx_1})/(Ae^{jkx_2} + Be^{-jkx_2}) \tag{14}$$

Using $R = B/A$ we get

$$H_{12} = (Ae^{jkx_2} + RAe^{-jkx_2})/(Ae^{jkx_1} + RAe^{-jkx_1}) \tag{15}$$

which can then be rearranged to find the reflection factor:

$$R = (H_{12}e^{jkx_1} - e^{-jkx_2})/(e^{-jkx_2} - H_{12}e^{-jkx_1}) \tag{16}$$

This reflection factor can then be used to calculate the absorption coefficient and acoustic impedance using the above equations.

The reflection and absorption coefficients are affected by factors such as porosity and surface finish of the material, both of which cause viscous energy losses. If the material is compressible, energy can also be lost to internal friction in the material as it is loaded and unloaded by the incident pressure wave. These additional losses will be influenced by the print quality and material used in the manufacture.

5.2 Rig and Sample Design

All the analysis in the previous sections assumed that the waves were all plane waves. Beneath the cut on frequency f_c only plane waves propagate in a duct, higher modes decay exponentially and so when the acoustic signal reaches microphone 1 it is composed of only plane waves. For a tube with circular cross section the cut on frequency is given by

$$f_c = 101/r \tag{17}$$

where r is the radius of the pipe in meters and f_c is in Hertz. For the current rig, the duct diameter is 40 mm and so the cut on is

$$f_c = 101/0.02 = 5050Hz \tag{18}$$

This means we can only perform tests reliably up to a theoretical maximum of 5050 Hz. The lower limit is determined by the speaker and is in the region of 300 Hz. On the left hand side of figure 10 (b) we can see the BMS 4591 speaker which is driven by the output signal of a National Instruments DAQ which has been amplified by a power amplifier. The speaker bolts on to the end of the tube to provide a tight seal with little leakage of sound. The square section on the right of figure 10 (b) is the sample holder which opens to hold cylindrical samples of 40 mm diameter and up to 50 mm thick. The sample holder is held shut by four long bolts with wing nuts.

GRAS 40PH array microphones were chosen to instrument the rig as they have a frequency response of 10 Hz - 20 kHz and upper limit of the dynamic range of 135 dB re 20 μPa allowing for testing up to high pressure amplitudes. The microphones are connected to the National Instruments DAQ and the signals are recorded in Matlab. The microphones are calibrated using the switching methods described in the standards to achieve a calibration transfer function which corrects for any differences in the behaviour of the microphones.

Figure 11 shows the ten layer deep DENORMS cell stacks produced by the three print methods. The high quality polymer prints produced by the Form 2 printer were limited to either single or dual layer disks shown in figure12. These were then stacked to produce a ten layer sample. The samples were simply manually aligned and held together under their own weight while mounted vertically in the impedance tube. This introduced a potential error as there may have been air gaps between disks and a slight misalignment of the channels, with the alignment error increasing further from the centre of the disk due to any rotation. In contrast the Ultimaker print had a low quality finish and many spurs within the channels. A photo of the print quality compared to the 3D systems sample is shown in figure 13 where these defects are visible. A section of the edge sample which included partially completed cells was chosen as a worst case example of the finish.

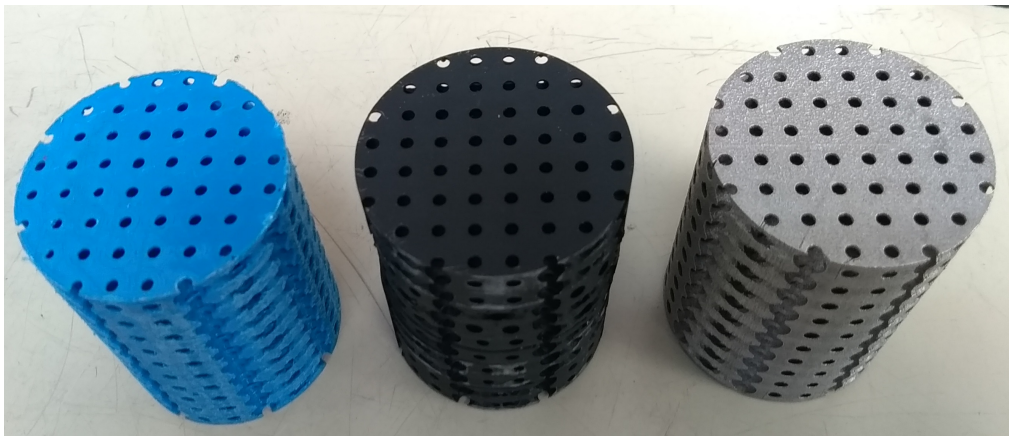


Figure 11: 10 cell deep samples: Left - Ultimaker, Centre - Form 2, Right - 3d Systems

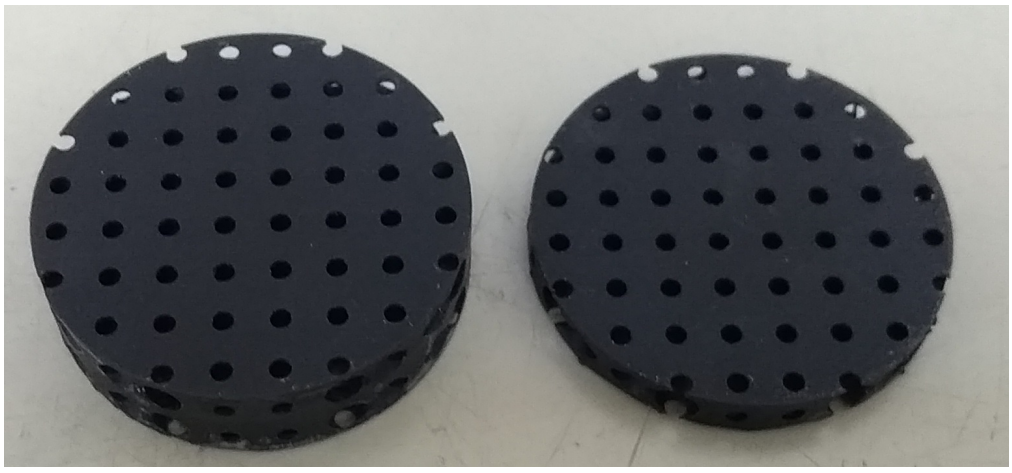


Figure 12: Form 2 single and dual layer disks

6 Experimental Results

The results for the ten layer deep prints from the three printers are shown in figure 14. From all three prints there is a double peak in the absorptivity in the regions of 1000 Hz and 3500 Hz. There is excellent agreement between the 3D systems sample and the Form 2 sample for the location and amplitude of the first peak while there is some divergence on the frequency of the second peak. The Ulitmaker sample produces both peaks at lower frequencies and high amplitudes. The increase in absorptivity can likely be attributed to the remaining spurs and low quality surface finish of the sample introducing additional losses within the

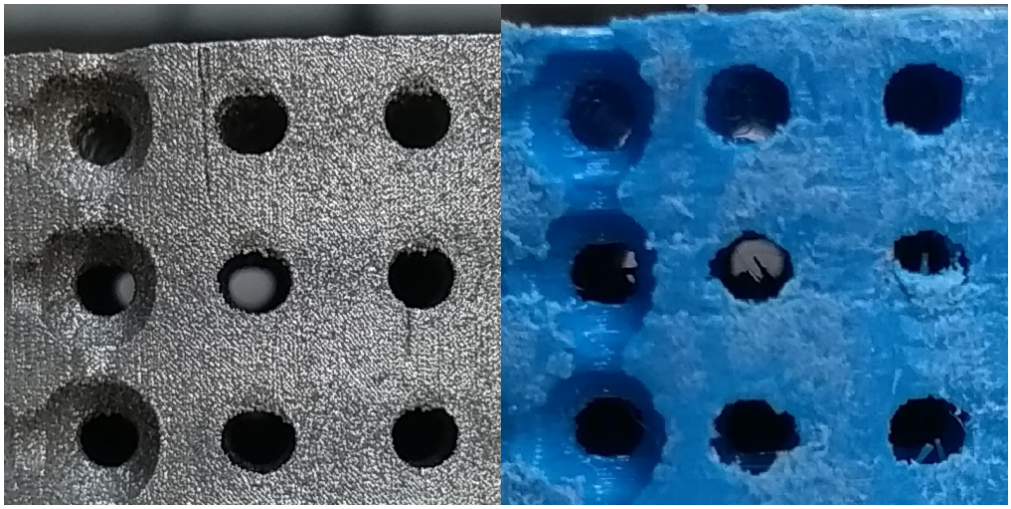


Figure 13: Comparison of print quality between the 3D systems (left) and Ultimaker (right) prints

channels. It appears from these results that any errors associated with the manual positioning of the polymer disks are of less importance than the quality of the interior geometry and from this we can conclude that the Form 2 may be a viable, low cost system suitable for producing sample for comparison to numerical models. The divergence of the Ulitmaker samples form the 3D systems sample is likely too great to allow it to be used for validation purposes.

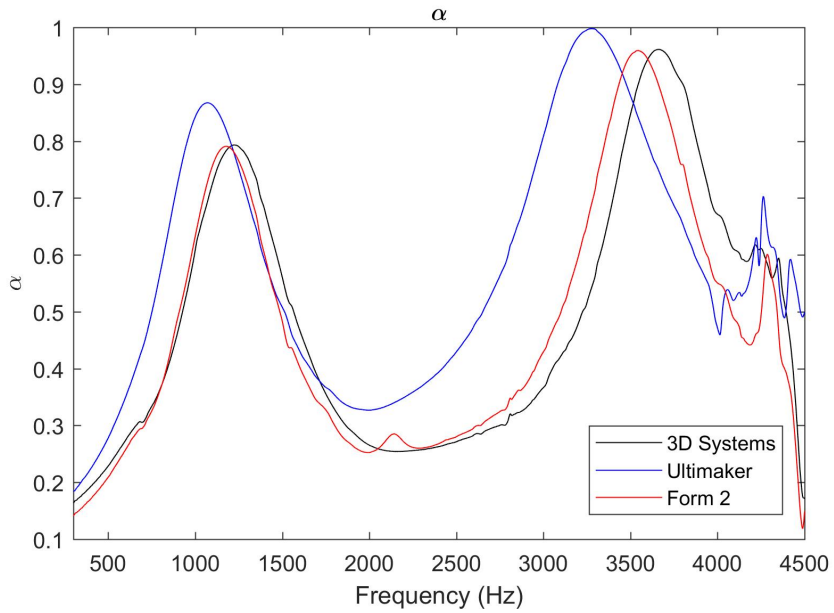


Figure 14: Absorption coefficient for three different prints of the 10 layer deep DENORMS cell

Due to the necessity to limit manufacture to single and dual layer disks on the Form 2 it was also possible to test other combinations of disks to produce different numbers of layers. Figure 15 reports the experimental results for five to ten layers deep. A clear trend can be seen in the location and magnitude of the peaks. As the number of layers decreases the location of both peaks shift to higher frequencies and the magnitude of the absorptivity drops.

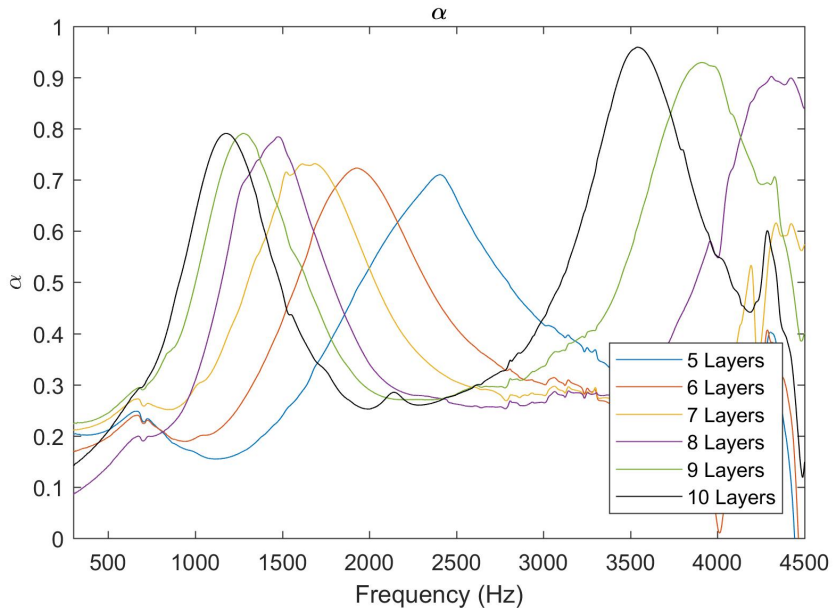


Figure 15: Absorption coefficient for 5-10 layers deep of the DENORMS cell printed on the Form 2

7 Conclusion

This work has reported on the design of a periodic acoustic metamaterial that is suitable for use as a benchmark validation case. The design was realised through three different additive manufacturing technologies which ranged from low cost desktop printers to state of the art machines. Experimental testing demonstrated good agreement between the Form 2 mid range printer and the state of the art 3D systems machine. This indicated that manufacture of a benchmark validation material may be possible at relatively low cost using current technologies. The use of a Ultimaker printer highlighted the potential for low quality prints to significantly influence the achieved performance, this is considered an obstacle for the production of validation data using this type of printer technology.

Clear trends as a function of depth were identified in the experimental results which were also achieved using a simple mounting procedure of the disks of high resolution low cost samples from the Form 2. The DENORMS design is therefore highly suitable for use as a benchmark and validation tool.

Initial modelling of the material was attempted in the COMSOL commercial tool set. At the time of writing this modelling was not complete and no comparison to the experimental results has been attempted. Further work will improve on the numerical results and attempt to match the experimental data.

The current scale of the design is at the limit of the low cost additive manufacturing technologies but finer scales can readily be achieved in the state of the art machines. Additional test samples at smaller scales are also planned to provide further data for model validation where parameters such as cell size, sphere size a cyclinder size.

Acknowledgements

as

This work was partially funded through the AERIALSIT project no: 723367 European Union H2020-EU.3.4. SOCIETAL CHALLENGES Smart, Green And Integrated Transport.

The authors wish to acknowledge the AMBER Additive Research Lab in the facilitating of the manufacturing of our metal test specimens and the AR Lab staff on providing training and guidance on the manufacturing

process. The AR-Lab has been enabled by a 3.3M award from Science Foundation Ireland as part of their Research Infrastructure program and an additional 1M investment from the European Research Council through our world leading investigators.

References

[1] Min Yang, Shuyu Chen, Caixing Fu, and Ping Sheng. Optimal sound-absorbing structures. *Materials Horizons*, 4(4):673–680, July 2017.

[2] Yifan Zhu, Xudong Fan, Bin Liang, Jianchun Cheng, and Yun Jing. Ultrathin Acoustic Metasurface-Based Schroeder Diffuser. *Physical Review X*, 7(2):021034, June 2017.

[3] Reza Ghaffarivardavagh, Jacob Nikolajczyk, R. Glynn Holt, Stephan Anderson, and Xin Zhang. Horn-like space-coiling metamaterials toward simultaneous phase and amplitude modulation. *Nature Communications*, 9(1):1349, April 2018.

[4] Changru Chen, Zhibo Du, Gengkai Hu, and Jun Yang. A low-frequency sound absorbing material with subwavelength thickness. *Applied Physics Letters*, 110(22):221903, May 2017.

[5] Yangbo Xie, Bogdan-Ioan Popa, Lucian Zigoneanu, and Steven A. Cummer. Measurement of a Broadband Negative Index with Space-Coiling Acoustic Metamaterials. *Physical Review Letters*, 110(17):175501, April 2013.

Study of sound absorption capability of silencers based on the acoustic black hole effect

N. Sharma[1], O. Umnova[1]
[1] Acoustic Research Centre, University of Salford,
Salford, M5 4WT - United Kingdom
E-mail: **n.sharma2@edu.salford.ac.uk**

Abstract
To keep up with the stringent norms and regulations, a lot of research has been put into the design and development of quieter moving parts and spaces, popularly involving improvisation in the technology of ducts and silencers. Prominent theoretical research based on the Acoustic Black Hole (ABH) effect has been developed that focuses on achieving total absorption of sound through retarding structures. Numerical and experimental visualization of this effect for sub-wavelength absorbers is currently an ongoing study across several acoustic groups. Passive muffling mechanisms based open termination structures with internal metamaterial lining have been studied semi-analytically and numerically on the ABH effect. In the present paper, 3D printed silencers with open expansion lined chambers are analysed numerically and validated experimentally for their absorption capability. Once optimized, this work can potentially contribute to the modern-day systems within the automotive and built environments.

1 Introduction

In accordance with the reports by professional bodies like the World Health Organization and the European Environment Agency, the impact of noise pollution is gaining attention. As an effect of this, the government based pollution control boards as also the OEMs (original equipment manufacturers) have raised the stringency in regulations pertaining to the generated noise. Quieter machinery and systems are being designed and fabricated, as a continuous effort to meet such requirements. For several applications, the industrial ducts and silencers have been modified to deliver the desired performance. In order to attain low overall noise levels, hybrid mufflers are being developed, that make use of both absorptive and reactive elements [1].

In recent times, technologies having significant contribution to the attenuation of low to medium frequency of sound are being explored. Prominent research work suggests the possibility of total absorption of sound through retarding structures having power law function based waveguides [2]. The work is based on the concept of Acoustic Black Holes (ABH) that have been theoretically realized. The numerical and experimental studies for such close termination structures that account for nearly perfect absorbers have been carried out by several research groups [3,4,5]. Based on the same principle, the ABH effect has been applied to silencing systems with essentially an open terminating structure. These silencers comprise of expansion chambers with varying wall admittance due to of the protruding flares having power law function based profiles. The theoretical and numerical modelling for several configurations with standard profiles have been analysed [6,7].

As an extension to the study of silencers based on the ABH effect, this research paper presents an experimental comparison between the linear and quadratic shaped profiles. The understanding developed with the numerical approach has been validated using 3D printed models. The study has been carried out for the transmission loss and sound absorption coefficients. The small B&K Impedance Tube setup has been used to characterize the performance of the silencer models in the low to medium frequency range (50 Hz – 4 kHz). The results show that there is good agreement between the numerical and experimental approaches

for both the flare profiles. Keeping in mind the practicalities of the techniques used, it is aimed that further optimization of the models would lead to the desired silencing capability from such structures.

2 Approach

2.1 Concept

In the present paper, the silencer models that have been experimented upon, have been initially analysed semi analytically. Using the first principles, plane wave propagating though an expansion chamber comprising of internal lined walls, is defined [6]. The lining of the walls accounts for the variation in the wall admittance to allow the visco-inertial exchanges. Solutions to the general wave equations, thus formulated in the presence of losses have been handled numerically using the Johnson-Champoux-Allard-Lafarge (JCAL) model. Transmission matrix approach as described in detail in the work [7] has been used to conveniently slice the chamber into periodic units. These units have been combined taking into consideration their variation across the profile of the flaring wall of the expansion chamber. Thus the progressing change in the external radius defines the waveguide to be either linear or quadratic.

2.2 Experimental Study

The impact of linear and quadratic profiles for the silencer was investigated by performing the experimental studies. The prototypes of the silencers to be tested upon were fabricated by 3D printing technology as a fast alternative. For the printings, the Computer Aided Models were built using SOLIDWORKS 2017. The different sectional views for the linear and quadratic profiles are as shown in figure (1).

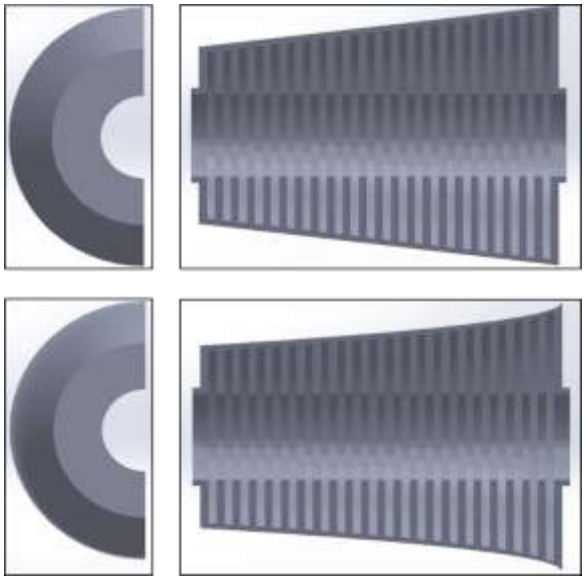


Figure 1: Side and Front sectional views of linear (top) and quadratic (bottom) profiles of silencer models

The prototypes are designed to be conveniently attached to the small B&K Impedance tube so that the complete frequency range (50 Hz – 6.4 kHz) can be observed for their performance. The inner radius of the chamber at its inlet and outlet section is 29 mm. The entire system is no longer than 100 mm and as wide as double the dimension of the inlet tube. The inner rings have a uniform thickness of 2mm arranged equidistantly in the chamber section. The PLA material based 3D printed prototypes are appended with metallic rings on both sides to maintain the flexibility in connection to the tube to accommodate both the

orientations. The different orientations have been termed as Narrow to Wide (N2W) and Wide to Narrow (W2N) for convenience in addressing simply based on the external flare variations. A detailed description of the experimental setup has been provided in a prior work [8].

3 Results and Discussion

Here the four different cases have been compared for their transmission loss and absorption characteristics. The cases include both the orientations for the linear and quadratic shaped silencer models. Figure (2) depicts the transmission loss (TL) characteristics for both configurations considering the waves being passed through W2N and N2W orientations. It can be seen that the quadratic silencers have higher TL over linear at low frequencies. It can also be noted that the curves trace a similar path for the two orientations in the functional frequency range.

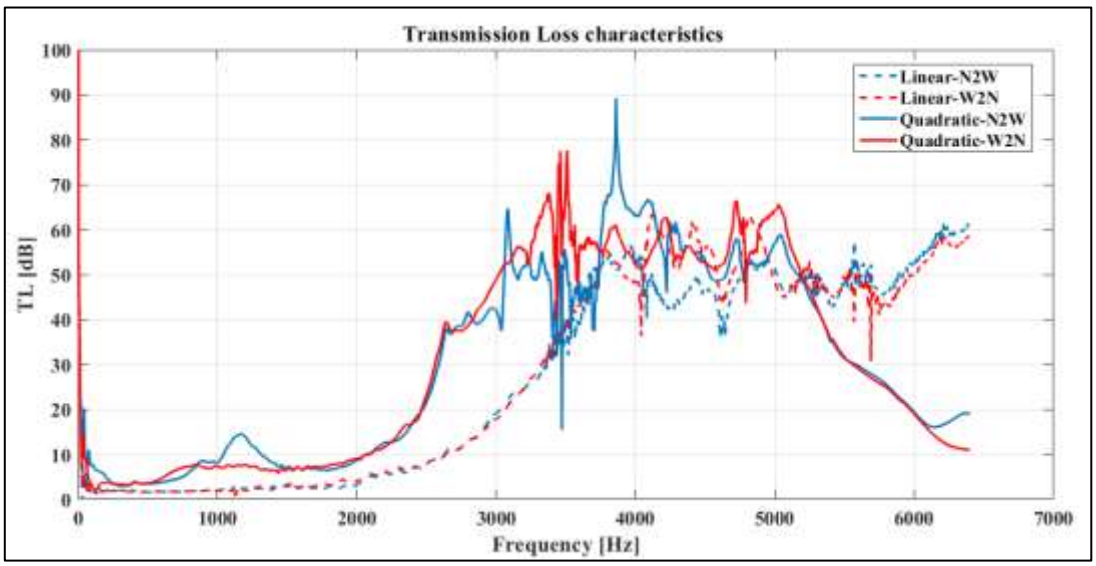


Figure 2: Comparison of the transmission loss characteristics between linear and conical flare profiles

The sound absorption coefficients have been plotted for the transmission regime as the open termination silencers are being studied. Figure (3) shows the dissipated absorption coefficient α_d which is calculated as

$$\alpha_d = 1 - [R]^2 - [T]^2 \quad (1)$$

Where $[R]^2$ and $[T]^2$ are the power reflection and power transmission coefficients respectively. At lower frequencies up to 2 kHz, the absorption capability of the linear profile is about 30-40% while that for the quadratic model, it starts from 30% and goes up to 80%. In the medium frequency range beyond 2 kHz, the N2W orientations for both linear and quadratic profiles reaches almost complete absorption indicating the ABH effect. The other orientation has much lower absorption, which could be due to the sudden expansion encountered by the waveguide on entering the system. The quadratic profile in both orientations shows better absorption capability over the linear profile. This again verifies the impact the higher order power-law functions have on the sound absorption as per the ABH theory.

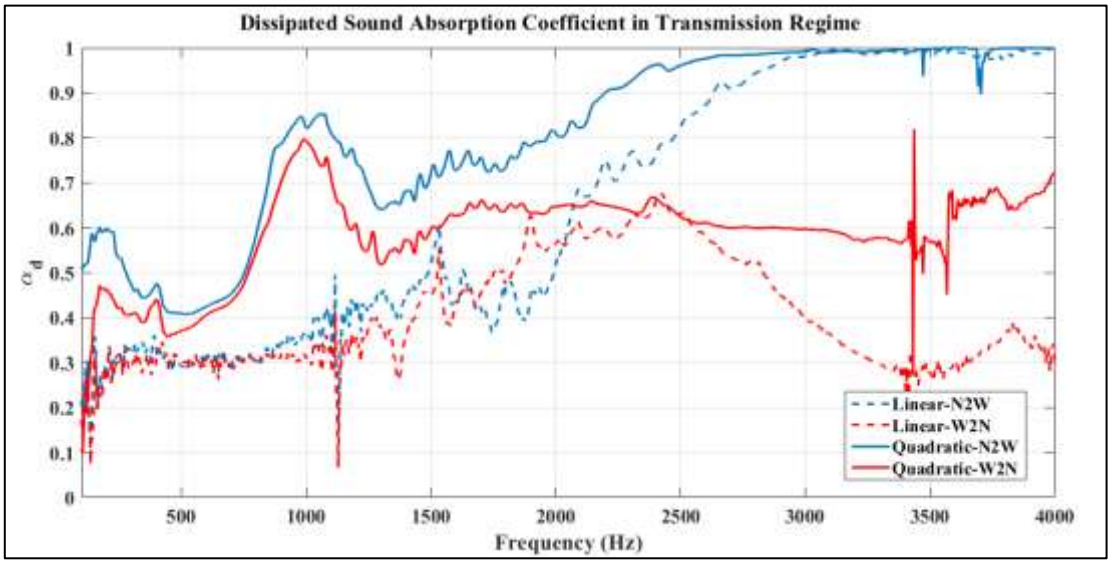


Figure 3: Comparison of the transmission regime based dissipated sound absorption coefficient between linear and conical flare profiles

Figure (4) and figure (5) present the power reflection and transmission coefficients that help to define α_d as in equation (1). The combined effects of the powered coefficients influence the overall dissipated absorption. For instance, at 1 kHz frequency, the quadratic curve has a trough for the power reflection coefficient tending to zero while the power transmission coefficient probes at 20%. The outcome of which appears at around 80% in terms of the absorption capability of the silencer.

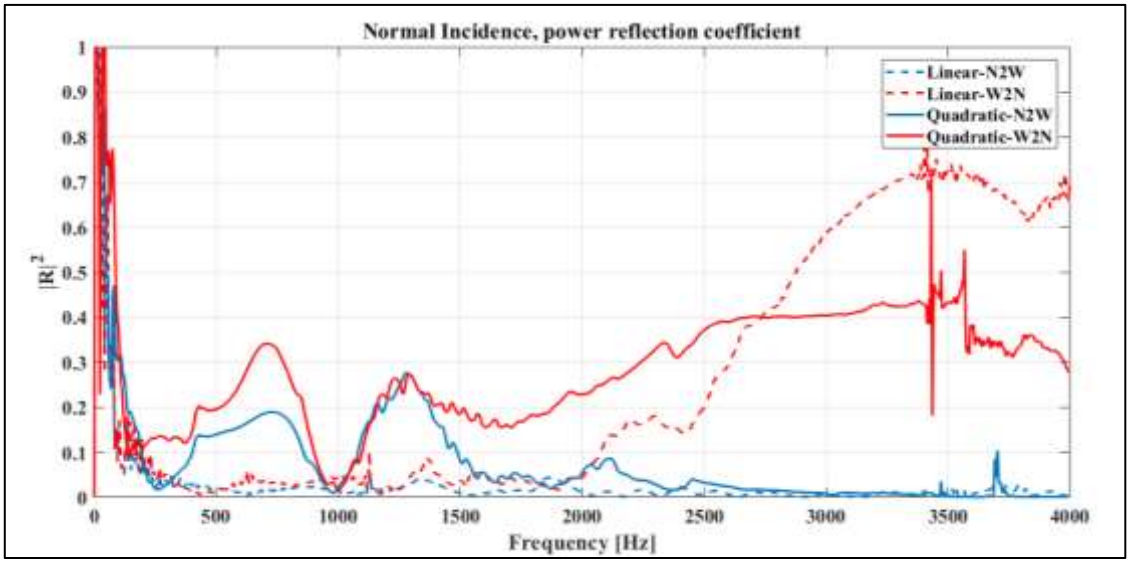


Figure 4: Comparison of the normal incidence, power reflection coefficient for anechoic termination between linear and conical flare profiles

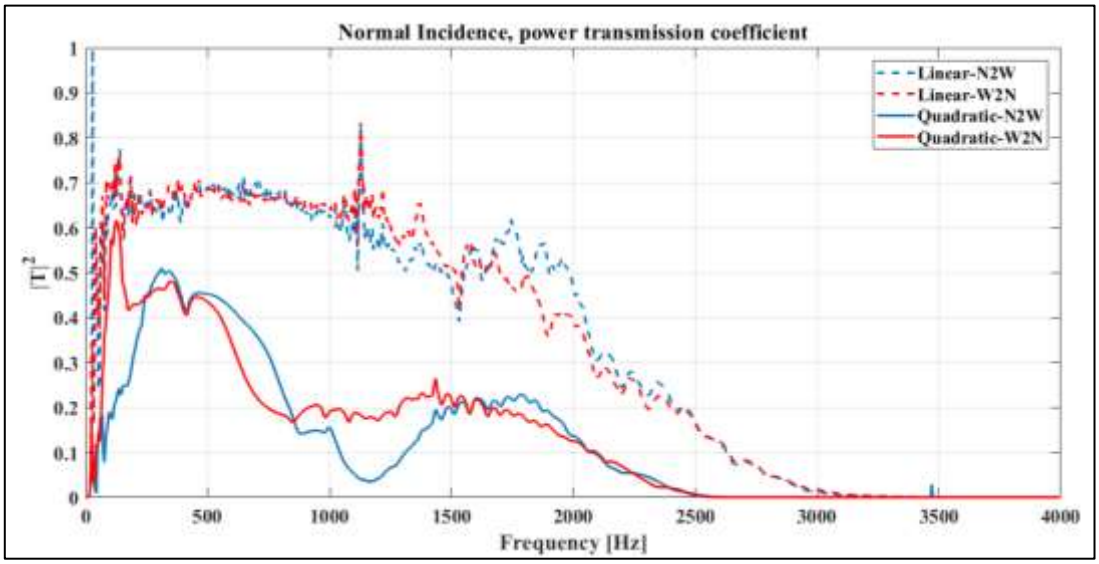


Figure 5: Comparison of the normal incidence, power transmission coefficient for anechoic termination between linear and conical flare profiles

The other sound absorption curve is considered with the presence of rigid termination as in figure (6). In comparison to the linear profile, the quadratic based plots have a higher variation with peak values reaching nearly complete absorption even at lower frequencies. After 2 kHz, the impact of orientations for both the configurations gains prominence. The W2N curves tend to show a decline in absorption capacity with the increase in frequency, which could be due to the narrowing of the silencing chamber. The N2W plots show continuous increase of the coefficient up to unity indicating total absorption satisfying the ABH principle.

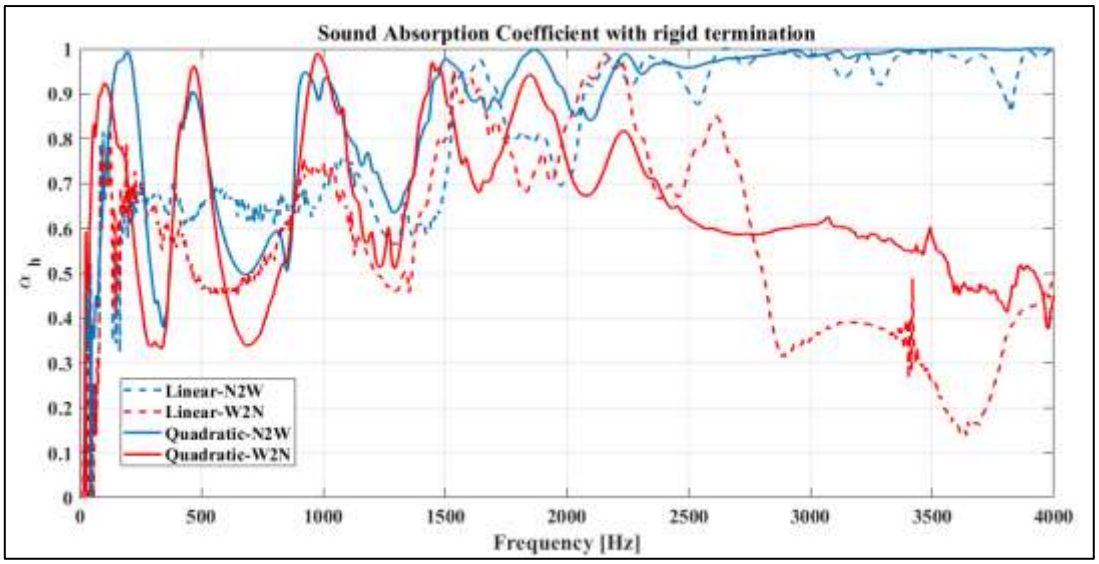


Figure 6: Comparison of the dissipated sound absorption coefficient with rigid hard backing between linear and conical flare profiles

4 Conclusion

In this experimental study, a comparative investigation between the silencer profile variation has been conducted. The profiles have been chosen as simple linear and quadratic being based on power-law function. As a validation to the numerical studies carried out earlier, the experiments have been designed and modelled accordingly. The transmission and sound absorption characteristics have been plotted to understand the contribution of the ABH effect. For the two profiles, linear and quadratic, both the orientations have been tested.

All through the frequency range and within its validity, there is significant transmission loss for both the configurations. The absorption coefficient is visibly higher at higher orders of the power function. At low frequencies, the effect of the flare profile is prominent while the orientation shows higher dominance for medium frequency range. It can be concluded that power-law profile contributes to ABH effect significantly even for open termination structures such as silencers.

As the models have been 3D printed, there could be chances of certain concerns due to probable leakages while connections and overall material infill during fabrication as well. The precision of the test has been ensured by repeatability of the experiments. The experimental comparison has presented the potential of ABH effect based silencers to behave as effective sound attenuating devices.

Acknowledgements

N.S. indebted to the University of Salford and her co-lab mates for the facility and constant support through the course of the research work. She is also thankful to her parents for their constant encouragement and motivation provided during the study.

References

[1] M. L. Munjal, *Acoustics of Ducts and Mufflers*, John Wiley, New York, (1987).

[2] M. A. Mironov and V. V. Pislyakov, *One-dimensional acoustic waves in retarding structures with propagation velocity tending to zero*, Acoustical Physics, 48 (3), (2002),347–352.

[3] V. V. Krylov, *Acoustic black holes: Recent developments in the theory and applications*, IEEE Transactions on Ultrasonics, Ferroelectrics, and Frequency Control, 61 (8), (2014), 1296-1306.

[4] O. Guasch, M. Arnela, P. Sanchez-Martin, *Transfer matrices to characterize linear and quadratic acoustic black holes in duct terminations*, Journal of Sound and Vibration, (2017), 395, 65-79.

[5] Azbaid El-Ouahabi, V. V. Krylov and D. J. O'Boy, *Investigation of the acoustic black hole termination for sound waves propagating in cylindrical waveguides*, INTER-NOISE and NOISE-CON Congress and Conference Proceedings, 250 (6) , (2015), 636-645.

[6] N. Sharma, O. Umnova, A. T. Moorhouse, *Analysis of a low frequency muffler based on the acoustic black hole effect*, Proceedings of the Institute of Acoustics, Acoustics 2016, 38 (1), (2016).

[7] N. Sharma, O. Umnova, A. T. Moorhouse, *Low Frequency Sound Absorption through a Muffler with Metamaterial Lining*, Proceedings of the 24th International Congress on Sound and Vibration, Acoustics 2017, (2017).

[8] N. Sharma, O. Umnova, A. T. Moorhouse, *Influence of Flare Variation on the Low Frequency Sound Absorption of Mufflers based on the Acoustic Black Hole Effect*, Proceedings of the Institute of Acoustics, Acoustics 2018, 40 (1), (2018).

Simplification of the transfer matrix model for acoustic screens

M. Gaborit [1,2], **P. Göransson**[1], **O. Dazel**[2]
[1] Marcus Wallenberg Laboratory, KTH Royal Institute of Technology, Stockholm, Sweden
e-mail: **gaborit@kth.se**

[2] LAUM UMR CNRS 6613, Le Mans Université, Le Mans, France

Abstract
Modern sound packages often feature coatings which are, in most cases, made of porous media. Their potentially strong impact on the acoustic performance underscores the need to include them in simulations although their small thickness is an obstacle to precise characterisation. The usual physical models for poro-elastic and porous media are either too crude to correctly account for the film effects (equivalent fluid, limp, etc.) or may seem over-refined for the task (Biot theory). In this paper, a simplified approach based on a transfer matrix representation and the Biot theory is presented and tested. It includes assumptions on the evolution of fields in the films and lead to a sparser transfer matrix than the usual Biot model. The proposed expression is shown to be accurate for a wide range of films and even outperforms other simplified representations in some cases (for instance in a stochastic context).

1 Introduction

Over the last years, the acoustics community devoted an important effort to the development of more efficient sound packages. The proposed strategies to mitigate noise often rely on the same design paradigm: a set of layers are arranged and tuned to form an absorbing panel. In these panels, one may distinguish the core (where most of the absorption occurs) from the other components (support, glue, coatings, etc.). The core has been the object of most contributions recently and different strategies emerged to improve its performance. For instance, some used the anisotropy inherent to poroelastic materials (PEM) as an advantage and tried to optimise the orientation of the different layers [1], others embedded (resonant) structures periodically to create meta-poroelastic materials [2, 3, 4], etc.

Independently from the type of core it uses, a sound package often bears coatings on its free surfaces. Serving protective or aesthetic purposes in most cases, these coating are thin (sub-millimetre) permeable layers (woven or not) bonded onto the absorber. Despite their size, the coatings tend to have a rather strong impact on the acoustic response [5] and thus must be included in the simulations. Their geometry and usual range of properties render their characterisation impractical though, and considerably lowers the confidence in the measurements of some parameters.

The available models for films have evolved a lot during the years, Pierce for instance was aware of the importance of the resistive effect and proposed to use a pressure jump approach [6]. The only parameter at the time was the flow based on power law such as the renown Delany-Bazley model (DB, see resistivity of the PEM which was already central to earlier empirical models from Delany and Bazley [7, 8]). Other approaches to model the dissipative effects emerged in the meantime and particularly, the Johnson-Champoux-Allard description (JCA, see Refs. [9, 10]) that provided semi-phenomenological expressions for a rigid-frame porous material. This approach was designed to be used in conjunction with the broaderly scoped Biot theory which describes both motion and stresses in the fluid and solid phases including the complex couplings at

play [11, 12].

While able to capture many effects accurately in a general PEM, the Biot theory seems slightly over-refined for very thin and plane layers. Indeed, one may argue that the complex interactions between the elastic and acoustic waves described by Biot will not actually take place along such short propagation lengths. The main advantage of this complete model is then to correctly account for the change of boundary condition between the core and surrounding media.

While others proposed alternative forms of the Biot equations including assumptions based on the typical properties of PEM [13], the present contribution intents to present a model based on the Biot theory assuming very short propagation paths and decoupling of some physical effects.

The model is introduced in section 2 and tested against Biot's theory in section 3. Section 4 challenges the proposed model in a stochastic context, comparing the generated envelope curves for one varying parameter with other models from the literature. Although incomplete, this opens the discussion about the use of simplified model to account for the effects of imperfect characterisation of the films most important properties in later works.

In this document, a positive ($e^{\mathrm{j}\omega t}$) time convention is assumed and all phenomena are considered time-harmonic. The quantities typeset in bold face are vectors or matrices and $\mathrm{j} = \sqrt{-1}$ which denotes the imaginary number. The document makes use of the Einstein convention on repeated indices and a subscripted comma followed by an axis denotes a partial derivative along this axis (e.g. $\mathbf{grad}\,\boldsymbol{u} = \boldsymbol{u}_{i,i}$).

2 Deriving the simplified model

The system under study is a plane poro-elastic material layer of infinite extent in the (x, y) plane and of thickness $d \ll 1$. In the present case, the model chosen for the film is the $\{\boldsymbol{u}^s, \boldsymbol{u}^t\}$ form of the Biot equations [14] which uses the total and solid displacement fields (resp. $\boldsymbol{u}^t$ and $\boldsymbol{u}^s$) to represent the acoustic behaviour. This formulation then defines two motion equations which, under time-harmonic assumption, read:

$$\hat{\sigma}_{ij,j} = -\omega^2 \tilde{\rho}_s u_j^s - \omega^2 \tilde{\rho}_{eq} \tilde{\gamma} u_j^t, \qquad -p_{,j} = -\omega^2 \tilde{\rho}_{eq} \tilde{\gamma} u_j^s - \omega^2 \tilde{\rho}_{eq} u_j^t \tag{1}$$

and two constitutive laws:

$$\hat{\sigma}_{ij} = \hat{A} u_{k,k}^s \delta_{ij} + N \left(u_{i,j}^s + u_{j,i}^s \right), \qquad p = -\tilde{K}_{eq} u_{k,k}^t \tag{2}$$

where $\hat{\sigma}_{xz}$ and $\hat{\sigma}_{zz}$ are the shear and compression components of the *in-vacuo* stress tensor, $u_i^{s,t}$ (with $i = x, z$) are the components of the solid and total displacement fields and p is the interstitial pressure. Concerning the other variables, $\tilde{\rho}_s$ and $\tilde{\rho}_{eq}$ are densities, $\tilde{\gamma}$ an fluid/solid coupling parameter, $\hat{A}$ and N the Lamé parameters (sometimes combined as $\hat{P} = \hat{A} + 2N$), $\tilde{K}_{eq}$ is a compressibility and δ_{ij} the Kronecker symbol. Note that $\tilde{\rho}_{eq}$ and $\tilde{K}_{eq}$ are equivalent fluid parameters.

A strategy to obtain a transfer matrix model of a poro-elastic slab is to rely on the so-called Stroh formalism which consists in rewriting (1) and (2) as a first order partial differential equation in the state vector $\boldsymbol{s}$ along z:

$$\boldsymbol{s}_{,z} = -\boldsymbol{\alpha}\boldsymbol{s}, \qquad \text{with } \boldsymbol{s} = \left\{ \hat{\sigma}_{xz},\ u_z^s,\ u_z^t,\ \hat{\sigma}_{zz},\ p,\ u_x^s \right\}^T \tag{3}$$

where each component of the state vector $\boldsymbol{s}$ implicitly depends on z and $\boldsymbol{\alpha}$ is the so-called *state matrix*

introduced in appendix A.1 of Ref. [15]:

$$\boldsymbol{\alpha} = \begin{bmatrix} 0 & 0 & 0 & \mathrm{j}k_x\frac{\hat{A}}{\hat{P}} & \mathrm{j}k_x\tilde{\gamma} & -\frac{\hat{A}^2-\hat{P}^2}{\hat{P}^2}k_x^2 - \tilde{\rho}\omega^2 \\ 0 & 0 & 0 & \frac{1}{\hat{P}} & 0 & \mathrm{j}k_x\frac{\hat{A}}{\hat{P}} \\ 0 & 0 & 0 & 0 & \frac{1}{\tilde{K}_{eq}} + \frac{k_x^2}{\tilde{\rho}_{eq}\omega^2} & -\mathrm{j}k_x\tilde{\gamma} \\ \mathrm{j}k_x & -\tilde{\rho}_s\omega^2 & -\tilde{\rho}_{eq}\tilde{\gamma}\omega^2 & 0 & 0 & 0 \\ 0 & \tilde{\rho}_{eq}\tilde{\gamma}\omega^2 & \tilde{\rho}_{eq}\omega^2 & 0 & 0 & 0 \\ \frac{1}{N} & \mathrm{j}k_x 0 & 0 & 0 & 0 & \end{bmatrix} \tag{4}$$

Solving this equation between the two sides of the layer (0 and d) leads to a transfer matrix expressed as a matrix exponential:

$$\boldsymbol{s}(0) = \boldsymbol{T}(d)\boldsymbol{s}(d), \qquad \text{with } \boldsymbol{T}(d) = \exp(-d\boldsymbol{\alpha}) \tag{5}$$

Considering the small thickness of the film ($d \ll 1$), one may use a first order Taylor expansion around $d = 0$ to get a linear approximation of the propagation phenomenon:

$$\boldsymbol{T}(d) \approx \boldsymbol{I} - d\boldsymbol{\alpha} + \mathcal{O}(d^2) \tag{6}$$

Such an expansion reduces the description of the propagation in the layer to a value jump for each field, proportional to the thickness d of the layer. Simplifying this model further implies identifying the components of the transfer matrix $\boldsymbol{T}$ which can be neglected.

Denoting by k_s the largest wave number in the layer (i.e. $k_s \geqslant k_{x,s}$) which often correspond to the solid-borne compressional wave and considering the first constitutive equation in (2) it comes:

$$|\hat{\sigma}_{xz}| \leqslant 2Nk_s(u_x^s + u_z^s), \qquad |\hat{\sigma}_{zz}| \leqslant k_s\left(\hat{P}u_z^s + \hat{A}u_x^s\right) \tag{7}$$

Substituting the expressions of $\boldsymbol{u}^s$ from the expanded transfer matrix (6), it is easily shown that:

$$|u_z^s(0) - u_z^s(d)| \leqslant k_s d\left(u_z^s(d) + 2\frac{\hat{A}}{\hat{P}}u_x^s(d)\right), \qquad |u_x^s(0) - u_x^s(d)| \leqslant k_s d\Big(2u_z^s(d) + u_x^s(d)\Big) \tag{8}$$

Provided that the thickness d or the frequency is small enough to have $k_s d \ll 1$, it can be considered that $\boldsymbol{u}^s(0) \approx \boldsymbol{u}^s(d)$. This allows to neglect all terms from lines 2 and 6 of $\boldsymbol{\alpha}$ in (6).

It is proposed as well to assume that two other effects are irrelevant in thin films: the influence of the saturating fluid on *in-vacuo* stresses and the coupling between tangential stresses and the normal displacement. These two assumptions lead to cancel T_{14}, T_{41}, T_{15} and T_{36}.

The last proposed simplification consists in neglecting the tortuosity effects in the film, setting $\alpha_\infty = 1$. This is supported by considered the small thickness and usual topology of the perforations (see-through coatings). Assuming such a property and using a low frequency approximation, one gets simplified expressions for the JCA equivalent fluid parameters:

$$\tilde{K}_{eq} \approx \frac{P_0}{\phi}, \qquad \tilde{\rho}_{eq} \approx \frac{\rho_0}{\phi} + \frac{\sigma}{\mathrm{j}\omega} \tag{9}$$

Note that the imaginary part of $\tilde{\rho}_{eq}$ corresponds to the pressure jump model proposed by Pierce [6] and that the real part is a correction term that mainly has an impact at high frequency. The simplified expression for $\tilde{K}_{eq}$ correspond to the isothermal limit of this parameter.

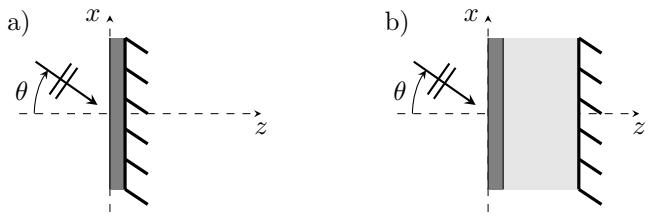


Figure 1: The two considered configurations featuring: a) a film directly laid on a rigid backing; b) an inserted, 20mm thick PEM.

Table 1: Physical parameters of the foam and films used in the validation cases of section 3. The woven and non-woven films parameters come from Ref. [16], the screen parameters from Ref. [17], Table 11.4 (Screen 2).

Parameters (unit)	Foam	Woven	Non-woven	Screen
ϕ	0.994	0.72	0.04	0.8
σ (N·s·m^{-4})	9045	87·10^3	775·10^3	3.2·10^6
$\tilde{\alpha}_\infty$	1.02	1.02	1.15	2.56
Λ' (μm)	197	480	230	24
Λ (μm)	103	480	230	6
ρ_1 (kg·m^{-3})	8.43	171	809	125
ν	0.42	0	0.3	0.3
E (Pa)	194.9·10^3	50·10^3	260·10^6	2.6·10^6
η	0.05	0.5	0.5	0.1

These approximations lead to the following simplified transfer matrix:

$$\boldsymbol{T}(d) = \boldsymbol{I} - d \begin{bmatrix} 0 & 0 & 0 & 0 & 0 & -\frac{\hat{A}^2-\hat{P}^2}{\hat{P}}k_x^2 - \tilde{\rho}\omega^2 \\ 0 & 0 & 0 & 0 & 0 & 0 \\ 0 & 0 & 0 & 0 & -\frac{1}{\tilde{K}_{eq}} + \frac{k_x^2}{\tilde{\rho}_{eq}\omega^2} & 0 \\ 0 & -\tilde{\rho}_s\omega^2 & -\tilde{\rho}_{eq}\tilde{\gamma}\omega^2 & 0 & 0 & 0 \\ 0 & \tilde{\rho}_{eq}\tilde{\gamma}\omega^2 & \tilde{\rho}_{eq}\omega^2 & 0 & 0 & 0 \\ 0 & 0 & 0 & 0 & 0 & 0 \end{bmatrix} \tag{10}$$

3 Agreement with Biot theory

In order to systematically validate the proposed approach, the results are compared with those given by a full Biot model (as defined in Ref. [15]). The configurations considered (rigid- and PEM- backing) are depicted in Figure 1 and are tested for two kinds of films (woven and non-woven). The material properties for the backing foam and the different films are given in Table 1. The angle of incidence θ is varied from 0°to 89°and the frequency from 10 to 4000 Hz. The graphs on Figure 2 then show the evolution of the error $\epsilon = |\alpha_{biot} - \alpha_{screen}|$ between the absorption coefficients computed with a complete or simplified model.

In the error maps of Figure 2, one clearly sees that the error, even if remaining low, increases with the incidence angle for both films. This effect is particularly seen on graphs 2.a and 2.b but is smoothed out by the absorption of the PEM on the other two. On these though one see a sudden rise of error near the resonance frequencies of the system. This effect is explained by the fact most of the elastic effects were neglected and some coupling are not accounted for in the simplified model albeit normally triggered at these frequencies. Figure 2.c shows as well an error increase when the frequency goes up which is linked to the approximations of the equivalent fluid properties $\tilde{\rho}_{eq}$ and $\tilde{K}_{eq}$.

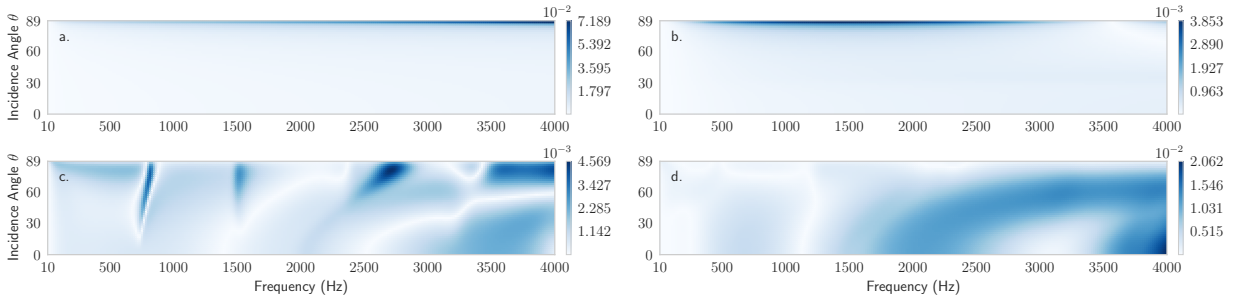


Figure 2: Evolution of the relative error in the (f, θ) plane. Left: (a. and c.) non-woven film; Right (b. and d.): woven film. Top: (a. and b.) configuration as in Figure 1.a; Bottom: (c. and d.) configuration as in Figure 1.b.

4 Ranged-defined parameters

The simplified model proposed in the present work was in the first place developed for statistical analysis. The films being difficult to characterise, the measured properties comes with low confidence and they may change vastly between samples. This effect associated with the potential strong impact films have on the response of system requires to consider the envelope curves of the response in place of a single plot.

In this second validation case, the proposed model is compared to the complete Biot model as for the preceding section but also to the so-called Limp model. This approach is based on the hypothesis that the material rigidity is negligible and leads to neglecting the term $\hat{\sigma}_{ij,j}$ in Equation (1). The result is a one compressional wave model that is similar to an equivalent fluid with the same compressibility $\tilde{K}_{eq}$ and the density $\tilde{\rho}_{limp}$ defined as [14]:

$$\tilde{\rho}_{limp} = \tilde{\rho}_{eq} \frac{\tilde{\rho}_s - \tilde{\gamma}^2 \tilde{\rho}_{eq}}{\tilde{\rho}_s}, \tag{11}$$

where the expressions of $\tilde{\rho}_{eq}$ and $\tilde{K}_{eq}$ are the complete ones [17]. Note that this model does not suppose a motionless skeleton and includes the fluid-related inertial effects.

This validation case considers a situation where the flow resistivity is a random variable following a normal paw. The draws are centred on the characterised value with a standard deviation of 10%. The statistical parameters are computed from 200 draws and the generator is reseeded between each film and each model. Figure 3 shows the standard deviation of the absorption coefficient for configuration shown in Figure 1.b (inserted PEM) for all three models

It is observed that both the simplified and limp models give similar results for two of the films but differs in the last case. Indeed, the (denoted Screen in Table 1) film is stiffer and this breaks the hypothesis underlying the limp approximation though the proposed model keeps up with the reference.

A similar trend is seen on the standard deviation of the envelope where, for these films, both the reference and proposed models agree while the limp model is inaccurate over the whole range. For a very soft veil such as the woven one though, as the proposed woven film, the limp model performs better, staying closer to the reference while the proposed approach drifts away as the frequency increases. Despite not fitting the reference exactly as precisely as the limp model, the proposed approach remains reasonably accurate.

5 Conclusion

In this work, a new simplified model for acoustic screen is proposed and tested. It is demonstrated that important assumptions on fields decoupling and parameters allow to drastically simplify the transfer matrix

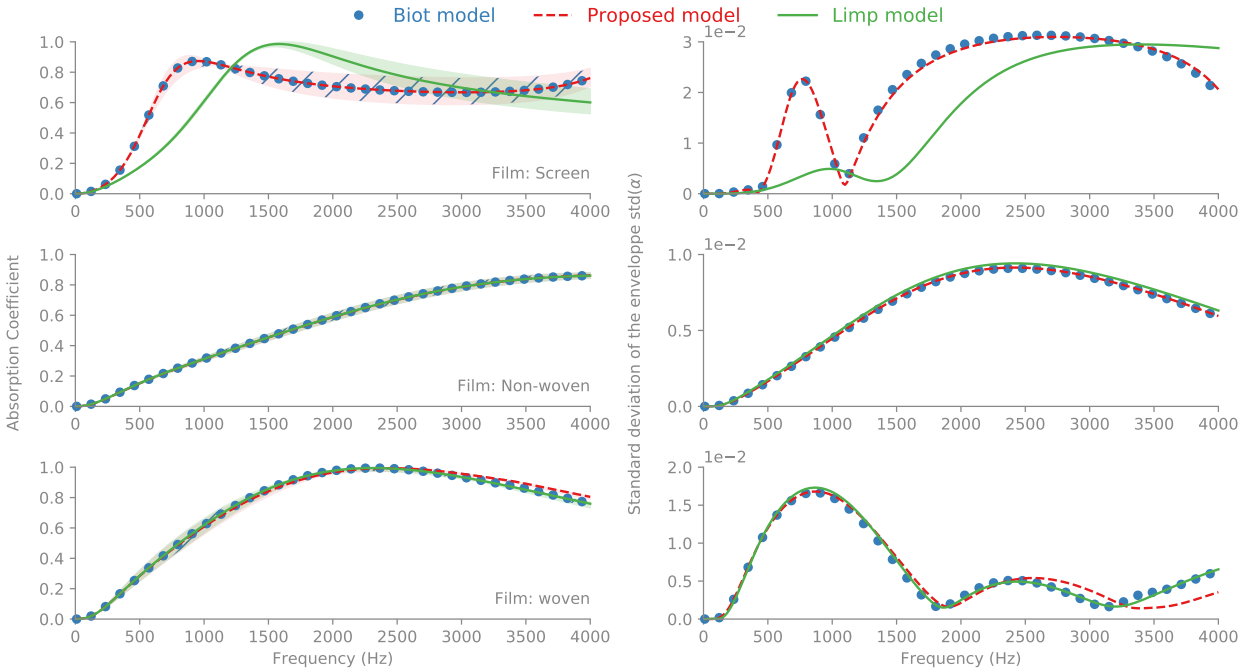


Figure 3: Figures generated for the films of Table 1 and the configuration of Figure 1.b at $\theta = 60°$ and with σ drawn from a normal distribution centred on the characterised value with a standard deviation of 10%. Left: Absorption coefficients and envelopes (the reference's is hatched). Right: standard deviation of the envelopes.

while still providing a reasonable accuracy. Initially developed for stochastic applications, the model is tested in the case of a parameter drawn from normal law. This test case shows that the results how the proposed models are comparable to those of a limp model for soft films and show a better accuracy for stiffer films. Although a more detailed study must be performed regarding the behaviour of the proposed model in a stochastic context, these preliminary results are encouraging for further application in such contexts.

References

[1] J. P. Parra Martinez, *On Multilayered System Dynamics and Waves in Anisotropic Poroelastic Media*, KTH Royal Institute of Technology, Stockholm (2016).

[2] J.-P. Groby, C. Lagarrigue, B. Brouard, O. Dazel, V. Tournat, B. Nennig, *Enhancing the Absorption Properties of Acoustic Porous Plates by Periodically Embedding Helmholtz Resonators*, Journal of the Acoustical Society of America, Vol.137, No.1 (2015), pp. 273–280. DOI:10.1121/1.4904534.

[3] C. Lagarrigue, J.-P. Groby, V. Tournat, O. Dazel, O. Umnova, *Absorption of Sound by Porous Layers with Embedded Periodic Arrays of Resonant Inclusions*, Journal of the Acoustical Society of America, Vol.134, No.6 (2013), pp. 4670–4680. DOI:10.1121/1.4824843

[4] T. Weisser, J.-P. Groby, O. Dazel, F. Gaultier, E. Deckers, S. Futatsugi, L. Monteiro, *Acoustic Behavior of a Rigidly Backed Poroelastic Layer with Periodic Resonant Inclusions by a Multiple Scattering Approach*, Journal of the Acoustical Society of America, Vol.139, No.2 (2016), pp. 617–629. DOI:10.1121/1.4940669

[5] F. Chevillotte, *Controlling Sound Absorption by an Upstream Resistive Layer*, Applied Acoustics, Vol.73, No.1 (2012), pp. 56–60. DOI:10.1016/j.apacoust.2011.07.005

[6] A. D. Pierce. *Acoustics: An Introduction to Its Physical Principles and Applications. 1989th ed.* Woodbury, Acoustical Society of America, New York (1989).

[7] M. E. Delany, E. N. Bazley, *Acoustical Properties of Fibrous Absorbent Materials*, Applied acoustics, Vol.3, No.2 (1970), pp. 105–116.

[8] Yasushi Miki, *Acoustical Properties of Porous Materials-Modifications of Delany-Bazley Models*, Journal of the Acoustical Society of Japan (E), Vol.11, No.1 (1990), pp. 19–24.

[9] D. L. Johnson, J. Koplik, and R. Dashen, *Theory of Dynamic Permeability and Tortuosity in Fluid-Saturated Porous Media*, Journal of fluid mechanics, Vol.176, No.1 (1987), pp. 379–402.

[10] Y. Champoux and J.-F. Allard, *Dynamic Tortuosity and Bulk Modulus in Air-Saturated Porous Media*, Journal of Applied Physics, Vol.70, No.4 (1991), p. 1975. DOI:10.1063/1.349482

[11] M. A. Biot, *Theory of Propagation of Elastic Waves in a Fluid-Saturated Porous Solid*, Journal of the Acoustical Society of America, Vol.28, No.2 (1956), p. 168. DOI:10.1121/1.1908239

[12] M. A. Biot, D. Willis, *The Elastic Coefficients of the Theory of Consolidation*, Journal of Applied Mechanics, Vol.24 (1957), pp.594-601.

[13] F.-X. Bécot, L. Jaouen, *An Alternative Biot's Formulation for Dissipative Porous Media with Skeleton Deformation*, Journal of the Acoustical Society of America, Vol.134 No.6 (2013), pp. 4801–4807. DOI:10.1121/1.4826175

[14] O. Dazel, B. Brouard, C. Depollier, S. Griffiths, *An Alternative Biot's Displacement Formulation for Porous Materials*, Journal of the Acoustical Society of America, Vol.121, No.6 (2007), pp. 3509-3516. DOI:10.1121/1.2734482

[15] O. Dazel, J.-P. Groby, B. Brouard, C. Potel, *A Stable Method to Model the Acoustic Response of Multilayered Structures*, Journal of Applied Physics, Vol.113, No.8 (2013), p. 083506. DOI:10.1063/1.4790629

[16] L. Jaouen, F.-X. Bécot, *Acoustical Characterization of Perforated Facings*, Journal of the Acoustical Society of America, Vol.129, No.3 (2011), pp. 1400–1406. DOI:10.1121/1.3552887

[17] J.-F. Allard, N. Atalla, *Propagation of Sound in Porous Media: Modelling Sound Absorbing Materials 2nd Ed.*, Hoboken, N.J: Wiley (2009).

A numerical study on the shielding performance of a periodic vibration protection device

L. Godinho[1], C. Albino[1], P. Alves-Costa[2], P. Amado-Mendes[1], A. Pinto[2], D. Soares Jr.[3]
[1]ISISE, Departamento de Engenharia Civil, Universidade de Coimbra
Rua Luís Reis Santos - Pólo II da Universidade
3030-788 Coimbra, Portugal
e-mail: **lgodinho@dec.uc.pt**

[2]Construct-FEUP, University of Porto
Rua Dr. Roberto Frias
4200-465 Porto, Portugal

[3]Structural Engineering Department, Federal University of Juiz de Fora
CEP 36036-330, Juiz de Fora, MG, Brazil

Abstract
The present paper describes a study on the concept of using a periodic buried structure, made of rigid elements (e.g. concrete), disposed with a geometrical arrangement that may allow an efficient filtering of vibrations at specific frequencies. The work makes use of a 3D finite element model, formulated using tetrahedral elements, to perform a set of numerical simulations, assessing the effectiveness of the proposed shielding device. The model simulates a set of elastic inclusions, buried in a homogeneous host soil, in which a propagating wave impinges. The simulation is performed using a time-marching algorithm, allowing an efficient calculation procedure. Time signals are then transformed to the frequency domain, and insertion loss results are calculated at receivers placed at different positions behind the shielding device. The computed results are promising, clearly revealing the existence of band gaps where large attenuation occurs.

1 Introduction

Mitigation of vibrations that can interfere with sensible constructions, human comfort and well-being has been under discussion since the middle of last century when high-speed trains, with speeds above 200 km/h, emerged as regular intercity transport [1–3]. In this scope, transportation infrastructures in urban regions should receive special attention, and this is particularly relevant in the case of railways since the demand for increasing the railway infrastructure capacity in European countries is defined in the roadmap for railway 2050. Indeed, this increase of railway infrastructure capacity will require efficient solutions for vibration mitigation in order to achieve the societal acceptance of this goal.

Existing technical and scientific literature reports a significant number of works related to the mitigation of vibrations induced by railway traffic, with different solutions being proposed and analysed. These solutions can typically be grouped in those acting at the source level, those acting at the receiver, and those acting in the propagation medium. The first group includes the introduction of resilient elements on the track structure, such as under sleeper pads ballast mats or floating slab systems [4,5][1]; in the second group, one can include global base-isolation systems, globally protecting a building [6,7]; the third group includes all solutions that can be introduced within the propagation medium between the source and the receiver in order to change the propagation patterns of elastic waves, as is the case of buried walls, trenches (empty or in-filled) or inertia blocks [3,8,9]. This last group is of significant interest, since it can help to protect groups of buildings or entire sites from traffic induced vibrations, complementing well interventions at the source

level. However, some difficulties are usually identified when dealing with trench solutions, since their efficiency is heavily based on their depth, in particular at low frequencies. As for in-filled tranches, recent studies by Barbosa et al [9] and by Coulier et al [10] show that stiff barriers provide protection mostly due to a wave guiding effect due to the coupling between surface waves propagating in the ground and the bending waves propagating in the barrier. A study by Van Hoorickx et al. [11] analysed the effect of double buried walls, showing that in general an improvement is registered when a second parallel buried wall is added to the system, although the resonances occurring between the two walls may give rise to a decrease in efficiency at some specific frequencies.

A recent trend in acoustic and vibratory protection is related to the introduction of a new paradigm based in the concept of metamaterials, which are, in essence, artificial materials engineered to have properties not directly found in nature. A particular case of such materials is that periodic structures, such as those usually designated as “phononic crystals”, which have the fascinating property of stopping the energy passage at specific frequency bands (band-gaps); some practical applications of these metamaterials can already be found for acoustic shielding as described in [12,13]. The successful studies already developed for acoustic applications indicate that such concepts may also be extended for elastodynamic applications, in the sense of blocking vibrations at specific frequency bands. Some works concerning “seismic” protection by periodic structures can indeed be found in the literature. Kim and Das [14], analysed the effect of a periodic structure in the creation of a shadow zone to seismic waves. Alagoz and Alagoz [15] presented numerical studies concerning the effect of what they called “seismic crystals”, indicating an effective attenuation of seismic waves. Brûle et al [16] reported what is possibly the first evidence of the efficiency of such structures as a shield to seismic waves. More recently, Krödel et al. [17] and Dertimanis et al. [18] have shown that the use of metastructures can reflect acoustic signals with wavelengths well above the characteristic size of the material’s internal structure, opening doors for a huge number of applications where low frequency band gaps are demanded. Preliminary work by the authors has also demonstrated the attenuating properties of arrays of elastic scatterers (see [19]) in a 2.5D scenario, although also identifying possible limitations related to the propagation of bending waves along the scatterers. However, an important finding of all works is that this possible new concept for vibration protection based on buried periodic structures or on metamaterials (see Figure 1) may constitute a powerful future solution.

The present paper follows previous works by the authors in which numerical simulations are used to better understand the propagation of vibrations in the presence of periodic buried structures [19–22]. Here, to help simulate the effect of the inclusion of those periodic structures, an innovative time-marching algorithm supported by the 3D finite element method was used [23].

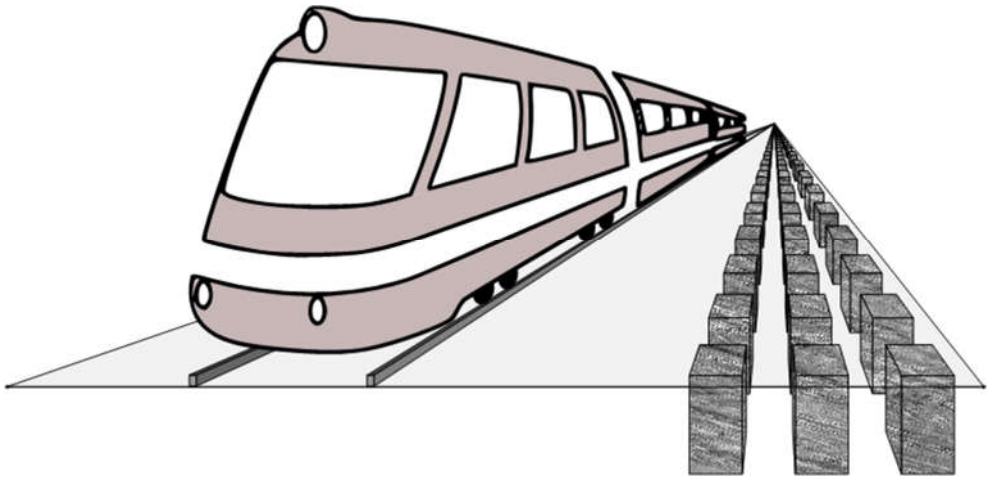


Figure 1: New mitigation devices (inclusions)

2 Numerical model

When a homogeneous halfspace is excited by a mechanical impulse, three important types of waves are generated. The compression waves (P) are those with the highest propagation velocity, defined by equation 1 (E, ν and ρ being the Young's modulus, Poisson's ratio and density). Those are longitudinal waves causing displacements in the medium, parallel to the direction of the wave. The shear waves (S) are transverse waves causing deformation at constant volume in the medium, giving rise to particle movements that are perpendicular to the direction of the propagation. These waves are slower than P waves and their speed is defined by equation 2. The surface waves are the slowest. For its low frequency, long duration and large amplitude these can usually be the most destructive. There are several types of surface wave (such as Rayleigh and Love in the case of layered ground). For the Rayleigh (R) waves, which propagate along the surface and are non dispersive in the case of homogenous ground, their velocity is approximately that defined in equation 3. These waves cause elliptical orbit displacements in the medium particles and their amplitude decreases rapidly with depth.

$$v_P = \sqrt{\frac{E(1-\nu)}{\rho(1+\nu)(1-2\nu)}} \tag{1}$$

$$v_S = \sqrt{\frac{E}{2\rho(1+\nu)}} \tag{2}$$

$$v_R = \frac{0.87+1.12\nu}{1+\nu}\sqrt{\frac{E}{2\rho(1+\nu)}} \tag{3}$$

In the context of the present paper, a numerical model is used to simulate the full wavefield generated in an elastic medium excited by a line load. All the simulations are performed in the time domain, using a time-marching algorithm.

The time-marching algorithm presented here is based on the 3D finite element method and, applied to a dynamic, multidimensional and damped system, can be mathematically defined by equation 4,

$$\mathbf{F}(t) = \mathbf{F}_{\mathrm{I}}(t) + \mathbf{F}_{\mathrm{D}}(t) + \mathbf{F}_{\mathrm{S}}(t) \tag{4}$$

were $\mathbf{F}(t)$ is the applied load, $\mathbf{F}_{\mathrm{I}}(t) = \mathbf{M}\mathbf{U}(t)$ is the inertial force, $\mathbf{F}_{\mathrm{D}}(t) = \mathbf{C}\mathbf{U}(t)$ is the damping force (considering a viscous damping) and $\mathbf{F}_{\mathrm{S}}(t) = \mathbf{K}\mathbf{U}(t)$ is the elastic force. $\mathbf{U}(t)$, $\mathbf{U}(t)$, $\mathbf{U}(t)$ are respectively the acceleration, velocity and displacement vectors dependent on time, t.

The governing equations of the algorithm and the time integration strategy are presented in [23], describing the basic aspects and the main parameters of this novel formulation using finite elements in the time domain. This paper presents only the time marching equations used in this new formulation, which are

$$\mathbf{E}\mathbf{U}^{n+1} = \overset{n+\frac{1}{2}}{\mathbf{F}} + \mathbf{M}\mathbf{U}^n \quad \frac{1}{2}\Delta t\mathbf{C}\mathbf{U}^n \quad \mathbf{K}\left(\Delta t\mathbf{U}^n + \frac{1}{2}\Delta t^2\mathbf{U}^n\right) \tag{5}$$

– the velocity equation – and

$$\mathbf{E}\mathbf{U}^{n+1} = \mathbf{E}\left(\mathbf{U}^n + \frac{1}{2}\Delta t\mathbf{U}^n + \frac{1}{2}\Delta t\mathbf{U}^{n+1}\right) \quad \frac{1}{2}\Delta t^2\mathbf{C}\mathbf{U}^{n+1} \quad \mathbf{K}\left[(\beta b_1 b_2)\Delta t^3\mathbf{U}^n + \left(\frac{1}{16} + \beta b_1\right)\Delta t^3\mathbf{U}^{n+1}\right] \tag{6}$$

– the displacement equation – where $\mathbf{C}$ is the damping matrix, $\mathbf{E} = \mathbf{M} + \frac{1}{2}\Delta t\mathbf{C}$ is the effective matrix, $\mathbf{M}$ and $\mathbf{K}$ stand for the mass and stiffness matrices, respectively; $\mathbf{U}$, $\mathbf{U}$ and $\mathbf{F}$ stand for the displacement, velocity and load vectors, respectively; n and Δt are the time-step number and time-step length, respectively; $\beta = 1$, $b_1 = 8.567 \times 10^{-3}$ and $b_2 = 8.590 \times 10^{-1}$ are the time integration parameters of the new method; $\overset{n+1/2}{\mathbf{F}} = \beta_1\Delta t\mathbf{F}^n + \beta_2\Delta t\mathbf{F}^{n+1}$, with $\beta_1 = \beta_2 = 1/2$, using trapezoidal quadrature rule or $\beta_1 = 1$ and $\beta_2 = 0$, extending the explicit feature of the technique to the load term (see [23] for more details).

The main features of this model, among others, are: the method is based only on single-step displacement-velocity relations; it requires no system of equations to be dealt with; it is second-order accurate. In other words, this model is very effective, being able to provide accurate analyses considering relatively large time steps (thus, also being very efficient). Moreover, since it has high stability limits, it minimizes the main drawback of explicit procedures, allowing time-steps that are usual in accurate implicit analyses, rendering good results at reduced computational costs [23].

3 Numerical results

The strategy used in this article to evaluate the effect of the presence of inclusions on the vibrations registered in receivers, placed in the downstream zone, was to determine the inclusions insertion loss and then compare the results with classical devices, in this case, using buried walls with the same material characteristics of the inclusions.

To determine the inclusions' insertion loss, it was performed a study without any type of mitigating devices and then, a set of three parallelepiped inclusions with quadrangular base. Sets of inclusions with three distinct depths, three distinct widths and two types of materials were studied. Finally, buried walls with the inclusion widths, at the distance of the closest inclusion of the load, with the same three depths and with the same material properties of the inclusions was considered. For all the studies a host medium with density ρ_m = 1700 kg/m^3, Young's modulus E_m = 115.76×10^6 Pa and Poisson's ratio ν_m = 0.33, was considered. These thirty-seven studies, summarized in the Table 1, where the mitigation devices material properties are defined, were performed using the finite element method that integrates the time-marching algorithm described above.

Study	Mitigating devices												
	M1	**I1**	**I2**	**I3**	**I4**	**I5**	**I6**	**W1**	**W2**	**W3**	**W4**	**W5**	**W6**
Type	(no mitigating devices)	3 Inclusions						Wall					
Width [m]		0.2, 0.4 and 0.6											
Depth [m]		1	3	5	1	3	5	1	3	5	1	3	5
Density [kg/m^3]		2100			2700			2100			2700		
Poisson's ratio		0.25			0.2			0.25			0.2		
Young's modulus [Pa]		2.7×10^9			27×10^9			2.7×10^9			27×10^9		

Table 1: Summary of studies carried out

The geometric scheme of the model is shown in Figure 3. Since the propagation domain is infinite it is considered only a slice to model. This slice contains the inclusion set, the loading line and adequate boundary conditions were used to simulate the infinite character of the problem.

Figure 3 shows the 1.2 m wide slice witch was modelled and that is repeated infinitely along one direction (y). In this figure, an absorption layer is shown, 6 m wide, necessary to simulate the effect of an infinite medium in the model. This layer, which has the width of at least one wavelength, is responsible for absorbing all the energy that enters it, avoiding unwanted reflections in the system under study. The system is excited by a Ricker pulse whose source is located 10 m to the right of the system's origin. The mitigation devices are placed 10 m to the right of the excitation point. Here, the mitigation devices composed of a set of three inclusions (along x) spaced 1.2 m between centres, and infinitely repeated along the y axis. Three sets of inclusions are considered, with different depths of (1, 3 and 5) m and for each depth the widths of (0.2, 0.4 and 0.6) m are tested. In addition, two different materials were considered for the inclusions (see Table 1). To analyse the efficiency of these devices, the effect of a buried wall, also placed 10 m from the source of excitation, was also studied. Similarly to the three sets of inclusions, three wall depths and three wall widths were considered with the same materials used in the inclusions. Finally, a set of receivers was placed on the surface, in the total width of the slice, between (25 and 30) m from the source (after the mitigation devices).

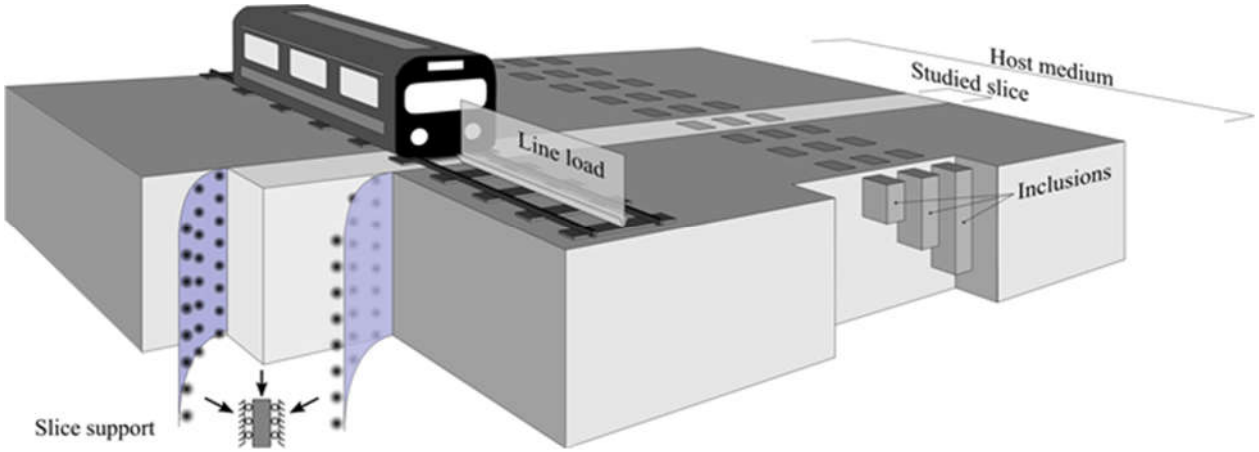


Figure 2: Schematic representation of the model used for the wave propagation analysis

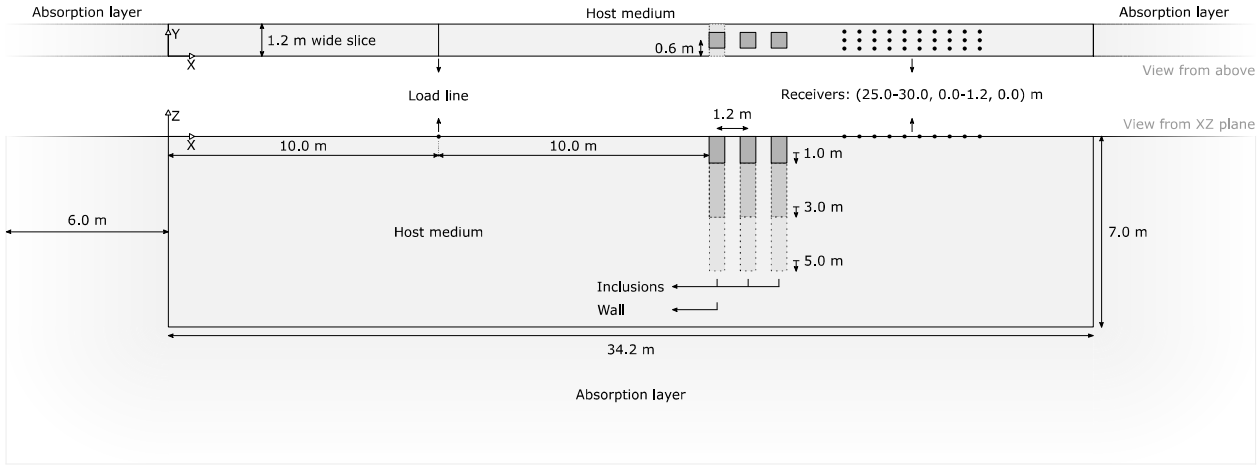


Figure 3: Schematic representation of the slice model used for the wave propagation analysis

Numerical simulations were performed using the above described 3D finite element method in the time domain, formulated using 2 162 160 regular tetrahedral elements whose smallest edges are 0.1 m. This mesh was obtained from the Gmsh program (version 2.16.0). The time marching algorithm described above was recently developed by Soares Jr. [23] and is adopted to render the numerical process more efficient. A damping factor equal to 1% and a propagating Ricker pulse with a central frequency of 60 Hz were considered.

Figure 4 shows the longitudinal amplitudes, over time, registered in a receiver placed at the surface of the medium, 25m from the source, in the alignment of the centre of inclusions. These results are obtained when a set of three lines of inclusions and a buried wall, both with 5 m depth, are considered. These responses are compared to homogeneous medium propagation considering different mitigation devices, with a) a poorer material and b) a stiffer material. Note that the modification in stiffness in the buried wall material does not lead to a significant difference in results. Of the studied cases, this difference is more pronounced in the 3 m depth wall (not shown). Another note that can be made by observing this figure is that the set of poorer inclusions produces practically the same result as the buried stiff wall.

Figure 5 shows snapshots of the wave field, in terms of horizontal displacements, computed in the presence of several sets of 5 m depth inclusions and different widths: a) 0.2 m, b) 0.4 m and c) 0.6 m. Note that the distance between centres of inclusions is 1.2 m in all situations. Here, the interference of the buried devices is clear, with a more complex wave pattern being visible when multiple inclusions are considered. Which becomes particularly evident for later times. These snapshots also evidence that a considerable fraction of

the energy is reflected back by all inclusions, showing the intended shielding effect. Additionally, from these figures surface waves seem to have a strong importance, as expected. It can also be seen that no spurious reflections from the artificial absorption layer seem to occur.

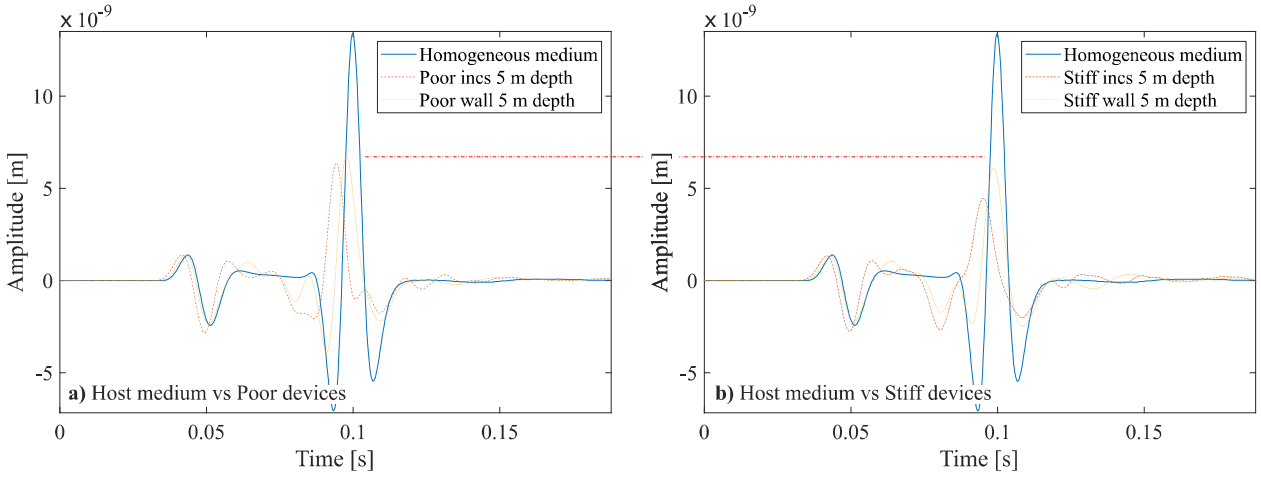


Figure 4: Comparison between mitigation devices types, 5 m depth, and their stiffness: a) poor and b) stiff

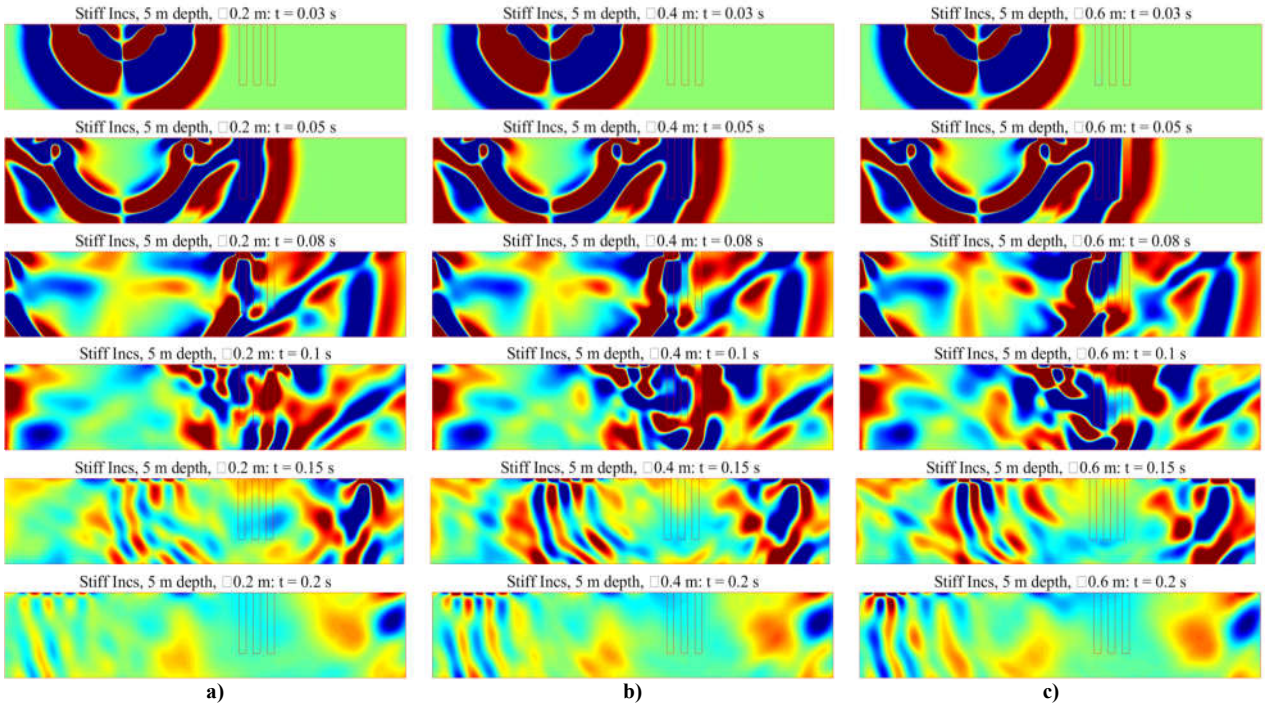


Figure 5: Time evolution of 5 m depth stiff inclusions: (0.2, 0.4, 0.6) m width, a), b) and c) respectively

Figure 6 shows the vibration levels average detected on surface receivers 25 m from the source, beyond the several sets of 5 m depth inclusions with a poorer material (a) and a stiffer material (b). The vibration levels correspond to the various widths of the studied inclusions. These levels are computed in the frequency domain, after application of a Fourier-transform to the time signals computed using the TD-FEM algorithm. To better observe the global behaviour, the response is grouped in frequency bands 16 Hz wide. From this figure, it can be seen that all sets of mitigation measures allow a reduction of the vibration levels, although acting differently throughout the frequency range. It is important to note that different reductions can be

identified between the stiffer and softer inclusions, and clearly the use of a stiffer material to build these inclusions leads to a better overall efficiency of the solution. Indeed, the higher contrast between the propagation medium and the elastic material of the embedded scatterers allows a larger portion of the incident energy to be reflected and thus enhances the visible effect of the structure. An additional point that must be stated is related with the effect of the dimension of the scatterers, which, for both materials, seems to be a dominant factor; for both cases, as larger scatterers ate modelled a reduction in the vibration levels seems to occur, indicating that larger filling fractions of the matrix have a beneficial effect.

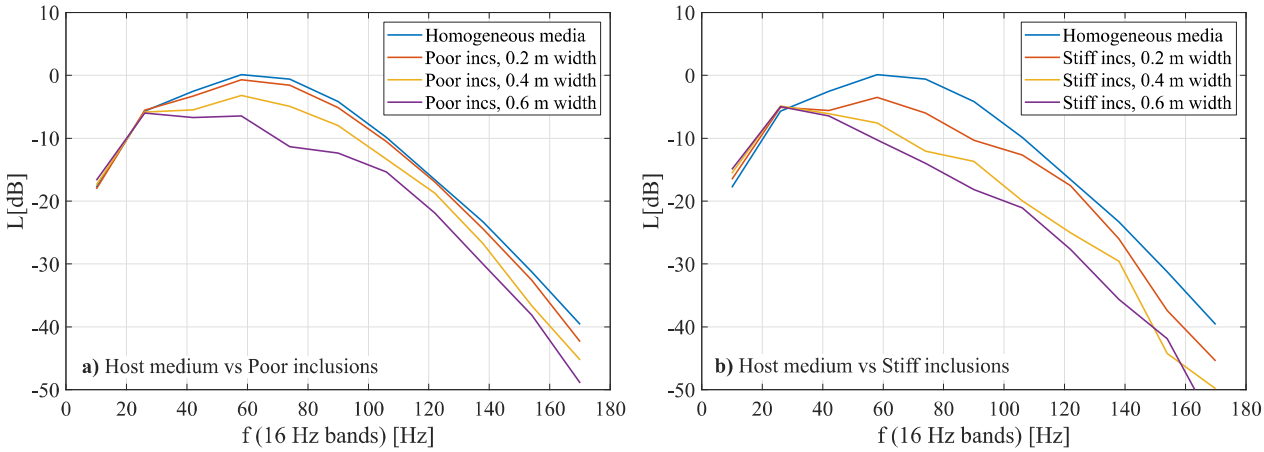


Figure 6: Vibration levels: 5 m depth a) poor and b) Stiff inclusions with several widths

Figure 7 shows the vibration levels average detected in the previously mentioned receivers, now comparing the various depths of inclusions (Figure 7a) and buried walls (Figure 7b), both with the same stiffer material and the same scatterer width (0.6 m). A qualitative comparison between both plots immediately allows identifying an important difference between the behaviour of both types of devices. When the discrete set of periodically spaced inclusions is considered, a larger vibration reduction is registered at intermediate frequencies, while the continuous walls seem to provide better vibration reduction at higher frequencies.

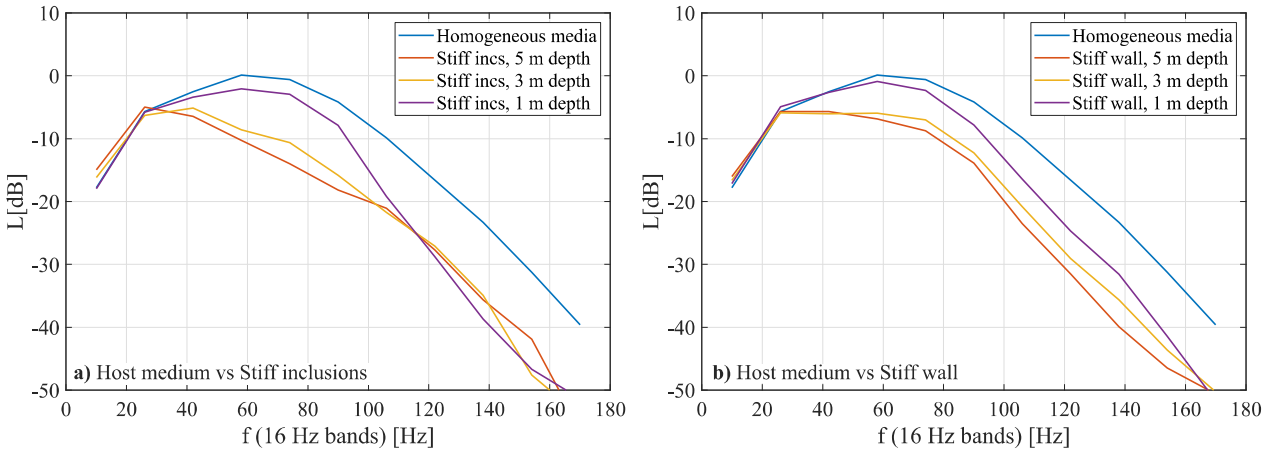


Figure 7: Vibration levels: a) stiff inclusions and b) Stiff wall, both with 0.6 m width

To better understand the results, Figure 8 shows the calculated reduction of vibration estimated for each scenario, for the three depths studied, and for the two types of elastic material composing the mitigation devices. To evaluate the effect of the presence of mitigation devices in the vibrations registered in the

previously mentioned receivers, the reduction is computed in terms of insertion loss, *IL*, that is defined as the difference between the vibration levels obtained in the presence of mitigation devices ($L1$) and the displacement vibration levels obtained without those devices ($L0$). The *IL* is given in dB by the following Equation 7:

$$IL = L0 \quad L1 = 20\log|u_0| \quad 20\log|u_1| \tag{7}$$

According to Equation 7, positive values correspond to a reduction of the displacement vibration levels in the presence of mitigation devices and negative values of the insertion loss stand for losing protective solutions efficiency.

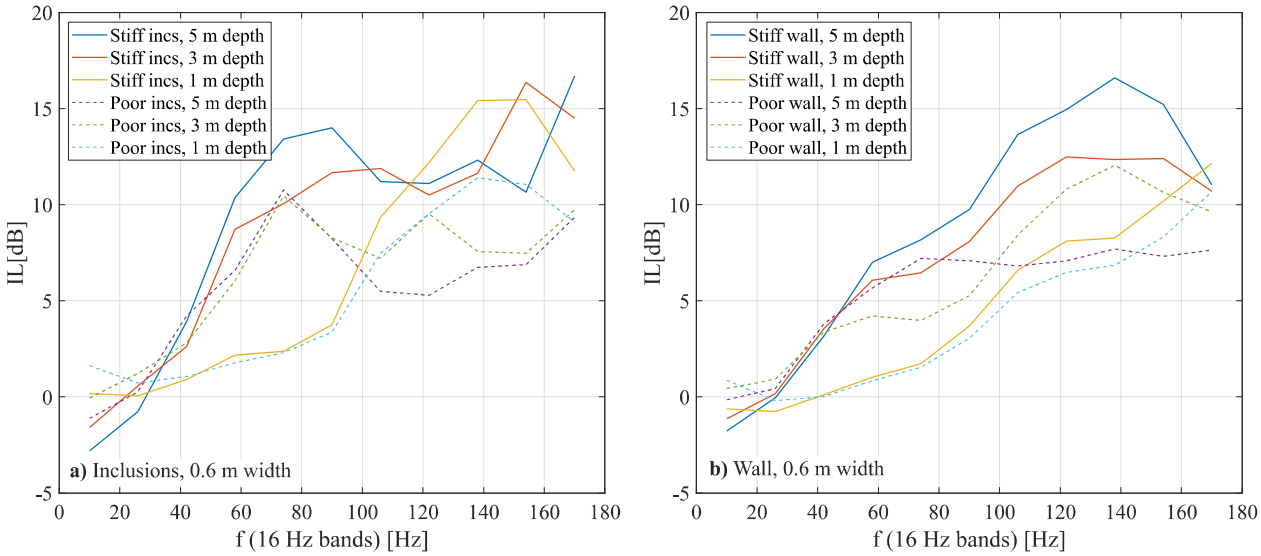


Figure 8: Insertion loss of the mitigation devices of 0.6 m width: a) set of inclusions and b) buried wall

From the results in Figure 8 it becomes clear that the insertion loss tends to increase with the frequency of the excitation load. However, it seems that for the case of the periodic array of inclusions, a), a peak in the insertion loss occurs between 40 and 100 Hz, for which frequencies the efficiency of this solution surpasses that of the traditional buried wall, b). If surface (Rayleigh) waves are considered, which propagate in the soil with an approximate velocity of c = 149 m/s, and taking into account that the inclusions are equally spaced d = 1.2 m, this frequency range seems to match what is usually considered as the band gap frequency (f) in sonic crystals ($f = c/2d$), which should occur around 62 Hz. This finding is quite important, and indicates that the mitigation solution can be tuned depending on the frequency band to mitigate and on the properties of the host medium. It should be noted that this effect is even more pronounced when inclusions (and walls) 5m deep are considered. For this case, a peak is quite evident in the identified frequency interval, for which *IL* values around 0.15 dB higher than those computed for the buried walls of the same material are registered. It should also be said that the more traditional solution of a buried wall seems to reach improved performance for higher frequencies, and to have a broader frequency range for which vibration attenuation is provided. More interestingly, it should be noted that in the case of the poorest material, the 3 m deep wall performs better than 5 m deep wall at higher frequencies.

Regarding the type of material used in the protection devices, it can be seen that, as expected and as previously commented for Figure 6, using a stiffer material leads to a better global performance for all tested depths, with higher values of insertion loss being reached. Indeed, for this case a stronger contrast of properties between the soil and the devices exists, and allows stronger energy reflections to occur.

When comparing the widths of mitigating devices (see Figure 9), it is concluded that they reproduce a more linear behaviour than the depth. That is, considering the cases studied and the bands between (40 and 140) Hz, it can be stated that the greater the width, the greater the mitigating power. If the depth figure (Figure 8) is taken into account, this linearity is not evident.

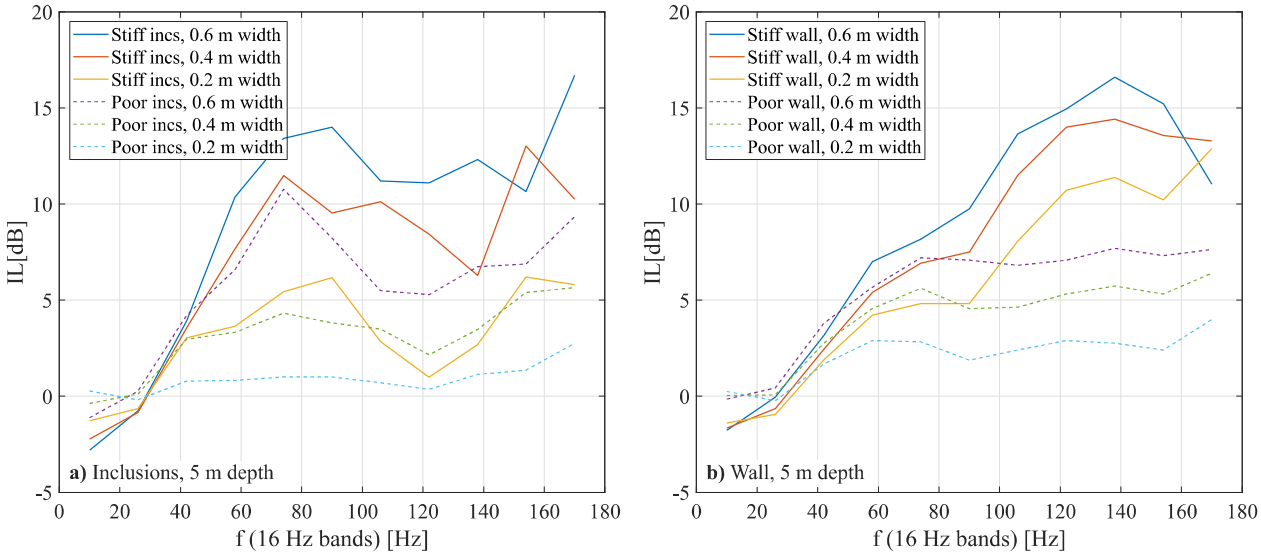


Figure 9: Insertion loss of the mitigation devices of 5 m depth: a) set of inclusions and b) buried wall

Although until now only sets of inclusions with the same depth have been analysed, it may be interesting to verify the behaviour of the periodic device when scatterers with different depths are considered. Some results obtained with inclusions 0.6 m wide and made of the stiffer material, now considering different depths, are presented below. The Figure 10 shows the comparison between the amplitudes, in time domain, resulting from sets of stiff inclusions with 3 (a) and 2 (b) different depths and the original set with a depth of 5 m. From plot (a) it is observed that the set of inclusions with (1, 3 and 5) m depth, positioned in this order relative to the source, leads to less favourable results, while the remaining combinations seem to lead to vibration reductions very close to those observed in the reference case. These conclusions can be confirmed in Figure 11 and Figure 12, which show the average vibration levels and insertion loss, respectively, detected on surface receivers 25 m from the source as mentioned before. From these images it is indeed visible that the configuration with (1, 3 and 5) m deep inclusion is significantly less effective when compared to the set of inclusions in which all of them are 5 m depth. The remaining sets seem to exhibit a better behaviour for frequencies above 90 Hz, although they also seem to be less effective in the region of the band gap above described (62 Hz). Overall, the plotted results seem to indicate that using a configuration with all inclusions 5 m deep still produces the best results.

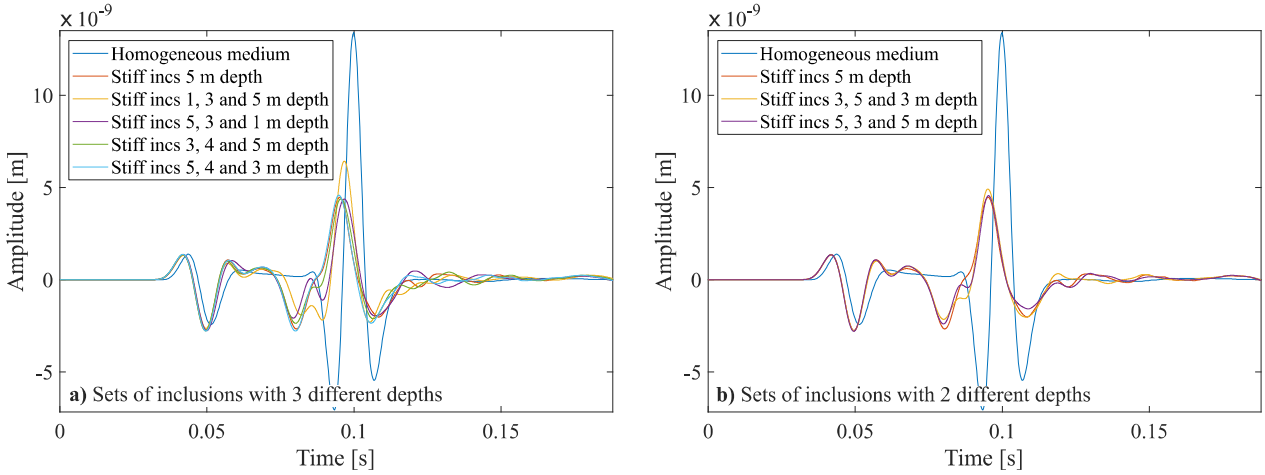


Figure 10: Comparison between set types of 3 inclusion, a) 3 and b) 2 different depths

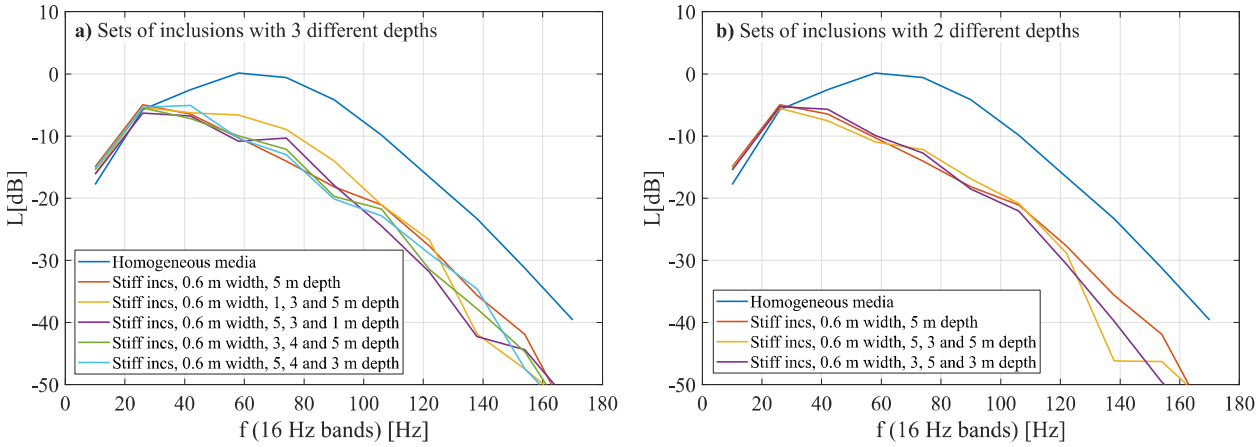


Figure 11: Vibration levels of set types of 3 inclusion, a) 3 and b) 2 different depths

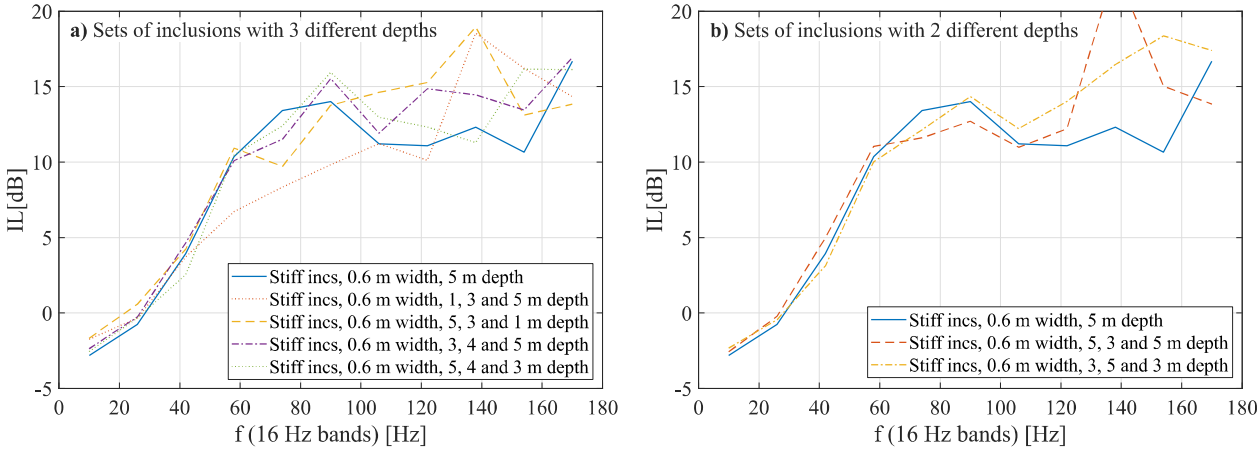


Figure 12: Insertion loss of set types of 3 inclusion, a) 3 and b) 2 different depths

4 Conclusions

This paper has presented and studied the effect of a periodic set of buried inclusions in the propagation of vibrations in a homogeneous soil. A TD-FEM algorithm is used for that purpose, making use of a recently proposed and efficient time marching scheme. Several simulations were performed in order to better understand the attenuation patterns provided by different configurations, varying the depth and width of the scatterers and their material. The results presented are quite promising, and reveal the existence of a specific frequency band for which higher vibration attenuation seems to occur. These band can be related to the effect of multiple interactions between the buried inclusions, as is usually seen in acoustics when analyzing sonic crystals. This indicates that using buried sets of periodically spaced inclusions can constitute an interesting solution for mitigation of vibrations at specific frequency bands, while still ensuring interesting attenuations outside these specific bands.

Acknowledgements

The authors acknowledge the financial support of FCT – Foundation for Science and Technology and COMPETE, through research project PTDC/ECM-COM/1364/2014 (METASHIELD). This work is also financed by FEDER funds through the Competitivity Factors Operational Programme - COMPETE and by national funds through FCT – Foundation for Science and Technology within the scope of the projects

POCI-01-0145-FEDER-007633 (ISISE) and POCI-01-0145-FEDER-007457 (CONSTRUCT). The authors acknowledge the financial support of Regional Operational Programme CENTRO2020 within the scope of the project CENTRO-01-0145-FEDER-000006 (SUSpENsE).

References

[1] I. Croy, M.G. Smith, K.P. Waye, Effects of train noise and vibration on human heart rate during sleep: an experimental study, BMJ Open. (2013). doi:10.1136/bmjopen-2013-002655.

[2] M.G. Smith, I. Croy, M. Ögren, K.P. Waye, On the Influence of Freight Trains on Humans: A Laboratory Investigation of the Impact of Nocturnal Low Frequency Vibration and Noise on Sleep and Heart Rate, PLoS One. 8(2): e558 (2013). doi:10.1371/journal.pone.0055829.

[3] Y.B. Yang, H.H. Hung, Wave Propagation for Train-Induced Vibrations. A Finite/Infinite Element Approach, World Scientific Publishing Co. Pte. Ltd., Singapore, 2009.

[4] P. Alves-Costa, R. Calçada, A.S. Cardoso, Ballast mats for the reduction of railway traffic vibrations. Numerical study, Soil Dyn. Earthq. Eng. 42 (2012) 137–150. doi:https://doi.org/10.1016/j.soildyn.2012.06.014.

[5] E. Bongini, G. Lombaert, S. François, G. Degrande, A parametric study of the impact of mitigation measures on ground borne vibration due to railway traffic, in: G. De Roeck, G. Degrande, G. Lombaert, G. Müller (Eds.), EURODYN 2011, Leuven, 2011: pp. 663–670.

[6] J. Talbot, Base-isolated buildings: Towards performancebased design, Proc. Inst. Civ. Eng. Struct. Build. 168(8) (2016) 574–582.

[7] J. Talbot, H. Hunt, On the Performance of Base-isolated Buildings and Isolation of Buildings from Rail-tunnel Vibration: a Review, in: B. Gibbs, J. Goodchild, C. Hopkins, D. Oldham (Eds.), Collect. Pap. Build. Acoust. Sound Transm., Multi-science, 2009.

[8] D.J. Thompson, J. Jiang, M.G.R. Toward, M.F.M. Hussein, E. Ntotsios, A. Dijckmans, P. Coulier, G. Lombaert, G. Degrande, Reducing railway-induced ground-borne vibration by using open trenches and soft-filled barriers, Soil Dyn. Earthq. Eng. 88 (2016) 45–59. doi:https://doi.org/10.1016/j.soildyn.2016.05.009.

[9] J. Barbosa, P. Alves-Costa, R. Calçada, Abatement of railway induced vibrations: Numerical comparison of trench solutions, Eng. Anal. Bound. Elem. 55 (2015) 122–139. doi:https://doi.org/10.1016/j.enganabound.2014.11.029.

[10] P. Coulier, S. François, G. Degrande, G. Lombaert, Subgrade stiffening next to the track as a wave impeding barrier for railway induced vibrations, Soil Dyn. Earthq. Eng. 48 (2013) 119–131. doi:https://doi.org/10.1016/j.soildyn.2012.12.009.

[11] C. Van hoorickx, M. Schevenels, G. Lombaert, Double wall barriers for the reduction of ground vibration transmission, Soil Dyn. Earthq. Eng. 97 (2017) 1–13. doi:https://doi.org/10.1016/j.soildyn.2017.02.006.

[12] R. Martínez-Sala, C. Rubio, L.M. García-Raffi, J. V Sánchez-Pérez, E.A. Sánchez-Pérez, J. Llinares, Control of noise by trees arranged like sonic crystals, J. Sound Vib. 291 (2006) 100–106. doi:https://doi.org/10.1016/j.jsv.2005.05.030.

[13] O. Umnova, K. Attenborough, C. Linton, Effects of covering on sound attenuation by periodic arrays of cylinders, J. Acoust. Soc. Am. 119 (2006) 278–284.

[14] S.-H. Kim, M. Das, Artificial Seismic Shadow Zone by Acoustic Metamaterials, Mod. Phys. Lett. B. 27 (2012).

[15] B. Alagoz, S. Alagoz, Towards Earthquake Shields: A Numerical Investigation of Earthquake Shielding with Seismic Crystals, Open J. Acoust. 1 (2011) 63–69.

[16] S. Brûlé, E.H. Javelaud, S. Enoch, S. Guenneau, Experiments on Seismic Metamaterials: Molding

Surface Waves, Phys. Rev. Lett. 112 (2014) 133901.

[17] S. Krödel, N. Thomé, C. Daraio, Wide band-gap seismic metastructures, Extrem. Mech. Lett. 4 (2015) 111–117. doi:https://doi.org/10.1016/j.eml.2015.05.004.

[18] V. K. Dertimanis, I. Antoniadis, E. Chatzi, Feasibility Analysis on the Attenuation of Strong Ground Motions Using Finite Periodic Lattices of Mass-in-Mass Barriers, J. Eng. Mech. 142 (2016) 4016060.

[19] L. Godinho, P. Amado-Mendes, P. Alves-Costa, C. Albino, MFS Analysis Of The Vibration Filtering Effect Of Periodic Structures In Elastic Media, Int. J. Comput. Methods Exp. Meas. 6 (2018) 1108–1119. doi:10.2495/CMEM-V6-N6-1108-1119.

[20] P. Amado-Mendes, L. Godinho, Reduction of Vibrations Transmitted Through the Soil by Multiple Buried Inclusions – Numerical Analysis, in: Z. et al. Dimitrovová (Ed.), 11th Int. Conf. Vib. Probl., Lisboa, 2013.

[21] C. Albino, L. Godinho, D. Dias-da-Costa, P. Amado-Mendes, The MFS as a tool for the numerical analysis of vibration protection devices, in: 22nd Int. Congr. Acoust. (ICA 2016), Buenos Aires, 2016.

[22] A.C. Pinto, P. Alves-Costa, L. Godinho, P. Amado-Mendes, Mitigation of vibrations induced by railway traffic though soil burried inclusions: a numerical study, in: A. Calvo-Manzano, A. Pérez-López (Eds.), 48º Congr. Español Acústica (TECNIACÚSTICA 2017), A Coruña, 2017: pp. 1078–1086.

[23] D. Soares Jr., A novel family of explicit time marching techniques for structural dynamics and wave propagation models, Comput. Methods Appl. Mech. Eng. 311 (2016) 838–855. doi:http://dx.doi.org/10.1016/j.cma.2016.09.021.

Perceptual evaluation of metamaterials as insulation partitions: A listening test within the COST action DENORMS (CA15125)

L. de Ryck [1], J. Cuenca [1], K. Jambrošić [2], C. Glorieux [3], M. Rychtarikova [3,4], V. Romero-Garcia [5], A. Cebrecos [5], N. Jiménez [5,6], J.-P. Groby [5]
[1] Siemens Industry Software NV,
Interleuvenlaan 68, B-3001 Leuven, Belgium
e-mail: **laurent.deryck@siemens.com**

[2] University of Zagreb, Faculty of Electrical Engineering and Computing (FER),
Unska ul. 3, 10000 Zagreb, Croatia

[3] KU Leuven, Laboratory for Soft Matter and Biophysics,
Celestijnenlaan 200D, B-3001 Leuven, Belgium

[4] Slovak University of Technology (STU), Dep. of building construction,
Vazovova 5, 812 43 Bratislava, Slovakia

[5] Laboratoire d'Acoustique de l'Université du Mans (LAUM) UMR CNRS 6613,
Avenue Olivier Messiaen, 72085 LE MANS cedex 9, France

[6] Universidad Politécnica de Valencia (UPV), Instituto de Instrumentación para Imagen Molecular,
Av. dels Tarongers, 14, 46011 València, Spain

Abstract
The need for improving indoor and outdoor acoustic comfort constantly drives the development of novel sound insulation and sound absorption solutions. Optimising their performance becomes reachable today by designing "metamaterials". A pending question is whether the non-uniform spectral characteristics of metamaterials is detrimental to the subjective appreciation of their sound absorption capabilities. By means of a headphone listening test, the present study aims at perceptually comparing the pleasantness from sounds transmitted through five office-like partitions, including classical- and meta- materials. The transmitted sounds were synthesised from partition models and replayed to jurors by pairs for each stimulus. This resulted in a ranking of the test sounds - and thus of the partitions – by order of annoyance. During the recent DENORMS workshop in Leuven (Feb. 6-7, 2018), 35 jurors volunteered for the test. Furthermore, insights are given towards a definition of a quantitative sound quality metric for acoustic material design.

Introduction

Working environments are rich of multiple noise sources causing annoyance/disturbance, while individuals search for comfort and privacy. Using acoustic materials to address such issues is common as these are passive and relatively cost-effective solutions. However, the final appreciation is deeply subjective and this must be accounted for beyond the sole sound reduction properties.

Metamaterials are widely studied in various branches of physics and engineering, especially with regards to electromagnetic [1], acoustical and structural wave propagation [2, 3]. Metamaterials are man-made structures that enhance or take advantage of physical principles not occurring naturally. Examples include negative refraction, super lenses, sub-wavelength resolution, cloaking [1, 3].

One aim of these metamaterials for audible acoustic applications is to increase performance in both absorption and transmission loss; if possible on the widest frequency band [6]. Another goal is to reach such performances without having to design bulky voluminous and expensive objects. A secondary aim is to include aesthetic aspects – or constraints, depending on the point of view – to the new metamaterials in order to include these in urban or indoor, e.g. home or office, environments [4].

A high interest in acoustic metamaterials resides in their tunability in terms of their effective bulk modulus and density (positive and negative), and in their suitability for design optimization. Typical examples are phononic crystals (periodic media with band gaps effect), and metamaterials exhibiting subwavelength-scale structures including for instance networks of resonators, which could be individually tuned [3, 5, 6].

Most of the studies focus on optimising objective markers such as the reflection and transmission coefficients on a large frequency range [5, 6]. However these numbers do not account for the human perception, and its appreciation of sound quality. Psychoacoustic studies could show that loudness is not the only factor for annoyance, disturbance or, conversely, pleasantness and comfort. Other metrics describe multiple aspects building the sound signature, when related to cognition, such as sharpness, roughness, fluctuation strength (both related to signal modulation), tonality, pitch... [10, 11]. In fact, the perceptual comparison of metamaterial insulation/absorption solutions to classical structures is a relatively new topic and the present study aims at contributing to defining the grounds for such a comparison.

One of the main research topics supported by the COST action DENORMS (CA15125) [12] is the understanding and design of metamaterials for sound absorption and insulation. The action encourages international cooperation, which has given rise to a group aiming at including psychoacoustics in models and experimental setups in order to characterise and design such materials. For this preliminary study, perception is at the central point of the test, and the COST action DENORMS provided an opportunity to organise a listening test during its recent workshop "Dedicated manufacturing and experimental techniques for acoustic metamaterials and acoustic treatments" that took place in Leuven in February 6-7th, 2018. The test gathered 35 experts from 17 countries, with a large age range and 20% of women.

The test complements the ongoing RISE project PAPABUILD [13] regarding listening tests and cognitive evaluation of partitions in building and architectural acoustics. In the present test, an office context is chosen in which listeners are sitting in front of an insulation partition. The test procedure consists in pair comparison of sounds from 4 different source signals transmitted through 'virtual' partitions, some being classical partitions (plexiglas, finite height rigid walls), some other being metamaterials (2 variants of a locally resonant sonic crystal [8] and a metamaterial with multiple tuned resonators [6]). The transmitted sounds were synthesised by performing a convolution of loudness-equalized source signals with each panel's transfer function at normal incidence and propagated to a single monaural receiver at the listener's position (facing the wall). The pair comparison criterion was to select the most annoying among two transmitted sounds, e.g. the one that would prevent concentration on the job to be done. The tests were run at the laboratory for Soft Matter and Biophysics of KU Leuven, in their silent room in which 6 parallel listening booths were setup. The listening tests were ran on laptops running LMS Test.Lab Jury Testing software and replayed through equalised Sennheiser HD600 open headphones. Finally, a comparison with objective sound quality metrics is performed in view to extract a number of perceptual features from the metamaterials tested. The end goal is to include such psychoacoustic targets as constraints in metamaterial design for use in everyday spaces.

1 Test scenario and test samples

As the present study aims at predicting the perception of insulation walls that do not exist yet, physical

models are used to synthesise sounds that could be replayed to listeners through headphones. This allows to fully design a virtual listening environment. In the present case, the following constraints are considered:

1. The listener is sitting in an 'infinite' or anechoic room
2. The listener is sitting at 1m facing the partition and 1m above the floor;
3. The response perceived by each ear is identical (monaural sound synthesis);
4. The source signal is convolved with the impulse response of the partition and then propagated identically to each ear, accounting for a generic Head & Torso equalisation. The latter aims at simulating the presence of a sitting person in the sound field;
5. Finally, another equalisation is applied to linearise for the response of the headphones.

To quantify the sound insulation from noise sources to the listener, the partitions from Table 1 are selected for their transmission characteristics. More details are provided in the two next sub-sections.

A	B	C	D	E
3mm Plexiglas	RSC(2)	RSC(4)	RTA	1.5m-high screen

Table 1: The five partitions used in the listening test. 'RSC(n)' stands for 'Resonant Sonic Crystal, with n referring to the number of unit cells in use; and 'RTA' stands for 'Rainbow Trapping Absorber'. These are described in section 1.2.

1.1 Classical samples

In view of comparing the sound transmission through metamaterials with classical sound insulation solutions that have similar advantages in terms of not totally blocking the visual connection between the locations to be acoustically insulated, we have considered a 3mm-thick Plexiglas panel and a 1.5m-high rigid wall, the former type of separation being fully optically transparent, and the latter one only blocking the view for the line of sight below 1.5m, relevant for subjects sitting, e.g. in an office.

For the calculation of the sound insulation of the Plexiglas panel, we assumed perpendicular incidence and neglected the existence of flexural waves. The sound propagation was thus modeled through a 1D 3-layer system air-Plexiglas-air. Table 2 summarises the properties of the plexiglas panel.

E (GPa)	σ	ρ (kg.m^{-3})	d (mm)
3.3	0.37	1190	3

Table 2: Properties of the plexiglas panel, E the Young's modulus, σ the Poisson's ratio, ρ the density and d the sample thickness.

For frequencies in the audio range, with wavelength significantly longer than the panel thickness, the acoustic insulation - or transmission loss TL - follows the mass-law [9]:

$$TL(f) = 10\log_{10}(1 + (m_A \pi f / Z_{\text{Air}})^2) \tag{1}$$

with $m_A = \rho d$ the surface mass density (kg.m^{-2}) and Z_{Air} (Pa.s.m^{-1}) the specific acoustic impedance of air. The impulse response is obtained by inverse discrete Fourier transform of the transmission spectrum, i.e., the inverse of the insulation spectrum, filtered by a 4^{th} order high-pass filter with a characteristic frequency of 10Hz in order to ensure numerical stability for the low frequency transmission.

For the calculation of the sound insulation of the 1.5m wall, we used a 2D finite difference model in 10m$\times$10m domain discretised by a staggered grid of 5000$\times$5000 elements. The 1.5m high panel modeled

was emulated by a infinitely rigid line with a thickness of 1 element, resting on the bottom in the middle of the domain, where the displacement was forced to zero. For the other boundaries we used perfectly matching layers of 20 elements thick. Figure 1 depicts the position of the Gaussian pressure source (radius r=2cm, corresponding with low pass filter effect with cut-off frequency of about c/r=340/0.02=17kHz), the panel, and the receiver.

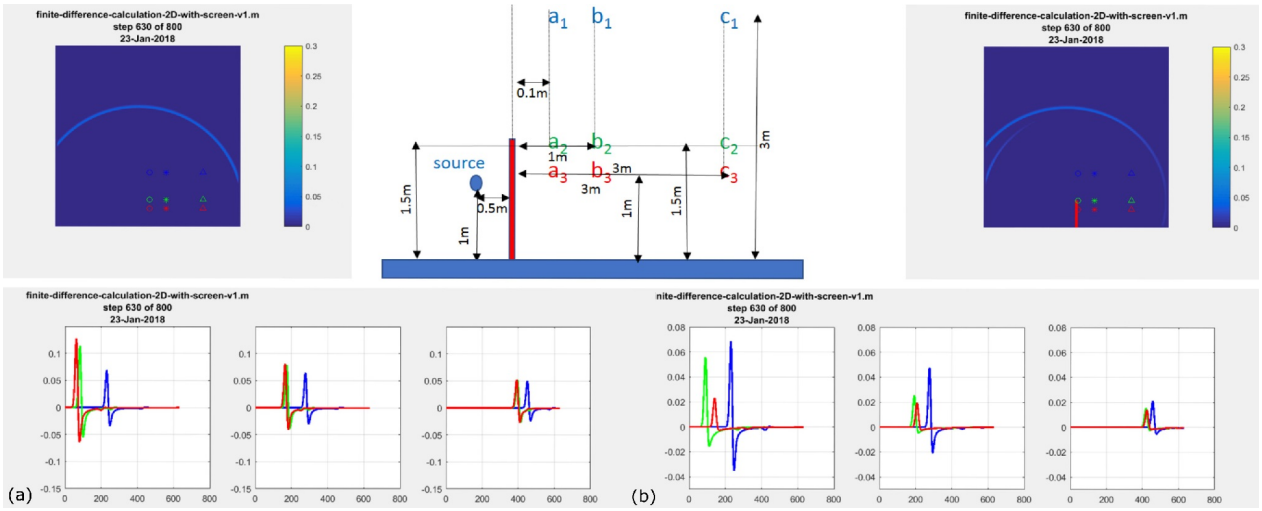


Figure 1: Finite difference propagation model for 1.5m screen. (a) and (b) show a snapshot of a propagating impulsive wave and response waveforms received at different locations behind the panel. The signal at 1m high and 1m from the panel was retained for convolution with the stimuli.

1.2 Metamaterial samples

In this work we have analyzed three samples based on Metamaterials. The first two ones consist of 2D resonant sonic crystals (RSCs) [8] with a broadband transmission loss (TL) in the range of frequencies between 350 Hz and 3220 Hz. The second one is an acoustic metamaterial [6] designed to present broadband quasi-perfect absorption in the range of frequencies between 300 Hz and 1000 Hz.

1.2.1 Resonant Sonic Crystals (RSC)

The 2D RSC is made of square cross-section scatterers arranged on a square lattice and incorporating both quarter-wavelength resonators (QWR) and Helmholtz resonators (HR) as shown in Fig. 2. Viscothermal losses are accounted for both in the QWR and HR resonators by using the Zwikker and Kosten formulae [7]. The unit cell is made of 4 square-rod scatterers placed face to face in the unit cell as shown in Fig. 2. Two differents RSC are studied in this work: One made of 2 unit cells and the second one made of 4 unit cells (see Fig. 2).

The scatterers consist of acoustically rigid square with cross-section side $L = 0.05$ m. The QWRs consist of a slit drilled along one of the scatterer's faces. Each QWR has a width $d_Q = 0.035$ m and depth $l_Q = 0.04$ m. HRs are obtained by inserting an l_n-thick PVC plate on top of the QWRs. The inner slit of each PVC annular plate plays the role of the HR neck. The neck width is $d_n = 0.004$ m and its length is $l_n = 0.004$ m. The width of the HR cavity is $d_c = 0.035$ m its depth $l_c = 0.036$ m.

Numerical simulations are performed using the two geometries shown in Fig. 2. The excitation signal consists in a plane wave impinging the structure from the left side, for frequencies in the range 100-24000 Hz having a frequency step of 10 Hz. The transfer function of both structures is measured at a point placed at a distance $L = 4 \times a_{xy}$, where $2 \times a_{xy}$ is the lattice constant of the metamaterial. The impulse response of

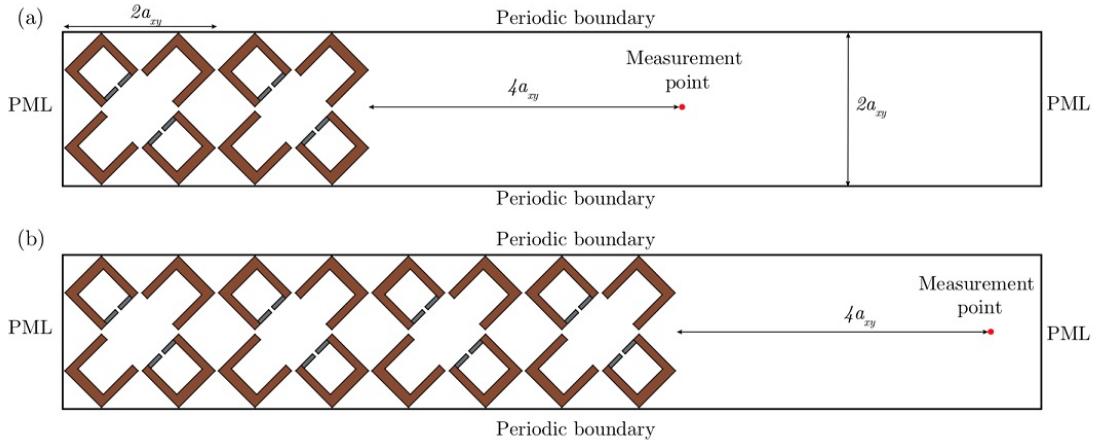


Figure 2: Schematic of the calculation domain including (a) 2 unit cells and (b) 4 unit cells of the metamaterial in the propagation direction. Periodic boundary conditions are considered in the y-axis, which makes the structure infinite in this direction. Anechoic conditions are simulated by means of perfectly matching layers (PML).

the system is obtained from the transfer function by applying the inverse Fourier transform to the recorded signal in the aforementioned point.

The combination of stop bands, due to local resonant scatterers generating multiple coupled resonances at low frequencies, with bandgaps, due to periodicity, is exploited to produce the broadest and largest possible value of the insertion loss (IL). The latter is the ratio of the transmitted energy through the RSC over the transmitted energy without RSC. Numerical predictions show a strong broadband attenuation, the RSC exhibits a large IL covering three and a half octaves from 350 Hz to 5000 Hz.

Figure 3 shows the results obtained for the structure having two (left) and four (right) unit cells. In both cases the dispersion relation of an infinite RSC having the same unit cell as the semi-infinite metamaterials under study is shown in the top of Fig. 3. The transfer function and the calculated impulse response are shown at the bottom of the figure for both structures.

1.2.2 Acoustic Metamaterial

The acoustic metamaterial selected for this listening test was designed to address the problem of perfect and broadband acoustic absorption using deep-subwavelength structures. The panels are composed of monopolar resonators with graded dimensions, namely *rainbow-trapping absorbers* (RTA). The designed panels present broadband, perfect and asymmetric sound absorption, and, due to slow sound, their thickness is reduced to the deep-subwavelength regime.

In particular, the structures are composed of a rigid panel, of thickness L, periodically perforated with series of identical waveguides of variable square cross-section loaded by an array of N Helmholtz resonators (HRs) of different dimensions, as shown in Figs. 4 (a, b). Each waveguide is therefore divided in N segments of length $a^{[n]}$, width $h_1^{[n]}$ and height $h_3^{[n]}$. The HRs are located in the middle of each waveguide section. In particular the *rainbow-trapping absorber* (RTA) was composed of $N = 9$ HRs as shown in Fig. 4 (b). The cost function was $\varepsilon_{\mathrm{RTA}} = \int_{f_1}^{f_N} |R^-|^2 + |T|^2 df$, i.e., to maximize the absorption in a broad frequency bandwidth, that was chosen from $f_1 = 300$ to $f_N = 1000$ Hz. In the case of the RTA the length of the panel was constrained to $L = 11.3$ cm, i.e. a panel 10 times thinner than the wavelength at 300 Hz. The geometrical parameters obtained by the optimization process are given in Table 3.

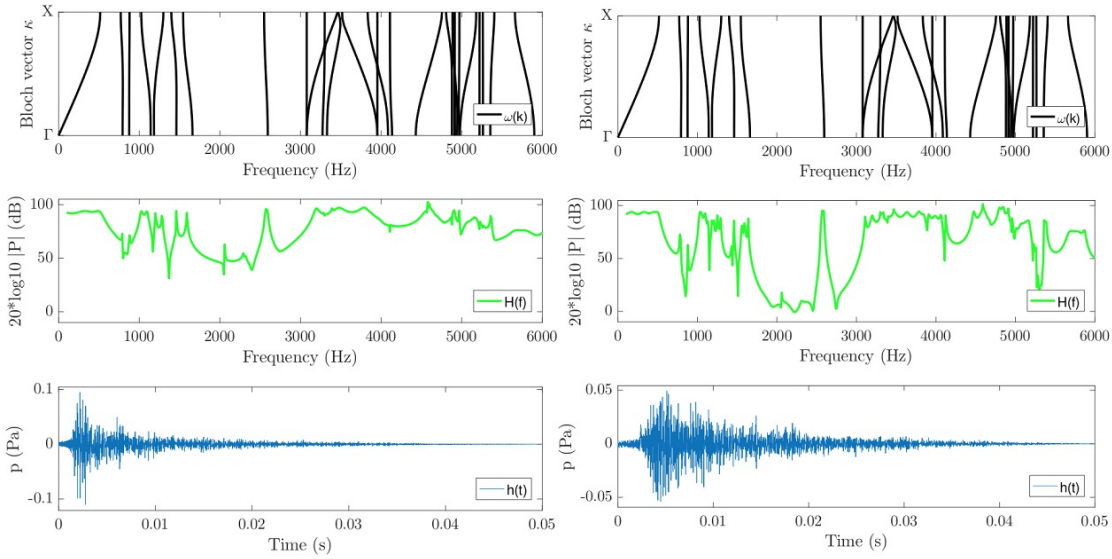


Figure 3: Numerical results for the metamaterials having two (left) and four (right) unit cells. Top: dispersion relation of the structures; middle: transfer functions $H(f)$; bottom: extracted impulse responses h(t).

n	$a^{[n]}$ (mm)	$h_3^{[n]}$ (mm)	$h_1^{[n]}$ (mm)	$l_{\mathbf{n}}^{[n]}$ (mm)	$l_{\mathbf{c}}^{[n]}$ (mm)	$w_{\mathbf{n}}^{[n]}$ (mm)	$w_{\mathbf{c},1}^{[n]}$ (mm)	$w_{\mathbf{c},2}^{[n]}$ (mm)
9	7.9	25.6	14.0	1.1	21.4	1.2	14.0	7.2
8	9.5	24.2	14.0	1.0	22.8	1.2	14.0	9.0
7	11.0	22.8	14.0	1.7	23.6	1.4	14.0	10.6
6	12.6	21.6	14.0	0.7	25.9	1.0	14.0	12.0
5	14.1	20.2	14.0	1.5	26.5	1.2	14.0	13.6
4	15.7	18.8	14.0	1.1	28.3	1.0	14.0	15.2
3	17.3	17.4	14.0	1.6	29.2	1.0	14.0	16.8
2	18.8	16.0	14.0	1.1	31.2	0.8	14.0	18.4
1	6.4	1.0	1.0	3.0	44.7	0.6	14.0	5.6

Table 3: Geometrical parameters for the Rainbow Trapping Absorber (RTA) $(N = 9)$.

2 Listening tests

The listening tests were conducted at the Physics department of KU Leuven on February 6^{th} and 7^{th}, 2018. Six sessions were held, each one hosting up to six volunteers taking the test in parallel.

This section details the design of the test, including the selection of stimuli or source signals, the generation and equalization of the transmitted signals to be replayed, the test type (A-B pair comparisons) and the questions submitted to the jurors.

2.1 Selected stimuli and test signals generation

Stimuli were selected to be meaningful in an office or working environment. For the listening tests to be comparable, each stimulus is scaled to equal loudness. The four selected stimuli ('source' signals) are listed in Table 4 together with their ISO532-1 loudness levels [15]. The pink noise stimulus was added to the list as a reference, and also to evaluate the correlation with the traffic noise test results.

The four equalized stimuli are convolved with the impulse response (transfer function) of each of the five panels from Table 1. Then, monaural signals are synthesized at the listener position, 1m away from the partition. These include a correction to account for a 'virtual' head and torso presence in the sound field. The ISO532-1 loudness levels were calculated for each transmitted signals and added to Table 4. It appears clearly that panel 'D', the Rainbow Trapping Absorber, efficiently reduce the loudness level by approximately 40

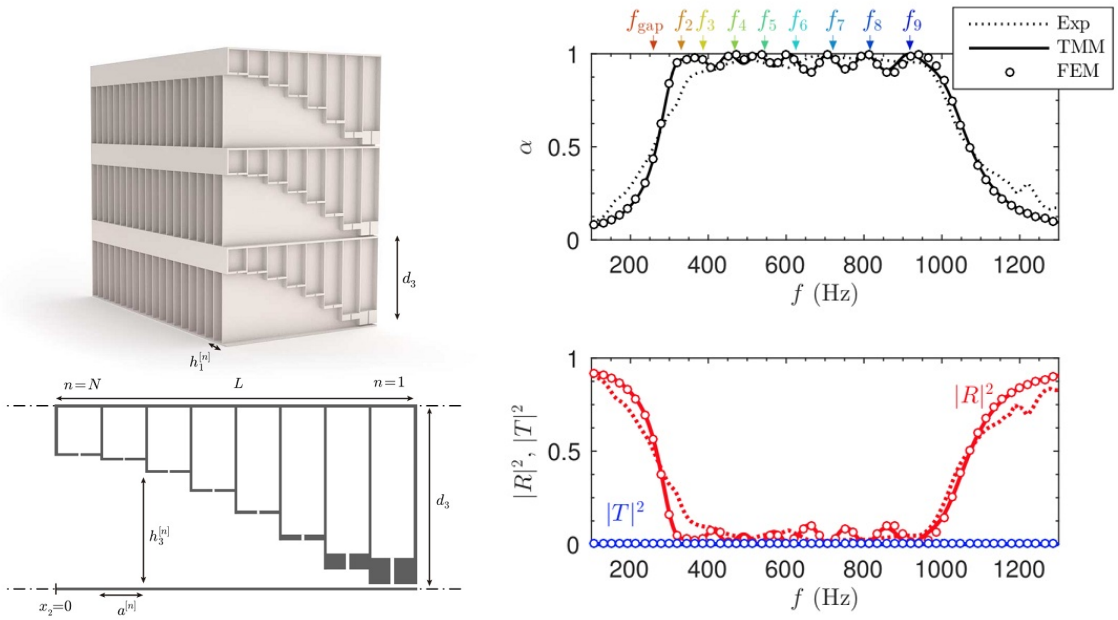


Figure 4: (Left panel) Conceptual view of a Rainbow Trapping Absorber (RTA) with $N = 8$ Helmholtz resonators. Scheme showing the geometrical variables for the RTA panels. (Right panel) Absorption obtained by using the Transfer Matrix Method (continuous line), Finite Elements simulations (circles) and measured experimentally (dotted line). (b) Corresponding reflection (red curves) and transmission (blue curves) coefficients.

phons. Then the plexiglas appears to be effective in loudness reduction, closely followed by the Resonant Sonic Crystal (RSC) with four unit cells, which only show a small improvement compared to the one with two unit cells. Finally, the 1.5m-high rigid screen only reduces the perceived loudness by slightly less than a factor 2 (=10 phons).

	LN (phon)					
	Source	A	B	C	D	E
Pink noise	80.6	62.9	66.2	64.5	42.5	71.3
Nokia phone	80.3	55.4	66.2	64.0	30.1	68.6
Voices (many)	80.4	65.4	65.1	63.7	45.5	72.6
Traffic noise	80.2	65.7	63.8	61.8	44.6	72.4

Table 4: ISO532-1 Loudness levels (LN) [15] of the equalized source signal (emission side of the panel), and transmitted through each of the five partitions from Table 1.

Twenty additional transmitted sounds were synthesized with the difference that these were equalized for loudness. The common loudness level was set to 67 phons. The goal of these extra tests (tagged 'EQ' throughout the paper) is to assess the contributions of other factors to the annoyance perception, such as frequency content and its relation to tonality and sharpness, which are loudness-independent features [10].

2.2 Set up with multiple jurors

Figure 5 shows a photograph of the jury test setup. The setup is based on the Siemens LMS Test.Lab Jury Testing application using a multi-channel output, enabling a total of 6 jurors to participate simultaneously. Calibrated Sennheiser HD 600 open headphones were used. Ideally, jurors need to be as isolated as possible from each other. The listening test took place in a silent room at the Physics department of the KU Leuven. The jurors were positioned in such a way as to avoid eye contact.



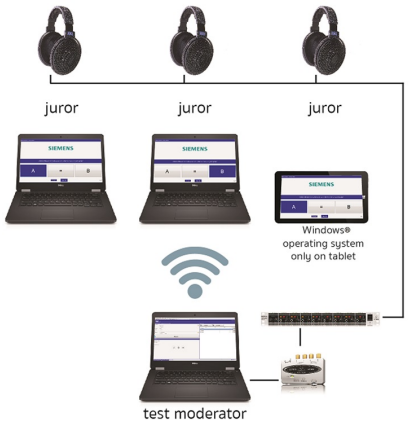


Figure 5: Jury test setup: Multiple jurors can participate via computers connected to a local network. The test moderator machine sends and receives the test questions, and sends accordingly identical audio to all calibrated headphones via a single, independent but synchronized audio chain.

The total duration of the listening test was about 30 minutes. The test sequence contained ten sub-parts: Eight independent tests, see Table 5 between preliminary and feedback questions, as given in Table 6.

Test 1	Test 2	Test 3	Test 4	Test 5	Test 6	Test 7	Test 8
Pink Noise	Voices	Traffic	Phone	Pink noise	Voices	Traffic	Phone
Non-EQ	EQ	EQ	Non-EQ	EQ	Non-EQ	Non-EQ	EQ
1m39s	1m30s	1m50s	1m10s	1m30s	1m30s	1m50s	1m10s

Table 5: Per test, the rows refer to the stimulus; then to the loudness of the transmitted signals, equalized ('EQ') or not to 67 phons; and finally each sub-test duration.

Preliminary questions	Feedback questions
What is your nationality?	Was the test easy or difficult?
What is your age range?	How did you find the test duration?
What is your gender?	Was the test representative?

Table 6: The preliminary questions are meant to build statistical groups, while the final questions are meant to gather direct feedback. A free text feedback was also offered to participants.

Each test consists of 10 pairs of sounds replayed one after the other. The number of pairs derive from the five panels under test, per stimulus and equalization status. The user is presented with three choices, 'A', 'B' or '=', allowing them to select A or B as the most annoying sound, or alternatively to judge them equally annoying. Owing to its simplicity, 'A-B comparison' tests [14] allow for a statistical analysis based on a relative ranking, in this case of the perceived annoyance.

2.3 Raw statistical results

The Siemens LMS Test.Lab Jury testing software produces direct statistics for each test on the answers gathered from all jurors.

The raw output of the tool consists of a distribution of the jurors based on their answers to the preliminary and feedback questions from Table 6. In addition, the concordance versus consistency per juror [14] is correspondingly displayed. Concordance provides a measure of the similarity of the ranking of sounds among jurors, and consistency provides a measure of the extent to which a juror repeats the same ranking of the test sounds. Figure 6 shows two examples of such raw statistical results.

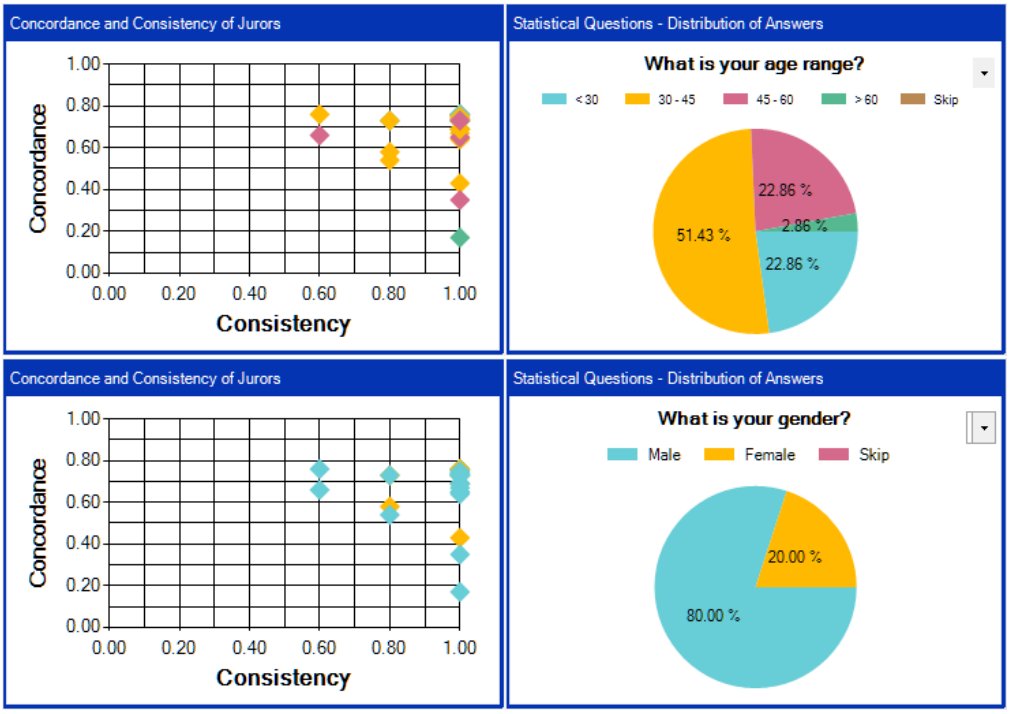


Figure 6: Examples of results from preliminary questions and Test 1 (see Tables 5 and 6). The markers indicate the concordance and consistency per juror, whose colors relate to a statistical group. The greater the consistency and concordance, the more reliable the test result is.

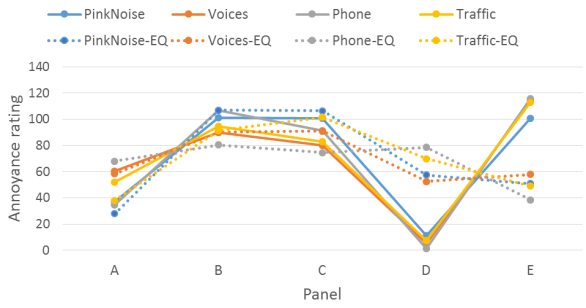
The most reliable results are those with both concordance and consistency scoring high. It is therefore possible to apply a filter removing outliers from the further statistical study based on both criteria. It follows that results from Figure 6 are reliable with few outliers with lower concordance. It is worth noting that outliers with poor concordance but high consistency are valuable as these represent listeners with very different perception than the rest of the jurors.

Results after performing this same analysis on the eight tests (see Table 5) are gathered on Figure 7. Figures 7a and 7b show the annoyance ratings from all tests, respectively without and with filtering. The latter focuses on answers with consistency greater than 80% and concordance greater than 50%. The minimum amount of jurors in all filtered cases was 11 among the total of 35 participants.

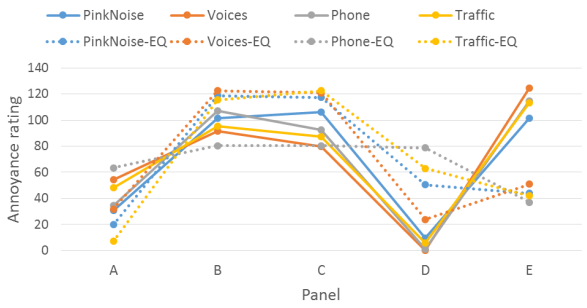
A low concordance can be observed for all equalized tests (tagged 'EQ'), and especially for the voices and phone stimuli. In fact, Figure 7c clearly shows that the concordance for the equalized phone sound is low, whether it is filtered for high consistency or not. However, for the other equalized cases showing a typical drop of concordance, the filtering among jurors led to greater concordance scores, therefore usable for further analysis.

Another result of interest is the weighted average of the annoyance ratings through all stimuli except for the unreliable phone sound, on Figure 7d. The weights apply to the filtered results to normalize the scores as if all 35 jurors were kept. This allows to compare filtered with non-filtered results. It is striking that for non-equalized test sounds, both filtered and non-filtered annoyance scores are almost identical. Indeed, as Figure 7c shows, concordances are high, as are consistencies. This allows to conclude that the corresponding annoyance rankings are highly reliable. With the phone stimulus excluded, the filtered and non-filtered results for equalized sounds show greater uncertainties, while the main ranking is kept for the five panels under test.

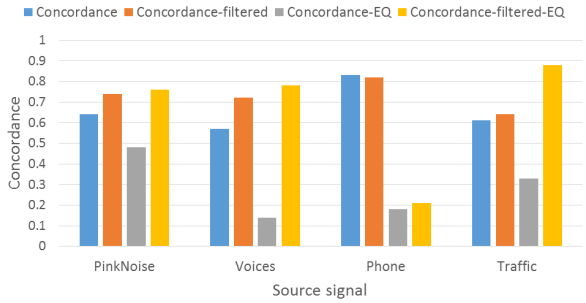
A final conclusion from Figure 7d is that the panels 'D' and 'E', respectively the Rainbow Trapping Absorber and the 1.5m high rigid screen, are highly affected by the equalization of the transmitted test sounds, inverting their ranking in terms of annoyance rating. Moreover, as summarized in Table 7, the classical partitions are



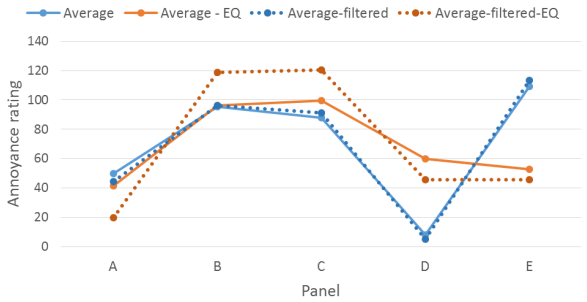
(a) Annoyance ratings including all 35 jurors.



(b) Annoyance ratings limited to highly consistent jurors.



(c) Concordance between all jurors (blue and gray bars); and within the subset (orange and yellow bars).



(d) Weighted average of the annoyance ratings (without the phone stimulus).

Figure 7: Statistical results from the listening test. In each figure, 'EQ' means that the transmitted signals have equalized loudness. The 'filtered' refer to subsets of jurors exhibiting a consistency greater than 80% and a concordance greater than 50% - except for the 'Phone' ring stimulus, for which concordance barely exceeds 20%. It clearly appears that with and without equalization, annoyance ratings remain similar for panels A, B and C, while panels D and E are highly impacted by loudness perception.

	A	B	C	D	E
Non-equalized	4	2	3	5	1
Equalized	5	2	1	3	4

Table 7: Ranking per order of annoyance of the five panels (1 representing the greatest disturbance). For the equalized sounds, panels 'D' and 'E' become ex-aequo after filtering jurors' answers (see Figure 7d).

the preferred ones when equalization of the transmitted sounds is applied. This gives a hint that there exist other sources of annoyance for the metamaterials. In most of the feedback, the frequency coloration (strong filtering induced by the severe sound reduction) was mentioned. This coloration is indeed strongly amplified in the equalized tests. Other sound quality metrics are needed to evaluate the annoyance based on frequency content in parallel to level perception alone.

3 Sound quality analysis and discussion

The responses to the listening tests, with their repeatable ratings and clear rankings of annoyance, call for the usual correlation study with objective sound quality metrics. These were defined throughout years of psychoacoustic research [10].

The starting point for further analysis is usually to compare the averaged spectra from the transmitted sounds with the ones from the source signals. This study is no exception and the A-weighted spectra for each stimulus are presented on Figure 8. The noticeable features are:

1. Very similar spectral features between pink noise and traffic noise, also in terms of levels;
2. Spectra from Resonant Sonic Crystals (RSC) and Rainbow Trapping Absorber (RTA) show peaks that could appear tonal, as well as a level increase at higher frequencies, which could be linked to sharpness;
3. The phone sound is definitely tonal, with largest components around 4kHz, a frequency the human ear is very sensitive to;
4. While the RTA shows an effective level decrease throughout the frequency range, the two RSC variants display a complex spectra with still a relatively high and constant averaged level.

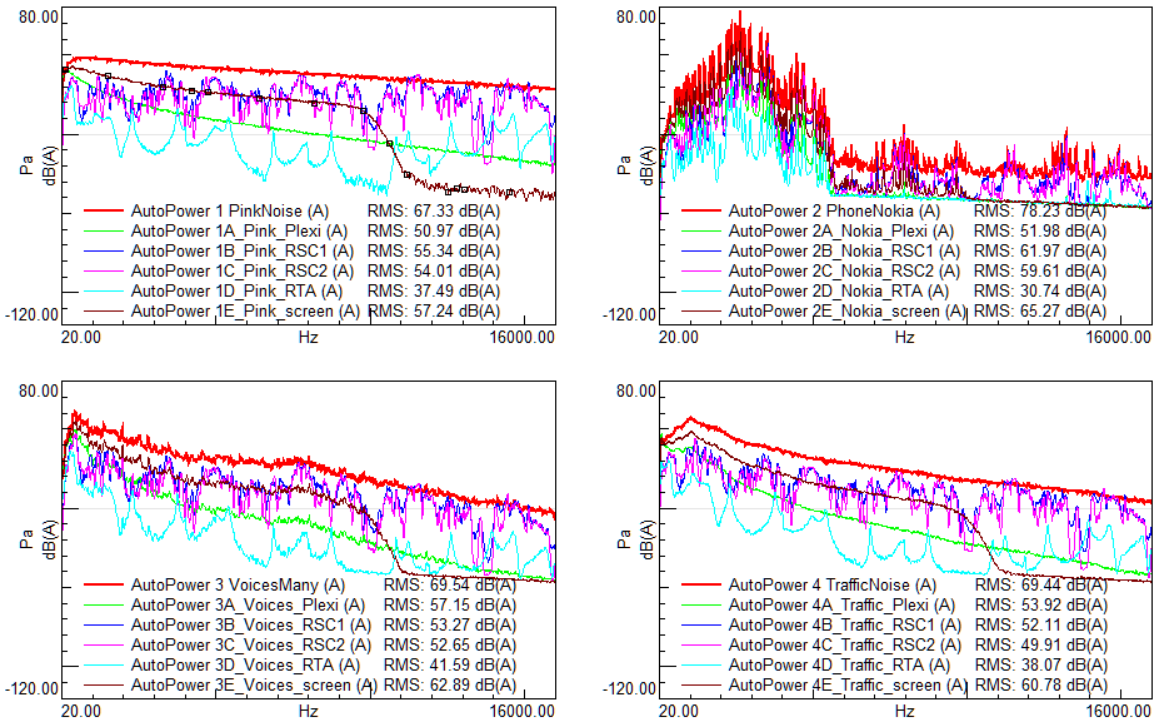


Figure 8: A-weighted spectra for each of the four stimuli (Pink noise, phone, voices and traffic noise). The references without partitions are the red spectra.

It is still difficult from spectra only to extract values that could be compared with the jury testing results. These give hints on what to apply as sound quality metrics, in which frequency range, etc. For instance, from time signals and spectra, tonal peaks appear as well as higher frequency content. Therefore, we target mostly tonal and speech metrics as well as sharpness as main metrics.

Regarding the features of the sounds and the test context, we focused on level, tonal and speech metrics, such as ISO532-1 loudness N (perceived sound level) [15], DIN45692 sharpness S (a normalized weighted loudness as a feature for annoyance) [16], articulation index AI (intelligibility of speakers towards an audience), and prominence ratio PR (quantifying the emergence of tonal components within critical bands) [17].

3.1 Sound quality metrics

Sound quality metrics are here presented, and calculated altogether in Siemens LMS Testlab software. For each metric, single values are extracted. Typical ones of greater use are linear averages, maxima and 5^{th} to 95^{th} percentiles.

For each source signal and partition, Table 8 groups the relative gains of each metric with respect to their references, i.e. the corresponding metrics values without partitions. For instance, it appears clearly that the RTA is the best material for loudness reduction; that the screen improves only slightly the intelligibility (AI); and that the three metamaterials induce a noticeable increase of sharpness (related to annoyance, thus negative), prominence ratios (associated with unpleasantness, tonality, negative as well), and articulation index (positive impact).

source	material	N gain (%)	S gain (%)	AI gain (%)	PR gain (%)
PinkNoise	Plexiglas	-66.88	-56.57	209.17	-21.19
PinkNoise	RSC(2)	-60.91	29.80	158.29	177.35
PinkNoise	RSC(4)	-64.90	31.15	173.56	293.21
PinkNoise	RTA	-89.50	-45.63	222.01	507.05
PinkNoise	screen	-44.85	-29.50	105.52	-2.52
Phone	Plexiglas	-81.24	-11.55	71.01	-0.89
Phone	RSC(2)	-64.89	8.41	40.28	4.85
Phone	RSC(4)	-69.67	10.00	46.94	9.37
Phone	RTA	-96.86	-7.32	96.84	-7.89
Phone	screen	-55.90	-6.78	32.10	-1.64
Voices	Plexiglas	-60.87	-48.76	182.89	-0.08
Voices	RSC(2)	-64.59	15.69	164.88	23.08
Voices	RSC(4)	-67.84	13.91	178.26	41.26
Voices	RTA	-88.36	-55.01	211.32	67.43
Voices	screen	-39.14	-25.48	106.63	0.91
Traffic	Plexiglas	-59.50	-51.59	210.86	-11.56
Traffic	RSC(2)	-65.44	18.08	179.14	39.00
Traffic	RSC(4)	-69.43	18.74	196.74	104.60
Traffic	RTA	-88.21	-53.19	240.24	175.11
Traffic	screen	-39.24	-26.03	115.15	-7.83

Table 8: Relative gains between the transmitted sounds and the source signals. Orange and red cells indicate moderate and noticeable deviations in directions opposite to targets. The three metamaterials impact negatively sharpness S and prominence ratio PR, assuming these should be as low as possible in an office environment. Finally N stands for Loudness and AI for Articulation Index.

A similar analysis can be performed on the equalized transmitted sounds, yielding similar results for the selected subsets of jurors, and loudness excluded. A side note is that for the phone stimulus, the AI only slightly improves. This can be interpreted as a desired feature since the aim of a phone ring is to trigger attention!

These results clearly show that sharpness and tonal metrics are key factors to account for in designing metamaterials for insulation partitions, and that their relationships toward these metrics are opposite to the ones of classical partitions.

3.2 Correlation, material design and discussion

The ultimate goal of this work is to establish correlations between material properties and perceptual metrics. Based on Table 8, the focus falls upon sharpness S, articulation index AI and prominence ratio PR.

To discard as much as possible the impact of loudness on subjective scores, the equalized results are selected, using the subset of jurors showing sufficient consistency and concordance. Figure 9 show that indeed for sharpness and prominence ratio, these tests give the best correlations. The correlation is logarithmic for prominence ratio because it is expressed in decibels.

For sharpness, the phone stimulus was indeed found to be a clear outlier, as concluded from the preliminary tests. In figure 9, it may be observed that the traffic results are also outliers despite its similarity with the pink noise stimulus. This conclusion poses the risk that in order to improve the linear regression, the amount of points is reduced. Reassuringly nevertheless, with and without the traffic results, the linear regressions are almost identical.

For the prominence ratio (PR), the correlation is limited to the three metamaterials, without the phone stimulus, which is too tonal in itself to describe an intrinsic feature of the panels. This was necessary as table 8 shows a specific trend in PR restricted to these materials.

For articulation index and loudness, the non-equalized test sounds must be used as these are level-dependent metrics. Results with and without the filtering of poorly consistent and/or concordant jurors can be compared. In both tests, it appears that the filtering of jurors has a low impact. Indeed, non-equalized test results show high consistency and concordance, with only a few outliers. For the articulation index, Figure 9 shows a good correlation for every stimumus, including that of the phone. Only the 1.5m high screen shows really off results, which could be imputed to the nearly unaltered broadband spectrum, except in level. Indeed metamaterials affect narrower frequency bands on which the articulation index calculation is based on.

For loudness, only the metamaterials are meaningful as the level reduction is a key feature of their design. This reduces drastically the number of points on which to perform the linear regression, but this gives a trend, found almost identical with and without juror filtering.

These trends in correlation need to be manipulated with care. First, the test accuracy must be assessed; then, the test data must be grouped in meaningful bundles (metamaterials together, level-dependent or not metrics...) on which a simple psychoacoustic model could be defined. Stability and reliability of these trends must be evaluated by testing under- and over-filtering. This is the present ongoing stage in this research, which aims at finding the best psychoacoustic model valuable for the different material characteristics under different stimuli by means of an optimization procedure. The psychoacoustic model would be able to rank the most probable preference for materials and stimuli similar to that obtained with human jurors.

4 Conclusion

The present jury testing activity within the COST action DENORMS (CA15125) is a preliminary study. The starting point was to compare how listeners (here mostly experts) would rank these new materials against classical partitions as used today.

The results is somehow surprising, the plexiglas panel performing better than the two variants of the resonant sonic crystals. The rainbow trapping absorber shows good scores due to an efficient broadband sound reduction, which also impacts positively the speech intelligibility, measured here with the articulation index. In order to understand other characteristics of such metamaterials, the tests were repeated with equalized transmitted sounds. These show that all metamaterials displayed an increase of sharpness and tonality induced by a severe alteration of the 'usual' sound spectra. This coloration was perceived as an annoyance factor by some jurors, thus reversing the preference ranking to the more classical partitions.

Both equalized and non-equalized tests were also useful to extract independent trends from sound quality metrics through correlation analysis; some common to all insulation panels (sharpness, articulation index), some specific to metamaterials (prominence ratio, loudness).

Future work will partly consist in building psychoacoustic models of such structured materials. These models could be included in upfront material design as constraints to reach known targets, e.g. privacy in an office, speech intelligibility in an auditorium, level reduction in outdoor environments such as streets or stations, while keeping key features so that safety constraints are guaranteed. The challenge therein is to get enough reliable subjective tests scores to optimally converge to such models.

Further research efforts in this field could also be concentrated on correlating sound quality metrics to the inner (micro)structure of the materials. This would allow to obtain an optimal set of design parameters such

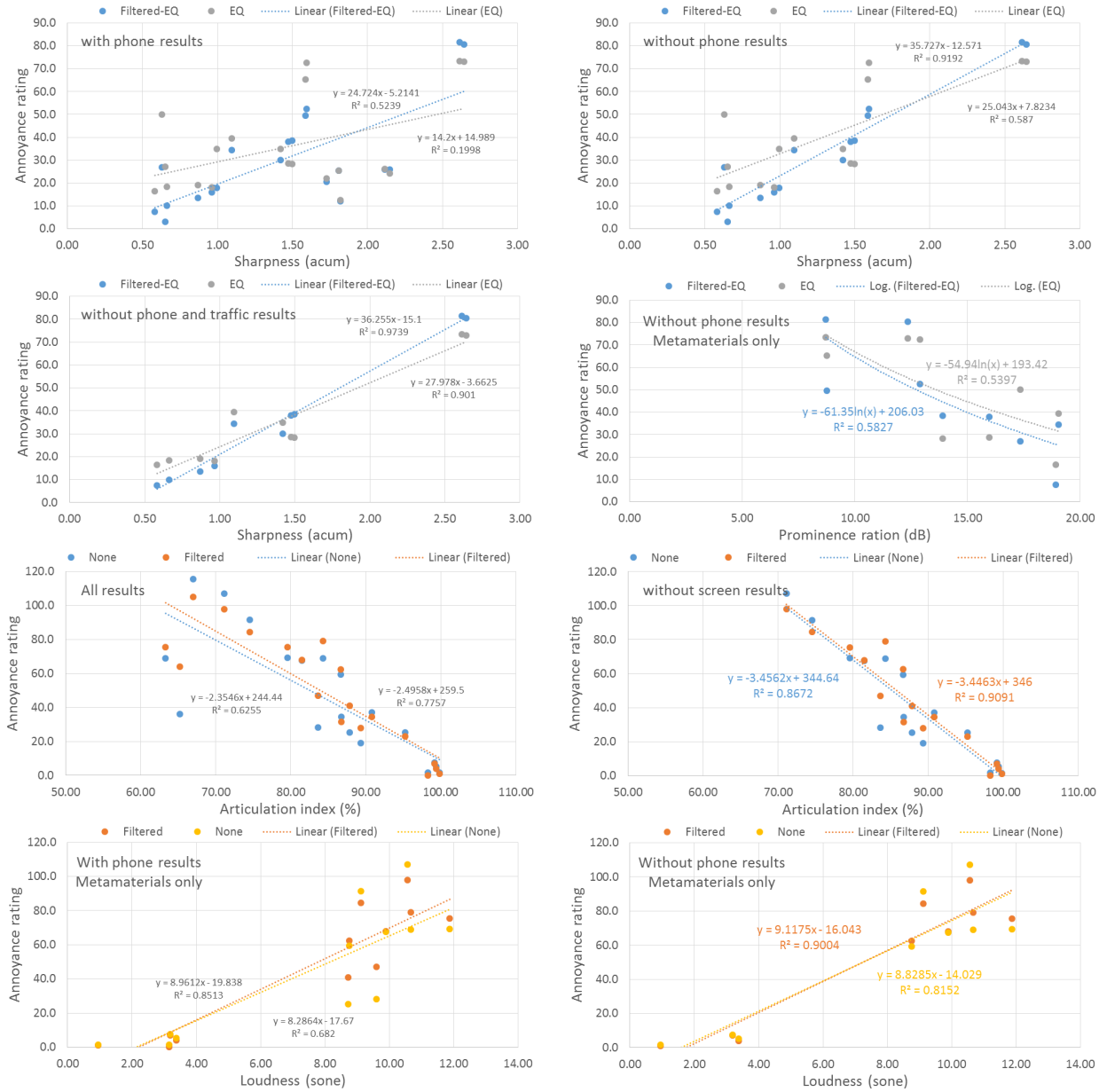


Figure 9: Correlations between calculated sound quality metrics and subjective annoyance ratings from the listening test. As expected, sharpness and prominence ratio give the best correlations from the equalized tests. Articulation index and loudness are level-dependent and therefore correlate better with the results from non-equalized test sounds. 'None' means no equalisation and no filtering.

as the geometry of the unit cell of a sonic crystal, thus allowing to reach a target sharpness value together with a target loudness reduction in transmission.

Acknowledgments

This article is based upon work from COST Action DENORMS CA15125, supported by COST (European Cooperation in Science and Technology) [The authors would like to thank for their support before and during the listening tests Prof. Nicolas Dauchez, Dr. Nicolas Côté, Agnieszka Mroz, Dr. Claudio Colangeli, Dr. Giampiero Accardo and Mansour Alkmim. Lastly, the authors would like to thank the 35 volunteers during the DENORMS workshop in Leuven in February 2018 for their participation to the test and for their valuable

comments and suggestions.

References

[1] Shamonina E. and Solymar L.; Metamaterials: How the subject started; *Metamaterials* **1** 12-18 (2007);

[2] Haberman M. R. and Guild M. D.; Acoustic metamaterials, *Physics Today* **69**, 6:42 (2016);

[3] Craster R. V. and Guenneau S. (eds); Acoustic metamaterials: Negative refraction, imaging, lensing and cloaking, *Springer Series in Materials Science 166* (2013);

[4] Martínez-Sala R., Sancho J., Sánchez J. V., Gómez V., Llinares J. and Meseguer F.; Sound attenuation by sculpture, *Nature* **378**, 241 (1995);

[5] Yang M. and Sheng P.; Sound Absorption Structures: From Porous Media to Acoustic Metamaterials, *Annual Review of Materials Research* **47**, 83-114 (2017).

[6] Jiménez N., Romero-García V., Pagneux V. and Groby J.-P.; Rainbow-trapping absorbers: Broadband, perfect and asymmetric sound absorption by subwavelength panels for transmission problems, *Scientific Reports*, 7:13595, 2017;

[7] Zwikker C. and Kosten C. W.; Sound Absorbing Materials, *Elsevier Publishing Company Inc* (1949).

[8] Lardeau A., Groby J.-P. and Romero-García V.; Broadband transmission loss using 3D locally resonant sonic crystals, *Crystals*, **6**, 51-62 (2016).

[9] Bies D.A. and Hansen C.H.; Engineering noise control: Theory and Practice, Chapter 8: Partitions, Enclosures and Barriers, *CRC press*, 3^{rd} edition (2003).

[10] Fastl, H. and Zwicker, E. *Psychoacoustics: Facts and models*. 3rd edition, Springer-Verlag Berlin Heidelberg, 2007.

[11] Ellermeier W., Zeitler A. and Fastl H.; Predicting annoyance judgments from psychoacoustic metrics: Identifiable versus neutralized sounds, *Proceedings Internoise 2004*, Prague (2004).

[12] Designs for Noise Reducing Materials and Structures (DENORMS), COST Action CA15125, European Cooperation in Science and Technology (COST),

[13] H2020-MSCA-RISE-2015 project 690970 PAPABUILD (*Advanced **P**hysical-**A**coustic and **P**sycho-**A**coustic diagnostic methods for innovation in **BUILD**ing acoustics*; ongoing project.

[14] Sound Quality Jury Testing, *Siemens PLM community wiki pages on Testing knowledge*, last viewed on 06/17/2018.

[15] ISO532-1:2017. Acoustics – Methods for calculating loudness – Part 1: Zwicker method

[16] DIN 45692:2009-08. Messtechnische Simulation der Hörempfindung Schärfe (*Measurement technique for the simulation of the auditory sensation of sharpness*).

[17] ECMA-74: Measurement of Airborne Noise emitted by Information Technology and Telecommunications Equipment; Annex D: Identification and evaluation of prominent discrete tones, *ECMA international, Geneva*, 14^{th} edition (2017).

A combined design-manufacturing-testing investigation of micro- to macro-scale tailoring of open poroelastic materials based on perturbed Kelvin cell micro-geometries.

L. Dowling[1], **H. Mao**[2], **L. Flanagan**[1], **J. Kennedy**[1], **J. Cuenca**[2], **H. Rice**[1], **D. Trimble**[1], **P. Göransson**[2]
[1] Trinity College Dublin, Department of Mechanical engineering,

[2] KTH Royal Institute of Technology, Aeronautical & Vehicle engineering,
100 44 Stockholm, Sweden,
e-mail: **pege@kth.se**

Abstract
The properties of open-cell porous materials for acoustic applications are known to be influenced by the micro-structure and micro-geometry of the material, possibly inducing anisotropy in the macroscopic properties of the material. This has obviously repercussions on the modelling of the elasto-acoustic behaviour of such materials. With the rapidly increasing quality and resolution of the additive manufacturing capabilities, some of these questions can now be studied in some more detail and under controlled conditions. The main contributions of this paper are to discuss a jointly pursued complete design-to-test of a Kelvin model based cell micro-structure. From a given micro-structure, the thickness of struts, the aspect ratio of the cell, the stiffness controlled by the joints between struts, etc., the macro-scale properties required for modelling the elasto-acoustic behaviour will be deduced from a combination of numerical simulations and inverse estimation techniques.

1 Introduction

The final objective of the current work is to design an anisotropic homogenised elastic constitutive material model on a macro level. We base our methods on previously published research focussed on anisotropic constitutive material properties and their influence on the vibroacoustic behaviour in different applications, see e.g. [1, 2, 3, 4, 5, 6, 7, 8, 9].

Our approach is to start from a defined micro-structural geometry that may be parametrised in a systematic and controlled way. We have chosen to work with the well-known Kelvin cell (KC), i.e. the tetrakaidecahedron which is known to fill space completely, see for example the original publication by Lord Kelvin, [10] which was recently reprinted as [11]. Some more recent works on KC mechanics include [12, 13, 14, 15, 16, 17, 18, 19].

In a dual-scale modelling approach, we build a micro-structural numerical model that is used to predict a certain physical field response, that is then used to extract a homogenised equivalent model through the steps outlined below.

2 From Micro to Macro elasticity modelling

We propose to employ a combined homogenisation-inversion method that takes a well-defined micro-structural geometry as a starting point. We then use the micro-structural model to extract elastic and acoustic properties for a homogenised, equivalent continuum.

For static elasticity this is achieved by computing a series of displacement fields for a given set of static loads and boundary conditions, that are replicated in a homogeneous continuum based elastic model, which is solved using (nominally) the same boundary conditions and loads.

Details on the applied procedures are given in the following. We will first give a general overview of the procedures developed and then get more specific in some cases investigated within the current framework.

2.1 Numerical Kelvin Cell Model

We start from a unit cell template as shown in Figure 1, holding 24 unique struts that may be repeated in x, y, z-directions to form a porous block with known micro-structural geometrical properties. The unit cell dimensions are defined through a set of parameters, i.e. L_x^{cell}, L_y^{cell} and L_z^{cell} of the length, width and height respectively. In addition to these, each of the 24 struts are assigned individual radii, $r_i, i = 1, ..., 24$. In the investigations performed, we have started our parametrisations from a fixed, nominally isotropic cell with the size H_c, and from this computed the lengths of the individual struts as $L_s = \sqrt{2}H_c/4$. We then introduce a set of scaling parameters that allow us to distort the unit cell, s_x, s_y, s_z, such that e.g. $L_x^{cell} = s_x 4L_s/\sqrt{2}$ etc.

To design a numerical test sample, we then choose the number of cells in each direction as N_x, N_y, N_z, and complement the missing struts at the boundaries, $x = 0$ and $x = N_x L_x^{cell}$; $y = 0$ and $y = N_y L_y^{cell}$; and $z = 0$, as illustrated in Figure 2 for $N_x = N_y = N_z = 15$. For ease of reference, the different faces of the cubic sample are indicated by their outgoing normal in the coordinate system attached to the sample, $x_-, x_+, y_-, y_+, z_-, z_+$. The displacement components are defined as $u = x_0 - x_1, v = y_0 - y_1$ and $w = z_0 - z_1$, where x_0, y_0, z_0 and x_1, y_1, z_1 are the positions of a point in the material before and after loading, respectively. The data used for the approach consists of a set of displacements from the KC model u^{kelvin}. A solid model is constructed to calculate the displacements u^{solid} for a set of elastic moduli, which are varied within an optimisation routine until the difference between measured and predicted displacements is minimised. In the present investigation, the displacements $u^{kelvin} = [u, v, w]$ are obtained as the result of a prescribed static compression d in the z direction. The shear displacement is applied subsequently in x and y directions, and three spatial components of the displacement are extracted at the four free faces of the sample.

Detail boundary and load conditions for inverse estimation during optimization simulations are

- Boundary conditions: all movements constrained on the z_+ surface nodes, where $u = v = w = 0$, Fig. 2.
- **Load Step 1**: Compression displacements $w = 0.01$ mm on z_- surface, Fig. 2.
- **Load Step 2**: Shear displacements $u = 0.01$ mm on z_- surface.
- **Load Step 3**: Shear displacements $v = 0.01$ mm on z_- surface.

2.2 Elastic Material Model

Biot [20] described the constitutive laws for porous materials consisting of a solid phase and a fluid phase in acoustic applications. In the case of open-cell porous materials, only the fluid phase takes part in the dynamic deformation. Therefore, the static structural properties of the material, such as elasticity, can conveniently be described in the absence of the fluid phase. Thus, only the solid frame of the material is considered here

and the Hooke's law for the anisotropic material in stiffness form is:

$$\sigma = \begin{bmatrix} \sigma_{xx} \\ \sigma_{yy} \\ \sigma_{zz} \\ \sigma_{xy} \\ \sigma_{xz} \\ \sigma_{yz} \end{bmatrix} = \begin{bmatrix} D_{1111} & D_{1122} & D_{1133} & D_{1112} & D_{1113} & D_{1123} \\ & D_{2222} & D_{2233} & D_{2212} & D_{2213} & D_{2223} \\ & & D_{3333} & D_{3312} & D_{3313} & D_{3323} \\ & & & D_{1212} & D_{1213} & D_{1223} \\ & & sym & & D_{1313} & D_{1323} \\ & & & & & D_{2323} \end{bmatrix} \begin{bmatrix} \varepsilon_{11} \\ \varepsilon_{22} \\ \varepsilon_{33} \\ \gamma_{12} \\ \gamma_{13} \\ \gamma_{23} \end{bmatrix} = \mathbf{H}_a \varepsilon \tag{1}$$

where $\mathbf{H}_a$ is the anisotropic stiffness or Hooke's matrix, $\sigma = [\sigma_{11}, \sigma_{22}, \sigma_{33}, \sigma_{12}, \sigma_{13}, \sigma_{23}]^{-1}$ is the stresses and $\varepsilon = [\varepsilon_{11}, \varepsilon_{22}, \varepsilon_{33}, 2\varepsilon_{12}, 2\varepsilon_{13}, 2\varepsilon_{23}]^{-1} = [\varepsilon_{11}, \varepsilon_{22}, \varepsilon_{33}, \gamma_{12}, \gamma_{13}, \gamma_{23}]^{-1}$ are the strains. If the structure is orthotropic, only 9 parameters are included in the Hooke's stiffness matrix $\mathbf{H}_o$,

$$\mathbf{H}_o = \begin{bmatrix} D_{1111} & D_{1122} & D_{1113} & 0 & 0 & 0 \\ & D_{2222} & D_{2233} & 0 & 0 & 0 \\ & & D_{3333} & 0 & 0 & 0 \\ & & & D_{1212} & 0 & 0 \\ & & sym & & D_{1313} & 0 \\ & & & & & D_{2323} \end{bmatrix} \tag{2}$$

If the cell structure is isotropic, the linear elastic materials have their elastic properties uniquely determined by any two moduli, e.g. Young's modulus, E, and ν, Poisson's ratio. The Young's modulus and Poisson's ratio can be calculated according to the relationship between moduli and stiffness parameters in Hooke's matrix, Equation 3.

$$D_{1111} = D_{2222} = D_{3333} = \frac{E(1-\nu)}{(1+\nu)(1-2\nu)}, \tag{3a}$$

$$D_{1122} = D_{1133} = D_{2233} = \frac{E\nu}{(1+\nu)(1-2\nu)}, \tag{3b}$$

$$D_{1212} = D_{1313} = D_{2323} = \frac{E}{2(1+\nu)}. \tag{3c}$$

2.3 Inverse estimation

The inverse estimation routine is implemented in Matlab using the globally convergent method of moving asymptotes (GCMMA) by [21, 22, 23]. The GCMMA routine pursues a strict decrease of the object function, guaranteeing a set of parameters which is a preferable solution. A detailed description of the GCMMA algorithm is given in the original paper [21]. The criterion to assess whether the optimisation is converged is that a variation in the objective function and in each of the parameters must be less than 10^{-4} between two subsequent iterations.

As has been discussed by Van der Kelen et al [9], the static inversion problem using prescribed displacements is undetermined and one of the moduli has to be estimated in a different numerical experiment. In the present work, prior to the optimization, a separate setup is required to estimate the stiffness component D_{3333} through a numerical compression test where constraints are set for all nodes $u = v = 0$. The estimated $D_{3333} = \sigma_{33}/\varepsilon_{33}$, where $\sigma_{33} = F^{r3}_{ZminSet}/A$, $\varepsilon_{33} = d_3/L_z$, $F^{r3}_{ZminSet}$ is the reaction force in z direction of on z_- nodes, A is the area of the z_- surface, d_3 is the compression displacement on the strain z_- surface, and L_z is the thickness of KC model in z direction. In the inverse estimation procedure, a the material model (moduli) is varied to approximate the measured displacements. In each iteration of the optimisation routine, a homogenised solid model representing the experimental setup is solved for a proposed set of constitutive parameters.

The error between the measured (here from a numerical experiment) and the predicted displacements using the solid model is used as the objective function, defined as the square of the L^2-norm of the difference between the predicted displacements and the measured displacements, summed over all free faces f, Figure 3, in each loading step s for all points per face,

$$\Pi_{total} = \sum_{s=1}^{3}\sum_{f=1}^{4} \frac{\left\| {}^{s}_{f}\mathbf{U}_k^{solid} - {}^{s}_{f}\mathbf{U}_k^{Kelvin} \right\|^2}{\left\| {}^{s}_{f}\mathbf{U}_k^{Kelvin} \right\|^2} \tag{4a}$$

$$\mathbf{U}^{solid} = [u, v, w]^{solid} \tag{4b}$$

$$\mathbf{U}^{Kelvin} = [u, v, w]^{kelvin} \tag{4c}$$

where $\mathbf{U}^{Kelvin}$ is the target displacements of the average displacements from **Load Steps** s, $\mathbf{U}^{solid}$ is the displacement of the solid model extracted at the same locations as in the KC model by interpolating the nearest point displacement on the solid material surface. Note that the average displacement of the individual KC was obtained from the displacement of its vertex nodes and compare to the solid ones. Thus increasing the KC number would decrease the possible displacement discontinuities from cell to cell and the fixed boundary effects on z_+ surface.

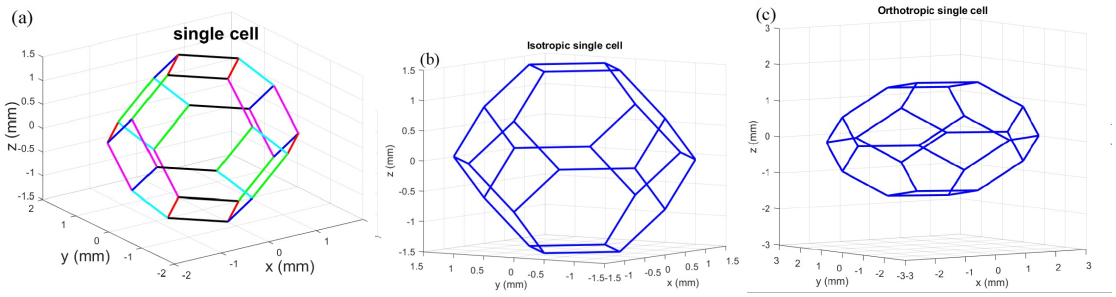


Figure 1: Single Kelvin cell: (a) single cell grouped beam elements based on directions; (b) isotropic cell with same beam elements in all direction; (c) orthotropic cell extended in x direction

To get an understanding of how the differences between simulated and measured displacements are spread, a symbolic representation of the measure of this difference is given for each loading step s,

$$\Pi_m^s = \sum_{f=1}^{4} \frac{\left\| {}_f\mathbf{U}_k^{solid} - {}_f\mathbf{U}_k^{Kelvin} \right\|^2}{\left\| {}_f\mathbf{U}_k^{Kelvin} \right\|^2} \tag{5}$$

which can be written as a matrix,

$$\mathbf{\Pi}_c = \begin{bmatrix} \Pi_u & \Pi_v & \Pi_w \end{bmatrix} = \begin{bmatrix} \Pi_{u,1} & \Pi_{v,1} & \Pi_{w,1} \\ \Pi_{u,2} & \Pi_{v,2} & \Pi_{w,2} \\ \Pi_{u,3} & \Pi_{v,3} & \Pi_{w,3} \end{bmatrix} \tag{6}$$

The component $\mu_{u,1}$ for example gives the square of L^2-norm difference on the displacement components u for **Load Step 1** in the x direction over all four free surfaces, relative to the displacement of the KC model. Note that the subscript c has been introduced in order to identify the results for the different cases tested and discussed in later sections.

2.4 Validation of The Inverse Estimation Approach

There are a number of different possible ways to validate the approach selected here, and we will recapitulate some interesting investigations that we have performed so far. We verified that the inversion would identify

an isotropic KC material, even when the optimization was performed using either an orthotropic constitutive model. Thus, the known material symmetry is not taken into account in the inverse estimation, and each material is addressed as if it were orthotropic.

We also investigated the effects of the number of Kelvin cells used, thus studying the influence of the boundaries; as well as the order of the (linear) beam elements used to model the struts; and finally the required mesh resolution in the solid model, i.e. the number of solid elements used in the simulated displacement computations.

In all the validation cases studied, it is expected that for a symmetric KC geometry, after the displacement error has reached a stable minimum, the estimated Hooke's matrix should have the relationship of Equation 3, where other parameters in the Hooke's matrix are small or close to zero.

We tested different number of cells as well as different beam element types of KC model, in order to investigate the boundary effects and the beam displacement approximation on the final optimization results. In the same way, different number of elements in the mesh of the solid FE model are used to find a reasonable mesh size for optimization.

Equation 7 shows the Hooke's law in compliance form found from the inverse of the compliance matrix in stiffness form Equation 2, where 9 elastic constants in orthotropic constitutive equations are comprised of 3 Young's moduli E_x, E_y, E_z, 3 Poisson's ratios ν_{xy}, ν_{xz}, ν_{xy}, and the 3 shear moduli G_{yz}, G_{zx}, G_{yz}.

$$\mathbf{H}_o = \begin{bmatrix} 1/E_x & -\nu_{yx}/E_y & -\nu_{zx}/E_z & 0 & 0 & 0 \\ -\nu_{xy}/E_x & 1/E_y & -\nu_{zy}/E_z & 0 & 0 & 0 \\ -\nu_{xz}/E_x & -\nu_{yz}/E_y & 1/E_z & 0 & 0 & 0 \\ 0 & 0 & 0 & 1/G_{xy} & 0 & 0 \\ 0 & 0 & 0 & 0 & 1/G_{xz} & 0 \\ 0 & 0 & 0 & 0 & 0 & 1/G_{yz} \end{bmatrix}^{-1} \tag{7}$$

where $\frac{\nu_{yz}}{E_y} = \frac{\nu_{zy}}{E_z}$, $\frac{\nu_{zx}}{E_z} = \frac{\nu_{xz}}{E_x}$, $\frac{\nu_{yz}}{E_y} = \frac{\nu_{zy}}{E_z}$.

The Young's moduli and Poisson's ratios for the isotropic KC model could be inverse calculated from following four methods with the optimized Hooke's matrix,

- **Method 1**: solve Equations 3(a)–(b);
- **Method 2**: solve Equations 3(a)–(c);
- **Method 3**: solve Equations 3(b)–(c);
- **Method 4**: solve Equations 2 and Equation 7;

The measure of the varition used in order to quantify and validate the proposed method is given by

$$\epsilon_m^E = \frac{\left|E_{opt,m} - \bar{E}_{opt}\right|}{\bar{E}_{opt}} \tag{8a}$$

$$\epsilon_m^\nu = \frac{\left|\nu_{opt,m} - \bar{\nu}_{opt}\right|}{\bar{\nu}_{opt}} \tag{8b}$$

where $\bar{E}_{opt}$ is the mean value of the Young's moduli $E_{opt,m}$ best fit of the model, resulting from the inverse estimation of **Method** m above.

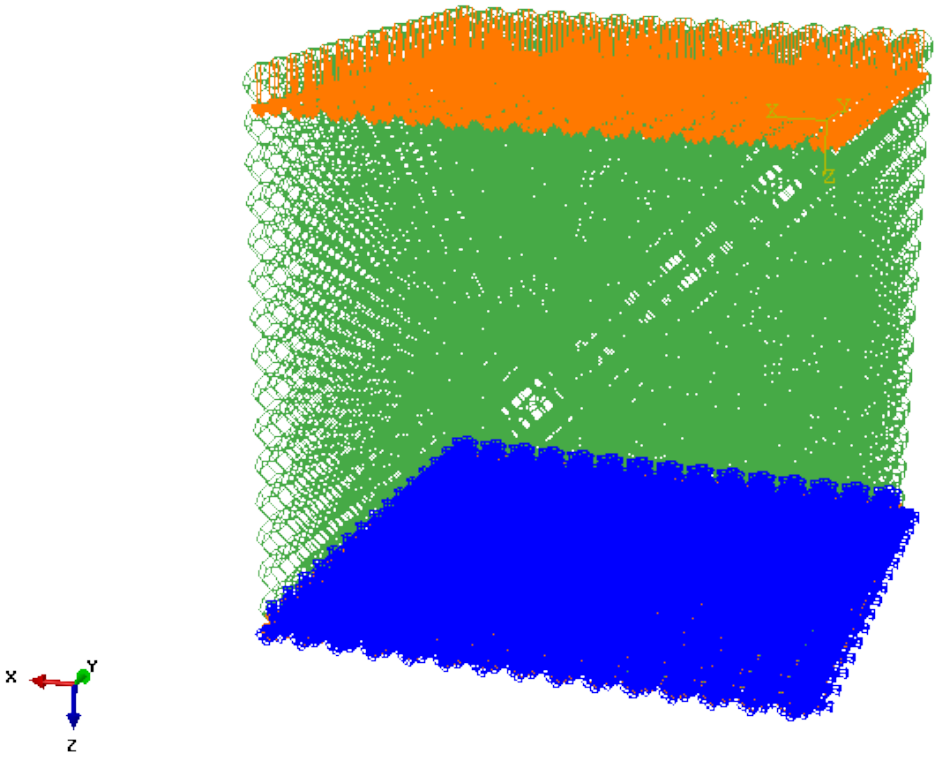


Figure 2: Boundary constraint on the surface nodes with maximal z surface z_+ and compression displacements on the minimal z surface z_-.

3 Validation of Inverse Estimation Method Results

3.1 Isotropic KC Models with Different Size

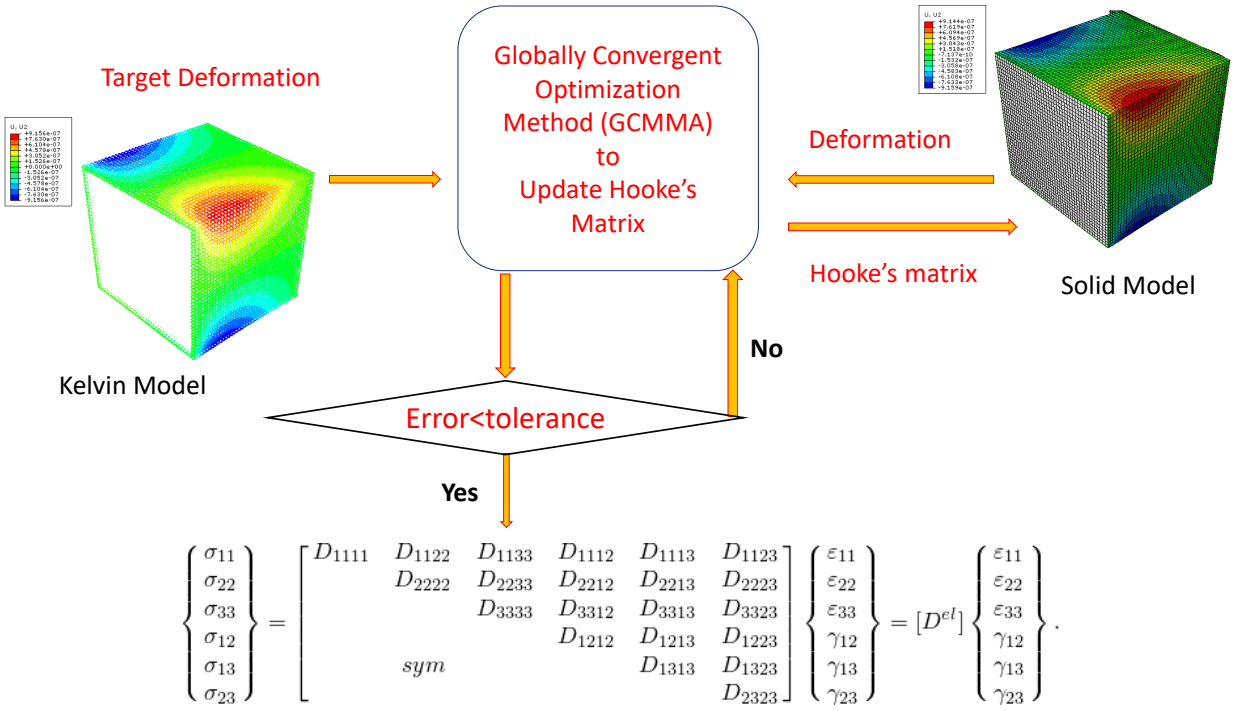
Three sizes ($15 \times 15 \times 15$, $30 \times 30 \times 30$ and $40 \times 40 \times 40$) of a symmetric (and thus expected to be isotropic) KC model were used to verify the inverse estimation method and find an economical and efficient size for both the experimental and the simulation model. Linear and quadratic beam elements were used for the struts (ligaments) of the KC models. As an example of the observations made, Figure 4 shows that the stiffness of D_{3333} decreases as the number of cells are increased in each direction or when using quadratic beam elements (B32) instead of linear elements (B31). This indicates that the stiffening effects of the boundaries are reduced (the KC model becomes softer) as the number of cells are increasing or when quadratic beam elements, but the influence on the estimated moduli is small ($< 3\%$).

In the solid FE model, 3D quadratic reduced Hex (hexahedral) mesh (C3D20R) elements. For the symmetric (isotropic) KC model, seven cases were addressed to verify the estimation method and find a proper balance between accuracy and computationa cost in modelling the structure,

1. Case 1: $15 \times 15 \times 15$ cell isotropic KC model with linear beam elements and $20 \times 20 \times 20$ Hex solid model, named '15Kelvin20Hex';

2. Case 2: $15 \times 15 \times 15$ cell isotropic KC model with quadratic beam elements and $20 \times 20 \times 20$ Hex orthotropic solid model, named as '15QKelvin20Hex';

3. Case 3: $30 \times 30 \times 30$ cell isotropic KC model with linear beam elements and $30 \times 30 \times 30$ Hex orthotropic solid model, named as '30Kelvin30Hex';



$$\begin{Bmatrix}\sigma_{11}\\ \sigma_{22}\\ \sigma_{33}\\ \sigma_{12}\\ \sigma_{13}\\ \sigma_{23}\end{Bmatrix} = \begin{bmatrix} D_{1111} & D_{1122} & D_{1133} & D_{1112} & D_{1113} & D_{1123} \\ & D_{2222} & D_{2233} & D_{2212} & D_{2213} & D_{2223} \\ & & D_{3333} & D_{3312} & D_{3313} & D_{3323} \\ & & & D_{1212} & D_{1213} & D_{1223} \\ & & sym & & D_{1313} & D_{1323} \\ & & & & & D_{2323} \end{bmatrix} \begin{Bmatrix}\varepsilon_{11}\\ \varepsilon_{22}\\ \varepsilon_{33}\\ \gamma_{12}\\ \gamma_{13}\\ \gamma_{23}\end{Bmatrix} = [D^{el}] \begin{Bmatrix}\varepsilon_{11}\\ \varepsilon_{22}\\ \varepsilon_{33}\\ \gamma_{12}\\ \gamma_{13}\\ \gamma_{23}\end{Bmatrix}.$$

Figure 3: Inverse estimation flowchart.

4. Case 4: $30 \times 30 \times 30$ cell isotropic KC model with quadratic beam elements and $30 \times 30 \times 30$ Hex orthotropic solid model, named '30QKelvin30Hex';

5. Case 5: $40 \times 40 \times 40$ cell isotropic KC model with linear beam elements and $40 \times 40 \times 40$ Hex orthotropic solid model, named '40Kelvin40Hex';

6. Case 6: $30 \times 30 \times 30$ cell isotropic KC model with quadratic beam elements and $30 \times 30 \times 30$ Hex anisotropic solid model, named '30QKelvin40HexAniso';

7. Case 7: $30 \times 30 \times 30$ cell isotropic KC model with quadratic beam elements and $40 \times 40 \times 40$ Hex orthotropic solid model, named '30QKelvin40Hex'.

As an alternative, for the isotropic KC model, an initial Poisson's ratio could have been estimated through a compression test instead of using a random value to improve the convergence, by comparing the deformation in x and y directions with a displacement loading in the z direction, where the KC model has a constraint $w = 0$ on the z_+ surface and a compression displacement $w = 0.01$mm on the z_- surface. A good starting point for the Hooke's matrix was given from Equation 3 with the estimated Poisson's ratio $\nu = 0.3786$ and D_{3333} in Figure 4. Note that the starting point for the optimisation can be chosen arbitrarily and the final solution does not depend on the chosen starting point.

Figure 5 shows the iteration history of the convergence error as the objective function in Cases 1–7 with the same starting Hooke's matrix. Cases 1–4 show the objective function does not change much even when quadratic beam elements (B32) were used instead of linear beam elements for KC model. Case 5 and Case 7 show increasing numbers of Kelvin cells could decrease the convergence error, which decreases the boundary effects. Case 4 and Case 7 show increasing mesh numbers of the solid model from $30\times30\times30$ to $40\times40\times40$ for the $30 \times 30 \times 30$ quadratic KC model could decrease the convergence error. Case 6 and Case 7 show that using an anisotropic solid model to simulate the isotropic KC model could also decrease the convergence error by over-fitting the boundary effects with 21 non-zero parameters of a full anisotropic matrix.

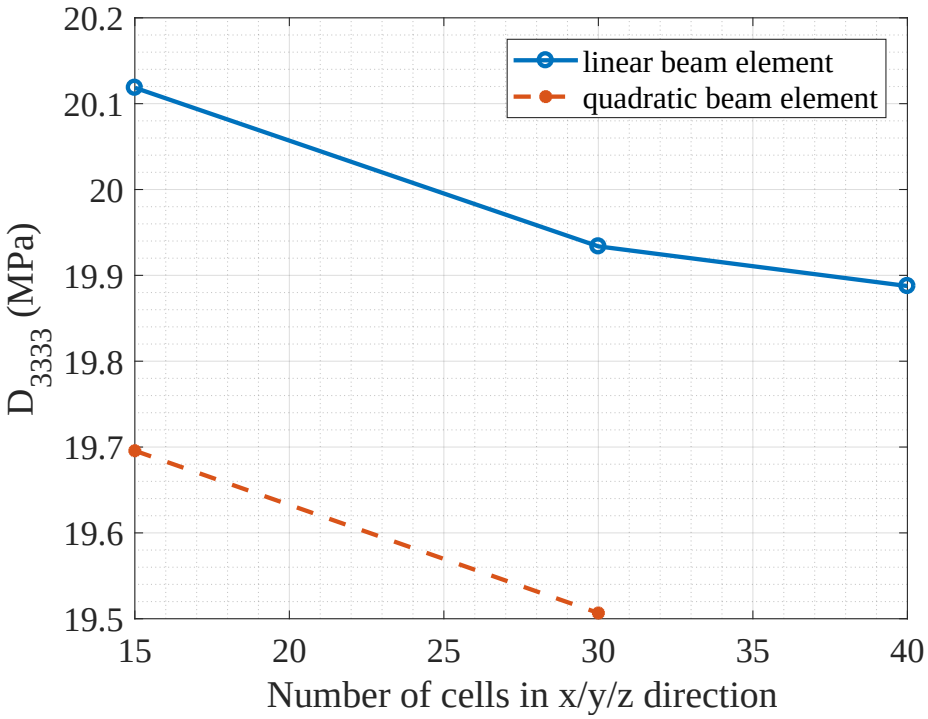


Figure 4: Estimated stiffness D_{3333} variation as the number of cells of KC model with linear and non-linear beam elements are varied.

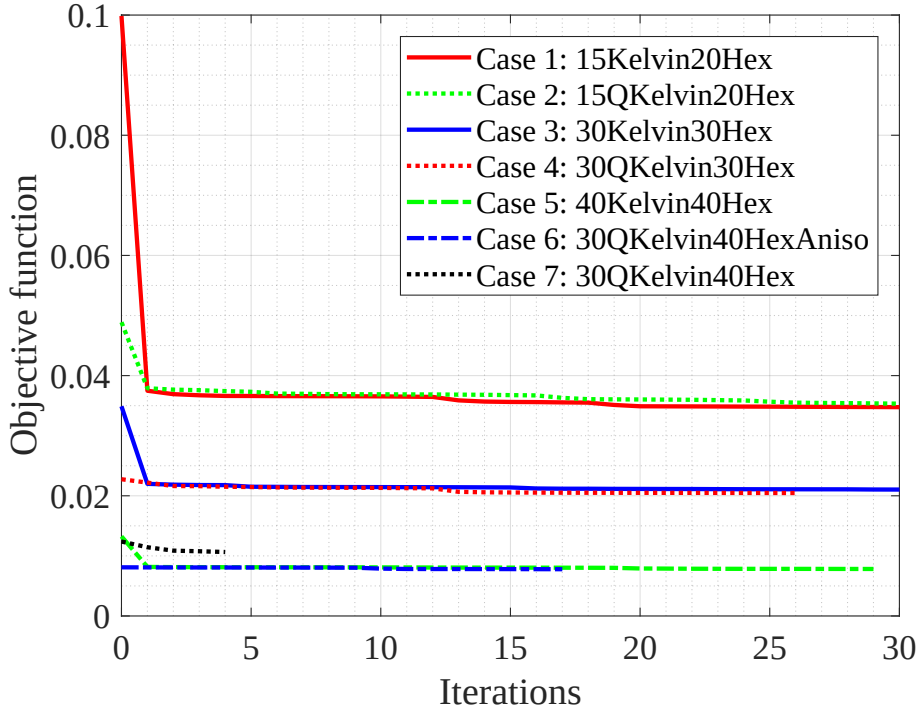


Figure 5: Iteration history of objective function for isotropic KC model.

Since the solid model needs to be solved many times before finding a convergent result, the computational time should be traded against the error in the cost function. Much larger computation times are required if we increase the solid meshes, e.g., from Case 4 and Case 7. Thus models of $30 \times 30 \times 30$ Hex and KC were suggested with a good convergence behaviour, final estimated moduli and acceptable computational time. A more accurate result could be obtained by using finer meshes with a starting point found from a coarse mesh, e.g., using the optimized Hooke's matrix of Case 1 as a starting point in Case 5.

Figure 6 shows the average Young's modulus ($E_{avg} = (E_x + E_y + E_z)/3$) and Poisson's ratio ($\nu_{avg} = \nu_x + \nu_y + \nu_z$) in Case 1, Case 3 and Case 5 estimated from **Methods 1–4**. **Method 1** and **Method 4** give very close results. As the cell numbers increased from 15 to 30 in each direction, the variation of the averaged Young's modulus and Poisson's ratio of the four methods decreased. The average Young's modulus of **Method 1–4** is 10.7MPa, 10.5MPa and 10.6MPa and the average Poisson's ratio is 0.378, 0.380 and 0.379 for Cases 1, 3 and 5, which are very close, within 2% of the average Young's modulus and 0.6% of the average Poisson's ratio.

Figure 7 shows the estimated stiffness and the convergence errors of the $30 \times 30 \times 30$ Kc quadratic beam model compared to the $10 \times 10 \times 10$, $20 \times 20 \times 20$, $30 \times 30 \times 30$, $40 \times 40 \times 40$ Hex solid models respectively. The same starting Hooke's matrix was given as for the other cases in this section. After 4 iterations, a stable convergence error was reached for all cases. Figures 7 (a)–(c) show that the case of $30 \times 30 \times 30$ Hex solid model gives a minimal variation of stiffness. The variation of coupling stiffness $[D_{1122}, D_{1113}, D_{2233}]$ and shear stiffness $[D_{1212}, D_{1313}, D_{2323}]$ decreases as the number of Hex increasing from $10 \times 10 \times 10$ to $30 \times 30 \times 30$. However, if the number of Hex increases to $40 \times 40 \times 40$, the variation increases a little since a finer solid model catches the boundary effects, but the convergence error decreases to less than 1%.

Table 1 shows the estimated engineering constants for the isotropic KC model in Cases 1–7 from **Method 4**. All cases give a modulus in each direction which is close but there exist small acceptable deviations, e.g., Young's moduli deviate $< 1\%$ in Case 6 from mean value of Cases 1–7. The solid orthotropic model with finer meshes, Case 7, gives the lowest deviations for Young's moduli, Poisson's ratios and shear moduli. One main reason is that a finer mesh solid structure is more close to the KC model since a single KC has more free points (24 for linear beam KC) than a Hex (20 point for C3D20R Hex). A solid model with coarse meshes would be stiffer than a KC model, which could be equivalent to a applied stiffer boundary constrain and generate a stiffer Young's modulus in the z-direction, Table 1.

Table 1: Engineering constants for the isotropic KC model

Eng.const	Case 1	Case 2	Case 3	Case 4	Case 5	Case 6	Case 7	mean
E_x [MPa]	10.84	10.68	10.75	10.43	10.77	10.73	10.51	10.67
E_y [MPa]	10.84	10.65	10.75	10.43	10.77	10.73	10.51	10.67
E_z [MPa]	12.01	11.1	11.37	10.30	11.13	11.13	10.31	11.05
ν_{xy} [-]	0.447	0.405	0.416	0.365	0.401	0.403	0.361	0.400
ν_{yx} [-]	0.447	0.404	0.416	0.365	0.401	0.403	0.361	0.400
ν_{xz} [-]	0.317	0.352	0.344	0.390	0.357	0.356	0.392	0.359
ν_{zx} [-]	0.351	0.366	0.364	0.385	0.369	0.369	0.384	0.358
ν_{yz} [-]	0.318	0.354	0.344	0.390	0.357	0.356	0.392	0.359
ν_{zy} [-]	0.352	0.369	0.364	0.385	0.369	0.369	0.384	0.370
G_{xy} [MPa]	3.85	3.77	3.81	3.77	3.81	3.80	3.72	3.79
G_{xz} [MPa]	3.66	3.62	3.78	3.57	3.77	3.79	3.56	3.68
G_{yz} [MPa]	3.64	3.61	3.78	3.57	3.77	3.78	3.56	3.67

3.2 Robustness of the Method

The robustness of the proposed characterisation method was studied for the isotropic KC model. The uncertainties in the experiment were studied, e.g., 5% of the measurement error of the loading displacement,

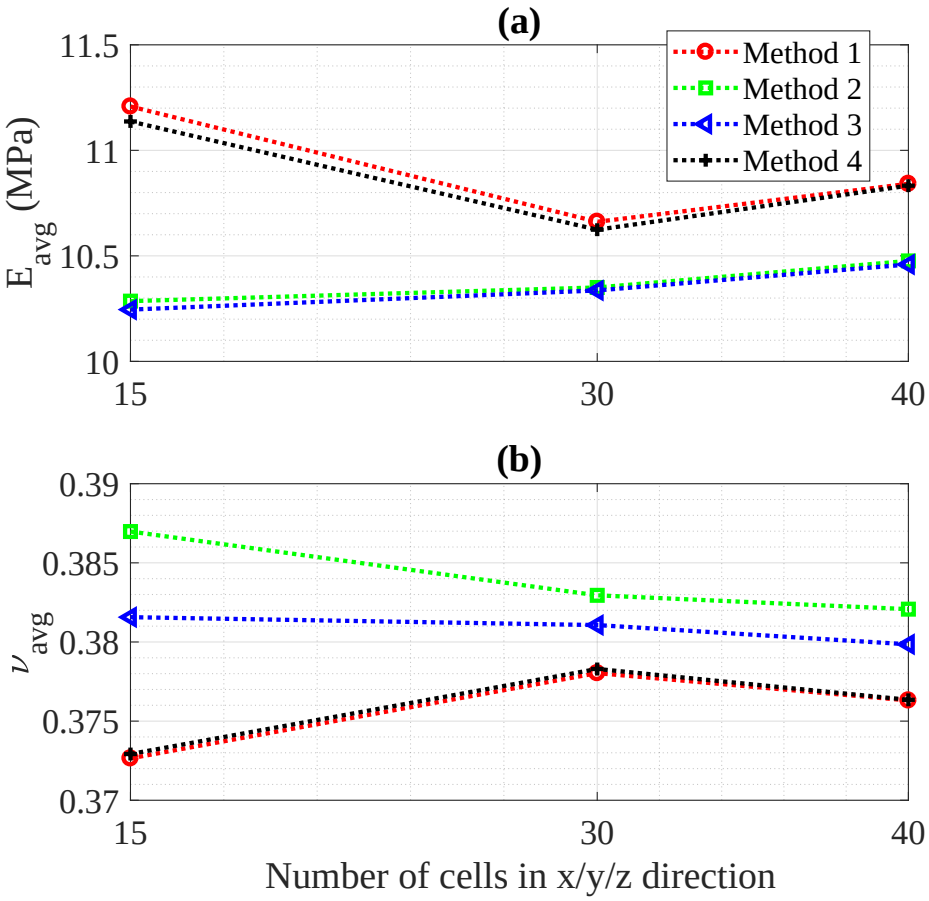


Figure 6: The average Young's modulus and Poisson's ratio for linear beam KC model by inverse estimated methods with data from optimization results, Section 2.4.

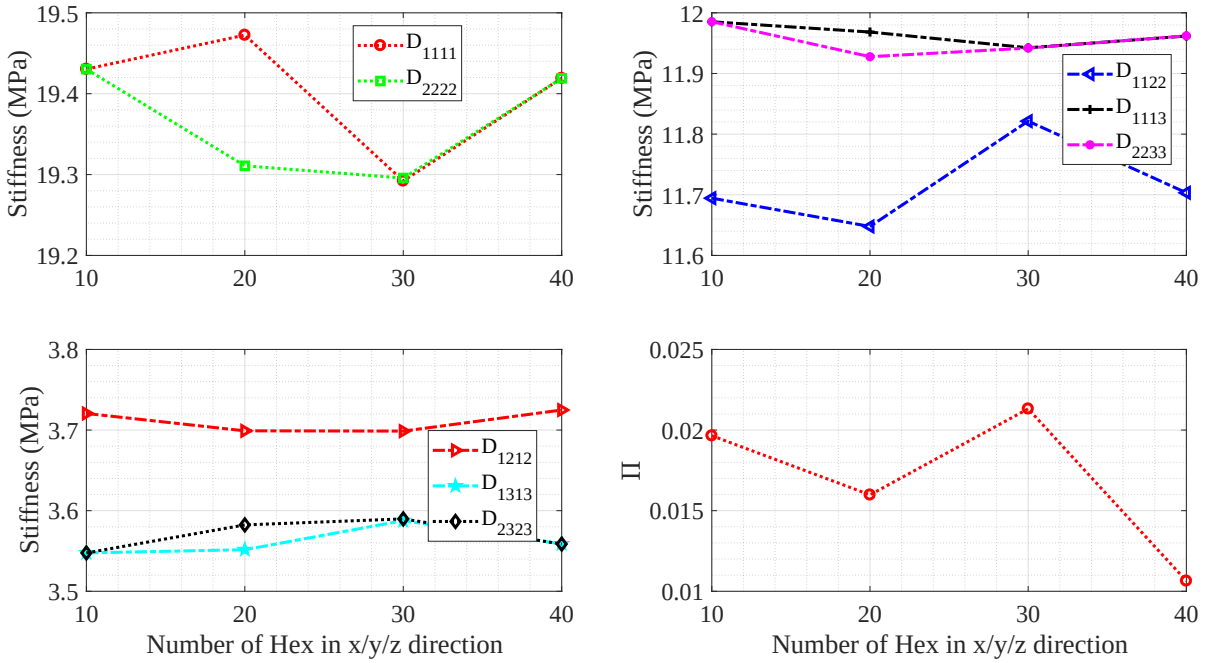


Figure 7: The estimated stiffness and convergent error for $30 \times 30 \times 30$ isotropic KC model respectively to different number of Hex in the solid model.

or 5% of the measurement error of the sample dimensions. The difference in the engineering constants is smaller than the uncertainty on the sample dimensions.

In the cases where an isotropic constitutive model was fitted using an orthotropic, the optimization tends to compensate for the error related to the boundariy effects, when fewer elements were used in the solid model than the number of cells in the KC model. For example, Figure 8 shows the shear modulus D_{1212} decreased from a convergence point (iteration 4) after 15 more iterations where Π_{total} decreased less than 10^{-4} but one component, Π_w, increased more than the decreased Π_{total}. Thus an over-fitting of the shear modulus G_{xy} might happen if a stiffer solid model was used after the convergence criterion was reached. In order to avoid this, the optimized Hooke's matrix could be checked if any of the error components ($\Pi_i, U = u, v, orw$) increased when the total error decreased when the convergent error decreased less than 10^{-4} after several iterations. One way to increase the robustness of the optimization is to use a starting point from a coarsely meshed optimization in a finely meshed solid model. Then only a few steps are required to capture a more accurate result for the shear modulus.

4 Orthotropic Kelvin Foam

The proposed method was subsequently applied to an orthotropic KC model, which is obtained by stretching the Kelvin cells in the x direction twice ($s_x = 2 \times s_y = 2 \times s_z$) but keeping the cell height H_z as before, Figure 1 (c). Here a KC model using $30 \times 30 \times 30$ and the same number of Hex elements were used. A starting point for the inverse estimation was taken from the isotropic Case 3 in Table 1. Table 2 shows the optimized results of convergence error, stiffness, Young's moduli and Poisson's ratios of the orthotropic Kelvin foam. The total convergence error is 2.34% and the v displacement has the smallest error compared to that of u and w. After applying the inverse estimation method, the cost function found a minimum and an equivalent Hooke's matrix was found. Comparing the obtained Young's moduli with mean data of the isotropic KC models in Table 1, E_x increased 76.3%, and E_y, E_z decreased 87.2% and 84.8% respectively.

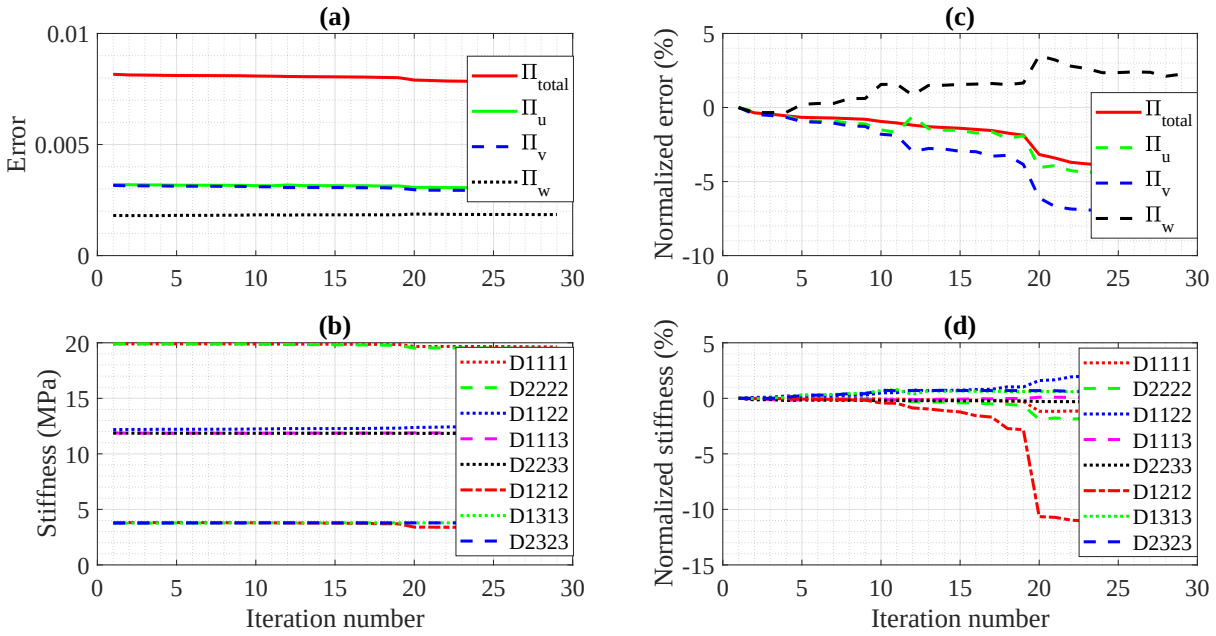


Figure 8: The iteration history of the cost function and the estimated stiffness of Case 5: (40Kelvin40Hex). (a), the cost function error and its contributions from components related to displacements u, v and w; (b), the estimated stiffness; (c), cost function and its components normalised to their initial iteration error; (d), the estimated stiffness components normalised to their initial iteration one.

5 Discussion of the Inverse Estimation Method

The proposed characterisation method is verified for symmetric Kelvin cell models, using different number of cells and shape function order in the beam elements in the experimental models and different number of elements in the solid models. For all cases, the objective function decreases monotonically as is expected for the optimisation algorithm used. For the isotropic KC model, the difference between different settings of the engineering constants is small and a finer meshed model gives a lower convergence error and deviations between moduli and Poisson's ratios in each direction. If a good start point was given from a coarse mesh or compression tests, the inverse estimation converged within a relatively small number of iterations. Note that, although the material is isotropic, the optimal Hooke's tensor deviates slightly from isotropy, as a result shear moduli D_{1212}, D_{1313} and D_{2323} are not converged to exactly the same value, and perfect isotropy is not reached. If the inverse estimation had been allowed similar freedoms (flexibility) in both solid and KC models, full convergence and perfect isotropy would have been reached. But even using coarse meshes for the solid model, the basic characteristics including shear moduli are found. The relative square of L^2-norm difference in displacement between KC and solid with finer meshes, Case 7, is smaller than 0.8% for all four surfaces, and is smallest for the longitudinal displacement components, Π_w.

The verified inverse estimation method was extended to the application of orthotropic models. The target displacements are obtained with very good accuracy for all components. These numerical examples confirm that the computational part of the inverse estimation works accurately, for structures from isotropic to fully anisotropic.

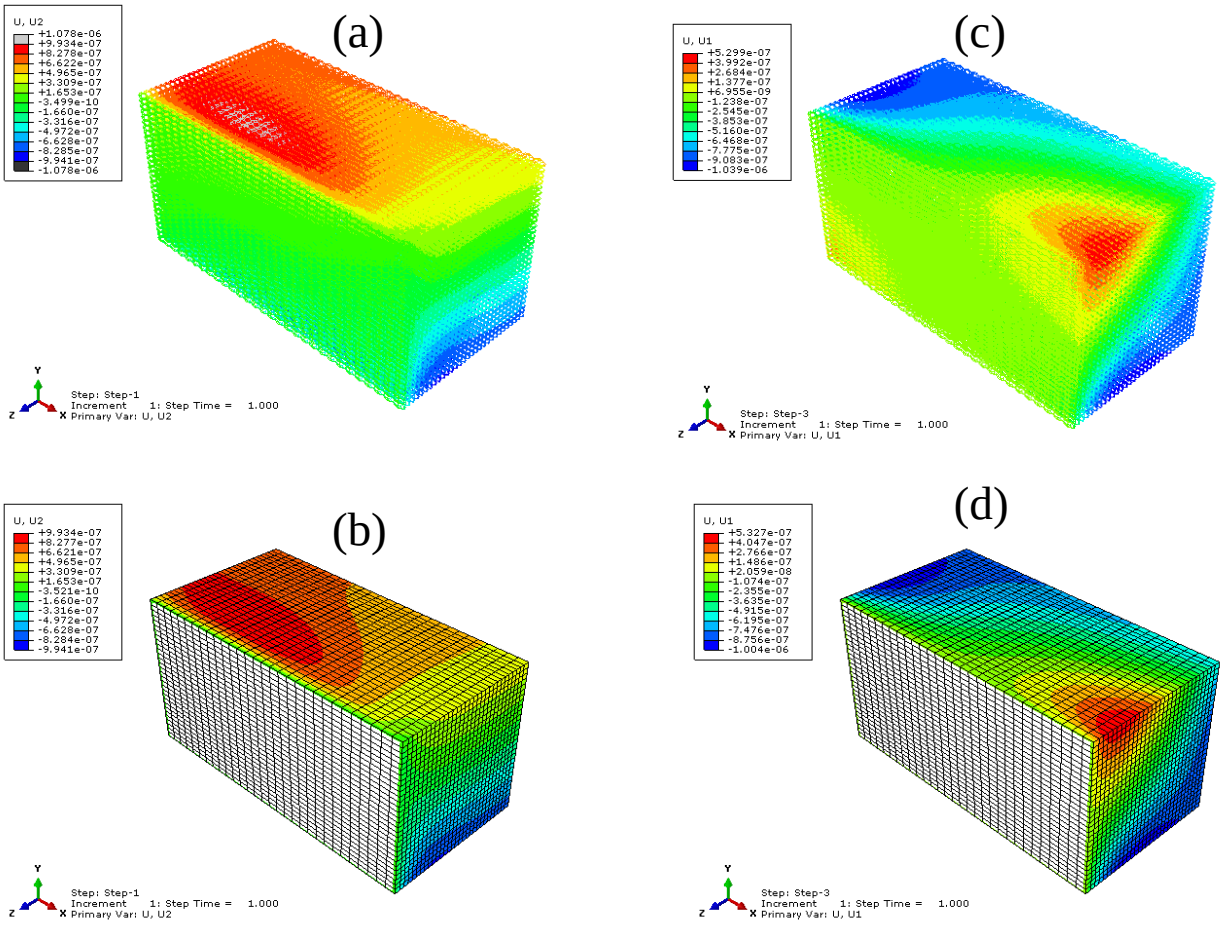


Figure 9: The displacements computed for a Kelvin cell model and for a solid FE model.

Table 2: Engineering constants for the orthotropic KC model

Quantity	Value	Unit
square of L^2-norm displacement error, Π	2.34	%
components of Π, $[\Pi_u, \Pi_v, \Pi_w]$	[0.78 1.08 0.49]	%
Stiffness parameters $[D_{1111}, D_{2222}, D_{3333}]$	[42.35, 3.38, 4.44]	MPa
Stiffness parameters $[D_{1122}, D_{1133}, D_{2212}]$	[7.68, 8.82, 1.89]	MPa
Stiffness parameters $[D_{1212}, D_{1313}, D_{2323}]$	[1.66,2.13,0.91]	MPa
Young's moduli, $[E_x, E_y, E_z]$	[18.82,1.95,2.57]	MPa
Poisson's ratios, $[\nu_{xy}, \nu_{xz}; \nu_{yx}, \nu_{yz}; \nu_{zx}, \nu_{zy}]$	[1.53, 1.34; 0.16, 0.11; 0.18, 0.14]	-

Acknowledgements

This work was partially funded through the AERIALIST project no: 723367 European Union H2020-EU.3.4. SOCIETAL CHALLENGES - Smart, Green And Integrated Transport, and partially by the Centre for ECO2 Vehicle Design at KTH.

The authors also wish to acknowledge the AMBER Additive Research Lab in the facilitating of the manufacturing of our metal test specimens and the AR Lab staff on providing training and guidance on the manufacturing process. The AR-Lab has been enabled by a €3.3M award from Science Foundation Ireland as part of their Research Infrastructure program and an additional €1M investment from the European Research Council through TCD world leading investigators.

The COST Action DENORMS CA15125, supported by COST (European Cooperation in Science and Technology) is acknowledged for the funding provided for mobility of some of the authors.

References

[1] Goransson, P., "A 3-D, symmetric, finite element formulation of the Biot equations with application to acoustic wave propagation through an elastic porous medium," *Int. J Num. Meth. Eng.*, Vol. 41, No. 1, 1998, pp. 167–192.

[2] Rice, H. J. and Gransson, P., "A dynamical model of light fibrous materials," *International Journal of Mechanical Sciences*, Vol. 41, No. 4-5, 1999, pp. 561–579.

[3] Göransson, P., Guastavino, R., and Hörlin, N.-E., "Measurement and inverse estimation of 3D anisotropic flow resistivity for porous materials," *Journal of Sound and Vibration*, Vol. 327, No. 35, 2009, pp. 354–367.

[4] Göransson, P. and Hörlin, N.-E., "Vibro-Acoustic Modelling of Anisotropic Porous Elastic Materials: A Preliminary Study of the Influence of Anisotropy on the Predicted Performance in a Multi-Layer Arrangement," *Acta Acustica united with Acustica*, Vol. 96, No. 2, 2010, pp. 258–265.

[5] Lind Nordgren, E., Göransson, P., Deü, J.-F., and Dazel, O., "Vibroacoustic response sensitivity due to relative alignment of two anisotropic poro-elastic layers." *J. Acoust. Soc. Am.*, Vol. 133, No. 5, May 2013, pp. EL426–30.

[6] Cuenca, J. and Göransson, P., "Inverse estimation of the elastic and anelastic properties of the porous frame of anisotropic open-cell foams," *J. Acoust. Soc. Am.*, Vol. 132, No. 2, 2012, pp. 621.

[7] Hörlin, N.-E. and Göransson, P., "Weak, anisotropic symmetric formulations of Biot's equations for vibro-acoustic modelling of porous elastic materials," *Int. J. Numer. Meth. Engng.*, Vol. 84, No. 12, 2010, pp. 1519–1540.

[8] Cuenca, J., Van der Kelen, C., and Göransson, P., "A general methodology for inverse estimation of the elastic and anelastic properties of anisotropic open-cell porous materials with application to a melamine foam," *J. Appl. Phys.*, Vol. 115, No. 8, Feb. 2014, pp. 084904.

[9] Van der Kelen, C., Cuenca, J., and Göransson, P., "A method for characterisation of the static elastic properties of the porous frame of orthotropic open-cell foams," *International Journal of Engineering Science*, Vol. 86, No. 0, 2015, pp. 44 – 59.

[10] Thomson, W., "On the division of space with minimum partitional area." *Phil. Mag.*, Vol. 24, 1887, pp. 503–514.

[11] Thomson, W., "LXIII. On the division of space with minimum partitional area (Reprinted)," *PHILOSOPHICAL MAGAZINE LETTERS*, Vol. 88, No. 2, 2008, pp. A503–A514.

[12] Sullivan, R. M., Ghosn, L. J., and Lerch, B. A., "A general tetrakaidecahedron model for open-celled foams," *INTERNATIONAL JOURNAL OF SOLIDS AND STRUCTURES*, Vol. 45, No. 6, 2008, pp. 1754–1765.

[13] Sullivan, R. M. and Ghosn, L. J., "Shear moduli for non-isotropic, open cell foams using a general elongated Kelvin foam model," *INTERNATIONAL JOURNAL OF ENGINEERING SCIENCE*, Vol. 47, No. 10, 2009, pp. 990–1001.

[14] Kumar, P., Topin, F., and Tadrist, L., "GEOMETRICAL CHARACTERIZATION OF KELVIN-LIKE METAL FOAMS FOR DIFFERENT STRUT SHAPES AND POROSITY," *JOURNAL OF POROUS MEDIA*, Vol. 18, No. 6, 2015, pp. 637–652.

[15] Kumar, P. and Topin, F., "Investigation of fluid flow properties in open cell foams: Darcy and weak inertia regimes," *Chemical Engineering Science*, Vol. 116, 2014, pp. 793 – 805.

[16] Storm, J., Abendroth, M., and Kuna, M., "Influence of curved struts, anisotropic pores and strut cavities on the effective elastic properties of open-cell foams," *Mechanics of Materials*, Vol. 86, 2015, pp. 1 – 10.

[17] Fanelli, P., Evangelisti, A., Salvini, P., and Vivio, F., "Modelling and characterization of structural behaviour of Al open-cell foams," *Materials & Design*, Vol. 114, 2017, pp. 167 – 175.

[18] Lu, Z.-x., Liu, Q., and Chen, X., "Analysis and simulation for tensile behavior of anisotropic open-cell elastic foams," *APPLIED MATHEMATICS AND MECHANICS-ENGLISH EDITION*, Vol. 35, No. 11, 2014, pp. 1437–1446.

[19] Jang, W.-Y., Kyriakides, S., and Kraynik, A. M., "On the compressive strength of open-cell metal foams with Kelvin and random cell structures," *International Journal of Solids and Structures*, Vol. 47, No. 21, 2010, pp. 2872 – 2883.

[20] Biot, M. A., "Theory of Propagation of Elastic Waves in a Fluid-Saturated Porous Solid. I. Low-Frequency Range," *The Journal of the Acoustical Society of America*, Vol. 28, No. 2, 1956, pp. 168–178.

[21] Svanberg, K., "A class of globally convergent optimization methods based on conservative convex separable approximations," *SIAM journal on optimization*, Vol. 12, No. 2, 2002, pp. 555–573.

[22] Svanberg, K., "MMA and GCMMA, versions September 2007," *Optimization and Systems Theory*, Vol. 104, 2007.

[23] Van der Kelen, C., Cuenca, J., and Göransson, P., "A method for the inverse estimation of the static elastic compressional moduli of anisotropic poroelastic foams–With application to a melamine foam," *Polymer Testing*, Vol. 43, 2015, pp. 123–130.

A periodic acoustic meta-material concept incorporating negative stiffness elements for low-frequency acoustic insulation/absorption

I. Antoniadis [1], **A. Paradeisiotis** [1]
[1] National Technical University of Athens, Department of Mechanical Engineering,
Heroon Polytechniou 9, 15780 Zografou Athens, Greece
e-mail: **antogian@central.ntua.gr**

Abstract
A class of periodic structures consisting of the repetition of unit cells exhibiting local resonances referred to as "acoustic/elastic meta-materials", achieve extreme properties via the combination of mechanical elements, resulting to negative effective stiffness and/or mass, at frequencies near these local resonances. Due to their unique wave propagation properties they are rendered especially suitable in low-frequency range applications. To overcome obstacles like heavy internal masses and narrow band-gaps, encountered in periodic structures based on traditional oscillators, a "KDamper" based structure is proposed. This concept, incorporates negative stiffness elements in addition to the internally resonating masses, leading to significantly lower required masses while exploiting the negative stiffness damping phenomenon. The dispersion relations of a 1D mass-in-mass lattice are derived via Bloch's theory. Preliminary results and comparisons with "m-k-m" and TMD based structures, indicate broader band-gaps and increased damping ratio in lower frequencies.

1 Introduction

The terms "acoustic/elastic meta-materials" [1] describe a class of periodic structures with unit cells exhibiting local resonance. An intuitive description of such designs lies in use of a simple "mass-in-mass" lumped parameter model, resulting in negative effective stiffness and/or mass at frequency ranges close to the local resonances. Unlike phononic crystals [2,3], which are based on Bragg scattering, this localized resonant structure has been shown [4–7] to exhibit band-gaps at wavelengths much longer than the lattice size, thus enabling low-frequency vibration attenuation, wave guiding, and filtering, among other applications. Preliminary applications include among others vibration absorption in beams [8,9] and plates [10,11].

However, low frequency range applications of such locally resonant meta-materials, may require very heavy internal moving masses, as well as additional constraints at the amplitudes of the internally oscillating locally resonating structures, which may prohibit their practical implementation. For example, current applications of locally resonant meta-materials in acoustics [12,13] often address frequencies well above 500 [Hz]. However, there are some notable applications in low frequency noise isolation based on thin membrane-type acoustic meta-materials, serving as a total reflection nodal surface at certain frequencies [14]. Another example is the sound absorption and reflection from a resonant meta-surface [15], achieving total sound absorption at resonance observed in an impedance tube, below 400 Hz. However, it should be mentioned, that in this frequency range, the performance of conventional noise insulation materials is quite poor.

To contribute to the solution of low frequency sound attenuation, the paper considers the application of the KDamping concept towards the design of highly dissipative low-frequency elastic/ acoustic meta-materials. The KDamper [16] is a novel passive vibration isolation and damping concept, based essentially on the optimal combination of appropriate stiffness elements, which include a negative stiffness element. The

KDamper can be considered as an extension of the traditional Tuned Mass Damper (TMD), by the addition of a negative stiffness element to the internal oscillating mass. This idea was first suggested in [16] and was further treated in a systematic way in [17], within the context of the design of a general class of tuned mass dampers. A preliminary review of the reported physical principles for the design of negative stiffness elements can be found in [17]. These principles include conventional pre-stressed elastic mechanical elements, such as post-buckled beams, plates, shells and pre-compressed springs arranged in appropriate geometrical configurations, or other sources of forces, such as gravitational, magnetic or electromagnetic.

Contrary to the TMD and its variants, the KDamper substitutes the inertial forces of the added TMD mass by the stiffness force of the negative stiffness element. Among others, this can provide significant comparative advantages, especially in the very low frequency range. As a result, the KDamper can achieve better damping characteristics, without the need of additional heavy masses, as in the case of the TMD. Moreover, since the isolation and damping properties of the KDamper essentially result from the stiffness elements of the system, further technological advantages can emerge, in terms of weight, complexity and reliability.

Based on the periodic repetition of KDamper elements, a novel class of meta-materials can be designed, in the same way that the periodic repetition of TMDs consists the conceptual framework under which the locally resonant meta-materials in [16] are analysed. Preliminary results [19, 20] confirm the efficiency of this approach. Towards this direction, it should be noted that recently, numerous periodic cellular structures with advanced dynamic behaviour have been also proposed, [21–24] combining high positive and negative stiffness elements, such as buckled beams or chiral structures.

Application of Bloch's theory (Subsec. 2.2) for the one- dimensional mass-in-mass lattice is analysed and the corresponding dispersion relations are derived. The results (Sect. 3) indicate significant advantages over the conventional mass-in-a mass lattice, such as broader band-gaps and increased damping ratio and reveal significant potential in the proposed solution. A preliminary feasibility analysis (Sect. 3) for low frequency acoustic isolation-damping confirms the strong potential and applicability of this concept.

2 KDamper Meta-materials

2.1 Overview of the KDamper Concept

Figure 1 presents the basic layout of the KDamper concept [17], which is designed to minimize the response $u_S(t)$ of an undamped SDoF system of mass m and static stiffness k_0 to an external excitation $f(t)$.

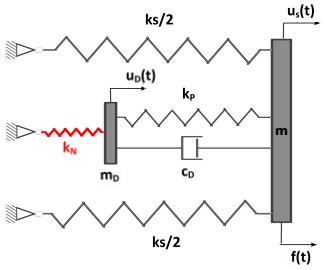


Figure 1: KDamper vibration absorption concept

In order to overcome limitations regarding the static loading capacity of the structure -which may result in unsolvable problems (e.g. collapse of structure), especially for vertical vibration isolation- the KDamper uses a negative stiffness element k_N along with the basic requirement that the overall static stiffness k_0 of the system is maintained as

$$k_0 = \frac{k_P k_N}{k_P + k_N} + k_S \tag{1}$$

and the natural frequency comes as

$$\omega_0 = \sqrt{k_0/m} \tag{2}$$

Compared to the conventional TMD, the additional negative stiffness element k_N, is inserted between the additional mass and the ground. Thus, the equation of motion of the KDamper becomes:

$$m\ddot{u}_S + c_D(\dot{u}_S - \dot{u}_D) + k_S u_S + k_P(u_S - u_D) = f(t) \tag{3}$$

$$m_D\ddot{u}_D - c_D(\dot{u}_S - \dot{u}_D) + k_N u_D - k_P(u_S - u_D) = 0 \tag{4}$$

Assuming a harmonic excitation in the form of $f(t)$ and a steady state complex response of $u_S(t)$, $u_D(t)$:

$$f(t) = \tilde{F}\, e^{\jmath\omega t} \tag{5}$$

$$u_S(t) = \tilde{U}_S e^{\jmath\omega t} \tag{6}$$

$$u_D(t) = \tilde{U}_D e^{\jmath\omega t} \tag{7}$$

the equations of motion of the KDamper can be expressed as

$$-\omega^2 m\tilde{U}_S + k_S\tilde{U}_S - \omega^2 m_D\tilde{U}_D + k_N\tilde{U}_D = \tilde{F} \tag{8}$$

$$-\omega^2 m_D\tilde{U}_D - \jmath\omega c_D(\tilde{U}_S - \tilde{U}_D) - k_P(\tilde{U}_S - \tilde{U}_D) + k_N\tilde{U}_D = 0 \tag{9}$$

Examination of Eq. (8) reveals that the amplitude F_{MD} of the inertia force of the additional mass m_D and the amplitude F_N of the negative stiffness force are exactly in phase, due to the negative value of k_N.

$$F_{MD} = -\omega^2 m_D\tilde{U}_D \tag{10}$$

$$F_N = k_N\tilde{U}_D \leq 0 \tag{11}$$

Thus, the KDamper presents an indirect way of increasing the inertia effect of the additional mass m_D without however increasing directly the mass m_D itself. Moreover, it should be noted that the value of $-\omega^2 m_D$, see Eq. (10), depends on the frequency, while the value of k_N, see Eq. (11), is constant in the entire frequency range, a fact which is of particular importance in low frequency vibration isolation.

The basic parameters of the KDamper concept [15] are μ,κ and ρ, which are defined as

$$\mu = m_D/m \tag{12}$$

$$\rho = \omega_D/\omega_0 \tag{13}$$

$$\kappa = -\frac{k_N}{k_N + k_P} \tag{14}$$

where $\omega_D = \sqrt{(k_P + k_N)/m_D}$. The optimal value of ρ where the transfer function of the displacement u_S (Fig.1) with regard to the excitation is minimized at a selected frequency, is defined as

$$\rho_{opt} = \sqrt{\frac{1}{(1+\mu+\kappa\mu)(1+\mu) - \kappa^2\mu}} \tag{15}$$

in terms of the parameters μ and κ.

By setting the denominator of ρ_{opt} equal to zero, the maximum value that can be reached for κ is determined as

$$\kappa_{max} = \frac{(1+\mu)(1+\sqrt{1+4/\mu})}{2} \tag{16}$$

Therefore the value of κ can be selected as a fraction of κ_{max}, namely

$$\kappa = (0:1)\cdot\kappa_{max} \tag{17}$$

As explained in detail in [17], the oscillator presents better vibration absorption capabilities when $\kappa \to \kappa_{max}$ but at the same time needs to be considered that for $\kappa \to \kappa_{max}$, the static stability margin of the oscillator tends to be nullified, because the overall static stiffness k_0 of the system in Eq. (1) becomes negative.

2.2 Bloch analysis

The KDamper based meta-materials essentially comprise a periodic repetition of unit lattice cells of KDamper elements, as presented in Fig. 2.

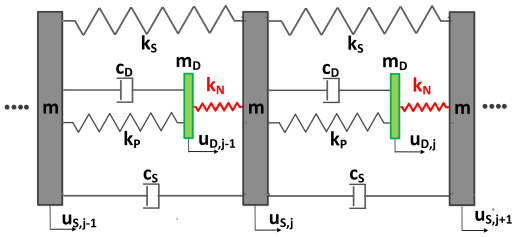


Figure 2: Unit cell of KDamper meta-material

As evident from Fig. 2, setting the value of the negative stiffness element of the KDamper unit cell as $k_N = 0$, makes it equivalent to the TMD based, acoustic/elastic locally resonant meta-materials. In view of Fig. 2, the equations of motion of a typical unit cell become:

$$m\ddot{u}_{S,j} + c_S(\dot{u}_{S,j} - \dot{u}_{S,j-1}) + c_S(\dot{u}_{S,j} - \dot{u}_{S,j+1}) + k_S(u_{S,j} - u_{S,j-1}) + k_S(u_{S,j} - u_{S,j+1}) + \\ + k_P(u_{S,j} - u_{D,j}) + k_N(u_{S,j} - u_{D,j-1}) = 0 \tag{18}$$

$$m\ddot{u}_{D,j} + c_D(\dot{u}_{D,j} - \dot{u}_{S,j}) + k_P(u_{D,j} - u_{S,j}) + k_N(u_{D,j} - u_{S,j+1}) = 0 \tag{19}$$

2.2.1 Application of Bloch's theorem

For each of the system of Eqs. (18) and (19), the generalized form [25] of Bloch's theorem is applied

$$u_{S,j} = U_S\, e^{\lambda t} \tag{20}$$
$$u_{S,j+1} = U_S\, e^{\jmath kl + \lambda t} = U_{S,j+1}\, e^{\lambda t} \tag{21}$$
$$u_{S,j-1} = U_S\, e^{-\jmath kl + \lambda t} = U_{S,j-1}\, e^{\lambda t} \tag{22}$$

$$u_{D,j} = U_D\, e^{\lambda t} \tag{23}$$
$$u_{D,j+1} = U_D\, e^{\jmath kl + \lambda t} = U_{D,j+1}\, e^{\lambda t} \tag{24}$$
$$u_{D,j-1} = U_D\, e^{-\jmath kl + \lambda t} = U_{D,j-1}\, e^{\lambda t} \tag{25}$$

where U_S, U_D are the wave amplitudes at node j, l is the unit-cell length, k is the wave number and λ is a complex frequency function that permits wave attenuation in time. In the limiting case of no damping, $\lambda = \jmath\omega$, and the usual form of Bloch's theorem is recovered. Substitution of Eqs. (20)-(22) and (23)-(25) into Eqs. (18)-(19), leads to:

$$[\lambda^2 m + \lambda(\gamma c_S + c_D) + (\gamma k_S + k_P + k_N)]U_S - (\lambda c_D + k_P + e^{\jmath kl} k_N)U_D = 0 \tag{26}$$

$$[\lambda^2 m_D + \lambda c_D + (k_P + k_N)]U_D - (\lambda c_D + k_P + e^{-\jmath kl} k_N)U_S = 0 \tag{27}$$

where

$$\gamma = 2 - (e^{\jmath kl} + e^{-\jmath kl}) = 2(1 - \cos kl) = 2(1 - \cos q) \tag{28}$$
$$q = kl \tag{29}$$

Substituting U_D from Eq. (27) into Eq. (26), leads to

$$[\alpha_4\lambda^4 + \alpha_3\lambda^3 + \alpha_2\lambda^2 + \alpha_1\lambda + \alpha_0]U_S = 0 \tag{30}$$

where

$$\alpha_4 = m_D m \tag{31}$$
$$\alpha_3 = (m_D + m)c_D + \gamma c_S m_D \tag{32}$$
$$\alpha_2 = (m_D + m)(k_P + k_N) + \gamma(c_S c_D + k_S m_D) \tag{33}$$
$$\alpha_1 = \gamma c_S(k_P + k_N) + \gamma c_D(k_S + k_N) \tag{34}$$
$$\alpha_0 = \gamma k_S(k_P + k_N) + \gamma k_P k_N \tag{35}$$

2.2.2 Bandgap estimation and properties

Equation (30) yields a characteristic equation of the form:

$$\alpha_4\lambda^4 + \alpha_3\lambda^3 + \alpha_2\lambda^2 + \alpha_1\lambda + \alpha_0 = 0 \tag{36}$$

The roots obtained from Eq. (36) may be expressed as:

$$\lambda_B = -\zeta_B(k)\omega_B \pm \jmath\omega_B\sqrt{1 - \zeta_B^2(k)}\,, B = 1, 2 \tag{37}$$

where $B = 1$ represents the lower branch number and $B = 2$ represents the upper branch number of the two dispersion curves and ω_B, ζ_B represent their corresponding natural frequency and damping ratio. Assuming an undamped system, the following are defined ($\alpha_3 = \alpha_1 = 0$, $\lambda_B = \pm\jmath\omega_B$):

$$\alpha_4 = m_D m \tag{38}$$
$$\alpha_2 = (m_D + m)k_I + \gamma\, k_S m_D = \alpha_{2,0} + \gamma\, \alpha_{2,\gamma} \tag{39}$$
$$\alpha_0 = \gamma[k_S(k_P + k_N) + k_P k_N] = \gamma\alpha_{0,\gamma} \tag{40}$$
$$k_I = k_P + k_N \tag{41}$$

The bandgap limits can be obtained from Eq. (42)

$$\alpha_4\omega^4 - (\alpha_{2,0} + \gamma\alpha_{2,\gamma})\omega^2 + \gamma\alpha_{0,\gamma} = 0 \tag{42}$$

which leads to:

$$\gamma = \omega^2\frac{\alpha_{2,0} - \alpha_4\omega^2}{\alpha_{0,\gamma} - \alpha_{2,\gamma}\omega^2} \tag{43}$$

Therefore

$$\cos q = 1 - \frac{\omega^2}{2}\frac{\omega_H^2\omega_I^2 - \omega^2}{\omega_0^2\omega_I^2 - \omega_S^2\omega^2} \tag{44}$$

where

$$\omega_I = \sqrt{k_I/m_D} \tag{45}$$
$$\omega_H = \omega_I\sqrt{1 + \mu} \tag{46}$$
$$\omega_S = \sqrt{(k_S/m)} \tag{47}$$

In view of the denominator and numerator of Eq. (44), the band gap limits are [26]:

$$\omega_L \leq \omega \leq \omega_H \tag{48}$$

where

$$\omega_L^2 = \frac{\omega_0^2}{\frac{1}{\rho^2} + \kappa(1 + \kappa)\mu} = \frac{\omega_I^2}{1 + \kappa(1 + \kappa)\mu\rho^2} \tag{49}$$

$$b_W = \frac{\omega_H - \omega_L}{\omega_L} = \sqrt{(1+\mu)[1+\kappa(1+\kappa)\mu\rho^2]} - 1 \tag{50}$$

$$\rho = \omega_I/\omega_0 \tag{51}$$

By setting $\kappa = 0$, the corresponding band-gap limits of the unit cell are obtained from Eqs. (49)-(51) as:

$$\omega_L \xrightarrow{\kappa\to 0} \omega_I = \omega_D = \sqrt{k_P/m_D} \tag{52}$$

$$b_W \xrightarrow{\kappa\to 0} \sqrt{1+\mu} - 1 \tag{53}$$

Observation of Eqs. (49) and (50), shows that the normalized band gap width b_W can be increased not only by increasing the parameter μ (i.e., the value of the internally oscillating mass m_D), but also the value of the parameter κ (i.e., the magnitude of the negative stiffness element k_N according to Eq. (14)). This can be considered among others as a consequence of Eq. (11), since the usage of a negative stiffness element can be considered as an indirect approach to artificially increase the inertia of the system.

Figure 3 presents the resulting normalized band gap widths b_W for a simultaneous variation of both the κ and μ parameters of the KDamper meta-material. As it can be observed, a normalized band gap width of $b_W = 3$ may already be achieved for values of κ close to κ_{max}, even for negligible values of the internal oscillating mass ($\mu \approx 0$) . Band-gaps of such a width may not be accomplished by conventional acoustic meta-materials, even for extremely high values of the internal oscillating mass ($\mu \geq 10$).

The value of ρ and consequently the value of κ, are determined according to the traditional KDamper design concept [17] from Eqs. (15)-(17).

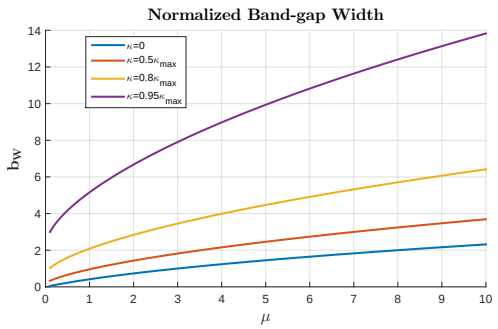


Figure 3: Normalized band-gap width as a function of the κ and μ KDamper parameters.

3 Application for Acoustic Isolation

Although the KDamper concept can find multiple applications in low-frequency damping and absorption, an indicative concept for the implementation of KDamper based meta-materials towards the design of acoustic isolation-absorption panels is examined here.

3.1 Examination of KDamper Metamaterial

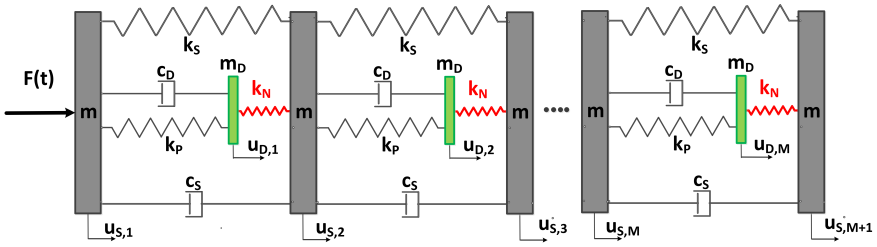


Figure 4: KDamper acoustic meta-material

For a selected value of the frequency f_L:

$$\omega_L = 2\pi f_L \tag{54}$$

and for a selected damping ratio ζ_D, the damping constant is calculated as:

$$c_D = 2\zeta_D\sqrt{(k_P + k_N)m_D} = 2\zeta_D\omega_I m_D \tag{55}$$

The values of ρ and κ, are determined from Eqs. (15)-(17) according to the selected parameter μ. Thus, from Eq. (49), the natural frequency should be:

$$\omega_0 = \omega_L\sqrt{\frac{1}{\rho^2} + \kappa(1+\kappa)\mu} \tag{56}$$

Finally the values of ω_I, ω_H and b_w can be calculated according to Eqs. (2),(46) and (50). Consequently, the equation of motion of the meta-material, for M number of unit cells is expressed in matrix formulation as:

$$\mathbf{M}\,\ddot{\mathbf{u}}(\mathbf{t}) + \mathbf{C}\,\dot{\mathbf{u}}(\mathbf{t}) + \mathbf{K}\,\mathbf{u}(\mathbf{t}) = \mathbf{F}\,\mathbf{f}(\mathbf{t}) \tag{57}$$

where $\mathbf{M}_{n\times n}$, $\mathbf{C}_{n\times n}$, $\mathbf{K}_{n\times n}\ddot{\mathbf{u}}_{n\times 1}$, $\dot{\mathbf{u}}_{n\times 1}$, $\mathbf{u}_{n\times 1}$, $\mathbf{F}_{n\times 1}$ and $n = 2M + 1$ is the number of degrees of freedom of the meta-material. For a single unit cell, M=1, the mass (**M**), damping (**C**) and stiffness (**K**) matrices are:

$$\mathbf{M} = \begin{bmatrix} m & 0 & 0 \\ 0 & m_D & 0 \\ 0 & 0 & m \end{bmatrix},\ \mathbf{C} = \begin{bmatrix} c_s + c_D & -c_D & -c_s \\ -c_D & c_D & 0 \\ -c_s & 0 & c_s \end{bmatrix}$$

$$\mathbf{K} = \begin{bmatrix} k_S + k_P & -k_P & -k_S \\ -k_P & k_P + k_N & -k_N \\ -k_S & -k_N & k_S + k_N \end{bmatrix},\ \mathbf{F} = \begin{bmatrix} 1 \\ 0 \\ 0 \end{bmatrix} \tag{58}$$

For $M > 1$, the above matrices of the single unit cell, are added appropriately. Therefore, the transfer functions of each degree of freedom to the excitation may be calculated via the following expression:

$$\mathbf{TF} = (-\omega^2\mathbf{M} + \jmath\,\mathbf{C} + \mathbf{K})^{-1}\mathbf{F} \tag{59}$$

where

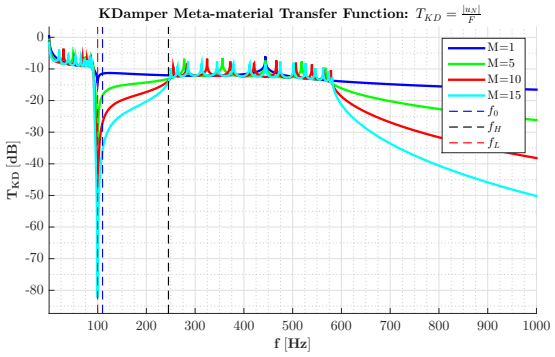
$$\mathbf{TF}_{n\times 1} = \left\{ \frac{\tilde{U}_{S,1}}{\tilde{F}} \quad \frac{\tilde{U}_{D,1}}{\tilde{F}} \quad \frac{\tilde{U}_{S,2}}{\tilde{F}} \quad \frac{\tilde{U}_{D,2}}{\tilde{F}} \quad \dots \quad \frac{\tilde{U}_{S,M+1}}{\tilde{F}} \right\}^T \tag{60}$$

The transfer function of the KDamper is defined as $T_{KD} = \frac{\tilde{u}_{S,M+1}}{\tilde{F}}$, which is subsequently examined further.

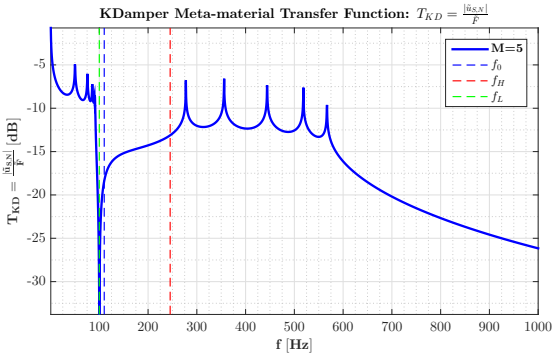
Figure 5.a shows a comparison between the transfer functions of the KDamper based meta-material for $M = 1, 5, 10$ and 15 number of unit cells for a selected low band-gap frequency $f_L = 100\ [Hz]$, damping ratios $\zeta = c_s/(2\omega_0 m) = 0.15$, $\zeta_D = 0.707$ and κ is taken as $0.9\kappa_{max}$.

It is observed that this meta-material offers satisfactory band-gap depth, namely over 20 $[dB]$ attenuation inside the band-gap, even for as low as $M = 5$ number of unit cells. Thus, for further examination regarding the behaviour of the meta-material at various frequencies f_L, the number of unit cells is chosen as $M = 5$. The corresponding transfer function for $f_L = 100$ is presented in Fig. 5.b.

(a)



(b)



(c)

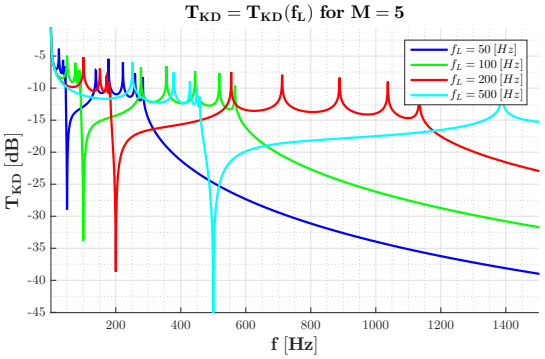


Figure 5: Transfer function of KDamper meta-material: (a) for increasing number of unit cells, (b) with M=5 number of unit cells for various frequencies f_L, (c) with M=5 number of unit cells

$f_L\ [Hz]$	50	100	200	500
$f_H - f_L\ [Hz]$	73	145	290	726

Table 1: Band-gap width for each f_L selection

The corresponding frequencies f_0,f_H and f_L are noted with dashed lines. In order to examine the effect of the low frequency choice f_L on the band-gap depth and width, Fig. 5.c is generated. In all cases the acoustic meta-material consists of $M = 5$ unit cells. The conclusion from this figure is that the width of the band-gap is decreased along with the selected frequency f_L which was expected. For $f_L < 100[Hz]$, the band-gap width becomes very narrow, but still offers considerable attenuation at the resonant frequencies.

3.2 Comparison of "m-k-m", TMD and KDamper Based Acoustic Metamaterials

A conventional "sandwich type" noise isolation panel, consisting of two plates with a noise insulation material between them and can be considered as a simple mass-spring-mass ("m-k-m") system, with some degree of internal damping. In view of Fig. 4, this corresponds to a system with $M = 1, m_D = c_D = k_N = k_P = 0$. Periodic repetition of this lattice results to a primitive form of a "phononic crystal" type of acoustic insulation meta-material. The introduction of an internal structure between the masses in the form of a TMD

($m_D, c_D, k_P \neq 0$) results to an acoustic meta-material design. The additional inclusion of a negative stiffness element ($k_N \neq 0$), results to a KDamper based meta-material.

The isolation-absorption properties of these three alternative concepts are compared here. The various meta-structures implemented have relevant unit lattice parameters summarized on Table 2 along with the resulting corresponding stiffness and damping elements in each case. The selection of the parameters ensures that all three unit lattice types have the same overall static stiffness. For this last reason, the overall static stiffness k_S of the periodic mass-spring-mass system is the same as the static stiffness of the TMD based meta- material. However, in view of Eq. (1), the value of k_S has to be increased for the KDamper meta-material, so that its overall static stiffness (now k_0) is equal to the overall static stiffness k_S of the other two types. Finally, the parameter κ of the KDamper meta-material is selected as $0.9\kappa_{max}$.

	μ	ζ	ζ_D
m-k-m	-	0.15	-
TMD	0.5	0.15	0.707
KDamper	0.01	0.15	0.707
	$f_L\,[Hz]$	$m[kg]$	$m_D[kg]$
m-k-m	-	0.035	-
TMD	100	0.035	$17.5 \times 10^{-}3$
KDamper	100	0.035	$0.35 \times 10^{-}3$
	$k_S\,[\frac{N}{m}]$	$k_0\,[\frac{N}{m}]$	$k_P\,[\frac{N}{m}]$
m-k-m	1.67×10^4	-	-
TMD	1.67×10^4	-	6.91×10^3
KDamper	9.98×10^4	1.67×10^4	8.69×10^3
	$k_N\,[\frac{N}{m}]$	$c_S\,[\frac{Ns}{m}]$	$c_D\,[\frac{Ns}{m}]$
m-k-m	-	7.26	-
TMD	-	-	31.10
KDamper	-7.87×10^3	7.26	0.76

Table 2: Values of the basic parameters of the meta-materials

Generally, Transmission Loss (TL) describes the accumulated decrease in intensity of a waveform energy, as a wave propagates through a certain type of structure and can be expressed as

$$TL = 10 \log_{10} \left| \frac{P_i}{P_t} \right| \, [dB] \tag{61}$$

where

- P_i : power of incident wave coming towards a structure,
- P_t : power of transmitted wave going away from a structure.

The theoretical prediction of the Transmission Loss in cases like this is a complicated procedure and sensitive to errors. However, the simplistic approach followed for this comparison provides an inside to the general behaviour of these meta-materials and the benefits of the demonstrated KDamper meta-material. Considering an incident plane wave on the surface of the 1st mass of the meta-material in question, with frequency $f = f_L = 100\,[Hz]$ which can be expressed in terms of acoustic pressure as:

$$p(r,t) = \tilde{p} e^{\jmath \omega t} \tag{62}$$

$$\tilde{p} = \hat{p} e^{\jmath \phi} \tag{63}$$

$$\phi = kr \tag{64}$$

where $\tilde{p}$ is the complex magnitude. Denoted by ϕ is the phase angle, where k is the wavenumber and r $[m]$ is the distance from the centre of the sound source. The surface in question is considered circular with an area $A = 0.01$ $[m^2]$. Consequently, considering a harmonic excitation force as:

$$F(t) = F_0 e^{\jmath 2\pi f_L t} \tag{65}$$

where

$$F_0 = \hat{p}A \ , \ \hat{p} = \frac{2}{\sqrt{2}} p_{ref} 10^{L_p/20} \tag{66}$$

$L_p = 70$ $[dB]$ is the considered sound pressure level and $p_{ref} = 20 \times 10^{-6}$ $[Pa]$. This level of noise is chosen in order to simulate the response of the meta-materials under typical conditions inside a car interior or an aircraft cabin.

Since the volume velocity is expressed as

$$Q = \upsilon A \tag{67}$$

and the sound power of the wave as

$$P = pQ \tag{68}$$

the power of the incident plane wave, assuming $r = 0$, comes as

$$P_i = \frac{\hat{p}^2}{\rho_0 c_0} A e^{2\jmath\omega t} \tag{69}$$

where ρ_0, c_0 are the air density and speed of sound respectively. Considering the surface of the last mass to be a source of sound waves equivalent to a circular piston in an infinite rigid baffle, the generated sound pressure is expressed as

$$p(r,t) = ZQe^{\jmath\omega t} \tag{70}$$

where

$$Z = \frac{\rho_0 c_0}{A}[e^{-\jmath kr} - e^{-\jmath k\sqrt{r^2+\alpha^2}}] \tag{71}$$

is the free space transfer impedance and α is the radius of the last mass. Therefore, for $r = 0$ considering the velocity $v = \dot{u}_{S,M+1}(t)$ as the velocity of the last mass, the power of the transmitted wave comes as

$$P_t = -\rho_0 c_0 A\omega^2 (1 - e^{-\jmath k^2}) \tilde{u}^2_{S,M+1} e^{\jmath 2\omega t} \tag{72}$$

Consequently the ratio of incident to transmitted sound power becomes:

$$\frac{P_i}{P_t} = \frac{1}{-A^2\omega^2(\rho_0 c_0)^2(1 - e^{-\jmath k\alpha^2})} \Big(\frac{\tilde{u}_{S,M+1}}{\tilde{F}}\Big)^{-2} = \frac{1}{-A^2\omega^2(\rho_0 c_0)^2(1 - e^{-\jmath k\alpha^2})} T_{KD}^{-2} \tag{73}$$

The comparisons between the three different concepts of the TL transfer function of each system are presented in Fig. 6. The "m-k-m" system essentially acts as a low pass filter for the noise with a cutoff frequency of $f_0 = 219.87[Hz]$. Observation of Fig. 6 indicates that the repetition of unit cells does not improve the low pass behavior. It just increases the high frequency filtering capability of this system. This behaviour is typical of the current noise isolation panels.

The TMD based meta-material retains this low pass filter behaviour, while introducing a deep but very narrow band gap. The width of this band-gap is approximately [100 Hz : 122 Hz]. However, in order to achieve this band-gap, an additional mass of 50% of the original mass of the meta-material is required. The repetition of unit cells does not improve the low pass behaviour or the band-gap boundaries. It just increases the high frequency filtering capability of this system, as well as the depth of the band-gap.

The KDamper meta-material essentially operates as a band-stop filter. Although its high frequency behaviour is less satisfactory than the periodic "m-k-m" system and the TMD based meta-material, it is very effective in introducing a very wide band gap of a [100Hz:245Hz] width while incorporating an added mass of only

1% of the value of the mass m. The repetition of unit cells, as presented in Fig. 6 increases the depth of the band-gap, while bearing a marginal effect on the high frequency behaviour of the system.

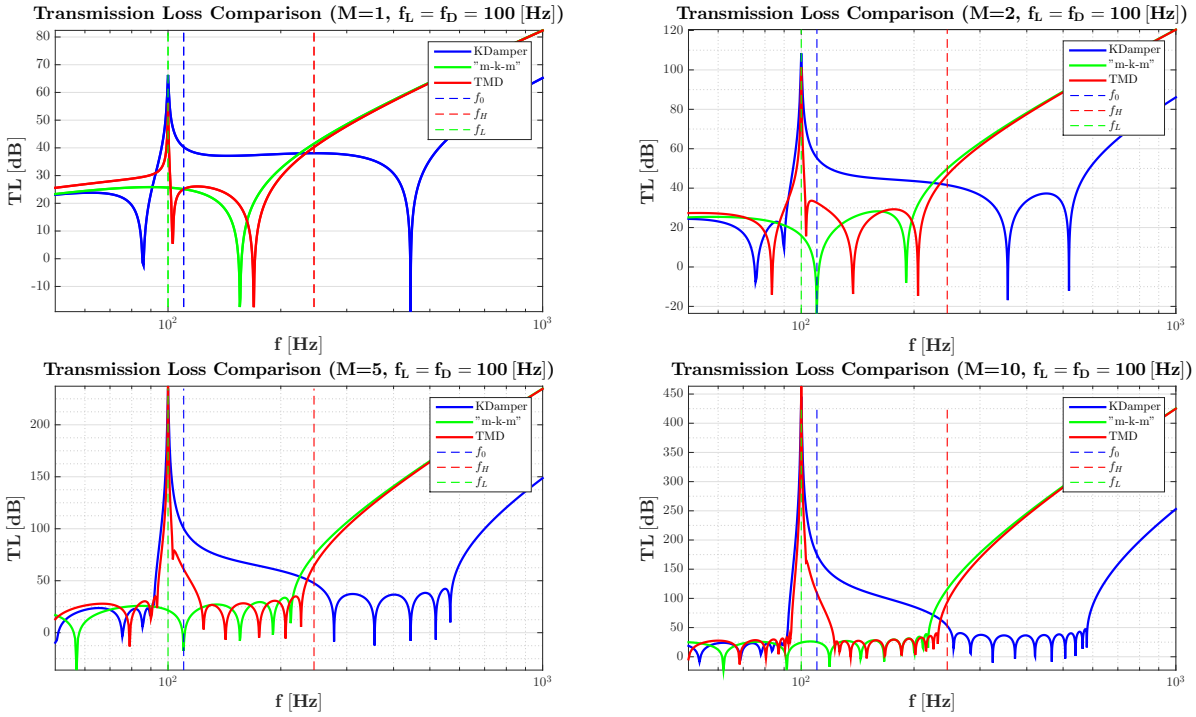


Figure 6: Comparison of the transmission loss (TL) transfer functions of the three acoustic isolation-absorption systems for $M = 1, M = 2, M = 5$ and $M = 10$ for $f_L = f_D = 100[Hz]$

3.3 Structural Realization of Negative Stiffness Element

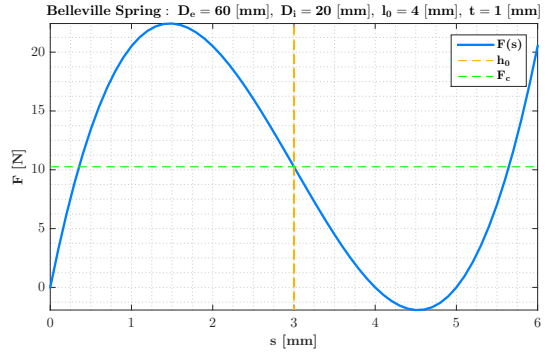
In structural mechanics, negative stiffness is generally obtainable through post-buckling processes (snap-through phenomenon). In this case, a single Belleville spring is chosen to act as the negative stiffness element of the oscillator. The exerted force and the equivalent stiffness of this type of springs, are non-linear functions of the vertical displacement s of the inner diameter D_i. The height of the spring is denoted by l_0, D_e is the external diameter and $h_0 \approx l_0 - t$, where t is the thickness. More specific informations are provided by manufacturers [27].



Figure 7: Structural realization of the negative stiffness element k_N, using a Belleville spring.

Figure 7 shows the shape of the spring along with the corresponding dimensions. As demonstrated in Fig.8, the range of the vertical displacement s corresponding to the snap- through region, exhibits the desired negative stiffness characteristics. This of course, translates to the application of a certain pre-stress condition on the spring, so that its stiffness falls in the negative stiffness region, at the equilibrium state of the oscillator.

(a)



(b)

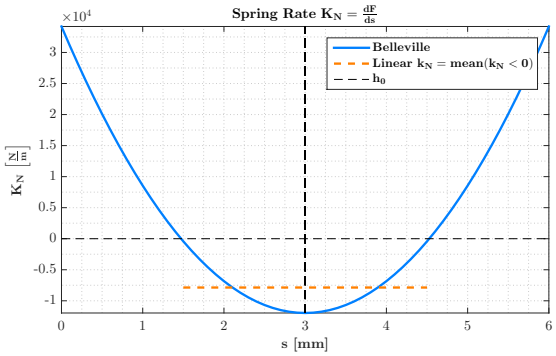


Figure 8: (a) Exerted force of the Belleville spring, as a function of the vertical displacement of its inner diameter. (b) Equivalent stiffness of the Belleville spring, as a function of the vertical displacement of its inner diameter.

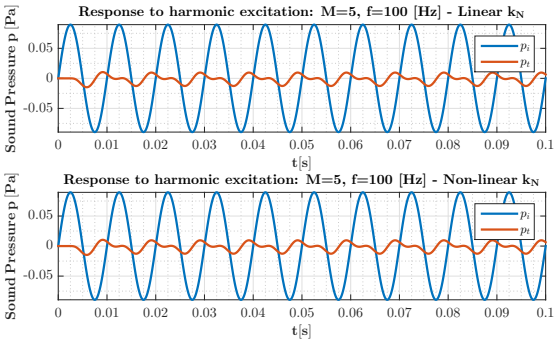
Figure 8.b shows the equivalent stiffness of the spring as a function of the vertical displacement s. The dotted orange line, indicates the mean value of k_N in the negative stiffness region, which corresponds to the k_N value used in the linear models, on which the dimensioning of the Belleville spring is based.

3.4 Response to Noise Excitation

3.4.1 Non-Linear Negative Stiffness - Pure Tone Sound Absorption

Initially, in order to investigate the time response of the meta-material and the effect of the non-linear negative stiffness element as realized via the Belleville spring, the same harmonic excitation is applied as in Sect.3.2.

(a)



(b)

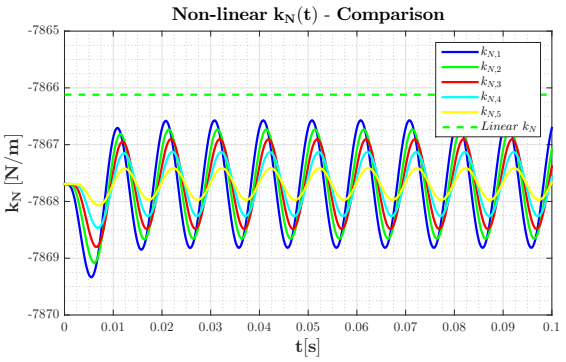


Figure 9: (a) Time response of KDamper meta-material with $M = 5$ unit cells to harmonic excitation with frequency $f = f_L = 100\ [Hz]$ (b) Time response of the non-linear stiffness of the negative stiffness elements realized with Belleville springs, for a KDamper meta-material with $M = 5$ unit cells. Comparison with linear k_N.

Observation of Fig.9.a, does not show any significant deviations between the linear and non-linear negative stiffness simulations. The required, initial, vertical displacement s of the Belleville springs (pre-stress), comes from the static equilibrium equations of the unit cell. Figure 9.b shows the time history of $k_{N,1}$ to $k_{N,M=5}$ values, along with the linear k_N stiffness, denoted by the green dotted line. Namely, the $k_{N,i}$ values of the Belleville springs, oscillate around the corresponding stiffness value of the aforementioned equilibrium position, which is approximating the linear k_N value.

3.4.2 Broadband Noise Absorption

In order to further examine the behaviour of the KDamper meta-material, a case of random noise acting as the excitation is considered. The content of this noise, is composed by a number of plane waves at frequencies between 100 and 300 Hz with random phase angles and amplitudes. Specifically, these features are generated as follows:

$$f_i = f_L \, (N(0,1) + 2) \tag{74}$$

$$\mathbf{F} = \sum_{i=1}^{h} |C_i| e^{\jmath 2\pi f_i t} \tag{75}$$

where

$$C_i = \alpha_0 e^{\jmath\phi} \tag{76}$$

$$\alpha_0 = F_0 \, N(0,1) \; , \; \phi = N(0,1) \tag{77}$$

and $N(0,1)$ are random numbers from a Gaussian distribution with zero mean and variance equal to unity. Considering a KDamper meta-material with M=5 unit cells, the response of the transmitted sound pressure along with the incident sound pressure is presented in Fig.10 (top). The corresponding sound pressure levels are displayed in Fig.10 (bottom).

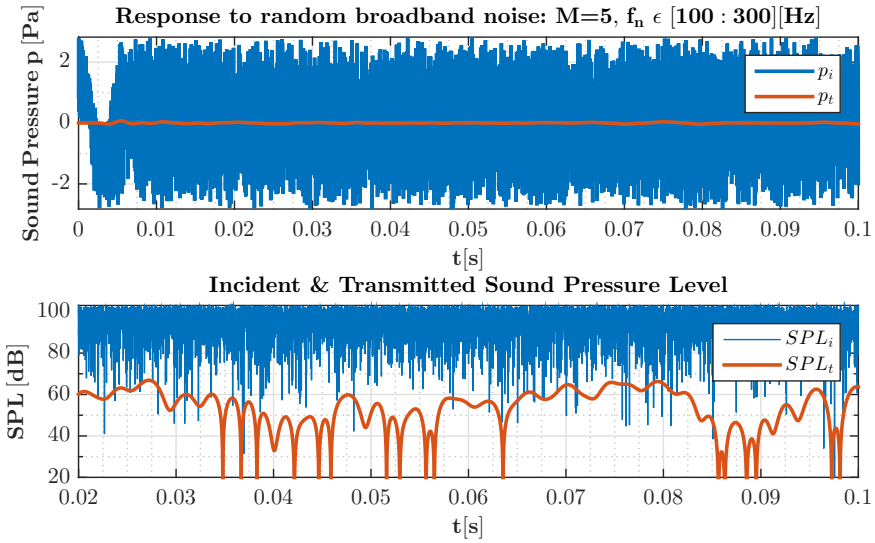


Figure 10: (Top) Time response of KDamper meta-material with $M = 5$ unit cells to random broadband noise with frequencies $f_n \, \epsilon \, [100 : 300] \; [Hz]$ (Bottom) SPL sample of the random broadband noise, with frequencies $f_n \, \epsilon \, [100 : 300] \; [Hz]$, used as excitation of the meta-material.

From Fig.10, comparing the incident sound (p_i, SPL_i) at the 1st mass to the transmitted sound (p_t, SPL_t) from the last mass/circular piston, the expected attenuation indicated by the corresponding TL transfer function presented in Fig.6.c is observed here.

4 Conclusion

Although acoustic meta-materials have been long considered to present the only available direction to create band-gaps at wavelengths much longer than the lattice size, and thus enable low-frequency vibration

attenuation, the width of the resulting band gaps is generally very narrow -especially when referring to the conventional "m-k-m" and TMD based periodic structures considered in the presented comparisons- since it depends on the ratio of the internal oscillating mass to the external mass of the unit lattice. Meta-materials based on the KDamper concept can overcome this disadvantage, since they exploit the additional synergy of a negative stiffness element inclusion. Thus, they prove highly efficient in generating wide band-gaps in low frequency applications, with only a small fraction of the external mass. Appropriate technological implementations of this concept can lead to drastic improvements in all types of low-frequency technological applications, with emphasis in low-frequency noise isolation-absorption. Future research objectives regarding this concept, include further examination of the meta-material response to broadband low frequency noise, involving computational simulations and experimental tests of practical implementations like panels, for determination of properties such as Transmission Loss and sound reflection among others.

References

[1] Hussein, M.I., Leamy, M.J., and Ruzzene, M. (2014). Dynamics of Phononic Materials and Structures: Historical Origins, Recent Progress, and Future Outlook. Applied Mechanics Reviews 66(4), 040802-040802-040838. doi: 10.1115/1.4026911.

[2] Sigalas, M.M., and Economou, E.N. (1992). Elastic and acoustic wave band structure. Journal of Sound and Vibration 158(2), 377-382. doi: http://dx.doi.org/10.1016/0022-460X(92)90059-7.

[3] Vasseur, J.O., Djafari-Rouhani, B., Dobrzynski, L., Kushwaha, M.S., and Halevi, P. (1994). Complete acoustic band gaps in periodic fibre reinforced composite materials: the carbon/epoxy composite and some metallic systems. Journal of Physics: Condensed Matter 6(42), 8759.

[4] Liu, Z., Zhang, X., Mao, Y., Zhu, Y.Y., Yang, Z., Chan, C.T., et al. (2000). Locally resonant sonic materials. Science 289(5485), 1734-1736.

[5] Huang, H., Sun, C., and Huang, G. (2009). On the negative effective mass density in acoustic metamaterials. International Journal of Engineering Science 47(4), 610-617.

[6] Auriault, J. L. and Bonnet, G. (1985). Dynamique des composites elastiques periodiques. Arch. Mech. 37:269-284.

[7] Auriault, J. L. (1994). Acoustics of heterogeneous media: Macroscopic behavior by homogenization. Current Topics in Acoust. Res. 1:63-90.

[8] Sun, H., Du, X., and Pai, P.F. (2010). Theory of Metamaterial Beams for Broadband Vibration Absorption. Journal of Intelligent Material Systems and Structures 21(11), 1085-1101. doi: doi:10.1177/1045389X10375637.

[9] Xiao, Y., Wen, J., Yu, D., and Wen, X. (2013). Flexural wave propagation in beams with periodically attached vibration absorbers: Band-gap behavior and band formation mechanisms. Journal of Sound and Vibration 332(4), 867-893. doi: http://dx.doi.org/10.1016/j.jsv.2012.09.035

[10] Pennec, Y., Djafari-Rouhani, B., Larabi, H., Vasseur, J.O., and Hladky-Hennion, A.C. (2008). Low-frequency gaps in a phononic crystal constituted of cylindrical dots deposited on a thin homogeneous plate. Physical Review B 78(10), 104105.

[11] Peng, H., and Frank Pai, P. (2014). Acoustic metamaterial plates for elastic wave absorption and structural vibration suppression. International Journal of Mechanical Sciences 89, 350-361. doi: http://dx.doi.org/10.1016/j.ijmecsci.2014.09.018.

[12] Groby, J.P., Lagarrigue, C., Brouard, B., Dazel, O., Tournat, V., and Nennig, B. (2014). Using simple shape three-dimensional rigid inclusions to enhance porous layer absorption. The Journal of the Acoustical Society of America 136(3), 1139-1148.

[13] Weisser, T., Schwan, L., Groby, J. P., Lagarrigue, C., Deckers, E., and Dazel, O. (2016, September). Poroelastic subwavelength absorber with both elastic and acoustic embedded resonator. In Proceedings of the 27th International Conference on Noise and Vibration Engineering, 2127-2136.

[14] Yang, Z., Dai, H. M., Chan, N. H., Ma, G. C., and Sheng, P. (2010). Acoustic metamaterial panels for sound attenuation in the 50-1000 Hz regime. Applied Physics Letters, 96(4), 041906.

[15] Schwan, L., Umnova, O., and Boutin, C. (2017). Sound absorption and reflection from a resonant metasurface: Homogenisation model with experimental validation. Wave Motion, 72, 154-172.

[16] Antoniadis I., Chronopoulos D., Spitas V. and Koulocheris D. (2015) Hyper-damping properties of a stable linear oscillator with a negative stiffness element, Journal of Sound and Vibration, 2015, 346, 37-52.

[17] Antoniadis, I.A., Kanarachos, S.A., Gryllias, K., and Sapountzakis, I.E. (2016). KDamping: A stiffness based vibration absorption concept. Journal of Vibration and Control, 24(3), 588-606.

[18] Sugino, C., Leadenham, S., Ruzzene, M., and Erturk, A. (2016). On the mechanism of bandgap formation in locally resonant finite elastic metamaterials. Journal of Applied Physics 120(13), 134501.

[19] Chronopoulos, D., Antoniadis, I., and Ampatzidis, T. (2017). Enhanced acoustic insulation properties of composite metamaterials having embedded negative stiffness inclusions. Extreme Mechanics Letters 12, 48-54.

[20] Chronopoulos, D., Antoniadis, I., Collet, M., and Ichchou, M. (2015). Enhancement of wave damping within metamaterials having embedded negative stiffness inclusions. Wave Motion 58, 165-179.

[21] Michelis, P., and Spitas, V. (2010). Numerical and experimental analysis of a triangular auxetic core made of CFR-PEEK using the Directionally Reinforced Integrated Single-yarn (DIRIS) architecture. Composites Science and Technology 70(7), 1064-1071.

[22] Virk, K., Monti, A., Trehard, T., Marsh, M., Hazra, K., Boba, K., et al. (2013). SILICOMB PEEK Kirigami cellular structures: mechanical response and energy dissipation through zero and negative stiffness. Smart Materials and Structures 22(8), 084014.

[23] Baravelli, E., and Ruzzene, M. (2013). Internally resonating lattices for bandgap generation and low-frequency vibration control. Journal of Sound and Vibration 332(25), 6562-6579.

[24] Wang, P., Casadei, F., Shan, S., Weaver, J.C., and Bertoldi, K. (2014). Harnessing buckling to design tunable locally resonant acoustic metamaterials. Physical review letters 113(1), 014301.

[25] Hussein, M.I., and Frazier, M.J. (2013). Metadamping: An emergent phenomenon in dissipative metamaterials. Journal of Sound and Vibration 332(20), 4767-4774.

[26] Huang, H.H., and Sun, C.T. (2009). Wave attenuation mechanism in an acoustic metamaterial with negative effective mass density. New Journal of Physics 11(1), 013003.

[27] Bauer, C. (2008, March 29). Disc springs-theory and practice. Retrieved from https://www.christianbauer.com/en/img-cust/3_Theory_and_practice.pdf

Influencing the wave-attenuating coupling of solid and fluid phases in poroelastic layers using piezoelectric inclusions and locally added masses

T. G. Zieliński [1], **M.-A. Galland** [2], **E. Deckers** [3,4]
[1] Institute of Fundamental Technological Research of the Polish Academy of Sciences,
ul. Pawińskiego 5B, 02-106 Warsaw, Poland
e-mail: **tzielins@ippt.pan.pl**

[2] Laboratoire de Mécanique des Fluides et d'Acoustique, Ecole Centrale de Lyon,
36 avenue Guy de Collongue, 69134 Ecully Cedex, France

[3] Department of Mechanical Engineering, KU Leuven,
Celestijnenlaan 300B box 2420, 3001 Heverlee, Belgium

[4] DMMS Lab, Flanders Make

Abstract
When airborne acoustic waves penetrate porous media their carrier becomes the air in pores, but also the solid skeleton – provided that it is sufficiently soft. Then, there is a coupled propagation of fluid-borne and solid-borne waves in a *poroelastic* medium. The coupling of fluid and solid phases of such media can be responsible for significantly better or weaker sound absorption in medium and lower frequency ranges. It has been observed that adding some well-localised small mass inclusions inside a poroelastic layer may improve its acoustic absorption in some medium frequency range, however, at the same time the absorption is usually decreased at some slightly higher frequencies. This situation can be improved by applying additionally an active approach using small piezoelectric inclusions which actively influence the vibrations of the solid skeleton with added masses, so that the interaction between the solid-borne and fluid-borne waves is always directed for a better mutual energy dissipation of the both types of waves.

1 Introduction

This work investigates the potential of an active enhancement of sound absorption in poroelastic foams by influencing the dissipative interaction between the solid and fluid phases by means of piezoelectric inclusions and locally added masses. Depending on its mounting, a piezoelectric inclusion can also play the role of a locally resonating mass (i.e., when it is *not* fixed to the backing wall). Thus, the work essentially combines the concepts of passive foams with inclusions and active acoustic foams.

A passive enhancement of acoustic treatments at some frequency ranges thanks to inserted inclusions was reported in many works. Experimental investigations by Kinder, Fuller and Gardner [1] showed a significant improvement of the insertion loss of standard acoustic blankets at lower frequencies by the addition of randomly placed masses. Yamamoto *et al.* [2] applied the techniques of topology optimization for passive layers consisting of one or two poroelastic media, elastic inclusions, and air cavities, in order to minimise the sound pressure levels in a coupled structural-acoustic system. The influence of small but heavy elastic inclusions on sound absorption of poroelastic foams was studied in [3] showing that the inclusion mass and scattering effects are important, while the elastic behaviour can be neglected for small compact (bulk) metal inclusions. The acoustic absorption of porous absorbers with different elastic inclusions was also the

subject of research in [4, 5, 6] where the fluid-equivalent models were used for porous media, assuming that their frames are rigid. Recently, the multiple scattering formalism has been applied in [7] to model sound absorbing poroelastic materials with embedded elastic inclusions.

The concept of smart acoustic foams was proposed by Gentry, Guigou, and Fuller [8, 9, 10] in experimental works on the application of control algorithms to polyurethane foams with pieces of piezoelectric PVDF film embedded inside. A piezoelectric composite smart foam for underwater noise reduction was also studied experimentally by Tang and Wang [11]. The feasibility of an active or adaptive enhancement of sound absorption and other desirable properties by applying a magnetic field was demonstrated on various samples of magnetorheological foams, i.e., highly porous materials coated with the magnetorheological fluid [12, 13, 14]. An experimental research was also conducted by Lee *et al.* [15] to investigate panels made up of a layer of sound-absorbing porous material and an aluminium faceplate with a piezoelectric patch, or two faceplates and an air gap in case of the so-called double panel. An advanced approach to model the problem of hybrid active-passive acoustic panels with poroelastic core was applied in a series of works [16, 17, 18, 19, 20], which present mainly a rigorous fully-coupled finite element modelling involving the Biot's poroelasticity [21] and the piezoelectric equations [22], but also some analytical developments and experimental tests. Active absorbers using a control system to cancel the acoustic pressure at the rear face of a porous layer, so as to obtain a purely real impedance at the front face (the value of which depends only on the resistivity and thickness of the porous material) was studied in [23, 24, 25]. Hybrid acoustic treatment was also investigated in [26] through experimental tests in a specific laboratory flow duct, as well as in modelling using the fluid-equivalent (rigid-frame) model for a porous material.

Smart foams with a PVDF film as a piezoelectric actuator embedded inside were extensively investigated by Leroy *et al.* [27, 28, 29], who performed finite element analyses (using, i.a., poroelastic finite elements) and some experimental validation tests to demonstrate the validity in the passive state. The acoustic absorption of poroelastic composites with active piezoelectric inclusions was examined in [30, 31, 32] using the fully-coupled modelling of poroelastic, elastic, piezoelectric, and acoustic media [33, 34].

The present work effectively combines the approaches proposed in [30, 31, 32] and [3, 35]. In Section 2 the problem configurations are described with all necessary geometric and material data. The applied poroelastic modelling and the passive state behaviour are discussed for one of the configurations in Section 3, while the active approach is analysed in Section 4 for both configurations and compared with the results of passive analyses (as well the sound absorption of the porolestic layer without inclusions).

2 The problem description and two configurations

Figure 1 shows a two-dimensional configuration of a 30 mm thick poroelastic layer (with inclusions) backed by a rigid wall. The adjacent semi-infinite layer of air is also depicted since a part of it will be considered in the model. The inclusions are embedded periodically every 16 mm along the poroelastic layer. There are two types of inclusions: (1) pieces of 0.25 mm thick PZT ceramics, (2) steel rods with diameter 0.8 mm.

Two configurations will be considered with respect to the attachment and cross-sectional length of the PZT ceramic actuators, namely: (A) the actuators are freely embedded inside the poroelastic layer at 5 mm distance from the wall 5 mm distance from and the steel rods on the other side; their cross-sectional length is 10 mm; (B) the actuators are fixed to the wall backing the poroelastic layer and their cross-sectional length is 15 mm. In both cases, the steel inclusions are set 10 mm from the layer's surface and 5 mm in front of the PZT actuators. Figure 1 depicts configuration A, although the alternative dimensions for the variant B are also shown (in the parenthesis). Both configurations are visualised in Figure 2, where the finite element meshes of modelled domains are presented. The modelled domains are drawn in Figure 1 as the adjacent rectangles $P_1P_2P_4P_3$ (the poroelastic domain) and $P_3P_4P_6P_5$ (the adjacent air domain). The symmetry along the lines $P_1P_3P_5$ and $P_2P_4P_6$ is accounted for, and the poroelastic domain contains only the upper halves of the PZT and steel inclusions. At the boundary P_5P_6 the normal-incidence plane wave pressure boundary condition is applied.

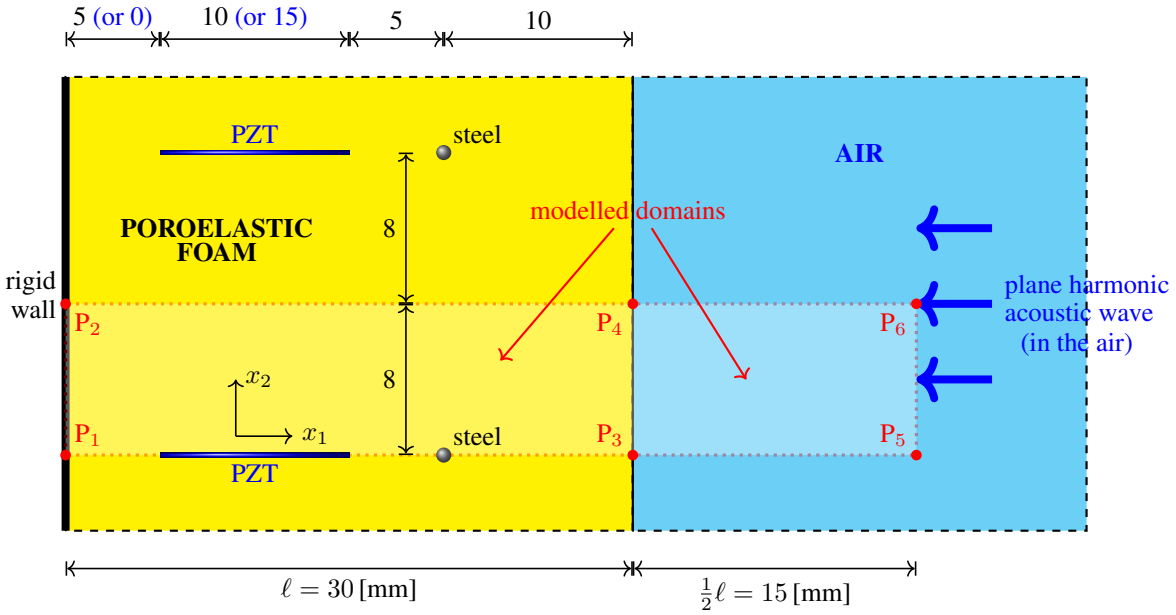
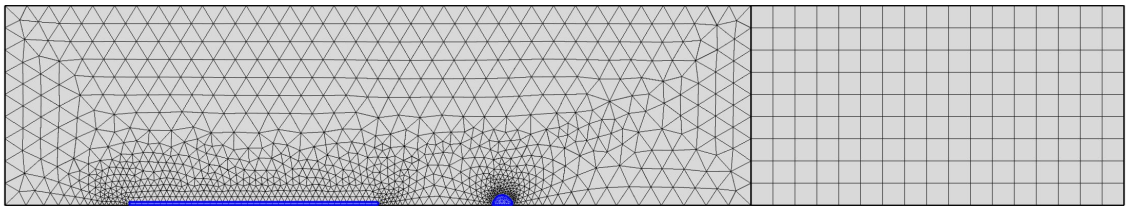


Figure 1: Poroelastic layer with inclusions and an adjacent air layer

CONFIGURATION **A**



CONFIGURATION **B**

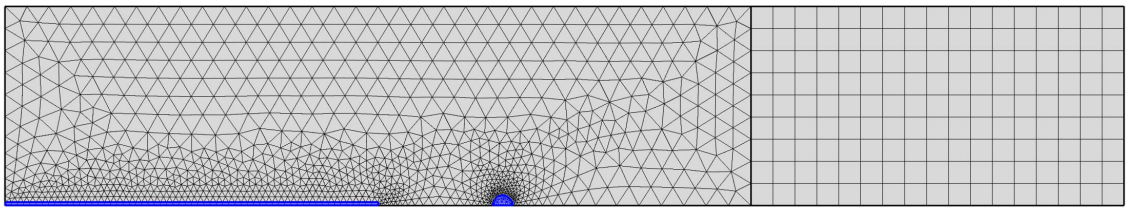


Figure 2: Finite element meshes for both configurations

The poroelastic material is a macroscopically-isotropic PU foam with properties listed in Table 1. The additional properties of pore-fluid (the mass density, the viscosity, the Prandtl number, the ratio of specific heats, and the ambient mean pressure) were taken as for air in standard conditions. The PZT ceramics are transversally-isotropic. For the material orientation as in Figure 1, where it is assumed that the material x_1-axis is horizontal and the x_2-axis is vertical, the relevant material constants for PZT are listed in Table 2. The problem is stated as two-dimensional using the plane-strain assumption, so only indispensable material constants are provided using the Voigt notation (where the fourth order elasticity tensor is represented by a symmetric matrix 6×6, and the third order piezoelectric tensor is represented by a matrix 3×6). Finally, the following properties of steel were used in calculations: the mass density $\varrho_{\text{steel}} = 7850\,\text{kg/m}^3$, the Young modulus $E_{\text{steel}} = 210\,\text{GPa}$, and the Poisson ratio $\nu_{\text{steel}} = 0.3$.

Parameter	Symbol	Unit	Value
porosity	ϕ	%	97
tortuosity	α_∞	–	2.52
flow resistivity	σ	kPa·s/m^2	87
viscous length	Λ	mm	0.037
viscous length	Λ'	mm	0.119
bulk density	ϱ_b	kg/m^3	31
bulk Poisson ratio	ν_b	–	0.3
shear modulus	μ_s	kPa	$55 \cdot (1 + 0.055\mathrm{i})$

Table 1: Poroelastic parameters of PU foam

mass density: $\varrho_\mathrm{PZT} = 7500\,\mathrm{kg/m^3}$
relevant elastic moduli (in the Voigt notation): $C_{11} = 127\,\mathrm{GPa}$, $C_{22} = 117\,\mathrm{GPa}$, $C_{12} = 84.7\,\mathrm{GPa}$, $C_{66} = 23\,\mathrm{GPa}$
relevant piezoelectric coupling coefficients (in the Voigt notation): $d_{21} = -274 \cdot 10^{-12}\,\mathrm{m/V}$, $d_{22} = 593 \cdot 10^{-12}\,\mathrm{m/V}$, $d_{26} = 0\,\mathrm{m/V}$

Table 2: Properties of PZT ceramics

3 Analyses in the passive state

The Biot-Allard or, more precisely, Biot-JCA model (JCA = Johnson-Champoux-Allard) [21, 36, 37, 38] was used for the poroelastic domian. The mixed displacement-pressure formulation [39, 40, 41] of the time-harmonic version of the Biot's equations of poroelasticity [21] was applied where the primary dependent variables are the complex amplitudes of the solid-phase displacements $\mathbf{u}^\mathrm{s}$ and the pore-fluid pressure p. The fluid-phase displacements $\mathbf{u}^\mathrm{f}$ and the total displacements $\mathbf{u}^\mathrm{t} = \phi\,\mathbf{u}^\mathrm{f} + (1-\phi)\mathbf{u}^\mathrm{s}$ are the secondary fields determined from the primary variables [39, 40].

In the model the symmetry conditions are applied on the boundaries $\mathrm{P_1P_3P_5}$ and $\mathrm{P_2P_4P_6}$. (The piezoelectric effect will be approximated with initial strains so there is no electric field in the model which otherwise would involve antisymmetry.) The sound hard boundary condition is set at the rigid wall boundary $\mathrm{P_1P_2}$ and the harmonic pressure condition of (amplitude) 1.0 Pa is applied at the boundary $\mathrm{P_5P_6}$. The coupling on the interfaces between the poroelastic material and elastic inclusions is naturally handled [40, 41] in the combined weak form of the relevant problems, so that only the continuity between the solid-phase displacements and elastic displacements must be satisfied, which allows to use the same variable $\mathbf{u}^\mathrm{s}$ also for the fields of displacements in elastic materials. Similarly, the continuity between the pore-fluid pressure and the pressure field in the adjacent air layer allows to use the same pressure variable p, although also an additional coupling integral must appear on the interface $\mathrm{P_3P_4}$ between both media.

Several numerical analyses were carried out for both configurations using the Finite Element Method (FEM) and the finite element meshes shown in Figure 2. At the first stage the analyses were for the passive state of the poroelastic composite, that is, when there is no voltage (nor electric field) applied and the PZT actuators are passive. Time-harmonic problems governed by the Biot's equations of poroelasticty (in the poroelastic domain $\mathrm{P_1P_2P_4P_3}$) coupled at the interface $\mathrm{P_3P_4}$ to the Helmholtz equation (in the air domain $\mathrm{P_3P_4P_6P_5}$) are solved yielding as results the complex-amplitude fields of the pore-fluid or acoustic pressure and the total or particle velocity, respectively, in the appropriate domains. This permits to compute the surface acoustic impedance at various points, in particular, at the surface of the poroelastic layer and at some distance from it in the air domain.

From the acoustic impedance, the reflection and acoustic absorption coefficients can be determined [36], and since the propagation in the open air is assumed lossless, the poroelastic layer/composite is solely responsible for the sound absorption computed from the double-layer configuration of the poroelastic domain $\mathrm{P_1P_2P_4P_3}$

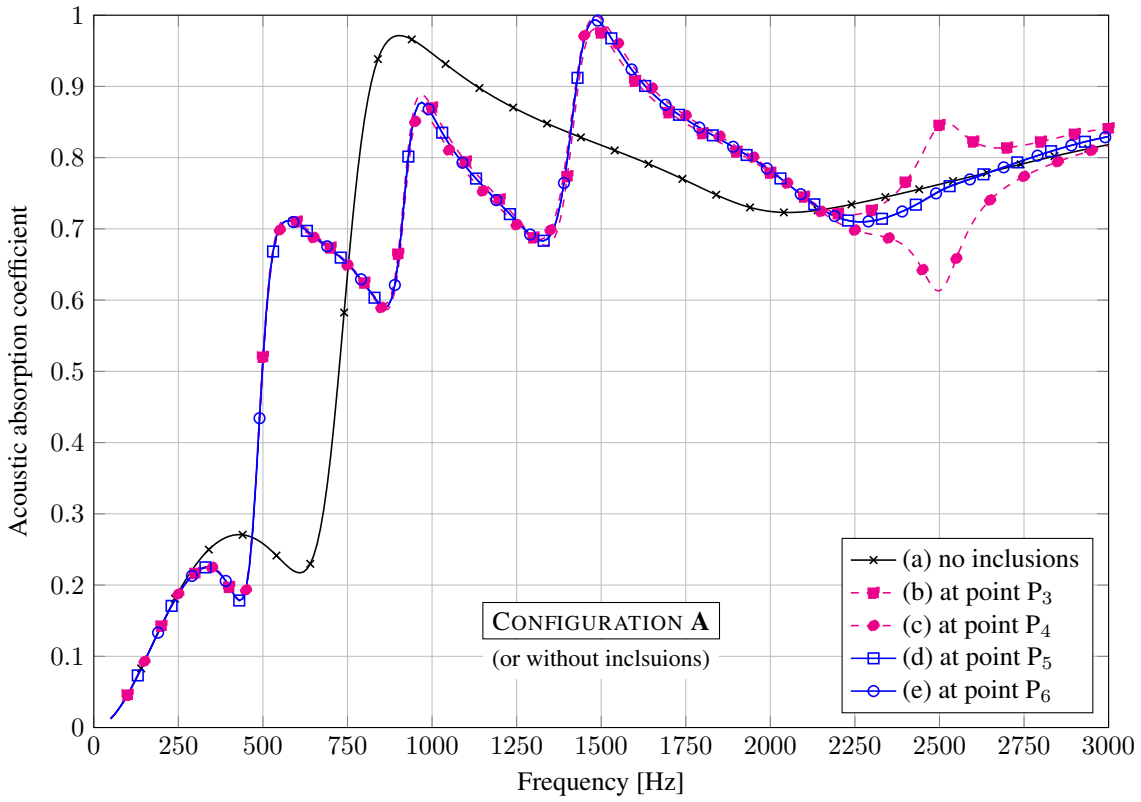


Figure 3: Sound absorption of the poroelastic layer (with passive inclusions in configuration A) computed at various points (see Figure 1) on the surface of in the lossless adjacent layer of air

and the adjacent domain of air $P_3P_4P_6P_5$. Therefore, one may speak here about the double-layer configuration only from the purely *computational* point of view. From the physical point of view, this is a single-layer absorber (with inclusions, so a non-homogeneous one). On the other hand, the obvious single-layer computational configuration, defined as the sole poroelastic domain $P_1P_2P_4P_3$ with the pressure excitation applied directly on the boundary P_3P_4, could be used only for some trivial or specific cases (see below), and *not* for the analyses of active approach. As a matter of fact, in case of the poroelastic layer *without* inclusions, the acoustic impedance (and therefore the acoustic absorption coefficient) is exactly the same no matter whether the calculations (which can be done analytically, see for example [42]) were carried out for the single- or double-layer computational configurations (although the pressure or velocity computed in various points are obviously completely different). The double-layer computational configuration is useful for the poroelastic composite, because the presence of inclusions locally violates the plane-wave regime and in some frequency ranges the vibrations and pressure may vary along the layer surface, whereas in the air at some distance from the layer the waves are plane. This is well illustrated in Figure 3, where the sound absorption results are compared for the layer without and with inclusions (for the configuration A): the absorption above 2200 Hz computed at points P_3 and P_4 on the poroelastic layer are fairly different from each other, although their mean value tends to be similar to the results computed in the air domain at points P_5 and P_6, which are practically identical. Below 2200 Hz the absorption results are almost the same for all calculation points on the interface P_3P_4 or on the boundary P_5P_6. It was found that, in practice, for the passive analyses in the frequency range of interest: (1) the single-layer approach could be used provided that the acoustic impedance is computed as an average from the integral taken on the boundary P_3P_4, or (2) in case of the double-layer computational configuration (which is obviously a little bit more computationally demanding) at least the thickness of air layer could be much smaller than the assumed half of the poroelastic layer.

The absorption curve for the layer with passive inclusions (configuration A) has three major peaks (see Figure 3): the one exceeding 0.7 at about 570 Hz, the value of about 0.87 at 950 Hz, and the maximal value

of nearly 1.0 at 1470 Hz. Two of them are manifestations of the presence of resonating inclusions fixed to the elastic skeleton and working as additional localised masses and wave scatterers inside the poroelastic domain. The first peak and the third one are responsible for the passively enhanced absorption (with respect to the case without inclusions) in the lower and higher frequency ranges, whereas the middle peak repeats to some extent the extreme performance found for the layer without inclusions in the medium frequency range. As a matter of fact, the absorption curve for the poroelastic layer without inclusions has a single major absorption peak of 0.97 at about 900 Hz. There is also a distinct absorption drop, observed at about 620 Hz for the layer without inclusions, which results from the first resonance of the elastic skeleton: it is the so-called quarter-wavelength resonance of the poroelastic layer set on the rigid wall [43]. In case of the layer with inclusions as in the configuration A, it is shifted to lower frequencies (namely, to 430 Hz), because of the added mass of inclusions – the mass effect is, therefore, more important than the locally added stiffness, which would shift the resonance to a higher frequency (see the discussion for the configuration B in Section 4). Finally, it seems that the effect of inclusions can be neglected above 2100 Hz: the difference in sound absorption is very small and tends to diminish completely when increasing the frequency. In the next Section, the active approach will be investigated for both configurations, A and B, in the frequency range up to 2 kHz.

4 Numerical analyses of the active approach

The active approach will be investigated in this Section, which means that a control signal is supplied to the electrodes of the PZT actuators and the piezoelectric effect plays an important role. However, since the PU foam is incomparably much softer than the stiff PZT ceramics a simplified approach can be applied to model the piezoelectric behaviour of the actuators. One may assume that the deformations of poroelastic foam caused by the acoustic waves induce no significant deformations inside the piezoelectric ceramics; only the other way around is possible. Thus, the direct piezoelectric effect can be neglected and instead of using the fully-coupled piezoelectric model only the inverse piezoelectric effect must be considered. This can be done is a simple way through the initial strains. It means that the PZT actuators can be treated as made up of a purely elastic material with some (time-harmonic) fields of initial strains, which happen to be caused by a dynamic external electric field. In that way the stress-strain relations of the material are affected as follows:

$$T_1 = C_{11}\big(S_1 - S_1^0\big) + C_{12}\big(S_2 - S_2^0\big), \quad T_2 = C_{22}\big(S_2 - S_2^0\big) + C_{12}\big(S_1 - S_1^0\big), \quad T_6 = C_{66}\big(S_6 - S_6^0\big). \tag{1}$$

Here, only the non-zero terms of the relations in the modelling plane are given, and the Voigt notation is used in which: $T_1 \equiv \sigma_{11}$, $T_2 \equiv \sigma_{22}$, and $T_6 \equiv \sigma_{12}$ are the relevant components of the stress tensor, $S_1 \equiv \varepsilon_{11}$, $S_2 \equiv \varepsilon_{22}$, and $S_6 \equiv \varepsilon_{12}$ are the relevant components of the elastic strain tensor, and similarly, $S_1^0 \equiv \varepsilon_{11}^0$, $S_2^0 \equiv \varepsilon_{22}^0$, and $S_6^0 \equiv \varepsilon_{12}^0$ are the relevant components of the tensor of initial strains. (See also Table 2 for the elastic material constants C_{11}, C_{12}, C_{22}, and C_{66}.) The initial strains are induced by an external electric field caused by a voltage signal sent to the electrodes of the PZT actuator, which are on the opposite lateral faces normal to the x_2-axis. Since the direct piezoelectric effect can be neglected, the electric field is spatially-constant in the whole domain of the PZT actuator, and moreover, $E_1 = E_3 \equiv 0\,\mathrm{V/m}$. Thus, only the E_2 component can be non-zero, and it generates the (dynamic) initial strains through the piezoelectric coupling coefficients (see Table 2), namely:

$$S_1^0 = d_{21}E_2\,, \qquad S_2^0 = d_{22}E_2\,, \qquad S_6^0 = d_{26}E_2\,. \tag{2}$$

(Notice that $S_6^0 = 0$, because $d_{26} = 0\,\mathrm{m/V}$, see Table 2.) The electric field depends (through the Maxwell's law) on the gradient of the electric potential, and in the simple case of the PZT actuator this relation can be written as follows:

$$E_2 = -\frac{U}{t_{\mathrm{PZT}}}, \tag{3}$$

where $t_{\mathrm{PZT}} = 0.25\,\mathrm{mm}$ is the thickness of PZT elements, while U is the electric voltage difference between

the two electrodes. The latter is here, in fact, the complex amplitude of the electric signal, namely:

$$U = U_{\text{amp}} \left(\cos(U_{\text{phase}}) + \mathrm{i} \sin(U_{\text{phase}}) \right), \tag{4}$$

where U_{amp} and U_{phase} are the real amplitude and phase shift of the electric voltage U, respectively. The phase shift U_{phase} is defined with respect to the acoustic pressure signal set on the boundary $\mathrm{P_5P_6}$ (which has no phase shift and therefore is real with the amplitude of 1.0 Pa).

The harmonic acoustic pressure of amplitude 1.0 Pa means the root-mean-square pressure of $1.0\,\text{Pa}/\sqrt{2} = 0.707\,\text{Pa}$ and sound pressure level of about 91 dB. It was found that such harmonic plane wave excitation, when applied to the layer of the poroelastic PU foam without inclusions, causes deformations of the solid skeleton phase of the order of 10^{-5}. The maximal amplitude of the normal solid phase strain $\varepsilon^{\text{s}}_{11}$ at about 5 to 10 mm from the rigid wall exceeds $2 \cdot 10^{-5}$ (at about 770 Hz). At this position (i.e., rather deep inside the layer) the piezoelectric inclusions would be embedded. For the amplitude $U_{\text{amp}} = 20\,\text{V}$ of the electric signal applied to the piezoelectric actuator, the amplitude of the initial strain $S^0_1 \equiv \varepsilon^0_{11}$ is almost $2.2 \cdot 10^{-5}$, and for $U_{\text{amp}} = 50\,\text{V}$ it's nearly $5.5 \cdot 10^{-5}$. The deformations of this order should satisfy the linear regime of vibrations of PU foam.

The introduced dynamic deformations of piezoelectric inclusions are supposed to move the elastic skeleton of PU foam so that the viscous interaction of the solid frame and the pore-fluid is directed in the way which increases the wave-attenuating effects. It has been shown (see Figures 3 and 4) that in the passive state the inclusions embedded inside the poroelastic layer may significantly change the sound absorption in some frequency ranges: the absorption is increased in the lower (470–750 Hz) and higher (above 1400 Hz) frequency ranges, however, it is moderately decreased at medium frequencies between 750 and 1400 Hz, although the peak at about 950 Hz is to some extent the major absorption peak observed for the layer without

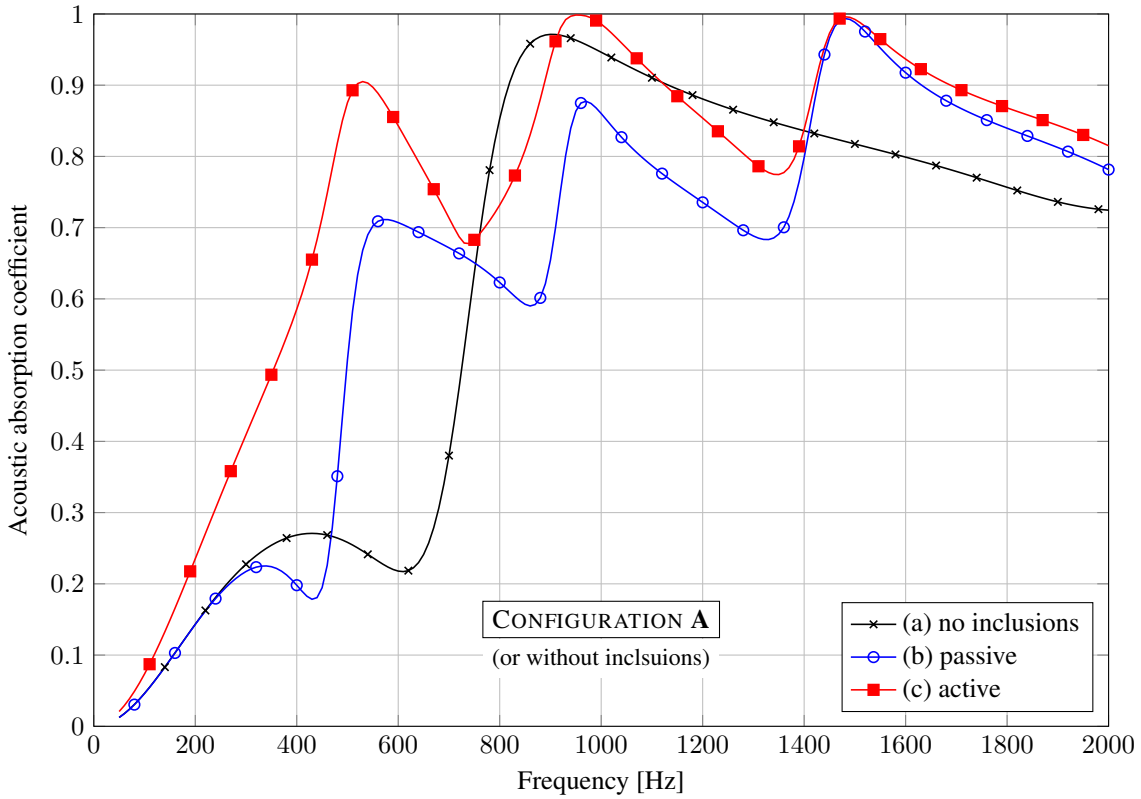


Figure 4: Sound absorption of the poroelastic layer (without or) with passive inclusions (configuration A) and for the active approach with the control signal of the fixed amplitude $U_{\text{amp}} = 50\,\text{V}$ and the optimised phase U_{phase}

inclusions at 900 Hz. The mechanism of passive influence is as follows: the steel inclusion and the non-fixed (in the configuration A) ceramic inclusion form two local masses which affect the vibrations of skeleton, but also they locally stiffen the foam, and moreover, they play a role of non-homogeneous scatterers. The active approach should affect the vibrational motion of both masses in order to: (1) increase or adjust the frequency-dependent amplitudes of the *relative* displacements of inclusions with respect to the displacements of elastic skeleton, and (2) appropriately change the relative phase shift between the vibrations of the solid frame (understood as the PU skeleton with the attached inclusions) and the pore-fluid. The superior goal is, of course, enhancement of the visco-thermal dissipation of the energy of acoustic waves penetrating the poroelastic composite. In the analyses presented below the amplitudes of the applied control signal are the same at each frequency – for the configuration A: $U_{\text{amp}} = 50$ V. Therefore, it is the relative phase shift U_{phase}, which is optimised for each (computational) frequency during the analyses of active approach.

Figure 4 compares the results of the active and passive approaches for the configuration A in the frequency range up to 2 kHz: the acoustic absorption for the control signal with the optimised phase is at each frequency higher than the absorption in the passive state, however, in some frequency ranges (i.e., 760–900 Hz and 1120–1400 Hz) it is slightly lower than the absorption of the poroelastic layer without inclusions. It is important to notice that a steady and significant enhancement in absorption is observed especially at low frequencies under 520 Hz, with the peak of 0.9 at this frequency. At about 750 Hz the enhancement is very weak, but this effect is isolated there to an extremely narrow band around this frequency. It fully exhibits itself above 1400 Hz where the active enhancement is very small or negligible, but the passive absorption is still clearly better than for the layer without inclusions.

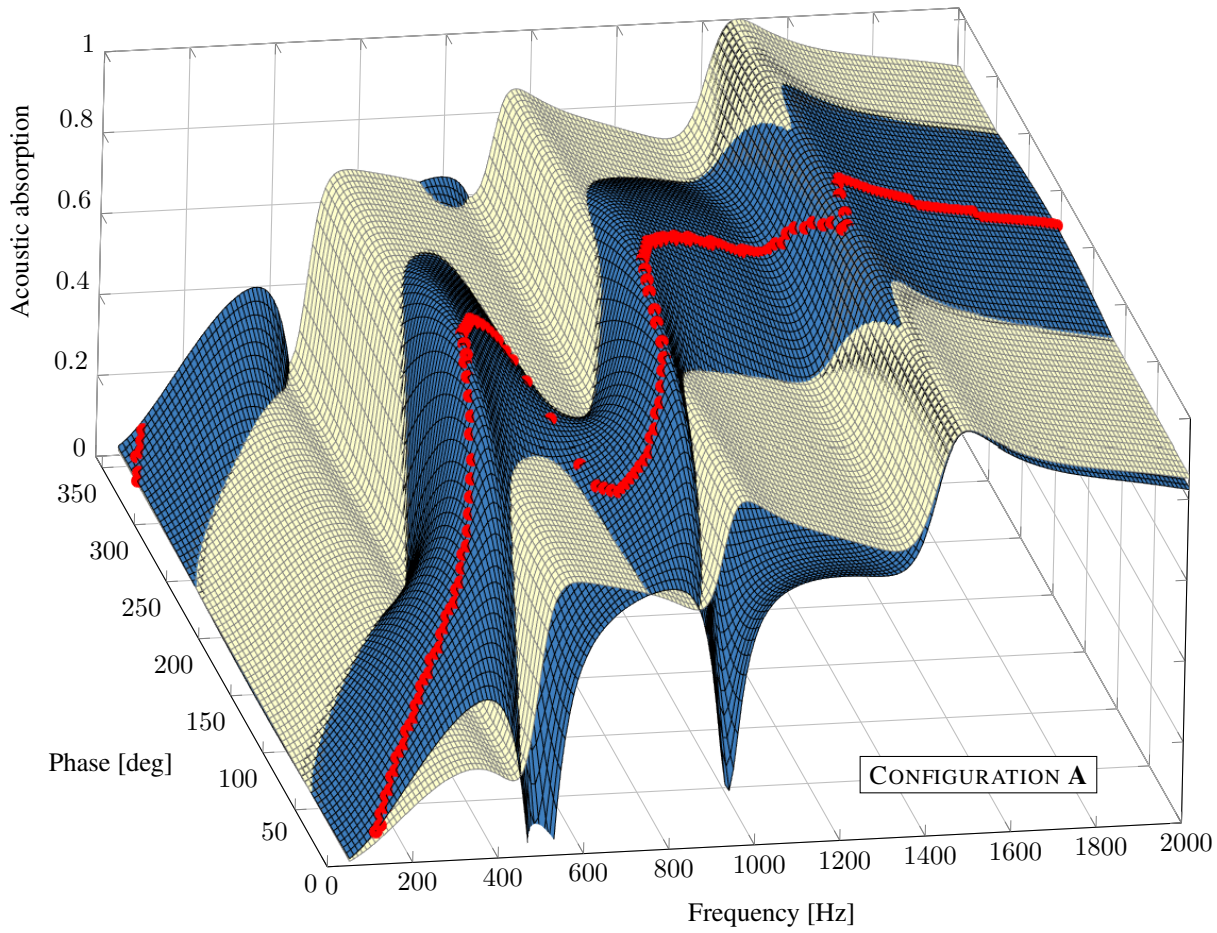


Figure 5: Sound absorption of the poroelastic layer with inclusions (configuration A): the phase-shift sweep for the active signal (the blue surface) and its optimal values (the red path, see also Figure 7 for 2D plot) compared with the passive state (the yellow surface constant along the phase axis)

The active absorption curve shown in Figure 4 was obtained for the optimal phase shift U_{phase}. The choice of a correct phase shift for each frequency is indispensable, since for active signals with wrong phases the absorption will be weakened instead of being enhanced. However, the choice of the signal phase may not be so precise, which is illustrated (for the configuration A) by Figure 5 showing the active sound absorption computed for the full sweeps of phase-shift carried out at each computational frequency from the considered range (i.e., every 10 Hz from 50 to 2000 Hz). Here, the active result is compared with the absorption of the passive state which is phase-independent (since no control signal is applied) to observe that at each frequency the phase-shift tolerance exceeds a hundred of degrees if we require simply that the active absorption must only be higher (that is, not worse) than the passive one. In Figure 5 the optimal phase-shift which ensures the best absorption enhancement is also shown as the red path on the active absorption surface.

Similar analyses of the sound absorption in the passive state and with the optimised active enhancement were carried out for the configuration B. In this configuration, the PZT actuators are fixed to the rigid wall backing the poroelastic layer. Therefore, the inertial effect of the ceramic inclusions is negligible, however, they significantly stiffen the interior of the poroelastic layer and scatter the waves. On the other hand, the advantage of this configuration is that the effect of active influence is much stronger, because the vibrating (and 50% longer) piezoelectric actuators are supported by the wall. Consequently, the control signal of a smaller voltage amplitude is required, e.g., $U_{\text{amp}} = 20$ V, in order to effectively drive the vibrations of the steel inclusions and the elastic skeleton.

The passive and active absorption results for the configuration B are confronted in Figure 6, where the passive-state result for the configuration A is also recalled for comparison, so it is easy to notice that the passive absorption for both configurations is practically identical for frequencies above 1 kHz. Under this frequency the passive absorption for the configuration B tends to be similar to the sound absorption of the

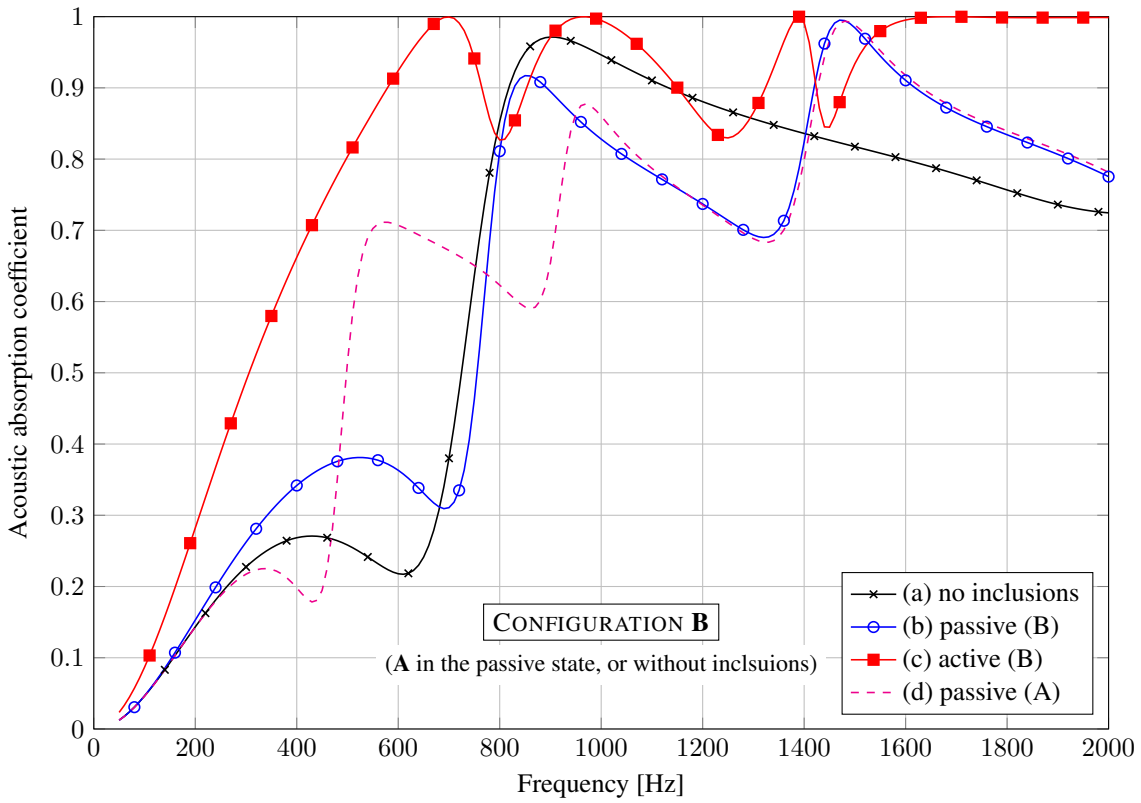


Figure 6: Sound absorption of the poroelastic layer (without or) with passive inclusions (both configurations) and for the active approach (configuration B) with the control signal of the fixed amplitude $U_{\text{amp}} = 20$ V and the optimised phase U_{phase}

layer without inclusions, although the maximal performance (at about 850–900 Hz) is slightly smaller when the inclusions are present, and in the lowest frequency range under 680 Hz the absorption is increased by the presence of inclusions. There is also a shift of the quarter-wavelength resonance from 620 Hz (no inclusions) to the higher frequency of 700 Hz (with inclusions in the configuration B), because the ceramic elements makes the poroelastic layer more stiff and their mass can be neglected since they are fixed to the rigid wall.

The active (phase-optimised) enhancement of the acoustic absorption in the configuration B is generally very good. The absorption is steadily increased at lower frequencies till 700 Hz where it is 1.0. Then, there are some fluctuations with peaks reaching again 1.0 around 950 Hz and 1400 Hz, however, one should notice that the active absorption anywhere above 500 Hz always exceeds the value of 0.8, and it becomes constantly 1.0 above 1600 Hz. Nevertheless, although the phase-shift is optimised, there are also two narrow band ranges, namely, 800–850 Hz and 1430–1530 Hz, where the active absorption is slightly lower than the passive one (which is generally very good there, with local peaks, and reaches the maximum 1.0 in the second of the two ranges). Obviously, it means that at these frequencies the active approach should be simply switched off.

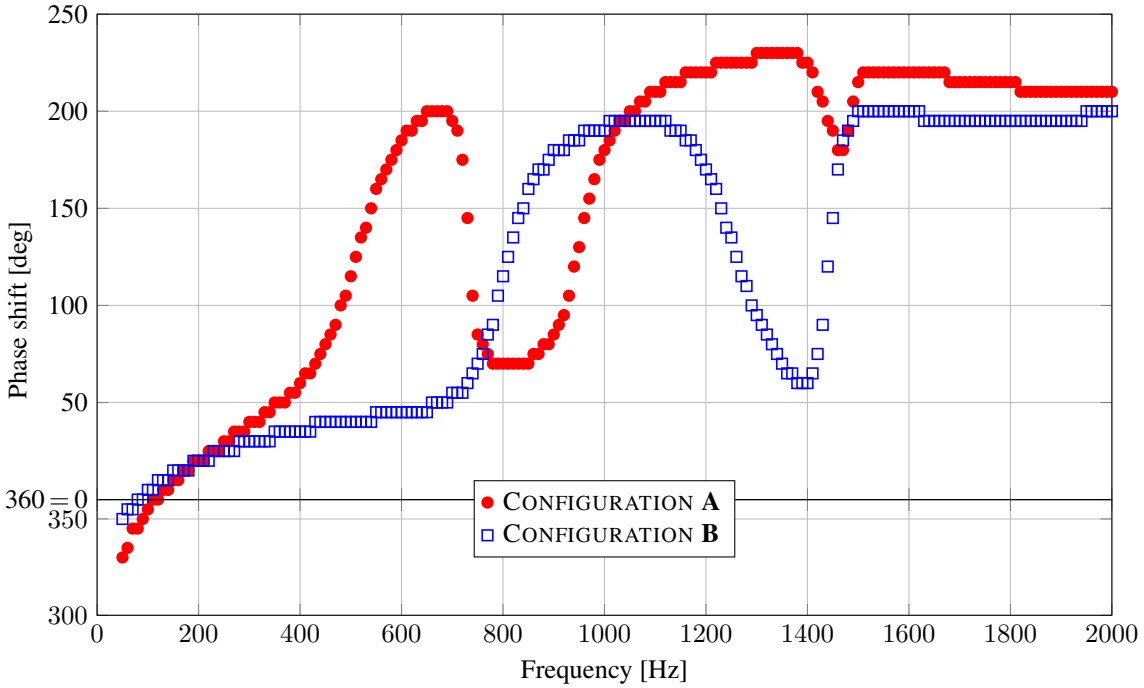


Figure 7: Optimal phase shift of the control signals for both configurations of PZT actuators

Figure 7 compares the optimal phase-shifts (at each computational frequency, i.e., every 10 Hz in the range 50–2000 Hz) for both analysed configurations. They are significantly different for most of the considered frequencies. They tend to be similar only at very low frequencies under 400 Hz, and also above 1450 Hz.

5 Final remarks

The analyses presented in this work show a great potential of the active-passive enhancement in sound absorption of poroelastic layers with various active and passive inclusions. The inclusions play the role of local masses (if they are not fixed to the backing wall) and wave scatterers; they also locally stiffen the poroelastic layer. Therefore, their presence has a substantial effect for the coupled wave propagation in the solid and fluid phases of a poroelastic material, which leads to a significant change in the acoustic wave dissipation in a wide frequency range. This mechanism can be to some extent controlled using the active inclusions which may locally drive the vibrations of the visco-elastic skeleton and other inclusions, but also induce local acoustic waves. More numerical analyses should allow for more theoretical developments

to better understand all these effects. In particular, investigations to optimise the locations and sizes of inclusions should be carried out. Regarding the further analysis of the obtainable numerical results it seems useful to find, for example, the relation between the essential enhancement in absorption and the correlated motion of the steel inclusion and/or the relative motions between the piezoelectric and steel inclusions which leads to such an enhancement. Such relations should be very helpful when developing a reliable control strategy. Even further research would be to design a feasible control filter able to reproduce a frequency response function close to the optimal one.

Acknowledgements

This article is based upon work from COST Action DENORMS CA15125: "*Designs for Noise Reducing Materials and Structures*", supported by COST (European Cooperation in Science and Technology). T. G. Zieliński would like to acknowledge the financial support of the project No. 2015/19/B/ST8/03979: "*Relations between the micro-geometry and sound propagation and absorption in porous and poroelastic media*", financed by the Polish National Science Centre (NCN). E. Deckers is a postdoctoral fellow of the Research Foundation – Flanders (FWO). M.-A. Galland and T. G. Zieliński would like to acknowledge the financial support of the Labex CeLyA, Université de Lyon, through the program *Investissements d'Avenir* (ANR-10-LABX-0060 / ANR-11-IDEX-0007) operated by the French National Research Agency (ANR).

References

[1] M. R. F. Kidner, C. R. Fuller, B. Gardner, *Increase in transmission loss of single panels by addition of mass inclusions to a poro-elastic layer: Experimental investigation*, J. Sound Vib., Vol. 294 (2006), pp. 466-472.

[2] T. Yamamoto, S. Maruyama, S. Nishiwaki, M. Yoshimura, *Topology design of multi-material soundproof structures including poroelastic media to minimize sound pressure levels*, Comput. Methods Appl. Mech. Engrg. Vol. 198 (2009), pp. 1439-1455.

[3] T. G. Zieliński, *Modelling of poroelastic layers with mass implants improving acoustic absorption*, in *19th International Congress on Acoustics 2007 (ICA'2007), 2-7 September 2007, Madrid, Spain*, Sociedad Española de Acústica, Madrid (2007), pp. 3155-3162.

[4] F.-C. Lee, W.-H. Chen, *On the acoustic absorption of multi-layer absorbers with different inner structures*, J. Sound Vib., Vol. 259 (2003), pp. 761-777.

[5] J.-P. Groby, A. Wirgin, L. De Ryck, W. Lauriks, R. P. Gilbert, Y. S. Xu, *Acoustic response of a rigid-frame porous medium plate with a periodic set of inclusions*, J. Acoust. Soc. Am., Vol. 126 (2009), pp. 685-693.

[6] J.-P. Groby, A. Duclos, O. Dazel, L. Boeckx, W. Lauriks, *Absorption of a rigid frame porous layer with periodic circular inclusions backed by a periodic grating*, J. Acoust. Soc. Am., Vol. 129 (2011), pp. 3035-3046.

[7] T. Weisser, J.-P. Groby, O. Dazel, F. Gaultier, E. Deckers, S. Futatsugi, L. Monteiro, *Acoustic behavior of a rigidly backed poroelastic layer with periodic resonant inclusions by a multiple scattering approach*, J. Acoust. Soc. Am., Vol. 139 (2016), pp. 617-629.

[8] C. A. Gentry, C. Guigou, C. R. Fuller, *Smart foam for applications in passive-active noise radiation control*, J. Acoust. Soc. Am., Vol. 101 (1997), pp. 1771-1778.

[9] C. Guigou, C. R. Fuller, *Adaptive feedforward and feedback methods for active/passive sound radiation control using smart foam*, J. Acoust. Soc. Am., Vol. 104 (1998), pp. 226-231.

[10] C. Guigou, C. R. Fuller, *Control of aircraft interior broadband noise with foam-PVDF smart skin*, J. Sound Vib., Vol. 220 (1999), pp. 541-557.

[11] J. Tang, T. Wang, *Piezocomposite smart foam for active control of underwater noise*, in *Proceedings of Global Congress on Intelligent Systems* (2009).

[12] F. Scarpa, F. C. Smith *Passive and MR fluid-coated auxetic PU foam – mechanical, acoustic, and electromagnetic properties*, J. Intell. Mater. Syst. Struct., Vol. 15 (2004), pp. 973-979.

[13] F. Scarpa, W. A. Bullough, P. Lumley, *Trends in acoustic properties of iron particle seeded auxetic polyurethane foam*, Proc. Inst. Mech. Eng. Part C: J. Mech. Eng. Sci., Vol. 218 (2004), pp. 241-244.

[14] T. G. Zielinski, M. Rak, *Acoustic absorption of foams coated with MR fluid under the influence of magnetic field*, J. Intell. Mater. Syst. Struct., Vol. 21 (2010), pp. 125-131.

[15] J.-K. Lee, J. Kim, C.-J. Rhee, C.-H. Jo, S.-B. Choi, *Noise reduction of passive and active hybrid panels*, Smart Mater. Struct., Vol. 11 (2002), pp. 940-946.

[16] T. G. Zieliński, M.-A. Galland, M. N. Ichchou, *Active reduction of vibroacoustic transmission using elasto-poroelastic sandwich panels and piezoelectric materials*, in *Proceedings of SAPEM'2005: Symposium on the Acoustics of Poro-Elastic Materials, 7-9 December 2005, Lyon, France*, Lyon (2005).

[17] T. G. Zieliński, M.-A. Galland, M. N. Ichchou, *Further modeling and new results of active noise reduction using elasto-poroelastic panels*, in *Proceedings of ISMA2006: International Conference on Sound and Vibration, Leuven, Belgium*, Vols. 1-8, Leuven (2006), pp. 309-319.

[18] C. Batifol, M. Ichchou, M.-A. Galland, *Component mode synthesis finite element model of a smart double-plate panel*, in *19th International Congress on Acoustics 2007 (ICA'2007), 2-7 September 2007, Madrid, Spain*, Sociedad Española de Acústica, Madrid (2007), pp. 3143-2148.

[19] C. Batifol, T. G. Zieliński, M. N. Ichchou, M.-A. Galland, *A finite-element study of a piezoelectric/poroelastic sound package concept*, Smart Mater. Struct., Vol. 16 (2007), pp. 168-177.

[20] T. G. Zieliński, M. N. Ichchou, M.-A. Galland, *Fully coupled finite-element modeling of active sandwich panels with poroelastic core*, J. Vib. Acoust., Vol. 134 (2012), 021007.

[21] M. A. Biot, *The theory of propagation of elastic waves in a fluid-saturated porous solid*, J. Acoust. Soc. Am., Vol. 28 (1956), pp. 168-191.

[22] A. Benjeddou, *Advances in piezoelectric finite element modeling of adaptive structural elements: a survey*, Comput. Struct., Vol. 76 (2000), pp. 347-363.

[23] M. Furstoss, D. Thenail, M.-A. Galland, *Surface impedance control for sound absorption: direct and hybrid passive/active strategies*, J. Sound Vib., Vol. 203 (1997), pp. 219-236.

[24] J.-B. Dupont, M.-A. Galland, *Active absorption to reduce the noise transmitted out of an enclosure*, Appl. Acoust., Vol. 70 (2009), pp. 142-152.

[25] B. Betgen, M.-A. Galland, *A new hybrid active/passive sound absorber with variable surface impedance*, Mech. Syst. Sig. Process., Vol. 25 (2011), pp. 1715-1726.

[26] N. Sellen, M. Cuesta, M.-A. Galland, *Noise reduction in a flow duct: Implementation of a hybrid passive/active solution*, J. Sound Vib., Vol. 297 (2006), pp. 492-511.

[27] P. Leroy, A. Berry, N. Atalla, P. Herzog, *Numerical analysis of smart foam for acoustic absorption*, in *Conference Proceedings of 19th International Congress on Acoustics ICA2007*, Madrid (2007).

[28] P. Leroy, P. Herzog, A. Berry, N. Atalla, *Experimental assessment of the performance of a smart foam absorber*, in *Conference Proceedings of Acoustics'08*, Paris (2008).

[29] P. Leroy, N. Atalla, A. Berry, P. Herzog, *Three dimensional finite element modeling of smart foam*, J. Acoust. Soc. Am., Vol. 126 (2009), pp. 2873-2885.

[30] T. G. Zielinski, *Active porous composites for wide frequency-range noise absorption*, in *Proceedings of ISMA2008: International Conference on Sound and Vibration, Leuven, Belgium*, Vols. 1-8, Leuven (2008), pp. 89-103.

[31] T. G. Zielinski, *Porous foams with active implants improving acoustic absorption*, in *SAPEM'2008 – Symposium on the Acoustics of Poro-Elastic Materials, 17-19 December 2008, Bradford, UK*, Bradford (2008).

[32] T. G. Zieliński, *Numerical investigation of active porous composites with enhanced acoustic absorption*, J. Sound Vib., Vol. 330 (2011), pp. 5292-5308.

[33] T. G. Zielinski, *Fundamentals of multiphysics modelling of piezo-poro-elastic structures*, Arch. Mech., Vol. 62 (2010), pp. 343-378.

[34] S. Rigobert, F. C. Sgard, N. Atalla, *A two-field hybrid formulation for multilayers involving poroelastic, acoustic, and elastic materials*, J. Acoust. Soc. Am., Vol. 115 (2004), pp. 2786-2797.

[35] T. G. Zieliński, Ł. Jankowski, K. Opiela, E. Deckers, *Modelling of poroelastic media with localised mass inclusions*, in *SAPEM'2017 – 5th Symposium on the Acoustics of Poro-Elastic Materials, 6-8 December 2017, Le Mans, France*, Univérsité du Mans, Le Mans (2017).

[36] J. F. Allard, N. Atalla, *Propagation of Sound in Porous Media: Modelling Sound Absorbing Materials, Second Edition*, Wiley (2009).

[37] D. L. Johnson, J. Koplik, R. Dashen, *Theory of dynamic permeability and tortuosity in fluid-saturated porous media*, J. Fluid Mech., Vol. 176 (1987), pp. 379-402.

[38] Y. Champoux, J.-F. Allard, *Dynamic tortuosity and bulk modulus in air-saturated porous media*, J. Appl. Phys., Vol. 70 (1991), pp. 1975-1979.

[39] N. Atalla, R. Panneton, P. Debergue, *A mixed displacement-pressure formulation for poroelastic materials*, J. Acoust. Soc. Am., Vol. 104 (1998), pp. 1444-1452.

[40] N. Atalla, M. A. Hamdi, R. Panneton, *Enhanced weak integral formulation for the mixed (u,p) poroelastic equations*, J. Acoust. Soc. Am., Vol. 109 (2001), pp. 3065-3068.

[41] P. Debergue, R. Panneton, N. Atalla, *Boundary conditions for the weak formulation of the mixed (u,p) poroelasticity problem*, J. Acoust. Soc. Am., Vol. 106 (1999), pp. 2383-2390.

[42] T. G. Zieliński, *Normalized inverse characterization of sound absorbing rigid porous media*, J. Acoust. Soc. Am., Vol. 137 (2015), pp. 3232–3243.

[43] J. F. Allard, C. Depollier, P. Guignouarad, P. Rebillard, *Effects of a resonance of the frame on the surface impedance of glass wool of high density and stiffness*, J. Acoust. Soc. Am., Vol. 89 (1991), pp. 999-1001.

Numerical and experimental study of first passage time of a steel strip subjected to forced and parametric excitations

E. Delhez [1], **H. Vanvinckenroye** [2], **J.-C. Golinval** [1], **V. Denoël** [2]
[1] University of Liège, Department of Aerospace and Mechanical Engineering,
Quartier Polytech 1, Allée de la Découverte, 9, 4000 Liège, Belgium.

[2] University of Liège, Department of Urban and Environmental Engineering.

Abstract
The first passage time refers to the time required for a dynamical system to reach a target energy level for the first time, departing from a known initial state. Analytical studies of the first passage time of a linear Mathieu oscillator under stochastic forced and parametric excitations defined as δ-correlated Brownian noises identified three behavioral regimes for the first passage time. The current work describes the design and use of an experimental set-up in order to validate the existence of the regimes. This paper successively describes the design and the finite element modeling of the set-up consisting in a pre-stressed steel strip, the reduction of the system to a single-degree-of-freedom system to match the framework of the theory, numerical studies on the influence of the frequency bands of the excitations on the first passage time and the experimental tests. Qualitatively, two of the three regimes are successfully observed in the experiment. Quantitatively, a good match is observed between the experimental and model results.

1 Introduction

The dynamics of many systems can be described by the Mathieu equation

$$z'' + 2\xi z' + [1 + u(\tau)]\, z = w(\tau), \tag{1}$$

where z is the dependent state variable, τ is a dimensionless time and ξ is the damping coefficient of the system. The right-hand side $w(\tau)$ represents an external force applied to the system and will be referred to as the forced excitation in the following. By contrast, the function $u(\tau)$ is a parametric excitation, as it induces variation in time of the stiffness of the oscillator. This equation can for instance model the oscillations of a pendulum in the gravity field when its support is subjected to a vertical motion, the parametric vibrations of cables subjected to axial oscillations at one extremity or the rotative equilibrium of a crane in a turbulent wind [4, 5, 8].

Equation (1) has been widely studied in the deterministic case, *i.e.* when the forced and parametric excitations have known deterministic analytical expressions, in particular in the harmonic case, with the aim of characterizing its steady-state solution and its stability [1, 6]. However, in most realistic applications, the system is slightly damped and the forced and parametric excitations are stochastic processes, so that the system spends most of its time in a stochastic transient regime. In the stochastic context, the classical stability theories are no longer relevant and the theory of first passage time has been developed as an efficient alternative. It consists in determining the statistics of the first passage time, defined as the time required for a stochastic process to leave a domain for the first time when starting from a given initial state inside the domain.

Closed-form expressions of the first and second order moments of the first passage time have been derived when both the forced and parametric excitations w and u are δ-correlated Brownian noises [9, 10]. These analytical developments, based on a multiple-scale approach, have highlighted the influence of some dimensionless groups impacting the dynamics and the existence of three different behavioral regimes, namely the additive, the incubation and the multiplicative regimes.

The aim of this paper is to design an experiment with an intrinsically multi-degree-of-freedom system to relate the equivalent linear Mathieu equation to the physical parameters of the system and to provide new experimental evidence of the existence of the three regimes identified in [9].

This paper starts with the description of the experimental set-up. Then, a finite element model of the structure is built and experimental modal analysis techniques are used to update this model. The multi-degree-of-freedom governing equations are then reduced to a set of decoupled single-degree-of-freedom equations to fit in the framework defined by the theory. The conditions under which an efficient use of the reduced model can be done are determined. They naturally lead to a numerical study of the first passage time of systems subjected to narrow-band excitations for which analytical results are not yet available. Eventually, first passage time maps are built experimentally and compared with the predicted results.

2 Experimental set-up description

The experimental part of the work is conducted in the "LTAS - Vibrations et Identification des Structures" (LTAS-VIS) laboratory unit of the Department of Aerospace and Mechanical engineering at the University of Liège. The experimental set-up consists in a vertical strip pre-stressed by a mass $m = 1.816$ kg. A schematic representation of the set-up is given in Fig. 1. The strip is characterized by a length $\ell = 0.501$ m, a width $w = 25$ mm and a thickness $t = 0.4$ mm. The structure is made of carbon steel (Young's modulus $E = 206$ GPa and density $\rho = 7\,767$ kg/m^3). The strip is clamped at its top end while a lateral guide constrains the bottom end of the strip to move only in the vertical direction.

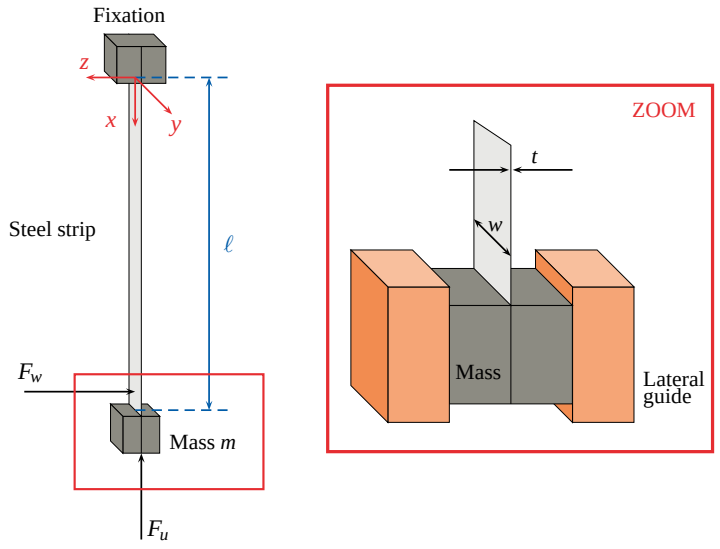


Figure 1: Schematic view of the designed experimental set-up.

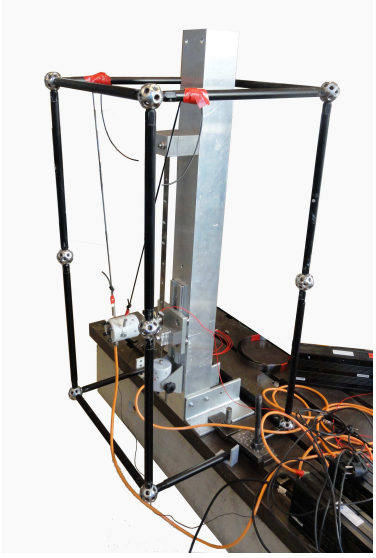


Figure 2: Experimental set-up.

The forced and parametric excitations F_w and F_u are applied by means of two electrodynamic vibration exciters. The first shaker is mounted horizontally and is used to excite the strip out of its plane close to its bottom fixation. This force constitutes the forced excitation of Mathieu equation (1). The second shaker is mounted vertically at the bottom of the structure, below the mass. This force modifies the pre-stress of the strip and therefore induces variation in time of the strip stiffness, giving rise to the parametric excitation of Mathieu equation. A picture of the physical prototype of the structure with the two shakers is given in Fig. 2.

Besides the two shakers, the structure is also instrumented with two impedance heads located at the two points where the shakers act and used to measure the force and the acceleration at these points. A Polytec MSA-400 OFV-552 laser transducer is used to measure the response of the structure in term of velocity at a single point. Data acquisition and signal processing are carried out using the LMS Test.Lab software and the LMS SCADAS Lab acquisition system [11].

3 Numerical modeling

In order to build an accurate numerical model of the physical set-up, both theoretical and experimental modal analyses are followed. The modal properties identified with these two approaches are then compared and the experimental results are used to update the finite element model. As a first step, a model of the non-instrumented structure (without the shakers) is built. Then, the influence of the shakers on the dynamics of the structure is modeled.

3.1 Non-instrumented structure

On the one hand, the steel strip is modeled in MATLAB using Bernoulli beam elements. The pre-stress is taken into account by the means of a geometrical stiffness matrix added to the usual linear stiffness matrix [3]. This numerical model is used to obtain a first estimate of the six lower natural frequencies and corresponding mode shapes of the strip.

On the other hand, experimental modal analysis is carried out on the real non-instrumented structure. The structure is excited close to its bottom fixation with an instrumented impact hammer and the response is successively measured at 8 other points equally spaced along the whole strip. The "Least Square Complex Exponential" (LSCE) and "Least Square Frequency Domain" (LSFD) methods are used to identify the modal properties of the structure [2].

The two sets of modal parameters obtained with the theoretical and experimental modal analyses are then compared. The natural frequencies obtained with the numerical model systematically overestimate the corresponding natural frequencies identified with the experimental modal analysis by 3-4%, which leaves room for improvement. The model is more rigid than the real structure. This can be ascribed to the modeling of the supports as perfect clampings. The finite element model is therefore corrected by introducing a stiffness in rotation about the y-axis (Fig. 1) at both ends of the strip. To simplify the analysis, the stiffness coefficient is assumed to be the same on both sides. The rigidity of the clamping is determined in such a way that it minimizes the difference (in a least-square sense) between the natural frequencies obtained with the numerical and experimental modal analyses. An optimum value of $k = 3.83$ Nm/rad is found.

This modification of the finite element model allows to decrease the relative errors on the natural frequencies below 0.2%. The Modal Assurance Criterion (MAC) [2] is used to quantify the correlation between the two sets of modes as represented in Fig. 3.

3.2 Instrumented structure

While the above derived model provides an accurate description of the dynamics of the strip itself, the shakers mounted on it have a non-negligible influence on the dynamics. Their influence has to be taken into account.

Experimental modal analysis is carried out by exciting the structure with the horizontal shaker located near the bottom fixation. The vertical shaker does not excite the structure but is mounted on it in such a way that its interaction with the structure is taken into account. The identification of the modal parameters of the structure is performed with the "Stochastic Subspace Identification" (SSI) method [7].

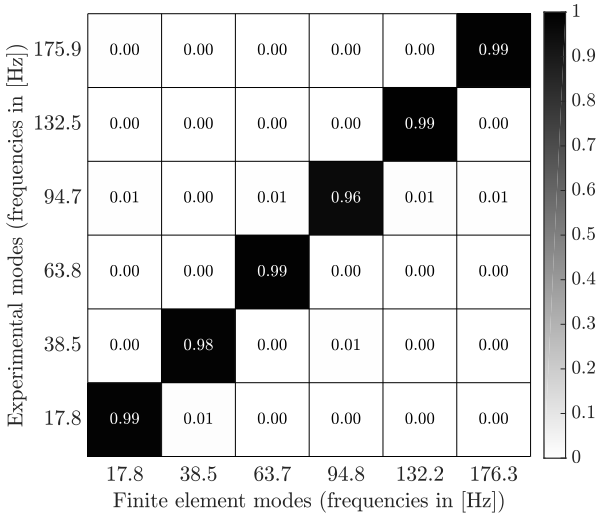


Figure 3: MAC matrix (non-instrumented structure).

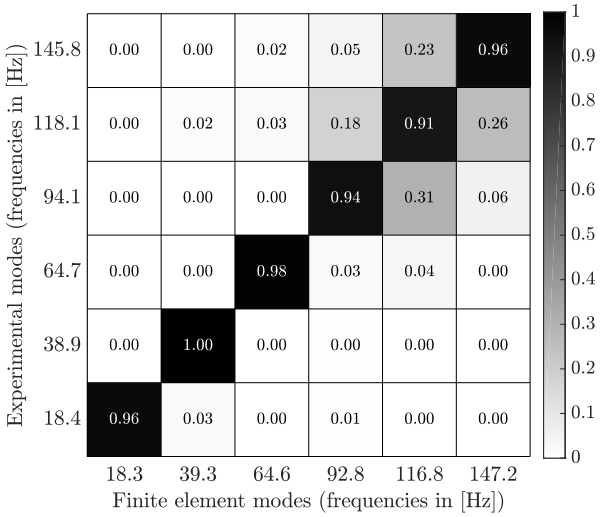


Figure 4: MAC matrix (instrumented structure).

The natural frequencies identified appear to differ by up to 20% from the natural frequencies computed with the original finite element model. The interaction of the shakers with the structure has therefore to be taken into account to get a reliable model.

The horizontal shaker, the stinger and the impedance head glued to the strip (Fig. 5) are modeled by a spring-mass system as shown in Fig. 6. The influence of the impedance head is modeled by adding a concentrated mass equal to the mass of the impedance head $m_{\text{head}} = 3 \cdot 10^{-2}$ kg where the horizontal shaker acts. The aluminum stinger connecting the shaker to the strip is modeled by a spring of stiffness $k_{\text{stinger}} = 4.5 \cdot 10^{6}$ N/m. The shaker itself is modeled by two masses connected by a spring. The mass $m_{\text{shaker}} = 1.7$ kg represents the main body of the shaker and the mass $m_{\text{moving}} = 1.5 \cdot 10^{-2}$ kg corresponds to the small moving mass. The spring of stiffness $k_{\text{suspension}} = 4 \cdot 10^{3}$ N/m represents the moving mass suspension. This modification of the finite element model reduces the relative errors on the natural frequencies below 5%.

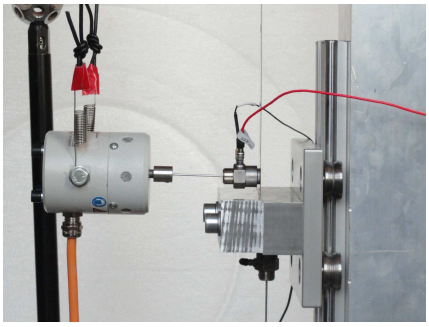


Figure 5: Horizontal shaker picture.

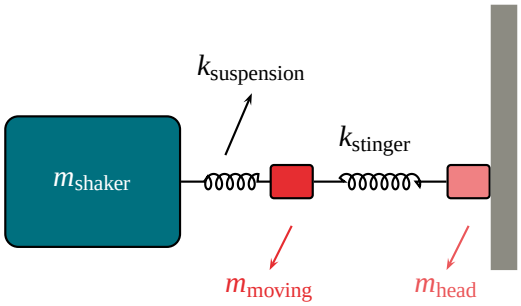


Figure 6: Horizontal shaker modeling.

The impedance head glued to the strip where the horizontal shaker acts prevents the strip from exhibiting significant curvature near the clamping. To reduce the errors, the stiffness of the finite elements in contact with the impedance head is artificially increased by 2%. This increased stiffness is adjusted to minimize the errors on the first six bending natural frequencies of the structure in a least square sense.

As a result of these two new modifications of the numerical finite element model of the structure, the relative errors on the natural frequencies are less than 1.2%. The corresponding MAC matrix is represented in Fig. 4 and shows a good correlation between the mode shapes and the corresponding frequencies. It is checked that the modes identified experimentally are real. A damping matrix that guarantees diagonal modal damping is built from the identified damping ratios using the assumption of proportional damping as proposed in [3].

4 From multiple-degree-of-freedom to single-degree-of-freedom equations of motion

The studied structure subjected to an external excitation $\mathbf{f}(t)$ is governed by the general equation of motion

$$\mathbf{M}\ddot{\mathbf{x}}(t) + \mathbf{C}\dot{\mathbf{x}}(t) + \mathbf{K}(t)\mathbf{x}(t) = \mathbf{f}(t), \tag{2}$$

where $\mathbf{x}$ is the vector of generalized coordinates, $\mathbf{M}$ the mass matrix, $\mathbf{C}$ the damping matrix and $\mathbf{K}(t)$ the time-varying stiffness matrix. The stiffness matrix can be decomposed into its constant and time-varying parts $\mathbf{K}(t) = \mathbf{K}_0 + \mathbf{K}_{\text{prestress}}(t)$, where $\mathbf{K}_0$ is the constant stiffness matrix and $\mathbf{K}_{\text{prestress}}(t)$ characterizes the time modulation of the stiffness induced by the zero mean parametric excitation $F_u(t)$. The multi-degree-of-freedom structure is therefore governed by a multi-dimensional version of the Mathieu equation.

The analytical results related to first passage time developed in [9] apply to single-degree-of-freedom Mathieu oscillators subjected to broadband forced and parametric excitations. In order to fit in the particular framework of the analytic model, several adaptations are required. This section focuses on the single-degree-of-freedom system model assumption. The multi-degree-of-freedom governing equations are reduced to a set of uncoupled single-degree-of-freedom Mathieu equations. The conditions under which a profitable use of this model reduction can be done are then identified.

4.1 Model reduction

The response of the structure $\mathbf{x}(t)$ can be written in the modal basis as $\mathbf{x}(t) = \mathbf{\Phi}\mathbf{q}(t)$, where $\mathbf{\Phi}$ is the modal matrix and $\mathbf{q}(t)$ is the vector of modal coordinates. Pre-multiplying the dynamical equation (2) by $\mathbf{\Phi}^{\mathrm{T}}$ and defining modal matrices and vectors as the projections of the physical structural matrices and vectors on the modal basis, the equation governing the dynamics of the modal coordinates can be written as

$$\mathbf{M}^*\ddot{\mathbf{q}}(t) + \mathbf{C}^*\dot{\mathbf{q}}(t) + [\mathbf{K}^* + F_u(t)\mathbf{K}^*_{\text{prestress,1}}]\mathbf{q}(t) = \mathbf{f}^*(t), \tag{3}$$

where $\mathbf{K}^*_{\text{prestress,1}}$ denotes the modal stiffness matrix due to the application of a unitary parametric force.

In the ideal case where $\mathbf{M}^*$, $\mathbf{C}^*$, $\mathbf{K}^*$ and $\mathbf{K}^*_{\text{prestress,1}}$ are diagonal, the N equations of system (3) can be decoupled and the dynamics of the structure in the different mode shapes can be studied separately. In such a case, the system of N coupled equations behaves like N single-degree-of-freedom uncoupled equations. By definition, matrices $\mathbf{M}^*$ and $\mathbf{K}^*$ are diagonal. Matrix $\mathbf{C}^*$ is also diagonal due to the assumption of modal damping. By contrast, there is no reason for matrix $\mathbf{K}^*_{\text{prestress,1}}$ to be perfectly diagonal. Actually, it can be verified that its diagonal elements are only one order of magnitude larger than its out-of-diagonal elements. As long as the product of $F_u(t)$ by the out-of-diagonal elements of $\mathbf{K}^*_{\text{prestress,1}}$ is well below the diagonal elements of $\mathbf{K}^*$, the coupling between modes remains small. In the following, parametric excitations of small amplitudes will be considered in order to limit the excitation of nonlinearities and to keep a quasi-Hamiltonian system. It is therefore expected that this condition will be met to good approximation.

According to these assumptions, the equations of motion can be decoupled for each modal coordinate. The single-degree-of-freedom equation governing the i-th modal coordinate takes the form

$$m_{\text{eq}}\ddot{z}(t) + c_{\text{eq}}\dot{z}(t) + [k_{\text{eq}} + F_u(t)k_{\text{p,eq}}]z(t) = p(t), \tag{4}$$

where $z(t) = q_i(t)$, the equivalent parameters m_{eq}, c_{eq}, k_{eq} and $k_{\text{p,eq}}$ are the generalized parameters of mode i defined according to [2] as the diagonal elements of the modal matrices normalized by $[\mathbf{\Phi}(x_i, i)]^2$, where x_i is the coordinate of an antinode of vibration of mode i, and $p(t)$ is the participation factor of the forced excitation to mode i,

$$p(t) = \frac{\mathbf{\Phi}(x_w, i)}{[\mathbf{\Phi}(x_i, i)]^2} F_w(t) = \alpha F_w(t), \tag{5}$$

where x_w is the coordinate where the forced excitation is applied.

In conclusion, for parametric excitations of sufficiently small amplitude, the modal responses of the structure are uncoupled. If the structure is excited in such a way that it responds only (or mainly) in a unique mode, then the response of the structure at a given point is the solution of an equivalent single-degree-of-freedom equation of the form (4), which is a linear Mathieu equation that can be rewritten in the dimensionless form of Equation (1). Indeed, introducing the characteristic time $T_{\text{charact}} = \sqrt{m_{\text{eq}}/k_{\text{eq}}}$ and the dimensionless time $\tau = t/T_{\text{charact}}$ and defining

$$\xi = \frac{c_{\text{eq}}}{2\sqrt{k_{\text{eq}} m_{\text{eq}}}}, \quad u(\tau) = F_u(\tau)\frac{k_{\text{p,eq}}}{k_{\text{eq}}} \quad \text{and} \quad w(\tau) = \frac{\alpha F_w(\tau)}{k_{\text{eq}}}, \tag{6}$$

Equation (4) becomes

$$z''(\tau) + 2\xi z'(\tau) + [1 + u(\tau)]z(\tau) = w(\tau), \tag{7}$$

where $z'(\tau)$ denotes the first derivative of z with respect to the dimensionless time τ.

4.2 Validity of the single-degree-of-freedom governing equation

Different aspects of the problem have to be taken into account to select the mode used for the reduction. First, the equivalent parameters of the selected mode must allow to cover the largest possible part of the first passage time map in a limited amount of time. Then, to ensure that the other modes have little influence on the dynamics, the selected mode must be such that the out-of-diagonal terms of $\mathbf{K}_{\text{prestress,1}}$ are much smaller than the diagonal elements. The chosen natural frequency must be far enough from other natural frequencies in order to avoid multi-modal excitation of the structure. Based on these remarks, the second bending mode is selected. It is characterized by the equivalent parameters

$$k_{\text{p,eq}} = 39 \text{ m}^{-1}, \quad k_{\text{eq}} = 3\,273 \text{ Nm}^{-1}, \quad c_{\text{eq}} = 0.08 \text{ N[m/s]}^{-1} \quad \text{and} \quad m_{\text{eq}} = 0.05 \text{ kg}. \tag{8}$$

The frequency of this second bending mode is $f_0 = 39.3$ Hz.

In order to identify the conditions under which an efficient use of the reduction of the multi-degree-of-freedom system can be done, both single-degree-of-freedom and multi-degree-of-freedom equations of motion are integrated forward in time using a Newmark integration scheme. On the one hand, the equations of motion of the multi-degree-of-freedom system (2) subjected to given stochastic forced and parametric excitations are solved and the response at an antinode of vibration of the studied mode is extracted. On the other hand, the reduced single-degree-of-freedom equation of motion (4) is solved for the same excitations. The objective is the determination of excitation characteristics that provide a satisfying superposition of the two responses. The modal responses are compared at an antinode of vibration in order to minimize the influence of the other modes.

The forced excitation needs to be defined on a limited frequency band centered on f_0, otherwise, several modes are excited and the single- and multi-degree-of-freedom governing equations provide qualitatively different solutions. When the system is subjected to a forced excitation only, a good match is observed between the responses of the single- and multi-degree of freedom governing equations as long as the frequency band is contained in $[0.8f_0\,;\,1.2f_0]$. When the frequency interval is expanded beyond [$0.8f_0$; $1.2f_0$], the closest modes are excited in such a way that the reduction is not legitimate anymore.

The uncoupling of the equation remains valid as long as the diagonalization of the equations is valid. F_u should therefore remain sufficiently small so that the out-of-diagonal elements of $F_u(t)\mathbf{K}^*_{\text{prestress,1}}$ remain small with respect to the diagonal elements of $\mathbf{K}^*$.

The well known theory of the deterministic Mathieu equation highlights that parametric instabilities occur for parametric excitation frequencies close to $2f_0/k$ (k integer) [1], even if the instability becomes less critical when damping increases. In this stochastic context, the frequency bandwidth of the parametric excitation must be sufficiently small to avoid triggering the other modes of the structure. It is numerically observed that the frequency interval should not include the second harmonics of the other bending modes, unless they are sufficiently damped.

5 Influence of narrow-band excitations on first passage time

The analytical results about first passage time of systems governed by Equation (7) rely on the assumption of broadband white noise excitations. The forced and parametric excitations w and u are characterized by constant power spectral densities S_w and S_u. The Hamiltonian of the quasi-Hamiltonian system (w, u and $\xi \ll 1$) is defined as

$$H = \frac{z^2}{2} + \frac{[z']^2}{2}. \tag{9}$$

The analytical studies conducted in the case of broadband excitations allowed to derive closed-form expressions of the mean first passage time U_1 [9]. They revealed that the reduced average first passage time $U_1 S_u/4$ only depends on the reduced initial energy and energy increment

$$H_0^* = \frac{H_0 S_u}{2S_w} \quad \text{and} \quad \Delta H^* = \frac{\Delta H S_u}{2S_w} \tag{10}$$

and on the damping factor $a = 8\xi/S_u$. This suggests to represent the results by maps of the reduced average first passage time $U_1 S_u/4$ as a function of H_0^* and ΔH^*. For instance, Fig. 7 (dotted lines) represents the analytical results for an undamped system and highlights the three regimes. For $H_0^* \ll 1$, $U_1 S_u/4$ is independent from H_0^*. This is called the additive regime. For $H_0^* \gg 1$, the curves show constant slope and the first passage time depends on by how much the initial energy level is multiplied to obtain the target energy level, which corresponds to the multiplicative regime. The incubation regime in which $U_1 S_u/4$ scales linearly with ΔH^* is identified for $\Delta H^* \ll 1 + H_0^*$.

In the current case, it was shown to be necessary to limit the frequency bands of the excitations for the response of the multi-degree-of-freedom system to be approximated by the response of an equivalent single-degree-of-freedom system. This section is therefore devoted to the numerical study of the influence of such limitations on the frequency band on the first passage time of the single-degree-of-freedom oscillator. The forced and parametric excitations w and u are defined as narrow-band random processes of constant power spectral densities S_w and S_u.

5.1 Influence of the frequency band of the forced excitation

As a first step, the system is studied for broadband parametric excitations and several different narrow frequency bands for the forced excitation (including the natural frequency f_0 of the oscillator or not). The first passage time maps are obtained numerically using Monte Carlo simulations. The Hamiltonian H of the single-degree-of-freedom system is computed at each time step. When it reaches a given maximal value, the simulation is stopped and a new simulation is initiated. The average first passage time is eventually obtained by averaging the results of a large set of simulations.

The three incubation, additive and multiplicative regimes can only be recovered if the frequency band of the forced excitation includes the natural frequency of the system. Fig. 7 compares the analytical map obtained under the assumption of broadband excitations with the numerical map built by Monte Carlo simulations of the oscillator subjected to broadband parametric excitation and narrow-band forced excitation in the interval $[0.8 f_0\,;\, 1.2 f_0]$ ($a = 0$, $S_u = 10^{-3}$, $S_w = 5 \cdot 10^{-4}$). For limited frequency intervals around the natural frequency of the oscillator, a nearly perfect match between the narrow-band and broadband results is observed in the whole map. The results are only significantly different in the bottom left corner corresponding to small values of H_0^* and ΔH^*. This is not surprising since the bottom left corner corresponds to the limit case where there is no parametric excitation; the forced excitation therefore has a dominant influence in this zone.

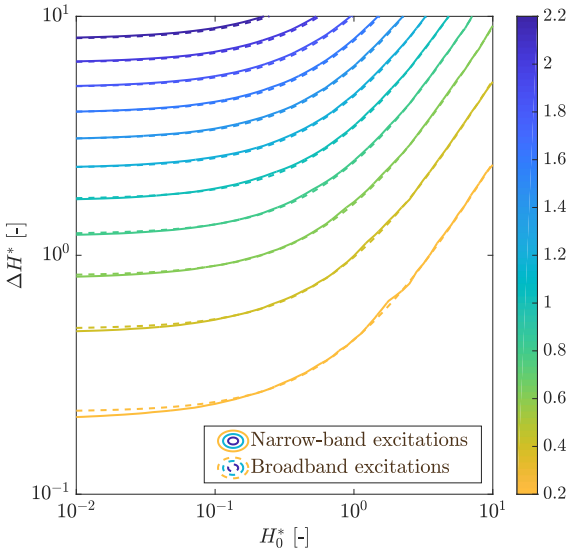


Figure 7: Reduced average first passage time $U_1 S_u/4$. Comparison of the maps obtained numerically for broadband u and narrow-band w on $[0.8f_0\,;\,1.2f_0]$ and analytically for broadband excitations ($a = 0$, $S_u = 10^{-3}$, $S_w = 5 \cdot 10^{-4}$).

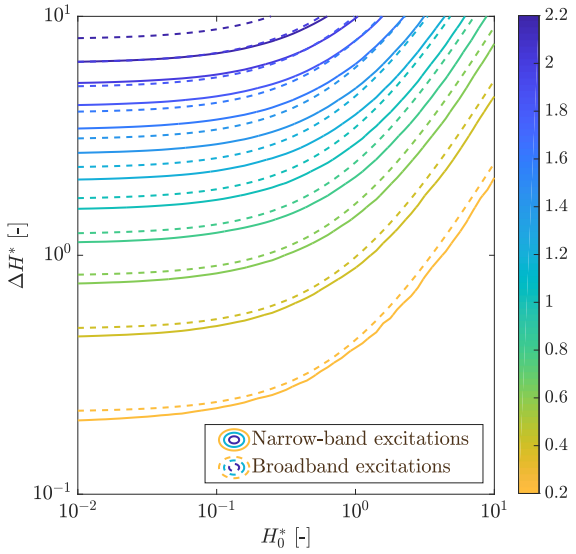


Figure 8: Reduced average first passage time $U_1 S_u/4$. Comparison of the maps obtained numerically for narrow-band excitations (u on $[0.1f_0\,;\,3f_0]$ and w on $[0.8f_0\,;\,1.2f_0]$) and analytically for broadband excitations ($a = 0$, $S_u = 10^{-3}$, $S_w = 5{\cdot}10^{-4}$).

5.2 Influence of the frequency band of the parametric excitation

Fig. 8 compares the maps obtained numerically for narrow-band excitations (F_u on $[0.1f_0\,;\,3f_0]$ and F_w on $[0.8f_0\,;\,1.2f_0]$) and analytically for broadband excitations in the absence of damping ($a = 0$, $S_u = 10^{-3}$, $S_w = 5 \cdot 10^{-4}$). Visual inspection of the maps reveals that the broadband results are not recovered when the system is subjected to narrow-band random processes. Although the additive, multiplicative and incubation regimes can still be clearly identified, the curves do not superimpose. This means that the analytical results obtained for broadband excitations do not simply transfer to narrow-band random processes. Here, the frequency band is limited and the corresponding first passage times are larger than those computed with broadband excitations. A more systematic study is required to characterize the influence of the parametric excitation.

The undamped system ($a = 0$) is studied. The parametric excitation is defined as a narrow-band process of constant power spectral density $S_u = 10^{-3}$ on the frequency interval $[f_1\,;\,f_2]$ and the bounds f_1 and f_2 are varied. The forced excitation is defined as a narrow-band process of constant power spectral density $S_w = 5 \cdot 10^{-4}$ on the frequency interval $[0.8f_0\,;\,1.2f_0]$, in agreement with the conclusions of the previous section.

An indicator I is introduced and defined as

$$I = \left| \frac{U_1^{\mathrm{NB}} - U_1^{\mathrm{BB}}}{U_1^{\mathrm{BB}}} \right|, \tag{11}$$

where U_1^{NB} and U_1^{BB} are respectively the mean first passage time obtained from Monte Carlo simulations with narrow-band processes at some observation point of the map and the corresponding analytical mean first passage time for broadband processes. Based on the comments of the previous section, the initial energy H_0^* and the energy increment ΔH^* are chosen far from the bottom left corner of the map where the influence of the narrow band of the forced excitation is large and for moderate values of H_0^* and ΔH^* to limit the computation time.

Fig. 9 shows the value of the indicator I (11) as a function of the lower and upper frequencies f_1 and f_2 (normalized by the natural frequency f_0) that define the parametric excitation at the observation point of the map characterized by $H_0^* = 10^{-1.5}$ and $\Delta H^* = 10^0$. This figure shows that it is necessary to include the second harmonic of the natural frequency, $2f_0$, in the frequency interval to be close enough to the analytical results for broadband excitations. In fact, when the second harmonic of the natural frequency does not belong to the frequency interval of the parametric excitation, the first passage time map looks completely different; even the three regimes do not appear. By contrast, it is not necessary to include the natural frequency itself in the frequency interval $[f_1\,;\,f_2]$. This can be supported by the deterministic theory of Mathieu equation [1]. Instabilities occur at frequency $2f_0/k$ (k integer). While the instability for $k = 1$, *i.e.* at $f = 2f_0$, is the most critical, the other instabilities do not develop when forced excitation or damping is introduced in the system unless the amplitude of the parametric excitation is large.

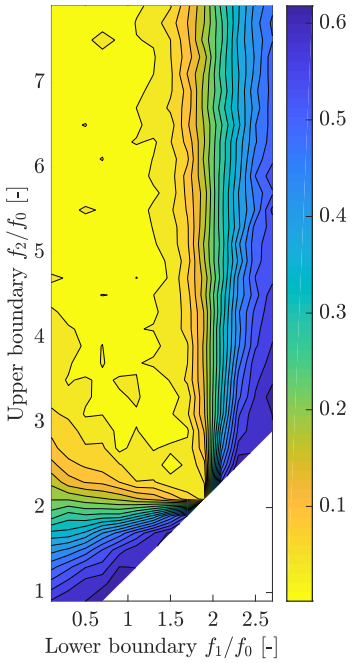


Figure 9: Indicator I (11) at point $H_0^* = 10^{-1.5}$ and $\Delta H^* = 10^0$ as a function of the lower and upper bounds of the frequency band of the parametric excitation ($a = 0$, $S_u = 10^{-3}$, $S_w = 5 \cdot 10^{-4}$).

It should be noted that, even if this study is based on a single point of the map located in the additive regime, the same exercise has been performed at other points located in other regimes and the same general conclusions have been drawn. The numerical study of systems characterized by other values of a, S_w and S_u also lead to the same general conclusions.

6 Experimental study of first passage time

The above numerical studies provide useful information to prepare the experimental study of first passage time. The forced excitation F_w and the parametric excitation F_u applied to the experimental set-up (Fig. 1) must be such that the conditions for the model reduction to be valid are verified and the influence of the narrow bands remains limited.

The forced excitation F_w is defined as a narrow-band process of constant power spectral density $\tilde{S}_w = 5 \cdot 10^{-3}$ N^2/Hz on the frequency interval $[0.87f_0\,;\,1.13f_0] = [34\,;\,44]$ Hz. This frequency interval does not cover any of the other natural frequencies of the set-up. The parametric excitation F_u is defined as a

narrow-band process of constant power spectral density $\tilde{S}_u = 5 \cdot 10^{-3}$ N^2/Hz on the frequency interval $[0.77 f_0\,;\, 2.57 f_0] = [30\,;\, 100]$ Hz. This frequency interval covers the natural frequency f_0 and its second harmonic. It can be regretted that the second harmonic of the first bending mode and the natural frequency of the third bending mode are also included. But, this is not an issue thanks to the high damping ratios of these modes.

Equation (6) shows that the dimensionless parameters a, S_w and S_u are related to the dimensional parameters through

$$a = \frac{4 c_{\text{eq}} k_{\text{eq}}}{k_{\text{p,eq}}^2 \tilde{S}_u} = 132,\ S_w = \frac{\tilde{S}_w}{T_{\text{charact}}} \left(\frac{\alpha}{k_{\text{eq}}} \right)^2 = 2.5 \cdot 10^{-10} \text{ and } S_u = \frac{\tilde{S}_u}{T_{\text{charact}}} \left(\frac{k_{\text{p,eq}}}{k_{\text{eq}}} \right)^2 = 1.8 \cdot 10^{-4}. \quad (12)$$

The force intensities S_w and S_u are much smaller than one, as required by the theory to have a quasi-Hamiltonian system. The high value of a does not mean that damping is intrinsically high ($\xi = 4 \cdot 10^{-3} \ll 1$) but, merely, that damping is high with respect to the amplitude of the parametric excitation.

The structure is excited by the horizontal and vertical shakers for 30 minutes and the velocity of the structure is measured at a vibration antinode with the laser transducer. The response is numerically integrated to compute the evolution of the position with time. It is then checked that the structure responds only in its second bending mode by analyzing the response in the frequency domain. The dimensionless Hamiltonian corresponding to Equation (7) is eventually computed by Equation (9).

The average first passage time map corresponding to the evolution of the Hamiltonian of the system with time can be built from the experimental results (solid lines in Fig. 10). If the time signal is sufficiently long, the same level of energy is reached several times and the system passes many times from initial energies H_0 to higher energies $H_c = H_0 + \Delta H$. Both energy axes are discretized in a finite number of values. The intervals between these values are chosen with uniform sizes on a logarithmic scale as this is the physical scaling suggested by the stochastic model. The mean first passage time corresponding to each point of the map (*i.e.* each combination of initial energy H_0^* and energy increment ΔH^*) is obtained by averaging all the first passage times corresponding to the transitions between these levels of energy [8].

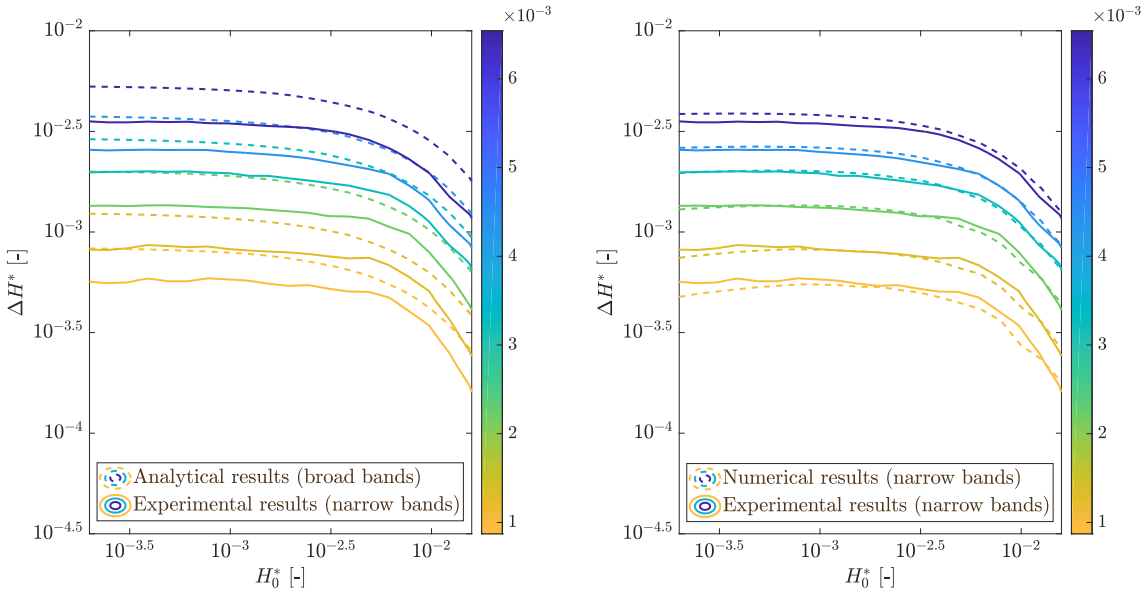


Figure 10: Reduced average first passage time $U_1 S_u / 4$ as a function of H_0^* and ΔH^*. Comparison of the maps obtained experimentally and numerically for narrow-band excitations (F_u on $[0.77 f_0\,;\, 2.57 f_0]$ and F_w on $[0.87 f_0\,;\, 1.13 f_0]$) and analytically for broadband excitations ($a = 132$, $S_w = 2.5 \cdot 10^{-10}$, $S_u = 1.8 \cdot 10^{-4}$).

Fig. 10(a) compares the experimental results with the analytical map obtained under the assumption of broad-band excitations. The results are qualitatively similar and the general trend of the average first passage time is recovered experimentally but, as expected, the curves do not superimpose.

Fig. 10(b) compares the experimental results with the map obtained by Monte Carlo simulations of the numerical system subjected to the same narrow-band excitations as in the experimental tests. Globally, a good match between the maps is observed and the global behavior of the mean first passage time is recovered. The different regimes can be analyzed separately.

The additive regime is well represented. In the left part of Fig. 10(b), the experimental curves tend towards horizontal asymptotes, at least for sufficiently large values of the increment ΔH^*. The incubation regime can be highlighted by considering cross-sections of the map at constant values of H_0^*. Fig. 11 shows the evolution of the average first passage time as a function of ΔH^* for $H_0^* = 2 \cdot 10^{-2}$ and $2 \cdot 10^{-3}$. As hinted by the linear trends represented as a guide, the average first passage times (cross markers) are fairly well aligned, which is the specific feature of the incubation regime.

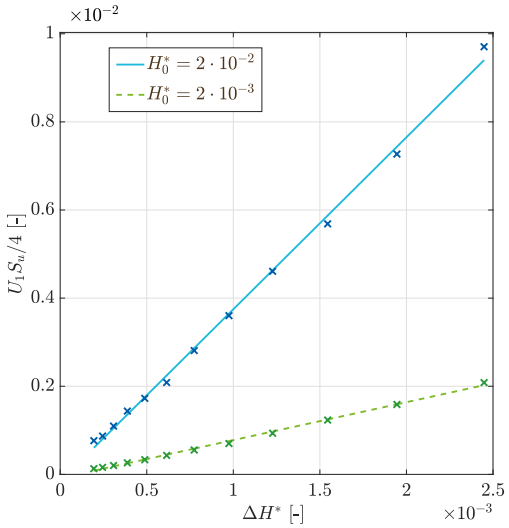


Figure 11: Cross-sections of the reduced average first passage time map (Fig. 10) in the incubation regime for $H_0^* = 2 \cdot 10^{-2}$ and $H_0^* = 2 \cdot 10^{-3}$. Experimental data (crosses) and linear trend (lines).

The multiplicative regime cannot be rigorously observed in Fig. 10(b). In the right part of the figure, the curves show the same negative slope but the multiplicative regime is not yet reached since the highest value of H_0^* is of the order of $10^{-1.5}$ while the multiplicative regime appears for $H_0^* \gg 1$. On the one hand, such high values of H_0^* must be avoided here since it can cause the excitation of nonlinearities in the system. On the other hand, for damped systems subjected to broadband excitations, the asymptotic slope in the multiplicative regime equals $2 - a$. This result is certainly not directly valid in the narrow-band excitations case but suggests that, given the high value of $a = 132$, the part of the multiplicative region reachable in a limited amount of time reduces to the bottom right corner. Because this corner is characterized by high coefficients of variation [10], very long time signals would be required to get a smooth map in this region.

The differences between the numerical and experimental results can be ascribed to different factors. The experimental conditions never match exactly the numerical ones. For instance, the power spectral densities of the excitations are not perfectly constant on the frequency band of definition, and do not drop to zero outside this interval. Then, the structure is inherently a multi-degree-of-freedom system and it is not possible to excite a single mode of the structure. Structure nonlinearities can also be a source of differences between the numerical and experimental results. Indeed, even if the intensities of the excitations have been chosen extremely small to limit the excitation of the nonlinearities, those are inherent to the structure.

7 Conclusions and perspectives

This work aims at designing and testing an experimental set-up to illustrate and provide empirical evidence of the main analytical results of the theory of first passage time described in [9]. The current theory applies to quasi-Hamiltonian linear single-degree-of-freedom systems subjected to broadband forced and parametric excitations (δ-correlated Brownian processes).

The selected structure consists in a vertical steel strip pre-stressed by a mass. First, a finite element model of the structure is built. The inherently multi-degree-of-freedom system is reduced to match the assumption of a single-degree-of-freedom system behind the theory of first passage time. This is done by defining the forced and parametric excitations as narrow-band random processes triggering only one bending mode of the structure. Since analytical results are not available for the first passage time of systems subjected to narrow-band excitations, a numerical study is performed and some general conclusions are drawn about the influence of the frequency bands of the forced and parametric excitations on the first passage time. The global behavior of the average first passage time is recovered in the whole map as long as the natural frequency of the oscillator is included in the frequency band of the forced excitation and the frequency band of the parametric excitation contains the second harmonic of the natural frequency. When these conditions are met, small quantitative differences can be observed when broadband or narrow-band excitations are used but the dynamics remains qualitatively similar.

The previous steps provide a rationale for selecting the appropriate parameters of the experimental testing. The experimental first passage time map is built and compared with the theoretical and model results. A good quantitative match is observed between the experimental map and the numerical results obtained with Monte Carlo simulations with narrow-band excitations. The experimental results are also qualitatively similar to the theoretical ones for broadband excitations. Both the additive and incubation regimes are clearly identified. Only the beginning of the multiplicative regime can however be observed.

This study contributes to broadening the scope of the first passage time theory introduced in [9, 10] beyond the context of single-degree-of-freedom linear systems subjected to broadband excitations considered so far by numerical and experimental studies of oscillators subjected to narrow-band processes. It is also a first physical evidence that the first passage time of real multi-degree-of-freedom mechanical systems can be characterized with the physical properties of the structure.

This study also suggests that work is still needed to go further with analytical, numerical and experimental studies of systems subjected to narrow-band excitations. In particular, analytical studies of the first passage time of systems subjected to colored excitations, and in particular to narrow-band excitations, could be conducted to get a better insight into the phenomena.

References

[1] M. Cartmell, *Introduction to Linear, Parametric and Nonlinear Vibrations*, Springer, 1st ed. (1990).

[2] D. Ewins, *Modal Testing: Theory, Practice and Application*, Research Studies Press Ltd, 2nd ed. (2000).

[3] M. Géradin, D. J. Rixen, *Mechanical Vibrations: Theory and Application to Structural Dynamics*, Wiley, 3rd ed. (2015).

[4] M. Gitterman, *Spring pendulum: Parametric excitation vs an external force*, Physica A: Statistical Mechanics and its Applications, Vol. 389 (2010), pp. 3101-3108.

[5] J. L. Lilien, A. Pinto da Costa, *Vibration Amplitudes Caused by Parametric Excitation of Cable Stayed Structures*, Journal of Sound and Vibration, Vol. 174 (1994), pp. 69-90.

[6] A. A. Prikhodko, A. V. Nesterov, S. V. Nesterov, *Analysis of Mathieu Equation Stable Solutions in the First Zone of Stability*, Procedia Engineering, Vol. 150 (2016), pp. 341-346.

[7] P. van Overschee, B. L. de Moor, *Subspace Identification for Linear Systems: Theory - Implementation - Applications*, Springer US, 1st ed. (1996).

[8] H. Vanvinckenroye, T. Andrianne, V. Denoël, *First passage time as an analysis tool in experimental wind engineering*, Journal of Wind Engineering and Industrial Aerodynamics, Vol. 177 (2018), pp. 366-375.

[9] H. Vanvinckenroye, V. Denoël, *Average first-passage time of a quasi-Hamiltonian Mathieu oscillator with parametric and forcing excitations*, Journal of Sound and Vibration, Vol. 406 (2017), pp. 328-345.

[10] H. Vanvinckenroye, V. Denoël, *Second-order moment of the first passage time of a quasi-Hamiltonian oscillator with stochastic parametric and forcing excitations*, Journal of Sound and Vibration, Vol. 427 (2018), pp. 178-187.

[11] Siemens website. `http://www.plm.automation.siemens.com`. Last view 24th May 2018.

Response of a curved panel subjected to local heating and base excitation

David A. Ehrhardt[1,2]**,Brian T. Gockel**[2]**,Timothy J. Beberniss**[2]

[1] Ehrhardt Engineering LLC, Monticello, IL 61856, USA.

[2] Structural Sciences Center, RQHF, Air Force Research Lab,
Wright Patterson Air Force Base, OH 45433, USA.

Abstract

Structures operating in aero-thermal environments greater than the speed of sound will experience large pressure and temperature gradients over small areas due to shock-wave impingement in addition to large amplitude distributed acoustic and/or mechanical loading from vehicle dynamics. Such combined environments complicate the dynamic response of these structures since the localized thermal loading affects their global dynamic response. This work experimentally explores the static and dynamic response of a 248 mm x 400 mm curved stainless steel panel subjected to localized thermal loading and distributed mechanical loading. The linear and nonlinear dynamic response of the panel is measured with high-speed 3D digital image correlation, and the temperature distribution is measured with a Forward Looking InfraRed camera. The resulting data set demonstrates how localized heating affects global dynamics in linear and nonlinear regimes.

1 Introduction

Structures operating in supersonic or hypersonic environments experience large temperature gradients over small surface areas as well as extreme acoustic and mechanical loading [1, 2]. Such temperature gradients, or localized thermal loading, modifies the local stiffness characteristics of these structures, and alters their dynamic response when combined with distributed acoustic and/or mechanical loading.

Experimentally producing controlled, repeatable, and local temperature gradients is difficult. Radiant heating with halogen lamps is widely used to thermally load structures in dynamic environments [3–5]. However, the time scale for heating and the distributed, radiant nature of halogen lamps makes their use in dynamic and local heating environments difficult. Radiant heating using infrared lasers, provides a shorter time scale for thermal loading and the benefit of pin point localization; however, loading over any larger area is difficult. Alternatively, inductive heating [6, 7], offers a method to quickly control a temperature distribution and modifying the coil of an inductive heater leads to a wide array of temperature distributions which are reproducible provided the coil geometry and distance from test article is kept constant. An inductive heater with a custom coil is used in this work to provide the desired temperature distribution.

The localization of temperature distribution and structural responses requires greater spatial measurement resolution. Full-field temperature measurement is typically limited to calibrated infrared cameras, such as the forward looking infrared (FLIR) camera used here, since large thermocouple arrays will effect the dynamic structural response. Full-field response measurement techniques include continuous scan [8, 9] or scanning [10] laser Doppler vibrometers (LDVs), accelerometer or strain gauge arrays, and 3D digital image correlation (3D-DIC) [11, 12]. Similar to thermocoules, accelerometer and strain gauge arrays affect the dynamic structural response. LDVs can be subject to error with large deformation and scanning techniques are a limit the type of measurable response. Alternatively, 3D-DIC has been used to measure large dynamic

deformations [9] and can be used at high temperatures with modification [13, 14]. A high speed 3D-DIC system is used in this work to provide full-field 3D coordinate of the panel deformation.

The dynamic behavior of a cylindrically curved stainless steel panel, previously examined in [15], is the focus of this work. The combination of localized thermal gradients and full field measurement techniques allows the identification of nonlinear coupling of resonant behavior under well defined thermal loading. The shape and location of the thermal loading is motivated by previous work examining shock-wave boundary layer interactions [16].

2 Experimental Setup

2.1 Overview

The 248 mm x 400 mm 304 stainless steel panel used in this study is cold rolled to a cylindrical curvature of 2540 mm and mounted to a slip table as shown in Fig. 1. This slip table, connected to a 110 kN shaker, provides 150 Hz-500 Hz band limited random base excitation at several excitation amplitudes. In addition to base excitation, a 6 kW inductive furnace is used to apply localized heating to the panel during excitation. Several measurement systems are used in tandem to fully capture the dynamic response of the panel to the outlined combined loading conditions. In addition to strain gauges and thermocouples mounted to the panel, two non-contacting fiber optic laser Doppler vibrometers (LDVs) and a non-contacting pyrometer are used to measure single point velocity and temperature, respectively. Images of the panel surface are measured at 2000 Hz using two Photron SAZ cameras for 3D-DIC and at 2 Hz using a FLIR camera and provide full field coordinates and temperature measurements, respectively.

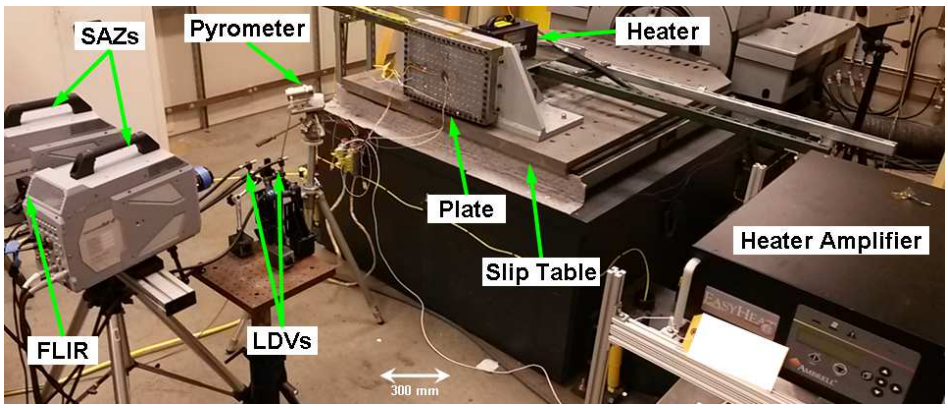
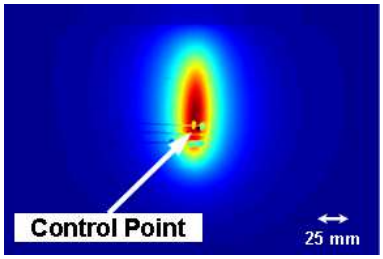


Figure 1: Experimental Setup

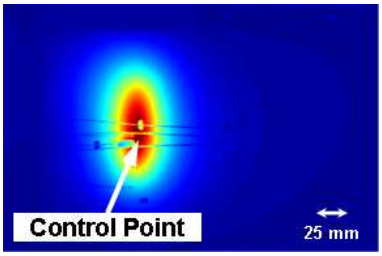
2.2 Loading Conditions

The 6 kW inductive furnace head and coil are mounted approximatly 300 mm behind the panel and suspended above the shaker slip table as shown in Fig. 1. This furnace, previously used in [7], heats the article by inducing eddy currents in the material with a magnetic field via an oscillating current through a coil attached to the head of the furnace [6]. A 860 mm copper tube is bent to specific shape and attached to the coil to induce localized temperature gradients the horizontal center line of the panel and the quarter line of the panel as shown in Fig. 2a and Fig. 2b, respectively. Throughout testing, the inductive heater is controlled at the single points shown using a Microepsilon pyrometer. During heating, A 110 kN electrodynamic shaker provides single axis base excitation controlled with a 10 mV/g PCB 352C22 uni-axial accelerometer mounted at the edge of the slip table. DataPhysics Abacus hardware and software is used to maintain control at a specified root-mean-squared (RMS) value of white noise acceleration in the frequency range of 150 Hz

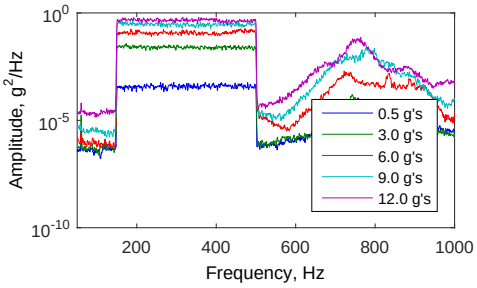
-500 Hz with 3 sigma clipping. Several RMS acceleration levels are selected to span from linear to nonlinear dynamic regimes. A measurement of the control signal at each RMS acceleration amplitude is shown in Fig. 2c. Motion outside of the frequency range of interest was recognized and attributed to dynamic motion from the slip table. At each base excitation amplitude, temperature at a single point within the compact thermal gradient is controlled at several temperatures between 30 °C and 260 °C.



(a)



(b)



(c)

Figure 2: Thermal and mechanical loading conditions. Induced temperature distribution at (a) 1/2 length and (b) 1/4 length. Red indicates an area of high temperature (260 °C) and blue indicates an area of low temperature (20 °C). (c) Profile of base excitation applied to the panel

2.3 Response Measurements

The full-field temperature response of the panel is measured at 2 Hz using a FLIR camera. A Surface Optics E10 reflectometer s used to measure the emissivity of the painted surface of the panel after the paint is cured. The emissivity of 0.94 at room temperature calibrates the FLIR temperature measurements. Additionally, the full-field coordinate position of the surface of the panel is determined post-test using 3D-DIC techniques on high speed images captured at 2000 Hz using Photron SAZ cameras following a similar procedure described in [9,17]. The calibration accuracy is 0.022 pixels and a facet size of 17 pixels x 17 pixels is used to determine the 3D coordinates of the surface in the grid shown in green in 3. Single point measurements include type-K thermocouples (T1, T2, and T3) sampled at 1Hz, fiber optic laser vibrometers (V1 and V2) sampled at 6000 Hz, and fiber optic strain gauges (ϵ 1 and ϵ 2) as shown in 3.

3 Results

3.1 Static Response to Varying Thermal Loading

The localized temperature distribution results in a local ‘in plane’ strain field which is dependent on the thermal state of the panel and frame, as well as the location of the coil. The thermal state of the panel in the frame is key to defining the ‘out of plane’ deformation the panel will undergo, similar to the buckled state of slender structures [18]. However, the curvature in the panel prevents buckling in the traditional sense,

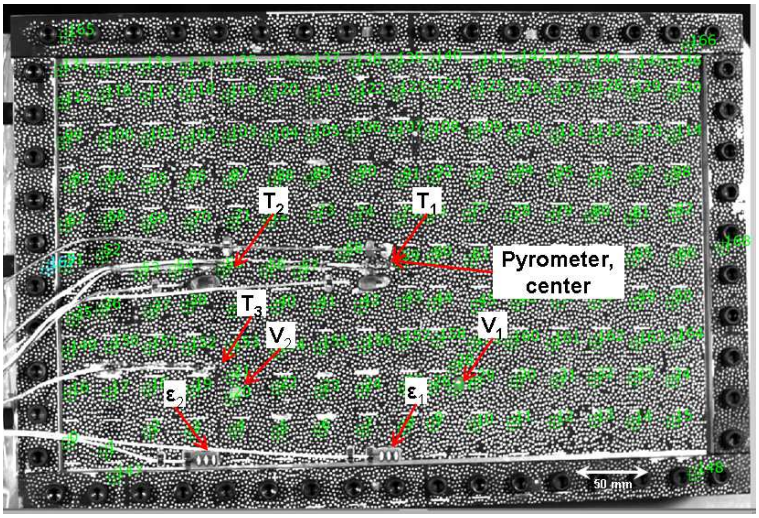
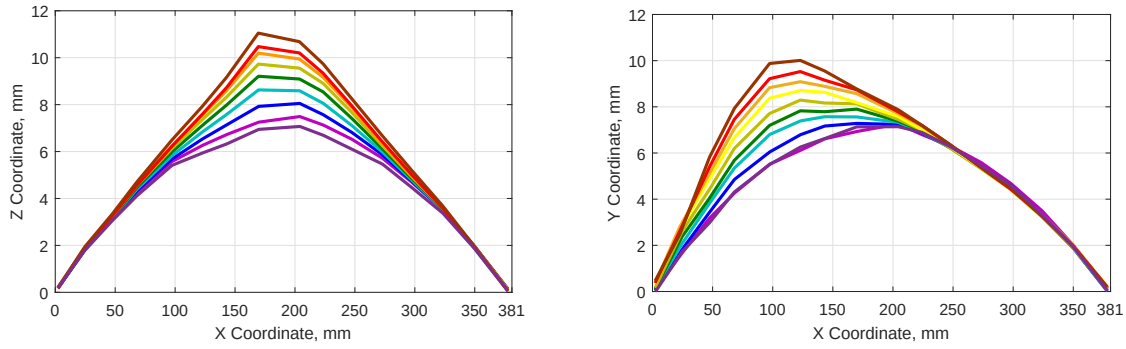


Figure 3: Image of panel illustrating single point sensor locations

so there is no bifurcation to an alternate equilibrium. Instead the 'out of plane' deformation will grow as temperature is increased.

The thermal strains induced on the panel are constant for each thermal loading case; therefore, the dynamic deformation of the panel for each case will occur around a different static equilibrium. The temperature dependent static equilibrium is identified by calculating the mean of the dynamically measured z-coordinate. The z-coordinate at each temperature step is shown for vertical center line of the panel in Fig. 4. When the coil is placed near the horizontal center line of the panel, the peak deformation of the panel is 4.2 mm at 260 °C. Similarly, when the coil is placed near the quarter line of the panel, the peak deformation of the panel is 4.4 mm at 260 °C. In each heating case, Fig. 4 shows the change from an initially cylindrically curved panel to a heavily biased curvature because of the local thermal gradients.



(a) (b)

Figure 4: Static deformation response to thermal loading when applied to the (a) center and (b) quarter point of the panel from 20 °C (purple) to 260 °C (dark red).

3.2 Dynamic Response with Varying Thermal Loading

At each temperature step, the dynamic response of the panel to a 0.5 g's RMS base acceleration is examined. For illustration, an averaged power spectral density (PSD) [19] of the velocity measured with laser Doppler vibrometers using a blocksize of 6000 samples is presented for the center line heating case (Fig. 5a) and for the quarter line heating case (Fig. 5b). For each heating case, the resonant behavior of the panel is identified by peaks in the PSD and plotted in the temperature vs. frequency domain (Fig. 5c and Fig. 5d) to identify

general trends as the panel is heated. The clearest distinction between the center heating case (Fig. 5c) and the quarter heating case (Fig. 5d) is how the first peak in PSD demonstrates a spring hardening (increase in frequency) for the center heating case, whereas a small spring softening (decrease in frequency) is observed for the quarter heating case. Additionally, for the quarter heating case, the peaks in the PSD coalesce into three distinct regions at higher temperatures, where the peaks in the PSD for the center heating case remain well separated after 150 °C. For both heating cases, the frequencies show strong variation because of heating and potentially lead to veering/crossing of the resonant behavior [20].

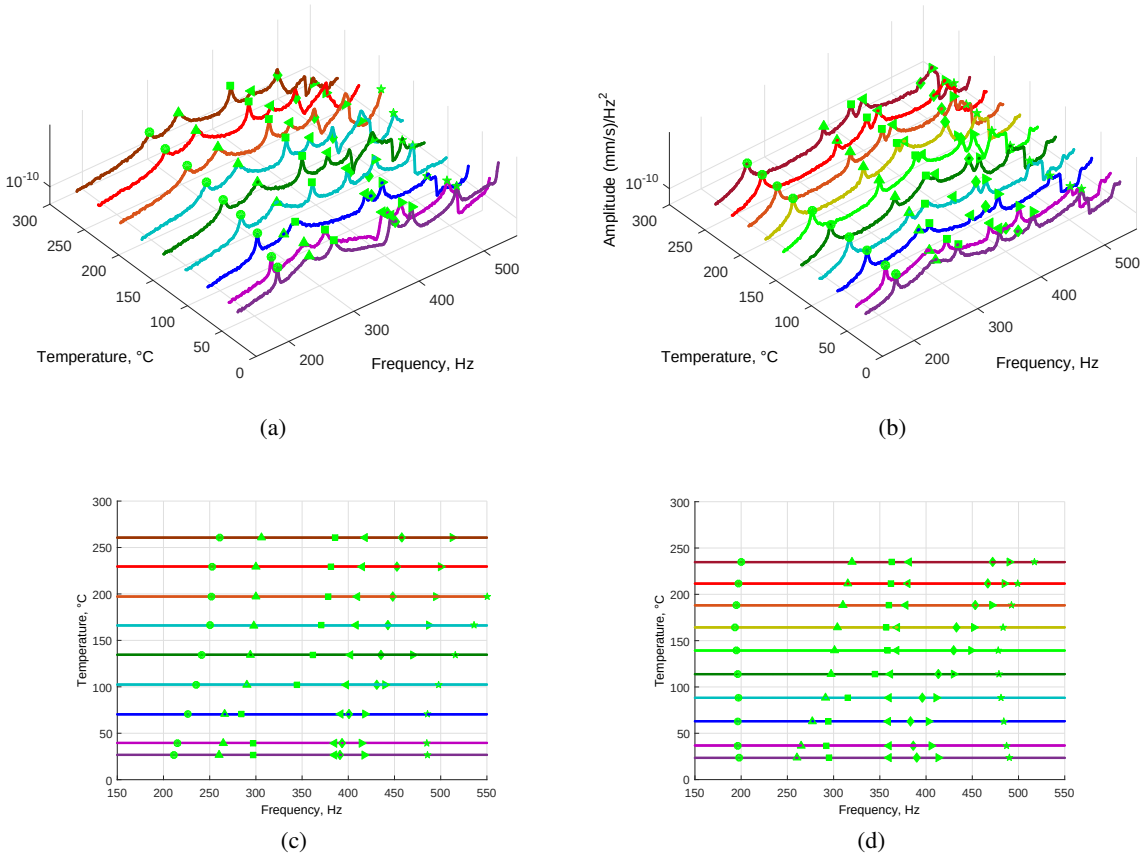


Figure 5: PSD of the panel measured with the laser Doppler vibrometers when heated at the (a) center line and (b) quarter line. The first 7 resonant peaks of the dynamic response were identified and detailed in the projection of temperature vs. frequency for heating at the (c) center linear and (d) quarter line.

In addition to the temperature dependent behavior of the resonant frequencies of the response, the deformation shapes of the panel at each resonant frequency are also temperature dependent. Using the methodology to compute frequency response functions of random data described in [19], the shape at each peak of the frequency response function (Gza) of the dynamic coordinates measured with 3D-DIC and the base acceleration is identified using singular value decomposition. For brevity, only a select number of shapes are presented in Fig. 6 for the center heating case and Fig. 7 for the quarter heating case.

The first five deformation shapes identified for the center heating case at 20°C (Fig. 6p-t) closely match the first five mode shapes of the curved panel previously identified in [15], as expected. For quantification, the RMS value of the maximum deformation across the panel is added in the caption, and the colormap scale can be identified from blue (negative value) to red (positive value). As temperature is increased the deformation shape corresponding to the first peak of the PSD is only active on the right side of the panel (Fig. 6a,f,k,p). Interestingly, the second peak's deformation shape is only active on the left of the panel at increased temperatures (Fig. 6b,g,l,q). The third peak's deformation shape initially merges to match the second peak's

shape, but at higher temperatures, the deformation shape resembles a mode 3 deformation. However, the third peak's deformation shape is primarily active in the lower part of the panel (Fig. 6c,h,m,r). The third and fourth peak's deformation shapes also initially couple then separate as the temperature increases, and both peak's shapes appear to interact at higher temperatures. It should also be noted, heating does not proportionally increase the rms value of the resonant peaks as quantified by the summation of RMS values. The resonant behavior has a total RMS value of 11.75 μm, 12.85 μm, 18.87 μm, and 18.92 μm at nominal temperature steps of 20 °C, 70 °C, 100 °C, and 260 °C, respectively. Finally, it is important to identify that the dominant resonance in the dynamic response becomes the second resonance peak at 260 °C, changing the frequency of importance from 250 Hz to 300 Hz.

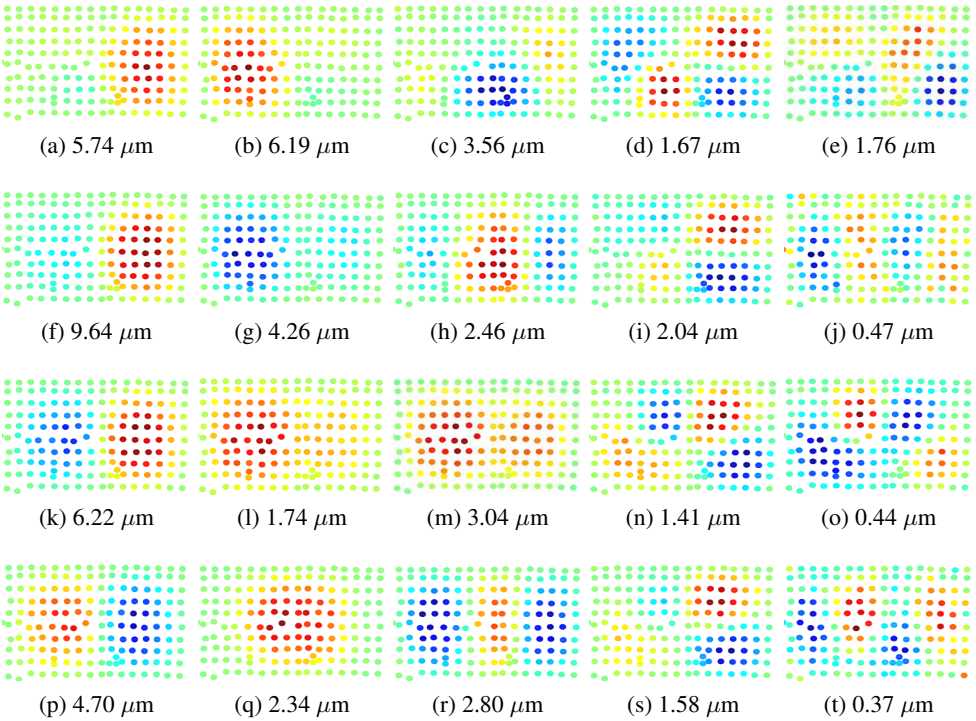
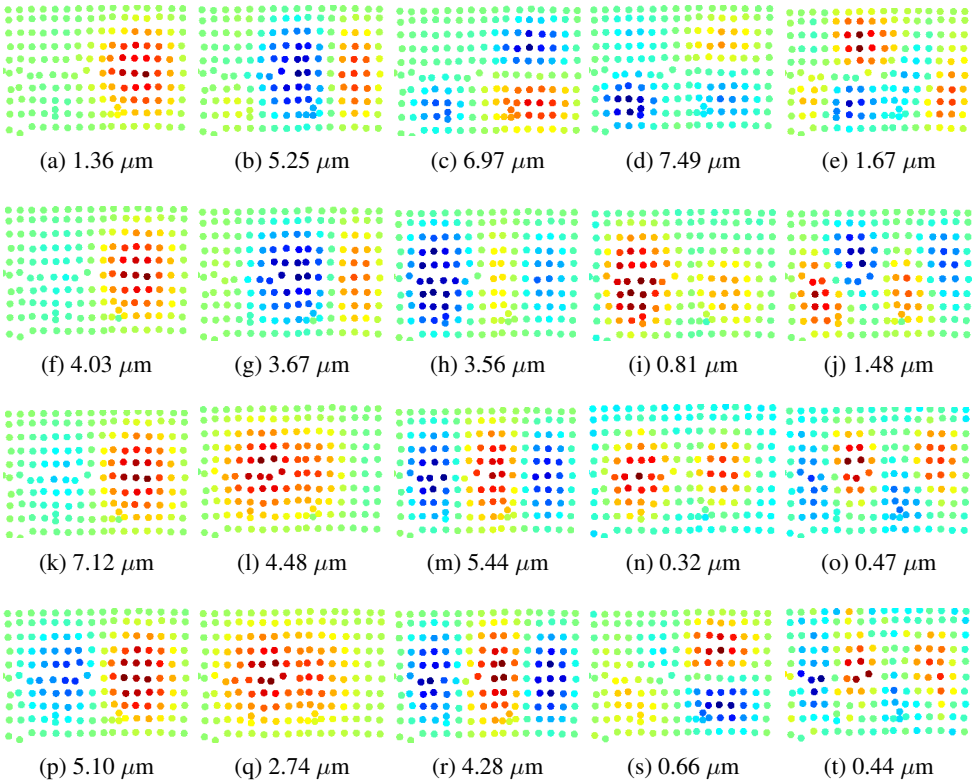


Figure 6: Resonant shapes of the first five peaks in the Gza during heating of the center line at temperature conditions Near 260 °C (a-e), 100 °C (f-j), 70 °C (k-o), and 20 °C (p-t). The color scale from blue to red is negative to positive deformation with the RMS value of the peak deformation given in the figure caption.

A similar examination of the temperature dependence of the resonant deformation shapes when the panel is heated at the quarter point of the panel is shown in Fig. 7. Again, the first five deformation shapes at room temperature resemble the experimental mode shapes identified in [15], and demonstrate consistency between the two tests. Similar to the center heating case, the first peak's deformation shape when heated at the quarter point becomes more active on the right side of the panel with increasing temperature (Fig. 7a,f,k,p). The second peak's deformation shape is also more active on the right side of the panel for increasing quarter line temperature (Fig. 7b,g,l,q) differing from the center heating case. As temperature is increased, the fourth peak's deformation shape couples with surrounding resonances (Fig. 7i,n,s), but the third and fifth peak's deformation shape remains consistent until the peak temperature is 260 °C. At 260 °C, the third peak's deformation shape (Fig. 7c) resembles the room temperature shape of the fourth peak (Fig. 7s), and the fourth and fifth peak's deformation shapes appear as combinations of several shapes (Fig. 7d and e, respectively). For the resonances of interest, the total RMS value at temperature steps of 20 °C, 70 °C, 100 °C, and 260 °C is 13.22 μm, 17.36 μm, 13.55 μm, and 22.47 μm, respectively. Finally, it is important to identify that the dominant resonances in the dynamic response become the third and fourth resonance peak at 260 °C, changing the frequencies of importance near 350 Hz.



(a) 1.36 μm (b) 5.25 μm (c) 6.97 μm (d) 7.49 μm (e) 1.67 μm

(f) 4.03 μm (g) 3.67 μm (h) 3.56 μm (i) 0.81 μm (j) 1.48 μm

(k) 7.12 μm (l) 4.48 μm (m) 5.44 μm (n) 0.32 μm (o) 0.47 μm

(p) 5.10 μm (q) 2.74 μm (r) 4.28 μm (s) 0.66 μm (t) 0.44 μm

Figure 7: Resonant shapes of the first five peaks in the PSD during heating of the quarter line at temperature conditions Near 260 °C (a-e), 100 °C (f-j), 70 °C (k-o), and 20 °C (p-t). The color scale from blue to red is negative to positive deformation with the RMS value of the peak deformation given in the figure caption.

3.3 Dynamic Response to Combined Loading

The dynamic response of the curved panel to a combination of large amplitude base acceleration and thermal loading leads to more interesting dynamic behavior. For brevity, only the dynamic response of the panel at 9g's of base excitation combined with thermal loading up to 260 °C is presented. Following the process outlined in 3.2, the composite PSD's for the center and quarter heating cases are shown in Fig. 8a and Fig. 8b, respectively. The temperature vs. frequency projection is shown in Fig. 8c and Fig. 8d. Similar to the center heating case presented in 3.2 with a base excitation of 0.5g's (Fig. 5c), the trend of the resonant frequencies for the center heating case at 9g's are a spring hardening as shown in Fig. 8c. However, at 160 °C, the first six resonant peaks appear to coalesce into three regions, and maintain this 'closeness' as temperature is further increased. This close behavior indicates strong coupling between the resonant peaks further detailed when we examine the deformation shapes at each peak. The first resonant peak for the quarter heating case at 9g's (shown in Fig. 8d) follows a similar trend when only 0.5g's of base excitation is examined (Fig. 5d). The next five resonant peaks also show a similar coalescence observed in the 0.5g's case; however, the 'closeness' is tighter. From these examples, it is shown that at high temperature and large base excitation, the trend of the resonant peaks is toward a tighter coalescence. This apparent interaction between resonant peaks greatly affects the deformation shapes observed at each peak.

The deformation shapes for the center heating case with a 9g's base excitation are presented in Fig. 9. The deformation shapes of the first (Fig. 9a,f,k,p) and second (Fig. 9b,g,l,q) resonant peaks follow the exact trend identified in the center heating cases under 0.5g's base acceleration. However, the deformation shapes of the third, fourth, and fifth resonant peaks demonstrate different behavior. This behavior is most notable at the 150 °C case (Fig. 9h-j). At this temperature, the deformation shapes of the third and fourth resonant peaks are a combination of their room temperature counterparts, and the deformation shape of the fifth resonant peak is rotated so the top half of the panel is out of phase with the bottom half of the panel. At 260°C (Fig. 9c-e),

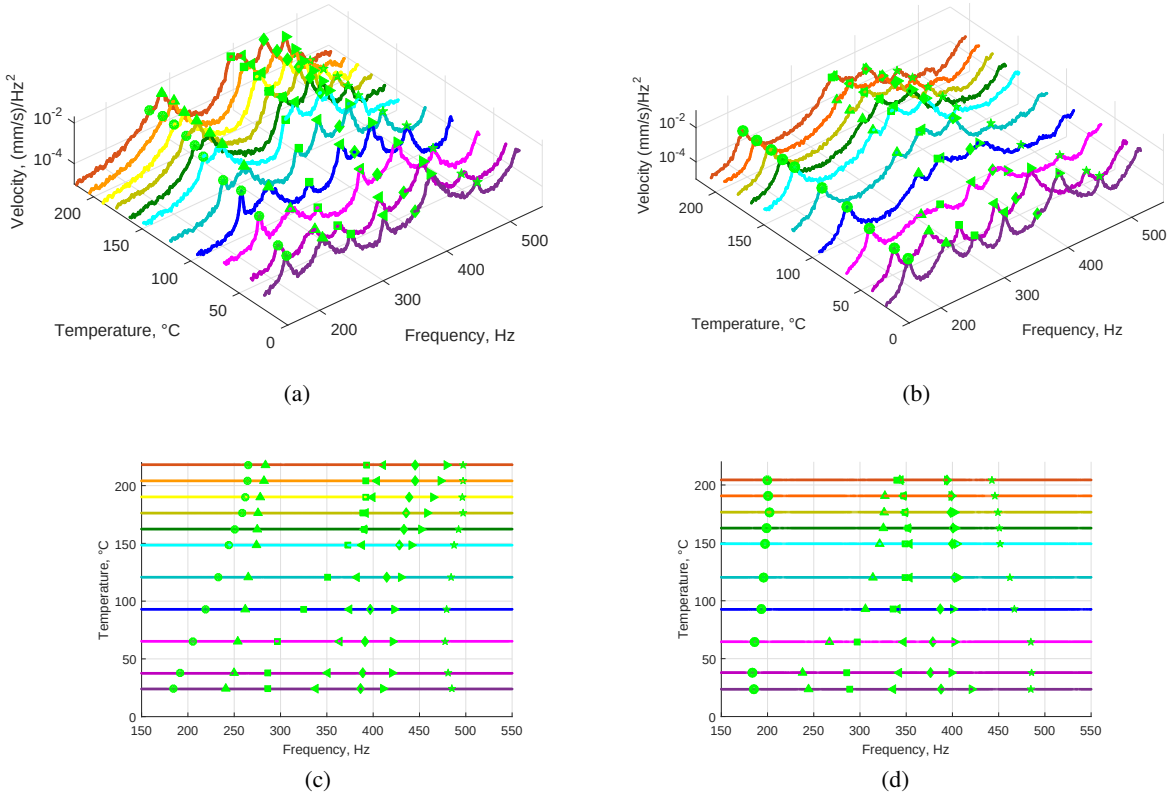
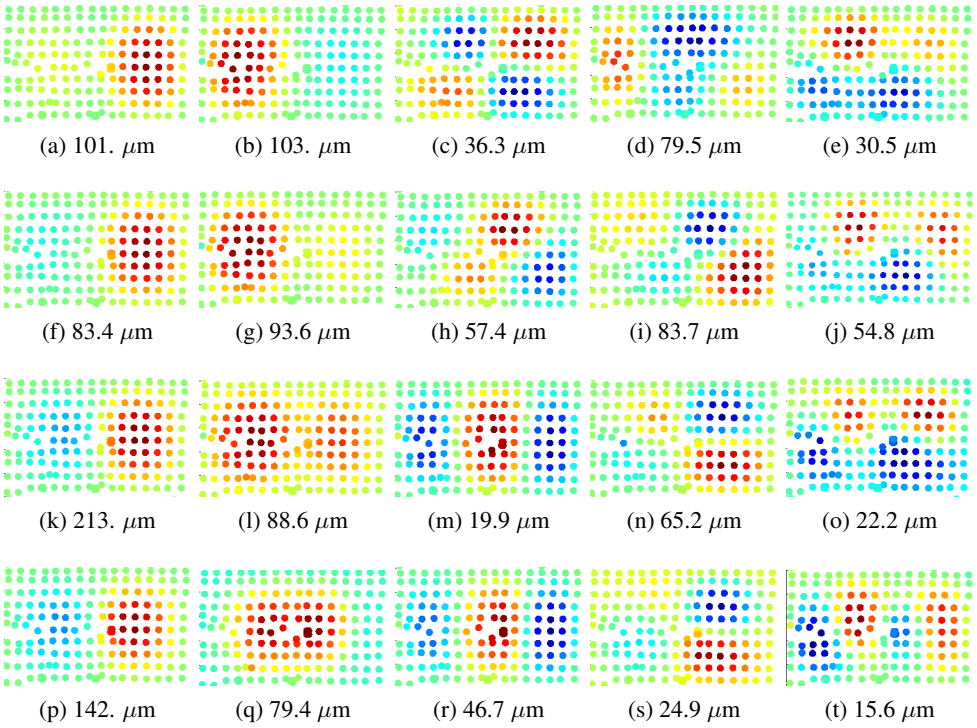


Figure 8: Composite power spectral densities of the panel measured with the laser Doppler vibrometers when heated at the (a) center line and (b) quarter line combined with a base excitation of 9 g's. The first 7 peaks of the dynamic response were identified and detailed in the projection of temperature vs. frequency for heating at the (c) center linear and (d) quarter line.

the deformation shapes of the third and fourth resonant peak change order with the deformation shape of the now fourth resonant peak resulting in a more active top half of the panel. For the resonances of interest, the total RMS value at temperature steps of 20 °C, 70 °C, 100 °C, and 260 °C is 309 μm, 409 μm, 373 μm, and 350 μm, respectively. Above 70 °C the 'smearing' of the resonant peaks results in a lower RMS value following a similar trend identified in [15] for large amplitudes of dynamic response. Finally, it is important to identify that the dominant resonances in the dynamic response are the first and second resonance peaks at 260 °C, changing the frequencies of importance near 260 Hz.

The deformation shapes for the quarter heating case with a 9g's base excitation are presented in Fig. 10. The deformation shapes of the first (Fig. 10a,f,k,p) and second (Fig. 10b,g,l,q) resonant peaks follow the exact trend identified in the quarter heating cases under 0.5g's base acceleration except in the case for the second resonant peak at 210 °C which resembles the third resonant peak at room temperature. The remaining deformation shapes presented have limited correlation to the room temperature shapes except in the case of the third resonant peak at 260 °C. For the resonances of interest, the total RMS value at temperature steps of 20 °C, 70 °C, 150 °C, and 260 °C is 300 μm, 363 μm, 421 μm, and 481 μm, respectively. It is interesting to note that the reduction in total mean resonant response observed in the center line heating case is not observed in the quarter heating case. Instead, an consistent increase is observed in the total RMS value and the first resonant response, setting 200 Hz as the resonance of interest for this thermal case.



(a) 101. μm (b) 103. μm (c) 36.3 μm (d) 79.5 μm (e) 30.5 μm

(f) 83.4 μm (g) 93.6 μm (h) 57.4 μm (i) 83.7 μm (j) 54.8 μm

(k) 213. μm (l) 88.6 μm (m) 19.9 μm (n) 65.2 μm (o) 22.2 μm

(p) 142. μm (q) 79.4 μm (r) 46.7 μm (s) 24.9 μm (t) 15.6 μm

Figure 9: Resonant shapes of the first five peaks in the Gza during heating of the center line at temperature conditions combined with 9g's of base acceleration near 260 °C (a-e), 150 °C (f-j), 70 °C (k-o), and 20 °C (p-t). The color scale from blue to red is negative to positive deformation with the RMS value of the peak deformation given in the figure caption.

4 Conclusions

The experimental methodology presented in this work demonstrates the ability to apply a controlled sharp temperature gradient in dynamic environments while measuring full field temperature and coordinates of a cylindrically curved stainless steel panel. The combined FLIR and 3D-DIC measurements result in rich data set for understanding the static and dynamic response of the panel. The full-field nature of the data also provides enough information for the validation of finite element models. Future work will explore localized heating in combined thermal and acoustic environments.

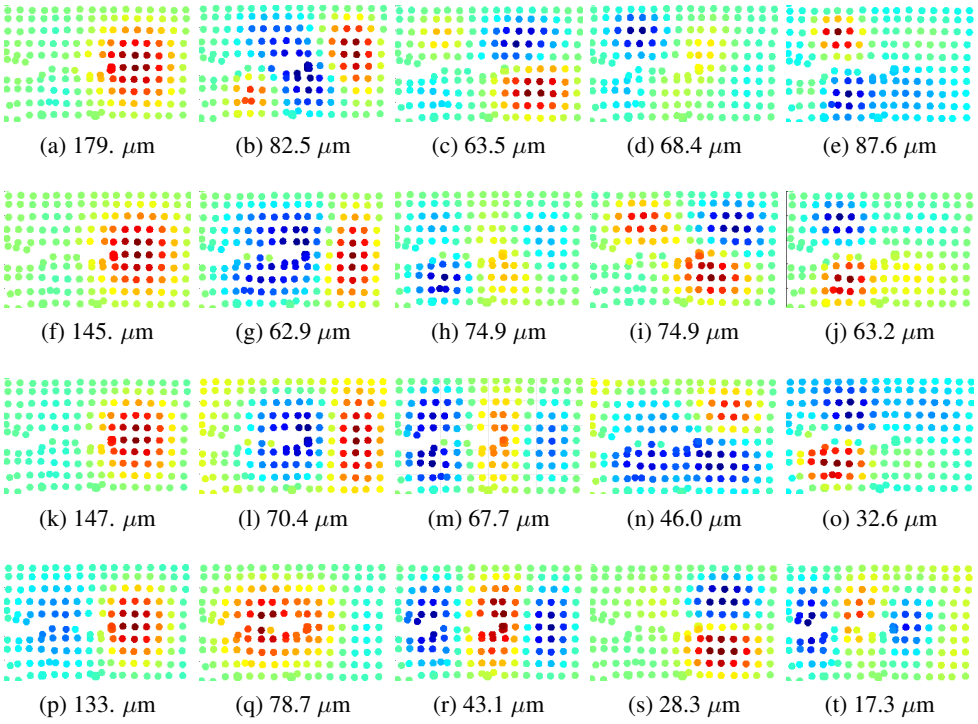
References

[1] B. Zuchowski. Predictive capability for hypersonic structural response of life prediction: Phase ii - detailed design of hypersonic cruise vehicle hot-structure. Technical report, Air Vehicle Integration and Technology Research, 2012.

[2] G. Tzong, R. Jacobs, and S. Liguore. Predictive capability for hypersonic structural response and life prediction: Phase 1-identification of knowledge gaps. Technical report, Air Vehicle Integration and Technology Research, 2010.

[3] S.A. Clevenson and E.F. Daniels. Capabilities of the thermal acoustic fatigue apparatus. Technical report, NASA, 1992.

[4] S.A. Rizzi and T.L. Turner. Enhanced capabilities of the nasa langley thermal acoustic fatigue apparatus. In Mei Ferguson, Wolfe, editor, *6th International Conference on Recent Advances in Structural Dynamics*, volume II, pages 919–933, 1997.



(a) 179. μm (b) 82.5 μm (c) 63.5 μm (d) 68.4 μm (e) 87.6 μm

(f) 145. μm (g) 62.9 μm (h) 74.9 μm (i) 74.9 μm (j) 63.2 μm

(k) 147. μm (l) 70.4 μm (m) 67.7 μm (n) 46.0 μm (o) 32.6 μm

(p) 133. μm (q) 78.7 μm (r) 43.1 μm (s) 28.3 μm (t) 17.3 μm

Figure 10: Resonant shapes of the first five peaks in the Gza during heating of the quarter line at temperature conditions combined with 9g's of base acceleration near 260 °C (a-e), 150 °C (f-j), 70 °C (k-o), and 20 °C (p-t). The color scale from blue to red is negative to positive deformation with the RMS value of the peak deformation given in the figure caption.

[5] J. Pearson. High-temperature acoustic test facilities and methods. In *Symposium on Impact of Acoustic Loads on Aircraft Structures*, 1994.

[6] S. Zinn and S.L. Semiatin. *Elements of induction heating: design, control, and applications*. ASM International, Metals Park, Ohio, 1988.

[7] B.T. Gockel, R.S. Kolesar, and A.D. Rollett. Experimental study of an aerospace titanium alloy under various thermal and tensile loading rate conditions. *Integrating Materials and Manufacturing Innovation*, 5(13), 2016.

[8] S. Yang and M.S. Allen. Harmonic transfer function to measure translational and rotational velocities with continuous-scan laser doppler vibrometry. *Journal of Vibration and Acoustics*, 136(2):021025–021025, 2014. 10.1115/1.4026350.

[9] David A. Ehrhardt, Matthew S. Allen, S. Yang, and Timothy J. Beberniss. Full-field linear and nonlinear measurements using continuous-scan laser doppler vibrometry and high speed three-dimensional digital image correlation. *Mechanical Systems and Signal Processing*, 2017.

[10] Phillip L. Reu, Daniel P. Rohe, and Laura D. Jacobs. Comparison of dic and ldv for practical vibration and modal measurements. *Mechanical Systems and Signal Processing*, 86, 03 2016.

[11] M. A. Sutton, W. J. Wolters, W. H. Peters, W. F. Ranson, and S. R. McNeill. Determination of displacements using an improved digital correlation method. *Image and Vision Computing*, 1(3):133–139, 1983.

[12] Timothy E. Schmidt, John Tyson, Konstantin Galanulis, Duane M. Revilock, and Matthew E. Melis. Full-field dynamic deformation and strain measurements using high-speed digital cameras. In *26th*

International Congress on High-Speed Photography and Photonics, volume 5580, pages 174–185, 2005. 10.1117/12.567142.

[13] R.B. Berke and J. Lambros. Ultraviolet digital image correlation (uv-dic) for high temperature applications. *Review of Scientific Instruments*, 85(045121), 2014.

[14] B. Pan, D. Wu, Z. Wang, and Y. Xia. High-temperature digital image correlation method for full-field deformation measurement at 1200c. *Measurement Science and Technology*, 22(1), 2011.

[15] R.W. Gordon and J.J. Hollkamp. Reduced order models for acoustic response prediction. Technical report, Air Force Research Lab, 2011.

[16] S. Michael Spottswood, T.J Beberniss, and T.G. Eason. Structural response prediction: Full-field, dynamic pressure and displacement measurements of a panel excited by shock boundary-layer interaction. Technical Report AFRL-RQ-WP-TP-2015-0046, Air Force Research Lab Structural Sciences Center, 2015.

[17] Timothy J. Beberniss and David A. Ehrhardt. High-speed 3d digital image correlation vibration measurement: Recent advances and noted limitations. *Mechanical Systems and Signal Processing*, 2017.

[18] Lawrence N. Virgin. *Vibration of Axially-Loaded Structures*. Cambridge University Press, 2007.

[19] William T. Thomson and Dahleh Marie Dillon. *Theory of Vibration with Applications*. Prentice-Hall Inc., Upper Saddle River, New Jersey, 5th edition, 1998.

[20] A.W. Leissa. On a curve veering aberration. *Journal of Applied Mathematics and Physics*, 25(1):99–111, 1974.

Effect of in-flight differential pressure in modal behaviour of an aircraft demonstrator using HS 3D-DIC

A.J. Molina-Viedma[1], A. González-Centeno[1], E. López-Alba[1], L. Felipe-Sesé[1], F. Díaz[1]
[1] Universidad de Jaén, Department of Mechanical and Mining Engineering
Campus Las Lagunillas, 23071, Jaén, Spain
e-mail: **ajmolina@ujaen.es**

Abstract
Experimental modal analysis is a useful tool in the aircraft industry to evaluate the effect of vibration in the structural endurance and the generation of noise in the cabin. Advances on High Speed Digital Image Correlation have made it possible to extend the use of this technique to real in service structures in a full-field non-invasive manner. In this work the passenger window area of a front fuselage full-scale demonstrator has been analysed. The natural frequencies and the full-field Operational Deflection shapes have been obtained to evaluate the effect of in-flight environmental conditions in the modal behaviour. An image decomposition procedure has been performed to reduce the full-field information to a vector of shape descriptors coefficients, without relevant loss of information. Results reveals the effect of static deflection due to the differential pressure in the deflection shapes and the stiffening in the natural frequencies shifting.

1 Introduction

In the aerospace industry the level of noise inside aircraft is a main concern where the selection of materials and design are critical issues regarding the modal behaviour. Moreover, the different environment conditions that aircrafts undergo alter the modal response. Therefore, experimental modal analysis provides fundamental background to improve the design and numerical models [1]. In this industry, this characterization is commonly performed using accelerometers or other pointwise transducers that introduce some sources of error due to their invasive nature. Moreover, the instrumentation is time consuming in this large structures with a very low spatial resolution.

Alternative techniques have been recently employed for experimental modal analysis providing contactless full-field information. Unlike traditional sensors, the dynamic response is not modified by mass and damping of transducers and cabling. Scanning Laser Doppler Vibrometry (LDV) is a interferometric technique that performs full-field velocity measurements in the laser beam direction by scanning the surface [2], [3]. In the last years digital image correlation with a stereoscopic system of high-speed cameras (HS 3D-DIC) is gaining popularity in experimental modal analysis [4]. It is an optical technique for displacement and strain measurement [5]. HS 3D-DIC for experimental modal analysis is still in its infancy a there is no commercial software that deals with the data and longer processing is required. Nevertheless, this technique is able to provide dynamic information with higher spatial resolution in the three spatial directions using a simpler setup [6]–[8]. Moreover, HS 3D-DIC currently involves a cost reduction for 3D measurements.

The full-field information is especially useful to characterise mode shapes and operational deflection shapes (ODS) using HS 3D-DIC. The most straightforward way is to carry out force normal excitation tests using sinusoidal signals at resonance of the system [6], [9]–[12]. Additionally, with broadband excitation it is also possible to obtain the full-field response of the specimen, such as frequency response functions (FRF) or other frequency domain transfer function. By analysing the peaks that maximize the response it is possible to estimate the natural frequencies and the damping ratios [7], [8], [13]–[16]. In some studies, image decomposition approaches have been proposed to reduce redundancies and the size of full-field data to just a few shape descriptors [17], [18].

Here, HS 3D-DIC has been explored for the evaluation of changes in the modal response of a front fuselage full-scale demonstrator due to different environmental conditions. In-flight conditions were experimentally simulated by applying differential pressure to the demonstrator. HS 3D-DIC measurements were conducted on the passenger window area, considered as relevant from the vibroacustic perspective. The experiments aimed for characterising the specific vibration modes with major significance in this sense. Firstly, sine tests were proposed for full-field ODS determination. Later, broadband random excitation test was applied to obtain the full-field transfer functions between the excitation and the window response. Hence, both natural frequencies and full-field ODSs could be obtained. For ODSs comparison, shape descriptor decomposition was performed to optimise the full-field data and find differences in the behaviour of the window. It was possible to identify changes in the modal behaviour and relate it with the deformation suffered due to pressure.

2 Experimental tests

Experiments were conducted using a full-scale composite cockpit demonstrator shown in Figure 1. This full-scale cockpit demonstrator was used for a comprehensive series of tests, including static and structural fatigue tests, impact damage tolerance, as well as vibroacoustic tests. It was in this context that the potential of HS 3D-DIC testing technology was evaluated for non-invasive structural dynamic testing, complementing conventional measurements using accelerometers.



Figure 1: Full-scale cockpit demonstrator.

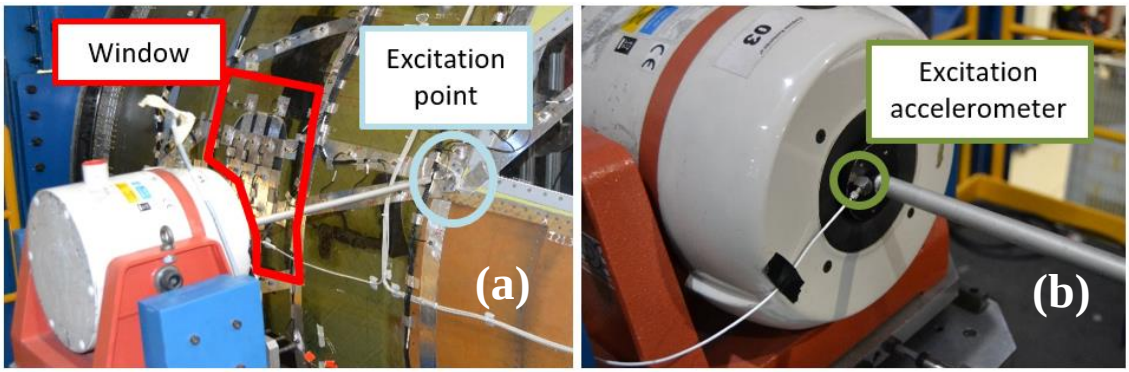


Figure 2: Excitation of the cockpit demonstrator using a shaker.

Measurements using HS 3D-DIC were performed in the window passenger area considering different types of tests hereafter described. The demonstrator was laterally excited by an electrodynamic shaker model LDS V450 (Bruel and Kjaer) using a stinger, as shown in Figure 2.

Under atmospheric pressure conditions, sine and random excitation signals were performed. In sine tests the ODSs at relevant natural frequencies of the structure were obtained. An impact hammer test was carried out to identify the natural frequencies for subsequent sine tests. A multi-input multi-output analysis was performed considering three measuring points and three excitation points. The location of these points was defined so that an optimal characterisation of the whole passenger window area could be made, as shown in Figure 3. The remaining accelerometers observed in the figure were intended for purposes unconnected with this study. A Photon+ Real Time Analyser of Bruel&Kjaer was employed to record the signals from three accelerometer together with Bruel&Kjaer 8206-003 hammer with a sampling frequency of 5120 Hz. Frequency Response Functions were obtained by processing these signal considering 16384 frequency lines and 10 averaged windows. Eventually, natural frequencies were detected using the principal response functions (PRFs) as indicator through single-value decomposition of the FRFs matrix [1]. Two significant frequencies are selected for sine tests from the first two PRFs, as highlighted in Figure 4. From random excitation tests using HS 3D-DIC, natural frequencies and ODSs could be obtained and compared with the sine tests results.

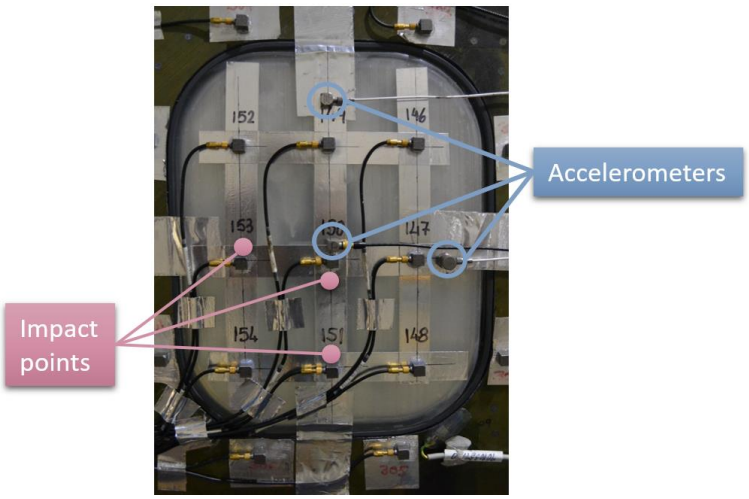


Figure 3: Setup for impact hammer tests on the passenger window (exterior view).

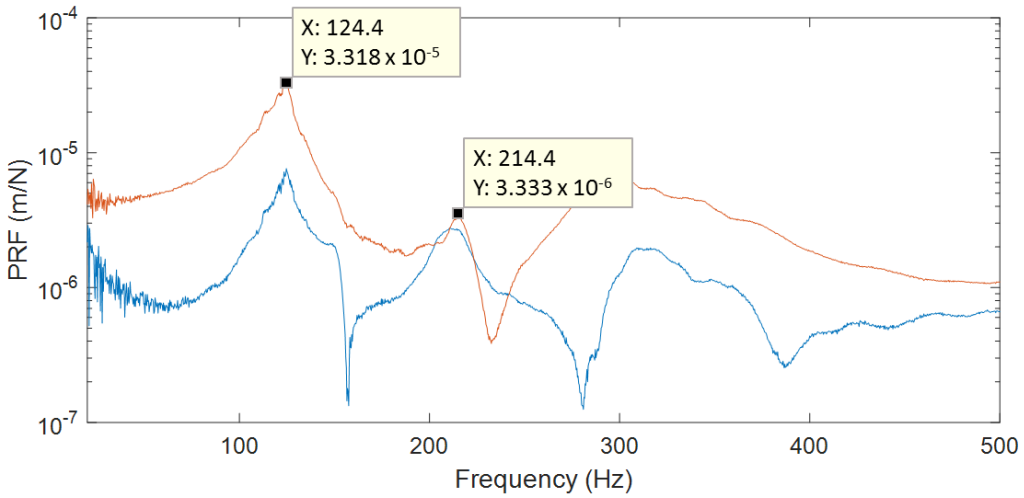


Figure 4: Two first principal response functions from impact hammer tests.

The influence of in-flight conditions was evaluated by applying a differential pressure of 5.5 psi (34,473.8 Pa). Under these conditions, random excitation was applied in order to reveal variations in the natural frequencies and ODSs previously studied under atmospheric conditions.

3 HS 3D-DIC full-field measurements

HS 3D-DIC measurements were carried out on the window from the inside. This setup consisted in two high speed cameras FASTCAM SA4 (Photron), providing a three-dimensional view, and a set of illumination lamps (Figure 5). In order to avoid the effect of the mass of these elements on the dynamic behaviour and isolate the cameras from vibration, the whole system was mounted on a rigid supporting bar which was designed to be fixed to the pressure bulkhead in the structure that supports the whole demonstrator.

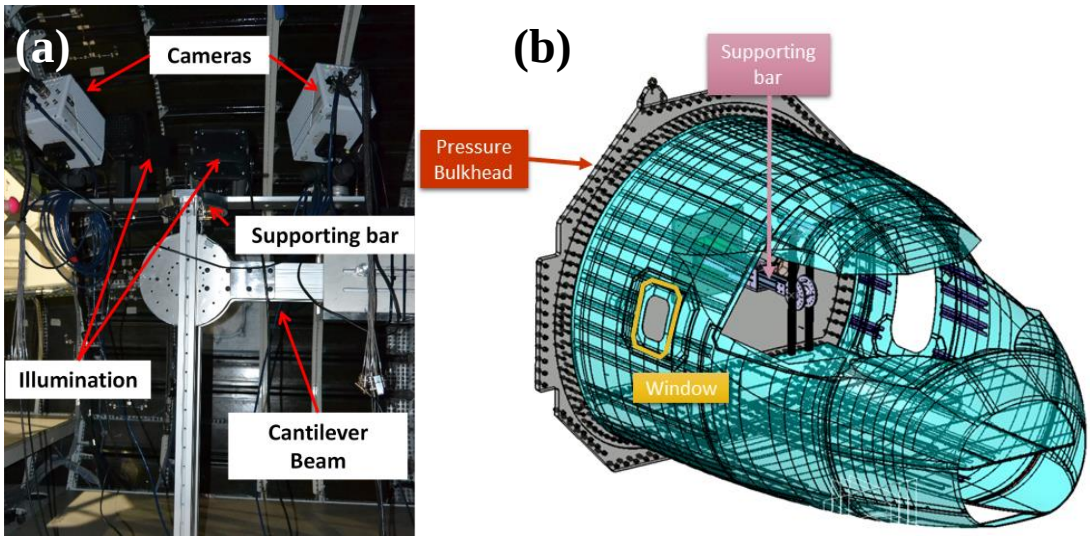


Figure 5: (a) Optical system mounted on the supporting bar. (b) 3D model of the global setup.

For the sine tests, cameras sampling was set at 2000 fps (frames per second) to achieve a good definition of the vibration cycle, considering that the highest mode was 240 Hz. The same frame rate was employed for random tests to analyse the spectrum from 0–640 Hz, satisfying the Nyquist criterion. The spectral analysis was performed considering a frequency resolution of 1 Hz, anti-leakage Hanning windows, and an overlap of 50%.

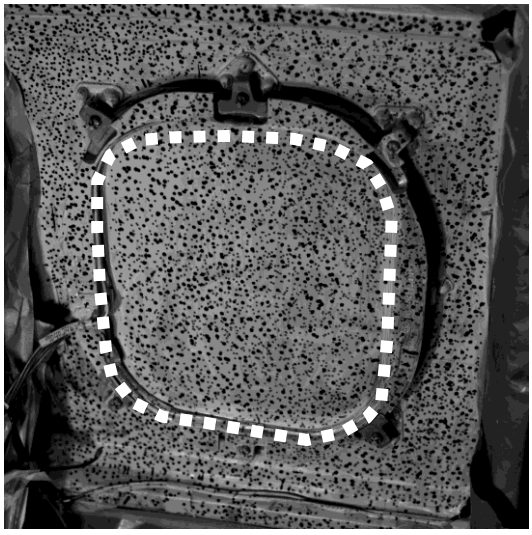


Figure 6: Speckle pattern painted on the passenger window. The area for shape descriptor analysis is highlighted in dotted line.

3D-DIC processing was performed using the commercial software Vic-3D by Correlated Solutions. The surface was treated with paint to provide a grey random speckle pattern (Figure 6) to enable the correlation. The analysis was conducted using 19 pixels facets with a 5 pixel overlap. Hence, about 35,000 measurement points were obtained. Despite that 3D-DIC also provide in-plane motion quantification, out-of-plane displacements were employed as the main direction for the bending deformation of the window.

Full-field transfer functions were obtained in random tests. The excitation was monitored by an accelerometer on the shaker armature, shown in Figure 2b. NI USB-6251 DAQ system (National Instrument) was employed to synchronise cameras and accelerometer sampling. The natural frequencies were identified by peak-picking and ODSs by full-field depicting the amplitude of the peaks for every single point.

4 Shape descriptors

In the tests, a very large number of points were obtained using HS 3D-DIC (~35000 points). In order to perform an efficient comparison of the results an image decomposition method was employed. This method essentially consists on compressing large amounts of two-dimensional data by reducing to a feature vector while preserving the information [19]. These feature vectors can be directly compared and are independent from original sized map or orientation [20]. The 2D data field could be reconstructed from a feature vector, as well. The adopted image decomposition method was based on Chebyshev polynomials $T_k(i,j)$ to decompose contours I(i,j) into a set of coefficients or shape descriptors, s_k, with the same units as the original sets of data:

$$I(i,j) = \sum_{k=0}^{N} s_k T_k(i,j) \quad (1)$$

In this work, this method was applied to full-field ODSs considering the transparent region of the window of analysis, as highlighted in Figure 6, where the largest displacements occur.

To ensure that the feature vector preserves the information, an appropriate number of shape descriptors must be used for the image decomposition. To find it, a sensitivity study was performed looking into improvements on the correlation coefficient between the original and the reconstructed results. In this case, only 20 shape descriptors are sufficient to represent the displacement (ODSs) maps analysed in this work with a correlation coefficient over 98%.

5 Results

From the impact tests, two natural frequencies were selected (124 Hz and 214 Hz) to obtain their ODSs during fixed-sine test. Analogous information can be extracted from random tests using HS 3D-DIC. In this case, the matrix of transfer functions represents the full-field behaviour of the window in the spectrum. By choosing a point at the centre of the window as representative of the main behaviour of the whole window, a wide variety of modes are detected from the transfer function, as shown in Figure 7. Although excitation covered up to 640 Hz, for illustration purposes the transfer function is truncated at 300 Hz, considering that the most relevant modes for this study were below this limit. Despite that the excitation was different for impact and random tests, similar resonance peaks to impact results were identified at 124 Hz y 214 Hz.

ODSs analyses were subsequently performed. Fixed-sine ODSs were obtained from displacement measurements at the window during excitation. ODSs from random tests were determined by depicting the response at local peaks of the full-field Transfer Functions. ODSs are shown in Figure 8 for each mode previously identified. They were normalized to enhance the visual and numerical comparison of the shape descriptors. Results show a good agreement between fixed-sine and random tests with a correlation coefficient between shape descriptors of 0.9803 for the first mode (124 Hz) and 0.9593 for the second mode (214 Hz). In the first mode the window experiences a single bending with maximum displacement in the middle. The second one is in a more complex shape as it is expected from a higher order mode, showing alternative bending regions.

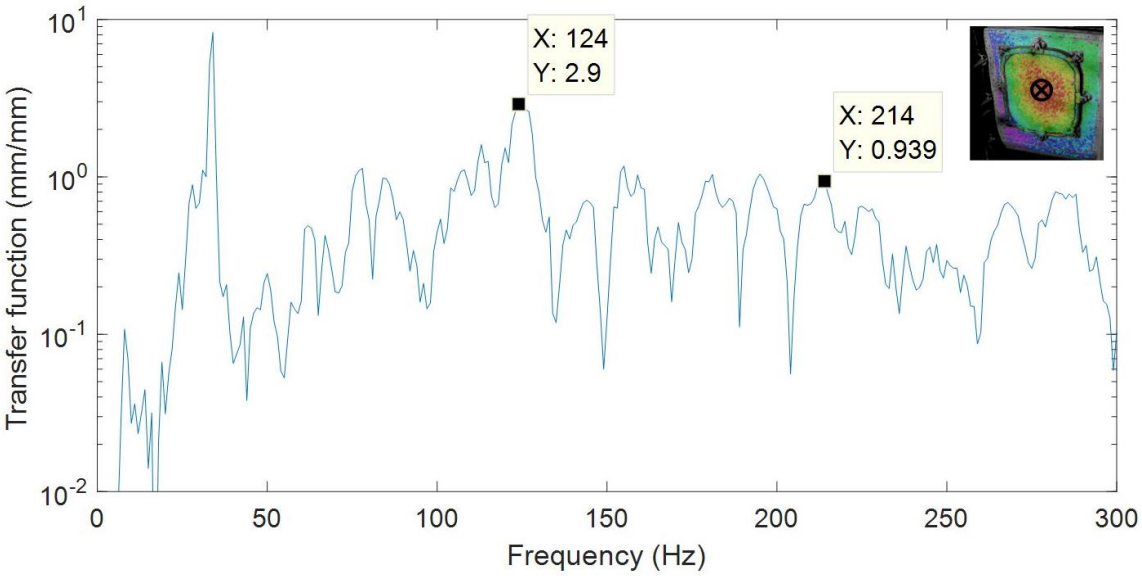


Figure 7: Transfer function obtained with HS 3D-DIC for a point at the centre of the window.

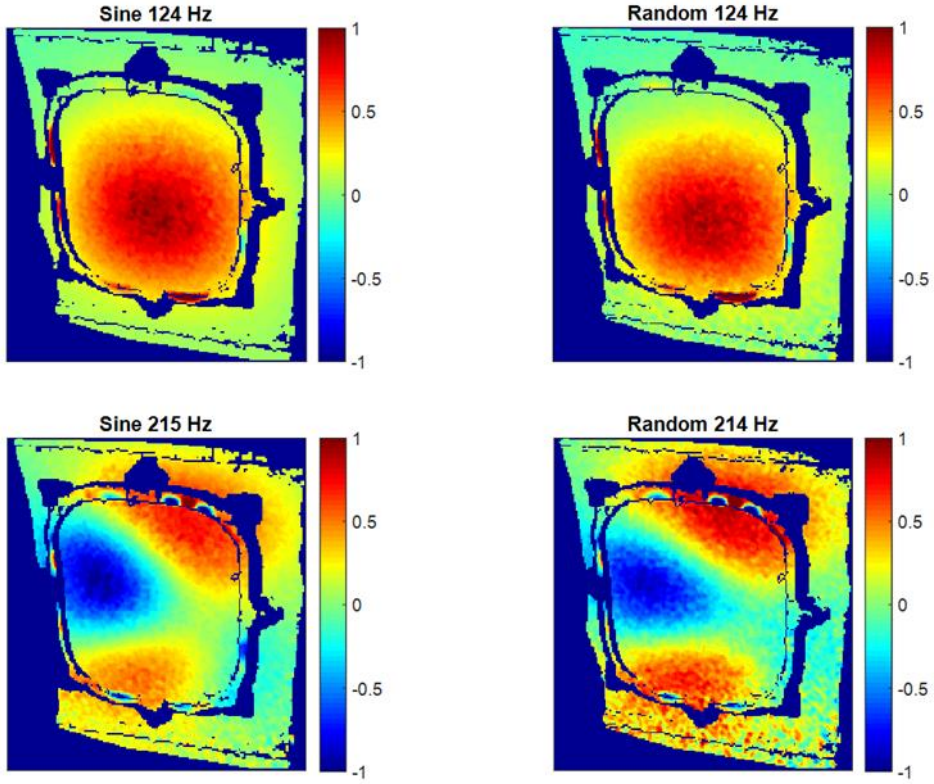


Figure 8: Normalised Operational Deflection Shapes obtained using DIC under different excitation signals.

Sine tests provide interesting advantages: the excitation energy is concentrated in just one single frequency considering ODSs and the results are less affected by noise due to higher displacements, additionally the execution and processing times are considerably shorter as only a small number of images are required. On the other hand, random test provides natural frequencies information in a broadband spectrum at a time and does not thus required additional tests. Despite that more structural information can be extracted, it is also more time-consuming if the number of modes is low and ODSs could be slightly noisier.

For instance, some additional resonance ODSs are shown in Figure 9 from random excitation. The resonance at 78 Hz corresponds to a global fuselage mode. In this study, impact energy is not enough to excite this sort of modes. The remaining two ODSs at 155 Hz and 267 Hz imply local behaviour and correspond to bending modes of increasing order of the window. Considering the high geometrical complexity of the presented ODSs, a sensor instrumentation, as that in Figure 3, would be sparse.

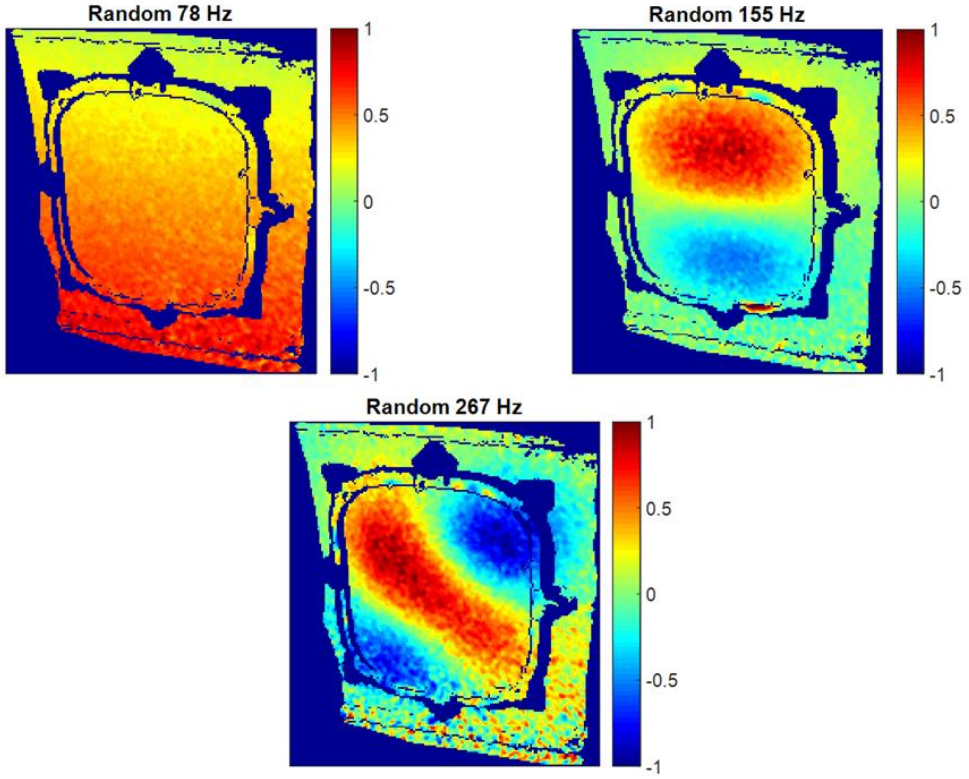


Figure 9: Additional normalised Operational Deflection Shapes obtained using DIC in random test.

5.1 Modal response under in-flight environmental conditions

Differential pressure introduces static deformation in the structure that modifies the modal behaviour. This deformation is shown in Figure 10 measured by 3D-DIC. It is observed that maximum deformation, more than 8 mm outwards, occurs at the centre of the window where the stiffness is lower. Hence the shape of the window has been perturbed, increasing the curvature and, thus, providing a stiffer configuration. In the random tests this fact is confirmed by the resonant frequency shifting of the corresponding modes in ambient conditions towards higher frequencies, as shown in Table 1.

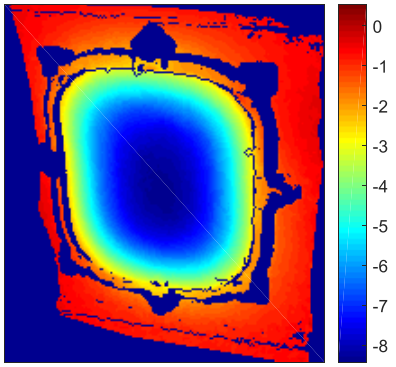


Figure 10: Static deflection under differential pressure.

Mode designation	Non-Pressurized (Hz)	Differential Pressure (Hz)
1	124	148
2	155	196
3	215	252
4	267	276

Table 1: Frequency shifting of the resonances identified in both pressurized states in specimen 1.

The ODSs are shown in Figure 11. To evaluate the variations of the four modes regarding the ambient behaviour, the differences between the features vector of both environmental states were reconstructed. Results of the subtractions are presented as percentages in Figure 12, considering the ambient state as a reference. It was found that the maximum positive difference is located in the centre of the window, where maximum static deformation due to pressure was found. Therefore, this region experienced more deformation with no differential pressure. Thus, the correlation between variations in ODSs and the pressure deformation is shown. The third mode is an exception as a consequence of the non-symmetrical shape.

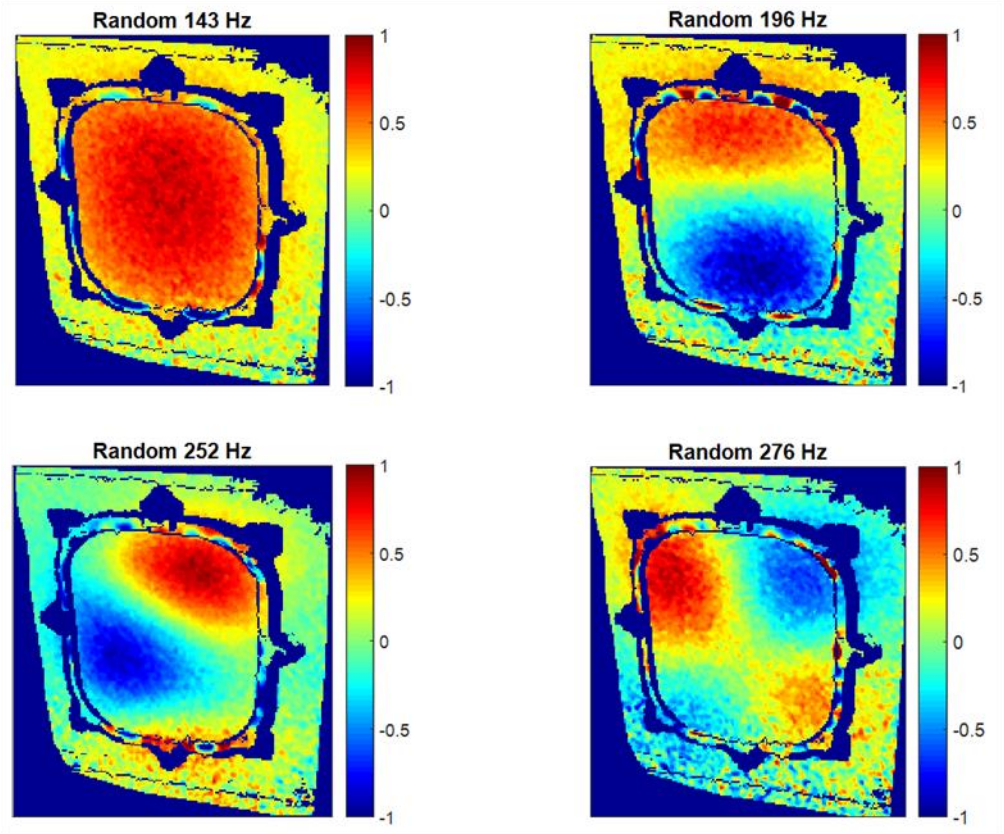


Figure 11: Normalised Operational Deflection Shapes obtained using DIC in random test under in-flight environmental conditions.

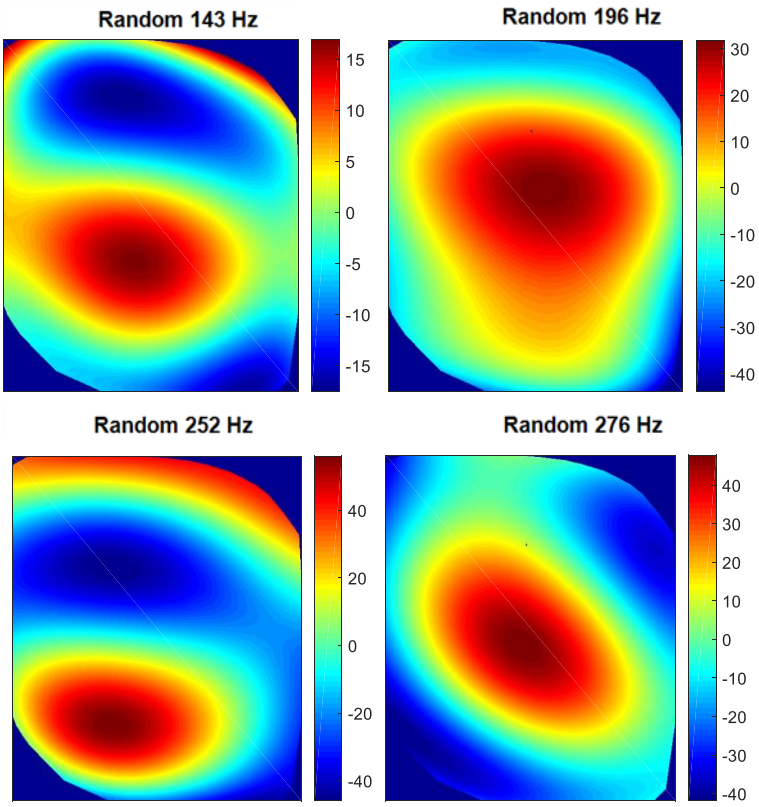


Figure 12: Normalised Operational Deflection Shapes obtained using DIC in random test under in-flight environmental conditions.

6 Conclusions

This work has presented the evaluation of the modal behaviour of the passenger window of a real aircraft structure using HS 3D-DIC under different environmental conditions. Additionally, the potential of HS 3D-DIC for sine and random excitation has been demonstrated. Sine excitation is more suitable to obtain low noise results of individual modes with few images. On the other hand, random allows to determine ODSs of many modes in a unique tests as well as natural frequencies.

It has been shown the effect of a local structural modification due to in-flight pressure conditions. The resonance shifting indicated the stiffening of the window. Moreover, the changes of ODSs showed a common deformation trend due to differential pressure. For this purpose, shape descriptor decomposition was employed to ease the managing and enhance the analysis of the full-field data.

Besides the advantages of the contactless measurement, the full-field results demonstrate the capabilities of the technique, avoiding spatial aliasing of pointwise sensors and showing potential for comparison with numerical simulations. Furthermore, this study involves an industrial application of HS 3D-DIC for modal characterisations in a final stage of assembly, presenting it as a complement to traditional instrumentations.

References

[1] D. J. Ewins, *Modal Testing: Theory, Practice, and Application*, 2nd ed., Research Studies Press LTD, Baldock, Hertfordshire, England (2000).

[2] A. B. Stanbridge, D. J. Ewins, *Modal testing using a scanning laser doppler vibrometer*, Mechanical Systems and Signal Processing, Vol. 13, No. 2, Elsevier (1999), pp. 255–270.

[3] L. Bertini, P. Neri, C. Santus, A. Guglielmo, *Automated Experimental Modal Analysis of Bladed Wheels with an Anthropomorphic Robotic Station*, Experimental Mechanics, Vol. 57, No. 2, Springer (2017), pp. 273–285.
[4] J. Baqersad, P. Poozesh, C. Niezrecki, P. Avitabile, *Photogrammetry and optical methods in structural dynamics – A review*, Mechanical Systems and Signal Processing, Vol. 86, Elsevier (2017), pp. 17–34.
[5] H. Schreier, J.-J. Orteu, M. A. Sutton, *Image Correlation for Shape, Motion and Deformation Measurements*, Springer US, Boston, MA (2009).
[6] M. N. Helfrick, C. Niezrecki, P. Avitabile, T. Schmidt, *3D digital image correlation methods for full-field vibration measurement*, Mechanical Systems and Signal Processing, Vol. 25, No. 3, Elsevier (2011), pp. 917–927.
[7] C. Warren, C. Niezrecki, P. Avitabile, P. Pingle, *Comparison of FRF measurements and mode shapes determined using optically image based, laser, and accelerometer measurements*, Mechanical Systems and Signal Processing, Vol. 25, No. 6, Elsevier (2011), pp. 2191–2202.
[8] P. L. Reu, D. P. Rohe, L. D. Jacobs, *Comparison of DIC and LDV for practical vibration and modal measurements*, Mechanical Systems and Signal Processing, Vol. 86, Elsevier (2017), pp. 2–16.
[9] N. S. Ha, T. Jin, N. S. Goo, *Modal analysis of an artificial wing mimicking an Allomyrina dichotoma beetle's hind wing for flapping-wing micro air vehicles by noncontact measurement techniques*, Optics and Lasers in Engineering, Vol. 51, No. 5, Elsevier (2013), pp. 560–570.
[10] D. A. Ehrhardt, M. S. Allen, S. Yang, T. J. Beberniss, *Full-field linear and nonlinear measurements using Continuous-Scan Laser Doppler Vibrometry and high speed Three-Dimensional Digital Image Correlation*, Mechanical Systems and Signal Processing, Vol. 86, Elsevier (2017), pp. 82–97.
[11] R. B. Berke, C. M. Sebastian, R. Chona, E. A. Patterson, J. Lambros, *High Temperature Vibratory Response of Hastelloy-X: Stereo-DIC Measurements and Image Decomposition Analysis*, Experimental Mechanics, Vol. 56, No. 2, Springer (2015), pp. 231–243.
[12] A. J. Molina-Viedma, L. Felipe-Sesé, E. López-Alba, F. A. Díaz, *3D mode shapes characterisation using phase-based motion magnification in large structures using stereoscopic DIC*, Mechanical Systems and Signal Processing, Vol. 108, Elsevier (2018), pp. 140–155.
[13] F. Trebuňa, M. Hagara, *Experimental modal analysis performed by high-speed digital image correlation system*, Measurement, Vol. 50, Elsevier (2014), pp. 78–85.
[14] Á. J. Molina-Viedma, E. López-Alba, L. Felipe-Sesé, F. A. Díaz, *Full-field modal analysis during base motion excitation using high-speed 3D digital image correlation*, Measurement Science and Technology, Vol. 28, No. 10, IOPscience (2017), p. 105402.
[15] R. Huňady, M. Hagara, *A new procedure of modal parameter estimation for high-speed digital image correlation*, Mechanical Systems and Signal Processing, Vol. 93, Elsevier (2017), pp. 66–79.
[16] Á. Molina-Viedma, E. López-Alba, L. Felipe-Sesé, F. Díaz, *Modal Identification in an Automotive Multi-Component System Using HS 3D-DIC*, Materials, Vol. 11, No. 2, MDPI (2017), p. 241.
[17] W. Wang, J. E. Mottershead, C. Mares, *Vibration mode shape recognition using image processing*, Journal of Sound and Vibration, Vol. 326, No. 3–5, Elsevier (2009), pp. 909–938.
[18] W. Wang, J. E. Mottershead, T. Siebert, A. Pipino, *Frequency response functions of shape features from full-field vibration measurements using digital image correlation*, Mechanical Systems and Signal Processing, Vol. 28, Elsevier (2012), pp. 333–347.
[19] G. Lampeas, V. Pasialis, X. Lin, E. A. Patterson, *On the validation of solid mechanics models using optical measurements and data decomposition*, Simulation Modelling Practice and Theory, Vol. 52, Elsevier (2015), pp. 92–107.
[20] C. Sebastian, E. Hack, E. Patterson, *An approach to the validation of computational solid mechanics models for strain analysis*, Journal of Strain Analysis for Engineering Design, Vol. 48, No. 1, Sage (2013), pp. 36–47.

Design and validation of a nonlinear test rig with hardening stiffness in multiple degrees of freedom

N. Pandiya [1], **R.J. Allemang** [2], **A.W. Phillips** [2]
[1] Engineering Vibration Reliability,
Robert Bosch GmbH, 70442 Stuttgart, Germany
e-mail: **nimish.pandiya@de.bosch.com**

[2] Structural Dynamics Research Laboratory
University of Cincinnati, Cincinnati, OH 45221, USA.

Abstract
An experimental approach was undertaken at the University of Cincinnati's Structural Dynamics Research Laboratory (UC-SDRL) to gather nonlinear data in a controlled sense from a real world, continuous mechanical specimen exhibiting multiple isolated modes in the frequency range of interest. The design phase consisted of preliminary hand calculations for setting the dimensions of the test rig and iterations on the finite element model, using both static and dynamic analyses results. The design was such that the dynamic interference of the support structure on the test specimen was minimized. The paper outlines the construction of the test rig and the testing carried out for validation post installation. Static stiffness test was used to identify the stiffness curve of the test specimen. Impact testing was used to verify dynamic behavior as a linear system (small amplitude oscillations) and sufficient isolation from the support structure's modes of vibration in the frequency range of interest, and signs of non-linearity for larger amplitudes of vibration.

1 Nomenclature

CMIF	-	Complex Mode Indicator Function
E	-	Modulus of Elasticity
FEM	-	Finite Element Method
FRF	-	Frequency Response Function
MIMO	-	Multiple Input Multiple Output
MPE	-	Modal Parameter Estimation
RFP-Z	-	Rational Fraction Polynomial - Z-domain
SDRL	-	Structural Dynamics Research Laboratory
UC	-	University of Cincinnati
ρ	-	density
ν	-	Poisson's ratio

2 Introduction

The importance of the study of nonlinear systems in structural dynamics has been increasing steadily with improving system models and higher computational power. Significant work has been done towards the identification, characterization and modelling of such systems [1]. Even though most commercial analyses use linear system methods by limiting ranges of interest, a more complete mathematical model in terms of structural dynamics is of widespread research interests. Under operating conditions, variations in amplitude

ranges and boundary conditions are some ways that can deteriorate the health of structures by introducing nonlinear dynamics into the picture. Numerical analyses during the design phase can only provide certainty up to the degree of robustness of the mathematical model, but experimentation for validation is critical. To develop such models, it is also imperative that real world data be used. This is the motivation of this project - to gather data from a physical structure vibrating in a nonlinear regime, for further research into system identification methods. Previous studies have been carried out at the UC-SDRL [2], [3], [4] for nonlinear system dynamic analysis, and the presented work would facilitate widening the scope of experimental validation for such studies [5].

Historical efforts towards experimental analysis of nonlinear vibrating systems have utilized either simulated data, or acquired data without leveraging the spatial aspect of the dynamic problem. Either (i) isolated modes in a continuous system [6], or (ii) rigid body modes in multiple degree of freedom systems with nonlinear connecting elements (nonlinear springs [7], for example) have been the basis of experimental evaluations.

Taking the experimental rig used by Ferreira [6] as a reference, a test rig was constructed such that experimental data could be gathered for a continuous test specimen, in a Multiple Input Multiple Output (MIMO) sense.

3 Theoretical background

The general equation for a single degree of freedom system is given as:

$$f_{inertial} + f_{damping} + f_{spring} = f_{external} \tag{1}$$

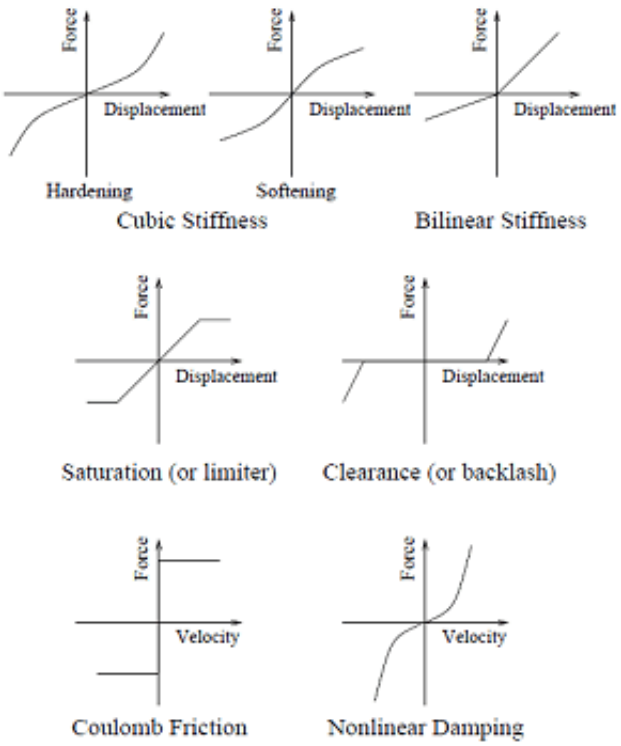


Figure 1: Common types of structural nonlinearities [8].

A special case of this equation is the linear, time-invariant form:

$$m\ddot{x} + c\dot{x} + kx = f \tag{2}$$

Here m, c and k represent the mass, damping and stiffness of the single degree of freedom system and are constants, rather than being time or amplitude dependent values.

Figure 1 indicates common types of nonlinearities observed in structural dynamics and more often than not, multiple types may be found to occur in a real world system. Typically, nonlinearities are classified into three types [8]:

1. **Geometric**: When assumptions of small angles and deflections do not hold true, nonlinear behavior may be observed for structures with fixed boundary conditions.
2. **Material**: Variation in thermal conditions or material exhibiting plastic deformation may result in material nonlinearities.
3. **Contact**: An example is a system with clearance, where being in contact with another body results in an abrupt stiffness change.

The Duffing oscillator equation (Eq. 3) is often used in analysis of nonlinear systems [8] and is the basis of construction of the test rig presented in this paper. Here, the spring force (f_{spring} in Equation 1) is represented in a polynomial sense (i.e. $f_{spring} = kx + k_0x^2 + k_1x^3$).

$$m\ddot{x} + c\dot{x} + kx + k_0x^2 + k_1x^3 = f \tag{3}$$

Assuming a symmetric cubic stiffness in the system, $k_0 = 0$. The "hardening" stiffness condition occurs when $k_1 > 0$, while for the "softening" condition $k_1 < 0$.

4 Test rig design

4.1 Theoretical considerations

For a thin fixed-fixed beam, undergoing vibrations of large amplitudes (greater than the thickness of the beam), the stiffness coefficients in Equation 3 may be obtained using [8]:

$$f_{spring} = 197.8\frac{EIY}{L^3} + 11.92\frac{EAY^3}{L^3} \tag{4}$$

Here Y is the deflection at the center point, E is the elastic modulus, A is the area of cross section, I is the area moment of inertia and L is the length of the beam. Hence,

$$k = 197.8\frac{EI}{L^3};\ k_1 = 11.92\frac{EA}{L^3} \tag{5}$$

Additionally, in the case of a thicker beam the polynomial stiffness may not come into the picture for the same deflections seen by the thin, fixed-fixed beam referred to above.[1] Figure 2 and Table 1 show the bending mode shapes and natural frequencies of fixed-fixed and cantilever beams made of steel ($E = 200\ GPa, \nu = 0.3, \rho = 7861\ kg/m^3$).

[1]For the sake of simplicity, the terms "thin" and "thick" in reference to the beams will refer to the dimensions and boundary conditions indicated in Table 1

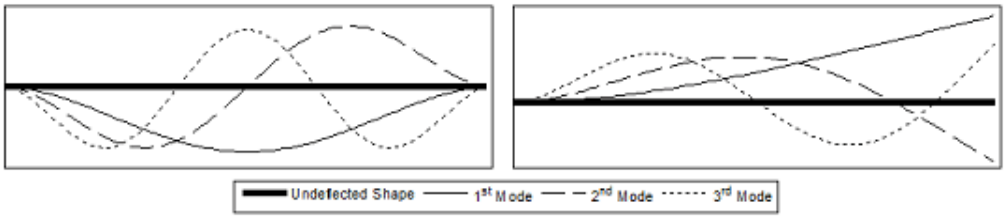


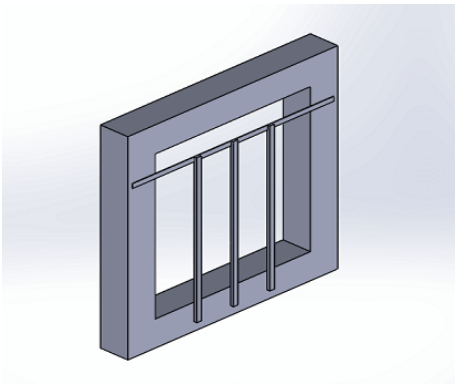
Figure 2: First three mode shapes of a fixed-fixed beam (left) and a cantilever beam (right).

Boundary Conditions	**"Thin" fixed-fixed**	**"Thick" cantilever**
Dimensions	$431.8 \times 12.7 \times 1.5875\,mm$	$381 \times 12.7 \times 7.9375\,mm$
Mode 1	39.4 Hz	44.58 Hz
Mode 2	108.6 Hz	279.41 Hz
Mode 3	212.9 Hz	782.36 Hz

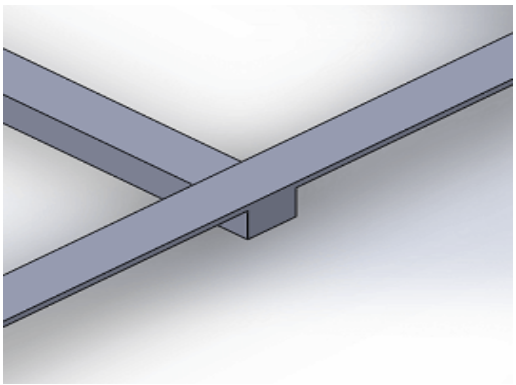
Table 1: Theoretically evaluated beam bending modes for steel specimens.

4.2 Preliminary simulations

Three cantilever beams were combined as shown in Figure 3 to create a three degree-of-freedom system. The modes of interest were the three combinations of the first bending mode of the cantilever beams, separated in modal frequencies due to their connection with the thin beam at its various locations.



(a) Preliminary design for support structure



(b) Junction of two beams

Figure 3: Preliminary test specimen as a single part, attached to the preliminary support structure.

There was also a need to design a support structure that would offer fixed supports to the specimen ends. The goal for the design of such a structure was high stiffness in the frequency range of interest. Also, a "vertical" orientation of the beam specimen was envisioned to prevent the static deflection due to gravity, which would introduce asymmetry in the stiffness curve. To begin with, a steel frame made of hollow square pipes was considered (Figure 3 (a)).

For initial simulations, welds, fillets etc. were ignored and all the connections were modelled as rigid. The aim of the preliminary simulations was to investigate the modal frequencies of the specimen and the frame, the interaction between them and to confirm the theoretical ideas.

4.2.1 Test Specimen simulations

The rectangular contact surfaces were split and assigned a "fixed" support. The same material properties were assigned as were used to derive the theoretical values of bending mode frequencies in Table 1. Meshing was done using tetrahedral elements with edge controls applied to obtain a structured mesh, resulting in about 3500 elements. Element mid-side nodes were included to capture bending effectively, and the first eight modes were computed (Figure 4).

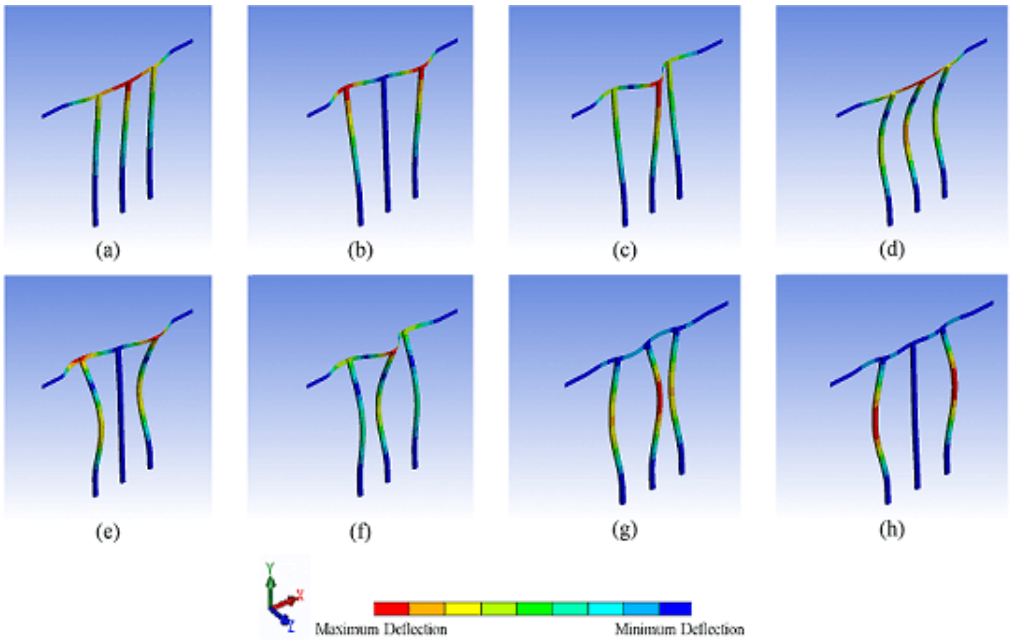


Figure 4: The first eight modal frequencies for the preliminary test specimen, corresponding to the respective mode shapes are, (a) 53.38 Hz, (b) 83.64 Hz, (c) 113.06 Hz, (d) 256.69 Hz, (e) 266.93 Hz, (f) 286.14 Hz, (g) 370.01 Hz, (h) 386.28 Hz.

The first three modes computed were the modes of interest, and were banded fairly close together - within about 60 Hz and separated from the higher modes by about 150 Hz. The fifth, seventh and eighth modes computed (Fig. 4 (e), (g) and (h)) indicated no modal displacement in the Z-direction. In an absence of excitation in the X-Y plane, these were expected to contribute minimally.

4.2.2 Frame Simulations

For the box-beam frame, meshing was done with high relevance and fine sizing applied resulting in about 26,000 elements. The bottom face was fixed and the first eight mode shapes were computed, as shown in Figure 5.

The second, fifth and eighth modes (Fig. 5 (b), (e) and (h)) indicated deflections in the X-Y plane and hence, were discarded from future considerations. The rest of the modes having deflections in the Z-direction especially the first and third modes (Fig. 5 (a) and (c)) needed to be pushed higher in frequency by stiffening the structure appropriately. The interaction between the specimen and the structure can be clearly seen in the results shown in Figure 6. The first eight modes computed were closely spaced with respect to modal frequencies. The fourth and eighth modes (Fig. 6 (d) and (h)) apparently required stiffening for non-interference with the specimen's modes of interest. Modes with deflections in the X-Y plane were not of importance again, since the Z-direction displacements were under consideration. Even so, it was recognized that the ideal application of unidirectional forces would be difficult.

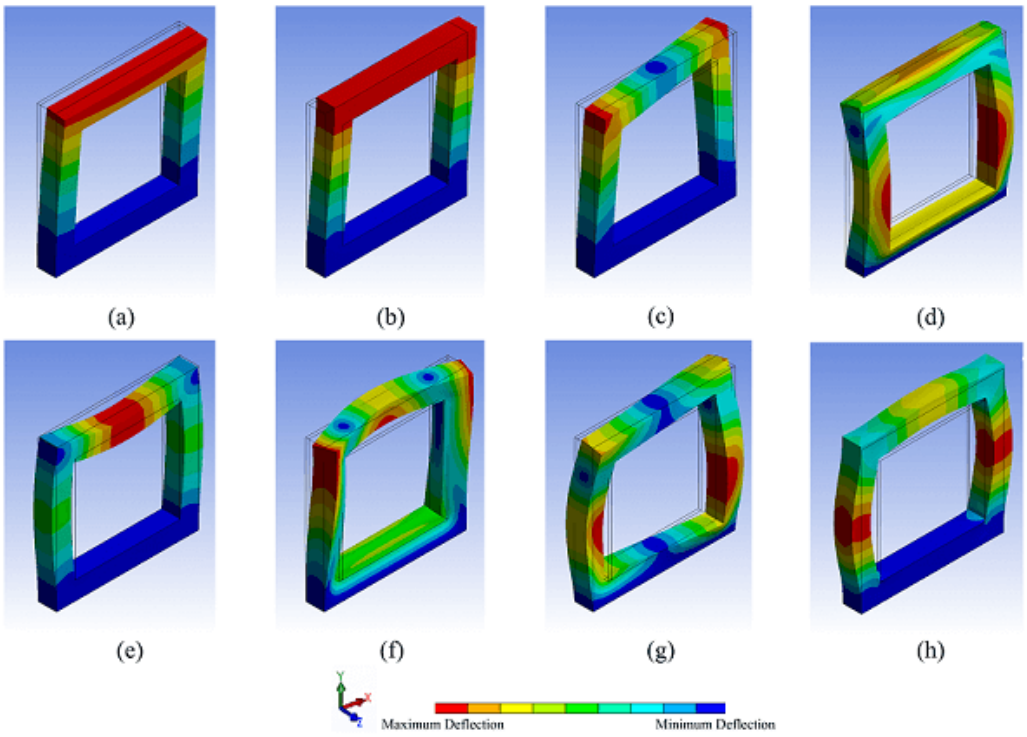


Figure 5: The first eight modal frequencies for the preliminary frame structure, corresponding to the respective mode shapes are, (a) 153.91 Hz, (b) 231.97 Hz, (c) 279.43 Hz, (d) 831.85 Hz, (e) 899.77 Hz, (f) 1044.5 Hz, (g) 1116.4 Hz, (h) 1315.7 Hz. The undeformed shape is also shown for easy visualization.

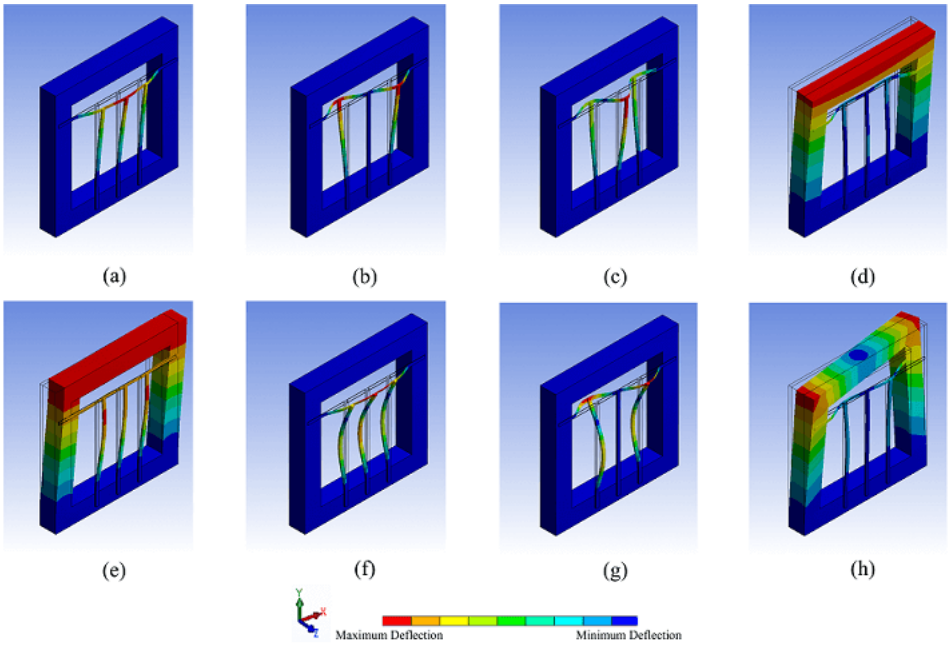


Figure 6: The first eight modal frequencies for the preliminary assembly of the frame and test specimen, corresponding to the respective mode shapes are, (a) 52.734 Hz, (b) 83.018 Hz, (c) 112.35 Hz, (d) 153.98 Hz, (e) 229.26 Hz, (f) 252.15 Hz, (g) 263.65 Hz, and (h) 279.09 Hz.

4.2.3 Static simulation

A static structural simulation was carried out for the assembly in the preliminary stage to confirm the cubic stiffness characteristic. The ramped input force was assigned at the junction of the thin (lateral) and the middle, thick (vertical) beam, labelled as node ”A” (Figure 7). Using the large deflection FEM analysis [9], a plot of the reactionary force and the displacements of the three junctions marked in Figure 7 as “A”, “B” and “C” was created (Figure 7), in which the hardening characteristic is clearly observed (compare with Figure 1, hardening stiffness).

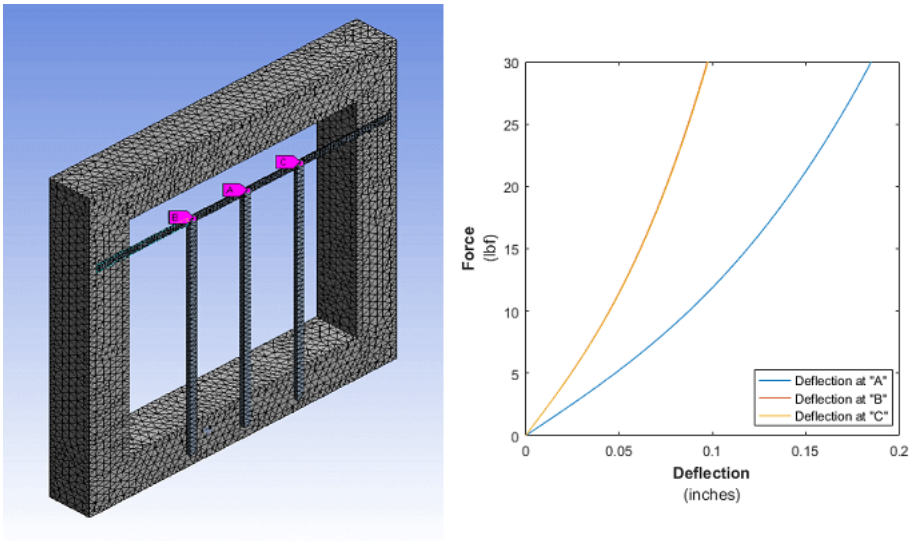


Figure 7: Mesh for the preliminary assembly for static analysis (left). The labels for the named selections of nodes at the center, left and right junctions are “A”, “B” and “C” respectively. Geometric hardening observed by plotting the applied static force at the center (A) junction, against the deflection caused by it at locations of the left (B), center(A) and right (C) junctions (right).

4.3 Finalizing the design

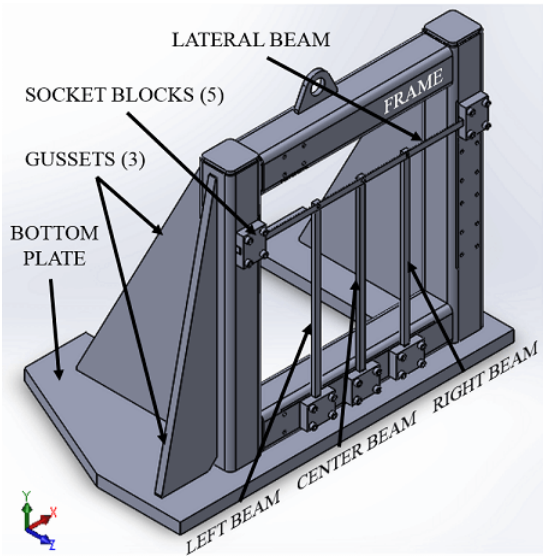


Figure 8: The solid model rendering of the final nonlinear test rig assembly.

Using the discussed simulation results, various configurations of stiffening members for the support structure were evaluated by means of similar FE workflows. The rendering of the final test rig is shown in Figure 8. The Y-Z motion was stiffened by two gussets and the X-Y plane motion was stiffened by a single smaller gusset. The final assembly's modal simulation results are shown in Figure 9.

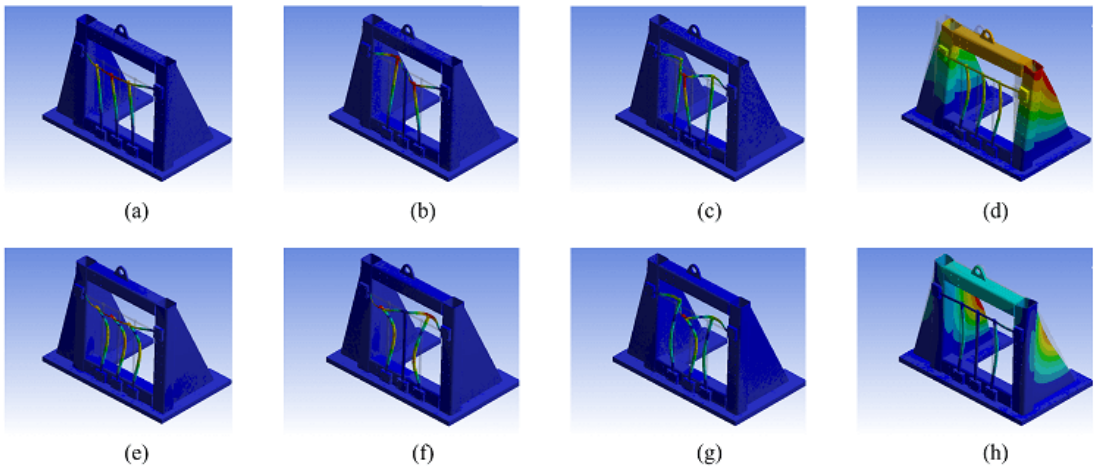


Figure 9: The first eight modal frequencies for the final assembly, corresponding to the respective mode shapes are, (a) 54.548 Hz, (b) 85.74 Hz, (c) 119.13 Hz, (d) 266.76 Hz, (e) 275.52 Hz, (f) 288.22 Hz, (g) 310.43 Hz, (h) 382.23 Hz.

For the modal simulation of the final test rig assembly meshing was done in a structured manner. Since the model was of greater complexity than the previous, simplified models, care was taken to include at least three layers of elements to capture bending effectively. Even so the mid-side nodes were included. The bottom plate was assigned a fixed boundary condition. The modal frequencies varied slightly from the previous results. This was mainly because of addition of stiffening members and small changes in the length of the beam due to manufacturing considerations like fillets and chamfers. A static stiffness curve was also plotted similar to Figure 7, and is shown in Figure 11.

4.4 Practical considerations

Post manufacturing, a few practical adjustments were made for the test rig's installation.

- The bottom surface of the base plate was skimmed flat to remove distortions resulting from welding operations. The base plate was then dog-clamped to a concrete isolation block, with rubber elements between all connection points between the rig and the ground.
- The test specimen was clamped onto the support frame and an equal torque of $3N.m$ was applied to all screws holding the specimen in place.
- With alternate placements of the support blocks and the shims holding the specimen in position, it is also possible to create clearance nonlinearity for further investigation.

5 Testing for model validation

5.1 Stiffness curve

The experimental setup is shown in Figure 10. A fishing line strung over a pulley with masses on one side was attached to the central node of intersection between the lateral and vertical beams. The force applied

due to the tension in the string was continually increased by placing masses of known value on the other end of the fishing line. The deflections of the three junctions were recorded using three dial gauges.

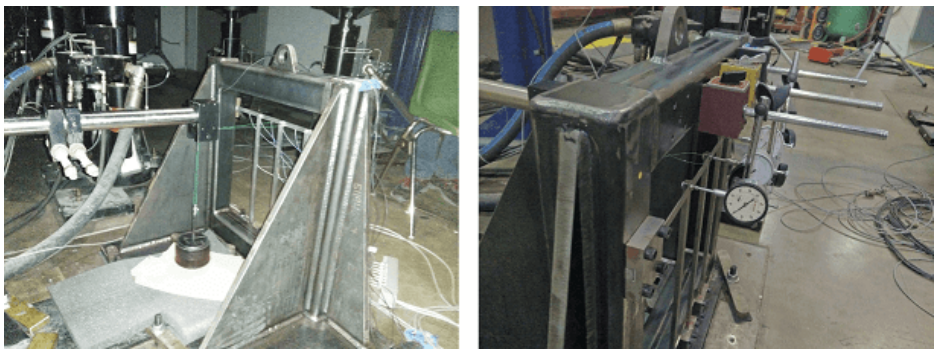


Figure 10: Fishing line wound over a pulley with a hanger with known masses on the other side, pulling on the center junction (left). Dial indicators attached magnetically to the frame to measure displacement (right).

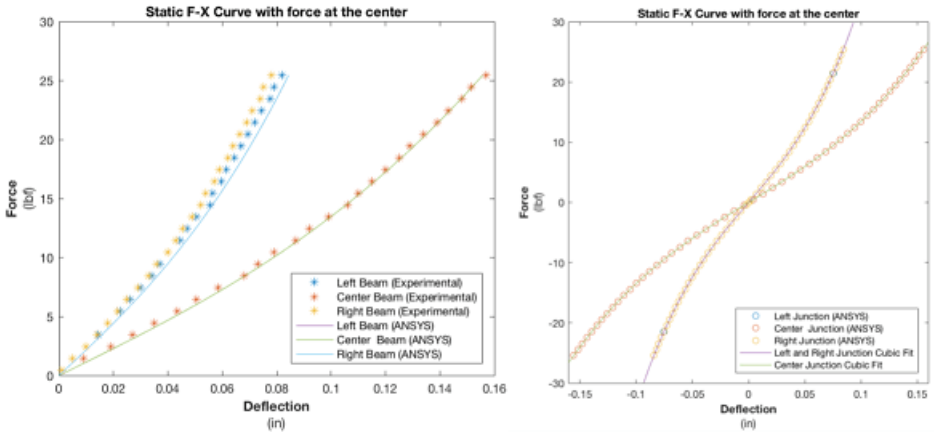


Figure 11: Comparison of static curves obtained experimentally and from the finite element model (left) and cubic polynomial fit for the static stiffness curve (right).

The applied static force was then plotted against the recorded deflections, to verify the cubic stiffness characteristic. Since the experiment was only performed for unidirectional force, and the agreement with the simulation results was good, the simulation values were used to obtain a cubic curve fit for positive and negative deflections (Fig. 11). The equations for the fitted curves in Figure 11 are shown in Table 2.

$Spring\ force(f_{spring}) = kx + k_1x^3$	
Left and Right Junctions	$f_{spring} = 11750.1x^3 + 218x$
Center Junction	$f_{spring} = 2034.2x^3 + 114.25x$

Table 2: Curve fit equations showing stiffness coefficients.

5.2 Impact testing

The wire-frame model indicating the reference and response points for impact testing is shown in Figure 13. Data acquisition was carried out using X-Modal III with a VXI system. The test specimen was instrumented with uniaxial (PCB 352C23) accelerometers having a nominal sensitivity of 0.5 $mV/(m/s^2)$ and weight of

0.2 grams while the support structure was instrumented using the larger uniaxial (PCB B352A56) accelerometers. Impacts on the specimen were performed using the PCB 086D80 “mini” hammer, while those on the frame were performed by the larger PCB 086C01 hammer (Fig. 12).

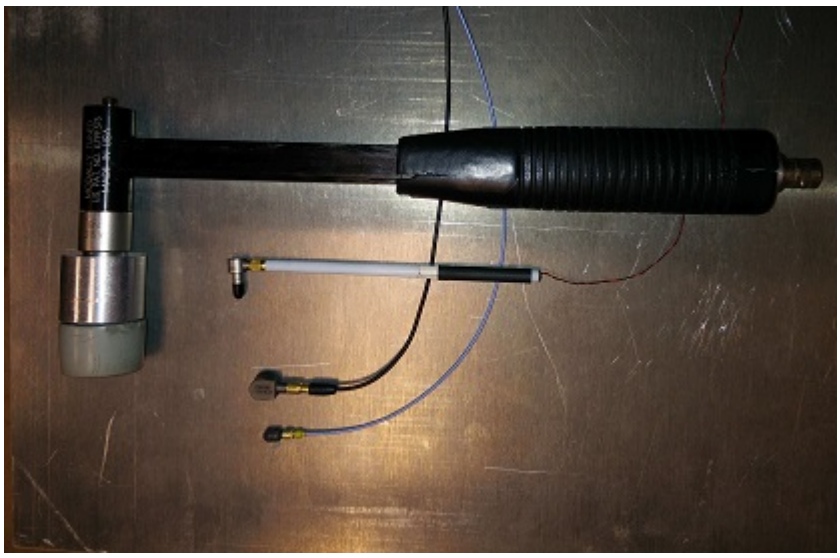


Figure 12: Sensors used for impact testing (bottom to top) PCB 352C23 accelerometer, PCB B352A56 accelerometer, PCB 086D80 impact hammer and PCB 086C01 impact hammer.

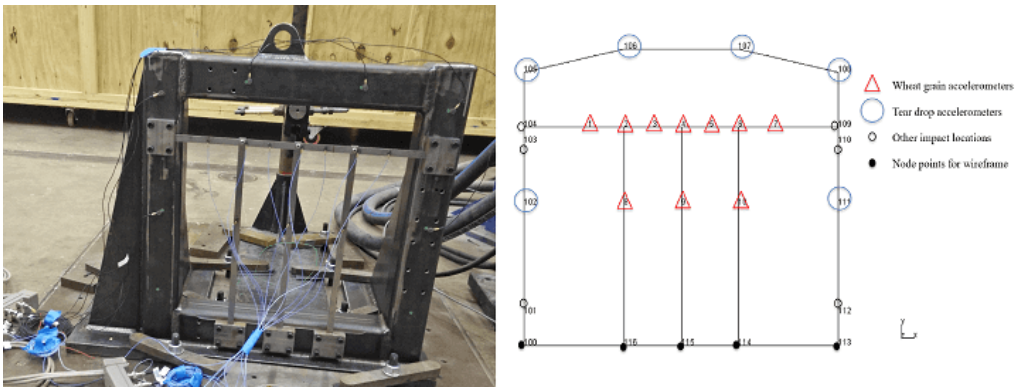


Figure 13: Instrumented test rig (left) and the corresponding wire-frame model (right).

5.2.1 Impacts on the support frame

Impacts were performed using an acrylic tip on the PCB 086C01 hammer (Fig. 12). The maximum frequency limit was set to 1600 Hz, with a frequency resolution of 0.5 Hz.

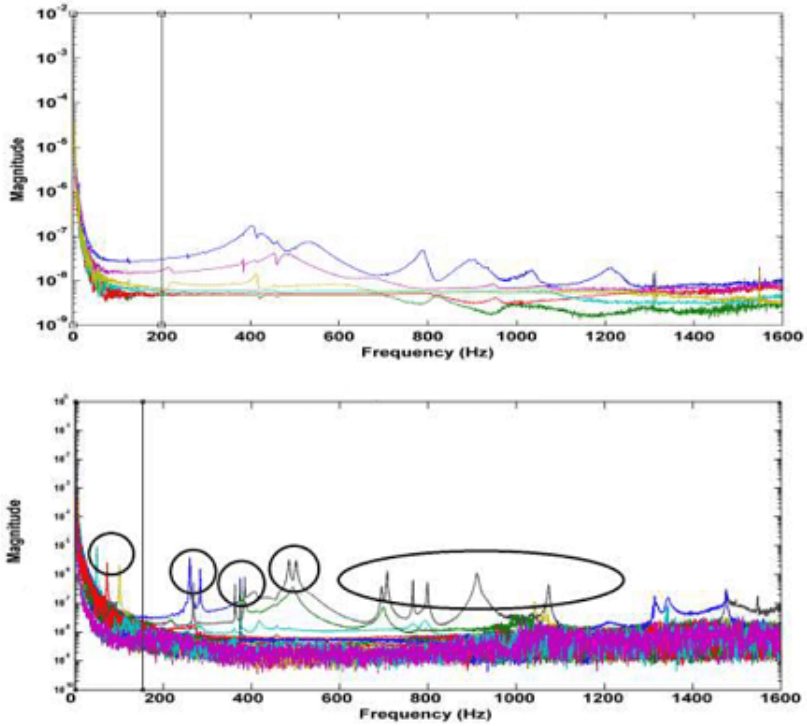


Figure 14: Complex Mode Indicator Function (CMIF) for impacts on the frame (bottom). A comparison with the CMIF with test specimen responses sieved out (top) indicates the modes circled do not appear in the figure at the top and are the test specimen modes of vibration.

The Complex Mode Indicator Functions (CMIFs) obtained from the Frequency Response Functions (FRFs) are shown in Figure 14 for the case with all the response degrees of freedom included and where those from the test specimen are sieved out.

The frame mode shapes obtained from modal parameter estimation are shown in Figure 15. These were about 300 Hz above the highest mode of interest, and hence would cause minimal interference modally.

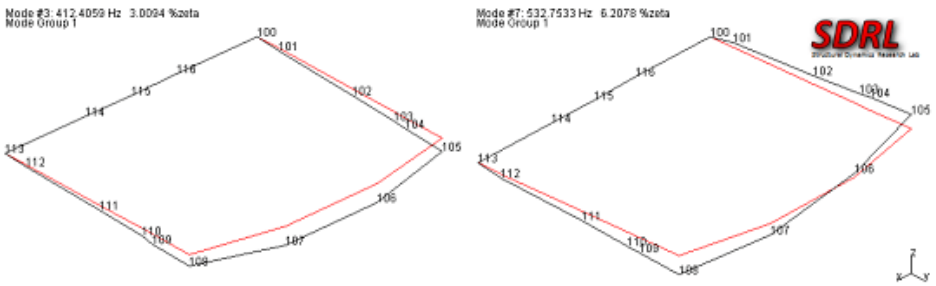


Figure 15: Modes of deflection at 412.41 Hz (left) and 532.75 Hz (right), obtained using impact testing on the frame and observing acceleration data on the frame.

5.2.2 Impacts on the test specimen

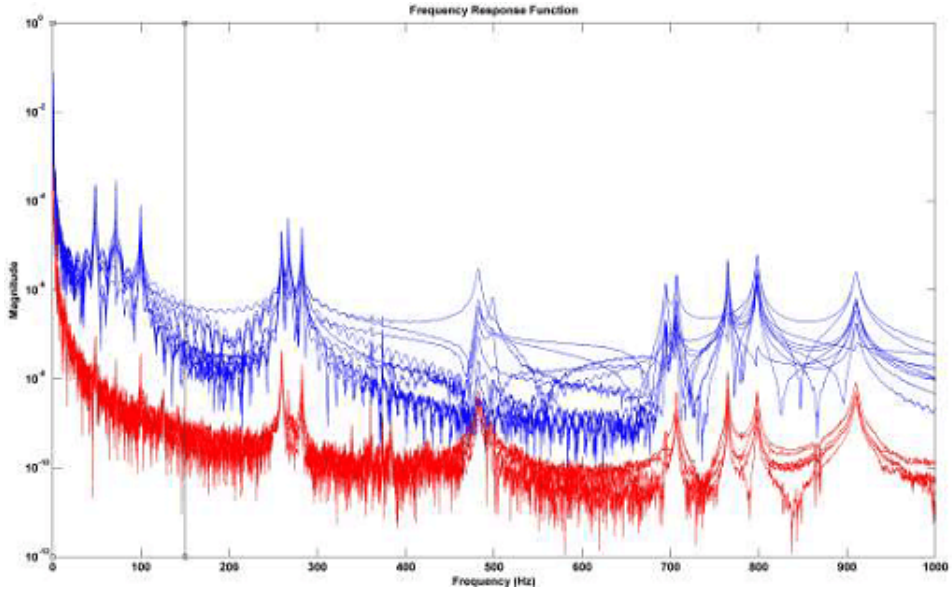


Figure 16: Frequency response functions for an impact on location 2 on the test specimen. The blue FRFs represent the responses from locations 1-10 on the test specimen, while those in red correspond the responses from the locations 102, 105, 106, 107, 108 and 111 on the frame.

The smaller PCB 086D80 was used with two rubber coverings on the tip to reduce high frequency overloads [10]. The frequency content was limited to 1000 Hz. Due to the lightness of the specimen and low damping of the system, double impacts and high frequency overloads were a recurring issue. Even so, for a preliminary check, the modal frequencies needed to be observed and impact testing provided sufficiently usable results.

As can be observed from Figure 16, the frame's response is not much more than the noise floor for the test specimen's response. This validates that the frame provides an almost rigid support in the frequency range of interest, marked by the vertical cursor in Figure 16.

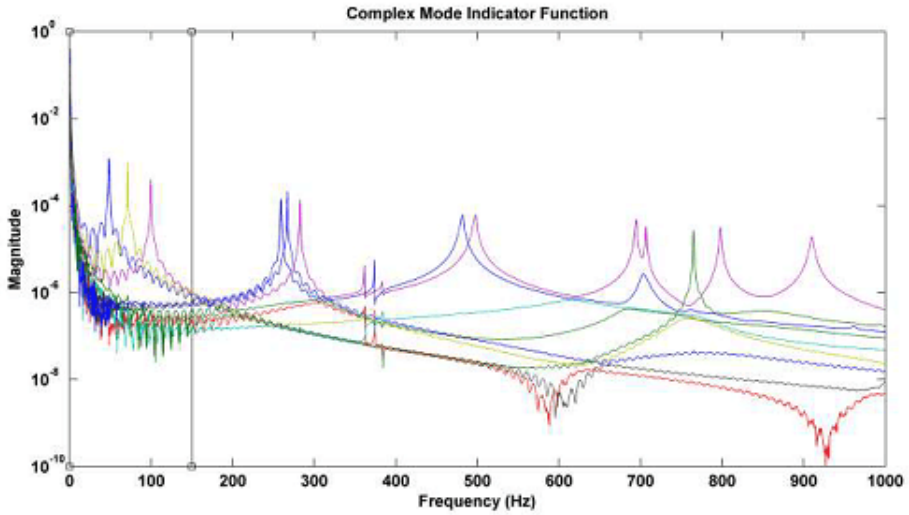


Figure 17: CMIF for impact on test specimen, with responses from the frame sieved out.

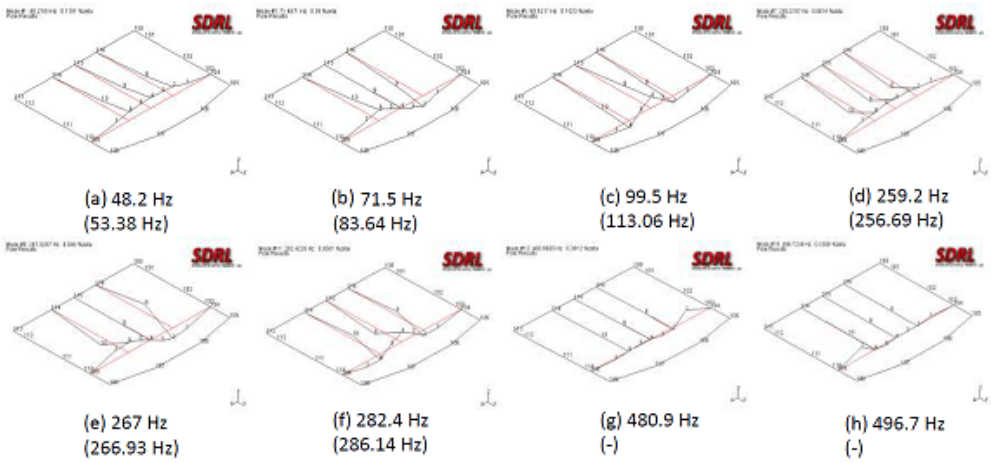


Figure 18: Experimentally obtained mode shapes using RFP-Z MPE algorithm in the range 20 Hz to 600 Hz.

From the Figure 17, the modes of interest can be identified to be at 48.2 Hz, 71.5 Hz and 99.5 Hz. A more complete set of mode shapes were computed using the Rational Fraction Polynomial - Z domain (RFP-Z) [11] in the frequency range 20-600 Hz and can be seen in Figure 18. The modal frequencies and shapes are compared to the frequencies from the simulation (in brackets) and are in general agreement with the simulation values. Due to the scope being limited to construction of a real nonlinear system, verification of the finite element model was not deemed necessary.

Impact tests were also carried out using the larger hammer with a view to elicit large deflection nonlinearity from the test specimen. Frequency content was limited by using a soft tip on the larger hammer (as seen in Fig. 12).

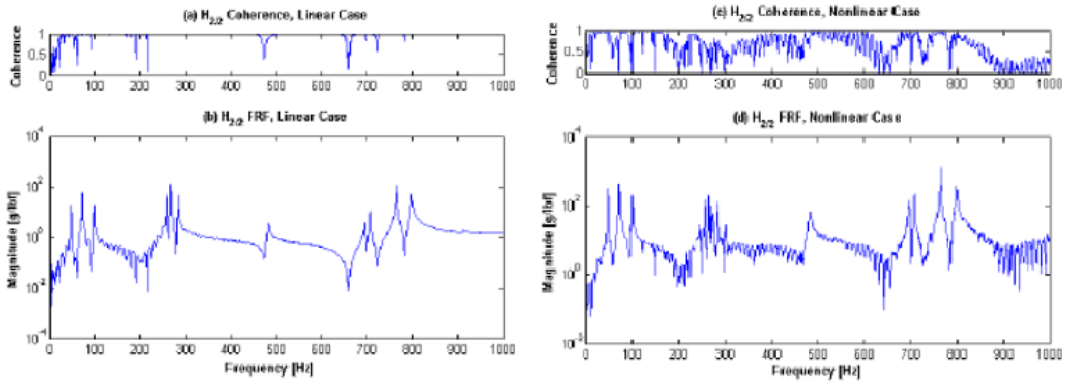


Figure 19: Comparison of coherence for the linear and nonlinear case ((a) and (c) respectively), and for the magnitudes for the linear and nonlinear case ((b) and (d) respectively).

As can be seen from visual comparison in Figure 19, the FRF was distorted for the “nonlinear” case. The low coherence observed also indicated that the nonlinearity in the measurement was not being captured by the linear formulation. Even though averaging was performed, which subdues the nonlinear characteristics, the test was carried out as proof of concept that when subjected to large deflections, the specimen would exhibit a cubic, hardening stiffness characteristic [3].

6 Conclusion

The iterative process behind the design of the nonlinear vibration test rig has been outlined. The experimental and simulation static stiffness curves match closely, and were approximated by cubic polynomial fits. The support structure was shown to interact minimally and provided a practically rigid base for the multi-degree of freedom test specimen. The modal frequencies of the test specimen were in general agreement with those obtained from finite element simulations, and the differences may be minimized by applying model updation techniques to the finite element model. Acquisition of data using impact testing was challenging due to presence of high frequency overloads and difficulties in eliminating double impacts.

Overall, the test rig provided an excellent specimen for gathering real data sets from a nonlinear system having hardening stiffness in multiple degrees of freedom. The design was kept modular and as an example, testing may be done by rotating the test specimen by 90° in addition to introducing clearances at contact locations.

References

[1] G. Kerschen, K. Worden, A. F. Vakakis and J. Golinval, *Past, present and future of nonlinear system identification in structural dynamics*, Mechanical Systems and Signal Processing, Vol. 20, No. 3 (2006), pp. 505 - 592.

[2] R. Arora, *Operational modal parameter estimation from short time-data series*, Master's thesis, University of Cincinnati, Ohio, USA (2014).

[3] S. M. Spottswood, *Identification of nonlinear parameters from experimental data for reduced order models*, PhD dissertation, University of Cincinnati, Ohio, USA (2006).

[4] D. E. Adams, *A spatial approach to nonlinear vibration analysis*, PhD dissertation, University of Cincinnati, Ohio, USA (2000).

[5] N. Pandiya, *Design and validation of a MIMO nonlinear vibration test rig with hardening stiffness characteristics in multiple degrees of freedom*, Master's thesis, University of Cincinnati, Ohio, USA (2017).

[6] J.V. Ferreira, *Dynamic response analysis of structures with nonlinear components*, PhD dissertation, Imperial College, London, UK (1998).

[7] P. Atkins, K. Worden, *Identification of a multi-degree-of-freedom nonlinear system*, in *Proceedings of the 15^{th} International Modal Analysis Conference, Vol. 3089* (1997), pp. 1023 - 1028.

[8] K. Worden and G. R. Tomlinson, *Nonlinearity in Structural Dynamics-Detection, Identification and Modeling*, Institute of Physics Publishing (2001).

[9] ANSYS, *Help System, ANSYS Academic Research, Release 16.2*, ANSYS, Inc. (2017).

[10] D. L. Brown, R. J. Allemang, A. W. Phillips, *Forty years of use and abuse of impact testing: a practical guide to making good FRF measurements*, in *Experimental Techniques, Rotating Machinery, and Acoustics*, Vol. 8 , Springer (2015), pp. 221-241.

[11] R. J. Allemang and A. W. Phillips, *The unified matrix polynomial approach to understanding modal parameter estimation: an update*, in *Proceedings of ISMA International Conference on Noise and Vibration Engineering, Katholieke Universiteit Leuven, Belgium* (2004), pp. 619-624.

Drives power reduction procedure to fill in the multiple-input multiple-output random control reference matrix

G. D'Elia [1], **U. Musella** [2], **E. Mucchi** [1], **B. Peeters** [2], **P. Guillaume** [3]
[1] University of Ferrara, Department of Mechanical Engineering,
via Saragat 1, 44122, Ferrara, Italy
e-mail: **giacomo.delia@unife.it**

[2] SIEMENS Industry Software NV,
Interleuvelaan 68, 3001, Leuven, Belgium

[3] Vrije University Brussel, Acoustics and Vibration Research Group,
Pleinlaan 2, 1050, Elsene, Belgium

Abstract
This paper proposes an innovative fully automatic target definition procedure to fill in the Multiple-Input Multiple-Output (MIMO) random reference matrix in cases where no information about the CSD terms is available. The developed method yields a set of coherences and phases of the CSD terms that is able to minimize the drives power needed to reach the test specifications. Additionally, the retrieved target complies with the required property of the spectral density matrix being positive semi-definite and with the constraint imposed on the PSDs, considered as test specifications. A series of tests with a three-axial electrodynamic shaker is carried out comparing the proposed target definition procedure with respect to other state-of-the-art solutions.

1 Introduction

Vibration control tests are performed to verify that a system and all its sub-components can withstand the vibration environment during the operational life. These tests aim to accurately replicate via controlled shaker excitation the in-service structural response of a unit under test in the main axis of vibration and in all the possible axes where the levels exceed the acceptance thresholds [1].
Due to the multidirectional nature of the field environments, multi-axis random control tests are the nowadays best solution to represent real-life structural responses of test specimen [2], [3], [4]. Although several works [5], [6], [7] underline the advantages of using Multiple-Input Multiple-Output (MIMO) vibration control strategies, their practice still needs to grow. The high degree of expertise needed to perform these tests and decades of single axis controlled excitation built meanwhile a legacy of Single-Input Single-Output (SISO) standards that currently represent the main reference for the environmental test engineers. For these reasons nowadays MIMO vibration control tests are still considered as a *pioneering* testing methodology.

There are different types of MIMO tests (random, sine, time waveform replication), depending on the environment a test article needs to be exposed. For automotive and aerospace systems and subsystems, a random vibration test is required for all the main mechanical and electrical components. This type of test is performed to simulate the response of the unit under test to a broadband random Gaussian vibration environment. For the SISO case the test specification is a Power Spectral Density (PSD, usually in g^2/Hz) profile that needs to be replicated for a user-defined control channel by exciting the unit under test with a single-axis shaker. In the MIMO case, it is possible to define required test levels for multiple control channels that will be controlled simultaneously. Additional information about the cross-correlation between the control channels is

also included. This information must be provided in terms of Cross Spectral Densities (CSDs) between pairs of control channels defining desired phase and coherence profiles [4], [8], [9]. The definition of these terms is essential to also replicate the cross-correlation that naturally exists between difference responses. These terms are also controlled by modern vibration controllers. For these systems the control target is thus a full reference Spectral Density Matrix (SDM). The target definition process plays already a key role for MIMO random control tests as documented in recent studies [10], [11].
Theoretically, a successful MIMO random control test can be performed in case the operational environment is fully replicated in the laboratory. As pointed out in [2], unfortunately operational measurements are not always available and often the test specifications are provided just in terms of PSDs at the control locations. This is due to several reasons. First of all, the gradual transition from sequential SISO testing to simultaneous multi-axial testing needs to face the aforementioned legacy of SISO standards and specifications, provided in terms of PSDs. Second, the standardization of the CSD terms is impractical to implement in a specification due to a lack of knowledge that makes challenging (and even impossibile) to average, smooth or envelope coherence and phase information from different operational conditions. In this case, the choice of setting appropriate values to fill in the full reference matrix *must reflect the desires of a knowledgeable environmental test engineer* [2]. Defining the reference matrix with no a-priori knowledge of the cross-correlation between control channels is very challenging. Filling in the off-diagonal terms, in fact, must guarantee that the reference matrix will have in the end a physical meaning (realizable). This is translated in the algebraic constraint that this matrix needs to be positive semi-definite and at the same time the test needs to guarantee the required PSDs at the control locations. The solution of finding a full reference matrix with fixed PSD terms is not unique. These considerations reflect the need of having a method rather than standardized values to define the specification of a multi-axial test.

The objective of this work is to provide a fully automated method to define the MIMO random reference matrix in case of missing operational measurements and the test specifications are provided in terms of (SISO) PSDs only. The full reference matrix returned by the method needs to be positive semi-definite in order to be used for actual testing and ensure good narrowband control performances on the provided PSDs. In [12] a solution to the aforementioned problems has been shown to be directly linked to the solution of the so-called problem of *meeting the minimum drives criteria* [2]. In [12] the author proposes the so-called Extreme Input/Output method. The idea behind the method is to find the CSDs that minimize the input power required to reach the (specified) PSDs. Unfortunately, this target definition procedure is not able to guarantee that the final target will be positive semi-definite. This makes the method not suitable for practical testing, as will be shown in the section 2. This issue is further tackled by the same author that proposes, in the later work [13], a constrained optimization algorithm to superimpose the required property.
Extending the work of Smallwood [12], rather than solving an optimization problem as proposed in [13], the fully automated procedure developed in this paper, named *Minimum (Maximum) Drives Method*, makes use of a direct phase selection as introduced in [14] and [15], to overcome the limitation of obtaining positive semi-definite target matrices.

Following this introduction, Section 2 explains the mathematical formulation of the Minimum (Maximum) Drives Method. In Section 3, a series of *normal-end* tests will be used to validate the developed procedure using an electrodynamic three-axial shaker. An industrial test case is considered to show how the method can be applied for testing automotive components.

Since in this work most of the derivations are in the frequency domain, all the arrays are functions of the frequency f (in Hz), if not specified otherwise. Vectors are denoted by lower case bold letters, e.g. $\mathbf{a}$, and matrices by upper case bold letters, e.g. $\mathbf{A}$. An over-bar $\overline{\square}$ is used to indicate the complex conjugate operation and the Hermitian superscript $\square^H$ to indicate the complex conjugate transpose of a matrix, e.g. $\overline{\mathbf{a}}$ and $\mathbf{A}^H$. The dagger symbol $\square^\dagger$ is used to indicate the Moore-Penrose pseudo-inverse of a matrix, whereas the hat $\hat{\square}$ is used to emphasize the estimation of a quantity, e.g. $\hat{\mathbf{A}}$ is an estimate of the matrix $\mathbf{A}$.

2 Drives power reduction procedure

In a MIMO random control test where m inputs (the so-called *drives*) and ℓ outputs (the so-called *controls* or *pilots*) are considered, if the full dynamic system is linear and time invariant, it is possible to write the Input-Output relation in terms of SDMs as [16]

$$\mathbf{S_{yy}} = \mathbf{H}\mathbf{S_{uu}}\mathbf{H}^H \tag{1}$$

where $\mathbf{S_{yy}} \in \mathbb{C}^{\ell\times\ell}$ and $\mathbf{S_{uu}} \in \mathbb{C}^{m\times m}$ are the output SDM and the input SDM respectively, and $\mathbf{H} \in \mathbb{C}^{\ell\times m}$ is the Frequency Response Functions (FRFs) matrix.
The objective of the MIMO random vibration control test is to replicate a full referecnce SDM $\mathbf{S_{yy}^{ref}}$. Theoretically, the test target can be directly achieved by sending the input drives that have the specified input spectral density matrix [17].

$$\mathbf{S_{uu}} = \mathbf{Z}\mathbf{S_{yy}^{ref}}\mathbf{Z}^H \tag{2}$$

where the $\mathbf{Z} = \mathbf{H}^\dagger \in \mathbb{C}^{m\times\ell}$ is often referred as the *System's Mechanical Impedance Matrix*.
In case a full set of measurements is not available and test specifications provided in terms of PSD-only breakpoints, the choice of setting the cross-correlation information between pairs of control channels is given to the test engineer. Most of the MIMO vibration controllers give the possibility of defining element-wise the CSDs in terms of (ordinary) coherence and phase profiles [2] (typical values of low coherence and high coherence are 0.01 - 0.05 and 0.95 - 0.98, respectively). All the CSDs are then easily computed as

$$S_{jk} = |S_{jk}|\exp(\mathrm{i}\phi_{jk}) = \sqrt{\gamma_{jk}^2\, S_{jj}S_{kk}}\exp(\mathrm{i}\phi_{jk}) \qquad \forall j,k \quad j \neq k \tag{3}$$

where i is the imaginary unit and j and k are the j-th and the k-th control channels, respectively.

2.1 The state-of-the-art solution: Extreme Inputs/Outputs Method

The idea of the method proposed in [12] is to find, with fixed PSD levels, the set of coherences and phases between the control channels that minimizes the trace of the drives SDM. The choice of the drive trace as quantity to be minimized is undoubtedly advantageous because a closed form expression can be derived in terms of the specified PSDs and the unknown coherences and phases between pairs of control channels. Considering the basic equation (2) for Linear Ttime Invariant (LTI) systems, the diagonal terms of the input SDM can be expressed as

$$S_{uu,ii} = \sum_{j=1}^{\ell}\sum_{k=1}^{\ell} Z_{ik}S_{yy,jk}^{ref}\bar{Z}_{ij} \qquad \forall i = 1:m \tag{4}$$

The trace of the drives SDM is the sum of the diagonal terms [18], where for the sake of brevity, the superscript $\square^{ref}$ will be dropped in the following derivation

$$P = \mathrm{Tr}(S_{uu}) = \sum_{i=1}^{m}\left(\sum_{j=1}^{\ell}\sum_{k=1}^{\ell} Z_{ik}S_{yy,jk}\bar{Z}_{ij}\right) = \sum_{j=1}^{\ell}\sum_{k=1}^{\ell} S_{yy,jk}\sum_{i=1}^{m}\bar{Z}_{ij}Z_{ik} \tag{5}$$

where the single sum on the right-hand-side of equation (5) can be interpreted as the kj-th entry of an hermitian matrix $\mathbf{F} \triangleq \mathbf{Z}^H\mathbf{Z}$.
By noticing that $\mathbf{S_{yy}^{ref}}$ needs to be hermitian too, the trace P must be a real number [18] and equation (5) can be rewritten as

$$P = \sum_{j=1}^{\ell}\sum_{k=1}^{\ell} S_{yy,jk}F_{kj} = \sum_{j=1}^{\ell} S_{yy,jj}F_{jj} + 2\sum_{j=1}^{\ell-1}\sum_{k=j+1}^{\ell}|S_{yy,jk}||F_{jk}|\cos(\phi_{jk}-\theta_{jk}) \tag{6}$$

where $S_{jk} = |S_{jk}| \exp(\mathrm{i}\phi_{jk})$ and $F_{jk} = |F_{jk}| \exp(\mathrm{i}\theta_{jk})$.
Equation (6) is explicit in the unknown reference matrix CSD terms. By using the relation (3), equation (6) can be finally expressed in terms of coherences and phases between the pairs of control channels (the information that needs to be provided to the vibration controller)

$$P = \sum_{j=1}^{\ell} S_{yy,jj} F_{jj} + 2 \sum_{j=1}^{\ell-1} \sum_{k=j+1}^{\ell} \sqrt{\gamma_{jk}^2} \sqrt{S_{yy,j} S_{yy,k}} \, |F_{jk}| \cos(\phi_{jk} - \theta_{jk}) \tag{7}$$

The matrix $\mathbf{F}$ can be easily computed from the identified system $\hat{\mathbf{H}}$, and therefore the terms $|F_{jk}|$ and θ_{jk} can be considered as known quantities. Also the PSD terms are known and considered as test specifications. The first term on the right hand side of equation (7) is always positive and fixed for the given test specifications and test setup. The second term contains the quantities ϕ_{jk} and γ_{jk}^2, unknowns of the target definition procedure. This term can be negative because of the cosine contained in the double sum and can therefore be a negative contribution, reducing the drive trace.
The expression in equation (7) has a minimum (maximum) when the coherences are all unitary and the cosines all equal -1 (1). This observation leads to the following conditions (addressed here as *Extreme Drives Conditions*) that lead to the theoretical minimum (maximum) drive traces

$$P \text{ is minimum} \iff \begin{cases} \gamma_{jk}^2 = 1 \\ \phi_{jk} = \theta_{jk} + \pi \end{cases} \qquad \forall j,k = 1:\ell, j \neq k \tag{8a}$$

$$P \text{ is maximum} \iff \begin{cases} \gamma_{jk}^2 = 1 \\ \phi_{jk} = \theta_{jk} \end{cases} \qquad \forall j,k = 1:\ell, j \neq k \tag{8b}$$

In the following the conditions (8a) and (8b) will be referred as the *Minimum Drives Condition* and the *Maximum Drives Condition*, respectively. All the other possible combinations of coherences and phases return drive traces that fall in the range between the minimum and the maximum value.

2.2 Proposed solution: Minimum (Maximum) Drives Method

Condition (8a) requires to fill in the MIMO reference matrix *element by element* with $\big(\ell(\ell+1)/2 - \ell\big)$ unitary coherence and phase profiles equal to the $(\theta + \pi)$ phase angle of the $\mathbf{F}$ matrix corresponding entry (the same considerations hold for (8b)). This could result in the reference matrix being negative definite. A mathematical proof can be found by analyzing the simple case of three control channels. Stated that the only physical values that the coherence can assume are between 0 and 1, for the reference matrix to be positive semi-definite it is necessary and sufficient that the Sylvester's Criterion holds [18] and therefore that

$$det(\mathbf{S}_{\mathbf{yy}}^{\mathbf{ref}}) = 1 - \gamma_{12}^2 - \gamma_{13}^2 - \gamma_{23}^2 + 2\cos(\phi_{12} - \phi_{13} + \phi_{23}) \sqrt{\gamma_{12}^2 \, \gamma_{13}^2 \, \gamma_{23}^2} \geq 0 \tag{9}$$

Unitary coherence implies also the cosine to be unitary, in order for the determinant to be greater or equal than zero and thus the cosine's argument must nullify

$$\begin{cases} det(\mathbf{S}_{\mathbf{yy}}^{\mathbf{ref}}) \geq 0 \\ \gamma_{12}^2 = \gamma_{13}^2 = \gamma_{23}^2 = 1 \end{cases} \quad \Rightarrow \quad \phi_{12} - \phi_{13} + \phi_{23} = 0 \tag{10}$$

A strong deterministic relation needs to exist between the phases to be selected. This can be physically explained by associating these phases to the ones of the respective recorded spectra, as shown in Figure 1. Setting the phases ϕ_{12} and ϕ_{13} means to set a *relative constraint* in the phase information carried by the two pairs of recorded signals, i.e. that between controls 1 and 2 and controls 2 and 3 there are phase angles (in radians) of ϕ_{12} and ϕ_{13}, respectively. Therefore, the phase ϕ_{23} between the control channels 2 and 3

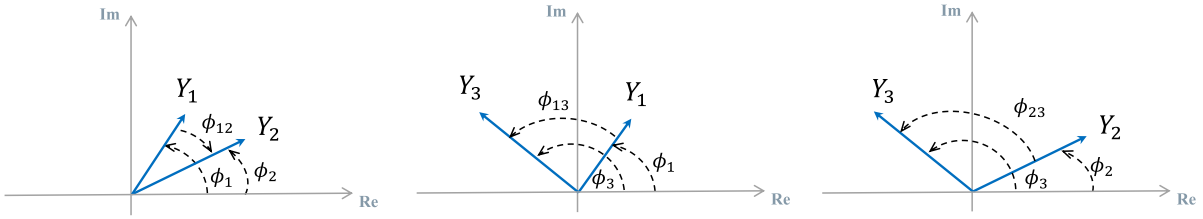


Figure 1: Example of phase relation for three fully coherent control channels. Given the phases ϕ_{12} and ϕ_{13}, the phase ϕ_{23} is unequivocally defined as the difference between the other two.

is unequivocally defined as the difference between ϕ_{13} and ϕ_{12}. Keeping unitary coherence, equation (10) highlights that, unless the $(\theta + \pi)$ angles does not already respect the aforementioned relation, a physical realizable target to be used for testing purposes cannot be set with the conditions (8).

Nevertheless, equation (7) still provides a solution to reduce the drives power. A positive semi-definite matrix can be obtained, according with the condition (8a), selecting just $(\ell - 1)$ phases equal to the respective $(\theta + \pi)$ phase angles whereas all the others needs to be obtained in order to fulfill the condition (10), i.e. as the difference between the selected ones. This means that an automatic target definition procedure can return positive semi-definite reference matrices and drastically reduce the drives power (without any modification on the PSDs) if these $(\ell - 1)$ phases are opportunely chosen and the remaining ones calculated in order to agree with this simple principle. Depending on the value of the resulting phase angle, they can contribute or not to the drive trace's reduction. It is worth to notice that, increasing the drive traces with respect to the one obtained from the standard method, is a direct consequence of the resulting reference matrix being positive semi-definite. A negative definite matrix can have a reduced traces due to the effect of negative eigenvalues (potentially, in the standard method, nothing prevents the drive traces to be also negative). In order to guarantee the biggest trace reduction, the $(\ell - 1)$ chosen phases can be defined as the one corresponding with the vectors with biggest amplitude $|F_{jk}|\sqrt{S_{yy,jj}\, S_{yy,kk}}$. More details of the proposed procedure can be found in [19].

The same procedure can be applied choosing the phases according to the condition (8b) in place of the condition (8a), hence maximizing the drive traces. However, although the advantages of having reduced drives are clear, the applicability (rather than purely comparative) of a method that requires maximum drives is still under investigation.

3 Test Cases

In order to show the general applicability of the algorithm, the Minimum (Maximum) Drives Method is tested with the electrodynamic three-axial shaker Dongling 3ES-10-HF-500 at the University of Ferrara, shown in Figure 2. This advanced actuation system is an assembly of three independent electrodynamic shakers, connected via a patented coupling hydrostatic bearing. The head expander is a squared 0.5 m plate with blunt corners and a total mass of 14 Kg. As data acquisition system and vibration controller, a Siemens LMS SCADAS Mobile SCM205V is used, driven by Simcenter LMS Test.Lab MIMO Random Control.
More details related to the applicability of the algorithm can be found in [19], where the developed procedure is tested considering different actuation mechanisms, number of drives and control channels.

Two different series of tests are performed. First, the bare head expander (HE) is tested for the maximum allowed bandwidth. Subsequently, an automotive component is tested in a single simultaneous three-axial test to match the single axis specifications (longitudinal, lateral and vertical) in a simultaneous three-axial test. In order to avoid possible energy sinks associated with the pseudo-inversion, just *square* well-conditioned configurations are considered with realizable PSDs [20].

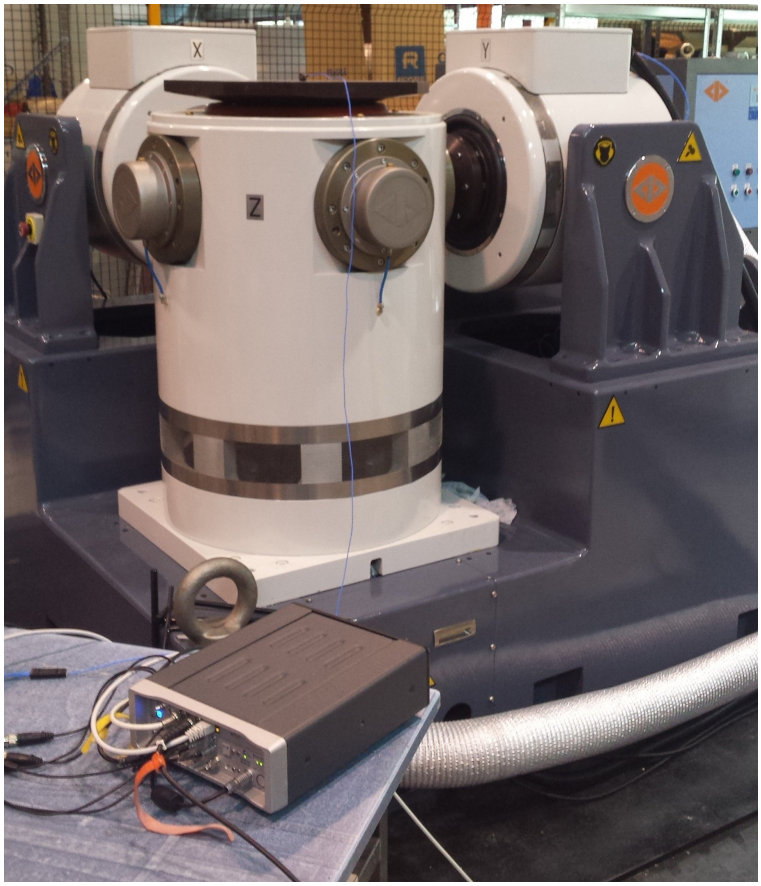
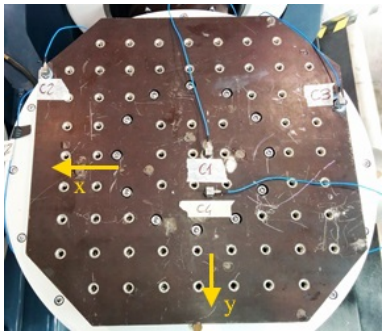


Figure 2: Dongling 3ES-10-HF-500 three-axial shaker at the University of Ferrara.

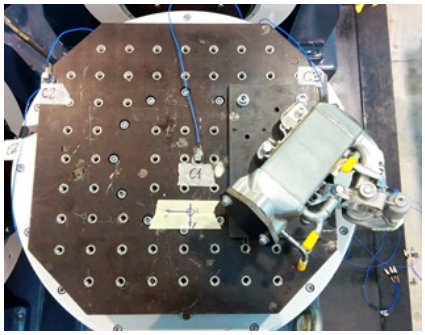
All the results are shown for *normal end* tests, meaning that the full level (0 dB) has been successfully run for 1 min (within the abort limits). The results in terms of control SDM are just shown for the tests run with the Minimum Drives Target. These results are illustrated in a matrix subplot fashion. The subplots on the diagonal show the reference profiles and the PSDs achieved at the normal end, together with the abort and alarm thresholds; in the upper and lower triangular parts of the plot the amplitude (in g^2/Hz) and phases (in degrees) of the upper triangular CSDs are reported, respectively. Since the matrices are positive semi-definite and therefore hermitian, the subplots are also representative for the lower triangular CSDs (complex conjugates). It is fundamental to notice that for the same test setup, different tests are run with the same PSD profiles, considered as test specifications, and different CSDs, coming from the application of the Minimum Drives Method and also with common choices of coherence and phases between control channels.

To show the advantage of the developed procedure, the comparison with other choices for the CSDs is shown in terms of:

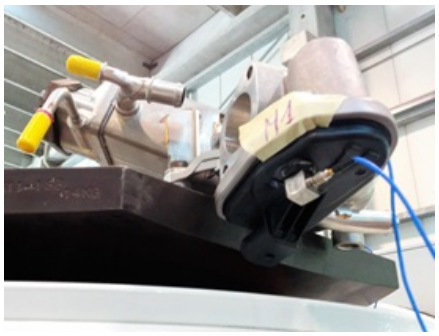
- predicted drives RMS from a system verification run prior to the test (to check the tests levels). These values are simply the RMS (over the selected bandwidth) calculated from the drive PSDs returned by equation (2);
- drive traces, to show the narrow band drive traces reduction;
- drive traces RMS, as global indicator for the drives' power reduction. During the test narrowband unpredictable differences could arise due to the several reason, such as the randomness of the process, the on-line control action that tunes the drives to match the target and/or system's non-linearities.



(a) bare head expander test configuration.



(b) test configuration with the EGR valve mounted on the head expander, top view.



(c) test configuration with the EGR valve mounted on the head expander, side view.



(d) test configuration with the EGR valve mounted on the head expander, front view.

Figure 3: test configuration for the tests performed with the three-axial shaker at the University of Ferrara.

3.1 Bare head expander

The HE is tested in the full frequency range allowed by the shaker's manufacturer ($[10 - 2000]$ Hz) with the test configuration shown in Figure 3a and a frequency resolution of 1.5625 Hz. The control channels are the X, Y and Z axis of the accelerometer C1. The bandwidth pushes the limits of the shaker system. In order to get meaningful PSDs to be set as diagonal elements for the MIMO random control test, an open-loop pre-test is run with uncorrelated drives (pseudo random signals with a random phase randomization). The X, Y and Z response RMS levels are 1.29, 1.25 and 1.45 g_{RMS}, respectively.

Figure 4 shows the predicted drive levels V_{RMS} and their sum from the pre-test System Verification. The different bars correspond to different choices in defining the CSDs. In the figure, the threshold for the overload of the data acquisition DAC is also reported. The figure allows to make some considerations. Low coherence between responses does not mean low power, as shown via the equation (8a). The phase information set between the control channels is playing a major role. Choosing the phases with the Minimum Drives Method returns minimum predicted drives power, compared to the other choices.

It is relevant to notice that the method shows a reduction of the single drives V_{RMS}. In case the test levels need to be increased, the method provides the biggest scaling factor. In case the same test levels are kept, choosing the CSDs with the Minimum Drives Method preserves the shakers and the amplifiers, subjected to lower voltages.

The control results for the normal end test with the target set with the Minimum Drives Method are shown in Figure 5 and the resulting drive traces are reported in Figure 6. The drive traces of the tests run by setting the CSDs with the Minimum and the Maximum Drives Method bound the drive traces returned by other phase and coherence selections.

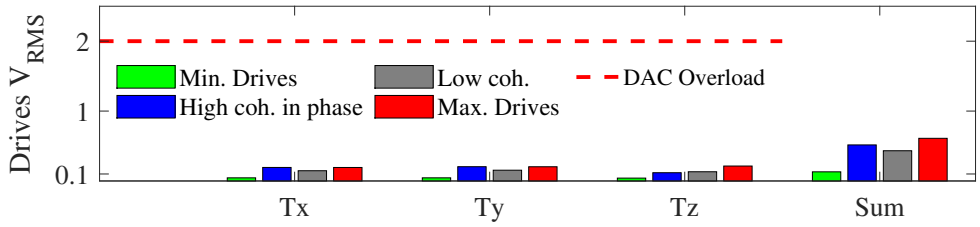


Figure 4: predicted drives and their sum, for the tests performed on the bare head expander with reference PSDs from an open loop pre-test.

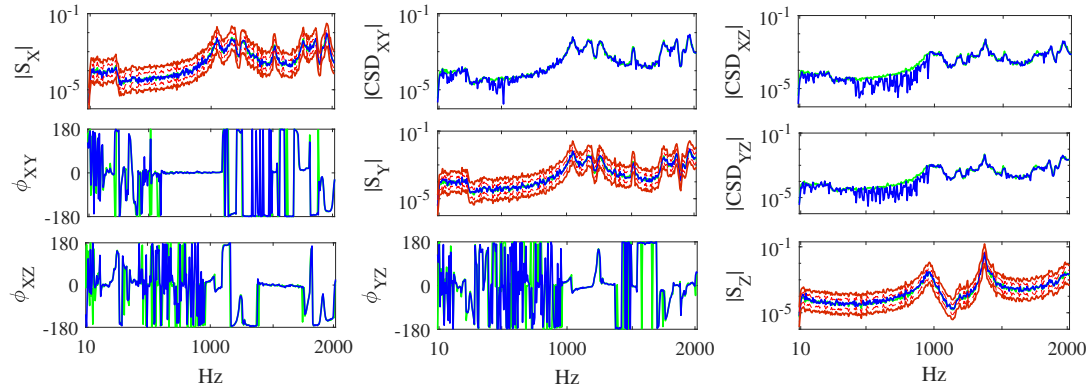


Figure 5: MIMO random control results (solid blue curve) for the test performed on the bare head expander of the three-axial shaker by setting the target (solid green curve) with the Minimum Drives Method. PSDs (diagonal subplots) and CSDs amplitudes (upper triangular subplots) in g^2/Hz, phase angles (lower triangular subplots) in degrees. The solid red and dashed orange lines are the abort and alarm thresholds, respectively.

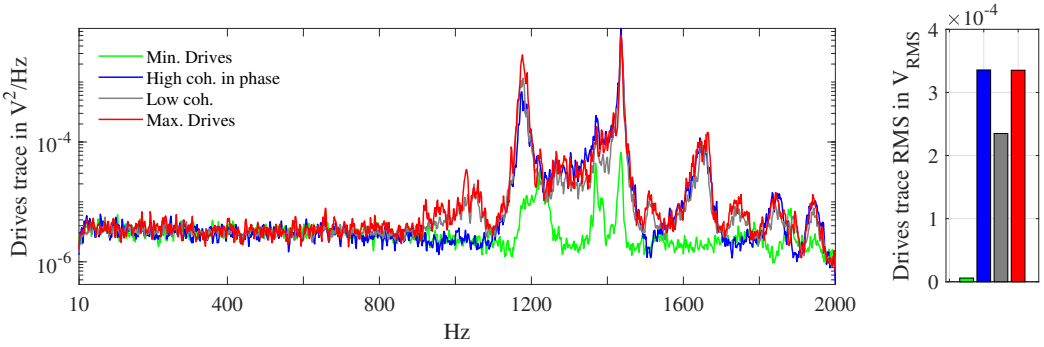


Figure 6: drive traces for the tests performed on the bare head expander with reference PSDs from an open loop test.

3.2 Automotive test article: Exhaust Gas Recirculation (EGR) valve

The successful tests motivated to use the Minimum Drives Method on an automotive OEM (Original Equipment Manufacturer) component to be tested to random vibration in the three different directions. The test specification are defined in terms of PSDs only, inherited from single axis test standard practices. The automotive component tested is an Exhaust Gas Recirculation (EGR) valve, used to reduce the internal combustion engines emissions. The test configuration is shown in the Figures 3b, 3c and 3d. For these tests, the same control channels adopted for the bare head expander test case are used. The PSD shapes come from single axis test specifications. They are defined in the frequency range $[10 - 500]$ Hz, with a frequency resolution of 1.5625 Hz.

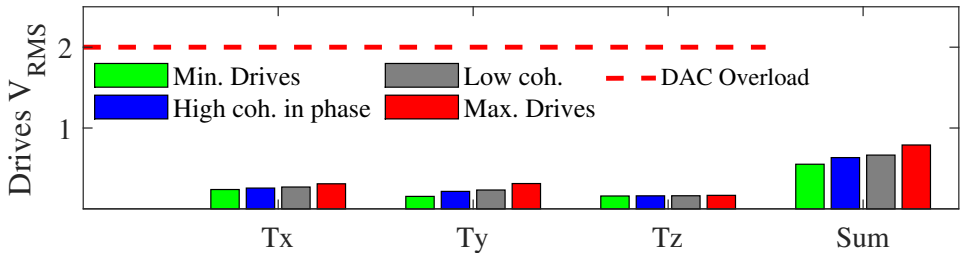


Figure 7: predicted drives and their sum, for the tests with the EGR valve mounted on the head expander.

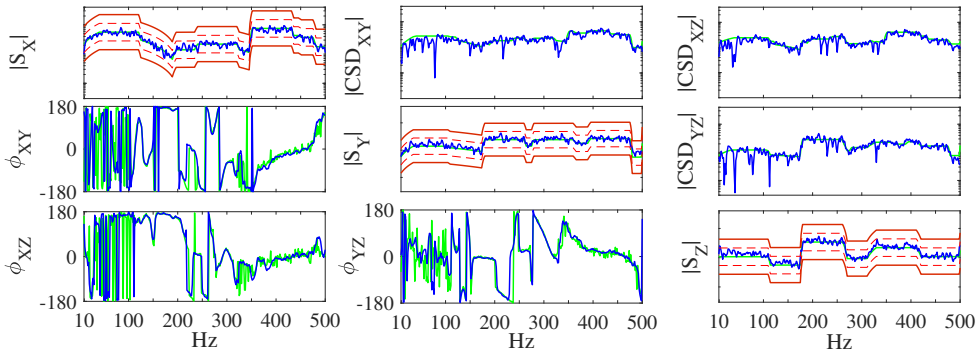


Figure 8: MIMO random control results (solid blue curves) for the test performed with the EGR valve mounted on the bare head expander of the three-axial shaker by setting the target (solid green curve) with the Minimum Drives Method. PSDs (diagonal subplots) and CSDs amplitudes (upper triangular subplots) in g^2/Hz, phase angles (lower triangular subplots) in degrees. The solid red and dashed orange lines are the abort and alarm thresholds, respectively.

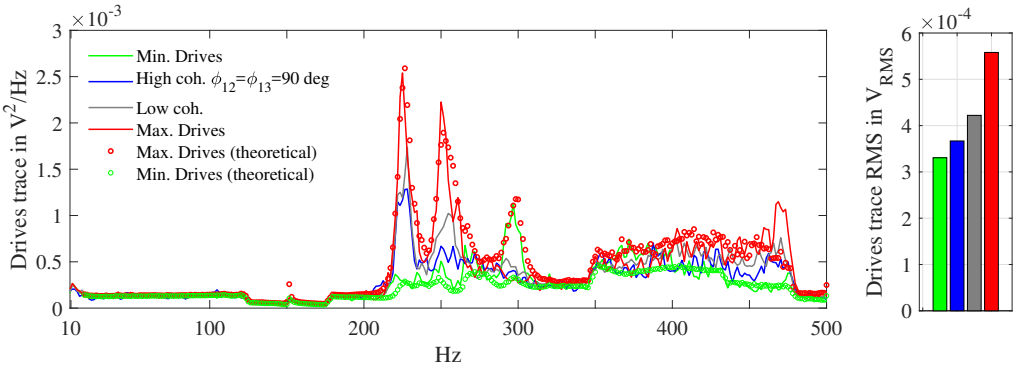


Figure 9: drive traces for the tests performed with the EGR valve mounted on the head expander.

The predicted drive voltages are illustrated in Figure 7 and show again the drives reduction obtained by the method. In this application the advantage in terms of voltage's reduction is evident but less significant compared to the previous test case. This is due to the reduced bandwidth, limited to a region where the cross-coupling between orthogonal axes is small and therefore the reference matrix's CSDs influence on the drives power reduces consequently.

Figure 8 shows the narrowband results of the MIMO random control process, with the response SDM controlled to achieve the Minimum Drives Target. The difference in the narrowband drive traces at the normal end can be seen in Figure 9, plotted in linear scale. The Minimum Drives Method shows a non negligible drives trace reduction. In the figure the theoretical Minimum (Maximum) drives trace are also reported. These traces are calculated substituting in equation (2) the response SDM with the target obtained applying the developed method and the system's FRF matrix with the one obtained from the system identification.

The only region with an unexpected behavior is a narrow band around 300 Hz, possibly due to the control action performed to try to control the system's non-linearities. The adaptive feature of the Siemens LMS MIMO Random Control can cope with system non-linearities, as shown in the good control results of Figure 8. On the contrary, the assumptions made to derive the Minimum Drives Target will be no longer valid and the effects of the drives correction could be unpredictable.

4 Conclusions

This paper proposes the Minimum (Maximum) Drives Method as innovative target definition procedure for MIMO random control tests. The only information needed for this target definition method is the System Identification, anyhow required for the vibration control algorithm, and the PSD profiles, representing the test specifications. The target definition process can therefore be fully automated.
With the developed procedure it is possible to generate the missing CSDs in such a way that (i) the reference matrix is positive semi-definite in the whole test bandwidth and (ii) the drives power needed to reach the test specifications (the PSDs) is systematically reduced with respect to other possible state-of-the-art solutions. These features open the possibility to candidate the proposed methodology as attractive solution to the problem of meeting *the minimum drives criteria* and therefore to be included in the current standard practice for multi-axial testing.
Compared to standard choices or methods currently used to fill in the CSDs, the added value of reducing the total drives power is undoubtedly advantageous: for fixed test response levels, it guarantees that the delicate and expensive excitation hardware (shakers and amplifiers) is driven with reduced voltages. In case the test levels need to be increased, the proposed solution would allows a maximum scale factor.
Furthermore, the generated targets incorporate information coming from the system identification, that could result in exciting the system in agreement with its dynamic behaviour.

References

[1] United States Department of Defence, *METHOD 514.6: Vibrations*, United States Military Standard 810G (2008).

[2] United States Department of Defence (2014), *METHOD 527.1: Multi-Exciter Test*, United States Military Standard 810G (2008).

[3] M. A. Underwood, *Multi-exciter Testing Applications: Theory and Practice*, *Proceedings of The Institute of Environmental Sciences and Technology*, (2002).

[4] B. Peeters, J. Debille, *Multiple-input-multiple-output random vibration control: theory and practice*, *Proceedings of The International Conference on Noise and Vibration Engineering*, (2002).

[5] M. Mršnik, J. Slavič and M. Boltežar, *Multiaxial Vibration Fatigue – A Theoretical and Experimental Comparison*, Mechanical Systems and Signal Processing 76-77, (2016), pp. 409 - 423.

[6] P. M. Daborn, P. R. Ind, *Next-Generation Random Vibration Tests*, *Proceedings of The 32nd IMAC Conference*, (2014).

[7] C. Roberts, D. J. Ewins, *Multi-Axis Vibration Testing of an Aerodynamically Excited Structure*, Journal of Vibration and Control 1–11, (2016).

[8] D. O. Smallwood, *Multiple Shaker Random Vibration Control - An Update*, Sandia National Laboratories, (1999).

[9] M. A. Underwood, T. Keller, *Recent system developments for multi-actuator vibration control*, Sound and Vibration 35, (2001), pp. 16–3.

[10] M. A. Underwood, R. Ayres, *Filling in the MIMO Matrix: part 1 - Performing Random Tests Using Field Data*, Sound and Vibration 1, (2011), pp. 5–14.

[11] L. Jacobs, M. Ross, G. Tipton, K. Cross, N. Hunter, J. Harvie, G. Nelson, *Experimental execution of 6-dof tests derived from field tests*, *Proceedings of The 35nd IMAC Conference*, (2017).

[12] D. O. Smallwood, *Multiple-Input Multiple-Output (MIMO) Linear Systems Extreme Inputs/Outputs*, Shock and Vibration 14, (2007), pp. 107–131.

[13] D. O. Smallwood, *Minimum Input Trace for Multiple Input Multiple Output Linear Systems*, Journal of the IEST 56, (2013), pp. 57–61.

[14] U. Musella, G. D'Elia, S. Manzato, B. Peeters, P. Guillaume, F. Marulo, *Analyses of Target Definition Processes for MIMO Random Vibration Control Tests*, *Proceedings of The 35th IMAC Conference*, (2017).

[15] U. Musella, G. D'Elia, B. Peeters, E. Mucchi, P. Guillaume, F. Marulo, *Tackling the Target Definition Processes for MIMO Random Vibration Control Tests*, *Proceedings of The 30th Aerospace Testing Seminar*, (2017).

[16] J. Bendat, A. G. Piersol, *Random data: analysis and measurement procedures*, John Wiley and sons, 729, New York, US (2011).

[17] D. O. Smallwood, T. Paez, *A Frequency-Domain Method for the Generation of Partially Coherent Normal Stationary Time-Domain Signals*, Shock and Vibration 1, (1993), pp. 45–53.

[18] C. D. Meyer, *Matrix analysis and applied linear algebra*, Society for Industrial and Applied Mathematics, Philadelphia (2000).

[19] U. Musella, G. D'Elia, A. Carella, B. Peeters, E. Mucchi, F. Marulo, P. Guillaume, *Minimum Drives Automatic Target Definition Procedure for Multi-Axis Random Control Testing*, Mechanical Systems and Signal Processing 107, (2018), pp. 452–468.

[20] M. G. Alvarez Blanco, K. Janssens, F. Bianciardi, *Experimental verification of projection algorithms and optimization routines for acoustic field uniformity enhancement in MIMO direct field acoustic control*, *Proceedings of The International Conference on Noise and Vibration Engineering*, (2016).

Fully automated vibration measurements of aircraft fuselages in the mid-frequency range

R. Winter[1], **S. Heyen**[1], **M. Böswald**[1]
[1] Deutsches Zentrum für Luft- und Raumfahrt e.V. (DLR), Institute of Aeroelasticity
Bunsenstr. 10, D-37073 Göttingen, Germany
e-mail: **rene.winter@dlr.de**

Abstract

In order to analyze the dynamic behavior of aircraft fuselage structures in the mid to high frequency range a large number of measurement positions is necessary. This is especially true if advanced methods of evaluation like structure intensity analysis (STI) are to be used. The amount of measurement positions necessary for the vibroacoustic evaluation of full sized aircraft fuselage structures has previously been shown to be in the order of multiple thousands requiring extensive measurement campaigns using hundreds of rowing sensors and a large team working for weeks. Presented here is a novel approach to Laser-Doppler-Vibrometer (LDV) based measurements of aircraft fuselages. A mobile laser scanning system capable of fully automatic vibration measurements of fuselage sections using a commercial single-point LDV was developed. The system can be deployed within the excited structure due to its vibration isolation and is able to autonomously match a predefined measurement geometry with the real structure using only a couple of reference markers.

1 Introduction

The vibration analysis of complex aircraft fuselage structures in the mid-frequency range requires a dense grid of measurement points. In 2014 the German Aerospace Center (DLR) measured and analyzed the dynamic behavior of the A400M acoustics fuselage demonstrator [1, 2], an actual aircraft fuselage re-purposed as a laboratory structure located at the Helmut Schmidt University of the Federal Armed Forces in Hamburg. Vibrations data was acquired at a total of approximately 2800 measurement positions with accelerometers deployed in a rowing sensor grid process. A total of 4 different excitation positions was used. Due to project requirements the campaign was repeated after several changes to the fuselage demonstrator. Each measurement campaign took a team of 5 scientists and technicians a total of 4 weeks. While the data was of high quality regarding signal-to-noise ratio an analysis at higher frequencies than 150 Hz was only possible using methods of spatial averaging [3], as the grid density was not sufficient.

In 2016 DLR performed another measurement aiming at the dynamic characterization of an aircraft fuselage structure, the Flight-LAB Acoustics Demonstrator [4, 5] located at the ZAL in Hamburg. The data needed to be of sufficient spacial density to allow for the updating of the Finite-Element-Model up to a frequency of 300 Hz. This was made possible by measuring a total of approximately 12000 positions using, again, accelerometers in a rowing grid configuration. The measurement was performed within 4 weeks. The higher number of measurement positions was possible due to trade-offs in data quality versus installation speed, no mass dummies were used and the sensors were fixed using wax instead of threaded mounts, and the Flight-LAB structure being more accessible than the A400M fuselage due to its lower diameter and central floor.

Both measurements were quite successful but several problems arose: The team members needed to carefully place and move hundreds of sensors following a predefined pattern and eventually evaluate the results and dismantle the system. This workflow is accompanied with a lot of repetitive work that demands concentration

and precision throughout the measurement campaign over the course of weeks. As every sensor also requires a wired connection to the measurement system a lot of effort is put into sustaining organized cable management. Overall the process is prone to errors alleviated only by constant on-site checks and occasional repetitions of configurations. In addition having a team of 4 to 5 people working for weeks is quite expensive and makes new measurements to confirm the effect of smaller changes to the structure unlikely due to cost and time constrains.

To alleviate these problems DLR developed a highly specialized laser scanning system dubbed ‘fuselage laser scanner’ (FLS). This system utilizes a single point Laser-Doppler-Vibrometer (LDV), a sensor allowing for velocity measurements along an optical axis and quite common in vibration measurements. A problem with LDV measurements [6] is the angle of incidence of the laser beam on the structure. The designed system is specifically built to measure aircraft fuselages or similar cylindrical structures. By designing the system to be deployed within the vibrating structure and close to its radial center the angle of incidence can be kept close to 90° for every measurement position, reducing the need for angular corrections. In addition the scanning unit is modular in longitudinal direction, in principle allowing for a cylinder of extreme length to be measured.

The system is designed to autonomously perform the task of acquisition and excitation of vibration data. It can be deployed and configured in a couple of hours by a 2 person team and performs the measurement automatically and without the need of downtime resulting in very cost efficient measurements. Due to a single point LDV based system operating effectively in serial mode, i.e. measuring one point after another, this does not necessarily transfer into an advantage when considering total measurement time depending on the parameters chosen. By designing the system to autonomously map its internal coordinates to a given structure and measurement grid once a couple of reference markers are glued to the target near perfect reproducability of tests is achieved. In principle a given structure can be reevaluated after every structural change if time allows. Without the need of a sizable team the costs for measurements are low.

To show the system is able to perform as designed several test were conducted. Besides smaller, component-wise laboratory tests of the system, a proof of usability in its intended environment was provided by two tests utilizing the system within actual aircraft structure. The system was used once within DLR’s DO728 aircaft as seen in Fig. 1 and another test was conducted returning to the A400M acoustics fuselage demonstrator.

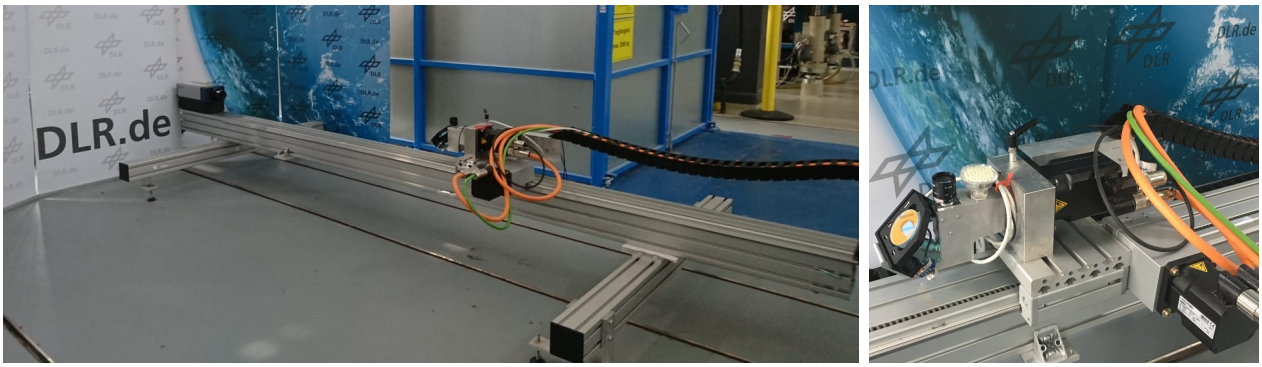


Figure 1: The fuselage scanning system deployed at the D728. Due to time constrains the fuselage was not completely freed of additions and secondary structures.

2 System overview and features

The fuselage scanning system is utilizes on a single-point LDV (PolyTec OFV-505) mounted at one end of an aluminum beam of variable length. A carriage carrying the scanning mirror, a digital camera (AVT Mako G-032 Mono 12) and a light source is placed on top of this beam. It is able to move along the beam utilizing a 'rack-and-pinion' setup allowing for a simple extension of the systems longitudinal span by adding more beams. The traverse beam is placed on top of two or more crossbeams.

Currently the system can be set up either with a 3 m or 6 m span. Expanding beyond this range can be done by getting more beams, longer cables and an accompanying cable carrier as long as the maximum measurement range of the vibrometer of up to 300 m (depending on the lens used with the Polytec OFV-505) is not exceeded. Utilizing two small brushless servomotors chosen from the Novotron NN3 series for their high precision encoders and the availability of controllers with CANopen protocoll support the carriage is the only moving part of the system. The LDV itself stays fixed at one end of the beam.



(a) Overview of the system setup in short configuration with a 3 m beam (b) Close-up of the scanning head.

Figure 2: The Laser-Doppler-Vibrometer scanning system in a laboratory environment

The longitudinal beam of the system is placed on two or more crossbeams. These are meant to either stand on their own on the floor of the structure to be measured or being directly fixed towards the rail system of an aircraft cabin. The longitudinal beam of the system is isolated from the crossbeams by a foam which functions as a vibration dampener. When loaded with the weight of the longitudinal beam and the carriage the foam functions as a low-pass vibration filter isolating the system from most vibrations over a desired frequency. The actual amount and type of foam elements used depends on the weight loaded upon them (i.e. the longitudinal beam length) and the isolation required for the task at hand. Using less dampening elements results in a lower suspension frequency and lower isolation frequency but also a less stiff system. Reducing the possible movement speeds of the servomotors due to self-induced vibrations.

2.1 System control

All control systems needed to operate the LFS, an embedded real-time controller (National Instruments CompactRIO or cRIO), the LDV controller and the two motor controllers are placed within a single rack forming the control unit.

The cRIO acts as the central controller of the whole system and due to its modular nature can be expanded with modules for data acquisition, output signal generation or inter-system communication among other options. It features a built-in FPGA processor and a complete Linux based operating System. Besides making use of the FPGA for analog data acquisition of currently 8 channels, providing analog output signals for excitation systems like shakers and performing image processing it is also utilized to control the servomotors through a CANopen Bus Network. The result is a real-time scanning system with a built-in controller unit that does

not need another PC to perform measurements. The current overhead (i.e. time in between the measurement of two points) of the system is in the range of 200-300 ms. Long compared to commercial LDVs (which have an overhead of about 50 ms [6]), but further optimization was currently not of interest due to average measurement times of 5-15 s per point in the mid-frequency range.

The embedded controller can be connected to a Host-PC through a TCP/IP network interface. The Host-PC is being used to configure the measurement, presenting a live preview of collected data and analyzing the data. Non of these are required to run the actual measurement once it is configured. The Host-PC can be (dis-)connected at any time during the measurement process.

2.2 Deployment and automated position calibration

Deployment of the FLS within a new measurement environment is rather simple. The traverse and crossbeam structure of desired length has to be set up, the carriage and LDV are positioned on the traverse and the beam optics have to be checked and if needed recalibrated. For optimal results the system should be placed as close to the radial center of the fuselage as possible. If that cannot be achieved corrections for the angle of incidence are applied in post-processing. In addition a couple of QR codes are placed on the structure at predetermined positions whose coordinates within the measurement grid are well known.

Once the system is in position it can determine its own position relative to the surrounding structure using the QR-Codes and a data file containing the QR-codes position in the desired measurement grid. The system can scan its full field of view using the camera mounted on the carriage for QR-Codes. It is also able to determine the position of the LDVs laser spot in the camera image. By centering the laser spot on the QR-Codes a lookup table of points coinciding in the predefined measurement grid and FLS coordinates is created. Using this lookup table an algorithm calculates the coordinate transformation between measurement grid and FLS system coordinates. In essence this process allows the system to repeat measurements even years later in the same structure if the QR-codes are placed with care and in the best case are kept on the structure. Deviations occurring due to slight LFS placement differences are suppressed by the self-calibration process. To this end all information which is needed to reproduce the a measurement is saved inside a database file accompanying each measurement.

3 Performance tests

Several small scale tests aiming for a component-wise validation of the systems capabilities were conducted. The results for reproducability of the measurements and the vibration isolation are shown below. In addition the long term stability of the system under high data loads was tested. The system was able to perform for 70 hours continuously without problems acquiring data at a sampling rate of up 51 kHz.

3.1 Repeatability of the positioning system

A design goal of the LFS system is high repeatablility of the LDV beam position on a given structure. A significant effort was put into the automated position calibration. Without a robust positioning that effort would yield no benefit. The electric motors used for mirror rotation and longitudinal positioning were chosen with that condition in mind. High repeatability was of primary concern. While the scanning mirror of the system is directly attached to the rotating motor and benefits directly from the motors capabilities the longitudinal axis uses a ”rack and pinion” setup. This comes along with slight clearance between the motors gear (pinion) and the linear gear (rack) of the beam. Even though this introduces a slight disadvantage compared to a toothed belt setup it makes that up in flexibility. The system can be setup at any length desired for the longitudinal axis.

To test the precision of the positioning system, the scanning system was instructed to repeatedly position itself on three different QR-markers. A total of 500 positioning events was analyzed by calculating the laser spot and marker position using image processing from the camera data. This data was used to calculate the precision of the systems in terms of a 3σ deviation. While this data includes an uncertainty caused by the cameras limited resolution and the efficiency of the processing algorithms it should be noted that analyzing the camera images is the only way a user of the system can see if the positioning was successful in an actual test. Thus the method chosen gives an estimation of the full systems reliability rather than an individual components.

Image Processing	3σ deviation at 1.68 m
Marker Pos. X / Y	0.70 / 0.87 mm
Laser Pos. X / Y	1.64 / 1.41 mm

(a) Image processing error

Axis	3σ deviation at 1.68 m
Rotation $\phi \rightarrow$ Y	$0.017^\circ \rightarrow 0.48$ mm
Longitudinal X	1.42 mm

(b) Total positioning error.

Table 1: Results of positioning testing by analyzing 500 repetitions. A 3σ deviation equals 99.7% (or 369 in 370) of positioning attempts falling within the given positioning precision. The system does not perform y-positioning. The angular positioning error was propagated to that axis as an estimate.

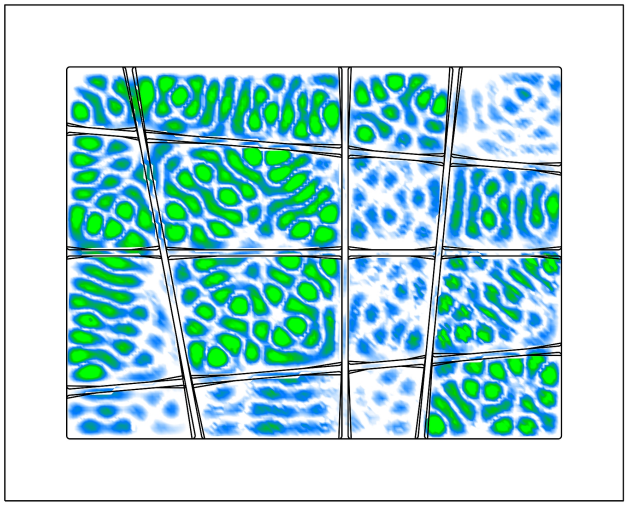
Results of these tests are compiled in Table 1. As shown there the total 3σ deviation of both axes is well below 2 mm. In fact, given a circle with a radius of 2 mm, approximately a 4σ area, only 1 in 15787 points would fall out of this area. These results show the robustness of the positioning of the system. An important characteristic when used in conjunction with the ability to repeat measurements at structures just be repeating the process of the automated positioning calibration. The system fully satisfies its design goal of high positioning precision and repeatability.

3.2 Positioning precision

With the repeatability of positioning shown, the quality of the positioning algorithm used to map a predefined grid to the structure was tested. A complex aluminum structure with easy to localize shapes was used for this test.



(a) The vibroacoustic test structure with 6 QR markers.



(b) An operational deflection shape (ODS) at 4 kHz.

Figure 3: The vibroacoustic test structure (a) is fitted with 6 QR markers providing positioning information. The markers placed on a skin field and a stiffener provide necessary depth information while the wide spread of the remaining markers help with the orientation of the structure. The ODS (b) shows a complex vibration pattern fitting well into the measured shape.

A measurement grid consisting of 32365 points, resulting in a spacing of 5 mm was matched to the plate using six QR markers placed to fully cover the geometry in all directions. According to the calculations done for the repeatability of positioning the measured grid is at the limit of what the system is currently capable of. The structure, a stiffened aluminum plate with irregular stiffeners and a measurement result are shown in Fig. 3. As can be seen the resulting operational deflection shape (ODS) is as expected. A multitude of vibration patterns, different for each of the irregular skin fields and confined to the skin fields.

3.3 Vibration isolation

The first out-of-lab test of the LFS system was performed in the DO728 aircraft structure located at the DLR in Göttingen. The structure is a real aircraft with no engines attached and clipped wings. Bosbach et. al. [7] provide further details on the DO728 laboratory. For the test performed it was important to simulate the intended use case of having the fuselage scanning system located within an aircraft structure to measure during vibration excitation. The structure was excited using the same Prodera EX 520 C50 modified for high frequencies as in [1, 2].

Fig. 1 shows the system set up in the DO728 cabin. Due to time constrains the fuselage was not fully rid of secondary structures like cables and tubes. While it was possible to test the systems vibration isolation without any problems, as the structure itself was of no concern for that, evaluating the more than 12000 points measurement was problematic. In principle the system was running well and performed the measurement without problems for more than 30 h. Checking the camera images saved for each measurement position also proved the positioning was working well. The acquired data itself was not useful for any structural analysis. Besides a lot of the measurement points being not on the structure itself but rather some of the tubes, cables and other systems it was also not possible to run the shaker at very high amplitudes due to noise concerns at the test facility as the test had to run over night.

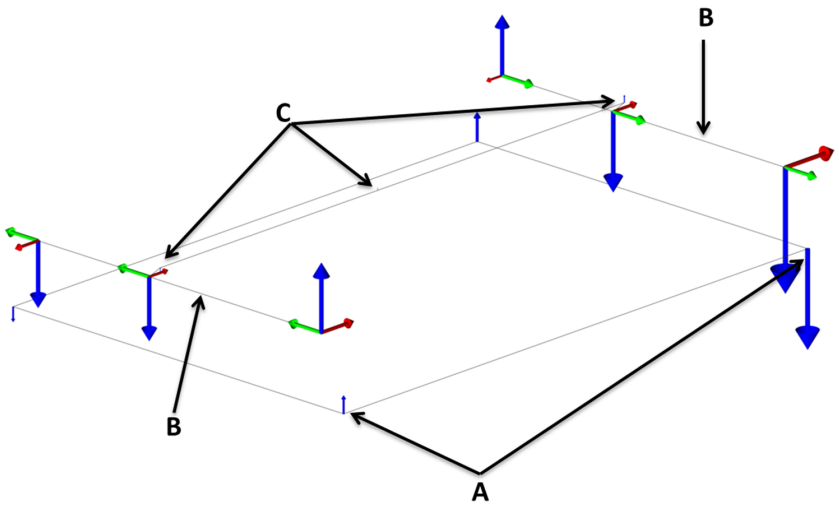


Figure 4: Example of measured vibration amplitudes and isolation efficiency of the scanning system at 52 Hz. (A) – Floor vibration near suspension points. (B) – Suspension beam vibrations. (C) Vibration of system traverse beam and carriage (barely visible due to low amplitude)

To test the efficiency of the vibration isolation the fuselage scanning system was fitted with accelerometers at its crossbeams, traverse beam and its mirror carriage. In addition accelerometers were placed at the floor close to the stands of the system to measure the undamped vibration transmitted into the system. The damping of the traverse beam and carriage is realized using foam dampers in between the crossbeam and the traverse beam. In the case of the 3 m traverse beam used for this test 8 die of 15 mm edge length of Cellasto MH 24-35 PUR foam (Elastogran GmbH) are used, resulting in rigid body eigenfrequency of 10.2 Hz. This is

well below the first bending mode of the traverse beam at 32 Hz and far below the desired excitation range for the fuselage of 50 Hz and upwards.

The test of the isolation was performed by exciting the DO728 structure using a multisine signal of 2-1000 Hz and measuring the acceleration at the previous described positions. Fig. 4 gives an overview of the setup and shows the resulting vibration amplitudes at 52 Hz. The isolation of the traverse beam and carriage from ground floor vibrations seem to work very well. To get a good estimation of the efficiency of the vibration isolation the relative vibration levels of the unisolated crossbeams and the traverse beam and carriage, as shown in Fig. 5 were analyzed. The vibration is show to drop to by an order of magnitude in the range of 50 Hz to 120 Hz. At higher frequencies it drops by two orders of magnitude.

There are several possible changes to the system to improve upon the current setup to get a better isolation. The simplest being to change the type and amount of foam used for isolation purposes and by changing to the feet of the system to include a second layer of isolation by using rubber isolation instead of the current rigid setup. Especially when using the system in a environment of transient, irregular low-frequency excitation events, as would certainly be the case in a flying aircraft, another step might be necessary. As shown in [8] LDV measurements can in principle be corrected for errors caused by measurement system vibrations. To this purpose an additional accelerometer can be fitted to the beam steering mirror of the scanning system and provide the necessary data to correct for external vibrations in post-processing.

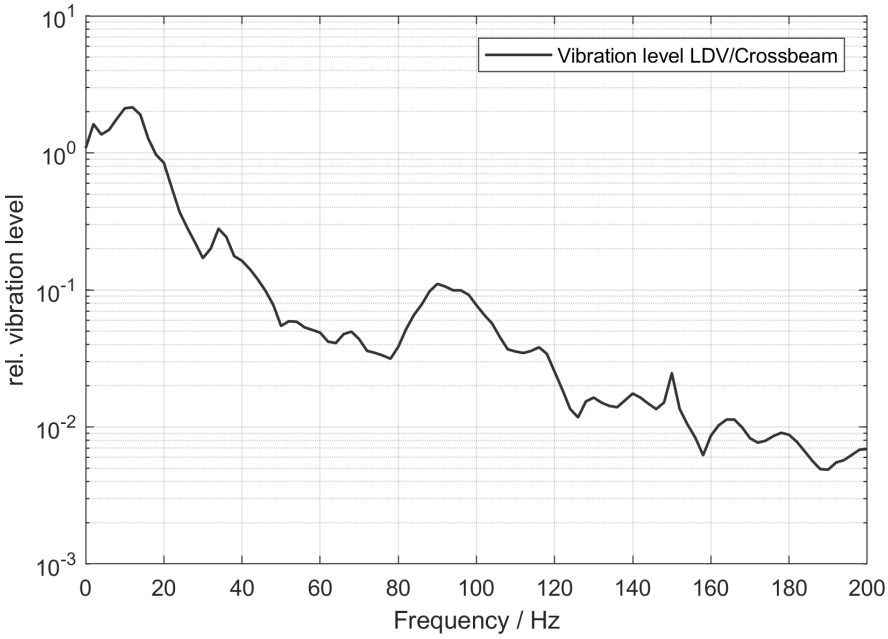


Figure 5: Efficiency of the vibration isolation as deployed in the DO728 fuselage. Shown here is the ratio of vibration measured on the beam steering mirror versus the vibration on the crossbeams carrying the traverse beam.

4 Preliminary test at A400M acoustics fuselage demonstrator

The dynamic characteristics of the A400M acoustics fuselage demonstrator has been analyzed by DLR in 2014 in great detail [1, 2]. The Flight-LAB project provided the opportunity to return to this facility. The fuselage has been slightly modified in the years in between measurements making a direct match of data impossible.

The fuselage scanning system was not used ‘as is’ in the A400M acoustics fuselage demonstrator but rather combined with an existing microphone array and its longitudinal traverse which uses a toothed belt setup

specifically fitted to that structure. The LDV scanners rotational axis and carriage setup was kept as is. All control elements were directly used from the fuselage scanning system, as the longitudinal axis of the A400M acoustics fuselage demonstrator setup could easily be integrated into the FLS controller. All relevant modules and functionalities for positioning control and measurement were kept as is.

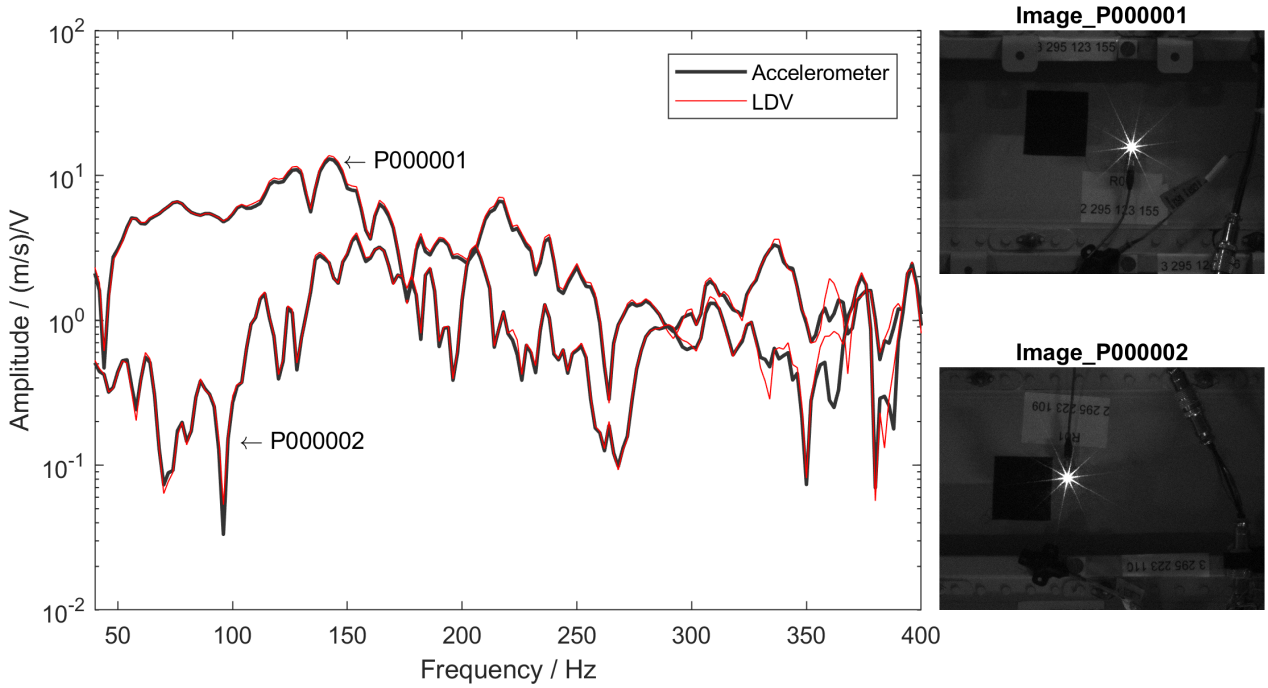


Figure 6: Comparison of LDV and accelerometer data (integrated to get velocity data) for two different positions on the A400M acoustics fuselage demonstrator. P000001 is close to the acoustic excitation while P000002 is at the opposite site of the structure. The data coincides well across a frequency range of 50-300 Hz.

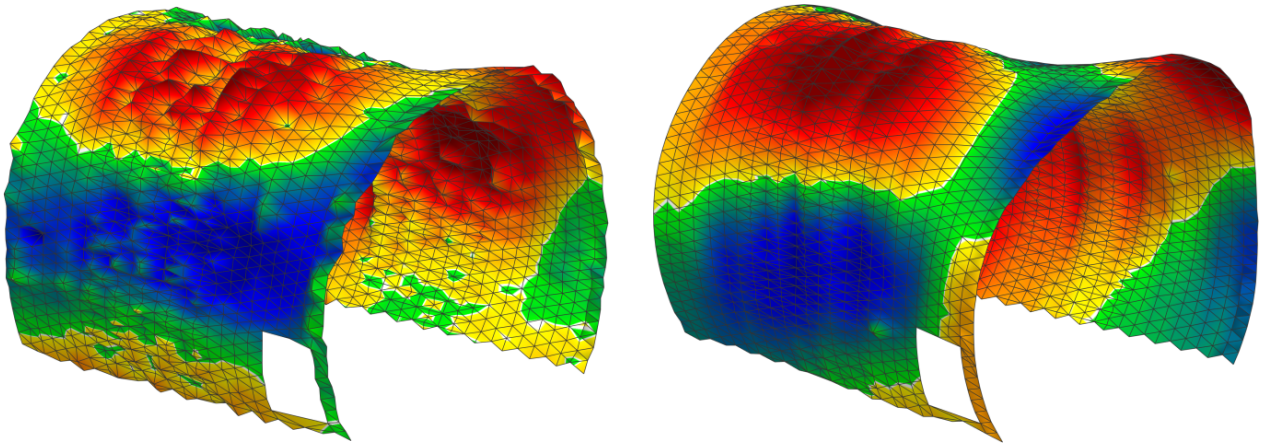
For these measurements the combination of the systems was not completed, but preliminary data showing the usability of the system is available. This data was acquired using a preliminary setup with some limitations in terms of stability. In Fig. 6 frequency response data as shown comparing the spectra of two sensors towards data measured using the LDV scanner positioned at the back of the sensor. For this test the excitation system was a loudspeaker array close to one side of the fuselage structure driven by a broadband random signal of 40-400 Hz. The acquisition time was 60 s. The whole structure was vibrating with the scanning system inside. The data of the LDV coincides well with the accelerometer data after integration in frequency domain. Up to 300 Hz the deviation is negligible. At higher frequencies deviations show but are more likely to originate from slight angle deviations between the two sensors. The acceleromter is perfectly perpendicular to the structures skin while the LDV will always have an angle of incidence depending on how close to the radial center it is.

Even though the setup at the A400M acoustics fuselage demonstrator is not yet finished, a first measurement aiming for a general prof of concept was performed. The high density measurement grid designed for the campaign in 2014 [1, 2] was reused to get some data to compare with previous measurements. The results of this effort are shown in Fig. 7.

The operational deflection shape shown at both measurements looks superficially similar. Several differences need to be pointed out: Since the measurements in 2014 several structural changes were applied to the A400M acoustics fuselage demonstrator. Most importantly a cargo-door mockup was installed closing the cavity and adding considerable weight. In addition previously installed acoustic boundaries where removed thus changing the dynamic characteristics of the structure.

The LDV data was acquired using only 6 s of acquisition time per point resulting in a total measurement time of 4 h. The accelerometer data is the result of an extensive measurement campaign taking 4 weeks and more crucially was acquired using 5 min of measurement time. In addition the accelerometer data used an 500 N

electromagnetic shaker with an excitation signal optimized for maximum response. For the quick test of the fuselage scanning system only acoustic excitation with a simple broad band random signal was available. The stark contrast in data quality is most certainly a result of these differences. As shown in Fig. 6 when using the same measurement time the data the FLS and an accelerometer do not differ much.



(a) LDV measurement with 6 s acquisition time per measurement position

(b) Accelerometer measurement with 5 min acquisition time per sensor

Figure 7: Comparison of deflection shapes of the A400M-MSN5 fuselage acquired at 47 Hz from broad band excitation. The LDV measurements are significantly more noisy due to a very short measurement time of 6 s versus 5 min for the accelerometer data.

5 Conclusion

The fuselage laser scanner (FLS) proved to be an easy to use and efficient system for fuselage vibration measurements. It operates within the desired specifications regarding the positioning precision and repeatability of measurements. A two person team is able to deploy it within a couple of hours inside a new structure and start a long term measurement if a measurement grid was defined before or if a generic grid can be used. Measurements run without failure for days due to a lot of stability optimization. A need to pause measurements can still be introduced. The excitation system might run hot, a problem more likely to occur when using loudspeakers instead of electromagnetic shakers for excitation. Or external factors like noise concerns at certain hours of the day might prevent 24 h non-stop measurements. A scheduled operation mode is available within the system software for this purpose.

The test at the DO728 showed the system working within a vibrating aircraft structure as intended. The vibration isolation was working as designed and a grid of 12000 points was scanned to repeat the amount of data acquired during the previous measurement campaign at the Flight-LAB acoustics demonstrator that used accelerometers for measurement. The data was not of any use for further dynamic characterization though, as the structure could not fully freed of secondary systems and the vibration amplitudes had to be kept very low for the long term stability tests. This was caused by time constrains within the project.

A second test within a real aircraft structure, the A400M acoustics fuselage demonstrator, was conducted. While this was only a rather short preliminary test it proved to be of success in two different ways: Using the system to measure at exactly the same spot as an accelerometer provides nearly identical data. A best case result considering the measurement system is still subject to some of the vibration inside the fuselage. In addition it was possible to measure an operational deflection shape with a high similarity to what has been measured with accelerometers before, although with much higher noise due to a very short measurement time.

Acknowledgements

The work presented here has been conducted in the joint research project Flight-LAB within the fifth Aeronautical Research Program (LuFo V). The project is funded by the Federal Ministry for Economic Affairs and Energy on the basis of a decision by the German Bundestag.

Supported by:

Federal Ministry for Economic Affairs and Energy

on the basis of a decision by the German Bundestag

References

[1] R. Winter, M. Norambuena, J. Biedermann, and M. Böswald, *Experimental characterization of vibro-acoustic properties of an aircraft fuselage*, in *ISMA 2014 - International Conference on Noise and Vibration Engineering*, 2014, pp. 2731–2748.

[2] R. Winter, J. Biedermann, M. Böswald, and M. Wandel, *Dynamic characterization of the A400M acoustics fuselage demonstrator*, in *INTER-NOISE 2016*, 2016, pp. 3296-3306.

[3] J. Biedermann, R. Winter, M. Wandel, M. Böswald, and M. Sinapius, *Advanced correlation criteria for the mid frequency range*, in *INTER-NOISE 2016*, 2016, pp. 3307-3318.

[4] J. Biedermann, R. Winter, M. Norambuena, M. Böswald, and M. Wandel, *Classification of the mid-frequency range based on spatial fourier decomposition of operational deflection shapes*, in *24th International Congress on Sound and Vibration (ICSV24)*, 2017.

[5] R. Winter, J. Biedermann, and M. Norambuena, *High-resolution vibration measurement and analysis of the flight-lab aircraft fuselage demonstrator*, in *INTER-NOISE 2018*, 2018.

[6] P. Castellini, M. Martarelli, and E. Tomasini, *Laser doppler vibrometry: Development of advanced solutions answering to technology's needs*, *Mechanical Systems and Signal Processing*, vol. 20, no. 6, pp. 1265–1285, 2006, Special Issue: Laser Doppler Vibrometry.

[7] J. Bosbach and T. Dehne, *Propagation of localized, unsteady heat loads in aircraft cabin air flows*, *CEAS Aeronautical Journal*, vol. 7, no. 1, pp. 57–68, Mar. 2016.

[8] B. J. Halkon and S. Rothberg, *Correction of laser doppler vibrometry measurements affected by steering mirror vibration*, 2016.

Robust algorithm for optimal configuration of a multi-type network of sensors

Mohamed Khalil[1,2]**; Christoph Heinrich**[2]**; Roland Wüchner**[1]**; Kai-Uwe Bletzinger**[1]
[1] Chair of Structural Analysis, Technische Universität München
Arcisstrasse 21. D-80333 München
e-mail: **mohamed.khalil@tum.de**

[2] Corporate Technology, Siemens AG
Otto-Hahn-Ring 6, D-81739 München

Abstract
An optimal configuration of sensors that maximizes the insight on the structure is essential for reliable condition monitoring. This work presents an approach for optimally placing sensors of different types. The objective of the optimization process doesn't only search for sensor locations that maximize the information gain of each sensor type, but rather builds a network of sensors that collectively reduce the estimation error as their signals are fused to reconstruct the structure's state. Fitness criterion is derived for each sensor type by extending the classical effective independence approach. Based on that, measures of system's observability are used as a metric of information gain and uniqueness for the respective sensor arrangements. Numerical studies are presented to demonstrate the robustness and effectiveness of the method in finding the optimal configuration for an electric motor and a steel structure operating under typical loading conditions and anomalies.

1 Introduction

Advances in 3D simulation and modeling as well as high performance computing make it possible to push designs of complex components to the limit, where weight can be reduced and borne loads conditions can be maximized. With the emergence of Internet of Things (IoT) and the Digital Twin (DT) concept into the industrial field, simulation is progressively contributing to modeling various operating scenarios, while coupling their input and output ends to sensing and control systems to extend insight on the machinery, leverage control precision, and improve steering decisions. One application which can be incubated in a digital twin environment is the optimization of sensor placement to capture the responses of the structure. Such captured signals can be exploited in state estimation, failure identification, damage assessment, and other forms of on-line condition monitoring.

The estimate of the structure's state involves uncertainties resulting from the limitations of the mathematical/simulation models, and measurement error in the acquired signal. The reliability of such estimations is, thus, very sensitive to the properties of sensors feeding them with signals and their deployment. An influential parameter in such is the positioning of sensors with respect to the structure, as well as their arrangement relative to one another.

Related Literature

An optimal sensors configuration that maximizes the insight on the structure is a challenging problem, that has been attempted over the last decades. Many methodologies have been proposed to find the optimal sensor positions that minimize the estimation error between the actual structure's responses and their expected

values estimated by mathematical models. Various methods derive the objective estimation error to be minimized based on the Fisher Information Matrix (FIM). One of which is the modal kinetic energy (MKE) first proposed in [1]; where the locations of maximum response amplitudes are favored as optimal. In [2] and [3], the Effective Independence (EI) method was proposed, where the positions that increase the independence between the significant estimated mode shapes are chosen. In [4] and [5], the locations of sensors are based on minimizing the information entropy (IE) - a scalar measure representing the uncertainty in the estimated response. In [6], Zhang et al. have proposed a more elaborate way to define the optimality criteria, based on the covariance error in a generalized-state reconstructed using Kalman filter. A significant advancement in this approach of deriving the estimation error is its robustness to tackle problems involving multiple sensor types. A similar approach has been used in [7]. The drawback, however, is the exhaustive underlying mathematical derivation and its involvement of matrices inversion, making it a tedious approach for structures with large number of degrees of freedom (DOFs). In [8] and [9], the authors focus on optimal sensors placement for parameter estimation in a multi-physics system; namely thermo-elastic systems. When employed to find the optimal positions for a group of sensors, the aforementioned methods can be tackled through heuristic/-greedy optimization approaches, summarized in [10], by step-wise addition or subtraction of optimal sensor locations from a given candidate set of possible locations. Zhang et al. in [11] have employed a heuristic approach for a Kalman-filter-based error estimation measure. An alternative approach to reach the optimal set of sensors is using genetic algorithms [7, 12] by iteratively exploring the domain of candidate sensor positions to find the optimal set. Papadimitriou in [5] concludes that heuristic approaches generally show a computational advantage over genetic algorithms, as they require less number of computation and, as the algorithm progresses, the domain of computation gets progressively smaller.

Another category of optimality measures for sensor locations is based on the observability of the system, quantified by the smallest eigenvalue, determinant, or trace of the inverse of the system's observability matrix or Gramian, as presented in [13]. Van der Berg et al. [14] and Georges [15] have utilized the concept in various applications involving linear systems. Singh and Hahn in their work [16] have employed this approach for non-linear system, and proven that it can be related to the FIM. The advantage however is the ability to account for the dynamic behavior of certain processes, overcoming such shortcoming in FIM-based approaches. The formulation of a minimization problem including the measures of a non-linear observability Gramian is difficult, especially with large systems, making it a challenge to incorporate such an approach [17]. Accordingly, Serpas et al. proposed the empirical observability Gramian as a computationally effective, yet less complex equivalent, to substitute the true observability Gramian. In such, the same measurements of the observability Gramian mentioned above are employed. In [17], the convexity of the scalar measure of the empirical observability Gramian is exploited to formulate a mixed-integer gradient-based constrained optimization problem, and propose a solution algorithm to solve it using non-linear programming methods. Hinson in [18] addresses the issues arising when employing mixed-integer programming to large systems, and proposes solutions to relax and regularize the associated binary constraints.

An additional objective to be borne in mind when using FIM-based approaches for sensor placement is the uniqueness of the sensor information. In civil applications, e.g. buildings and bridges, where it is common to approximate the spatial and physical models of the structure by simplified mathematical models, e.g. beam or truss finite elements, this might be irrelevant since the spatial distance between the model's evaluation points (nodes in FEM context) guarantee the uniqueness of sensor information. This, however, is particularly important for structures described by mathematical models involving dense spatial discretization, e.g. non-isogeometric solid finite elements, where nodes can be closely positioned to one another to ensure the model's accuracy. Without considering the uniqueness of information as an objective, the FIM-based algorithm alone can result in clustered sensor positioning, which are chosen because they satisfy the formulation's *fitness* criteria (maximizing the FIM), yet don't account for the information correlation gained from the existing sensors and the sensor to be added to the optimal set. In this regard, different methods have been proposed to tackle this problem. Gibanica has extended Kammer's classical EI approach to reject positions contributing to redundant information based on the their corresponding contribution to the trace of the observability Gramian [19]. Feng et al. have derived a modal-shapes-based measure to evaluate the similarity between the modes observed by adding a new sensor to the optimal set and the already existing

optimal sensors [20]. Liu et al. in [21] have utilized the nodal contribution to the structure's stiffness matrix to evaluate its redundancy with respect to the existing optimal sensor positions.

Structure of Work

This work presents an approach for optimally placing sensors of different types; namely yet without losing generality, accelerometers, strain gages and displacement probes. As an optimal sensor configuration should minimize the estimation error between the expected and measured states, the objective of the optimization process doesn't only search for sensor locations that maximize the information gain for each sensor type, but rather builds a network of sensors, that collectively reduce the estimation error when their signals are fused to reconstruct the structure's state. This inherently considers maximizing the uniqueness of information obtained from the deployed sensor configuration.

In section 2, the problem statement for the multi-type optimal sensor placement is derived. First, a fitness criterion is defined for each sensor type by utilizing the classical effective independence approach. Based on the calculated fitness criteria, measures of system's observability are investigated to determine an adequate metric of both information gain and uniqueness for the respective sensor arrangements.

In section 3, numerical studies are presented to demonstrate the robustness and effectiveness of the method. An industrial example of this work in the field of rotary machines is exhibited by applying the algorithm on an electric motor operating under loading conditions and anomalies commonly experienced in ventilation applications. Another application of the algorithm is demonstrated through a steel structure subject to random ground vibrations.

2 Theoretical Formulation

Problem Statement

In systems theory, e.g. [22], the equation of motion describing the dynamics of a system, having n degrees of freedom (DOFs) and is getting excited by p inputs, is given by

$$\boldsymbol{M}\ddot{\boldsymbol{z}}(t) + \boldsymbol{V}\dot{\boldsymbol{z}}(t) + \boldsymbol{K}\boldsymbol{z}(t) = \boldsymbol{L}\boldsymbol{u}(t), \tag{1}$$

where $\boldsymbol{M}, \boldsymbol{V}, \boldsymbol{K} \in \mathbb{R}^{n\times n}$ are the system's mass, damping and stiffness matrices, respectively, $\boldsymbol{u} \in \mathbb{R}^p$ and $\boldsymbol{z} \in \mathbb{R}^n$ are the inputs and displacements vectors, respectively, and $\boldsymbol{L} \in \mathbb{R}^{n\times p}$ is the mapping matrix relating the system DOFs to the excitation inputs. The suffix (t) denotes the time dependency of displacements, and the $\dot{(\cdot)}$ and $\ddot{(\cdot)}$ operators denote the first and second time derivatives.

Applying the coordinate transformation $\boldsymbol{z} = \boldsymbol{\Phi}\boldsymbol{q}$ and pre-multiplying eq. (1) by $\boldsymbol{\Phi}$, where $\boldsymbol{\Phi} \in \mathbb{R}^{n\times n}$ is the mass-normalized mode shapes matrix (obtained by performing an eigenvalue analysis on the undamped system in eq. (1)), results in the modal representation of the equation of motion, given by

$$\ddot{\boldsymbol{q}} + 2\boldsymbol{\Xi}\boldsymbol{\Omega}\dot{\boldsymbol{q}}(t) + \boldsymbol{\Omega}^2\boldsymbol{q} = \boldsymbol{\Phi}^{\mathsf{T}}\boldsymbol{L}\boldsymbol{u}(t), \tag{2}$$

where $\boldsymbol{\Xi} \in \mathbb{R}^{n\times n}$ and $\boldsymbol{\Omega} \in \mathbb{R}^{n\times n}$ are diagonal matrices holding the modal damping ratios ξ_i, and modal eigen frequencies ω_i, where $i \in \{1..n\}$. Deriving the state-space representation of the equation of motion based on the modal representation, the system dynamics are described as

$$\begin{gathered}\boldsymbol{x}(t) = \begin{Bmatrix}\boldsymbol{q}(t)\\ \dot{\boldsymbol{q}}(t)\end{Bmatrix},\ \boldsymbol{y}(t) = \begin{Bmatrix}\boldsymbol{x}(t)\\ \boldsymbol{\varepsilon}(t)\\ \ddot{\boldsymbol{x}}(t)\end{Bmatrix}\\ \dot{\boldsymbol{x}}(t) = \boldsymbol{A}\boldsymbol{x}(t) + \boldsymbol{B}\boldsymbol{u}(t)\\ \boldsymbol{y}(t) = \boldsymbol{C}\boldsymbol{x}(t) + \boldsymbol{D}\boldsymbol{u}(t)\end{gathered} \tag{3}$$

where the system matrices are defined as:

$$\boldsymbol{A} = \begin{bmatrix} \boldsymbol{0} & \boldsymbol{I} \\ -\boldsymbol{\Omega}^2 & -2\boldsymbol{\Xi}\boldsymbol{\Omega} \end{bmatrix}, \qquad \boldsymbol{B} = \begin{bmatrix} \boldsymbol{0} \\ \boldsymbol{\Phi}^{\mathsf{T}}\boldsymbol{L} \end{bmatrix},$$
$$\boldsymbol{C} = \begin{bmatrix} \boldsymbol{\Phi} & \boldsymbol{0} \\ \boldsymbol{\Psi} & \boldsymbol{0} \\ -\boldsymbol{\Phi}\boldsymbol{\Omega}^2 & -2\boldsymbol{\Phi}\boldsymbol{\Xi}\boldsymbol{\Omega} \end{bmatrix}, \quad \boldsymbol{D} = \begin{bmatrix} \boldsymbol{0} \\ \boldsymbol{0} \\ \boldsymbol{\Phi}\boldsymbol{\Phi}^{\mathsf{T}}\boldsymbol{L} \end{bmatrix}, \tag{4}$$

where $\boldsymbol{A} \in \mathbb{R}^{2n\times 2n}$, $\boldsymbol{B} \in \mathbb{R}^{2n\times p}$, $\boldsymbol{C} \in \mathbb{R}^{m\times 2n}$ and $\boldsymbol{D} \in \mathbb{R}^{m\times p}$ are the state, input, output and transmission matrices, respectively, m is the number of outputs, and $\boldsymbol{\Psi} \in \mathbb{R}^{n\times n}$ is the strain mode shapes matrix. Due to the measurement noise associated with real applications, a discrepancy between the actual output of the system $\boldsymbol{y}^{(a)}$, and the estimated output $\boldsymbol{y}^{(e)}$ is prone to exist. The measurement noise is denoted by $\boldsymbol{v} \in \mathbb{R}^m \sim N(0, \boldsymbol{R})$, where $\boldsymbol{R} = r\boldsymbol{I}, \boldsymbol{I} \in \mathbb{R}^m$ is the noise covariance, assuming that the noise at each sensor r is identical to and independent from others. Herein, the covariance matrix of the estimation error $\boldsymbol{P}$ can be defined as

$$\boldsymbol{P} = \mathbb{E}\left[\left(\boldsymbol{y}^{(a)} - \boldsymbol{y}^{(e)}\right)\left(\boldsymbol{y}^{(a)} - \boldsymbol{y}^{(e)}\right)^{\mathsf{T}}\right] = \overset{\text{simplifying to}}{\cdots} = \left[\boldsymbol{\Phi}^{\mathsf{T}} R^{-1}\boldsymbol{\Phi}\right]^{-1} = \frac{1}{r}\left[\boldsymbol{\Phi}^{\mathsf{T}}\boldsymbol{\Phi}\right]^{-1} = \boldsymbol{Q}^{-1}, \tag{5}$$

where $\boldsymbol{Q}$ is the known Fisher Information Matrix (FIM). Hence, the reduction in the estimation covariance is directly related to, and can be achieved through maximizing the FIM; precisely one of its norm measures, e.g. the determinant. In most cases, the noise term r is dropped from the formulation of $\boldsymbol{Q}$, thus reducing the definition in eq. (5) to $\boldsymbol{Q} = \boldsymbol{\Phi}^{\mathsf{T}}\boldsymbol{\Phi}$.

Optimal Sensor Placement

Exploiting the mathematical model of the structure, different input vectors, corresponding to different operation modes, can be simulated and the estimated system's output $\boldsymbol{y}^{(e)}(t)$ can be evaluated. Adopting a time space discretization scheme, as common in many transient FE solvers, the output can be evaluated only at distinct time steps $t_i \in \{t_1, t_2, .., t_s\}$ that can sufficiently describe the dynamics of the system.

Let $\boldsymbol{Y} = [\boldsymbol{y}_1, \boldsymbol{y}_2, .., \boldsymbol{y}_s] \in \mathbb{R}^{n\times s}$ be the matrix of responses snapshots captured at discrete time steps. The column space spanning $\boldsymbol{Y}$ can be represented in a reduced space in terms of d linearly-independent columns $\boldsymbol{U}_f \in \mathbb{R}^{n\times d}$, if a proper set of the snapshots is chosen, where $d = \min(n, s)$ [23]. Singular value decomposition (SVD) guarantees the existence of real, positive eigenvalues $\sigma_1 > \sigma_2 > .. > \sigma_d > 0$, and two sets of orthogonal basis vectors $\boldsymbol{U}_f \in \mathbb{R}^{n\times d}$ and $\boldsymbol{Z}_f \in \mathbb{R}^{s\times d}$ such that

$$\boldsymbol{Y} = \boldsymbol{U}_f\, \boldsymbol{\Sigma}_f\, \boldsymbol{Z}_f^{\mathsf{T}}; \quad \boldsymbol{\Sigma}_f = \text{diag}(\sigma_1, \sigma_2, .., \sigma_d) \in \mathbb{R}^{d\times d} \tag{6}$$

According to [24], for such a set of snapshots $\boldsymbol{Y}$, having orthogonal basis vectors $\boldsymbol{U}_f$ and $\boldsymbol{Z}_f$, there exists a reduced sub-space represented by fewer basis vectors $\boldsymbol{U}_r$ that can express the data contained in $\boldsymbol{Y} \in \mathbb{R}^{n\times r}$ and $\boldsymbol{Z}_r \in \mathbb{R}^{s\times r}$, whose components are given by

$$\begin{aligned} \boldsymbol{U}_{r,\,ij} &= \boldsymbol{U}_{f,\,ij} \quad \text{for } i \in \{1..n\}\ ,\ j \in \{1..r\}, \\ \boldsymbol{Z}_{r,\,ij} &= \boldsymbol{Z}_{f,\,ij} \quad \text{for } i \in \{1..s\}\ ,\ j \in \{1..r\}, \end{aligned} \tag{7}$$

where r is defined as

$$\sigma_1 > \sigma_2 > .. > \sigma_r \gg \sigma_{r+1} > .. > \sigma_d \quad i \in \{1..d\}, \quad \text{such that } \delta(r) = \frac{\sum_{i=1}^{r}\sigma_i}{\sum_{i=1}^{d}\sigma_i} \approx 1 \tag{8}$$

In [25], Park and Kim have proven that for an existent $\boldsymbol{Y}$, the formulation of FIM in eq. (5) can be re-written based on the SVD set of vectors $\boldsymbol{U}_f$, given as $\boldsymbol{Q} = \boldsymbol{U}_f^{\mathsf{T}}\boldsymbol{U}_f$. Introducing the definition of reduced

basis vectors in eq. (7) (which, from here on, will be referred to as $\boldsymbol{U}$, without the subscript r, for notation simplicity), $\boldsymbol{Q}$ can eventually be defined as

$$\boldsymbol{Q} = \boldsymbol{U}^{\mathsf{T}}\boldsymbol{U} \tag{9}$$

In relation to the optimal sensor placement problem, the minimum number of sensors N_{min} should equal to the reduced number of basis vectors r representing the structure's responses; $N_{min} \geq r$.

To identify minimal set of optimal sensors indices $\mathcal{S}_{min}$, the definition of effective independence (EI) is recalled. From the matrix $\boldsymbol{U}$, a projection matrix $\boldsymbol{P} \in \mathbb{R}^{n\times n}$ can be defined, whose diagonal terms are proportional to the leverage gained by each estimated value, $\boldsymbol{y}^{(e)}$, on its actual measurement, $\boldsymbol{y}^{(a)}$, in eq. (3) [10]. From this definition, the EI values are defined as

$$\boldsymbol{E} = \text{diag}\left(\boldsymbol{P}\right) = \text{diag}\left(\boldsymbol{U}\boldsymbol{Q}^{\text{-1}}\boldsymbol{U}^{\mathsf{T}}\right) \tag{10}$$

The purpose, however, of utilizing the EI is not to determine the final solution, but rather to filter the minimal set of optimal sensors indices, $\mathcal{S}_{min}$. $\mathcal{S}_{min}$ is defined as the subset of the candidate nodal indices, $\mathcal{S}_c$, at which the EI value is maximum for each EI iteration, where $\mathcal{S}_{min} \subseteq \mathcal{S}_c \subseteq \mathcal{S}_f,\ \mathcal{S}_f = \{1, 2, .., n\}$. The process of determining $\mathcal{S}_{min}$ through EI iterations is described in full detail in literature such as [2], [26] and [27], and a similar approach would be applied in this work on the definition in eq. (10).

Given the objective of the work to determine an optimal configuration of positions for different sensor types, the filtering process of the minimum set of optimal indices should be repeated for each sensor type; that's determine the minimal set of optimal sensor positions to monitor a given physical response. The sets would be denoted $\mathcal{S}^{\vartheta}_{min}$, where the superscript $\vartheta \in \Theta = \{\boldsymbol{x}, \boldsymbol{\varepsilon}, \ddot{\boldsymbol{x}}\}$ distinguishes the corresponding measured physical properties. It should be understood that any $\mathcal{S}^{\vartheta}_{min}$ is a sub-optimal solution for our problem, and that uniqueness of information within such sub-optimal solution could not be guaranteed, as it is possible for a certain index to be present in more than one $\mathcal{S}^{\vartheta}_{min}$; i.e. sensors of different types could end up being placed at the same position.

Attempting to find the optimal configuration comprising different sensor types is achieved through exploiting the properties of the observability Gramian, $\boldsymbol{W}_o$, of the linear time-invariant system in eq. (3), evaluated by solving the following discrete Lyapunov equation [28]

$$\boldsymbol{A}^{\mathsf{T}}\boldsymbol{W}_o\boldsymbol{A} - \boldsymbol{W}_o = -\boldsymbol{C}^{\mathsf{T}}\boldsymbol{C} \tag{11}$$

According to [22], for a given linear time-invariant system, the system is considered observable if observability Gramian $\boldsymbol{W}_o$ is non-singular. The Gramian characterizes the degree of observability, or correspondingly unobservability [29], of the system, through quantifying how far $\boldsymbol{W}_o$ is from being singular. Various Gramian norm functions can be defined to measure the observability of the system, e.g. the determinant, the condition number, the max-to-min singular value ratio, the trace [29]. In [30], Hinson has demonstrated the adequacy of using those observability measures as metrics for the optimality of the sensor placement. Their adequacy is proven on the basis of the inherent relationship between the effective independence and the different metrics of the estimation error ellipsoid, and their relation to the covariance matrix of estimation error of the system in eq. (5). Herein, the optimal sensor placement problem is an optimization problem with an objective to find an optimal set of indices $\mathcal{S}_o$ of the system output matrix $\boldsymbol{C}$ including information about the locations and the types of the sensors. This can be formulated as

$$\begin{gathered}\mathcal{S}_o = \underset{i\in n, j\in\Theta}{\arg\max}\ \varphi\left(\boldsymbol{W}_o(\tilde{\boldsymbol{C}})\right) \neq \{\phi\}, \quad \tilde{\boldsymbol{C}} = \left(C^l_k\right) \forall\ (k,l) \in \tilde{\mathcal{S}} \\ \tilde{\mathcal{S}} = \bigcup_{\vartheta\in\Theta} \tilde{\mathcal{S}}^{\vartheta}_{min}, \quad \tilde{\mathcal{S}}^{\vartheta}_{min} \in \mathcal{C}^{\vartheta}_{min} = \{\phi\} \cup C\begin{pmatrix}\mathcal{S}^{\vartheta}_{min} \\ \nu\end{pmatrix}\ \forall\ \nu \in \{1, ..., N^{\vartheta}_{min}\},\end{gathered} \tag{12}$$

where $\{\phi\}$ is the empty set, $\bigcup_{\vartheta}$ is the set union operator running over all sensor types, $C\begin{pmatrix}\mathcal{S}^{\vartheta}_{min} \\ \nu\end{pmatrix}$ is the set of combinations of ν elements in the set of minimum optimal indices of the sensor type ϑ, N^{ϑ}_{min} is

minimum number of sensors of the corresponding type and $\tilde{\mathcal{S}}^{\vartheta}_{min}$ is an element of the union set containing the aforementioned combinations and the empty set. $\varphi\left(\boldsymbol{W}_o(\tilde{\boldsymbol{C}})\right)$ is a Gramian norm function, where the Gramian is calculated by solving eq. (11) given the test output matrix $\tilde{\boldsymbol{C}}$, holding only rows corresponding to the sensor types and locations dictated by $\tilde{\mathcal{S}}$.

The complete workflow of the proposed method to find an optimal network of multi-type sensors is summarized in algorithm 1.

Algorithm 1 Algorithm for the Optimal Sensor Placement Problem

1: Define the set of sensor types, $\Theta = \{\theta_1, \theta_2, ...\}$.
2: Define the set of candidate sensor indices for each sensor type, $\mathcal{S}^{\vartheta}_c$.
3: Build the state space system of equations in eq. (3).
4: **procedure** FILTER THE SETS OF MINIMUM OPTIMAL POSITIONS, $\mathcal{S}^{\vartheta}_{min}$
5: **for all** $\vartheta \in \Theta$ **do**
6: Solve eq. (3) for s time steps to build the matrix of response snapshots, $\boldsymbol{Y} = [\boldsymbol{y}_1, \boldsymbol{y}_2, .., \boldsymbol{y}_s]$.
7: Solve the SVD problem in eq. (6); $\boldsymbol{Y} = \boldsymbol{U}_f\, \boldsymbol{\Sigma}_f\, \boldsymbol{Z}_f^{\mathsf{T}}$.
8: Reduce $\boldsymbol{U}_f$ to $\boldsymbol{U}_r = \boldsymbol{U}$, according to eq. (7).
9: Apply a proper EI algorithm to eq. (10) to find $\mathcal{S}^{\vartheta}_{min}$
10: **end for**
11: **end procedure**
12: **procedure** FIND THE OPTIMAL SENSOR COMBINATION, $\mathcal{S}_o$
13: Generate the sets of possible *filtered* sensor combinations, $\mathcal{C}^{\vartheta}_{min}\ \forall\ \vartheta \in \Theta$
14: **for all** $\tilde{\mathcal{S}}^{\vartheta}_{min} \in \mathcal{C}^{\vartheta}_{min}$ **do**
15: Generate a network of sensors, $\tilde{\mathcal{S}} = \bigcup_{\vartheta \in \Theta} \tilde{\mathcal{S}}^{\vartheta}_{min}$
16: Build the selected output matrix, $\tilde{\boldsymbol{C}}$
17: Evaluate and store the Gramian norm function, $\varphi\left(\boldsymbol{W}_o(\tilde{\boldsymbol{C}})\right)$
18: **end for**
19: Identify the sensor network $\mathcal{S}_o$ corresponding to the highest value of φ
20: **end procedure**

The method proposed here outperforms the classic EI approach by introducing the influence of sensor output combination on the estimation error. In addition, the FIM-based approaches fail to describe the dynamics of the system. Both drawback are proposed to be overcome by observability-based approaches [18]. Comparing the proposed method to the observability-based approaches for linear, time-invariant systems in [14] and [15], one can see that the sheer effort of formulating a discrete gradient-based optimization problem and deriving a consistent objective function derivative with respect to the design variables is spared. Even the empirical Gramian evaluation proposed by [16] can be seemingly more exhaustive, since the empirical functional has to evaluated at each DOF of the system. This can be computationally costly, especially in real-world applications, where systems with large number of DOFs can be typically encountered. On the other hand, through the pre-requisite filtering process, the size of the problem can reduced down drastically to $m \ll n$ DOFs.

3 Numerical Investigation

The proposed algorithm for finding the optimal sensor configuration can be used for industrial various applications. In this section, two demonstration examples, a steel structure and an electric motor, are presented to investigate the efficiency of the method in maximizing the system's observability. An intuitive interpretation of the results of the algorithm is also discussed for each case.

Electric Motor

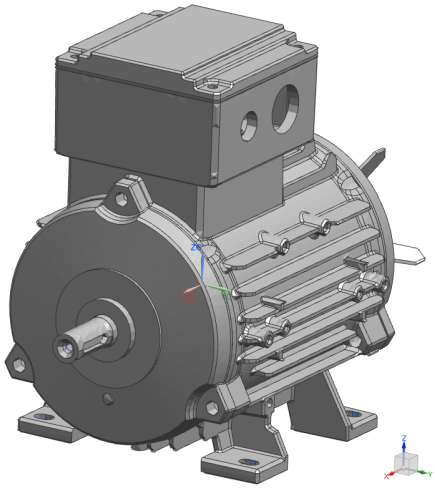


Figure 1: Electric Drive

The first investigated example is a 250-Watts asynchronous electric drive, see fig. 1, typically used for ventilation applications and domestic appliances. The drive's four feet are fully supported, an 8 N.m torque is exerted on its shaft's drive end. The intention of this sensor deployment is to be able to monitor the health condition of the motor during operation and identify the presence of failures. One of the most frequent failures a motor is prone to is misalignment in its shaft's drive-end. This in turn can cause severe overloading on the bearings and high cyclic loading on the shaft's root, both which can in practice drastically shorten the life of the motor in service. In this case, the drive is subjected to a 0.1 mm parallel misalignment at its drive-end, simulated by the external excitation.

For this investigation, finding the optimal network is attempted given three sets of sensor; (a) a set of only uni-axial accelerometers in x-, y-, and z-directions, (b) a set of only uni-axial strain gauges oriented in x-, y- and z-directions, and (c) a set of both uni-axial accelerometers and uni-axial strain gauges. The purpose of this study is to examine the extent to which the proposed algorithm can reduce the hardware required for observing the structure's. The initial unfiltered result of eq. (10); i.e. the nodes corresponding to the minimal set of sensors indices for each sensor type $\mathcal{S}^{\vartheta}_{min}$, are summarized in tables 1 to 3, along with evolution of each set when the network optimization problem in eq. (12) is solved to obtain $\mathcal{S}_o$. Additionally, the second and third best network configurations are also listed, denoted by the subscript suffixes, 2 and 3, respectively. The positions of the sensors on the motor's housing are displyed in fig. 2

Table 1: Initial optimal set for each sensor type $\mathcal{S}^{\vartheta}_{min}$ and final optimal network configuration $\mathcal{S}_o$ for attempt (a)

		Initial Sets	**Optimal Networks**		
Sensor type	ϑ	$\mathcal{S}^{\vartheta}_{min}$	$\mathcal{S}_o$	$\mathcal{S}_{o,2}$	$\mathcal{S}_{o,3}$
accelerometer x	$\ddot{\boldsymbol{z}}_x$	319413	319413	319413	-
accelerometer y	$\ddot{\boldsymbol{z}}_y$	323914	323914	-	323914
accelerometer z	$\ddot{\boldsymbol{z}}_z$	307903	307903	307903	307903
$\varphi(\boldsymbol{W}_o)$		-1.05×10^{-3}	-1.05×10^{-3}	-1.06×10^{-3}	-1.06×10^{-3}

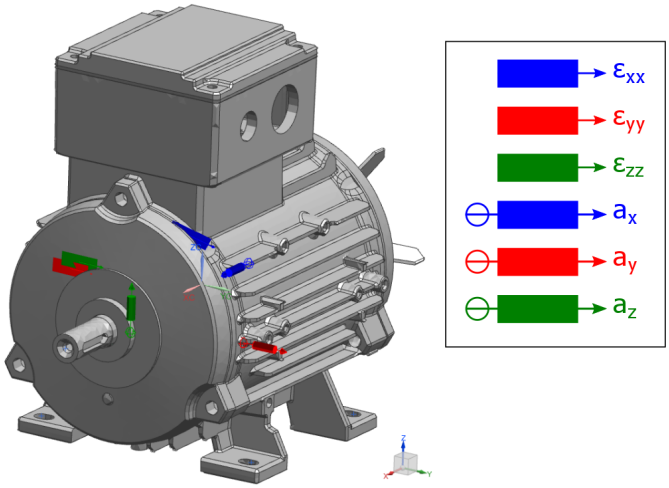


Figure 2: Positions of the initial set of sensors on the electric drive

Table 2: Initial optimal set for each sensor type $\mathcal{S}^{\vartheta}_{min}$ and final optimal network configuration $\mathcal{S}_o$ for attempt (b)

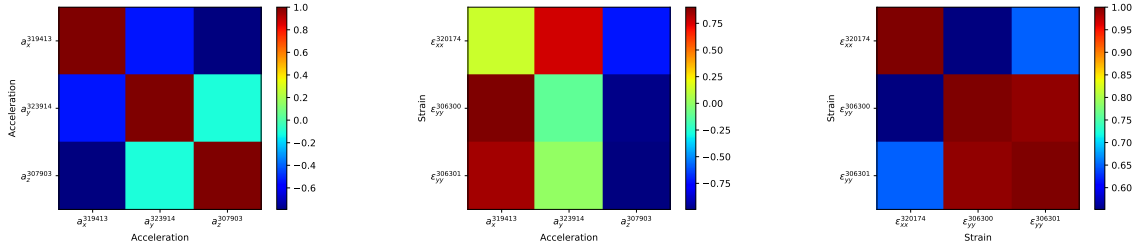
		Initial Sets	**Optimal Networks**		
Sensor type	ϑ	$\mathcal{S}^{\vartheta}_{min}$	$\mathcal{S}_o$	$\mathcal{S}_{o,2}$	$\mathcal{S}_{o,3}$
strain gauge xx	ε_{xx}	320174	320174	-	320174
strain gauge yy	ε_{yy}	306300	306300	306300	-
strain gauge zz	ε_{zz}	306301	306301	306301	306301
$\varphi(\boldsymbol{W}_o)$		4.6×10^{-4}	4.6×10^{-4}	4.55×10^{-4}	4.54×10^{-4}

It is clear from tables 1 and 2 that trying to find a further optimal configuration of sensors using eq. (12) after applying the EI algorithm doesn't change the results. Even the second and the third optimal configurations are only one-sensor different from the optimal one. That is explained by the relationship between the observability Gramian, and correspondingly its metrics, and the Fisher Information Matrix $\boldsymbol{Q}$ in eq. (5), which the objective of the EI approach is to maximize. On the other hand, observing the configurations in table 3, a significant reduction in the sensors required can be observed between the individual sets generated by EI and the optimal and two sub-optimal sets. When attempting to deploy sensors to monitor different signal types, the EI has the shortcoming that it can only handle the reduction of estimation covariance for the different sensors independently. The observability metrics, on the other hand, overcome such a deficiency, as they consider the presence of other system outputs.

Figure 3 shows the correlation between accelerometers' signals, and strain gauge signals. Let a^i_x denote the acceleration signal in x-direction at node i, and respectively for other signals. Figure 3b shows an existent correlation between the the strain signals y and z, and the acceleration signals in x and z. It also shows another correlation between the strain signal x and the acceleration signals y and z. Although the correlation between the acceleration signals is not as high, yet, the redundancy of information in the acceleration signals with respect to the strain signals can be observed. This explains the rejection of the accelerometers from the optimal configuration in table 1. A strong correlation can be also observed between the strain signals in y- and z-directions. Referring to fig. 2, this can be explained by the close spatial positioning of the two sensors. In theory, either of those two sensors could have been excluded as well since it is not adding any unique information about the structure's strain behavior. Exactly these are the two sub-optimal configurations in table 3, with a reduction in the objective function of 1 %.

Table 3: Initial optimal set for each sensor type $\mathcal{S}_{min}^{\vartheta}$ and final optimal network configuration $\mathcal{S}_o$ for attempt (c)

		Initial Sets	**Optimal Networks**		
Sensor type	ϑ	$\mathcal{S}_{min}^{\vartheta}$	$\mathcal{S}_o$	$\mathcal{S}_{o,2}$	$\mathcal{S}_{o,3}$
accelerometer x	$\ddot{z}_x$	319413	-	-	-
accelerometer y	$\ddot{z}_y$	323914	-	-	-
accelerometer z	$\ddot{z}_z$	307903	-	-	-
strain gauge xx	ε_{xx}	320174	320174	320174	320174
strain gauge yy	ε_{yy}	306300	306300	306300	-
strain gauge zz	ε_{zz}	306301	306301	-	306301
$\varphi(\boldsymbol{W}_o)$		-1.04×10^{-3}	4.6×10^{-4}	4.55×10^{-4}	4.54×10^{-4}



(a) acc. vs. acc. **(b)** acc. vs. SG **(c)** SG vs. SG

Figure 3: Cross-correlation between the electric drive signals

As mentioned before in section 2, the number pf modes resulting from the SVD of the snapshots corresponds to the least number of sensors required to observe the system. Hence, a trivial approach to configure an optimal sensor network would be to compile all results from eq. (10); i.e. position sensors at their corresponding locations for each sensor type. However, it can be shown from table 3 that considering the dependency of sensor positions on one another in proposed method results in notably less number of sensors than the least requirement when the dependency between sensors is overlooked.

Steel Structure

The steel structure shown in fig. 4 consists of an arrangement of connected I-beams. The structure dimensions are $4\ m \times 5\ m \times 9\ m$, and its four bottom nodes are subject to the 10-seconds long random displacement excitation shown in fig. 5 in the Y-direction of an amplitude varying between -1 and 1 mm.

For this example, the sensor pool investigated consisted of three uni-axial accelerometers (x-, y-, z-directions) and a uni-axial strain gauge in the x-direction. Similar to the previous investigation example, the network consisting of all initial sets of individual sensors $\mathcal{S}_{min}^{\vartheta}$, the optimal network as well as the second and third optimal networks are compared. The results are summarized in table 4.

The optimization algorithm in eq. (12) iterated over 255 sensor combinations. The advantage of the algorithm is clearly indicated by the significant reduction in the hardware required to maximize the system's observability. For an optimal configuration, only the strain gauges were necessary, and the accelerometers were all rejected. As well, none of the second and third optimal network did comprise any accelerometers. The locations of the sensors resulting from the initial and the optimal sets are shown in fig. 6.

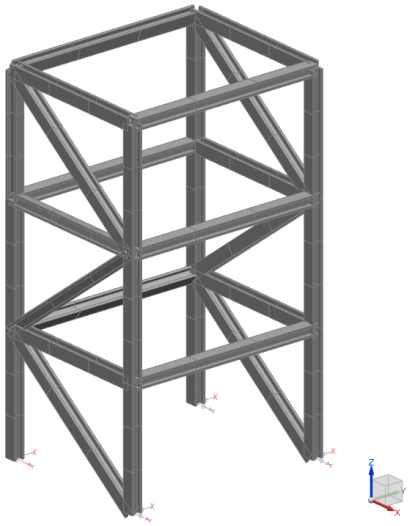


Figure 4: Steel Structure

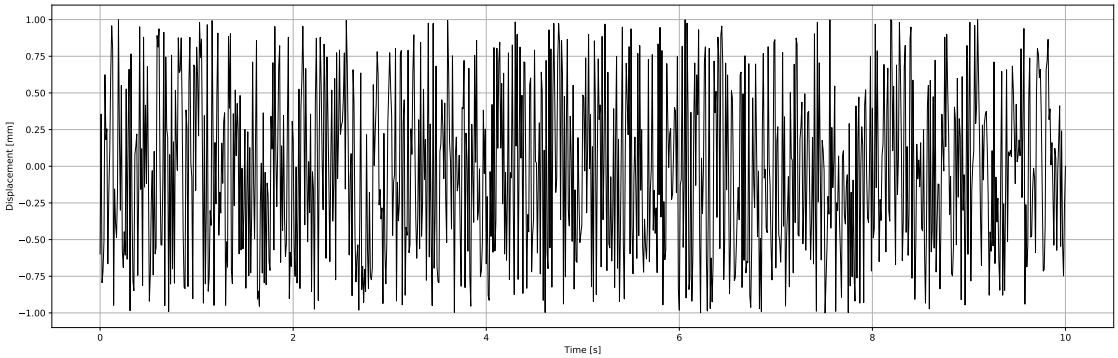
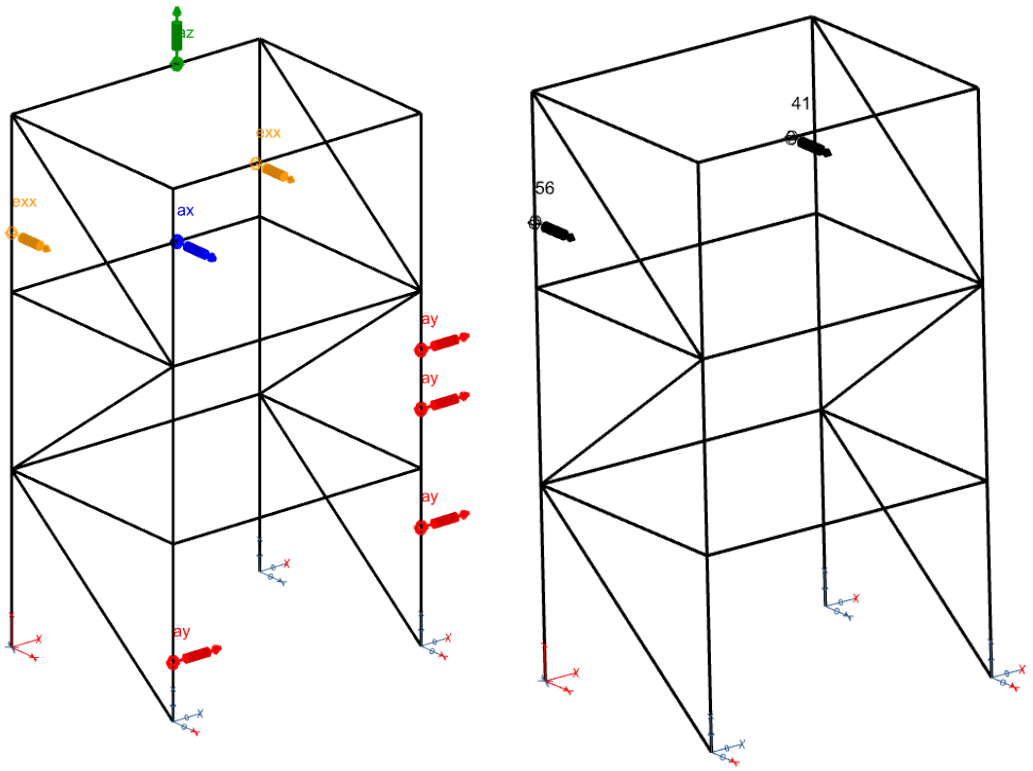


Figure 5: Random excitation signal



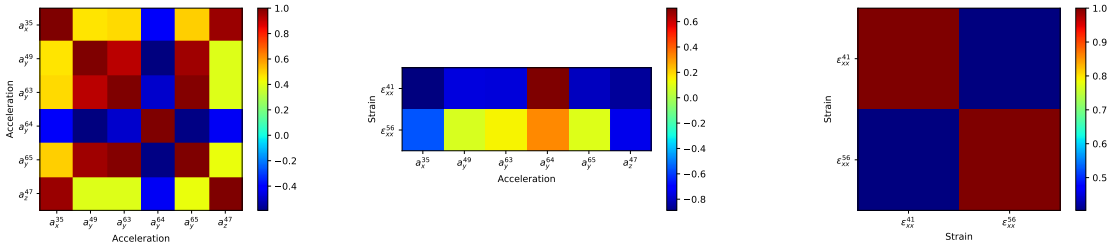
(a) Initial network **(b)** Optimal network

Figure 6: Positions of sensors on the steel structure

Table 4: Initial optimal set for each sensor type $\mathcal{S}_{min}^{\vartheta}$ and final optimal network configuration $\mathcal{S}_o$

		Initial Sets	**Optimal Networks**		
Sensor type	ϑ	$\mathcal{S}_{min}^{\vartheta}$	$\mathcal{S}_o$	$\mathcal{S}_{o,2}$	$\mathcal{S}_{o,3}$
accelerometer x	$\ddot{\boldsymbol{z}}_x$	35	-	-	-
accelerometer y	$\ddot{\boldsymbol{z}}_y$	49, 63, 64, 65	-	-	-
accelerometer z	$\ddot{\boldsymbol{z}}_z$	47	-	-	-
strain gauge xx	ε_{xx}	41, 56	41, 56	41	56
$\varphi(\boldsymbol{W}_o)$		-4.69×10^{-3}	1.07×10^{-3}	1.05×10^{-3}	1.01×10^{-3}

In contrast to what would be presumed, table 4 shows that the observability metric $\varphi(\boldsymbol{W}_o)$ increases notably when the accelerometers are removed from the network. This can be interpreted by examining the correlation coefficients between the signals. Figure 7 shows the correlation between accelerometers' signals, and strain gauge signals. Let a_x^{35} denote the acceleration signal in x-direction at node 35, and respectively for other signals. It is clearly shown the correlation coefficients are notably high between different accelerometers, indicating a large correlation (positive or negative) among accelerometers' signals. Additionally, correlation can be observed between the strain gauge signal at node 41 and the accelerometers' signals. One can hence conclude that the additional information obtained from the accelerometers are redundant with respect to one another, and with respect to the strain gauge at node 41. In comparison, the cross-correlation coefficients between the two strain gauges responses in fig. 7c indicates almost no correlation between the two signals, hence no redundancy of information resulting from adding the second strain gauge. This result goes in line with the inherent property of the observability metrics as being a viable measure of information redundancy, as well as a measure of system observability [30].



(a) acc. vs. acc. **(b)** acc. vs. SG **(c)** SG vs. SG

Figure 7: Cross-correlation between the signals of the steel structure

4 Conclusion

In this paper, a method was proposed to optimally configure a network of sensors of multiple types; namely, accelerometers, displacement probes, and strain gauges. The method is based on the simulation results of the structure's behavior under given operating conditions and excitation loads. The method runs in two steps: first, an initial set of sensors for each type are independently obtained using the classic EI approach, from which sensor network configurations are created. Following, observability metrics are used as objective functions to evaluate the respective configurations. The proposed method was evaluated on two industrial applications; an electric drive and a steel structure under typical operating conditions. The results have demonstrated the strength of the method to configure multi-type sensor networks and exclude sensors with redundant information. Additionally, it has been shown that the method is able to propose sensor networks

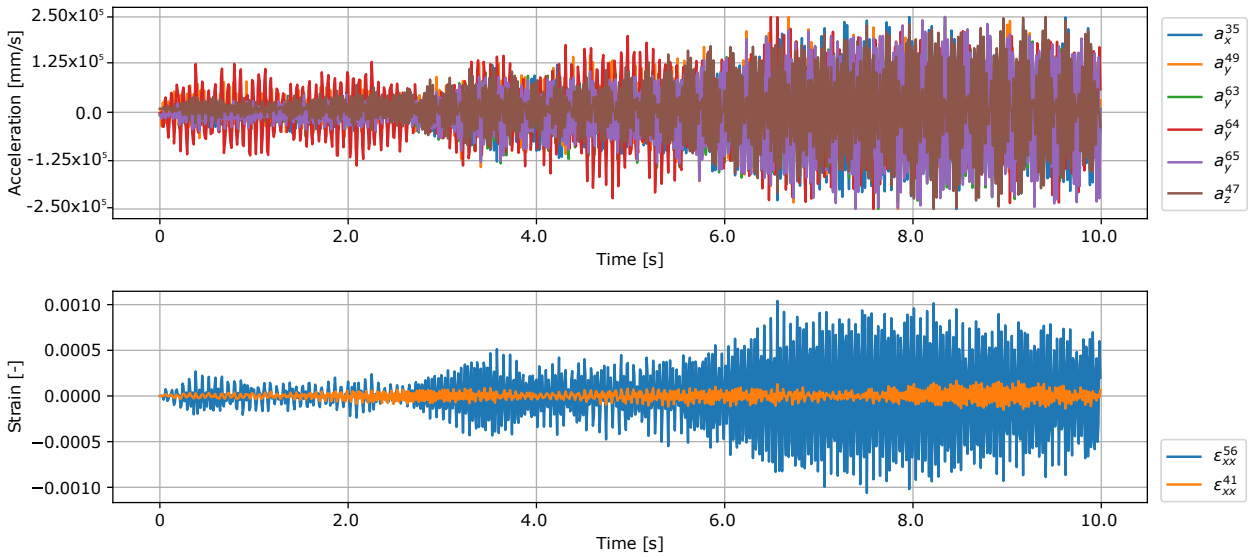


Figure 8: Output signals for accelerometers (top) and strain gauges (bottom) at the different positions of the initial sensor set $\mathcal{S}_{min}^{\vartheta}$

containing less hardware when compared to methods that find optimal sensor positions individually without accounting for the dependency among sensors.

In the context of this work, the approach was only derived for uni-axial sensors; i.e. the sensor positions are spatially independent. This is not the case for tri-axial accelerometers and strain-gauge rosettes, which are frequently used in industrial applications for structural health monitoring. Further, as an outlook, the efficiency of the method should also be investigated in finding the optimal sensor configuration for state estimation of the structure.

References

[1] D. C. Kammer, "Sensor placement for on-orbit modal identification and correlation of large space structures," *Journal of Guidance, Control, and Dynamics*, vol. 14, no. 2, pp. 251–259, 1991.

[2] D. C. Kammer and R. Brillhart, "Optimal sensor placement for modal identification using system-realization methods," *Journal of guidance, control, and dynamics*, vol. 19, no. 3, pp. 729–731, 1996.

[3] D. C. Kammer and M. L. Tinker, "Optimal placement of triaxial accelerometers for modal vibration tests," *Mechanical systems and signal processing*, vol. 18, no. 1, pp. 29–41, 2004.

[4] C. Papadimitriou and G. Lombaert, "The effect of prediction error correlation on optimal sensor placement in structural dynamics," *Mechanical Systems and Signal Processing*, vol. 28, no. 4, pp. 105–127, 2012.

[5] C. Papadimitriou, "Optimal sensor placement methodology for parametric identification of structural systems," *Journal of sound and vibration*, vol. 278, no. 4, pp. 923–947, 2004.

[6] C. Zhang and Y. Xu, "Optimal multi-type sensor placement for response and excitation reconstruction," *Journal of Sound and Vibration*, vol. 360, pp. 112–128, 2016.

[7] J.-F. Lin, Y.-L. Xu, and S.-S. Law, "Structural damage detection-oriented multi-type sensor placement with multi-objective optimization," *Journal of Sound and Vibration*, vol. 422, pp. 568–589, 2018.

[8] R. Herzog, I. Riedel, and D. Ucinski, "Optimal sensor placement for joint parameter and state estimation problems in large-scale dynamical systems with applications to thermo-mechanics." TU Chemnitz, 2017.

[9] P. Benner, R. Herzog, N. Lang, I. Riedel, and J. Saak, "Comparison of model order reduction methods for optimal sensor placement for thermo-elastic models." TU Chemnitz, 2017.

[10] D. Li, *Sensor placement methods and evaluation criteria in structural health monitoring*. PhD thesis, Universitat Siegen, 2012.

[11] J. Zhang, G. D. Roeck, E. Reynders, and G. Lombaert, "Optimal sensor placement for modal identification of repetitive structures," in *Proceedings of ISMA 27*, (Leuven, Belgium), pp. 2355–2364, the International Conference on Noise and Vibration Engineering, September 2016.

[12] U. Muthuraman, M. S. Hashita, N. Sakthieswaran, P. Suresh, M. R. Kumar, and P. Sivashanmugam, "An approach for damage identification and optimal sensor placement in structural health monitoring by genetic algorithm technique," *Circuits and Systems*, vol. 7, no. 06, p. 814, 2016.

[13] P. Müller and H. Weber, "Analysis and optimization of certain qualities of controllability and observability for linear dynamical systems," *Automatica*, vol. 8, no. 3, pp. 237–246, 1972.

[14] F. Van den Berg, H. Hoefsloot, H. Boelens, and A. Smilde, "Selection of optimal sensor position in a tubular reactor using robust degree of observability criteria," *Chemical engineering science*, vol. 55, no. 4, pp. 827–837, 2000.

[15] D. Georges, "The use of observability and controllability gramians or functions for optimal sensor and actuator location in finite-dimensional systems," in *Decision and Control, 1995., Proceedings of the 34th IEEE Conference on*, vol. 4, pp. 3319–3324, IEEE, 1995.

[16] A. K. Singh and J. Hahn, "On the use of empirical gramians for controllability and observability analysis," in *American Control Conference, 2005. Proceedings of the 2005*, pp. 140–141, IEEE, 2005.

[17] M. Serpas, G. Hackebeil, C. Laird, and J. Hahn, "Sensor location for nonlinear dynamic systems via observability analysis and max-det optimization," *Computers & Chemical Engineering*, vol. 48, pp. 105–112, 2013.

[18] B. T. Hinson and K. A. Morgansen, "Observability-based optimal sensor placement for flapping airfoil wake estimation," *Journal of Guidance, Control, and Dynamics*, vol. 37, no. 5, pp. 1477–1486, 2014.

[19] M. Gibanica, T. J. Abrahamsson, and D. C. Kammer, "Redundant information rejection in sensor localisation using system gramians," in *Topics in Modal Analysis & Testing, Volume 10, Proceedings of the 34th IMAC, A Conference and Exposition on Structural Dynamics*, pp. 325–333, Springer, 2016.

[20] S. Feng and J. Jia, "Acceleration sensor placement technique for vibration test in structural health monitoring using microhabitat frog-leaping algorithm," *Structural Health Monitoring*, p. 1475921716688372, 2017.

[21] W. Liu, W.-c. Gao, Y. Sun, and M.-j. Xu, "Optimal sensor placement for spatial lattice structure based on genetic algorithms," *Journal of Sound and Vibration*, vol. 317, no. 1-2, pp. 175–189, 2008.

[22] D. J. Inman, *Vibration with control*. John Wiley & Sons, 2017.

[23] K. Kunisch and S. Volkwein, "Optimal snapshot location for computing pod basis functions," *ESAIM: Mathematical Modelling and Numerical Analysis*, vol. 44, no. 3, pp. 509–529, 2010.

[24] S. Volkwein, "Proper orthogonal decomposition: Theory and reduced-order modelling." Lecture Notes, Aug. 2013. Lecture Notes.

[25] Y.-S. Park and H.-B. Kim, "Sensor placement guide for model comparison and improvement," in *PROCEEDINGS-SPIE THE INTERNATIONAL SOCIETY FOR OPTICAL ENGINEERING*, pp. 404–409, SPIE INTERNATIONAL SOCIETY FOR OPTICAL, 1996.

[26] D. C. Kammer, "Sensor set expansion for modal vibration testing," *Mechanical systems and signal processing*, vol. 19, no. 4, pp. 700–713, 2005.

[27] D. C. Kammer and J. A. Peck, "Mass-weighting methods for sensor placement using sensor set expansion techniques," *Mechanical Systems and Signal Processing*, vol. 22, no. 7, pp. 1515–1525, 2008.

[28] B. Moore, "Principal component analysis in linear systems: Controllability, observability, and model reduction," *IEEE transactions on automatic control*, vol. 26, no. 1, pp. 17–32, 1981.

[29] A. J. Krener and K. Ide, "Measures of unobservability," in *Decision and Control, 2009 held jointly with the 2009 28th Chinese Control Conference. CDC/CCC 2009. Proceedings of the 48th IEEE Conference on*, pp. 6401–6406, IEEE, 2009.

[30] B. T. Hinson, *Observability-based guidance and sensor placement*. PhD thesis, University of Washington, 2015.

Nonlinear system identification using digital image correlation

D. Roettgen[1], E. Jones[1], A. Brink[1], P. Reu[1], D. Rohe[1], J. Wagner[1]
[1] Sandia National Laboratories*

Abstract

Mechanical and aerospace structures often contain nonlinearities arising from frictional contact at joints. In order to calibrate response predicting models, these nonlinearities must be experimentally quantified to provide information about the type and strength of nonlinearity. For amplitude dependent nonlinearities, such as frictional contact, the nonlinear response is obtained by gathering ring down accelerometer data from impact testing with varying amplitudes. These accelerations are then spatially filtered to obtain a single degree-of-freedom response, which is used to identify a pseudo-modal model. This work examines a small test article with embedded frictional nonlinearities, in which accelerometers cannot be placed. Using a laser doppler vibrometer (LDV) to determine linear mode shapes and digital image correlation (DIC) to obtain response data during various amplitude hammer strikes, the nonlinearity in this small system is quantified.

* Sandia National Laboratories is a multimission laboratory managed and operated by National Technology and Engineering Solutions of Sandia, LLC., a wholly owned subsidiary of Honeywell International, Inc., for the U.S. Department of Energy's National Nuclear Security Administration under contract DE-NA-0003525.

1 Introduction

Most real-world structures include nonlinearities introduced due to frictional contact, like those observed at the interface within bolted joints. These nonlinear surface interactions are extremely difficult to model. Even when joints behave in a linearly, the stiffness and damping properties can be non-repeatable and difficult to predict. Often this modeling task is neglected and experimental measurements and conservative design margin are used to compensate for this inaccuracy.

Recently researchers have shown that many bolted structures tend to display weakly nonlinear behavior. In such cases, the mode shapes of the structure do not change with amplitude, instead small changes in frequency and damping are observed. In addition, the energy transfer between modes of the structure are assumed to be negligible in the frequency range of interest; thus, any effects of modal coupling are ignored. Several bolted assemblies have been analyzed in this weakly nonlinear framework using traditional accelerometer measurements. [1-3]

In this work, the structure of interest is so small that it is not feasible to instrument the structure with enough accelerometers to develop a quality pseudo-modal model. Instead full-field (laser doppler vibrometer and digital image correlation) techniques are implemented to assess the structure's nonlinear behavior. This offers some distinct advantages for this type of model identification as spatial density of your measurements locations must form an independent basis for each of the nonlinear modes of interest.

This paper is organized as follows. Section 2 contains an overview of the approach used for the identification of nonlinear modal models as well as a few of the tools used to analyze the system nonlinearity. Section 3 describes the experimental setup as well as some of the challenges with testing the small hardware of interest. Section 4 shows an example set of results from the nonlinear modal testing. Finally, Section 5 contains closing remarks and plans for future work.

2 Theory

2.1 Nonlinear Pseudo-Modal Model Identification

The pseudo-modal model identification process used here has been thoroughly detailed in previous works [2, 3] for many large structures. The main methodology and process is repeated here in order to focus on the portions that are affected by the use of full-field laser doppler vibrometer (LDV) and digital image correlation (DIC). In a typical linear system, the dynamics of a structure are represented by a sum of modal degrees of freedom, or modal models. Each modal model contains a modal mass connected to ground with a modal spring, representing the frequency, and modal damper, representing the modal dissipation.

A nonlinear pseudo-modal model augments the traditional linear system with the addition of a nonlinear forcing element. This element can take any form from a cubic polynomial spring and damper to a complex constitutive model like a Palmov [4, 5] or Iwan [6, 7] model. In this work, a cubic and quadradic polynomial spring and damper are used to represent the nonlinear dynamics for each mode of interest. An example linear modal model and nonlinear pseudo-modal model are shown in Fig. 1

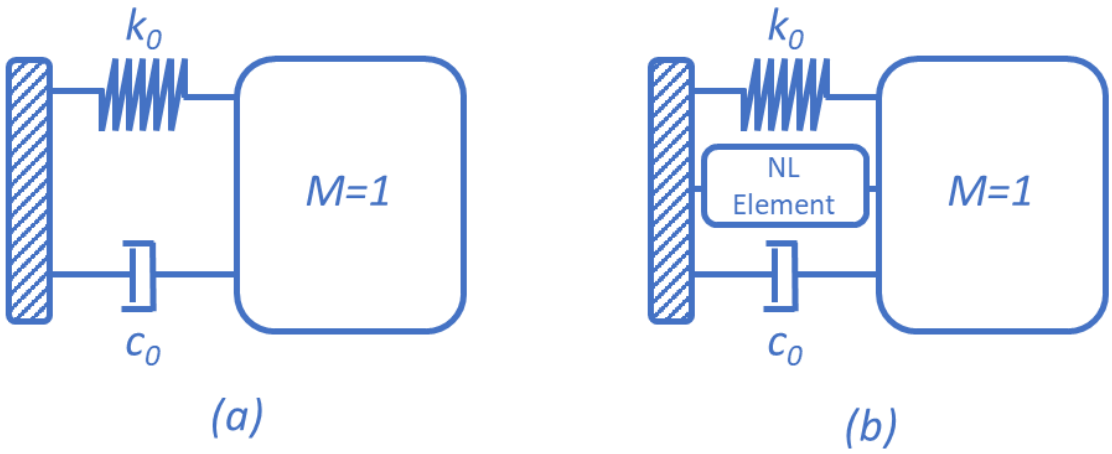


Figure 1: (a) Linear modal model (b) Nonlinear pseudo-modal model

A restoring force surface approach is implemented to identify these nonlinear parameters from high-level modal testing. This requires a series of tests at both high and low-levels of input excitation. Because the system is so small, usual accelerometer placement would not provide enough measurement locations for spatial filtering. Instead full-field measurement techniques were implemented to gather both linear and nonlinear information on the system. To begin, a low level modal test is performed, with a laser doppler vibrometer, in order to capture the linear mode shapes, frequencies, and damping ratios of the system at low vibration amplitude. Next, the system is tested with a high level of excitation to induce its nonlinear dynamics. This response is measured using a digital image correlation set-up as this allows all the data to be taken in one measurement frame which is essential to the nonlinear post processing. These measurements are spatially filtered using the linear shapes in order to develop a single degree-of-freedom system that is fit using the restoring force surface method.

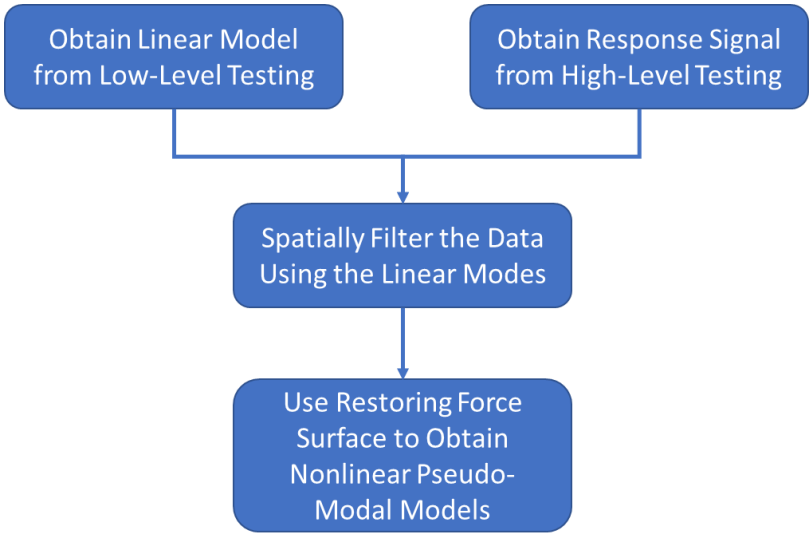


Figure 2: Process flowchart

In this work, depending on the measurement system, velocity or displacements are used instead of the acceleration measurements that would typically be achieved in a dynamic test using traditional instrumentation A simple numerical integration or differentiation in the frequency domain is used to obtain the displacement, velocity, and acceleration measurements. With these measurements a modal filter can be used to obtain a single degree-of-freedom response for each mode of interest. This modal filter is shown in Eqn. 1 using a pseudo-inverse of the mode shapes to transform from physical measurements, $\ddot{x}$, to modal signals, $\ddot{q}$. Because of the weakly nonlinear assumptions, the mode shapes are assumed to not change with amplitude and thus the linear mode shape matrix can be used to complete this filtering.

$$\ddot{q} = \Phi^{+}\ddot{x} \tag{1}$$

The equation of motion for a linear modal model is shown in Eqn. 2

$$\ddot{q} + c_0\dot{q} + k_0 q = \Phi^T F \tag{2}$$

while the nonlinear pseudo-modal model is shown in Eqn. 3 with the addition of quadradic and cubic polynomial terms.

$$\ddot{q} + c_0\dot{q} + k_0 q \; + c_1\dot{q}|\dot{q}| + c_2\dot{q}^3 + k_1 q|q| + k_2 q^3 = \phi^T F \tag{3}$$

The nonlinear forces can be gathered into a single nonlinear restoring force,

$$F_{rs} = c_1\dot{q}|\dot{q}| + c_2\dot{q}^3 + k_1 q|q| + k_2 q^3 \tag{4}$$

The values for c_0, k_0, and Φ can be obtained from a linear low-level modal test, while measurements of the modal acceleration, $\ddot{q}$, velocity, $\dot{q}$, and displacement q are obtained from a high-level test using integration and differentiation in the frequency domain. The only remaining unknowns are in the nonlinear coefficients c_2, k_2, c_2, and k_2. The equation of motion from Eqn. 3 can be set up to solve these coefficients in a least squares sense as shown in Eqn. 5 and Eqn. 6. The process from [2,3] is followed to complete these least squares, in particular real and imaginary signals are stacked and these equations are solved in the frequency domain.

$$\phi^T F - \ddot{q} - c_0\dot{q} - k_0 q \; = [\dot{q}|\dot{q}| \quad \dot{q}^3 \quad q|q| \quad q^3] \begin{bmatrix} c_1 \\ c_2 \\ k_1 \\ k_2 \end{bmatrix} \rightarrow \bar{U} = P \begin{bmatrix} c_1 \\ c_2 \\ k_1 \\ k_2 \end{bmatrix} \tag{5}$$

$$\begin{bmatrix} c_1 \\ c_2 \\ k_1 \\ k_2 \end{bmatrix} = P^{+}\bar{U} \tag{6}$$

As a simple approximation of amplitude-dependent damping and frequency, the nonlinear model's stiffness and dissipation terms can be gathered and related to linear damping and frequency. From linear modal theory we can relate k_0 to natural frequency.

$$k_0 q = \omega_n^2 q \tag{7}$$

Using the stiffness terms in the nonlinear pseudo-modal modal we can get an estimate for effective natural frequency.

$$k_0 q + k_1 q|q| + k_2 q^3 = (k_0 + k_1|q| + k_2 q^2)q \ = \omega_{n_{eff}}^2 q \tag{8}$$

A similar effective damping ratio can be obtained using the dissipation terms as shown in Eqn. 9. These nonlinear modal estimates are not perfect and would benefit from a more rigorous multiple-scales perturbation approach but they provide a quick sanity check while testing in the lab.

$$c_0\dot{q} + c_1\dot{q}|\dot{q}| + c_2\dot{q}^3 = (c_0 + c_1|\dot{q}| + c_2\dot{q}^2)\dot{q} \ = 2\zeta_{eff}\omega_{n_{eff}}\dot{q} \rightarrow \zeta_{eff} = \frac{(c_0 + c_1|\dot{q}| + c_2\dot{q}^2)}{2\omega_{n_{eff}}} \tag{9}$$

2.1.1 Hilbert Transform

Beyond simply investigating the nonlinear pseudo-modal model, the Hilbert transform [7-8] was used to investigate the nonlinear characteristics of measured responses. This tool is widely used for nonlinear system identification. The Hilbert transform is usually used on ringdown data from an impact hammer test. First, it is assumed that the modal response can be rewritten in an exponential form as shown in Eqn. 10 where $\psi_r(t)$ is the Hilbert envelope and $\psi_i(t)$ is the unwrapped phase.

$$\ddot{q} = e^{\psi_r(t) + i\psi_i(t)} \tag{10}$$

The amplitude envelope and unwrapped phase obtained in this exponential form can be used to find time varying damped natural frequency and dissipation.

$$\omega_d(t) = \frac{d\psi_i}{dt} \tag{11}$$

$$-\zeta\omega_n(t) = \frac{d\psi_r}{dt} \tag{12}$$

These values can then be plotted against response amplitude to obtain amplitude dependent curves for frequency and dissipation to quantify the nonlinearity observed in each mode.

3 Experimentation

3.1 Experimental System and Challenges

The experimental structure of interest is shown disassembled in Fig. 3. It consists of two shelled-beam specimens that connect with two bolted interfaces in the center of the beam. The goal of the experiment was to extract amplitude dependent frequency and damping relationships to aid in the finite element model updating for the small structure.



Figure 3: *Two beam specimen with modal hammer for size comparison*

This structure provided many experimental challenges. The beam has two internal gages shown in the sketch from Fig. 4 but when exciting the structure at high force levels the internal sensors would over-range or reach the nonlinear saturation of the sensor, making it difficult to determine if the measured nonlinearity was from the jointed structure of the sensor response. In addition, two sensors would not be adequate to perform the spatial filter as calculated in Eqn. 1. The spatial resolution of the measurement locations would not be able to separate the measurements into single degree-of-freedom modes; thus, full-field measurement was necessary for this application.

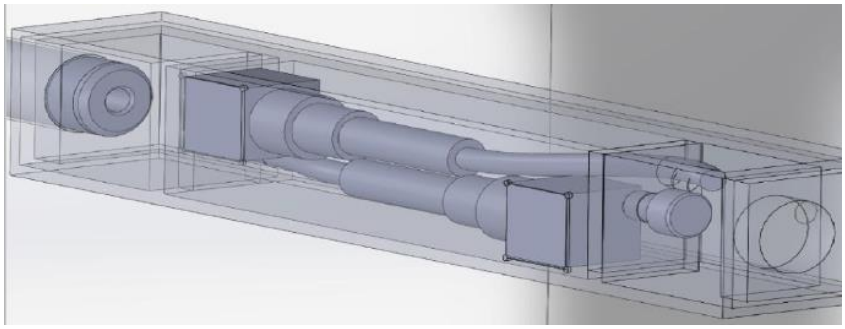


Figure 4: Assembled two beam specimen internal view showing instrumentation

The nonlinear analysis presented in Eqns. 3-6 requires that all measurement points be taken with a consistent loading. With accelerometers this is a simple task but it is much more difficult with a LDV system that scans point by point. This process was considered but would require a highly repeatable force in order to obtain the same nonlinearity at each measurement location. Instead, the team chose to pursue a digital image correlation (DIC) measurement technique using high-speed cameras to capture the motion of the beam specimen under high loading. This decision came with more challenges, mainly the noise floor of DIC measurements. In the free-free configuration a large enough force was difficult to obtain while remaining in depth of field for the camera system. Several individual hammer strikes were obtained but averaging tended to wash out the nonlinearity as repeatable hammer strikes were not obtainable. To alleviate this issue, the system was attached to a large fixture from a higher-level assembly. This frame provided a sturdier structure for modal testing, allowing for larger force levels bringing the signal out of the noise floor of the system.

3.2 Experimental Set-Up

The final framed experimental setup is shown in Fig. 5. DIC speckle patterns were applied to the beam while 66 accelerometer measurements were placed onto the framed structure. The structure was suspended by bungees to represent a free-free boundary condition on the entire fixture-beam assembly.

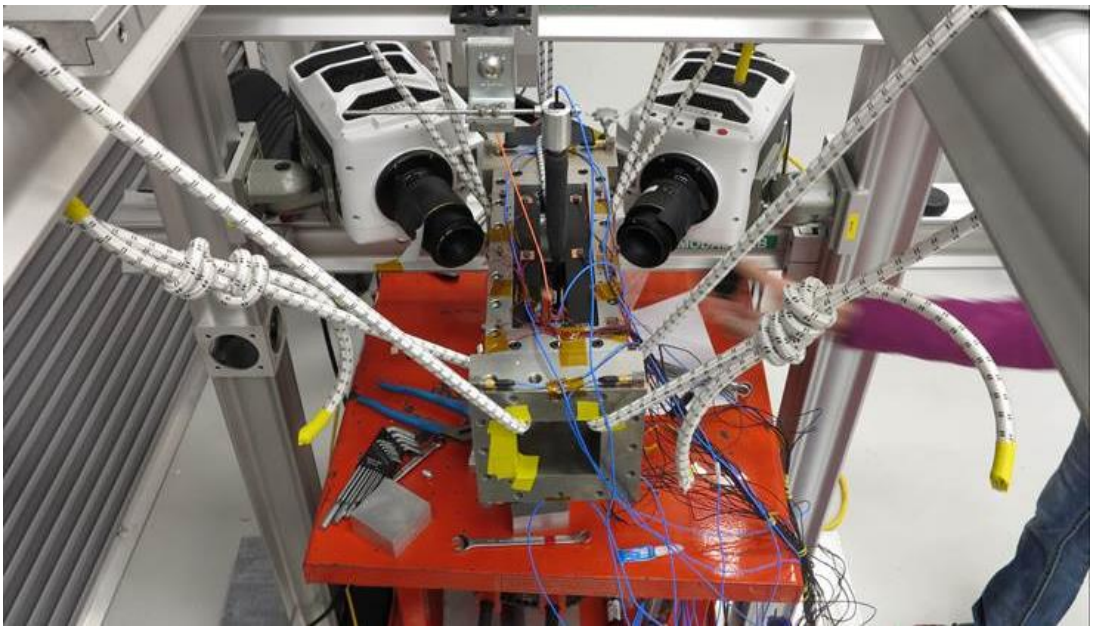


Figure 5: Experimental system setup with cameras

The speckle pattern used for DIC analysis is shown in Fig. 6. Note, the hammer blocks a significant portion of the view so only measurements where the speckle subset is identified for all time steps are used in this analysis.

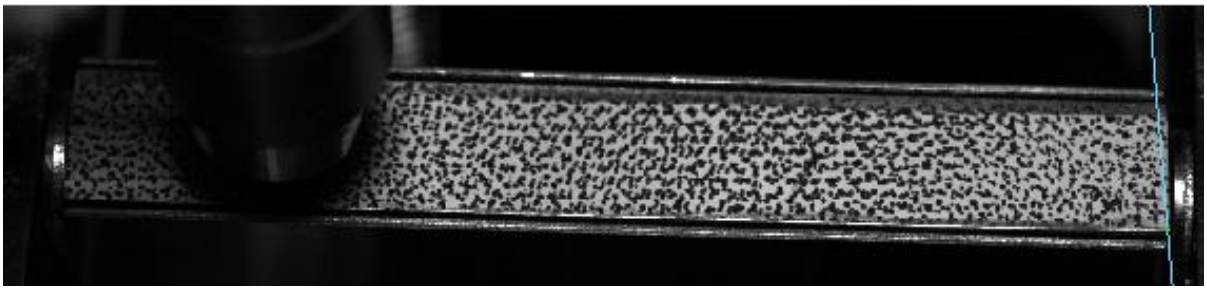


Figure 6: Experimental DIC speckle pattern

Nonlinear, high-level, testing was performed with an impact hammer swung from a pendulum to strike the beam at the same location with approximately the same force. The testing was completed at multiple forces to assess the nonlinearity of the joint in various configurations and loadings. These high-level impact measurements were processed through a series of signal manipulations (filtering etc.) to obtain useful nonlinear relationships between vibration amplitude and damping.

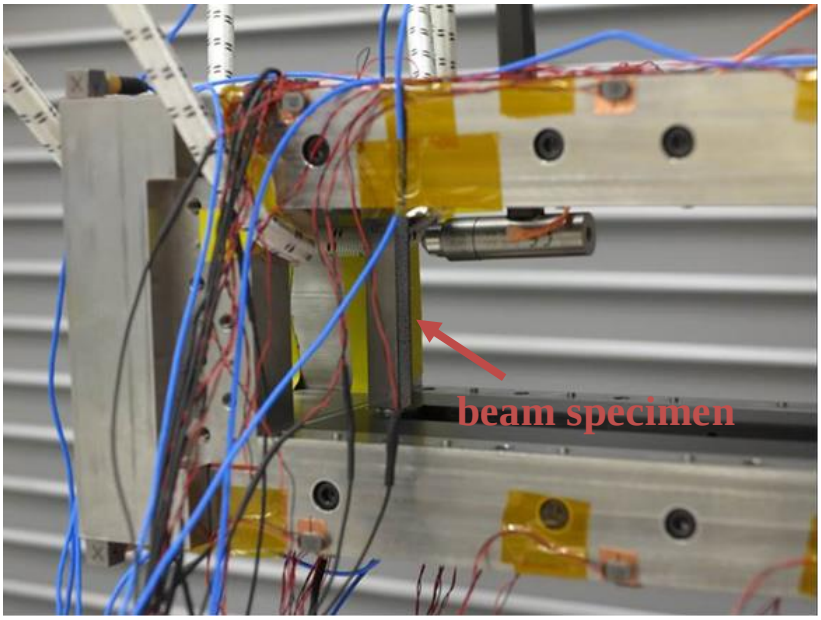


Figure 7: Hammer pendulum picture

4 Example Experimental Results

This section will walk through the processing of a single data set and then overlay the results of many data sets to see the experimental repeatability of this test practice. This section will highlight any unique processing that occurs due to the mix of modal digital image correlation measurements and more traditionally used modal accelerometer measurements.

To begin, the digital image correlation measures displacements which contains rigid body motion and high frequency noise. A bandpass filter is used to remove this unwanted frequency content, an example signal is shown in Fig. 8.

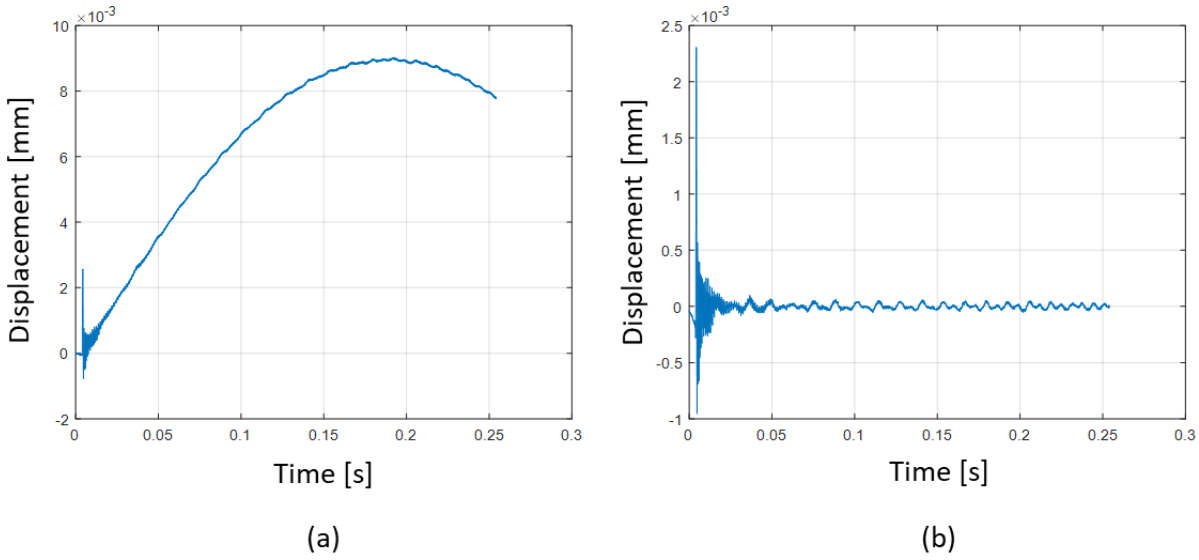


Figure 8: (a) Raw DIC response for a single point (b) Filtered DIC response for a signle point

After filtering, the displacement measurements were converted to acceleration in the frequency domain. The data from the DIC measurement and the accelerometers must be combined into one set to complete the modal filter calculation. The data from both sets was resampled at a high rate and then decimated so the signals had the same temporal resolution. Because the cameras and modal accelerometer DAQ were not synchronized the signals needed to be aligned in time. To do this the displacement measurements were shifted in time until the phase of the DIC and accelerometer measurements were aligned. At this point the data sets could be combined into one file containing a force, acceleration measurements from the accelerometers, and calculated acceleration measurements from the DIC system.

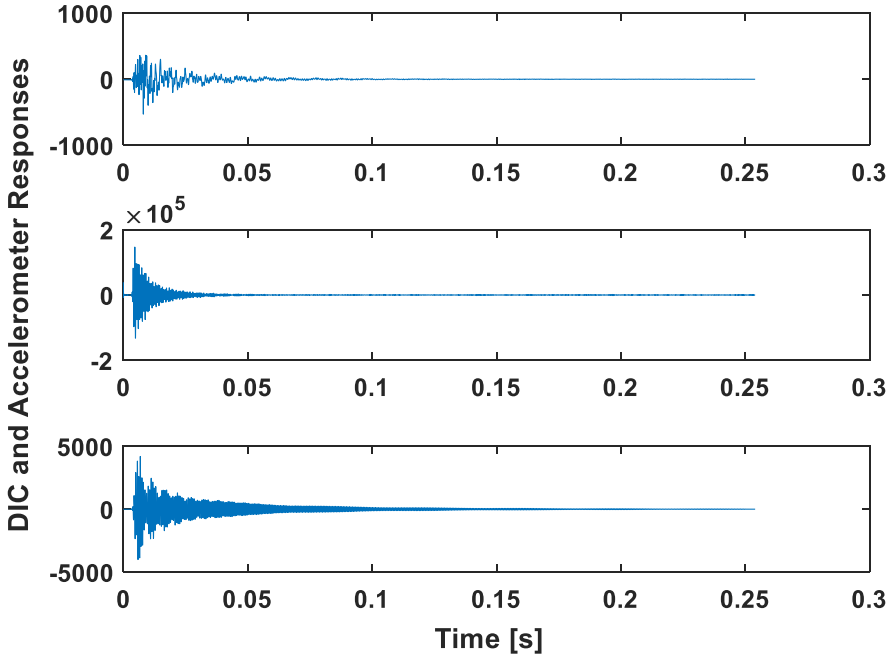


Figure 8: Combined responses from DIC and Accelerometers

Using Eqn. 1 the signals can be spatially filtered into single degree-of-freedom responses. In this work, the filter was successful at removing nearby frequencies for the two modes of interest but did not successfully remove much of the low frequency (under 1000 Hz) content. This undesired frequency content was removed with a high-pass filter. The results from the spatial filter are shown in Fig. 10.

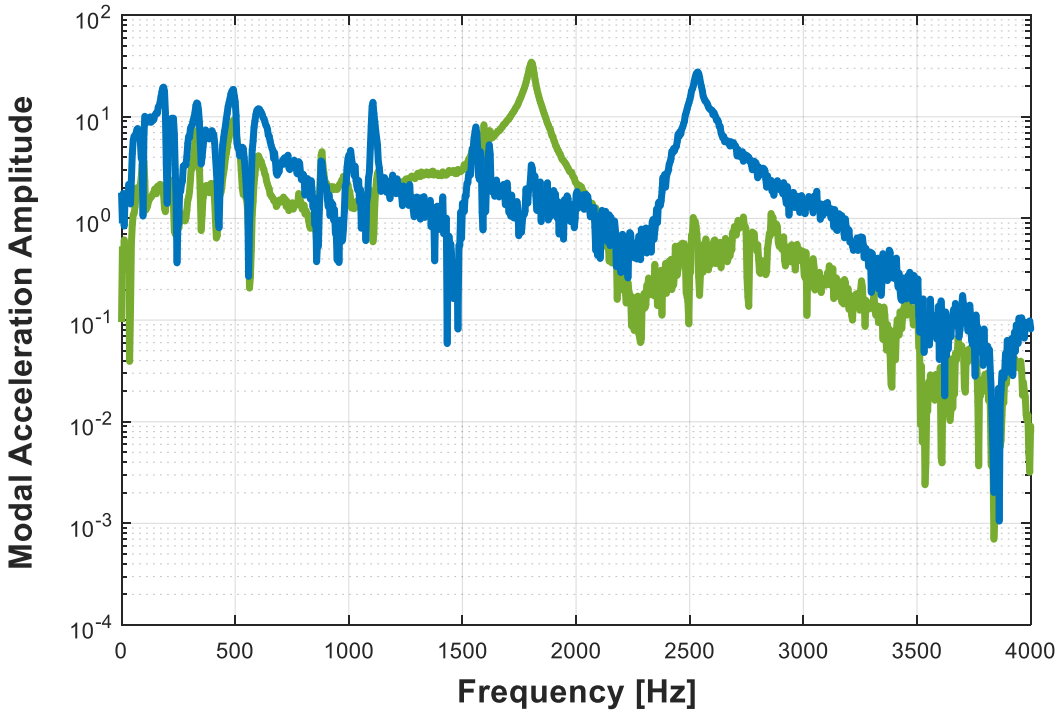


Figure 10: Spatially filtered modal acceleration signals

A nonlinear pseudo-modal model was created using the process from Eqns. 3-6, where the linear parameters were found from low-level excitation tests, and the filtered high-level data was used to obtain the modal states q, $\dot{q}$, and $\ddot{q}$. For the tested force level, the nonlinear coefficients were determined in a least squares sense from Eqns. 5-6 for the first bending mode of the beam specimen. These coefficients are contained in Table 1.

Parameter	Value
k_1	-4.45E11
k_2	1.20E15
c_1	1449
c_2	-2472

Table 1: Nonlinear pseudo-modal model coefficients

The obtained nonlinear pseudo-modal model was simulated using a high-level impact excitation force and compared to modally filtered test response data to ensure the accuracy of the obtained modal model. Figure 11 shows the results of this time-domain simulation. Here the amplitude of the modal response at early and late time correlate very well, meaning the nonlinear pseudo-modal model obtained from test data provided a quality fit.

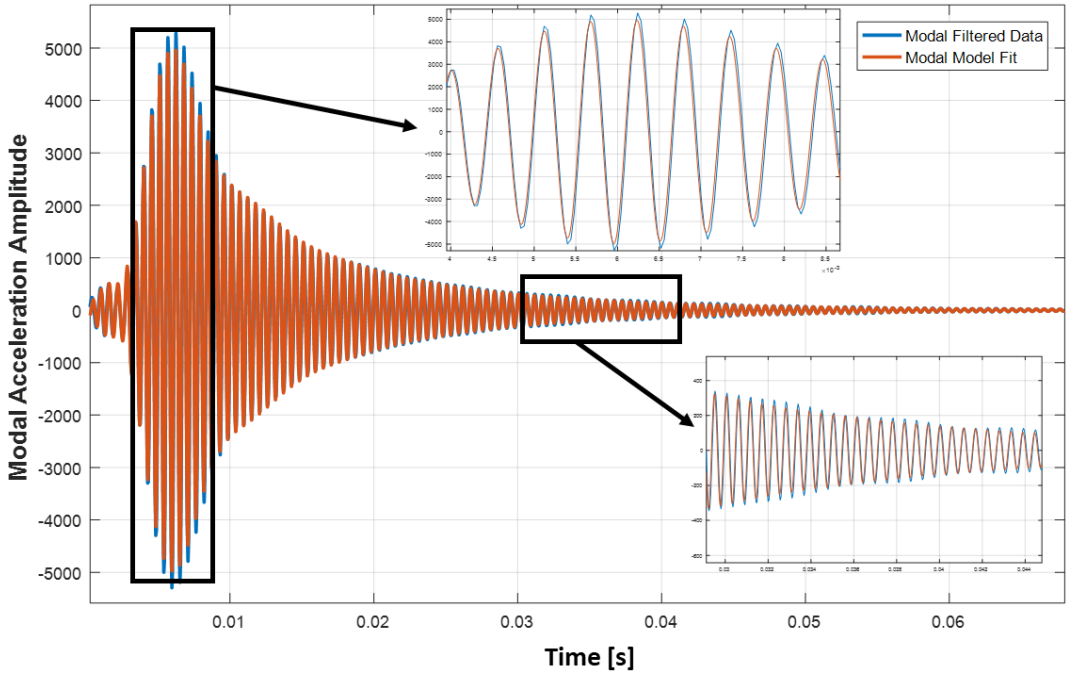


Figure 11: Nonlinear pseudo-modal model simulation

The RFS estimate, from Eqns. 8-9, and Hilbert transform, from Eqns. 10-12, were used to determine the amplitude-dependent frequency and damping for the first bending mode of the structure. Figure 11 shows the amplitude dependent damping which provides a quality match between both the RFS estimate and the Hilbert approach. At low level the two estimates agree to a similar damping ratio (around 0.006). This is significant because the RFS low level damping is determined solely by the low level linear test of the system. At higher levels we see similar levels of increased damping, with added end-effects due to the polynomial nature of the Hilbert approach.

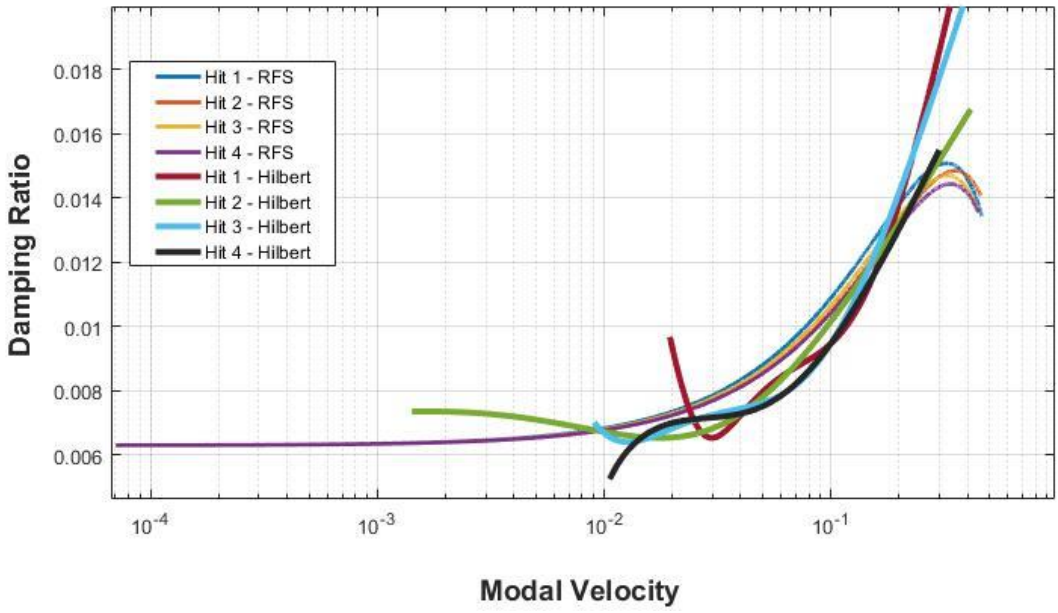


Figure 11: Nonlinear amplitude dependent damping

Figure 12 shows the nonlinear amplitude-dependent frequency calculation and here we can see a large discrepancy between the Hilbert and RFS estimate of frequency. As can be observed in Fig. 12 both methods have around the same level of linear frequency. The Hilbert method observes a very small change in frequency (~0.2%), while the RFS estimate see a much larger shift at high levels (2%). The Hilbert results suggest that the mode really had very little nonlinear stiffness change, future work will investigate modes such as this using RFS to fit damping only, versus damping and stiffness nonlinear pseudo-modal models.

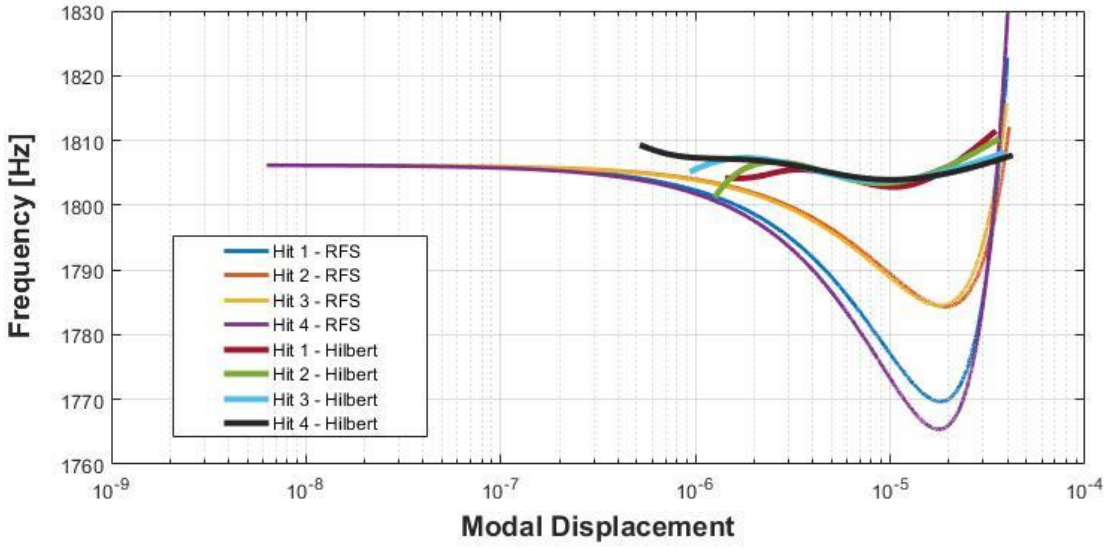


Figure 12: Nonlinear amplitude dependent frequency

Additional hammer impacts were taken at higher load levels. Figure 13 shows the nonlinear damping results of these high-level hits. Here, both loading cases agree (as expected) at lower levels, additionally, the high-level response data follows a similar microslip trend as the low-level impacts. This means in future work on this structure high-level impacts with appropriate ringdown can be used to capture the entire amplitude range of interest.

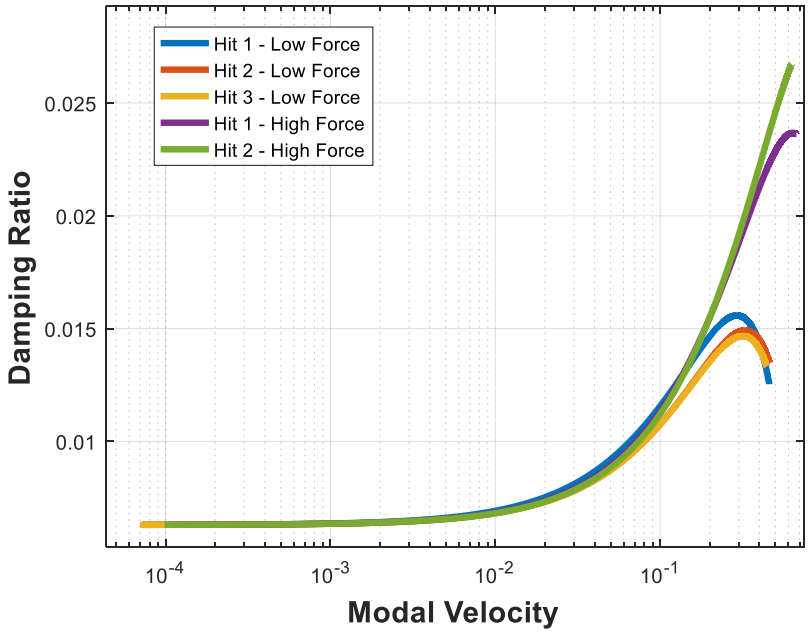


Figure 13: High versus low-level comparison

5 Conclusions and Future Work

This paper provided a nonlinear identification example using both accelerometer and digital image correlation data. To identify the desired nonlinear pseudo-modal models a nonlinear restoring force surface technique was used. The pseudo-modal models were assumed to be cubic and quadradic polynomial elements and were able to capture the nonlinearity present in the main mode of interest for this beam specimen. The Hilbert transform was implemented to understand the degree of nonlinearity present in the main mode of interest. A simple calculation was performed using the form of the nonlinear pseudo-modal model to validate the nonlinearity observed in the Hilbert response. In addition to the identification exercises the bolted specimen was tested at multiple levels to see if the nonlinearity would shift as force was slightly increased.

There are a few follow-up tasks from which this study would greatly benefit. First, the range in which the pseudo-modal model is accurate could be increased by testing at even higher force levels. Ideally a model would span a large range, but a study comparing the model extracted at different forcing levels could provide insight into some of the pitfalls of this methodology. Second, some optimization would could be done on the node selection from the DIC measurements. Spatial averaging may be implemented to eliminate drop the noise floor at higher frequencies and allow this technique to target higher frequency modes otherwise riddled with noise. Finally, investigating data at multiple torque levels (especially lower ones), would allow the system to experience more micro-slip and potential observe larger stiffness changes. These tasks would help to prove out and enlighten the nonlinear community on what appears to be a promising technique for nonlinear joint measurement and model identification.

References

[1] D. Roettgen and M. Allen, *Nonlinear characterization of a bolted, industrial structure using a modal framework*, Mechanical Systems and Signal Processing, (2016).

[2] R. Mayes, B. Pacini and D. Roettgen, *A Modal Model to Simulate Typical Structural Dynamic Nonlinearity*, in *Proceedings of the XXXIV International Modal Analysis Conference*, Orlando, FL, 2016.

[3] B. Pacini, R. Mayes, B. Owens and R. Schultz, *Nonlinear Finite Element Model Updating, Part I: Experimental Techniques and Nonlinear Modal Model Parameter Extraction*, in *Proceedings of the XXXV International Modal Analysis Conference*, Garden Grove, CA, 2017.

[4] D. Segalman, et al., *Experimental Assessment of Joint-Like Modal Models for Structures*, presented at *the International Design Engineering Technical Conferences & Computers and Information in Engineering Conference IDETC/CIE* Boston, MA, 2015.

[5] V. Palmov, *Vibrations of Elasto-Plastic Bodies*: Springer, 1998.

[6] D. J. Segalman, *A Four-Parameter Iwan Model for Lap-Type Joints*, Journal of Applied Mechanics, Vol. 72, (2005), pp. 752-760.

[7] B. Deaner, et al., *Application of Viscous and Iwan Modal Damping Models to Experimental Measurements From Bolted Structures*, ASME Journal of Vibrations and Acoustics, Vol. 137, (2015), pp. 12, 2015.

[8] M. W. Sracic, et al., *Identifying the modal properties of nonlinear structures using measured free response time histories from a scanning laser Doppler vibrometer*, in *Proceedings of the XXX International Modal Analysis Conference*, Jacksonville, Florida, 2012.

Detecting cavitation inception in external gear pumps by means of vibro-acoustic measurements

M. Battarra [1], **E. Mucchi** [1]
[1] University of Ferrara, Engineering Deptartment,
Via G. Saragat, 1 - 44122, Ferrara, Italy
e-mail: **mattia.battarra@unife.it**

Abstract

The present work investigates cavitation in external gear machines by means of a dedicated experimental campaign. Four different pump prototypes have been designed and manufactured to perform this research, one of them specifically built up to not be affected by such a phenomenon. Vibro-acoustic measurements performed by a hydrophone and a high-frequency accelerometer are put in comparison with measurements of inlet and outlet pressure ripple, in order to enlighten their capability to follow the development of the phenomenon. Waterfall spectra are investigated and later Root Mean Square (RMS) values of the filtered signals are shown with respect to the cavitation number and compared with efficiency measurements. Results demonstrate that vibro-acoustic measurements associated to a dedicated signal processing procedure represent a powerful tool to detect cavitation inception in gear pumps. In addition, effect of oil temperature is investigated, showing its contribution in spreading the phenomenon on a wider speed range.

1 Introduction

Cavitation detection in fluids machinery represents a central but demanding task in defining the performances of pumps and turbines throughout a wide range of working conditions. Characterizing the machines behavior from the onset of the phenomenon until its full development usually requires a well-assessed measurement procedure and accurate post-processing. One of the first works on this subject pertains to I. S. Pearsall [1], that focused the attention on determining the effects of cavitation by means of acoustic measurements on the performances of various hydraulic machines, such as axial-flow and centrifugal pumps, as well as Francis and Kaplan turbines. Measured data demonstrated that acoustic measurements were more sensitive to the phenomenon inception than efficiency one. These first results have been later supported by more extended experimental campaigns performed on centrifugal pumps [2], demonstrating the effective capability to detect cavitation inception by using hydrophone sensors.

The measurements approach described in [1, 2] has been lately developed and applied to various Kaplan and Francis turbine prototypes [3, 4], underlining the chance to improve the experimental detection with blade-passage frequency demodulation techniques. More recently, different signal processing techniques have been proposed for detecting cavitation inception: M. Čudina demonstrated the possibility to characterize the phenomenon in centrifugal pumps by using audible sound [5]; later, uncertainty of the results was evaluated by the same authors [6]. Adamkowski et al. focused the investigation on monitoring the pump shaft torsional vibrations induced by cavitation erosion [7]. In the same years, Zhaoli et al. presented an assessed method to detect cavitation in pumps with the help of phase demodulated ultrasonic signals [8]. More recently, Azizi et al. developed an algorithm to estimate the severity of the phenomenon in centrifugal pumps [9].

Various other experimental studies on this challenging subject may be found in the literature, however, despite the wide interest shown by the scientific community, a lack of results concerning the detection of cavitation in volumetric machines has been observed by the authors. A small amount of research regards the

effects produced by air release/absorption and oil vaporization in volumetric pumps and motors. Moreover, such works are generally restricted to the numerical approach and focused on the assessment of models for performance prediction. In particular, in [10] Borghi et al. evaluated the influence of cavitation in external gear pumps and motors by proposing a lumped parameter model restricted to the meshing zone, only. More recently, in [11, 12] Zhou et al. presented a lumped parameter approach to evaluate external gear pumps performances under cavitation conditions based on simplified transport equations. The model described in [12] is supported by experimental data referring to the pressure ripple around gears, but no effective data regarding the cavitation detection are provided. Several other works are focused on determining the pump performance taking into account a number of design parameters and working conditions [13, 14, 15, 16], but the cavitation phenomenon is always neglected.

As far as the authors are aware of, the only one experimental work focused on cavitation monitoring in volumetric pumps pertains to Buono et al. [17], that presented an experimental campaign aiming at characterizing the phenomenon in gerotor pumps by means of pressure ripple and vibration measurements. Experimental measurements on cavitation in gear pumps cannot be found in the literature even if this machine type is commonly known to be affected by such a phenomenon [10, 12, 18, 19]. This lack of data might be justified by considering that gear pumps are traditionally driven by electric motors or low speed engines since the requested delivery flow rate is obtained by increasing the pump displacement. Nowadays, in particular in the automotive field, the need to reduce weight and dimensions of the overall system requires to reduce the pump displacement as much as possible and then to guarantee the requested delivery flow rate by increasing the working speed. Based on this brief literature review, the goal of the present work is to characterize cavitation in gear pumps experimentally and define a systematic procedure to detect the inception of the phenomenon with respect to the pump working speed. For this reason, results obtained from the signal processing of different sensors such as accelerometers, hydrophone and pressure pulsation sensors are shown and discussed. Moreover, the analysis of measured data referring to different pumps is supported by measurements of volumetric efficiency and actual detection of various damages produced by cavitation.

The following Section describes the characteristics of the cavitation phenomenon in fluid machines. Section 3 outlines the test setup, concentrating on the description of the test bench adopted to evaluate both pumps efficiency and vibro-acoustic performances, the data acquisition system together with the various transducers installed on the rig and, lastly, the four external gear pumps designed for the experimental campaign and the measurement procedure. Section 4 describes the signal processing techniques applied to measured data, while Section 5 presents the obtained results, with the aim at characterizing gear pumps behavior under cavitating conditions. Finally, last section is devoted to concluding remarks.

2 Cavitation in fluid machinery

The literature survey in Section 1 demonstrates that the cavitation phenomenon in axial/centrifugal pumps and turbines has been widely studied throughout the last five decades. Several experimental campaigns contributed in addressing its characteristics, from a machine performance point of view, as in refs. [1, 2], as well as from a physical point of view, as in ref. [20]. The former approach is based on the evaluation of the machine efficiency with respect to its working condition, which is usually defined in terms of the cavitation number σ:

$$\sigma = \frac{p_{in} - p_{sat}}{0.5\rho u^2} \tag{1}$$

where p_{in} is the mean inlet pressure, p_{sat} is the saturation pressure at the reference oil temperature, ρ is the oil density at the reference temperature and u is the mean flow velocity at the inlet port. As described in ref. [21], the cavitation number is a scaling parameter adopted to extrapolate data from one working condition to another by assuming complete similitude guaranteed by a constant cavitation number itself. However, in practice, σ does not include all the variables influencing the phenomenon, e.g. boundary geometry, absolute pressure, local velocity or pressure drop, and therefore such a parameter is still affected from scale effects.

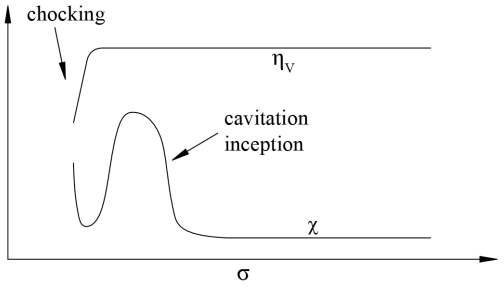


Figure 1: Qualitative trend of volumetric efficiency η_V and generic vibro-acoustic quantity χ with respect to the cavitation number.

Once the cavitation number is assumed as a control parameter, starting from a cavitation-free working condition, by reducing σ the generic turbomachine cross three main regions: the first one coincides with the initial condition, then as the machine approaches the cavitation inception region, small, isolated and localized bubbles start appearing. As σ keeps decreasing, the phenomenon intensifies till the machine enters the fully-developed cavitation region and starts working in chocked conditions.

These considerations explain the results obtained in [1, 2], which demonstrated that efficiency measurements cannot follow the evolution of the phenomenon entirely, since the delivery flow rate starts being influenced by cavitation when the machine enters the fully-developed cavitation region. On the contrary, measurements based on hydrophones, accelerometers, acoustic emission sensors and pressure transducers were shown to be much more sensitive to the phenomenon, being able to detect it from the inception to its complete development. In particular, several experiments demonstrated that vibro-acoustic measured quantities always follow a common trend as the cavitation number is decreased from the free-of-cavitation region till the fully-developed one, as shown in Figure 1. Volumetric efficiency η_V remains unaltered till the chocked condition, when it finally shows a sharp drop; on the contrary, generic vibro-acoustic quantity χ starts increasing as soon as the inception takes place, it reaches a maximum and then suddenly drops down as the phenomenon intensifies. If σ is further decreased, chocking starts appearing and χ starts increasing again.

These results are usually obtained by executing a large number of measurements where σ is gradually decreased by reducing the inlet pressure while the working speed is set as a constant. The practical advantage given by this kind of approach stands in the possibility to fully characterize the phenomenon by simply regulating a valve placed on the inlet side. Moreover, since this kind of machines is typically designed to work at a fixed constant speed while the inlet pressure depends on the installation layout, the proposed approach also gives an accurate representation of the real case.

In order to have a complete overview of the problem, it must be clarified that the necessity to detect cavitation inception comes from a practical reason. Although fully-developed cavitation affects volumetric efficiency seriously, it is proved to be less damaging than the inception condition in terms of wear and erosion. As explained in refs. [21, 22], when cavitation becomes well developed, the flow aggressiveness tends to decrease due to a smaller production of vapor bubbles or weaker implosions. For this reason, detecting cavitation from its inception becomes a crucial task to define the working condition range where the machine can operate safely.

Despite the large amount of specialized literature regarding cavitation on hydraulic machines, similar studies have never been performed for gear pumps. For this reason, a clear description regarding how and where the phenomenon takes place and evolves is not available in the literature. Concurrently, experimental data for correlating cavitation in gear pumps with respect to vibro-acoustic measurements cannot be found. However, by taking advantage of the numerical results in ref. [11] regarding the vapor and air mass fractions evolution around the gears, it is possible to assume a realistic description of its development. Since bubble generation

requires a consistent drop of the local pressure, air release and vaporization must necessarily take place in the meshing zone, when the trapped volume opens to the inlet chamber. Within this context, the oil suddenly flows from a high pressure zone to a low pressure one by means of an extremely small orifice, which causes the flow velocity to increase significantly. Since oil speed sudden increases, a further decrease of the local pressure is produced with the consequent effect of promoting cavitation. Once bubbles are generated, they can either collapse in the suction chamber or be trapped by gear pockets, dragging them into the pressurizing zone. As soon as the pressure inside the pockets increases, bubbles collapse and produce undesired noise, vibration and, potentially, wear.

On the basis of this description, it is clear that both working speed and suction pressure are crucial parameters. If the speed is increased, the oil pressure inside the meshing zone tends to increase as well and therefore the subsequent pressure drop becomes more and more intense. Moreover, the speed increase produces a slight reduction of the mean suction pressure that contributes in intensifying the phenomenon. On the other hand, cavitation can be also induced by decreasing the mean inlet pressure till the bubble generation can take place directly inside the suction chamber. Although the two mechanisms lead to the same final effect of promoting cavitation inside the pump, they cannot be considered equivalent since speed increase and suction pressure reduction have a different influence on the pressure course around the gears. As described by Mucchi et al. in [23, 24], the speed increase produces a consistent reduction of the pump sealing capability; since the pressure increase in the pressurizing zone is delayed, the bubble collapse is also expected to be delayed. The proposed explanation clarifies the reason why cavitation tests in gear pumps for automotive applications should be performed by increasing the working speed rather than reducing the inlet pressure. This kind of pumps are designed to work safely throughout an extended speed range, while the installation layout is fixed; in this way, each specific pump is designed for a specific lubrication system. Therefore, in this framework, the inlet pressure does not actually represent a control parameter of the phenomenon, which appears to be mainly governed by the working speed.

3 Experimental setup

3.1 Test rig description

The test rig adopted to carry out the experimental campaign is shown in Figure 2. The gear pump is installed inside a sealing box that makes it working submerged and driven by a brushless AC motor with speed controller; a torque meter is located along the shaft connecting the pump with the electric motor. The pipeline for the oil supply system is constituted by two branches: one connecting the tank to the sealing box and the other one connecting the pumps outlet chamber to the tank. An automatic servo valve located on the latter branch of the pipeline allows for the fast regulation of the oil delivery pressure. The oil temperature is regulated with an additional pipeline connected to the tank and controlled by a dedicated system, namely the temperature controller. Such a system monitors the oil inside the tank by using a thermocouple and regulates the temperature with a number of electric resistances.

Both pipeline systems described above are equipped with a drainage system, various valves and filters in order to allow for a safe and easy management of the test rig during the measurement procedures. The description of such auxiliary parts of the test rig is neglected being out of the scope of the present work.

3.2 Sensors and data acquisition system

Two different sets of transducers have been adopted to carry out the experimental campaign. As shown in Figure 2, a first set of sensors has been used to control the test rig and monitor the working condition of the pump under examination. In particular, two digital pressure gauges have been placed on the suction and delivery ports, respectively, in order to check the mean inlet and outlet pressure. A Kracht Gear Type Flow

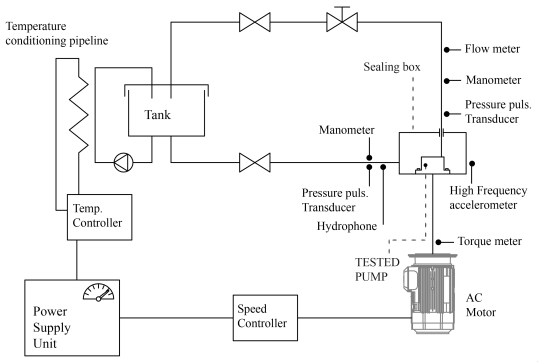


Figure 2: Test rig configuration and sensors disposition adopted for the experimental campaign.

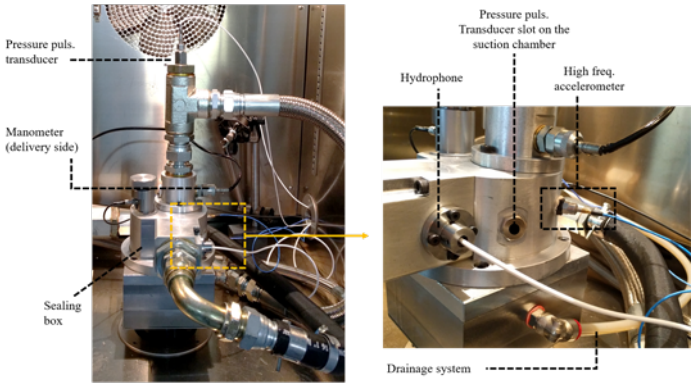


Figure 3: Transducers setup in the real test configuration. As underlined in Section 3.1, the sealing box does not allow for a direct access to the pump casing.

Meter has been used to measure the outlet flow rate, while the instantaneous angular speed can be directly acquired from the tachometer connected to the speed controller of the electric motor.

The second set of sensors has been specifically designed to detect the presence of cavitation by means of vibro-acoustic measurements (see Figure 3). With this purpose, two high frequency piezoelectric transducers (model PCB S102B with resonant frequency above 500kHz) have been place on the suction and delivery ports respectively, in order to measure the pressure ripple generated by the pump. Moreover, a miniature hydrophone (model B&K 8103), located in proximity of the suction chamber and connected to a conditioning amplifier (model B&K Nexus 2692), monitors the acoustic pressure of the oil. Finally, a high-frequency single-axis accelerometer (model PCB 352A60 with resonant frequency above 95kHz) has been located on the sealing box, close to the beginning of the pressurizing zone related to the driving gear. This choice is justified by the fact that while bubbles are generated in the last part of the meshing zone, they are supposed to collapse in the first part of the pressurizing zone. This assumption is supported by direct observation of the wear produced by cavitation on the pump casing. This second set of sensors, together with the signal provided by the tachometer, has been acquired with a LMS Scadas 305 acquisition system and then postprocessed in Matlab environment. In order to capture the signature produced by cavitation phenomena, the sample frequency f_s has been set to the maximum value allowed by the adopted acquisition system, which is equal to 204800Hz.

3.3 Gear pumps type and measurement procedure

Four different gear pump prototypes have been designed and manufactured in order to perform a wide experimental campaign allowing for a satisfactory characterization of the phenomenon. The first prototype, namely Pump A, is constituted by helical gears, with 14 teeth on the driving gear and 9 teeth on the driven one. Since the pump casing is made by steel, no running in process is required and therefore radial clearances between gears and casing are entirely defined by design. The second prototype, namely Pump B, is composed by the same gearpair used for Pump A, but the casing is milled from a single block of aluminum. For this reason, radial clearances are reduced during the design process since the gear pair can mill its own grooves into the casing during the running in process. The third prototype, namely Pump C, is made up by a spur gearpair, with 13 teeth on the driving gear and 10 teeth on the driven one. As described for Pump B, Pump C has an aluminum casing that requires the running in process before the pump can be considered ready to be tested. Finally, the last prototype, namely Pump D, is made by an aluminum casing and helical gears, with 11 teeth and transmission ratio equal to one. All the four prototypes have similar global dimensions and displacement (around $14cm^3/rev$). Pump D has been specifically designed to avoid the presence of cavitation inside the range of working conditions tested. The main design features of the four described prototypes are summarized in Table 3.3.

The four pumps have been tested by following the same measurement procedure: the prototype is installed on the test rig and the servo valve is set to maintain a mean delivery pressure equal to 30bar. The oil temperature is set at 60^oC and kept as a constant by the temperature controller. With these constraints settled up, each pump is tested at different speed values, starting from 800rpm till 6000rpm, with a constant step of 100rpm. The maximum speed is limited by the maximum torque provided by the electric motor. Moreover, experimental tests regarding prototype A have been repeated at 90^oC and 120^oC in order to evaluate the influence of the oil temperature. Tests have been performed without reducing the inlet pressure by regulating a valve in the inlet piping, but the speed increasing solely induces cavitation. Despite this testing procedure is uncommon when evaluating the influence of cavitation in fluid machines, it is a more realistic representation of the phenomenon that may take place in actual gear pump applications, e.g. in the auxiliary systems for automotive applications. These pumps are usually driven by the engine and therefore must properly work throughout a wide speed range; on the contrary, the installation can be designed to minimize pressure losses on the inlet pipeline making this parameter less dominant on the evolution of the phenomenon.

Pump Type	z_1/z_2	**Tooth Type**	**Case Material**	p_{out}
A	$14/9$	Helical	Cast iron	30bar
B	$14/9$	Helical	Aluminum	30bar
C	$13/10$	Spur	Aluminum	30bar
D	$11/11$	Helical	Aluminum	30bar

Table 1: Main design characteristics of the four tested prototypes.

In order to verify the presence/absence of cavitation in each pump prototype, endurance tests have been performed on each gear machine and later the potential presence of wear has been assessed. Endurance tests have been performed for 60 hours at the most severe working condition, which corresponds to a combination of angular speed/delivery pressure equals to 6000rpm/30bar. As expected, wear has not been detected on pump prototype D, while various marks of erosion due to cavitation have been observed on prototype A, B and C. In particular, endurance tests on various samples of pump prototype A had to be stopped before the expected time due to severe wear that compromised the correct machines operation.

4 Post processing

The early detection of cavitation phenomena in hydraulic machines by means of vibrational and acoustic measurements requires the design of specific post processing procedures, typically based on the evaluation

of the demodulated signal at the blade passage frequency [3, 4, 20, 25]. However, the application of these methods in the present study did not provide any valuable result. It is the author's belief that such a negative outcome is linked to the methodology adopted in this study to promote cavitation, which is induced by increasing the working speed of the pump, without modifying any other working condition parameter. This method differs considerably from the classical approach that has been described in the literature since the very first publications, in which cavitation is promoted by the reducing the suction pressure at constant nominal speed. This latter method has the benefit to freeze the dynamics of the machine with respect to the working condition; as a consequence, any change recorded in the machine response can be attributed to the cavitation development. Concurrently, as explained in Section 2, the approach is a well representation of real cases: axial/centrifugal machines are designed to work at fixed nominal speed, but they may encounter different suction pressure values depending on the installation layout. On the contrary, gear pumps are often designed to be installed on a specific layout, e.g. in the automotive field a specific pump is designed for a specific driveline transmission, but they are required to work safely throughout a wide speed range. Within this framework, it is therefore clear that promoting cavitation by increasing the working speed is a more realistic reproduction of the real case, even if the machine dynamics becomes to be influenced by both the working condition and the cavitation development. As a matter of fact, the speed increase causes the amplitude of the harmonics of the mesh frequency, together with their sidebands potentially present, to vary through the considered speed range depending on (i) the dynamics of the gearpair, (ii) the dynamics of the overall pump body and (iii) the fluid-dynamics of the machine. This particular behavior masks the signature of cavitation throughout the low frequency range typically excited by the first $10-15$ harmonics of the mesh frequency.

On the basis of these considerations, the phenomenon has been characterized by using an energetic approach applied to a frequency range less involved by the pump dynamics. The first step of the developed procedure consists of calculating the waterfall diagrams of the acquired signals. Waterfall charts are not determined by performing a Short Time Fourier Transform on a single run up, since they can be directly estimated by piling the data acquired at constant speed and expressed in frequency domain on a single chart. By repeating this procedure for each sensor, a general overview of the pump behavior is obtained and the frequency limit value that bounds the low frequency range can be defined by direct observation of such charts. Moreover, as it will be shown in Section 5, waterfall diagrams allow for a preliminary and qualitative evaluation of the presence of cavitation.

The second step of the post processing procedure starts with filtering the data by using a high-pass filter with cutoff frequency equals to the frequency limit value determined in the previous step. Filtered signals at each working speed are then analyzed by calculating their RMS value and displayed with respect to cavitation number σ [2]. The methodology is able to determine the presence of high frequency cavitation noise, in particular when enlightened by the presence of resonances inside the analyzed frequency range.

5 Results and discussion

In the current section, results obtained from the signal processing procedure described in Section 4 are shown and discussed. Attention is particularly focused on showing the signature caused by the presence of cavitation and the different capability of the four adopted sensors in capturing the phenomenon. Moreover, in order to misleading conclusions, the capability to distinguish the cavitation noise from the structural one is verified by applying the the proposed method to a non-cavitating pump.

In order to better understand the importance of the first step of the post processing procedure, waterfall charts of the signals referred to pumps B and D are reported in Figure 4. The latter is specifically designed to not be affected by cavitation in the analyzed working range conditions. Results, that are displayed in logarithmic scale, have been previously normalized by their minimum value and divided by the reference value $k = 10^{-3}$ (the normalized quantity is indicated with symbol $\tilde{X}$). For each plot, two main regions can be distinguished: the low frequency region, which extends to the 40kHz limit in the currently analyzed pumps, and the high

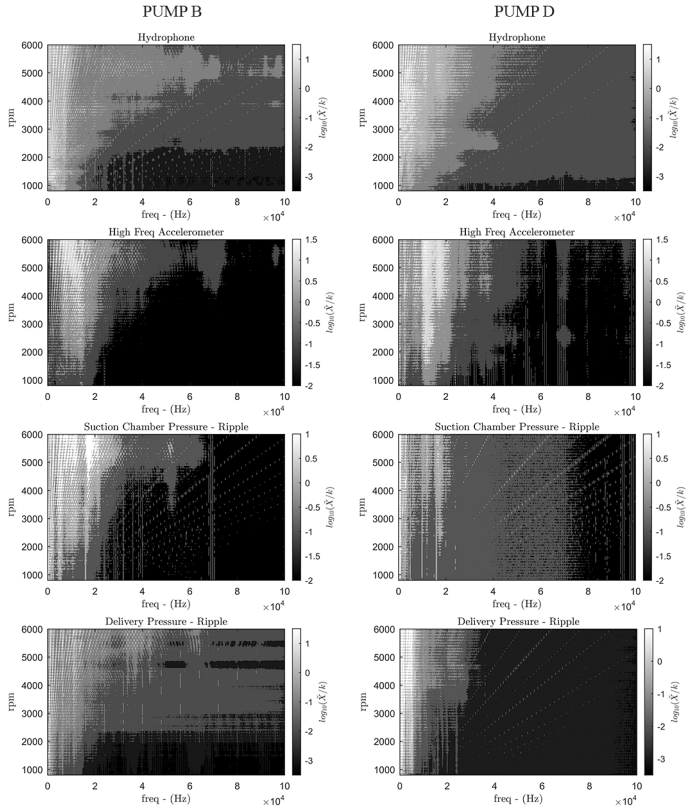


Figure 4: Waterfall plots (in logarithmic scale) of the acquired data referred to pump prototype B, affected by cavitation, and prototype D, not affected by cavitation. In each plot, symbol $\tilde{X}$ refers to the measured quantity normalized by its maximum value.

frequency region, which involves the remaining frequency range. The former region is mainly influenced by the periodic components of the signal, typically harmonics of the angular speed and the mesh frequency. The latter, on the contrary, refers to a frequency range that is usually too high to be crossed by harmonics of the mesh frequency with a relevant amplitude. Concurrently, as also observed in [2, 3, 20], the high frequency range is usually the one characterized by the cavitation signature. Based on these considerations, the waterfall plots become a powerful tool for the determination of the frequency limit that will be used to set the cutoff frequency of the high-pass filter in the following step of the post processing.

Waterfall charts in Figure 4 represent also a valuable tool for a preliminary detection of cavitation. Focusing the attention on the suction chamber pressure ripple, for example, the signals referred to the two pumps show a completely different behavior in the high frequency region. For each arbitrary frequency band within this region, the noncavitating one (prototype D) is characterized by the absence of amplitude gradient along the entire speed range, except for the presence of some high order harmonics of the mesh frequency. On the contrary, the signal referred to the cavitating one (prototype B) outlines the presence of high frequency broadband components between 40 and 70kHz. Such broadband components start being appreciable, in terms of amplitude, qualitatively from 4200rpm, reach a maximum amplitude value at around 5500rpm and then a decrease is observed. The described phenomenon is recognized also in the signals obtained from the other transducers; in particular, hydrophone measurements appear to be the most sensitive, since such a behavior is present throughout the entire bandwidth of the high frequency region.

By following the signal processing procedure defined in Section 4, data referred to pump prototypes B and D have been high-pass filtered at 40kHz and then the RMS value for each transducer at each working speed condition has been calculated (Figure 5). Results are reported together with the measured volumetric

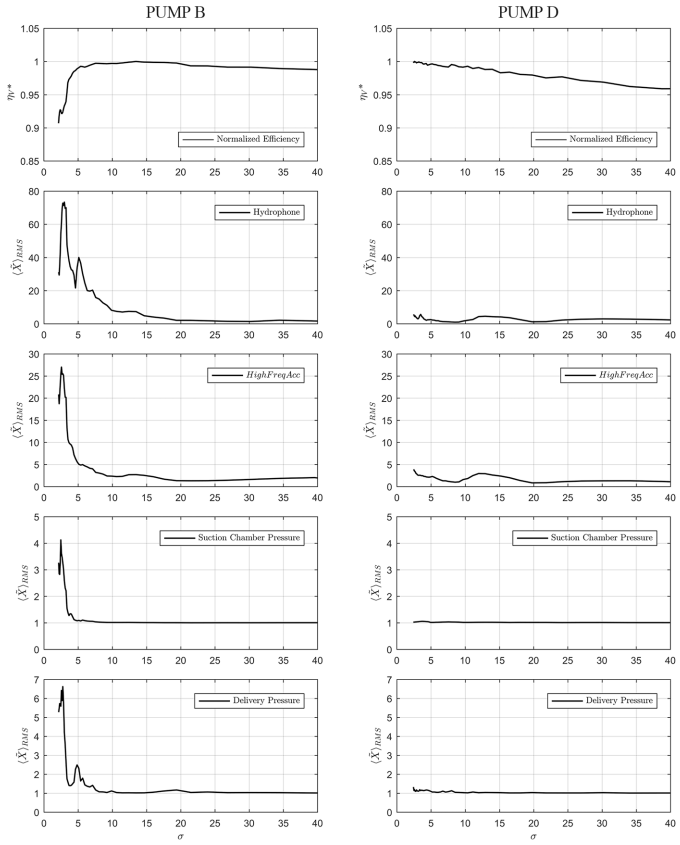


Figure 5: RMS values of the four measured signals and volumetric efficiency as a function of the cavitation number σ, for pump prototypes B and D. In each plot, symbol $\tilde{X}$ refers to the measured quantity normalized by its minimum value, while symbol η_V^* refers to the volumetric efficiency normalized by its maximum value.

efficiency and expressed with respect to the cavitation number σ. For the sake of clarity, measurements performed with hydrophone, accelerometers and pressure transducers are normalized by their respective minimum value. Volumetric efficiency is normalized with respect to its maximum value for confidentiality reasons. As can be appreciated from Figure 5, the efficiency referred to pump B shows the typical sharp drop caused by the presence of intense cavitation; on the contrary, no efficiency reduction is detected for pump D. By focusing the attention on the cavitating one, it is possible to observe that in conformity with the efficiency drop that starts taking place at about $\sigma = 5$, all the four signals show a strong increment of the RMS value. Moreover, as often described in the literature [1, 2, 25, 5], the RMS value reaches a maximum when cavitation is close to the fully developed condition and then starts decreasing. It is therefore clear that intense cavitation phenomena are captured by pressure pulsation measurements as well as acceleration and acoustic measurements. However, since it is well known that incipient cavitation takes place well before the efficiency drop [1, 2, 25], it is interesting to notice that pressure pulsation measurements appear not to be able to detect it. In particular, suction chamber pressure pulsation results to be the least sensitive to the phenomenon since the RMS value begins to increase when the efficiency drop is already developed. On the contrary, both acceleration and acoustic measurements start rising considerably before the efficiency drop, and in particular around $\sigma = 15$. In analogy to the observations made in [25], it is reasonable to assume that incipient cavitation takes place in the range between $\sigma = 10$ and $\sigma = 15$, where pressure pulsation measurements are not affected by a significant variation in their RMS values.

The behavior described by vibration and acoustic measurements can be also appreciated in Figure 6, which reports the results of the post processing applied to acoustic measurements performed on prototype A at three

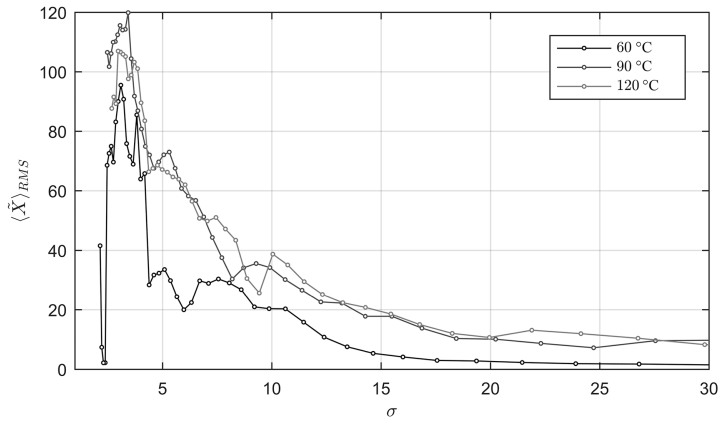


Figure 6: RMS values referred to the hydrophone measurements on pump prototype A at different oil temperature. Symbol $\tilde{X}$ refers to the measured quantity normalized by the minimum value recorded for the 60^oC case, while symbol η_V^* refers to the volumetric efficiency normalized by its maximum value.

different temperature values. The cutoff frequency of the high-pass filter has been set at 45kHz and results have been normalized by the minimum value obtained for the 60^oC case. By focusing the attention on the 60^oC case, it can be noted that the analyzed speed range (from 800rpm to 6000rpm) is able to characterize the entire development of the phenomenon, which starts being detected at $\sigma = 14$. By increasing the speed, i.e. by reducing the cavitation number, RMS value increases and reaches a maximum at $\sigma = 3.10$; after this value, the RMS of the filtered signal shows a sharp drop till the minimum value recorded at $\sigma = 2.38$ and it then starts raising again. Such a particular behavior has been described several times in the literature for rotordynamic machines [1, 2, 25, 5, 26] but no similar data are already available in the literature for positive-displacement machines. Figure 6 allows also for the evaluation of the effect produced by the oil temperature on the cavitation phenomenon. As it can be appreciated, temperature variation does not cause a significant modification of the overall behavior since the maximum of each curve is bounded by $\sigma = 2.97$ and $\sigma = 3.43$. However, since for a given working speed the temperature increasing makes the cavitation number to reduce, measurements performed at 90^oC and 120^oC cannot describe the development of the phenomenon entirely. Practically speaking, the increase of oil temperature spreads the phenomenon on a wider speed range and, in particular, it moves the fully developed cavitation condition at higher speed values.

The comparison between pump prototypes A and B allows for the evaluation of the effects related to the choice of a different casing technology. As described in Section 3.3, pump A has been designed with a cast iron casing that does not require running in processes; this means that radial clearances are entirely defined during the design procedure. On the contrary, prototype B is constituted by an aluminum casing, which undergoes a dedicated running in process allowing for the gearpair to produce a certain amount of wear and therefore modify the radial clearances by itself. Apart from this aspect, the two pumps are identical. On the basis of these considerations, Figure 7 shows the comparison between the two pumps in terms of the vibro-acoustic response, normalized with respect to the minimum value calculated for pump prototype A; measured efficiency is given as standard proof of the presence of cavitation. Although the overall behavior is similar, RMS values referred to pump B are considerably smaller in the range where the cavitation takes place; on the contrary, outside this range, calculated values are similar both regarding acoustic and acceleration measurements. It is therefore reasonable to assume that, since the running in process permits the gearpair to self-adjust its radial clearances through a controlled wear, it also actively contributes in reducing the intensity of the cavitation phenomenon. As underlined in Section 3.3, the higher intensity of cavitation in pump prototype A is also proved by the presence of an excessive amount of wear observed by performing endurance tests on various samples of such a prototype. From these considerations, it results that vibro-acoustic measurements performed on external gear pumps are able to quantitatively define the intensity of

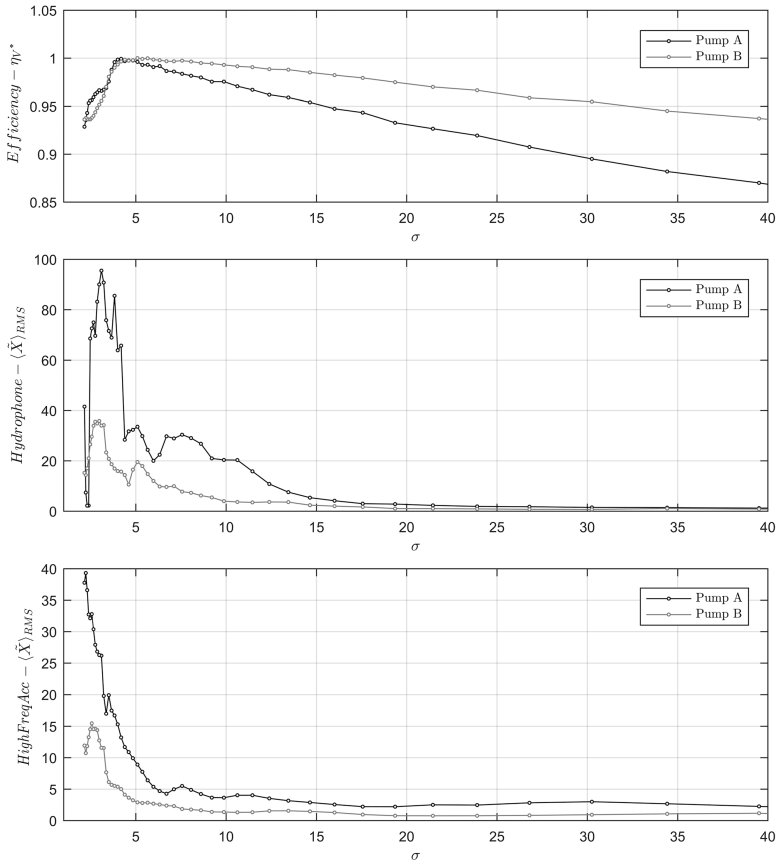


Figure 7: Comparison between pump prototypes A and B in terms of hydrophone and accelerometer response (RMS values); efficiency measurements are shown as a benchmark indicator. In each plot, symbol $\tilde{X}$ refers to the measured quantity normalized by its minimum value recorded for pump prototype A, while symbol η_V^* refers to the volumetric efficiency normalized by its maximum value.

the cavitation phenomenon, in addition to their capability to detect it in advance with respect to pressure ripple and efficiency measurements.

6 Concluding remarks

An extended experimental campaign aiming at detecting cavitation in external gear pumps by means of acceleration and acoustic measurements has been presented. With this purpose, a dedicated test rig has been instrumented with a hydrophone and a high frequency accelerometer, together with pressure ripple transducers located both on the suction and delivery chambers. Moreover, a flow meter, a tachometer and two digital pressure gauges complete the set of transducers adopted to control the pump working conditions.

In order to perform the present study, four different pump prototypes have been designed with the aim at evaluating the phenomenon under the effects of different design solutions. In particular, last prototype has been specifically designed to not be affected by cavitation throughout the entire working conditions range examined; this characteristic makes it as the reference point to assess the results. The effective presence/absence of cavitation in the four prototypes has been checked with the help of efficiency measurements and endurance tests, showing examples of various cavitation erosion marks observed.

The application of the post processing procedure has underlined the necessity of a general overview of the signals, which is achieved with the help of waterfall spectra extended to the entire measured frequency range.

This first step identifies two different regions: the low frequency one, which is mainly influenced by the mesh frequency and its harmonics, and the high frequency one, which is mainly characterized by the wideband cavitation noise.

Experimental data are filtered to enlighten the high frequency region and then RMS values of such signals are plotted with respect to the cavitation number. Comparison between pump B (cavitating) and D (not cavitating) has underlined the effective capability of the procedure in detecting the presence of the phenomenon. In particular, acceleration and acoustic measurements appeared to be highly sensitive to the phenomenon if compared to efficiency measurements as well as pressure ripple measurements. All the calculated results qualitatively reproduce the behavior usually detected in rotordynamic pumps and turbines, demonstrating that the cavitation phenomenon can be analyzed also in volumetric pumps in a similar manner. Results obtained on pump prototypes A and C (both cavitating) confirm these observations.

Influence of the oil temperature has been evaluated by reproducing the tests at three different temperature values: 60^oC, 90^oC and 120^oC. Results seem demonstrating that the temperature increasing tends to spread the development of cavitation throughout a wider speed range and, in particular, to move the fully developed cavitation condition at higher speed values. Moreover, influence of the casing technology has been evaluated: pumps made by aluminum casings resulted to be less affected by cavitation. This result may be explained by considering that aluminum casings require the pumps to undergo a dedicated running in process that allows the gearpair to self-adjust its radial clearances through a controlled wear process. This aspect seems to contribute in reducing the intensity of the cavitation phenomenon, as verified by endurance tests performed on various samples of pump prototypes A and B. The capability of the proposed procedure to capture the intensity of the phenomenon, a characteristic that efficiency curves cannot detect, can be clearly appreciated by comparing the maximum RMS values calculated for the two pump prototypes. As a consequence of this assessment, the method resulted to be able to evaluate the severity of the cavitation in gear pumps.

The proposed study therefore demonstrates that vibro-acoustic measurements coupled with a dedicated signal processing procedure are a powerful tool for the early detection of cavitation in external gear pumps and a quantitative estimation of the intensity of the phenomenon. However, it also underlines that such a phenomenon is still not completely addressed and further studies should be devoted to analyze the nature of cavitation in gear pumps in correlation with the nature of the produced signals.

References

[1] I. S. Pearsall, Acoustic detection of cavitation, Proceedings of the Institution of Mechanical Engineers 181 (1966) paper 14.

[2] P. J. McNulty, I. S. Pearsall, Cavitation inception in pumps, Journal of Fluids Engineering 104 (1) (1982) 99–104.

[3] P. A. Abbot, Cavitation detection measurements on Francis and Kaplan hydro turbines, in: R. E. A. Arndt, M. L. Billet, W. K. Blake (Eds.), Proceedings of the Third International Symposium on Cavitation, Noise and Erosion in Fluid Systems, San Francisco, CA, 1989, pp. 55–61.

[4] P. A. Abbot, C. J. Gedney, D. L. Greeley, Cavitation monitoring of two axial-flow hydroturbines using novel acoustic and vibration methods, in: Proceedings of the 13th IAHR Symposium, Vol. 1, Montreal, Canada, 1986, p. paper 23.

[5] M. Čudina, Detection of cavitation Phenomenon in a centrifugal pump using audible sound, Mechanical Systems and Signal Processing 17 (6) (2003) 1335–1347.

[6] J. Černetič, M. Čudina, Estimating uncertainty of measurements for cavitation detection in a centrifugal pump, Measurement 44 (7) (2011) 1293–1299.

[7] A. Adamkowski, A. Henke, M. Lewandowski, Resonance of torsional vibrations of centrifugal pump shafts due to cavitation erosion of pump impellers, EFA 70 (2016) 56–72.

[8] Z. Yan, J. Liu, B. Chen, X. Cheng, J. Yang, Fluid cavitation detection method with phase demodulation of ultrasonic signal, Applied Acoustics 87 (2015) 198–204.

[9] R. Azizi, B. Attaran, A. Hajnayeb, A. Ghanbarzadeh, M. Changizian, Improving accuracy of cavitation severity detection in centrifugal pumps using a hybrid feature selection technique, Measurement 108 (2017) 9–17.

[10] M. Borghi, M. Milani, F. Paltrinieri, B. Zardin, The Influence of Cavitation and Aeration on Gear Pumps and Motors Meshing Volumes Pressures, in: ASME IMECE 2006, Chicago, 2006, pp. 1–10.

[11] J. Zhou, A. Vacca, B. Manhartsgruber, A Novel Approach for the Prediction of Dynamic Features of Air Release and Absorption in Hydraulic Oils, Journal of Fluids Engineering 135 (9) (2013) 091305.

[12] J. Zhou, A. Vacca, P. Casoli, A novel approach for predicting the operation of external gear pumps under cavitating conditions, Simulation Modelling Practice and Theory 45 (2014) 35–49.

[13] E. Mucchi, G. Cremonini, S. Delvecchio, G. Dalpiaz, On the pressure ripple measurement in variable displacement vane pumps, Journal of Fluids Engineering 135 (2013) 091103.

[14] E. Mucchi, G. Dalpiaz, A. Fernandez Del Rincon, Elasto-dynamic analysis of a gear pumpPart IV: Improvement in the pressure distribution modelling, Mechanical Systems and Signal Processing (2014) 1–21.

[15] M. Battarra, E. Mucchi, G. Dalpiaz, A model for the estimation of pressure ripple in tandem gear pumps, in: ASME IDETC/CIE, 2015, p. V010T11A018; 9 pages.

[16] M. Battarra, E. Mucchi, A method for variable pressure load estimation in spur and helical gear pumps, Mechanical Systems and Signal Processing 76-77 (2016) 265–282.

[17] D. Buono, D. Siano, E. Frosina, A. Senatore, Gerotor pump cavitation monitoring and fault diagnosis using vibration analysis through the employment of auto-regressive-moving-average technique, Simulation Modelling Practice and Theory 71 (2016) 61–82.

[18] D. del Campo, R. Castilla, G. A. Raush, P. J. Gamez-Montero, E. Codina, Numerical Analysis of External Gear Pumps Including Cavitation, Journal of Fluids Engineering 134 (8) (2012) 081105.

[19] D. del Campo, R. Castilla, G. A. Raush, P. J. Gamez-Montero, E. Codina, Pressure effects on the performance of external gear pumps under cavitation, Proceedings of the Institution of Mechanical Engineers, Part C: Journal of mechanical engineering science 228 (16) (2014) 2925–2937.

[20] X. Escaler, E. Egusquiza, M. Farhat, F. Avellan, M. Coussirat, Detection of cavitation in hydraulic turbines, Mechanical Systems and Signal Processing 20 (4) (2006) 983–1007.

[21] J. P. Tullis, Hydraulics of Pipelines - Pumps, Valves, Cavitation, Transients, John Wiley & Sons, Inc., 1989.

[22] S. C. Li, Cavitation in hydraulic machinery, Imperial College Press, London, 2000.

[23] E. Mucchi, G. Dalpiaz, A. Rivola, Dynamic behavior of gear pumps: Effect of variations in operational and design parameters, Meccanica 46 (6) (2011) 1191–1212.

[24] M. Battarra, E. Mucchi, Evaluating time dependent pressure forces and torques in external gear machines by means of an analytical approach, in: INTER-NOISE, Hong Kong, 2017, pp. 6737–6748.

[25] T. Rus, M. Dular, B. Sirok, M. Hocevar, I. Kern, An Investigation of the Relationship Between Acoustic Emission, Vibration, Noise, and Cavitation Structures on a Kaplan Turbine, Journal of Fluids Engineering 129 (September) (2007) 1112.

[26] M. Čudina, J. Prezelj, Detection of cavitation in operation of kinetic pumps. Use of discrete frequency tone in audible spectra, Applied Acoustics 70 (4) (2009) 540–546.

Spectral optical flow imaging - measuring full-field sub-pixel oscillations without a high-speed camera

J. Slavič [1], **J. Javh** [1], **M. Boltežar** [1]
[1] University of Ljubljana, Laboratory for Dynamics of Machines and Structures,
Aškerčeva 6, 1000 Ljubljana, Slovenia
e-mail: **janko.slavic@fs.uni-lj.si**

Abstract
In recent years high-speed cameras have seen great progress, both in hardware performance as well as in the progress of image processing methods. Digital image correlation methods have been around for decades, but only in recent years those methods have been extended to the experimental modal analysis. If compared to classical still cameras, the high-speed cameras are expensive. Still as well as high-speed cameras offer great spatial resolution.
This article presents a new approach, the Spectral Optical Flow Imaging (SOFI), where classical (still) cameras are used to capture spectral components (real and imaginary) of a vibrating structure. It is shown that one spectral component can be obtained from three still pictures. Theoretical background is supported with an experiment; the results are compared to the high-speed camera approach.

1 Introduction

Photogrammetric displacement measurements using high-speed cameras and various optical flow image processing algorithms such as digital image correlation [1] and other frequency based methods [2, 3], are increasingly being used in modal analysis [4]. Displacement measurements from images are non-contact and produce dense, simultaneous, full-field measurements accurate to within 1/100 of a pixel between frames and 1/10000 of a pixel in the amplitude spectrum [5]. Implementing a stereoscopic camera set-up, three-dimensional displacements can be measured [6].

Photogrammetric measurements suffer from high equipment costs in case of using high-speed cameras, which typically cost many tens of thousands of euros, and up to a few hundred thousand euros for a stereoscopic pair of higher-end cameras. To reduce the equipment costs, single-camera measurement approaches have been explored; the stereo information can be acquired with repeated measurements at different angles [7] or by using a dividing mirror, producing two viewing angles for a single camera [8, 9]. A number of researchers have used lower-speed cameras to measure structural dynamics, by under-sampling and remapping the time instances [10], or by using frequency zooming and allowing for aliasing [11], also the researchers that extracted sound from vibrations in videos [12] were able to use the rolling-shutter effect to sample high frequencies from a normal DSLR camera video. Compared to high-speed cameras, still-frame cameras typically boast a higher colour-intensity resolution (typically 14-bit) and a higher pixel resolution, ranging in multiple tens of mega-pixels, at a cost of only 500–2000 euros.

This research reviews the Spectral Optical Flow Imaging (SOFI) measurement technique introduced in [13] that uses a still-frame camera and harmonically varying illumination to measure individual displacement spectral components.

2 Spectral Optical Flow Imaging

Spectral optical flow imaging (SOFI) was introduced in [13]. The method is briefly explained here, however, for more details, please refer to the original publication.

A radiance field $r((x,y),L)$ is produced by light L being reflected from the structure's surface $P(x,y)$ (where (x,y) are the coordinates of the camera's image plane):

$$r\big((x,y),L\big) = P(x,y)\,L \tag{1}$$

The radiance is converged by a lens and projected on the camera's sensor where it gets integrated over a set exposure time T_e to produce pixel intensities $I(x,y)$:

$$I\big((x,y),L\big) = \int_0^{T_e} r\big((x,y),L\big)\,\mathrm{d}t, \tag{2}$$

By assuming small displacements, a displacement s will produce a change in the radiance approximately equal to:

$$r\big((x,y)+s,L_0\big) = r\big((x,y),L_0\big) + s\,\nabla r\big((x,y),L_0\big), \tag{3}$$

where ∇r is the radiance gradient. Relation (3) is based on brightness conservation and is commonly used to estimate the displacements based on the intensity gradient in Optical Flow methods, such as Lucas-Kanade [1]. The equation is typically written in the form of pixel intensities instead of radiance. Unlike typical Optical Flow, Spectral Optical Flow implements a harmonically varying illumination:

$$L(t) = L_0 + L_A\,\sin(\omega_l\,t), \tag{4}$$

which produces the following radiance relation:

$$\begin{aligned} r\Big((x,y)+s\big((x,y),t\big),L(t)\Big) &= \frac{L(t)}{L_0}\,r\Big((x,y)+s\big((x,y),t\big),L_0\Big) = \\ &= \frac{L(t)}{L_0}\Big(r\big((x,y),L_0\big) + s\big((x,y),t\big)\,\nabla r\big((x,y),L_0\big)\Big) \end{aligned} \tag{5}$$

By integrating both sides of the equation (5) over the exposure time T_e and neglecting non-significant terms, the following relation can be produced:

$$\begin{aligned} \underbrace{I\Big((x,y)+s\big((x,y),t\big),L(t)\Big)}_{\text{blinking \& vibrations image}} &= \underbrace{I\big((x,y),L_0\big)}_{\text{reference image}} + \\ + \underbrace{\frac{L_A}{L_0}}_{\substack{\text{illumination}\\ \text{scaling}}}\ \underbrace{\nabla I\big((x,y),L_0\big)}_{\substack{\text{reference image}\\ \text{gradient}}}\ \underbrace{\frac{S_s\big((x,y),\omega_l\big)}{2}}_{\substack{\text{displacement}\\ \text{spectral}\\ \text{component}}} & \end{aligned} \tag{6}$$

the above equation indicates that an image of a vibrating structure illuminated with a harmonically varying light (blinking & vibrations image) is composed of a motionless image under constant illumination (reference image) and the distortion caused by the displacement spectral component, which is a product of the illumination scaling, the reference image gradient and the displacement spectral component $S_s\big((x,y),\omega_l\big)$ of the frequency equal to the frequency of the varying light ω_l. The displacement spectral component $S_s\big((x,y),\omega_l\big)$ can be obtained as:

$$S_s\big((x,y),\omega_l\big) = \frac{I\Big((x,y)+s\big((x,y),t\big),L(t)\Big) - I\big((x,y),L_0\big)}{\frac{1}{2}\,\frac{L_A}{L_0}\,\nabla I\big((x,y),L_0\big)} \tag{7}$$

By using different illumination frequencies ω_l and by changing the phase of the lights relative to the vibrations, other spectral components can be measured. The frequency of interest is not limited by the camera and can be very high (in the range of kHz) as long as the displacements are significant enough to be identified. Relatively small displacement amplitudes can be measured, because a typical displacement resolution between two images is in the range of a hundredth of a pixel, provided that the gradient in the pixel (x, y) is appropriate [5].

The displacement amplitudes $S_s((x, y), \omega_n)$ and $S_c((x, y), \omega_n)$ are displacements in the direction of the image gradient only. The 2D displacements can be determined by identifying displacements of larger subsets of the image (e.g. 20×20) containing various gradient directions. Perhaps the most prominent 2D Optical Flow is the Lucas-Kanade method. To obtain appropriate 2D results using SOFI, the identified displacements using Lucas-Kanade need to be scaled according to the illumination $1/(L_A/L_0)$, as indicated by Equation (7).

3 Practical considerations

Spectral Optical Flow Imaging is analogous to the Fourier transform and is therefore affected by windowing effects [14]. To avoid windowing effects, the exposure time T_e should preferably match multiples of the displacement and illumination harmonic periods.

To obtain valid results, the cumulative motion should be very small, so as not to violate the small motion assumptions made in Equation (3). The motion should not exceed the area of gradient linearity, the size of which depends on the filmed pattern, however a rough value would be 1 pixel of motion.

When performing experiments a problem was made apparent. It was observed that sequential frames captured by the consumer camera produced apparent displacement fields. Since SOFI works by identifying displacements between frames, these apparent displacements can cause erroneous data. The apparent displacements were observed for completely stationary conditions measured on a vibro-isolated granite block. We believe that the source of the apparent displacements is the result of the jerk caused by the retraction of the mirror and the operation of the mechanical shutter of the camera taking still images. It is believed that the jerk causes shifts of the lenses, thereby distorting the image ever so slightly. Figure 1 shows an example of such apparent displacements. The apparent displacements typically range around 0.1 pixel, which is significant. The problem can be solved by filming a video instead of taking still images, because in that case no

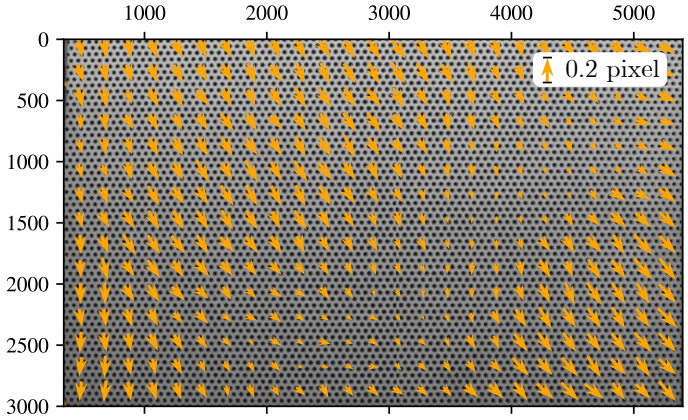


Figure 1: Apparent displacement fields believed to be caused by the jerk of the camera shutter and / or the mirror retraction

mechanical operation is present during the capture. Still images can be produced from video by setting the exposure time to match the period of the camera's frame rate, this way no significant discontinuation of the intensity integration (2) are present when cumulating the video frames into a still frame.

Another reason for displacements between frames can be the result of actual displacements, such as rigid motion between the reference image taken for stationary conditions and the blinking & vibrations image. To account for these displacements we would acquire the reference image during operation, but keeping the light constant. This is because such an image is approximately equal to the reference image:

$$\begin{aligned} & I\Big((x,y)+s\big((x,y),t\big),L_0\Big) = \\ & = \int_0^{T_e} \Big(r\big((x,y),L_0\big) + s\big((x,y),t\big)\,\nabla r\big((x,y),L_0\big)\Big)\mathrm{d}t \approx \\ & \approx I\big((x,y),L_0\big), \end{aligned} \tag{8}$$

because the integral of the $s\big((x,y),t\big)\,\nabla r\big((x,y),L_0\big)$ part is zero for harmonic motion when the exposure time T_e is a multiple of the periods of motion $s(t)$ and the displacements are small (within the area of gradient linearity).

4 Experimental set-up

To capture a frequency component three images need to be acquired; a reference image, an image at sine phase illumination and an image at cosine illumination. Figure 2 shows an example of a capture procedure with orange indicating the excitation force, which for the given case was single harmonic, and blue indicating the measured light intensity. The close-up shows the three different illumination conditions, which each produce their separate images. During the acquisition of the separate images the response is considered to be indifferent. It should be noted that the excitation does not need to be single harmonic for SOFI to work,

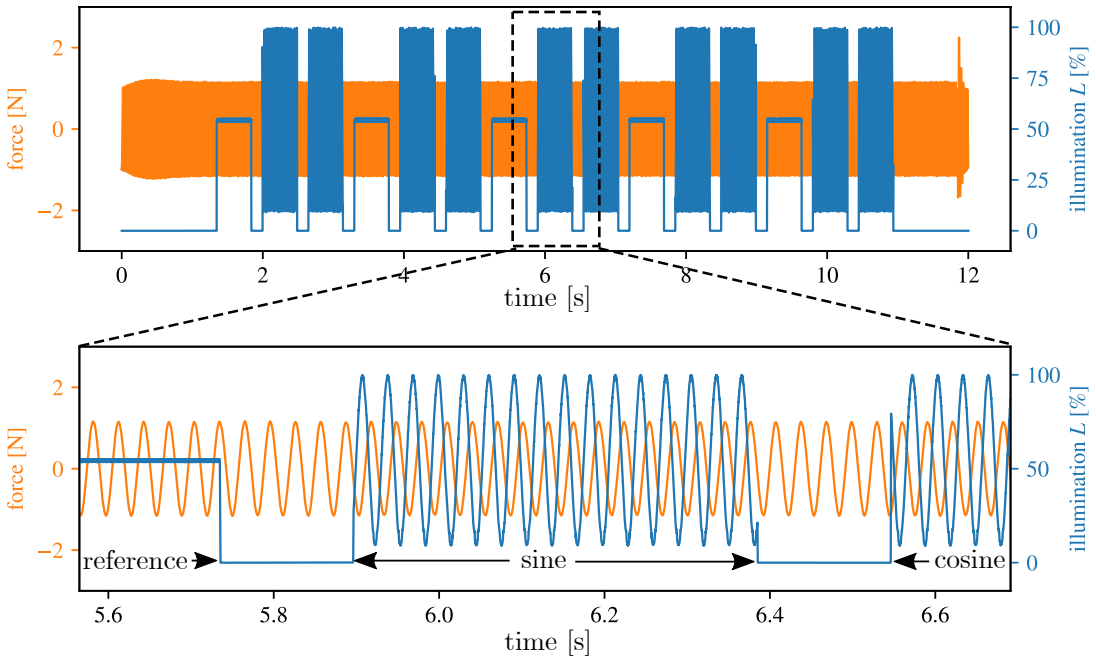


Figure 2: Measured illumination and force during five repetitions of a SOFI measurement for the frequency component $f_l = 32.71$ Hz

SOFI captures only a selected frequency component even for a multisine excitation (for example see [13]).

The phase matching between the SOFI measurement and the force measurement is achieved by syncing the illumination with the excitation.

To produce a harmonically varying illumination a simple feedback-loop circuit can be created to linearly control the LEDs (Light Emitting Diodes), or some other light source. The feedback should preferably be intensity based, for instance from the current sense of a reference photodiode placed in line of the illumination. Another control strategy could be using pulse width modulation (PWM) to power the LEDs. Our experiments were produced using the feedback regulation.

5 Operational modal analysis experiment

SOFI was demonstrated for an operational case of an electric motor running at a set frequency in [13]. The motor's frequency of rotation was PID-controlled and set to be 125 Hz. The PID kept the motor's rotation in phase with the lights with an error lower than $4.5°$ over the 3 s required to capture the reference image and the two images with varying illumination. This experiment was performed before the inconsistencies between frames were noticed, this is why the still images were acquired with a Nikon D5300 DSLR consumer camera at 24 megapixel (the area of interest was later limited to 3576×3616 to fit the front of the motor fixture). The DSLR exposure time was set to $1/5\ s$ to be in line with the assumptions made in Section 3. The other capture settings were fixed to produce an optimal exposure spanning the full 14-bit intensity resolution of the camera. The colour images were transformed to black and white and blurred with a 8×8 subset before processing. A high-contrast dotted sticker was stuck on the face of the motor fixture, to make the displacements more apparent due to high gradients.

The experimental set-up is shown in Figure 3. The high-speed camera in Figure 3 is present to monitor the process, after the SOFI measurement it replaced the DSLR to produce results for the comparison shown in Figure 4. Figure 4 shows the reconstructed trajectories from the SOFI (DSLR) and the high-speed camera

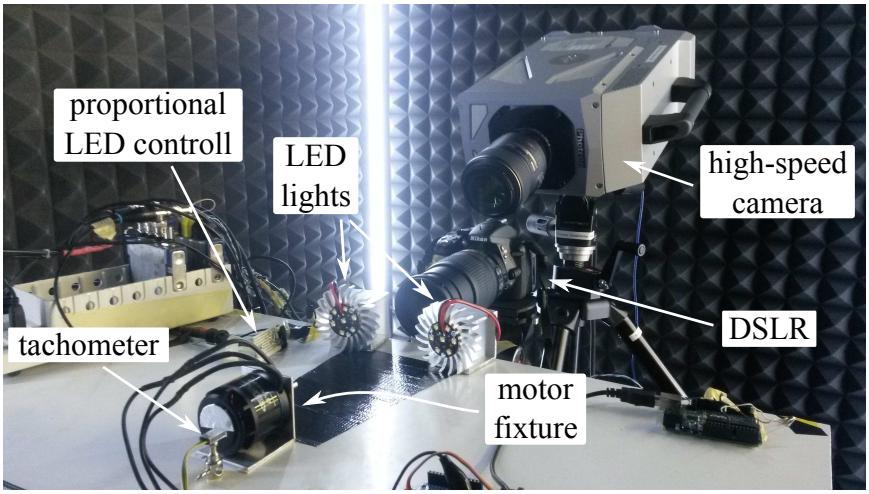


Figure 3: The SOFI electric motor experiment set-up

(HS) for the 125 Hz component. The elliptical trajectories are scaled by a factor of $250\times$ and overlaid on the image captured by the DSLR. The comparison shows agreeing results. The divergence is now believed to be mostly the result of the inconsistencies between frames caused by the shutter operation, although other effects, such as non-stationary response, spectral leakage and the small motion assumption may have an effect as well.

6 Experimental modal analysis experiment

In a later study [15] SOFI was used to perform an experimental modal analysis of a cymbal.

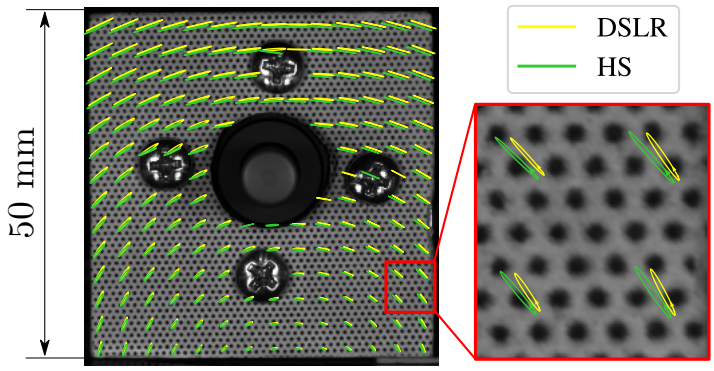


Figure 4: Overlaid reconstructed trajectories of the measured 125 Hz harmonic using the DSLR (SOFI) and the high-speed camera (HS). Trajectories are scaled by a factor of $250\times$.

The cymbal was rigidly fixed at its centre hole and excited using a shaker attached close to the ridge as indicated in Figure 5.

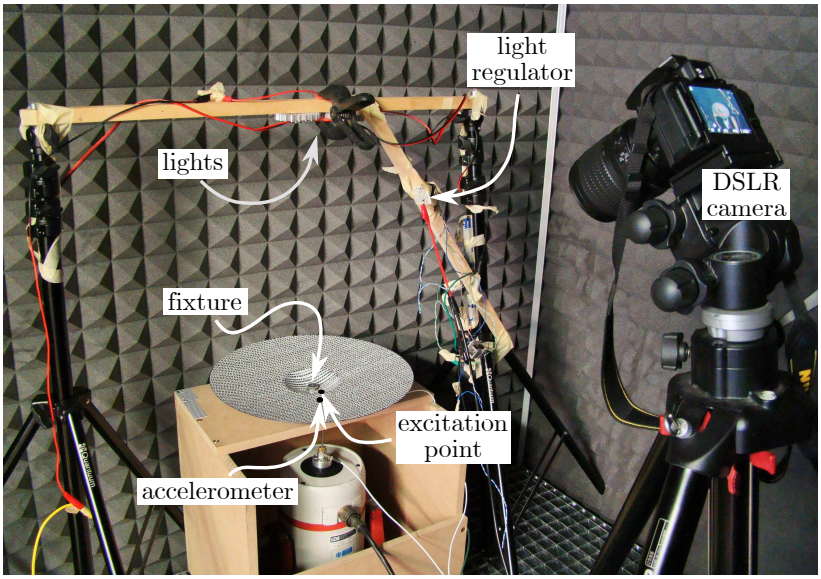


Figure 5: The SOFI cymbal experiment using shaker excitation

Alongside the images captured by the Nikon consumer camera the excitation force and responses in two points were measured (one using an accelerometer and one using a laser vibrometer). The single point response measurements produced by the accelerometer and the laser vibrometer were used to identify the eigenvalues of the cymbal. The eigenvalues were then combined with 39 full-field frequency components, measured using SOFI, in a hybrid modal parameter identification [16] to produce the full-field mode shapes.

Figure 6 shows some of the 39 mode shapes (modal constants) obtained from the SOFI measurement in the hybrid modal parameter identification with the accelerometer eigenvalues. Each shape is accompanied by the identified eigenvalue in the form of an eigenfrequency f_r and damping ζ_r. Green colour indicates the real values of the modal constants and red indicates the imaginary values. The intensity of the colours indicate the magnitude.

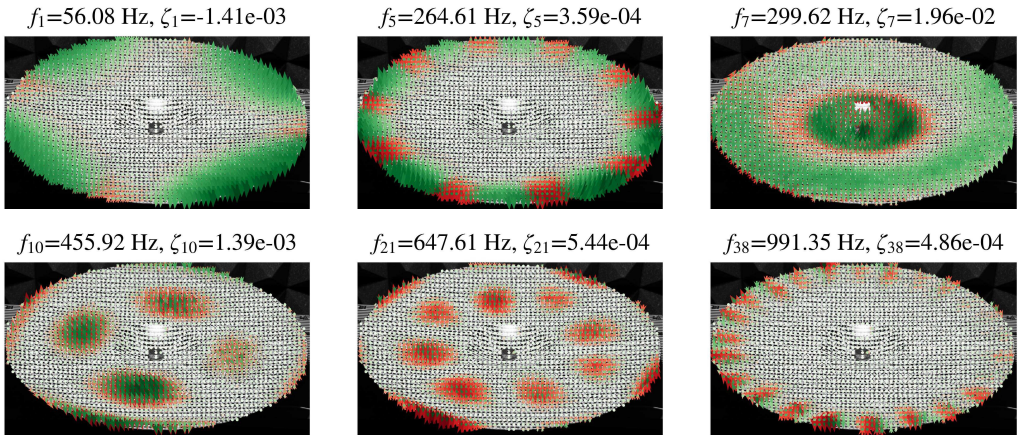


Figure 6: Set of identified mode shapes using the consumer camera and SOFI

7 Conclusion

Spectral Optical Flow Imaging enables the acquisition of full-field operational shapes for frequencies far above the camera's sampling rate (frame rate), enabling modal measurements using consumer cameras. Examples of use are demonstrated for a case of operational modal analysis and experimental modal analysis.

Compared to high-speed camera measurements SOFI is much cheaper, because it works with affordable still-frame cameras, which have the added benefit of a high pixel count and high bit depth. SOFI produces valid results comparable to high-speed cameras, however it has proved to be considerably sensitive, due to the required assumptions. The method requires a set time-varying illumination and only works for small displacements in the range of approximate gradient linearity. Since the method typically uses three sequential frames to produce a single frequency component, any inconsistencies between frames produce errors. The inconsistency between frames caused by the shutter operation force the use of video acquisition instead of still-frame images, limiting the image quality and resolution. Also, compared to high-speed measurements, SOFI measurements do not benefit from the noise reduction due to the effect of dithering enabled by high counts of acquired images [5].

References

[1] B. Lucas, T. Kanade, An iterative image registration technique with an application to stereo vision, International Joint Conference on Artificial Intelligence (1981) 674–679.

[2] H. Foroosh, Z. B. Zerubia, M. Berthod, Extension of phase correlation to subpixel registration, IEEE Transactions on Image Processing 11 (3) (2002) 188–200.

[3] D. J. Fleet, A. D. Jepson, Computation of component image velocity from local phase information, International journal of computer vision 5 (1) (1990) 77–104.

[4] J. Baqersad, P. Poozesh, C. Niezrecki, P. Avitabile, Photogrametry and optical methods in structural dynamics - a review, Mechanical Systems and Signal Processing 86 (2017) 17–34.

[5] J. Javh, J. Slavič, M. Boltežar, The subpixel resolution of optical-flow-based modal analysis, Mechanical Systems and Signal Processing 88 (2017) 89–99.

[6] P. F. Luo, Y. J. Chao, M. A. Sutton, W. H. Peters, Accurate measurement of three-dimensional deformations in deformable and rigid bodies using computer vision, Experimental Mechanics 33 (2) (1993) 123–132.

[7] T. G. Ryall, C. S. Fraser, Determination of structural modes of vibration using digital photogrammetry, Journal of Aircraft 39 (1) (2002) 114–119.

[8] M. Pankow, B. Justusson, A. M. Waas, Three-dimensional digital image correlation technique using single high-speed camera for measuring large out-of-plane displacements at high framing rates, Applied Optics 49 (17) (2010) 3418–3427.

[9] L. Yu, B. Pan, Single-camera high-speed stereo-digital image correlation for full-field vibration measurement, Mechanical Systems and Signal Processing 94 (2017) 374–383.

[10] Y. Liu, H. Gao, J. Zhuge, J. Zhao, Research of under-sampling technique for digital image correlation in vibration measurement, Shock & Vibration, Aircraft/Aerospace, Energy Harvesting, Acoustics & Optics 9 (2017) 49–58.

[11] J. Javh, M. Brumat, J. Slavič, M. Boltežar, A high-speed camera measurement set-up for deflection shape analysis, Proceeding of ISMA2016-USD2016 (2016) 1043–1050.

[12] A. Davis, M. Rubinstein, N. Wadhwa, G. Mysore, F. Durand, W. T. Freeman, The visual microphone: Passive recovery of sound from video, ACM Transactions on Graphics (Proc. SIGGRAPH) 33 (4) (2014) 1–10.

[13] J. Javh, J. Slavič, M. Boltežar, Measuring full-field displacement spectral components using photographs taken with a DSLR camera via an analogue fourier integral, Mechanical Systems and Signal Processing 100 (2018) 17–27.

[14] K. Shin, J. Hammond, Fundamentals of signal processing for sound and vibration engineers, John Wiley & Sons, 2008.

[15] J. Javh, J. Slavič, M. Boltežar, Experimental modal analysis on full-field dslr camera footage using spectral optical flow imaging, submitted to Journal of Sound and Vibration.

[16] J. Javh, J. Slavič, M. Boltežar, High frequency modal identification on noisy high-speed camera data, Mechanical Systems and Signal Processing 98 (2018) 344–351.

Hardware in the loop testing using a hydraulic shaking table

M. Böswald[1], M. Tang[1]
[1] Deutsches Zentrum für Luft- und Raumfahrt (DLR)
Institute of Aeroelasticity, Department for Structural Dynamics and System Identification
Bunsenstraße 10, D-37073 Göttingen, Germany
e-mail: **Marc.Boeswald@DLR.de**

Abstract
In aerospace engineering, experimental testing is mandatory for certification. In case of assembled structures, the interaction of dynamic loads between substructures largely determines the overall dynamic behavior. However, testing of large assembled structures is not always feasible or may be unreasonable from economic considerations. Hardware-in-the-loop (HIL) simulation is a testing technique based on dynamic substructuring of large assembled structures, where one part of an assembled structure is available as hardware while the remaining part is represented by a simulation model. The interaction between the virtual and the physical substructure requires the measurement of interface forces and the emulation of interface motion using a dedicated test facility. In this paper, the feasibility of HIL is investigated using a six-axis hydraulic shaking table. The theoretical foundation for HIL is reviewed and the critical factors for the success of HIL are being discussed. An exemplary application is presented.

1 Introduction

The Institute of Aeroelasticity of the German Aerospace Center (DLR) operates the six-axis hydraulic shaking table MAVIS (Multi-Axial VIbration Simulator), see Figure 1. Its hydraulic and mechanical hardware components originate from the 1980's but still meet state-of-the-art requirements for hydraulic test facilities. The multi-axis vibration controller of MAVIS has been upgraded with a retro-fit solution compatible with the existing hydraulic and mechanical hardware in November 2015. Next to the standard test sequences for qualification tests like random, sine or swept-sine in single or even multiple axes, the new vibration controller can process uploaded long duration time-histories (e.g. results of a numerical simulation) to be used as target signals for the table motion. Furthermore, the new controller has a provision for the input of external transient signals to be used as instantaneous target motion signals for all six axes simultaneously.

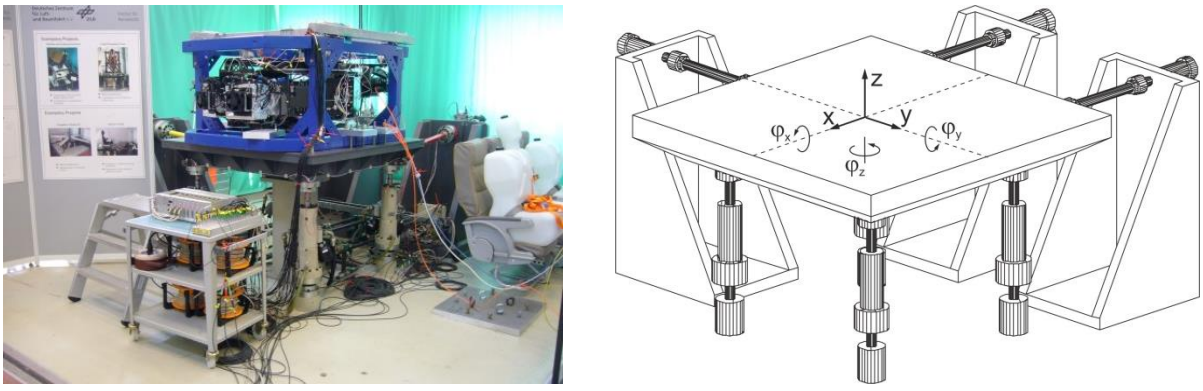


Figure 1: Six-axis hydraulic shaking table MAVIS

The feasibility of HIL testing on MAVIS with its new vibration controller has been investigated within a Master Thesis conducted at the DLR Institute of Aeroelasticity, [1]. The setup for HIL is sketched in Figure 2: A state-space model of the virtual substructure is implemented on a real-time controller. This controller analyses in real-time the displacement at the interface of the virtual and the physical substructure comprising all 6 degrees-of-freedom (DoFs). The state-space model uses the interface forces measured with a 6-axis force measurement platform (force measurement device, FMD) as input. The calculated 6-axis displacement responses are provided to the MAVIS facility as transient external signals for the target displacements. The physical substructure is installed on the table of the MAVIS facility and responds dynamically to the enforced base excitation. The resulting dynamic constraint forces of the physical substructure (i.e. the interface forces) are fed as input into the real-time controller. As a consequence of the coupling, the dynamic response of the physical substructure corresponds represents the response of the overall assembled system. The six-axis hydraulic test facility MAVIS is the key enabler for HIL, because it provides the controlled interface motion in six axes simultaneously.

2 Theoretical background and modelling considerations

Reasons for HIL testing are manifold. It is a means to investigate the local dynamic behavior of a specific substructure of an overall assembled structure. The particular advantage over component testing is that the dynamic interactions between the physical substructure and the rest of the structure are taken into account. Consequently, the local dynamic behavior of the substructure is observed with the correct boundary conditions (i.e. frequency dependent mechanical impedance) representative for the in-situ installation in an assembly of substructures. The essential feature is: one substructure is hardware (i.e. the physical substructure), and the other substructure is a simulation model (i.e. the virtual substructure). Continuous real-time simulation is required for real-time dynamic interaction between simulation and test. This is mostly achieved by employing numerically efficient state-space models solved on a dedicated real-time controller. To reduce the computational effort, these are realized in most cases as discrete-time state-space models, modal state-space models, or even a combination of the two.

In the applications considered here, the setup shall be limited to two substructures, i.e. one physical substructure and one virtual substructure. Furthermore, the two substructures shall have a single statically determined interface, i.e. no more than 6 DoFs in case of 3 dimensional substructures. In this case, the MAVIS test facility is able to emulate the interface motion.

The following discussion of the interactions of substructures in a HIL setup and the related notation of quantities refers to Figure 2 and to references [2], [3], and [4]. The superscript *p* in Figure 2 indicates quantities of the physical substructure, while the superscript *v* indicates quantities of the virtual substructure. The subscript *a* indicates unconstrained DoFs, whereas the subscript *b* indicates constrained DoFs, or respectively, interface DoFs.

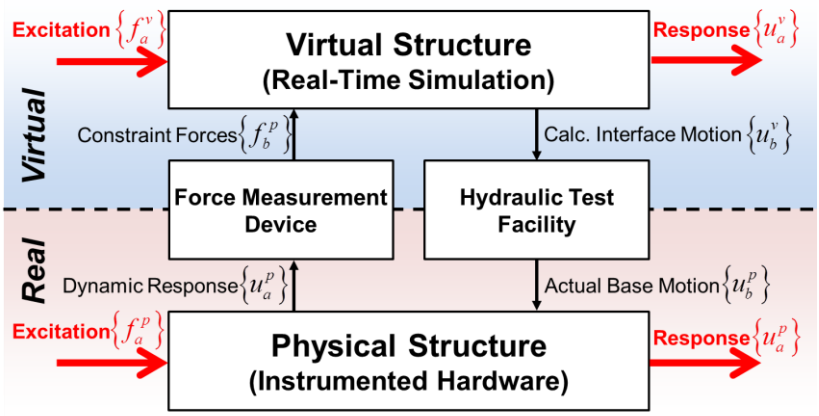


Figure 2: Subsystems and dynamic interactions of a Hardware-in-the-Loop simulation

Like in all substructuring applications, two basic requirements must be fulfilled also in HIL: (i) compatibility of the motion and (ii) equilibrium of forces at the interface. The peculiarity with HIL is that one substructure is physically available while the other is represented by a simulation model. The compatibility of the motion at the interface is ensured by the hydraulic test facility. Its vibration table can move as a rigid body in all six axes and the physical substructure must be installed properly on the vibration table. Compatibility requires that the motion $\{u_b^p\}$ at the interface (subscript *b*) of the physical substructure (superscript *p*) and the motion $\{u_b^v\}$ at the interface (subscript *b*) of the virtual substructure (superscript *v*) are identical:

$$\{u_b^p\} = \{u_b^v\} \tag{1}$$

It remains as a difficulty to ensure that the motion of the vibration table accurately emulates the interface motion calculated in real-time with the simulation model of the virtual substructure. This can be achieved e.g. by proper control of the test facility within a frequency range of interest.

The equilibrium of forces at the interface requires that the constraint forces $\{f_b^p\}$ at the interface (subscript *b*) of the physical substructure (superscript *p*) and the constraint forces $\{f_b^v\}$ at the interface (subscript *b*) of the virtual substructure (superscript *v*) compensate each other:

$$\{f_b^p\} = -\{f_b^v\} \tag{2}$$

Also here, the difficulty is that the interface forces between the substructures must be measured, e.g. using an FMD. The measured forces are being provided as input to the simulation model of the virtual substructure

2.1 Modelling of the virtual substructure

The virtual substructure is addressed first, because the corresponding models are easier to obtain. According to Figure 2, the constraint forces $\{f_b\}$ are the input into the virtual substructure and the calculated interface motion $\{u_b\}$ is the output of the virtual substructure (the superscript *v* for virtual substructure is skipped in this subchapter). In general, the virtual substructure is considered as multi-degree of freedom systems. The notation used here refers to [5].

For HIL testing, a real-time simulation model is required for the virtual substructure. Consequently, a state-space model must be derived from the equation of motion of this substructure.

$$[M]\{\ddot{u}\} + [D]\{\dot{u}\} + [K]\{u\} = \{f\} \tag{3}$$

In general, the DoFs may be partitioned into unconstrained DoFs (index *a*) and interface DoFs (index *b*):

$$\{u\} = \begin{Bmatrix} u_a \\ u_b \end{Bmatrix} \quad , \quad \{f\} = \begin{Bmatrix} f_a \\ f_b \end{Bmatrix} \tag{4}$$

Conversion of a structural system into state-space models is discussed e.g. in [6] for single-input, single-output systems, and in [7], [8] for multiple-input, multiple-output systems. The state-space model for time-domain simulation comprises two equations. The first one is the state equation with the system inherent dynamics (i.e. differential equation of motion), whereas the second is the output equation whose matrices are strongly dependent on the desired outputs or the physical output quantities:

$$\{\dot{x}\} = [A_c]\{x\} + [B_c]\{u_e\} \tag{5}$$

$$\{y\} = [C_c]\{x\} + [D_c]\{u_e\} \tag{6}$$

The index *c* indicates that the state-space model is defined in continuous time-domain. The corresponding vectors and matrices of this continuous-time state-space model are:

$$\{x\} = \begin{Bmatrix} u \\ \dot{u} \end{Bmatrix} \ , \ \{u_e\} = \{f_b\} \ , \ \{y\} = \{u_b\} \tag{7}$$

$$[A_c] = \begin{bmatrix} 0 & I \\ -M^{-1}K & -M^{-1}D \end{bmatrix} , \ [B_c] = \begin{bmatrix} 0 \\ M^{-1}I_b^T \end{bmatrix} , \ [C_c] = [I_b \quad 0] , \ [D_c] = [0] \tag{8}$$

It should be noted that the matrix $[I_b]$ as part of the matrices $[B_c]$ and $[C_c]$ is a boolean matrix selecting the interface DoFs from the full displacement vector:

$$\{u_b\} = [I_b]\{u\} \ , \ \{f\} = [I_b]^T \{f_b\} \tag{9}$$

If acceleration responses are required as physical output quantities of the virtual substructure, the matrices $[C_c]$ and $[D_c]$ change correspondingly and also the output vector $\{y\}$:

$$\{y\} = \{\ddot{u}_b^v\} \ , \ [C_c] = \left[-I_b M^{-1}K \quad -I_b M^{-1}D\right] \ , \ [D_c] = \left[M^{-1}I_b^T\right] \tag{10}$$

Next to the state-space model of the virtual substructure, the frequency-domain transfer function matrix $[G_v]$ is required for stability analysis using the Nyquist criterion later on. It can be obtained by transforming the equation of motion into the frequency domain:

$$\left(-\Omega^2[M] + j\Omega[D] + [K]\right)\{\hat{u}\} = \{\hat{f}\} \tag{11}$$

Solving this frequency-domain equation of motion in a direct manner for the desired complex response vector $\{\hat{u}\}$ as a function of the complex excitation $\{\hat{f}\}$ yields the transfer function matrix $[G_v]$ involving all DoFs of the virtual substructure:

$$\{\hat{u}\} = [G_v]\{\hat{f}\} \quad \rightarrow \quad [G_v] = \left(-\Omega^2[M] + j\Omega[D] + [K]\right)^{-1} \tag{12}$$

In this application, only the partition related to the interface DoFs (index *b*) is required from the full matrix $[G_v]$. In this case, a modal series expansion is more appropriate to improve the numerical efficiency in processing the simulation model of the virtual substructure:

$$\{\hat{u}_b\} = [G_{v,bb}]\{\hat{f}_b\} \quad \rightarrow \quad [G_{v,bb}] = \sum_r \frac{\{\phi_{b,r}\}\{\phi_{b,r}\}^T}{m_r\left(\omega_r^2 - \Omega^2 + j2D_r\omega_r\Omega\right)} \tag{13}$$

The modal parameters of the virtual substructure required to compute the above mentioned modal series expansion can also be used to establish a modal state-space in the time-domain. A truncated set of mode shapes covering the frequency range of interest can be used in this case which significantly reduces the order of state equation of the state-space model.

2.2 Modelling of the physical substructure

In principle, no model is required for the physical substructure for HIL tests, because it is available as hardware. However, when the overall HIL setup shall be simulated in the time-domain during the preparation of the test, a state-space model of the physical substructure is required. Furthermore, when stability assessment is considered, a frequency-domain transfer function matrix of the physical substructure is required.

The physical substructure is mounted on the table of the hydraulic test facility. Therefore, the DoFs of this substructure can be partitioned into index *a*, i.e. unconstrained DoFs with unknown displacement $\{u_a\}$ but known excitation forces $\{f_a\}$, and index *b*, i.e. DoFs at the interface to the virtual substructure with known displacement $\{u_b\}$ but unknown constraint forces $\{f_b\}$, see [5].

$$\begin{bmatrix} M_{aa} & M_{ab} \\ M_{ba} & M_{bb} \end{bmatrix} \begin{Bmatrix} \ddot{u}_a \\ \ddot{u}_b \end{Bmatrix} + \begin{bmatrix} C_{aa} & C_{ab} \\ C_{ba} & C_{bb} \end{bmatrix} \begin{Bmatrix} \dot{u}_a \\ \dot{u}_b \end{Bmatrix} + \begin{bmatrix} K_{aa} & K_{ab} \\ K_{ba} & K_{bb} \end{bmatrix} \begin{Bmatrix} u_a \\ u_b \end{Bmatrix} = \begin{Bmatrix} f_a \\ f_b \end{Bmatrix} \tag{14}$$

The input into this physical substructure is the base motion $\{u_b\}$ which generates a dynamic response $\{u_a\}$ at the unconstrained DoFs. This is contained in the upper partition of the equation of motion:

$$[M_{aa}]\{\ddot{u}_a\} + [D_{aa}]\{\dot{u}_a\} + [K_{aa}]\{u_a\} = \{f_a\} - [M_{ab}]\{\ddot{u}_b\} - [D_{ab}]\{\dot{u}_b\} - [K_{ab}]\{u_b\} \tag{15}$$

It is reasonable to separate the dynamic response at the unstrained DoFs into a quasi-static part and a relative dynamic part:

$$\{u_a\} = \{u_a\}^{static} + \{u_a\}^{rel} \tag{16}$$

The quasi-static response would occur if the enforced interface motion was applied infinitely slow. It therefore represents a rigid body motion where the structure perfectly follows the enforced motion of the interface. The relative dynamic part represents the additional response due to the system inherent dynamics. It should be noted that the interface motion $\{u_b\}$ does not have a relative dynamic part. Figure 3 illustrates the two parts of the dynamic response of a structure with enforced interface motion.

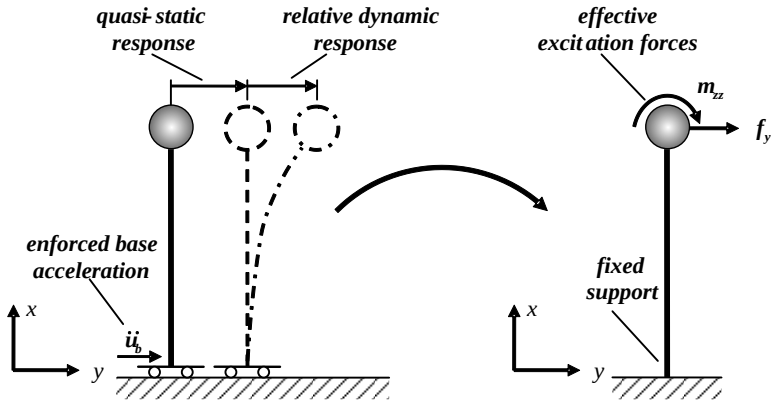


Figure 3: Illustration of quasi-static and relative dynamic response in case of enforced interface motion

In case of statically determined interfaces as considered here, the quasi-static response at the unconstrained DoFs $\{u_a^{static}\}$ is a rigid body displacement. When assuming small interface motion, a simple linear relationship can be formulated between the quasi-static part of the response at the unconstrained DoFs $\{u_a^{static}\}$ and the enforced interface motion $\{u_b\}$:

$$\{u_a\}^{static} = -[K_{aa}]^{-1}[K_{ab}]\{u_b\} = [T_G]\{u_b\} \tag{17}$$

In particular, when assuming small interface rotations the time-derivative of the matrix $[T_G]$ can be neglected and the following relations exist for the quasi-static velocity and acceleration response:

$$\{\dot{u}_a\}^{static} = [T_G]\{\dot{u}_b\} \tag{18}$$

$$\{\ddot{u}_a\}^{static} = [T_G]\{\ddot{u}_b\} \tag{19}$$

When inserting these relations into the upper partition of the equation of motion, the following differential equation can be established from which the relative dynamic response can be determined. This relative dynamic response comprises all elastic deformations that occur due to the dynamic nature of the enforced motion. The enforced interface motion can be converted into an equivalent effective excitation force vector $\{f_{eff}\}$:

$$\begin{aligned}\left[M_{aa}\right]\left\{\ddot{u}_a^{rel}\right\}+\left[D_{aa}\right]\left\{\dot{u}_a^{rel}\right\}+\left[K_{aa}\right]\left\{u_a^{rel}\right\}&=\left\{f_{eff}\right\}\\ \left\{f_{eff}\right\}=\left\{f_a\right\}-\left(\left[M_{ab}\right]+\left[M_{aa}\right]\left[T_G\right]\right)\left\{\ddot{u}_b\right\}-\left(\left[D_{ab}\right]+\left[D_{aa}\right]\left[T_G\right]\right)\left\{\dot{u}_b\right\}&\end{aligned} \tag{20}$$

The coupling of the unconstrained and interface DoFs by inertia forces or damping forces can be neglected in most cases so that a simpler, approximate relation exists for the effective excitation force vector:

$$\left\{f_{eff}\right\}=\left\{f_a\right\}-\left[M_{aa}\right]\left[T_G\right]\left\{\ddot{u}_b\right\}-\left[D_{aa}\right]\left[T_G\right]\left\{\dot{u}_b\right\} \tag{21}$$

When lightly damped systems are considered, the viscous damping part in the effective excitation force vector is considerably smaller than the part from the inertia forces:

$$\left\{f_{eff}\right\}=\left\{f_a\right\}-\left[M_{aa}\right]\left[T_G\right]\left\{\ddot{u}_b\right\} \tag{22}$$

Inserting this simplified relation into the equation of motion allows for the determination of the relative dynamic acceleration response at the unconstrained DoFs:

$$\left\{\ddot{u}_a^{rel}\right\}=-\left[M_{aa}\right]^{-1}\left[K_{aa}\right]\left\{u_a^{rel}\right\}-\left[M_{aa}\right]^{-1}\left[D_{aa}\right]\left\{\dot{u}_a^{rel}\right\}+\left[M_{aa}\right]^{-1}\left\{f_a\right\}-\left[T_G\right]\left\{\ddot{u}_b\right\} \tag{23}$$

Now, modelling for HIL requires the dynamic constraint forces $\{f_b\}$ as output, see Figure 2. These constraint forces can be determined from the lower partition of the equation of motion:

$$\begin{aligned}\left\{f_b\right\}=&\left[M_{ba}\right]\left\{\ddot{u}_a^{rel}\right\}+\left[D_{ba}\right]\left\{\dot{u}_a^{rel}\right\}+\left[K_{ba}\right]\left\{u_a^{rel}\right\}+\dots\\ &\dots\left(\left[M_{ba}\right]\left[T_G\right]+\left[M_{bb}\right]\right)\left\{\ddot{u}_b\right\}+\left(\left[D_{ba}\right]\left[T_G\right]+\left[D_{bb}\right]\right)\left\{\dot{u}_b\right\}+\left(\left[K_{ba}\right]\left[T_G\right]+\left[K_{bb}\right]\right)\left\{u_b\right\}\end{aligned} \tag{24}$$

It can be shown that in the absence of external forces $\{f_a\}$ at the unconstrained DoFs, the last term on the right hand side vanishes:

$$\left[K_{ba}\right]\left[T_G\right]+\left[K_{bb}\right]=\left[0\right] \tag{25}$$

This relation actually means that in case of a statically determined interface, a displacement of the interface does not produce constraint forces. Consequently, the following equation remains for the determination of dynamic constraint forces:

$$\begin{aligned}\left\{f_b\right\}=&\left[M_{ba}\right]\left\{\ddot{u}_a^{rel}\right\}+\left[D_{ba}\right]\left\{\dot{u}_a^{rel}\right\}+\left[K_{ba}\right]\left\{u_a^{rel}\right\}+\dots\\ &\dots\left(\left[M_{ba}\right]\left[T_G\right]+\left[M_{bb}\right]\right)\left\{\ddot{u}_b\right\}+\left(\left[D_{ba}\right]\left[T_G\right]+\left[D_{bb}\right]\right)\left\{\dot{u}_b\right\}\end{aligned} \tag{26}$$

Of course, the damping term and the damping coupling term can be neglected compared to the inertia effects on the constraint forces and the following simplification is reasonably accurate:

$$\left\{f_b\right\}=\left[M_{ba}\right]\left\{\ddot{u}_a^{rel}\right\}+\left[D_{ba}\right]\left\{\dot{u}_a^{rel}\right\}+\left[K_{ba}\right]\left\{u_a^{rel}\right\}+\left(\left[M_{ba}\right]\left[T_G\right]+\left[M_{bb}\right]\right)\left\{\ddot{u}_b\right\} \tag{27}$$

Now, equation (23) for the acceleration response $\{\ddot{u}_a^{rel}\}$ at the unconstrained DoFs can be inserted here:

$$\begin{aligned}\left\{f_b\right\}=&\left(\left[K_{ba}\right]-\left[M_{ba}\right]\left[M_{aa}\right]^{-1}\left[K_{aa}\right]\right)\left\{u_a^{rel}\right\}+\left(\left[D_{ba}\right]-\left[M_{ba}\right]\left[M_{aa}\right]^{-1}\left[D_{aa}\right]\right)\left\{\dot{u}_a^{rel}\right\}+\dots\\ &\dots\left[M_{ba}\right]\left[M_{aa}\right]^{-1}\left\{f_a\right\}+\left[M_{bb}\right]\left\{\ddot{u}_b\right\}\end{aligned} \tag{28}$$

This is a differential equation for the desired dynamic constraint forces $\{f_b\}$ required as output from the physical substructure. A state-space model can now be established for the physical substructure:

$$\left\{\dot{x}\right\}=\left[A_c\right]\left\{x\right\}+\left[B_c\right]\left\{u_e\right\} \tag{29}$$

$$\left\{y\right\}=\left[C_c\right]\left\{x\right\}+\left[D_c\right]\left\{u_e\right\} \tag{30}$$

Here again, the index *c* denotes a state-space model defined in continuous time-domain. The corresponding vectors and matrices of this continuous-time state-space model are:

$$\{x\} = \begin{Bmatrix} u_a^{rel} \\ \dot{u}_a^{rel} \end{Bmatrix}, \{u_e\} = \begin{Bmatrix} f_a \\ \ddot{u}_b \end{Bmatrix}, \{y\} = \{f_b\} \tag{31}$$

$$[A_c] = \begin{bmatrix} 0 & I \\ -M_{aa}^{-1}K_{aa} & -M_{aa}^{-1}D_{aa} \end{bmatrix}, [B_c] = \begin{bmatrix} 0 & 0 \\ M_{aa}^{-1} & -T_G \end{bmatrix} \tag{32}$$

$$[C_c] = \begin{bmatrix} K_{ba} - M_{ba}M_{aa}^{-1}K_{aa} & D_{ba} - M_{ba}M_{aa}^{-1}D_{aa} \end{bmatrix}, [D_c] = \begin{bmatrix} M_{ba}M_{aa}^{-1} & M_{bb} \end{bmatrix} \tag{33}$$

With this state-space model, the constraint forces of the physical substructure can be calculated from the interface acceleration input into the system.

For time-domain simulation of the complete HIL setup, i.e. for preparation of the HIL test, it is required that the state-space model of the virtual substructure provides the acceleration response at the interface output, because this interface acceleration is used as input for the state-space model of the physical substructure. In HIL tests as discussed later on, the displacement response at the interface is required as output from the physical substructure, because this output quantity is used as target commands for controlling the hydraulic test facility. Furthermore, a state-space model of the physical substructure is not required for HIL tests, because this part is available as real hardware.

When stability assessment using the Nyquist criterion is addressed, the frequency-domain transfer function of the physical substructure $[G_p]$ is required. This model would provide the constraint forces $\{f_b\}$ as output with the enforced interface motion $\{u_b\}$ as input:

$$\left(-\Omega^2[M_{aa}] + j\Omega[D_{aa}] + [K_{aa}]\right)\{\hat{u}_a\} = \{\hat{f}_a\} - \left(-\Omega^2[M_{ab}] + j\Omega[D_{ab}] + [K_{ab}]\right)\{\hat{u}_b\} \tag{34}$$

External forces $\{\hat{f}_a\}$ can be ignored when using the Nyquist criterion and the following relation between the response at unconstrained DoFs $\{\hat{u}_a\}$ and the response at the interface DoFs $\{\hat{u}_b\}$ can be established:

$$\{\hat{u}_a\} = -\left(-\Omega^2[M_{aa}] + j\Omega[D_{aa}] + [K_{aa}]\right)^{-1}\left(-\Omega^2[M_{ab}] + j\Omega[D_{ab}] + [K_{ab}]\right)\{\hat{u}_b\} \tag{35}$$

The constraint forces $\{\hat{f}_b\}$ are determined from the lower partition of the equation of motion in case of enforced interface motion $\{\hat{u}_b\}$:

$$\left(-\Omega^2[M_{ba}] + j\Omega[D_{ba}] + [K_{ba}]\right)\{\hat{u}_a\} + \left(-\Omega^2[M_{bb}] + j\Omega[D_{bb}] + [K_{bb}]\right)\{\hat{u}_b\} = \{\hat{f}_b\} \tag{36}$$

Inserting the relation between the response at the unconstrained DoFs $\{\hat{u}_a\}$ and at the interface DoFs $\{\hat{u}_b\}$ into this equation yields the required transfer function matrix $[G_p]$ of the physical substructure:

$$\begin{aligned} \{\hat{f}_b\} = [G_p]\{\hat{u}_b\} = \Big[\left(-\Omega^2[M_{bb}] + j\Omega[D_{bb}] + [K_{bb}]\right) - \left(-\Omega^2[M_{ba}] + j\Omega[D_{ba}] + [K_{ba}]\right)\cdot\ldots \\ \ldots\cdot\left(-\Omega^2[M_{aa}] + j\Omega[D_{aa}] + [K_{aa}]\right)^{-1}\left(-\Omega^2[M_{ab}] + j\Omega[D_{ab}] + [K_{ab}]\right)\Big]\{\hat{u}_b\} \end{aligned} \tag{37}$$

3 Stability analysis

As HIL is a closed-loop application. Therefore, stability of the overall setup must be checked a priori. Two approaches for stability analysis are presented in the following, namely the Nyquist criterion and the eigenvalue analysis of the system matrix of the state-space model of the closed-loop system. Both have specific advantages which will be highlighted accordingly.

3.1 Nyquist criterion

The stability margin of the system in closed-loop can be assessed from the open-loop transfer function, see e.g. [6]. At this point, ideal transfer behavior with unit magnitude and zero phase is assumed for the hydraulic test facility and for the force measurement platform. In addtion, the process time delay of the real time simulation is neglected. The underlying block diagram of this simplified setup is shown in Figure 4 and will be used for the determination of the critical delay time that must not be exceeded e.g. by the hydraulic test facility and/or the process time delay of the real-time simulation.

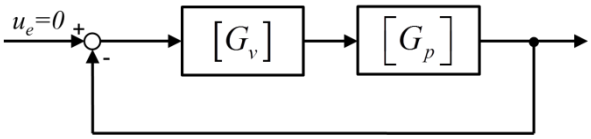


Figure 4: Simplified block diagram of closed-loop HIL system with transfer functions of virtual and physical substructure

When neglecting the feedback in Figure 4, the so-called open-loop transfer function $[G_o]$ can be obtained from the transfer functions of the physical and the virtual substructures arranged in series:

$$[G_o] = [G_p][G_v] \tag{38}$$

The closed-loop transfer function $[G_c]$ can be obtained from the open-loop transfer function:

$$[G_c] = \left([I] + [G_o]\right)^{-1}[G_o] = \left([I] + [G_p][G_v]\right)^{-1}[G_p][G_v] \tag{39}$$

According to the Nyquist criterion, the stability margin of the closed-loop system can be determined from open-loop transfer function. In case of HIL, the open-loop transfer function has no physical unit, i.e. it is dimensionless. The magnitude of this complex quantity is the gain of the open-loop system and the argument is the phase delay. An example open-loop transfer function is illustrated in Figure 5. As a stability requirement for the closed-loop system, it must be ensured that the Nyquist plot of the open-loop transfer function does not encircle the point (-1,0) in the complex plane, i.e. the black point in the Nyquist plot on the right hand side of Figure 5.

The simplified Nyquist stability criterion shall be introduced here, see [6]. It is valid for single-input, single-output (SISO) systems only. Even though a generalized Nyquist criterion has been proposed for multiple-input, multiple-output (MIMO) systems, see [7] and [9], the simplified Nyquist criterion can be applied to the individual elements of the transfer function matrix. The benefit of the simplified Nyquist criterion over the generalized one is the allocation of the stability margin, which is typically not provided by the generalized Nyquist criterion as proposed in [7]. If the open-loop transfer function G_o of a SISO system crosses the point (-1,0) in the complex plane, the denominator of the closed-loop transfer function, i.e. $1+G_o$, would become zero, i.e. 1+(-1)=0. In this case, the closed-loop system would have an undamped pole (critically stable). If the point (-1,0) is encircled by the open-loop transfer function, the pole of the closed-loop system will be unstable. When the point (-1,0) is not encircled, like shown in the Nyquist plot in Figure 5, the pole of the closed-loop system will be stable.

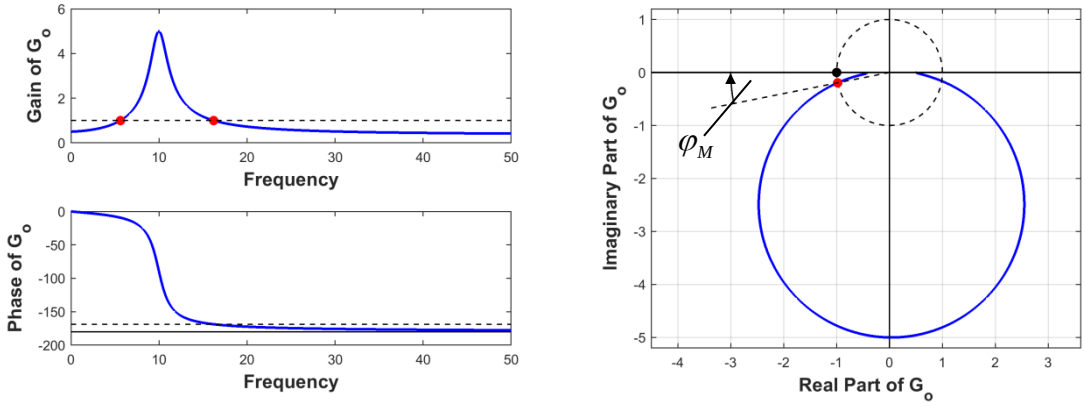


Figure 5: Bode plot (left) and Nyquist plot (right) of open-loop transfer function

It can be seen from the Nyquist plot in Figure 5 that the open-loop transfer function crosses two times the unit gain circle – one time with positive slope of the gain curve, one time with negative slope of the gain curve. These points can also be observed as red points in the Bode plot in Figure 5 where the magnitude of the open-loop transfer function crosses 1 (or respectively 0 dB). The corresponding frequencies will be referred to as cross-over frequencies Ω_c in the following.

The black point in the Nyquist plot of Figure 5 indicates the stability limit. It is placed on the unit circle at -180° phase angle. The difference in phase angle at the red marked cross-over point to the black marked stability limit point at -180° phase angle is referred to as the phase margin φ_M:

$$\varphi_M = -\pi - \arg\left(G_o\left(\Omega_c\right)\right) \tag{40}$$

So far, the stability of closed-loop systems has been addressed from analyzing the open-loop transfer function. Now, the maximum delay can be deduced from this simplified analysis. This maximum delay must not be exceeded by the delay of the hydraulic test facility and of the real-time simulation of the virtual structure. In general, a delay-time will lead to a linear increase of the phase angle of the open-loop transfer function with frequency, while the magnitude of the open-loop transfer will remain unaffected. For stability of the closed-loop system, it must be ensured that the critical delay-time τ_{crit} does not fully consume the phase margin φ_M at the cross-over frequency Ω_c:

$$\varphi_M \geq \Omega_c \tau_{crit} \quad \rightarrow \quad \tau_{crit} \leq \frac{\varphi_M}{\Omega_c} \tag{41}$$

When inspecting the phase angles at the two cross-over frequency in the phase response of Figure 5, it can be seen that the distance to the phase angle of -180° is significantly higher at the cross-over frequency below the resonance. At the cross-over frequency beyond the resonance the phase margin is significantly lower and consequently, the conditions at this specific point determines the stability margin.

In HIL applications, the actuation system will always have a delay time and these should be considered as a system property which cannot be changed. Accordingly, it can be seen from equation (41) that for a given delay time the stability margin is higher for lower delay times. It can also be seen, that the stability margin can be increased by shifting the cross-over frequencies towards lower frequencies. For a given system with multiple resonances, it can be concluded that those having higher cross-over frequencies are most critical for stability. It should be noted that not all resonances of the open-loop transfer function have cross-over frequencies. If the gain of the resonance remains below 1 (or respectively below 0 dB) no cross-over frequencies will occur and the corresponding resonance will not make the closed-loop system unstable.

The effect of damping on the stability margin is illustrated in Figure 6. The dashed light blue line in the diagrams represents the system with nominal damping as shown in Figure 5. The solid blue line represents the same system with damping increased by a factor of two. It can be seen from the Bode plot that damping is not sensitive to shift the cross-over frequencies. However, the sensitivity of damping can be

observed in the phase response of the Bode plot. It increases the phase distance to the -180° phase angle and thus increasing the phase margin for the stability of the closed-loop system.

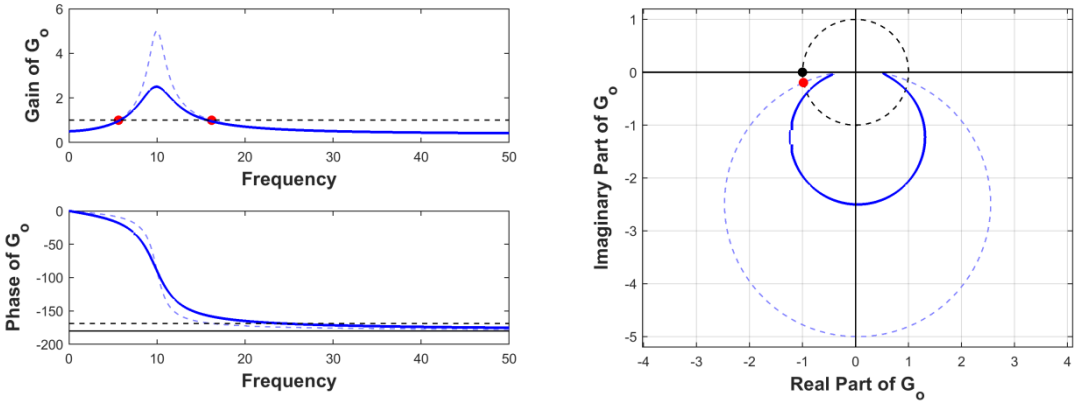


Figure 6: Bode plot (left) and Nyquist plot (right) of open-loop transfer functions with different damping levels

As a closing statement of this section on stability assessment using the Nyquist criterion, it should be mentioned that the open-loop transfer function can be obtained from either numerical models, from experiments, or from a combination of the two. The particular advantage is that stability assessment of the closed-loop system is performed on the open-loop transfer functions. Furthermore, a stability margin is provided which indicates the distance from unstable conditions. Next to the phase margin, the Nyquist criterion also indicates a gain margin. This is an important parameter needed for adjusting the static gain of a controller in open-loop while taking into account the stability of the closed-loop system. This criterion has not been used here.

3.2 Eigenvalue analysis of system matrix of discrete-time state-space model

The stability of the closed-loop system can be assessed from the eigenvalues of the state matrix of a state-space model representing the closed-loop system. For example, a series arrangement of the state-space models of the virtual and the physical substructure forms the state-space model of the open-loop system. The output of this state-space model can be fed back to its input to form the closed-loop system. These operations can easily be performed using the MATLAB Control System Toolbox and the corresponding commands “series” or “feedback” applicable to dynamic system objects. The different possibilities for setting up numerically efficient state-space models have been mentioned at the end of chapter 2.1. In particular the discrete-time state-space models are interesting for stability assessment of systems with delay. The modelling of systems with delay can be obtained easily when assuming that the total delay in the closed-loop system is an integer multiple of the process delay (i.e. the sampling interval) of the real-time simulation. State-space models can be transformed into the discrete-time domain by introducing a constant sampling interval Δt and integrating the state equation over one time interval, see e.g. [8]. As a consequence, the resulting state matrix $[A_d]$ and the input matrix $[B_d]$ are then dependent on the sampling interval, but at the same time, the state equation is no longer a differential equation:

$$\{x_{i+1}\} = [A_d]\{x_i\} + [B_d]\{u_{e,i}\} \tag{42}$$

$$\{y_i\} = [C_c]\{x_i\} + [D_c]\{u_{e,i}\} \tag{43}$$

$$[A_d] = e^{[A_c]\Delta t} \quad , \quad [B_d] = \int_t^{t+\Delta t} e^{[A_c]\Delta t} dt\,[B_c] \tag{44}$$

In case of a delay for a single input of three sampling intervals, a closed-form discrete-time state-space model can be defined as follows, see e.g. [7]:

$$\begin{Bmatrix} x_1(i+1) \\ x_2(i+1) \\ x_3(i+1) \end{Bmatrix} = \begin{bmatrix} 0 & 1 & 0 \\ 0 & 0 & 1 \\ 0 & 0 & 0 \end{bmatrix} \begin{Bmatrix} x_1(i) \\ x_2(i) \\ x_3(i) \end{Bmatrix} + \begin{Bmatrix} 0 \\ 0 \\ 1 \end{Bmatrix} u_e(i) \tag{45}$$

$$y(i) = \begin{bmatrix} 1 & 0 & 0 \end{bmatrix} \begin{Bmatrix} x_1(i) \\ x_2(i) \\ x_3(i) \end{Bmatrix} \tag{46}$$

At first, the input u_e is assigned to the state x_3 and the output y is 0. In the next loop, the state x_3 is assigned to the state x_2 and still the output y is 0. In the third loop, the state x_2 is assigned to the state x_1 and the output y is the input from 3 sampling intervals ago. The advantage is that this model has memory that transfers the input some sampling intervals later. The disadvantage of this model is the increased number of states. When the delay is long, i.e. many sampling time intervals, the model will become inefficient. In case of a delay of n sampling intervals, n additional states per input signal are required for modelling the delay. Furthermore, if this model is arranged in series with other state-space models, n additional eigenvalues (or poles) will appear due to the n additional states. These may have to be separated from the original eigenvalues of the system under consideration. Nonetheless, eigenvalues and eigenvectors can be computed from eigenvalue analysis of the state matrix of a discrete-time state-space model of the closed-loop system including delay. This can be repeated for a set of different delay times and the changes in eigenfrequencies and damping ratios can be tracked and plotted as a function of the delay time. This is the main advantage of this method over the simplified Nyquist criterion. While the Nyquist criterion indicates the stability margin, the eigenvalue analysis (when performed for a set of different delay times) indicates changes of poles/eigenvalues of the closed-loop system.

When approaching the critical delay time, it is quite interesting to note that none of the structural modes becomes unstable. Instead, one of the additional poles introduced by the additional states from the delay model turns the closed-loop system into unstable condition. The damping of the critical pole becomes zero at the stability limit and its frequency corresponds to the critical cross-over frequency. In Figure 7, an example of stability diagrams are presented for a simple mass-spring-damper system as virtual substructure coupled with an additional mass as the physical substructure. The blue line in the lower diagram of Figure 7 represents the evolution of damping of the coupled system (i.e. the closed-loop system) with increasing delay. At about 7 ms, the damping reaches a maximum and decreases afterwards until it becomes unstable at about 9 ms (i.e. damping crosses zero). Approximately at the same delay, the corresponding eigenfrequency (blue line in the upper diagram) increases from 4.5 Hz to 5.5 Hz. It can be seen that the frequency of a second pole (i.e. the red line) is entering into the upper diagram of Figure 7. It is a consequence from modelling of the delay using a discrete-time state-space model according to equations (45) and (46). For delays longer than 6 ms, coupling of the additional pole with the structural pole can be observed. Finally, the interaction with the additional pole makes the structural pole to become unstable. As will be shown in the example in chapter 5 later on, this is not a numerical artefact, but it is confirmed by experimental validation.

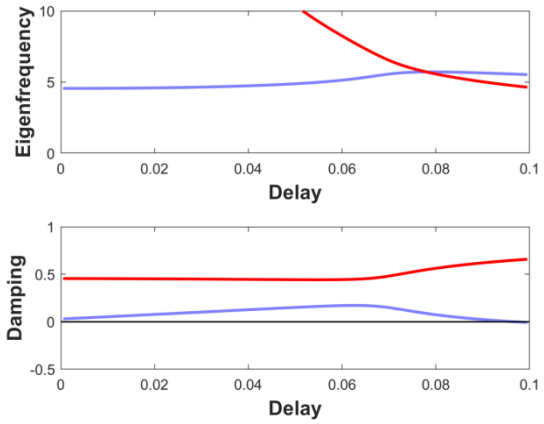


Figure 7 Stability diagram for a simple spring-mass-damper system as virtual substructure with an additional mass as physical substructure with delay in the coupling

4 Hydraulic shaking table MAVIS

The hydraulic shaking table MAVIS (Multi-Axial Vibration Simulator, see Figure 1) is a dynamic testing facility which has been used for qualification testing of spacecraft structures, earthquake simulation of piping components of power-plant cooling systems, road-load simulation of large battery-packs of electric vehicles and passenger comport related investigations with human test persons. The vibration table is a rib-stiffened steel platform having the dimensions of 1,5m x 1,5m x 0.2m and a mass of approximately 500 kg. The table is driven by 7 hydraulic actuators: 4 actuators in vertical z-direction (each having 40kN static force), 2 actuators in the x-direction (each having 80 kN static force), and a big single actuator in y-direction (120kN static force). The maximum stroke of the cylinders is ±50mm. In order to allow unconstrained table motion in multiple directions, ball joints are installed at the connection points of the actuators to the table and at the connection points of the actuators to their static reaction support. The stroke of the actuators allows for table rotations of about ±4.5° about each rotational axis.

The 6-axis vibration controller has an internal signal generator for the standard operating modes like sine, sine-sweep, random. For these operating modes, a frequency-domain controller actively controls the motion of the vibration table. This can run in multiple axes simultaneously.

For HIL testing, transient external signals are fed into the vibration table controller and are used as target signals. For this operation, each actuator has a PID-controller on its own whose parameters can be adjusted to tune the transfer behaviour. So called modal control provides multiple drive signals for the actuators involved in the desired motion of the vibration table. It is based on the coordinates of the actuator connection points and on the actuator directions. For example, if displacement in pure x-direction is requested, the modal control will generate quasi identical target signals for the 2 x-direction actuators, whereas all other actuators will receive a zero target command.

At the beginning of the experimental HIL validation tests, the transfer functions of the table have been identified in all 6 axes with the default PID-settings. The blue curve in Figure 8 shows the initial transfer function of the shaking table in x-direction. Since there was significant drop of the magnitude of the transfer function in the targeted frequency range up to 30Hz, tuning of the PID settings was performed. In particular the gain for the P (proportional) part and the gain of the D (differentiating) part were increased. Afterwards, the magnitude and the phase of the transfer functions were significantly improved as indicated by the red curve. The amplitude is represented well in the investigated frequency range but the phase shows a nearly linear drift, just like a pure delay element. In order to further improve the phase drift in the transfer function of the vibration table, a model based feed-forward control has been applied. The transfer function of the shaking table with improved PID settings was curve-fitted by a rational function in frequency domain, i.e. numerator and denominator polynomial. With an analytical expression for the transfer function at hand, the inverse of this transfer function has been used as a filter to modify the input

signal for the shaking table. Since the inverse of a stable transfer function is unstable, an additional low pass filter has been to be introduced for stabilization purposes. Of course, this additional low pass filter will increase again the delay, but as the green curve in Figure 8 indicates, the phase drift in the transfer function is significantly improved. Also a slight improvement can be observed for the amplitude of the transfer function.

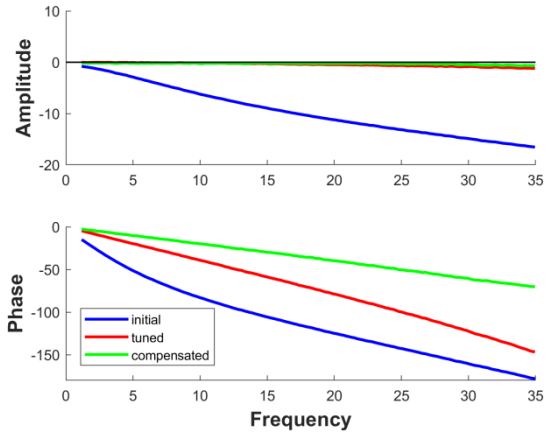


Figure 8 Transfer function of the x-axis. The initial state in blue, tuned PID parameters in red and delay commpensation in green.

The slope of the linear phase drift of the transfer function indicates the delay time of the hydraulic shaking table. Finally, with the compensated transfer function, the remaining delay time is about 6 ms.

5 Test case: Coupling of a virtual rod with a rigid mass

The analytical equations for response analysis and stability assessment of HIL tests were derived in the previous sections. The applicability of the theory will be demonstrated in this section on an illustrative example. As sketched in Figure 9, the virtual substructure consists of a rod fixed at one end. The physical substructure is a point mass to be coupled with the free end of the virtual rod. The rod has a single output displacement DoF at the interface to the physical substructure. Several modes may however contribute to the dynamic response in the longitudinal direction of the rod. It can therefore be considered as a SISO system with multiple interior dynamic DoFs.

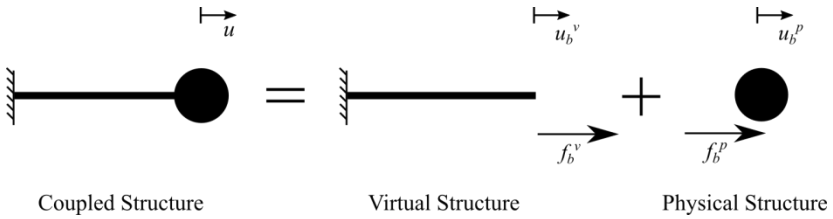


Figure 9: Virtual substructure (rod) and physical substructure (point mass) with interface

Usually the eigenfrequencies of a rod with reasonable cross-sectional dimensions are quite high. Therefore, the material parameters of the rod were artificially adapted to achieve multiple eigenfrequencies below 30 Hz envisaged for HIL applications with the hydraulic test facility. In order to maintain stability, the virtual model of the rod had to be reduced the first two modal DoFs only (i.e. the first two eigenfrequencies as listed in Table 1). The first eigenfrequency is at 4.03 Hz and the second at

12.19 Hz. The modal damping ratio has been set to 1% for both modes. The weight of the rigid mass is 12.5 kg.

Table 1 Modal paramemmeters of the rod without the rigid mass attached up to 30 Hz

f_r [Hz]	D_r [%]	m_r [kgm^2]
4.03	1.0	53.78
12.19	1.0	52.04
20.65	1.0	48.73
29.61	1.0	44.17

Even though the setup of this example appears to be constructed, artificial and far away from the targeted HIL applications, it is nonetheless adequate and appropriate to verify the feasibility of HIL with the six-axis hydraulic shaking table.

First, the Nyquist criterion according to chapter 3.1 is applied for the determination of the stability of the closed-loop system and the critical delay which indicates the stability limit. In a second step, the state-space approach of chapter 3.2 is employed to study the changes in the dynamic behavior for an array of different delays from which the stability diagrams are generated. Finally, the HIL test is conducted for validation purposes.

For application of the Nyquist criterion, the frequency-domain transfer functions of the virtual and physical substructure are needed. The modal representation of the transfer function of the virtual substructure is shown in equation (13) and was evaluated with the modal parameters of rod shown in Table 1. The rod has a single output DoF and mode shape scaling has been used so that the mode shape at this single output DoF is equal to 1. The transfer function of the physical substructure according to equation (37) is simple to establish for the rigid mass. In this case, no unconstrained DoFs (index *a*) exist in the physical substructure but just interface DoFs (index *b*). Consequently, no coupling matrices exist among the unconstrained DoFs and the interface DoFs. What remains from equation (37) is the following:

$$\left\{ \hat{f}_b^{\,p} \right\} = -\Omega^2 \left[M_{bb} \right] \{ \hat{u}_b \} \quad \rightarrow \quad \hat{f}_b^{\,p} = -\Omega^2 m \hat{u}_b = -\hat{f}_b^{\,v} \tag{47}$$

$$G_p = \frac{\hat{f}_b^{\,p}}{\hat{u}_b} = -m\Omega^2 = -\frac{\hat{f}_b^{\,v}}{\hat{u}_b} \tag{48}$$

When arranging the virtual and the physical substructures in series, the open-loop transfer function without delay is obtained according to equation (38). In Figure 10, the Bode plot of the open-loop transfer function is shown. The two resonances of the rod can be observed together with the four cross-over frequencies related to the resonances. A statement with respect to the limitation to only two modal contributions: With the contribution of the third and/or fourth mode of the rod to the open-loop transfer function, the gain of the open-loop transfer function converges towards a value larger than one. This makes the system unstable, because disturbances with high frequency content would always be amplified.

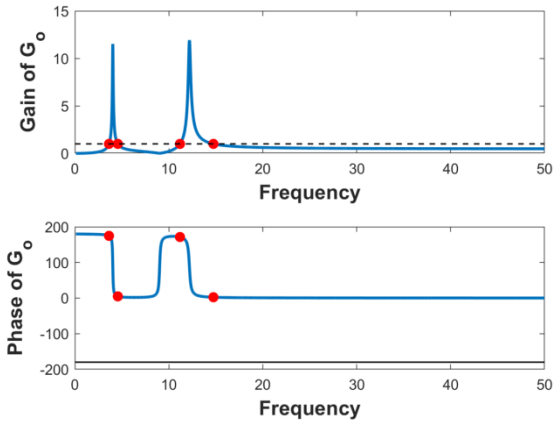


Figure 10: Open-loop transfer function for the virtual rod with point mass example

In general, four different critical delays can be computed from the four cross-over frequencies in the open-loop transfer function. The smallest critical delay determines the stability limit. Two of the cross-over frequencies are uncritical in this respect, namely those, where the gain-curve has positive slope (i.e. the cross-over frequencies located below the resonance peaks). For the other two, the one with the higher frequency is more critical, because a given delay produces a linearly increasing (negative) phase drift and consequently consuming more phase margin at higher frequencies. In this example, the highest crossover frequency is at 14.7 Hz and the corresponding phase is 2.3°, i.e. the phase margin to the critical phase of -180° is 182.3°. From this phase margin, a critical delay of 34.3 ms can be deduced according to equation (41). With an approximate delay time of 6 ms for the hydraulic shaking table (identified from the phase drift of the optimized experimental transfer functions), it can be concluded that there is enough phase margin to ensure stability of the closed-loop system.

Now, the second approach based on eigenvalue analysis of the system matrix of the time discrete state space models is utilized to investigate the dynamic behavior when approaching the stability limit. The closed-loop system must be considered in this case. Equations (5) to (9) are used to establish the state-space model of the virtual substructure, whereas equations (29) to (33) are used for the physical substructure. These equations are formulated in continuous-time domain. Transformation into discrete-time domain is needed and can be performed according to equations (42) to (44). The discrete-time state-space models of the virtual substructure, the physical substructure and the delay can be arranged in series (i.e. the output of the first system is equals the input into the second system, etc.) to form the open-loop system. Afterwards, the closed-loop system is established by feedback of the output of the open-loop system to its input. The eigenvalues of the closed-loop system matrix can then be computed, where the delay is explicitly part of the model. It should be noted that the hydraulic test facility has a delay of 6 ms after optimization of the transfer functions. An additional delay was introduced to study the change in the dynamic behavior when approaching the stability limit. This additional delay has been varied systematically and the eigenvalues of the closed-loop system have been analyzed for discrete values for the delay. The eigenfrequencies and damping ratios of the closed-loop system can then be plotted as a function of the delay and the poles can be tracked until zero-crossing of one of the damping ratios. This indicates the stability limit.

In Figure 11, the stability diagram computed for the virtual rod and the point mass are shown. As already discussed in section 3.2 the number of eigenvalues increase with increasing delay because of the additional states introduced by the model of the delay. In this diagram, only the first three eigenvalues are plotted but additional (high frequency and high damping) eigenvalues can be found but are omitted from the display. It is anticipated that the eigenfrequencies of the closed-loop system are lower than those of the open-loop system due to adding a rigid mass to the tip of the rod. The theoretical eigenfrequencies of the first two modes drop from 4.03 Hz to 3.62 Hz and from 12.19 Hz to 10.98 Hz when attaching the rigid mass to the tip of the rod.

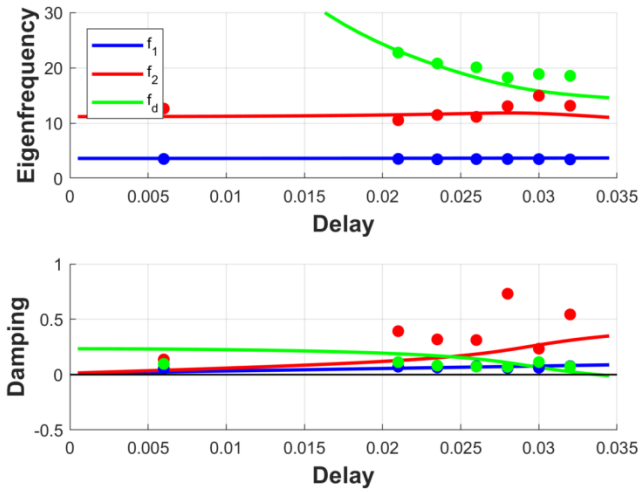


Figure 11: Variation of the delay time and its impact on the stability of the closed-loop system

With increasing delay in the closed-loop system, the two eigenfrequencies of the rod vary slightly. It is also observed that the damping ratios of these two modes are increasing with increasing delay. But the most interesting phenomenon is the new eigenfrequency which appears as a consequence of the delay model and shown as a green line in the upper diagram of Figure 11. It starts from infinite frequency at zero delay and converges towards the critical cross-over frequency when reaching the stability limit. The corresponding damping ratio of this additional pole is about 20% for small delays. But with increasing delay, the damping ratio starts to decrease until it becomes negative. At this point, the closed-loop system goes unstable.

Time-domain simulations have been conducted with the state-space model of the closed-loop system but are not shown here. They give the proof that both methods indicate the same stability limit. However, the second approach based on eigenvalue analysis provides more engineering insight into the behavior of the closed-loop system. Only with this approach it is possible to understand that the additional pole from the delay drives the closed-loop the system into unstable conditions.

The numerical stability analysis with the two different methods has been validated experimentally. The real-time simulation of the virtual rod is performed on an ADwin Pro II controller. The implementation of the simulation model on the controller hardware is achieved with MATLAB and Simulink and dedicated compilers to transform Simulink models into executables to run on the CPU of the controller. The displacement of the hydraulic test facility is measured by displacement sensors integrated in the hydraulic actuators of the test facility. An acceleration sensor has been placed on the rigid mass for an independent acceleration measurement. The coupled structure is excited using an impulsive virtual force. It has been generated with a battery connected to a push-button operated manually. The output of this simple impulse generator was introduced into one of the analog input channels of the real-time controller. Inside the Simulink model running on the controller, the impulse excitation is transformed into a force introduced at the interface DoF. It has to be mentioned, however, that the repeatability of the impulse generated from manual execution of the push-button was not satisfactory. It was “just good enough” for disturbing the closed-loop system and observing a decay or a growth of the impulse response.

In general, the response to an impulse is a free vibration. It has been measured in terms of the actual displacement of the hydraulic test facility in this example. This has been repeated for different values of artificial delay until the system turned unstable. Afterwards, the Least-Squares Complex Exponential modal parameter estimator, see [10], has been applied to the recorded free vibrations in order to determine the damping ratios and the eigenfrequencies of the closed-loop system. The identified frequencies and damping ratios were compared to the simulated behavior obtained from eigenvalue analysis. Variation of the delay has been achieved by manipulating a delay block in the Simulink model and re-compiling the model for the real-time simulation on the ADwin Pro II controller. This artificial delay is added on top of the delay of the test facility which cannot be changed. The total delay is the sum of the delay of the test

facility and the artificial delay. With this total delay, the poles identified from the measured impulse responses were plotted as discrete points into the stability diagram in Figure 11. The simulated and the measured poles are matching quite well for the first mode of the coupled system (i.e. blue curve in Figure 11). It does not match very well for the damping of the second mode (i.e. red curve in the lower diagram of Figure 11). The reason is the poor excitation of this mode from the impulse generated manually with the push-button. It is known from practical experience with modal analysis, that the damping of poorly excited modes is hard to identify accurately.

In Figure 12, impulse responses recorded for different delays are shown. The curve in the left diagram corresponds to a delay slightly below the critical limit. It can be seen that towards the end of the recording, an oscillation at a higher frequency does not seem to decay. When slightly increasing the delay, the system becomes unstable and the diagram on the right hand side is obtained with exponential growth of the response. The frequency related to this growing amplitude oscillation was found to be the critical cross-over frequency. Such impulse excitation and recording of the response has performed for a set of different delay times but only two particular examples are presented here.

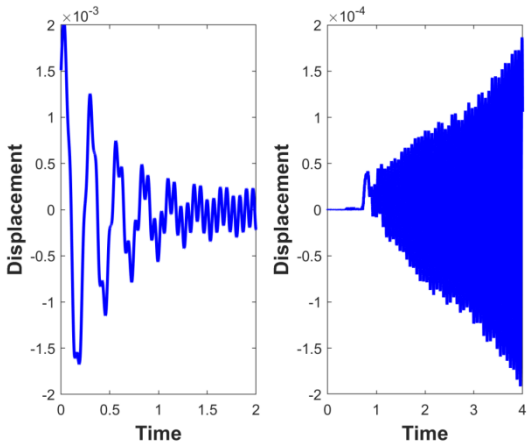


Figure 12: Impulse responses recorded in closed-loop HIL conditions
stable with exponential decay (left) – unstable with exponential growth (right)

With this example, the feasibility of HIL on the DLR six-axis hydraulic shaking table MAVIS has been demonstrated. Here, a single axis has been used but the theoretical foundation has been presented for the generic case of 6-DoFs interfaces.

6 Summary and conclusions

The modelling aspects for hybrid dynamic substructuring tests have been discussed. In the form presented here, the equations are directly applicable to generic MIMO systems for the physical and for the virtual substructure. However, due to the targeted application using a six-axis hydraulic shaking table, the assumption of a single and statically determined interface between the two substructures has been introduced and must be taken into account when adapting the theoretical foundation to other applications.

The feasibility of hardware in the loop testing with the DLR six-axis shaking table MAVIS has been demonstrated numerically and subsequently by experimental verification. Two different approaches for stability analysis have been employed: i) using the simplified Nyquist criterion based on the open-loop transfer function to assess the stability margin of the closed-loop system, ii) based on eigenvalue analysis of the state matrix of a discrete-time state-space model of the closed-loop system including a model for the total delay. The first approach provides the safety margin, whereas the second approach provides insight into the dynamic behavior of the closed-loop system with delay when approaching stability limit.

The frequency range up to 30Hz has been addressed here for HIL. This is the relevant frequency range for the targeted applications in aeronautic research like testing of aircraft wing stores using the HIL approach. In the test case of chapter 5, the limitation mainly arises from the delay time of the hydraulic shaking table. The process time delay of the real-time simulation of the virtual substructure is one order of magnitude smaller in this case, mainly due to the simplicity of the simulation model. However, when more complex models for the virtual substructure must be solved, the process time delay of the real-time simulation will become more significant leading to a further reduction of the stability margin.

A rather simple test case with only a single DoF at the interface has been considered where the physical structure is not a flexible body but a rigid mass. A more complex demonstration test case is currently under investigation with flexible dynamic MIMO systems for the virtual and for the physical substructure. In this test case, not only stability will be addressed, but also the concept of virtual excitation and additional virtual responses. This is already indicated in Figure 2. With this more complex setup, frequency response functions of the fully assembled system will be measured and the feasibility of experimental modal analysis from HIL tests will be assessed, and in particular, the impact of the total delay on the accuracy of the identified modal parameters.

References

[1] Tang, M.: Hardware-in-the-Loop Simulation mit dem hydraulischen Versuchsstand MAVIS, Master Thesis of the Faculty of Mechanical Engineering, Technical University of Braunschweig, published as DLR Report No. DLR-IB-AE-GO-2017-196, 2017

[2] Füllekrug, U.: *Determination of Effective Masses and Modal Masses from Basedriven Tests, Proceedings of 14th IMAC, Dearborn, Michigan, 1996, S.671-681*

[3] Stoten, D.P., Gomez, E.G.: *Adaptive control of shaking tables using the minimal control synthesis algorithm*, In: Philosophical Transactions of the Royal Society of London A: Math., Phys. And Eng. Sci., 359 (2001), 1786

[4] Terkovics, N., Neild, S.A., Lowenberg, M., Szalai, R., Krauskopf, B.: Substructurability: *The effect of the interface location on a real-time dynamic substructuring test. In: Proceedings of the Royal Society of London A: Math., Phys. and Eng. Sci., 472 (2016), 2192*

[5] Link, M.: *Finite Elemente in der Statik und Dynamik*, Springer, 2014

[6] Lunze, J.: *Regelungstechnik 1*, Springer, 2016

[7] Lunze, J.: *Regelungstechnik 2*, Springer, 2014

[8] Juang, J.N.: *Applied System Identification*, Prentice Hall, 1994

[9] Emami-Naeini, A., Kosut, R.L.: *The generalized Nyquist criterion and robust margins with applications, In: 51st IEEE Conference on Decision and Control, CDC 2012, 2012, pp. 226-231*

[10] Vold, H., Rocklin, G.T.: *The numerical implementation of a multi-point modal estimation method for mini-computers, In: Proceedings of the 1st IMAC I, Orlando, Florida, 1982*

Statistical analysis of cup-horn ultrasonic proximity sensor output

S. Jackson[1], A.J. Croxford[1], B.W. Drinkwater[1]
[1] University of Bristol, Department Mechanical Engineering
e-mail: **sj17322@bristol.ac.uk**

Abstract
Cup-horn transducers are ultrasonic transducers with very consistent resonant frequencies. This makes them ideal for applications requiring a focused array, such as particle manipulation/levitation. In this paper, we present a statistical analysis of the variation in transducer response at the quoted resonance of 40 kHz, as well as the variation in electrical impedance. The results show that variation in Q-factor is significantly greater than variation in resonant frequency. Despite the statistically significant variation between individual transducer outputs, the implication for arrays is minimal, with a predicted maximum loss in peak focal pressure of 1.25 dB. Finally, we show that the response of the coupled electro-mechanical structure of the transducer is highly nonlinear. The same nonlinear phenomena are less significant at low excitation voltages, as would be used for sensing applications. This nonlinearity has implications for the design and selection of transducers for high power applications.

1 Introduction

Arrays of ultrasonic transducers have been developed for many applications, including noncontact manipulation of particles in air, microfluidic particle manipulation and micro-surgery [1] [2]. An ultrasonic transducer type of particular interest is the cup-horn transducer, which is most commonly utilised for proximity sensing applications, for example car parking sensors. Recently, cup-horn ultrasonic proximity sensor transducers have been utilised in research applications requiring large arrays of transducers operating in air, as they produce reliable and controllable acoustic fields with desired characteristics at a competitive price. Such applications include ultrasonic levitation [3] and low cost parametric speakers [4]. Such transducers consist of a piezoelectric disk, with a cup shaped horn attached using adhesive. Cup-horn transducers have several major advantages, including low cost, low operating voltages (10-20 V) and very stable and repeatable resonant frequencies in comparison to other options, such as Langevin horn transducers. Whilst the variability of such transducers is known to be low, manufacturers don't provide statistical data on transducer output. In particular, data is not available as to the variation in phase and output sound power between transducers of the same model, how this varies with driving voltage, and how transducers of different models compare.

In this paper, we provide a statistical analysis of the performance and variability of two off the shelf cup-horn transducers, the Prowave 400ST160 [5] and the Murata MA40S4S [6], both of which are relatively cheap and readily available from multiple suppliers. Both transducers are designed for proximity sensing applications and have a rated resonant frequency of 40 kHz. In Section 2, the statistical variation in acoustic output and phase for both transducers is presented. In addition, the relative efficiency of each transducer is assessed as a function of excitation voltage. In Section 3, the frequency response of both transducers is presented, highlighting a nonlinear response that is dependent on the excitation voltage. The frequency response was measured to try and understand the source of the measured output variation. In Section 4, an analysis of the influence of individual transducer variation on the peak acoustic pressure generated by a focused array is assessed. Finally, we presented our proposed future work based on the findings in this paper in Section 5.

2 Transducer Variation at Resonance

To test and quantify the variation in performance, 10 Prowave and 10 Murata transducers were randomly selected from a batch of several hundred transducers purchased from 3rd party suppliers. The response of each transducer was measured at the quoted resonant frequency of 40 kHz using a microphone at a distance of 70 mm from the transducer surface (Figure 1). As well as the acoustic response of the microphone, the excitation voltage and current applied to the transducer was also recorded to ensure phase and power draw could be quantified. The microphone used is a GRAS 46BG high pressure microphone coupled to a GRAS 12AX power module. To generate the required sine wave input signal, an Iso-Tech AFG-21005 function generator was used in conjunction with an A.A. Lab A-303 high voltage amplifier, with a gain of 20. The current applied to the transducer was measured using a CP35 current probe. In all measurement cases, the function generator was set to supply a sine wave at 40 kHz with a user determined rms voltage. Prior to each measurement, a transducer is located in the transducer mount for testing. All data was acquired using the National Instruments LabView software in conjunction with an NI 9222 acquisition module and an NI 9171 chassis. All data processing was performed using Matlab and statistical analysis was performed using Minitab.

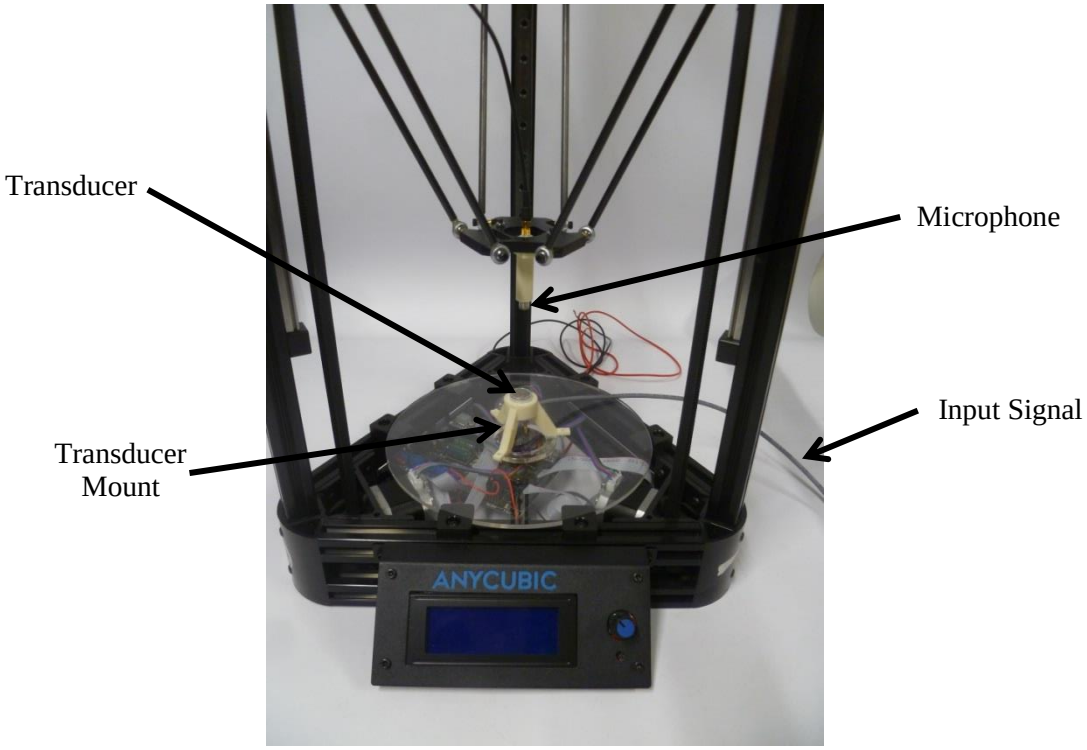


Figure 1: Test rig used for characterizing transducer output.

2.1 Statistical Variation

The measured response of the transducer samples are presented in Figure 2 for the Prowave transducers and Figure 3 for the Murata transducers. The response characteristics recorded for each transducer are the rms acoustic pressure amplitudes measured by the microphone at a distance of 70 mm from the transducer surface, the true rms voltage amplitude of the excitation signal, the rms current amplitude of the excitation signal, and the phase difference between the acoustic pressure and the excitation voltage. 70 mm was chosen as a reasonable trade-off between maximizing the signal to noise ratio and limiting the reflections from the microphone interfering with the acoustic field. Data was recorded at three rms excitation voltages; 6 V, represented a low power signal that would be used for sensing applications; 14 V, represented a mid-level power signal; and 22 V, representing a high power signal at the upper limit of the transducer power rating and relevant to particle manipulation.

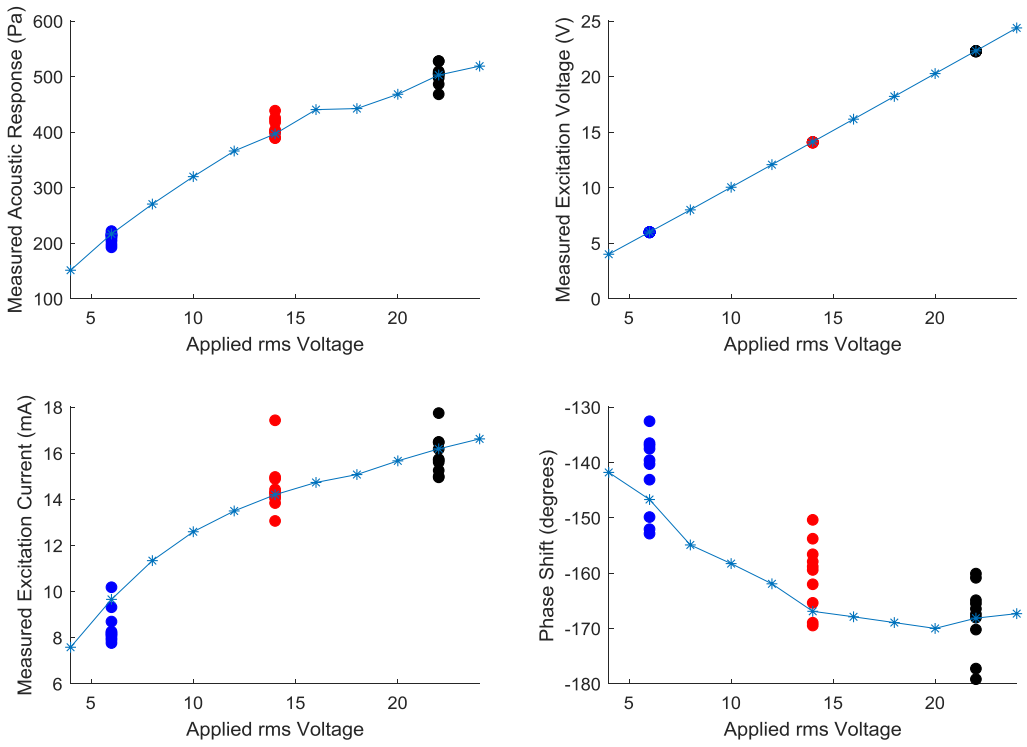


Figure 2: Response measurements of 10 randomly selected Prowave transducers at low (6 V_{rms}, blue markers), medium (14 V_{rms}, red markers) and high (22 V_{rms}, black markers) excitation voltages. The stared line is the response of a single transducer at intervals of 2 V_{rms}.

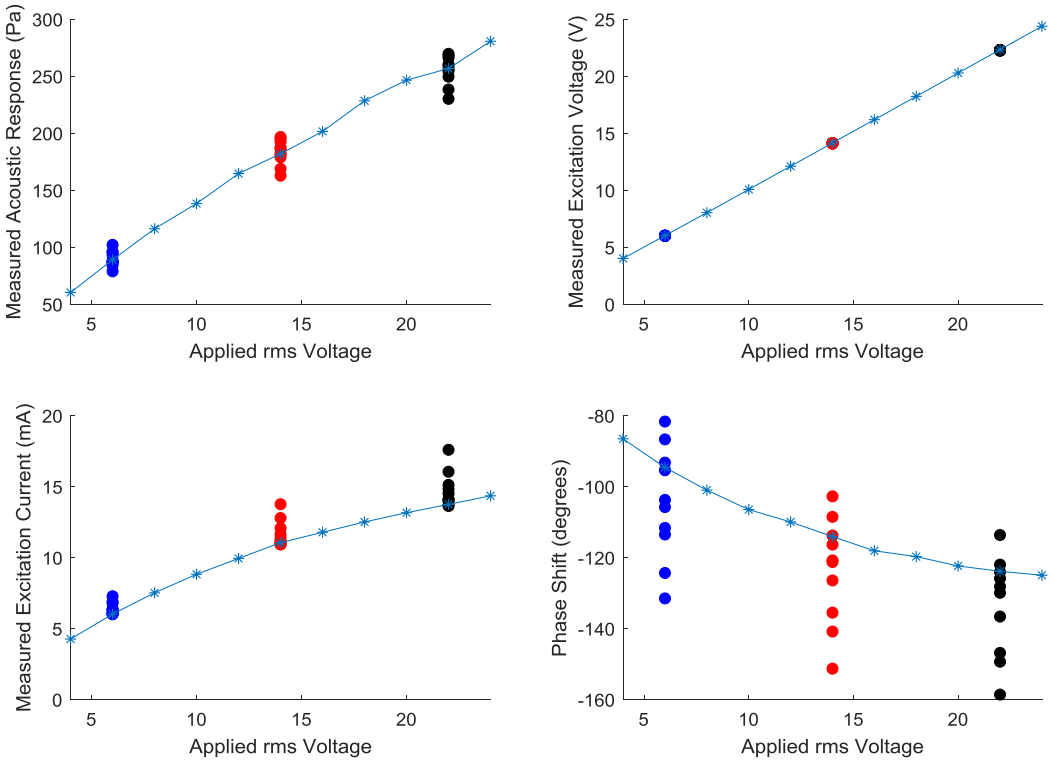


Figure 3: Response measurements of 10 randomly selected Murata transducers at low (6 V_{rms}, blue markers), medium (14 V_{rms}, red markers) and high (22 V_{rms}, black markers) excitation voltages. The stared line is the response of a single transducer at intervals of 2 V_{rms}.

In addition to measuring the response of each of the 10 sample transducers, 10 repeat measurements were taken for one transducer, with the transducer removed from and placed back into the mount between each test. This was done to estimate the statistical error of the test setup itself, which is presented as part of the statistical results in Table 1. By comparing the statistical error between 10 transducers and 1 repeated transducer, the significance of the variation in output between different transducers over random error could be estimated. The full statistical results are presented in Table 1. The statistical results are presented for low and high excitation voltages only, as these are of most interest in terms of comparing sensing and particle manipulation applications.

Transducer	Excitation Voltage	Measurement	μ_{comp}	σ_{comp}	σ_{ref}	σ_{ratio}	P-value
Prowave	6 V_{rms}	Response (Pa)	208.50	8.12	5.95	0.733	0.433
		Excitation Current (mA)	8.46	0.75	0.46	0.607	0.411
		Phase (deg)	-142.12	7.12	2.50	0.351	0.008
	22 V_{rms}	Response (Pa)	503.77	17.69	6.21	0.351	0.031
		Excitation Current (mA)	15.92	0.80	0.25	0.302	0.027
		Phase (deg)	-167.98	6.22	1.75	0.282	0.011
Murata	6 V_{rms}	Response (Pa)	90.16	6.76	2.34	0.346	0.013
		Excitation Current (mA)	6.43	0.40	0.05	0.112	0.000
		Phase (deg)	-104.67	16.00	2.68	0.168	0.000
	22 V_{rms}	Response (Pa)	255.49	12.85	3.68	0.286	0.020
		Excitation Current (mA)	14.78	1.20	0.05	0.039	0.000
		Phase (deg)	-133.42	14.08	1.41	0.100	0.000

Table 1: Statistical analysis of the response, excitation current and phase of 10 Prowave and 10 Murata transducers when excited with a low (6 V_{rms}), medium (14 V_{rms}) and high (22 V_{rms}) excitation voltage. μ_{comp} is mean value from 10 transducers, σ_{comp} is the standard deviation between 10 transducers, σ_{ref} is the standard deviation of 10 repeated tests with one transducer, σ_{ratio} is the ratio of σ_{comp} and σ_{ref}, Given is the P-value of the likelihood that there is no difference between σ_{comp} and σ_{ref}.

In order for the data to be a valid representation of the error in transducer response, the standard deviation ratio should be less than 1 with a high confidence. Apart from the response of a Prowave transducer with a low excitation voltage, it can be said with at least 95% confidence that there is a statistically significant difference in the standard deviation of the response of the 10 tested Prowave and Murata transducers compared to a single transducer repeated 10 times (P-value less than 0.05). As all ratios are less than 1, it can be said that the measurement error of the test rig is smaller than the error between individual transducers, validating the data obtained. This statement is less valid for the Prowave transducer at a low excitation voltage due to the relatively high ratio and P-value. In this paper, we are predominantly interested in the high voltages cases.

It is noted that there is not a significant difference in the output variation of the tested Prowave and Murata transducers, with the Murata having a more consistent response in terms of output sound power and the Prowave having a more consistent phase. It cannot be reasonably said that the performance of either model is better or worse with regards to variation between apparently identical transducers.

2.2 Transducer Efficiency Comparison

The data presented in Figure 2 and Figure 3 was used to calculate the throughput of the transducers at each of the three voltage levels. Throughput is measured as the pressure recorded at 70 mm above the transducer per Watt of power usage. It is clear that there is a difference between the Prowave and Murata transducers, however, as the measurement is taken at a single point, it does not take into account differences in directivity, and hence cannot be used to compare the efficiency of the two types. What is of interest is the change in throughput of both transducer types as a function of voltage, which represents the relative change in efficiency. It can be seen in Table 2 that the throughput drops by two thirds from the low voltage to high voltage levels. The potential cause of this efficiency loss is discussed in the next section.

Transducer	Applied Excitation Voltage	Throughput (Pa/W)	Throughput Ratio (6V/22V)
Prowave	6 V(rms)	4132	
	14 V(rms)	1996	2.91
	22 V(rms)	1420	
Murata	6 V(rms)	2326	
	14 V(rms)	1109	3.00
	22 V(rms)	775	

Table 2: Throughput of both transducers as a function of excitation voltage.

3 Frequency Response

As well as a statistical analysis of the response at resonance, it is of interest to analyse the frequency dependent response of both transducer models. This is to try and link the observed statistical variation in output to the transducer operation, as well as to quantify variation in resonant frequency and Q-factor. Two methods were used to do this. The impedance of each sample transducer was measured without load using a Cypher Instruments C-60 and the CypherGraph software. This information is used to assess the variability of the transducers when unloaded in terms of both resonant frequency and Q-factor, both of which are calculated within the software. Secondly, frequency sweeps were performed using the test equipment shown in Figure 1. To do this, the microphone was moved to a height of 270 mm above the transducer surface and the acoustic response and excitation current were recorded whilst sweeping the frequency of the excitation signal around 40 kHz using the function generator.

3.1 Impedance Measurements

The statistical analysis from the impedance measurements is presented in Table 3 for resonant frequency and Table 4 for Q-factor. The results are a measure of the electro-mechanical impedance of the transducers, and do not correlate directly to acoustic output as the acoustic impedance of the horn is not directly included in the measurement. It can be seen that the variation in resonant frequency is indeed very low compared to the magnitude of the mean for both transducer types. There is, however significant variation in the Q-factor. This variation in Q-factor will result in a variation in output acoustic power when driving all transducers at a constant frequency of 40 kHz, as at least some of the transducers in the sample will be driven off-resonance. It is therefore likely that the high variation in Q-factor can at least partly explain the variation in output acoustic power presented in Table 1.

Transducer	Mean Resonant Frequency	σ_{comp}	σ_{ref}	Coefficient of Variation
Prowave	40203 Hz	99.5 Hz	33.6 Hz	0.20%
Murata	40205 Hz	77.3 Hz	30.0 Hz	0.19%

Table 3: Statistical analysis of the resonant frequency of 10 Prowave and 10 Murata transducers. σ_{comp} is the standard deviation between 10 transducers, σ_{ref} is the standard deviation of 10 repeated tests with one transducer and the coefficient of variation is the ratio of the standard deviation to the mean.

Transducer	Mean Q-factor	σ_{comp}	σ_{ref}	Coefficient of Variation
Prowave	33.06	3.69	0.60	11.16%
Murata	22.60	2.16	0.22	9.56%

Table 4: Statistical analysis of the Q-factor of 10 Prowave and 10 Murata transducers. σ_{comp} is the standard deviation between 10 transducers, σ_{ref} is the standard deviation of 10 repeated tests with one transducer and the coefficient of variation is the standard deviation to the mean.

3.2 Acoustic Response Measurements

The measured frequency response of the 10 sample transducers subject to low, medium and high excitation voltages are depicted in Figure 4 for the Prowave transducers and Figure 5 for the Murata transducers. Frequency sweeps were conducted between 34 and 54 kHz to capture all phenomena of interest in the vicinity of the quoted resonant frequency of 40 kHz. The responses were measured with the microphone at a distance of 270 mm to minimize reflections from the microphone interfering with the acoustic field. The signal to noise ratio of the magnitude of the field was not a consideration as we are not comparing absolute magnitude values.

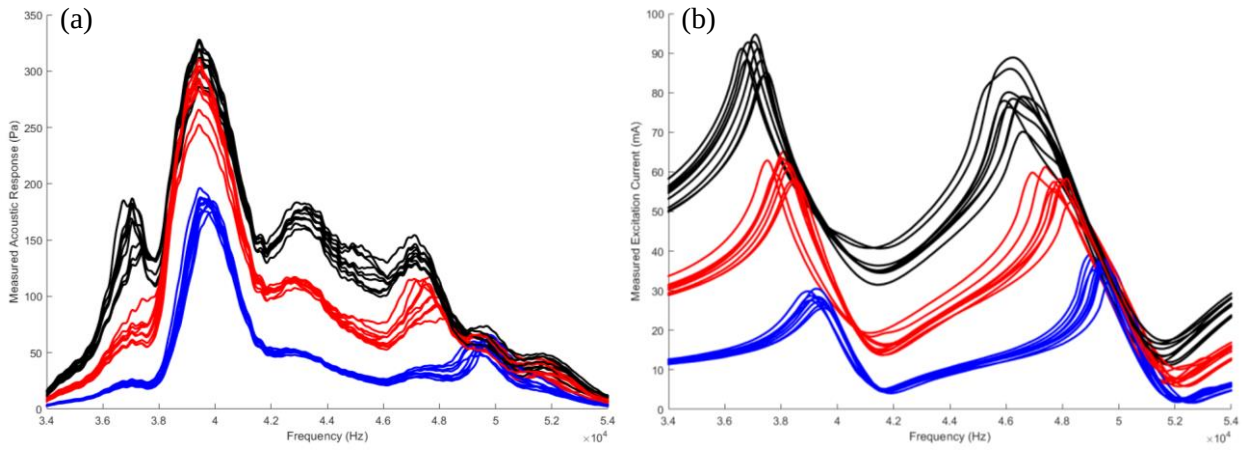


Figure 4: Frequency response of 10 Prowave Transducers at low (6 V_{rms}, blue), medium (14 V_{rms}, red) and high (22 V_{rms}, black) excitation voltages. (a) acoustic intensity measured at 270 mm from the transducer surface, (b) excitation current.

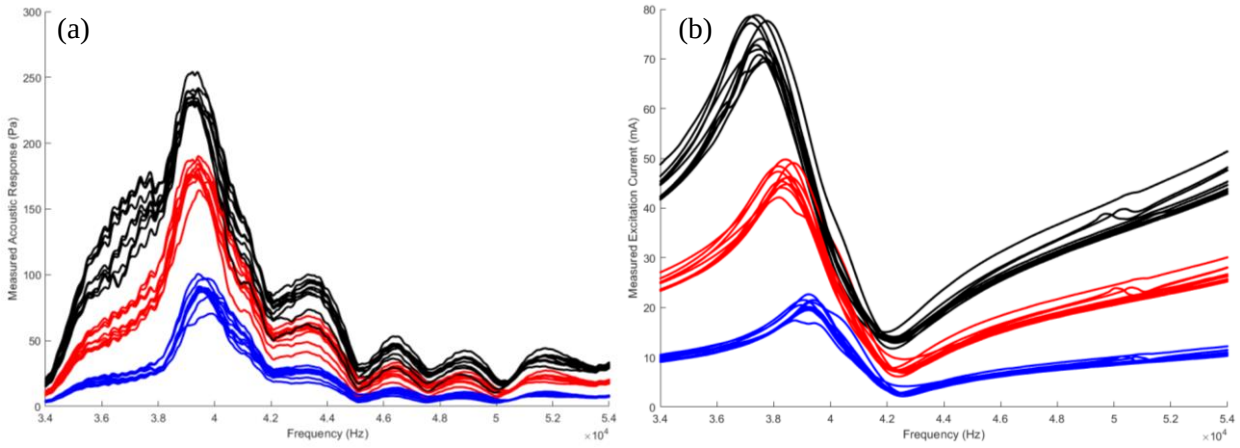


Figure 5: Frequency response of 10 Murata Transducers at low (6 Vrms, blue), medium (14 Vrms, red) and high (22 Vrms, black) excitation voltages. (a) acoustic intensity measured at 270 mm from the transducer surface, (b) excitation current.

The measured excitation current with a constant excitation voltage (Figure 4b and Figure 5b) suggest that both the Prowave and Murata transducers demonstrate a nonlinear softening behaviour, with the impedance minimum (maximum current) shifting down by approximately 2 kHz in both cases. This phenomenon is manifested in the acoustic output of the transducers (Figure 4a and Figure 5a), which depict a secondary resonant peak forming below the 40 kHz resonance (between 36 and 38 kHz) for the case of high voltage inputs. The secondary peak is better resolved in the Prowave transducer response due to the higher Q-factor. In addition to the secondary peak, the response at 40 kHz is a nonlinear function of voltage, as is apparent from the acoustic response curves of Figure 2 and Figure 3. Despite the nonlinear softening behaviour observed in the excitation current as a function of excitation voltage, the acoustic response remains strongest at 40 kHz for both transducer types, with no statistically significant frequency shift observed. This would suggest a relatively linear response with input voltage. A possible hypothesis is that the nonlinearity of the driving piezo is responsible for the nonlinear response observed in the current signal, whilst the emitting horn itself is very linear, resulting in the consistent resonant peak observed in the acoustic response signal. The coupling between the nonlinear driving piezo and the linear emitting horn could produce the observed response. A model of the full coupled physics would be required to verify this hypothesis, which is discussed in the Future Work section.

The nonlinearity of the frequency response could also explain the observed drop in throughput efficiency that was highlighted in Section 2.2. As the point of minimum impedance of the transducer shifts to lower frequencies, the impedance at 40 kHz increases as a function of voltage. The result is a greater loss of energy through heating, reducing the efficiency of the transducer to convert input electrical power into acoustic power.

Finally, it is interesting to note that a secondary peak occurs in the excitation current response of the Prowave transducer in the region of 46-50 kHz. However, the same phenomenon is not observed in the Murata transducer response. The cause of this secondary peak is not fully understood, but is likely a secondary resonant mode of the piezo disk element itself. This secondary peak does appear to manifest in the acoustic response of the Prowave transducer, however, the acoustic amplitude is significantly lower than the main peak at 40 kHz, suggesting high acoustic impedance from the emitting horn. To confirm this hypothesis, it would be desirable to study the resonant properties of the driving piezo disk and compare this to the design parameters of both transducer models. This is discussed further in the Future Work section.

4 Simulated Array Variation

The statistical data from Section 2 was used to simulate the variation in peak acoustic pressure of a focused array as a representation of the variation in acoustic radiation force. The response of a single transducer at a single point in space can be assumed to be harmonic with a variable amplitude and phase term.

$$P = A\mathrm{e}^{i(\omega t-\phi)}, \tag{1}$$

where A is the output pressure amplitude of the transducer, ω is the excitation angular frequency and ϕ is the phase of the transducer output. For a focused array of N transducers, the total acoustic pressure at the focal point will be a simple summation.

$$P_{tot} = \left(\sum_{n=1}^{N} A_n \mathrm{e}^{-i\Phi_\mathrm{n}}\right)\mathrm{e}^{i\omega t} \tag{2}$$

Using the statistical data from Table 1 (μ_{comp} and σ_{comp}), the 5th and 95th percentile can be found for any sized array using a Monte Carlo simulation and equation (2). The results are presented in Table 5 for the Prowave transducers and Table 6 for the Murata transducers. The transducers are assumed to have a Gaussian distribution. A total of 100,000 trials were run for each case, at which point sufficient convergence was achieved.

No. Transducers	**5th and 95th percentile due to Transducer Variation 6 V_{rms} (dB)**		**5th and 95th percentile due to Transducer Variation 22 V_{rms} (dB)**	
	5th	95th	5th	95th
1	-1.38	1.19	-0.90	0.82
10	-0.81	0.17	-0.59	0.10
50	-0.56	-0.11	-0.42	-0.10
100	-0.50	-0.18	-0.37	-0.15

Table 5: Variation in focused array acoustic pressure due to individual variation in transducer output for an array of Prowave transducers. The 5th and 95th percentiles are in dB relative to the acoustic pressure from an array of identical, mean valued transducers operated at 6 V_{rms} and 22 V_{rms}.

No. Transducers	**5th and 95th percentile due to Transducer Variation 6 V_{rms} (dB)**		**5th and 95th percentile due to Transducer Variation 22 V_{rms} (dB)**	
	5th	95th	5th	95th
1	-0.69	0.64	-0.62	0.58
10	-0.28	0.15	-0.24	0.15
50	-0.16	0.03	-0.14	0.04
100	-0.14	0.00	-0.11	0.01

Table 6: Variation in focused array acoustic pressure due to individual variation in transducer output for an array of Murata transducers. The 5th and 95th percentiles are in dB relative to the acoustic pressure from an array of identical, mean valued transducers operated at 6 V_{rms} and 22 V_{rms}.

The variation in output is more pronounced at lower excitation voltages for both transducer types, predominantly due to the greater variation in phase. At high excitation voltages, as would be used for particle manipulation/levitation applications, the variation in individual transducer output results in no more than a -0.9 dB reduction in peak focal acoustic pressure, compared to pressure levels in the region of 160 dB often used for particle manipulation applications [7]. The variation in output of the two tested models of cup-horn transducers hence should not be a significant issue when incorporating them into arrays for particle manipulation applications. It is noted that both the range and the lower bound loss in peak acoustic intensity of the $95^{\%}$ confidence interval reduces as the array size increases. This is due to the reduced phase deviation between individual transducers, as the number of transducers increase whilst the individual variation in phase remains constant.

5 Future Work

This paper has presented an experimental analysis of two cup-horn transducers used in research applications involving large arrays operating in air. It has been demonstrated experimentally through frequency response analysis that the operating mode of two existing off-the-shelf cup-horn transducers varies significantly depending on the applied excitation voltage. It is important to understand not only how this influences the application of cup-horn transducers, but also how design parameters influence the voltage dependent operating mode. To complete the picture, it would be desirable to construct a model of the coupled system, consisting of an approximately linear resonant horn and nonlinear piezoelectric-actuated disk. An analysis of the coupling between the two would give an insight into how the frequency response of a cup-horn transducer varies with excitation voltage, and would be a valuable tool for specifying design parameters, depending on whether a transducer is required for high or low power applications (for example sensing vs. acoustic levitation).

6 Conclusion

The results of our experimental investigation demonstrate that while the tolerances on resonant frequency are well controlled (less than 1%), there is measurable variation in measured Q-factor (on the order of 10%). It is suggested that this variation in Q-factor is the main driver of variation in sound power output for a given driving voltage. In addition to resonant frequency and output sound power/Q-factor, we measure the frequency response of both transducers at high and low excitation voltages. The results show a significant nonlinearity of the transducer, with two coupled resonances forming at high voltages, which we propose is a result of the coupling of a relatively linear resonant horn and a highly nonlinear piezoelectric disk. Taking into account the measured variation in transducer response when considering a focused array, a maximum variation in peak focal acoustic pressure of 1.38 dB at the 5^{th} percentile was calculated for high voltage excitation. This is a small deviation compared to the acoustic pressures normally required for particle manipulation/levitation applications (on the order of 160 dB) and is unlikely to be a significant consideration.

References

[1] A. Marzo, S. A. Seah, B. W. Drinkwater, D. R. Sahoo, B. Long and S. Subramanian, "Holographic acoustic elements for manipulation of levitated objects," *Nature Communications,* vol. 6, no. 1, p. 8661, 2015.

[2] M. Wiklund, R. Green and M. Ohlin, "Acoustofluidics 14: Applications of acoustic streaming in microfluidic devices," *Lab on a Chip,* vol. 12, no. 14, pp. 2438-2451, 2012.

[3] A. Marzo, A. Barnes and B. W. Drinkwater, "TinyLev: A multi-emitter single-axis acoustic levitator," *Review of Scientific Instruments,* vol. 88, no. 1, p. 085105, 2017.

[4] W.-S. Gan, E.-L. Tan and S. M. Kuo, "Audio projection: directional sound and its applications in immersive communication.," *IEEE Signal Processing Magazine,* vol. 28, no. 1, pp. 43-57, 2011.

[5] Pro-Wave Electronics Corporation, "Air Ultrasonic Ceramic Transducers 400ST/R160," New Taipei City, 2005.

[6] Murata Manufacturing Co. Ltd., "Ultrasonic Sensor Application Manual," Kyoto, 2009.

[7] A. Marzo, M. Caleap and B. W. Drinkwater, "Acoustic Virtual Vortices with Tunable Orbital Angular Momentum for Trapping of Mie Particles," *Physical Review Letters,* vol. 120, no. 1, p. 044301, 2018.

Easy sensor localization using an RGB camera

S. Sels[1], B. Bogaerts[1], S. Vanlanduit[1], R. Penne[12]
[1] Universiteit Antwerpen, Faculty of Applied Engineering department Electromechanics
Groenenborgerlaan 171, 2020 Antwerpen
e-mail: **Seppe.Sels@uantwerpen.be**

[2] Universiteit Antwerpen, Department Mathematics, 2020 Antwerpen, Belgium

Abstract
When performing an experimental modal test, the user has to define (i.e. draw) a geometry of the structure which includes the 3D locations and orientations of the vibration sensors (accelerometers, strain gages, etc.). This step is often tedious and time-consuming, especially for complex geometries containing a large number of sensors. Incorrect placement of sensors can lead to important errors [1].

In this paper, we propose a camera based method to semi-automatically link the geometry of an object under test with an available geometry in a CAD file. The technique uses low-cost equipment (a compact camera).

Our method will be demonstrated on three test objects: a car, a bicycle frame and a drone aircraft model. In the case of the drone, the curved shape of the wing makes it very difficult to measure the position and orientation of the sensors manually. We show that we are able to detect the sensors with an accuracy of about 5 mm in the studied cases.

1 Introduction

When performing an experimental modal test, the user has to define (i.e. draw) a geometry of the structure which includes the 3D locations and orientations of the vibration sensors (accelerometers, strain gages, etc.). This step is often tedious and time-consuming, especially for complex geometries containing a large number of sensors. Incorrect placement of sensors can lead to important errors [1].

In this paper, we propose a camera based method to semi-automatically link the geometry of an object under test with an available geometry in a CAD file. Our methodology can assist vibration test engineers in two ways:

Our camera-based method can be used to determine the positions and orientations of vibration sensors which are attached to a structure. The coordinates of the sensor positions are then transferred to the corresponding locations (and orientations) in a CAD geometry.

The used technique uses low-cost equipment (a compact RGB camera). The proposed procedure allows users to test prototypes faster and in a more repetitive manner because physical measurement positions are determined with less user interaction.

The proposed procedure consists of two main steps.

1. Firstly, a camera image of the object under test is recorded (it is assumed that parts of the contours of the object are visible in the camera image).

2. Next, the camera is aligned with a 3D CAD file using an image segmentation technique and pose estimation [2]. To do this, the user first manually aligns both geometries after which an optimization technique is used to improve the accuracy of the alignment.

Although the method relies on a camera our method does not need a calibration procedure to obtain the position between the camera and object. The fact that we do not need this calibration allows the user to quickly switch between large and small objects by simply zooming and focusing the camera.

Our method will be demonstrated on three test objects: a car , a bicycle frame and a drone aircraft model. In the case of the drone, the curved shape of the wing makes it very difficult to measure the position and orientation of the sensors manually. We show that we are able to detect the sensors on this complex shape object with a reasonable accuracy (of about 5 mm).

2 Methodology

2.1 State-of-the-art

The main idea is to align an image with a 3D CAD model of a test object. With this alignment sensors can be indicated in the image and the 3D location on the object can be calculated. In this work, the alignment of an image with a 3D CAD model is called pose estimation.

Algorithms for fully automatic pose estimation exist, but they need a large training set of images with known poses and/or accurate and textured 3D models of the test object [3,4]. Obtaining this training set and textures can be hard and time-consuming. Therefore in this work, it is assumed that this data is not available. Also, pose estimation using 3D range cameras exist, but material properties (colour, high surface reflectivity (metal),…) can often distort the 3D range image and disrupt the pose estimation [5]. Also, the size of the objects is limited to the used sensor. This work proposes a methodology with low-cost equipment that can be applied on various objects with various material properties and both small and large sizes. Therefore we propose a method using standard 2D cameras (smartphone camera, compact camera,…) that are low cost, easy to use, and by simply zooming or focusing they can be used to photograph small and large objects. Also, the pose estimation algorithm should be robust to small errors in the 3D CAD model.

There are various algorithms used for pose estimation of 3D models using 2D cameras. The most common algorithms for pose estimation use solutions of the perspective-n-point-problem (pnp-problem). The pnp-problem solutions estimate the 3D location of a camera to an object given a set of N 3D points in a chosen world coordinate system and their corresponding 2D projection in the image. In practice, this means that a user can select 2D points in an image, and when corresponding points are selected in a 3D CAD-model, the pnp-solution can calculate the position of the camera to the 3D model. Although in theory this should work, when the user only selects 4-6 points, the pose will not likely to be a good estimate since the algorithm is not robust to noise, outliers (wrongly selected points) and even the camera resolution will distort the results when using few points. Therefore an extra optimization algorithm is needed to calculate a good pose. In this paper a Matlab implementation of optimization algorithms described in [2,3,6] is used. Other (commercial) libraries exist like vuforia [7] and visionlib [8] that have similar working principles and results.

The original PWP3D pose estimation [2,6] assumes that the camera parameters are known. In this methodology this is not needed because we are not interested in the exact position of the camera, only the mapping between the image and 3D CAD model is needed. Therefore we only need to know the resolution of the camera. A rough estimate of the perspective angle can be used for the camera parameters. Errors on this estimate will not alter the alignment between the image and 3D CAD model.

2.2 Tools and Methodology

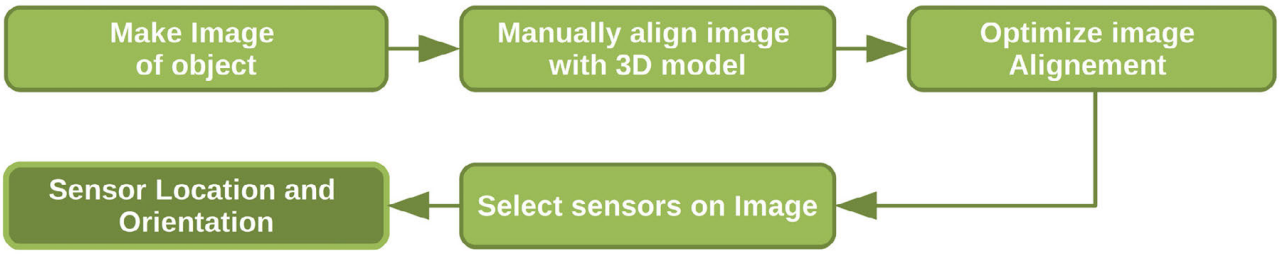


Figure 1 Flowchart of summarized methodology.

The methodology (Figure 1) starts with taking an image of a test object with sensors attached (Figure 2 a). Next the user roughly aligns the image with the 3D model by selecting points on the mesh and corresponding points in the image (Figure 2 b-c). Subsequent the pose of the object is optimized with the PWP3D optimization routine (Figure 2 d). After this optimization the sensor location can be manually selected in the image (Figure 2 e). The position of the sensor on the 3D model can then be calculated with the previously calculated pose (Figure 2 f). In this work we assume that the measuring direction (blue arrow Figure 2 f) of the sensor is normal to the surface of the measured object.

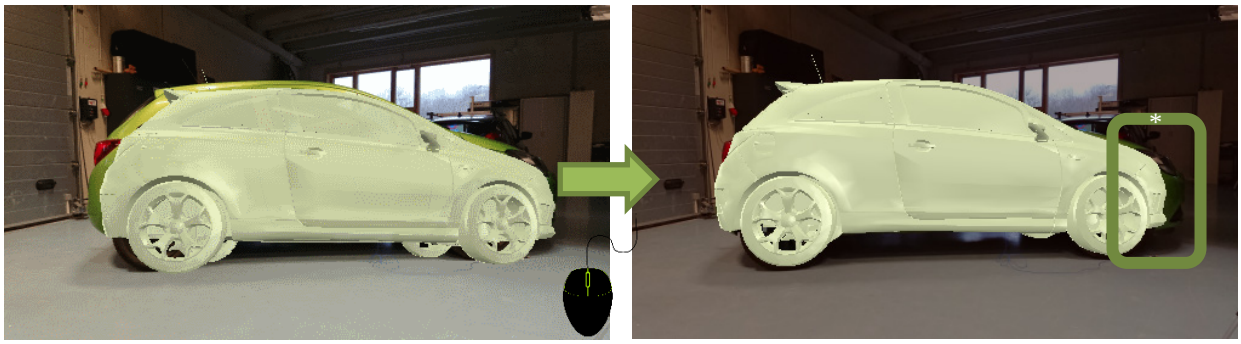
Figure 2 shows that the method also works when the 3D model slightly deviates from the real object. In this example the real car is an Opel Corsa 2016 while the CAD file corresponds to a 2014 model. This can be seen at the rear spoiler, rear light and the front bumper (Figure 2 d).

The method is tested with a standard compact camera (Nikon Coolpix S6300). The method allows to use any standard camera or smartphone camera given that the lens distortion (e.g. fish-eye effect) is low or compensated [9]. As a virtual rendering environment, an educational version of Vrep 3.5 [10] is used. This environment is linked with Matlab (r2017a). The pose of the object is initialized with the standard settings of the pnp solution of OpenCV (solvePnPRansac() [11]), and optimized using PWP3D. Due to speed and memory constraints of the link between Matlab and Vrep, images are downsampled to 500x275 pixels where the original image is 5500 x 3096 pixels. When properly implemented in C++ with GPU processing this downsampling is not needed as stated in [2,6].



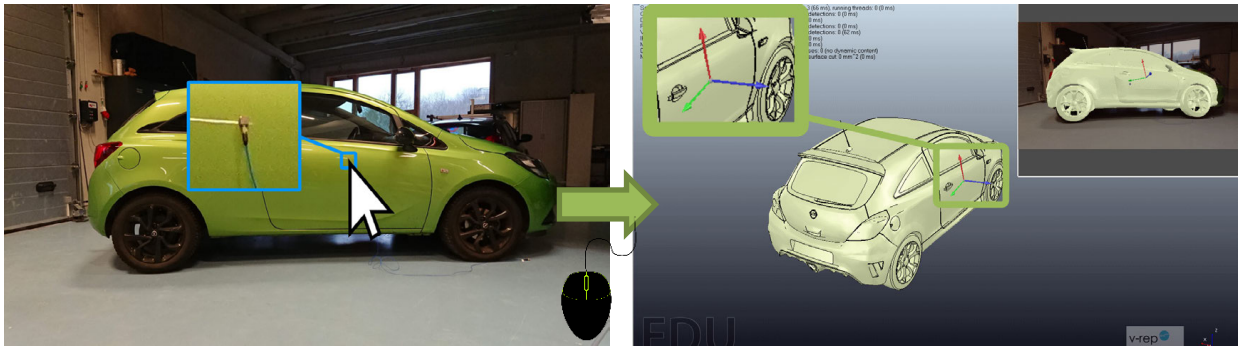
(a) Picture of object with sensor attached

(b) 3D model and picture with selected points highlighted for visualisation



(c) Picture of object initial pose (manually set in Vrep-model environment)

(d) 3D model pose after pose optimization. *misalignment due to error in 3D model



(e) Sensor is manually selected in image

(f) Sensor located on CAD file. (red-green-blue coordinate system)

Figure 2 Methodology in pictures. The user starts with taking an image of the test object and ends with the location and orientation of the attached sensor in the 3D model coordinate system. (a) reference image (b) 3D model (c) initial pose (d) optimized pose (e) image sensor (f) sensor location

3 Case studies

3.1 Car

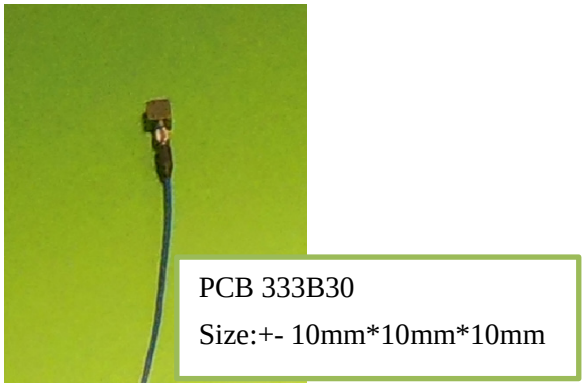
An accelerometer is placed at two position on a car. Two pictures are taken of the car (Figure 2 a-b). The method described in 2.2 is executed for each picture (2 pose estimations). As a result sensor locations where obtained (Figure 3 d). Only the measurement direction is plotted in the image. In this case this direction is assumed to be normal to the car-surface.



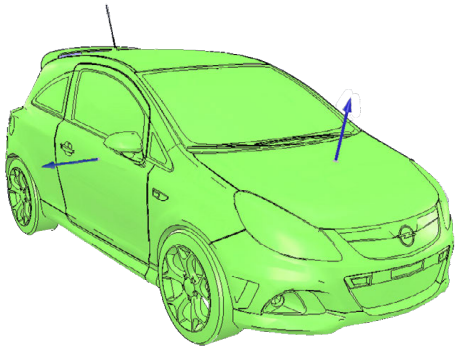
(a) Image sideview



(b) Image front view



(c) Sensor (zoomed from figure a)



(d) Sensors location and direction (blue arrow) on CAD model

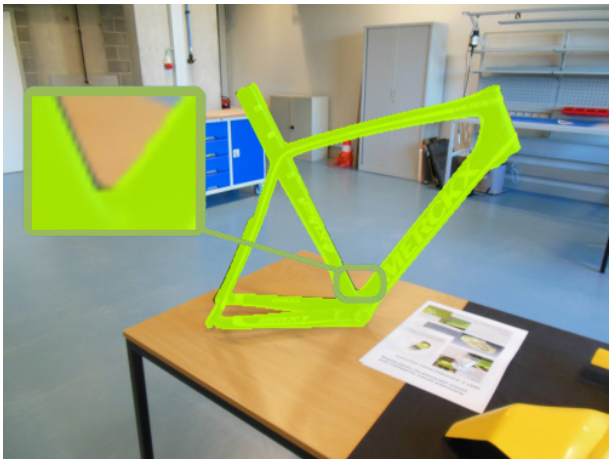
Figure 3 (a) Accelerometer placed on door panel (b) Accelerometer placed on bonnet (c) close up of accelerometer (picture not used in methodology) (d) Placement of sensors (blue arrows) on 3D model using images (a) and (b).

3.2 Bicycle Frame

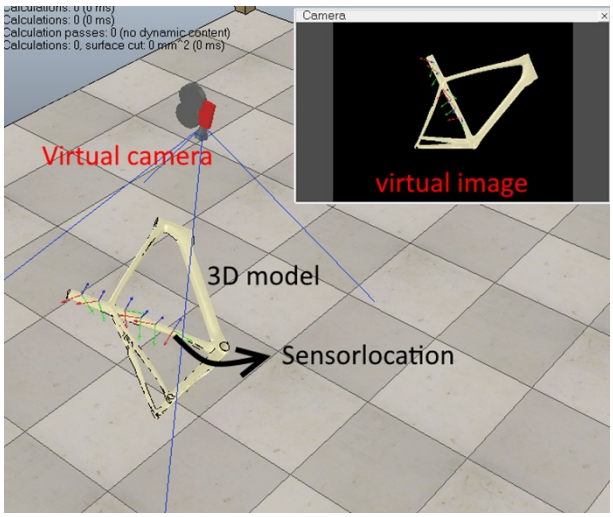
A bicycle frame is placed on a table and an image is taken with a relatively cluttered background. In this case sensor locations where indicated with white stickers (Figure 4 a). The bicycle frame is initialized by selecting 4 corresponding points in the 3D model and image. The optimized pose is visible in Figure 4 b. Only a small deviation (1 pixel) is visible in some parts of the image. The sensor locations are selected manually in the original image and plotted on the 3D model (Figure 4 c). The Z-direction (blue arrows) are normal to the surface other directions (x,y ; red, green arrow) are chosen randomly.



(a) Image bicycle frame (with zoomed part of locations)



(b) 3D model (green) plotted on original image



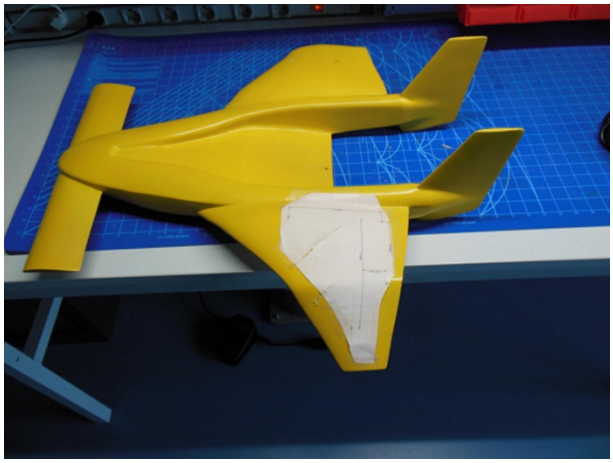
(c) Sensor locations in Vrep-enviroment

Figure 4 Example of sensor location selection on a bicycle frame (a) Image of frame (b) Image aligned with 3D model (c) Sensor locations

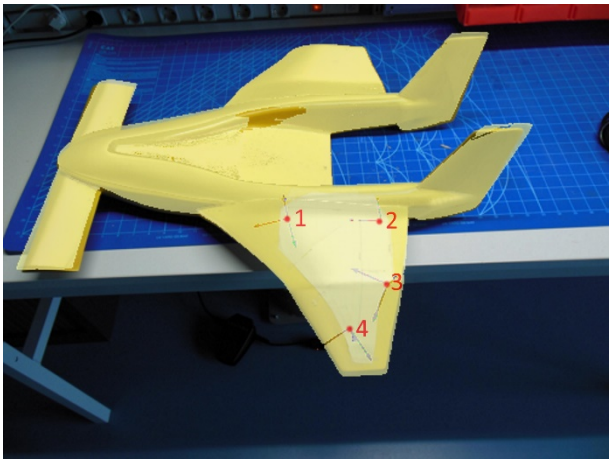
3.3 Model Drone

To benchmark the accuracy of the pose estimation with real world images, a piece of mm-paper is placed on a curved wing of a model drone. Locations are indicated on this paper (see Figure 5 a). The exact distance between points on paper is summarized in Table 1. After placing the paper with indicated points, the complete methodology is executed (see Figure 5 b-d). After selecting the indicated points (i.e. sensor locations) the distances between points are calculated (see Table 1).

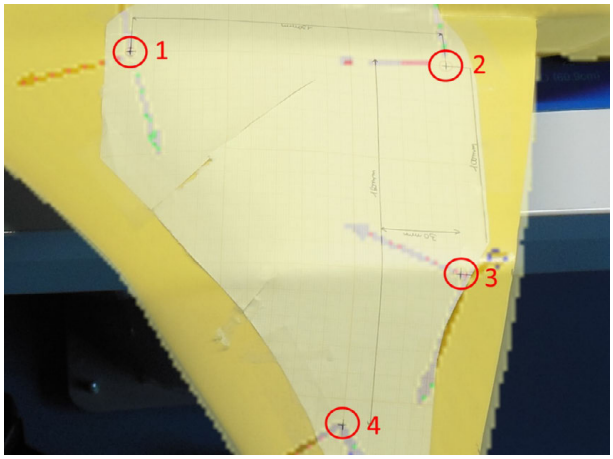
In this small benchmark the maximum deviation is 4 mm. The spatial resolution of the image is approximately 1.2 mm per pixel (on the left wing). The deviation is dependent on the indication of the points and the pose estimation. Note that the measured distance is the Euclidian distance between points and the added distance due the curvature is neglected. As a more reliable test a semi-synthetic repeatability test is executed in section 4.



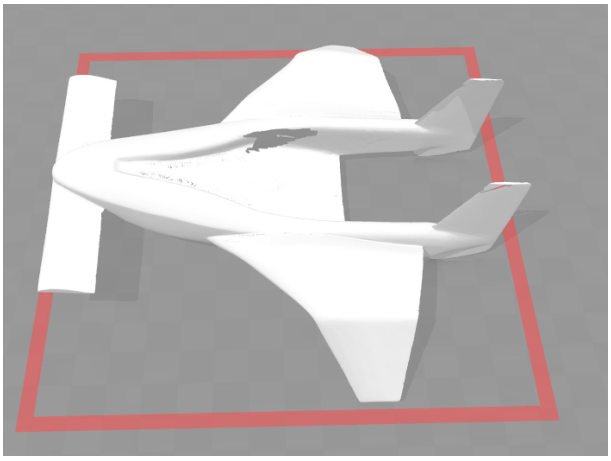
(a) Image of drone with mm-paper attached to left wing



(b) 3D model (light-yellow) plotted on orignal image.



(c) Zoomed image (orignal resolution) with an overlay of the 3D model. Locations are numbered in red.



(d) 3D scanned mesh model of (top part) of the drone.

Figure 5 Example of Pose estimation on a model of a drone. (a) Image of drone (b) Image aligned with 3D model (c) Sensor locations (d) Used 3D model

Table 1 Measurement results

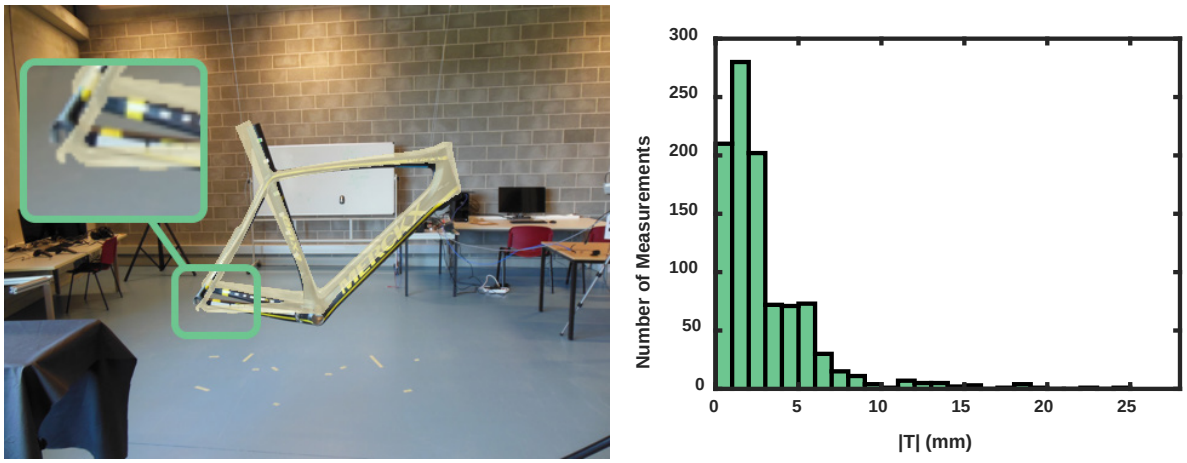
Point	Point	Distance (mm)	Distance Measured (mm)	Deviation (mm)
1	2	130	133	3
2	3	100	96	4
3	4	70	68	2

4 Validation

As a (synthetic) repeatability test we manually initialized the pose on an image of a bicycle frame. This initialization is used as the standard initialization. The initialized pose is randomly translated and rotated (slightly) to mimic other manual initializations. Next the PWP3D routine optimizes this pose. The random initialization and optimization is repeated a thousand times. From all the calculated poses the amplitude of the translation is saved. The procedure is summarized in Figure 6. An example of the initialization is given in Figure 7 (a). The deviation of the calculated amplitude is plotted in Figure 7 (b). This figure shows that for this experiment 95% of the measurements had a deviation (relative to the mean amplitude) less than 7.5 mm. 99% of the measurements is below 15.5 mm and 66% of the measurements have a deviation below 2.8 mm.

1. *Manual initialization of pose*
2. *Add noise on this initialization (Translation +- 12,5 mm, Rotation +- 0.5°)*
3. *Optimizer Pose*
4. *Save Translation*
5. *Repeat step 2 to 5 a 1000 times*
6. *Calculate Amplitude of Translation*
7. *Calculate Mean Translation*
8. *Amplitude of Translation = abs(Amplitude of Translation – mean(Amplitude of Translation))*

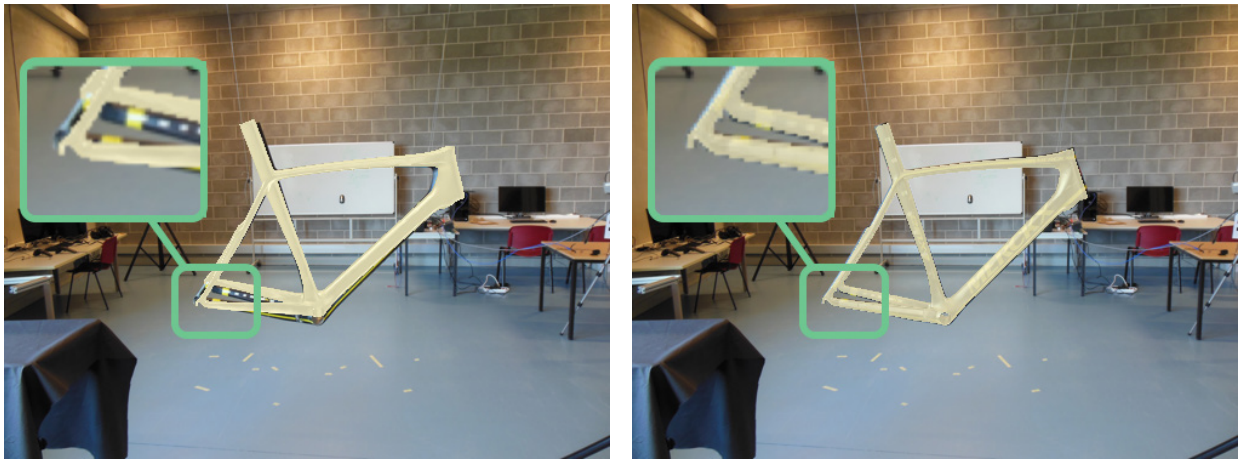
Figure 6 Synthetic repeatability tests



(a) (b)

Figure 7 (a) Example of a (semi) random initialized pose (b) Distribution of the amplitude of the calculated translation. Total number of measurements = 1000.

In our experience when the deviation is larger than 5 mm the user can easily see that the pose is not optimal. In this case/image 5 mm corresponds with approximately 8 pixels In Figure 8 a visually bad pose and visually good pose is shown. The visually bad pose had a deviation on the amplitude of 8.5 mm and the good pose has a deviation of 2 mm.



(a) Visually Bad Pose Estimation |T| = 8.5mm (b) Visually Good Pose Estimation |T| = 2 mm

Figure 8 Example of (a) a visually good pose and (b) a visually bad pose.

5 Conclusion

In this work a system is proposed that locates sensor locations and orientation from a picture taken with a standard compact camera.

The proposed system is aimed at industrial testing, prototyping and quality control where it is important to know the location of placed sensors on a test object. This location can be used for visualization, documentation and/or comparison with finite element simulations. A repeatability test shows that in our setup 95% of the sensor localization had a deviation of below 7.5 mm.

Parts of the methodology require manual intervention. This is specifically done to avoid object detection techniques that often require large data-set of images and/or highly accurate and textured models of the object. These conditions are often not achieved, and the proposed manual intervention also forces/allows the user to visually check the positions of the calculated sensor positions.

6 References

[1] Kammer DC, Tinker ML. Optimal placement of triaxial accelerometers for modal vibration tests. Mech Syst Signal Process 2004;18:29–41. doi:10.1016/S0888-3270(03)00017-7.

[2] Tjaden H, Schwanecke U, Schömer E. Real-time monocular segmentation and pose tracking of multiple objects. Lect. Notes Comput. Sci. (including Subser. Lect. Notes Artif. Intell. Lect. Notes Bioinformatics), vol. 9908 LNCS, 2016, p. 423–38. doi:10.1007/978-3-319-46493-0_26.

[3] Tjaden H, Schwanecke U, Schömer E. Real-Time Monocular Pose Estimation of 3D Objects using Temporally Consistent Local Color Histograms. ICCV 2017, 2017. doi:10.1109/ICCV.2017.23.

[4] Pauwels K, Kragic D. Pauwels, Karl and Kragic, Danica, "SimTrack: A Simulation-based Framework for Scalable Real-time Object Pose Detection and Tracking", IEEE/RSJ International Conference on Intelligent Robots and SimTrack: A Simulation-based Framework for Scalable Real-time Object Pose Detection and Tracking n.d.

[5] Rusu RB, Marton ZC, Blodow N, Beetz M. Persistent point feature histograms for 3D point clouds. Intell Auton Syst 10, IAS 2008 2008:119–28. doi:10.3233/978-1-58603-887-8-119.

[6] Prisacariu VA, Reid ID. PWP3D: Real-Time Segmentation and Tracking of 3D Objects. Int J Comput Vis 2012;98:335–54. doi:10.1007/s11263-011-0514-3.

[7] PTC. Vuforia | Augmented Reality n.d.

[8] Visionlib. Weblet Importer n.d.

[9] Zhang Z, Zhang Z. A Flexible New Technique for Camera Calibration. IEEE Trans Pattern Anal Mach Intell 2000;22:1330–1334.

[10] Robotics C. Coppelia Robotics V-REP: Create. Compose. Simulate. Any Robot. n.d.

[11] Documentation O. OpenCV: Camera Calibration and 3D Reconstruction n.d.

Optimal positioning of continuous optical fiber sensors for the modal analysis of turbine blades with optical backscatter reflectometer technology

P. Pennacchi[1], G. Cazzulani[1], M. Chieppi[1], A. Colombo[1]
[1] Politecnico di Milano, Department of Mechanical Engineering
Via G. La Masa 1, I-20156, Milan, Italy
e-mail: **paolo.pennacchi@polimi.it**

Abstract
There are many methods described in the literature for the modal analysis of turbine blades, using well-established technologies. The aim of this paper is the introduction of a new method, based on continuous optical fiber sensors and on optical backscatter reflectometer (OBR) technique. Contrary to other methods, the sensor is not invasive and all the measuring points are aligned in sequence on the same wire (i.e. the same optical fiber) characterized by a limited length. In the literature, many optimal positioning methods for the sensors have been proposed, but none of them considers sensors arranged sequentially along the same wire, limiting to independent sensors, such as strain gauges or accelerometers. On the contrary, in this paper, an optimal method is proposed and illustrated in detail to arrange the optical fiber along the blade to perform the modal analysis. Finally, some numerical and experimental tests performed on a blade will be presented.

1 Introduction

Experimental modal analysis (EMA) is well-known and material tool for the identification of the dynamic characteristics of a structure [1],[2], including also blades employed in rotating machines [3]. In this case, the analysis is aimed at:

- predicting the locations of possible energy introduction. This permits the determination of fluid-structure interactions, which could be critical for the blade structure, and the design of devices for vibration damping [4]-[7];
- identifying the presence of possible cracks from the mode shapes and, with a suitable real-time system, controlling fatigue crack growth [8],[9];
- validating FE models, when complex geometries or inhomogeneous materials are used.

To completely decouple EMA from the use of numerical models, a high number of sensors is required to properly fit the different mode shapes of the structure and to distinguish between them, avoiding the so-called *spillover effect* [10].

One of the most promising solutions for this purpose is the use of optical fiber sensors [11]-[13], like the well-known fiber Bragg grating (FBG) sensors. Recently, other measurement techniques based on optical fiber sensors have been developed, allowing a continuous strain measurement along the fiber. This is the case, for example, of the optical backscatter reflectometer (OBR) technology, which is considered in this paper.

A further advantage consists in the fact that the optical fiber sensor can be embedded into blades made of composite material, e.g. the optical fiber can be directly woven inside the carbon fiber matrix or can be installed between different layers composing the blade (see Figure 1). This technical solution allows the sensor to be always installed in the blade, so that it can perform continuously the condition monitoring of

this component. Given these remarkable advantages, the exploitation of the great potential of this type of sensor must be done by positioning the optical fiber correctly along the turbine blade.

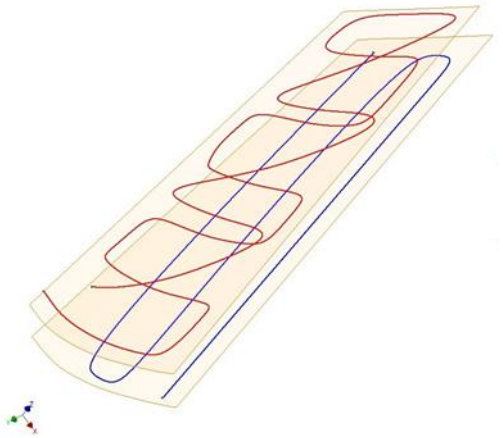


Figure 1. Optical fiber arrangement on layers.

Indeed, differently from classical sensors, which can be placed independently from the others, in this case all the measurement points are placed on the same wire (the fiber itself) and this wire is characterized by a finite length. Moreover, due to the physical characteristics of the fiber, some constraints on how the fiber is placed, such as the maximum allowed fiber curvature, must be considered, especially for highly twisted blades. Moreover, blade strains are measured and a proper position is required to be able to properly reconstruct the displacement modal shapes from strain measurements.

Many optimal placement methods for sensors have been proposed in the literature [14]-[18], but they are generally referred to independent sensors, like accelerometers, strain gauges, etc., while no methods can be found for this kind of continuous sensors, to the best knowledge of the authors. Aim of this paper is to propose an optimal method for continuous optical sensor placing on the structure for modal analysis.

After a brief recall of the optical sensing technology considered here (section 2), the paper describes the optimal placement method, based on genetic algorithms (section 3). Finally, section 4 shows some significant numerical and experimental tests, which prove the good results obtained by using the proposed approach.

2 Optical backscatter reflectometry sensors

Fiber optic sensors are an excellent solution for embedding in composite materials, thanks to their reduced cross-section and the consequent negligible load effect on the structure. Moreover, they can be embedded inside the structure during the manufacturing process, thus avoiding any surface alteration that may compromise the correct working of the structure, for example when a specific surface shape is required for fluid-structure interaction (e.g. turbine blades), or a free surface is necessary for the interaction with other components (e.g. mechanisms or joints).

Many different sensing technologies based on optical fibers are available, each one suitable for a range of applications depending on many parameters like the number of sensors, the fiber length or the frequency range. Among them, one interesting solution for vibration monitoring and modal analysis purposes is represented by OBR sensors [19],[20].

OBR fiber optics relies on the optical backscatter reflectometry physical principle: when an electromagnetic radiation, like a light beam or a laser, propagates in a medium, it collides and interacts

with the incident atoms causing secondary electromagnetic waves, called *"scattered"*, which are coherent and interact in a constructive way defining a weak, but detectable signal. If the medium is not homogeneous in terms of density (thus, in terms of refraction index), as a real fiber, the propagating wave gets scattered and then a back scattered wave is created. This phenomenon is called *spontaneous Rayleigh scattering*.

By varying the frequency of the laser wave, a periodic signal is created at the light sensor, whose frequency depends on the location of the respective fiber segment that scatters the light back. The further the segment away from the light sensor, the greater the frequency of the interference signal. As the light sensor receives the backscattered signal from all the segments simultaneously, the total signal must be split into its frequency components using a Fourier transform technique. The frequencies then correspond to the signal location along the fiber. The amplitude of each frequency component indicates the strength of the respective reflection.

When a commercially available optical fiber is scanned, a fluctuating intensity profile of the Rayleigh scattering along the fiber will be detected. This profile is stable when the measurement is repeated under unaltered external conditions (i.e. no loads are applied), so that it represents a characteristic *"fingerprint"* for a given fiber segment. This phenomenon is typical of Rayleigh scattering, being caused by the elastic scattering process and refractive index variations at local defects. If the temperature varies, or an external mechanical load is applied to the fiber, its fingerprint is spatially stretched or compressed. This phenomenon is at the basis of the Rayleigh sensor technology, since the changes to the local Rayleigh pattern can be converted into local temperature or strain values.

3 Optimal sensor placement method

3.1 From strain measurements to displacement estimation

The procedure for optimal placement of continuous sensors should allow reconstructing the displacement modal shape of the structure starting from the available measurements

Being the measurement output a strain measure, a strain-to-displacement procedure has to be implemented to obtain the structure displacements. In the literature, this is typically obtained by using the so-called DST-matrix method [21], which is based on a full a-priori knowledge of the modal shapes of the structure (displacement and strain modal shapes are linked by the numerical model itself). Anyway, for the purpose of this work, the modal shape estimation should rely on the model as less as possible. For this reason, the reconstruction of the displacement field of the structure must be obtained from the measurement of the strain in a number of points and in a given direction (i.e. the fiber direction in that points).

Considering the strain theory for thin plates, the surface strain of the plate can be expressed as

$$\varepsilon_{xx} = \frac{\partial u}{\partial x} = -z\frac{\partial^2 w}{\partial x^2},\ \varepsilon_{yy} = \frac{\partial u}{\partial y} = -z\frac{\partial^2 w}{\partial y^2} \tag{1}$$

$$\varepsilon_{xy} = \frac{1}{2}\left(\frac{\partial u}{\partial y} + \frac{\partial v}{\partial x}\right) = \frac{1}{2}\left(-z\frac{\partial^2 w}{\partial x \partial y} - z\frac{\partial^2 w}{\partial x \partial y}\right) = -z\frac{\partial^2 w}{\partial x \partial y} = -\frac{1}{2}\gamma_{xy} \tag{2}$$

where x, y and z represent the reference system (see Figure. 2), u, v and w are the displacements along x, y and z respectively, ε_{xx} and ε_{yy} are the axial strain along x and y, while γ_{xy} represents the planar shear strain at 45°. All the other strain terms generally present in 3-D structures are equal to zero for thin plates.

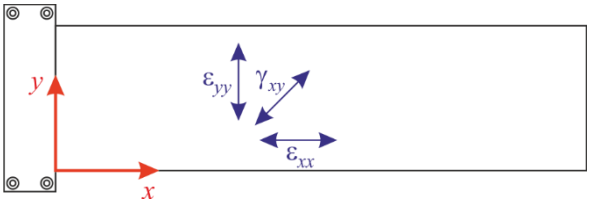


Figure. 2. Reference system for the thin plate under analysis.

Under a theoretical point of view, to obtain the displacement field (w), a few surface strain measurements with any direction are sufficient, since the displacement field can be obtained by double-integrating the strain field based on one of the two expressions in eq. (1). In practice, this leads to non-robust results, because "information" from one direction only is employed, without considering what happens along the other ones.

For this reason, a different approach is adopted with the aim at considering strain information coming from different directions. Starting from

$$\begin{Bmatrix} \varepsilon_{xx} \\ \varepsilon_{yy} \\ \gamma_{xy} \end{Bmatrix} = \begin{bmatrix} \cos^2\theta_1 & \sin^2\theta_1 & \cos\theta_1 \sin\theta_1 \\ \cos^2\theta_2 & \sin^2\theta_2 & \cos\theta_2 \sin\theta_2 \\ \cos^2\theta_3 & \sin^2\theta_3 & \cos\theta_3 \sin\theta_3 \end{bmatrix}^{-1} \begin{Bmatrix} \varepsilon_{\theta 1} \\ \varepsilon_{\theta 2} \\ \varepsilon_{\theta 3} \end{Bmatrix} \tag{3}$$

where $\varepsilon_{\theta i}$ represents the axial strain along a general i-th direction in a certain structure point, the shear strain γ_{xy} can be computed in the same structure point. Then, once the shear strain is known, the displacement w is computed by integrating twice the expression in eq. (1). To do that, the complete strain field along at least three directions must be known. By placing the optical fiber sensors along three directions, it is possible to interpolate them, obtaining the complete axial strain field along these directions and then to calculate γ_{xy} by using eq. (2). An example of this procedure is shown in Figure. 3, while Figure. 4 shows an example comparing the displacement reconstruction obtained with this approach and using the axial strain measurements along the x-axis only. Both results are obtained considering 20 "virtual" sensors placed randomly on the structure.

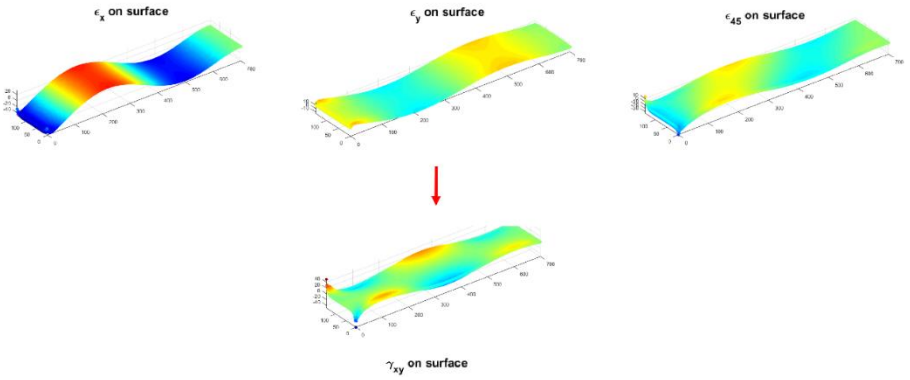


Figure. 3. Computation of the shear strain field from axial strain measurements.

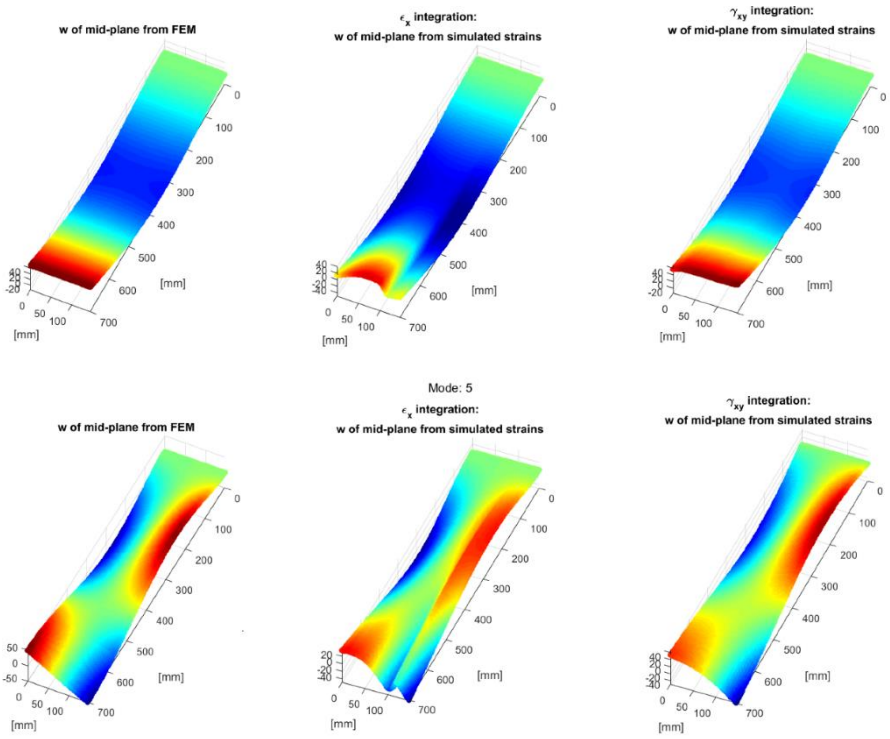


Figure. 4. Computation of the displacement field from axial strain along x (center) and from shear strain (right) compared with the correct displacement (left): lower order mode (on the top) and higher order mode (on the bottom)

3.2 Optimal sensor placing algorithm

The optimal placing algorithm proposed in this paper is based on genetic algorithms (GA) [19]. Unlike FBG optical sensors, for which some optimal sensor placement methods can be found in the literature [14], OBR optical-fiber contains a huge number of embedded gauges. GA has to place the fiber dealing with a physically constrained continuous device. The continuity of the fiber-sensor is a tricky constraint to be dealt with. No kind of suggestion has been found in the literature concerning how to manage this specific aspect. Therefore, some new procedures have been implemented according to this fact.

It is necessary to develop a fiber-placement algorithm that works in the GA framework and tracks a potentially valid path for the fiber starting from a reduced number of encoded design variables (DVs). This approach permits producing valid sensor arrangements at each generation, depending on a fixed logic. As a matter of fact, too many constraints exist to allow the survival of whichever valid configuration, after a crossover if the whole fiber-path is encoded. For these reasons, the genetic coding and crossover procedure will not involve the whole fiber arrangement, but just a set of *outstanding* positions. These points, namely their position and orientation, represent the genes of each individual and build the chromosome, as represented in Figure. 5. The position is described by a number univocally representing a structure point, while orientation is described by another number representing the possible orientations allowed. In this example three possible orientations, identified by numbers 1, 2, and 3, are considered.

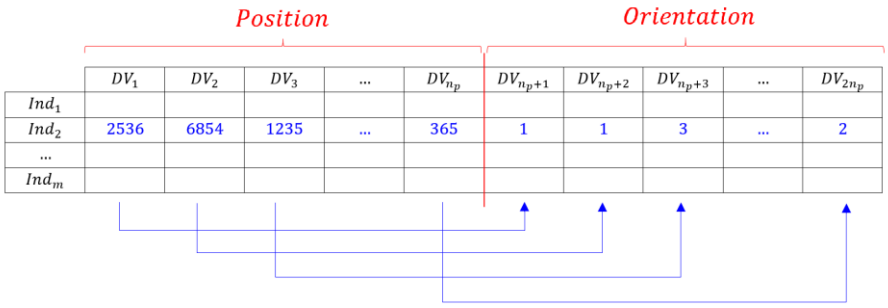


Figure. 5. Structure of the individual chromosome.

To obtain the full fiber path, these points will be connected in deterministic manner, providing the complete configuration of the fiber. Then, the individual fitness is computed accounting for the information available by the complete configuration. If the configuration exceeds the maximum fiber length, it is excluded by setting the corresponding fitness function to zero. Being the connection strategy deterministically dependent on the relative position and orientation of the *outstanding* locations, the genetic heritability of fiber arrangement is guaranteed among generations. Figure. 6 resumes how the fitness function of the GA is calculated, as described above.



Figure. 6. Procedure for the definition of the fitness function of the genetic algorithm.

The fitness function, to be maximized by the GA, has been defined based on the scope of the algorithm and on the physical constraints the OBR sensor is subject to:

$$Fitness = \left\{ MSE_{weighted} \left[1 + \left(1 - \frac{\det FIM_{fiber}}{\det FIM_{global}} \right) + AutoMAC + \left(1 - \frac{bends_{\min}}{bends_{fiber}} \right) \right] \right\}^{-1} \quad (4)$$

The fitness function is composed by:

- a main contribution ($MSE_{weighted}$), representing the mean square error between the estimated and real modal shape for all the considered modes. The weight is an user-defined coefficient that can be introduced to provide more importance to some modes;
- a penalty function ($detFIM_{fiber}$) able to drive the optimization procedure to those points containing more significant strain information if compared to the global strain information of the structure;
- a penalty function, based on *AutoMAC*, to avoid fiber configurations for which two different modes cannot be distinguished one from the other;
- a penalty function ($bends_{fiber}$) to penalize configurations containing more fiber curves along the path than the minimum required ones.

While the first three elements of the fitness function depend on the target of the optimization procedure, the last one is strongly sensor-dependent and it is due to the fact that OBR sensors are characterized by a strong reduction of the measurement quality if the fiber is placed with many low-radius bends. The same optimization method can be used for any other kind of continuous sensor without losing generality, just removing this last penalty element.

4 Experimental tests

The proposed method for the experimental modal analysis has been tested on two structures. The first one is a simple PVC thin plate, while the second one is a more realistic structure, consisting in a scaled model of a gas turbine.

4.1 Test rig setup with a simple plate

For the first test setup, a thin rectangular plate made by PVC has been equipped with a 2 m OBR optical fiber. The optimal fiber configuration has been obtained considering the following parameters:

- available optical fiber length equal to 1.5 m (this value is due to the fact that the first part of the fiber length must remain free as suggested by the producer);
- targeted modes from the 2nd to the 9th except to the 8th: the algorithm will optimize the fiber position to optimally identify these modes;
- minimum fiber radius equal to 10 mm (limit imposed by the loss of light and consequent reduction of signal quality induced by small-radius curves);
- three possible sensor directions (0°, 45° and 90° with respect to the *x*-axis).
- 100 individuals for the genetic algorithm;
- mutation probability of 0.4.

Figure. 7 shows the result obtained for the algorithm in this case. The segments of the fiber along the three allowed directions, representing the portions of the optical fiber that is used for the mode estimation, are represented with dots having different colors, namely blue for 0°, black for 45° and yellow for 90° with respect to the *x*-axis. The thin red lines represent the parts of the fiber used to connect the active measuring portions.

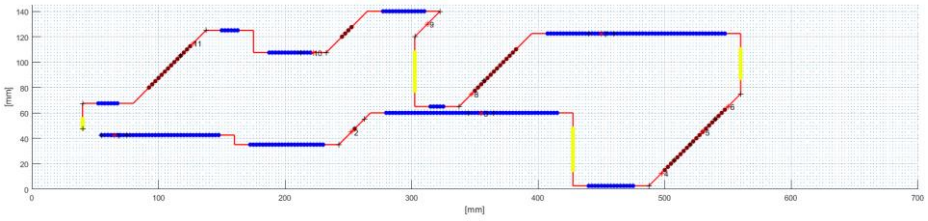


Figure. 7. Fiber configuration provided by the optimization algorithm.

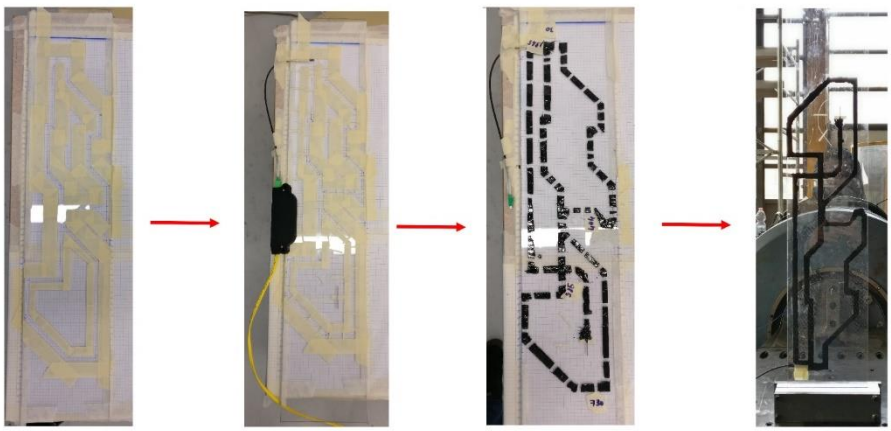


Figure. 8. Application of the optical fiber on the structure following the path identified by the optimal placing method.

As shown in Figure. 8, the fiber has been glued to the plate surface using an epoxy glue following the profile provided by the optimal placing method. The structure has then been tested on an electromechanical shaker, forcing both torsional and bending modes (Figure. 9).



Figure. 9. Plate clamped at his basement and mounted on the shaker to excite the torsional modes (on the left) and the bending modes (on the right).

4.2 Numerical and experimental mode estimation results

Both numerical and experimental tests have been carried out on the setup shown in the previous section. The numerical tests have been done simulating the optical fiber and forcing the FEM numerical model of the structure through an imposed movement of the clamp constraint. The experimental tests have been done replicating the same behavior through the shaker excitation, as shown in the previous section.

Numerical and experimental results are expected to be similar, since the structure is very simple and thus easy to model precisely. Anyway, some differences can be found in the measurement system, since the numerical tests are performed assuming ideal sensor output, while the experimental measurements are affected by poor signal quality and quantization. As a consequence, the experimental output of the modal analysis could be significantly worse than the numerical one.

In order to reduce this negative effect, the experimental modal analysis have been performed by averaging the output obtained by multiple vibration cycles. Thus, the modal analysis of the structure cannot be performed punctually (i.e. a point-by-point estimation cannot be performed unless a high estimation error is accepted), but it must be performed on an acquisition window. Anyway, it must be underlined that the general validity of the proposed procedure is not nullified by this issue, being it a characteristic of the particular fiber type used in this test setup.

In the following, some results obtained on some significant modes are reported. All the figures are organized as follows: the left figure represents the ideal modal shape (from FEM model), the central figure shows the result obtained by the numerical estimation, while the right one shows the results of the experimental modal analysis. In particular, figure Figure. 10 and Figure. 11 show the estimation result for 5^{th} mode (second torsional one) and 6^{th} mode (fourth bending one). It can be observed that in both cases the modal shape reconstruction provided by both numerical and experimental data are able to reproduce the real characteristics of the mode.

Different considerations can be drawn when analyzing the reconstruction of 8^{th} mode (see Figure. 12), which was intentionally not included in the optimization procedure.

In this case the mode shape reconstruction is not satisfactory, neither in the case it is computed from simulated strains, neither in the case of experimental measurements. Anyway, for the algorithm validation, this is a very good result, confirming the effectiveness of the fiber-placement. Indeed, since 8^{th} mode was not included as target mode in the optimization process, its correct reconstruction is not considered by the algorithm itself, and thus it cannot be guaranteed.

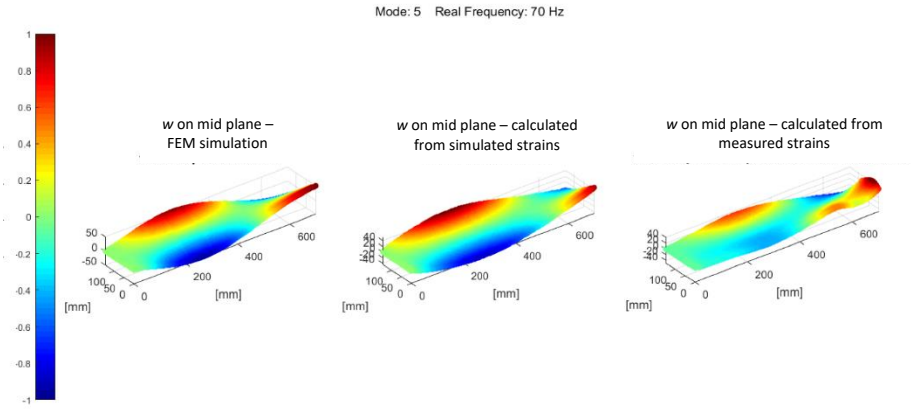


Figure. 10. Estimation results for the 5th mode: real mode from FEM (left), mode reconstructed from numerical data (center) and experimental data (right).

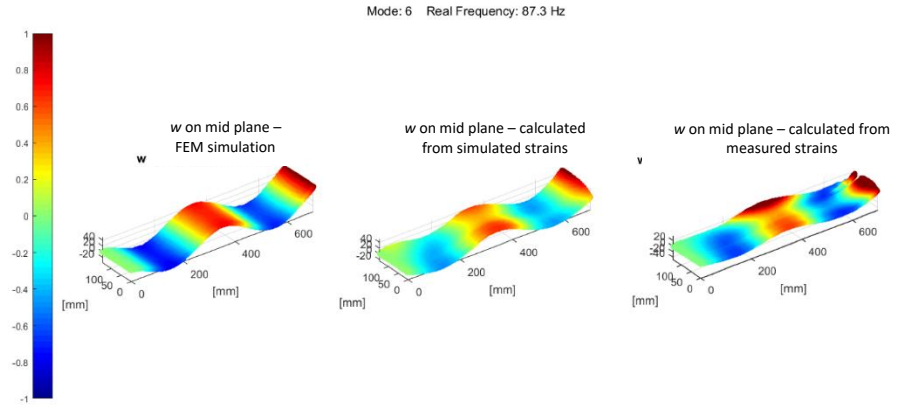


Figure. 11. Estimation results for the 6th mode: real mode from FEM (left), mode reconstructed from numerical data (center) and experimental data (right).

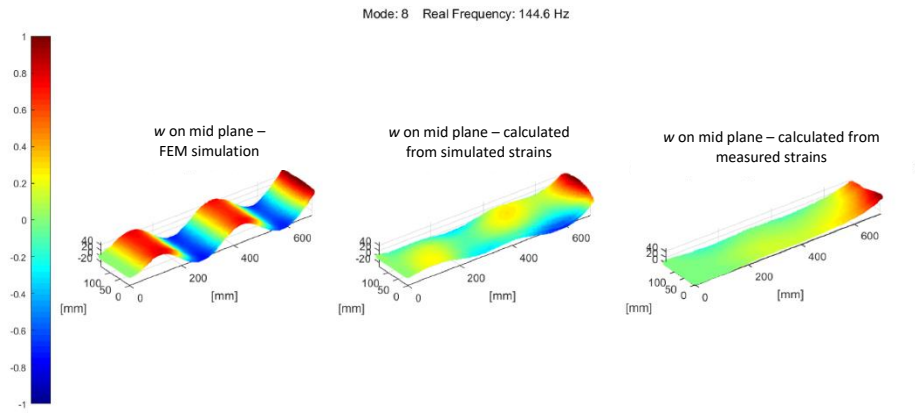


Figure. 12. Estimation results for the 6th mode: real mode from FEM (left), mode reconstructed from numerical data (center) and experimental data (right).

4.3 Tests on a composite blade

Once the good results obtained by the placing algorithm and by the measurement technique has been verified by means of the simple thin plate, a second test set-up has been considered. This setup is more

representative on a real condition, since modal analysis on turbine blades is a very important research topic.

Due to the simplicity of construction and to some frequency limitation of the used optical fiber measurement system (limitations which can be overcome with the new designed OBR interrogators), the blade used for the tests was made of ABS by additive manufacturing. The blade geometry was reproduced by means of the 3D reconstruction of a standard steam turbine blade (Figure. 13), but due to the different material the natural frequencies are scaled down, while the modal shapes remain the same.

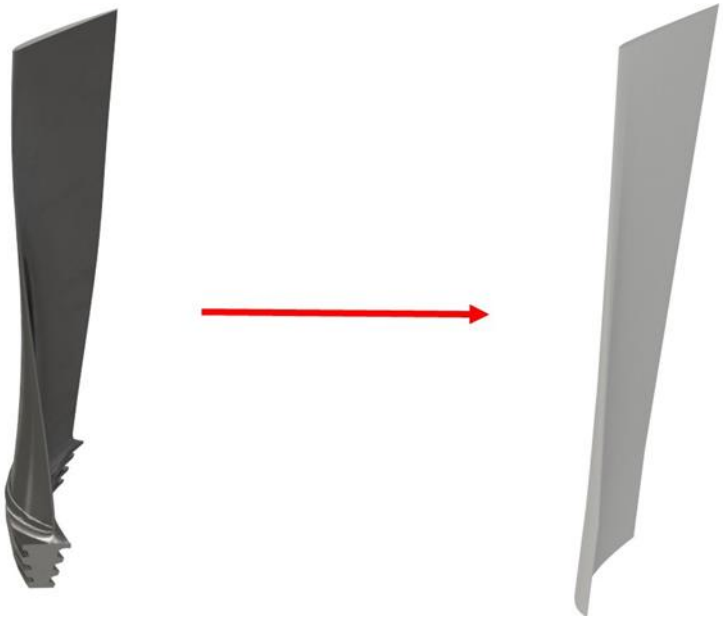


Figure. 13. From the 3D model of the real blade to the ABS model

In this setup, the accentuated 3D geometry due to the blade twist involves two remarkable differences with respect to the thin plate case described in section 0 and 4.2:

- The strain theory for 3D solids requires a modification of the procedure shown in section 2, which is based on the idea of flat 2D structures;
- The second difference is relative to the precise 3D reference for the positioning of the optical fiber on the blade. This fact has required the development of a suitable blade mapping algorithm.

Also in this case, the optical fiber sensor has been glued to the blade surface, optimizing its arrangement according to the algorithm introduced in section 3.2. The blade has then been mounted on the shaker through a properly designed support simulating the real connection between the blade and the rotor. Only one mounting condition has been considered since due to the blade twist bending and torsional modes are coupled and can be excited simultaneously. The results are shown in Figure. 14 and Figure. 15 for the first two blade modes and for the displacements along the three reference axes (x,y,z from left to right) and are compared with those obtained with the FEM model of the blade. The results show a good estimation of the modal shapes and, at the same time, a good fitting between numerical results (obtained assuming ideal sensors) and experimental results obtained using the OBR sensors.

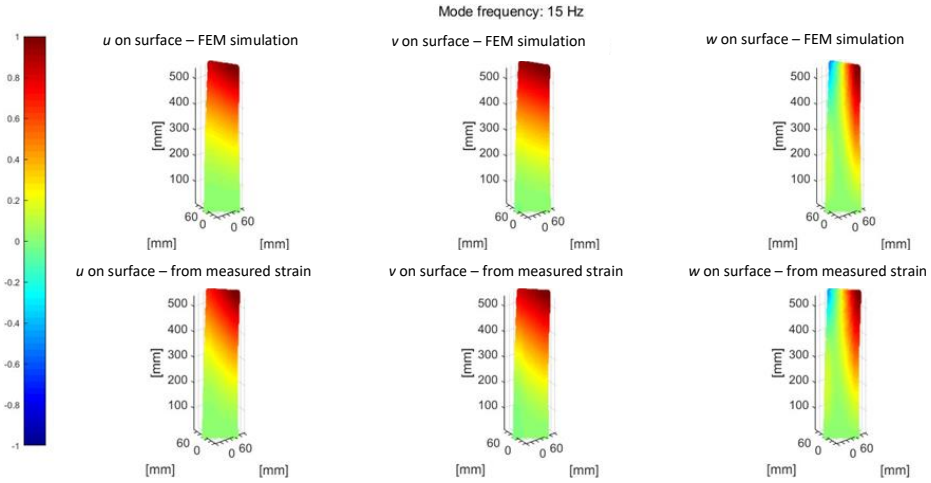


Figure. 14. 3D-blade 1st mode-shape at 15 Hz: numerical (top figures) and experimental (bottom figures).

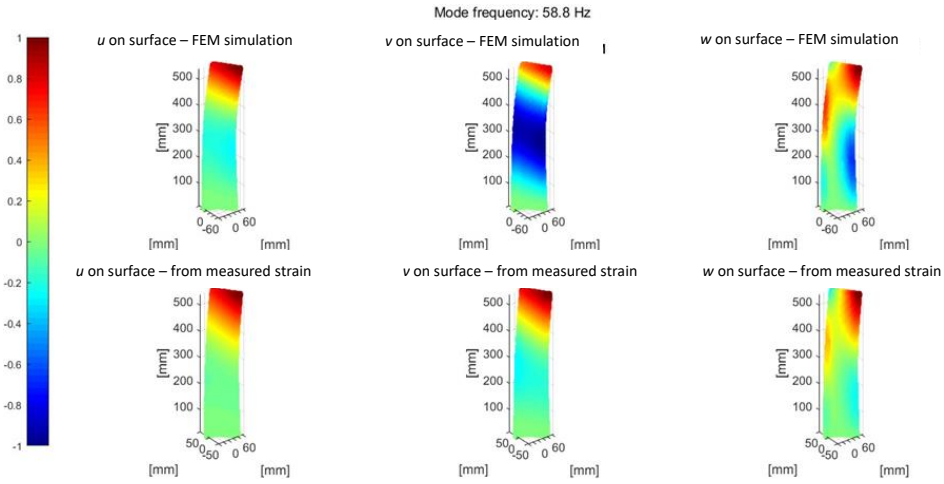


Figure. 15. 3D-blade 2st mode-shape at 58.8 Hz: numerical (top figures) and experimental (bottom figures).

5 Conclusions

A new method for optimally placing continuous sensors such as optical fiber ones for modal analysis purpose is proposed in this paper. This method finds the best fiber configuration to identify a number of structure modes under some constraints through a genetic algorithm.

The paper describes this method and proposes some numerical and experimental tests to validate it. The tests are firstly performed on a simple 2D thin plate and then on a scaled model of a steam turbine blade. In both cases the optical fiber sensor placed following the output of the optimization algorithm is able to correctly reconstruct the desired modes both in the numerical analysis and in the experimental validation.

Thanks to the advantages of optical fiber sensors, this approach can be used in several of applications, such as vibration monitoring of composite structures, where the optical fiber can be embedded in the structure during the lamination process.

References

[1] Ewins, D.J.: Modal testing: theory and practice. John Wiley & Sons, NY, USA (1984).

[2] Friswell, M., Mottershead, J.E.: Finite element model updating in structural dynamics. Springer, Berlin, Germany (1995).

[3] Kuts, V.A., Nikolaev, S.M., Voronov, S.A.: The procedure for subspace identification optimal parameters selection in application to the turbine blade modal analysis. Procedia Engineering 176, 56–65 (2017).

[4] Pennacchi, P., Chatterton, S., Bachschmid, N., Pesatori, E., Turozzi, G.: A model to study the reduction of turbine blade vibration using the snubbing mechanism. Mechanical Systems and Signal Processing 25(4), 1260–1275 (2011).

[5] Madhavan, S., Jain, R., Sujatha, C., Sekhar, A.S.: Vibration based damage detection of rotor blades in a gas turbine engine. Engineering Failure Analysis 46, 26–39 (2014).

[6] Firrone, C.M., Zucca, S.: Underplatform dampers for turbine blades: The effect of damper static balance on the blade dynamics. Mechanics Research Communications 36(4), 515–522 (2009).

[7] Zhang, D., Hong, J., Ma, Y., Chen, L.: A probability method for prediction on High Cycle Fatigue of blades caused by aerodynamic loads. Advances in Engineering Software 42(12), 1059–1073 (2011).

[8] Ciang, C.-C., Lee, J.-R., Bang, H.-J.: Structural health monitoring for a wind turbine system: a review of damage detection methods. Measurement Science and Technology 19(12), 1–20 (2008).

[9] Schroeder, K., Eckel, W., Apitz, J., Lembke, E., Lenschow, G.: A fibre Bragg grating sensor system monitors operational load in a wind turbine rotor blade. Measurement Science and Technology 17(5), 1167–1172 (2006).

[10] Yuan, Y.: Structural Dynamics Model Updating with Positive Definiteness and No Spillover. Mathematical Problems in Engineering 2014, 1–6 (2014).

[11] Cusano, A., Capoluongo, P., Campopiano, S., Cutolo, A., Giordano, M., Felli, F., Paolozzi, A., Caponero, M.: Experimental modal analysis of an aircraft model wing by embedded fiber Bragg grating sensors. IEEE Sensors Journal 6(1), 781–800 (2006).

[12] Rapp, S., Kang, L.-H., Mueller. U.C., Hana, J.-H., Baier, H.: Displacement field estimation for a two-dimensional structure using fiber Bragg grating sensor. Smart Materials and Structures 18, 534–542 (2009).

[13] Kang, L.-H., Kim, D.-K., Han, J.-H.: Estimation of dynamic structural displacements using fiber Bragg grating strain sensors. Journal of Sound and Vibration 305, 534–542 (2007).

[14] Geng Lu, Zhu Xiaojin, Zhang Hesheng, Gao Zhiyuan, and Liu Kaining, “Opti-mal Placement of FBG Sensors for Reconstruction of Flexible Plate Structures Using Modal Approach,” 34th Chinese Control Conference, (2015)

[15] Castro-Triguero, R. , Murugan, S., Friswell, M.I., Gallego, R.: Optimal Sensor Placement for Structures under Parametric Uncertainty. In: Proceedings of the 31st IMAC, Garden Grove, CA USA (2012)

[16] Meo, M., Zumpano, G.: On the optimal sensor placement techniques for a bridge structure. Engineering Structures 27, 1488–1497 (2005).

[17] Papadimitriou, C., Beck, J.L., Au, S.K.: Entropy-based optimal sensor location for structural model updating. Journal of Vibration and Control 6, 781–800 (2000).

[18] Tong, K.H., Bakhary, N., Kueh, A.B.H., Mohd Yassin, A.Y.: Optimal sensor placement for mode shapes using improved simulated annealing. Smart Structures and Systems 13(3), 389–406 (2013).

[19] Huang, K.-Y., Carter, G.M.: Coherent optical frequency domain reflectometry (OFDR) using a fiber grating external cavity laser. IEEE Photonics Technology Letters 6(12), 1466–1468 (1994).

[20] Soller, B.J., Gifford, D.K., Wolfe, M.S., Froggatt, M.E.: High resolution optical frequency domain reflectometry for characterization of components and assemblies. Optics Express 13, 666–674 (2005).

[21] Rapp, S., Kang, L.-H., Han, J.-H., Mueller, U.C., Baier, H.: Displacement field estimation for a two-dimensional structure using fiber Bragg grating sensors. Smart Materials and Structures 18(2), 1-12 (2009).

[22] Zhang, H., Lennox, B., Goulding, P.R., Leung, A.Y.T.: Float-encoded genetic algorithm technique for integrated optimization of piezoelectric actuator and sensor placement and feedback gains. Smart Materials and Structures 9(4), 552–557 (2000).

Experimental evaluation of pressure dependent tangential contact stiffness

M. Kreider[1], C.W. Schwingshackl[1]
[1] Imperial College London, Department of Mechanical Engineering
Exhibition Road, London, SW7 2AZ, UK

Abstract

The modelling of nonlinear dynamic behaviour of interfaces is of great interest, with one of the main challenges being the provision of reliable friction interface parameters. One of these parameters is the tangential contact stiffness which represents the in-plane compliance at the interface. It is traditionally assumed to be constant, but recent findings in the literature indicate a dependence of the tangential contact stiffness on the normal load.

To investigate this behaviour in detail, the 1D friction rig at Imperial College London was fitted with a High-Speed Camera and Digital Image Correlation system to initially validate its accuracy and then investigate the relationship between tangential contact stiffness and contact pressure. A strong increase of contact stiffness at low contact pressure was observed, followed by a saturation of the contact stiffness at higher values. An increase in contact stiffness due to wear was also present, indicating that current modelling approaches may need to be refined.

1 Introduction

The modelling of the nonlinear dynamic behaviour of interfaces is of great importance, since every assembled structure contains a large amount of joint interfaces, which all provide potential sources of nonlinearity to the system. Advanced modelling techniques [1]-[4] are available today to predict such nonlinear dynamic behaviour which allow for very detailed modelling. These simulations heavily rely on the provided interface input data, which often are the friction coefficient, μ, which in combination with the contact pressure, p, governs the transition from stick to slip, and the tangential and normal contact stiffness, k_t and k_n, which represent the elastic compliance at the interface in in-plane and out of plane direction. The most common approach to obtain these interface parameters accurately is to measure them with the help of an experimental setup [5]-[12] under varying test conditions.

Often the assumption is being made that the frictional input parameters are independent of the contact interface conditions and that they can be represented with constant parameters in the analysis. Recent observations for low frequency tests at the University of Oxford [11] have shown that this may not be strictly true, and that in particular the tangential contact stiffness, k_t, depends on the contact pressure, p, at the interface. Unfortunately, an accurate measurement of this behaviour under high frequency cyclic oscillation is not straight forward and it has been so far neglected in most measurements and analysis.

To obtain a better understanding of the importance of such pressure dependent tangential contact stiffness under high frequency loading, an evaluation was conducted with the help of the 1D friction rig [9] at Imperial College London. For this purpose, the rig was equipped with a high speed camera and DIC setup to ensure

accuracy of the measurement system, and a series of different tests were conducted to quantify the tangential contact stiffness behaviour under different contact pressures.

2 Experimental setup

Friction input parameters for a nonlinear dynamic analysis are predominantly measured with the help of experimental test rigs. One of the available rigs thereby is the 1D friction rig at Imperial College London.

2.1 1D friction rig

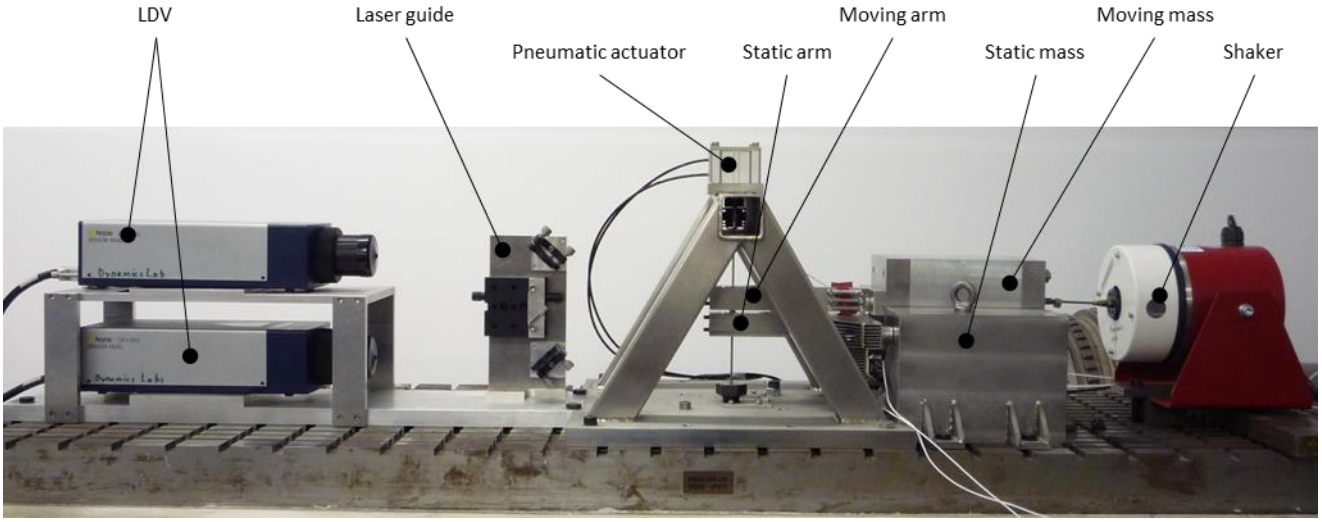


Figure 1 1D friction rig at Imperial College London

The 1D friction rig in the Dynamics and Vibration Laboratory at Imperial College London (see Figure 1) was recently developed [9] to replace a previous design [10] providing a stronger clamping force, a minimisation of the number of joints, a better measurement system and a stiffer frame, to ensure fast and accurate measurements of the friction coefficient, μ, and the tangential contact stiffness, k_t. A detailed description of the working principle of the rig can be found in [9], but a short discussion will be included here for completeness.

The rig is excited via an electro dynamic shaker (Data Physics V20) which drives a large inertia mass, siting on leave springs, to ensure a harmonic displacement of the test specimen (see Figure 1). Attached to the mass via the knife edge joint in Figure 2b) is the moving arm which contains the actual specimen at its free end. The round specimens from Figure 2a) have normally a 1mm contact flat, where the moving upper specimen is oriented orthogonally to the static lower specimen, providing a nominal $1mm^2$ contact area. The static arm is attached via three force gauges to the static mass, which provides a rigid ground connection. A pneumatic actuator system is used in combination with a static load cell to apply and monitor the normal contact loading, N_0, to the upper specimen, which in combination with the contact area, A, provides the nominal contact pressure, p. Two single point Laser Doppler Vibrometers are used to measure the absolute displacement of the moving and static specimen as close as possible to the contact interface (see Figure 2c).

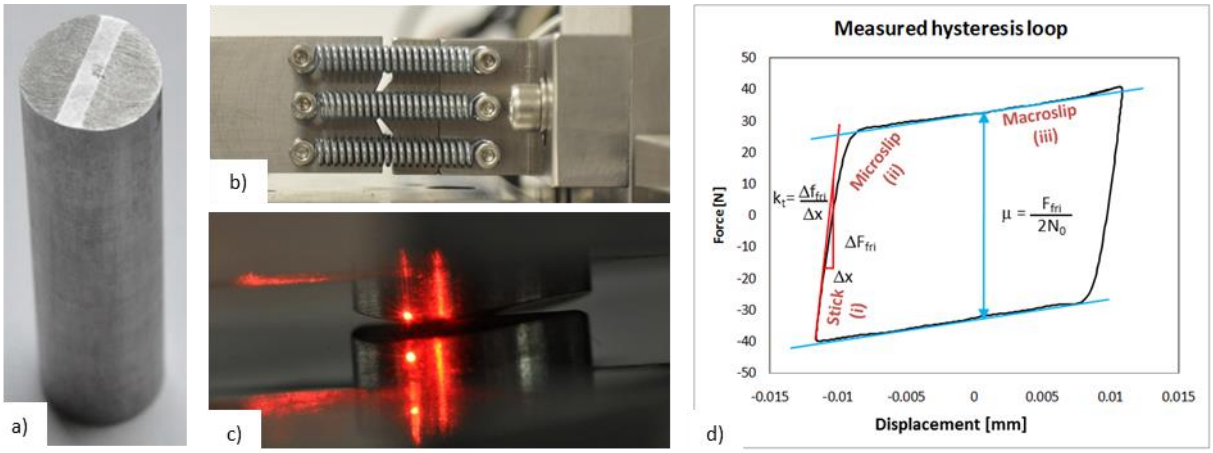


Figure 2 Details of the test rig: a) one specimen with manufactured contact area, b) knife edge joint of the moving arm, c) relative velocity measurement location and d) measured hysteresis loop

During a measurement the moving mass is excited at a constant frequency somewhere between 20-200Hz, normally at 100Hz, leading to a harmonic horizontal motion of the upper specimen. Due to the applied normal load, elastic and/or friction forces are transmitted via the contact zone to the lower specimen, which are measured with the help of the force transducers on the static arm. Combining the measured forces with the computed relative displacement between the two specimens from the LDV data, leads to a hysteresis loop such as in Figure 2d).

A major factor for the accuracy of the measurement is the reliability of the relative displacement extraction between the moving and the static specimen. It will determine the gradient of the tangential contact stiffness, k_t, which can have a significant impact on the nonlinear dynamic response of a system. The use of the two single point LDVs to obtain the relative displacement data is highly efficient and deemed accurate enough for standard input parameter testing, but with the intended evaluation of the pressure dependency of the tangential contact stiffness, highest accuracy at very small amplitudes must be ensured. Experience with the rig has shown that: (i) during very low level excitation a significant amount of measurement noise can be observed and resolution limits can be reached, resulting in poor data quality; (ii) the distance between the laser measurements cannot be decreased below 1 mm due to the chamfer of the bottom specimen (see Figure 2c), raising the question of contact versus specimen deflection due to bulk material properties; iii) linked to the latter is a potential additional compliance in the system due to the specimen clamping mechanism.

To investigate the scale of these uncertainties in the rig on the measurement accuracy and ensure an accurate measurement can be provided for the following tangential contact over contact pressure measurements, a high-speed camera setup in combination with digital image correlation (DIC) was introduced to obtain higher resolution measurements closer to the contact surface, minimising the impact of the rig and specimen compliance.

2.2 DIC setup for the 1D friction rig

A high-speed camera system was set up to verify the accuracy of the LDV setup and to gain further knowledge of the specimen motion during excitation. A Photron FASTCAM Mini UX100 was used in combination with a Navitar x12 Microscopic lens, set to its highest magnification level. The camera lens was placed 30-40 mm away from the contact interface as seen in Figure 3a). Considering the 10° chamfer of the top specimen in Figure 2a), the camera was rotated by 5° out of the horizontal plane in order to allow focusing directly on the outer edge of the surface contact.

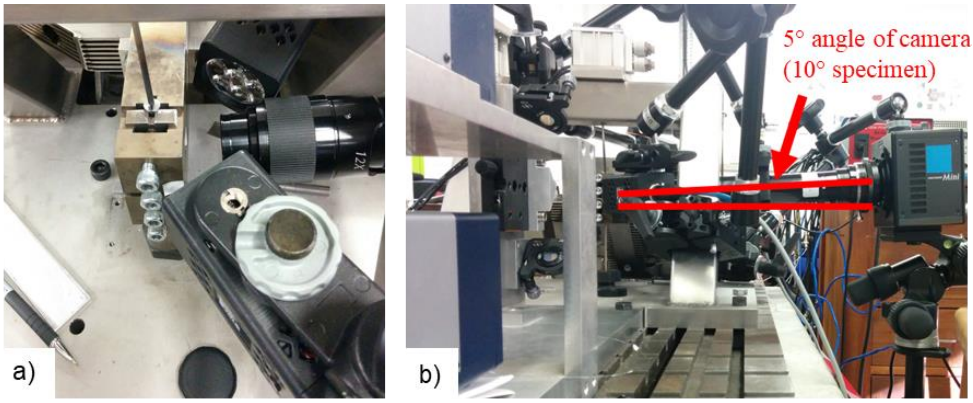


Figure 3 The DIC test setup

Two VD-7000LP LED spots with 7280 lm each were used to light the contact surfaces. A major problem thereby was to get enough light onto the edge of the contact, due to the small gap between the upper and lower arm (see Figure 3b). It was found that the LEDs placed at a 45° angle in plane with the gap provided the highest illumination for the high speed camera. The camera was set to its widest aperture to allow as much light as possible onto the sensor and a shutter speed of 1/12000s was used and minimise blur. This allowed a frame capture at 4000fps at full HD resolution, which was deemed more than satisfactory for the 100Hz vibration of the contact interface.

A few vibration cycles were recorded with the high speed camera for each test, and the post processing was conducted with the open source software NCORR v1.2 [13] in MATLAB. This tool allows the analysis of individual images to track relative motion of subsets of pixels in the area of interest (ROI). In this particular case it can be used to track the vibrational motion of the upper and lower specimen at the interface, from which a highly accurate relative motion can be computed. Initial tests to gauge the influence of the post processing parameters including region of interest (ROI), DIC subset radius and spacing led to an optimised DIC setup which was used throughout.

Figure 4 shows the high speed camera image of the interface edge. The coloured region thereby contains the analysed data in the ROI, while the red boxes highlight the areas on the moving and static specimen from which an average displacement was extracted to compute the relative motion between the upper and lower specimen. The DIC system was calibrated against the LDV data for an unloaded test, where the free motion of the moving arm resulted in a sensitivity of 6.2µm/pixel for the used lens setup.

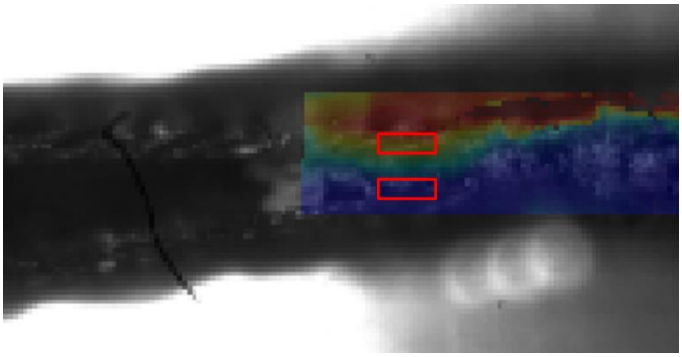


Figure 4 NCORR data processing at interface with ROI in color and actual displacement measurement regions in the red boxes.

2.3 Tangential contact stiffness extraction

The tangential contact stiffness, k_t, can be extracted from the hysteresis loop in Figure 2. Initially the absolute displacement of the top and bottom specimens are measured, from which the relative displacement can be computed. Plotting this over the transmitted tangential force in the contact then leads to the hysteresis loop. The tangential contact stiffness, k_t, is then extracted from the slope of the stuck zone, where it is assumed that only elastic deformations of the contact asperities occurs, and no plastic or frictional motion is present. The extracted values are then normalised by the contact area to provide generally applicable input parameters with the unit of N/mm^3 to the analysis.

To investigate the impact of the contact pressure at the interface on the tangential contact stiffness, k_t, a series of tests were conducted with contact pressures, p, ranging from 10-180MPa. Experience from previous tests [9] has shown, that the specimen undergo a running in phase during which the contact condition changes due to wear at the interface. In order to take this effect into account, tests were conducted at different instances in time, to gain a better understanding of the time dependence of the tangential contact stiffness.

3 Results

3.1 DIC calibration of the LDV system

Figure 5a) shows a comparison of the relative displacement measured by the LDV and DIC data along with the resulting hysteresis loop in Figure 5b). It can be seen that a very good agreement between the two measurement systems was achievable for both the time and hysteresis trace. The results confirmed the accuracy of the LDV setup to capture the relative motion, and demonstrate that any compliance from the rig or the bulk material of the specimens does not affect the measured relative motion between the two interfaces. The good agreement also highlighted the ability of the developed High Speed Camera DIC setup to measure vibration amplitudes in the order of μm accurately, demonstrating the great potential that such a system has to study interface motion of dynamic joints.

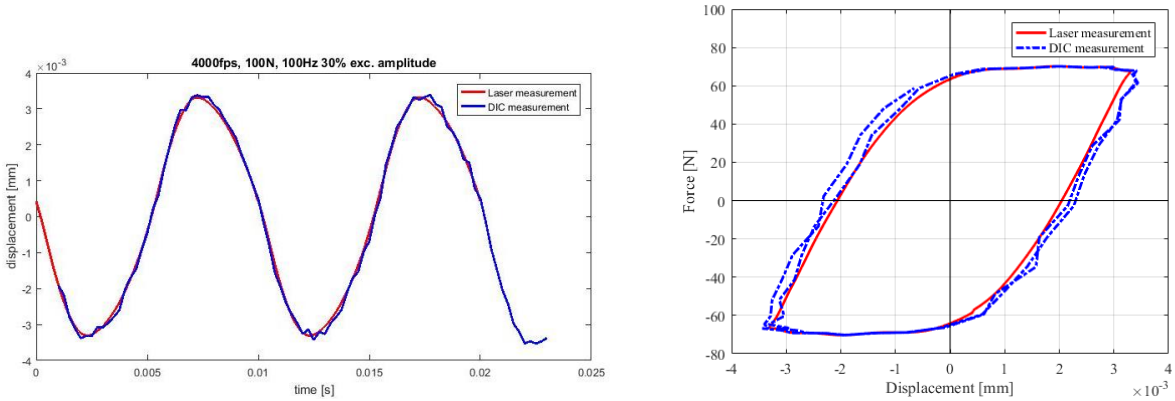


Figure 5 Comparison of DIC and LDV measurement for a 100N load and 100 Hz excitation a) relative displacement and b) resulting hysteresis loop.

In addition to confirming the accuracy of the LDV measurement system in the horizontal sliding direction, the analysis of the DIC data also revealed a small motion in the vertical plane. The specimens thereby experience a downward motion when the contact moves forward, and an upward motion during its return. To better understand the impact of the vertical motion on the global behaviour of the rig, the displacement difference between the front and back end of the contact area of each specimen was computed. The resulting relative displacement over one vibration cycle for each specimen can be seen in Figure 6. The vertical

displacement of the top and bottom specimen are similar in phase and amplitude, indicating that the surfaces do not separate or rotate in respect to each other during a vibration cycle, and consequently not affecting the contact condition at the interface. A further concern was the impact on the horizontal motion due to the rotation, but it could be shown that the impact was less than 0.5 % due to the small angles which was deemed negligible. It should be mentioned that the normal load supplied by the pneumatic actuator may show some periodic variations as a result of this vertical movement, which will need to be further investigation in the future to ensure an accurate extraction of the friction coefficient.

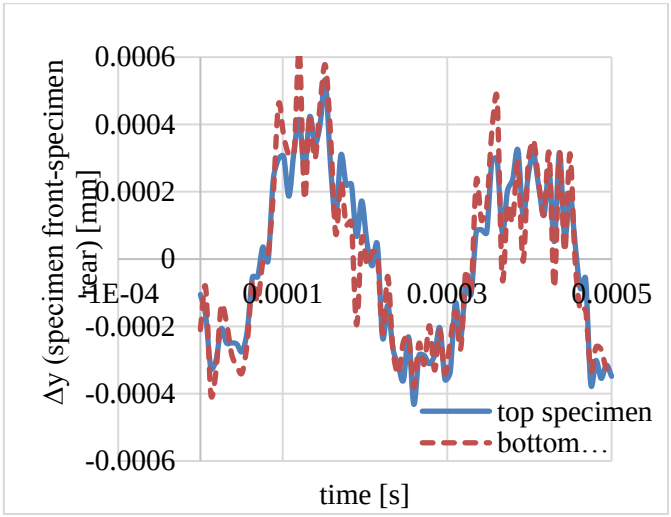


Figure 6 Relative vertical displacement between the front and rear of the top and bottom contact surface edge.

Overall the DIC measurement confirmed that the current LDV setup is of sufficient accuracy to determine the relative displacement of the two specimens in the sliding direction, making the latter approach the system of choice for the following investigation due to its significantly easier setup and lighter post processing requirements.

3.2 Tangential contact stiffness measurements

After confirming the accuracy of the LDV measurement system with the high speed camera and DIC setup, the investigation focused on the contact pressure dependency of the tangential contact stiffness, k_t.

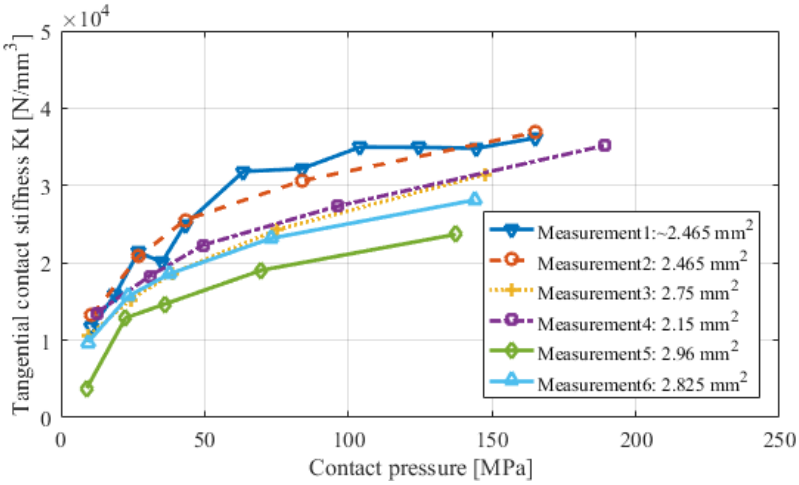


Figure 7 Change of tangential contact stiffness with contact pressure for different contact areas

Initially six independent measurements of the tangential contact stiffness, k_t, were performed. Each test consisted of the mounting of the specimen pair (304 steel) to the rig, loading the contact with a predetermined normal load, and then very gently exciting the system to ensure that no micro or macroslip was present in the measured loops. Six measurements using three available specimen sets of the same material were conducted. For each new test the contact surface was refurbished by removing any onset of a wear scar that may have developed during testing, leading to slightly different contact areas for each test. Figure 7 shows the resulting contact stiffness measurements, which have been normalised with regards to the contact area, *A*. A strong increase of the contact stiffness at low contact pressure was observed, followed by a gentler and more linear increase of the contact stiffness at higher pressure values. This is in good agreement with the findings from the literature [11], and highlights the fact that the tangential contact stiffness can strongly vary at low contact pressures. The contact stiffness behaviour with regards to the contact pressure is very repeatable, but the scatter of the absolute values is somewhat large, highlighting the great challenge to get repeatable results out of a joint reassembly. It should also be noted that there is no apparent link between contact area and stiffness behaviour, indicating that the normalisation by contact area is a good approach to provide design independent contact stiffness data to the analysis.

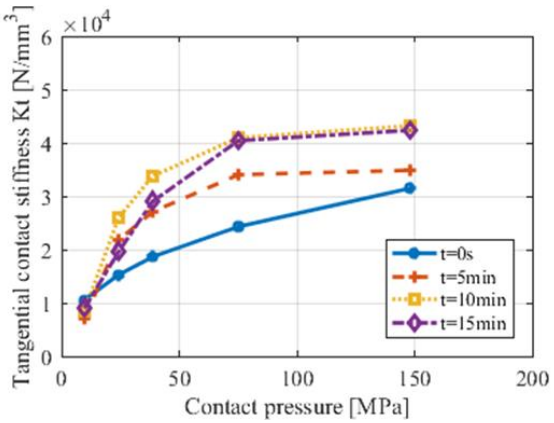
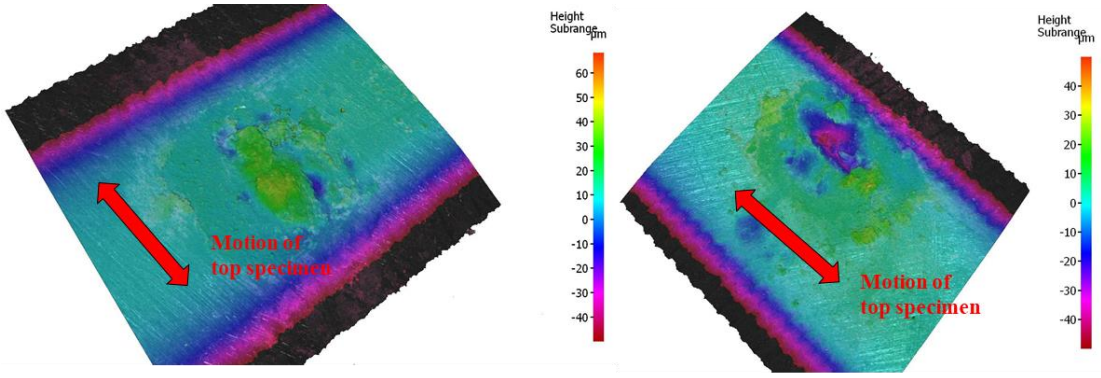


Figure 8 Time dependency of the tangential contact stiffness

Wear at the contact interface during the previous tests, also minimal due to the small excitation amplitudes, could not be entirely prevented, and a further test was conducted to gauge the influence of wear at the interface on the stiffness behaviour. To induce a significant amount of wear at the interface, the contact was excited under full slip condition, leading to a fully developed hysteresis loop. Initial measurements were taken right at the beginning of the test (0s), followed by measurements after 5-10-15 minutes. At the beginning of each 5-minute wear period the normal contact pressure was varied quickly to obtain a set of loops for different contact pressures. During the three 5-minute periods the slip distance was held constant at 33μm resulting in an accumulated total sliding distance of ~2950 mm at 100Hz. Figure 8 shows that the pressure dependency of the tangential contact stiffness stays intact, but as time progresses a steeper increase in stiffness at low pressures and a much flatter behaviour for higher contact pressures develops. While the stiffness does not saturate under the maximum applied pressure for the shorter runs, this is nearly the case for the 15 min runs. These results suggest that a similar running in period, similar to the previously identified requirement for stable friction coefficient, μ, extraction [10], is needed for the tangential contact stiffness.

To better understand this time dependency, a profilometer measurement of the worn contact surface was carried out (see Figure 9). The images, taken after 15min of running time, show the formation of an elevation on the bottom specimen and a corresponding groove on the upper specimen. These strong contact features are assumed to lock much faster than the smooth initial contact patch, helping to explain the higher pressure dependency of the worn specimen at lower contact pressures and the relatively flat behaviour at higher pressures.



Bottom specimen Top specimen

Figure 9 Profilometer measurement of worn contact surface after 15 minutes for measurement 3

To further investigate the impact of the large-scale contact features which develop over time, an additional test was carried out. After taking the initial stiffness-contact pressure measurement at t=0s, the measurement was repeated after 5 minutes of sliding, after which the test was stopped, and the specimen contact surface was un– and reloaded and the test started again. The same process was repeated at 15min. Figure 10 shows the resulting tangential contact stiffness to pressure behaviour. Not surprisingly the first five miutes of testing time lead to an increase in stiffness, but once the contact is separated and newly loaded (no refurbishment), the contact behaviour is reset. Indeed, the resulting contact stiffness is below the original one, which may indicate that due to the development of an elevation and a small misalignment between the two specimens after reloading, not all of the contact surface is properly engaged at this stage. Running the specimens for 15 minutes, brings everything back to the expected behaviour, with a strong increase in tangential contact stiffness at lower values, and a relatively flat behaviour for higher ones. Unloading and reloading in this case seems to have less of an impact, probably due to the much larger wear features at the interface, which are less likely to misalign during reloading, and leading to a more repeatable joint reassembly.

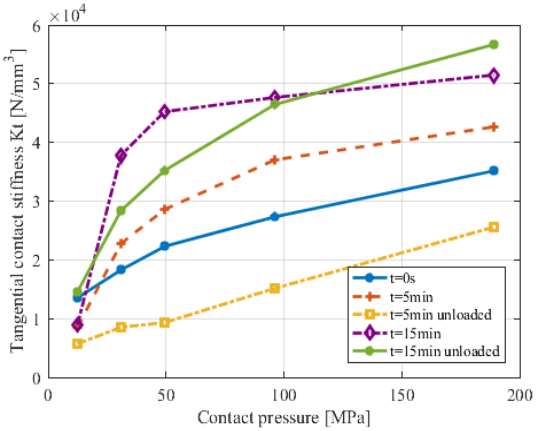


Figure 10 : Influence of unloading & reloading of specimen on tangential contact stiffness.

4 Conclusion

The contact pressure dependency of the tangential contact stiffness at an interface was investigated with the help of the 1D friction rig at Imperial College London. To ensure accuracy, initially a high-speed camera and DIC setup was developed to validate the accuracy of the traditionally used LDV measurement system and to gain more detailed insight on the motion of the specimens.

The measurements of the tangential contact stiffness revealed a very sensitive dependence on the contact pressures for low loading values, and a more constant behaviour above 70 MPa where the tangential contact stiffness values were changing from 10-50kN/mm^3. The behaviour was repeatable across several tests and seemed to be independent of the contact area. Further measurements showed a dependence of the contact stiffness behaviour on time, which could be linked to the wearing of the contact interface.

References

[1] M. Krack, L. Salles, F. Thouverez, Vibration prediction of bladed disks coupled by friction joints, Arch. Comput. Methods Eng. 24 (3) (2016) 1–48.

[2] C.M. Firrone, S. Zucca, M.M. Gola, The effect of underplatform dampers on the forced response of bladed disks by a coupled static/dynamic harmonic balance method, Int. J. Non-Linear Mech. 46 (2) (2011)

[3] E.P. Petrov, A high-accuracy model reduction for analysis of nonlinear vibrations in structures with contact interfaces, J. Eng. Gas Turbines Power 133(10) (2011)

[4] D. Süß, K. Willner, Investigation of a jointed friction oscillator using the multiharmonic balance method, Mech. Syst. Signal Process. 52–53 (2015) 73–87.

[5] Cabboi, A., T. Putelat, and J. Woodhouse (2016). "The Frequency Response of Dynamic Friction: Enhanced Rate-and-State Models". In: Journal of the Mechanics and Physics of Solids 92, pp. 210–236.

[6] Filippi, S., A. Akay, and M. M. Gola (2004). "Measurement of Tangential Contact Hysteresis During Microslip". In: ASME Journal of Tribology 126, pp. 482–489.

[7] Kartal, M. E. et al. (2011a). "Determination of the Frictional Properties of Titanium and Nicekl Alloys Using the Digital Image Correlation Method". In: Experimental Mechanics 51, pp. 359–371.

[8] Lavella, M., D. Botto, and M. M. Gola (2013). "Design of a High-Precision, Flat-on-Flat Fretting Test Apparatus with High Temperature Capability". In: Wear 302, pp. 1073–1081.

[9] Schwingshackl, C. W. (2012). "Measurement of Friction Contact Parameters for Nonlinear Dynamic Analysis". In: 30th International Modal Analysis Conference (IMAC XXX). Jacksonville, FL.

[10] Schwingshackl, C. W., E. P. Petrov, and D. J. Ewins (2012). "Measured and Estimated Friction Interface Parameters in a Nonlinear Dynamic Analysis". In: Mechanical Systems and Signal Processing 28, pp. 574–584.

[11] Mulvihill, D. M. et al. (2011). "Investigation of Non-Coulomb Friction Behaviour in Reciprocating Sliding". In: Wear 271, pp. 802–816.

[12] Segalman, D. J., L. A. Bergman, and D. J. Ewins (2010). Report on the SNL/AWE/NSF International Workshop on Joint Mechanics, Dartington, United Kingdom, 27-29 April 2009. Technical Report SAND2010-5458. Sandia National Laboratories, Albuquerque, NM.

[13] Blaber, J. , Adair, B., Antoniou, A (2015). Ncorr: Open-Source 2D Digital Image Correlation Matlab Software. Experimental Mechanics. 55(6).

Consideration of estimation error in multiple coherence approaches: application to the inside/ outside coherence analysis of aircraft flight tests

Q. Leclere [1], **J. Antoni** [1], **E. Julliard** [2], **A. Pintado-Peño** [2]
[1] Univ Lyon, INSA-Lyon, LVA EA677, F-69621, Villeurbanne, France
e-mail:**quentin.leclere@insa-lyon.fr**

[2] Airbus Operations S.A.S, Acoustics Department, Toulouse, France

Abstract
Multiple coherence analysis is a well-known approach to address MIMO problems. It allows the estimation of the contribution of partially coherent inputs to one or several outputs. This analysis can be conducted either in the frame of waterfall subtraction [1] or using a diagonalization of the inputs [2]. Those techniques are well established when dealing with converged cross-spectral estimates. However, some difficulties can appear in practice because those quantities have never completely converged, due to the finite nature of time records. The purpose of this work is to introduce some statistical significance tests in those approaches to avoid the systematic overestimation of the multiple coherence that is due to estimation errors. The proposed approach is applied to signals recorded inside and outside the cabin of an aircraft during a flight test. The multiple coherence is applied either from outside to inside signals, to analyse the contribution of outside noise sources to the interior noise.

1 Introduction

The Coherent Output Power Spectrum [3], introduced in the 70's, is a concept related to noise source identification, in which a linear relationship is assumed between an output signal and a given reference. A linear relationship is estimated ($H1$ estimator) and the Coherent Output Power Spectrum is obtained by combining the Reference Power Spectrum and the estimated filter. In multiple input cases, this approach is limited by the correlation between inputs. This issue led to the development of more advanced analysis techniques, like partial and multiple coherence approaches[4, 5, 1], or virtual source analysis [2, 6, 7], that have proven some efficiency in several industrial applications [8, 9, 10, 11]. Coherence-based methods have been extensively used in the field of aeroacoustics [12, 13, 14, 15], which can be explained by the fact that aeroacoustic sources are often physically distributed with relatively short coherence lengths, facilitating their separation using statistical approaches. The difficulty is then to be able to represent the source of interest with a sufficient number of references, in a context where the SNR can be strongly affected by flow noise.

The originality of the present work is to propose the implementation of a thresholding step in the multiple coherence calculation based on the consideration of the statistical laws of coherences estimated on finite length time records. The first section is dedicated to theoretical aspects, including the establishment of asymptotic probability laws for the coherence and multiple coherence. An hypothesis test is proposed so as to determine if a coherence is significantly greater than 0 or not. An approach based on a Principal Component Analysis of the reference cross spectral matrix is proposed to implement the test for the multiple coherence. Those

theoretical developments are then illustrated in a second section dedicated to an experimental application to microphone signals recorded during aircraft flight tests.

2 Theoretical aspects

2.1 Probability laws of the estimated coherence between uncorrelated signals

Let $x(t)$ and $y(t)$ be two uncorrelated Gaussian signals. Let X and Y be the Fourier coefficients of these two signals at a given frequency (excluding 0 and Nyquist frequency bins), X and Y are random variables following centered complex Gaussian laws. The expected value and variance of instantaneous auto and cross spectra are in this case

$$E(|X|^2) = \sigma_x^2 \quad ; \quad V(|X|^2) = \sigma_x^4 \tag{1}$$
$$E(|Y|^2) = \sigma_y^2 \quad ; \quad V(|Y|^2) = \sigma_y^4 \tag{2}$$
$$E(X\overline{Y}) = 0 \quad ; \quad V(X\overline{Y}) = \sigma_x^2\sigma_y^2 \tag{3}$$

where σ_x^2 and σ_y^2 represent by definition the expected value of the power spectral density of signals at the frequency of interest. If instantaneous auto and cross spectra are averaged over a number N of time snapshots with N high enough to apply the central limit theorem, then averaged results are following in the limit Gaussian laws (complex for the cross spectrum) :

$$S_{xx} = \langle |X|^2 \rangle_N \underset{N \to +\infty}{\sim} \mathcal{N}\left(\sigma_x^2; \sigma_x^2/\sqrt{N}\right) \tag{4}$$
$$S_{yy} = \langle |Y|^2 \rangle_N \underset{N \to +\infty}{\sim} \mathcal{N}\left(\sigma_y^2; \sigma_y^2/\sqrt{N}\right) \tag{5}$$
$$S_{xy} = \langle X\overline{Y} \rangle_N \underset{N \to +\infty}{\sim} \mathcal{N}_c\left(0; \sigma_x\sigma_y/\sqrt{N}\right) \tag{6}$$

The coherence function is defined as the following ratio

$$\gamma_{xy}^2 = \frac{|S_{xy}|^2}{S_{xx}S_{yy}} \tag{7}$$

The probability law of the estimated coherence function of two uncorrelated signals is given by Carter [16] :

$$f_{\gamma_{xy}^2}(x) = (N-1)(1-x)^{N-2} \quad \text{for } 0 < x < 1 \tag{8}$$
$$f_{\gamma_{xy}^2}(x) = 0 \quad \text{for } x < 0 \text{ or } x > 1$$

Asymptotically, assuming that N is high enough to replace S_{xx} and S_{yy} by their expected values, then the probability law of the coherence can be approximated by a chi-squared with 2 degrees of freedom:

$$\gamma_{xy}^2 \underset{N \to +\infty}{\sim} \frac{\chi_2^2}{2N}, \tag{9}$$

with an expected value and variance equal to $1/N$ and $2/N$, respectively. In order to illustrate the convergence of this approximation, simulations are conducted for different values of N. For each value of N, 10^5 realizations are drawn using complex centered normal distributions. The resulting histograms are drawn in Fig. 1 together with the approximation (9). It can be seen that for values above $N = 50$, the histogram perfectly fits the approximation.

These probability laws are obtained for non overlapping time segments. When using some overlap between time segments, the number of average can artificially strongly increase, however it does not change the

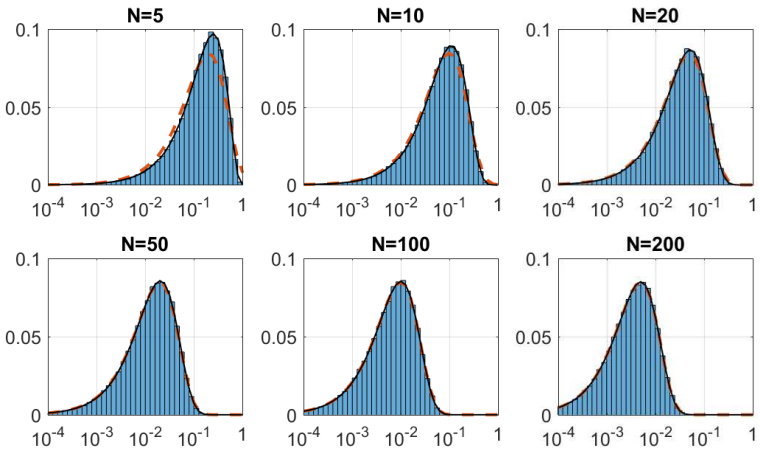


Figure 1: Histograms of coherence values for different average sizes. Solid lines : theoretical pdf (solid black), asymptotic distribution (dashed red).

total record length and induces some redundancy between time snapshots [17]. However, using a Hanning window, it is found that for an overlap greater or equal to 65%, the probability law of the coherence is

$$\gamma_{xy}^2 = \frac{\chi_2^2}{2\kappa\, N_0} = \chi_2^2 \frac{n_{snap}}{2\,\kappa\, n_{tot}}, \tag{10}$$

where n_{snap} and n_{tot} are the number of samples of a snapshot and of the total record, respectively, verifying $n_{tot} = N_0 n_{snap}$, and where $\kappa = 2.07$ (Hanning window).

2.2 An hypothesis test for the significance of the coherence

The probability law of the coherence given by Eq. (10) can be used to implement a statistical test so as to decide if the two signals can be assumed as fully uncorrelated or not. Under a H_0 hypothesis that the two signals are fully uncorrelated, there is a user-defined small probability α (risk of the test) that the coherence is greater than a given threshold depending on α and N_0. If the observed value is smaller than the threshold, the coherence is considered as not significantly different from 0 (signals are uncorrelated). If the observed value is greater than the threshold, the H_0 hypothesis is rejected, the value of the estimated coherence is kept as is. The threshold is given in the following table for different values of α and N_0, with a Hanning window and an overlap greater than or equal to 65%:

α	5%	1%	0.1%
$N_0 = 50$	0.0289	0.0445	0.0667
$N_0 = 200$	0.0072	0.0111	0.0167
$N_0 = 500$	0.0029	0.0044	0.0067

Table 1: Threshold T such that $p(\gamma_{xy}^2 > T \mid H_0) = \alpha$, Hanning window, overlap $\geq 65\%$.

2.3 The coherent output power for SISO and MISO cases

Let $x(t)$ and $y(t)$ be two signals recorded simultaneously in a given experimental context. Assuming that x is an input, the Coherent Output Power (COP) of y (with respect to x) is defined by

$$S_{yy}^{(x)} = \gamma_{yx}^2 S_{yy}, \tag{11}$$

and can be interpreted as the part of S_{yy} that is linearly explained by x at the frequency of interest. If y represents a source signal, $S_{yy}^{(x)}$ is the contribution of x to y. The COP is in fact related to the H1 estimator of the FRF Y/X that assumes that the noise is on the output signal only:

$$S_{yy}^{(x)} = \gamma_{yx}^2 S_{yy} = \frac{|S_{yx}|^2}{S_{xx}S_{yy}} S_{yy} = \frac{|S_{yx}|^2}{S_{xx}} = \left|\frac{S_{yx}}{S_{xx}}\right|^2 S_{xx} = |\mathrm{H1}_{yx}|^2 S_{xx}, \tag{12}$$

where $\mathrm{H1}_{yx} = S_{yx}/S_{xx}$. It is clear using that formulation that the the COP represents the contribution of x to y, the remaining part of S_{yy} (equal to $(1-\gamma_{yx}^2)S_{yy}$) representing the contribution of the noise.
In some situation it can be interesting to estimate the contribution of n reference signals, $a(t)$, $b(t)$, $c(t)$, ... $\mu(t)$ to the output $y(t)$. However, reference signals are rarely uncorrelated, such that the energy of the output cannot be simply defined as the sum of the COPs with respect to each reference. Bendat and Piersol proposed 40 years ago [] to proceed iteratively, reference by reference (Conditioned Spectral Analysis - CSA framework). The COP is firstly calculated with respect to a :

$$S_{yy}^{(a)} = \gamma_{ya}^2 S_{yy} = \frac{|S_{ya}|^2}{S_{aa}}. \tag{13}$$

Then the contribution of the first reference is removed from auto and cross spectra of other channels :

$$S_{ij.a} = S_{ij} - \frac{S_{ia}S_{aj}}{S_{aa}}, \forall i,j \in \{y,b,c...\mu\}. \tag{14}$$

$S_{ij.a}$ are called auto and cross spectra conditioned by a. The second step is to calculate a COP with respect to a second reference b using quantities conditioned by a :

$$S_{yy.a}^{(b)} = \frac{|S_{yb.a}|^2}{S_{bb.a}}. \tag{15}$$

The contribution of the second reference is removed to obtain cross spectral quantities conditioned by a and b :

$$S_{ij.a,b} = S_{ij.a} - \frac{S_{ib.a}S_{bj.a}}{S_{bb.a}}, \forall i,j \in \{y,c,...\mu\}, \tag{16}$$

and so on up to the last reference. At the end, the multiple coherent output power can be obtain as follows :

$$S_{yy}^{(a,b,...\mu)} = S_{yy}^{(a)} + S_{yy.a}^{(b)} + S_{yy.a,b}^{(c)} + ...S_{yy.a,b,...}^{(\mu)}, \tag{17}$$

the multiple coherence coresponding to the ratio between this result and the total output power :

$$\gamma_{y(a,b...\mu)}^2 = \frac{S_{yy}^{(a,b,...\mu)}}{S_{yy}} \tag{18}$$

This multiple coherence can be interpreted as the part of the ouptut signal that can be linearly explained by the set of references. If the reference are representing sources, the multiple coherent output power can be interpreted as the contribution of the referenced sources to the output signal.
An alternative to Conditioned Spectral Analysis for the estimation of the multiple coherence is obtained through the Virtual Source Analysis (VSA), proposed by Price and Bernhard [] in the 80's. This approach leads theoretically to the same result for the multiple coherence than CSA, yet it is more suited for the further developments proposed in present work. VSA is based on an eigen decomposition of the cross spectral matrix of the reference signals. Let λ_v^2 be the v^{th} (real positive) eigenvalue and Φ_{jv} the j^{th} element of the v^{th} eigenvector ($v,j \in [1...n]$). Eigenvalues can be interpreted as a set of n uncorrelated virtual sources contributing to reference channels. The cross spectrum between the output and the v^{th} virtual source is

$$S_{vy} = \sum_{j=1}^{n} \overline{\Phi_{jv}} S_{jy} \tag{19}$$

The virtual coherence represents the contribution of the virtual source to the output:

$$\gamma_{vy}^2 = \frac{|S_{vy}|^2}{S_{vv}S_{yy}} = \frac{1}{\lambda_v^2 S_{yy}} \left| \sum_{j=1}^{n} \overline{\Phi_{jv}} S_{jy} \right|^2 \tag{20}$$

with a corresponding virtual COP given by

$$S_{yy}^{(v)} = \gamma_{vy}^2 S_{yy} \tag{21}$$

Virtual sources have the property to be uncorrelated, such that their contribution can be simply added energetically :

$$S_{yy}^{(1,2,...n)} = \left(\gamma_{1y}^2 + \gamma_{2y}^2 + ...\gamma_{ny}^2\right) S_{yy} \tag{22}$$

Thus, the multiple coherence is simply obtained by adding virtual coherences between the output and each virtual source component.

$$\gamma_{y(1,2...n)}^2 = \sum_{v=1}^{n} \gamma_{vy}^2 \tag{23}$$

2.4 Probability law of the multiple coherence

As suggested by Eq. (23), if the number of averages is sufficiently high to satisfy Eq. (9), and under the assumption that the output is fully incoherent with references, then the multiple coherence is the sum of n independent random variables following chi-squared laws with 2 dofs. This is true whatever the level of coherence between inputs, as far as it is considered that a set of n inputs can always be split into n incoherent sources through eigen decomposition. In those conditions, the multiple coherence follows a chi-squared law with 2n dofs :

$$\gamma_{y(1,2...n)}^2 = \frac{\chi_{2n}^2}{2\kappa\, N_0} \tag{24}$$

The expected value of the multiple coherence is $\frac{n}{\kappa\, N_0}$ and its variance $\frac{n}{\kappa^2\, N_0^2}$. In order to validate and illustrate this result, the multiple coherence is estimated between $n = 1, 5, 20$ uncorrelated reference signals and one output (Hanning window, $N_0 = 100$, overlap=70%). Histograms of multiple coherence values are drawn in Fig. 2 together with theoretical pdfs (Eq. (24)). The effect of increasing the number of references is

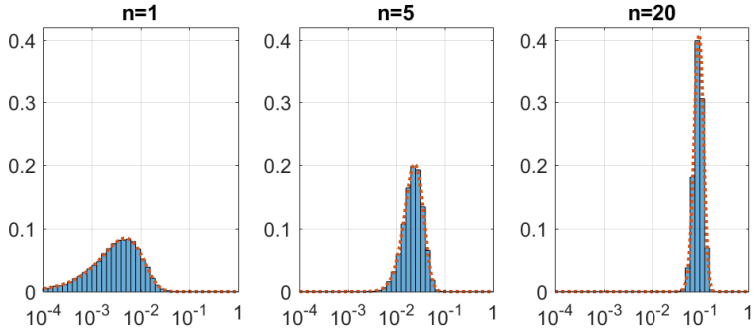


Figure 2: Histograms of multiple coherence values for different number of references (from left to right : $n = 1, 5, 20$) with $N_0 = 100$. Solid lines : theoretical asymptotic distributions.

clearly illustrated by Fig. 2 : the expected value increases, and the dispersion decreases. For instance, for $n = 20$, half of coherence values are between 8 and 11%. Of course, this can lead to difficulties in the analysis because it means that phenomena that are contributing to less than 10% of the output energy will not be detected. However, it is possible to implement the significance test proposed in section 2.2 to try to improve the detectability. The test can be easily verified for each of the n virtual components, using the virtual coherences (20).

3 Experimental application to aircraft flight tests

Developments proposed in this work are used in the frame of the analysis of aircraft flight tests involving a set of 14 interior microphones (distributed in the cabin) and a set of 35 external microphones (distributed along the fuselage, on one side of the plane, downstream to the wing). The source of interest here is composed of all noise sources that are located outside, mainly the engine and the trailing edge of the wing. External microphones are strongly disturbed by the turbulent boundary layer developed on the fuselage, with a signal to noise ratio that can be extremely poor (negative values). Internal microphone records are composed of external source contributions (transferred through the fuselage, here considered as the *signal*) but also of contribution of several interior sources such as the ventilation system (here considered as *noise*). In this application, several outputs are considered, and a global multiple coherence is defined as the ratio between the average output COP and the average output :

$$\gamma^2_{glob(1,2...n)} = \frac{\sum_i \gamma^2_{y_i(1,2...n)} S_{y_i y_i}}{\sum_i S_{y_i y_i}} \tag{25}$$

Internal and external microphones are recorded simultaneously during stationary flight conditions. The total record length is 60s, the cross spectral matrix is calculated with a resolution of 4Hz (Hanning window, overlap 70%, $N_0 = 240$). Output signals are internal sensors, and references are external ones distributed on the fuselage. The global multiple coherence (Eq. (25)) is calculated for different values of $\alpha = 100\%$, 5% and 1%, the $\alpha = 100\%$ case corresponding to the classical approach without the thresholding step. Results are drawn in Fig. 3, with the global COP on the left and the global multiple coherence on the right. The global

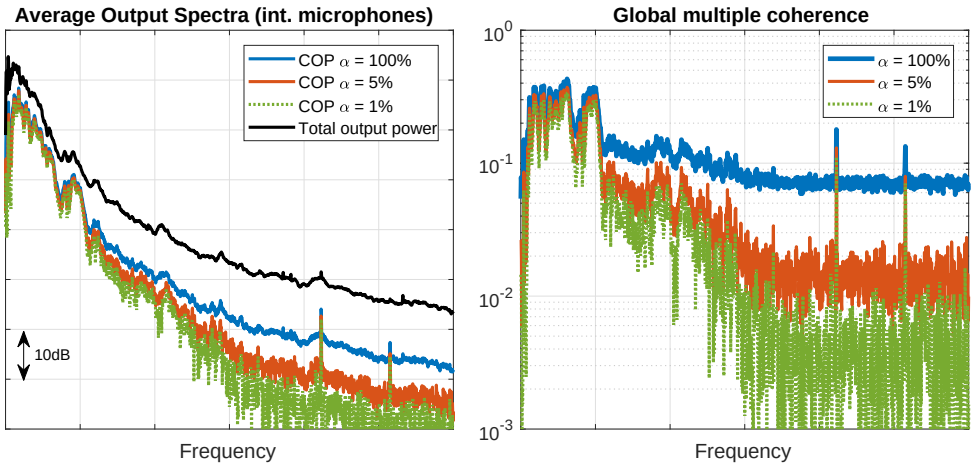


Figure 3: Left : total (black) and Coherent (colours) output spectra with the classical approach ($\alpha = 100\%$, blue) and with $\alpha = 5\% - 1\%$ (red− green). Right : Global multiple coherence with the classical approach ($\alpha = 100\%$, blue) and with $\alpha = 5\% - 1\%$ (red − green).

multiple coherence can be interpreted here as the contribution of external sources located on the left side of the plane to interior noise, because external sensors that are used as references are distributed exclusively on the left side of the fuselage. This explains why the global coherence never exceeds 50% (maximum global coherence at about 35 to 45% in the low frequency range). Assuming a symmetry between the contribution of external sources on both sides, this global coherence could be multiplied by 2 to account for the contribution of external sources on the right side. In mid and high frequency, the global multiple coherence decreases, and strong differences are observed between the different values of α used for the test. For $\alpha = 100\%$, the coherence never goes below about 7 or 8%, this value corresponding to the theoretical expected value of the multiple coherence for uncorrelated signals ($\frac{n}{\kappa\, N_0}$ see section 2.4, with $N_0 = 240$ and $n = 35$ here). Using the proposed test for the thresholding of the virtual coherence, the multiple coherence drops to 2%

($\alpha = 5\%$) and even less than 1% ($\alpha = 1\%$). Some tonal components, that can be seen on either COPs or coherences, are emerging in the high frequency range. The emergence of these tonal components on microphones installed on the fuselage skin, as compared to the background noise of the COP, is strongly improved using the proposed approach : the emergence of these tonal components, equal to 3 to 5dB for $\alpha = 100\%$, increases to 8 to 10 dB and even to 12 to 15dB for $\alpha = 5\%$ and 1%, respectively.

4 Conclusion

The originality of this work is to propose the implementation of a simple statistical test to put to zero coherence values of two finite length time signals that cannot be considered as significant. A development for MISO cases is also proposed, for the multiple coherence, a situation that can be problematic using the standard approach with several references. The method has been applied to aircraft flight tests, illustrating its efficiency, in a case with several references with a poor SNR, to identify the contribution of external acoustic sources to interior noise. Future work will be dedicated to the use of the method to denoise microphones placed on the fuselage.

Acknowledgements

This work was performed within the framework of the Labex CeLyA of Université de Lyon, operated by the French National Research Agency (ANR-10-LABX-0060/ANR-11-IDEX-0007), and of the Clean Sky 2 Joint Undertaking, European Union (EU), Horizon 2020, CS2-RIA, ADAPT project, Grant agreement no 754881.

References

[1] J.S. Bendat and A.G. Piersol. *Engineering applications of correlation and spectral analysis*. Wiley-Interscience, New York, 1980.

[2] S.M. Price and R.J. Bernhard. Virtual coherence : A digital signal processing technique for incoherent source identification. In *Proceedings of IMAC 4*, Schenectady, NY, USA, 1986.

[3] W. G. Halvorsen and J. S. Bendat. Noise source identification using coherent output power spectra. *Sound and Vibration*, 9(8):15, 18–24, 1975.

[4] C.J. Dodds and J.D. Robson. Partial coherence in multivariate random process. *Journal of Sound and Vibration*, 42(2):243–249, 1975.

[5] J.S. Bendat. Solutions for the multiple input/output problem. *Journal of Sound and Vibration*, 44(3):311–325, 1976.

[6] N. Okubo and K. Kumazawa. Application of principal spectrum analysis to identify the vibration sources. In *Proceedings of ISMA 13*, Leuven, Belgium, 1988.

[7] M.S. Kompella, P. Davies, Bernhard R.J., and D.A. Ufford. A technique to determine the number of incoherent sources contributing to the response of a system. *Mechanical System and Signal Processing*, 8(4):363–380, 1994.

[8] P.R. Wagstaff, B. Bouizem, X. Bohineust, and J.C. Henrio. Source identification using partial coherence virtual coherence and principal inputs. In *Proceedings of Inter-Noise 88*, Avignon, France, 1988.

[9] C. Giangreco, P.R. Wagstaff, J.C. Henrio, and E. Langlois. Use of conditioned spectra to differentiate between flow noise and machinery noise. In *Proceedings of Inter-Noise 95*, Newport Beach, CA, USA, July 1995.

[10] M.F. Albright. Conditioned source analysis, a technique for multiple input system identification with application to combustion energy separation in piston engines. *S.A.E. Technical paper series*, (951376), 1995.

[11] Q. Leclere, C. Pezerat, B. Laulagnet, and L. Polac. Application of multi-channel spectral analysis to identify the source of a noise amplitude modulation in a diesel engine operating at idle. *Applied Acoustics*, 66:779–798, 2005.

[12] J. Y. Chung. Rejection of flow noise using a coherence function method. *The Journal of the Acoustical Society of America*, 62(2):388–395, 1977.

[13] B. N. Shivashankara. High bypass ratio engine noise component separation by coherence technique. *Journal of Aircraft*, 20(1), 1983.

[14] J. Hsu and K. Ahuja. A coherence-based technique to separate ejector internal mixing noise from farfield measurements. In *proceedings of the 4th AIAA/CEAS Aeroacoustics Conference*, Toulouse,France, 1998.

[15] Ian Davis and Gareth Bennett. Experimental investigations of coherence based noise source identification techniques for turbomachinery applications - classic and novel techniques. In *17th AIAA/CEAS Aeroacoustics Conference 2011 (32nd AIAA Aeroacoustics Conference)*, 06 2011.

[16] G. C. Carter and A. H. Nuttall. Statistics of the estimate of coherence. *Proceedings of the IEEE*, 60(4):465–466, April 1972.

[17] Jérôme Antoni and Johan Schoukens. Optimal Settings for Measuring Frequency Response Functions With Weighted Overlapped Segment Averaging. *IEEE Transactions on Instrumentation and Measurement*, 58(9):3276 – 3287, September 2009.

Model validation of an aeroelastically-tailored forward swept wing using fibre-optical strain measurements

Y. Govers[1], M. Y. Meddaikar[1], K. Sinha[1]
[1]DLR - German Aerospace Center, Institute of Aeroelasticity
Bunsenstr. 10, 37073 Göttingen, Germany
e-mail: **Yves.Govers@dlr.de**

Abstract
The Institute of Aeroelasticity of the German Aerospace Center (DLR) in Göttingen has analysed means to passively minimise gust load encounters within the DLR project ALLEGRA. One goal was to develop and test a highly flexible forward-swept wind tunnel model which is aeroelastically optimised for maximum tip deflection while constraining the tip twist. Stiffness optimisation tools offer the possibility to design wings with very specific aeroelastic constraints. From the optimised stiffness distribution a feasible stacking sequence needs to be derived to reach the full potential of the stiffness optimisation process. After manufacturing, the wind tunnel model needs to be validated thoroughly. Here, a two-step validation process will be shown. First, static tests obtaining deflection and strain measurements are utilised to adjust the finite element model by a computational model updating (CMU) approach [1-3]. Second, experimental eigenfrequencies and strain shapes are used to check the validity of the updated model

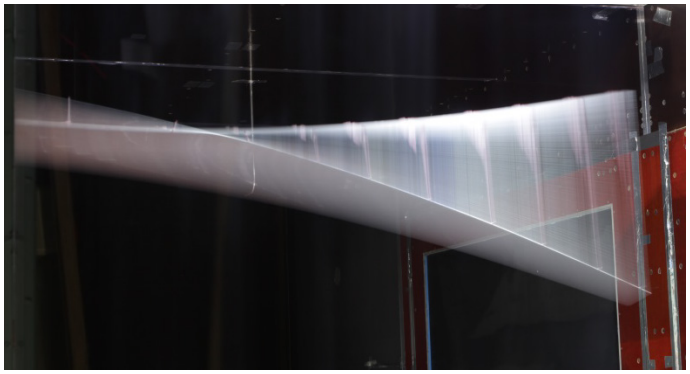


Figure 1: long exposure photo for angle of attack variation during wind tunnel testing

1 Introduction

The main objective of this work is to integrate new measurement technique in the model validation process. Composite structures offer the possibility to vary the stiffness properties of a wing fluently in span direction. Abrupt stiffness changes result in strain discontinuities under static and dynamic loading, which can hardly be identified from conventional measurements like displacement, velocity or acceleration signals.

Most commonly acceleration measurements are employed to determine mode shapes from modal identification for validation purposes. There are two simple reasons for this: an acceleration sensor is easy to apply and deflection mode shapes can directly be estimated from acceleration signals by experimental or operational modal analysis techniques. In the past strain gauges have played a minor role in modal identification because they were of single use and more difficult to apply. Another drawback is that strain

modes do not represent deflections and are not easy to interpret. They need to be converted into deflection modes [4]. Recent progress in strain measurement technology with fibre-optical strain sensors offering spatially near-continuous measurements at sampling rates of 250Hz raise the interest especially for aeroelastic applications [5].

Within DLR's internal project ALLEGRA, passive load alleviation techniques have been studied thoroughly. A special task within this project was to validate the design of an aeroelastic tailored composite wing structure optimized with the in-house tool chain. Therefore new measurement techniques have been explored. For this reason a fibre-optical strain sensor was installed during the manufacturing process to analyze the strain distribution along the span during static, dynamic and wind tunnel testing. The strain sensor offers a spatial resolution of 2.5mm for a total length of 2m at a sampling rate of 250Hz.

The benefits of these measurements for model validation of composite structures will be highlighted in this work. The wing model used in this study is a forward-swept aeroelastically tailored composite wing [6]. The wing was designed for maximum flexibility using an in-house aeroelastic tailoring framework. Wind-tunnel tests demonstrated a maximum deflection of ~20% of the wing semi-span. The wing was fabricated with an optical strain measurement fibre, embedded in the lower skin. Static and dynamic tests were performed outside the wind-tunnel while deformations and strains were measured for the purpose of model-updating.

In the present paper, finite element model updating is performed using experimental data from different tests. The updated model is validated with measurements that have not been integrated in the updating process.

2 Design and manufacturing of an aeroelastically tailored wing

2.1 Model design

The wing model used in this experimental study is a forward-swept wing with a sweep angle of 15°, a wing half-span of 1.6*m*, root and tip chord of 0.36*m* and 0.12*m* respectively, a full wing aspect ratio of 13.33 and a custom unsymmetrical airfoil. In order to tap the stiffness-tailoring potential of composites, the entire wing was designed having five design fields each in the upper and lower skin. Each design field is defined as a region having constant stiffness properties, effectively constant laminate stacking sequence. Laminate blending rules are followed in order to ensure ply continuity while manufacturing and improve structural integrity between the regions with varying laminates. The geometry of the wing and the distribution of the design fields are shown in Figure 2.

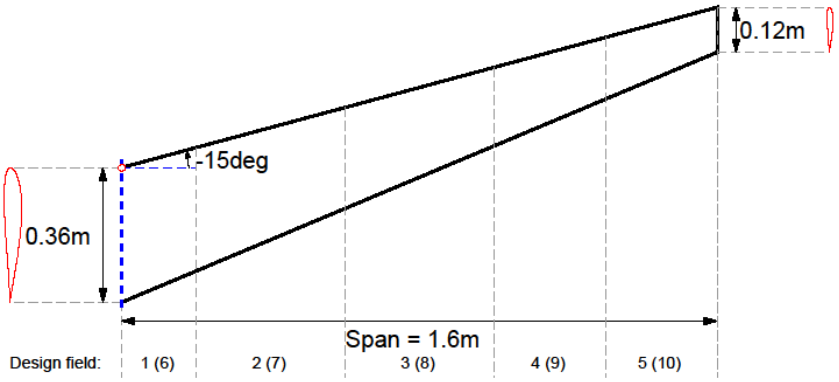


Figure 2: Wing planform showing distribution of the design fields in the skins (shown within brackets are design field numbers in lower skin)

The wing was tailored for maximum flexibility, while ensuring that the resulting twist-deformation at the tip was zero. The requirement on the twist was placed in the optimization, since forward-swept wings tend to produce a nose-up twist when bending upwards, which then aggravates toward static aeroelastic instability in the form wing divergence. Figure 3 shows the polar distribution of the A_{11} term in the ABD composite stiffness matrix of the upper skin. This distribution highlights the main direction of stiffness in the upper skin of the wing. In this case, it is a distribution characteristic of bend-twist coupling that aims to produce a nose-down twist when experiencing an upward-bending deflection. Details of the wing design and the DLR in-house aeroelastic tailoring framework is presented in [6].

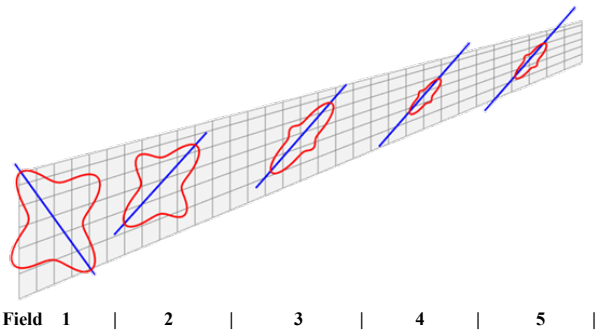


Figure 3: Design stiffness distribution in upper skin

Field	6	7	8	9	10
Plies	30°	30°	30°		
	90°	90°			
	30°	30°	30°	30°	30°

Table 1: Optimized ply layup of design fields in lower skin

2.2 Manufacturing

With wing flexibility being the design objective of the wing, a uni-directional glass fibre material (E-glass/epoxy) was used in the design. A load-carrying skin concept was applied in order to keep the modelling and manufacturing simple, while a foam core (Styrodur 3035CS) filled between the upper and lower skin ensured structural stability. The wing was manufactured using a hand layup and vacuum-bagging technique.

The optic strain measurement fibre was placed along the 25%-chord line at the interface between the lower skin and the foam core. Near the root of the wing, the chord-wise position was adapted in order to allow a safe transition while exiting the wing. From this root segment until the adapter outside, the entire fibre is enclosed within protective tubing in order to prevent any possible damage whilst manufacturing and handling during tests.

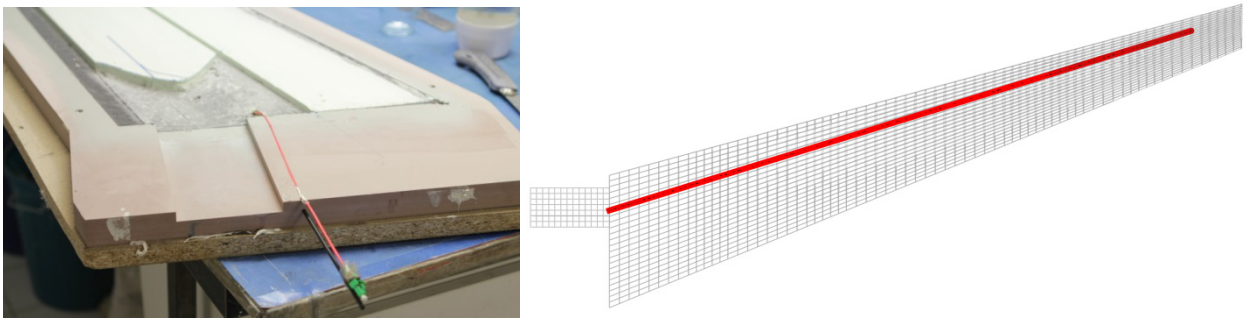
2.3 Sensor instrumentation

The aeroelastically tailored wing can be characterized by a very complex stiffness distribution along the wing span which is realized by stiffness variations that can only be made with composite material. The manufacturer gets a ply book with the composite layer setup. Angles and number of plies must exactly match the ply book which itself must match the stiffness distributions. This process describes that the stiffness properties from the manufacturing are much more uncertain.

To identify errors in the stiffness properties of the manufactured wing experimental tests are needed to compare with results from finite element method (FEM). Stiffness variations from ply drops result in discontinuities of strain. Therefore a measurement technique was chosen which yields continuously strain information along a 2m fibre. The strain fibre was installed in the lower skin of the wing. In contrast to the technology of fibre Bragg grating for measuring strain at a maximum of ~30 locations the fibre used can measure a very high spatial resolution with up to 800 locations. Additionally to static measurements the system can acquire data at a sampling rate of 250Hz. The technology behind is the optical frequency

domain reflectometry (OFDR) described in [7]. OFDR is already available since late 90's. Applications to structural health monitoring in the field of aerospace have been demonstrated in [8, 9]. Since the technology is still improving it now gets interesting for dynamical measurements and therefore also modal identification.

The sensor itself is easy to install and just needs to be bonded with superglue to the skin of the monitored structure.



a) Fibre installation b) Fibre position in structure

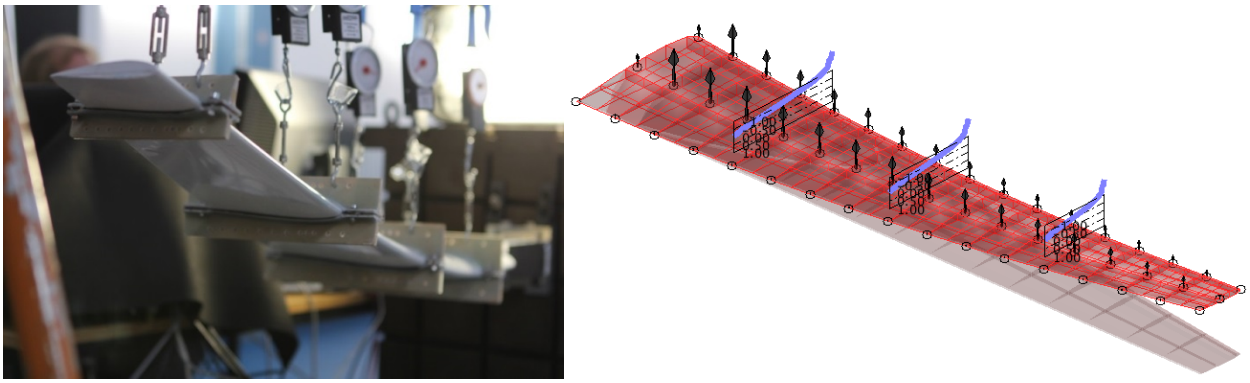
Figure 4: Strain fibre sensor

3 Experimental characterization of the composite structure

The experimental characterization was done in three steps using (i) an ultimate load test, (ii) a static test and (iii) a vibration test. While the ultimate load test was to validate the design and manufacturing process for maximum stress and to ensure wind tunnel testing safety the two other tests should gain data for model validation.

3.1 Limit load testing

Prior to testing the wing in a wind-tunnel, a limit load test was performed with the forward swept wing structure. The limit loads for which the wing was sized were applied during static testing. This was done to ensure validity of the assumed allowable for the material and the modelling process. Equivalent loads were introduced at four sections using load-scissors, such that the resulting displacements were as close as possible to the actual distributed aeroelastic loads. Figure 5 shows the setup and the deflection of the wing in the limit load test together with force and pressure c_p-distribution from the NASTRAN aeroelastic analysis using the Doublet Lattice Method (DLM).



a) Limit load test with equivalent aerodynamic loading b) DLM forces and c_p for angle of attack α=10° and v = 50m/s

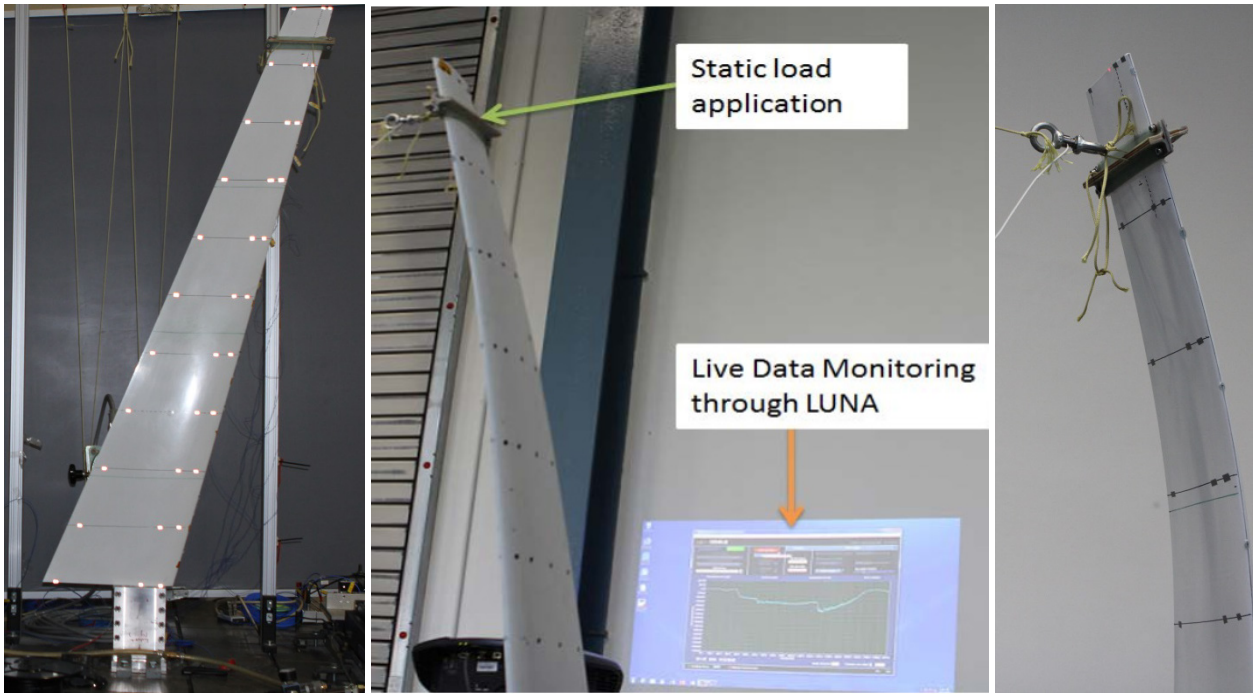
Figure 5: Calculation of aerodynamic forces and application to limit load test

3.2 Static testing

Static tests were conducted on the wing structure with the LUNA ODiSi-B measurement system designed to read and process the optical strain data from strain fibre embedded inside the wing. The objective of the measurements was to obtain model validation data and concurrently demonstrate the utility of optical strain fibres for such measurements. In the Figure 6b, instant data visualization through the LUNA system is depicted along with the wing in loaded condition. The live data monitoring enabled a quick check of the structural response and therefore, ensured that the deflection did not exceed allowable limits. The strain variation was measured along the full length of the strain fibre at a high spatial resolution.

Measurements using the Polytec Laser Doppler Vibrometer were also taken in tandem with the strain measurements as a check for wing deflection under bending loading. Here, the geometry laser was used to measure the deflections along different sections of the wing span. Since the deflection cannot directly be measured the difference between the actual laser point position under load and the zero position was calculated. The measurement points can be identified by the reflector marks in Figure 6a.

A single point force was introduced into the structure near the tip at approximately 1.5 m from the base of the wing. The applied load was introduced using a clamp for uniform load distribution across the cross-section. The loading was done using physical weights and a measure of the applied load was taken using load cells attached at the point of load introduction which is depicted in Figure 6c.



a) Reflector marks for deflection scan b) Setup with optical strain fibre system c) Static deflection

Figure 6: Measurement setup for static tests

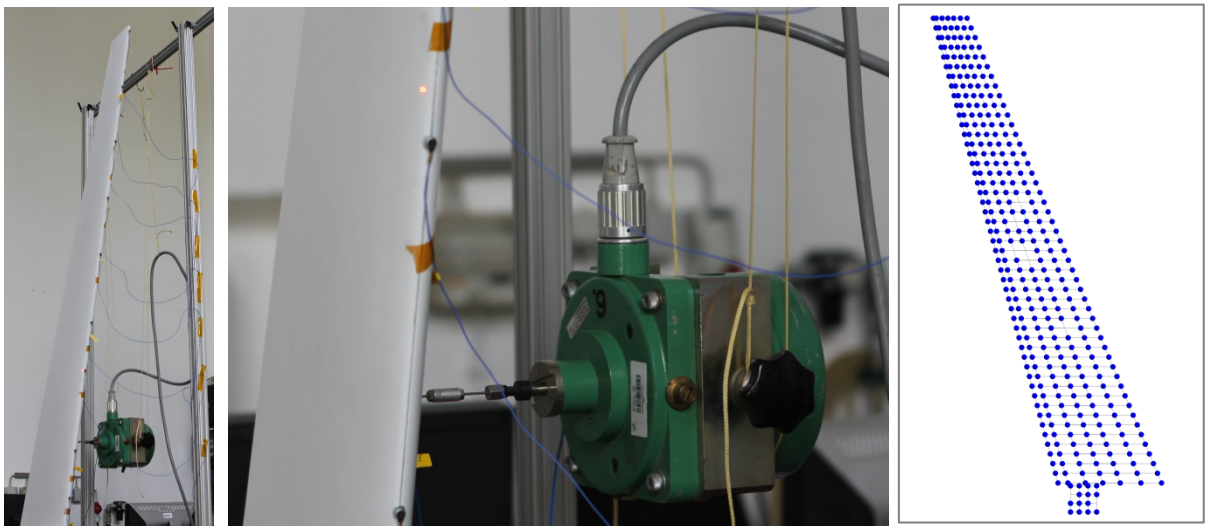
3.3 Vibration testing

A ground vibration test (GVT) was performed on the forward swept wing using to identify the structural dynamic properties. To excite the structure an electrodynamic shaker was used. The responses were measured (i) with a Polytec PSV-400 Laser Doppler Vibrometer (LDV) using a high spatial resolution of measurement points and (ii) with the LUNA ODiSi-B system using the continuous fibre optic sensor with a spatial resolution of 2.5mm and a sampling frequency of 250Hz.

The structure was excited with an electrodynamic shaker using a random signal in the frequency range from 10 to 1200 Hz. The shaker was connected to the structure by superglue. A force cell between structure and stinger provided the input force signal. The shaker was supported by ropes as depicted in Figure 7a and b. This type of suspension decouples the excitation from the supporting structure. In the higher frequency range > 100 Hz each supporting structure will show its own resonance frequencies, which can interfere with the test object. Additionally the test was carried out on DLR's seismic block that can also be decoupled from the building by air cushions. The fixation of the structure was the same than for the static test.

3.3.1 LDV and accelerometer measurements

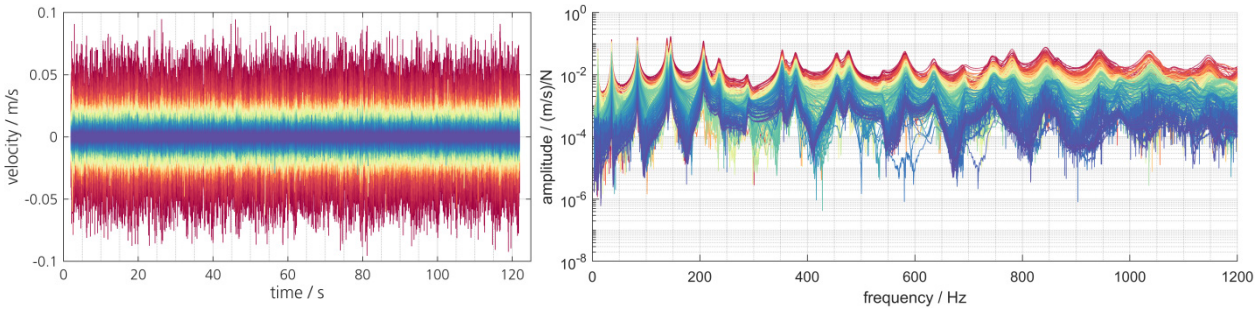
Before setting up the test the structure was treated with a reflector spray to enhance the signal quality of the laser. Random excitation with signal duration of 125 seconds was applied for each scan point. The random signal was generated before and played as user defined signal for each scan point again to guarantee high repeatability. A sampling frequency of 2.56 kHz was used. The complete structure was scanned at 343 measurement points across the wing surface and 16 points on the clamp at the wing root. Additionally 10 accelerometers used for in-plane vibration measurement have been installed on the leading edge of the wing. LDV measurements have been carried out with a Polytec Scanning Vibrometer PSV-400 while the accelerometers have been acquired with an LMS Scadas III measurement system. On both systems time data signals of the input force and the structural responses were stored together with the time data from reference an accelerometer at the driving point. Modal testing was carried over three consecutive days due to the high scan density of the measurement grid.



a) Wing with shaker b) Close up of shaker attachment c) Valid scan points on structure

Figure 7: Experimental setup and scan points of LDV measurements

The recorded time data signals shown in Figure 8a have been processed into velocity frequency response functions (FRF) by referencing on the input force measured by the force cell in order to estimate mode shapes within the framework of experimental modal analysis. As depicted by missing points in Figure 7c some of the time data signals were corrupted and needed to be eliminated for further modal analysis. A good indicator for corrupt measurement signals from random excitation is to look at the skewness or kurtosis which describe the 3rd and 4th statistical moment of the time data signals. These values indicate bad measurement signals and need to be eliminated before further analysis.



a) Time data from random excitation

b) Velocity frequency response functions

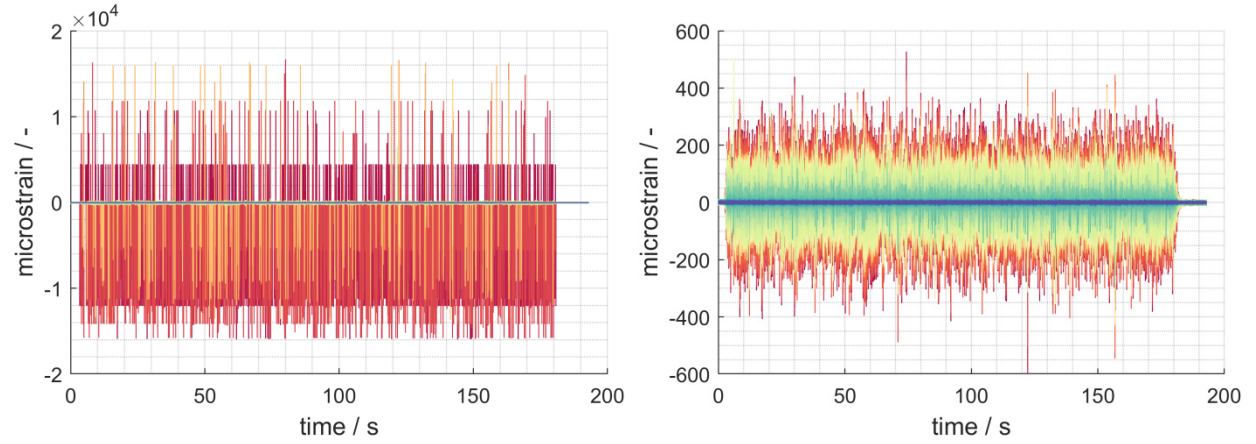
Figure 8: Data acquisition and signal processing of LDV measurements

Transfer functions have been obtained using the H1 estimator by applying Welch's modified periodogram [10] with an overlapping Hanning window. The signal processing has been performed using DLR's object-oriented modal analysis MATLAB toolbox. The FRFs obtained from flap-wise excitation are presented in Figure 8b. The transfer functions in log-scale show very clear resonance peaks up to the maximum excitation frequency of ~1200Hz.

3.3.2 Strain fibre measurements

The strain fibre measurements make use of the OFDR technique as explained in [7]. T vibration measurements have first been carried out in the same boundary and shaker conditions as for the LDV measurements. Unfortunately the sampling frequency was only set to 10 Hz which was recognized after the test was disassembled. Nevertheless data from shaker testing before wind tunnel entry was available for analysis with a maximum sampling rate of 250 Hz. Though the structural dynamic characteristics between fixation on seismic block and wind tunnel wall do slightly differ the results are similar and the capabilities of such a fibre can be discussed in this paper.

The model mounted to the wind wall was also excited with an electrodynamic shaker using random excitation. The length of the excitation was this 180 seconds. The data was stored in a raw data format on the computer attached to the LUNA ODiSi-B system. One drawback of the current system is that no external analogue signal can be measured as reference signal and therefore the input force is not available. Also time synchronization is not available for the ODiSi-B system, but seems to be implemented in the current system.



a) Time data before correction

b) Time data after correction

Figure 9: Data acquisition and signal processing of strain sensor

The recorded time data signals shown in Figure 9 have been processed into strain cross power spectral density functions (CPSD) by referencing on a stain sensor location itself in order to estimate mode shapes within the framework of operational modal analysis. As depicted in Figure 9a many time data signals were corrupted and needed to be purified for further modal analysis. Missing data points needed to be interpolated using common splining functions within MATLAB. After purifying the data nice random signals could be obtained.

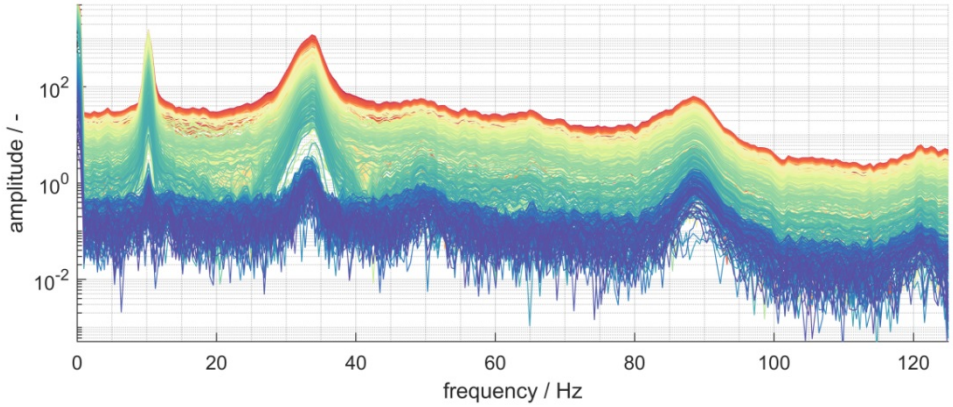


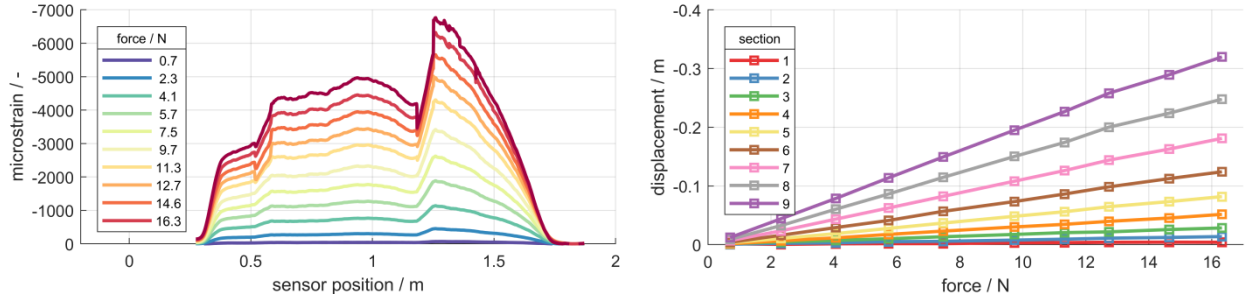
Figure 10: cross power spectral density functions of strain fibre

From 819 time data signals cross power spectral densities (CPSDs) were calculated in the same manner as described for the LDV data. The reference sensor was chosen according to strain mode amplitudes after first modal identification results had been processed. It is important to reference on a sensor location with a significant strain mode contribution. The CPSDs already indicate some resonance frequencies (see Figure 10).

4 Results

4.1 Static data

The load application was done in a sequence of 11 steps up to the estimated maximum allowable load. Strain and displacement measurements were stored for each of these 11 load steps. Due to frictional forces acting along the load application path, the actual bending loads measured at the force cell were smaller than the applied load. The strain and displacement results are depicted in Figure 11. In the strain vs length diagram, strain discontinuities are clearly visible at distinct positions within the structure. These indicate the change in the composite layup within different sections of the wing. The applied load steps varied from 0.7 to 16.3 N for maximum tip deflection. The increase in load is clearly implied in Figure 11a through the superimposed strain plots for the different load steps.



a) Strain variation along the length of the fibre

b) Displacement increment with load

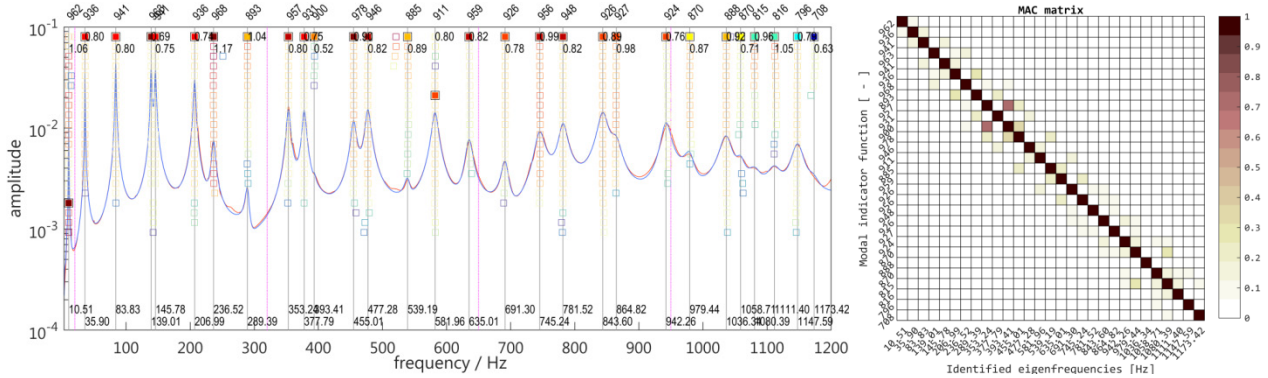
Figure 11: Strain and displacement response from the static tests

In Figure 11b, displacements at 9 different measurement locations along the span with increasing load magnitudes are shown. The deflection curves, as expected, are found to have a linear variation with load increments. The peak deflection near the tip was observed at 32 cm for an applied load of 16.3 N which is 20% of the wing span.

4.2 Modal identification

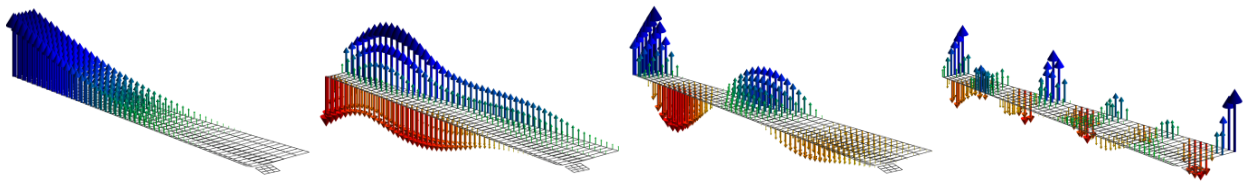
4.2.1 Identification of displacement modes

Figure 12a shows the stabilization diagram of the FRF modal analysis including a summation of experimental (red) and fitted (blue) FRF amplitudes. The eigenvalues and eigenvectors are estimated using the well-known least-squares complex frequency method (LSCF) [11], from which the stabilization diagram is constructed using the DLR's Modal Analysis MATLAB toolbox.



a) Stabilization diagram and curve fit of sum of absolute values of FRFs d) MAC matrix for identified modes

Figure 12: modal identification results from LDV and accelerometers



a) 1st wing bending 10.5Hz b) 1st wing torsion 139 Hz c) 4th wing bending 146 Hz d) higher torsion mode782 Hz

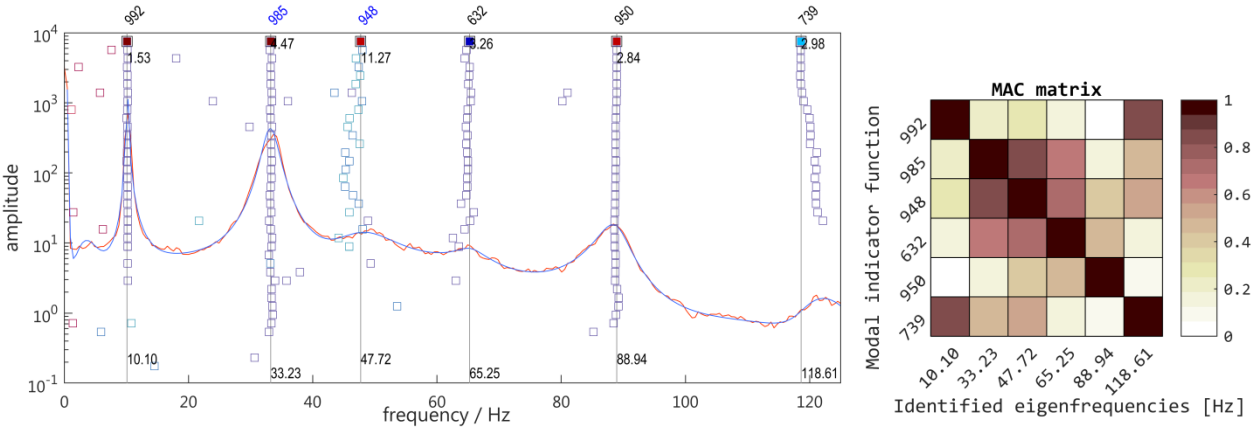
Figure 13: some bending and torsions modes from LDV measurements

The Auto-MAC matrix in Figure 12b shows a number ~30 modes that are well separated from each other. A selection of identified modes is presented in Figure 13. The identification of modes was possible even above 1200

4.2.2 Identification of strain modes

Strain gauge modal analysis can be applied on strain transfer functions in the same way as on transfer functions calculated from acceleration, velocity or displacement signals. Figure 14a shows the stabilization diagram of the strain modal analysis including a summation of experimental (red) and fitted (blue) SCPSD amplitudes. The eigenvalues and eigenvectors are also estimated using the well-known least-squares complex frequency method (LSCF) [11], from which the stabilization diagram is constructed using the DLR's Modal Analysis MATLAB toolbox.

Within the frequency range up 125 Hz six stable poles can be detected see Figure 14a. The curve fit in the same figure shows a good representation of the SCPSDs. The MAC matrix in Figure 14b shows



a) Stabilization diagram and curve fit of sum of absolute values of SCPSD's d) MAC matrix for identified modes

Figure 14: modal identification results from strain sensor

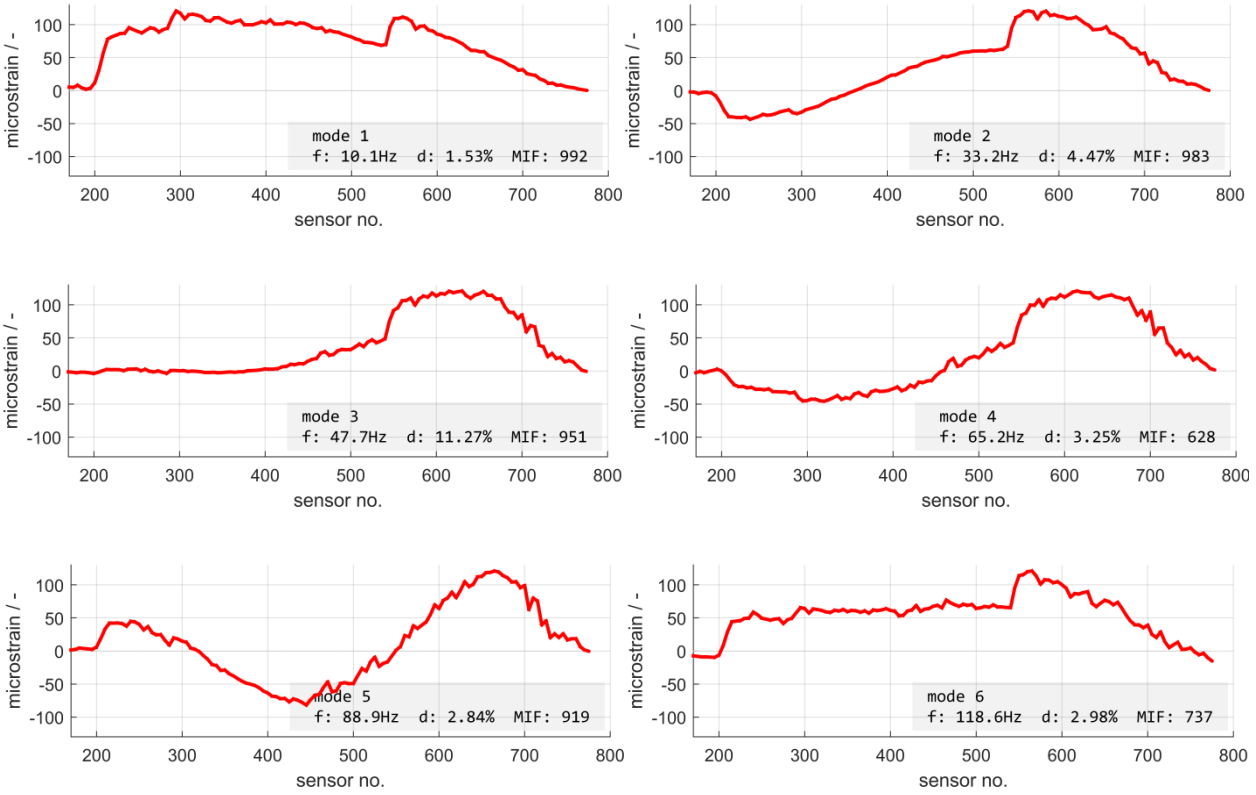


Figure 15: strain modes

The identified strain modes are depicted in Figure 15. Though six modes could be identified, two of them are spurious modes which do exist neither in finite element model nor in results from LDV modal identification. The spurious modes are already indicated by the low mode indicator function value (MIF), which is plotted into the text field of each graph. Mode 1, 2 and 5 represent flap bending modes while mode 3 is an edge bending mode.

5 Model updating and validation

Differences between the idealized simulations models used in a structural design and the actual behavior observed in experiments are inevitable and can arise from several sources. In the present case, the design of the wing with the aeroelastic tailoring process uses GFEM/dynamic type of FE models that are well-suited for structural dynamic and aeroelastic applications. For the model generation, the parametric model generator ModGen [12] at the DLR – Institute of Aeroelasticity is used. Such a model typically includes an approximate representation of the non-structural masses for instance, glue, additional resin and paint. The mass in the FE model is then adapted to the measured wing mass and the center of gravity. A second important source of difference results from deviations arising out of material scatter and manufacturing discrepancies, observable only after the structure is manufactured.

In order to update the simulation FE models such that they represent the actual manufactured structure, information from static or vibration tests can be used to update the FE models.

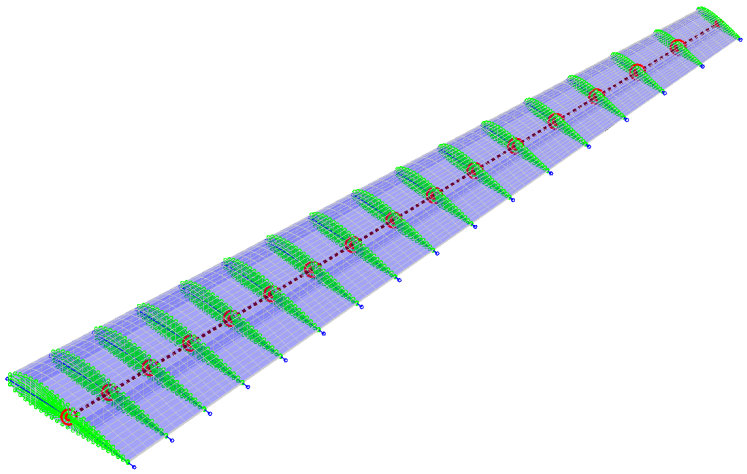


Figure 16: Wing FE model showing tuning beams (in red) connected to inner structure of wing

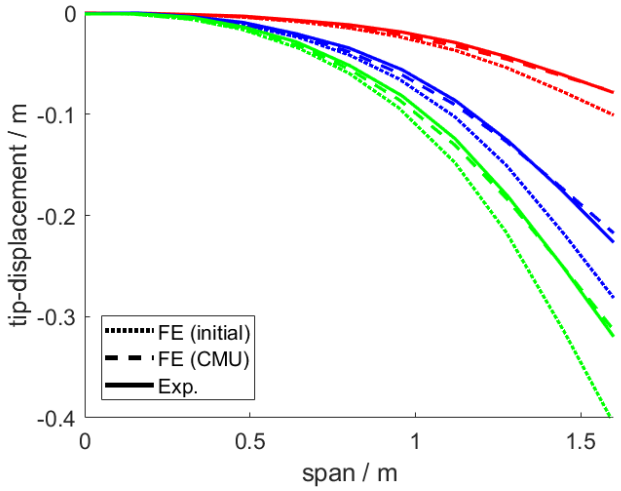
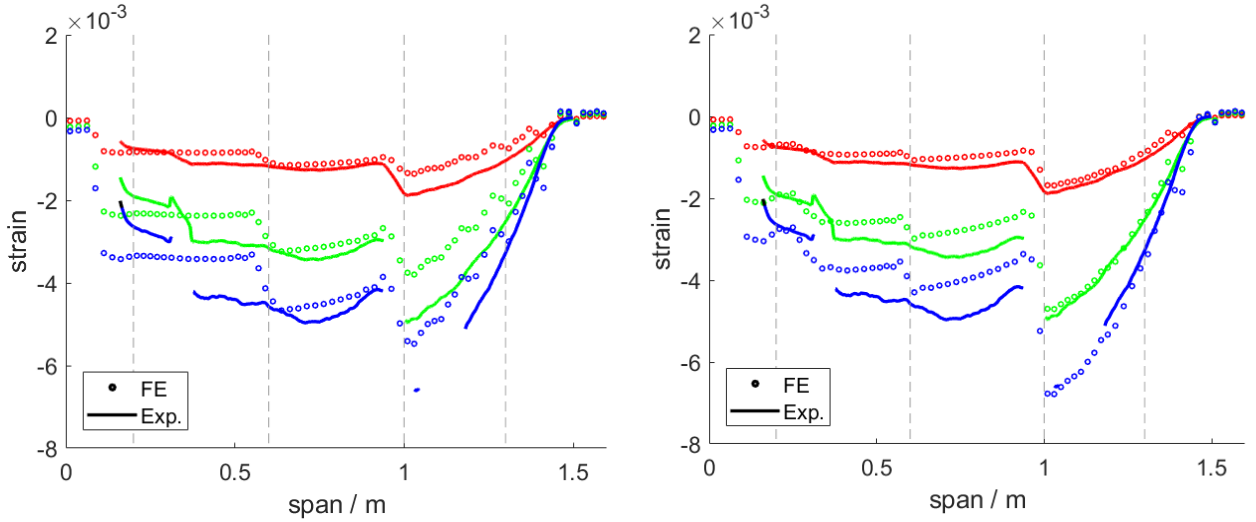


Figure 17: Tip-displacement for Model-1 – initial FE model, FE model after CMU, experimental results (for three different load magnitudes)

In this case, the static tests explained in the previous section were used to update the FE model with a CMU approach. The FE model shown in Figure 16 contains dummy ribs that are used for the aero-structure splining. ‘Tuning-beams’ are added between two ribs totaling 16 such beams in this case. The

properties of the beams are grouped such that 5 unique beams exist. Using the bending-stiffness term of these tuning beams as design variables, an optimization problem is setup within NASTRAN's optimization framework – the SOL 200. The objective of the optimization is to minimize the difference between the displacements at defined points in the measured test results and the FE model. The drawback of using such a tuning-beam is that the update is a purely mathematical adaptation of the model without necessarily providing any metric of the physical parameters changed. However, as a first quick approach at model-updating, it is effective on account of its simplicity.

The results from the CMU step are shown in Figure 17. The displacement from the experiments corresponding to the largest load (shown in green) is used as the target displacement in the optimization. The updated model (denoted as Model-1) agrees well with the experimental measurements for other measurement points as well, thus showing the consistency of the update over the different load sets.



a) Model-1 b) Model-2

Figure 18: Span-wise strain distribution along the strain-fibre and in the FE model (dashed lines represent the boundaries of the design regions in the lower skin)

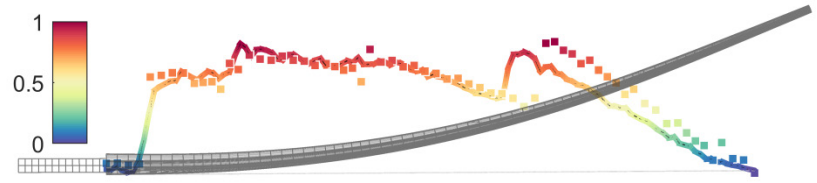
The strains measured using the optic fibre are compared with the updated Model-1 in Figure 18a. The trends observed are comparable and of particular interest are the sharp jumps in strain observed at the interfaces between two design regions, between which plies are dropped. A noticeable discrepancy between the experimental results and strains in Model-1 occurs at the first ply-drop junction between design regions 1 and 2 (at span location 0.20m). The FE model predicts a sharp increase in strain, which can be expected given the sudden drop in thickness. This drop is observable in the experimental results shifted slightly outward (at a span location of ~0.40m).

A possible explanation could be a simple manufacturing defect wherein the ply in consideration was dropped at a false location further outboard than had been initially planned. Such a manufacturing oversight is quite difficult to detect once the wing has been assembled and closed.

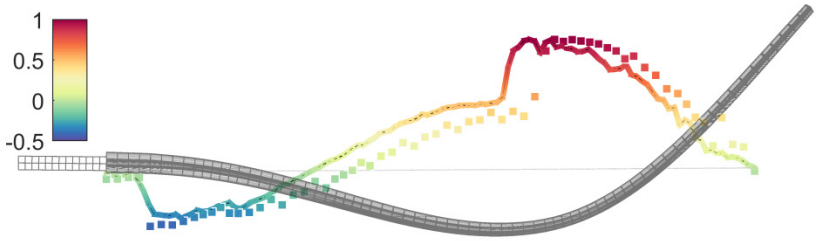
In order to further investigate on this, the FE model was re-generated with the possibly shifted ply-drop location, a CMU was performed similar to Model-1 using the experimental displacements as objective and the strains were recalculated. For the sake of convenience, this model is denoted as Model-2 henceforth. A strain comparison between the FE model and the experiment for Model-2 is shown in Figure 18b. Even though the comparison for the strains in the mid-span section is slightly deteriorated, the strains near the root and tip seem to have a much better correlation with the FE model. This manufacturing defect could in fact be present in the actual wing and the complete set of measured data will be next processed in order to confirm this.

An observable artefact in the measured strain data are the gaps in measured strains. This arises due to the sharp gradient in the experimental strains along the span, mostly at the ply-drop locations, which is beyond the specification limits of the used optic-fibre.

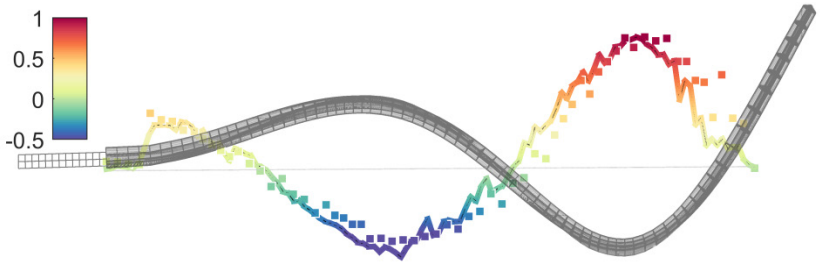
For comparisons with strain mode shapes measured using the fibre, strain modal data was extracted using a SOL103 analysis in Nastran. First, the FEM elements were correlated to the previously measured strain fibre location in the wing and an element set was created for strain computation. The strains in Nastran were computed in the material coordinate system, of which the x-axis aligns approximately with the direction of strain fibre and therefore, strain transformation along the direction of the strain fibre was not necessary. The comparisons for the static analysis and mode shapes have been done with a direct utilization of local x-strain for each element extracted from the SOL103.



a) 1st wing bending strain mode



b) 2nd wing bending strain mode



c) 3rd wing bending strain mode

Figure 19: comparison of strain modes from experimental fibre (solid line) and numerical results (square)

The analytical and measured strain modes are compared for all flap bending modes in Figure 19a-c. The figure shows analytical (squares) vs. experimental strain (solid line). The color code and vertical position gives the strain mode values while in gray the finite element deflection mode shape of the wing is overlaid. The plot shows quite nicely that the strain curves match quite well. Mode 1 and 2 indicate still a slight discrepancy in position for the last ply drop. Also turning points of mode shape bending can be detected as points of zero strain.

6 Conclusions and Outlook

An aeroelastically tailored forward swept wing has been designed for high flexibility and zero tip twist. To realize maximum flexibility a glass fibre – epoxy based material was chosen in the design. The manufacturing of the wing was done using hand layup and vacuum bagging technique. The OFDR measurement technique was employed using a strain fibre for continuous static and dynamic strain information along the span of the forward swept wing. The sensor was embedded within the wing during the manufacturing. The wing was then subjected to a sequence of experimental tests to determine its characteristics. An initial limit load test was conducted to validate the assumed design allowable in the FEM structural model. A static test was then conducted with simultaneous strain measurement using the optical strain fibre and relative displacement measurement using geometry laser of an LDV. The strain variation plotted along fibre length was found to be a good indicator of the composite layup in different sections of the manufactured wing. The displacement data at several points on the wing obtained using the LDV was then utilized for a computational model update of the FEM model. A comparison of the experimental displacement measurements with the updated model shows a good agreement. Furthermore, a comparison of the element strain along the fibre location in the FEM model with the strain data obtained from the strain sensor gives a reasonably good correlation. This, to some extent, gives a good validation of the experimental measurement using strain fibre.

Vibration tests with a classical GVT were also conducted for the wing to obtain a dynamic characterization of the wing. A good prediction of the mode shapes and modal frequencies of the wing was obtained using measurements from the LDV and the in-house DLR tool for data analysis. The sampling rate of 250 Hz for the strain fibre of 2 m length provided time response for >800 sensor locations. It was possible to extract all four strain modes of the structure within the frequency range up to 100 Hz. After update the match between analytical and experimental strain modes was fairly good.

Such strain fibres provide detailed data about the stiffness distribution of a composite structure. It is much more sensitive than other measurement techniques like displacements and accelerations. Since now even modal identification is possible the value of this technique has risen significantly. In the future the strain modes will be integrated in the CMU process. Furthermore the strain sensor information should be used to do real time monitoring during wind tunnel testing.

Acknowledgements

This work was founded by DLR programmatic research in the project ALLEGRA.



References

[1] M. Link, *Updating of Analytical Models – Basic Procedures and Extensions*, in Modal Analysis and Testing, J.M.M. Silva and N.M.M. Maia, Editors. 1999, Kluwer Academic Publishers: Dordrecht, Netherlands. pp. 281-304.

[2] M.I. Friswell , J.E. Mottershead, *Finite element model updating in structural dynamics*. Solid mechanics and its applications, v. 38. 1995, Dordrecht; Boston: Kluwer Academic Publishers.

[3] J.E. Mottershead, M. Link , M.I. Friswell, *The sensitivity method in finite element model updating: A tutorial*. Mechanical Systems and Signal Processing, 2011. 25(7): pp. 2275-2296.

[4] A. Geeraert , C. Stephan. *EXPERIMENTAL RESULTS BY STRAIN PATTERN ANALYSIS*. in International Forum on Aeroelsticity and Structural Dynamics. 2015. St. Petersburg, Russia. pp. 2015-23.

[5] Y. Govers, G. Jelicic , T. Akbay, *The use of strain sensors for modal identification of aeroelastic structures*, in International Conference on Noise and Vibration Engineering2016: KU Leuven, Belgium. pp. 2207-2216.

[6] M.Y. Meddaikar, J. Dillinger, M.R. Ritter , Y. Govers. *Optimization & Testing of Aeroelastically-Tailored Forward Swept Wings*. in International Forum on Aeroelasticity and Structural Dynamics. 2017. Como, IT.

[7] M. Froggatt , J. Moore, *High-spatial-resolution distributed strain measurement in optical fibre with Rayleigh scatter*. Applied Optics, 1998. 37(10): pp. 1735-1740.

[8] H. Murayama, H. Igawa, K. Omichi , Y. Machijima. *Application of distributed sensing with longlength FBG to structural health monitoring*. in 9th International Conference on Optical Communications and Networks (ICOCN 2010). 2010. pp. 18-24.

[9] S.G. Allison, W.H. Prosser, D.A. Hare, T.C. Moore , W.S. Kenner. *Optical fibre distributed sensing Structural Health Monitoring (SHM) strain measurements taken during cryotank Y-joint test article load cycling at liquid helium Temperatures*. in SPIE. 2007. Boston, MA, United States: The International Society for Optical Engineering.

[10] P. Welch, *The use of fast Fourier transform for the estimation of power spectra: A method based on time averaging over short, modified periodograms*. IEEE Transactions on Audio and Electroacoustics, 1967. 15(2): pp. 70-73.

[11] B. Peeters, H. Van der Auweraer, P. Guillaume , J. Leuridan, *The PolyMAX frequency-domain method: a new standard for modal parameter estimation?* Shock and Vibration, 2004. 11(3): pp. 395-409.

[12] T. Klimmek, *Parameterization of topology and geometry for the multidisciplinary optimization of wing structures*, in CEAS 2009 European Air and Space Conference2009.

Top 10 mechanical experiments for the teaching of sound and vibration in mechanical engineering

M. A. Peres[1], A. Barnard[2]
[1] The Modal Shop, Inc.
3149 E Kemper Rd, Cincinnati, OH 45241, USA
e-mail: **mperes@modalshop.com**

[2] Michigan Technological University, Department of Mechanical Engineering – Engineering Mechanics
1400 Townsend Dr., Houghton, MI 49931, USA

Abstract
The use of experimental tools such as electrodynamic shakers, hammers, accelerometers, and microphones are reviewed as part of the educational curriculum for the young mechanical engineer and science degree student. A list of unique 10 laboratory experiments are described as part of a good foundation for engineers interested in the fields of vibration dynamics, acoustics, and mechanical systems.

1 Introduction

Mechanical engineering curriculum includes many facets of dynamics, thermodynamics, fluids, control systems, design, manufacturing, and other fields. One important sub-field within mechanical engineering is Noise, Vibration, and Harshness (NVH). Mechanical product designers and test engineers need to have an introduction to NVH in order to design consumer products that meet customer expectations in terms of sound and vibration quality. Excess vibration in mechanical systems can lead to product damage/failure or user discomfort. Mechanical engineering curriculum varies worldwide in terms of the content of NVH materials taught to undergraduate and graduate students.

The objective of this paper is to present 10 NVH experiments that we have found useful in teaching fundamental NVH concepts to mechanical engineering students. These experiments cover both acoustics and vibration and provide a basis for graduates with basic knowledge in NVH principles. These experiments may be useful to the new professor developing a program in NVH, the seasoned professor looking to update current classes, or the industry professional interested in training new NVH engineers.

Because of the nature of this paper, the format is developed to present each experiment in a single page format as a figure that incorporates text and images to portray the experiment. Figures 1-10 in the Experiments section show an overview of the 10 experiments.

2 Experiments

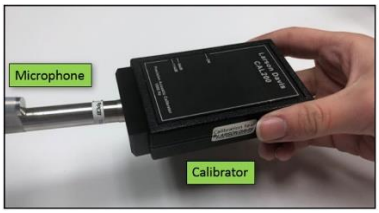
Measurement chain calibration and noise floor

Motivation for the lab:
Many mistakes in collecting data can be avoided by some up-front understanding of the measurement system. Making a good measurement starts early in the process. This lab emphasizes performing calibration of sound and vibration equipment as an entire signal chain, not just a single transducer. Understanding the system noise floor is also important to interpreting the recorded data. The importance of background noise testing is demonstrated.



Frequency = 159.2 Hz
(ω = 1000 rad/s)
Acceleration = 1 g (9.81 m/s^2)

Required equipment:
- Free-field microphone
- Pistonphone and/or speakerphone
- Accelerometer
- Accelerometer calibrator
- Cables and signal conditioners
- Data acquisition system
- 50 Ohm terminator



Frequency = 1000 Hz
SPL = 94 dB or 114 dB

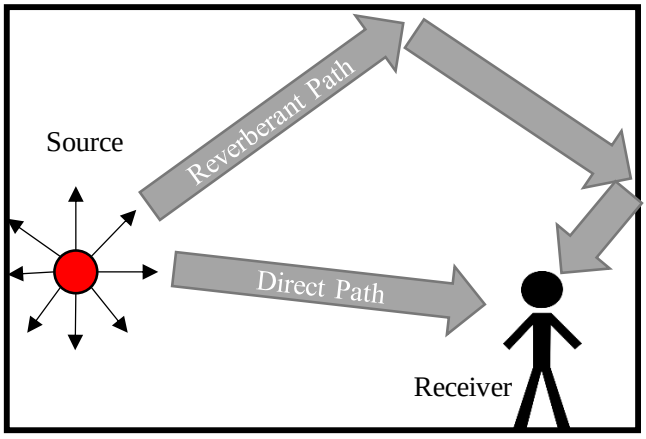
Process:
1. Calibrate the microphone data chain using the speakerphone or pistonphone. Calibrate at different SPL levels (94 dB and 114 dB) and discuss the importance of linearity. Change the gain of the signal conditioner to demonstrate sensitivity changes of the system with the same sensor.
2. Calibrate the accelerometer data chain using the calibrator. Have students calibrate using RMS and Peak acceleration. Change the gain of the signal conditioner and repeat.
3. Measure the background electrical noise floor spectra of the system using the 50 Ohm terminator at the data acquisition system and calibrate it using the sensitivity for the sensor.
4. Measure the background noise spectra in the facility (sound pressure and acceleration) using the now-calibrated sensors.
5. Compare the background noise spectra of the data system and the facility. Test at different gain settings to understand the importance of gain selection.

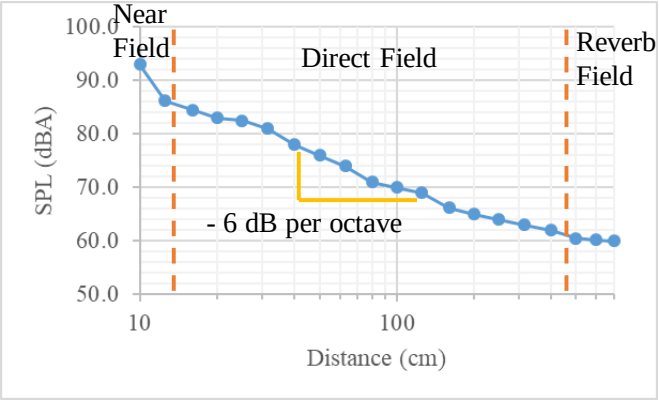
Outcomes and suggestions:
Students should understand that a good NVH test starts and ends with calibration of the entire in-situ signal chain and understanding of the ambient noise floor. It is helpful to discuss the 10 dB signal-to-noise ratio rule-of-thumb with students during this lab and, if possible, demonstrate a low SNR measurement compared to a high SNR measurement. Students should understand that analog gain can be used to increase the sensor signal above the noise floor of the data acquisition system, but not to separate desired signal from extraneous signals in the facility also picked up by the sensor. This lab provides a good hands-on introduction to use and handling of NVH instrumentation.

Figure 1. Experiment #1 – calibration and noise floor

Sound propagation: direct field vs. diffuse field

Motivation for the lab:
This lab will help students understand how sound propagates from a source. They will observe the difference between a direct field and a reverberant field. It serves as a good introduction to hand-held sound level meters and how to use them correctly. A simple demonstration of the source-path-receiver paradigm, this lab instills the fact that as the source is held constant, the receiver measurement changes due to a changing path.





Required equipment:
- Handheld Sound Level Meter (SLM) or free-field microphone and data acquisition system
- Sound source (a band limited white noise from a speaker works well)
- Tape measure or ruler
- Tape to mark positions on the floor

Process:
1. Place the source on the edge of a table. Using the tape and tape measure, mark out distances on the floor moving away from the source in a straight line. A room where you can get at least 4 m away from the speaker works best. Logarithmically spaced locations works best.
2. Calibrate the SLM and measure background noise in the room.
3. Play band limited white noise through the source so that the Sound Pressure Level (SPL) is about 90 dB(A) near the source.
4. Do not use tones as they will not produce good results due to destructive interference effects.
5. Have the students measure SPL using the SLM at the same height as the source at each horizontal location marked on the floor. Ensure students hold the SLM correctly so their bodies do not provide extraneous reflections.
6. Plot the SPL data versus logarithmic distance. The slope should be -6 dB per doubling the distance in the direct field and start to flatten out in the reverberant field.

Outcomes and suggestions:
Intuitively, students know that sources sound quieter as they move farther away from them. However, they don't know about the transition between the direct and reverberant fields in an enclosed space. This lab helps to reinforce the concept of the reverberation radius. It also helps the students to think in terms of logarithmic distances, common in acoustics, but not intuitive for the beginner. Discuss point source and spherical spreading and the inverse square law using these results to provide an Ah-Ha moment. Later in the class, these results can be revisited to discuss room absorption coefficients.

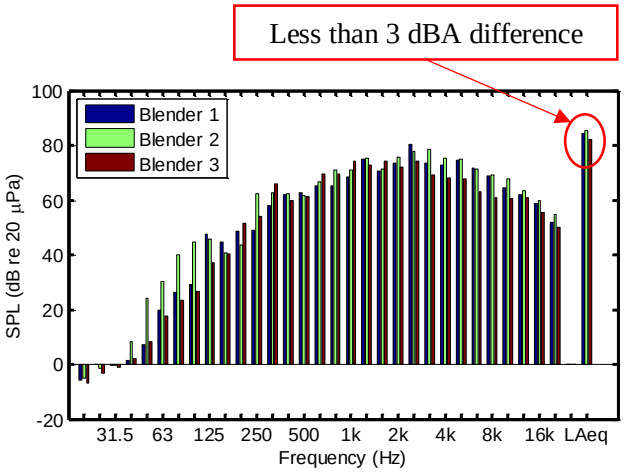
Figure 2. Experiment #2 – direct field vs. diffuse field

Product sound quality

Motivation for the lab:
Sound from mechanical devices is everywhere. The noise control engineer's job is to make these systems pleasant for the customer. Different customer segments have different expectations for product noise. Sound quality testing helps the engineer to match objective measurements with subjective customer feedback. One way this is achieved is through comparative measurements, or benchmark testing.

Required equipment:
- Free-field microphone and data acquisition system
- Several versions of a consumer product (blenders, hair dryers, power tools, etc.)
- A black sheet to conceal the products from the students





Process:
1. Develop a survey for the students. Ask questions like "Which product sounds more powerful?", "Which product sounds cheaper?", or "Which product would you buy based on sound?" Conduct a short jury study in class where the students can't see the products.
2. Compile the jury data and show the students the products. Have them guess which one had which sound based on looks. Reveal the sounds and discuss cost relative to sound.
3. Make operator ear sound pressure level measurements of each of the products. View the data in the time domain and as spectra and compute overall levels.
4. Try to identify what parts of the sound pressure spectra contributed to the results of the jury study and how the poorer rated products may be improved.

Outcomes and suggestions:
The students will appreciate the importance of sound quality in product design. It is surprising that loud products are usually the least expensive but also have lower power ratings than more expensive and quieter products. This is a great time to discuss the economics of NVH design and the different demands of different customer segments. Another observation is that more expensive parts with tighter tolerances typically produce better sounding products. We have conducted this experiment with 3 blenders ranging from $20 USD to $150 USD, and students almost always say they prefer to buy the loudest (least expensive) blender because it sounds like it is the most powerful, even though it is not.

Figure 3. Experiment #3 – product sound quality

Source sound power

Motivation for the lab:
Sound power is a source specific quantity that is important for the noise control engineer to understand. When trying to quiet a loud product, the engineer may quantify the product sound using sound power techniques. This type of measurement is independent of the path and receiver and is, therefore, a good way to characterize sources. This lab helps students to see the difference between sound pressure and sound power. Noise labeling is becoming a practice for some consumer products, e.g. dish washers.

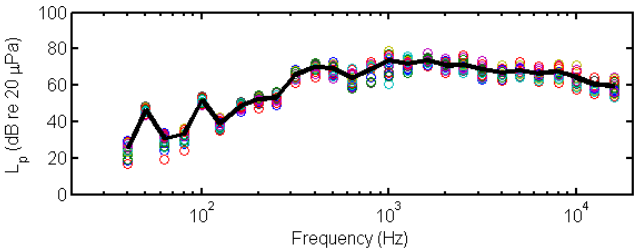
Required equipment:
- 2-4 Free-field microphones
- Data acquisition system
- Measuring device
- Small mechanical product to test
- ISO 3744 or ISO 3745

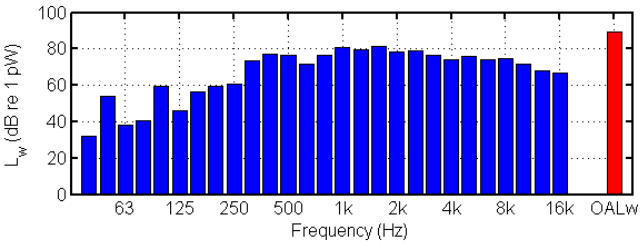
Optional equipment:
- Indexing turntable
- Anechoic chamber



7 bar compressor







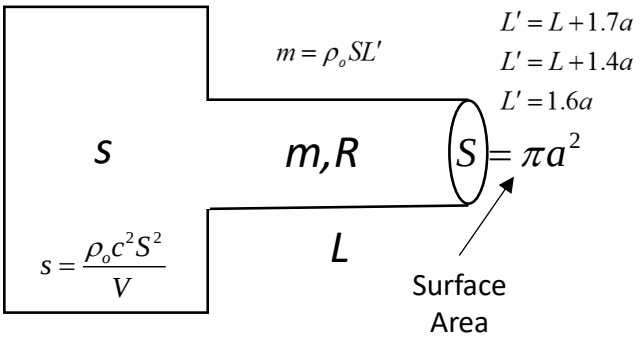
Process:
1. Set up the sound source on a hard surface and select a measurement radius (1-2 meters works well for small sources and high frequencies). The source can be put on the turntable for indexing.
2. Locate one microphone in a stationary position directly over the source. Place the other roaming microphones at locations from the standards in your measurement hemisphere.
3. Measure sound pressure on all of your microphones simultaneously.
4. Move the roaming microphones to all the other locations in the standard and record sound pressure level. Repeat as necessary, each time recording the stationary microphone as well
5. Compare all data from the stationary microphone position to ensure no changes over the test
6. Use ISO standards to compute sound power based on averaged mean-square sound pressure
7. Optionally, use other measurements techniques to compare and show the same measured sound power levels

Outcomes and suggestions:
Students will learn how to conduct a sound power test. Importantly, they will see the difference between sound power and sound pressure. They can also look at the measured SPL data as a function of measurement angle to observe product directivity. Using the standards will help students to understand how to read and follow a standard, a useful skill in industry. By using fewer than the required number of microphones, students will learn the challenges of making measurements with real-world restrictions. If you don't have an anechoic chamber, this can be done outside in a paved parking lot away from reflecting sources like cars or buildings.

Figure 4. Experiment #4 – source sound power

Acoustic resonators

Motivation for the lab:
Acoustic resonators are used to silence mechanical equipment through exhaust or intake pipes and ducts. They are an important tool for the noise control engineer. The fundamentals of a Helmholtz resonator will connect single degree of freedom (SDOF) vibratory systems with SDOF acoustic systems. Mode splitting of a tuned mass damper can also be demonstrated with this lab.



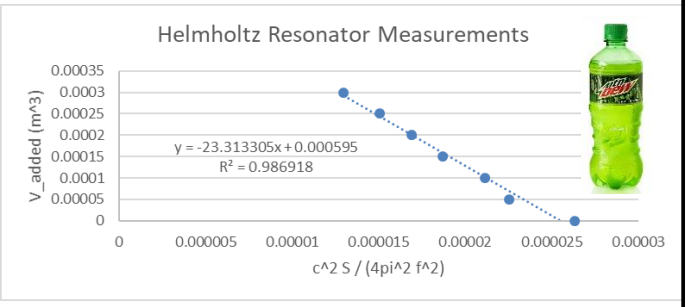
$$\omega_n = \sqrt{\frac{s}{m}} = c\sqrt{\frac{S}{L'V}}$$

$$V = V_o - V_{added}$$

$$V_{added} = -\frac{1}{L'}\frac{c^2 S}{4\pi^2 f_n^2} + V_o$$

Required equipment:
- Free-field microphone and data acquisition system with spectrum analyzer
- Beaker and graduated cylinder
- Beverage bottle

Option equipment:
- PVC pipe connected to a speaker and open on one end



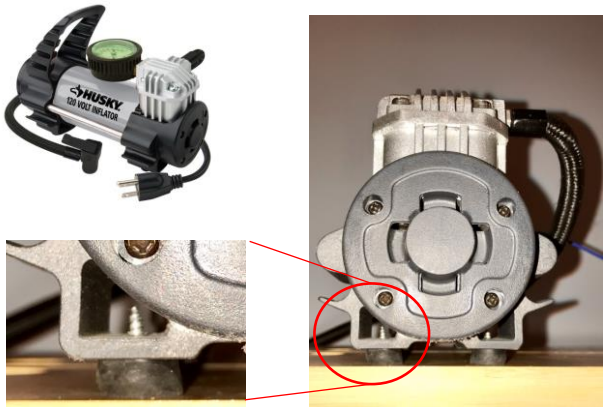
Process:
1. Explain the fundamentals of Helmholtz resonators
2. Hold microphone near the bottle neck and blow over the bottle (like a flute) to create a Helmholtz tone
3. Measure and record the frequency of the tone using the microphone and a spectrum analyzer
4. Add 50 mL of water to the bottle using the graduated cylinder and repeat step 3
5. Continue adding water in 50 mL increments and recording the frequency of the resonator
6. Linearize the natural frequency equation and plot added water volume (V_{added}) as a function of the variable shown above. The result is a line whose slope is the negative inverse of the effective neck length and whose offset is acoustic volume
7. Use this information to predict how much water would need to be added to attenuate a sound of known frequency

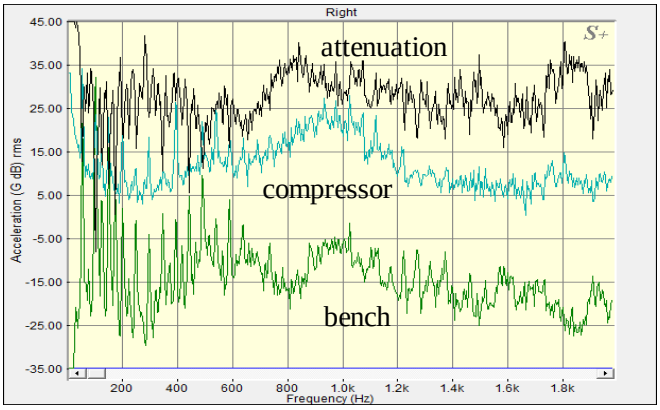
Outcomes and suggestions:
Students learn about Helmhotz resonators and relate to understood concepts of a SDOF vibratory system. Linearizing an equation to use a least-squares fitting approach is good to review in a practical situation. It is fun to create a game with step 7 using an driven open ended pipe with a hole in the side wall to insert the resonators. The students try to predict the amount of water needed to attenuate a tone and must account for the difference between a flanged and unflanged end condition. They compete with other groups to get the best attenuation and many groups try many times. When they get an increase in SPL at the end of the pipe, it's a good time to discuss mode splitting of tuned dampers.

Figure 5. Experiment #5 – acoustic resonators

Vibration isolation

Motivation for the lab:
Machinery vibration can easily be transmitted through floors and foundations and quickly become the source of structure-borne noise problems in buildings such as hotels, hospitals or schools. Refrigeration machines, chillers, air compressors, pumps, fans, boilers, rooftop HVAC equipment, can be vibration isolated so to limit the overall impact of vibration on people, structures, and other equipment nearby.





Required equipment:
- Two general purpose accelerometers, data acquisition system with spectrum analyzer software
- Mini air compressor
- Anti-vibration rubber mounts

Optional equipment:
- 1g handheld vibration calibrator

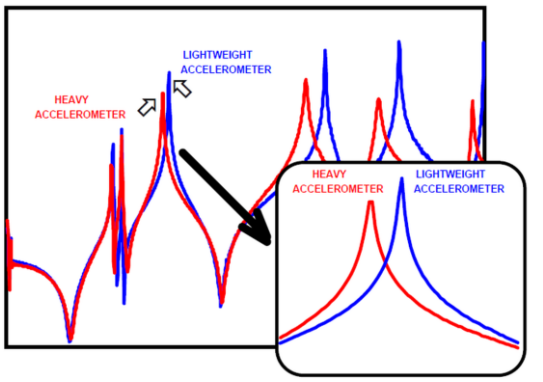
Process:
1. Check the data acquisition and measurement chain using the 1g hand-held shaker (see Lab 1)
2. Place the compressor on the laboratory bench, mount an accelerometer on the compressor (near its foot) and one accelerometer on the working bench.
3. Measure the vibration with the compressor turned off to stablish a baseline. Measure the vibration again with the compressor turned on and compare the difference
4. Install 4 isolation rubber mounts under the compressor and repeat the measurement with the compressor running. How does it look like?
5. Look at the vibration spectrum and its frequency content. Zoom in the lower frequencies and identify its fundamental frequency and its harmonics

Outcomes and suggestions:
1. Discuss the basic principles of vibration isolation and the equations of motion of a single degree of freedom spring-mass-damper system
2. Analyze the different regions of the transmissibility curve for an isolated system, discuss how the isolation system must be designed with a natural frequency much lower than any major frequency present in the compressor (vibration source)
3. Discuss how the principles of vibration isolation apply not only for isolating unwanted machinery vibration to be transmitted to its surroundings, but also to prevent environmental excitation (e.g. aerodynamic turbulences, highway and railroads, earthquakes) to impact critical equipment such as microscopes, telescopes, MRI (Magnetic resonance imaging) machines, etc.

Figure 6. Experiment #6 – vibration isolation

Using accelerometers and mass loading

Motivation for the lab:
In physics, the **observer effect** is the theory that simply observing a situation or phenomenon necessarily changes that phenomenon. Instrumentation is generally perceived as non-intrusive, but, in reality, it is. The accelerometer used to measure vibration will affect the vibration itself. As we know, the natural frequency of a structure is related to the square root of the ratio of stiffness to mass. This lab analyses the mass loading effect of an accelerometer while measuring the natural frequency of a structure.



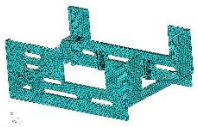
FRF with Two Different Accelerometer Masses

Required equipment:
1. Impact hammer with force sensor
2. Accelerometers with same sensitivity: lightweight teardrop style, general purpose accelerometer
3. Lightweight disk drive bracket
4. Bungee cords to suspend the bracket in a free-free boundary condition
5. Data acquisition system



1.2 gram vs. 27 gram ceramic vs. quartz 100 mV/g piezoelectric accelerometers




Disk drive bracket

Process:
1. Hang the bracket using the bungee cords and glue the small accelerometers under one of the edges of the bracket.
2. Tap the plate with the impact hammer on top, directly above the accelerometers and measure the Frequency Response Function between the force and acceleration (drive point measurement).
3. Repeat the experiment using the heavier accelerometer.
4. Compare the measurements and watch for natural frequency peaks (resonances) and any frequency shifts of these peaks.

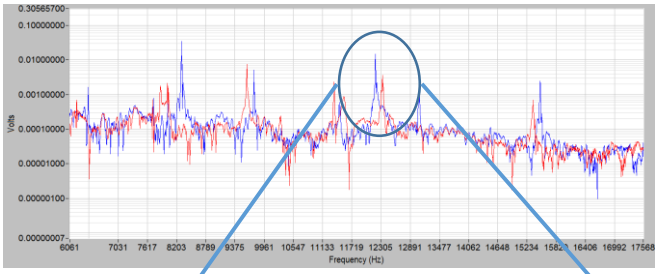
Outcomes and suggestions:
1. Discuss in general how the test set up can have an effect over measurement data especially on lightweight structures.
2. Review the frequency response function again and note how the higher frequencies experience a larger frequency shift while the two lower frequency peaks don't appear to be significantly affected by the mass of the accelerometers. Discuss how the mass loading effect won't be perceived if the accelerometer is mounted on a node of a mode.
3. Discuss different accelerometer design and its impact on accelerometer sensitivity and frequency range

Figure 7. Experiment #7 – accelerometers and mass loading

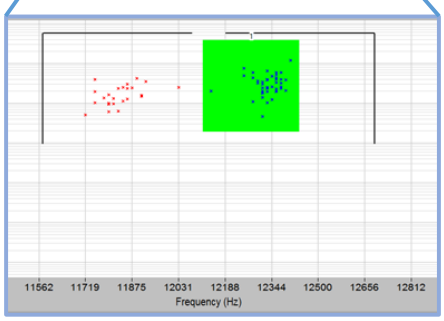
Fundamentals of mechanical resonance

Motivation for the lab:
Mechanical resonances occur when dynamic forces excite the natural frequencies of a structure. Resonance measurements can be used to understand the vibration behavior of structures, from musical instruments to machines, vehicles and buildings. An impact hammer or an electrodynamic shaker are ideal tools to excite a structure at all frequencies while a dynamic transducer such as an accelerometer or microphone can be used to capture the structure's resultant motion and acoustic response signature.

Required Equipment:
- Impulse hammer with force sensor
- Microphone (or accelerometer)
- 2 channel data acquisition system
- A sample structure. A metal part (vehicle component) works great
- Some rubber bands (or a piece of foam or exercise bands) to support the structure (free-free boundary condition)



Two parts, same geometry, different materials.





Statistical distribution a natural frequency of several metal parts with the same exact geometry, but made with two different types of steel.

Process:
1. Use a rubber band and a pencil to hang the sample metal part with one hand
2. Use the other hand to hit the metal part with the impact hammer
3. Measure the response using an accelerometer and using a microphone and compare the results
4. Repeat the impact measurement 5 times averaging out the measurements in the frequency domain
5. Repeat the measurements with the other sample and compare the results
6. Imagine how this measurement can be implemented to perform 100% inspection on hundreds of parts on the plant floor, as part of a an end-of-line quality check system. What type of information can be obtained from the test?

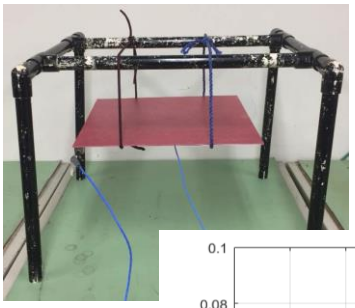
Outcomes and suggestions:
Students will learn how to perform impact testing to measure the natural frequencies of a structure. Explain the relationship between natural frequency, mass and stiffness, and how to use this relationship to tune a particular structure. Discuss how damping affec the width of the resonant peak. Introduce the concepts of Frequency Response Function (FRF) and Coherence Function measurements used in experimental modal analysis.

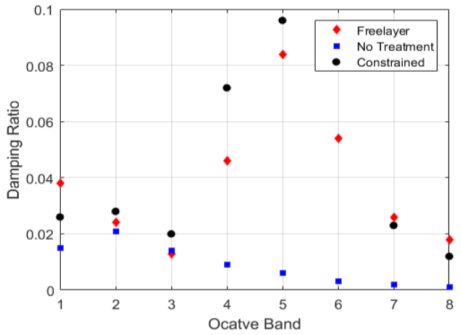
Figure 8. Experiment #8 – mechanical resonance

Principles of mechanical damping

Motivation for the lab:
Damping is an important concept for the NVH engineer. When mechanical structures are vibrating near resonance, large displacement, velocity, acceleration can occur. This can have adverse effects on the structure (such as fatigue and failure) or on people (such as high noise and vibration exposure levels). Damping is one way to limit high vibration levels. This lab will explore free-layer and constrained-layer damping treatments and ways to measure damping.

Required equipment:
- Instrumented impact hammer
- Lightweight accelerometer
- Thin plates (3), fiberglass or metal
  1. Bare plate
  2. Plate with free-layer damping
  3. Plate with constrained-layer damping
- Bungee cords to suspend the plate in a free-free boundary condition
- Data acquisition system





$c =$ damping coefficient

$\zeta =$ damping ratio $= \frac{c}{c_c} = \frac{c}{2\sqrt{km}}$

$\eta =$ loss factor $= 2\zeta$

$Q =$ Quality Factor $= \frac{1}{\eta} = \frac{\omega_n m}{c} = 2\pi \frac{\omega_n E_{Stored}}{\Pi_{Dissipated}} = \frac{f_n}{2}\frac{\partial \phi}{\partial f}$

T_{60} = Reverberation Time $= \frac{2.2}{f\eta}$

Process:
1. Hang the bare plate using the bungee cords or strings and glue accelerometers at the center and corner, under the plate
2. Tap the plate with the impact hammer on top, directly above the accelerometers and measure the Frequency Response Function between the force and acceleration (drive point measurement), and the time domain decay of the accelerometer
3. Evaluate damping as a function of frequency using several techniques (-3 dB bandwidth, slope of the phase at resonance, log decrement, reverberation time)
4. Repeat the experiment for the free-layer and constrained-layer damped plates
5. Discuss the importance of shear in damping treatments and discover why constrained-layer damping may perform better than free-layer damping

Outcomes and suggestions:
Students will learn the challenges in making a good damping measurement. Several techniques can be tested and compared. Pros and cons of each method can be evaluated. For example, if there are closely spaced modes at higher frequencies, the -3 dB bandwidth method may not produce accurate results due to high modal overlap. Using different methods also provides an opportunity to discuss data quality and selecting the right method based on the quality of results. Students should learn the differences between free-layer and constrained-layer damping, and that adding damping is an effective NVH mitigation technique when a system vibrates at a mechanical resonance.

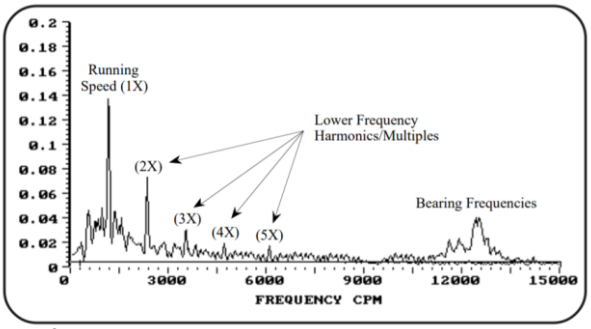
Figure 9. Experiment #9 – mechanical damping

Machine-Health monitoring

Motivation for the lab:
Vibration is a great indication of machine-health. It reflects the behavior of a machine's mechanical components as they react to internal and external forces. Vibration measuring and trending provides a picture of component wear, helping with maintenance planning, saving time and money by preventing unexpected machinery failure. Through vibration monitoring, and analysis, it is possible to detect common faults such as unbalance, mechanical looseness, misalignment, and local bearing or gear faults.



Required equipment:
1. Accelerometer
2. Data acquisition system
3. Running motor or other rotating machine
4. Laser tachometer



Ref.: SKF Vibration Diagnostic Guide (CM5003)

Process:
1. Mount the accelerometer to the machine using a mounting base or a magnet base
2. Mount the laser tachometer to measure the shaft speed of the device under test
3. While the machine is running, record averaged vibration data simultaneously with motor RPM Block sizes of 1-2 seconds work well with 20-50 averages. Synchronous averaging is also good to demonstrate here
4. Look at the overall RMS vibration levels in acceleration and velocity units
5. Look for peaks, shapes, and patterns present in the vibration signature spectrum
6. Try to identify and correlate those peaks with potential machine issues, e.g. high 1x RPM is an indication of out of balance, gear mesh frequencies, 2x RPM as indication of misalignment

Outcomes and suggestions:
Vibration is a big part of a condition based maintenance program. Instead of a "running to failure" approach, companies can take advantage of vibration measurements and analysis to perform machine-health monitoring and decide the right time for maintenance, not too early, not too late. The benefits of vibration monitoring include improved predictability, reliability, safety (e.g. avoid catastrophic failures), increased maintenance intervals, time and money savings, and peace of mind.

Figure 10. Experiment #10 – machine-health monitoring

3 Conclusion

We have described ten laboratory experiments that can provide engineering and science students with good hands on experience and exposure to practical aspects of sound and vibration measurements, equipment, and real world problems. The labs can be used in support or in addition to existing sound and vibration undergraduate classroom curriculum.

As it is not possible to cover all the details of every experiment in a short paper, the authors efforts are to provide a concise teaching laboratory framework covering most of the import concepts that will be valuable for the future sound and vibration practitioner. The authors would encourage the teaching community to use and modify these labs as needed, provide feedback, create and add labs that can be shared with universities and with the sound and vibration community around the world.

Acknowledgements

The authors would like to thank previous acoustics and vibration professors who motivated several of these experiments including Dr. Chuck Van Karsen, Dr. Jason Blough, Dr. Mohan Rao, Dr. Harold Evensen, Dr. William Shapton, Dr. Peter Avitabile, and others.

References

[1] H. Lord, W. Gatley, H. Evensen, *Noise Control for engineers*, McGraw-Hill, New York, NY, (1980).

[2] A. Frey, A. Coppens, J. Sanders, L. Kinsler, *Fundamentals of Acoustics*, John Wiley and Sons, New York, NY, (2000).

[3] S. Rao, *Mechanical Vibrations*, Pearson Education, London, England, (2018).

[4] S. Kelly, *Fundamental of Mechanical Vibrations*, McGraw-Hill, New York, NY, (2000).

Impact testing lightweight structures

R. J. Allemang [1], **A. W. Phillips** [1], **D. L. Brown** [1]
[1] Structural Dynamics Research Lab (UC-SDRL), Mechanical and Materials Engineering,
University of Cincinnati,, Cincinnati, OH 45221-0072
e-mail: **Randall.Allemang@uc.edu**

Abstract

Impact testing has always been an attractive method when exciting all types of structures to estimate frequency response functions (FRFs). For most structures, the option of using single or multiple input excitation with shakers is also a reasonable possibility. Lightweight structures made of carbon fiber construction, thin metal panels or plastics pose problems for both excitation methodologies. For these lightweight structures, the use of shaker excitation, even with very small shakers, is often undesirable since the attachment of the shaker(s) may result in constraining or altering the structure. While impact testing does not have these constraints, using very small excitation hammers create practical problems as well. Some of these are well known (like multiple impacts) and some are less well known (high energy signal distortion in the delta-sigma ADCs). This paper reviews some of these problems, shows examples of data collected demonstrating these problems and suggests ways that these problems can be minimized once the problems are understood.

1 Introduction

The validation of models for lightweight structures raises several practical problems that, while similar to past testing situations, raise new concerns with respect to the excitation of these structures. Lightweight structures are those made of carbon fiber or fiberglass construction, thin metal panels or plastics which have high stiffness to mass ratios with very low weight. These types of structures are used more frequently in various current products and need to be experimentally tested in order to validate an associated dynamics model. The experimental testing is critical since there is more uncertainty in these models due to the evolving nature of the materials and associated material properties. In any fiber based materials, the orientation of the fiber ply material in multiple layers, with different potential orientations of the fiber ply material, together with the fiber density and the amount of resin impregnation means that these materials, even in a simple validation coupon structure (for example, flat rectangular plates), are difficult to model accurately. Examples of these types of structures are shown in Figure 1 and Figure 2. Structures that have been recently tested include the structures in Figures 1 and 2 along with the blade for an aero-drone and military aircraft helmet.

Experimental testing of these lightweight structures is mostly conducted in a free-free environment to match an associated modeling boundary condition. Due to the lightweight structure, great care must be taken to minimize the effect of instrumentation on the dynamics of the structure. Small lightweight accelerometers are most often used to measure response. Non-contacting sensors like laser velocimeters are desirable but the amount of rigid body motion in a free-free test configuration frequently will cause the laser to fall out of registration. The small mass of an accelerometer can be added to the associated model as a small lumped mass for most validation exercises. As long as the mass is accurately located and not moved during the testing, small accelerometers are quite acceptable. Excitation is quite another concern. Small shakers are a possibility but the structural impedance associate with attaching the shaker, stinger and load cell is a significant problem. With free-free testing, the constraint that a small shaker adds to the test is notable and not easy to model. All in all, impact testing provides minimum issues when compared to small shakers.

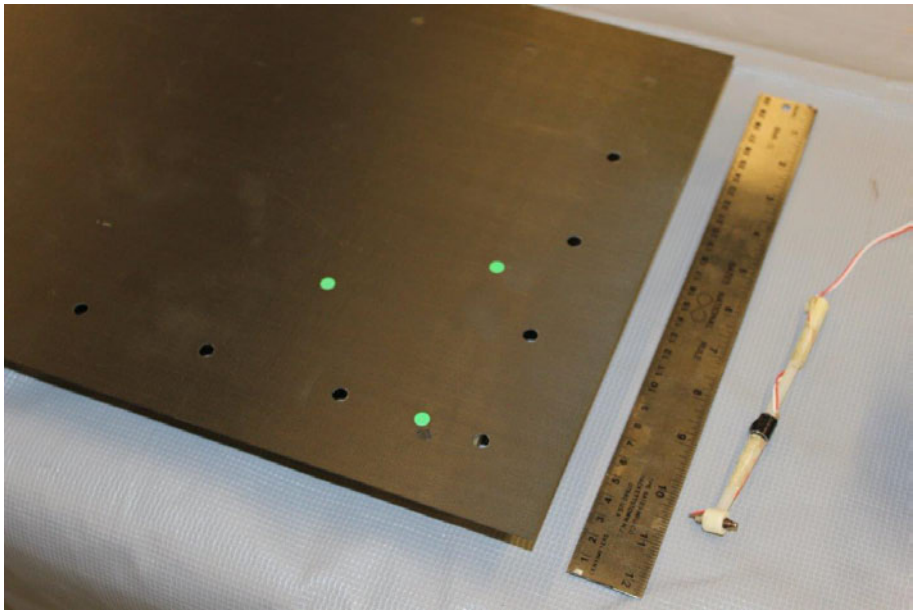


Figure 1: Validation Coupon Structure Example



Figure 2: Small Engine Intake Plenum Example

2 Impact testing (pulse testing, tap testing)

Impact testing has been used for structural dynamics testing since the late 1960s when the FFT was starting to be available in stand-alone testing equipment [2]. The seminal reference reviewing many of the advantages and limitations of impact testing is the paper by Halvorsen and Brown [5]. Since those early days, many references have appeared that discuss many aspects and nuances of impact testing applied to various test situations (see references [1]).

A recent paper [1] summarized the particular issues associated with impact testing and various digital signal processing hardware, particularly delta-sigma ADCs. This information is reviewed in the following sub-sections.

3 Data acquisition issues

Data acquisition concepts/issues related to impact testing and, particularly, modern delta-sigma ADCs need to be reviewed. While these modern ADCs effectively involve the same sampling-quantization result, the mechanisms that are used are a little different. This causes some particular concerns with respect to impact testing. Some of the subtle differences include anti-aliasing filters (both analog and digital), the location and purpose of the anti-aliasing filters, the number of bits in the ADC that are available to quantify the amplitude of the time domain signal, the detection of signals that are too large for the input gain chosen (overloads), the location of the detection of the overloads and the number of simultaneous channels. The year 1980 is chosen as the crossover point where the hardware began moving toward fewer sampling frequencies with fewer analog filters to the design of the current delta sigma (or sigma delta) ADC technology with only one sampling frequency and one analog anti-aliasing filter, relying increasingly on digital filtering. By 1980, most hardware systems had added the ability to pre- and post-trigger, the last piece of hardware and software technology that is commonly used in impact testing today. Note that most of the current impact testing guidelines and techniques were developed long before the introduction of current ADC hardware/software in the time period of 1970 to 1990.

3.1 Historical ADC hardware/software (pre-1980)

Figure 3 gives a block diagram of the typical hardware that was used prior to 1980 for each channel of the data acquisition. It is important to note that there were generally not more than four channels of simultaneous data acquisition in the Fourier transform analyzers of this time period. From the first commercial Fourier transform analyzers, the traditional frontend hardware input utilized a user selectable, low-pass filter (LPF) that was placed before the analog gain portion of the ADC to protect against the aliasing error (noted by location A in Figure 3). This filter was not generally part of the Fourier analyzer during this time period and the user had to choose the LPF based upon the Nyquist frequency that would be used in the ADC. The general rule was to choose the cutoff frequency of the LPF around 80 percent of the Nyquist frequency to eliminate the frequency information above the Nyquist frequency, thus avoiding the aliasing error.

Several design issues are important to note. The analog, anti-aliasing LPF needs to have significant roll-off to prevent the aliasing error based upon the 80 percent, Nyquist frequency rule and the same filter must be applied to all channels of data acquisition to prevent phase mismatch between channels. This requires an instrumentation quality filter to be both adjustable and to have the desirable pass band characteristics. The overload detection was generally a visual indicator on each channel (LED) but the software interface with the hardware rarely provided any feedback to the user. The overload detection circuitry that triggered the visual indicator was in the output of the analog gain section of the ADC or in the input of the digital section of the ADC (location B in Figure 3). The ADC typically had only 10-12 bits together with numerous input gain settings to allow for optimization of the analog signal to the ADC. The optional digital filter (noted by location C in Figure 3) was limited by the computer performance of the mini-computers available in these

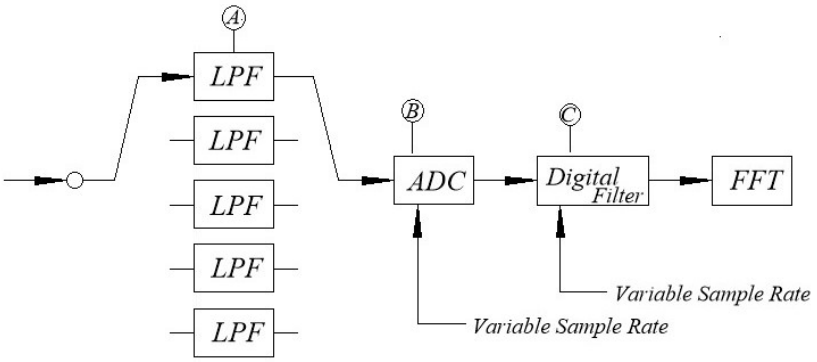


Figure 3: Historical ADC Design

data acquisition systems (computer speed, computer word size, computer memory, etc.). For this reason, the digital filter was only used to perform banded frequency analysis within the chosen Nyquist frequency bandwidth. With respect to impact testing, it is important to note that the analog, anti-aliasing LPF performed a secondary function that is distinctly different in the current ADC design. Since the cutoff frequency of the LPF filter was always set at 50-80 percent of the desired Nyquist frequency, this filter removed the frequency information (energy) above the Nyquist frequency on every signal before the signal entered the analog gain section of the ADC (at location B). This allowed the input gain to be set according to the signal frequency content that was in the users frequency band of interest. Note that in the mid 1980s, when DSA manufacturers first integrated the LPF into the frontend, it was not uncommon for the manufacturer to choose a maximum frequency (cutoff frequency equal to 50-80 percent of the Nyquist frequency) to protect the quality of the users data through an additional frequency guard-band (frequency band from maximum frequency to Nyquist frequency). The high cost of this ADC design had a significant cost per channel that made multiple channel analyzer designs cost prohibitive. The high cost was a function of both the design of the ADC itself and the requirement for an instrumentation quality filter for each ADC channel.

3.2 Current ADC hardware/software (post-1995)

Figure 4 gives a block diagram of the typical hardware that is now used for each channel of the data acquisition. The delta-sigma design currently used allows for a digital signal analyzer to have a much lower cost per channel since this design takes advantage of the delta-sigma ADC/DAC design that is widely used throughout many consumer electronics devices (CD and DVD players, HD-TV systems, etc.). The delta-sigma ADC design uses a different process that takes advantage of the bundling of the operations into a single electronics chip along with increased computer speed, computer word size and computer memory to give a superior final result (24 bits) at a much lower cost. This means that more channels can be made available at a lower and lower cost per channel. The changes in the design concept give the same final result but the operation is a bit different. In Figure 4, the significant difference in the delta-sigma design is the single sampling rate that is utilized. The ADC is a one-bit ADC with a sampling rate at a very high frequency when compared to structural testing, or even acoustic testing, requirements. The actual sampling rate is often in the 5-10 MHz region, (noted by location B in Figure 4) and is generally chosen at 128 times the effective sampling rate associated with the highest effective Nyquist frequency. Note that other oversampling rates are used in specialized application areas when the decimated frequency may be chosen to match a particular application need; for example in audio applications where the effective sampling rate is chosen to match the CD audio data rate. As an example, if the highest desired Nyquist frequency is 25 kHz, then the highest effective sampling rate would be 50 kHz. The actual sampling rate would then be 6.4 MHz. The 24 effective bits of the delta-sigma ADC, at the highest effective sampling rate, comes via the digital filtering and down-sampling that occurs

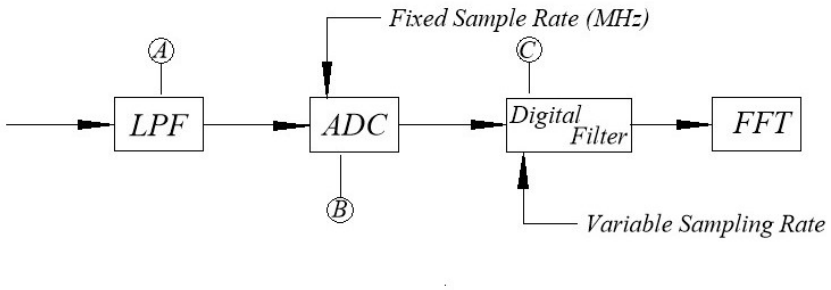


Figure 4: Current ADC Design

in the delta-sigma ADC chip beginning with the one bit sampling that occurs at 6.4 MHz. The user selected Nyquist frequency is determined by the digital filter characteristics (noted by location C in Figure 4). The difference in the delta-sigma ADC design that affects experimental testing, and particularly impact testing, comes from the analog, anti-aliasing LPF that is utilized (noted by location A in Figure 4). Note that the analog, anti-aliasing LPF (at location A) is positioned early in the signal processing and separated from the digital filter that is set by the user selected Nyquist frequency (at location C). In the example cited above, the cutoff frequency of the LPF can be chosen anywhere between 80 percent of the highest effective Nyquist frequency (25 kHz) up to 80 percent of the actual Nyquist frequency (3.2 MHz). Since the digital filter (at location C) removes the high frequency energy in the signal after the input gain and quantization, the input gain cannot be optimized as in the historical ADC design. In order to make sure that the characteristics of the LPF do not affect the magnitude and phase characteristics of any data in the frequency range up to the effective Nyquist frequency, vendors will often choose a less aggressive anti-aliasing filter design set at a frequency that is well above the effective Nyquist frequency. This gives an effective anti-aliasing design at a minimum cost per channel.

Regardless of the oversampling rate, the type of anti-aliasing filter that is used and/or the cutoff frequency chosen by the vendor in a delta-sigma design, the anti-aliasing filter no longer limits the higher frequency energy that may be present in impact testing. At a minimum, this cutoff frequency would be at 80 percent of the highest Nyquist frequency (25 kHz) in a digital signal analyzer. Most structural testing involving impact testing is at 5 kHz or below. While there are no issues involving the aliasing error, the anti-aliasing LPF now allows this high frequency energy from the impact input or response to reach the ADC.

The overload detection in a delta-sigma ADC design occurs at the same location as in the historical ADC design. The overload is detected at the output of the analog gain section of the ADC or in the input of the digital section of the ADC. The problem for impact testing is that the data signals now have energy in the frequency range well above the actual Nyquist frequency desired (100-500 Hz). This means that the analog, input gain on each channel will be set using the higher energy level of the frequency range up to the analog, anti-aliasing LPF. This is distinctly different from the historical ADC design. As an example, the delta-sigma ADC may require that the input gain be set to a plus/minus 10 volt range to satisfy the high frequency characteristics in the data (25 KHz or above) but the final time waveforms may be only a volt or less once the digital filter reduces the data to the desired Nyquist frequency (100 Hz). This means that the choice of the hammer and hammer tip, to limit the frequency content above the desired Nyquist frequency, is critical. This will be discussed further in a later section concerning auto-ranging, overloads and overload detection.

3.3 Other data acquisition hardware/software issues

There are a number of other issues concerning the delta-sigma ADC design that affect impact testing. With the move to a delta-sigma ADC design with 24 effective bits (more dynamic range than previous designs),

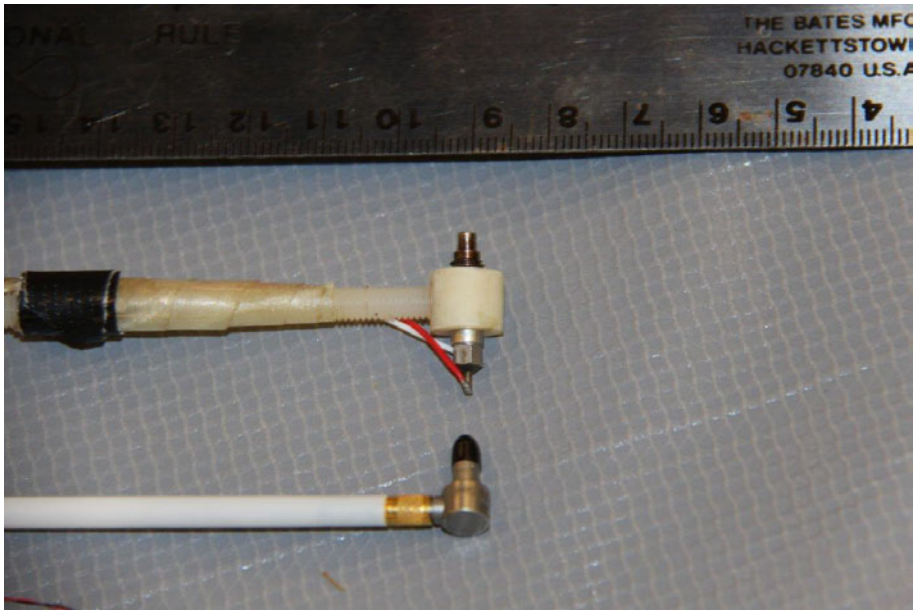


Figure 5: Typical Mini Hammers

most manufacturers have reduced the number of input gain settings as the number of effective bits in the ADC have increased.

While the need for fewer input ranges may be true for most steady state testing situations, it is another complication for impact testing since there are fewer input ranges to choose from to avoid the overload problem.

Other changes that are common in current ADC designs involve a number of trends. Most systems have more channels than previously with 8 to 16 channels very common. More channels means that visual checking of each channel for overload or undesirable characteristics is often overlooked or compromised. To reduce this problem, most overload detection is now integrated with the software so that a hardware overload is communicated to the data acquisition software. This allows for a software auto-ranging algorithm to assist the user in detecting overloads. Current data acquisition designs also offer the ability to pre- and/or post-trigger to make sure that the initial portion of transient signals, like those involved in impact testing, is not missed.

4 Data acquisition sensors

When testing lightweight structures the size and mass of the sensors needs to be very small as well. The hammers are nothing more than the tiniest load cell mounted on the end of a small plastic tube (see Figure 5). This configuration means that the hammer will be tapped on the structure to input the force (truly the meaning of a tap test). Alternatively, since the handle is now a small plastic tube, the input force can be achieved by bending or pre-loading the plastic tube and releasing the hammer head in a flicking motion. This gives a much higher force input.

While it is desirable to use non contacting response sensors, this is often not possible since free-free boundary conditions are most often used. Even the small force input will cause sufficient rigid body motion in the structure. This will often cause a non-contacting sensor like a laser vibrometer to lose registration with respect to the structure.

Generally, very small accelerometers like those in Figure 6 are used. These accelerometers must be very small with low mass in order to avoid alteration of the modal parameters, particularly modal frequencies,

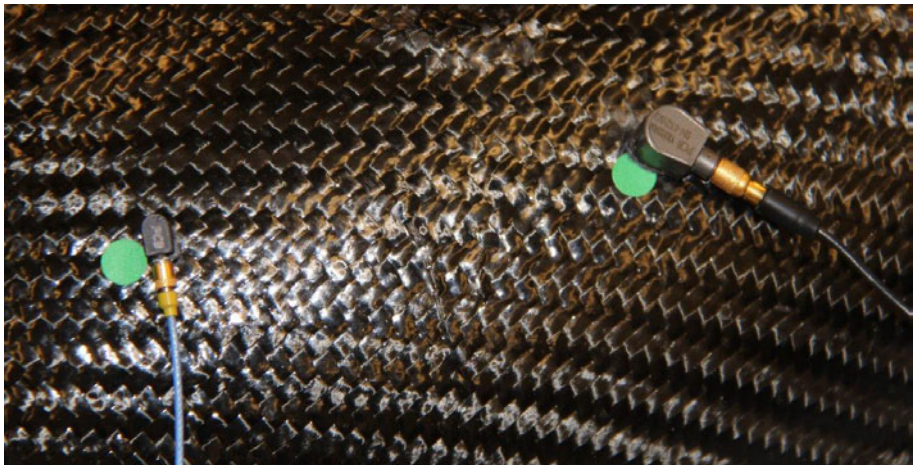


Figure 6: Typical Small Accelerometers

of the structure. It is very difficult to find small sensors with reasonable sensitivity (0.1V/g or greater). Normally very small accelerometers have very minimal sensitivity as they are used in shock environments. Low sensitivity is complicated by the small amplitude impacts (taps) as well as the limited number of input gains available in delta sigma ADCs.

5 Impact testing guidelines - revisited

Impact testing lightweight structures requires that all of the guidelines for traditional impact testing need to be reconsidered due the challenging characteristics of the testing environment. Figure 7 is representative of a typical test environment with a lightweight structure. Impact testing is normally performed with several response sensors held at fixed locations with the impact force moved to each degree of freedom (DOF) of interest. This form of impact testing is single-input, multiple output (SIMO) and is referred to as a multiple reference impact test. Since most modern data acquisition systems can be configured with four, eight or sixteen data acquisition channels, it is easy and efficient to utilize three, seven or fifteen references for each input DOF. This SIMO data, repeated at each input DOF is an excellent test method that acquires FRF data needed for multiple reference (polyreference) modal parameter estimation. The lightweight structure, an engine intake plenum in this example is supported on foam to approximate a free-free boundary condition.

Several impact testing guidelines are reviewed in the following subsections. These are not new guidelines but many are even more difficult to achieve, and may need to be redefined, when impact testing lightweight structures.

5.1 High frequency energy

Many of the problems associated with impact testing in delta sigma ADCs are a function of the analog to digital conversion process that occurs well above the user's frequency range of interest along with the summation and down-sampling that occurs when the digital signal is processed into the final frequency range of interest. The high frequency energy (from the user's desired maximum frequency to the analog aliasing filter's frequency cutoff) arises from the nature of the small hammer and resulting impact force spectrum. Due to the small physical nature of the impact hammer, it is difficult to adjust the force spectrum of the impact hammer. The only possible frequency spectrum adjustment may be utilization of a viscoelastic tip cover. The possible force spectrum versus frequency achievable in such a small hammer is shown in Figures 9 and 10.

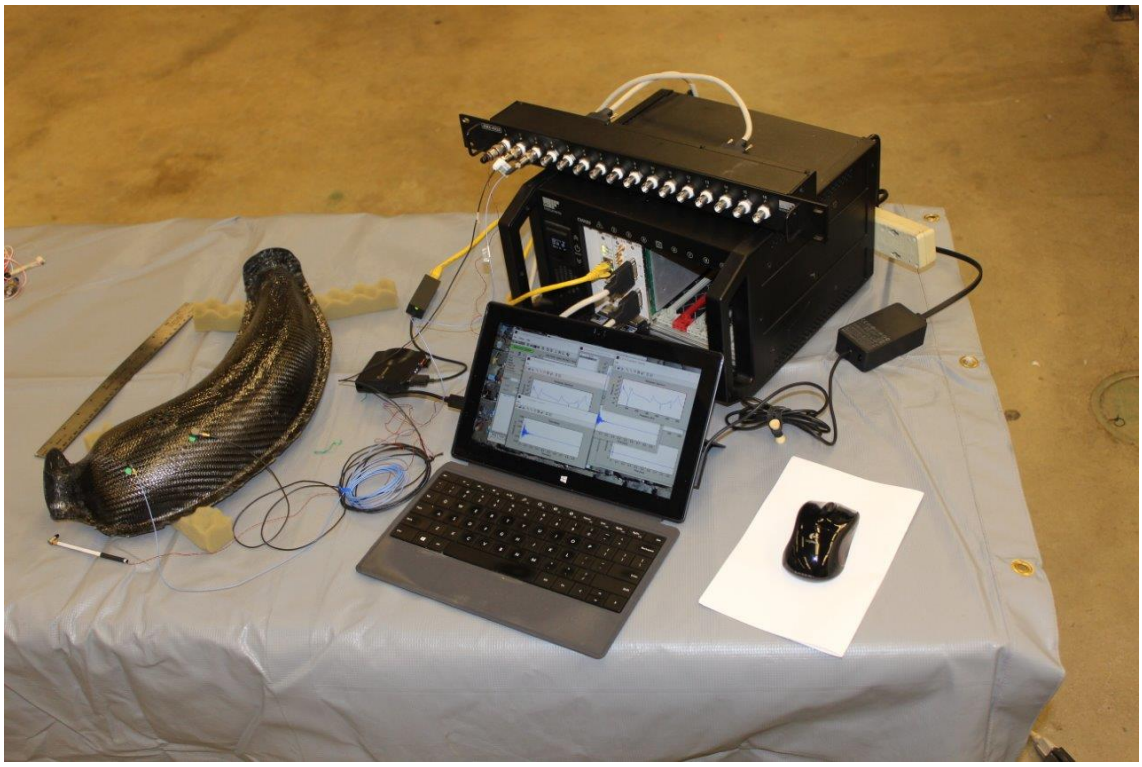


Figure 7: Typical Test Setup

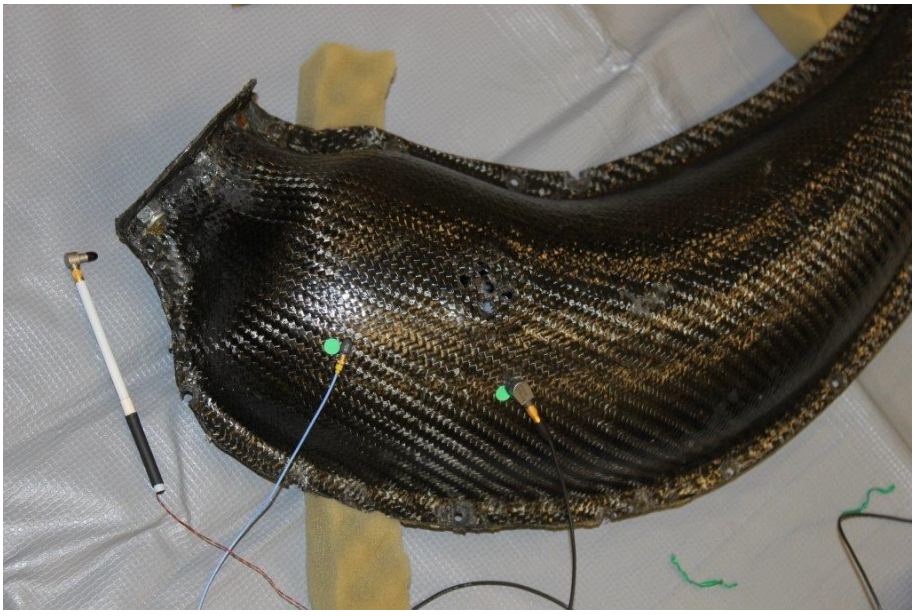


Figure 8: Typical Test Object, Engine Intake Plenum

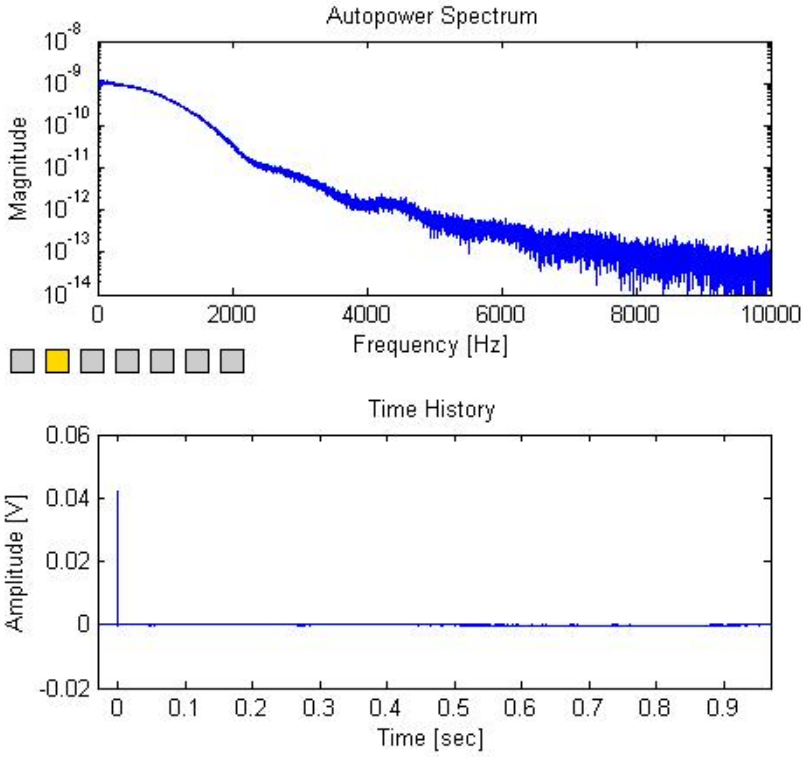


Figure 9: Impact With Tip Cover

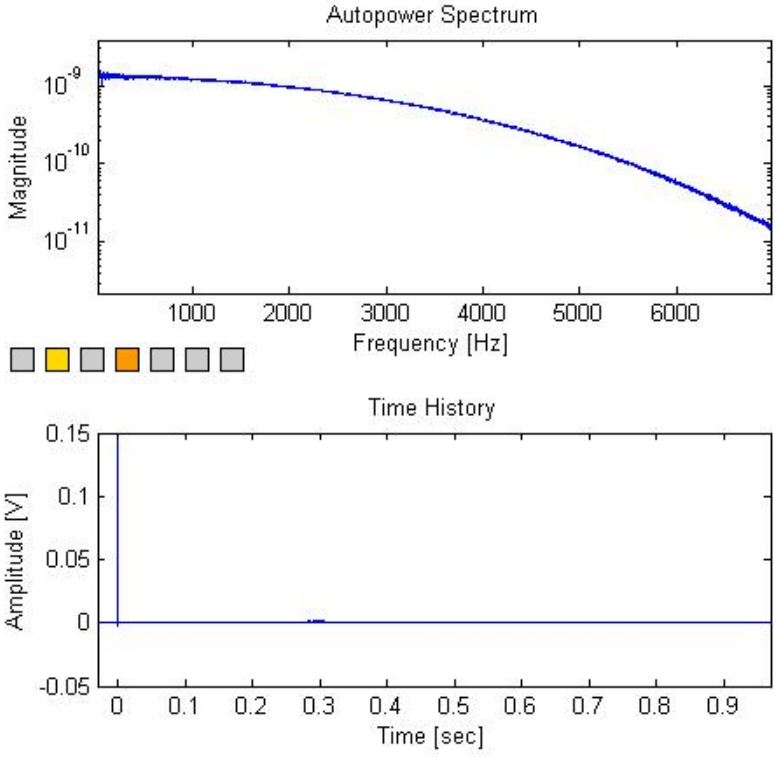


Figure 10: Impact Without Tip Cover

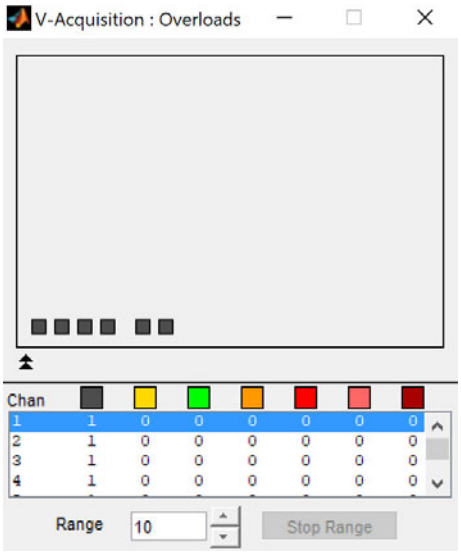


Figure 11: Overload Indication GUI

It is imperative that frequency range analysis be initially conducted at 5-10 times the user's desired maximum frequency in order to fully understand the nature of the force spectrum. This is particularly important in order to understand the overload characteristics of both the input and the response.

5.2 Overloads

Overloads can occur due to the voltage signal in the input and/or response for two different reasons. First, the measured voltage can too large with respect to the analog nature of the signal limited by the analog anti-aliasing filter frequency cutoff (above the input gain setting). This frequency is fixed as a function of the fixed sampling rate of the delta sigma ADC and may be as high as 3.2 MHz. This is often a quite high frequency relative to the frequency range of interest. Overload detection hardware/software can easily detect this situation but the clipping of the time domain signal is not normally visually observed due to the delta-sigma processing (digital filtering and summation) from one bit to 24 bits of dynamic range.

The second reason for which an overload can occur is due to the level of the high frequency energy associated with the magnitude of the frequency spectrum in the frequency region from the desired maximum frequency (approximately at the digital anti-aliasing filter cutoff) up to the analog anti-aliasing cutoff frequency. Overload detection hardware/software has a more difficult time detecting this situation. Likewise, if this sort of overload occurs at one of the downsampling/processing stages of the delta-sigma ADC, it will be hard to detect visually in the time domain signal.

For both overload cases, the user must trust the overload detection hardware/software. Sometimes this is a single overload indicator (red LED) that does not delineate the nature of the problem. Frequently, there may be more than one overload indicator as shown in Figure 11. In this example, there is a series of colored indicators that indicate the status of the voltage level for each channel.

The meaning of the colors of the status of the voltage signal, based upon the current input gain setting are shown in Table 1.

5.3 Dynamic range optimization

In general, for steady state data acquisition, it is desirable to optimize the input gain setting on each data acquisition channel to be above, but as close as possible, to the maximum voltage level of the signal on each

Color	Data signal meaning
black	Low data signal (below 10 percent)
yellow	Minimum data signal (below 50 percent)
green	Good data signal (50 - 100 percent)
orange	High data signal (above input range but below overload)
red	Analog overload
pink	Common mode ground signal overload
dark red	Digital overload (high frequency energy)

Table 1: Meaning of Overload Indicators

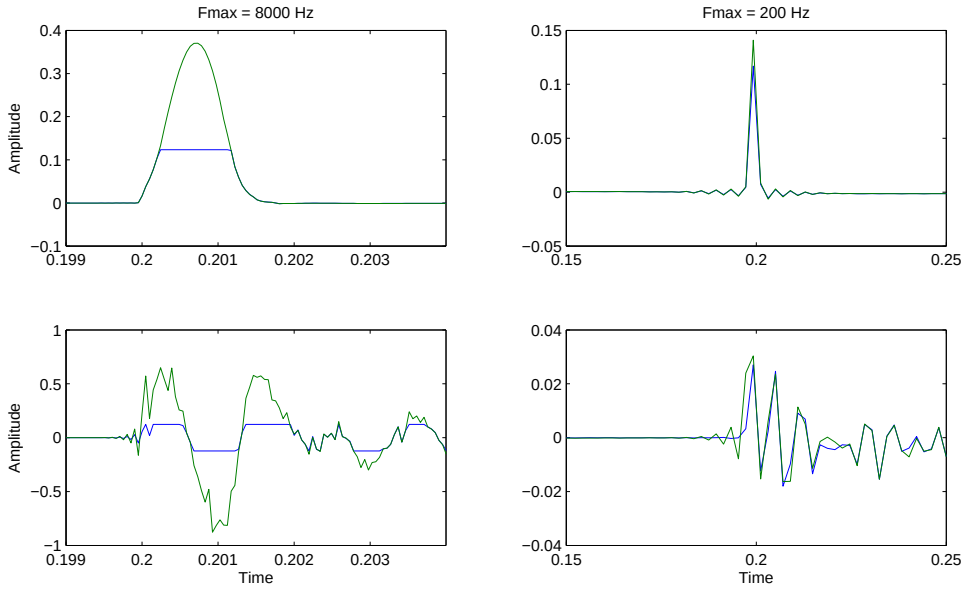


Figure 12: Time Domain Signal, No Filtering

channel. With fewer analog gain settings on each channel (no more than 5-10), this is more complicated than in historical data acquisition systems that had as many as 32 analog voltage gain settings. A further complication is that the time domain voltage signal is only observable after the delta-sigma processing has been completed. In the case of impact testing, the maximum level of the transient signal will often appear to be quite low when compared to the input gain setting for that channel. This occurs due to the high frequency energy that is above the maximum frequency of interest.

Unfortunately, the true levels of the analog signal cannot be observed in modern data acquisition systems. It is difficult if not impossible for the average user to turn off the digital and/or analog anti-aliasing filters to see what is going on. One way to check for the associated filtering problems is to ”tee” the input analog signal to a high frequency scope to observe the actual signal. This is not practical for the average data acquisition situation but can be instructive in order to understand what is really happening. Sometimes, this will be observable by viewing the data at an increased sampling rate as shown in Figure 12.

The green curves are the signals with a proper input gain setting. The blue curves exhibit an overload situation that should be captured by the hardware/software overload detection. The important observation is that at an improper input gain situation, there is little visual difference in the green and blue curves at the lower (digital) anti-alias setting associated with the lower maximum frequency (200 Hz) even for severely clipped data. Note that all data for Figure 12 was taken from the same two input/output analog signals.

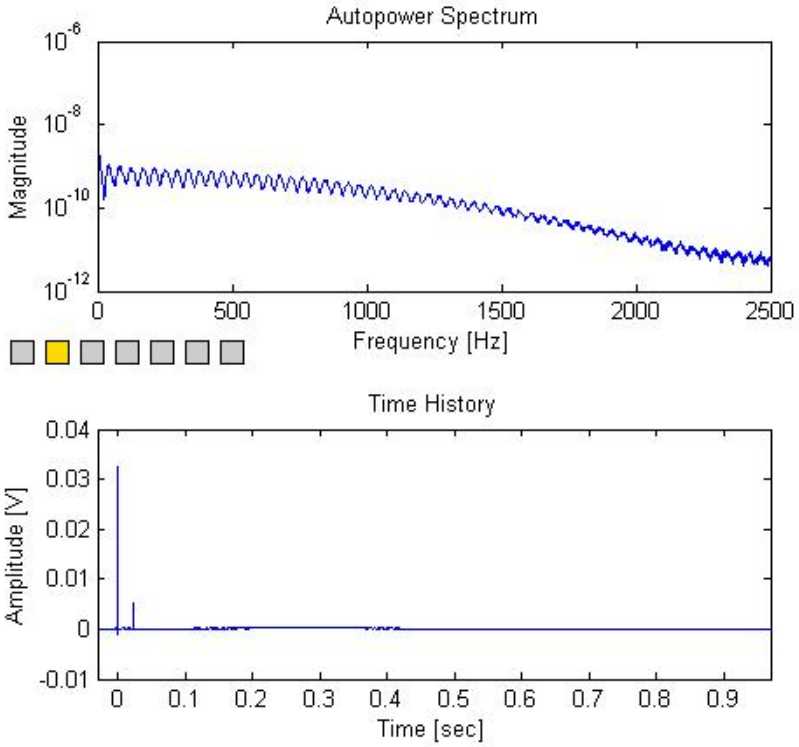


Figure 13: Double Impact Signal- Single Ensemble

For the above reason, it is very important to trust the analog input gain setting from the auto-ranging process (and very important to auto-range with each new input DOF location/direction). Frequently, this will mean using an input gain setting that gives a visual time domain signal that seems very small compared to the channel gain setting. This is also indicated in Figure 12 when the magnitudes of the acquired signals are compared, from the higher frequency sampling rate to the lower frequency sampling rate. The actual voltage levels (associated with the high frequency energy) require a gain setting four to ten times greater than the apparent voltage level at the lower digital anti-aliasing filter cutoff frequency associated with lower maximum frequency. This is detailed further in [1].

This situation means that the input gain setting will often be higher than what is apparently necessary. With the limited gain settings available, it is advisable to utilize the overhead or headroom feature associated with each channel of data acquisition during auto-ranging. This feature allows the user to set a percentage (above 100 percent) of the observed maximum voltage witnessed during auto-ranging to be used in the choice of the available input gain. This prevents getting into the voltage level region that is not easily detected by the hardware/software overload detection process. It is much better to give an gain setting that is larger than necessary rather than to risk the distortion caused by an undetected overload condition.

5.4 Multiple impacts

The general rule in impact testing is to avoid double or multiple impacts. With lightweight structures and small hammers, it is very difficult to not have multiple impacts. However, there is no theoretical reason that double or multiple impact data cannot be utilized. The fundamental rule is that the observed input and response must be totally observed. This is not a problem for the hammer input signal but for very lightly damped systems, having double or multiple inputs will extend the response signal in time and may cause leakage (time domain truncation) issues. In both cases, though, the conventional force and response

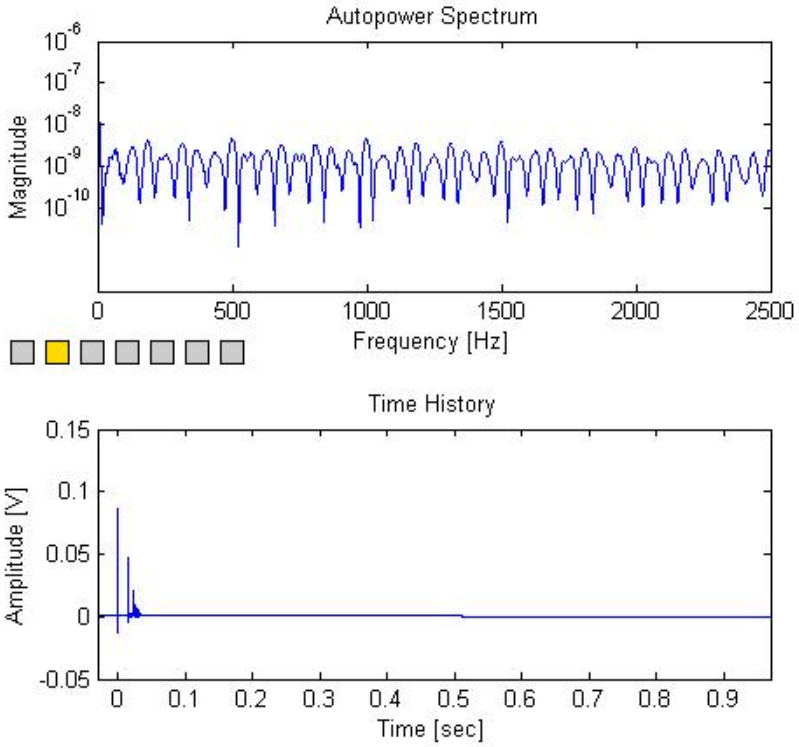


Figure 14: Poor Impact Signal - Single Ensemble

windows may need to be altered so that the windows do not remove portions of the signals that are valid. Figure 13 is a typical example of a double impact input signal.

If the spacing between the double impacts is not the same for each ensemble, the oscillation in the magnitude of the force frequency spectrum will be different for each ensemble. The average will then be a smoother auto power spectrum. As long as really poor impacts are not included, as in Figure 14, the result can be acceptable.

Figure 15 shows the result with three averages. Some evidence of the double impact data is observable but overall, this result is not unreasonable. With more averages, the result can become quite smooth. Impact data with ten ensembles normally smooths the low level oscillation in the FRF data. However, with the difficulty obtaining clean impact data on a lightweight structure, moving to more ensembles is sometimes not easy. The focus should be on taking clean data (low noise) with a reduced focus on avoiding double impacts.

5.5 Digital aliasing filter

Frequently, the digital anti-aliasing filter may be observed in the time domain signals, particularly on the input. The oscillation that is observed in the time domain signal in Figures 16 and 17 is the convolution of the transient data with the digital anti-aliasing characteristics. This is normal and should not be construed as a multiple impact signal.

5.6 Impact location issues

In addition to all the previously mentioned measurement challenges, the very nature of the test article affects the process of acquiring quality data. For structural objects made of layered materials, as can be seen in Figure 8, the surface variations can include surface roughness issues. Because of the very small size of

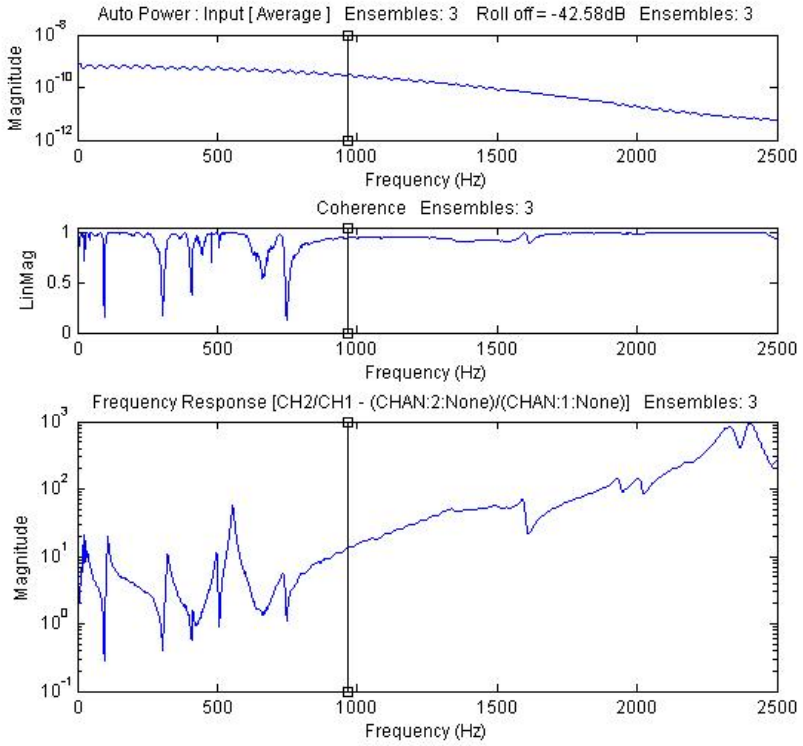


Figure 15: FRF: 3 Averages Including Double Impacts

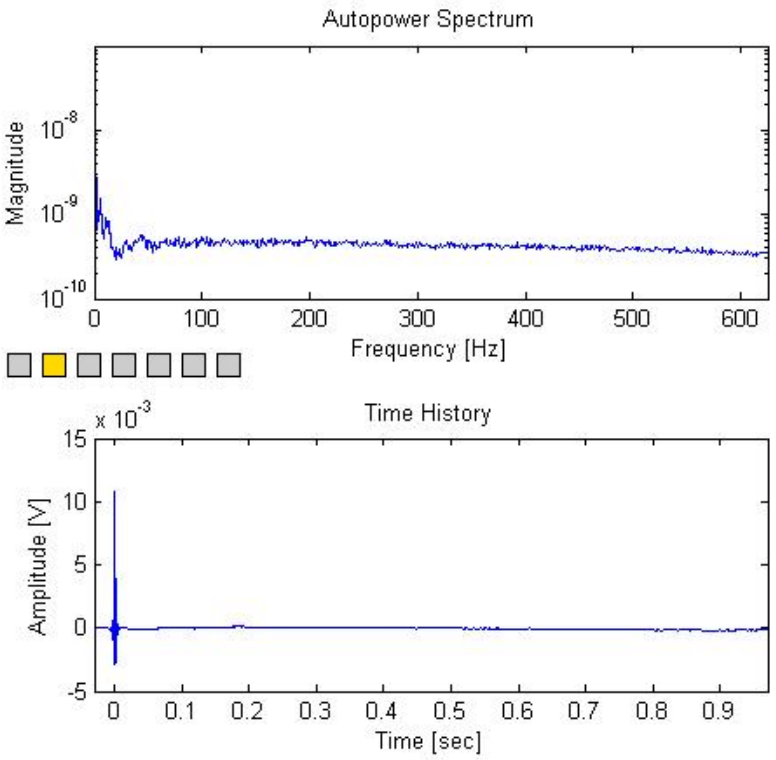


Figure 16: Impact with noticeable aliasing filter artifact

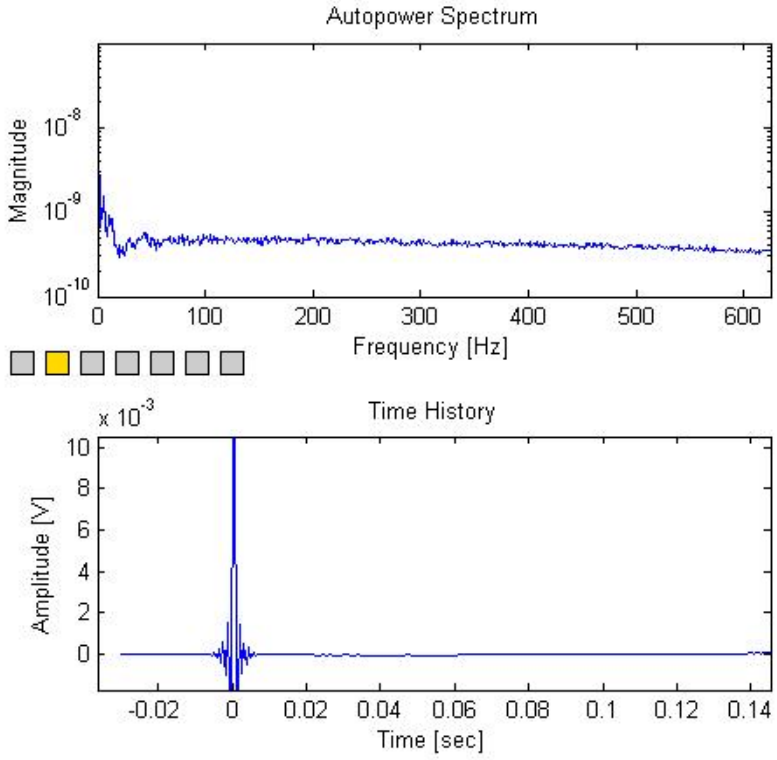


Figure 17: Impact with noticeable aliasing filter artifact

the impact hammer tip, it can become difficult to impact the structure to a desired force level or in the same location/direction consistently. A tip cover (viscoelastic) can widen the impact hammer contact and, in addition to altering the frequency content of the force spectrum, can make effects due to the surface roughness less noticeable.

The small size of these lightweight test structures also makes it very difficult to tap at the same location and in the same direction. Even small shifts in the impact location from ensemble to ensemble, which can be exacerbated by the limited manual dexterity of the tester, results in significant distortions in the computed FRFs. This distortion is generally accompanied by a loss of coherence and an obviously bad FRF measurement.

6 Conclusions and future work

In this paper, it has been shown that impact testing techniques on light weight structures can, just as in larger structures, be used successfully. However, the dynamic characteristics of these types of structures, often of small size, high stiffness, low mass and associated small sensors means that greater care must be used in these situations. Just getting consistent impact and response data, that satisfies known impact testing guidelines, is much more difficult. Good quality FRF measurement results can be obtained with great patience. However, the nature of these structures increases the need for careful testing techniques.

References

[1] Brown, D.L., Allemang, R.J., *Forty Years of Use and Abuse of Impact Testing: A Practical Guide to Making Good FRF Measurements*, Proceedings, Society of Experimental Mechanics-International Modal

Analysis Conference, (2015).

[2] Morse, I.E., Shapton, W.R., Brown, D.L., Kuljanic, E., *Application of Pulse Testing for Determining Dynamic Characteristics of Machine Tools*, 13th International Machine Tool Design and Research Conference, University of Birmingham, England, (1972).

[3] Hewlett Packard Corporation, *Dynamic Testing of Mechanical Systems Using Impulse Testing Techniques*, HP Application Note 140-3, (1972).

[4] Allemang, R.J., Graef, T., Powell, C.D., *Dynamic Characteristics of Rotating and Non-Rotating Machine Tool Spindles*, ASME Paper Number 73-DET-29,(1973). ASME Transactions, Journal of Engineering for Industry, Vol. 96, Series B, No. 1, (1974), pp. 343-347.

[5] Halvorsen, W.G., Brown, D.L., *Impulse Technique for Structural Frequency Response Testing*, Sound and Vibration Magazine, November, (1977), pp. 8-21.

[6] W.A. Fladung, *Multiple-Reference Impact Testing*, MS Thesis, University of Cincinnati, Department of Mechanical Engineering, (1994).

[7] Tamhane, S.K., *Feasibility of Impact Technique for Studying Nonlinear Systems*, Proceedings, Society of Experimental Mechanics-International Modal Analysis Conference, (1984).

[8] Sohaney, R.C., Nieters, J.M., *Proper Use Of Weighting Functions For Impact Testing*, Proceedings, Society of Experimental Mechanics-International Modal Analysis Conference, (1985).

[9] Chouychai, T., Vinh, T., *Impact Testing Of Non-Linear Structures*, Proceedings, Society of Experimental Mechanics-International Modal Analysis Conference, (1987).

[10] Tretheway, M.W., J.A. Cafeo, J.A., *Tutorial: Signal Processing Aspects of Structural Impact Testing*, International Journal of Analytical and Experimental Modal Analysis, Vol. 7, No. 2, (1992), pp. 129-149.

[11] Fladung, W.A., Brown, D.L., *Multiple Reference Impact Testing*, Proceedings, Society of Experimental Mechanics-International Modal Analysis Conference, (1993).

[12] McConnell, K.G., Varoto, P.S., *The Effects of Window Functions and Trigger Levels on FRF Estimations from Impact Tests*, Proceedings, Society of Experimental Mechanics-International Modal Analysis Conference, (1995)

[13] Fladung, W.A., *Windows Used for Impact Testing*, Proceedings, Society of Experimental Mechanics-International Modal Analysis Conference, (1997).

[14] Van Karsen, C.D., Little, E.F., *The Strengths of Impact Testing*, Proceedings, Society of Experimental Mechanics-International Modal Analysis Conference, (1997).

[15] Brown, D.L., *The Weaknesses of Impact Testing*, Proceedings, Society of Experimental Mechanics-International Modal Analysis Conference, (1997), pp. 1672-1676.

[16] Napolitano, K., N. Yoder, R. Brillhart, *A Comparison of Multiple Impact Testing Methods*, Proceedings, Society of Experimental Mechanics-International Modal Analysis Conference, (2012), pp. 331-345.

Vibration-based monitoring of the quality of clutch engagement in a forklift truck

A. Van Campen[1], T. Ooijevaar[1], C. Mannaerts[1], C. De Buyser[2], K. Janssens[3], A. Bartic[1]
[1] DecisionS, Flanders Make
Oude Diestersebaan 133, 3920 Lommel, Belgium
email: {**anke.vancampen, ted.ooijevaar}@flandersmake.be**

[2] Dana Belgium N.V
Ten Briele 3, 8200 Brugge, Belgium

[3] Siemens Industry Software
Researchpark 1237, 3001 Leuven, Belgium

Abstract
Professional drivers of off-road vehicles are often exposed to high levels of vibrations. The continuous exposure to those vibrations can lead to discomfort and physical injuries. Clutch engagement is one of the sources of vibrations. Accelerometers are in general appropriate sensors to measure vibrations. However, due to the historical cost of these sensors, current strategies to control the clutch engagement do typically not take vibration data into account, they mostly rely on rotational shaft speed data. Nowadays, affordable accelerometers are available. Yet, little is known about the feasibility to include accelerometer data into the feedback loop of the clutch control strategy. The goal of this study was to assess the feasibility of quantifying the clutch engagement quality based on accelerometer data and based on a comfort metric resulting from frequency-weighted accelerometer data. It has been demonstrated that the quality of the clutch engagement can be monitored based on accelerometer data acquired at the transmission of the vehicle.

1 Introduction

Driving an off-road vehicle, operators are nearly continuously subjected to vibrations resulting from one or multiple sources. Vibrations result from extrinsic sources such as the interaction between the tyres and the road surface, and from intrinsic sources such as the motor and the clutch system e.g. [1], [2], [15]. This study focusses on the vibration phenomenon that occurs during the clutch engagement process, referred to as judder [15], in a forklift truck. Clutch judder is a friction-induced vibration between sliding-contact masses resulting in (torsional) vibrations and oscillations of the driveline. They excite the vehicle body frame causing a forward-afterward vibration of the vehicle at low frequencies.

As any vibrations, judder is transferred from the excitation source to the driver's seat, where it can be sensed by the driver. The impact on the driver's comfort depends on the transfer path and the driver's subjective perception [8]. Especially in case of off-highway vehicles, such as forklift trucks, where high torques are transmitted between input and output shaft under strongly varying operating conditions, these torsional vibrations may become cumbersome in light of the driver's comfort as well as lifetime of the clutch components [10], [18].

Accelerometers are the dedicated measurement instruments to obtain information about vibrations. In automotive for example, the control of (semi-) active suspensions relies on the accelerometer data to minimize the amount of vibrations and hence, to maximize the driver's comfort [17]. Typically, control of clutch engagement in forklift trucks does not rely on accelerometer data. The reason for this is historical: accelerometers were too expensive, and as such, excluded from implementation on the transmission. Nowadays, low-cost accelerometers are available. This opens perspectives towards incorporation of

accelerometers in the control loop of clutch engagement to impose a smooth clutch engagement and hence to maintain driver's comfort in the future. Before we can close the control loop, as schematically presented in figure 1, we need to gain insight in the feasibility of using accelerometers to quantify the quality of clutch engagement which depends on the controller parameters. Earlier, [12] described the need of smooth clutch

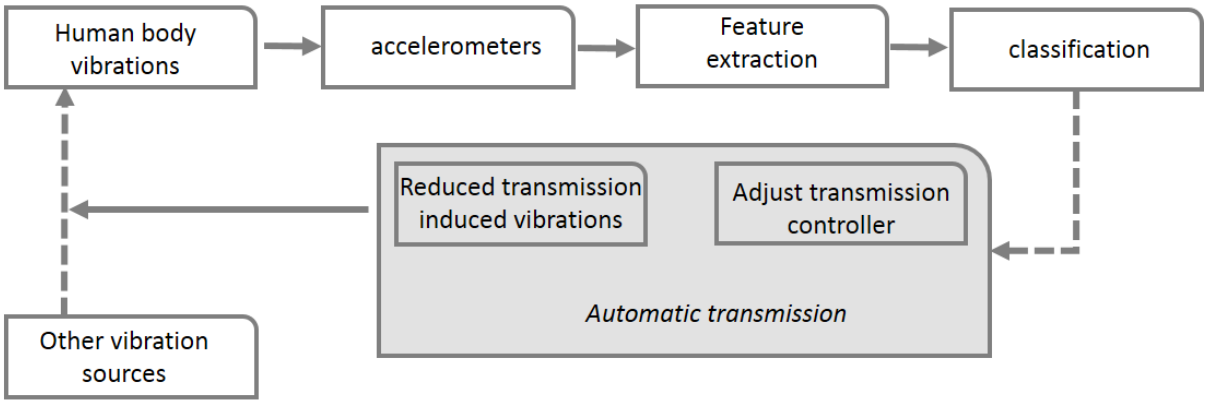


Figure 1: A schematic representation of the control loop, including virtual comfort sensor, to enhance the comfort of drivers.

engagement in relation to comfort in a tractor. They avoid to use accelerometers under the assumption that the signal is contaminated, hence not only capturing vibrations related to clutch engagement, but also resulting from other vibration sources. Apart from this, a major concern towards their approach lies in the presented reference slip profile. In this profile, discontinuities are present indicating that the jerk, being the second derivative of the slip, reaches infinity. As the jerk is strongly related to discomfort, a comfortable shift is achieved by minimizing the maximum jerk in the slip profile [18]. As a consequence of the choice of their slip profile, it is unlikely that the shifts in the tractor of [12] are perceived as 'comfortable'.

In our study, we start from the idea of a virtual comfort sensor which later on can be included in a control loop as schematically presented in figure 1. Accelerometers are mounted on the seat of the driver, and on the transmission. The accelerometers on the seat allow us to extract a comfort metric conform the metrics described in ISO standard 2631-1 [8]. The aims of our study are to gain insight in the feasibility of using (i) accelerometer data, and (ii) a comfort metric [8] to quantify the quality of clutch engagement in a forklift truck.

Our paper is organized as follows: *Section 2* provides background information on wet clutches and comfort metrics. The experimental set-up, the data acquisition and data processing are described in *Section 3*. *Section 4* presents the results, whereas *Section 5* provides the discussion of the results. Finally, *Section 6* summarizes our conclusion and lists future steps.

2 Background

2.1 Wet clutches and controller parameters

A wet clutch transmits power from input to output shaft when it is engaged. The ratio between input and output torque is defined by the size of the gears and is referred to as the transfer ratio. The gearbox of the forklift truck contains five wet clutches with different transfer ratios. Friction plates are installed on the shafts, coupling of the shafts is realized by pressing the plates together. Whenever the shafts are aligned, torque is transmitted.

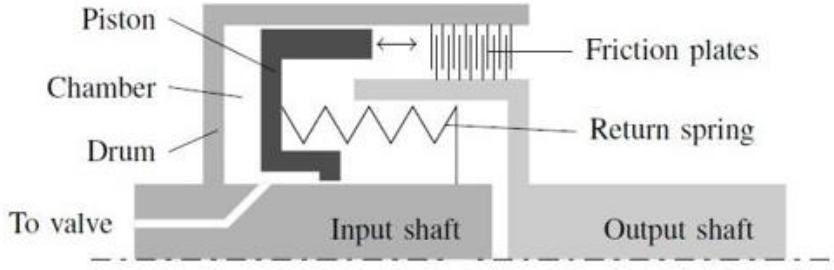


Figure 2: Schematic representation of a clutch, which transfers power from the input shaft to the output shaft when the friction plates are pressed together by internal oil pressure.

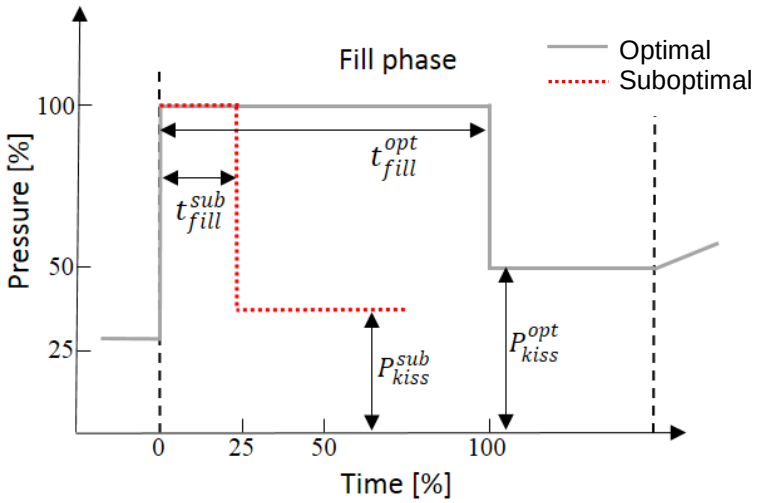


Figure 3: For a fill phase indicated by the vertical dashed lines, a good tuning (opt) of kiss (P) and fill (t) parameters is shown in solid line, and a suboptimal (sub) tuning of these parameters is shown by the dotted line. When tuning is suboptimal, (i) the speed of oil inflow is much higher than in the case of optimal tuning: the piston moves fast towards the friction plates; (ii) the pressure drop is high, the deceleration of the piston is fast. As a result, the impact of the piston on the friction plates is higher compared to optimally tuned parameters, and the level of vibrations induced by engagement of the clutch rises.

Figure 2 illustrates the physical appearance of a clutch. The input shaft of the clutch is connected to a drum, which is a hollow cylinder with grooves on the inside. Through these grooves, a first set of friction plates can slide. This set is referred to as the clutch friction plates. The second set of friction plates, can slide over a grooved bus that is connected to the output shaft. To engage the clutch, a signal is sent to the valve in the hydraulic line of the clutch. When the valve opens, oil flows to the clutch chamber which fills up and the pressure starts to raise. At a certain point in time, the pressure is sufficiently high to compress the return spring and the piston starts to move towards the friction plates. This is the so called filling phase of the clutch engagement and is controlled by two process parameters, a fill parameter and a kiss parameter. The fill parameter determines the speed of the oil inflow, the kiss parameter determines the pressure drop. When the piston has advanced far enough to start pressing the friction plates together, oil flows out the chamber and the pressure drops so that the impact between piston and friction plates would be minimized. At this moment, the slip phase begins and torque starts to be transferred from input to output shaft. At the transition from filling phase to slip phase, the dynamics change considerably, causing strong vibrations [18]. These torsional vibrations are transferred to the wheels resulting in a forward/backward vibration of the vehicle's body frame.

The fill and kiss parameter of the filling phase control the piston, hence the possible impact between piston and friction plates causing the vibrations and affecting the driver's comfort. A non-smooth clutch

engagement is the result of e.g. a fast oil inflow making the piston move fast forward and a high pressure drop avoiding a proper deceleration of the piston as illustrated in figure 3. As a result, the contact between piston and friction plates is harsh and clearly experienced by the driver.

2.2 ISO 2631-1 for comfort quantification

Discomfort is an important issue in automotive industry, and is regulated by e.g. the international standards ISO 2631-1 and -4 [8] on 'Mechanical vibration and shock: Evaluation of human exposure to whole-body vibration'. The standard basically models the generalized subjective comfort perception of humans to vibrations. It is applicable to motions transmitted to the human body via supporting surfaces, hence the seat surface and back of a driver's seat are relevant location of measurement. Because the driver's comfort is frequency dependent, the standard prescribes frequency weightings which should be applied depending on the location of the measurements and on the considered direction. For comfort, the frequency weighting curves are shown in figure 4: frequencies are attenuated below 0.5 Hz and above 80 Hz.

To combine vibrations in multiple directions, specific multiplication factors are provided to scale the frequency weighted vibrations again depending on location and direction. The vibrations are combined to a single comfort metric which reflects the perceived comfort level by the driver. The comfort metric can be interpreted in light of the discomfort scale provided in the standard ranging from not uncomfortable for a value below 0.315 m/s^2 to extremely uncomfortable for a value larger than 2 m/s^2. An in-depth description of the standard is presented in e.g. [13]. There are numerous studies on this topic aiming at capturing comfort perception of the driver under different circumstances and for different vehicles, see e.g. [11], [14].

3 Experimental Set-up

3.1 Experimental set-up and data acquisition

Experiments were performed with a Hyster forklift truck at the test infrastructure of Dana Belgium NV in Brugge, Belgium. The forklift truck was equipped with an automatic transmission comprising five clutches: forward, reverse and high, first and second.

Three tri-axial MEMS accelerometers (type ADXL326) were placed: one at the driver's seat surface, one at the back of the seat, and one on the transmission as shown in figure 5. The sensors measured linear acceleration in X- (forward/backward), Y- (lateral) and Z- (vertical) direction. For each clutch, a digital progress signal was logged indicating the state of the clutch. When this signal is high it indicates the instance the clutch reached the friction plates. A push button was pressed whenever an experiment was started and stopped. Data were logged at 3 kHz using a DEWESoft DAQ Sirius and DEWE-43 system. The clutch progress signals were also logged with the DEWE-43 system at 50 Hz on the forklift truck, corresponding to the sampling frequency of the transmission controller.

In the preprocessing step, we removed the DC offset of the vibration signals, which is intrinsic to MEMS-based accelerometers.

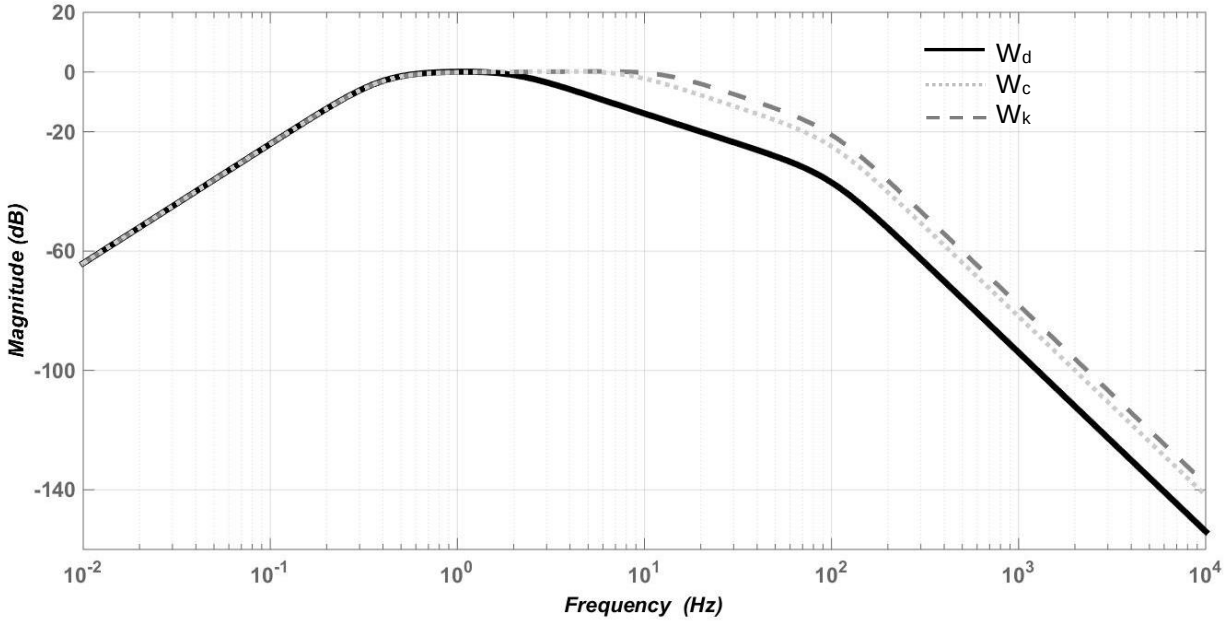


Figure 4: Frequency weighting filter curves for comfort vibrations measurement at seat and back of the driver's chair. The black is the W_d filter applied for the seat in X (scale factor: 1) and Y (scale factor: 1) and for the back in Y (scale factor: 0.5) and Z (scale factor: 0.4). The dotted silver line is the W_c filter applied for the back in X (scale factor: 0.8). The striped grey line is the W_k filter applied for the seat in Z (scale factor: 1).

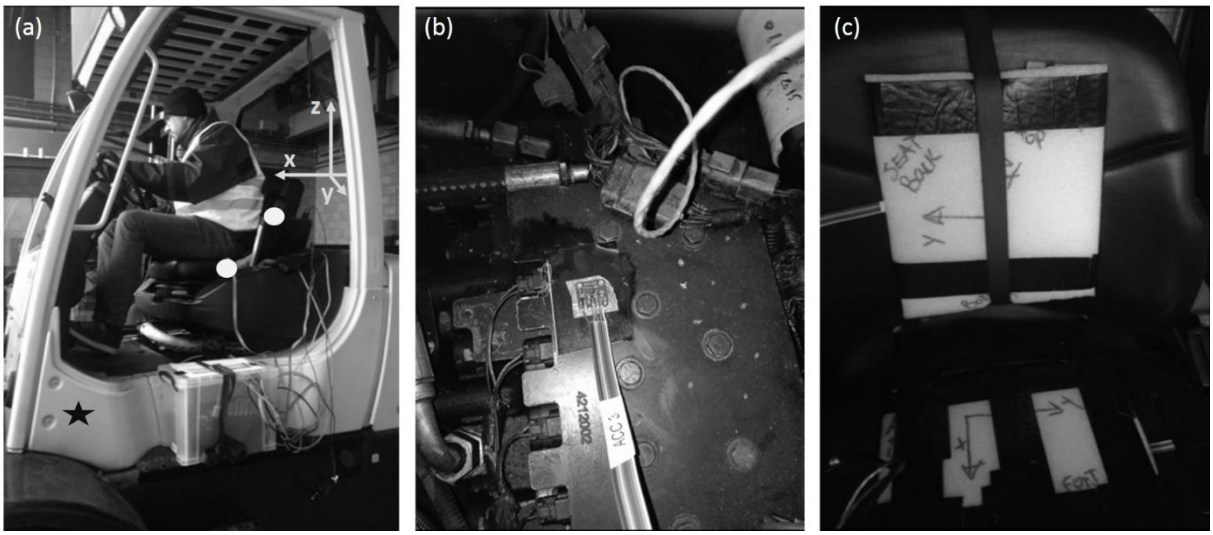


Figure 5: Experimental setup showing the mounting of the MEMS accelerometers and the DAQ system on the test vehicle. The dots in figure (a) indicate the position of the accelerometers at the driver's seat, the star represents the accelerometer at the transmission, XYZ-directions are indicated. Figure (b) shows the accelerometer on the transmission, figure (c) shows the mounting of the accelerometers on the seat.

3.2 Experimental protocol

We performed power reversal (PR) experiments during which the vehicle with slick tires, drove back and forward on a straight and flat track while the vehicle speed was rather low and the forklift was unloaded. We have focused our experiment on the shifts from gear 1 to gear 2 to evaluate the smoothness of the clutch engagement. In this case clutch 1 opens, while clutch 2 engages. Clutch forward remains engaged.

We perturbed these kiss and fill parameter stepwise from 0%, 33%, 67% to 100% in a 1/1 ratio, hence when kiss was perturbed with 33%, fill was also perturbed with 33%. The most optimal and suboptimal controller settings were empirically defined. The best case values (i.e. 0%) for clutch 2 were 0.86 s and 2.7 bar for the kiss and fill parameter respectively. The worst case values (i.e. 100%) for clutch 2 were 0.4 s and 1.6 bar for the kiss and fill parameter respectively. The effect of the fill and kiss parameter perturbation on the pressure profile is illustrated in figure 3. For each perturbation level, three experiments were conducted. An experiment contained 10 repetitions of the vehicle maneuver. Hence, in total, we performed 120 tests for the PR experiments. The order of the experiments was randomized as shown in table 1 in order to avoid bias by habituation of the driver.

Test no	**1**	**2**	**4**	**5**	**6**	**7**	**8**	**9**	**10**	**11**	**12**
Perturbation level (%)	67	0	100	33	67	0	100	33	100	33	67

Table 1: Randomized experimental protocol.

3.3 Data processing

Vibration data were captured during the power reversal tests. As we are interested in vibrations resulting from clutch engagement, we isolated the time intervals where the vibrations of interest occur in the signal, and hence the vehicle is excited by the clutch engagement. The rising edge of the progress signal indicated the start t_{start} of the clutch engagement. Typically, the influence of clutch engagement lasts 1.5 s. Hence, the end t_{end} of the clutch engagement is set at $t_{start} + 1.5\,s$. Upshifts are grouped per parameter perturbation level. Outliers defined as follows (1), were removed:

$$Q_3 + W\ IQR < Outlier < Q_1 - W\ IQR \tag{1}$$

Where Q1 and Q3 are the 25% and 75% percentile respectively, IQR is the interquartile range defined as the difference between Q3 and Q1 and W is the whisker, here set to 1.

In the time domain, we evaluated two different ways of signal processing. In the first case, we segmented and low pass filtered (2nd order Butterworth filter with cutoff frequency at 100 Hz) the accelerations for the upshift from 1st to 2nd gear in each direction. The low-pass filter was applied since the clutch-induced vibrations are expected in the lower frequency bands e.g. [15]. We used the root mean square (RMS) to obtain scalarized quantifications of the vibration levels. In the second case, we segmented the accelerations for the upshift from 1st to 2nd gear and calculate the comfort metric according to [8]. All vibration responses were also combined over the directions per sensor (2):

$$a_s = \sqrt{k_x^2\ a_{wx}^2 + \ k_y^2\ a_{wy}^2 + \ k_z^2\ a_{wz}^2} \tag{2}$$

With k the scale factors, a_w the frequency-weighted RMS accelerations, a_s the vibration total per accelerometer with $s = 1 \ldots S$ with S=3 here. The frequency weightings and scale factors are discussed in *subsection 2.2*. For the transmission sensor, we applied the same frequency weightings as for the seat surface sensor. Hence, we introduced a virtual seat surface which should enable us to compare the difference in comfort perception. The change in vibration levels are calculated for the different parameter perturbation levels. The optimal parameter settings are used as a reference.

In the frequency domain, the amplitude spectrum of the segmented signal is calculated using a fast Fourier transform, which converts the time-domain discrete signal in the frequency domain discrete spectrum. The spectra are compared between the perturbation levels and between the sensor locations.

4 Results

4.1 Low-pass filtered data

Figure 6 summarizes the results for the PR experiments for low-pass filtered accelerometer data. The combined amount of vibrations (shown in figure 6a) are more than twice as large for the transmission sensor compared to the back and the seat support sensor: e.g. for 100% perturbation, the levels are 3.3 m/s^2 for the transmission sensor versus 1.3 m/s^2 and 1.2 m/s^2 for the back and the seat sensor respectively.

As shown in figures 6b, 6d and 6f, the differences between the sensor on the transmission and the sensors on seat and back are between 0.44 and 0.49 m/s^2 in the X-direction, and between 1.83 and 2.12 m/s^2 in the Y-direction. Standard deviations on the vibrations levels resulting from back and the seat support sensors are between 0.18 m/s^2 and 0.23 m/s^2 in the X-directions, and between 0.07 m/s^2 and 0.13 m/s^2 in the Y- and Z-directions. Standard deviations on the vibrations levels resulting from transmission sensor are between 0.03 m/s^2 and 0.07 m/s^2 except for the Y-direction at 0% perturbation which is 0.11 m/s^2.

The difference in the amount of vibrations with respect to the optimal situation (0% perturbation) is shown in figures 6c, 6e and 6g. The effect of perturbing the controller parameters is manifested in the X-direction (forward/backward direction) for the back rest and the seat support sensor: the difference increases gradually between 0% and 100% perturbation to 0.15 m/s^2. The maximum differences in Y and Z are -0.04 m/s^2 and 0.02 m/s^2 respectively, although there is no specific correlation with the level of perturbation of the controller parameters. The effect of perturbing the controller parameters is clearly manifested in the X- and Y-direction (forward/backward and lateral) for the sensor on the transmission (see figure 6g). The differences increase gradually between 0% and 100% perturbation to 0.14 m/s^2 in X-direction and 0.25 m/s^2 in Y-direction. Maximum difference in Z-direction is -0.04 m/s^2. Again, for the Z-direction no specific trend is observed in relation to the level of perturbation of the controller parameters.

4.2 Comfort filtered data according to ISO 2631-1

Figure 7 summarizes the results for the PR experiments for accelerometer data filtered according to ISO standard 2361-1 [8] for the estimation of the perceived comfort. The combined amount of vibrations (shown in figure 7a) are the comfort metrics according to ISO standard 2631-1 [8] (i.e. frequency weighted and weighted for combining each direction). In terms of the comfort classification prescribed by the ISO standard, the vibrations at the seat are classified as ‘uncomfortable’, at the back as ‘a little uncomfortable’, and at the transmission (when evaluated as a ‘virtual’ seat surface) as ‘fairly uncomfortable’.

The average amount of frequency weighted vibrations in each direction is shown in figures 7b, 7d and 7f. For the transmission, vibrations related to comfort are between 0.33 m/s^2 and 0.44 m/s^2 (all directions) whereas standard deviations are between 0.11 m/s^2 and 0.19 m/s^2. For the seat support sensor, vibrations related to comfort are always lower than 0.12 m/s^2 with standard deviations lower than 0.04 m/s^2. For the back sensor, there is a gradual increase in the level of frequency weighted vibrations for all directions between 0.27 m/s^2 and 0.51 m/s^2 with a maximum standard deviation of 0.2 m/s^2.

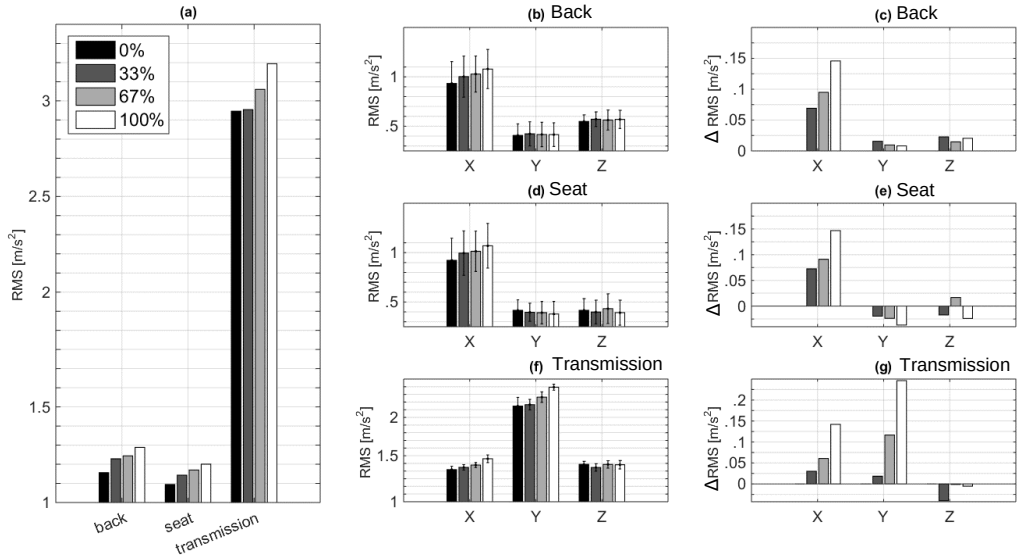


Figure 6: Vibrations levels as resulted from low pass filtered acceleration data (cutoff 100Hz) for three sensors: 'back' is placed on the backrest of the driver's chair, 'seat' is placed on the seat support of the driver's chair and 'transmission' is placed on the transmission of the forklift truck. (a) are the combined averaged vibration levels; (b), (d), (f) are the averaged vibration levels in each direction for back, seat and transmission respectively, standard deviations are provided by the error bars; (c), (e), (g) are the absolute differences between vibration levels under optimal controller conditions (0%) and the different levels of perturbation for back, seat and transmission respectively.

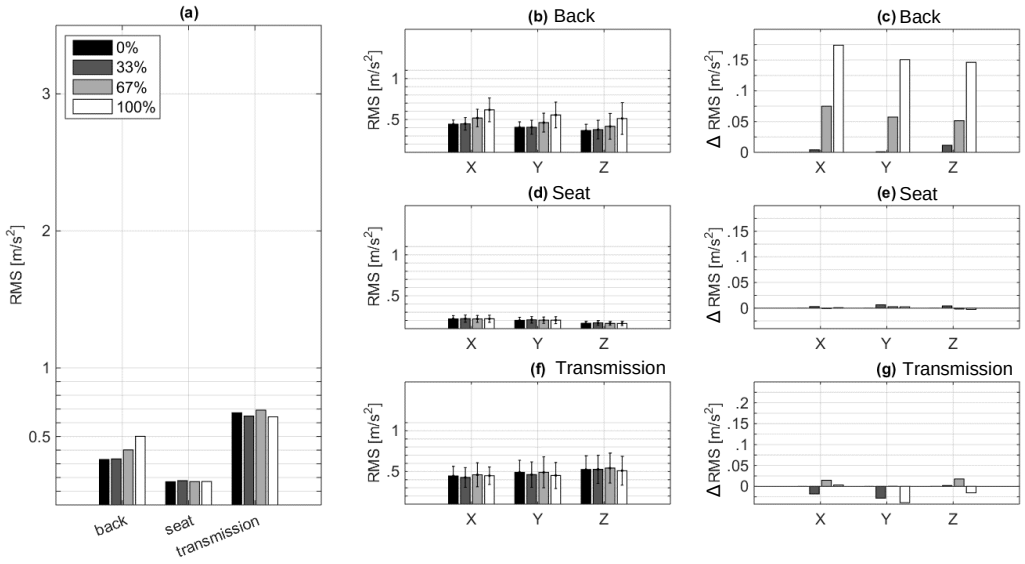


Figure 7: Vibrations levels as resulted from comfort metrics as described by ISO standard 2631-1 for three sensors: 'back' is placed on the backrest of the driver's chair, 'seat' is placed on the seat of the driver's chair and 'transmission' placed on the transmission of the forklift truck. (a) are the combined averaged frequency weighted (fw) vibration levels representing the comfort metric; (b), (d), (f) are the averaged fw vibration levels in each direction for back, seat and transmission respectively, standard deviations are provided by the error bars; (c), (e), (g) are the absolute differences between fw vibration levels under optimal controller conditions (0%) and the different levels of perturbation for back, seat and transmission respectively.

The differences in the amount of frequency weighted vibrations with respect to the optimal situation (0% perturbation) are shown in figures 7c, 7e and 7g. The difference increases gradually with increasing levels of perturbation for back sensor for all directions: up to 0.17 m/s^2 in the X-direction, up to 0.15 m/s^2 in the Y- and Z-direction. There is no consistent correlation to the level of perturbation observed for the seat and the transmission sensors after applying the ISO frequency weightings.

4.3 Amplitude spectra

The amplitude spectra of the accelerations measured at the seat, the seat back and the transmission are shown in figure 8. For the low-pass filtered vibrations in the X-direction, all sensors show the presence of a large amount of vibrations in the frequencies lower than 15 Hz in comparison to the Y- and Z-direction. Besides that, the vibrations measured at the transmission are dominated by vibrations between 60 and 80 Hz. Those higher frequency vibrations are also present in the spectrum of the seat support sensor (mainly in X-direction), but the amplitude is much lower compared to what is observed for the transmission.

The increased vibration amplitudes between 60 and 80 Hz are severely attenuated in the amplitude spectra of the frequency weighted accelerations that are used for the comfort analysis according to ISO 2631-1. There is some content left in the lower frequencies: in the X-, Y-, Z-direction peaks occur lower than 5 Hz, 3 Hz and between 3 and 15 Hz respectively.

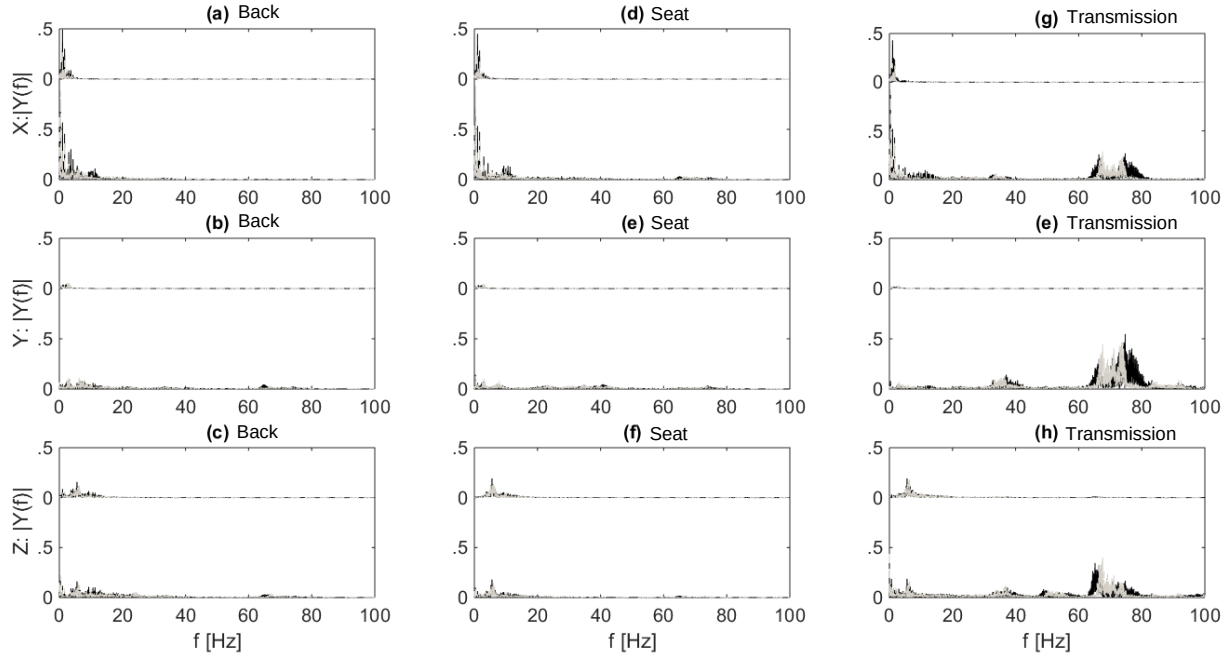


Figure 8: The amplitude spectra of low-pass filtered acceleration data and the frequency weighted acceleration data according to ISO standard 2631-1 are shown in all directions for back (a, b, c), seat (d, e, f), and transmission (g, e, h). In each subfigure, the lower spectra result from low-pass filtered acceleration data, the upper spectra result from the frequency weighted acceleration data. In every subfigure, the black spectra result from an experiment where controller parameters were suboptimal (100% parameter perturbation), the gray spectra result from an experiment where controller parameters were optimal (0% parameter perturbation).

5 Discussion

5.1 Low-pass filtered data

In the amplitude spectra of all sensors, we observed dominant frequencies in the lower frequency bands (< 15 Hz), mainly in the X-direction during clutch engagement of the 2nd gear. This is consistent with literature: Reitz et al. [15] state that forward/backwards vibrations mainly occur between 5-20 Hz. Khaksar et al. [9] found dominant frequencies below 10 Hz at the seat support in all directions for experiments with a tractor, albeit for a combined influence of excitations during the entire experiment. Ahlin et al. [1] state that low frequencies, < 7 Hz, are typically not well damped by the chair, and hence whenever those low frequency are measured due to clutch engagement at the transmission, they are undamped transferred to the driver's seat. Indeed, in our result we observe that the lower frequencies are barely damped between the transmission and the driver's seat. At the higher frequencies, we also observed an increased amplitude spectrum between 60 and 80 Hz for the transmission sensor in all directions. These higher frequency components are also shown in the spectrum (X-direction) of the seat support sensor, albeit to a lesser extent, and is barely visible in the spectrum of the back sensor. This suggests that its origin lies within the transmission, and that the vibrations are damped when passed to the seat surface, closest to the transmission, and even more damped when further passed to the back-rest [1]. Hence, the driver will therefore only be limited subjected to the vibrations within this 60-80 Hz frequency range. The results of Khaksar et al. [9] also show some increased frequency content mainly in X- and Y-direction between 40 and 50 Hz measured by accelerometers at the driver's seat. Yet, the authors do not discuss this as they focused on the dominant low frequencies. Altogether, our data indicate that the gear shifting mainly results in vibrations in the lower frequency bands (< 15 Hz), and between 60-80 Hz.

In the time-domain analysis shown in Figure 6a, we observed the highest combined vibration levels at the transmission sensor. Again this is expected as we measure at the source of excitation of the judder whereas these vibrations are damped when transferred to the driver's seat. For the sensors at the driver's seat, shown in Figure 6b, the vibrations in the X-direction (forward/backward) are dominant, whereas at the transmission the dominating direction is the Y-direction (lateral).

For the seat support and back rest sensor, we found that the vibrations levels in the X-direction rise as a function of the controller parameter perturbations (see Figure 6c). The rising trend is clearly present when the controller parameters are set to optimal versus the suboptimal parameters. In contrast, we observed no trend related to parameter perturbation in Y and Z direction. Yet, we measured vibration components both in Y and Z-direction, but these vibrations are most likely resulting from other sources of excitation as among others the road surface (mainly Z-direction) e.g. [1], [5], [16] or the engine [4], [16]. Hence, we can state that the main change in vibrations due to clutch engagement measured at the driver's seat is observed in the forward/backward X-direction. This observation matches with what has been reported in literature regarding judder related effects [7], [15].

For the transmission sensor, in contrast to the observations at the driver's seat, we found that the vibration levels rise as a function of the controller parameter perturbations in both the forward/backward (X) and lateral (Y) directions. The largest vibration levels are measured in the Y-direction. The sensor at the transmission is directly subjected to the torsional vibrations which result from the impact between the piston and the friction plates. These torsional vibrations are exciting the sensors in the X- and Y-direction. These vibrations are passed to the vehicles body, resulting in forward/backward vibrations which are captured by the sensors at the driver's seat. We can state that the main change in vibrations due to clutch engagement measured with an accelerometer at the transmission is observed in the forward/backward direction (X) and lateral direction (Y).

Considering the standard deviations at each sensor location, these are up to seven times larger for data resulting from the accelerometers at the driver's seat and seat back than compared to the accelerations measured at the transmission. The smaller the standard deviation, the higher the repeatability of the experiments. During our experiments, the accelerometer at the transmission appears to capture consistently the clutch behavior over repetitions for specific sets of controller parameters. The variability between

repetitions can at least partly be ascribed to the interaction with the road as this is not strictly repeatable [16]. The large standard deviations as observed for the accelerometers at the driver's seat indicate an inferior repeatability. Again this can be explained by the interaction between the vehicle as well as the movements of the drive itself. Altogether, we observed that the best results were obtained by the sensor at the transmission itself instead of the sensors at the driver's seat to monitor the quality of the clutch engagement.

5.2 Comfort filtered data according to ISO 2631-1

Comparing the amplitude spectra of the low-pass filtered data with the amplitude spectra of frequency weighted accelerations for comfort estimation, the amplitudes of the higher frequencies are strongly attenuated, as shown in Figure 8. For the lateral (Y) direction of the transmission, barely any frequency content remains. The evaluation of the accelerations measured at the transmission gives us insight in the transformation of the comfort perception between the source of excitation and the actual driver's seat. Also, we are not studying the comfort during the entire experiment, but specifically want to quantify the comfort as perceived during clutch engagement. Related to the time interval under consideration for comfort evaluation, the ISO standard does not define the length of the interval, but states that 'the reactions at various magnitudes depend on passenger expectations with regard to trip duration and the type of activities passengers expect to accomplish'. Earlier studies stated that the standard is applicable to off-highway vehicles [6] to quantify comfort perception. The standard is intensively applied for quantification of comfort both in lab setups (overview in [14]) as in outdoors experiments e.g. [9], [16]. However, the standard has never been applied to verify whether it can be used to relate the comfort metric to the quality of the clutch engagement.

In the time-domain, frequency weighted vibrations are largest at the back rest sensor instead of at the transmission sensor in contrast to the results obtained from the raw data. For the seat support and back rest, we can compare the levels of vibration to literature. E.g. Paddan et al. [11] report frequency weighted accelerations of 0.53-1.00 m/s^2 in the most severe axis of a lift truck; Khaksar et al. [9] found a combined metric at the seat support between 0.4-1.6 m/s^2 depending on the experimental conditions; Scarlett et al. [16] report frequency weighted accelerations between 0.5-0.75 m/s^2 at low speed for a tractor; Deboli et al. [5] report combined frequency weighted accelerations between 0.15-0.42 m/s^2 for a tractor driving on an asphalt track via a sensor at the cabin's floor close to the seat mounting point. Although our results show comparable values, there is no evidence about the feasibility of extracting information on the quality of the clutch engagement based on the comfort metric. Moreover, we did not find a difference in perceived comfort at the seat surface nor at the transmission as a function of perturbation of the controller parameters which is an effect of the frequency weighting. We can state that applying the ISO standard for comfort filters at least part of the information related to gear shift quality out. Therefore, it is not feasible to relying on the ISO comfort metric to identify the clutch engagement quality, but that it is more feasible to rely on the low-pass filtered accelerations as discussed in Section 5.1.

6 Conclusions

The aim of our study was twofold: analyzing the feasibility of monitoring clutch engagement quality (i) based on accelerometers mounted both on the driver's seat or/and the transmission and (ii) based on comfort metrics resulting from frequency weighted accelerometer data after applying ISO standard 2631-1 [8].

Our results showed that it is feasible to capture clutch engagement quality based on lowpass filtered accelerometer data. Relying on one accelerometer mounted on the transmission is the most promising approach given the high repeatability. To quantify the clutch engagement quality, both lateral and forward/backward accelerations should be taken into account. If one would choose to rely on accelerometers mounted on the driver's seat despite the lower repeatability, only the forward/backward accelerations should be taken into account.

In contrast, our results did not show a reliable correlation between the comfort metric defined according to ISO standard 2631-1 [8] and the quality of clutch engagement.

The fact that the quality of clutch engagement can be obtained with one accelerometer placed on the transmission, is particularly interesting for manufacturers of transmissions. The monitoring solution can, first of all, be used to gain insight in the quality of the clutch engagement. Secondly, it can also be used to optimize the working of an automatic transmission of an off-road vehicle to improve the gear shift quality and hence increase the comfort perception and reduce health risks of drivers. In the latter case, the monitoring system could be integrated in a feedback loop, as presented in the virtual sensor node in figure 1. Therefore, future work should contain the determination of the relation between the vibration level and the perturbation of the controller parameters for all clutches, and merging these results with a dedicated rule-based algorithm for clutch control as e.g. presented by Witters et al. [18].

Acknowledgements

The research from DEWI project (www.dewi-project.eu) leading to these results has received funding from the ARTEMIS Joint Undertaking under grant agreement n° 621353 and from the VLAIO.

References

[1] K. Ahlin, N.O.J. Granlund. *Relating road roughness and vehicle speeds to human whole body vibration and exposure limits*. International Journal of Pavement Engineering, Vol. 3 (2002), pp. 207-216.

[2] M. Bartram, G. Mavros, S. Biggs. *A study on the effect of road friction on driveline vibrations.* Proceedings of the Institution of Mechanical Engineers, Part K: Journal of Multi-body Dynamics. Vol. 224.4 (2010), pp. 321-340.

[3] G. Beard, M.J. Griffin. *Discomfort during lateral acceleration: Influence of seat cushion and backrest.* Applied Ergonomics. Vol. 44.4 (2013), pp. 588-594.

[4] R. Burdzik. *Research on the influence of engine rotational speed to the vibration penetration into the driver via feet-multidimensional analysis.* Journal of Vibroengineering. Vol. 15.4 (2013), pp. 2114-2123.

[5] R. Deboli, A. Calvo, C. Petri, G. Paletto. *Whole body vibration (WBV) transmitted to the operator by tractors equipped with radial tires.* Proceedings. International Conference Innovation Technology to Empower Safety, Health and Welfare in Agriculture and Agro-food Systems, Ragusa, Italy (2008).

[6] P. Els. *The applicability of ride comfort standards to off-road vehicles.* Journal of Terramechanics, Vol 42.1 (2005), pp. 47-64.

[7] N. Fatima, P. Marklund, R. Larsson. *Influence of clutch output shaft inertia and stiffness on the performance of the wet clutch.* Tribology Transactions, Vol. 56 (2013), pp. 310-319.

[8] INTERNATIONAL ORGANIZATION FOR STANDARDIZATION ISO 2631-1. *Mechanical vibration and shock—Evaluation of human exposure to whole-body vibration. Part 1: General requirements.* 1997.

[9] K. Khaksar, S.S. Mohtasebi. *Whole body vibration analysis of tractor operators using power spectral density.* Journal of Mechanical Engineering and Technology, Vol. 1.1 (2013), pp. 6-12.

[10] A. P. Ompusunggu. *Intelligent monitoring and prognostics of automotive clutches*. Diss. Ph. D. thesis, Katholieke Unversiteit Leuven, Department of Mechanical Engineering, Division PMA, Leuven (2012).

[11] G.S. Paddan, M.J. Griffin. *Evaluation of whole body vibration in vehicles.* Journal of Sound and Vibrations, Vol. 253 (2002), pp. 195-213.

[12] G. Panzani, M. Tanelli, S. Savaresi. *Transmission control for power-shift agricultural tractors.* American Control Conference 2010. IEEE (2010).

[13] F. Petre, F. Bouwens, S. Gillijns, F. Masse, M. Engels, B. Gyselinckx, K. Vanstechelman, C. Thomas. *Wireless vibration monitoring on human machine operator*. In: Communications and Vehicular Technology in the Benelux (SCVT), 2010 17th IEEE Symposium on. IEEE (2010) pp. 1-6.

[14] S. Rakheja, R.G. Dong, S. Patra, P.E. Boileau, P. Marcotte, C. Warren. *Biodynamics of the human body under whole-body vibration: Synthesis of the reported data.* International Journal of Industrial ergonomics, Vol. 40 (2010), pp. 710-732.

[15] J. Reitz, W. Biermann, P. Kelly. *Special test bench to investigate NVH phenomena of the clutch system.* Inst fur Kraftfahrwesen Aachen, 1999.

[16] A. Scarlett, J. Price, R. Stayner. *Whole-body vibration: Evaluation of emission and exposure levels arising from agricultural tractors.* Journal of Terramechanics, Vol. 44.1 (2007), pp. 65-73.

[17] M. Witters. *Nonlinear black-box identification and control of a semi-active damper for passenger cars.* Diss. Ph. D. thesis, Katholieke Unversiteit Leuven, Department of Mechanical Engineering, Division PMA, Leuven (2010).

[18] M. Witters, A. De Mare, S. Vandenplas, M. Versteyhe. *Experimental validation of iterative learning control for power shifts on a transmission with wet clutches in a heavy duty forklift.* Proceedings of The 14th Mechatronics Forum International Conference Mechatronics June 16-18, Karlstad University, Sweden (2014).

Experimental evaluation of a new two-microphone method for the mode detection and radiation of broadband noise in ducts

J. Chen[1, 2], J. Melling[1] and P. Joseph[1]
[1] Institute of Sound and Vibration Research,
University of Southampton, Southampton SO17 1BJ, UK

[2] Department of Engineering, University of Leicester,
University Road, Leicester, LE1 7RH, UK
e-mail: **jc734@leicester.ac.uk**

Abstract
This paper attempts to experimentally evaluate a new two-microphone measurement technique for determining the modal amplitude distribution and far-field radiation of the broadband noise from hard walled ducts. The new technique is based only on the complex coherence function of the acoustic pressure measured by two closely spaced microphones located at the duct wall. Particularly, the cuton ratio, rather than an index couple of azimuthal and radial mode orders (m, n), was introduced to represent the behaviour of individual propagating modes. The hard-walled circular duct was excited at one end by a diffuse sound field, and the other open end is terminated within an anechoic chamber with which to measure the radiated sound field. The measured complex coherence was used to infer the mode amplitude distribution and far field directivity, based on the underlying Fourier transfer relationship. The results verified the good agreement between direct measurements of sound power and directivity.

1 Introduction

Various common noise sources radiate sound into finite-length ducts, from which the sound escapes into the far field via radiation from an un-baffled open end. Examples are exhaust mufflers, large exhaust stacks, and aircraft turbofan engines. The sound field within a duct can be considered as the superimposition of propagating modes. In-duct modal analysis allows the amplitude of each modal component to be determined from the sound pressure measured at the duct wall. The mode amplitude distribution can be used for source diagnostics and for the in-duct liner design. Meanwhile, it is also important to understand the far field directivity and sound power radiating from the duct opening, either as an index of insertion loss in order to assess silencer performance, or as a means of quantifying and ranking the total noise output for predicting community annoyance.

Broadband noise generally comprises all propagating modes, which would require at least as many microphones to deduce the amplitude for each mode index pair (m, n). At the blade passing frequency of a typical aeroengines, for example, the number of modes can easily exceed 100, making the simultaneous measurements of all modes unrealistic. One current method to determine the amplitude of each mode (m, n) requires a large circumferential array that typically requires a large number of microphones in each ring [1-4]. A second method requires long axial arrays within the duct to determine modal amplitude distribution versus propagation angle [5]. Both methods use a large number of microphones, and they are not very efficient, financially or practically, as the microphones required to take such measurements are expensive and each requires calibration. Therefore, the new measurement technique [6] validated in this paper is only based on the complex coherence function of two measurement points at the duct wall, and is has the potential to replace current techniques at a reduced cost and increased productivity. Moreover, in the case exhaust stack and turbofan engines, for example, locating microphones in the far field is difficult.

In the case of turbofan engines very large anechoic facilities are needed. In new two-microphone method, far field noise measurements can be inferred from measurements of the coherence function from two closely space microphones located at the duct wall. In this paper, the experimental prediction of the far field noise directivity by using two-microphone method were also evaluated.

2 Theory of two-microphone method

2.1 Mode amplitude distribution

The detail of the theory basis of the two microphone method can be found in Ref. [6]. In this paper we only briefly introduce the important deviation to the final formulas which was used in the measurement and data analysis. A uniform mean flow were included in the derivation in the Ref. [6], but in this paper the effects of flow are ignored for consistency with the measurements presented in Section 3.

Above its cutoff frequency, a single mode propagating along the duct of pressure amplitude A_{mn} at a single (angular) frequency ω can be written as

$$p_{mn}^{\pm}(y,x) = e^{-i\omega t} A_{mn}^{\pm} \Psi_{mn}(\boldsymbol{y}) e^{\pm \alpha_{mn} k x} \tag{1}$$

Here, the superscript ± denotes the modes propagating in the positive and negative x directions, respectively. A point on the duct cross section is represented by $\boldsymbol{y} = (r, \theta)$, and x denotes the axial distance along the duct relative to some arbitrary origin. $\Psi_{mn}(\boldsymbol{y})$ denotes the modal shape function with the normalisation property, $A^{-1}\int_A |\Psi_{mn}(\boldsymbol{y})|^2 \, dA(\boldsymbol{y}) = 1$, where A is the duct cross sectional area, and $k = \omega/c$ is the free space wavenumber and c is the sound speed. Of central importance in Eq. (1) is the non-dimensional quantity α_{mn}, which is referred to as the modal cuton ratio

$$\alpha_{mn} = \sqrt{1 - (\kappa_{mn}/k)^2} \tag{2}$$

where α_{mn} are a set of eigenvalues that are characteristic of the duct cross section such that the corresponding mode shape functions Ψ_{mn}, defined by $(\nabla_{\perp}^2 + \kappa_{mn}^2)\Psi_{mn}(y) = 0$, also satisfy the duct-wall boundary conditions and the normalization condition $A^{-1}\int_A |\Psi_{mn}(y)|^2 \, dA(y) = 1$ [6]. The cuton ratio $\alpha = 0$ corresponds to the modal cutoff frequency $\omega = \omega_{mn} = \kappa_{mn} c$, and while $\alpha = 1$ corresponds to $\omega / \omega_{mn} \to \infty$, and the modes well above cuton.

The significance of the cuton ratio, or its related quantity cutoff ratio $(1-\alpha^2)^{-1} = k/\kappa$, to duct acoustics was highlighted in the seminal work of Rice [7]. It is an important quantity in duct acoustics for various reasons: (1) Different modes with the same cuton ratio have similar transmission and radiation characteristics [7]. (2) Cuton ratio is uniquely related to the angle with which the mode propagates along the duct and therefore the angle radiated most strongly to the far field (the angle of the main lobe). (3) The mode amplitude distribution for many physical source distributions are a smoothly varying function of α.

Joseph [6] has recently shown that providing the relative mode amplitude distribution is independent of frequency, and can therefore be written in the form

$$\frac{\pi}{T} \mathrm{E}\left[\left| A_{mn}^{\pm}(\omega) \right|^2 \right] = S(\omega) \overline{a^2}(\alpha_{mn}) \tag{3}$$

where $S(\omega)$ is a source strength with units of squared pressure per unit frequency, the non-dimensional mode amplitude distribution $\overline{a^2}(\alpha_{mn})$ versus α_{mn} can be deduced from only the complex coherence

function $\psi_{12}(\hat{\omega})$ between two acoustic pressure measurements made at the duct wall separated by a distance Δx . In the high frequency limit ($ka = \omega a/c > 10$ has been found to be sufficient, where a is the duct radius), we may treat $\overline{a^2}(\alpha_{mn})$ as a continuous variable so that the discrete summation over $\overline{a^2}(\alpha_{mn})$ may be replaced by an integration over α. Finally, it has been shown that $\overline{a^2}(\alpha)$ and $\psi_{12}(\hat{\omega})$ are related via the Fourier Transform relationship,

$$\overline{a^2}(\alpha) = \frac{1}{2\pi|\alpha|}\int_{-\infty}^{\infty}\psi_{12}(\hat{\omega})e^{-i\hat{\omega}\alpha}d\hat{\omega} \tag{4}$$

where $\hat{\omega} = \omega\Delta x/c$ and $\psi_{12}(\hat{\omega})$ is given by,

$$\psi_{12}(\hat{\omega}) = \frac{S_{12}(\hat{\omega})}{\sqrt{S_{11}(\hat{\omega})S_{22}(\hat{\omega})}}\left(0 \le \left|\psi_{12}(\hat{\omega})\right|^2 \le 1\right) \tag{5}$$

where $S_{12}(\hat{\omega})$ is the acoustic pressure cross spectrum between the two measurement positions and $S_{11}(\hat{\omega})$ and $S_{22}(\hat{\omega})$ are the acoustic pressure Power Spectral Densities measured at the two microphones. Note that in Eq. (4) positive and negative a values refer to positive and negative-going modes, respectively, i.e., $\overline{a_+^2}(\alpha_{mn}) = \overline{a^2}(\alpha_{mn}),(\alpha \ge 0)$ and $\overline{a_-^2}(-\alpha_{mn}) = \overline{a^2}(\alpha_{mn}),(\alpha \le 0)$.

2.2 Far field directivity

Knowledge of the mode amplitude distribution versus α is sufficient to determine the variation of far field PSD, $S_{ff}(\omega,\theta)$ versus polar radiation angle θ measured relative to the duct axis. Given that, $\alpha = \cos\theta$ in Ref. [6] we show that

$$\frac{S_{ff}(\omega,\theta)}{S_{11}(\omega)} = \frac{1}{8\pi}\left(\frac{a}{R}\right)^2 \cos\theta\int_0^{\infty}\psi_{12}(\hat{\omega})\mathrm{e}^{-\mathrm{i}\hat{\omega}\cos\theta}\mathrm{d}\hat{\omega} \quad (0 \le \theta \le \pi/2) \tag{6}$$

The integral expression on the right hand side of Eq. (6) is an integral over $\hat{\omega}$ and is therefore frequency-independent. A consequence of making the separability assumption of Eq. (3), therefore, is that the normalised directivity function, similar to the mode amplitude function, is independent of frequency. The validity of this prediction will be examined experimentally in Section 3.

2.3 Sound power radiation

The mode amplitude distribution versus α is sufficient to determine exactly the sound power transmitted along the duct on both positive and negative direction. Joseph [6] has shown that the sound power $W^{\pm}(\omega)$ may be computed directly from the complex coherence function from the expression,

$$\frac{4\pi W^{\pm}(\omega)\rho c}{S_{11}(\omega)A} = \int_0^{\infty}\psi_{12}(\hat{\omega})\Omega^{\pm}(\hat{\omega})d\hat{\omega} \tag{7}$$

In the absence of flow and reflections, $\Omega^{+}(\hat{\omega})$ is given by

$$\Omega^{+}(\hat{\omega}) = \frac{\mathrm{e}^{\mathrm{i}\hat{\omega}}(1-\mathrm{i}\hat{\omega})-1}{\hat{\omega}^2} \tag{8}$$

2.4 Assumptions and limitations

The validity of Eq. (4) relating the mode amplitude distribution to the coherence function relies on the following assumptions about the multi-modal sound field in the duct:

- The modes in the sound field are mutually uncorrelated.
- The separability assumption of Eq. (3) is met. Rice [7] and more recently Joseph [6] have shown that this is a valid assumption for a broad class of physically important mode amplitude distribution functions such as spatial distributions of monopoles, dipoles and the case where each mode has identical energy.
- The excitation frequency is sufficiently high to ensure that there are a sufficient number of modes so that its distribution versus a may be approximated as a continuous function. This is believed to be correct for $ka > 10$.

3 Experiments

This section describes the experimental arrangement used to validate the measurement theory outlined in Section 2. In order to validate this new measurement technique, two different sets of measurements were taken of broadband sound propagating through a duct. The first of these measurements was taken by two in-duct electret microphones, from which the complex coherence could be calculated. The second set of measurements taken was the direct measurement of the sound in the far-field radiated from the end of the duct, measured using a microphone array. By comparing the results obtained from the application of the theory to the in-duct microphones with the direct far-field measurements the validity of the method can be gauged.

A schematic of the experimental set up is shown in Figure 1, with the duct spanning reverberant (left) and anechoic (right) room, and the arrow represents the direction of the propagating sound field. A circular duct manufactured from hard plastic duct of 0.2m internal radius and 4.34m in length was located through the wall separating a reverberation chamber (on the right) and an anechoic chamber (on the left). Four loudspeakers positioned in the corners of the reverberation chamber were driven by independent broadband random signals to generate a broadband reverberant sound field in the reverberation chamber. The sound field in the source room approximates to a diffuse sound field. The random sound field impinging on the open of the duct was then transmitted through the duct, which was then partially transmitted to the other side and then radiated into the anechoic chamber from the open end. Two electret microphones on the duct wall separated by a distance Δx and x_D from the source end was used to measure the complex coherence function. The location of the microphone pair x_D was varied between x_D = 0.5m to x_D = 3.0m (x_D = 0m corresponds to the position at the source room end of the duct. The separation distance between the microphones was varied between $\Delta x = 0.01\text{m}$ and 0.1m in increments of 0.01m. Eleven Bruel and Kjaer microphones distributed over an arc in the anechoic chamber at a distance of R = 3m from the duct centre were used to measure the directivity and sound power from the duct. The directly measured directivity and sound power were then compared against that predicted from the in-duct measurement.

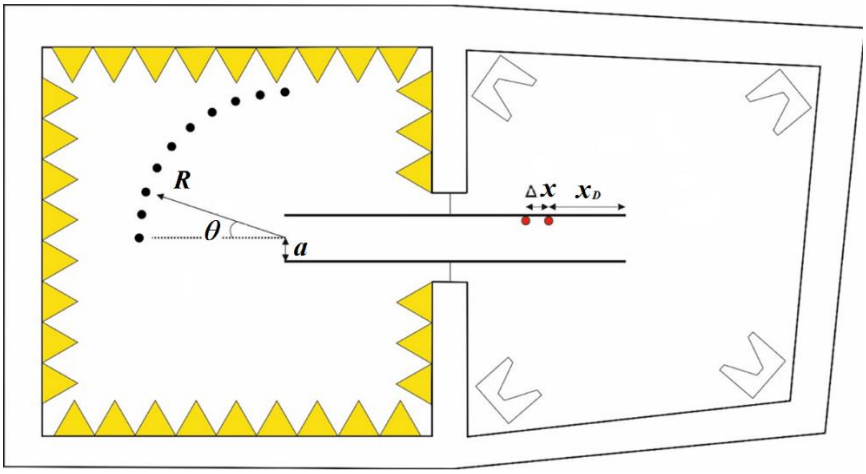


Figure 1: Basic layout (not to scale) of the experimental set-up

3.1 Measurement procedure

Acoustic pressure data was acquired at a sampling frequency of 50 kHz for a duration of 10s. For a sound field with fully uncorrelated mode amplitudes, Eq. (5) predicts that the coherence function, and hence inferred mode amplitude distribution function, are independent of the microphone separation distance and position within the duct. To assess the validly of this assumption the In-duct acoustic pressure measurements were made using pairs of microphones at varying distances along the duct and different separation distances.

Measurements were taken in order to ensure that the experiment had been conducted in accordance with the assumptions and limits outlined in Section 2.4. Assumption 1 was not directly tested as this was not possible, however the electronic setup ensured that sound sources were uncorrelated. Further to this, a set of measurements were taken in the source room to ensure that the sound field was diffuse. These measurements were taken for a variety of different microphone and speaker positions and spectrums checked for any frequency spikes. Secondly, the assumption that the sound field was uniform and the same everywhere within the duct was tested. In order to test that the sound field was uniform, in-duct measurements were taken at 90 degree intervals around the duct wall. The separability assumption is not one that can be physically tested as it is a statistical assumption which has previously shown to be true [7].

3.2 Data processing for far-field measurement

The generic equation for calculating the sound power spectrum across an angular region from 0° to 90° can be calculated by

$$W(\omega) = \int_0^{\pi/2} \frac{S_{ff}(\omega,\theta_i)}{\rho c} 2\pi R^2 \sin\theta \, d\theta \tag{9}$$

To implement Eq. **Fout! Verwijzingsbron niet gevonden.**, continuous data would be required across all angles in order to apply the integral correctly. The experiment was not carried out with a continuous array of microphones in the far-field, an array of 11 microphones was used. These were equally spaced from 0° to 100° at a radius of 2.5m from the end of the duct. In order to complete the calculation, the power spectral densities of each of the 11 signals were averaged in neighbouring pairs to give new power spectral densities in 10° intervals between 5° to 95°.

As the variable being integrated over was discrete rather than continuous, the integral was replaced with a summation. The result of this is Eq. (1), which was applied to calculate the directly measured far-field power PSD.

$$W(\omega) = 2\pi R^2 \sum_{i=1}^{11} \frac{S_{ff}(\omega,\theta_i)}{\rho c} \sin\theta_i \Delta\theta_i \tag{1}$$

To obtain the directly measured far-field directivity as a function of both angle and frequency, the PSDs averaged between each position (as outlined above) were plotted directly onto polar plots (one plot per frequency and mirrored about 0°) with no further calculation required. As the averaging meant that no PSD was calculated for the central 10° of the plot, the results were shifted to avoid having a large gap in the centre of the polar plot.

3.3 Data processing for in-duct measurement

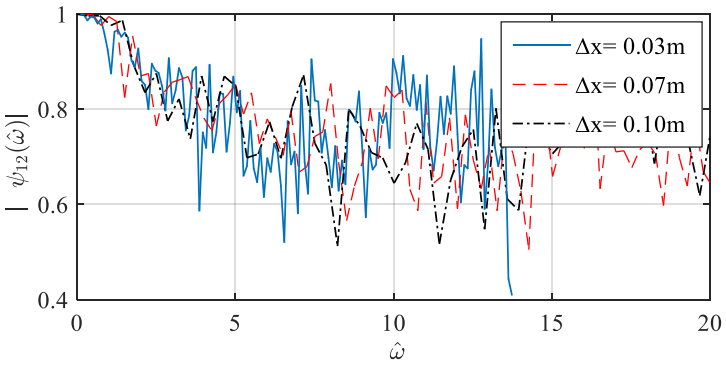
The modal amplitude distribution within the duct was evaluated by Eq. **Fout! Verwijzingsbron niet gevonden.**. As the independent variable in this equation is not one that could be physically measured, the calculation was done by looping the equation through a pre-defined vector of the cuton ratio ranging from $-1 \leq \alpha \leq 1$. Eq **Fout! Verwijzingsbron niet gevonden.** outlines how far-field directivity can be calculated from the complex coherence at the duct wall. Directly evaluating the left hand side of Eq. **Fout! Verwijzingsbron niet gevonden.**; the ratio of the pressure PSD of the far-field radiation to the pressure PSD at the duct wall, leads to a results which is independent on frequency. One can multiply both sides of Eq. **Fout! Verwijzingsbron niet gevonden.** by the pressure PSD to obtain the directivity $S_{ff}(\omega,\theta)$ which was dependent on frequency.

4 Results and analysis

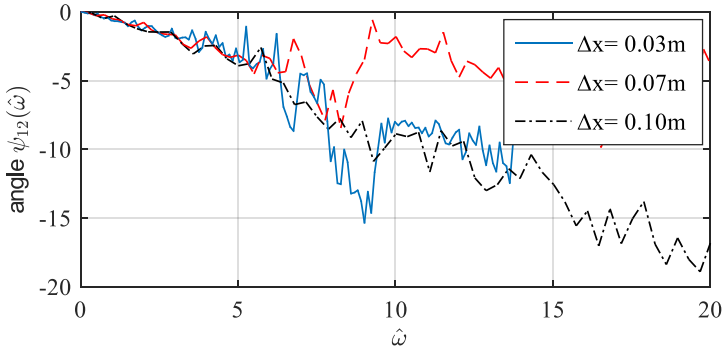
4.1 Complex coherence function

The underlying assumption of the two-microphone method is that the frequency dependence mode amplitude can be separated as a purely frequency-dependence source terms and a non-dimensional mode amplitude distribution, as shown in Eq. (3). A consequence of making this assumption is that the complex coherence function is only a function of the non-dimensional frequency $\hat{\omega} = \omega\Delta x/c$, as indicated in Eq. (4) and explained more fully in ref [6]. We now test this assumption on the measured in-duct pressure data by computing the magnitude and phase of the complex coherence function up to a maximum frequency of 25kHz at the three microphone separation distances of Δx = 0.03, 0.07 and 0.10m located arbitrarily at x_D =1.5m along the duct. The magnitude and phase are plotted against $\hat{\omega}$ in Figure 2. Note that $ka/\hat{\omega} = a/\Delta x$. Good collapse of the measured magnitude and phase are observed over the frequency range $\hat{\omega} < 14$ where the spectra overlap. The jump in the phase spectrum for Δx = 0.07m in the frequency range $\hat{\omega} > 7$ arise due to 2π phase unwrapping issues. The main assumption made in the measurement technique therefore appears to be reasonably valid in this test.

A notable feature of Figure 2 is the slow rate of decay of the coherence function with increasing frequency for $\hat{\omega}$ up to about 6. Above this frequency the coherence function remains roughly flat with an average value of about 0.7 over the frequency range shown and beyond. The reason for this behaviour is mostly likely due to the presence of strong axial standing waves in the pipe rig even though the phase spectrum is indicative of waves propagating away from the source. Note that the coherence measurements presented in Figures 2 were repeated at different positions x_D along the duct and found to have comparatively little effect on the results, and are therefore not shown here.



(a) Magnitudes of coherences



(b) Phases of conherences

Figure 2: Measured complex coherences

4.2 Mode amplitude distribution

The measured coherence functions at the three microphone separation distance Δx = 0.03, 0.07 and 0.10m were used to predict the mode amplitude distribution versus cuton ratio α propagating in the duct. The non-dimensional normalised mean square amplitude distribution $\overline{a^2}(\alpha)$ deduced from Eq. (4) is plotted in Figure 3 versus α for the three cases.

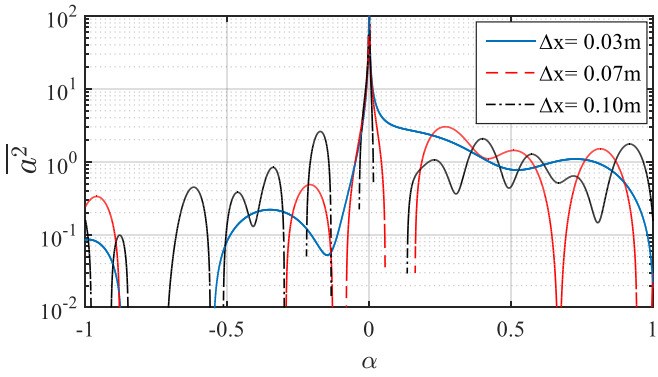


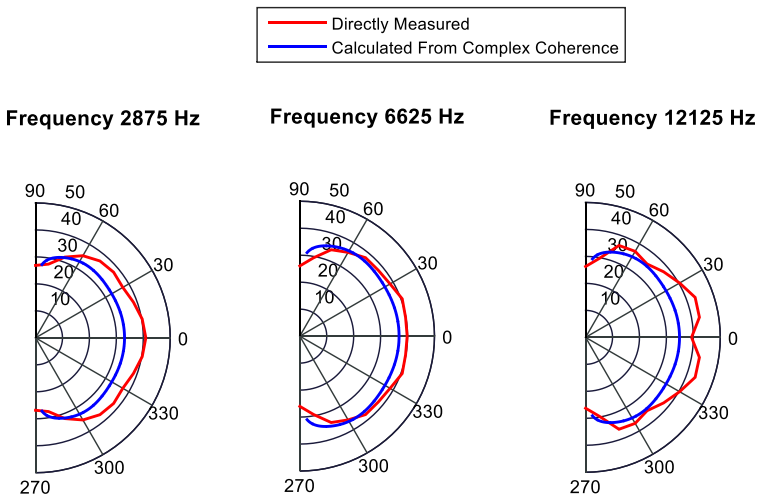
Figure 3: Predicted modal amplitude distribution

The upper non-dimensional frequency limit $\hat{\omega}_{max}$ is related to the maximum frequency f_{max} of the frequency spectrum (equal to half the sampling frequency) through $\hat{\omega}_{max} = 2\pi f_{max}\Delta x/c$. The separation distance Δx should therefore be sufficiently large to ensure that the coherence function due to the acoustic field has decayed to sufficiently low levels so that it is fully captured by the spectrum. Figure 3 shows a clear dominance of modes propagating in the direction away from the source represented by $\alpha \geq 0$. Modes propagating towards the source due to multiple reflections between the open ends of the duct, represented by $\alpha \leq 0$, are observed to be about 10dB below that of the 'incident' modes. For modes propagating away from the source $\alpha \geq 0$ the predicted mode amplitude distribution is reasonably consistent, with variations being less than about 3dB for a values greater than 0.2. For a values less than 0.2, associated with modes close to cutoff. The estimates deviate considerably more than 3dB. These modes radiate more strongly in the sideline directions.

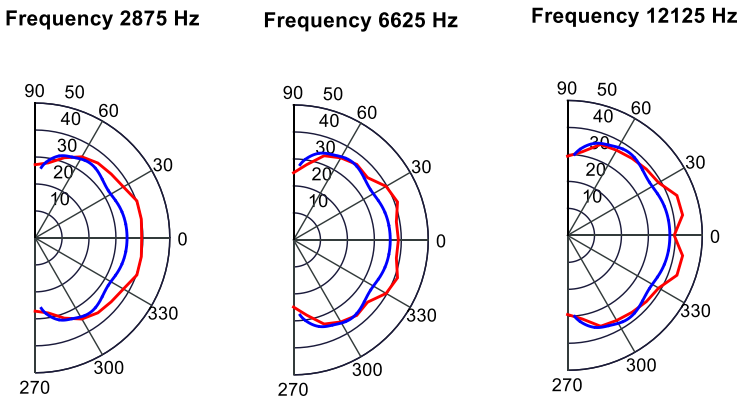
4.3 Far-field directivity

As the far-field directivity is a function of both radiation angle and frequency, only a small selection of the results are able to be presented in this paper. Plots have been chosen to represent certain features of the results, although discussion about a larger portion of the data set will be included in this section. For further ease of discussion, results will be split into low, middle and high frequency ranges. It can be seen that there is a definite match in overall shape and amplitude at nearly all frequencies between the two data sets, although there are patterns that can be become more pronounced with increasing frequency.

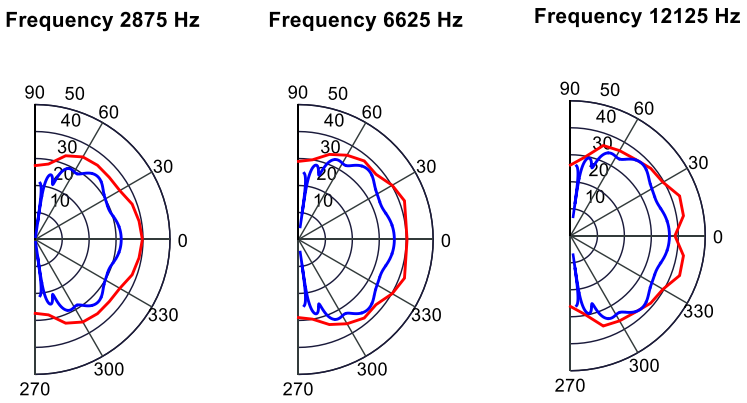
Figure 4 shows the comparison of the directivities which were directly measured and calculated from the complex coherences, for the separation distances of $\Delta x = 0.03$, 0.07 and 0.10m, at three frequencies (at low frequency - 2875Hz, middle frequency - 6625Hz and high frequency - 12125Hz). The larger the microphone separation distance, the more 'lobed' the directivity pattern becomes. Lobing is a high frequency characteristic of radiation from ducts and the larger non-dimensional frequency range one obtains when measuring with a larger microphone separation distance gives rise to the lobes in the directivity calculation. For the Δx = 0.03 and 0.10m, the overall calculated shape is reasonable, but the amplitude is an underestimate at nearly all angles, especially with approximately 5dB difference in the central radiation angles. For the Δx= 0.07m, the agreement across all radiation angles is excellent with a near perfect match at low, middle and high frequencies. But in overall, the directivity evaluated by the complex coherence is reasonable accurate.



(a) $\Delta x = 0.03$m



(b) $\Delta x = 0.07$m



(c) $\Delta x = 0.10$m

Figure 4: Directivity comparison at different frequencies

4.4 Far-field sound power PSD

Figure 5 show that the spectra obtained from the direct measurement of the far-field sound at $\Delta x = 0.07$m. It is clear that the application of Eq. (10) has been successful in calculating the far-field sound power PSD from the complex coherence and PSD at the duct wall. The calculated spectra (blue) not only follows the overall shape of the measured spectra (red), but is accurate to the extent of matching the prominent peaks and dips in the measured spectra.

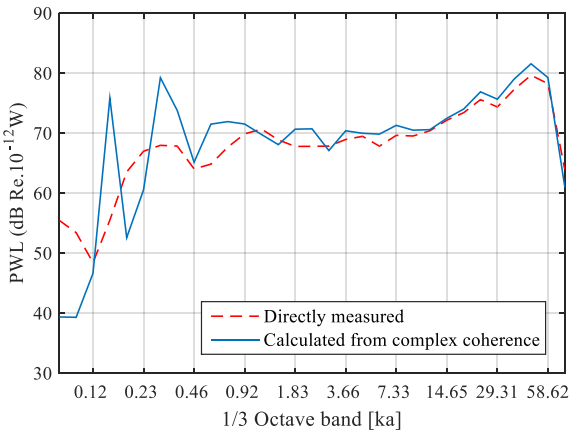


Figure 5. Comparison of the calculated ($\Delta x = 0.07$m) and measured far-field sound power PSD

Where the measured spectra exhibits a peak, the calculated curve does but also the peak tends to be exaggerated in amplitude. This can be explained by the inclusion of the S_{11} term in Eq. (7). The theory behind this measurement technique states that the far-field spectra is the same as the in-duct spectra multiplied by the area of radiation, impedance of the propagation medium and the integral of the complex coherence. This means that the spectrum shapes will be the same with the amplitude of determined by the other factors in Eq. (7).

5 Conclusions

This paper has used experiments to verify the two-microphone method in mode decomposition and far-filed directivity of in-duct sound field. Using the complex-coherence to calculate the modal amplitude distribution inside the duct was successful. Although there were limited means of predicting the distribution, the results agreed with what was expected and the variation in the microphone separation distance had little effect on the observed behaviour. Perhaps the most successful application of the measurement technique was the agreement between the measured and calculated far-field spectra. The theory relies on the in-duct and far-field spectra having the same shape and this has been shown to be true. Overall, the comparisons between the calculated and measured far-field characteristics of the sound radiated from the duct have proved the new measurement technique to be valid for the case of zero Mach number. As the potential applications of this new measurement technique are so vast and have specific potential in the aeronautical industry and turbo-fan jet engine design, and we would recommend that the experiment is repeated with flow (of various Mach numbers) present in the duct. Overall, the accurate mode detection and far-filed directivity prediction on the broadband noise in ducts by using the new technique provides a critical guidance for acoustics liner designer in modern turbo-fan jet engines.

References

[1] P. Sijtsma, *Feasibility of in-duct beamforming*, in *13th AIAA/CEAS Aeroacoustics Conference*, AIAA-2007-3696, Rome, Italy (2007).

[2] R. P. Dougherty, J.M. Mendoza, *Nacelle in-duct beamforming using modal steering vectors*, in *14th AIAA/CEAS Aeroacoustics Conference*, AIAA-2008-2812, Vancouver, Canada (2008).

[3] L. Enghardt, A. Holewa and U. Tapken, *Comparison of different analysis techniques to decompose a broad-band ducted sound field in its mode constituents*, in *13th AIAA/CEAS Aeroacoustics Conference*, AIAA-2007-3520, Rome, Italy (2007).

[4] L. Enghardt, C. Lowis and L. Neuhaus, *Radial mode analysis of broadband noise in flow ducts using a combined axial and azimuthal sensor array*, in *20th AIAA/CEAS Aeroacoustics Conference*, AIAA 2014-3318, Atlanta, USA (2014).

[5] C. R. Lowis, P. F. Joseph and A. J. *Kempton, Estimation of the far-field directivity of broadband aeroengine fan noise using an in-duct axial microphone array*, Journal of Sound and Vibration, Vol. 329, No.19 (2010), pp.3940-3957.

[6] P. Joseph, *A two-microphone method for the determination of the mode amplitude distribution in high-frequency ducted broadband sound fields*, Journal of the Acoustical Society of America, Vol. 142, No. 4 (2017), pp. 2019–2029.

[7] E. J. Rice, *Multimodal far-field acoustic radiation pattern using mode cutoff ratio*, AIAA Journal, Vol. 16 (1978), pp.906-911.

Huddle test of optical inertial sensors combined with slightly damped mechanics

B. Ding[1], G. Zhao[1], J. Watchi[1], C. Collette[1,2]
[1] Université libre de Bruxelles, Precision Mechatronics Laboratory (PML),
Department of Bio-, Electro- And Mechanical Systems
av. F.D. Roosevelt 50, CP 165/56, B-1050 Brussels, Belgium
e-mail: **binlding@ulb.ac.be**

[2] Université of Liège, Department of Aerospace and Mechanical Engineering
Allée de la Découverte 9, B-4000, Liège, Belgium.

Abstract
Precise seismic measurements and active isolation in the low-frequency domain are more and more required. In order to meet the requirements, an optical inertial sensor is developed, where a lightly damped mechanical structure (high Q factor) is employed. The sensor consists of two parts. The first part is a homemade interferometric readout which has a resolution below 1 pm/√Hz at 1 Hz, and the other one is a mechanical part which has a low resonance frequency and a high Q factor. For the developed sensor at hand, the mechanical structure of STS-1 vertical seismometer is used and adapted for hosting the interferometric readout. The sensor is then placed inside a vacuum chamber to be immune from the ambient noise. The sensor resolution is experimentally examined using huddle tests.

Keywords: Q factor, interferometric, low-frequency domain, huddle test.

1 Introduction

Inertial sensors are often used to measure either linear or angular motions. A good review about rotation sensors can be found in Lee *et al*. [1]. In this paper, only linear motion is considered, and a thorough discussion about this kind of sensors can be found in Collette *et al*. [2]. Inertial sensors are widely used in many fields like seismology, structural engineering, and navigation. However, traditional inertial sensors cannot meet the requirements for active vibration isolation of large instruments like the Laser Interferometer Gravitational-Wave Observatory (LIGO). Novel inertial sensors are required which should incorporate the features of a high resolution in a low-frequency domain, an ambient noise (magnetic field, temperature variations, etc.) insensitivity, and a low tilt-horizontal coupling [3, 4].

In order to improve the performance of inertial sensors, one way is to use homodyne quadrature interferometric readout to increase the sensor resolution. The advantages of using optical readouts are twofold: they are coil free and thus insensitive to magnetic field; the quadrature interferometric signal processing methods [5-7] provide a picometer resolution. Using the optical readout, a vertical sensor based on leaf springs structure was developed by Otero *et al* [8, 9], which reaches the resolution around 1 pm/√Hz at 1 Hz. A horizontal sensor based on a folded pendulum structure was developed by Acernese *et al.* [10, 11], the resolution of which is lower than 1 pm/√Hz at 1 Hz.

Developments of optical inertial sensors are also conducted by the PML of ULB [12-13]. Currently, it is coupled with the mechanics of an STS-1V seismometer [14], which has a Q factor of 30 and resonant frequency of 0.28 Hz. In this paper, recent developments of our prototype are presented. A description of the optical readout and mechanical part is discussed in Section 2. Section 3 presents and discusses the results of the huddles tests of two optical inertial sensors and two Guralp CMG-6T sensors. Section 4 contains the conclusions and presents the future plans.

2 Optical inertial sensor

Our optical inertial sensor is designed to measure the vertical motion, which is shown in Figure 1. A is our homemade optical readout. B is the STS-1V seismometer. C is the horizontal pendulum of the seismometer, on which a corner cube is mounted. D is a mirror mounted at 45 degrees to reflect the laser beam. When the horizontal pendulum vibrates, the laser beam is reflected by the corner cube and the 45 degrees mounted mirror, the relative motion between the horizontal pendulum and the monolithic structure can be obtained by the optical readout. E is a vacuum chamber which can provide a vacuum environment down to 0.5 mBar in order to avoid disturbances from the air fluctuation.

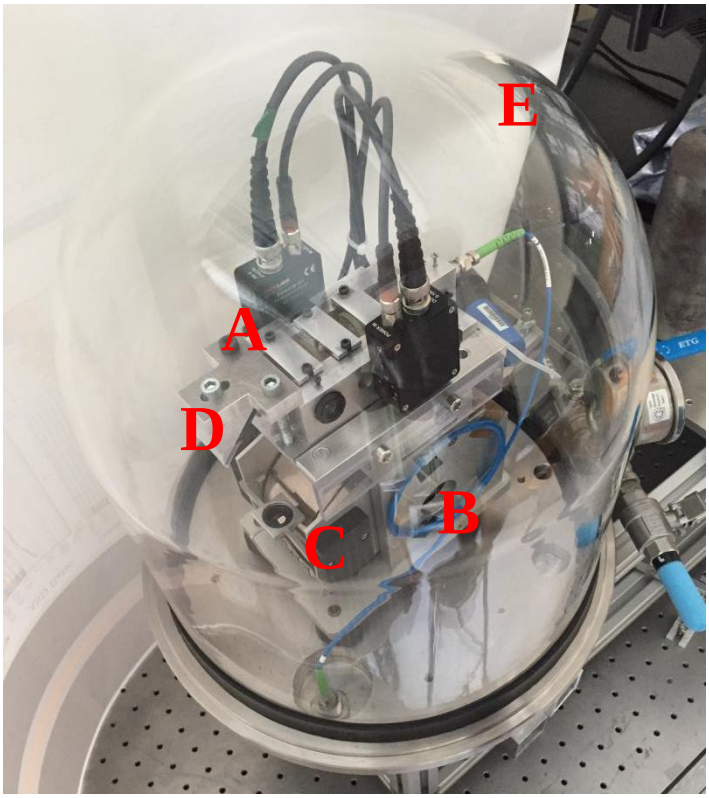


Figure 1. The overall view of the inertial sensor

2.1 Optical readout

As Shown in Figure 1, the homemade optical readout is one of the important parts of the inertial sensor. The size of the monolithic readout is around 120mm × 80 mm × 60mm, which can be easily combined with the mechanical structure of STS-1V. The optical readout is schematically shown in Figure 2.

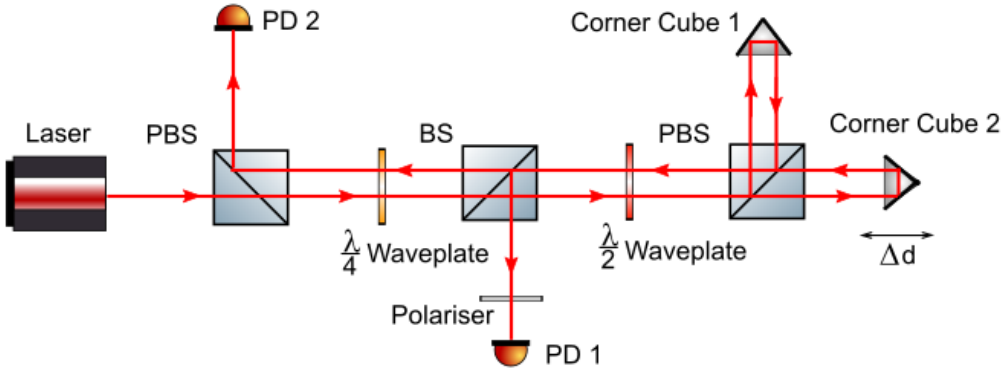


Figure 2. Scheme of the optical readout. [15]

The laser is a 1550 nm fibered laser source, which generates a single polarization laser beam. The red arrows show the propagation direction of the laser beam. After passing through a polarizing beamsplitter (PBS), a quarter-wave plate, a non-polarizing beamsplitter (BS) and a half-wave plate, the two polarization states of the laser beam are separated by a PBS and the two beams with orthogonal polarization states are reflected by corner cubes. The corner cube 1 is a fixed reflector in the reference arm. The corner cube 2 is a movable reflector in the measuring arm. When the laser beam is reflected by the corner cube 2, the information of the displacement of the corner cube 2 is carried by the laser beam. After reflection, the two beams recombine and arrive at the BS where one part of the laser beam reaches the photodiode 1 (PD1) and the other reaches the photodiode 2 (PD2). Thanks to different polarizing components, the orthogonal polarization states of the two laser beams reaching on the two photodiodes are guaranteed. Ignoring the non-linearity and noises in measurements, the power of the laser beams measured by the PD 1 and PD 2 are given by

$$P_{PD1} = \frac{P_0}{8}(1+\sin(\frac{4\pi}{\lambda}\Delta d)) \tag{1}$$

$$P_{PD2} = \frac{P_0}{8}(1+\cos(\frac{4\pi}{\lambda}\Delta d)) \tag{2}$$

where P_0 is the original laser power from the laser source; λ is the wavelength of the laser beam, which is 1550 nm; Δd is the path difference between the reference arm and the measurement arm. Then, the unwrapping dynamic range of Δd is calculated by

$$\Delta d = \frac{\lambda}{4\pi}\text{atan2}((P_{PD1}-\frac{P_0}{8}),(P_{PD2}-\frac{P_0}{8})) \tag{3}$$

However, several noises affect the performance of this optical readout, which includes the intensity noise from the laser source, electronic noises in photodiodes, and analog to digital converter (ADC) noise from the data acquisition (DAQ) system. To study the properties of different sources of noise, and their influence on the optical readout, a noise budgeting analysis is provided in Watchi *et al.* [13]

In order to measure the resolution of the optical readout, the movable corner cube 2 was blocked during the measurement. The output power of the laser source is 8 mW, and the amplitude of the two photodiodes is set to 20 dB. A 16-bit DAQ system with a sampling frequency of 2 kHz is used to record the data. The amplitude spectrum density (ASD) of the optical readout resolution is shown in Figure 3.

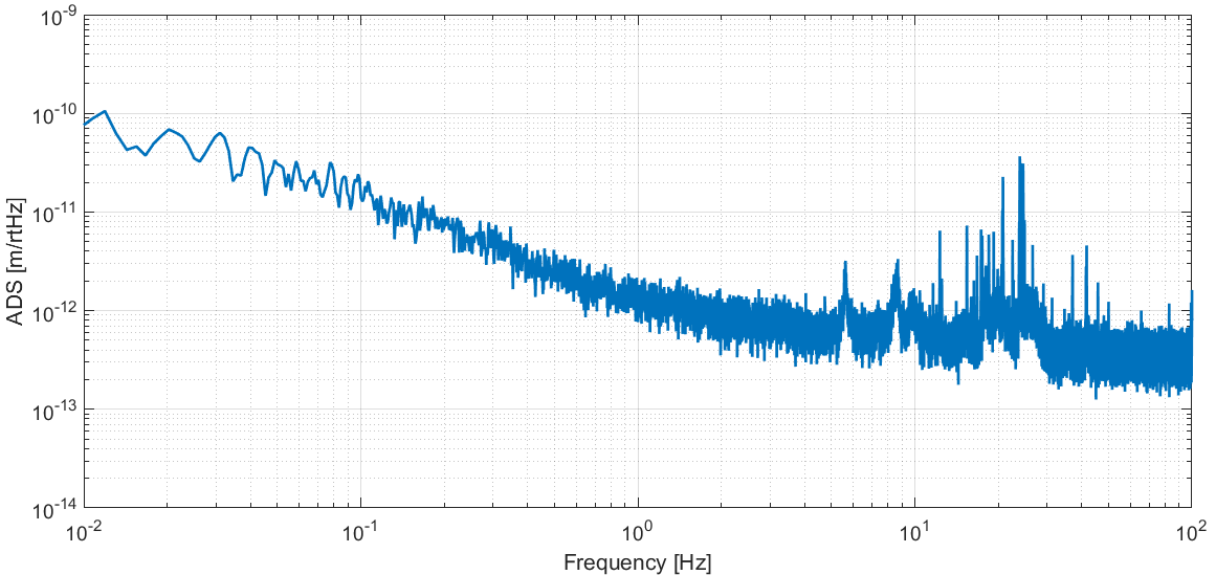


Figure 3. The optical readout resolution.

The resolution of the optical readout is around 3×10^{-13} m/√Hz above 10 Hz, 1×10^{-12} m/√Hz at 1 Hz,

1×10^{-11} m/√Hz at 0.1 Hz and 1×10^{-10} m/√Hz at 0.01 Hz. Peaks around 20 Hz are the resonance frequencies of the optical table.

2.2 Mechanical structure of STS-1V

As the inertial sensor is dedicated for the low-frequency applications, the mechanical structure is required to have a very low fundamental resonance frequency, which provides a good sensitivity curve in the desired low-frequency domain. Meanwhile, the material of the mechanical structure also needs to be carefully designed to reduce the thermal noise of the optical inertial sensor. At this stage, three optical inertial sensors with the mechanical structures of three STS-1V seismometers have been built. The original electronic readout of the seismometer is a pair of linear variable differential transducers (LVDT), which has been replaced by our optical readout in the project. The mechanical part of the STS-1V is based on a Lacoste suspension structure, which is a horizontal pendulum coupled with a spring. The horizontal pendulum swings vertically, and the spring is a leaf spring to counterbalance the gravity. According to the manual of the STS-1V, the original fundamental resonance frequency is around 0.3 Hz. To mount a corner cube, the horizontal pendulum of the STS-1V is modified slightly (shown in Figure 1) and the resonance frequency after modification is 0.28 Hz.

The dynamic equation of the STS-1V reads

$$m\ddot{y} + c\dot{y} + ky = -m\ddot{w} \tag{4}$$

where, c is the dashpot, x is the displacement of the seismic mass, w is the ground motion and g is the gravity constant. The gravity is counterbalanced by the leaf spring. As the optical readout measures the relative motion between the mass displacement and the ground displacement, $y = x - w$.

Transforming Eq.4 to the Laplace domain, the transfer function between the ground motion $W(s)$ and the relative motion $Y(s)$ is derived

$$H(\mathrm{s}) = \frac{Y(s)}{W(s)} = \frac{-ms^2}{ms^2 + cs + k} \tag{5}$$

Where s is the Laplace operator. Once the resonance frequency ω_0 and the Q factor are known, the Eq. 5 can be rewritten in the Fourier domain as

$$H(\omega) = \frac{\omega^2}{-\omega^2 + i\omega\omega_0/Q + \omega_0^2} \tag{6}$$

Thermal noise is one of important noise source in low frequency range [16], and it can be estimated by

$$\Phi_{thermal} = \sqrt{\frac{4k_B T k \phi}{\omega}} \Big/ (m\omega^2) \quad [\mathrm{m}/\sqrt{\mathrm{Hz}}] \tag{7}$$

where, ϕ is the loss factor of the material, which is approximated as $\phi = 1/Q$. Q is the quality factor (Q factor) of the horizontal pendulum known from the datasheet of STS-1V. k_B is the Boltzmann constant, T is the Kelvin temperature, k is the spring constant and be modeled as $k = \omega_0^2 m$, m is the mass of the structure of the STS-1V. The ω^2 in the denominator is to convert the acceleration to displacement. The numerical values of the above mentioned parameters are shown in Table 1

No.	Parameter	Symbol	Numerical values	Unit
1	Loss factor	ϕ	0.05	[-]
2	Q factor	Q	20	[-]

3	Boltzmann constant	k_B	1.38×10^{-23}	$[m^2 \cdot kg \cdot s^{-2} \cdot K^{-1}]$
4	Kelvin temperature	T	300	[K]
5	Spring constant	k	1.857	$[N \cdot m^{-1}]$
6	Mass	m	0.6	[Kg]
7	Resonance frequency	ω_0	0.28	[Hz]

Table 1: Numerical Values of Parameters

2.3 Theoretical resolution of the Optical inertial sensor

Based on the optical readout and the mechanical structure of STS-1V, the theoretical resolution (blocked test) of the optical inertial sensor is shown in Figure 4. The green curve is the model of the thermal noise based on Eq. 7. The blue curve is the measured optical readout resolution (shown in Figure 3) multiplied with the inverse dynamics of the mechanical structure. The red curve is the resolution of the inertial sensor which includes the thermal noise and the readout noise. For the sake of comparison, we also show the resolution of Geotech Instrument GS-13 (the gray dash-dot line), which is a first choice geophone, and Nanometrics Trillium T-240 (the black dash-dot line), which is a first choice broadband seismometer.

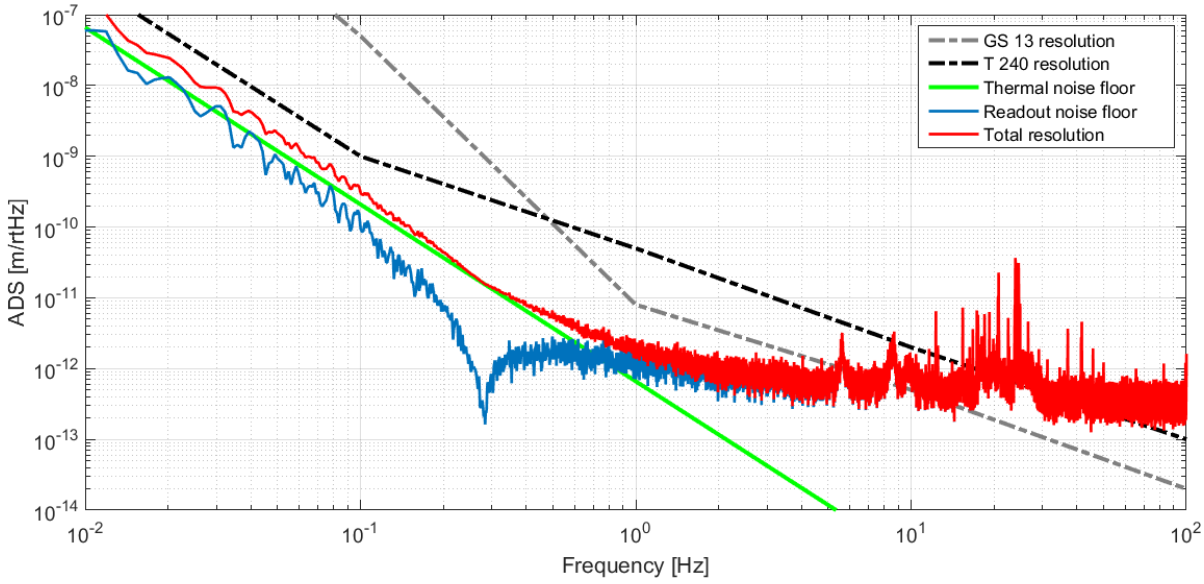


Figure 4. The theoretical resolution of the inertial sensor.

3 Huddle test of Optical inertial sensors

Huddle test is often used to determine the incoherent noise floor of a sensor. The working principle of the huddle test is discussed in Holcomb [17]. When at least two sensors are placed close to each other to capture the same motion (coherent signal), the incoherent noise of the sensors can be extracted from the sensors outputs. Meanwhile, we also use two Guralp CMG-6T sensors as a reference to measure the vertical motion.

The layout of the instruments on the optical table is shown in Figure 5. A is two CMG-6T sensors. B and C are the optical inertial sensors inside two vacuum chambers.

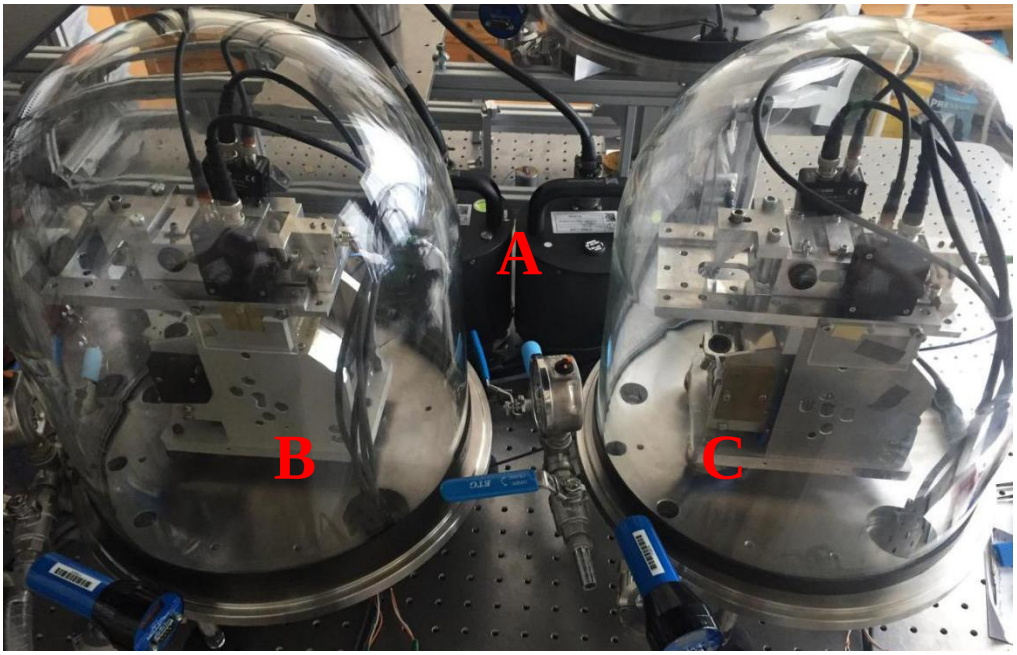


Figure 5. The layout of the huddle test

The coherence of signals from different sensors is plotted in Figure 6. The blue and the orange curves are the coherence between one of the optical inertial sensors and the same CMG-6T sensor. They show that the coherence is good below 30 Hz. The yellow curve is the coherence between two optical inertial sensors. The purple curve is the coherence between two CMG-6T sensors.

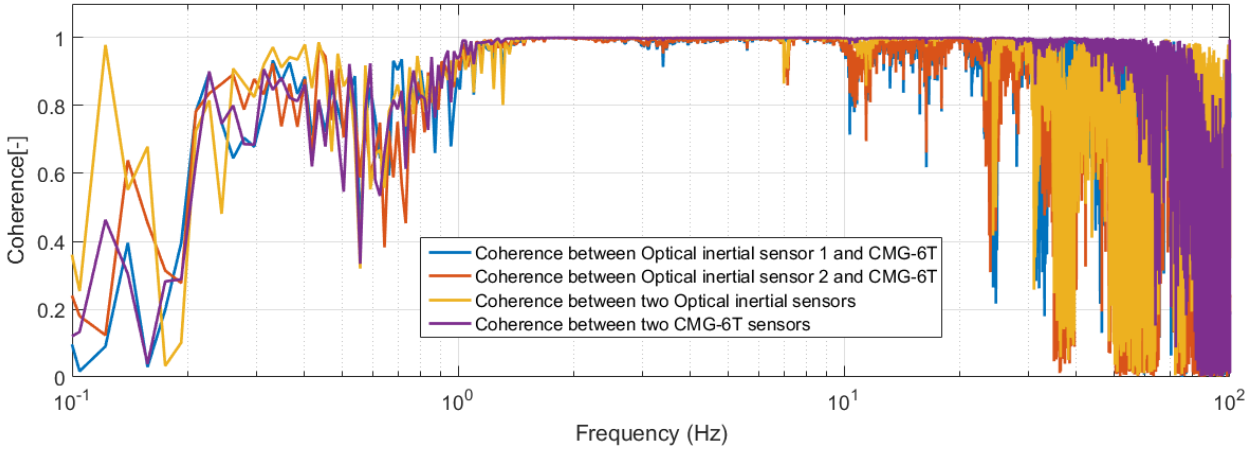


Figure 6. The coherence between sensors during the measurement.

The noise floor of the two optical inertial sensors and two Guralp CMG-6T sensors are extracted from the huddle test and are shown in Figure 7. The blue and the purple curves are the signals extracted from the sensor signals, which refer to the vertical table motion. They show that both of optical inertial sensors and both of Guralp CMG-6T sensors output similar signals, which indicate that our homemade optical inertial sensors work well. The green curve is the noise of the data acquisition system (DAQ) multiplied with inverse dynamics of CMG-6T, which predicts the resolution of a CMG-6T sensor with a 16-bits DAQ. The red curve is the theoretical resolution of our optical inertial sensor (in blocked mass tests), which is taken from Figure 4. The curve is used to predict the noise floor of the optical inertial sensor in the huddle test. The

black and gray dashed-dot curves are the resolution of T-240 and GS-13, which are references from Figure 4.

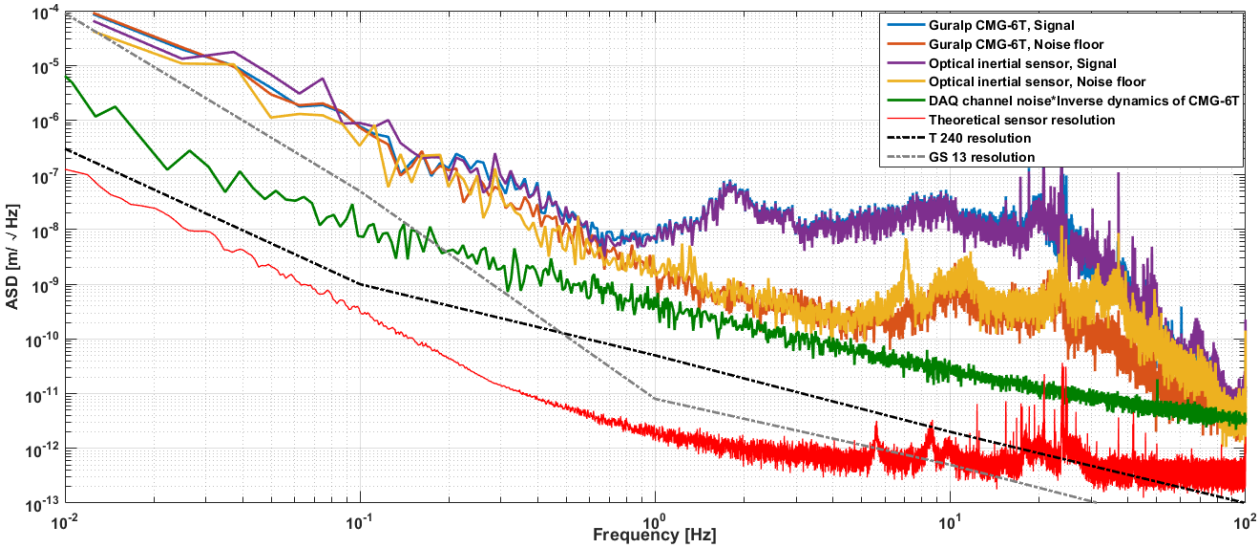


Figure 7. The results of the huddle test and the resolution comparison.

The orange curve is the noise floor of the two Guralp CMG-6T extracted from the huddle test. Compared with the green curve, it is close to the DAQ noise above 1 Hz, but there is a gap below 1 Hz. The yellow curve is the noise floor of the two optical inertial sensors. It is close to the noise floor of the two Guralp CMG-6T, which is higher than the prediction of the red curve. About 30 Hz, the yellow curve is close to the purple curve (signal from the optical inertial sensor), which means the two sensors measure incoherent signals. Both of the noise floors are higher than the predicted resolution. Below 0.7 Hz, due to the drop in the coherence in Figure 6, the difference between coherence signal and incoherence noise is not obvious in Figure 7.

The reason for the difference between the resolution from the huddle test and the resolution from the blocked mass test is investigated. Firstly, the two optical inertial sensors are not on the optical table directly. To avoid air fluctuation in low-frequency domain, they are put inside two vacuum chambers. Therefore, it is not a compacted surface for both optical inertial sensors. Secondly, the culture noise is relatively high during the measurement. We need an isolation platform to hold all sensors and perform the huddle test on a relatively quiet condition. Thirdly, in the low-frequency domain different noise sources will be investigated in the next step. Fourthly, the two mechanical structures of the STS-1V seismometers are assumed as linear systems, which might be not the case in practice leading to the estimation errors for the huddle test.

4 Conclusion

An optical inertial sensor is presented in this paper. The optical readout and the mechanical structure of the inertial sensor are introduced. The sensors are compared with Guralp CMG-6T sensors, and the resolution from blocked mass test and huddle tests are shown. There is a difference between the resolution from the huddle test and blocked mass test. In the future, the quality of the huddle test will be improved.

Acknowledgment

The authors gratefully acknowledge the CSC for funding Binlei Ding(Grant number: 201607650017), and Brussels Capital Region (Innoviris) and the FRS-FNRS for funding this research (IGOR project F453617F). Many thanks to the researchers from the Federal Institute for Geosciences and Natural Resources in Hanover and the Royal Observatory of Belgium. They kindly lend the STS-1V seismometers in the tests. The authors

also gratefully acknowledge the members of the LIGO Seismic Working Group for their comments and inspiring discussions. This document was assigned with LIGO Document: LIGO-P1800193.

References

[1] Lee, W. H. K., Celebi, M., Todorovska, M. I., & Diggles, M. F. (2007). Rotational Seismology and Engineering Applications: Proceedings for the First International Workshop, Menlo Park, California, USA—September 18 to 19, 2007. US Geol. Surv. Open File Rep, 1144.

[2] Collette, C., Janssens, S., Fernandez-Carmona, P., Artoos, K., Guinchard, M., Hauviller, C., & Preumont, A. (2012). Inertial Sensors for Low-Frequency Seismic Vibration Measurement. Bulletin of the seismological society of America, 102(4), 1289-1300.

[3] Rodgers, P. W. (1969). A note on the response of the pendulum seismometer to plane wave rotation. Bulletin of the Seismological Society of America, 59(5), 2101-2102.

[4] Matichard, F., & Evans, M. (2015). Tilt-free low-noise seismometry. Bulletin of the Seismological Society of America, 105(2A), 497-510.

[5] Birch, K. P. (1990). Optical fringe subdivision with nanometric accuracy. Precision Engineering, 12(4), 195-198.

[6] Zumberge, M. A., Berger, J., Dzieciuch, M. A., & Parker, R. L. (2004). Resolving quadrature fringes in real time. Applied optics, 43(4), 771-775.

[7] Downs, M. J., & Raine, K. W. (1979). An unmodulated bi-directional fringe-counting interferometer system for measuring displacement. Precision engineering, 1(2), 85-88.

[8] Otero, J. D. (2009). Development and characterization of an observatory-class, broadband, non-fedback, leaf-spring interferometric seismometer. University of California, San Diego.

[9] Zumberge, M., Berger, J., Otero, J., & Wielandt, E. (2010). An optical seismometer without force feedback. Bulletin of the seismological society of America, 100(2), 598-605.

[10] Acernese, F., Giordano, G., Romano, R., De Rosa, R., & Barone, F. (2008). Mechanical monolithic horizontal sensor for low frequency seismic noise measurement. Review of scientific instruments, 79(7), 074501.

[11] Acernese, F., Giordano, G., Romano, R., & Barone, F. (2012, September). Compact tunable monolithic sensors for vibration monitoring and control of structures and very low frequency large band characterization of sites. In 15th World Conference in Earthquake Engineering (pp. 24-28).

[12] Collette, C., Nassif, F., Amar, J., Depouhon, C., & Gorza, S. P. (2015). Prototype of interferometric absolute motion sensor. Sensors and Actuators A: Physical, 224, 72-77.

[13] Watchi, J., Ding, B., Matichard, F., & Collette, C. (2016). Development of a high-resolution optical inertial sensor for sub-hz seismic isolation (ISMA2016 International Conference on Noise and Vibration Engineering, 19-21 September 2016 (Leuven, Belgium))

[14] Wielandt, E., & Streckeisen, G. (1982). The leaf-spring seismometer: Design and performance. Bulletin of the Seismological Society of America, 72(6A), 2349-2367.

[15] Ponceau, D., Millier, P., & Olivier, S. (2008, April). Subnanometric Michelson interferometry for seismological applications. In Optical Sensors 2008 (Vol. 7003, p. 70030U). International Society for Optics and Photonics.

[16] Saulson, P. R. (1990). Thermal noise in mechanical experiments. Physical Review D, 42(8), 2437.

[17] Holcomb, L. G. (1989). A direct method for calculating instrument noise levels in side-by-side seismometer evaluations. HISTORY, 2, 1.

Experimental investigation on the acoustic impedance of Helmholtz resonators using an accelerometer for the volume velocity source

G. P. Guimarães[1], I. T. Ribeiro[1]
[1] Universidade Federal de Ouro Preto, Escola de Minas, Department of Mechanical Engineering
Campus Morro do Cruzeiro, S/N, Ouro Preto - MG, Brazil
e-mail: **paulinelli.gpg@ufop.edu.br**

Abstract
Helmholtz resonators (HR) are devices used to control the acoustic field inside cavities in a specific frequency band. Its impedance depends on the geometry, the radiation and viscous damping effects, whose models need to be improved. This study consists of an experimental investigation using a cylindrical cavity, a loudspeaker and some HRs. The volume velocity of the source is estimated by a lightweight accelerometer attached to the loudspeaker cone and the sound pressure is measured by a microphone inside the cavity. The Frequency Response Functions measured represent the acoustic impedance itself (ratio between sound pressure and volume velocity). Four HR were used (two tuned to 170 Hz and two tuned to 250 Hz, having its volumes as the difference). The main results are: (i) well measured impedance functions using the proposed volume velocity source, (ii) identification of the HR behavior on the functions, and (iii) possibility in discriminating the acoustic attenuation capacity of each device.

1 Introduction

Helmholtz resonators (HR) are devices with resistive and reactive characteristics widely used to control the acoustic behavior inside cavities in a narrow frequency band [1]. Its natural frequency depends on the dimensions and geometry of the HR and it is tuned to the frequency whose amplitude must be suppressed into the cavity.

A HR consists of a cavity and a neck. For this work, the HR is attached to a tube (Figure 1), at which the sound will be attenuated. The HR dimensions must be smaller than the minimum wavelength of interest in order to consider it as an element with lumped parameters connected to a geometric discontinuity. The condition of attachment is that the oscillatory volume flow in the neck is equal to that imposed on the fluid in the cavity, thus the air elastic property of the neck fluid is neglected, being treated as an incompressible volume [2].

Acoustic impedance [2] is related to how coupled regions of fluid or the contact of fluid and solid system interacts between them, indicating their acoustic properties. It can be possible to determine quantitatively the reflection and transmission of the sound wave between two fluid volumes with different shapes and the sound absorption, reflection and transmission occurred in the fluid and solid system.

The formulation for acoustic impedance (Z) is basically expressed by the ratio of complex amplitude of harmonic pressure (p) to the associated volume velocity (Q). Thus, the acoustic impedance is a complex quantity and can be stated as [2]:

$$Z = \frac{p}{Q} = \frac{p}{v.S} \tag{1}$$

where v is the particle velocity and S the associated surface area.

The acoustic impedance of a tube, with a source at one end inducing a velocity inside it, can be obtained at a central point on the surface (the same one where it is applied the excitation). It can be expressed as [2]:

$$Z_{tube} = \left(\frac{\rho c}{S}\right) j \cdot \cot K l_T \tag{2}$$

where K is wave number represented for $K = \omega/c$, S is the cross-sectional area of the tube, c is the sound velocity, ω is the frequency and l_T is the length of tube.

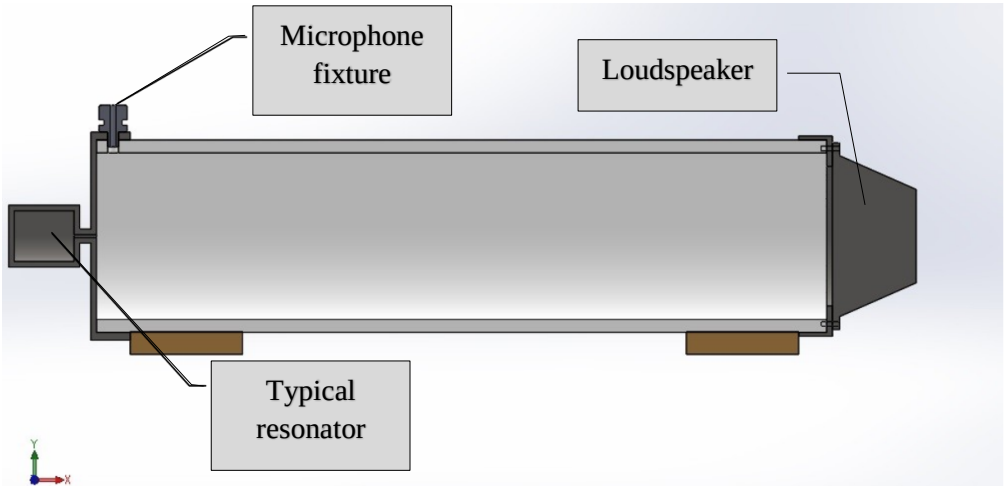


Figure 1: Schematic of a HR attached to a tube

For the HR, the reactance (imaginary part of impedance) depends on the resonator geometry and the frequency. It is well modelled and validated. The resistance (real part of impedance) models need to be improved. The RH resistance is explained by two portions: (i) the radiation resistance of the neck, and (ii) the viscous damping effect of the air mass while it oscillates inside the neck. In this way, the manufacturing issues (as neck roughness or neck termination) influence the resistance behavior.

The natural frequency of a Helmholtz Resonator depends on its dimensions:

$$\omega_{RH} = c\sqrt{\frac{A_p}{l_{eff} V_c}} \tag{3}$$

where and Ap is the neck area, Vc is the cavity volume and l_{eff} is the effective neck length, which includes a correction factor (δ) for mass-loading due to air entrainment at the neck extremities $l_{eff} = l + \delta$ [3].

The acoustic impedance can be written as a function of frequency and can characterize acoustic systems [4]. In this way, such impedance can be obtained as a function of frequency, a sort of Frequency Response Function.

This work presents an experimental investigation on the acoustic impedance estimation using a volume velocity source based on the measurement of the loudspeaker cone acceleration. The goal focuses on the identification of HR behavior when coupled to a cavity.

2 Acoustic impedance function estimation

ASTM E1050-12 standardizes a well-known method to measure acoustic impedance of absorbing material, using the two-microphones methodology. Such standard method uses a cylindrical tube as main cavity. At one end is mounted the specimen and a sound source is placed at another end, which provides a broad band signal. Two microphones are placed near the specimen. In order to guarantee a plane wave propagation for a specific frequency range inside the tube, its dimensions are calculated [5].

The present study considers a tube as main cavity also. A sound source is located at one extremity and a fixture is placed at the other extremity to receive the Helmholtz resonator under test (Figure 1). A lightweight accelerometer is attached to the sound source (loudspeaker cone). The pressure response can be measured by a microphone in some points inside the tube, but one at a time.

In this way, it is presented here the estimation of the acoustic impedance via one microphone e one volume velocity sensor approach.

Since the volume velocity of a portion of fluid very closed to a surface can be approximated by the velocity of such surface, the volume velocity of a loudspeaker cone can be estimated by the product of the velocity and the cone surface, as can be seen from equation (1): $Q = v.S$.

Based in the fact that the measurement of acceleration implies in low cost instrumentation in recent years, the cone velocity can be expressed by the acceleration signal integration, and the volume velocity can be estimated from the cone area (*S*) and acceleration (*a*) by:

$$Q(t) = \mathrm{S} \int a(t) \cdot dt \tag{4}$$

Considering the estimation process [6] of frequency response of a time-invariant system, the Frequency Response Function (FRF) *H(ω)* of an acoustic system (whose volume velocity (*Q*) is the input and pressure (*p*) is the output) can be reached [4] by:

$$H_{pQ}(\omega) = \frac{G_{Qp}}{G_{QQ}}, \text{ whose unit is } \left[\frac{Pa}{m^3/s}\right] \tag{5}$$

where G_{Qp} is the cross spectral density function between volume velocity and pressure, and G_{QQ} is the power spectral density function of the volume velocity.

The acoustic impedance from equation (1) can be rewritten as the Acoustic Impedance Function, which depends on the frequency:

$$Z(\omega) = \frac{P(\omega)}{Q(\omega)} \tag{6}$$

If the acoustic system input is the volume velocity quantity and the output is pressure quantity, the estimated FRF is the acoustic impedance function itself:

$$Z(\omega) = \frac{G_{Qp}}{G_{QQ}} \tag{7}$$

3 Methodology

A test rig was developed to estimate the acoustic impedance function of cavities. Four Helmholtz resonators were coupled, one at a time, to the cavity. Five test configurations were performed. The first one considers the tube without HR (one end closed, the other end with the sound source). The other configuration considers each one of the HR presented below.

A comparative analysis was done indicating the effect of each HR on the behavior of the tube, using the acoustic impedance function approach.

3.1 Experimental setup

The experimental setup shown in Figure 2 consists of a steel tube 650 mm long and 155.6 mm in diameter. Such dimensions allow a frequency range up to 1000 Hz, as calculated by the standard [5]. The sound source (loudspeaker JBL 6W4P Selenium Pro Woofer) was installed in right extremity of the tube. The loudspeaker low frequency cutoff is around 80 Hz. Then, the setup frequency band is considered from 80 to 1000 Hz. The source was supplied by an amplifier (NCA – AB 100, mono, 100 W @ 4 Ohms) which is controlled by a notebook soundboard, that provides a random noise covering the frequency band of interest.

The HR under test was installed at the left extremity, one at a time. Two microphone positions were considered: one very close to the loudspeaker (10 mm distance), whose acquisition and processing provides the point FRF; the other close to the resonator (10 mm distance), that provides the transfer FRF.

The microphone (G.R.A.S., Type 40PH. Sensitivity: 49.84 *mV/Pa*) positioning details can be observed in the Figure 3 (left).

The volume velocity of the source (or source strength) was estimated using a lightweight low-cost MEMS accelerometer (Analog Devices ADXL335 triaxial. Sensitivity 0.3 *g/V*) attached to the loudspeaker cone (Figure 3 - right). The accelerometer yields signals related to three axes. In this way it was possible to perform a compensation for misalignment and/or positioning errors of the sensor.

The sensors were connected to the acquisition module (National Instruments, NI 9234, ±5 V, IEPE, 4 Analog input, 51.2 kS/s/ch) that is connected to a notebook with LabVIEW 2015 SP1.

The algorithm was developed in LabVIEW. It performs the acquisition of the sound pressure and the acceleration simultaneously. The signal from the accelerometer are integrated to achieve the cone velocity and then multiplied by the cross-sectional area of the cavity (as presented in equation (4)), in order to estimate the instantaneous volume velocity (units in m^3/s) of the source.

The FRF is calculated considering the volume velocity as the excitation and the sound pressure (units in *Pa*) as the response (equation (5)). In such configuration, the FRF is the acoustic impedance function itself (equation (7)).

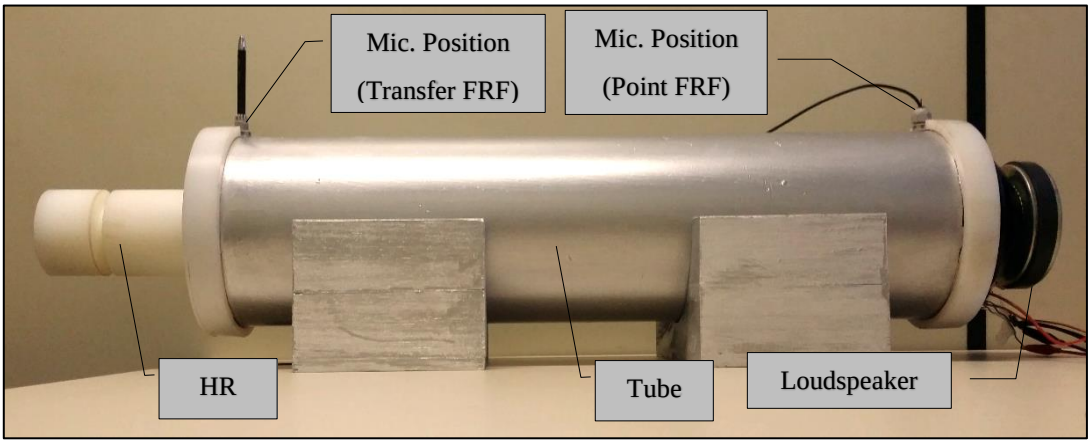


Figure 2 – Experimental setup overview

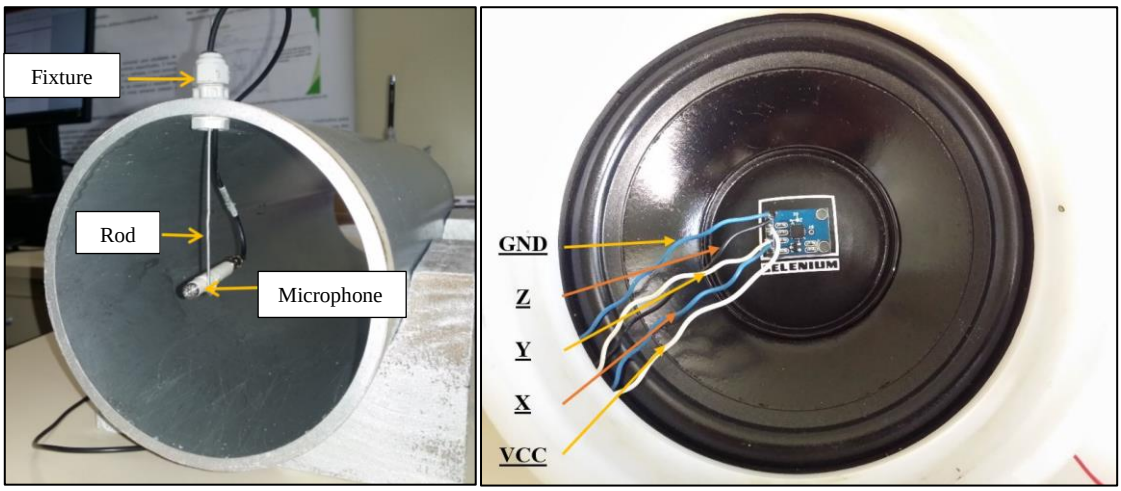


Figure 3 - Microphone positioning (left) and the accelerometer attached to the loudspeaker cone (right)

3.2 Helmholtz resonators

Four HRs were used into the investigation. The HRs topology were based on a cylindrical shape, having a piston to vary the cavity volume (Figure 4) and hence its natural frequency (the tuning process).

Two HRs were tuned to 170 Hz and the other two tuned to 250 Hz. In fact, there are one type of resonator with a smaller neck volume (type *A*) and another with a larger neck volume (type *B*) to each tuned frequency. The HRs dimensions can be observed in Table 1.

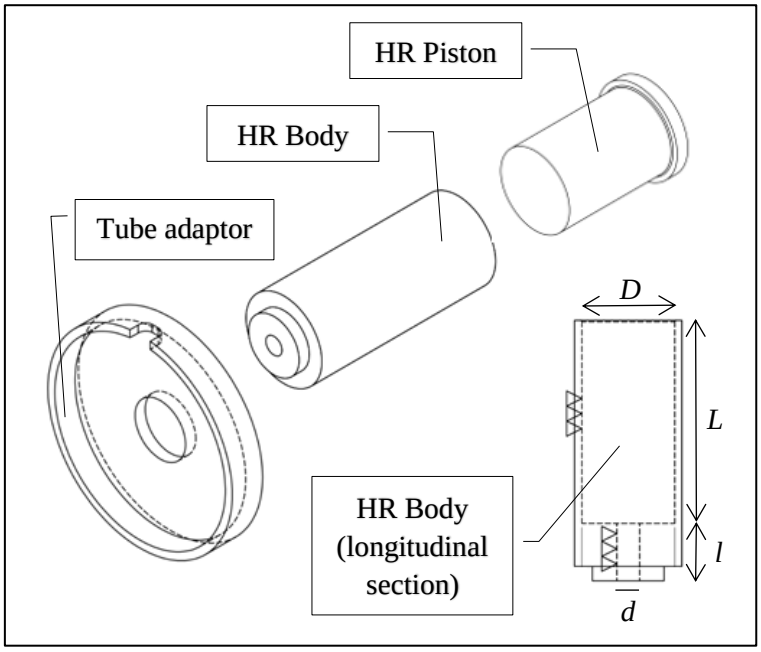


Figure 4: Helmholtz resonator topology

[*mm*]	**170-A**	**170-B**	**250-A**	**250-B**
d	5	16	5	16
D	20	40	20	40
l	45	65	45	65
L	53.1	121.7	23.2	55.0

Table 1: Helmholtz resonators dimensions

4 Results and discussion

The module and phase angle plots for point and transfer FRFs, or the acoustic impedance functions, related to the tube without HR (or with closed end) can be observed in Figure 5. Such functions presented clear resonance peaks and phase angle inversions of 180 degrees at the acoustic natural frequencies of the cavity. The anti-resonances could be observed between two resonance peaks in the point FRF module for acoustic system as it is verified in mechanical (solid) systems [7]. The high pass filter roll of related to the microphone channel can also be observed close to 20 Hz. The results outside the nominal frequency range (80 up to 1000 Hz) were also presented. In general, the measured impedance functions presented an expected behavior using the proposed volume velocity source.

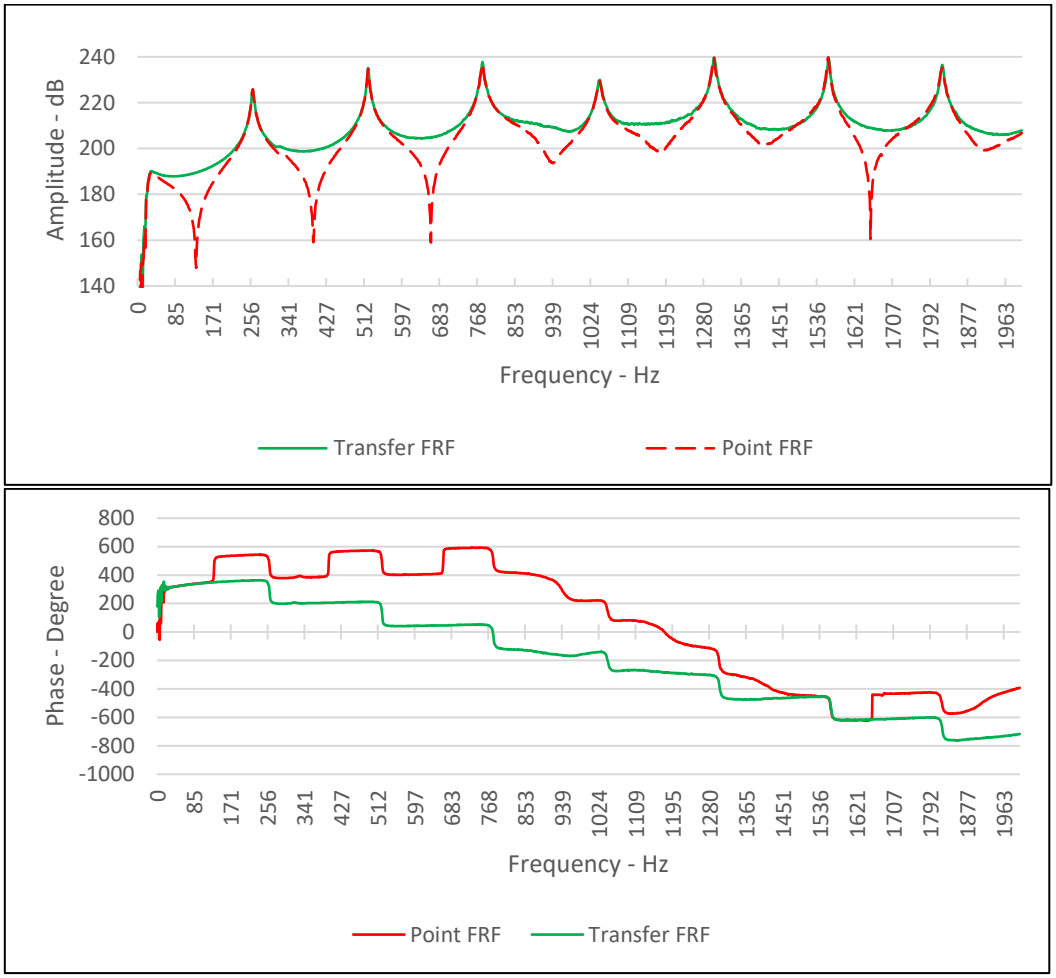


Figure 5: Module (above) and phase angle (below) for closed tube: Point and Transfer FRFs

A comparison among the impedance functions (point FRFs) measured for the cavity without resonator and with each one of the HRs are presented in Figure 6 (tuned to 170Hz) and Figure 7 (tuned to 250Hz).

The influences of the HRs tuned to 170 Hz (Figure 6) are evidenced when compared to the impedance function of the closed tube. Such frequency corresponds to the FRFs low pressure (response) levels region. Nevertheless, the presence of the HR behavior could be verified. For the smaller volume HR (170-A) a very slight variation was observed in the impedance function around 170Hz. For the larger volume HR (170-B) an extra resonance peak is present, comparing to the closed tube. This behavior was expected, considering the HR as an additional one-degree-of-freedom system attached to the tube. The resonator with smaller volume presented smaller influence over the impedance function, while the resonator with larger volume presented higher effect on the tube impedance function.

In the closed tube impedance function (without resonator), there is an acoustic natural frequency in 250 Hz (Figure 7). For the HRs tuned to this frequency, two resonance peaks in the impedance functions became present around the closed tube natural frequency for the first mode. Such behavior is similar to the last case (Figure 6), but the efficiency in attenuating the response is higher. For the smaller HR (250-A) the average attenuation is 10 dB at the frequencies around the tube natural frequency. Two smoothed peaks were noted, confirming the degree-of-freedom increment. For the larger HR (250-B) the attenuation at the natural frequency of the tube is higher than 25 dB. The two peaks are more spaced each other, creating a band with considerable attenuation. Again, the difference between both HR could also be verified and can be associated to the HR neck volume: the higher the HR neck volume, the higher the attenuation.

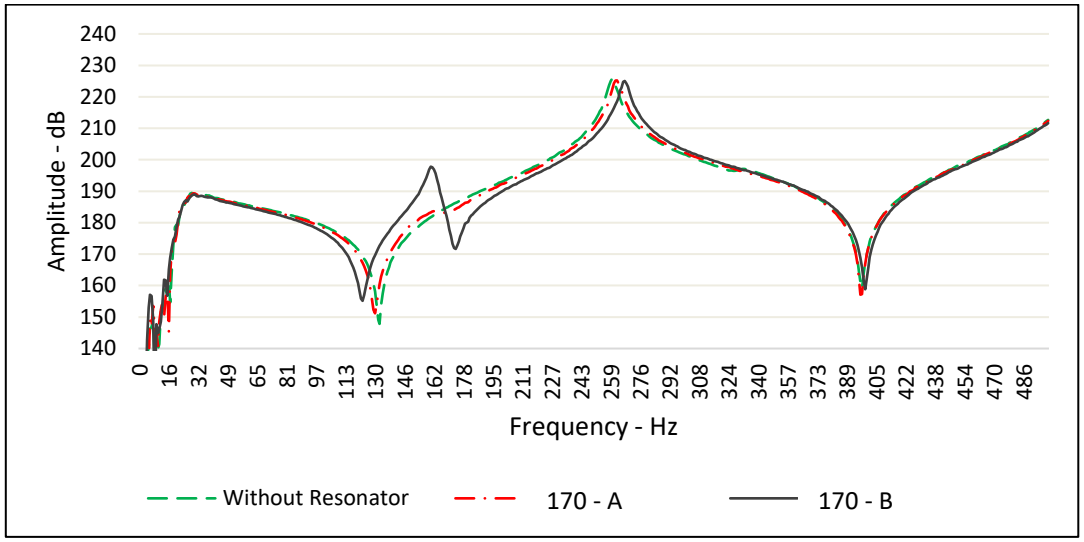


Figure 6: Impedance functions (point FRF) for 170 Hz resonators

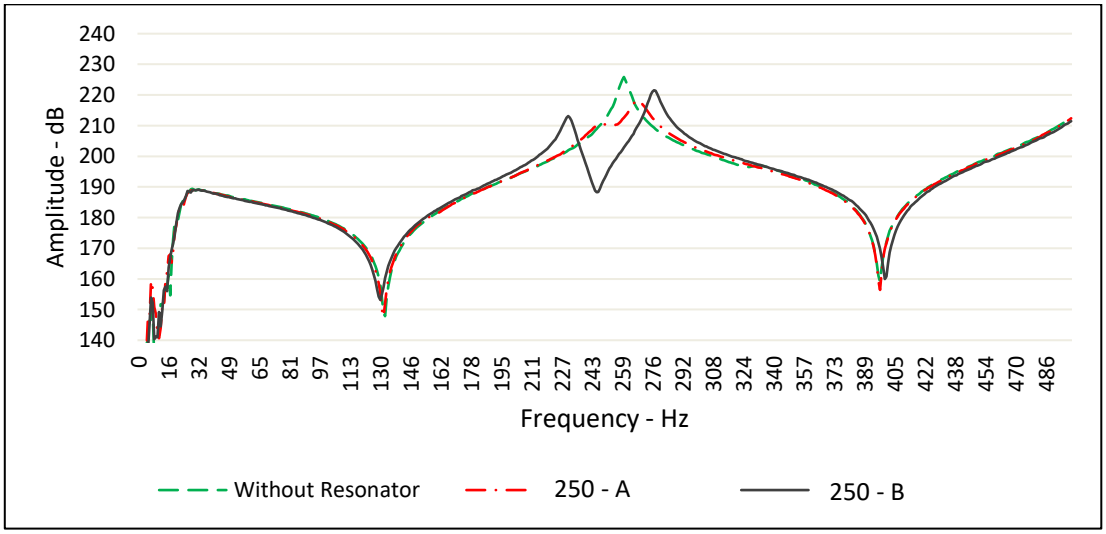


Figure 7: Impedance functions (point FRF) for 250 Hz resonators

5 Conclusion

This investigation indicates that the proposed volume velocity estimation (using the accelerometer as the sensor) for the acoustic source resulted in well measured impedance functions. Similar behavior could be observed in FRFs obtained from commercial volume velocity sources [4]. More investigation need to be made to promote the method to a higher level of development, including the measurement uncertainty analysis.

It was possible to identify the HR behavior on the functions when compared to the cavity without resonator. In addition, it was possible to discriminate the acoustic attenuation capacity of each device. The higher the volume of the resonator neck, the greater the mass of air contained in this region and consequently the greater the attenuation, as well as presented in the results from an equivalent numerical study [8].

The results were considered suitable to continue the development in the next steps of the research, that aims the identification of the HR parameters, i. e., to perform the parametric identification from the non-parametric model (impedance functions).

Acknowledgements

This work was financially supported by the Research Support Foundation of Minas Gerais (FAPEMIG), the National Council for Technological and Scientific Development (CNPq), the Coordination for the Improvement of Higher Education Personnel (CAPES) and the Gorceix Foundation. The authors gratefully acknowledge to the School of Mines and the Federal University of Ouro Preto (UFOP) for the support.

References

[1] H. S. Sang, H.K. Yang, *Silencer Design by using array resonators for low-frequency band noise reduction*. Journal Acoustic Society of America, Vol. 118, No.4, (2005) pp. 2332–2338

[2] F. J. Fahy, *Foundations of engineering acoustics*, Academic Press, London (2001).

[3] J. M. de Bedout, M. A. Franchek, R. J. Bernhard, L. Mongeau, *Adaptive-passive noise control with self-tuning Helmholtz resonators*, Journal of Sound and Vibration, Vol. 202, No. 1, (1997) pp. 109-123.

[4] G. P. Guimarães, R. Pirk, C. D'A. Souto, L. C. S. Góes, *Analysis of the acoustical behavior of cavities using impedance functions*, Journal of the Brazilian Society of Mechanical Sciences and Engineering, Vol. 38, No. 4, Springer (2016), pp. 1103-1111

[5] ASTM standards: E1050-12, *Standard Test Method for Impedance and Absorption of Acoustic Material using a Tube, Microphones and a Digital Frequency Analysis System*.

[6] J. S. Bendat, A. G. Piersol, *Random data: analysis and measurament of procedures*. Hoboken : John Wiley & Sons (2000).

[7] D. J. Ewins, *Modal Testing: Theory, Practice and Application*. 2ª. ed. Hertfordshire: Research Studies Press LTD. (2000).

[8] B. O. Mendes; G. P. Guimarães. *Numerical study of the Helmholtz Resonators behavior using impedance functions*. In: *Proceedings of the 23rd ABCM International Congress of Mechanical Engineering, Rio de Janeiro, Brazil, 2015 December 6-11*, (2015).

Compressive sensing-moving horizon estimator for periodic loads: experimental validation in structural dynamics with video-based measurements

M. Kirchner [1,2], **J. Croes** [1,2], **F. Cosco** [1,2], **B. Pluymers** [1,2], **W. Desmet** [1,2]
[1] KU Leuven, Department of Mechanical Engineering,
Celestijnenlaan 300, B-3001, Leuven, Belgium
e-mail: **matteo.kirchner@kuleuven.be**

[2] DMMS Core Lab, Flanders Make

Abstract
The compressive sensing-moving horizon estimator (CS-MHE) is an approach for joint state/input estimation. It integrates compressive sensing principles into a moving horizon estimator, enabling to exploit shape functions to model an input, resulting in better observability and wider input bandwidth in comparison to other input models. The authors have recently extended the CS-MHE to the estimation of complex quantities. In particular, Fourier shape functions can be instrumental to model a load which exhibits some form of periodicity. This paper presents an experimental validation in which a structure is excited by a shaker with several force profiles whose Fourier transforms include up to four components. This allows to investigate the performance of the CS-MHE on a physical setup, by taking into account aspects such as the necessary window length of the MHE and the number of measurements points for a certain sparsity, which is governed by the spectral content of the force input.

1 Introduction

The compressive sensing-moving horizon estimator (CS-MHE) is a multi step time domain approach for joint state/input estimation [1, 2, 3]. It exploits the capabilities of the moving horizon estimator (MHE) of minimizing the noise while correlating a model with measurements [4, 5], together with compressive sensing (CS) principles [6], which enable the observation of a relatively large number of input locations for a small set of measurements, whereas other existing techniques are characterized by intrinsic limitations when estimating multiple input locations, due to an observability decrease [2]. Furthermore, compressive sensing for input representation [7, 8, 9, 10, 11, 12] offers an alternative to the widely employed random walk model [13, 14]. In comparison to the latter, CS allows to efficiently model a high input bandwidth by exploiting a known input shape, resulting in the need for a coarser sampling.

The CS-MHE has been shown able to jointly estimate the states and a force impulse on a mechanical system in terms of input magnitude, time and position, provided that the input is sparse [1]. Furthermore, its applicability was recently extended to the estimation of complex quantities, which can be instrumental to model a load which exhibits some form of periodicity (*e.g.*, through Fourier components). Specifically, handling complex representations such as Fourier basis functions can be instrumental to estimate forces and torques in rotating machines, since their characteristics are of quasi-periodic nature [3]. This is particularly relevant, since physical quantities such as forces and torques are important for condition monitoring and control engineering, but are difficult or even impossible to be measured in a cheap, accurate and non intrusive manner.

This paper summarizes the formulation of the CS-MHE in case of a complex input representation through Fourier components (section 2), and presents an experimental validation in which a structure (a “U shaped”

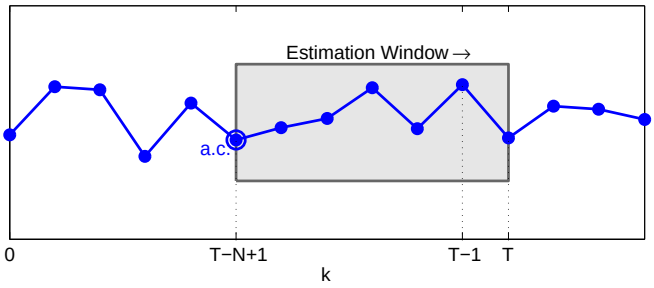


Figure 1: MHE strategy. Figure reproduced from [2].

assembly consisting of a horizontal beam clamped between two vertical mounts) is excited by a shaker with several force profiles whose Fourier transforms include up to four components (section 3). The structure is modeled by finite elements (FE), being such representation widely employed for industrial applications. The model is then reduced to a few mode shapes (each associated to a structural eigenfrequency). The measurement system relies on high-speed camera recordings, since they offer the possibility to build a flexible sensor array with respect to number of measurement points and their positioning, without modifying the system dynamics. Consequently, section 3 includes the image processing steps to extract displacement information from a sequence of images. The experiments allow us to discuss a few aspects related to the practical applicability of the CS-MHE, such as the window length of the MHE and the number of measurements points required for a certain input sparsity, which is governed by the spectral content of the load. Section 4 contains the experimental results, which we discuss in section 5.

2 The CS-MHE with a Fourier dictionary

This section gives the formulation of the CS-MHE for the case of an input described by Fourier components, which we employ for the experiments in this paper. Further details can be found in [3]. The formulas consider a generic discrete time state-space system such as eqs. (1–2), where x_k is the state vector, and the input u_k is represented by a linear superposition of (Fourier) basis functions ψ_j multiplied by a scale factor α_k. Subscript k denotes the current time step, and the elements $\psi_{k,j}$ belong to a (Fourier) dictionary Ψ. Subscripts k and j refer to a sampling point and to a Fourier component, respectively, *i.e.*, each column of Ψ models one basis function of the dictionary [3]. We employ regular sampling and equal amount of samples and Fourier components, and consequently Ψ is a square matrix of size $N-1$ that applies the inverse discrete Fourier transform (DFT) to a signal [15]. An estimation window of length N is defined between the discrete time steps $k = T-N+1$ and $k = T$, as shown in Fig. 1. w_k and v_k are two noise terms associated to model and measurements, respectively. Under the hypothesis of additive noise (which can always be satisfied thanks to discretization [14, 16]), the noise terms can be written down explicitly and substituted in the CS-MHE problem, that we present in eqs. (3–4) [2, 3]. Eqs. (1–2) are linear, and can also be obtained by linearizing a nonlinear system.

$$x_{k+1} = A_k x_k + B_k u_k + w_k = A_k x_k + B_k \sum_{j=T-N+1}^{T-1} \psi_{k,j}\alpha_k + w_k \tag{1}$$

$$y_k = C_k x_k + D_k u_k + v_k = C_k x_k + D_k \sum_{j=T-N+1}^{T-1} \psi_{k,j}\alpha_k + v_k \tag{2}$$

$$
\begin{aligned}
\underset{x_k,\alpha_k}{\text{minimize}} \quad & \left(x_{T-N+1} - \bar{x}_{T-N+1}\right)^\top P_a^{-1} \left(x_{T-N+1} - \bar{x}_{T-N+1}\right) \\
& + \sum_{k=T-N+1}^{T-1} \left(x_{k+1} - A_k x_k - B_k \sum_{j=T-N+1}^{T-1} \psi_{k,j}\alpha_k \right)^\top Q_k^{-1} \left(x_{k+1} - A_k x_k - B_k \sum_{j=T-N+1}^{T-1} \psi_{k,j}\alpha_k \right) \\
& + \sum_{k=T-N+1}^{T} \left(y_k - C_k x_k - D_k \sum_{j=T-N+1}^{T-1} \psi_{k,j}\alpha_k \right)^\top R_k^{-1} \left(y_k - C_k x_k - D_k \sum_{j=T-N+1}^{T-1} \psi_{k,j}\alpha_k \right) \\
& + \left(\alpha - \bar{\alpha}\right)^\top P_\alpha^{-1} \left(\alpha - \bar{\alpha}\right) + \lambda \sum_{k=T-N+1}^{T-1} \|\alpha_k\|_{\ell_1} \qquad (3)
\end{aligned}
$$

$$
\text{subject to} \quad x \in \left[x^{\mathrm{LB}}, x^{\mathrm{UB}}\right], \alpha \in \left[\alpha^{\mathrm{LB}}, \alpha^{\mathrm{UB}}\right] \qquad (4)
$$

Eq. (3) is the cost function of the optimization problem that the CS-MHE solves at every time step, and contains five terms to be minimized, which are weighted through covariance matrices. From top to bottom, they refer to the arrival cost $P_a \in \mathbb{R}^{N_S \times N_S}$, the model error $Q_k \in \mathbb{R}^{N_S \times N_S}$ and the measurement error $R_k \in \mathbb{R}^{n_r \times n_r}$, where N_S and n_r are the number of states and transducers, respectively. Q_k and R_k are related to the noise terms in eqs. (1–2), being $w_k \sim \mathcal{N}(0, Q_k)$ and $v_k \sim \mathcal{N}(0, R_k)$. Furthermore, covariance P_α weights the propagation of any estimated input to the next time step [1], and finally the ℓ_1-norm minimization of the sparse representation α_k of the input is balanced with the other components of the cost function through a constant weight λ, *i.e.*, λ balances the noise on model and measurements with the input sparsity. In fact, the ℓ_1-norm minimization promotes a sparse solution [17]. P_a and P_α in eq. (3) weight any information prior to the current estimation window, which is marked with a bar ($\bar{x}_{T-N+1}$ for the arrival cost and $\bar{\alpha}$ for any input). The arrival cost (a.c. in Fig. 1) carries the information from $k = 0$ to $k = T - N + 1$. We computed it through a smoothing approach, exploiting the covariance matrix of the optimization problem [18, 19, 20]. Finally, eq. (4) contains some bounds on the optimization variables (superscripts LB and UB denote lower and upper bounds, respectively).

The optimization problem (3–4) can be written in matrix form. It includes complex variables and it can be recast into a standard form second order cone problem (SOCP) [3, 21, 22]. We solved the SOCP in MATLAB® by exploiting the modeling language YALMIP [23] and the solver MOSEK [24].

3 Experimental test setup

The test setup on which we demonstrate the CS-MHE for the estimation of a periodic load consists of a 1 m long aluminum beam clamped on each side to a vertical mount, which is fixed to the ground (Fig. 2). Nine steel masses are attached to the beam every $\Delta x = 0.1$ m with the aim of lowering the eigenfrequencies and add complexity to the system. Table 1 indicates the geometry of the beam. The reference system is sketched in Fig. 2 (the y axis forms a right handed reference system with x and z), the origin being on the neutral axis of the beam at the left mount.

We built a FE model of the beam assembly and we updated it based on a series of three experimental modal analyses (EMAs) [25], using three uniaxial accelerometers at a fixed location and one impact hammer. We extracted the experimental eigenmodes in LMS Test.Lab [26]. First we considered solely the aluminum bar in free-free conditions in order to determine its Young's modulus (given its mass and Poisson ratio). Next we added the nine masses and we characterized the stiffness of the contact between the aluminum steel (we chose to model the contact as a uniform isotropic stiffness of the steel $\mathrm{E}_{\mathrm{steel}}$, given its mass and Poisson ratio). Finally we determined the stiffness of the vertical mounts $\mathrm{E}_{\mathrm{mount}}$, including the clamping stiffness. Table 2 reports the material properties that resulted from all three model updating procedures.

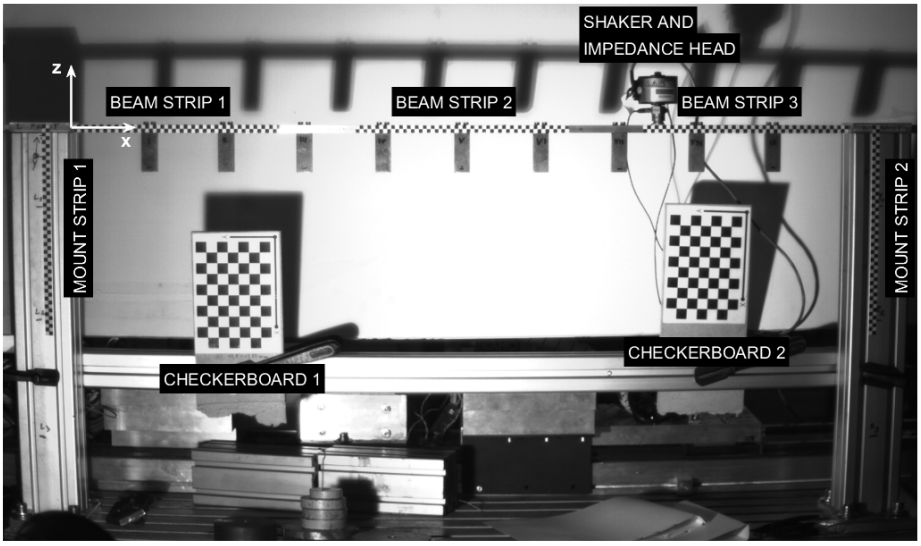


Figure 2: Beam setup.

Feature	Along axis	Size [m]
Beam length (L)	x	1.000
Beam width	y	0.015
Beam thickness	z	0.010
Steel mass height	z	0.050
Steel mass width	x	0.020
Steel mass thickness	y	0.015
Mount height	z	0.500
Mount cross-section	plane xy	0.080×0.080

Table 1: Geometry of the beam setup.

Part	Property	Value
Aluminum beam	ρ_{alu} $[\mathrm{kg/m^3}]$	2655.56
	$\mathrm{E}_{\mathrm{alu}}$ [GPa]	63.84
	ν_{alu}	0.33
Steel masses	ρ_{steel} $[\mathrm{kg/m^3}]$	8013.33
	$\mathrm{E}_{\mathrm{steel}}$ [GPa]	198.93
	ν_{steel}	0.29
Vertical mounts	ρ_{mount} $[\mathrm{kg/m^3}]$	2700.00
	$\mathrm{E}_{\mathrm{mount}}$ [GPa]	43.45
	ν_{mount}	0.33

Table 2: Material properties after model updating.

The model updating considered nine eigenfrequencies (up to 200 Hz) involving all three Cartesian planes, including a torsional mode around x. However, for the experiment that we discuss in this paper we applied a force along z (see the shaker position in Fig. 2), and three eigenmodes in the plane xy govern the dynamical behavior of the system. Table 3 and Fig. 3 show the results of the model updating for these three eigenmodes and their shapes, respectively. The ID numbers 1, 3, 8 derive from the whole mode set. We made use of the

Mode ID	Freq. EMA [Hz]	Freq. MoUp [Hz]	Error [%]
1	25.74	25.79	0.19
3	68.93	69.19	0.38
8	134.71	136.00	0.96

Table 3: Model update for the first three beam modes in plane xz.

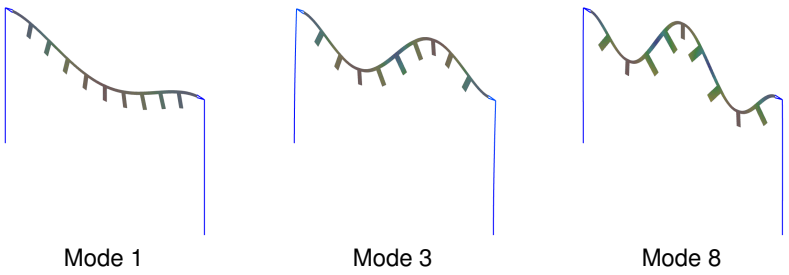


Figure 3: Mode shapes of the first three beam eigenmodes in plane xz.

model update procedure implemented in Siemens NX, which is parametric and works on a reduced model. The structure is made of simple components, such that beam and shell elements can represent the dominant mode shapes. In particular, we chose shell elements for the beam and the masses, and beam elements for the vertical mounts (we modeled the vertical mounts as a beam with cross-section 0.050×0.050 m). We set the damping values by comparing several FRFs between the FE model and the EMA acceleration measurements. We modeled each of the two clamping points through two rigid connections going from the top node of the vertical mounts to the top and bottom nodes of the aluminum beam.

In order to run the CS-MHE, we need the model of the test setup to be available in MATLAB®. We tackled this problem by extracting the FE mass and stiffness matrices and projecting them on modal coordinates [25]. This allows to build a reduced order state-space model in the form of eqs. (1–2), that takes into account only the eigenmodes under examination. Literature offers a few model order reduction (MOR) techniques [27, 28], but for the beam setup we selected the mode shapes based on the participation factors of the excitation configuration. This allows to improve the observability of the system at the expense of a very small loss of modeling accuracy.

Beside the state-space representation, we employed camera based measurements to investigate the influence of the number of measurement points. Compared to other sensor arrays (*e.g.*, accelerometers and strain sensors), camera measurements offer high spatial resolution and contact-less properties, such that a huge amount of information is available in one picture, and the model does not have to include any extra mass related to a sensor. In other words, a high speed camera is a flexible measurement system for what sensor number and placement are concerned. This choice is also supported by recent advances in vision technology and high-speed recording. We cite references [29, 30, 31, 32, 33, 34] for a few applications of camera measurements in structural dynamics.

If we look back at Fig. 2 we see how the beam was instrumented. In particular, there are three adhesive paper strips on the beam, each of them resulting in 53 markers equally distributed on a length of 0.260 m, *i.e.*, a marker every 0.005 m. Due to the lighting condition, we employ only the central strip ("BEAM STRIP 2" in Fig. 2). This corresponds of having up to 53 contact-less displacement transducers spanning the range from $x = 0.370$ m to $x = 0.630$ m. Furthermore, there are one shaker (THE MODAL SHOP Miniature Inertial Shaker K2002E01) and one impedance head (PCB ICP® 288D01), both located at $x = 0.750$ m and acting along the z axis. The impedance head measures the shaker force for validation purposes. Additional marker patterns are located on the beam for calibrating the system.

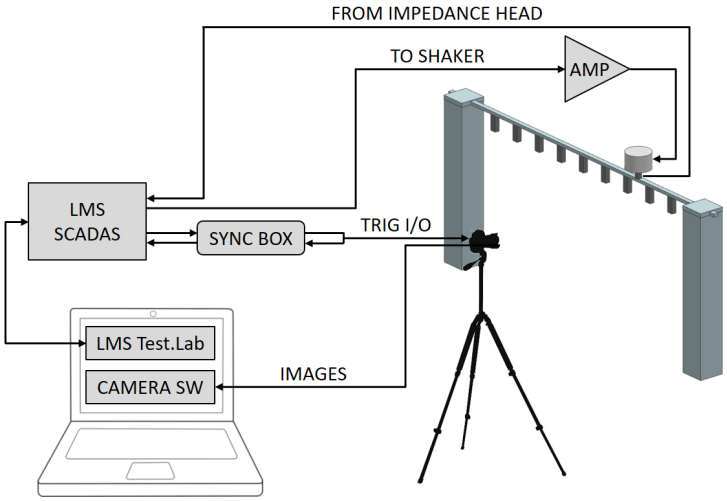


Figure 4: Schematic representation of the test setup.

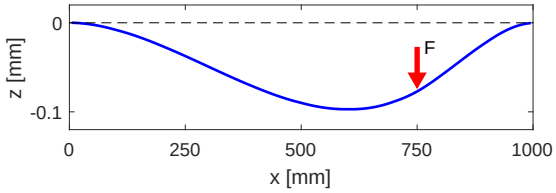


Figure 5: Beam deformed under the static load of the shaker (F), obtained through a FE analysis.

Next, Fig. 4 shows the schematic data flow when an experiment is running. The settings for the data acquisition system (LMS SCADAS) and for the camera (Ximea MQ042CG-CM) are defined via two dedicated programs. In LMS Test.Lab we set the duration of the experiment, the sampling rate, the signal for the shaker and the trigger for the camera. In the camera software we set the camera such that each frame is activated by the rising edge of the trigger signal and the exposure has a fixed duration. Furthermore, a signal indicating the exposure time is sent back to the LMS SCADAS for synchronization purposes. The camera software takes also care of saving the images on the PC. The LMS SCADAS is a data acquisition system with multiple inputs and outputs. Two outputs send the signal to the shaker and a trigger to the camera, while two inputs record the validation signal from the impedance head and an *exposure active* signal from the camera.

When performing vision based measurements, the first phase involves the estimation of the parameters for correcting the lens distortions (typically barrel or pincushion distortions) as well as the parameters to calibrate the scene, *i.e.*, transforming the pixel information into metric measurements. This requires standard digital image processing techniques, which can be found in references such as [35, 36]. Their implementation in MATLAB® is documented in [37], and many functions are now available in the image processing and computer vision toolbox (MATLAB® R2017a). For this reasons, we refer the interested reader to the MATLAB® help and references therein.

Once all the parameters of the camera and of the scene are available, we can apply a procedure to all images (*i.e.*, to every frame of a video acquired during an experiment) in order to extract displacement information in metric units. First, we determine the markers position up to sub-pixel resolution, and then we apply all adjustments. Finally, we need to correct the displacement measurements with the model. This step is not a standard procedure in image processing, and we will discuss it further here. If the shaker is attached to the structure and it is not active, we expect the beam to be deformed under its static weight (Fig. 5). Unfortunately, the displacement measurements do not match the expected deformation shape. This is the

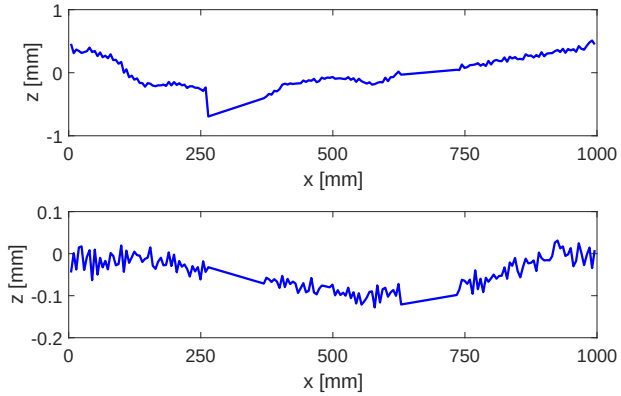


Figure 6: Displacement measurements at the first time step. From image processing (top) and corrected with the FE deformed shape (bottom).

consequence of multiple systematic uncertainties such as the boundary conditions of the beam (in particular the geometry of the connection, since it can cause static deformations) and the gluing of the marker strips, as well as stochastic uncertainties such as the markers printing accuracy and errors during image processing. We can spot some of these issues in Fig. 6 (top), which shows the measurements at the first frame of the simulation, *i.e.*, when the shaker is still off. For this reason, we corrected the measurements with the FE static simulation, obtaining the displacements in Fig. 6 (bottom). We applied such correction to all frames.

3.1 Observability considerations of the experimental setup

Before presenting the experimental results, let us briefly discuss the observability of the system in relation to number of measurements (n_r), number of inputs (n_u) and window length (N). For the system to be observable, matrices A and C of the state space representation need to satisfy condition $rank(\mathcal{O}) = N$, where $\mathcal{O}$ is the observability matrix in Eq. 5 (left) [14, 38], which holds also in case of an augmented system for joint state/input estimation. Fig. 7 (left) shows the region in which observability is satisfied, assuming a random walk model for the input representation [2, 13], and referring to the best theoretical situation in which the locations of both inputs and measurements are not critical. In fact, observability can decrease due to local problems (typically sensor and/or load applied to a nodal line. In such situation, other tests such as the Popov-Belevitch-Hautus (PBH) test for local observability can provide further information [38, 39]. Each plane in Fig. 7 (left) refers to a constant number of inputs. We note that the system is not observable with less than 2 sensors and 3 time steps, and observability gets more critical with a higher number of inputs.

$$\mathcal{O} = \begin{bmatrix} C \\ CA \\ \vdots \\ CA^{N-1} \end{bmatrix} \qquad n_r \geq \mathrm{c} \cdot S \log\left(\frac{N}{S}\right) \tag{5}$$

The rank of the observability matrix saturates quite fast, *i.e.*, after the rank is satisfied it is not worth to add any further information (that may come from additional sensors or time steps). Accordingly, we can infer that the random walk works well for a short window. On the other hand, let us consider Eq. 5 (right) of compressive sensing [6], which indicates how the number of required measurements scales with the signal length N and its sparsity $S \leftrightarrow n_u$, *i.e.*, S is the number of nonzero components of a signal of length N, and it is connected to the number of inputs [2] (c is a small constant).* Fig. 7 (right) shows a numerical example of Eq. 5 (right) for a signal up to $N = 100$ and $S = 50$ (with $\mathrm{c} = 3$). We note that n_r scales strongly with

*For the details concerning the validity of Eq. 5 (right) we refer to reference [6].

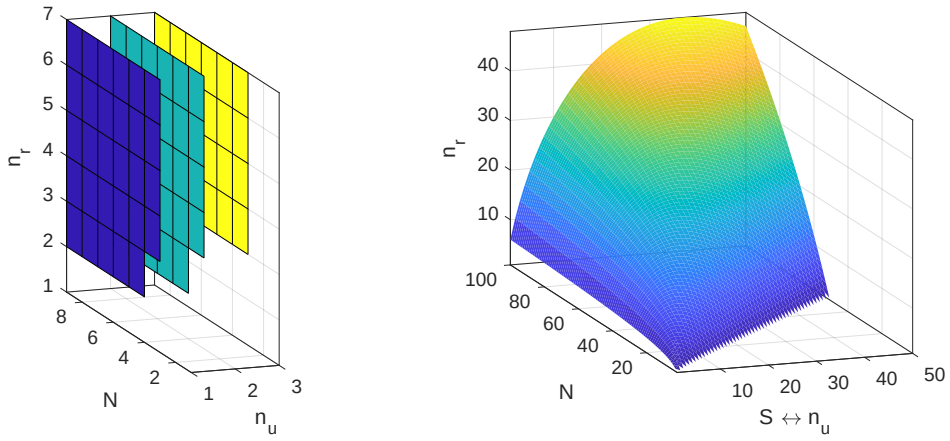


Figure 7: Left: region of observability in function of the number of time steps (N), inputs (n_u) and measurement points (n_r). Right: number of measurements required by compressive sensing in function of signal length N and sparsity S, according to Eq. 5 (right), with $\mathrm{c}=3$.

S and smoothly with N especially for small values of S, indicating that given a certain sparsity S a longer signal may bring in extra information at a price of a very reasonable amount of extra measurements. In other words, a long MHE window may be worth if CS is used for input modeling. In a previous research we have already indicated that the number of measurements required by the CS-MHE scales with S [2], and for the specific case of this paper the CS-MHE requires a higher number of measurements in comparison with the random walk model, especially in the case of the estimation of multiple Fourier components (since S increases). However, it can generate very accurate results at a relatively low sampling rate. In this sense, we can consider compressive sensing as a complementary approach to other approaches for input modeling such as the random walk. The exact domain of applicability of compressive sensing requires further investigation, and remains an interesting open point for future developments of the CS-MHE.

4 Experimental results

In this section we present the experimental results, and we investigate the influence of a force input composed by an increasing number of sine waves on the CS-MHE accuracy. We remind that input sparsity is a key ingredient of the CS-MHE. In Fourier domain, this means that only a few shape functions belonging to a dictionary should represent the load. An increasing amount of sines deteriorates the sparsity, and the major aim of the experiment is to investigate how to cope with this issue. Table 4 shows the settings for a series of tests. Notation "$\min(n_r)$" in the third column refers to the minimum number of measurement points which is required to satisfy an observability requirement, and scales linearly with the number of sines (*i.e.*, with the input sparsity) [2]. The electrical signal that goes to the shaker has the same amplitude for each component. However, the dynamic response of the system composed by shaker and structure acts as a filter (with a low-pass tendency), causing the smoothing of higher frequencies. We acquired the data at 512 Hz, *i.e.*, the camera operated at 512 frames per second (fps).

From the fourth column of Table 4 we notice that the window length N varies with the number of sine waves. We made this choice *a posteriori* by choosing the smallest window length that generates a sufficient sparsity and guarantees that all frequencies are modeled, in order to avoid spectral leakage that would degenerate the sparsity level. We remind that a single sine wave consists of two complex conjugate peaks, and a further nonzero element is due to the static weight of the shaker (DC component).

Let us now present the estimation results. Fig. 8 refers to one sine and three measurement points (located at $x=0.370$ m, $x=0.500$ m, $x=0.630$ m). The two graphs on left hand side refer to the state estimation (three

Sinusoid #	Sinusoid Freq. [Hz]	$\min(n_r)$	N
1	128	3	17
2	64 128	5	33
3	64 128 192	7	33
4	64 128 160 192	9	33

Table 4: Settings for the experiment with multiple sines.

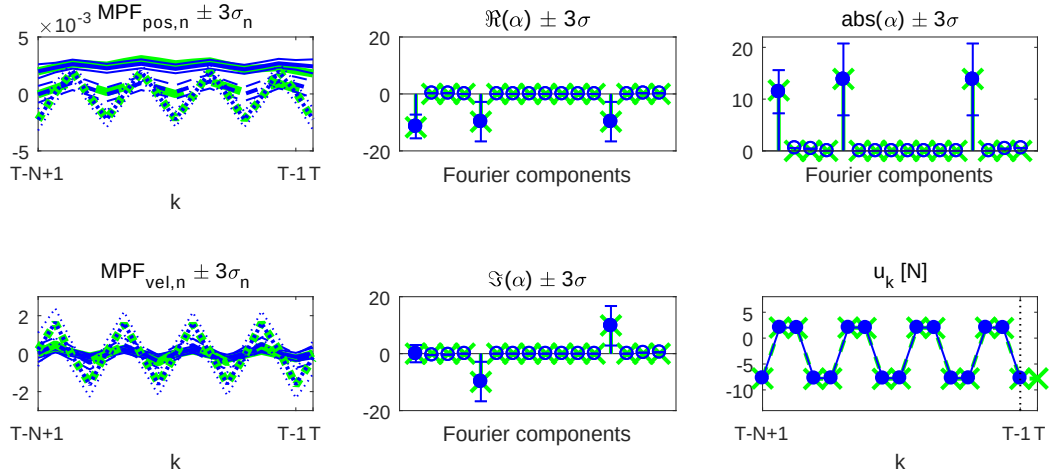


Figure 8: Results at iteration 1 for one sinusoid, obtained by considering 3 displacement sensors. Legend (state estimation): 1st mode (——); 2nd mode (- - -); 3rd mode (· · ·). The thick green lines are a reference from the model, the thick blue lines are the CS-MHE estimation, confined into two thin blue lines that represent the confidence level (MPF$_n$ $\pm$ $3\sigma_n$). Legend (input estimation): reference values (- - -×); CS-MHE estimation (——○); CS-MHE nonzero components (——●).

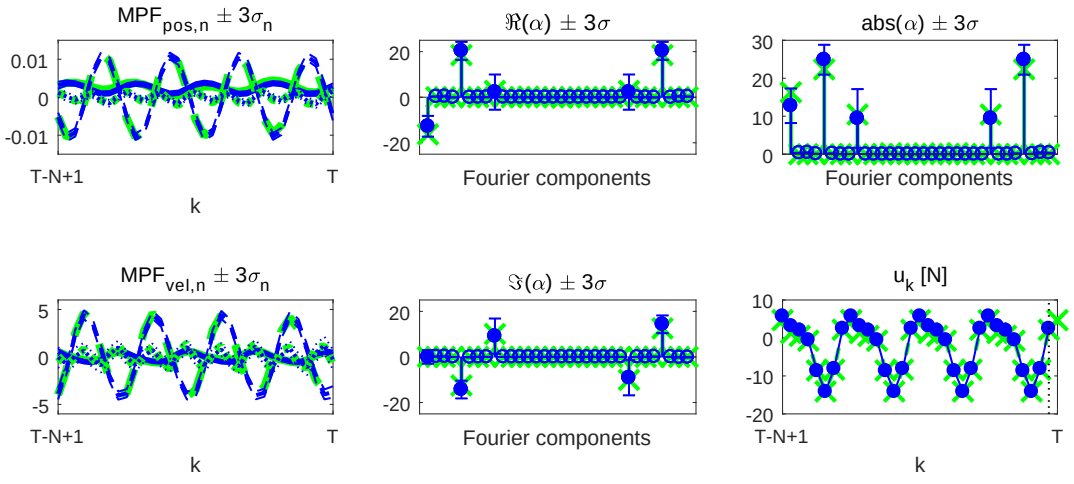


Figure 9: Results at iteration 1 for two sinusoids, obtained by considering 5 displacement sensors. Legend: see Fig. 8.

position modal participation factors (MPFs) – top, and their time derivatives – bottom). We obtained the green curves by evaluating the states with the model and the measured force, while the CS-MHE estimates are in blue. Consequently, a mismatch between those curves indicates a poor model accuracy for that specific load. The third eigenmode (mode ID 8 in Table 3) dominates the beam response, not surprisingly since this

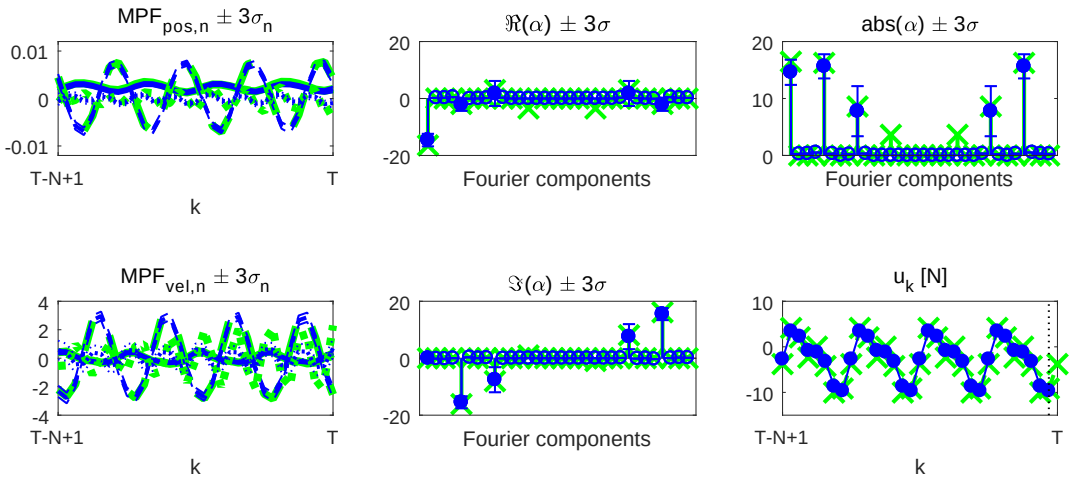


Figure 10: Results at iteration 1 for three sinusoids, obtained by considering 7 displacement sensors. Legend: see Fig. 8.

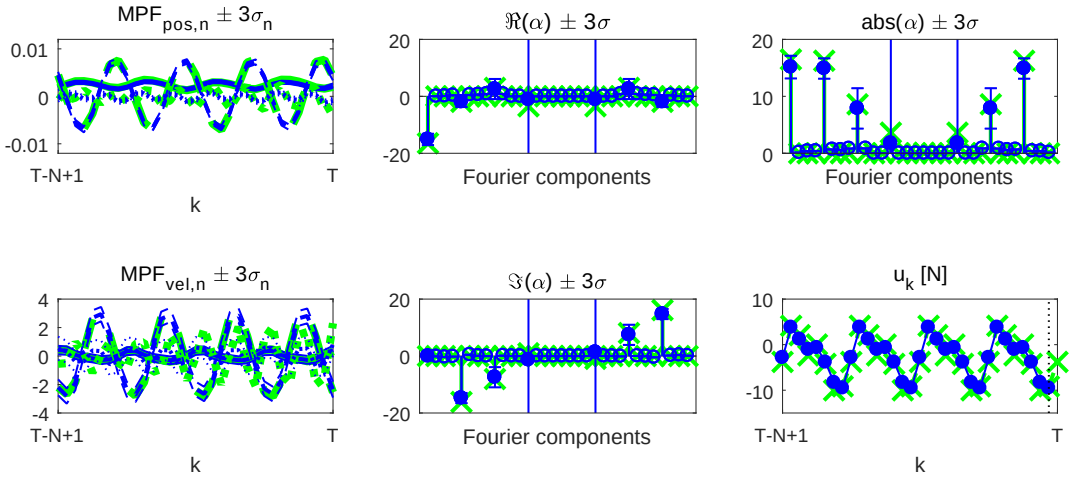


Figure 11: Results at iteration 1 for three sinusoids, obtained by considering 15 displacement sensors. The $\pm 3\sigma$ interval that falls outside the graph equals approximately ± 30. Legend: see Fig. 8.

eigenmode is the closest to the excitation frequency. The results of the input estimation are in the remaining four graphs of Fig. 8 (middle and right hand side). The reference values (green curves) come from the impedance head, to which we added the static weight of the shaker. By looking at the real and imaginary parts of the input (middle graphs) as well as the magnitude and time domain transformation (right graphs), we see that the input estimation (solid blue) follows well the measurements.

Next, Fig. 9 shows the results with two sine waves. We did not manage to estimate accurately both components keeping the same window length as the previous case, due to the deteriorated sparsity resulting from the extra component. Consequently, we chose $N = 33$, being this the next smallest number that includes the two frequencies indicated in Table 4. For an idea about the sparsity requirements we refer again to Eq. 5 (right) [6]. It is worth mentioning that in general every combination of number of sensors and sparsity requires a different calibration of the system, and this applies especially for the balancing weight λ. Accordingly, we tuned each scenario following the procedure indicated in reference [1].

Adding a third component produces the results of Figs. 10 and 11, where the importance of a good calibration becomes clear. From Fig. 10 we see that the third component is not being captured, which may suggest that

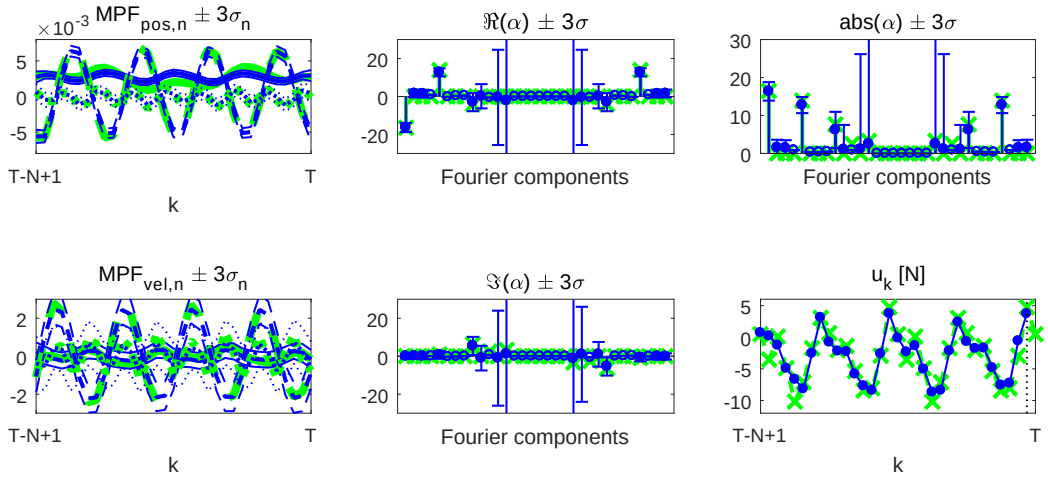


Figure 12: Results at iteration 1 for four sinusoids, obtained by considering 9 displacement sensors. Legend: see Fig. 8.

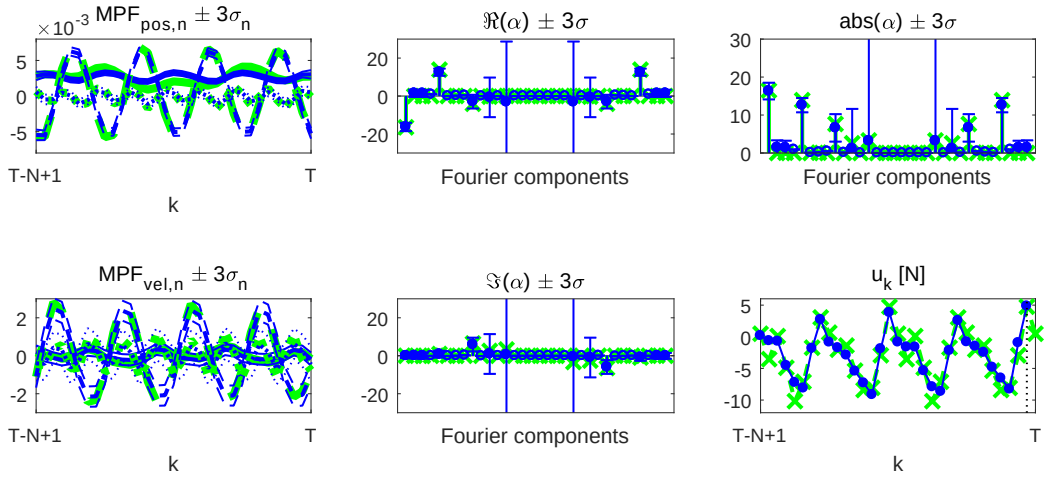


Figure 13: Results at iteration 1 for four sinusoids, obtained by considering 15 displacement sensors. Legend: see Fig. 8.

the window is too short. However, we can detect all components by keeping the same window length and adding measurement points (Fig. 11). This encourages the following two considerations:

- In case we want a minimum number of measurement points (governed by observability requirements), we may need to rely on the results in Fig. 10. These offer the smallest mean square error (MSE) for the given set of tuning parameters. The third component has a small amplitude in comparison with the other components, and it is likely that the filter treats it as noise.
  In case the third component is crucial for a specific application, we could attempt a finer tuning or alternatively we could choose a lower λ in order to relax the weight on the sparsity requirement, at the price of a possible higher MSE [1].

- In case the number of measurement points is not fixed, then adding measurements may be the way to proceed, as we pointed out in Fig. 11. In this context, it is important to underline that adding measurements also come with additional noise, which clearly reflects on the covariance of the optimization problem. In other words, adding a measurement does not always generate better results, since it may

# sines	N	n_r	λ	ε_Q	ε_R $[\mathrm{mm}^2]$	Error [%]	Fig.
1	17	3	0.34	2.0	$2{\cdot}10^{-4}$	0.6	8
2	33	5	0.17	1.9	$1{\cdot}10^{-3}$	4.1	9
3	33	7	0.17	0.3	$1{\cdot}10^{-3}$	5.2	10
3	33	15	0.21	0.3	$1{\cdot}10^{-3}$	4.8	11
4	33	9	0.04	0.3	$1{\cdot}10^{-3}$	6.7	12
4	33	15	0.07	0.3	$1{\cdot}10^{-3}$	6.8	13

Table 5: Settings for the experiment with multiple sines.

deteriorate the matrix conditioning. Such aspect plays an important role with our camera based measurements, where each point offers a different uncertainty due to the quality of the marker detection (that involves the marker itself in terms of typology, condition, positioning and light level), which we assumed to be the same for each marker. We can see how this affects the numerical stability of the covariance matrix by looking at the wide uncertainty bands of the third component in Fig. 11. Concerning this aspect, we believe that a rigorous noise assessment of the camera measurement system can improve the estimation results.

Finally, Figs. 12–13 show the results with four Fourier components and $n_r = 9$ and 15, respectively. To obtain these graphs we lowered λ not to fall into the problems that we already mentioned with regard to Fig. 10. In Fig. 12 we can see that with 9 sensors the CS-MHE does not capture the component with the lowest amplitude, whereas its neighboring frequencies become active instead. Having 15 sensors such as in Fig. 13 overcomes this issue. Further simulations indicated that this tendency applies also in case of longer windows, suggesting that it is not worth to further extend the estimation window.

5 Discussion and conclusions

We preformed the exercise of an increasing number of Fourier components in order to investigate the requirements and limits of the CS-MHE in terms of number of measurements, window length (and consequently number of basis functions in the dictionary) and tuning parameters (covariances and weight of the CS term) for an increasing sparsity. We showed good estimation results, but at the same time we are not yet able to identify clear relations that would bring the CS-MHE to a more mature technological stage. Table 5 shows the settings for the CS-MHE, where ε_Q and ε_R are weights on the diagonal of the model and measurements covariances (Q and R), respectively. In the second-last column we indicate an error in time domain (*i.e.*, after the inverse Fourier transform), averaged within the estimation window and computed as percentage with respect to the peak-to-peak amplitude that results from the sum of all active Fourier components. It is not a rigorous metric since a small phase discrepancy can have a big influence, but it gives an indication on the results accuracy, which we expect to further increase after a few iterations of the CS-MHE.

The model error has a significant effect on the experimental results, especially in relation to the input, *i.e.*, the accuracy of the modal participation factors is a key element for the force estimation. Different Fourier components at different frequencies do not have the same weight in the estimation, since their amplitude is scaled according to the dynamics of the system. Furthermore, different Fourier components excite the structure eigenmodes in a different way. Each eigenmode has a certain modeling error, resulting in the need to vary the covariance associated to the model in order for the filter to perform better. Accordingly, a comparison that takes into account only the number of Fourier components can be misleading, since their magnitude and frequency (connected to a certain modeling error) play an important role. In addition, a poorly modeled damping (which is likely to happen in practice) affects the dynamic response in neighborhood of the eigenmodes in a much stronger way than in other portions of the spectrum. In other words, a model may result to be less accurate in case of a broadband excitation. All these statements are typical considerations in model based estimation problems, where in general a good model improves the estimation accuracy.

Several factors determine the accuracy of the measurements. These include systematic as well as stochastic phenomena. First, the light has a strong influence on the measurement error. Furthermore, the quality of the markers, the accuracy of their locations and the chosen image processing algorithm cause systematic errors. At the same time, the stochastic behavior which is typical of measurement system is present. All uncertainties are also linked to the hardware, and in particular to the camera location, resolution, quantization and optics. Consequently, different measurement points have a different accuracy. Some points add less noise to the problem than others, and thus an increase in the amount of measurements may result in an improvement as well as a deterioration of the estimates. This aspect links to numerical stability and constitutes an interesting open point for future research.

The size of a Fourier dictionary depends on the length of the estimation window, within which the input should be as sparse as possible due to compressive sensing and observability requirements. This raises the question weather a relatively long window (static or possibly shifting in time by a whole window length) would outperform a more traditional MHE scheme for what the accuracy of the input estimation is concerned (we refer to a traditional MHE scheme as a MHE that aims at a short window for computational speed, shifting in time by one time step and relying on an accurate arrival cost). In the experiments of this paper we did not vary the window length by unity steps, not to introduce spectral leakage, *i.e.*, we always made sure that the frequencies of all active Fourier components of the input were modeled within the window. Current research is investigating a few approaches to cope with possible spectral leakage.

In this paper we showed a few experimental examples in which we employed a Fourier dictionary in order to model a periodic load. We chose a linear model, but the procedure can be extended to nonlinear systems provided that the state-space matrices are adapted accordingly. Possible applications include rotating machinery, where loads have a quasi-periodic nature. The experiments involved the topics of FE modeling, modal analysis, model update, model order reduction and high-speed camera measurements. We presented a series of experimental tests with an increasing number of Fourier components, in order to assess the feasibility domain of the CS-MHE in terms of number of measurement points, window length and system calibration needed in relation to sparsity. The experiments showed an accurate input estimation and at the same time they allowed to spot a few open points for future research, with the final aim of finding mathematical relationships that can bring the CS-MHE to a more mature technological stage.

Acknowledgments

This research was partially supported by Flanders Make, the strategic research center for the manufacturing industry, within the MoForM project. The Research Fund KU Leuven is also gratefully acknowledged for its support.

References

[1] M. Kirchner, J. Croes, F. Cosco, W. Desmet, *Exploiting input sparsity for joint state/input moving horizon estimation*, Mechanical Systems and Signal Processing, Vol. 101, (2018), pp. 237–253.

[2] M. Kirchner, J. Croes, F. Cosco, B. Pluymers, W. Desmet, *Compressive sensing-moving horizon estimator for combined state/input estimation: an observability study*, P. Sas, D. Moens, A. van de Walle, Editors, *Proceedings of ISMA2016 including USD2016, Leuven, Belgium*, 2947–2962.

[3] M. Kirchner, J. Croes, F. Cosco, W. Desmet, *Compressive sensing-moving horizon estimator for distributed loads*, Procedia Engineering, Vol. 199, No. C, (2017), pp. 447–452.

[4] C. V. Rao, J. B. Rawlings, *Constrained process monitoring: Moving-horizon approach*, AIChE Journal, Vol. 48, No. 1, (2002), pp. 97–109.

[5] E. L. Haseltine, J. B. Rawlings, *Critical evaluation of extended kalman filtering and moving-horizon estimation*, Industrial & Engineering Chemistry Research, Vol. 44, No. 8, (2005), pp. 2451–2460.

[6] E. Candes, M. Wakin, *An introduction to compressive sampling*, Signal Processing Magazine, IEEE, Vol. 25, No. 2, (2008), pp. 21–30.

[7] D. Ginsberg, C.-P. Fritzen, *New approach for impact detection by finding sparse solution*, P. Sas, D. Moens, H. Denayer, Editors, *Proceedings of ISMA2014 including USD2014, Leuven, Belgium*, (2014), pp. 2043–2056.

[8] A. Rezayat, V. Nassiri, B. D. Pauw, J. Ertveldt, S. Vanlanduit, P. Guillaume, *Identification of dynamic forces using group-sparsity in frequency domain*, Mechanical Systems and Signal Processing, Vol. 70-71, (2016), pp. 756–768.

[9] B. Qiao, Z. Mao, X. Chen, *Sparse representation for the inverse problem of force identification*, P. Sas, D. Moens, A. van de Walle, Editors, *Proceedings of ISMA2016 including USD2016, Leuven, Belgium*, 1685–1696.

[10] B. Qiao, X. Zhang, J. Gao, X. Chen, *Impact-force sparse reconstruction from highly incomplete and inaccurate measurements*, Journal of Sound and Vibration, Vol. 376, (2016), pp. 72–94.

[11] B. Qiao, X. Zhang, J. Gao, R. Liu, X. Chen, *Sparse deconvolution for the large-scale ill-posed inverse problem of impact force reconstruction*, Mechanical Systems and Signal Processing, Vol. 83, (2017), pp. 93–115.

[12] B. Qiao, X. Zhang, C. Wang, H. Zhang, X. Chen, *Sparse regularization for force identification using dictionaries*, Journal of Sound and Vibration, Vol. 368, (2016), pp. 71–86.

[13] F. Naets, J. Croes, W. Desmet, *An online coupled state/input/parameter estimation approach for structural dynamics*, Computer Methods in Applied Mechanics and Engineering, Vol. 283, (2015), pp. 1167–1188.

[14] D. Simon, *Optimal State Estimation: Kalman, H Infinity, and Nonlinear Approaches*, Wiley-Interscience (2006).

[15] M. Kirchner, E. Nijman, *Cylindrical nearfield acoustical holography using compressive sampling: feasibility and numerical examples*, P. Sas, D. Moens, H. Denayer, Editors, *Proceedings of ISMA2014 including USD2014, Leuven, Belgium*, 1531–1546.

[16] R. A. DeCarlo, *Linear Systems: A State Variable Approach with Numerical Implementation*, Prentice-Hall, Inc., Upper Saddle River, NJ, USA, (1989).

[17] S. Boyd, L. Vandenberghe, *Convex Optimization*, Cambridge University Press, New York (2004).

[18] C. V. Rao, J. B. Rawlings, J. H. Lee, *Constrained linear state estimation–a moving horizon approach*, Automatica, Vol. 37, No. 10, (2001), pp. 1619–1628.

[19] R. Lopez Negrete de la Fuente, *Nonlinear programming sensitivity based methods for constrained state estimation*, Ph.D. thesis, Carnegie Mellon University (Pittsburgh, PA), Department of Chemical Engineering (2011).

[20] R. Lopez Negrete de la Fuente, B. T. Lorenz, *A moving horizon estimator for processes with multi-rate measurements: A nonlinear programming sensitivity approach*, Journal of Process Control, Vol. 22, No. 4, (2012), pp. 677–688.

[21] S.-J. Kim, K. Koh, M. Lustig, S. Boyd, D. Gorinevsky, *An interior-point method for large-scale ℓ_1-regularized least squares*, IEEE Journal of Selected Topics in Signal Processing, Vol. 1, No. 4, (2007), pp. 606–617.

[22] M. S. Lobo, L. Vandenberghe, S. Boyd, H. Lebret, *Applications of second-order cone programming*, Linear Algebra and its Applications, Vol. 284, No. 1, (1998), pp. 193–228.

[23] J. Löfberg, *YALMIP : A toolbox for modeling and optimization in MATLAB*, *Proceedings of the CACSD Conference*, Taipei, Taiwan (2004).

[24] MOSEK ApS, *MOSEK Quickstart Guide Version 7.1 (Revision 60)* (2015).

[25] W. Heylen, S. Lammens, P. Sas, *Modal Analysis Theory and Testing*, KU Leuven, Department of Mechanical Engineering, PMA Section (2007).

[26] B. Peeters, H. Van der Auweraer, P. Guillaume, J. Leuridan, *The polymax frequency-domain method: A new standard for modal parameter estimation?*, Shock and Vibration, Vol. 11, No. 3-4, (2004), pp. 395–409.

[27] B. Besselink, U. Tabak, A. Lutowska, N. van de Wouw, H. Nijmeijer, D. Rixen, M. Hochstenbach, W. Schilders, *A comparison of model reduction techniques from structural dynamics, numerical mathematics and systems and control*, Journal of Sound and Vibration, Vol. 332, No. 19, (2013), pp. 4403–4422.

[28] R. R. Sanchez, m. Buchschmid, G. Müller, *Model order reduction techniques in structural dynamics*, M. Papadrakakis, V. Papadopoulos, G. Stefanou, V. Plevris, Editors, *ECCOMAS Congress 2016 – VII European Congress on Computational Methods in Applied Sciences and Engineering*.

[29] D. Feng, M. Q. Feng, *Identification of structural stiffness and excitation forces in time domain using noncontact vision-based displacement measurement*, Journal of Sound and Vibration, Vol. 406, No. Supplement C, (2017), pp. 15–28.

[30] J. Javh, J. Slavič, M. Boltežar, *The subpixel resolution of optical-flow-based modal analysis*, Mechanical Systems and Signal Processing, Vol. 88, (2017), pp. 89–99.

[31] J. Javh, J. Slavič, M. Boltežar, *High frequency modal identification on noisy high-speed camera data*, Mechanical Systems and Signal Processing, Vol. 98, No. Supplement C, (2018), pp. 344–351.

[32] J. Javh, J. Slavič, M. Boltežar, *Measuring full-field displacement spectral components using photographs taken with a dslr camera via an analogue fourier integral*, Mechanical Systems and Signal Processing, Vol. 100, No. Supplement C, (2018), pp. 17–27.

[33] R. H. Nady, M. Hagara, *A new procedure of modal parameter estimation for high-speed digital image correlation*, Mechanical Systems and Signal Processing, Vol. 93, (2017), pp. 66–79.

[34] L. Yu, B. Pan, *Single-camera high-speed stereo-digital image correlation for full-field vibration measurement*, Mechanical Systems and Signal Processing, Vol. 94, (2017), pp. 374–383.

[35] R. Gonzalez, R. Woods, *Digital Image Processing (2nd Edition)*, International Edition, Prentice Hall (2002).

[36] W. Pratt, *Digital Image Processing: PIKS Scientific Inside (4th Edition)*, A Wiley-Interscience publication, Wiley (2007).

[37] R. Gonzalez, R. Woods, S. Eddins, *Digital Image Processing Using MATLAB*, Pearson Prentice Hall (2004).

[38] S. Korovin, V. Fomichev, *State Observers for Linear Systems with Uncertainty*, De Gruyter Expositions in Mathematics, No. 51, De Gruyter, Berlin, Boston (2009).

[39] B. K. Ghosh, J. Rosenthal, *A generalized popov-belevitch-hautus test of observability*, IEEE Transactions on Automatic Control, Vol. 40, No. 1, (1995), pp. 176–180.

Accurate structural excitation through adaptive control

M. Norambuena[1], R. Winter[1] and J. Biedermann[1]
[1] German Aerospace Center (DLR), Institute of Aeroelasticity
Bunsenstr. 10, D-37073, Göttingen, Germany
e-mail: **Marco.Norambuena@dlr.de**

Abstract
In order to study the phenomena that surrounds structure-borne noise mechanisms, it is necessary to have complete control over the structural excitation source, or equivalently, control over the forces injected into a structure. In other words, it is necessary to accurately reproduce operational forces on the structure under study. The control over the excitation source is usually managed simply by defining a desired input signal with a particular amplitude or frequency profile. However, this approach is rather incomplete since the profile defined does not take into account the modifications resulting from the interaction between source and structure. If the idea is to inject into the structure an exact copy of a reference force signal, an active controller can be used prior to the amplification stage in order to adjust amplitude and phase to obtain such copy of the reference force at the injection point on the structure. The following work describes the adaptive controller implemented for such an objective and discusses test results obtained in the laboratory.

1 Introduction

In the aeronautics industry, Ground Vibration Tests (GVT's) are a well stablished testing procedure meant to characterize structural behavior of aircrafts. Such applied methodology serves as key part not only in the understanding of aeroelastic stability but also provides relevant data used to validate analytical models that ultimately become part of the certification process of airworthiness [1]. In summary, GVT's are able to accurately describe the fuselage response by means of artificial excitation of the structure. There are two other closely related methods to achieve similar objectives, Taxi Vibrations Tests (TVT) and Flight Vibrations Tests (FVT), the former consists in the replacement of the artificial shaker excitation by the natural vibrations generated during aircraft taxiing [2] and the later uses the operational vibration generated on the fuselage during flight [3].

Any current structural testing procedure in the field of aeronautics uses one, or a variation, of these methods. From the excitation point of view, the most common strategy is to use arbitrary, but known, excitation signals, e.g. white noise or sine sweeps. This provides the necessary flexibility to obtain, for instance, frequency response functions, modal parameters, etc.

One could easily argue that a FVT will provide the perfect type of excitation since it is in fact an operational condition, however the elevated costs associated with flight tests make this option unfeasible in most cases. Moreover, such type of excitation, although ideal for many applications, is completely unknown and difficult to quantify since there are multiple sources acting on the fuselage during flight. The unavailability of such excitation reference will limit the types of processing that can be performed, e.g. modal masses can't be obtained.

During recent years [4], vibroacoustic topics had drawn considerable attention in the aeronautic industry. This is given by the fact that concerns have been shifted from safety and reliability topics of previous decades of research to cabin quality and passenger comfort. This current trend has pushed the

development of new tools and methodologies in order to face these new challenges [5]. A set of refocused topics has emerged from the interest in understanding how vibroacoustics play a crucial role in the cabin noise.

Given the fact that the starting points of all vibroacoustic phenomena are vibrations propagating on a structure, it is necessary to have a suitable excitation system capable of reproduce real flight operational conditions. If we forget for one second the effect of the Turbulent Boundary Layer, the solely source responsible for vibrations on the fuselage at low frequencies are the loads generated by the rotating components of the engines.

Through simulation, it is possible to accurately calculate the loads generated at connection points between engines and fuselage. However, a key problem arises at the moment when you try to reproduce those loads on the structure, since there is no way to compensate for the modifications introduced by the system created between amplifier, shaker and structure. Such unaccounted system will certainly change the predefined reference loads. Nonetheless, if the reference loads signal is available, it can be used to design an active excitation system able to generate and inject into the structure an exact copy of the simulated loads. As we will show in the following sections, such real-time excitation system is based on an adaptive controller. As part of the development process, as a first step a single-input single-output (SISO) controller was investigated and implemented. The fundamentals of this system served later on as a stepping stone for the more complex multi-input multi-output (MIMO) controller. Such multichannel system is part of our long-term goal to create a system able to reproduce forces in the three directions of space plus its associated moments.

Therefore, if we could implement a system able to excite a structure in a realistic manner, mimicking true loads, such system will allow to study the vibroacoustic behavior of a structure in the most accurate way possible. Such opportunity will help, for example, in the better understanding of structure—borne noise mechanisms of different parts of a fuselage or will assist in the determination of relevant energy transmission paths between sources and receivers.

2 Controlled excitation

The type of problem presented in this scenario, where it is required to inject on a structure a copy of an arbitrary reference force signal, seems to be a perfect candidate for an active control solution. The two main reasons for this are the availability of a reference signal, in this case the load forces, and the need to compensate a relatively stable plant. In this particular case the plant consists of the path created between amplifier, electrodynamic shaker, the structure and a force cell used to quantify the injected force, Figure 1 shows the configuration of the plant.

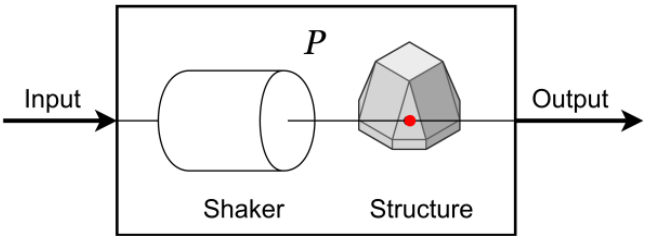


Figure 1: Schematic of the plant which consists of a shaker, a structure and a force cell (denoted by the red dot) that quantify the injected force into the structure.

The type of configuration described above is known as inverse control, since the task of adaptive process is to generate an inverse system $\hat{C}$ of the plant P. If this is successfully accomplished, the output of the plant will be an unmodified copy of the reference force signal. The typical schematic of an idealized inverse controller is shown in Figure 2, where $\hat{C}$ represents the compensation filter of the plant P, driven by the adaptive procedure. The error signal represents the deviation of the output of the plant in comparison with the reference force signal at the input of $\hat{C}$.

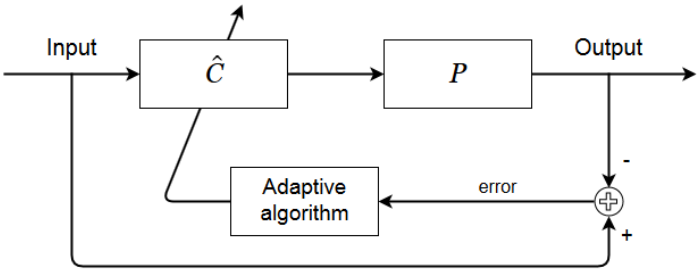


Figure 2: Diagram of an idealized adaptive inverse controller.

There are multiple options available to implement the adaptive algorithm. From the most simple and reliable LMS variations to the most sophisticated and demanding RLS variations.

According with this type of application, the following algorithms were tested in order to find the best tradeoff between speed of convergence and overall quality of output signal: NLMS, Correlation-LMS, DCT-LMS and RLS. The comparisons showed that all algorithms performed fairly well. After this comparison and considering that there is no requirement of high speed tracking of the reference signal, it was decided that the NLMS was the proper choice at this stage. Having the simplicity of an NLMS algorithm will make it easier to debug any problem that could potentially appear during the implementation on hardware.

The idealized system shown in Figure 2 is the most basic configuration for an inverse controller. However this simplicity helps to illustrate how such configuration works. Unfortunately, such idealized controller is not able to work properly on a real implementation since it requires conditions that are almost impossible to obtain, e.g. that there is no internal disturbance at the output of *P*. One of the options suggested in the literature [6] that can be used for an actual implementation, has a configuration similar to what is called *filtered-x* LMS (Fx-LMS) algorithm. This configuration is well known and widely used in Active Noise Control applications [7].

One of the characteristics of this configuration is that the control filter $\hat{C}$ is not applied directly to the plant P but rather to a modeled version $\hat{P}$ of the plant. The Fx-NLMS configuration ensures stable inverse control of the plant even in the case where there are errors in the modeling of $\hat{P}$. Independently of how $\hat{P}$ is modeled, online or offline, the complete control system can be summarized in Figure 3. In this schema it is assumed that on a previous process the plant $\hat{P}$ was identified and now a copy is connected at the input of the control filter $\hat{C}$. Under certain conditions it could be desired that the plant does not track directly the *Reference* signal but rather a delayed or modified version of the *Reference*. The introduction of the *Reference model M* serves this purpose.

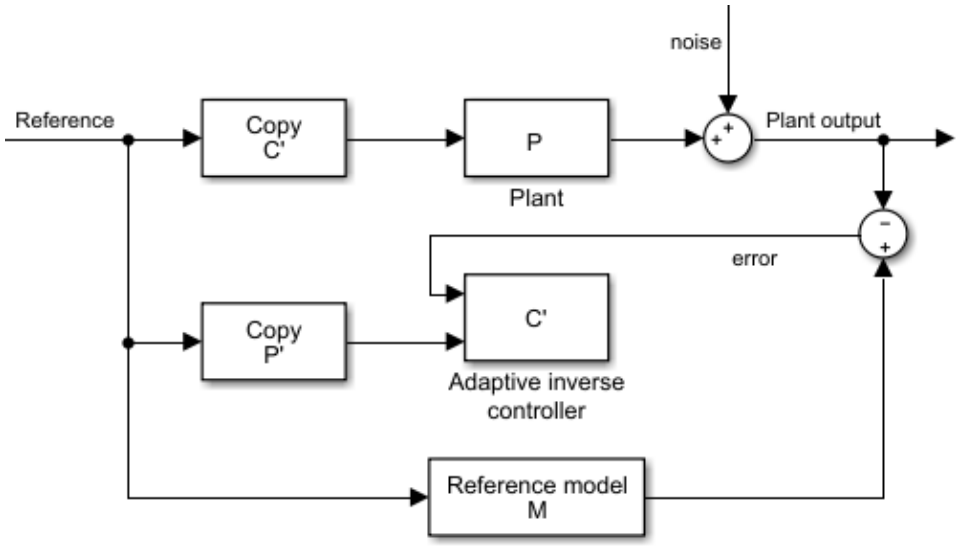


Figure 3: Diagram of inverse controller with added reference model.

3 Simulations

Although multiple simulations were performed during the development processes in order to test different algorithms, a simple example is presented here for the purpose of illustrating the general behavior of the controller. In this example, an arbitrary plant *P* with a low-pass characteristic was chosen. This fact is evidenced by the spectral profile of the *Control OFF* curve in Figure 5, which will be discussed shortly. The reference signal was defined as the sum of four sinusoids with frequencies 30, 50, 170 and 240 Hz.

In the following figures, time and frequency comparisons are presented between the *Reference* that represents the desired signal that should be injected into the structure, *Control OFF* that represents the signal obtained at the output of the plant when no control is performed (bypassing $\hat{C}$) and *Control ON* is the same as the latter but now the controller $\hat{C}$ is operating. All these curves are shown in Figure 4 and Figure 5. The time domain comparison, in Figure 4, presents two important characteristics, firstly, the evident difference between the *Reference* signal and the *Control OFF* signal given by the effect of the transfer function of the plant *P*. This means that when there is no control applied, the injected signal into the structure does not resemble the predefined *Reference* signal. The second characteristic worth to mention is the evolution of the *Control ON* signal and its convergence to the *Reference* signal as time passes. This means that, as it was designed, after some time the controller $\hat{C}$ will compensate the influence of the plant *P* and will inject a proper copy of the *Reference* signal into the structure. The spectral comparison presented in Figure 5 shows a similar result, a disparity between *Reference* and *Control OFF* signals; and subsequently a perfect matching between *Reference* and *Control ON* signals.

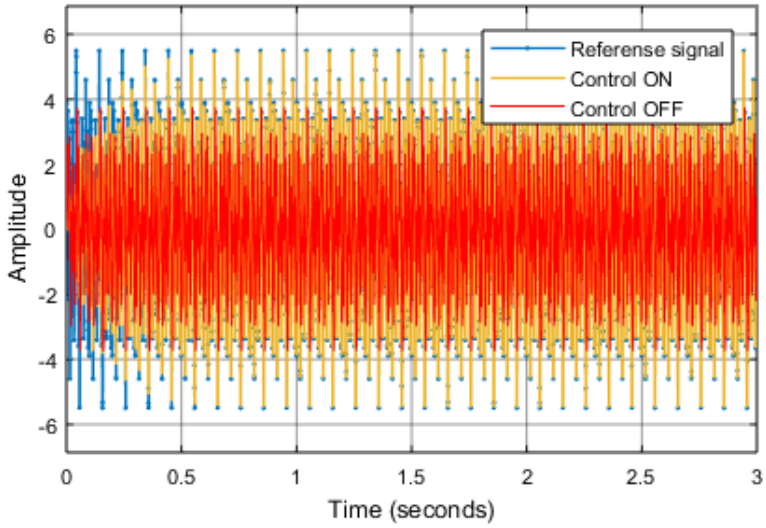


Figure 4: Comparison of signals evolution.

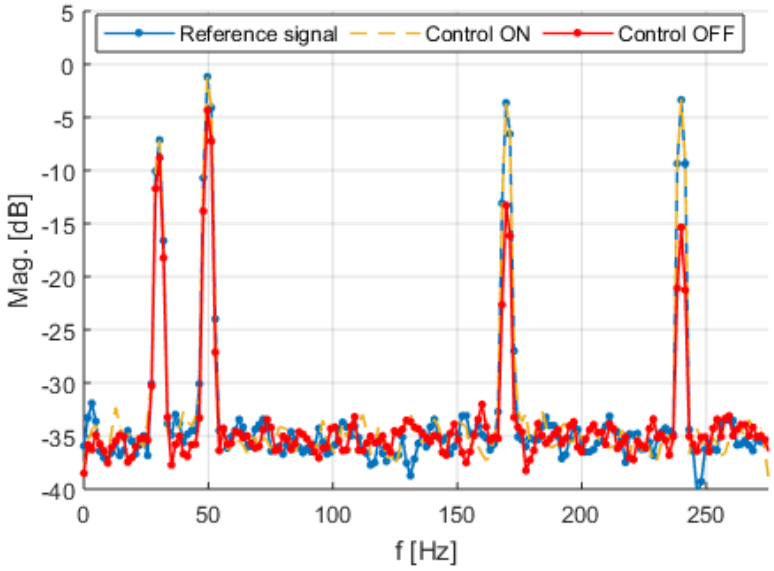


Figure 5: Comparison of resulting spectra.

The task performed by the adaptive filter $\hat{C}$ can be described by the evolution of its coefficients. Equally important, at the core of the adaptive process is the evolution of the error signal, which is responsible for driving the coefficients of $\hat{C}$ in the update equation of the LMS algorithm. The relationship between the progression of the error and the controller $\hat{C}$ can be observed in Figure 6.

4 Hardware realization and Experimental results of a SISO system

The last stage in the development process of the active controller was the implementation of the previously described algorithm into specialized hardware running in real time. The whole controller was implemented in two separate steps, firstly the plant *P* was identified and then a copy of *P* was used to run the Fx-NLMS inverse control. For this purpose the algorithm was developed using Simulink and an ADwin-Pro II T12 system.

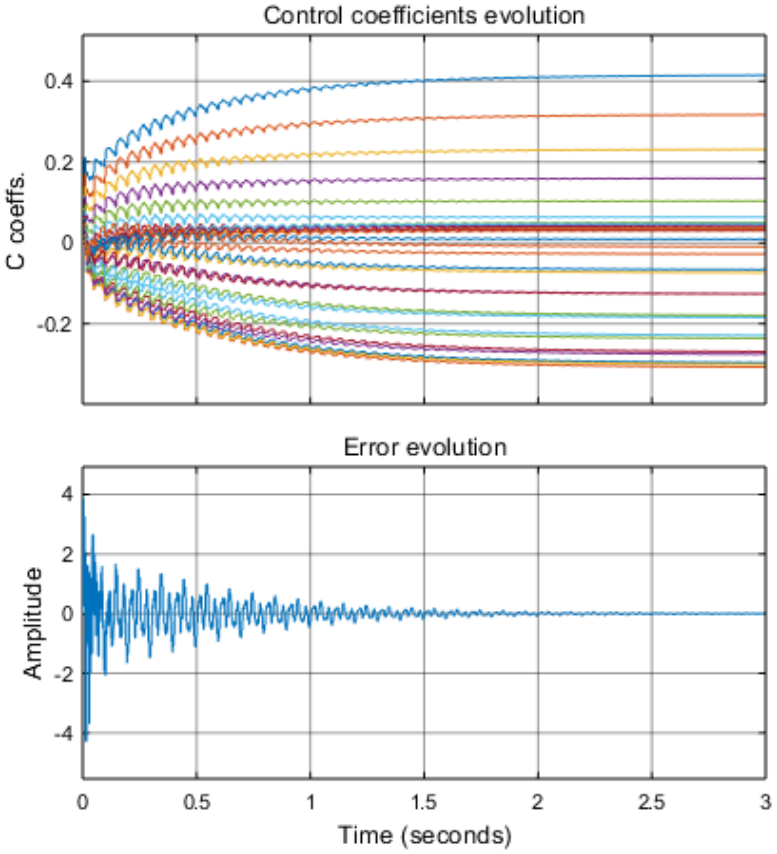


Figure 6: Illustration of error and coefficients evolution of the presented simulation.

In order to evaluate the correct operation of the system, a laboratory experiment was designed. The idea was to define a reference signal with a narrow band profile that resembles a low pass filter characteristic but with a non-flat response, as seen in Figure 7. In this way, the performance of the controller will be evaluated under, although limited, broadband condition that is still relevant for the use cases of structural excitation. The chosen frequency range was from 0 to 120 Hz.

The test structure used was a single aluminum plate of 1 x 0.8 x 0.03 m, with an asymmetric milled pattern that resembles the skin fields, stringers and frames typically found in fuselage structures. The thickness of the skin fields, stringers and frames was 1, 5 and 10 mm respectively. The plate was suspended using bungee cords in order to generate free displacement boundary conditions. As seen in Figure 8, a shaker and an impedance head were screwed to an anchor point of the plate. From the impedance head, the force signal was used to generate the error signal by comparing the actual injected force with the predefined force reference signal.

A spectral comparison of the reference and control signals is shown in Figure 7; there it is possible to assess the correct operation of the controller under narrow band excitation. In addition, a second evaluation is made by calculating the transfer function between the input and the output of the whole system, from the *Reference* signal fed into the controller $\hat{C}$ up to the output of the plant using the signal coming from the force cell. As before, two conditions are evaluated, *Control ON* and *OFF*. The comparison of the frequency response function for both conditions is made in terms of their magnitude and phase, as shown in Figure 9. The results presented there provide evidence about the correct operation of the controller. Firstly, the adjustment of the magnitude around 1 means a close match between the injected force into the structure and the predefined reference. Secondly, a similar behavior takes place with the phases of both cases, where the *Control ON* condition displays a relatively flat line around 0 rad. All this means that the controller is properly working and is able, for the most part, to calibrate the injected force using the predefined *Reference* signal.

There are, however, three distinctive peaks that appear in the higher frequency region, this peaks are associated with the natural modes of the plate. Their presence there is somewhat expected; it is possible to identify two important factors that can influence their appearance here. In the first place, the structure used is highly undamped which can greatly increase the interaction between the injected force and response of the plate. Near resonances, any small out-of-phase displacement between the structure and the force cell can generate a seemingly large signal at the output of the force cell. Secondly, the assumption that the shaker is behaving as a linear time invariant (LTI) system is not necessarily true, at least up to some degree. One option to minimize this effect could be to perform an online identification of the plant $\hat{P}$ in order to compensate any variation over time while the inverse controller is running.

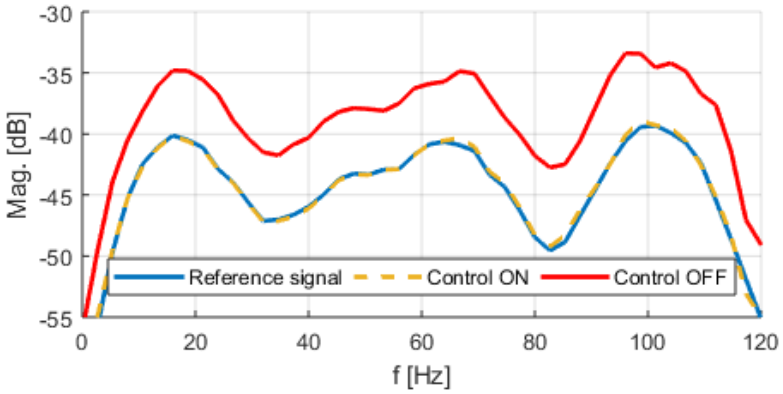


Figure 7: Spectral comparison of reference and control signals.



Figure 8: Aluminum plate used as test structure in a SISO configuration.

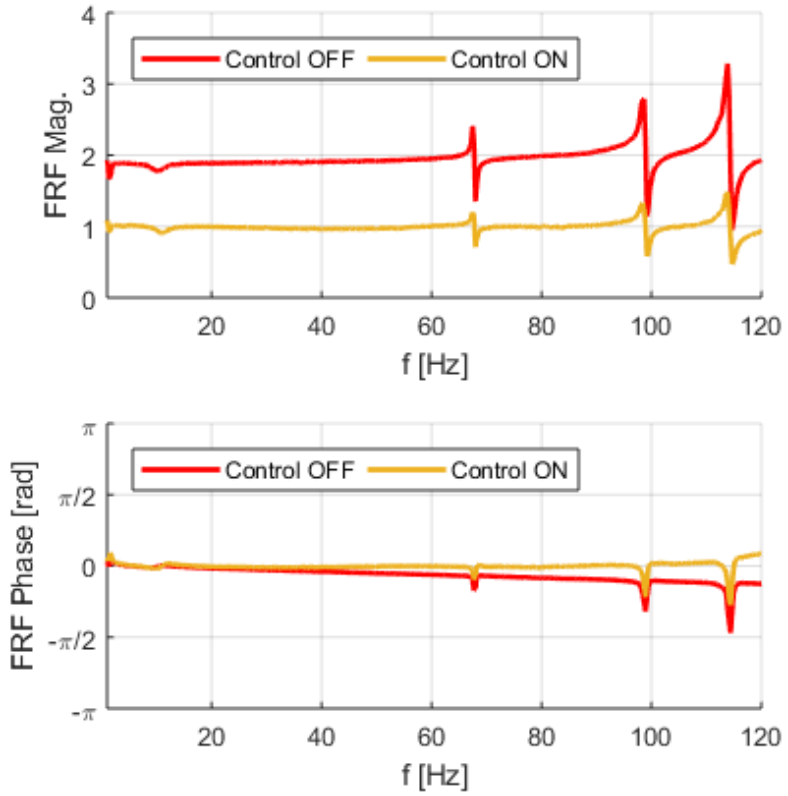


Figure 9: Frequency response function comparison in terms of magnitude and phase relatively to the reference signal.

5 Hardware realization and Experimental results of a MIMO system

The next step in the development of the system was to extend its capabilities to be able to provide three-dimensional controlled excitation, i.e. in each direction of space. The extension from a SISO controller, as described previously, to a MIMO implementation required certain modifications of the algorithms. The previously shown implementation relies on the fact that SISO system are commutative, i.e. $P(z)\,C(z) = C(z)\,P(z)$. However, such a property is in general not true for MIMO systems as pointed out by Plett [8]. Special care needs to be taken in the order of how the transfer function matrix of the controller C is manipulated. Plett also introduces a highly efficient controller by using a Recursive Least Square (RLS) update strategy. It is a well-known fact that RLS algorithms, although fast, are computationally demanding. During the development phase it was clear that the AD-win system was not able to run the controller at the required sampling rate with a RLS algorithm. Therefore, a simplified version was implemented with an LMS algorithm, in a similar manner as the SISO controller. The cost of this decision is carried by the speed of convergence, however for our application it has a low impact if we have to wait a little longer before the control coefficients settle and the optimal solution is reached.

For the evaluation of the MIMO implementation, the same aluminum plate was used but this time three shakers were attached, one per spatial direction as seen in Figure 10. In this case, three different frequency profiles were arbitrarily defined. As in the previous SISO case, these profiles serve as the target reference that the controller will try to replicate at the injection point of the structure. The profiles were integrated into the controller as part of the reference model M, see Figure 3. The input signal was wide band white noise. The result of the evaluation is summarized in Figure 11, where the *Reference* profiles and the *Control ON* condition are shown. There, each color represents one direction in space, the solid and dashed lines represent the *Reference* and the *Control ON* respectively. From Figure 11 it is possible establish the correct operation of the controller. The good agreement among references and resulting profiles illustrates the proper generation of control coefficients and the successful application of the compensation filter *C* to the input signal. In X direction, it is possible to notice a relatively small difference of 0.6 dB between

Reference and *Control ON* in the region of interest. In Y direction, vertical excitation, the difference between both curves seems to increase in the upper frequency range. We assume that in this direction the suspension of the plate negatively affects the result. It is not unreasonable to assume that the non-linear effect of the bungee cords suspension escapes the control capabilities of the system making it appear as a less favorable result. In order to validate this assumption, a new configuration of suspension is being designed to minimize its influence and will be evaluated in the near future. The Z direction presents an almost perfect match between *Reference* and *Control ON* profiles.



Figure 10: Aluminum plate with MIMO configuration.

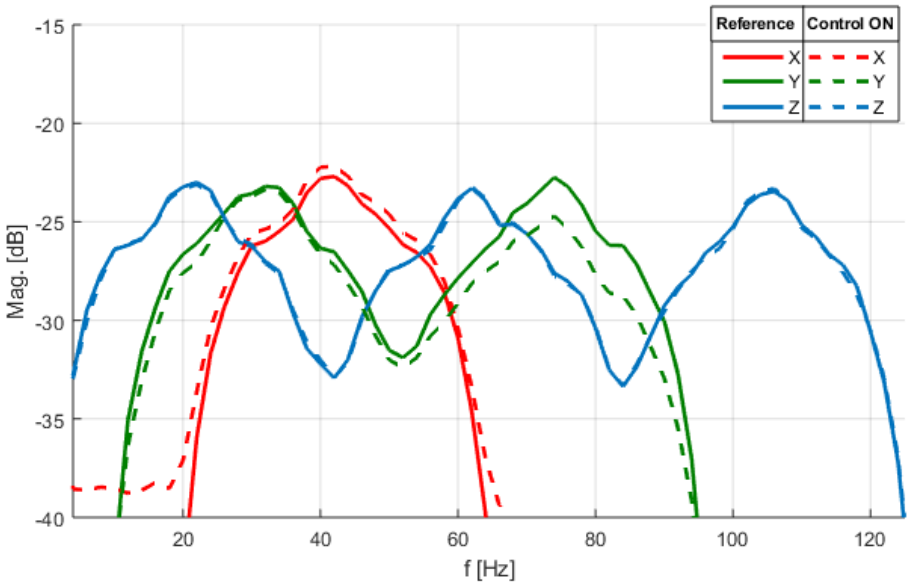


Figure 11: Spectral comparison of MIMO controller, references vs. control ON condition.

Concluding remarks

In this paper we examine the application of an active system to perform controlled structural excitation. Simulations and laboratory test show that it is possible to successfully apply a calibrated excitation for either multi-tonal or broadband signals in accordance with an arbitrary predefined signal reference or model reference. A SISO and a more sophisticated MIMO controller were presented and evaluated. The successful implementation of both configurations was demonstrated through laboratory experiments. Both controllers were able to reproduce reference forces with great accuracy.

Future work will move forward by improving control around resonances, improve speed of convergence and extending the current system to be able to control moments.

Acknowledgement

This project has received funding from the Clean Sky 2 Joint Undertaking under the European Union's Horizon 2020 research and innovation programme under grant agreement No CS2-LPAGAM-2014-2015-01.

References

[1] D. Göge, M. Böswald, U. Fullekrug and L. Pascal, "Ground Vibration Testing of Large Aircraft - State-of-the-Art and Future Perspectives," in *Proceedings of the 25th International Modal Analysis Conference (IMAC XXV)*, Orlando, 2007.

[2] M. Böswald and Y. Govers, "Taxi Vibration Testing - An Alternative Method to Ground Vibration Testing of Large Aircraft," in *Proceedings of the International Conference on Noise and Vibration Engineering - ISMA 2008*, Leuven, 2008.

[3] J. Meijer, "Introduction to Flight Test Engineering - "Aeroelasticity"," RTO AGARDograph 300 Vol. 14, 2005.

[4] J. Biedermann, R. Winter, M. Norambuena and M. Böswald, "Classification of the mid-frequency range based on spatial Fourier decomposition of operational deflection shapes," in *24th International Congress on Sound and Vibration (ICSV24)*, London, 2017.

[5] R. Winter, J. Biedermann, M. Böswald and M. Wandel, "Dynamic characterization of the A400M acoustics fuselage demonstrator," in *Inter-Noise 2016*, Hamburg, 2016.

[6] B. Widrow and E. Walach, Adaptive Inverse Control, Prentice-Hall Inc., 1995.

[7] S. Elliott, Signal Processing for Active Control, London: Academic Press, 2001.

[8] G. Plett, "Efficient linear MIMO adaptive inverse control," *Adaptation and learning in control and signal processing*, vol. 34, no. 14, pp. 89-94, 2001.

Microphone random arrangements for near-field acoustic holography based on compressive sampling

B. Du[1], X. Liu[1], X. Wu[1], Z. Wang[1]
[1] Kunming University of Science and Technology, Faculty of Mechanical and Electrical Engineering
No. 727 Jingming South Road, Kunming, Yunnan, China
e-mail: **liuxqsmile@gmail.com**

Abstract
In traditional near-field acoustic holography (NAH), regular grid array microphone is used and distance between adjacent microphones has to be less than half wavelength of the highest frequency. This makes unacceptable array cost for large sound sources. The Microphones can be arranged randomly in NAH based on compressive sampling, which can reduce microphones potentially. In this paper, NAH principle with compressive sampling is introduced firstly. Then reconstruction accuracy of random arrangements is compared with grid ones on premise of signal sparse representation. To reduce the microphone number further, random arranged microphones are optimized by Particle Swarm Optimization. It shows that most microphones are concentrated on the sound sources. Finally, the method of microphone arrangement with mixture Gaussian distribution is proposed. Both simulation and experimental results show that this method can achieve better reconstruction results with less microphones than random arrangement.

Keywords: planar near-field acoustic holography; compressive Sampling; microphone arrangement; mixture Gaussian distribution

1 Introduction

Near-field acoustical holography (NAH), firstly proposed by Maynard et. al., is an effective sound source localization and sound field visualization technology [1, 2]. The NAH theory research and development of the measurement system are mostly based on spatial Fourier transform, which has many advantages such as completeness, easy to implement, and fast calculation [2-4]. However, the method requires that the microphones of holography must be arranged regularly as grid, and the interval between adjacent microphones should be less than half of minimum wavelength of the sound, according to the spatial sampling theorem. A large number of microphones are needed to perform NAH on large sound sources with high frequency. The limits the application of NAH [5]. In 2010, Mingsian R. Bai compared microphone arrays of sparse, random and regular arrangement based on Equivalent Source Method (ESM), and concluded that the reconstruction accuracy has no particular advantage when the microphone is arranged randomly [6].

In 2012, Gilles Chardon introduced Compressive Sampling (CS) into planar NAH, and the feasibility of the method was verified by experiment [7]. The main advantage of this method is that high reconstruction accuracy can be obtained with fewer microphones placed sparsely and randomly on holography, which brings great potential for the practical application of NAH.

Literature [7] proves that if the microphones on the array are arranged randomly or pseudo-randomly under the condition of signal sparsity, the velocity distribution of the planar sound source can be reconstructed with high accuracy. Hald recommends using random, uniform microphone arrays in Wideband Acoustical Holography (WBH) as well [8]. However, the sound sources of literature [7] are from the modes of an aluminum plate, whose vibration states are more uniform on the natural frequencies of excitation signal, which means, the noise source are evenly distributed. In real applications, the actual noise source is uneven in many cases, and the number and location of the noise sources are predictable generally. If the

microphones on the array can be arranged according to the predictive information, it will be able to obtain higher reconstruction precision with fewer microphones.

In this paper, firstly, the method of NAH based on Compressive Sampling is analyzed from three aspects: signal sparse representation, measurement matrix design and signal optimization and reconstruction. Then the reconstruction results are compared between regular arrangement and random arrangement of the microphone array on uniformly distributed sound sources. On this basis, the microphone distribution is optimized with Particle Swarm Optimization (PSO) method on the sound sources of uneven distribution. Finally, a random placement method based on mixture Gaussian distribution for microphone array is proposed, and the effectiveness of the method is verified by simulation and experiment.

2 Planar NAH based on compressive sampling

Compressive sampling based NAH is an innovative application of the compressive sampling theory to solve the inverse problem of acoustic radiation. The procedure of the method includes the sparse representation of the signal, the linear observation of the signal and the reconstruction of the signal [9].

2.1 Sparse representation

The sparsity of the signal is the basis and premise of the theory of compressive sampling. Whether the sparsity of the signal can be represented flexibly and comprehensively, indicates a direct impact on the perceived efficiency of the signal [10]. In planar NAH, it is assumed that the particle velocity of the reconstructed surface is approximately sparse in an appropriate transform basis:

$$V_z(x, y, z_s) \approx D\theta \tag{1}$$

Where $V_z(x, y, z_s)$ denotes the particle velocity of on the reconstruction plane located at z_s in wave number domain, x and y denote the spatial coordinates on directions x and y, $D \in R^{N\times N}$ denotes the transformation base, and $\theta \in R^{N\times 1}$ denotes the sparse coefficient.

For different transformation base, the numbers of nonzero elements in the sparse coefficients θ are different. The less the nonzero elements, the sparser the particle velocity is on the transform base, and the original signal can be reconstructed with higher precision.

According to Kirchhoff-Love, the particle velocity of the planar source can be decomposed as propagating waves and evanescent waves:

$$v_z(x, y, z_s) \approx \left(\sum_n (\propto_n e^{i\overrightarrow{k_n}\cdot\vec{x}} + \beta_n e^{\overrightarrow{k_n}\cdot\vec{x}})\right) \cdot 1_S\left(x, y\right) \tag{2}$$

In the equation (2), $1_S\left(x, y\right)$ limits the plane wave to the range of the source S, which is a rectangular region of the wavenumber field, and the length and width are $L_x = 2\pi/k_x$, $L_y = 2\pi/k_y$ respectively.

Since the distance between the holography surface and the reconstruction surface is very small, evanescent waves are approximated as propagating waves in the sparse representation of the particle velocity. In other words, the particle velocity is sparse on the Fourier transform base, and the Fourier transform of the sparse coefficient θ can obtain the particle velocity on the reconstruction surface.

2.2 Measurement matrix

Theoretically, it is necessary to construct the measurement matrix to observe the particle velocity of the reconstruction surface, and obtain the sound pressure values on the holography surface. In NAH based on compressive sampling, the measurement matrix is corresponding to the pattern of the microphone array. Each column of measurement matrix $H \in R^{N\times N}$ ($M \ll N$) can be regarded as a sensor and senses part of

the information of particle velocity on holography surface v_z. The measured sound pressure $p_z(x, y, z_H) \in R^{M\times 1}$ is obtained by the linear observation of v_z by H, as equation (3).

$$P_z(x, y, z_H) \approx HV_z(x, y, z_s) \tag{3}$$

where $H = F(h_N(x, y, z_H))$, and F represents two-dimensional Spatial Fourier Transform, and

$$h_N(x, y, z_H) = -i\rho ck\frac{e^{-ik\vec{r}}}{2\pi\vec{r}} \tag{4}$$

Where c is the velocity of sound in the air, ρ is the air density, k is the wave number, and $\vec{r}$ is the position of the microphone.

The time domain convolution of the equation (3) is calculated to avoid the truncation caused by the spatial Fourier transform, as equation (5).

$$p_z(x, y, z_H) = h_N(x, y, z_H)\otimes v_z(x, y, z_s) \tag{5}$$

2.3 Optimization and reconstruction

By combining equations (1) and (3), the sound pressure P_z on the holography surface can be calculated by:

$$P_z(x, y, z_H) = HD\theta \tag{6}$$

The reconstruction of the signal is achieved by solving an optimization problem as the following equations :

$$\begin{cases}\min\|\theta\|_0 \\ s.t. P_z(x, y, z_H) = HD\theta_0\end{cases} \tag{7}$$

According to the above equation, a unique sparse coefficient θ_0 can be found. The particle velocity $V_{z.}$ of the reconstruction surface can be restored by multiplying θ_0 with the dictionary D. However, equation (7) is a non-convex optimization problem under l_0 pseudo-norm. In order to solve the sparse coefficient θ_0, we must search all possible nonzero combinations in θ.

Obviously, solving the above problems is extremely difficult. Donohue et al. proposed that the non-convex optimization objective of equation (7) can be replaced by the l_1 norm under the condition that the matrix *HD* satisfies the Restricted Isometry Property (RIP) [11].

$$\begin{cases}\min\|\theta\|_1 \\ s.t. P_z(x, y, z_H) = HD\theta\end{cases} \tag{8}$$

Thus, the optimization problem of (7) is transformed into a convex optimization problem, which can be solved by optimization algorithms. In practice, due to the presence of noise, it is necessary to balance the reconstruction accuracy and computational complexity. If the required accuracy is too high, the calculation will consume a lot of time. In this paper, the Basis Pursuit De-Noising (BPDN) algorithm developed by M. P. Friedlander is used to solve the convex optimization problem [12]. The reconstruction error is denoted by ε , and equation (8) can be rewritten as:

$$\begin{cases}\min\|\theta\|_1 \\ s.t. \|P_z(x, y, z_H) - HD\theta\|_2^2 \le \varepsilon\end{cases} \tag{9}$$

3 Array optimization for evenly distributed sound sources

3.1 Simulation settings

In order to compare the reconstruction results of microphone arrays with the regular grid arrangement and random arrangement, 25 uniformly distributed point sources are combined as a planar sound source. The point sources are on a 5×5 rectangular grid with grid interval of 0.6m. The radius of each sound source is

0.01m. The square holography surface with edge of 4m is 0.1m parallel to the sound source. A total of 1600 microphones on a 40×40 square grid (grid size 0.1m) are placed on the holography surface. The reconstruction results from the 1600 microphones are used as reference for other settings.

Three simulations are carried out with the frequencies of the sources are set to 300, 1600, and 3200Hz, respectively. For each simulation, a regular grid array and a random array with the same number of microphones are constructed on the same holography surface of the 1600-microphone array. The number of microphones for the three frequencies are 144, 400, and 784, respectively. Therefore, the regular arrays for the three frequencies are 12×12, 20×20, and 28×28.

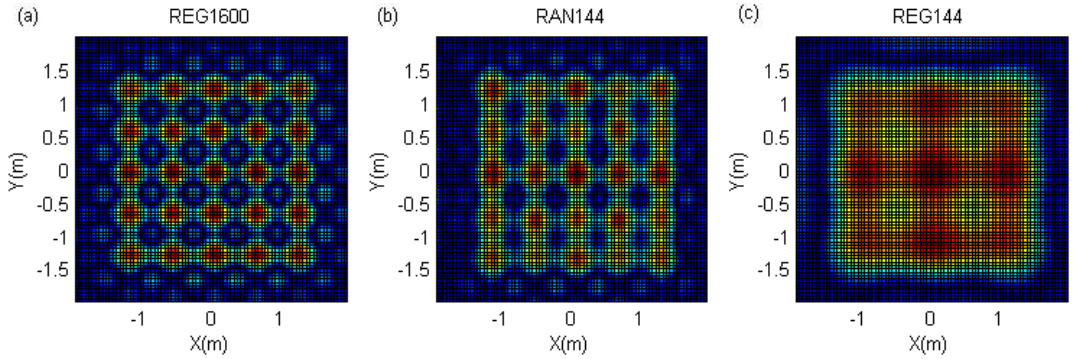
To quantitate the reconstruction errors of different arrays, the particle velocity reconstructed from the 1600-microphone array is taken as true value. The reconstruction errors on particle velocity of other arrays are calculated by the correlation coefficient between the arrays and the 1600-microphone array, as in equation (10).

$$Error = 1 - \frac{v_z(x,y,z_S)^T v_z(x,y,z_R)}{\|v_z(x,y,z_S)\|_2 \cdot \|v_z(x,y,z_R)\|_2} \tag{10}$$

Where $v_z(x, y, z_S)$ is the particle velocity of regular 1600-microphone array, and $v_z(x, y, z_R)$ is particle velocity of regular or random array with less microphones.

3.2 Simulation results

Figure 1 shows the particle velocity of the reconstruction surfaces from the three arrays when the frequency of the sound sources is 300 Hz. Compared with the particle velocity obtained by reference array (Figure 1a), the random array with 144 microphones (Figure 1b) can also identify the exact location of the 25 sources, and the boundaries between neighboring sources are clear. While on the regular grid array (Figure 1c), the 25 sources are mismatched as 9 sources only.

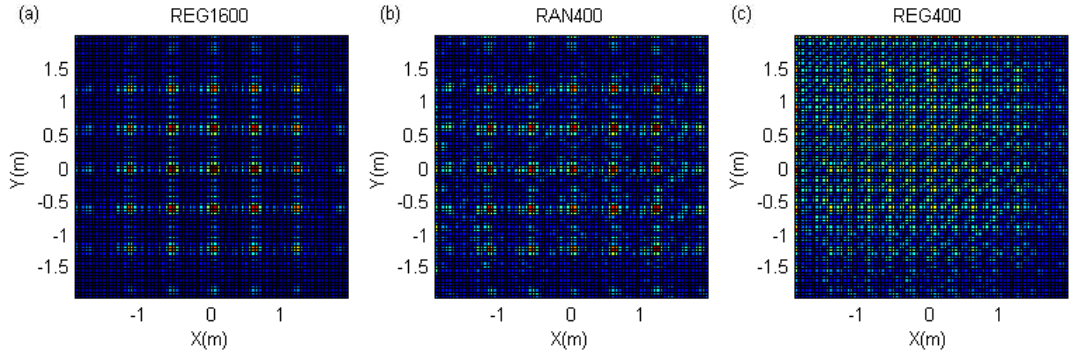


a) 40×40 grid array; b) random array of 144 microphones; c) 12×12 grid array;

Figure 1: Particle velocity on reconstruction surface of source frequency 300Hz

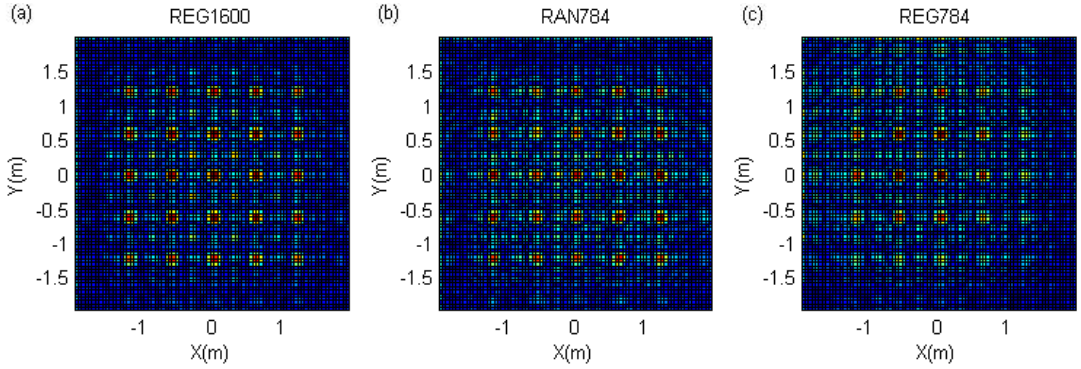
Figure 2 shows the results of sound sources with frequency 1600Hz. The reconstructed result of random array with 400 microphones (Figure 2b) is nearly identical to the result of reference array (Figure 2a). While the sound sources cannot be identified from the result of grid array with 400 microphones (Figure 2c). Similar results are obtained on sound sources of 3200Hz with arrays of 784 microphones, shown in Figure 3.

Figure 4a shows the reconstruction errors of the regular and random microphone arrays with different number of microphones calculated by the equation (10). For sound of 300Hz, when the reconstruction error is below 0.2, more than 200 microphones are needed on the grid array, while only about 100 microphones are needed on the random array. For all three frequencies, the random array shows great precision with less microphones than the regular array.



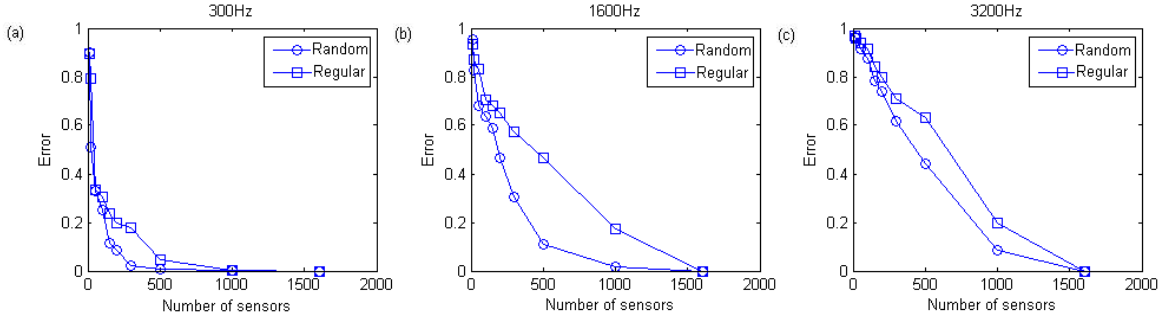
a) 40×40 grid array; b) random array of 400 microphones; c) 20×20 grid array;

Figure 2: Particle velocity in reconstruction surface of source frequency 1600Hz



a) 40×40 grid array; b) random array of 784 microphones; c) 28×28 grid array;

Figure 3: Particle velocity on reconstruction surface of source frequency 3200Hz



a) sound sources of 300Hz b) sound sources of 1600Hz c) sound sources of 3200Hz

Figure 4: Reconstruction errors of regular and random arrays with respect to the number of microphones

From Figure 4, we can see that as the frequency increases, the number of points required to achieve the same precision also increases. In general, it is better to arrange the measuring points randomly than regularly when the microphone number is limited, and the advantage is more obvious in the middle and low frequency band.

4 Array optimization for unevenly distributed sound sources

We have proved that random array needs fewer microphones than the grid array for evenly distributed sources. In practice, the distribution of the sound sources is generally uneven on the measurement surface. The number of microphones may be reduced further by placing microphones densely on the sources. In this section, Particle Swarm Optimization (PSO) is used to study the patterns of the optimal arrays for unevenly distributed sound sources.

4.1 Particle swarm optimization

PSO is a random search algorithm which simulates the foraging behavior of birds. The algorithm is widely used and easy to implement. The flowchart of PSO is shown in Figure 6.

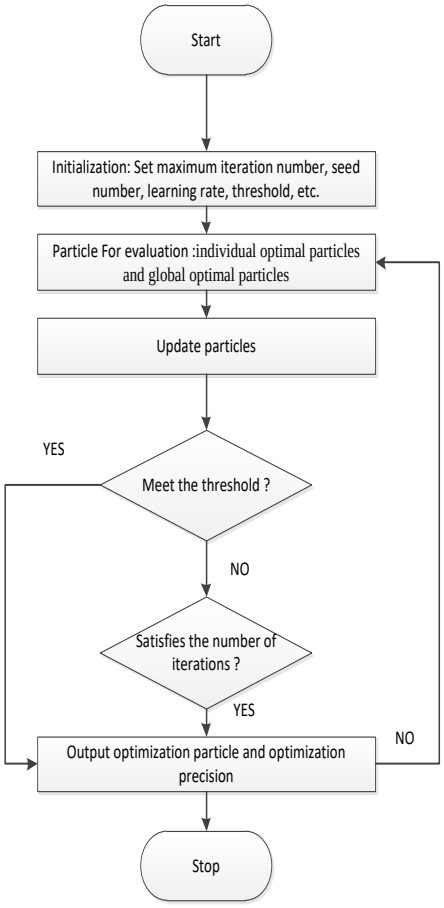


Figure 6: flow chat of PSO

Firstly, the initial population of M arrays are generated. Each array is an individual or a particle in the PSO. The microphones' positions on each array are generated randomly. Then the optimized array can be fund by updating generations. In every iteration, each particle is updated by following two "best" values. The first one is called *pbest*, and is the best solution (fitness) this particle has achieved so far. Another value is a global *gbest* that is the best value obtained so far by any particle in the population.

After finding the two best values, the particle updates its velocity as equation (11).

$$v_i(t+1) = v_i(t) + c_1 \times rand() \times (pbest_i - p_i(t)) + c_2 \times rand() \times (gbest_i - p_i(t)) \quad (11)$$

Where $v_i(t+1)$ is the new velocity for the *i*-th particle, c_1 and c_2 are the weighting coefficients for the personal best and global best positions respectively, $p_i(t)$ is the *i*-th particle's position at time t, $pbest_i$ is the *i*-th particle's best known position, and $gbest_i$ is the best position known to the population. The $rand()$ function generates a uniformly random variable $\in [0, 1]$.

The position of a particle is updated using:

$$p_i(t+1) = p_i(t) + v_i(t+1) \quad (12)$$

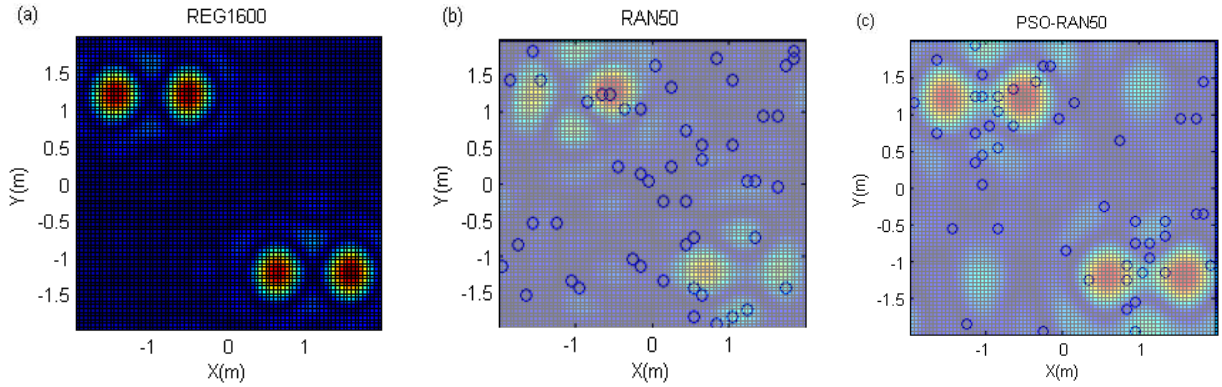
The best values are found by evaluating the particle, which is to calculate the fitness of each particle in the population. In this paper, the fitness function is the reconstruction accuracy calculated by the equation (10). The algorithm does not need additional auxiliary information for judgment and only the fitness function is used to distinguish the individual's adaptability, which is the basis for the further operation of the subsequent particle group.

If the maximum number of iteration is reached, or the change of fitness values between adjacent iterations is less than a given threshold, the process terminates, and the particle with the best fitness is taken as the optimal solution, otherwise, the iteration continues.

4.2 Simulation of array optimization

Four point sound sources are simulated, two of which are located on the upper left corner and the other two on the lower right corner of the source plane(Figure 7). Sound source's frequency is 300Hz, and the other options are the same as that in Section 3.1. Arrays containing 50 microphones are taken as particles in the particle swarm optimization algorithm. The population has 24 particles.

The optimized array is shown in Figure 7c as small circles. And the particle velocity recovered is shown as color map at back ground. Figure 7a shows the reconstruction of particle velocity from the 40×40-microphone array as ground truth of the sources. Figure 7b shows the recovered result and the pattern of a random array with 50 microphones.



b) regular array of 1600 microphones b) random array of 50 microphones c) optimized random array of 50 microphones

Figure 7: Particle velocity of reconstruction with respect to arrays of microphones

Compared to the result of the random array of Figure 7b, PSO optimized random array in Figure 7c achieves better reconstruction accuracy. The four sources can be distinguished nearly as clearly as the 40×40 array. Moreover, it can be seen that the microphones on the optimized array are mainly distributed on the sound sources or their vicinities.

In compressive sampling based NAH, the construction of the measurement matrix is equivalent to the arrangement of the microphones' positions. Candes states that the measurement matrix obeying the Gaussian distribution is irrelevant to any orthogonal dictionary or over-completed dictionary [13]. As two-dimensional Gaussian distribution has more samples on the center, which is similar to the optimized array shown in Figure 7c. So the Gaussian random matrix can be used as a universal measurement matrix.

5 Microphone array of mixture Gaussian distribution

5.1 Theory

For the case where the sound sources are not evenly distributed, arrays obeying two dimensional Gaussian distribution are setup for the sources. Each array is concentered on a source or serval sources in conjunction.

The probability density function of two-dimensional Gaussian distribution is defined as equation (11):

$$N(x, y, \mu_x, \mu_y, \sigma_x, \sigma_y) = \frac{1}{2\pi\sigma_x\sigma_y} exp\left[-\frac{1}{2}\left(\frac{(x-\mu_x)^2}{{\sigma_x}^2} + \frac{(x-\mu_y)^2}{{\sigma_y}^2}\right)\right] \quad (11)$$

Where x and y are the ordinates of the microphone position, respectively. u_x, u_y are the means of the distribution. σ_x, σ_y are the standard deviations of the distribution, which represent the lateral and longitudinal ranges of the array. For multiple sound sources, the probability density of the microphones obeys the mixture Gaussian distribution (MGD), which is defined as:

$$p(x,y) = \sum_{k=1}^{c} \frac{1}{C} N\left(x, y, \mu_x^k, \mu_y^k, \sigma_x^k, \sigma_y^k\right) \tag{12}$$

Where *C* is the number of two-dimensional Gaussian distributions. μ_x^k and μ_y^k are the means of *i*-th Gaussian distribution. σ_x^k and σ_y^k are the standard deviations of the *i*-th Gaussian distribution.

In practical application, if we know the possible locations and sizes of the sources, the parameters in equation (12) can be estimated, and a microphone array obeying the distribution can be generated.

5.2 Simulation and results

In the simulation, the sound sources are the same as in Section 4.2. The four sources are placed at the upper left and lower right corners. Two Gaussian distributions located on the two corners overlap to compose the mixture Gaussian distribution as equation (12). The standard deviations of the two Gaussian distributions are the same. The other parameters are shown in Table 1. The 50 microphone positions generated from the mixture Gaussian distribution are shown in Figure 8 as small circles. The reconstruction results are also shown in Figure 8. The recovered sound sources are as clear as in Figure 7c by PSO method. The four sources are separated from each other, and the equality of the strength of the four sources is also preserved.

ϕ	k=1	k=2
μ_x	-1.1	1.1
μ_y	1.2	-1.2
σ_x	0.9	0.9
σ_y	0.4	0.4

Table 1: Parameters of Mixture Gaussian Matrix

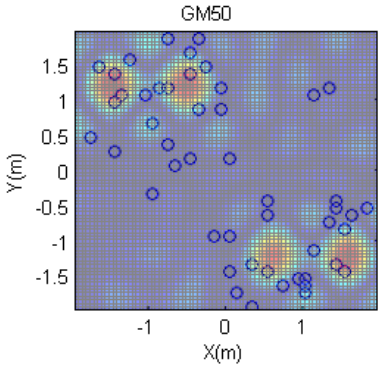


Figure 8: Particle velocity of reconstruction surface from microphones of MGD

6 Experimental verification of mixture Gaussian distribution array

6.1 Experiment settings

The experimental measurement is carried out on a refrigerator in a semi-anechoic chamber, shown in Figure 9. The main sound sources of the refrigerator are the compressor at the bottom and the fan in the middle. The back of the refrigerator (0.65m on width and 1.8m on height) is taken as the reconstruction surface, and the holography surface is 0.1m from the reconstruction surface. The linear array of 10 microphones (MPA416, BSWA, China) spacing at 2.5cm is used to scan the entire holography surface, with the reference microphone off the back of the refrigerator. The linear array scans 3 positions on the width direction and 80 positions on the height direction, thus a total number of 2400 points on the 30 × 80 grid (spacing 2.5cm) are measured on the holography surface. The data acquisition device is LMS SCADASIII and the Spectrum Test module in LMS Test.Lab software is used to record the data.

The mixture Gaussian distribution contains two two-dimensional Gaussian distributions located on the compressor and the fan respectively. The measurement points generated by the mixture Gaussian distribution are selected approximately from the 2400 grid points, shown as circles in Figure 10b.

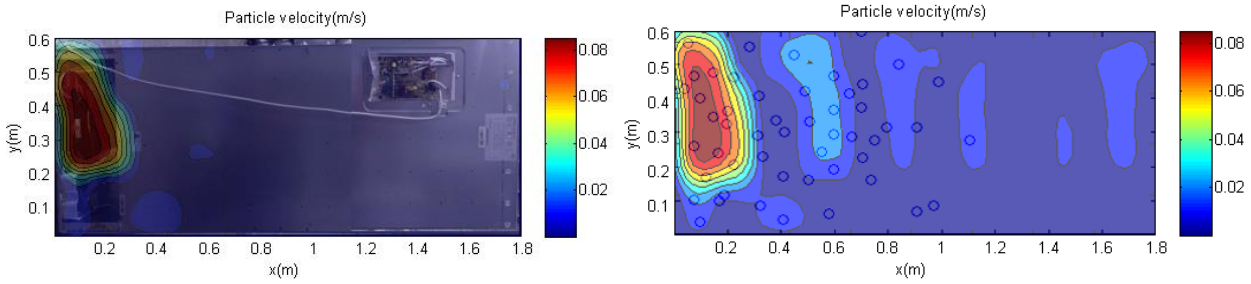


Figure 9: Experimental setup

6.2 Experiment results

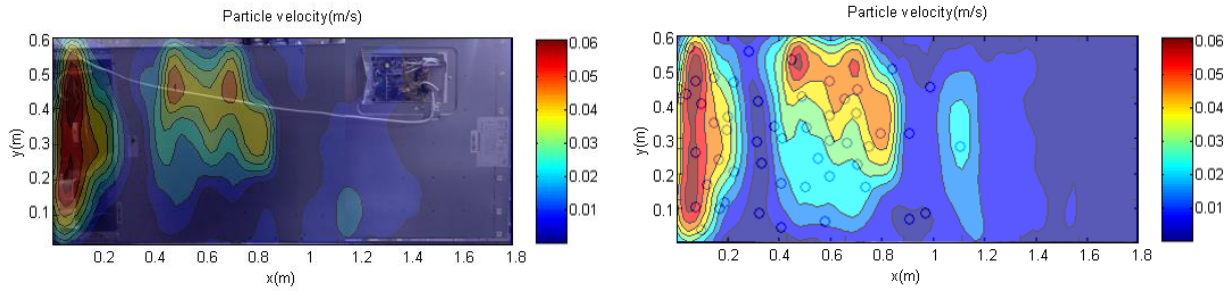
Figure 10a shows the contour map of particle velocity of 63Hz by 2400-microphone array, while figure 10b is obtained by a 50-point array from mixture Gaussian distribution. Comparing Figure 10a with Figure 10b, the reconstruction results of two methods are similar, and both of them can show that the main sound source on the reconstruction map is the compressor. The boundary and strength of the sound from the compressor are also reserved. The drawback of the MGD method with much less microphones is the presence of the false sound sources above the compressor. As the false sound sources are very weak compared to the compressor, the identification and estimation of the main sound source can still be done with high accuracy.

Figure 11a and Figure 11b show the contour maps of particle velocity of 230Hz by the 2400-point array and 50-point array from MGD method (same as the array in Figure10b), respectively. Three sources indicated by the three peaks in the Figure 11b are identical to that of the figure 11a. The boundaries and strength of the three sources are also nearly the same on Figure 11a and Figure 11b. There is a false sound source located on x =1.1m in Figure 11b, and the particle velocity is relatively low, thus the false source has no significant effect on the sound source identification.



b) 30×80 grid array; b) random array of 50 microphones from MGD

Figure 10: Particle velocity of 63Hz on reconstruction surfaces of the refrigerator



a) 30×80 grid array; b) random array of 50 microphones from MGD

Figure 11: Particle velocity of 230Hz on reconstruction surfaces of the refrigerator

7 Conclusions

The Nearfield Acoustic Holography based on Compressing Sampling has the advantage of retrain the reconstruction accuracy with much less microphones compared to traditional NAH using grid array. As sound sources usually take a small area compared to the entire measurement surface, this paper proves that further less microphones are needed to achieve nearly the same reconstruct accuracy when the microphone array obeys mixture Gaussian distribution and is centered on the sources. This method is practical because the possible locations of sound sources can be estimated in many cases, and the microphone array obeying two dimensional Gaussian distribution can also be built. This research has the potential to greatly improve the applicability of NAH method on large objects.

Acknowledgements

This work is supported by the National Science Foundation of China (No. 51465022).

References

[1] Maynard J D, Williams E G, Lee Y. *Nearfield acoustic holography: I. Theory of generalized holography and development of NAH* [J]. Journal of the acoustical society of America,1985,78(4): 1395-1413

[2] Veronesi W A, Maynard J D. *Near-field acoustic holography (NAH):II. Holography reconstruction algorithms and computer complementation* [J]. Journal of the acoustical society of America, 1987, 81(5): 1307-1322

[3] WANG Ran,CHEN Jin,DONG GuangMing. *Patch near-field acoustic holography based on modified Helmholtz equation least square method* [J].Journal of Vibration and Shock,2014,33(10):157-161

[4] LU WenBo,JIANG WeiKang. *Near-field acoustic holography based fault diagnosis and its system development* [J].Journal of Vibration and Shock,2013,32(5):48-51

[5] Williams E G, Maynard J D,Skuarzyk E. *Sound source reconstruction using a microphone array* [J]. Journal of the acoustical society of America, 1980, 68: 340-344

[6] Mingsian R.Bai,Jia-Hong Lin,Kwan-Liang Liu. *Optimized microphone deplomen*t *for near-field acoustic holography:To be,or not to be random, that is the question* [J].Journal of Sound and Vibration,2010,329:2809-2824

[7] Gilles Chardon, Laurent Daudet. *Nearfield Acoustic Holography using sparsity and compressive sampling* [J]. Journal of the acoustical society of America，2012，132(3)：1152-1534

[8] Hald.*Wideband acoustical holography*.Proc INTER-NOISE 2014

[9] D Donoho. *Compressed sensing* [J]. IEEE Transactions on Information Theory, 2006, 52(4):1289-1306

[10] JIAO LiCheng, YANG ShuYuan, LIU Fang et, al. *Development and prospect of compressive sensing* [J]. Acta Electronica Sinica, 2011,39(7):1651-1662

[11] D Donoho, Y Tsaig. *Extensions of compressed sensing* [J]. Signal Processing, 2006, 86(3):533-548

[12] E. van den Berg, M. P. Friedlander. *SPGL1: A solver for large-scale sparse reconstruction*. 2007 http://www.cs.ubc.ca/labs/scl/spgla

[13] E Candes, J Romberg, T Tao. *Robust uncertainty principle: exact signal reconstruction from highly incomplete frequency information* [J]. IEEE Transactions on Information, 2006, 52(2):489-509

Validation of PIRAT, a novel tool for beam-like structures subject to seismic induced misalignment of guiding sleeves

M.S. Bonney [1], **M. Zabiégo** [1]
[1] CEA Cadarache
CEA/DEN/CAD/DEC/SESC/LECIM
13108 St Paul lez Durance Cedex
e-mail: **matthew.bonney@cea.fr**

Abstract

This paper is a comparison of analytical and numerical evaluations for a model system, which consists of a suspended beam-like structure, guided by a pair of sleeves subjected to transverse displacements. The goal of these analyses is to evaluate and describe the mechanical behavior of this system during situations involving significant misalignment of the guiding sleeves caused by seismic motion. The analytical evaluation of the beam is performed using a solver in the novel tool PIRAT, and the numerical calibration uses a finite element solver called Cast3M. Illustrative computations are performed in order to verify that both methods are able to produce the same results / trends using a static deformation profile for the guiding sleeves. Additionally, the preliminary dynamic response of the system is also presented. The work in this paper signifies the next step in developing a set of tools for considering dynamic responses to ensure the proper behavior of such systems during seismic activities through the use of analytical evaluations.

1 Introduction / Background

Because they ensure essential safety functions, Reactivity Control Systems (RCS) are critical components for any nuclear reactor. Seismic events, which require operational RCS, in order to achieve reactor shutdown with a high reliability, represent the most challenging situations for the RCS design. Indeed, the large structural deformations that an earthquake could induce have the potential of preventing the anti-reactivity insertion into the reactor core, necessary to stop the nuclear reaction,.

This topic applies to a large variety of reactor types: Pressurized Water Reactors (PWR) [1, 2], Boiling Water Reactors (BWR) [3] and Sodium-cooled Fast Reactors (SFR) [4, 5, 6, 7]. As illustrated in Figure 1, RCS designs, such as the CSR and the RBC systems, respectively described in [8] and [7], both instances for SFR-type reactors, are typically composed of:

- A Mobile Part (MP), which embeds the neutron absorbing material, retracted above the fissile core during reactor operation, and inserted into it during shutdown phases.
- Two static sleeves, which guide the MP during the insertion phase triggered by the reactor scram. The sleeves are respectively suspended underneath the Above Core Structure (ACS), for the Upper Sleeve (US), and supported by the Below Core Structure (BCS), for the Lower Sleeve (LS), which is surrounded by neighboring fuel assemblies forming a densely packed lattice.

Under seismic situations:

- The collective movements of the core assemblies, induced by the horizontal BCS excitation, lead to bending deformations of the LS. Because of the important stiffness provided by the close packing of

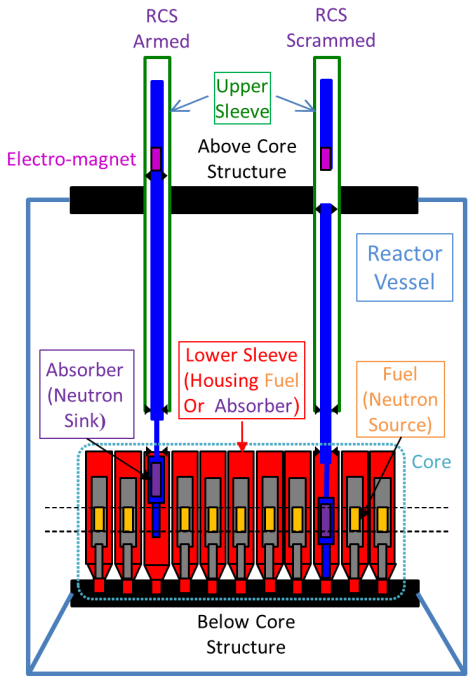


Figure 1: Example RCS Components

core assemblies, the LS deformation constitutes a rigid boundary condition for the lower part of the MP.

- The US also undergoes bending deformations, induced by the horizontal ACS excitation, albeit of lesser amplitude. These deformations constitute a semi-rigid boundary condition for the upper part of the MP, due to the finite stiffness of the US and absence of close packed structures surrounding it.

As illustrated in Figure 2, the resulting misalignment between the LS and the US can generate multiple contacts with the MP, implying horizontal reaction forces that could be detrimental in two ways:

- Friction forces, resulting from these contacts, could counter-balance the gravitational force that drives the passive insertion of the MP into the reactor core, and thus delay reactor shutdown.
- Bending deformations and contact pressure, could induce various damages, such as excessive stress, relative to accepted design limits, and premature wear of the coated guide levels, where contacts are nominally expected to occur.

The French Atomic & Alternative Energy Commission (CEA) recently started a multi-year program to develop a set of simulation tools, and the associated experimental qualification tests, dedicated to RCS insertion reliability assessment. This work plan was initiated with a static tool, referred to as RC3, developed with the Cast3M Finite Element solver [9]. It is presently continued with the ongoing development and validation of a set of tools, based on analytic formulations and implemented with the Python programming language, within a toolbox called the Python Implementation for Reliability Assessment Tools (PIRAT) to cover:

- Static studies: the Static Bresse Implementation tool (StaBI) is a finalized substitute for a finite element analysis, based on the Bresse formulation [10], designed for computing reaction forces (and resulting deformations, contact pressures, etc) induced by static displacements imposed by the sleeves.

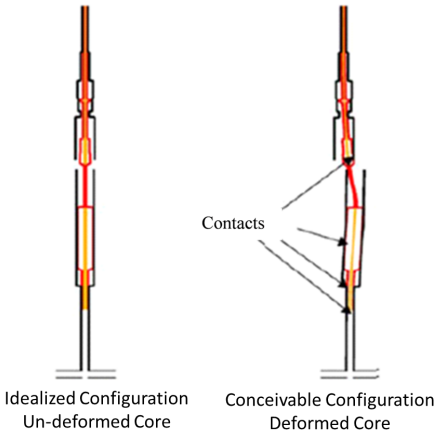


Figure 2: Possible Contacting Surfaces

- Dynamic studies: the Dynamic Euler-Bernoulli Implementation for Seismic Events tool (DEBSE), whose development is in progress, solves the dynamic Euler-Bernoulli equation, designed for producing outputs similar to those of StaBI, but taking into account their time evolution under some dynamic excitation relevant to seismic situations.
- Kinetic studies: the Step-by-step Insertion Kinetic Implementation tool (SIKI) will be developed to perform an iterative computation of the MP insertion, by relying on friction forces evaluated by means of the static/dynamic tool for each time step of the shutdown sequence, starting from scram, and until full insertion, including the final damping phase.

This paper discusses the progress and validation of the first two studies.

2 PIRAT

PIRAT uses Python as the script interpreter. Possible future development of the analysis performed by PIRAT, currently in discussion, could be to develop within the Cast3M framework. The current use of PIRAT is for an exploratory analysis that was only previouslly performed in [7] with issues that created a desire for analytical robustness. This desire was to allow a more flexible implementation for various geometries and desired outputs. The modular structure offered by PIRAT, in addition to the simple interface for numerical tools, are well adapted to the exploratory work considered. Within PIRAT, the full static solver and the preliminary work on the dynamic solver are presented in this section. Results from both of these solvers are compared against similar computations made with custom implementations of Cast3M to verify the accuracy, pending future comparison to experimental testing.

One of the unique characteristics of PIRAT, thanks to the Python implementation, is the ability to easily create new geometries and material properties. Geometry is inputted into PIRAT using an Excel spreadsheet containing the geometric properties and a material flag to be matched to user-defined properties. Adjusting the geometry, for example increasing the diameter of a section, is a simple change in the spreadsheet. With RC3, any geometric changes require a new model to be generated, meshed, and then analyzed. This is more time consuming since the intended use of PIRAT is for the initial design phases. During this phase, the geometry can vary over many iterations that can accumulate to a large amount of time for remodeling.

2.1 StaBI

For the first solver, a 1-to-1 replacement for RC3 is envisioned. The mathematics used in the StaBI solver are based on the Bresse formulations as presented in [10] and summarized as:

$$\theta(z) = \theta(z_0) + \int_{z_0}^{z} \frac{M_{fy}(\zeta)}{E(\zeta)I_{Gy}(\zeta)} \cdot d\zeta \tag{1}$$

$$\nu(z) = \nu(z_0) + \theta(z_0) \cdot (z - z_0) + \int_{z_0}^{z} \frac{M_{fy}(\zeta)}{E(\zeta)I_{Gy}(\zeta)} \cdot (z - \zeta) \cdot d\zeta, \tag{2}$$

where $\theta(x)$ is the angular displacement, $\nu(x)$ is the transverse displacement, $M_{fy}(x)$ is the effective moment, $E(x)$ is the Young's modulus, and $I_{Gy}(x)$ is the area moment of inertia at location x. Since the system of interest is a combination of multiple sections, the analysis is split into sections with both the transverse and angular displacement being continuous across each transition.

One of the major desired outputs of StaBI is the contact force values and locations between the MP and the sleeves (LS and US). Due to this, the effective bending moment is not known *a priori*. In order to calculate the force values, the superposition principle is used. At each location of possible contact, the response of the beam is computed for a unitary force. These responses are then collected into a matrix and used to solve for the forces via

$$F_k = [\bar{V}(z_k)]^{-1} \cdot [\Delta(z_k)], \tag{3}$$

with $[\Delta(z_k)]$ being the collection of displacements caused by the sleeves and $[\bar{V}(z_k)]$ is the collection of responses at each contact location due to a unitary force at each contact z_k. Then these forces are used to determine the final deflection of the MP and can be post-processed in order to get relevant data such as friction magnitude and bending stress in the beam.

The current implementation of StaBI has several assumptions; some are based on the Bresse theory and other are based solely on current implementations. The first assumption is that the beam is cantilevered at one end. Due to previous testing using RC3, this assumption is not expected to have a large effect on the results as compared to being pinned at the end. Past RC3 computations indicate that there is no large effect on the force locations and magnitudes due to the boundary condition at the top of the MP. Secondly, the force due to contact is assumed to be a point force that does not cause any surface deformation. This is to allow a simple determination of the applied forces due to the contact. Another implementation assumption is that for each section in the model is treated as a homogeneous and uniform cylinder. This creates the opportunity to avoid numerical integration; For a single point force, the effective moment within the beam can be known and then integrated analytically. The simplification comes in Equations 1 and 2 where the integrals are determined external to Python and the resultant is programmed in, reducing computational time and complexity in the program. There is a version of StaBI that utilizes numerical integration. However, there is a very large increase in computational time for the systems tested. For example, one evaluation using specific parameters using the analytical integration would take StaBI approximately one minute, and the same parameters but using a numerical integrator that is built into Python takes approximately 17 minutes on a fairly standard desktop computer. If only a single analysis is performed, this is still acceptable, but this might be constraining if StaBI is used for a kinetic evaluation that assumes quasi-static state at each time step via SIKI.

The last major assumption, which creates the most challenge, is how StaBI detects contact. This is done differently from the method used in RC3, which assigns a constraint on the stiffness matrix in order to account for contact. StaBI is a solver that does not require a mesh in order to determine the deflection of the MP, which RC3 requires. However, in order to determine if there is contact, a conforming mesh is assigned to all parts of the system. The current algorithm sweeps through that mesh and determines if the outer radius of the MP is in contact or past contact with the inner radius of the sleeves. Then StaBI assigns the point with the largest discrepancy as another contact point, and the algorithm is looped until there are no additional contact points. One major caveat found during testing is that enforcing a displacement very close to the actual sleeve

location will result in the algorithm detecting contact very close to previously determined locations, since each force is treated as a point force. This creates force values that are very large and nonphysical. In order to alleviate this issue, a clearance adjustment factor is used. This makes it such that there is a very small gap between the MP and the sleeve. Doing this generally produces larger force values, but allows for a more robust analysis. For the majority of the work performed in this paper, an adjustment factor of 80% of the clearance is applied. This is selected as an all-around value for the systems tested to produce reasonable results with no numerically determined parasitic contact.

2.1.1 Pseudo-code

While there are many detailed steps in StaBI, the general work flow is broken-up into four major parts: 1) Setup and Geometry, 2) Quasi-Rigid Convergence, 3) Contact Determination, and 4) Post-Processing. These are the steps currently implemented into the static solver and are similar steps to those that are expected to be implemented into the dynamic solver as well. Step 1 is specific to each system tested. This includes: generating the geometry, setting material properties, determining convergence criteria, setting the sleeve locations, and determining the step size for the contact determination. These all are different depending on the system being investigated and what the user desires. Step 2 is a large loop that contains step 3 within it. If a subsystem (US for example) is determined to be quasi-rigid, then iterations on the displacement of that subsystem must be performed to create a quasi-static equilibrium state of the system. Currently, this is done by comparing the calculated force value on the MP and the force value on the quasi-rigid subsystem at the same location. Step 3 loops through adding contact locations until there is no additional contacts found. Once step 2 is converged, then the post-processing of the data can occur in step 4. This would output values such as: bending stress, total friction in the system, and Hertzian contact pressure. A more detailed step flow chart is presented in Figure 3.

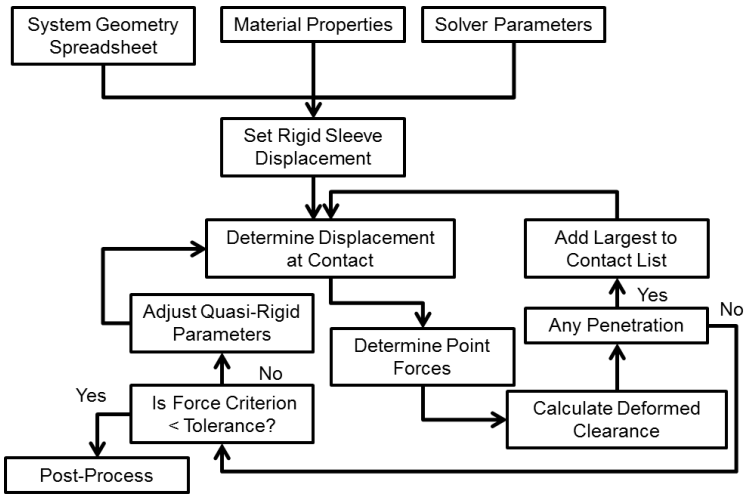


Figure 3: Flow Chart of StaBI for Guided Systems with Both Rigid and Quasi-Rigid Sleeves

2.2 Preliminary DEBSE

One of the main goals of the PIRAT tool is to perform the analysis in the dynamic domain to ensure the insertion reliability during a seismic event. Initially, the expansion of PIRAT to handle dynamic situations is to replace the Bresse's equations of motion with the dynamic Euler-Bernoulli beam equations of motion. This increases the dimension of the system by introducing a dependency of time. Current use of one dimension in space is a simplification for the current work that can be expanded in the future to account for any drop velocity. The governing differential equation of motion becomes:

$$\frac{\partial^2}{\partial x^2}(EI(x)\frac{\partial^2 w(x,t)}{\partial x^2}) + \rho A(x)\frac{\partial^2 w(x,t)}{\partial t^2} = q(x,t), \tag{4}$$

where $w(x,t)$ is the transverse displacement of the beam, $EI(x)$ is the structural rigidity, $\rho A(x)$ is the linear mass density, and $q(x,t)$ is the externally applied distributed load. One thing to note is that this formulation does not account for axial stretching. As will be discussed in the comparison of DEBSE to Cast3M, this stretching might be an important factor for select modes. For the majority of the analysis in this paper, it is assumed that all driving loads are either internal to the system or are applied as a time-dependent boundary conditions. The implementation of these boundary conditions are similar to the method used in [11]. Simply, the displacement of the beam is a combination of the free-vibration and the time-dependent boundary conditions. One example of how this can be written is:

$$w(x,t) = \phi_0(t)\delta(x) + \phi_L(t)\delta(x-L) + u(x,t) \tag{5}$$

where $\phi_x(t)$ is the time dependent boundary condition at x, $\delta(x)$ is the Dirac delta function, and $u(x,t)$ is the free-vibration of the beam subject to elementary boundary conditions such as: pinned, clamped, and free.

With the knowledge that future work will include free-vibration, the preliminary dynamic analysis is a verification of the dynamic properties of the example system, in particular the MP subsystem. The free-vibration analysis being used in DEBSE is currently based on modal decomposition. This allows for a separation of time and space in the governing equations of motion and can be written as:

$$u(x,t) = \sum_n \psi_n(x) q_n(t), \tag{6}$$

where $\psi_n(x)$ are the deflection shapes, also called mode shapes, and $q_n(t)$ is the time dependent contribution of mode n [11]. While this summation is countably infinite, it is typically truncated based on frequency via the natural frequencies. Using this modal decomposition allows for the partial differential equation in Equation 4 to become a summation of independent ordinary differential equations.

This system of interest contains some interesting aspects that require some special considerations. The major interesting aspect is the geometric discontinuities across different sections of the MP. Each section of the MP is modeled as a homogeneous, uniform cylinder with the difference between sections occur instantaneously, providing no derivative at that point of the beam. The cylinder model is a current simplification to allow for a more simple evaluation. There are analytical representations of mode shapes for functionally variant cross-sections [12, 13, 14] that will be included as this tool is further developed. This is mainly an issue with the first term in Equation 4 that looks at how the structural rigidity changes along the beam. In order to account for this step change, each section is thought up as a homogeneous beam with specified boundary conditions, similarly to the method used in [15]. The external boundary conditions are still enforced, but at the internal boundaries, mode shape continuity is enforced. This can be expressed as:

$$\psi_{n,i}(L_i) = \psi_{n,i+1}(0) \tag{7a}$$

$$\frac{\partial \psi_{n,i}}{\partial x}(L_i) = \frac{\partial \psi_{n,i+1}}{\partial x}(0) \tag{7b}$$

$$EI_i\frac{\partial^2 \psi_{n,i}}{\partial x^2}(L_i) = EI_{i+1}\frac{\partial^2 \psi_{n,i+1}}{\partial x^2}(0) \tag{7c}$$

$$EI_i\frac{\partial^3 \psi_{n,i}}{\partial x^3}(L_i) = EI_{i+1}\frac{\partial^3 \psi_{n,i+1}}{\partial x^3}(0), \tag{7d}$$

with L_i being the length and $\psi_{n,i}$ being the mode shape of section i for mode n. Using this formulation, it is assumed that each section has a local coordinate system and the modal deflection at any location can be determined by:

$$\psi_n(x) = \psi_{n,i}(x - x_{0i}) \text{ if } x \in [x_{0i}, x_{fi}], \tag{8}$$

where x_{0i} is the starting location and x_{fi} is the ending location of section i in the global coordinate system.

For the validation of DEBSE, Cast3M is used to provide natural frequencies and mode shapes for the MP system. These are chosen in order to test the basic uses for the dynamic solver. Both natural frequencies and mode shapes are not dependent on user-input. Other dynamic data, such as frequency response functions and time history, require the analyst to decide some damping factor and time-dependent boundary conditions in order to evaluate. Since this can be chosen to be the same for Cast3M and DEBSE, any differences found in these two are primarily due to the differences in the mode shapes and frequencies.

Applying the modal decomposition to Equation 4, the space component of this equation becomes:

$$\frac{\partial^4 \psi_{n,i}(x)}{\partial x^4} = \beta_{n,i}^4 \psi_{n,i}(x), \tag{9}$$

where $\beta_{n,i}$ is an unknown coefficient that is related to the natural frequency of the mode n and the material properties of section i. The general solution to this differential condition is:

$$\psi_{n,i}(x) = a_{1,n,i} \sin(\beta_{n,i}x) + a_{2,n,i} \sinh(\beta_{n,i}x) + a_{3,n,i} \cos(\beta_{n,i}x) + a_{4,n,i} \cosh(\beta_{n,i}x), \tag{10}$$

with $a_{k,n,i}$ being unknown coefficients for the mode shapes. These coefficients are determined based on the constraints of the system, which can be written as:

$$\begin{bmatrix} Ex & 0 \\ 0 & D \\ G & \end{bmatrix} \begin{bmatrix} \vdots \\ \mathbf{a}_{n,i} \\ \vdots \end{bmatrix} = [0] \tag{11}$$

or

$$[B][\mathbf{a}_n] = [0], \tag{12}$$

where Ex is the external boundary condition for $x = 0$ and D is the external boundary condition at $x = L$ applied to the mode shapes, G is the continuity conditions given in Equation 7, and $\mathbf{a}_n$ are the collection of mode shape coefficients with $\mathbf{a}_{n,i} = [a_{1,n,i}, a_{2,n,i}, a_{3,n,i}, a_{4,n,i}]^T$.

The constraint matrix $[B]$ is a function of the coefficient β that is a function of frequency. When the frequency is set to a natural frequency, the constraint matrix is rank deficient, meaning that the determinate is equal to zero [16]. In order to determine the natural frequency in DEBSE, a Newton-Raphson method is used on the determinate of the constraint matrix. For the initial points of the Newton-Raphson method, the natural frequency of a uniform beam containing the mean properties of the MP subject to the external boundary conditions is used. Since a uniform beam with elementary boundary conditions contains a known analytical solution, that value is used. This makes the assumption that this mean natural frequency is relatively close to the true natural frequency. In order to ensure this, a redundancy check is performed on the natural frequencies to ensure that the same mode is not considered multiple times. Additionally, the natural frequencies found in Cast3M are also inputted as initial points to determine the natural frequencies before the redundancy check. It was found during testing, that using an uniform beam with average material properties would occasionally skip a mode of vibration. Alternate initial starting points for the Newton-Raphson method are being investigated, such as an interactive input showing the frequency response function to ensure that each peak is selected and evaluated. The mode shapes are determined at each natural frequency by setting one component to a specified value since the constraint matrix is rank deficient.

Once these are determined in DEBSE, they can be compared to the results from Cast3M. The error on the natural frequencies is calculated by a percent difference once the desired mode in the model is selected. In

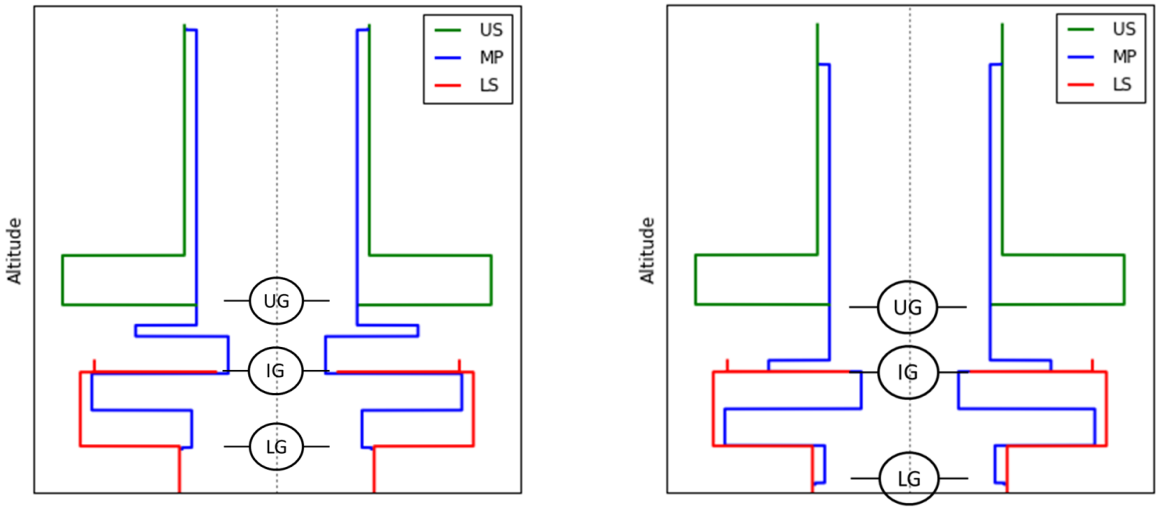
order to select which DEBSE mode corresponds to the Cast3M mode, a comparison between the mode shapes is required. For this analysis, the modal assurance criterion (MAC) is used. The MAC can be determined by:

$$MAC_{ij} = \frac{(\psi_i^T \psi_j)^2}{(\psi_i^T \psi_i)(\psi_j^T \psi_j)}, \tag{13}$$

where i and j are mode numbers. The MAC calculation is performed for each mode generated by DEBSE and by Cast3M. This MAC value has a range of $[0, 1]$ with a MAC value of 0 implying that there is no correlation between the modes and a value of 1 implying that there is a perfect correlation between the modes. An important note to make is that the MAC values do not prove orthogonality, they just imply correlation. This is similar to the saying "Correlation does not ensure dependency" from the statistics field. Using a method like this will allow a quantitative proof of the corresponding mode shapes. This is used to filter out motion that is not described by a method, in this report the axially coupled modes of Cast3M, and show if there is any issue with the convergence of the Newton-Raphson approach to determine the natural frequencies.

3 Example System

In order to test PIRAT, a simplified but realistic RCS system is used. The requirement for the type of system is a beam like object that is guided by sleeves, such as the one pictured in Figure 4. This is taken as a similar system to the one analyzed in [5, 6, 7]. There are some differences in these systems and the dimensions are not given. An estimation of the length of the beam and comparative dimensions was performed, resulting in the example system used in this work. In order to represent the sleeves, a polynomial is used for the LS and the US is treated as quasi-rigid. Some features, such as the dash-pot, are removed for simplification since previous testing showed no significant changes due to these additional complexities.



(a) Zero Stroke (b) Full Stroke

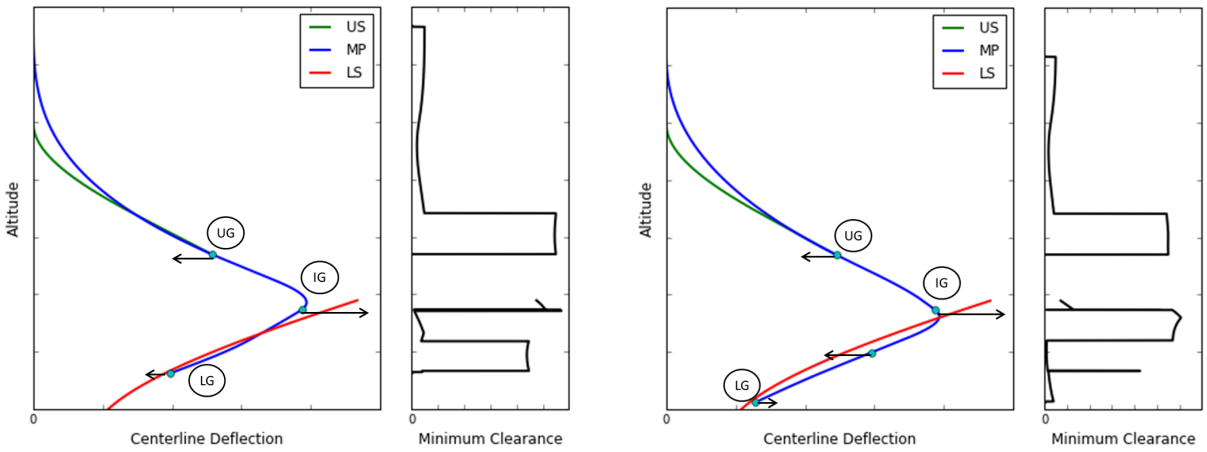
Figure 4: Geometric Configuration of the Example System

This system has a maximum stroke around $1000mm$, meaning that the MP can move vertically by that amount. To test this range, stroke values from 0 to $1000mm$ in increments of 10% the maximum stroke are simulated using StaBI. There are three main points of reference that correspond to expected guide regions shown in Figure 4. The first is the bottom section of the MP, thus causing the contact location to vary in

the global coordinate system. If the global reference frame is considered, the Lower Guide (LG) produces a moving contact, which could add some difficulties to the dynamic analysis if the MP is allowed to drop. The second area is the guide region at the top of the LS, call the Intermediate Guide (IG). This area has a larger clearance compared to the other guide regions, but is expected to produce the largest contact force due to the large imposed displacements. The final expected contact location is the Upper Guide (UG). This is located at the bottom of the US and has the smallest clearance. The UG is also the location used for the quasi-rigid convergence loop.

4 Static Misalignment

For this static solver, both StaBI and RC3 produced the same contact points for stroke values up to $800mm$. In the cases with stroke values greater than $800mm$, StaBI detected a parasitic contact between the LG and the IG. The first result to report is the deformation shape of the MP in Figure 5a. This figure shows the center-line deflection of the three subsystems, contact locations (as cyan dots), and the minimum clearance of the MP at each altitude point for the case of a stroke value of $0mm$. This shows that there is contact at each of the guide areas that contain a reduced clearance resulting in a total of three nominal contacts. One interesting aspect of Figure 5a is the near parasitic contact within the US. Figure 5b shows the same data for when there is a full stroke. Some interesting things to note are the parasitic contact between the LG and IG and the change in sign for the contact force of the LG.



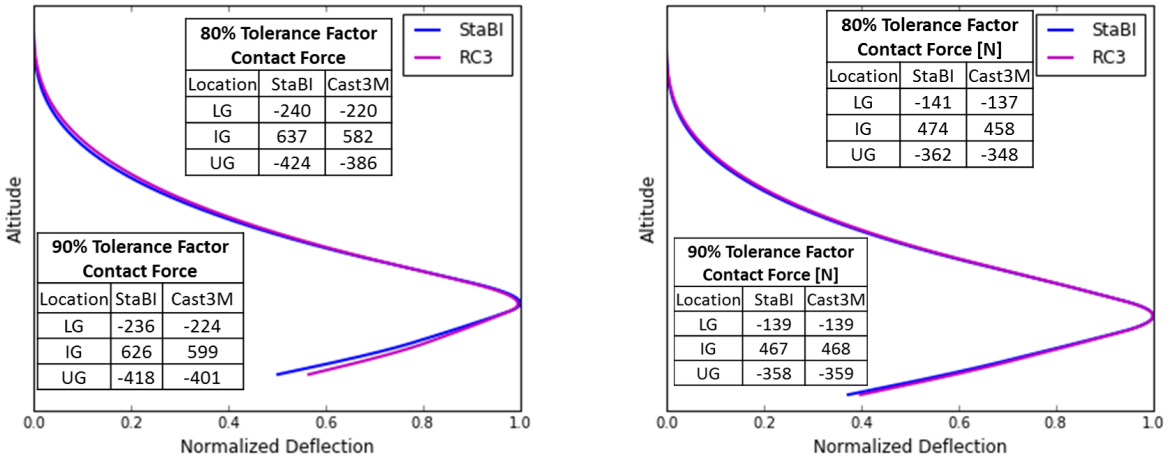
(a) Zero Stroke

(b) Full Stroke

Figure 5: Example Deformation Shape of Example System with Vectors Representing Relative Force Magnitude and Direction

These deflections are compared to the results from RC3 using the same displacement for the quasi-rigid US, which is scaled to the displacement at the UG, and can be seen in Figure 6a. In Figure 6, the values for the detected contacts are also presented. These include both using a tolerance adjustment factor of 80% and 90% to show the increase in accuracy. One thing to note, the RC3 simulations are re-performed for each adjustment factor. This is due to each case having a slightly different US profile due to the deflection at the UG.

There is some small differences between RC3 and StaBI shown in Figure 6a. First, for the areas that are bounded by the sleeves, StaBI reports less deflection than RC3 and the opposite of that when the MP is not bounded by the sleeves (between the IG and UG). Besides that small shift, there is a noticeable discrepancy near the LG. The cause of this is unknown, since there is a tight tolerance at the LG level. One possibility is the discrepancy between StaBI and RC3 on the force magnitude. For the LG on this particular example, StaBI



(a) Stroke Value of 0 mm

(b) Stroke Value of 700 mm

Figure 6: Comparison of Deflected Shape of Example System

detected a force of $240N$ while RC3 detected a force of $220N$. This is one of the largest differences found between the two methods but is still within 10%. Another possibility is based on the contact algorithm. The contact algorithm used in RC3 sweeps through the mesh on the sleeves and finds the closest mesh point of the MP within tolerance. There is a possibility that for this stroke value, the algorithm did not evaluate a mesh point on the LG, but only to another section of the MP. One thing to note is that for a stroke value of $0mm$, StaBI and RC3 has the worst agreement among the cases where the same contact zones are determined. To show a closer agreement, a stroke value of $700mm$ is shown in Figure 6b. This shows that there is almost no difference between StaBI and RC3 except a very small shift that was also noted in Figure 6a, but with a smaller magnitude of difference.

Qualitatively, the benchmark between StaBI and RC3 produces satisfactory results. By looking at the percentage difference between the magnitude of the contact forces, a similar conclusion can be determined. For the cases where StaBI and RC3 produced the same contact zones, there was an average percent difference of 5.6% with a maximum difference of 9.9%. This level of accuracy is sufficient to say that when the contact algorithms detect the same locations, either StaBI or RC3 will give a good result.

It is an important note that these results used a tolerance adjustment factor of 0.80, meaning that 80% of the clearance is enforced for the contacts. If this factor is increased to 90%, the accuracy increases. For this system, the average percent difference is 1.5% with a maximum of 5.0% in magnitude. One interesting effect of this increase is that the forces from StaBI are not always higher in magnitude compared to RC3. This shows that there is not a guaranteed conservative estimate on the contact forces as originally thought. When the adjustment factor is increased to 95%, StaBI detects parasitic contact within the same zones as other previously determined contact locations. In particular, StaBI usually detects a second contact at the LG causing the forces at the LG to increase substantially, on the order of $100N$ to $20,000N$. There is still future work in the determination of the tolerance adjustment factor and the contact algorithm in general. This can only be done with either a known benchmark (simplified system tested by various methods) or some experimental validation.

5 Preliminary Dynamic Analysis

In order to test the accuracy of the DEBSE solver, six different configurations are tested for the MP using a combination of free (F), clamped (C), and pinned (P) boundary conditions applied to the top of the MP and

the LG. These same configurations were also used in Cast3M in order to verify the natural frequencies and mode shapes. The algorithm used in Cast3M for modal analysis requires one of two inputs, a set number of modes or a range of frequencies. For this comparison, the frequencies of interest are those less than $100Hz$. This was chosen since the seismic frequencies are expected to be in the low range. The MP has between 10 and 13 elastic natural frequencies within this range depending on the boundary conditions.

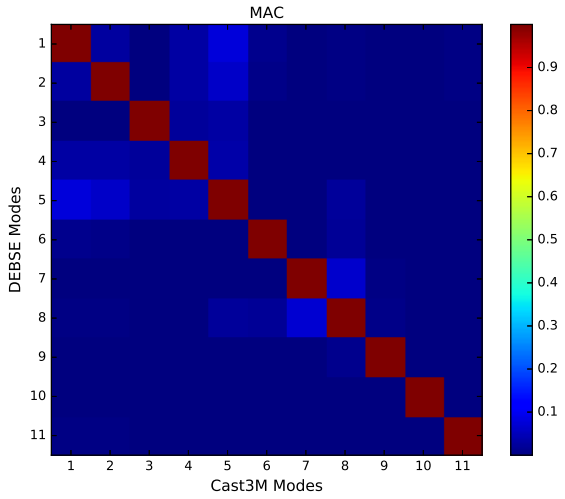
The first results for validation purposes is the comparison of mode shapes. This is done by applying the MAC formula in Equation 13 to the modes generated by DEBSE and the modes generated by Cast3M. The results from these calculations can be seen in Figure 7 for the six combinations of boundary conditions. As a note of nomenclature, the first word in the sub-caption refers to the boundary condition at the bottom of the MP, the LG, and the second word refers to the condition at the top. For the majority of the modes, there is an almost one-to-one relationship between the DEBSE modes and the Cast3M modes. In a typical analysis, a MAC value greater than 0.90 would be considered the same mode.

For the majority of the modes, the MAC value is around 0.99 for the corresponding mode and values less than 0.10 for the non-corresponding modes with the exception of the Free-Pin and Free-Clamped boundary conditions. In the Free-Pin configuration, there is no Cast3M mode for the tenth elastic mode discovered in DEBSE. Additionally, the tenth mode in Cast3M is very similar to the ninth mode from DEBSE producing a MAC value of 0.63. These four modes are shown in Figure 8a with the blue curves being from Cast3M and the red curves being from DEBSE. The first thing to note is that Mode 9 for both Cast3M and DEBSE overlap nearly perfectly and are indistinguishable from each other on this plot. Mode 10 for each produce similar shapes, but with a phase shift and different amplitudes. The true cause of this is unknown, but it is expected to be due to in part by the stepped-beam properties. With drastic changes in the geometry and material properties, there is a possibility of local stretching that is characterized in Cast3M that is undetectable by DEBSE in the current implementation. DEBSE uses the small deformation version of the Euler-Bernoulli beam equation. Alternate formulations are possible that can account for axial stretching, but it not currently implemented. Further investigation is being performed to determine the exact cause of this discrepancy. A similar case can be seen for the Free-Clamped boundary conditions. For this, there is no missing DEBSE mode, but there is a strong coupling between Cast3M mode 10 and 11. The MAC value for DEBSE mode 10 and Cast3M mode 11 is 0.835. This is a very large MAC value for separate modes. To further investigate, these modes shapes are plotted in Figure 8b. Cast3M and DEBSE mode 10 are almost identical with mode 11 from Cast3M matching the curve but with different amplitudes further along the beam. The cause of this is also unknown, but might be due to the local stretching that was previously discussed for the Free-Pin boundary condition.

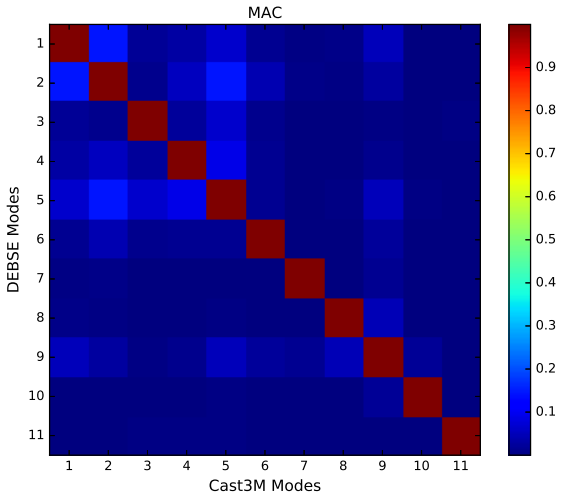
The other main validation is the difference in natural frequencies between the two methods. This is computed as a percentage difference of the corresponding modes that contained MAC values larger than 0.90. The results from this comparison can be seen in Table 1. For the modes that matched well, there is very good agreement in the natural frequencies, resulting in a maximum percent difference of 0.36%. This shows that for a given bending mode, DEBSE is able to correctly identify the natural frequency and mode shape.

Boundary Conditions	N_{modes}	Mean Difference [%]	Max Difference [%]
Clamp-Clamp	11	0.14	0.34
Pin-Pin	11	0.13	0.33
Free-Free	11	0.16	0.36
Free-Pin	10	0.13	0.34
Free-Clamp	12	0.14	0.34
Pin-Clamp	11	0.14	0.33

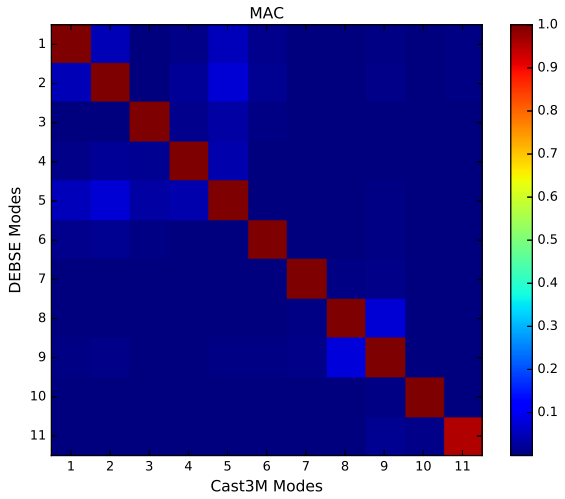
Table 1: Mean and Maximum Percentage Difference Between DEBSE and Cast3M



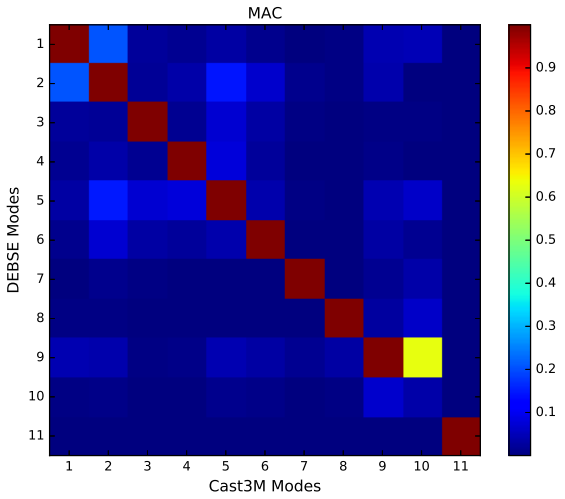
(a) Pin-Pin



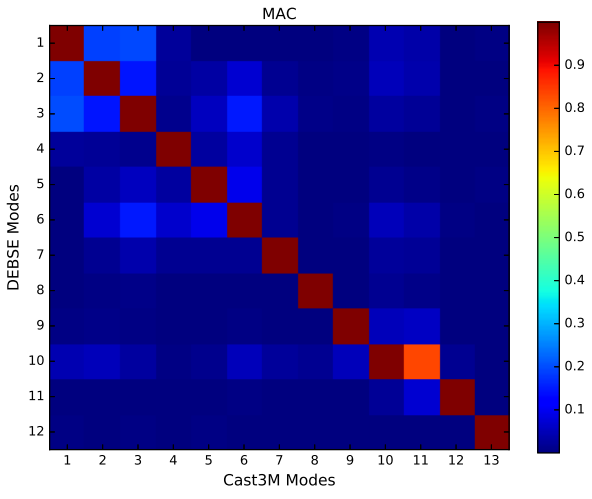
(b) Free-Free



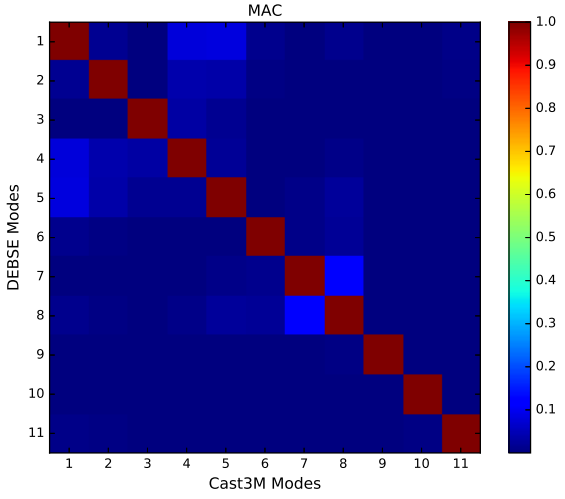
(c) Clamp-Clamp



(d) Free-Pin

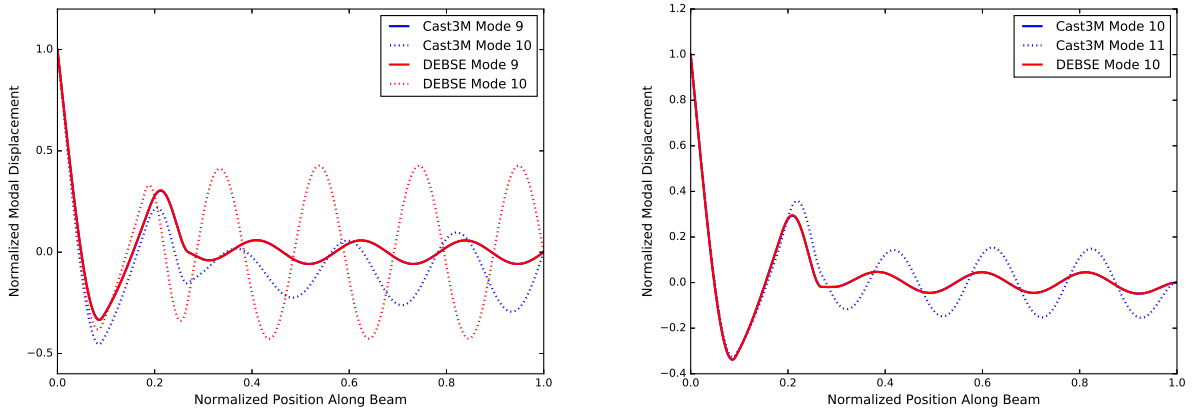


(e) Free-Clamp



(f) Pin-Clamp

Figure 7: MAC Plots for Various Boundary Conditions



(a) Free-Pin

(b) Free-Clamp

Figure 8: Normalized Mode Shapes for Select Boundary Conditions

6 Remarks/Future Work

The static solver, StaBI, is shown to produce similar results to RC3 when the contact algorithms produce the same contact locations. This is the major part of the future work for this solver. The contact algorithm of adding an additional contact for each iteration with no ability to remove a contact is the portion of the solver that requires the most investigation. It is currently unknown how this algorithm will be changed, but it is difficult to determine which algorithm is a better match to the real system without any experimental data to compare to. Gathering of this experimental data is currently being discussed and planned. This data is expected to be gathered at either the CARNAC facility in Cadarache [17] or at the TAMARIS facility in Saclay [18].

The next step for using the static solver would be to introduce the SIKI tool using the StaBI solver. This system is expected to drop in case of a seismic event. So in order to get some information about this insertion, a kinetic analysis is expected to be performed. This entails using an explicit ”time-marching” algorithm with each time step being treated as quasi-static. The analysis would not require much changes to the solver, but might require some optimization in order to allow for performing the analysis within a reasonable time.

While the natural frequencies and mode shapes are not the desired end result for the dynamic expansion, they do provide a useful foundation to show that the solver can handle the simple calculations. There is a possible issue when it comes to computational time for each simulation. Since the natural frequencies are determined by taking the determinate of the constraint matrix, as the matrix increases in size, the required time to determine each natural frequency increase. This matrix increases in size as more sections are introduced since there are four additional coefficients and four continuity equations that are added to the system. While this is not an issue for just looking at the MP, this might become more of an issue when contact is added. One possible method to introduce contact is to replace the location of contact with a moving Pin boundary condition. Using this method, along with modal decomposition, would require an initial determination of frequencies and an additional determination for each addition and removal of contact locations. Currently for the MP, it takes roughly ten minutes to compute the first fifteen natural frequencies while checking for duplicates. It also takes approximately ten minutes to calculate the mode shapes for the MP with 1206 node points. One expected future work is to better optimize these procedures or find an alternative approach to determine the time history of the system. A possible alternative would be to apply the contact as constraints on the system. This would allow for a single modal characteristics evaluation and provides extra equations that might allow for the determination of the contact force required.

The next steps in DEBSE are to essentially perform the same analysis as the static solver, but also as a func-

tion of time. This includes: contact determination, force calculation at contact locations, contact removal, modeling contact, and moving contact. One interesting aspect about performing this dynamic analysis is that this type of analysis has not previously been performed at CEA. Previous iterations used a quasi-static approach to simulations and then used experimental systems to ensure dynamic capabilities for qualification. Using this dynamic simulations will be able to replicate the dynamic experiments at a fraction of the cost, and allow for additional information to be determined providing more information to the design engineers. While a dynamic experiment will still be required for qualification, there is less chance of geometric changes due to failure resulting in requiring additional experimentation with a new geometry. Using this PIRAT tool will allow for engineers to produce a safer system at an expectantly lower cost.

7 Conclusions

PIRAT is a novel tool that allows the calculation of contact location and forces using an analytical approach. The static solver uses the Bresse's formulations that allow for the determination of the displacement of a system due to a force and also allows for an inverse solution in order to determine the force magnitudes due to constrained displacements. This tool is used on an example prototype system and is compared to previous work done using finite elements in Cast3M called RC3. These two methods show very good agreement for the majority of cases. This agreement did not occur when the different contact algorithms produced different contact locations. Without experimental validation data, it is unsure of which algorithm is more realistic to the physical system, thus experimental testing is currently being planned.

The final desire for this PIRAT tool is to perform the same analysis in a dynamic sense. While this is a complicated expansion, some preliminary work has been performed for the dynamic solver. This work is comprised of a modal analysis of the Mobile Part with no contact with the Lower or Upper Sleeve. The results presented are the natural frequencies and the mode shapes of the step-changed Mobile Part beam. These results are compared to a similar analysis performed in Cast3M using the built-in eigen solvers. This compares the shape and natural frequencies for the modes less than $100Hz$. DEBSE was able to produce nearly identical results for the natural frequencies and mode shapes except when there was possibly axially stretched modes found in Cast3M, which uses 2D finite elements compared to 1D equations of motion for DEBSE. For modes that had a MAC value larger than 0.90, the difference in the natural frequency was less than 0.4%.

This StaBI tool has proven to be accurate for the static analysis compared to the work previously performed using finite elements in a custom implementation in Cast3M. While there are differences in the contact algorithms, these tools provide very similar results for most cases tested. The differences between the algorithms and the physical system are not yet known, but are in planning. Since the desire of analysis is to predict if there is a failure during a seismic event, preliminary steps are performed in creating a dynamic solver within PIRAT. Initially, this work compares the natural frequencies and mode shapes of DEBSE and those produced by finite elements in Cast3M. DEBSE shows to be extremely accurate while being much easier to make design changes compared to Cast3M due to the implementation. The PIRAT tool is able to take beam-like structures that are bounded by guiding sleeves and determine the contact force and deflection caused primarily by the seismic induced misalignment.

References

[1] K. Fujita, Y. Shinohara, K. Nanbu, T. Nakatogawa, and T. Nomura. Scram characteristics of control rods of pressurized water reactor under seismic conditions. *JSME international journal*, 30(267):1450–1457, 1987.

[2] B Collard. Rod cluster control assembly drop kinetics with seismic excitation. In *Proceedings of the 11th international conference on nuclear engineering ICONE 11*, Tokyo, Japan, April 2003. ICONE-36419.

[3] Y Watanabe and Y Motora. Analysis of cr scrammability characteristics on the condition of the forced vibration of fuel assemblies. In *Transactions of the 7. international conference on structural mechanics in reactor technology. Vol. F*, 1983.

[4] A. Morrone, A.N. Nahavandi, and W.G. Brussalis. Scram and nonlinear reactor system seismic analysis for a liquid metal fast reactor. *Nuclear Engineering and Design*, 38(3):555 – 566, 1976.

[5] D. Brochard and P. Buland. Seismic qualification of SPX1 shutdown systems - tests and calculations. In *Proceedings of the ICONE-11 Conference*, Bologna, Italy, October 1987.

[6] M.N. Sundaran, R. Vijayashree, S. Raghupathy, and P. Puthiyavinayagam. Experimental seismic qualification of diverse safety rod and its drive mechanism of prototype fast breeder reactor. In *Proceedings of the FR17 Conference*, Yekaterinburg, Russia.

[7] M. Zabiégo, D. Lorenzo, T. Helfer, and E. Guillemin. Insertion reliability studies for the RBC-type control rods in ASTRID. In *Proceedings of FR17 Conference*, Yekaterinburg, Russia, June 2017. Paper IAEA-NC-254-120.

[8] V. R. Babu, R. Veerasamy, S. Patri, S. I. S. Raj, S.C.S.P. K. Krovvidi, S.K. Dash, C. Meikandamurthy, K.K. Rajan, P. Puthiyavinayagam, P. Chellapandi, et al. Testing and qualification of control & safety rod and its drive mechanism of fast breeder reactor. *Nuclear Engineering and Design*, 240(7):1728–1738, 2010.

[9] CAST3M. Cast3M is a research fem environment; its development is sponsored by the French Atomic and Alternative Energy Commission. http://www-cast3m.cea.fr.

[10] J. Courbon. Théorie des poutres. *Techniques de l'ingénieur*, (C2010), 1980. (In French).

[11] P. F. Gou and K. K. Panahi. Analytical solution for beam with time-dependent boundary conditions versus response spectrum. In *Proceedings of the* 9^{th} *International Conference on Nuclear Engineering*, Nice, France, April 2001.

[12] S. Y. Lee and S. M. Lin. Dynamic analysis of nonuniform beams with time-dependent elastic boundary conditions. *Journal of applied mechanics*, 63(2):474–478, 1996.

[13] D. W. Chen and J. S. Wu. The exact solutions for the natural frequencies and mode shapes of non-uniform beams with multiple spring–mass systems. *Journal of Sound and Vibration*, 255(2):299–322, 2002.

[14] Y. Huang and X. F. Li. A new approach for free vibration of axially functionally graded beams with non-uniform cross-section. *Journal of sound and vibration*, 329(11):2291–2303, 2010.

[15] M. A. Koplow, A. Bhattacharyya, and B. P. Mann. Closed form solutions for the dynamic response of Euler–Bernoulli beams with step changes in cross section. *Journal of Sound and Vibration*, 295(1-2):214–225, 2006.

[16] M. Avcar. Free vibration analysis of beams considering different geometric characteristics and boundary conditions. *International Journal of Mechanics and Applications*, 4(3):94–100, 2014.

[17] T. Catterou, V. Blanc, G. Ricciardi, S. Bourgeois, and B. Cochelin. Numerical strategy for dynamic simulations of impacts on SFR fuel pins and experimental validation. *Journal of Nuclear Engineering and Design*. In Submission.

[18] Tamaris. http://www-tamaris.cea.fr.

Influence of diaphragm modelling on the dynamic performance of a reinforced concrete high-rise building

N. J. Savnik[1,2], E. I. Katsanos[1], S. D. R. Amador[1], C. E. Ventura[3], R. Brincker[1]
[1] Technical University of Denmark, Department of Civil Engineering
Brovej, Building 118, 2800, Kgs. Lyngby, Denmark
e-mail: **niels@savnik.dk**

[2] Read Jones Christoffersen Ltd.,
1285 W Broadway suit 300, Vancouver, BC V6H 3X8, Canada

[3] The University of British Columbia, Department of Civil Engineering
6250 Applied Science Lane, V6T 1Z4, Vancouver BC, Canada

Abstract
The present study investigated the dynamic behaviour of an irregular 32-storey reinforced concrete, Vancouver-style, high-rise, podium tower by assessing the influence of the floor diaphragm modelling stiffness assumptions on the structure's modal properties. The state-of-the-art diaphragm modelling approaches and their effect on structures' dynamic performance are currently related to symmetrical buildings with multiple shear walls. The influence of horizontal floor diaphragms on the dynamic behaviour of irregular, high-rise buildings with concrete core has not been sufficiently investigated either on a numerical or experimental basis. In this context, the primary objectives of the current study are: (a) to enhance the comprehension of the horizontal floor diaphragm behaviour of a high-rise building with a concrete core and, (b) to quantify the effect of varying diaphragms modelling approaches on the dynamic properties of the structure.

1 Introduction

Most existing civil engineering structures as buildings, bridges and other infrastructures are unique structures and the real dynamic performance capacity of these structures are relatively uncertain. For designers' convenience and saving computational power, the code-confronted design of structural systems is commonly subjected to several simplifications and crude assumptions that may not reflect the actual static and, primarily, dynamic performance of structural systems. The latter is more profound for complex structures that deviate from symmetrical configurations and typical structural systems with regular distribution of the mass and stiffness both in plan and elevation. Today engineers are challenged more than never by the request of designing irregular and code-breaking structures, where the fundamental engineering principles are deficient as the design basis. Therefore, it is of high importance to address the accuracy of those assumptions thoroughly and investigate their effect on the structural response evaluation that, in turn, constitutes the concrete basis of any decision needs to be made by the relevant stakeholders for repairing or retrofitting of existing structures. Future design of structures and infrastructure systems can benefit and be optimised by revising the primary design considerations, and quantifying their impact on the actual structural performance. Designers frequently treat the horizontal plates at each storey level, as rigid diaphragms and this simplification, though a convenient approach regarding modelling perspective, dominates the current design practice. Such an infinite stiffness assumption for the diaphragm modelling may be suitable for somewhat regular and symmetrical reinforced concrete (RC) buildings. For complex structures, the validity of this assumption is questionable, in which the diaphragms response affects the lateral performance of the entire structural system. The engineering society is missing, how accurate is the

real diaphragm performance captured both in experimental and numerical investigations, to identify a refined modelling approach for the diaphragms.

Current research efforts describe the suitability of the rigid diaphragms modelling approach, evaluated for different structural systems. For example, Saffarini and Qudaimat [1], investigated 37 reinforced concrete structures of varying height, structural configuration and dimensions for the storeys as well as the columns and the shear walls. They concluded that the rigid-floor assumption captures less accurately the dynamic response of buildings with shear walls compared to structural systems that the beam-column frames have been designed to resist the lateral forces. Moreover, Ju and Lin [2] undertook a thorough response analysis of 520 buildings with varying configurations, i.e., T-shaped, U-shaped and rectangular shaped buildings, and they highlighted that the rigid diaphragm assumption was found to be associated with the less accurate calculation of the building response compared to the flexible diaphragm approach. A study to assess the influence of floor diaphragm flexibility on the dynamic response of torsional-sensitive asymmetric buildings was carried out by Basu and Jain [3], and they found the flexible diaphragms modelling approach is somewhat deficient in capturing the accuracy of lateral performance of buildings with torsional sensitivity. Additionally, the lateral performance of three existing building systems, modelled with both flexible and rigid floor diaphragms respectively, was comparatively assessed by Tena-Colunga and Abrams [4] revealing higher deformations (i.e., accelerations and displacements) calculated for the building systems with the flexible diaphragms. The torsional response was also found reduced by increasing the diaphragms flexibility that, in turn, affected the dynamic properties of the building by elongating their natural building period.

Moeini and Rafezy [5], assessed the diaphragm modelling relation to the code provision, who performed modal response spectrum analysis of RC buildings with T-shaped, U-shaped and rectangular structural configuration. The study divides existing building codes and standards into two categories regarding the recommended diaphragm modelling assumptions. Primarily, according to the Eurocode 8 (EN1998-1), the New Zealand code (NZS4203) and the Chinese one (GSC-2000) the decision regarding the diaphragms modelling is based on qualitative criteria associated with the shape of the floor diaphragm. On the other hand, the Iranian 2800 code as well as the UBC 97, SEAOC-90 and FEMA-273, prescribe quantitative criteria related to the in-plane deformation of the plates to define whether the diaphragm should be treated as fixed or flexible. However, the latter approach was concluded deficient due to the deformation of the diaphragm is dependent on the acting force. Moeini and Rafezy [5] were in favour of modelling the horizontal floor plated with shell elements rather than beam finite elements, widely used in the engineering practice.

The studies mentioned above addressed the influence of different diaphragms modelling approaches on the dynamic properties (i.e., Eigen frequency and mode shapes) and the numerically-calculated response of various structures, missing the investigation of typical RC high-rise podium towers with irregular distribution of mass and stiffness along the height and in-plane. Therefore, the City Crest Tower, being an emblematic tall building from early 1990's located in downtown Vancouver (British Columbia, Canada), was chosen as the testbed to investigate whether the rigid or flexible diaphragm modelling approach respectively captured more accurately the actual dynamic response. To this end, the measured response data sets were used to identify the modal properties of the building that, in turn, enabled the refinement of a detailed finite element model increasing, eventually, the reliability and accuracy of the investigation results. The primary objectives of the current study are summarised below:

- Identification of the benchmark structure's modal properties based on the measured response data that was obtained during the ambient vibration tests.
- Development of the structure's finite element model, which is refined further by experimentally, identified dynamic properties.
- Investigation of the suitability of the different diaphragms modelling approaches and the related assumptions (i.e., rigid or flexible diaphragm) for the specific structural system accounting for the identified dynamics properties.
- Assessment of the effect the diaphragm modelling assumptions have on the dynamic response for the high-rise RC building presented in this study.

2 Constraints of Diaphragms and Numerical Modelling Aspects

Floor diaphragms/slabs in multi-storey buildings are often modelled as shells elements and discretisation of the diaphragms can be considered massive computational power-wise. To avoid massive computational models kinematic constraints are applied, and the constraints are often "master-slave" nodes for many automated structural analysis programs. A floor system in three dimensions with the shape of a rectangle and has four corner nodes. Each node has six degrees of freedom three translations and three rotations ones before any constraints are applied. If a structural element as columns or beams is attached to the floor system, this introduces additional six degrees of freedom per node. For large structures, the in-plane definition of the lower floors is often considered to be small compared with the horizontal inter-storey drift, and the applied master-slave approach will provide safe computation power, [6]. Reducing the degrees of freedom has disadvantages regarding the response of the floor system. Simplifying the behaviour of the floor leads to significant errors and non-conservative estimations, [3]. Figure 1, illustrates the master-slave approach for the floor system, the centre of mass is located at the point O, and a random point i is considered. By assuming the kinematic constraint, the diaphragm is rigid; the displacement of any node can be expressed as a linear function of the master node, in the point O. The figure shows displacements in the x-direction is illustrated as $u_x^{(O)}$, the corresponding y-direction is $u_y^{(O)}$ and the rotational displacement is illustrated as $u_{\theta z}^{(O)}$, [7].

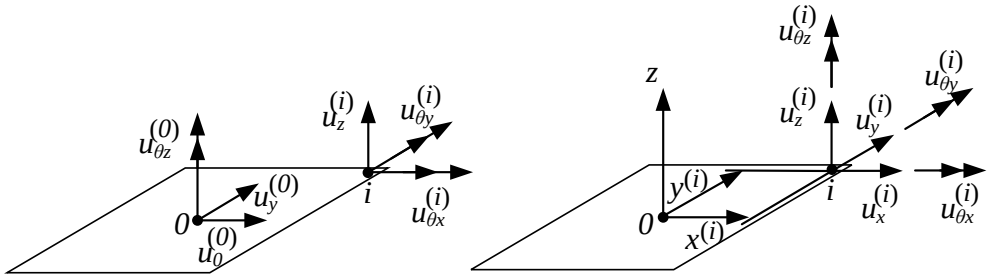


Figure 1: Master-slave diaphragm assumption. Left: 6 degrees of freedom node. Right: slave node with 3 degrees of freedom.

The compatibility equations yields, the displacement of any slave node is

$$\begin{aligned} u_x^{(i)} &= u_x^{(O)} - y^{(i)} u_{\theta z}^{(O)} \\ u_y^{(i)} &= u_x^{(O)} + x^{(i)} u_{\theta z}^{(O)} \\ u_\theta^{(i)} &= u_{\theta z}^{(O)} \end{aligned} \tag{1}$$

The kinematic constraints further yields any external force $\mathrm{f}_x^{(Oi)}$ associated with the rigid displacements, estimated with the equation above, is transform with respect to the master node. By static equilibrium, the slave node force is transformed to the master node, which yields, [7].

$$\begin{aligned} \mathrm{f}_x^{(Oi)} &= \mathrm{f}_x^{(i)} \\ \mathrm{f}_y^{(Oi)} &= \mathrm{f}_y^{(i)} \\ \mathrm{f}_{\theta z}^{(Oi)} &= \mathrm{f}_{\theta z}^{(Oi)} - y^{(i)} \mathrm{f}_x^{(i)} + x^{(i)} \mathrm{f}_y^{(i)} \end{aligned} \tag{2}$$

3 The City Crest Tower

The building adopted for investigation by the current study is the City Crest Tower (Figure 2), which is a Vancouver style high-rise 32-storey RC building reaching 83.2 m in height. The high-rise podium was constructed from autumn 1992 to January 1994 and is located in downtown Vancouver (British Columbia, Canada). The structure is representative of high-rise podium towers in Vancouver and was designed according to Vancouver Buildings By-law 6134, CAN/CSA-S413-87 for the parking structure and the Canadian RC concrete design standard CSA CAN3-A23.3-M84. The basement of the tower and a pair of walkway bridges constructed at the second level are used to facilitate the connection between the high-rise building and a two-storey townhouse. However, the latter is not a central part of the primary structural system of the tower and hence, is not further considered in this study. The typical storey height is 2.6 m except for the ground floor, designed deliberately higher, i.e., 4.0 m, to facilitate commercial activities.



Figure 2: South-East (left) and South-West (right) side of the City Crest Tower.

The main seismic force resisting system of the high-rise tower is the concrete core, located in the centre of each floor above the ground and designed to resist lateral forces. Additionally, the columns are a part of the load-bearing gravity system. The core and edge columns are continuous at each floor to support the in situ-cast floor slabs. From the 30th level and above, the columns at the perimeter are replaced with walls of 204 mm thickness. Regarding the concrete core per se, it measures 10.3 m by 7.6 m in the plan (Figure 3) with a varying wall thickness from 457 mm at the basement to 356 mm at the top floors. The core houses mechanical and electrical conduits, stairwells and elevator shafts. Figure 3 also illustrates the plan layouts for different floor levels. The lower floors (3-10) measure 24.7 m in East-West and 22.4 m in North-South direction respectively while the floor area is reduced thought out the height of the tower, from 600 m^2 for levels three to ten, 500 m^2 for levels 11 to 25, and the floor area is further reduced from levels 25 to 32. Additionally, the floor slabs are typically 191 mm thick with varying reinforcement, concentrated mainly around the columns and the concrete core while diaphragm reinforcement is placed along the slab edges. Significant variation regarding size, geometry and material properties (Table 1) are found for the columns, the shear walls and the beams designed for the entire building stemming from its basement up to higher elevations.

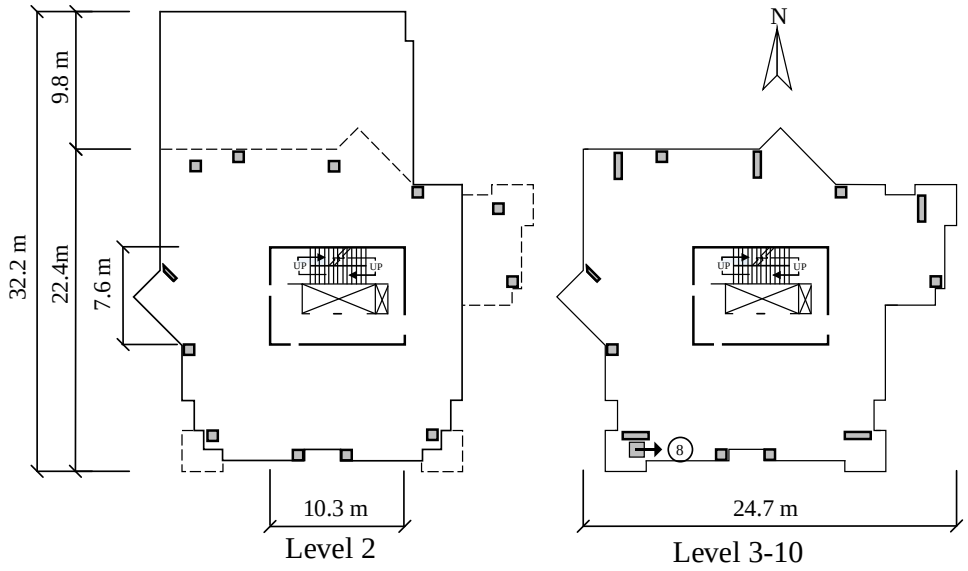


Figure 3: Level 2 (left) and level 3-10 (right) floor layout of the City Crest Tower.

Structural element/description	Strength [MPa]
Footings and walls	25
Tower core walls	
Level P6 – 5	25
Level 6 - 32	30
Suspended slabs and beams and retaining walls	30
Columns	
Level P6 – 4	40
Level 5 – 9	35
Level 10 – 19	30
Level 20 - 32	25
Exterior slabs, driveways, and other surfaces subject to de-icing salts (Class C-1 exposure)	35
All other concrete	20
Reinforcing steel	Grade 400

Table 1: Material properties adopted for designing the City Crest Tower [8].

An extensive setback, found from level 10 at the Southeast corner of the City Crest Tower (Figure 2), reduces the number of the perimeter columns introducing, in such a way, non-uniform mass and stiffness distribution along the height of the structure's height. The latter, commonly considered as a primary source of structural irregularity, is heightened by additional, smaller though, setbacks that can be found for the higher floors of the tower. The extension of the second floor by 9.8 m, being connected to the tower with a monolithic slab connection, contributes further to the asymmetric configuration of the high-rise tower increasing its structural irregularity. It is notable that the slab of the extended second floor has been designed with a varying thickness between 178 mm and 229 mm while the slab thickness of the second floor's central area is 216 mm.

Regarding the basement of the podium tower, six staggered levels were constructed to accommodate parking areas measuring 62.3 m in the East-West direction and 35.8 m in the North-South direction while the sixth parking level is located 9.4 m below the ground surface. Different types of slab bands with varying thickness, i.e., from 406 mm to 457 mm, were applied for the parking-related levels. Finally, both strip and footing foundations were used to support the entire building and designed to undertake loads of the columns. The footing foundations are varying significantly regarding their size since the smaller ones measure 2.1 m by

2.4 m in plan and 0.7 m thick while the most massive footing column foundations were calculated to be square of 4.1 m length and 1.2 m thickness. The concrete core was also supported by a stiff mat foundation measuring 12.8 m by 16.2 m with a thickness of 3.1 m. The line foundations varying in width (0.6 m up to 1.8 m) and thickness (0.3 m up to 0.5 m) were used to support the shear walls.

4 Ambient Vibration Tests and Operational Modal Analysis

The ambient vibration test of the City Crest Tower was performed in the summer of 1993 with eight Kinematic Inc. force balance sensors, i.e., the FBA-11 accelerometer, connected with the signal conditioner by using cables of 90 m up to 300 m length. The signal conditioner filtered and amplified the raw FBA signals that, afterwards, were converted from analogue to digital format. The sensor locations, as illustrated in Figure 4, were carefully chosen to capture the dynamic characteristics of the building, i.e., the natural frequencies and mode shapes efficiently. Primarily, the guidelines of the California Strong Motion Instrumentation Program, [9], were followed to place the sensors and ensure adequate isolation of the translational and rotational vibrations at each storey level in both the North-South and East-West direction respectively. It is worth mentioning that during the ambient vibration tests, the City Crest Tower was under construction and partition walls had been installed only for the first five floors while the building's roof had been cast two weeks prior the test. The sensors were mounted with anchor bolts to the concrete floor slabs. The ambient vibrations experimental campaign included 19 different test setups, with four roving sensors and four reference sensors each. The latter was placed at the 29th floor at antinodes of the vibration modes of interest. The sampling rate was set to 40 Hz, ensuring a Nyquist frequency of 20 Hz while the acceleration measurements were filtered onsite with a high pass filter of 0.1 Hz and a low pass filter of 12.5 Hz. The duration of each measured acceleration signal was 13 minutes and 39.2 seconds, corresponding to 32768 data points.

The measured response of the City Crest tower during the ambient vibration tests was used to identify the dynamic properties of the building by applying the Operational Modal Analysis (OMA) is a widely used method for system identification [10] of civil engineering structures. Figure 5 (left) illustrates the geometrical model of the high-rise structure created by using the commercial software ARTeMIS Pro Modal (v4) [11], applied to perform the OMA. The blue arrows represent the data channels being associated with the reference sensors placed on the 29th floor while the pink and the green arrows are the projection and data channels respectively. Furthermore, the singular values of the spectral densities, calculated for calculated for all measurement setups by using ARTeMIS Pro Modal (v4), were plotted by Figure 5 showing well identified (tapered bell shape) natural frequencies of the high-rise structure within the frequency range of 0-12 Hz. It is notable that the spectral density estimation/segment size used was taken equal to 1024 while no additional filters were applied to derive the singular values.

A pair of OMA-based identification techniques, namely the Enhanced Frequency Domain Decomposition (EFDD) and the Stochastic Subspace Identification – Unweight Principal Component (SSI - UPC) technique respectively, was used to estimate the dynamic properties of the City Crest Tower including the natural frequencies and the modal damping as well as the mode shapes. Table 2 lists the identified properties for the first eight translational and first four rotational modes respectively ranging, regarding natural frequencies, from 0.55 Hz (NS – first translational mode, EFDD) to 10.27 Hz (fourth rotational mode, SSI-UPC). Furthermore, the first two translational modes along the North-South and East-West directions were identified as closely spaced modes since the EFDD identification technique resulted in 0.55Hz and 0.65 Hz respectively. The first rotational mode was identified with a natural frequency of 1.29 Hz. As can be seen, by Table 2, the two identification techniques, i.e., the EFDD and the SSI – UPC, led to estimating somewhat similar natural frequencies for the 12 modes investigated with the highest difference being of 4.4%. On the other hand, the EFDD and SSI-UPC techniques resulted in slightly different estimates for the modal damping ratios that were found to be in the range of 0.8% to 3.53% with a maximum difference of 130.1%. The latter is mainly attributed to the increased uncertainty, generally related to the damping estimation. It is to the best knowledge of the authors that the SSI-UPC technique usually provides estimates of modal damping ratios with higher accuracy compared to the EFDD-based estimates especially when the duration of the acceleration signals is shorter than 20 minutes [12]. Finally, the first four translational (NS1, EW1,

NS2 and EW2) modes and the first two torsional modes (T1 and T2) determined with the SSI – UPC method, are illustrated at Figure 6.

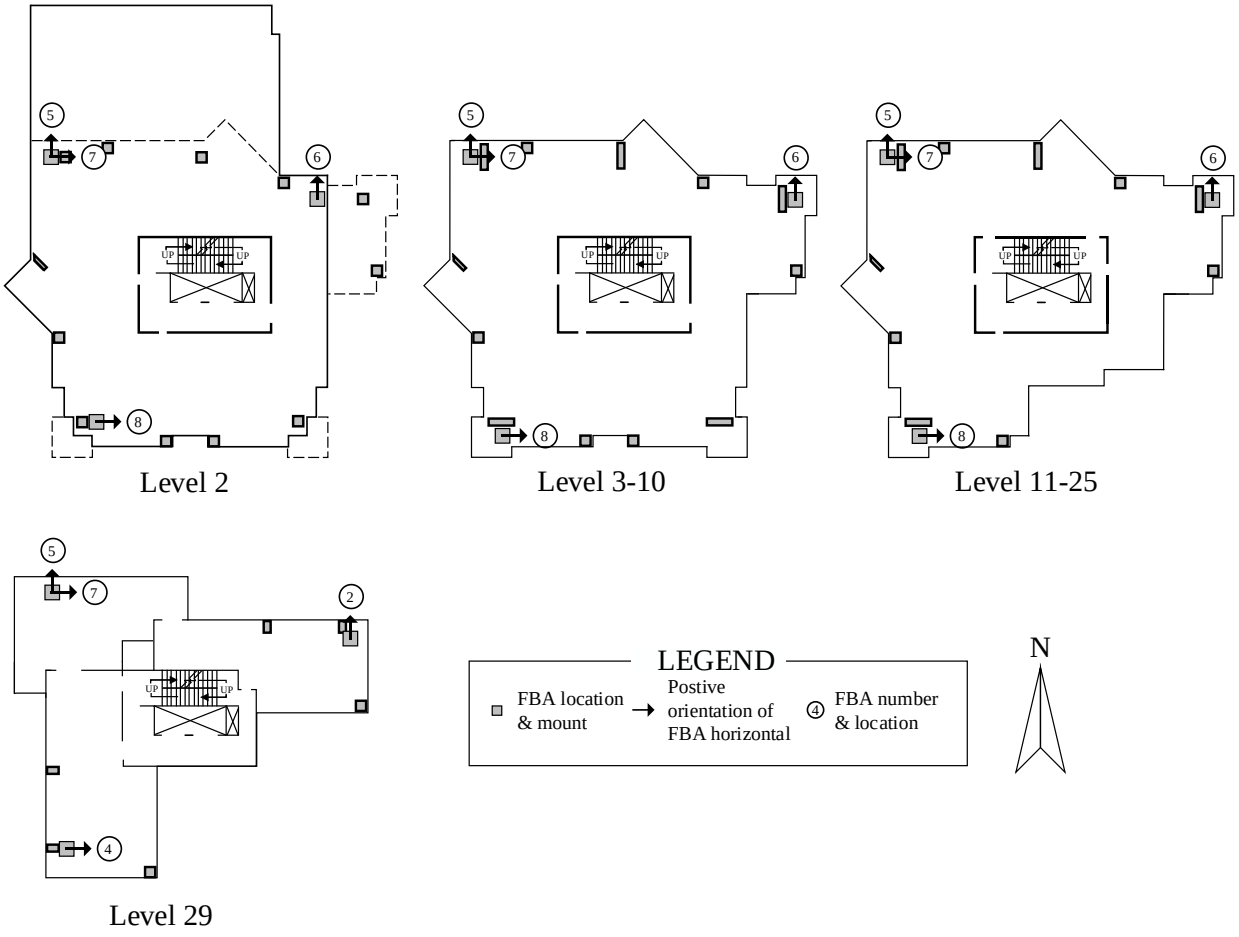


Figure 4: Sensors layout at different levels

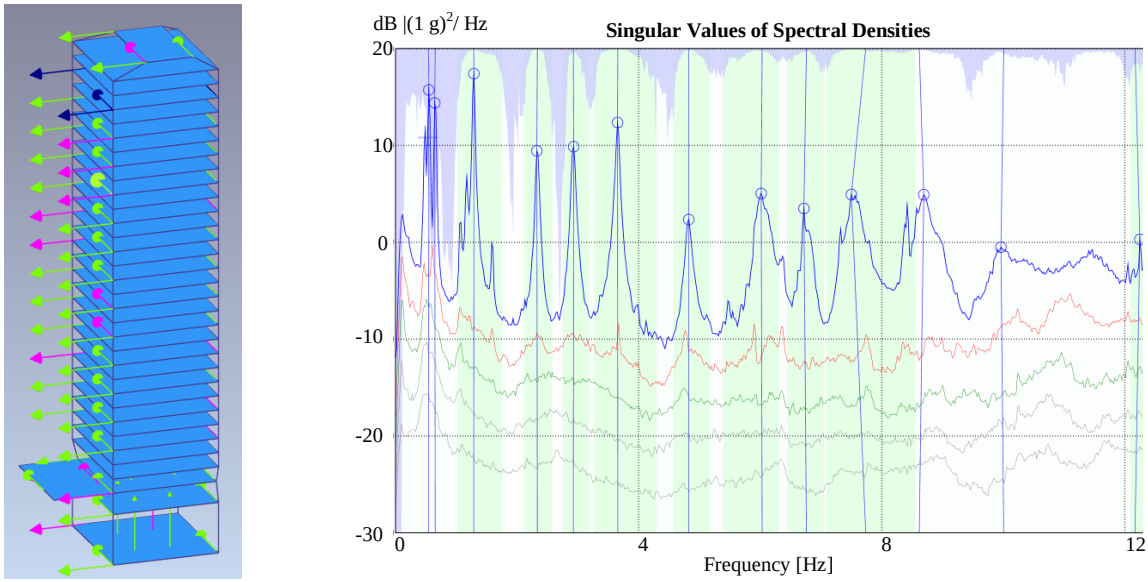


Figure 5: Computer model in ARTeMIS for the Operational Modal Analysis (left) and the singular values of spectral densities (right).

Method Mode	EFDD Frequency [Hz]	SSI - UPC Frequency [Hz]	Frequency Difference (%)	EFDD Damping (%)	SSI - UPC Damping (%)	Damping Difference (%)
NS 1	0.55	0.57	4.4	3.53	2.88	-18.4
EW 1	0.65	0.64	-2.0	2.09	3.41	63.7
T 1	1.29	1.26	-2.1	1.04	2.31	121.8
NS 2	2.33	2.35	0.8	1.05	1.71	62.4
EW 2	2.92	2.93	0.2	1.04	0.92	-11.8
T 2	3.66	3.55	-2.8	0.80	1.42	77.6
NS 3	4.82	4.83	0.2	1.17	1.61	37.7
EW 3	6.03	6.03	0.0	1.62	1.94	19.9
T 3	6.76	6.80	0.6	1.20	1.91	59.3
NS 4	7.74	7.49	-3.2	1.67	1.93	16.0
EW 4	8.62	8.79	2.1	1.71	2.06	20.5
T 4	10.01	10.27	2.6	1.35	3.11	130.1

Table 2: Natural frequencies and damping ratios identified from the ambient vibration test

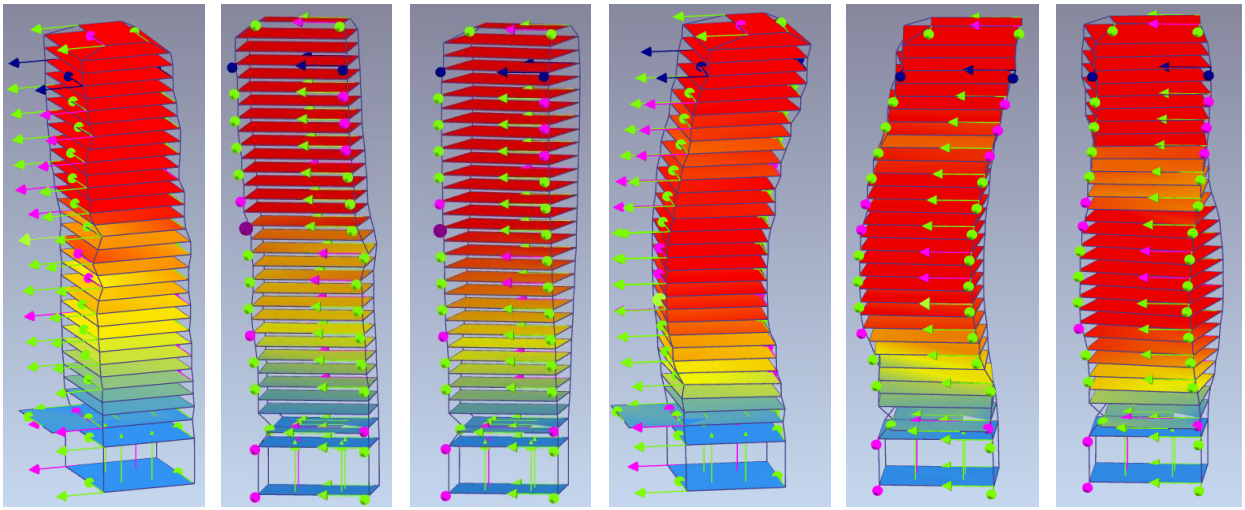


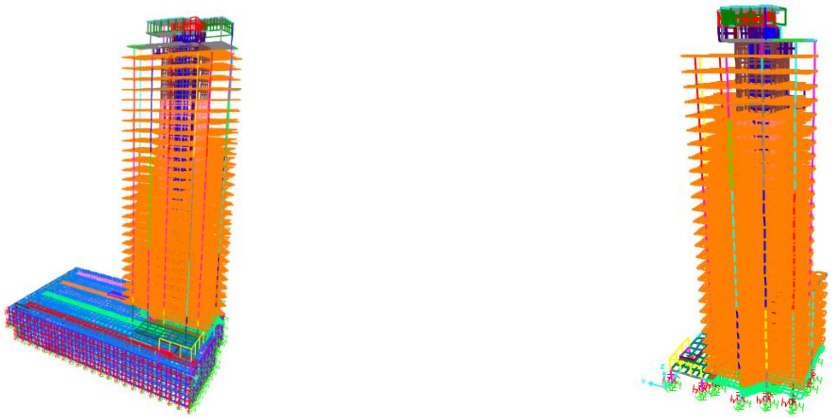
Figure 6: The first six mode shapes from the ambient vibration test.

5 Finite Element model

A linear Finite Element (FE) model of the City Crest Tower was developed to investigate the effect of different diaphragms modelling approaches on the dynamic performance of the high-rise structure. By strictly following the building's drawings being available to the authors, a high level of details were applied for the development FE model, with beams, columns, shear walls and slabs of varying size and complexity, found at each floor level, was modelled by the use of SAP2000 [13]. To utilise the OMA-based identification of the dynamic properties of the structure, for the refinement of the finite element model, the FE model should reflect precisely the structure, for which the ambient tests were performed. Therefore, under normal operating conditions of a building the opening and closing of microcracks in the elements of a building is very small and that the assumption of an "uncracked" section is justifiable. The detailed modelling of the reinforcement was outside the scope of the current study. Hence, the applied concrete mass density was

adopted equal to 2500 kg/m^3 accounting, in such a way, for the additional mass density related to the reinforcement steel bars [14]. Moreover, the different strength used for the concrete material (Table 1) led to different values for Young's modulus that was applied for the structural members modelled as either beam elements (columns and beams) or shell elements (floor slabs, shear walls and basement walls). The shell elements enable modelling of the transverse shear deformation by the Mindlin/Reissner formulation, while the bending shell stiffness is also considered [15].

Regarding the diaphragms considered at each story level, three modelling approaches were adopted to investigate their influence on the structure's global dynamic response, captured already during the ambient vibration test campaign. Along these lines, the diaphragms were modelled by the current study as flexible, semi-flexible and rigid ones. For the latter case, being the most common chosen for designers and engineers due to the computation power savings and simplicity, a constraint is applied to the nodes of the slab and the total mass is concentrated at the centre of the diaphragm condensing, in such a way, the associated stiffness matrix. Infinite in-plane stiffness properties are also related to the rigid diaphragm while, for the earthquake-induced lateral loads, the accidental eccentricity is applied to the centre of mass of the diaphragm [15]. On the other hand, no constraints are assigned for the diaphragms flexible modelling approach, and the floor-associated masses are not lumped while no modification is applied to both the flexural and shear stiffness of the shell elements, used to model the diaphragm. The semi-rigid diaphragm assumption, which lies between the rigid and the flexible assumptions, accounts for the actual in-plan stiffness of the slab. The accidental eccentricity, generally considered in seismic analysis, is applied to each node of the shell elements.



FE-Model with basement FE-Model without basement

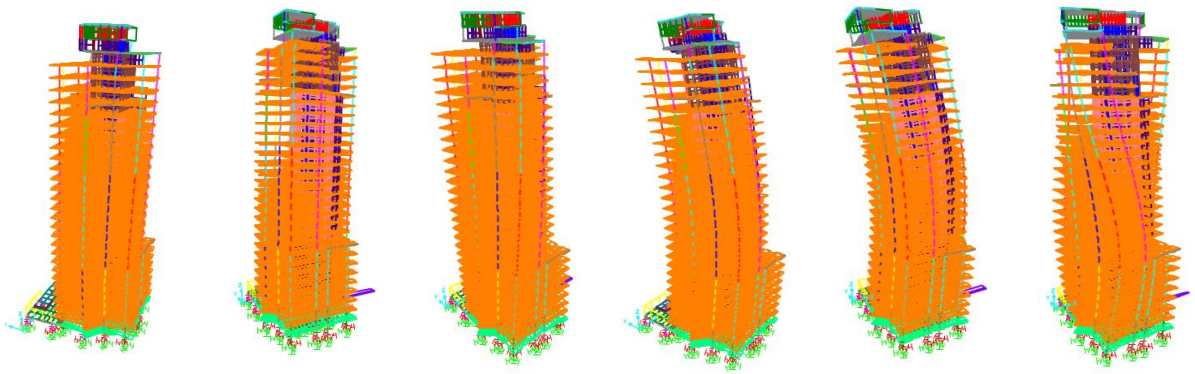
Figure 7: The two FE-models with and without the basement.

As it concerns the RC tower's six-story basement, an investigation was carried out to identify the effect that such a rigid RC block underneath the soil surface may have on the dynamic performance of the high-rise building studied. To this end, two numerical models were created with and without the multi-storey basement (Figure 7). For both FE models, fixed boundary conditions were considered due to the firm soil found on the structure's site, i.e., Soil Class C according to NBCC 2015 with average shear wave velocity at the upper 30 m of the soil profile (v_{s30}) equal to 450 m/s [16] that limits the soil-structure interaction phenomena [17]. The results of the eigenvalue analysis, carried out by using SAP2000, are presented by Table 3 listing the modal frequencies for both the FE models, i.e., with and without the basement. For the 12 modes considered, the numerical model of the high-rise structure without the basement led to estimating natural frequencies that are in better agreement with the experimentally derived ones in section four. Notably, the average difference between the FE model and the experimental frequencies for the first three modes was found to be equal to 11.0 % and 9.1 % for the model with and without the basement respectively. Therefore, the authors chose to disregard the FE model of the high-rise structure with the basement and continue the investigation by using the FE model without the basement since its associated frequencies were found to be in closer agreement with the experimentally derived modal frequencies. The investigation concerning the effect of the diaphragms modelling approaches on the dynamic response of the City Crest

Tower was solely based on the non-basement numerical model. The latter was found to be associated with mode shapes (Figure 8) that are in agreement with ones estimated using the ambient vibration analysis results (Figure 6).

	OMA (SSI)	Without basement		With basement	
	Frequency	Frequency	Difference	Frequency	Difference
Mode	[Hz]	[Hz]	(%)	[Hz]	(%)
NS 1	0.57	0.54	-5.3	0.49	-14.0
EW 1	0.64	0.68	6.3	0.61	-4.7
T 1	1.26	1.46	15.9	1.44	14.3
NS 2	2.36	2.50	5.9	2.30	-2.5
EW 2	2.93	3.18	8.5	2.91	-0.7
T 2	3.55	4.33	22.0	4.25	19.7
NS 3	4.83	5.38	11.4	5.08	5.2
EW 3	6.03	6.82	13.1	6.49	7.6
T 3	6.80	7.31	7.5	7.08	4.1
NS 4	7.49	8.38	11.9	8.07	7.7
EW 4	8.79	9.32	6.0	9.10	3.5
T 4	10.27	10.58	3.0	10.01	-2.5

Table 3: Frequencies and the modal mass participation ratios for both FE models.



NS 1 EW 1 T 1 NS 2 EW 2 T 2

Figure 8: The first six mode shapes from the FE model without the basement

6 Effect of diaphragms assumptions on dynamic performance

Engineers use analysis to verify the design of a structure, and need to make simplifications and implement modelling assumptions that can affect significantly the reliability of the analysis results, and could potentially lead to erroneous conclusions about the expected behaviour of the structure. Along these lines, the choice of the most appropriate diaphragm modelling approach is not a trivial task, and hence, the rigid, semi-rigid and flexible diaphragm's numerical modelling approaches considered enabled investigating their influence on the estimated dynamic properties of the City Crest Tower. To this end, Table 4 provides the basis for a thorough comparative assessment modal behaviour (i.e., vibration frequencies), estimated by performing eigenvalue analysis of the FE model of the high-rise building with different diaphragm's modelling approaches. The suitability of the diaphragm above's assumptions is assessed by comparing the

FE model-estimated modal frequencies with the ones identified by performing OMA on the measured vibration responses. Comparing the first four translational (NS1, EW1, NS2 and EW2) and the first two torsional FE model-related modes (T1 and T2) with their experimental counterparts obtained by using the SSI-UPC technique, it is seen that the rigid diaphragm modelling approach led to natural frequencies that deviate significantly (i.e., the average difference is equal to 35.1 %) from the OMA-identified ones. On the other hand, both the semi-rigid and the flexible diaphragm modelling approaches were found to result in modal frequencies being significantly closer to the ones identified by using the measured vibration responses, i.e., the average relative difference was calculated to be equal to 9.9 % and 8.7 % for the semi-rigid and flexible diaphragms modelling approach respectively. Indeed, for the first two translational modes along the main directions of the high-rise building (NS, EW), the latter two approaches led to quite accurate prediction of the modal frequencies since the relative difference from the OMA-identified ones were found to be within the range of 5.3 % and 8.5 %. Contrarily, the rigid diaphragm modelling approach led to translational frequencies deviating from the experimental ones with relative difference higher than 54%. Slightly lower, though still excessive, deviation (i.e., relative difference up to 44%) was calculated for the first two rotational modes-related frequencies, which were estimated almost identically by applying the semi-rigid and flexible diaphragm's modelling approaches leading to a maximum relative difference of 22.0% from the OMA-identified frequencies.

	OMA (SSI)	**Flexible**		**Semi-rigid**		**Rigid**	
Mode	**Frequency [Hz]**	**Frequency [Hz]**	**Difference (%)**	**Frequency [Hz]**	**Difference (%)**	**Frequency [Hz]**	**Difference (%)**
NS 1	0.57	0.54	-5.3	0.54	-5.3	0.88	54.4
EW 1	0.64	0.68	6.3	0.68	6.3	0.97	51.6
T 1	1.26	1.46	15.9	1.45	15.1	1.79	42.1
NS 2	2.35	2.50	6.4	2.50	6.4	2.61	11.1
EW 2	2.93	3.18	8.5	3.17	8.2	3.14	7.2
T 2	3.55	4.33	22.0	4.31	21.4	5.12	44.2

Table 4: Experimental and FE model-based natural frequencies of the benchmark building accounting for the three different diaphragm modelling approaches considered.

Based on the results presented by Table 4 and briefly discussed above, the rigid diaphragm assumption, widely adopted by building designers, was found to result in natural frequencies significantly different than the experimental ones. The latter, estimated significantly higher than the corresponding OMA-identified natural frequencies, can be attributed to the artificially high floor stiffness, being related to the simplified modelling approach of rigid diaphragms. On the other hand, such a deviating modal behaviour was not detected for the semi-rigid, and flexible diaphragms are modelling approaches since the corresponding FE model-related estimates for the natural frequencies are in good agreement with those experimentally identified from the actual vibration response of the 32-storey RC building. It is observed that the first NS translational natural frequency estimated by the FE model accounting for either the semi-rigid or the flexible diaphragms, was found slightly lower than the OMA-identified one while, for the rest five frequencies presented (Table 4), the FE-model based estimates were lower than the experimental ones. This peculiar result, already reported by Schuster [18] by OMA identification results for the City Crest Tower, may be attributed to deviations between the designed structural members and the ones eventually constructed at the building's site. For example, construction imperfections regarding the appropriate reinforcement of the tower's walls can modify the stiffness distribution along the height of the structure that, in turn, affects the vibration frequencies. A thorough on-site investigation is necessary to elaborate on this peculiar result identification result.

In addition to evaluating the effects of diaphragm flexibility on the modal frequencies, these effects were also investigated by comparing the modes shapes obtained from the FE-models and those obtained experimentally. This was done by using the Modal Assurance Criterion (MAC) to compare the vectors of the mode shapes. Notably, the MAC values calculated higher than 91% (Table 5 for the semi-rigid and the

flexible diaphragm modelling approaches corroborate their superiority in predicting with increased reliability the modal behaviour of City Crest Tower. The less accurate prediction of the building's mode shapes was found to be associated with the rigid diaphragm since an average MAC value of 73.0 % was calculated for the first translational and two rotational modes considered.

Mode Shapes	Flexible MAC (%)	Semi-rigid MAC (%)	Rigid MAC (%)
NS 1	95.3	95.3	85.8
EW 1	97	97.0	76.1
T 1	98.2	98.2	88.3
NS 2	95.3	95.3	60.4
EW 2	91.9	91.9	58.2
T 2	92.8	92.7	69.3

Table 5: Modal Assurance Criterion values for the three different diaphragm-modelling approaches.

7 Conclusion

The outcome of the current study carried out for an existing RC high-rise irregular building located in Vancouver, Canada, highlights the effect of three different, widely adopted though, floor diaphragms modelling approaches on the reliable prediction of the global modal behaviour of the structure. Along these lines, the natural frequencies of the City Crest Tower, being a single RC core structural system with irregular stiffness distribution both in-plane and elevation, were experimentally identified by applying OMA techniques. These modal estimates were compared with the natural frequencies found on FE model basis accounting for three diaphragm's modelling approach: flexible, semi-flexible and rigid. The latter approach led to natural frequencies deviating significantly from the experimentally obtained ones (i.e., the relative difference was calculated, on average, equal to 35.1 % considering the first four translational and the first two rotational modes). On the contrary, both the flexible and the semi-rigid diaphragm modelling approaches resulted in natural frequencies that deviate, on average, from the experimental ones with less than 10 % considering the first four translational and first two rotational modes respectively. The assumptions of flexible and the semi-rigid diaphragm in the FE model led to closer modal results (frequencies and mode shapes) with those obtained experimentally than those obtained based on a rigid-floor assumption. MAC values higher than 91% were calculated for the FE models with the semi-rigid and flexible diaphragms while, on the other hand, the rigid diaphragm affected the estimation of the mode adversely shapes adversely since the associated, on average, MAC value for the six modes considered was calculated equal to 73.0%.

Acknowledgements

The authors acknowledge the funding received from Centre for Oli and Gas – DTU/Danish Hydrocarbon Research and Technology Centre (DHRTC). The first author also acknowledges Read Jones Christoffersen Ltd. for providing him with the necessary monetary resources to register and attend the ISMA 2018 conference. The authors would like to thank Dr Freddy Pina, President of PBRV Consulting Ltd., for sharing his experience and expertise in Vancouver style high-rise buildings.

References

[1] H. S. Saffarini and M. M. Qudaimat, "In-Plane Floor Deformations in RC Structures," *Journal of Structural Engineering - ASCE,* vol. Vol 118, no. No 10, pp. 3089-3102, 1992.

[2] S. H. Ju and M. C. Lin, “Comparison of Building Analyses Assuming Rigid or Flexible Floors,” *Journal of Structural Engineering - ASCE,* vol. Vol 125, no. No 1, pp. 25-39, 1999.

[3] D. Basu and S. Jain, "Seismic Analysis of Asymmetric Buildings with Flexible Floor Diaphragms," *Journal of Structural Engineering - ASCE,* vol. Vol 130, no. No 8, pp. 1169 - 1176, 2004.

[4] A. Tena-Colunga and D. P. Abrams, "Seismic Behavior of Structures with Flexible Diaphragms," *Journal of Structural Engineering - ASCE,* vol. Vol. 122, no. No 4, pp. 439 - 445, 1996.

[5] M. Moeini and B. Rafezy, "Investigation into the Floor Diaphragms Flexibility in Reinforced Concrete Structures and Code Provision," *Global Journal of Researches in Engineering,* vol. Vol. 11, no. No 1, pp. 25 - 35, 2011.

[6] E. L. Wilson, Three-Dimensional Static and Dynamic Analysis of Structures - A Physical Approach With Emphasis on Earthquake Engineering, Third ed., Berkeley: Computers and Structures, Inc., 2002.

[7] P. Paultre, Dynamics of Structures, Hoboken: ISTE Ltd and John Wiley & Sons, Linc, 2011.

[8] B. Pao, "Structural Drawings of the City Crest Tower," Bogdonov Pao Associates Ltd., 1992.

[9] A. Shakal, M. Reichle, C. Ventura, T. Cao, R. Sherburne, M. Savage, R. Darragh and C. Petersen, “CSMIP strong-motion records from the Santa Cruz Mountains (Loma Prieta), California Earthquake of 17 October 1989,” California Department of Conservation Division of mines and geology office for strong motion studies report OSMS 89-06, Sacramento, 1989.

[10] R. Brincker and C. E. Ventura, Introduction To Operational Modal Analysis, 1 ed., West Sussex: John Wiley & Sons, 2015.

[11] Structural Vibration Solutions A/S, "ARTeMIS Pro Modal Version 4," Aalborg, Denmark, 2017. www.svibs.com.

[12] F. Magalhães, R. Brincker and Á. Cunha, “Damping Estimation Using Free Decays and Ambient Vibration Tests,” *Proceedings of the 2nd International Operational Modal Analysis Conference Vol. 2,* pp. 513-521, 2007.

[13] Computers & Structures, Inc., “CSI SAP2000 Pro v19,” Walnut Creek, California, USA, 2017.

[14] P. K. Mehta and P. J. M. Monteiro, “Concrete - Microstrictires, Properties, and Materials,” Mc-Graw Hill Education, 2014.

[15] CSI - Computers and Structures Inc, "CSI Knowledge Base - Manual," CSI - Computer and Structures Inc, 2018. [Online]. Available: https://wiki.csiamerica.com. [Accessed 28 June 2018].

[16] N. R. Canada, "Determine 2015 National Building Code of Canada seismic hazard values," 10th February 1026. [Online]. Available: http://www.earthquakescanada.nrcan.gc.ca/hazard-alea/interpolat/index_2015-en.php. [Accessed 12th January 2018].

[17] T. K. Sen, Fundamentals of Seismic Loading on Structures, First ed., West Sussex: John Wiley and Sons, Ltd, 2009.

[18] N. D. Schuster, "Dynamic Characteristics of a 30 Storey Building During Construction Detected From Ambient Vibration Measurements," The University of British Columbia, Vancouver, 1994.

Mass loading and temperature compensation for long-term ambient measurement data of a freeway bridge

T. Furtmüller [1], **C. Adam** [1], **R. Veit-Egerer** [2]
[1] University of Innsbruck, Unit for Applied Mechanics
Innsbruck, Austria
e-mail: **thomas.furtmueller@uibk.ac.at**

[2] VCE Vienna Consulting Engineers ZT GmbH
Vienna, Austria

Abstract
This contribution addresses the compensation of disturbing effects on performance indicators in the framework of structural health monitoring of bridge structures. Basis of this study is the ambient acceleration response of a freeway bridge located in the Austrian Alps, recorded in a long-term monitoring campaign over five years. The two investigated effects are the non-stationary added mass of the traffic volume and the exposure of the bridge to seasonal ambient temperature changes. In the first part, the impact of added mass on an identified natural frequency is quantified. With trucks crossing the bridge modeled as rigid lumped mass, the mass loading effect on the performance indicator is rather small. In the second part, three different black-box input-output models for compensating the influence of the ambient temperature on the identified frequency are developed. It is shown that the developed black-box models facilitate at least partially the desired compensation of the temperature effect on the considered bridge frequency.

1 Introduction

The basic idea of structural health monitoring (SHM) is to continuously or periodically monitor a kinematic response quantity (strains, deformations, velocities, accelerations) that serves as input for performance indicators of the considered structure. A change of a performance indicator indicates a modification of the structural state due to degradation or damage, and allows to take immediate appropriate measures. Many SHM approaches and aspects have been discussed in the literature, see for instance literature survey [1]. So-called operational modal analysis (OMA), also referred to as output-only SHM methodology, is based on the ambient dynamic structural response due to inherent excitation, such as micro-seismicity, wind loads, and traffic loads ([2],[3]). Since the spatial and time evolution of these, in general, non-deterministic excitation sources without pre-defined load pattern is not explicitly known, in a common assumption ambient excitation is modeled as a stochastic stationary Gaussian white noise process. Consequently, frequency response functions (FRFs) of the monitored structure can be derived using only the recorded response data. Then, in the next step, system identification algorithms are applied to the FRFs to identify modal structural parameters (natural frequencies, damping values, mode shapes) [4], which may serve itself as performance indicator (i.e. damage sensitive parameter) or may be processed to performance indicators [5]. Particularly for bridges, where the time-varying traffic is the main excitation source, the stationarity assumption is a rather crude description of the reality. In practical applications, thus, before parameter identification, FRFs from several time frames of the observation period are sufficiently averaged.

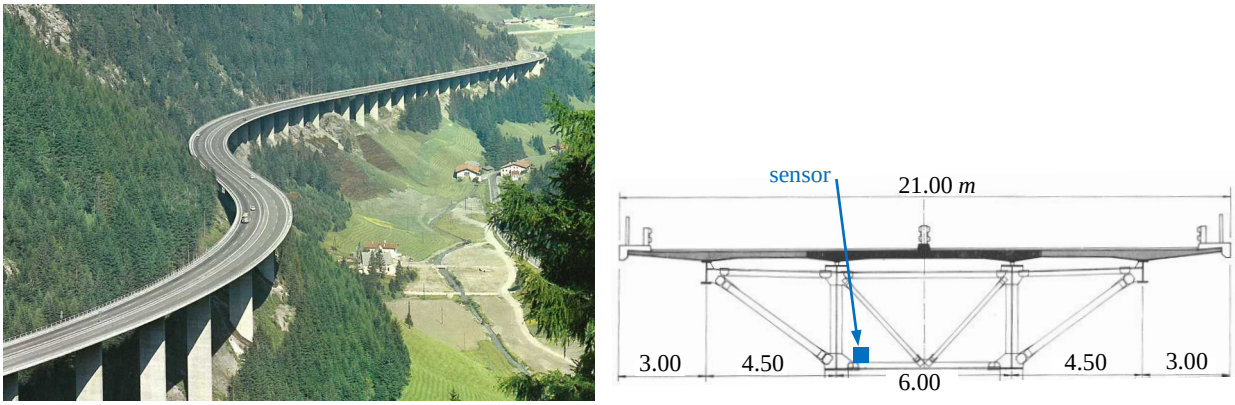
Although in the last decades various SHM methodologies have been developed, their application in engineering practices still faces several difficulties. In particular, the effect of pronounced varying environmental

boundary conditions such as the ambient temperature on the structural response may distort performance indicators, thus, potentially hiding structural damage. Yet another difficulty in SHM of bridges is related to the crossing of heavy goods traffic because any significant additional mass (truck, train, etc.) changes the modal system properties.

In the present contribution, several approaches to reducing the impact of both ambient temperature and mass loading on performance indicators are proposed and discussed. These approaches are derived from the ambient acceleration response of a freeway bridge located in the Austrian Alps, recorded in a long-term measurement campaign [6], [7].

2 Considered bridge, traffic volume, and environmental condition

The *Lueg* bridge, located close to the *Brenner Pass* in Austria, carries the four-lane *Brenner* freeway along a mountain slope connecting Austria and Italy. The bridge, which was completed in 1969, is separated into five segments of about equal length and exhibits a total span of $1800\,m$. Four segments are made of prestressed concrete, whereas the cross-section of the central segment is composed of a steel truss and a concrete deck.



(a) Arial photograph [8]

(b) Composite cross-section of the central bridge segment, adopted from [8]

Figure 1: *Lueg* bridge of the *Brenner* freeway, Austria

At an altitude of $1370\,m$ the *Brenner Pass* is the only major mountain pass within the area, and hence, the *Brenner* freeway represents one of the most important transit routes between Northern and Southern Europe both for freight and holiday traffic. Figure 2 shows the total number of vehicles passing the bridge per day in 2008. As observed, during the holiday seasons the traffic volume is higher, with peaks on Saturdays throughout the year. In [9] the number of trucks (i.e. vehicles exceeding a mass of $8.7\,t$) crossing the *Europa* bridge, which is also part of the *Brenner* freeway, is specified for this observation period. It is reasonable to assume that the *Lueg* bridge carries the same trucks, because the *Europa* bridge is situated only $25\,km$ north without major exits in-between. In Figure 2 the counted trucks per day are shown by red circular markers, except for the period mid of May till the end of June, where no data are available. In contrast to the total traffic volume, the daily truck traffic is from Monday to Saturday relatively constant throughout the year, with a mean of about 7000 trucks per day. However, on Sundays and on public holidays a significant drop of the heavy goods traffic is observed, due to the truck driving ban in Austria from Saturday 3 p.m. to Sunday 10 p.m. and on public holidays from midnight to 10 p.m. This ban is also in place every night from 10 p.m. to 5 a.m.

From these data, for every day of 2008 the diurnal variation of traffic across the bridge can be presented in terms of a histogram, here selecting one hour intervals. When normalizing the total area below the histogram to one, it represents an approximation of the corresponding probability function of the daily traffic. Then, the

normalized histograms of all Mondays (Tuesdays, Wednesdays, etc.) in the observation year 2008 are added up and divided by the number of Mondays (Tuesdays, Wednesdays, etc.). In this respect, public holidays are treated as Sundays, i.e. the histogram of Sunday also includes the traffic information of those holidays. As the result of this statistical analysis, in Figure 3(a) the arithmetic mean normalized histograms of the daily traffic volume is displayed. Inspection of Figure 3(a) confirms that most of the traffic crosses between 5 a.m. and 10 p.m. the bridge, partially due to the driving ban on heavy goods traffic beyond this time period. It is also observed that during weekdays the daily distribution of the traffic is similar, however, on Saturdays and Sundays the characteristics of the traffic flow is different.

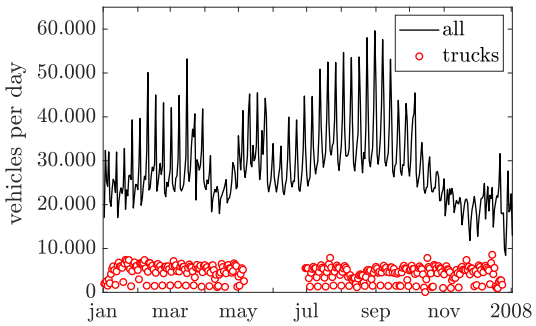
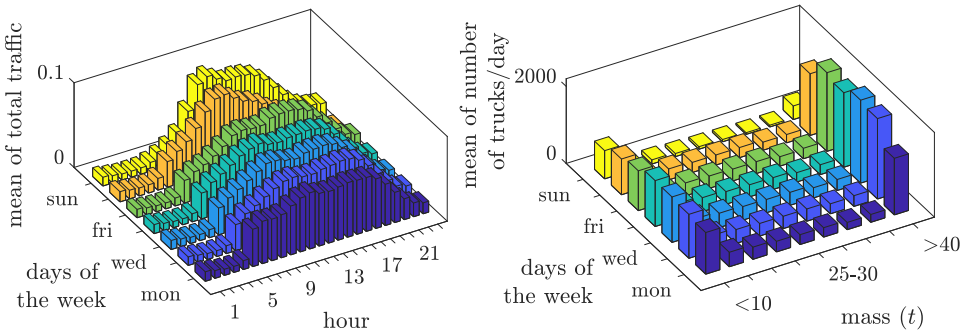


Figure 2: Number of all crossing vehicles and trucks per day recorded close to the *Lueg* bridge in 2008



(a) Daily distribution of total traffic

(b) Daily number of trucks as a function of vehicle mass

Figure 3: Arithmetic mean histograms of the daily traffic distribution crossing the *Lueg* bridge in 2008

According to Figure 2, trucks represent approximately 20% of the total traffic volume. Considering that in Austria the gross vehicle mass of trucks is limited to 44 metric tons (t), which is one order of magnitude larger than the mass of passenger cars, this implies that the mass added to the bridge is dominated by the heavy goods traffic. In [9], the mass of each truck crossing the *Europa* bridge in 2008 is specified, and the trucks are categorized into nine mass classes: mass class 1 (8.7-10t) collects the vehicles carrying little to no loads, whereas mass class 9 (40-44t) comprises the fully loaded trucks. Figure 3(b) shows for each mass class the arithmetic mean truck number of each day of the week, evaluated over the observation period 2008. Public holidays are treated as Sundays, as before. It is readily observed that most of the trucks belong to mass classes 1 and 9. The number of unloaded trucks is relatively stationary throughout the week, however, on Sundays the quantity of fully laden trucks is much smaller compared to the remaining six days of the week. Despite the traffic ban, due to exception permits, on the weekends the heavy goods traffic is still considerably. From this discussion it can be concluded that the traffic across the *Lueg* bridge is highly non-stationary.

Since located at an altitude of about $1300\,m$, the *Lueg* bridge is exposed to pronounced climatic seasonal changes. Figure 4 shows the annual ambient temperature, recorded in 2008 close-by at the *Brenner Pass*. As

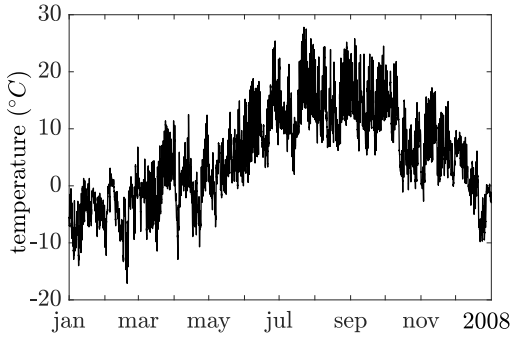


Figure 4: Daily ambient mean temperature recorded close to the *Lueg* bridge in 2008

observed, the ambient temperature fluctuates in a range of $45\,^{\circ}C$, and frost is present during half of the year.

3 System identification

In a long-term monitoring campaign, conducted in the framework of a funded research project [10], the company VCE Vienna Consulting Engineers ZT GmbH recorded from December 2006 to September 2011 ambient accelerations of the *Lueg* bridge continuously at a sample rate of $100\,Hz$. The position of the *Kinemetrics* triaxial force-balance accelerometer in the steel truss of the central bridge segment, which measured the acceleration data used in this study, is shown in Figure 1(b). Based on these data, subsequently a characteristic natural frequency of the bridge structure is identified. This frequency is considered as the performance indicator of the bridge.

To identify the characteristic natural bridge frequency, the recorded acceleration signals serve as input for Welch's estimator [11], applied to estimate the power spectral densities (PSDs) of these signals. The frequency resolution of the PSDs depends on the considered time frame of the signals. In general, the required time frame increases, the lower the expected natural frequencies and damping coefficients are. Rules of thumb for estimating the time frame are provided, for instance, in [2], [3]. In the present study, PSD analysis is based on a time frame of $14400\,s = 4\,h$ to obtain the targeted frequency resolution of $0.0025\,Hz$. To stationarize the signal in the time frame, it is divided into a sequence of 100 partial segments with 64% overlap. The arithmetic mean of the 100 segment PSDs is the representative PSD of the signal in the considered time frame, implying that non-stationary effects have been minimized through averaging. The PSD of the next time frame is based on the signal with 75% overlap to the signal of the previous time frame, thus, resulting in a PSD update rate of $1\,h$.

As an example, Figure 5 depicts the resulting auto PSDs, S_{xx}, of the three orthogonal acceleration components recorded at two different seasons in logarithmic scale. The underlying signals of the left plot were recorded in winter at night (December 10 2006) from midnight to 4 a.m., the PSDs of the right plot are based on accelerations measured in summer at noon (June 29 2007) from 10 a.m. to 2 p.m. As observed, the longitudinal vibrations are orders of magnitude smaller than in the other directions, and therefore, they are not further considered. On the other hand, PSDs of the transverse and vertical vibration components are of the same scale, and they exhibit in the depicted frequency domain from 1 to $4\,Hz$ several pronounced resonance peaks. The bridge is supported by long piers of up to $50\,m$ (see Figure 1(a)), and thus, the recorded transverse response in mainly associated with bending of the piers. Since the focus of this study is on the structural condition of the bridge deck but not on the piers, the transverse response component is not elaborated in more detail.

In both subplots of Figure 5, the PSD of the vertical acceleration shows at a frequency of about $2.2\,Hz$ a well separated peak. This apparent natural frequency is chosen as performance indicator for potential structural

changes in the bridge deck. Since only one sensor output is available, peak-picking is the obvious choice to identify the frequency at this peak from the PSDs in one hour intervals in the entire observation time from December 2006 to September 2011. In Figure 6 this identified natural frequency, f_{id}, is depicted for two time intervals of 50 days in the winter and summer seasons: the left plot refers to the December-January period of three different winters, and the right plot to the July-August period of three subsequent years. This figure reveals that the frequency is not stationary over time.

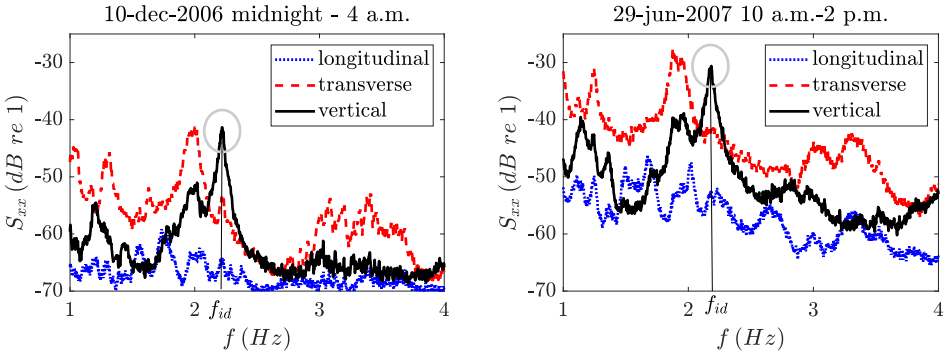
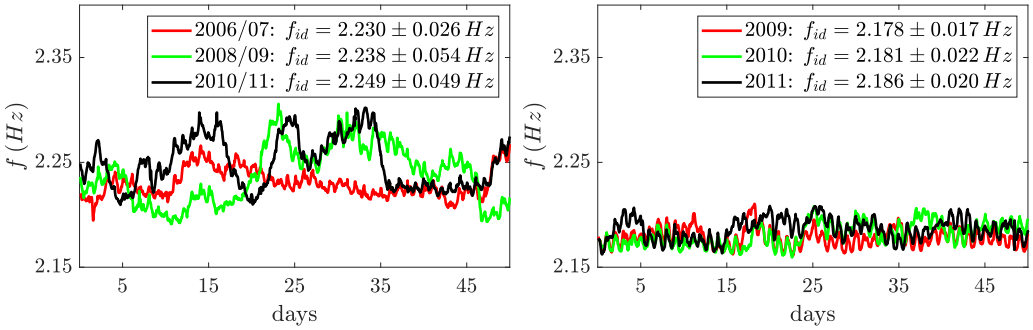


Figure 5: Auto spectral density of the three acceleration components for two different periods of time

Since in the entire monitoring period no structural damage was observed, it can be, thus, concluded that the bridge structure is sensitive to the variable mass-loading effect and/or the environmental impact. The frequency varies in the range from $2.15\,Hz$ (summer) to $2.35\,Hz$ (winter), which can be attributed mainly to seasonally different climatic different conditions. In the cold season the mean of this frequency is larger, because subsoil, abutment (due to formation of ice), asphalt, etc. are stiffer at low temperatures. It is also observed that the frequency fluctuation in winter is larger than in summer, a result of frost-thaw cycles in the winter. The small variations of the frequency in the summer period are most likely related to the variation of the heavy goods transport over the day and the week, as discussed before. In the legends of Figure 6, mean $\pm$ two times the standard deviation σ of this natural frequency in the considered time intervals are specified. Assuming a normal distribution, the range $\pm 2\sigma$ approximates the 95% confidence interval of the frequency, representing its uncertainty.



(a) December-January period (b) July-August period

Figure 6: Variation of the identified natural frequency in two 50 day periods of three subsequent years

This natural frequency may only serve as performance indicator if the effects of traffic volume and ambient temperature in this frequency are compensated. That is, the scatter with respect of time is eliminated, or at least, reduced, thus resulting in a significant decrease of the 95% confidence interval of the frequency. Subsequently, those effects on the identified frequency are quantified, and procedures for their compensation proposed, tested, and evaluated.

4 Assessment of mass-loading effect

At first, effect and extent of variable mass-loading on the identified natural frequency is discussed, based on stochastic finite element (FE) simulations of the bridge-truck system. To this end, a two-dimensional FE beam model of the considered bridge segment is built. The fundamental frequency of this bridge model without truck loading is $f_{sim,0} = 2.292\,Hz$.

Heavy goods traffic on the bridge is stochastically simulated. Fundamentals of this simulation are the statistically evaluated data of the counted traffic for every day of the week, as described in section 2, compare with Figure 3. The number of trucks of each mass class is assumed to be a standard-normal distributed random variable, with mean according to Figure 3(b) and corresponding standard deviation. These random variables are combined in vector $\mathbf{x}_1 \in \mathbb{R}^9 \sim \mathcal{N}(0,1)$. Random vector $\mathbf{x}_2 \in \mathbb{R}^{24} \sim \mathcal{N}(0,1)$ contains the set of 24 standard normal-distributed random variables describing the distribution of the heavy goods traffic in one-hour intervals during the course of the day, taking into account mean values depicted in Figure 3(a) and corresponding standard deviations. The arrival time x_3 of the individual trucks at the bridge in each one-hour interval is assumed to be uniformly distributed. The mass of a truck in a mass class is captured by another uniformly distributed random variable denoted as x_4. A further assumption is that the trucks cross the bridge with constant but random speed with mean $50\,km/h$ and standard deviation $10\,km/h$. As such, at each time instant, the position of a truck on the bridge can be determined.

Lumped masses representing the truck are attached to the two adjacent nodes of the FE beam bridge model. Modal analysis of 100 random coupled bridge-truck samples is performed at discrete time instants in ten-seconds intervals for the seven days of a week. Averaging results in one-hour intervals yields estimates for the considered natural frequency $f_{sim,\Delta m}$ taking into account mass-loading. Figure 7 shows the range of this frequency in terms of mean values $\mu \pm 2$ standard deviations σ. It can be concluded that the lumped mass truck model reduces consistently the considered natural bridge frequency at all time instants. The extent of reduction is directly related to the diurnal variation of the traffic, compare with Figure 3(a). Consequently, on Sundays and during the nights the predicted frequency shifts are much lower. According to Figure 7 the maximum mean frequency reduction due to the heavy goods traffic is less than $0.02\,Hz$, i.e. 1%. Variations of the identified natural frequency observed in summer can, thus, be attributed partially to mass-loading effects, compare with Figure 6. However, the larger deviations observed in winter still remain to be tackled.

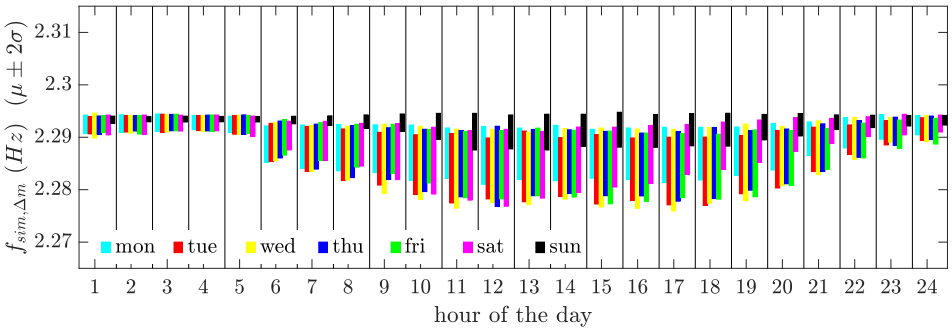


Figure 7: Simulated natural bridge frequency (mean ± 2 standard deviations) considering the traffic variation of one week

5 Compensation of temperature effect

The main input variable for compensating the temperature effect on the selected performance parameter is the ambient temperature recorded continuously at the closely located meteorological station on the *Brenner Pass*, shown in Figure 4.

The complex physical processes, which govern the relation between ambient temperature and the dynamic bridge properties, are unknown, and thus, no thermo-mechanical model can be developed. Instead, empirical black-box models in the form of input-output relations $y(t) = g\left(u(t)\right)$ are established, where the input $u(t)$ is the ambient temperature, and the output $y(t)$ the identified natural frequency.

The most basic and straightforward approach assumes a static relation, $y = g(u)$, representing a direct correlation between actual temperature and frequency. In reality, the underlying processes are more dynamic than static. The dynamic nature of such processes may be captured by a linear time-invariant (LTI) model with a single input and a single output (so-called SISO model). Most generally, a time-discrete SISO LTI system subjected to additive random disturbances is mathematically structured as [12]

$$A(q)y(t) = \frac{B(q)}{F(q)}u(t) - \frac{C(q)}{D(q)}e(t) \tag{1}$$

where $e(t)$ is an additional noise process, and $A(q)$, $B(q)$, $C(q)$, $D(q)$, $F(q)$ are polynomials in q in the form, for instance,

$$B(q) = b_1 q^{-1} + b_2 q^{-2} + \ldots + b_n q^{-n} = \sum_{k=1}^{n} b_k q^{-k} \tag{2}$$

Parameter q represents the forward shift operator [12] with the properties $qu(t) = u(t+1)$ and $q^{-1}u(t) = u(t-1)$. Variables are, thus, parameters b_k ($k = 1, ..., n$), analogously, parameters a_k, c_k, d_k, f_k, and the corresponding model orders n, which are not necessarily equal for all polynomials.

From the time-discrete SISO LTI model, Equation 1, several special cases can be deduced that are typically used in system identification. For instance, choosing $A(q) = 1$ yields the class of Box-Jenkins (BJ) models, $F(q) = D(q) = 1$ ARMAX (auto-regressive moving average with exogenous input) models, and $A(q) = C(q) = D(q) = 1$ Output Error (OE) models. When only the dynamics of the process but not the noise is of interest (i.e. the relation between $u(t)$ and $y(t)$), OE models are a common choice [13]. Note that Equation 1 is equivalent to a model described in the z-domain [14], typically used for describing discrete-time systems. Assuming a discrete-to-continuous time conversion method of any choice (e.g. bilinear transform $s = \frac{2}{t_s}\frac{z-1}{z+1}$ with sampling time t_s), the transfer function can be expressed in the Laplace domain as $G(s) = B(s)/F(s)$.

From another perspective, the input-output relation between ambient temperature $u(t)$ and frequency $y(t)$ can be modeled in terms of process models known from control engineering. For instance, a plant including a proportional gain K and a time constant T linked with underlying energy storage and delayed response is described by the following transfer function in the Laplace domain [14],

$$G(s) = \frac{K}{Ts+1} = \frac{Y(s)}{U(s)} \tag{3}$$

or, alternatively, in the time domain by the first-order differential equation $T\dot{y}(t) + y(t) = Ku(t)$. This model describes, for instance, non-stationary heat exchange problems, which are expected to govern the underlying relation between temperature and natural frequency. SISO LTI systems can be extended either to linear parameter-varying (LPV) systems or to nonlinear models. In a more sophisticated approach, Equation 1 is extended by multiple inputs instead of one. Such models are referred to as MISO systems.

In the present study, the following three models are developed to reduce the temperature effect on the identified natural frequency:

- For model 1 ("direct correlation") a static relation between current ambient temperature ϑ and natural frequency $f_{sim,\Delta\vartheta}$ is developed.

- Model 2 ("OE(2,3)") applies a discrete-time Output-Error-Model with polynomial orders $n_b = 2$ for $B(q)$ and $n_f = 3$ for $F(q)$, and an input-output delay of one sample, i.e. of the form $y(t) = \frac{b_1 q^{-1} + b_2 q^{-2}}{1 + f_1 q^{-1} + f_2 q^{-2} + f_3 q^{-}} u(t) - e(t)$ (compare with Equation 1).
- In model 3 ("MISO") two first-order systems according to Equation 3 are connected in parallel. In one subsystem the temperature variable serves as input, in the second one the temperature gradient, i.e. the time derivative of the temperature. The input-output relation reads as $y(t) = g\left(u(t), \dot{u}(t)\right)$. A block diagram of the model structure is depicted in Figure 8.

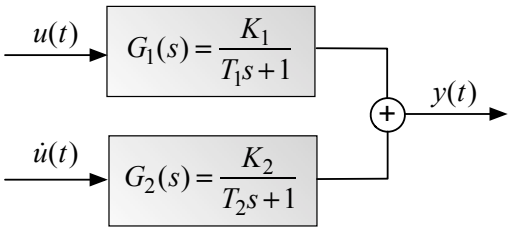


Figure 8: Structure of model 3 (MISO)

To find the "best" analytical static frequency-temperature relation of model 1, initially at each discrete time instant the identified natural frequency and the corresponding mean temperature of the four hour time frame for data acquisition (as described in section 3) is paired. These data are clustered in temperature bins with a width of $1°C$, and histograms are computed for each bin. The histograms are normalized to a maximum value of 1, and interpolation between the individual histograms yields a density function, shown in Figure 9 in terms of a contour plot.

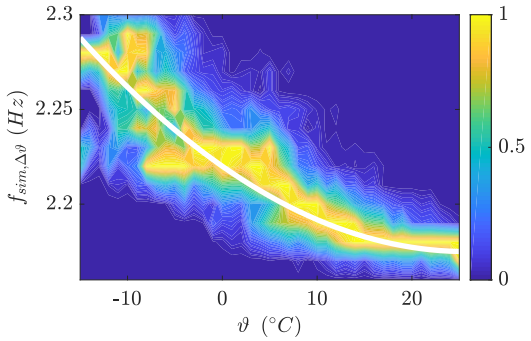


Figure 9: Correlation function applied for model 1

This figure reveals that ϑ and $f_{sim,\Delta\vartheta}$ are correlated, however, particularly for temperatures below the freezing point a rather large scatter is observed. Application of regression analysis to the peak values of the density function displayed in Figure 9 yields the following quadratic function $f_{sim,\Delta\vartheta}(\vartheta)$,

$$f_{sim,\Delta\vartheta}(\vartheta) = 2.22 - 3 \cdot 10^{-3}\vartheta + 5 \cdot 10^{-5}\vartheta^2 \tag{4}$$

which represents model 1 for temperature compensation. Application of Equation 4 to the identified natural frequency $f_{id}(t)$ at a certain time instant t, utilizing the temperature recorded at t as input, results in the frequency $f_{model}(t)$. Then, the compensated natural frequency is obtained as

$$f_{comp}(t) = f_{id}(t) - f_{model}(t) + f_{ref} \tag{5}$$

where f_{ref} is the reference natural frequency to be monitored.

The structure of model 2 (OE(2,3) with input-delay of one is the result of a parametric study on the identified natural frequency of nine time frames of 50 consecutive days each (compare Figure 6). Three of the time frames contain the frequency data of the December-January winter period, three the March-April spring period, and the last three the July-August summer period. As such, the full ambient temperature range of a year is captured. When testing different approaches, for a single time frame higher order models (i.e. models with $n_b > 2$ and $n_f > 3$) have shown to compensate better the temperature effect on the frequency. However, when condensing the individual models derived for each time frame to a global model applicable to the entire monitoring period, lower-order models have proven to be more robust. Yet no general single model for predicting the temperature effect uniformly throughout the monitoring period could be found. Instead, two OE(2,3) sub-models have been developed. The first one is calibrated to data recorded in December and January, thus referred to as winter sub-model, whereas the second one is calibrated to data from July and August (summer sub-model). The derived transfer function of the winter and the summer sub-model, respectively, in the Laplace domain read as

$$\begin{aligned} G_{winter}(s) &= \frac{1.34 \cdot 10^{-4} s^3 + 1.30 \cdot 10^{-11} s^2 - 4.12 \cdot 10^{-11} s - 4.01 \cdot 10^{-18}}{s^3 + 3.29 \cdot 10^{-4} s^2 + 6.52 \cdot 10^{-9} s + 6.75 \cdot 10^{-19}} \\ G_{summer}(s) &= \frac{3.15 \cdot 10^{-4} s^3 - 1.81 \cdot 10^{-11} s^2 - 9.71 \cdot 10^{-11} s + 5.60 \cdot 10^{-18}}{s^3 + 6.27 \cdot 10^{-4} s^2 + 1.10 \cdot 10^{-7} s - 4.53 \cdot 10^{-19}} \end{aligned} \tag{6}$$

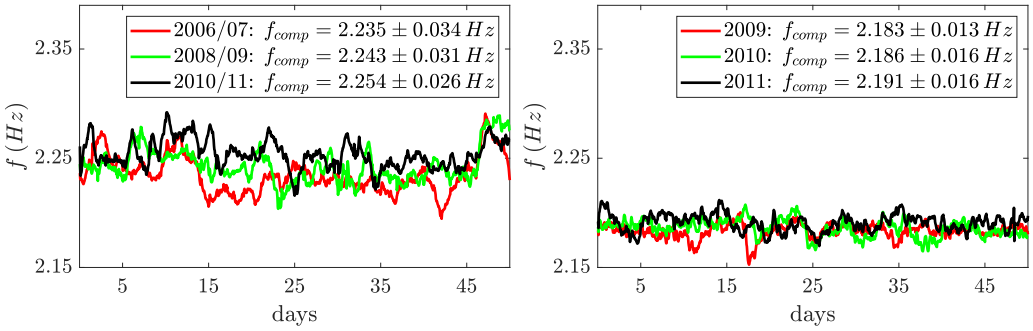
An optimization procedure is applied to determine the four model parameters of MISO model 3 according to Figure 8, providing that the frequencies of the nine considered time frames are approximated as good as possible by a single model. The normalized root-mean-square-error between model output and identified frequency is used as objective function to be minimized [13]. This procedure yields the following expressions for the transfer functions,

$$\begin{aligned} G_1(s) &= \frac{K_1}{T_1 s + 1} \quad \text{with } K_1 = -0.0025\, Hz/^\circ C\ ,\ T_1 = 0.4\, h \\ G_2(s) &= \frac{K_2}{T_2 s + 1} \quad \text{with } K_2 = 0.1\, Hz/\left(^\circ C/h\right)\ ,\ T_2 = 44\, h \end{aligned} \tag{7}$$

Application of model 2 yields the compensated natural frequency shown in Figure 10 for the underlying time frames. The outcomes of Figure 10(a) are based on the winter sub-model, application of the summer sub-model yields the graphs shown in Figure 10(b). Comparing Figure 10 with the original data displayed in Figure 6 shows visually that this model reduces the scatter of the natural frequency with respect to time significantly. Mean $\pm$ two standard deviations specified in the legends of Figures 10 and 6 confirm this observation, i.e. the standard deviation is considerably reduced after implementation of compensation model 2.

Now, the performance of all three developed compensation models is discussed in more detail based on the 95% confidence interval (i.e. two times the standard deviation) specified in Table 1 for both original and compensated frequency data. For each of the nine considered time frames and each model the confidence interval (in Hz) and its relative change, Δ, in $\%$ with respect to the raw data is provided separately. A negative Δ $(\%)$ indicates the desired reduction of the confidence interval. In this respect, model 1 ("CI direct corr.") does not perform satisfactorily, because both a reduction and amplification of the confidence interval, depending on the time frame, is observed. For instance, performance is worst for the time series March-April 2010, where an increase of 55% is observed. Model 2 ("CI OE(2,3)"), which combines a winter and a summer sub-model, reduces significantly the 95% confidence interval in winter and summer periods (with one exception in December-January 2006/07). In the time frames of the spring season, where the climatic conditions of winter and summer interfere, the summer sub-model can only compensate partially the

temperature effect, i.e. the reduction of the confidence interval is minor (approximately 6% mean reduction). Application of the winter sub-model to this transition period even increases the scatter of the frequency. From the results it can be concluded that model 2 does not capture appropriately the seasonal transition periods. Application of model 3 ("CI MISO"), on the other hand, yields a reduction of the confidence interval in all but one time frame (March-April 2010). It is, thus, the most favorable model developed here to compensate the effect of ambient temperature on the identified natural frequency. However, the confidence intervals of the winter and spring periods still remain considerably larger than in summer, also when employing this model. Mean confidence intervals are 0.03 and $0.01\,Hz$, respectively. In future investigations it should be studied whether more sophisticated models may further reduce this gap.



(a) December-January period (b) July-August period

Figure 10: Variation of the temperature compensated natural frequency according to model 2 in two 50 day periods of three subsequent years

period		CI raw	CI direct corr.		CI OE(2,3)		CI MISO	
		(Hz)	(Hz)	$\Delta\,(\%)$	(Hz)	$\Delta\,(\%)$	(Hz)	$\Delta\,(\%)$
dec/jan	06/07	0.025	0.031	+24.0	0.034	+33.8	0.019	-26.8
	08/09	0.054	0.041	-24.1	0.031	-42.8	0.043	-20.1
	10/11	0.048	0.035	-27.8	0.026	-45.9	0.034	-29.6
mar/apr	2008	0.029	0.031	+5.9	0.027	-7.7	0.025	-16.5
	2010	0.027	0.041	+55.4	0.026	-3.1	0.031	+14.5
	2011	0.044	0.039	-10.8	0.040	-7.6	0.037	-16.1
jul/aug	2009	0.015	0.015	+2.1	0.013	-11.1	0.012	-23.5
	2010	0.020	0.017	-17.6	0.016	-22.6	0.012	-42.6
	2011	0.019	0.017	-11.3	0.016	-16.4	0.013	-32.2

Table 1: 95% confidence interval (CI) of the mean of the performance indicator in nine 50 day periods before and after temperature compensation, and relative change in $\%$

6 Summary, conclusions, and outlook

In this contribution, from acceleration response data of the *Lueg* bridge located in the Austrian Alps, continuously recorded in a long-term monitoring campaign over five years, a characteristic natural frequency has been identified at discrete time instants of the observation time. In the framework of structural health-monitoring, this frequency serves as performance indicator. Since in the monitoring period no damage has been reported, temporal scatter of this frequency has been attributed to disturbance effects. Two possible sources of the observed frequency scatter have been addressed. That is, (i) the non-stationary variation of the mass due to the heavy goods traffic crossing the bridge, and (ii) the ambient temperature, which is significantly different in winter with long frost periods and summer with peak temperatures up to $+\,30\,^{\circ}C$.

A numerical study utilizing a finite element model of the bridge and a simple mechanical model of a truck, the mass-loading effect has been quantified to reveal how the traffic mass contributes to the frequency scatter. The crossing traffic volume has been modeled stochastically, based on statistical data of the diurnal traffic variation, and the hourly and weekly distribution of the truck mass. From the results of this analysis it can be concluded that the overall impact of the mass-loading effect on the identified natural frequency of the bridge is rather small.

The second study concerns the impact of the ambient temperature recorded at a close meteorological station on the considered bridge frequency and its compensation. Since the underlying processes between temperature and dynamic bridge properties (respectively stiffness) is not well understood, three different black-box models have been developed, describing empirically a relation between recorded temperature (and/or temperature gradient) and identified natural frequency. As first model, a static relation between temperature and natural frequency has been established, thus, neglecting the dynamic character of the underlying thermo-mechanical process. The second approach, a linear time-invariant single input-single output model has been calibrated to the temperature and frequency data, accounts for this process dynamics in a simple manner. Since no uniform model applicable to an entire year has been found, it consists of two separate Output-Error sub-models, one for the cold season and one for the summer season. In an effort to create a single temperature-frequency relation, in the third model the time derivative of the temperature serves as second input variable. It was shown that the static model cannot capture the temperature effect on the identified frequency. Both dynamic models, and here in particular the most sophisticated model 3, have their merits to compensate the temperature induced scatter of the frequency in the seasons of less pronounced temperature variations (winter and summer). However, in the transition periods between winter and summer and vice versa the performance of both models is less satisfying.

Additional studies are needed to find better models for temperature compensation that can be applied throughout the year. Such models can be either nonlinear or linearly time-varying. On the other hand, sources of disturbance not directly related to ambient temperature should be considered.

Acknowledgements

This work is part of the research project *Street Life* (project number 849045) partially funded by the *Austrian Research Promotion Agency (FFG)*.

References

[1] H. Sohn, C. R. Farrar, F. M. Hemez, D. D. Shunk, D. W. Stinemates, B. R. Nadler, J. J. Czarnecki, *A Review of Structural Health Monitoring Literature: 1996-2001*, Los Alamos National Laboratory Report LA-13976-MS (2004)

[2] C. Rainieri, G. Fabbrocino, *Operational Modal Analysis of Civil Engineering Structures*, Springer, New York (2014)

[3] R. Brincker, C. Ventura, *Introduction to operational modal analysis*, Wiley (2015)

[4] W. Heylen, S. Lammens, P. Sas, *Modal Analysis Theory and Testing*, Katholieke Universiteit Leuven, Departement Werktuigkunde, Leuven (1997).

[5] A. Tributsch, C. Adam, *An enhanced energy vibration-based approach for damage detection and localization*, Structural Control and Health Monitoring 25 (1), pp. 528-36 (2018)

[6] T. Furtmüller, C. Adam, *Compensation of temperature effects in long-term monitoring of a highway bridge located in the Austrian Alps*, Procedia Engineering 199, pp. 2078-83 (2017)

[7] T. Furtmüller, C. Adam, R. Veit-Egerer, *Temperatur- und Massenkompensation für Langzeit-Brückenüberwachung* (Temperature and mass compensation for long-term bridge monitoring, in German), Bauingenieur 92, pp. 528-36 (2017)

[8] Brenner Autobahn AG, *Die Brenner-Autobahn* (the Brenner freeway, in German), Verlag Tiroler Nachrichten, Innsbruck, Austria (1972)

[9] R. Veit-Egerer, *Entwicklung eines neuen, Monitoring basierten dynamischen Gewichtserfassungssystems zur Beschreibung des realen Einwirkungskollektivs von Schwerverkehrseinheiten und Analyse der Konsequenz für die resultierende Lastmodellierung von Stahlbrücken am Beispiel der Europabrücke* (Development of a novel, monitoring-based dynamic weighing system to describe realistically the load collective of heavy traffic and analyis of its consequence on the resulting load models on steel bridges, exemplified for the *Europa* bridge, in German), PhD thesis, TU Wien (2014)

[10] R. Veit-Egerer, M. Widmann, H. Wenzel, *HOT SPOT - Advanced Weakness Determination & Assessment of Bridges*, FFG project 811355 / 3381 - GLE/BLC, Technical Report (2008)

[11] P. D. Welch, *The use of Fast Fourier Transform for the estimation of power spectra. A method based on time averaging over short, modified periodograms*, IEEE Transactions on Audio and Electroacoustics 15 (2), pp. 70-73 (1967)

[12] L. Ljung, *System Identification: Theory for the User*, Prentice Hall PTR, Upper Saddle River, NJ (1999)

[13] Mathworks Inc., *System Identification Toolbox User's Guide* (2018)

[14] A. V. Oppenheim, A. S. Willsky, *Signals & Systems, Second Edition*, Prentice Hall (1997)

Soil-structure interaction and the added-foundation effect of surface foundations with application to ground-borne vibration in buildings

G. Sanitate, J. P Talbot
University of Cambridge, Department of Engineering,
CB2 1PZ Cambridge, United Kingdom
e-mail: **gs528.cam.ac.uk**

Abstract
Ground-borne vibration and re-radiated noise are an important design consideration for many modern buildings that are close to railways. The induced vibration field may be assumed as an incoming wavefield. The response of the soil-foundation-building system can be then obtained in two stages with reference to the sub-modelling technique. This paper refers to the first stage that is associated with the modification of the free-field vibration due to the coupling of a foundation to the ground (i.e. added-foundation effect). Here, the foundation model consists of a series of rigid regions representing the subsequent coupling points with a building. Iguchi's method is investigated as a simplified procedure to obtain the response of surface rigid foundations resting on a homogeneous and elastic half-space subjected to incoming plane wavefields. The case of rigid footings on an elastic layer overlying the half-space (i.e. slab foundation) is also investigated. The results obtained with Iguchi's method and the rigorous boundary-element model are in good agreement.

1 Introduction

Ground-borne vibration and re-radiated noise, generated by surface and/or underground railways, are an important design consideration for modern buildings. This is particularly so in metropolitan cities because of the expanding transportation infrastructure and the available areas for new residential and office buildings, which are often located in the vicinity of railways. The vibration generated at the source propagates through the ground and reaches the building through its foundation. The ultimate concern is the disturbance of the occupants caused by the vibration and re-radiated noise in the interior of a building. Because of the multidisciplinary nature of the topic, research efforts involve the study of the excitation mechanisms at the source, the propagation of vibration through the ground, the dynamic response of the building and potential mitigation measures [1, 2]. The latter have the goal of reducing the ground-borne vibration by acting either at the source [3, 4], along the propagation path [5] or at the receiver (building) [6]. A rather common example of mitigation at the receiver is the implementation of a thick slab foundation [7, 8] at the base of the building. Significant literature exists on the soil-foundation interaction of both flexible [9–11] and rigid foundation systems [12–15] subjected to incoming wavefields. The response of the foundation is often considered rigid in earthquake-related problems, which involve low frequencies and long wavelengths. With reference to ground-borne vibration induced by railway traffic, the frequency range of interest lies between approximately 20 Hz and 200 Hz, reflecting both the frequency content of the source and the range of human perception. Therefore, problems related to ground-borne vibration involve relatively short wavelengths that may be comparable with the dimensions of a typical concrete slab foundation. In this case, the flexibility of the slab should be considered. Previous work by Auersch [16] has considered the response of finite and infinite plates resting on a half-space to Rayleigh wave excitation. The case of a slab foundation as an infinite elastic layer on an elastic half-space subjected to incoming P-, SV-, or Rayleigh waves has been investi-

gated [17] by means of the Dynamic Stiffness Method (DSM) [18] and the Elastodynamics Toolbox [19] in MATLAB [20].
In the framework of ground-borne vibration, this paper adopts Iguchi's method [13, 15] as a simplified procedure for obtaining approximate transfer functions between the *free-field vibration* amplitude of the ground as a homogeneous and elastic half-space subjected to incoming plane wavefields, and the *free-surface vibration* amplitude at the foundation level. The procedure refers to rigid regions that represent the subsequent coupling points with a portal-frame building. The rigid regions may be thought either as rigid foundations, in the case of direct coupling with the half-space, or rigid footings, if they are on top of a flexible foundation resting on the ground. The following section presents the general soil-structure interaction problem with the focus on the added-foundation effect.

2 Soil-Structure Interaction and the Added-Foundation Effect

Let us consider the general case of the construction of a building in the vicinity of a source of vibration represented by buried or surface train lines. Figure 1 shows the main construction stages that are also representative of the modelling steps for such a vibration problem. The vibration generated at the source can be expressed in terms of a *free-field* displacement $\mathbf{u_0}(x, y, 0, t)$ that may represent either on-site vibration measurements that are taken prior any construction activities or the displacement field obtained by some source-propagation modelling of the railway and the ground. For sake of simplicity, the wavefield is assumed to be harmonic so that $\mathbf{u_0}(x, y, 0, t) = \tilde{\mathbf{u}}_\mathbf{0}(x, y, 0)\, e^{i\omega t}$ where ω is the angular frequency and the exponential term in the time variable t is omitted in the following. The construction of a foundation at the free-surface of the ground modifies the initial *free-field* displacement because of the soil-foundation interaction (added-foundation effect), with the resulting *free-surface* displacement field $\tilde{\mathbf{u}}_\mathbf{f}(x, y, h_f)$ at the top of the foundation. The vibration levels are further changed with the construction of the building. The coupling between the structure and the soil-foundation system leads to a displacement field $\tilde{\mathbf{u}}_\mathbf{b}(x, y, h_f)$ at the foundation-building interface (added building effect).
This paper presents a discussion of the added-foundation effect with an attempt at applying well-known soil-foundation interaction concepts to problems related to ground-borne vibration. In a general scenario as illustrated in Figure 1, the building can be modelled by means of a beam-bar formulation of its main frame. This is convenient when looking for simplified models that are able to give physical insights with regard to specific aspects of the problem (i.e. added-building effect [21]).

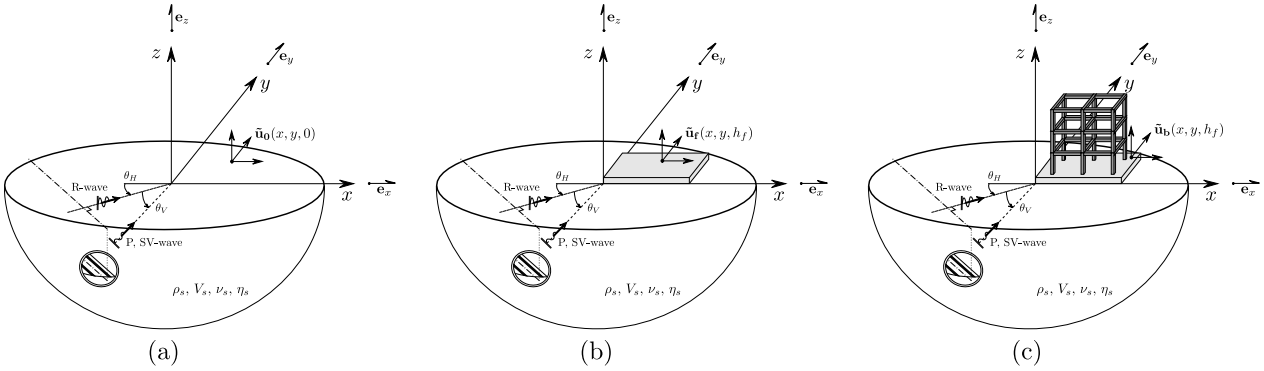


Figure 1: Overview of the general vibration problem: (a) *free-field* displacement generated by underground and/or surface railways; (b) *free-surface* displacement field on the upper surface of the foundation accounting for soil-foundation interaction; (c) displacement field at the base of the building accounting for soil-foundation-building interaction.

It is then necessary to ensure the compatibility of the displacement field at the foundation-building interface with regard to the degrees of freedom of the rigid regions at the base of the building's columns. The soil-foundation model must then refer to rigid foundations or alternatively to rigid footings on a larger domain of a flexible foundation (i.e. slab foundation). The soil-foundation models used in this paper refer to the

application of the Boundary Element Method (BEM) [22, 23] by means of the BEMFUN [24] and EDT [25] toolbox in MATLAB [20]. The EDT toolbox can conveniently provide fundamental solutions for an elastic and layered half-space that can be used in the BEM formulation for evaluating the response of rigid footings resting on a layered soil. Hence, the presence of a flexible foundation of infinite extent along the x and y directions may be obtained by including an elastic layer with appropriate material properties (i.e. concrete) on top of the half-space representing the ground. The response of rigid footings, representing the rigid regions on top of the flexible foundation, can be obtained with the same BEM formulation used for the case of rigid foundations.

The use of a rigid foundations and/or footings model limits the range of incoming wavefields that can be properly studied because of the relatively short wavelengths involved in ground-borne vibration. Similar to the argument valid for the discretization in finite-element analysis, the discussion is then limited to incoming wavefields whose shortest apparent wavelengths are at least 5-8 times larger than the dimension of the column [26, 27]. Considering typical soil and column properties encountered in practice (see Table A.1), this condition can be generally satisfied up to about 80 Hz, which covers only partially the frequency range of interest in ground-borne vibration. While the latter argument sets limitations on the use of a rigid foundations and/or footings model in ground-borne vibration, the authors believe that it is a necessary assumption for approaching the soil-structure interaction problem in its simplest form.

The following section presents a review of the response of rigid foundations subjected to an incoming wavefield.

3 Multiple rigid foundations subjected to an incoming wavefield

This section presents a review of the formulation for the evaluation of the response of a number (n_f) of rigid foundations subjected to an incoming wavefield [12, 14]. The discussion is extended to Iguchi's method for obtaining an approximate solution of the response [13, 15]. The general case of embedded rigid foundations is presented and reduced to the case of surface foundations. Figure 2 illustrates such a foundation model for two embedded foundations with the soil-foundation interfaces Ω_1 and Ω_2.

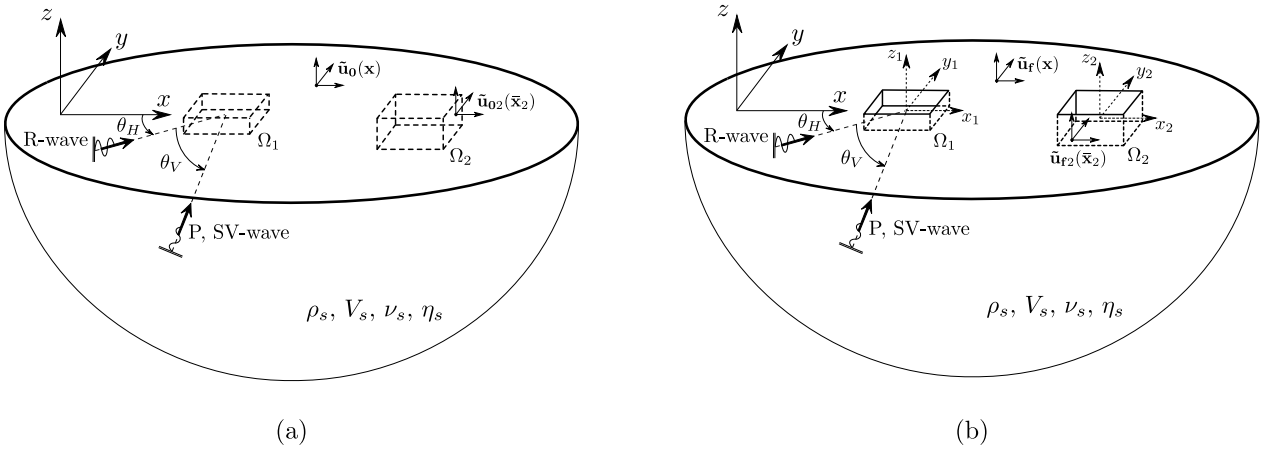


Figure 2: Multiple, embedded, rigid foundations in a homogeneous and elastic halfspace: a) the incoming wavefield, in absence of foundations, is represented by $\tilde{\mathbf{u}}_{\mathbf{0}}(\mathbf{x})$ at a generic location $\mathbf{x}$ in the half-space and by $\tilde{\mathbf{u}}_{\mathbf{0}i}(\bar{\mathbf{x}}_i)$ at a location $\bar{\mathbf{x}}_i$ on the domain Ω_i of the i^{th} foundation; b) the displacement field in the presence of foundations is represented by $\tilde{\mathbf{u}}_{\mathbf{f}}(\mathbf{x})$ at a generic location $\mathbf{x}$ in the half-space and by $\tilde{\mathbf{u}}_{\mathbf{f}i}(\bar{\mathbf{x}}_i)$ at a location $\bar{\mathbf{x}}_i$ on the domain Ω_i of the i^{th} foundation.

The ground is represented by a homogeneous and elastic half-space that is subjected to an incoming wavefield with a resulting free-field displacement $\tilde{\mathbf{u}}_{\mathbf{0}}(\mathbf{x}, \omega)$ expressed as:

$$\tilde{\mathbf{u}}_{\mathbf{0}}(\mathbf{x}, \omega) = \mathcal{U}_0(\mathbf{x}, \omega)\, \mathbf{u}_{\mathbf{0}} \tag{1}$$

where $\mathcal{U}_0(\mathbf{x},\omega)$ is a describing function of the incoming wavefield at $\mathbf{x} \equiv (x,y,z)$ for the angular frequency ω. Examples of incoming wavefields are P-, SV-, SH- or Rayleigh waves propagating in the half-space from a given source. The latter is assumed to reside in the far-field so that the source-receiver interaction can be neglected [28]. For sake of simplicity, the propagating waves are assumed to be plane, as shown in Figure 2, with a vertical incidence angle θ_V ($\theta_V = 0$ for Rayleigh waves), and an horizontal incidence angle θ_H. The describing function of the incoming wavefield can then be expressed as:

$$\mathcal{U}_0(x,y,z,\omega) = \exp\{\tfrac{-i\omega\cos\theta_V}{V}\,(x\cos\theta_H + y\sin\theta_H + z\tan\theta_V)\} \tag{2}$$

with V the velocity of the propagating wave. The vector $\mathbf{u_0} = [u_{0x}\ u_{0y}\ u_{0z}]^{\mathrm{T}}$ is the free-field amplitude at the origin of the reference system. It depends on the type of incoming wave, the incidence angles θ_V and θ_h, and the properties of the half-space.
In general, the presence of a foundation induces a scattered wavefield in terms of displacement $\tilde{\mathbf{u}}_\mathbf{s}(\mathbf{x},\omega)$ and traction $\tilde{\mathbf{t}}_\mathbf{s}(\mathbf{x},\omega)$ such that:

$$\tilde{\mathbf{u}}_\mathbf{f}(\mathbf{x},\omega) = \tilde{\mathbf{u}}_\mathbf{0}(\mathbf{x},\omega) + \tilde{\mathbf{u}}_\mathbf{s}(\mathbf{x},\omega) \tag{3a}$$

$$\tilde{\mathbf{t}}_\mathbf{f}(\mathbf{x},\omega) = \tilde{\mathbf{t}}_\mathbf{0}(\mathbf{x},\omega) + \tilde{\mathbf{t}}_\mathbf{s}(\mathbf{x},\omega) \tag{3b}$$

with $\tilde{\mathbf{u}}_\mathbf{f}(\mathbf{x},\omega)$ and $\tilde{\mathbf{t}}_\mathbf{f}(\mathbf{x},\omega)$ representing the free-surface displacement and traction field accounting for the added-foundation effect and $\tilde{\mathbf{t}}_\mathbf{0}(\mathbf{x},\omega)$ the traction field originated by the incoming wavefield.
The n_f rigid foundations of arbitrary shape are embedded in the half-space with the centroids O_i being the origin of the local reference systems $\mathbf{x_i}$. The free-surface displacement on the footprint of the i^{th} footing can be expressed as:

$$\tilde{\mathbf{u}}_{\mathbf{f}i}(\bar{\mathbf{x}}_i,\omega) = \mathcal{S}_i(\bar{\mathbf{x}}_i)\,\mathbf{u}_{\mathbf{f}i}(\omega) \qquad \text{with} \quad \bar{\mathbf{x}}_i \in \Omega_i, \quad (i = 1,\ldots,n_f) \tag{4}$$

with $\mathbf{u}_{\mathbf{f}i} = [u_{fi}\ \ v_{fi}\ \ w_{fi}\ \ \varphi_{fxi}\ \ \varphi_{fyi}\ \ \varphi_{fzi}]^{\mathrm{T}}$ the rigid displacement of the i^{th} foundation referring to the 6 degrees-of-freedom. The 3×6 transformation matrix $\mathcal{S}_i(\bar{\mathbf{x}}_i)$ can be expressed as:

$$\mathcal{S}_i(\bar{\mathbf{x}}_i) = \begin{bmatrix} 1 & 0 & 0 & 0 & z_i & -y_i \\ 0 & 1 & 0 & -z_i & 0 & x_i \\ 0 & 0 & 1 & y_i & -x_i & 0 \end{bmatrix} \tag{5}$$

The force that the i^{th} rigid foundation exerts on the soil can be evaluated as:

$$\mathbf{f}_{\mathbf{f}i}(\omega) = \int_{\Omega_i} \mathcal{S}_i^{\mathrm{T}}(\bar{\mathbf{x}}_i)\,\tilde{\mathbf{t}}_{\mathbf{f}i}(\bar{\mathbf{x}}_\mathbf{i},\omega)\,d\Omega_i \tag{6}$$

with $\mathbf{f}_{\mathbf{f}i} = [f_{fxi}\ \ f_{fyi}\ \ f_{fzi}\ \ q_{fxi}\ \ q_{fyi}\ \ q_{fzi}]^{\mathrm{T}}$. The global equilibrium condition for the i^{th} foundation can be obtained by pre-multiplying Equation 3b by $\mathcal{S}_i^{\mathrm{T}}(\bar{\mathbf{x}}_i)$ and integrating over the domain Ω_i so that:

$$\mathbf{f}_{\mathbf{f}i}(\omega) = \mathbf{f}_{\mathbf{0}i}(\omega) + \mathbf{f}_{\mathbf{s}i}(\omega) = \int_{\Omega_i} \mathcal{S}_i^{\mathrm{T}}(\bar{\mathbf{x}}_i)\,\tilde{\mathbf{t}}_{\mathbf{0}i}(\bar{\mathbf{x}}_i,\omega)\,d\Omega_i + \int_{\Omega_i} \mathcal{S}_i^{\mathrm{T}}(\bar{\mathbf{x}}_i)\,\tilde{\mathbf{t}}_{\mathbf{s}i}(\bar{\mathbf{x}}_i,\omega)\,d\Omega_i \tag{7}$$

with $\mathbf{f}_{\mathbf{0}i}$ and $\mathbf{f}_{\mathbf{s}i}$ the forces induced by the incoming wavefield and by the scattered wavefield respectively. Introducing the Green's function matrix $\mathcal{G}(\mathbf{x},\mathbf{x}',\omega)$ that relates the displacement $\tilde{\mathbf{u}}(\mathbf{x},\omega)$ to the traction

$\tilde{\mathbf{t}}(\mathbf{x}', \omega)$, the scattered displacement field is given by:

$$\tilde{\mathbf{u}}_{\mathbf{s}i}(\bar{\mathbf{x}}_\mathbf{i}, \omega) = \sum_{j=1}^{n_f} \int_{\Omega_j} \mathcal{G}_{ij}(\bar{\mathbf{x}}_\mathbf{i}, \bar{\mathbf{x}}'_\mathbf{j}, \omega)\, \tilde{\mathbf{t}}_{\mathbf{s}j}(\bar{\mathbf{x}}_\mathbf{j}, \omega)\, d\Omega_j \tag{8}$$

Following the approach of Thau [29], the scattered traction field can be divided in one part directly related to the unknown rigid displacement of the foundations and another one required to make the foundation system immobile under the incoming wavefield:

$$\tilde{\mathbf{t}}_{\mathbf{s}i}(\bar{\mathbf{x}}_\mathbf{i}, \omega) = \sum_{j=1}^{n_f} \mathcal{T}_{jiR}(\bar{\mathbf{x}}_\mathbf{i}, \omega)\, \mathbf{u}_{\mathbf{f}j}(\omega) - \mathcal{T}_{iD}(\bar{\mathbf{x}}_\mathbf{i}, \omega) \tag{9}$$

The matrix $\mathcal{T}_{jiR}(\bar{\mathbf{x}}_\mathbf{i}, \omega)$ gives the traction field across the domain $\bar{\mathbf{x}}_i \in \Omega_i$ of the i^{th} foundation due to a rigid motion $\mathbf{u}_{\mathbf{f}j}$ of the j^{th} foundation. Let us consider Equation 3a for the i^{th} foundation and substitute the term $\tilde{\mathbf{u}}_\mathbf{s}(\bar{\mathbf{x}}, \omega)$ as in Equation 8 with the traction expressed as in Equation 9. The following integral equations related to the i^{th} foundation and referring to the two distinct radiation (Equation 10a) and diffraction (Equation 10b) problems are obtained:

$$\mathcal{S}_i(\bar{\mathbf{x}}_i)\, \mathbf{u}_{\mathbf{f}i}(\omega) = \sum_{j=1}^{n_f} \int_{\Omega_j} \mathcal{G}_{ij}(\bar{\mathbf{x}}_\mathbf{i}, \bar{\mathbf{x}}'_\mathbf{j}, \omega) \sum_{r=1}^{n_f} \mathcal{T}_{rjR}(\bar{\mathbf{x}}'_\mathbf{j}, \omega)\, \mathbf{u}_{\mathbf{f}r}(\omega)\, d\Omega_j \tag{10a}$$

$$\tilde{\mathbf{u}}_{\mathbf{0}i}(\bar{\mathbf{x}}_i, \omega) = \sum_{j=1}^{n_f} \int_{\Omega_j} \mathcal{G}_{ij}(\bar{\mathbf{x}}_\mathbf{i}, \bar{\mathbf{x}}'_\mathbf{j}, \omega)\, \mathcal{T}_{jD}(\bar{\mathbf{x}}_\mathbf{j}, \omega)\, d\Omega_j \tag{10b}$$

Equation 10a may be further divided into the n_f integral equations that yield the unknown matrix $\mathcal{T}_{ijR}$:

$$\mathcal{S}_i(\bar{\mathbf{x}}_i) = \sum_{j=1}^{n_f} \int_{\Omega_j} \mathcal{G}_{ij}(\bar{\mathbf{x}}_\mathbf{i}, \bar{\mathbf{x}}'_\mathbf{j}, \omega)\, \mathcal{T}_{ijR}(\bar{\mathbf{x}}'_\mathbf{j}, \omega)\, d\Omega_j \tag{11a}$$

$$0 = \sum_{j=1}^{n_f} \int_{\Omega_j} \mathcal{G}_{ij}(\bar{\mathbf{x}}_\mathbf{i}, \bar{\mathbf{x}}'_\mathbf{j}, \omega)\, \mathcal{T}_{rjR}(\bar{\mathbf{x}}'_\mathbf{j}, \omega)\, d\Omega_j \quad \text{with} \quad r = 1, \dots, n_f \wedge r \neq i \tag{11b}$$

By definition of the matrix $\mathcal{T}_{jiR}(\bar{\mathbf{x}}'_\mathbf{i}, \omega)$, the dynamic stiffness matrix relating the forces at the i^{th} foundation due to the rigid displacement at the j^{th} foundation is given by:

$$\mathbf{K}_{\mathbf{f}ij}(\omega) = \int_{\Omega_i} \mathcal{S}_i^{\mathrm{T}}(\bar{\mathbf{x}}_i)\, \mathcal{T}_{jiR}(\bar{\mathbf{x}}'_\mathbf{i}, \omega)\, d\Omega_i \tag{12}$$

The forces associated with the i^{th} foundation originated by the scattered wavefield can be then expressed as:

$$\begin{aligned} \mathbf{f}_{\mathbf{s}i}(\omega) &= \int_{\Omega_i} \mathcal{S}_i^{\mathrm{T}}(\bar{\mathbf{x}}_i) \left[\sum_{j=1}^{n_f} \mathcal{T}_{jiR}(\bar{\mathbf{x}}_\mathbf{i}, \omega)\, \mathbf{u}_{\mathbf{f}j}(\omega) - \mathcal{T}_{iD}(\bar{\mathbf{x}}_\mathbf{i}, \omega) \right] d\Omega_i = \\ &= \sum_{j=1,2} \mathbf{K}_{\mathbf{f}ij}(\omega)\, \mathbf{u}_{\mathbf{f}j}(\omega) - \int_{\Omega_i} \mathcal{S}_i^{\mathrm{T}}(\bar{\mathbf{x}}_i)\, \mathcal{T}_{iD}(\bar{\mathbf{x}}_\mathbf{i}, \omega) d\Omega_i \end{aligned} \tag{13}$$

Consider the i^{th} foundation to be massless and free of external forces so that from Equation 7:

$$\mathbf{f}_{\mathbf{s}i}(\omega) = -\mathbf{f}_{\mathbf{0}i}(\omega) \tag{14}$$

The rigid displacement $\mathbf{u}_{\mathbf{f}i}(\omega)$ can then be expressed as:

$$\mathbf{u}_{\mathbf{f}i}(\omega) = \sum_{j=1}^{n_f} \mathbf{H}_{\mathbf{f}ij}(\omega) \int_{\Omega_j} \mathcal{S}_j^{\mathrm{T}}(\bar{\mathbf{x}}_j)\, \mathcal{T}_{jD}(\bar{\mathbf{x}}_j, \omega)\, d\Omega_j - \sum_{j=1}^{n_f} \mathbf{H}_{\mathbf{f}ij}(\omega)\, \mathbf{f}_{\mathbf{0}j}(\omega) \quad \text{with} \quad i = 1, \dots, n_f \tag{15}$$

Equation 15 yields the displacement of multiple, massless, rigid foundations embedded in an elastic half-space subjected to an incoming wavefield but free of external forces. The term $\mathcal{T}_{jD}(\bar{\mathbf{x}}_j, \omega)$ is related to the displacement wavefield $\tilde{\mathbf{u}}_{\mathbf{0}}(\mathbf{x}, \omega)$ by Equation 10b while the forces $\mathbf{f}_{\mathbf{0}j}(\omega)$ can be retrieved by the traction field $\tilde{\mathbf{t}}_{\mathbf{0}}(\mathbf{x}, \omega)$ (see Equation 7). The frequency response function (FRF) matrix $\mathbf{H}_{\mathbf{f}}(\omega)$ can be found as the inverse of the dynamic stiffness matrix $\mathbf{K}_{\mathbf{f}}(\omega)$.
Let us consider the special case of massless and surface foundations. Because of the free-surface condition, the force $\mathbf{f}_{\mathbf{0}i}(\omega)$ is null and by substituting Equation 13 into Equation 14 we obtain:

$$\mathbf{f}_{\mathbf{s}i}(\omega) = \int_{\Omega_i} \mathcal{S}_i^{\mathrm{T}}(\bar{\mathbf{x}}_i) \left[\sum_{j=1}^{n_f} \mathcal{T}_{jiR}(\bar{\mathbf{x}}_\mathbf{i}, \omega)\, \mathbf{u}_{\mathbf{f}j}(\omega) - \mathcal{T}_{iD}(\bar{\mathbf{x}}_\mathbf{i}, \omega) \right] d\Omega_i = 0 \tag{16}$$

A sufficient condition for the latter Equation is that:

$$\sum_{j=1}^{n_f} \mathcal{T}_{jiR}(\bar{\mathbf{x}}_\mathbf{i}, \omega)\, \mathbf{u}_{\mathbf{f}j}(\omega) = \mathcal{T}_{iD}(\bar{\mathbf{x}}_\mathbf{i}, \omega) \tag{17}$$

Equation 17 can be related to Equations 10a and 10b by considering the rigid displacement of the r^{th} foundation. Pre-multiplying the left- and right-hand side by $\sum_{i=1}^{n_f} \mathcal{G}_{ri}(\bar{\mathbf{x}}_r, \bar{\mathbf{x}}_i', \omega)$ and integrating over the domain Ω_i, the following identity holds:

$$\sum_{i=1}^{n_f} \int_{\Omega_i} \mathcal{G}_{ri}(\bar{\mathbf{x}}_\mathbf{r}, \bar{\mathbf{x}}_\mathbf{i}', \omega) \sum_{j=1}^{n_f} \mathcal{T}_{jiR}(\bar{\mathbf{x}}_\mathbf{i}', \omega)\, \mathbf{u}_{\mathbf{f}j}(\omega)\, d\Omega_i = \sum_{i=1}^{n_f} \int_{\Omega_i} \mathcal{G}_{ri}(\bar{\mathbf{x}}_r, \bar{\mathbf{x}}_i', \omega)\, \mathcal{T}_{iD}(\bar{\mathbf{x}}_i', \omega)\, d\Omega_i \tag{18}$$

By substituting Equations 10a and 10b in the latter identity one can relate the rigid displacement $\mathbf{u}_{\mathbf{f}r}(\omega)$ of the r^{th} foundation to the displacement field $\tilde{\mathbf{u}}_{\mathbf{0}r}(\bar{\mathbf{x}}_r, \omega)$ on the footprint of the same foundation:

$$\mathcal{S}_r(\bar{\mathbf{x}}_r)\, \mathbf{u}_{\mathbf{f}r}(\omega) = \tilde{\mathbf{u}}_{\mathbf{0}r}(\bar{\mathbf{x}}_r, \omega) \tag{19}$$

Equation 19 represents only an approximate solution since the condition in Equation 17 is not a necessary condition. For instance, it is clear, by physical intuition, that Equation 19 completely neglects the through-soil coupling between the foundations and that the same expression is obtained for the case of a single foundation subjected to an incoming wavefield. Moreover, by inspection of the transformation matrix $\mathcal{S}_r(\bar{\mathbf{x}}_r)$, it is clear that the solution of Equation 19 can only be found in approximate terms for instance by means of the least square method [13]. The rigid displacement of the foundation can then be found as a weighted average

of the displacement field on its footprint (Iguchi's method):

$$\begin{aligned} \mathbf{u_f}_r(\omega) &= \mathbf{P}_r^{-1} \int_{\Omega_r} \mathcal{S}_r^{\mathrm{T}}(\bar{\mathbf{x}}_r)\, \tilde{\mathbf{u}}_{\mathbf{0}r}(\bar{\mathbf{x}}_r, \omega)\, d\Omega_r \\ \text{with} \quad \mathbf{P}_r &= \int_{\Omega_r} \mathcal{S}_r^{\mathrm{T}}(\bar{\mathbf{x}}_r)\, \mathcal{S}_r(\bar{\mathbf{x}}_r)\, d\Omega_r \end{aligned} \tag{20}$$

It can be shown that by choosing the origin of the coordinate system at the centroid of the foundation the matrix $\mathbf{P} = \mathrm{diag}[A_f, A_f, A_f, I_{fx}, I_{fy}, I_{fz}]$ is diagonal with the components being the area A_f, the second moment of area I_{fx} and I_{fy}, and the polar moment of area I_{fz} of the single rigid foundation.
The integral equations presented in the previous discussion can be reduced to sets of algebraic equations expressed at collocation points $\bar{\mathbf{x}}_\mathbf{c}$ of boundary elements [24] and both the rigorous and approximate rigid-body displacement of the foundation can be expressed as:

$$\mathbf{u_f}(\omega) = \mathbf{A}(\omega)\, \mathbf{u_0} \tag{21}$$

The following sections present the validation and a general discussion for the case of a single [12] and two adjacent [14] squared, surface, rigid foundations resting on a homogeneous and elastic half-space subjected to incoming plane P- and SV-waves.

3.1 The case of a squared rigid foundation

In the case of a single rigid foundation, the matrix $\mathbf{A}$ in Equation 21 for an incoming plane wave impinging the free-field at a vertical angle θ_V and a horizontal angle $\theta_H = 0$ can be expressed as:

$$\mathbf{A} = \begin{bmatrix} A_{xx} & 0 & A_{xz} \\ 0 & A_{yy} & 0 \\ A_{zx} & 0 & A_{zz} \\ 0 & A_{\varphi_x y} & 0 \\ A_{\varphi_y x} & 0 & A_{\varphi_y z} \\ 0 & A_{\varphi_z y} & 0 \end{bmatrix} \tag{22}$$

The components of the matrix $\mathbf{A}$ in Equation 22 for the case of a surface and square foundation are reproduced and reported in Figure 3 for the cases obtained by Wong [12] (Poisson's ratio $\nu_s = 1/3$). Considering the case of incoming P- or SV-waves, one can notice that the horizontal-vertical contributions A_{xz} and A_{zx} have limited values when compared with the direct terms A_{xx} and A_{zz} respectively. So that, the latter terms will dominate the translational response u_f and w_f of the rigid foundation. Similarly, the rocking response φ_{fy} depends mostly on the component $A_{\varphi_y z}$ related to the vertical displacement u_{0z}. Figure 4 shows the application of Iguchi's method for a square, surface, rigid foundation subjected to an incoming P- or SV-wave at $\theta_V = 45^\circ$ and $\theta_H = 0^\circ$. The comparison of the foundation response with the rigorous solution is favourable with the approximate magnitude response that oscillates about the rigorous solution [30].

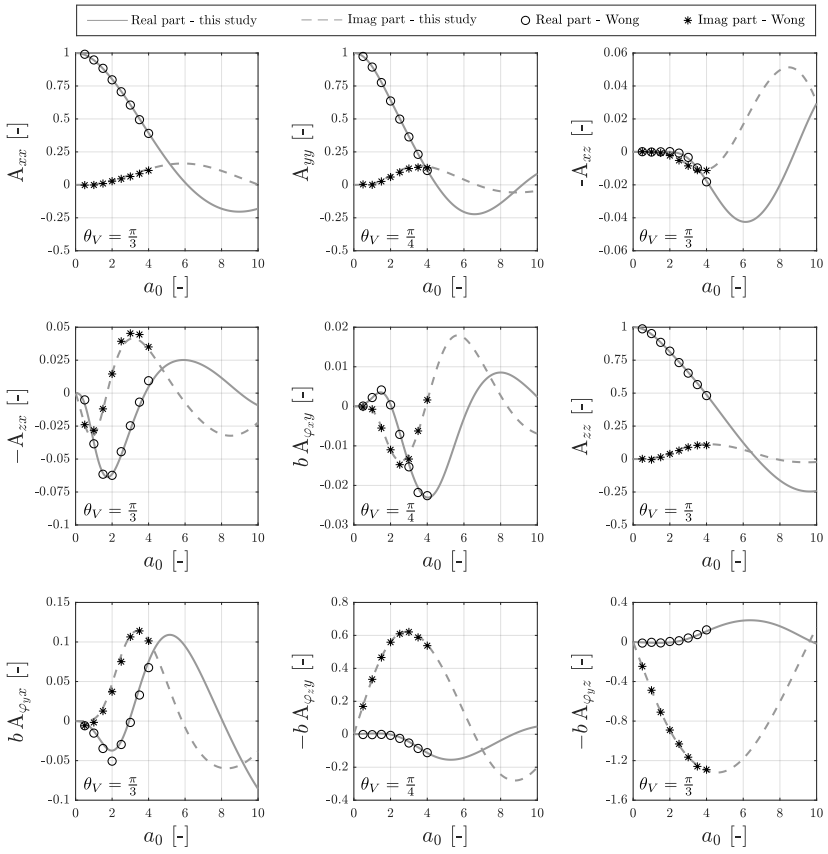


Figure 3: Components of the matrix $\mathbf{A}$ obtained for incoming wavefield at a vertical incidence angles $\theta_V = 45°$ and $60°$, and horizontal incidence angle $\theta_H = 0°$ for a homogeneous and elastic half-space with Poisson's ratio $\nu_s = 1/3$. Comparison is made with the result of Wong [12] by using 8 x 8 constant elements for the rigid foundation.

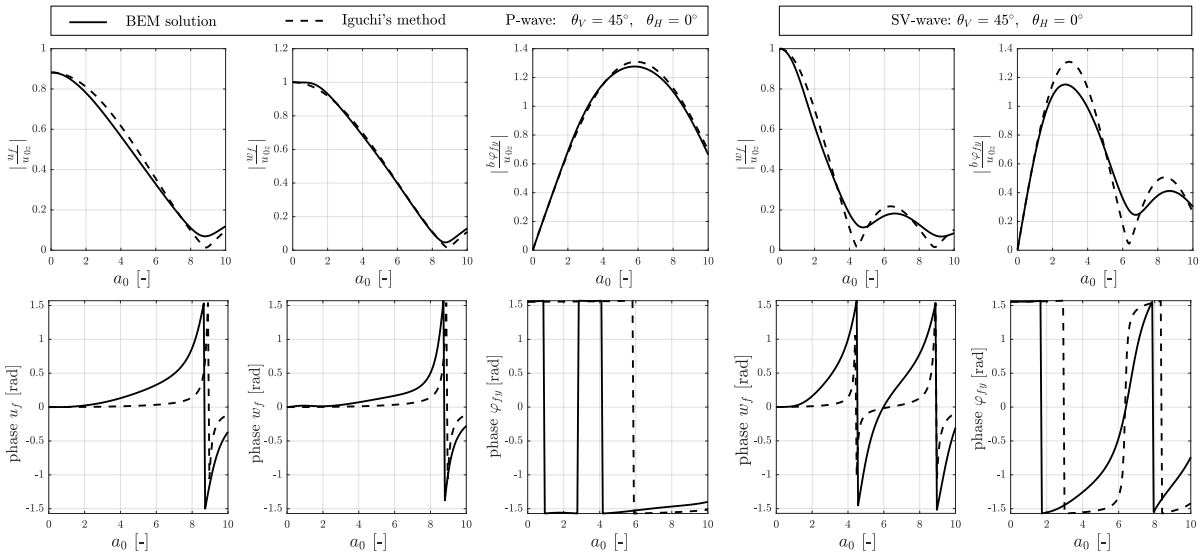


Figure 4: Results for the horizontal u_f, vertical w_f and rocking φ_{fy} response of a square, surface rigid foundation on a homogeneous and elastic half-space (Poisson's ratio $\nu_s = 1/3$) subjected to incoming plane P- (left) and SV-waves (right) at an incidence angle $\theta_V = 45°$. Comparison is made for the magnitude (top) and phase (bottom) of the rigid-body displacement between the rigorous solution obtained with BEM (using 8 x 8 quadratic elements) and the solution obtained with Iguchi's method.

3.2 Two adjacent rigid foundation

The discussion in Section 3 illustrates the validity of Iguchi's method to the case of multiple rigid foundations on the free-field or embedded in an elastic half-space. This can be explored with reference to two square, surface rigid foundations of half-width b at a centre-to-centre distance d (along x axis) and subjected to incoming plane P- or SV-waves. An extensive study on the rigid-body response of such a foundation system has been undertaken by Qian [14] via application of the BEM. The purpose of the present paper is not to extend such an investigation, but rather to contextualize the case of multiple rigid foundations to the application of Iguchi's method. Figure 5 shows a comparison of the magnitude of the response for the upstream and downstream rigid foundations between the rigorous BEM solution and the one obtained by means of Iguchi's method. The fluctuation of the amplitude of the rigorous solution can be noted for both the translational and rotational response, with the latter being more accentuated, as anticipated by Qian [14]. A qualitative result from the study of Qian states that the intensity and the "period" of such fluctuations along the frequency-spectrum decrease with increasing the foundation separation d.
The purpose of this paper is to apply Iguchi's method for evaluating the added-foundation effect, as described in Section 2, in the case of rigid foundations representing the subsequent coupling regions with a beam-bar representation of a portal-frame building. With reference to typical building typologies (e.g. reinforced concrete and/or steel buildings), the centre-to-centre distance d is most likely greater than $2.5\,b$. Due to space limitations, only the results attaining the specific case in Figure 5 are shown.

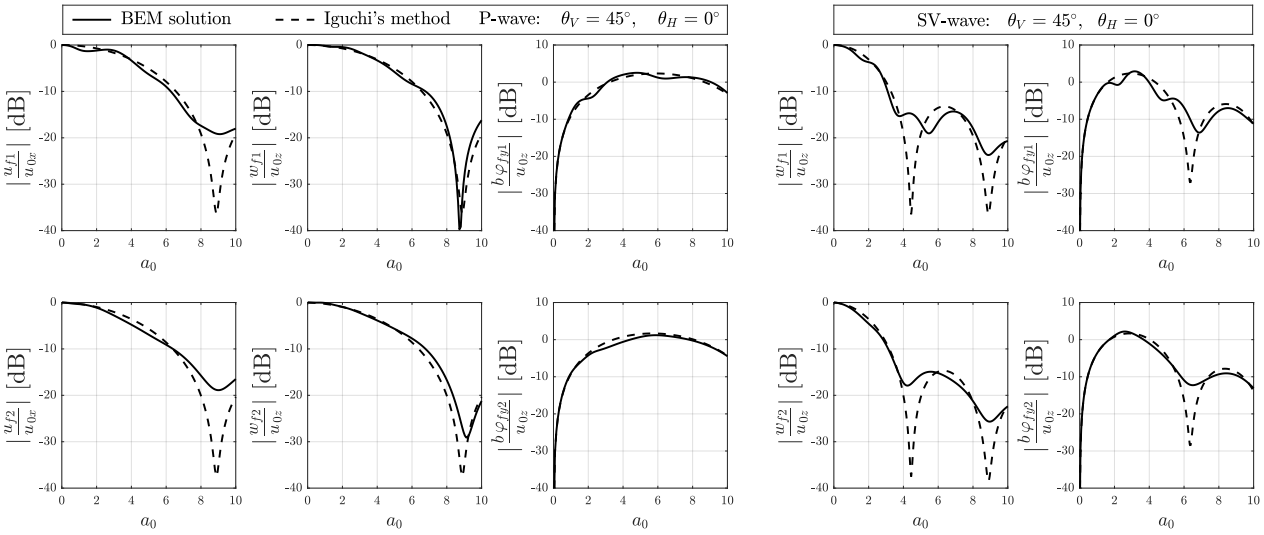


Figure 5: Results for the horizontal u_f, vertical w_f and rocking φ_{fy} response of two square, surface rigid foundations on a homogeneous and elastic half-space at a centre-to-centre distance $d = 2.5\,b$ subjected to incoming plane P- (left) and SV-waves (right) at $\theta_V = 45°$ and $\theta_H = 0°$. Comparison is made for the magnitude of the response for the upstream (top) and downstream (bottom) foundation between the results obtained with the rigorous solution (BEM - 8 x 8 quadratic elements for each foundation) and that with Iguchi's method.

Although the aforementioned fluctuations of the actual response are in general different depending on the distance d/b, the type of the incoming wavefield and the Poisson's ratio of the soil, the approximate solution is in good agreement with the results obtained with the rigorous BEM. Iguchi's method can then be adopted as a simplified procedure for considering the added-foundation effect in ground-borne vibration of buildings. The next section examines the more realistic case of rigid footings on top of a flexible foundation (e.g. concrete slab) resting on the half-space representing the ground.

4 Rigid footings on a flexible foundation

The presence of a flexible foundation on top of the ground can be modelled, as a first approximation, as an elastic layer of infinite extent along both the x and y direction with density ρ_c, shear wave velocity V_c, Poisson's ratio ν_c and damping loss factor η_c that can be representative, for instance, of a concrete slab foundation. As for the previous discussion, incoming plane P- or SV-waves can be considered at some vertical and horizontal incidence angle θ_V and θ_H with the resulting free-field displacement $\tilde{\mathbf{u}}_\mathbf{0}(\mathbf{x}, \omega)$.

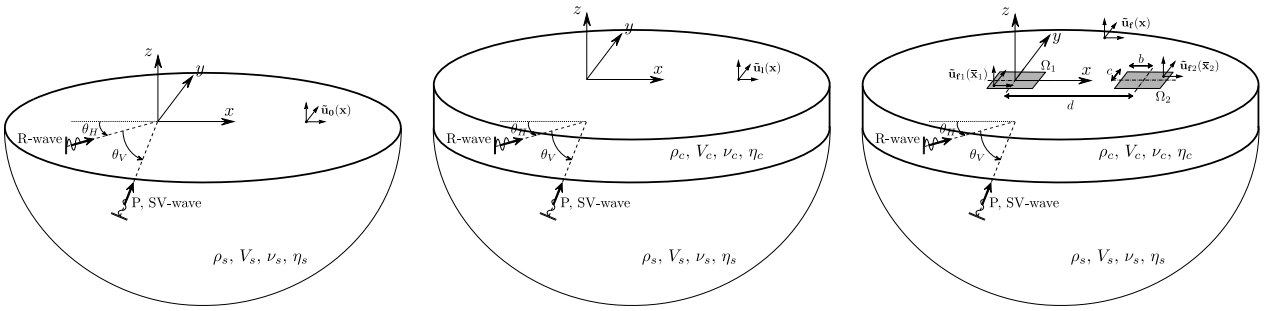


Figure 6: Schematic of the added-foundation effect with reference to rigid footings on a flexible foundation. a) A homogeneous and elastic half-space representing the soil is subjected to an incoming wavefield due to P-, SV- or Rayleigh waves with the resulting free-field displacement $\tilde{\mathbf{u}}_\mathbf{0}(\mathbf{x})$; b) the addition of a flexible foundation as an elastic layer leads to the displacement $\tilde{\mathbf{u}}_\mathbf{l}(\mathbf{x})$ at the free-surface of the layer; c) consideration of rigid footings as regions that will be coupled with a beam-bar representation of a portal-frame building leads to the modified displacement $\tilde{\mathbf{u}}_\mathbf{f}(\mathbf{x})$ at the free-surface and the displacement $\tilde{\mathbf{u}}_{\mathbf{f}1}(\mathbf{x_1})$ and $\tilde{\mathbf{u}}_{\mathbf{f}2}(\mathbf{x_2})$ on the domain Ω_1 and Ω_2 of the two rigid footings.

Prior to the coupling of the elastic layer, the displacement field $\tilde{\mathbf{u}}_\mathbf{0}(\mathbf{x}, \omega)$ is related to the displacement amplitude $\mathbf{u_0}$ by means of Equation 2. The addition of a flexible foundation changes the displacement field at the surface of the half-space into $\tilde{\mathbf{u}}_\mathbf{1}(\mathbf{x}, \omega)$ with the resulting displacement field $\tilde{\mathbf{u}}_\mathbf{l}(\mathbf{x}, \omega)$ at the free-surface of the elastic layer. The displacement field at the lower and upper surface of the elastic layer can then be written as:

$$\tilde{\mathbf{u}}_\mathbf{1}(\mathbf{x_1}, \omega) = \mathcal{U}_0(\mathbf{x_1}, \omega)\, \mathbf{u_1}(\omega) \tag{23a}$$

$$\tilde{\mathbf{u}}_\mathbf{l}(\mathbf{x_l}, \omega) = \mathcal{U}_0(\mathbf{x_l}, \omega)\, \mathbf{u_l}(\omega) \tag{23b}$$

where $\mathcal{U}_0(\mathbf{x}, \omega)$ is the describing function of the incoming wavefield as in Equation 2 and $\mathbf{u_1}(\omega)$ and $\mathbf{u_l}(\omega)$ represent the displacement amplitude vectors at the lower and upper surface of the layer respectively. They can be related to the traction amplitude vectors at the same z locations by considering the dynamic stiffness matrix $\mathbf{K_c}(\omega)$ of the elastic layer [18]:

$$\begin{pmatrix} \mathbf{t_l}(\omega) \\ \mathbf{t_1}(\omega) \end{pmatrix} = \begin{bmatrix} \mathbf{K_c^{(ll)}}(\omega) & \mathbf{K_c^{(l1)}}(\omega) \\ \mathbf{K_c^{(1l)}}(\omega) & \mathbf{K_c^{(11)}}(\omega) \end{bmatrix} \begin{pmatrix} \mathbf{u_l}(\omega) \\ \mathbf{u_1}(\omega) \end{pmatrix} \tag{24}$$

Similarly, the traction and displacement amplitude vectors at the surface of the half-space are related through the dynamic stiffness matrix $\mathbf{K_s}$. By consideration of the equilibrium and compatibility between the half-space and the layer, the resulting displacement amplitude $\mathbf{u_1}(\omega)$ at their interface can be found as:

$$\mathbf{u_1}(\omega) = \left[\mathbf{I} + [\mathbf{K_s}(\omega)]^{-1}\, \mathbf{K_c^{(11)}}(\omega)\right]^{-1} \mathbf{u_0} \tag{25}$$

The displacement amplitude vector at the free-surface of the layer can be found by imposing the traction-free condition by means of Equation 24, so that:

$$\mathbf{u_l}(\omega) = -[\mathbf{K_c^{(11)}}(\omega)]^{-1}\,\mathbf{K_c^{(11)}}(\omega)\,\mathbf{u_1}(\omega) \tag{26}$$

For the results shown herein, the displacement amplitude vectors $\mathbf{u_1}$ and $\mathbf{u_l}$ are obtained from Equations 25 and 26 by using the dynamic stiffness matrices from EDT [19]. The addition of an elastic layer, on top of the half-space, restrains the vibration levels at relatively high-frequencies. The extent to which this effect manifests depends, in general, on the type of the incoming wavefield, on the material properties of both the layer and the half-space and on the dimensionless frequency $a_0 = \omega\, h_f/V_s$, with h_f the thickness of the layer, as summarily described in Equation 27.

$$\frac{u_l}{u_0} \propto \Psi\left(\frac{V_s}{V_c}, \frac{\rho_s}{\rho_c}, \nu_s, \nu_c, \theta, \frac{\omega h_f}{V_s}\right) \tag{27}$$

For the vertical displacement component, a region of amplification at relatively low-frequencies precedes the restraining effect so that there is a divide somewhat analogous to the concept of coincidence frequency in thin plates [16, 17, 31].

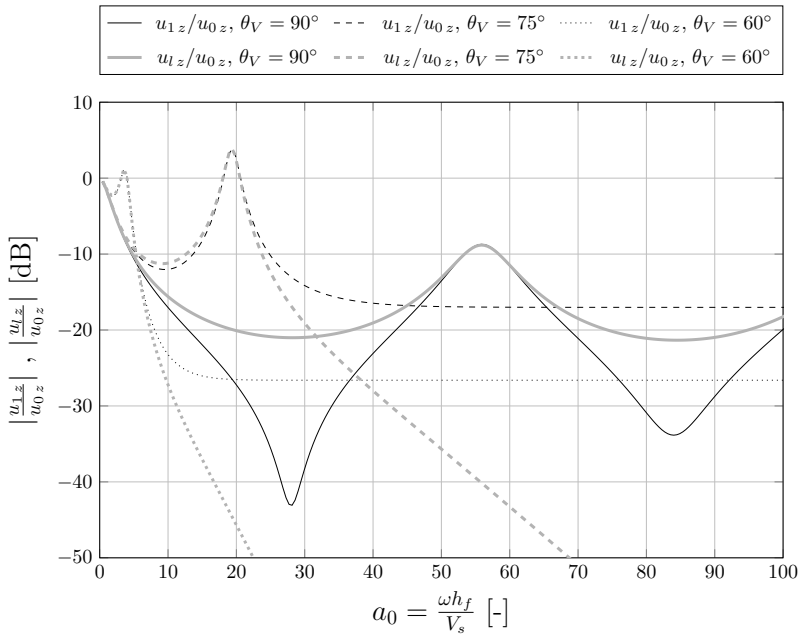


Figure 7: Restraining effect on the vertical displacement amplitude of a concrete foundation modelled as an elastic layer of infinite extent along x and y axes and resting on top of a homogeneous and elastic half-space representing the ground. Incoming plane P-waves at vertical incidence angles $\theta_V = 60°, 75°$ and $90°$ are considered.

Figure 7 shows such a feature for incoming P-waves at vertical incidence angles of $75°$ (dashed line) and $60°$ (dotted line). For these values of the incidence angle θ_V, the restraining effect is evident with a constant high-frequencies limit for the interface displacement amplitude u_{1z} and a free-surface displacement amplitude u_{lz} that tends to the null value. The solid line in Figure 7 explores the case of normally incident P-waves, for which the interface displacement u_{1z} is restrained at the dimensionless frequencies $a_0 = \frac{\pi}{2}\frac{V_c}{V_s}(2n+1)$ and released at $a_0 = \pi\frac{V_c}{V_s}(n+1)$ when the layer is dynamically de-coupled from the half-space with regard to the normally incident wavefield. Although general comments have been presented here, the reader is redirected to the relevant literature for a more thorough discussion on the influence of slab

foundations on ground-borne vibration levels [16, 17].
Let us consider the case for which, in the framework of soil-foundation-structure interaction as shown in Figure 1, the building is represented by a portal-frame model referring to a beam-bar formulation with the implications already mentioned in Section 2. The foundation-building coupling regions on top of the flexible foundation can be then idealised as surface, rigid footings on the elastic layer as schematically illustrated in Figure 6c. The displacement field $\tilde{\mathbf{u}}_\mathbf{l}(\mathbf{x})$ at the free-surface of the layer can be obtained by Equation 23b, and the response of the rigid footings on the free-surface of the elastic layer can be approached as in Section 3. The equivalence of Equation 18 to Equation 19 in Section 3 still holds so that Iguchi's method is applicable with the due limitations related to the conditions in Equations 16 and 17. The approximate response of the rigid footings can be then obtained as weighted average of the displacement field $\tilde{\mathbf{u}}_\mathbf{l}(\mathbf{x})$ on the footprint of the rigid regions.

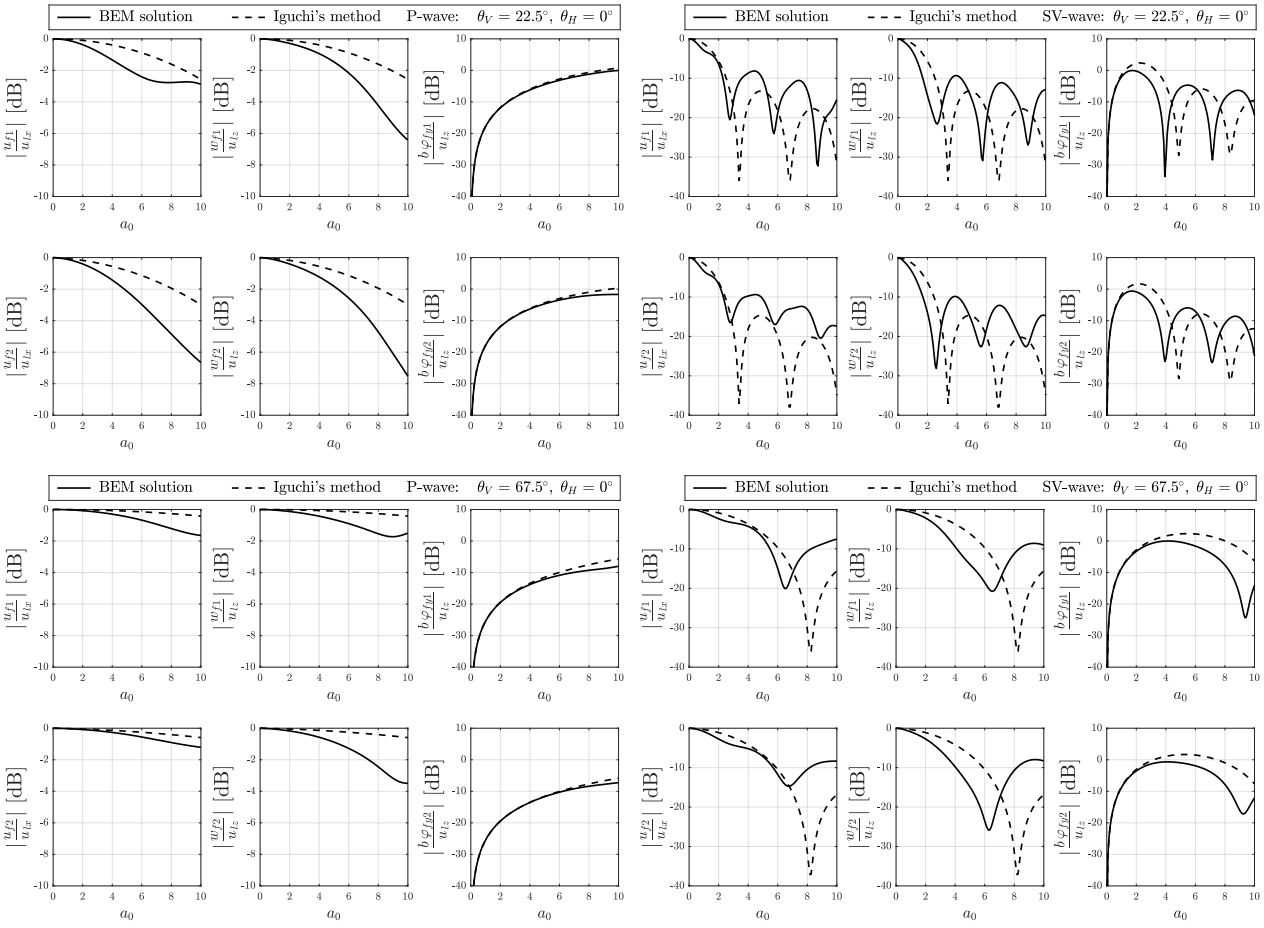


Figure 8: Results for the horizontal u_f, vertical w_f and rocking φ_{fy} response of two square, surface rigid footings on an elastic layer, representing a flexible foundation, resting on a homogeneous and elastic half-space subjected to incoming plane P- (left) and SV-waves (right) at $\theta_V = 22.5°, 67.5°$ and $\theta_H = 0°$. The centre-to-centre distance of the rigid footings is set to $d = 2.5\,b$. Comparison is made for the magnitude of the response for the upstream (top) and downstream (bottom) footing between the results obtained with the rigorous solution (BEM - 8 x 8 quadratic elements for each foundation) and those obtained with Iguchi's method.

The magnitude in decibels of the horizontal u_{fi}, vertical w_{fi} and rocking φ_{fyi} displacements referring to two square footings at a distance $d = 2.5\,b$ are shown in Figure 8 for the upstream ($i = 1$) and downstream ($i = 2$) footings subjected to incoming plane P- and SV-waves at vertical incidence angles $\theta_V = 22.5°$, $67.5°$ and horizontal incidence angle $\theta_H = 0°$. The rigid footings response is scaled to the related horizontal or vertical component of the displacement amplitude vector $\mathbf{u}_\mathbf{l}$ of the incoming wavefield at the free-surface of the layer. Iguchi's method provides approximate solutions that agree reasonably at low-frequencies with the

rigorous counterparts, especially for the rocking motion of the footings. However, the agreement seems to be limited at higher frequencies. In general, the agreement of the approximate solution improves for larger centre-to-centre distances between adjacent footings.

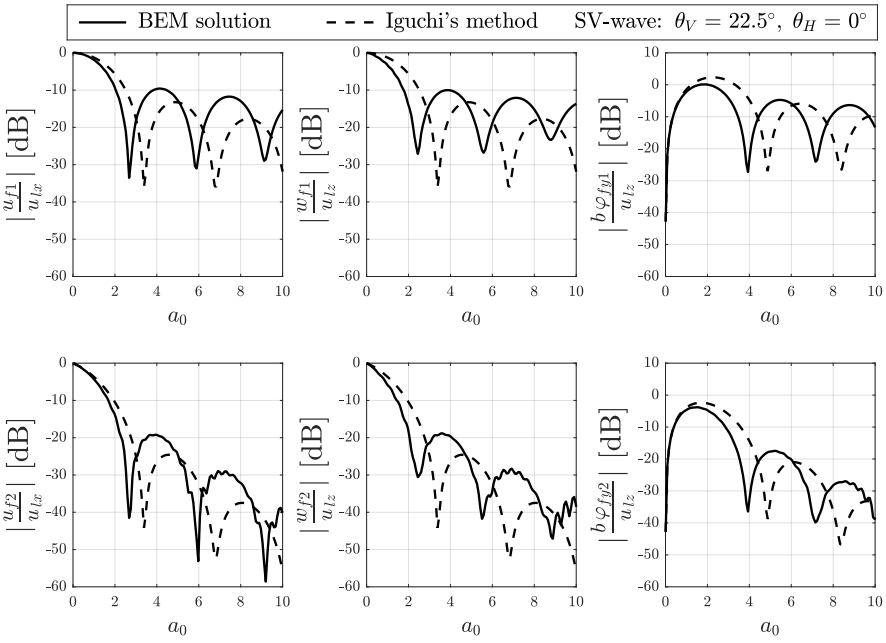


Figure 9: Results for the horizontal u_f, vertical w_f and rocking φ_{fy} response of two square, surface rigid footings on an elastic layer, representing a flexible foundation, resting on a homogeneous and elastic half-space subjected to incoming plane SV-waves at $\theta_V = 22.5°$ and $\theta_H = 0°$. The centre-to-centre distance of the rigid footings is set to $d = 20\,b$. Comparison is made for the magnitude of the response for the upstream (top) and downstream (bottom) footing between the results obtained with the rigorous solution (BEM - 8x8 quadratic elements for each foundation) and those obtained with Iguchi's method.

This is evident in Figure 9, which shows the response of two squared rigid footings at a distance $d = 20\,b$ to incoming plane SV-wave at $\theta_V = 22.5°$. This represents a more realistic scenario for common building typologies (e.g. reinforced concrete buildings). From the results in Figure 8 and 9, it is possible to acknowledge the influence of the rigid footings assumption, whenever can be deemed valid, with an order of 0-20 dB reduction of the vibration levels depending on the specific incoming wavefield.

5 Conclusions

This paper has presented a general overview of the response of surface foundations to incoming wavefields with the application to ground-borne vibration. Iguchi's method has been reviewed and adopted as a simplified procedure for the response of rigid foundations resting on the ground and subjected to incoming wavefields. Both the case of rigid foundations resting directly on the ground or rigid footings on a flexible foundation resting on the ground have been considered. The simplified procedure aims at obtaining approximate transfer functions between the *free-field vibration* amplitude of the ground as a homogeneous and elastic half-space subjected to incoming plane wavefields, and the *free-surface vibration* amplitude at the foundation level. The rigid foundations and/or footings are representative of rigid regions for the subsequent coupling of a portal-frame building.

Iguchi's method holds favourable agreement with rigorous solutions for the response of adjacent rigid foundations, even for relatively short centre-to-centre distances between the foundations and for typical soil properties (as in Table 1). The agreement is, in general, less satisfactory in the case of adjacent rigid footings with relatively short centre-to-centre distances. This is probably due to the interaction of the rigid footings

through the elastic layer representing the concrete slab. However, considering more realistic values for the centre-to-centre distance between the footings, typical of common building typologies (e.g. reinforce concrete buildings), the effect of the through-slab coupling between adjacent footings may be less significant.

Acknowledgements

The authors wish to thank Prof. Geert Degrande and colleagues in KU Leuven for providing the EDT and BEMFUN Toolbox and the industrial partner WSP for providing the funding for the research.

A Reference data

Footing	Area	$A_f = 0.25$ m^2	**Slab**	Young's Modulus	$E_c = 3 \text{ x } 10^{10}$ N/m^2
	half-width	$b = 0.25$ m		Density	$\rho_c = 2400$ kg/m^3
				Poisson ratio	$\nu_c = 0.15$
				thickness	$h_f = 1.5$ m
				Damping loss factor	$\eta_c = 0.1$
Soil	Shear wave velocity	$V_s = 200$ m/s			
	Poisson ratio	$\nu_s = 1/3, \underline{0.49}$			
	Density	$\rho_s = 1980$ kg/m^3			
	Damping loss factor	$\eta_s = 0.03$			

Table 1: Reference data for the soil and the foundation properties

REFERENCES

[1] D. P. Connolly, G. Kouroussis, O. Laghrouche, C. L. Ho, and M. C. Forde, "Benchmarking railway vibrations - Track, vehicle, ground and building effects," *Constr. Build. Mater.*, vol. 92, pp. 64–81, 2014.

[2] G. Lombaert, G. Degrande, S. François, and D. J. Thompson, "Ground-borne vibration due to railway traffic: A review of excitation mechanisms, prediction methods and mitigation measures," *Notes Numer. Fluid Mech. Multidiscip. Des.*, vol. 126, pp. 253–287, 2015.

[3] P. Alves Costa, R. Calçada, and A. Silva Cardoso, "Ballast mats for the reduction of railway traffic vibrations. Numerical study," *Soil Dyn. Earthq. Eng.*, vol. 42, pp. 137–150, 2012.

[4] J. P. Talbot, "Lift-over crossings as a solution to tram-generated ground-borne vibration and re-radiated noise," *Proc. Inst. Mech. Eng. Part F J. Rail Rapid Transit*, vol. 0, no. 0, pp. 1–9, 2013.

[5] P. Coulier, V. Cuéllar, G. Degrande, and G. Lombaert, "Experimental and numerical evaluation of the effectiveness of a stiff wave barrier in the soil," *Soil Dyn. Earthq. Eng.*, vol. 77, pp. 238–253, 2015.

[6] J. P. Talbot, "Base-isolated buildings: towards performance-based design," *Proc. Inst. Civ. Eng. - Struct. Build.*, pp. 1–9, 2016.

[7] J. T. Nelson and W. E. Blazier, Jr., "Influence of foundation design on environmental vibration," in *Vib. Control Microelectron. Opt. Metrol.* (C. G. Gordon, ed.), vol. 1619, (San Jose, CA, United Sates), pp. 127–135, feb 1992.

[8] B. R. Barben and L. M. Hanagan, "Investigation of a Slab on Grade Supporting Sensitive Equipment," in *Dyn. Civ. Struct. Vol. 4* (F. N. Catbas, ed.), Conference Proceedings of the Society for Experimental Mechanics Series, Cham: Springer International Publishing, 2014.

[9] M. A. Oien, "Steady motion of a rigid strip bonded to an elastic half space," *J. Appl. Mech. - Trans. ASME*, vol. 38, no. 2, pp. 328–334, 1971.

[10] L. Auersch and G. Schmid, "A simple boundary element formulation and its application to wavefield excited soil-structure interaction," *Earthq. Eng. Struct. Dyn.*, vol. 19, pp. 931–947, oct 1990.

[11] L. Tham, J. Qian, and Y. Cheung, "Dynamic response of a group of flexible foundations to incident seismic waves," *Soil Dyn. Earthq. Eng.*, vol. 17, pp. 127–137, feb 1998.

[12] H. L. Wong and J. E. Luco, "Dynamic response of rectangular foundations to obliquely incident seismic waves," *Earthq. Eng. Struct. Dyn.*, vol. 6, no. 1, pp. 3–16, 1978.

[13] M. Iguchi, "An approximate analysis of input motions for rigid embedded foundations," *Trans. Archit. Inst. Japan*, vol. 315, no. 315, pp. 61–75, 1982.

[14] J. Qian and D. E. Beskos, "Harmonic wave response of two 3-D rigid surface foundations," *Soil Dyn. Earthq. Eng.*, vol. 15, no. 2, pp. 95–110, 1996.

[15] M. Iguchi, "An approximate evaluation method of foundation input motions for adjacent embedded foundations," *J. Struct. Constr. Eng. (Transactions AIJ)*, vol. 81, no. 721, pp. 515–523, 2016.

[16] L. Auersch, "Response to harmonic wave excitation of finite or infinite elastic plates on a homogeneous or layered half-space," *Comput. Geotech.*, vol. 51, pp. 50–59, jun 2013.

[17] G. Sanitate and J. P. Talbot, "The influence of slab foundations on ground-borne vibration from railways," *24th Int. Congr. Sound Vib.*, pp. 1–8, 2017.

[18] E. Kausel and J. M. Roesset, "Stiffness matrices for layered soils," *Bull. Seismol. Soc. Am.*, vol. 71, no. 6, pp. 1743–1761, 1981.

[19] M. Schevenels, "Elastodynamics toolbox for matlab," *Civ. Eng.*, no. July, 2010.

[20] "MATLAB 2015a, The MathWorks, Natick, Massachusetts, United States,"

[21] G. Sanitate and J. P. Talbot, "Soil-Structure Interaction and the added-building effect: simplified models for assisting with the prediction of ground-borne vibration in buildings," *25th Int. Congr. Sound Vib.*, pp. 1–8, 2018.

[22] H. L. Wong and J. E. Luco, "Dynamic response of rigid foundations of arbitrary shape," *Earthq. Eng. Struct. Dyn.*, vol. 4, no. 6, pp. 579–587, 1976.

[23] J. Qian, L. Tham, and Y. Cheung, "Dynamic analysis of rigid surface footings by boundary element method," *J. Sound Vib.*, vol. 214, no. 4, pp. 747–759, 1998.

[24] S. François, M. Schevenels, and G. Degrande, "Bemfun: Matlab toolbox for boundary elements in elastodynamics," no. May, 2009.

[25] M. Schevenels, S. François, and G. Degrande, "EDT: An ElastoDynamics Toolbox for MATLAB," *Comput. Geosci.*, vol. 35, no. 8, pp. 1752–1754, 2009.

[26] R. L. Kuhlemeyer and J. Lysmer, "Finite element method accuracy for wave propagation problems," *J. Soil Mech. Found. Div.*, vol. 99, no. SM5, pp. 421–427, 1973.

[27] J. Lysmer, T. Udaka, C.-F. Tsai, and H. B. Seed, "FLUSH - a computer program for approximate 3D analysis of soil-structure interaction problems," tech. rep., Earthquake Engineering Research Center, 1975.

[28] P. Coulier, G. Lombaert, and G. Degrande, "The influence of source-receiver interaction on the numerical prediction of railway induced vibrations," *J. Sound Vib.*, vol. 333, no. 12, pp. 2520–2538, 2014.

[29] S. A. Thau, "Radiation and Scattering From a Rigid Inclusion in an Elastic Medium," *J. Appl. Mech.*, vol. 34, no. 2, p. 509, 1967.

[30] A. L. Pais and E. Kausel, "On rigid foundations subjected to seismic waves," *Earthq. Eng. Struct. Dyn.*, vol. 18, no. 4, pp. 475–489, 1989.

[31] F. Fahy and P. Gardonio, "Sound and Structural Vibration," in *Radiation, Transm. Response*, Elsevier, 2007.

Influence of transverse bracing beams on the dynamic behaviour of Arroyo Bracea I bridge in Madrid-Sevilla High-Speed railway line

E. Moliner [1], **P. Galvín** [2], **M.D Martínez-Rodrigo** [1], **A. Romero** [2]
[1] Universitat Jaume I, Department of Mechanical Engineering and Construction,
Avda Sos Baynat S/N, 12071, Castellón, Spain
e-mail: **molinere@uji.es**

[2] Universidad de Sevilla, School of Engineering,
Camino de los descubrimientos S/N, 41092, Sevilla, Spain

Abstract
In this contribution the dynamic response of a short simply-supported girder bridge belonging to a High-Speed railway line is analysed with the aim of evaluating the influence of a proper modelling of decks with a significant participation of modes different from the longitudinal bending one (torsion, transverse bending) and also the influence of the transverse beams usually present at the supports position bracing the longitudinal girders of the deck. The numerical results will be compared with the measurements from an experimental campaign in terms of frequencies, mode shapes and deck vertical acceleration response. Additionally, a representative ensemble of girder bridges has been studied to numerically evaluate the influence of the deck characteristics (deck skewness, span length and flexibility of the neoprene bearings) on the effect of the bracing beams.

1 Introduction

The increase of the operating train velocity with the advent of the modern railway transport systems can entail harmful consequences on the railway infrastructures, since the resonance effects caused by the trains at circulating speeds above 200 km/h can induce inadmissible levels of vertical acceleration on the railway bridge decks. In this regard short-to-medium span simply supported (SS) bridges are especially critical, due to their low mass and structural damping [1, 2] and therefore, the Serviceability Limit State of vertical acceleration prescribed by The European Standard Eurocode (EC) ([3]), limited to 3.5 m/s^2 for ballasted tracks, is one of the most demanding specification for the design or upgrading of these structures. Therefore the development of accurate numerical models able to realistically predict the dynamic response of the structure with a reasonable computational cost becomes crucial.

Traditionally planar numerical SS beam models and other numerical methods based on Bernoulli-beam theory have been quite popular in literature due to their low computational costs, however they are only valid for bridges with a dynamic response mainly governed by the contribution of longitudinal bending modes [4, 5, 6], which could not be the case for skewed or double-track bridges [7]. The quick development of the computational technologies has encouraged the use of more sophisticated three dimensional models, especially for research purposes [8, 9]. Their application to bridge dynamic analysis in engineering consultancies is still less frequent unless a singular structure is designed, since they are a tool to guarantee that the prescriptions of the regulations in force at each particular country are met. In these cases, superfluous refinements are to be avoided.

According to [10] the dynamic response of short-to-medium-span SS bridges is difficult to predict during the design or upgrading stages, due to the uncertain influence of several aspects such as super-structure components (rails, ballast) or the environment. In this context the calibration of numerical models with experimental measurements becomes an issue and a number of research works on this topic have been presented [11, 12, 13]. The cited studies, performed on bridges of long spans, are focused on the determination of the modal parameters of the structure from ambient or train induced vibrations. The documented experimental campaigns devoted to short SS structures are less common in literature unless a particular behaviour of the bridge is expected, as is the case of portal frames or soil-steel composite railway bridges [14, 15], where the soil-structure interaction effects (SSI) can play an important role.

The authors of the present manuscript have performed in a previous work an experimental campaign on a short SS girder bridge belonging to a High-Speed railway line in Spain (Arroyo Bracea I bridge) [16]. The bridge was chosen due to the high level of obliquity of the deck, with a skew angle of 45°, and due to the main dimensions, with a span length similar to the deck width, which make this structure susceptible of experiencing a dynamic response with a significant contribution of modes different from the ones of a beam-like structure. In the work several FE models which adopt common assumptions in engineering practice are updated with the experimental measurements, showing a reasonable good correspondence in terms of frequencies and mode shapes, and also in terms of the deck vertical acceleration response under the passage of High-Speed trains. However, the calibration of the first torsion mode and other modes with transverse deformation is less accurate. In the authors opinion this could be caused by the presence of transverse beams bracing the longitudinal girders of the deck at the supports position, which were not included in the numerical models.

In the present work the effect of the transverse bracing beams on the dynamic response of the deck is analysed in Arroyo Bracea I bridge. The study is extended to an ensemble of SS girder bridges of short-to-medium spans, in a view to evaluate how several aspects such as the span length, deck stiffness and flexibility of the elastomeric bearings at the supports, can influence the effect of the transverse bracing beams on the dynamic response, with the main purpose of contributing to the development and validation of safe an accurate numerical models useful for practical applications.

2 Case studies: SS girder bridges

2.1 Arroyo Bracea I bridge

This bridge belongs to the first High-Speed railway line opened in Spain in 1992, Madrid-Sevilla. The structure is a double ballasted track railway bridge composed by two identical SS bays with a span length of 15.25 m, and crosses the Bracea stream with a 45° skew angle. As can be seen in Figure 1 each deck consists of a 25 cm thick, 11.6 m width concrete slab resting over five prestressed concrete longitudinal I girders. The girders rest on the supports through laminated rubber bearings. As per the substructure, the bridge deck is supported on reinforced concrete abutments in its outermost sections and on a pile foundation in the inner ones. At the supports position, the ends of the longitudinal girders are tied one another with a cast-in-situ transverse bracing beam.

As regards the railway track, the rails have a UIC60 cross section and are supported by rail pads and fixed with clips on monoblock concrete sleepers with a spacing of 0.6 m, The monoblock sleepers are 2.60 m long, 0.30 m wide at the base and 0.24 m high, the total mass being 533 kg/m along each of the two tracks.

On the 22^{nd} and the 23^{rd} of July 2016 the authors performed an experimental campaign on this bridge, which included a dynamic characterisation of the soil and of the structure. A detailed description of the experimental tests can be found in [16]. As regards the structure, the acceleration response was measured at 11 points of the lower flange of the pre-stressed concrete girders (points 1-11 in Figure 2) and at the pile abutment upper horizontal surface close to the girders support (point 12 in Figure 2), using Endevco model 86 piezoelectric accelerometers. The sensors, with a nominal sensitivity of 1000 mV/g and a low frequency

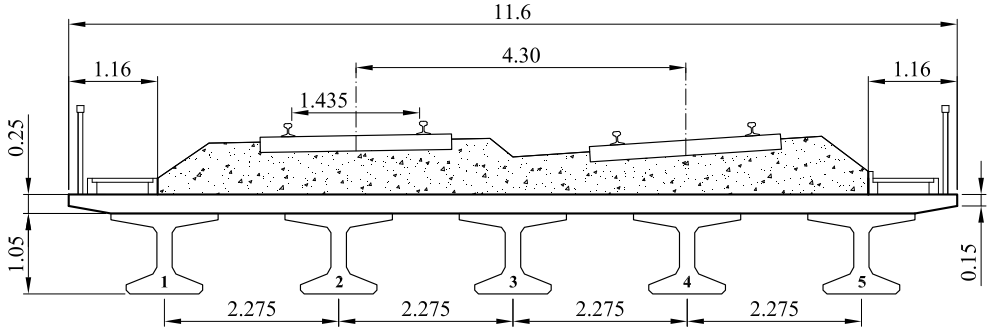


Figure 1: Deck cross section of Arroyo Bracea I bridge (Units [m]).

limit of 0.1 Hz, were attached to the lower flange of the girders using circular aluminium plates of 0.09 m diameter and 0.006 m thickness, glued with epoxy resin.

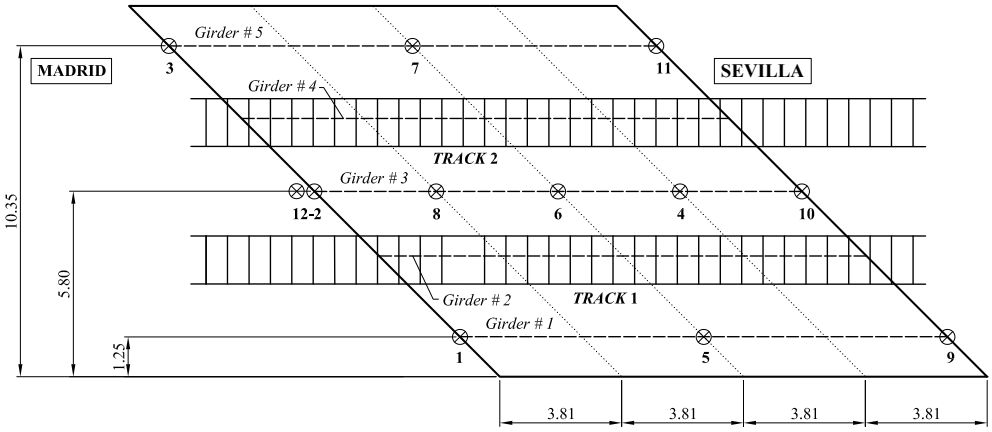


Figure 2: Sensor location.

The ambient vibration response was acquired in 4184 s per channel, and the signals were decimated by 16 to carry out data analysis in the frequency range of interest 0-30 Hz. Also two third-order Chebyshev filters with high-pass and low-pass frequencies of 1 Hz and 30 Hz were applied to the signals. From these data five modes were identified, which correspond to the first longitudinal bending, first torsion and first transverse bending mode shapes. Table 2 and Figure 6 show, respectively, the identified frequencies and mode shapes.

2.2 Representative ensemble of girder bridges

Apart from Bracea I bridge, a representative ensemble of girder bridges, covering the range of span lengths [10 25] m and with slenderness ratio (depth/span) lower than 1/13, has been dimensioned to numerically evaluate the influence of the span length and other bridge properties on the effect of the transverse bracing beams. Figure 4 shows a general cross section of the decks, where the main dimensions h, d_g and h_g and other mechanical properties are provided in Table 1.

The first row of Table 1 corresponds to the mechanical properties of Bracea I bridge after performing a model updating in terms of frequencies and mode shapes with the measurements of the experimental setups. For each span length a different number of longitudinal girders N_g is considered and also several stiffness ratios L/δ (span length/maximum vertical displacement under static UIC-71 train loading [17]) in the range 2000-4000, which is the stiffness ratio usually found in girder bridges belonging to conventional and high-speed lines. Additionally, each deck will be calculated considering rigid supports $k_{v,dyn}$=rigid and also considering



Figure 3: Accelerometers setup.

the flexibility of the laminated rubber bearings as a vertical stifness $k_{v,dyn}$. Furthermore, two different levels of deck skewness will also be considered, 0° and 45°.

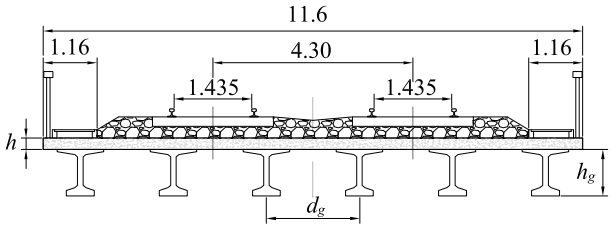


Figure 4: Cross section of the girder bridges of study.

3 Numerical model

A finite element (FE) model which adopts common assumptions in engineering practice has been implemented in the commercial code ANSYS to numerically evaluate the dynamic behaviour of the girder bridges (see Figure 5). The main features are the following: (i) the upper slab deck behaviour is simulated by means of and isotropic thin place discretised in shell elements with 6 degrees of freedom (dof) per node; (ii) different mass density elements are defined in order to concentrate the weight of the ballast, sleepers and rails over the central portion of the plate; (iii) the longitudinal girders and the transverse bracing beams located at the abutment position are included in the model as beam elements with 6 dof per node; (iv) The longitudinal girder nodes are connected to the upper plate by means of rigid kinematic constraints that couple the dofs of the beam nodes to those of the plate nodes right above them, and also the same constraints are used to link the transverse bracing beams to the upper slab and also to the end nodes of the longitudinal girders; (v) the laminated rubber bearings of the bridge are introduced in discrete positions by means of longitudinal springs with vertical stiffness $k_{v,dyn}$; (vi) a point load model is adopted for the railway excitation, therefore neglecting vehicle-structure interaction effects; (vii) the dynamic equations of motion are transformed into modal space and numerically integrated by the Newmark-Linear Acceleration algorithm.

Bridge	Slab		Girders					Mass	Supports	L/δ
	h (m)	E (Pa)	N_g	d_g (m)	h_g (m)	I_h(m^4)	E (Pa)	(kg/m)	$k_{v,dyn}(N/m)$	
Bracea I	0.27	3.99E10	5	2.275	1.05	0.08802	4.59E10	28355	1.4E9	3847
L=10 m	0.25	3.34E10	5	2.275	0.6	0.01098	3.85E10	19066	rigid, 9.7E8	2049
	0.22	3.34E10	6	2.0	0.6	0.01098	3.85E10	18765	rigid, 8.34E8	2119
	0.25	3.34E10	5	2.275	0.65	0.02150	3.85E10	21395	rigid, 1.57E9	3320
	0.22	3.34E10	6	2.0	0.65	0.02150	3.85E10	21560	rigid, 1.47E9	3740
L=12.5 m	0.25	3.34E10	6	2.0	0.8	0.02278	3.85E10	19995	rigid, 7.56E8	2229
	0.22	3.34E10	5	2.275	0.85	0.04446	3.85E10	21542	rigid, 1.60E9	3607
	0.22	3.34E10	6	2.0	0.85	0.04339	3.85E10	22100	rigid, 1.31E9	3560
L=15 m	0.22	3.34E10	5	2.275	1.05	0.03703	3.85E10	19485	rigid, 8.93E8	2154
	0.25	3.34E10	6	2.0	1.0	0.03961	3.85E10	20355	rigid, 7.44E8	2154
	0.25	3.34E10	5	2.275	1.05	0.08258	3.85E10	23221	rigid, 1.54E9	3710
	0.25	3.34E10	6	2.0	1.05	0.07423	3.85E10	23510	rigid, 1.26E9	3657
L=17.5 m	0.25	3.34E10	5	2.275	1.2	0.09131	3.85E10	22018	rigid, 9.89E8	2506
	0.25	3.34E10	6	2.0	1.2	0.06195	3.85E10	20715	rigid, 6.88E8	2090
	0.25	3.34E10	5	2.275	1.25	0.11476	3.85E10	22745	rigid, 1.22E9	3079
	0.25	3.34E10	6	2.0	1.25	0.11476	3.85E10	24050	rigid, 1.01E9	3495
L=20 m	0.25	3.34E10	5	2.275	1.4	0.13457	3.85E10	22393	rigid, 9.26E8	2441
	0.25	3.34E10	6	2.0	1.4	0.09029	3.85E10	21075	rigid, 6.42E8	2031
	0.25	3.34E10	5	2.275	1.45	0.17098	3.85E10	23896	rigid, 1.27E9	3387
	0.25	3.34E10	6	2.0	1.45	0.16571	3.85E10	24590	rigid, 1.06E9	3351
L=22.5 m	0.25	3.34E10	5	2.275	1.6	0.18768	3.85E10	24590	rigid, 8.72E8	2383
	0.25	3.34E10	6	2.0	1.6	0.18768	3.85E10	24078	rigid, 8.27E8	2717
	0.25	3.34E10	5	2.275	1.65	0.23652	3.85E10	24396	rigid, 1.18E9	3387
	0.25	3.34E10	6	2.0	1.65	0.22778	3.85E10	25130	rigid, 9.85E8	3223
L=25 m	0.25	3.34E10	5	2.275	1.7	0.21812	3.85E10	22956	rigid, 7.26E8	2037
	0.25	3.34E10	6	2.0	1.7	0.21812	3.85E10	24303	rigid, 6.89E8	2320
	0.25	3.34E10	5	2.275	1.85	0.131500	3.85E10	24896	rigid, 1.11E9	3126
	0.25	3.34E10	6	2.0	1.85	0.16087	3.85E10	25670	rigid, 9.23E8	3106

Table 1: Main properties of the girder bridges of study

4 Results

4.1 Dynamic behaviour of Arroyo Bracea I bridge

In the following subsections the results of the experimental campaign performed on Bracea I bridge and the comparison with the numerical predictions are shown and discussed.

4.1.1 Natural frequencies and mode shapes

The experimental campaign performed in July 2016 allowed the identification of the modal parameters of the bridge from ambient vibration by state-space models using MACEC software [18]. Table 2 shows the identified natural frequencies for the first five modes (f_{exp}), where the lowest ones in frequency order correspond to the first longitudinal bending, first torsion and first transverse bending mode shapes. The Modal Phase Collinearity (MPC) provided in Table 2 shows the consistency of the identified structural modal parameters, with values higher than 0.95.

This table also shows the numerical natural frequencies provided by the updated FE model using two approaches: neglecting the beam elements used for the transverse bracing beams of the bridge (f_{num}) and

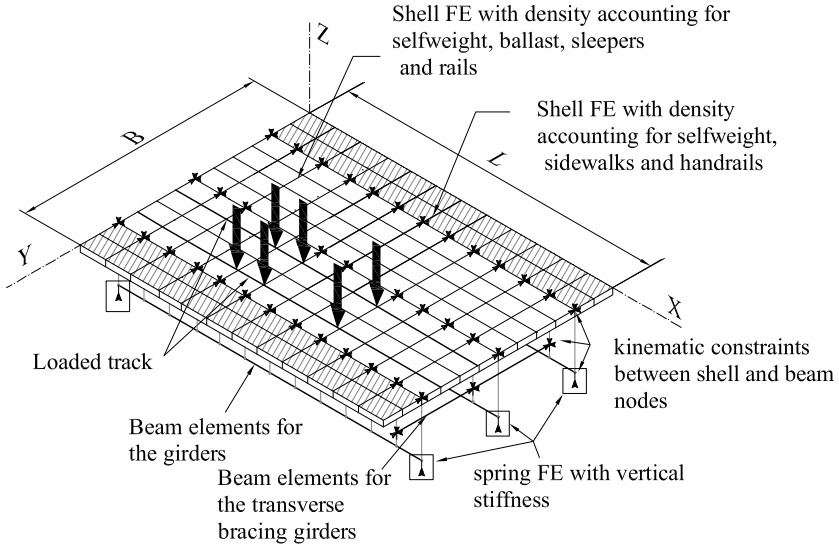


Figure 5: FE model.

including them as commented in section 3, ($f_{num,brace}$). The Modal Assurance Criterion (MAC), which is a measure of the level of correspondence between the experimental and numerical mode shape, is also provided. MAC values vary from 0 to 1, where MAC=1 implies perfect correlation between the compared mode vectors.

	f_{exp} (Hz)	MPC (-)	f_{num} (Hz)	$f_{num,brace}$ (Hz)	MAC$_{exp,num}$ (-)	MAC$_{exp,brace}$ (-)
1	9.25	0.99	9.13	9.13	0.95	0.96
2	10.63	0.97	9.86	10.17	0.93	0.93
3	12.75	0.99	11.83	12.81	0.95	0.96
4	17.92	0.99	16.71	18.89	0.96	0.95
5	24.57	0.99	24.62	28.12	0.98	0.96

Table 2: Experimental and numerical natural frequencies, AutoMAC and MPC values.

As can be seen the correspondence between the experimental measurements and the numerical predictions is reasonably accurate with both numerical approaches in terms of frequencies and mode shapes. The presence of the transverse bracing beams in the numerical model is especially affecting the frequencies of the modes with significant transverse deformation (all the modes different from the first one), leading to an increment of them. As a result, the numerical model that neglects the transverse bracings predicts the deck natural frequencies with errors lower than 8% for the first five modes. However, in the model with transverse beams the errors are lower than 6% for the first four ones, since the prediction of the second and third frequencies corresponding to the first torsion and first transverse bending mode are significantly improved. Conversely, the prediction of the fifth natural frequency worsens with respect to the model without transverse bracings.

The experimental and numerical mode shapes for the first five modes are plotted in Figure 6. In this case the influence of the transverse bracing beams is almost negligible, as can be derived from the observation of the MAC values, due to the discrete position of these elements that are only present along the deck edges at the supports. Both numerical approaches provide MAC values higher than 0.95 for all the modes different from the first torsion one, in which the MAC value attains 0.93 and is not improved by the presence of the transverse bracing system in the FE model.

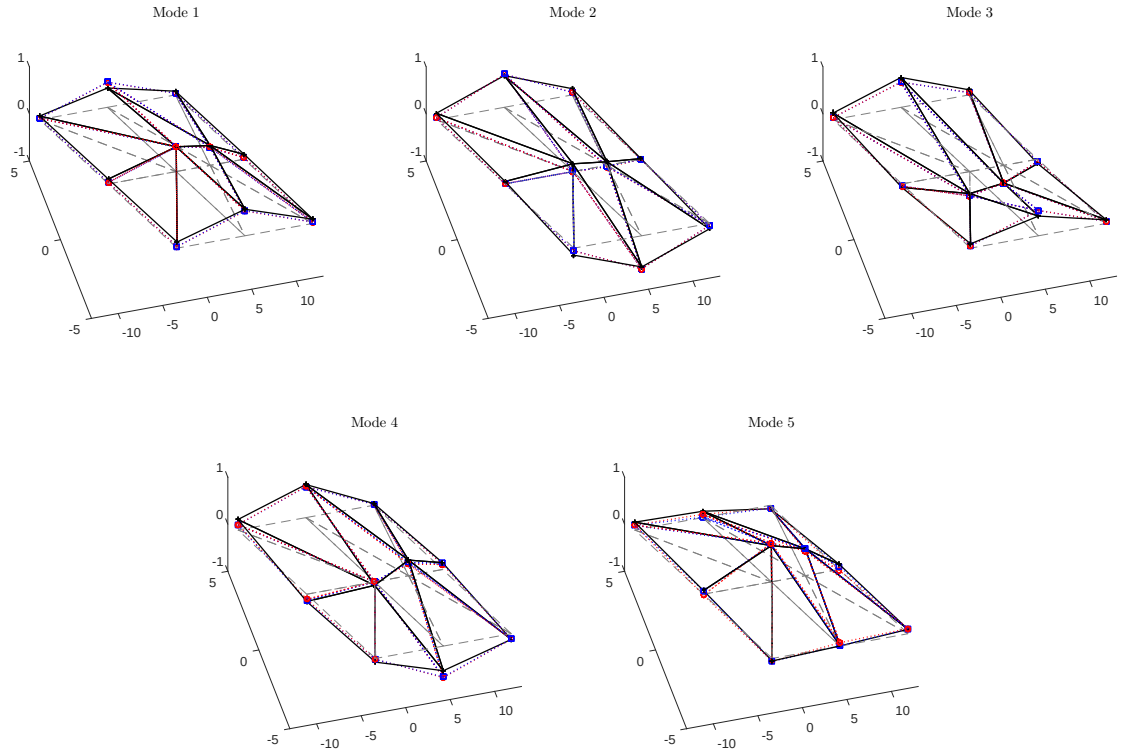


Figure 6: Experimental (black solid line) vs. numerical with transverse bracing beams (red dotted line) and numerical without transverse bracing beams (blue dotted line) first five identified mode shapes. Undeformed shape (dashed grey line).

4.1.2 Bridge response under High-Speed traffic

During the experimental campaign several trains crossed Bracea I bridge with circulating velocities in the range [100 280] km/h. In what follows the experimental and numerical vertical acceleration response of the deck due to the circulation of two of these trains, RENFE Class 103 (ICE 3 or S103) and 130 (Talgo 250 or S130), is shown and discussed. S103 and S130 have been chosen in this work due to their speeds of circulation along the structure. The circulating velocity of S103 is 279 km/h, which is very close to the theoretical third resonance speed of the fundamental mode (275 km/h); and S130 circulates at 247 km/h, which is also close to a second resonance speed of one of the modes more affected by the transverse bracing beams, the second mode (251.4 km/h).

RENFE Class 103 is a train with distributed traction, with powered bogies located in alternate carriages, being the coach distribution a-6xb-a (eight cars, with an integrated driver and passenger car at each end). Renfe Class 130 has two power cars, with a coach distribution L-a-9xb-a-L. Figure 7 shows the axle schemes and coach distribution of both trains.

Figures 8 and 9 show, respectively the vertical acceleration response under the passage of S103 and S130 trains at different points of the deck, corresponding to point 5 (mid-span girder number 1), 6 (mid span girder number 3) and 10 (second abutment girder number 3). The response is plotted in the time domain (first row of the figures) and frequency domain (last row of the figures). In all the plots the experimental response is represented in solid black trace, the predictions without transverse bracing beams in blue, and the numerical response including the transverse bracing beams in red colour. The measurements and predictions at point 5 are shown in the first column of the figures, the results at point 6 in the second column and the response at point 10 in the third one.

As expected the dynamic response of the structure is caused by different mode contributions apart from the longitudinal bending one, due to the length to width aspect ratio of the bridge and the skewness, that make



Renfe Class 103



Renfe Class 130

Train	Renfe S103						Renfe S130		
	d [m]	***P*** [kN]		***d*** [m]	***P*** [kN]		***d*** [m]	***P*** [kN]
Axle 1	3.51	147.2	**Axle 21**	4.9	145	**Axle 1**	4.4	180
Axle 2	2.5	147.2	**Axle 22**	2.5	145	**Axle 2**	2.8	180
Axle 3	14.875	141.4	**Axle 23**	14.875	154.7	**Axle 3**	7.85	180
Axle 4	2.5	141.4	**Axle 24**	2.5	154.7	**Axle 4**	2.8	180
Axle 5	4.9	149.3	**Axle 25**	4.9	154.3	**Axle 5**	6.67	156
Axle 6	2.5	149.3	**Axle 26**	2.5	154.3	**Axle 6**	8.97	161
Axle 7	14.875	148.5	**Axle 27**	14.875	154.6	**Axle 7**	13.14	170
Axle 8	2.5	148.5	**Axle 28**	2.5	154.6	**Axle 8**	13.14	167
Axle 9	4.9	149.4	**Axle 29**	4.9	148.4	**Axle 9**	13.14	159
Axle 10	2.5	149.4	**Axle 30**	2.5	148.4	**Axle 10**	13.14	166
Axle 11	14.875	142.5	**Axle 31**	14.875	153.1	**Axle 11**	13.14	166
Axle 12	2.5	142.5	**Axle 32**	2.5	153.1	**Axle 12**	13.14	170
Axle 13	4.9	133.5				**Axle 13**	13.14	166
Axle 14	2.5	133.5				**Axle 14**	13.14	170
Axle 15	14.875	130.9				**Axle 15**	13.14	166
Axle 16	2.5	130.9				**Axle 16**	8.97	163
Axle 17	4.9	128.8				**Axle 17**	6.67	180
Axle 18	2.5	128.8				**Axle 18**	2.8	180
Axle 19	14.875	135				**Axle 19**	7.85	180
Axle 20	2.5	135				**Axle 20**	2.8	180

Figure 7: Train coach distribution and axle distances

this structure to behave different from that of a beam structure. However, in Figure 8 a predominant mode contribution of the fundamental frequency is clear from the observation of the frequency domain plots, with a very poor contribution of other modes. This is caused by the resonance of the fundamental mode induced by S103 at 279 km/h, which is perceptible in the time-history plot as a progressive increase of the acceleration amplitude. In this particular case, the bridge behaves as a beam-like structure. The circulation of S130 also induces a resonance of the torsion mode, which is also perceptible in Figure 9, but its effects in terms of acceleration amplitudes are less noticeable when compared to the resonance of the fundamental mode. This can be explained due to the presence of a theoretical cancellation speed in the vicinity of the circulation speed of S130 [16].

The numerical predictions are reasonably accurate with both approaches, especially for the sensors located at mid-span (points 5 and 6) and in the frequency range 1-13 Hz, which is the frequency interval of the first three modes of the structure. The frequency peak associated to the excitation and corresponding to the bogie passing frequency (4.5 Hz for S103 in Figure 8 and 5.2 Hz for S130 in Figure 9) is present in all the plots and well predicted by the numerical models. Also the peak corresponding to the contribution of the first mode of the structure, which is more noticeable in Figure 8, is well predicted by both numerical models, as could be expected due to the good correspondence in terms of frequency and MAC value with the experimental measurements. Both models predict the amplitude of this peak with the same level of accuracy, leading to a certain overestimation with respect to the experimental measurements at points 5 and 6, that is more visible in the resonant recordings of Figure 8. The contribution of the torsion mode is also visible both experimentally

and numerically, with the peak amplitude being higher in point 5 of Figure 9. In this recording it can be observed that the numerical model with transverse bracing beams reproduces the frequency and amplitude associated to the torsion mode more accurately than the model without them, which is consistent with the better correspondence in terms of torsion frequency with the experimental measurements.

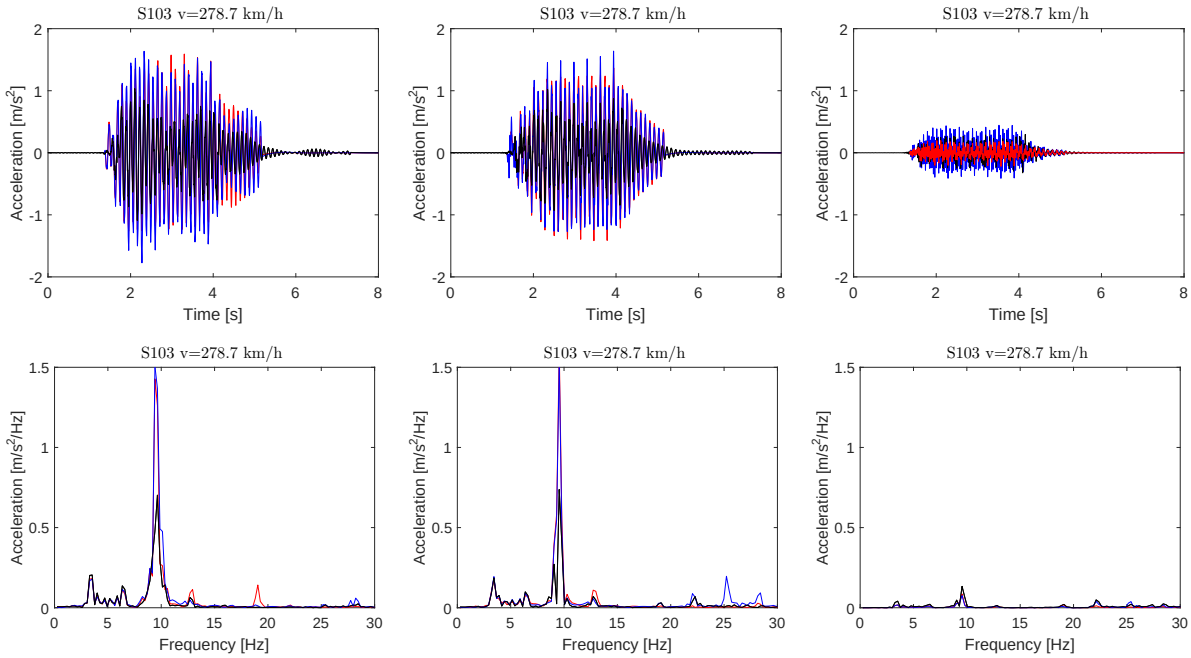


Figure 8: Time history and frequency content of the acceleration at point 5 (left), point 6 (centre) and point 10 (right) induced by S103 Renfe class train: experimental (black line), numerical without transverse bracing beams (blue line) and numerical with transverse bracing beams (red line).

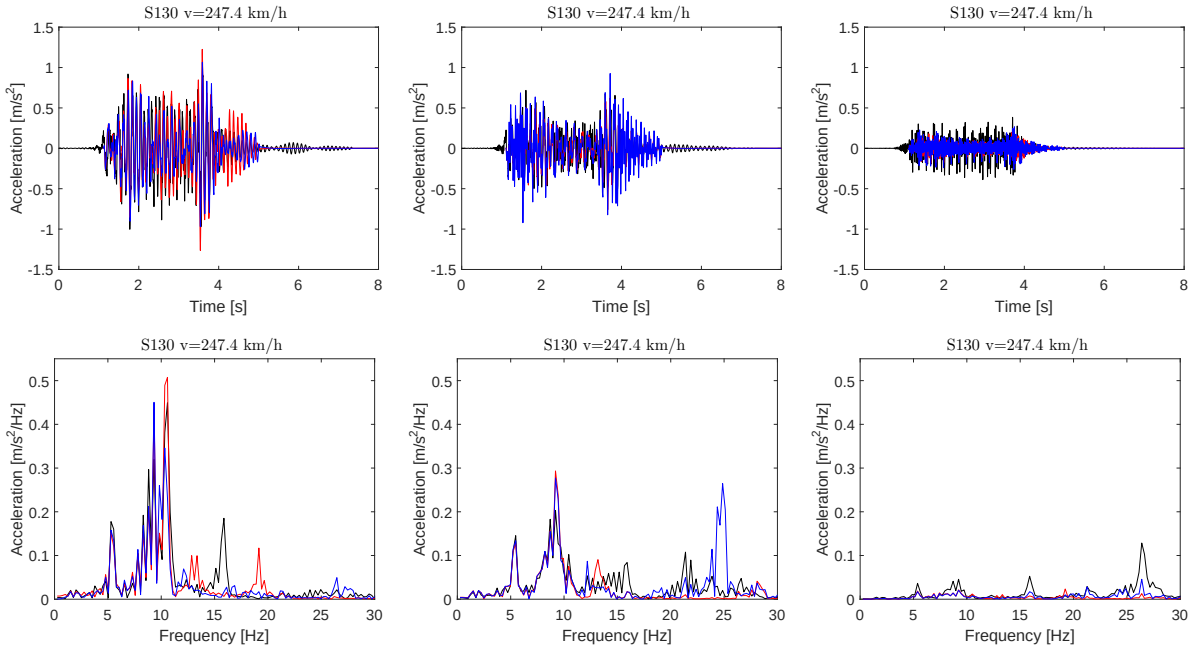


Figure 9: Time history and frequency content of the acceleration at point 5 (left), point 6 (center) and point 10 (right) induced by S130 Renfe class train: experimental (black line), numerical without transvere bracing beams (blue line) and numerical with transverse bracing beams (red line).

The difference between the accuracy of the predictions of the two numerical approaches is minor in the

frequency range 1-13 Hz. The model with bracing beams improves the prediction of the torsion mode contribution and by contrast, however, the predictions at higher frequencies do not appear better than the ones of the model without bracing beams: it is noticeable at point 5 the appearance of a peak at a frequency around 18 Hz predicted by the model with bracing beams that is not present in the experimental response; and conversely, the peak that appears at point 6 at a frequency around 25 Hz with the model without bracing beams is not predicted by the other model nor present in the experimental response.

In general, at the points far from the abutments (points 5 and 6) both numerical models tend to overestimate the dynamic response, as can be derived from the observation of the time-history curves. At the points close to the abutments (point 10) the acceleration response is, in general, underestimated by the numerical models with the exception of the results at point 10 shown in Figure 8, where the acceleration predicted by the model with transverse bracings in the time domain shows a similar amplitude with respect to the experimental response. It can be concluded that the introduction of the transverse bracing beams in the numerical model does not appear to significantly improve the prediction of the vertical acceleration levels in Bracea I bridge.

4.2 Dynamic behaviour of the representative ensemble of girder bridges

In this subsection the dynamic response of the set of girder bridges of Section 2.2 is analysed in a view to evaluate whether the effect of the transverse bracing beams is influenced by other aspects such as the deck stiffness, skewness, number of longitudinal girder beams, the span length or the flexibility of the laminated rubber bearings. With this purpose their natural frequencies and mode shapes are calculated with the numerical model of Figure 5 using also the two approaches already employed with Bracea I: neglecting the transverse bracing beams and including them in the FE model as seen in Figure 5. Additionally, the frequencies and modes have been calculated for two skew angles, 0 and 45°.

Since in this case experimental results are not available to compare with the numerical predictions, the comparison is only made between the results obtained with the two approaches used in the numerical model. The attention is focused on the first three frequencies and mode shapes, since the frequencies of the second and third mode are significantly influenced by the transverse bracing beams.

4.2.1 Natural frequencies and mode shapes

First of all, in Figure 10 the fundamental frequency f_1 of all the bridges of study, which corresponds to the first longitudinal bending mode, is presented as a function of the span length. As can be seen, all the values are enclosed by the two solid black lines that represent the frequency band of EC, which entails that at speeds lower than 200 km/h significant vibrations are not expected.

Figures 11 and 12 show the differences in terms of frequency in the prediction of the first three modes of the bridges, corresponding to the first longitudinal bending, first torsion and first transverse bending mode. This difference is defined as (Equation (1))

$$\text{Diff } f_i(\%) = \frac{f^i_{num,brace} - f^i_{num}}{f^i_{num}} \cdot 100, \tag{1}$$

where *i* is the mode number. In both figures the markers in grey correspond to bridges with a stiffness ratio L/δ in the range 2000-3000, which is an usual ratio for girder bridges belonging to conventional railway lines. The results in black correspond to stiffness ratios between 3000-4000, which is more common in high-speed lines. Bracea I bridge belongs to this category, with L/δ= 3847. Furthermore, the square marker has been assigned to bridges with N_g= 6 longitudinal girders, whereas the diamonds correspond to bridges with N_g= 5. For a better visualisation, note that the scale of the vertical axes changes for each mode.

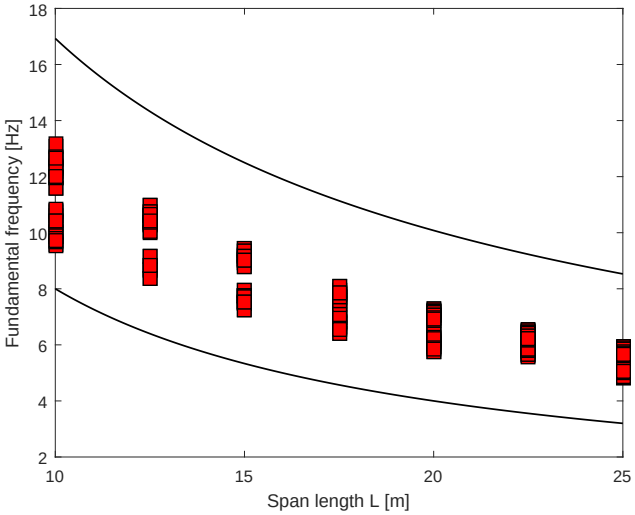


Figure 10: First natural frequency of the bridges of study versus their span length

Figure 11 shows the results obtained when considering rigid supports (i.e. the flexibility of the laminated rubber bearing is not included in the numerical model) in the girder bridges. The plots on the top of the figure correspond to non-skewed decks, while the plots of the bottom to decks with 45° skew angle. In Figure 12 the results considering the vertical stiffness of the laminated rubber bearings are shown; a new marker in red appears that corresponds to the results of Bracea I bridge.

As can be seen from the plots, the presence of transverse bracing beams leads, in general, to an increment of the natural frequencies of the deck. This increment of the frequencies is more noticeable for the modes with significant transverse bending, such as the first torsion mode and the first transverse bending mode, where the differences may attain values up to 15% for the frequency of the third mode. For the fundamental mode the effect of the transverse bracing beams is less noticeable, with maximum differences lower than 2% and also some negative differences have been measured specially for the bridges with elastic supports shown in Figure 12.

Additionally, the results show that effect of the transverse bracing beams on the prediction of the natural frequencies of the first two modes (longitudinal bending and first torsion) appears to be more significant for the skewed decks and the shortest spans (L= 10 m). The highest differences in these bridges have been found for the stiffness ratio L/δ in the range 2000-3000 and with the lower number of longitudinal beams, with values that attain 1.2% and 5.8% for the frequencies of the first and second mode, respectively. However, as regards the third mode, this tendency is only observed for the bridges with rigid supports (Figure 11), where the maximum difference attains 10.8% for the shortest span.

Finally, the influence of the vertical stiffness of the laminated rubber bearings $k_{v,dyn}$ on the differences in the frequency prediction caused by the transverse bracing beams does not seem an issue. As regards the mode shapes, no results have been shown since the variation of the mode vectors caused by the introduction of the transverse bracing beams in the numerical model is almost negligible, as was also seen in the MAC values of Bracea I bridge shown in Table 2.

5 Conclusions

This work evaluates the influence of the transverse bracing beams, usually present at the supports position in many girder bridges, on the dynamic response of railway girder bridges of short-to-medium span lengths. With this purpose a numerical FE model that adopts common assumptions in engineering practice, where the transverse bracing beams can be introduced, is implemented to predict the dynamic behaviour of several

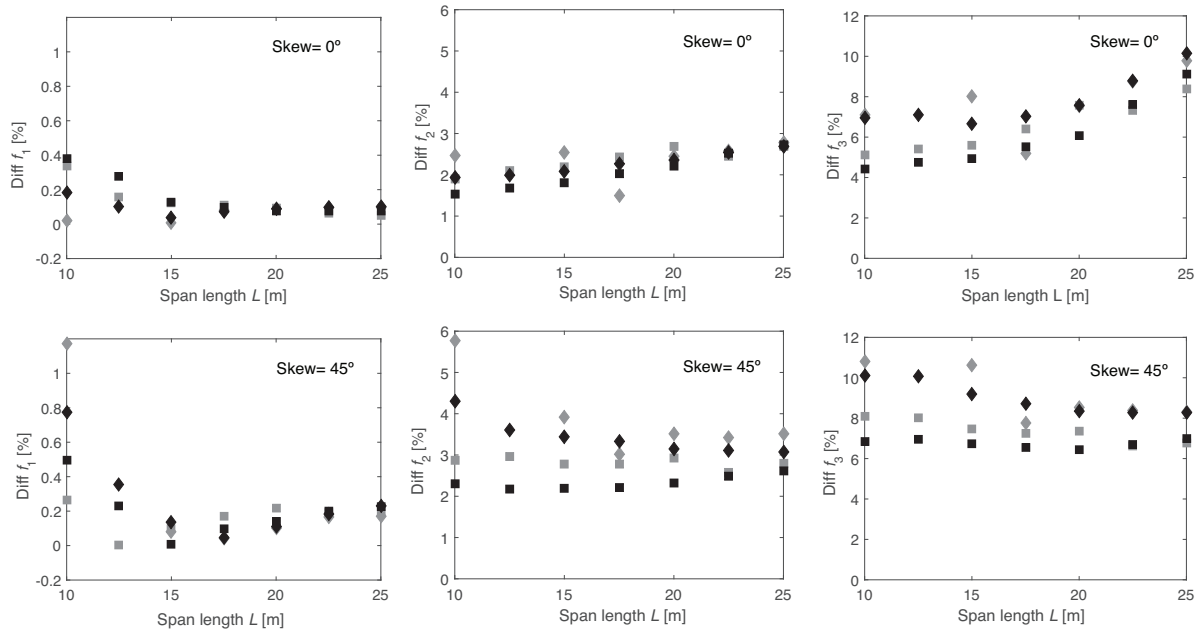


Figure 11: Differences in the prediction of the first three natural frequencies caused by the effect of the transverse bracing beams for the bridges with rigid supports ($k_{v,dyn}$=rigid): results for deck skewness = $0°$ (top), deck skewness = $45°$ (bottom).

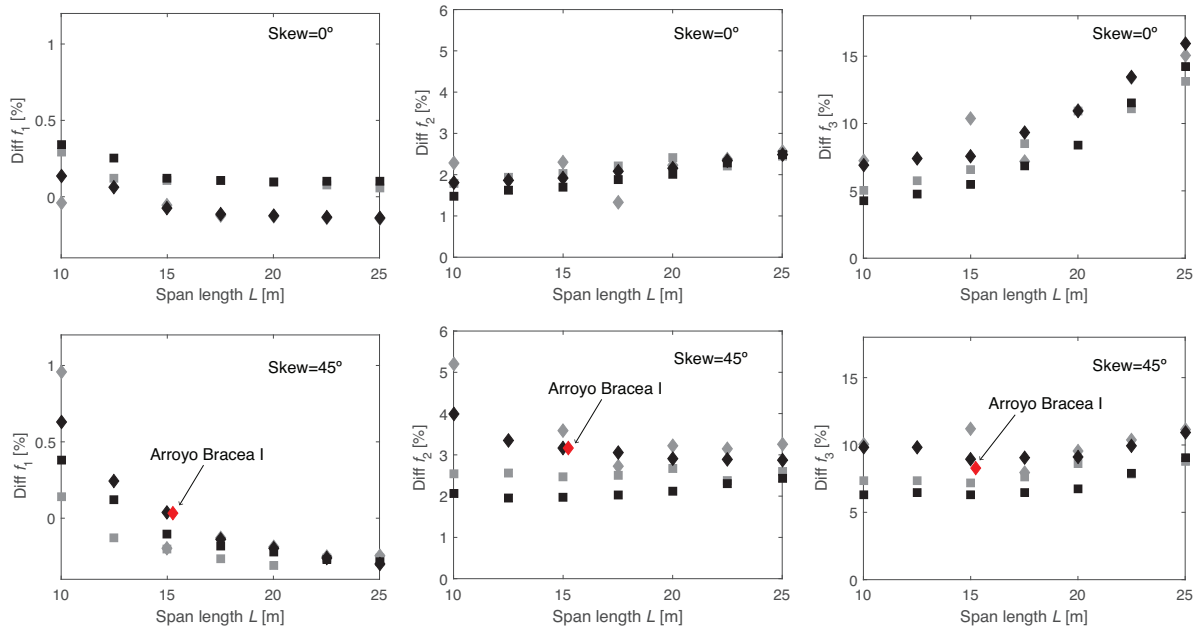


Figure 12: Differences in the prediction of the first three natural frequencies caused by the effect of the transverse bracing beams for the bridges with elastic supports $k_{v,dyn} \neq 0$: results for deck skewness = $0°$ (top), deck skewness = $45°$ (bottom).

bridges of study. The numerical results are compared with the measurements from an experimental campaign performed on a real short simply-supported girder bridge (Arroyo Bracea I bridge) in terms of frequencies, mode shapes and deck vertical acceleration response. Furthermore, in a view to obtain more general conclusions and to evaluate the potential influence of other aspects such as the deck stiffness, skewness, number of longitudinal girder beams, the span length or the flexibility of the laminated rubber bearings on the effect of the transverse bracing beams, the natural frequencies and mode shapes of a representative ensemble of girder

bridges have also been calculated and compared. The following main conclusions are derived:

- The transverse beams bracing the longitudinal girder along the deck edges at the supports position lead to an increment of the natural frequencies of the structure, which is more noticeable for the mode shapes with significant transverse deformation, such as the first torsion mode and the first transverse bending mode.
- Due to the discrete position of the transverse bracing beams in the bridge deck, their effect on the predominant mode shapes of the structure in terms of MAC values is almost negligible.
- Among the different girder bridges that have been analysed, the effect of the transverse bracing beams on the natural frequencies of the first two modes is, in general, more significant for the skewed decks with the shortest spans (L= 10 m), with a stiffness ratio L/δ in the range 2000-3000 and with the lowest number of longitudinal beams. However, this tendency is not clear for the frequency of the third mode since it has only been observed when the flexibility of the laminated rubber bearings is neglected in the numerical model.
- The comparison of the numerical predictions with the results from an experimental campaign performed on a short SS girder bridge (Arroyo Bracea I) has shown that the introduction of the transverse bracing beams in the numerical FE models allows a better calibration of the first torsion and first transverse bending mode of the structure in terms of frequency. However, the level of correspondence with their corresponding experimental mode shapes in terms of the MAC values is almost unaffected. In terms of deck vertical acceleration response, the introduction of the transverse bracing beams in the numerical model does not appear to significantly improve the prediction of the maximum dynamic response when compared to the experimental measurements.

Acknowledgements

The authors would like to acknowledge the financial support provided by (i) the Spanish Ministry of Economy and Competitiveness under the research project [BIA2013-43085-P], (ii) the Andalusian Scientific Computing Centre (CICA) and (iii) Universitat Jaume I under the research project [P1-1B2015-54]. This work falls within the research project BIA2016-75042-C2 financed by the Spanish Ministry of Economy and Competitiveness.

References

[1] ERRI-D-214/RP9, *Ponts Rails pour vitesses > 200km/h. Rapport final*, European Committee for Standardization, Brussels (2000).

[2] L. Frỳba, *Dynamic behaviour of bridges due to high-speed trains*, in *Workshop Bridges for High-Speed Railways, Porto, Portugal, 2004 June*, Porto (2004), pp. 137-158.

[3] CEN, *Eurocode: Basis of structural design. Annex A2: Application for bridges. Final version*, European Committee for Standardization, Brussels (2005).

[4] Y. B. Yang J.D. Yau, L. C. Hsu, *Vibration of simple beams due to trains moving at high speeds*, Engineering Structures, Vol. 19, No. 11, Elsevier (1997), pp. 936-944.

[5] L. Frỳba, *Vibration of solids and structures under moving loads*, Thomas Telford (1999).

[6] C. Johansson, C. Pacoste, R. Karoumi *Closed-form solution for the mode superposition analysis of the vibration in multi-span beam bridges caused by concentrated moving loads*, Computers & Structures, Vol. 119, Elsevier (2013), pp. 85-94.

[7] E.Moliner, M.D. Martínez-Rodrigo, P. Museros, *Dynamic performance of existing double track railway bridges at resonance with the increase of the operational line speed*, Engineering Structures, Vol. 132, Elsevier (2017), pp. 98-109.

[8] Y-S. Lee, S-H Kim, *Structural analysis of 3D high-speed train-bridge interactions for simple train load models*, Vehicle System Dynamics, Vol. 48, 2, Taylor & Francis (2010), pp. 263-281.

[9] W. W. Guo, H. Xia, G. De Roeck, K. Liu, *Integral model for train-track-bridge interaction on the Sesia viaduct: Dynamic simulation and critical assessment*, Computers & Structures, Vol. 112-113, Elsevier (2012), pp. 205-216.

[10] C. Rebelo, L. Simoes da Silva, C. Rigueiro, M. Pircher, *Dynamic behaviour of twin single-span ballasted railway viaducts. Field measurements and modal identification*, Engineering Structures, Vol. 30, Elsevier (2008), pp. 2460-2469.

[11] K. Liu, E. Reynders, G. De Roeck, G. Lombaert, *Experimental and numerical analysis of a composite bridge for high-speed trains*, Journal of Sound and Vibration, Vol. 320, Elsevier (2009), pp. 201-220.

[12] J. Malveiro, D. Ribeiro, R. Calçada, R. Delgado, *Updating and validation of the dynamic model of a railway viaduct with precast deck*, Structure & Infrastructure Engineering, Vol. 10, 11, Taylor & Francis (2014), pp. 1484-1509.

[13] D. Ribeiro, R. Calçada, R. Delgado, M. Brehm, M. Zabel, *Finite element model updating of a bowstring-arch railway bridge based on experimental modal parameters*, Engineering Structures, Vol. 40, Elsevier (2014), pp. 413-435.

[14] M. Ülker-Kaustell, R. Karoumi, C. Pacoste, *Simplified analysis of the dynamic soilstructure interaction of a portal frame railway bridge*, Engineering Structures, Vol. 32, 11 Elsevier (2010), pp. 3692-3698.

[15] P. Mellat, A. Andersson, L. Pettersson, R. Karoumi, *Dynamic behaviour of a short span soil-steel composite bridge for high-speed railways Field measurements and FE-analysis*, Engineering Structures, Vol. 69, Elsevier (2014), pp. 49-61.

[16] P. Galvín, A. Romero, E. Moliner, M.D. Martínez-Rodrigo, *Two $\{FE\}$ models to analyse the dynamic response of short span simply-supported oblique high-speed railway bridges: Comparison and experimental validation*, Engineering Structures, Vol. 167, Elsevier (2018), pp. 48-64.

[17] CEN, EN 1991-2, *Eurocode 1: Actions on Structures - Part 2: Traffic loads on bridges*, European Committee for Standardization, Brussels (2002).

[18] E. Reynders, *System Identification Methods for (Operational) Modal Analysis: Review and Comparison*, Archives of Computational Methods in Engineering, Vol. 19,1, Springer (2012), pp. 51-124.

Specific dynamic response of truss railway bridge identified using operational modal analysis as an extension of typical dynamic load testing

G. Poprawa[1], M. Salamak[1], S. Pradelok[1]
[1]Silesian University of Technology, Faculty of Civil Engineering
ul. Akademicka 5, 44-100, Gliwice, Poland
e-mail: **marek.salamak@polsl.pl**

Abstract
The paper describes the use of operational modal analysis (OMA) as a tool that can contribute to the improvement of quality and unambiguity of results obtained in dynamic load trials that bridge structures are subjected to. Three experiments of varying scope and at various stages of use were carried out on the selected double truss railway bridge. Apart from the effective identification of basic modal parameters, these experiments have revealed the phenomenon of interaction between two trusses supported on common abutments. Dynamic response specific to truss bridges was observed. OMA has confirmed its usefulness in the process of dynamic load testing of a complex railway bridge.

1 Introduction

Dynamic tests in the form of dynamic load trials of newly built bridges are common practice in many European countries. In Poland, the law enforces the dynamic load trials, among others, for all newly constructed steel railway bridges with a theoretical span length of more than 21 m. Dynamic response is particularly important in the case of railway bridges. This is due to the specific load in the form of sets of evenly distributed forces moving with varying, often very high speeds. The most common approach applied to this type of tests, consisting of vibrations forcing with various passages of the heavy locomotive, vibration recording with just a few sensors, and the use of simple signal analysis methods to extract modal data, is unfortunately often insufficient.

The goal of the majority of dynamic bridge tests is to search for information on the modal model of the tested structure in the range of vibration frequencies important for dominant forcing. In the case of simple beam structures, this information can be obtained from recorded free response data gathered using a small number of appropriately located vibration transducers and basic signal processing methods. However, in the case of structures with a complex dynamic response, with high modal density, e.g., trusses, this approach may lead to incorrect identification.

Dynamic testing of responsible structures requires the unambiguity of the results obtained. The specific test conditions described in this contribution allow the use of only Operational Modal Analysis (OMA) [1]. Therefore, the proposed solution for improving the quality of identification of modal parameters in dynamic load tests is the expansion of the measurement chain. Additional transducers for the registration of useful OMA signals are required. This can be done without interfering with the typical dynamic load trial program. Thanks to this approach, the requirements of contemporary tests are still met, and the duration of the experiment is not extended significantly. Therefore OMA can be seemingly integrated into the routine commissioning dynamic trials of newly built and renovated bridges.

Operational modal analysis has been proven in the dynamic studies of many types of complex structures. Especially those where the use of controlled excitations is difficult or very expensive. This group includes building and civil structures [2]. An example of the use of OMA in the study of a railway bridge under normal traffic is described in the paper [3]. Dynamic interaction of two adjacent spans with common ballast

was observed. Another example of dynamic testing of a railway bridge, this time a double track truss railway bridge was studied in [4]. The examined truss had a span of 128.6 m, and the measurements were carried out under the normal traffic. The possibility of conducting tests without the necessity for closing traffic is one of the greatest advantages of OMA.

2 Dynamic load tests of railway bridges

The load tests are a specific form of tests to which newly constructed, modernized or existing bridge structures are subjected. Their goal is to get to know/assess the real behavior of these structures in response to the known load [5]–[8]. Such tests are often part of the commissioning procedures that the bridge must go through before it is put into operation. In the case of railway bridges, they usually consist of two types of tests, static and dynamic.

In a static test, a known load (usually a heavy locomotive or multiple locomotives) is used to induce measurable deflections in the structure. Their measurement serves primarily as indirect verification of the rigidity of the structure. The paper focuses on dynamic load tests. In Poland, a dynamic load test usually consists of a series of passages of a particular type of rolling stock with different gradually increasing speeds. Usually, due to financial constraints, it is the same vehicle that was used in the static load test i.e., one or more heavy locomotives. The speed of the test vehicle starts from the quasi-static one (usually 10 km/h) up to the maximum possible for the available rolling stock. Displacements and accelerations of few representative points of the bridge located usually in the middle of the bridge span are observed. The attempt to identify modal parameters is usually made by the analysis of the free vibration response (after the test vehicle left the structure and its mass is not influencing dynamic response) of the tested bridge. The identification of modal parameters is based on the Spectral Analysis (SA) of registered free response signals. Identified modal parameters in the form of natural frequencies and mode shapes can be used to indirectly verify the Finite Element (FE) model regarding stiffness and mass of the structure. The actual damping properties of the structure can be described by the identified modal damping parameters. Also, during the tests, the relation of the passage speed of the test vehicle to the dynamic response level of the tested span is observed. The primary purposes of the dynamic load trials include:

- identification of modal parameters – natural frequencies, mode shapes and modal damping,
- indirect verification of design assumptions,
- observation of the dynamic response caused by the passing vehicle.

Test loads of new bridges are usually carried out on a track that is under temporary administration of construction company. This involves problems of a formal and technical nature. Usually, at this stage, the railway track is not yet adapted to the target traffic speed. Also, restrictions related to other works carried out on access roads to the bridge may be an issue. Available section of the closed track may be insufficient to achieve the desired speeds of the test vehicle. Therefore, the use of OMA may contribute to the improvement of the quality of such experiments without the need to modify the procedures used so far.

The significant natural frequencies of railway bridges are usually in the range of 0-30 Hz. In case of medium span bridges as one described in this contribution the lower end of the range is the most important. Reliable identification of basic modal parameters is even more important the higher the allowed speed on a given bridge. It stems from the possible problem of resonance of rolling stock traveling with various speeds (being a stream of evenly distributed and rhythmically applied forces) and a bridge [9], [10].

2.1 Selected aspects of Operational modal analysis in dynamic load tests

By using the most significant advantage of OMA that is to use freely available alternate sources of excitation and performing experiment under regular rail traffic goals specified above could be achieved without the necessity for expensive renting of vehicles for dynamic trials. However, infrastructure managers in Poland rarely decide on such a solution. For this reason, work on the use of OMA as an extension of the standard test program without significant interference in contemporary procedures has been undertaken.

It should be remembered that the load tests in Poland are almost routine. Therefore they are often limited by time and financial constraints. The test date must be adapted to the ongoing construction works. Therefore, tests are usually carried out immediately before putting the bridge into operation. In turn, the range of measurements, i.e. number of measurement locations and the duration of the experiment are also limited. This translates, for example, into the fact that experiments with many setups of accelerometers (such as those described in the paper [11]) do not work well in routine dynamic load tests. Single setup experiments are preferred. Single setup experiment should enable unambiguous identification of the most critical modes of vibrations. Renting test vehicles is a significant cost of the static and dynamic trials. The striving to optimize the costs associated with the tests means that there could be several bridges to be tested in one day. This is an additional obstacle to the implementation of time-consuming experiments with many transducer setups, mainly when the measuring system uses standard wired connections. Single setup with a limited number of transducers is the tradeoff between identified modes observability and measurement time (cost).

3 Tested structure



Figure 1: Discussed truss railway bridge

The subject of the described research is a truss railway bridge crossing the Biala River near Tarnow in Poland (Figure 1). This modern truss was built during the modernization of the Third Pan-European corridor: Brussels - Aachen - Cologne - Dresden - Wroclaw - Katowice - Krakow - Lviv - Kiev. The new truss replaced the old deteriorated bridge (an open deck truss with parabolic upper chord). The new commercial speed on the described bridge is 160 km/h. Modernization of the line (also the replacement of civil structures), was carried out with the constant maintenance of rail traffic on one track. It required dividing the construction works into stages. Likewise, commissioning load tests were carried out in stages, the elements of which was the work described in the contribution.

3.1 Structure characteristics

The bridge consists of two steel truss spans; each carries one ballasted railway track (Figure 3). Trusses are supported on common abutments. Beside common supports, the two trusses are in principle independent. They share only small-sized elements supporting inspection ladders (visible in Figure 1). The lower chord, the upper chord, and the extreme diagonals are designed as box cross-sections. The deck is made as a steel-concrete composite. Reinforced concrete deck slab is supported by transverse steel I-beams. The basic dimensions of the structure are shown in Figure 2 and Figure 3.

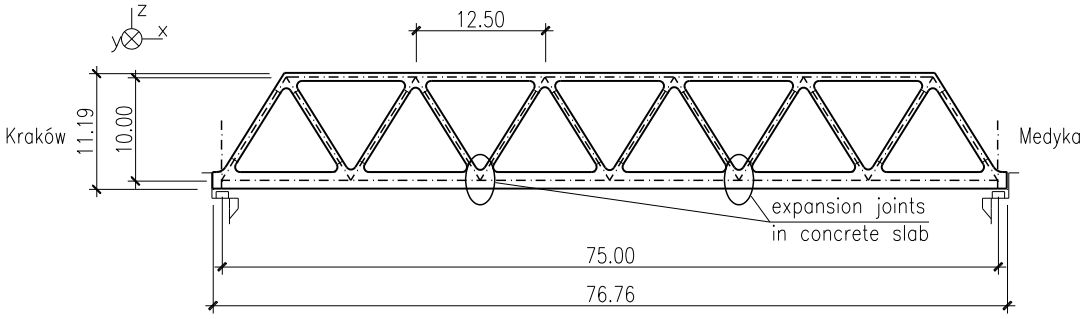


Figure 2: Side view of the analyzed truss

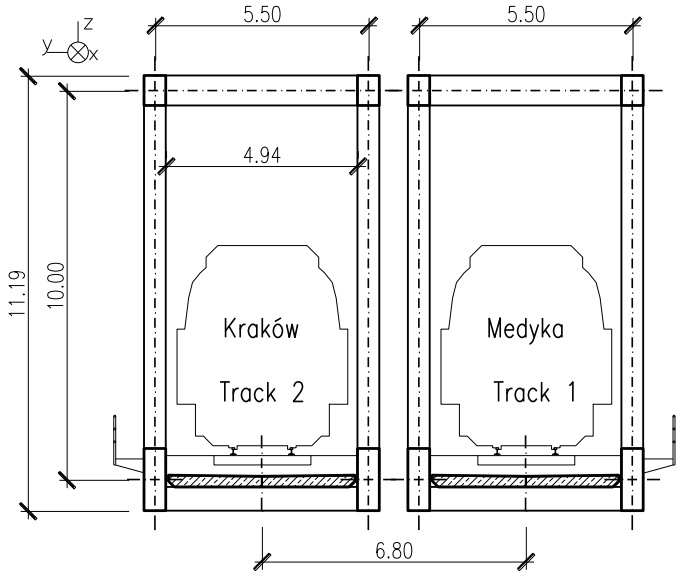


Figure 3: Cross section of analyzed truss

The discussed structure has been subjected to dynamic load tests five times in total (Table 1). The first two experiments (not described in the contribution) were ordinary load tests (as described in pt 2). Three others were supplemented with additional measurements (pt 4) specially selected for the acquisition of time data useful from the OMA perspective.

Order	Structure	Year	Type of test	Description
1	Track 1	2013	SA	A previous experiment with SA
2	Track 2	2014	SA	A previous experiment with SA
3	Track 1	2016	OMA	First OMA experiment (see 4.1)
4	Track 2	2017	OMA	Second OMA experiment (see 4.2)
5	Track 1 and 2	2017	OMA	Third OMA experiment (see 0), additional dynamic trials with faster locomotive

Table 1: Conducted experiments

4 Field tests

Initially, the concrete deck slab was constructed as a continuous element along the entire span. However, it cracked and was leaking, so repair of the slab was requested by the investor. The deck slab was replaced by a new one. Two expansion joints marked in Figure 2 were introduced to the new slab. These structural

changes were the reason for additional load tests, during which OMA was applied. Because OMA was an extension of a typical dynamic load test, standard test program had to be executed. In Table 2 all the trial runs completed during all five experiments are listed. Each of them was conducted at least twice – in both directions.

Order of DLT	Track	Dynamic Load Test trial speed													Type of locomotive
		10	20	30	40	50	60	70	80	100	120	140	160	30b	
SA 1		o		o		o	o							o	Class ST43
OMA 1	1	x	x	x	x	x	x	x	x					x	Class TEM2
OMA 3		x		x		x		x		x	x	x	x		Class EP09
SA 2		o		o		o		o						o	Class TEM2
OMA 2	2	x		x		x		x						x	Class M62
OMA 3		x		x		x		x		x	x	x	x		Class EP09

o – structure before modification of deck slab – typical dynamic load test (Spectral Analysis)

x – structure after modification of deck slab – dynamic load test with additional OMA measurements

Table 2: Summary of the completed trial runs during all conducted Dynamic Load Tests

Additional measurements were to have the least impact on the current approach to this type of tests. In addition to the typical dynamic trail runs (passage of a single locomotive with various speeds – unusable from the perspective of OMA), available sources of excitation forces included the influence of wind (very useful due to developed spatial form of the bridge), pedestrian traffic and the passage of trains on the active track. In the case of each OMA experiment, efforts were made to maximize the length and sustain sufficient quality of recorded time histories of accelerations. Measurements were recorded in the form of long time histories with a duration ranging from 600 to 1800 sec. The research team performing the tests is part of the Bridge Structures Research Laboratory with the ISO/IEC 17025 accredited quality system. The measurements were carried out using the LMS Scadas Mobile Frontend. Accelerations of the superstructure were recorded with piezoelectric accelerometers with a sensitivity of 1 V/g (with simultaneous measurement by 12 to 14 single axis accelerometers). Vertical displacements were recorded with two LVDT linear displacement transducers. The Test.Xpress software was used for the management of the test equipment. For the estimation of modal parameters, a two-step Stochastic Subspace Identification algorithm based on correlation functions (SSI-COR) was used [12].

4.1 First OMA experiment – track 1

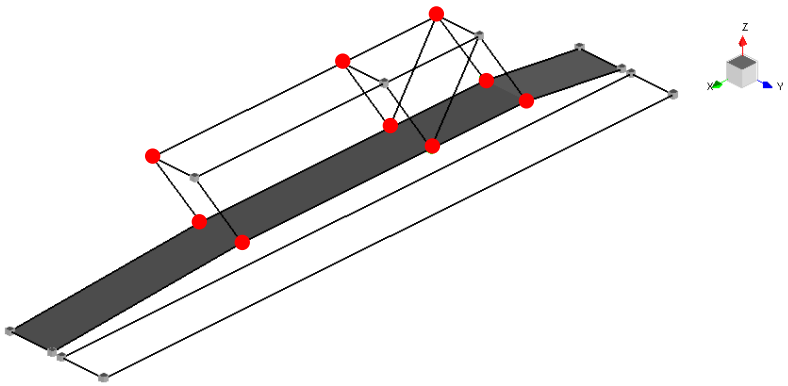


Figure 4: Schematic measurement layout in the first experiment

In the first experiment, truss span carrying track no. 1 was tested. Twelve single-axis accelerometers were used for measurements of vibrations time histories. The test was planned as two setup experiment, where six of available transducers were reference points. This allowed measuring vibrations of eighteen degrees

of freedom. The location of the measurement points is shown in Figure 4. In each of the three observed cross sections, six accelerometers were installed what was schematically drawn in Figure 5a. This approach has proven to be too time-consuming.

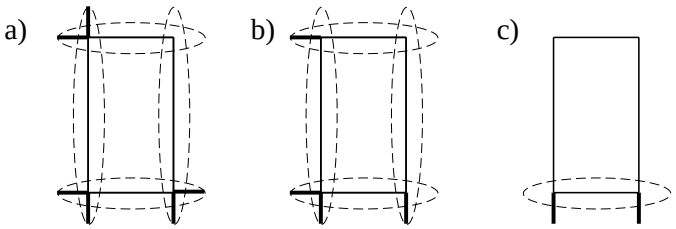


Figure 5: Schematic layout of measurement directions instrumented with single axis accelerometers in typical cross sections of a truss: a) six transducers; b) four transducers; c) two transducers

4.2 Second OMA experiment – track 2

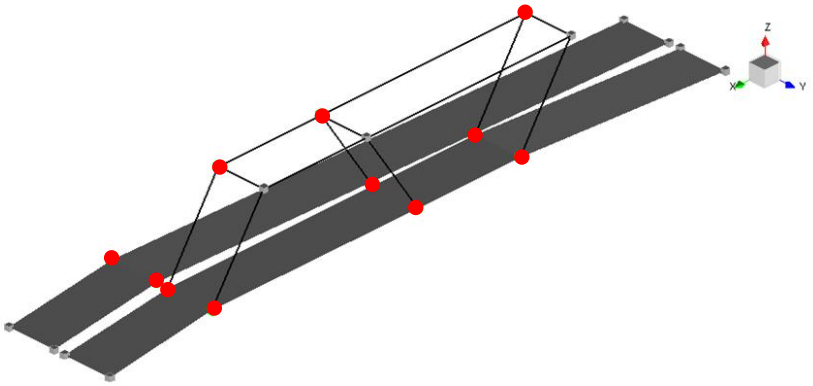


Figure 6: Schematic measurement layout in the second experiment

In the second experiment truss span carrying track no. 2 was tested. Due to the difficulties encountered in the identification process of the first experiment (e.g., closely spaced and repeated modes of vibrations) the measurement strategy was changed. The number of accelerometers in the observed cross-sections has been reduced (Figure 6) from six to four (Figure 5a, b). Two of the six accelerometers were acquiring redundant information. The transducer layout has been reorganized to obtain an unambiguous picture of the basic modes in one setup of accelerometers (12 measurement directions). It was decided that in addition to the examined span the neighboring one will also be observed. Two single axis accelerometers were mounted on it (Figure 6). Two additional accelerometers were oriented according to Figure 5c. This decision was made because of the difficulties encountered previously in the identification of basic global modes of vibrations, especially vertical bending and torsional. As mentioned earlier in the first experiment, repeated forms of vibration were observed. One possible reason was the dynamic interaction of two adjacent lattice spans. Described transducers layout was planned, e.g., to verify this hypothesis.

4.3 Third OMA experiment – track 1 I 2

The third experiment was carried out during additional dynamic tests conducted after the completion of all construction works. In this case, the tests included structures in both tracks and were carried out during the night closures of the railway line that was fully functional at that time. Scheduled test runs (of light and fast electric locomotive) included speeds ranging from 10 to 160 km/h (Table 2). Three cross-sections in each truss were observed (Figure 7). In all cross sections, two accelerometers were installed according to the sketch in Figure 5c. The tests had to be carried out with one setup of sensors, so it was decided to use this

opportunity to finally verify the observations made in the second experiment. That is the observed interaction of the two truss spans.

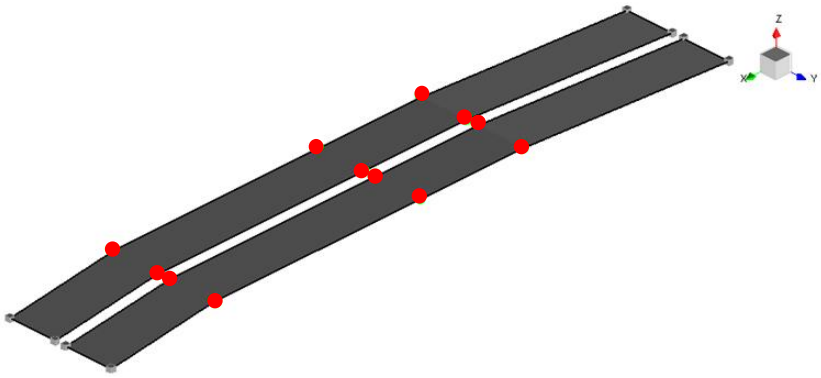


Figure 7: Schematic measurement layout in the third experiment

5 Results

The most important effect of using modal operational analysis is the unambiguous identification of basic modes of vibrations. This is something that would not be possible to achieve using spectral analysis. Especially in the case of this structure, which is characterized by a complex dynamic behavior.

Spatial distribution of transducers used in the first and second experiment (described in point 4) allowed for unambiguous observation of almost all basic forms of natural vibrations up to the second, vertical bending mode. It was possible to observe several higher order modes. However, only some of them were characterized by satisfactory observability. The results of the first experiment, in which only one truss was observed, indicated the repeated modes.

Mode description	Mode Number OMA	f_{OMA} [Hz]	$U(f_{OMA})$ [Hz]	ξ_{OMA} [%]	$U(\xi_{OMA})$ [%]
horizontal bending	1	1.83	0.02	1.39	1.10
torsional	2	2.93	0.01	0.44	0.22
vertical bending	3	3.10	0.01	0.31	0.37
horizontal bending II	4	4.46	0.07	1.35	0.48
torsional II	5	6.27	0.05	1.04	0.57
torsional – alternative form	6	6.80	0.06	0.26	0.07
vertical bending II	7	6.95	0.06	1.20	0.68

Table 3: First experiment - identified global modes of vibration

In Table 3 the results of identification carried out in the first experiment i.e., obtained during measurements on the structure in track no. 1 (Figure 3) are presented. At the stage of the first experiment, the possible interaction of two trusses was not taken into account. In the case where one of the modes was identified as a repeated root, it was concluded that the most important (of the physical meaning) is one that had more energy content in the vibration spectrum. In addition to the frequency of the identified mode (f_{OMA}) the table shows the damping estimate (ξ_{OMA}) and extended experimental uncertainties ($U(f_{OMA})$ i $U(\xi_{OMA})$) of those parameters.

In Table 4 the results of identification carried out in the second experiment, i.e., obtained during measurements on the structure in track no. 2 (Figure 3), were presented. Two of the seven modes were identified as conjugate pairs. Not every identified mode had its conjugated counterpart identified. This may be due to low excitation of these modes or ineffective identification.

Mode description	Mode Number OMA	f_{OMA} [Hz]	$U(f_{OMA})$ [Hz]	ξ_{OMA} [%]	$U(\xi_{OMA})$ [%]
horizontal bending	1	1.82	0.02	1.05	0.28
torsional	2	2.94	0.01	0.84	1.23
vertical bending in phase	3	2.95	0.03	1.37	0.77
vertical bending out of phase	3	3.15	0.02	0.67	0.70
horizontal bending II	4	4.48	0.09	1.69	0.70
torsional II	5	5.79	0.03	0.29	0.86
torsional (alternative form) in phase	6	6.74	0.01	0.25	0.07
vertical bending II	7	7.01	0.03	0.96	0.35
torsional (alternative form) out of phase	6?	7.74	0.24	0.36	0.18

Table 4 Second experiment - identified global modes of vibration

Despite the annual gap between experiments no. 1 and 2, and the fact that they focused on various trusses, the results overlap quite well (Table 3 and Table 4). The only significant difference is the frequency of the second torsional mode, which takes the value of:

- in experiment no. 1 – 6,27±0.05 Hz,
- in experiment no. 2 – 5.79±0.03 Hz.

This may indicate an identification error or a pair of repeated characters. Where in different experiments two variants of the same mode were observed.

The detailed results of the third experiment were not cited. Observations made in it coincided with those described above. However, most of the forms had observability issues. It stems from the adopted layout of vibration transducers. The primary purpose of this experiment was to verify the occurrence of duplicated conjugate modes and was programmed to identify global modes with the dominant vertical component.

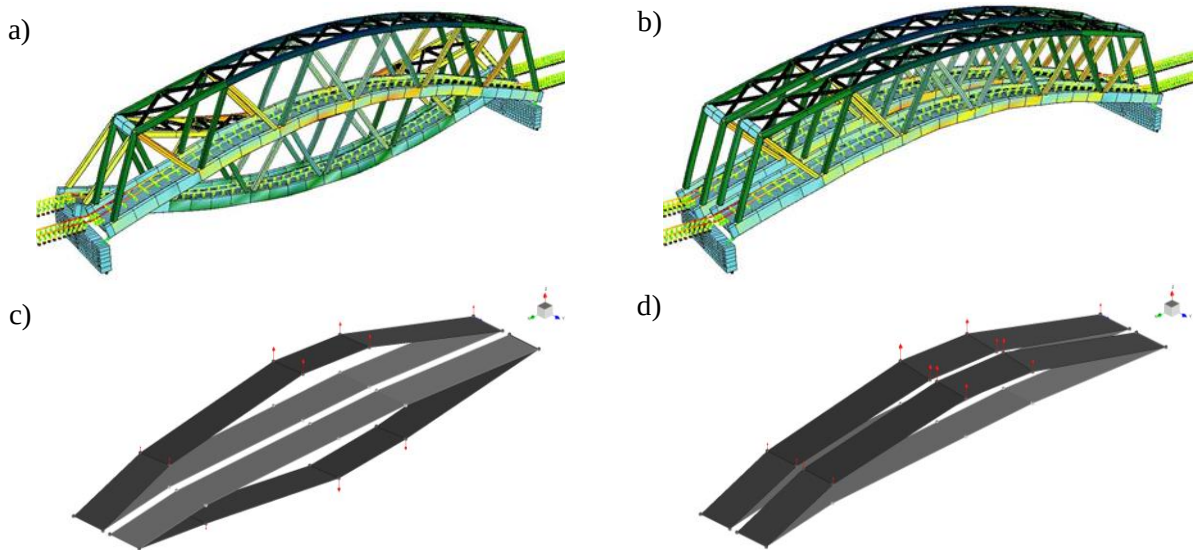


Figure 8: Two warrants of first vertical bending mode identified in the third experiment compared against FE model prediction: a) FEM out of phase; b) FEM in phase; c) OMA out of phase 2.92 Hz; d) OMA in phase 3.17 Hz

Experiment two and three (see pt 4.1 and 4.2) allowed observation of the dynamic interaction of two trusses. In Figure 8 an example of a pair of conjugate vertical bending modes is shown. The two calculated from the FE model and identified during the identification experiment are shown. Additionally, in Figure 9 an example of a pair of conjugate higher-order modes associated with one of the torsional vibration modes are shown.

The effect of expansion joints introduced to the deck slab was not observed in any of the three experiments (see 4). This may be due to the insufficient number of measurement points within the structure deck. The results of previous dynamic load tests (using less reliable transducers and basic signal processing see 3.1) were considered unreliable and therefore could not provide information on the impact of the discussed changes of the structural system on the modal parameters. Significant limitations of the conducted research were:

- a limited number of available vibration transducers,
- conditions encountered on the site in individual experiments - water level in the river, access to the structure, other works carried out on the bridge or in its vicinity,
- the sensor layout did not allow the integration of results from various experiments
- the third experiment had an insufficient number of transducers to identify any modes with significant transverse motions unambiguously.

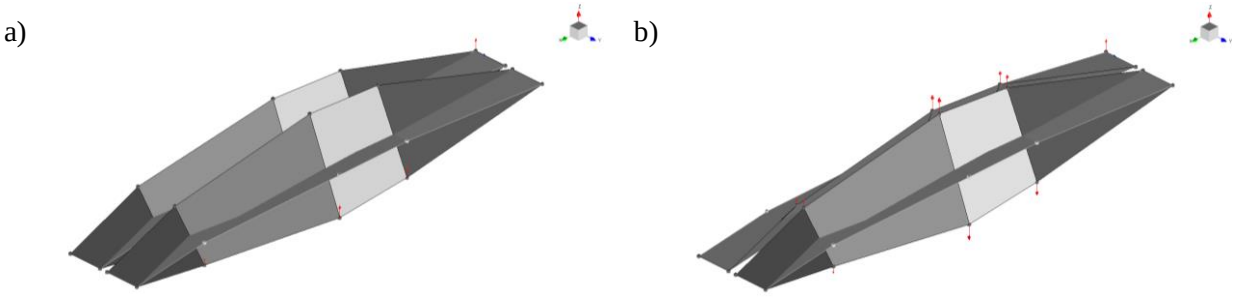


Figure 9: Two variants of one of the torsional modes identified in the third experiment: a) – 6.78 Hz; b) 7.0 Hz

5.1 Comparison with other tested railway trusses

The described truss exhibits dynamic behavior similar to other truss bridges of a similar type. In Figure 10 the frequency relationship of three primary forms of natural vibrations against the background results obtained by authors on other truss railway bridges (OMA was used in all those cases) is shown. Attention should be paid to the closely spaced vertical bending and torsional modes of vibrations. In addition to the dynamic interaction of the two spans described above, it is the proximity of these two modes that cause the greatest identification difficulties. Therefore, the use of simple signal analysis methods may lead to misidentification. The most troublesome is the reliable detection of a torsional form of vibrations.

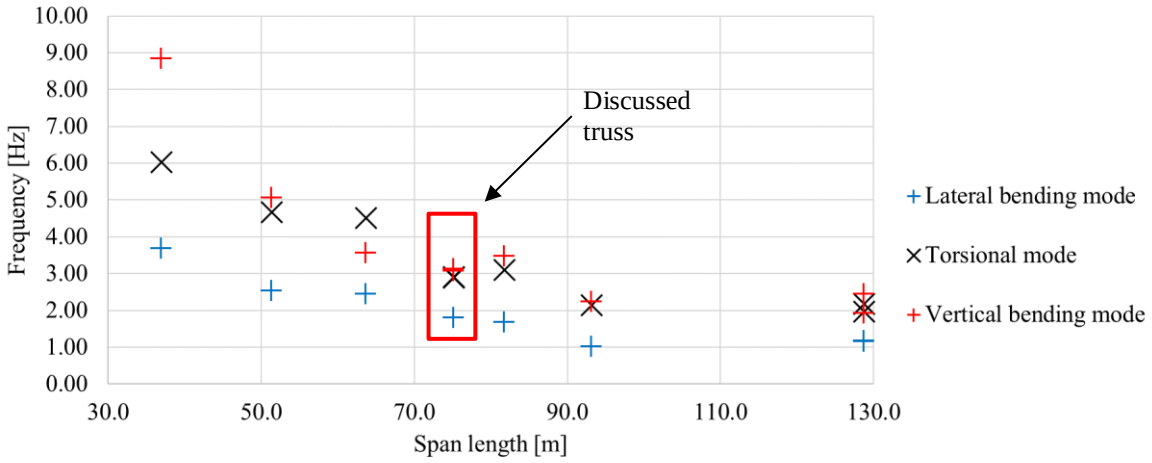


Figure 10: First three fundamental modes of vibration compared to other similar structures tested by authors using OMA

6 Discussion and conclusions

The described research was carried out during an identification experiment which was an extension of a typical dynamic load test. Operational modal analysis fits well into the practice of performing the load tests on dynamic railway bridges. The advantages of OMA are particularly visible in the analysis of complex structures such as truss bridges. The spatial character of their vibration forms is undisputed, and it is necessary to include this observation in the planning process of identification experiments. The correct identification of dynamic parameters of these bridges is made more difficult by the frequent occurrence of closely-spaced modes of vibrations.

The applied research approach allowed to disambiguate the identified modal model together with the extension of the range of identified modes of vibrations over what is possible using simple signal analysis methods. The conducted experiments showed the phenomenon of interaction between two trusses based on a common supports. Repeated conjugate modes of vibrations were observed. The first of the described experiments focusing only on one truss gave results difficult to interpret, e.g., repeated forms of vibrations. Only simultaneous measurements on two trusses allowed to explain the source of these difficulties.

Multi-setup experiments are impractical in case of routine commercial dynamic load tests. The inability to give up the test runs of rented locomotives means that it is necessary to carry out this type of work efficiently. Changing the location of transducers based on wired technology is too time-consuming. With one setup experiments, it is possible to perform tests of several neighboring bridges on the section of the railway line in one day. This allows for optimization of the costs of renting rolling stock.

The identified modal model can be used to confirm the validity of design assumptions made at the design stage, in the process of updating the numerical model and as a dynamic bridge metric for future use.

References

[1] R. Brincker and C. Ventura, *Introduction to operational modal analysis*. Chichester, West Sussex: John Wiley and Sons, Inc, 2015.
[2] A. Cunha and E. Caetano, "Experimental modal analysis of civil engineering structures," *Sound Vib.*, vol. 6, no. 40, pp. 12–20, 2006.
[3] R. Cantieni, M. Brehm, V. Zabel, T. Rauert, and B. Hoffmeister, "Ambient testing and model updating of a filler beam bridge for high-speed trains," in *Proceedings of 7th European Conference on Structural Dynamics (EURODYN), Southampton, UK*, 2008, pp. 7–9.
[4] G. Poprawa, S. Pradelok, M. Salamak, and P. Łaziński, "Operational modal analysis in model updating of a truss railway bridge," in *Proceedings of 7th IOMAC*, Ingolstadt, 2017, pp. 64–67.
[5] R. Karoumi, A. Andersson, and H. Sundquist, "Static and Dynamic Load Testing of the New Svinesund Arch Bridge," presented at the International Conference on Bridge Engineering – Challenges in the 21st Century, Hong Kong, 2006.
[6] P. Łaziński and S. Pradelok, "Load Test of Railway Viaduct Built Using Crosswise Launching Technology," *Procedia Eng.*, vol. 161, pp. 530–537, 2016.
[7] Ł. Pyrzowski, M. Miśkiewicz, J. Chróścielewski, and K. Wilde, "Load Testing of GFRP Composite U-Shape Footbridge," *IOP Conf. Ser. Mater. Sci. Eng.*, vol. 245, Oct. 2017.
[8] M. Malinowski, A. Banas, M. Jeszka, and A. Sitarski, "Imaginative footbridge in Mikolajki, Poland," *Stahlbau*, vol. 87, no. 3, pp. 248–255, Mar. 2018.
[9] L. Frýba, *Dynamics of Railway Bridges*, 2nd revised edition. London: Thomas Telford Ltd., 1996.
[10] M. Szafrański, "Vibration of the bridge under moving singular loads - theoretical formulation and numerical solution," *J. Appl. Math. Comput. Mech.*, vol. 15, no. 1, pp. 169–180, Mar. 2016.
[11] B. Peeters, F. Dammekens, F. Magalhães, H. Van der Auweraer, E. Caetano, and A. Cunha, "Multi-run Operational Modal Analysis of the Guadiana cable-stayed bridge," in *Proceedings of IMAC XXIV*, St. Louis, 2006.
[12] B. Peeters and G. De Roeck, "Reference-based stochastic subspace identification for output-only modal analysis," *Mech. Syst. Signal Process.*, vol. 13, no. 6, pp. 855–878, 1999.

Modeling of a prestressed concrete bridge with 3D finite elements for structural health monitoring using model updating techniques

S. Schommer[1], T. Kebig[1], V.-H. Nguyen[1], A. Zürbes[2], S. Maas[1]
[1] University of Luxembourg, Faculty of Science, Technology and Communication
6, rue Richard Coudenhove-Kalergi, L-1359, Luxembourg, Luxembourg
e-mail: **tanja.kebig@uni.lu**

[2] Bingen University of Applied Sciences, Department 2
Berlinstraße 109, D-55411, Bingen am Rhein, Germany

Abstract
This paper presents a linear finite element model for a prestressed concrete beam, which was part of a real bridge. Static and dynamic tests were carried out and compared to the numerical simulation responses. A solid finite element model was created including the prestressed concrete beam, permanent dead load, two additional live loads and a shaker. A well planned finite element model is very important for later detection and localization of damage. Therefore, a mapped mesh was used to define so-called 'slices', which enables describing stiffness changes, e.g. damage. The model validation was performed by comparing simulated results to measured responses in the healthy state of the beam. After validation of the reference model, it is possible to modify the bending stiffness along the longitudinal axis of the beam by modifying Young's moduli of different slices to adapt for the effect of damage.

1 Introduction

Model updating is often used for damage detection in civil engineering structures. Prerequisite is a parameterized model using finite element method to validate at first the healthy reference state. For a successful damage assessment, the reference model has to present the real structure as accurately as possible. The model updating includes a complex procedure, containing also model errors resulting from idealizations and assumptions. On the other hand, measurements of physical properties are never absolutely accurate due to measurement uncertainty. An elaborated review on numerical and application aspects for model updating was reported in [1]. It described the choice of updating parameters and the definition of residuals, which may be used to compare the physical measurements and analytical results. The difference between measured and simulated physical quantities may be reflected by a weighted sum of the residual vector which is the core of an objective function. An optimal model parameter set can be found to minimize this function.

The number of parameters to be updated is often an important issue as it largely influences the computational cost or the convergence. The definition of 'damage function', proposed by Abdel Wahab et al. [2], allows reducing efficiently the number of parameters. The technique was further developed by Teughels et. al. [3] by combining element groups and using dimensionless parameters. As revealed clearly in its name, damage function can describe mathematically a damage for example by modeling stiffness reduction. In [3, 4], damage localizations were carried out with beam models and a number of damage functions summing up Legendre polynomials.

The present study examines a part of a real prestressed concrete bridge in Luxembourg that artificial damage was provoked with increasing severity. Static and dynamic responses were measured in each damage scenario. Further than the simple beam models in [3, 4], the damage localization is here performed with a

more detailed solid model including prestressed tendons. Moreover, only one damage function was used, based on a Gaussian Bell curve, which enables a fast model updating procedure. Differences between model responses and measurements are assessed and summed-up in an objective function, which depends of course on chosen parameters. At a second stage, a set of measurements is considered and the model is updated by varying parameters in order to minimize the objective function. It is recommended to keep the number of parameters low to reduce computational effort and to achieve convergence. But the focus of the present paper is the generation of the solid model and its important features for its later use in model updating with damage functions.

2 Test set-up

The tests were carried out on a part of a real prestressed concrete bridge. The original bridge crossed the river Mosel between Grevenmacher (Luxembourg) and Wellen (Germany). Built from 1953 to 1955, the bridge was demolished in 2013 for safety reasons. It was a 5-span bridge and each field composed of 5 adjoining concrete T-section beams. These beams were prestressed by internal steel tendons in longitudinal direction.

For the test set-up, two of these beams with a length of 46 m and a mass of approximately 120 t each, were transported to the port of Mertert (Luxembourg). One of them with 19 tendons was used as the test beam and was supported at the two ends by a sliding and a fixed bearing. For the fixed bearing, the beam was molded with concrete and the sliding bearing was realized by two steel plates. Grease was spread between the two steel plates to reduce the friction. Before the demolition of the original bridge, the asphalt layer had been removed. However, a purpose of the test was to reproduce the condition during the lifetime of the bridge as far as possible. A part of the second beam with a length of 12 m and a weight of about 30 t was used to simulate an additional dead load due to the removed asphalt layer. Live load due to traffic was represented by two additional loads of about $2 \cdot 13$ t = 26 t put on top of the test beam. During the static tests with the live loads, the additional dead load stayed on top of the beam. For vibrational testing, an electromagnetic shaker was positioned between the additional dead load and the live loads. The whole test set-up is shown in Figure 1.

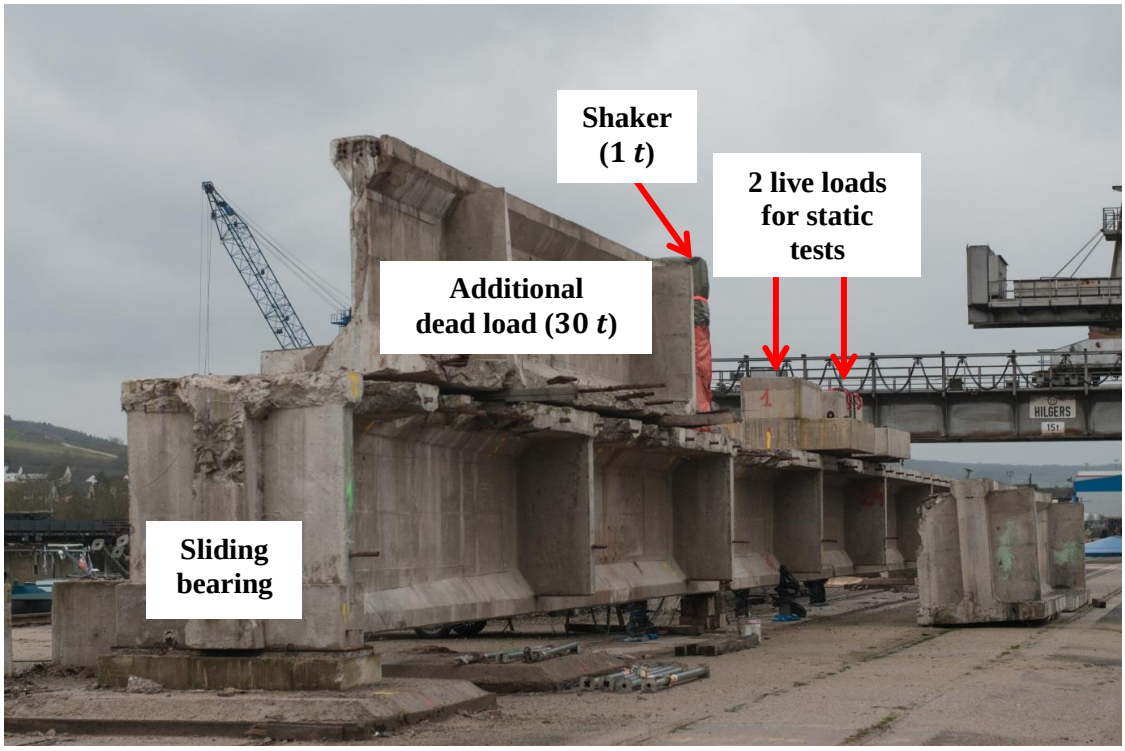


Figure 1: Test set-up at the port of Mertert

The beam was equipped with 8 displacement transducers, 8 temperature sensors and 26 accelerometers for the vibrational testing. The location of the sensors is presented in Figure 2. During the whole test period of about 1 month, the vertical deflection versus ground was recorded by 7 transducers (SV1-SV6, SV8) at the bottom of the beam. Another sensor (SH7) was attached to register horizontal displacement of the sliding bearing. In addition, the concrete temperature (T1-T7) and the ambient air temperature (T_{amb}) were measured.

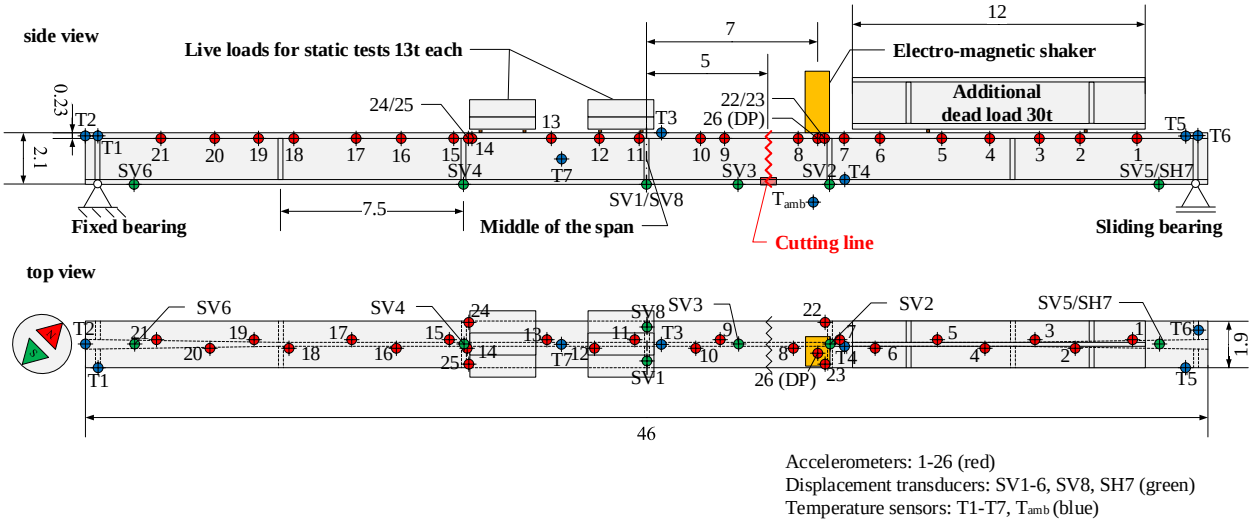


Figure 2: Side and top view of test set-up with sensors

Artificial damage was applied in 4 steps by cutting tendons at a distance of 5 m off the middle of the beam, as shown by the cutting line in Figure 2. Hence, totally 5 pre-defined damage scenarios (DS) were studied. The first DS#0 represents the undamaged reference state and DS#4 the most severe damaged state of the beam. DS#1 to DS#4 correspond to the cutting of 2, 4, 6 and finally 9 tendons. The damage was always introduced symmetrically on both sides of the beam. Figure 3 demonstrates the lower part of the cross-section at the damage location with the position of the 19 tendons. In the last scenario DS#4, 6 tendons were only partly cut, when clearly visible cracking was observed. Fully cut cables are marked by a cross, while a partially cut is marked by a half-filled circle.

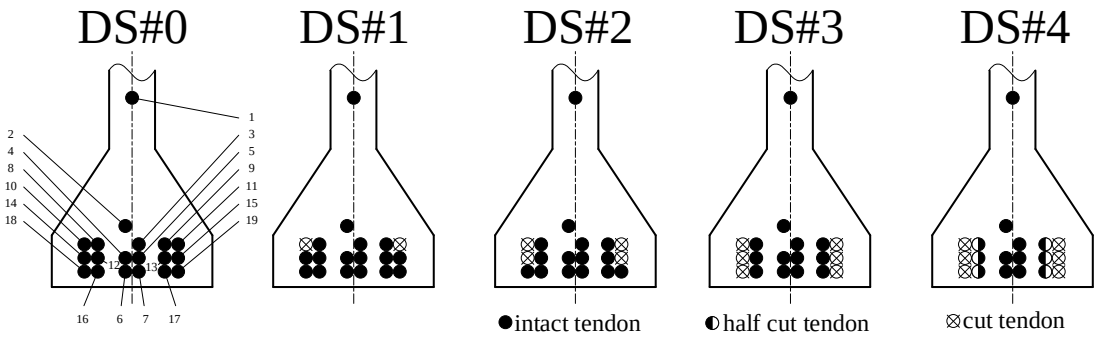


Figure 3: Damage scenarios

3 Finite Element (FE) Model

The measurements were analyzed and used for a model updating procedure based on a parameterized FE-model in order to identify local stiffness reduction. Hence, the chosen parameters should be able to represent stiffness reductions in the model. Damage may be evaluated by tracking the selected parameters starting from the initial model in the healthy state. The main characteristics of the T-shaped cross-section of the beam are shown in Figure 4.

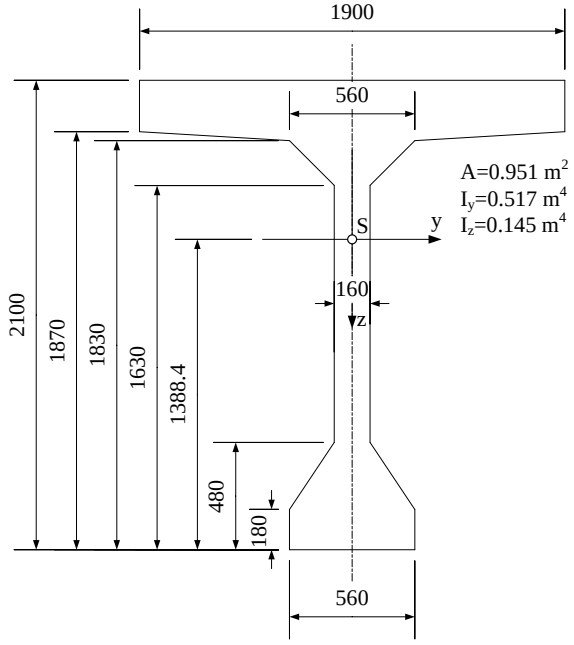


Figure 4: Cross section of the beam in the middle of the span (dimensions in [mm])

A finite element model was prepared with ANSYS Classic 17.0. The Ansys Parametric Design Language (APDL) was used to create the parametric model and to implement batch processing allowing large numbers of automatic simulations that optimization often requires. Therefore, a linear model was chosen. In addition to linear elastic material models, the contact conditions were defined in a way so that no nonlinearities (e.g. contact) occurred in the model. A volume model of the test set-up was created with mainly solid elements. Table 1 shows the most important elements used in the model.

Type	Description	Node number	Usage	Important options
SOLID186	Structural Solid	20	Hexahedral elements for mapped meshing	Sometimes used as tetrahedral- or as pyramid-shaped elements
BEAM188	Beam	2	Beam elements for the tendons, Dummy-Beams to connect the tendons to the concrete	Timoshenko beam theory
MPC184-Revolute	Multipoint Constraint Element, Revolute Joint	2	To model a revolute joint at the sliding bearing	
MPC184-Planar	Multipoint Constraint Element, Planar Joint	2	To model a planar joint without friction at the sliding bearing	

Table 1: Element types

A local stiffness loss due to cracking or reduction of stiffness along the beam's length can be simulated by reducing YOUNG'S modulus. The idea was to split the beam into narrow "slices", whose stiffness can be reduced as a whole to limit the number of free parameters. This was implemented by a mapped mesh. "SOLID186" – a hexahedral element with 20 nodes and with "brick" shape was used allowing an easy definition of slices. Each slice can be defined and assigned with its own material. At the beginning, the material properties were uniform and Young's moduli can be modified during the model updating. The mapped mesh does not only reduce the number of elements compared to a free mesh but also avoids distorted elements and thus increases the mesh quality.

Figure 5 illustrates the mapped meshing with solid elements, e.g. around the sliding bearing side. Different colors present different materials and material properties can be varied individually. In the present model, the beam was divided into 227 individual "slices" of 20 cm thickness. The YOUNG's modulus of the concrete was initially set to 30.000 MPa and for the steel tendons to 200.000 MPa.

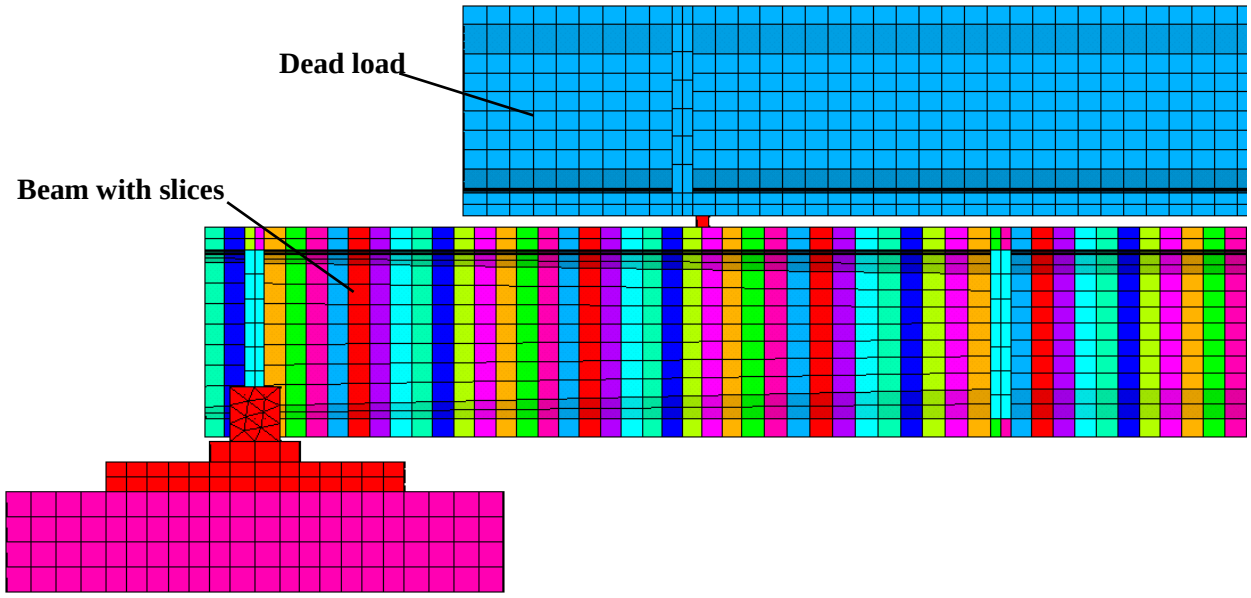
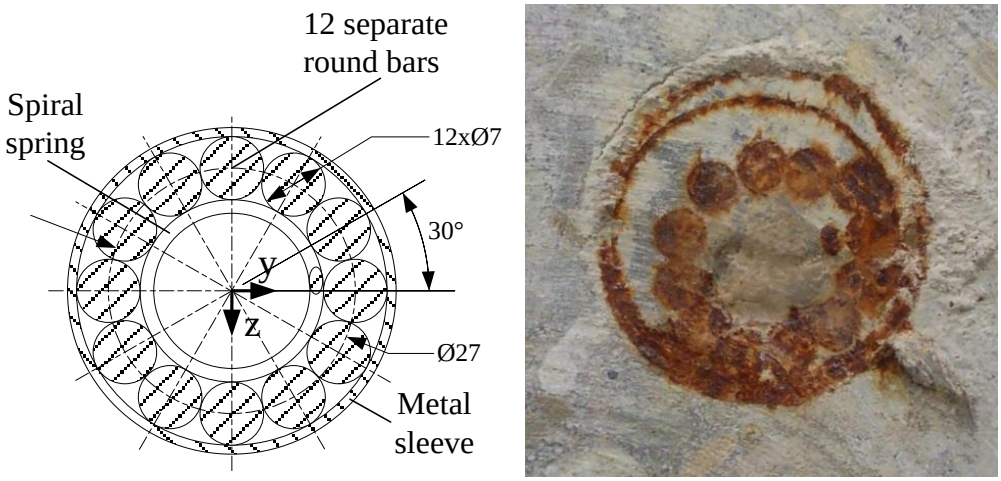


Figure 5: FE-model of the test set-up with mapped mesh; diverse colors show different materials

The tendons in longitudinal direction were also simulated and meshed with the concrete beam. In reality, each tendon consists of 12 individual round bars with a diameter of 7 mm. They were arranged in a thin jacket pipe and held in position by a spiral spring. After a pre-tensioning the tendons were grouted as illustrated in Figure 6. In this model, a tendon is represented by a pipe with area and moment of inertia equivalent to the ensemble of 12 round bars. It was assumed here that the round bars did not move relatively to each other due to the grouting. Thus, the tendons were simulated by pipe with an inner diameter di = 21.4 mm and an outer diameter da = 32.4 mm.



a) drawing with dimensions

b) photo of a real tendon of a cut beam, filled with mortar

Figure 6: Cross section of the tendons

Then in order to connect the tendons to the surrounding concrete elements, node-to-node connections were created by additional dummy (beam) elements as detailed in Figure 7. Those dummy elements had material properties like the tendons, but zero density, and hence they added no mass to the system. As a beam element has 6 Degrees of Freedom (DOFs) per node and a solid element has only 3 translational DOFs, the 3 rotational DOFs of a beam element remain free in such a connection. To solve this problem, each node of the tendons was in addition connected to 3 nearest neighboring nodes of concrete (solid) elements. These multiple connections allow transmitting moments between the connected elements. An overview of the prestressed-tendons is shown in Figure 8.

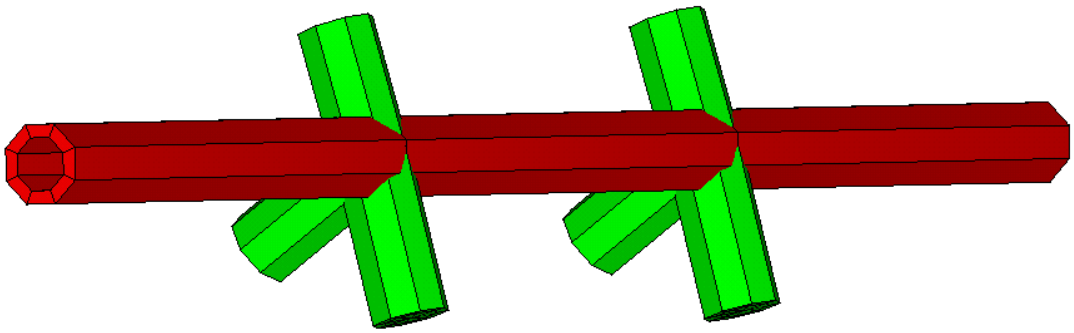


Figure 7: Part of a tendon (red) with additional dummy beam elements (green) connecting it in the model to the concrete

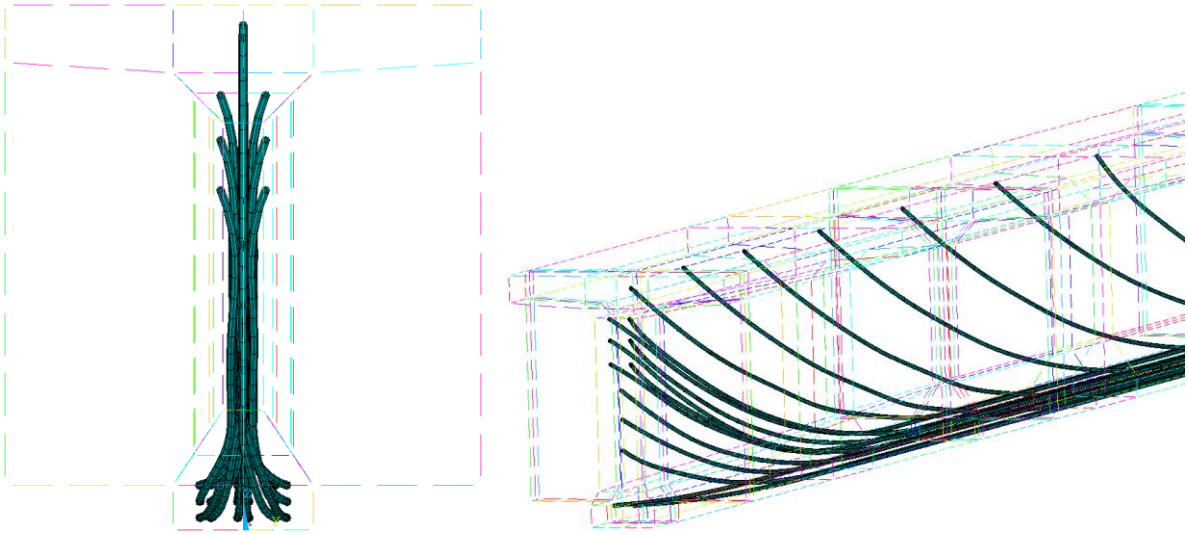


Figure 8: Internal tendons inside the test beam

Then the permanent additional dead load of 30 t was also modeled by elements without intermediate nodes (SOLID185). The last step concerns the modeling of the bearings. The bridge part was set up as a simply supported beam but in reality, the fixed bearing and especially the sliding bearing did not show behavior of ideal bearings. On the fixed bearing, the beam was surrounded by concrete for a length of about a half meter. So it was not only supported at one point, but in a certain area. The concrete of the bearings was quite young and hence not completely rigid. Therefore, a rotation around the transverse axis was possible but not completely free. The sliding bearing was realized by two steel plates with grease between. The cast concrete including the foundation and a part of the soil were also modeled as volume elements. In addition to the contact between these volume bodies, the contact between the bearings and the beam had to be defined. Therefore, surface contact elements with the “always bonded” option were used for both bearings, which hence merged the two FE-meshes. Furthermore for the sliding bearing, additional movement possibilities had still to be modeled. Therefore two joints were simulated by using elements of type MPC184-revolute and -planar joint. Nonlinearity can be avoid by switching off the alteration of underlying constraint equations in case of large deformations for the MPC184-elements. The soil under a bearing was modeled by a cube as shown in Figure 9. To fix the soil, the movements of 3 surfaces of this cube were blocked in the direction perpendicular to the surfaces. As the sliding bearing was not perfect, its horizontal displacement was blocked for the dynamic test due to friction, while the friction was zero for the static loading. For this phase, elements of type MPC184-planar was changed by MPC184-rigid.

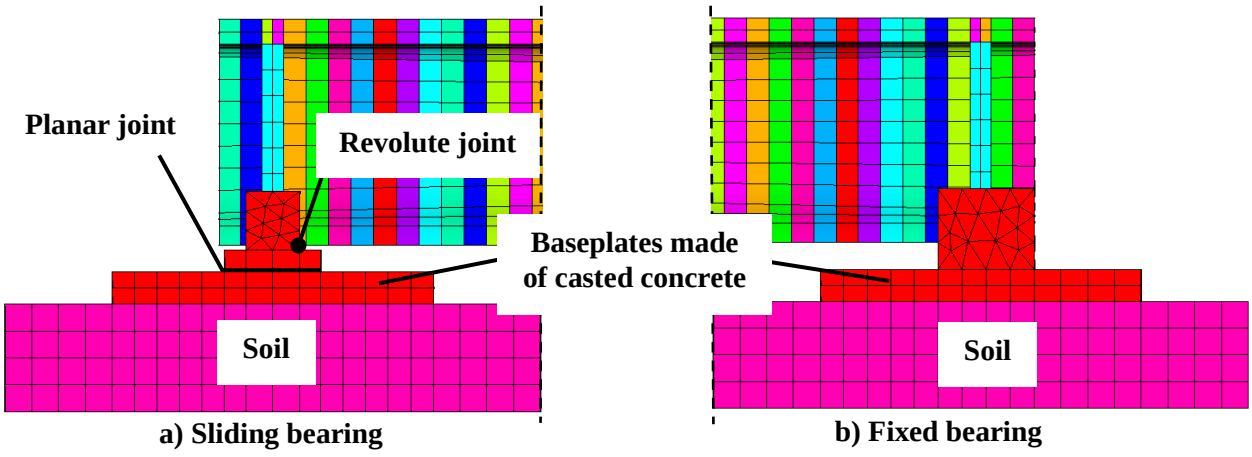


Figure 9: FE-models of the bearings

The shaker used for vibration tests was represented by a lumped mass. Furthermore, 'live loads' including two 13 t weights put on the beam only for static loading tests were also considered. Their weight was represented by pressure load on the contact area between two supporting wooden beams and the tested concrete bridge. The present paper does not describe the model updating procedure and its criteria in detail, which will be done in another paper. The focus is here the modeling itself: solids clustered in slices with a mapped mesh and beams for the tendons.

4 Model Validation

The validation of the model is performed by comparing simulated results to the measurements in the healthy state (DS#0). Figures 10-15 present the simulation in comparison to the measurements. The first result shows the deflection in a loaded state. Figure 10 reveals that the measured and the simulated results match well. The measured displacements had been compensated for temperature effects, which is detailed in a former paper [5].

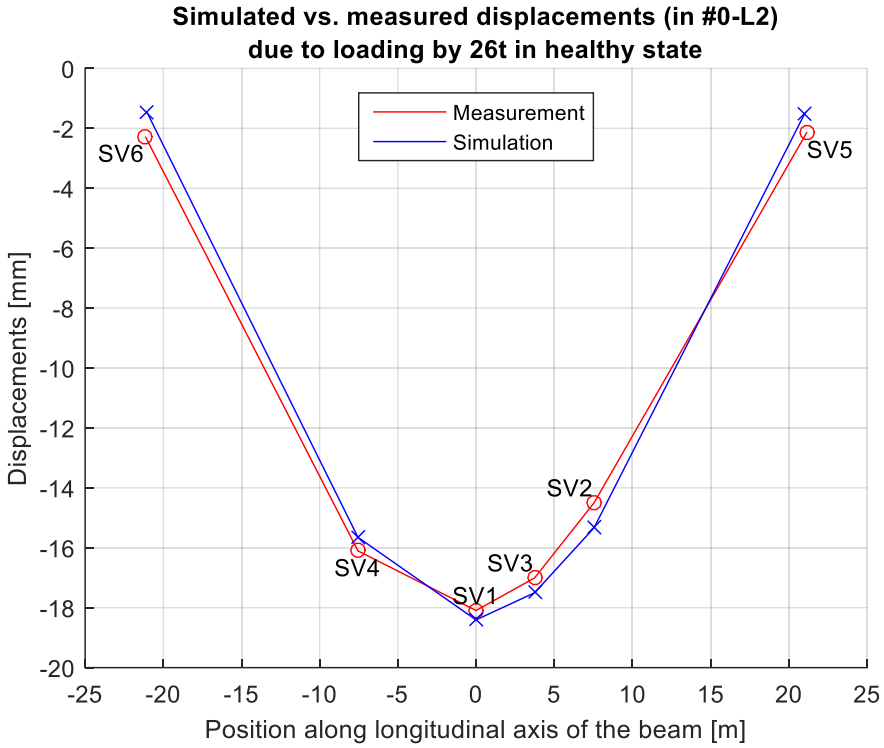


Figure 10: Comparison of the measured deflection in a loading - healthy state due to test weights and simulated vertical displacements

Results of the modal analysis are displayed in the following. The first simulated mode is bending in the horizontal plane, i.e. x-y plane in Figure 11, however this mode was not identified by the Experimental Modal Analysis (EMA), as only vertical DOFs were measured. The second simulated mode at 3.00 Hz shown in Figure 12 is a vertical bending mode, which could be correlated to the measured mode named B1, identified at 2.88 Hz. The correlation based on Modal Assurance Criterion (MAC) between these two mode shapes led to a good value with MAC = 0.982.

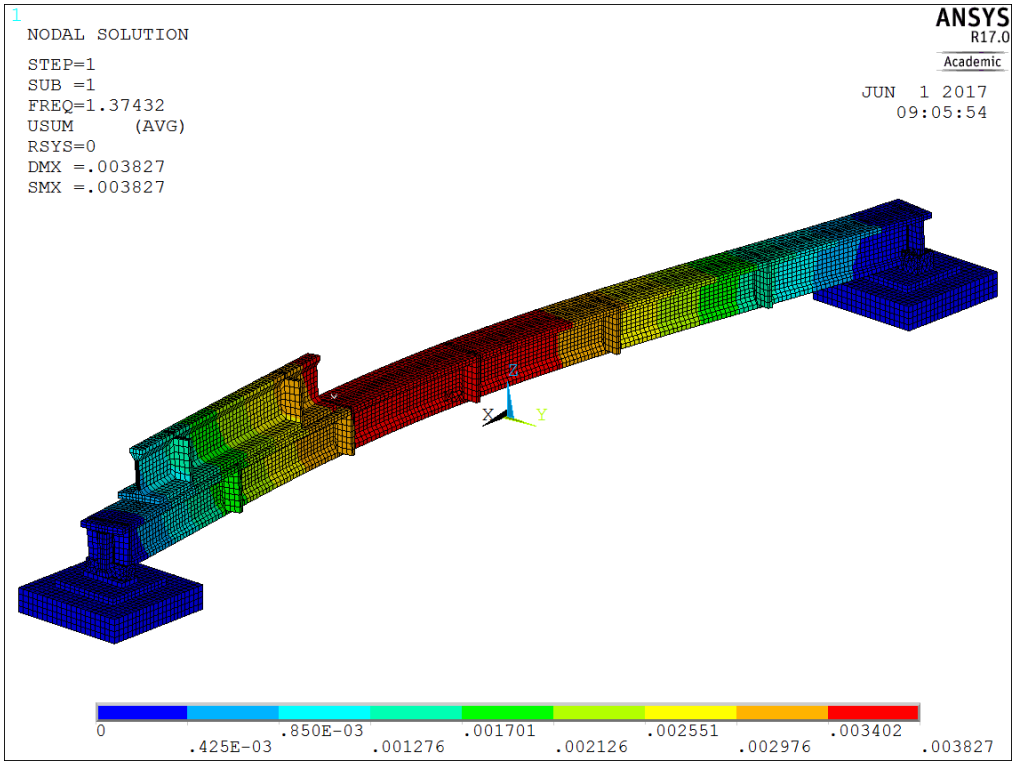


Figure 11: Bending mode in y direction at 1.37 Hz

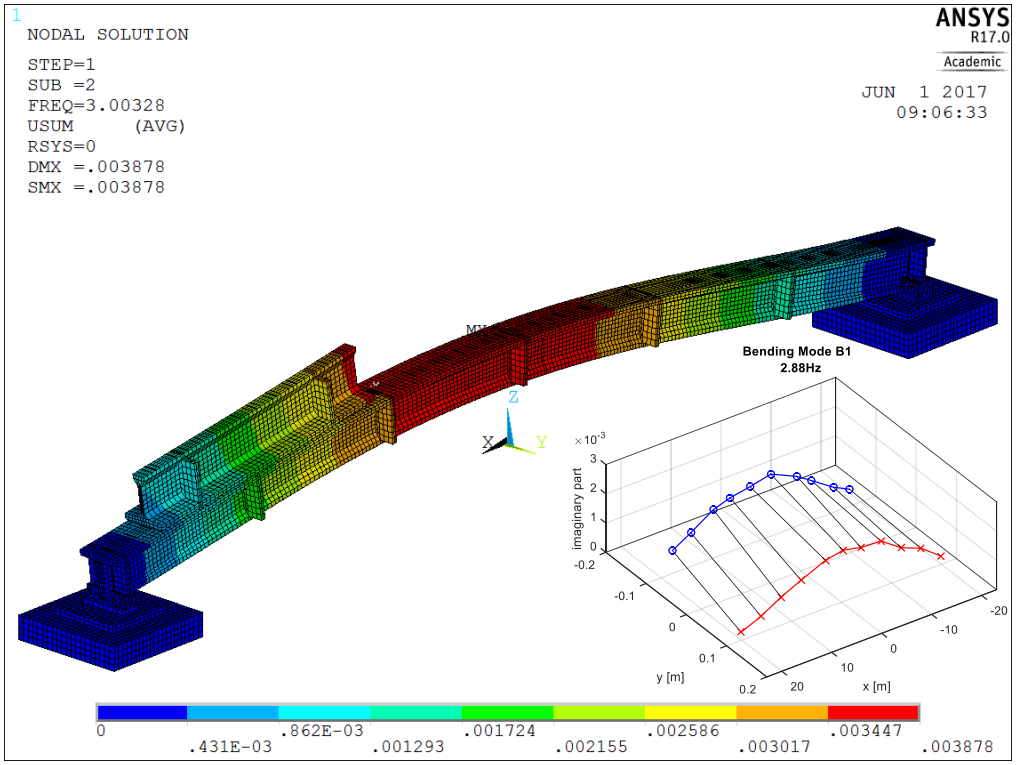


Figure 12: Simulated bending mode at 3.00 Hz juxtaposed with measured mode B1 at 2.88 Hz (MAC = 0.982)

The next two simulated modes are torsional; mode at 5.21 Hz correlated with mode T1 measured at 4.48 Hz. Torsional modes were not well identified in the EMA, because the sensors were positioned too close to the middle of the web of the beam, resulting in inadequate MAC values.

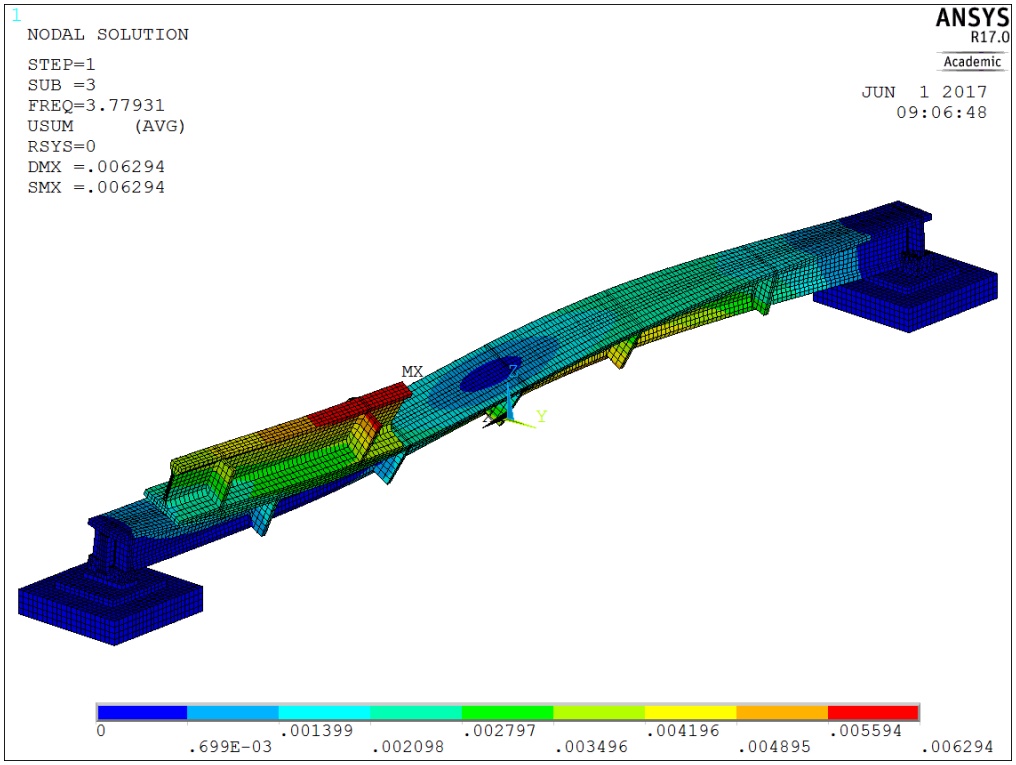


Figure 13: Torsional mode at 3.78 Hz

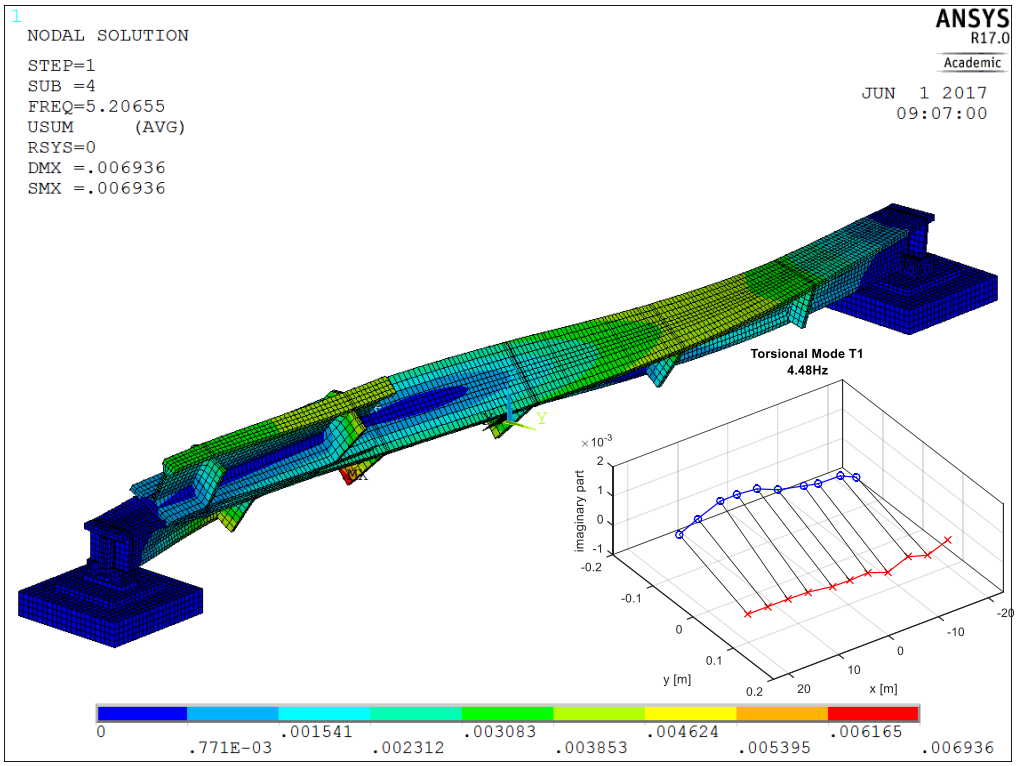


Figure 14: Simulated torsional mode at 5.21 Hz compared with mode T1 measured at 4.48 Hz (MAC = 0.632)

The correlation between simulated and experimental modes scores better with the next bending mode as shown in Figure 15. In the next step of model updating, 3 modes B1, T1 and B2 shown in Figure 12, 14 and 15 are used with their corresponding MAC values and eigenfrequencies.

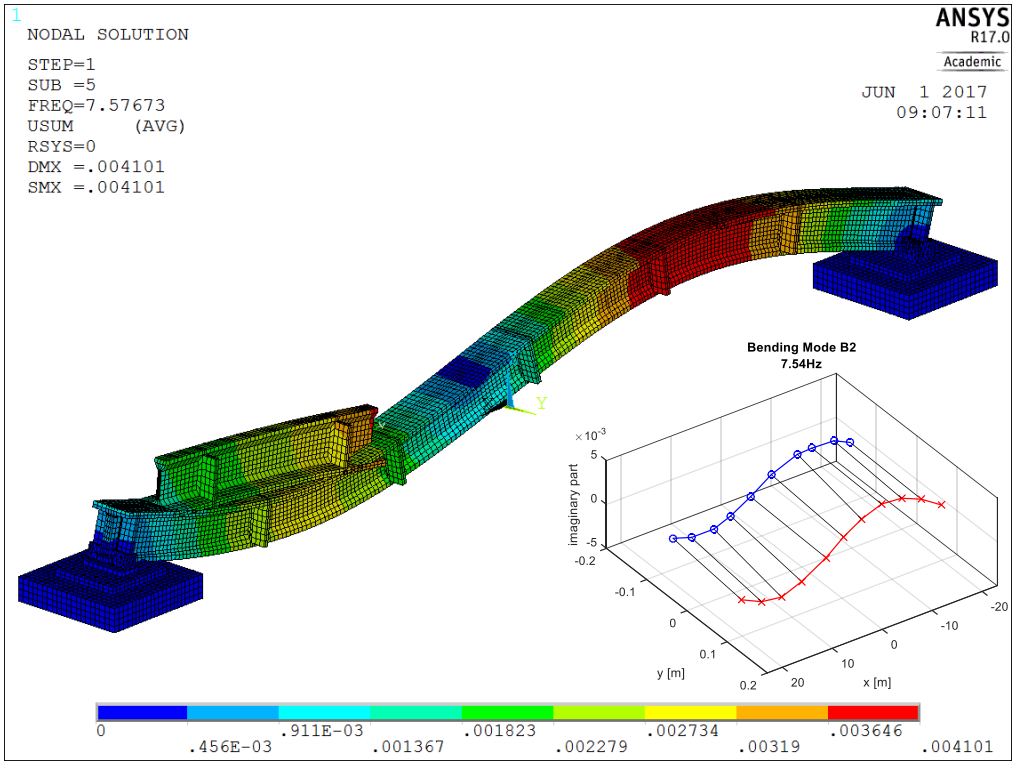


Figure 15: Simulated bending mode at 7.58 Hz correlated with mode B2 measured at 7.54 Hz (MAC = 0.970)

After the validation of the initial reference model, the effect of damage can be simulated by modifying the bending stiffness along the longitudinal axis of the beam. This is done by changing Young's moduli of the predefined slices. Totally 227 slices in the model lead to 227 parameters that describe the bending stiffness. This number of free parameters is too large for updating and hence has to be reduced. An interesting approach is 'damage function', introduced by Abdel Wahab et al. [2], Teughels et. al. [3]. It consists in using dimensionless parameters and in combining element groups and so that only some parameters of these groups are used for the updating. The damage function uses a predefined pattern reflecting the influence of damage on stiffness. It thus enables a physically reasonable optimization with reduced number of variables. Those damage functions are described and discussed in our former works [6, 7] and are not presented in detail in this paper.

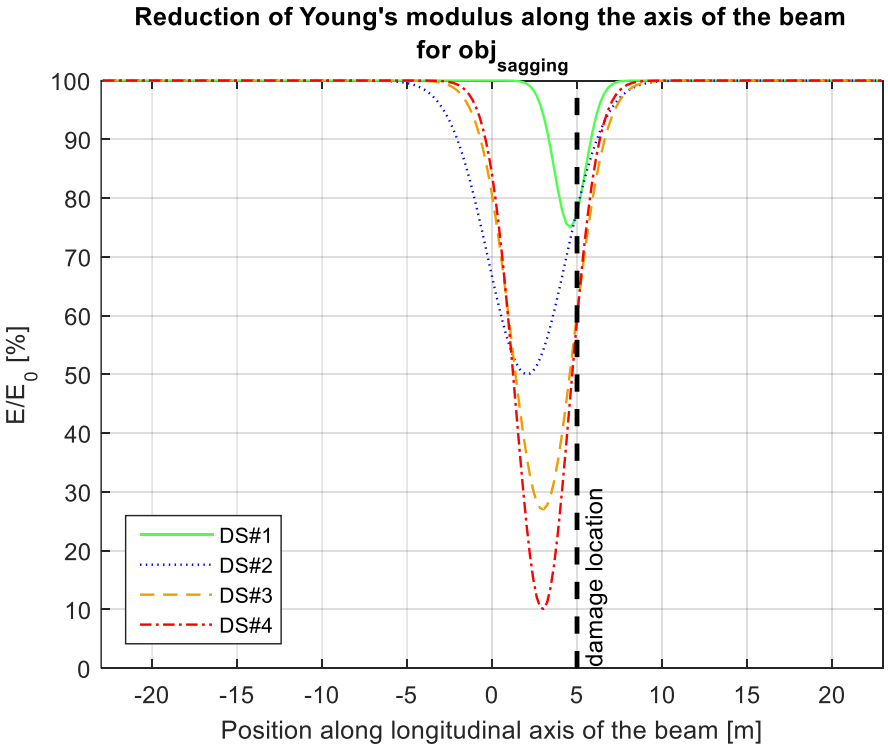


Figure 16: Reduction of Young's modulus along the longitudinal axis by the optimal parameter sets

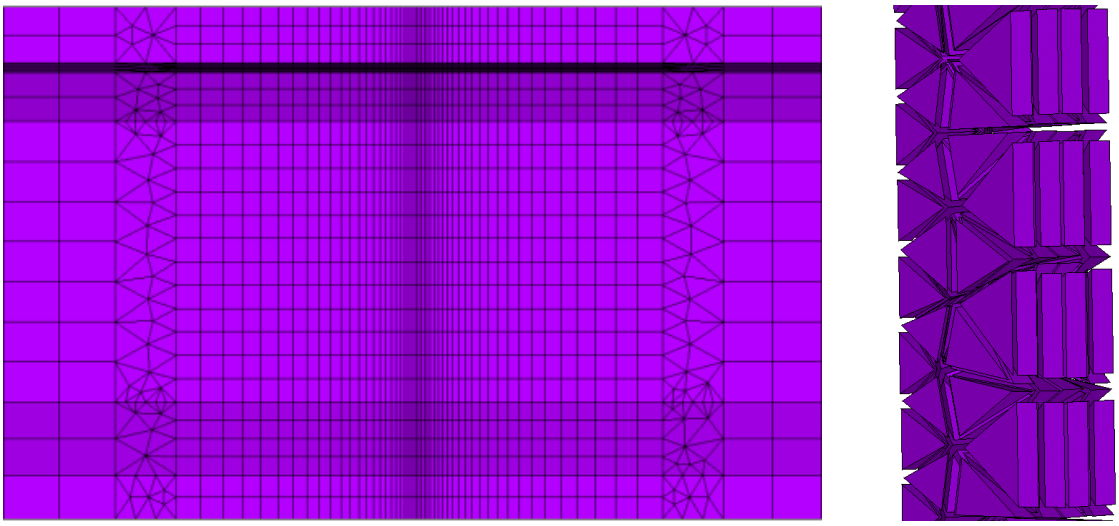
In our current model, the slices have an axial length of about 20 cm and so lead to a quite coarse localization of damage. The results given in Figure 16 and distinguish well the level of stiffness reduction and show the damage locus near the cutting line. The abscissa presents the length of the beam that the origin is defined in the middle and the cutting line is 5 m off the origin.

In order to improve the accuracy of the localization, the axial widths of the slices need to be reduced. As the width of a crack is only in the order of magnitude of millimeters, the mesh has to permit very local stiffness reduction. On the other hand, a large stiffness reduction occurs directly at the location of a crack due to the diminution of the cross-section. But at only small distance from the crack, the cross-section is intact again. In the current work, a damage function with the shape of a Gaussian Bell curve was used, which is given by

$$p \cdot e^{-0.5\left(\frac{x-\mu}{\sigma}\right)^2} \tag{1}$$

Hence the 3 parameters describe damage provided the axial mesh is sufficiently fine: p for the maximal reduction, σ for the width of the curve and μ for localization. With a finer mesh, we can define a more narrow bell curve, that allows a more accurate localization of damage. Of course, any reduction of the element size evolves higher computing effort.

As the outputs from the coarse meshing provide us already a coarse localization of damage, the mesh at the identified location can be refined. The idea was carried out with a second model with refined mesh in a region of 1 m left and right of the cutting line. The axial width of slices was there reduced to 10 mm in the middle of this region as shown in Figure 17. To avoid skewed elements with large ratio of height to width, the element size in the vertical direction were also reduced. Simultaneously a transition needs to be created between the refined and the coarse mesh. For this purpose, a transitional mesh was generated with the same elements of SOLID186, however with tetrahedral or pyramidal shapes. The resulting mesh in the refined region is shown in Figure 17.



a) Refined mesh **b) Transition mesh shown with shrinked elements**

Figure 17: Mesh refinement in the refined region

This refined mesh leads to a more accurate damage localization, as shown in Figure 18. The damage was localized exactly at 5 m off the middle of the beam for state DS#1, DS#3 and DS#4; corresponding exactly to the cutting line. Only in DS#2, there is a little deviation of less than 20 cm due to convergence issue. However, by considering the whole length of the beam, the detection based on the refined mesh gives good results.

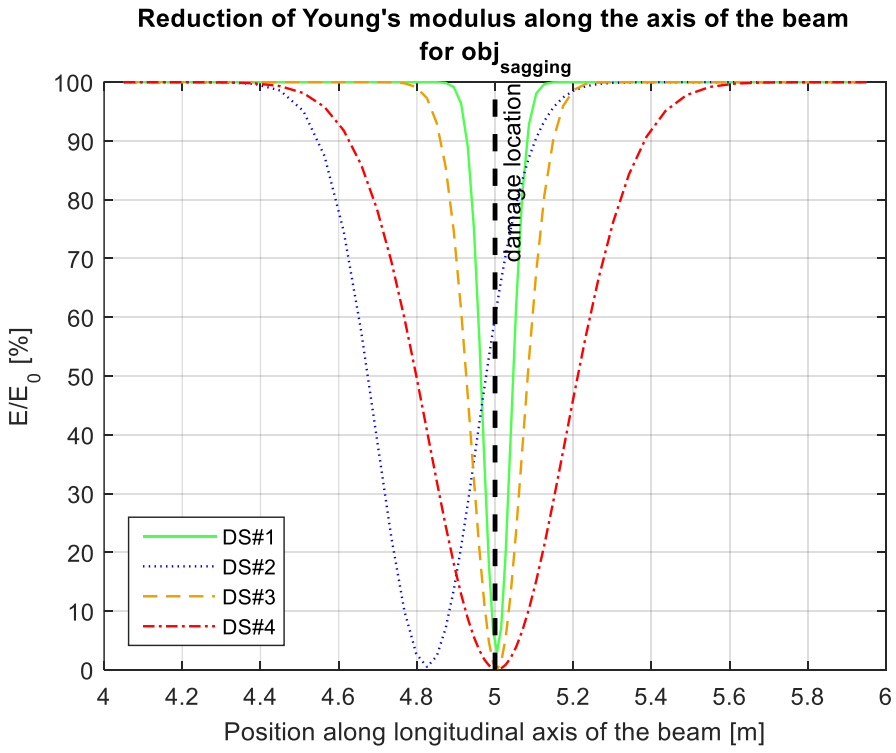


Figure 18: Reduction of Young's modulus along the beam in the refined FE-model

5 Conclusion

A part of a prestressed concrete bridge was tested in the presented work. The test-structure was exposed to real environmental conditions, such as temperature fluctuations and solar radiation, so the assessment was confronted with the same challenges as testing of a bridge still in operation. The FE-model consisting of solid elements allowing better accuracy than a classical simple beam analysis. An advantage is the mapped mesh allowing reduction effectively the computation cost and furthermore splitting the beam into controllable narrow slices. In this manner, it was possible to reduce the YOUNG's modulus of groups including adjacent elements to simulate the decrease of local stiffness due to cracks or reduction of the bending stiffness along the length of the beam.

Regardless of nonlinearities presented in bridges, the current work choose a linear FE-model for reasons of efficiency and practical application. Therefore, the model can be improved by considering nonlinearities, for instance on contact conditions. Another perspective relies to substructure-techniques that could reduce the computational effort.

References

[1] M. Link, *Updating of analytical models – review of numerical procedures and application aspects*, In: Proc., Structural Dynamics Forum SD2000, Research Studies Press, Baldock (1999), pp. 193-223.

[2] M.M. Abdel Wahab, G. De Roeck, B. Peeters, *Parameterization of damage in reinforced concrete structures using model updating*, Journal of Sound and Vibration, Vol. 228, No. 4, Elsevier (1999), pp. 717-730.

[3] A. Teughels, J. Maeck, G. De Roeck, *Damage assessment by FE model updating using damage functions*, Computers & Structures, Vol. 80, No. 25, Elsevier (2002), pp. 1869-1879.

[4] A. Teughels, G. De Roeck, *Structural damage identification of the highway bridge Z24 by FE model updating*, Journal of Sound and Vibration, Vol. 278, No. 3, Elsevier (2004), pp. 589-610.

[5] V.-H. Nguyen, S. Schommer, S. Maas, A. Zürbes, *Static load testing with temperature compensation for structural health monitoring of bridges*, Engineering Structures, Vol. 127, Elsevier (2016), pp. 700-718.

[6] S. Schommer, *Damage detection in prestressed concrete bridges based on static load testing, sagging and modal parameters, using measurements and model updating*, PhD dissertation, University of Luxembourg, Luxembourg (2017).

[7] S. Schommer, V.-H. Nguyen, T. Kebig, A. Zürbes, S. Maas, *A Gaussian Bell curve-based damage function together with a sliced finite element meshing for damage assessment using model updating*, Mechanical Systems and Signal Processing, under Review (2018).

Simplified design of filler beam railway bridges for high-speed traffic

H. Bigelow[1], B. Hoffmeister[1], M. Feldmann[1]
[1] RWTH Aachen University, Institute of Steel Construction
Mies-van-der-Rohe-Str. 1, 52074 Aachen, Germany
e-mail: **bigelow@stb.rwth-aachen.de**

Abstract

Filler beam railway bridges are usually constructed as single span beam bridges. Due to high slenderness of this bridge type, calculated fundamental frequencies are usually in a range where resonance effects at rather slow crossing speeds are expected. Measurements however show repeatedly that filler beam bridges behave much better than predicted and resonance effects eventually may occur at significantly higher speeds.

In Europe, design of filler beam bridges usually requires a high number of simulated train crossings. To reduce modelling effort and computational time, the authors present a simplified approach using an equivalent single degree of freedom (SDOF) system. All parameters relevant for the design are considered and response values required can be determined. Furthermore, positive restraining effects of tracks exceeding bridge ends can be included to the design without increasing the computational time. The simulation results obtained with the new method are significantly enhanced in comparison to conventional design methods.

1 Introduction

Filler beam railway bridges have proven themselves as reliable and durable constructions. They have been built in Germany since the 19th century. Currently, approximately a quarter of all German railway bridges are filler beam bridges [1][2][3]. They usually have ballast beds and are constructed as simply supported beam systems. They are very popular replacement structures due to their relatively small construction heights. A typical example is given in Figure 1.

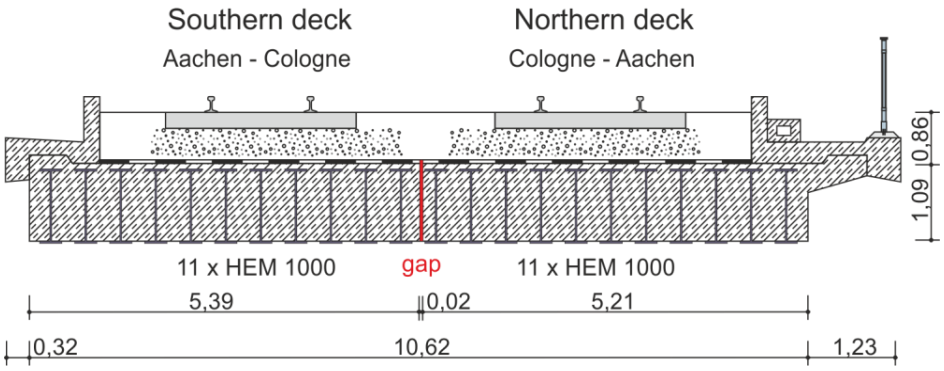


Figure 1: Cross section of sample bridge *EÜ Erfttalstraße*

The bridge *EÜ Erfttalstraße* in Figure 1 is a twin bridge, i.e. it consists of two decks separated by a longitudinal gap, which share a joint ballast bed. If necessary, the decks could thus be replaced individually.

Though measurements have revealed interaction between twin decks of several bridges via their shared ballast beds (e.g. [4][5][6][7]), the decks are usually considered individually in dynamic design. Therefore, only the southern deck of the bridge in Figure 1 will be used as a sample structure throughout this paper.

The bridge *EÜ Erfttalstraße* is part of the European high-speed connection between Brussels, Aachen and Cologne with a local maximum design speed of 69 m/s (250 km/h). It has been discussed previously in [2][3][4][6][8]. The span length L is 24.6 m. As usually with filler beam bridges, mass and stiffness properties of the simply supported beam system are constant over the span length. The fundamental frequency n_0 of such a system (see Figure 2b) can thus be calculated with Equation (1) [9][10].

$$n_0 = \frac{\pi}{2L^2}\sqrt{\frac{EI}{\mu}} \tag{1}$$

Where EI is the bending stiffness and μ is the mass per length. The southern deck (EI = 29796 MNm², μ = 25.98 t/m) has a fundamental frequency n_0 =2.8 Hz, when calculated according to (1). The fundamental frequency is of great importance in the design process.

As railway bridges are subjected to periodic excitation due to regular distances between train axes, designers have to predict if one of the natural frequencies of the bridge can be excited in resonance during a train passage. When performing simulations of train passages on filler beam bridges using numerical models, one can expect amplified dynamic structural responses at resonance speeds according to Equation (2) [10], where $L_{üP,k}$ is the wagon length of the respective train type k and i is 1, 2 ,3 or 4 (i^{th} harmonic excitation). In Germany generally all vertical bending frequencies n_j up to the upper limit in Equation (3) have to be considered, where n_2 is the third bending frequency. Eurocode 1 [9] considers it sufficient for simply supported bridges to consider only n_0 in Equation (2).

$$v_{res,i,j,k} = n_j \frac{L_{üP,k}}{i} \tag{2}$$

$$n_j \leq n_{max} = max\{30\ Hz, 1.5 \cdot n_0, n_2\} \tag{3}$$

Anyway, it is very likely that the decisive dynamic reactions will occur at resonance speeds dependent on n_0. Moreover, as demonstrated for ICE1 trains crossing the sample deck in Table 1, the resonance speeds related to higher frequencies often exceed the possible maximum speeds of current train types.

	nominally pinned beam system			**beam system with rotational springs**		
n_j **[Hz]**	n_0 **= 2.78**	n_1 **= 11.11**	n_2 **= 25.00**	n_0 **= 3.14**	n_1 **= 11.50**	n_2 **= 25.39**
$v_{res,1,j,ICE1}$	**264**	1056	2376	**299**	1093	2413
$v_{res,2,j,ICE1}$	132	528	1188	**149**	547	1207
$v_{res,3,j,ICE1}$	88	352	792	100	364	804
$v_{res,4,j,ICE1}$	66	**264**	594	75	**273**	603

Table 1: Critical velocities $v_{res,i,j,ICE1}$ [km/h] of an ICE1 on the southern deck of *EÜ Erfttalstraße* [11]

For simply supported bridges with spans $L \leq 40$ m (this applies to most German filler beam bridges) and design speeds $\leq$ 55.6 m/s (200 km/h), it can be sufficient to check the fundamental frequencies n_0 of unloaded decks against lower and upper limits of a simplified resonance check according to [9][10]. In case of simply supported bridges the respective limits depend on the span length L, see Figure 2. If n_0 is between the limits, dynamic train loads can be exclusively represented by static load models, combined with dynamic factors. If n_0 is outside the limits, additional dynamic simulations of train passages have to be performed.

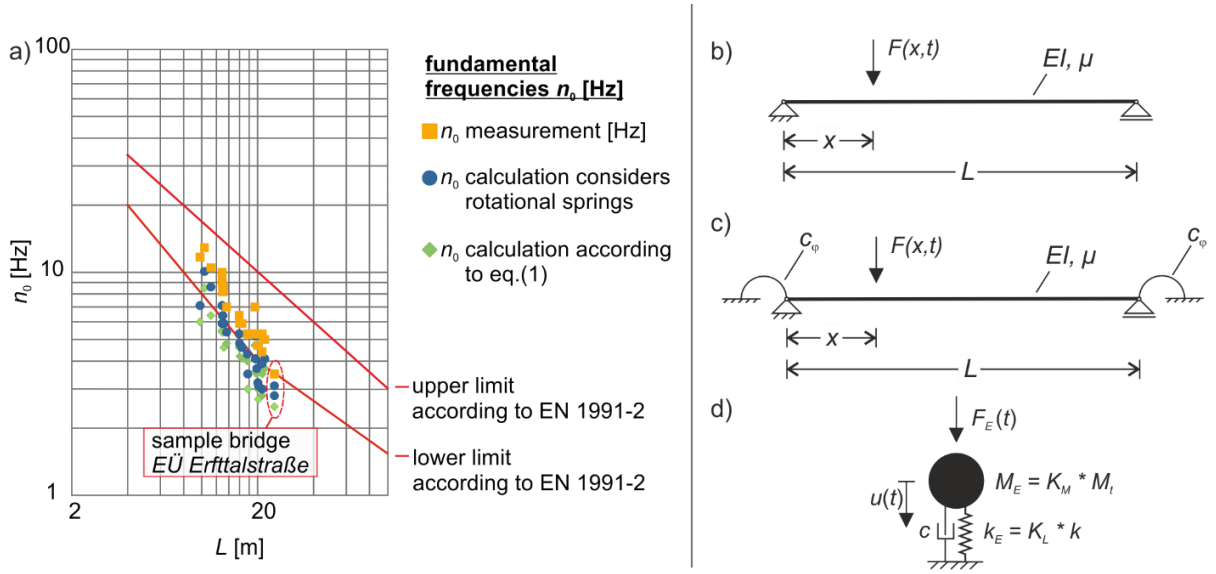


Figure 2: a) Calculated and measured fundamental frequencies n_0 of filler beam bridges [16] b) nominally pinned beam system c) beam system with rotational springs d) equivalent SDOF system

Figure 2a compares calculated and measured fundamental frequencies of 28 filler beam decks to their respective limits, among them the sample deck of *EÜ Erfttalstraße*. The bridges were investigated before introducing the *ICE3* train to the German railway network [2][3]. While most of the fundamental frequencies calculated with Equation (1) (depicted with green diamonds) are below the lower limits, the measured values (depicted with orange squares) are mostly between the limits. The measured frequency n_0 of both decks of *EÜ Erfttalstraße* is 3.5 Hz, which is just the lower limit according to Equation (4) (for 20 m< $L \leq$ 100 m).

$$n_{02} = 23{,}58 \cdot L^{-0{,}592} = 23{,}58 \cdot 24.6^{-0{,}592} = 3.54\ Hz \tag{4}$$

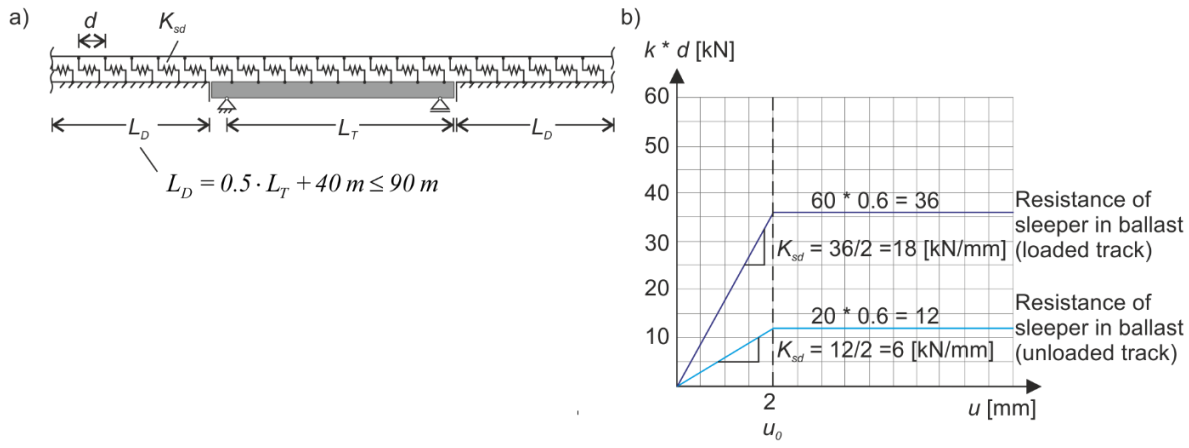


Figure 3: a) Combined track/structure system b) Resistance of sleeper in ballast, converted to a sleeper distance d = 0.6 m

Such differences between calculations and measurements have been observed for a while and are usually attributed to additional stiffness contributions of non-structural elements, such as ballast bed, rails, etc. [2][3][6]. Though there is a lot of ongoing research regarding possible additional stiffness contributions, e.g. of the ballast bed [2][4][5][11][12][13][14][15], current standards [9][10] permit only the consideration

of restraining effects of tracks exceeding the bridge ends (Figure 3) and restoring forces in bearings (the latter are negligible for filler beam bridges, which usually have elastomer supports).

A consideration of a combined track/structure system as in Figure 3a causes an increased modelling effort and usually a high increase of computational time. Practical engineers therefore usually neglect this additional contribution to system stiffness.

To minimize the effort, an equivalent rotational spring characteristic was derived in [11][16][17], which can be applied to the beam system (Figure 2c). Using the (linear) rotational spring stiffness c_φ of unloaded tracks can already improve the results of n_0 visibly (see Figure 2a, where the respective values are depicted with blue circles). The calculated frequency of the *EÜ Erfttalstraße* sample deck (c_φ= 897 MNm/rad) can be improved by 11 % to n_0 = 3.1 Hz. The simplified resonance check still cannot be satisfied for this particular bridge though (n_{02} =3.5 Hz). A high number of (high speed) train crossing simulations have to be performed between 40 m/s (lower limit for passenger trains [9][10]) and 83 m/s (300 km/h = 1.2 local maximum design speed). However, the respective critical speeds are enhanced (see Table 1). As n_0 is below the lower limit n_{02}, [9][10] permit simulations of train crossings with series of moving loads (if n_0 exceeds the upper limit, simulations considering train/track interaction are mandatory).

2 Equivalent SDOF system

2.1 Initial systems

To minimize the modelling and computational effort of train passage simulations, both systems given in Figure 2b and c can be represented by an equivalent single degree of freedom (SDOF) system (Figure 2d). It consists of an equivalent mass M_E, equivalent stiffness k_E and is subjected to an equivalent load vector F_E, which represents a crossing train. Equation (5) displays the linear differential equation of motion of the system, where c is damping, $\ddot{u}$ vertical acceleration, $\dot{u}$ vertical velocity and u vertical deflection.

$$M_E \cdot \ddot{u} + c \cdot \dot{u} + k_E \cdot u = F_E(t) \tag{5}$$

With the approach given by [18], the total mass of the initial system M_t can be transformed into M_E using a mass factor K_M. The stiffness k of the initial system (inverse of vertical deflection in mid-span due to a given load distribution) can be transformed into k_E with a load factor K_L. With Equation (6) respective load factors K_L for systems with distributed loads p can be derived. If the initial system is subjected to single loads F_r, K_L can be derived with Equation (7). As filler beam bridges have uniformly distributed masses, Equation (8) can be used to calculate the respective mass factors K_M; [18] gives additional equations for systems with single masses. Equations (6) to (8) require a shape function $\Phi(x)$ according to Equation (9), which is the product of stiffness k and bending line $w(x)$ of the initial system and thus depends on the load distribution. The selected approach assumes that $\Phi(x)$ is also affine the fundamental mode shape of the initial system.

$$K_L = \frac{\int_0^L p \cdot \Phi(x) dx}{p \cdot L} \tag{6}$$

$$K_L = \frac{\sum^r F_r \Phi_r}{\sum^r F_r} \tag{7}$$

$$K_M = \frac{\int_0^l \mu \cdot \Phi^2(x) dx}{\mu \cdot L} \tag{8}$$

$$\Phi(x) = k \cdot w(x) \tag{9}$$

Table 2 lists the respective parameters k, K_L, and K_M for an nominally pinned system (rows I, II) according to [18] and of a system with additional rotational springs (rows III, IV) according to [11][16]. In both cases distributed loads and a single load in mid-span are distinguished. The parameters in row I are based on $\Phi(x)$ according to Equation (10), those in row II are based on $\Phi(x)$ according to Equation (11); both are given in

[18]. For rows III and IV an auxiliary parameter $\tilde{c}$ according to Equation (12) is required. The parameters in row III are based on $\Phi(x)$ according to Equation (13). A derivation of this $\Phi(x)$ is given in [11][16][17].

$$\Phi(x) = \frac{16}{5L^4}(L^3x - 2Lx^3 + x^4) \tag{10}$$

$$\Phi(x) = \frac{x}{L^3}(3L^2 - 4x^2) \tag{11}$$

$$\tilde{c} = L + \frac{2EI}{c_\varphi} \tag{12}$$

$$\Phi(x) = \frac{16\tilde{c}}{(5L^3\cdot\tilde{c}-4L^4)} \cdot \left[\frac{x^4}{L} - 2x^3 + \frac{L^2x^2}{\tilde{c}} + L^2 \cdot x\left(1 - \frac{L}{\tilde{c}}\right)\right] \tag{13}$$

$$M(x) = F\left(\frac{1}{2}x - \frac{L^2}{8\tilde{c}}\right) \text{ (for } x \le L/2) \tag{14}$$

$$w(x) = \iint \frac{-M(x)}{EI}dx = \frac{F}{16\cdot EI}\left[-\frac{4}{3}x^3 + \frac{L^2}{\tilde{c}}x^2 + \left(L^2 - \frac{L^3}{\tilde{c}}\right)x\right] \tag{15}$$

$$\Phi(x) = \frac{3}{L^3\cdot\left(1-\frac{3L}{4\tilde{c}}\right)} \cdot \left[-\frac{4}{3}\cdot x^3 + \frac{L^2}{\tilde{c}}\cdot x^2 + \left(L^2 - \frac{L^3}{\tilde{c}}\right)\cdot x\right] \tag{16}$$

The parameters in row IV are based on $\Phi(x)$ according to Equation (16); Equations (14)(15) present steps of its derivation [11].

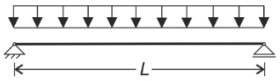
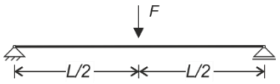
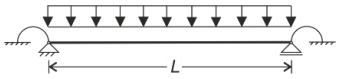
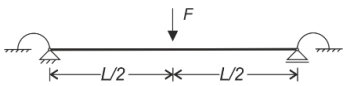
	Loading	k	K_M	K_L
I		$\frac{384\,EI}{5L^3}$	$\frac{3968}{7875} \cong 0.50$	$\frac{16}{25} = 0.64$
II		$\frac{48\,EI}{L^3}$	$\frac{17}{35} \cong 0.49$	1.0
III		$\frac{384\cdot\tilde{c}\cdot EI}{5L^3\cdot\tilde{c}-4L^4}$	$\frac{256\tilde{c}^2}{(5L^3\cdot\tilde{c}-4L^4)^2}\cdot\left[\frac{31}{630}L^6 - \frac{17}{210}\frac{L^7}{\tilde{c}} + \frac{1}{30}\frac{L^8}{\tilde{c}^2}\right]$	$\frac{8(6\tilde{c}-5L)}{15(5\tilde{c}-4L)}$
IV		$\frac{48\cdot EI}{L^3\cdot\left(1-\frac{3}{4}\frac{L}{\tilde{c}}\right)}$	$\frac{18}{\left(1-\frac{3}{4}\frac{L}{\tilde{c}}\right)^2}\cdot\left[\frac{17}{630} - \frac{61}{1440}\frac{L}{\tilde{c}} + \frac{1}{60}\frac{L^2}{\tilde{c}^2}\right]$	1.0

Table 2: Transformation factors [11][16][18]

The fundamental frequency of the equivalent SDOF can be calculated according to Equation (17). Though the form functions $\Phi(x)$ of the initial systems under distributed loads (rows I, III) technically are in slightly better agreement with the actual mode shape, the differences between n_0 calculated with the respective parameters given in rows I and II are very small. The same applies to the differences between n_0 calculated according to rows III and IV.

$$n_0 = \frac{1}{2\pi}\cdot\sqrt{\frac{k_E}{M_E}} = \frac{1}{2\pi}\cdot\sqrt{\frac{K_L\cdot k}{K_M\cdot M_t}} \tag{17}$$

For the simulation of train crossings the parameters given in rows II and IV have to be considered, as the passing trains are considered as series of (moving) single loads. As the equivalent SDOF represents one point in mid-span of the initial system, the load vector has to be applied here.

2.2 Equivalent load vector

One moving load *F* crossing a beam system can be approximated quite well if it is applied only in mid-span as a half sine function *F(χ)*, see Figure 4 and Figure 5. The complete load vector to be applied to the equivalent SDOF system can be created with Equation (18).

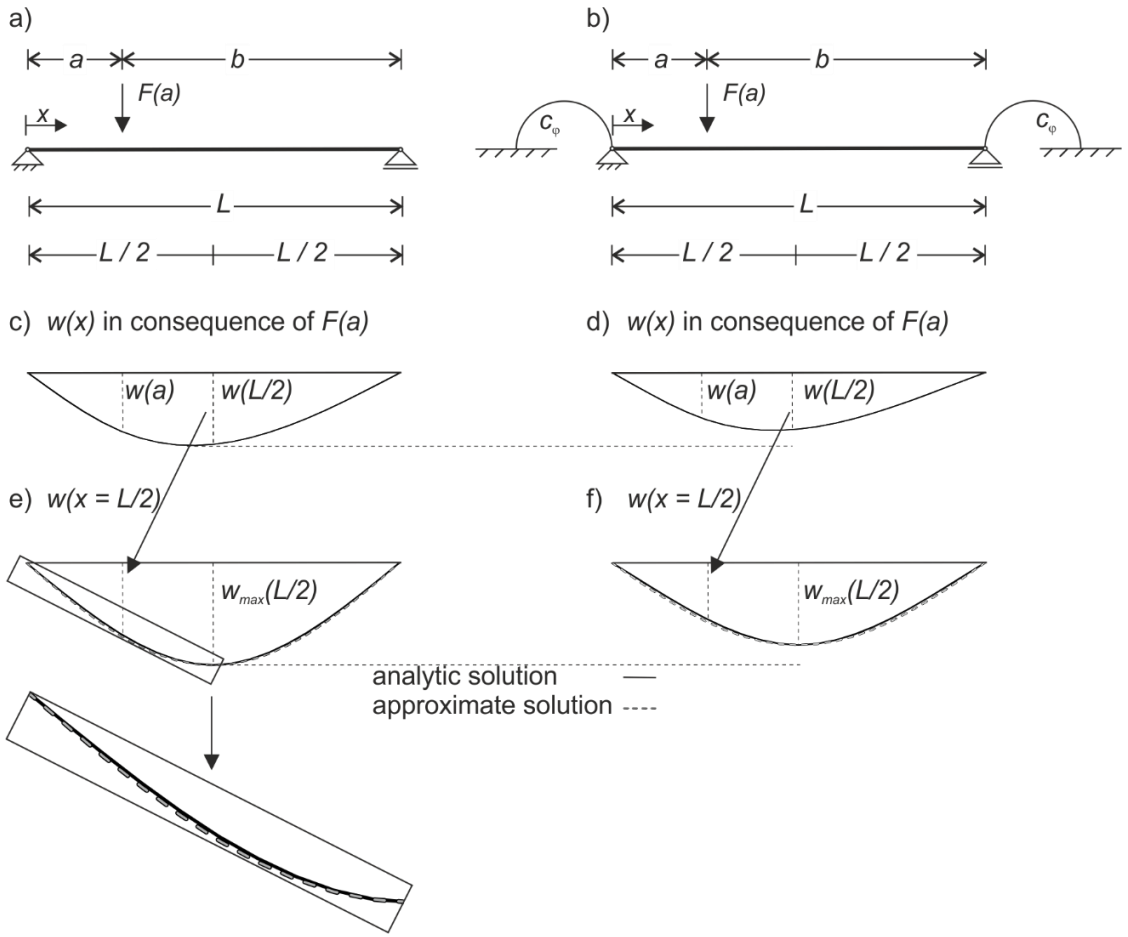


Figure 4: Beam system under moving load a) nominally pinned, b) with rotational springs, c) d) bending lines resulting to load F at position a, e), f) deflection in mid-span: analytical vs. approximate solution [11]

$$F_E(t) = \sum F_i(t) = \sum F_i \cdot sin(\Omega \cdot t) = \sum F_i \cdot sin\left(\frac{v \cdot \pi}{L} \cdot t\right) \tag{18}$$

Figure 4 compares the two discussed systems under a moving load *F*. Consideration of the additional springs has a positive effect on the vertical deflection. Nonetheless, the rotational spring stiffness c_φ is sufficiently small to allow the vertical deflection in mid-span to be approximated with the half sine function. In case of fully fixed supports the shown approximation leads to false results.

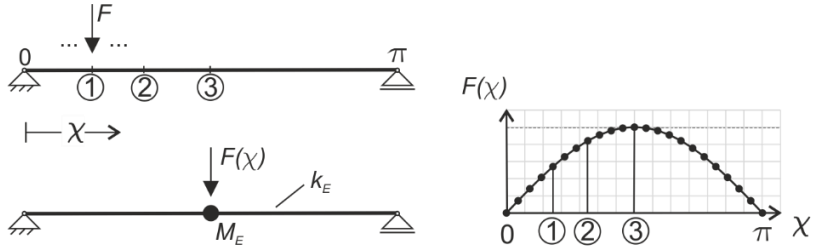


Figure 5: Representation of a moving load with a single load in mid-span [11]

2.3 Derivation of further parameters

Solving Equation (5) delivers vertical accelerations, velocities and deflections in mid-span of the respective initial system. The results presented within this paper were obtained using a numerical approach (Newmark algorithm, see e.g. [19]).

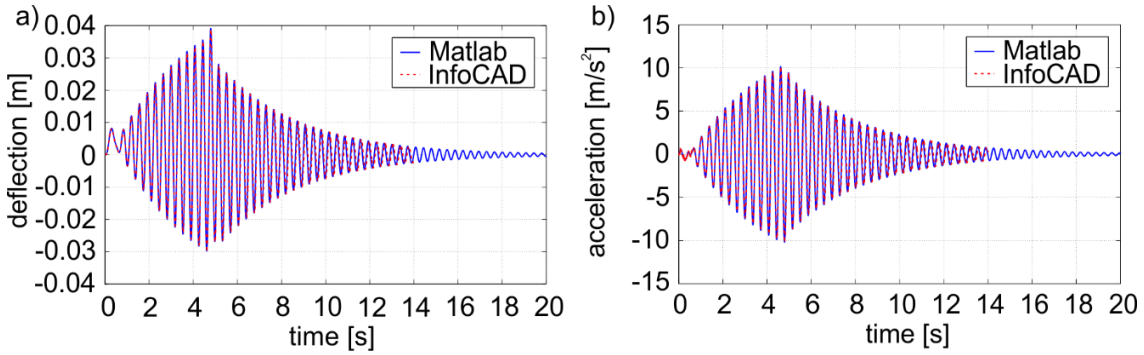


Figure 6: Vertical reactions in mid-span to an ICE 1 crossing at $v_{res,1,j,ICE1}$ = 299 km/h a) deflections b) accelerations

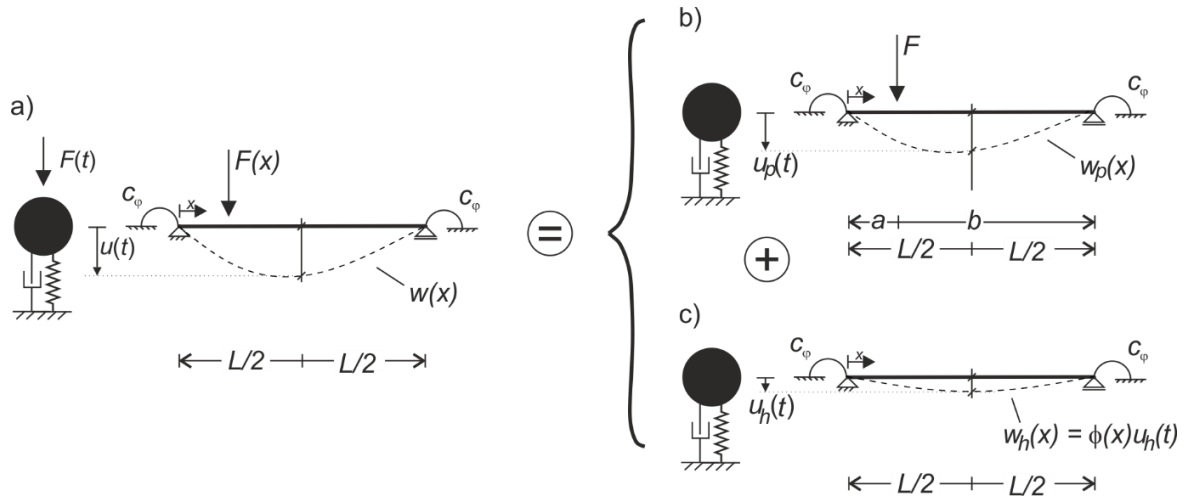


Figure 7: Solution of differential equation $u(t)$ b) inhomogeneous solution $u_p(t)$ c) homogeneous solution $u_h(t)$ [11]

To perform the simulations with the SDOF systems a MATLAB [20] routine was written. The code is given in [11]. Comparative calculations were performed using a commercial software InfoCAD [21] to simulate moving loads crossing a beam system. As demonstrated in Figure 6 for the southern deck of *EÜ Erft-talstraße*, the obtained results are very similar. Depicted are the results due to an ICE1 crossing the system with rotational springs (Figure 2c, with c_φ= 897 MNm/rad) at resonance speed $v_{res,1,j,ICE1}$ = 299 km/h (83 m/s) according to Equation (2). To derive further parameters relevant for design, static and dynamic part of the vertical deflection in mid-span have to be separated, as visualized with Figure 7 and Figure 8.

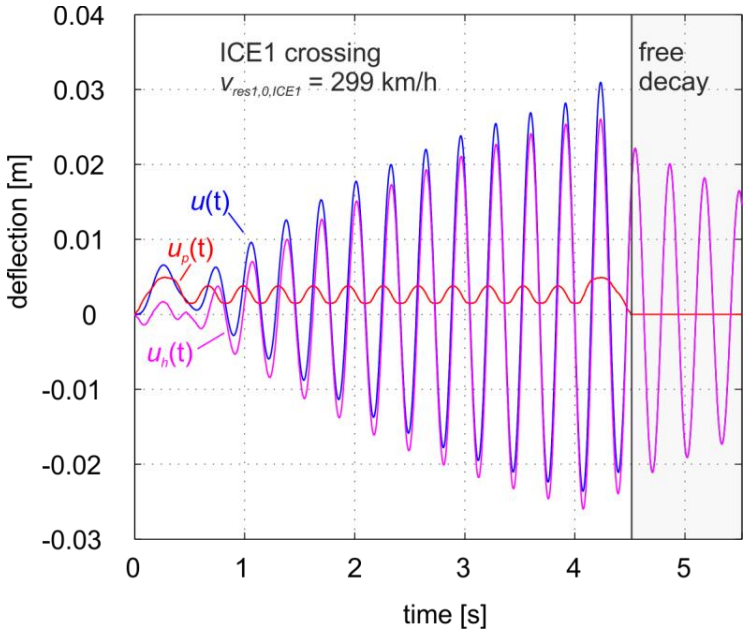


Figure 8: Total, inhomogeneous and homogeneous solution of an ICE1-crossing [11]

The static or inhomogeneous part of the solution $u_p(t)$ can be easily calculated with Equation (19). Subtracting it from the total solution $u(t)$ obtained by the numerical simulations delivers the dynamic or homogeneous part of the solution.

$$u_p(t) = \frac{F_E(t)}{k_E} \tag{19}$$

$$u_h(t) = u(t) - u_p(t) \tag{20}$$

The static reactions to the crossing trains can easily be calculated for any position in the initial system. Equations (21) to (27) are valid for the initial system with rotational springs (Figure 2c). They can also be used for the nominally pinned system ($c_\varphi \to 0$).

$$\varphi_p(x,t) = w'(x,t) \tag{21}$$

$$w'(x=0) = \frac{F}{6 \cdot EI} \cdot \left[\frac{a}{L}(a-L)(a-2L) - \frac{ab}{EI} \frac{(a-b)\left(\frac{L}{EI}+\frac{2}{c_\varphi}\right)+3L\left(\frac{b}{EI}+\frac{2b}{c_\varphi L}+\frac{2}{c_\varphi}\right)}{\left(\frac{L}{EI}+\frac{2}{c_\varphi}\right)\left(\frac{L}{EI}+\frac{6}{c_\varphi}\right)} \right] \tag{22}$$

$$w'(x=L) = \frac{F}{6 \cdot EI} \cdot \left[-3aL + 2\frac{ab(a-b)}{EI\left(\frac{L}{EI}+\frac{6}{c_\varphi}\right)} + \frac{a}{L}(a^2+2L^2) + 3\frac{abL}{EI} \frac{\left(\frac{b}{EI}+\frac{2b}{c_\varphi L}+\frac{2}{c_\varphi}\right)}{\left(\frac{L}{EI}+\frac{2}{c_\varphi}\right)\left(\frac{L}{EI}+\frac{6}{c_\varphi}\right)} \right] \tag{23}$$

$$M_p(x,t) = \begin{cases} \left(\frac{F(L-a)}{L} + \tilde{\tilde{C}}\right)x + \tilde{C} & for\ x \le a \\ \left(\frac{-Fa}{L} + \tilde{\tilde{C}}\right)x + Fa + \tilde{C} & for\ x > a \end{cases} \tag{24}$$

$$V_p(x,t) = \begin{cases} \left(\frac{F(L-a)}{L} + \tilde{\tilde{C}}\right) & for\ x \le a \\ \left(\frac{-Fa}{L} + \tilde{\tilde{C}}\right) & for\ x > a \end{cases} \tag{25}$$

$$\tilde{C} = \frac{-F \cdot a(L-a)}{EI} \frac{\left(\frac{L-a}{EI} + \frac{2(L-a)}{c_\varphi L} + \frac{2}{c_\varphi}\right)}{\left(\frac{L}{EI} + \frac{2}{c_\varphi}\right) + \left(\frac{L}{EI} + \frac{6}{c_\varphi}\right)} \tag{26}$$

$$\tilde{\tilde{C}} = \frac{F \cdot a(L-a)(L-2a)}{EI \cdot L^2\left(\frac{L}{EI} + \frac{6}{c_\varphi}\right)} \tag{27}$$

Dynamic rotations and bending moments can be calculated with Equations (28) to (35) considering Equation (12). Here $\Phi(x)$ of the initial system under distributed load has to be considered according to Equation (16) or (10) respectively, as it is in better accordance with the actual mode shape.

$$\varphi_h(x,t) = u_h(t) \cdot \frac{\Phi'(x)}{\Phi\left(\frac{L}{2}\right)} = u_h(t) \cdot \Phi'(x) \tag{28}$$

$$M_h(x,t) = -u_h(t) \cdot EI \cdot \frac{\Phi''(x)}{\Phi\left(\frac{L}{2}\right)} = -u_h(t) \cdot EI \cdot \Phi''(x) \tag{29}$$

$$\Phi'(x) = \frac{16\tilde{c}}{(5L^3\tilde{c} - 4L^4)}\left[4\frac{x^3}{L} - 6x^2 + 2\frac{L^2 x}{\tilde{c}} + L^2\left(1 - \frac{L}{\tilde{c}}\right)\right] \tag{30}$$

$$\Phi''(x) = \frac{32\tilde{c}}{(5L^3\tilde{c} - 4L^4)}\left[6\frac{x^2}{L} - 6x + \frac{L^2}{\tilde{c}}\right] \tag{31}$$

$$\Phi'(0) = \frac{16(\tilde{c} - L)}{(5L\tilde{c} - 4L^2)} \tag{32}$$

$$\Phi'(L) = -\Phi'(0) = \frac{16(L - \tilde{c})}{(5L\tilde{c} - 4L^2)} \tag{33}$$

$$\Phi''(0) = \Phi''(L) = \frac{32}{(5L\tilde{c} - 4L^2)} \tag{34}$$

$$\Phi''(L/2) = \frac{16(2L - 3\tilde{c})}{(5L\tilde{c} - 4L^3)} \tag{35}$$

To calculate dynamic vertical forces one has to consider the system's inertia force *I*, see Figure 9. *I* is distributed in accordance with $\Phi(x)$ [18]. Dividing the system in half (Figure 9b), where the resulting ½ *I* acts in the distance $x_{S,\Phi}$ (37) from the support, and solving the equilibrium of forces leads to the vertical forces at the supports in Equation (38).

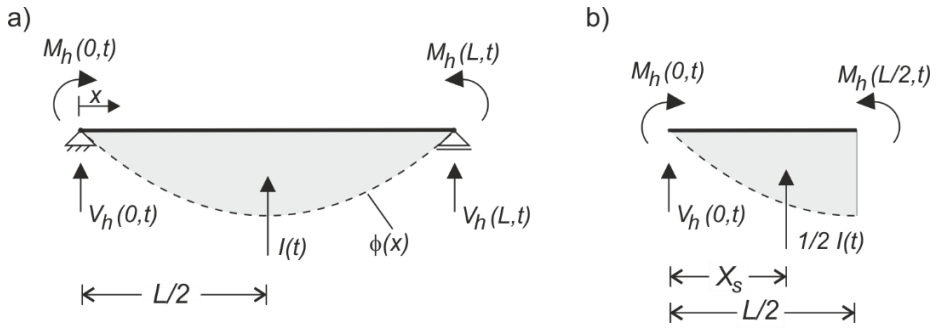


Figure 9: Dynamic equilibrium of homogeneous solution a) complete bridge b) half bridge [11]

$$A_\Phi = \int_0^{L/2} \Phi(x)dx = \frac{2\cdot L(12\cdot\tilde{c}-10\cdot L)}{15(5\cdot\tilde{c}-4\cdot L)} \tag{36}$$

$$x_{S,\Phi} = \frac{1}{A_\Phi}\int_0^{L/2} x\cdot\Phi(x)dx = \frac{L(61\cdot\tilde{c}-50\cdot L)}{16(12\cdot\tilde{c}-10\cdot L)} \tag{37}$$

$$V_h(0,t) = V_h(L,t) = \frac{M_h(L/2,t)-M_h(0,t)}{x_{S,\Phi}} \tag{38}$$

Combining dynamic and static part of the respective solution leads to the total solution in consequence of a passing train. Figure 10 shows again a very good agreement between results obtained with the SDOF system and the beam system. Here, exemplarily bending moment and vertical force at the left support due to a train crossing the initial system with rotational springs at resonance speed $v_{res,1,j,ICE1}$ = 299 km/h (83 m/s) are presented.

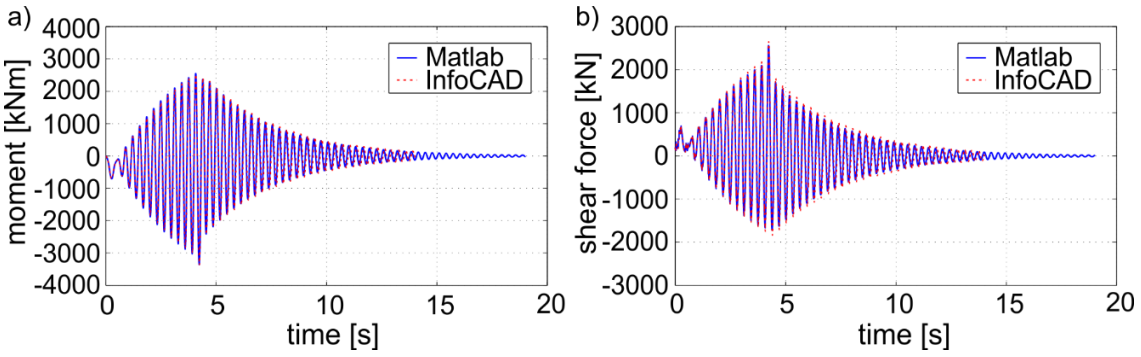


Figure 10: a) Reactions at left support to an ICE 1 crossing at $v_{res,1,j,ICE1}$ = 299 km/h bending moments b) shear forces [11]

Figure 11 compares vertical deflections and accelerations in mid-span due to an ICE1 crossing at $v_{res,4,j,ICE1}$ =273 km/h (resonance speed of the second bending frequency n_1), see also Table 1. The results are also very good considering the fact that the SDOF only represents the fundamental mode shape. Moreover, a comparison to the reactions to a train crossing with different velocities (selected maximum and minimum reactions are plotted against the respective crossing velocity v in Figure 12), shows that the resonance speed $v_{res,1,j,ICE1}$ = 299 km/h (see also Figure 6) is decisive for design.

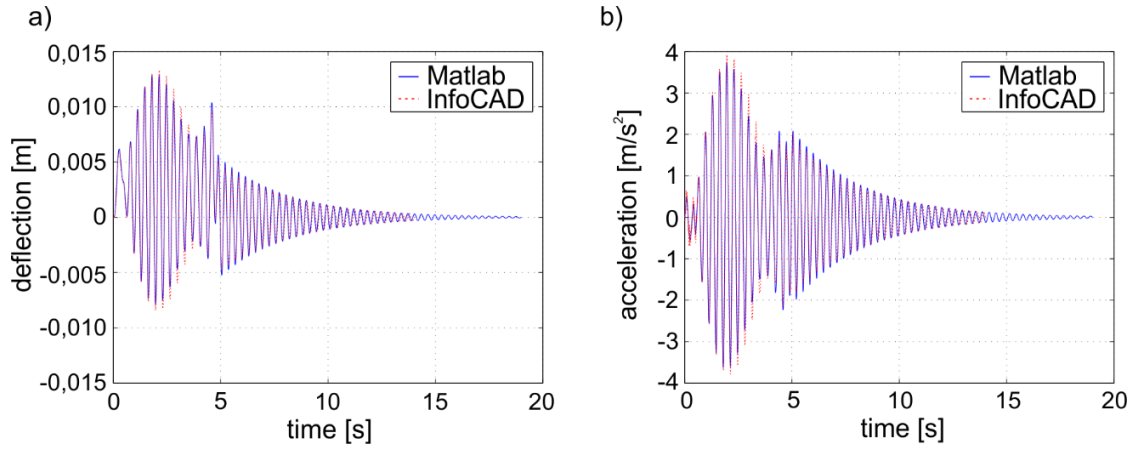


Figure 11: ICE1 crossing with $v_{res,4,j,ICE1}$ =273 km/h; mid-span: a) deflections b) accelerations [11]

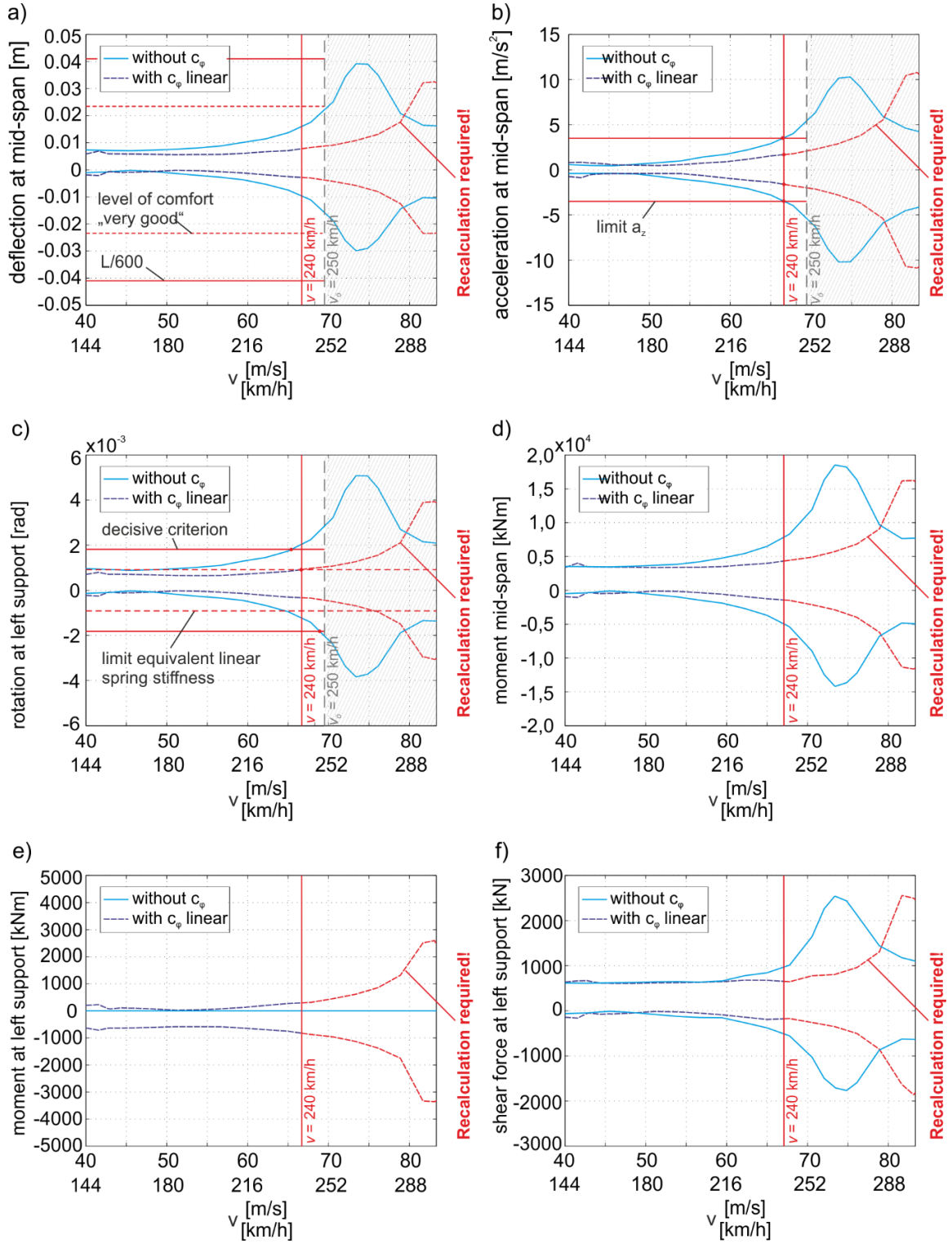


Figure 12: Comparison of maximum values due to ICE1 crossings a) deflection in mid-span b) acceleration in mid-span c) rotation at left support d) bending moment in mid-span e) bending moment at left support f) vertical force at left support [11]

2.4 Discussion of results

Figure 12 plots minimum and maximum reactions to ICE1 trains crossing the southern deck of *EÜ Erft-talstraße* against the respective crossing velocity *v*. For verifications in the Serviceability Limit States *SLS* velocities up to the maximum design speed of 250 km/h (69/s) have to be considered (Figure 12 a-c). For verifications in the Ultimate Limit States *ULS* velocities up to 300 km/h (83/s) have to be considered (1.2 • maximum design speed). A consideration of the additional rotational spring stiffness c_φ= 897 MNm/rad already improves the obtained results visibly (to create conservative results only the stiffness of an unloaded track on the embankment is used during the complete calculation). While some of the maximum and minimum reactions (a deflection, c rotation, d moment in mid-span) are also reduced in their amount by consideration of the additional rotational stiffness, the key benefit is that the decisive resonance speed $v_{res,1,j,ICE1}$ is increased from 264 km/h to 299 km/h. *SLS* criterions given by [9][10] regarding maximum vertical acceleration ($a_z \leq 3.5$ m/s²) and rotation cannot be satisfied with the nominally pinned system (without c_φ) but can be satisfied with the system with rotational springs (with c_φ).

However, it has to be acknowledged that the rotation limit ($9.14 \cdot 10^{-4}$ rad) for the linear spring stiffness c_φ= 897 MNm/rad is exceeded for velocities *v* >240 km/h (67 m/s). This means that at least one of the spring elements on the embankment (Figure 3a) reaches the critical value u_0 (Figure 3b), which (slightly) decreases the stiffness. Strictly speaking a recalculation of all ICE1 crossings with *v* >240 km/h would be necessary. As shown in [11], the stiffness decrease is very small and the results differ only slightly in the range of the resonance speed.

3 Conclusions

Dynamic simulations of train passages on filler beam bridges can be performed with equivalent SDOF systems. The SDOF system represents the mid-span of the initial beam system. Required bridge parameters for the simulations are span length *L*, bending stiffness *EI*, total mass M_t and damping. Compared to computations of complete beam systems, this procedure saves effort and especially computational time as vertical accelerations, velocities and deflections are calculated in mid-span only and any additional design parameters are derived afterwards at required points of interest everywhere else in the initial system.

The additional stiffness contribution of a combined track/super structure system can be included by adding equivalent rotational springs (with stiffness c_φ) at the supports of the initial beam system. This adjusted initial system can also be represented with an equivalent SDOF system without increasing the computational time. As the equivalent spring characteristic c_φ is non-linear, rotations at the support have to be checked against a bridge specific rotation. The presented sample calculations were performed using a linear spring stiffness c_φ. It was shown that the rotation, until which the stiffness characteristic c_φ is linear was exceeded for crossing velocities over 240 km/h (67 m/s). Next, recalculations of these train crossings will be performed considering a non-linear spring characteristic.

Further steps will also include a discussion if higher rotational a spring stiffness (representing a loaded track on the embankment) can be considered during parts of the train crossing simulation.

References

[1] Schmitt, V., Seidl, G., Vogel, C., Schülke, B., Koch, E.: *Untersuchungen zum verstärkten Einsatz von Stahlverbundkonstruktionen bei Brücken kleiner und mittlerer Stützweiten*, Forschungsvorhaben P 629, Verlag und Vertriebsgesellschaft mbH, Düsseldorf, 2005.

[2] Rauert, T.: *Zum Einfluss baulicher Randbedingungen auf das dynamische Verhalten von WiB-Eisenbahnbrücken*, D 82 (Dissertation RWTH Aachen University), SHAKER Verlag (2011), ISBN 978-3-8440-0360-4

[3] Rauert, T.; Bigelow, H.; Hoffmeister, B.; Feldmann, M.; Patz, R.; Lippert, P.: *Zum Einfluss baulicher Randbedingungen auf das dynamische Verhalten von WIB-Eisenbahnbrücken, Teil 1: Einführung und Messuntersuchungen an WiB-Brücken*, BAUTECHNIK 87 (2010) 11, p. 665-672, DOI: 10.1002/BATE.201010044

[4] Rauert, T.; Bigelow, H.; Hoffmeister, B.; Feldmann, M.: *On the prediction of the interaction effect caused by continuous ballast on filler beam railway bridges by experimentally supported numerical studies*, ENGINEERING STRUCTURES (2010), 12, p. 3981-3988

[5] Bigelow, H.; Rauert, T.; Hoffmeister, B.; Feldmann, M.: *Steifigkeitsbeiträge durchgängiger Schotterschichten auf Eisenbahnbrücken mit Längsfugen - Interaktion zwischen baulich getrennten Überbauten durch ein gemeinsames Schotterbett*, STAHLBAU 87 (2018), p. 215-224, DOI: 10.1002/STAB.201810577

[6] Rauert, T.; Bigelow, H.; Hoffmeister, B.; Feldmann, M.; Patz, R.; Lippert, P.: *Zum Einfluss baulicher Randbedingungen auf das dynamische Verhalten von WIB-Eisenbahnbrücken, Teil 2: Numerische Untersuchungen und Bemessungsvorschläge*, BAUTECHNIK 87 (2010) 12, p. 751-760

[7] Bigelow, H., Pak, D., Herrmann, R., Schneider, S., Marx, S., Petraschek, T., Feldmann, M.; Hoffmeister, B., *Dynamische Messungen an einer Eisenbahnbrücke als Stahlbetonverbundrahmen*. STAHLBAU 86 (2017): p. 778–788. doi:10.1002/stab.201710524

[8] Rauert, T., Hoffmeister, B., Cantieni, R., Brehm, M., Zabel, V.: *Experimental modal analysis of a twin composite filler beam railway bridge for high-speed trains with continuous ballas*t, Proceedings of the IABMAS'08 Conference (InternationaL Association for Bridge Maintenance and Safety), Seoul, Korea, 2008.

[9] EN 1991-2: Eurocode 1: Actions on structures - Part 2: Traffic loads on bridges

[10] DB NETZ AG: *Richtlinie 804:Einsenbahnbrücken (und sonstige Ingenieurbauwerke) planen, bauen und instand halten*, 2013.

[11] Bigelow, H.: *Vereinfachte dynamische Bemessung von WiB-Eisenbahnverbundbrücken für den Hochgeschwindigkeitsverkehr*, D 82 (Dissertation RWTH Aachen University), to be published 2018

[12] Mähr, T. *Theoretische und experimentelle Untersuchungen zum dynamischen Verhalten von Eisenbahnbrücken mit Schotteroberbau unter Verkehrslast*, Dissertation TU WIEN, 2009.

[13] Fink J.; Kirchhofer J. *Experimentelle Untersuchungen zum dynamischen Verhalten von Eisenbahnbrücken mit Schotteroberbau*, STAHLBAU 80 (2011) 5, p. 317-323. DOI: 10.1002/STAB.201101427.

[14] Kirchhofer J.; Fink J. *Analyse des dynamischen Verhaltens des Eisenbahnschotteroberbaues: Einfluss der Schwingungsamplitude und anderer Randbedingungen auf das Steifigkeits- und Dämpfungsverhalten*, STAHLBAU 82 (2013) 5, p. 370-377. DOI: 10.1002/STAB.201310050

[15] Baeßler M.: *Lageveränderung des Schottergleises durch zyklische und dynamische Beanspruchungen*, D 83 (Dissertation TU BERLIN), 2008.

[16] Bigelow, H., Feldmann, M., Hoffmeister, B., Zabel, V: *Zur Einspannwirkung von Eisenbahngleisen: Die Auswirkung auf die erste Biegeeigenfrequenz bei Einfeldträgerbrücken*, BAUTECHNIK 93 (2016) 7, p.462-469, DOI: 10.1002 / BATE.201600006.

[17] Feldmann, M., Hoffmeister, B., Bigelow, H., Könke, C., Zabel, V., Höll, S., Reichert, I.: Forschungsvorhaben P 941 / S 024/10187/11: *Dynamische Auslegung von Eisenbahnbrücken in Stahl- und Stahlverbundbauweise mit kleinen und mittleren Spannweiten für den Hochgeschwindigkeitsverkehr (DYNABRIDGE)*, Verlag und Vertriebsgesellschaft MBH, DÜSSELDORF, ISBN 978-3-942541-70-1

[18] Biggs, L. M.: *Introduction to Structural Dynamics*, MCGRAW-HILL, 1964

[19] Bathe, K.-J: *Finite-Elemente-Methoden*, ISBN 3-540-15602-X, 1990.

[20] MATLAB software version 2014A, MATHWORKS, 2014.

[21] InfoCAD software version 14.00x64, InfoGraph GmbH, www.infocad.de, 2014.

Examining the impact of critical building substructural elements on the building's rail induced vibration responsiveness

J. D'Avillez
WSP, Acoustics
WSP House, 70 Chancery Lane, London, United Kingdom WC2A 1AF
e-mail: **Jorge.DeAvillez@wsp.com**

Abstract

Rail induced ground-borne vibration, which often causes structure-borne noise, adversely impacts on human wellbeing and building serviceability. As current architectural trends are to adopt complex lightweight structures, centered on stronger, more lightly damped materials, a general rise in building vibration responsiveness should be expected. In limiting the impact of rail induced ground-borne vibration, countermeasures may turn out to be highly complex, incurring significant additional costs. Given that the vibration propagation is affected by the structural design, structural elements can be tuned to control, to some extent, the transfer of vibration. To assess the contribution, in terms of ground-borne noise reduction, of critical substructural elements, sensitivity analysis has been carried out via 3d numerical modelling. The study investigates the benefits of tuning the raft foundation, the secant wall and basement/ground floor slabs (i.e. unisolated slabs).

1 Introduction

Vibration generated by the track-train interaction, if not adequately mitigated, has the potential to be transmitted through the ground to adjacent buildings, setting floorplates and walls in to a vibratory motion. More often than not, this causes plate-like structural elements to radiate noise into sensitive spaces, giving rise to general annoyance, discomfort, potential sleep disturbance and interference with specific activities, including the operation of vibration sensitive devices.

With the densification of urban spaces, the tendency is for deeper basements, occasionally bringing buildings closer to underground rail tunnels. In addition, modern construction tends to rely on complex lightweight structures centered on stronger, more lightly damped, materials (e.g. pre-stressed concrete and steel frames, with fewer joints) raising the building's responsiveness.

Depending on the characteristics of the impinging vibration, countermeasures may turn out to be highly complex, often incurring significant additional costs to the development, not only financially, but also in terms of design impact, constructability and maintenance. As vibration propagation, and the manner in which it manifests itself, is affected by the structural design (including materials and geometry) [1], structural elements can be tuned to reduce the transfer of vibration. Tuning structural components, such as thickening the raft foundation, have been suggested (via industrial studies) in assisting mitigation strategies.

To assess the scope of potential countermeasures, mainly through the tuning of structural elements, this paper presents a theoretical study that centers on a contemporary lightweight structural building design. A sensitivity analysis is then carried out to evaluate potential rail-induced ground-borne noise isolation benefits as a function of structural tuning.

After evaluating the ground-borne noise isolation benefits when employing the conventional "Base-isolation" strategy, this study will go on to investigate the benefits of tuning a set of substructural elements,

as measured by the reduction in ground-borne noise throughout the building. The substructural elements under investigation are the raft foundation, the basement slabs and the secant wall.

2 General Mitigation Strategies

2.1 Base-isolation

Rail-induced ground-borne vibration, and subsequently radiated noise, can be mitigated by disrupting the vibration path. An effective way of controlling incoming vibration is to employ the "Base-isolation" concept, isolating the entire building at its foundations (or part of the building at a designated point).

The principle of Base-isolation is to decouple, using isolation units, the superstructure from the substructure resting on the ground which is affected by vibration, thus breaking the vibration path. Isolation units (e.g. helical springs or elastomeric bearings) are basic elements of the isolation system that enables the mechanical decoupling. Whether the building should be isolated using helical springs or elastomeric bearings depends on the degree of isolation required, which is given in terms of frequency and magnitude requirements. When considering buildings, spring systems can naturally isolate down to 3 Hz, whilst elastomeric bearing will typically only go down to 6 Hz (although, there are bearing manufactures that have managed to bring the isolation frequency down to 3.5 Hz).

The Base-isolation performance is dependent on the natural frequency of the isolation unit (which is a function of exerted load and stiffness), the damping of the isolation unit, number of isolation units (and how they're mounted, either in parallel or series, which will impact differently) and the mechanical properties of the ground structure in which the building is implanted [1].

The drawback with Base-isolation is that it impacts on the building's firmness making it vulnerable mainly to lateral motions; such effects will need to be counteracted through additional means, raising complexity to the structural design. As a rule of thumb: lowering the isolation frequency will raise the complexity of the required countermeasures.

According to isolation unit manufactures and suppliers, spring systems, although more effective, require higher level of maintenance as oppose to elastomeric bearings. Additionally, with elastomeric bearings, a higher degree of control over the lateral movement can be achieved. Therefore, from a structural engineering point of view, the preferable option, if the isolation requirement allows, tends to be elastomeric bearings.

2.2 Structural Tuning

As vibration flows from one medium to another a change in vibration magnitude (and/or phase) will occur as the incoming signal becomes modified by either the boundary and/or the different characteristics of the consecutive intervening medium (e.g. density), causing a rise or decay in vibration levels as a function of frequency [2]. When considering buildings, the structural elements, such as beams, columns and slabs, make up the media through which vibration travels. Generally, the greater the impedance mismatch between both coupled structures, the greater the loss in vibration levels when transferring from one structural element to another. In some cases, depending on the relationship between both intervening structural elements, a significant portion of vibration energy will fail to transfer due to reflections at the boundaries of both intervening structures. This feature can be exploited by thickening the raft foundation – more mass, more reflections will be expected. Another aspect that impacts on the vibration transfer is the mechanical joints coupling structure elements, such as bolts, rivets and welds; however, mechanical joints are outside the scope of this study.

In line with the above, isolation can be achieved by tuning key parameters of the influential structural elements. The "structural tuning" method can also be used to complement the Base-isolation mitigation scheme. It has the potential to lower the Base-isolation requirements (subsequently raising the natural

frequency of the isolation units), hence lowering the degree of complexity that the structural design will have to address.

Within the substructure there may be some structural components that have a higher influence on the building's response than others. However, their degree of influence is linked to extraneous conditions such as ground composition and building design [1]. As this study only examines a specific building arrangement planted onto a soft ground, conclusions should not be generalized without caution.

To carry out the study, a numerical model has been used, which is presented in the section below.

3 Numerical Model

When considering Base-isolation, the ground, which acts as a spring in line with its mechanical properties (e.g. stiffness), needs to be considered [3]. Because of the ground's elasticity, the isolated building can no longer be considered as a mass on a spring attached to a fixed frame. Therefore, simple dynamic models cannot be used.

Although numerical models have proved to be a highly efficient tool for studying rail-induced vibration phenomena, their accuracy, in terms of absolute levels, are somewhat questionable due to the difficulty in acquiring accurate actual data concerning the properties of the components of the model [4]. However, due to their geometrical flexibility when representing complex structures, numerical models are justified when predicting the insertion loss (i.e. relative changes) offered by a mitigation scheme of a complex. Additionally, as demonstrated in reference [5], the ground in which the building lays is required to be included in the model as it will bring the evaluated response closer to the actual response of the building.

Given the size of the domain being modelled, FINDWAVE® [6], a finite-difference time-domain method (FDTD), offers a way of computing the generation, propagation and reception of vibration for establishing relative changes to rail-induced noise and vibration levels [7]. Structure-borne noise is then evaluated by employing an empirical formulation, commonly referred to as the Kurzweil formula [8], which converts the vibration levels measured (or predicted) at the room floor into a sound level.

4 Scenario Being Examined

The building is an 9-storey, steel frame structure, built off a concrete substructure, with four basement levels. The substructure, which is 30m long and 20m wide, is approximately 20m deep.

The ground in which the building sits consists of an upper layer formed of approximately 2m of made ground, 3.5m Alluvium (silts) layer and 2.5m Gravels (terrace) layer above London clay.

4.1 Substructure

The substructure (see Figure 1) is formed by a secant pile wall (pile diameters are approximately 900mm) lined with a 250mm reinforced concrete wall. Male piles extend downwards beyond the raft foundation by circa 8m. The embedded retaining wall (the secant walls) are supported by five levels of 200mm thick reinforced concrete slabs. A 1.2m deep reinforced concrete raft slab is provided at Basement 4 to support the vertical loads of the whole building and to prop the base of the wall.

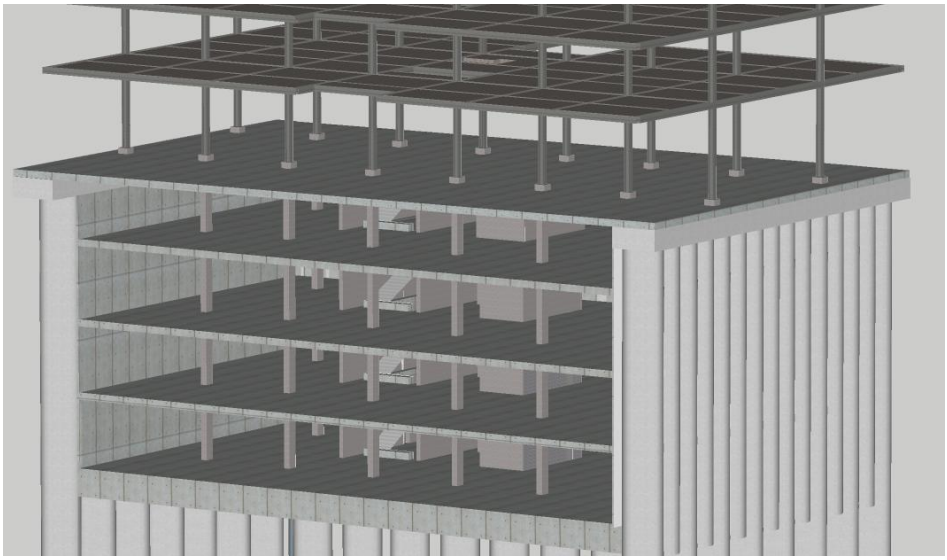


Figure 1: Substructure of the specimen building

The closest railway tunnel runs parallel to the secant wall, approximately 7m from the nearest edge of the raft foundation. There are twelve internal reinforced concrete columns located directly beneath the main columns of the superstructure. These columns are approximately 650mm square.

4.2 Superstructure

The superstructure (see Figure 2) is supported on a regular grid of closely spaced steel columns positioned within the middle third of the building. The 16 steel columns continue through the basement as reinforced concrete columns.

A 150mm thick concrete slab (see Figure 3) is provided throughout the superstructure floors. The slab acts compositely with MD60 trapezoidal decking. The floor slabs span circa 3.3m in the north-south direction between steel floor beams, and approximately 4.5m in the east west direction. Primary floor beams are typically 300mm deep internally and 350mm deep on the perimeter. The typical maximum depth of the internal steel floor beams is 300mm. The beams are positioned so that the top flanges are at the same level as the top of the slab.

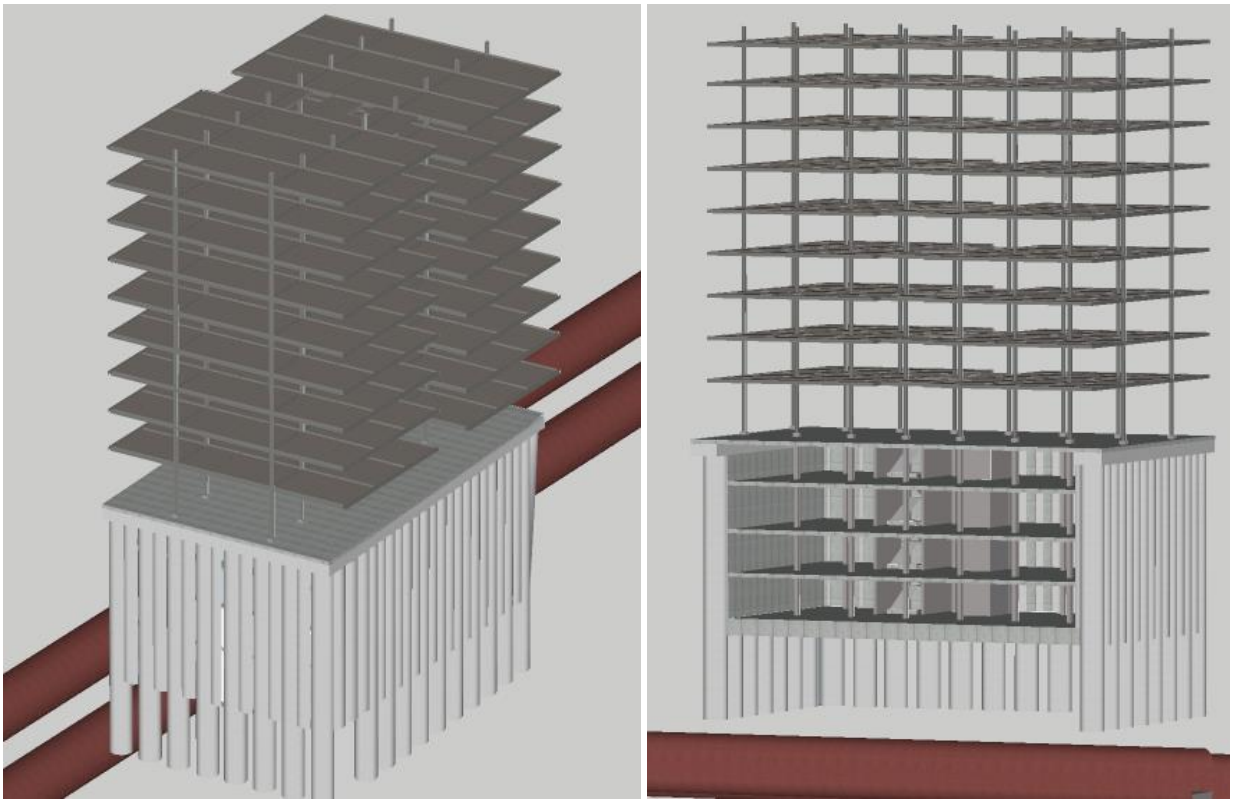


Figure 2: Substructure of the specimen building
(left: view from the south-west; right: view from the north)

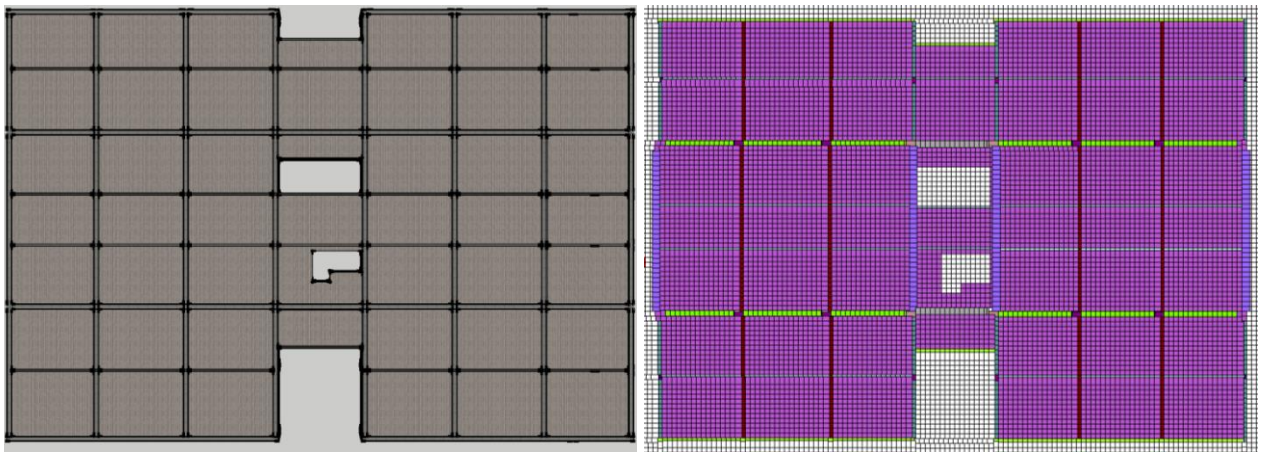


Figure 3: First floor level slab (same throughout the entire superstructure)
(left: representation of the slab and beams arrangement; right: FDTD discretization)

5 Assessment

As shown in Figure 4, the rail induced vibration levels are unevenly distributed across the floorplate, which is commonly taken to be the main radiating surface throughout the superstructure. As expected the floorplate expresses lower vibration levels around areas close to its supporting beams. Note that vibration velocity levels in Figure 4 have been A-weighted so as to conform to the Kurzweil formulation, enabling a direct comparison to the expected sound pressure level experienced throughout the floorplate.

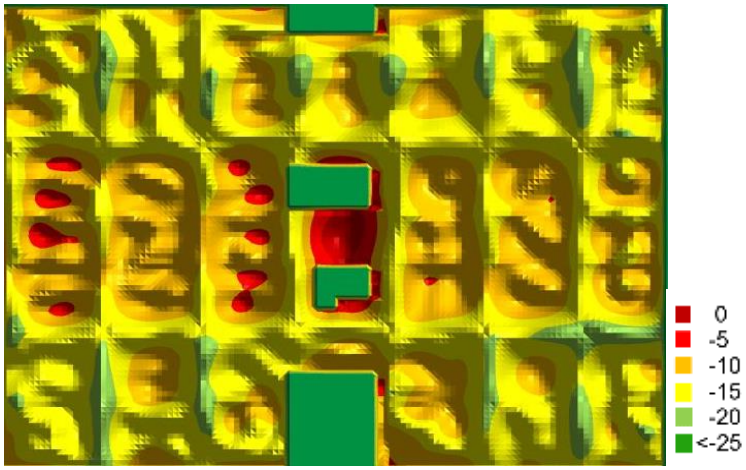


Figure 4: Evaluated rail induced vibration at the floorplate of the first floor level (normalized A-weighted vibration velocity levels)

5.1 Base-isolation

In contrasting the Base-isolation requirements, as given by the natural frequency of the isolation system, with the isolation performance, as measured by the evaluated A-weighted ground-borne noise level, a set of rail induced ground-borne noise evaluations using a range of Base-isolation frequencies have been carried out. Figure 5 reveals how ineffective a 10 Hz bearing is for this specific scenario (i.e. ground characteristics and building design), reducing the vibration transfer into the superstructure by circa 4 dB around the frequencies of interest.

Note that the isolation performance given herein cannot be generalized. As demonstrated in references [9] the isolation effectiveness is a function of the ground conditions, meaning that this same configuration under a different set of ground conditions could achieve a much higher isolation performance.

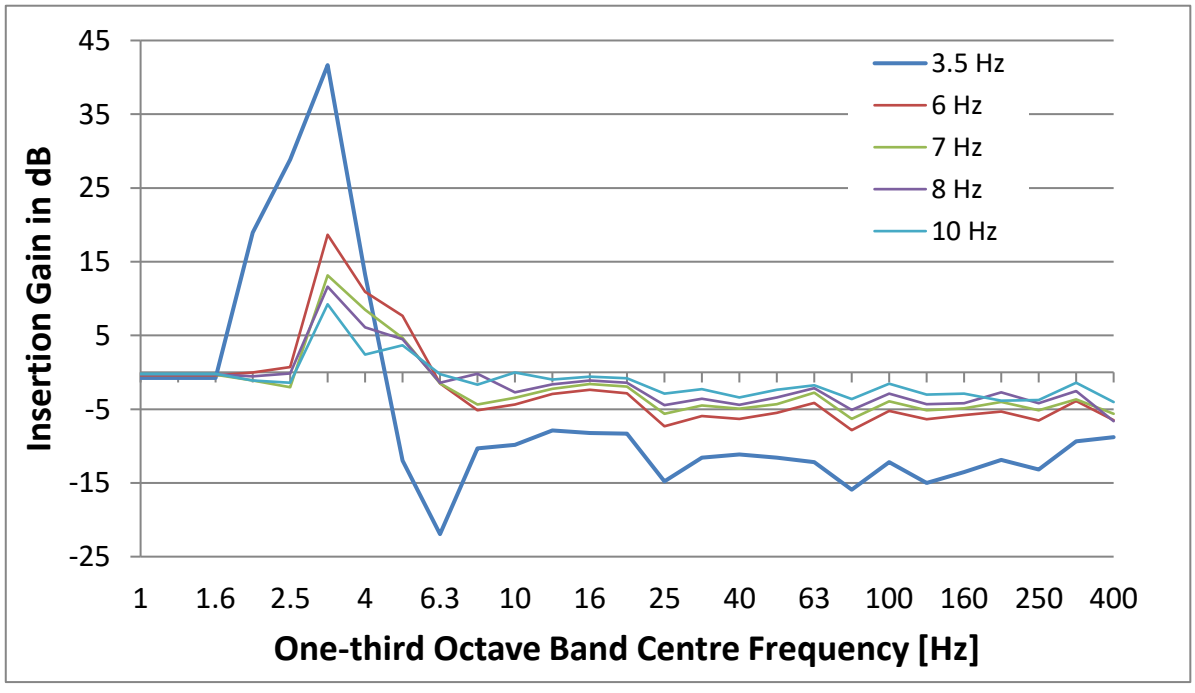


Figure 5: Relative change in vibration levels as a function of isolation system measured at a specific point on the floorplate of first floor level

Figure 6 maps out the ground-borne noise isolation benefits, in terms of $L_{Amax,s}$ (as given by the Kurtzweil formulation), for a set of Base-isolation frequencies. The noise levels, in dB(A), have been normalized to the noise response of the unisolated building; positive values represent the A-weighted evaluated noise reduction for a given Base-isolation frequency. The $L_{Amax,s}$ values, which are then used for assessing the relative ground-borne noise reduction, are computed by averaging a set of evaluated $L_{Amax,s}$ values across the floorplate. As seen by the missing blue bars, not all isolation frequency points were evaluated. As illustrated by the green curve in Figure 6 (which has been sketched to characterise a plausible regression curve), modelling results suggest a slight deviation from a linear relation between isolation frequency, in Hz, and isolation performance, in dB. This, to a degree, enables interpolating the isolation performance when approximating the optimal bearing isolation frequency.

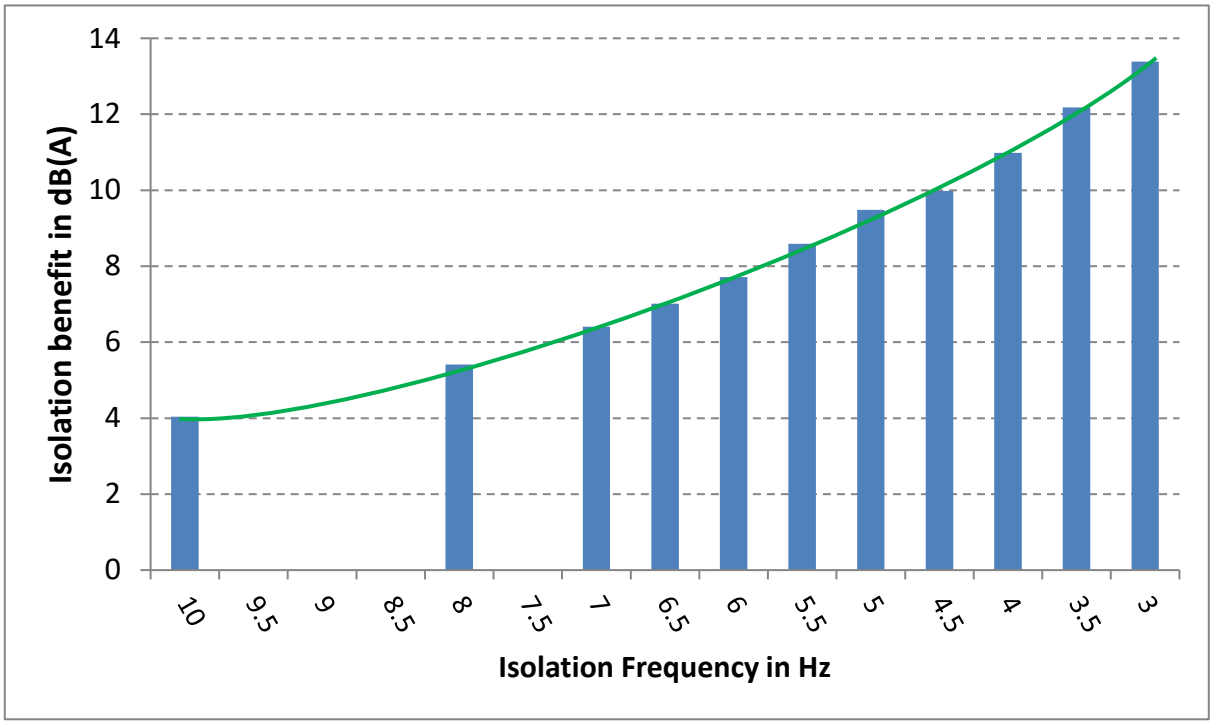


Figure 6: Normalized noise isolation benefits as a function of Base-isolation frequency (blue bar: evaluated through modelling; green curve: sketched arc depicting a representative regression curve)

Whenever the isolation frequency is required to go below 6 Hz, the mitigation strategy tends to employ helical springs; however, if the preference is for elastomeric bearings (which may arise due to maintenance and constructability requirements), the design might consider tuning structural elements so as to increase the required isolation frequency.

5.2 Structural Tuning

By thickening the raft foundation, a change in vibration transfer is expected. To evaluate the benefits of thickening the raft foundation, three observation points were chosen: basement level -2 (unisolated substructure); ground floor level (unisolated substructure); and first floor level (6 Hz isolated superstructure). Figure 7 shows the isolation benefits at each of the locations being assessed. For the ground floor and first floor level there is a diminishing return on isolation benefit, suggesting that there is an optimum raft thickness: 2.5m for first floor level and 3m for the ground floor. At the basement, given the base configuration, there seems to be an ever-increasing benefit in thickening the raft foundation (at least up to 4m thick).

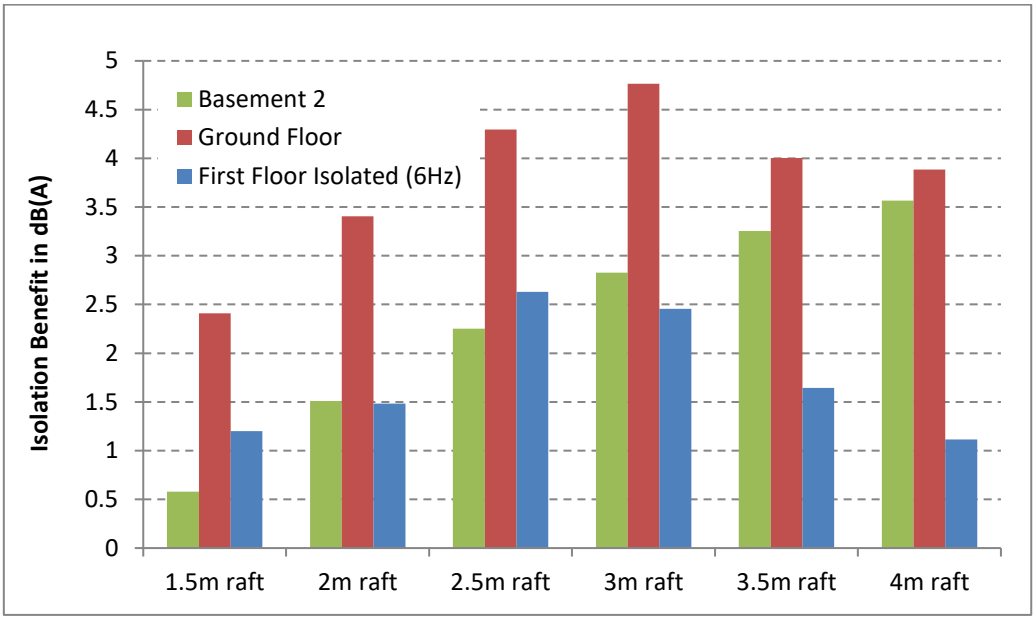


Figure 7: Contrasting the impact on ground-borne noise reduction at three areas of the building as a function of raft foundation thickness

Assuming the substructure is somewhat behaving as a lattice structure (as given by the columns-slabs arrangement), this study goes on to assess the isolation benefits of stiffening the lattice structure via thickening the substructure slabs (i.e. basement and ground floor slabs). This is believed to limit the vibratory motion of the substructure as a whole, limiting the freedom of movement. The sensitivity analysis evaluating the benefits in changing the substructure slab thickness, from 200mm to 400mm in steps of 100mm, fixes the raft foundation at 1.2m. Figure 8 reveals some isolation benefits, especially at ground level where the ground-borne noise falls by as much as 7 dB if the basement slabs are to increase from 200mm to 400mm. Another aspect worth noting is that the benefit of thickening the baseman slabs are not consistent throughout every floor level.

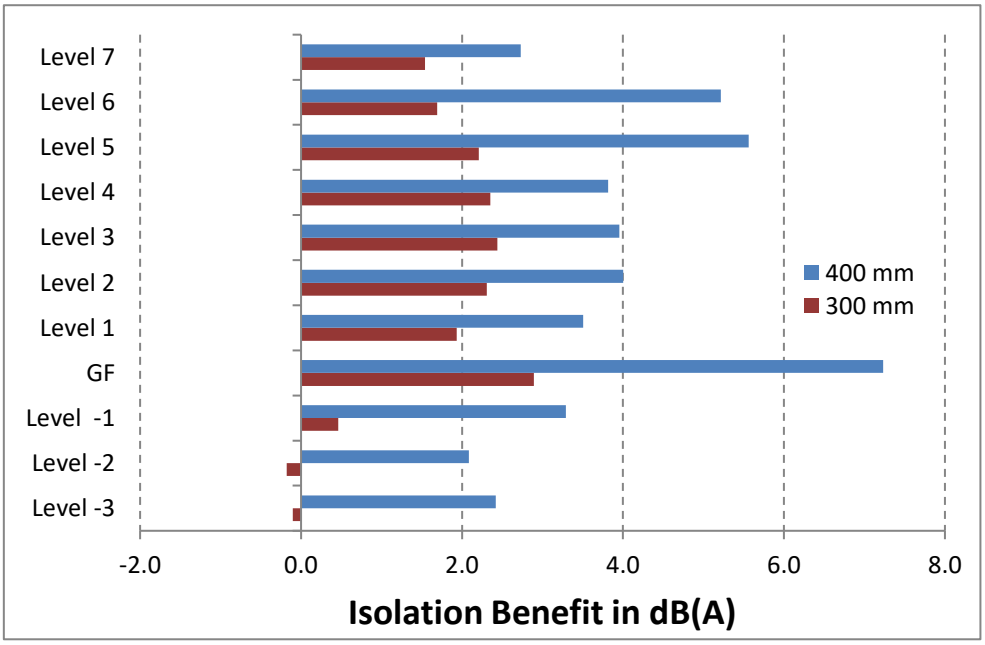


Figure 8: Evaluating the changes in ground-borne noise as a function of substructure slab thickness

Fixing the raft foundation thickness at 2.5m and the basement slab thickness at 400mm, this study goes on to investigate whether there are further ground-borne noise isolation benefits by thickening the secant wall from 1.25m to 1.75m. Figure 9 reveals a slight ground-borne noise reduction as a result of thickening the secant wall. This suggests that, under these selected circumstances, and considering practical structural adjustments, the reduction in ground-borne-noise through the substructure tuning process is reaching its limit. However, it is possible that higher ground-borne noise isolation benefits could be achieved if the sensitivity analysis employed, for its fixed conditions, a 200mm slab thickness throughout its substructure.

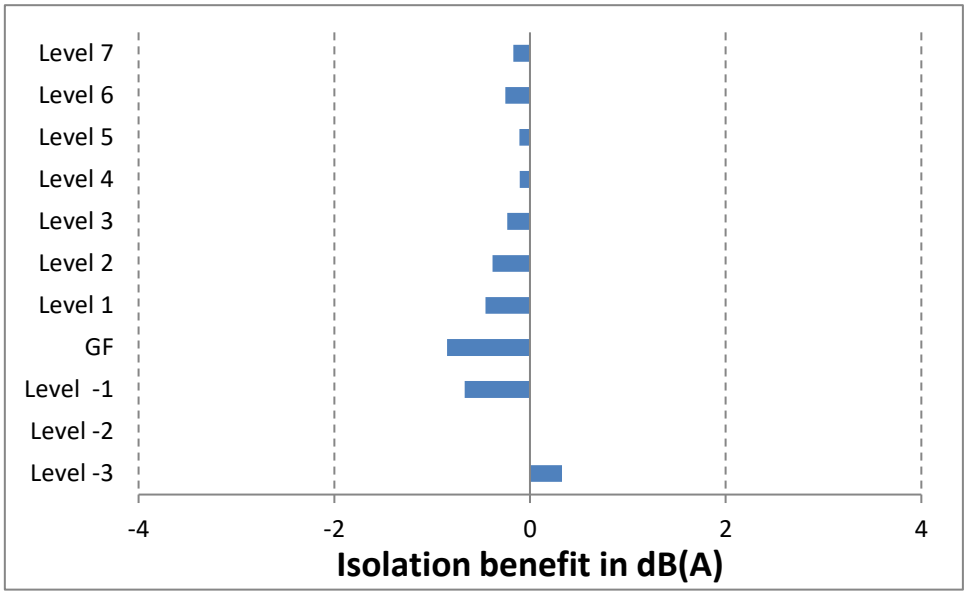


Figure 9: Evaluating the changes to ground-borne noise as a function of secant wall thickness: from 1.25m to 1.75m.

6 Conclusion

A representative contemporary lightweight structural building design has been used to assess the contribution of critical substructure elements to the dynamic response of the building, as measured by the A-weighted rail-induced ground-borne noise across relevant parts of the building.

The Base-isolation preliminary study demonstrated that not all scenarios (i.e. combination of ground properties and building design) respond effectively to high frequency Base-isolation (e.g. >10 Hz); hence it follows that structural tuning could be employed to relax the Base-isolation requirements.

The study confirmed that a share of ground-borne noise levels can be reduced via tuning specific substructure elements. For the selected scenario, a 9-storey steel frame structure built off a four-basement levels concrete substructure sitting in London clay, up to 7 dB reduction was attained by thickening the basement and ground floor slabs. Whilst assessing the response to structural changes, the study also revealed diminishing returns on ground-borne noise isolation benefit, indicating that there are optimum structural configurations.

References

[1] R. Thornely-Taylor. *Numerical modelling of groundborne noise and vibration from underground railways: Geotechnical considerations*, Proceedings of the 12th International Congress on Sound and Vibration, Lisbon, Portugal, 2005 July 11–14

[2] L.V. Socco and C. Strobbia, 2004, *Surface-wave method for near surface characterization: a tutorial*, Near Surface Geophysics. Vol. 2, pp. 165–185

[3] H. Verbraken, S. Francois, G. Degrande, G. Lombaert, *Verification of an empirical prediction method for ground borne vibration in building due to high speed railway traffic*. ECCOMAS Thematic Conference on Computational Methods in Structural Dynamics and Earthquake Engineering, Corfu, Greece, 2011 May 25-28

[4] J. Avillez, M. Frost, S. Cawser, C. Skinner, A. El-Hamalawi, and P. Shields, *Procedures for Estimating Environmental Impact from Railway Induced Vibration: A review*, Proceedings of the Internoise 2012/ASME NCAD, New York City, NY, USA, 2012 August 19-22 (IN12-1083)

[5] M. O'Connor, K. Jefferson and J. D'Avillez, *An investigation of numerical procedures to assess rail-induced vibration responce of tall builidings*, . Proceedings of The 23th International Congress on Sound and Vibration, Athens, Greece, 2016 July 10-14

[6] R. Thornely-Taylor. *The use of numerical methods in the prediction of vibration*. Proceeding of the Institute of Acoustics, United Kingdom, 2007; 29:14–21

[7] R. Thornely-Taylor: *The relationship between floor vibration from an underground source and the airborne sound pressure level in the room*, International Journal of Rail Transportation (2016), DOI: 10.1080/23248378.2016.1219240

[8] L.G. Kurzweil, *Ground-borne noise and vibration from underground rail systems*, Journal of Sound and Vibration (1979), vol. 66 (3), 363-370

[9] R. Thornely-Taylor, *Evaluating uncertainty in the prediction of the performance of base-isolation systems designed to reduce groundborne noise in buildings*. Proceedings of The 24th International Congress on Sound and Vibration, London, United Kingdom, 2017 July 23-27

Dynamic effects at sudden structural rebuilding of the “beam-foundation” system

V. A. Gordon[1], O. V. Pilipenko[1] ,V. A. Trifonov[2]
[1] Orel State University, Department of Further Mathematics
95 Komsomolskaya Str., Orel, 302026, Russia
email: **gordon1312@mail.ru**

[2]GAZPROM-SOCINVEST
St. Petersburg, Russia

Abstract
The authors constructed a mathematical model of a dynamic process in a loaded beam on the elastic Winkler foundation in a sudden formation of a defect in the form of a change in the boundary conditions. The solution of the static problem of bending of the beam pinched at the ends served as the initial condition for the process of forced vibrations hinged supported at the ends of a beam, which arose after a sudden break in the connections that prevented the rotation of the end sections. The authors determined the dynamic increments of stresses in a beam for various combinations of a beam and foundation parameters.

1 Introduction

An important problem of construction mechanics is the analysis of the sensitivity of load-bearing structures to structural rearrangements under load such as suddenly disconnected connections, cracks, fractures, etc. Obtaining such information for real constructions requires the development of special methods, since this problem cannot be solved by universal methods. From the standpoint of structural mechanics in these problems, it becomes necessary to calculate such systems as constructively nonlinear, changing the design scheme under load, i.e. with dynamic overloads, caused by sudden beyond projected effects.

In the present work, the task is to construct a mathematical model of transient dynamic processes in a beam on an elastic foundation when a defect is suddenly formed in the form of a change in the boundary conditions. Before the formation of a defect, the reaction of the structure is determined by a static action. The sudden formation of a defect leads to a reduction in the overall rigidity of the structure, which does not ensure the static equilibrium of the system. The inertial forces that have arisen cause a dynamic reaction, redistribution and growth of strains and stresses. As a result, there may be a violation of the regular functioning of the structure, or loss of load capacity and destruction.

2 Statement of the problem

The elastic beam with flexural stiffness EI rests on the entire length l on the elastic Winkler foundation with stiffness coefficient k, rigidly clamped at the ends. The uniformly distributed intensity load q and the foundation reaction affect the outer layers of the beam. It is assumed that at some point in time $t = 0$, the connections in a statically deformed beam, which prevent the rotation of the end sections in the supports, suddenly collapsed, forming hinges in the place of sealing. The static state of the loaded beam ceases to be

in equilibrium and the beam will move into motion $\upsilon(x,t)$, during which the deformations and stresses in the beam acquire dynamic increments.

3 Solution of the problem

The problem is solved in the following sequence:

1) we determine the static deflection of a ("undamaged") beam with clamped ends on an elastic foundation, which is used subsequently as the initial condition of a dynamic process, which is initiated in the system by a sudden transformation of the boundary conditions;
2) we determine the frequencies and forms of bending vibrations of a ("damaged") beam with hinged ends on an elastic foundation;
3) we study the forced bending vibrations of a loaded beam. In this case, the load, the static deflection of the "undamaged" beam and the desired dynamic deflection are decomposed into series according to the modes of natural vibrations of the "damaged" beam.

3.1 The static bending of a beam, which is pinched at the ends on Winkler foundation, in dimensionless variables and parameters

$$\xi = \frac{x}{l}, \quad w_{st} = \frac{\upsilon}{l}, \quad \bar{q} = \frac{ql^3}{EI}, \quad \alpha = \sqrt[4]{\frac{kl^4}{4EI}}.$$

is described by equation [1, 2]

$$\frac{d^4 w_{st}}{d\xi^4} + 4\alpha^4 w_{st} = \bar{q}, \tag{1}$$

The general solution of equation (1) in the case of pinching ends has the form [1, 2]

$$w_{st} = \frac{\bar{q}}{4\alpha^4}\left(1 - k_4(\alpha\xi)\right) + w_0'' k_2(\alpha\xi) + w_0''' k_1(\alpha\xi), \tag{2}$$

where $k_i(\alpha\xi)\ (i = 1 \div 4)$ is Krylov function of the form

$$k_1(\alpha\xi) = \frac{\sin\alpha\xi ch\alpha\xi - \cos\alpha\xi sh\alpha\xi}{4\alpha^3}, \quad k_2 = k_1', \quad k_3 = k_2', \quad k_4 = k_3';$$

w_0'', w_0''' are the initial parameters, respectively, the dimensionless bending moment and the shear force at the origin $\xi = 0$.

$$w_0'' = \frac{\bar{q}}{k_2^2(\alpha) - k_1(\alpha)k_3(\alpha)}\left(\frac{k_4(\alpha) - 1}{4\alpha^4}k_2(\alpha) + k_1^2(\alpha)\right),$$

$$w_0''' = \frac{\bar{q}}{k_1(\alpha)k_3(\alpha) - k_2^2(\alpha)}\left(\frac{k_4(\alpha) - 1}{4\alpha^4}k_3(\alpha) + k_1(\alpha)k_2(\alpha)\right).$$

The dimensionless bending moment in a static state is determined by the function

$$w_{st}'' = \bar{q}k_2(\alpha\xi) + w_0'' k_4(\alpha\xi) + w_0'''(\alpha\xi). \tag{3}$$

Figure 1 shows the diagrams of bending moments in a beam with clamped ends for various values of the generalized rigidity of the "beam-foundation" system $\lambda = 4\alpha^4$. It is worth paying attention to the somewhat "unusual" form, which takes the moment epures with increasing rigidity of the system – the

moments in the central part of the beam are much lower than in the quarter of spans. This is the result of the combined effect of external unloading on the beam and the reaction of the elastic foundation.

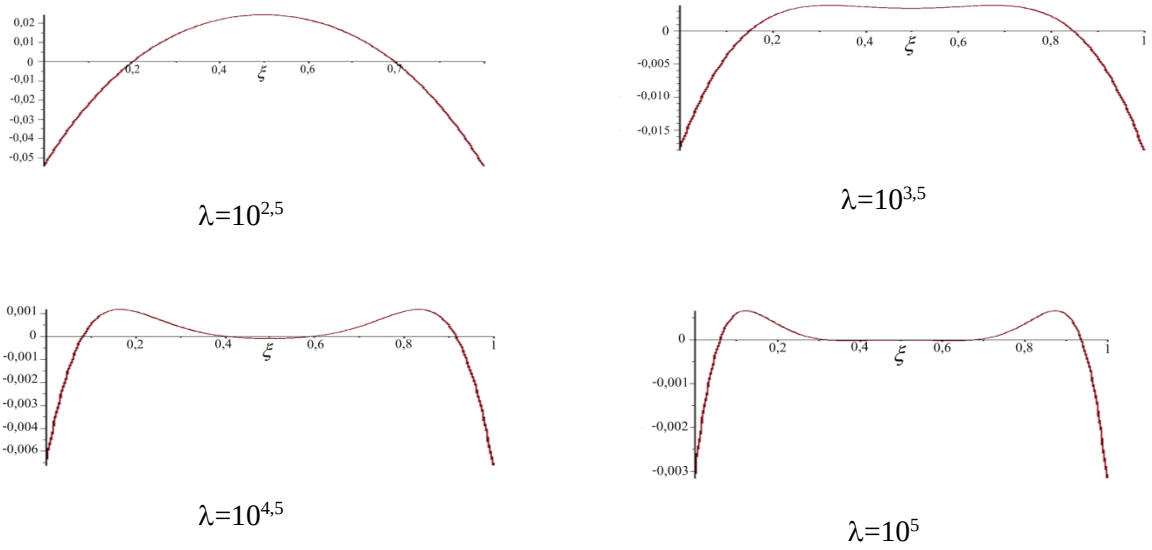


Figure 1: Epures of bending moments in the initial static state, depending on the rigidity index of the "beam-foundatio" system λ

3.2 The resulting motion $\upsilon_{dyn} = \upsilon(x,t)$ after a sudden transformation of the restraints of the beam into the hinges is described by equation [2]

$$\frac{\partial^4 w_{dyn}}{\partial \xi^4} + 4\alpha^4 \left(w_{dyn} + \frac{\partial^2 w_{dyn}}{\partial \tau^2} \right) = \bar{q}, \tag{4}$$

where $w_{dyn} = \frac{\upsilon(x,t)}{l}$, $\tau = w_0 t$. $w_0 = \sqrt{\frac{k}{\rho A}}$ is a parameter having a frequency dimension and, therefore, called a "conventional" frequency.

Equation (4) describes the forced vibrations of a loaded beam. The Winkler model does not imply dynamic phenomena in the elastic foundation. The required eigenfunctions and frequencies of the problem will be obtained from equation (4) with the zeroed right-hand side, which after separation of the variables by representation

$$w_{dyn} = W(\xi) \sin \bar{\omega} \tau, \tag{5}$$

takes the form

$$\frac{d^4 W}{d\xi^4} + 4\alpha^4 \left(1 - \bar{\omega}^2\right) W = 0, \tag{6}$$

where $\bar{\omega} = \frac{\omega}{\omega_0}$ is a dimensionless eigenfrequency of the bending vibrations of a beam on an elastic foundation.

Using the "conventional" frequency ω_0, characterizing stiff and inertial properties of the "beam-

foundation" system, and the known basic frequency of bending vibrations of a free beam supported in the same way (without foundation support)

$$\omega_{1f} = \left(\frac{\pi}{l}\right)^2 \sqrt{\frac{EI}{\rho A}},$$

we bring the equation to the form (6)

$$\frac{d^4W}{d\xi^4} = \pi^4\left(-\bar{\omega}_0^2 + \tilde{\omega}^2\right)W, \tag{7}$$

where $\bar{\omega}_0 = \frac{\omega_0}{\omega_{1f}}$ is a relative "conventional" frequency; $\tilde{\omega} = \frac{\omega}{\omega_{1f}}$ is a relative required frequency.

Using Euler substitution

$$W = Ae^{r\xi}, \tag{8}$$

we find the characteristic equation for differential equation (7)

$$r^4 + \pi^4\left(\bar{\omega}_0^2 - \tilde{\omega}^2\right) = 0,$$

roots of which can be represented in two ways, depending on the ratios of frequencies $\bar{\omega}_0$ and $\tilde{\omega}$:

1) if $\tilde{\omega} > \bar{\omega}_0$, then the roots of equation (9) are real and purely imaginary

$$r_{1,2} = \pm\beta_1, \quad r_{3,4} = \pm i\beta_1, \quad \beta_1 = \pi\sqrt[4]{\tilde{\omega}^2 - \bar{\omega}_0^2}, \tag{10}$$

the deflection function (8) has the form

$$W = A_1 ch\beta_1\xi + A_2 sh\beta_1\xi + A_3\cos\beta_1\xi + A_4\sin\beta_1\xi; \tag{11}$$

2) if $\tilde{\omega} < \bar{\omega}_0$, then the roots of equation (9) are complex

$$r_{1,2,3,4} = \left(\pm i \pm 1\right)\beta_2, \quad \beta_2 = \frac{\pi}{\sqrt{2}}\sqrt[4]{\bar{\omega}^2 - \tilde{\omega}^2} \tag{12}$$

and the deflection function

$$W = A_1 sh\beta_2\xi\sin\beta_2\xi + A_2 sh\beta_2\xi\cos\beta_2\xi + A_3 ch\beta_2\xi\sin\beta_2\xi + A_4 ch\beta_2\xi\cos\beta_2\xi. \tag{13}$$

It was shown in [3, 4] that for a beam completely supported on the Winkler foundation, in the case of canonical boundary conditions – pinch- pinch, pinch - hinge, hinge-hinge, console – only variant (10) is realized.

Using the initial parameters

$$W_0 = W(0), \quad W_0' = W'(0), \quad W_0'' = W''(0), \quad W_0''' = W'''(0)$$

instead of integration constants $A_i\left(i = 1 \div 4\right)$, we write the relations characterizing the state of arbitrary cross-section ξ of the beam, using version (10), (11).

In this case, the deflection function has the form

$$W(\xi) = W_0 R_4(\beta_1\xi) + W_0' R_3(\beta_1\xi) + W_0'' R_2(\beta_1\xi) + W_0''' R_1(\beta_1\xi), \tag{16}$$

where $R_i\left(i = 1 \div 4\right)$ – Krylov functions of the form

$$R_1(\beta_1\xi)=\frac{sh\beta_1\xi-\sin\beta_1\xi}{2\beta_1^3};\quad R_2=R_1';\quad R_3=R_2';\quad R_4=R_3'.$$

The state of the arbitrary beam section is described by the matrix equation

$$\bar{W}(\xi)=V_1(\xi)\bar{W}_0, \tag{17}$$

where $\bar{W}(\xi)$ is a state vector of arbitrary section ξ

$$\bar{W}(\xi)=\{W(\xi)\ W'(\xi)\ W''(\xi)\ W'''(\xi)\};$$

$\bar{W}_0(\xi)$ is a vector of initial parameters

$$\bar{W}_0=\{W_0\ W_0'\ W_0''\ W_0'''\};$$

$V_1(\xi)=\{\upsilon_{ij}\}$ is a functional matrix of influence of initial parameters on the state of section ξ

$$V_1(\xi)=\begin{pmatrix} R_4(\beta_1\xi) & R_3(\beta_1\xi) & R_2(\beta_1\xi) & R_1(\beta_1\xi)\\ \beta_1^4R_1(\beta_1\xi) & R_4(\beta_1\xi) & R_3(\beta_1\xi) & R_2(\beta_1\xi)\\ \beta_1^4R_2(\beta_1\xi) & \beta_1^4R_1(\beta_1\xi) & R_4(\beta_1\xi) & R_3(\beta_1\xi)\\ \beta_1^4R_3(\beta_1\xi) & \beta_1^4R_2(\beta_1\xi) & \beta_1^4R_1(\beta_1\xi) & R_4(\beta_1\xi)\end{pmatrix}.$$

3.3 We will conduct an analysis of free frequencies and forms of flexural vibrations of a beam on an elastic foundation when the ends are hinged. In this case, the boundary conditions and the deflection function have the form

$$\begin{aligned} W_0=W_0''=0,\\ W(1)=W''(1)=0. \end{aligned} \tag{18}$$

$$W(\xi)=W_0'R_3(\beta_1\xi)+W_0'''R_1(\beta_1\xi). \tag{19}$$

Satisfying the second pair of boundary conditions (18), from function (19) and its second derivative, we obtain a system of two algebraic equations of relatively unknown initial parameters and W_0' и W_0'''

$$\begin{cases} W_0'R_3(\beta_1)+W_0'''R_1(\beta_1)=0,\\ W_0'\beta_1^4R_1(\beta_1)+W_0'''R_3(\beta_1)=0. \end{cases} \tag{20}$$

The condition for the existence of nonzero solutions of a given homogeneous system is that the determinant of the coefficient matrix of this system is equal to zero

$$\begin{vmatrix} R_3(\beta_1) & R_1(\beta_1)\\ \beta_1^4R_1(\beta_1) & R_3(\beta_1)\end{vmatrix}=0. \tag{21}$$

Expanding the determinant, we obtain the frequency equation

$$4\sin\beta_1 sh\beta_1=0,$$

whence it follows that

$$\sin\beta_1=0$$

$$\beta_{1n}=n\pi\ \ (n=1,2,3,...).$$

Taking into account formula (10), we obtain the frequency spectrum

$$\tilde{\omega}_n = \sqrt{\bar{\omega}_0^2 + n^4}. \tag{22}$$

From any equation of the system (20) with $\beta_n = n\pi$, it follows that

$$\frac{W_0'''}{W_0'} = -(n\pi)^2,$$

then, according to (19), the *n-th* form with frequency $\bar{\omega}_n$, has the form

$$W_n(\xi) = A_n \sin n\pi\xi, \tag{23}$$

where n is a number of half-waves of a sinusoid on length l of a beam;

A_n is an unknown amplitude of vibrations in *n-th* form.

Thus, the forms of free vibrations of the beam on an elastic foundation remain the same as for the free beam, but with frequencies ω_n, which are larger than the corresponding frequencies of the free beam ω_{f_n} in $\sqrt{\bar{\omega}_0^2 + n^4}$ times, i.e. according to (22)

$$\omega_n = \sqrt{\bar{\omega}_0^2 + n^4}\,\omega_{f_n}.$$

3.4 The solution of the differential equation of forced vibrations (4) will be sought by expanding the function $w_{dyn}(\xi,\tau)$ in a series of eigenfunctions $W_n(\xi)$ (23) with coefficients in the form of unknown time functions $Q_n(\tau)$

$$w_{dyn} = \sum_{n=1}^{\infty} Q_n(\tau) W_n(\xi). \tag{24}$$

We find functions $Q_n(\tau)$ using the following procedures: substituting the series (13) and the expression (2) into equation (4), multiplying both sides of this equation by $W_n(\xi)$, integrating both parts of ξ from 0 to 1 and, using the property of orthogonality of the modes of free vibrations $W_n(\xi)$, we obtain the differential equation for defining functions $Q_n(\tau)$

$$\frac{d^2 Q_n}{d\tau^2} + \bar{\omega}_n^2 Q_n = S_n, \tag{25}$$

where $S_n = \dfrac{2\bar{q}}{\pi^4 \bar{\omega}_0^2} \dfrac{\sin^2 \dfrac{n\pi}{2}}{\dfrac{n\pi}{2}}$.

The general solution of the inhomogeneous equation (25)

$$Q_n = D_{1n} \cos \frac{\tilde{\omega}_n}{\bar{\omega}_0}\tau + D_{2n} \sin \frac{\tilde{\omega}_n}{\bar{\omega}_0}\tau + \frac{S_n}{\bar{\omega}_n^2} \tag{26}$$

is a sum of the solution of the relevant homogeneous equation (the first two terms) and the particular solution corresponding to the right-hand side of (25) (the third term).

Now, according to (24), the dynamic deflection function takes the form

$$w_{dyn} = \sum_{n=1}^{\infty} \left(D_{1n} \cos \frac{\tilde{\omega}_n}{\bar{\omega}_0} \tau + D_{2n} \sin \frac{\tilde{\omega}_n}{\bar{\omega}_0} \tau + \frac{S_n}{\bar{\omega}_n^2} \right) \sin n\pi\xi. \tag{27}$$

The constants of integration D_{1n} and D_{2n} are determined from the initial conditions

$$w_{dyn}(\xi, 0) = w_{cm}(\xi), \qquad \left. \frac{\partial w_{dyn}}{\partial \tau} \right|_{\xi,0} = 0. \tag{28}$$

From the second condition (28) we determine one constant

$$D_{2n} = 0. \tag{29}$$

Multiplying both sides of the first condition (28), taking into account (27) and (29), by $\sin n\pi\xi$, and integrating on ξ from 0 to 1, we obtain another constant

$$D_{1n} = B_n - \frac{S_n}{\bar{\omega}_n^2}, \tag{30}$$

where $B_n = 2\int_0^1 w_{st}(\xi) \sin n\pi\xi d\xi.$

Substituting (29) and (30) into (27), and taking into account the trigonometric identity

$$1 - \cos \frac{\tilde{\omega}_n}{\bar{\omega}_0} \tau = 2 \sin^2 \frac{\tilde{\omega}_n}{2\bar{\omega}_0} \tau,$$

we get

$$w_{dyn} = \sum_{n=1}^{\infty} \left(B_n \cos \frac{\tilde{\omega}_n}{\bar{\omega}_0} \tau + C_n \sin^2 \frac{\tilde{\omega}_n}{2\bar{\omega}_0} \tau \right) \sin n\pi\xi, \tag{31}$$

where $C_n = \frac{4\bar{q}}{\pi^4 \tilde{\omega}_n^2} \frac{\sin^2 \frac{n\pi}{2}}{\frac{n\pi}{2}}.$

The dimensionless bending moment is obtained by differentiating the series (31) twice

$$w''_{dyn} = -\pi^2 \sum_{n=1}^{\infty} n^2 \left(B_n \cos \frac{\tilde{\omega}_n}{\bar{\omega}_0} \tau + C_n \sin^2 \frac{\tilde{\omega}_n}{2\bar{\omega}_0} \tau \right) \sin n\pi\xi,$$

4 A numerical example

The Maple software package helped to calculate the dimensionless deflections $w(\xi)$ and bending moments $w''(\xi)$ in a beam, which is loaded by a uniformly distributed intensity load $\bar{q} = 1$, on the elastic Winkler foundation

- in an initial static state, when the ends are pinched: $w_{st}(\xi)$, $w''_{st}(\xi)$;

- in a static state formed after a quasi-static transformation of pinches into hinges $w_q(\xi)$, $w_q''(\xi)$;
- in a dynamic process that occurs when in a sudden transformation of pinches into hinges: $w_{dyn}(\xi, \tau)$, $w_{dyn}''(\xi)$.

In practical calculations, 20 series members (19) and (20) were taken into account. In this case, we obtain a practical coincidence of epures of the dynamic deflection $w_{dyn}(\xi, 0)$ and the static deflection $w_{st}(\xi)$, that is,

$$\sum_{n=1}^{20} B_n \sin n\pi\xi \approx w_{st}(\xi).$$

The results of the calculations are shown in Figures 2 and 3, as well as in Table 1. In Figures 2 and 3 are shown respectively: epures of bending moments $w_q''(\xi)$ in a beam after quasi-static of transformation of pinches into hinges, and during vibrations $w_{dyn}''(\xi, \tau_0)$ after sudden transformation of pinches into hinges at the time τ_0 of reaching the highest values. The epures are constructed for different values of the stiffness parameter of the "beam-foundation" system λ.

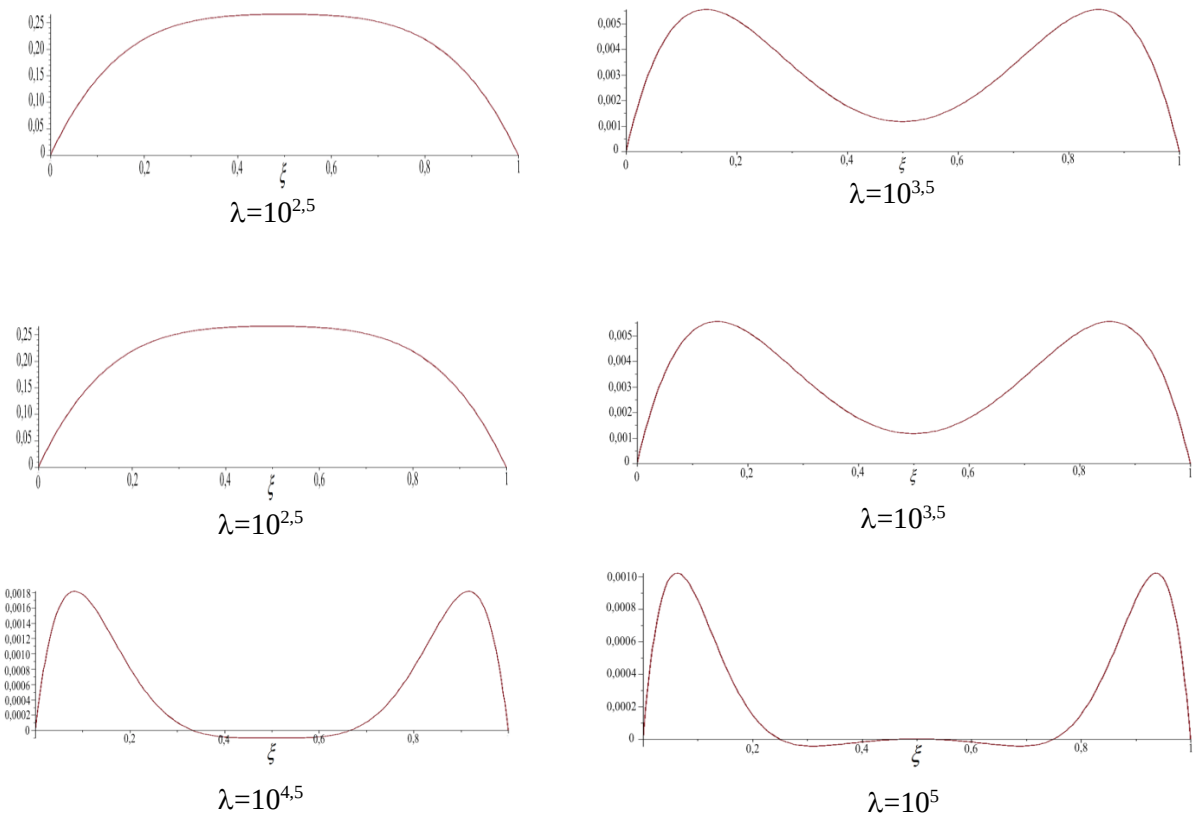


Figure 2: Epures of bending moments after quasi-static transformation of boundary conditions depending on the rigidity index of the "beam-foundation" system λ

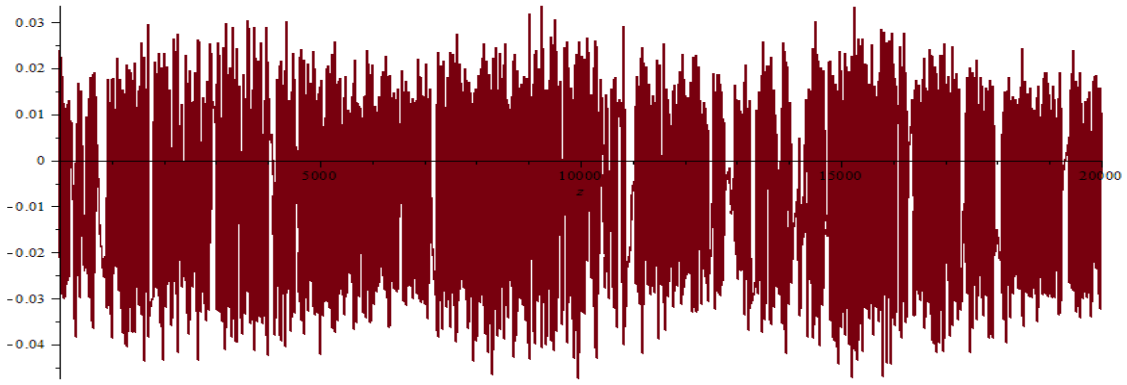


Figure 3: Moments in the cross section $\xi = 0{,}16$ (time scanning). $M_{\max} = 0{,}047$

λ	$\left\lvert w''_{st} \right\rvert_{\max}$	$w''_{q\,\max}$	K_{st}	$w''_{dyn\,\max}$	K_{dyn}
0	0,083	0,125	1,506	0,3	3,614
10	0,082	0,112	1,366	0,269	3,28
$10^{1,5}$	0,079	0,093	1,177	0,225	2,848
10^{2}	0,071	0,06	0,845	1,156	2,197
$10^{2,5}$	0,0544	0,0265	0,487	0,07	1,287
10^{3}	0,0334	0,0104	0,311	0,0346	1,036
$10^{3,5}$	0,018	0,0055	0,305	0,0186	1,033

Table 1: Influence of the rigidity of the "beam-foundation" system on the increment of bending moments

5 Conclusions

If we consider the transformation of the boundary conditions in the given "beam-foundation system" under the load as a defect, then the conducted study shows that the quasi-static formation of a defect, that is, a reduction in the rigidity of the end supports, leads to an insignificant increase in the maximum stresses in the beam ($K_{st} > 1$) if there is no foundation ($\lambda = 0$) and low values of the indicator of the "beam-foundation" system ($0 < \lambda \leq 10^{1,79}$). For beams resting on more rigid foundations ($\lambda > 10^{1,79}$), the formation of the same defect, on the contrary, leads to a decrease in the greatest stresses ($K_{st} < 1$).

A sudden formation of a defect gives more than three times ($K_{dyn} = 3{,}614$) an increase in the maximum stress in a free beam ($\lambda = 0$). For systems with higher rigidity, the effect of transforming the boundary conditions is reduced. There is a redistribution of stresses along the span, but the greatest stress at $\lambda > 10^4$ does not exceed the initial static value ($K_{dyn} = 1$). In addition, regardless of the rate of defect formation with increasing rigidity of the system, the greatest stresses move from the center of the beam to the periphery of the span.

The work was conducted within the framework of the basic part of the state task 1.5265.2017/BP (1.5265.2017/8.9)

References

[1] Gordon V. *Vibration of loaded beam initiated by fully or partially destruction of the elastic foundation* / V. Gordon, O. Pilipenko // Proceedings of the 22 Intern. Congress on sound and vibration. Florence, Italy, (2015).

[2] Gordon V. *Beam's dynamical stresses increments after partial deconstruction of foundation* / V. Gordon, O. Pilipenko // Proc. European congress on computational methods in applied sciences and engineering. Crete, Greece (2016), Vol. 3:5533-5549.

[3] Gordon V.A. *Variants of the solution of eigenvalue problems for beams on an elastic foundation* / V.A. Gordon, E.V. Bruma, T.B. Poturaeva // Fundamental and Applied Problems of Engineering and Technology. Orel: OSU named after I.S. Turgenev (2017), Vol. 1 (321): 8-14. (in Russian)

[4] GordonV.A. *The analysis of free frequencies of transverse vibrations of a beam on an elastic foundation* / V.A. Gordon, E.V. Bruma // Vibration technologies, mechatronics and controlled machines: collection of scientific articles in 2 parts. South-West State University. Kursk (2016), pp.182-191. (in Russian)

Resonance and cancellation mechanisms in existing High-Speed railway bridges with an orthotropic plate behaviour

M.D. Martínez-Rodrigo[1], E. Moliner[1], A. Romero[2], P. Galvín[2]
[1] Universitat Jaume I, Mechanical Engineering and Construction Department
Castellón, 12071, Spain
e-mail: **mrodrigo@uji.es**

[1] Universidad de Sevilla, Escuela Técnica Superior de Ingeniería
Sevilla, 41092, Spain

Abstract
Railway bridges may experience important vertical vibrations under the circulation of High-Speed (HS) convoys. Especially critical in this regard are short simply-supported (S-S) structures composed by slab or girder decks, with usually associated low masses and damping levels. The dynamic amplification experienced by a S-S bridge under the passage of equidistant moving loads is intimately related with resonance and cancellation phenomena. In this contribution the free vibration response of rectangular S-S orthotropic plates after the circulation of a single load travelling at constant speed is first formulated, following an analytical approach. Secondly, the effect of the plate obliqueness, supports flexibility and structural damping on the cancellation and maximum free vibration conditions are numerically investigated. Then, the phenomena of cancellation of resonance and maximum resonance are presented and their effects are shown through the experimental measurements performed on a bridge from the Spanish railway network.

1 Introduction

Short-to-medium span S-S railway bridges may experience excessively high deck vertical accelerations under passing trains, especially as the operating speed increases. For this reason the Serviceability Limit State for traffic safety [1] has become one of the most restrictive design limits in such structures. Since the opening of the first HS railway lines in Europe and Japan, there has been experimental evidence of excessive transverse vibrations in railway bridges which was attributed to resonance of the bridge deck [2]. Resonance takes place when the loading frequency of the equidistant axle or bogie loads coincides with a natural frequency of the structure. Resonance is generally characterized by a noticeable dynamic amplification of the structural response. A resonant behaviour builds up from the free vibrations that each axle load leaves on the structure after exiting it. The amplitude of these free vibrations depends on the ratio between the load speed and the deck natural frequency. Maximum free vibration and cancellation conditions have been formulated for S-S and elastically supported (E-S) beams in the past [3]-[4], but not for plates as far as the authors know. In the resonant case, depending on the amplitude of these free vibration waves and on how they combine with each other when a train of loads crosses the structure, resonances entailing noticeable amplification levels or almost imperceptible ones could develop.

For what has been previously said, understanding the free vibration behaviour of bridges under a single moving load and its dependence on the travelling speed becomes crucial. In what follows, the conditions for maximum free vibration and cancellation, as well as those for resonance and cancellation of resonance are studied in the case of S-S rectangular orthotropic plates. Double track bridges with length to width ratios close to unity or with oblique plans can present modes different from the longitudinal bending ones (i.e. torsion and transverse bending modes) with natural frequencies below 30 Hz that may significantly contribute to the total response. Therefore, the dynamic response of such structures should not be analysed

using beam-type models. Due to the usual typologies of bridges with lengths in the range 12-25 m (slab, girder decks etc.) an orthotropic plate model is selected instead. These conditions are formulated analytically for rectangular S-S orthotropic plates and their evolution with the level of obliquity, structural damping and supports vertical flexibility are numerically evaluated.

The importance of understanding the phenomena of cancellation or maximum free vibration under a single load is the relation of this issue with the amplification at resonance when a train of successive loads acts on the bridge. If the resonant velocity coincides or is close to a cancellation condition, the resonance peak will be moderate or sometimes even imperceptible. On the other hand, when resonance takes place close to a maximum free vibration situation an important amplification of the structural response should be expected. Equating resonance conditions with maximum free vibration or cancellation conditions, length to train characteristic distance ratios are derived leading to these two scenarios.

Finally, the experimental response of a bridge belonging to the Madrid-Sevilla HS railway line is presented illustrating the conclusions derived in the previous sections.

2 Free vibration of rectangular S-S orthotropic plates after de circulation of a single moving load at constant speed

2.1 Analytical formulation

The partial differential equation governing the transverse oscillations $w(x,y,t)$ of a thin orthotropic rectangular plate under a generic load distribution $q_z(x,y,t)$ (Figure 1a) neglecting shear deformation and rotary inertia, and being X and Y the principal directions of orthotropy, is given by

$$D_x \frac{\partial^4 w}{\partial x^4} + 2H \frac{\partial^4 w}{\partial x^2 \partial y^2} + D_y \frac{\partial^4 w}{\partial y^4} + \rho h \frac{\partial^2 w}{\partial t^2} = q_z(x,y,t) \tag{1a}$$

$$q_z(x,y,t) = -\sum_{k=1}^{N_P} \left(\mathrm{H}\left(t - \frac{d_k}{V} \right) - \mathrm{H}\left(t - \frac{d_k + L}{V} \right) \right) P_k \, \delta(x - Vt + d_k) \delta(y - y_P) \tag{1b}$$

where D_x and D_y are the flexural rigidities per unit of length of the plate with respect to the XZ and YZ planes (moment-curvature proportionality constants), respectively, $2H=D_1+D_2+2(D_{xy}+D_{yx})$, D_1 and D_2 are the coupling rigidities and D_{xy} and D_{yx} the torsional rigidities with respect to the same planes [5]. Equation (1b) represents the particular source of excitation of a train of constant moving loads travelling parallel to the X axis (Figure 1b) at constant speed V. In equation (1b) H and δ stand for the Heaviside unit and Dirac Delta functions.

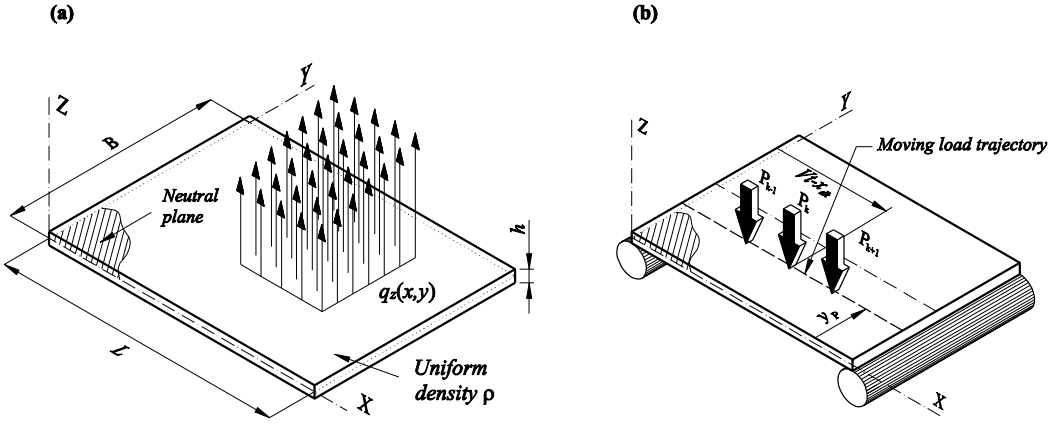


Figure 1: Orthotropic rectangular plate subjected to (i) a generic transverse load distribution and (ii) a set of moving loads. Axes nomenclature and dimensions

Admitting S-S conditions on two opposite sides of the plate, the transverse displacement of the neutral plane $w(x,y,t)$ under the circulation of the moving loads may be expressed as a linear combination of the normal modes of vibration $\Phi_{ij}(x,y)$

$$w(x,y,t)=\sum_{i=1}^{N_m}\sum_{j=1}^{N_n}\psi_{ij}(t)\Phi_{ij}(x,y)=\sum_{i=1}^{N_m}\sum_{j=1}^{N_n}\psi_{ij}(t)\sin\left(\frac{i\pi x}{L}\right)Y_{ij}(y)C_{ij} \tag{2}$$

where C_{ij} is a constant depending on the mode normalization. For the details of the derivation of the natural frequencies and mode shapes of a rectangular S-S orthotropic plate the reader is referred to [6]. In equation (2):

$$Y_{ij}(y)=\frac{\delta_{ij}\cosh(\phi_{ij}y/L)+\gamma_{ij}\cos(\vartheta_{ij}y/L)}{\gamma_{ij}\delta_{ij}(\cosh(\phi_{ij}B/L)-\cos(\vartheta_{ij}B/L))}-\frac{\vartheta_{ij}\gamma_{ij}\sinh(\phi_{ij}y/L)+\phi_{ij}\delta_{ij}\sin(\vartheta_{ij}y/L)}{\vartheta_{ij}\gamma_{ij}^2\sinh(\phi_{ij}B/L)-\phi_{ij}\delta_{ij}^2\sin(\vartheta_{ij}B/L)} \tag{3a}$$

$$\phi_{ij}=\frac{i\pi}{\sqrt{D_y}}\left[\left(H^2-D_xD_y+\frac{\rho hD_yL^4\omega_{ij}^2}{i^4\pi^4}\right)^{1/2}+H\right]^{1/2} \qquad \delta_{ij}=D_y\vartheta_{ij}^2+i^2\pi^2\frac{D_1+D_2}{2} \tag{3b}$$

$$\vartheta_{ij}=\frac{i\pi}{\sqrt{D_y}}\left[\left(H^2-D_xD_y+\frac{\rho hD_yL^4\omega_{ij}^2}{i^4\pi^4}\right)^{1/2}-H\right]^{1/2} \qquad \gamma_{ij}=D_y\phi_{ij}^2-i^2\pi^2\frac{D_1+D_2}{2} \tag{3c}$$

In equations (3b-c), ω_{ij} is the circular frequency of the orthotropic plate which is related to the roots of the frequency equation (4b) ϕ_{ij} as per

$$\omega_{ij}=\frac{\sqrt{D_y\phi_{ij}^4-2i^2\pi^2H\phi_{ij}^2+i^4\pi^4D_x}}{L^2\sqrt{\rho h}} \tag{4a}$$

$$(\vartheta_{ij}^2\gamma_{ij}^4-\phi_{ij}^2\delta_{ij}^4)\sinh\left(\phi_{ij}\frac{B}{L}\right)\sin\left(\vartheta_{ij}\frac{B}{L}\right)+2\phi_{ij}\vartheta_{ij}\gamma_{ij}^2\delta_{ij}^2\left(\cosh\left(\phi_{ij}\frac{B}{L}\right)\cos\left(\vartheta_{ij}\frac{B}{L}\right)-1\right)=0 \tag{4b}$$

Expressing $w(x,y,t)$ as a linear combination of $N_m \times N_n$ modes and in virtue of the modes orthogonallity condition [6], the differential equation governing the *mn-th* modal amplitude neglecting structural damping may be expressed as

$$\ddot{\psi}_{mn}(t)+\omega_{mn}^2\psi_{mn}(t)=-\frac{1}{M_{mn}}\sum_{k=1}^{N_P}\left(\mathrm{H}\left(t-\frac{d_k}{V}\right)-\mathrm{H}\left(t-\frac{d_k+L}{V}\right)\right)P_k\ \Phi_{mn}(Vt-d_k,y_P) \tag{5}$$

where M_{mn} stands for the *mn-th* modal mass. If only one load crosses the plate at a constant velocity, equation (5) presents the following solution

$$\psi_{mn}(t)=-\frac{PC_{mn}Y_{mn}(y_P)}{M_{mn}\omega_{mn}^2}\cdot\frac{1}{1-K_{mn}^2}\left[\sin(K_{mn}\omega_{mn}t)-K_{mn}\sin(\omega_{mn}t)\right] \qquad 0\le t\le\frac{L}{V} \qquad K_{mn}\neq 1 \tag{6a}$$

$$\psi_{mn}(t)=-\frac{PC_{mn}Y_{mn}(y_P)}{M_{mn}\omega_{mn}^2}\cdot\frac{1}{2}\left[\sin(\omega_{mn}t)-\omega_{mn}t\cos(\omega_{mn}t)\right] \qquad 0\le t\le\frac{L}{V} \qquad K_{mn}=1 \tag{6b}$$

In equation (6b) K_{mn} is a nondimensional speed defined as

$$K_{mn}=\frac{m\pi V}{\omega_{mn}L} \tag{7}$$

Notice that in the previous equations m corresponds to the number of half-sine waves travelled by the load when crossing the plate admitting a deformation of the *mn-th* mode. As the load travels parallel to the X axis the modal deflection along the load path is always a sinusoidal function multiplied by a constant. When the

load exits the plate, the latter is left in free vibration. The amplitude of this free vibration stage may be obtained solving equation (8) with initial conditions given by equation (6) at $t=L/V$.

$$\ddot{\psi}_{mn}(t)+\omega_{mn}^2\psi_{mn}(t)=0 \qquad t \geq L/V \tag{8}$$

If the amplitude of the free vibrations is divided by the static solution, ψ_{mn}^{st}, a nondimensional amplitude in free vibration may be defined and expressed as

$$R_{mn}=\frac{\Psi_{mn}}{\psi_{mn}^{st}}=\frac{K_{mn}\sqrt{2}}{1-K_{mn}^2}\sqrt{1-\cos(m\pi)\cos\left(\frac{m\pi}{K_{mn}}\right)} \qquad \psi_{mn}^{st}=\left|-\frac{PC_{mn}Y_{mn}(y_P)}{M_{mn}\omega_{mn}^2}\right| \tag{9}$$

Figure 2 shows the evolution of R_{mn} with the nondimensional speed K_{mn} in S-S rectangular orthotropic plates computed analytically for modes with m=1,2,3. On the right hand side of each graph three mode shapes with 1, 2 and 3 half-sine waves along a hypothetical load path are represented as examples. Provided the nondimensionalization of R_{mn}, curves of R_{mn} (K_{mn}) are superimposed for different values of n (*i.e.* different modes with the same number of half-sine waves along the load path).

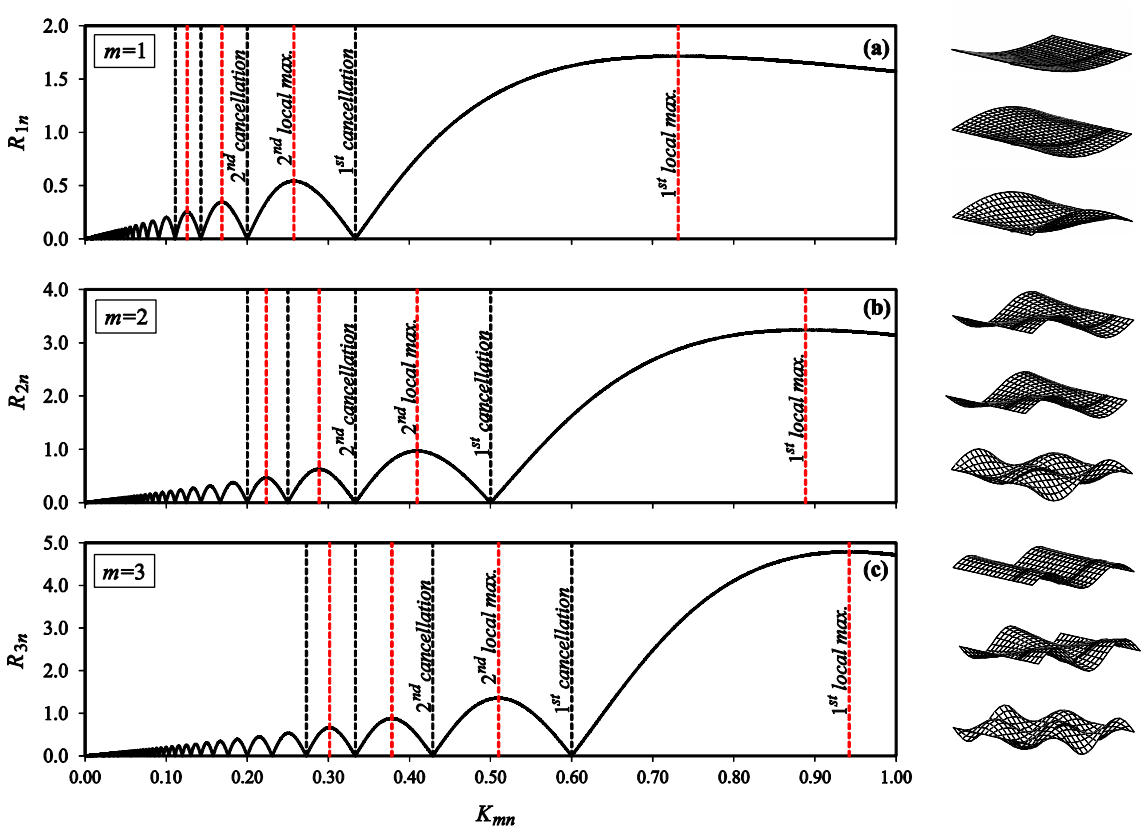


Figure 2: Amplitude of the free vibrations R_{mn} for modes of orthotropic S-S rectangular plates with m=1,2,3 computed analytically

2.2 Cancellation and maximum free vibration conditions

The amplitude of the free vibrations in a particular mode of the orthotropic plate after the circulation of a moving load depends on the nondimensional velocity K_{mn}. From Figure 2 it can be concluded that maximum free vibration and cancellation conditions alternate as the velocity increases. From equation (9) these conditions may be obtained as:

$$R_{mn}\left(K_{mn}\right)=0\rightarrow K_{mn}^{ci} \qquad \frac{\partial R_{mn}\left(K_{mn}\right)}{\partial K_{mn}}=0\rightarrow K_{mn}^{\max i} \tag{10}$$

In equation (10) K_{mn}^{ci} for i=1, 2… stand for the values of K_{mn} for cancellation as the velocity decreases (*i.e.* K_{mn}^{c1} is the first cancellation taking place at the highest speed of circulation). Likewise, $K_{mn}^{\max i}$ designates the nondimensional speeds leading to a local maxima of the plate free vibrations, corresponding $K_{mn}^{\max 1}$ to the maximum taking place at the highest speed. In Table 1 the values for the first four cancellation and maximum free vibration speeds are included for modes with m=1, 2 and 3.

K_{mn}^{ci}	i=1	i=2	i=3	i=4	$K_{mn}^{\max i}$	i=1	i=2	i=3	i=4
m=1	0.3333	0.2000	0.1429	0.1111	m=1	0.7314	0.2576	0.1687	0.1258
m=2	0.5000	0.3333	0.2500	0.2000	m=2	0.8883	0.4094	0.2886	0.2235
m=3	0.6000	0.4286	0.3333	0.2727	m=3	0.9422	0.5096	0.3782	0.3015

Table 1: Maximum free vibration and cancellation conditions for a S-S orthotropic plate corresponding to modes with m=1,2,3

The analytical expression of normalized R_{mn} coincides with that of a S-S Bernouilli-Euler (B-E) beam [14]. Therefore, in the absence of damping, the nondimensional conditions for maximum free vibration and cancellation of rectangular S-S orthotropic plates for modes with 1, 2 and 3 half-sine waves along the load path (Table 1) coincide with those of a S-S B-E beam for the first, second and third longitudinal bending modes of vibration (Figure 3a).

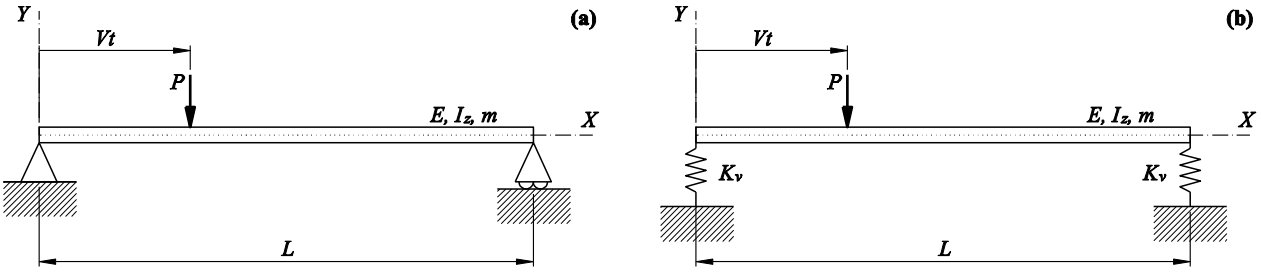


Figure 3: (a) Simply-supported and (b) elastically-supported Bernouilli-Euler beams

In the following section the influence of the plate obliquity, level of structural damping and supports flexibility on the cancellation and free vibration conditions of orthotropic plates are numerically investigated.

3 Influence of plate obliquity, structural damping and supports flexibility on the cancellation and maximum free vibration conditions

In what follows a particular orthotropic plate Finite Element (FE) model is considered. The plate properties are obtained from a real railway bridge with two S-S 15.25 m span identical bays and double track pre-stressed concrete girders deck. The structure is fully described in section 4. This bridge has been selected in particular as (i) the span length to with ratio is close to unity; (ii) it presents a pronounced obliquity (45º skew angle); (iii) experimental measurements are available under ambient vibrations and railway traffic. Due to the deck geometry and the eccentric excitation several modes contribute to the dynamic response of

the bridge deck under railway traffic, and its behaviour considerably differs from that of a beam type structure. The plate properties are included in Table 2:

Orthotropic plate constants		*Plate dimensions*		*Parametric analysis*	
D_x (Nm)	4.5505E9	L (m)	15.25	α (º)	[0, 45]
D_y (Nm)	5.1950E7	B (m)	11.60	ζ (%)	[0.0-5.0]
$D_{1,2}$ (Nm)	1.0390E7	h (m)	11.25	κ (--)	[0.0, 0.15]
D_{xy} (Nm)	1.0864E8	M (kg/m)	26256		
D_{yx} (Nm)	4.1560E7				

Table 2: Orthotropic plate properties and ranges for parametric analysis variables

In this section the variation with (i) the plate obliquity, (ii) structural damping and (iii) the supports vertical flexibility of the cancellation and maximum free vibration conditions after the passage of a single load are investigated.

3.1 Influence of the plate obliquity

The plate is subjected to the circulation of a load travelling parallel to the longitudinal axis X with an eccentricity equal to ¼ of the width of the plate (i.e. y_P=2.9 m). R_{mn} (equation (9)) is obtained for the first 20 modes in a wide range of circulating velocities ($K_{mn} \in$ [0.0, 0.7]), considering two levels of the plate obliquity, α=22.5º and α=45º. α is defined as the complementary angle to the angle formed between the track direction and the plate supported border. It must be stated at this point that K_{mn}=0.5 is a realistic upperlimit considering existing structures and railway lines design velocities. Figure 4 shows the aforementioned results for modes with m=1 and n=1,2 (plots (a-d)), modes with m=2 and n=1,2 (plots (b-e)) and modes with m=3 and n=1,2 (plots (c-f)). In each plot the natural frequencies of the two modes represented along with the deformed shape along the load trajectory are included. Also, in red continuous trace R_{mn} for the plate with straight angles (α=0) is superimposed, which is obtained analytically (Eq. 9). Finally the analytical conditions for cancellation and maximum free vibration neglecting the plate obliquity (those included in Table 1) are also represented in black and red dashed lines, respectively.

From the analysis performed it can be concluded that as long as the mode deformed shape along the load path is approximately sinusoidal, (i) cancellation conditions do occur (leading to zero free vibration levels in the absence of damping); (ii) maximum free vibration conditions take place in between two cancellation conditions; and (iii) the values of K_{mn} for these two situations may be approximated with analytical values for straight plates. For the particular plate under study, it can be observed that for the first bending and first torsion modes (modes 11 and 12), represented in Figure 4 (a)-(d), the free vibration amplification, R_{mn}, is almost coincident with the analytical trace even for the highest level of obliquity considered (α=45º). This fact is important as these two modes (first bending and first torsion modes) participation in the total response is in general of major importance in these structures.

3.2 Influence of structural damping

Secondly, the influence of structural damping on the evolution of R_{mn} with the non-dimensional speed is evaluated considering modal damping values in the interval [0.0, 5.0]%. In Figure 5 R_{mn} is represented for the first 20 modes of the straight plate and for four levels of structural damping. Modes with m=1 are included in plot (a). All the modes with the same number of half sine waves along the load path (same value of m) and the same modal damping overlap. Plots (b) and (c) represent R_{mn} for m=2 and m=3, respectively. The analytical solution given by Eq. (9) coincides with the curves of 0% damping. Analytical cancellation and maximum free vibration conditions for the rectangular plate neglecting damping are also represented in discontinuous traces.

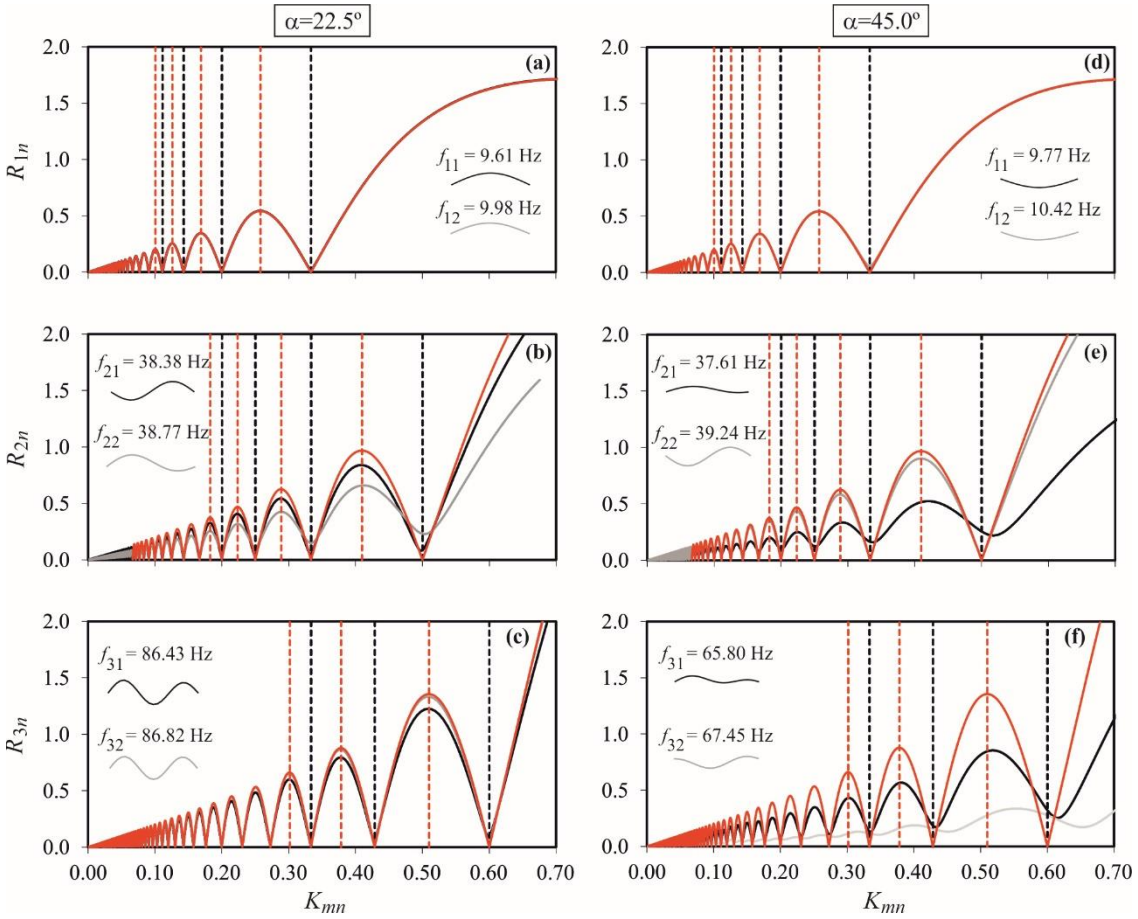


Figure 4: R_{mn} of orthotropic S-S plate under study for modes with m=1,2,3 and n=1,2 considering skew angles of 22.5º and 45º. Red trace: analytical evolution of R_{mn} for rectangular plates. Black and red dashed lines: analytical cancellation and maximum free vibration conditions for straight plates

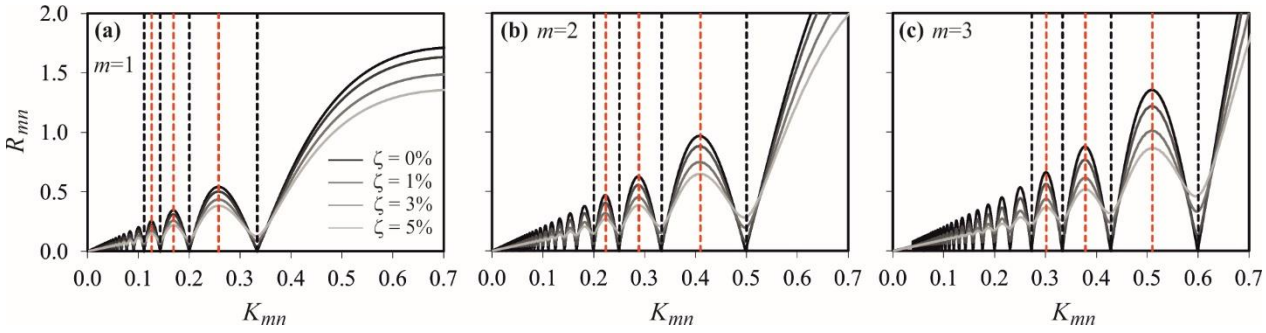


Figure 5: R_{mn} of orthotropic S-S rectangular plate under study for modes with m=1,2,3 for different structural damping levels. Black and red dashed lines: analytical cancellation and maximum free vibration conditions (ζ=0) for undamped straight plates

According to standards [7] prescribed values of damping to be assumed for design purposes in bridges are considerably low. Considering span lengths in the range [10, 25] m, recommended damping values lie between 1-1.7% for pre-stressed concrete bridges and between 0.5-1.75% for steel and composite bridges. Nevertheless, a higher interval has been considered in this analysis to clearly observe the main tendencies. Due to the low damping that generally characterizes these structures modal parameters do not vary significantly with it. For this reason, as shown in Figure 5, cancellation and maximum free vibration conditions remain unmodified, even for the highest level of damping considered. As damping increases, the amplification in free vibration far from the cancellation velocities decreases. Also, in the presence of

damping, the modal response of the bridge when the load travels at a cancellation velocity does not completely vanish. The higher the level of damping, the lower the amplification at maximum free vibration and the higher the amplification at cancellation.

3.3 Influence of the supports flexibility

As a third step in the sensitivity analysis the existence of neoprene bearings introducing certain vertical flexibility at the supports sections (x=0 and x=L) is considered. In the orthotropic plate model this is included in a first approach as a uniform distributed vertical stiffness along the plate supported borders. A nondimensional parameter κ is used as an approximation of the ratio between the flexural rigidity of the plate and the stiffness of the supports, using a beam analogy. The fundamental frequency of a E-S beam leaning on constant vertical linear springs may be approximated by the following expression (see [4]):

$$\omega_1^{ESB} = \omega_1^{SSB}\sqrt{\frac{\pi+4\kappa}{\pi+8\kappa+2\pi\kappa^2}} \tag{11}$$

where ω_1^{SSB} is the circular frequency of the beam in the S-S case, $\kappa=EI_z\pi^3/(K_v L^3)$, and E, I_z, L and K_v are the beam Elastic Modulus, moment of inertia, length and supports vertical stiffness. The plate distributed stiffness along the borders is adjusted such that the first natural frequency accomplishes equation (11) for two levels of supports flexibility: κ=0.05 and κ=0.15. κ=0 corresponds to infinitely rigid supports (S-S case) and the supports flexibility increases with κ. In the structures under study generally $\kappa \leq 0.1$.

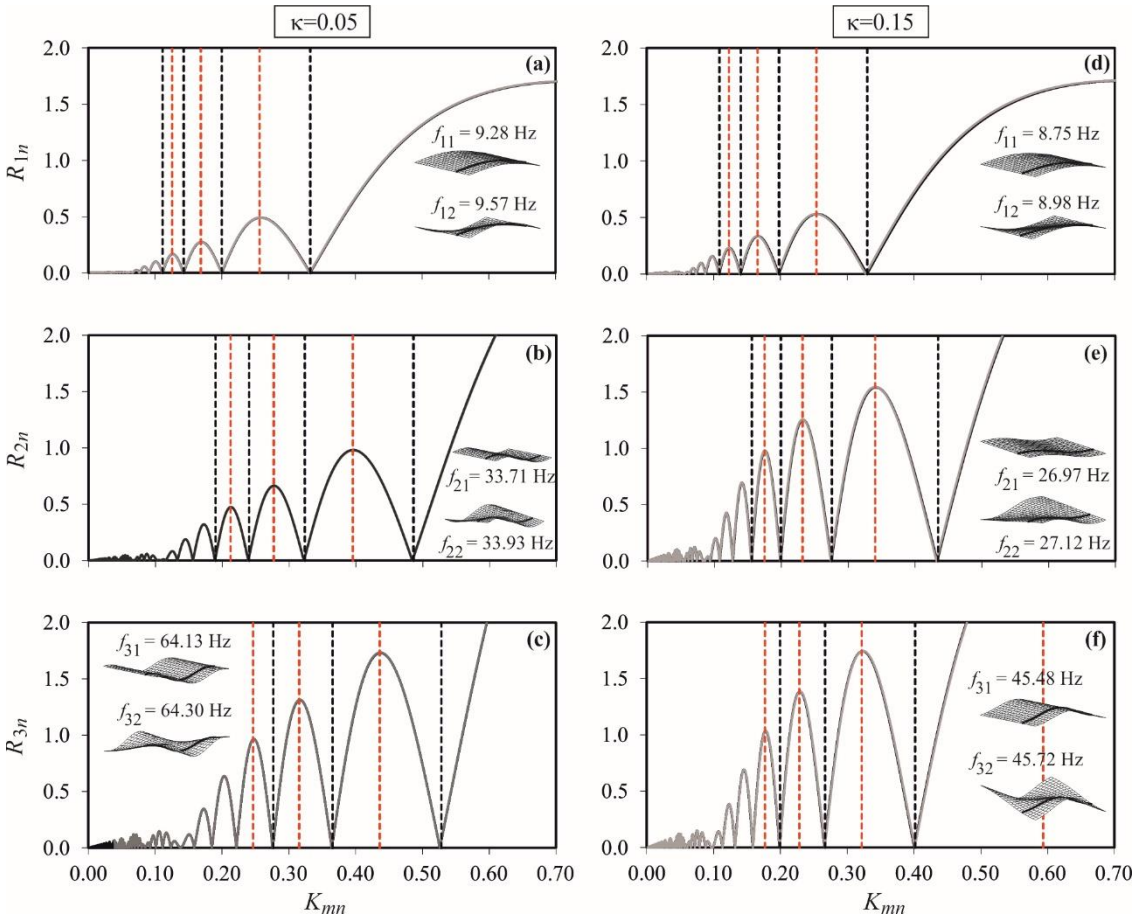


Figure 6: R_{mn} of orthotropic S-S rectangular plate under study for modes with m=1,2,3 and n=1,2 for different support flexibility levels (κ). Black and red dashed lines: analytical cancellation and maximum free vibration conditions for the E-S B-E beam 1st, 2nd and 3rd bending modes

In Figure 6, R_{mn} is represented for the first two modes with m=1, 2 and 3. Plots (a)-(b)-(c) correspond to the most rigid supports (κ=0.05) and plots (d)-(e)-(f) to the most flexible ones (κ=0.1). In all the graphs the corresponding modal shapes and natural frequencies are included. In dashed black and red lines the analytical cancellation and maximum free vibration conditions for a E-S beam are also represented. At this point it should be noted that the nondimensional velocity in the abscissa axis is defined as in equation (7), that is to say referred to the circular frequency in the S-S case. This is convenient because this ratio is independent of κ. From the analysis of Figure 6 it can be concluded that (i) the evolution of the amplitude of the free vibrations presents a similar form when flexible distributed supports are included, i.e. cancellation and maximum free vibration situations take place as the load speed increases; (ii) the cancellation and maximum free vibration conditions reduce mildly as a consequence of the reduction experienced by the plate natural frequencies when the supports are introduced; (iii) in the particular case under consideration the analytical cancellation conditions derived from the analytical E-S B-E beam equations predict excellently the real cancellation conditions in the case of the first two modes in frequency order with a number of half-sine waves m=1,2 and 3. The particular values of these conditions may be consulted in [4]; (iv) the cancellation phenomenon does take place in the elastically supported case implying that when individual modal contributions are considered and in the absence of damping the free vibration levels following the circulation of a single load travelling at constant speed theoretically vanish.

4 Maximum resonance and cancellation of resonance

The main application of the investigation presented herein is the dynamic response of bridges under railway traffic. Railway convoys consist of groups of axle loads regularly spaced. Repetitive distances between the loads are usually known as *characteristic distances*. When the time interval between the passages of these repetitive actions is a multiple of one of the structure natural periods, resonance takes place. At resonance, the free vibrations that each axle load leaves on the bridge when exiting it accumulate, leading to a progressive increase of the dynamic amplification and, in certain cases, to excessive vertical accelerations at the platform area. Therefore, the amplification that should be expected at resonance depends not only on the periodicity of the loads but also on the amplitude of these free vibrations. If the resonant velocity coincides or is close to a cancellation condition, the resonant peak will be moderate or sometimes even imperceptible. On the other hand, when resonance takes place close to a maximum free vibration condition an important amplification of the structural response should be expected.

Let d_k be the characteristic distance causing resonance in a train of loads. Resonant speeds associated to the mn-th mode are then given by:

$$V_{mn,j}^{r} = \frac{d_k f_{mn}}{j} \quad j = 1,2,3... \tag{12}$$

Values of j indicate resonance orders: *i.e.* a second resonance (j=2) implies that mode mn-th experiences two complete cycles of oscillation between the passage of two loads separated the characteristic distance d_k. As the resonance order is higher, generally the amplification is lower as only the first cycle happens under loading and the rest of the cycles tend to damp out due to damping mechanisms. If the resonant speed is expressed as a non-dimensional speed:

$$K_{mn,j}^{r} = \frac{m\pi V_{mn,j}^{r}}{\omega_{mn} L} = \frac{m d_k}{2 jL} \tag{13}$$

Equating expression (13) with the analytical cancellation or maximum free vibration conditions included in Table (1) it is possible to obtain L/d_k ratios causing very soft (Equation 14a) or considerably amplified resonances (Equation 14b):

$$K_{mn}^{ci} = K_{mn,j}^{r} \rightarrow \left(\frac{L}{d_k} \right)_{mj}^{ci} = \frac{m}{2j} \frac{1}{K_{mn}^{ci}} \tag{14a}$$

$$K_{mn}^{\max i} = K_{mn,j}^{r} \rightarrow \left(\frac{L}{d_k}\right)_{mj}^{\max i} = \frac{m}{2j}\frac{1}{K_{mn}^{\max i}} \tag{14b}$$

In Table 3 L/d_k values for maximum resonance and cancellation of resonance in a generic rectangular orthotropic S-S plate are included for m=1,2 (modes with 1 or 2 half-sine waves along the load path), $j \in [1,4]$ (first 4 resonance orders) and $i \in [1,4]$ (first 4 cancellation and maximum free vibration conditions):

$\left(\frac{L}{d_k}\right)_{1j}^{ci}$	i=1	i=2	i=3	i=4	$\left(\frac{L}{d_k}\right)_{1j}^{\max i}$	i=1	i=2	i=3	i=4
j=1	1.5000	2.5000	3.5000	4.5000	j=1	0.6836	1.9411	2.9640	3.9737
j=2	0.7500	1.2500	1.7500	2.2500	j=2	0.3418	0.9705	1.4820	1.9869
j=3	0.5000	0.8333	1.1667	1.5000	j=3	0.2279	0.6470	0.9880	1.3246
j=4	0.3750	0.6250	0.8750	1.1250	j=4	0.1709	0.4853	0.7410	0.9934

$\left(\frac{L}{d_k}\right)_{2j}^{ci}$	i=1	i=2	i=3	i=4	$\left(\frac{L}{d_k}\right)_{2j}^{\max i}$	i=1	i=2	i=3	i=4
j=1	2.0000	3.0000	4.0000	5.0000	j=1	1.1257	2.4424	3.4656	4.4750
j=2	1.0000	1.5000	2.0000	2.5000	j=2	0.5629	1.2212	1.7328	2.2375
j=3	0.6667	1.0000	1.3333	1.6667	j=3	0.3752	0.8141	1.1552	1.4917
j=4	0.5000	0.7500	1.0000	1.2500	j=4	0.2814	0.6106	0.8664	1.1188

Table 3: L/d_k ratios for cancellation of resonance and maximum resonance of an orthotropic S-S rectangular plate for modes with m=1,2

As the cancellation and maximum free vibration conditions for an orthotropic S-S rectangular plate (Table 1) are the same as the conditions for a S-S B-E beam [4], the L/d_k ratios for modes with 1 and 2 half-sine waves along the load path correspond to those of the S-S B-E beam for the first and second longitudinal bending modes. In the following section the response of a real bridge under High-Speed railway traffic is presented. Resonance is detected for two different trains leading to different amplification levels.

5 Real response of an existing structure

5.1 Structure description

Arroyo Bracea bridge belongs to the Madrid-Sevilla High-Speed railway line. It is composed by two identical S-S bays of 15.25 m of span. The deck is made of a 25 cm thick concrete slab resting over five prestressed concrete girders (see Figure 7 and 8). The girders lean on the supports through laminated rubber bearings. As per the substructure, the bridge deck is supported on reinforced concrete abutments in its outermost sections and the inner sections of both bays lean on a pile foundation. The structure crosses the Bracea stream forming an angle of 45º. The deck accommodates a double track ballasted platform. The singularity of this structure is that due to the span to width ratio and deck typology, it presents 5 natural modes below 30 Hz. Also, due to the eccentricity of the excitation and the skew angle, the contribution of modes different from the longitudinal bending ones (i.e. first torsion and first transverse bending modes) is

of importance. This bridge dynamic behaviour was numerically analysed by the authors in the past using an orthotropic plate FE model which showed a good correspondence between numerical predictions and experimental measurements, both under ambient vibration and under railway traffic [8].



Figure 7: Arroyo Bracea bridge photographs

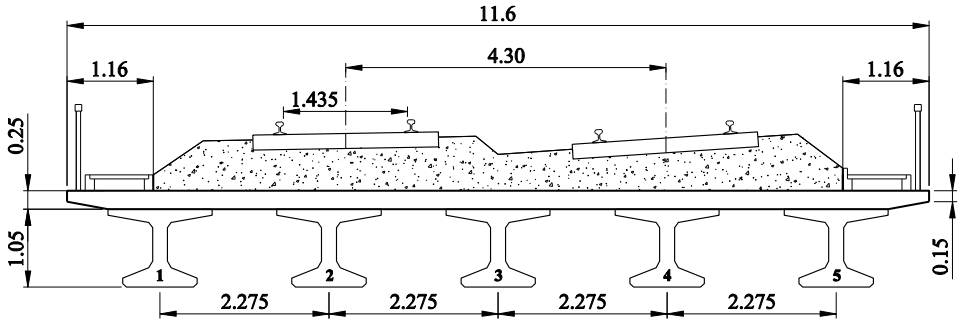


Figure 8: Arroyo Bracea bridge deck cross section

5.2 Experimental campaign

In 2016 the authors carried out an experimental campaign with the purpose of characterizing the structure and soil dynamic properties along with the bridge dynamic response under railway traffic. During the campaign, the vertical acceleration of the bridge deck was measured at 11 points of the lower flange lower horizontal face of the pre-stressed concrete girders (points 1 - 11 in Figure 9), and at the pile foundation upper horizontal surface, close to the central girder support (point 12 in Figure 9).

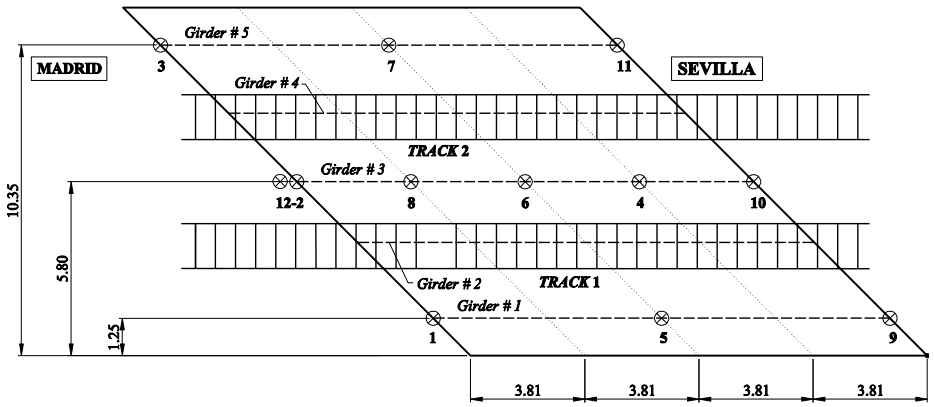


Figure 9: Arroyo Bracea bridge plan and sensors locations

First, the modal parameters of the bridge were identified from ambient vibration data by state-space models using MACEC software [9]. Five modes were identified with frequencies below 30 Hz, in particular: 9.25 Hz, 10.63 Hz, 12.75 Hz, 17.92 Hz and 24.57 Hz. The first three modal shapes correspond to the first longitudinal bending, first torsion and first transverse bending modes. Modal damping values were identified as well for the first five modes as 2.0%, 1.61%, 1.30%, 0.80% and 0.95 %.

5.3 Bridge response under railway traffic. Detection of resonances

During the campaign, several trains crossed the bridge with circulating velocities in the range [100, 280] km/h. In this paper the structural response under two of these trains is presented as the velocity was in the vicinity of a theoretical resonant velocity for the first two modes of the structure. These trains are RENFE Class 103 (ICE 3 or S103) and RENFE Class 130 (Talgo 250 or S130). The circulating velocities for these two trains were 279 and 247 km/h, respectively. In Table 4 the theoretical resonant velocities associated to the first and second modes of the bridge deck and to the characteristic distances of both trains are included for the first 3 resonance orders. The characteristic distance may be any repetitive distance, but the length of the passengers coaches has been selected in this case as it is the one usually associated with maximum acceleration values when resonance takes place in this type of bridges [10]. For the S103 and S130 trains these distances are 24.8 and 13.1 m, respectively. In Table 4 two resonant speeds are highlighted: the third resonance of the fundamental mode induced by S103 train and the second resonance of the first torsion mode induced by S130 train. It can be observed that these two theoretical resonant velocities are in the vicinity of actual circulating velocities of the trains and, therefore, could lead to a certain structural amplification.

Train V (km/h)	d_k (m)	$V^r_{11,1}$ (km/h)	$V^r_{11,2}$ (km/h)	$V^r_{11,3}$ (km/h)
S103 (279)	24.8	825.0	412.5	**275.0**
	d_k (m)	$V^r_{12,1}$ (km/h)	$V^r_{12,2}$ (km/h)	$V^r_{12,3}$ (km/h)
S130 (247)	13.1	502.8	**251.4**	167.6

Table 4: First three resonant speeds for first and second modes associated to the length of the passengers cars

In what follows the structural response is shown for these two convoys. In Figure 10 the bridge vertical acceleration is represented at sensor number 5 located at mid-span below girder #1 for the two trains S103 and S130 travelling at 279 and 241 km/h, respectively. Plots (a) and (b) show the acceleration time history and plots (c) and (d) the frequency content. From Figure 10 it is evident that train S103 travelling at 279 km/h induces resonance of the fundamental mode. The response progressively builds up and a peak in the frequency domain close to the identified fundamental frequency (9.25 Hz) prevails. This type of response is observed as well in the rest of the sensors. It should be stressed at this point that the maximum acceleration of the bridge is admissible despite the resonant situation according to the Serviceability Limit State of vertical acceleration in ballasted bridges (a_{max} < 3.5 m/s^2).

On the other hand, the circulation of S130 train at 247 km/h induces a second resonance of the first torsion mode as well. The comparison of the bridge responses at sensors 5 and 6 (not included) confirms this statement. Also, in Figure 10(d) it may be observed that the acceleration peak at the second mode frequency (torsion mode) of 10.63 Hz exceeds that of the fundamental mode.

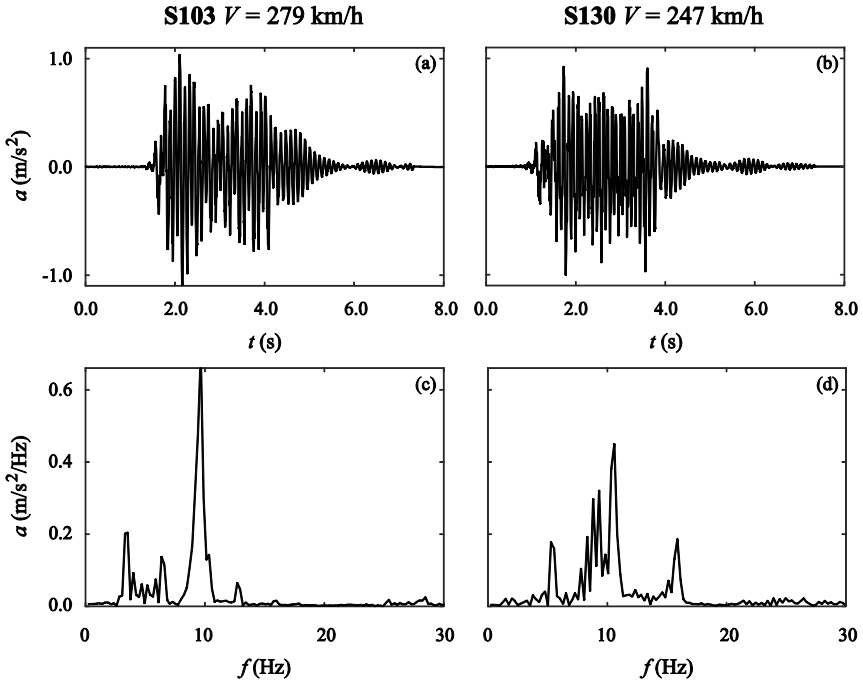


Figure 10: Vertical acceleration at point 5 in the time and frequency domains induced by trains S103 (a)-(c) and S130 (b)-(d)

It can be affirmed that both trains induce resonance on the bridge. Nevertheless, the amplification associated to the circulation of train S103 is more evident than the one associated to train S130, even though the former is a third resonance (one loaded and two empty cycles of oscillation between repetitive loads) and the latter is a second resonance (one loaded and one empty cycle of oscillation). In the view of the authors this difference in amplitude could be related, at least partially, with the level of free vibrations that every axle load leaves on the structure at the particular velocity of circulation in each mode. If ratios L/d_k are calculated for both trains neglecting the flexibility of the supports in a first approach:

$$\left(\frac{L}{d_{S103}}\right)=\frac{15.25}{24.8}=0.61\approx\left(\frac{L}{d_k}\right)_{1,\,j=3}^{\max,i=2}=0.6470 \tag{15a}$$

$$\left(\frac{L}{d_{S130}}\right)=\frac{15.25}{13.1}=1.16\approx\left(\frac{L}{d_k}\right)_{1,\,j=2}^{c,i=2}=1.25 \tag{15b}$$

Equation (15a) shows how the L/d_k ratio for the S103 train is close to a condition of maximum resonance for the third resonance of modes with m=1 (one half-sine wave in the longitudinal direction) (see Table 3). On the other hand, equation (15b) shows that the L/d_k ratio for the S130 train is close to a cancellation condition for second resonances of also modes with m=1.

6 Conclusions

First, the free vibration response of rectangular S-S orthotropic plates under the circulation of a single load travelling at constant speed has been investigated. As the speed increases, the amplitude of the free vibrations associated to every normal mode may be maximum or may cancel out in the absence of damping. Nondimensional velocities for these two situations are obtained analytically. It is shown how the nondimensional conditions for maximum free vibration and cancellation of a rectangular S-S orthotropic plate for modes with m half-sine waves along the load path coincide with those of a S-S B-E beam for the m-th longitudinal bending mode of vibration.

Second, the influence the plate obliquity, structural damping and flexibility of the plate supports on the free vibration response of the plate is investigated numerically. Concerning the plate obliquity the following is concluded: as long as the mode deformed shape along the load path is approximately sinusoidal, (i) cancellation conditions do occur (leading to zero free vibration levels in the absence of damping); (ii) maximum free vibration conditions take place in between two cancellation conditions; and (iii) the values of the nondimensional speed for these two situations may be approximated with analytical values for straight plates.

Regarding the presence of structural damping, cancellation and maximum free vibration conditions remain unmodified when compared to the undamped case, even for the highest level of damping considered. As damping increases, the amplification in free vibration far from the cancellation velocities decreases. Also, in the presence of damping, the modal response of the bridge when the load travels at a cancellation velocity does not completely vanish.

As per the flexibility of the supports, it is concluded that (i) the evolution of the amplitude of the free vibrations presents a similar form when flexible distributed supports are included; (ii) the cancellation and maximum free vibration conditions reduce as a consequence of the reduction experienced by the plate natural frequencies when the supports are introduced; (iii) in the particular case analysed considering the analytical cancellation conditions derived from the E-S B-E beam equations predicts excellently the real cancellation conditions in the case of the first two modes in frequency order with a number of half-sine waves m=1,2 and 3.

Finally, ratios of length-characteristic distance leading to maximum resonance and cancellation of resonance when the plate is subjected to a train of equidistant loads are determined for the analytical case (rectangular straight plates with no damping and rigid supports). To support the conclusions derived theoretically, the experimental response of a real bridge from the Spanish HS railway network is presented and two resonant situations with different amplitudes are shown and analysed.

Acknowledgements

The authors would like to acknowledge the financial support provided by (i) the Spanish Ministry of Economy and Competitiveness under the research project [BIA2016-75042-C2]; and (ii) the Andalusian Scientific Computing Centre (CICA).

References

[1] CEN/TC250, *Eurocode: Basis of structural design. Annex A2: Application for bridges. Final version*, European Committee for Standardization (2005).

[2] ERRI D214, *Rail bridges for speeds >200 km/h. Final report. Part A. Synthesis of the results of D 214 research*, European Rail Research Institute (1999).

[3] A.V. Pesterev, B. Yang, L.A. Bergman, C.A. Tan, *Revisiting the moving force problem*, Journal of Sound and Vibration, Vol. 261, (2003), pp. 75-91.

[4] P. Museros, E. Moliner, M.D. Martínez-Rodrigo, *Free vibrations of simply supported beam bridges under moving loads: maximum resonance, cancellation and resonant vertical acceleration*, Journal of Sound and Vibration, Vol. 332, (2012), pp. 326-345.

[5] M.D Martínez-Rodrigo, P. Museros. *Optimal design of passive viscous dampers for controlling the resonant response of orthotropic plates under high-speed moving loads*, Journal of Sound and Vibration, Vol. 330, (2011), pp. 1328-1351.

[6] N.J. Huffington, W.H. Hoppmann, *On the transverse vibrations of rectangular orthotropic plates*, Journal of Applied Mechanics Vol. 25, (1958), pp. 389-395.

[7] CEN/TC250, *Eurocode 1: Actions on structures. Part 2: Traffic loads on bridges*, European Committee for Standardization (2005).
[8] P. Galvín, A. Romero, E. Moliner, M.D. Martínez-Rodrigo, *Two FE models to analyse the dynamic response of short span simply-supported oblique high-speed railway bridges: Comparison and experimental validation*, Engineering Structures, https://doi.org/10.1016/j.engstruct.2018.03.052, (2018).
[9] E. Reynders, *System identification methods for (operational) modal analysis: review and comparison*, Archives of Computational Methods in Engineering, Vol. 19(1), (2012), pp. 51-124.
[10] M.D. Martínez-Rodrigo, J. Lavado, P. Museros, *Dynamic performance of existing high-speed railway bridges under resonant conditions retrofitted with fluid viscous dampers*, Engineering Structures Vol. 32(3), (2010), pp. 808-828.

Ship roll control and energy harvesting using a U-tube anti-roll tank

N. Alujević[1,*], I. Ćatipović[1], Š. Malenica[2], I. Senjanović[1], N. Vladimir[1]
[1] University of Zagreb, Faculty of Mechanical Engineering and Naval Architecture,
Department of Naval Architecture and Ocean Engineering
Ivana Lučića 5, 10 000 Zagreb, Croatia
E-Mail: **neven.alujevic@fsb.hr**

[2] Bureau Veritas Group, Marine and Offshore Division, Research Department,
Le Triangle de l'Arche, 8 Cours du Triangle - CS 50101,
92937 Paris La Defense Cedex, France

Abstract
In the traditional design of passive anti-roll tanks (ART), the energy associated with the tank fluid motion is dissipated. The work reported in this paper explores the possibility that this energy is instead harvested. It is analytically determined in the paper how the natural frequency and the damping ratio of a U-tube ART should be tuned to maximise the power absorbed by the tank fluid. To this end, a perfectly flat spectrum of the moment representing the excitation of the ship by waves has been assumed. It is found that a tuning that maximises the power absorbed by the ART fluid motion also minimises the average kinetic energy of the ship roll. This is a result of the fact that the power input of the wave excitation moment into the ship plus tank system does not depend on how the ART is tuned. Therefore, different tunings of the ART natural frequency and damping ratio only affect the distribution of the power dissipated by the ship roll damping and the power absorbed by the ART.

1 Introduction

Whereas all angular degrees of freedom (roll, pitch and yaw) are important for sea-keeping characteristics of any ship, roll motion is known to be the critical one [1–3]. This is because ship roll is typically lightly damped and the restoring moment of the ship is small in the cross-plane in comparison with the other planes. As a result, excessive roll can occur under unfavourable or extreme sea conditions. This can lead to reduced effectiveness of the crew, damaged or lost cargo, limited operability of the on-board equipment, or even to catastrophic sea accidents which include capsizing of the ship and the loss of human lives.

Roll reduction devices include keels, fin stabilizers, [4,5], rudders, [6], gyro stabilizers [7,8], azimuthing propellers, [9], and anti-roll tanks (ARTs), [10–14]. Among these devices, anti-roll tanks have raised a considerable attention. Contrary to fin stabilisers, ARTs are effective at low forward speeds. This is relevant, for example, for offshore service vessels such as the wind farm installation vessels, [15]. ARTs do not cause highly concentrated loads, like for example gyro stabilisers, and do not require complicated mechanisms such as Weis–Fogh flapping fin stabilizers, [16]. The operational costs related to ARTs are low. A drawback of ART technology is a remarkable space required for the installation which reduces the space available for transport of cargo. Also, the tank free surface effect reduces the metacentric height of the ship.

Probably the first attempt to use a fluid-filled tank to control the ship roll was at the end of the 19th century [11,17,18]. In 1911 an ART in the shape of a U-tube was proposed, having the horizontal channel below the centre of gravity of the ship, [10]. U-tube ARTs were installed in over 1,000,000 tons of German shipping before WWII, [12]. By 1975 nearly two thousand ships of various types had been fitted with different types of tank stabilisation systems, [19]. Later on, many authors developed mathematical models for analysis of

seakeeping of ships equipped with ARTs, and evaluated the ART performance with respect to the control of roll motion, either actively or passively, [20–24], including the control of parametric roll [13,14,25]. For example, a linearized two-degree-of-freedom (dof) model for the analysis of the roll of a ship equipped by a U-tube ART has been developed by Stigter, [26]. The two dofs are the angle of the ship roll and the angle of the free surface of the tank fluid. The author also discussed the validity of the model by a comparison with experimental results on a scaled model.

Contemporary anti-roll tanks can be designed either in the form of a free-surface ("flume") tank or in the form of a U-tube tank, [5]. A theoretical and experimental comparison of the two designs can be found in [19,27]. With free-surface tanks, an existing liquid reservoir on board can be adapted to perform additional function, that is, to impede the roll motion [19,28]. This may be done without major interventions into the tank construction, apart from installing flooded baffles in order to the increase the damping of the oscillatory fluid sloshing [29,30]. The control of the period of sloshing requires adjusting the level of the liquid in the tank: the higher the level, the lower the period, [19]. On the other hand, U-tube tanks are designed so as to have separated port and starboard portions of the tank connected by a channel between them, [10]. The damping ratio is normally tuned through the size and shape of an orifice (a valve) in the connecting channel of the U-tube. The natural frequency is controlled by a careful sizing of the device. This is predominantly done through choosing the width of the two portions of the tank and their separation distance, which enable adjusting the moment of inertia of the free surface with respect to the symmetry line of the tank installation. Fine tuning can be achieved with the level of filling of the U-tube and dimensioning the height of the connecting channel. If properly designed, a U-tube tank can reduce the roll motion of a ship excited by waves in a way similar to how Tuned Vibration Absorbers (TVA) reduce the response of a mechanical structure to simple harmonic or stochastic forcing, [31–34]. In fact, apart from proposing his U-tube anti roll tank, Frahm had also patented in 1911 an entirely mechanical “device for damping vibrations of bodies”, [31]. This device, effectively a TVA, can be modelled as a mass suspended to the controlled structure through a spring and a damper. It creates an anti-resonance condition at its natural frequency. A U-tube ART works in a similar manner and it can be represented by a simplified mechanical scheme with lumped parameters and linear motions. The equivalent mechanical scheme, however, is somewhat more complex than the TVA scheme [35]. Thus the various optimum tuning strategies developed for TVAs [36–40], cannot be directly used to tune ARTs.

The natural frequency and the damping ratio of ARTs have been typically tuned according to the H_∞ criterion. This criterion aims at minimising the amplitude of the ship roll angle at wave excitation frequencies where maxima of the roll response occur. The roll of a ship without the ART installation is characterised by one such frequency, roughly corresponding to the roll natural frequency. However, the roll of a ship equipped with a lightly damped ART is characterised by two resonance frequencies, due to the additional degree of freedom of the liquid in the tank. Then the optimum natural frequency and damping ratio of the tank can be determined using the H_∞ criterion by employing the so-called “fixed point theory”, originally introduced by Den Hartog [32] for the control of mechanical vibrations, and adapted to the problem of tuning a U-tube ART for ship roll control by Stigter [26]. Using this criterion minimises (and equalises) the roll response at the two resonance frequencies.

The energy associated with the tank fluid motion in traditional U-tube ARTs is normally dissipated, mostly through the viscous damping at the valve in the channel connecting the port and starboard reservoir of the U-tube. The investigation reported in this paper explores the possibility that this energy is instead harvested.

In fact, the specific aim of the work presented in this paper is twofold. On one hand, it is investigated how the natural frequency and damping ratio of an ART should be tuned to maximise the power absorbed by the ART. On the other hand, it is investigated how this tuning corresponds to a tuning that minimises the kinetic energy of the ship roll. The two tuning criteria are compared assuming a perfectly flat spectral distribution of the moment representing the excitation of the ship by waves. Although this assumption is far from the real conditions at sea, it facilitates analytical estimation of the optimum natural frequency and damping ratio of the ART.

The paper is structured as follows. In Section 2 the mathematical model for the analysis of the roll of a ship equipped with an ART is presented. Equations of motion are given and the balance of the power input into the ship plus tank system with the power dissipated by the system is introduced. In Section 3 the roll of a

ship equipped with an ART is discussed assuming the flat spectrum of the roll excitation moment. Analytical expressions for the natural frequency and damping ratio of the ART either to minimise the average kinetic energy of the ship roll, or to maximise the power absorbed by the ART installation are derived.

2 Mathematical model

2.1 Equations of motion

The schematic representation of the ship equipped with an anti-roll tank is shown in Figure 1.

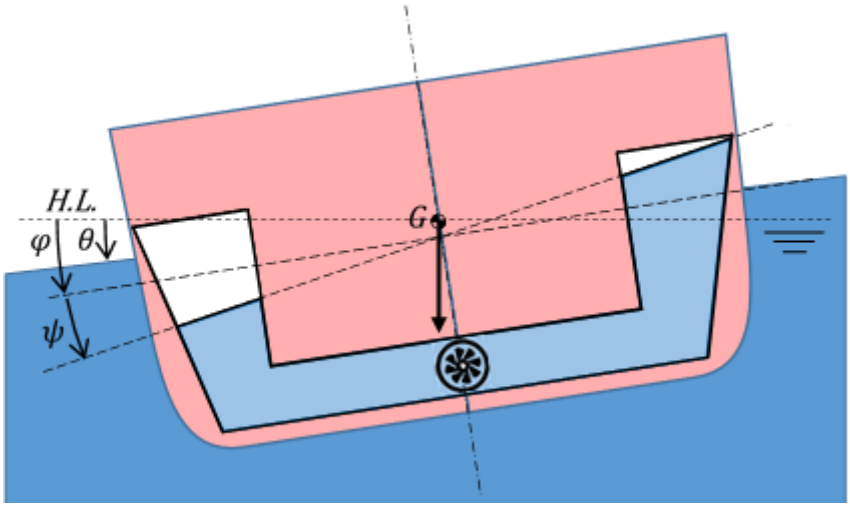


Figure 1: The scheme of a ship equipped with an anti-roll tank

According to Stigter's linearized model of a ship plus tank, [26], equations of motion can be written as :

$$a_1\ddot{\varphi} + a_2\dot{\varphi} + a_3\varphi + c_1\ddot{\psi} + c_3\psi = m_\theta\,, \tag{1}$$

$$c_1\ddot{\varphi} + c_3\varphi + b_1\ddot{\psi} + b_2\dot{\psi} + b_3\psi = 0\,, \tag{2}$$

where φ is the ship roll angle, ψ is the tank fluid angle measured relative to the ship (Figure 1), an m_θ is the wave excitation moment.The coefficients $a_i, b_i,$ and c_i are:

$a_1 =$ the moment of inertia of the ship+ART system, assuming a "frozen" tank fluid (kgm^2),

$a_2 =$ the linear roll damping coefficient of the hull (Nms/rad),

$a_3 =$ the righting moment of the ship+ART system assuming a "frozen" tank fluid (Nm/rad),

$b_1 =$ the moment of inertia of the tank fluid assuming a motionless ship (kgm^2)

$b_2 =$ the total linear angular damping coefficient between the tank fluid and the tank walls (Nms/rad)

$b_3 =$ the restoring moment of the tank fluid assuming a motionless ship (Nm/rad)

$c_1 =$ the moment of inertia of the "frozen" tank fluid (kgm^2)

$c_3 = b_3$, [26].

All moments of inertia, restoring moments and the righting moment are with reference to the centre of gravity of the ship plus ART system ([26]). Full details on how to calculate all model coefficients for a given

ship can be found in [26]. A discussion on the assumptions required to derive the linearized model and its experimental validation can also be found in the reference.

The equations of motion (1) and (2) can be written in the matrix form as:

$$\mathbf{M}\ddot{\mathbf{x}} + \mathbf{C}\dot{\mathbf{x}} + \mathbf{K}\mathbf{x} = \mathbf{F}\,, \tag{3}$$

where **M** is the generalised inertia matrix, **K** is the generalised restoring moment matrix, **C** is the damping matrix, $\mathbf{x}(t)$, $\dot{\mathbf{x}}(t)$, $\ddot{\mathbf{x}}(t)$ are the angular displacement, velocity and acceleration column vectors respectively, and **F**(*t*) is the generalised excitation moment column vector. These matrices/vectors are given by the following expressions:

$$\mathbf{M} = \begin{bmatrix} a_1 & c_1 \\ c_1 & b_1 \end{bmatrix},\ \mathbf{C} = \begin{bmatrix} a_2 & 0 \\ 0 & b_2 \end{bmatrix},\ \mathbf{K} = \begin{bmatrix} a_3 & c_3 \\ c_3 & b_3 \end{bmatrix}, \tag{4 a-c}$$

$$\mathbf{x} = \begin{bmatrix} \varphi(t) \\ \psi(t) \end{bmatrix}, \mathbf{F} = \begin{bmatrix} m_\theta(t) \\ 0 \end{bmatrix}. \tag{5 a-b}$$

Assuming a simple harmonic oscillation of the wave excitation moment, $m_\theta = \Re\left\{\hat{M}_\theta \mathrm{e}^{-\mathrm{i}\omega t}\right\}$, the steady state forced response of the ship and the tank are also simple harmonic, $\varphi = \Re\left\{\hat{\Phi}\mathrm{e}^{-\mathrm{i}\omega t}\right\}$, and $\psi = \Re\left\{\hat{\Psi}\mathrm{e}^{-\mathrm{i}\omega t}\right\}$, where $\mathrm{i} = \sqrt{-1}$ and $\Re$ stands for the real part. Therefore Eq. (3) can be written as:

$$\mathbf{S}(\mathrm{i}\omega)\mathbf{x}(\mathrm{i}\omega) = \mathbf{F}(\mathrm{i}\omega), \tag{6}$$

where **S**(iω) is a dynamic stiffness matrix with the following form:

$$\mathbf{S}(\mathrm{i}\omega) = -\omega^2\mathbf{M} + \mathrm{i}\omega\mathbf{C} + \mathbf{K}\,. \tag{7}$$

The solution of Eq. (6) can be obtained by inversion of the dynamic stiffness matrix **S**(iω) as

$$\mathbf{x}(\mathrm{i}\omega) = \mathbf{S}^{-1}(\mathrm{i}\omega)\mathbf{F}(\mathrm{i}\omega)\,. \tag{8}$$

Differentiating Eq. (8) in order to obtain ship roll and tank fluid angular velocities results in the following expression:

$$\dot{\mathbf{x}}(\mathrm{i}\omega) = \mathbf{Y}(\mathrm{i}\omega)\mathbf{F}(\mathrm{i}\omega), \tag{9}$$

where $\dot{\mathbf{x}}(\mathrm{i}\omega) = \mathrm{i}\omega\,\mathbf{x}(\mathrm{i}\omega)$ is a vector containing ship and tank free surface angular velocities and $\mathbf{Y}(\mathrm{i}\omega) = \mathrm{i}\omega\,\mathbf{S}^{-1}(\mathrm{i}\omega)$ is the angular mobility matrix (2×2) containing frequency response functions (FRFs) between angular velocities and excitation moments:

$$\mathbf{Y}(\mathrm{i}\omega) = \begin{bmatrix} Y_{\dot{\varphi},m_\theta} & Y_{\dot{\varphi},m_\psi} \\ Y_{\dot{\psi},m_\theta} & Y_{\dot{\psi},m_\psi} \end{bmatrix}. \tag{10}$$

Taking into account Eq. (5b), the steady-state angular velocity responses of the ship and tank system to the moment exciting the ship, are the two FRFs located in the first column of the angular mobility matrix $Y_{\dot{\varphi},m_\theta}$, and $Y_{\dot{\psi},m_\theta}$. $Y_{\dot{\varphi},m_\theta}$ is the FRFs between the ship roll angular velocity, $\dot{\varphi}$, and the excitation wave moment, m_θ, whereas $Y_{\dot{\psi},m_\theta}$ is the FRFs between the angular velocity of the tank free surface, $\dot{\psi}$, and the excitation wave moment, m_θ. The wave excitation moment m_θ can be represented in terms of the wave slope θ, [26], as:

$$m_\theta = a_3\theta\,, \tag{11}$$

so that the two FRFs expressed in terms of the wave slope are:

$$Y_{\dot\varphi,\theta} = a_3 Y_{\dot\varphi,m_\theta}\,, \tag{12}$$

$$Y_{\dot\psi,\theta} = a_3 Y_{\dot\psi,m_\theta}\ . \tag{13}$$

By taking **M**, **K** and **C** matrices from Eq. (4)a-c, and noting that $c_3 = b_3$, the two FRFs in Eqs. (12),(13) can be calculated as

$$Y_{\dot\varphi,\theta} = \frac{a_3 b_1 (\mathrm{i}\omega)^3 + a_3 b_2 (\mathrm{i}\omega)^2 + a_3 b_3 (\mathrm{i}\omega)}{\left(b_1 a_1 - c_1^{\,2}\right)(\mathrm{i}\omega)^4 + \left(b_2 a_1 + b_1 a_2\right)(\mathrm{i}\omega)^3 + \left(\left(a_1 - 2c_1\right)b_3 + b_2 a_2 + b_1 a_3\right)(\mathrm{i}\omega)^2 + \left(b_3 a_2 + b_2 a_3\right)(\mathrm{i}\omega) + b_3\left(a_3 - b_3\right)}\,, \tag{14}$$

$$Y_{\dot\psi,\theta} = \frac{-a_3 c_1 (\mathrm{i}\omega)^3 - a_3 b_3 (\mathrm{i}\omega)}{\left(b_1 a_1 - c_1^{\,2}\right)(\mathrm{i}\omega)^4 + \left(b_2 a_1 + b_1 a_2\right)(\mathrm{i}\omega)^3 + \left(\left(a_1 - 2c_1\right)b_3 + b_2 a_2 + b_1 a_3\right)(\mathrm{i}\omega)^2 + \left(b_3 a_2 + b_2 a_3\right)(\mathrm{i}\omega) + b_3\left(a_3 - b_3\right)}\,. \tag{15}$$

The minus sign in the tank free surface angular velocity FRF is due to use of the relative angle ψ, i.e. if the tank free surface remains parallel to the calm sea level, then the angle $\psi = -\varphi$.

2.2 The power balance

As can be seen by inspecting Eqs. (1),(2) the only dissipative terms are the total coefficient of the linear damping of the ship roll, a_2, and the coefficient of the tank linear damping, b_2. Therefore, the power input into the ship plus tank system must be a sum of the power dissipated by the ship roll and the power absorbed by the tank fluid motion:

$$P_{IN} = P_S + P_T\,. \tag{16}$$

The power dissipated by the ship roll motion can be written as:

$$P_S(\mathrm{i}\omega) = \frac{1}{2}\Re\left\{m^*_{a_2}(\mathrm{i}\omega)\dot\varphi(\mathrm{i}\omega)\right\}, \tag{17}$$

where $()^*$ denotes complex conjugate, and the moment m_{a_2} is the moment produced by the damping of the ship roll, which is given by:

$$m_{a_2}(\mathrm{i}\omega) = a_2\dot\varphi(\mathrm{i}\omega), \tag{18}$$

so that using Eq. (17) the power dissipated by the ship roll equals:

$$P_S(\mathrm{i}\omega) = \frac{1}{2}a_2\left|\dot\varphi(\mathrm{i}\omega)\right|^2. \tag{19}$$

Assuming that the wave slope, θ, is represented by its spectrum, $S_{\theta,\theta}$, the mean squared value of the angular velocity of the ship roll (i.e. the expectation value of the squared velocity) can be written as:

$$E\left[\left|\dot{\varphi}\right|^2\right]=\int_{-\infty}^{\infty}\left|Y_{\dot{\phi},\theta}\left(\mathrm{i}\omega\right)\right|^2 S_{\theta,\theta}\mathrm{d}\omega \tag{20}$$

where $E[\ ]$ denotes the expectation value. The mean power dissipated by the ship roll damping is thus

$$P_S=\frac{a_2}{2}E\left[\left|\dot{\varphi}\right|^2\right]=\frac{a_2}{2}\int_{-\infty}^{\infty}\left|Y_{\dot{\phi},\theta}\left(\mathrm{i}\omega\right)\right|^2 S_{\theta,\theta}\mathrm{d}\omega\,. \tag{21}$$

On the other hand, the power absorbed by the tank water motion is equal to that absorbed through the total coefficient of the linear damping of the tank, b_2, which can be written as:

$$P_T=\frac{1}{2}\Re\left\{m_{b_2}^*\left(\mathrm{i}\omega\right)\dot{\psi}\left(\mathrm{i}\omega\right)\right\}, \tag{22}$$

where the moment m_{b_2} is the moment produced by the damping of the tank fluid motion given by:

$$m_{b_2}\left(\mathrm{i}\omega\right)=b_2\dot{\psi}\left(\mathrm{i}\omega\right). \tag{23}$$

This is because $\dot{\psi}$ is the angular velocity of the tank free surface relative to the tank structure. Therefore the power absorbed by the ART equals:

$$P_T\left(\mathrm{i}\omega\right)=\frac{1}{2}b_2\left|\dot{\psi}\left(\mathrm{i}\omega\right)\right|^2. \tag{24}$$

The expectation value of the squared angular velocity of the tank fluid is:

$$E\left[\left|\dot{\psi}\right|^2\right]=\int_{-\infty}^{\infty}\left|Y_{\dot{\psi},\theta}\left(\mathrm{i}\omega\right)\right|^2 S_{\theta,\theta}\mathrm{d}\omega\,. \tag{25}$$

Thus the mean power absorber by the tank fluid motion is

$$P_T=\frac{b_2}{2}E\left[\left|\dot{\psi}\right|^2\right]=\frac{b_2}{2}\int_{-\infty}^{\infty}\left|Y_{\dot{\psi},\theta}\left(\mathrm{i}\omega\right)\right|^2 S_{\theta,\theta}\mathrm{d}\omega\,. \tag{26}$$

3 Maximisation of the power absorbed by the tank - minimisation of the roll kinetic energy

3.1 Absorbed power, dissipated power and input power

At this point it is convenient to express the steady state response of the system by using the following six dimensionless parameters:

$$f = \frac{\omega_T}{\omega_S} \qquad \eta_1 = \frac{a_2}{2\sqrt{a_1 a_3}}$$
$$\mu_1 = \frac{c_1}{\sqrt{b_1 a_1}} \qquad \eta_2 = \frac{b_2}{2\sqrt{b_1 b_3}} \tag{27a-f}$$
$$\mu_2 = \frac{b_1}{\sqrt{b_1 a_1}} = \sqrt{\frac{b_1}{a_1}} \qquad \Omega = \frac{\omega}{\omega_S}$$

where

$$\omega_S = \sqrt{\frac{a_3}{a_1}}, \tag{28}$$

is the natural frequency of the ship roll assuming a "frozen" tank liquid, and

$$\omega_T = \sqrt{\frac{b_3}{b_1}}, \tag{29}$$

is the natural frequency of the tank fluid free oscillation in an otherwise motionless ship. The frequency ratio f is thus the ratio between the two natural frequencies, η_1 is the damping ratio of the ship roll free oscillations assuming again a frozen tank liquid, η_2 is the damping ratio of the tank fluid free oscillations assuming again a motionless ship. Furthermore, μ_1 is the frozen tank fluid rotary moment of inertia ratio, and μ_2 is the tank fluid rotary moment of inertia ratio assuming a motionless ship. Finally, Ω is the dimensionless frequency, that is, the ratio of frequency to the ship natural frequency.

Two dimensionless frequency response functions can now be defined in the form analogue to that in Eqs. (14),(15) as:

$$\Upsilon_{\dot{\phi},\theta}(\mathrm{i}\Omega) = \omega_s Y_{\dot{\phi},\theta}(\mathrm{i}\Omega) = \frac{B_3(\mathrm{i}\Omega)^3 + B_2(\mathrm{i}\Omega)^2 + B_1(\mathrm{i}\Omega) + B_0}{A_4(\mathrm{i}\Omega)^4 + A_3(\mathrm{i}\Omega)^3 + A_2(\mathrm{i}\Omega)^2 + A_1\mathrm{i}\Omega + A_0}, \tag{30}$$

$$\Upsilon_{\dot{\psi},\theta}(\mathrm{i}\Omega) = \omega_s Y_{\dot{\phi},\theta}(\mathrm{i}\Omega) = \frac{C_3(\mathrm{i}\Omega)^3 + C_2(\mathrm{i}\Omega)^2 + C_1(\mathrm{i}\Omega) + C_0}{A_4(\mathrm{i}\Omega)^4 + A_3(\mathrm{i}\Omega)^3 + A_2(\mathrm{i}\Omega)^2 + A_1\mathrm{i}\Omega + A_0}, \tag{31}$$

where

$$\begin{aligned} A_0 &= f^2 - f^4 {\mu_2}^2 \\ A_1 &= 2f^2\eta_1 + 2\eta_2 f \\ A_2 &= 1 - (2\mu_2\mu_1 - 1) f^2 + 4\eta_2 f \eta_1 \\ A_3 &= 2\eta_2 f + 2\eta_1 \\ A_4 &= 1 - {\mu_1}^2 \end{aligned} \qquad \begin{aligned} B_0 &= 0 \\ B_1 &= f^2 \\ B_2 &= 2\eta_2 f \\ B_3 &= 1 \end{aligned} \qquad \begin{aligned} C_0 &= 0 \\ C_1 &= -f^2\mu_2 \\ C_2 &= 0 \\ C_3 &= -\mu_1 \end{aligned} \tag{32}$$

If it is assumed that the spectrum of the wave slope, $S_{\theta,\theta}$ is independent of frequency, i.e. the wave slope spectrum has the characteristics of white Gaussian noise, the power dissipated by the ship roll expressed in terms of the dimensionless FRFs can be obtained by using (30) and (32):

$$P_S = 2\Omega_{sh}{}^4 a_1 S_{\theta,\theta} \eta_1 \int_{-\infty}^{\infty} \left| \Upsilon_{\dot{\phi},\theta}(\mathrm{i}\Omega) \right|^2 \mathrm{d}\Omega \ . \tag{33}$$

The corresponding dimensionless power ratio, can be expressed as:

$$\Pi_S = \frac{P_S}{a_1 \omega_S{}^4 S_{\theta,\theta}} \ . \tag{34}$$

Note that the unit of $S_{\theta,\theta}$ is second, so that the denominator of (34), used to make the power index dimensionless, has the dimension of power in Watts.

Similarly, the power absorbed by the tank fluid motion expressed in terms of the dimensionless FRFs using (31) and (32) can be written as:

$$P_T = 2\, f a_1 \Omega_{sh}{}^4 \eta_2 S_{\theta,\theta} \int_{-\infty}^{\infty} \left| \Upsilon_{\dot{\psi},\theta}(\mathrm{i}\Omega) \right|^2 \mathrm{d}\Omega \, . \tag{35}$$

The corresponding dimensionless power ratio is:

$$\Pi_T = \frac{P_T}{a_1 \omega_S{}^4 S_{\theta,\theta}} \, . \tag{36}$$

The integrals in Eqs. (33) and (35) can be respectively calculated as [41]:

$$\int_{-\infty}^{\infty} \left| \Upsilon_{\dot{\phi},\theta}(\mathrm{i}\Omega) \right|^2 \mathrm{d}\Omega = \pi \frac{A_0 B_3^2 \left(A_0 A_3 - A_1 A_2 \right) + A_0 A_1 A_4 \left(2B_1 B_3 - B_2^2 \right) - A_0 A_3 A_4 \left(B_1^2 - 2B_0 B_2 \right) + A_4 B_0^2 \left(A_1 A_4 - A_2 A_3 \right)}{A_0 A_4 \left(A_0 A_3^2 + A_1^2 A_4 - A_1 A_2 A_3 \right)} , \tag{37}$$

and

$$\int_{-\infty}^{\infty} \left| \Upsilon_{\dot{\psi},\theta}(\mathrm{i}\Omega) \right|^2 \mathrm{d}\Omega = \pi \frac{\left(A_0 C_3{}^2 \left(A_0 A_3 - A_1 A_2 \right) + A_0 A_1 A_4 \left(2C_1 C_3 - C_2{}^2 \right) - A_0 A_3 A_4 \left(C_1{}^2 - 2C_0 C_2 \right) + A_4 C_0{}^2 \left(A_1 A_4 - A_2 A_3 \right) \right)}{A_0 A_4 \left(A_0 A_3{}^2 + A_1{}^2 A_4 - A_1 A_2 A_3 \right)} . \tag{38}$$

By substituting from (32) into (37) and (38), and using (34) and (36) it is obtained:

$$\Pi_S = \frac{\pi \eta_1 \begin{pmatrix} \eta_2 \left(\mu_1{}^2 - \mu_2{}^2 - 1 \right) f^4 + 4\left(\left(\mu_1{}^2 - 1 \right) \eta_2{}^2 - 1/4 \left(\mu_1 - \mu_2 \right)^2 \right) \eta_1 f^3 + \\ 4\eta_2 \left(\left(\mu_1{}^2 - 1 \right) \eta_2{}^2 + 1/2 \mu_2 \mu_1 + 1/2 - 1/2 \mu_1{}^2 - \eta_1{}^2 \right) f^2 - 4\eta_1 f \eta_2{}^2 - \eta_2 \end{pmatrix}}{\left(\mu_1{}^2 - 1 \right) \begin{pmatrix} f^5 \mu_2{}^2 \eta_2{}^2 - 2\eta_1 \eta_2 \left(\mu_2 \mu_1 - \mu_2{}^2 - 1/2 \right) f^4 + \left(\left(4\eta_1{}^2 - 2\mu_2 \mu_1 \right) \eta_2{}^2 + \eta_1{}^2 \left(\mu_1 - \mu_2 \right)^2 \right) f^3 + \\ 2\eta_1 \eta_2 \left(2\eta_1{}^2 + 2\eta_2{}^2 + \mu_1{}^2 - \mu_2 \mu_1 - 1 \right) f^2 + \eta_2{}^2 \left(\mu_1{}^2 + 4\eta_1{}^2 \right) f + \eta_1 \eta_2 \end{pmatrix}} \tag{39}$$

for the dimensionless index of the dissipated power for the ship, and

$$\Pi_T = -\frac{\pi f \eta_2 \left(f^4 \eta_2 \mu_2^{\,2} + \eta_1 \left(\mu_1 - \mu_2\right)^2 f^3 + 4\mu_1 \left(\mu_1 \eta_1^{\,2} - 1/2\mu_2\right) \eta_2 f^2 + 4 f \eta_2^{\,2} \mu_1^{\,2} \eta_1 + \eta_2 \mu_1^{\,2} \right)}{\left(\mu_1^{\,2} - 1\right) \left(\begin{array}{l} f^5 \mu_2^{\,2} \eta_2^{\,2} - 2\eta_1 \eta_2 \left(\mu_2 \mu_1 - \mu_2^{\,2} - 1/2\right) f^4 + \left(\left(4\eta_1^{\,2} - 2\mu_2 \mu_1\right) \eta_2^{\,2} + \eta_1^{\,2} \left(\mu_1 - \mu_2\right)^2 \right) f^3 + \\ 2\eta_1 \eta_2 \left(2\eta_1^{\,2} + 2\eta_2^{\,2} + \mu_1^{\,2} - \mu_2 \mu_1 - 1\right) f^2 + \eta_2^{\,2} \left(\mu_1^{\,2} + 4\eta_1^{\,2}\right) f + \eta_1 \eta_2 \end{array} \right)} \tag{40}$$

for the dimensionless absorbed power index for the tank.

The sum of the two dimensionless powers is the dimensionless power input, which using (39) and (40) greatly simplifies and becomes:

$$\Pi_{IN} = \Pi_S + \Pi_T = \frac{\pi}{1 - \mu_1^{\,2}}. \tag{41}$$

where

$$\Pi_{IN} = P_{IN} / a_1 \omega_S^{\,4}. \tag{42}$$

It can be seen that the power input $P_{IN} = a_1 \omega_S^{\,4} \Pi_{IN}$ does not depend on how the ART is tuned. Furthermore, the rotational inertia ratio μ_1, can be neglected in Eq. (41), since the value of c_1 is normally small in comparison with a_1 and b_1, Eq. (32), see also [26]. Therefore, it can be stated with sufficient accuracy that the power input only depends on the moment of inertia of the ship plus tanks system, a_1 multiplied by the natural frequency of the ship roll to the power of four. Since the sum $\Pi_S + \Pi_T$ is invariant, even if $\mu_1^{\,2}$ in Eq. (41) is not neglected, it becomes clear that maximising the power absorbed by the ART, Π_T, minimises the power dissipated by the ship roll, Π_S. Given that the average kinetic energy of the roll of the ship is proportional to the mean squared angular roll velocity through the moment of inertia of the ship plus tank system, a_1, minimising the power dissipated by the ship roll is equivalent to minimising the roll kinetic energy. Therefore a maximisation of the power absorbed by the tank also leads to minimisation of the roll kinetic energy.

3.2 H_2 optimisation

A type of optimisation which minimises (or maximises) energy in signals is often referred to as H_2 optimisation. This is in contrast to the other widely used criterion, H_∞, which optimises for the maximum expected amplitudes. The combination of the frequency ratio f and the tank fluid damping ratio η_2 which maximises the power absorbed by the tank can be obtained by requiring that the derivatives of the dimensionless absorbed power index of the tank, Π_T, by the frequency ratio f and by the tank damping ratio η_2 both vanish. Alternatively, the same procedure can be used to minimise the power dissipated by the ship, Π_S which, according to Eq. (41) must yield the same result. The rotational inertia ratio μ_1, can be neglected in the expressions for the two derivatives. Also, the ship roll damping ratio, η_1 ,is normally low, especially if the ship is not equipped with bilge keels, and can also be neglected in the expressions for the two derivatives. The conditions that must be satisfied for the two simplified derivatives to vanish are:

$$\begin{aligned} \frac{\partial \Pi_T}{\partial f} = 0 \quad &\Rightarrow \quad 5 + \left(12\eta_2^{\,2} - 6\right) f^2 + \left(1 + \mu_2^{\,2}\right) f^4 = 0 \\ \frac{\partial \Pi_T}{\partial \eta_2} = 0 \quad &\Rightarrow \quad 4 f^2 \eta_2^{\,2} + 2 f^2 - 1 - \left(1 + \mu_2^{\,2}\right) f^4 = 0. \end{aligned} \tag{43}$$

Solving (43) simultaneously for f and η_2 results in eight roots, of which the physically meaningful one for a typical ship plus ART system, which maximises the power absorbed by the ART is:

$$f_{OPT} = \frac{\sqrt{2\left(1+\mu_2{}^2\right)\left(3-\sqrt{1-8\mu_2{}^2}\right)}}{2(1+\mu_2{}^2)}, \qquad \eta_{2,OPT} = \frac{\sqrt{1-\sqrt{1-8\mu_2{}^2}}}{4}. \tag{44}$$

The validity of the expressions (44) is limited to the inertia ratios μ_2 below the ratios of at most 35%. However the inertia ratio μ_2 is normally less than that, since the moment of inertia of the tank fluid, b_1, is smaller than the moment of inertia of the ship plus frozen tank, a_1. In fact, given that μ_2^2 is small in comparison to one, the optimum frequency ratio is just above unity. It is a physically sound and acceptable result that the best power absorption by the tank is obtained by tuning its natural frequency close to the natural frequency of the ship roll, $f_{OPT} \approx 1$. Even when applying different optimisation criteria on other types of oscillation absorber systems [34,36–40] the optimum natural frequency ratio close to unity has been obtained.

An illustrative example of a ship equipped with a U-tube ART is considered next. The system is characterised by the following dimensionless parameters: $\mu_1 = 0.048$, $\mu_2 = 0.192$, and $\eta_1 = 0.075$. The example ship is taken from [26]. It is assumed for convenience that $S_{\theta,\theta} = 1$ s, and $\omega_S = 1\ \mathrm{s}^{-1}$. Two tuning criteria of the ART are compared, the H_∞ criterion, aiming at minimising the maximum roll angle, and the present H_2 criterion, aiming at maximising the power absorbed by the ART. It is seen in Figure 2 that both tuning criteria significantly reduce either the roll angle or the roll angular velocity squared in comparison to the situation where the ship is not equipped with an ART.

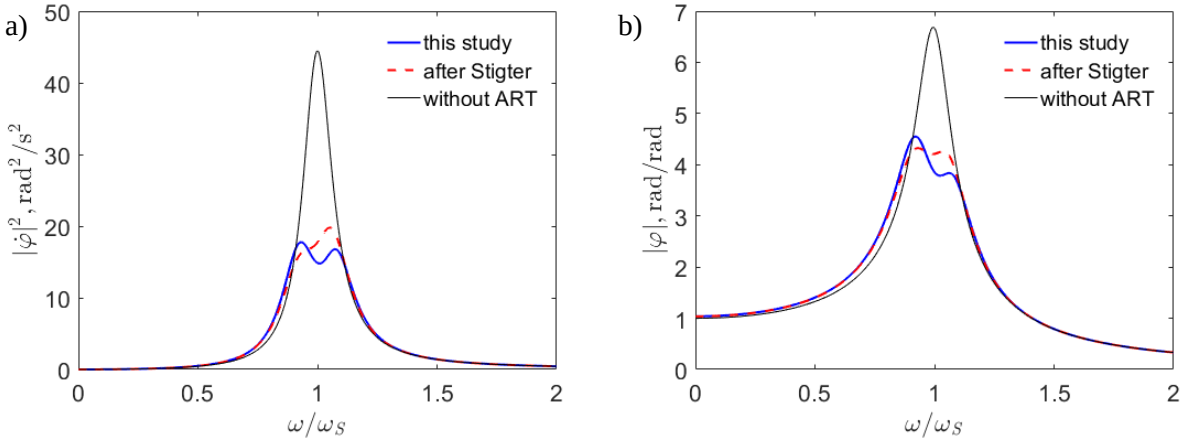


Figure 2: a) the roll velocity squared b) the roll angle as a function of frequency per unit excitation wave angle

The area under the solid curve in Figure 2a) is in fact minimised by using the optimum tuning parameters of Eq. (44). If interpreted in terms of the maximum ship roll angle, Figure 2 b), it is seen that the present tuning is somewhat inferior to the tuning using the H_∞ criterion, as one would expect, given the different aims of the two tuning principles. Still, the increased roll angle near the first natural frequency of the H_2 optimised ship plus ART system is not excessive, as seen by comparing the solid line with the dashed line at the frequency of about $0.9\omega_S$.

Figure 3a) shows the dimensionless index of the power dissipated by the ship and Figure 3b) shows the dimensionless index of the power absorbed by the ART.

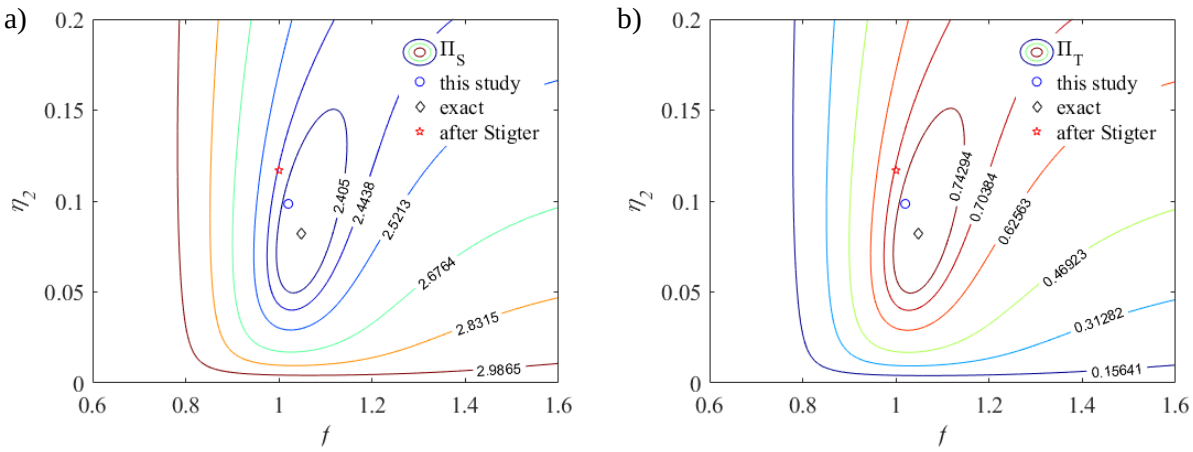


Figure 3: a) The dimensionless absorbed power index of the tank and b) the dimensionless index of the power dissipated by the ship, as functions of the frequency ratio and the ART damping ratio with $\mu_1 = 0.046$, and $\eta_1 = 0.075$

Both powers are calculated using Eqs. (39),(40) and plotted are as functions of the frequency ratio and the ART damping ratio. It can be seen that the maximum of the power absorbed indeed corresponds to the minimum of the power dissipated, as shown by the diamond markers in the two plots. Also note that the levels of corresponding contours in each plot sum to approximately π. However, the optimum damping-frequency ratio pair, calculated using Eqs. (44) and designated by the circle, does not exactly correspond to the extreme values calculated by numerically maximising Π_T (minimising Π_S) of the two power indices, designated by the diamond marker.

This is due to the combined effects of neglecting the ship roll damping ratio, η_1, and the moment of inertia ratio, μ_1. In order to illustrate that the discrepancy is due to the neglects made, a situation is considered in which the ship roll damping ratio, η_1, and the moment of inertia ratio, μ_1, are both reduced by a factor of ten.

As shown by Figure 4, the optimum damping-frequency ratio pair, calculated using Eqs. (44) now overlaps with the exact extreme values of the two power indices. The optimum tuning pair obtained using the H_∞ criterion on the roll angle is designated by the pentagon markers in Figure 3, indicating somewhat smaller optimum damping and frequency ratios than those obtained in this study. Both criteria suggest the frequency ratio of about unity and a tank damping ratio of about 10% for the example ship considered.

The absorbed power is in fact mostly dissipated through the boundary layer friction between the tank fluid and its walls, the vortices that occur due to the non-ideal flow of the water in the two reservoirs, and the losses in the “knee” between the reservoirs and the connection conduit. Therefore only a fraction of total absorbed power could be converted to, for example, electricity. This could be done by integrating a turbine in the channel connecting the port and starboard reservoirs of the ART that drives an electrical generator. If the generator is shunted with a variable electrical load, then, even if this load is a pure resistance, the temperature developed on the load could be monitored in order to maximise the power absorbed, by varying the load. This could potentially enable an automatic tuning of the damping ratio of the ART which would ensure a maximum power absorbed as the conditions at sea change. As discussed in Section 2 this means also a minimum of the expected value of the roll angular velocity which is a valid criterion for the performance of roll control techniques.

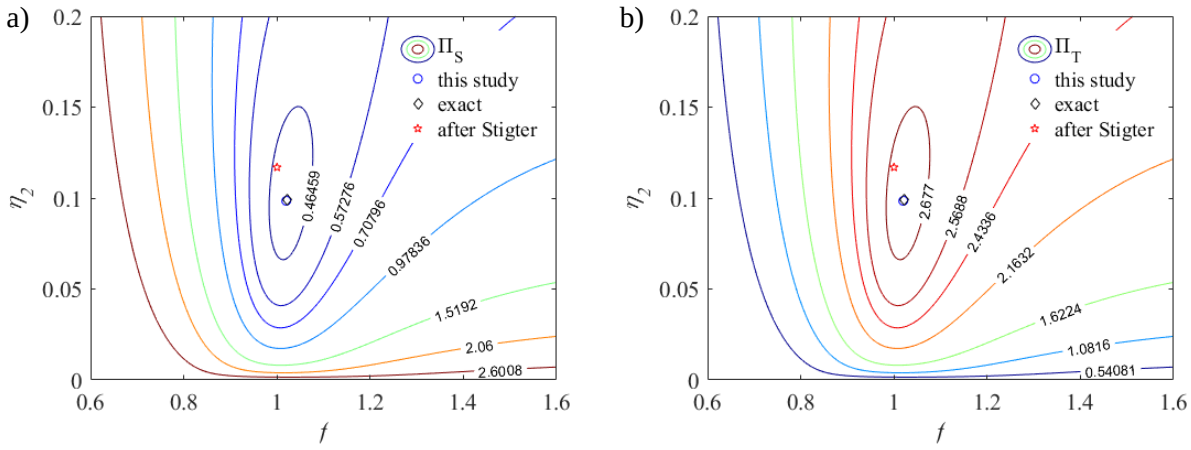


Figure 4: a) The dimensionless absorbed power index of the tank and b) the dimensionless index of the power dissipated by the ship, as functions of the frequency ratio and the ART damping ratio with $\mu_1 = 0.0046$, and $\eta_1 = 0.0075$

4 Conclusions

In this paper it is investigated how the natural frequency and the damping ratio of an ART should be tuned to maximise the power absorbed by the tank. It is also studied how this tuning corresponds to a tuning that minimises the kinetic energy of the ship roll. It is found that the two tuning criteria are exactly equivalent assuming the flat spectrum of the roll moment. This is a result of the fact that the power input of the wave excitation moment into the ship plus tank system does not depend on how the ART is tuned. Rather, different tunings of the ART natural frequency and damping ratio only affect the distribution of the power dissipated by the ship roll damping and the power absorbed by the ART. The optimum tuning parameters, the natural frequency and the damping ratio of the ART are calculated analytically assuming the flat spectrum of the wave excitation moment. The optimum tuning parameters are found not to be particularly different from those minimising the maximum roll angle for the example ship considered. The power input into the ship plus tank system is found to be proportional to the natural frequency of the ship roll to the power of four multiplied by the moment of inertia of the ship for the flat spectrum of the wave slope. According to this theoretical result, if specialised offshore installations are considered for harvesting the wave energy by using U-tube ARTs, they should be designed with an as high roll natural frequency as possible. Finally, it is important to emphasize that the study is carried out using a linearized model in which a number of effects has been neglected, like, for example, sloshing of the fluid in the ART.

Acknowledgements

This project has received funding from the European Union's Horizon 2020 research and innovation programme under the Marie Sklodowska-Curie grant agreement no. 657539 STARMAS. The third and fifth authors acknowledge the support of the National Research Foundation of Korea (NRF) grant funded by the Korea Government (MSIP) through GCRC-SOP (Grant No. 2011-0030013)

References

[1] S. Kastner, V.L. Belenky, N.B. Sevast'ianov, L.K. Kobylinski, *Stability and safety of ships*., Elsevier, Amsterdam; Boston, 2003.

[2] T. Perez, M. Blanke, *Ship roll damping control*, Annu. Rev. Control. 36 (2012) 129–147.

[3] I. Senjanović, J. Parunov, G. Ciprić, *Safety analysis of ship rolling in rough sea*, Chaos, Solitons & Fractals. 8 (1997) 659–680.
[4] W. Burger, A.G. Corbet, *Ship Stabilizers: Their Design and Operation in Correcting the Rolling of Ships: a Handbook for Merchant Navy Officers*, Pergamon Press, 1966.
[5] A.R.J.M. Lloyd, *Seakeeping : ship behaviour in rough weather*, E. Horwood, 1989.
[6] A.E. Baitis, L. V. Schmidt, *Ship Roll Stabilization in the U.S. Navy*, Nav. Eng. J. 101 (1989) 43–53.
[7] E. Schlick, *The gyroscopic effect of flywheels on board ship*, Trans. Inst. Nav. Archit. 23 (1904) 117–134.
[8] A. Donaire, T. Perez, *Energy-based Nonlinear Control of Ship Roll Gyro-stabiliser with Precession Angle Constraints*, IFAC Proc. Vol. 46 (2013) 328–333. doi:10.3182/20130918-4-JP-3022.00046.
[9] K.A. McTaggart, *Active Roll Stabilization of a Coastal Naval Vessel Using Azimuthing Propellers*, Eighteenth Int. Offshore Polar Eng. Conf. (2008).
[10] H. Frahm, *Results of trials of the anti-rolling tanks at sea*, J. Am. Soc. Nav. Eng. 23 (1911) 571–597.
[11] W. Froude, *Considerations respecting the rolling of ships at sea*, Ina Trans. 14 (1874) 96–116.
[12] A.F.A.A. Gawad, S.A. Ragab, A.H. Nayfeh, D.T. Mook, *Roll stabilization by anti-roll passive tanks*, Ocean Eng. 28 (2001) 457–469.
[13] M.A.S. Neves, J.A. Merino, C.A. Rodríguez, *A nonlinear model of parametric rolling stabilization by anti-roll tanks*, Ocean Eng. 36 (2009) 1048–1059.
[14] M.A.S. Neves, C.A. Rodríguez, J.A. Merino, J.E.M. Vivanco, J.C.V. Rosales, R. AgarwaL, *Control of Unstable Ship Motions Using Anti-Rolling Tanks: Erosion of Safe Basins*, in: ASME 2010 29th Int. Conf. Ocean. Offshore Arct. Eng., American Society of Mechanical Engineers, 2010: pp. 119–125.
[15] J. Bard, F. Thalemann, *Offshore Infrastructure: Ports and Vessels*, A Rep. off-Shore Renew. Energy Convers. Platforms-Coordination Action. Fraunhofer IWES. (2011).
[16] H. Jin, W. Yu, Z. Qi, G. Jin, H. Jin, W. Yu, Z. Qi, G. Jin, *Study on Lift Generation of Weis-Fogh Flapped Fin Stabilizer at Zero Speed*, in: 2006 SICE-ICASE Int. Jt. Conf., IEEE, 2006: pp. 1521–1524. doi:10.1109/SICE.2006.315591.
[17] P. Watts, *On a method of reducing the rolling of ships at sea*, Trans. Inst. Nav. Archit. 24 (1883) 165–190.
[18] P. Watts, *The use of water chambers for reducing the rolling of ships at sea*, Trans. Inst. Nav. Archit. 26 (1885).
[19] S.B. Field, J.P. Martin, *Comparative effects of U-tube and free surface type passive roll stabilisation systems*, Nav. Archit. (1976).
[20] K.S. Youssef, S.A. Ragab, A.H. Nayfeh, D.T. Mook, *Design of passive anti-roll tanks for roll stabilization in the nonlinear range*, Ocean Eng. 29 (2002) 177–192.
[21] K.S. Youssef, D.T. Mook, A.H. Nayfeh, S.A. Ragab, *Roll stabilization by passive anti-roll tanks using an improved model of the tank-liquid motion*, Modal Anal. 9 (2003) 839–862.
[22] C. Holden, T.I. Fossen, *A nonlinear 7-DOF model for U-tanks of arbitrary shape*, Ocean Eng. 45 (2012) 22–37.
[23] O.A. Marzouk, A.H. Nayfeh, *Control of ship roll using passive and active anti-roll tanks*, Ocean Eng. 36 (2009) 661–671.
[24] R. Moaleji, *Adaptive control for ship roll stabilization using anti-roll tanks*, University of London, University College London (United Kingdom), 2007.
[25] N. Umeda, H. Hashimoto, S. Minegaki, A. Matsuda, *An investigation of different methods for the prevention of parametric rolling*, J. Mar. Sci. Technol. 13 (2008) 16–23.
[26] C. Stigter, *The performance of U-tanks as a passive anti-rolling device*, Delft, 1966.
[27] J. Bootsma, J.J. Van den Bosch, *The efficiency of two different roll damping tanks*, Shipp. World Shipbuild. (1967).
[28] M. Zalar, L. Diebold, E. Baudin, J. Henry, X.-B. Chen, *Sloshing Effects Accounting for Dynamic Coupling Between Vessel and Tank Liquid Motion*, (2007) 687–701.
[29] V. Armenio, A. Francescutto, M. La Rocca, *On the roll motion of a ship with partially filled unbaffled and baffled tanks - Part 2: Numerical and experimental analysis*, Int. J. Offshore Polar Eng. 6 (1996) 283–290.

[30] V. Armenio, A. Francescutto, M. La Rocca, *On the roll motion of a ship with partially filled unbaffled and baffled tanks - Part 1: Mathematical model and experimental setup*, Int. J. Offshore Polar Eng. 6 (1996) 275–282.
[31] H. Frahm, *Device for damping vibrations of bodies*, (1911). US patent US989958A.
[32] J.P. Den Hartog, *Mechanical vibrations*, McGraw-Hill, 1956.
[33] G.B. Warburton, *Optimum absorber parameters for various combinations of response and excitation parameters*, Earthq. Eng. Struct. Dyn. 10 (1982) 381–401.
[34] M. Zilletti, S.J. Elliott, E. Rustighi, *Optimisation of dynamic vibration absorbers to minimise kinetic energy and maximise internal power dissipation*, J. Sound Vib. 331 (2012) 4093–4100.
[35] N. Alujević, I. Ćatipović, Š. Malenica, I. Senjanović, N. Vladimir, *Ship roll control and energy harvesting using a U-tube anti-roll tank*, Submitt. to Ocean Eng. (2018).
[36] O. Nishihara, T. Asami, *Closed-Form Solutions to the Exact Optimizations of Dynamic Vibration Absorbers (Minimizations of the Maximum Amplitude Magnification Factors)*, J. Vib. Acoust. 124 (2002) 576.
[37] H. Yamaguchi, *Damping of transient vibration by a dynamic absorber.*, Trans. Japan Soc. Mech. Eng. Ser. C. 54 (1988) 561–568.
[38] D.W. Miller, E.F. Crawley, $ B A Ward, *Inertial Actuator Design for Maximum Passive and Active Energy Dissipation in Flexible Space Structures*, in: Struct. Struct. Dyn. Mater. Conf., American Institute of Aeronautics and Astronautics, Orlando FL, 1985: pp. 536–544.
[39] S. Krenk, Frequency A*nalysis of the Tuned Mass Damper*, J. Appl. Mech. (2005).
[40] Y. Iwata, *On the construction of the dynamic vibration absorber*, Japanese Soc. Mech. Eng. 820 150–152. 820 (1982) 150–152.
[41] D.E. Newland, *An introduction to random vibrations, spectral and wavelet analysis*, Dover Publications, 2005.

Modeling of partially covered piezoelectric energy harvester connected to SEH interface circuit

G. Hu[1], B. Zhao[2], L. Tang*[1], J. Liang[2], R. Das[3]
[1]Department of Mechanical Engineering, University of Auckland,
20 Symonds Street, Auckland 1010, New Zealand
e-mail: **l.tang@auckland.ac.nz**

[2]School of Information Science and Technology, ShanghaiTech University,
393 Middle Huaxia Road, Shanghai 201210, China

[3]School of Engineering, RMIT University,
GPO Box 2476, Melbourne, VIC 3001, Australia

Abstract
In this paper, a modelling methodology of a partially covered piezoelectric energy harvester (PEH) connected to an standard energy harvesting (SEH) interface circuit is developed. The PEH is based on a cantilevered beam structure. First, the free end of the PEH cantilever is assumed to be mounted with a tip mass that is much heavier than the weight of the cantilevered beam itself. The PEH is represented by a single-degree-of-freedom (SDOF) model and the equivalent lumped parameters are derived. Subsequently, for the case when the tip mass is removed, a correction factor is proposed to ensure the accuracy of the SDOF model. The developed SDOF models of the PEH are verified by finite element analysis. Finally, the equivalent impedance method (EIM) is modified and employed for analysing the derived SDOF PEH model with SEH interface circuit. The results are compared with those obtained by using the existing analytical method.

1 Introduction

Vibration energy harvesting has attracted considerable research interests in the past decade [1, 2], as this technology has a promising potential for enabling widely utilized micro-electromechanical systems (MEMS) to substitute electrochemical batteries in some circumstances where environmental vibrations exist. A comprehensive study of a practical energy harvester often requires the consideration of both mechanical and electrical aspects. Hence, reliable modelling methods for both the mechanical structures and electrical interfaces are the fundamentals for the research in this field. In addition, bridging the mechanical and electrical models is essential to achieve accurate estimation.

One of the most typical design of piezoelectric energy harvesters (PEHs) is a cantilevered beam covered with one or multiple piezoelectric transducers. When the structure is excited around its resonant frequencies (especially the fundamental one), the cantilevered PEH could deliver a maximum power output. Several modelling methods have been proposed for describing the behavior of this type of PEHs and predicting the energy harvesting performance. Erturk and Inman [3] introduced the mathematical representation of the cantilevered PEH using a continuous model and derived the close-form analytical solution. However, in that model the piezoelectric layer was assumed to cover the entire substrate of the beam. In a lot of other research, the cantilevered PEH is represented by using a SDOF model [4, 5]. Erturk and Inman [6] then pointed out that the commonly used SDOF model may yield a significant prediction error and proposed to use a correction factor to improve the SDOF model. However, their study was only based on a plain beam without piezoelectric coverage. Thus, their corrected SDOF model only has the ability to describe the mechanical behavior of the cantilevered beam, but is incapable of including the

piezoelectric effect into consideration for predicting the energy harvesting performance. Yang and Tang [7] proposed an equivalent circuit representation for the cantilevered PEH. The advantage of this modelling method is that after the equivalent circuit representation of the mechanical structure, the mechanical and the electric parts of the PEH system are bridged and can incorporate more complicated structures and nonlinear circuits. However, in their model, the piezoelectric layer was also assumed to cover the entire cantilevered beam. In other reported literature, the cantilevered beam is partially covered by piezoelectric layer but the modeling is simplified during the derivation of equivalent parameters [8, 9]. Therefore, the main aim of this paper is to develop a model of the cantilevered PEH with partially covered piezoelectric layer for predicting the energy harvesting performance.

In addition, practical design of a PEH often requires a standard energy harvesting circuit (i.e., an AC-DC interface circuit) [10] to power real applications, or sometimes a complicated nonlinear interface circuit for efficiency improvement, such as, synchronized charge extraction (SCE) [11, 12], synchronized switch harvesting on inductor (SSHI) [13-15] etc. The existence of the complicated interface circuits poses difficulty to investigate the energy harvesting performance analytically. A simplest way to evaluate the power output of a PEH shunted to a SEH interface circuit is by uncoupling the mechanical part and the electrical part [4]. However, this method is only valid for weakly coupled systems. A method for estimating the energy harvesting output of a PEH shunted to a SEH or SSHI circuit is presented in [15] by assuming that the external forcing function and the velocity of the mass are in phase. It can be anticipated that the in-phase assumption is also only valid in limited circumstances where the electro-mechanical coupling is not strong. Shu and Lien [4] later proposed an analytical method to model PEHs with SEH interface circuit that is accurate for both weak and strong couplings. By comparing with simulation and experimental results, the reliability of that method was confirmed. Based on the same idea, Shu *et al.* [14] extended this analytical method for the analysis of the P-SSHI interface circuit. From another point of view, by using the harmonic decomposition method and only taking the fundamental component, Liang and Liao [15] presented an equivalent impedance modelling (EIM) method that was capable of analyzing the SEH, P-SSHI and S-SSHI interface circuits even for strong coupling cases. However, in that method, the final expression of the harvested power is a function of the rectifier block angle and cannot calculate the rectified voltage. Therefore, another objective in this paper is to make an improvement of the EIM method, and together with the proposed SDOF modelling method, to give a comprehensive modelling of practical cantilevered PEH with partial piezoelectric coverage and shunted to a SEH interface circuit.

The content of this paper is arranged as follows: In section 2, the cantilevered PEH that carries a tip mass with partial piezoelectric coverage is represented by a SDOF model. The equivalent lumped parameters of the SDOF model are derived. The developed SDOF model is then compared with a finite element model. In section 3, the same cantilevered PEH model but without tip mass is considered. After removing the tip mass, the prediction performance of the SDOF model declines significantly. A correction factor to improve the SDOF model is derived. In order to simplify the calculation procedure of the correction factor, an approximate method is then proposed. The corrected SDOF model is then also compared with a corresponding finite element model. In section 4, the EIM method is modified and improved for the modeling of the PEH shunted to a SEH interface circuit and the results are compared with those obtained by analytical method proposed in [4].

2 SDOF model of partially covered PEH with tip mass

2.1 Derivation of equivalent lumped parameters

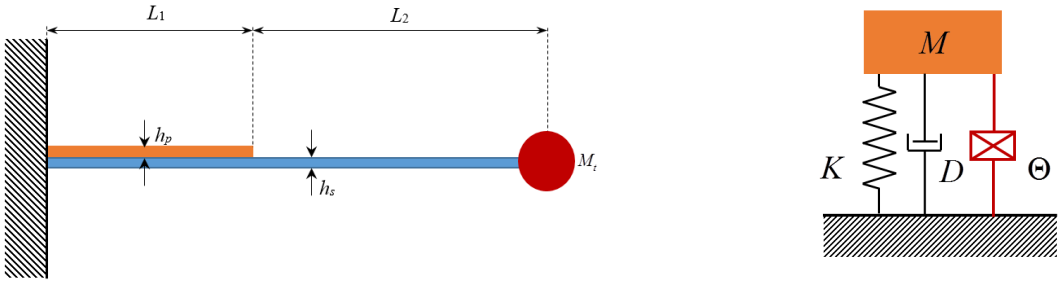
The cantilevered PEH with partial piezoelectric coverage is shown in Figure 1(a). The beam sections with and without piezoelectric coverage are of lengths L_1 and L_2, respectively. M_t is the tip mass which is regarded as a point mass. Throughout this paper, the subscripts 1 and 2 will be used to denote the beam sections with and without piezoelectric coverage, respectively. Assuming that the piezoelectric layer and

the substrate layer are of the same width b, the masses per unit length and the bending stiffnesses for the two beam sections can then be calculated:

$$\begin{cases} m_1 = (\rho_s h_s + \rho_p h_p) b & EI_1 = \left[b\left(Y_s\left(h_b^3 - h_a^3\right) + Y_p\left(h_c^3 - h_b^3\right)\right)\right] / 3 \\ m_2 = \rho_b h_s b & EI_2 = Y_s b h_s^3 / 12 \end{cases} \tag{1}$$

where ρ_s and ρ_p are the mass densities of the substrate and the piezoelectric materials, respectively; Y_s and Y_p are their Young's modulus; and h_s and h_p are their thickness. Setting the origin of the coordinate system along the composite cross section be at the neutral axis, h_a is the distance from the bottom of the substrate layer to the neutral axis. h_b and h_c are the distances from the bottom and the top of the piezoelectric layer to the neutral axis, respectively. They are determined by the two component material properties and the thicknesses of the two component layers.

$$\begin{cases} h_a = -\left(Y_p h_p \left(h_p/2 + h_s\right) + Y_s h_s^2/2\right) / \left(Y_p h_p + Y_s h_s\right) \\ h_b = h_s + h_a \\ h_c = h_p + h_b \end{cases} \tag{2}$$



(a) (b)

Figure 1: (a) Cantilevered PEH with partial piezoelectric coverage; (b) the equivalent SDOF model.

By using the relationships between the bending moment and the beam deflection from Euler beam theory, the functions that describe the static deflections under gravity of the two beam sections with and without piezoelectric coverage are derived. For the section with piezoelectric coverage (i.e., $0 \le x \le L_1$):

$$y_1(x) = \frac{g}{24EI_1}\left[m_1 x^4 - 4\left(m_1 L_1 + m_2 L_2 + M_t\right) x^3 + 6\left(m_1 L_1^2 + m_2 L_2\left(2L_1 + L_2\right) + 2M_t\left(L_1 + L_2\right)\right) x^2 \right] \tag{3}$$

where g is the gravitational constant. Combining with the continuity conditions of displacement and slope at the intersection, the deflection of the section without piezoelectric coverage (i.e., $0 \le x \le L_2$) is:

$$y_2(x) = \frac{1}{24EI_2}\left[m_2 g x^4 - 4\left(m_2 L_2 + M_t\right) g x^3 + 6\left(m_2 L_2^2 + M_t L_2\right) g x^2 \right] + y_1'(L_1)\, x + y_1(L_1) \tag{4}$$

To represent the cantilevered PEH by a linear SDOF model as shown in Figure 1(b), the equivalent lumped parameters (i.e., the equivalent stiffness K and the equivalent mass M) are assumed to be concentrated at the free end. The following procedure determines K and M. First, the static deflection at the free end of the beam under gravity is calculated:

$$\frac{\left(M_{static}+M_t\right)g}{K}=y_2\left(L_2\right) \tag{5}$$

where M_{static} is the equivalent static mass of the beam. Also the static deflection at the free end caused by the weight of the beam only without tip mass is:

$$\frac{M_{static}g}{K}=y_2\left(L_2,M_t=0\right) \tag{6}$$

Combining Eq.(5) and (6), the equivalent stiffness of the beam can be derived:

$$K=\frac{M_t g}{y_2\left(L_2\right)-y_2\left(L_2,M_t=0\right)}=\frac{3EI_1EI_2}{EI_1L_2^3+3EI_2L_1L_2^2+3EI_2L_1^2L_2+EI_2L_1^3} \tag{7}$$

The Rayleigh's method is used to find the natural frequency of the cantilevered beam without tip mass, then the dynamic equivalent mass at the free end of the beam. The maximum potential energy P in the beam is:

$$P=\frac{EI_1}{2}\int_0^{L_1}\left(\frac{d^2y_1}{dx^2}\right)^2dx+\frac{EI_2}{2}\int_0^{l_2}\left(\frac{d^2y_2}{dx^2}\right)^2dx \tag{8}$$

The maximum kinetic energy T in the beam is:

$$T=\frac{1}{2}m_1\omega_n^2\int_0^{L_1}y_1^2dx+\frac{1}{2}m_2\omega_n^2\int_0^{L_2}y_2^2dx \tag{9}$$

where ω_n is the natural frequency. Equating P and T yields:

$$\omega_n^2=\sum_{p=0}^{5}n_pL_1^p\Big/\sum_{q=0}^{9}d_qL_1^q \tag{10}$$

where

$$\begin{cases}n_5=2268m_1^2EI_1EI_2^2\\ n_4=11340m_1m_2EI_1EI_2^2L_2\\ n_3=\left(7560m_1+15120m_2\right)m_2EI_1EI_2^2L_2^2\\ n_2=22680m_2^2EI_1EI_2^2L_2^3\\ n_1=11340m_2^2EI_1EI_2^2L_2^4\\ n_0=2268m_2^2EI_1^2EI_2L_2^5\end{cases}\quad\begin{cases}d_9=182m_1^3EI_2^2\\ d_8=1638m_1^2m_2EI_2^2L_2\\ d_7=\left(1584m_1+4968m_2\right)m_1m_2EI_2^2L_2^2\\ d_6=\left(420m_1^2+9828m_1m_2+5040m_2^2\right)m_2EI_2^2L_2^3\\ d_5=\left(7812m_1+15120m_2\right)m_2^2EI_2^2L_2^4\\ d_4=\left(567m_1EI_1+\left(2520m_1+19845m_2\right)EI_2\right)m_2^2EI_2L_2^5\\ d_3=\left(13230m_2EI_2+\left(546m_1+1512m_2\right)EI_1\right)m_2^2EI_2L_2^6\\ d_2=\left(2772EI_1+3780EI_2\right)m_2^3EI_2L_2^7\\ d_1=1638m_2^3EI_1EI_2L_2^8\\ d_0=182m_2^3EI_1^2L_2^9\end{cases}$$

Recall that the equivalent stiffness of the beam at the free end is already derived in Eq.(7), the equivalent dynamic mass of the beam itself is thus:

$$M_{dynamic} = \frac{K}{\omega_n^2} \tag{11}$$

By including the tip mass M_t, the total equivalent mass of the system is:

$$M = M_{dynamic} + M_t \tag{12}$$

Note that this is an electromechanical system, because there is a piezoelectric transducer. Therefore, for the piezoelectric effect, one more lumped parameter is needed to be determined which is the equivalent electromechanical coupling coefficient of the piezoelectric transducer. The linear-electroelastic constitutive relation for the piezoelectric material is expressed as:

$$D = e_{31}S + \varepsilon_{33}^S E_3 \tag{13}$$

where S is the strain, D is the electric displacement, e_{31} is the piezoelectric constant, ε_{33}^S is the permittivity at constant stress. The electric field in the piezoelectric transducer in terms of the voltage across it can be expressed as:

$$E_3(t) = -\frac{v(t)}{h_p} \tag{14}$$

Therefore, from the constitutive equation of the piezoelectric materials, one obtains:

$$D(x,t) = e_{31}S(x,t) + \varepsilon_{33}^S \frac{v(t)}{h_p} \tag{15}$$

According to beam theory, the average bending strain in the piezoelectric transducer can be expressed as:

$$S(x,t) = -h_{pc}\frac{\partial^2 w(x,t)}{\partial x^2} \tag{16}$$

where h_{pc} is the distance of the center of the piezoelectric layer to the neutral axis of the cross section of the piezoelectric covered beam section, $w(x,t)$ is the transverse deflection of the beam during vibration. Substituting Eq.(16) into Eq.(15) gives:

$$D(x,t) = -e_{31}h_{pc}\frac{\partial^2 w(x,t)}{\partial x^2} + \varepsilon_{33}^S \frac{v(t)}{h_p} \tag{17}$$

Integrating the electric displacement over the electrode area and then differentiating with respect to time gives the current $i(t)$ flowing out of the piezoelectric transducer as follows.

$$i(t) = \int_{x=0}^{L_1} -e_{31}h_{pc}b\frac{\partial^3 w(x,t)}{\partial x^2 \partial t}dx + \frac{\varepsilon_{33}^S bL_1}{h_p}\frac{dv(t)}{dt} \tag{18}$$

The clamped boundary condition at $x = 0$ implies that $\frac{\partial^2 w(0,t)}{\partial x \partial t} = 0$, Eq.(18) thus becomes:

$$i(t) = -e_{31} h_{pc} b \frac{\partial^2 w(L_1,t)}{\partial x \partial t} + \frac{\varepsilon_{33}^S b L_1}{h_p} \frac{dv(t)}{dt} \tag{19}$$

In order to evaluate the equivalent parameters at the free end $x = L_2$, Eq.(19) is rearranged as:

$$i(t) = \left[-e_{31} h_{pc} b \frac{\partial^2 w(L_1,t)}{\partial x \partial t} \frac{1}{w(L_2,t)} \right] w(L_2,t) + C_p \frac{dv(t)}{dt} \tag{20}$$

where $C_p = \varepsilon_{33}^S b L_1 / h_p$ is the capacitance of the piezoelectric transducer. By using the modal superposition method and representing the transverse deflection *w*(*x*,*t*) by using the series of mode shape functions.

$$w(x,t) = \sum_{r=1}^{\infty} \phi_r(x) \eta_r(t) \tag{21}$$

where $\phi_r(x)$ and $\eta_r(t)$ are mode shape functions and modal coordinates of the beam. Only the dynamic behavior around the first mode is of interest. Substituting Eq.(21) into Eq.(20) and keeping the first mode only yields:

$$i(t) = \left[-e_{31} h_{pc} b \frac{d\phi_1(L_1)}{dx} \frac{1}{\phi_1(L_2)} \right] \phi_1(L_2) \frac{d\eta_1(t)}{dt} + C_p \frac{dv(t)}{dt} \tag{22}$$

$\phi_1(L_2) d\eta_1(t)/dt$ is actually the velocity of the beam at the free end, i.e., $dw(L_2,t)/dt$. The electromechanical coupling coefficient is obtained as:

$$\Theta = -e_{31} h_{pc} b \frac{d\phi_1(L_1)}{dx} \frac{1}{\phi_1(L_2)} \tag{23}$$

And the circuit governing equation is obtained as:

$$i(t) = \Theta \frac{dw(L_2,t)}{dt} + C_p \frac{dv(t)}{dt} \tag{24}$$

By using the previously derived static deflection function to approximate the first mode shape function of the beam, the equivalent electromechanical coupling coefficient can be expressed as:

$$\Theta = \frac{4EI_2 L_1^3 m_1 + 12EI_2 L_1 L_2 (L_1 + L_2) m_2 + 12EI_2 L_1 (L_1 + 2L_2) M_t}{\left\{ \begin{array}{l} EI_2 L_1^3 (3L_1 + 4L_2) m_1 + \left[3EI_1 L_2^4 + EI_2 L_1 L_2 (12L_2^2 + 18L_1 L_2 + 8L_1^2) \right] m_2 \\ +8 \left[EI_1 (L_1^3 + L_2^3) + 3EI_2 L_1 L_2 (L_1 + L_2) \right] M_t \end{array} \right\}} \tag{25}$$

Therefore, the dynamic behavior of the cantilevered PEH with partial piezoelectric coverage can be equivalently represented by the SDOF model and the governing equations can be expressed as:

$$\begin{cases} M\ddot{u} + D\dot{u} + Ku + \Theta v = -M\ddot{u}_b \\ \dfrac{v}{R} + C_p \dot{v} - \Theta \dot{u} = 0 \end{cases} \tag{26}$$

where $D = 2\zeta M\omega_n$ is the damping coefficient that can be calculated according to the damping ratio ζ of the continuous system, R is the electric resistor connected to the piezoelectric transducer, and u_b is the base displacement. The displacement at the free end $w(L_2,t)$ is redefined as u for conciseness. In fact, this electromechanical system has an additional electrical degree-of-freedom (DOF). Throughout of this paper, it is simply referred to as a SDOF system as this system has only one mechanical DOF.

2.2 Comparison with finite element model

To verify the equivalent SDOF representation, a finite element (FE) model is developed by using the commercial software ANSYS for comparison. In this case study, the substrate material of the beam is steel and modelled by using the 3D 20-node structural solid element (SOLID186 in ANSYS). The piezoelectric material is modelled by using the 3D 20-node coupled-field solid element SOLID226 to take into account the piezoelectric effect. The voltage DOFs on the top and bottom surfaces of the piezoelectric sheet are coupled separately to ensure uniform electrical potentials, thus to emulate the electrodes. The displacement DOFs of the left hand side of the beam are forced to be zero in the dynamic analysis to reflect the clamping condition. An acceleration field $a_{cc} = 1\,m/s^2$ is applied onto the whole structure to ensure a constant input power level over the spectrum under investigation. A harmonic analysis is then performed to investigate the steady-state open-circuit voltage output of the system. The detailed parameters of the FE model are listed in Table 1.

Parameters	Values	Materials	Parameters	Values
Substrate beam length	62.5 mm	Steel	Mass density	7800 kg/m^3
Substrate beam width	10 mm		Young's Modulus	180 GPa
Substrate beam thickness	1 mm	Piezo	Mass density	5440 kg/m^3
Piezoelectric layer length	28 mm		Young's Modulus	30.336 GPa
Piezoelectric layer width	10 mm		d_{31}	-170 pC/N
Piezoelectric layer thickness	0.2 mm		ε_T	1.3281×10-8 F/m

Table 1: Geometry parameters and material properties of the sample system

For the FE model with the given parameters, by using the proposed SDOF representation method, the equivalent lumped parameters are calculated as: $M = M_{dynamic} + M_t$, $M_{dynamic}$ = 0.4 g, K = 907.5 N/m, Θ = 4.5097×10^{-4} N/V, C_p = 18.59 pF. The damping ratio of the system is set as 0.008 in this case study. Under the same constant acceleration field, by sweeping the excitation frequency, the open-circuit voltage of the SDOF and the FE models with tip mass M_t = 10 g are obtained (Figure 2). The natural frequencies predicted by the SDOF and the FE models are 47.3 Hz and 47.22 Hz, respectively. The maximum open-circuit voltage amplitudes predicted by the SDOF and the FE models are 17.26 V and 17.47 V, respectively. The prediction errors of the SDOF model, as compared to the FE model, in terms of the natural frequency and maximum open-circuit voltage amplitude are about 0.17% and 1.20%, respectively.

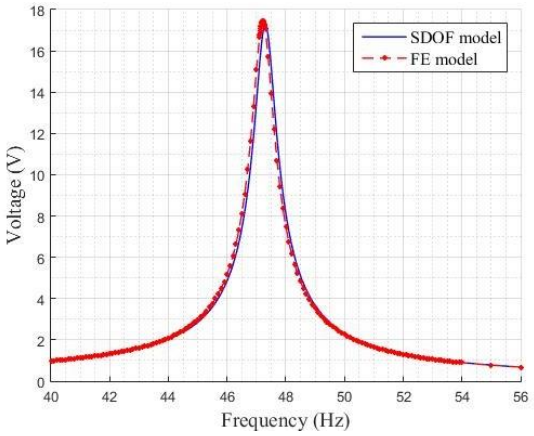


Figure 2: Open-circuit voltage of the developed SDOF and FE models with tip mass M_t = 10 g

Table 2 lists more comparison results by varying the tip mass M_t. It can be found that with the increase of the tip mass M_t, the prediction error for the natural frequency based on the SDOF model slightly varies, while the prediction error for the maximum open-circuit voltage becomes evidently smaller.

M_t	**Natural Frequency**			**Maximum** $\lvert V_{oc} \rvert$		
	SDOF model	FE model	Relative error	SDOF model	FE model	Relative error
6 g	60.30 Hz	60.21 Hz	0.14 %	10.66 V	10.92V	2.45 %
7 g	56.08 Hz	55.99 Hz	0.16 %	12.31 V	12.56V	2.01 %
8 g	52.63 Hz	52.55 Hz	0.16 %	13.96 V	14.20V	1.68 %
9 g	49.75 Hz	49.67 Hz	0.16 %	15.61 V	15.84V	1.42 %
10 g	47.30 Hz	47.22 Hz	0.17 %	17.26 V	17.47V	1.20 %
11 g	45.18 Hz	45.10 Hz	0.18 %	18.91 V	19.11V	1.03 %
12 g	43.32 Hz	43.24 Hz	0.19 %	20.57 V	20.75V	0.88 %

Table 2: Comparison of the natural frequencies and maximum open-circuit voltage amplitudes predicted by the developed SDOF model and FE model with different tip masses

In general, it can be stated that the proposed SDOF model demonstrates almost the same dynamic behavior of the original continuous model around the first natural frequency. With an acceptable accuracy, the proposed SDOF representation provides a fast and concise means to evaluate the performance of such kind of piezoelectric energy harvesters.

3 SDOF model of partially covered PEH without tip mass

3.1 Analytical model

For the sake of simplicity and by using the Euler-Bernoulli beam theory, the piezoelectric effect (or short circuit the piezoelectric transducer) is excluded. The governing equation of the beam section with piezoelectric coverage can be expressed as:

$$EI_1 \frac{\partial^4 w_1(x_1,t)}{\partial x_1^4} + m_1 \frac{\partial^2 w_1(x_1,t)}{\partial t^2} = -m_1 \ddot{u}_b \tag{27}$$

The governing equation of the beam section without piezoelectric coverage is in a similar form as:

$$EI_2 \frac{\partial^4 w_2(x_2,t)}{\partial x_2^4} + m_2 \frac{\partial^2 w_2(x_2,t)}{\partial t^2} = -m_2 \ddot{u}_b \tag{28}$$

where $w_1(x_1,t)$ and $w_2(x_2,t)$ represent the relative displacements to the base of the beam sections in $0 \le x_1 \le L_1$ and $0 \le x_2 \le L_2$, respectively. Using the modal superposition method, the relative displacement along the beam can be expressed as the series of the product of mode shape functions and modal coordinates as:

$$\begin{cases} w_1(x_1,t) = \sum_{r=1}^{\infty} \phi_{1,r}(x_1)\eta_r(t) \\ w_2(x_2,t) = \sum_{r=1}^{\infty} \phi_{2,r}(x_2)\eta_r(t) \end{cases} \tag{29}$$

where $\phi_{1,r}(x_1)$ and $\phi_{2,r}(x_2)$ are the r^{th} mode shapes of the beam sections in $0 \le x_1 \le L_1$ and in $0 \le x_2 \le L_2$, respectively. By using the boundary conditions at the two ends of the beam and the continuity conditions at the intersection, one can obtain the following orthogonal relations.

$$\begin{cases} \int_{x_1=0}^{L_1} \phi_{1,s}(x_1) m_1 \phi_{1,r}(x_1) dx + \int_{x_2=0}^{L_2} \phi_{2,s}(x_2) m_2 \phi_{2,r}(x_2) dx = \delta_{rs} \\ \int_{x_1=0}^{L_1} \phi_{1,s}(x_1) EI_1 \frac{d^4 \phi_{1,r}(x_1)}{dx_1^4} dx + \int_{x_2=0}^{L_2} \phi_{2,s}(x_2) EI_2 \frac{d^4 \phi_{2,r}(x_2)}{dx_2^4} dx = \omega_r^2 \delta_{rs} \end{cases} \tag{30}$$

Substituting Eq.(29) into Eqs.(27) and (28), multiplying by $\phi_{1,r}(x_1)$ and $\phi_{2,r}(x_2)$, integrating over each beam section, and then using the orthogonal relations, the modal governing equation can be obtained:

$$\frac{d^2\eta_r(t)}{dt^2} + 2\zeta_r\omega_r \frac{d\eta_r(t)}{dr} + \omega_r^2 \eta_r(t) = \left[-m_1 \int_{x_1=0}^{L_1} \phi_{1,r}(x_1) dx - m_2 \int_{x_2=0}^{L_2} \phi_{2,r}(x_2) dx \right] \ddot{u}_b \tag{31}$$

The modal response can then be obtained as:

$$\eta_r(t) = \frac{\left[m_1 \int_{x_1=0}^{L_1} \phi_{1,r}(x_1) dx + m_2 \int_{x_2=0}^{L_2} \phi_{2,r}(x_2) dx \right] \omega^2 U_b}{\omega_r^2 - \omega^2 + 2j\zeta_r\omega_r\omega} e^{j\omega t} \tag{32}$$

where U_b is the magnitude of the base displacement, ω and ω_r are the excitation and r^{th} natural frequencies, respectively, and j is the unit of imaginary number. The relative displacement transmittance at the free end of the beam can thus be expressed:

$$T_{rel} = \sum_{r=1}^{\infty} \phi_{2,r}(L_2) \frac{\left[m_1 \int_{x_1=0}^{L_1} \phi_{1,r}(x_1) dx + m_2 \int_{x_2=0}^{L_2} \phi_{2,r}(x_2) dx \right] \omega^2}{\omega_r^2 - \omega^2 + 2j\zeta_r\omega_r\omega} \tag{33}$$

3.2 Correction factor for the SDOF model without tip mass

From the mechanical governing equation of the SDOF model,

$$M\ddot{u} + C\dot{u} + Ku = -M\ddot{u}_b \tag{34}$$

one can easily obtain the relative displacement transmittance as follows:

$$T_{rel}^{SDOF} = \frac{\omega^2}{\omega_1^2 - \omega^2 + j2\zeta_1\omega_1\omega} \tag{35}$$

In order to represent the continuous beam model with equivalent lumped parameters only around the first natural frequency, contributions from higher modes are neglected in Eq.(33) to give:

$$T_{rel} = \phi_{2,1}(L_2)\frac{\left[m_1\int_{x_1=0}^{L_1}\phi_{1,1}(x_1)dx + m_2\int_{x_2=0}^{L_2}\phi_{2,1}(x_2)dx\right]\omega^2}{\omega_1^2 - \omega^2 + 2j\zeta_1\omega_1\omega} \tag{36}$$

where $\phi_{1,1}(x_1)$ and $\phi_{2,1}(x_2)$ are the first mode shapes of the sections in $0 \le x_1 \le L_1$ and in $0 \le x_2 \le L_2$, respectively. Based on the comparison between Eq.(35) and (36), a correction factor μ should be introduced to improve the prediction based on the SDOF model as given below.

$$\mu = \phi_{2,1}(L_2)\left[m_1\int_{x_1=0}^{L_1}\phi_{1,1}(x_1)dx + m_2\int_{x_2=0}^{L_2}\phi_{2,1}(x_2)dx\right] \tag{37}$$

The analytical mode shape function of the beam with varying cross-section is difficult to be calculated. Therefore, to simplify the calculation of μ, the derived static deflection functions Eq.(3) and Eq.(4) are used to approximate the exact first mode shape. μ can thus be derived in the explicit form:

$$\mu = \frac{\left[EI_2L_1^3(4L_2 + 3L_1)m_1 + (3EI_1L_2^4 + 12EI_2L_1L_2^3 + 18EI_2L_1^2L_2^2 + 8EI_2L_1^3L_2)m_2\right]}{24EI_1EI_2}\omega_n^2 \tag{38}$$

Therefore, the forcing term in (34) should be corrected by multiplying μ and the governing equations of the electromechanical system become:

$$\begin{cases} M\ddot{u} + D\dot{u} + Ku + \Theta v = -\mu M\ddot{u}_b \\ \dfrac{v}{R} + C_p\dot{v} - \Theta\dot{u} = 0 \end{cases} \tag{39}$$

3.3 Comparison with the finite element model

The open-circuit voltage of the corrected SDOF model and the corresponding FE model are compared. The same system parameters listed in Table 1 are used, except that the tip mass is removed. The loading and boundary conditions are the same as used in the previous case study. Figure 3 shows the open-circuit voltage responses of the SDOF model with and without the correction factor and the corresponding FE model. It can be seen that the maximum open-circuit voltage amplitudes of the uncorrected SDOF, corrected SDOF model and the FE model are 0.72 V, 1.16 V and 1.15 V, respectively. So, the relative

errors for the uncorrected SDOF model and the corrected SDOF model are 37.64% and 0.89%, respectively. The natural frequency of the uncorrected SDOF and the corrected SDOF models are the same of 242.7 Hz, and the natural frequency of the FE model is 239.94 Hz, indicating a prediction error of 0.97%. It can be seen that after introducing the corrected factor, the SDOF model is greatly improved.

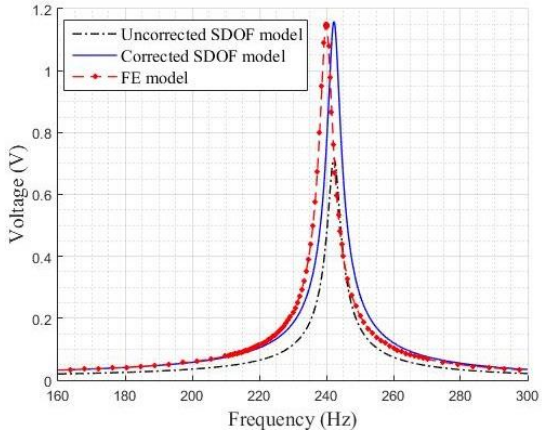


Figure 3: Open-circuit voltage of the uncorrected SDOF, corrected SDOF and FE models without tip mass

4 SEH circuit interface

In this section, the cantilevered PEH with tip mass is connected to a SEH interface circuit. The equivalent impedance method is introduced, modified and applied for analyzing the system.

4.1 Equivalent impedance modelling

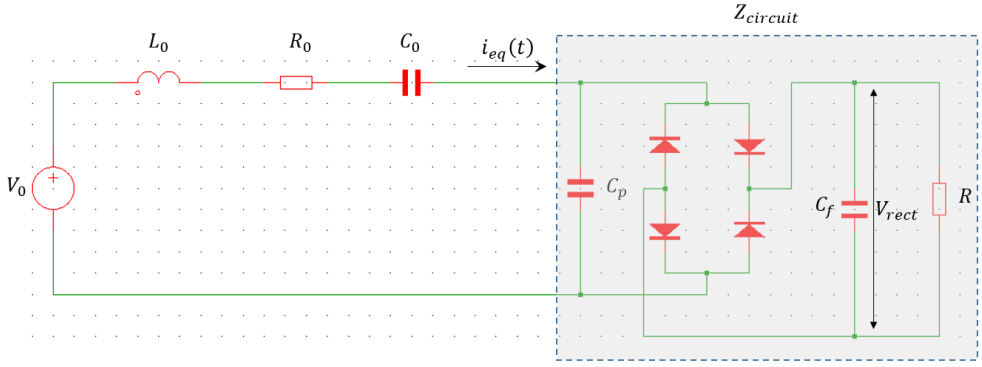


Figure 4: Equivalent circuit representation of a SDOF PEH shunted to a SEH interface circuit

By using the mechanical-electrical analogies, the mechanical part can be equivalently represented by an electrical model. The mechanical part and the electric circuit part are bridged as shown in Figure 4. The mechanical parameters are correspondingly converted into the electrical parameters as follows.

$$L_0 = M/\Theta^2 \quad C_0 = \Theta^2/K \quad R_0 = D/\Theta^2 \quad V_0 = -M\ddot{u}_b/\Theta \quad i_{eq}(t) = \Theta\dot{u} \tag{40}$$

Due to the existence of the full-wave rectifier bridge, nonlinearity is introduced in the system. The characteristic waveform of the voltage across the piezoelectric element is not harmonic anymore. By using the equivalent impedance modelling (EIM) method which decomposes the voltage response into harmonic

components and only takes the fundamental one $V_{p,F}$, the equivalent impedance of the SEH interface circuit can be derived as [15]:

$$Z_{circuit} = \frac{V_{p,F}}{I_{eq}} = \frac{1}{\pi\omega C_p}\left[\sin^2\varphi + j\left(\sin\varphi\cos\varphi - \varphi\right)\right] \tag{41}$$

where φ is the rectifier blocked angle in a half cycle that is related to the rectified voltage V_{rect} by:

$$\cos\varphi = 1 - 2\frac{V_{rect}}{V_{oc}} \tag{42}$$

where V_{oc} is related to the displacement amplitude by [15]:

$$V_{oc} = \frac{\Theta U}{C_p} \tag{43}$$

where U is the magnitude of the relative displacement. From Eq.(41), it is to be noted that the resistance and the reactance corresponding to the real and imaginary components of the equivalent impedance for the SEH interface circuit are R_h and X_E, respectively.

$$R_h = \frac{1}{\pi\omega C_p}\sin^2\varphi, \quad X_E = \frac{1}{\pi\omega C_p}\left(\sin\varphi\cos\varphi - \varphi\right) \tag{44}$$

It is known that the imaginary component (i.e., reactance) stores and releases energy periodically but does not dissipate energy. Only the real component (i.e., resistance) of the equivalent impedance absorbs energy from the source, i.e., converts mechanical energy into electric energy. Assuming that the full-wave rectifier bridge can realize the AC-to-DC conversion ideally, the harvested energy by the SEH interface circuit can then be evaluated by the energy consumed by the real component R_h.

$$P_h = \frac{V_{eq}^2}{2}\frac{R_h}{\left(X_{L_0} + X_{C_0} + X_E\right)^2 + \left(R_0 + R_h\right)^2} \tag{45}$$

where X_{L_0} and X_{C_0} are the reactances of L_0 and C_0, respectively.

4.2 Derivation of power

When the system is under steady state which implies that the variation of the charge stored in the filtering capacitance is null over a cycle, by considering the balance of the charge flowing through the DC resistance load, the rectified voltage can be expressed by the amplitude of the displacement as follows [4].

$$V_{rect} = \frac{2\omega\Theta R}{2\omega R C_p + \pi}U \tag{46}$$

Combining Eq.(46) and Eq.(43) gives:

$$\frac{V_{rect}}{V_{oc}} = \frac{2\omega R C_p}{2\omega R C_p + \pi} \tag{47}$$

Substituting Eq.(47) into Eq.(42), one can express the rectifier block angle by using the resistance load R as:

$$\varphi = \arccos\left(\frac{-2\omega RC_p + \pi}{2\omega RC_p + \pi}\right) \tag{48}$$

The expression of the harvested power is then obtained by substituting Eq.(44) into Eq.(45).

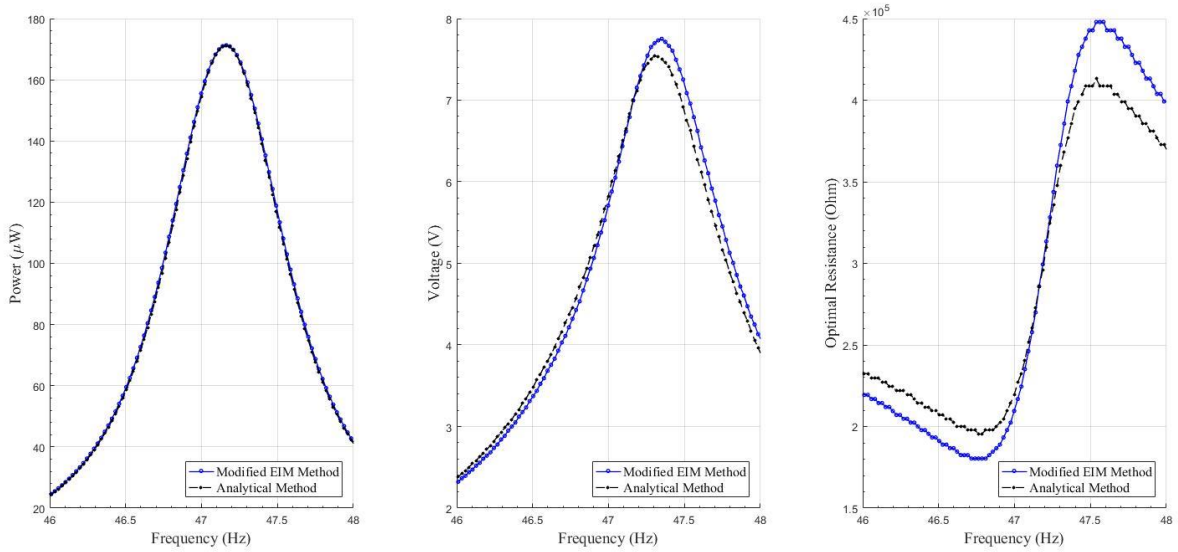
$$P_h = \frac{4R\left(\frac{MA_{cc}}{\Theta}\right)^2}{\left(2\omega RC_p + \pi\right)^2\left[\left(\omega\frac{M}{\Theta^2} - \frac{K}{\omega\Theta^2} + \frac{1}{\pi\omega C_p}\left(\sin\varphi\cos\varphi - \varphi\right)\right)^2 + \left(\frac{C}{\Theta^2} + \frac{8R}{\left(2\omega RC_p + \pi\right)^2}\right)^2\right]} \tag{49}$$

Thus, instead of using φ, we could express the harvested power in terms of R, which is the modification to the conventional EIM method [15], that gives the advantage of determining the optimal resistance. As the rectified voltage V_{rect} is nearly constant under steady-state operation and has the relationship with the harvested energy as $P_h = V_{rect}^2 / R$, the rectified voltage can thus be calculated:

$$V_{rect} = \sqrt{P_h R} \tag{50}$$

4.3 Comparison with analytical method

The mechanical part of the cantilevered PEH is already represented by the developed SDOF model and converted into an equivalent circuit model (Figure 4). The SEH interface circuit is also converted to an equivalent AC electrical component by using the modified EIM method. The energy harvesting performance of this system can then be evaluated. Figure 5 shows the optimal power response by tuning R at each frequency, the corresponding rectified voltage and the optimal resistances, respectively. The results obtained by using the analytical method proposed by Shu and Lien [4] are also provided for comparison. In terms of the optimal power, the results from the modified EIM method match well with those from the analytical method. For the rectified voltage and the optimal resistance, when near the resonant frequency, the predictions by both the methods are almost the same. When farther away from the resonant frequency, there appears a non-negligible difference, especially in the predictions of the optimal resistance. However, from the perspective of the optimal power prediction, the modified EIM method shows a satisfied accuracy.



(a) (b) (c)

Figure 5: Comparison of the results from the modified EIM method and the analytical method (a) the optimal power response, (b) the rectified voltage, and (c) the optimal resistance

5 Conclusions

In this paper, we propose a modelling methodology for a partially covered cantilevered PEH that is connected to a SEH interface circuit. A SDOF representation method is first proposed to describe the dynamic mechanical behavior. In the first case, the free end of the cantilevered beam is mounted with a tip mass that is much heavier than the beam weight. The equivalent lumped parameters concentrated at the free end are derived. A corresponding FE model built by using the program ANSYS confirms the reliability of the developed SDOF model. In the second case, the tip mass is removed. By comparing the relative displacement transmittances at the free end of the analytical model and the lumped SDOF model, a correction factor is proposed to improve the SDOF model and ensure the accuracy. The corrected SDOF model is verified by the corresponding FE model. The EIM method is modified and improved for converting the SEH interface circuit into an equivalent AC electrical component that is then connected with the equivalent circuit representation of the developed SDOF mechanical model. Finally, the energy harvesting performance of the partially covered PEH can then be evaluated and the results have been validated by the existing analytical method for SDOF model.

Acknowledgements

This work is financially supported by the Energy Education Trust of New Zealand (no. 3708242) and the PhD scholarship from China Scholarship Council (no. 201608250001).

References

1. K. Tao, L. Tang, J. Wu, S.W. Lye, H. Chang, and J. Miao, *Investigation of multimodal electret-based MEMS energy harvester with impact-induced nonlinearity.* Journal of Microelectromechanical Systems, 2018. **27**(2): p. 276-288.

2. G. Hu, L. Tang, R. Das, and P. Marzocca, *A two-degree-of-freedom piezoelectric energy harvester with stoppers for achieving enhanced performance.* International Journal of Mechanical Sciences, 2017.

3. A. Erturk and D.J. Inman, *A distributed parameter electromechanical model for cantilevered piezoelectric energy harvesters.* Journal of Vibration and Acoustics, 2008. **130**(4): p. 041002.

4. Y.C. Shu and I.C. Lien, *Analysis of power output for piezoelectric energy harvesting systems.* Smart Materials & Structures, 2006. **15**(6): p. 1499-1512.

5. N.E. duToit, B.L. Wardle, and S.G. Kim, *Design considerations for MEMS-scale piezoelectric mechanical vibration energy harvesters.* Integrated Ferroelectrics, 2005. **71**(1): p. 121-160.

6. A. Erturk and D.J. Inman. *Mechanical considerations for modeling of vibration-based energy harvesters*. in *Proceedings of the ASME IDETC 21st Biennial Conference on Mechanical Vibration and Noise*. 2007.

7. Y.W. Yang and L.H. Tang, *Equivalent Circuit Modeling of Piezoelectric Energy Harvesters.* Journal of Intelligent Material Systems and Structures, 2009. **20**(18): p. 2223-2235.

8. L. Tang and Y. Yang, *A nonlinear piezoelectric energy harvester with magnetic oscillator.* Applied Physics Letters, 2012. **101**(9): p. 094102.

9. J. Xu and J. Tang, *Multi-directional energy harvesting by piezoelectric cantilever-pendulum with internal resonance.* Applied Physics Letters, 2015. **107**(21): p. 213902.

10. E. Lefeuvre, A. Badel, C. Richard, and D. Guyomar, *Piezoelectric energy harvesting device optimization by synchronous electric charge extraction.* Journal of Intelligent Material Systems and Structures, 2005. **16**(10): p. 865-876.

11. W. Liu, C. Zhao, A. Badel, F. Formosa, Q. Zhu, and G. Hu, *Compact self-powered synchronous energy extraction circuit design with enhanced performance.* Smart Materials and Structures, 2018. **27**(4): p. 047001.

12. L. Zhao, L. Tang, and Y. Yang, *Synchronized charge extraction in galloping piezoelectric energy harvesting.* Journal of Intelligent Material Systems and Structures, 2016. **27**(4): p. 453-468.

13. D. Guyomar, A. Badel, E. Lefeuvre, and C. Richard, *Toward energy harvesting using active materials and conversion improvement by nonlinear processing.* IEEE transactions on ultrasonics, ferroelectrics, and frequency control, 2005. **52**(4): p. 584-595.

14. Y. Shu, I. Lien, and W. Wu, *An improved analysis of the SSHI interface in piezoelectric energy harvesting.* Smart Materials and Structures, 2007. **16**(6): p. 2253.

15. J. Liang and W.-H. Liao, *Impedance modeling and analysis for piezoelectric energy harvesting systems.* IEEE/ASME Transactions on Mechatronics, 2012. **17**(6): p. 1145-1157.

A nonlinear vibration energy harvester for spacecraft

H. P. Liu[1,2], D. Zhou[1], Y. B. Wang[1,2]
[1] Beijing Institute of Spacecraft System Engineering
104 Youyi Road, Haidian District, 100094, Beijing, China

[2] Beijing Key Laboratory of Intelligent Space Robotic System Technology and Application
104 Youyi Road, Haidian District, 100094, Beijing, China
e-mail: **lhpvibration@163.com**

Abstract

A nonlinear energy sink, which using a compressed beam as nonlinear stiffness element, is constructed for whole-spacecraft vibration reduction. The beam is fixed at both ends. A two-degree-of-freedom equivalent model of the scaled whole-spacecraft with the NES is presented. The systematic dynamic equations under the transient loading are solved by using 4th-order Runge-Kutta method. Based on these calculating results, it is shown that the NES exhibits the efficiency of energy transfer from the whole-spacecraft system as well as broad band vibration absorption. Furthermore, this study explores the potential of using the nonlinear energy sink for energy harvesting. The electromagnetic system is included in the equations of motion for the equivalent model. Using the compound model, a simulation is carried out to investigating the device's performance under transient responses in terms of energy harvesting. According to the calculating results, the system is shown to be capable of harvesting energy.

1 Introduction

The nonlinear energy sink (NES), as a useful method to suppress vibration without introducing new natural frequencies into the primary system, has attracted many researchers' attention [1-3]. In contrast to a linear vibration absorber, the NES exhibits some advantages, for instance, absorbing vibration energy over a wide spectrum of frequency, relatively small mass and without the need for additional energy. These merits are very important in the cases of whole-spacecraft and some key payloads that are subjected to complicated excitations during the launch stage and on-orbit stage, respectively.

Recent years, the nonlinear energy sink is used to capture vibration energy. This research field is getting more and more active. Some attempts to combine the functions of vibration reduction and energy harvesting have been conducted [4-5]. Kremer provided a novel electromagnetic energy harvester using

NES, which refers to several key parameters determined by using experimental identification [4]. Apparently, this method can be used to parametric study with the designing values of the NES. Li et al. [5] mainly focused on the energy transfer mechanism for the whole-spacecraft with the NES-piezoelectric system.

To enlarge the application range of NES-electromagnetic system, this paper investigates the dynamic performance of an equivalent scaled whole-spacecraft model with a NES-electromagnetic system. The content is organized as follows. Section 2 addresses the modelling procedure of the NES based on fixed-fixed beam. Section 3 develops a combined model of the whole-spacecraft with the NES-electromagnetic system. Section 4 the nonlinear dynamic equations are solved by using 4th-order Runge-Kutta method under transient excitations in time domain. The last part of this manuscript summarizes the conclusions based on calculating results.

2 Modelling of Nonlinear Energy Sink

The model of the nonlinear energy sink (NES) is built by a single beam fixed at both ends and a lumped mass located in the middle position of the beam, as shown in Figure 1.

The force along X direction can be obtained from the potential energy stored in the deflected beam. The stored potential energy in the beam is given by

$$U_c = \frac{1}{2}\frac{AE}{l_0}u_y^2 \tag{1}$$

where a slender beam held at a constant axial displacement u_y under compressed force P, l_0 and l_c represents the free length and the compressed length of the beam, respectively, A is the cross-sectional area of the rectangle beam, E is the Young's modulus of the material.

The transverse shape of the deflected Euler beam with fixed-fixed boundary follows the first-modeshape

$$x(y) = \frac{u_x}{2}\left[1-\cos\left(\frac{2\pi y}{l_c}\right)\right] \tag{2}$$

where u_x represents the displacement in the direction X induced by the transverse force F_t and y represents the distance of the beam along the direction Y.

The reduction of the compressed beam under the transverse load equals to the change of the arc length of the deflected beam.

$$L(x(y)) = \int_0^{l_c}\{1+\frac{1}{2}[\frac{\pi u_x}{l_c}\sin(\frac{2\pi y}{l_c})]^2\}dy \cong \frac{u_x^2\pi^2}{4l_c}+l_c \tag{3}$$

The corresponding decrease ΔU_c in the potential energy stored in the deflected beam can be provided by equation (4) due to the changing of the beam's length.

$$\Delta U_c = \frac{1}{2}\frac{AE}{l_0}\left(u_y-\frac{u_x^2\pi^2}{4l_c}\right)^2 \tag{4}$$

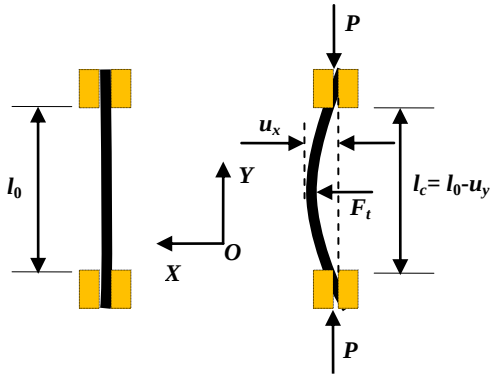


Figure 1: Schematic of the nonlinear energy sink

The bending energy in the deflected beam due to the influence of transverse F_t yields

$$U_b = \frac{\pi^4 EI}{l_c^3} u_x^2 \tag{5}$$

where I represents the area moment of inertia of the rectangle beam, $I=bt^3/12$.

The work from the force F_t over distance u_x equals to the total change in energy from the initial compressed state to the final bending shape for the deflected beam. The corresponding expression is defined as follows

$$F_t = \frac{\partial U}{\partial u_x} = \frac{\partial}{\partial u_x}(\Delta U_c + U_b) = (\frac{2\pi^4 EI}{l_c^3} - \frac{AE}{2l_0}\frac{\pi^2}{l_c} u_y) u_x + \frac{AE}{2l_0}\frac{\pi^4}{4l_c^2} u_x^3 \tag{6}$$

It can be easily known that the transverse force F_t is combined by linear and nonlinear components. Based on the results from reference [1], the linear component can be omitted. For simplicity, a new term k_3 is introduced as follows

$$F_t \approx k_3 u_x^3 \approx \frac{AE}{2l_0}\frac{\pi^4}{4l_c^2} u_x^3 \tag{7}$$

3 Modelling of Whole-spacecraft with NES and Energy Harvester

In launch phase of the satellite, all types of shocks are induced due to stage separation, fairing jettisoning and clamped-band release. And then, these transient loads propagate through the launcher structure and the payload adaptor up to the sensitive device interface. To control the influences from these transient excitations on the satellite, a NES-electromagnetic system is introduced into the whole-spacecraft, as shown in Figure 2. A combined model, which includes a two-degree-freedom equivalent whole-spacecraft model, a NES and an electromagnetic harvester, is developed in order to investigate the influences of the NES and the harvester on the dynamic responses of whole-spacecraft under transient excitations.

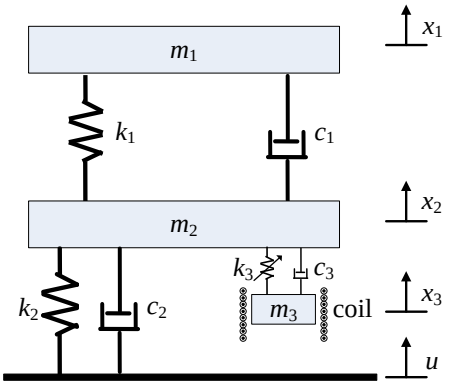


Figure 2: Equivalent model of whole-spacecraft with NES-electromagnetic system

The electrical circuit of the electromagnetic harvester is exhibited in Figure 3.

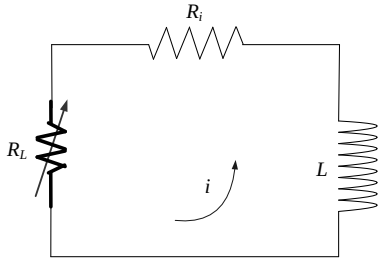


Figure 3: Electrical circuit of the energy harvester

The dynamic equations of the coupling system can be obtained

$$\begin{cases} m_1\ddot{x}_1 + c_1\left(\dot{x}_1 - \dot{x}_2\right) + k_1\left(x_1 - x_2\right) = 0 \\ m_2\ddot{x}_2 + c_2\left(\dot{x}_2 - \dot{u}\right) + k_2\left(x_2 - u\right) + c_1\left(\dot{x}_2 - \dot{x}_1\right) + k_1\left(x_2 - x_1\right) + c_3\left(\dot{x}_2 - \dot{x}_3\right) + k_3\left(x_2 - x_3\right)^3 = 0 \\ m_3\ddot{x}_3 + c_3\left(\dot{x}_3 - \dot{x}_2\right) + k_3\left(x_3 - x_2\right)^3 + F_e = 0 \end{cases} \quad (8)$$

where m_i, k_i, and c_i (i =1,2) represent the masses, linear stiffnesses and damping coefficients of the whole-spacecraft's equivalent model, m_3, k_3 and c_3 represent the mass, the nonlinear stiffness and the damping coefficient of the NES, x_1, x_2 and x_3 represent the displacements of the first rigid mass, the second rigid mass and the NES, F_e represents the electromagnetic force induced by the interaction of the oscillating magnet and the coils, $u=U\sin(\Omega t)$ represents a harmonic excitation.

Based on Lenz's law, the electromagnetic force is proportional to the coil current i

$$F_e = k_t i \quad (9)$$

where k_t is the transduction factor.

According to Kirchoff's voltage law to the electrical circuit of Figure 3, the equation of electrical circuit is obtained

$$L\frac{di}{dt} + \left(R_L + R_i\right)i = k_t\left(\dot{x}_3 - \dot{x}_2\right) \quad (10)$$

where L is the inductance of the coil, R_i is the internal resistance of the coil and R_L is the resistance of the external load.

For simplification, the coil inductance is omitted in the equation of electrical circuit. Letting L=0 and rearranging equation (10) yields

$$\left(R_L + R_i\right) i = k_t \left(\dot{x}_3 - \dot{x}_2\right) \tag{11}$$

An equation for induced voltage in the electrical circuit is provided by applying Faraday's law

$$\varepsilon = k_t \left(\dot{x}_3 - \dot{x}_2\right) \tag{12}$$

The relationship for the power delivery to the electrical load is given by

$$P_L = i^2 R_L = \frac{k_t^2 R_L}{\left(R_L + R_i\right)^2} \left(\dot{x}_3 - \dot{x}_2\right)^2 \tag{13}$$

4 Numerical Simulations

4.1 Parameters for calculations

The initial parameters for the equivalent model of the whole-spacecraft are: m_1=60kg, m_2=12kg, c_1=300Ns/m, c_2=10Ns/m, k_1=1.8677×10^{6}N/m, k_2=2.1346×10^{6}N/m.

Above values are based on reference [2]. The parameters of the NES and the energy harvester are: m_3=6kg, k_3=4×10^{8}N/m^3, c_3=50Ns/m; R_L=500Ω, R_i=200Ω, k_t=100Tm

4.2 Dynamic responses

In order to compare, all responses are induced by the displacement of the primary system, that is, $x_1(0) = X$, $x_2(0) = \dot{x}_3(0) = 0$, $\dot{x}_1(0) = \dot{x}_2(0) = \dot{x}_3(0) = 0$, $u(0) = 0$.

The influences of the NES and NES-electromagnetic system designing parameters on controlling the input energy will be studied in order to estimate the effectiveness of the NES-electromagnetic system. From the view of energy, the initial energy is stored in the spring k_1 obtained as follows

$$E_{\text{int}} = \frac{k_1 X^2}{2} \tag{14}$$

The energy dissipated by the NES is given by

$$W_{\text{NES}}(t) = \int_0^t c_3 \left[\dot{x}_3(\tau) - \dot{x}_2(\tau)\right]^2 d\tau \tag{15}$$

The power dissipated by the external load of the energy harvester defined by

$$W_{\text{elec}}(t)=\int_0^t P_L(\tau)d\tau=\int_0^t \frac{k_t^2 R_L}{(R_L+R_i)^2}\left[\dot{x}_3(\tau)-\dot{x}_2(\tau)\right]^2 d\tau \tag{16}$$

The energy dissipated by the whole-spacecraft system is expressed as follows

$$W_{\text{P}}(t)=\int_0^t c_1\left[\dot{x}_1(\tau)-\dot{x}_2(\tau)\right]^2 d\tau+\int_0^t c_2\dot{x}_2^2(\tau)d\tau \tag{17}$$

To better understand the performance of different components in the combined system, the percentage of the initial energy dissipated by the whole-spacecraft system, the NES and the energy harvester are addressed.

The percentage of the input energy dissipated by the NES is given by

$$\eta_{\text{NES}}(t)=\frac{W_{\text{NES}}(t)}{E_{\text{int}}}\times 100\% \tag{18}$$

The percentage of the input energy dissipated by the energy harvester is expressed as follows

$$\eta_{\text{elec}}(t)=\frac{W_{\text{elec}}(t)}{E_{\text{int}}}\times 100\% \tag{19}$$

The percentage of the energy dissipated by the dampers of the whole-spacecraft is given by

$$\eta_{\text{P}}(t)=\frac{W_{\text{P}}(t)}{E_{\text{int}}}\times 100\% \tag{20}$$

A simulation is conducted to investigate the effects of the initial displacement $x_1(0)$ on the percentage of the dissipated energy by the NES damper in Figure 4.

Figure 4 displays that there is an optimized value (about $X\approx 0.014$m) for the initial input energy where the NES exhibits the highest efficiency in vibrational absorbing. In addition, the influence from the electromagnetic harvester is also considered in this plot. It can be found that the energy dissipated percentage of the NES reduced in the displacement range of 0.013m～0.05m due to the input energy dissipated by the energy harvester partially. In two cases, the maximum energy is dissipated by the NES about 41% and 36%, respectively.

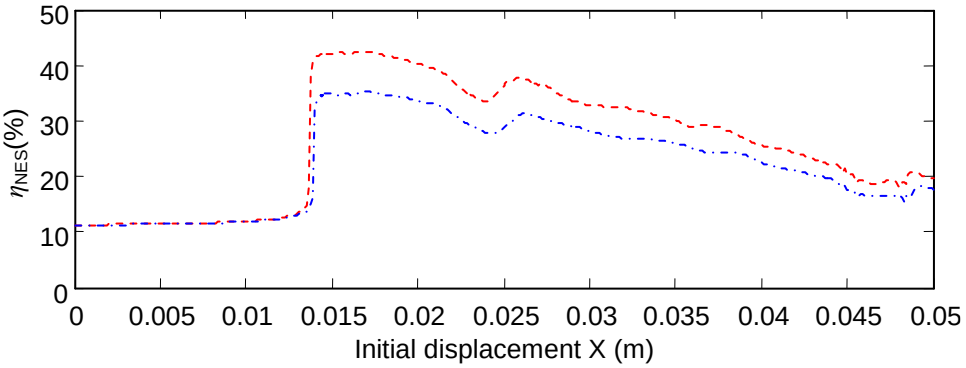


Figure 4: Percentage of the NES dissipated energy as a function of the initial displacement: – – only with NES, – . – with NES and energy harvester

Figure 5(a) and Figure 5(b) describe the percentage of dissipated energy by the whole-spacecraft system and the electromagnetic harvester under the same input displacement values, respectively. Compared with the NES and the NES-electromagnetic system, it can be seen that the varying trend of the dissipated energy by the primary system dampers is reversed. Especially, the input energy (X=0.014m) is harvested by the harvester amounts to about 7.1%.

The displacement responses of the primary mass m_1 among different systems under the initial displacement X=0.014m are obtained in Figure 6. It can be observed that the NES could reduce the response amplitudes significantly. Moreover, it can be seen that the displacement amplitude of the primary system, which includes the NES and the energy harvester, are larger than the one only with the NES.

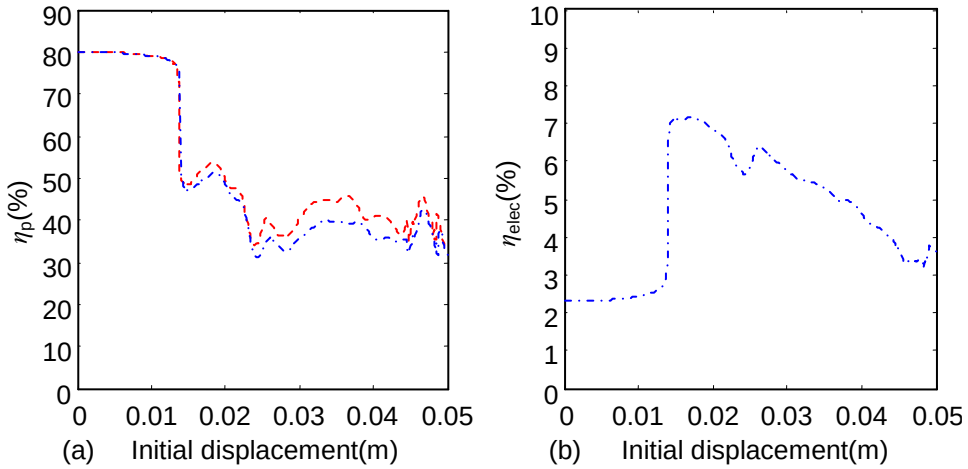
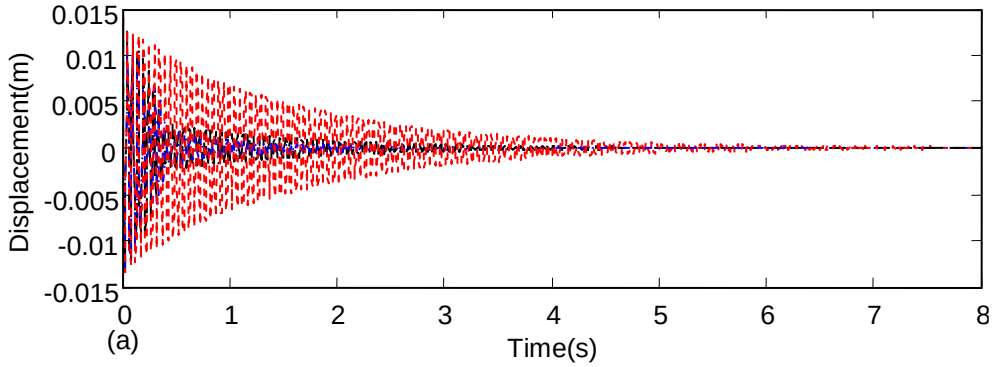


Figure 5: Percentage of the dissipated energy as a function of the initial displacement: (a) the whole-spacecraft system and (b) the electromagnetic harvester, – – only with NES, – . – with NES-electromagnetic system



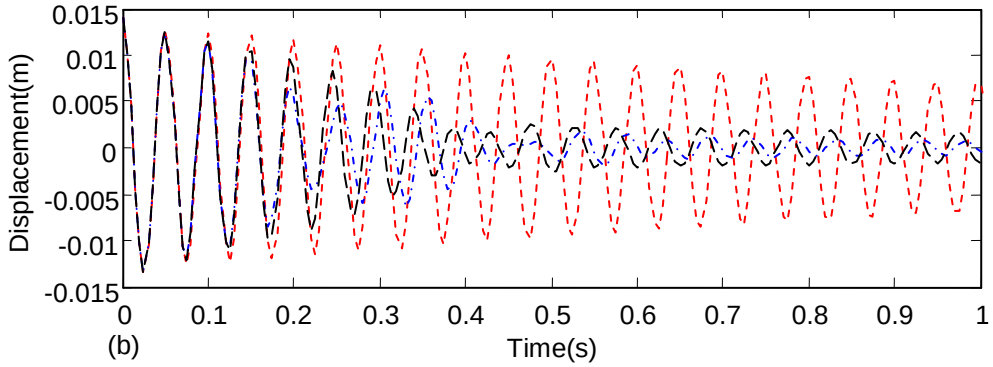


Figure 6: Displacement responses in the time history for the primary mass m_1: (a) 0s～8s and (b) 0s～1s, - - without NES and energy harvester, – . – only with NES， – – with NES and energy harvester

Figures 7(a), 7(b) and 7(c) depict the percentages of the energy dissipated by the whole-spacecraft dampers $\eta_P(t)$, the NES damper $\eta_{NES}(t)$ and harvested by the electromagnetic harvester $\eta_{elec}(t)$, respectively. The captured input energy for the system only with the NES is dissipated by the primary system and the NES about 50% and 41%, respectively. Under the same situation in the system with the electromagnetic harvester, the effectiveness of the NES is weakened, the corresponding values is about 53% and 32%. Beside, the harvested energy by the electromagnetic harvester is about 6.5%. It is evident that, a part of input energy can be harvested or stored as electric energy.

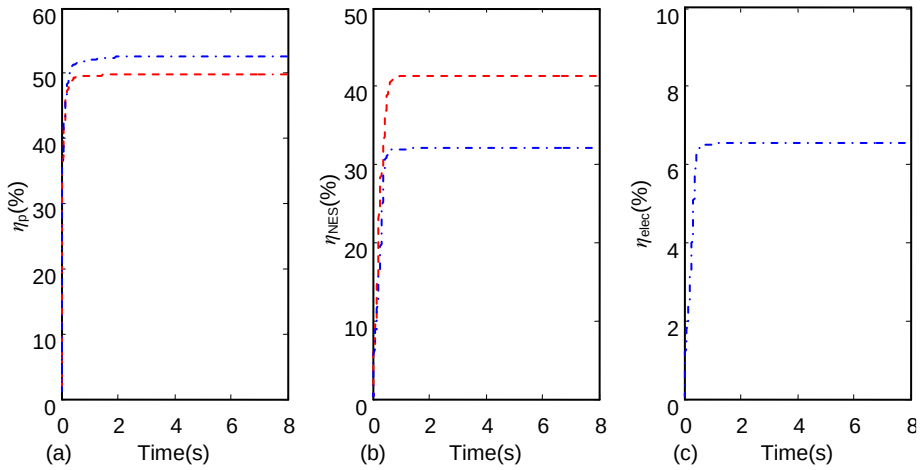


Figure 7: Percentage of energy dissipated or harvested by the compound systems: (a) the whole-spacecraft system, (b) the NES, (c) the energy harvester, - - only with NES, – . – with NES and energy harvester

The simulation results are presented at the initial displacement X=0.014m, as shown in Figure 8. In this section, the Morlet mother wavelet is used to process the time history. Figure 8(a) and 8(b) describe the displacement responses of the mass m_1 and its wavelet transform spectra. As it can be seen, the response is dominated by the primary system oscillating at its first-order natural frequency about 20Hz. There is some voltage induced in the coils and electric power available across the load resistor.

Figure 9 describes the transient relative displacement responses among the mass m_2, the

NES-electromagnetic harvester system, and the corresponding wavelet transform spectra. As displayed in Figure 8(b), the main frequency of the whole-spacecraft system is nearly 20Hz, while the relative displacement response of the NES-electromagnetic system exhibits frequency components over a large frequency band between 10Hz and 20Hz, as shown in Figure 9(b). After about 0.5s, the escaping phenomenon from resonance capture occurs due to the input energy decreased. For investigating the influences from the harvester on the energy dissipated by the NES, the transient response among the mass m_2, the NES, and the wavelet transform spectra, which are shown in Figure 10. Compared with the NES-electromagnetic system, the transient response of the NES has two main frequency components at about 20Hz and 24Hz, at the same time, the NES exerts the effect over the frequency range between 10Hz and 30Hz. From the view of vibration control, the NES presents great efficiency than the NES-electromagnetic system under the same conditions.

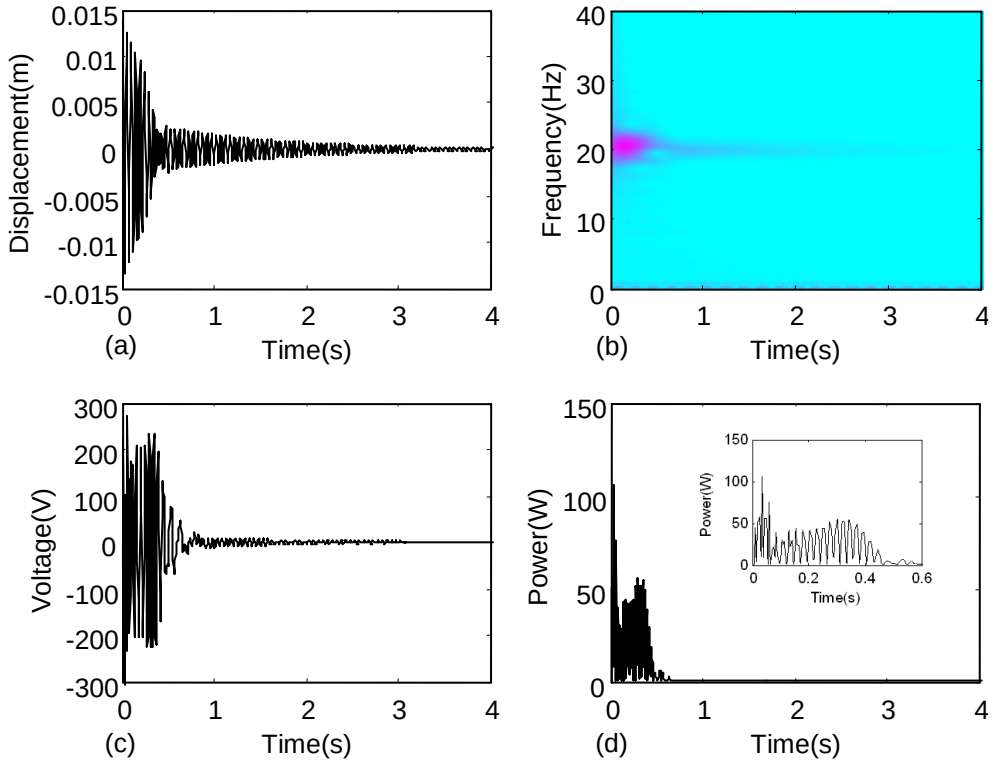


Figure 8: Simulation results for initial displacement of X=0.014m: (a) displacement curve of the primary mass m_1, (b) wavelet transforms, (c) voltage across the external load, (d) electrical power

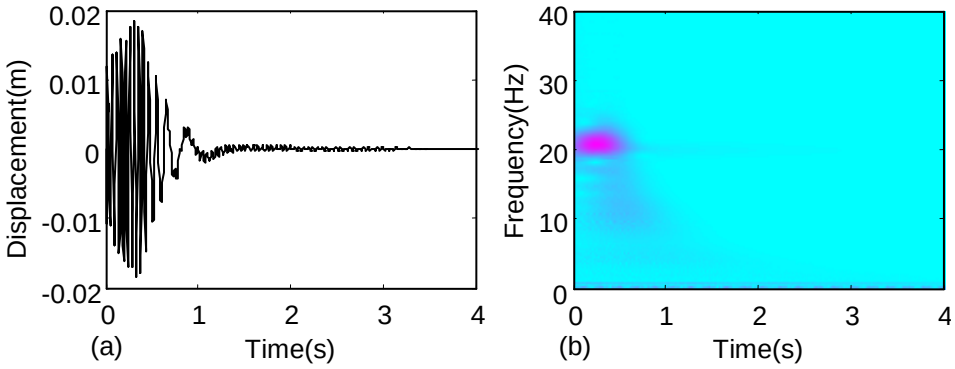


Figure 9: Relative response between the primary mass m_2 and the NES-electromagnetic system: (a) relative displacement x_3-x_2, (b) wavelet transforms

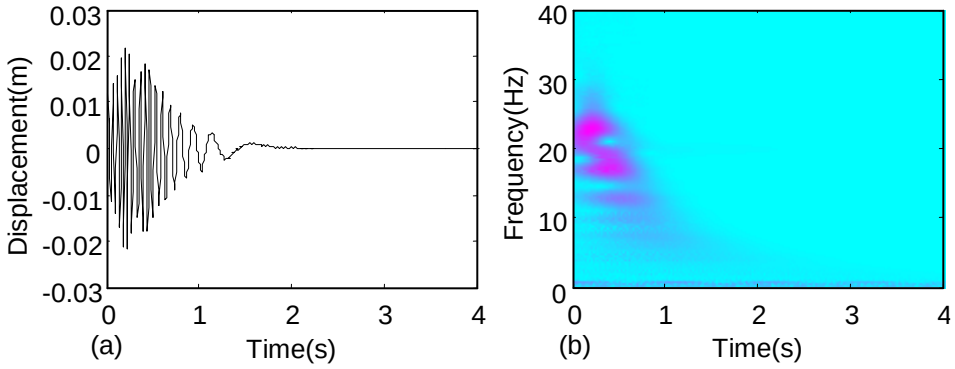


Figure 10: Relative response between the primary mass m_2 and the NES: (a) relative displacement x_3-x_2, (b) wavelet transforms

5 Conclusions

A compound model, which includes the whole-spacecraft, NES and electromagnetic harvester, has been conducted. In order to investigate the efficiency of the NES-electromagnetic harvester under transient excitations, the numerical calculations are performed by using the 4th-order Runge-Kutta method. The dynamic characteristics of the developed system subject to different initial displacement have been studied. It has been displayed that a well-defined critical threshold of the initial energy where the NES and the electromagnetic harvester perform well. Compared with the combined system only with the NES, the latter system presents great efficiency than the NES-electromagnetic system under the same conditions. The Morlet mother wavelet transforms are used to describe the phenomenon of transient resonance capture between the primary system and the NES. In addition, the efficiency and the difference between the NES and the NES-electromagnetic harvester are also been verified based on the time-frequency analysis results.

Acknowledgements

This research was supported by the National Natural Science Foundation of China (NSFC) under grant NO. 51405014.

References

[1] H.P. Liu, Y.B. Wang, *Construction and study on dynamic performance of a novel nonlinear energy sink under transient excitation*, Journal of Vibration and Shock, Vol. 37, No. 11, (2018), pp: 55-60. (in Chinese)

[2] K. Yang, Y.W. Zhang, H. Ding, T.Z. Yang, Y. Li, L.Q. Chen, *Nonlinear energy sink for whole-spacecraft vibration reduction, Journal of Vibration and Acoustics*, Vol. 139, No. 2, (2017), pp: 021011-1-021011-19.

[3] O. Gendelman, L.I. Manevitch, A.F. Vakakis, R. M'Closkey, *Energy pumping in nonlinear mechanical oscillator I: dynamics of the underlying Hamiltonnian system*, Journal of Applied Mechancis, Vol. 68, No. 1, (2001), pp: 34-41.

[4] D. Kremer, K.F. Liu, *A nonlinear energy sink with an energy harvester: Transient response*, Journal of Sound and Vibration, Vol. 333, No. 20, (2014), pp: 4859-4880.

[5] X. Li, Y.W. Zhang, H. Ding, L.Q. Chen, *Integration of a nonlinear energy sink and a piezoelectric energy harvester*, Applied Mathematics and Mechanics, Vol. 38, No. 7, (2017), pp: 1019-1030.

Tuned mass dampers as energy harvesters for railways

G. Nerubenko[1], A. Bograd[1], P. Kolomier[1]
[1] NER*MAR Limited
270 Palmdale Drive, Toronto, ON, M1T 3N8 Canada
e-mail: **optimalproject@hotmail.com**

Abstract

Increasing challenges on recovering of wasted energy has opened the new directions in railway technologies. The example of such technology applied for railway sleepers (crossties) is the implementation of novel type of energy harvesters developed recently. The approximate estimates show that the usage of proposed crossties equipped by energy harvesters allows get around 500 kW per one running US or Canadian freight train. It must be underline that these 500 kW now are known as lost energy and never used. The composed vibration energy harvester consists of two main components: regular tuned mass damper and electricity generator. The results of theoretical analysis combined with experiments on prototypes illustrate the proof of selected mathematical modeling. Test results illustrate the high efficiency of proposed vibration energy harvesters and some new opportunities for their applications.

1 Introduction

The energy harvesting is the nowadays technology allowing capture, convert and transfer small amount of wasted power [1], [2]. Energy harvesting is widely used for instance for feeding autonomous electronic devices. The authors did not include in present paper the detailed analysis of a various published materials regarding considered subject trying to concentrate only on authors results. First Vibration Energy Harvesters (VEH) developed by authors in [3] – [5] were based on controlled tuned mass dampers. The implementation of VEH in railways was dictated by two combined reasons: necessity of a reduction of intensive vibrations and proper usage of damped vibration energy. The interesting results were obtained using electromagnetic and piezoelectric schemes ([6] – [8], [16]-[23]). The application of developed VEH in railway environment for reaching two goals: reduction of vibration levels and effective usage of wasted vibration is demonstrated in current study. An evaluation of possible maximal power **Po** obtained from one running US or Canadian freight train could be done approximately based on formula from theory of vibrations for certain vibrating object: $\mathbf{Po} = 0.5\beta\, \mathbf{A_m}^2\, \omega^2$, where $\mathbf{A_m}$ is a resonance amplitude of object, ω is a resonance frequency, β is a viscous damping coefficient. Taking the conservative numbers for amplitude as 2 mm, and resonance frequency as 10 Hz, the values of the possible maximal extracted power would be in the range 495 kW – 550 kW for regular running freight train (2,000 meters long). The schematic and structural components of proposed compositions are presented. Theoretical modeling and analysis are supported by recommendation of parameter's selection. Further the dynamical behaviour of device is analyzed and advantages of different approaches are discussed. The results of the theoretical analysis are supported by experimental tests showing the effectiveness of implementation of proposed VEH. It is highlighted that the usage of controlled tuned mass damper scheme for purpose of vibration energy harvesting in railway application provides the independent reliable source of electrical power for the electricity consumers.

2 General scheme of vibration energy harvester

There are several types of energy harvesters however Electromagnetic Vibration Energy Harvesters (EVEHs) are nominated for usage in railway industry, the main reason for this choice is that running train operates practically with constant speed. EVEH is presented in “rectilinear vibration operation” general version. The core graphical model of rectilinear operating EVEH ([9] – [14]) is shown in Figure 1.

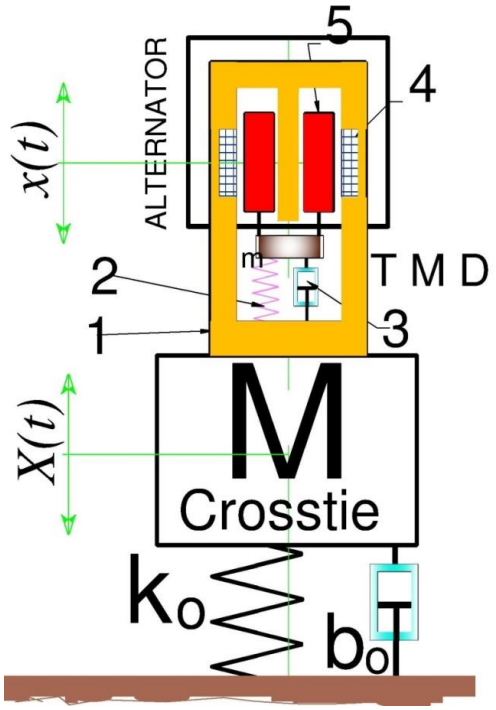


Figure 1: EVEH arrangement for linear one-dimension application.

Let's assume that a certain object (for instance, a crosstie) is vibrating along coordinate axis X as shown in Figure 1. The mass of vibrating object is **M**. The body 1 of EVEH is attached firmly to object. EVEH consists of two major parts: tuned mass damper and alternator. Tuned mass damper having mass **m** is attached to EVEH's body by means of spring 2 and damping element 3. Alternator part consists of pick-up coil 4 and magnet 5 (for instance, configured as a ring). Magnet 5 is attached firmly to the mass **m** of tuned mass damper. Tuned mass damper has to have own resonant frequency equal to crosstie operational frequency. The amplitude of mass **m** vibrations would be maximal in this case, and “productivity” of an alternator would be the maximal as well. Hence the accepted scheme for that study is described as EVEH mounted in a crosstie (see Figure 2).



Figure 2: Typical crosstie / sleeper

Since EVEH is coupled to a crosstie, it could be assumed that the external force is caused by a train moving with constant speed. The mono harmonic low frequency (up to 30 Hz) vibrations of concrete crosstie would be considered for that simplified case. A crosstie is modeling by solid body.

3 Parametric modeling of EVEH

The simplified modeling of EVEH could be done using the scheme shown in Figure 1. Let's suppose that the object - crosstie **M** is mounted on site and assembly is modeling by spring having stiffness **ko** and viscosity factor **bo**. Let's consider that it would be vibrating in one direction only. Its movement coordinate is **X(t)**, where **t** is time. The outer casing of EVEH is firmly attached to the crosstie, and the mass of casing is included in **M**. Tuned mass damper **m** is connected to casing by means of springs having the stiffness **k1** and viscosity factor **b1.** Mass **m** is vibrating in the same direction as mass **M**. The coordinate of vibrations of **m** is **x(t)**. The electromagnetic subsystem is inducing current **i**, and **L** is inductance, **R** is electrical resistance, where **Rc** is coil resistance and **Rd** is load resistance, and **R** = **Rc** + **Rd.** The EVEH dynamics is described by system of ordinary differential equation (see for instance [1], [2], [5], [17], [21], [22])

$$\mathbf{M}X'' + \mathbf{k_o}\,x + \mathbf{b_o}\,x' + \mathbf{k_1}\,(X - x) + \mathbf{b_1}\,(X' - x') = \mathbf{H}\sin(\omega t) \quad (1)$$

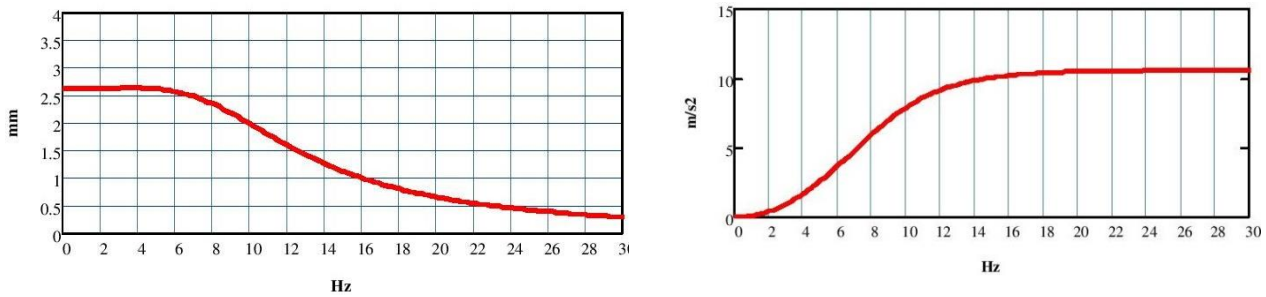
$$\mathbf{m}x'' - \mathbf{k_1}\,(X - x) - \mathbf{b_1}\,(X' - x') + \Phi_m\,\mathbf{i} = 0 \quad (2)$$

$$\mathbf{L}i' + \mathbf{R}i - \Phi_e\,\mathbf{i} = 0 \quad (3)$$

where **H** is the magnitude of external force, **ω** is the frequency of external force, **Φm** is the linkage factor between mechanical and electromagnetic subsystems in mechanical terms, **Φe** is the linkage factor between electromagnetic and mechanical subsystems in electromagnetic terms.

The system of equations (1) – (3) is written purposely focusing on specific link between vibrations of tuned mass damping subsystem (equation (2)) and dynamic behaviour of current generating subsystem (equation (3)). Furthermore it is possible to pay attention on a specific of the dynamic properties of tuned mass damper coupled to an alternator.

Assuming that at considered case for crosstie: M=300 kg, bo=25000 kg/s, ko=1.2*10^6 kg/s^2, H=3140 kg m/s^2, it is possible to build the amplitude - frequency characteristic (red solid curve) as shown in Figure 3A or linear acceleration – frequency characteristic as shown in Figure 3B. The abscissa horizontal axis is for excitation frequency in these Figures (further similar on following Figures) and ordinate vertical axis is for amplitude (mm) in Figure 3A, and for linear acceleration (m/s2) in Figure 3B.



A **B**

Figure 3: Dynamical characteristics for crosstie.

Analyzing the amplitude - frequency characteristic in Figure 3A, one can see that the amplitude of 2.6 mm is presented at all excitation frequencies starting from 0 up to 6 Hz, and then it declines with raised frequencies. On the contrary the analysis of linear acceleration – frequency characteristic in Figure 3B shows that the values of acceleration are climbing up with increasing of excitation frequencies to number of 10.6 m/s2, and after that the value of acceleration is practically stable.

The model presentation of crosstie's dynamical behaviour in form of the amplitude - frequency characteristic is very convenient for the applied analysis, for example, one can see that amplitude of vibrations at 10 Hz is equal to 2.0 mm. It means that the selected crosstie will be operating at 10 Hz having amplitude of 2.0 mm if there is no additional devices installed on that crosstie, for example, no tuned mass dampers. Using the approximate evaluation of possible maximal power **Po** obtained from one such vibrating crosstie, one can get the result equals to 115 Watt.

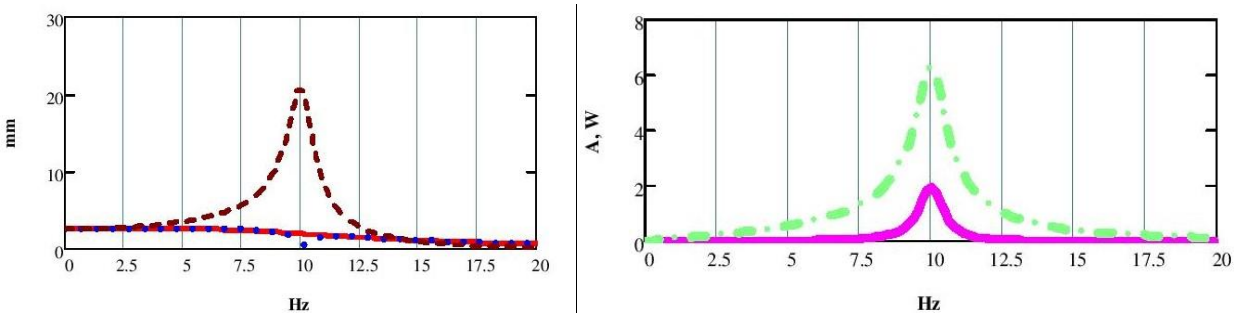
Prior to examination of implementation of EVEH into crosstie structure let's formulate the purpose of this implementation. The main target of design of proposed EVEH is to satisfy two conditions: **a.** generation of an additional power which could be used, **b.** possible reduction of the vibration levels of crosstie by controlled tuned mass dampers.

There is no information at the beginning of study, so suppose that the mass of tuned mass damper is selected equal to 10% of crosstie's mass following the standard recommendations. This tuned mass damper will be tuned to 10 Hz. Let's assume for simplicity that the initial parameters of an alternator for trial study are dimensionless, $\Phi m = \Phi e = \Phi$, and all of them are equal to unit, or L=1, R=1, $\Phi = 1$.

The amplitude - frequency characteristics of considered system (case 1) is presented in Figure 4A. A red curve reflects the vibration behaviour of main system (mass M) without installed EVEH, and this curve coincides to red curve in Figure 3A.The amplitude - frequency characteristic of tuned mass damper could be reflected by brown dashed curve as shown in Figure 4A.The resonant amplitude of tuned mass damper is equal to 20.868 mm at 10 Hz. The blue dotted curve in Figure 4A stands for damped vibrations of main system (tuned mass damper installed). The resulted damped amplitude (according to blue dotted line) is 0.554 mm at 10Hz, so the reduction of resonance amplitude is in 2/0.533= 3.617 times, which is sufficient for technical system.

EVEH induced current would be presented by green dash – dotted curve as shown in Figure 4B, and EVEH peak of useful power could be plotted by solid magenta curve in Figure 4B. EVEH useful power is calculating by formula $\mathbf{P(\omega)} = 0.5\ \mathbf{Rd}\ \mathbf{i}^2$, where $\mathbf{Rd} = 0.5\ \mathbf{R}$.

One can see that the shape and location of green dash – dotted curve (induced current) in Figure 4B is coinciding with the shape and location of brown dashed curve (tuned mass damper) in Figure 4A. The shape and location of magenta solid curve (peak of useful power) in Figure 4B is coinciding with the shape and location of green dash – dotted curve (induced current) in this figure. It is the confirmation that alternator's parameters are dictated by dynamics of tuned mass damper. The maximal values at 10 Hz are: for induced current is 6.27 A, peak of useful power is 1.97 Watt, such result is very far from desired 115 Watt, and demonstrates the 10% mass of tuned mass damper allows get sufficient vibration level reduction, but does not work as the energy harvester.



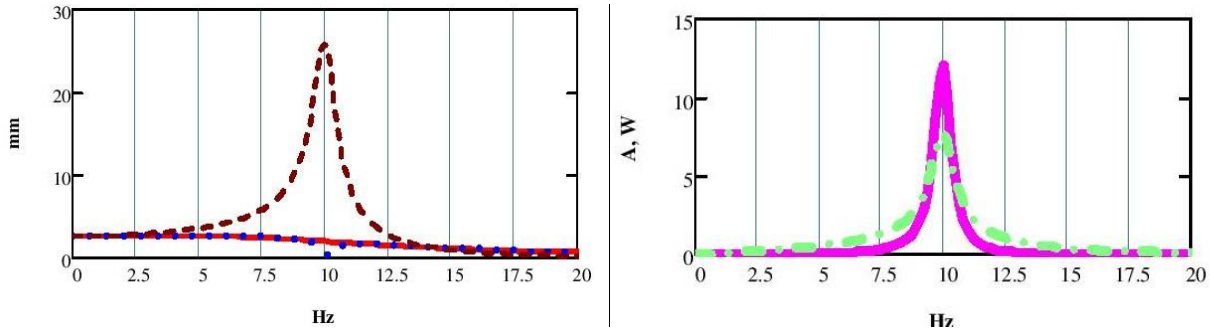
A B

Figure 4: Dynamical characteristics for crosstie when EVEH installed. Case 1.

There are the results of model simulation for considered system in Figure 5 when the mass of tuned mass damper still is equal to 10% of crosstie's mass and the initial dimensionless parameters of an alternator are equal to 4, or L=4, R=4, $\Phi = 4$ (case 2).

The resonant amplitude of tuned mass damper (brown dashed curve in Figure 5A) is equal to 25.827 mm at 10 Hz. The resulted damped amplitude (according to blue dotted line) is 0.439 mm at 10Hz, so the

reduction of resonance amplitude is in 4.556 times, which is sufficient for technical system. The maximal values at 10 Hz are: for induced current is 7.76 A, peak of useful power is 12.04 Watt, and again that result is very far from desired 115 Watt.
The preliminary cycle of study indicates that the parameter's selection of tuned mass damper in first approximation mass should be equal to 1% of crosstie's mass: m=3 kg, and b1=51 kg/s, k1=1.2*10^4 kg/s^2 . Let's examine the impact of each electromagnetic parameter on tuned mass damper amplitude and useful power. Suppose that each of parameter variation is in interval (1...4), or $1 < L < 4$; $1 < R < 4$;$1 < \Phi < 4$; and $\omega = 62.8$ 1/s = 10 Hz.



A B

Figure 5: Dynamical characteristics for crosstie when EVEH installed. Case 2.

The relationship between amplitude of tuned mass damper and an inductance L is plotted by blue curve in Figure 6; and on the same figure there is a relationship between the peak of useful power P and an inductance L plotted by red curve. Other parameters are R= Φ = 1. The horizontal axis (dimensionless) is standing for inductance, and the vertical axis is standing for amplitude of tuned mass damper (in cm), and useful power (in Watt). The analysis of this chart shows that the amplitudes of tuned mass damper are reducing slightly with increased numbers of inductance, and values of useful power are falling down with increased numbers of inductance. It could be concluded that for power efficiency it is better to select the inductance with minimal values.
The relationship between amplitude of tuned mass damper and a resistance R is plotted by the similar blue curve in Figure 7; and a relationship between the peak of useful power P and a resistance R is plotted by red curve. Other parameters are Φ = L = 1. The horizontal axis (dimensionless) is standing for resistance, and the vertical axis is the same as per Figure 6. The analysis of this graph shows that the amplitudes of tuned mass damper are reducing slightly down to some minimum, and the values of useful power at this time are reducing as well. It could be stated that for power efficiency it is better to select the resistance values with minimal numbers.

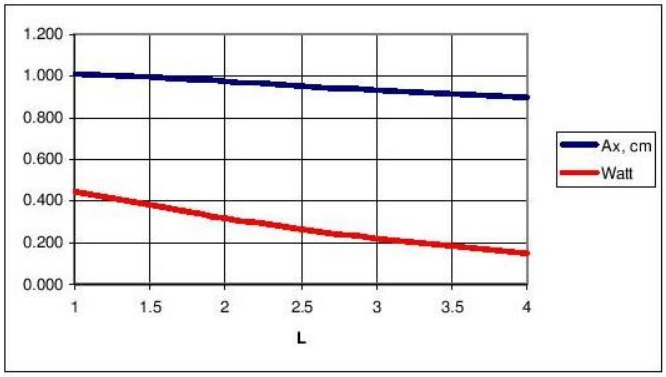


Figure 6: Amplitude of tuned mass damper and peak of useful power vs. inductance

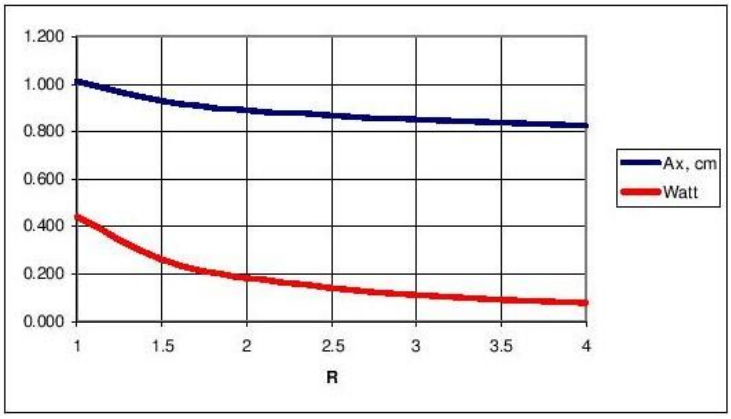


Figure 7: Amplitude of tuned mass damper and peak of useful power vs. resistance

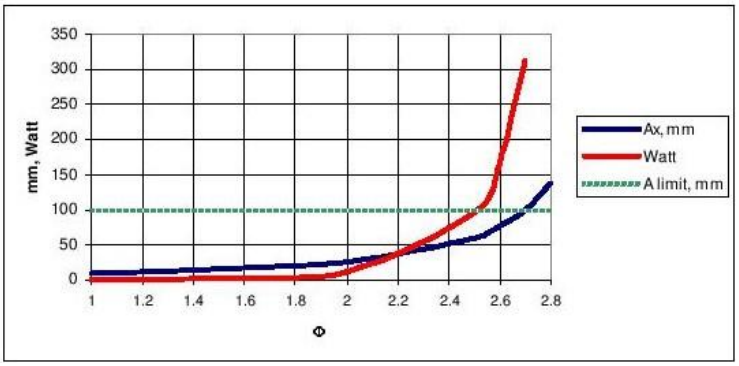


Figure 8: Amplitude of tuned mass damper and peak of useful power vs. linkage factor

The relationship between amplitude of tuned mass damper and a linkage factor Φ is plotted by the similar blue curve in Figure 8; and a relationship between useful power P and a linkage factor Φ is plotted by red curve. Other parameters are R = L = 1. The horizontal axis (dimensionless) is standing for the linkage factor, and the vertical axis is the same as in Figure 6.

The analysis of this graph shows that the amplitudes of tuned mass damper are growing up, and the values of useful power are growing up significantly. The rise of amplitudes is restricted by technical requirements – amplitude of tuned mass damper vibrations could not be more than 100 mm. The values of useful power may reach more than 300 W. It is necessary to highlight that the upper magnitude of a linkage factor was less than planned Φ =4 because of the vibration amplitude restrictions. It could be stated that for power efficiency it is better to select the maximally possible linkage factor values in this case.

This study illustrates that the implementation of an alternator subsystem into tuned mass damper design leads to changes of magnitudes of its amplitudes, and increasing values of useful power means the reduction of tuned mass damper 's amplitudes numbers. The analysis of graphs presented in Figures 6 – 8 tells that the linkage factor provides the most significant influence on amplitudes of tuned mass damper.

It was assumed until now that the external excitation force has unchangeable constant frequency, for example 10 Hz. If the frequency does not have the constant nature, the additional control apparatus [15] could adjust properly the EVEH parameters using the algorithms “catch and match frequency”.

4 Rectilinear EVEH prototype design

A crosstie is an example of a solid object vibrating in one line direction (rectilinear) or objects having single degree of freedom. Its model is shown in Figure 1 and can be described by system of equations (1) – (3). An attachment of tuned mass damper completed with an alternator to a crosstie is providing two

opportunities to engineer: a reduction of level of body vibrations and an effective conversion of damped vibrations into useful power. Actually these opportunities could involve tuned mass damper completed with an alternator in conflict situation.
Trying to reach the best result for reduction of a crosstie vibration at 10 Hz, there were considered two options: “heavy” EVEH having the mass of tuned mass damper equal to 1.9% of crosstie mass, and: “light” EVEH having the mass of tuned mass damper was equal to 1.0% of crosstie mass. The “heavy” version of a system was readjusted in the following way: the viscosity coefficient b1 was selected as b1=51 kg/s, an inductance was nominated as L=2, the electrical resistance was selected as R=1.52, and a linkage factor was assumed to be 3.03.The “light” version of a system was readjusted in the following way: the viscosity coefficient b1 was selected as b1=50 kg/s, an inductance was nominated as L=1.5, the electrical resistance was selected as R=1.2, and a linkage factor was assumed to be 2.924.

The dynamical characteristics of “heavy” system are shown in Figure 9. The abscissa axis stands for frequency (in Hz) of external force in Figure 9, and ordinate axis stands for **a.** amplitudes of tuned mass damper vibrations in mm **b**. peak value of useful power in W.

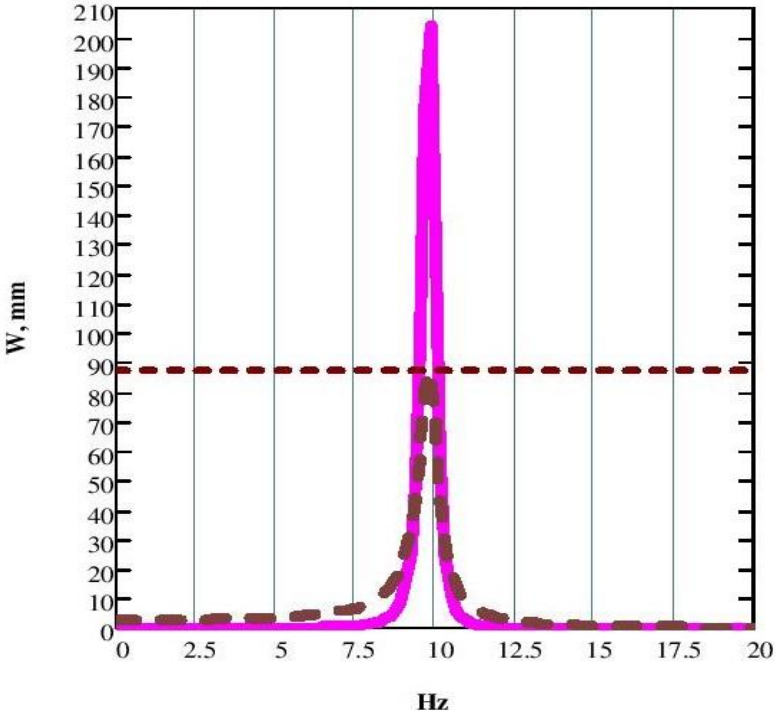


Figure 9: The dynamical characteristics of “heavy” system.

On that chart the amplitude - frequency characteristic of tuned mass damper could be reflected by brown dashed curve, and relationship of useful power vs. frequency reflected by magenta solid curve. The maximum value of amplitude of tuned mass damper is 86.36 mm at 10 Hz, and maximal number of useful power is 204.2 W. There is a straight line in Figure 5 equals to 87 mm. It was found during design that the actual maximum value of amplitude of tuned mass damper must be limited geometrically to 87 mm.

The dynamical characteristics of “light” system are shown in Figure 10. The coordinate axis and curves are similar to those presented in Figure 9. The maximum value of amplitude of tuned mass damper is 86.89 mm at 10 Hz, and maximal number of useful power is 218.5 W, or it means that average extracted useful power is 109.25 W, which is close to desired 115 Watt. The analysis of obtained results demonstrates that the proper selection of EVEH parameters could provide the sufficient values of expected useful power, but it would be done at expense of quality of reduction of crosstie’s vibration levels, for instance the magnitude of damped resonant amplitude for the last case is 1.86 mm (amplitude reduction in 1.075 times), or practically no appreciable result of a reduction.

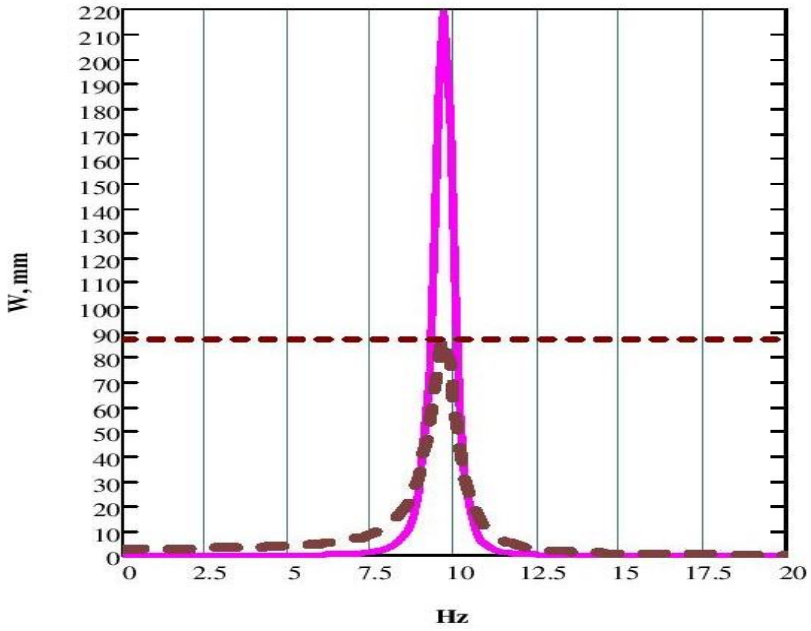


Figure 10: Dynamics of EVEH focused on “light” system

Hence there is an attractive result in using the wasted power, but practically no vibration reduction in latest case. This case is illustrating the design of EVEH focused on the effectiveness of using wasted power only. Furthermore, it is obvious that the case of “light” system is more preferable in comparison to case of “heavy” system – less weight, less mass – geometry characteristics, and more useful power.

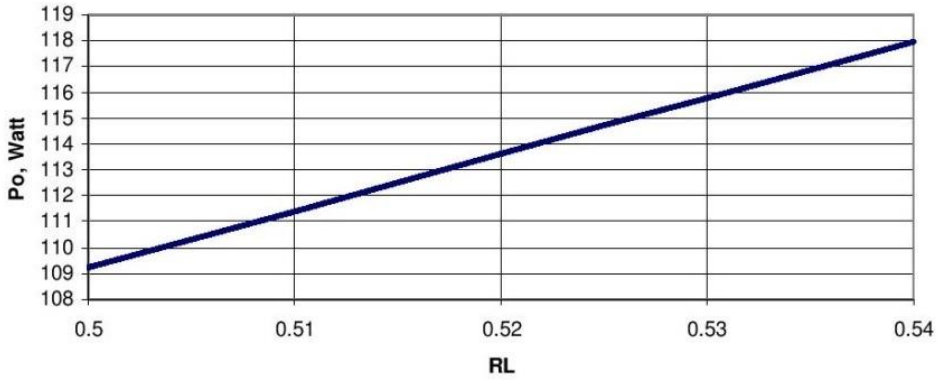


Figure 11: Selection of load resistance.

The final step in design parameters selection is the elaboration of relationship between **Rd** load resistance and average extracted useful power. The results of a digital analysis are presented in Figure 11 (abscissa axis is the dimensionless **Rd**, and ordinate axis is average useful power). The designer could see that the modelling predicted power would be obtained at **Rd** = 0.53.

5 EVEH prototype test

The prototype of EVEH focused on extracting the possibly maximum power from vibrating crosstie was designed and fabricated. The design parameters were composed specifically for prototype mounting on a crosstie vibrating at 10 Hz with amplitude 2 mm. Its main characteristics were based on values presented in last modelling case. EVEH was vertically installed. The EVEN photo is shown in Figure 12 in left side,

and pick-up coil (solenoid) is in right side of Figure 12. There was a specifically designed shaker used for experiments (see Figure 13).

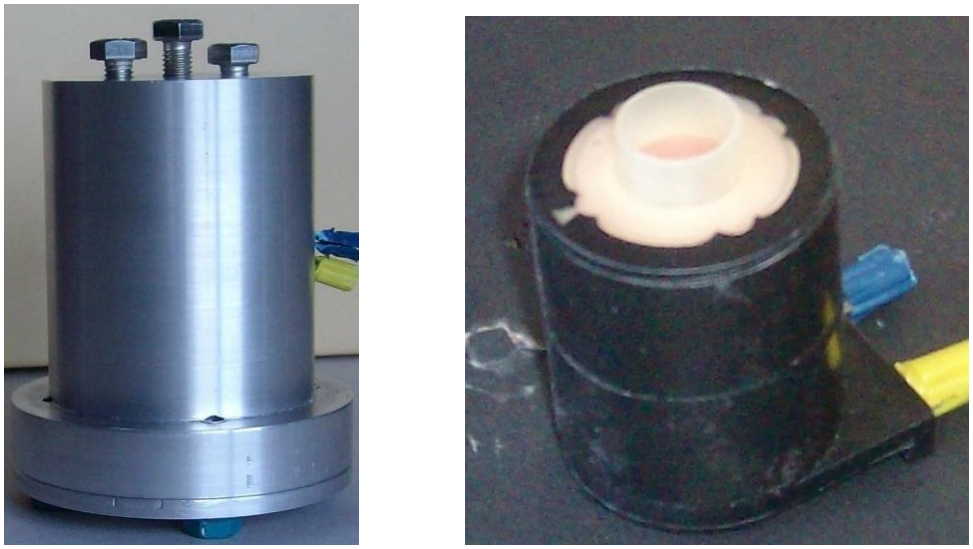


Figure 12: Rectilinear EVEN

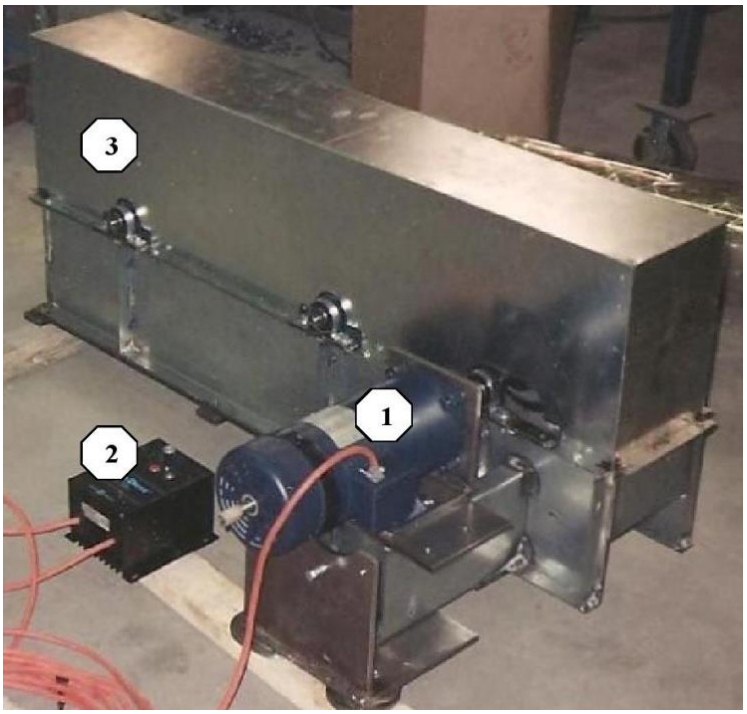


Figure 13: General photo of Shaker

The shaker has the driving device – DC Motor 1, electrically connected to speed controller 2 for controlling DC rpm. The DC Motor is providing rotation to input shaft of shaker 3 through clutch. The shaker was configured (see Figure 14) to generate a steady state sinusoidal force acting in the vertical direction. For that purpose the input shaft has the drive gear 4 (see Figure 14) contacted to two counter – rotating wheels 5, each of counter – rotating wheels are equipped by counter - rotating masses 6. Such design provides a shaker by the adjustable controllable speeds (hence, the frequencies of excitation). The shaker could have the stable certain vertical vibrations in frequency range of 1.5 Hz – 20 Hz. The shaker was installed on test platform (see Figure 15).

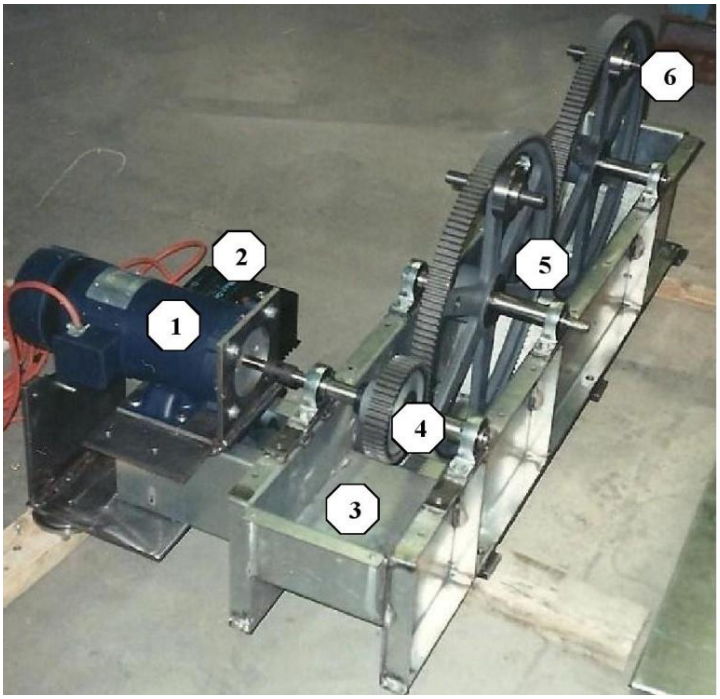


Figure 14: Internal view of shaker



Figure 15: Shaker on test platform

The vibration of test platform were recorded, analyzed and control by means of Hewlett Packard Handheld Dynamic Spectrum Analyzer 3 (see Figure 16) getting signal from measuring accelerometer 2. A speed controller marked as 1 is shown in Figure 16 as well. The EVEH prototype focused on getting power was assembled on test platform and experimentally examined. The comparison of magnitudes measured in an experiment to data obtained in previous theoretical study was done. The recorded useful power was visualized specifically for convenience purposes as a graph in coordinates “useful power in W” vs. “time in seconds” (see Figure 17). The analysis of presented graph brings us to conclusion that the measured average useful power is 114.03 Watt.



Figure 16: Data recording

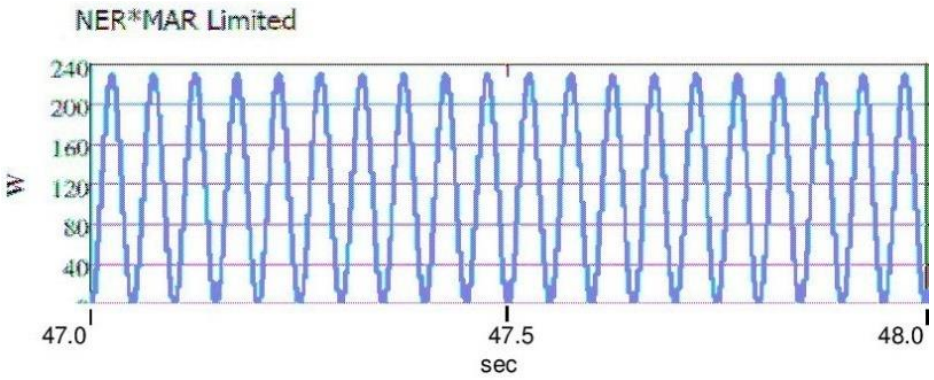


Figure 17: The recorded useful power

The comparison of values metered during test to data received theoretically (115.78 Watt) shows that the deviation of obtained data from theoretically predicted ones is 1.53% and one can say that this result confirms that it is a satisfactory compliance of real manufactured EVEH to theoretically predicted model.

6 EVEH application for tuned mass damper feeding

One of the perspective ways of EVEH usage was practically missed in R&D practice. It is the rerouting of produced power to tuned mass damper subsystem for reducing its viscosity factor **b1** [10],[11]. Such EVEH usage significantly improves the tuned mass damper efficiency. It could be demonstrated graphically as shown in Figure 18 which reflects the modelling and simulation of system (1) - (3) for "heavy" option.

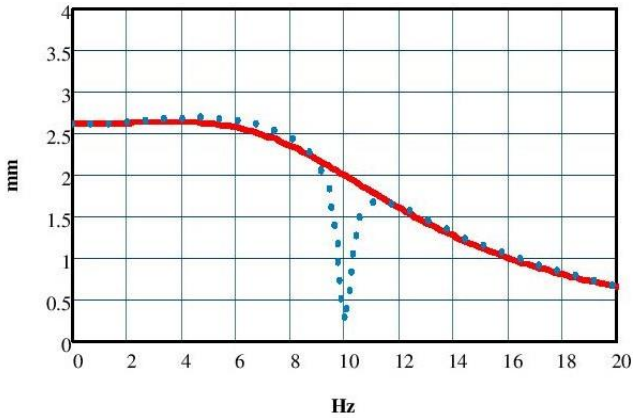


Figure 18: Amplitude – frequency charts for system without EVEH and with improved EVEH installed

Figure 18 is built similar to Figure 4A, but the amplitudes of tuned mass damper are not plotted. During modelling and plotting these graphs it was accepted that all EVEH useful power was directed for compensation of viscosity factor.

The red solid curve reflects the initial dynamical behaviour (amplitude – frequency chart) of previously examined crosstie without tuned mass damper. The value of amplitude is 2 mm at 10 Hz. The amplitude - frequency characteristic of a crosstie equipped by tuned mass damper could be reflected by blue dotted curve as shown in Figure 18. Now the value of amplitude is 0.294 mm at 10 Hz, or reduction of amplitude level is in 6.8 times. The engineer can see that the rerouting the useful power signal for viscous factor compensation gives the magnificent opportunity for further suppression of negative crosstie vibrations. However the designer must take into account that this phenomenon is caused by increasing amplitude of tuned mass damper [18], which could cause (in its turn) the further raising of magnitudes of useful power. It is important to keep that process of damper's displacements increasing combined to power rising in stable dynamic zone. It should be done using, for instance, the control schemes described in [15].

It is necessary to mention that the presented design solutions are not restricted, and they could be applicable in various situations in railways generally.

7 Summary / Conclusions

Elaborated vibration energy harvesters based on electromagnetic tuned mass dampers has several improved features. The universality of application of proposed scheme for “rectilinear vibration operation” is one of the most important issues among others. The main purpose of design and implementation of proposed electromagnetic vibration energy harvester demonstrated in current study is to serve dual goals:

- reduction of the vibration levels of a crosstie by controlled tuned mass dampers,
- generating an additional power which could be used in an industry.

The implementation of suggested electromagnetic vibration energy harvesters gives flexibility in applications: it gives a possibility to use them in such formats as

- focused on tuning damping of crosstie vibrations,
- focused on reasonable balance between tuning damping of crosstie vibrations and effectiveness of using wasted power,
- focused on the effectiveness of using wasted power only.

Usage of proposed design solutions allows redirect the useful power for compensation of tuned mass damper’s viscous factor. Due to composed control system it is possible to build electromagnetic vibration energy harvester operating in stable zones.

The developed electromagnetic vibration energy harvesters could be installed and used successfully in various branches of railway business having vibrating modules, units and parts.

References

[1] Priya, S and D. L, Inman. *Energy Harvesting Technologies*. Sprinder. Verlag. 2009.

[2] Francesco Cottone. *Energy Harvesting: introduction*. NiPS Summer School 2015 – July 7-12th - Fiuggi (Italy). 50 p.

[3] George Nerubenko et al. *Tuned Mass Damper.* USSR Patent 464730, 25.03.75.

[4] George Nerubenko et al. *Generator of Electrical Signals.* USSR Patent 841077. 23.06.1981.

[5] Eliseev, S. V. and Nerubenko G. P. *Tuned Mass Dampers,* NAUKA, Novosibirsk, 1982 (in Russian).

[6] John J. Wang ; G. P. Penamalli ; Lei Zuo. *Electromagnetic energy harvesting from train induced railway track vibrations. 2012 IEEE/ASME International Conference on Mechatronics and Embedded Systems and Applications (MESA),* 2012, IEEE, Suzhou, China.

[7] V G Cleante, M J Brennan, G Gatti, D J Thompson. *Energy harvesting from the vibrations of a passing train: effect of speed variability.* Journal of Physics: Conference Series, Volume 744, Number 1, 2016.

[8] Francisco Duarte, Adelino Ferreira. *Energy harvesting on railway tracks: state-of-the-art.* Proceedings of the Institution of Civil Engineers – Transport. Volume 170 Issue 3, June, 2017, pp. 123-130

[9] Babitsky V. I., Kobrinsky A. E. *Electromagnetic Dynamical Vibration Damper.* USSR Patent 151533. 01.11.1962

[10] George Nerubenko. *Vibration Damper.* USSR Patent 1275169. 04.12.84.

[11] George Nerubenko, Greg Sidorenko. *Tuned Mass Damper.* USSR Patent 1469223. 30.03.1989.

[12] Francesco Cottone, Suresh Goyal, Jeff Punch. *Energy harvester apparatus having improved efficiency.* US Patent 8,350,394. January 8, 2013.

[13] Roy Freeland, Stephen Roberts. *Electromechanical generator for converting mechanical vibrational energy into electrical energy.* US Patent 7,999,402 Aug 16, 2011.

[14] Alexander Veprik, Vladimir Babitsky. *Ultra-light weight undamped tuned dynamic absorber for cryogenically cooled infrared electro-optic payload.* Elsevier. Cryogenics. Volume 83, April 2017, Pages 22–30.

[15] George Nerubenko. *Torsional Vibration Damper of a Rotating Shaft.* US Patent 7,464,800, Dec 16, 2008

[16] Jianjun Wang, Zhifei Shi, Hongjun Xiang, Gangbing Song. *Modeling on energy harvesting from a railway system using piezoelectric transducers. Smart Materials and Structures*, Volume 24, Number 10. September 2015

[17] Hongxin Sun, Yifan Luo, Xiuyong Wang, Lei Zuo. 2445. *Seismic control of a SDOF structure through electromagnetic resonant shunt tuned mass-damper-inerter and the exact H2 optimal solutions.* Journal of vibroengineering. May 2017, VOL. 19, ISSUE 3. ISSN 1392-8716. JVE INTERNATIONAL LTD. pp.2063 – 2079.

[18] Daqaq M. F. et al., *Investigation of Power Harvesting via Parametric Excitations*, Journal of Intelligent Material Systems and Structures, Mar. 1, 2009, pp. 545-557, vol. 20, No. 5,

[19] Zhou, Wanlu et al., *An Efficient Vibration Energy Harvester with a Multi-mode Dynamic Magnifier*, Smart Materials and Structures, 21 (2012) 015014, Dec. 20, 2011, 9 pages.

[20] Tang, Xiudong et al., *Enhanced Design of Vibration Energy Harvester Using Dual Masses*, *Proceedings of the ASME 2011 International Design Engineering Technical Conferences & Computers and Information in Engineering Conference*, IDETC/CIE, Aug. 28-31, 2011, 9 pages, Washington DC, USA.

[21] Qian Zhang, Eun Sok Kim. *Vibration Energy Harvesting Based on Magnet and Coil Arrays for Watt-Level Handheld Power Source.* Proceedings of the IEEE. Vol. 102, No. 11, November 2014 p. 1747-1761.

[22] Pratik Patel. *Development of Electromagnetic Micro-Energy Harvesting Device*. A thesis presented to the University of Waterloo. Waterloo, Ontario, Canada, 2013.

[23] Xiudong Tang, Lei Zuo. *Self-powered Active Control of Structures with TMDs*. Proceedings of the IMAC-XXVIII, February 1–4, 2010, Jacksonville, Florida USA, 12 p.

Analytical modeling of a cantilever beam type vibration energy harvester with a lever mechanism

S. Ertarla[1], C. V. Karadag[1], N. Topaloglu[1,2]
[1] Yeditepe University, Department of Mechanical Engineering
Atasehir 34755, Istanbul, Turkey
[2]e-mail: **nezih.topaloglu@yeditepe.edu.tr**

Abstract
Energy need have increased in time, hence there is an obvious trend in seeking non-traditional energy sources, such as ambient mechanical vibrations. This paper focuses on the energy harvesting efficiency of piezoelectric-based cantilever beam type vibration energy harvesters. The aim is to increase efficiency by homogenizing the axial stress along the beam. For this purpose, a counter mass is attached to the beam via a simple lever mechanism. This way, an inertial force is applied on the beam, having a direction opposite of the inertia force of the tip mass, thereby obtaining a loading close to pure moment. A detailed analytical model for this structure is constructed. The analytical model is used to assess the effect of two design parameters on efficiency. It is shown that efficiency increases by means of the proposed method. The future work includes finite element analysis and experimental verification.

1 Introduction

The interest in generating energy from vibrations has increased over the past years. Typical current and prospective applications of vibration energy harvesters (VEH) comprise wireless sensor networks, body sensor networks, implanted biomedical devices and portable electronics [1,2]. Three main transduction methods have been the focus of vibration energy harvesting research: electromagnetic [3], electrostatic [4] and piezoelectric [5]. The focus of this paper is a popular and promising harvester type: piezoelectric-based cantilever beam VEH.

There is a great effort on increasing the efficiency of piezoelectric-based cantilever beam VEHs. During vibration, voltage is generated on the piezoelectric layer at the surface of the beam, and this voltage is proportional to average axial stress on the beam surface [6]. In a typical cantilever beam with uniform width, the axial stress is maximum at the base of the cantilever beam and is close to zero at the beam tip [7]. This situation poses a serious limitation on the energy harvesting efficiency, due to the non-uniform stress distribution along the cantilever beam surface.

To improve the stress distribution in piezoelectric based beam VEHs, various solutions were offered. As an example, Kong et al produced micro-sized cantilever beams with piezoelectric thin films, at which the polarization of the piezoelectric layer is tilted from the out-of-plane direction [8]. Although this method increases the overall efficiency, it cannot be applied to batch fabricated piezoelectric patches. Introducing cavities into the beam cross-section also resulted in improved stress profile, but posed difficulty in fabrication [9,10].

Using a varying beam width profile to improve stress distribution was first proposed by Roundy et al [7]. It was suggested to use a tapered beam, i.e. a beam with linearly decreasing width profile from the base to the tip. However, no theoretical or experimental study was presented. Recently, it was shown via theory [14,15], finite element analysis [16] and experiments [15] that tapered beams exhibit higher efficiency compared to beams with uniform width.

Recently, Ma et al proposed an outer mechanism with compliant hinges to improve the cantilever beam stress distribution [11]. By affecting the dynamic load at the beam tip with the proposed mechanism, it was possible to obtain a more homogenous stress distribution on the beam surface. In another research, the response of a pre-stressed piezoelectric beam to vertical impact loads have been analyzed [12]. In a recent study, the stress distribution is homogenized by using a mechanical amplifier [13]. Both of these researches resulted in improved stress distribution, but the proposed devices are suitable to harvest energy only from impact type excitations.

In this study a force, in opposite direction of inertial force due to tip mass motion, is applied to the beam during oscillation. Thus, it is aimed to obtain approximately a pure moment as the net load acting on the beam. Because of this, a counter mass is used with a simple lever mechanism, connected to the beam with a hinge. The inertial force affecting the counter mass is applied to the beam by changing direction, with the help of the lever mechanism. In this paper, a comprehensive analytical model of the proposed approach is explained and the preliminary results are presented.

2 Working Principle

The main goal of the proposed method is to obtain a more uniform stress distribution on the cantilever beam during harmonic excitation. To achieve this goal, a counter mass is connected to the beam with a lever mechanism. The counter mass is located at the left end of the lever beam, and the other end of the lever beam is pin connected to a rigid link, which is pin-connected to the beam. The lever is also connected to the support with an L-shaped frame. A simple schematic of the mechanism is shown in Figure1(a).

During oscillation, the inertia forces exerted by the tip mass and the counter mass will have the same direction (see Figure1(b)). Due to the lever mechanism, the counter mass inertia force on the beam will have a direction opposite to the inertia force of the tip mass. This way, these two forces acting on the cantilever beam will have a moment effect, which in turn will result in a more uniform stress distribution on the beam.

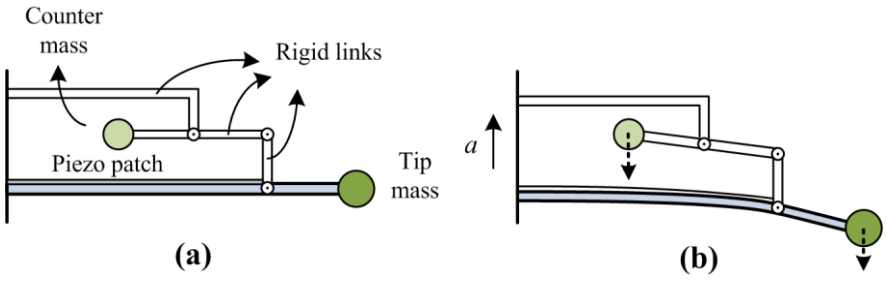


Figure 1: Schematic of the proposed structure when there is no oscillation (a), when there is oscillation (b).

To assess the effect of geometrical parameters on the stress uniformity and demonstrate the improvement on stress uniformity with the proposed mechanism, a mathematical model is constructed, which is presented next.

3 Mathematical modeling

An extensive model of the proposed design is given in this section. The model includes the lever mechanism model, modal analysis of the beam and finally the harmonic response analysis based on modal expansion method.

Some assumptions are used to facilitate the modeling process; which are listed below:

- The piezoelectric beam is modeled using the Euler-Bernoulli beam theory, so the length to thickness ratio of the beam is assumed to be large. In addition, it is assumed that the beam consists of a single homogenous material. The effect of piezoelectric layer on beam response is neglected.
- The links that form the mechanism are assumed to be rigid and massless. All the joints that form the mechanism are assumed to be frictionless hinges. The tip mass and the counter mass are assumed to be point masses.
- The beam is rectangular, therefore it is assumed that the stress on the beam does not vary in the z (i.e. width) direction.
- The damping on the beam is assumed to be viscous and to depend on the beam deflection rate with respect to the beam base. The damping effects on the lever mechanism are neglected.
- The rigid link which connects the lever to the beam is assumed to remain vertical during oscillation. As a result of this assumption, the force transmitted to the beam by this link will be in the transverse direction.
- The beam possesses small deformations, and the angle of rotation of the lever is assumed to be small.
- The stress induced on the beam in the static case is neglected.

3.1 Modeling of the lever mechanism

The static analysis is skipped based on the assumption that the stresses induced on the beam when there is no vibration is negligible. Figure 2(a) shows the lever and the beam on the same schematic at an arbitrary time during oscillation. The angle of rotation of the lever is given as $\beta(t)$, measured positive counter clockwise. The lengths of the left and right portion of the lever are L_1 and L_2, respectively. The counter mass is denoted as m_c.

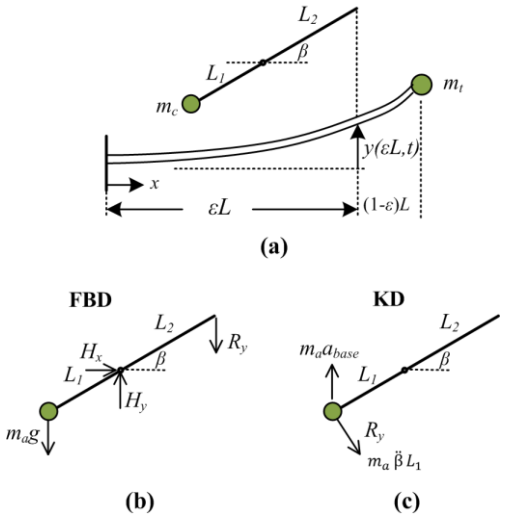


Figure 2: The design parameters of the lever and the beam (a); the free-body diagram (b) and the kinetic diagram (c) of the lever.

A vertical link connects the right end of the lever to the beam, at the location $x = \varepsilon L$. The deflection of the beam as a function of spatial coordinate and time is $y(x,t)$, and thus the deflection at $x = \varepsilon L$ will be $y(\varepsilon L, t)$. From geometry, and by using small angle assumption for the lever angle, the relation between the lever angle and the beam deflection is given as

$$\beta(t) = y(\varepsilon L, t)/L_2 \tag{1}$$

The free-body diagram and the kinetic diagram of the lever are given in figures 2(b) and 2(c). The acceleration due to support motion is given as a_{base}. If the base excitation is harmonic, i.e. $y_b(t) = Y_0 \cos \omega t$, then

$$a_{base}(t) = -Y_0 \omega^2 \cos \omega t \tag{2}$$

where Y_0 and ω are amplitude and the frequency of harmonic base excitation, respectively. The equation of motion by summing moments about the lever support gives

$$\left(R_y L_2 - m_c g L_1\right) \cos \beta(t) = m_c(-Y_0 \omega^2 \cos \omega t) L_1 \cos \beta - m_a \ddot{\beta}(t) L_1^2 \tag{3}$$

Using the small angle approximation $\cos \beta(t) \approx 1$ and using equation (1) for equation (3) will give the following expression for $R_y(t)$:

$$R_y(t) = \frac{L_1}{L_2} m_c \left(g - Y_0 \omega^2 \cos \omega t - \ddot{y}(\varepsilon L, t) \frac{L_1}{L_2}\right) \tag{4}$$

Equation (4) is a summation of three terms. The first term is the static term due to gravity, and its effect on the beam is neglected. The second term is the desired harmonic force due to the oscillation of the counter mass. The third term is the inertia force due to the accelerated rotation of the counter mass. The application of $R_y(t)$ on the beam and derivation of the beam deflection function is provided in the next sections.

3.2 Modeling of the cantilever beam

The transverse vibration of a cantilever beam with harmonic base excitation is an extensively analyzed problem in mechanical vibrations. However, application of the force $R_y(t)$, given by equation (4), on the beam requires attention. The first term of $R_y(t)$ is neglected, so only the second and third term should be applied to the beam. However, third term, $-m_c \ddot{y}(\varepsilon L, t)(L_1/L_2)^2$ includes an unknown function $\ddot{y}(\varepsilon L, t)$. Applying a force with this unknown term complicates the solution for the beam deflection function, $y(x,t)$. Since $\ddot{y}(\varepsilon L, t)$ equals the acceleration of the beam at the location $x = \varepsilon L$, it is possible to represent the third term as a virtual point mass, located at $x = \varepsilon L$. As seen in figure 3, this virtual mass is shown with m_v. To accurately model the third term in $R_y(t)$, the following equation should be set

$$m_v = m_c(L_1/L_2)^2 \tag{5}$$

Excluding the first and third term from $R_y(t)$, the force that is applied to the cantilever beam, denoted as *f(t)*, can be expressed as

$$f(t) = -\frac{L_1}{L_2} m_c Y_0 \omega^2 \cos \omega t \tag{6}$$

The solution for deflection function for the problem shown in figure 3 involves two steps. In the first step, the external force is omitted and a modal analysis is performed for the undamped beam. After solving for the natural frequencies and the mode shapes, harmonic response is solved for the forced and damped beam, using mode superposition method.

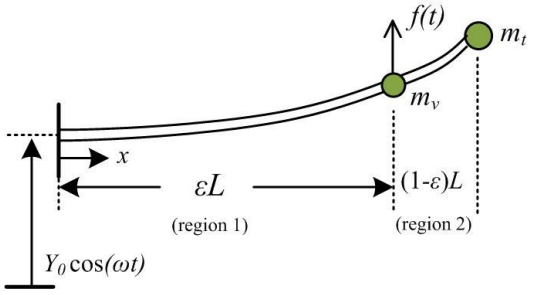


Figure 3: The flexible beam with virtual intermediate mass m_v, with base excitation.

3.3 Modal analysis

To perform the modal analysis of the cantilever beam with a tip mass and an intermediate mass, the beam length is divided into two regions with deflection functions defined as $y_1(x,t)$ and $y_2(x,t)$. These regions are shown in figure 3. Using the Euler-Bernoulli theory, the dynamic equation for the pure transverse oscillation of the unforced and undamped beam can be written as

$$EIy_i^{IV}(x,t) + \rho A\ddot{y}_i(x,t) = 0 \tag{7}$$

for *i = 1, 2*. In this equation, *E*, *I*, ρ and *A* are the Young's modulus, area moment of inertia for transverse bending, density and section area, respectively. The boundary conditions for the left and right end can be expressed as

$$y_1(0,t) = 0 \tag{8}$$

$$y_1'(0,t) = 0 \tag{9}$$

$$EIy''(L,t) = 0 \tag{10}$$

$$EIy'''(L,t) = m_t\ddot{y}(L,t) \tag{11}$$

For the location $x = \varepsilon L$, the contiunity equations are given below

$$y_1(\varepsilon L,t) = y_2(\varepsilon L,t) \tag{12}$$

$$y_1'(\varepsilon L,t) = y_2'(\varepsilon L,t) \tag{13}$$

$$y_1''(\varepsilon L,t) = y_2''(\varepsilon L,t) \tag{14}$$

$$EIy_1'''(\varepsilon L,t) - m_v\ddot{y}_1(\varepsilon L,t) - EIy_2'''(\varepsilon L,t) = 0 \tag{15}$$

The last continuity equation includes the change in internal shear due to the inertia force of the intermediate mass.

For both regions, modal expansion is applied and the deflection function is written as the infinite summation of temporal and spatial terms:

$$y_i(x,t) = \sum_{r=1}^{\infty} \emptyset_{ir}(x)T_{ir}(t) \tag{16}$$

Here, $\emptyset_{ir}(x)$ and $T_{ir}(t)$ are the mode shape function and the temporal term for mode *r* of region *i*, respectively. Using equation (16) in equation (7), the dynamic equation becomes

$$c^2\emptyset_i^{IV}(x)T_i(t) + \emptyset_i(x)\ddot{T}_i(t) = 0 \tag{17}$$

where $c^2 = EI/\rho A$. Arranging equation (17) gives

$$c^2\frac{\emptyset_i^{IV}(x)}{\emptyset_i(x)} = -\frac{\ddot{T}_i(t)}{T_i(t)} = \omega_i^2 \tag{18}$$

which yields two differential equations

$$\emptyset_i^{IV}(x) - \beta_i^4\emptyset_i(x) = 0 \tag{19}$$

$$\ddot{T}_i(t) + \omega_i^2 T_i(t) = 0 \tag{20}$$

with $\beta_i = \sqrt{\omega_i/c}$.

The general solution for the mode shape functions is expressed as

$$\emptyset_{1i}(x) = c_{1i}sin(\beta_{1i}x) + c_{2i}cos(\beta_{1i}x) + c_{3i}sinh(\beta_{1i}x) + c_{4i}cosh(\beta_{1i}x) \tag{21}$$

$$\emptyset_{2i}(x) = c_{5i}sin(\beta_{2i}x) + c_{6i}cos(\beta_{2i}x) + c_{7i}sinh(\beta_{2i}x) + c_{8i}cosh(\beta_{2i}x) \tag{22}$$

where the terms c_{1i} to c_{8i} are the coefficients for mode *i*. Applying the boundary conditions (8-11) and the continuity equations (12-15) results in

$$\beta_{1i} = \beta_{2i} = \beta_i \tag{23}$$

$$\omega_{1i} = \omega_{2i} = \omega_i \tag{24}$$

Hence, the mode shape functions (equations (21-22)) can be rewritten as

$$\emptyset_{1i}(x) = c_{1i}sin(\beta_i x) + c_{2i}cos(\beta_i x) + c_{3i}sinh(\beta_i x) + c_{4i}cosh(\beta_i x) \tag{25}$$

$$\emptyset_{2i}(x) = c_{5i}sin(\beta_i x) + c_{6i}cos(\beta_i x) + c_{7i}sinh(\beta_i x) + c_{8i}cosh(\beta_i x) \tag{26}$$

Equations (25-26) lead to the eigenvalue problem, where the eigenvalues are the β_is and the eigenvectors are the related mode shape functions. Finding the eigenvalues and eigenvectors by using the boundary conditions and continuity equations completes the modal analysis part.

3.4 Harmonic Response Analysis

The modal analysis results will be used to determine the response to harmonic base excitation. As seen in Fig.3, the beam is subjected to harmonic base excitation, and as a result of the lever mechanism, a force *f(t)* is applied at $x = \varepsilon L$. Since the third term of the force $R_y(t)$ derived in equation (4) is already modeled as a virtual mass (equation (5)) and the static effects (i.e. the gravity term in equation (4)) are neglected; the force *f(t)* will only include the inertia due to harmonic base excitation on the counter mass:

$$f(t) = -\frac{L_1}{L_2}m_c Y_0\omega^2\, cos\,\omega t \tag{27}$$

The dynamic equation for the whole beam can be expressed as

$$EIy^{IV}(x,t) + \rho A\ddot{y}_t(x,t) + \gamma\dot{y}(x,t) = F(x,t) \tag{28}$$

where

$$y_t(t) = y(t) + Y_0 cos(\omega t) \tag{29}$$

$$F(x,t) = f(t)\delta(x - \varepsilon L) \tag{30}$$

Arranging equation (28) we reach

$$EIy^{IV}(x,t) + \rho A\ddot{y}(x,t) + \gamma\dot{y}(x,t) = f(t)\delta(x - \varepsilon L) + \bar{Y}cos(\omega t) \tag{31}$$

where

$$\overline{Y} = \rho A Y_0 \omega^2 \tag{32}$$

Applying modal expansion theorem to the deflection function, we reach

$$\begin{aligned} EI\sum_{r=1}^{\infty} \emptyset_r^{IV}(x)T_r(t) + \rho A\sum_{r=1}^{\infty} \emptyset_r(x)\ddot{T}_r(t) + \gamma\sum_{r=1}^{\infty} \emptyset_r(x)\dot{T}_r(t) \\ = \bar{Y}\,cos\,\omega t + f(t)\,\delta(x - \varepsilon L) \end{aligned} \tag{33}$$

The mode shape function $\emptyset_r(x)$, defined for the whole beam, can be expressed as a combination of mode shape functions defined for each region (equations (25-26)), using the Heaviside step function:

$$\emptyset_r(x) = \emptyset_{1r}(x)\big(u(x) - u(x - \varepsilon L)\big) + \emptyset_{2r}(x)u(x - \varepsilon L) \tag{34}$$

To solve equation (33), each term is multiplied by the mode shape $\emptyset_s(x)$ and integrated over the beam length. The function arguments shown in parentheses are omitted for clarity.

$$\begin{aligned} EI\sum_{r=1}^{\infty} T_r\int_0^L \emptyset_r^{IV}\emptyset_s dx + \rho A\sum_{r=1}^{\infty} \ddot{T}_r\int_0^L \emptyset_r\emptyset_s dx + \gamma\sum_{r=1}^{\infty} \dot{T}_r\int_0^L \emptyset_r\emptyset_s dx \\ = \int_0^L \overline{Y}\,\emptyset_s\,cos(\omega t)dx + f(t)\int_0^L \emptyset_s\delta(x - \varepsilon L)dx \end{aligned} \tag{35}$$

Since the mode shapes are orthogonal, the integrals on the right-hand side of equation (35) will be non-zero only when $r = s$. Therefore, equation (35) simplifies as

$$\left[EIT_s(t){\beta_s}^4 + \gamma\dot{T}_s(t) + \rho A\ddot{T}_s(t)\right]\Psi = \overline{Y}cos(\omega t)\,\Gamma + f(t)\emptyset_s(\varepsilon L) \tag{36}$$

where

$$\Psi = \int_0^L \emptyset_s^2(x)dx \tag{37}$$

$$\Gamma = \int_0^L \emptyset_s(x)dx \tag{38}$$

Substituting equation (27) in equation (36) results in

$$\omega_s^2 T_s(t) + \frac{\gamma}{\rho A}\dot{T}_s(t) + \ddot{T}_s(t) = \frac{cos(\omega t)}{\Psi}\left[\overline{Y}\Gamma - \frac{L_1}{L_2}\emptyset_s(\varepsilon L)m_c Y_0\omega^2\right] \tag{39}$$

The steady-state temporal solution to the above differential equation is [19]

$$T_s(t) = \frac{\overline{Y}\Gamma - \frac{L_1}{L_2}\emptyset_s(\varepsilon L)m_c Y_0\omega^2}{\Psi\sqrt{({\omega_s}^2 - \omega^2)^2 + (2\zeta_s\omega_s\omega)^2}}cos\left(\omega t - tan^{-1}\frac{2\zeta_s\omega_s\omega}{{\omega_s}^2 - \omega^2}\right) \tag{40}$$

where

$$\zeta_s = \gamma/(2\rho A\omega_s\omega) \tag{41}$$

Finally, the temporal function $T_s(t)$ and the mode shape function $\phi_s(x)$ are multiplied and infinite summation is performed, to obtain the deflection function.

$$y(x,t) = \sum_{s=1}^{\infty} \emptyset_s(x) T_s(t) = \sum_{s=1}^{\infty} Y_s(x)\, cos\left(\omega t - tan^{-1}\frac{2\zeta_s \omega_s \omega}{{\omega_s}^2 - \omega^2}\right) \tag{42}$$

where

$$Y_s(x) = \emptyset_s(x)\frac{\overline{Y}\Gamma - \frac{L_1}{L_2}\emptyset_s(\varepsilon L) m_c Y_0 \omega^2}{\Psi\sqrt{({\omega_s}^2 - \omega^2)^2 + (2\zeta_s\omega_s\omega)^2}} \tag{43}$$

The expression of $\emptyset_s(x)$ in equation (43) is already given in equation (34). If it is assumed that the phase ($\tan^{-1}\frac{2\zeta_s\omega_s\omega}{{\omega_s}^2-\omega^2}$) is negligible, then the deflection function can be simplified as follows

$$y(x,t) = Y(x)\, cos(\omega t) \tag{44}$$

where

$$Y(x) = \sum_{s=1}^{\infty} Y_s(x) \tag{45}$$

Deriving the deflection function $y(x,t)$ completes the mathematical modelling.

4 Results and Discussion

There are various geometrical parameters and material properties that are expected to affect the stress uniformity on the beam. Assuming that the piezoelectric patch spans the top surface of the beam within the range $(0, \varepsilon L)$, the uniformity parameter, denoted by η, is calculated as follows

$$\eta = \frac{\int_0^{\varepsilon L} Y(x)'' dx}{\max(Y(x)'')} \tag{46}$$

The second derivative of deflection with respect to *x* is proportional to stress, according to the Euler-Bernoulli beam theory. The numerator of equation (46) represents the area-averaged surface axial stress of the beam. Dividing this value to the maximum value of stress, the uniformity is found.

In this study, the effect of two non-dimensional parameters on fundamental frequency and uniformity are analyzed and preliminary results are presented. These parameters are the non-dimensional counter mass, defined as the counter mass to tip mass ratio (m_c/m_t), and the leverage ratio L_1/L_2. The non-dimensional counter mass is varied from 0 to 2, with increments of 0.5, and the leverage ratio is varied from 0 to 1, with increments of 0.25. The other geometrical parameters and material properties are provided in table 1. The modal summation is performed by using the first five modes and the damping ratio is taken as 0.01 for all modes.

Parameter	Value	Unit
Beam length	100	mm
Beam width	10	mm
Beam thickness	2	mm
$\boldsymbol{\varepsilon}$	0.8	-
Tip mass	0.01	kg
Young's modulus	69	GPa
Density	2700	kg/m^3
$\boldsymbol{\zeta_s}$	0.01	-

Table 1: Parameters used in the simulation

The effect of non-dimensional counter mass and leverage ratio on the fundamental natural frequency is analyzed first. The analysis is performed by plotting the tip deflection as a function of frequency, as seen in figure 4. The frequency response when there is no lever mechanism is also included in the plots for comparison. Each frequency response is divided to its maximum for normalization. As seen from the plots, increasing the counter mass, as well as the leverage ratio results in a decrease in the fundamental natural frequency. The results are expected, since increasing these parameters results in a higher effective inertia.

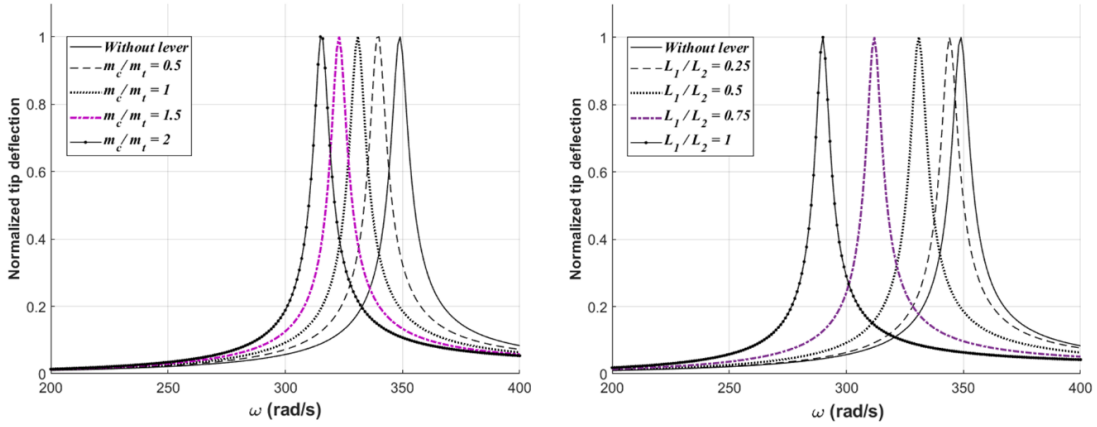


Figure 4: The normalized tip deflection as a function of excitation frequency. m_c/m_t is varied when $L_1/L_2 = 0.5$ (a); L_1/L_2 is varied when $m_c/m_t = 1$ (b).

To assess the effect of m_c/m_t and L_1/L_2 on uniformity, the mean uniformity within the excitation frequency range 200-400 rad/s is computed, and tabulated in table 2 for different m_c/m_t and L_1/L_2 values. The standard deviation of uniformity within the same range is also given.

$\boldsymbol{m_c/m_t}$	$\boldsymbol{L_1/L_2}$	mean($\boldsymbol{\eta}$)	stdev($\boldsymbol{\eta}$)	$\boldsymbol{m_c/m_t}$	$\boldsymbol{L_1/L_2}$	mean($\boldsymbol{\eta}$)	stdev($\boldsymbol{\eta}$)
0.5	0.25	0.5748	0.0074	1.5	0.25	0.5981	0.0087
0.5	0.50	0.5420	0.0239	1.5	0.50	0.5732	0.0008
0.5	0.75	0.5925	0.0089	1.5	0.75	0.5582	0.0027
0.5	1	0.5737	0.0015	1.5	1	0.5445	0.0050
1	0.25	0.5467	0.0231	2	0.25	0.5864	0.0021
1	0.50	0.5819	0.0019	2	0.50	0.5678	0.0018
1	0.75	0.5673	0.0011	2	0.75	0.5513	0.0040
1	1	0.5551	0.0029	2	1	0.5367	0.0066
0	-	**0.58**	**0.0051**				

Table 2: Mean and standard deviation of uniformity within 200-400 rad/s excitation frequency range. The results when there is no lever mechanism are shown in bold.

The last row of the table shows that the mean uniformity when there is no lever mechanism ($m_c/m_t = 0$) equals 0.58. Mean uniformity values greater than this value are highlighted with gray color. The results clearly show that it is possible to obtain higher stress uniformity on the beam with the proposed lever mechanism. It is also advantageous to have low variation of uniformity within the given frequency range. The combination $m_c/m_t = 2, L_1/L_2 = 0.25$ has a mean uniformity of 0.5864 and a low standard deviation of 0.0021. Both of these values are improved, compared to the case without lever mechanism. It can be inferred that the once the design parameters are correctly tuned, the proposed mechanism exhibits higher efficiency in a wide frequency range, compared to a conventional piezoelectric beam energy harvester.

The results given in table 2 reveals that the effect of non-dimensional counter mass and leverage ratio on performance is complex, and requires further investigation. These parameters influence the virtual mass m_v and the external harmonic force *f(t)*, which in turn affect the natural frequencies, mode shapes as well as harmonic response. This preliminary study demonstrates the possible benefits of the lever mechanism.

5 Conclusion

In this paper, the analytical model of a cantilever beam type vibration energy harvester with a lever mechanism and a counter mass has been proposed. The objective is to increase energy conversion efficiency by obtaining a more uniform stress distribution within the piezoelectric cantilever beam. A comprehensive analytical model is constructed using the Euler-Bernoulli beam theory. The effect of counter mass and leverage ratio on stress uniformity within the excitation frequency range 200-400 rad/s are analyzed. It is shown that by tailoring the non-dimensional counter mass and leverage ratio values, stress uniformity can be improved, compared to a conventional cantilever beam energy harvester. As for future work, a thorough optimization on stress uniformity will be performed and the analytical model will be verified with finite element analysis and experimental study.

Acknowledgements

This research has been funded by TUBITAK (The Scientific and Technological Research Council of Turkey) under Grant No. 117M101.

References

[1] F.K. Shaikh, S. Zeadally, *Energy harvesting in wireless sensor networks: A comprehensive review, Renew Sustain Energy Reviews,* Vol.55, (2016), pp. 1041-1054..

[2] T.Starner, *Human-powered wearable computing*, Vol. 35, No. 3.4, IBM Systems Journal (1996), pp. 618-629.

[3] L. Xie, R. Du, *Frequency Tuning of a Nonlinear Electromagnetic Energy Harvester,* Journal of Vibration and Acoustics, Vol. 136, No. 1, 2013, pp. 011010-011010-7.

[4] Y. Naruse, N. Matsubara, K. Mabuchi, M. Izumi, K.Honma, Electrostatic Micro Power Generator from Low Frequency Vibration such as Human Motion, 2008, pp. 19-22.

[5] Xu Wang, L. Lin, *Dimensionless optimization of piezoelectric vibration energy harvesters with different interface circuit,* Smart Materials and Structures, Vol. 22, No. 8, 2013, pp. 85011-20

[6] A. Wickenheiser, *Analysis of Energy Harvesting Using Frequency Up-Conversion by Analytic Approximations In: Small-Scale Energy Harvesting*, 2012.

[7] S. Roundy, E.S. Leland, J. Baker, et al., *Improving power output for vibration-based energy scavengers*, IEEE Pervasive Computing, Vol. 4, No. 1, 2005.

[8] L. Kong, J. Zhang, H. Wang, et al., *Simulation study of MEMS piezoelectric vibration energy harvester based on c-axis tilted AlN thin film for performance improvement,* AIP Advances Vol. 6, No.12, 2016.

[9] A.R. Reddy, M. Umapathy, D. Ezhilarasi, G. Uma, *Cantilever beam with trapezoidal cavity for improved energy harvesting,* International Journal of Precision Engineering and Manufacturing, Vol. 16, No. 8, 2015, pp. 1875-1881.

[10] S.S. Raju, M. Umapathy, G. Uma , *Cantilever piezoelectric energy harvester with multiple cavities. Smart Mater Struct,* Vol. 24, No. 11, 2015, pp. 115023.

[11] X. Ma, A. Wilson, C.D. Rahn, S. Trolier-McKinstry, *Efficient Energy Harvesting Using Piezoelectric Compliant Mechanisms: Theory and Experiment*, Journal of Vibration and Acoustics, Vol. 138, No. 2, 2016, pp. 21005.

[12] H.S. Yoon , *Modeling, Optimization, and Design of Efficient Initially Curved Piezoceramic Unimorphs for Energy Harvesting Applications*, Journal of Intelligent Material Systems and Structures, Vol. 16, No. 10, 2015, pp. 877-888.

[13] X. Xie, C. Livermore, *A high-force, out-of-plane actuator with a MEMS-enabled microscissor motion amplifier*, Journal of Physics, Conference Series, 2015, pp. 660-12026.

[14] E. Halvorsen, T. Dong, *Analysis of Tapered Beam Piezoelectric Energy Harvesters,* Proceedings of PowerMEMS(June 2017), pp. 241-244.

[15] M. Rosa, C. De Marqui Junior, *Modeling and analysis of a piezoelectric energy harvester with varying cross-sectional area,* Shock and Vibration, 2014.

[16] X. Xiong, S. Olutunde Oyadiji, *Tapered Two-Layer Broadband Vibration Energy Harvesters,* Journal of Vibration and Acoustics, Vol. 137, No. 3, 2015, pp. 31011-31014.

[17] L. Meirovitch, *Fundamentals of Vibrations*, McGraw-Hill (2001).

[18] A. Erturk, D. J. Inman, On *Mechanical Modeling of Cantilevered Piezoelectric Vibration Energy Harvesters,* Journal of Intelligent Material Systems and Structures, Vol. 19, No. 11, 2015, pp. 1311-1325.

[19] D. J. Inman, *Engineering Vibration*, Englewood Cliffs, N.J. Prentice Hall (1994).

Energy in random vibration – reduce, resist, recycle

A. Wasenczuk[1], I. Corni[2], N. Symonds[2]
[1] Perpetuum Ltd.
Abbey Park Industrial Estate, Romsey, SO51 9DT, UK
e-mail: **adam.wasenczuk@perpetuum.com**

[2] University of Southampton, nC² Engineering Consultancy
Wolfson Building, SO17 1BJ, UK

Abstract
Random vibration of a structure dissipates energy at a rate proportional to the Power Spectral Density of the vibration and the mass of the structure. This energy must be directed away from damaging processes, especially fatigue, into non-damaging damping mechanisms. A portion of the available energy can be extracted as useful work, for example to power a condition monitoring system. Perpetuum manufacture just such a system. The issues raised by this approach are the extraction of the highest proportion of the available energy, and the overall durability of the system in its environment. This paper reports efficiency measurements of an energy harvesting condition monitoring system applied to a rail vehicle, along with a design rule and figures of merit for operation in harsh environments.

1 Introduction

It is often necessary to operate equipment under severe mechanical vibration. For example, the wheel-rail interface of a rail vehicle is a high-speed, high-load, metal-to-metal contact, exposed to the elements without intentional surface coating or lubrication. Surface degradation in service is almost certain. It may be desirable to mount equipment near the wheel, axle, or axle-bearing, for purposes of condition monitoring (CM) [1]. This region is below the vehicle suspension and the structure has low compliance. Any surface imperfections in the rail, wheel or bearing can be expected to give rise to large forces and accelerations. By implication, however, small or even subsurface defects may be perceptible.

An *energy harvester* is essentially a tuned mass damper in which energy is extracted as electrical current which can perform useful work. Perpetuum have commercialised a complete wireless CM system powered by electromagnetic energy harvesting, which avoids technical issues associated with access, connection, or battery changes in environments where these are unwelcome – for example, retrofit to the underside of a train bogie. However, new issues are raised by this approach:

- What power can be extracted from the vibration environment?
- How might such a system be made most resistant to the environmental vibration?

1.1 Wheel-rail interface

Forces at the wheel-rail interface can be expected to vary as the vehicle travels along the rails. That is, the force will have a substantially ‘random’ character, as opposed to any repeating waveform, and this means

that there will be components of the vibration across a continuous range of frequencies. This range of frequencies will almost certainly excite resonances in the structure.

Random vibration is described as a function of frequency by a measure known as Power Spectral Density (PSD). It is known that the energy dissipated by random vibration in a structure with a resonant frequency f depends only on the modal mass and the PSD at f [2]. This energy must be dissipated *somewhere*, and it is this that drives the use of tuned mass dampers where resonances cannot otherwise be avoided. The vibrational energy must be diverted away from the damaging processes of fretting and fatigue.

The aims of this work are to address two issues arising from the use of an electromagnetic mass damper in this way:

- *Efficiency* – what is the greatest proportion of the available power that can be extracted from a given PSD?
- *Durability* – could the power extraction be designed so as to optimise the mechanical durability of the system?

Brennan *et al.* [3] have shown that, for random vibration, an optimised energy harvester can act as an optimised mass damper.

2 Background to vibration energy

The calculation of resonant response to random vibration is commonly credited to Miles [4]. Crandall's text [5] is more direct: the mean squared displacement $\overline{y^2}$ is given by equation (1),

$$\overline{y^2} = \frac{\pi}{2}\frac{S_0}{\zeta\omega_n^3} \tag{1}$$

Here ω_n is the resonant frequency in radians per second and the value ζ represents the damping in the structure, otherwise expressed by the *Q*-factor, equation (2):

$$Q = 1/2\zeta \tag{2}$$

Vibration is an acceleration signal, and S_0 is the Power Spectral Density (PSD) of the vibration at frequency ω_n, in $(m/s^2)^2$ per radian per second. Importantly, S_0 is defined at both positive and negative frequencies. We would rather concern ourselves with a more intuitive definition of PSD, A, such that frequency f is in Hertz, there are no negative frequencies, and $A(f)\cdot df$ simply 'represents the contribution to the *variance* from frequencies between f and $(f + df)$' [6]. In other words,

$$A = 4\pi S_0 \tag{3}$$

We note that the mean squared velocity $\overline{v^2}$ of the resonant response is given by equation (4):

$$\overline{v^2} = \omega_n^2\overline{y^2} \tag{4}$$

Substituting (2-4) into (1),

$$\overline{v^2} = \frac{AQ}{4\omega_n} \tag{5}$$

Now consider the moving (modal) mass in the resonance, m. Clearly the average energy $\bar{E}$ (elastic + kinetic) stored in the resonant motion is given by equation (7):

$$\bar{E} = m\overline{v^2} \tag{6}$$

Substituting into (5),

$$\bar{E} = \frac{mAQ}{4\omega_n} \tag{7}$$

The *Q*-factor is defined so that the average power $\bar{P}$ dissipated in the system is given by equation (8):

$$\bar{P} = \frac{\omega_n\bar{E}}{Q} \tag{8}$$

By substitution again, $$\bar{P} = \frac{mA}{4} \tag{9}$$

This means that the power dissipated in a system by random vibration depends only on the modal mass m and the PSD A at the resonant frequency. This is a remarkable result, not least for its recent 'rediscovery' in the fields of energy harvesting [2] and automotive suspensions [7]. Recent authors [8-11] have shown that equation (9) holds for all nonlinear resonators, though this might be suspected from dimensional analysis. The only exception would seem to be a potential increase in effective m caused by rotational motion in the system [12].

For a designer, equation (7) is pertinent. It implies that a structure must store elastic energy which depends only on mass, PSD, and the value of Q/ω_n. The presence of ω_n here must not be taken too seriously: Q/ω_n should rather be interpreted as the characteristic decay time t of the system. Alternatively, for viscous damping c (force proportional to velocity) acting on a mass m,

$$\frac{m}{c} = \frac{Q}{\omega_n} = t \tag{10}$$

In other words, the only way to control the total stored elastic energy in a structure of a given mass exposed to random vibration is to manage the *damping* in the structure. Finite element analysis can help *distribute* the energy beneficially, but it cannot easily comment on structural damping.

3 Durability of an energy harvester

Following Williams [13] (though similar illustrations can be found at least as far back as 1954 [14-15]), an electromagnetic energy harvester is completely described by the equivalent circuit of Figure 1, where a is mounting-point acceleration, v is response velocity, and V is the EMF (electromotive force) induced in the coil:

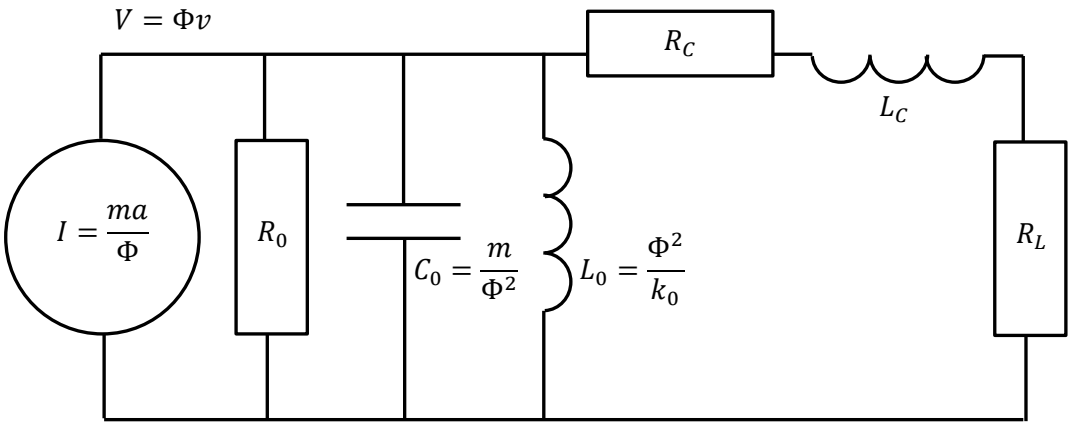


Figure 1 – Harvester equivalent circuit after Williams [13]

We omit the coil self-capacitance, which is negligible at the frequencies of interest. The system is then described by the parameters listed in Table 1. Note subscripts '*C*' for coil parameters and '0' for mechanical parameters. Similar presentations exist in the literature, e.g. [11-12, 16].

Parameter	Symbol	Unit
Coil resistance	R_C	Ω
Coil inductance	L_C	Ω
Load resistance	R_L	Ω
Moving mass	m	kg
Spring stiffness	k_0	$N \cdot m^{-1}$
Magnetic coupling	Φ	$N \cdot A^{-1}$, $V \cdot s \cdot m^{-1}$
Mechanical damping, represented by an internal shunt resistor	R_0	Ω

Table 1 – Parameters of an electromagnetic energy harvester

For random vibration, there are three dissipative elements, R_C, R_0 and R_L, and the total average power dissipated in these elements is fixed by the mass m and the PSD a, equation (9). The system therefore reduces to Figure 2:

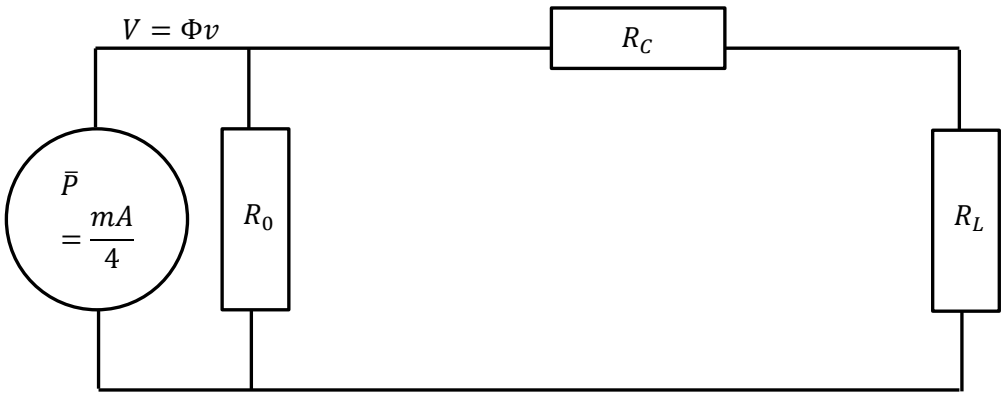


Figure 2 – Simplified equivalent circuit at resonance

3.1 Design for durability

A system is most resistant to applied vibration when the energy $\bar{E}$ stored in the resonance is minimised. Equation (7) indicates that this occurs for a harvester when the damping is maximised. Therefore, the harvester is most durable when $R_L = 0$. Unfortunately this results in zero power delivery to the load! A better question is therefore this:

What load resistance maximises load power P_L for a given stored energy $\bar{E}$?

At resonance, C_0 and L_0 cancel, and we assume that L_C is small (for inductive corrections, see [17-18]).

The voltage V dissipates fixed power $\bar{P}$ in a total resistance R_T given by equation (11):

$$R_T = \frac{(R_L + R_C)R_0}{R_0 + R_L + R_C} \tag{11}$$

From (8) and (10) we have

$$\bar{P} = \frac{c\bar{E}}{m} \tag{12}$$

and we know from first principles $$\bar{P} = c\overline{v^2} = \frac{\overline{V^2}}{R_T} = \frac{\overline{v^2}\Phi^2}{R_T} \tag{13}$$

Now from (13) we can see $$c = \frac{\Phi^2}{R_T} \tag{14}$$

so combine (12) and (14) to get $$\bar{P} = \frac{\Phi^2 \bar{E}}{R_T m} \tag{15}$$

We are interested in the power in the load $\overline{P_L}$, and it's fairly easy to show that

$$\frac{\overline{P_L}}{\bar{P}} = \frac{R_0 R_L}{(R_0 + R_L + R_C)(R_L + R_C)} \tag{16}$$

Multiplying (15) and (16), $$\overline{P_L} = \frac{\Phi^2 \bar{E}}{m} \cdot \frac{R_L}{(R_L + R_C)^2} \tag{17}$$

For fixed $\bar{E}$, m, R_C and Φ, this is maximised for $R_L = R_C$, at which point,

$$\overline{P_L} = \frac{\Phi^2 \bar{E}}{4 R_C m} \tag{18}$$

In equation (18) we can clearly see that a *figure of merit* for the energy harvester is given by $\Phi^2/R_C m$, or in other words the electrical damping at short-circuit divided by the mass. This figure of merit has units of s^{-1}, and can be physically interpreted as the reciprocal of the characteristic decay time of oscillations due to electromagnetic damping.

For a given energy stored in the spring, an energy harvester with a higher figure of merit will produce more power. Note that this figure of merit is somewhat different to those derived by other authors, [16-17]; this will be discussed later.

3.2 Measuring durability figure of merit

To measure the figure of merit $\Phi^2/R_C m$ which characterises the durability of an energy harvester, we must measure the coil resistance R_C and the electromagnetic coupling Φ. A Perpetuum harvester with moving mass m = 0.6kg was obtained for this purpose.

The mechanical motion of the harvester was temporarily suppressed, so that the coil resistance R_C = 26Ω and inductance L_C = 22mH could measured with a standard impedance meter. Then the harvester was mounted axially on a small permanent-magnet shaker (DataPhysics V55) to measure the magnetic coupling Φ.

Measurements of the magnetic coupling Φ were performed with a sine wave excitation a at the resonant frequency, with the coil inductance L_C cancelled at this frequency by a suitable series capacitor. The fixed-power source of Figure 2 is therefore replaced with the current source of Figure 1, resulting in Figure 3:

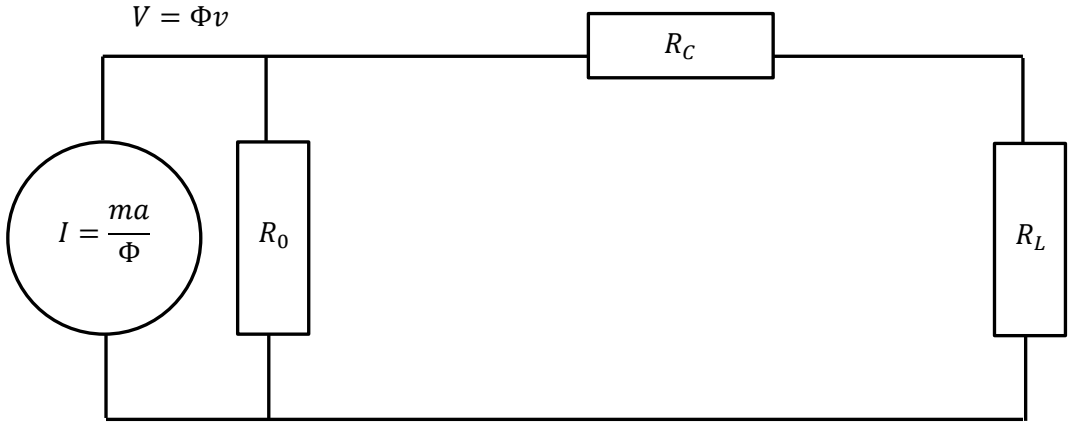


Figure 3 – Harvester being driven at resonance with appropriate series capacitor

The procedure is to start with large R_L and small a, so that the output is most sensitive to frequency, and to find the resonant frequency for a particular amplitude of motion (indicated by V). Note that:

- the measured load voltage is always less than V by a factor $R_L/(R_C + R_L)$.
- nonlinearities in the harvester will tend to inject overtones into the acceleration signal, unless the shaker has a very large 'ballast' mass, so acceleration must be measured carefully at the fundamental frequency only.
- the acceleration must be kept constant as the frequency is varied.

The resonant frequency at V = 1V_{RMS} was found to be 68.59Hz, giving ω_n = 431 radians·s^{-1}. This necessitated a series capacitor of $1/L_C\omega_n^2$ = 250μF.

The object is then to measure load current I_L as a function of a, at constant V (constant amplitude). The load current is given by equation (19):

$$I_L = \frac{ma}{\Phi} - \frac{V}{R_0} \tag{19}$$

A plot of R_L against a will then have slope m/Φ and negative y-intercept V/R_0.

3.3 Durability figure of merit: results

Measurements of the magnetic coupling Φ, for a Perpetuum energy harvester of mass m = 0.6kg, are plotted in Figure 4:

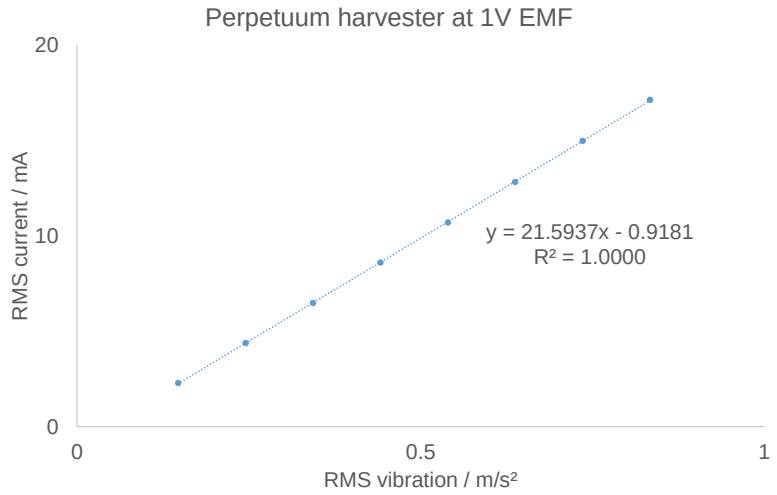


Figure 4 – Shaker measurement of Perpetuum energy harvester magnetic coupling

The results of the measurements are summarised in Table 2:

Mass	m	0.6 kg
Slope	m/Φ	21.594 mA/m·s^{-2}
Negative y-intercept	R_0	1089 Ω
Magnetic coupling	Φ	27.8 N·A^{-1}
Figure of merit	$\Phi^2/R_C m$	49.5 s^{-1}

Table 2 – Measured parameters of Perpetuum harvester

4 Efficiency of an energy harvester

As we have seen, for a given PSD, total dissipated power $\bar{P}$ is fixed. For reasons of brevity we leave it as an exercise for the reader to show from equation (16) that:

$\overline{P_L}$ is maximised for $$R_L = R_C\sqrt{1+\frac{R_0}{R_C}} \tag{20}$$

at which point the efficiency is $$\eta = \frac{\sqrt{1+\frac{R_0}{R_C}}-1}{\sqrt{1+\frac{R_0}{R_C}}+1} \tag{21}$$

As R_C is fixed for a given harvester, it remains to measure R_0. The figure of merit in this case is R_0/R_C, which can be interpreted as the ratio of the short-circuit electrical damping to the mechanical damping, in agreement with [16].

R_0 is a function of mechanical amplitude. There are many contributions to R_0 [19]. In addition it may be desirable to introduce extra mechanical damping in high-vibration environments, to prevent the harvester resonant response becoming excessive.

In general, it is observed that R_0 decreases with increasing mechanical amplitude. In other words, the damping increases with amplitude. This allows us to take the novel step of building the harvester into a test circuit which is essentially a bridge oscillator, Figure 5:

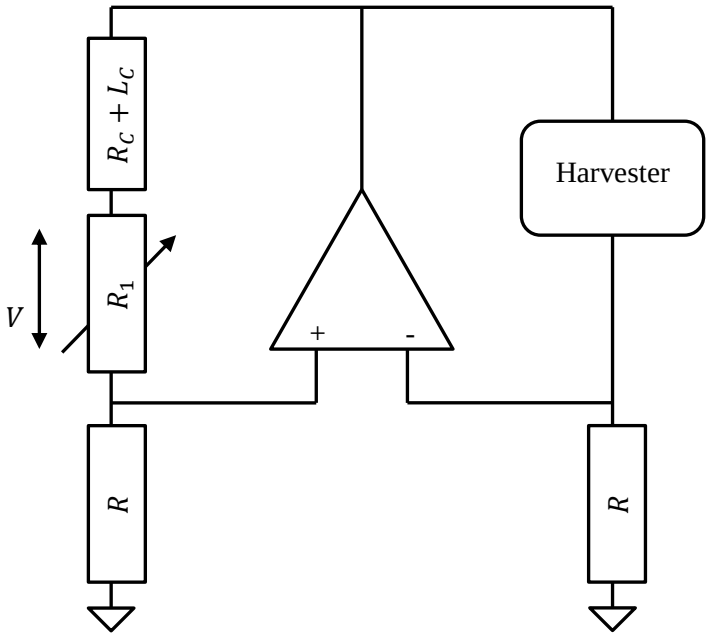


Figure 5 – Measuring harvester damping

First we mount the harvester on a large suspended ('floating') mass M so that it can resonate freely, with minimal interaction with the wider environment. This has the effect of replacing the mass m with the 'reduced mass' m' (equation 22), as shown in Figure 6:

$$m' = \frac{mM}{m+M} \tag{22}$$

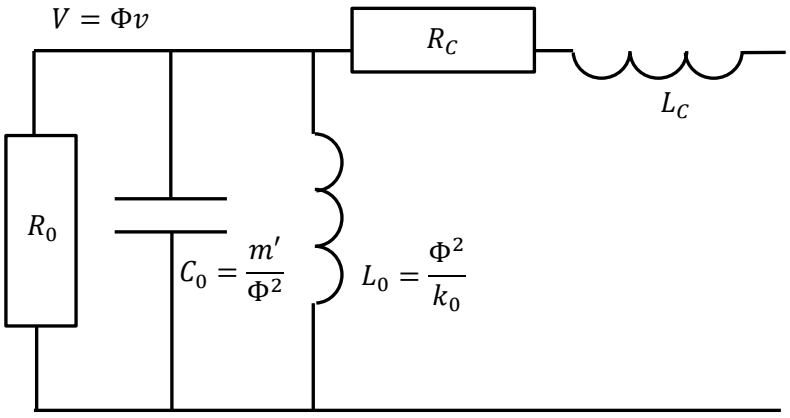


Figure 6 – Equivalent circuit for harvester isolated on 'floating' mass

The impedance of the harvester is a maximum, $R_0 + R_C + L_C$, at the system resonance. If this is greater than the impedance $R_1 + R_C + L_C$ in the positive-feedback arm of Figure 5, then the resonance will increase in amplitude, and *vice-versa*. The resonant amplitude will change until $R_0 = R_1$.

At that point the harvester EMF, $V = \Phi v$, is duplicated across R_1, where it can be measured.

With a pair of measurements, (V, R_0) we can calculate the optimum load resistor (equation 20) and the optimum efficiency (equation 21). We can then calculate (equation 17) the power that would be dissipated in an *installed* harvester with this load, operating at the point (V, R_0), which gives us an *estimate* of the random PSD associated with the point (V, R_0). Finally we can associate estimated PSD with efficiency and optimum load.

4.1 Efficiency measurements: results

A Perpetuum harvester with R_C = 26Ω, L_C = 22mH, and m = 0.6kg was measured as described above. Optimum load, equation (20), was estimated as a function of PSD A and also load power $\overline{P_L}$. The calculated values are shown in Figure 7:

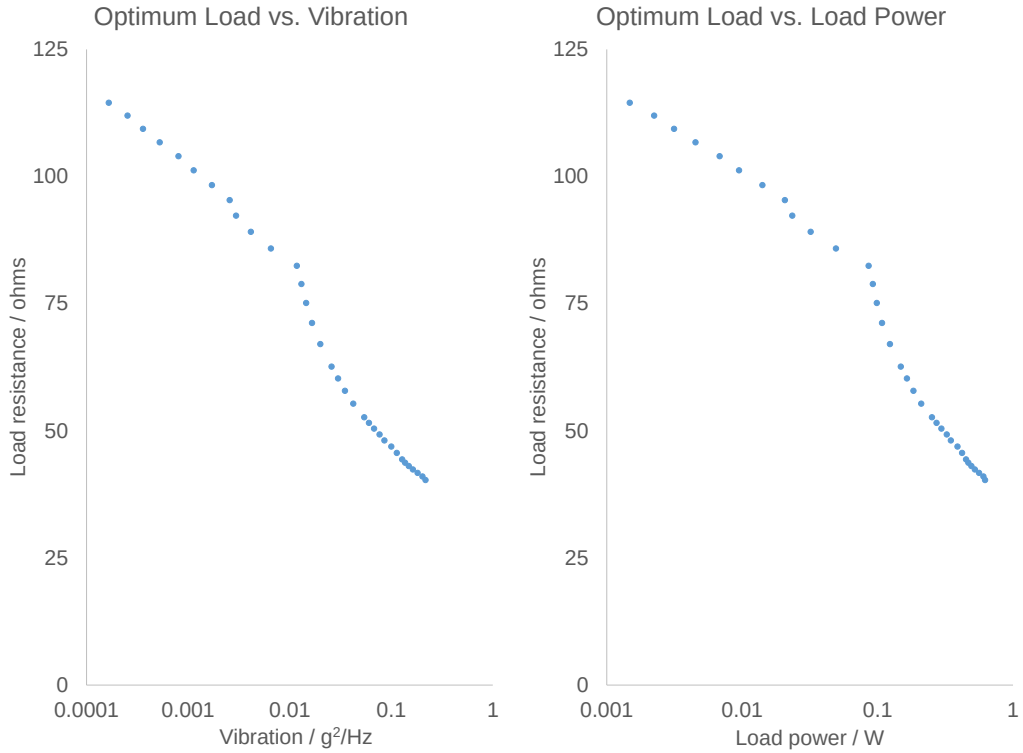


Figure 7 – Estimated optimum load for Perpetuum energy harvester

Ways of achieving specified resistive loads, and yet supplying constant DC voltage to payload electronics, are suggested in [17, 20-21].

Estimated efficiency, equation (21), is shown in Figure 8, again as a function of PSD A and load power $\overline{P_L}$. In this case, the data can be approximated by a piecewise straight line fit on log-linear axes:

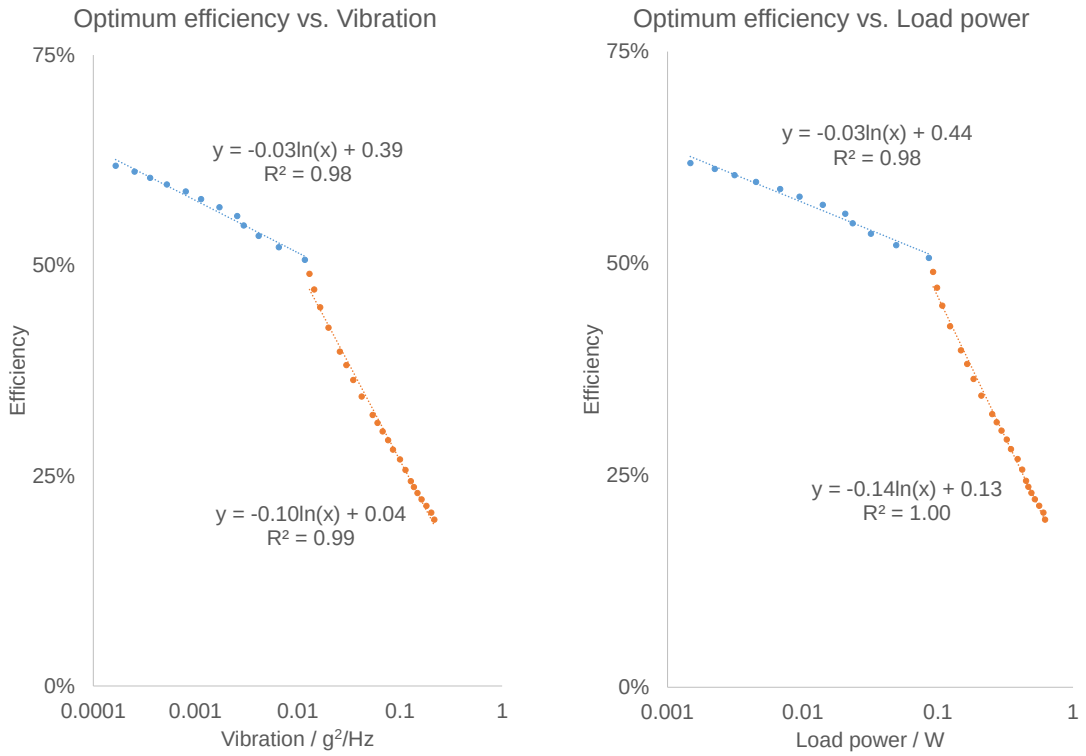


Figure 8 – Estimated efficiencies for Perpetuum energy harvester

5 Discussion

5.1 Design for durability

The electromagnetic durability figure of merit for the Perpetuum energy harvester was measured to be $\Phi^2/R_C m$ = 49.5 s^{-1} (Table 2). This is the reciprocal of the characteristic decay time of oscillations due to electromagnetic damping.

We can compare this with data from other authors who publish electromagnetic parameters, Table 3:

Author	Moving mass m / kg	$(\Phi^2/R_C m)$ / s^{-1}
Present authors	0.6	49.5
Hendijanizadeh *et al.* [12]	8	5.5
Elliott & Zilletti, [16]	2.2	45.5

Table 3 – Comparison of Perpetuum device with those of other authors

It would seem that the Perpetuum device performs well because of its relatively low moving mass. Moving mass is easy to increase, but at the cost of reduced durability, unless the magnetic circuit is strengthened accordingly.

The mechanical damping of the Perpetuum device at V = 1V$_{RMS}$ was Φ^2/R_0 = 0.71 N/m·s^{-1} [13]. The frequency was 68.59Hz, giving ω_n = 431 radians·s^{-1}. Two electrical damping conditions were considered: a simple mass damper ($R_L = 0$) and an energy harvester designed for maximum power at a given stored

energy ($R_L = R_C$). Table 4 gives us insight into the proportional bandwidth, $1/Q$, of the Perpetuum device:

Condition	Electrical damping	Total damping c	$Q = \omega_n m/c$	Bandwidth
$R_L = 0$	Φ^2/R_C = 29.7 N/m·s^{-1}	30.4 N/m·s^{-1}	8.5	12%
$R_L = R_C$	$\Phi^2/2R_C$ = 14.9 N/m·s^{-1}	15.6 N/m·s^{-1}	16.6	6%

Table 4 – Bandwidth of Perpetuum device as mass damper and maximally durable harvester

5.2 Design for efficiency

Figure 7 and Figure 8 show the optimum load and efficiency estimated for the Perpetuum energy harvester, over several orders of magnitude of power. As the optimum load varies from 120Ω to 40Ω, the efficiency drops accordingly from 60% to 20%, equation (21). This variation in required load has been discussed by Halvorsen [17] and Ghandchi-Tehrani & Elliott, [22]. Theoretical optimisation of efficiency is further discussed by Hawes & Langley, [18]. Note that equation (20) implies that the optimum load should never drop below the durability condition, $R_L = R_C$.

Comparable efficiency *measurements* in the literature are few and far between. However, we can present the data in terms of the figure of merit R_0/R_C proposed by [16], as shown in Figure 9:

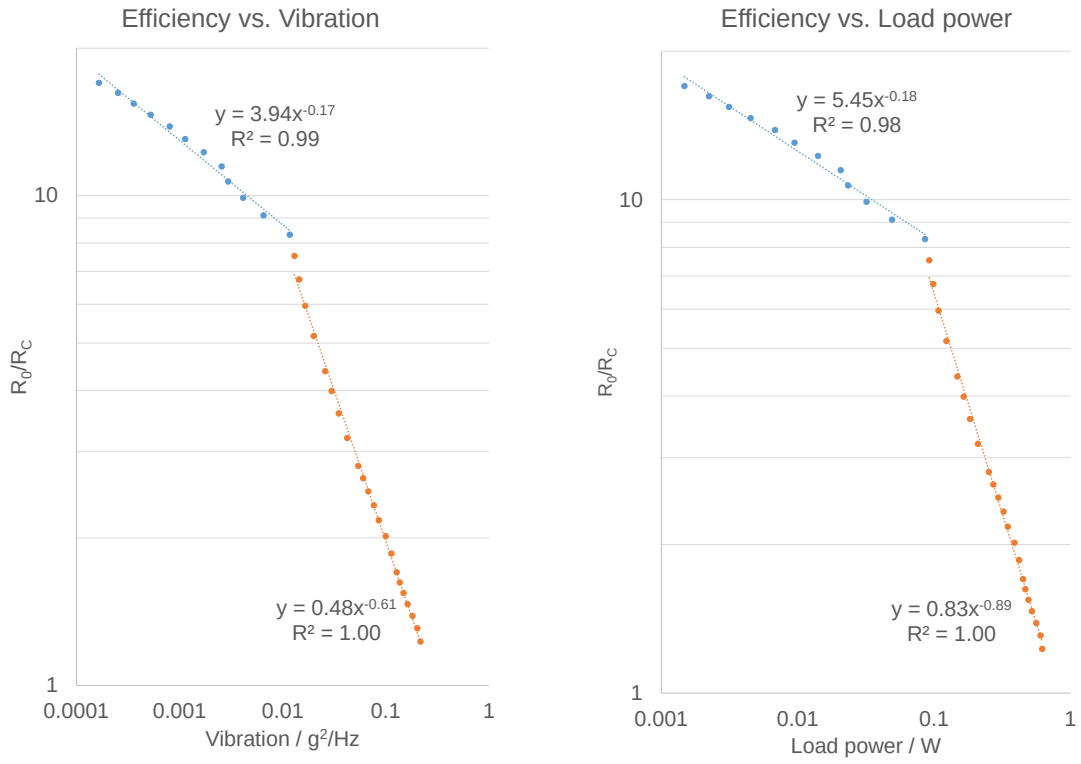


Figure 9 – Measured efficiency presented as ratio of electrical to mechanical damping

The measured values of R_0/R_C shown in Figure 9 are for the most part substantially higher than the value of ~1 proposed by [16]. Note the piecewise *power-law* fit in this case.

5.3 Dynamic range

The dynamic range of the measurements might at first seem excessive. However, it is known [23-26] that the vibration of a typical vehicle in service is not well characterised by a single PSD measurement; rather, the vibration is best characterised as non-stationary [27]. The statistics of some related non-stationary processes are discussed by Beck [28]. For our purposes, a constraint on the behaviour is that the power dissipated in the vibration must be finite, which means that any distribution of PSD must have a defined mean. (A general introduction to some systems which do not behave in this way is given in [29].)

In the range of PSD from 0.0001 to 0.2 g^2/Hz, we estimate optimised power delivery to vary between 1mW and 0.6W. Standards for accelerated vibration tests, e.g. EN 61373, tend to specify PSD levels towards the high end of the measurements presented here.

The breaks in the curves of Figure 7, Figure 8 and Figure 9 are associated with a deliberately engineered increase in mechanical damping and spring rate at high amplitudes, as discussed in e.g. [2, 8-11, 22]. Although these nonlinearities cause the displacement and acceleration response of the system to deviate from a Gaussian distribution, the energy constraints discussed above cause the velocity to remain Gaussian [10-11]. Similar behaviour in a more complex system is discussed in [30-31]. The implication of well-behaved kinetic energy is well-behaved strain energy, meaning that some traditional fatigue analyses, e.g. [32-34], remain applicable.

6 Conclusions

The aims of this work were to characterise the efficiency and durability of an energy harvester applied in a condition monitoring system.

An electromagnetic energy harvester used to power a commercial condition monitoring system was found to be able to extract between 60% and 20% of the available vibration energy, a range of 1mW to 0.6W, by measurement in a novel bridge circuit. This efficiency is greater than some recent literature might suggest.

Calculation shows that these systems can be expected to be most durable when the load impedance equals the coil impedance, at which point a figure of merit for the system is given by the square of the magnetic coupling ($N \cdot A^{-1}$ or $V/m \cdot s^2$), divided by the coil resistance and the moving mass. The figure of merit for this 0.6kg device was found to be 49.5 s^{-1}, in excess of results suggested in the literature.

Acknowledgements

Particular thanks are due to Professor Stephen Elliott of the University of Southampton, for reading through and commenting on a draft of this manuscript.

References

[1] N. Symonds, I. Corni, R.J.K. Wood, A. Wasenczuk & D. Vincent, *Observing early stage rail axle bearing damage*, J. Eng. Failure Analysis 56 (2015) pp. 216-232

[2] R.S. Langley, *A general mass law for broadband energy harvesting*, J. Sound & Vibration 333 (2014) pp. 927-936

[3] M.J. Brennan, B. Tang, G. Pechoto Melo & V. Lopes Jr., *'An investigation into the simultaneous use of a resonator as an energy harvester and a vibration absorber*', J. Sound & Vibration 333 (2014) pp. 1331-1343

[4] J.W. Miles, *On Structural Fatigue Under Random Loading*, J. Aero. Sci. 21 (1954) pp. 752-762

[5] S.H. Crandall & W.D. Mark, *Random Vibration in Mechanical Systems*, Academic Press (1963)

[6] R.B. Blackman & J.W. Tukey, *The Measurement of Power Spectra*, Dover (1959)

[7] M.C. Smith & S.J. Swift, *Power Dissipation in Automotive Suspensions*, Vehicle System Dynamics 49 (2011) pp. 59-74

[8] J.M.C. Clark & M.C. Smith, *Power Absorbtion Invariance for Brownian Spring Forcing*, Proc. 51st IEEE Conf. Decision & Control (2012) pp. 4396-4399

[9] R.S. Langley, *Bounds on the vibrational energy that can be harvested from random base motion*, J. Sound & Vibration 339 (2015) pp. 247-261

[10] E. Halvorsen, *Energy Harvesters Driven by Broadband Random Vibrations*, J. Microelec. Syst. 17 (2008) pp. 1061-1071

[11] P.L. Green, K. Worden, K. Atallah & N.D. Sims, *Scaling of electromagnetic transducers for shunt damping and energy harvesting*, J. Sound & Vibration 333 (2014) pp. 2185-2195

[12] M. Hendijanizadeh, S.J. Elliott & M. Ghandchi-Tehrani, *Extending the dynamic range of an energy harvester with a variable load resistance*, J. Intelligent Mat. Syst. & Struct. 28 (2017) pp. 2996-3005

[13] C.B. Williams, C. Shearwood, M.A. Harradine, P.H. Mellor, T.S. Birch & R.B. Yates, *Development of an electromagnetic microgenerator*, IEEE Proc. Circuits Devices Systems 148 (2001) pp. 337-342

[14] W.W. Soroka, *Analog methods in Computation and Simulation*, McGraw-Hill (1954)

[15] S.H. Crandall, D.C. Karnopp, E.F. Kurtz & D.C. Pridmore-Brown, *Dynamics of Mechanical and Electromechanical Systems*, McGraw-Hill (1968)

[16] S.J. Elliott & M. Zilletti, *Scaling of electromagnetic transducers for shunt damping and energy harvesting*, J. Sound & Vibration 333 (2014) pp. 2185-2195

[17] E. Halvorsen, *Optimal Load and Stiffness for Displacement-Constrained Vibration Energy Harvesters*, arXiv:1603.01909v1 (2016)

[18] D.H. Hawes & R.S. Langley, *Limits on the power available to harvest from broadband random excitation*, J. Sound & Vibration 399 (2017) pp. 244-256

[19] F. Ayazi, L. Sorenson & R. Tabrizian, *Energy Dissipation in Micromechanical Resonators*, in T. George, M. Saif Islam & A.K. Dutta eds., Proc. SPIE 8031, *Micro- and Nanotechnology Sensors, Systems, and Applications III*, 803119 (2011)

[20] T. Paing, J. Shin & R. Zane, *Resistor Emulation Approach to Low-Power RF Energy Harvesting*, IEEE Trans. Pow. Elect. 23 (2008) pp. 1494-1501

[21] G.D. Szarka, *Review of Power Conditioning for Kinetic Energy Harvesting Systems*, IEEE Trans. Pow. Elect. 27 (2012) pp. 803-815

[22] M. Ghandchi-Tehrani & S.J. Elliott, *Extending the dynamic range of an energy harvester using nonlinear damping*, J. Sound & Vibration 333 (2014) pp. 623-629

[23] V. Rouillard, *On the Statistical Distribution of Stationary Segments Lengths of Road Vehicles Vibrations*, Proc. World Congress on Eng. (2007)

[24] V. Rouillard, *On the Non-Gaussian Nature of Random Vehicle Vibrations*, Proc. World Congress on Eng. (2007)

[25] P. Wolfsteiner & W. Breuer, *Fatigue assessment of vibrating vehicle bogie components under non-Gaussian random excitations using power spectral densities*, J. Sound & Vibration 332 (2013) pp. 5867-5882

[26] P. Wolfsteiner, *Fatigue assessment of non-stationary random vibrations by using decomposition in Gaussian portions*, Int. J. Mech. Sci. 127 (2017) pp. 10-22

[27] J.S. Bendat & A.G. Piersol, *Random Data: Analysis and Measurement Procedures*, Wiley (1971)

[28] C. Beck, *Superstatistics: Theoretical concepts and practical applications*, in Klages *et al.*, eds., *Anomalous Transport: Foundations and Applications*, Wiley (2008)

[29] J. Klafter, M.F. Shlesinger & G. Zumofen, *Beyond Brownian Motion*, Physics Today (February 1996) pp. 33-39

[30] T. Butlin, *A comparison of worst-case predictions with experimental results for a locally nonlinear beam*, Proc. ISMA (2014) pp. 2989-3003

[31] T. Butlin, *Response bounds for complex systems with a localised and uncertain nonlinearity*, J. Sound & Vibration 384 (2016) pp. 227-252

[32] A.F. Desmond, *On the distribution of the time to failure for the simple linear oscillator*, Probabilistic Eng. Mech. 2 (1987) pp. 214-218

[33] S.H. Smith, *Fatigue Crack Growth under Axial Narrow and Broad Band Random Loading*, in Trapp & Forney, eds., *Acoustical Fatigue in Aerospace Structures*, Syracuse UP (1965)

[34] S.A. Clevenson & R. Steiner, *Fatigue Life Under Random Loading for Several Power Spectral Shapes*, NASA Technical Report R-266 (1967)

Response predictions of reduced models with whole joints

R.J. Kuether[1], D.A. Najera-Flores[2]
[1] Sandia National Laboratories
Albuquerque, New Mexico, USA

[2] ATA Engineering, Inc.
San Diego, California, USA
e-mail: **rjkueth@sandia.gov**

Abstract
Structural dynamic models of mechanical, aerospace, and civil structures often involve connections of multiple subcomponents with rivets, bolts, press fits, or other joining processes. Recent model order reduction advances have been made for jointed structures using appropriately defined whole joint models in combination with linear substructuring techniques. A whole joint model condenses the interface nodes onto a single node with multi-point constraints resulting in drastic increases in computational speeds to predict transient responses. One drawback to this strategy is that the whole joint models are empirical and require calibration with test or high-fidelity model data. A new framework is proposed to calibrate whole joint models by computing global responses from high-fidelity finite element models and utilizing global optimization to determine the optimal joint parameters. The method matches the amplitude dependent damping and natural frequencies predicted for each vibration mode using quasi-static modal analysis.

1 Introduction

Due to their cost effectiveness, mechanical interfaces from joining processes are commonly found within structural assemblies and introduce nonlinear behavior localized in these regions. Common types of joints include welds, bolted connections and compression fits, all of which introduce frictional contact between mating surfaces. In the aerospace and defense industries, vibration mitigation in electronic and electromechanical devices can be achieved by press fitting shock and vibration sensitive components within foam packaging material. This leads to mechanical interfaces that maintain their strength with normal contact pressure and friction to resist relative slipping between subcomponents. Under time-varying loads, these normal pressures fluctuate and the tangential pressures vary with time, and may ultimately exceed slip values. These interfaces can have a significant influence on the overall stiffness and dissipation of a built-up assembly, which can account for up to 90% of the damping in a structure [1].

Many strategies have been developed over several decades to model structures with frictional contact. Review papers by Gaul and Nitsche [2] and Bograd et al. [3] summarize various friction models that have been developed to model joint forces. The most common and readily available approach in industry is the finite element method with Coulomb friction. Commercially available software packages include frictional contact algorithms in both implicit and explicit solvers to predict the nonlinear response of structures with detailed geometries and complex material models. While many commercially available software exists, this paper uses the Sierra Solid Mechanics (Sierra/SM) finite element code [4] developed at Sandia National Laboratories to perform the high-fidelity model simulations. The drawback to using this approach to solve problems involving contact is the computational burden associated with the iterative contact solvers. Commercial finite element codes require an excessive amount of computational resources to solve transient response simulations with direct time integration.

Simplified representations of jointed interfaces have been developed over several decades to overcome the excessive computational cost of full-scale problems. This paper utilizes the four-parameter Iwan element developed by Segalman [5] to capture the constitutive behavior of the frictional interface. The Iwan element is a one-dimensional constitutive model that is a parallel arrangement of spring and slider elements with a power-law distribution describing the population density of slider strengths. A reduced order structural dynamics model is developed by connecting Hurty/Craig-Bampton superelements [6, 7] with whole joint models to capture the nonlinear physics localized at the joint. In these reduced representations, the nonlinear element forces are applied at a single node location that is constrained to multiple nodes along the interface surface using multi-point constraints (MPCs). Other simplified joint models in the literature include various Iwan type elements [8, 9], Bouc-Wen hysteresis models [10, 11], and parallel Jenkins elements [2, 12].

One practical challenge associated with simplified, whole joint modeling is parameter identification of the constitutive model. Typically, the unknown parameters require calibration with either experimental data or simulated data from high-fidelity finite element analysis. The whole joints are optimized by searching for the optimal parameter set that best matches data metrics readily measured or extracted from the reference system. Examples of parameter identification of whole joint models include the work by Charalampakis et al. [13, 14] who developed a method to determine Bouc-Wen element parameters using different global optimization schemes. Recent work by Dong et al. [15] has extended the Iwan element to capture non-zero stiffness in the macro-slip regime and curve-fit the parameters of a single bolted joint using high-fidelity FEA simulations of oscillatory and monotonic loading. Wang et al. [16] presented a joint model updating scheme using analytical mode decomposition to extract the instantaneous modal characteristics of the measured and numerically time integrated response. Oldfield et al. [12] fit the parameters of a Bouc-Wen and parallel Jenkins element to match the joint hysteresis predicted from a detailed finite element model.

This paper presents a framework that calibrates a reduced order model of a structure assembled with whole joint models to capture the global response of the assembly. This is achieved by defining a multi-objective function with the amplitude-dependent natural frequencies and damping ratios computed from a high-fidelity solid mechanics model using quasi-static modal analysis (QSMA) [17, 18]. QSMA applies a quasi-static modal force to the preloaded model to estimate the frequency and damping as a function of the modal response amplitude. Lacayo has recently demonstrated this approach on experimentally obtained data from a beam structure with a lap-joint [19], and Jewell et al. [20] extended this approach to high-fidelity finite element models. This technique provides two unique advantages for optimization of whole joints that are not readily captured by existing techniques. First, the simulated data does not require expensive dynamic simulations and can be readily obtained from both high-fidelity and reduced order models with Iwan elements. Second, the QSMA captures the amplitude-dependent modal behavior of the assembly and reveals how the joints influence the global response with increasing amplitudes. QSMA provides the opportunity to choose which frequency bandwidth to preserve by tailoring which modes to calibrate to the reference data. The genetic algorithm implemented in [21] is combined with the multi-objective function and QSMA to search for the optimal parameters of the four-parameter Iwan elements in a reduced order model.

The paper is organized as follows. Section 2 develops an overview of the whole joint reduced order modeling framework to represent high-fidelity models with mechanical interfaces. The calibration workflow is described along with a brief overview of the QSMA theory. Section 3 introduces the Ministack hardware consisting of a foam-to-metal interface held together with a press fit joint. The results of the QSMA and model calibration are applied to the Ministack example and discussed in Section 4, followed by the conclusions in Section 5.

2 Whole Joint Modeling

A flowchart of the model calibration is shown in Fig. 1. Section 2.1 reviews the theory of model order reduction with whole joint representations created from preloaded finite element models. The preloaded

model is simulated using the QSMA algorithm in Section 2.2 to estimate the nonlinear damping and natural frequencies as a function of modal response amplitude. The high-fidelity model data combined with the reduced order model feed into the multi-objective optimization routine in Section 2.3 to determine the correct whole joint model parameters to capture the nonlinear physics at the frictional interface.

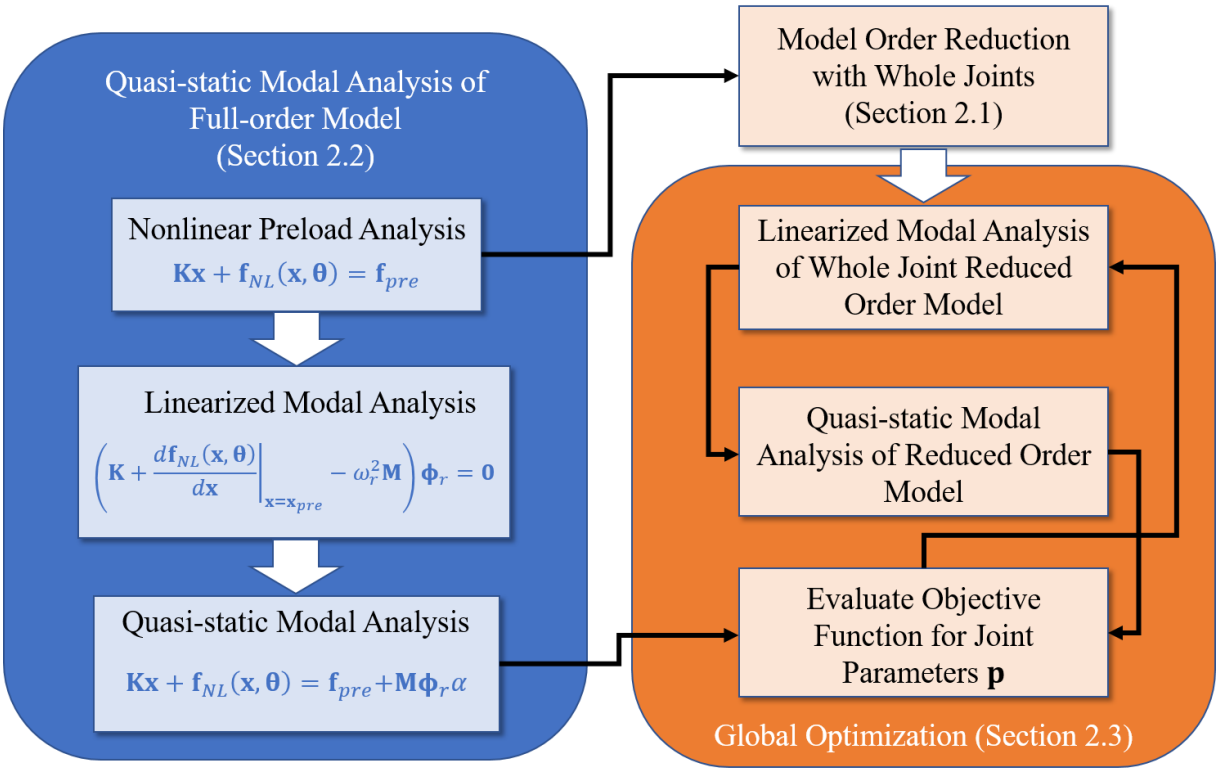


Figure 1. Flowchart of whole joint reduced order model calibration.

2.1 Hurty/Craig-Bampton Reduction with Whole Joint Models

A whole joint modeling approach provides efficient structural dynamic models that speed up computation time required to predict expensive transient responses of nonlinear dynamical systems. A whole joint model condenses the frictional interface down to a single, discrete nodal location. An example of this for a lap-joint with three bolted connections is shown in Fig. 2 (note that the exploded view helps visualize the modeling approach). The orange lines represent rigid bar elements tying a single point to a patch of nodes along the assumed contact area of the bolted interface. The red bars represent the pointwise constitutive model, referred to as the whole joint, between two discrete nodal locations to describe the linear or nonlinear behavior at the interface. Each whole joint has six linearly independent degrees-of-freedom that can be connected by various element types (e.g. linear springs, dashpots, four-parameter Iwan elements, etc..). A whole joint model significantly reduces the time and length scales of the mechanical interfaces for time simulations requiring many time steps. Rigidly tying each interface to a single point assumes that the local kinematics at the interface do not significantly contribute to the response.

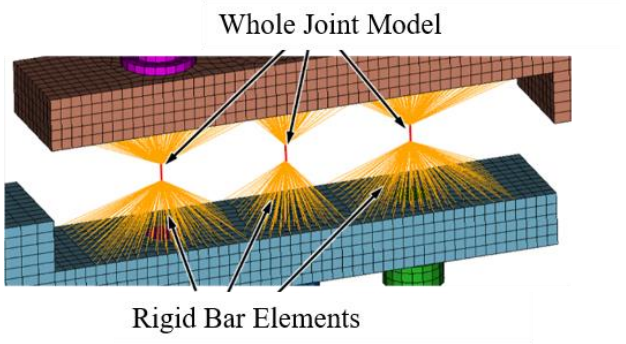


Figure 2. Example of a whole joint model of three bolts in a lap-joint [19].

The modeling approach assumes that each individual subcomponent behaves linearly (i.e. linear elastic materials, small deformations, etc..) in the absence of joints. The linear portion of the model is reduced using the Hurty/Craig-Bampton (HCB) substructuring approach [6, 7], which reduces the linear, interior degrees-of-freedom (DOF) with a truncated set of fixed-interface dynamic modes. The interface DOF are preserved with static constraint modes. Each linear subcomponent is represented with the standard HCB equations-of-motion,

$$\begin{bmatrix} \mathbf{I}_{kk} & \widehat{\mathbf{M}}_{kb} \\ \widehat{\mathbf{M}}_{bk} & \widehat{\mathbf{M}}_{bb} \end{bmatrix} \begin{Bmatrix} \ddot{\mathbf{q}}_k \\ \ddot{\mathbf{x}}_b \end{Bmatrix} + \begin{bmatrix} \mathbf{\Lambda}_{kk} & \mathbf{0} \\ \mathbf{0} & \widehat{\mathbf{K}}_{bb} \end{bmatrix} \begin{Bmatrix} \mathbf{q}_k \\ \mathbf{x}_b \end{Bmatrix} = \begin{Bmatrix} \mathbf{0} \\ \mathbf{f}(t) + \mathbf{r}(t) \end{Bmatrix} \tag{1}$$

The $N_k \times 1$ vector $\mathbf{q}_k$ represents the truncated fixed-interface modal coordinates and the $N_b \times 1$ vector $\mathbf{x}_b$ corresponds to the physical boundary DOF of the whole joint interface nodes. The $N_k \times N_k$ matrices $\mathbf{I}_{kk}$ and $\mathbf{\Lambda}_{kk}$ respectively correspond to the identity matrix and diagonal matrix of fixed-interface mode natural frequencies. The unknown $N_b \times 1$ vector $\mathbf{r}(t)$ accounts for the unknown reaction force applied at the interface between adjacent structure(s).

Without loss of generality, assume that two subcomponents denoted with superscripts (A) and (B) are assembled by applying a nonlinear joint model, $\mathbf{f}_{NL}(\mathbf{x}_b, \boldsymbol{\theta})$, at the physical boundary DOF, $\mathbf{x}_b$. These joint forces replace the unknown reaction force, $\mathbf{r}(t)$, resulting in the assembled equations,

$$\begin{bmatrix} \mathbf{I}_{kk}^{(A)} & \widehat{\mathbf{M}}_{kb}^{(A)} & \mathbf{0} & \mathbf{0} \\ \widehat{\mathbf{M}}_{bk}^{(A)} & \widehat{\mathbf{M}}_{bb}^{(A)} & \mathbf{0} & \mathbf{0} \\ \mathbf{0} & \mathbf{0} & \mathbf{I}_{kk}^{(B)} & \widehat{\mathbf{M}}_{kb}^{(B)} \\ \mathbf{0} & \mathbf{0} & \widehat{\mathbf{M}}_{bk}^{(B)} & \widehat{\mathbf{M}}_{bb}^{(B)} \end{bmatrix} \begin{Bmatrix} \ddot{\mathbf{q}}_k^{(A)} \\ \ddot{\mathbf{x}}_b^{(A)} \\ \ddot{\mathbf{q}}_k^{(B)} \\ \ddot{\mathbf{x}}_b^{(B)} \end{Bmatrix} + \begin{bmatrix} \mathbf{\Lambda}_{kk}^{(A)} & \mathbf{0} & \mathbf{0} & \mathbf{0} \\ \mathbf{0} & \widehat{\mathbf{K}}_{bb}^{(A)} & \mathbf{0} & \mathbf{0} \\ \mathbf{0} & \mathbf{0} & \mathbf{\Lambda}_{kk}^{(B)} & \mathbf{0} \\ \mathbf{0} & \mathbf{0} & \mathbf{0} & \widehat{\mathbf{K}}_{bb}^{(B)} \end{bmatrix} \begin{Bmatrix} \mathbf{q}_k^{(A)} \\ \mathbf{x}_b^{(A)} \\ \mathbf{q}_k^{(B)} \\ \mathbf{x}_b^{(B)} \end{Bmatrix} + \cdots$$

$$\cdots + \begin{Bmatrix} \mathbf{0} \\ \mathbf{f}_{NL}\left(\mathbf{x}_b^{(A)}, \mathbf{x}_b^{(B)}, \boldsymbol{\theta}\right) \\ \mathbf{0} \\ -\mathbf{f}_{NL}\left(\mathbf{x}_b^{(A)}, \mathbf{x}_b^{(B)}, \boldsymbol{\theta}\right) \end{Bmatrix} = \begin{Bmatrix} \mathbf{0} \\ \mathbf{f}(t)^{(A)} \\ \mathbf{0} \\ \mathbf{f}(t)^{(B)} \end{Bmatrix} \tag{2}$$

The nonlinear joint forces, $\mathbf{f}_{NL}$, are generally dependent on the physical displacements of the interface nodes, $\mathbf{x}_b$, and any applicable internal variables of the whole joint model or frictional contact elements, $\boldsymbol{\theta}$.

In this work, the shear frictional forces in the mechanical interface are modeled as four-parameter Iwan elements originally derived for lap-type joints in [5]; the theory is briefly reviewed here. This constitutive model captures the nonlinear dependence of damping and loss of stiffness with increasing response amplitude, which are the result of microslip. The force of a parallel-series Iwan model is written as,

$$f_{NL} = \int_0^\infty \rho(\phi)[u(t) - x(t,\phi)]d\phi \tag{3}$$

with the stick/slip condition definitions,

$$\dot{x}(t) = \begin{cases} \dot{u}(t) & \text{if } \|u(t) - x(t,\phi)\| = \phi \text{ and } \dot{u}(t)[u(t) - x(t,\phi)] > 0 \\ 0 & \text{otherwise} \end{cases} \tag{4}$$

The dimensionless values, $x(t,\phi)$, are the displacements of the Jenkins elements with a slip displacement, ϕ. The population density of Jenkins elements is $\rho(\phi)$, and $u(t)$ and f_{NL} are the joint displacement and internal nonlinear force, respectively.

The population density of the Jenkins elements assumes a power-law distribution that is terminated at a finite displacement as,

$$\rho(\phi) = R\phi^{\chi}[H(\phi) - H(\phi - \phi_{\max})] + S\delta(\phi - \phi_{\max}) \tag{5}$$

Substituting the power-law distribution into Eq. (3) results in the force-displacement relationship,

$$f_{NL} = \int_0^{\phi_{\max}} [u(t) - x(t,\phi)] R\phi^{\chi} d\phi + S[u(t) - x(t,\phi_{\max})] \tag{6}$$

where the parameters of the Iwan element are defined as,

$$R = \frac{F_s(1+\chi)}{\phi_{\max}^{\chi+2}\left(\beta + \left(\frac{\chi+1}{\chi+2}\right)\right)} \tag{7}$$

$$S = \frac{F_s\beta}{\phi_{\max}\left(\beta + \left(\frac{\chi+1}{\chi+2}\right)\right)} \tag{8}$$

$$\phi_{\max} = \frac{F_s(1+\beta)}{K_T\left(\beta + \left(\frac{\chi+1}{\chi+2}\right)\right)} \tag{9}$$

The Iwan element in Eq. (6) in conjunction with Eqns. (7) - (9) is completely defined by the following parameters:

- Slip force, F_s
- Joint stiffness when no slip occurs, K_T
- Exponent describing slope of force-dissipation curve, χ
- Shape parameter of the force-dissipation curve near transition to macroslip, β

As discussed in [5], these parameters are preferred since they are "measureable" quantities. The slip force has physical meaning since it can be estimated from the normal force calculations with an assumed Coulomb friction coefficient. The joint stiffness is estimated by performing vibration tests at low excitation levels. Determining the values for χ and β is more challenging, requiring specific experiments or simulations to calibrate.

2.2 Quasi-Static Modal Analysis

The recently developed quasi-static modal analysis approach [17, 18] shows promise as an efficient method to estimate the amplitude dependent frequency and damping with quasi-static simulations within commercial finite element software. The technique is amenable to computational models, such as reduced order models with Iwan elements [17] or high-fidelity finite element models [20], but does not have an experimental counterpart since it relies on an external force proportional to the mode shape of interest. We start from the discretized equations-of-motion of a system with frictional contact nonlinearities,

$$\mathbf{M}\ddot{\mathbf{x}} + \mathbf{C}\dot{\mathbf{x}} + \mathbf{K}\mathbf{x} + \mathbf{f}_{NL}(\mathbf{x},\boldsymbol{\theta}) = \mathbf{f}_{ext}(t) \tag{10}$$

These equations generally represent any nonlinear system, such as the reduced order model in Eq. (2) or the full-order equations within a commercial finite element package. Ignoring the mass and damping terms in Eq. (10), and defining a static preload force, $\mathbf{f}_{pre}$, results in the quasi-static form of the equations,

$$\mathbf{K}\mathbf{x} + \mathbf{f}_{NL}(\mathbf{x},\boldsymbol{\theta}) = \mathbf{f}_{pre} \tag{11}$$

These equations are solved directly using an appropriate nonlinear static solver to calculate the preloaded deformation, $\mathbf{x}_{pre}$. The system is linearized about this preloaded state to approximate the low amplitude, linear vibration modes of the preloaded structure. The eigenvalue problem is obtained by linearizing the nonlinear internal force vector, $\mathbf{f}_{NL}(\mathbf{x},\boldsymbol{\theta})$, about the deformed state, resulting in,

$$\left(\mathbf{K} + \frac{d\mathbf{f}_{NL}(\mathbf{x},\boldsymbol{\theta})}{d\mathbf{x}}\Big|_{\mathbf{x}=\mathbf{x}_{pre}} - \omega_r^2\mathbf{M}\right)\boldsymbol{\phi}_r = \mathbf{0} \tag{12}$$

where $\boldsymbol{\phi}_r$ is the r[th] mode shape vector and ω_r is the corresponding natural frequency. The quasi-static modal analysis defines a static external force proportional to the r[th] mode shape to be applied to the preloaded equations in Eq. (11). This applied force statically deforms the system into the linear mode shape of interest at low amplitudes (i.e. when the joint remains stuck). Mathematically, this is achieved by defining the r[th] modal force vector,

$$\mathbf{f}_r(\alpha) = \mathbf{M}\boldsymbol{\phi}_r\alpha \tag{13}$$

where α is a scalar amplitude of the modal force. The modal force is appended to the righthand side of Eq. (11) and solved for displacements over a range of modal force amplitudes, $\mathbf{x}(\alpha)$. For low amplitudes, the joint remains stuck and the external force leads to a deformation shape isolating only the r[th] mode shape. For increasing values of α, the joint begins to slip within low-pressure regions of the interface (i.e. microslip), resulting in a change in stiffness and dissipation of the modal response. This phenomenon is observed by applying a modal filter to the full-field displacements,

$$q_r(\alpha) = \boldsymbol{\phi}_r^{\mathrm{T}}\mathbf{M}\mathbf{x}(\alpha) \tag{14}$$

Following the theory in [17], the natural frequency as a function of amplitude is approximated using the secant of the modal hysteresis curve,

$$\omega_r(\alpha) = \sqrt{\frac{\alpha}{q_r(\alpha)}} \tag{15}$$

while the amplitude dependent damping ratio is defined as,

$$\zeta_r(\alpha) = \frac{D(\alpha)}{2\pi[q_r(\alpha)\omega_r(\alpha)]^2} \tag{16}$$

The modal dissipated energy is determined using Masing's rules [17],

$$D(\alpha) = 2\int_{-q_r(\alpha)}^{q_r(\alpha)}\left[f_r\left(\frac{q_r(\alpha)+q_r}{2}\right) + f_r\left(\frac{q_r(\alpha)-q_r}{2}\right) - \alpha\right]dq_r \tag{17}$$

The amplitude dependent natural frequencies and damping ratios in Eqs. (15) and (16), respectively, are used as metrics in the objective function to calibrate the four-parameter Iwan elements in the reduced order model. The advantage to using QSMA is that the unknown parameter space in the reduced order model can be sampled quickly since the model only needs to be simulated for static loads. Furthermore, the amplitude dependent modal parameters capture the change in stiffness and dissipation for each mode of interest, capturing the global response of the structure rather than the local response of the joint in isolation.

2.3 Multi-Objective Optimization

The parameters of the Iwan element(s) in the whole joint reduced order models are calibrated using multi-objective optimization with reference data generated from QSMA on the full-order finite element model. The algorithm used in this paper is the Non-dominated Sorting Genetic Algorithm II (NSGA-II), which is implemented in Python using the DEAP package [21]. NSGA-II was chosen because it has been shown to outperform other multi-objective optimization algorithms [22] in its ability to find a better spread of solutions by explicitly diversifying the pareto front. NSGA-II generates a random population of candidate solutions which are assigned a "fitness" based on whether they are considered being non-dominated or not. Non-domination is satisfied when there is no alternative solution with a better fitness in at least one of the objectives. The best candidates are chosen based on their fitness and recombined with other solutions. The set of best solutions from the original population and their offspring make it to the next generation and the process is repeated. NSGA-II pays special attention to "crowding distance" which is a measure of the uniformity of the spread of the Pareto-optimal front. The Pareto-optimal front is composed of all the non-dominated individuals in a population.

The multi-objective fitness function to be minimized is defined as,

$$\Gamma_{\mathrm{GA}} = \left[\frac{1}{N_\alpha}\sum_{i=1}^{N_\alpha}\left|\frac{\omega_r(\alpha_i)-\tilde{\omega}_r(\alpha_i,\mathbf{p})}{\max(\omega_r(\alpha_i))}\right|, \frac{1}{N_\alpha}\sum_{i=1}^{N_\alpha}\left|\frac{\zeta_r(\alpha_i)-\tilde{\zeta}_r(\alpha_i,\mathbf{p})}{\max(\zeta_r(\alpha_i))}\right|\right] \tag{18}$$

The amplitude dependent natural frequencies, $\tilde{\omega}_r(\alpha_i,\mathbf{p})$, and damping ratios, $\tilde{\zeta}_r(\alpha_i,\mathbf{p})$, are computed from the whole joint reduced order model using QSMA for an arbitrary set of whole joint parameters, $\mathbf{p}$. The modal data from the full-order model, $\omega_r(\alpha_i)$ and $\zeta_r(\alpha_i)$, are computed offline. The advantage to using the QSMA in the reduced model is the cost efficiency to evaluate one instance of the objective function. Other approaches that rely on dynamic, time integrated solutions are costlier to simulate, and more difficult to automate with signal processing tools within an optimization scheme.

3 Ministack Assembly Models

The model calibration is demonstrated on the Ministack assembly, a benchmark structure developed at Sandia National Laboratories to better understand the nonlinear damping and stiffness behavior of compression fit interfaces. A schematic and picture of the hardware is shown in Fig. 3. The structure consists of an outer can that houses an aluminum slug that fits tightly in between two foam cups. The foam-slug subassembly fits into the can, and a cover plate is inserted to apply a nominal preload force. Once preloaded, the threaded ring nut is fastened to the can to maintain the compressive load on the foam-slug subassembly. The foam-to-metal interfaces are the primary source of nonlinear energy dissipation due to frictional losses when the slug vibrates within the foam packaging.

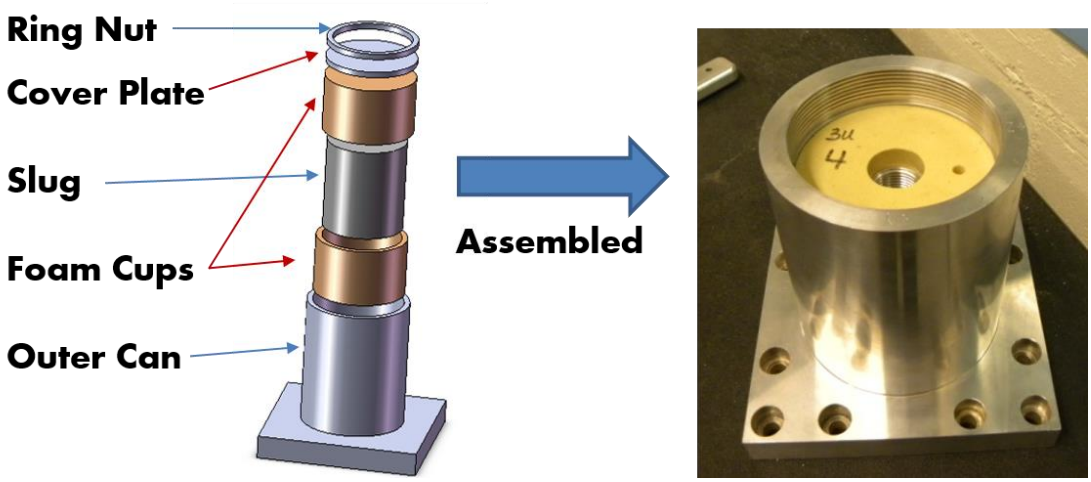


Figure 3. Ministack assembly.

A finite element model of the Ministack geometry was created using 406,720 first order hexahedral elements; a schematic of the mesh is shown in Fig. 4a. The materials of each subcomponent (i.e. ring nut, cover plate, outer can, foam cups, slug) are modeled with the linear elastic properties given in Table 1. For simplicity, the foam is assumed to behave as a linear elastic material and no other viscous damping is included, leaving the only source of energy dissipation within the model as slip occurring at the frictional interfaces. Frictional contact is defined between all blocks using the Dash search algorithm, augmented Lagrange enforcement, and face-face constraints [4]. A Coulomb friction value of 0.4 is used at all interfaces denoted with black dashed lines in Fig. 4b. An implicit solver is used within Sierra/SM to gradually apply a preload as a distributed force to the top face of the retaining ring. The preload is maintained by applying glued constraints between the ring nut and aluminum can, as shown by the red dashed lines in Fig. 4b, and removing the externally applied force. The bottom of the can is fixed during all simulations and this preloaded state is used as the equilibrium for the linearized modal analyses presented in Section 4.1.

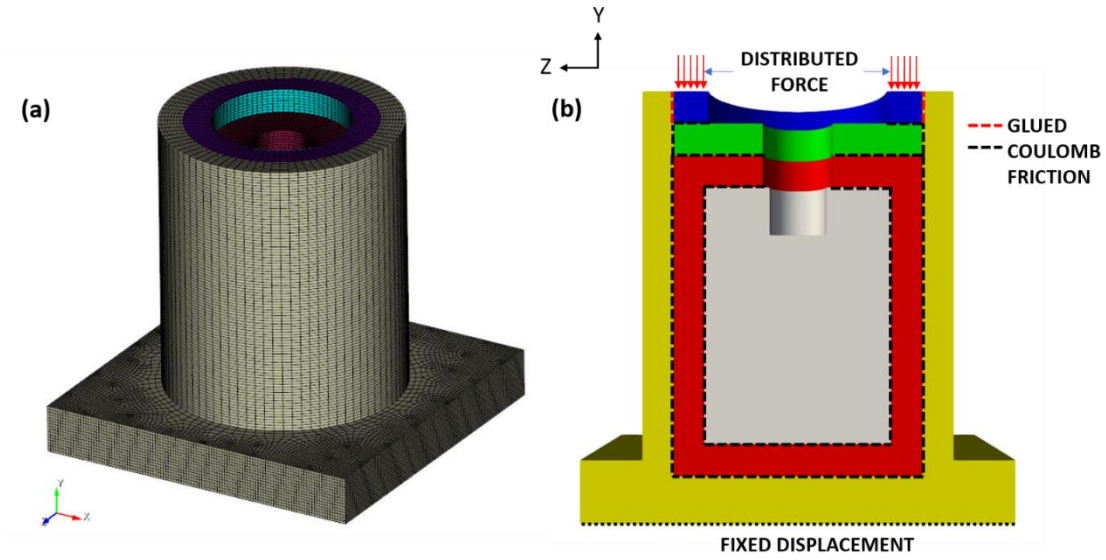


Figure 4. Finite element mesh of Ministack model.

Table 1. Linear elastic material properties of Ministack.

Material	Component(s)	Young's Modulus	Density	Poisson's Ratio
Aluminum 6061-T6	Slug, Outer Can	68.9 GPa	2644 kg/m^3	0.33
Structural Steel	Ring Nut, Cover Plate	206.8 GPa	7800 kg/m^3	0.33
PMDI10	Foam Cups	162 MPa	288.6 kg/m^3	0.30

A reduced order model was created from the mesh in Fig. 4a by adding rigid bar elements to constrain the nodes on the frictional interfaces of interest down to a single node at the midpoint of the surface. The schematic in Fig. 5 shows the locations of the constraints on the side, top, and bottom slug-to-foam interfaces. Two variants of reduced order models are created: a one-joint model with only the side interface represented, and a three-joint model with the side, top and bottom interfaces. A HCB model was generated for each case with a total of 25 fixed-interface modes (up to 14.6 kHz) and either 18 or 42 static constraint modes for the one- and three-joint models, respectively. These constraint mode sets include an additional 6 DOF to account for the spidered node at the bottom surface of the can. The reduced order models are augmented with linear spring and Iwan elements to create the whole joint model between the spidered nodes; these elements are summarized in Table 2. The DOF corresponding to rotation about the y-axis is modeled with four-parameter Iwan elements since these rotational DOF are expected to slip during modal excitation, as discussed further in the next section. The remaining DOF of the whole joint are modeled as stiff springs.

Table 2. Element definitions at HCB interfaces.

DOF	Side Interface	Top Interface	Bottom Interface
X	Linear Spring	Linear Spring	Linear Spring
Y	Linear Spring	Linear Spring	Linear Spring
Z	Linear Spring	Linear Spring	Linear Spring
RX	Linear Spring	Linear Spring	Linear Spring
RY	Four-parameter Iwan	Four-parameter Iwan	Four-parameter Iwan
RZ	Linear Spring	Linear Spring	Linear Spring

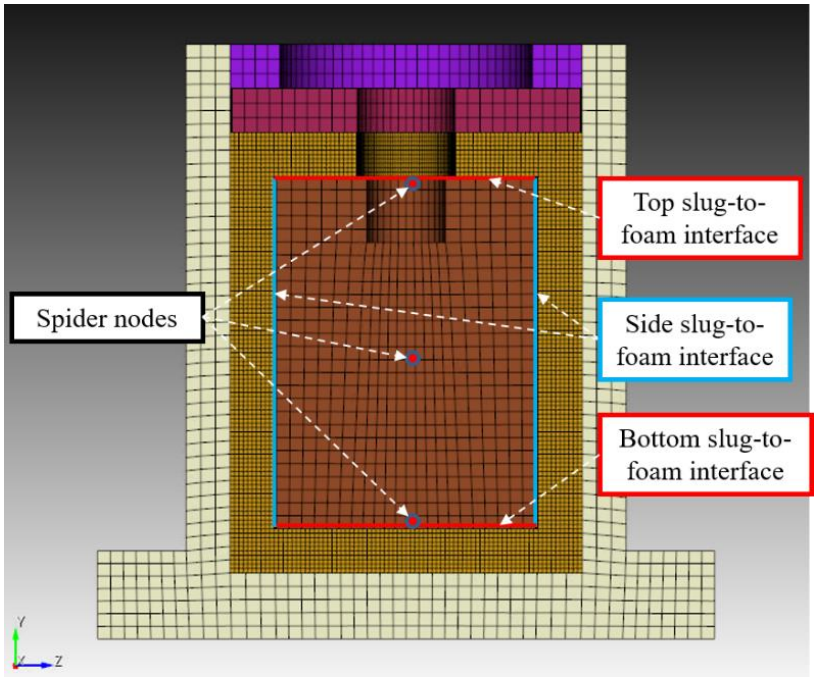


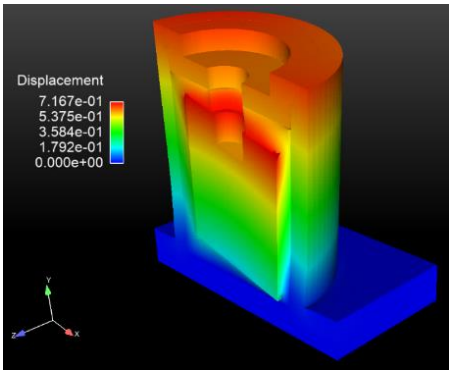
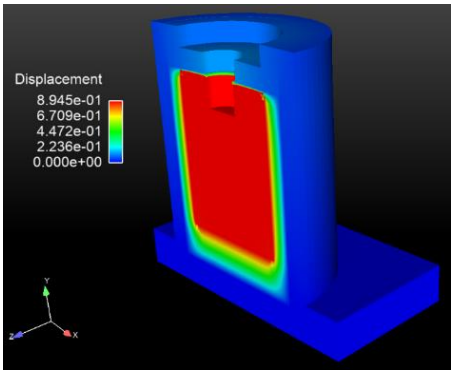
Figure 5. Ministack reduced order model with whole joints between slug-to-foam interfaces.

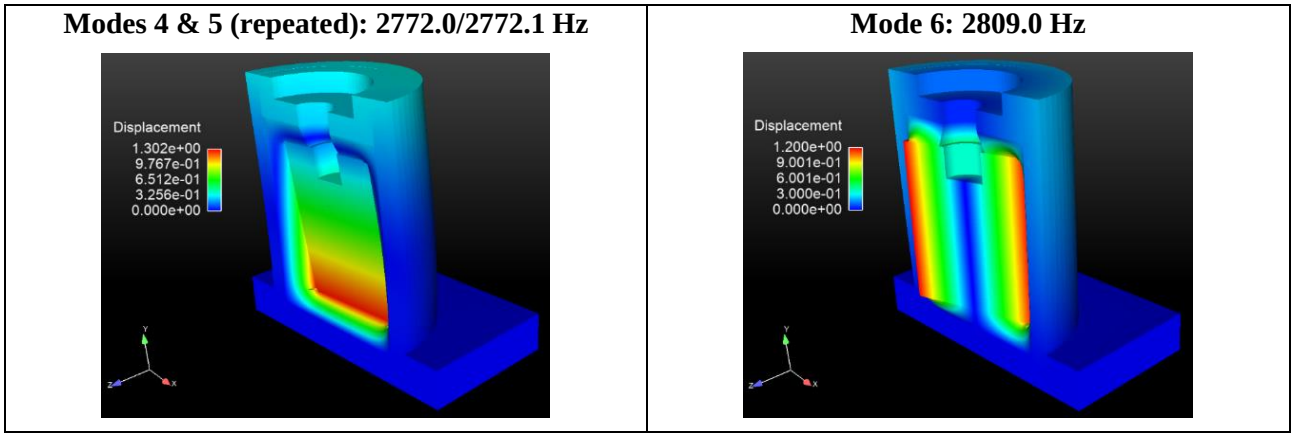
4 Numerical Results

4.1 Quasi-Static Modal Analysis

The QSMA results for the full-order Ministack finite element model were computed using the Sierra Solid Mechanics software [4]. The model was first preloaded to 3,114 N to simulate the assembly process. From the preloaded equilibrium, the deformation and stress states were transferred to the Sierra Structural Dynamics software [23] for the computation of the linearized vibration modes. The code used a search algorithm to tie nodes and faces within a certain distance from one another with multi-point constraints. All the nodes and faces along the slug-to-foam and foam-to-can interfaces were in contact following the preload simulation. The first six linear vibration modes with fixed boundary conditions at the base are provided in Table 3, corresponding to the preloaded, linearized modes in Eq. (12). The mass normalized mode shapes show that these first few elastic modes were dominated by slug translations and rotations within the foam packaging.

Table 3. Linear vibration modes of preloaded Ministack assembly.

Mode 1 & 2 (repeated): 1649.4/1649.5 Hz	**Mode 3: 2390.7 Hz**
	



Mode 6 was chosen as the mode shape of interest to demonstrate the model reduction and calibration for an isolated modal response. The 6th mode shape in Table 3 corresponds to a pure rotation of the slug about the vertical y-axis, and thus was expected to load the frictional interfaces between the slug and foam subcomponents. The modal force in Eq. (13) was calculated using the displacements of the 6th mode shape and the mass matrix, and the force was applied to the preloaded model at 150 values over a log-scale ranging from 1e0 to 1e5 to compute the QSMA results. The amplitude dependent natural frequency and damping ratio are shown in Fig. 6 as a function of the modal displacement, $q_6(\alpha)$. The quasi-static results were solved with a nonlinear implicit solver to obtain solutions at each modal force amplitude needed to calculate the modal backbone curve.

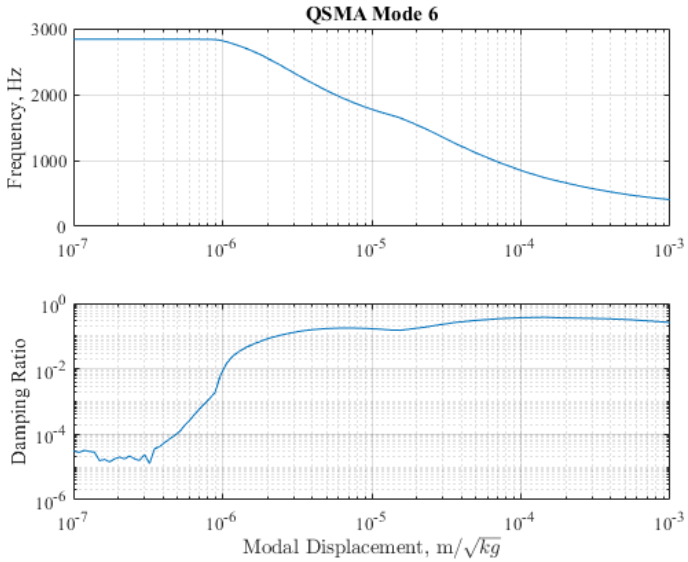


Figure 6. Quasi-static modal analysis results for mode 6 of Ministack assembly.

At low amplitudes, the slug-to-foam interface remained stuck and thus the natural frequency remained unchanged for modal displacements less than $10^{-6}m/\sqrt{kg}$. Similarly, the damping ratio was relatively small below this amplitude since no frictional losses contributed to the energy dissipation. Above a displacement of $10^{-6}m/\sqrt{kg}$, the frictional interface began to slip as evidenced by the drop in natural frequency and sharp increase in damping ratio. This data serves as the reference data to calibrate the whole joint reduced order models in Section 4.3.

The QSMA damping ratio in Fig. 6 was estimated from the modal backbone curve using Masing's rules to construct the cyclic hysteresis curve. This assumption was investigated by directly calculating the modal hysteresis curve by loading/unloading the structure over three cycles to a maximum loading amplitude of $\alpha = 970\ N/\sqrt{kg}$. The third cycle of the modal hysteresis loop was assumed to reach steady state and is compared to the Masing's hysteresis curve in Fig. 7. The backbones from each simulation were essentially

identical, and the hysteresis curves were in relatively good agreement. The modal dissipated energy calculated from Eq. (17) was $7.0 \times 10^{-3}\ N-m/kg$ for the Masing's rule approach and $7.5 \times 10^{-3}\ N-m/kg$ for the direct approach, resulting in approximately 6.7% error in the damping ratio estimate. The efficiency and accuracy of the QSMA approach relies on the assumption that Masing's rules apply for the interfaces and that the modal hysteresis curve can be adequately reconstructed from the backbone curve.

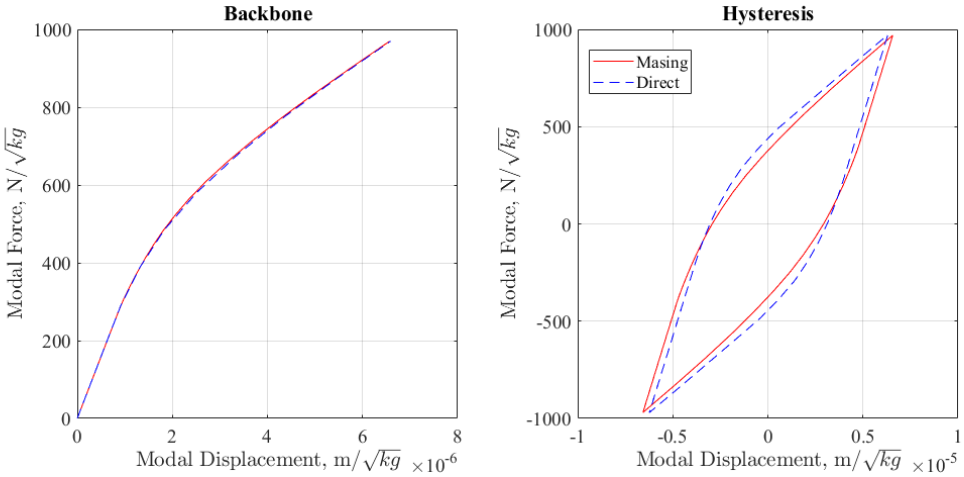


Figure 7. Comparison of modal hysteresis curve computed directly and indirectly using Masing's rules.

4.2 Self-Calibration

A self-calibration study was performed on the one-joint reduced order model to assess the ability of the global optimizer to find a known solution. A single Iwan element corresponding to the radial slug-to-foam interface was defined by an arbitrary set of parameters for F_s, K_T, χ, and β, and the amplitude dependent frequency and damping ratio for the multi-objective function were computed using the QSMA approach on the reduced order equations. The global optimizer was then used to minimize this multi-objective function and evaluate how well it could recover the known parameters. The known and optimized parameters are listed in Table 4 and Fig. 8a shows the comparison between the amplitude dependent frequency and damping ratio obtained with the known solution and the optimized parameters.

The difference between the target Iwan element parameters and the parameters found by the optimizer is less than 1%. The natural frequencies were in near perfect agreement over the entire response range. The damping ratio was also in near perfect agreement for modal amplitude greater than $10^{-6} m/\sqrt{kg}$, but there were noticeable differences at amplitudes below this value. It was observed that the damping ratio was particularly sensitive to small perturbations in the parameter space. This discrepancy at low damping levels was not considered important because the interfaces tend remain stuck at low response amplitudes and do not contribute to energy dissipation in the system. The plot in Figure 8b shows the fitness of the frequency and damping objectives for the entire population in the genetic algorithm history. The evolution trend was fairly linear towards the known solution (shown in red). The known solution does not have an absolute zero objective value because there is interpolation involved during the error calculation of Eq. (18).

Table 4. Comparison of target and optimized Iwan element parameters.

	Target	**Optimization**	**Difference**
K_T	3.74E+07	3.76E+07	0.47%
F_s	10.00	10.00	0.00%
χ	-0.650	-0.653	0.48%
β	0.0040	0.0040	-0.54%

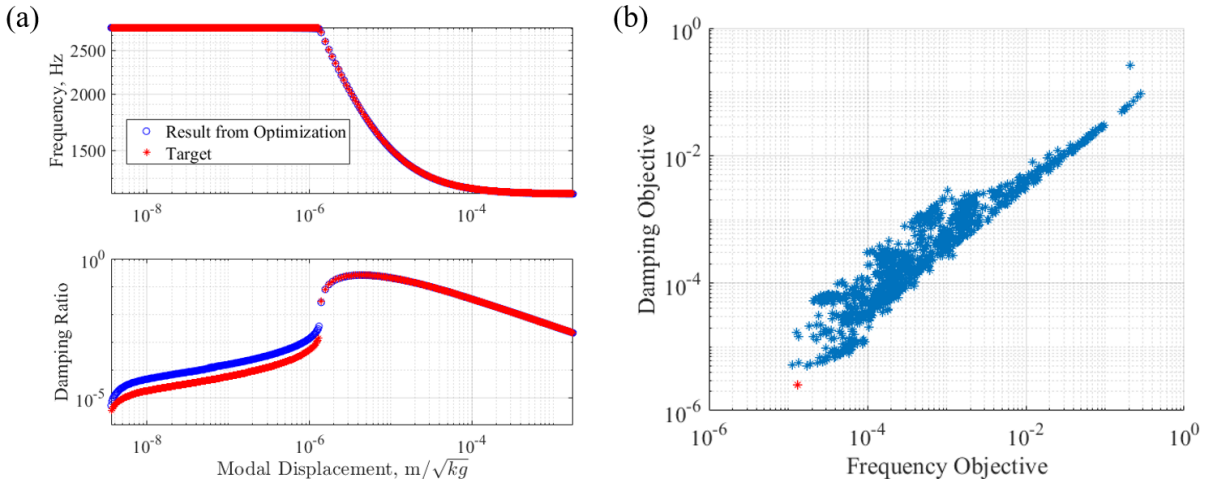


Figure 8. Plot in (a) shows response comparison using known and optimized Iwan parameters of one-joint reduced order model. Plot in (b) shows frequency and damping ratio objective for (blue) entire population of genetic algorithm history and (red) known solution objective value.

4.3 Whole Joint Calibration with Full-order Model Data

The Ministack whole joint calibration was performed by running the global optimization algorithm to find the optimal set of Iwan parameters in the one- and three-joint reduced order models. This was achieved by minimizing the objective function defined by the amplitude dependent natural frequency and damping ratio for the sixth vibration mode such that the reduced order models reproduce the modal characteristics of the high-fidelity model. The one-joint reduced order model with a single Iwan element is presented and discussed first. As discussed in the previous section, the single Iwan element represents the radial slug-to-foam interface in the Ministack assembly. The high-fidelity QSMA results were truncated below a modal response amplitude of $10^{-5}m/\sqrt{kg}$ since the data appears to contain a unique bend in the frequency and damping curves. This data feature indicates that a second interface slipped and the one-joint reduced order model would not capture this since it only contains a single nonlinear interface.

As described in Section 2.3, a multi-objective optimization technique was used to find the optimal set of Iwan parameters that reproduce the high-fidelity response. Figure 9a shows the fitness of the frequency and damping objectives for the entire population of the genetic algorithm history, with the pareto front shown in green. It was observed that both objectives could not be minimized simultaneously, and the optimization algorithm found a pareto front of solutions that best approximated the target. The comparison of the amplitude dependent frequency and damping ratio between the optimized reduced order model and the high-fidelity model are shown in Fig. 9b such that the reduced order model was assigned a subset of the solutions residing in the pareto front. The solutions were close to the target data in the range of 10^{-6} to $10^{-5}m/\sqrt{kg}$, the region in which the interface began to slip. At low amplitude, the damping ratio was in significant disagreement with the reference solution. It was expected that the high-fidelity QSMA damping data was in error since the model should not dissipate energy at low levels and the damping estimate was in the noise of the implicit solver tolerance. At higher response levels above $10^{-5}m/\sqrt{kg}$, the one-joint reduced order model was unable to match the QSMA results, likely due to other interfaces beginning to tangentially slip in this forcing range.

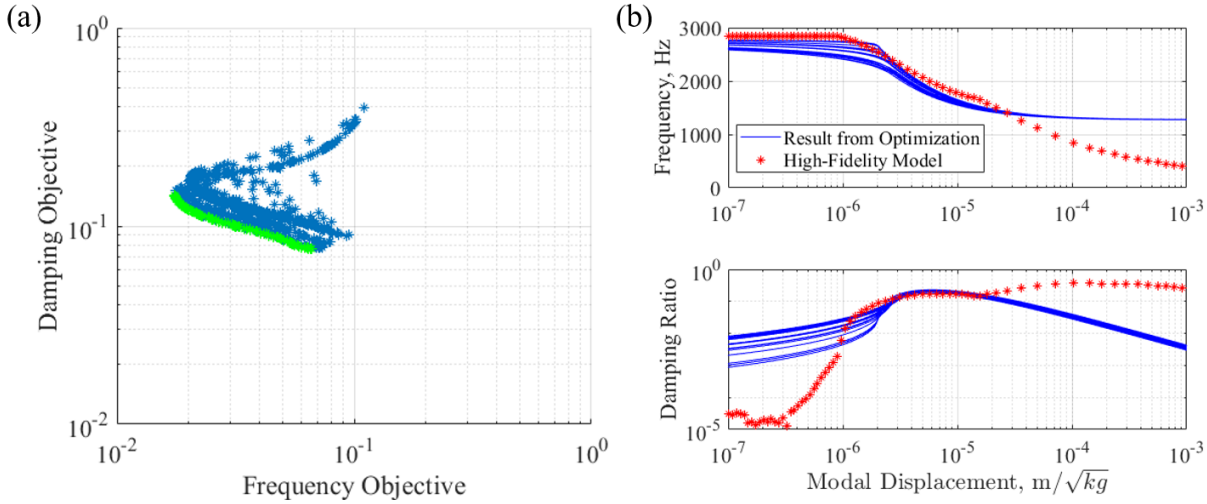


Figure 9. One-joint reduced order model calibration: (a) frequency and damping ratio objective for (blue) entire population of genetic algorithm history, and (green) resulting pareto front; (b) comparison of the (red) QSMA results and (blue) reduced order model using parameters from pareto front.

Two additional nonlinear interfaces were added to the reduced order model to account for the second slip feature observed in the high-fidelity data. The three-joint model included Iwan elements for the top and bottom slug-to-foam interfaces, as well as the radial interface from the one-joint model. This resulted in a total of 12 independent joint parameters to be optimized for each four-parameter Iwan element. The optimization algorithm ran over 350 generations with 90 individuals per generation. The plot in Fig. 10a shows the fitness of the frequency and damping objective for the entire population of the genetic algorithm history, with the pareto front shown in green. The pareto front shows that it was difficult to minimize both objectives at the same time, although the error in Fig. 10a is lower compared to the one-joint model optimization in Fig. 9a. The comparison of pareto front solutions in Fig. 10a show that the large error values stem from the difficulty in matching damping at very low levels; frequency matched well at all amplitudes, even above $10^{-5}m/\sqrt{kg}$. In the linear frequency estimate, the smallest difference was only 4 Hz compared to 40 Hz for the one-joint model.

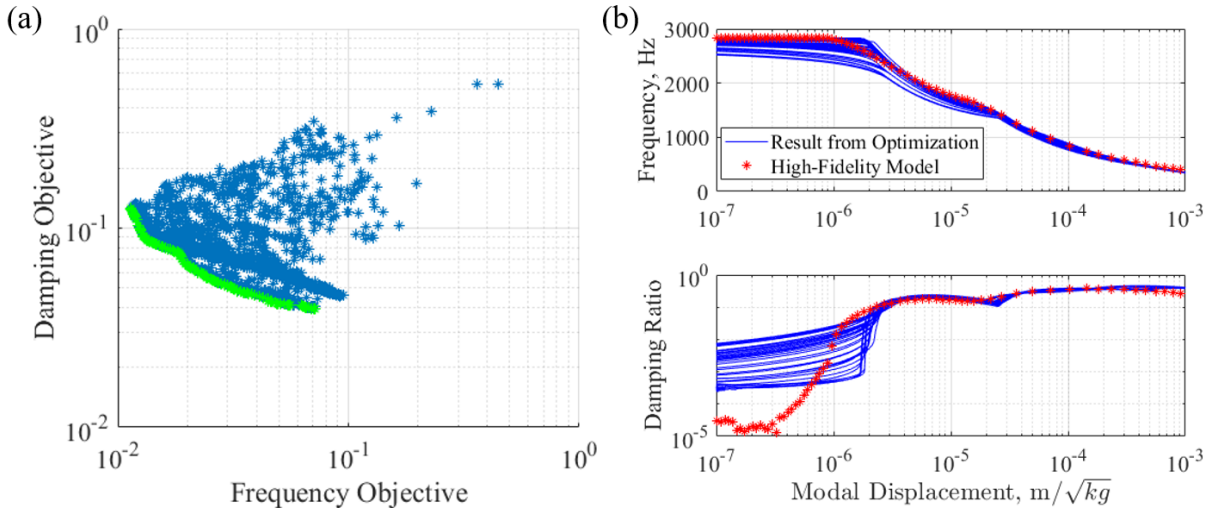


Figure 10. Three-joint reduced order model calibration: (a) frequency and damping ratio objective for (blue) entire population of genetic algorithm history, and (green) resulting pareto front; (b) comparison of the (red) QSMA results and (blue) reduced order model using parameters from pareto front.

The improvement in response calibration suggests that it was important to model all the relevant interfaces that could slip during modal excitation, even at low amplitudes. Capturing these additional interfaces in the three-joint reduced order model resulted in good agreement of the overall shape of the amplitude dependent damping and frequency with the high-fidelity model. The most difficult region of the data to

match was the onset of slip of the first interface. The high-fidelity model had a more gradual transition (more evident in the damping) than the reduced order model, which appeared to change more abruptly. For reference, the Iwan parameters corresponding to the best match in frequency from Fig. 10a are provided in Table 5. The top interface had a higher slip force, F_s, and a relatively lower stiffness value than the side and bottom interfaces. This difference is a bit unexpected since the preload forces on the top interface should be similar to the bottom interface. Nevertheless, this set of parameters provided optimal solutions to match the full-order model response.

Table 5. List of optimized Iwan element parameters.

	Radial Iwan	**Top Iwan**	**Bottom Iwan**
K_T	1.73E8	9.15E5	5.49E8
F_s	12.65	50.00	24.14
χ	-0.8140	-0.9843	-0.2644
β	1.05E-5	4.33E-5	0.0016

5 Conclusion

A whole joint model calibration routine was developed and demonstrated on the Ministack finite element model to evaluate how modeling decisions of frictional interfaces affect the ability to obtain an optimal parameter set that predicts matching responses. A multi-objective function is defined based on the amplitude dependent frequency and damping ratio for a mode of interest computed from the quasi-static modal analysis technique recently developed in [17, 18]. The reference data is calculated from high-fidelity model simulations that are obtained from a nonlinear statics solver available within most commercial finite element codes. A whole joint reduced order model of the structure is developed by reducing the linear portion of the model with Hurty/Craig-Bampton substructured models and reducing the nonlinear, frictional interfaces down to a single node location with multi-point constraints. A whole joint model connects the linear substructured models, and four-parameter Iwan element are used to represent the nonlinear slip behavior.

The results from the Ministack example reveal that the reduced order model needs sufficient flexibility in the interface degrees-of-freedom to accurately represent the slip occurring within the full-order model. Even after optimization, the one-joint reduced order model only captured a small portion of the modal response. However, adding more nonlinear degrees-of-freedom with two additional slip interfaces allowed for the optimization to better match solutions from the high-fidelity model. In future works, these models will be validated by comparing transient response predictions from the calibrated reduced order model to high-fidelity model simulations. In addition, this work will extend the multi-objective optimization to simultaneously fit whole joint parameters to two or more nonlinear modes for capturing excitations beyond a single mode response.

Acknowledgements

The authors would like to thank Professor Matthew S. Allen from the University of Wisconsin-Madison for providing the codes to perform the quasi-static modal analysis. Sandia National Laboratories is a multimission laboratory managed and operated by National Technology & Engineering Solutions of Sandia, LLC, a wholly owned subsidiary of Honeywell International Inc., for the U.S. Department of Energy's National Nuclear Security Administration under contract DE-NA0003525. SAND2018-6002 C

References

[1] C. F. Beards, "Damping in structural joints," *The Shock and Vibration Digest,* vol. 24, no. 7, pp. 3-7, 1992.

[2] L. Gaul and R. Nitsche, "The Role of Friction in Mechanical Joints," *Applied Mechanics Reviews,* vol. 54, no. 2, pp. 93-106, 2001.

[3] S. Bograd, P. Reuss, A. Schmidt, L. Gaul, and M. Mayer, "Modeling the dynamics of mechanical joints," *Mechanical Systems and Signal Processing,* vol. 25, no. 8, pp. 2801-2826, 2011.

[4] Sierra Solid Mechanics Team, "Sierra/SolidMechanics 4.42 User's Guide," SAND2016-9916 O, Sandia National Laboratories, Albuquerque, NM, October 2016.

[5] D. J. Segalman, "A Four-Parameter Iwan Model for Lap-Type Joints," *Journal of Applied Mechanics,* vol. 72, no. 5, pp. 752-760, 2005.

[6] R. R. J. Craig and M. C. C. Bampton, "Coupling of Substructures for Dynamic Analysis," *AIAA Journal,* vol. 6, no. 7, pp. 1313-1319, 1968.

[7] W. C. Hurty, "Vibrations of structural systems by component mode synthesis," *Journal of the Engineering Mechanics Division,* vol. 86, no. 4, pp. 51-70, 1960.

[8] Y. Li and Z. Hao, "A six-parameter Iwan model and its application," *Mechanical Systems and Signal Processing,* vol. 68–69, pp. 354-365, 2016.

[9] M. P. Mignolet, P. Song, and X. Q. Wang, "A stochastic Iwan-type model for joint behavior variability modeling," *Journal of Sound and Vibration,* vol. 349, pp. 289-298, 2015.

[10] R. Bouc, "Forced vibration of mechanical systems with hysteresis," presented at the Fourth Conference on Non-linear Oscillation, Prague, Czechoslovakia, 1967.

[11] Y.-K. Wen, "Method for random vibration of hysteretic systems," *Journal of the engineering mechanics division,* vol. 102, no. 2, pp. 249-263, 1976.

[12] M. Oldfield, H. Ouyang, and J. E. Mottershead, "Simplified models of bolted joints under harmonic loading," *Computers & Structures,* vol. 84, no. 1, pp. 25-33, 2005.

[13] A. E. Charalampakis and C. K. Dimou, "Identification of Bouc–Wen hysteretic systems using particle swarm optimization," *Computers & Structures,* vol. 88, no. 21–22, pp. 1197-1205, 2010.

[14] A. E. Charalampakis and V. K. Koumousis, "Identification of Bouc–Wen hysteretic systems by a hybrid evolutionary algorithm," *Journal of Sound and Vibration,* vol. 314, pp. 571-585, 2008.

[15] D. Wang, C. Xu, X. Fan, and Q. Wan, "Reduced-order modeling approach for frictional stick-slip behaviors of joint interface," *Mechanical Systems and Signal Processing,* vol. 103, pp. 131-138, 2018.

[16] Z.-C. Wang, Y. Xin, and W.-X. Ren, "Nonlinear structural joint model updating based on instantaneous characteristics of dynamic responses," *Mechanical Systems and Signal Processing,* vol. 76–77, pp. 476-496, 2016.

[17] M. S. Allen, R. M. Lacayo, and M. R. W. Brake, "Quasi-static Modal Analysis based on Implicit Condensation for Structures with Nonlinear Joints," presented at the ISMA2016 - International Conference on Noise and Vibration Engineering, Leuven, Belgium, 2016.

[18] H. Festjens, G. Chevallier, and J.-l. Dion, "A numerical tool for the design of assembled structures under dynamic loads," *International Journal of Mechanical Sciences,* vol. 75, pp. 170-177, 2013.

[19] R. M. Lacayo, "An investigation on Iwan models for capturing the amplitude-dependent behavior of structures with bolted joints," M.S. Thesis, University of Wisconsin-Madison, 2017.

[20] E. A. Jewell, M. S. Allen, and R. M. Lacayo, "Predicting Damping of a Cantilever Beam with a Bolted Joint Using Quasi-Static Modal Analysis," presented at the ASME 2017 International Design Engineering Technical Conferences IDETC/CIE, Cleveland, OH, 2017.

[21] F.-A. Fortin, F.-M. D. Rainville, M.-A. Gardner, M. Parizeau, and C. Gagné, "DEAP: Evolutionary algorithms made easy," *Journal of Machine Learning Research,* vol. 13, pp. 2171-2175, 2012.

[22] D. Kalyanmoy, S. Agrawal, A. Pratap, and T. Meyarivan, "A Fast Elitist Non-Dominated Sorting Genetic Algorithm for Multi-Objective Optimization: NSGA-II," in *International Conference on Parallel Problem Solving from Nature*, Paris, France, 2000, pp. 849-858: Springer

[23] Sierra Structural Dynamics Development Team, "Sierra Structural Dynamics-User's Notes," SAND2016-3046 O, Sandia National Laboratories, Albuquerque, NM, April 2016.

Modal impact testing for estimating bolted joint tightness

M. Brøns [1], **J.J. Thomsen** [1], **A. Fidlin**[2], **D. Tcherniak**[3], **S.M. Sah**[1]
[1] Technical University of Denmark, Department of Mechanical Engineering,
Nils Koppels Allé B404, 2800 Lyngby, Denmark
e-mail: **maribr@mek.dtu.dk**

[2] Karlsruhe Institute of Technology, Department of Mechanics,

[3] Brüel & Kjær Sound and Vibration Measurement A/S

Abstract
The tension level in a bolt is difficult to determine and control. Based on simple hammer impacts, a novel technique is proposed to quantify the level of bolt tightness by analyzing natural frequencies and damping ratios of the bolt. The technique is investigated experimentally by testing two different bolts (short and long) and measuring accelerations in the transverse directions. At low tension the squared natural frequency of the first bending mode increases strongly with tension. As the bolt is gradually tightened, the squared frequency starts changing more weakly and approximately linearly with tension. By signal processing the transient response from the hammer impact, and treating problems of beat-frequencies due to the near cross sectional symmetry in the bolt, the corresponding effective linear damping ratios can also be obtained. Further, a scanning laser Doppler vibrometer (SLDV) is used to measure the mode shapes of the long bolt and it is studied how these change with tension.

1 Introduction

Bolts are used in numerous engineering structures and the tightness of a bolted joint is of high importance, especially if the joint secure e.g. wind turbine blades or large machinery elements, where failure is unsafe and unacceptable. If the tightness of a bolted joint could be estimated by analysing measured accelerations from a single impulse hammer impact, it could reduce maintenance costs and allow a way to check the health of a bolted joint without using heavy equipment such as hydraulic tensioners.

Various techniques are used to estimate bolt tension, most commonly torque control [1], turn control [1], and ultrasonic methods [2, 3, 4]. Here the potential in estimating bolt tension from transient bolt vibrations is studied, by analysing a set of experiments. Signal analysis of a transient response in a bolt, when impulse hammer impacted, is used to examine the first transverse natural frequency and corresponding damping ratio. To see how these dynamic properties relate to tension, it is studied how these change when subjected to different levels of tension. Furthermore a scanning laser Doppler vibrometer (SLDV) is used to measure mode shapes of a bolt when tightened to different levels of tension, to reveal how the boundary conditions effectively change as the bolt is tightened.

2 Experimental setup

Figure 1 shows the experimental setup. A single bolt is tightened with a nut to a solid aluminium structure with washers on the outside, and uni-axial accelerometers (B&K 4397) are mounted on the bolt head to

measure vibrations. A force washer (HBM KMR 100kN) is placed beneath the bolt head to measure the tension. The setup is isolated mechanically as it is placed on a foam block. The hit surface is filed flat, and the impact is applied by a pendulum hammer to decrease variations between hits.

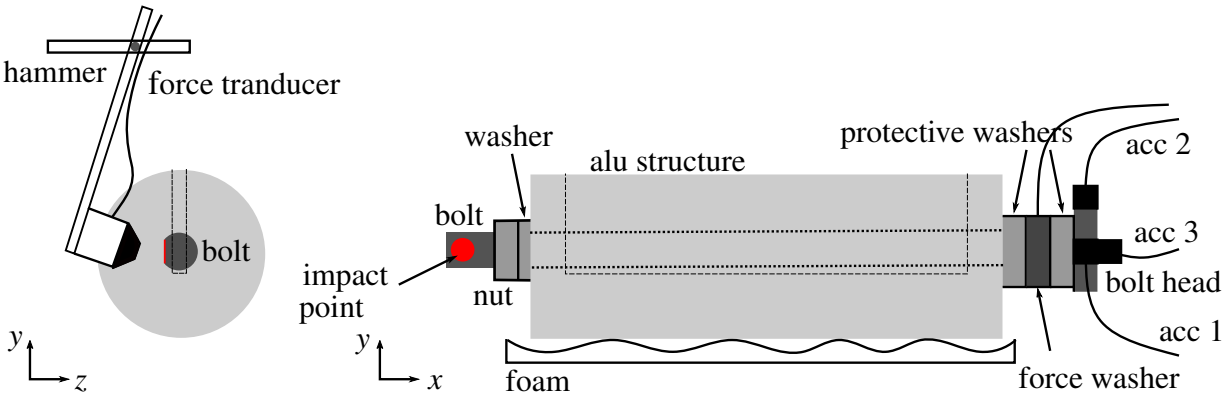


Figure 1: Experimental setup

Tests are made on two bolts with the same properties except for the length: one is referred to as *short* (M12×140) the other as *long* (M12×250). The bolts are tightened in ten load steps between σ/σ_y = 0.05 and σ/σ_y = 0.79, where $\sigma_y = 640$ MPa is the bolt material yield stress, and σ the actual axial stress. The nominal tension in a bolt is typically $\sigma/\sigma_y \approx 0.7$ [1]. The tightening is done with a hydraulic tensioner (HBM model HTS 9 M12×1.75). The force F applied by the tensioner translates to stress σ by $\sigma = F/A_s$, where A_s is the stressed cross section of the bolt [1]. After ten load steps the bolted structure is disassembled and reassembled before the test is repeated (3 tests for each bolt).

A long narrow gap in the aluminium structure enables the SLDV (Polytec PSV-500 [6]) to measure vibrations along the bolt length so the mode shapes can be obtained. Figure 2 shows the scanning points on the long bolt. There are fourty points along the bolt length. A hammer impact is applied, and the SLDV measures one point, then a new impact is applied, and the next point is measured, and so on. The boundaries are of most interest because they are expected to change with tension [5]. However, near the bolt ends, vibrations can only be measured on nut and force washer, and not directly on the bolt shaft, which will unavoidably introduce some error in the extracted mode shapes. Despite this obstacle, the end points are still relevant, because it is expected that if vibrations are measured on the nut and force washer then the bolt must be vibrating too.

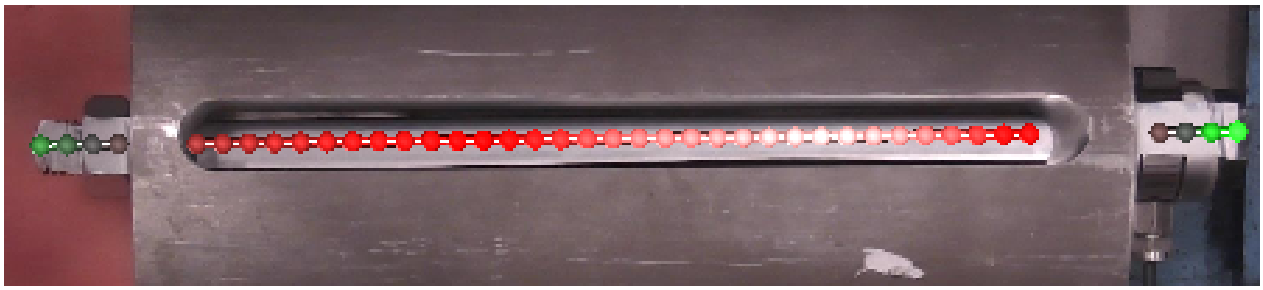


Figure 2: SLDV measurement points (red/green dots) for the long bolt.

3 Theoretical natural frequencies for an axially stressed clamped-clamped beam

A simple model is to consider a bolt as a Bernoulli-Euler beam exposed to axial tension. The j'th transverse natural frequency can then be calculated as [7]:

$$\omega_j = \frac{\lambda_j^2}{ls}\sqrt{\frac{E}{\rho}\left(1+\frac{\sigma}{E}\left(\frac{K_j s}{\lambda_j^2}\right)^2\right)}, \tag{1}$$

where λ_j is an eigenvalue for mode j (depends on the boundary conditions), l the bolt length, E Young's modulus, ρ the density, σ the applied axial stress, K_j a mode shape dependent constant, $s = l\sqrt{A/I}$ the slenderness ratio, where A is the cross-sectional area of the bolt and I the area moment of inertia. The squared natural frequencies increase linearly with axial stress σ in Eq.(1), with a proportion depending on the slenderness s of the bolt; the more slender a bolt, the bigger the influence of the axial stress term on natural frequency. In the particular case of a clamped-clamped beam $\lambda_1 = 4.73$, $\lambda_2 = 7.85$, $K_1^2 = 12.3026$, and $K_2^2 = 46.05$. In Section 5.1 Eq. (1) is compared to the experimental data for varying σ.

4 Signal processing

At each level of tension the accelerations of freely decaying vibrations measured at the bolt head are signal processed to obtain the dynamic properties. Figure 3 shows a typical acceleration time history after an impulse hammer impact, prior to signal processing. Figure 4 shows this signal filtered with a 4th order Butterworth passband filter, so that it only contains energy from the first transverse natural frequency ω. Figure 5 shows the Fourier transforms of the unfiltered signal, and also the signal filtered around each of the first two transverse natural frequencies. As wanted, the first filtered signal only has a significant magnitude at the first natural frequency peak, and likewise for the second natural frequency.

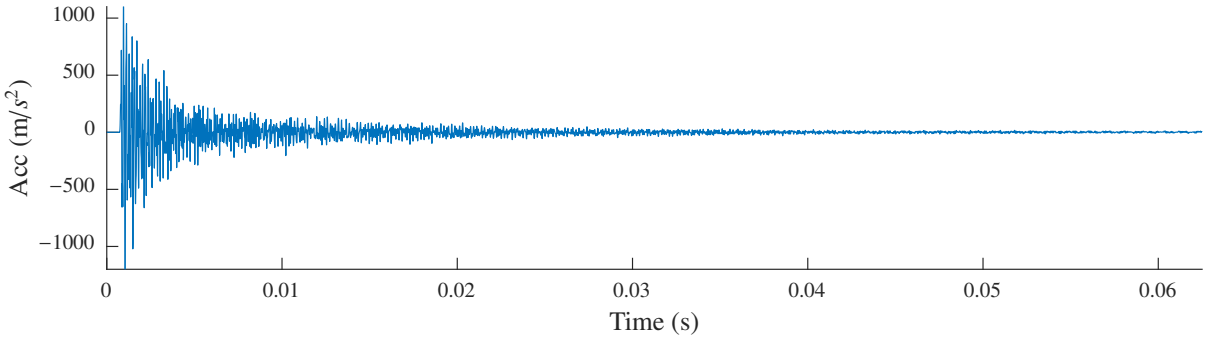


Figure 3: Free decay of acceleration (stress σ/σ_y=0.43).

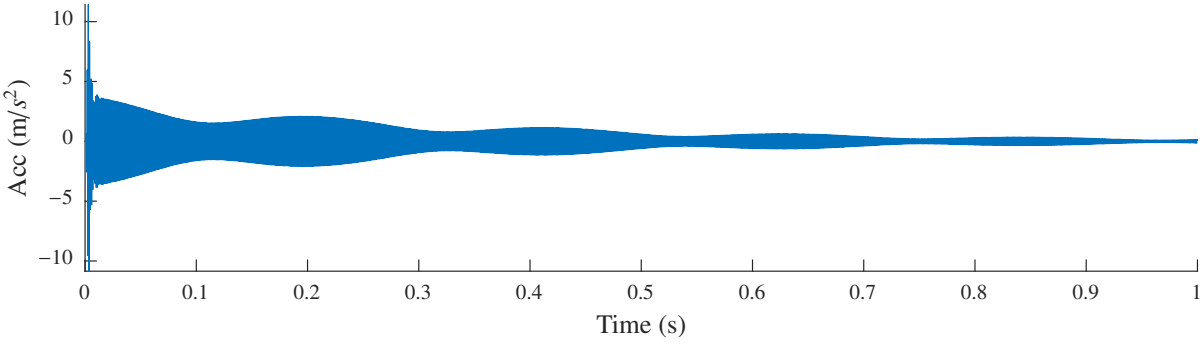


Figure 4: Filtered acceleration signal, 1st natural frequency.

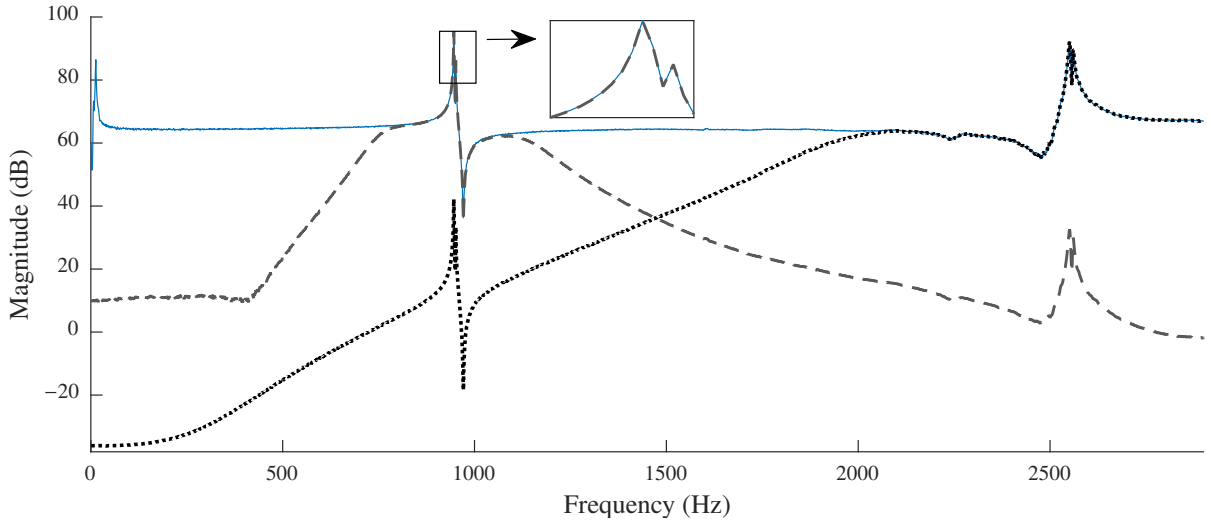


Figure 5: Fourier Transforms of accelerations. Solid line: unfiltered signal; Dashed line: filtered around 1st natural frequency; Dotted line: filtered around 2nd natural frequency; Box insert: zoom of the double peaks, 5 Hz apart.

The equivalent linear damping ratio ζ of the first transverse mode can be estimated by fitting an exponential decay envelope to the filtered signal in Figure 4. The exponential fit function has the form $A_0 e^{-\beta t}$, where A_0 is the initial amplitude, and $\beta = \zeta\omega$ the decay rate. However, the signal in Figure 4 is beating, i.e. the amplitude is slowly modulated, due to the near-symmetry in the bolts. The two transverse frequencies in the xy and xz plane (cf. Figure 1) are almost identical. In this example they are 5 Hz apart, which also shows as a double peak in the box insert on Figure 5. To overcome this problem, the accelerations measured by the accelerometer perpendicular to the impact directions are also used, and the total vibration amplitude is calculated as:

$$A = \sqrt{A_1^2 + A_2^2} \tag{2}$$

where A_1 and A_2 is the vibration amplitude in each transverse direction. Figure 6 shows the filtered signals, in both directions, of mode 1, and the corresponding envelope, and also the total envelope determined from (2). Using the total amplitude eliminates the beating, and a reasonable exponential envelope fit and a meaningful decay rate β can be obtained. In this way, the effective linear damping ratio ζ can be estimated for the bolts at each tension level.

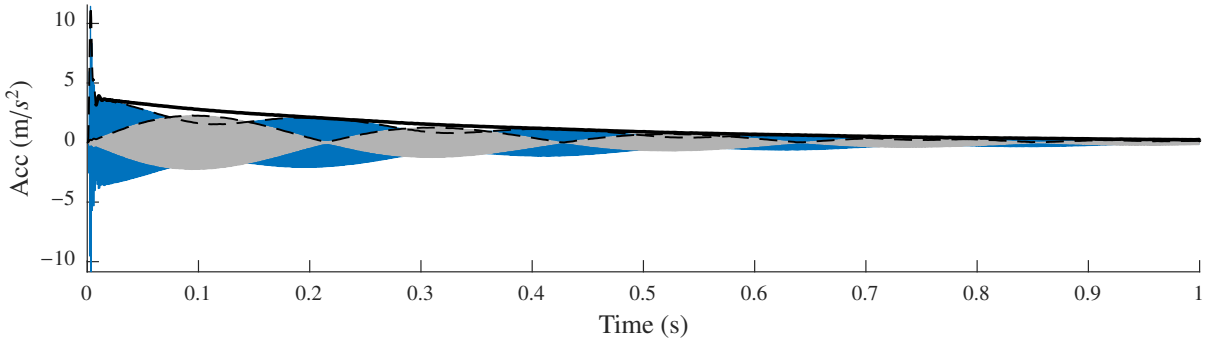


Figure 6: Filtered time signal of 1st natural frequency in two directions and envelopes. Dark/blue: direction of hit; Light/grey: perpendicular to hit direction; Dashed line: A_1 and A_2; Solid line: A.

5 Results

5.1 Natural Frequency

Figure 7a and 7b shows the squared first transverse natural frequency as a function of tension for the long and short bolt, respectively. The dashed line is the squared frequency as a function of axial stress σ for a clamped-clamped beam (cf. Eq. (1)). The model fits the data well for the long bolt (Fig.(a)), when the bolt is tightened more than about $\sigma/\sigma_y = 0.2$, suggesting that the boundaries are effectively clamped. In [5] Sah sets up a model that explains the frequency increase for the whole tension range by a beam model with linear springs at the boundaries, whose stiffness increase with tension. For the short bolt (Fig.(b)) the gradient of the linear beam model does not fit as good as for the long bolt. This can partially be attributed to the bolt's short length: for very short bolts the Bernoulli-Euler beam model is insufficient, as rotary inertia and shear deformation significantly influence beam vibrations which the model does not account for. For every tension level there are three successive hammer hits, but as the measured frequency is the same for all hits it does not show on the figure. The three test series (given by different markers), with full axial unloading in between, follow the same frequency-tension relation. Conclusively, the estimated natural frequencies are reproducible for the setup, both in case of immediate repetition, and when the setup has been reassembled.

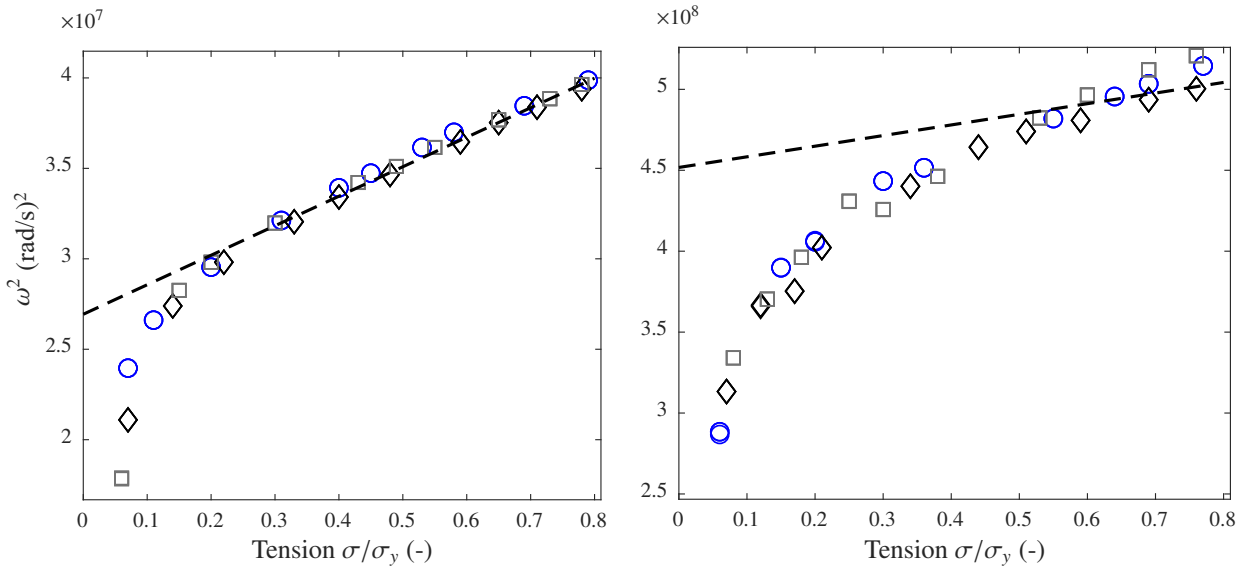


Figure 7: Measured 1st natural frequency squared as a function of tension. **(a)** long bolt **(b)** short bolt. Each test series indicated by ○, ◇, □. For every tension level there are three measurements. Dashed line: squared natural frequency for a clamped-clamped beam as a function of axial tension (cf. (1))

5.2 Damping ratio

Figure 8 shows the estimated linear damping ratio as function of tension for the two bolts. As appears, the damping ratio decreases with tension for both bolts. For tension below about σ/σ_y = 0.2 the damping ratio is significantly larger than for the more tightened bolt. While measuring, one can by listening to the dull sound from the hammer impact hear that the bolt is weakly tightened. The short bolt's first mode is much more damped than the long bolt, possibly ascribed to the fact that the boundaries make up a larger part of the bolt, thus the boundary friction influence more. A similar damping-tension relation (not shown) exists for the second mode, but the decrease in damping with tension is less pronounced.

For every tension level there are three successive hammer hits. For the lowest tension level the estimated damping ratio vary slightly between hits, but for higher tension there is only insignificant variation between hits. The three test series (given by different markers) generally follow the same damping ratio-tension relation, although there is more variation than for the natural frequencies (cf. Figure 7). Conclusively, the estimated damping ratios are generally reproducible for the setup, both in case of immediate repetition, and when the setup has been reassembled.

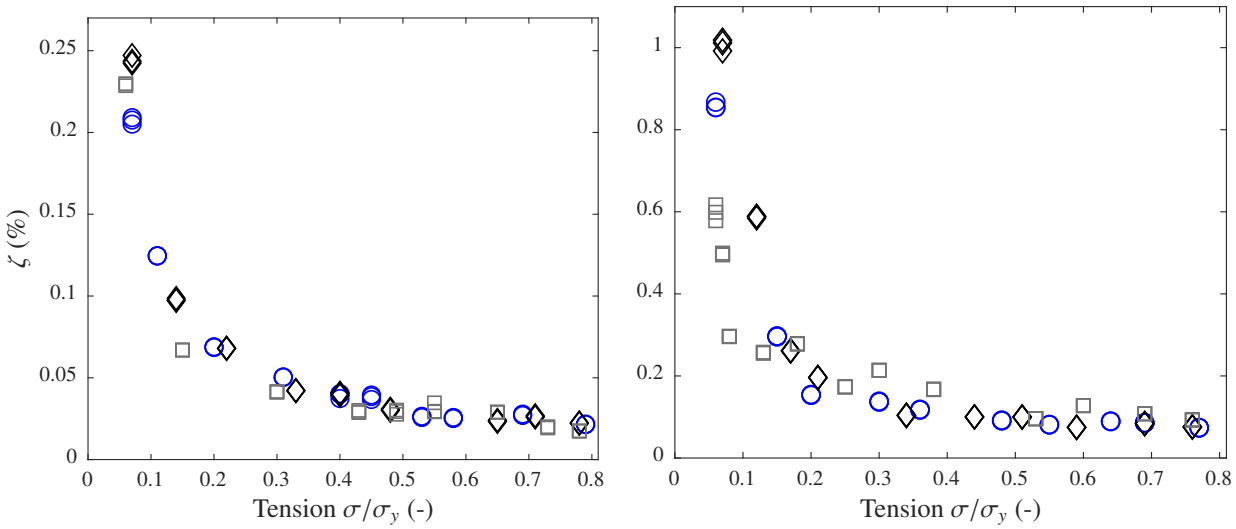


Figure 8: Damping ζ as a function of tension. **(a)** long bolt **(b)** short bolt. Markings as for Figure 7.

5.3 Mode shapes

The lowest mode shapes for the long bolt are measured with the SLDV. Figure 9 shows the first three transverse bending modes. The measured modes to the left are of a weakly tightened bolt, along with the theoretical mode shapes for a free-free Bernoulli-Euler beam. The right shows the modes for three higher levels of tension together with the corresponding theoretical mode shape for a clamped-clamped Bernoulli-Euler beam. For the weakly tightened bolt the S/N-ratio for the first mode is small, why the emphasis in this case is on the second and third mode. Here there are deformations and slopes at the boundaries, however not to the degree of the free-free beam model, thus indicating that the small tension in the bolt induces at least some elastic stiffness at the boundaries. Beside this, the curvature at the boundaries is small, also indicating that the boundaries are not completely free, but weakly elastic. As soon as the bolt is tightened to $\sigma/\sigma_y = 0.19$ no significant deformations at the boundaries are observed, and the slope of the mode shapes approaches zero at the boundaries, supporting the theory of the well-tightened bolt effectively behaving as a clamped-clamped beam (cf. the dashed line in Figure 7a).

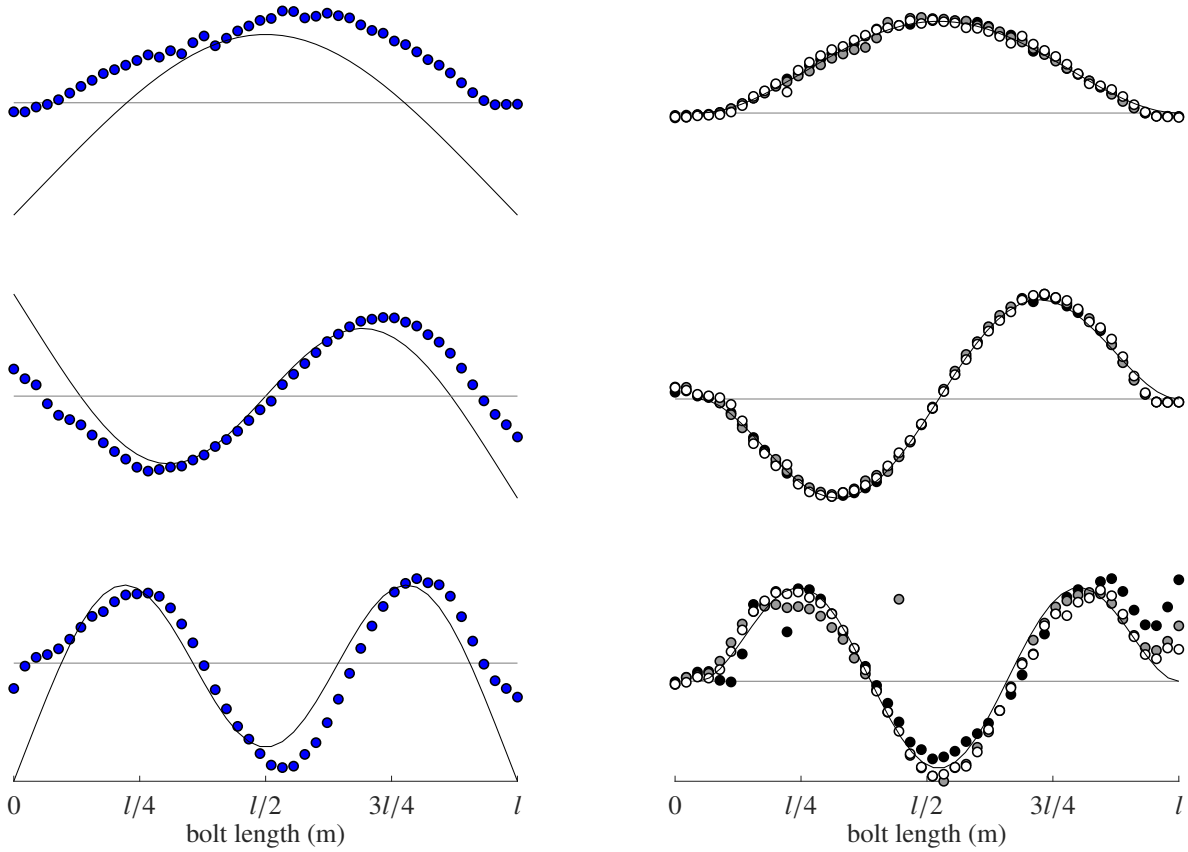


Figure 9: The first three mode shapes of the long bolt for different tension levels. Left: Measured modes (filled circle markers) for a weakly tightened bolt ($\sigma/\sigma_y = 0.03$), and theoretical free-free beam modes (solid line); Right: Measured modes ([black, grey, white] circle markers) for a stronger tightened bolt (σ/σ_y = [0.19, 0.34, 0.65]), and theoretical clamped-clamped beam modes (solid line).

6 Conclusions

The mode shape tests are not applicable for estimating tension, as bolts are can be hidden inside structures, but the tests support the theory of bolts gradually approaching an effectively clamped-clamped beam as tightened. The mode shapes show that there is less and less translation and rotation movement at the boundaries when the bolt is tightened. Therefore it is expected that the boundary friction decreases, which seems to also be the case, as the experimentally estimated damping ratio decreases with tension.

If a bolt is so weakly tensioned that it is unsafe, a single hammer hit could reveal it, as the damping ratio will be strikingly large; it is a good measure for discovering a not strongly tightened bolt without much effort. During initial mounting, one could carry out three successive hits, tightening the bolt in between; if the damping ratio stops decreasing between the second and third impact, the bolt could be considered tight enough. Along with the measured first bending natural frequency, this can give an indication of the tightness of the bolt so far.

The tests show that the measured vibrations depend on bolt tension, and the results contributes insights into a vibration based estimation of bolt tension. Future tests could be to study the effect of impact strength, amplitude level, other bolt dimensions, and multi-bolt structures, as well as in-situ tests of real structures, to see how robust these changes are.

Acknowledgements

This work is financially supported by the Danish Council for Independent Research, grant DFF-6111-00385.

References

[1] J. H. Bickford, *Introduction to the Design and Behavior of Bolted Joints, Non-Gasketed Joints* (Fourth Ed.), CRC Press (2007).

[2] E. Persson, A. Roloff, *Ultrasonic tightening control of a screw joint : A comparison of the clamp force accuracy from different tightening methods*, in *Proceedings of the Institution of Mechanical Engineers Part C-Journal of Mechanical Engineering Science* (2016), 230 (15), pp. 2595-2602.

[3] S. A. Nassar, A. B. Veeram, *Ultrasonic control of fastener tightening using varying wave speed*. Journal of Pressure Vessel Technology-Transactions of the Asme, Vol. 128, No.3, (2006), pp.427-432.

[4] S. G. Joshi, R. G. Pathare, *Ultrasonic Instrument Bolt Stress*, Ultrasonics, Vol. 22, No.6,(1984), pp.270-274.

[5] S. M. Sah, J. J. Thomsen, M. Brøns, A. Fidlin, D. Tcherniak, *Estimating bolt tightness using transverse natural frequencies*, Journal of Sound and Vibration (accepted for publication).

[6] M.Brøns, J. J. Thomsen, *Scanning Laser Vibrometry for Vibration Analysis* [abstract], in *Proceedings of the 1st International Symposium on Multi-Scale Experimental Mechanics - ISMEM 1*, DTU Risø Campus, Roskilde, October 5, (2016), 2 pp.

[7] J. J. Thomsen, *Vibrations and Stability : Advanced Theory, Analysis, and Tools*, Springer-Verlag (2003).

Identification of contact parameters for dry friction joints

K. Willner [1]
[1] FAU, Lehrstuhl für Technische Mechanik,
Egerlandstraße 5, 91058 Erlangen, Germany
e-mail: **kai.willner@fau.de**

Abstract

We present a strategy for identification of contact parameters for dry friction joints. The contact stiffness in normal and tangential direction is obtained from a halfspace simulation of the rough surface contact, while the slip limit and a slip stiffness are identified from measured hysteresis data. Calculated FRF obtained from time domain calculations simulating a swept sine measurement and a multi-harmonic balance solution are compared to measured FRF data of a Gaul-type resonator.

1 Introduction

The efficient identification of contact parameters for friction joints is still an interesting topic in structural dynamics. The present paper proposes a mixed approach, where the contact stiffness in normal and tangential direction are determined by a halfspace simulation of the contacting rough surfaces [8]. This step can be done a priori without any dynamic measurements. The slip limit however has to be determined from measured hysteresis data, since there is so far no reliable way to predict friction coefficients exactly.

This approach is demonstrated on an isolated friction joint experiment, the so-called Gaul-resonator, introduced by Gaul and Bohlen in [2] and subsequently investigated in [3, 6, 7]. The identified parameters are subsequently used in the time-domain simulation of a swept-sine measurement of the resonator experiment. Frequency response functions (FRFs) obtained from actual and simulated measurements show very good agreement. Comparison with FRFs obtained from a multi-harmonic balance method show also good agreement, however a very high number of harmonics has to be used.

The following two sections introduce the resonator experiment and the corresponding finite element model with some basic parameter identification regarding global masses and stiffness, respectively. The identification of the contact parameters is shown in Sec. 4. Time domain results are presented in Sec. 5 and compared to frequency domain results in Sec. 6. Finally, a short conclusion is given in Sec. 7.

2 Experimental set-up

The experimental set-up consists of two monolithic masses shown in Fig. 1.

One of the masses (the left one in Fig. 1) has a cut-out such that the thin remaining bars can act as bending springs. The parts can be joined by a simple bolted lap joint to form the two-mass system shown in Fig. 2. The system is driven by an electromagnetic shaker at the left mass. Accelerations are measured at the left mass opposite to the excitation point (a_1), opposite to the joint (a_2), and on the right mass (a_3). Compared to the soft bending spring, the masses can be assumed rigid, such that the transmitted joint force T can be simply evaluated by

$$T = ma_3 \ , \tag{1}$$

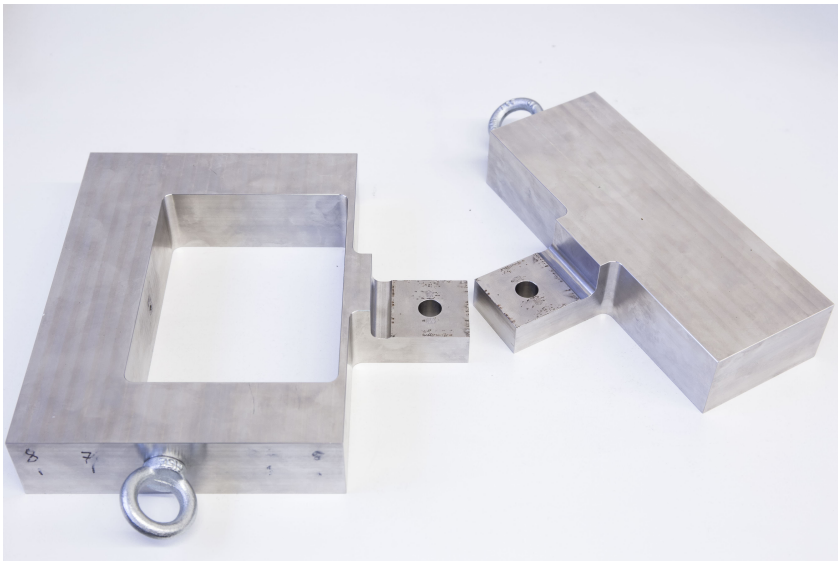


Figure 1: Gaul-type resonator: Parts

where m is the mass of the right part. The relative displacement in the joint can be obtained by integrating twice the differential acceleration

$$\Delta a = a_3 - a_2 \ . \tag{2}$$

The bolt is instrumented by strain gauges to measure the normal load and a washer-like piezo-actor is used to adjust the normal load.

By driving the system close to the first resonance frequency comparatively large transmitted forces can be generated in an isolated joint free from other boundary conditions except for the unavoidable suspension.

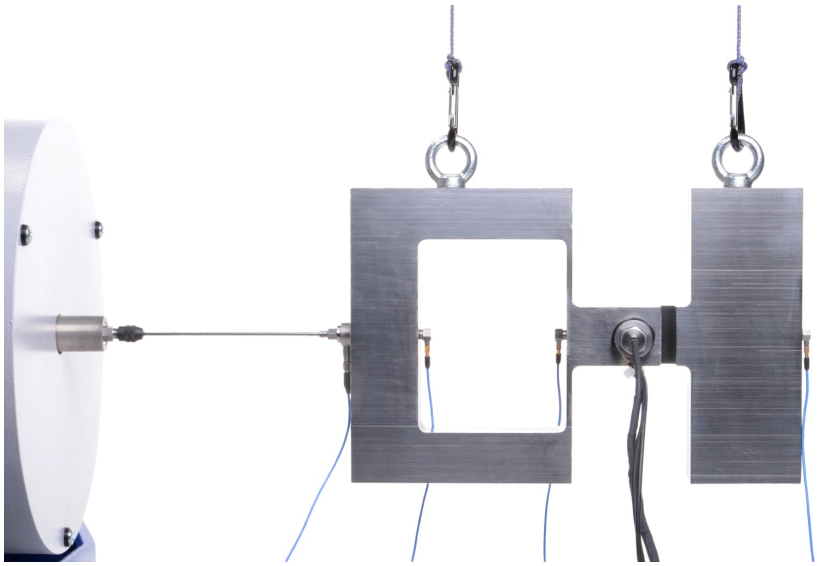


Figure 2: Gaul-type resonator: Experimental set-up

3 Finite element model

The resonator is meshed with a total of 1100 HEX8-elements and 2031 nodes, the contact interface is meshed using 48 zero-thickness elements. The bolt is modeled by a single beam element, which is coupled to the resonator parts by kinematic constraints. The bolt head, nut, and the piezo-actor are accounted for by simple lumped masses. The normal force N is applied by an initial overlap of the contact interface.

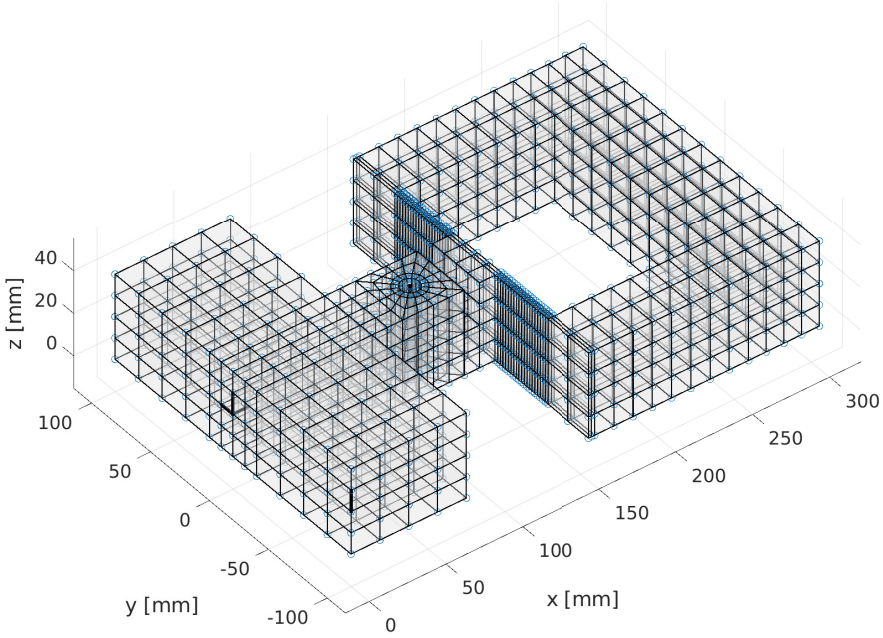


Figure 3: Finite element mesh

3.1 Identification of material parameters

Material data is given in Table 1, where the density is fitted to match the masses of the parts, see Table 2, while the Young's modulus is fitted to match the first eigenfrequencies of the mass with spring, which are obtained by standard EMA, as shown in Table 3.

ϱ	E	ν	N
$8040\,\mathrm{kg/m^3}$	$2.07 \cdot 10^{11}\,\mathrm{N/m^2}$	0.32	$2\,\mathrm{kN}$

Table 1: Material and loading parameters

Mass	Measured	Calculated
with spring	$5.900\,\mathrm{kg}$	$5.900\,\mathrm{kg}$
without spring	$5.225\,\mathrm{kg}$	$5.257\,\mathrm{kg}$

Table 2: Masses of the resonator parts including eye-bolts

Mode	Measured	Calculated
1	541 Hz	541 Hz
2	834 Hz	843 Hz
3	1120 Hz	1127 Hz

Table 3: Measured and calculated eigenfrequencies of mass with spring

4 Identification of contact parameters

4.1 Rough surface measurements

The surface roughness is measured by an optical measurement system (GOM-ATOS) providing STL-data of the surface with a lateral resolution of about $\Delta x = 50\,\mu$m and a vertical resolution of about $\Delta z = 1\,\mu$m. The raw measured surface data for the mass without spring together with the height distribution data is shown in Fig. 4. Obviously, the height distribution is close to Gaussian as can be expected for a polished surface. Since we are only interested in the elastic deformation of the surfaces, assuming that all plastic deformation will take place during the initial loading, only the long-wave content of the surface roughness is relevant. Therefore the relative low resolution of the ATOS-system compared to a stylus profilometer or an optical interferometer is acceptable. Figure 5 shows a representative surface element with height data interpolated from the STL-data of the ATOS-measurements.

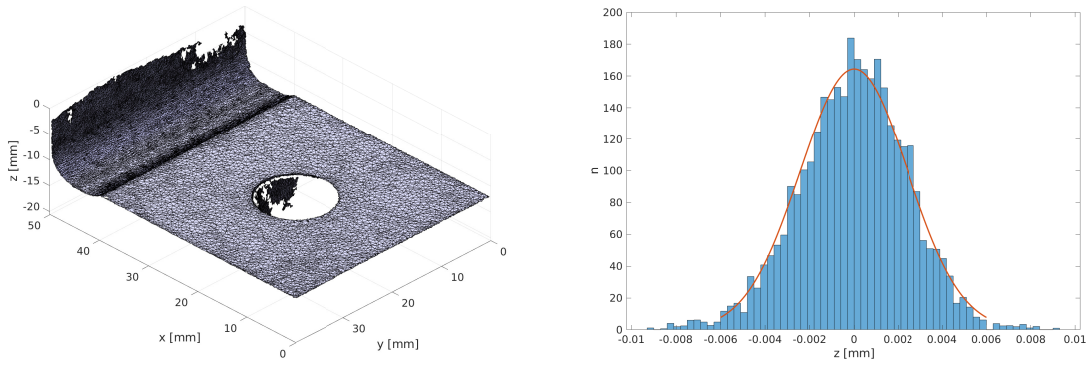


Figure 4: ATOS measurement: STL data (left), height distribution (right)

4.2 Halfspace model

The contact between the the two rough surfaces was simulated employing an elastic halfspace model [8] with a local Coulomb friction law with an assumed local friction coefficient of $\mu = 0.45$.

The normal contact behavior is then obtained as the nominal pressure p as a function of the average approach g, see Fig. 6. The halfspace results are fitted using a least-squares method by

$$p(g) = p_1 \left[\exp\left(p_2 \frac{g}{R_q} \right) - 1 \right] , \tag{3}$$

where the approach g is normalized by the rms roughness R_q of the joint surfaces. The identified parameters are shown in Table 4.

The tangential contact behavior shown in Fig. 7 is fitted by an Iwan-model with five parallel Jenkin-elements. Each Jenkin-element has the same pressure dependent stiffness c_k, which is given by

$$c_k = \frac{p}{x_t} , \tag{4}$$

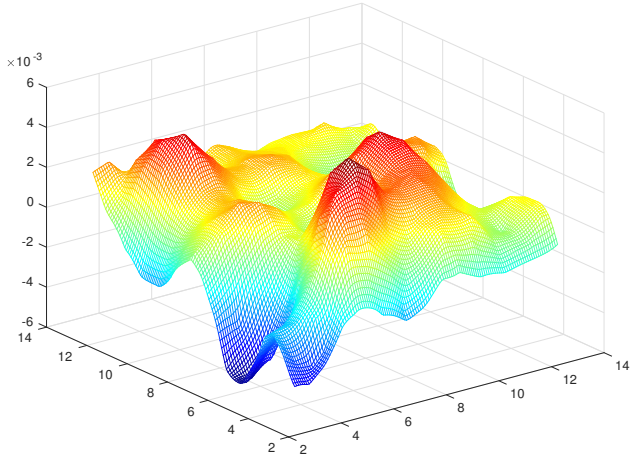


Figure 5: Representative surface element

p_1	p_2	R_q
0.5443 N/mm^2	3.1589	0.0031 mm

Table 4: Parameters for normal contact model

with the elastic slip distance x_t. The slip distance and the individual friction coefficients for each Jenkin-element are again identified by a least-squares fit to the halfspace results and given in Table 5.

Since the friction coefficients depend on the assumed value of the local friction coefficient μ in the halfspace simulation, the absolute values are not yet determined. However, the distribution of the friction coefficients is close to linear, such that we can assume a distribution of the form given by (5)

$$\mu_k = \mu_0 \frac{k}{\sum_{k=1}^{n} k} , \tag{5}$$

where we will use the value of μ_0 to fit our experimental data.

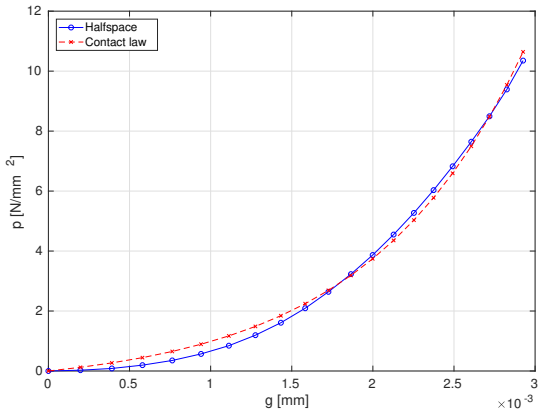


Figure 6: Normal contact law: Halfspace simulation and fitted contact law (3)

x_t	0.0068 mm
μ_1	0.0266
μ_2	0.0561
μ_3	0.0867
μ_4	0.1180
μ_5	0.1500
$\mu_0 = \sum \mu_k$	0.4374

Table 5: Parameters for tangential contact

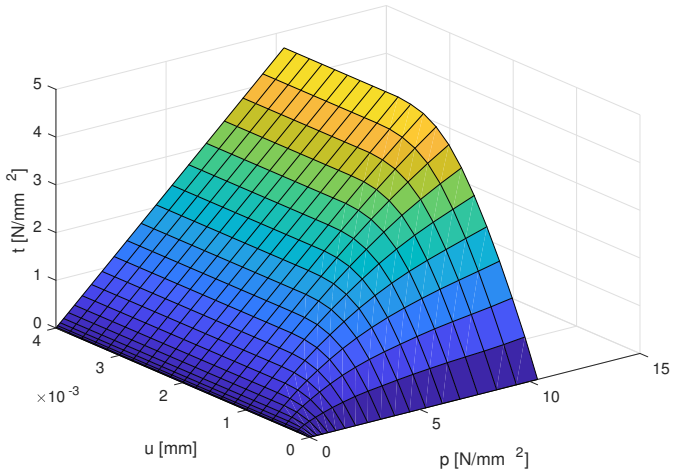


Figure 7: Tangential contact: Halfspace simulation

4.3 Identification of friction coefficient

The unknown friction coefficient μ_0 is identified from a comparison of a static hysteresis calculation to a measured hysteresis close to resonance, where the normal contact parameters are taken from Tab. 4 and the slip distance x_t from Tab. 5. The static solution is obtained using the finite element model by fixing the right part (mass without spring) at the accelerometer attachment point and applying a given displacement at the left part at the shaker attachment point,[1] see Fig. 2. Since the measured hysteresis shows a significant stiffness during "full slip" an additional slip stiffness c_0 has to be added to the Iwan-model. The reason for this additional stiffness are cold welded junctions formed by severe fretting of the rough surfaces during the experiments as shown in Fig. 8.

The slip stiffness c_0 and the total friction coefficient μ_0 are obtained using Matlab's `fminsearch`, where the objective function is the weighted sum of the least squares deviations of the time histories of relative displacement Δx and tangential force T over one period. Optimized parameters are shown in Tab. 6 and the resulting hysteresis in Fig. 9.

[1] Additionally, some soft springs have to be used to suppress rigid body modes.



Figure 8: Surface with severe fretting

c_0	μ_0
$156\,\mathrm{N/mm^3}$	0.576

Table 6: Slip stiffness and friction coefficient

4.4 Modal analysis

As a first check, an experimental modal analysis of the assembled system is performed using very light hammer excitation to stay in the linear regime at full stick. The results are compared to the numerical results in Tab. 7 for the first four modes with very satisfactory agreement.

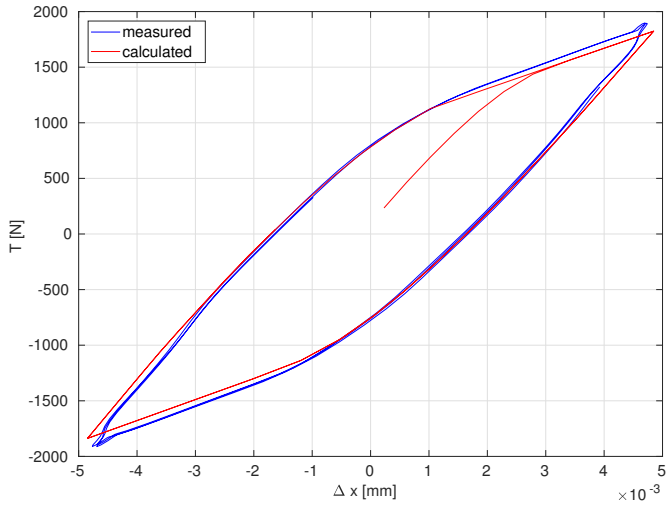


Figure 9: Fit of calculated static hysteresis to measured hysteresis at $f = 329.7\,\mathrm{Hz}$

Mode	Measured	Calculated	Error
1	150 Hz	150 Hz	0.0%
2	191 Hz	190 Hz	0.5%
3	340 Hz	337 Hz	0.9%
4	441 Hz	428 Hz	2.9%

Table 7: Measured and calculated eigenfrequencies of assembled system

5 Time domain results

The assembled finite element system is now subjected to a simulated swept-sine-measurement in the frequency range $f = 320\,\text{Hz}$ to $f = 340\,\text{Hz}$ with a sweep rate of $\dot{f} = 1\,\text{Hz/s}$, resulting in a sweep duration of $t_{\text{sweep}} = 20\,\text{s}$. The excitation force is $F_0 = 50\,\text{N}$. Time integration is performed using standard Newmark's method with $\gamma = 0.5$ and $\beta = 0.25$ without any numerical damping. The fixed time step size is $\Delta t = 5 \cdot 10^{-5}\,\text{s}$ resulting in $n = 400000$ time steps. The system is completely free without any boundary conditions. In order to avoid rigid body drift resulting from start-up disturbances, the system is initialized using a linear harmonic solution (full stick) at the start frequency.

In the following, we will compare the measured and calculated frequency response function (FRF) of the first harmonic of the acceleration signal at the right mass (mass without spring) due to a harmonic force excitation at the left mass (mass with spring), simulating the experiment shown in Fig. 2. The FRF is obtained by short-time FFT using a moving Tukey-window with window size $t_{\text{window}} = 0.5\,\text{s}$.

5.1 Original data

Figure 10 shows the calculated FRFs for a up- and a down-sweep in comparison to the measured data. The agreement is quite good. Beside a small difference in amplitudes, there is some offset in the resonance frequencies between measured and calculated data and also a slight difference between the numerical up- and down-sweep data.

The latter effect can be attributed to a too high sweep rate, since calculations with higher sweep rates show an even greater difference, which vanishes with decreasing sweep rates. However, a calculation with a lower sweep rate was not deemed feasible, since a single sweep at the given time steps size and sweep rate takes already about a week wall time on a standard PC. So, the chosen values are already a compromise between accuracy and calculation time.

Both eigenfrequencies, measured and calculated, are below the corresponding eigenfrequencies of the linear system at full stick, see Tab. 7. This is to be expected, since the stiffness is reduced during slip in the nonlinear case. However, the drop is more significant in the experiment ($\Delta f \approx 10\,\text{Hz}$) than in the simulations ($\Delta f \approx 2\,\text{Hz}$). The reason for this effect is not clear and will be the topic of future investigations.

5.2 Tuned damping

To obtain a better fit of the amplitudes, some Rayleigh damping is added to the model. Using stiffness proportional damping only with a damping factor of $d_k = 10^{-6}$ results in the FRFs shown in Fig. 11.

5.3 Tuned Young's modulus

To obtain a better fit of the eigenfrequencies, we will finally tune the Young's modulus to $E = 2.014\,\text{N}/\text{mm}^2$. The resulting FRFs are given in Fig. 12, showing an excellent agreement between measured and calculated data.

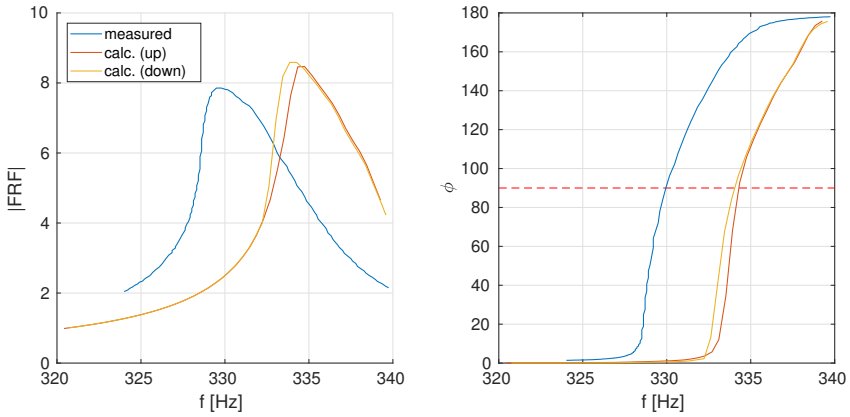


Figure 10: Comparison between measured and calculated FRFs (Original data)

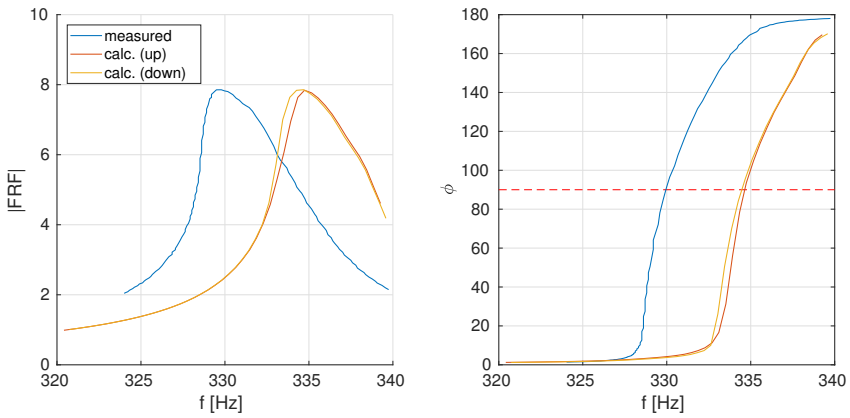


Figure 11: Comparison between measured and calculated FRFs (Added damping)

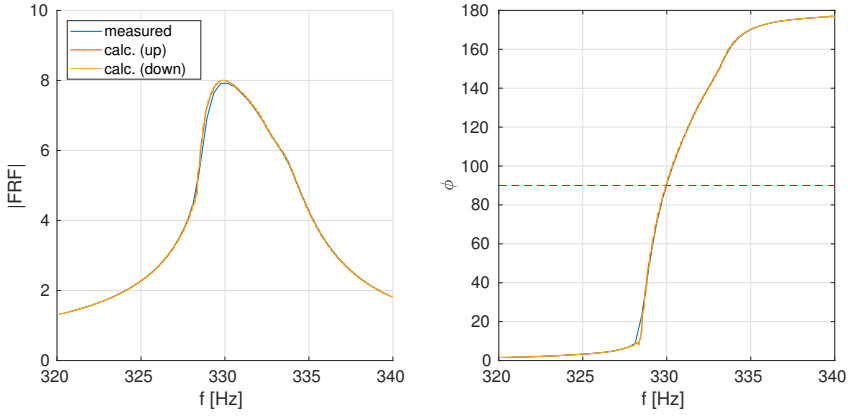


Figure 12: Comparison between measured and calculated FRFs (Tuned Young's modulus)

6 Frequency domain results

Using the tuned data from the time domain calculations, we perform a multi-harmonic balance analysis [7], where the nonlinear terms are treated by the alternating-frequency/time domain method (AFT) [1]. One period was discretized using $n = 64$ time steps. The tangent matrix was obtained by finite differencing, resulting in an inefficient but robust and general scheme.

Figure 13 shows the calculated FRFs for different numbers of used harmonics. Obviously, a very high number of harmonics is needed to obtain a converged result. Convergence is also non-monotonous, since the amplitude curve for 19 harmonics is slightly higher than for $n_{\text{harm}} = 13$. However, the result for 19 harmonics seems to be converged, since a calculation with 25 harmonics (not shown) will give the same result in the eyeball norm.

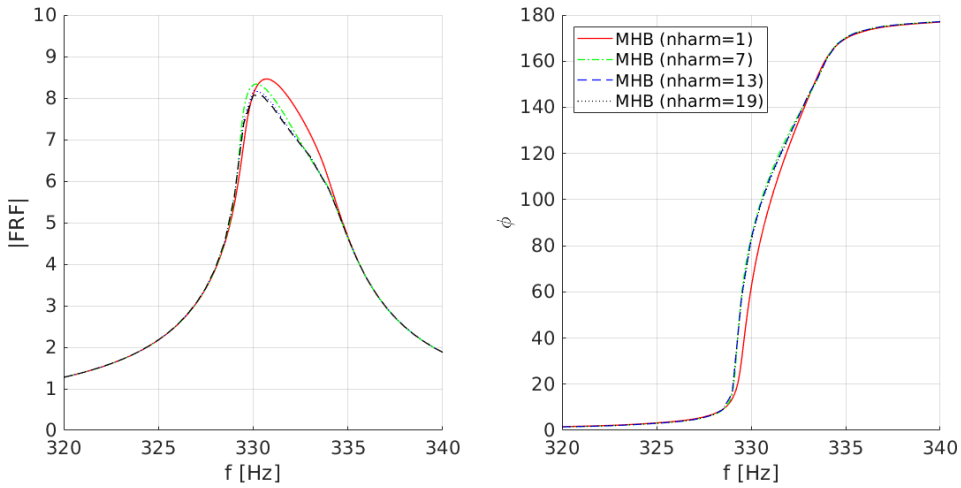


Figure 13: FRFs from multi-harmonic-balance method using different numbers of harmonics

Interestingly, a comparison of the MHB result with the FRF obtained from the time integration shows some differences, see Fig. 14. There is a very slight shift in the resonance frequency. This shift can be attributed to the Newmark integration scheme, which has some numerical dispersion leading to a period prolongation, which results in turn in an underestimation of the resonance frequency [4]. Also the amplitude is not exactly the same, this may be attributed to a still insufficient number of harmonics. However, a higher number of harmonics would require an even finer time discretization during the time-domain part of the AFT method, resulting in very long calculation times. The calculation for $n_{\text{harm}} = 19$ in the given frequency range and using a coarse frequency increment of $\Delta f = 0.5\,\text{Hz}$ takes already about 5 days wall time on a standard PC, thus coming close to the time domain calculations.

7 Conclusions

The presented method of parameter identification for dry frictions joints shows, at least for the quite simple demonstration problem, excellent results. A comparison between time domain and frequency domain results shows some small differences, which can be attributed to some deficiencies of either method. Since a very high number of harmonics seems necessary in the multi-harmonic balance method, no clear advantage in terms of computing time for the frequency domain method can be observed. This can be improved by substituting the finite difference approximation of the MHB tangent, by a more efficient approximation, see for example [5], albeit at some loss of generality. But the same holds true for the time domain method, which would benefit from a proper model reduction.

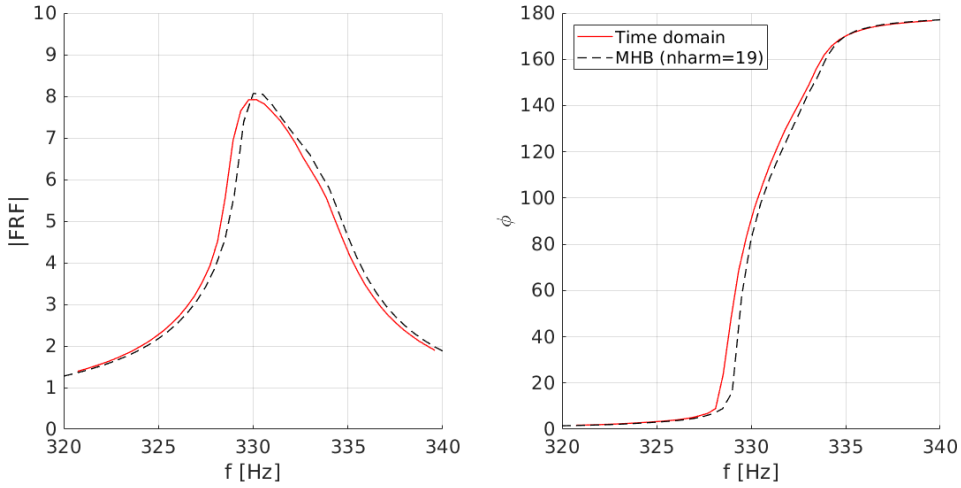


Figure 14: Comparison between FRFs from time-integration and multi-harmonic-balance method

Acknowledgments

The author would like to thank Mr. R. Stadter from LFT at FAU for conducting the surface roughness measurements using the GOM-ATOS system.

References

[1] T. M. Cameron, J.H. Griffin, *An alternating frequency/time domain method for calculating the steady-state response of nonlinear systems*, Journal of Applied Mechanics, Vol. 56, ASME (1989), pp. 149-154.

[2] L. Gaul, S. Bohlen *Zum nichtlinearen Übertragungsverhalten von Fügestellen*, Zeitschrift für angewandte Mathematik und Mechanik, Vol. 64, GAMM (1984), pp. T45-T48.

[3] L. Gaul, J. Lenz *Nonlinear Dynamics of Structures Assembled by Bolted Joints*, Acta Mechanica, Vol. 125, Springer (1997), pp. 169-181.

[4] Th. J. R. Hughes, *The Finite Element Method*. Dover Publications, Mineola, NY (2000).

[5] E. P. Petrov, D. J. Ewins *Analytical formulation of friction interface elements for analysis of nonlinear multi-harmonic vibrations of bladed disks*, Journal of Turbomachinery, Vol. 125, ASME (2003), pp. 364-371.

[6] D. Süß, J. Geisler, K. Willner, *Numerical and Experimental Investigations of Dynamic Contact Phenomena in Jointed Structures*, PAMM, Vol. 10 (2010), pp. 263-264.

[7] D. Süß, K. Willner, *Investigation of a Jointed Friction Oscillator Using the Multiharmonic Balance Method*, Mechanical Systems and Signal Processing, Vol. 52-53, Elsevier (2015), pp. 73-78.

[8] K. Willner, *Fully Coupled Frictional Contact Using Elastic Halfspace Theory*, Journal of Tribology, Vol. 130, ASME (2008), pp. 031405-1–031405-8.

A block-Gauss Seidel algorithm with static reduction to predict damping in bolted joints

Iman Zare and Matthew S Allen[1]
[1] University of Wisconsin - Madison, Department of Engingeering Physics,
1500 Engineering Drive, 525 ERB, Madison, Wisconsin, USA
e-mail: **msallen@engr.wisc.edu**

Abstract
Bolted joints in assembled structures are responsible for much of the structure's damping and give rise to nonlinear behavior. This work explores the application of a new static reduction method to reduce the computation costs associated with analyzing built-up structures. This novel method applies a Gauss-Seidel algorithm to a model that has been statically reduced to retain only the DOF at the contact interface in which the geometry, contact pressure and friction in the joint are modeled in detail. The problem considered consists of two 2D cantilever beams in a sandwich configuration, with a load applied to simulate a bolt joining the beams at the tip. The quasi-static simulations were used to predict the damping in the first mode of vibration of the sandwich beam. It was found that the static reduction method resulted in dramatic computational savings while providing good accuracy as compared to simulations in commercial finite element software. This approach could facilitate future studies in which different friction laws are applied between the interfaces.

1 Introduction

Airplanes, automobiles and various machines are all constructed from multiple parts joined by bolts or other fasteners, and one of the greatest challenges in structural dynamics is to predict the damping in a structure due to slip in the interfaces between its parts. When two parts are bolted together, the clamping pressure provided by the bolt and the Poisson effect creates a distribution of contact pressure at the interface, which possibly goes to zero if the joint opens up away from the contact. It is possible, although not trivial, to predict the area of contact for a bolted joint if the interface geometry and friction behavior are known. In contrast, damping is much more challenging to model since it arises due to slip in small regions at the edges of the contact, where a very fine mesh is needed to resolve slip accurately; to date no truly predictive models have been both presented and effectively validated. The fine mesh and the nonlinear nature of the contact makes the problem very computationally expensive.

A nonlinear simulation of a bolted interface includes several steps. First, the preload step must be simulated, where the torque applied to the bolt clamps the connecting members together. As the members come into contact, friction is generated at the joint interface that limits lateral motion. In a second step, external forces or displacements are applied, causing the bolted surfaces to try to slip relative to each other. As the strength of the external forces increases, the contacting members will experience microslip, or slipping near the edge of contact where the clamping pressure is lowest. For very large forces the joint may slip completely and transition from microslip to macroslip where in the macroslip regime, severe nonlinearity can be observed. Microslip is responsible for energy dissipation at the joint and therefore causes damping, up to 90 percent of the damping in some systems [**?**], and softening in the joint that varies with loading as the microslip region evolves. Various studies have shown that structures with bolted joints can exhibit variations in damping of hundreds of percent with response amplitude, so a new analysis method for bolted joints should examine a spectrum of loads. If dynamic loads are of interest, then the area of contact, frictional forces, stresses,

etc... must be solved for at every time step and, extrapolating based on the static simulations presented in [**?**], computation times within conventional FEA can be expected to be measured in decades or centuries. In an attempt to reduce the costs required to simulate the response of a structure with joints, Festjens et al. [**?**] proposed a model reduction technique that spatially decomposes a structure into a linear domain away from the joint and a nonlinear domain near the joint. Then the inertial term in the joint domain is neglected and the joint is assumed to behave quasi-statically. Allen et al. later [**?**] presented a variant on this method, known as Quasi-Static Modal Analysis, and applied it to structures where the joints were modeled as discrete Iwan elements. It was found that Quasi-Static Modal Analysis produces very accurate estimates of nonlinear behavior of the joint, especially the amplitude-dependent modal damping and natural frequency when the response is dominated by a single mode.

For Lacayo and Allen's work, Iwan elements were selected since they can capture the opening and closings experienced by the joint, which gives rise to energy dissipation and nonlinear behavior of the joint (to be discussed later). However, Iwan elements require four parameter inputs that must be tuned based upon prototype experiments since they cannot be deduced from first principles [**?**],[**?**]. Thus a better method would simply require a full element model of the assembly which would eliminate the need for prototype experimenting and producing a new model for every variation of joint geometry, preload, material, etc. Using the best available methods to date, this is still very computationally expensive. For example, Jewell et al. [**?**] implemented quasi-static modal analysis method within a commercial finite element package. In that work they found computation times ranging from 16-50 hours for relatively simple 3D finite element models with one or two bolted joints. Ahn and Barber [**?**] proposed a static reduction procedure as a way to speed up contact mechanics simulations. This work proposes to combine their approach with quasi-static analysis to seek to predict the nonlinear stiffness and damping of a joint at a significantly reduced cost compared to existing analysis methods. Several enhancements are presented for the approach in [**?**] to speed up the analysis, in order to make it practical for the joints that are of interest.

The following sections review the quasi-static modal analysis method and the approach used by Ahn and Barber. Then, the proposed enhancements are outlined and the algorithm is applied to a test structure.

2 Review of the quasi-static modal analysis method

The Quasi-Static Modal Analysis method implemented in this paper is similar to one developed by Festjens, Chevallier, and Dion, [**?**], where the effective natural frequency and modal damping ratios are extracted from a nonlinear static analysis. This is done by imposing a quasi-static load to the model that would excite only a single mode of the linearized structure. Allen and Lacayo, [**?**] recently elaborated on this method, and used the modal load-displacement curves to construct a hysteresis curve from which the effective natural frequency and damping were estimated. The method is reviewed below.

Suppose that a preload is applied to a structure such that the members come into contact in at least one location. The equation of motion for the coupled structure(s) can then be written as,

$$\mathbf{M}\ddot{\mathbf{x}} + \mathbf{C}\dot{\mathbf{x}} + \mathbf{K}\mathbf{x} + \mathbf{f}_j(x,\theta) = \mathbf{f}_{ext}(t) \tag{1}$$

where $\mathbf{M}$, $\mathbf{C}$, and $\mathbf{K}$ are, respectively, the mass, damping, and stiffness matrices of the system, and $\mathbf{x}$, $\dot{\mathbf{x}}$, and $\ddot{\mathbf{x}}$ are the displacement, velocity, and acceleration vectors, respectively. The vector $\mathbf{f}_j$ represents the internal forces due to a joint model containing internal sliders, and θ is a vector that captures the state (slip or stick) of each slider element.

At low amplitudes the joints can be replaced with springs equivalent to the zero-load equilibrium stiffness of the joints,

$$\mathbf{K}_T = \frac{\partial \mathbf{f}_J}{\partial \mathbf{x}}|_{\mathbf{x}=\mathbf{0}} \tag{2}$$

and an eigenvalue problem can be solved to estimate the mass-normalized mode shapes, Φ_0 , of the structure

$$([\mathbf{K}_T + \mathbf{K}] - \lambda_r \mathbf{M})\Phi_{0_r} = 0 \tag{3}$$

To characterize the effect of the joints on each mode of vibration, a force $\mathbf{f}_{ext} = \mathbf{M}\Phi_{0_r}$ is applied which distributes a load over the entire structure such that only mode r of the system would respond if the structure were linear. Using the approach in [**?**],[**?**], this force is applied to the nonlinear model resulting in the following quasi-static problem,

$$\mathbf{K}\mathbf{x} + \mathbf{f}_j(x, \theta) = \mathbf{M}\Phi_{0_r}\alpha \tag{4}$$

where α is a scalar which sets the load amplitude. This is then solved to find $\mathbf{x}(\alpha)$, which can then be mapped onto the rth mode using:

$$q_r(\alpha) = \Phi_{0_r}^T \mathbf{M}\mathbf{x} \tag{5}$$

Using this approach, the hysteresis curve can be constructed from a single, linearly increasing loading from 0 to α if the nonlinear forces are independent of the velocity and if each mode obeys the Masing assumptions, Using mass-normalized mode shapes, the modal force is

$$f_r(\alpha) = \Phi_{0_r}^T \mathbf{M}\alpha = \alpha \tag{6}$$

Then using Masing'rules, the force (and similarly displacement) over a full loading cycle can be estimated from the following forward and reverse loading curves.

$$\hat{f}_1(q_r) = 2f_r(\frac{q_r + q_r(\alpha)}{2}) - \alpha \tag{7a}$$

$$\hat{f}_1(q_r) = \alpha - 2f_r(\frac{q_r - q_r(\alpha)}{2}) \tag{7b}$$

The secant of this hysteresis curve is then used to estimate the instantaneous natural frequency of the mode in question:

$$\omega_r(\alpha) = \sqrt{\frac{\alpha}{q_r(\alpha}}) \tag{8}$$

The area enclosed by the loop is the total energy dissipated $D^(\alpha_j)$ per cycle of vibration, which is readily obtained with trapezoidal integration of the difference $(\hat{f}_1^j(q_r) - (\hat{f}_2^j(q_r)$ with respect to q_j. Then, using an energy balance between the dissipation and an equivalent viscous damper, the effective damping ratio can then be calculated as follows.

$$\xi_r(\alpha) = \frac{D(\alpha)}{2\pi(q_r(\alpha)\omega_r(\alpha))^2} \tag{9}$$

Jewell et al. [**?**] used this approach within a commercial finite element package to estimate $\mathbf{x}(\alpha)$, which proved costly and the static solver was not always reliable. As mentioned previously, this work will employ static reduction and an algorithm based on [**?**] to solve the reduced problem.

3 Static Reduction

In this section, the mathematical and theoretical basis of the static reduction procedure is described. First, the case of a single elastic body in contact with a rigid surface is considered, which is then extended to the case of contact between two elastic bodies.

3.1 Single Elastic Body

Following [**?**] and using equation (**??**), as done in [**?**] we relate the dynamic response to the quasi-static response over a single loading cycle. For example, in the case study that follows we have a finite element model containing 2158 nodes, of which 124 are located at the interface and may potentially come into contact. The force vector may also be partitioned between the forces at the interface $\mathbf{f}^C$and the other forces $\mathbf{f}^E$. A standard Guyan reduction [**?**] is performed to reduce the system to only the nodes at the interface, with displacements u^C and to obtain the reduced stiffness matrix $\mathbf{K}^C$. Then we can write the equilibrium for the contact nodes as,

$$\mathbf{f}^C = \mathbf{f}^w + \mathbf{K}^C u^C \tag{10}$$

where the force and displacement vectors can be decomposed into forces and motions normal to and parallel to the surface as,

$$\mathbf{f}^C = \begin{bmatrix} Q \\ P \end{bmatrix}; \mathbf{f}^w = \begin{bmatrix} Q^w \\ P^w \end{bmatrix}; u^C = \begin{bmatrix} v \\ w \end{bmatrix} \tag{11}$$

where, Q^w and P^w are the time-varying nodal reaction forces in the lateral and vertical directions respectively, that would be generated by the given external load if all the nodes were restrained from moving. The displacement of the contact nodes, are denoted v in the lateral direction and w in the direction normal to the surface.

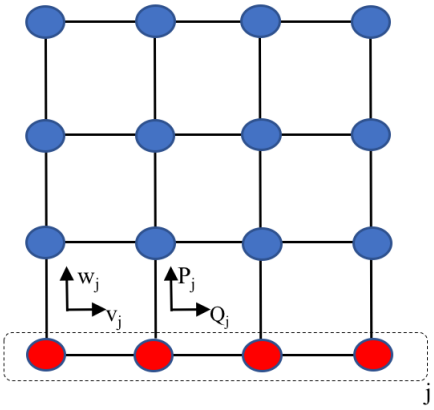


Figure 1: Example of a mesh with the directions of the displacements and loading specified. The mesh is statically reduced so that only the interface or contact nodes, shown in red, are retained.

3.2 Two Elastic Bodies

To extend this procedure to the case of two elastic bodies in contact, first, a separate finite element model must be created for each body, the global stiffness matrix of each individual model must then be extracted, and the reduced contact stiffness matrix $\mathbf{K}_j^C$, and the loading vectors $\mathbf{f}_j^w$, must be computed by fixing the interface nodes and computing the reaction forces at the interface when the external loading of interest is applied to the structure.

When the two bodies are in contact, Newton's third law requires that the forces between the bodies be equal and opposite, which is equivalent to the statement $\mathbf{f}^C = \mathbf{f}_1^C = \mathbf{f}_2^C$, where the subscripts 1, 2 denote the body to which the vector of contact force relates. Therefore, we can write the following.

$$\mathbf{f}_1^C = \mathbf{f}_1^w + \mathbf{K}_1^C u_1^C \tag{12a}$$

$$\mathbf{f}_2^C = \mathbf{f}_2^w + \mathbf{K}_2^C u_2^C \tag{12b}$$

The contact displacements must satisfy the following conditions.

$$u_1^C = u_2^C + u_2^C \tag{13}$$

We merge the equations (**??**) and (**??**) and finally, for two elastic bodies we can write,

$$\mathbf{f}^C = \mathbf{f}^w + \mathbf{K}^C u^C \tag{14}$$

where

$$\mathbf{f}^w = [\mathbf{K}_1^C[\mathbf{K}_2^C]^{-1} + \mathbf{I}]^{-1} + (\mathbf{f}_1^w + \mathbf{K}_1^C[\mathbf{K}_2^C]^{-1}\mathbf{f}^w]) \tag{15a}$$

$$\mathbf{K}^C = [\mathbf{K}_1^C[\mathbf{K}_2^C]^{-1} + \mathbf{I}]^{-1}\mathbf{K}_1^C. \tag{15b}$$

Hence, a contact problem involving two bodies has been reduced to a form equivalent to contact between one body and a rigid surface, and the same algorithm can be used for both. Therefore, from this point forward the focus is on an algorithm to solve eq. (**??**).

4 Solution Algorithm: Block Gauss Seidel

To solve the contact problem, the authors initially employed the algorithm by Barber et al [**?**], which uses a standard Gauss Seidel algorithm and iterates one node at a time, adjusting the forces and contact conditions at each node until equilibrium is satisfied. This algorithm may have advantages in some cases, but in the applications explored here this approach was found to be somewhat expensive since many iterations were often required to obtain convergence. Furthermore, since the authors' ultimate goal is to apply this reduction to 3D Finite Element models, and Gauss Seidel is known to perform poorly in three dimensions, an alternative was sought.

Therefore, a variation on the Block Gauss Seidel [**?**] procedure was developed for this application. For this method, the displacements at nodes beyond the contact interface are assumed to remain unchanged. Then the nodes at the contacting surfaces are placed into one of three baskets (nodes that are stuck, slipping, or separated) at each point in time. The algorithm then cycles over the basket until the governing equations at all basket nodes are satisfied to within a set tolerance. Then the nodes are evaluated and updated and the procedure repeats for the remainder of the contact analysis. In order to speed up the analysis further, two types of baskets were used: temporary and final. All nodes for which the contact condition is uncertain at a given time step t are place in a temporary basket, while nodes that either cease to change state for two successive iterations, or have never changed, are placed into a "final" basket. Doing this, the algorithm does not need to check the contact conditions for many of the nodes and this can help to speed up the computations. However, if convergence involves large changes in the displacements of the nodes then there is a risk that the solution would be inaccurate if some nodes end up in the wrong baskets.

4.1 Baskets

4.1.1 Contact/Stuck region (Contact region basket):

The nodes are in contact and there is no relative motion, so for each node in this category,

$$w_i = 0 \dot{v}_i = 0. \tag{16a}$$

For this state to hold, the normal reaction must be compressive and the tangential reaction must satisfy the Coulomb friction inequality, giving

$$P_i > 0; -\mu P_i \leq Q_i \leq \mu P_i \tag{16b}$$

where μ is the friction coefficient.

4.1.2 Separation region (Separation region basket):

The node is not in contact, so the reaction forces are zero, giving

$$P_i = 0; Q_i = 0 \tag{17a}$$

For this to hold, the gap between the block and the plane surface must be non-negative, which requires

$$w_i \geq 0 \tag{17b}$$

4.1.3 Slip region (Slip region basket):

The node is in contact and slipping, so

$$w_i = 0; \dot{v}_i \neq 0 \tag{18a}$$

The normal contact reaction must be compressive and the Coulomb friction law implies that sum of Q_i and P_i opposes the motion, giving

So we will find the Q_i and P_i as follows

$$Q_i = sign(Q_i)\mu P_i \tag{18b}$$

4.2 Algorithm

A flow chart documenting the algorithm is given in Figure 2. The algorithm begins each time step by placing all contact nodes in the temporary contact/stuck basket. From this assumption, the reaction forces at the interface are found and the inequalities in equations (**??**) and (**??**) above are checked. If equation (**??**) or (**??**) is found to be satisfied, the nodes are moved into the final contact basket, if not, they would move into the appropriate temporary sliding or temporary separation basket. Then the algorithm progresses to the next basket as shown in Fig.1, and the procedure is repeated and each of the baskets checked again until every node is in the final basket, or in other words until the status of each node has remained unchanged for two iterations so that it is transfered to the final basket.

The convergence tolerance is defined based on the change in displacements. Specifically, in each iteration the changes Δv_i, Δw_i in the displacements v_i , w_i at all slipping and separated nodes during the last iteration are less than a given proportion of the corresponding displacement. In other words, when $\epsilon_0 \leq \epsilon$, where

$$\epsilon = max_{v_i,w_i} \left(\frac{\Delta v_i}{v_i}, \frac{\Delta w_i}{w_i} \right). \tag{19}$$

The tolerance is then checked and if it is not satisfied then another iteration begins in which the final baskets of the previous iteration become the temporary ones for the new iteration (i.e. moving the nodes from the final basket of the contact/stuck region to the temporary basket of the contact/stuck region, and similarly for the separation and slip). Typically a few iterations are required until the tolerance would be satisfied for the current time. Then we can proceed to the next time step with the same procedure as before. .

5 Modeling, Results and Discussion

5.1 Modeling

In this section the algorithm is applied to evaluate its robustness and also the results are compared with the result from a commercial software package, Abaqus®. A 2D model was constructed consisting of two cantilever beams stacked on each other with a bolted joint joining the free ends. Hence, when the joint sticks

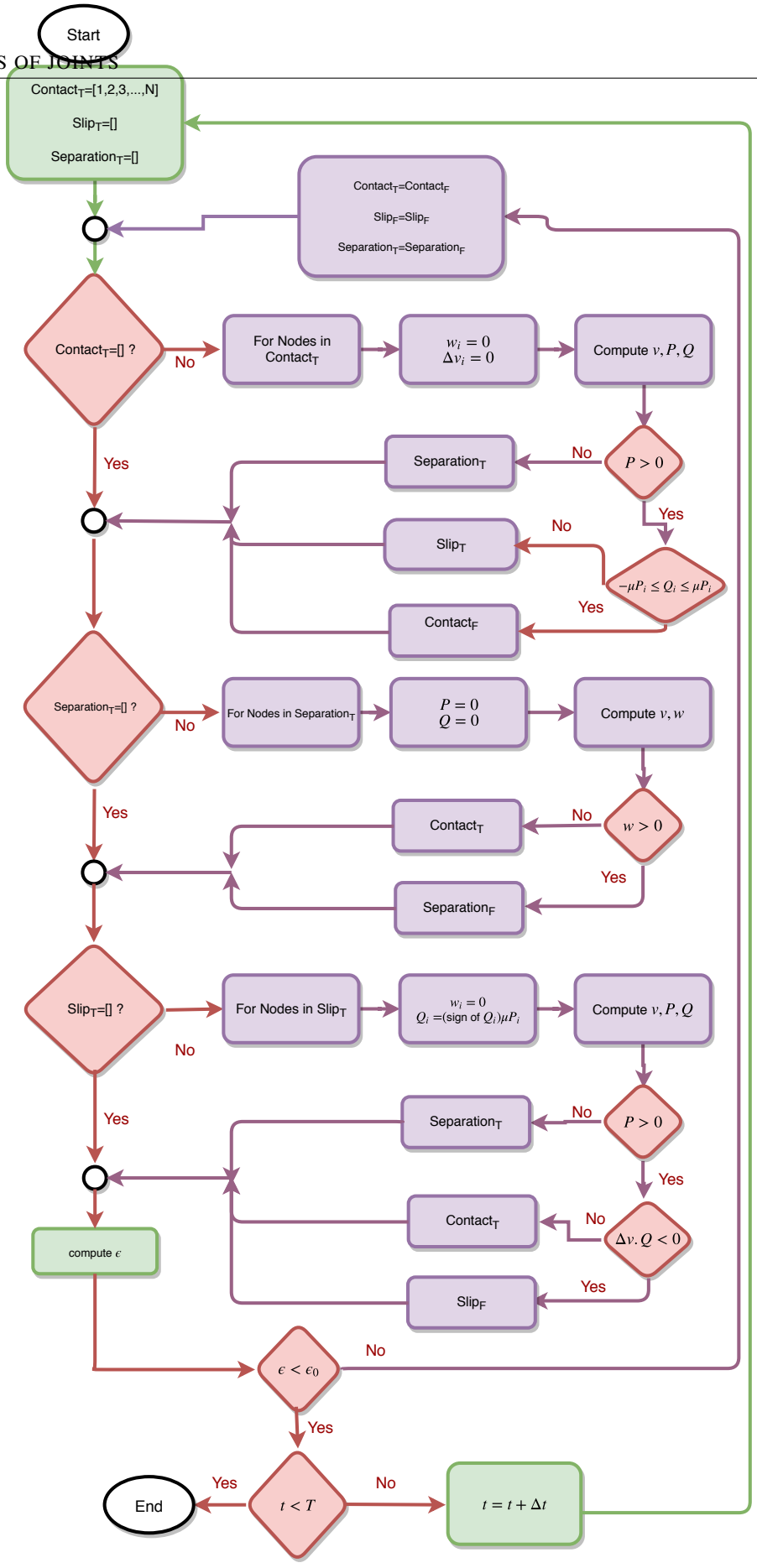


Figure 2: Flow chart explaining the proposed algorithm

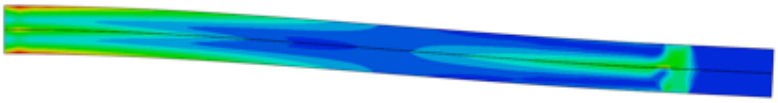


Figure 4: Von Mises stress results from quasi-static modal analysis on 2D model.

axially the beam has an effective height that is twice as large. Each beam is 203 mm [8 in] long, 6.35 mm [0.25 in] thick and is assumed infinite in width due to the selection of plane strain CPE4 elements. A fixed boundary condition is applied to one end of the structure. The bolt is modeled by a line pressure load on both the top and bottom faces of the stacked beams in a 6.35 mm [0.25 in] wide section 25.4 mm [1 in] from the free end of the structure. A pressure of 288 Nm [2546 lb-in] is applied on each segment, corresponding to the clamping pressure that would be applied by a 6.35 mm [0.25 in] diameter bolt with 4450 N [1000 lb] of preload.

Both the bolt and beams were made of steel with material properties E = 200 GPa, $\nu = 0.285$, and $\rho = 6600$ kg/m^3. The material is linear elastic so that the only damping in the model comes from Coulomb friction and material damping is neglected since it can be readily added after the analysis if need be. The structure is then meshed with smaller elements around the bolt and washer regions which are expected to experience microslip. The final mesh used for the quasi-static analysis is shown in Fig. **??** where the elements are colored to highlight key regions within the model. The contact is considered only near the bolt and not along the full length of the beams, with a coefficient of friction $\mu = 0.6$. This same structure was considered in [**?**] using Abaqus®to solve the quasi-static problem so it provides a good test case for this new algorithm.

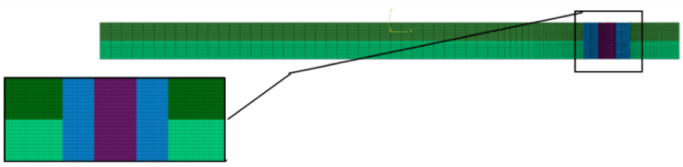


Figure 3: Finite element model of 2D bolted structure model composed of top beam (dark green), bottom beam (light green), bolt region with pressure line loads (maroon), and washer region (blue).

5.2 Quasi-Static Analysis

After creating the finite element model, the quasi-static analysis method was implemented. The analysis procedure consists of three parts, 1.) Pre-processing, which includes computing the forces acting on the beam for each time step, 2.) Solving for the displacements $x = \left[u^{\mathrm{T}}\ v^{\mathrm{T}}\right]^{\mathrm{T}}$ using the proposed algorithm , 3.) Post processing the displacements to construct the force-displacement curve and compute the effective natural frequency and damping ratio.

5.2.1 Pre-processing: Loading

For this part, the first bending mode was extracted from a modal analysis using Abaqus (shown in Fig. **??**) and it is the focus of further analysis. Once the first mode shape was extracted, the shape of the load in Eq. **??** was determined. The load magnitude was specified by giving a desired vertical tip deflection at the free end of the structure. This displacement value was then translated to a maximum forcing amplitude that would scale the forced mode shape to yield the specified tip deflection at the final analysis step. The distributed load was then applied to the beams with the interface nodes fixed in order to compute the reaction force at the interface nodes, $\mathbf{f}^w$ in Eq. **??**.

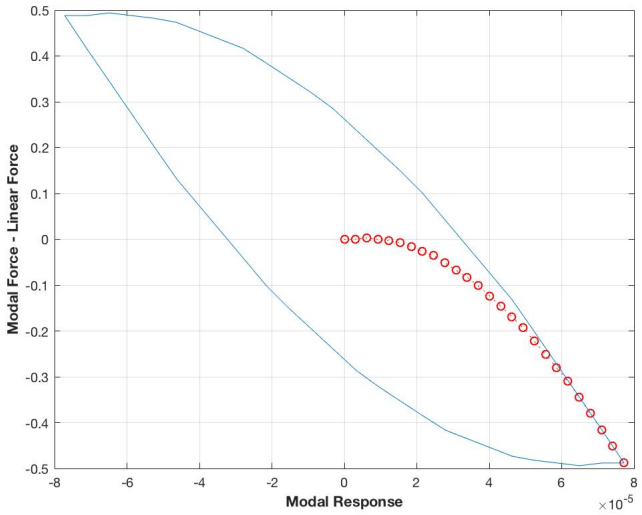


Figure 5: The force-displacement curve,

5.2.2 Solving the Quasi-Static equation

The force, $\mathbf{f}^w$, found above, was applied to the reduced model and the corresponding displacement u^C was found in each step using the enhanced GaussSeidel algorithm. The results from this quasi-static analysis were requested at 50 points. After solving the problem for the first time step, the time required to solve the problem would significantly be reduced because the force varies minimally between each time step and we can use the result from the previous step as a guess for the next time step. Therefore, the number of iteration in each time step decreases making the algorithm more efficient.

5.2.3 Post-processing

After computing u^C at each time step, the displacement of full model is reconstructed by finding u^C for both beams and using the recovery procedure associated with the static reduction. Also, Eq. 5 is then used to compute the modal displacement at each load step. The nonlinear part of force displacement curve is constructed, shown in Fig. **??**. The algorithm computes only the loading portion of the force-displacement curve (red circles) from which Masing's rules were used to obtain the complete hysteresis curve, shown in blue. The energy dissipation was then calculated from the full hysteresis curve using the trapezoidal rule from which Eq. **??** was used to calculate the damping ratio that the structure would have when vibrating in this mode. Then the secant of the hysteresis curve was used in Eq. **??** to determine the natural frequency as a function of amplitude. The resulting damping ratios and natural frequencies are plotted versus the peak velocity amplitude in Fig. **??** and the results are compared with the Abaqus solution.

5.3 Discussion

To solve the 51 load cases in Abaqus took 201 seconds. In contrast, the algorithm presented here took approximately 4 seconds on a 2.2GHz Intel i7 mac in Matlab using uncompiled code. This represents a 50x speed up compared to Abaqus.

Upon examining the natural frequency plot, the lowest forcing magnitudes gave an initial natural frequency around 198 Hz. This is in quite close agreement with the first mode found by the eigensolver at 198.4 Hz, which therefore confirms the accuracy of the stiffness in the quasi-static model. Moreover, the damping curve matches that computed in Abaqus almost identically, and the damping is seen to change by a factor of about

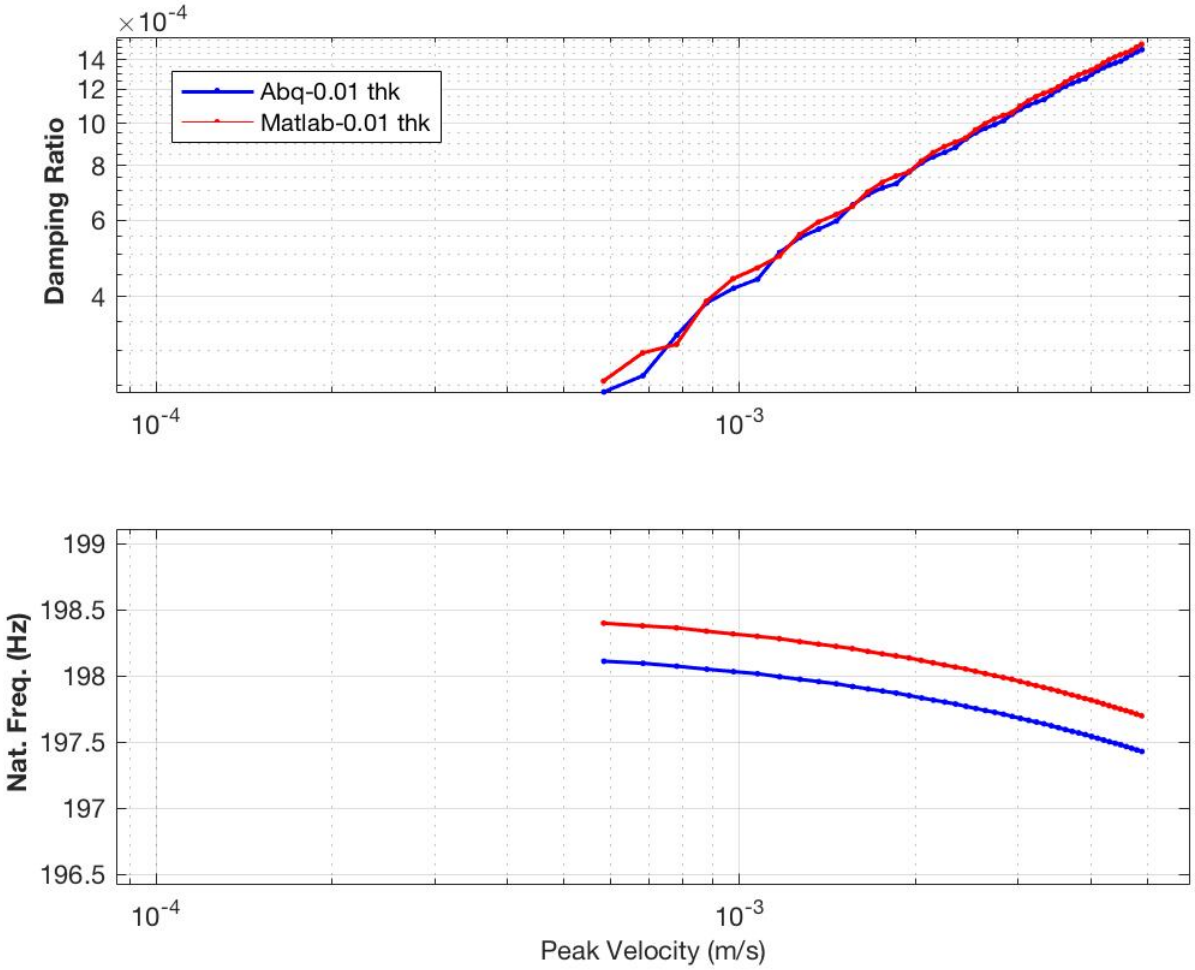


Figure 6: Damping ratio and natural frequency of the model versus the peak velocity, compared to the Abaqus results,

3 for the range of loading amplitudes considered. This is encouraging because the study in [**?**] revealed that it was challenging to be sure that Abaqus did not contaminate the damping due to the forces used to stabilize the solution, and having a second, independent solution that agrees is encouraging. At this point, the cause of the small offset between the natural frequency computed by Abaqus and by this algorithm is unknown. There could be inaccuracy in the stiffness computed by this algorithm due to static reduction or the way in which the applied load at the interface is approximated as the load when the interface is completely fixed. This will be explored further in future studies.

6 Conclusion

This work has presented a variant of a method used in the contact mechanics community that combines the standard Guyan static reduction method with a block Gauss-Seidel algorithm efficiently simulate contact problems. Recent works such as [**?**, **?**] show that the dynamics of low frequency modes are governed by the quasi-static response at the interface, and so using the methods there one can apply approaches such as these to dynamic problems. A basket concept was developed that solves the largest possible portion of the whole model at each iteration, while allowing the contact condition of the nodes to change between iterations. The algorithm was found to provide a dramatic reduction in computational cost compared to commercial software. This provides a welcome alternative to commercial code, which is more difficult to customize should different friction laws be of interest. Future works will seek to extend this algorithm to 3D models, where QSMA has been found to take between 16-50 hours even for relatively simple models.

References

[1] Allen, M. S., Lacayo, R., and Brake, M. R. W., 2016 *Quasi-static Modal Analysis based on Implicit Condensation for Structures with Nonlinear Joints*. International Seminar on Modal Analysis (ISMA)Leuven, Belgium.

[2] Young Ju Ahn, J.R. Barber. *Response of frictional receding contact problems to cyclic loading*. Department of Mechanical Engineering, University of Michigan, Ann Arbor, MI 48109-2125, USA.

[3] Suhas V. Patanker. *Numerical Heat Transfer and Fluid Flow*. pages 62-64.

[4] Festjens, H., Chevallier, G., and Dion, J.-L. 2013 *A numerical tool for the design of assembled structures under dynamic loads*. International Journal of Mechanical Sciences, 75, pp. 170-177.

[5] Beards, C. F., 1979 *Damping in Structural Joints*. The Shock and Vibration Digest, 11(9), pp. 35-41.

[6] Emily A. Jewell, Matthew S. Allen , Robert Lacayo *Predicting Damping of a Cantilever Beam with a bolted joint using quasi-static modal analysis* . IDETC/ MSNDC 2017 August 6-9, 2017, Cleveland, OH, USA

[7] Segalman, D. J., 2005 *A Four-Parameter Iwan Model for Lap-Type Joints*. Journal of Applied Mechanics, 72(5), pp. 752-760.

[8] Deaner B.J., Allen M.S., Starr M.J., Segalman D.J. (2014) *Investigation of Modal Iwan Models for Structures with Bolted Joints.*. In: Mayes R., Rixen D., Allen M. (eds) Topics in Experimental Dynamic Substructuring, Volume 2. Conference Proceedings of the Society for Experimental Mechanics Series. Springer, New York, NY

[9] R. J. Guyan. (1965) *Reduction of stiffness and mass matrices*. AIAA J., 3, p. 380 (1965)

[10] R. Lacayo and M. S. Allen, *Updating Structural Models Containing Nonlinear Iwan Joints Using Quasi-Static Modal Analysis*. Mechanical Systems and Signal Processing, vol. Submitted Sept 2018, 2018

Extracting natural frequencies and damping from time histories. Better than the frequency domain?

H. G.D. Goyder[1], D. P.T. Lancereau[1]
[1]Cranfield University, Centre for Defence Engineering
Shrivenham, Swindon, SN6 8LA UK
E-mail: **h.g.d.goyder@cranfield.ac.uk**

Abstract
If measurements are made of the free vibration decay of a structure, then, the usual approach is to use Fourier transforms to give a spectrum which separates out all the resonance peaks. Each resonance may then be analysed to determine natural frequencies and damping ratios. A novel alternative method is proposed here. This method involves narrow band filtering the vibration decay to extract a simple oscillating decay curve for each resonance. The advantage of this method is that nonlinear decay curves can be analysed. A particular feature of the method is that the data is reversed in time before the filtering is performed, thus, avoiding the excitation of filter resonances which would otherwise contaminate the data. This procedure is illustrated using nonlinear experimental data and theoretical data. It is shown that for a linear decay time history the filtering method does not alter the natural frequency and damping ratio of the data. For nonlinear decays, a method is given for removing minor distortions of the data.

1 Introduction

A measured time history of free vibration decay contains information about natural frequencies and damping ratios. The challenge is to extract this information. A novel method is presented here for analysing decaying time histories. A significant benefit is that it can be used on data that is nonlinear.

A standard procedure in experimental modal analysis is to determine the natural frequencies and damping ratios of the resonances of a structure. Extensive techniques are available for this process with the restriction that the structure must behave in a linear manner. These methods are described in Ewins [1] and consist of two stages; i) an experimental stage where the structure is set into vibration and response data captured and ii) a data analysis stage where the measured data is processed to extract the natural frequencies and damping ratios. Many software packages are available to assist with these tasks.

Stage ii) typically involves Fourier transforms to convert the measured data into frequency response functions. For linear structures, these frequency response functions can be modelled as rational polynomials with frequency as the independent variable. These models can then be fitted to the measured frequency response functions and in this process the natural frequencies and damping ratios of the structure determined. A review of these methods may be found in Formenti and Richardson [2].

The analysis approach above is restricted to linear systems. When a structure is nonlinear, there is no standard method to determine how to proceed. The key difficulty is that parameters such as natural frequency and damping ratio may no longer exist with the vibration frequency and damping depending on the amplitude of the vibration.

A key issue when analysing a decaying time history is that it is generally composed of the response of several modes of vibration with the responses of each mode being combined in the data. The use of spectra to separate the frequencies associated with each mode makes the spectral approach very attractive. However, when the response is nonlinear, the spectra are very difficult to interpret and for this reason a time domain approach has been developed. The challenge is to separate modes with different frequency content in the time domain.

An alternative to working in the frequency domain in stage ii) is to work in the time domain. Here for linear structures is the well-established Prony algorithm, and its variants, which dates back to 1795 [3]. These methods are also reviewed in Formenti and Richardson [2]. Methods involving the Hilbert transform are being developed by Feildman [4], Roettegen [5] and Sracic, Allen and Sumali [6]. The Hilbert transform is useful once a simple decaying time history is obtained which is part of the objectives of this work. Attempts to use the frequency domain to determine instantaneous methods for natural frequency and damping are also ongoing. The method by Kuether and Brake [7] involves taking short intervals of a decay time history and then transforming them into the frequency domain. A similar approach has been developed by Allen and Mayes [8] who take intervals of the decay curve starting at various times within the decay and then continuing to the end of the data. Both these methods enable the resonances to be sorted into individual frequency bands and allow the development of nonlinearities to be observed.

The new method proposed here is based on conducting stage ii) in the time domain but not making the assumption of linear behaviour. As will be explained the method relies on using narrow band filters to determine details of the behaviour.

2 The method of reverse filtering

The measurement method proposed here starts, in the same way as a standard experimental modal analysis, by exciting the structure with an instrumented hammer (or any equivalent method). The response to this excitation is captured, sampled and stored as a digital signal. An example of a response time history is shown in Figure 1. This data is taken from a beam-like structure with bolted connections. Details are available in [9]. It can be seen that there are many frequencies superimposed. Figure 2 is the Fourier transform of this response time history. Unlike a normal modal analysis, this spectrum is not divided by the Fourier transform of the excitation time history. Two resonances of the structure are shown; many more were also present in the spectrum at higher frequencies. Care must be taken in calling the peaks resonances since there are clear nonlinear features. However for simplicity the term resonance peak will continue to be used. For the resonance at approximately 188 Hz, there are two peaks one rounded and one sharp which are difficult to interpret since they express nonlinear features. The peak at approximately 270 Hz also has nonlinear characteristics. It is clear that due to the nonlinearity not much progress can be made by continuing in the frequency domain.

A fourth order narrow band Butterworth filter was applied to the data in Figure 1 with a bandwidth of 167 Hz to 208 Hz (the bandwidth is shown in Figure 2). This revealed the time history shown in Figure 3 (a). This time history clearly explains the data seen in the spectra of Figure 1. There are two parts to this time history. For times between 0 s and 0.13 s, the time history decays rapidly with a relatively low frequency. After 0.13 s the time history decays very slowly with a relatively high frequency. These two frequencies explain the two peaks see in Figure 1 at approximately 188Hz. Figures 3 (b) and 3 (c) will be discussed later. They relate to corrections to the filtered data and the error involved in the filtering process.

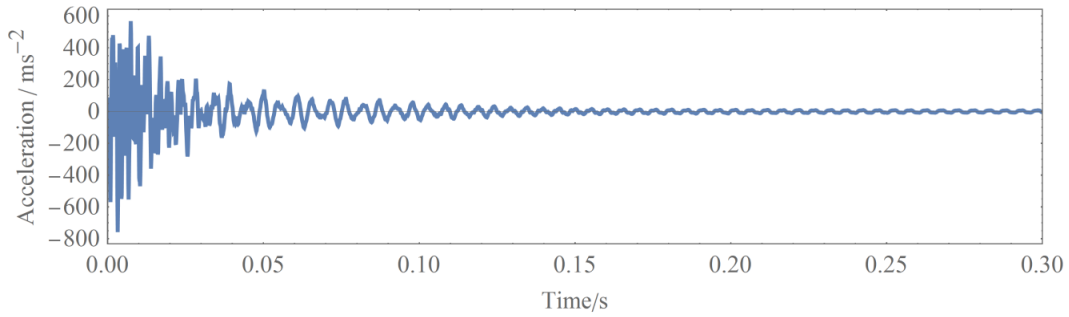


Figure 1. A measured time history.

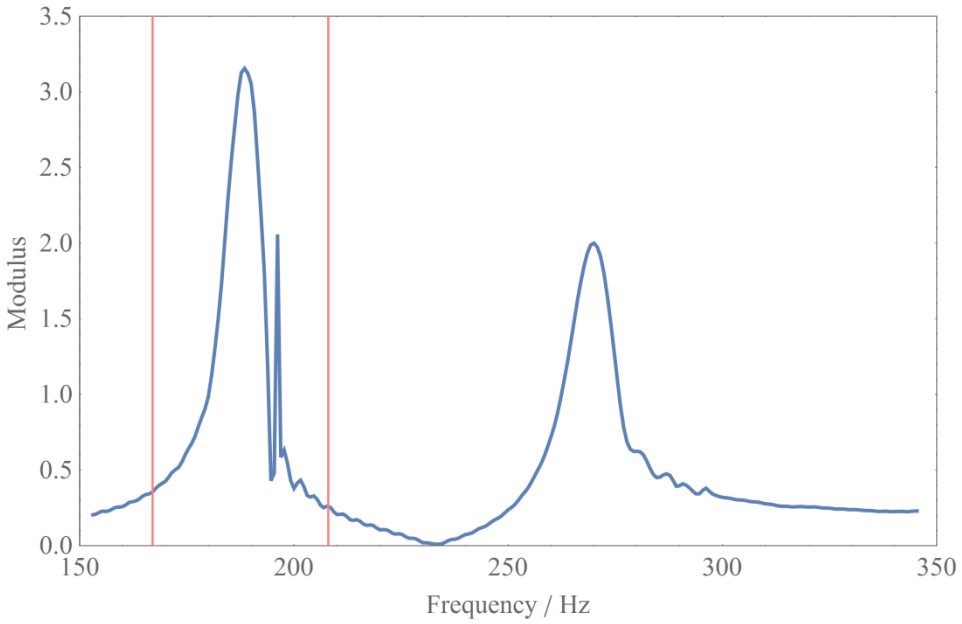


Figure 2. Spectrum of data in Figure 1 derived via a Fourier transform. The pink lines show the bandwidth of the filter.

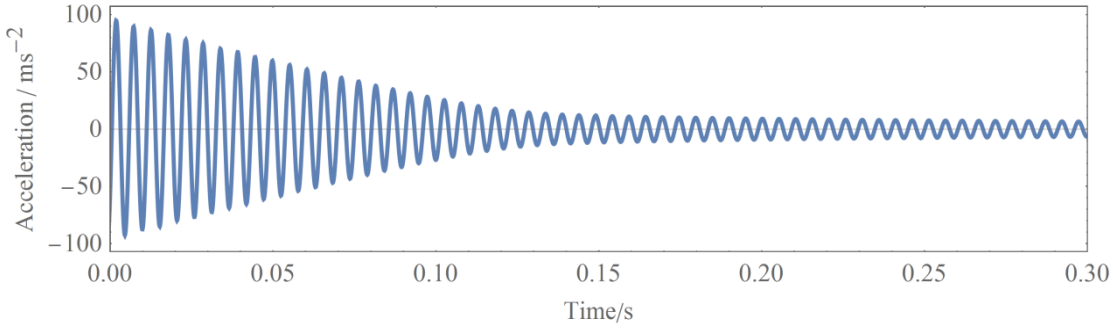


Figure 3 (a). Data in Figure 1 reverse filtered.

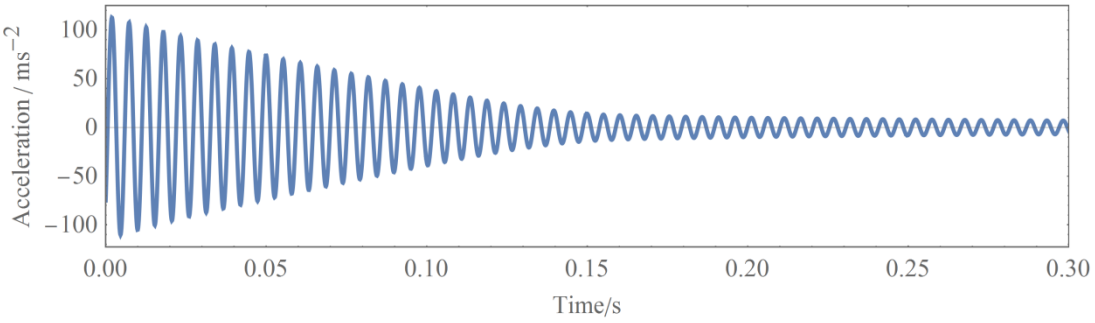


Figure 3 (b). A corrected (deconvolved) version of Figure 3 (a)

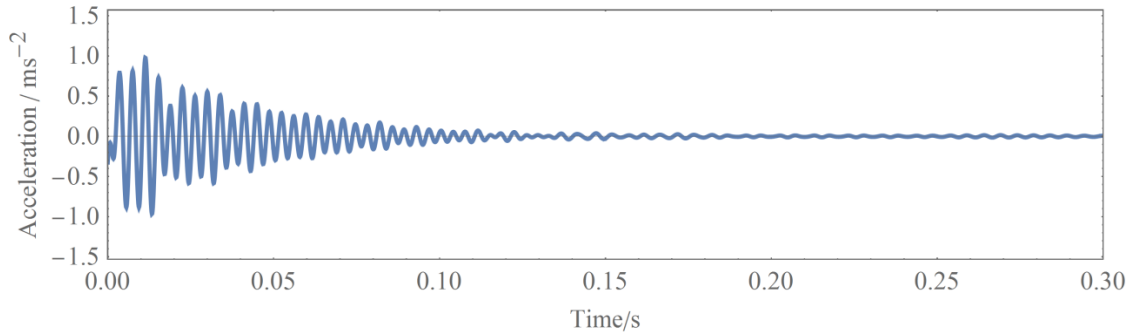


Figure 3 (c). The error in the filtering process.

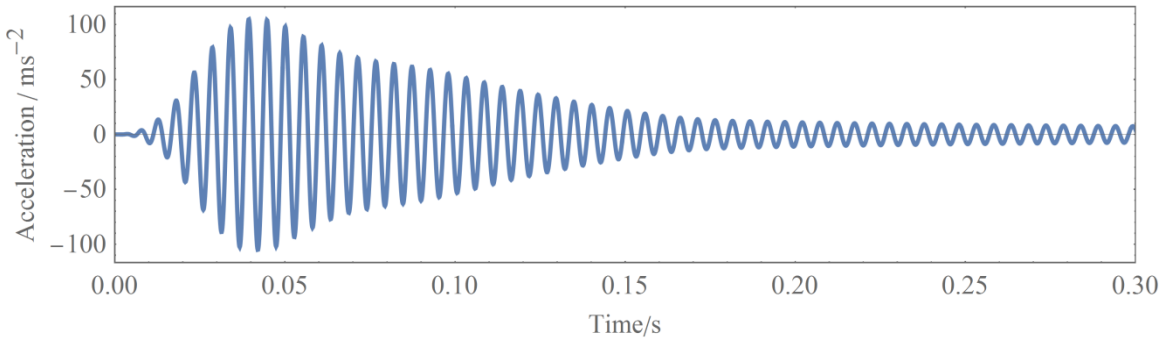


Figure 4. Data in Figure 1 forward filtered.

It is important to note that the narrow band filtering was not performed in a conventional manner. The data was reversed in time before passing it through the filter. This was done to avoid the filter resonance being excited. The difficulty with narrow band filters is that they have resonances which can ring and their characteristics can pollute the desired time history. By reversing the time history this effect is avoided.

When reversed, the amplitude of the data starts at zero and grows slowly and finally comes to an abrupt finish. This avoids initiating transients in the filter. After the filtering is completed the filtered data is reversed again so that it is in its original order. If the time history is not reversed before filtering, then a filtered response such as that shown in Figure 4 is produced.

It can be seen that filtering in a conventional manner, Figure 4, considerably distorts the time history particularity at the start. Note that in Figure 4 the effects of the filter last until about 0.1 s. This is a considerable loss of fidelity. The procedure of reversing the time history before filtering will be called reversed filtering while the conventional filtering process will be called forward filtering.

The nonlinear effects shown in Figure 3 are due to friction in the bolted joint. At large amplitudes, the joint has a slipping contact patch that causes damping and a low frequency, while at small amplitudes the contact path locks-up resulting in small damping and a relatively high frequency. More details in [9].

Instantaneous values for damping and natural frequency can easily be extracted from time histories such as those shown in Figure 3(a). The advantages of reverse filtering are clear in this example and provide a much better approach for understanding the dynamics of this structure, than working in the frequency domain. For this reason, this method of reverse filtering is being developed.

From the signal processing viewpoint, the key question is how the time history is affected by the reverse filtering process. To what extent is the time history shown in Figure 3(a) contaminated by the filter? Do corrections have to be made to get the true information? These important questions are investigated in the rest of this paper.

3 The effect of reverse filtering a linear system decay time history

As a starting point, the effect of reverse filtering the decay time history from a linear, single-degree-of-freedom (SDOF), system is examined. This process can be analysed by using Laplace transforms. Since reverse time histories are being considered it is necessary to use a double sided Laplace transform so that negative times can be considered. Details of Laplace transforms may be found in Bracewell [10]. The Laplace transform and its inverse are given by

$$X(s) = \int_{-\infty}^{\infty} x(t)e^{-st}\,dt \quad \text{and} \quad x(t) = \frac{1}{2\pi i}\int_{-\infty}^{\infty} X(s)e^{st}\,ds \tag{1}$$

where $x(t)$ is the time history and $X(s)$ its Laplace transform. Here t is time and s is the Laplace variable.

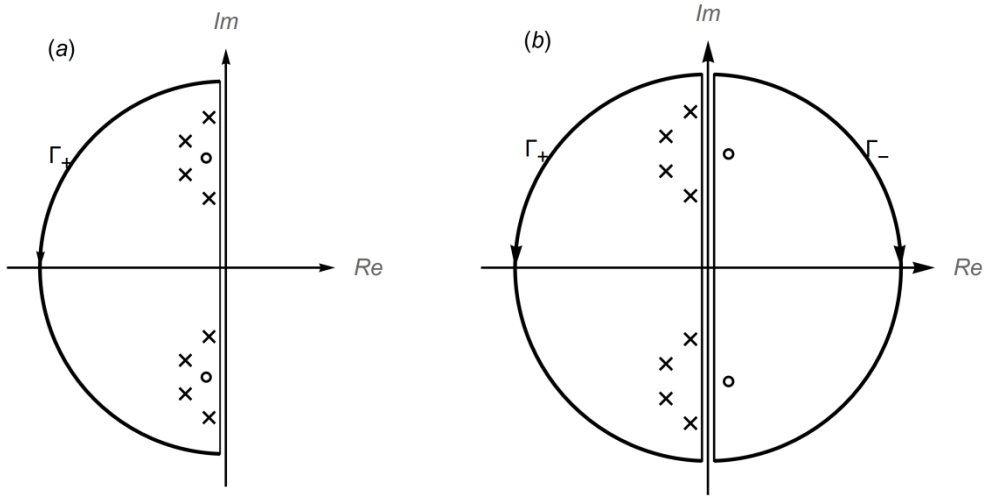


Figure 5. The poles in the complex plane; the poles of the SDOF are shown as circles. The poles of the filter as crosses. Contours of integration are shown as Γ_+ and Γ_-.

In the theory of Laplace transforms the output of the filter, $Y(s)$, is given by

$$Y(s) = H(s)X(s) \tag{2}$$

where $H(s)$ is the Laplace transform of the filter transfer function and $X(s)$ the Laplace transform of the time history that is input to the filter (i.e. the measured time history).

To determine the time history of the filter output, the inverse Laplace transform of $Y(s)$ must be calculated. This is best done by considering the poles of both $X(s)$ and $H(s)$.

Figure 5 shows the Laplace plane for a SDOF system filtered by a fourth-order Butterworth filter. The configuration for forward filtering is shown in Figure 5 (a) while for reverse filtering the configuration is shown in Figure 5 (b). The SDOF system has two complex conjugate poles marked by circles. For the forward filtering case, these are shown on the left half plane while for the reverse case these are shown on the right half plane. Their position on the right half plane follows naturally if it is recognised that the reversed time history looks like an unstable system.

The poles of the Butterworth filter are shown on the left half plane and are marked by crosses. The poles of the filter occur in complex conjugate pairs and are clustered in half-circles centred on the mid frequency of the pass band.

In order to calculate the time history of the filtered signal, the inversion integral is used. This integral must be applied carefully so that convergence is achieved. For times less than zero, the integral is completed using a contour on the right half plane (Γ_- in Figure 5 (b)). For times greater than zero the integral must use the contour on the left half plane (Γ_+ in Figure 5 a and b). Use of the Cauchy integration theorem may be made where the integral is equal to $2\pi i$ times the sum of the residues. The problem with forward filtering is thus clear; use of the contour on the left hand plane will result in the response of the SDOF time history and the response of the filter as well. Thus for the fourth order filter illustrated, there will be four oscillating decaying responses from the filter as well as the oscillating decaying response from the SDOF system. These responses interact to produce a composite oscillating decaying output. This is unsatisfactory because it is a mixture of the characteristics of the structure as well as the filter. The mixture is clearly seen in the start of Figure 4. For the reverse filtering case there are two parts. For times

less than zero, the output of the filter is that of the SDOF system only. For times greater than zero, the output is from the filter only. For reverse filtering and times greater than zero, the filter output can be ignored.

How does the reverse filtering effect the measured time history? This important question can be completely answered for a SDFS. Let the time history of the filter input, $x(t)$, be

$$x(t) = e^{-\beta\, t}(A\cos(\alpha\, t) + B\sin(\alpha\, t)) \tag{3}$$

where the poles of the SDOF system are $-\beta \pm i\alpha$ and *A* and *B* are coefficients which can be used to select the initial conditions. In more standard terminology

$$\alpha = \sqrt{1+\zeta^2}\omega_0 \text{ and } \beta = \zeta\omega_0 \tag{4}$$

where ω_0 is the undamped natural frequency in radians per second and ζ is the damping ratio.

Calculation of the filter output for the reverse filtering case gives

$$y(t) = e^{-\beta\, t}|H|\,(A\cos(\alpha\, t+\phi) + B\sin(\alpha\, t+\phi)) \tag{5}$$

where

$$|H| = \sqrt{H_r^2 + H_i^2} \text{ and } \tan(\phi) = -H_i/H_r \text{ with } H_r + iH_i = H(\beta + i\alpha) \tag{6}$$

Here the filter transfer function, *H*, has entered the solution during the evaluation of the residue at the poles of the SDOF system. Note that just the magnitude and phase of the filter at one pole is used. Examination of Equation 5 shows that the output of the filter is just the same as the input with a factor, $|H|$, scaling the amplitude and with a phase shift of ϕ. Thus the filter has made a negligible change to the input time history.

In contrast for the forward filtering case the time history of the response is much more complicated and is given by

$$\begin{aligned} y(t) = e^{-\beta\, t}|H|(A\cos(\alpha\, t+\phi) + B\sin(\alpha\, t+\phi)) \\ + \sum_{n=1}^{N} e^{-\beta_n\, t}(R_n\cos(\alpha_n\, t) + S_n\sin(\alpha_n\, t)) \end{aligned} \tag{7}$$

where the summation covers the response from the poles of the filter. For a forth order filter $N = 4$ and there are filter poles at $-\beta_n \pm i\alpha_n$. The coefficients R_n and S_n are values that determine the initial conditions for the filter. They also contain contributions from the residues of the SDOF.

The important point to note is that the frequency and damping of the SDOF are unaltered by reverse filtering. In contrast, for forward filtering, the SDOF decay time history is contaminated by the decay of the filter, and it is difficult to pick out the SDOF from the characteristics of the filter. This is illustrated in Figure 6 (a), (b) and (c)

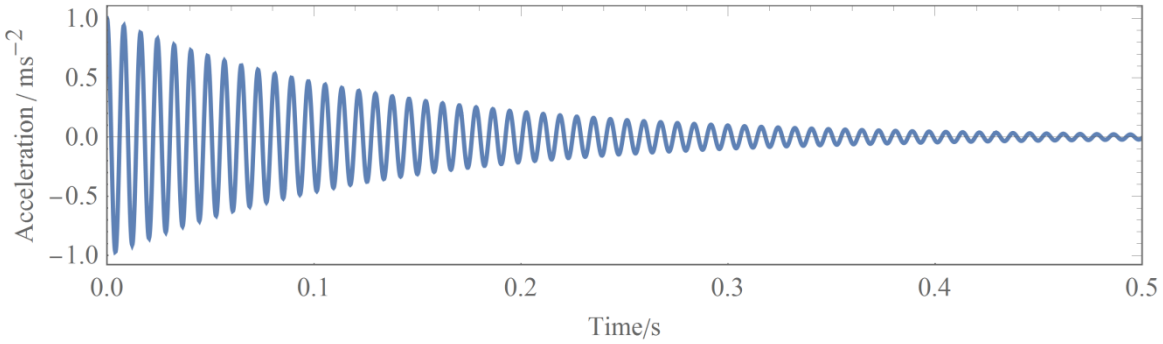


Figure 6 (a). Time history of a SDOF system

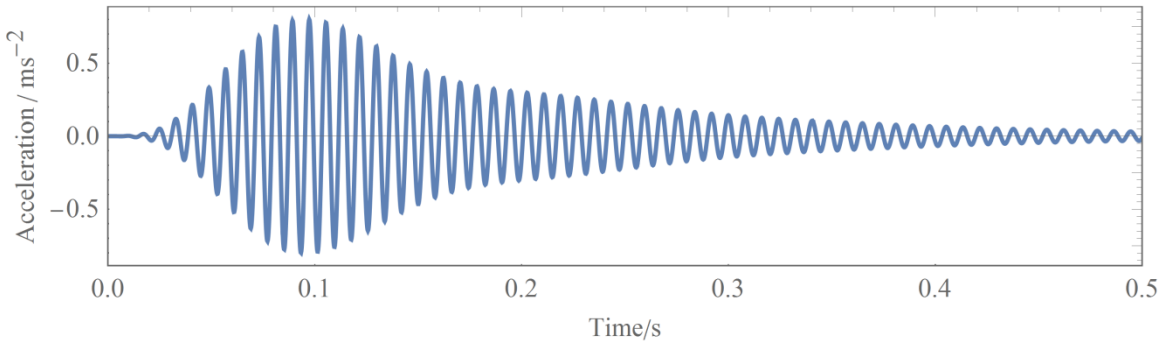


Figure 6 (b). Data in Figure 6 (a) forward filtered.

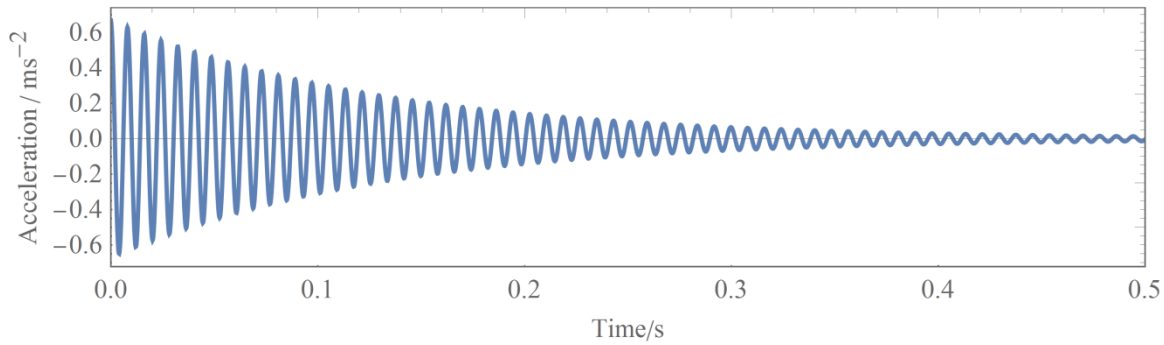


Figure 6 (c). Data in Figure 6 (a) reverse filtered.

It can be seen that forward filtering, Figure 6 (b), considerably distorts the data while reverse filtering, Figure 6 (a) leaves it uncontaminated except for a decrease in amplitude and a change in phase.

A further stage in signal processing would be to use a curve fitting method to determine the value of the natural frequency and damping precisely. The data in Figure 6 (c) would be fitted to the model in Equation 3. A method for doing this is described in Goyder and Lancereau [11]. This method is valid for fitting linear or nonlinear decay time histories. If the phase angle and scaling factor $|H|$ need to be removed from the output, this can be done easily since they can be deduced from Equation 6 once the frequency and damping are determined. Reverse filtering a nonlinear system decay time history

A nonlinear example is examined in this section. The objective is to see how a nonlinear decay is affected by reverse filtering. The synthetic decaying time history investigated here has two intervals each with different natural frequencies and damping ratios. The details are given in Table 1.

	Time ranges (s)	Natural frequency Hz	Damping ratio	A	B
Interval 1	$0 \leq t \leq 0.15$	123.4	0.015	1	0.5
Interval 2	$0.15 < t$	135.74	0.005	0.3190	-0.1753

Table 1. Parameters for a decaying time history composed of two intervals.

The amplitude values for the second interval are chosen so that the function and its derivative are continuous at the junction of the two intervals. This corresponds to displacement and velocity being continuous; while the acceleration is discontinuous. This system is similar to the measured example shown in Figure 1.

The nonlinear time history and the reverse filtered version are shown in Figure 7 and Figure 8. It can be seen that the reverse filtering has reduced the amplitude of the time history but that the time histories are substantially similar. Unlike the case of the linear system, there is no easy way of determining how to correct the decrease in amplitude that is due to the filter.

The general problem of correcting a time history for the effects of a filter is known as deconvolution. There is an extensive literature on deconvolution which is a problem that is known to be ill poised and sensitive to noise [12]. Much of the literature considers continuous time histories, rather than the transient ones of interest here. The standard method for deconvolving a continuous time history is Weiner deconvolution [13]. It should be noted that the simple expedient of dividing $Y(s)$ by $H(s)$ in Equation 2 to calculate $X(s)$ is not appropriate since this will just bring back the original time history with all the resonances superimposed.

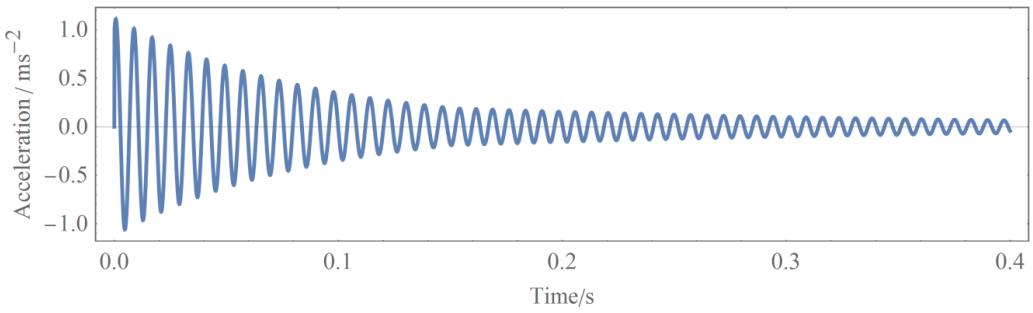


Figure 7. A nonlinear time history composed of two intervals with different properties

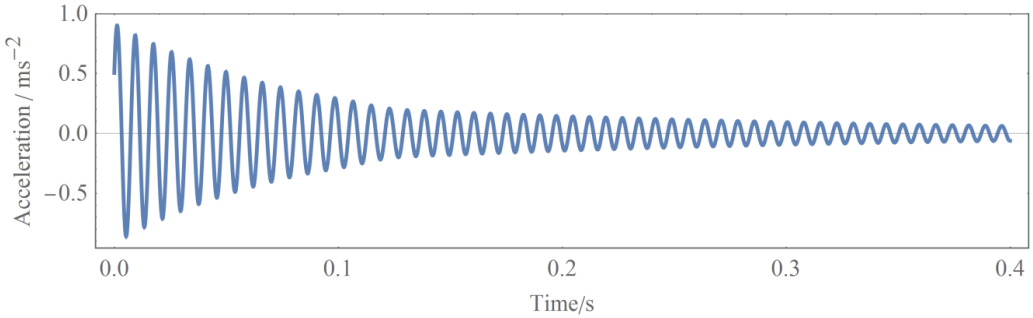


Figure 8. The data in Figure 7 reverse filtered.

An interesting point to note is that if a candidate for a deconvolved time history is available, then it may be checked to see if it correct by applying the reverse filtering procedure and comparing this output to the output obtained from the original reverse filtered time history. They should be identical. If they are not

then an error time history can be generated by subtracting one from the other. This idea forms part of an iterative method developed by Van Cittert [14] and Bracewell and Roberts [15]. The problem, however, is to determine the candidate for the deconvolved time history.

A novel approach has been developed for deconvolving the time history for the type of transient being investigated here. It can be noted that forward filtering approximately compensates the effects of reverse filtering. Thus if the reverse filtered data is forward filtered the decrease in amplitude is compensated by an increase in amplitude. However, as has been seen, forward filtering results in the contamination of the time history by filter components. The approach used here to avoid this contamination is to extrapolate the reverse filtered time history backwards to times less than zero. If this extrapolation is carried back far enough then when forward filtering the filter components will have decayed before time zero is reached.

This approach has been developed and Figure 9 shows the deconvolved time history. Most importantly an error signal, Figure 10, is also constructed between the original reverse filtered time history and the reverse filtered time history of the deconvolved signal. As can be seen this error signal is small suggesting a successful deconvolution.

This deconvolution process was also applied to the data in Figure 3 (a). The results of the deconvolution and the error in the process are shown in Figures 3 (b) and 3 (c) respectively.

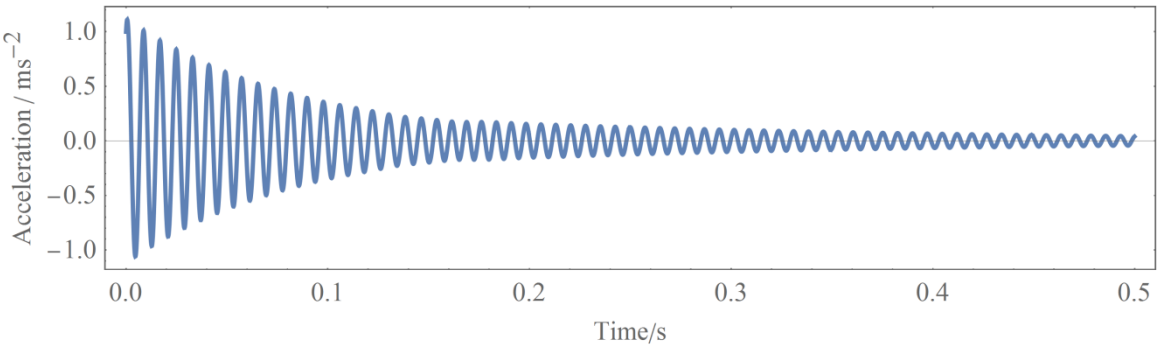


Figure 9. The deconvolved time history of Figure 8.

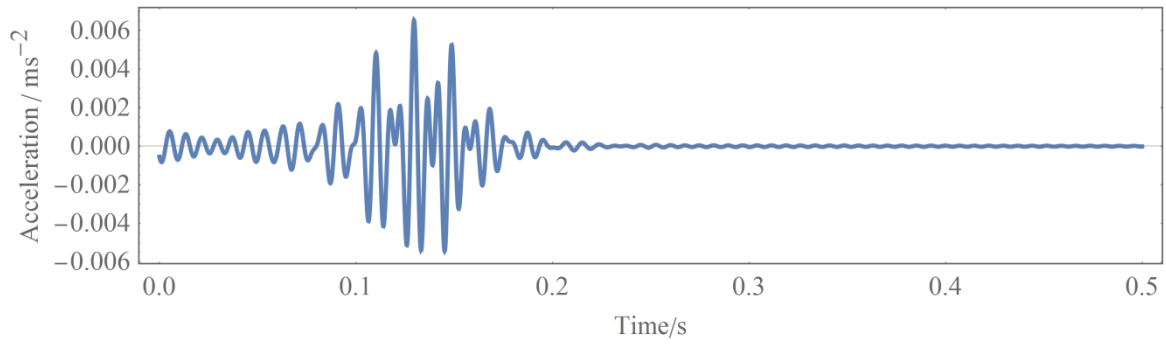


Figure 10. The error in the deconvolution process of Figure 8.

4 Discussion

The examples show that the reverse filtering technique can extract one resonance from a decaying time history and reject other resonances. This is the key starting point of the method. Further, the contamination of the data by the filter is small. In particular, the reversing of the data prevents filter oscillations from combining with the desired output. This is clearly a useful tool, particularly for nonlinear time histories.

The example with a linear system shows that the natural frequency and damping ratio are not influenced by the filtering process. This is another strong argument in favour of this method.

For the nonlinear system there is an issue with deconvolution. The challenge is to correct for the minor modifications to the data due to the filter. This modification is mostly a change in amplitude and a small shift in phase. A method has been presented that requires the data to be extrapolated backwards and then forward filtered. Other methods are probably possible and some are being considered. However, the corrections required for deconvolution are small, so this is a secondary problem.

A good feature of the reverse filtering method is the ability to check the quality of the data by calculating an error signal. One approach is to model the data obtained from reverse filtering. This model can be useful in providing instantaneous values of natural frequency and damping ratio. Further, the model can be used to generate a set of model data and this data can be reverse filtered and compared to the measured reverse filtered data. This approach, as well as providing a basis for an error time history, can add confidence to the whole data analysis process.

The deconvolution method described can also produce an error time history, and in this case, there is no need to generate a model (except for the backward extrapolation).

A question that has not been investigated here is how narrow a filter band can be used. Narrow filter bands are useful in separating close natural frequencies. The limitation will be the need for the decay time of the filter to be much shorter than the decay time of the resonance being investigated. This requirement can be formulated in the frequency domain for a linear system where the resonance has a bandwidth that depends on the damping ratio. The resonance bandwidth is given by $2\zeta f_0$ where ζ is the damping ratio and f_0 the natural frequency (in Hz). The filter similarly has a bandwidth and the requirement would be that this bandwidth be larger than the resonance bandwidth. This condition should be straightforward to satisfy.

In the title of this paper, it is suggested that the reverse filtering technique, operating in the time domain, is better than working in the frequency domain. For the nonlinear example with the spectrum shown in Figure 2, it would be difficult to see how working in the frequency domain could proceed. The clarity of the reverse filtered data in Figure 3 (a) explains the entire nonlinear phenomenon. For data with only a small nonlinearity, it is often difficult to spot that nonlinearity is present from examination of the spectrum. However, with the reverse filtering technique even small nonlinearities are clear in the time domain. The disadvantage of the reverse filtering technique is that some deconvolution may be necessary. For a linear system the deconvolution is trivial. For a nonlinear system a method has been proposed, i.e. extrapolating and then forward filtering, which has been found to be adequate.

The reverse filtering method has been successfully used for investigating nonlinear behaviour [9] and it is recommended as a good approach.

5 Conclusions

The following conclusions may be drawn.

1. Using a narrow band filter allows individual decaying oscillations from a resonance to be selected. This selection works even when there are other oscillations from other decaying resonances present.
2. Reversing the time history prior to filtering prevents the filter ringing and avoids contamination of the data by the filter.
3. It has been shown that for a linear system, the reverse filtering method results in a time history that preserves the natural frequency and damping ratio exactly.
4. Some second order modifications are made to the output time history by the filtering process. For a linear system these are just a change in scale and a phase shift. A process of deconvolution has been demonstrated that enables almost all these modifications to be corrected.
5. Either by deconvolution or by developing a model using curve fitting it is possible to determine an error time history. This gives confidence to the reverse filtering method.

6 Acknowledgements

The authors acknowledge the support of Cranfield University. One of the authors is also supported by AWE Aldermaston.

References

[1] Ewins DJ 2000, *Modal Testing: Theory, Practice and Applications,* . Research Studies Press. ISBN 0863802184.

[2] Formenti D and Richardson M, *Parameter Estimation From Frequency Response Measurements Uisng Rational Fraction Polynomials (Twenty Years of Progress).* IMAC 20, Los Angeles CA USA (2002),

[3] Prony GRB, *Essai experimental et analytic.* J l'Ecole Polytech. (Paris) vol 1 pp24-76 (1795e)

[4] Feldman M. *Hilbert transform application in mechanical vibrations*. John Wiley and Sons Ltd. ISBN 9780470978276. (2011)

[5] D. R. Roettgen and M. S. Allen, *Nonlinear characterization of a bolted, industrial structure using a modal framework*, Mech. Syst. Signal Process., vol. 84, pp. 152–170, (2017)

[6] M. W. Sracic, M. S. Allen, and H. Sumali, *Identifying the Modal Properties of Nonlinear Structures Using Measured Free Response Time Histories from a Scanning Laser Doppler Vibrometer* in *Topics* in Nonlinear Dynamics, Volume 3, Proceedings of the 30th IMAC, A Conference on Structural Dynamics, pp. 269–286. (2012)

[7] R. J. Kuether and M. R. W. Brake, *Instantaneous Frequency and Damping from Transient Ring-Down Data*, Int. Modal Anal. Conf., (2016).

[8] M. S. Allen and R. L. Mayes, *Estimating the degree of nonlinearity in transient responses with zeroed early-time fast Fourier transforms*, Mech. Syst. Signal Process., vol. 24, no. 7, pp. 2049–2064, (2010).

[9] Goyder HGD, Lancereau DPT, Ind P and Brown D. *Friction and Damping Associated with Bolted Joints: Results and Signal Processing.* ISMA International Conference on Noise and Vibration Engneering. KU Leuven (2016)

[10] Bracewell RN, *The Fourier Transform and its Applications* McGraw-Hill Book Co. ISBN 0 07 116043 (1999)

[11] Goyder HGD and Lancereau DPT. *Methods for the measurement of non-linear damping and Frequency in built-up structures.* Proceedings of the ASME 2017 International Design Engineering Technical Conferences & Computers and Information in Engineering Conference IDETC 2017,August 6-9, Cleveland, Ohio, USA (2017)

[12] Xu C, Aissaoui I, Jacquey S. *Al;gebraic analysis of the Van Cittert iterative method of deconvolution with a general relaxation factor.* J Opt. Soc. Am. A/Vol. 11 No. 11 November (1994)

[13] Press WH, Flannery BP, Teukolsky SA and Vetterling WT. *Numerical Recipes.* Cambridge University Press. ISBN 0 521 30811 9. pp417-420 (1987)

[14] Van Cittert PH, *Zum Einfluss der Spaltbreite auf die Intensitatswerteilung in Spektrallinen II.* Z. Phsy. 69 298 (1931)

[15] Bracewell RN and Roberts JA, *Aerial smoothing in rado astronomy.* Aust. J Phys. 7, 616-640 (1954)

The surrogate system hypothesis for joint mechanics: statement and evaluation through empirical parameter estimation

N. N. Balaji [1], **M. R.W. Brake** [1]
[1] Rice University, Department of Mechanical Engineering,
6100 Main Street, Houston, TX 77005, USA
e-mail: **brake@rice.edu**

Abstract
In modeling jointed interfaces, it becomes necessary to understand how properties of joints, estimated in situations removed from the contexts of their assemblies, correspond to the system-level dynamical behavior of the total assembly. The current study presents, along with the results of preliminary efforts at examining it, the Surrogate System Hypothesis for Joint Mechanics. The hypothesis states that joint interface properties are independent of the structural context it is found in. If the hypothesis finds support, experimental characterization of surrogate structures can be used to develop predictive models for jointed assemblies, which will enable significant advances in the design and optimization of jointed structures. In the current study, the dynamics of modified versions of the Brake-Reuß Beam (BRB) are captured using an established joint model (Segalman's 4-parameter Iwan friction elements) tuned using experimental data from a regular BRB. Quasi-Static Modal Analysis (QSMA) and related methods are employed for the numerical characterization.

1 Introduction

The lack of accurate predictive models for capturing the dynamics of jointed connections is an issue that has persisted in the community for a long time now [24, 3]. The main sources of difficulty in modeling interfacial friction may broadly be understood as two-fold: (1) Uncertainty in characterizing the interface and its evolution, and (2) computational overhead in incorporating the local kinematics of the interface in a macro-level simulation. There are several studies working on developing constitutive models with increasing sophistication (see, for example, [13, 11, 10]) as well as developing better experimental setups & techniques for hysteresis measurements [12]. The most popular alternative to fully predictive models is the use of experimentally derived empirical models. The key drawback here lies in the fact that this necessitates expensive, often destructive testing of assembled structures. The current work strives to provide a cheaper alternative to this by attempting to establish the correlation between experimental measurements of identical joints in dissimilar structural contexts. Parameter sets for different friction models are evaluated using experimental data for three different lap-jointed (bolted) beams by first posing the estimation problem in a Multi-Objective Optimization framework (MOOP), and then using the resulting model form deviation metrics for the analytics.

In applying friction constitutive models in a system-level model, one is sure to come across the second challenge — computational expense. Physically, since friction is thought to be a multi-scale phenomenon; with micro-scale interfacial characteristics influencing the macro-scale system level performance, it is neither possible nor practical (with the current state-of-the-art) to develop minutely resolved full-scale computational models for simulating real world structures. Consequently, various reduced order modeling techniques have been employed to facilitate simulations [20, 21, 18, 14]. In the current study, a fairly simple interface

reduction methodology is followed, in order not to make simulations prohibitively expensive, while at the same time retaining computational accuracy. The interfaces are reduced to "patches" governed by the so-called whole-joint models [24], with dynamic simulations cast into a quasi-framework as in [1].

2 Background

2.1 Quasi-Static Modal Analysis

Following the developments in [14], the authors in [1] developed a framework for the simulation of weakly nonlinear systems. The method uses the linearized mode shapes of the full dynamical system in order to apply "modal" forcing on the nonlinear structure in a quasi-static manner. Employing Masing friction models enables one to obtain the steady state dynamic response using quasi-static simulations alone. The low computational cost of the method allows one to conduct fairly sophisticated parameter estimation procedures in a reasonable amount of time. The interested reader is referred to [1] and [2] for a detailed exposition of the same.

2.2 Modeling

Figure 1 illustrates the whole-joint patches used in the current study. Discretization is not conducted along the Y direction since the mode-shape of interest is not expected to have tangential relative displacements in that direction.

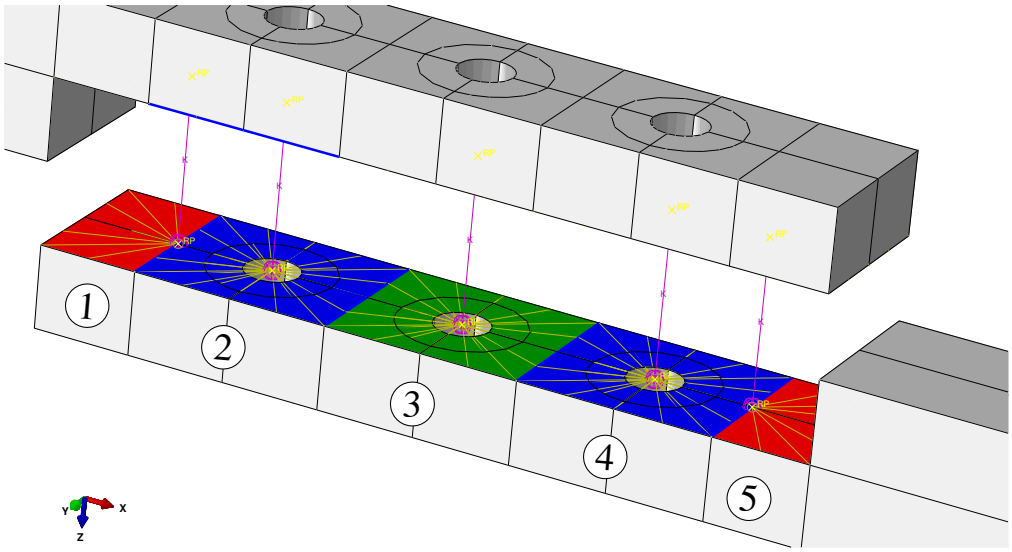


Figure 1: The five-patch whole-joint interface with correspondingly labeled regions. By symmetry, regions 1 & 5 and 2 & 4 can be taken to have identical properties.

Each patch is represented by a "virtual node" whose six Degrees-Of-Freedom (DOFs) are all retained for the model reduction step that follows. A Hurty/Craig-Bampton component mode dynamic substructuring [15, 7] is conducted retaining the said DOFs as well as 26 constrained modes for each structure. This provides a comparatively small system (86×86 matrices) representing the structure.

The Masing model [4] places the following conditions on the hysteresis loop of a friction model,

- The forward part of the hysteresis curve is identical to the reverse part of the hysteresis curve, only stretched by a factor of two and reflected across the axes when oscillating between two extremes.

- The equation of any hysteretic response curve is determined from the last point of the loading cycle before reversal and requiring that if the loading curve crosses a previous loading curve, it must correspond to the previous loading curve.

Essentially, this allows one to establish a functional relationship between the hysteretic backbone and the loop itself. There are however a large class of models which do not follow these rules. The violations arise mostly because of explicit normal force dependence which is absent in most Masing models. The previously described quasi-static framework may still be used in order to simulate such systems, but the quasi-static solver will have to trace out the full hysteretic loop as opposed to just the backbone for Masing models. The current study uses Segalman's four-parameter Iwan model [23], which is an example of a model that follows Masing's conditions strictly. These models, as the name suggests, are formulated with four unknown parameters, the estimation of which will form the crux of the current work.

2.3 Systems of Interest

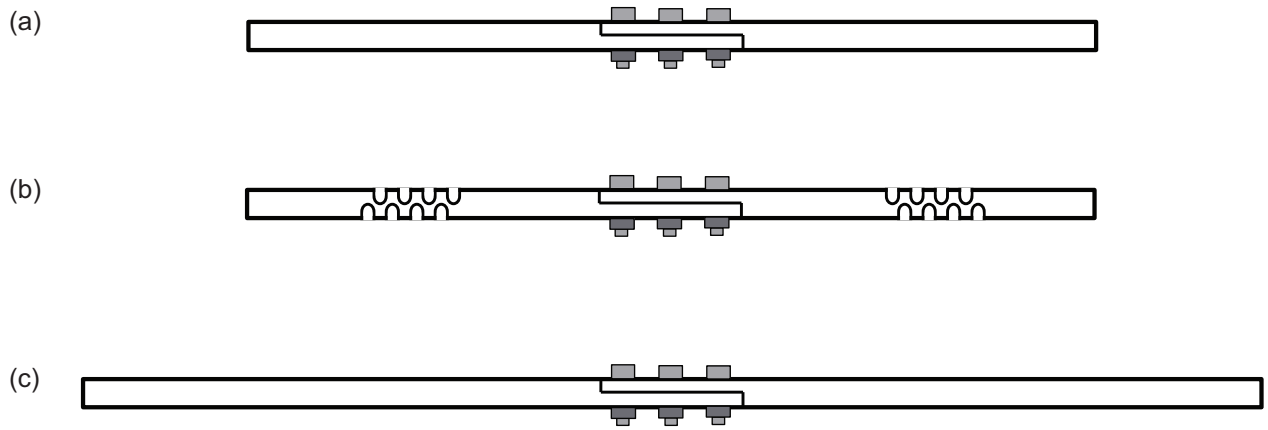
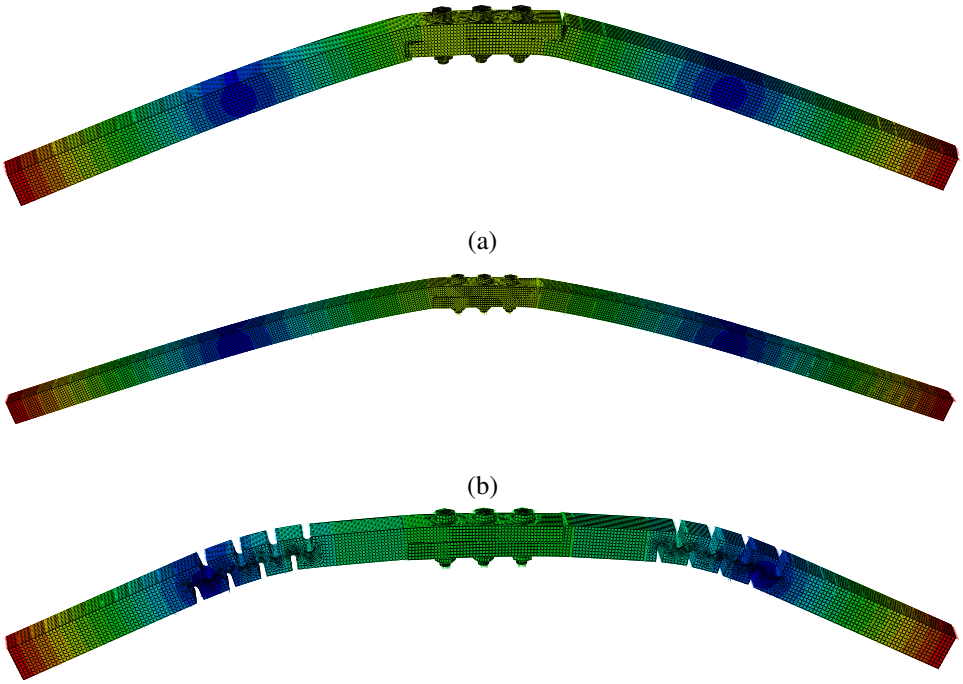


Figure 2: Three different configurations of the Brake-Reuß Beam: (a) Nominal (BRB), (b) Spring-modified (SBRB), and (c) Length-modified (LBRB) [6].

Figure 2 depicts the three different configurations of the Brake-Reuß Beam (BRB) that will be considered presently. The nominal configuration consists of two steel half beams bolted together through a lap-joint with three bolts torqued to 20Nm. The length of the total assembly is 720cm, with the cross-sections described by a square of side 1 inch (25.4cm). As can be seen, the other two modifications, the SBRB & the LBRB, modify different aspects the nominal system, rendering different structural contexts for the bolted lap joint in the middle. The main aspect that will be dealt with here will be the viability of considering one of the structures as a "surrogate structure" for the others, i.e., using information collected from experimental measurements of just one of the beams to develop predictive models for the others. The interested reader is directed to [2] for the exact dimensional drawings of the beams.

Figure 3 depicts the linearized mode shapes corresponding to the first bending mode of each of the beams. As previously stated, the frictional excitation is majorly expected to be in the relative X direction. All of the models have a static prestress load applied along the bolt axes corresponding to the 20Nm bolt torque (calculated to be 11,580N for the current geometry [16, 5]).

Table 1 summarizes the low amplitude experimental behavior of the assembled beams in terms of the natural frequency and damping factor. As a representation of the nonlinearity, fig. 4 depicts the deviation of these modal properties for varying displacement amplitudes. A Hilbert transform technique was used to process ring down experimental data into amplitude dependent characteristics (see [17] and references therein for details). The signs of the deviations are retained in order to illustrate the fact that increasing displacement amplitudes will result in reduced frequencies and increased dissipation (damping factors). Both of these are oft-observed phenomena in numerical (as well as experimental) investigations of stick-slip friction [19, 4].

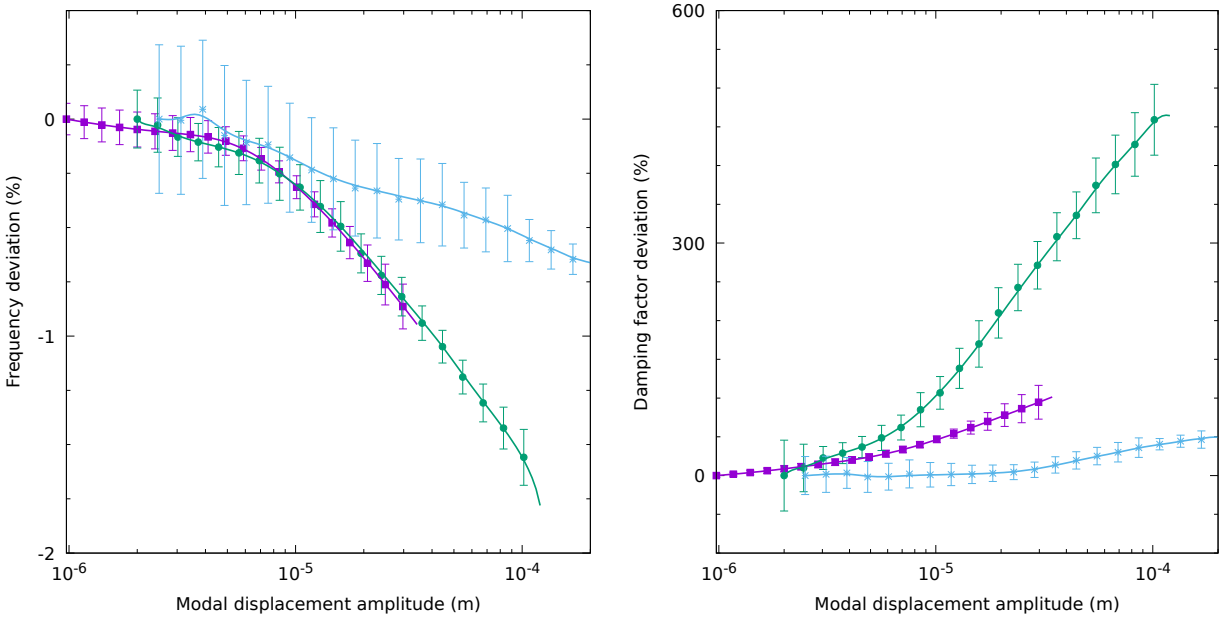


(a)

(b)

(c)

Figure 3: Linear mode shapes of (a) the BRB, (b) the LBRB, and the (c) the SBRB (Contours colored by displacement magnitude)



(a) (b)

Figure 4: Experimental (a) frequency and (b) damping factor deviations from low-amplitude values, shown for the BRB ( ), LBRB ( ), and the SBRB ( ).

Table 1: Mean low amplitude modal parameters for the different beam configurations

Beam	Frequency (Hz)	Damping factor ($\times 10^{-6}$)
BRB	169.48	1665.9340
LBRB	80.82	924.3096
SBRB	91.96	946.0959

2.4 Multi-Objective Optimization

In order to use the experimental data in fig. 4 for fitting friction models to the interface, the first aspect that will have to be understood is that there are two seemingly independent quantities (natural frequency and the damping factor) that any acceptable model will have to predict. This naturally lends itself to a Multi-Objective Optimization Problem (MOOP) wherein a lot of features not readily apparent in single objective problems start coming up. For example, it may not always be possible to find one optimal model that will be able to best predict the trends in terms of all the objectives. Instead, one may obtain what are referred to as Pareto optimal/nondominated sets of solutions. A set of solutions (referred to interchangeably as designs) is said to be nondominated if no solution in the set performs better than any other solution in terms of both the objectives [8]. Using this as a criterion, it is also possible to rank the designs based on the number of designs that "dominate" it. Rank 1 designs are those which have no other solution that dominates them, while rank 2 are those which are dominated by rank 1 alone, and so on.

Another important issue that comes up in MOOPs is the diversity of population. Any unbiased design exploration must result in diverse population in both the parameter as well as the error-space. There are evolutionary algorithms (see [9], for example) which tackle the same in order to obtain the nondominated set for a given problem. But when the parameter space is very large (say 15 independent parameters), clustering tends to happen in the parameter space. This effect scales up dramatically with dimension. For the current investigation however, large numbers of random samples are generated and numerical studies conducted on them.

Several ranked pareto sets are extracted and their parameter distributions studied. While it is true that a strict optimization study will reject all solutions except the rank 1, this is not followed here since in most cases, there might be many higher ranked solutions that will still have satisfactory predictive capabilities. When interpreting parameter distribution estimates, it must be noted that the there is a high tendency for spurious clustering and bias owing to the dimensionality of the problem (see "curse of dimensionality" in [22]). Although little can be done about the bias, a better picture, sans the spurious peaks, may be obtained by considering pareto solutions of multiple ranks. Using too many ranks may however lead, once again, to wrong results. Thus, a trade-off will have to be achieved for choosing the number of ranks.

3 Results and Discussions

Table 2: Parameter limits for design exploration

Parameter	Min.	Max.	Sampling
F_S	10^1N	10^{11}N	Log-scale
K_T	10^2Nm^{-1}	10^{14}Nm^{-1}	Log-scale
χ	-0.99	-0.01	Linear-scale
β	10^{-4}	10^4	Log-scale
K_Z	10^2Nm^{-1}	10^{14}Nm^{-1}	Log-scale

Design exploration was conducted on the three beam models using 5,000,000 Latin Hypercube Sampled (LHS) points. The parameter limits (fixed through trial & error to obtain well-pronounced Pareto sets) are given in table 2. In (a)-(c) of fig. 5, the error-space plots of the design exploration for each of the three beams are depicted along with several ranks of non-dominated sets. Designs showing more than 1Hz rms frequency deviation are not considered for the Pareto analysis. It can be observed that the larger ranked designs tend to cluster together in the error-space, i.e., rank improvement offers lesser and lesser utility. Another important feature that can be made out is the dense error space structure for the SBRB. For ranks larger than about 100, the Pareto sets become approximately horizontal, meaning that the two objectives are no longer completely independent and an absolute minima becomes more and more well-defined. In (d), kernel density estimates [1] of the fraction of designs as a function of the non-dominated rank is provided. As expected, SBRB has the maximum designs in the range 1-100, while the corresponding region is 1-1000 for the other two.

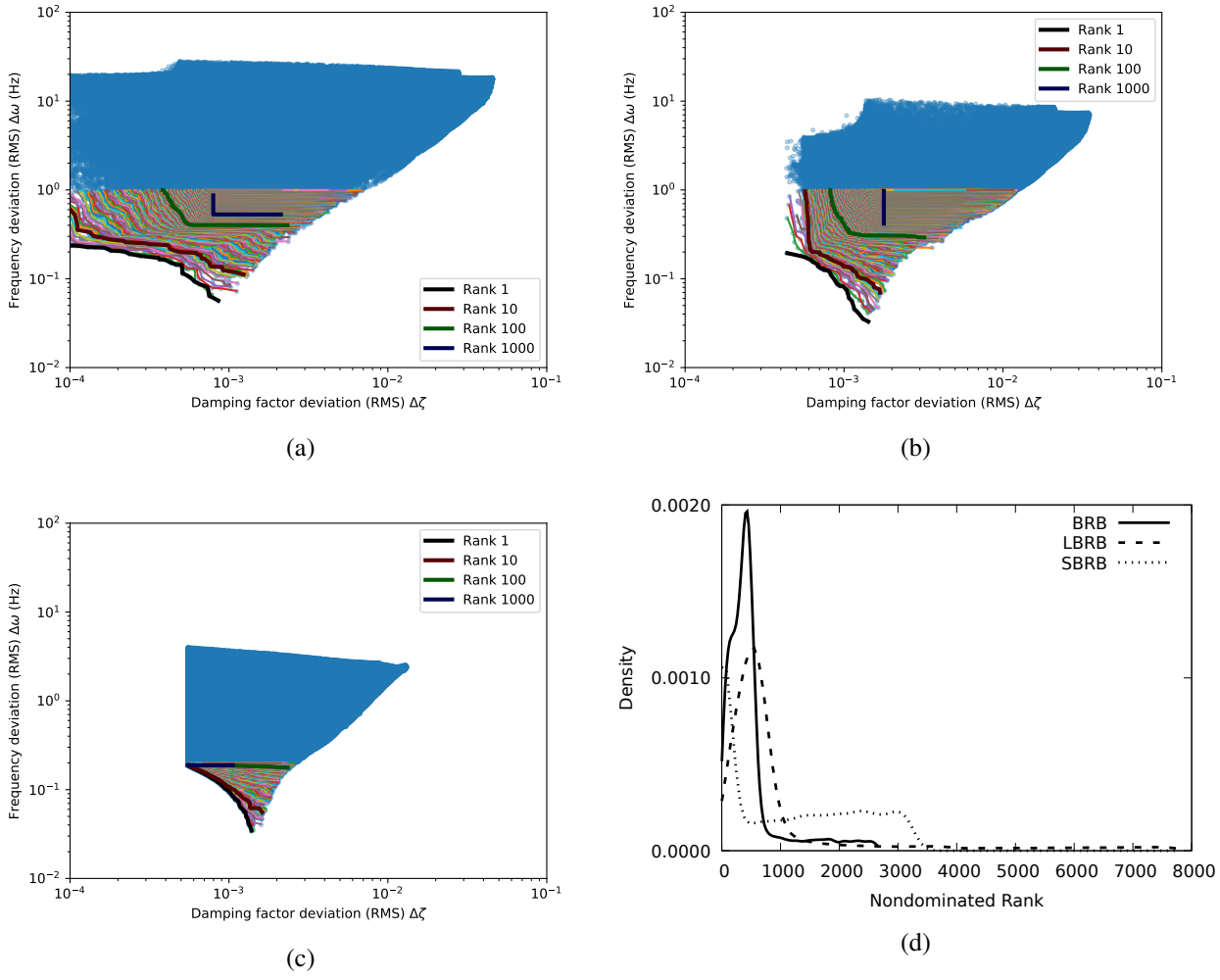


Figure 5: Error space design exploration for the (a) BRB, (b) LBRB, and (c) SBRB, with sorted non-dominated sets. (d) Distribution of number of designs with Pareto rank. Designs with rms frequency deviation of more than 1Hz were rejected directly.

In order to understand why the results are all slightly different for the SBRB, one has to observe the nature of the interfacial loading. In fig. 3, it is evident that in both the BRB as well as the LBRB the largest amount of bending energy is borne at the nonlinear interface. But for the SBRB, the far-field stiffness modifications show considerable bending which seems to result in a reduced loading condition for the interface[2].

[1] Gaussian Kernel's with Scott's normal reference bandwidth [22] used everywhere unless otherwise stated

[2] This is observed experimentally where the SBRB is nearly linear (near-horizontal response curves in fig. 4).

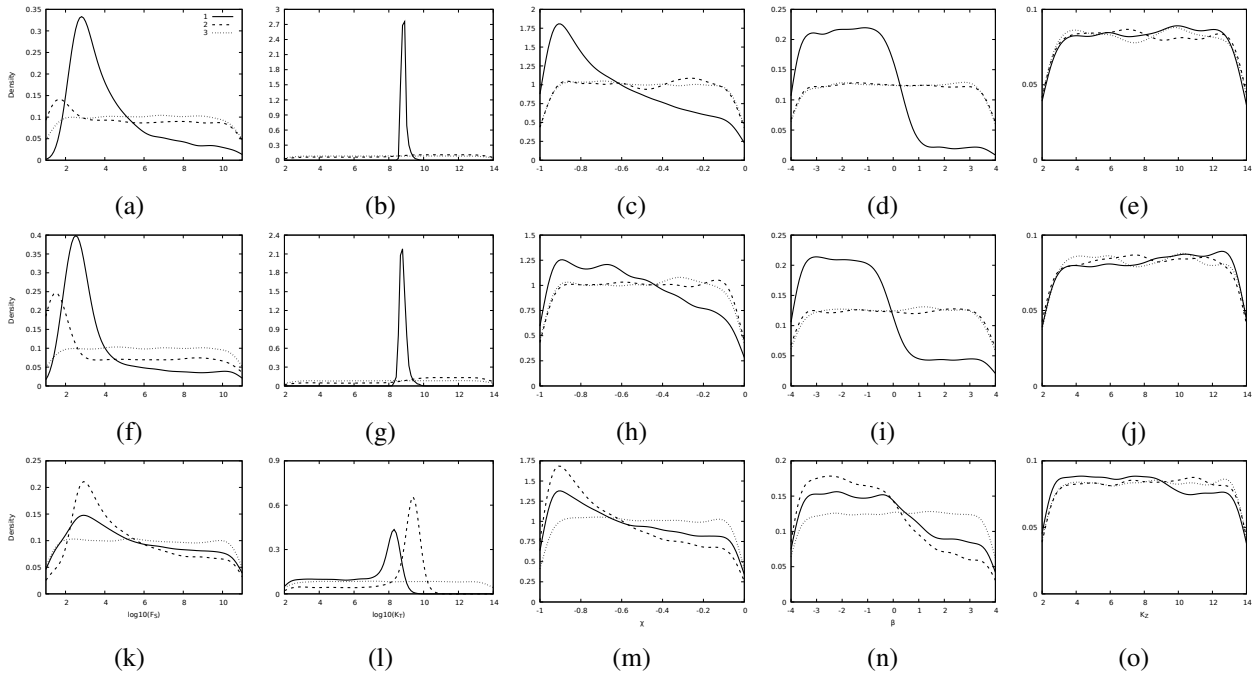


Figure 6: Parameter distribution estimates on the first one hundred nondominated sets for the (a)-(e) BRB, (f)-(j) LBRB, and (k)-(o) SBRB. (a),(f),(k) shows the estimation for F_S, (b),(g),(l) for K_T, (c),(h),(m) for χ, (d),(i),(n) for β, and (e),(j),(o) for K_Z. Also depicted in each figure is the distribution for each patch (labeled 1,2 & 3).

Figure 6 depicts the parameter distribution estimates for the first 100 ranked non-dominated designs for the three beams. The BRB, LBRB & the SBRB have 6337, 6999, and 14599 designs respectively (out of a total sample of 5 million each). Each panel depicts the density of a parameter in all the three regions, labeled accordingly. It can be observed that the peaks in each distribution fall close to each other in the estimates of all the three beams, but there are significant disparities in the tail regions. This is also reflected in the absolute values of the density estimates at each value, where a larger tail will bring the peak down, while a thinner tail will increase the density at the peak location. The tail effect seems to be most pronounced in the case of the SBRB. As mentioned earlier, the extent of non-linearity that gets excited in the case of the SBRB is lesser in comparison to the other two. Hence, many of the nonlinear parameters have very little to no influence on the actual response. This leads to what may be regarded as a large "plateu" (or a degenerate set) of minima in the design-space which leads to the tailing behavior. This is also the reason why the SBRB has more than twice the number of designs as compared to the other beams in the same 100 ranks.

On the other hand, the agreement between the BRB and the LBRB estimates are remarkably similar. Although these fail any classical sampled hypothesis test due to the smaller features, the importance of the structure has to be understood. The similar but non-identical structure of the density indicates that only a subset of the selected designs belong to the same family, and there are still some factors contributing to dissimilarity.

In [2], the authors have expanded on this idea of "incomplete equivalence", where the choice of designs has been made based on a region in the error-space and fractions of designs falling within have been used to come up with a metric of confidence with which estimates from one beam can be used for making predictions in another. A factor-level study is also conducted in order to estimate the dependence on various modeling choices. The current investigation, based on density estimates serves as a supplement to the study in confirming the numbers obtained therein.

Figure 7 depicts the same estimates for the first five hundred ranks. It can be observed that the tails are thicker and in a few places, have even made the peaks imperceptible. But the basic trends are intact.

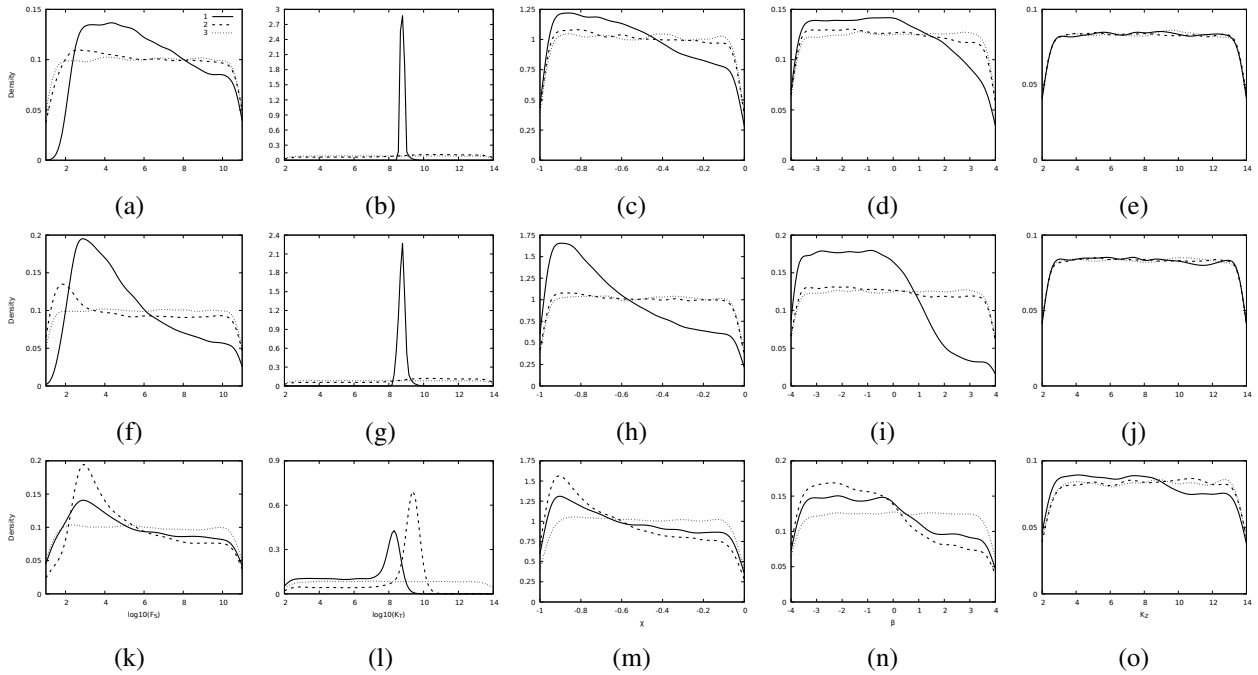


Figure 7: Parameter distribution estimates on the first five hundred nondominated sets for the (a)-(e) BRB, (f)-(j) LBRB, and (k)-(o) SBRB. (a),(f),(k) shows the estimation for F_S, (b),(g),(l) for K_T, (c),(h),(m) for χ, (d),(i),(n) for β, and (e),(j),(o) for K_Z. Also depicted in each figure is the distribution for each patch (labeled 1,2 & 3).

It must, however be noted that both the sets of estimates in figs. 6 to 7 represent only single-dimensional densities. The actual parameter space is 15-dimensional and one must be very cautious in making conclusions from just the above figures.

4 Conclusions

The Quasi-Static Modal Analysis (QSMA) technique offers a highly efficient way of computing the amplitude-dependent modal properties of nonlinear systems using quasi-static simulations alone. This was exploited in the current study to fit experimental data to a computational model and observing the trends in the resulting parameter estimates. The MOOP framework followed provides interesting ways of looking at the estimation problem, in terms of Pareto optimality. The markedly similar trends in the parameter density estimates indicate at least partial support to the surrogate system hypothesis. In order to proceed further, it will be necessary to obtain quantitative estimates of the confidence. A preliminary effort may be found in [2], where a slightly different approach has been taken to tackle the problem. However, characterizing the high dimensional density structure is an issue that persists.

References

[1] M. S. Allen, R. M. Lacayo, and M. R. W. Brake. Quasi-static modal analysis based on implicit condensation for structures with nonlinear joints. In *International Conference on Noise and Vibration Engineering*, Leuven, Belgium, September 2016.

[2] N. N. Balaji and M. R. W. Brake. The surrogate system hypothesis for joint mechanics, In preparation.

[3] M. R. W. Brake, C. W. Schwingshackl, and P. Reuß. On the observed variability and repeatability in jointed structures. *Mechanical Systems and Signal Processing*, Under Review.

[4] M. R.W. Brake. An overview of constitutive models. In *The Mechanics of Jointed Structures*, pages 207–221. Springer, 2018.

[5] R. G. Budynas and K. Nisbett. *Shigley's Mechanical Engineering Design*. McGraw Hill, 10th edition, 2014.

[6] S. B. Cooper, M. Rosatello, A. Mathis, K. Johnson, M. R. W. Brake, M. S. Allen, A. A. Ferri, D. R. Roettgen, B. R. Pacini, and R. L. Mayes. Effect of far-field structure on joint properties. In *35th International Modal Analysis Conference (IMAC XXXV)*, Garden Grove, CA, January 2017.

[7] R. R. Craig and M. C. C. Bampton. Coupling of substructures for dynamic analyses. *AIAA Journal*, 6 (7):1313–1319, 1968.

[8] K. Deb. *Multi-objective optimization using evolutionary algorithms*, volume 16. John Wiley & Sons, 2001.

[9] K. Deb, A. Pratap, S. Agarwal, and T. Meyarivan. A fast and elitist multiobjective genetic algorithm: NSGA-II. *IEEE transactions on evolutionary computation*, 6(2):182–197, 2002.

[10] M. Eriten, A. A. Polycarpou, and L. A. Bergman. Surface roughness effects on energy dissipation in fretting contact of nominally flat surfaces. *ASME Journal of Applied Mechanics*, 78:Art. 021011, 2011.

[11] M. Eriten, A. A. Polycarpou, and L. A. Bergman. Physics-based modeling for fretting behavior of nominally flat rough surfaces. *International Journal of Solids and Structures*, 48:1436–1450, 2011.

[12] D. J Ewins. A survey of contact hysteresis measurement techniques. In *The Mechanics of Jointed Structures*, pages 149–179. Springer, 2018.

[13] J. A. Greenwood and J. B. P. Williamson. Contact of nominally flat surfaces. *Proceedings of the Royal Society of London, Series A*, 295:300–319, 1966.

[14] J. J. Hollkamp and R. W. Gordon. Reduced-order models for nonlinear response prediction: Implicit condensation and expansion. *Journal of Sound and Vibration*, 318(4-5):1139–1153, 2008.

[15] W. C. Hurty. Dynamic analysis of structural systems using component modes. *AIAA Journal*, 3:678–685, 1960.

[16] R. M. Lacayo, L. Pesaresi, D. Fochler, J. Gross, J. Armand, L. Salles, M. R. W. Brake, and C. W. Schwingshackl. A comparison of numerical approaches for predicting the dynamics of a beam with a lap joint. In *35th International Modal Analysis Conference (IMAC XXXV), Springer, Garden Grove, California*, 2017.

[17] R. M. Lacayo, L. Pesaresi, J. Groß, D. Fochler, J. Armand, L. Salles, C. W. Schwingshackl, M. S. Allen, and M. R. W. Brake. Nonlinear modeling of structures with bolted joints: a comparison of two approaches based on a time-domain and frequency-domain solver. *Mechanical Systems and Signal Processing*, Under Review.

[18] M. P. Mignolet, A. Przekop, S. A. Rizzi, and S. M. Spottswood. A review of indirect/non-intrusive reduced order modeling of nonlinear geometric structures. *Journal of Sound and Vibration*, 332:2437–2460, 2013.

[19] E. P. Petrov and D. J. Ewins. Analytical formulation of friction interface elements for analysis of nonlinear multiharmonic vibrations of bladed discs. *ASME Journal of Turbomachinery*, 125:364–371, 2002.

[20] F. Pichler, W. Witteveen, and P. Fischer. Reduced-Order Modeling of Preloaded Bolted Structures in Multibody Systems by the Use of Trial Vector Derivatives. *Journal of Computational and Nonlinear Dynamics*, 12(5):051032–051032–12, July 2017. ISSN 1555-1415. doi: 10.1115/1.4036989.

[21] D. R. Roettgen, B. Seegar, W. C. Ttai, S. Baek, T. Dossogne, M. S. Allen, R. J. Kuether, M. R. W. Brake, and R. L. Mayes. A comparison of reduced order modeling techniques used in dynamic substructuring. In *34th International Modal Analysis Conference (IMAC XXXIV)*, Orlando, FL, February 2016.

[22] D. W. Scott. *Multivariate density estimation: theory, practice, and visualization*. John Wiley & Sons, 2015.

[23] D. J. Segalman. A four-parameter Iwan model for lap-type joints. *ASME Journal of Applied Mechanics*, 72:752–760, 2005.

[24] D. J. Segalman, D. L. Gregory, M. J. Starr, B. R. Resor, M. D. Jew, J. P. Lauffer, and N. M. Ames. *Handbook on Dynamics of Jointed Structures*. Technical Report SAND2009-4164. Sandia National Laboratories, Albuquerque, NM, 2009.

Two types of dynamic joint behaviour: theoretical and experimental analysis

H. G.D. Goyder[1], D. P.T. Lancereau[1], P. Ind[2], D. Brown[2]
[1]Cranfield University, Centre for Defence Engineering
Shrivenham, Swindon, SN6 8LA UK
E-mail: **h.g.d.goyder@cranfield.ac.uk**

[2] AWE Aldermaston, Berkshire, UK RG7 4PR

Abstract
The joints in a structure may be a significant source of damping and may have uncertain stiffness properties. Experimental and theoretical investigations are presented that suggest there are two extreme types of bolted lap joint. If the joint has a limited contact patch, due to the bolt stress, then the edges of the contact patch have large static normal stresses which prevent sliding under dynamic loading. Alternatively, if the contact patch occurs naturally, due to bolting two surfaces together, then outside the contact patch the joint interfaces will separate. This type of joint can slip at the edges of the contact patch and this can lead to changes in the stiffness and the generation of significant damping. It is shown that the joint behaviour is nonlinear with damping increasing and stiffness decreasing as vibration amplitudes are increased. It is suggested that all joint damping falls between the extremes of a limited contact patch and a natural contact patch.

1 Introduction

Which type of joint on a structure causes damping? This is an important question because damping from joints is difficult to model in computer simulations. Further very little is known about how joints provide stiffness and damping. This paper describes two types of joints which are believed to be the two extreme cases for joint dynamic behaviour.

A typical structure is built-up from components connected together by joints. A component may be a single homogeneous manufactured block of material. Each component is attached to other components by connections which may be bolted joints, glues or fasteners. In this paper, we only consider bolted lap joints.

The long term objective of the work considered here is to enable computer simulations to model built-up structures with many joints correctly. This is currently not feasible, and there is no guidance on how to model joints dynamically.

The objective of the work presented here is to suggest that there are two bolted joint configurations that represent the extremes of behaviour. For one case there is constant stiffness and no damping. For the opposite case there is significant damping and variable stiffness. It is suggested that typical joints fall between these two extremes. The important consideration is the nature of the contact patch that connects the two parts of the joint.

The approach taken here combines both experimental measurements and simulation studies. Joint behaviour is very nonlinear, so special experimental methods have been devised to enable the stiffness and damping to be investigated. Similarly, special computer simulations have been conducted to help better understand the behaviour of a bolted joint.

Bolted joints are usually designed for static considerations. The bolt tension is selected to prevent the joint slipping due to the loads. Bolt tensions range from about 50% of yield to 100% yield. The static design does not usually consider dynamics which is the main concern of this study.

Previous work on the dynamics of joints has recently been assembled in a book edited by Brake [1]. Reviews of significant experimental work on joints have been performed by Gaul [2], Seagleman [3] and Peyret, Dion and Chevallier [4]. The main conclusion from these reviews is that the joint behaviour is nonlinear in stiffness and damping [5].

The nonlinearity causes difficulties for experimental work when extracting information while undertaking the necessary signal processing to determine relevant parameters such as natural frequencies and damping ratios. Kuether and Brake [6] use short time Fourier transforms which identify the nonlinearity as the amplitudes change. Allen and Mayes [7] have a method that involves examining free vibration decay time histories by choosing a range of starting times. The method used in this paper has been developed by Goyder and Lancereau [8] using special filtering methods and curve fitting to obtain instantaneous natural frequencies and damping values (see below). Recent experimental work has shown the importance of the size of the contact patch within a joint; Lancereau and Goyder [9].

Typical computational investigations have been made by introducing Iwan models [10] into finite element descriptions of a structure and tuning them to experimental results. This approach is usually successful and has been performed by Denear and Allen [11] and Schwengshackl [12]. There has been no detailed stress analysis of contact patches under dynamic loading.

2 Joint Contact Patches

The forces acting at a joint location consist of three types. First there is the static force generated by the tightening of the bolt and nut. Second there are static forces generated by the structure. Finally there are the dynamic forces that exercise the joint during operation.

Figure 1 (a) and (b) show two types of lap joint. In Figure 1 (a) the contact patch has been constructed to

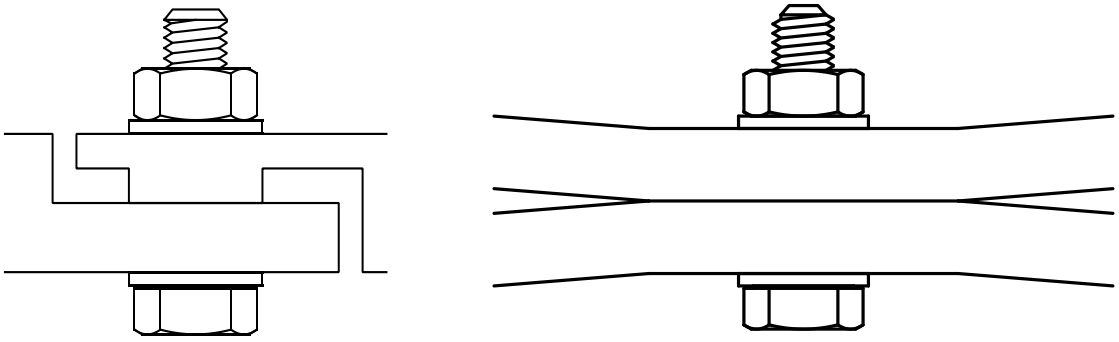


Figure 1. (a) A joint with a limited contact patch (complete contact).

(b) A joint with flat surfaces which has a gap surrounding the contact patch (receding contact).

be of a specific size; in this case the same size as the washer. In Figure 1 (b) the joint has been constructed to hold two flat surfaces together. In this case the surfaces find their own contact patch size and spring apart in a region outside the contact patch. This may be identified as the natural contact patch which is larger than the limited contact patch in Figure 1 (a). These contact patches arise from the static loading due to the bolt tension. An important question is how these contact patches are altered by the application of dynamic loading.

The investigation of static contact patches has received considerable attention due to their importance in stress calculations where loads are applied to structures. The basic contact patch was first described by

Hertz for a sphere pressed into a surface. Various different types of contact patches have been identified; for basic information see Hill, Nowell and Sackfield [14].

The two joint types identified in Figures 1 (a) and (b) are known as complete contacts and receding contacts respectively. More details on this type of contact may be found in Hills and Parel [15] and Ramish and Hills [16].

In order to gain an understanding of the stresses involved in a contact patch simplified calculations have been made using the two-dimensional model illustrated in Figure 2.

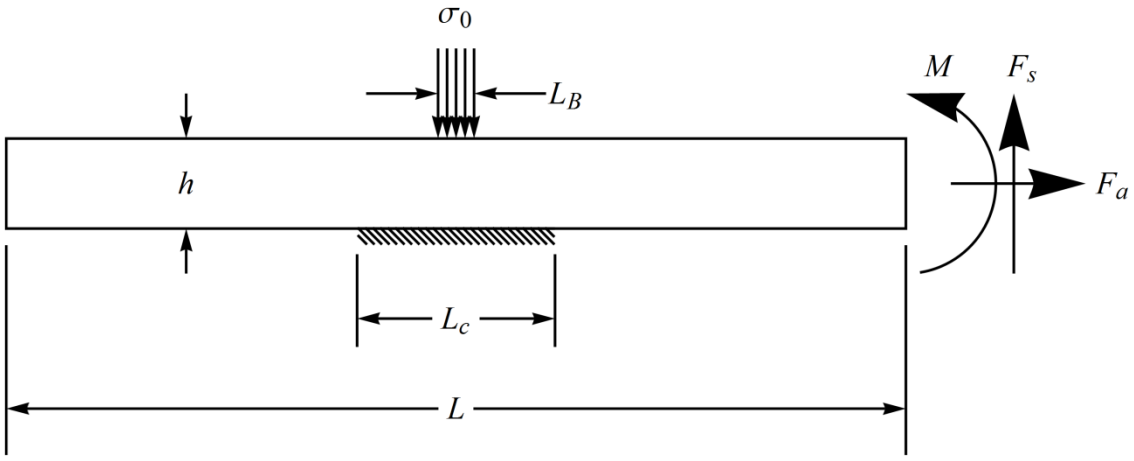


Figure 2. Simplified version of a joint in two dimensions. A rectangular strip of material of length L and height h is pressed on a rigid contact patch of length L_c. The stress applied by the bolt is σ_0 distributed over a length L_B. External dynamic forces M, F_s and F_a may also be applied.

The joint is modelled as a rectangular component (plain stress) which is pressed onto a contact patch of length L_c by a bolt acting on the top surface. The bolt applies a stress of magnitude σ_0 over a length of L_B. The length of the strip, L, is long compared to the strip height, h. This is because the bolt stress does not spread out far beyond the contact patch so that the dimension L can be ignored. The lengths in the calculation can be rendered non-dimensional by dividing by the height, h. It is assumed that the inertial effects due to the mass of the joint are negligible compared to the dynamic forces so that the joint may be considered as a static component loaded by the dynamic forces generated within the surrounding structure.

The dynamic loads are indicated by a moment, M, a shear force F_s and an axial force F_a. The effect of the shear force and bending moment are similar and only the effect of the bending moment has been investigated. The effect of the axial force F_a is not reported here. Although these are dynamic loads the assumption of ignoring the inertia of the joint itself means that they can be treated as static loadings.

The calculations have been made using a finite element code within the Mathematica computer program [17]. Particular attention was paid to the mesh size at the contact patch which was refined to check that the stress calculations converge. The calculations were performed with the bolt stress distributed over a length equal to $L_B/h = 0.5$.

The contact patch due to the bolt stress was investigated first with all other forces (M, F_s and F_a) set to zero. Figure 3 shows the normal stress for various lengths of the contact patch. The notable feature is the large value of the stress at the edge of the contact patch. This holds the edge of the contact patch firmly and will prevent slipping. As the contact patch is made larger the stress at the edges decreases and the stress in the middle of the contact patch increases. It can be expected that for small contact patches the joint is held firmly together and no slipping will occur when dynamic loads are applied. This is the typical behaviour of a complete contact.

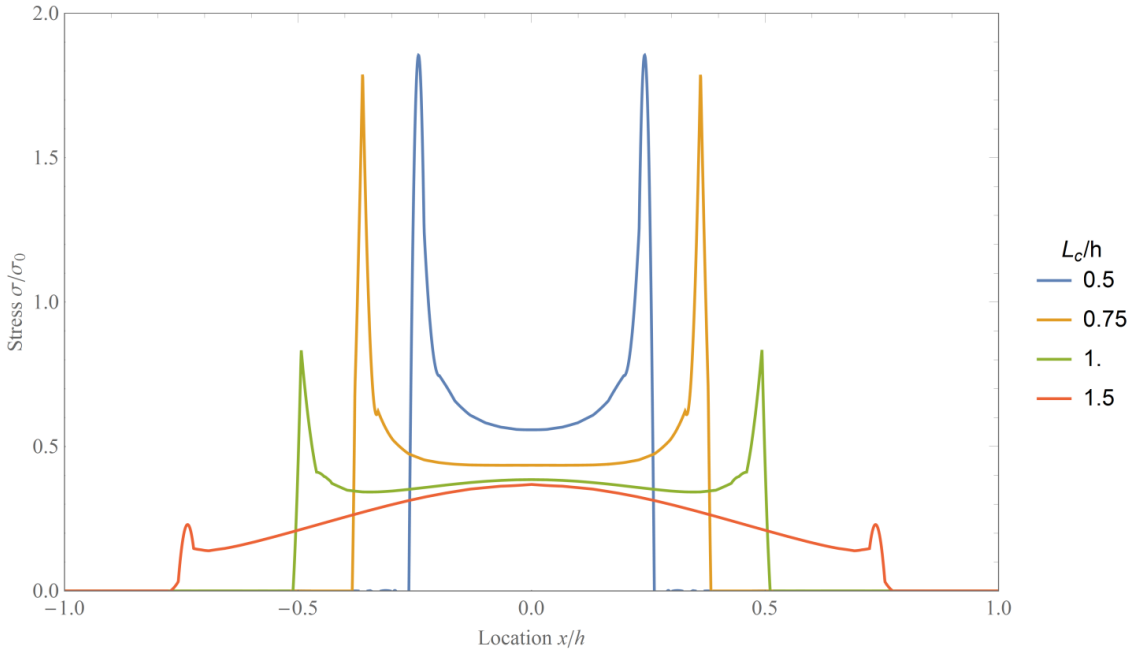


Figure 3. Stress on a complete contact patch for a range of contact patch lengths.

Figure 4 shows the stress on the contact patch of a receding contact. The precise positions of the edges of the contact patch have to be found by iteration. Outside of the contact patch the joint surfaces separate as shown in Figure 1 (b). It is notable that the location of the edge of the contact patch is independent of the load. For this receding contact the stress is largest in the middle and drops to zero at the edges. Consequently for receding contacts it can be expected that slip may occur at the edges of the contact patch when the joint is loaded dynamically.

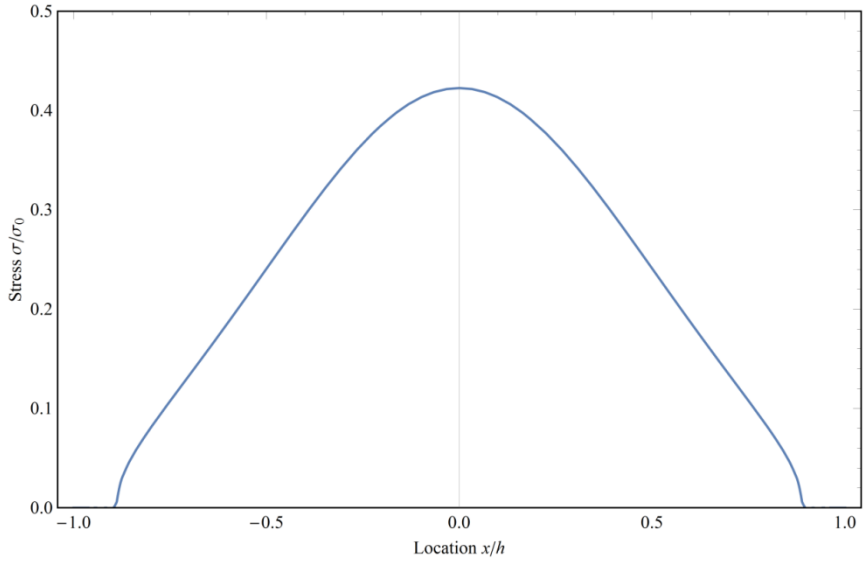


Figure 4. The stress on the contact patch of a receding contact. The location of the edges of the contact patch is found by iteration.

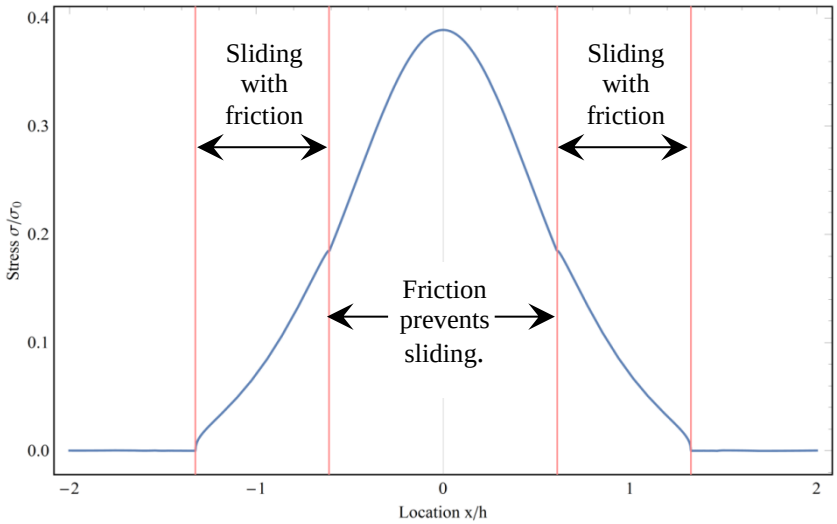


Figure 5. Stress on a receding contact showing regions where friction is acting. Internal region friction prevents sliding. External region sliding with friction can occur.

A more complicated variant of Figure 4 is shown in Figure 5. Here the vertical lines separate different regions of frictional constraint. In the inner region the shear stress is insufficient to cause slipping, and the surfaces are locked together by friction. Here the coefficient of friction is 0.7. In the outer region slipping may occur. This type of condition arises when the two thicknesses of the joint parts are unequal or additional forces are applied. The location of these lines must be found by iterating their location until constraints on stress and deflection conditions are satisfied.

Figure 6 shows the influence of a bending moment on a contact patch for receding conditions. The loading from the bolt is the same as those in figure 5. However, the addition of a bending moment (positive according to Figure 2) has caused asymmetry with a shorter slipping region on one side and a longer slipping region on the other side. The portion where sliding is prevented has also moved.

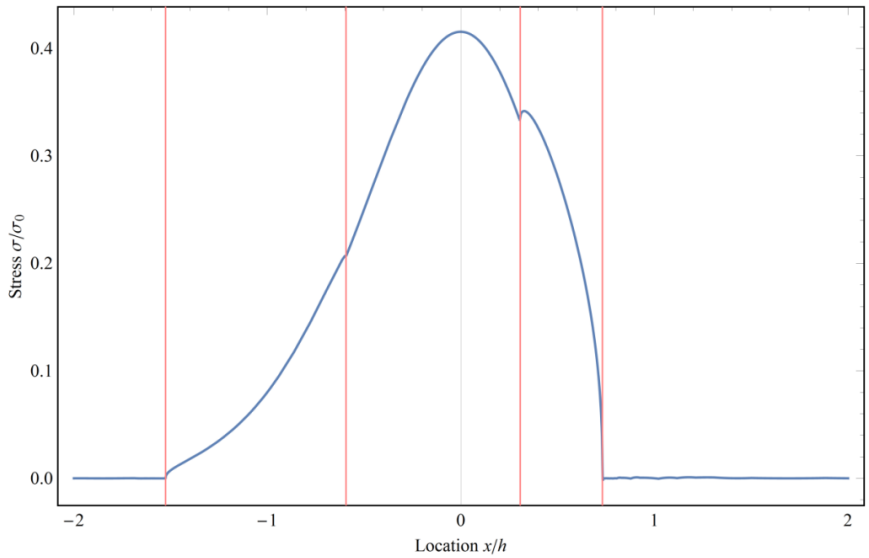


Figure 6. The stress on the contact patch with a moment applied to the joint. The central region, where slip cannot occur has moved. The outer regions have changed their dimensions.

The change in the stress on the contact patch, due to the moment, is significant for stiffness and damping. It can be seen that the evolution of the surfaces in the outer regions will lead to damping. Further the change in the location of the central contact patch has implications for stiffness.

For complete contacts the large forces at the edges of the contact patch may stop any sliding when a bending moment is applied. However, if the bending moment is sufficient to overcome these large forces then some sliding could occur.

3 Experimental method

Experimental measurements were made on joints that are both complete contacts and receding contacts. For both cases a series of small beams was assembled into a chain of bolted joints. The two configurations are shown in Figure 7 (a) and (b). For configuration (a) the component beams were made with a circular boss the size of a washer (outside diameter 20mm) at the joint interface. This corresponds to a complete contact. Previous experiments using these complete contacts have been described by Goyder, Ind and Brown [17]. For configuration (b) each component beam had a uniform cross-section. These beams were simply bolted together to give receding contacts. In each case, there are 11 bolts and 12 component beams. The overall length of the assembled beam for configuration (a) was 478 mm with each component beam being 60 mm × 50 mm × 12mm. The overall length of the assembled beam for configuration (b) was 1160 mm with each component beam being 170 × 30 × 10 mm. For both assemblies, there was a 10.2 mm clearance hole taking an M10 bolt with two washers and a nut. All joint interfaces were ground to give a flat finish.

Considerable attention was given to the suspension system so that the beam was supported in a free-free configuration. Support strings of 1350 mm were located at the nodes of the first mode of vibration and tied onto a stiff overhead beam.

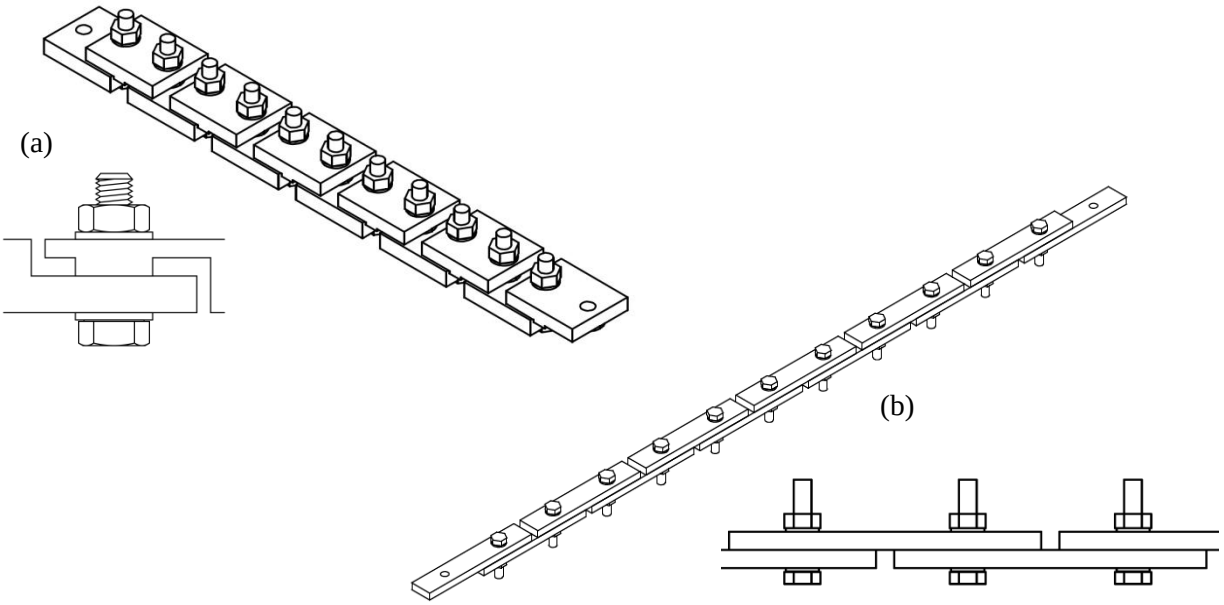


Figure 7 (a) and (b). The two beam configuration used in the experimental study. The configuration (a) is a complete contact with a circular boss forming the joint interface. Configuration (b) has simple lap joints.

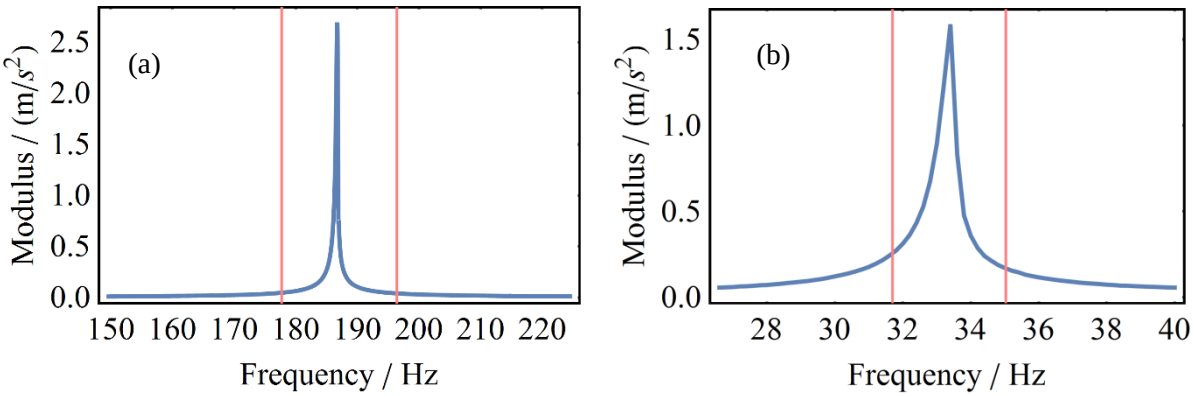


Figure 8. Fourier transform of time history from (a) beam with complete contacts (b) beam with receding contacts. The pink lines indicate the bandwidth of the filter that was applied to the time history.

The experimental method had four stages. First, the beam was set into excitation by means of a standard modal impact hammer applied at one end. The vibration data were collected using an accelerometer located at the other end. The data were digitized using a sample rate of 10000 samples/second. The vibration was allowed to decay over 30 seconds for configuration (a) and 15 seconds for configuration (b). Second, the discrete Fourier transform of the acceleration was determined and examples of the spectra obtained are shown in Figure 8. Note that these spectra were not divided by the Fourier transform of the force as is usual in modal analysis. The first resonance frequency of each beam is shown in the spectra.

In the third stage, each time history was filtered using a second order bandpass Butterworth filter with a bandwidth corresponding to the position of the pink lines shown in Figure 8. The filtering was done using the reverse filtering technique described in Goyder and Lancereau [8]. In this procedure, the time history is reversed before it is passed through the filter and then returned to its original sequence afterwards. This resulted in time histories of decay that are shown in Figure 9.

In the final stage, the data was divided into intervals of about four cycles of vibration and a curve fitting procedure was used to determine the instantaneous frequency, damping ratio and amplitude.

The experiments were repeated 10 times and the four stages applied each time to build-up a good set of data. The instantaneous frequency and damping as a function of time are shown for the complete contact in Figure 10 (a) and (b). Similar plots for the receding contact are shown in Figure 11 (a) and (b).

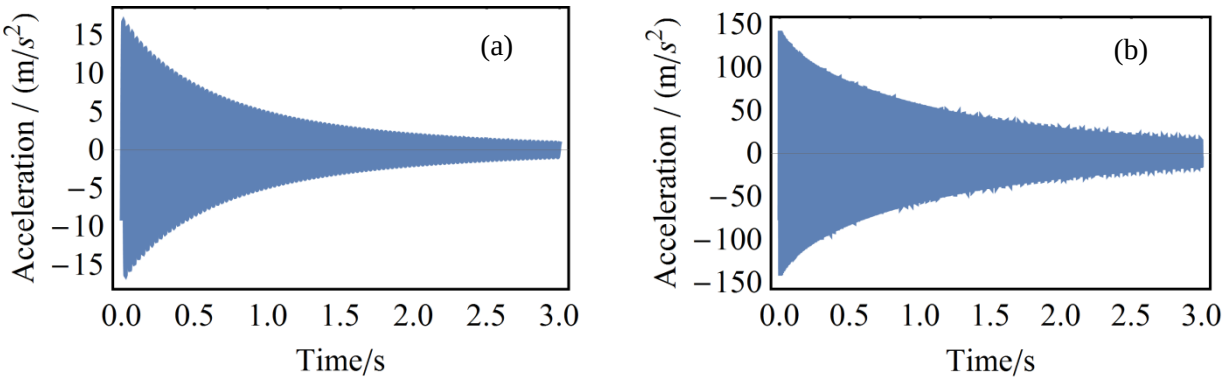


Figure 9. Filtered data for the first mode of (a) beam with complete contacts and (b) beam with receding contacts.

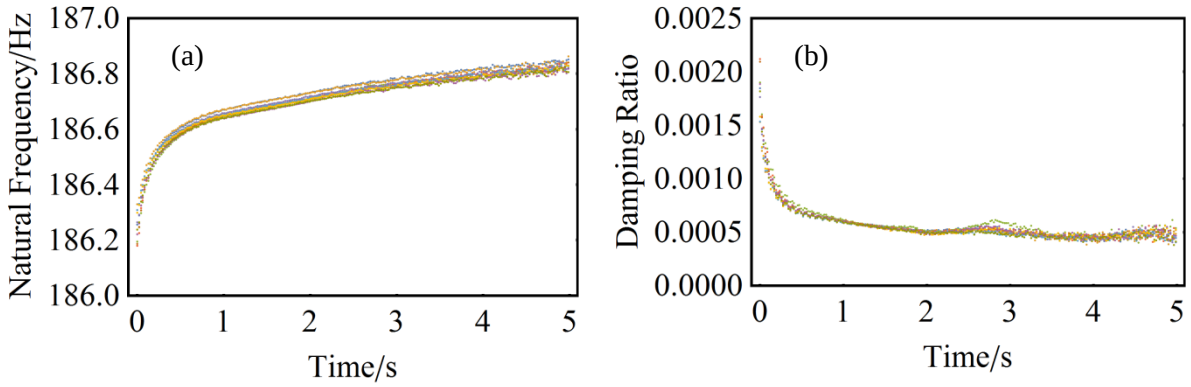


Figure 10. Results of 10 tests and curve fitting for the beam with complete contacts. (a) Instantaneous natural frequency and (b) instantaneous damping ratio as a function of time.

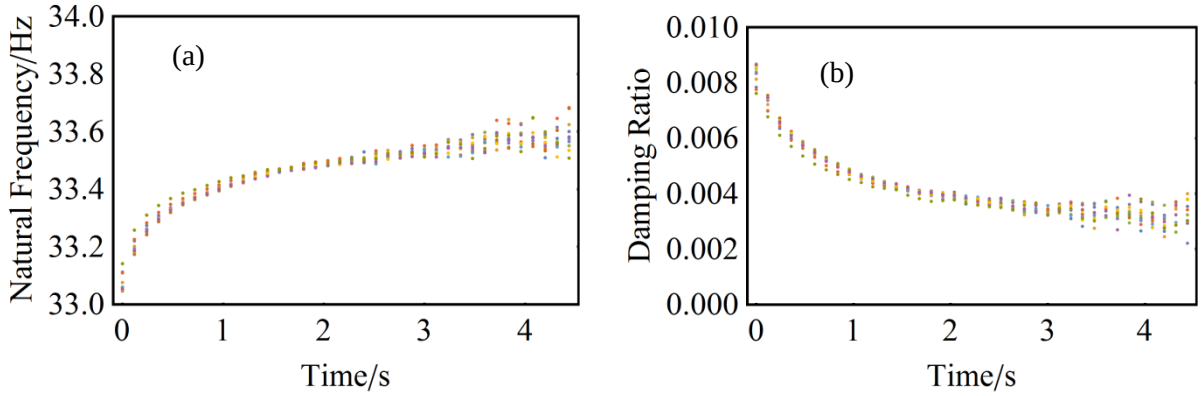


Figure 11. Results of 10 tests and curve fitting for the beam with receding contacts.
(a) Instantaneous natural frequency and (b) instantaneous damping ratio as a function of time.

In order to compare the results for the two beams, the data are plotted again on the same graph. For the instantaneous natural frequency, the percentage change in frequency is most relevant. The absolute frequency is determined by the mass and stiffness of the structure while the change in frequency is due to the change in stiffness of the joint. The percentage change was calculated by determining a mean value for the final natural frequency reached as the decay was completing and entering the noise floor. The percentage change in natural frequency was then determined using the equation

$$100\frac{f - f_m}{f_m} \tag{1}$$

Where f is the value of the instantaneous frequency at one time and f_m is the mean value of the frequency at the end of the decay. The mean values were 186.8 Hz and 33.6 Hz for the complete contact case and receding contact case respectively. Figure 12 shows the percentage change as a function of amplitude. The damping ratios for both beams are plotted against amplitude on Figure 13.

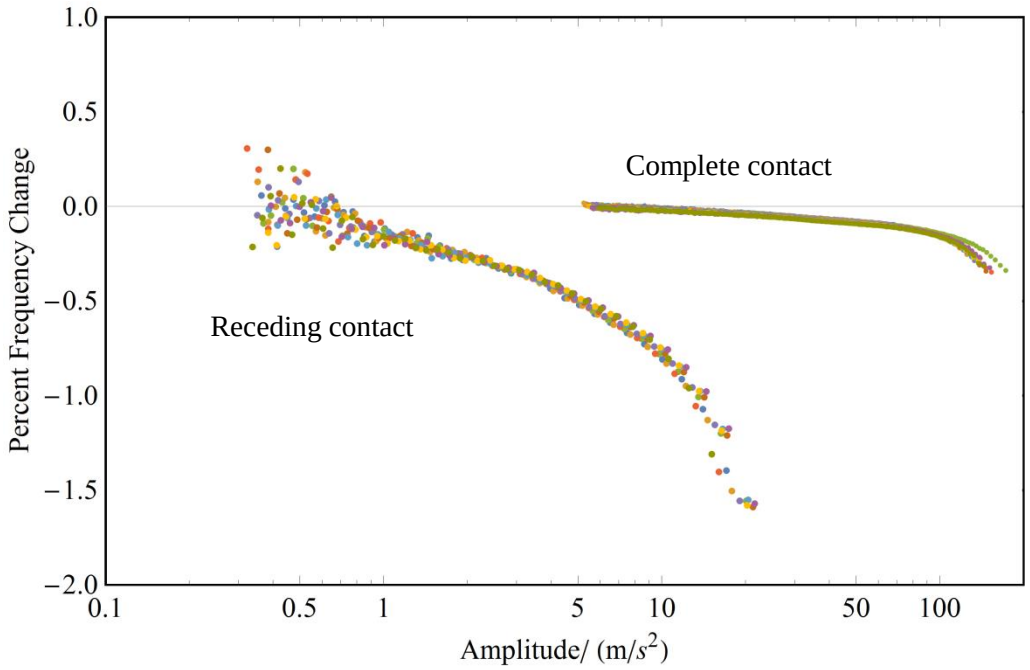


Figure 12. Percent change in natural frequency as a function of amplitude, all tests.

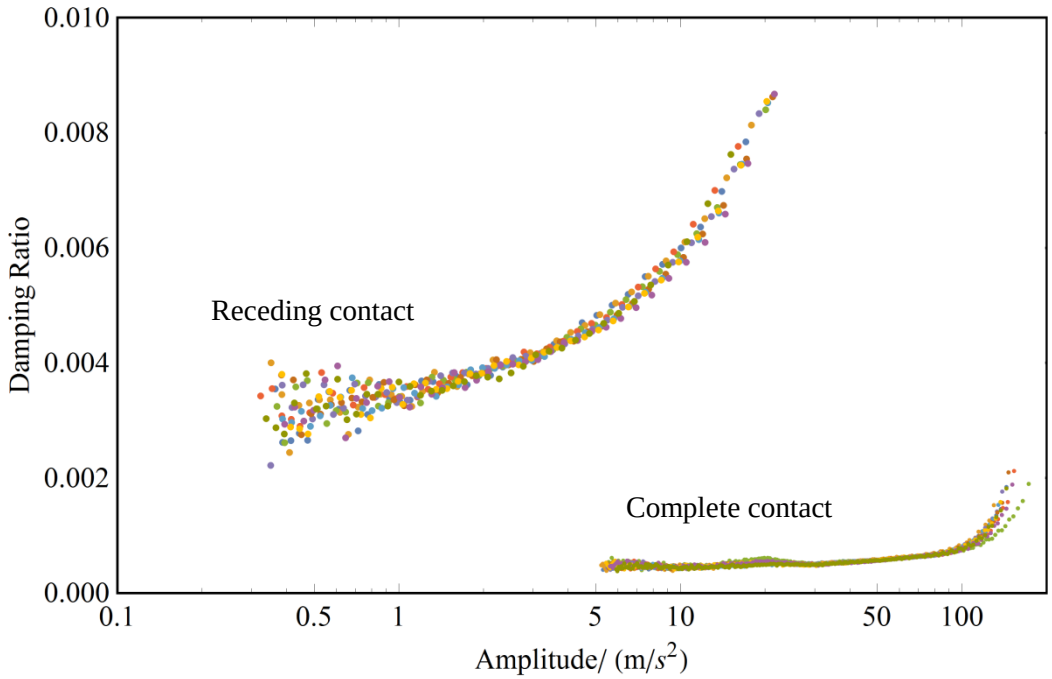


Figure 13. Damping ratio as a function of amplitude, all tests.

4 Discussion

Examination of the experimental results shows that as the vibration decays and the amplitude decreases the natural frequency increases and the damping decreases. This is most marked for the beam with receding contacts. For the beam with complete contacts there is a notable initial change in frequency and damping but the subsequent change is small. The increase in frequency suggests that the constraint provided by the joints is increasing with decreasing amplitude. This observation can be explained by an amplitude dependant change in the size of the contact patch. The damping can be explained by sliding of surfaces within the contact patch.

The theoretical calculations for the contact patch of the complete contact suggested that this configuration had large forces around the edges of the contact patch and that these large forces would prevent slip at the interface of the joints. In contrast the theoretical calculations for the receding contact suggested that the normal stress was decreasing to zero at the edges of the contact patch, thus allowing slip.

These suggestions are supported by the measured data. Examination of the percentage changes in natural frequency in Figure 12 shows that there was a considerable change in frequency for the receding contact, about 1.5%, while only a 0.35% change for the complete contact. For the damping the relatively large values for damping ratio (≈ 0.005) and spread in values for the receding contact suggests that there is considerable friction and slip occurring. In contrast for the complete contact the damping ratio is small ($\approx$ 0.0005) and only changes slightly for large amplitudes.

The small change in frequency and damping for the complete contact at large amplitudes may be due to some slipping of the contact patch when the amplitudes are large. Once the amplitude drops then the complete contact has only small damping and a small change in frequency.

The suggestion was made at the beginning of the paper that joints with receding contacts and complete contacts represent extremes of behaviour. The complete contact is one extreme that appears to prevent all sliding and thus has only a small contribution to damping and preserves a constant stiffness. However, if the amplitudes are large, then this joint configuration may allow some slip. This lack of slip is attributed to the large normal stresses generated at the edge of the contact patch.

In contrast, joints with receding contacts have a very different behaviour. When the bolt is tensioned, a gap appears between the joint surfaces leaving a contact patch which has small normal forces at the periphery and a large force in the centre. When an external bending moment is applied, due to the dynamics of the vibration, sliding can occur at the joint interfaces. This leads to a loss of stiffness and large values of damping. The receding contact is thus the opposite extreme to the complete contact.

5 Conclusions

The following conclusions may be drawn:

1. The geometry of the contact patch in a bolted joint has a large effect on the dynamic behaviour. If a contact patch is made with a limited size this is a complete contact and this configuration prevents sliding at the edges.
2. If a contact patch is formed by bolting two surfaces together and the size of the contact patch is not limited, then, there are small forces at the edge of the contact patch and a gap opens outside of the contact patch. This is known as a receding contact.
3. The small forces at the edge of a receding contact allow slip of the interfaces within the joint. This leads to significant damping and a variation of stiffness depending on the amplitude of vibration.
4. The experimental results show a considerable difference in behaviour between joint interfaces forming a complete contact and a receding contact. The receding contact shows large values of damping and significant changes in natural frequency as vibration amplitude changes. Whereas a complete contact has a small change in frequency and damping.
5. Joints with complete contacts and receding contacts represent extremes of behaviour. Typical joint conditions will fall between these extremes.

Acknowledgements

The authors acknowledge the support of Cranfield University and AWE Aldermaston.

References

[1] M. R. W. Brake, *The Mechanics of Jointed Structures*. Springer Nature, 2017.

[2] L. Gaul and R. Nitsche, "The Role of Friction in Mechanical Joints," *Appl. Mech. Rev.*, vol. 54, no. 2, p. 93, 2001.

[3] D. J. Segalman, "A Modal Approach to Modeling Spatially Distributed Vibration Energy Dissipation," 2010.

[4] N. Peyret, J. L. Dion, and G. Chevallier, "A framework for backbone experimental tracking: Piezoelectric actuators, stop-sine signal and Kalman filtering," *Mech. Syst. Signal Process.*, vol. 78, pp. 28–42, 2016.

[5] H. R. Kess, N. J. Rosnow, and B. C. Sidle, "Effects of Bearing Surfaces on Lap Joint Energy Dissipation," in *The 20th International Modal Analysis Conference*, 2002.

[6] R. J. Kuether and M. R. W. Brake, "Instantaneous Frequency and Damping from Transient Ring-Down Data," *Int. Modal Anal. Conf.*, 2016.

[7] M. S. Allen and R. L. Mayes, "Estimating the degree of nonlinearity in transient responses with zeroed early-time fast Fourier transforms," *Mech. Syst. Signal Process.*, vol. 24, no. 7, pp. 2049–2064, 2010.

[8] H. G. D. Goyder and D. P. T. Lancereau, "Methods for the Measurement Of Non-Linear Damping and Frequency in Built-Up Structures," in *ASME 2017 International Design Engineering Technical Conferences and Computers and Information in Engineering Conference, Volume 8: 29th Conference on Mechanical Vibration and Noise*, 2017, pp. 1–10.

[9] D. P. T. Lancereau, H. G. D. Goyder, P. Ind, and D. Brown, "Some Dynamic Properties of Contact Patches in Bolted Joints," in *Volume 8: 29th Conference on Mechanical Vibration and Noise*, 2017.

[10] W. D. Iwan, "A distributed-element model for hysteresis and its steady-state dynamic response," *J. Appl. Mech.*, pp. 893–900, 1966.

[11] B. J. Deaner, M. S. Allen, M. J. Starr, and D. J. Segalman, "Application of Viscous and Iwan Modal Damping Models to Experimental Measurements From Bolted Structures," vol. 137, no. April 2015, pp. 1–12, 2017.

[12] C. W. Schwingshackl, "Identification reassembly uncertainties for a basic lap joint," 2017, p. 35th IMAC, A Conference and Exposition on Structur.

[13] D. A. Hills, D. Nowell, and A. Sackfield, "Essential solid mechanics," *Mech. Elastic Contacts*, vol. i, pp. 3–42, 1993.

[14] K. S. Parel and D. A. Hills, "Frictional receding contact analysis of a layer on a half-plane subjected to semi-infinite surface pressure," *Int. J. Mech. Sci.*, vol. 108–109, pp. 137–143, 2016.

[15] R. Ramesh and D. Hills, “Recent progress in understanding the properties of elastic contacts,” *Proc. Inst. Mech. Eng. Part C J. Mech. Eng. Sci.*, vol. 229, no. 12, pp. 2117–2126, 2015.

[16] Mathematica. Wolfram Research, Inc., Version 11.3, Champaign, IL 2018.

[17] HGD Goyder, P Ind, D Brown. Measurement of Damping in a chain of Bolted Joints. *Proceedings of the ASME 2014 International Design Engineering Technical Conferences & Computers and Information in Engineering Conference Buffalo New York*. 2013

Dynamic response and energy loss in jointed structures using finite element methods: application to an aero-engine casing assembly

X. Chi[1], D. Di Maio[2], N. A. J. Lieven[1]
[1] Department of Aerospace Engineering, University of Bristol, Queens Building, University Walk, Bristol, BS8 1TR, England, UK

[2] Department of Mechanical Engineering, University of Bristol, Queens Building, University Walk, Bristol, BS8 1TR, England, UK
e-mail: **xintian.chi@bristol.ac.uk**

Abstract
The purpose of this research is to identify the influences caused by local changes in contact regions of an aero-engine casing assembly on its dynamic and thermal behaviours through Finite Element (FE) methods. The creation and updates of the FE model are demonstrated in this paper. Two types of FE analyses are performed in this research. The first analysis is in the frequency domain, which focuses on the changes in natural frequencies caused by the different contact conditions. The second analysis is in the time domain to study the changes in frictional heat generation caused by alternate contact conditions of the interface regions.

In the concluding observations of this paper, results from these two types of analyses are interpreted to demonstrate that the local changes in contact regions can alter the dynamic and thermal responses of the aero-engine casing assembly by affecting several determining parameters differentially, and these changes caused by the different contact conditions are summarised, analysed and explained.

1 Introduction

Engineering structures are tending to become more complex with an increasing number of components. The components are usually connected by bolts, which creates jointed interfaces. There is a possibility that these joints and interfaces can cause noticeable changes to the dynamic and thermal behaviours of the structure, which must be fully understood to ensure the structure functions stably and safely.

There are several parameters that may determine the effects caused by the joints and the interfaces, which include the bolt preload, material type and size of the bolts, contact area of the interface regions, and bolt tightening sequence [1]. This research focuses on the influences caused specifically by changes in the contact area of the interface regions.

Experimental studies on the effects caused by different contact areas can be arduous because it requires several samples of the structure to be made, each having a contact region with a different profile. These experimental tests are economically achievable for small and simple structures that do not require high manufacturing time and cost. However, due to the fact that the dynamic behaviours of larger and more complex structures are more difficult to predict, analyses of these structures appear to be more necessary.

The structure being studied in this research is an aero-engine casing assembly, which has three components: a Combustion Chamber Outer Casing (CCOC), a High-Pressure Chamber (HPC) and a Low-Pressure Chamber (LPC). There are two jointed interfaces in this assembly, which are between the CCOC and HPC and between the HPC and LPC. As explained above, making several samples of this complex structure for experimental testing is economically impractical. Instead, Finite Element (FE) methods can be used.

In the preparation phase of this research, the dimensions of the aero-engine casing assembly are measured, based on which a preliminary FE model is created. The FE model is then updated according to the modal parameters acquired from an Experimental Modal Analysis (EMA). Two criteria, the Modal Assurance Criterion (MAC) and Natural Frequency Difference (NFD), are used to evaluate the updated FE model. After the FE model is updated to an acceptable level, subsequent FE models are created, which all have contact interfaces with different profiles.

Firstly, a frequency domain FE modal analysis is performed on each model. The natural frequency is selected as the parameter to be studied, which aims to identify the effects caused by the different profiles of the contact regions on the dynamic responses and modal parameters of the structure. Strain energy density is used to analyse and explain the changes in the natural frequencies.

After the completion of the frequency domain analysis, several simplified models are created for the time domain coupled temperature-displacement dynamic analysis. In the time domain analysis, each model is excited by a single-point sinusoidal force for a same amount of time. The thermal data, namely temperature increase and frictional heat generation, at the end of each analysis are collected to evaluate the changes in friction and energy loss caused by the different contact conditions of the interface regions.

2 Preliminary FE modelling and frequency domain modal analysis

In the first stage of this research, an FE model of the aero-engine casing assembly needs to be created. The structure is composed of three parts – a CCOC, an HPC and an LPC, as shown in Figure 1 (a). The CCOC and HPC are connected by 60 bolts and the HPC and LPC are connected by 80 bolts. The total mass of the aero-engine casing assembly is 266 kg, with the exact dimensions and material properties being unknown.

The dimensions of the aero-engine casing assembly are measured, based on which a preliminary FE model is created. Most major geometric features are included in the FE model. Minor features that are considered unable to alter its dynamic behaviours significantly are excluded from the FE model to reduce computational time. The created preliminary FE model is shown in Figure 1 (b).

It is not necessary to model the bolts physically because the FE software Abaqus has built-in engineering fastener features that can be used to simulate the bolts while saving the computational costs. 140 engineering fasteners are added corresponding to their actual locations, for which proper connector properties are defined so that stiffness properties are added for one Degree of Freedom (DOF), with the other DOFs being fully constrained [2]. The interaction properties are defined for the interface regions so that there are tangential behaviours which model the friction, normal behaviours which prevent penetration of the surfaces [3], as well as thermal behaviours including heat generation and thermal conductance which model the heat generation and transfer that will be involved in the time domain analysis section of this research.

As for material properties, because the exact material of the structure is unknown, a density value of 4.25×10^3 kg/m^3 is used, so the total mass of the FE model matches the real mass of the structure. A Young's modulus value of 100 GPa is used in this preliminary model for the ease of model update as it is between the Young's modulus of several potential materials of this structure. Similarly, a Poisson's ratio value of 0.30 is used. The boundary condition is set to be free-free to match the condition in the EMA.



(a) (b)

Figure 1: The aero-engine casing assembly and its FE model

The FE analysis step used in this part is a frequency domain eigenvalue extraction procedure that calculates the natural frequencies and mode shapes of the structure. The first 20 no-rigid modes are requested to match the number of modes from EMA. Lanczos algorithm is used because of its general capabilities [4].

The last step before the FE simulation becoming executable is to mesh the structure. Considering that during this step of the analysis, the parameters being studied are the natural frequencies and mode shapes of the structure and that 20 modes are studied, it is essential to create a fine-mesh model of the entire structure. A coarse mesh on any part of the structure is possible to cause inaccuracies in the results of at least one mode.

Due to the high complexity of the structure, only the tetrahedral element shape is usable. Mesh convergence is performed to calculate the proper element size, which decides that a 20 mm global element size with 10% minimum element size control is small enough to obtain accurate results. However, because the profiles of the interfaces will be changed which creates smaller areas, the element size of these regions is further decreased to 5 mm for improved accuracy. Eventually, the interface regions have a 5 mm initial element size and 0.5 mm minimum element size. The rest of the model has a 20 mm initial element size and 2 mm minimum element size. The results from the FE modal analysis will be shown in the next section.

3 Experimental Modal Analysis (EMA) results and model updates

An EMA is performed on this aero-engine casing assembly to measure the natural frequencies and mode shapes of the first 20 non-rigid modes of the structure. The results of natural frequencies from the EMA are shown in Table 1. The first 10 mode shapes from the EMA are shown in Figure 2. Because of the symmetry of the structure, each mode has its pair with almost identical natural frequency and mode shape. Only the first 10 modes are used for the model updates, as keeping the accuracy of FEA results will be increasingly difficult for higher order modes because of more complex deformation shapes and dynamic responses.

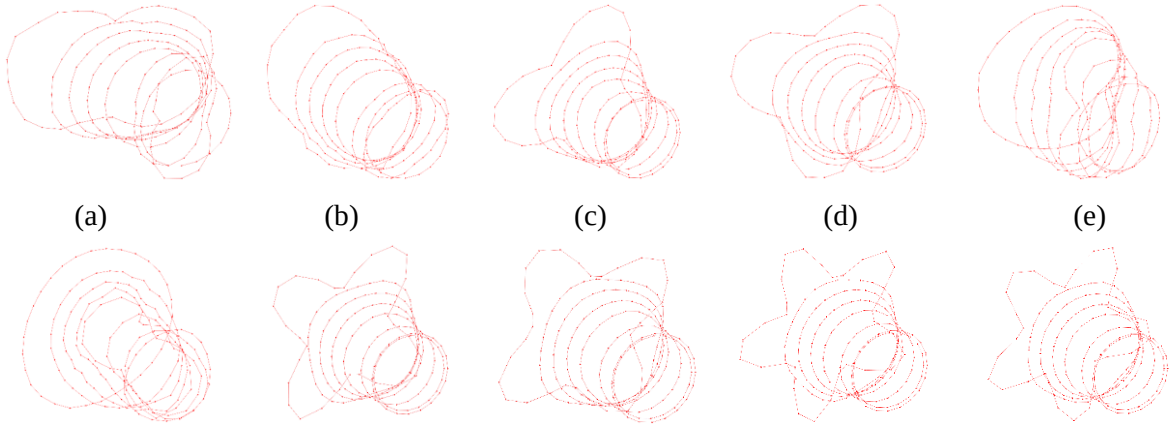


Figure 2: Mode shapes of the first 10 non-rigid modes measured from EMA

The results of the natural frequencies calculated from the FE analysis and their differences from the EMA results are listed in Table 2. The NFD is used to compare the natural frequencies from EMA and FE modal analysis, which is defined as shown in Equation 1, where f_{FE} is the natural frequency calculated from FE modal analysis, and f_{EMA} is the natural frequency calculated from EMA.

$$\text{NFD} = \frac{f_{FE} - f_{EMA}}{f_{EMA}} \times 100\% \tag{1}$$

The mode shapes calculated from the FE modal analysis are shown in Figure 3.

Mode	1	2	3	4	5	6	7	8	9	10
Freq (Hz)	39.141	39.685	53.128	53.21	58.51	58.935	82.256	82.348	125.73	125.8
Mode	11	12	13	14	15	16	17	18	19	20
Freq (Hz)	180.50	180.56	187.68	189.35	196.75	201.06	206.03	229.84	230.28	232.72

Table 1: Natural frequencies of the first 20 non-rigid modes measured from EMA

Mode	1	2	3	4	5	6	7	8	9	10
Freq (Hz)	38.951	39.129	60.304	60.307	75.056	75.119	99.926	99.932	155.51	155.52
NFD (%)	-0.49	-1.40	13.51	13.34	28.28	27.46	21.48	21.35	23.69	23.62

Table 2: Natural frequencies of the first 10 non-rigid modes calculated from the preliminary FE analysis

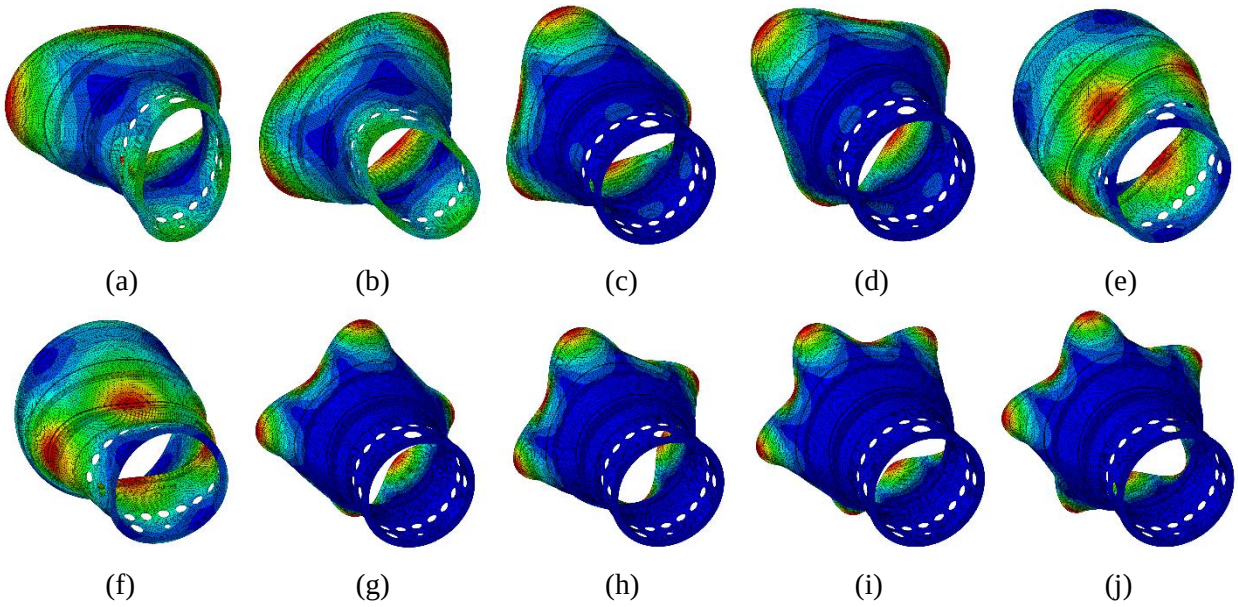


Figure 3: Mode shapes of the first 10 non-rigid modes calculated from the preliminary FE analysis

It can be observed that, although there are discrepancies between natural frequencies, in general the mode shapes and their sequences in the FE modal analysis results match those in the EMA results. However, it is important to note that, despite the visual agreements in the mode shapes between the FE results and EMA results, quantitative methods are still required to evaluate the correlations.

Before comparing the mode shapes quantitatively, the first step of model update should be improving NFD. Theoretically, the entire model updating process can be completed automatically as there are several software packages available to perform this task, most of which update the model based on NFD and MAC. However, these engineering fasteners used in this model, as explained in the previous section, are part of the built-in features of Abaqus, hence unable to be read and processed by the model updating software.

There are several potential solutions to this problem. Firstly, the bolts can be modelled without using the engineering fastener features so that they can be processed by the model updating software. However, modelling the bolts will increase the number of components in this structure. Moreover, these bolts will require high-quality mesh with very small element sizes, which increases computational cost significantly.

The second solution is to update the three components separately using modal updating software. This method requires the mass properties and modal parameters of each component of the structure, which needs disassembly of the structure. Considering the difficulties in practical execution, this solution is not optimal.

The third solution involves editing the input file generated by Abaqus that is going to be imported into model updating software, where the sections containing the engineering fasteners can be forced to be skipped by

the model updating software and added back when the model updating software uses Abaqus as the external solver to perform FE modal analyses with the updated parameters. However, this method is only achievable if the model updating software interacts with Abaqus and uses Abaqus as the external solver.

The last solution, which is most general and straightforward, is to update the model manually without relying on any model updating software. This process seems arduous, but if the relationship between the natural frequencies and the potential determining factors can be found, a manual model update is achievable.

Firstly, the parameters to be updated need to be selected. The determining factors to the modal parameters of the FE model include density, Young's modulus and Poisson's ratio of the material, the geometry of the structure and minor factors such as contact properties and properties of the engineering fasteners.

The geometry of the FE model should be kept unchanged, as changing it will require the largest amount of work. The density of the material for each part is also preferably unchanged because the mass of the FE model already matches the actual mass of the structure. Between Young's modulus and Poisson's ratio, the model update should begin with changing Young's modulus because the Poisson's ratio values of all possible materials are very close, changing Poisson's ratio is not expected to make a considerable difference.

Theoretically, for an undamped system, if the geometry and density remain unchanged, its natural frequencies should be in direct proportion to stiffness. When damping is considered, the positive correlation between natural frequencies and stiffness still exists, although the mathematical relationship becomes more complicated. Changing Young's modulus of material will alter the stiffness matrix of the structure. A higher value of Young's modulus will increase the natural frequencies of the structure because of the increased stiffness. Following this relationship between Young's modulus and natural frequency, it is possible to perform the model update iteratively in a more strategic way.

By inspecting the results in Table 2, it can be observed that apart from the first two modes, all other FE modes appear to have higher natural frequencies, which indicates the overall stiffness of the FE model is higher than the actual value. Reducing the Young's modulus of all three components blindly can be misleading, as the natural frequencies of the first two modes are very close between FE and EMA results. In these two modes, the large deformations appear to be on the CCOC and LPC. Compared to the first two modes, the deformations on the CCOC are significantly smaller in the other eight modes. Reducing the Young's modulus of HPC and LPC while increasing the Young's modulus of CCOC is possible to decrease the natural frequencies of the other modes while keeping the first two modes relatively unchanged.

For HPC and LPC, the Young's modulus of both parts should be decreased. Mode 5 and 6 have the largest NFD, where the large deformations concentrate on HPC, while both CCOC and LPC deforms moderately.

Based on these analyses, the Young's modulus of LPC should be decreased moderately while the Young's modulus of HPC should be decreased by a larger percentage. The Young's modulus of CCOC should be increased moderately, as the sole purpose of increasing Young's modulus for CCOC is to balance the natural frequency decrease in the first two modes because of the changes in HPC and LPC.

As described in the previous section, the initial Young's modulus is 100 GPa for all three parts. After several iterations, it is decided to increase the Young's modulus of CCOC by 30 GPa, decrease the Young's modulus by 30 GPa for LPC and 60 GPa for HPC. The results after the First Model Update (MU1) are shown in Table 3. It should be noted that, because of the excluded features and inaccurate geometries in the FE model, the Young's modulus of the materials in the FE model may not reflect the values of the materials used in the real structure, especially in the HPC where the thickness is very difficult to measure, and many small features are excluded during the creation of the FE model.

Mode	1	2	3	4	5	6	7	8	9	10
Freq (Hz)	39.198	39.391	49.332	49.334	57.755	57.818	82.572	82.577	129.59	129.59
NFD (%)	0.15	-0.74	-7.15	-7.28	-1.29	-1.90	0.38	0.28	3.07	3.01

Table 3: Results of natural frequencies from FE analysis after MU1

The results verified that the overall strategy of the model update is correct, although mode 3 and 4 are overly adjusted. Following the same algorithm, the Young's modulus of LPC is increased, and to balance the first

two modes, the Young's modulus of CCOC is decreased. Eventually, the Young's modulus of HPC is adjusted slightly to fine-tune the natural frequencies.

The material properties after the model updates and the results from the FE modal analysis after the final model update are displayed in Table 4 and Table 5 respectively.

	CCOC (Initial)	HPC (Initial)	LPC (Initial)	CCOC (MU1)	HPC (MU1)	LPC (MU1)	CCOC (Final)	HPC (Final)	LPC (Final)
Young's modulus (GPa)	100	100	100	130	40	70	125	42	80

Table 4: Changes in material properties during the model updates

Mode	1	2	3	4	5	6	7	8	9	10
Freq (Hz)	39.379	39.569	52.808	52.811	58.674	58.737	89.684	89.689	141.03	141.03
NFD (%)	0.61	-0.29	-0.60	-0.75	0.28	-0.34	9.03	8.91	12.17	12.11

Table 5: Results of natural frequencies from FE analysis after the final model update

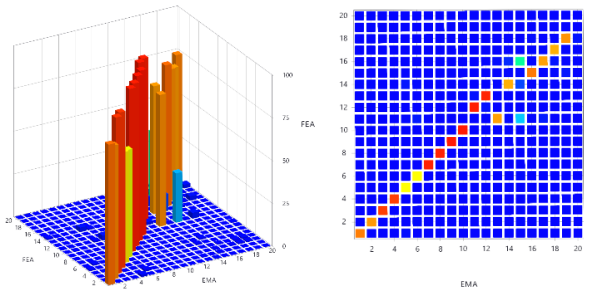
As the modal updating theory suggests, although the NFD values for the first six modes are very small, as the mode number increases, the discrepancies between the FE modal analysis results and EMA results increase correspondingly. Considering that the FE model is created manually based on the measured dimensions, as well as the exclusion of small features, the FE model after the final model update is considered acceptable in terms of natural frequencies.

With the natural frequencies of the FE model updated successfully, it is now necessary to compare the FE results and EMA results quantitatively in terms of the mode shapes. The quantitative method used to compare the mode shapes is Modal Assurance Criterion (MAC), which is defined as shown in Equation 2, where $\{\varphi_{FE}\}_i$ is the i^{th} mode shape of the FE model and $\{\varphi_{EMA}\}_j$ is the j^{th} mode shape from the EMA.

$$\mathrm{MAC}(i,j) = \frac{\left|\{\varphi_{FE}\}_i^T \{\varphi_{EMA}\}_j^*\right|^2}{\left(\{\varphi_{FE}\}_i^T \{\varphi_{FE}\}_i^*\right)\left(\{\varphi_{EMA}\}_j^T \{\varphi_{EMA}\}_j^*\right)} \tag{2}$$

A MAC value equal to one indicates a perfect correlation, and a MAC value equal to zero indicates zero correlation between these two mode shapes [5]. Generally, 80% is used as the threshold for good correlation between the two mode shapes. However, there is not a formal standard as MAC values vary from case to case. Simpler models tend to have higher MAC values while achieving an equivalently high MAC value for a complex model is significantly more difficult.

All mode shapes from the EMA and the FE modal analysis after the final model update are used to calculate the MAC. Necessary rotations of mode shapes were performed due to the symmetry of the structure. The calculated MAC plot is shown in Figure 4. The matched mode pairs and their MAC values are listed in Table 6, where mode pairs are in this format: EMA mode – paired FEA mode.



(a) (b)

Figure 4: MAC plot, FEA modes vs EMA modes

Mode Pair	1-1	2-2	3-3	4-4	5-5	6-6	7-7	8-8	9-9	10-10
MAC (%)	82.1	78.2	91.5	91.3	64.9	62.9	95.5	95.5	96.7	96.7
Mode Pair	11-13	12-12	13-12	14-14	15-16	16-15	17-16	18-17	19-18	20
MAC (%)	77.0	96.1	95.3	74.8	42.5	82.7	77.1	74.7	79.1	

Table 6: MAC values, EMA modes vs FEA modes

By inspecting the MAC values, it can be observed that in the first ten EMA modes, seven modes have found their correlated FE modes with MAC values greater than 80%. In the first 20 modes, there are ten mode pairs with MAC values greater than 80%, with another six MAC values close to 80%. By observing the mode shapes shown in Figure 3, modes with large deformations on LPC have higher MAC values while modes with large deformations on HPC have lower MAC values.

In summary, the FE model is acceptable in terms of both natural frequency and mode shape. The natural frequencies for the first 6 modes are very close between the EMA and FE results. As for mode shape, seven out of the first ten non-rigid FE modes have found their correlated EMA mode with MAC value greater than 80%. The LPC region has the highest correlation while the HPC region contributes poorly to the MAC values. The most likely reason is that there are many small features on the HPC of the aero-engine casing assembly that are excluded in the FE model, as shown in Figure 1. The accurate thickness of the HPC region is very difficult to measure, which is another possible factor that leads to the discrepancies. As a comparison, the LPC region has few small features so that a high agreement between the FE and EMA results is easily achieved.

Additionally, techniques such as Coordinate Modal Assurance Criterion (COMAC) can be used to identify the more precise locations of the nodes contributing poorly to the MAC values, so the inaccurately modelled regions can be located [6]. Because of the algorithm of COMAC, which is shown in Equation 3, it has high precision so that every individual node can be sorted according to its contribution to the MAC values. The geometries and material properties of these locations can be further updated to improve the correlations between the FEA and the EMA results.

$$\mathrm{COMAC}(k) = \frac{\left(\sum_{i=1}^{n} \left|(\varphi_A)_{ik}(\varphi_X)_{ik}^{*}\right|\right)^2}{\sum_{i=1}^{n}(\varphi_A)_{ik}^2 \sum_{i=1}^{n}(\varphi_X)_{ik}^{*2}} \tag{3}$$

In Equation 3, $(\varphi_A)_{ik}$ is the value, such as displacement, of the k^{th} element in the i^{th} analytical mode shape, $(\varphi_X)_{ik}$ is that value for the i^{th} experimental mode and n is the total number of correlated mode pairs. The COMAC, which is a vector, has the same size as the original mode shape vector and every node can be placed back to their original location, so the locations of the regions that contribute poorly to the MAC values can be revealed clearly. Although COMAC is not necessary here for model updating of this FE model, it is used and interpreted in this research, which is demonstrated in the next section of this paper.

4 Effects of changes in contact condition on dynamic behaviours

After the completion of the model update, several subsequent models are created, where different profiles are created for the interfaces. Figure 5 demonstrates the creation of the interfaces with different profiles, where a 2 mm deep annular gap is created on the top and bottom surfaces of HPC respectively. The location of the gap is selected so that the engineering fasteners pass through the gaps, by which the gaps can have considerable impacts on the behaviours of the fasteners. In total, 19 subsequent FE models are created, where the widths of the gaps are from 1 to 19 mm. The same FE modal analysis procedure is performed on every model. The changes in natural frequencies of the first six modes as the width of the gap increases are shown in Figure 6 (a) to (f) respectively, where OM represents 'Original intact model after the final model update' and CMx represents 'Created model with x mm wide gap'.

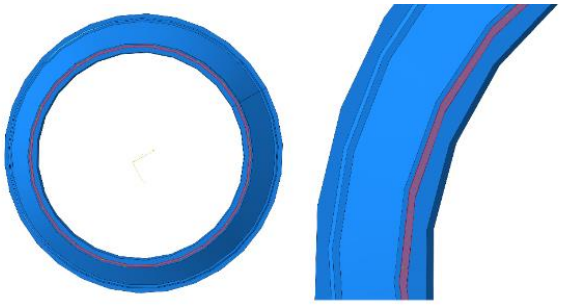
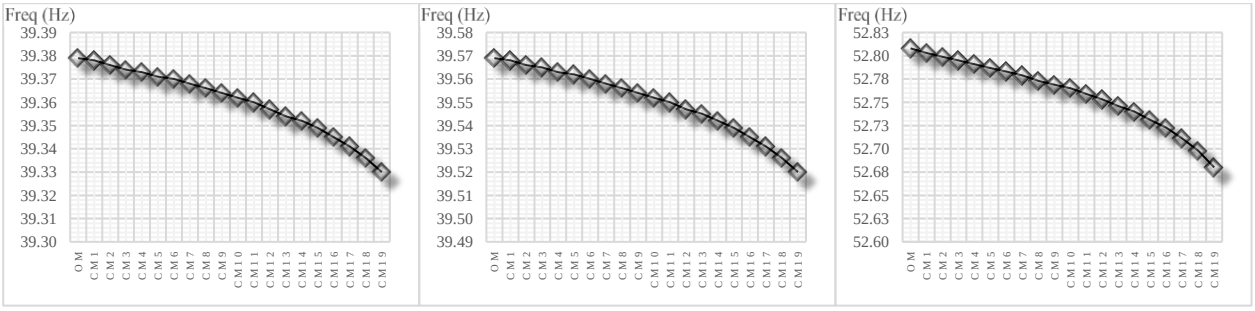
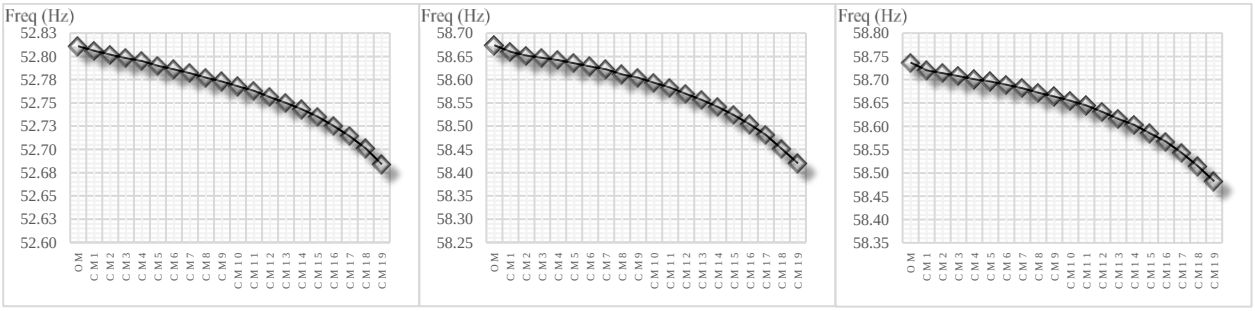


Figure 5: Creation of the alternate contact interface profile



(a) (b) (c)



(d) (e) (f)

Figure 6: Changes in natural frequencies of the first six modes as the width of the gap increases

As demonstrated clearly in Figure 6, for every mode the natural frequency decreases monotonically as the width of the gap increases. Additionally, as the size of the gap increases, the changes in natural frequencies appear to be more drastic. The percentage changes in natural frequencies between OM and CM19 are listed in Table 7.

Mode	1	2	3	4	5	6	7	8	9	10
OM (Hz)	39.379	39.569	52.808	52.811	58.674	58.737	89.684	89.689	141.03	141.03
CM19 (Hz)	39.330	39.520	52.680	52.684	58.420	58.482	89.574	89.579	140.95	140.96
NFD (%)	-0.124	-0.124	-0.242	-0.240	-0.433	-0.434	-0.123	-0.123	-0.057	-0.050

Table 7: Percentage changes in natural frequencies between OM and CM19

This result seems counter-intuitive considering that the total mass of the model decreases as the width of the gap increases, which theoretically should increase the natural frequencies of the structure. A possible explanation is that the reduction of contact area changed both the mass and stiffness matrix of the model. Although the decrease in mass suggests increased natural frequency, the overall decreasing trend of natural frequencies as the width of the gap increases indicates that the stiffness of the structure has decreased. It is theoretically comprehensible that the overall stiffness of the structure decreases because the gaps created on

the interfaces make the model more flexible, which decreases the local stiffness. However, this explanation needs to be verified on this model.

Mathematically, strain energy can be used to reveal the changes in flexibility. The strain energy density for a volume element subjected to arbitrary stress can be calculated as described in Equation 4.

$$u = \frac{1}{2}\left(\sigma_{xx}\varepsilon_{xx} + \sigma_{yy}\varepsilon_{yy} + \sigma_{zz}\varepsilon_{zz}\right) + \left(\sigma_{xy}\varepsilon_{xy} + \sigma_{yz}\varepsilon_{yz} + \sigma_{zx}\varepsilon_{zx}\right) \tag{4}$$

$$= \frac{1}{2E}\left(\sigma_{xx}^2 + \sigma_{yy}^2 + \sigma_{zz}^2\right) - \frac{\nu}{E}\left(\sigma_{xx}\sigma_{yy} + \sigma_{yy}\sigma_{zz} + \sigma_{zz}\sigma_{xx}\right) + \frac{1}{2\mu}\left(\sigma_{xy}^2 + \sigma_{yz}^2 + \sigma_{zx}^2\right)$$

If the model has a higher strain energy after the gap is created, it suggests an increase in flexibility hence the decrease in stiffness. Strain energy density data for the first ten non-rigid modes of all 20 models are extracted. The strain energy density map of the 6th mode from the intact model OM, which is superimposed on its mode shape, is displayed in Figure 7 as an example to show the strain energy density distribution.

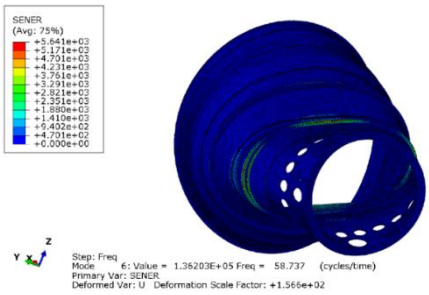


Figure 7: Strain energy density of the 6th mode from the original model

As for the data extraction, strain energy density at the integration points are selected, instead of the values at the individual nodes (element corners). In FE analysis, the integration points provide data with the highest accuracy, while the nodal solutions are extrapolated from the results at the integration points.

With the strain energy density data for every integration point extracted, the average strain energy density of the whole model can be calculated. The changes in average strain energy density of the first six modes as the width of the gap increases are shown in Figure 8 (a) to (f) respectively.

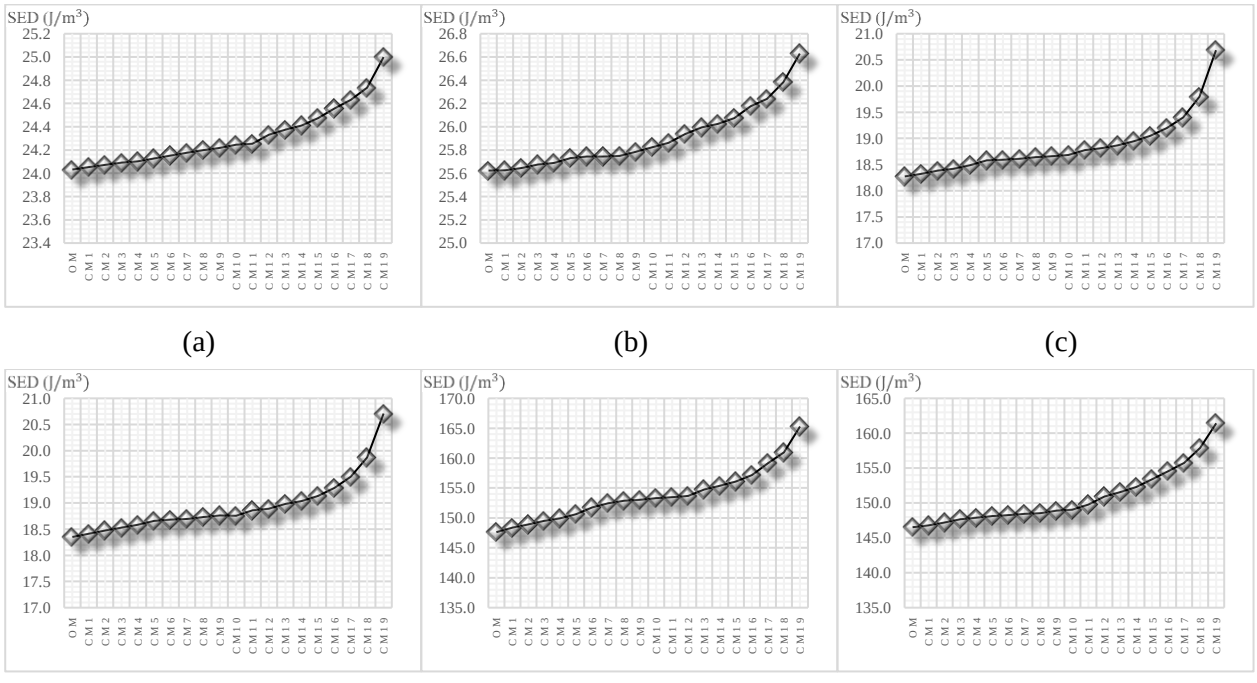


Figure 8: Changes in average strain energy density as the width of the gap increases

The average strain energy density of the structure increases monotonically with the size of the gap. The monotonic increase of average strain energy density confirms that the structure becomes more flexible as the size of the gap increases, which indicates the decrease in stiffness of the structure. Additionally, as the size of the gap increases, the decrease in stiffness becomes more drastic. Mathematically, the strain energy density in the interface regions is expected to approach infinity as the area of contact approaches zero because of the extremely high stress caused by the infinitesimal contact area, which can be derived based on Equation 4. This explains the reason why the natural frequencies change more drastically as the size of the gap increases.

By using strain energy, the decreases in the natural frequency of the structure have been explained. However, as demonstrated in Table 7, the natural frequencies changed differentially for the ten modes. It can be observed that the changes in mode 5 and 6 are significantly larger than the changes in other modes.

This phenomenon can be explained using strain energy as well. As the changes in geometry are made at the interface regions of the structure, the average strain energy density of the interface regions can be calculated for each mode and compared with the average strain energy density of the whole structure, based on which the relative impacts from the local changes in the interface regions on the overall dynamic behaviours of the structure can be evaluated.

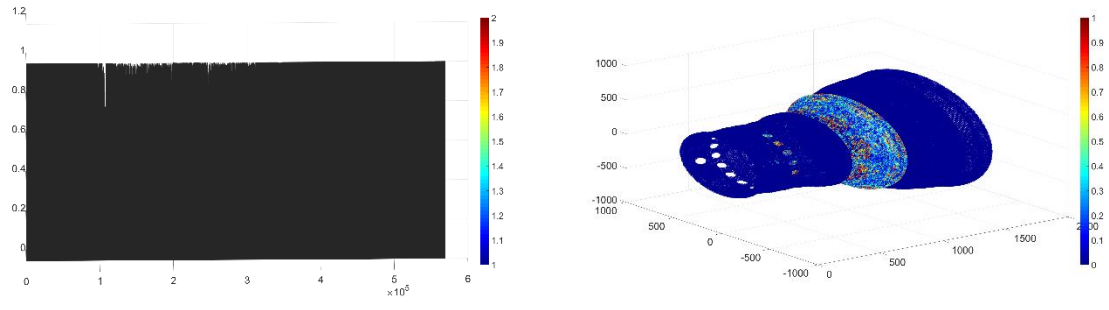
To perform this task, the strain energy density data for both interfaces of the OM model are extracted, which include the strain energy density of integration points on all four surfaces constituting the two interface regions. The average strain energy density data of the interface regions are calculated and listed in Table 8, which also has the average strain energy density of the whole model and the ratio between them.

Mode	1	2	3	4	5	6	7	8	9	10
$u_{int.}$ (J/m^3)	17.50	18.58	22.94	22.99	291.81	293.16	25.14	21.66	18.45	18.54
u_{model} (J/m^3)	24.03	25.62	18.27	18.35	147.63	146.53	35.86	31.19	59.29	59.38
Ratio	0.7680	0.7251	1.2554	1.2527	1.9767	2.0007	0.7011	0.6943	0.3113	0.3122

Table 8: Average strain energy density data of model OM

As displayed in Table 8, in mode 5 and 6 the average strain energy density in the interface regions are significantly higher than the average strain energy density of the whole model. The ranking of the ratio between strain energy densities matches exactly the ranking of the natural frequency change. In mode 5 and 6, the local changes in the interface regions have the highest impacts to the stiffness of the structure, which causes that the natural frequency changes in these two modes are significantly higher than the changes in the other modes. Similarly, in mode 9 and 10, the influences caused by the local changes in the interface regions are relatively small, which leads to smaller changes in natural frequencies.

To confirm that the changes in average strain energy density are caused by the gaps created on the interfaces, instead of other unexpected factors acting on other locations of the model, COMAC is used to compare the strain energy density data of CM1 and CM19. The strain energy density data for the first 10 non-rigid modes of both models are used. The calculated COMAC values of all nodes constituting the FE model and the recovered model with superimposed COMAC values are shown in Figure 9 (a) and (b).



(a) (b)

Figure 9: COMAC between the first 10 non-rigid modes of CM1 and CM19

In Figure 9 (a), it is shown that for most of the nodes, their strain energy density values did not change or changed very slightly between CM1 and CM19. There are two regions in Figure 9 (a) that have noticeable decreases in COMAC, which indicates the strain energy density changed significantly in these regions. In order to determine the locations of these regions, the COMAC values are then superimposed onto the geometric grid of the engine model, which is created by exporting the coordinates of the nodes from Abaqus and importing them into MATLAB. The created figure is shown in Figure 9 (b). As a matter of fact, it is '$1 - \mathrm{COMAC}$' that is used in Figure 9 (b), so that nodes with smaller COMAC values will be in red hence more noticeable. In Figure 9 (b), it can be observed clearly that, these two regions with noticeably smaller COMAC values are the areas around these two interfaces. Nodes on HPC experience overall greater changes in terms of strain energy density compared to nodes on CCOC and LPC, which is comprehensible because they are influenced by both interfaces, while for nodes on CCOC or LPC the influence from one interface is always very small, even almost negligible.

By using COMAC, the locations with the most significant changes in strain energy density have been identified. It has been verified that the changes in natural frequencies are caused by the effects of creating gaps on the interfaces locally, which leads to a reduction in stiffness of the structure.

From this section of the research, it can be observed that, despite the decrease in mass of the structure caused by the creation of the gap on the interfaces, the natural frequencies of the structure still decrease because of the increased flexibility. The decrease in stiffness has been verified by the use of strain energy density. The extent to which the natural frequencies change can be evaluated based on the ratio between the average strain energy density of the interface regions and the average strain energy density of the whole model. It has also been shown that, apart from mode shapes, the COMAC is also capable of being used on other parameters, such as strain energy density in this case, to determine and locate the discrepancies between two sets of data.

5 Effects of changes in contact condition on thermal behaviours

In the second part of this research, the effects of changes in contact conditions on the thermal behaviours caused by the friction on the interfaces are studied. This is achieved by focusing on the energy loss due to friction using thermal parameters including temperature increase and frictional heat generation.

An important reason for studying the friction through energy loss is that contact friction is one of the main causes of nonlinear behaviours in coupled structures. If contact friction can be decreased, the nonlinear behaviours in the structure can be reduced effectively.

Theoretically, friction causes energy loss, during which heat is generated. The total frictional heat generation on area A over time t can be calculated as shown in Equation 5, where P_{fr} is frictional heat generation of a unit area over time t, τ is shear stress and γ is total length of the overall slip path, which is the total distance of the relative movement between the two surfaces [7].

$$P_A = \iint P_{fr}\, dA = \iint \tau\gamma\, dA \tag{5}$$

Shear stress in contact regions can be calculated from the contact pressure p and friction coefficient μ:

$$\tau = \mu p \tag{6}$$

Theoretically, the creation of gap on the interfaces will increase contact pressure, which increases shear stress hence accelerates frictional heat generation in a unit area on the contact region. However, the reduction in contact area is likely to decrease the total frictional heat generation. Additionally, the increased contact pressure is also possible to cause slip rate and slip distance to decrease.

All three factors determining the total frictional heat generation are affected by the changes in contact area. The contact pressure will increase, which causes an increase in shear stress but decrease in slip rate. The total contact area will also decrease. The combined effects of changes in the three factors make the total frictional heat generation very difficult to predict theoretically.

Because of the challenges in predicting the frictional heat generation theoretically and performing the test experimentally, accurate FE simulations must be performed to identify the effects caused by the changed contact conditions on the frictional heat generation and temperature increase in this structure.

In order to obtain accurate thermal results from FE analysis, a coupled temperature-displacement dynamic analysis must be used because of the mutual influences between the thermal and dynamic behaviours.

In general, the coupled temperature-displacement analysis requires extreme computational cost and time, which is one of the reasons that alternative methods have been used extensively for this type of analyses. Exporting the results from a dynamic analysis and importing them back to a thermal analysis is one of these theoretically sensible methods. This method requires considerably lower computational cost and time. However, the interactions between the thermal and dynamic behaviours are neglected in this method. These interactions can only be reflected in a fully coupled temperature-displacement analysis.

The FE model used in the first part of this research is too complicated for a coupled temperature-displacement analysis. Performing a coupled temperature-displacement analysis on it will be practically impossible even with a supercomputer. A new FE model is created, in which the model is further decreased to a more basic shape. The meshed model is shown in Figure 10. The element size for the interface regions is 20 mm with 10% minimum element size control. The rest of the model is meshed with 100 mm tetrahedral elements with 10% minimum element size control. The model is updated following a similar strategy used in the first part of this research.

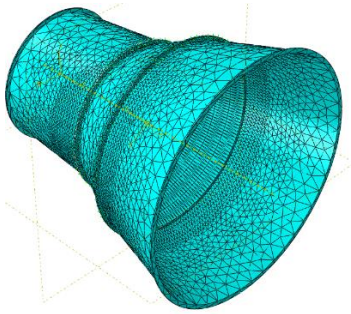


Figure 10: Meshed FE model for coupled temperature-displacement analysis

The input force has a frequency matching the natural frequency of the 5th and 6th mode of the structure to achieve resonance. The selection of this frequency for excitation is because it has been concluded that the interface regions have the highest impacts on the overall behaviours of the structure in these two modes. For the same reason, the location of the input force is selected to be located approximately at the middle of the outer surface of the HPC section, so that both interface regions can be excited effectively. The exact location is determined based on an algorithm for automatic selection of candidate sensor locations [8].

Due to the high computational cost and time of this analysis, the time period of the analysis cannot be extended to match a realistic test. As a compensation, a very high force magnitude is selected to scale the simulation so that there is a detectable amount of heat generation within the short time period of the simulation, which is only one second. It should be noted that plastic behaviours are excluded in this FE model, which means the model will not experience plastic deformation or damage under large forces, so the high force magnitude only acts for scaling purposes without being able to cause unexpected behaviours.

Additional material properties including thermal conductivity and specific heat capacity have been added, so that heat transfer can be simulated correctly. The boundary condition of this analysis is set to be free-free so only phenomena caused by the vibration of the structure itself are considered. The initial temperature of the structure is set to 20 degrees Celsius, so as the environmental temperature. Average temperature and frictional heat generation of the model are calculated at the end of the analyses, which are listed in Table 9.

It needs to be noted that, despite the decrease in complexity of the model and the use of a supercomputer, performing a coupled temperature-displacement analysis is still time-consuming. In this research, the coupled temperature-displacement analyses are performed on BlueCrystal, a High-Performance Computing (HPC) machine of University of Bristol. 64 Intel Xeon E5-2670 processors and 256GB of Random Access

Memory (RAM) are requested for each analysis, with which each analysis takes approximately 100 hours to complete.

Temp. (℃)	Average	Increase	Percentage	Heat Gen. (W/m^2)	Average
OM	20.00907	0.00907	0.045349%	OM	2.57788×10^2
CM3	20.21050	0.21050	1.052498%	CM3	1.25427×10^4
CM6	20.19675	0.19675	0.983756%	CM6	8.29843×10^3
CM9	20.12195	0.12195	0.609764%	CM9	4.12921×10^3
CM12	20.06030	0.06030	0.301520%	CM12	2.13393×10^3
CM15	20.03463	0.03463	0.173170%	CM15	1.21155×10^3
CM18	20.02543	0.02543	0.127148%	CM18	9.47077×10^2

Table 9: Thermal data at the end of the coupled temperature-displacement dynamic analyses

It can be observed from the results that, after the gap is created, the frictional heat generation decreases as the size of the gap increases, which is likely caused by the decreased slip rate and reduced total contact area. However, due to the location of the gap, the creation of the gap will affect the effectiveness of the fasteners significantly, which is expected to have high impacts on the relative movement between the contact surfaces. The increased slip rate caused by this will benefit the frictional heat generation and temperature increase, which explains the significant discrepancies between the model OM and the models with the gap created.

It is comprehensible that the contact pressure will increase due to the reduced contact area, however, the changes in the slip rate and distance still need to be verified. In order to achieve this, the average total slip distance of the nodes (the total distance of the relative movements between the nodes in the two surfaces) on the interfaces are calculated and listed in Table 10.

Slip dis. (m)	Int. 1	Int. 2	Average	Slip dis. (m)	Int. 1	Int. 2	Average
OM	0.00026	0.00001	0.00013	CM12	0.00122	0.00049	0.00085
CM3	0.00310	0.00051	0.00181	CM15	0.00117	0.00040	0.00079
CM6	0.00233	0.00069	0.00151	CM18	0.00091	0.00037	0.00064
CM9	0.00145	0.00056	0.00100				

Table 10: Average total length of the slip path of the nodes on the interfaces

It is demonstrated clearly that, as the width of the gap increases, the average slip distance of nodes on the interfaces decreases monotonically, which verifies the assumptions made at the beginning of this section. Similar to the phenomena observed in the thermal data, the creation of gap alters the relative motion between the contact surfaces significantly, which causes distinct differences between models with and without the gaps on the interfaces.

In summary, as the width of the gap increases, the contact pressure will increase but the slip rate and total contact area will decrease. Despite the fact that the increased contact pressure may accelerate frictional heat generation in each unit area on the contact region, the reductions in contact area, slip rate and slip distance are able to cause more significant influences that surpass the influences from increased contact pressure so a monotonic relationship between the frictional heat generation and size of the gap is obtained. The combined effects of the three parameters cause total frictional heat generation to decrease as the size of the gap increases. However, the creation of the gap will affect the effectiveness of the fasteners, which increases the temperature rise and total frictional heat generation significantly.

For the sake of completeness, running a coupled temperature-displacement dynamic analysis on a complex FE model is achievable by using mass scaling to alter the time increment so that the total number of iterations

can be controlled. However, mass scaling can only be used situationally as using mass scaling can put the accuracy of the results in risk [9], which is one of the main reasons that it is not used in this research.

6 Discussions and conclusions

In this research, the effects of changing contact conditions of interface regions in an aero-engine casing assembly on its dynamic and thermal behaviours have been studied by using FE methods.

Firstly, the creation of the FE model and the mesh configurations have been explained. The model updating strategy for a manual model update of a complex coupled structure, such as the aero-engine casing assembly in this research, has been demonstrated. It has been shown that, without the usage of model updating software, performing model updates on a complex coupled structure is still possible to succeed. It has also been demonstrated that MAC and NFD can be used as the two main criteria for a model update to guide the model updating process to success. Additionally, the COMAC is available for more precise model improvements if model updates based merely on MAC and NFD are unable to obtain a decent FE model.

In the frequency domain analysis section of this research, it has been confirmed that local changes on the interfaces in a coupled structure are able to alter its dynamic responses and modal parameters. This research shows that, despite the decrease in total mass of the structure due to the creation of the gap on the interfaces, the natural frequency is still possible to decrease because of the increased flexibility and decreased stiffness in the structure. Additionally, it has been demonstrated that the sensitivity to same changes in contact conditions can be different for each mode. Some modes appear to be more sensitive than the others, which has been explained by calculating the ratio of average strain energy density in the interface regions to the average strain energy density of the whole model. The results showed high agreements between the trends of changes in strain energy density and changes in natural frequency, which concludes that strain energy density is capable of predicting and explaining the changes in dynamic responses and modal parameters of the structure by revealing the changes in stiffness. Additionally, it has been shown that the COMAC is capable of being used on parameters apart from mode shapes, such as strain energy density in this research, where it demonstrates successfully that it is the creation of gaps locally on the interfaces that affected the dynamic behaviour of the entire structure.

In the time domain part of this research, frictional heat generation and temperature increase are used to demonstrate that, besides dynamic behaviours, local changes on interfaces are also able to alter the thermal behaviours of the structure. The mathematical relationship between the temperature increase (or total frictional heat generation) and size of the gap is apparently monotonic, despite the opposite influences from the three determining parameters. The creation of the gap, however, alters the effectiveness of the fasteners significantly because of its location, which amplified the frictional heat generation greatly.

It has been shown that alternate designs for the interfaces are able to change the friction in the contact areas, which may benefit the control of nonlinear behaviours. Although the alternate profile of contact regions in this research caused an increase in friction because of the location of the gap, it shows the possibility of controlling the friction in the interface regions using an alternate contact profile, with which the nonlinear behaviours in the structure can be reduced effectively.

Despite the successes of obtaining and analysing the results and observations in this research, there are several potential improvements that can be made.

Firstly, it is possible to increase the quality of the FE model further by using COMAC to locate the small regions on the FE model that have large disagreements with the EMA structure.

In the frequency domain analysis, despite the changes in the width of the gaps, its depth was kept constant at 2 mm in this research. It is worth studying if a deeper gap is able to cause different results. As a matter of fact, the change in mass caused by a 2 mm deep gap is very small. It is possible that with a deeper gap or a change in profile, the effects from reduced mass may surpass the effects caused by the reduced stiffness, which eventually lead to an overall increase in natural frequency. Moreover, the changes in natural frequencies are not very large in this research, performing a similar study on a coupled structure with more and larger interface regions can be valuable. For this specific research on the aero-engine casing assembly,

it is also possible to continue increasing the width of the gap, to verify if the changes in strain energy density and local stiffness of the interface regions and changes in the natural frequencies of the structure are still able to become more drastic as the size of the gap increases.

In the time domain analysis, it has been mentioned that a simplified FE model was used due to the limitations of computational time and cost. It is possible to use an FE model with a higher quality mesh, like the model used in the frequency domain analysis of this research, to repeat this time domain analysis and study if the results can be different. In this research, the structure was stimulated by a single-point sinusoidal force that matches the natural frequency of the 5th and 6th mode. Changing the excitation frequency so that it matches the natural frequency of the first 10 or 20 non-rigid modes respectively to study if the differences in sensitivity between modes that appeared in the frequency domain analysis are still significant in the time domain analysis is also a potential direction for the future work of this research. Additionally, it might be necessary to study the changes in parameters when several random loads are applied at several different locations on the structure simultaneously, which is closer to the actual working condition of the structure so that the results can have higher values for practical applications. For this specific research, the size of the gap can be further increased to evaluate if the monotonic relationship between total frictional heat generation and size of the gap still holds when the size of the gap keeps increasing.

Finally, it might be worth trying to repeat the analyses performed in this research experimentally, although a simpler coupled structure could be used as an alternative because of the high cost for producing several samples of this complex aero-engine casing assembly.

References

[1] D. Di Maio, Z. Mitha, J. V. Paul and X. Chi, "Variability of Dynamic Response in Jointed Structures," in *Dynamics of Coupled Structures, Volume 4. Proceedings of the 35th IMAC, A Conference and Exposition on Structural Dynamics 2017*, Garden Grove, CA, USA, 2017.

[2] R. L. Norton, Design of Machinery, New York City: McGraw-Hill Education, 2008.

[3] "37.1.2 Contact pressure-overclosure relationships," in *Abaqus Analysis User's Guide*, Dassault Systèmes Simulia Corp., 2016.

[4] "6.3.5 Natural frequency extraction," in *Abaqus Analysis User's Guide*, Dassault Systèmes Simulia Corp., 2016.

[5] R. J. Allemang, "The Modal Assurance Criterion (MAC): Twenty Years of Use and Abuse," University of Cincinnati, Cincinnati, OH, USA, 2003.

[6] N. A. J. Lieven and D. J. Ewins, "Spatial Correlation of Mode Shapes, The Coordinate Modal Assurance Criterion (COMAC)," in *Proceedings of the Sixth International Modal Analysis Conference*, Orlando, FL, USA, 1988.

[7] H. Schmidt, J. Hattel and J. Wert, "An analytical model for the heat generation in friction stir welding," *Modelling and Simulation in Materials Science and Engineering*, vol. 12, p. 143–157, 2004.

[8] FEMtools Pretest and Correlation Analysis User's Guide, Dynamic Design Solutions, 2016.

[9] "11.6.1 Mass scaling," in *Abaqus Analysis User's Guide*, Dassault Systèmes Simulia Corp., 2016.

Estimation of normal contact stiffness for different contact pairs: experiments and numerical approach

D. Tonazzi[1], F. Massi[1], L. Baillet[3], M. Salipante[1], Y. Berthier[2]
[1)] DIMA, Department of Mechanical and Aerospace Engineering, ‘‘La Sapienza’’ University of Rome, via Eudossiana 18, 00184 Rome, Italy.
E-mail:**davide.tonazzi@uniroma1.it**

[2)] LaMCoS, Contacts and Structural Mechanics Laboratory, Université de Lyon, CNRS, INSA Lyon, UMR 5259, 20 rue des Sciences, F-69621 Villeurbanne, France.

[3)] ISTerre, Institut des Sciences de la Terre, CNRS, Joseph Fourier University, Grenoble 1381 rue de la Piscine, Domaine universitaire, 38400 St. Martin D’Heres, France.

Abstract
Modelling of frictional contact systems with high accuracy needs the knowledge of several contact parameters that are mainly related to the properties of the contact interfaces. While the interface parameters cannot be directly obtained by performing local measurements, the values estimated by means of analytical/numerical models are not reliable to describe the contact behavior, which affects in a prominent way the complex contact phenomena. This work presents a newer approach for identifying reliable values of the normal contact stiffness between rough surfaces as a function of contact pressure, surface roughness and materials. The combination of dynamic experimental tests, on a dedicated set-up, with finite element modelling allowed for an indirect determination of the normal stiffness at the contact.

1 Introduction

The correct modeling of contact interfaces is a key factor in many engineering applications that inherently include contacts between components: e.g. joints, clamping devices, robotic contacts, rolling bearings [1, 2], brake systems [3], etc. The contact mechanics between component surfaces plays also a key role for understanding many tribological processes such as, contact induced vibrations [4-6], frictional instability[4, 7, 8], stick-slip phenomena [9], adhesion and wear [10]. Accurate contact modeling of such systems requires knowledge of interface contact parameters [11], such as contact stiffness, which are not easily available and completely understood. The first works dealing with contact stiffness dealt with analytical approach of simple elastic model using Hertzian spherical contact. In the GW model [12] the contact interface is considered nominally flat with single scale roughness where the contact stiffness is obtained by statistical model. Less common are papers dealing with direct techniques for measuring the properties of rough contacts. Many attempt in estimation of contact stiffness were made and, for instance, Hattori and Serpa [13] have proposed the use of an artificial neural networks. Drinkwater et al. [14] measured the contact stiffness of an aluminum–aluminum interface using an acoustic technique. Mulvihill et al. [15] compared contact stiffness that it has been measured by using Digital Image Correlation (DIC) and ultrasound techniques. A completely different method to measure contact stiffness is based on ultrasonic methods where high frequency waves are used to derive the stiffness from the interface [14]. Another method to measure contact stiffness and damping at the nano-scales has been presented by Asif et al [16]. A few works [17, 18] in literature are based on combined experimental and analytical/numerical approach for indirect measurement of the contact stiffness [19]. In this context the objective of the present work is the estimation of surface contact stiffness using a newer methodology that combines experiments and finite element approach for an indirect measure of its value in static and sliding condition. On one hand, an experimental

setup has been developed for measuring the contact stiffness both in sticking and sliding conditions, for different surface topographies, materials and average contact pressures. The frequency analysis of the system response allowed for identifying its dynamics, which is related to both the dynamics of the considered system and the interface contribution. On the other hand, a finite element model of the experimental setup has been developed, taking into account the dynamics of the system and the contact interface contribution. Comparison between numerical and experimental results allows for estimating the normal contact stiffness for different contact pairs.

2 Methodology

The proposed methodology for the estimation of the normal contact stiffness of the materials in contact is based on a dynamic method, developed through a combined numerical and experimental approach (Figure 1). By an experimental point of view, a newer setup has been designed and then used to perform dynamic tests, controlling and identifying its dynamic response. Afterwards, a 3D finite element model, updated and to be representative of the experimental setup, has been utilized to compare the numerical and experimental results for estimating the normal contact stiffness between the investigated materials in contact.

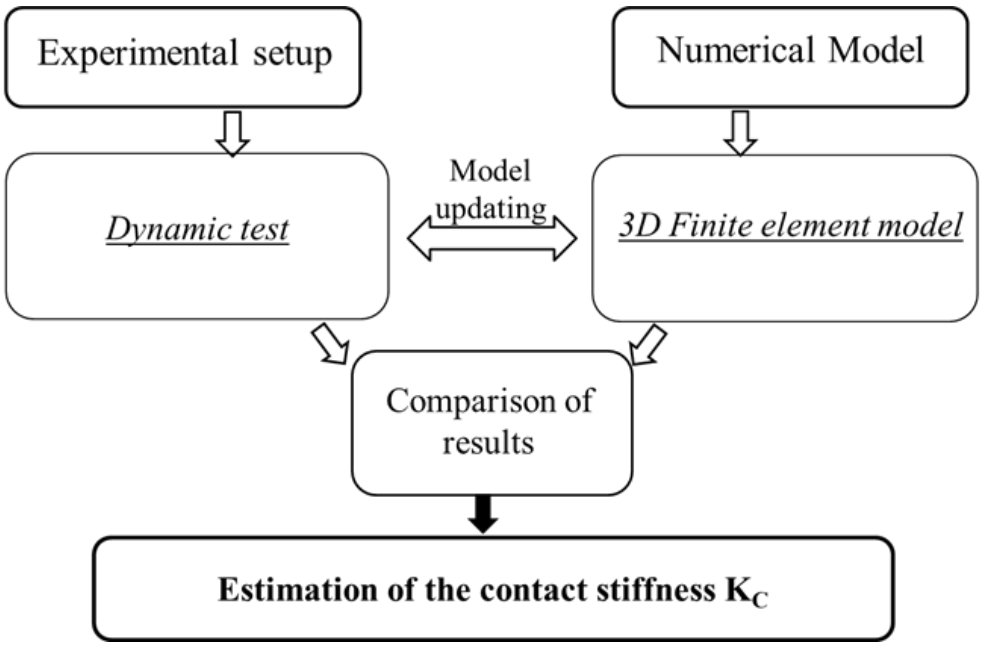


Figure 1. Overview of the proposed approach for the estimation of the contact stiffness.

Through the comparison between the results from the numerical model and the system frequency response from experiments, the value of the normal contact stiffness can be estimated by fitting the numerical eigen-frequencies with the results of the frequency analysis performed on the experimental setup.

3 Experimental setup

The experimental tribometer, designed to perform the experiments dedicated to the contact stiffness estimation, is presented in Figure 2. The setup has been designed to perform tests with different materials (samples) in contact, different length of the samples and a range of the average contact pressure up to 1 MPa. The system is mainly characterized by a material sample in contact with a disc and loaded by the weight of a massive support. In order to minimize the friction between the massive support and the frame, along the normal direction to the contact surface, an air bearings technology is used. In such a way, the

massive support is free to move and vibrate in the normal direction. The experimental setup is equipped with a DC motor and a digital motion controller, making possible to perform measurements in both static and sliding condition at a well-controlled rotational speed. After the characterization of the geometry and the mechanical properties of the tested material, the samples have been machined obtaining three different lengths to ensure reproducibility of the results. After the cutting process, a face milling is used with a right combination of cutting head (diameter and cutters shape), rotational and feeding speed, allowing for obtaining a surface with desired surface parameters (Ra) and topography. After the milling process, the specimens have been cleaned in an ultrasound cleaning machine and then left to dry. At this point, every single sample has been visually inspected and then tested by a profilometer in order to compute the roughness parameter in terms of Ra. The specimens which surfaces have met the roughness and planarity requirement have been used for the contact stiffness evaluation tests. Each measurement is carried out by placing the specimen in contact between the disc surface and the guide bar; successively, a dead mass is added on the top of the guide bar to obtain a desired average pressure at the contact interface between the sample and the disc. The dynamic response of the system to an impulsive excitation (hammer impact) is recorded, by an accelerometer placed at the top of the guide bar (Figure 2). The signal of the impulsive force and the system response have been recorded by a signal acquisition system with a sampling frequency of 10 kHz.

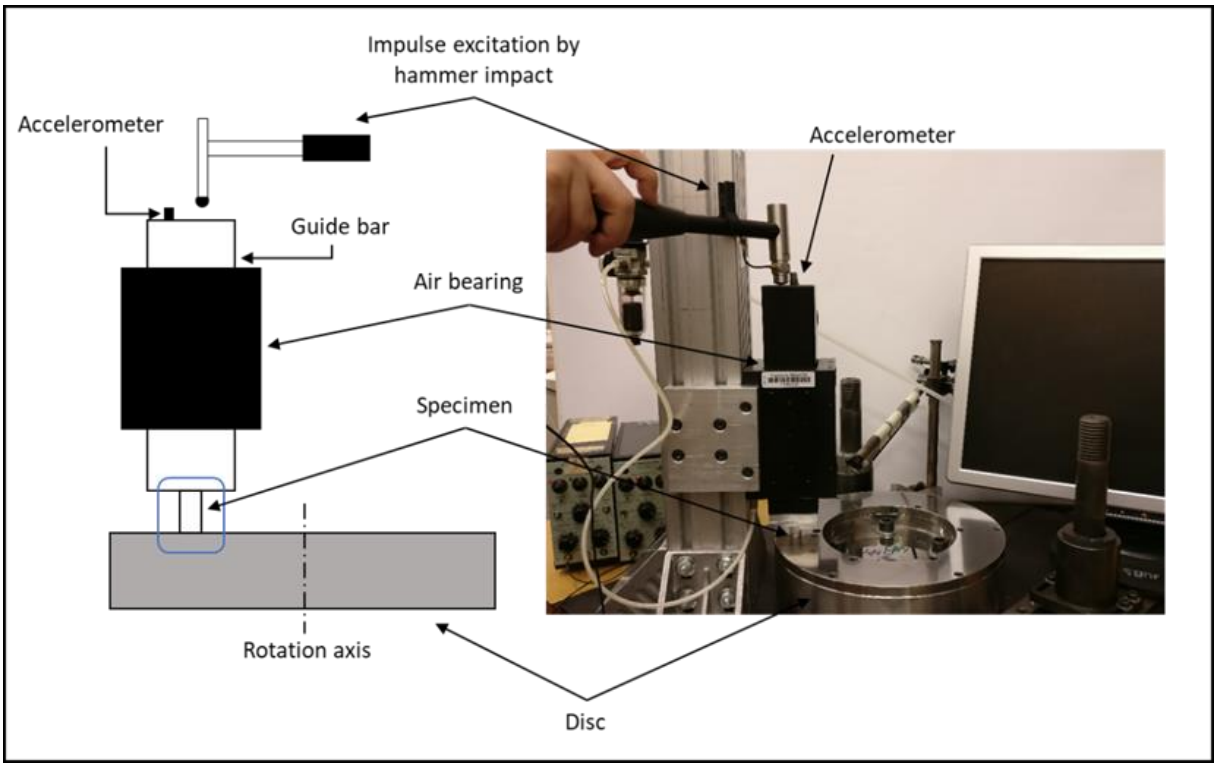


Figure 2: Scheme (left) and photograph(right) of the setup.

4 Finite element model

A finite element model (Figure 3) of the experimental setup has been developed using the ANSYS software; in order to reduce the model size and the complexity of the system, the numerical model includes only the disc assembly and the air bearing support with its guide bar. The presence of the shaft and bearings, the belt and the drive motor and the related global dynamic contributions, have been taken into account adding an elastic support on the base of the disc assembly with a stiffness value calculated by updating the model with preliminary dynamic tests.

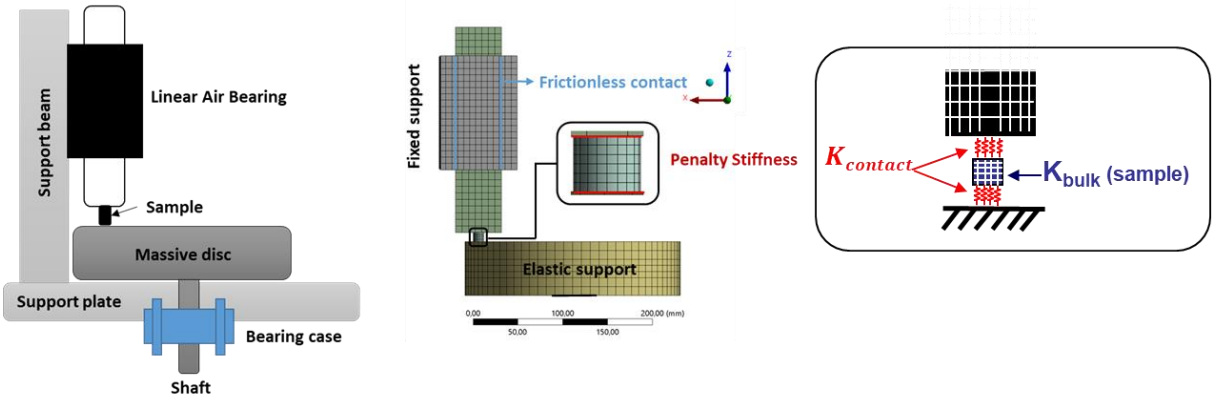


Figure 3: Finite element model of the developed experimental setup and zoom related to the sample in contact.

A hexahedral-dominated mesh has been used in the numerical model. Each 3D solid element has 16 nodes, for a total of 48 degrees of freedom. The model is composed of four main bodies: the disc, the guide bar, the air bearing and the specimen. A fine mesh has been used for the specimen meshing, while a coarser mesh turned out to be sufficient for an accurate description of the other bodies, for a total of 13884 elements in the model. The contact region between the guide bar and the air bearing has been modelled as frictionless; a pure penalty method has been used to describe the contact between the specimen surfaces, the disc and the guide bar. The same contact stiffness value has been introduced for both the contact between specimen and disc and the contact between the specimen and guide bar. A fixed support on the side of the air bearing has been added, in order to model the effect of the support beam. A point mass on top of the guide bar is used to vary the average contact pressure on the specimen surfaces and to account for the dynamic effect of the dead mass on the guide bar as in the experimental setup. As shown in Figure 3 an elastic support on the joint between disc and shaft has been placed where the disc physically joins the shaft, with a magnitude of 20N/mm2 in order to modelling the stiffness of the shaft bearings assembly.

The updating of each component and then of the whole system have been carried out by experimental dynamic tests. In the first step, the normal contact stiffness has been simulated introducing in the model an equivalent layer on the top and on the bottom of the sample in contact with the disc. In a second step, the method has been also validated by taking in account the contact stiffness directly by the value of the contact stiffness parameter in the penalty modelling of the interfaces. The results of the modal analysis (frequency of the investigated mode) of the updated numerical model have been compared with the experiments (frequency response function) to fit as better as possible the value of the contact stiffness. A parametrical modal analysis has been performed as a function of the different lengths of the sample and as a function of different average contact pressures imposed experimentally.

5 Contact stiffness estimation

5.1 PMMA material

An extensive measurement campaign has been conducted for the estimation of the contact stiffness in static conditions for PMMA material samples.

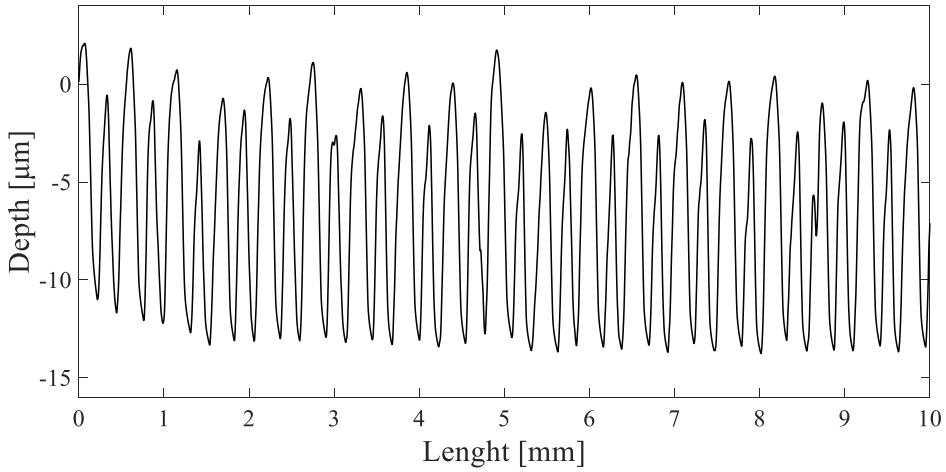


Figure 4: 1D-profile for PMMA material and roughness parameter Ra=6µm.

Three specimens for each length (L=10 mm, L=15 mm, L=20 mm) and for two values of the roughness parameter, Ra=1 µm and Ra=6 µm (1D-profile in Figure 4), have been tested, according to the following protocol:

- At first, the specimen is put in contact between the disc and the guide bar;
- In the second phase, the system is excited with an hammer impact on the top of the bar and then the impulsive system response is recorded by the accelerometer positioned in the normal direction respect to the contact (Figure 5);
- At the end, the recorded signals are used to compute the frequency response function in order to identify the natural frequency of the investigated mode (Figure 5).

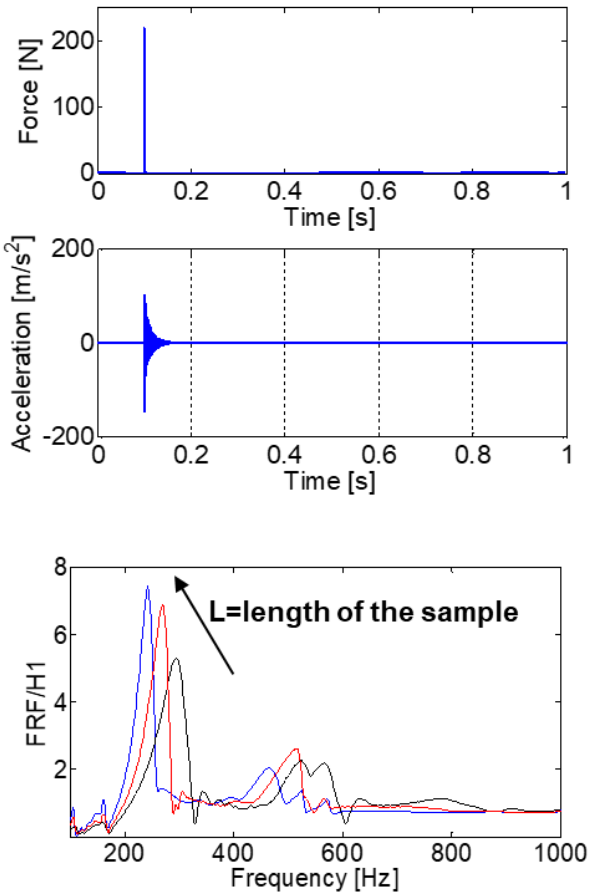


Figure 5: (Up) Acceleration and force signals over the time recorded due to the impact excitation for a single measurement; (down) frequency response function of the system for different lengths of the tested samples.

The previous mentioned protocol has been repeated, maintaining the same material sample, for each of the following average contact pressure values: 0.14 MPa, 0.25 MPa, 0.35 MPa, 0.57 MPa and 1 MPa. After performing the test with the highest pressure, a last measurement is made with the lower value of the average contact pressure in order to verify the repeatability of the test and to verify as well the occurrence of residual plastic deformation at the interface that could modify the natural frequency of the investigated mode. However, for the tested pressure range, no plastic deformation is emerged from the measurements.

Figure 6 shows a comparison of the results between numerical and experimental tests in terms of the natural frequency of the investigated system mode. A good quantitative agreement between experiments and numerical results is shown in the figure for an average contact pressure of 0.14 MPa and for a surface roughness of Ra=1 μm.

With the same model and same boundary conditions used in the previous case, the default penalty contact stiffness value, calculated automatically by the software as a function of different parameters (penetration tolerance, mesh size, contact pressure, etc) has been introduced in the model. The comparison with the experiments highlights a crucial difference in term of natural frequency of the considered system mode, confirming the unrealistic values of the contact stiffness in the commercial codes, which lead to completely wrong results, overestimating the frequency of the investigated mode (grey point in Figure 6).

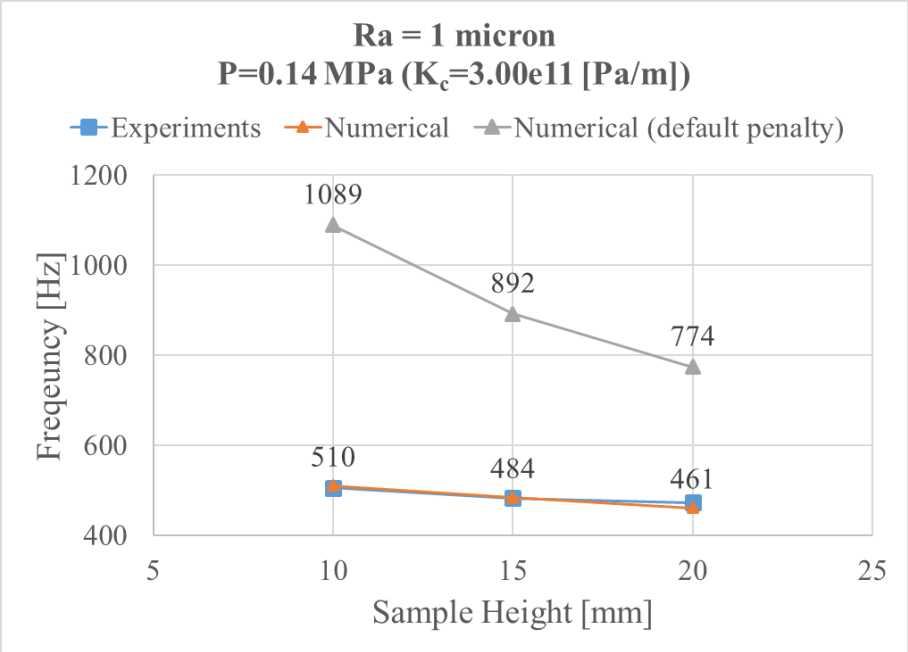


Figure 6: Experimental and numerical results for PMMA samples and for surface roughness of Ra=1μm and average contact pressure of P=0.14 MPa.

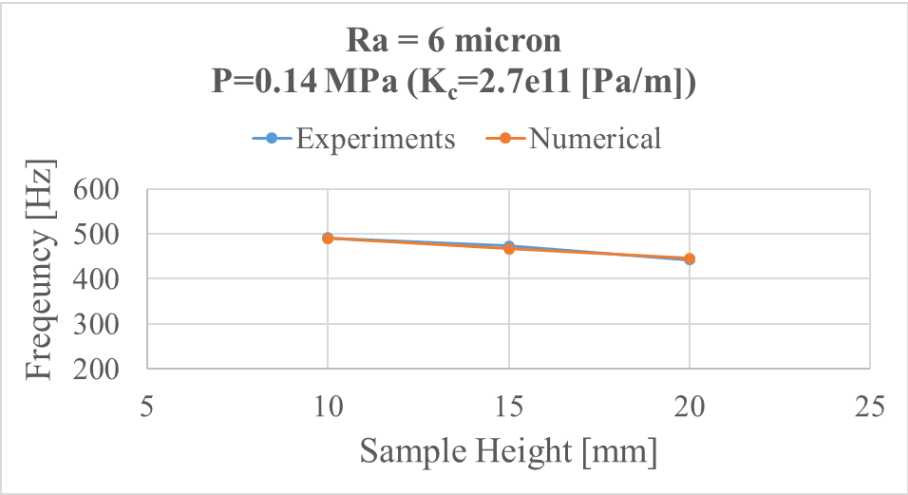


Figure 7: Experimental and numerical results for PMMA samples and for surface roughness of Ra=6μm and average contact pressure of P=0.14 MPa.

Figure 7 shows the numerical and experimental results for PMMA material in the case of roughness value of Ra=6 μm. The value of the contact stiffness (Kc=2.7e11 [Pa/m]), introduced in the numerical model allowed for a good fitting with the experiments in terms of the natural frequency of the investigated mode. Varying the contact stiffness parameter, used in the penalty method to solve the contact, it has been possible to fit the value of the natural frequencies for each combination of specimens, average contact pressure and surface roughness parameter (Ra). Figure 8 shows the trend of the contact stiffness as a function of the average contact pressure for both surface roughness parameters of Ra=1 μm and Ra=6 μm for PMMA material. Figure 6 highlights how the contact stiffness value increases as a function of the average contact pressure for both roughness parameters, as found in the literature by analytical and simplified numerical models [12, 17]. A difference in the contact stiffness value is remarkable (Figure 8) as a function of the different surface roughness and as expected a lower surface roughness leads to a higher contact stiffness value for the entire investigated pressure range.

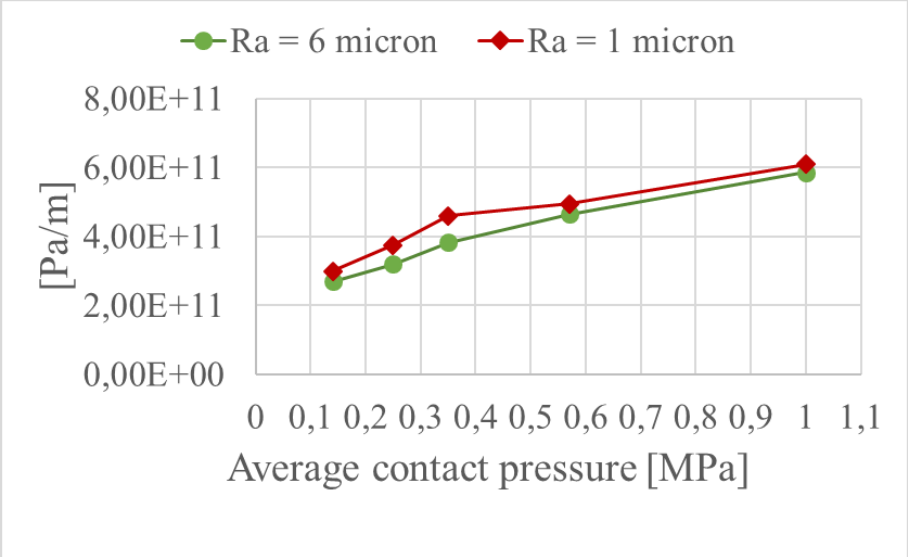


Figure 8: Normal contact stiffness as a function of the average contact pressure: surface roughness parameter of Ra=1µm (red curve) and Ra=6µm (green curve) for PMMA material.

5.2 Aluminum alloy material

Once the model has been validated using PMMA material, only two different specimen heights, 15mm and 20mm, have been used for the contact stiffness estimation for aluminum alloy material, which is stiffer than PMMA. As for PMMA material, the specimens have been cut and then machined with well-controlled parameters (rotational and feeding speed) in order to obtain the two desired values (Ra=1 µm and Ra=6 µm) of the surface roughness to be tested. The same protocol, explained in the section 5.1, is applied for Aluminum specimen as well. Figure 9 shows the experimental frequencies (blue points) calculated from the Frequency Response Function (FRF) of the system and the natural frequencies coming out from the numerical model for a contact stiffness value of Kc=1.15e12 [Pa/m]. Aluminum material is stiffer than PMMA material and as expected the measured frequency are higher respect to PMMA (Figure 8) both for h=15 mm and h=20 mm (the frequency contribution is due to the bulk stiffness and the stiffness of the contact interface of the sample). The results highlighted a good matching between experiments and numerical results in terms of the frequency of the investigated mode.

Figure 10 shows the evolution of the contact stiffness as a function of the average contact pressure for Aluminum alloy material. The contact stiffness increases as a function of the contact pressure for both roughness values (Ra=1 µm and Ra=6 µm). As expected, an higher roughness value leads to a lower contact stiffness as found for PMMA material.

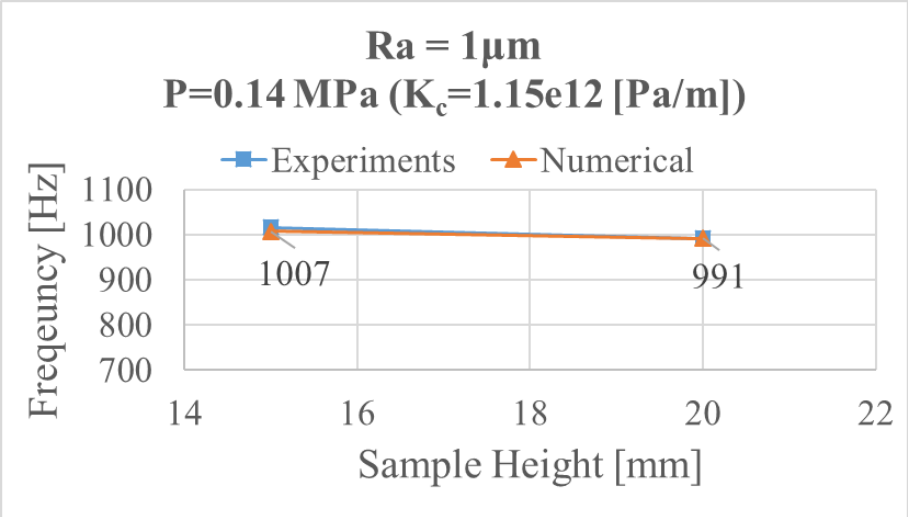


Figure 9: Experimental and numerical results for Aluminum alloy samples and for surface roughness of Ra=1µm and average contact pressure of P=0.14 MPa

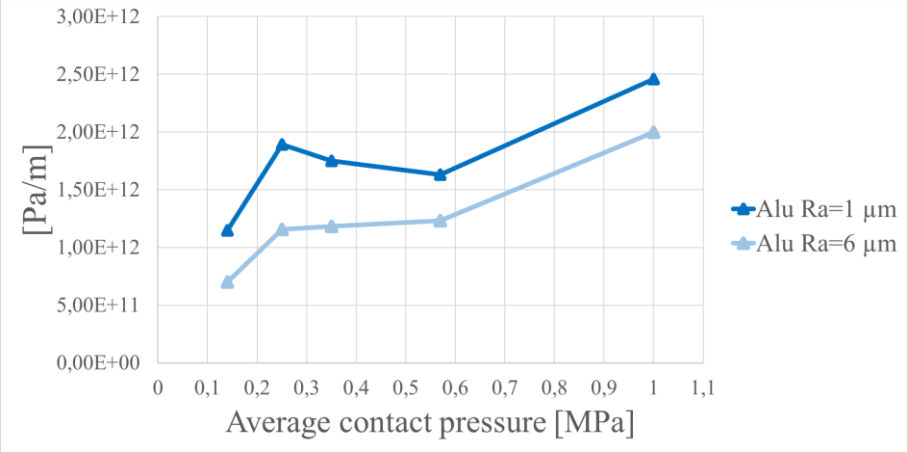


Figure 10: evolution of contact stiffness as a function of the average contact pressure for aluminum alloy material.

5.3 Frictional material

In this section, a preliminary result on contact stiffness estimation for frictional material for automotive brake application is shown. The cylindrical specimens have been cut directly from the disc brake pads and three different heights were tested: 3mm, 9.3 mm and 13 mm. For each sample height, two different diameters, 12 mm and 20 mm were tested as well. The same protocol, explained in section 5.1, is adopted and a parametrical analysis has been carried out as a function of the following average contact pressures: 0.05, 0.15, 0.5 and 1 MPA. The surface topography and roughness is preserved the same as in the commercial pads and a pairs of each sample height is tested in order to investigate the effect of the heterogeneities of such complex material as well.

Figure 11 shows the numerical and the experimental results for sample diameter of 12 mm and for a contact pressure of 0.15 MPa and 1 MPa. The results highlighted a dispersion of the experimental results in terms of the measured natural frequencies of the tested samples. The dispersion of the results could be attributed to the heterogeneity of the bulk and surface material properties. However, with the developed approach it has been able to identify an average value of the contact stiffness $\bar{\boldsymbol{K}}$ for each value of the average contact pressure as shown in Figure 11 and summarized in Figure 12.

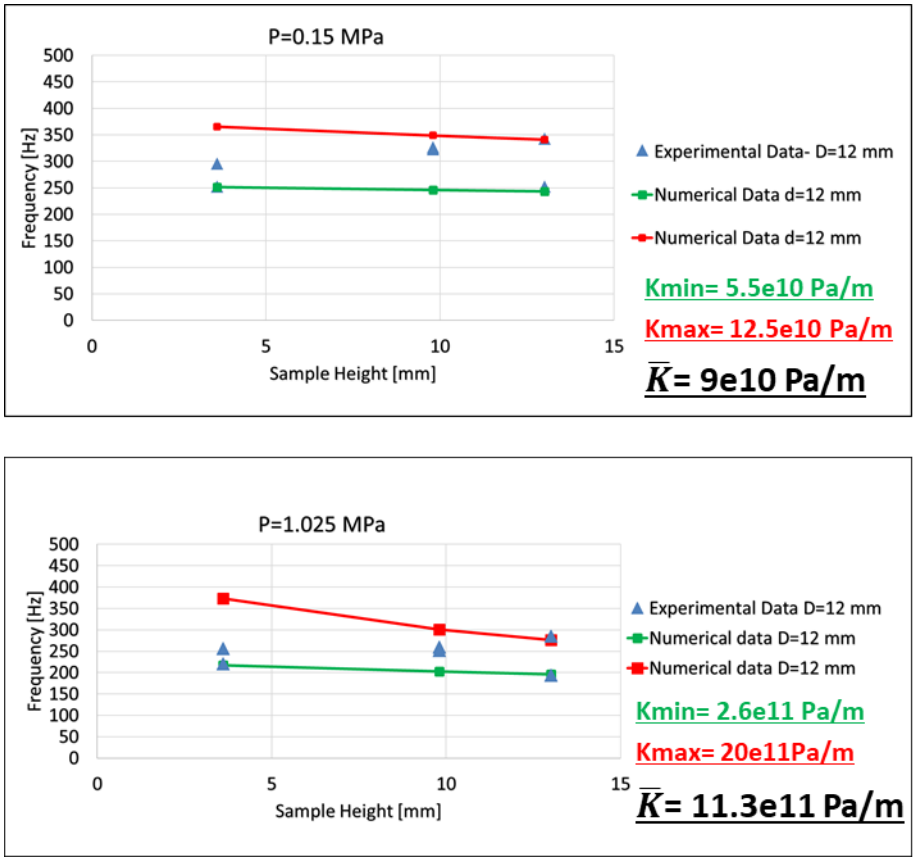


Figure 11: Comparison between numerical results and experiments for average contact pressure of 0.15 MPa (Up) and 1 MPa (down) for sample diameter of 12mm.

Figure 12 shows the evolution of the contact stiffness for all tested materials: PMMA, aluminum alloy and friction material. The figure highlighted the increasing of the contact stiffness as a function of the average contact pressure for all tested materials. Moreover, frictional material and PMMA have a lower contact stiffness with respect to Aluminum alloy in the pressure range from 0.1 MPa up to 1 MPa.

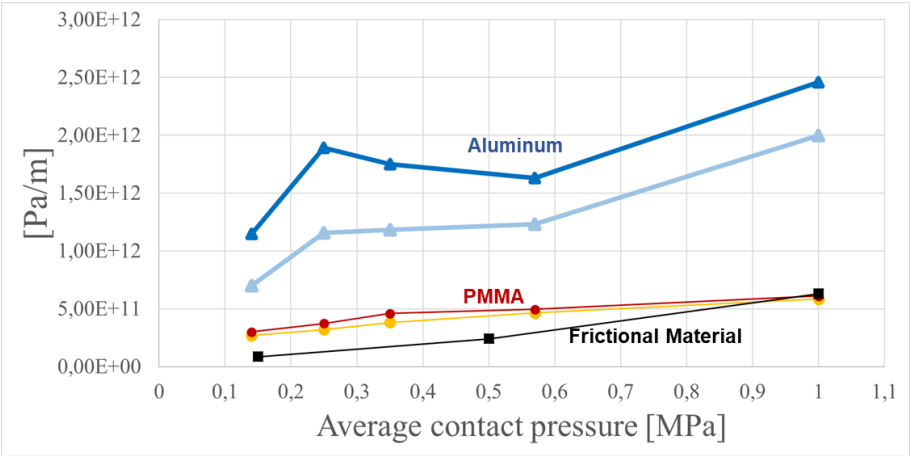


Figure 12: Comparison of the contact stiffness for different contact pairs as a function of the average contact pressure.

6 Conclusions

The quantitative estimation of contact stiffness between bodies in contact represents a significant improvement in the finite element modelling of frictional systems. To achieve such a result, an experimental and numerical procedure has been designed, allowing to investigate the contact stiffness evolution as a function of the contact pressure, surface roughness for different contact material pairs , obtaining consistent and reproducible results. In frictional systems, the contact stiffness affects both the global dynamic response of the system and the local contact behaviour (stress and strain at the contact interface). The developed approach allows for estimating the contact stiffness in sticking conditions under well controlled parameters, useful to be introduced into finite element models for both static and dynamic contact simulations, such as, for example, CEA and nonlinear transient analysis for brake squeal prediction.

Acknowledgements: the present research work has been partially supported by the French National Research Agency (Grant number ANR-12-VPTT-0006).

References

[1] D. Tonazzi *et al.*, "Numerical analysis of contact stress and strain distributions for greased and ungreased high loaded oscillating bearings," *Wear,* vol. 376-377, pp. 1164-1175, 2017/04/15/ 2017.

[2] I. Ghezzi *et al.*, "Damage evolution and contact surfaces analysis of high-loaded oscillating hybrid bearings," *Wear,* vol. 406-407, pp. 1-12, 2018/07/15/ 2018.

[3] J. Brunetti, F. Massi, W. D′Ambrogio, and Y. Berthier, "A new instability index for unstable mode selection in squeal prediction by complex eigenvalue analysis," *Journal of Sound and Vibration,* vol. 377, pp. 106-122, 2016/09/01/ 2016.

[4] D. Tonazzi *et al.*, "Experimental and numerical characterization of system response under dry frictional contact," in *ISMA- International Conference on Noise and Vibration Engineering*, ed. Leuven, 2014.

[5] M. Di Bartolomeo, F. Morelli, D. Tonazzi, F. Massi, and Y. Berthier, "Investigation of the role of contact-induced vibrations in tactile discrimination of textures," *Mechanics & Industry,* 10.1051/meca/2017027 vol. 18, no. 4, // 2017.

[6] J. Brunetti, F. Massi, W. D'Ambrogio, and L. Baillet, "Steady state of modal coupling instabilities as a dynamic energy equilibrium," in *Proceedings of ISMA 2014 - International Conference on Noise and Vibration Engineering and USD 2014 - International Conference on Uncertainty in Structural Dynamics*, 2014, pp. 1827-1842.

[7] D. Tonazzi, F. Massi, L. Baillet, J. Brunetti, and Y. Berthier, "Interaction between contact behaviour and vibrational response for dry contact system," *Mechanical Systems and Signal Processing,* vol. 110, pp. 110-121, 2018/09/15/ 2018.

[8] D. Tonazzi, F. Massi, A. Culla, A. Fregolent, and Y. Berthier, "Role of damping on contact instability scenarios," presented at the 5° World Tribology Congress, Turin, Italy, 2013-09-08, 2013.

[9] D. Tonazzi, F. Massi, L. Baillet, A. Culla, M. Di Bartolomeo, and Y. Berthier, "Experimental and numerical analysis of frictional contact scenarios: from macro stick–slip to continuous sliding," (in English), *Meccanica,* pp. 1-16, 2014/07/08 2014.

[10] M. Renouf, F. Massi, N. Fillot, and A. Saulot, "Numerical tribology of a dry contact," *Tribology International,* vol. 44, no. 7–8, pp. 834-844, 7// 2011.

[11] J. Brunetti, F. Massi, W. D'Ambrogio, and Y. Berthier, "Dynamic and energy analysis of frictional contact instabilities on a lumped system," (in English), *Meccanica,* pp. 1-15, 2014/08/07 2014.

[12] "Contact of nominally flat surfaces," *Proceedings of the Royal Society of London. Series A. Mathematical and Physical Sciences,* 10.1098/rspa.1966.0242 vol. 295, no. 1442, p. 300, 1966.

[13] G. Hattori and A. L. Serpa, "Contact stiffness estimation in ANSYS using simplified models and artificial neural networks," *Finite Elements in Analysis and Design,* vol. 97, pp. 43-53, 2015/05/01/ 2015.
[14] R. S. Dwyer-Joyce, B. W. Drinkwater, and A. M. Quinn, "The Use of Ultrasound in the Investigation of Rough Surface Interfaces," *Journal of Tribology,* vol. 123, no. 1, pp. 8-16, 2000.
[15] D. M. Mulvihill, H. Brunskill, M. E. Kartal, R. S. Dwyer-Joyce, and D. Nowell, "A Comparison of Contact Stiffness Measurements Obtained by the Digital Image Correlation and Ultrasound Techniques," *Experimental Mechanics,* vol. 53, no. 7, pp. 1245-1263, 2013/09/01 2013.
[16] S. A. Syed Asif, K. J. Wahl, R. J. Colton, and O. L. Warren, "Quantitative imaging of nanoscale mechanical properties using hybrid nanoindentation and force modulation," *Journal of Applied Physics,* vol. 90, no. 3, pp. 1192-1200, 2001/08/01 2001.
[17] D. P. Hess and N. J. Wagh, "Evaluating Surface Roughness From Contact Vibrations," *Journal of Tribology,* vol. 117, no. 1, pp. 60-64, 1995.
[18] M. Gonzalez-Valadez, A. Baltazar, and R. S. Dwyer-Joyce, "Study of interfacial stiffness ratio of a rough surface in contact using a spring model," *Wear,* vol. 268, no. 3, pp. 373-379, 2010/02/04/ 2010.
[19] A. A. Polycarpou and A. Soom, "Boundary and Mixed Friction in the Presence of Dynamic Normal Loads: Part I—System Model," *Journal of Tribology,* vol. 117, no. 2, pp. 255-260, 1995.

Experimental and numerical modal analysis of dry friction-induced contact damping in assembled structures

B. Magyar [1], **G. Csernak** [1], **R. Zana** [1], **R. Wohlfart** [1], **G. Stepan** [1]
[1] Budapest University of Technology and Economics, Department of Applied Mechanics,
Muegyetem rkp. 5, H-1111, Budapest, Hungary
e-mail: **magyar@mm.bme.hu**

Abstract

Finite element (FE) modal analysis of monolithic structures with negligible damping belongs to routine tasks even in the industry. However, in case of assemblies, there is no off-the-shelf solution due to the stiffness uncertainties and the unavoidable increase in damping due to contacts. A relevant part of structural damping originates in dry friction between the conforming surfaces of the assembled machine parts, and the modelling of this mechanism is extremely challenging. Our goal is the quantification of dry friction-induced modal damping by experiments in order to enhance the quality of existing contact models in FE algorithms. First, a new theoretical model was set up for the prediction of the friction-induced additional damping of each mode shape based on the FE analysis of a monolithic assembly. Second, the fundamentals of a new practical method were established that can be used for the designed increase of damping in certain structures.

1 Introduction

In mechanical engineering, design processes are mainly based on numerical simulation methods, like the finite element (FE) method. The FE analysis of structures provides reliable results – based on geometrical data and material properties – if static problems are considered. The accurate treatment of dynamic problems is more challenging since the damping characteristics of structures are related to several different phenomena. In this case, the parameters of the FE model cannot be determined merely on the basis of material parameters, but experimental validation is also necessary. Luckily, the internal (material) damping of metals is usually quite small, which means that the aforementioned problem does not lead to large errors if vibrations of monolithic structures are examined.

However, in case of assemblies, a relevant part of damping is related to the dry friction contact among the various components of the structure. Even small modifications of the assembled structure may lead to significant changes of damping, requiring the repetition of experiments for the validation of the new FE model. Moreover, the proper numerical modelling of contacts is a rather difficult task and the simulations are time consuming, see e.g. [1] and [2]. In some cases, damping of a mechanical structure plays a key role in the stability of the process, particularly in case of high speed machining [3], [4]. A significant part of the damping is related to dry friction in this case, too.

The goal of the present contribution is to propose a method for the estimation of contact damping by the modal analysis of the monolithic structure. The method is based on the idea that each vibration mode can be characterized by a dimensionless quantity δ_i, describing the possible dissipative processes on a chosen internal surface – where the contact is realized in the assembled structure. According to our assumption, relevant δ_i values can be determined by simple FE analysis and contact-related modal damping can be characterized by them. A possible application of this approach is the validation of friction models in forthcoming finite element solvers.

To check the proposed idea, two test-specimens had been designed and manufactured. One of the specimens is monolithic, the other one consists of two shrink-fitted parts. The shrink-fitted disc has the same geometry as the monolithic one and the overlap of the shrink-fitting was designed to obtain a contact pressure distribution that corresponds to a realistic case: the spindle-tool holder connection in a medium-size industrial machine tool.

An automated pneumatic ball shooter (see [5] and [6]) was used for the excitation to ensure the initial conditions to be as identical as possible. Free vibration decays had been measured both by laser Doppler vibrometers and lightweight accelerometers. Short-time Fourier transform was applied on the acquired velocity and acceleration signals, and characteristic amplitude peaks had been traced during the decays. The measured modal damping values were compared with the dimensionless δ_i parameters that were determined by the FE modal analysis of the monolithic disc and the traced peaks were selected based on the finite element results.

2 Design and numerical analysis of the test specimens

2.1 Preliminary studies, design process

The test specimens had been designed to be suitable for both free vibration decay experiments and forced vibration experiments by using an available electrodynamic shaker. In order to achieve higher amplitudes on a shaker, the weight of the specimens was kept reasonably small, and to exploit the optimal frequency ranges of the accelerometers and laser Doppler micrometers, natural frequencies were tuned to the preferred 300 Hz - 3 kHz range.

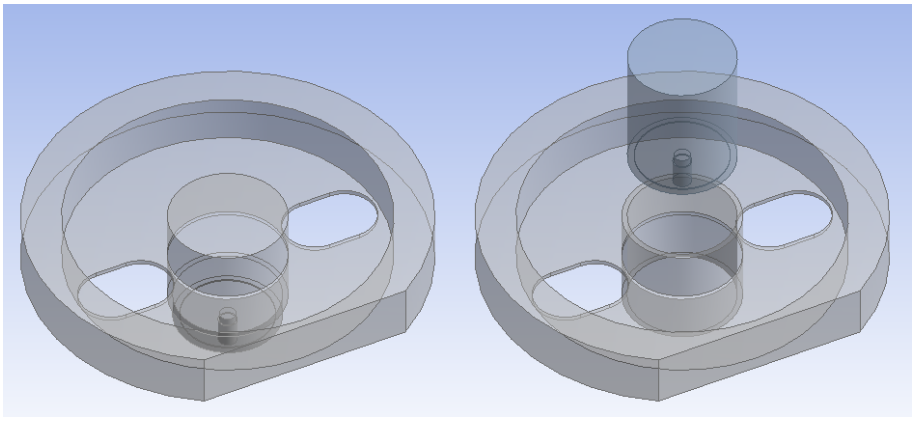


Figure 1: Test specimen geometries, left: monolithic, right: shrink fitted assembly.

For the proper evaluation of the measurement results, well-defined contact surface geometry and pressure distribution are preferred: threads should be avoided because of their relatively complex shape, and shrink-fit is preferred to provide prestress.

The realized specimen geometries are shown in Figure 1. In case of the specimen that consists of two bodies (Figure 1, right panel), the overlap of the shrink-fitted cylindrical surfaces is 0.03 mm in diameter, and the magnitude of the calculated prestress on the contacting surfaces varies between 10 and 40 MPa. The outer part was heated to 180 °C prior to the shrink-fitting. After the assembly, the two specimens were adjusted on an ultra precision milling machine, hence ensuring that the two discs are as identical as possible.

In order to avoid duplex modes, the rims were snipped by electrical discharge machining and two oval windows were also cut in the membranes of both specimens. In a previous study [7], the results regarding to axisymmetric specimens were presented, where beat phenomena occured due to the relatively close natural frequencies.

Since the aim of the experiment is to quantify damping, contactless devices, like laser Doppler vibrometers (LDVs) were preferred in order to avoid the increase of damping and/or mass. These vibrometers were used in two different measurements setups. First, forced vibration experiments were performed by using an electrodynamic shaker. Unfortunately, the power of the shaker was not sufficient, and at frequencies close to resonance (520-530 Hz) the vibration amplitude of the disc core was not in the detectable range of the LDVs. After that, an experiment was performed with suspended specimens, but the LDVs were not usable in this case either because of the large-amplitude swinging motion.

2.2 Modal analysis of the monolithic disc

In order to identify mode shapes and natural frequencies of the test specimens, modal analysis was carried out by using ANSYS finite element software and 3D solid elements. Figure 2 presents the result regarding the monolithic disc.

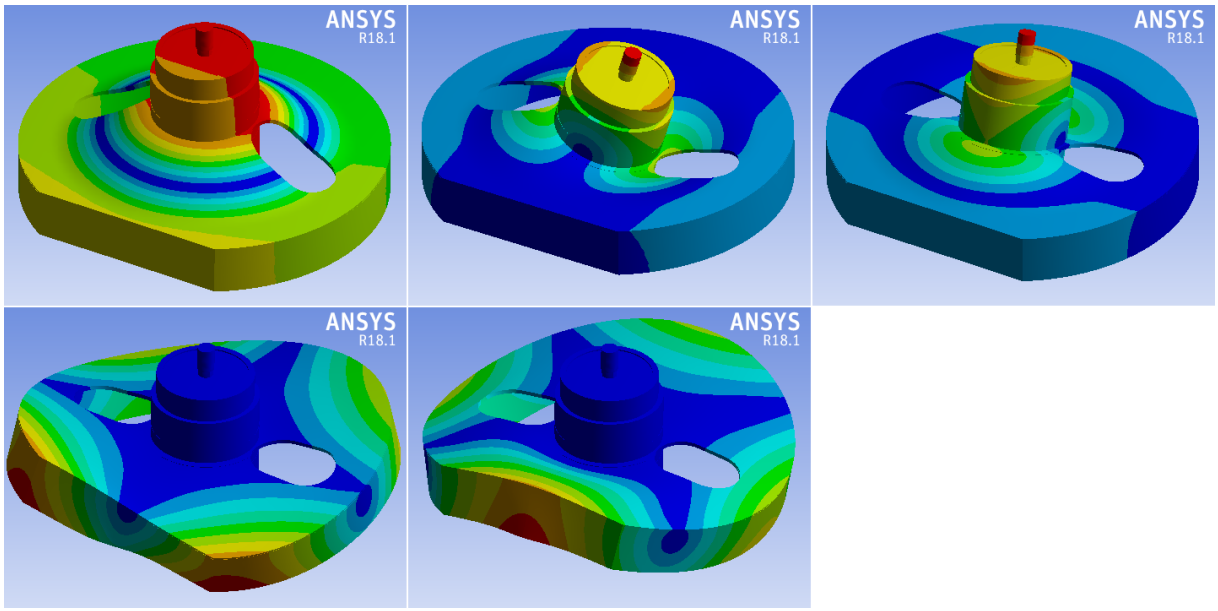


Figure 2: Natural frequencies and mode shapes of monolithic disc. Top row: 486.4 Hz, 602.3 Hz, 709.7 Hz; bottom row: 2018.6 Hz, 2448.6 Hz

The natural frequency of the first mode is 486.4 Hz, and this mode corresponds to the translational motion of the outer rim opposite to the inner core. The second and third natural frequencies are 602.3 Hz and 709.7 Hz, which belong to the tilting motions of the rim. The fourth and fifth natural frequencies are 2018.6 Hz and 2448.6 Hz, and these correspond to the bending vibrations of the outer rim.

3 Ultralight accelerometers

After the unfavourable experiences with contactless vibrometers, ultralight MEMS based accelerometers were tested (Xtrinsic FXLN8361QR1). These accelerometers were mounted on a printed circuit board (PCB), and the power supply was also constructed. The total weight of the accelerometer with the PCB was 0.065 grams, and the wire diameters were 0.08 mm. Compared to the 1590 grams of a disc, both the stiffness of the wires and the mass of the sensors could be neglected.

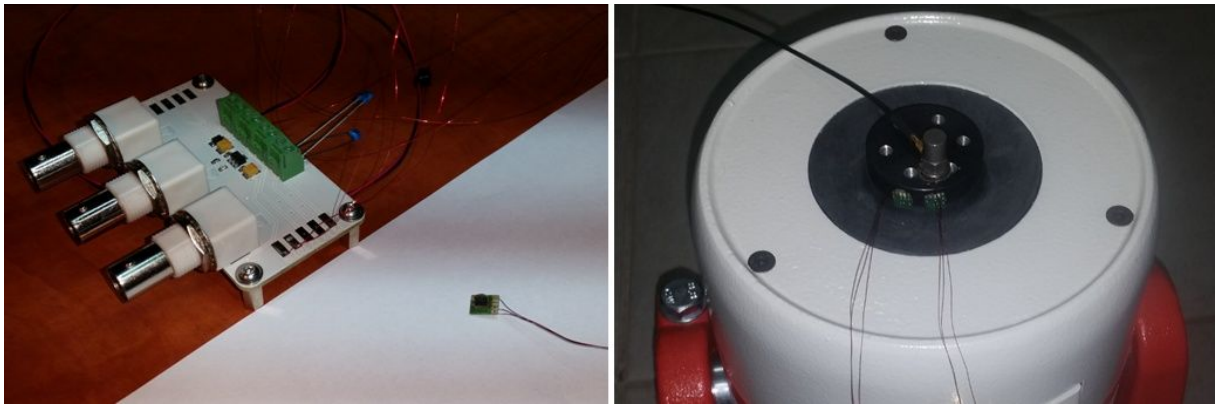


Figure 3: Left: ultralight accelerometer, power supply. Right: calibration of the accelerometers.

3.1 Calibration with Bruel & Kjaer accelerometers

The product sheet of the Xtrinsic sensors specified 2.7 kHz as the upper frequency limit, therefore the calibration of these sensors was necessary. Two Xtrinsic sensors were placed on an electro-dynamic shaker with a Bruel & Kjaer DeltaTron Type 4397 accelerometer as a reference for the calibration. The shaker was driven with an exponential chirp signal from 10 Hz to 10 kHz, and the three channels were recorded with a sampling frequency of 100 kHz.

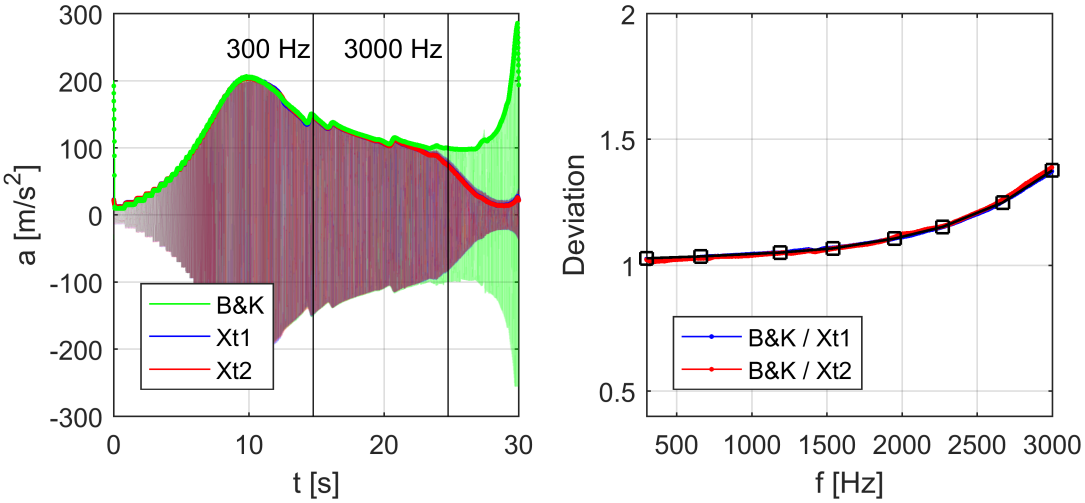


Figure 4: Calibration of the MEMS based accelerometer. Left panel: time signals, right panel: deviation curve in the frequency domain.

The time signal (thin curves) together with the RMS $*\sqrt{2}$ values (thick curves) are presented in the left panel of Figure 4, and the ratio of the Bruel & Kjaer and Xtrinsic RMS values are shown in the right panel in the 300 Hz - 3 kHz frequency range. A low pass FIR filter was created with a cut-off frequency of 3 kHz, and the frequency response of the filter was adjusted to the fitted curve in the right panel of Figure 4, hence compensating the inaccuracies of the Xtrinsic sensors.

4 Free vibration decay measurements

4.1 Measurement setup

Free vibration decays had been measured on both the monolithic and the shrink-fitted discs. The discs were drilled through the rims at $\pm 60^\circ$ positions relative to the top quadrant point, and suspended with kevlar fishing lines. An automated pneumatic ball shooter was used for the excitation to ensure the initial conditions to be as identical as possible. The places of impacts were at -45° on the rim. Between +30° and +165° relative to the top quadrant point, 8 locations were selected to measure accelerations. On each disc 40 vibration decays were recorded at these points.

Figure 5 illustrates the measurement setup. In the left panel, the automated pneumatic ball shooter can be seen with the suspended disc, a red laser dot shows the place of impact. In the right panel the Xtrinsic accelerometers are shown attached on the side of the assembled disc.



Figure 5: Left: suspended disc, automated pneumatic ball shooter. Right: Xtrinsic accelerometer attached on the side of the rim.

4.2 Measurement results

The accelerometer signals were recorded with 100 kHz sampling frequency with a Rohde & Schwarz RTE 1104 digital oscilloscope. The free vibration decay time signals are shown in the top row of Figure 6. The difference in the decays can be clearly seen between the monolithic (top left panel) and the shrink-fitted disc (top right panel).

In order to identify the natural frequencies, fast Fourier transform (FFT) of the two decays were calculated on 5 s samples as illustrated in the bottom panels of Figure 6. The identified frequencies in case of the monolithic disc were in good accordance with the FEM results; moreover, there were no significant differences either between the frequency peaks of the shrink-fitted disc and the FEA results with the monolithic disc. These frequencies are listed in panel headers of Figure 7.

In Figure 7, the decays of the acceleration magnitudes are shown; each curve corresponds to the average of 10 shots. A 0.25 s wide Blackman-Harris window [8] was used for the short-time Fourier transform with a window overlap of 95%.

Charts in the left column correspond to the monolithic disc, charts on the right correspond to the shrink-fitted assembly. Each row shows the decays of different acceleration magnitude peaks, i.e., vibration modes. Different colours belong to different measurement locations, and solid lines represent the average decays in response to 10 shots.

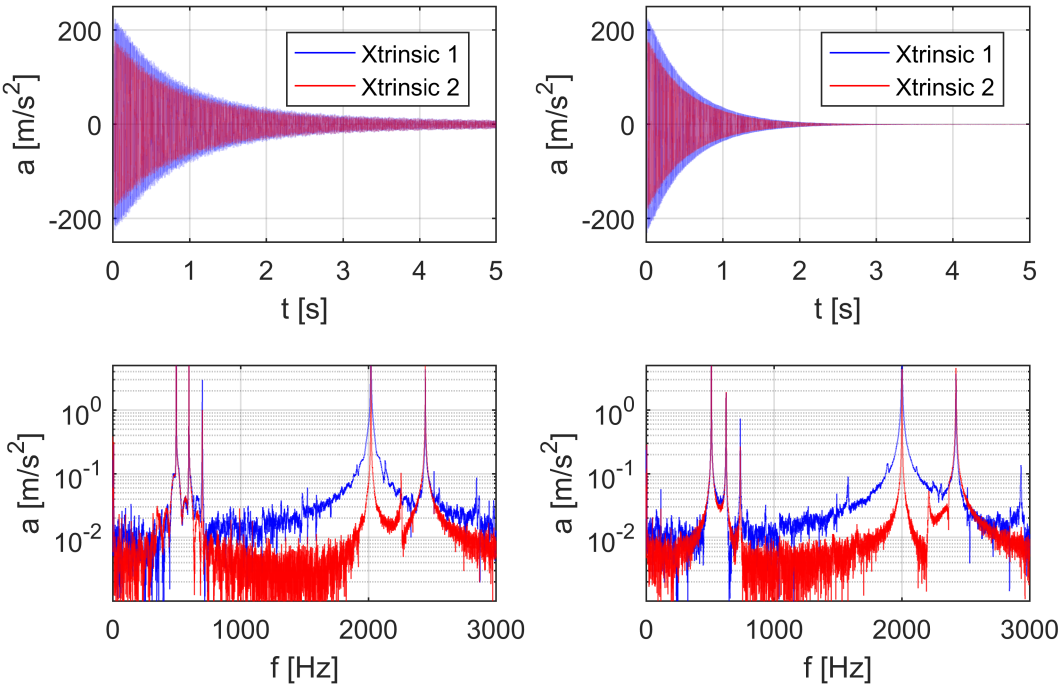


Figure 6: Free vibration decays. Left: monolithic disc, right: shrink-fitted assembly.

Exponential curves were fitted onto the measured decays, these fitted curves are illustrated by the dashed lines. The fitted ζ decay ratios are listed in the legends of these charts.

According to the results, a significant difference was experienced in the decay ratios between the monolithic disc and the shrink-fitted assembly, which cannot be explained by the differences in material damping or air resistance, since both the material properties and the macroscopic geometry were identical of the specimens.

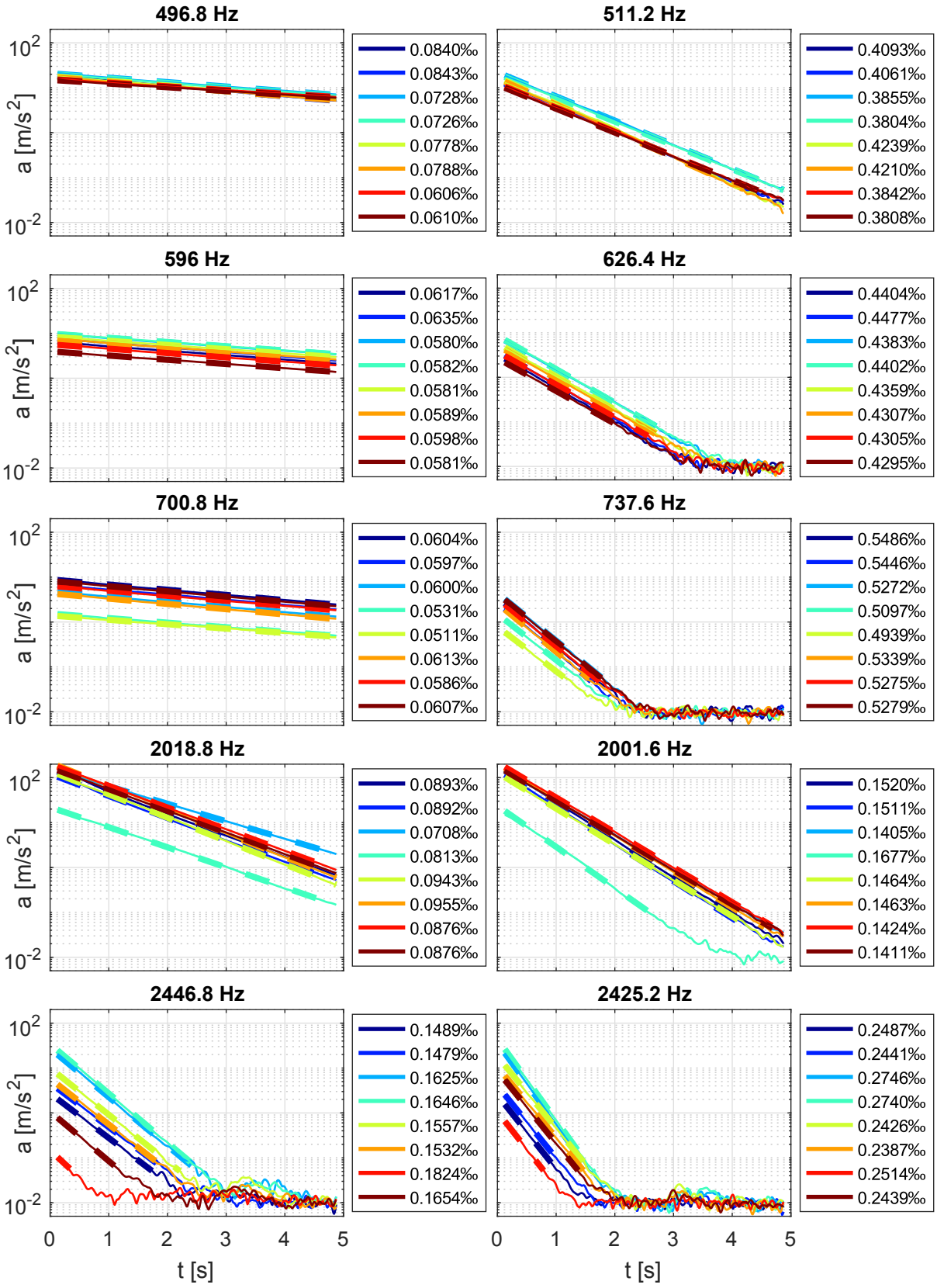


Figure 7: Free vibration decays of the acceleration magnitude peaks at eight points of the specimens. Left: monolithic disc, right: shrink-fitted assembly.

5 Analysing friction-induced contact damping

Since the only feasible approach of the finite element modelling of vibrating assemblies with dry friction is the use of full transient solution, it is an excessively intensive task from computational viewpoint. On the other hand, finite element modal analysis of the monolithic structure can be carried out much faster, and besides nodal displacements, stress and strain distribution is also resulted, however, the resulted values of stresses and strains do not have physical meanings, only their ratios, just as in case of displacements.

Let us define the $\overline{\sigma}_{\mathrm{eq}}$ average equivalent stress as follows:

$$\overline{\sigma}_{\mathrm{eq}} = \frac{\int_{(V)}(\sigma_1 - \sigma_3)dV}{V}, \tag{1}$$

where σ_1 and σ_3 are the highest and lowest principal stresses, respectively, and V is the volume of the body. We can describe the possible dissipative processes on a chosen internal surface by a dimensionless quantity, δ_i, calculated as the ratio of σ_{cmax} maximal equivalent stress on the contact surface and $\overline{\sigma}_{\mathrm{eq}}$, the average equivalent stress:

$$\delta_i = \frac{\sigma_{\mathrm{cmax}}}{\overline{\sigma}_{\mathrm{eq}}} \tag{2}$$

Based on the fitted results presented in Figure 7, the increase in the decay ratios can be determined. In the vertical axis of Figure 8, ζ_{a} denotes the damping ratio regarding to the shrink fitted assembly, and ζ_{m} correspond to the monolithic body, therefore the friction-induced modal damping can be characterized by $\zeta_{\mathrm{a}}/\zeta_{\mathrm{m}}$, and can be computed for the 5 examined modes and 8 measurement locations. The correlation between the damping increase and δ_i appears to be convincing.

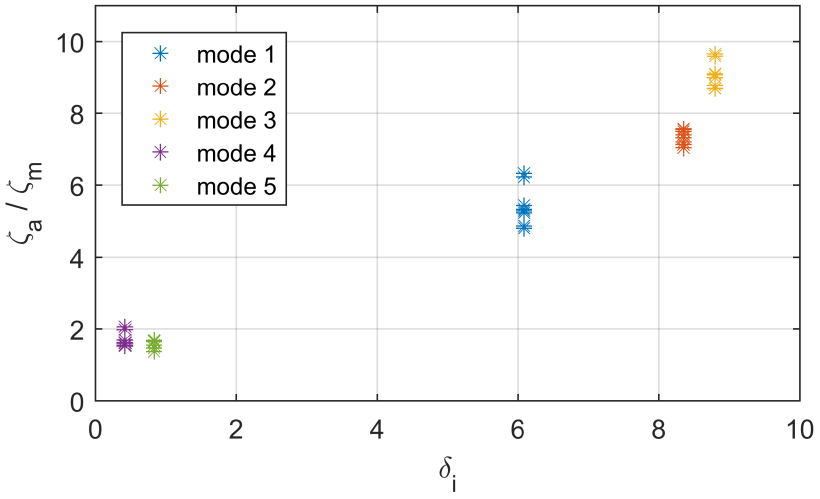


Figure 8: Friction-related damping ratio increase versus dimensionless contact stress

6 Conclusions

According to the presented free-vibration decay experiments, a significant difference was experienced in the damping ratios between the monolithic disc and the shrink-fitted assembly. Since both the material properties and the macroscopic geometry were identical, the source of the damping increase was identified as the dry friction on the contact surface. Based on these measurement results, the particular damping increases of each modes were determined. By using finite element modal analysis, a dimensionless quantity, δ_i was introduced,

and a strong correlation was found between the dry friction-induced damping increase and the numerically determined δ_i values corresponding to the particular modes.

On basis of the aforementioned correlation, it is possible the predict the extent of the additional damping related to dry friction, and also to differentiate the induced damping increase between particular mode shapes. This correlation depends on surface quality, surface measure, material properties and static prestress. These relationships are willing to be explored in future experiments.

Acknowledgements

The research leading to these results has received funding from the European Research Council under the European Unions Seventh Framework Programme (FP/2007-2013) / ERC Advanced Grant Agreement n. 340889.

References

[1] B. J. Lazan, *Damping of materials and members in structural mechanics*, Oxford: Pergamon Press; (1968).

[2] C. W. de Silva, *Vibration damping, control and design*, CRC Press; (2007).

[3] S. A. Tobias, *Machine tool vibration*, London: J. Wiley; (1965).

[4] G. Stepan, *Delay-differential equation models for machine tool chatter*, Dynamics and Chaos in Manufacturing Processes (1988); 471152935:165-192.

[5] D. Takacs, R. Wohlfart, A. Miklos, G. Krajnyak, A. Tth, G. Stepan, *Measurement of the modal parameters of rotating spindles by ball shooting impact excitation*, 8th CIRP Conference on High Performance Cutting (2018)

[6] S. Berezvai, A. Kossa, D. Bachrathy, G. Stepan, *Numerical and experimental investigation of the applicability of pellet impacts for impulse excitation*, International journal of impact engineering 115: pp. 19-31. (2018).

[7] B. Magyar, R. Zana, R. Wohlfart, G. Csernak, G. Stepan, *Measuring modal damping of a multibody system with dry friction*, 24th International Congress on Sound and Vibration (2017).

[8] J. O. Smith, *Spectral Audio Signal Processing*, W3K Publishing, (2011), ISBN 978-0-9745607-3-1.

Extension of the multi-stage cyclic symmetry methodology and application to modal and dynamic response analyses

N. C. Kill[1], F. D'Ambrosio[1]

[1]SAMTECH S.A.
Rue des Chasseurs Ardennais 8, B4031 Angleur,
Belgium e-mail: **norbert.kill@siemens.com**

Abstract

Multi-stage cyclic symmetry is used since several years for the modal and dynamic response analyses of turbo-machineries where it allows the use of detailed models at limited cost. With this method, each stage of the machine is cyclically modelled and inter-stage coupling combines the different stages. The coupling is either mesh compatible or not. Though it is an approximate method, it provides high quality results in the low frequency range. For higher frequencies, approximations may occur and they are mainly detected at the inter-stage junctions. The use of harmonic decomposition allows to detect missing harmonics for some stages. The method has therefore been enriched in order to automatically add basic fundamental harmonics. The different cyclic fields are then coupled at the inter-stage junctions.

1 Introduction

The design of aerospace turbomachines is the result of multiple compromises between performance, mass and thermo-mechanical behavior. From the mechanical point of view, these evolutions result in refined designs with respect to previous experience, including a strong reduction in the number of mechanical connections between components. Some turbomachine bladed disks, the most mechanically loaded components, are increasingly made in a single piece (BLISK). Conventional bolted connections between bladed disks give way to continuous connections, obtained for example by inertial friction. These advances in manufacturing and machining processes lead to significant gains in on-board weight compared to conventional technologies and, to a lesser extent, the aerodynamic performance of the machine. On the other hand, the reduction in the number of these mechanical links generates a significant reduction in the structural damping of the rotor as well as the appearance of greater dynamic coupling between components. The evolution of these technologies therefore poses new vibration problems for turbine engine designers. In this context, it is more important than ever for engine manufacturers to have reliable prediction tools for the dynamic behavior of their machines, at the earliest of the design phase, in order to prevent vibration fatigue problems and costly induced re-designs.

Design methods based on mono-stage dynamic analysis, exploiting the properties of cyclic symmetry, do not respond adequately to the technology evolution. Vibration phenomena, previously unobserved, coupling several bladed disks, whether adjacent or not, have been identified on some turbomachines.

On the other hand, a direct approach based on the modeling of the 360 ° complete multi-stages assembly remains very expensive in terms of data setting, computation time and post-processing. As a result, the possibility to analyze multi-stage assemblies in a nearly similar manner as the one used for the mono-stage case is an asset.

However, the multi-stage methodology is an approximated one. It gives good results in the lower frequency range but at higher frequencies, approximations may occur and they are mainly detected at the inter-stage junctions. A way to remove these approximations consists to simultaneously use several fundamental harmonics.

2 Theoretical Background

2.1 Mono-Stage Cyclic Symmetry

A cyclically periodical structure is a structure composed of a set of identical sectors which closes on itself to form the complete structure. If a finite element discretization of these structures is performed, the corresponding structural matrices are block circulant and a discrete Fourier transform produces block diagonal matrices. These diagonal matrices are expressed in cyclic coordinates and the number of diagonal blocks is equal to the number *N* of sectors. The eigenvalue problem to be solved to obtain the eigen-modes is replaced by a set of reduced eigenvalue problems each one function of the propagation wave number *n*.

$$n = 0,1,\cdots,{}^{N}/_{2} \qquad N\ even \quad ; \quad n = 0,1,\cdots,{}^{(N-1)}/_{2} \qquad N\ odd \tag{1}$$

The number of different wave numbers or fundamental harmonics is bounded by the number of sectors. Usually, a complex formalism is used to describe the cyclic coordinates and the wave number is included in the mathematical constraint linking the right and left boundaries of the sector [1].

$${}^{l}\mathbf{q} = e^{\frac{2j\pi n}{N}}\,{}^{r}\mathbf{q} = e^{j\beta}\,{}^{r}\mathbf{q} \tag{2}$$

The reduced eigenvalue problem has still the classical form for a rotating structure described in the rotating frame

$$\left[\lambda^2\mathbf{M} + \lambda(\mathbf{B} + \Omega\mathbf{C}) + \left(\mathbf{K_0} + \mathbf{K_\sigma} - \Omega^2\mathbf{N}\right)\right]\mathbf{q} = \mathbf{0} \tag{3}$$

Or

$$[\lambda^2\mathbf{M} + \lambda\mathbf{B} + \mathbf{K}]\ \mathbf{q} = 0 \tag{4}$$

For a not rotating structure modelled in the inertial frame; where **M** is the mass matrix, **B** the viscous damping matrix, **C** the Coriolis matrix, $\mathbf{K_0}$ the elastic stiffness matrix, $\mathbf{K_\sigma}$ the geometrical stiffness matrix and **N** the centrifugal stiffness matrix.

2.2 Harmonic Decomposition

The harmonic content related to one fundamental harmonic is described by the so-called Zigzag diagram. For the wave number n, its contents is

$$m = n, N-n, N+n, \cdots, kN-n, kN+n, \cdots, \infty \tag{5}$$

In some industrial cases, a sector of a bladed disk may be made of several blades. This is for example due to assembly methodology where the blades are grouped by packet and where the cyclic periodical property is lost for a sector made of one blade. An analysis performed for a given wave number yields modes with a mixed harmonic content. If the number of blades of the sector is equal to *M*, the sector is considered to be made of *M* subsectors. Each node of the finite element model of the first subsector is related to (*M-1*) nodes of the other subsectors. If the meshes of the subsectors are not identical, the displacements of these nodes are obtained by interpolation. The displacements are expressed in cylindrical coordinates in order to perform the harmonic decomposition.

$$\begin{bmatrix} 1 & 1 & \dots & 0 & 0 & \dots \\ \cos\beta_1 & \cos\beta_2 & \dots & -\sin\beta_1 & -\sin\beta_2 & \dots \\ \vdots & \vdots & \ddots & \vdots & \vdots & \ddots \\ \cos M\beta_1 & \cos M\beta_2 & \cdots & -\sin M\beta_1 & -\sin M\beta_2 & \cdots \\ \cos(M+1)\beta_1 & \cos(M+1)\beta_2 & \cdots & -\sin(M+1)\beta_1 & -\sin(M+1)\beta_2 & \ddots \\ \vdots & \vdots & \ddots & \vdots & \vdots & \end{bmatrix} \begin{bmatrix} u_1^R \\ u_2^R \\ \vdots \\ u_1^I \\ u_2^I \\ \vdots \end{bmatrix} = \begin{bmatrix} q_1^R \\ q_2^R \\ \vdots \\ q_1^R cos\beta - q_1^I sin\beta \\ q_2^R cos\beta - q_2^I sin\beta \\ \vdots \end{bmatrix} \quad (6)$$

Where

$$\begin{aligned} \beta &= \frac{2\pi n}{N} \\ \beta_1 &= \frac{2\pi n}{MN} \\ \beta_2 &= \frac{2\pi(N-n)}{MN} \\ \beta_3 &= \frac{2\pi(N+n)}{MN} \\ &\vdots \end{aligned} \quad (7)$$

This decomposition is performed for each node of the subsector. By weighting the obtained decomposed displacements with respect to the maximum displacement of the mode and by summing the weighted decompositions, it is possible to assign at each harmonic a percentage of its contribution to the mode. The process may be done for the radial, axial and azimuthal displacements. It is therefore possible to classify the modes as mainly radial, axial, azimuthal or mixed.

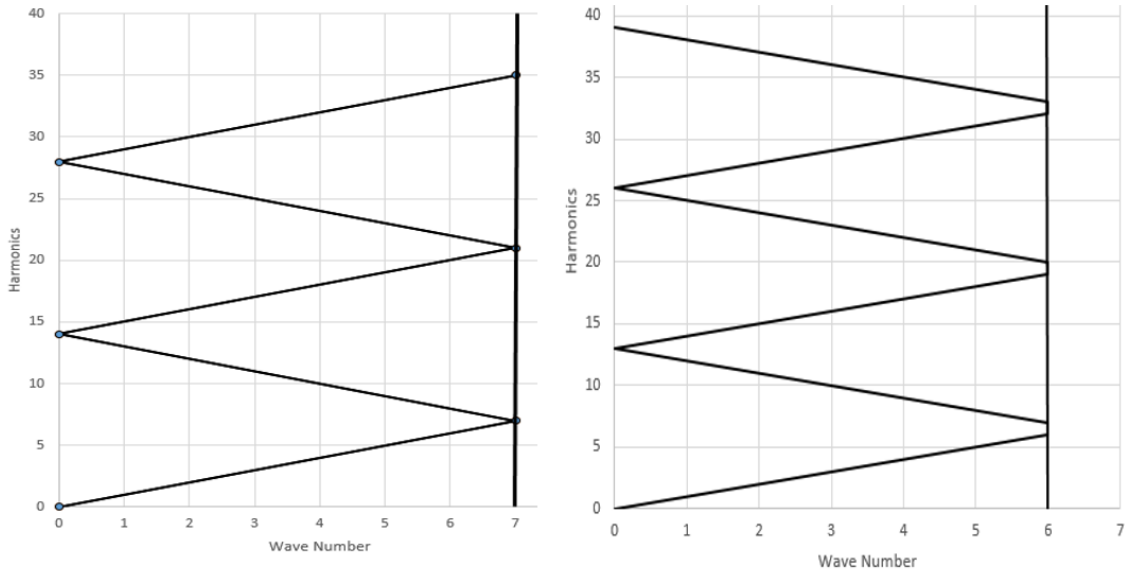


Figure 1: Zigzag Diagram (even or odd number of sectors)

2.3 Multi-Stage Cyclic Symmetry

The direct multi-stage cyclic symmetry has been proposed by Laxalde [2] and is, for example, implemented in the SAMCEF code [3]. The method is direct with respect to other approaches where each stage model is separately condensed and a reduced assembled multi stage model is analysed. With the direct method, the idea is to describe each stage *i* by its basic sector with the classical wave propagation condition applied on its left and right boundaries

$$- {}^{l}\mathbf{q}^{(i)} = e^{\frac{2j\pi n}{N_i}} {}^{r}\mathbf{q}^{(i)} = e^{j\beta_i} {}^{r}\mathbf{q}^{(i)} \tag{8}$$

Where ^{l} and ^{r} indexes correspond to the left and right boundaries of stage *i* made of N_i sectors. The **q** vectors are complex. The fundamental wave number (number of nodal diameters, engine order) *n* is the same for each stage. The fundamental wave number is bounded by the number of sectors N_{min} of the stage with the lower number of sectors. For the other stages, based on their number of sectors and on the fundamental wave number, additional wave numbers may be taken into account. These additional wave numbers are obtained from the zigzag diagram and are bounded by the number of sectors of the considered stage:

$$m = n, N_{min} - n, N_{min} + n, \cdots, kN_{min} - n, kN_{min} + n, \cdots, \leq {}^{N_i}/_{2} \tag{9}$$

It is then necessary to express the continuity of the displacement field at the inter-stage junction. Based on the number of sectors of each stage, the condition is either expressed on 360 degrees or on a sector. In order to manage industrial applications, the finite element meshes may not be congruent at the inter-stage junctions. In this case, the condition linking one node of stage 1 to a facet of stage 2 is written as follows

$$\mathbf{C}_1((j-1)\beta_1)\mathbf{q}^{s} = \mathbf{B}_1((k-1)\beta_2)\mathbf{q}^{m} \tag{10}$$

Where ^{s} and ^{m} indexes respectively correspond to the slave node and the master nodes of the facet. The **C** matrix rotates the slave node *(j-1)* times at a physical location where it is projected on a facet. The **B** matrix includes the *(k-1)* times rotation and the projection. Based on the numbers of sectors in stage 1 and 2, the same slave node will appear in *N* continuity constraints corresponding to different physical locations. On compact form, these constraints may be written

$$\mathbf{D}\mathbf{q}^{s} = \mathbf{A}\mathbf{q}^{M} \tag{11}$$

Where ^{M} index corresponds to all the master nodes necessary to define the N different facets used by the constraints.

In order to include these constraints in the cyclic symmetrical formalism, it is necessary to come back to the cyclic coordinates. As the **D** matrix is made of a set of rotation matrices, we have

$$\mathbf{q}^{s} = \frac{1}{N}\mathbf{D}^{T}\mathbf{A}\mathbf{q}^{M} \tag{12}$$

In practice, the mathematical constraint is applied using N gluing elements sharing the same Lagrangian multipliers. In the cyclic coordinates, the continuity at the inter-stage junction is only expressed in a weak form.

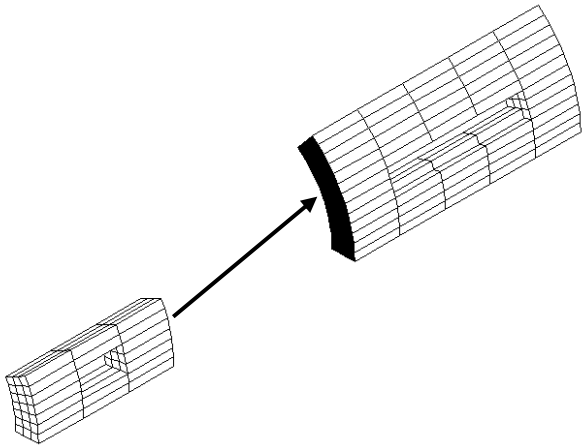


Figure 2 Two stages case with 7 and 13 sectors

If the finite element meshes are compatible at the inter-stage junction, equation (12) only expresses that the displacements of the slave node in cylindrical coordinates are the mean values of the displacements of a set of master nodes. This weak character of the constraint is related to the approximation of the method. The exact solution requires the use of several harmonics in order to express the continuity of the displacement field at the inter-stage junction.

For example, for a structure made of stages having different prime numbers of sectors as shown in figure 2, the final assembly is no longer isotropic with respect to the structure axis. Normal modes with nodal diameters don't anymore exist in orthogonal pairs. Assuming that each normal mode of the whole structure is only described by the contribution of one fundamental wave family per stage removes the asymmetry of the system. This assumption has to be kept in mind when using this method. Recombined results show that the continuity at the inter-stage junction is not respected when strong asymmetrical cases are considered.

If a Fourier harmonic decomposition of the obtained solution is performed, the application of (5) to the different stages where the numbers N_i of sectors are different gives different lists of harmonics. If some of these harmonics have an important contribution to the solution of one stage in the junction area and are missing in the coupled stage, the continuity of the solution may strongly be not respected at the inter-stage junction.

The harmonic decomposition described in section 2.2 may also be applied in multi-stage cyclic symmetry. In this case, an additional weighting is performed based on the contribution of each stage to the kinetic energy of the modes. For each stage, the harmonic content corresponds to

$$m_i = n, N_i - n, N_i + n, \cdots, kN_i - n, kN_i + n, \cdots \tag{13}$$

Where the number of harmonics is based on the number of subsectors of the stage.

2.4 Improved Multi-Stage Cyclic Symmetry

According to relation (13), the harmonic content usually differs from one stage to the other except for the fundamental harmonic. The improvement of the method consists to use several fundamental harmonics in the same analysis. For example, if the first additional harmonic of stage *i* has to be included, the additional fundamental harmonic is obtained as follows based on the zigzag diagram of the stage with the lower number of sectors.

$$n_{add} \pm kN_{min} = m_i = N_i - n \tag{14}$$

This procedure is repeated for each stage. In practice, adding a cyclic field for one sector corresponds to automatically duplicate the finite element model of the sector and to update the cyclic constraints on its boundaries by using the corresponding additional fundamental harmonic. The coupling between the harmonics is done by the inter-stage junctions.

$$\sum_{i=1}^{ns} \mathbf{C}_i\,((j-1)\beta_i)\mathbf{q}_i^s = \sum_{i=1}^{ms} \mathbf{B}_i\,((j-1)\beta_i)\mathbf{q}_i^s \tag{15}$$

Where *ns* is the number of fundamental harmonics of the slave stage and *ms* the number of fundamental harmonics of the master stage.

3 Applications

Let us consider an academic structure made of two stages with respectively 50 and 60 blades. It is the idealization of a bladed drum where the deformation of the drum induces coupling between both stages.

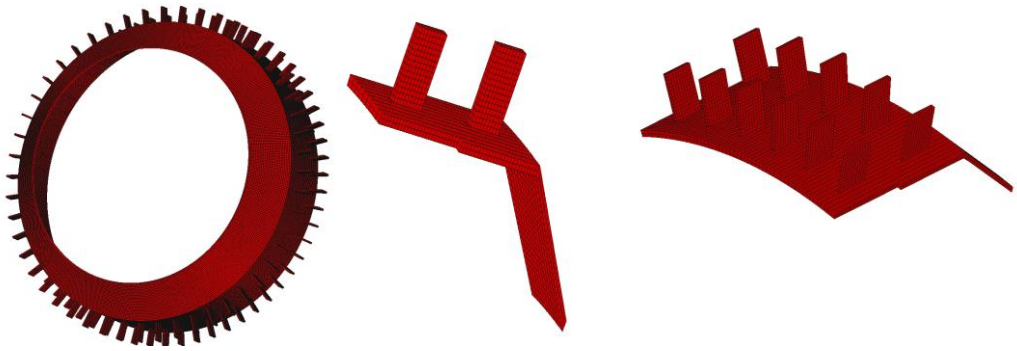


Figure 3 Two stages with 50 and 60 blades

The structure may either be modelled by one sector including 5 blades of stage 1 and 6 of stage 2 or be modelled by two sectors including one blade.

The mono-stage cyclic symmetry approach yields exact results used as reference. The standard multi-stage approach yields correct results for low frequencies and for modes where the main harmonic corresponds to the fundamental one (figure 4).

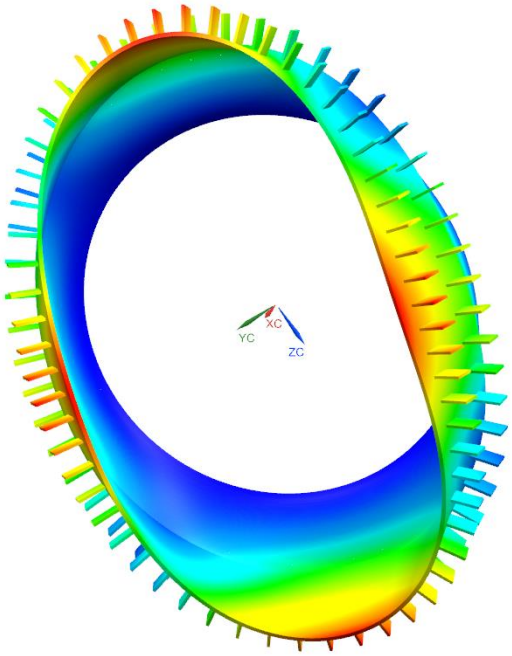


Figure 4 Low frequency correct mode

For higher frequencies and for some modes, the standard multi-stage approach produces approximated frequencies and discontinuity at the inter-stage junction (figure 5).

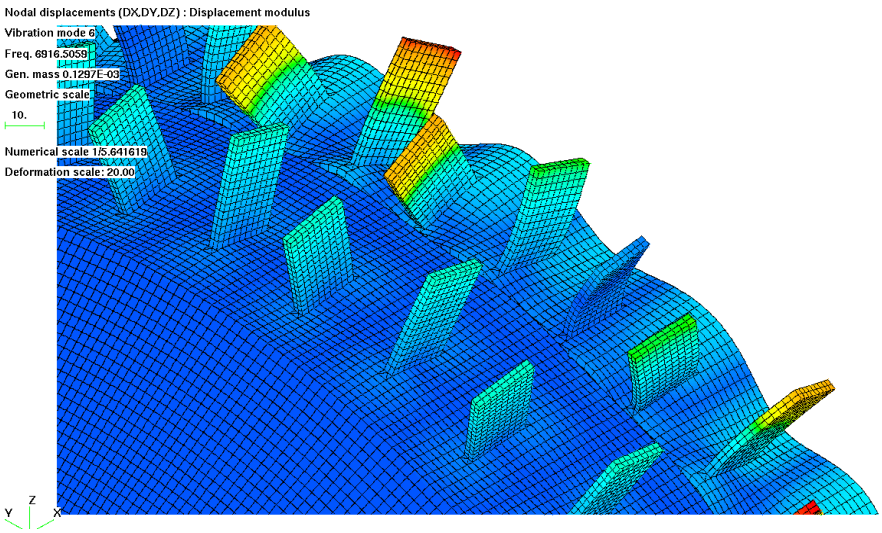


Figure 5 Harmonic 25 – 6925 Hz Approximation

By adding one fundamental harmonic, it is possible to reach the exact solution and to improve the continuity at the inter-stage junction (figure 6).

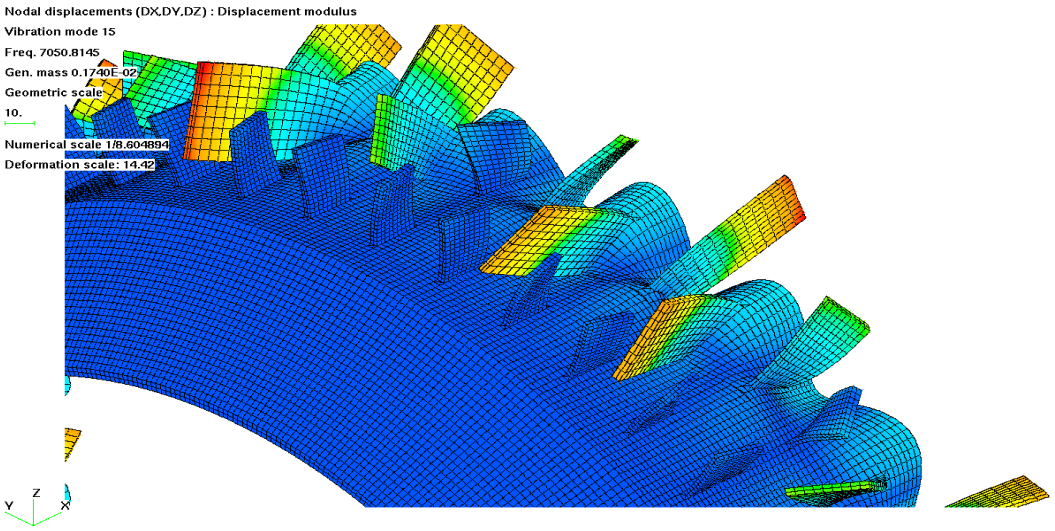


Figure 6 Harmonics 25 and 17 – 7050 Hz Exact

Conclusions

The extension of the multi-stage cyclic symmetry methodology has been presented. Its application to a simple two stages structure shows the efficiency and the interest of such method. When applied to rotors of turbo-machines like compressor rotors of aero-engine, this method allows the taking into account of 3D models at affordable computing costs.

The method has been integrated in the finite element system SAMCEF [3].

References

[1] Thomas, D.L., *Dynamics of rotationally periodic structures*, Int. J. for Num. Meth. In Eng., **14** (1979), pp. 81-102.

[2] Laxalde D., Thouverez F., Lombard J.P. *Dynamical analysis of multi-stage cyclic structures*, Mechanics Research Communications, Vol. **34,** Issue 4 (2007), pp 379-384.

[3] SAMCEF 18.1, Siemens PLM Software (2017)

Numerical and experimental vibration analysis of a two-pole induction motor mounted on an elastic machine test bed

S. Mathes[1], U. Werner[1], C. Bauer[2]
[1] University of Applied Sciences Georg Simon Ohm Nuremberg
Keßlerplatz 12, 90489, Nuremberg, Germany
e-mail: **sebastian.mathes@th-nuernberg.de**

[2] Siemens AG, Process Industries and Drives Division, Large Drives, Simulation
Vogelweiherstraße 1-15, 90441, Nuremberg, Germany

Abstract
This paper describes the analysis of natural and forced vibrations of a two-pole induction motor mounted on an elastic steel frame foundation. A simplified vibration model is derived which can be used for calculating the natural vibrations in the transversal plane of an electrical motor mounted on a soft foundation. The natural vibrations of the motor are calculated using the simplified vibration model as well as a numerical calculation using a finite element model. These calculations are compared to each other and validated by measurements using experimental modal analysis. In addition to the natural frequencies, also forced vibrations are measured while the motor is operated by a converter. The frequency spectrum is analyzed by using FFT, regarding the forced vibrations.

1 Introduction

Vibration problems often occur for induction motors in the upper power range (> 1 MW). The most common reason is that large induction motors are usually designed for operation on a massive foundation, but in the application, the motors are often mounted on an elastic steel frame (Figure 1). Therefore, the vibrational behavior of the motor changes completely, compared to the measurements, carried out at the motor manufacturer, where the motor is mounted on a massive foundation [1-3]. The electrical motors are tested on a massive foundation because the vibrations of the motor itself shall be proved. The problem now is, that a motor which runs perfectly on a massive foundation may show high vibrations when it is mounted on a steel frame foundation and operated near or in resonances.

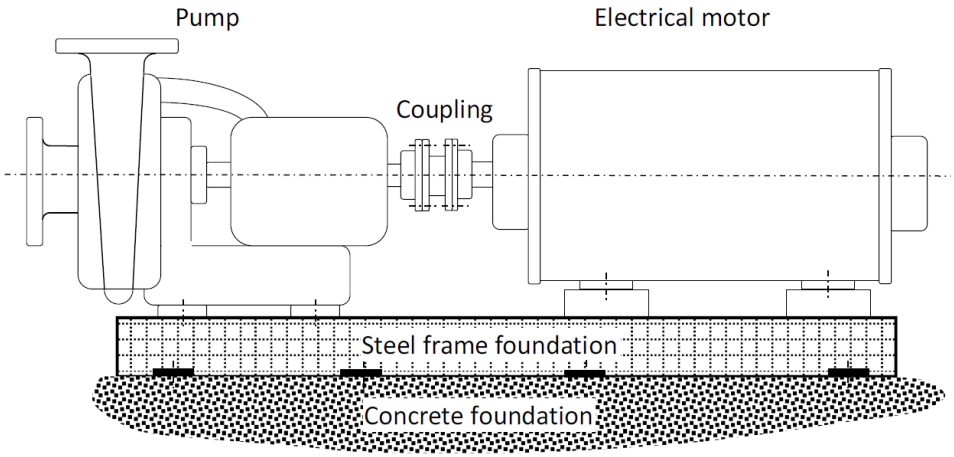


Figure 1: Powertrain mounted on an elastic steel frame foundation [4]

The idea now is to solve this problem by using an active vibration control system, where actuators are mounted between the motor feet and the steel frame foundation (Figure 2), to influence the vibration behavior actively [4], [5]. Since the investigation of the concept for an induction motor with a power of 1 MW and higher is difficult, the concept is first examined using a small induction motor. For the small motor similar conditions have to be created such as for huge motors, because this vibration problems usually occur only for motors with high power. Therefore, a machine test bed consisting of a small two-pole induction motor (11 kW) and a steel frame foundation was developed which can be extended by actuators later. To check the suitability of the machine test bed, natural vibrations as well as forced vibrations are investigated.

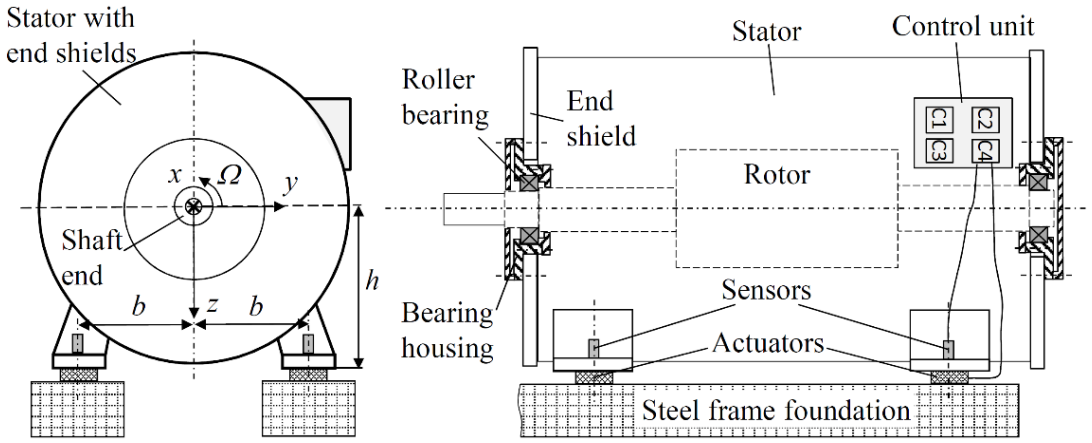


Figure 2: Electrical motor with actuators between the motor feet and elastic steel frame foundation [5]

2 Rotor eccentricities

Different kinds of excitations exist which cause vibrations in electrical motors. In addition to mechanical excitation there are also electromagnetic forces. The cause for these excitations is often rotor eccentricity. Generally there are two different kinds of rotor eccentricity, static eccentricity and dynamic eccentricity [6]. The difference between both is, that the smallest air gap remains at the same position for static eccentricity and changes for dynamic eccentricity (Figure 3).

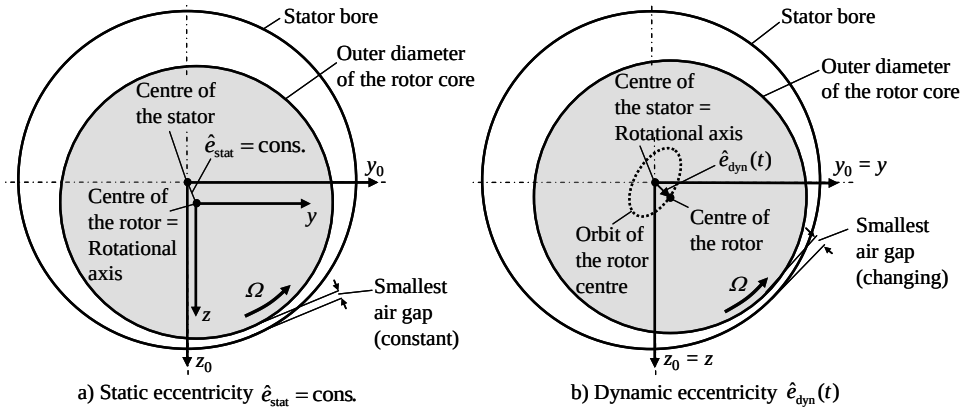


Figure 3: Two different kinds of eccentricity. a) Static eccentricity and b) dynamic eccentricity [6]

2.1 Static eccentricity

Reference [7] shows a number of reasons causing static rotor eccentricity in electrical motors with roller bearings. The most common reasons are production tolerances (Figure 4a), radial bearing clearance (Figure 4b) and static deflection (Figure 4c).

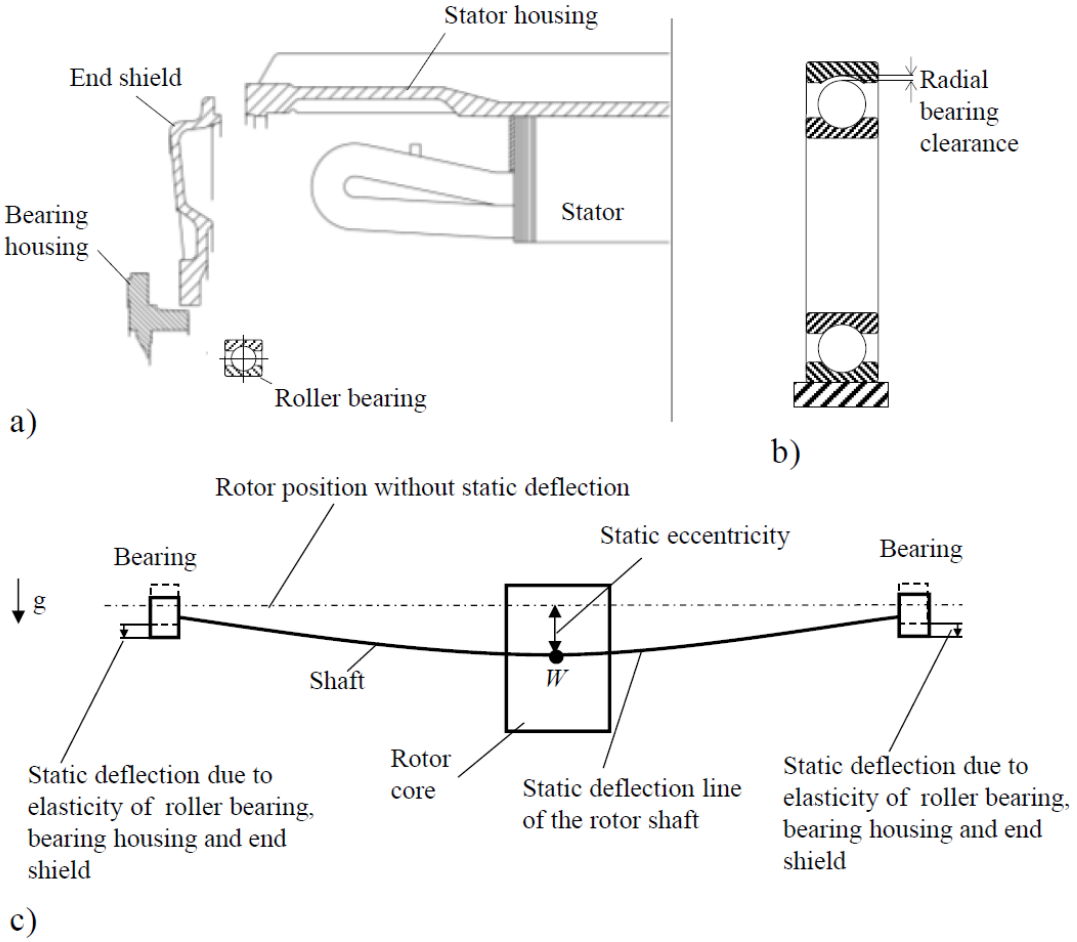


Figure 4: Static rotor eccentricities of an electrical motor caused by a) production tolerances, b) radial bearing clearance, c) static deflection [7]

Static rotor eccentricity leads to an unequal air gap in the induction motor and results in an electromagnetic force – which acts between rotor and stator – oscillating with double angular supply frequency $2 \cdot \omega_1$ [7-9]. For two-pole induction motors (pole pair number: $p = 1$) the double angular supply frequency $2 \cdot \omega_1$ can be assumed to be equal to the 2x rotational angular frequency ($2 \cdot \Omega$) of the rotor when the slip is very small ($s << 1$) [7]. This is the case when the motor is operated in steady state.

$$\Omega = \frac{\omega_1 \cdot (1 - s)}{p} \quad \xrightarrow{p = 1;\, s \approx 0} \quad \Omega \approx \omega_1 \tag{1}$$

Thus the excitation angular frequency ω_F of the oscillating magnetic force becomes [7]:

$$\omega_F = 2 \cdot \omega_1 \approx 2 \cdot \Omega \tag{2}$$

2.2 Dynamic eccentricity

There are different kinds of dynamic eccentricity in electrical motors. The most important are eccentricity of rotor mass (Figure 5a), magnetic eccentricity (Figure 5b) and bent rotor deflection (Figure 5c) [4]. Eccentricity of rotor mass results in mechanical unbalance. This is caused e.g. by residual unbalance, which remains in the rotor after balancing. Magnetic eccentricity e.g. is caused by a deviation of concentricity between the inner and outer diameter of the rotor core. Bent rotor deflection e.g. is caused by unequal thermal expansion of the rotor or plastic deformation of the shaft. All these excitations occur with rotor angular frequency Ω.

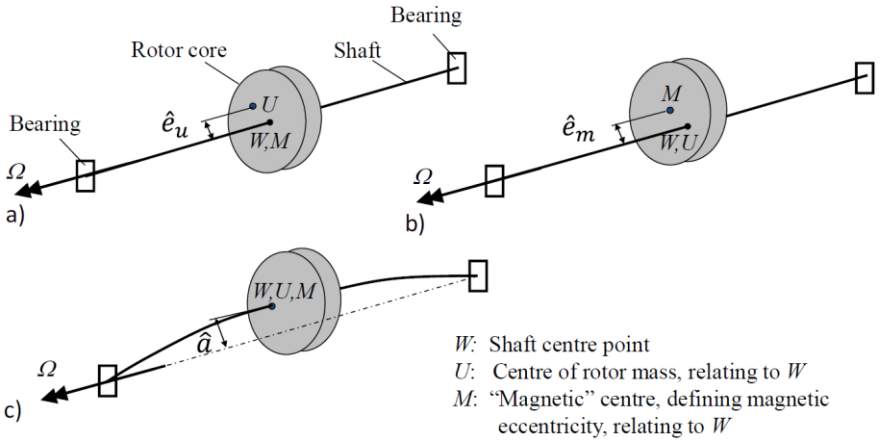


Figure 5: Dynamic rotor eccentricities of an electrical motor caused by a) eccentricity of rotor mass, b) magnetic eccentricity, c) bent rotor deflection [4]

3 Analytical vibration model

First a theoretical investigation of the natural vibration behavior of the motor on an elastic steel frame foundation is done. In [10] a simplified analytical vibration model is used for calculating the natural vibrations in the transversal plane (yz plane) of an electrical motor mounted on a soft foundation. It is shown, that the used vibration model shows good results regarding the calculation of the natural vibration behavior. Since the motor of the machine test bed is mounted on a steel frame foundation and therefore the motor is mounted on a soft foundation, a similar vibration model following [10] is used to calculate the natural vibrations. Reference [10] has shown that the angular foundation stiffness has nearly no influence on the natural frequencies and thus the angular foundation stiffness is neglected in the analytical vibration model (Figure 6) of this paper. In the analytical vibration model from [10] the mass of the foundation is neglected because the mass of the foundation is much lower than the mass of the motor in that case. However, for the machine test bed the masses of motor and foundation (steel frame foundation) are in the same range. To investigate the influence of the mass of the foundation on the natural vibrations, the natural frequencies are calculated once with and without the mass of the foundation.

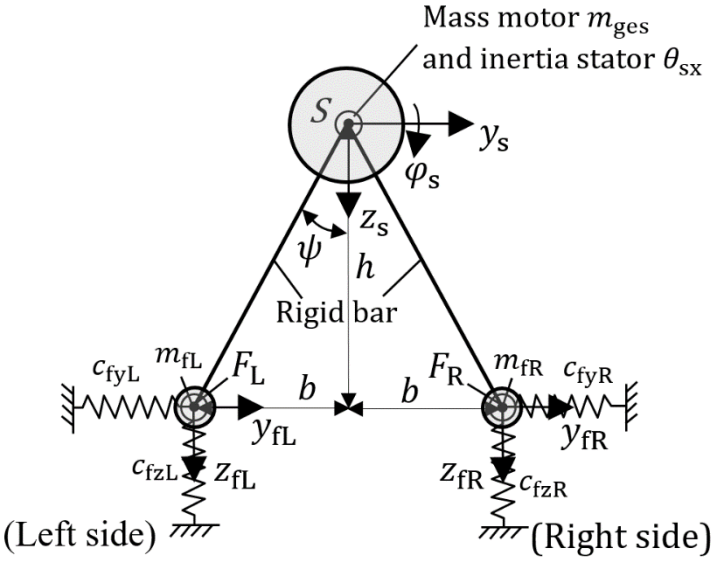


Figure 6: Vibration model of an electrical motor mounted on a soft foundation (Based on [10])

The mass m_{ges} of the motor is concentrated at the centre of gravity S and has the inertia θ_{sx}. The inertia θ_{sx} is only the inertia of the stator, because the rotor must be free to rotate around the x-axis. The structure of the motor is assumed to be rigid compared to the soft foundation. This assumption is only valid when the

motor is mounted on a soft foundation or on soft rubber elements. The points F_L (L: left side) and F_R (R: right side) describe the foundation points, where the motor feet are fixed to the foundation and where the modal masses of the foundation m_{fL} and m_{fR} are positioned. The foundation stiffness is described by the stiffness coefficients c_{fyL}, c_{fyR}, c_{fzL} and c_{fzR} and the damping of the foundation is neglected, because it has only a small influence on the natural frequencies. Three fixed coordinate systems are included in the vibration model. The movement of the mass m_{ges} is described by the coordinate system (z_s, y_s, φ_s) which is positioned in the point *S*. The coordinate system (z_{fL}, y_{fL}) is positioned in the point F_L and describes the movement of the mass m_{fL} and the left motor foot. The movement of the mass m_{fR} and right motor foot is described by the coordinate system (z_{fR}, y_{fR}) which is positioned in the point F_R.

4 Mathematical description

To derive the mathematical description, the vibration system is cut free (Figure 7) and the equilibriums of forces and moments have to be analyzed.

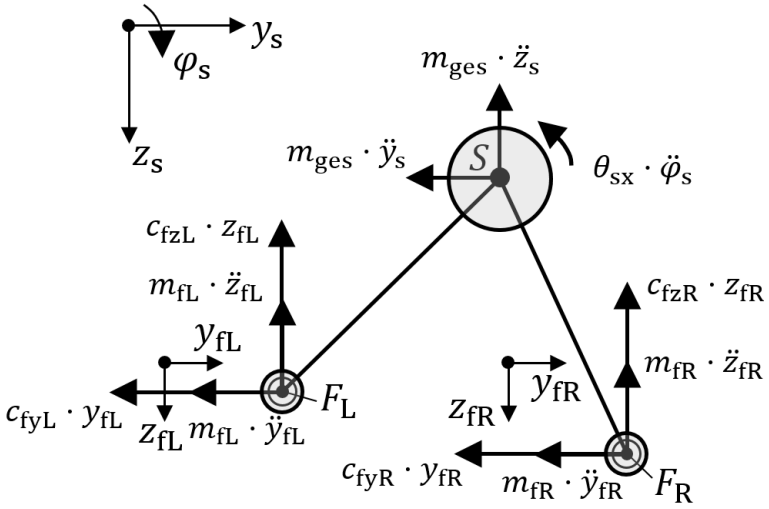


Figure 7: Vibration system cut free

Equilibrium of forces in vertical direction:

$$m_{ges} \cdot \ddot{z}_s + m_{fL} \cdot \ddot{z}_{fL} + m_{fR} \cdot \ddot{z}_{fR} + c_{fzL} \cdot z_{fL} + c_{fzR} \cdot z_{fR} = 0 \tag{3}$$

Equilibrium of forces in horizontal direction:

$$m_{ges} \cdot \ddot{y}_s + m_{fL} \cdot \ddot{y}_{fL} + m_{fR} \cdot \ddot{y}_{fR} + c_{fyL} \cdot y_{fL} + c_{fyR} \cdot y_{fR} = 0 \tag{4}$$

Equilibrium of moments around *S*:

$$\begin{aligned} &\theta_{sx} \cdot \ddot{\varphi}_s + m_{fR} \cdot \ddot{z}_{fR} \cdot b + c_{fzR} \cdot z_{fR} \cdot b - m_{fR} \cdot \ddot{y}_{fR} \cdot h - c_{fyR} \cdot y_{fR} \cdot h \\ &- m_{fL} \cdot \ddot{z}_{fL} \cdot b - c_{fzL} \cdot z_{fL} \cdot b - m_{fL} \cdot \ddot{y}_{fL} \cdot h - c_{fyL} \cdot y_{fL} \cdot h = 0 \end{aligned} \tag{5}$$

Due to the small displacements of the motor mass z_s, y_s, φ_s, compared to the dimensions of the motor *h*, *b*, ψ, an linearization is possible. The displacements of the mass from the foundation z_{fL}, z_{fR}, y_{fL}, y_{fR} can be described by the displacements of the stator mass z_s, y_s, φ_s: [10]

$$z_{fL} = z_s - \varphi_s \cdot b \qquad z_{fR} = z_s + \varphi_s \cdot b \tag{6}$$

$$y_{fL} = y_s - \varphi_s \cdot h \qquad y_{fR} = y_s - \varphi_s \cdot h \tag{7}$$

Foundations are usually designed, that the mass and the stiffness is identical for both sides and following additional simplifications can be made:

$$m_{fL} = m_{fR} = m_f \qquad c_{fzL} = c_{fzR} = c_{fz} \qquad c_{fyL} = c_{fyR} = c_{fy} \tag{8}$$

With the kinematic constraints, the movement of the masses from the foundation can be described by the movement of the centre of gravity. The equations (6) and (7) are inserted in the equations (3) – (5) and the simplifications in (8) are applied, so the following equations can be deduced:

Equilibrium of forces in vertical direction:

$$m_{\mathrm{ges}} \cdot \ddot{z}_{\mathrm{s}} + m_{\mathrm{f}} \cdot \left(\ddot{z}_{\mathrm{s}} - \ddot{\varphi}_{\mathrm{s}} \cdot b\right) + m_{\mathrm{f}} \cdot \left(\ddot{z}_{\mathrm{s}} + \ddot{\varphi}_{\mathrm{s}} \cdot b\right) + c_{\mathrm{fz}} \cdot \left(z_{\mathrm{s}} - \varphi_{\mathrm{s}} \cdot b\right) + c_{\mathrm{fz}} \cdot \left(z_{\mathrm{s}} + \varphi_{\mathrm{s}} \cdot b\right) = 0 \tag{9}$$

Equilibrium of forces in horizontal direction:

$$m_{\mathrm{ges}} \cdot \ddot{y}_{\mathrm{s}} + m_{\mathrm{f}} \cdot \left(\ddot{y}_{\mathrm{s}} - \ddot{\varphi}_{\mathrm{s}} \cdot h\right) + m_{\mathrm{f}} \cdot \left(\ddot{y}_{\mathrm{s}} - \ddot{\varphi}_{\mathrm{s}} \cdot h\right) + c_{\mathrm{fy}} \cdot \left(y_{\mathrm{s}} - \varphi_{\mathrm{s}} \cdot h\right) + c_{\mathrm{fy}} \cdot \left(y_{\mathrm{s}} - \varphi_{\mathrm{s}} \cdot h\right) = 0 \tag{10}$$

Equilibrium of moments around *S*:

$$\begin{aligned} &\theta_{\mathrm{sx}} \cdot \ddot{\varphi}_{\mathrm{s}} + m_{\mathrm{f}} \cdot \left(\ddot{z}_{\mathrm{s}} + \ddot{\varphi}_{\mathrm{s}} \cdot b\right) \cdot b + c_{\mathrm{fz}} \cdot \left(z_{\mathrm{s}} + \varphi_{\mathrm{s}} \cdot b\right) \cdot b - m_{\mathrm{f}} \cdot \left(\ddot{y}_{\mathrm{s}} - \ddot{\varphi}_{\mathrm{s}} \cdot h\right) \cdot h - c_{\mathrm{fy}} \cdot \left(y_{\mathrm{s}} - \varphi_{\mathrm{s}} \cdot h\right) \cdot h \\ &- m_{\mathrm{f}} \cdot \left(\ddot{z}_{\mathrm{s}} - \ddot{\varphi}_{\mathrm{s}} \cdot b\right) \cdot b - c_{\mathrm{fz}} \cdot \left(z_{\mathrm{s}} - \varphi_{\mathrm{s}} \cdot b\right) \cdot b - m_{\mathrm{f}} \cdot \left(\ddot{y}_{\mathrm{s}} - \ddot{\varphi}_{\mathrm{s}} \cdot h\right) \cdot h - c_{\mathrm{fy}} \cdot \left(y_{\mathrm{s}} - \varphi_{\mathrm{s}} \cdot h\right) \cdot h = 0 \end{aligned} \tag{11}$$

Based on the equilibrium of forces and moments, following homogenous differential equations system can be derived with the mass matrix **M**, the stiffness matrix **C** and the coordinate vector **q**:

$$\mathbf{M} \cdot \ddot{\mathbf{q}} + \mathbf{C} \cdot \mathbf{q} = \mathbf{0} \tag{12}$$

The homogenous differential system becomes:

$$\begin{pmatrix} m_{\mathrm{ges}} + 2 \cdot m_{\mathrm{f}} & 0 & 0 \\ 0 & m_{\mathrm{ges}} + 2 \cdot m_{\mathrm{f}} & -2 \cdot m_{\mathrm{f}} \cdot h \\ 0 & -2 \cdot m_{\mathrm{f}} \cdot h & \theta_{\mathrm{sx}} + 2 \cdot m_{\mathrm{f}} \cdot \left(b^2 + h^2\right) \end{pmatrix} \cdot \begin{pmatrix} \ddot{z}_{\mathrm{s}} \\ \ddot{y}_{\mathrm{s}} \\ \ddot{\varphi}_{\mathrm{s}} \end{pmatrix} + \begin{pmatrix} 2 \cdot c_{\mathrm{fz}} & 0 & 0 \\ 0 & 2 \cdot c_{\mathrm{fy}} & -2 \cdot c_{\mathrm{fy}} \cdot h \\ 0 & -2 \cdot c_{\mathrm{fy}} \cdot h & 2 \cdot \left(c_{\mathrm{fz}} \cdot b^2 + c_{\mathrm{fy}} \cdot h^2\right) \end{pmatrix} \cdot \begin{pmatrix} z_{\mathrm{s}} \\ y_{\mathrm{s}} \\ \varphi_{\mathrm{s}} \end{pmatrix} = \begin{pmatrix} 0 \\ 0 \\ 0 \end{pmatrix} \tag{13}$$

It can be seen from the differential equation system that it can be split into two independent differential equation systems. One system describes the vertical movement and one system the horizontal and angular movement.

The translation z_{s} of the centre of gravity without horizontal and angular movement ($y_{\mathrm{s}} = 0$; $\varphi_{\mathrm{s}} = 0$) can be described by:

$$\left(m_{\mathrm{ges}} + 2 \cdot m_{\mathrm{f}}\right) \cdot \ddot{z}_{\mathrm{s}} + 2 \cdot c_{\mathrm{fz}} \cdot z_{\mathrm{s}} = 0 \tag{14}$$

In vertical direction only one natural angular frequency occurs:

$$\omega_{0,\,\mathrm{z},\,1} = \sqrt{\frac{2 \cdot c_{\mathrm{fz}}}{m_{\mathrm{ges}} + 2 \cdot m_{\mathrm{f}}}} \tag{15}$$

Figure 8 shows the mode shape of the natural frequency in vertical direction. Here only a vertical translation occurs.

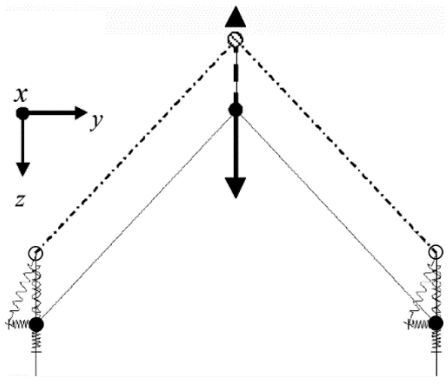


Figure 8: Mode shape in vertical direction (Based on [11])

The horizontal translation y_s and rotation φ_s of the centre of gravity S without vertical translation ($z_s = 0$) can be described by:

$$\begin{pmatrix} m_{ges} + 2 \cdot m_f & -2 \cdot m_f \cdot h \\ -2 \cdot m_f \cdot h & \theta_{sx} + 2 \cdot m_f \cdot \left(b^2 + h^2\right) \end{pmatrix} \cdot \begin{pmatrix} \ddot{y}_s \\ \ddot{\varphi}_s \end{pmatrix} + \begin{pmatrix} 2 \cdot c_{fy} & -2 \cdot c_{fy} \cdot h \\ -2 \cdot c_{fy} \cdot h & 2 \cdot \left(c_{fz} \cdot b^2 + c_{fy} \cdot h^2\right) \end{pmatrix} \cdot \begin{pmatrix} y_s \\ \varphi_s \end{pmatrix} = \begin{pmatrix} 0 \\ 0 \end{pmatrix} \tag{16}$$

Here also a differential equation system in the form $\mathbf{M} \cdot \ddot{\mathbf{q}} + \mathbf{C} \cdot \mathbf{q} = \mathbf{0}$ occurs. The formulation with the eigenvalue λ and eigenvector $\mathbf{q}$

$$\mathbf{q} = \hat{\mathbf{q}} \cdot e^{\lambda \cdot t} \tag{17}$$

results in the eigenvalue equation:

$$\left[\mathbf{C} + \lambda^2 \cdot \mathbf{M}\right] \cdot \hat{\mathbf{q}} = \mathbf{0} \tag{18}$$

To determine the eigenvalues of the differential equation the determination equation is established:

$$\det\left[\mathbf{C} + \lambda^2 \cdot \mathbf{M}\right] = 0 \tag{19}$$

In contrast to the vertical translation, in horizontal direction two natural angular frequencies occur:

$$\omega_{0,\,y\varphi,\,1} = \sqrt{\frac{B - \sqrt{B^2 - 4 \cdot A \cdot C}}{2 \cdot A}} \tag{20}$$

$$\omega_{0,\,y\varphi,\,2} = \sqrt{\frac{B + \sqrt{B^2 - 4 \cdot A \cdot C}}{2 \cdot A}} \tag{21}$$

With:

$A = m_{ges} \cdot \left(\theta_{sx} + 2 \cdot m_f \cdot b^2\right) + 2 \cdot m_f \cdot \left(m_{ges} \cdot h^2 + \theta_{sx} + 2 \cdot m_f \cdot b^2\right)$

$B = 2 \cdot \left(c_{fy} \cdot \theta_{sx} + 2 \cdot m_f \cdot b^2 \cdot \left(c_{fy} + c_{fz}\right) + m_{ges} \cdot \left(c_{fy} \cdot h^2 + c_{fz} \cdot b^2\right)\right)$

$C = 4 \cdot c_{fy} \cdot c_{fz} \cdot b^2$

Figure 9 shows the mode shapes of the horizontal angular frequencies. In both mode shapes a horizontal translation occurs, coupled with a rotation around the x-axis. In the first mode shape (Figure 9a) translation and rotation are inphase, in the second mode shape (Figure 9b) translation and rotation are out of phase.

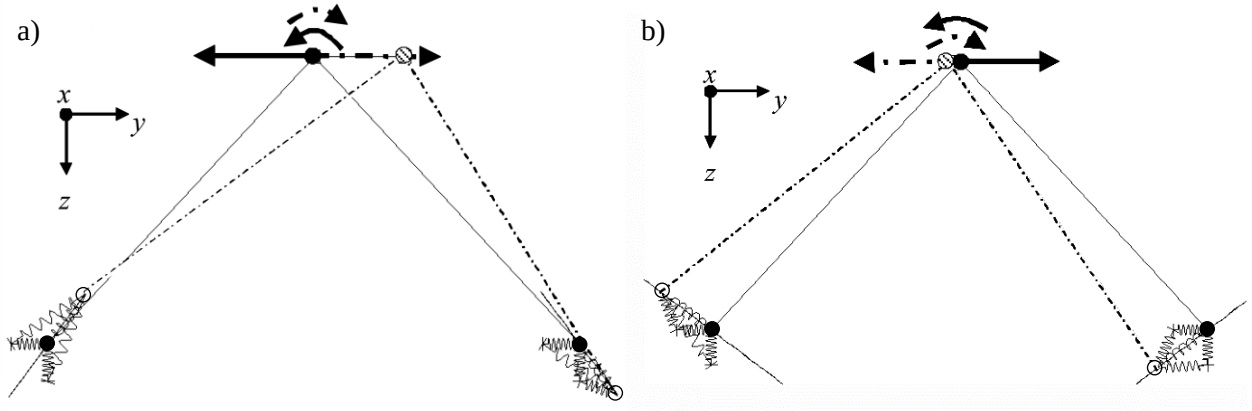


Figure 9: Mode shapes in horizontal direction (Based on [11])

5 Machine test bed

The machine test bed (Figure 10) which was developed consists of a two-pole induction motor (Table 1) which is mounted on a steel frame foundation and this system is mounted on a machine bed foundation. The steel frame foundation consists of two square hollow profiles to which the motor is screwed. The motor is mounted on the steel frame foundation so the motor feet are in the middle of the hollow profiles with regard to the front view of the shaft. The steel frame foundation is designed so that a second motor can be mounted on the steel frame and coupled to the induction motor later. Therefore, the concept for active vibration damping can also be tested for a whole powertrain. The machine test bed was developed, so three natural frequencies occur in the operating speed range of the motor and they can be excited by 1x-excitation. Since it was difficult to reduce the natural frequencies so that they occur in the speed range of the motor, another special design, regarding the mounting of the motor feet was necessary. In [10] it is shown that natural frequencies of a motor on a soft foundation can be strongly influenced by varying the contact area between the motor feet and the foundation. Therefore, steel blocks were placed between the motor feet and the steel frame to reduce the contact area and thus the natural frequencies. Since the machine test bed should mainly be used stationary, the square hollow profiles were mounted on a huge steel plate and screwed to it. This system – consisting of motor, steel frame and steel plate – is anchored to a machine bed foundation with clamping claws. The machine bed foundation itself is mounted on soft rubber elements which decouple the machine bed foundation from concrete foundation with regard to vibrations.

Data of the two-pole induction motor		
Rated power	P_N	11 kW
Rated voltage in star connection	U_N in Y	400 V
Rated current in star connection	I_N in Y	21.2 A
Rated speed	n_N	2915 1/min
Rated frequency	f_N	50 Hz
Limiting frequency	f_{max}	80 Hz
Mass of the motor	m_{ges}	62 kg
Moment of inertia of the stator	θ_{sx}	0.5055 kg·m²
Distance between feet	$2b$	254 mm
Height of the centre of gravity	h	158 mm
Data of the steel frame foundation		
Square hollow profile	EN 10219	150 x 100 x 3
Height of the profile	h_p	100 mm
Width of the profile	b_p	150 mm
Thickness of the profile	s_p	3 mm
Length of the profile	l_p	1100 mm
Width of the steel blocks	b_{sb}	20 mm
Length of the steel blocks	l_{sb}	20 mm
Modal mass of the foundation per side (identical for both sides)	$m_{fL} = m_{fR}$	2.15 kg
Substitute foundation stiffness vertical direction per side (identical for both sides)	$c_{fzL} = c_{fzR}$	4.47 kN/mm
Substitute foundation stiffness horizontal direction per side (identical for both sides)	$c_{fyL} = c_{fyR}$	5.2 kN/mm

Table 1: Data of the two-pole induction motor and data of the steel frame foundation

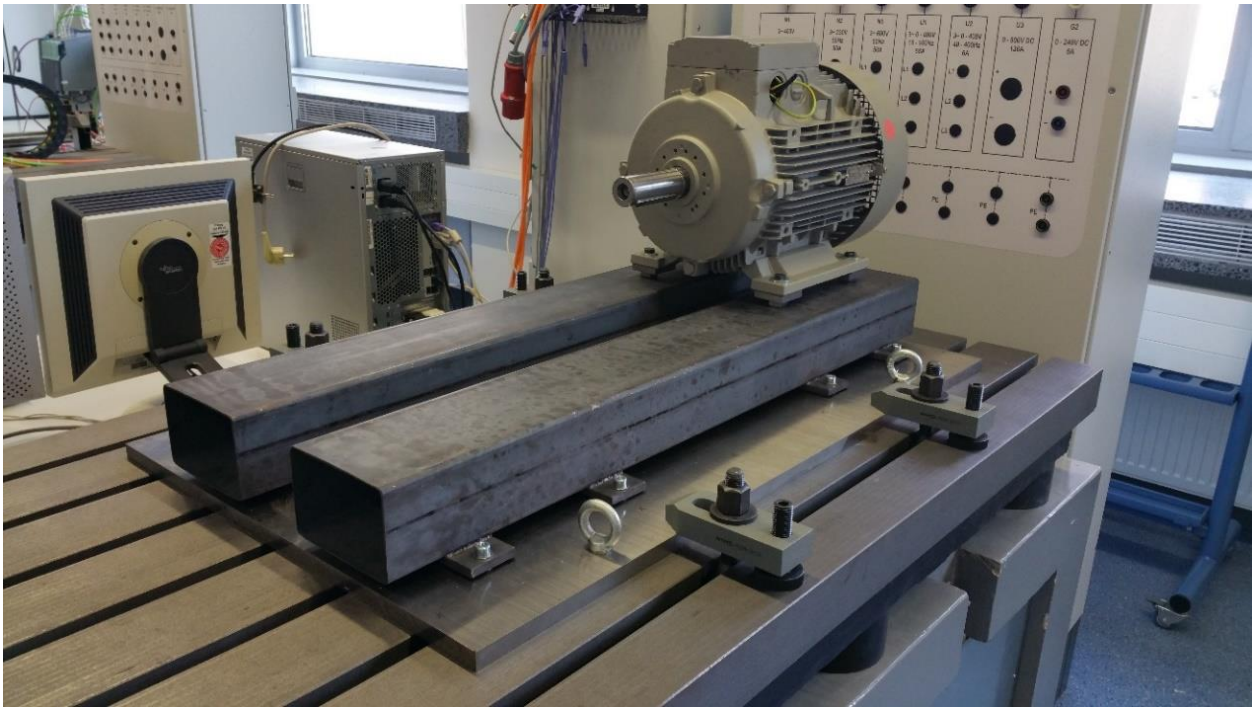


Figure 10: Machine test bed: Two-pole induction motor on steel frame foundation and machine bed foundation

6 Semi-analytical calculation of natural frequencies

The natural frequencies of the machine test bed are determined in this chapter. Therefore, the analytical vibration model from chapter 3 is used to calculate the natural frequencies semi-analytically. The calculation is named semi-analytical because the foundation stiffness coefficients c_{fyL}, c_{fyR}, c_{fzL} and c_{fzR} were derived using numerical calculation, like it is shown in [10]. Also the modal masses of the foundation m_{fL} and m_{fR} were determined with finite element calculation, so the calculation of the natural frequencies according to chapter 4 is not only analytical. Table 1 shows the data of the motor and the foundation which are used for the analytical vibration model. Since the derivation of the modal masses from the foundation is usually very difficult, a simplified finite element model was used to determine the modal masses of the foundation roughly. To investigate the influence of the modal masses from the foundation to the natural frequencies, the natural frequencies are calculated once with and without ($m_f = 0$) the masses of the foundation (Table 2). The results show, there is a small deviation (< 4 %) in the first two natural frequencies when considering and neglecting the modal masses of the foundation. For the third natural frequency, the values clearly differ from each other. The deviation for mode 3 is about 18 %.

Mode	Mode shape	Natural frequency considering foundation mass	Natural frequency neglecting foundation mass
1	Horizontal translation coupled with rotation at the x-axis (inphase)	36 Hz	36.4 Hz
2	Vertical translation	58.4 Hz	60.4 Hz
3	Horizontal translation coupled with rotation at the x-axis (out of phase)	128.9 Hz	152.2 Hz

Table 2: Natural frequencies of the analytical vibration model considering and neglecting foundation mass

7 Numerical analysis of natural vibrations

To validate the results from the semi-analytical calculation, a complete three dimensional finite element model of the machine test bed (Figure 11) is used. The soft rubber elements under the machine bed foundation are implemented in the finite element model using substitute stiffnesses by springs in x-, y-, and z-direction. The concrete foundation under the rubber elements is not considered in the model, because it has nearly no influence regarding the vibrations. The values for the substitute stiffnesses of the rubber elements were derived using experimental modal analysis. For this, the natural frequencies of the machine bed foundation itself – without motor and steel frame foundation – mounted on the rubber elements were determined. So this system can be assumed simplified as one mass oscillator and the substitute stiffnesses of the rubber elements were derived from the natural frequencies of the rigid body modes of the machine bed foundation.

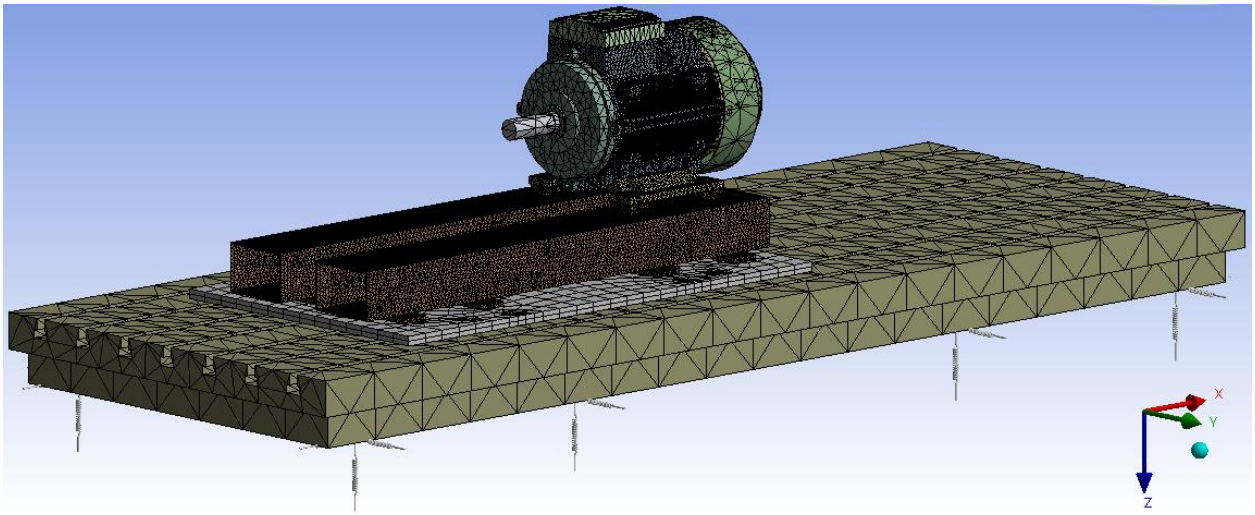


Figure 11: Finite element model of the whole System: Machine bed foundation with induction motor and steel frame foundation

Figure 12 shows the first four mode shapes of the whole system, where the motor performs the main movement. Table 3 shows the corresponding natural frequencies. Before the first mode of the motor occurs, six rigid body modes – translation in x-, y- and z-direction and rotation around the x-, y- and z-axis – of the machine test bed occur. There the whole system – motor, steel frame foundation and machine bed foundation – moves nearly as rigid body. However, this paper only focuses only on the mode shapes where the deformation of the steel frame is dominant. In the first mode (Figure 12a) a rotation of the motor around the transverse axis (y-axis), coupled with an axial translation (x-direction) occurs at a frequency of 31.4 Hz. In the second mode (Figure 12b) the motor performs a horizontal translation (y-direction), coupled with a rotation around the rotor axis (x-axis) at a frequency of 37.1 Hz. In the third mode (Figure 12c) a vertical translation (z-direction) of the motor occurs at a frequency of 53.9 Hz. The fourth mode (Figure 12d) occurs at a frequency of 114 Hz. In the fourth mode the motor performs a horizontal translation (y-direction), coupled with a rotation around the rotor axis (x-axis). However, the translation and rotation are out of phase.

Mode	Mode shape	Natural frequency
1	Axial translation coupled with rotation at the y-axis	31.4 Hz
2	Horizontal translation coupled with rotation at the x-axis (inphase)	37.1 Hz
3	Vertical translation	53.9 Hz
4	Horizontal translation coupled with rotation at the x-axis (out of phase)	114 Hz

Table 3: Natural frequencies calculated with the finite element model

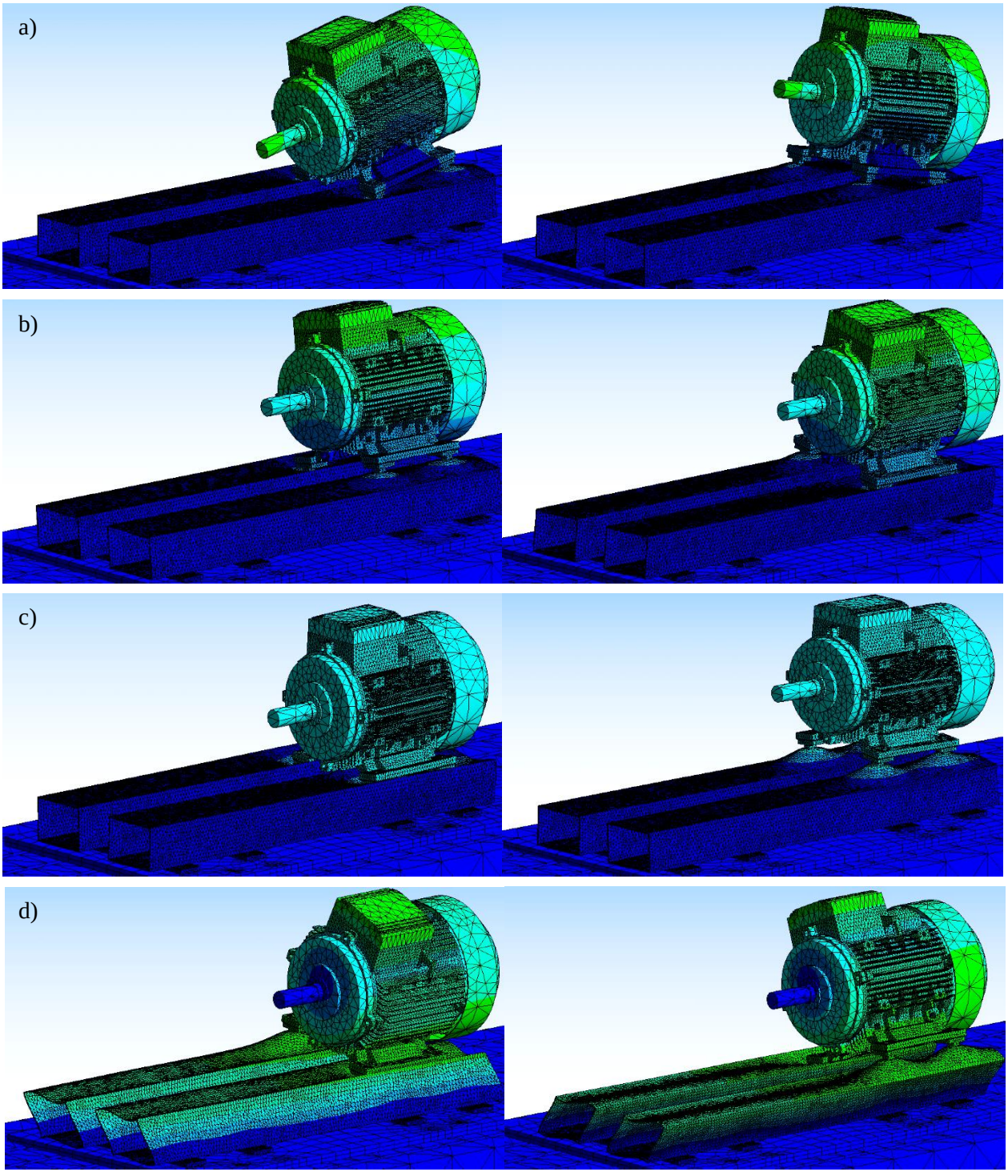


Figure 12: Mode shapes finite element model: a) mode 1; b) mode 2; c) mode 3; d) mode 4

8 Experimental analysis of natural vibrations

After the theoretical investigation of the natural vibration behavior of the machine test bed, experimental modal analysis is used to validate the simulation results and results from the semi-analytical calculation. The result of the experimental modal analysis is the transfer function of the system. Figure 13 shows exemplary the amplitude and phase response of the system in horizontal direction. From the transfer function the natural frequencies of the system can be determined on the basis of the resonances. Here in horizontal

direction, two dominant resonances occur. The first dominant resonance is the natural frequency of mode 2 and the second dominant resonance is the natural frequency of mode 4. Table 4 shows the natural frequencies of the first four modes of the motor.

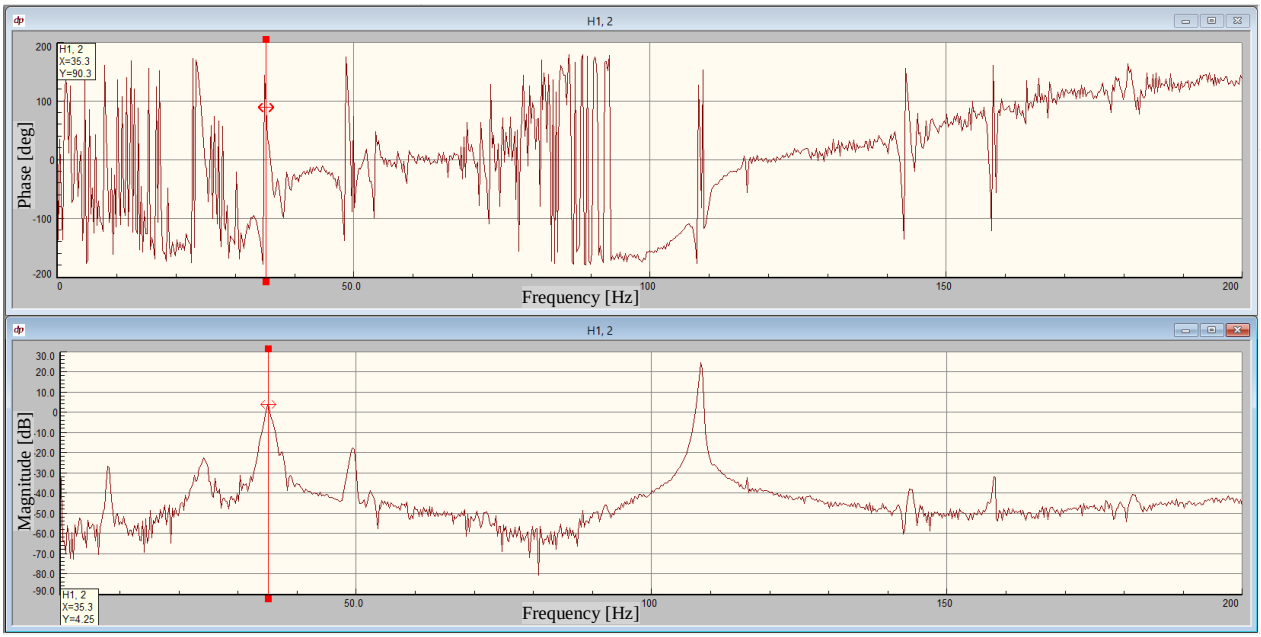


Figure 13: Amplitude and phase response of the experimental modal analysis in horizontal direction

Mode	Mode shape	Natural frequency
1	Axial translation coupled with rotation at the y-axis	30.5 Hz
2	Horizontal translation coupled with rotation at the x-axis (inphase)	35.3 Hz
3	Vertical translation	52.8 Hz
4	Rotation at the x-axis coupled with horizontal translation (out of phase)	109 Hz

Table 4: Natural frequencies measured using experimental modal analysis

9 Comparison between semi-analytical calculation, numerical and experimental analysis

In this paper the natural frequencies of the motor were determined in different ways. Semi-analytical calculation – using a plane vibration model – was used as well as numerical modal analysis and experimental modal analysis. Now the results from different analyses are compared to each other. Table 5 shows the natural frequencies of the first four modes for the semi-analytical calculation with and without the mass of the foundation, the numerical analysis using the finite element model and the experimental modal analysis. In brackets the percentage deviations of the natural frequencies for the semi-analytical calculation and the simulation with the finite element model regarding the results of the experimental analysis are shown. Since the vibration model in the semi-analytical calculation is only a plane model which describes the natural vibrations in the transversal plane (yz plane), the mode shape of the motor is not captured where an axial translation coupled with a rotation at the y-axis occurs. Thus, the numbering of the mode shapes for the semi-analytical calculation, the finite element model and experimental analysis is different. Therefore, the letters *A* to *D* are used for the mode shapes and the comparison.

The natural frequencies derived from the finite element model fit good to the measured natural frequencies for all modes from *A* to *D*. The maximum deviation occurs for mode *B* and is +4.85 %. For the semi-

analytical calculations with and without the mass of the foundation, the deviations increase with the higher modes. For mode *B* the results for both semi-analytical calculations fit good to the measured natural frequencies. Thus the mass of the foundation in the semi-analytical calculation has nearly no influence for mode *B*. For mode *C* the results from the semi-analytical calculations differ more clearly. One reason for this is the steel plate under the steel frame. The stiffness of the foundation was calculated for the static case and there the influence of the high mass of the steel plate mostly disappears, but there is a dynamic system here, where the mass of the steel plate influences. The deviation is +9.59 % when considering and +12.58 % when neglecting the mass of the foundation. Here also the mass of the foundation has only a small influence. For mode *D* the deviations of the semi-analytical calculations are clearly higher than for mode *C*. Here the influence of the steel plate occurs again. The deviation of the semi-analytical calculation with foundation mass is +15.44 % and without foundation mass even +28.38 %. Different to the modes before, the influence of the foundation mass in the semi-analytical calculation is obvious for mode *D*, because in the corresponding mode shape a large, related movement of the steel frame foundation occurs.

Mode	Mode shape	Semi-analytical calculation neglecting foundation mass	Semi-analytical calculation considering foundation mass	Finite element model	Experimental modal analysis
A	Axial translation coupled with rotation at the y-axis	-	-	31.4 Hz (+2.87 %)	30.5 Hz
B	Horizontal translation coupled with rotation at the x-axis (inphase)	36.4 Hz (+3.02 %)	36 Hz (+1.94 %)	37.1 Hz (+4.85 %)	35.3 Hz
C	Vertical translation	60.4 Hz (+12.58 %)	58.4 Hz (+9.59 %)	53.9 Hz (+2.04 %)	52.8 Hz
D	Horizontal translation coupled with rotation at the x-axis (out of phase)	152.2 Hz (+28.38 %)	128.9 Hz (+15.44 %)	114 Hz (+4.39 %)	109 Hz

Table 5: Comparison natural frequencies analytical model, finite element model and measurements

10 Experimental analysis of forced vibrations

In addition to the natural vibrations of the machine test bed, also forced vibrations are investigated. Therefore, the bearing housing vibrations are measured while the motor is operated by a converter and in no-load. The results are derived from different rotor speeds and when the motor is driven in steady state condition. The focus is on the vibrations caused by the oscillating magnetic force with double supply frequency (chapter 2.1) and by the 1x-excitation (chapter 2.2). Regarding the investigation of the 1x-excitation, the vibrations are measured once with inserted half feather key – the rotor is half-key balanced so only the residual unbalance after the rotor balancing occurs – and once without the half feather key, so there is a large mechanical unbalance. For the investigation of the vibrations resulting from the $2 \cdot f_1$-excitation, the measurements are done for half and full magnetization of the motor ($\frac{U}{f}$ = const.). Figure 14 shows the bearing housing vibration velocity (RMS) in horizontal direction for different supply frequencies. The vibration limits according ISO 10816-3 [12] are not exceeded in the measurements, so the vibrations could not be measured for all frequencies. Also, the measurements without half feather key are only done up to a frequency of 25 Hz, because the unbalance force increases by the square of the speed and so very high vibrations could occur for high rotor speeds.

The results (Figure 14) show, that the highest vibrations in horizontal direction occur at a frequency of about 17.5 Hz with full magnetization of the motor. This is due to the magnetic force oscillating with double

supply frequency which excites the second mode (Mode *B*: natural frequency: 35.3 Hz). By reducing the magnetization of the motor, the vibrations in the range of 17.5 Hz decrease clearly. Figure 15 shows the corresponding FFT (0-peak) at a supply frequency of 17.1 Hz with full and half magnetization of the motor. Here is clearly illustrated that the vibrations are mostly caused by $2 \cdot f_1$-excitation and also the influence of the magnetization on the amplitude of the $2 \cdot f_1$-excitation is shown. For supply frequencies up to about 20 Hz, the 1x-excitation – caused by unbalance from the missing half feather key – has nearly no influence on the vibrations. With higher supply frequencies the influence of the 1x-excitation increases. The vibrations in horizontal direction also show higher values at a frequency of about 35.5 Hz. Here now the 1x-excitation causes mostly the higher vibrations and the effect of the magnetization is small.

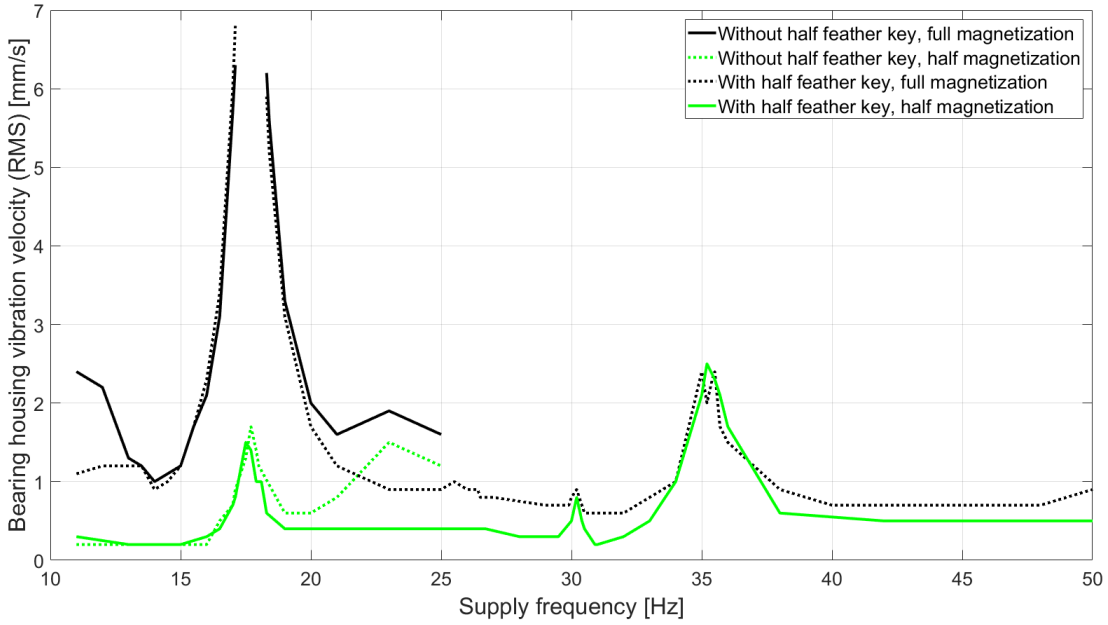


Figure 14: Bearing housing vibration velocity in horizontal direction (RMS)

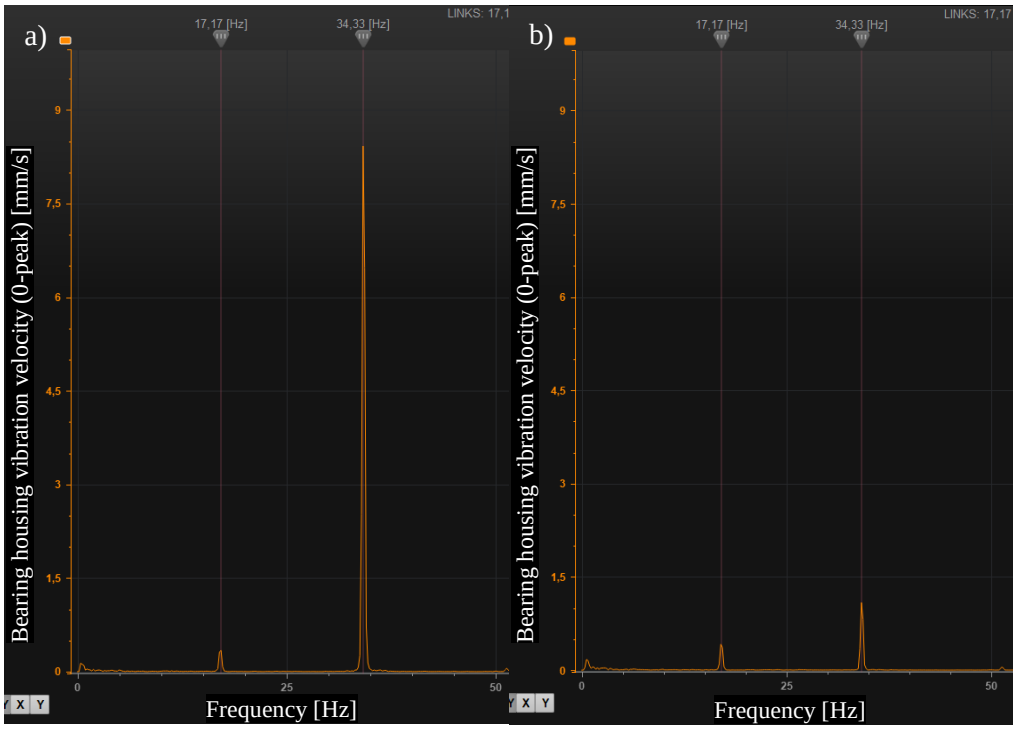


Figure 15: FFT bearing housing vibrations (0-peak) horizontal direction at supply frequency of 17.1 Hz
a) full magnetization; b) half magnetization

11 Conclusion

Vibration problems often occur for induction motors in the upper power range (> 1 MW) mounted on an elastic steel frame foundation. The idea to solve this problem is using an active vibration control system, where actuators are mounted between the motor feet and the steel frame foundation, to influence the vibration behavior actively. Therefore, a machine test bed consisting of a small two-pole induction motor and a steel frame foundation was developed. The aim of this paper is the investigation of the machine test bed regarding natural and forced vibrations. A simplified vibration model is derived which can be used for calculating the natural vibrations in the transversal plane of an electrical motor mounted on a soft foundation. The natural vibrations of the motor are calculated using a simplified vibration model as well as a numerical calculation using a finite element model. These calculations are compared to each other and validated by measurements using experimental modal analysis. The natural vibration analyses have shown that the results of the finite element model fit good to those of the experimental modal analysis. Only for low frequencies, the calculation based on the vibration model shows good accordance. The forced vibrations are measured while the motor is operated by a converter. High vibrations are clearly seen according to 1x-excitation and according to $2 \cdot f_1$-excitation. By reducing the magnetization of the motor, the vibration amplitudes with double supply frequency decrease clearly, which was expected from theoretical view.

References

[1] J. S. Rao, *Rotor Dynamics*. John Wiley & Sons, New York, (1996).

[2] R. Gasch, R. Nordmann, H. Pfützner, *Rotordynamik*, Springer-Verlag, Berlin-Heidelberg, (2002).

[3] J. M. Vance, F. J. Zeidan, B. Murphy, *Machinery Vibration and Rotordynamics*, John Wiley & Sons, Inc. Hoboken, New Jersey, (2010).

[4] U. Werner, *Analysis of active vibration reduction for soft mounted electrical machines based on a multibody model*, IJAM – International Journal of Applied Mechanics, Vol. 8, No. 8, (2017).

[5] U. Werner, *Vibration control of large induction motors using actuators between motor feet and steel frame foundation*, Journal MSSP-Mechanical Systems and Signal Processing, Vol. 12, (2017), pp. 319-342.

[6] U. Werner, *Theoretical vibration analysis of soft mounted electrical machines regarding rotor eccentricity based on a multibody model*, Multibody System Dynamics, SPRINGER, Vol. 24, No. 1, (2010), pp. 43-66.

[7] C. Bauer, U. Werner, *Method to detect the critical bending speed of an induction motor by using static rotor eccentricity for deriving the roller bearing stiffness*, 11th International Conference on Vibrations in Rotating Machinery, Manchester, UK, (2016), pp. 177-185.

[8] H. Jordan, R.-D. Schroeder, H. O. *Seinsch, Zur Berechnung einseitiger magnetischer Zugkräfte in Drehfeldmaschinen, Archiv der Elektrotechnik*, 63, Springer-Verlag, (1981), pp. 117-124.

[9] R. Belmans, A. Vandenput, W. Geysen, *Calculation of the flux density and the unbalanced pull in two pole induction machines*, Archiv der Elektrotechnik, 70, Springer-Verlag, (1987), pp. 151-161.

[10] U. Werner, *Derivation of a plane vibration model for electrical machines on soft machine foundations*, Engineering Research, SPRINGER, Vol. 74, No. 4, (2010), pp. 185-205.

[11] U. Werner, *An analytical method to minimize dynamic foundation forces caused by transit torques in the air gap of an asynchronous machine*, International Conference on Power Engineering, Energy and Electrical Drives, POWERENG, Setúbal, Portugal, (2007), pp. 6-11.

[12] ISO 10816-3 (International Organization of Standardization) *Mechanical vibration - Evaluation of machine vibration by measurements on non-rotating parts - Part 3: Industrial machines with nominal power above 15 kW and nominal speeds between 120 r/min and 15 000 r/min when measured in situ*, (2009).

Frictional effects on the synchronisation of partial contact in rotating machinery

E T Chipato [1], **A D Shaw** [1], **M I Friswell**[1]
[1] College of Engineering, Swansea University Bay Campus, Fabian Way,
Crymlyn Burrows, Swansea SA1 8EN, UK
e-mail: **687949@swansea.ac.uk**

Abstract
An overhung rotor model is explored to determine the effect of friction on the nonlinear dynamics of an aero-engine. The model has two degrees of freedom with rotor stator contact and the equations of motion are non-dimensionalised. A parametric study of the friction coefficient and eccentricity is conducted and the results displayed on bifurcation plots, waterfall plots, orbit plots, Poincaré maps and Lyapunov spectra. In the presence of friction, for bouncing type motion, the synchronisation of rotor spin speed, backward whirl and forward whirl is the main driver in sustaining such motion. Furthermore, it was observed from the bifurcation plots that besides the primary resonance there is a region with high radial displacement. In this region the dominant frequency component was the backward whirling frequency of the stiffened system. The region with backward whirling solutions expands as the friction coefficient is increased.

1 Introduction

Efficiency in rotors is often achieved through high operating speeds, bearings with reduced clearances and lighter shafts. These changes increase the probability of faults such as rub and fatigue cracking. Internal resonance can lead to the onset of bouncing-type partial contact motion away from the primary resonance [1, 2] and this leads to the approximate prediction of speeds at which contact occurs [3]. Most studies do not account for the gravitational and frictional effects in sustaining such bouncing-type solutions and whether the synchronisation condition holds in the presence of such phenomena. Studies on the effect of introducing imperfections to a system via a gravity sag or simply the effect of gravity on the internal resonance and synchronisation prove that gravity should be included for low shaft stiffness but for high shaft stiffness gravity can be ignored [2, 4]. For the case with gravity, internal resonance still led to the onset of bouncing-type motion but additional solutions not seen in earlier studies were found, such as chaotic solutions and multi-periodic solutions for different values of the gravity parameter.

Alber and Markert [5] gave a compact and comprehensive overview of rotor-stator contact in rotordynamics. A general two degrees of freedom system with no gyroscopic effects that accounts for most of the phenomena in the rotor-stator contact problem was described. A variety of motion patterns was observed including synchronous, subhamornic, super-harmonic, backward whirling (BW), forward whirling (FW) and chaotic motion. It was observed in their studies that dry friction in the contact surfaces causes backward components in the frequency spectrum and led to backward whirling. Other authors such as [6, 7, 8, 9, 10] also observed the same effect of friction from numerical and experimental studies. Some authors such as Nelson [11] have argued that the BW mode vector is orthogonal to the unbalance force vector and therefore energy cannot be fed into the BW and thus its inception can safely be attributed to a frictional effect. BW is also referred to as dry friction whirl, dry friction whip or counter whirl and can either be BW rolling or BW sliding. Some work, such as in [12], have modelled the rotor system as a continuous rotor including gyroscopic effects and modelled the rotor system using partial differential equations

Varney and Green [13] developed a novel model for rotor stator rub which they argued replicates reality by treating the contact surfaces as a series of stochastically distributed asperities. For a more comprehensive explanation of how the method is implemented readers are directed to a second paper by Varney and Green in [14]. The motivation for the new model was that most studies employ the simple piecewise-smooth linear-elastic contact model (LECM) where the rotor switches between non-contacting and contacting states. They argued that though useful as a first step, the LECM relies on a contact stiffness estimate, in addition to assuming point contact which does not fully emulate the actual contacting surface. A comparison between shaft speed bifurcation diagrams obtained for LECM and the new method showed significant differences between the predicted dynamics. Furthermore, the results they obtained showed that the new contact model worked well for partial/light rubs in which the primary mechanism for contact is actually asperity deformation.

Alzibdeh *et al*. [15] analysed the effect of drive speed modulation on a rotor with continuous stator contact. The drill string was modelled as an extended Jeffcott rotor and has a torsional degree of freedom with sinusoidal modulation. Their results show that for a rotor that is whirling either forward or backward, the addition of sinusoidal excitation to the drive speed (modulation) can cause an increase in the equivalent torsional stiffness, smooth the discontinuous friction force at the contact and the region with negative slope in the variation of friction coefficient with respect to relative velocity became smaller. Experimental studies with a laboratory scale drill string showed a good correlation with the simulation from a reduced order model. The results obtained also show that drive-speed modulation is useful in reducing drill string vibrations.

In this work, the role friction plays in influencing the dynamics and its effect in sustaining bouncing-type partial contact solutions and synchronisation is revealed. The model used is an overhung disc with contact, has two degrees of freedom and the equations of motion are non-dimensionalised. The equations are similar to those used in [2] and [3] except that friction is included. Following studies done by [2] and [4] for stiff rotors such as aero-engines where gravity can be ignored, here we also ignore gravity as we assume that the rotor is very stiff. This is advantageous to this study because any qualitative changes in the nature of the dynamics will solely be attributed to the inclusion of friction in the system. ODE45 in MATLAB is employed to calculate the solutions of the nonlinear differential equations. Three dimensional bifurcation diagrams with rotor spin speed for different values of the coefficient of friction are plotted with their corresponding Lyapunov exponents to characterize the nature of the solutions. Vibration responses, orbit trajectories, Poincaré maps and waterfall plots are presented and a discussion of the effect of friction is given.

2 Theoretical model

A lumped parameter model of the rotor is used which is described using differential equations. This work makes use of a two degrees of freedom model whose formulation was inspired by Zilli *et al*. [3] and further work by Chipato *et al*. [2]. The idealized model is shown in Figure 1.

The equations of motion were derived using the Lagrange method and are given by

$$\begin{cases} J_s\ddot{\phi_y} - J_p\dot{\theta}\dot{\phi_x} + D\dot{\phi_y} + k_\phi\phi_y = ame(\dot{\theta}^2\cos\theta + \ddot{\theta}\sin\theta) + M_{\phi_y} \\ J_s\ddot{\phi_x} + J_p\dot{\theta}\dot{\phi_y} + D\dot{\phi_x} + k_\phi\phi_x = ame(\ddot{\theta}\sin\theta - \dot{\theta}^2\cos\theta) + M_{\phi_x} \\ M_{\phi_y} = H(||r_c|| - c^*)k_s b^2(\phi_y + \alpha\mu\phi_x)\left(\frac{c}{b\sqrt{\phi_x^2+\phi_y^2}} - 1\right) \\ M_{\phi_x} = H(||r_c|| - c^*)k_s b^2(-\phi_x + \alpha\mu\phi_y)\left(\frac{c}{b\sqrt{\phi_x^2+\phi_y^2}} - 1\right) \end{cases} \tag{1}$$

where ϕ_x and ϕ_y are rotations about the x and y axes respectively, D is the damping, m is the mass of disk, k_ϕ represents the angular stiffness of the bearing, g is the acceleration due to gravity, θ is the rotation angle, J_s is the equivalent moment of inertia of the overhung rotor system and is given by $J_s = (J_t + a^2m)$, J_t is the transverse moment of inertia, J_p is the polar moment of inertia, e is mass unbalance eccentricity, M_{ϕ_x}

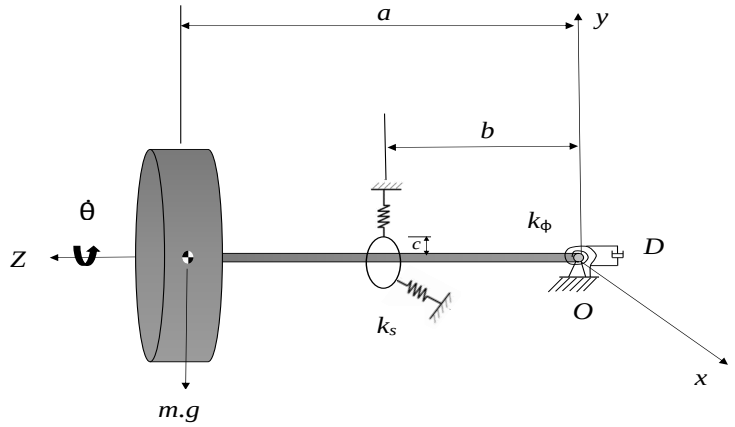


Figure 1: Schematic of the overhung rotor

and M_{ϕ_y} are the generalized moments associated with the normal snubbing force F_n and tangential snubbing force F_t due to friction and k_s is the stator stiffness. The equations of motion of this system are given in dimensionless form as

$$\begin{cases} \hat{\phi}_y'' - \hat{J}_p\theta'\hat{\phi}_x' + 2\zeta\hat{\phi}_y' + \hat{\phi}_y = \hat{m}\hat{e}(\theta'^2\cos\theta + \theta''\sin\theta) + \hat{M}_{\phi_y} \\ \hat{\phi}_x'' + \hat{J}_p\theta'\hat{\phi}_y' + 2\zeta\hat{\phi}_x' + \hat{\phi}_x = \hat{m}\hat{e}(\theta''\sin\theta - \theta'^2\cos\theta) + \hat{M}_{\phi_x} + \hat{m}\hat{g} \\ \hat{M}_{\phi_y} = H(||\hat{r_c}|| - 1)\beta(\hat{\phi}_y + \alpha\mu\hat{\phi}_x)\left(\frac{1}{\sqrt{\hat{\phi}_x^2+\hat{\phi}_y^2}} - 1\right) \\ \hat{M}_{\phi_x} = H(||\hat{r_c}|| - 1)\beta(-\hat{\phi}_x + \alpha\mu\hat{\phi}_y)\left(-\frac{1}{\sqrt{\hat{\phi}_x^2+\hat{\phi}_y^2}} + 1\right) \end{cases} \tag{2}$$

where a caret ($\hat{}$) and apostrophe ($'$) represents a nondimensional quantity and a derivative with respect to nondimensional time respectively. Nondimensional time is given by $\tau = \omega_n t$, where $\omega_n^2 = k_\phi/J_s$, and the rotations are scaled as $\hat{\phi}_x = \phi_x\frac{a}{c^*}$ and $\hat{\phi}_y = \phi_y\frac{a}{c^*}$. $H(||r_c|| - 1)$ is the Heaviside step function which activates the equations for the generalized moments $\hat{M}_{\phi_y}$ and $\hat{M}_{\phi_x}$ when there is contact in the system and introduces non-linearities in the equations of motion. r_c is the radial displacement of the disk's centre given by $\sqrt{\hat{\phi}_x^2 + \hat{\phi}_y^2}$, c is the radial clearance, $c^* = \frac{ca}{b}$ is the displacement of the disk centre that leads to contact, $\hat{m} = \frac{ma^2}{J_s}$ is the equivalent mass, $\hat{e} = e/c^*$ is the eccentricity, β is the ratio between the snubbing stiffness and the linear stiffness of the rotor, that is the degree of non-linearity, $\frac{k_s}{k_r}$, $k_r = \frac{k_\phi}{b^2}$ and $\hat{g} = \frac{g}{c^*\omega_n^2}$ is the gravity parameter which in this study is zero because we assume the rotor is very stiff.

Friction has been reported to cause instability in numerical simulations using time marching methods [16] and therefore one has to exercise caution when handling friction. The friction force opposes the motion of the rotor and thus can lead to a reduced rotor spin speed or even result in the sticking of the rotor. In these cases the relative velocity between the stator and the rotor will have to be checked for each iteration/ time step to ensure that an appropriate direction of the friction force is chosen. The appropriate direction of the frictional force is obtained by assigning a value to α.

$$\alpha = \begin{cases} \text{-1} & \text{if } v_{rel} > 0 \\ 0 & \text{if } v_{rel} = 0 \\ 1 & \text{if } v_{rel} < 0 \end{cases} \tag{3}$$

The relative velocity is obtained as

$$v_{rel} = \theta' + \hat{\phi}'_x \left(\frac{\hat{\phi}_x}{r_c} \right) - \hat{\phi}'_y \left(\frac{\hat{\phi}_y}{r_c} \right) \tag{4}$$

For a system with friction the motion of the rotor can be sliding, rolling or sticking. In sliding motion there is relative motion at the contact point between the rotor and stator. If the rotor is rolling then the contact point has no motion but the rotor keeps spinning. When stuck the driving force of the rotor has completely been overcome by the frictional force. For the chosen parameters of this system no sticking was observed. In this study the Coloumb friction model is used. The variation of the coefficient of friction, μ, with relative velocity, v_{rel}, for the Coulomb friction model is shown in Figure 2. It is apparent from this figure that the friction force is discontinuous when the relative velocity at the contact point is zero. Reality dictates that if there is no relative slipping then the friction force can take any bounded value, and this leads to problems with the numerical integration. To solve this problem, the friction coefficient is modified to $(v_{rel}/v_{min}))\mu$ if $v_{rel} < v_{min}$ where v_{min} = 0.01 for the red line in Figure 2. This force can be further smoothed using the function $\mu = \mu_0 \tanh(v_{rel}/v_0)$, where μ_0 is the maximum friction coefficient and v_0 is a parameter to change the profile of required curve.

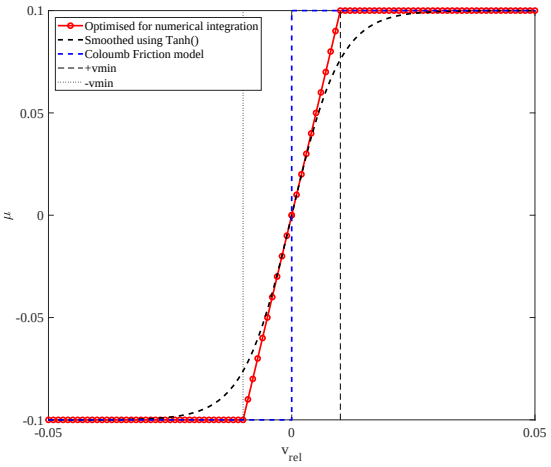


Figure 2: Coloumb friction model

3 Numerical analysis and results

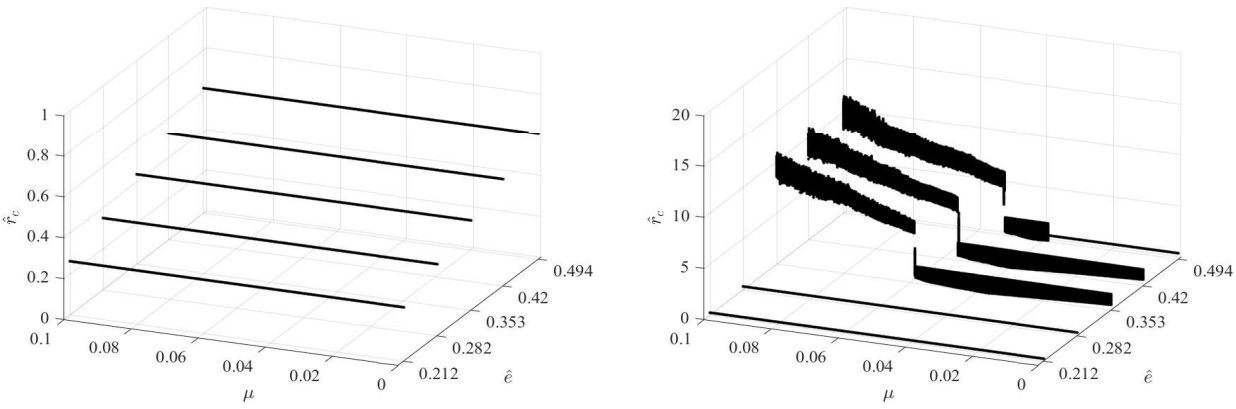
In this study numerical calculations were performed using ODE45 in MATLAB. Representative test parameters are shown in Table 1 following the studies done by Chipato *et al.* [2]. Nonlinear systems can exhibit a number of different qualitative solutions or responses. For the bifurcation diagrams, the simulation was run for a thousand forcing periods to ensure that the initial transients die out and then the last two hundred cycles are sampled to give the Poincaré return points. In this way, periodic solutions on the bifurcation diagram will appear as a single point, and multi-periodic solutions will appear as multiple points, for example, for period-2 solutions only two Poincaré return points will be observed on the bifurcation diagram.

Figure 3 shows three dimensional bifurcation plots with μ as the control parameter for different values of unbalance forcing. The two figures are plotted for two different values of rotor spin speed. Figure 3(a) is for a rotational speed where no contact occurs and Figure 3(b) is for a rotational speed with contact. It is evident from these two plots that for the non-contacting rotor spin speed, for five different levels of unbalance forcing, the dynamics of the system remain periodic as shown by a single Poincaré return point for all values of the control parameter μ which give straight lines on the bifurcation diagrams. However as the forcing increases

Table 1: Nondimensionalised system parameters

Symbol	Parameter	Value
$\hat{m}$	Normalised mass	0.9285
$\hat{J}_p$	Normalised polar moment of inertia	0.143
β	Stiffness nonlinearity	1.32
$\hat{e}$	Normalised rotor eccentricity	0.494
μ	Coefficient of friction	0.1
ζ	Damping ratio	0.01

the response amplitude in the form of the radial displacement, $\hat{r_c}$, grows. This is expected since when the system is not contacting, it is a linear system and any quantitative change in the system's parameters, in this case $\hat{e}$, results in a quantitative change in the nature of the response and thus $\hat{r_c}$ increases. For the contacting speed, we see that for the first two eccentricities we get similar periodic solutions as obtained in Figure 3(a). For higher eccentricities a series of Poincaré return points appear as quasi-periodic solutions. It is also observable that after a particular cut off value of μ the solution jumps to larger values of $\hat{r_c}$. This analysis therefore helps in making sure that one captures all the values of eccentricity, $\hat{e}$ with interesting nonlinear phenomena.

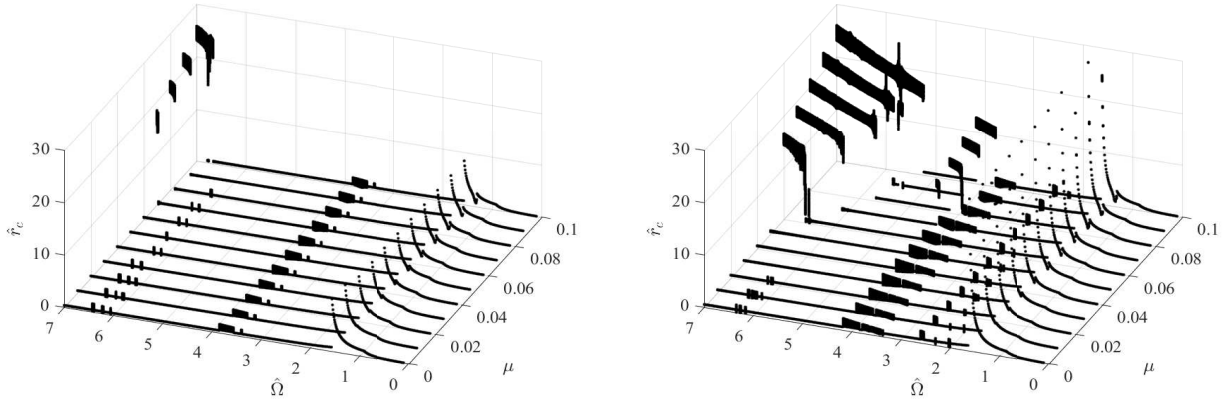


(a) $\hat{\Omega}$ = 3.0 (b) $\hat{\Omega}$ = 3.8

Figure 3: Three dimensional bifurcation plots with μ as the control parameter for varying levels of forcing

To better understand the nature of dynamics being experienced in this system, two values of eccentricity were chosen based on results obtained from Figure 3 for further analysis, namely $\hat{e}$ = 0.353 and 0.494. Furthermore, bifurcation diagrams with $\hat{\Omega}$ as the control parameter for different values of μ are shown in Figure 4.

Figure 5 shows the bifurcation, Lyapunov spectra, and waterfall plots for $\hat{e}$ = 0.353. Figure 6(a) shows a quasi periodic solution for μ = 0.1 at $\hat{\Omega}$ = 3.39. Figure 7(a) shows the Campbell diagram for the linear system which can safely be used to predict the natural frequencies at a given rotor spin speed with minimal difference for partial contacting cycles. The FFT in Figure 6(b) clearly shows that for this value of unbalance forcing, in the presence of friction, the synchronisation of the three frequencies namely, FW, BW and $\hat{\Omega}$, still holds the key to causing bouncing type solutions in the presence of friction. Also at higher speeds between $\hat{\Omega}$ = 6 and $\hat{\Omega}$ = 7 we see a bifurcation occurring from periodic to very high amplitude quasiperiodic. Figure 6(c) shows an orbit taken at $\hat{\Omega}$ = 6.9, where the Poincaré section that is superimposed to the orbit is a closed loop and the Lyapunov exponent is close to zero and therefore this is a quasiperiodic solution. A look at the FFT of this orbit in Figure 6(d) sheds more light on the exact type of solution, as there are two peaks identifiable



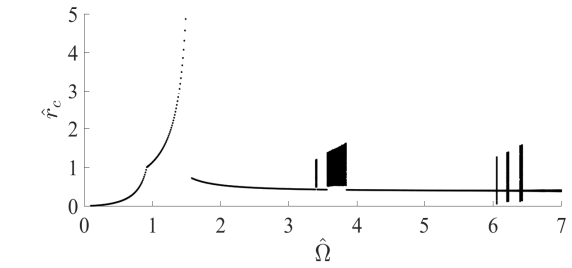
(a) $\hat{e}$ = 0.353 (b) $\hat{e}$ = 0.494

Figure 4: Three dimensional bifurcation plots with $\hat{\Omega}$ as the control parameter for varying levels of friction at different levels of unbalance forcing obtained from Figure 3

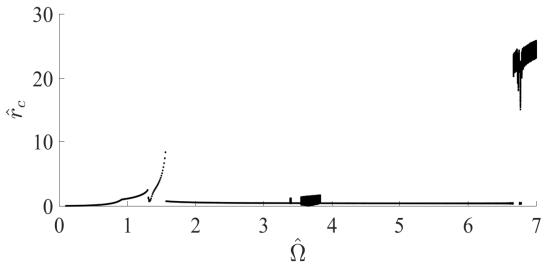
at 1.10 and 6.90. Clearly the 6.9 corresponds to the rotor spin speed and the 1.10 is something else. The natural frequencies of the linear system are 1.61 and 0.62 and there is no relationship with the peak at 1.10. A closer look at the orbit in Figure 6(c) shows that the orbit is in a full annular rub and thus the natural frequencies of the linear system will not be related to the frequencies in the FFT for this orbit. To investigate this problem we use the Campbell diagram for the nonlinear stiffened system, which assumes that the system is always in contact. Therefore, after considering equilibrium at one of the bending planes of the model, the linear stiffness terms in Eq. (2) are scaled by $(1 + \beta)$.

Figure 7(b) shows the Campbell diagram of the stiffened system and gives the natural frequencies at the corresponding speed. The natural frequencies of the nonlinear stiffened system at $\hat{\Omega}$ = 6.9 now become 2.0945 and 1.10, which are the FW and BW frequencies of the stiffened system. Therefore, it is apparent that the other peak in the FFT which is dominating the response is in fact the BW natural frequency and therefore the solution at $\hat{\Omega}$ = 6.9 is a quasiperiodic backward whirling solution.

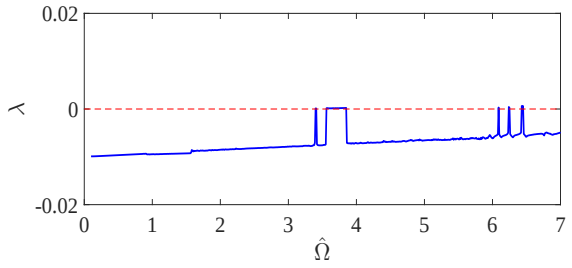
For higher levels of forcing, that is $\hat{e}$ = 0.494, we see that for the zero friction case, there is an increase in the number of contacting solutions shown in Figure 8(a) than the previous case shown in Figure 5(a) . Furthermore, for the case with friction, for $\hat{e}$ = 0.353 we see that backward whirling solutions start to appear at speeds above $\hat{\Omega}$ = 6. For $\hat{e}$ = 0.494 we see that backward whirling solutions start to appear as early as $\hat{\Omega}$ = 3.78 and all solutions above $\hat{\Omega}$ = 5.24 are backward whirling solutions. The Lyapunov exponents for both friction cases are either negative or equal to zero and therefore only periodic and quasiperiodic solutions exist. The waterfall plots in Figure 8 show that for bouncing solutions at higher forcing, the synchronisation condition still holds. Figure 9(b) shows a close up of the FFT of a typical bouncing solution for $\hat{\Omega}$ = 3.39 and clearly shows the three frequencies required for synchronisation. Furthermore, a close up look at the waterfall plot in Figure 8(f) shows the shifting of the backward whirling solution frequencies towards higher frequencies, which shows that there is more stiffening in the BW solutions compared to the bouncing partial contacting solutions. Figures 9(c) and 9(d) shows the orbit and FFT of the BW solution is similar to Figure 6 with the FFT showing peaks at 1.22 and 4. The Campbell diagram predicts the BW natural frequency as 1.26, which is close to the peak frequency. Also, the magnitude of the rotor spin speed peak is higher than the $\hat{e}$ = 0.353 case and this could be due to the increase in unbalance forcing in this case.



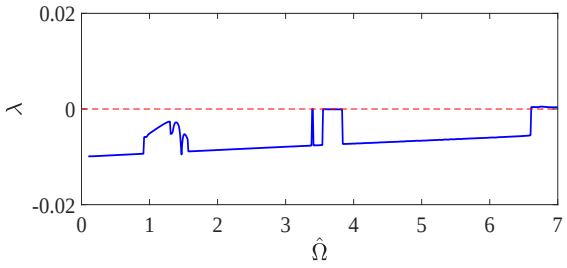
(a) $\mu = 0$



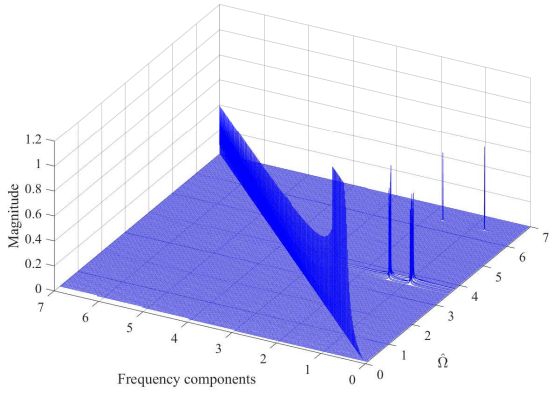
(b) $\mu = 0.1$



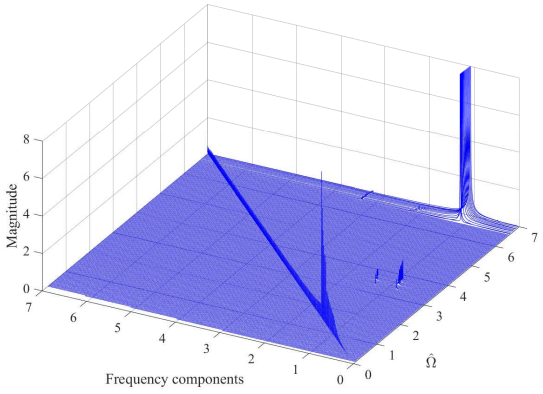
(c) $\mu = 0$



(d) $\mu = 0.1$

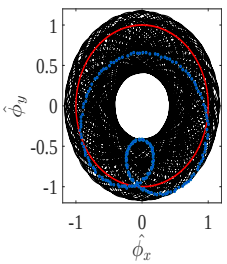


(e) $\mu = 0$

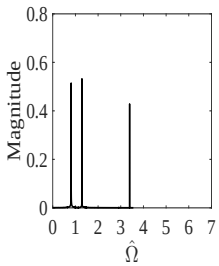


(f) $\mu = 0.1$

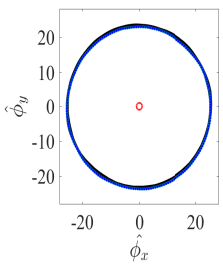
Figure 5: Bifurcation, Lyapunov spectrum and waterfall plots for $\hat{e} = 0.353$ at two different values of μ



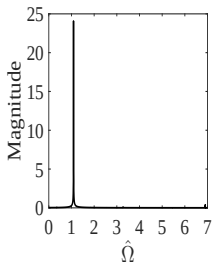
(a) $\hat{\Omega}$ =3.39



(b) $\hat{\Omega} = 3.39$

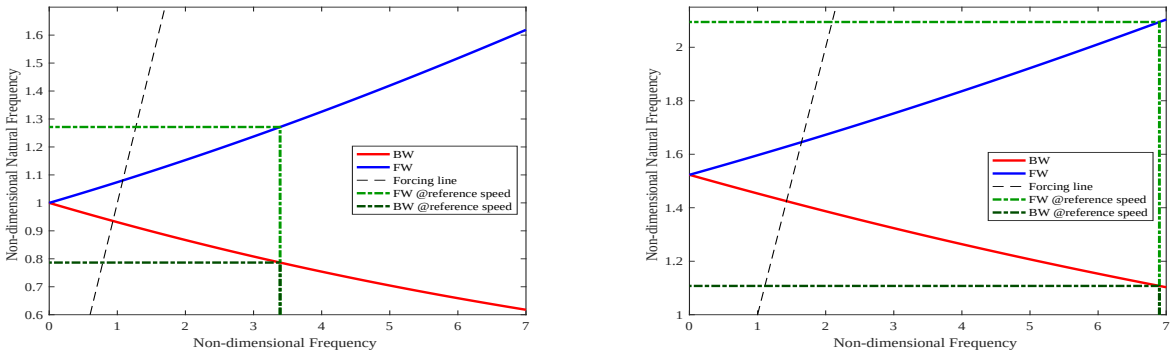


(c) $\hat{\Omega} = 6.9$



(d) $\hat{\Omega} = 6.9$

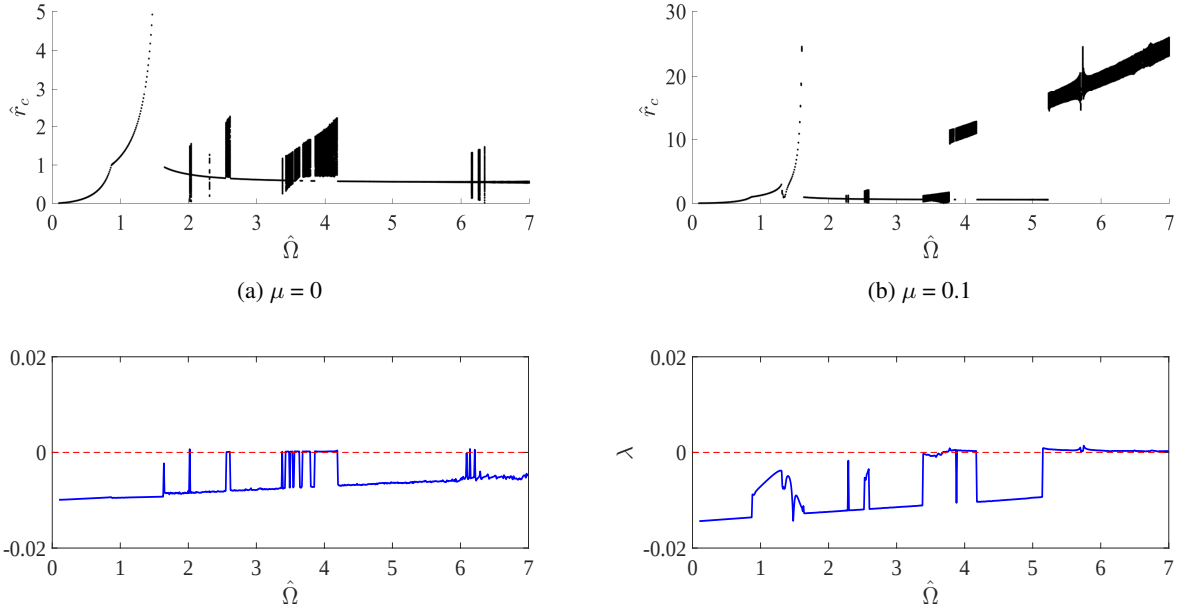
Figure 6: Quasiperiodic and BW orbit and their corresponding FFTs at $\hat{\Omega} = 3.39$ and 6.9 at $\mu = 0.1$



(a) Linear system

(b) System in contact

Figure 7: Campbell diagram showing forward and backward whirl frequencies

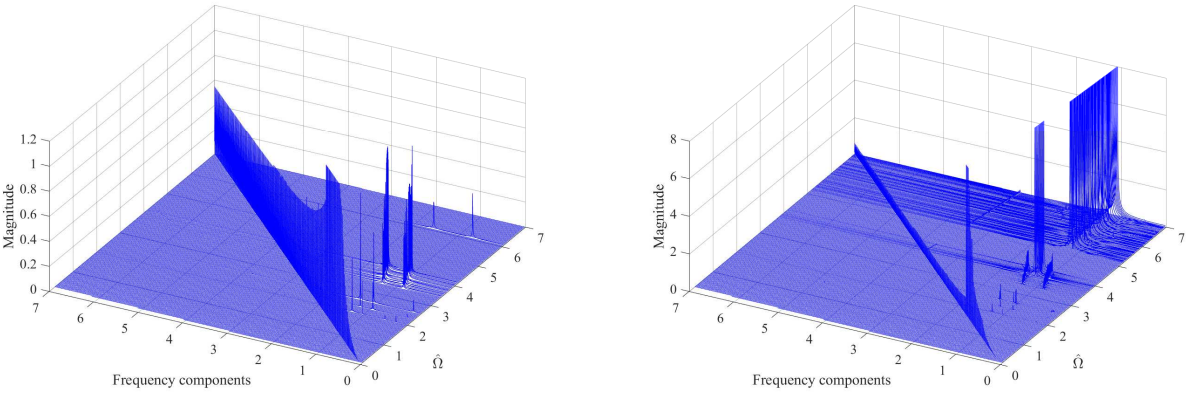


(a) $\mu = 0$

(b) $\mu = 0.1$

(c) $\mu = 0$

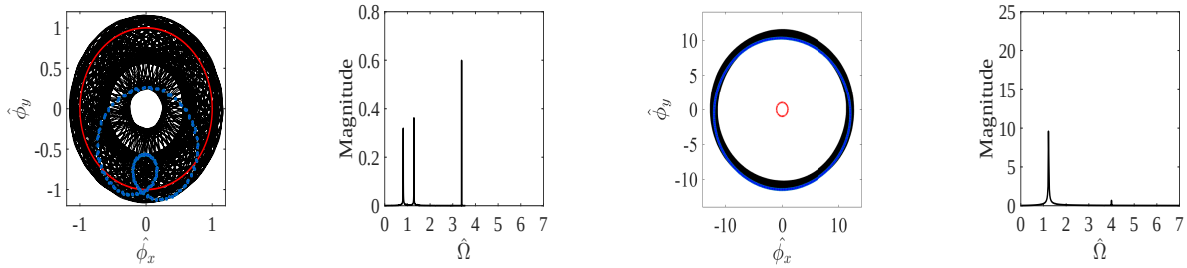
(d) $\mu = 0.1$



(e) $\mu = 0$

(f) $\mu = 0.1$

Figure 8: Bifurcation, Lyapunov spectrum and waterfall plot for $\hat{e} = 0.494$ at two different values of μ



(a) $\hat{\Omega}$ =3.39 (b) $\hat{\Omega}$ = 3.39 (c) $\hat{\Omega}$ = 4 (d) $\hat{\Omega}$ = 4

Figure 9: Quasi-periodic bouncing orbit and Quasiperiodic backward whirling orbit and their corresponding FFTs at $\hat{\Omega}$ = 3.39 and 4 at $\mu = 0.1$

4 Conclusions

This paper has explored the effects of friction on the synchronisation of partial contact in an overhung rotor which is subjected to different unbalance excitation. A two degrees of freedom system with gyroscopic effects included was used. The equations of motion are non-dimensionalised with respect to time and normalised. The nonlinear equations were then placed in state space form for numerical integration using ODE45 in MATLAB. It was observed that for different values of unbalance forcing, in the presence of friction, the synchronisation condition holds as seen by the presence of the BW, FW and $\hat{\Omega}$ frequency components in the bouncing type solutions. A high amplitude response was also observed for lower unbalance forcing, and the frequency content of this response showed that the BW frequency was the dominant frequency component followed by a highly attenuated rotor spin speed peak. For lower unbalance forcing the backward whirling solutions are only observed at higher rotational speeds for a very small region but as the forcing becomes stronger, the region with backward whirling solutions is seen to expand towards lower rotor spin speed values. The waterfall plots also showed that these BW solutions, which have full annular contact have a frequency content that migrates towards higher frequency values because of the stiffening effect as compared to the bouncing type solutions. For this reason the natural frequencies of the BW solutions were predicted better using the Campbell diagram of the stiffened system where permanent contact is assumed.

Acknowledgements

The research leading to these results has received funding from Swansea University via the ZCCE PhD scholarship.

References

[1] A. D. Shaw, A. R. Champneys, M. I. Friswell. *Asynchronous partial contact motion due to internal resonance in multiple degree-of-freedom rotordynamics*. In *Proc. R. Soc. A*, vol. 472. The Royal Society (2016).

[2] E. Chipato, A. D. Shaw, M. I. Friswell. *Effect of gravity-induced asymmetry on the nonlinear vibration of an overhung rotor*. Communications in Nonlinear Science and Numerical Simulation, vol. 62 (2018), pp. 78–89.

[3] A. Zilli, R. J. Williams, D. J. Ewins. *Nonlinear dynamics of a simplified model of an overhung rotor subjected to intermittent annular rubs*. Journal of Engineering for Gas Turbines and Power, vol. 137, no. 6 (2015), p. 065001.

[4] P. Varney, I. Green. *Nonlinear phenomena, bifurcations, and routes to chaos in an asymmetrically supported rotor–stator contact system*. Journal of Sound and Vibration, vol. 336 (2015), pp. 207–226.

[5] O. Alber, R. Markert. *Rotor-stator contact–overview of current research*. In *Materials Science, Engineering and Chemistry Web of Conferences*, vol. 16. EDP Sciences (2014), p. 03001.

[6] S. Lahriri. *On the Rotor to Stator Contact Dynamics with Impacts and Friction-Theoretical and Experimental Study*. Ph.D. thesis, Technical University of Denmark (DTU) (2012).

[7] S. Ahmad. *Rotor casing contact phenomenon in rotor dynamicsliterature survey*. Journal of Vibration and Control, vol. 16, no. 9 (2010), pp. 1369–1377.

[8] G. Jacquet-Richardet, M. Torkhani, P. Cartraud, F. Thouverez, T. N. Baranger, M. Herran, C. Gibert, S. Baguet, P. Almeida, L. Peletan. *Rotor to stator contacts in turbomachines. review and application*. Mechanical Systems and Signal Processing, vol. 40, no. 2 (2013), pp. 401–420.

[9] J. Jiang. *The analytical solution and the existence condition of dry friction backward whirl in rotor-to-stator contact systems*. Journal of vibration and acoustics, vol. 129, no. 2 (2007), pp. 260–264.

[10] Y. Chen, G. Yao, J. Jiang. *The forward and the backward full annular rubbing dynamics of a coupled rotor-casing/foundation system*. International Journal of Dynamics and Control, vol. 1, no. 2 (2013), pp. 116–128.

[11] F. C. Nelson. *Rotor dynamics without equations*. International Journal of Condition Monitoring and Diagnostic Engineering Management, vol. 10, no. 3 (2007), p. 2.

[12] M. F. A. Azeez, A. F. Vakakis. *Numerical and experimental analysis of a continuous overhung rotor undergoing vibro-impacts*. International journal of non-linear mechanics, vol. 34, no. 3 (1999), pp. 415–435.

[13] P. Varney, I. Green. *Rotordynamic analysis of rotor–stator rub using rough surface contact*. Journal of Vibration and Acoustics, vol. 138, no. 2 (2016), p. 021015.

[14] P. Varney, I. Green. *Rough surface contact of curved conformal surfaces: An application to rotor–stator rub*. Journal of Tribology, vol. 138, no. 4 (2016), p. 041401.

[15] A. AlZibdeh, M. AlQaradawi, B. Balachandran. *Effects of high frequency drive speed modulation on rotor with continuous stator contact*. International Journal of Mechanical Sciences, vol. 131 (2017), pp. 559–571.

[16] G. Von Groll, D. J. Ewins. *A mechanism of low subharmonic response in rotor/stator contactmeasurements and simulations*. Journal of vibration and acoustics, vol. 124, no. 3 (2002), pp. 350–358.

Balancing rotating structures using slow-speed data via optimized parametric excitation and nonlinear feedback

A. Dolev[1]*, S. Tresser[1] and I. Bucher[1]
[1] Dynamics Laboratory, Mechanical Engineering, Technion
Technion City, Haifa 3200003, Israel
*e-mail: **amitdtechnion@gmail.com**

Abstract
The paper presents an improved mass balancing procedure for fast rotating machinery, while it is being rotated at speeds considerably slower than the "critical speeds", where dangerously high vibration amplitudes may arise. By utilizing tuned dual frequency parametric excitation along with optimized nonlinear feedback terms, the slow imbalance forces are projected onto a chosen mode of vibration. This allows to identify the imbalance projection on that specific mode, and to cancel these forces by adding or reducing mass. The scheme benefits from two kinds of parametric excitation yielding combination and principal parametric resonances. The former is used to project the imbalance forces onto a selected vibration mode, and the latter significantly amplifies the response. By tuning the parametric excitation and the nonlinear terms in an optimal manner, a pseudo-linear behavior is formed. This behavior enables to increase both amplification and sensitivity to the imbalance forces without having to compromise between the two.

1 Introduction

Mechanical vibrations in rotating machinery is an undesired phenomenon, and its main excitation source is rotor imbalance. Because the local center of mass at each cross-section along the rotor does not coincide with the geometric center, a rotating distributed force arises at the rotation frequency. This force excites all the vibration modes of the structure, and each mode's participation in the response is proportional to the imbalance projection on it [1,2]. To minimize the imbalance, a mass balancing procedure (MBP) is often carried out, where small correction masses are added or removed. Usually, the MBP is performed at the machinery full operational speed range.

Rotors exhibiting bending oscillations at their operational speed range are referred to as “flexible”, and are common in high speed machinery. This kind of machinery is customarily designed to operate close to a specific critical speed where a single "flexible mode" dominates the response. Implementation of MBP for such machinery is impossible in many cases due to safety reasons or harsh conditions, e.g. high temperatures or inaccessibility, which prevent the ability to take measurements or even to run the system at such speeds. The inability to perform flexible MBP may lead to conservative over-design, adding damping elements which add weight and unacceptable complexity [3,4], and performing MBP using commercial balancing machines [5], where the rotor is not balanced in its full operational speed range. The latter assumes a rigid rotor type of behavior, hence the projection of the imbalance on flexible modes is not seen by sensors. At the related critical speeds which are not balanced, large vibrations are exhibited during operation [6,7].

In all MBP approaches designed for flexible rotors (e.g., “Influence Coefficient Method”, “Modal Balancing” and “Unified Balancing Approach” [6–14]), the machinery is span in the vicinity of critical speeds within its full operational speed range and the vibration levels are measured [6,8–10]. Then, these data are post-processed to calculate the correction masses. Since these methods are based on vibration readings, a sufficiently good signal to noise ratio is required. The latter is achieved when the vibration levels are sufficiently high, therefore, it is required to rotate the machinery close to its critical speeds [6]. Furthermore, when this occurs, a single vibration mode dominates the response, allowing separating its

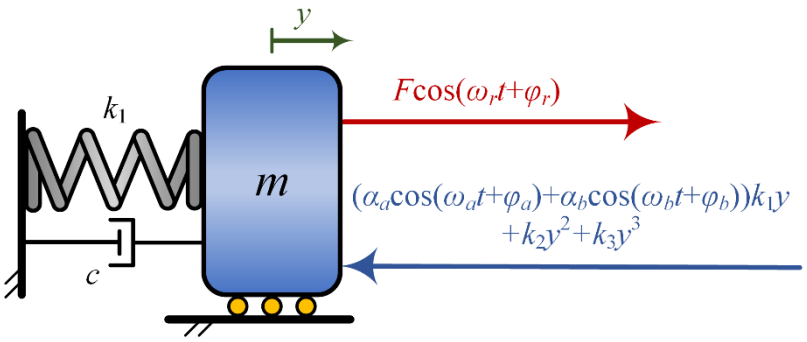


Figure 1: A linear SDOF oscillator subjected to a controlled force.

contribution to the measured response. This procedure has to be repeated for all modes of interest, therefore at several critical speeds. The latter cannot be carried out unless all critical speed in the range are balanced.

Recently, a different MBP approach was reported [15,16], based on [17–20], which enables to detect the imbalance projection on high frequency modes while rotating at speeds much lower than the critical speeds. The reported scheme allows to overcome the aforementioned limitations by utilizing dual-frequency parametric excitation (also known as pumping) along with a cubic nonlinear feedback term which limits the vibration levels and leads to a steady oscillation amplitude. The latter approach was implemented in [15,16], and it was shown that the imbalance can be found with high accuracy both numerically and experimentally. It was found in [16] that the suggested MPB is robust, however, when very weak imbalance forces are considered, high precision in the amplifier's parameters estimation is needed. Moreover, lower sensitivity levels were obtained with respect to cases with larger imbalance. This fact leads to a compromise, when tuning the parameters, between the amplification and sensitivity levels.

An improved scheme for which optimal parameters tuning is given in a closed form was recently introduced [21]. The scheme was developed for a nonlinear single-degree-of-freedom (SDOF) parametric amplifier, which behaves in a pseudo-linear manner. This unique dynamic behavior is achievable by a carful tuning of the cubic and quadratic nonlinear terms [21–23]. Furthermore, it eliminates the need to make a comprise between amplification and sensitivity levels, and permits to lower the precision requirement in the amplifier parameter estimation. In what follows, the scheme of [21] is extended to accommodate a multi-degree-of-freedom (MDOF) rotating machinery dynamic behavior. The ability to detect the imbalance force projection on any desired vibration mode, while rotating much slower than the critical speeds, without the aforementioned compromise is demonstrated via a test case.

The paper begins with a brief mathematical summary of the pseudo-linear parametric amplifier scheme, and the stages required to tune the amplifier parameters. Then, the improved MBP scheme is introduced, followed by a concise mathematical description of the scheme extension to a rotating MDOF system. In the following sections, a numerical verification of the suggested optimal scheme is carried out, and the performance is compared to the previously reported scheme.

2 Approximate analytical solution of a pseudo-linear parametric amplifier

A linear SDOF oscillator which is subjected to the aforementioned controlled external force is analyzed in this section. The discussion below is related to a oscillator and the nature of forces acting on it as illustrated in Figure 1. The model considered here consists of an ordinary differential equation having lumped parameters and is characterized by a point mass m, linear dashpot c and a linear stiffness k_1. The applied force consists of three components: (1) a dual-frequency parametric excitation term with frequencies ω_a, ω_b, appropriate phase shifts φ_a, φ_b and corresponding magnitudes α_a, α_b, (2) nonlinear stiffness feedback terms – quadratic (k_2) and cubic (k_3), and (3) an external force at a known frequency, ω_r, and unknown phase shift φ_r and amplitude F. The third term, the harmonic force (at frequency ω_r), is the input signal to be amplified.

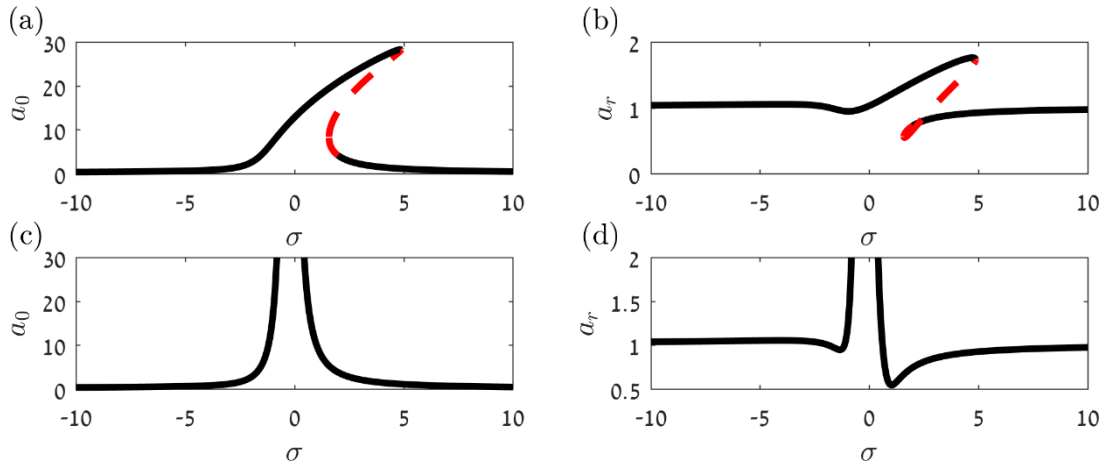


Figure 2: (a) The amplitude of the harmonic term near the natural frequency and (b) at the external force frequency vs. the detuning parameter when κ_e =5. (c) The amplitude of the harmonic term near the natural frequency and (d) at the external force frequency vs. the detuning parameter, when κ_e =0. Continuous lines represent stable solutions while dashed lines represent unstable solutions.

The governing equation of motion is:

$$m\ddot{y}+c\dot{y}+\left(\left(1+\alpha_a\cos\left(\omega_a t+\varphi_a\right)+\alpha_b\cos\left(\omega_b t+\varphi_b\right)\right)k_1+k_2 y+k_3 y^2\right)y=F\cos\left(\omega_r t+\varphi_r\right). \tag{1}$$

The analytical solution is approximated by utilizing the multiple scales perturbation method [24], therefore the equation of motion is transformed to the following:

$$x''+x=P\cos\left(\Omega_r\tau+\varphi_r\right)-\varepsilon\left(2\zeta x'+\left(\gamma_a\cos\left(\Omega_a\tau+\varphi_a\right)+\gamma_b\cos\left(\Omega_b\tau+\varphi_b\right)\right)x+\kappa_2 x^2\right)-\varepsilon^2\kappa_3 x^3$$

$$x=y/\varepsilon^2 \quad \tau=\omega_n t, \quad \omega_n=\sqrt{k/m}, \quad \Omega_\bullet=\frac{\omega_\bullet}{\omega_n}, \quad \zeta=\frac{c}{2\varepsilon m\omega_n}, \tag{2}$$

$$\gamma_\bullet=\alpha_\bullet/\varepsilon, \quad \kappa_2=\frac{\varepsilon k_2}{m\omega_n^2}, \quad \kappa_3=\frac{\varepsilon^2 k_3}{m\omega_n^2}, \quad P=\frac{F}{m\varepsilon^2\omega_n^2}.$$

Whereas, $\partial\bullet/\partial\tau=\bullet'$, and it is assumed that the amplifier is lightly damped $\varepsilon\sim O\left(c/2\sqrt{km}\right)=1$. Considering a second order expansion in the form

$$x(\varepsilon,\tau)=x_0\left(\tau_0,\tau_1,\tau_2\right)+\varepsilon x_1\left(\tau_0,\tau_1,\tau_2\right)+\varepsilon^2 x_2\left(\tau_0,\tau_1,\tau_2\right), \quad \tau_i=\varepsilon^i\tau, \tag{3}$$

and setting the pumping frequencies as:

$$\Omega_a=2\left(1+\varepsilon\sigma\right), \quad \Omega_b+\Omega_r=1+\varepsilon\sigma, \tag{4}$$

whereas σ is a detuning parameter. The selected frequencies in Eq.(4) mean pumping the system at a frequency (Ω_a) close to twice the natural frequency yielding a principal parametric resonance [25], and a frequency combination (Ω_b+Ω_r) close to the natural frequency yielding a combination resonance [25]. For the assumed scaling of the parameters, the steady-state approximated solution consist two dominating harmonic terms: one close to the natural frequency $\Omega_a/2$ and the other at the external force frequency Ω_r.

$$x=a_0\cos\left(\frac{\Omega_a}{2}\tau-\psi_0\right)+a_r\cos\left(\Omega_r\tau-\psi_r\right)+O\left(\varepsilon^2\right). \tag{5}$$

The detailed derivation of the parameters a_0, a_r, ψ_0 and ψ_r is provided in [21], and a_0 as a function of the various parameters is provided in Appendix A, Eq.(A.1).

The nonlinear stiffness terms have a significant influence on the response and their mutual contribution can be quantified by a single parameter κ_e, which is the effective nonlinear stiffness:

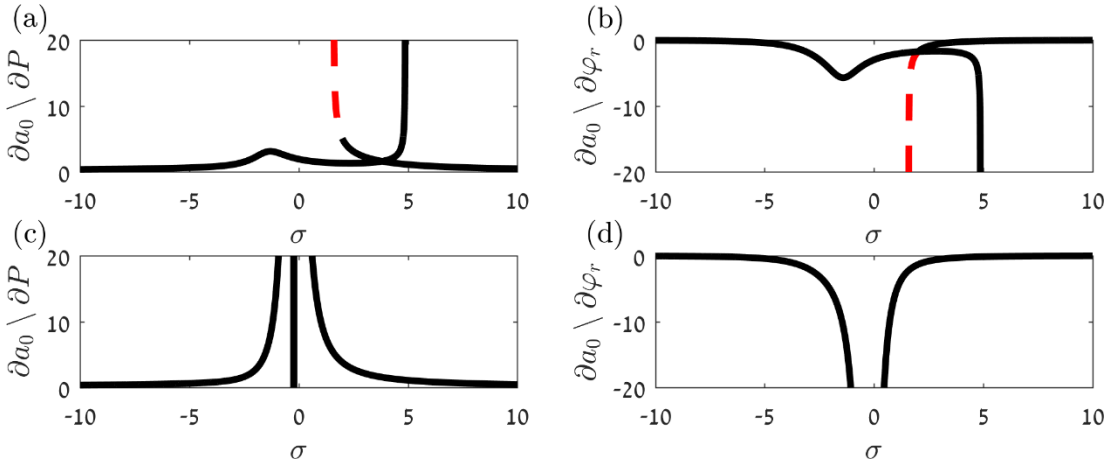


Figure 3: (a) The sensitivity with respect to the external force amplitude, P and (b) with respect to the external phase, φ_r when κ_e =5. (c) The sensitivity with respect to the external force amplitude, P and (d) with respect to the external phase, φ_r, when κ_e =0. Continuous lines represent stable solutions while dashed lines represent unstable solutions.

$$\kappa_e = 3\kappa_3 - \frac{10}{3}\kappa_2^2 . \tag{6}$$

Setting positive effective stiffness leads to a hardening type system, while setting it negative leads to a softening type system [26]. By setting κ_e to zero, the amplifier behaves linearly up to the second order (i.e., ε^2). Analytically computed characteristic frequency sweeps for two cases are shown in Figure 2. In the first case, depicted in Figure 2 (a) and (b), the effective stiffness is positive, and one can witness a stiffening behavior. In the second case, depicted in Figure 2 (c) and (d), the effective stiffness equals zero, and the amplifier behaves pseudo-linearly.

Another important attribute of the amplifier is its sensitivity to variations in the external force amplitude, and phase φ_r, which can be computed in a closed form as shown in Appendix B of [21]. The sensitivities for the previous cases are depicted in Figure 3. It is noticeable, that when a single stable solution exists (for κ_e =5, $\sigma<-2$ or $4.8<\sigma$, and for κ_e =0 the whole σ domain) higher sensitivity levels can be achieved when κ_e =0. Observing Figure 2 and Figure 3, it is also noticeable that the pseudo-linear amplifier sensitivities and amplitude a_0 behave similarly with respect to σ, which means that no compromise has to be made between the two, unlike when $\kappa_e \neq 0$.

2.1 Optimal parameters tuning

By properly setting the tunable parameters of the scheme parameters, the oscillator becomes as a sensitive amplifier. To produce large amplification while maintaining the sensitivities, it was found that the effective stiffness should be tuned to zero, therefore, it is suggested to set κ_2=1 and κ_3=10/9. The pumping magnitudes should be tuned to allow the linear system to lose its stability, thus producing large amplitudes. The suitable value of γ_a as a function of the system parameters and γ_b can be computed by solving a sixth order polynomial:

$$G_6\left(\varepsilon,\Omega_r\right)\gamma_a^6 + G_4\left(\varepsilon,\Omega_r,\gamma_b,\zeta\right)\gamma_a^4 + G_2\left(\varepsilon,\Omega_r,\gamma_b,\zeta\right)\gamma_a^2 + G_0\left(\Omega_r,\zeta\right) = 0. \tag{7}$$

The functions G_i are provided in Appendix A of [21]. Because γ_b is unknown prior to the computation of γ_a, one can set the maximum allowable stiffness modulation (Δk_1, $0< \Delta k_1<1$) as a design parameter. Then, the following algebraic relation can be substituted to Eq.(7):

$$\varepsilon\left(\gamma_a + \gamma_b\right) = \Delta k_1, \tag{8}$$

for simple computation of the pumping magnitudes.

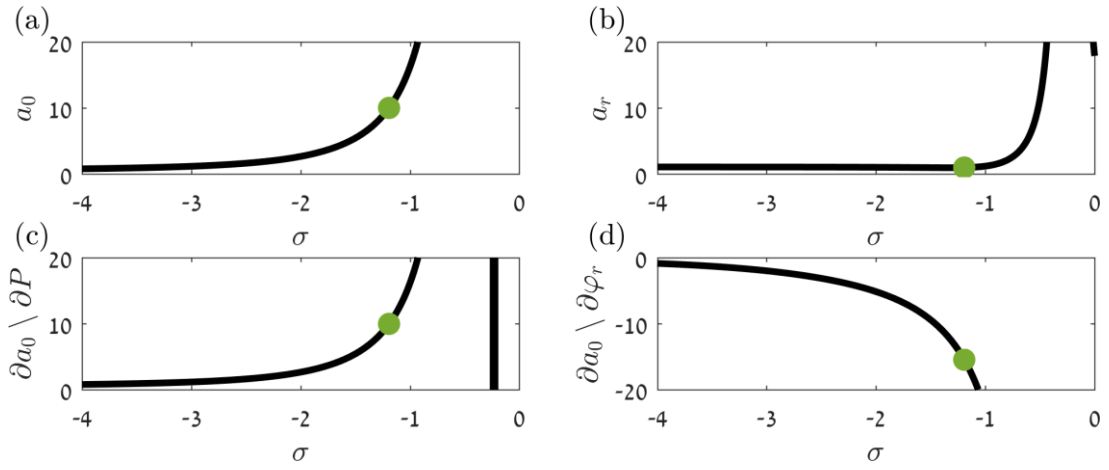


Figure 4: κ_e =0, the response amplitudes and sensitivities vs. the detuning parameter. (a) The amplitude of the harmonic term near the natural frequency and (b) at the external force frequency. (c) The sensitivity with respect to the external force amplitude, and (d) with respect to the external phase. The dots mark $\sigma \approx -1.19$.

Once the nonlinear stiffness terms and pumping magnitudes were computed the detuning parameter σ should be set. This can be done graphically, as shown in Figure 4, where the selected detuning parameter was chosen to be -1.19, and is marked in the subfigures by a circular marker. Finer adjustments can then be made by tuning φ_a [21], while φ_b is used to obtain φ_r as briefly explained in Section 3; a detailed explanation is provided in [16].

3 Suggested mass balancing procedure exploiting the amplifier

During the MBP one seeks the distribution of the imbalance forces, amplitude and phase along the rotor. To simplify the discussion, consider the case of an unbalanced rigid disc mounted on a flexible weightless shaft as shown in Figure 5. As depicted in the figure, the center of mass does not coincide with the geometrical center, and is located at a phase φ_r relative to the initial position.



Figure 5: Two views of an unbalanced rigid disc mounted on a weightless flexible shaft.

The resulting imbalance force has the general form $A\Omega_r^2\cos(\Omega_r t+\varphi_r)$ where Ω_r is the rotation speed and A is related to the imbalance magnitude. When the SDOF scheme is implemented (i.e., tuned parametric excitation), and the amplitude of vibration close to the natural frequency due to the imbalance is plotted as a function of $\varphi_b+\varphi_r$, it has a period of π, as shown analytically and numerically in Figure 6.

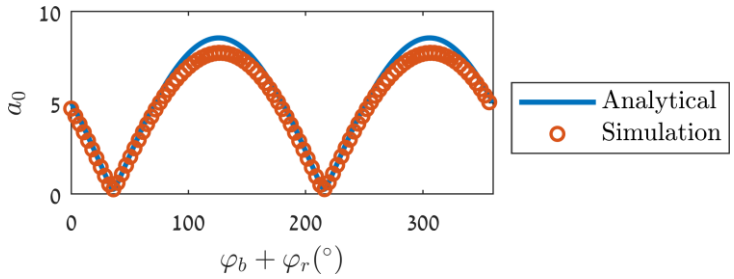


Figure 6: The amplitude of the harmonic term near the natural frequency vs. the sum of phases φ_b+φ_r. Analytically computed (continuous lines) and numerically simulated responses (hollow circular markers).

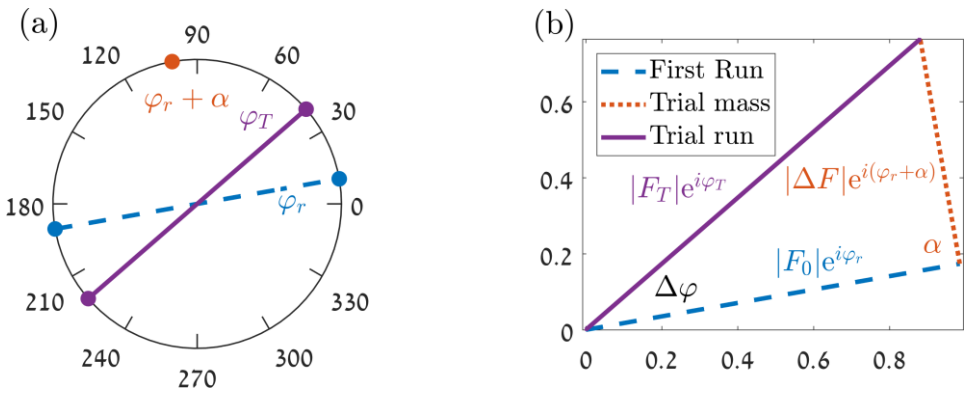


Figure 7: (a) Possible solutions for φ_r in the first and the trial runs. (b) Extraction of the imbalance.

Because φ_b and φ_r have the same influence on the system [16,18,19,21], and φ_b is controllable, identifying the minima (or maxima) of a_0 vs. φ_b is equivalent to identifying the imbalance phase. However, because the two minima are π radians apart, an additional, controlled measurement is required, where a trial mass is placed at a known phase.

First, the amplitude vs. the phase φ_b is measured until a minimum is found, this phase is denoted φ_{b0}. The location of the imbalance, φ_r is found according to the analytical solution of $a_0(\varphi_{b0}+\varphi_r)$, (e.g., for the SDOF discussed in Section 2 see Eq.(A.1), and for a MDOF system see Eq.(16) and Eq.(20)). To distinguish between the two possible locations of φ_r (π radians apart, as shown in Figure 7(a)), a trial mass is added, and the total imbalance force at the trial run is:

$$|F_T|e^{i\varphi_T} = |F_0|e^{i\varphi_r} + |\Delta F|e^{i(\varphi_r+\alpha)}, \tag{9}$$

whereas $|F_0|$ is the force due to the unknown imbalance, $|\Delta F|$ is the force due to the trial mass, and φ_r+α is the total trial mass phase. The phase φ_T is found by sweeping φ_b (two possible solutions π radians apart, as shown in Figure 7(a)). The trial mass should be placed about $\pi/2$ apart from φ_r to achieve maximum change in φ_r. Since the imbalance at the trial run must lie between φ_r and φ_r+α, the true location of φ_r can be found. And the imbalance magnitude is computed as:

$$|F_0| = \frac{|\Delta F|\sin(\alpha+\Delta\varphi)}{\sin(\Delta\varphi)}, \tag{10}$$

graphical explanation is depicted in Figure 7(b).

4 Extension of the method to a rotating MDOF system

In this section, the scheme is extended to accommodate rotating structures via a test case, for which an experimental rig was designed and built. As shown in Figure 8, two rigid discs are fixed to a rigid rotor which is mounted on a plate free to move only in the horizontal plane (x-z). A lumped parameters model of

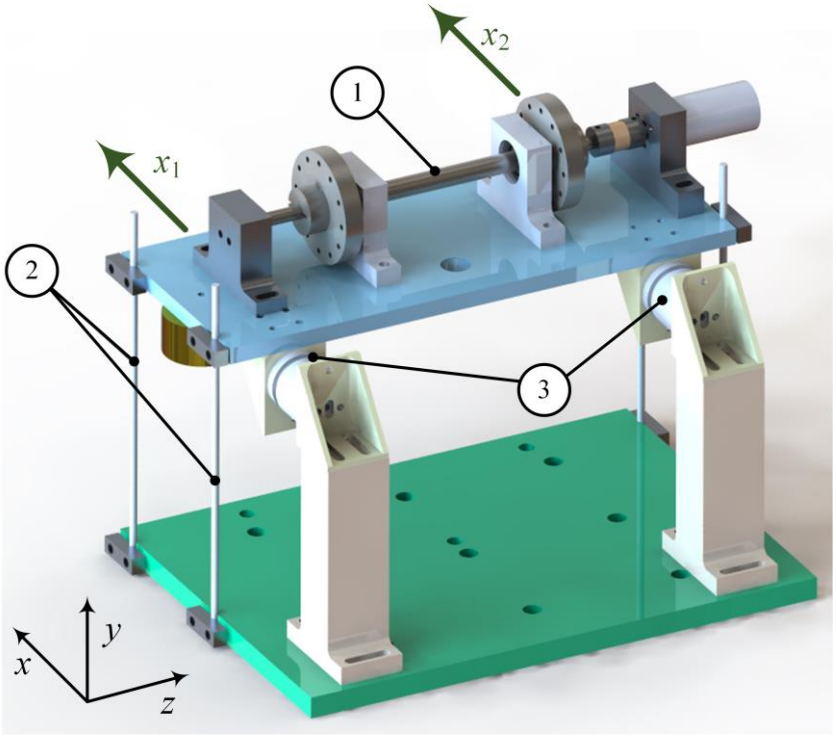


Figure 8: Rotor balancing demonstrator, comprises a rotating rigid shaft and discs (1), flexible foundation supports (2), and two linear voice coil actuators (3) that induces position and time dependent forces.

the system is used, and the governing equations of motion in matrix and vector notation are:

$$\mathbf{M}\ddot{\mathbf{x}} + \mathbf{C}\dot{\mathbf{x}} + \left(\mathbf{K} + \mathbf{K}_{\mathbf{p}}(t)\right)\mathbf{x} + \mathbf{f}_{\mathbf{nl}}\left(\mathbf{x}^2, \mathbf{x}^3\right) = \Omega_r^2 \mathbf{f}_{\mathbf{ib}} \tag{11}$$

Here, $\mathbf{M}$ is the mass matrix, $\mathbf{C}$ the damping matrix, $\mathbf{K}$ the stiffness matrix, $\mathbf{K_p}$ the pumping matrix, $\mathbf{f_{nl}}$ the nonlinear feedback force vector and $\Omega_r^2\mathbf{f_{ib}}$ is the imbalance force vector. In this case, the matrix $\mathbf{K_p}$ and force vector $\mathbf{f_{nl}}$ are fully controllable and are manipulated to excite every desired system vibration mode as described below.

By assuming low damping levels, setting the parametric excitation and nonlinear forces to the same order of magnitude, and using the mass normalized modes of the linear undamped system, the equations of motion can be transformed to the following:

$$\mathbf{I}\boldsymbol{\eta}'' + \boldsymbol{\chi}^2\boldsymbol{\eta} = \mathbf{P}(\tau) - \varepsilon\left(2\zeta\boldsymbol{\chi}\boldsymbol{\eta}' + \mathbf{K}_{\gamma}(\tau)\boldsymbol{\eta} + \boldsymbol{\kappa}_2\boldsymbol{\eta}_2^2\right) - \varepsilon^2\boldsymbol{\kappa}_3\boldsymbol{\eta}_3^3. \tag{12}$$

Here the time was scaled as $\tau = \omega t$, and $\boldsymbol{\eta}$ is the modal coordinate vector which is related to the physical ones according to Eq.(B.4). A detailed mathematical description regarding the transformation from Eq.(11) to Eq.(12), and parameter definitions are provided in Appendix B.

4.1 Approximate analytical solution

To derive the approximate analytical solution, the method of multiple scales is employed. First the imbalance force projection on the first mode is computed, hence $\omega = \omega_1$. It proves convenient to apply the controlled forces in a manner leading to minimal coupling between the modes, while choosing the frequencies leading to combination and principal parametric resonances. Therefore, the following parametric excitation matrix is used:

$$\mathbf{K}_{\gamma}(\tau)=\begin{pmatrix}\chi_1^2\left(\gamma_{a1}\cos\left(\chi_{a1}\tau+\varphi_{a1}\right)+\gamma_{b1}\cos\left(\chi_{b1}\tau+\varphi_{b1}\right)\right) & 0\\ 0 & 0\end{pmatrix},$$
$$\chi_{a1}=2\left(1+\varepsilon\sigma\right),\quad \chi_{b1}+\mu_1\chi_1=1+\varepsilon\sigma,\quad \chi_r=\mu_1\chi_1. \tag{13}$$

Moreover, the nonlinear forces should also have minimal influence on the unexcited mode:

$$\boldsymbol{\kappa}_2=\frac{\left|\boldsymbol{\Phi}\right|^2\beta_{11}}{\omega^2}\begin{pmatrix}\frac{\phi_{11}}{\phi_{22}^2} & 0 & -\frac{\phi_{12}}{\phi_{21}\phi_{22}}\\ 0 & 0 & 0\end{pmatrix},\quad \boldsymbol{\kappa}_3=\frac{\left|\boldsymbol{\Phi}\right|^2\delta_{11}}{\omega^2}\begin{pmatrix}\frac{\phi_{11}^2}{\phi_{22}^2} & 0 & -\frac{3\phi_{11}\phi_{12}}{\phi_{21}\phi_{22}} & -\frac{\phi_{12}\left(\phi_{12}\phi_{21}+\phi_{11}\phi_{22}\right)}{\phi_{21}^2\phi_{22}}\\ 0 & 0 & 0 & 0\end{pmatrix},$$
$$\left|\boldsymbol{\Phi}\right|^2=\left(\phi_{12}\phi_{21}-\phi_{11}\phi_{22}\right)^2. \tag{14}$$

Following the multiple scales procedure up to the 2nd order, as detailed in [21], the solution in modal coordinates is:

$$\eta_1=a_{10}\cos\left(\frac{\chi_{a1}}{2}\tau-\psi_0\right)+a_{r1}\cos\left(\chi_r\tau-\psi_{r1}\right),\quad \eta_2=a_{r2}\cos\left(\chi_r\tau-\psi_{r2}\right). \tag{15}$$

Whereas,

$$a_{10}=\frac{\gamma_{b1}P_1}{2\chi_1^2\left(\mu_1^2-1\right)}\begin{pmatrix}4\varepsilon\zeta_1\left(3+\mu_1\left(\mu_1+\mu_1^2-13\right)\right)\cos\left(\psi_0+\varphi_{b1}+\varphi_1\right)+\\ \left(1+\mu_1\right)\begin{pmatrix}\gamma_{a1}\varepsilon\left(7+\left(\mu_1-4\right)\mu_1\right)\sin\left(\psi_0+\varphi_{a1}-\varphi_{b1}-\varphi_1\right)+\\ 4\left(\mu_1-3\right)\left(\mu_1-1\right)\left(2-\varepsilon\sigma\right)\sin\left(\psi_0+\varphi_{b1}+\varphi_1\right)\end{pmatrix}\end{pmatrix}$$
$$\times\left(4\left(\mu_1-3\right)\left(\mu_1-1\right)\left(\mu_1+1\right)\left(4\zeta_1+\gamma_{a1}\left(1-\varepsilon\sigma\right)\sin\left(2\psi_0+\varphi_{a1}\right)\right)\right)^{-1} \tag{16}$$

It is clear that Eq.(16) is practically the same as Eq.(A.1), therefore the optimal parameters can be tuned as described in Section 2.1. Furthermore, the suggested balancing procedure (Section 3) can be employed and the imbalance projection on the first mode can be found.

To find the imbalance projection on the second mode, the parameters are tuned to have minimal influence on the first mode. In this case, $\omega=\omega_2$ and the pumping and nonlinear terms are tuned as:

$$\mathbf{K}_{\gamma}(\tau)=\begin{pmatrix}0 & 0\\ 0 & \chi_2^2\left(\gamma_{a2}\cos\left(\chi_{a2}\tau+\varphi_{a2}\right)+\gamma_{b2}\cos\left(\chi_{b2}\tau+\varphi_{b2}\right)\right)\end{pmatrix},$$
$$\chi_{a2}=2\left(1+\varepsilon\sigma\right),\quad \chi_{b2}+\mu_2\chi_1=1+\varepsilon\sigma,\quad \chi_r=\mu_2\chi_1. \tag{17}$$

$$\boldsymbol{\kappa}_2=\frac{\left|\boldsymbol{\Phi}\right|^2\beta_{22}}{\omega^2}\begin{pmatrix}0 & 0 & 0\\ -\frac{\phi_{21}}{\phi_{11}\phi_{12}} & 0 & \frac{\phi_{22}}{\phi_{11}^2}\end{pmatrix},\quad \boldsymbol{\kappa}_3=\frac{\left|\boldsymbol{\Phi}\right|^2\delta_{22}}{\omega^2}\begin{pmatrix}0 & 0 & 0 & 0\\ -\frac{\phi_{21}\left(\phi_{12}\phi_{21}+\phi_{11}\phi_{22}\right)}{\phi_{11}\phi_{12}^2} & -\frac{3\phi_{21}\phi_{22}}{\phi_{11}\phi_{12}} & 0 & \frac{\phi_{22}^2}{\phi_{11}^2}\end{pmatrix}\delta_{22}. \tag{18}$$

And the solution is:

$$\eta_1=a_{r2}\cos\left(\chi_r\tau-\psi_{r2}\right),\quad \eta_2=a_{20}\cos\left(\frac{\chi_{a2}}{2}\tau-\psi_0\right)+a_{r2}\cos\left(\chi_r\tau-\psi_{r2}\right). \tag{19}$$

Whereas,

$$a_{20}=\frac{\gamma_{b2}P_2}{2\chi_1^2\left(\mu_2^2-1\right)}\begin{pmatrix}4\varepsilon\zeta_2\left(3+\mu_2\left(\mu_2+\mu_2^2-13\right)\right)\cos\left(\psi_0+\varphi_{b2}+\varphi_2\right)+\\ \left(1+\mu_2\right)\begin{pmatrix}\gamma_{a2}\varepsilon\left(7+\left(\mu_2-4\right)\mu_2\right)\sin\left(\psi_0+\varphi_{a2}-\varphi_{b2}-\varphi_2\right)+\\ 4\left(\mu_2-3\right)\left(\mu_2-1\right)\left(2-\varepsilon\sigma\right)\sin\left(\psi_0+\varphi_{b2}+\varphi_2\right)\end{pmatrix}\end{pmatrix}$$
$$\times\left(4\left(\mu_2-3\right)\left(\mu_2-1\right)\left(\mu_2+1\right)\left(4\zeta_2+\gamma_{a2}\left(1-\varepsilon\sigma\right)\sin\left(2\psi_0+\varphi_{a2}\right)\right)\right)^{-1}. \tag{20}$$

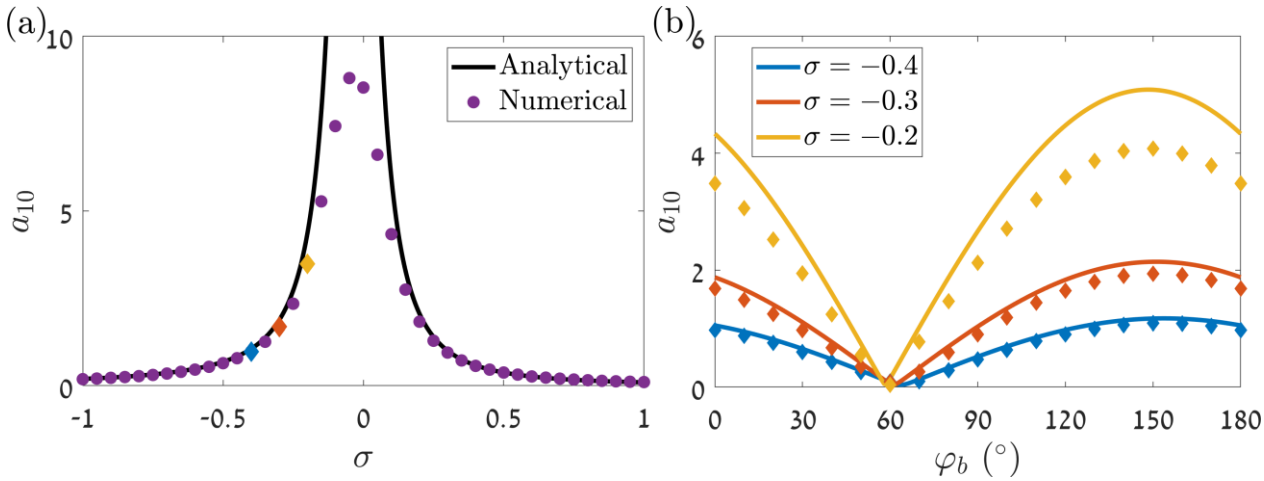


Figure 9: first mode amplitude close to the natural frequency (a_{10}) (a) vs. σ, and (b) vs. φ_b. Analytical solutions are shown bycontinous lines, and numerical results by markers.

As before, Eq.(20) is practically the same as Eq.(A.1). The optimal parameters can be tuned as previously described, and the suggested balancing procedure can be employed.

4.2 Numerical verification

In the following section a numerical verfication of the suggested optimal schem is performed via simulations. The parameters used in the simulation match the experimental rig shown in Figure 8, and were experimentally identified:

$$\Phi = \begin{pmatrix} 0.6411 & 0.6312 \\ 0.6230 & -0.6645 \end{pmatrix}, \quad \Omega_n = \begin{pmatrix} 18.9 & 0 \\ 0 & 29.1 \end{pmatrix} (\text{Hz}), \quad \zeta = \begin{pmatrix} 1 & 0 \\ 0 & 0.45 \end{pmatrix}. \tag{21}$$

The numerical verification shown herein was performed for a known level of imbalance. The goal was to find its projection on each mode, and to study the ability to change the sensitivity by tuning the pumping frequency, σ.

First, the imbalance projection on the first mode was sought, therefore the parameters were tuned according to Eqns.(13) and (14), where $\boldsymbol{\kappa}_{2,11}$ and $\boldsymbol{\kappa}_{3,11}$ were chosen according to Eq.(6) leading to κ_e=0. Moreover, the pumping magnitudes γ_{a1} and γ_{b1} were tuned according to Eqns.(7) and (8), where Δk=0.1. In Figure 9 (a) the analytical and numerical results of the amplitude close to the natural frequency (a_{10}) vs. the detuning parameter σ are shown. The analytical solution is shown by a black continuous line, while, the numerical results are depicted by markers. The values depicted by diamond shaped markers in Figure 9 (a) are used in the following stage, the phase (φ_b) sweep. One can witness the good agreement between the analytical and numerical solutions for relatively low amplitudes. As the amplitude grows the solutions deviate due to nonlinear effects, this is anticipated whereas the analytical model was derived for small amplitudes. Moreover, it is noticeable that according to the analytical model a single solution exists at each frequency, in contrast to the previous method. A discussion regarding that is provided in Section 4.3.

The following stage is a frequency sweep as shown in Figure 9 (b) for different detuning values. The numerical solutions (markers) are in agreement with the analytical solution (continuous lines), and the agreement is better as the amplitude decreases. Because the numerical solution agrees with the model, the imbalance phase φ_r can be computed from Eq.(16). As discussed in Section 2, the amplification and sensitivity behave similarly with respect to σ when the equivalent stiffness is set to zero. This phenomenon can be seen in Figure 9 (b); as the detuning parameter is increased higher amplitudes are produced and also better sensitivity is achieved. The sensitivity can be interpreted as the difference between the maximum and minimum measured amplitudes in the phase sweep.

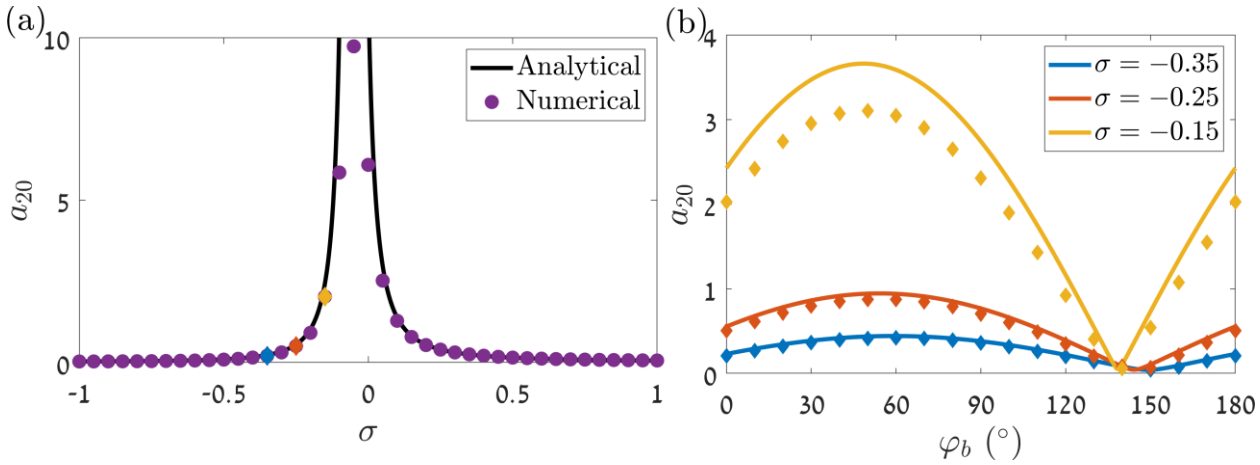


Figure 10: second mode amplitude close to the natural frequency (a_{10}) (a) vs. σ, and (b) vs. φ_b. Analytical sulutions are shown by lines, and numerical results by markers.

A similar process to identify the imbalance projection on the second mode was preformed, and shown in Figure 10. For this case, the parameters were tuned according to Eqns.(17) and (18) where $\boldsymbol{\kappa}_{2,21}$ and $\boldsymbol{\kappa}_{3,21}$ were chosen according to Eq.(6) leading to κ_e=0. Moreover, the pumping magnitudes γ_{a1} and γ_{b1} were tuned according to Eqns.(7) and (8), where Δk=0.1. The observations in this case are similar to the ones in the previous case, hence the imbalance phase φ_r can be computed from Eq.(20), and the amplification and sensitivity are controllable via σ.

4.3 Comparison to the previous MBP method

The previous MBP method, which is discussed in [15-20], differs from the current by two main aspects. It neither includes a quadratic stiffness term, nor it includes the parameter optimization stage for selecting the parametric excitation magnitudes. Therefore, the previous method has two main drawbacks: (1) a compromise between amplification and sensitivity has to be made, and (2) multiple stable solution branches may exist very close to each other for the same σ. In practice, two close branches results in a major decrease of the sensitivity, since the solution jumps from one stable branch to the other as shown Figure 11 (and [16]), by the circular and diamond shaped markers. These results, depicting two close stable solution branches were obtained experimentally.

By implementing the quadratic nonlinear stiffness, the system behavior is pseudo-linear, hence omits the need to compromise between sensitivity and amplification, and it also eliminates the second stable solution. The use of optimized pumping magnitudes enables higher sensitivity, and also results with a single stable solution, because the pumping level of the principal parametric resonance is lower than its linear threshold [21].

Comparison between the two methods applied to the same system [16] is shown in Figure 11. It is noticeable that while similar maximal amplitudes were produced, the sensitivity is about five times higher when the optimal method is used. Note that the methods result in different values for φ_{b0}, since the phase of the response ψ differs. For the experimental results, φ_{b0} is located at the minimum of the black dashed line (~84°), while for the optimal method it is located around 60°.

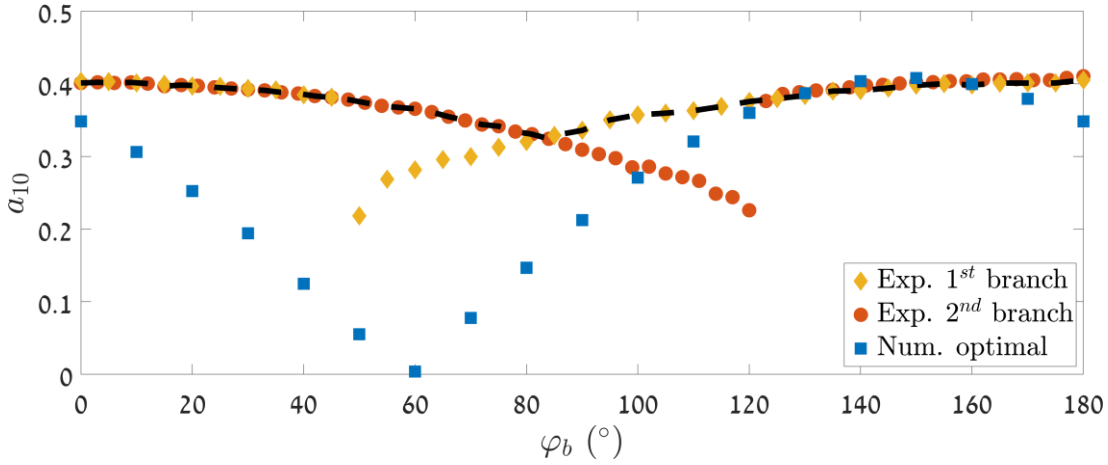


Figure 11: first mode amplitude close to the natural frequency (a_{10}) vs. φ_b, a comparison between the current optimal to the previous metod. Previous method, experimentally obtained results: circular orange (diamond shaped yellow) markers depict the first (second) stable solution branch. Current method, numerically obtained results are shown by blue square markers.

5 Summary and conclusions

A modified optimal mass balancing procedure scheme has been introduced, whose performance surpassed the previous one [16], as discussed in Section 4.3. The current scheme is an extension of the SDOF parametric amplifier scheme, which was discussed in Section 2, to a rotating MDOF system. The current MBP utilizes tuned dual frequency parametric excitation and nonlinear feedback term, to project the distributed imbalance force on any selected vibration mode, while rotating the structure slowly. The latter enables to identify the imbalance and correct it by adding or removing mass from the rotor, while avoiding the difficulties and risks involved in rotating the rotor close to a critical speed.

Implementing tuned dual parametric excitation leads to two kind of resonances. First, a combination resonance that couples the external signal (i.e., the imbalance force) with one of the vibration modes, which is appropriate to a selected natural frequency. Second, a principal parametric resonance that considerably amplifies the response close to the selected natural frequency. The resulting dynamic response due to both resonances is the underlying mechanism that allows energy transfer from the imbalance force at frequency ω_r to the rotor's response close to a selected natural frequency $\sim \omega_n$. The optimal parameters tuning by which the pumping magnitudes are selected, leads to a marginally stable system [21], thus making it very sensitive. In addition, proper tuning of the nonlinear feedback term (i.e., setting the equivalent stiffness to zero) leads to a pseudo-linear dynamic behavior. As a result, the amplification and sensitivity behaves similarly with respect to the detuning parameter σ, therefore no compromise between the two has to be made as in the previous method.

In Section 4.3, a comparison between the optimal and previous methods was briefly discussed. The data for the previous method was obtained experimentally, while for the current method it was simulated. In future work, the optimal method would be implemented experimentally on the same system to validate its superiority. In addition, the method will be tested on a different system which has "flexible" modes [27].

Acknowledgements

The first author would like to acknowledge the generous financial support of the Israeli Ministry of Science and Technology (3-13336) for the Applied Science scholarship for engineering PhD students 2016.

References

[1] I. Bucher, D.J. *Ewins, Modal analysis and testing of rotating structures*, Philos. Trans. R. Soc. London A Math. Phys. Eng. Sci. 359 (2001) 61–96. doi:10.1098/rsta.2000.0714.

[2] M. Géradin, D.J. Rixen, *Mechanical Vibrations: Theory and Application to Structural Dynamics*, third ed., Wiley, Chichester, 2015.

[3] A. Tonoli, N. Amati, A. Bonfitto, M. Silvagni, B. Staples, E. Karpenko, *Design of Electromagnetic Dampers for Aero-Engine Applications*, J. Eng. Gas Turbines Power. 132 (2010) 112501. doi:10.1115/1.4000801.

[4] R. Holmes, *The Control of Engine Vibration Using Squeeze Film Dampers*, J. Eng. Power. 105 (1983) 525. doi:10.1115/1.3227447.

[5] H. Nguyen-Schäfer, *Rotordynamics of Automotive Turbochargers*, 2nd ed., Springer Science + Business Media, 2015. doi:10.1007/978-3-319-17644-4.

[6] M.S. Darlow, *Balancing of High-Speed Machinery*, Springer-Verlag New York Inc., 2012. doi:10.1007/978-1-4612-3656-6.

[7] R.E.D. Bishop, A.G. Parkinson, *On the Use of Balancing Machines for Flexible Rotors*, J. Eng. Ind. 94 (1972) 561–572. doi:10.1115/1.3428193.

[8] G. Genta, D*ynamics of rotating systems*, Springer Science + Business Media, Inc., 2007.

[9] Y. Ishida, T. Yamamoto, *Linear and nonlinear rotordynamics: a modern treatment with applications*, John Wiley & Sons, 2001.

[10] W.C. Foiles, P.E. Allaire, E.J. Gunter, *Rotor balancing*, Shock Vib. 5 (1998) 325–336. doi:10.1155/1998/648518.

[11] W.D. Pilkey, J.T. Bailey, *Constrained balancing techniques for flexible rotors*, J. Mech. Des. 101 (1979) 304–308. doi:10.1115/1.3454053.

[12] R.M. Little, W.D. Pilkey, *A Linear Programming Approach for Balancing Flexible Rotors*, J. Eng. Ind. 98 (1976) 1030–1035. doi:10.1115/1.3438997.

[13] C.D. Untaroiu, P.E. Allaire, W.C. Foiles, *Balancing of Flexible Rotors Using Convex Optimization Techniques: Optimum Min-Max LMI Influence Coefficient Balancing*, J. Vib. Acoust. 130 (2008) 21006. doi:10.1115/1.2730535.

[14] M.S. Darlow, A.J. Smalley, A.G. Parkinson, *Demonstration of a Unified Approach to the Balancing of Flexible Rotors*, J. Eng. Power. 103 (1981) 101–107. doi:10.1115/1.3230679.

[15] T. Shachar, I. Bucher, *A Method for Balancing High-Speed Rotors Using Low Rotation Speed Measured Data Through Parametric Excitation*, in: Proc. 11th Int. Conf. Vib. Rotating Mach., manchester, UK, 2016.

[16] S. Tresser, A. Dolev, I. Bucher, *Dynamic balancing of super-critical rotating structures using slow-speed data via parametric excitation*, J. Sound Vib. 415 (2017) 59–77. doi:https://doi.org/10.1016/j.jsv.2017.11.029.

[17] A. Dolev, I. Bucher, *A Parametric Amplifier for Weak, Low-Frequency Forces*, in: ASME 2015 Int. Des. Eng. Tech. Conf. Comput. Inf. Eng. Conf., ASME, Boston, Mass., USA, 2015: p. V006T10A046. doi:10.1115/DETC2015-46273.

[18] A. Dolev, I. Bucher, *Tuneable, non-degenerated, nonlinear, parametrically-excited amplifier*, J. Sound Vib. 361 (2016) 176–189. doi:10.1016/j.jsv.2015.09.048.

[19] A. Dolev, I. Bucher, E*xperimental and Numerical Validation of Digital, Electromechanical, Parametrically Excited Amplifiers*, J. Vib. 138 (2016). doi:10.1115/1.4033897.

[20] A. Dolev, I. Bucher, *Dual frequency parametric excitation of a nonlinear, multi degree of freedom mechanical amplifier with electronically modified topology*, J. Sound Vib. 419 (2018) 420–435.

doi:10.1016/j.jsv.2018.01.008.

[21] A. Dolev, I. Bucher, *Optimizing the dynamical behavior of a dual-frequency parametric amplifier with quadratic and cubic nonlinearities*, Nonlinear Dyn. (2018). doi:10.1007/s11071-018-4174-5.

[22] L.D. Zavodney, A.H. Nayfeh, *The response of a single-degree-of-freedom system with quadratic and cubic non-linearities to a fundamental parametric resonance*, J. Sound Vib. 120 (1988) 63–93. doi:10.1016/0022-460X(88)90335-5.

[23] L.D. Zavodney, A.H. Nayfeh, N.E. Sanchez, *The response of a single-degree-of-freedom system with quadratic and cubic non-linearities to a principal parametric resonance*, J. Sound Vib. 129 (1989) 417–442. doi:10.1016/0022-460X(89)90433-1.

[24] A.H. Nayfeh, *Perturbation Methods*, Wiley-VCH, Weinheim, 2008.

[25] A.H. Nayfeh, D.T. Mook, *Nonlinear Oscillations*, Wiley-VCH, Weinheim, 2008.

[26] I. Kovacic, M.. Brennan, *The Duffing equation: Nonlinear oscillators and their behaviour*, 1st ed., John Wiley & Sons, 2011. doi:10.1002/9780470977859.

[27] A. Ferdinskoif, *Laboratory Platform for Simulation, Validation and Design of High-Speed Rotors*, Technion – Israel Institute of Technology, 2018.

Appendix A

The analytical solution of a_0, as reported in [21]:

$$a_0 = \frac{\gamma_b}{2\left(\Omega_r^2-1\right)}\left(\begin{array}{l} 4\varepsilon\zeta\left(3+\Omega_r\left(\Omega_r^2+\Omega_r-13\right)\right)\cos\left(\psi_0+\varphi_b+\varphi_r\right)+ \\ \left(1+\Omega_r\right)\left(\begin{array}{l}\gamma_a\varepsilon\left(7+\left(\Omega_r-4\right)\Omega_r\right)\sin\left(\psi_0+\varphi_a-\varphi_b-\varphi_r\right)+ \\ 4\left(\Omega_r-3\right)\left(\Omega_r-1\right)\left(2-\varepsilon\sigma 2\right)\sin\left(\psi_0+\varphi_b+\varphi_r\right)\end{array}\right)\end{array}\right) \\ \times\left(4\left(\Omega_r-3\right)\left(\Omega_r-1\right)\left(\Omega_r+1\right)\left(4\zeta+\gamma_a\left(1-\varepsilon\sigma\right)\sin\left(2\psi_0+\varphi_a\right)\right)\right)^{-1}. \tag{A.1}$$

Whereas, ψ_0 are the roots of a 10th order polynomial, whose coefficient are omitted for brevity.

Appendix B

The governing equations of the experimental rig are:

$$\underbrace{\begin{pmatrix} m_{11} & m_{12} \\ m_{21} & m_{22} \end{pmatrix}}_{\mathbf{M}}\begin{pmatrix} \ddot{x}_1 \\ \ddot{x}_2 \end{pmatrix}+\underbrace{\begin{pmatrix} c_{11} & c_{12} \\ c_{21} & c_{22} \end{pmatrix}}_{\mathbf{C}}\begin{pmatrix} \dot{x}_1 \\ \dot{x}_2 \end{pmatrix}+\underbrace{\begin{pmatrix} k_{11} & k_{12} \\ k_{21} & k_{22} \end{pmatrix}}_{\mathbf{K}}\underbrace{\begin{pmatrix} x_1 \\ x_2 \end{pmatrix}}_{\mathbf{x}}+ \\ \underbrace{\begin{pmatrix} k_{p11}(t) & k_{p12}(t) \\ k_{p21}(t) & k_{p22}(t) \end{pmatrix}}_{\mathbf{K_p}}\begin{pmatrix} x_1 \\ x_2 \end{pmatrix}+\underbrace{\begin{pmatrix} b_{11} & b_{12} \\ b_{21} & b_{22} \end{pmatrix}}_{\mathbf{B}}\begin{pmatrix} x_1^2 \\ x_2^2 \end{pmatrix}+\underbrace{\begin{pmatrix} d_{11} & d_{12} \\ d_{21} & d_{22} \end{pmatrix}}_{\mathbf{D}}\begin{pmatrix} x_1^3 \\ x_2^3 \end{pmatrix}=\underbrace{\Omega_r^2\begin{pmatrix} f_1\cos\left(\Omega_r t+\varphi_1\right) \\ f_2\cos\left(\Omega_r t+\varphi_2\right) \end{pmatrix}}_{\mathbf{Q}} \tag{B.1}$$

It is assumed that using the normal modes of the linear system, the parametric excitation matrix can be made diagonal:

$$\mathbf{\Phi}^T\mathbf{K_p}\mathbf{\Phi}=\mathbf{K_{p\eta}}, \tag{B.2}$$

whereas, $\mathbf{\Phi}$ is the modal matrix of the linear undamped system, containing the normal modes of the system in the following form:

$$\mathbf{\Phi}=\begin{pmatrix}\phi_1 & \phi_2\end{pmatrix} \tag{B.3}$$

Next, the following transformation is defined:

$$\mathbf{x} = \varepsilon^{\alpha}\boldsymbol{\Phi}\boldsymbol{\eta}, \quad \varepsilon \sim O\left(\hat{\zeta}\right) \tag{B.4}$$

Here, ε is some measure of the modal amplitudes and is assumed small, and $\hat{\zeta}$ is the modal damping. Substituting Eq.(B.4) to Eq.(B.1) and pre-multiplying it by $\boldsymbol{\Phi}$, the equations reduce to:

$$\begin{gathered}\mathbf{I}\ddot{\boldsymbol{\eta}} + 2\hat{\boldsymbol{\zeta}}\boldsymbol{\Omega}_n\dot{\boldsymbol{\eta}} + \boldsymbol{\Omega}_n^2\boldsymbol{\eta} + \mathbf{K}_{\mathbf{p\eta}}(t)\boldsymbol{\eta} + \varepsilon^{\alpha}\boldsymbol{\Phi}^T\mathbf{B}\left(\boldsymbol{\Phi}\boldsymbol{\eta}\right)^2 + \varepsilon^{2\alpha}\boldsymbol{\Phi}^T\mathbf{D}\left(\boldsymbol{\Phi}\boldsymbol{\eta}\right)^3 = \varepsilon^{-\alpha}\Omega_r^2\boldsymbol{\Phi}^T\mathbf{Q} \\ \hat{\boldsymbol{\zeta}} = \begin{pmatrix}\hat{\zeta}_1 & 0\\ 0 & \hat{\zeta}_2\end{pmatrix} \quad \boldsymbol{\Omega}_n = \begin{pmatrix}\omega_1 & 0\\ 0 & \omega_2\end{pmatrix} \\ \mathbf{K}_{\mathbf{p\eta}}(t) = \begin{pmatrix}\omega_1^2\begin{pmatrix}\alpha_{a1}\cos\left(\omega_{a1}t+\varphi_{a1}\right)+\\ \alpha_{b1}\cos\left(\omega_{b1}t+\varphi_{b1}\right)\end{pmatrix} & 0\\ 0 & \omega_2^2\begin{pmatrix}\alpha_{a2}\cos\left(\omega_{a2}t+\varphi_{a2}\right)+\\ \alpha_{b2}\cos\left(\omega_{b2}t+\varphi_{b2}\right)\end{pmatrix}\end{pmatrix}\end{gathered} \tag{B.5}$$

Introducing the dimensionless time $\tau = \omega_{\bullet}t$, where $\omega_{\bullet}$ is the response typical frequency, to Eq.(B.5):

$$\begin{gathered}\mathbf{I}\boldsymbol{\eta}'' + 2\hat{\boldsymbol{\zeta}}\boldsymbol{\chi}\boldsymbol{\eta}' + \boldsymbol{\chi}^2\boldsymbol{\eta} + \frac{1}{\omega_{\bullet}^2}\mathbf{K}_{\mathbf{p\eta}}(\tau)\boldsymbol{\eta} + \frac{1}{\omega_{\bullet}^2}\varepsilon^{\alpha}\boldsymbol{\Phi}^T\mathbf{B}\left(\boldsymbol{\Phi}\boldsymbol{\eta}\right)^2 + \frac{1}{\omega_{\bullet}^2}\varepsilon^{2\alpha}\boldsymbol{\Phi}^T\mathbf{D}\left(\boldsymbol{\Phi}\boldsymbol{\eta}\right)^3 = \frac{\Omega_r^2}{\omega_{\bullet}^2}\varepsilon^{-\alpha}\boldsymbol{\Phi}^T\mathbf{Q} \\ \boldsymbol{\chi} = \begin{pmatrix}\chi_1 & 0\\ 0 & \chi_2\end{pmatrix}, \quad \chi_{\bullet} = \frac{\omega_{\bullet}}{\omega_{\bullet}}\end{gathered} \tag{B.6}$$

Where $\partial/\partial\tau \equiv \bullet'$. Moreover, Eq.(B.6) can be written as Eq.(12) where light damping, weak pumping and large nonlinearity are assumed:

$$\begin{gathered}\hat{\zeta} = \varepsilon\zeta, \quad \alpha_{\bullet} = \varepsilon\gamma_{\bullet} \quad \rightarrow \quad \frac{1}{\omega_{\bullet}^2}\mathbf{K}_{\mathbf{p\eta}}(\tau) = \varepsilon\mathbf{K}_{\gamma}(\tau) \\ \frac{1}{\omega_{\bullet}^2}\varepsilon^{\alpha}\boldsymbol{\Phi}^T\mathbf{B}\left(\boldsymbol{\Phi}\boldsymbol{\eta}\right)^2 = \varepsilon\boldsymbol{\kappa}_2\boldsymbol{\eta}_2, \quad \boldsymbol{\eta}_2 = \begin{pmatrix}\eta_1^2 & \eta_1\eta_2 & \eta_2^2\end{pmatrix}^T \\ \frac{1}{\omega_{\bullet}^2}\varepsilon^{2\alpha}\boldsymbol{\Phi}^T\mathbf{D}\left(\boldsymbol{\Phi}\boldsymbol{\eta}\right)^3 = \varepsilon^2\boldsymbol{\kappa}_3\boldsymbol{\eta}_3, \quad \boldsymbol{\eta}_3\begin{pmatrix}\eta_1^3 & \eta_1^2\eta_2 & \eta_1\eta_2^2 & \eta_2^3\end{pmatrix}^T \\ \mathbf{P}(\tau) = \begin{Bmatrix}p_1\cos\left(\chi_r\tau+\varphi_1\right)\\ p_2\cos\left(\chi_r\tau+\varphi_2\right)\end{Bmatrix} = \frac{\Omega_r^2}{\omega_{\bullet}^2}\varepsilon^{-\alpha}\boldsymbol{\Phi}^T\mathbf{Q} \\ p_1 = \varepsilon^{-\alpha}\chi_r^2\sqrt{f_1^2\phi_{11}^2 + f_2^2\phi_{21}^2 + 2f_1f_2\varphi_{11}\varphi_{21}\cos\left(\varphi_I - \varphi_{II}\right)} \\ p_2 = \varepsilon^{-\alpha}\chi_r^2\sqrt{f_1^2\phi_{12}^2 + f_2^2\phi_{22}^2 + 2f_1f_2\varphi_{12}\varphi_{22}\cos\left(\varphi_I - \varphi_{II}\right)} \\ \varphi_1 = \arctan\left(\frac{f_1\phi_{11}\sin\left(\varphi_I\right) + f_2\phi_{21}\sin\left(\varphi_{II}\right)}{f_1\phi_{11}\cos\left(\varphi_I\right) + f_2\phi_{21}\cos\left(\varphi_{II}\right)}\right) \\ \varphi_2 = \arctan\left(\frac{f_1\phi_{12}\sin\left(\varphi_I\right) + f_2\phi_{22}\sin\left(\varphi_{II}\right)}{f_1\phi_{12}\cos\left(\varphi_I\right) + f_2\phi_{22}\cos\left(\varphi_{II}\right)}\right)\end{gathered} \tag{B.7}$$

Rotor-to-seal rubs in a steam turbine caused by deposits of carbonized oil

A. Vania[1], P. Pennacchi[1], S. Chatterton[1], F. Cangioli[1]
[1] Politecnico di Milano, Dept. of Mechanical Engineering
Via La Masa 1, I-20156, Milano, Italy
e-mail: **andrea.vania@polimi.it**

Abstract
Sometimes, deposits of carbonized oil may cause the obstruction of the available radial clearance between shaft and oil deflectors in the area close to oil-film journal bearings of steam turbines. As a result, the friction forces generated by light rotor-to-stator rubs usually cause a shaft thermal bow and changes in the synchronous vibration. Owing to the continuous increase of vibration levels and rub-induced contact forces, the blocking material can be abraded quickly. Therefore, intermittent onsets of high peaks in the shaft vibration may occur also under stable operating conditions. This paper shows a case history in which deposits of carbonized oil caused rubbing phenomena in a steam turbine. A diagnostic method that has allowed the cause of the fault to be identified is described. Besides, comparisons between experimental data and numerical results obtained with a model-based diagnostic method are also shown.

1 Introduction

The diagnosis of faults in rotating machinery is often based on the analysis of the symptoms pointed out by vibration data collected by condition monitoring systems. However, some different faults can cause similar symptoms. This may make it difficult to perform a proper diagnosis of the malfunction. Therefore, in order to obtain reliable results, diagnostic techniques must be able to take into account additional information like the historic trend of vibration data and process parameters, along with some basic mechanical and geometrical characteristics of the rotating machine.

The friction forces generated by rotor-to-stator rubs often cause a shaft thermal bow whose main effect on the machine dynamic behaviour is a progressive change in the synchronous (1X) vibration. However, most of the rotor-to-stator rubs are a consequence of a further primary fault that causes an initial increase of the vibration level such as to exceed the radial clearance between shaft and stationary parts. For instance, this primary fault can be represented by residual imbalances and shaft thermal bows, thermally induced changes in the machine alignment, blade loss events, wrong adjustments of the radial clearance of some machine components carried out during maintenance actions. Therefore, if the machine alignment is correct and the available radial clearance between rotating and stationary parts is sufficiently high, it is rather unlikely that rubbing phenomena start when the vibration levels, caused by common excitations, are low. However, the accidental presence of hard carbonized coke-like deposits in the radial clearance between rotating and stationary parts, like lube oil labyrinth seals, may cause occasional obstructions of the clearance. As a result, rubbing phenomena and a consequent shaft thermal bow are generated.

This malfunction, which commonly occurs at the machine operating speed, can cause intermittent severe peaks of the 1X vibration. In fact, owing to the continuous increase of the shaft bow and vibration levels, as well as of the contact forces between the shaft and the deposit of carbonized oil, the hard and brittle material that obstruct the radial clearance can be abraded. As a consequence of that, the rubbing phenomenon extinguishes and the heat input vanishes. Hence, the magnitude of the shaft thermal bow decreases. Owing to this, and to the rotary motion of the shaft, which is often characterized by a rather high angular speed, a fairly fast and complete straightening of the rotor occurs. However, a new deposit of carbonized oil can

again obstruct the radial clearance between rotating and stationary parts, so that a further event of rotor-to-stator rubs may take place after an unpredictable time interval.

Owing to the particular characteristics of this fault, the symptoms caused, in the machine vibration, by the rub-induced thermal bow are similar to those due to Newkirk effects and spiral vibrations. However, the casual repetition of the rub events and the absence of a cyclicality of the vibration peaks make this machine dynamic behavior quite different from that represented by common spiral vibrations that can cause a limit cycle or an outward spiraling of the 1X vector whose magnitude expands, continuously, until a machine trip is triggered.

This paper shows a case history in which the 1X vibration of a steam turbine, monitored in operating condition, have been affected by temporary very high levels. The shaft vibration continuously increased and decreased without any significant change of the process parameters. The events of high 1X vibration were intermittent and casual. According to these symptoms it was suspected the occurrence of light rotor-to-stator rubs. However, it was unclear why these phenomena also started when the vibration levels were rather low. Besides, it was not clear what caused the temporary cessation of the rubs and the subsequent occurrence of further onsets of similar phenomena, after time intervals whose length was causal.

In fact, the effects of an unbalance, like that caused by a blade loss, are permanent, while the amplitude of the spiral vibration due to a rub-induced thermal bow of the shaft tends to increase continuously or to be affected by a limit cycle, especially when rather light rubs occur. In the latter case, the 1X vibration is often affected by recurrent changes, of both amplitude and phase, which are nearly periodic. Conversely, in the present case study, the peak values of the shaft vibration approached or exceeded the alarm limit only for short time intervals. Moreover, the recurrent peaks of the vibration levels did not happen at regular intervals and their maximum amplitudes were fairly different from time to time.

A visual inspection allowed finding the presence of a large amount of deposits of carbonized oil in the oil deflectors mounted in the area close to a turbine journal bearing. The formation of hard carbonized coke-like deposits caused occasional temporary obstructions of the radial clearance between the shaft and the oil deflectors. The friction forces due to the consequent rubs caused a shaft thermal bow and changes in the synchronous vibration. Sometimes, spiral vibrations, characterized by a short spiraling of the 1X vectors, occurred. The increase of the vibration level caused an increase of the contact forces. As a result, the hard and brittle deposits of carbonized oil were abraded and the rubbing phenomena ceased, until a new obstruction of the radial clearance occurred again. This caused unusual intermittent peaks in the historic trend of the 1X vibration.

Rotor-to-seal rubs caused by the presence of deposits of carbonized oil is not one of the most common faults in rotating machines but when this phenomenon occurs the consequences in the rotor-system vibration can be rather serious, while the fault symptoms may be as evident as ambiguous. In fact, the occurrence of intermittent peaks of the 1X vibration, detected at the rated speed, even when only negligible changes in the process parameters happen, is really an uncommon behaviour.

The analysis of the case history described in the paper has been carried out with a diagnostic method that can provide some indications that are useful to confirm the suspect of the occurrence of rubbing phenomena caused by the presence of deposits of carbonized oil. Rather complex mathematical models can be used to simulate the spiral vibrations induced by rotor-to-stator rubs, rigorously [1-8]. Conversely, in the present investigation, a simplified method that simulates the dynamic effects caused by the rub-induced thermal bow of the shaft has been applied. The numerical results obtained with this method are shown and compared to the corresponding experimental data.

2 Case history

The dynamic behavior of a 135 MW steam-turbine power unit that has been affected by rotor-to-seal rubs has been analyzed. This paper shows some results of this diagnostic analysis. The steam-turbine unit was installed in a 360 MW combined cycle power plant. This unit could operate as a stand-alone machine-train, being it separated from the turbogas power unit. Figure 1 shows the machine diagram of the unit, which was composed of a generator, a high-pressure (HP) steam turbine, an intermediate-pressure (IP) and a low-

pressure (LP) steam turbine. The stages of the HP turbine were mounted on a shaft supported on a single oil-film journal bearing, while the stages of the IP and LP turbines were mounted on a shaft supported on two oil-film journal bearings. The turbine shafts were connected by means of a rigid coupling. Each support was equipped with a pair of XY proximity probes. The support numbering and the angular position of the proximity probes are shown in Figure 1. An elliptical journal bearing was mounted at the support #2 while six shoes tilting-pad journal bearings, having a load-on-pad (LOP) configuration, were mounted at the supports #1 and #3. The rated speed of the shaft-train was 3000 rpm. A distributed control system (DCS) performed the continuous basic monitoring of machine vibrations and process parameters.

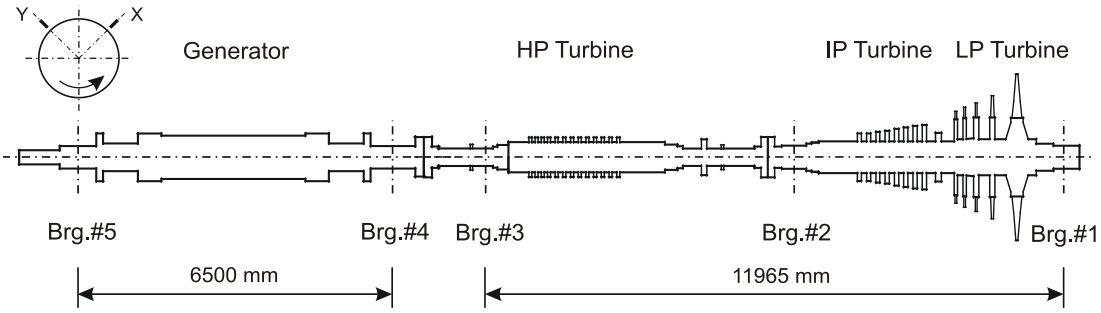


Figure 1: Machine-train diagram

The overall amplitude of the turbine vibration measured in operating condition, with a nearly constant load, suddenly experienced temporary peaks that occasionally reached considerable levels. This abnormal dynamic behavior occurred at all the supports of the steam turbines. Figure 2 shows the historic trend of the overall amplitude of the vibrations measured at bearings #1, #2 and #3, in the X direction, during a time interval of about thirteen hours. The highest amplitude of the turbine vibration approached 140 μm pp. In correspondence of each peak the vibration amplitude increased continuously, starting from rather low values, then it reached a maximum level that remained at the peak value only for a few minutes. In the end, it decreased with a rate of change just a little slower than that with which it had raised. Each peak of vibration affected the machine dynamic behavior for about one hour. The decreases of the vibration amplitude always occurred without doing any significant change of the main process parameters of the plant. Every time, at each measurement point, the vibration level returned to low starting values. That is, the phenomenon of the abnormal vibration was recurrent and almost reversible, but the length of the period that separated two consecutive peaks of vibration was rather casual. Moreover, the maximum vibration amplitude sometimes occurred at bearing #2, while other times it occurred at bearing #3. The vibration of the two turbines was actually affected by intermittent peaks that occasionally reached considerable levels.

Figure 3 shows the overall amplitude of the vibrations measured at bearings #1, #2 and #3, in the X direction, during a planned coastdown. In this case, the unit slowdown started when the vibration level was rather low at all three supports of the steam turbines. However, when the rotational speed approached the range from 1200 rpm to 1800 rpm, which contains the first two flexural critical speeds of the turbine shafts, the vibration levels increased significantly. The maximum amplitude, which occurred at bearing #2, reached 262 μm pp. These vibration levels were noticeable and quite different from those experienced during previous runups and coastdowns of the unit. However, it was possible to exclude the occurrence of rotor-to-bearing rubs because of the normal values of the white-metal temperature measured during the machine coastdown.

Conversely, it was suspected that rubbing phenomena between rotating and stationary parts occurred, likely in the area of the turbine shafts where packing-glands were mounted. That is, in the area before the first stages of both HP and IP turbines. In the latter case, the gland seals are rather close to the journal bearing #2 (Figure 4). An advanced monitoring system that performed the order analysis of the machine vibrations, continuously, was installed in order to detect the recurrent noticeable intermittent peaks of the turbine vibration that occurred in the operating condition. This monitoring activity has allowed finding out that the harmonic content of the turbine vibration measured at the rated speed was always dominated by the 1 × rev. (1X) harmonic order, as proved below.

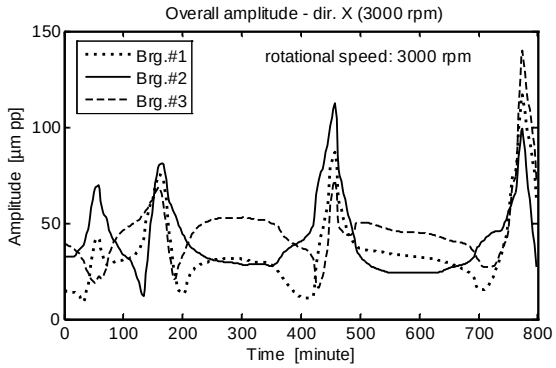


Figure 2: Overall amplitude of the shaft vibrations measured at bearings #1, #2 and #3, in the X direction, in operating condition (3000 rpm)

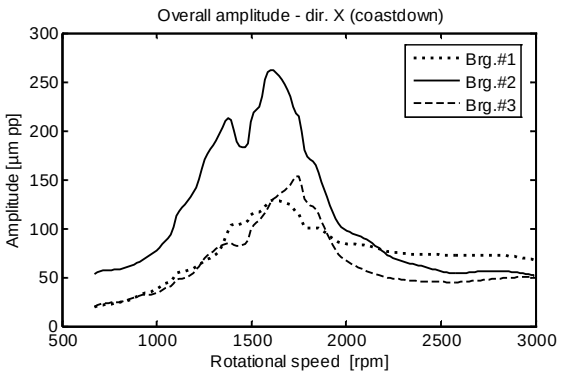


Figure 3: Overall amplitude of the shaft vibrations measured at bearings #1, #2 and #3, in the X direction, during a coastdown

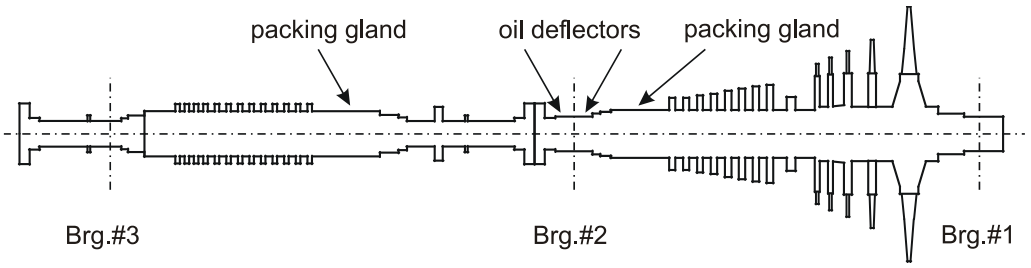


Figure 4: Steam turbine shafts

Figure 5 shows the historic trend of amplitude and phase of the uncompensated 1X vibrations measured at bearings #1, #2 and #3, in the X direction, in a time period during which a significant peak amplitude occurred (Case A). This abnormal behavior was detected in operating condition, with a nearly constant load. It is possible to note that when the vibration peak occurred, the corresponding phase was affected by a significant change. Besides, when the abnormal dynamic behaviour ceased, both amplitude and phase of the 1X vibrations returned to the values of the respective “reference vibrations” that correspond to the 1X vectors measured before the occurrence of the peak amplitude.

This confirmed that the residual imbalance of the shafts was rather low and that the malfunction was caused by a reversible phenomenon. However, the phase of the 1X vibration vector caused, at each measurement point, by the unidentified fault was not the same in occasion of each occurrence of a peak amplitude. Therefore, the maximum vibration level sometimes occurred at different bearings of the turbine shafts. Figure 6 shows the historic trend of the so called “not-1X” amplitude of the vibrations measured at bearings #1, #2 and #3, in the X direction, during the time period of the Case A. The curves shown in this figure confirm that during the occurrence of the rubbing phenomena the machine dynamic behaviour was dominated by the 1X vibration, while the contribution of both sub-synchronous and super-synchronous vibrations was negligible.

In order to bring out the effects caused by the fault, the 1X reference vectors measured at 3000 rpm, with the unit operating in normal state, that is with low stable vibrations like those occurred at the beginning of the observation period, were subtracted from the corresponding 1X vibration data collected at any time instant. This data processing is similar to the run-out compensation sometimes used for the analysis of the vibration data collected during machine runups. This investigation method is based on the assumption that the nonlinear effects caused by the unidentified phenomenon were unimportant. Figure 7 shows the historic trend of the shaft vibrations obtained compensating the 1X vectors previously illustrated in Figure 5. It is possible to note that the amplitude of the 1X vibration that can be mainly ascribed to the fault increases continuously before reaching its maximum value. Similarly, after having reached the top of the peak, the vibration amplitude decreases continuously and it nullifies asymptotically.

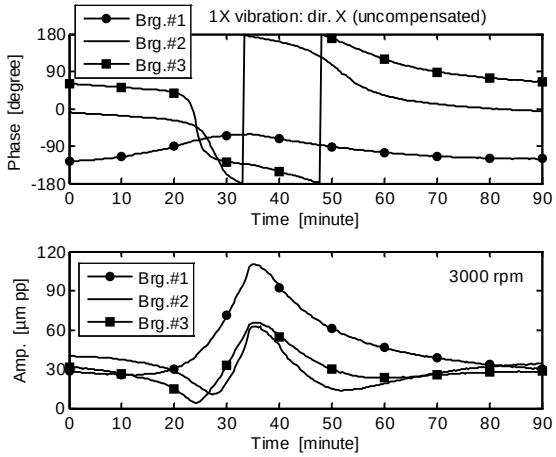


Figure 5: Case A: historic trend of the 1X vibrations (uncompensated) measured at bearings #1, #2 and #3, in the X direction, in operating condition (3000 rpm), during the occurrence of a rubbing phenomenon

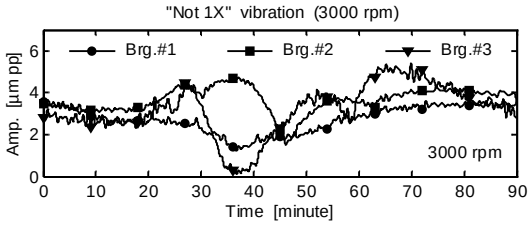


Figure 6: Case A: historic trend of the not-1X amplitude of the vibrations measured at bearings #1, #2 and #3, in the X direction, in operating condition (3000 rpm), during the occurrence of a rubbing phenomenon

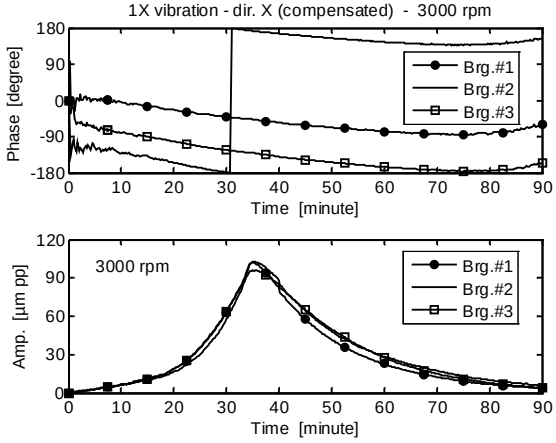


Figure 7: Historic trend of the compensated 1X vibrations measured at bearings #1, #2 and #3, in the X direction, in operating condition, during the occurrence of a rubbing phenomenon (Case A)

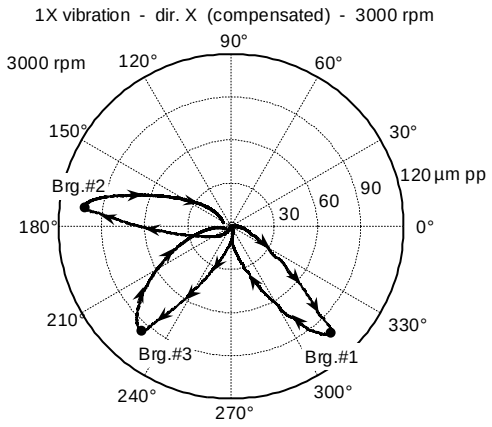


Figure 8: Polar plot of the compensated 1X vibrations measured at bearings #1, #2 and #3, in the X direction, at 3000 rpm, during the occurrence of a rubbing phenomenon (Case A)

The phase of the compensated 1X vibration is affected by a slow continuous rotation. With reference to the data illustrated in Figure 7, the rate of change of amplitude and phase of the compensated 1X vibration vectors is nearly the same at all journal bearings of the turbine shafts. These characteristics of the compensated 1X vibration are clearly pointed out by the polar plot shown in Figure 8. When the vibration levels decrease, the values of the 1X phase are different from those found during the continuous increase of the vibration amplitude. Nevertheless, when the additional 1X vibration caused by the fault nullifies, the phase of the uncompensated vibration tends to return to the corresponding reference value. The main symptoms of this phenomenon are consistent with the occurrence of rubs between rotating and stationary parts of the steam turbine. In fact, it was possible to suppose that the friction forces generated by the rubs caused a reversible shaft thermal bow that, in turn, caused additional 1X vibrations of the turbine shafts. However, it was not clear what primary fault caused the rotor-to-stator contacts since the amplitude of the turbine vibration always started increasing from rather low levels. This was not in accordance with normal values of the available radial clearance of seals and journal bearings.

The amplitude of the 1X vibration measured in operating condition by a given proximity probe increased continuously, or it showed a more complex trending, depending on the relative phase between the additional 1X vibration caused by the shaft thermal bow and the respective 1X reference vector. The sudden extinction of this phenomenon and the consequent continuous decrease of the shaft vibration levels could be explained as a temporary end of the rubs. If the rotor heating caused by the friction forces generated by the rubs nullifies, the high rotational speed is able to straighten the shaft in a rather short time period. However, it was not clear what caused the sudden extinction of the rubs and the intermittent recurrence of this phenomenon.

Figure 9 shows the 1X filtered orbits evaluated, at bearings #1, #2 and #3, considering the compensated data collected, in operating condition, in concomitance with the occurrence of the maximum vibration amplitude. The major axis of the 1X elliptical orbit evaluated at bearing #3 is nearly horizontal. This orbit, which is the largest one, is also rather flat. These characteristics are rather unusual for an orbit measured at a six shoes tilting-pad journal bearing whose anisotropy is not so much important as that of elliptical oil-film journal bearings. Therefore, it was possible to suspect that the rubbing phenomena were caused by a machine misalignment, perhaps influenced by the machine thermal state.

Figure 10 shows the polar plots of the compensated 1X vibrations measured, at bearings #1, #2 and #3, in operating condition, over a time period of thirteen minutes, in occasion of a further event (Case B) of a temporary peak of the turbine vibration levels, caused by rubbing phenomena occurred in operating condition. In this case, since the maximum vibration amplitude exceeded the precautionary trip level that had been set to prevent serious damage, an automatic shutdown of the power unit occurred. The comparison between the polar plots illustrated in Figures 8 and 10 points out that the phase of the 1X vibration vectors caused by the fault, in the two case studies, at the corresponding measurement points, is quite different. Conversely, the relative phase of the compensated 1X vibrations measured at each pair of measurement points is nearly the same for both case studies A and B. These findings confirmed the suspect that the temporary increase of the 1X vibration amplitude was caused by rotor-to-seal rubs. However, with reference to the area of the rotor that was affected by the rubs, the angular position of the point of the shaft orbit at which the rotor-to-seal contacts occurred was not the same for each rubbing event. This is in accordance with the readings of different phase values of the 1X additional vibrations caused by the rubs. Therefore, the unidentified fault that caused the rubs gave rise to dynamic effects that were not entirely repetitive.

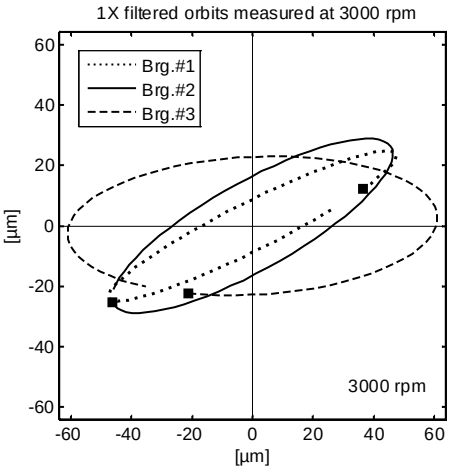


Figure 9: 1X filtered orbits obtained considering the compensated vibrations measured at bearings #1, #2 and #3, at 3000 rpm, in concomitance with the maximum vibration amplitude (Case A)

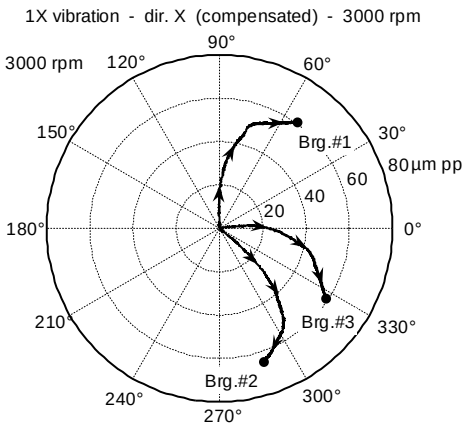


Figure 10: Polar plot of the compensated 1X vibrations measured at bearings #1, #2 and #3, in the X direction, in operating condition, during a rubbing onset (Case B)

Figure 11 shows the Bode plot of the 1X vibrations of the steam turbines measured at bearings #1, #2 and #3, in the X direction, during the machine shutdown. Since the vibration levels were just rather high even

at the beginning of the turbine slowdown, being the turbine shaft already affected by a thermal bow, the vibration amplitudes increased considerably when the rotational speed crossed the flexural critical speeds contained in the range from 1200 rpm to 1800 rpm. The highest vibration amplitude measured on bearing #2 reached 488 μm pp at the rotational speed of 1685 rpm. Also in this case the white-metal temperature of all journal bearings was normal and almost unaffected by the vibration levels. This confirmed the suspect that rubbing phenomena occurred at some seals rather than at the turbine bearings. In this case, it is likely that when the rotational speed approached the first balance resonance with vibration levels that were already rather high, further light rubs also occurred at the packing glands of the IP turbine, which are close to bearing #2. It is also possible to note that the amplitude of the 1X vibration measured in the final part of the machine slowdown is very low. This means that the rubs, and the consequent friction forces, caused only a temporary shaft thermal bow, which disappeared during the coastdown, after crossing the first balance resonance of the turbine shafts. The rotor straightening, which occurred in about thirty minutes, confirmed that the rotor-to-stator contacts certainly ceased during the machine slowdown, when the rotational speed was lower than the first flexural speed of 1670 rpm. It is well known that reversible shaft thermal bows may vanish in a rather short time, if the heat input is eliminated, by operating the machine at a significant rotational speed. Otherwise, the unit can be operated in barring mode, that is at a very low rotational speed, for a longer time.

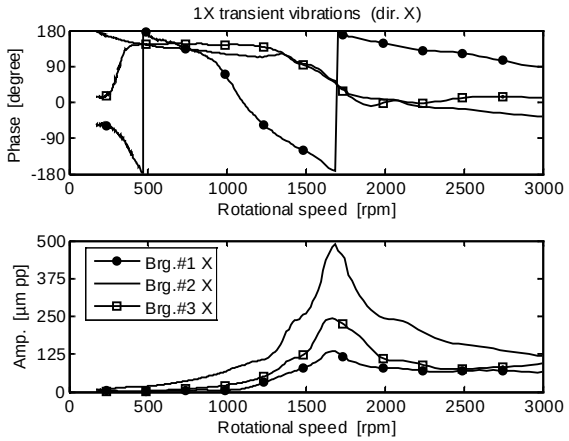


Figure 11: Bode plot of the 1X vibrations of the shaft measured at bearings #1, #2 and #3, in the X direction, during a machine coastdown

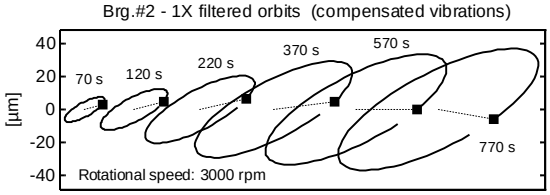


Figure 12: Evolution over time of the 1X filtered orbits measured at bearing #2, at 3000 rpm, during the occurrence of rotor-to-seal rubs

The vibration data illustrated in Figure 10 show that the phase of the 1X vectors collected at each measurement point, at the rated rotational speed, is affected by a slow but continuous rotation that approached 35° degrees, over a time interval of only thirteen minutes. This symptom is in accordance with the occurrence of spiral vibrations [1-13]. The increasing spiraling motion of the rub induced thermal bow happens in a direction opposite to that of the shaft rotation. This is a typical phenomenon that may affect the dynamic behavior of rotating machines that are subjected to light rubs between rotating and stationary components, especially when the rotational speed is lower than a flexural critical speed and not very far from it. This behavior is confirmed by the analysis of the 1X filtered orbits obtained processing the compensated synchronous vibrations measured at bearing #2 during the rub evolution (Case B).

Figure 12 shows the evolution of the shape of the above mentioned orbits measured at different times during the rubbing phenomenon. The orbit flatness is weakly affected by the rubs although its amplitude increased significantly in the time as a result of the growing magnitude of the shaft thermal bow. The angular position of the key-phasor dot, as well as that of the hot spot, moves backwards along the orbit. This phenomenon has been pointed out in Figure 12 by drawing the segment that connects the key-phasor dot with the center of the corresponding elliptical orbit. This segment rotates continuously during the rub evolution, in the opposite versus of the shaft rotation, in accordance with the symptoms of common spiral vibrations.

As a consequence of these findings, it was decided to stop the unit and perform a visual inspection of the oil deflectors mounted at both sides of bearing #2. Figure 13 shows a picture of one of these components that were both found significantly damaged. Besides, a large amount of deposits of carbonized oil was found in the machine area close to the journal bearing #2.

These deposits are agglomerations of hard and brittle material that occasionally caused the obstruction of the available radial clearance between shaft and seal (Figure 14). Therefore, rotor-to-seal rubs started occurring even when the amplitude of the turbine vibration was rather low, but sufficient to cause contacts between shaft and blocking material. Moreover, the continuous increase of the vibration levels and the consequent increase of the contact forces abraded the deposits of carbonized oil that temporarily occluded the seal radial clearance. This explains the sudden cessation of the rubs detected during the machine monitoring in operating conditions during which the process parameters were nearly constant.



Figure 13: Oil deflector mounted at bearing #2 and deposits of carbonized oil

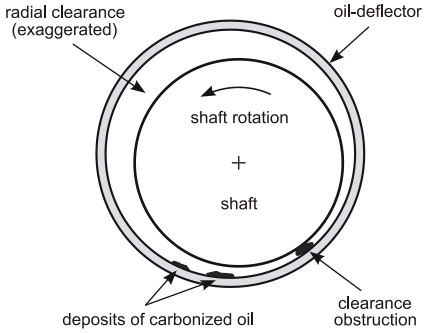


Figure 14: Example of a radial clearance obstruction

Since the angular position where these occlusions formed was casual, the phase of the 1X additional vibration induced by the consequent shaft thermal bow was not repetitive. Therefore, in accordance with the experimental findings, the 1X vibration measured by the probes, given by the sum of the synchronous additional vibration vector and the corresponding 1X reference vibration, could reach the maximum level at different journal bearings of the turbine shafts. The blockage of the radial clearance occurred occasionally, at the unit rated speed. However, this phenomenon was more likely during rotational speed transients when the crossing through the first balance resonance of the shaft caused an unavoidable increase of the vibration amplitude and possible interactions with deposits of carbonized oil. Likely, the hot alignment of the machine-train was improper. This may have caused lube oil to leak into the area, close to bearing #2, between oil rings and the seal vacuum chamber.

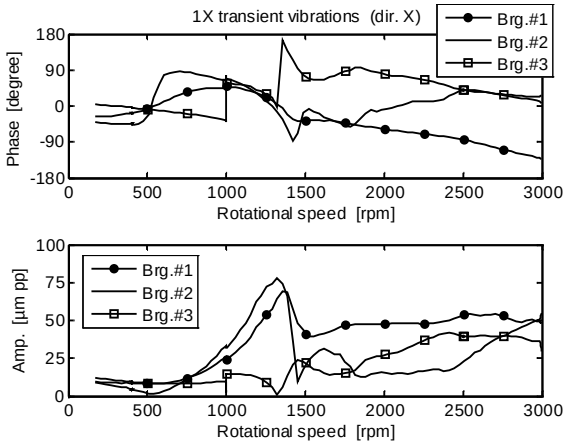


Figure 15: Bode plot of the 1X vibrations of the shaft measured at bearings #1, #2 and #3, in the X direction, during a machine runup performed after the maintenance

Under this assumption, high-temperature-steam and oil-vapor mixed together in the vacuum chamber. Besides, the flow of this mixture through the turbine may have came in contact with hot spots. Therefore, the consequent thermal loading suffered by the oil caused the buildup of hard carbonized coke-like deposits that occasionally blocked the clearance between shaft and oil deflectors [11, 18-19].

At the end of a maintenance outage, during which the deposits of carbonized oil were removed and the oil deflectors substituted, the power unit was restarted without doing any rotor balancing or modifying the machine alignment. Figure 15 shows the Bode plot of the 1X vibrations measured at bearings #1, #2 and #3, in the X direction, during the machine runup. When the rotational speed crossed the range from 1200 rpm to 1800 rpm the amplitude of the 1X vibration of the steam turbines reached a maximum level of only 75 μm pp. This amplitude is significantly lower than that measured before removing the deposit of carbonized oil because of the absence of a rub-induced thermal bow of the shaft, caused by temporary obstructions of the oil deflector radial clearance. The amplitude of the turbine vibration was sufficiently low also at the operating speed, in accordance with the low value of the residual imbalance of the shaft. A long-term monitoring of the unit dynamic behavior showed that rotor-to-seal contacts no longer occurred.

3 Model-based analysis

Spiral vibrations in rotating machines can be studied and simulated by means of well-known methods based on mathematical models of the rotor system [1-8]. A finite element model of the shaft-train is integrated with further mechanical parameters that allow the effects caused by the dynamic stiffness of the journal bearings and those caused by the machine supporting structure to be taken into account. Moreover, these investigation methods allow one to simulate both heavy and light contacts between rotating and stationary parts, as well as to estimate the heat introduced into the shaft by the friction forces generated by the rubbing phenomena. These methods need to integrate, in the time domain, partial differential equations based on the Fourier's law. As a result of the local heating of the rotor, a thermal bow is generated in the area close to the hot-spot [1-8]. This phenomenon causes changes in both shaft imbalance and machine response. In particular, the phase lag between excitation and shaft vibration can be subjected to a continuous change. Therefore, the solution of the differential equations contained in the thermal model must be combined with the integration of the equations of motion of the rotor system. This study often needs a high computational time. Moreover, it needs a preliminary fine tuning of the model of rotating and stationary parts.

In addition to this, the results obtained with these methods can be significantly influenced by some parameters of the thermal model whose values are often rather uncertain. A further critical aspect of the simulation of rubbing phenomena is that the growth of the shaft thermal bow is considerably slower than the period of a complete revolution of the shaft. This problem is often solved assigning equivalent values to the most important parameters of the thermal model of the system in order to obtain a growth of the shaft bow, similar to the real one, in a much shorter time period. Therefore, an accurate reliable estimate of the amount of the thermally-induced bow of the rotor may be difficult to obtain. However, these methods can provide an interesting qualitative simulation of the main physical phenomena caused by rotor-to-stator rubs, like the buildup of the shaft thermal bow, the consequent increase of the additional imbalance and the phase lagging of the 1X vibration vectors caused by the continuous changes of the rubbing spot.

In the case studies considered in this paper many parameters that needed to be taken into account in the thermal model of the rotor system were unknown. Unfortunately, it was impossible to obtain reliable results from investigations based on rigorous methods that need to use an accurate model of the rub-induced thermal phenomena, like that described in [4], as the geometrical and mechanical characteristics of the obstacle, represented by the deposits of carbonized oil, were unknown. Therefore, it was preferred to apply an alternative technique in which the shaft bow caused by the rotor-to-stator contacts is roughly modeled by means of a pair of opposite coplanar bending moments, which rotate with the rotor, whose magnitude and phase depend on the rub evolution over time [14, 15]. As said above, the dynamic behaviour of rotating machines can be studied with methods in which the shaft-train is represented by finite element models (FEM). In general, beam finite elements are used to model short portions of the shaft, having a circular cross-section, which are characterized by a constant diameter. The mechanical characteristics of the journal bearings that support the shafts can be modelled by means of dynamic stiffness coefficients that can depend

on the machine rotational speed. In the end, the dynamic effects caused by pedestals and foundation structure can be simulated with different techniques [14, 16, 17], here not described in detail for the sake of brevity. Figure 16 shows the finite element model (FEM) of the shafts of generator and steam turbines. The equation of motion of the rotor-system can be written in the following matrix form:

$$\left[\mathbf{M}\right]\ddot{\mathbf{x}} + \left(\left[\mathbf{C}\right] + \left[\mathbf{G}(\Omega)\right]\right)\dot{\mathbf{x}} + \left[\mathbf{K}\right]\mathbf{x} = \mathbf{F}(t) \tag{1}$$

where $\mathbf{M}$, $\mathbf{C}$ and $\mathbf{K}$ are the mass, damping and stiffness matrices, respectively, of the fully assembled system, while $\mathbf{G}$ is the gyroscopic matrix of the shaft-train. The vector $\mathbf{x}$ contains the displacements and rotations of shafts and foundation. Besides, the vector $\mathbf{F}$ contains the system excitations, that is, forces and moments that can be applied to the degrees of freedom of the model.

The most important faults in rotating machines can be simulated by means of suitable sets of equivalent excitations represented by harmonic orders of forces and moments whose magnitude, phase and axial position along the rotor-train can be identified by minimizing the error between experimental vibration data and the corresponding numerical results provided by the machine model [14, 15]. In the present case study the axial position of the equivalent excitations was known, as the cross-section where the rotor-to-stator rubs occurred, and the consequent shaft thermal bow was generated, had been identified with a visual inspection. By assuming that the nonlinearities of the system are negligible, the following equation can be written for each harmonic component, of order *n*, of the machine excitations:

$$\left[-(n\Omega)^2\mathbf{M} + in\Omega\left(\mathbf{C} + \Omega\mathbf{G}\right) + \mathbf{K}\right]\mathbf{X}_n e^{in\Omega t} = \mathbf{F}_n(n\Omega)\, e^{in\Omega t} \tag{2}$$

where Ω is the shaft angular velocity, while the terms contained in vector $\mathbf{F}_n$ are the equivalent harmonic excitations used to model the fault that must be identified. The harmonic content of the excitations, as well as the number of not-null terms of vector $\mathbf{F}_n$, depends on the type of the fault. The quantity contained in the square brackets of eq.(2) is the mechanical impedance matrix of the system. Eq.(2) can be solved to evaluate the harmonic component of order *n* of the machine vibration. This can be obtained as follows:

$$\mathbf{X}_n = \left[-(n\Omega)^2\mathbf{M} + in\Omega\left(\mathbf{C} + \Omega\mathbf{G}\right) + \mathbf{K}\right]^{-1}\mathbf{F}_n(n\Omega) \tag{3}$$

Let us denote $\mathbf{H}_n$ the transfer matrix obtained as the inverse of the mechanical impedance matrix. That is:

$$\mathbf{H}_n = \left[-(n\Omega)^2\mathbf{M} + in\Omega\left(\mathbf{C} + \Omega\mathbf{G}\right) + \mathbf{K}\right]^{-1} \tag{4}$$

Therefore, we can rewrite eq.(3) as:

$$\mathbf{X}_n = \mathbf{H}_n\, \mathbf{F}_n(n\Omega) \tag{5}$$

The absolute vibrations of the shafts are commonly measured at a limited number of cross-sections that are often rather close to the machine supports. Therefore, the theoretical lateral displacements associated with the degrees of freedom along which the radial vibrations of shafts and supports are measured can be inserted into a vector $\mathbf{X}_m$. In the present case study the machine dynamic behaviour must be investigated only at the rated speed. Therefore, eq.(5) must be solved for a unique value of the angular speed Ω. The rows of the matrices contained in eq.(5) can be rearranged, partitioning the transfer matrix $\mathbf{H}_n$, in order to split the vector $\mathbf{X}_m$ from the vector $\mathbf{X}_r$, the terms of which are the displacements evaluated at the remaining degrees of freedom of the rotor-system model. Therefore, eq.(5) can be rewritten in the following form, in which any dependence on both Ω and order *n* has been omitted for the sake of brevity:

$$\begin{aligned}\mathbf{X}_m &= \mathbf{H}_m\,\mathbf{F}_n \\ \mathbf{X}_r &= \mathbf{H}_r\,\mathbf{F}_n\end{aligned} \tag{6}$$

The experimental lateral vibrations that correspond to the terms of vector $\mathbf{X}_m$ can be inserted into a vector $\mathbf{X}_{exp}$. This way, it is possible to evaluate the error, δ, between theoretical vibrations and experimental data:

$$\delta = \mathbf{X}_m - \mathbf{X}_{exp} = \mathbf{H}_m \mathbf{F}_n - \mathbf{X}_{exp} \tag{7}$$

The corresponding squared error, ε, can be defined as:

$$\varepsilon = \left[\mathbf{X}_m - \mathbf{X}_{exp}\right]^{*T} \left[\mathbf{X}_m - \mathbf{X}_{exp}\right] \tag{8}$$

Then, magnitude and phase of the equivalent excitations $\mathbf{F}_n$ can be estimated by means of least squares error methods. A preliminary tuning of this model, including the dynamic stiffness coefficients of the oil-film journal bearings, has been carried out comparing the eigenvalues of the model to the corresponding experimental findings obtained by the analysis of vibration monitoring data collected during machine runups and coastdowns. Afterwards, a pair of opposite coplanar bending moments, M_1 and M_2, have been applied to the nodes of the FEM mesh of the shaft located at the opposite sides of the journal bearing #2 (Figure 16), mounted on the IP-LP steam turbine. These two cross-sections are close to the axial position of the oil deflectors where the rotor-to-seal rubs occurred in the operating condition. Since these bending moments rotate with the shaft and the model of the rotor system is linear, only synchronous vibrations are generated by these excitations. In this investigation, the two bending moments, M_1 and M_2, are the only not null terms of vector $\mathbf{F}_n$.

The identification of magnitude and phase of these bending moments has been carried out at six time instants spaced over the period, thirteen minutes long, during which the rubbing phenomena that are the subject of this investigation occurred (Case B). Only the compensated 1X vibrations of shafts have been considered in this investigation, in order to simulate the response only caused by the rub-induced thermal bow.

In order to facilitate the comparison between the numerical response of the rotor system and the corresponding experimental data, at each cross-section of interest of the shaft-train, the main parameters that allow the 1X journal orbit to be defined, have been evaluated. These parameters are the major and minor principal axes of the 1X elliptical orbit, along with the angle formed by the horizontal axis and the aforementioned major axis of the orbit. With reference to the major and minor axes of the 1X orbits evaluated at bearings #1 and #2, Figure 17 shows a comparison between the numerical results provided by the mathematical model and the corresponding experimental findings. The accordance between numerical results and experimental data is really satisfactory over the whole period during which the rubbing phenomena occurred.

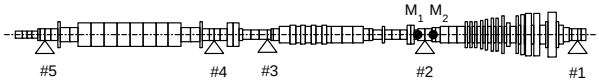


Figure 16: Finite element model of the shafts of generator and steam turbines along with the axial position of the bending moments M_1 and M_2

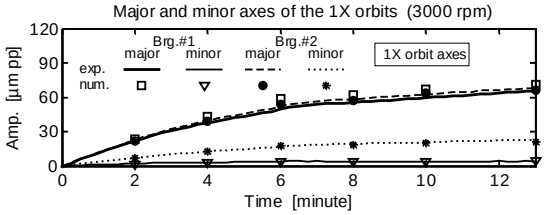


Figure 17: Major and minor principal axes of the 1X orbits: comparison between experimental data and numerical results

All the estimates of the major and minor axes of the 1X orbits evaluated, at the bearings #1, #2 and #3 of the steam turbine, by processing the numerical results provided by the model have inserted into a vector denoted $\mathbf{Z}_{th}$. Conversely, the values of the principal axes of the same orbits, evaluated by processing the experimental 1X vibrations measured during the rubbing phenomena, have inserted into a vector denoted

$\mathbf{Z}_{exp}$. The accuracy of the results provided by the model has been estimated by means of the Coherence Factor, CF, given by:

$$CF = \frac{\left| \mathbf{Z}_{exp}^{*T} \mathbf{Z}_{th} \right|^2}{\mathbf{Z}_{exp}^{*T} \mathbf{Z}_{exp} \mathbf{Z}_{th}^{*T} \mathbf{Z}_{th}} \tag{9}$$

The value of this factor is 0.9862. The accuracy of the estimate of the evolution over time of the 1X bending moments that simulate the changes in the rub-induced thermal bow of the shaft can be assumed satisfactory as the value of the Coherence Factor is rather close to the ideal unity value. Besides, the comparison between the experimental and theoretical values of the inclination angle of the major axis of the 1X elliptical orbits evaluated at bearings #1 and #2 is shown in Figure 18. Also in this case, the accordance between experimental data and numerical results is fairly good, especially with reference to the bearing #2.

In the end, Figure 19 shows the evolution over time of the magnitude and phase of the identified bending moments that have been used to simulate the rub-induced thermal bow of the turbine shaft. It is possible to note that the phase of these bending moments deceases continuously. That is, it rotates in the opposite versus of the shaft rotation, slowly. This phenomenon is in accordance with the phase lagging caused by the continuous changes of the rubbing spot position. In this case study, the magnitude of the equivalent bending moments and then that of the shaft thermal bow seems to reach an asymptotic value.

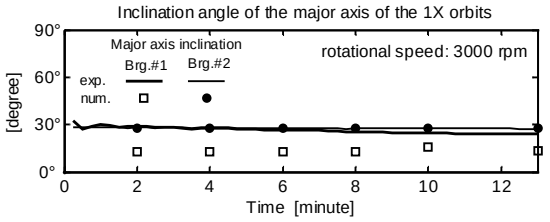


Figure 18: Inclination angle of the major axis of the 1X elliptical orbits at bearings #1 and #2: comparison between experimental data and numerical results

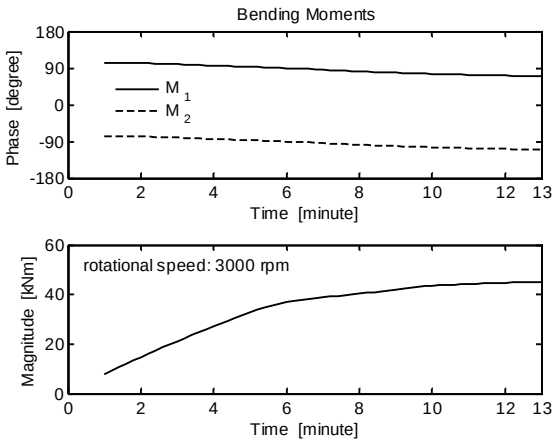


Figure 19: Evolution over time of the identified bending moments that simulate the rub-induced thermal bow of the shaft

4 Conclusions

Light rubs between shaft and stationary parts is one of the most common faults in rotating machines. However, rubs are always the secondary effect of primary faults like: high imbalances, machine misalignments, thermal expansions, inaccurate adjustments of the radial clearance of seals. The friction forces generated by the rubs usually cause a shaft thermal bow and additional synchronous vibrations. Sometimes, unstable lasting spiral vibrations are generated. However, it is also possible that deposits of carbonized oil form in the area close to oil-film journal bearings, especially in steam turbines. These deposits may cause the obstruction of the available radial clearance between shaft and oil deflectors. In this case, light rubs can be generated even starting from rather low vibration amplitudes of the shaft.

As a consequence of the continuous increase of vibration levels and rub-induced contact forces the blocking material can be quickly abraded. This causes the end of the input, into the shaft, of the heat generated by the

friction, as well as a continuous decrease of the shaft thermal bow and vibration amplitudes. Therefore, intermittent onsets of high vibration levels may occur in the operating condition. Owing to these uncommon ambiguous symptoms, standard root-cause-analysis techniques may involve the identification of false faults.

A case history in which deposits of carbonized oil have caused recurrent temporary peaks of the 1X vibration levels of a steam turbine has been shown in this paper. The analysis of the compensated 1X vectors has allowed the additional vibrations caused by the rub-induced thermal bow of the shaft to be estimated. Owing to this, some typical symptoms of rotor-to-seal rubs, like those of spiral vibrations, have been better highlighted.

Complex rigorous methods can be applied to simulate the shaft vibration caused by rubbing phenomena. However, as some parameters of the system thermal model were unknown, it has been preferred to simulate the experimental behaviour of the steam turbine by means of an approximated approach in which the rub-induced thermal bow has been modeled with a pair of coplanar opposite bending moments applied to suitable cross-sections of the shaft. The evolution over time of magnitude and phase of these 1X bending moments has been studied, in the frequency domain, with methods based on parameter identification. The satisfactory accordance between numerical results and experimental data has confirmed the effectiveness of this investigation method, which can be used for diagnostic purposes successfully.

References

[1] W. Kellenberger, *Spiral vibrations due to seal rings in turbogenerators thermally induced interaction between rotor and stator*, Journal of Mechanical Design, Vol. 102, No. 1 (1980), pp. 177-184.

[2] L. Eckert, J. Schmied, *Spiral Vibration of a Turbogenerator Set: Case History, Stability Analysis, Measurements and Operational Experience*, Journal of Engineering for Gas Turbines and Power, Vol. 130, No. 1 (2008), pp. 012509-1-10.

[3] R. Liebich, *Rub induced non-linear vibrations considering the thermos-elastic effect*, Proc. of 5th *IFToMM Int. Conference on Rotor Dynamics*, Darmstadt (1998), pp. 802-815.

[4] N. Bachschmid, P. Pennacchi, A. Vania, *Thermally Induced Vibrations Due to Rub in Real Rotors*, Journal of Sound and Vibration, Vol. 299, No. 4-5, 2007, pp. 683-719.

[5] P. Pennacchi, A. Vania, S. Chatterton, R. Ricci, *Spiral vibrations in power units: modeling and experimental evidences*, Proc. of ISMA-2010, *Int. Conf. on Noise and Vibration Engineering*, Sept. 20-22, Leuven, Belgium (2010), pp. 2905-2919.

[6] N. Bachschmid, P. Pennacchi, A. Vania, *Modelling of Spiral Vibrations Due to Rub in Real Rotors*, paper ISROMAC10-2004-096, Proc. ISROMAC-10 *Conference*, March, Honolulu, Hawaii (2004), pp. 1-10.

[7] N. Bachschmid, P. Pennacchi, A. Vania, *Spiral Vibrations Due to Rub: Numerical Analysis and Field Experiences*, Proc. of *Schwingungen in Rotierenden Maschinen V*, H. Irretier, R. Nordmann, H. Springer Editors, Vieweg Verlag, Braunschweig/Wiesdaden, Germany (2001), pp. 61-74.

[8] A. Muszynska, *Rotordynamics*, CRC Taylor & Francis Group, New York, (2005).

[9] J.T. Sawicki, A. Montilla-Bravo, Z. Gosiewski, *Thermomechanical Behavior of Rotor with Rubbing*, Int. Journal of Rotating Machinery, Taylor & Francis, Vol. 9, No. 1 (2003), pp. 41-47.

[10] P. Goldman, A. Muszynska, D.E. Bently, *Thermal Bending of the Rotor Due to Rotor-to-Stator Rub*, Int. Journal of Rotating Machinery, Vol. 6, No. 2, (2000), pp. 91-100.

[11] P. Sharma, *Vibration Monitoring Identifies Steam Turbine Seal Rub*, Orbit, Vol. 33, No. 3 (2013), pp. 33-43.

[12] N. Péton, C. Grislin, G. Christin, *Compressor rub verified by rotating phase symptoms*, Proc. of *Int. Conference Surveillance 7*, October 29-30, Chartres, France (2013), pp. 1-6.

[13] W. Wang, K. Feng, T. Dimond, P. Allaire, *Steam Turbine Vibration Caused by Oil Coking Rubs: Case Studies and Numerical Simulation*, Proc. of IDETC/CIE 2013 *ASME 2013 Int. Design Engineering Technical Conf. and Computer and Information in Engineering Conf.*, August 4-7, Portland, Oregon, USA, (2013), VA No. DETC2013-13713, pp. V008T13A060; 10 pages, doi 10.1115/DETC2013-13713.

[14] N. Bachschmid, P. Pennacchi, A. Vania, *Identification of multiple faults in rotor systems*, Journal of Sound and Vibration, 254, No. 2, 2002, pp.327-366.

[15] P. Pennacchi, A. Vania, N. Bachschmid, *Increasing the robustness of fault identification in rotor dynamics by means of M-estimators*, Mechanical System and Signal Processing, Vol. 21, No. 8, 2007, pp. 3003-3029.

[16] M. Lalanne, G. Ferraris, *Rotordynamics Predictions in Engineering*, 1998, John Wiley & Sons Inc., Chichester, England.

[17] M. Adams, *Rotating machinery vibration*, 2001, Marcel Dekker Inc., New York, N.Y., USA.

[18] J. Sandre, *Steam Turbine Oil Challanges*, LE White Paper www.LElubricants.com 800-537-7683, Lubrication Engineers, Inc., 2012.

[19] W. Moehle, V. Ghatto, G. Livingstone, D. Wooton, *Practical Approaches to Controlling Sludge and Varnish in Turbine Oil*, Lubrication Excellence 2007 Conference Proceedings, Noria Corp., May 2007.

Vibration dynamics in non-linear dual mass flywheels for heavy-duty trucks

L. Wramner [1,2], **V. Berbyuk** [1], **H. Johansson** [1]
[1] Chalmers University of Technology, Department of Mechanics and Maritime Sciences,
SE-412 96 Göteborg, Sweden
e-mail: **lina.wramner@chalmers.se**

[2] AB Volvo, Group Trucks Technology

Abstract
A non-linear model for simulations of a dual mass flywheel (DMF) for heavy-duty applications is proposed. The model includes internal clearances and friction. LuGre friction model is used, which depends on normal force, relative velocity between the two surfaces and an internal deflection variable. Measurements on the DMF are performed in a test rig and the test rig properties are analysed. The correlation shows that the general behaviour of the DMF is reproduced by the proposed simulation model. The viscous part of the friction is dominant for the analysed cases with zero mean torque, and a conventional Coulomb friction model would not suffice for this application. Near resonances, the model also shows a high sensitivity to internal clearances and spring stiffness. This indicates that correlation could be improved further if the static stiffness was measured with good accuracy for the relevant range of deflection angles.

1 Background

The increasing demand for higher efficiency in engines currently drives development towards down-sized and down-speeded engines and higher cylinder pressure. This leads to increased torsional vibrations and as a consequence puts higher demands on the driveline vibration damping capabilities.

Dual mass flywheels (DMFs) have the past decades proved their ability to significantly reduce torsional vibrations in passenger cars. In heavy-duty commercial vehicles conventional flywheels are still standard though and there is a need to better understand the potentials of DMFs for such applications. This work focuses on simulations of DMFs in heavy-duty applications, with the goal to accurately predict torsional vibrations in powertrains with DMFs for the complete operating speed and torque range.

A DMF consists of two flywheels torsionally connected by a series of springs at a radius. By exchanging a conventional flywheel for a DMF, the torsional resonance frequencies in the powertrain are affected in an advantageous way, leading to less excitation in the operating speed interval.

The most common way to connect the two flywheels is by means of curved springs, so called arc springs, located in a channel in the primary flywheel. Modelling and simulation approaches for this type of DMF for passenger cars have been studied before. In [1], [7], [5] and [3] the arc springs are modelled as several lumped masses connected by massless springs and with Coulomb friction introduced between these masses and the primary flywheel. In [4] a lumped mass model of the arc spring is combined with a LuGre friction model. The LuGre friction depends on the normal force, the relative velocity between the two contact surfaces and an internal deflection variable.

An alternative way to design the DMF is to instead of arc springs have several straight shorter springs connected by sliding shoes. This type of DMF exists for heavy-duty applications with engine torques up to

3500 Nm. No previous work regarding simulations for this type of DMF has been found. Although similar modelling as for the arc springs can be used, there is a need to build experience regarding realistic parameter values and to investigate the validity of the models for operating points valid for heavy-duty applications. In this paper a model for this type of DMF is proposed and evaluated.

2 The DMF

The analysed DMF has an outer diameter of about 490 mm to fit in an industry-standard SAE1 engine-gearbox interface. It is composed of a primary flywheel and a secondary flywheel torsionally connected by three parallel spring sets. Each spring set consists of two sliding shoes and two spring caps connected by three spring packages in series. This is illustrated in figure 1.

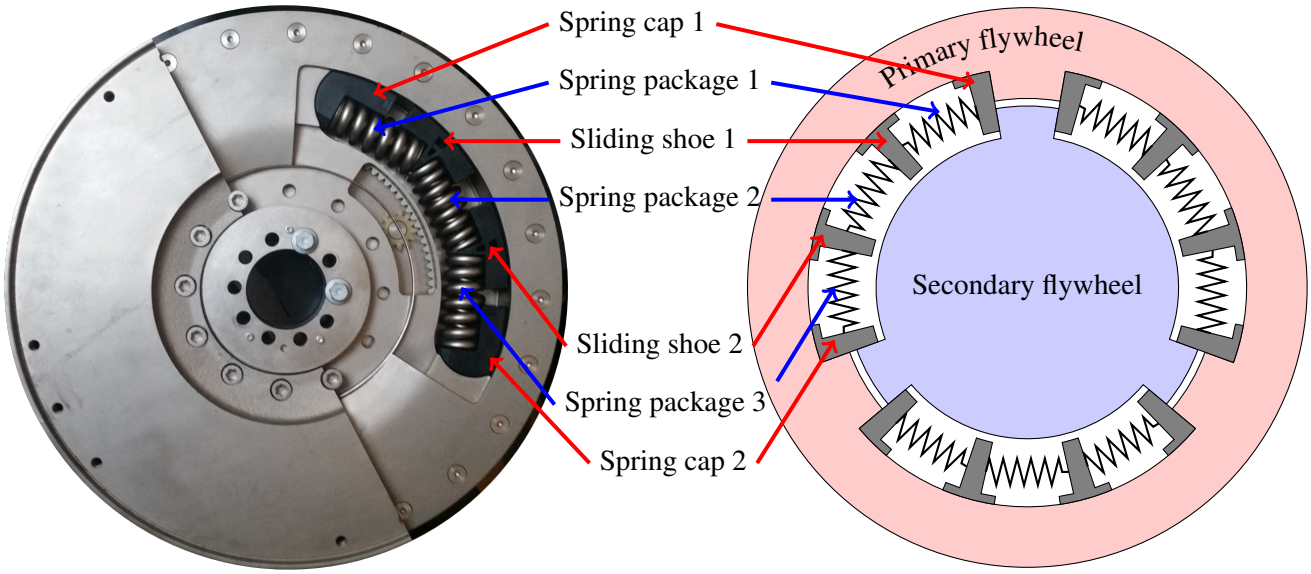


Figure 1: DMF design

The spring packages consist of two or three springs located inside each other and with slightly different lengths. The spring sets are located in a channel in the primary flywheel, with friction occurring at the contact surfaces between the primary flywheel and the sliding shoes and spring caps. When the spring packages are compressed and decompressed, the sliding shoes and spring caps slide against the primary flywheel. This results in friction forces. The normal forces at the contact surfaces depend on the compression of the springs and the centrifugal action. There is grease between the sliding shoes and the primary flywheel, and the resulting coefficient of friction will depend on the properties of the grease. These properties are generally very temperature dependent. All this means that the properties of the DMF are highly non-linear and detailed models are needed in order to accurately simulate the DMF.

2.1 Engineering model

In figure 2, the proposed torsional engineering model for the DMF in study is shown. The mass moment of inertia j_p corresponds to the primary flywheel and j_s to the secondary flywheel. It is assumed that all three spring sets are equivalent and they are modelled as one spring set represented by moments of inertia j_1 to j_4. Each spring cap can be in contact with either the primary or the secondary flywheel. For spring cap 1 this is modelled as gap activated springs with impact stiffness b_1 and gap angles θ_{1p} and θ_{1s} to primary and secondary flywheel respectively. For spring cap 2 the modelling is similar, with impact stiffness b_5 and gap

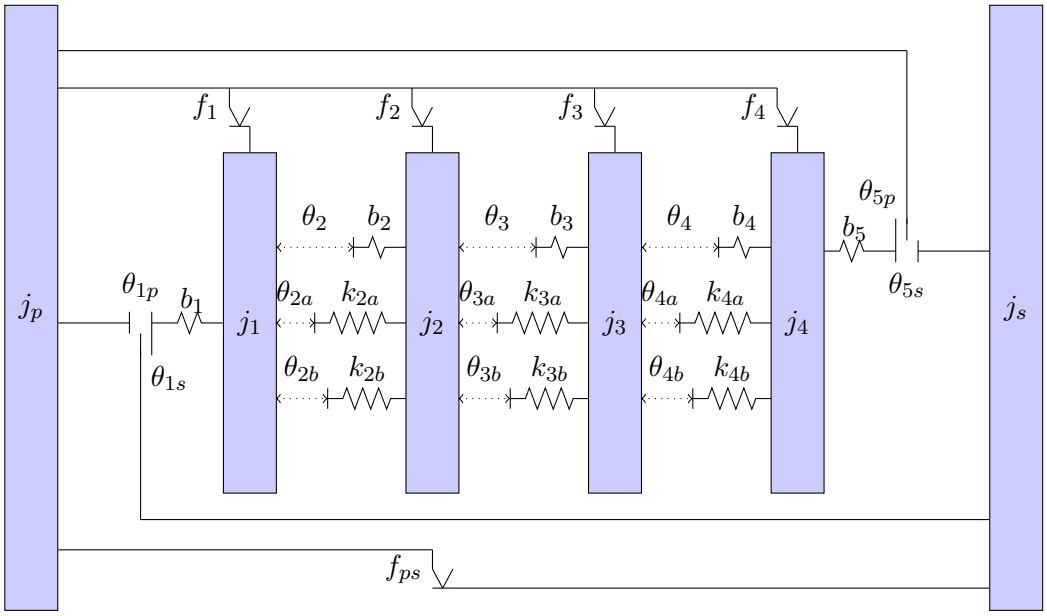


Figure 2: Engineering model of the DMF

Table 1: DMF model data

Moments of inertia	Gap angles	Stiffness
j_p = 1.8000 kgm^2	θ_{1p} = 0 rad	b_1 = 3.00e9 Nm/rad
	θ_{1s} = 0 rad	
j_1 = 0.0297 kgm^2	θ_{2a} = 0 rad	k_{2a} = 2.10e4 Nm/rad
	θ_{2b} = 0.0070 rad	k_{2b} = 5.35e4 Nm/rad
j_2 = 0.0426 kgm^2	θ_{3a} = 0 rad	k_{3a} = 1.02e4 Nm/rad
	θ_{3b} = 0.0030 rad	k_{3b} = 5.26e3 Nm/rad
j_3 = 0.0426 kgm^2	θ_{4a} = 0 rad	k_{4a} = 2.10e4 Nm/rad
	θ_{4b} = 0.0070 rad	k_{4b} = 5.35e4 Nm/rad
j_4 = 0.0297 kgm^2	θ_{5s} = 0 rad	b_5 = 3.00e9 Nm/rad
	θ_{5p} = 0 rad	
j_s = 0.9000 kgm^2		

angles θ_{5p} and θ_{5s}. If cases with low average torque are to be analysed, it is important to model the individual springs in each spring package separately. This is because the small differences in lengths of the different springs result in a non-linear stiffness which will influence the resonance behaviour. Spring package 1 is represented by springs k_{2a} and k_{2b}, spring package 2 by springs k_{3a} and k_{3b} and spring package 3 by springs k_{4a} and k_{4b}. Table 1 shows the data used. The torque in the measurements is not large enough for the spring caps and sliding shoes to be in contact, so the angular gaps between spring caps and sliding shoes, θ_2, θ_3, and θ_4 and the corresponding impact stiffnesses b_2, b_3 and b_4 will not affect the simulation results presented in this paper.

The friction torques at the contact surfaces between the spring caps and sliding shoes to the primary flywheel are represented by f_1 to f_4. The friction between the primary and secondary flywheel is represented by f_{ps}. The main part of this friction is believed to occur in the bearings between the two flywheels.

2.2 Friction

The geometry of the tangential connection between the flywheels and the spring caps is such that it will also take up much of the radial force. It will therefore be assumed that the friction between the spring caps and the primary flywheel will be only viscous. The friction between the sliding shoes and the primary flywheel will be modelled with the LuGre friction model. This model is described and evaluated in [6]. The friction force F depends on the relative velocity v between two surfaces, a deflection variable z and the normal force, F_n, at the interface. Equations (1) describe the standard parametrisation of the model used in this work.

$$\begin{aligned} F =& \sigma_0 z + \sigma_1 \dot{z} + \sigma_2 v \\ \dot{z} =& v - \sigma_0 \frac{|v|}{g(v)} z \\ g(v) =& F_c + (F_s - F_c) e^{-\left(\frac{v}{v_S}\right)^2} \end{aligned} \tag{1}$$

The Coulomb friction force F_c at each contact is a function of the corresponding normal force F_n and given as $F_c = \mu_c F_n$. The normal force depends on spring compressions, the angles between the sliding shoes and spring caps, the radial position of the springs and on the centrifugal action. The static friction force F_s is calculated as $F_s = \min(\mu_s F_n, F_t)$, where F_t is the total tangential force at the friction surface. In table 2, the used friction parameters are shown. The parameters are presented for one spring set and for translational direction. The friction between the primary and secondary flywheel f_{ps} is estimated as viscous damping coefficient of 5 Nms/rad. The static and kinetic friction coefficients are the same, since parameter studies have shown no significant influence of the static coefficient of friction for the analysed load cases. For higher mean torques and higher rotational speeds, the influence is expected to be higher.

Table 2: Friction parameters

Parameter	Description
$\sigma_0 = 10^5$ N/m	stiffness parameter
v_s = 0.01 m/s	Stribeck velocity
σ_1 = 350 Ns/m	velocity dependent damping coefficient
σ_2 =120 Ns/m	viscous damping coefficient
μ_c = 0.08	kinetic coefficient of friction
μ_s = 0.08	static coefficient of friction
r = 0.166 m	radial position of springs
r_f = 0.191 m	friction contact radius
$\alpha_{2,3,4}$ = 0.547 rad	angle between sliding shoes and between sliding shoes and spring caps

3 Measurements

Measurements have been performed in order to study the properties of the DMF and to enable validation of the simulated results. A rig was used that consisted of a large flywheel connected to a propeller shaft, which had a universal joint set at an angle. For a constant input angular speed, the universal joint creates an oscillating speed with oscillation frequency twice that of the input speed. The angular velocity of the rig flywheel was accelerated and then kept at a constant speed by means of a belt connected to an electric motor. The DMF was connected to the other side of the propeller shaft with some adapters and a torque meter in between as shown in figure 3. Measurements were performed for propeller shaft angles ranging

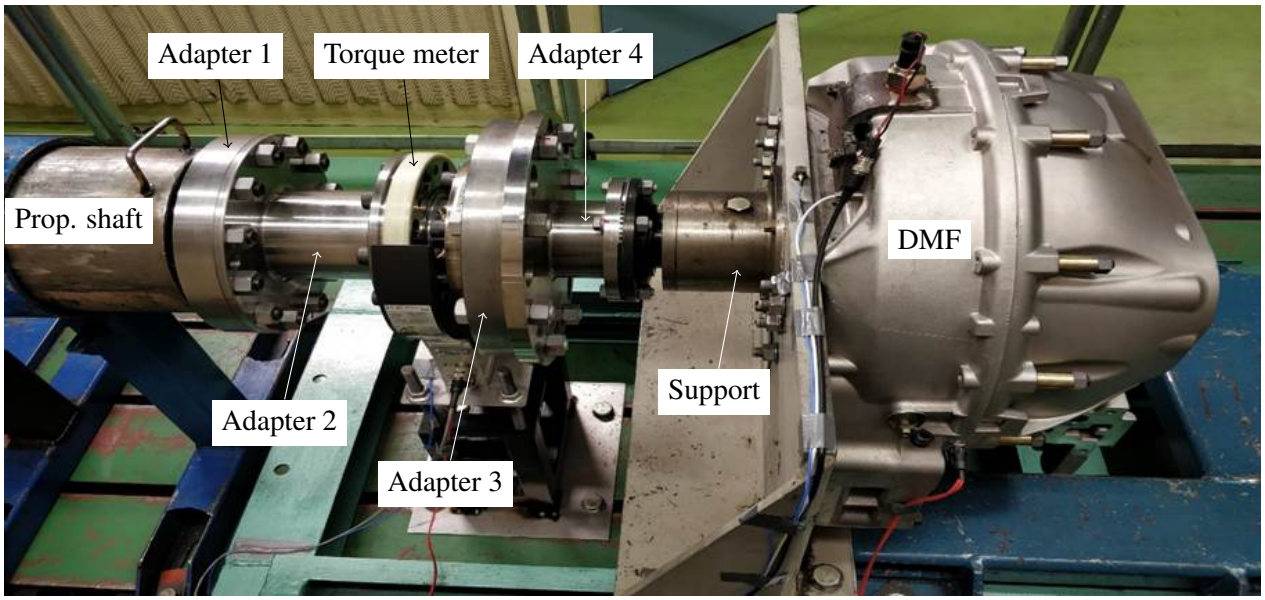


Figure 3: Rig

between 3 and 15 degrees and rotational speeds up to 1200 revolutions per minute (rpm). Angular velocities were measured at the rig flywheel and at the primary flywheel of the DMF with magnetic pickups, detecting motion of gear wheels connected to the flywheels. The number of gear teeth was 60 on the rig flywheel and 153 on the primary flywheel of the DMF. The angular velocity of the secondary DMF flywheel was measured using an optic sensor and a zebra tape with 60 black and white fields glued to the flywheel.

The friction between the sliding shoes and the primary flywheel depends on the properties of the grease. Since these properties are believed to be very temperature dependent it was considered important to measure and control the temperature. Initially, the DMF was heated until a temperature of 80 °C was obtained at the DMF surface. The temperature inside the flywheel at a distance of about 3 mm from the contact surface between the sliding shoes and the primary flywheel was recorded during the measurements. These temperatures were very stable during all measurements with values around 55 °C. The repeatability of the results was evaluated by measuring at 700 rpm both at the beginning of the measurements for a specific joint angle and after measurement had been done for all speeds under evaluation. No big deviations between the 700 rpm measurements could be seen which indicates that there were no huge differences in friction properties between the measurements. More information regarding the test procedure can be found in [2].

Table 3: Rig model structural parameters

Part	Stiffness / [Nms/rad]	Moment of inertia / [kgm^2]	label
Rig flywheel		40.0000	rig
Half propeller shaft		0.0640	joint
Propeller shaft	356000		prop
Half propeller shaft		0.0640	
Adapter 1		0.1800	
Adapter 2		0.1100	
Half torque meter		0.0485	
Bolts		0.0629	
		Total: 0.4654	
Torque meter+adapter	5997256		tm
Half torque meter		0.0485	
Adapter 3		0.3700	
Adapter 4		0.2100	
Bolts		0.0740	
		Total: 0.7025	
Support	853000		fw1
Primary flywheel		1.8	
Secondary flywheel	Non-linear	0.9	fw2

3.1 Rig modelling

In measurements a resonance around 15 Hz was observed, involving mainly the DMF. There also appear to be resonances of higher frequencies that depend on propeller shaft joint angles. A good model of the rig contributes to the understanding of the measured vibrations and simplifies evaluation.

For steady-state conditions and linear rig properties, the displacements at different positions in the rig can be estimated based on the measured torque τ_{tm} and the measured angular velocity at the primary flywheel $\dot{\varphi}_{fw1}$ as follows.

A lumped mass system of the rig can be formed according to figure 4. Here τ denotes torque and φ angular displacement. How the different parts have been lumped is shown in table 3. For steady-state solutions, the

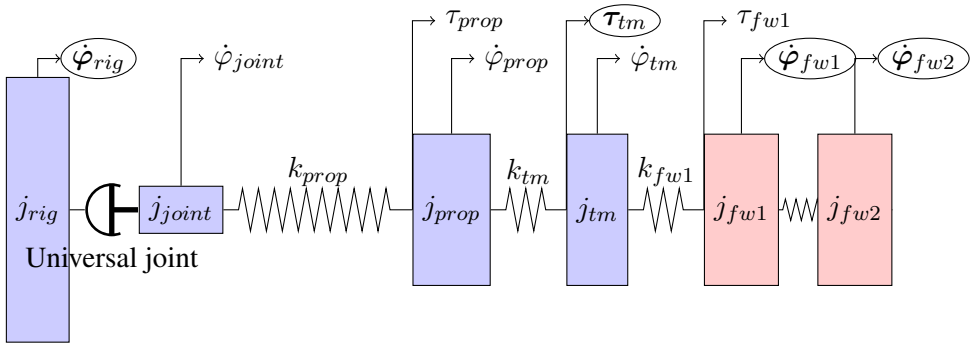


Figure 4: Schematic picture of the rig (encircled variables are measured)

different variables can be estimated as complex series according to equation (2).

$$\varphi_{tm} = \sum_{q=-n}^{n} A_q e^{iq\omega t},\ \varphi_{fw} = \sum_{q=-n}^{n} B_q e^{iq\omega t},\ \tau_{tm} = \sum_{q=-n}^{n} T_q e^{iq\omega t} \tag{2}$$

Here A_q, B_q and T_q are complex constants, t is the time and ω is the average angular velocity. The integer n is selected in order to estimate the measured signals with good accuracy. In this work, a value of 8 has been used. The angular velocities and accelerations can also be expressed accordingly. From angular momentum balance, we obtain

$$\begin{aligned} j_{tm}\ddot{\varphi}_{tm} =& \tau_{tm} + k_{fw1}(\varphi_{fw1} - \varphi_{tm}) \\ \Rightarrow j_{tm}\ddot{\varphi}_{tm} + k_{fw1}\varphi_{tm} =& \tau_{tm} + k_{fw1}\varphi_{fw1} \end{aligned} \tag{3}$$

Inserting the expressions from (2) into (3) gives

$$\sum_{q=-n}^{n} \left(-\omega^2 q^2 j_{tm} A_q + k_{fw1} A_q\right) e^{iq\omega t} = \sum_{q=-n}^{n} \left(T_q + k_{fw1} B_q\right) e^{iq\omega t} \tag{4}$$

Due to the orthogonality of the functions $e^{iq\omega t}$ we have for all q that

$$A_q = \frac{T_q + k_{fw1} B_q}{-\omega^2 q^2 j_{tm} + k_{fw1}}. \tag{5}$$

Once φ_{tm} is calculated, φ_{prop} can be obtained from equation (6).

$$\varphi_{prop} = \frac{\tau_{tm} + k_{tm}\varphi_{tm}}{k_{tm}} \tag{6}$$

The displacement, on the DMF side of the universal joint, φ_{joint} is then given by equation (7).

$$\varphi_{joint} = \frac{j_{prop}\ddot{\varphi}_{prop} + \tau_{tm} + k_{prop}\varphi_{prop}}{k_{prop}} \tag{7}$$

Based on this, τ_{prop} can be calculated according to equation (8).

$$\tau_{prop} = -k_{prop}(\varphi_{prop} - \varphi_{joint}) \tag{8}$$

The equations presented here are based on linear stiffness and no damping. It should be noted, that for higher orders, a correct timing between the signals and very accurate stiffness in the model are of extreme importance. Small deviations in timing can introduce unrealistically high oscillations for higher orders.

4 Simulations

4.1 Computational method

Due to the big number of gap activated springs in the model, conventional time integration methods require very small time steps in order to converge. In the correlation work, a method inspired by [8] has been used. The algorithm first solves a linear complementary problem, assuming that the friction forces are the same as the previous time step and then iterates in order to solve for the updated friction forces. The steady-state harmonic response of a linearised model has been used to impose realistic initial conditions. The simulations have been run until steady-state and the last two cycles have been used for evaluation.

4.2 System modelling

There are several alternatives for the engineering model used in simulation that can be considered in correlation work. The simplest approach is to include only the DMF in the model and impose the measured angular velocities at the primary flywheel in the simulation. Another alternative is to include all parts between torque meter and DMF and apply the measured torque in the simulation. The drawback with these alternatives is that resonance frequencies in the models differ from the full rig system.

A third alternative is to include the rig in the model. The universal joint in the propeller shaft imposes some problems, though. Besides difficulties with implementation and increased simulation time, there are some uncertainties regarding internal clearance, joint angle and joint angular position. A simplification is to model the rig system from the propeller shaft joint to the DMF and apply φ_{joint}, as derived in section 3.1, as a boundary condition.

In figure 5 the relative displacement amplitudes between the primary and secondary flywheel in the DMF are shown for the second vibration order for different propeller shaft joint angles and different rotational speeds. Measured results are shown as solid lines. Simulated results, using only the DMF in the model, are shown as dashed lines. We see that the correlation is not as good for speeds below 500 rpm as for the higher speeds.

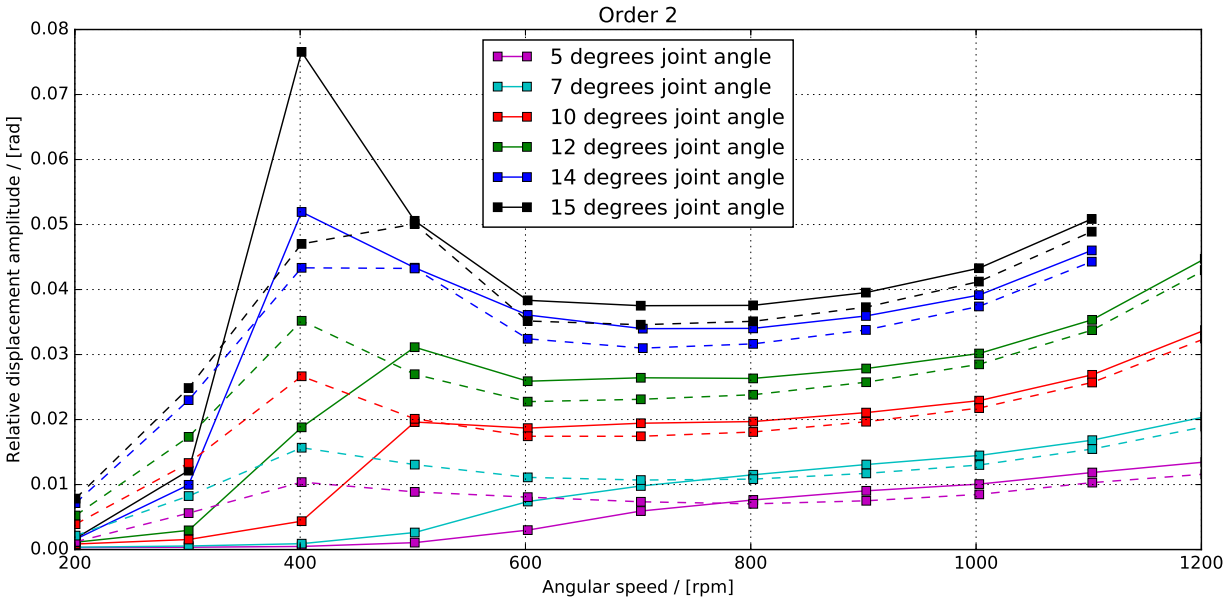


Figure 5: Measured (solid lines) and simulated (dashed lines) relative displacement amplitudes between primary and secondary flywheel

In particular, there is a clear resonance peak in the measurements with 14 and 15 degrees joint angle at 400 rpm that is not captured very well in the simulations. The resonance peak is only visible for the two highest propeller shaft joint angles. Considering that the stiffness of the DMF is lower for lower deflection angles, resonance peaks for lower joint angles can be expected at lower speeds. This is not what is observed in the measurements.

The explanation to this is probably the non-linearities in the rig propeller shaft. As shown in section 3.1, the displacement φ_{prop} at the propeller shaft end closest to the DMF can be estimated from the measured signals τ_{tm} and $\dot{\varphi}_{fw1}$. If the angular position of the universal joint relative the rig flywheel is known, the velocity just after the joint (assuming a stiff joint), can be calculated based on the joint angle and the measured rig flywheel velocity, $\dot{\varphi}_{rig}$. If calculated this way, it will be labelled $\hat{\varphi}_{joint}$. The relative displacement in the propeller shaft can then be estimated as

$$\Delta_{prop} = \varphi_{prop} - \hat{\varphi}_{joint} \tag{9}$$

In this work, the angular position of the rig flywheel could be determined thanks to small deviations in the rig timing gear geometry. These deviations caused reoccurring spikes in the measured signal that were used to determine the position. How the universal joint is rotated relative the rig flywheel determines the phase of the angular velocity oscillation after the joint. By inspecting the angular velocity after the joint, $\dot{\varphi}_{joint}$, as derived in section 3.1, the angular position of the universal joint relative the rig flywheel could be estimated.

Figure 6 shows the relationship between the estimated second order of the torque at the end of the propeller shaft τ_{prop} as a function of the second order of the estimated propeller shaft deflection, Δ_{prop}. The squares denote speeds below 700 rpm and the dashed line shows the propeller shaft stiffness calculated from the geometry. As can be seen we have a fairly linear relationship for speeds at 700 rpm and higher. The curve

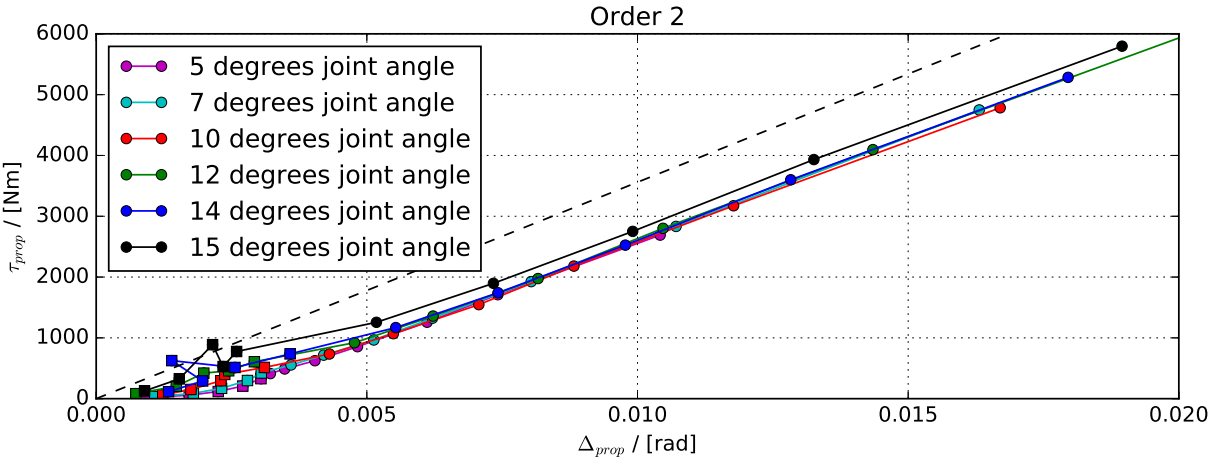


Figure 6: Propeller shaft stiffness

follows the expected stiffness of the propeller shaft well, but with an offset. This indicates that there is an internal clearance and a very non-linear stiffness in the propeller shaft joint for small deflection angles. At small deflection angles, the resonance behaviour is governed both by high non-linearities in the DMF and in the propeller shaft joint.

Several different rig modelling approaches have been used and compared, in order to capture the resonances in a better way. Improvement for some joint angles lead to worse results for other angles. Apart from near resonances, there are small differences in the results from the different approaches.

Since the focus of this work is the DMF model and not the rig it was decided to concentrate on correlation for speeds above the resonance. Results for the lowest propeller shaft joint angles were also omitted in the correlation work, since those results are extremely sensitive to the internal clearances in the DMF. Additional measurements are needed in order to model these non-linearities in an accurate way.

In section 5, the simulated results are based on the model including only the DMF and with measured angular velocities as boundary conditions for the primary flywheel.

5 Correlation

In figure 7, the relative angular displacement between the primary and secondary flywheel is shown for measurements and simulations. Far from resonance, the friction and damping parameters have relatively small influence on the relative displacement, so the good correlation is not surprising. In order to better assess the

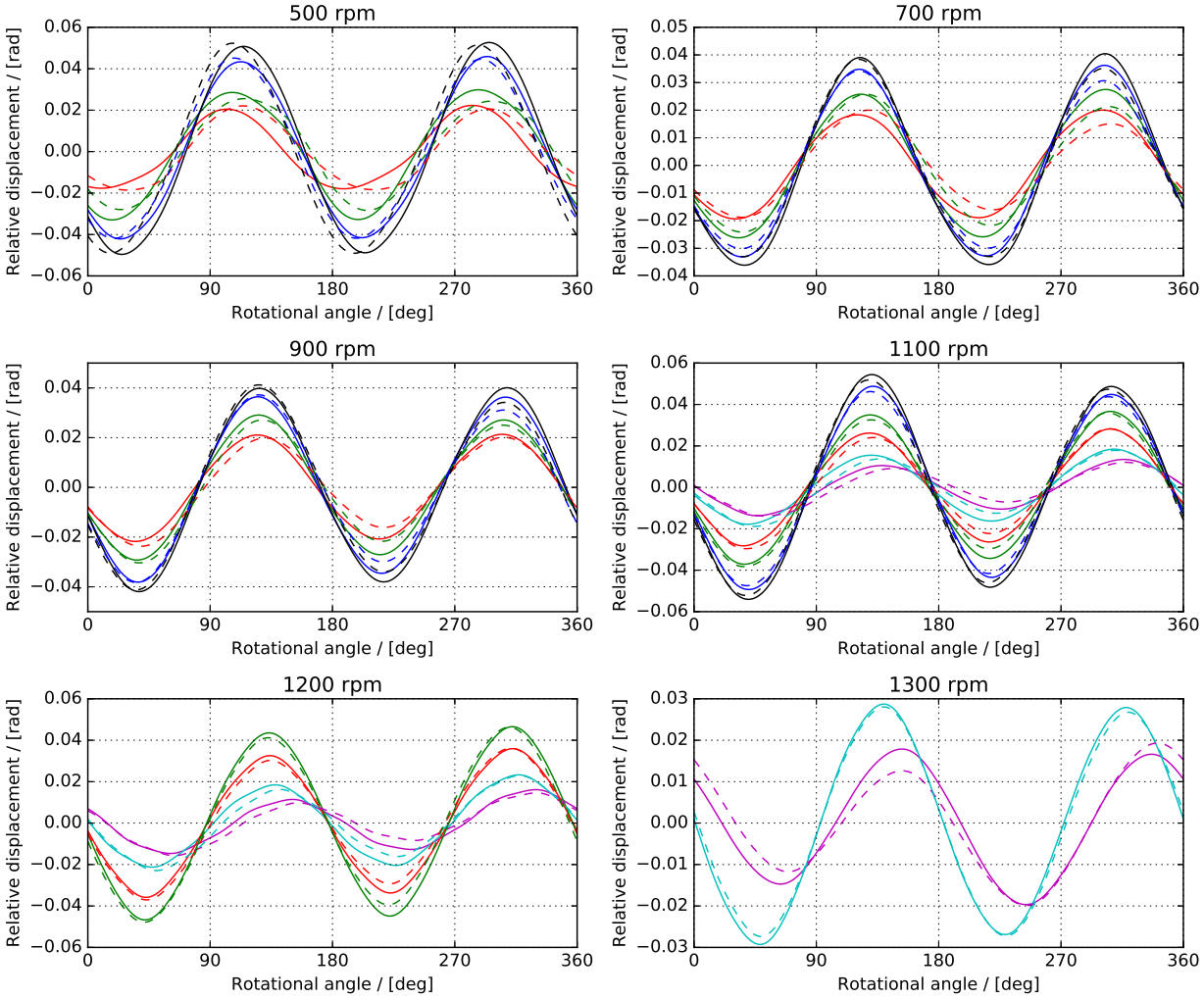


Figure 7: Relative angular displacement between secondary and primary flywheel for different speeds from measurements (solid lines) and simulations (dashed lines). Colours denote joint angles as in figure 5.

validity of the friction model the hysteresis curves are analysed. In figure 8, the torque into the secondary flywheel is shown as a function of the relative displacement between the two flywheels. Only orders up to 12 are included in order to filter out noise and high-frequency vibrations. It should be noted that small measurement errors in the angular velocity of the secondary flywheel can have a significant impact on the higher orders of the calculated torque. It has been difficult to determine if the deviations between measurements and simulations that exist are due mainly to the modelling or to the resolution in the measurements.

Even though the measured results are not exactly reproduced, the general behaviour of the DMF is captured. We can see clear trends of higher energy dissipation per cycle at higher speeds and also higher effective stiffness. At higher speeds the sliding shoes do not move in a uniform manner, which explains the non-linear variation of the torque.

The effect of the Coulomb coefficient of friction is illustrated in figure 9a for the case with rotational speed of 800 rpm and 15 degrees propeller shaft joint angle. Simulated results are shown with coefficients of friction

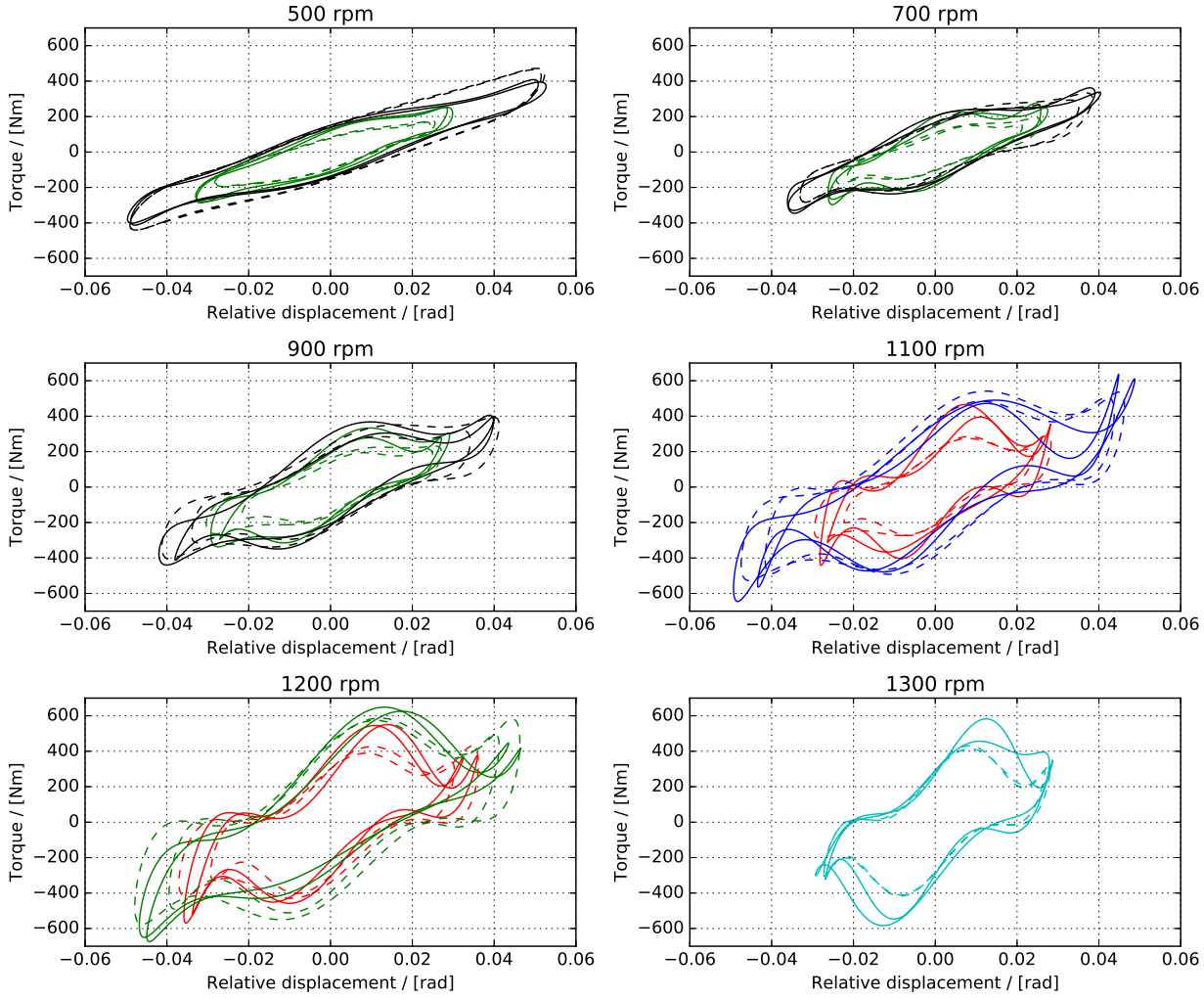


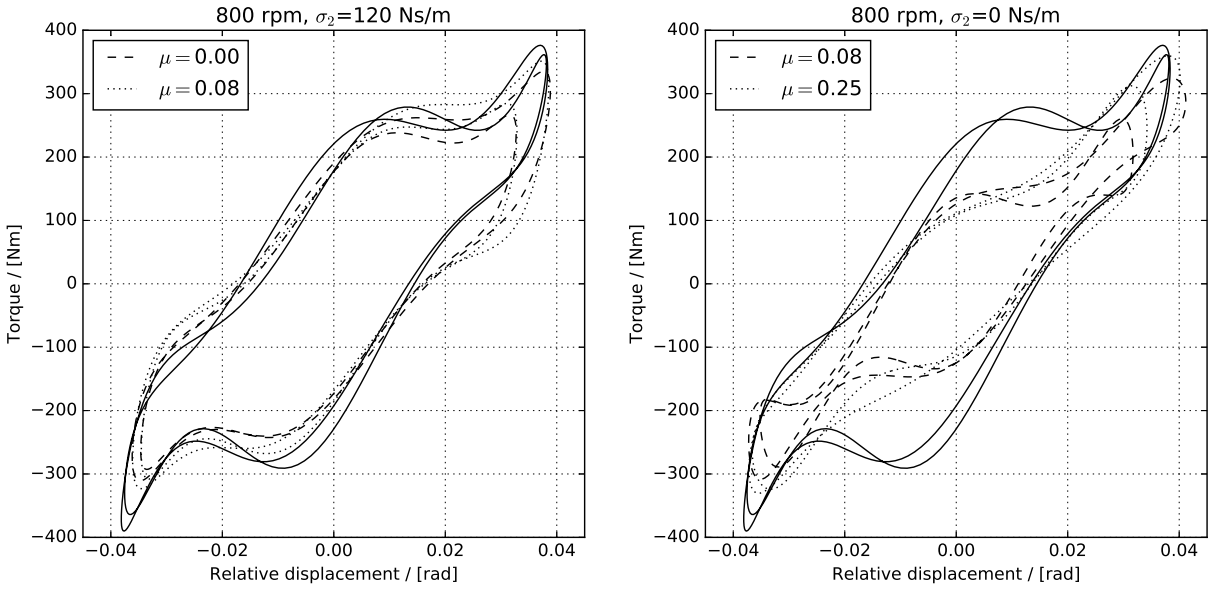
Figure 8: Torque-displacement relationship at different speeds from measurements (solid lines) and simulations (dashed lines). Colours denote joint angles as in figure 5.

of zero and 0.08. The difference is quite small and the reason is the low normal force. For higher mean torques the coefficient of friction is expected to affect the results in a more significant way.

In the measurements there is generally a steep increase in torque at secondary flywheel for small relative displacements. This indicates that there is significant viscous damping, since this is where the relative velocities between the sliding shoes and the primary flywheel are high. In figure 9b simulated results without the viscous part in the friction model are shown for two different coefficients of friction. We can note much lower torque magnitudes at small relative displacements than in corresponding results from the measurements. The impact of the different friction parameters is similar at higher speeds.

6 Conclusions

The proposed model of the DMF has shown to produce realistic results for a big range of speeds and load amplitudes. The results indicate that there is a significant amount of viscous damping between the sliding shoes and primary flywheel. This must be included in the friction modelling and considering only Coulomb friction does not produce satisfactory results. The effect of the Coulomb friction in the analysed model is quite small compared to the viscous part, but it is expected to be more important for higher average torque and higher rotational speeds.



(a) With viscous damping

(b) Without viscous damping

Figure 9: Torque-displacement relationship from measurements (solid lines) and simulations (dashed and dotted lines) with different parameter settings

There are several resonances in the analysed system and accurate modelling of the internal gaps and spring stiffnesses is very important to capture the oscillating behaviour of the systems near these resonances. Correlation could be improved further with accurate measurements of the internal clearances. However, for higher mean torques which corresponds to normal operating conditions, the impact of internal clearances is not as big.

Future work will focus on the validity of the model for higher mean torques at different load amplitudes and frequencies.

Acknowledgements

The measurements referred to in this paper were performed by Johan Karlsson as part of his master thesis and we would like to express our gratitude for his valuable contribution to this work. Many thanks also to all Volvo employees who helped with the measurements and rig preparation.

We also want to offer a very special thanks to Anders Hedman, AB Volvo, for his continuous support, encouragement and useful assistance in all phases of this project. His broad knowledge and experience have been great assets.

This research is part of the doctoral project ”Reduced vibration transmissions - reduced energy consumption and environmental impacts together with an increased competitiveness” which is funded by the Swedish Energy Agency (project No. 42100-1).

References

[1] A. Albers et al. “New Methodology for Power Train Development in the Automotive Engineering - Integration of Simulation, Design and Testing”. In: *SAE Technical Papers*. 2001.

[2] J. Karlsson. *Investigation of dynamic friction properties of a dual mass flywheel for commercial vehicles*. M. Sc. thesis. Chalmers University of Technology. 2018.

[3] P. Kelly et al. “Dual mass flywheel as a means of attenuating rattle”. In: *Tribology and Dynamics of Engine and Powertrain* (2010), pp. 857–877.

[4] T. H. Kim et al. “Analysis of Dual Mass Flywheel Using Discrete Arcspring Model”. In: *Key Engineering Materials* 326-328 (2006), pp. 1607–1610. ISSN: 1662-9795.

[5] T. Mahl and O. Sawodny. “Modelling of an automotive Dual Mass Flywheel”. In: *IFAC Proceedings Volumes (IFAC-PapersOnline)*. Vol. 43. 18. IFAC, 2010, pp. 517–523. ISBN: 9783902661760.

[6] H. Olsson. “Control Systems with Friction”. PhD thesis. Lund Institute of Technology, 1996. ISBN: 0280-5316.

[7] U. Schaper et al. “Modeling and torque estimation of an automotive dual mass flywheel”. In: *Proceedings of the American Control Conference*. 2009, pp. 1207–1212. ISBN: 9781424445240.

[8] S. D. Yu. “An efficient computational method for vibration analysis of unsymmetric piecewise-linear dynamical systems with multiple degrees of freedom”. In: *Nonlinear Dynamics* 71.3 (2013), pp. 493–504. ISSN: 0924090X.

Dynamic characterisation of rolling-element bearings - implementation of smooth contact-state transition

M. Razpotnik [1], **G. Čepon** [1], **M. Boltežar** [1]
[1] University of Ljubljana, Faculty of Mechanical Engineering,
Aškerčeva ulica 6, 1000 Ljubljana, Slovenia
e-mail: **matej.razpotnik@fs.uni-lj.si**

Abstract
Predicting the response of a system containing rolling-element bearings often encounters numerical difficulties when time integration is performed. The problem originates in a sudden contact-state transition, which is governed by the bearing clearance and the bearing nonlinear contact characteristics. The response of a shaft-bearing-housing assembly can be especially unstable in the transient regions, e.g., at the start of a system run-up or when passing the critical speed of a system. In this paper, a new analytical bearing-stiffness model is presented that is capable of overcoming these problems by smoothing the nonlinear bearing deformation-, force- and stiffness-displacement characteristics in the discontinuous regions. Based on a simple case study it is shown that already a small value of the smoothing parameter significantly improves the numerical simulation in terms of speed and stability.

1 Introduction

The transmission of vibrations through rolling-element bearings is one of the main topics of interest with respect to rotating machinery. Thus, the dynamic characterization of rolling bearings has been investigated for many decades; however, due to its complexity it remains an important matter in ongoing research. Due to the nonlinear nature of the contact formulation in rolling bearings, the prediction of the system's response remains a demanding task.

Over the past few decades, many approaches and results have been presented in the field of bearing models. A first general theory for elastically constrained ball and roller bearings was developed by Jones [1] and later on further derived by Harris [2]. This theory was in fact very general and it was not able to properly determine the cross-coupling stiffness between the radial, axial and the tilting deflections. Simplified bearing models were instead introduced by other researchers, where the bearings were modelled as ideal boundary conditions for the shaft, as presented by Rao [3]. Meanwhile, the idea of interpreting the bearings with a simple one- or two-degrees-of-freedom (DOFs) model with linear springs was introduced by While [4] and Gargiulo [5]. Later, more precise bearing models were derived. A major improvement in predicting the vibration transmission through rolling-element bearings was made by Lim and Singh [6], who derived a model that provides a comprehensive bearing-stiffness matrix. The model is capable of properly describing the nonlinear relation between the load and the deflection, taking into account all 6 DOFs and their interplay. The model of Lim and Singh was the basis for many subsequent investigations. Later, Royston and Basdogan [7] introduced a model for predicting the vibration transmission through self-aligning (spherical) rolling-element bearings. Liew and Lim [8] extended the model of Lim and Singh to analyse the time-varying rolling element bearing characteristics that occur due to the pass of the rolling element. A bearing-stiffness matrix formulation for double raw angular contact ball bearings was derived by Gunduz and Singh [9]. Lee and Choi [10] presented an analysis approach where they investigated the speed-dependent ball-bearing stiffness in a flexible rotor with a nonlinear bearing characteristic based on Jones' model. Sheng et al. [11] studied and derived the

bearing speed-varying stiffness model. With the development of the finite-element-method (FEM) models, new techniques for calculating the proper bearing dynamics have appeared. Guo and Parker [12] proposed a stiffness matrix calculation for a rolling-element bearing using a finite-element/contact-mechanics model. The authors precisely modelled each integral part of the bearing and implemented a special contact model between the rolling elements and both raceways. Recently, Zhang et al. [13] presented a general model for preload calculation and stiffness analysis for combined angular contact ball bearings.

Many authors have studied the bearing dynamics by analysing a rotor-bearing-housing assembly. Lim and Singh investigated a geared-rotor system [14] and performed a statistical energy analysis [15]. Bai et al. [24] went step further and analysed the acoustic response. They evaluated the radiation noise of the bearing applied to the ceramic motorized spindle based on the sub-source decomposition method. Čermelj and Boltežar [17] presented an indirect approach to investigate the dynamics of a structure with ball bearings. Lately, Razpotnik et al. [18] investigated the vibration transmission in a statically indeterminate system that is supported by bearings. The dynamic behaviour of a system containing bearings where the time response was calculated was presented by Xu and Li [19, 20] for a planar multibody system with multiple deep groove ball-bearing joints. Fonseca et al. [21] studied the influence of unbalance levels on nonlinear dynamics of a rotor-backup rolling bearing system. Wang et.al. [22] conducted dynamic modelling of moment wheel assemblies with nonlinear rolling bearing supports. They performed dynamic tests to verify the nonlinear dynamic model. The effect of bearing preload on the modal characteristics of a shaft-bearing assembly was investigated by Gunduz et al. [23]. Similarly, the effect of the axial preload of the ball bearings on the nonlinear dynamic characteristics of a rotor-bearing system was investigated by Bai et al. [16]. It was shown that the bifurcation margins of an unbalanced rotor-bearing system enhance markedly when the axial preload increases and relates to the system's resonance speed.

Predicting the response of a system with rolling bearings often encounters numerical difficulties when a time integration is performed. The problem originates in a sudden contact-state transition, which is governed by the bearing clearance and the nonlinear force- and stiffness-displacement characteristics. Several attempts have been made to increase the stability of the calculation. Fleming and Poplawski [25] showed that a moderate amount of damping eliminated the bistable region in their response, but this damping is not inherent in the ball bearings and introduces additional artificial forces. Another approach was presented by Xia et al. [26] for the rotor-bearing system with journal bearings. They presented two calculation methods (the Ritz model and a one-dimensional FEM) to overcome the numerical shortcomings of the extremely time-consuming Reynolds equations.

We present a new formulation for the contact-state transition in rolling-element bearings, operating under radial clearance, to ensure a stable numerical calculation. The original non-smooth contact-dynamics formulation implies numerical issues in a time-integration process. In order to avoid these problems the proposed formulation introduces smoothing of bearing deformation-displacement characteristics in the region of the impact contacts. The idea is somehow similar to the modelling of a non-smooth friction force using an approximate single-valued friction law [27]. The bearing model from Lim and Singh [6] represents the basis for our study. The formulation proposes the smoothing of deformations, therefore the whole existing bearing model has to be reformulated and new equations have to be derived. Finally, a comprehensive bearing-stiffness matrix is obtained. The modularity of the proposed bearing model allows the implementation of an arbitrary smoothing value for each individual rolling element. The applicability of the developed bearing model is demonstrated on a simple unbalanced rotor that is supported by two bearings. It is shown that already a small value of the smoothing parameter significantly improves the numerical simulation in terms of speed and stability.

2 Assumptions

Besides the assumptions given in [6] the following also have to be taken into account:

1. The radial load is dominant.
2. It is applicable to bearings that operate under a radial clearance. Therefore, ball and cylindrical roller bearings are of primary interest.
3. The coordinate system follows the direction of the radial load (always pointing directly to one rolling element). Consequently, any fluctuation due to a rolling-element pass cannot be modelled.

3 The existing analytical bearing model

Having the bearing mean-load vector $\mathbf{f}_b = \{F_x,\, F_y,\, F_z,\, M_x,\, M_y,\, M_z\}^{\mathrm{T}}$ and the bearing mean-displacement vector $\mathbf{q}_b = \{\delta_x,\, \delta_y,\, \delta_z,\, \beta_x,\, \beta_y,\, \beta_z\}^{\mathrm{T}}$ as shown in Fig. 1, we can express the radial and axial displacements

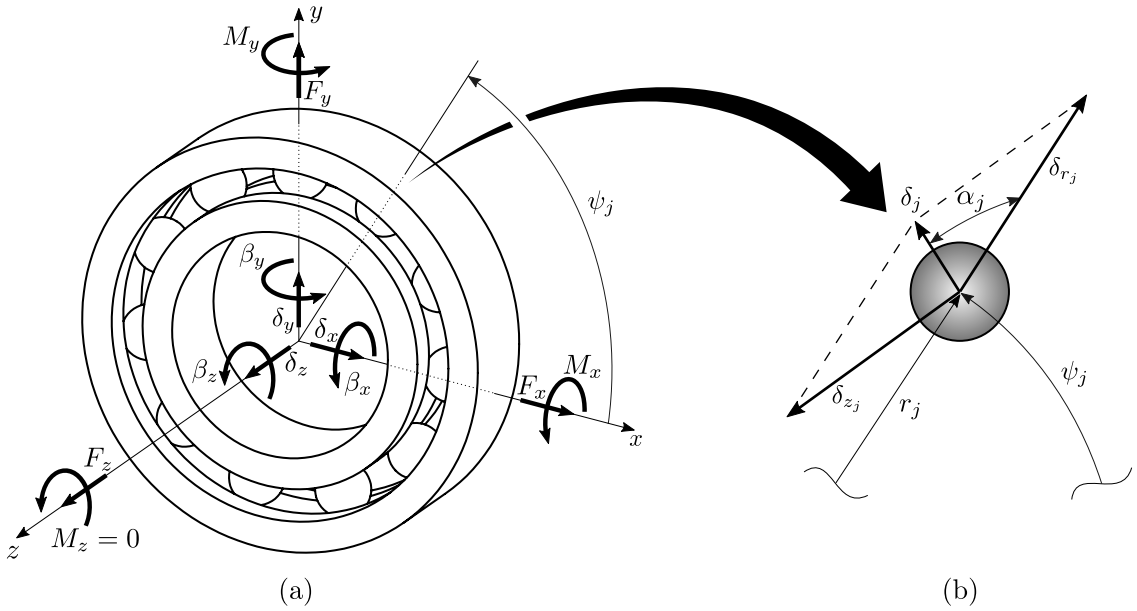


Figure 1: Rolling-element bearing loads and displacements; (a) Global representation (inner ring relative to the outer ring), (b) Local displacements of the jth rolling element.

of the jth rolling element as

$$\delta_{r_j} = \delta_x \cos\psi_j + \delta_y \sin\psi_j - r_c \tag{1}$$

and

$$\delta_{z_j} = \delta_z + r_j(\beta_x \sin\psi_j - \beta_y \cos\psi_j), \tag{2}$$

where x and y point to the radial direction and z to the axial direction (Cartesian coordinate system). The moment around z-axis is zero by default (no friction). For ball bearings the contact angle of the jth ball is defined as $\tan\alpha_j = \frac{\delta^*_{z_j}}{\delta^*_{r_j}}$, where $\delta^*_{z_j} = A_0 \sin\alpha_0 + \delta_{z_j}$ and $\delta^*_{r_j} = A_0 \cos\alpha_0 + \delta_{r_j}$. For cylindrical roller bearings it is assumed that $\alpha_j = \alpha_0 = 0$. The loaded distance between the inner- and outer-raceway curvature centres for the jth ball is given as:

$$A(\psi_j) = A_j = \sqrt{(\delta^*_{r_j})^2 + (\delta^*_{z_j})^2}. \tag{3}$$

From the ball-bearing kinematics, the resultant elastic deformation of the jth ball is defined as:

$$\delta_{B_j} = \begin{cases} A_j - A_0, & \delta_{B_j} > 0 \\ 0, & \delta_{B_j} \leq 0 \end{cases}, \tag{4}$$

whereas for cylindrical roller bearings, the resultant elastic deformation of the jth roller is equal to:

$$\delta_{R_j} = \begin{cases} \delta_{r_j}, & \delta_{R_j} > 0 \\ 0, & \delta_{R_j} \leq 0 \end{cases}. \tag{5}$$

Following the Hertzian contact stress principle as $F_j = K_n \, \delta_j^n$ (n is equal to $^3/_2$ for ball bearings and $^{10}/_9$ for roller bearings), we can connect $\mathbf{f}_b$ and $\mathbf{q}_b$ by summing the contribution from the rolling elements:

$$\mathbf{f}_b = \begin{Bmatrix} F_x \\ F_y \\ F_z \\ M_x \\ M_y \end{Bmatrix} = \begin{Bmatrix} \sum_{j=1}^{z} F_j \cos\alpha_j \cos\psi_j \\ \sum_{j=1}^{z} F_j \cos\alpha_j \sin\psi_j \\ \sum_{j=1}^{z} F_j \sin\alpha_j \\ \sum_{j=1}^{z} r_j \, F_j \sin\alpha_j \sin\psi_j \\ -\sum_{j=1}^{z} r_j \, F_j \sin\alpha_j \cos\psi_j \end{Bmatrix}, \tag{6}$$

where z is the number of all the rolling elements in a bearing. Finally, the symmetrical bearing-stiffness matrix with dimension five is expressed as:

$$\mathbf{K}_b = \frac{\partial \, \mathbf{f}_b}{\partial \, \mathbf{q}_b} = \begin{bmatrix} k_{xx} & k_{xy} & k_{xz} & k_{x\beta_x} & k_{x\beta_y} \\ & k_{yy} & k_{yz} & k_{y\beta_x} & k_{y\beta_y} \\ & & k_{zz} & k_{z\beta_x} & k_{z\beta_y} \\ & \text{sym.} & & k_{\beta_x\beta_x} & k_{\beta_x\beta_y} \\ & & & & k_{\beta_y\beta_y} \end{bmatrix}. \tag{7}$$

It is important to note that $\mathbf{K}_b$ is symmetrical and in general with dimension 6×6; however, due to the zero stiffness terms connected with β_z we obtain a matrix with a rank of five.

The existing bearing model is of great use in all kinds of implicit calculations. However, when it comes to explicit dynamics – using either the Finite Element Method (FEM) model or Multi-Body Simulations (MBS) – some numerical difficulties arise due to the bearing clearance. The derived equations for deformation, force and stiffness are not smooth functions, i.e., are not continuously differentiable, which originates from the piecewise definition of the bearing deformation.

When running explicit calculations it is important to have a system whose integral parts exhibit continuously differentiable stiffness-displacement characteristics. Otherwise, a time step during the integration process decreases significantly. Consequently the calculation might results in a longer computational time or even leads to non-converged solutions.

4 Smoothing the contact-state transition

When the transition of a contact change from open to closed is very fast in terms of time, we can talk about impacts. They change the dynamic properties of a system significantly in a very short time. In the case of bearings, this happens when the rolling elements eliminate the clearance and suddenly hit the raceways. This sudden change of the bearing load vector and the corresponding bearing stiffness represents the root cause of many problems in a time-integration procedure.

An efficient way to improve the calculation of a system with a sudden contact-state transition is to derive the smoothed deformation, force and the corresponding stiffness characteristics in the area of the transition. A sudden hit appears every time each single rolling element eliminates the clearance and hits between both raceways. The transition is especially problematic for the first rolling element coming into a contact. The

smooth contact transition introduces "simplification", which helps the integration process to pass that region flawlessly. Smoothing a function implies an approximate final solution in the region where the smoothing is applied. Obviously, there is a trade-off between the exact solution with numerical difficulties and the approximate one with numerical ease.

4.1 Theoretical background

A sudden transition of the force- and stiffness-displacement characteristics originates in piecewise-defined ball- and roller-bearing kinematics as given in Eq. (4) and (5). Thus, it is reasonable to smooth the function regulation in the region between both pieces. Furthermore, this change is to be conducted on the deformation level so that the derived expressions for the force- and stiffness-displacement characteristics are to be smoothed as well. From Eq. (4) and (5) it follows that

$$A_j - A_0 = 0 \quad \text{and} \quad \delta_{r_j} = 0 \tag{8}$$

represent the points between both function intervals of the jth rolling element for a ball and cylindrical roller bearing, respectively. Since radial load is dominant and most sensitive to the impacts, we have to find the roots of Eq. (8) in radial (x') direction. The roots represent the radial displacement of each jth rolling element (as a function of all other DOFs), needed to overcome a clearance. First, we define a new rotating Cartesian coordinate system as shown in Fig. 2. The axes z' and z are aligned, whereas the axes x' and y' rotate

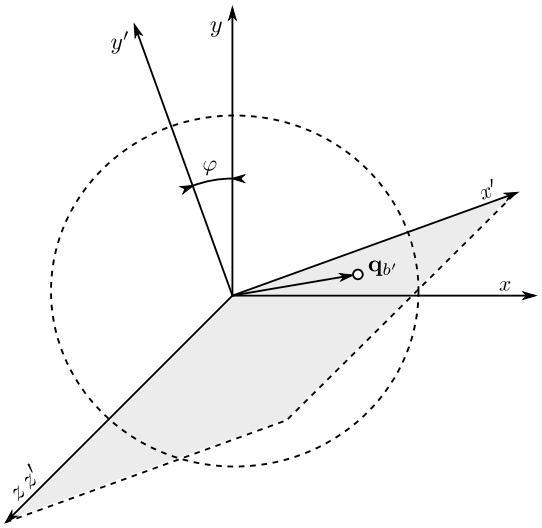


Figure 2: Fixed and rotating coordinate systems.

around z'. Such a coordinate system enables the definition of a radial displacement entirely in the $x'z'$ plane, having a displacement in the y' direction always equal to zero. The new mean-load and mean-displacement vectors are defined as:

$$\begin{aligned} \mathbf{f}_{b'} &= \{F_{x'},\, F_{y'} = 0,\, F_{z'},\, M_{x'},\, M_{y'}\, M_{z'} = 0\}^{\mathrm{T}}, \\ \mathbf{q}_{b'} &= \{\delta_{x'},\, \delta_{y'} = 0,\, \delta_{z'},\, \beta_{x'},\, \beta_{y'}\, \beta_{z'}\}^{\mathrm{T}}. \end{aligned} \tag{9}$$

The transformation from the fixed to the rotating coordinate system is equal to

$$\mathbf{q}_{b'} = \mathbf{R}\, \mathbf{q}_b, \tag{10}$$

where $\mathbf{R}$ is a rotational transformation matrix. Hereinafter, all the parameters and properties that refer to the rotating coordinate system are denoted as $(...)'$.

4.1.1 Ball bearings

By transforming Eq. (8) to the rotating coordinate system we can express the roots of Eq. (8) in x' direction as a function of all other displacements and rotations:

$$\begin{aligned} A_{j'} - A_0 &= 0 \\ \left(A_0 \cos\alpha_0 + \delta_{x'} \cos\psi'_j - r_c\right)^2 &= \left(A_0^2 - (\delta^*_{z'_j})\right)^2 \\ \delta_{x'_{B0j}} &= \frac{1}{\cos\psi'_j}\left(r_c - A_0\cos\alpha_0 + \sqrt{A_0^2 - (\delta^*_{z'_j})^2}\right) \end{aligned} \tag{11}$$

Having an arbitrary $\mathbf{q}_{b'}$, Eq. (11) gives the exact radial displacement $\delta_{x'_{B0j}}$ at which every jth ball is coming into contact. Going back to Eq. (4) with all the radial roots $\delta_{x'_{B0j}}$ known, we have to make the transition smooth. In order to achieve that, the value of the deformation $\delta_{B'_j}$ below which the smoothing is to be applied has to be defined. This value is initially given by the user and we denote it as μ_{0j}. If $\delta_{B'_j}$ is a linear function (valid only when all the other than radial displacement are equal to zero), we calculate the corresponding radial displacement as:

$$\lambda_j = \delta_{x'_{B0j}} + \frac{\mu_{0j}}{k_{0j}}, \tag{12}$$

where k_{0j} is the slope of $\delta_{B'_j}$ at $\delta_{x'_{B0j}}$. However, in general $\delta_{B'_j}$ is not linear (Eq. (3)) and the slope in the radial direction is a function of $\mathbf{q}_{b'}$, which can be expressed as:

$$k_j = k_j(\mathbf{q}_{b'}) = \frac{\partial\,\delta_{B'_j}}{\partial\,x'} = \frac{\delta^*_{r'_j}}{A'_j}\cos\psi'_j. \tag{13}$$

Thus, an exact deformation μ_j, which is equal to $\delta_{B'_j}(\lambda_j)$ differs slightly from μ_{0j}, as demonstrated in Fig. 3. Based on the initial μ_{0j} we can calculate the parameters λ_j, μ_j and k_j, which are crucial to define a

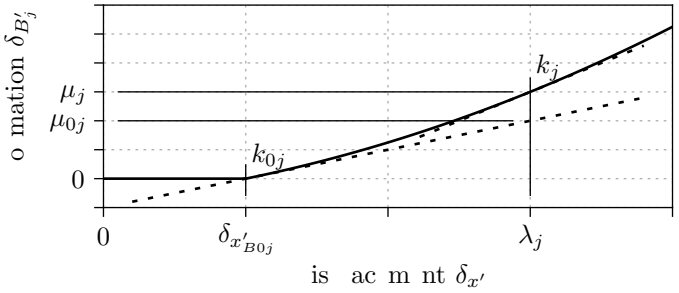


Figure 3: The parameters of the smoothing algorithm.

smoothing function. For the latter we use a hyperbolic tangent function of the form:

$$\delta_{T'_j} = \mu_j\left(\tanh\left(\frac{k_j}{\mu_j}\left(\delta_{x'} - \lambda_j\right)\right) + 1\right). \tag{14}$$

Fig. 4 shows $\delta_{B'_1}$ and $\delta_{T'_1}$ as a function of the radial displacement $\delta_{x'}$ for a chosen bearing with $r_c = 20\,\mu$m. It is clear that a combination of the functions $\delta_{B'_j}$ and $\delta_{T'_j}$ results in a smooth, i.e., continuously differentiable function, since their values and derivatives at λ_j are exactly the same.

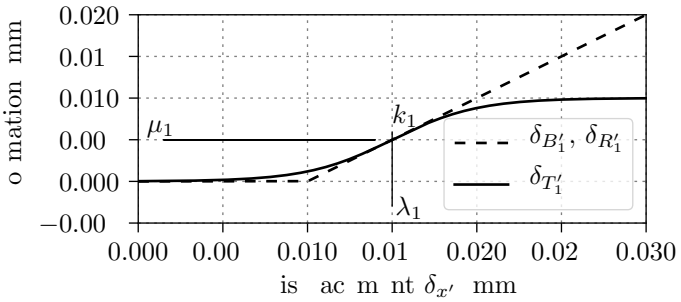


Figure 4: Resultant elastic deformation and corresponding smoothing function for the 1st rolling element of the chosen bearing.

4.1.2 Cylindrical roller bearings

Analogously to the derivation of the roots in the radial direction for ball bearings, we can write the roots of Eq. (8) for cylindrical roller bearings as:

$$\begin{aligned} \delta_{r'_j} &= 0 \\ \delta_{x'_{R0j}} &= \frac{r_c}{\cos\psi'_j} \end{aligned} \tag{15}$$

Concerning the cylindrical roller bearings, loads other than radial loads are negligible [6]. Therefore, $\delta_{R'_j}$ can be treated as a linear function of the radial displacement $\delta_{x'}$. As for ball bearings we define:

$$\lambda_j = \delta_{x'_{R0j}} + \frac{\mu_{0j}}{k_{0j}}, \tag{16}$$

where $\mu_{0j} = \mu_j$ and $k_{0j} = k_j$ due to the linear δ_{R_j} characteristics for cylindrical roller bearings. The slope of $\delta_{R'_j}$ is equal to:

$$k_j = \frac{\partial\,\delta_{R'_j}}{\partial\,x'} = \cos\psi'_j. \tag{17}$$

By knowing all the necessary parameters (λ_j, μ_j, k_j) we use a smoothing function of the form given in Eq. (14). Consequently, the deformation characteristics are smoothed as shown in Fig. 4.

4.2 Application of the smoothing algorithm to the existing bearing model

The idea of smoothing a piecewise-defined bearing kinematics is applied to the well-established bearing model of Lim and Singh [6].

4.2.1 Ball bearings

The resulting elastic deformation of the jth ball is redefined as:

$$\delta_{B'_j} = \begin{cases} A'_j - A_0, & \delta_{B'_j} > \mu_j \\ \mu_j \left(\tanh\left(\frac{k_j}{\mu_j}\left(\delta_{x'} - \lambda_j\right)\right) + 1\right), & \delta_{B'_j} \leq \mu_j \end{cases}. \tag{18}$$

It is important to note that $\delta_{B'_j}$ in Eq. (18) cannot be smaller than zero, since the defined hyperbolic tangent function asymptotically approaches zero. Additionally, a radial displacement $\delta_{x'}$ is never negative due to the

definition of the rotating coordinate system. Taking into account that $\cos\alpha_j = \frac{\delta^*_{r_j}}{A_j}$ [6] we can write the force in the radial direction as:

$$F_{x'} = K_n \sum_{j=1}^{z} \delta^n_{B'_j} \frac{\delta^*_{r'_j}}{A'_j} \cos\psi'_j. \tag{19}$$

By inserting Eq. (18) into Eq. (19) we obtain:

$$F_{x'} = K_n \sum_{j=1}^{z} \frac{\delta^*_{r'_j}}{A'_j} \cos\psi'_j \begin{cases} (A'_j - A_0)^n, & \delta_{B'_j} > \mu_j \\ \left(\mu_j \left(\tanh\left(\frac{k_j}{\mu_j}\left(\delta_{x'} - \lambda_j\right)\right) + 1\right)\right)^n, & \delta_{B'_j} \le \mu_j \end{cases}. \tag{20}$$

Other elements of the load vector $\mathbf{f}_{b'}$ retain the original form (except $F_{y'} = 0$ as defined in Eq (9)). The stiffness in the radial direction is further derived as:

$$k_{B'_{xx}} = K_n \sum_{j=1}^{z} \left(\frac{\partial}{\partial x'} \left(\delta^n_{B'_j}\right) \frac{\delta^*_{r'_j}}{A'_j} + \delta^n_{B'_j} \frac{\partial}{\partial x'} \left(\frac{\delta^*_{r'_j}}{A'_j}\right) \right) \cos\psi'_j. \tag{21}$$

Due to the piecewise definition of $\delta_{B'_j}$, Eq. (21) has the form:

$$k_{B'_{xx}} = K_n \sum_{j=1}^{z} \begin{cases} P_{Bi}, & \delta_{B'_j} > \mu_j \\ R_{Bi}, & \delta_{B'_j} \le \mu_j \end{cases}, \tag{22}$$

where

$$P_{Bi} = \frac{1}{(A'_j)^3}(A'_j - A_0)^n \cos^2\psi'_j \cdot \left(\frac{n\, A'_j (\delta^*_{r'_j})^2}{A_j - A_0} + (A'_j)^2 - (\delta^*_{r'_j})^2 \right) \tag{23}$$

and

$$R_{Bi} = \delta^n_{B'_j} \left(\frac{n\, k_j\, \delta^*_{r'_j}}{\delta_{B'_j}\, A'_j} \left(1 - \tanh^2\left(\frac{k_j}{\mu_j}\left(\delta_{x'} - \lambda_j\right)\right)\right) + \frac{(\delta^*_{n'_j})^2}{(A'_j)^3} \cos\psi'_j \right) \cos\psi'_j. \tag{24}$$

When $\delta_{B'_j} > \mu_j$, Eq. (22) yields the same expression as in the existing 6-DOFs model [6]. However, when $\delta_{B'_j} \le \mu_j$, a new, smooth force and stiffness characteristic is calculated.

4.2.2 Cylindrical roller bearings

Similarly to the ball bearings, the resultant elastic deformation of the jth roller is redefined as:

$$\delta_{R'_j} = \begin{cases} \delta_{x'} \cos\psi'_j - r_c, & \delta_{R'_j} > \mu_j \\ \mu_j \left(\tanh\left(\frac{k_j}{\mu_j}\left(\delta_{x'} - \lambda_j\right)\right) + 1\right), & \delta_{R'_j} \le \mu_j \end{cases}. \tag{25}$$

The force in the radial direction can be expressed as:

$$F_{x'} = K_n \sum_{j=1}^{z} \delta^n_{R'_j} \cos\psi'_j. \tag{26}$$

After considering Eq. (25) we obtain:

$$F_{x'} = K_n \sum_{j=1}^{z} \cos\psi'_j \cdot \begin{cases} \left(\delta_{x'} \cos\psi'_j - r_c\right)^n, & \delta_{R'_j} > \mu_j \\ \left(\mu_j \left(\tanh\left(\frac{k_j}{\mu_j}\left(\delta_{x'} - \lambda_j\right)\right) + 1\right)\right)^n, & \delta_{R'_j} \le \mu_j \end{cases}. \tag{27}$$

So like in the ball-bearing formulation, the other elements of the load vector $\mathbf{f}_{b'}$ retain their original form. The radial stiffness term transforms to:

$$k_{R'_{xx}} = K_n \sum_{j=1}^{z} \left(\frac{\partial}{\partial\, x'} \left(\delta_{R'_j}^{n} \right) \cos \psi'_j \right). \tag{28}$$

By inserting Eq. (25) into Eq. (28) we obtain the following expression:

$$k_{R'_{xx}} = K_n \sum_{j=1}^{z} \begin{cases} P_{Ri}, & \delta_{R'_j} > \mu_j \\ R_{Ri}, & \delta_{R'_j} \leq \mu_j \end{cases}, \tag{29}$$

where

$$P_{Ri} = n\, \delta_{R'_j}^{n-1} \cos^2 \psi'_j \tag{30}$$

and

$$R_{Ri} = k_j\, \delta_{R'_j}^{n-1} \left(1 - \tanh^2 \left(\frac{k_j}{\mu_j} \left(\delta_{x'} - \lambda_j \right) \right) \right) \cos \psi'_j \tag{31}$$

Again, when $\delta_{R'_j} > \mu_j$, Eq. (29) yields the same expression as in the existing 6-DOFs model for the cylindrical roller bearings [6]. Additionally, when $\delta_{R'_j} \leq \mu_j$, a smooth stiffness characteristic is obtained.

The proposed model introduces a smooth transition between the open- and the closed-contact states in the radial direction. Initially, it is necessary to specify the level of deformation μ_{0j} (for every jth rolling element), below which the smoothing is applied. All the μ_{0j} are joined together in a bearing-smoothing vector:

$$\mathbf{m} = \{\mu_{01},\, \mu_{02} \ldots \mu_{0z}\}^{\mathrm{T}}. \tag{32}$$

It is important to note that the first element in $\mathbf{m}$ represents the first rolling element coming into contact. If the smoothing vector $\mathbf{m}$ contains zeros only, no smoothing is applied and the theory yields the formulation of the existing 6-DOFs model.

4.3 Comparison between the existing and the proposed bearing models

Chosen ball and cylindrical roller bearings are investigated. Fig. 5 shows the deformation as a function of the radial displacement. The characteristics for the ball and the cylindrical roller bearings are identical due

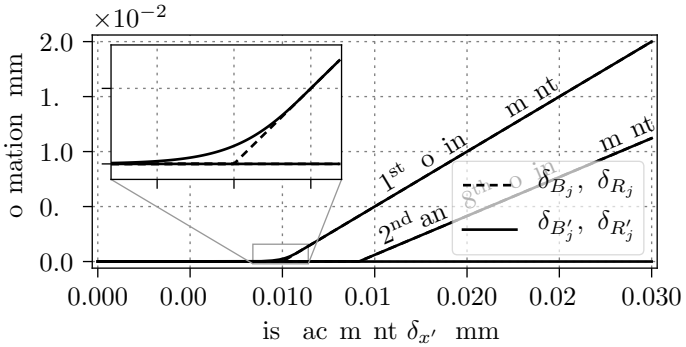


Figure 5: Comparison of deformations between existing and proposed bearing models ($\mu_{01} = 1\,\mu$m).

to them having the same main geometry and equal number of rolling elements. As seen from the zoomed-in region, the smoothing is applied to the first rolling element coming into contact ($\mu_{01} = 1\,\mu$m). The other rolling elements are left without smoothing. Such a smoothed deformation characteristic leads to the modified force- and stiffness-displacement relations, as shown in Fig. 6 and Fig. 7 for ball and cylindrical roller bearings, respectively. Already a small value of smoothing, e.g., 1 μm, causes a significant change in the force and stiffness characteristics.

Ball bearings in comparison to the cylindrical roller ones express additional dependency on the other DOFs. For instance, if a ball bearing is already a bit axially displaced, but still within the clearance area, a smaller radial displacement will cause an impact as in the case where there is no axial displacement. Fig. 8 illustrates the phenomenon, presenting an interplay of the axial and radial displacements on the radial stiffness. The characteristics before and after the smoothing are shown. Similar applies also to rotational DOFs, yielding comparable plots. The applied smoothing vector $\mathbf{m}$ contains the elements as follows: $\mu_{01} = 2\,\mu$m and $\mu_{0j} = 1\,\mu$m, $j = 2,\, 3 \ldots 8$. The effect of the smoothing is clearly shown in all the transitions where a certain ball is coming or leaving the contact. The proposed analytical bearing model has a modular nature, i.e., every contact adjustment can be achieved with smoothing vector $\mathbf{m}$.

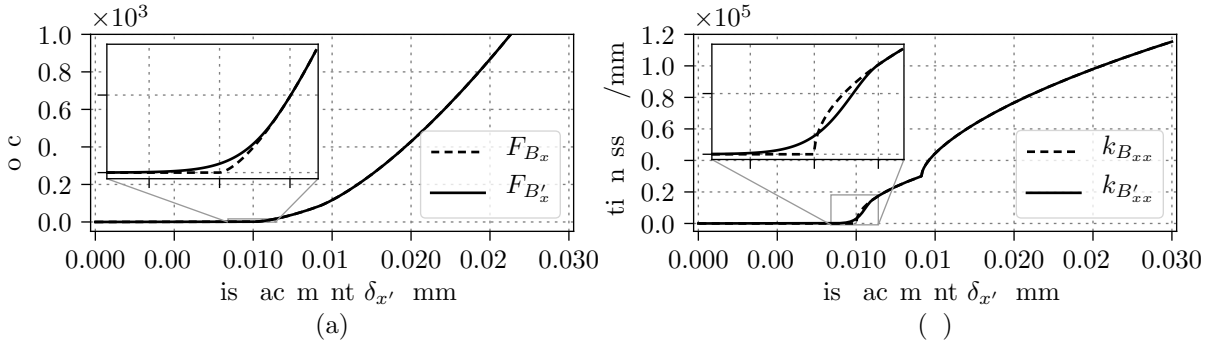


Figure 6: Existing and proposed ball-bearing models ($\mu_{01} = 1\,\mu$m); (a) Force-displacement characteristic, (b) Stiffness-displacement characteristic.

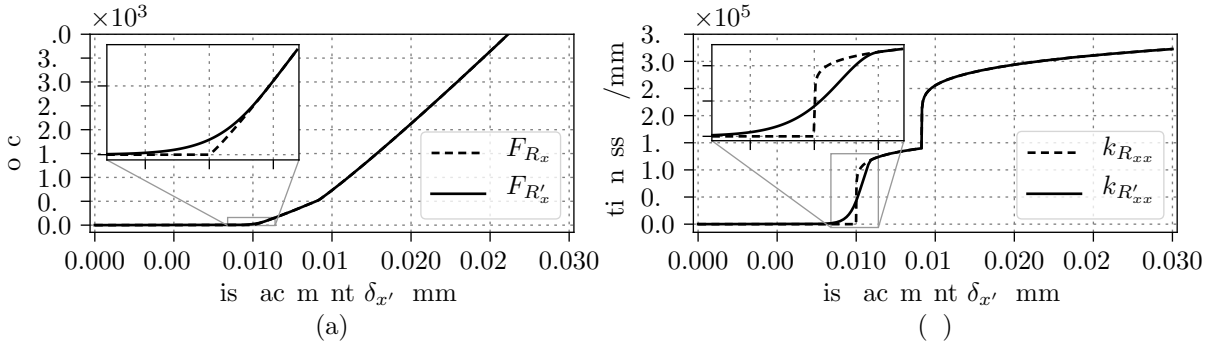


Figure 7: Existing and proposed cylindrical roller bearing models ($\mu_{01} = 1\,\mu$m); (a) Force-displacement characteristic, (b) Stiffness-displacement characteristic.

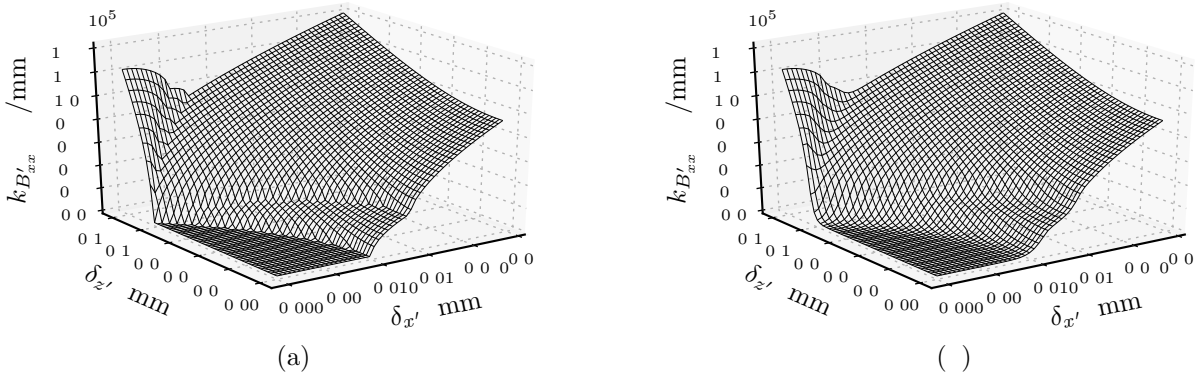


Figure 8: Radial stiffness vs. radial and axial displacements of a ball bearing; (a) Existing model, (b) Proposed model with $\mu_{01} = 2\,\mu$m and $\mu_{0j} = 1\,\mu$m, $j = 2,\, 3 \ldots 8$.

5 Case study

The applicability of the proposed bearing model is presented in a case study. A simple FEM model assembly (Fig. 9) consists of a shaft, two different bearings (ball and cylindrical roller) and a housing, connected to the rigid base. Two separate masses simulate the dynamic load. The geometrical parameters of the bearings

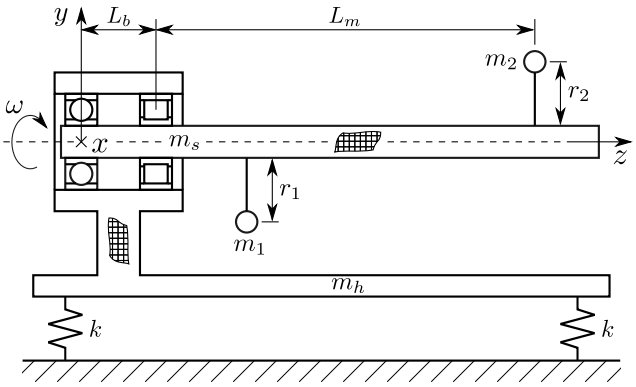


Figure 9: Schematically presented FEM model assembly used for the case study.

are given in Table 1. The inner and outer rings of both bearings are modelled with conventional FEM solid

type	code	d [mm]	D [mm]	r_c [μm]	z	r_b [mm]	l_{eff} [mm]
ball	6306	30	72	20	8	6	/
roler	N306	30	72	45	12	/	11

Table 1: Properties of the ball and cylindrical roller bearings for the presented case study.

elements, whereas the rolling elements are not modelled, but incorporated into the bearing-stiffness matrix. Both raceways of a single bearing are connected into two separate central nodes. The analytically calculated nonlinear bearing-stiffness matrix is prescribed between both central nodes, as demonstrated in Fig. 10.

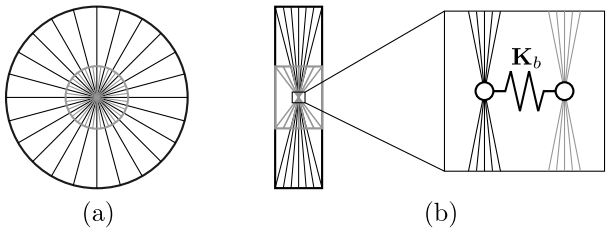


Figure 10: A bearing in the FEM model (black – outer ring, grey – inner ring); (a) Spider elements connecting both raceways, (b) Bearing-stiffness matrix prescribed between the central nodes.

The aim of our case study is to present the time response during the system's run-up. The shaft (and eccentric masses), together with both bearing's inner rings and associated spider elements rotate by prescribed movement. In every time step the displacements and rotations between both central nodes of each bearing are calculated (displacement vector $\mathbf{q}_b$). Based on $\mathbf{q}_b$ the bearing stiffness is provided. The original and the proposed bearing models are utilized. For the latter we prescribe $\mu_{01} = 2\,\mu$m, whereas the other elements of the smoothing vector are equal to zero. It is important to note that μ_{01} has, in general, the greatest influence on the performance of the calculation. The shaft is governed by a constant angular acceleration $\dot{\omega} = 0.8\,\text{rev/s}^2$, starting with $\omega = 0$. The damping ratio used in the FEM model is equal to 0.1 and the numerical method employed for the time integration is Runge-Kutta-Fehlberg.

The initial stage of run-up represents the first 8 seconds of the simulation. The initial conditions are as follows: both bearings have their inner and outer rings concentrically aligned and the shaft is not rotating. When the simulation starts, the inner rings of both bearings move towards the rolling elements due to gravity and eliminate the clearance (the rolling elements collide with both raceways). At the same time the shaft is subjected to a constant angular acceleration. The radial response $\delta_{x'}$ is shown in Fig. 11 for both bearings. It

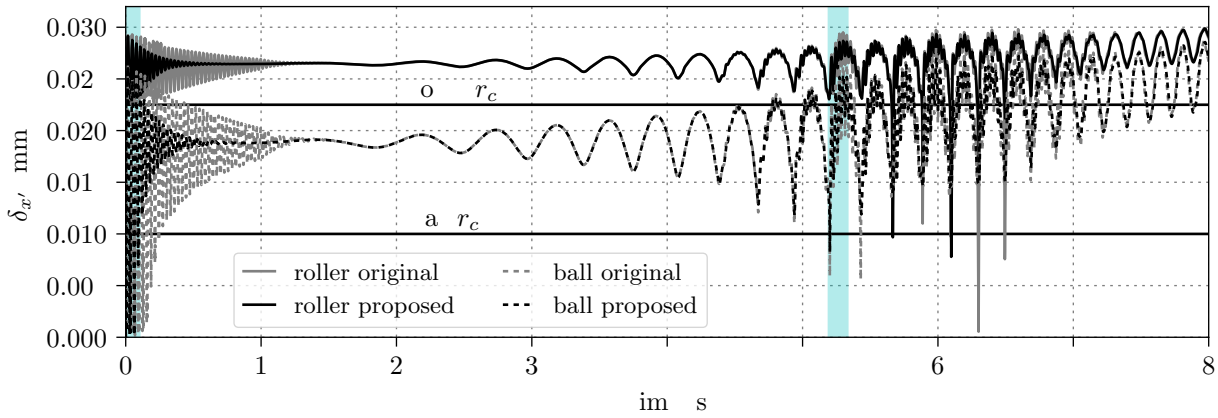


Figure 11: Radial response of both bearings for the original and the proposed bearing model.

is clear that the results obtained with the proposed bearing model exhibit a much more attenuated response. The effect is especially significant in the first second of the simulation, when the shaft reaches the equilibrium position. A small oscillations in the original bearing model appear due to numerical issues, i.e., a high contact force and a stiffness change in a very short time. Two sections, A and B, (Fig. 11) are shown separately in Fig 12. The areas A and B reveal details of how the proposed bearing model follows the general behaviour of

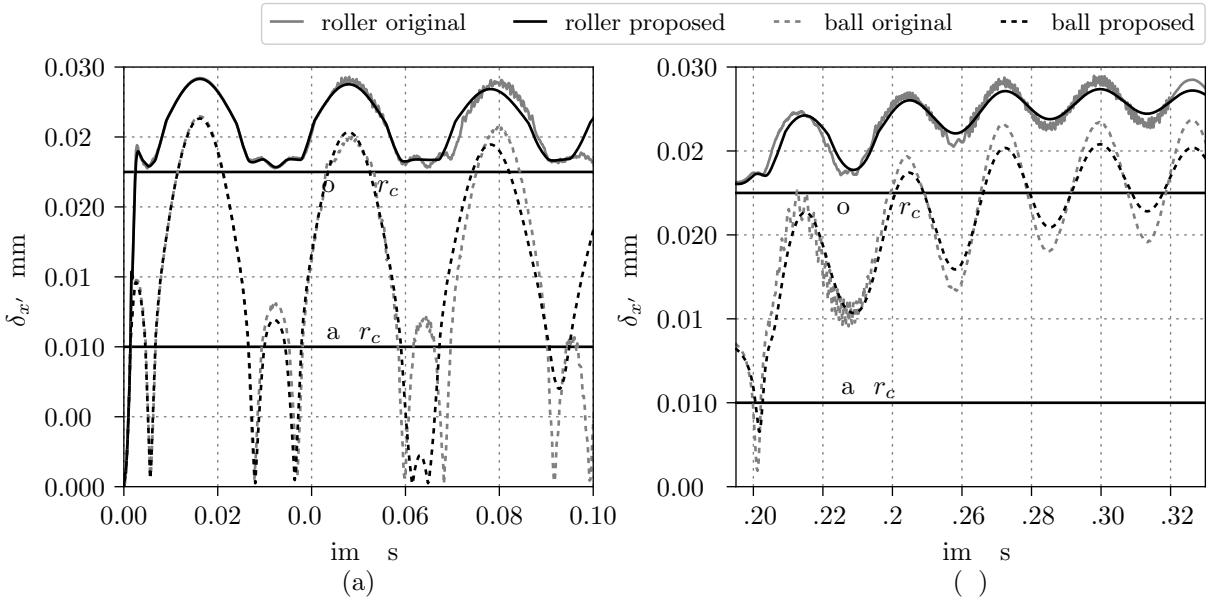


Figure 12: Radial response of both bearings for the original and the proposed bearing model; (a) Region A, (b) Region B.

the original bearing model. Besides the amplitude of the displacement response in a time domain, the orbital motion of both bearings is also shown in Fig. 13 and Fig. 14. Both figures consist of orbits obtained using the original bearing formulation as well as with the proposed one. The clearance of the bearing is marked as a grey circle in the centre. The attenuated response is also clearly seen in the orbital motion, especially for the ball bearing at the beginning of the simulation. After both bearings reach their equilibrium positions

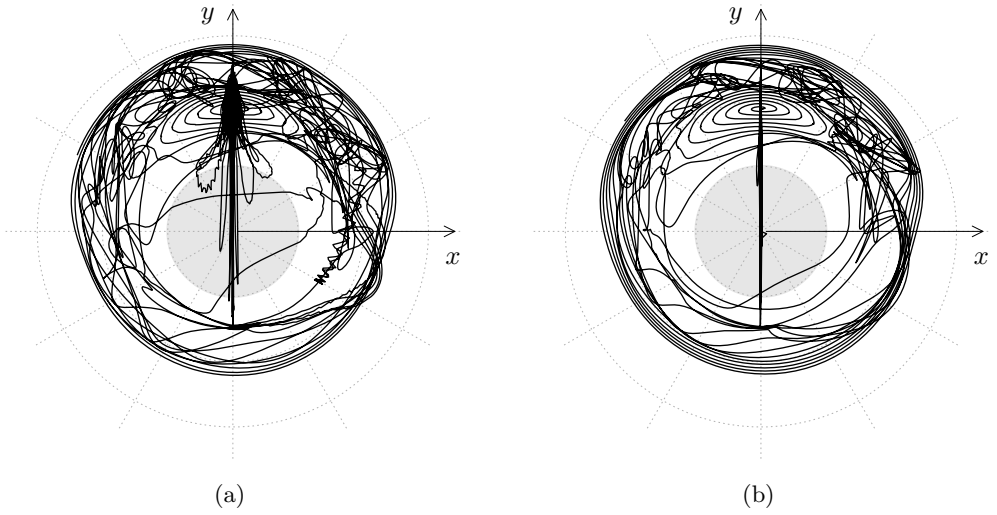


Figure 13: Orbit of a ball bearing (0 to 8 s); (a) Original bearing model, (b) Proposed bearing model.

they enter into another region, where a sudden hit from one side to another occurs. This happens since the centrifugal force of the rotating shaft at a certain speed is not yet high enough to push both bearings to the side completely (Fig. 11, region B). The region expresses unstable movement of the inner ring with respect to the outer ring. After the angular velocity and, consequently, the centrifugal force are high enough, the inner ring starts to rotate together with the shaft. It is clear that the smoothed bearing model does not provide exactly the same orbits as the original one; however, the motion, in general, is the same.

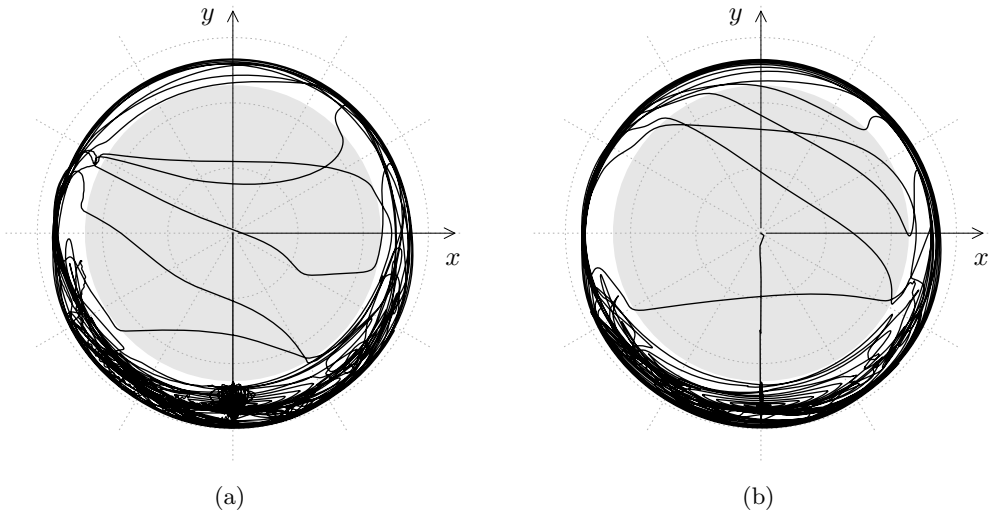


Figure 14: Orbit of a cylindrical roller bearing (0 to 8 s); (a) Original bearing model, (b) Proposed bearing model.

One of the main advantages of the proposed bearing model is a reduction in the computational time. Fig. 15 shows the comparison of the computational times for the first 8 seconds at different smoothing levels. The presented case study with $\mu_{01} = 2\,\mu$m reduced the computational time by up to 40 % compared to the original bearing model. Employing a smoothing value only helps to a certain extent. Small smoothing values help to avoid numerical issues in the contact-state transition, whereas larger smoothing values do not contribute any further to a reduction in the computational time.

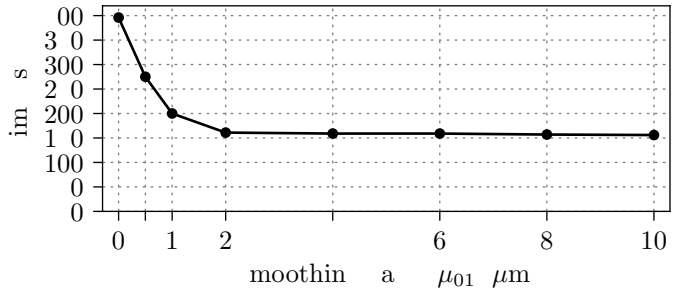


Figure 15: The effect of smoothing value μ_{01} on the overall computational time for the first 8 s of the simulation.

6 Conclusion

An improved dynamic model of rolling-element bearings is presented. The proposed bearing model is able to smooth the deformation-, force- and stiffness-displacement characteristics in the region of the contact-state transition. It is applicable for explicit calculations of the bearings that operate under radial clearance and are subjected to a dominant radial load. The smoothed bearing's nonlinear dynamic characteristics lead to a more stable calculation and a reduced computational time.

Acknowledgements

The authors would like to thank the ZF Friedrichshafen AG for supporting this research.

References

[1] A. B. Jones, *A General Theory for Elastically Constrained Ball and Radial Roller Bearings Under Arbitrary Load and Speed Conditions*, Journal of Basic Engineering, ASME, Vol. 180, (1960), pp. 309-320.

[2] T. A. Harris, *Rolling bearing analysis*, John Wiley, New York (1984).

[3] J. S. Rao, *Rotor dynamics*, John Wiley, New York (1983).

[4] M. F. While, *Rolling Element Bearing Vibration Transfer Characteristics: Effect of Stiffness*, Journal of Applied Mechanics, ASME, Vol. 46, (1979), pp. 677-684.

[5] E. P. Gargiulo, *A simple way to estimate bearing stiffness*, Machine Design, Vol. 52, (1980), pp. 107-110.

[6] T. C. Lim, R. Singh, *Vibration transmission through rolling element bearings, part 1: bearing stiffness formulation*, Journal of Sound and Vibration, Vol. 139, No. 2, (1990), pp. 179-199.

[7] T. J. Royston, I. Basdogan, *Vibration transmission through self-aligning (spherical) rolling element bearings: Theory and experiment*, Journal of Sound and Vibration, Vol. 215, No. 5, (1998), pp. 997-1014.

[8] H. V. Liew, T. C. Lim, *Analysis of time-varying rolling element bearing characteristics*, Journal of Sound and Vibration, Vol. 283, (2005), pp. 1163-1179.

[9] A. Gunduz, R. Singh, *Stiffness matrix formulation for double row angular contact ball bearings: Analytical development and validation*, Journal of Sound and Vibration, Vol. 332, No. 22, (2013), pp. 5898-5916.

[10] D. S. Lee, D. H. Choi, *A Dynamic Analysis of a Flexible Rotor in Ball Bearings with Nonlinear Stiffness Characteristics*, International Journal of Rotating Machinery, Vol. 3, (1997), pp. 73-80.

[11] X. Sheng, B. Li, Z. Wu, H. Li, *Calculation of ball bearing speed-varying stiffness*, Mechanism and Machine Theory, Vol. 81, (2014), pp. 166-180.

[12] Y. Guo, R. G. Parker, *Stiffness matrix calculation of rolling element bearings using a finite element/contact mechanics model*, Mechanism and Machine Theory, Vol. 51, (2012), pp. 32-45.

[13] J. Zhang, B. Fang, J. Hong, S. Wan, Y. Zhu, *A general model for preload calculation and stiffness analysis for combined angular contact ball bearings*, Journal of Sound and Vibration, Vol. 411, Supplement C (2017), pp. 435-449.

[14] T. C. Lim, R. Singh, *Vibration transmission through rolling element bearings, part 3: geared rotor system studies*, Journal of Sound and Vibration, Vol. 152, No. 1, (1991), pp. 31-54.

[15] T. C. Lim, R. Singh, *Vibration transmission through rolling element bearings, part 4: statistical energy analysis*, Journal of Sound and Vibration, Vol. 153, No. 1, (1992), pp. 37-50.

[16] C. Bai, H. Zhang, Q. Xu, *Effects of axial preload of ball bearing on the nonlinear dynamic characteristics of a rotor-bearing system*, Nonlinear Dynamics, Vol. 53, No. 3, (2008), pp. 173-190.

[17] P. Čermelj, M. Boltežar, *An indirect approach to investigating the dynamics of a structure containing ball bearings*, Journal of Sound and Vibration, Vol. 276, (2004), pp. 401-417.

[18] M. Razpotnik, T. Bischof, M. Boltežar, *The influence of bearing stiffness on the vibration properties of statically overdetermined gearboxes*, Journal of Sound and Vibration, Vol. 351, (2015), pp. 221-235.

[19] L.-X. Xu, Y.-G. Li, *An approach for calculating the dynamic load of deep groove ball bearing joints in planar multibody systems*, Nonlinear Dynamics, Vol. 70, No. 3, (2012), pp. 2145-2161.

[20] L.-X. Xu, *A general method for impact dynamic analysis of a planar multi-body system with a rolling ball bearing joint*, Nonlinear Dynamics, Vol. 78, No. 2, (2014), pp. 857-579.

[21] C. A. Fonseca, I. F. Santos, H. I. Weber, *Influence of unbalance levels on nonlinear dynamics of a rotor-backup rolling bearing system*, Journal of Sound and Vibration, Vol. 394, Supplement C (2017), pp. 482-496.

[22] H. Wang, Q. Han, R. Luo, T. Qing, *Dynamic modeling of moment wheel assemblies with nonlinear rolling bearing supports*, Journal of Sound and Vibration, Vol. 406, Supplement C (2017), pp. 124-145.

[23] A. Gunduz, J. T. Dreyer, R. Singh, *Effect of bearing preloads on the modal characteristics of a shaft-bearing assembly: Experiments on double row angular contact ball bearings*, Mechanical Systems and Signal Processing, Vol. 31, (2012), pp. 176-195.

[24] X. T. Bai, Y. H. Wu, K. Zhang, C. Z. Chen, H. P. Yan, *Radiation noise of the bearing applied to the ceramic motorized spindle based on the sub-source decomposition method*, Journal of Sound and Vibration, Vol. 410, (2017), pp. 35-48.

[25] D. P. Fleming, J. V. Poplawski, *Unbalance response prediction for rotors on ball bearings using speed- and load-dependent nonlinear bearing stiffness*, International Journal of Rotating Machinery, Vol. 2005, No. 1, (2005), pp. 53-59.

[26] Z. Xia, G. Qiao, T. Zheng, W. Zhang, *Nonlinear modeling and dynamic analysis of the rotor-bearing system*, Nonlinear Dynamics, Vol. 57, No. 4, (2009), pp. 559-577.

[27] R. I. Leine, N. v. d. Wouw, *Stability and convergence of mechanical systems with unilateral constraints*, Lecture Notes in Applied and Computational Mechanics, Springer, Dordrecht, (2008).

Relative cyclic component mode synthesis and its application to nonlinear vibration analysis of mistuned bladed disks with friction joints

S. Mehrdad Pourkiaee[1], Stefano Zucca[1], Robert G. Parker[2]
[1] Politecnico di Torino, Department of Mechanical and Aerospace Engineering
Corso Duca degli Abruzzi 24, Torino, Italy
e-mail: **mehrdad.pourkiaee@polito.it**

[2] Department of Mechanical Engineering, Virginia Tech, Blacksburg, VA 24061, USA
Visiting Professor, Politecnico di Torino, Department of Mechanical and Aerospace Engineering

Abstract
A new reduced order modelling technique based on Relative Cyclic Component Mode Synthesis (RCCMS) is presented. RCCMS results in an efficient and highly compact reduced-order model (ROM) suitable for nonlinear forced response analysis of mistuned bladed disk with friction interfaces. Implementation of relative coordinates not only reduces the computational time but also enhances the CB-CMS basis by incorporating the fully stuck modeshapes. In the proposed ROM, it is possible to introduce the small sector-level mistuning directly into the reduced model. In this way, reduction is performed only once in case of multiple analyses, necessary for statistical characterization of the nonlinear response levels of the system. Numerical simulations revealed a very good accuracy between the ROM and the baseline for nonlinear forced response analysis of a mistuned bladed disks.

1 Introduction

Bladed disk in turbomachinery applications, are critical components with peculiar characteristics. Because of their high modal density, crossing the resonance frequencies in the broad operating range of the engine, is inevitable. This could result in high amplitude vibrations of the blades and makes them susceptible to high cycle fatigue (HCF) [1].

To limit the vibration amplitudes of the blades and the related stresses, the dry friction damping is extensively incorporated in the design of bladed disks. Due to the presence of friction interfaces (e.g. as shrouds, blade roots and rigid/flexible dampers) the bladed disk behavior is nonlinear.

In practice, the nominally identical sectors of a bladed disk are slightly different, because of operating conditions, wear and manufacturing tolerances. These small structural deviations are called mistuning. The lack of cyclic symmetry properties increases the computational burden, since, the full-order model is needed for design purposes. It is shown that, even in the presence of small mistuning, forced response levels of blades increase remarkably [2].

The design of bladed disks in realistic operating conditions, demands forced response analysis in the presence of mistuning and nonlinearities, to accurately assess the maximum vibration amplitudes and avoid HCF [3]. Also, because of the random nature of mistuning, it is necessary to statistically characterize the forced response levels. The large size of Finite Element (FE) models of industrial bladed disks (typically millions of degrees of freedom per sector) makes the analysis of the full-order model unfeasible. Therefore, efficient and accurate reduced order models (ROMs) are needed to reduce the computational time.

In contrast to mistuning modeling of linear system (in the absence of friction contacts), the research on mistuning modeling of nonlinear systems (in the presence of friction contacts) is few. The effects of contact mistuning on dynamics of shrouded bladed disk was investigated in [4]. The same authors, showed in [5] that a set of mode shapes (Adaptive Microslip Projections) corresponding to linear system with different contact states, can be used as a basis for system-level reduction of the tuned/mistuned bladed disks with contact interfaces. Reduced order models for nonlinear dynamics of blisks with friction ring dampers in the presence of small and large geometric mistuning were developed in a series of work [6,7]. Recently, a reduced order model based on a triple nonlinear modal synthesis was proposed for nonlinear dynamics of bladed disks in the presence of structural mistuning [8].

This study introduces a new reduced order modeling technique based on Relative Cyclic Component Mode synthesis (RCCMS). In its development, the following requirements and features are addressed:

1. The ROM must be obtained by performing only sector-level calculations.
2. The whole reduction must be performed once, and then the small mistuning is directly introduced into the final ROM.
3. The ROM should be capable of modeling the mistuning in sector-levels (i.e. for both blade and disk).
4. It is preferable that the ROM retains only physical degrees-of-freedom (DOFs) at contact interfaces, to avoid transitions between modal and physical DOFs, during forced response calculations.
5. It is preferable to enhance the accuracy of fixed interface component modes, as their boundary conditions differ from actual kinematics at friction interfaces.
6. It is preferable to implement system-level reductions, to obtain compact ROMs and avoid ending up with component assembly and the need of multiple secondary reductions.

RCCMS results in an efficient and highly compact ROM suitable for nonlinear forced response analysis of mistuned bladed disk with friction interfaces. The developed ROM consists of two steps: First, representing the absolute displacements of the nodes lying on adjacent friction interfaces in terms of relative displacements between the node pairs. Afterwards, performing the Craig-Bampton Component Mode Synthesis (CB-CMS) on the full-order model already transformed into relative coordinates.

Implementation of relative coordinates is beneficial in different ways. First, it results in efficient forced response calculations by reducing the number of unknowns by half. Secondly, in the CB-CMS framework, by selecting the relative displacements of contact node pairs as master DOFs, the fixed interface normal modes yield fully stuck modeshapes (system modes with merged friction interfaces). This will increase the accuracy of the reduction basis especially for microslip regime.

The idea of using relative coordinates was first introduced in [9], for forced response analysis of cracked bladed disks. Later in [10], the idea of relative DOFs was used for the same application. They implemented the Component Mode Mistuning (CMM) [12] to model small blade mistuning in the pristine/uncracked structure, in the absence of contact interactions between crack surfaces. The relative notation has been used more often to reduce the computational burden of nonlinear forced response calculations [4,5].

In this research the application of relative notation is extended and generalized for nonlinear forced response analysis of mistuned bladed disks with friction interfaces.

In RCCMS coordinates, the final ROM is composed of a statically reduced component corresponding to relative contact DOFs (referred to as nonlinear partition), and a modal reduced component corresponding to the linear system with merged friction interfaces (referred to as linear partition).

This makes the RCCMS unique and very flexible for the mistuning modeling. Since it allows analysts and designers; in a systematic way; to benefit from powerful theories of mistuning modeling of linear system

(e.g. SNM [11], CMM [12], IMM [13] and NEWT [14]) for mistuning analysis of nonlinear system with friction interfaces.

In particular, the current study introduces the small mistuning in the sector-level by employing the principle assumption of the SNM theory. This results in a highly reduced ROM by using system-level modes. However, all the calculations are performed only on a single sector. In RCCMS, the reduction is performed only once in case of multiple analyses, necessary for statistical characterization of the nonlinear response levels of the system.

In the following, the theory of RCCMS is first described for tuned systems. Afterwards, the introduction of small mistuning directly into the final ROM (at sector-levels) is discussed. Finally, RCCMS is applied on a mistuned bladed disk with blade root friction damping, to evaluate its performance in predicting nonlinear forced response levels. The last section contains concluding remarks on the new developed reduction technique.

2 Methodology

2.1 Equations of motion

The equations of motion of a general bladed disk system can be represented as:

$$M\ddot{x}(t) + C\dot{x}(t) + Kx(t) = F_{nl}(x(t), \dot{x}(t)) + F_{ex}(t) \tag{1}$$

where $\boldsymbol{M}$ and $\boldsymbol{K}$ are system mass and stiffness matrix, respectively. $\boldsymbol{C}$ denotes the linear viscous damping and is assumed to be proportional to mass and stiffness (i.e. $C = \alpha M + \beta K$). $\boldsymbol{x(t)}$ denotes the displacement vector of the full system. $\boldsymbol{F_{nl}}$ represents the vector of nonlinear friction forces and is dependent on relative displacements and velocities at contact nodes. $\boldsymbol{F_{ex}}$ denotes the external periodic forces applied on the system.

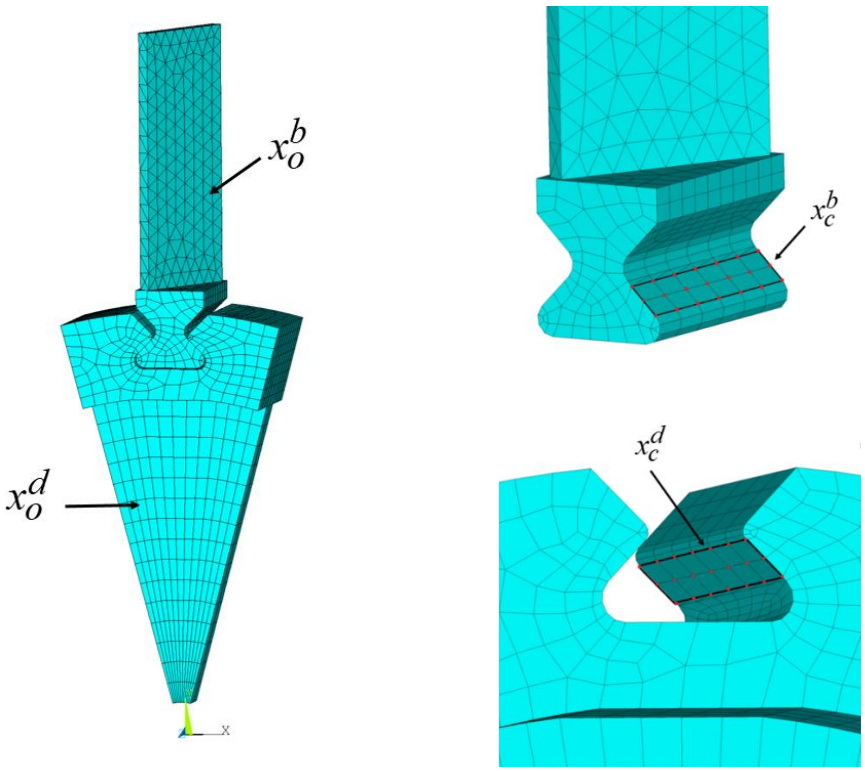


Figure 1: Fundamental sector of the studied bladed disk and its partitioned DOFs

Figure. 1 shows the fundamental sector of the studied mock up bladed disk and the defined partition of DOFs. To assess the friction damping at blade roots, the nodes laying on blade-disk interfaces, are denoted as contact nodes (subscripts ***c***). Other remaining DOFs are denoted by subscripts ***o***. Superscripts ***b*** and ***d*** are used to distinguish between the blade and the disk degrees-of-freedom.

Prior to performing the new reduction steps, it is convenient to first reorder the full displacement vector and the corresponding structural matrices, as follows:

$$x=\begin{Bmatrix} x_c^b \\ x_c^d \\ x_o^b \\ x_o^d \end{Bmatrix}\ ,\ K=\begin{bmatrix} K_{cc}^b & 0 & K_{co}^b & 0 \\ 0 & K_{cc}^d & 0 & K_{co}^d \\ K_{oc}^b & 0 & K_{oo}^b & 0 \\ 0 & K_{oc}^d & 0 & K_{oo}^d \end{bmatrix},\ M=\begin{bmatrix} M_{cc}^b & 0 & M_{co}^b & 0 \\ 0 & M_{cc}^d & 0 & M_{co}^d \\ M_{oc}^b & 0 & M_{oo}^b & 0 \\ 0 & M_{oc}^d & 0 & M_{oo}^d \end{bmatrix} \tag{2}$$

It should be noted that, Eqn. (1) represents the partitioned full displacement vector of the system and for instance, x_c^b, denotes the contact DOFs of all blades. As evident from Fig. 1, the partitions corresponding to blade DOFs are block diagonal and the partition corresponding to other DOFs of the disk (i.e. K_{oo}^d and M_{oo}^d) are block circulant, due to the coupling between the interfaces of disk sectors.

2.2 RCCMS theory

2.2.1 Relative coordinates

The first step in RCCMS is to represent the absolute displacements of contact nodes in terms of the relative displacements between contact node pairs. The relative displacements between contact nodes can be determined by:

$$x_{rel}=x_c^b-x_c^d \tag{3}$$

Note that, $\boldsymbol{x_{rel}}$ denotes relative displacements in local coordinate systems of contact surfaces. Accordingly, the full displacement vector can be expressed in relative coordinates by using Eqn. (3) and introducing the following transformation [10]:

$$\begin{Bmatrix} x_c^b \\ x_c^d \\ x_o^b \\ x_o^d \end{Bmatrix}=\begin{bmatrix} I & I & 0 & 0 \\ 0 & I & 0 & 0 \\ 0 & 0 & I & 0 \\ 0 & 0 & 0 & I \end{bmatrix}\begin{Bmatrix} x_{rel} \\ x_c^d \\ x_o^b \\ x_o^d \end{Bmatrix}=[T]\{x_r\} \tag{4}$$

It is evident that, the displacement vector in relative coordinates (i.e. $\boldsymbol{x_r}$ in Eqn. (4)), can be divided into two distinct groups, namely nonlinear and linear DOFs, as follows:

$$x_r=\begin{Bmatrix} [x_{rel}]=x_N \\ \begin{bmatrix} x_c^d \\ x_o^b \\ x_o^d \end{bmatrix}=x_L \end{Bmatrix}=\begin{Bmatrix} x_N \\ x_L \end{Bmatrix} \tag{5}$$

In Eqn. (5), $\boldsymbol{x_N}$ is the vector of nonlinear coordinates and only contains relative displacements of contact nodes which is used to calculate nonlinear friction forces. On the other hand, $\boldsymbol{x_L}$ is the vector of linear coordinates and contains DOFs of the linear system with no friction interfaces. In fact, $\boldsymbol{x_L}$ denotes a linear system in fully stuck condition (i.e. merged contact nodes).

Introducing Eqn. (4) into Eqn. (1), yields the transformed equations of motion in relative coordinates:

$$M_r \begin{Bmatrix} \ddot{x}_N \\ \ddot{x}_L \end{Bmatrix} + C_r \begin{Bmatrix} \dot{x}_N \\ \dot{x}_L \end{Bmatrix} + K_r \begin{Bmatrix} x_N \\ x_L \end{Bmatrix} = \begin{Bmatrix} f_{nl} \\ 0 \end{Bmatrix} + \begin{Bmatrix} 0 \\ f_{ex} \end{Bmatrix} \tag{6}$$

where

$$K_r = T^T K T = \left[\begin{array}{c|ccc} K_{cc}^b & K_{cc}^b & K_{co}^b & 0 \\ \hline K_{cc}^b & K_{cc}^b + K_{cc}^d & K_{co}^b & K_{co}^d \\ K_{oc}^b & K_{oc}^b & K_{oo}^b & 0 \\ 0 & K_{oc}^d & 0 & K_{oo}^d \end{array}\right] = \begin{bmatrix} K_{NN} & K_{NL} \\ K_{LN} & K_{LL} \end{bmatrix}$$

$$M_r = T^T M T \ , \ C_r = T^T C T \tag{7}$$

In Eqn. (7), $\boldsymbol{M_r}$ and $\boldsymbol{C_r}$ matrices are partitioned in the same fashion as the stiffness matrix and are not shown here for brevity. $\boldsymbol{F_{nl}}$ is the vector of nonlinear friction forces, acting on nonlinear (relative) partition. $\boldsymbol{F_{ex}}$ is the vector of external force and it is assumed that it applies on linear partition only. Note that, in RCCMS, moving to relative coordinates is a preliminary step, and size reduction comes only afterwards. The benefits of this transformation will become apparent in the following sections.

2.2.2 CB-CMS

Full FE models of an industrial bladed disk may contain millions of degrees of freedom. Thus, computing the forced response levels of the full order model by solving Eqn. (7) is prohibitively expensive. To overcome this, the CB-CMS reduction technique is employed to reduce the size of the full order model. The objectives of performing the CB-CMS on equations of motion in relative coordinates, is threefold:

1. First, to retain the relative contact DOFs after the reduction, for nonlinear forced response calculations.
2. Second, to enhance the accuracy of the reduction basis by employing normal modes with fully stuck boundary conditions.
3. Third, to achieve a highly reduced ROM by taking the advantage of system level modeshapes during the reduction.

It should be noted that, in classical CB-CMS techniques, the contact nodes laying on both blade and the disk interfaces are retained as master nodes. This could result in a final ROM with large number of retained nodes (usually a secondary reduction technique should be performed as an extra step [8]). Moreover, the utilized modeshape have boundary conditions (clamped at interface), different from real kinematics of friction interfaces. Consequently, to reduce the errors arisen from the choice of modal bases, usually more number of modes should be retained in the reduction basis.

Performing the new reduction technique; based on RCCMS; could alleviate many of these difficulties. To do so, $\boldsymbol{x_N}$ (relative DOFs) is retained as master DOFs while $\boldsymbol{x_L}$ is represented by modal coordinates. The final reduced displacement vector in RCCMS coordinates is given by:

$$x_r = \begin{Bmatrix} x_N \\ x_L \end{Bmatrix} = R_{cb} x_{rom} = \begin{bmatrix} I & 0 \\ \Psi_c & \Phi_f \end{bmatrix} \begin{Bmatrix} x_N \\ \eta \end{Bmatrix} \tag{8}$$

where $\boldsymbol{R_{cb}}$ is the CB-CMS transformation matrix composed of static constraint modes ψ_c and fixed interface modeshapes Φ_f. In the relative context, constraint modes can be obtained by imposing a unitary relative displacement at each retained contact node pair while holding the other node pairs fixed. Moreover, fixed interface modeshapes are normal modes of a bladed disk system with zero relative

displacement at contact node pairs, which are in fact the vibration modes of a fully stuck system. At this step, both Φ_f and ψ_c can be computed using the cyclic symmetry properties of the system.

The equations of motion of the final reduced system in RCCMS coordinates can be represented as:

$$M_{rom}\begin{Bmatrix}\ddot{x}_N\\ \ddot{\eta}\end{Bmatrix}+C_{rom}\begin{Bmatrix}\dot{x}_N\\ \dot{\eta}\end{Bmatrix}+K_{rom}\begin{Bmatrix}x_N\\ \eta\end{Bmatrix}=F_{nl}+F_{ex} \tag{9}$$

where

$$K_{rom}=R_{cb}^T K_r R_{cb}=\begin{bmatrix}K_{Guyan} & 0\\ 0 & \Lambda_i\end{bmatrix},\ M_{rom}=R_{cb}^T M_r R_{cb}=\begin{bmatrix}M_{Guyan} & M_{N\eta}\\ M_{\eta N} & I\end{bmatrix}$$

$$F_{nl}=\begin{Bmatrix}f_{nl}\\ 0\end{Bmatrix},\ F_{ex}=\begin{Bmatrix}F_{ex}^n\\ F_{ex}^l\end{Bmatrix}=\begin{Bmatrix}\Psi_c^T f_{ex}\\ \Phi_f^T f_{ex}\end{Bmatrix} \tag{10}$$

Different partitions of final reduced mass and stiffness matrices are given below:

$$K_{Guyan}=K_{NN}-K_{NL}K_{LL}^{-1}K_{LN},\ \Lambda_i=\Phi_f^T K_{LL}\Phi_f$$

$$M_{Guyan}=M_{NN}+\Psi_c^T M_{LN}+M_{NL}\Psi_c+\Psi_c^T M_{LL}\Psi_c,\ M_{N\eta}=M_{NL}\Phi_f+\Psi_c^T M_{LL}\Phi_f \tag{11}$$

2.3 Mistuning modeling in RCCMS

Since the proposed reduction technique is a CMS-based approach, in general, it is suitable for both small and large mistuning problems. However, the focus of this study is on small sector-level mistuning.

A general reduced stiffness matrix of a mistuned system can be written as:

$$K_{rom}^{mist}=\begin{bmatrix}\Psi_{mist}^T K_r^{mist}\Psi_{mist} & \Psi_{mist}^T K_r^{mist}\Phi_{mist}\\ \Phi_{mist}^T K_r^{mist}\Psi_{mist} & \Phi_{mist}^T K_r^{mist}\Phi_{mist}\end{bmatrix}=\begin{bmatrix}K_{Guyan}^{mist} & 0\\ 0 & \Lambda_i^{mist}\end{bmatrix} \tag{12}$$

where $\Psi_{mist}=\begin{bmatrix}I & \Psi_c^{mist}\end{bmatrix}^T$ are mistuned static constraint modes.

In RCCMS coordinates, the final ROM is composed of two distinct partitions:

1. Statically reduced component corresponding to relative displacements between contact node pairs (retained for nonlinear forced response calculations); called the nonlinear partition.
2. Modal reduced component corresponding to the fully stuck system (with merged friction interfaces); called the linear partition.

This will split the introduction of mistuning into a classical linear mistuning problem (for the linear partition) and the mistuning problem of the static component (for the nonlinear partition). In practice, these two components are dealt with, independently.

This makes the RCCMS unique and very flexible for mistuning modeling. Since, powerful classical theories (e.g. SNM, CMM, and etc.), are readily applicable for the reduction of the so-called linear partition.

In this research, the principle assumption of SNM theory is employed, to make the ROM suitable for statistical analyses and also to obtain a highly compact ROM by using system-level modes. Accordingly,

it is assumed that modeshapes of the mistuned system can be represented as a linear combination of the tuned system modes (in the presence of small mistuning). This assumption yields:

$$K_{rom}^{mist} = \begin{bmatrix} K_{Guyan}^{mist} & 0 \\ 0 & \Phi^T K_r^{mist} \Phi \end{bmatrix} \tag{13}$$

where Φ are cyclic tuned modeshapes of the linear system in fully stuck conditions. It should be noted that, even implementing tuned modeshapes in Eqn. (13), the linear and nonlinear partitions/DOFs of the system are still statically uncoupled.

In practice, the lower right partition of the mistuned ROM stiffness matrix (Eqn. (13)), is calculated by sector-level calculations. One may only need sector-level tuned modeshapes that are computed by imposing cyclic symmetry boundary conditions at disk interfaces.

By defining a non-dimensional mistuning parameter δ_n, as small deviations of nominal Young's modulus of the fundamental sector, the final stiffness matrix of the mistuned ROM can be determined by:

$$K_{rom}^{mist} = \begin{bmatrix} K_{Guyan}^{mist} & 0 \\ 0 & \sum_{n=1..N} (1+\delta_n)\Phi_{\gamma,n}^T K^0 \Phi_{\gamma,n} \end{bmatrix} \tag{14}$$

where K^0 is the tuned stiffness matrix of a single sector and $\Phi_{\gamma,n}$ are tuned sector-level modeshapes of *n*th sector DOFs. More details on performing this sector-level projection can be found in [15].

The next step in mistuning modeling; which is needed whenever contact node pairs are retained for nonlinear forced response analysis; would be the computation of the $K_{Guyan}^{mist} = K_{NN}^{mist} - K_{NL}^{mist}\left(K_{LL}^{mist}\right)^{-1} K_{LN}^{mist}$, which in general could become a formidable task. Since, it demands the inversion of the stiffness matrix of the fully stuck system.

Accordingly, to alleviate the computational burden of computing the relative constraint modes of the full wheel, a simplifying assumption is made by restricting the relative static modes to the sector-level.

In many industrial applications, the disk might be much stiffer than the blades. In this case, strain energy is mostly confined in blades rather than in the disk. So, it can be assumed that, the relative constraint modes are restricted to the sector level and are not distributed along the full wheel, considerably.

In RCCMS coordinates, relative constraint modes are static responses of the system, while a unitary relative displacement is applied on a retained contact node pair at blade-disk interface, while other node pairs are held fixed. When the disk component is much stiffer than the blade, it can be assumed that the relative static response is only confined to the sector-level and does not propagate beyond the disk interfaces.

Accordingly, sector-level relative constraint modes can be simply computed by clamping each sector at its interfaces. This will isolate each sector and will result in zero static response in other remaining sectors. Moreover, by isolating the relative static modes, the nonlinear partition (i.e. statically reduced component of the ROM) is computed once and mistuning can be directly introduced into it.

It should be noted that, this assumption is only applied on the nonlinear component of the final ROM, and the linear partition remains unaffected.

Consequently, the final stiffness matrix of the mistuned ROM; computed with isolated relative static modes and sector-level calculations; can be computed by:

$$K_{rom}^{mist} \approx \begin{bmatrix} \underset{n=1..N}{Bdiag}\left[(1+\delta_n)K_{Guyan}^{0}\right] & 0 \\ 0 & \sum_{n=1..N}(1+\delta_n)\Phi_{\gamma,n}^{T}K^{0}\Phi_{\gamma,n} \end{bmatrix} \tag{15}$$

where ***Bdiag*** denotes a block diagonal matrix and K_{Guyan}^{0} is the tuned Guyan stiffness matrix of a tuned sector with fixed interfaces. The same logic is applied to the mass matrix which is not shown here for brevity. The mistuned stiffness matrix defined in Eqn. (15), is obtained based on sector-level calculations. In addition, the mistuning is directly introduced into the final ROM, which makes the ROM suitable for statistical nonlinear forced response analyses.

3 Numerical solution

In this study, node-to-node state-of-the-art contact elements are used to model the nonlinear friction forces [18]. In the final ROM, semi-3D contact elements (two perpendicular Jenkins contact elements with variable normal load) are imposed at all retained contact node pairs to model the friction contacts. Nonlinear friction forces are then calculated based on the contact states and relative displacements at each contact node pair [18].

The steady state response of the system is computed using the Harmonic Balance Method [16]. It is assumed that the response of the system under a periodic excitation is periodic. Accordingly, the displacements and forces in Eqn. (10), are approximated as a sum of harmonic functions:

$$\begin{aligned} x_{rom}(t) &\approx x_{rom}^{0} + \mathrm{Re}\left(\sum_{h=1..H} x_{rom}^{(h)} e^{ih\omega t}\right) \\ F_{nl}(t) &\approx F_{nl}^{0} + \mathrm{Re}\left(\sum_{h=1..H} F_{nl}^{(h)} e^{ih\omega t}\right) \\ F_{ex}(t) &\approx F_{ex}^{0} + \mathrm{Re}\left(\sum_{h=1..H} F_{ex}^{(h)} e^{ih\omega t}\right) \end{aligned} \tag{16}$$

where the ***H*** denotes the number of considered harmonics and ω is the frequency of the excitation force. The zeroth harmonic terms x_{rom}^{0}, F_{nl}^{0} and F_{ex}^{0} represent static equilibrium solutions, static contact and static external forces, respectively. It is assumed that the static solutions are not affected by dynamic state of the system. Thus, the static equilibrium state and the corresponding static nonlinear forces are calculated by applying nodal static loads (due to centrifugal forces) to contact node pairs and solving the zeroth order balance equation.

Substituting Eqn. (16) into Eqn. (10) and performing a Galerkin projection, yields the following algebraic balance equations for each harmonic *h*:

$$\begin{bmatrix} D_{NN} & D_{NL} \\ D_{LN} & D_{LL} \end{bmatrix}^{h} \begin{bmatrix} x_N \\ \eta \end{bmatrix}^{h} = \begin{bmatrix} F_{nl} \\ 0 \end{bmatrix}^{h} + \begin{bmatrix} F_{ex}^{n} \\ F_{ex}^{l} \end{bmatrix}^{h} \tag{17}$$

where $D = \left(-(h\omega)^2 M + ih\omega C + K\right)$ is the so-called dynamic stiffness matrix. An iterative scheme (predictor-corrector) based on the Alternating Frequency/Time (AFT) approach [17], is used to first solve the nonlinear core of the balance equations:

$$\left[D_{NN} - D_{NL} D_{LL}^{-1} D_{LN} \right]^h x_N^h = F_{nl}^h + \left[F_{ex}^n - D_{NL} D_{LL}^{-1} F_{ex}^l \right]^h \tag{18}$$

And only afterwards, the solution of the linear partition, is readily available by:

$$\eta^h = D_{LL}^{-1h} \left(F_{ex}^{l\ h} - D_{LN}^h x_N^h \right) \tag{19}$$

It is evident from Eqn. (18) that one another advantage of relative coordinates is that it reduces the number of final unknowns (to be solved iteratively) by half, which result in a highly efficient ROM.

It should be noted that, the nonlinear friction forces are dependent on all harmonic functions of the displacement vector. So, the algebraic balance equations (h=1..H) are coupled to each other through the nonlinear F_{nl}^h terms, and they should be solved simultaneously. To increase the efficiency, the Jacobian of the residual function in Eqn. (18) is computed analytically. Finally, forced response curves are obtained using a path following technique based on the pseudo-arclength continuation.

4 Results and discussions

The developed reduction technique and numerical simulations are performed on a mock up bladed disk with 12 blades, shown in Fig. 2. The bladed disk is made of steel of Young's modulus $E = 200\text{GPa}$, density $\rho = 8000\text{kg/m}^3$ and Poisson's ratio $\nu = 0.3$. The full-order FE model where the blades are attached to the disk, comprises 42,432 nodes and 127,296 DOFs in total. Each contact surface contains 21 contact node pair and the full-order model is composed of 1512 relative contact DOFs.

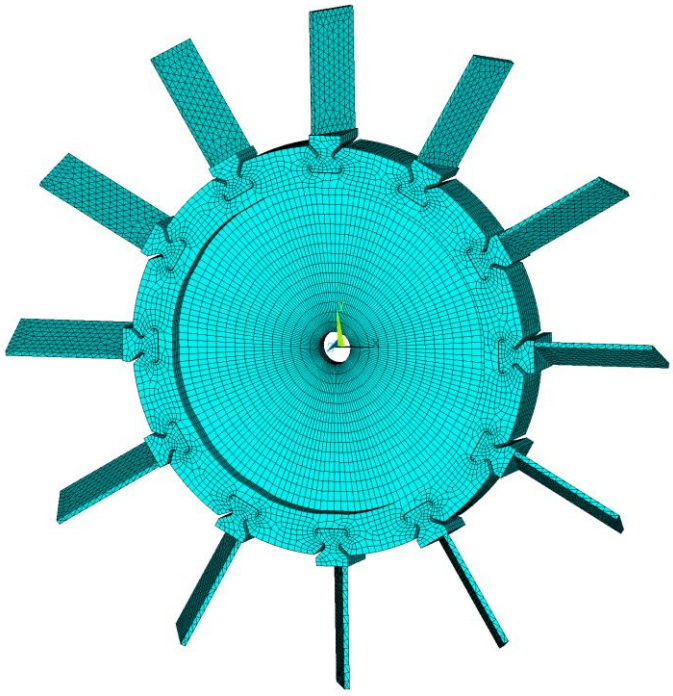


Figure 2: Full wheel FE model of the mock up bladed disk

The contact stiffness in both normal and tangential directions is considered identical. This user defined value is equal to $k_t = 100\ \text{N}/\mu\text{m}$, and is defined in a way to make the stuck natural frequencies of the ROM (computed by introducing linear springs of k_t stiffness into the ROM) close to the ANSYS stuck natural

frequencies (computed by merging contact node pairs). The reference model for forced response results, is a CB-CMS ROM of the full wheel. A convergence analysis was performed for the ROM in the considered frequency range of the study. The mistuned bladed disk model is obtained by defining a random mistuning pattern with uniform distribution and standard deviation of 3%.

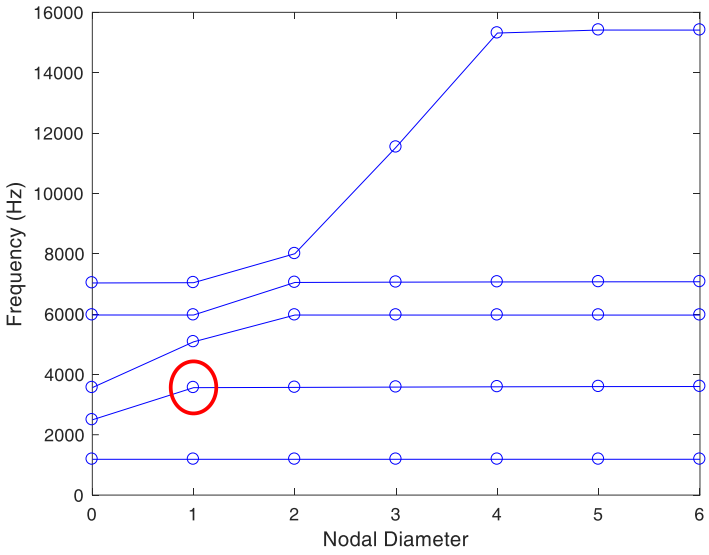


Figure 3: Natural frequencies versus nodal diameters for the tuned bladed disk in fully stuck condition

Natural frequencies versus the number of nodal diameters plot for the tuned bladed disk in fully stuck is shown in Fig 3. Red circle shows Nodal Diameter one (ND1) mode of the second frequency family. All forced response calculations are performed under engine order one excitation (eo1) of amplitude F0 and near the depicted mode of the second family, unless otherwise stated. Static loads are modeled by applying a constant normal preload (i.e. N0) on all the retained contact node pairs. Forced response levels are computed based on a mono-harmonic balance procedure. The tangential component of steady state solutions (calculated for a response node located at the tip of nominal blade #1) are plotted here.

Forced response level of the mistuned bladed disk in fully stuck condition is depicted in Fig. 4. As it is seen, RCCMS can mimics the Baseline behavior very good. A frequency shift of $\approx$ 0.12% is evident in the RCCMS predicted response. This is because of the simplifying assumption made on computation of the relative static modes. In fact, restricting the relative static modes into the sector level, introduces more stiffness into the ROM. This becomes more evident for the bladed disk with a thinner disk component (like the case study in this paper) and near lower ND modeshapes.

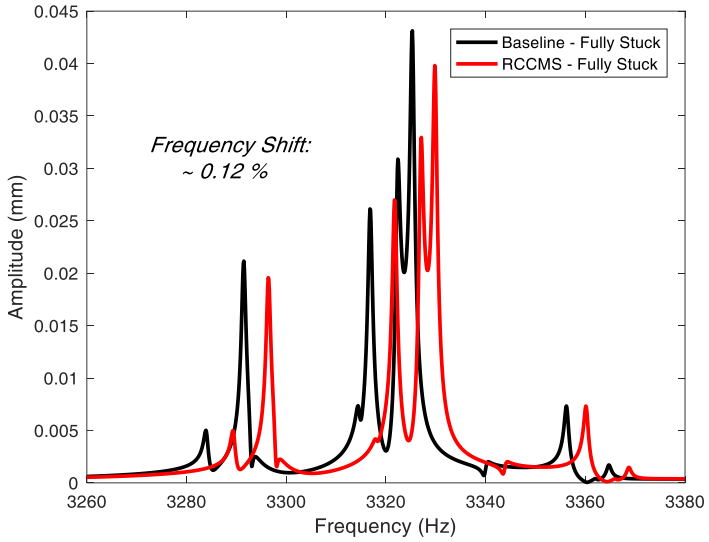
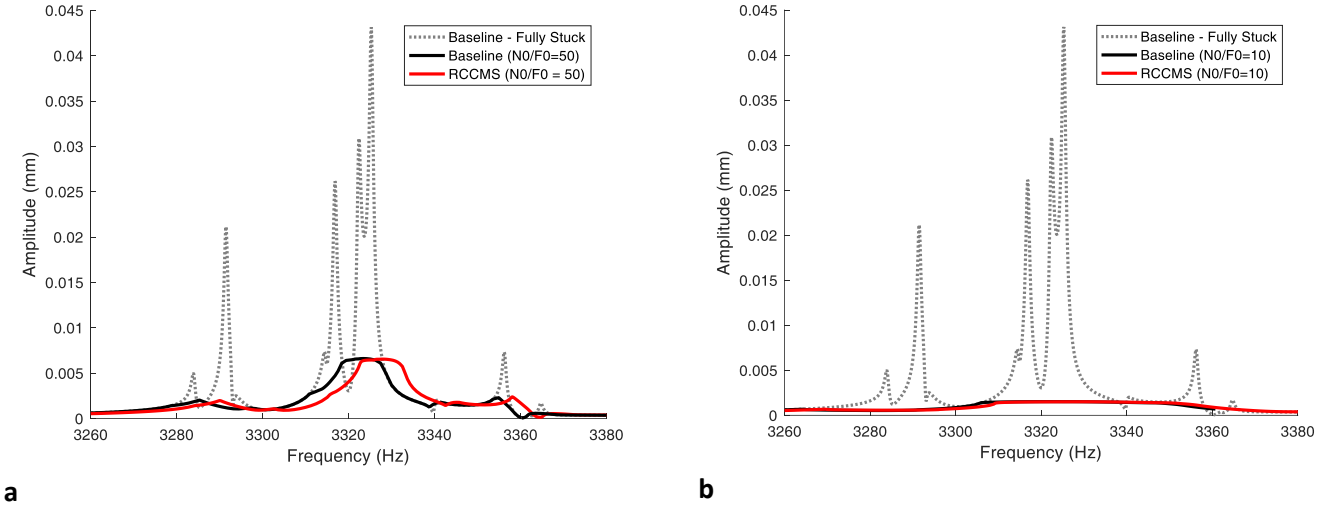


Figure 4: Forced response level of the mistuned bladed disk in fully stuck (eo1 excitation)

Figure 5 shows nonlinear forced response levels of the mistuned bladed disk in microslip regime. RCCMS shows a good accuracy in predicting the nonlinear behavior of the system. A slight frequency shift is seen for higher values of N0/F0 ratio and near the resonance peaks. The effect of preload-to-excitation ratio on the damping performance is evident in Figs. 5(a) to (b). Near high amplitude resonance peaks, because of high relative displacements at contact nodes, contacts are in microslip and the friction damping decreases the response amplitude. By further decreasing of N0/F0 ratios, contact states will change into gross slip and as a result, the amplitude of the vibration will be damped within the full frequency range.



a b

Figure 5: Nonlinear forced response levels of the mistuned bladed disk in microslip regime (eo1 excitation)

The studied mock up bladed disk is composed of a rather thin disk component. It is also favorable to evaluate the performance of the RCCMS in predicting the forced response levels of systems with a stiffer disk component. To this end, the Young's modulus of the disk component was artificially doubled to resemble a stiffer disk component.

Figure 6 shows the forced response levels of the mistuned bladed disk with an artificially stiffer disk component. The system is under an eo5 excitation. As it can be seen, RCCMS has predicted forced

response levels with an excellent accuracy. In fact, restricting the relative constraint modes to sector levels, becomes a more valid assumption as the disk stiffness increases.

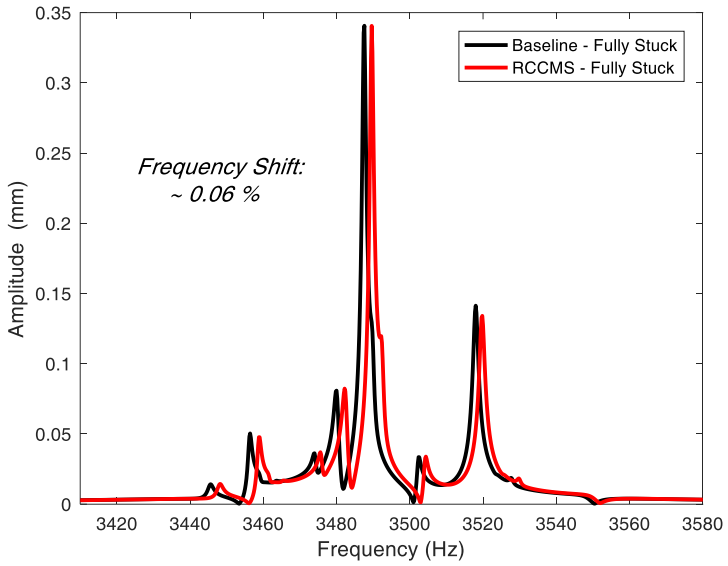
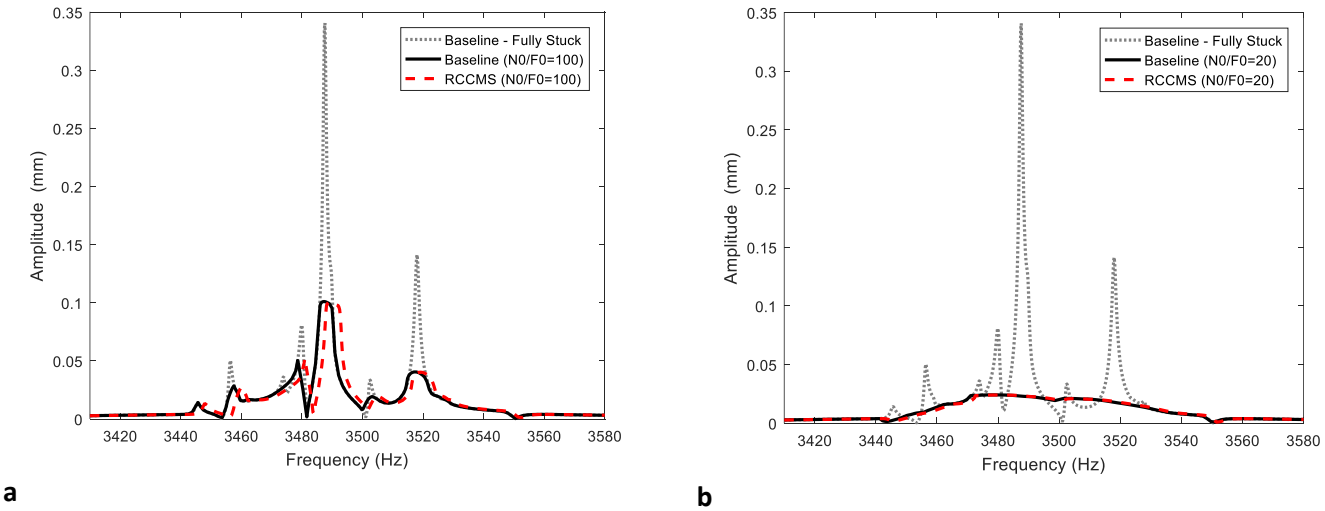


Figure 6: Forced response level of the mistuned bladed disk with an artificially stiffer disk component, in fully stuck (eo5 excitation)

Figure 7 shows nonlinear forced response levels of the mistuned bladed disk under eo5 excitation, for the system with the stiffened disk component. Results reveal the high accuracy of RCCMS in predicting the response of system in microslip. In fact, the simplifying assumption of using sector-level relative constraint modes for computation of RCCMS, will result in highly accurate ROMs for systems with a stiff disk component.



a b

Figure 7: Nonlinear forced response levels of the mistuned bladed disk with an artificially stiffer disk component in microslip regime (eo5 excitation)

5 Conclusions

In this paper, a new reduction technique was developed based on Relative Cyclic Component Mode Synthesis (RCCMS). RCCMS results in an efficient and highly compact ROM suitable for nonlinear forced response analysis of mistuned bladed disk with friction contacts. The final ROM in RCCMS coordinates benefits from different features, such as:

- Final ROM is obtained by performing sector-level calculations
- Mistuning is introduced directly into the final ROM at sector-levels (i.e. both blade and disk).
- Physical DOFs corresponding to relative displacements of contact nodes are retained for highly efficient forced response calculations.
- Fully stuck modeshapes are implemented in the reduction basis, with boundary conditions more similar to kinematics of friction interfaces.
- Highly compact ROM, due to the implementation of system-level modes, with no need of secondary reduction techniques.

It was shown that, in mistuning modeling, RCCMS allows analysts to readily employ powerful classical theories in the construction of the final ROM. To perform all calculations on single-sector only, a simplifying assumption was made. It was assumed that relative constraint modes are restricted to sector-levels. The accuracy of the ROM in predicting the nonlinear forced response levels of a mistuned bladed disk with blade root friction damping was evaluated. Numerical simulations revealed a good accordance between the ROM and the baseline results. It was shown that implementing isolated relative constraint modes (restricted to sector-level) gives even more accurate results for bladed disks with a stiffer disk component.

References

[1] Srinivasan, A.V., 1997. Flutter and Resonant Vibration Characteristics of Engine Blades. Journal of Engineering for Gas Turbines and Power 119, 742. doi:10.1115/1.2817053

[2] Castanier, M., Pierre, C., 2006. Modeling and Analysis of Mistuned Bladed Disk Vibration: Current Status and Emerging Directions. Journal of Propulsion and Power 22, 384–396. doi:10.2514/1.16345

[3] Seinturier, E. Forced response computation for bladed disks industrial practices and advanced methods. Lecture Series-Von Karman Institute For Fluid Dynamics, 2007, 2:5.

[4] Mitra, M., Zucca, S., Epureanu, B.I., 2016. Effects of Contact Mistuning on Shrouded Blisk Dynamics. ASME, p. V07AT32A026. doi:10.1115/GT2016-57812

[5] Mitra, M., Zucca, S., Epureanu, B.I., 2016. Adaptive Microslip Projection (AMP) for Reduction of Frictional and Contact Non-linearities in Shrouded Blisks. Journal of Computational and Nonlinear Dynamics. doi:10.1115/1.4033003

[6] Tang W, Baek S, Epureanu BI. Reduced-order models for blisks with small and large mistuning and friction dampers. Journal of Engineering for Gas Turbines and Power. 2017 Jan 1;139(1):012507

[7] Tang W, Epureanu BI. Nonlinear dynamics of mistuned bladed disks with ring dampers. International Journal of Non-Linear Mechanics. 2017 Dec 1;97:30-40

[8] Joannin C, Thouverez F, Chouvion B. Reduced-order modelling using nonlinear modes and triple nonlinear modal synthesis. Computers & Structures. 2018 Jul 1;203:18-33

[9] Kharyton V, Laine JP, Thouverez F, Kucher O. Cracked blade detection from bladed disk forced response. InASME Turbo Expo 2009: Power for Land, Sea, and Air 2009 Jan 1 (pp. 353-362). American Society of Mechanical Engineers

[10] Marinescu O, Epureanu BI, Banu M. Reduced order models of mistuned cracked bladed disks. Journal of Vibration and Acoustics. 2011 Oct 1;133(5):051014

[11] Yang, M.-T., Griffin, J.H., 2001. A Reduced-Order Model of Mistuning Using a Subset of Nominal System Modes. Journal of Engineering for Gas Turbines and Power 123, 893. doi:10.1115/1.1385197

[12] Lim SH, Bladh R, Castanier M, Pierre C. A compact, generalized component mode mistuning representation for modeling bladed disk vibration. In44th AIAA/ASME/ASCE/AHS/ASC Structures, Structural Dynamics, and Materials Conference 2003 (p. 1545)

[13] Vargiu, P., Firrone, C.M., Zucca, S., Gola, M.M., 2011. A reduced order model based on sector mistuning for the dynamic analysis of mistuned bladed disks. International Journal of Mechanical Sciences 53, 639–646. doi:10.1016/j.ijmecsci.2011.05.010

[14] Fitzner, C., Epureanu, B.I., Filippi, S., 2014. Nodal energy weighted transformation: A mistuning projection and its application to FLADETM turbines. Mechanical Systems and Signal Processing 42, 167–180. doi:10.1016/j.ymssp.2013.08.027

[15] Madden A, Epureanu BI, Filippi S. Reduced-order modeling approach for blisks with large mass, stiffness, and geometric mistuning. AIAA journal. 2012 Feb;50(2):366-74

[16] Cardona, A., Coune, T., Lerusse, A., Geradin, M., 1994. A multiharmonic method for non-linear vibration analysis. International Journal for Numerical Methods in Engineering 37, 1593–1608. doi:10.1002/nme.1620370911.

[17] Cameron, T. M., & Griffin, J. H. (1989). An alternating frequency/time domain method for calculating the steady-state response of nonlinear dynamic systems. Journal of applied mechanics, 56(1), 149-154

[18] Siewert C, Panning L, Wallaschek J, Richter C. (2010). Multiharmonic Forced Response Analysis of a Turbine Blading Coupled by Nonlinear Contact Forces. ASME. J. Eng. Gas Turbines Power, 132(8):082501-082501-9. doi:10.1115/1.4000266.

Solution of rotor stator contact problems with the method of normal forms

A.D. Shaw [1], **A.R. Champneys** [2], **M.I. Friswell** [1]
[1] Swansea University, College of Engineering,
Bay Campus, Fabian Way, Swansea, SA1 8EN, UK
e-mail: **a.d.shaw@swansea.ac.uk**

[2] University of Bristol, Queen's Building,
University Walk, Bristol, BS8 1TR, UK

Abstract
Rotor stator contact is an issue affecting many industrial applications, and causes some very rich dynamic responses. There is a need for new analytical approaches in these systems, due to the current reliance on costly brute force numerical methods. Recent work has shown that many contacting limit cycles are an internal resonance between two whirling modes. This insight makes these responses ideally suited to analysis with the method of normal forms, which works by reducing a system to just its resonant components, in a form that can be solved exactly. After briefly outlining the method, this paper applies it to single and multiple rotor systems, and uses it to gain insights into the effects of system parameters such as damping and stator stiffness.

1 Introduction

Rotor stator contact is an issue affecting many industrial applications, and causes some very rich dynamic responses [1–24]. Out of the huge variety of responses and phenomena seen in these systems, an intruiging subset are asynchronous bouncing solutions. These are solutions where the fundamental frequency has no obvious relation to the shaft drive speed, and are inherently harder to deal with for the following reasons:

1. They are aperiodic in the stationary coordinate system.
2. The response frequency cannot be directly inferred from the forcing frequency.
3. They can occur at drive speeds significantly removed from the critical speeds of the rotor [25].

These solutions are high amplitude limit cycles involving repeated contacts with the stator, and therefore can be very destructive. They occur in rotor systems that may be considered isotropic. There is a need for new analytical approaches in these systems, due to the current reliance on costly brute force numerical methods to investigate these behaviours.

Two general insights make these responses far easier to understand, and guide the current approach. Firstly, asynchronous responses are found to be periodic in a coordinate system that rotates with the shaft [26]. Secondly, it has been shown that they typically occur as an interaction between the underlying linear resonances of the rotor, and in fact this becomes a straightforward case of internal resonance when viewed in the rotating coordinate system [25,27]. The fact that these cycles are interactions of typically just two interacting modes makes them ideal for analysis with the method of Normal Forms, which works by transforming the system

to a simpler one that consists of the resonant response components [28-32]. However, in this case it must be adapted for use with complex modes and for non-smooth nonlinearity.

In what follows, the analysis method is briefly outlined in Section 2. Then it used to investigate the effects of various system paramters on a single disc rotor in Section 3 and then a multi-disc rotor in Section 4.

2 Normal Form analysis

What follows is a relatively brief outline of the method; for more detail please see [33]. The systems under consideration have the following form in a coordinate system that rotates with the shaft:

$$\mathbf{M}\ddot{\mathbf{q}} + \Omega\mathbf{G}\dot{\mathbf{q}} + \mathbf{K}\mathbf{q} + \mathbf{C}\dot{\mathbf{q}} + \mathbf{K_c}\mathbf{q} + \mathbf{n_q}(\mathbf{q}, \dot{\mathbf{q}}) = \mathbf{b} \tag{1}$$

where $\mathbf{M}$, $\mathbf{G}$, $\mathbf{K}$ and $\mathbf{C}$ are the mass, gyroscopic, stiffness and damping matrices respectively and Ω is the shaft speed in radians per second. Note that $\mathbf{G}$ and $\mathbf{K}$ will contain inertial terms that arise from the time-varying transformation from stationary coordinates. The matrix $\mathbf{K_c}$ contains 'stiffness like' terms that arise from applying the rotating transformation of damping effects and $\mathbf{n_q}(\mathbf{q}, \dot{\mathbf{q}})$ represents the nonlinearity. The vector $\mathbf{b}$ represents the out of balance forcing, which becomes a constant term in the rotating coordinate system; note that this system is autonomous whereas the stationary definition is not. The form of equation (1) is chosen to separate linear conservative terms from everything else.

System (1) is transformed into first order form:

$$\dot{\mathbf{y}} = \mathbf{A}\mathbf{y} + \mathbf{n_y}(\mathbf{y}) \tag{2}$$

where $\mathbf{y} = \{\mathbf{q}, \dot{\mathbf{q}}\}^T$, $\mathbf{A} = \begin{bmatrix} \mathbf{0} & \mathbf{I} \\ -\mathbf{M^{-1}K} & -\Omega\mathbf{M^{-1}G} \end{bmatrix}$ contains the underlying linear conservative terms, and therefore all nonconservative and nonlinear terms are contained within $\mathbf{n_y}(\mathbf{y})$. The system is then transformed to complex modal form using the eigensolutions of $\mathbf{A}$:

$$\dot{\mathbf{p}} = \mathbf{\Lambda}\mathbf{p} + \mathbf{n_p}(\mathbf{p}) \tag{3}$$

where $\mathbf{\Lambda}$ is a diagonal matrix of eigenvalues and $\mathbf{y} = \Re(\mathbf{\Phi}\mathbf{p})$ and $\mathbf{\Phi}$ contains eigenvectors. Note that this system has the same number of degrees of freedom as system (1) because only one of each conjugate pair of eigensolutions is used. Furthermore, the retained eigenvalues have form $\pm j\omega_i$ where it is important that the sign reflects the direction of the physical whirling i.e. positive if it is the same as the shaft rotation.

The method of normal forms seeks a near-identity transformation $\mathbf{p} = \mathbf{u} + \mathbf{h}(\mathbf{u})$ such that the variable $\mathbf{u}$ results in a system

$$\dot{\mathbf{u}} = \mathbf{\Lambda}\mathbf{u} + \mathbf{n_u}(\mathbf{u}) \tag{4}$$

that is much simpler equation than (3) to solve, and can be solved exactly. Note that the actual form of the transformation is decided in the frequency domain as a trial solution is implemented. If we subtract (4) from (3) we obtain:

$$\dot{\mathbf{p}} - \dot{\mathbf{u}} = \dot{\mathbf{h}} = \mathbf{\Lambda}\mathbf{h} + \mathbf{n_p}(\mathbf{p}) - \mathbf{n_u}(\mathbf{u}) \tag{5}$$

A problem occurs in trying to eliminate $\mathbf{p}$ from this equation; this has to be done by approximation. Many texts apply the approximation $\mathbf{n_p}(\mathbf{p}) \approx \mathbf{n_p}(\mathbf{u})$ to accuracy $\mathcal{O}(\mathbf{h})$. In this method the more accurate approximation

$$\mathbf{n_p}(\mathbf{p}) \approx \mathbf{n_p}(\mathbf{u} + \mathbf{h_{-1}}) = \mathbf{n_p}(\mathbf{p_{-1}}) \tag{6}$$

may be used with accuracy of $\mathcal{O}(\mathbf{h_0} - \mathbf{h_{-1}})$ where $\mathbf{h_{-1}}$ is an estimate from a previous iteration or initial guess and $\mathbf{h_0}$ is the true value for $\mathbf{h}$. After incorporating this approximation equation (5) can be rearranged to give

$$\dot{\mathbf{h}} - \mathbf{\Lambda}\mathbf{h} - \mathbf{n_p}(\mathbf{u} + \mathbf{h_{-1}}) + \mathbf{n_u}(\mathbf{u}) = \mathbf{0} \tag{7}$$

The general solution of (4) is assumed to be of form:

$$\mathbf{u} = \sum_{i=-n_f/2}^{n_f/2-1} \mathbf{U}_i \mathrm{e}^{ij\omega_r t} = \mathbf{U}\mathbf{t} \tag{8}$$

i.e. a summation of vectors multiplied by exponential time functions, so that each transformed modal variable is a complex Fourier series with unknown fundamental frequency ω_r and signed harmonics. In the matrix form $\mathbf{U}\mathbf{t}$, $\mathbf{U}$ will have dimensions $N \times n_f$ where n_f indicates the length of the Fourier transform, and $\mathbf{t}$ is a vector of all the terms $\mathrm{e}^{ij\omega_r t}$ with length n_f. The aim is a system where $\mathbf{u}$ is simple, and therefore it is desirable that $\mathbf{U}$ is as sparse as possible. Similar representations are made for all other variables:

$$\begin{gathered} \mathbf{h} = \mathbf{H}\mathbf{t} \ , \ \mathbf{n_u}(\mathbf{u}) = \mathbf{N_u}\mathbf{t} \ , \ \mathbf{n_p}(\mathbf{u}+\mathbf{h_{-1}}) = \mathbf{N_p}\mathbf{t} \ , \\ \mathbf{h_{-1}} = \mathbf{H_{-1}}\mathbf{t} \ , \ \mathbf{p_{-1}} = \mathbf{P_{-1}}\mathbf{t} \end{gathered} \tag{9}$$

Differentiation can also be achieved by noting that

$$\dot{\mathbf{h}} = \mathbf{H}\dot{\mathbf{t}} = \mathbf{H}\mathbf{\Psi}\mathbf{t} \tag{10}$$

where $\mathbf{\Psi}$ is an $n_f \times n_f$ diagonal matrix where the diagonal entries are all of form $ij\omega_r$. Thus equation (7) may be written:

$$\mathbf{H}\mathbf{\Psi}\mathbf{t} - \mathbf{\Lambda}\mathbf{H}\mathbf{t} - \mathbf{N_p}\mathbf{t} + \mathbf{N_u}\mathbf{t} = \mathbf{0} \tag{11}$$

In order to evaluate the trial nonlinear frequency components $\mathbf{N_p}$ the Alternating Frequency/Time (AFT) method is used. This consists of firstly approximating the time series of $\mathbf{p}$ at all time steps using $\mathbf{p} = (\mathbf{U} + \mathbf{H_{-1}})\,\mathbf{t}$ (obtained from using the forms of (9) in (6)). Then, all nonlinear and nonconservative forces $\mathbf{n_p}(\mathbf{p})$ are evaluated based on this time series. Finally a Fast Fourier Transform is used to return the frequency components of the forces $\mathbf{N_p} = \mathbf{F}(\mathbf{n_p}(\mathbf{p}))$. Note that because our state variables give velocity as well as displacement, there is no need to know ω_r to evaluate this stage. Note that $\mathbf{U}$ is to be very sparse, whereas $\mathbf{H_{-1}}$ is a matrix of constants from a previous solution or initial guess, and is in general full except where $\mathbf{U}$ is nonzero.

The corresponding elements k, ℓ of the matrices in (11) can be compared separately because they each relate to a different harmonic of a different modal variable. Hence equation (11) (with $\mathbf{t}$ eliminated) can be considered term by term:

$$H_{k,\ell}\Psi_{\ell,\ell} - \Lambda_{k,k}H_{k,\ell} - N_{p(k,\ell)} + N_{u(k,\ell)} = 0 \tag{12}$$

At this point a slight shorthand is introduced; since we have to deal with negative (or perhaps zero) harmonics we allow the index representing harmonics ℓ to be zero or negative. Clearly, matrix indices need to be positive integers so when ℓ is non-positive, it should really be converted to whichever positive value is needed. But for brevity we ignore this and just assume that when needed matrices have columns relating to negative values.

In general, because we want to simplify equation (4), equation (12) is solved by choosing:

$$N_{u(k,\ell)} = 0 \ , \ H_{k,\ell} = \frac{N_{p(k,\ell)}}{\Psi_{\ell,\ell} - \Lambda_{k,k}} \tag{13}$$

However, if $\Psi_{\ell,\ell} \approx \Lambda_{k,k}$, this will cause $H_{k,\ell}$ to be large, violating the assumption of a near identity transformation. These terms are known as resonant terms and must be solved by choosing:

$$N_{u(k,\ell)} = N_{p(k,\ell)} \ , \ H_{k,\ell} = 0 \tag{14}$$

Typically interesting solutions (i.e. not simply synchronous whirling in or out of contact) occur when exactly two modes become internally resonant [27]. Therefore, expressing the harmonic components of the resonant equation of motion (4) will give a harmonic balance problem of the form:

$$\begin{gathered} U_{i,j}\Psi_{j,j} - \Lambda_{i,i}U_{i,j} - N_{u(i,j)} = 0 \\ U_{k,\ell}\Psi_{\ell,\ell} - \Lambda_{k,k}U_{k,\ell} - N_{u(k,\ell)} = 0 \end{gathered} \tag{15}$$

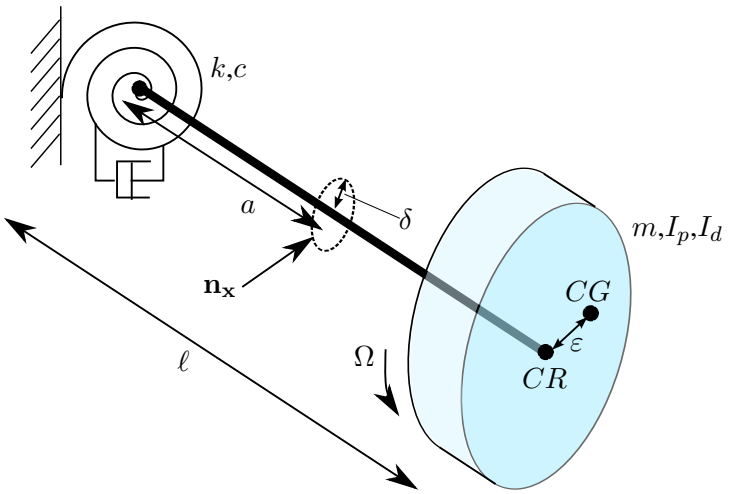


Figure 1: A snubbed overhung rotor.

Hence our system of N degrees of freedom results in this greatly reduced form. Equation (15) has 5 unknowns; the real and imaginary parts of $U_{i,j}$ and $U_{k,\ell}$ and also the unknown fundamental frequency ω_r which is within $\Psi_{j,j}$ and $\Psi_{\ell,\ell}$ (see the definition of $\mathbf{\Psi}$ following equation (10)). However, we may impose that one of the transformed modal variables is purely real; this constrains the phase of this modal variable and therefore locks the solution in time. Therefore, with this imposition equation (15) is solvable.

In order to start solving the problem, a guess for $\mathbf{h_{-1}}$ and the resonant variables must made. It seems that typically $\mathbf{h}$ is close to the linear synchronous out of balance response, so this is chosen for the intial $\mathbf{h_{-1}}$. The guesses for resonant variables can be chosen to just give a reasonable amount of stator penetration, and perhaps try different phase angles between the complex amplitudes. After a solution of the resonant variables, $\mathbf{h}$ can be populated with equations (13) and (14), and then this value can be used as $\mathbf{h_{-1}}$ in another iteration. In this way repeated iterations of the process improve accuracy.

The method outlined is very general with regard to the form of nonlinearity in $\mathbf{n_q}(\mathbf{q}, \dot{\mathbf{q}})$ due to the use of the AFT step. Furthermore, it is also very general with regard to the size of the system matrices, so should scale to rotor systems with many degrees of freedom with appropriate modal truncations.

3 An overhung rotor

3.1 System description

This is a two degree of freedom system similar to that presented in [25]. The disc is supported on a rigid inertialess shaft which in turn is mounted on a rotational spring damper with stiffness and damping represented by k and c respectively. The disc has mass m, polar moment of inertia I_p and diametral moment of inertia I_d. Out of balance forcing occurs due to the mass centre of the disc at CG being slightly away from its rotational centre CR. Nonlinearity occurs due to the snubber ring at distance a from the root, which exerts a force whenever the shaft at this point exceeds clearance δ and this is represented by the nonlinear force $\mathbf{n_x}$ in the stationary frame.

The system is nondimensionalised using the undamped natural frequency of the underlying nonrotating system $\omega_n = \sqrt{\frac{k}{m_{eff}\ell}}$ to scale time where $m_{eff} = m + \frac{I_d}{\ell^2}$ is the effective inertia, and the displacement required to make contact with the stator $\Delta = \frac{\delta\ell}{a}$ is used to scale displacement:

$$\begin{gathered} \tau = \omega_n t \quad , \quad \hat{u} = \tfrac{u}{\Delta} \quad , \quad \hat{v} = \tfrac{v}{\Delta} \quad , \quad \hat{I}_p = \tfrac{I_p}{m_{eff}\ell^2} \\ \hat{\Omega} = \tfrac{\Omega}{\omega_n} \quad , \quad \hat{f} = \tfrac{\varepsilon}{\Delta} \quad , \quad \zeta = \tfrac{c}{2\ell^2\omega_n m_{eff}} \end{gathered} \tag{16}$$

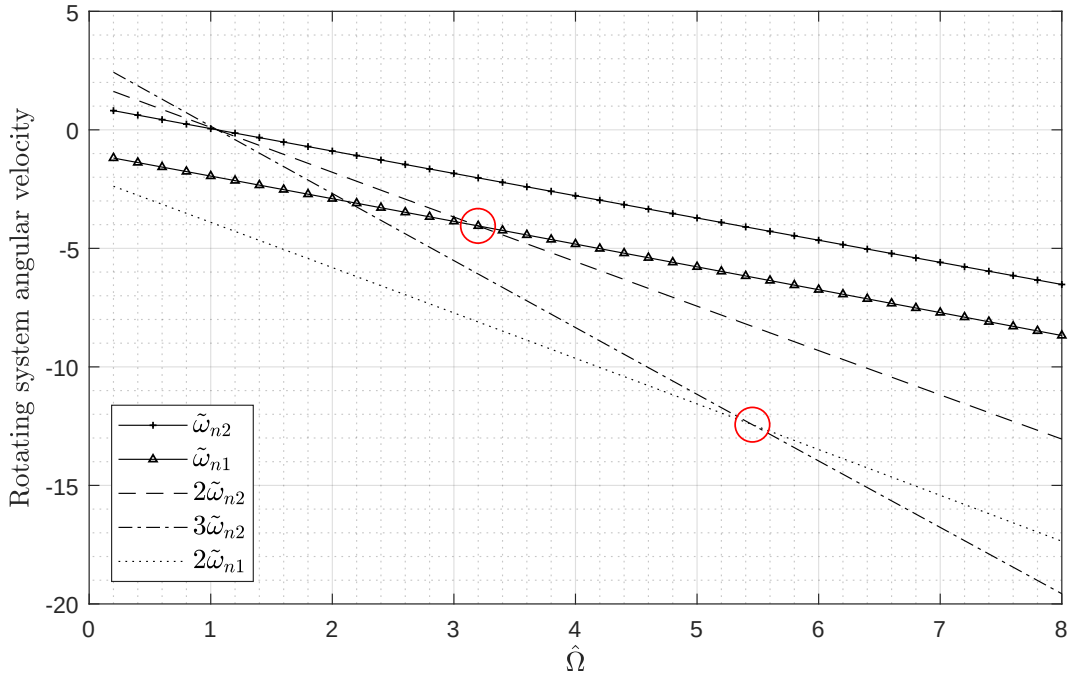


Figure 2: Campbell diagram showing rotating coordinate system whirl velocities for the underlying undamped linear rotor. Circles at $\hat{\Omega} = 3.198$ and $\hat{\Omega} = 5.455$ indicate the nonlinear critical speeds for 2:1 and 3:2 internal resonance respectively.

This leads to equations of motion of the form of equation (1) with matrices as follows:

$$\begin{gathered}\mathbf{M} = \mathbf{I}_{2\times 2}\ ,\ \mathbf{G} = -(\hat{I}_p - 2)\mathbf{J}\ ,\ \mathbf{K} = (1 - \hat{\Omega}^2(1 - \hat{I}_p))\mathbf{I}_{2\times 2} \\ \mathbf{C} = 2\zeta\mathbf{I}_{2\times 2}\ ,\ \mathbf{K_c} = -2\zeta\hat{\Omega}\mathbf{J}\ ,\ \mathbf{b} = \left\{\hat{f}\hat{\Omega}^2, 0\right\}^T\end{gathered} \tag{17}$$

and

$$\mathbf{n_q}(\mathbf{q}) = \begin{cases} -\beta(|\mathbf{q}| - 1)\left\{q_1, q_2\right\}^T/|\mathbf{q}|, & \text{if } |\mathbf{q}| \geq 1 \\ \left\{0, 0\right\}^T, & \text{if } |\mathbf{q}| < 1, \end{cases} \tag{18}$$

where $\beta = \frac{k_s a}{k}$ expresses the ratio of stator stiffness to the underlying linear stiffness and $\mathbf{J} = \begin{bmatrix} 0 & -1 \\ 1 & 0 \end{bmatrix}$. The vector $\mathbf{q}$ represents the horizontal and vertical deflections of the point CR, taken in the rotating coordinate frame. Note that since the nonlinearity is isotropic and purely a function of radial displacement, the rotating coordinate system nonlinear force function $\mathbf{n_q}$ is in this case identical to the the stationary coordinate function $\mathbf{n_x}$.

3.2 Results

The results are presented for a rotor with $\hat{I}_p = 0.1$ (Note that this parameter and the drive speed $\hat{\Omega}$ completely define the linear conservative part of the system). Figure 2 shows the Campbell diagram for this system; note that unlike the traditional representation that shows unsigned whirl frequencies from the stationary frame, this shows signed whirl velocities from the rotating frame (for more detail see [33]). Figure 2 also includes some multiples of the whirl velocities, and it may be seen that these having crossing points. We describe these drive speeds as *nonlinear critical speeds* because they indicate the lower bound of a region of $\hat{\Omega}$ where internally resonant responses may be encountered.

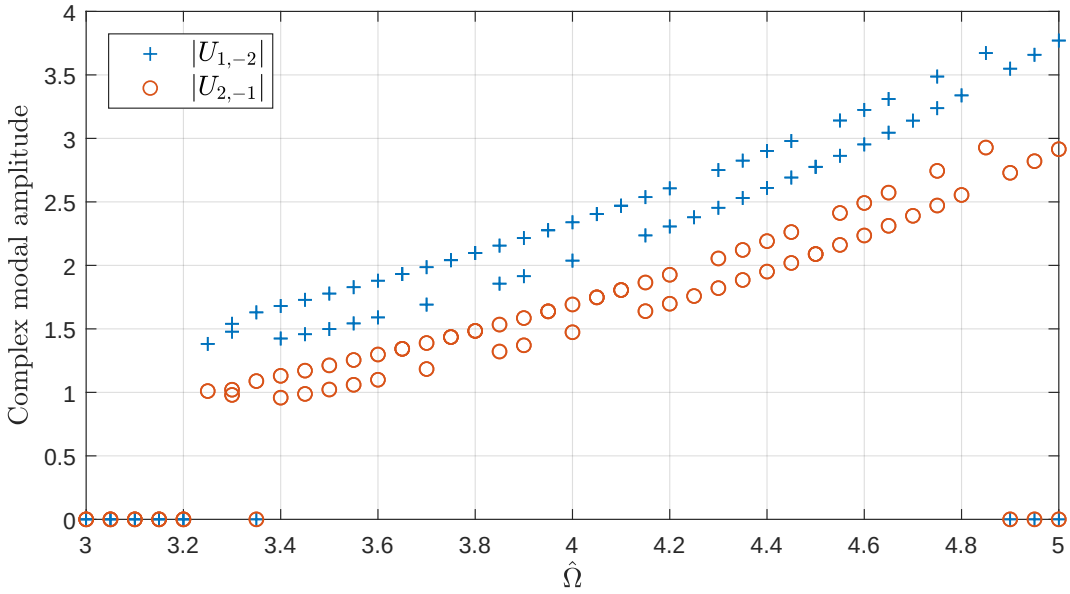


Figure 3: Amplitudes of the resonant complex variables in 2:1 resonance against nondimensional drive speed for $\zeta = 0.01$, $\hat{f} = 0.100$, $\beta = 5$.

3.2.1 2:1 resonance

A range of results are shown in Figure 3 for a rotor with $\zeta = 0.01$, $\hat{f} = 0.100$, and $\beta = 5$. The drive speeds are considered in the region of the 2:1 nonlinear critical speed in Figure 2, and $n_f = 1024$. The intial value for $\mathbf{h_{-1}}$ is chosen as the linear out of balance solution, and 3 iterations are performed. In order to enforce our assumption of 2:1 resonance, we populate equation (15) with $i = 1$, $j = -2$, $k = 2$ and $\ell = -1$. The indices are found with reference to Figure 2 ; in words we are looking for a response where complex modal variable 1 responds at -2 times the response frequency ω_r, and modal variable 2 responds at $-\omega_r$, and both are responding at close to their linear natural frequencies.

The results of this are shown in Figure 3. The results where both variables are zero are linear synchronous whirls which for the purpose of this paper are considered trivial. As expected, the non-trivial solutions begin at just above the nonlinear critical speed of $\hat{\Omega} = 3.198$ found in Figure 2 . We then see two rows of solutions (the upper and lower branches correspond for each modal variable).

As an example of stable and unstable orbits, the orbits of two solutions found at $\hat{\Omega} = 3.4$ are shown in Figure 4, superimposed on time simulation results intiated at the same inital condition as the predicted orbit. The time simulation runs for 25 periods of the predicted cycle. The orbit in Figure 4 (a) comes from the higher amplitude solution from Figure 3, and as can be seen the match with time simulation is perfect. This is because this solution has included the full system dynamics, with a high value for n_f. In principle, with further iterations and a higher n_f any required accuracy could be reached. By contrast the time simulation in Figure 4 (b) follows the analytical orbit initially, but then gradually divergese. The fact that the solution is followed initially suggests that it is not erroneous, however it is clear that this solution is not stable. This trend of the lower amplitude being unstable is followed throughout the results in Figure 3, and as the drivespeed increases it is seen that the divergence becomes more rapid.

The advantage of having an analytical method to explore this system's behaviour is that it is now far quicker to explore the effect of various parameters than was previously possible when relying on brute simulation approaches such as those used in [27]. Given the observation that solutions always appear at a drive speed slightly above the nonlinear critical speed, a key question is what governs this differnce. To begin answering this, a series of parameter sweeps taken near the nonlinear critical speed are presented.

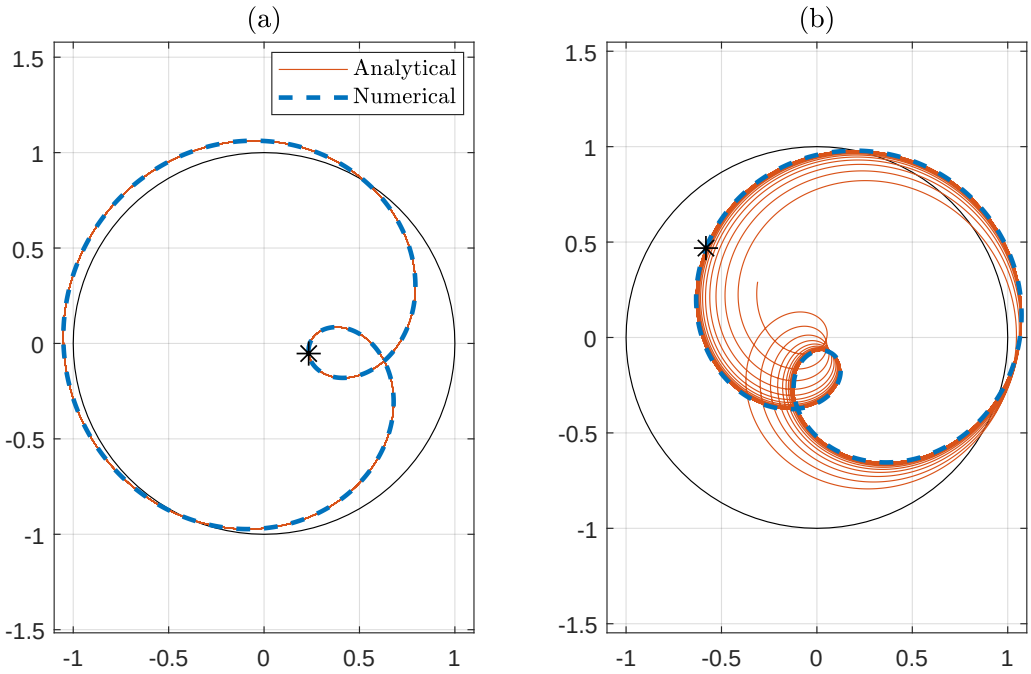


Figure 4: Orbit paths in rotating coordinates 2:1 resonance at for $\hat{\Omega} = 3.4$. (a) Stable orbit. (b) Unstable orbit. Circle indicates the threshold for stator contact, asterisk ($*$) indicates the beginning of the analytical orbit and numerical time simulation.

In Figure 5, the effect of the non-contact damping ratio ζ is seen. As the damping ratio falls, the onset of limit cycles is seen to move further toward the nonlinear critical speed. Note that there appears to be a single line of 'stray' solutions found beyond the main region of stable and unstable solutions. These never seem to be stable, but are the subject of ongoing investigation.

The effect of the out of balance forcing term $\hat{f}$ is shown in Figure 6. With regard to the onset drivespeed for stable responses, it seems to have an opposite effect to that of damping, with higher $\hat{f}$ moving the onset point toward the nonlinear critical speed. However, it is seen that increasing the out of balance forcing also seems to increase the separation between the amplitudes of the upper and lower branches.

The contact stiffness parameter is seen in Figure 7 to have a noticeable effect on the onset drive speed, but it is less dramatic than the effects of out of balance and damping. It also has an effect on the separation of the upper and lower solution branches. As expected for a parameter that governs the amount of nonlinear stiffening, it also appears to affect the rate that amplitude increases with regard to drive speed.

3.2.2 3:2 resonance

The process is repeated in the region of the nonlinear critical speed for 3:2 resonance, found to be $\hat{\Omega} = 5.455$ in Figure 2. Solutions of equation (15) are sought with $i = 1$, $j = -3$, $k = 2$ and $\ell = -2$, again using $n_f = 1024$ and three iterations for a rotor with $\zeta = 0.01$, $\hat{f} = 0.100$, and $\beta = 5$. The results are shown in Figure 8. As seen in the 2:1 case, regions of higher and lower amplitude response start at drivespeeds slightly above the nonlinear critical drive speed. Again, these branches give stable and unstable orbits, and example orbits are shown in Figure 9. Similar trends regarding non-contact damping, out of balance forcing and stator stiffness to the 2:1 case may also be observed although they are omitted here for brevity.

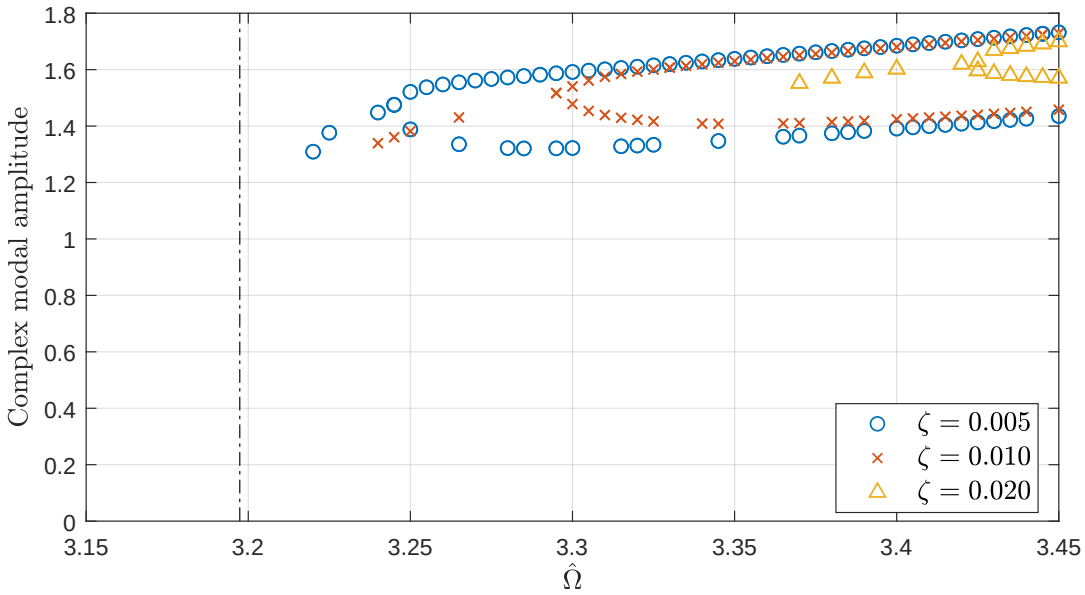


Figure 5: Sweeps with varying ζ showing $|U_{1,-2}|$ near the nonlinear critical speed critical speed for 2:1 resonance of a rotor with $\hat{f} = 0.100$, $\beta = 5$. The vertical dot-dash line marks the nonlinear critical speed as predicted using Figure 2.

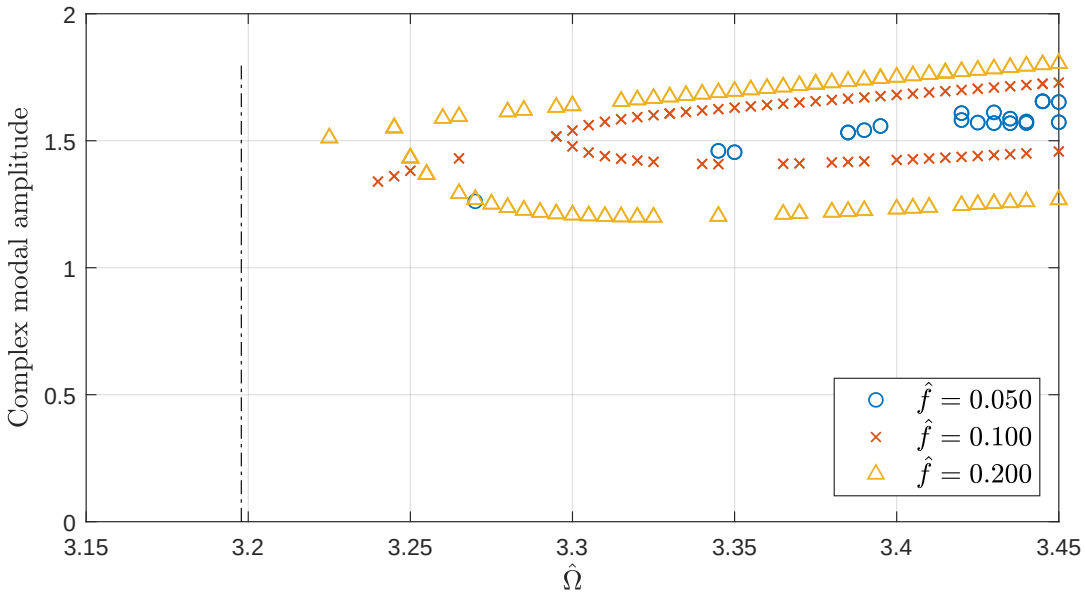


Figure 6: Sweeps with varying $\hat{f}$ showing $|U_{1,-2}|$ near the nonlinear critical speed critical speed for 2:1 resonance of a rotor with $\zeta = 0.010$, $\beta = 5$. The vertical dot-dash line marks the nonlinear critical speed as predicted using Figure 2.

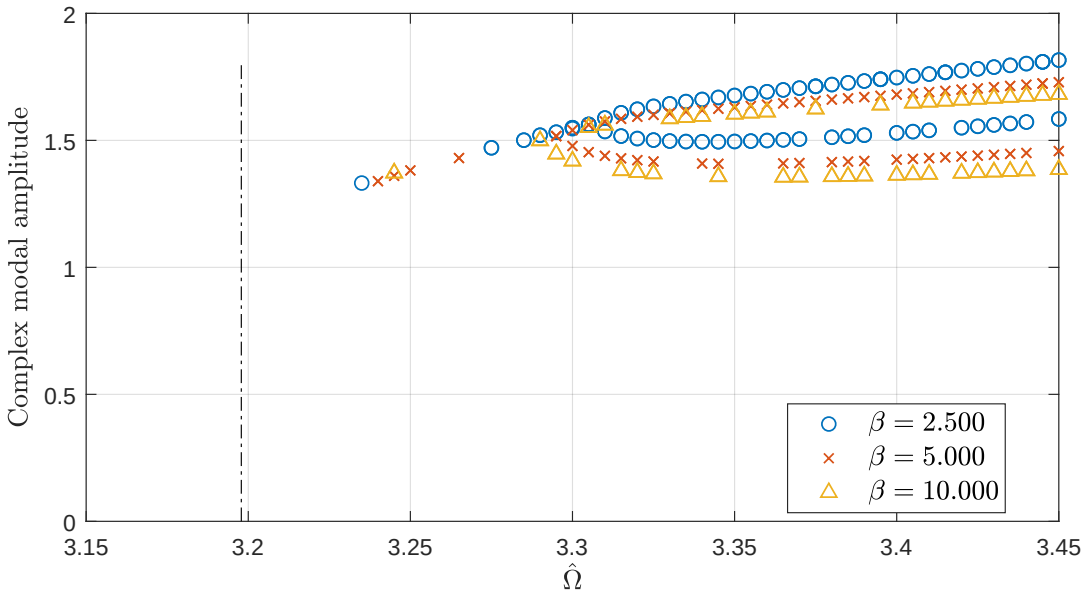


Figure 7: Sweeps with varying β showing $|U_{1,-2}|$ near the nonlinear critical speed critical speed for 2:1 resonance of a rotor with $\zeta = 0.010$, $\hat{f} = 0.1$. The vertical dot-dash line marks the nonlinear critical speed as predicted using Figure 2.

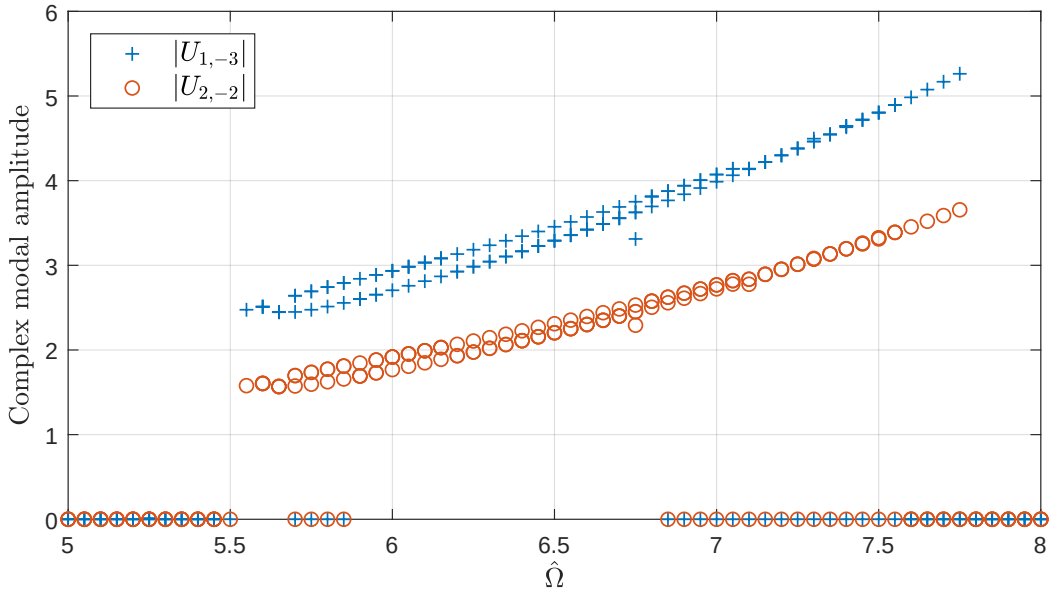


Figure 8: Amplitudes of the resonant complex variables in 3:2 resonance against nondimensional drive speed for $\zeta = 0.01$, $\hat{f} = 0.100$, $\beta = 5$.

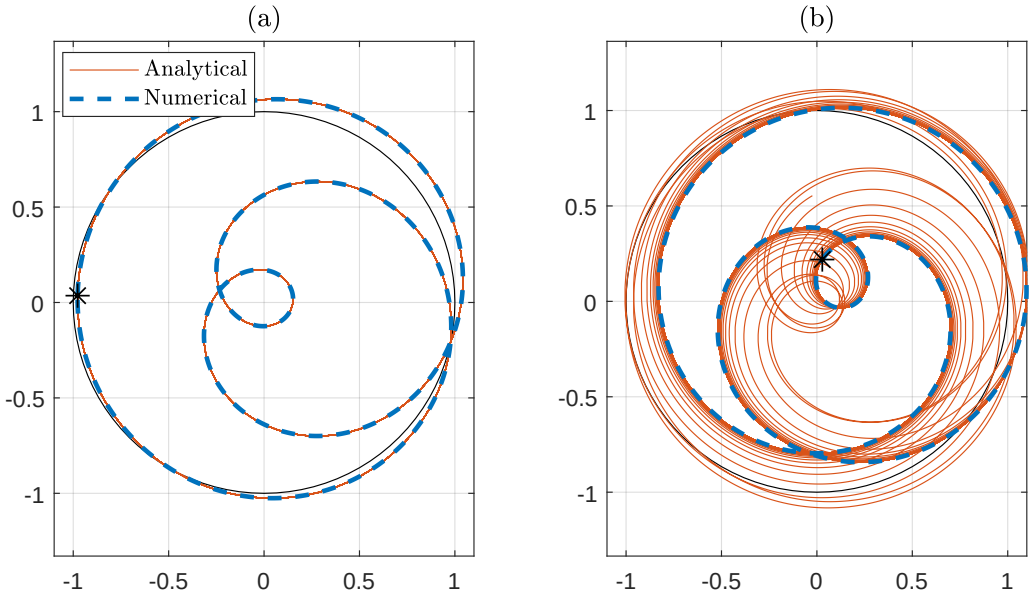


Figure 9: Orbit paths in rotating coordinates for 3:2 resonance at $\hat{\Omega} = 5.8$. (a) Stable orbit. (b) Unstable orbit. Circle indicates the threshold for stator contact, asterisk ($*$) indicates the beginning of the analytical orbit and numerical time simulation.

4 A multi disc rotor

In this section we consider a four disc rotor, with a stator clearance at the centre as shown in Figure 10. The shaft is a hollow tube with inner diameter of 3mm, outer diameter 5mm, length 500mm and made from steel assumed to have Young's modulus 210GPa, Poisson's ratio 0.3 and density 7810kg/m^3. The shaft is simply supported at each end. There is an inertialess stator at the midpoint of the shaft, with a clearance of 1mm and a contact stiffness of 10N/mm. Using standard methods such as those described in [34], this may be represented by an 80 degree-of-freedom finite element model and transformed to the rotating coordinate system using the approach found in [27]. The rotating system Campbell diagram showing just the lower modes of this system is given in Figure 11, and it is clear that there are many potential nonlinear critical speeds for this system.

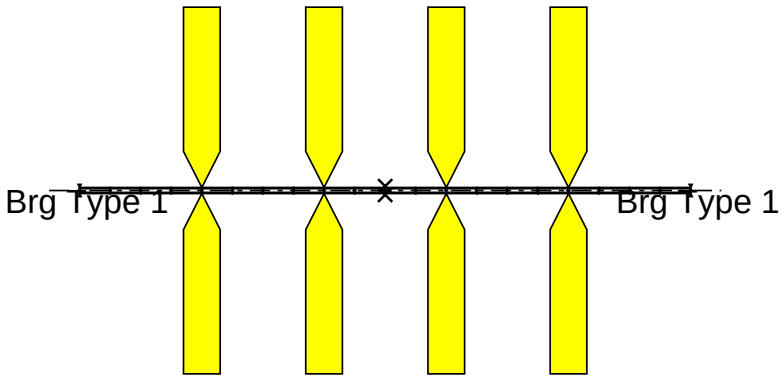


Figure 10: A four disc rotor.

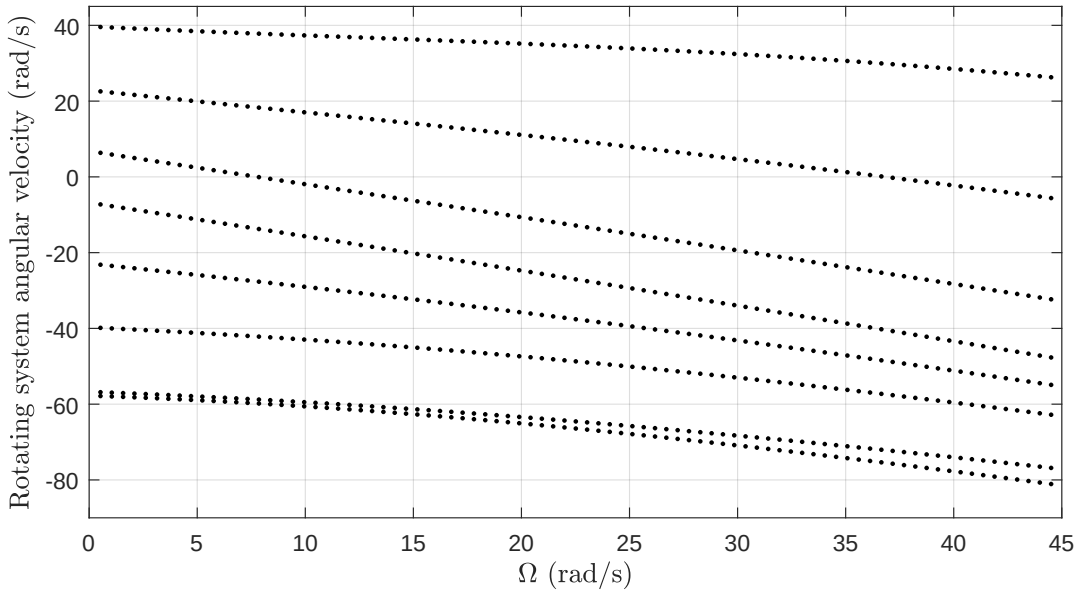


Figure 11: Signed rotating system Campbell diagram for the four disc rotor in Figure 10.

The method set out in Section 2 is very general and can be scaled to larger systems quite easily. However it is found that the inclusion of higher harmonics can cause very large $H_{k,\ell}$ values to arise from equation (13); these are not physical and they can prevent the solution from converging. Therefore, it is necessary to truncate higher harmonics from the response of larger systems, although a high n_f can still be beneficial to deal with potential issues such as aliasing. In some cases more than two modes can become resonant and in these cases it is necessary to add extra equations to (15). However, despite the additional complexity, many results and features can be found that are very similar to the phenomena seen in the simple two degree of freedom system presented earlier.

Figure 12 (a) shows a typical orbit for a 2:1 resonance between the first backward and the first forward linear whirl modes of the rotor. and shows the familiar 'double loop' shape seen for the overhung rotor in Figure 4. In Figure 12 (b) the harmonic content of this response is represented. Firstly, note that at $\ell = 0$ there are visible contributions from all modes. This is the synchronous component of the response, and although classified as non-resonant this has an important symmetry-breaking role in the solution. However, away from this component the response is dominated by the resonant terms, as marked by asterisks. Note that the content for $|\ell| \geq 3$ has been zeroed as discussed above; in a fully physical solution there would be some low amplitude noise here. Figure 12 (a) compares the analytical solution to a time simulation, and it can be seen that the time solution does not exactly follow the analytical orbit. However, it does settle on a very similar orbit suggesting that the analytical solution has closely approximated a stable response, with some accuracy lost due to the truncation of higher harmonics.

5 Conclusions

This work has discussed how the method of normal forms adapted for complex modes and using an AFT step can be used to explore intermittently contacting responses of a rotor stator system. Results are highly accurate for a simple rotor, as there is no requirement to truncate higher harmonics from the response. For a more complex rotor, the need to truncation means that solutions are approximate, but still useful.

The approximate onset of these limit cycles can be predicted using a Campbell diagram approach, using the underlying linear modes to predict a so-called nonlinear critical speed. However it has been observed

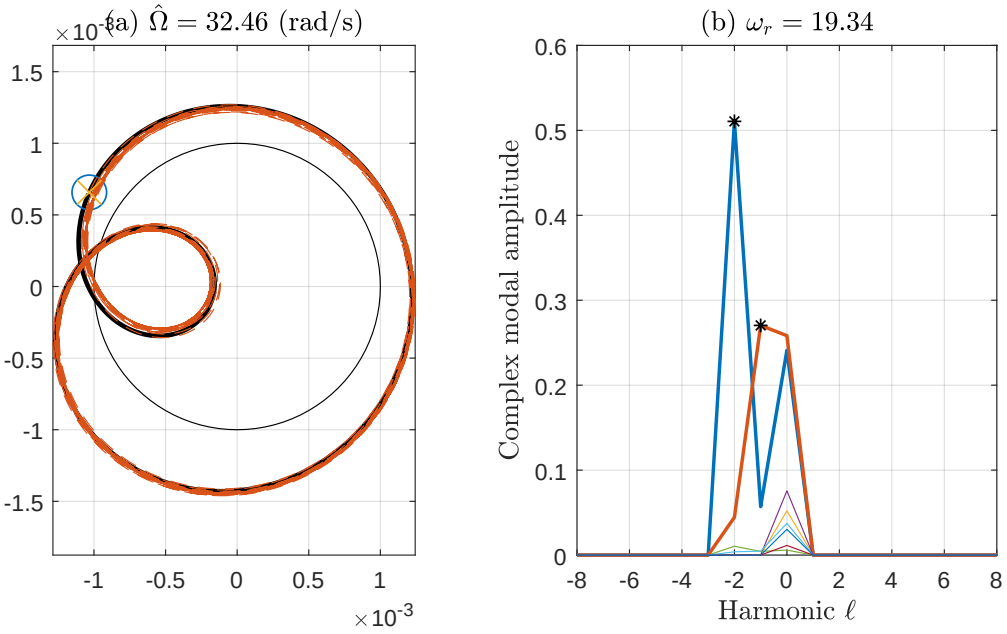


Figure 12: (a) Orbit taken at the midpoint of the four disc shaft. Circle shows threshold for contact. Thick black line shows analytical orbit, dashed orange line shows time simulation. (b) Fourier components of the analytical solution, showing all modes of the shaft. The resonant modes are in thicker lines, and their resonant harmonics are marked with asterisks.

that this always slightly under predicts the onset drivespeed. The normal forms analysis has been used to show that the difference between the nonlinear critical speed and the true onset of limit cycles is governed primarily by damping and out of balance forcing. Increasing damping moves the true onset point further away from the nonlinear critical speed, whereas increasing the out of balance force has the opposite effect. The contact stiffness only has a secondary effect on the onset drivespeed.

Acknowledgements

References

[1] G. Jacquet-Richardet, M. Torkhani, P. Cartraud, F. Thouverez, T. N. Baranger, M. Herran, C. Gibert, S. Baguet, P. Almeida, L. Peletan, *Rotor to stator contacts in turbomachines. review and application*, Mechanical Systems and Signal Processing, Vol. 40, No. 2, Elsevier (2013), pp. 401 – 420.

[2] J. Jansen, *Non-linear rotor dynamics as applied to oilwell drillstring vibrations*, Journal of Sound and Vibration, Vol. 147, No. 1, Elsevier (1991), pp. 115 – 135.

[3] S. Ahmad, *Rotor casing contact phenomenon in rotor dynamics – literature survey*, Journal of Vibration and Control, Vol. 16, No. 9, Sage (2010), pp. 1369–1377.

[4] F. F. Ehrich, *Observations of nonlinear phenomena in rotordynamics*, Journal of System Design and Dynamics, Vol. 2, No. 3, ASME (2008), pp. 641–651.

[5] F. F. Ehrich, *Sum and difference frequencies in vibration of high speed rotating machinery*, Journal of Engineering for Industry, Vol. 94, No. 1, AMSE (1972), pp. 181–184.

[6] F. F. Ehrich, J. OConnor, *Stator whirl with rotors in bearing clearance*, Journal of Engineering for Industry, Vol. 89, No. 3, ASME (1967), pp. 381–389.

[7] R. Neilson, A. Barr, *Dynamics of a rigid rotor mounted on discontinuously non-linear elastic supports*, Proceedings of the Institution of Mechanical Engineers, Part C: Journal of Mechanical Engineering Science, Vol. 202, No. 5, IMechE (1988), pp. 369–376.

[8] W. Szczygielski, *Application of chaos theory to the contacting dynamics of high-speed rotors*, Rotating machinery dynamics, (1987), pp. 319–326.

[9] F. F. Ehrich, *High order subharmonic response of high speed rotors in bearing clearance*, Journal of Vibration, Acoustics, Stress, and Reliability in Design , Vol. 110, No. 1, ASME (1988), pp. 9–16.

[10] A. Muszynska, P. Goldman, *Chaotic responses of unbalanced rotor/bearing/stator systems with looseness or rubs*, Chaos, Solitons & Fractals, Vol. 5, No. 9, Elsevier (1995), pp. 1683–1704.

[11] F. Chu, Z. Zhang, *Bifurcation and chaos in a rub-impact Jeffcott rotor system*, Journal of Sound and Vibration, Vol. 210, No. 1, Elsevier (1998), pp. 1–18.

[12] S. Edwards, A. W. Lees, M. I. Friswell, *The influence of torsion on rotor/stator contact in rotating machinery*, Journal of Sound and Vibration , Vol. 225, No. 4, Elsevier (1999), pp. 767–778.

[13] Y. Ishida, *Nonlinear vibrations and chaos in rotordynamics*, JSME international journal. Ser. C, Dynamics, Control, Robotics, Design and Manufacturing, Vol. 37, No. 2, (1994), pp. 237–245.

[14] E. V. Karpenko, M. Wiercigroch, E. E. Pavlovskaia, M. P. Cartmell, *Piecewise approximate analytical solutions for a Jeffcott rotor with a snubber ring*, International Journal of Mechanical Sciences, Vol. 44, No. 3, Elsevier (2002), pp. 475–488.

[15] E. V. Karpenko, M. Wiercigroch, M. P. Cartmell, *Regular and chaotic dynamics of a discontinuously nonlinear rotor system*, Chaos, Solitons & Fractals, Vol. 13, No. 6, Elsevier (2002), pp. 1231–1242.

[16] E. Pavlovskaia, E. Karpenko, M. Wiercigroch, *Non-linear dynamic interactions of a Jeffcott rotor with preloaded snubber ring*, Journal of Sound and Vibration , Vol. 276, No. 1, Elsevier (2004), pp. 361–379.

[17] E. Karpenko, M. Wiercigroch, E. Pavlovskaia, R. Neilson, *Experimental verification of Jeffcott rotor model with preloaded snubber ring*, Journal of Sound and Vibration, Vol. 298, No. 4, Elsevier (2006), pp. 907–917.

[18] F. Chu, W. Lu, *Experimental observation of nonlinear vibrations in a rub-impact rotor system*, Journal of Sound and Vibration, Vol. 283, No. 3, Elsevier (2005), pp. 621–643.

[19] M. Torkhani, L. May, P. Voinis, *Light, medium and heavy partial rubs during speed transients of rotating machines: numerical simulation and experimental observation*, Mechanical Systems and Signal Processing, Vol. 29, Elsevier (2012), pp. 45–66.

[20] Y. Ishida, T. Inoue, *Nonstationary oscillations of a nonlinear rotor during acceleration through the major critical speed: influence of internal resonance (special issue on nonlinear dynamics)*, JSME International Journal Series C Mechanical Systems, Machine Elements and Manufacturing, Vol. 41, No. 3, (1998), pp. 599–607.

[21] Y. Ishida, T. Inoue, *Internal resonance phenomena of the Jeffcott rotor with nonlinear spring characteristics*, Journal of Vibration and Acoustics, Vol. 126, No. 4, ASME (2004), pp. 476–484.

[22] Y. Ishida, T. Inoue, *Internal resonance phenomena of an asymmetrical rotating shaft*, Modal Analysis, Vol. 11, No. 9, Sage (2005), pp. 1173–1193.

[23] T. Inoue, Y. Ishida, *Chaotic vibration and internal resonance phenomena in rotor systems*, Journal of Vibration and Acoustics, Vol. 128, No. 2, ASME (2006), pp. 156–169.

[24] P. Keogh, M. Cole, *Rotor vibration with auxiliary bearing contact in magnetic bearing systems part 1: Synchronous dynamics*, Proceedings of the Institution of Mechanical Engineers, Part C: Journal of Mechanical Engineering Science , Vol. 217, No. 4, IMechE (2003), pp. 377–392.

[25] A. Zilli, R. J. Williams, D. J. Ewins, *Nonlinear dynamics of a simplified model of an overhung rotor subjected to intermittent annular rubs*, Journal of Engineering for Gas Turbines and Power, Vol. 137, No. 6, ASME (2015), pp. 065001.

[26] M. Cole, P. Keogh, *Asynchronous periodic contact modes for rotor vibration within an annular clearance*, Proceedings of the Institution of Mechanical Engineers, Part C: Journal of Mechanical Engineering Science, Vol. 217, No. 10, IMechE (2003), pp. 1101–1115.

[27] A. D. Shaw, A. R. Champneys, M. I. Friswell, *Asynchronous partial contact motion due to internal resonance in multiple degree-of-freedom rotordynamics*, Proc. R. Soc. A, Vol. 472, No. 2192, The Royal Society (2016), pp. 20160303.

[28] D. J. Wagg, S. A. Neild, *Nonlinear Vibration with Control*, Springer, Dordrecht, 2009.

[29] S. A. Neild, D. J. Wagg, *Applying the method of normal forms to second-order nonlinear vibration problems*, Proc. R. Soc. A, Vol. 467, No. 2128, The Royal Society (2011), pp. 1141 – 1163.

[30] S. A. Neild, A. R. Champneys, D. J. Wagg, T. L. Hill, A. Cammarano, *The use of normal forms for analysing nonlinear mechanical vibrations*, Phil. Trans. R. Soc. A, Vol. 373, No. 2051, The Royal Society (2015), pp. 20140404.

[31] L. Stolovitch, *Progress in normal form theory*, Nonlinearity, Vol. 22, No. 7, IOP Publishing (2009), pp. R77.

[32] M. H. Fredriksson, A. B. Nordmark, *On normal form calculations in impact oscillators*, Proceedings of the Royal Society of London A: Mathematical, Physical and Engineering Sciences, Vol. 456, No. 1994, The Royal Society (2000), pp. 315–329.

[33] A. D. Shaw, A. R. Champneys, M. I. Friswell, *Normal form analysis of bouncing cycles in isotropic rotor stator contact problems*, Under review.

[34] M. I. Friswell, J. E. T. Penny, S. D. Garvey, A. W. Lees, *Dynamics of Rotating Machines*, Cambridge, 2010.

Effects of geometrical nonlinearities for a rotating intentionally mistuned bladed-disk.

A. Picou [1,2], **E. Capiez-Lernout** [1], **C. Soize** [1], **M. Mbaye** [2]
[1] Université Paris-Est, Laboratoire Modélisation et Simulation Multi-Echelle, MSME UMR 8208 CNRS, 5 bd Descartes, 77454 Marne-La-Vallée Cedex 02, France

[2] Safran Tech - Safran Group, 78114 Magny-Les-Hameaux, France
e-mail: **anthony.picou@u-pem.fr**

Abstract
The present paper describes a computational methodology adapted to the analysis of the nonlinear dynamical behavior of a detuned bladed disk. The context of the analysis is the following : (1) the detuning is taken into account by voluntarily breaking the cyclic symmetry of the structure with the use of a pattern constituted of different blade types; (2) the structure is assumed to undergo large strain/displacements induced by the geometrical nonlinear effects; (3) the prestresses and the gyroscopic effects induced by the rotating motion are considered in the nonlinear dynamical analysis. The computational strategy has to be compatible with the industrial context. Consequently, a particular attention is paid to the construction of an adapted nonlinear reduced-order model. Finally, the proposed methodology is applied on a complex bladed disk structure.

1 Introduction

In turbomachinery, the mistuning of bladed-disks structures caused by the manufacturing tolerances and the small variations in the mechanical properties from blade to blade is known to amplify and to localize the dynamical response of some blades [1, 2]. There have been various researches concerning the computational modeling of mistuned structures, with the development of reduced-order models (see for instance [3, 4, 5] for linear reduced-order models and [6, 7] for nonlinear reduced-order models) and probabilistic approaches [8, 9]. One possible strategy is also to intentionally mistune (detuning) the structure by assembling generating sectors of different types according to a given pattern [10, 11, 12]. The pattern optimization is known to be efficient for reducing the response amplitudes in the linear context. Nevertheless, geometrical nonlinear effects can no longer be neglected with the current technological improvements, including the use of more flexible and lighter materials which sometimes leads to large displacements and strains. In this context, the present research is devoted to the computational analysis of geometrical nonlinear effects on a rotating detuned bladed disk. The research is focused on a computational strategy for which a nonlinear reduced-order model compatible with the consideration of both mistuning and detuning phenomena is introduced. In the present context, we limit the investigation only to the case of detuning. The paper is organized as follows. The first Section is devoted to the development of the methodology. In particular, an adapted nonlinear reduced-order basis is constructed for the detuned structure with a double projection method. Such method involves a first projection of the nonlinear dynamical response on the usual eigenmodes of vibrations followed by a Proper Orthogonal Decomposition of the related nonlinear response including the gyroscopic coupling effects. In a second Section, a numerical application concerning a realistic computational model of bladed-disk is considered. The nonlinear responses of the tuned rotating structure and of a detuned rotating structure corresponding to a given pattern are analyzed.

2 Methodology

In this Section, a methodology adapted to the nonlinear dynamical analysis of a rotating detuned bladed-disk is developed. In this context of detuning, it is assumed that the bladed-disk is constituted of N sectors that can be different from one sector to another one. A detuned bladed disk is constructed according to a given pattern $\mathcal{P}$ which defines the distribution of the different sectors that constitute the detuned bladed-disk structure. Furthermore, the constitutive equations are assumed to be linear elastic but the external loads are assumed to be sufficiently large so that the structure undergoes geometrical nonlinear effects induced by the large displacements and strains.

2.1 Nonlinear finite element model of the detuned bladed-disk

The computational model is constructed by using three-dimensional isoparametric solid finite elements. Let P be the number of available sectors whose mesh is assumed to be compatible at the interface of each sector. The full bladed-disk is constructed by the assembly of each sector type according to a given pattern $\mathcal{P}$. Let n be the number of dofs of the finite element mesh. The nonlinear finite element computational model that describes the nonlinear dynamical behavior of the detuned structure at a given rotational velocity Ω consists in finding the $\mathbb{R}^n$-vector $\mathbf{U}$ of the displacements, solution of the following nonlinear differential equation

$$[M]\ddot{\mathbf{U}}(t) + \Big([D] + [C_g(\Omega)]\Big)\dot{\mathbf{U}}(t) + \Big([K_e] + [K_c(\Omega)] + [K_g(\Omega)]\Big)\mathbf{U}(t) + \mathbf{F}^{\mathrm{NL}}(\mathbf{U}(t)) = \mathbf{F}(t)\,, \qquad (1)$$

in which the $(n \times n)$ real matrices $[M]$, $[D]$, $[C_g(\Omega)]$, $[K_e]$, $[K_c(\Omega)]$ and $[K_g(\Omega)]$ are respectively the mass matrix with symmetry and positive definiteness properties, the damping matrix with symmetry and positive semi-definiteness properties, the gyroscopic coupling matrix with antisymmetry property, the elastic stiffness matrix with symmetry and positive definiteness properties, the centrifugal stiffness matrix with symmetry and negative definiteness properties, and the geometrical stiffness matrix with symmetry and positive definiteness properties. Matrix $[K_g(\Omega)]$ is beforehand constructed using the stress state issued from a linear static analysis for which each type of sector is subjected to a centrifugal load [13]. It is assumed that the finite element matrix $[K_e] + [K_c(\Omega)] + [K_g(\Omega)]$ remains symmetric positive-definite for the considered valued of Ω. In equation (1), the $\mathbb{R}^n$-vector $\mathbf{F}(t)$ is issued from the discretization of the external loads and the $\mathbb{R}^n$-vector $\mathbf{F}^{\mathrm{NL}}(\mathbf{U}(t))$ describes the nonlinear finite element internal forces induced by the geometrical nonlinearities. In the present strategy, we are interested in analyzing the nonlinear forced response in the time domain. In consequence, the external load is defined for $t \in \mathbb{R}$. A Fourier transform performed on the solution of Eq.(1) allows then the nonlinear dynamical response in the frequency domain to be analyzed.

2.2 Nonlinear reduced-order model for a detuned bladed-disk

In this Section, the method used for constructing the nonlinear reduced-order model of the detuned bladed-disk is presented. The main idea is to use a double projection method. A first projection basis is constructed by solving the generalized eigenvalue problem related to the conservative and homogeneous dynamical equation for which the gyroscopic coupling is ignored. In a second step, this projection basis is used for constructing the nonlinear reduced-order model related to Eq.(1) (that includes the gyroscopic coupling effects). A new projection basis is then computed from this nonlinear reduced-order response with the Proper Orthogonal Decomposition method [14].

2.2.1 Construction of the first projection basis

First, let us consider the following generalized eigenvalue problem

$$\Big([K_e] + [K_c(\Omega)] + [K_g(\Omega)]\Big)\,\boldsymbol{\varphi_\alpha} = \lambda_\alpha\,[M]\,\boldsymbol{\varphi_\alpha}\,. \qquad (2)$$

Note that such projection basis does not correspond to the homogeneous conservative equation since the gyroscopic coupling term is ignored in the definition of the present generalized eigenvalue problem (if the gyroscopic coupling was taken into account, a nonsymmetric complex eigenvalue problem should be solved). In (2), the eigenvalues λ_α, $\alpha = \{1, ..., n\}$ related to the elastic modes $\boldsymbol{\varphi_\alpha}$ are sorted by increasing order $0 < \lambda_1 \leqslant \lambda_2 \leqslant \cdots \leqslant \lambda_n$. The $m \lll n$ eigenvectors related to the first m eigenvalues are computed. Let $[\Phi]$ be the $(n \times m)$ real modal matrix defined by

$$[\Phi] = [\boldsymbol{\varphi_1} \ldots \boldsymbol{\varphi_m}] \,. \tag{3}$$

2.2.2 Construction of the second projection basis

The second projection basis is obtained by considering the first nonlinear reduced-order model that is constructed by projection of Eq. (1) on the subspace spanned by $\{\boldsymbol{\varphi_1}, \ldots, \boldsymbol{\varphi_m}\}$,

$$\mathbf{U}(t) = [\Phi]\, \mathbf{Q}_0(t) \quad , \tag{4}$$

$$[\mathcal{M}_0]\ddot{\mathbf{Q}}_0(t) + \Big([\mathcal{D}_0] + [\mathcal{C}_0(\Omega)] \Big) \dot{\mathbf{Q}}_0(t) + [\mathcal{K}_0(\Omega)]\mathbf{Q}_0(t) + \boldsymbol{\mathcal{F}}^{NL}(\mathbf{Q}_0(t)) = \boldsymbol{\mathcal{F}}_0(t) \,, \tag{5}$$

in which the $\mathbb{R}^m$-vector $\mathbf{Q}_0(t) = (Q_1(t), \cdots, Q_m(t))$ is the vector of the generalized coordinates and where the generalized mass, damping, gyroscopic coupling, and stiffness matrices $[\mathcal{M}_0]$, $[\mathcal{D}_0]$, $[\mathcal{C}_0(\Omega)]$, and $[\mathcal{K}_0(\Omega)]$ are defined by

$$\begin{aligned} [\mathcal{M}_0] &= [\Phi]^T[M][\Phi] \quad , \quad [\mathcal{D}_0] = [\Phi]^T[D][\Phi] \quad , \quad [\mathcal{C}_0(\Omega)] = [\Phi]^T[C_g(\Omega)][\Phi] \\ [\mathcal{K}_0] &= [\Phi]^T \Big([K_e] + [K_g(\Omega)] + [K_c(\Omega)] \Big) [\Phi] \end{aligned} \tag{6}$$

In Eq. (5), the $\mathbb{R}^m$-vectors of the reduced external load and of the nonlinear reduced internal load are written as

$$\boldsymbol{\mathcal{F}}_0(t) = [\Phi]^T \mathbf{F}(t) \quad , \quad \boldsymbol{\mathcal{F}}^{NL}(\mathbf{Q}_0(t)) = [\Phi]^T \mathbf{F}^{\mathrm{NL}}([\Phi]\, \mathbf{Q}_0(t)) \,. \tag{7}$$

In the present context, the reduced nonlinear stiffness operators are first explicitly constructed with the finite element method from the knowledge of the projection basis [15] and the nonlinear reduced internal loads are computed from these nonlinear reduced operators. Note that such strategy is compatible with the possibility of implementing random uncertainties [16], which is not considered in the present work. The nonlinear differential equation (5) is solved in the time domain and the corresponding solution $\mathbf{Q}_0(t)$ is then used for constructing a new reduced-order basis with the POD method. Let n_t be the number of time steps and let $\{t_j, j = 1, \ldots, n_t\}$ be the sampling time points. We then introduce the $(m \times n_t)$ real matrix $[Y]$ and the $(m \times m)$ real correlation matrix $[A]$ such that

$$[Y]_{ij} = Q_{0,i}(t_j) \sqrt{t_j - t_{j-1}} \quad , \quad [A] = [Y]\,[Y]^T \,. \tag{8}$$

The projection basis is then defined as the eigenvectors $\mathcal{W}_1, \cdots, \mathcal{W}_p$ of the correlation matrix $[A]$ related to the p most contributing eigenvalues $\mu_1 \geq \cdots \geq \mu_p$ such that

$$[A]\, \mathcal{W}_\alpha = \mu_\alpha\, \mathcal{W}_\alpha \,. \tag{9}$$

Let $[\mathcal{W}]$ be the $(m \times p)$ matrix whose columns are these p eigenvectors. The new projection basis that will be used for solving the nonlinear dynamical problem is characterized by the $(n \times p)$ matrix $[\Psi]$ such that

$$[\Psi] = [\Phi][\mathcal{W}] \,. \tag{10}$$

The nonlinear reduced-order model is then obtained by projecting the solution $\mathbf{U}$ of the nonlinear finite element equation such that

$$\mathbf{U}(t) = [\Psi]\mathbf{Q}(t) \quad , \tag{11}$$

in which $\mathbf{Q}(t)$ is the $\mathbb{R}^p$-vector of the generalized coordinates solution of the nonlinear differential equation

$$[\mathcal{M}]\ddot{\mathbf{Q}}(t) + \Big([\mathcal{D}] + [\mathcal{C}(\Omega)]\Big)\dot{\mathbf{Q}}(t) + [\mathcal{K}]\mathbf{Q}(t) + \boldsymbol{\mathcal{F}}^{\mathrm{NL}}(\mathbf{Q}(t)) = \boldsymbol{\mathcal{F}}(t)\,, \tag{12}$$

in which the generalized mass, damping, gyroscopic coupling, and stiffness matrices $[\mathcal{M}]$, $[\mathcal{D}]$, $[\mathcal{C}(\Omega)]$, $[\mathcal{K}(\Omega)]$, the reduced external load vector $\boldsymbol{\mathcal{F}}(t)$ and the nonlinear reduced internal load vector $\boldsymbol{\mathcal{F}}^{\mathrm{NL}}(\mathbf{Q}(t))$ are defined similarly to (7).

This nonlinear reduced-order model can be useful for two main reasons. For instance, let us consider all the patterns related to a given number of sectors for each sector type. This leads us to parameterize the nonlinear reduced-order model with respect to a given parameter μ for which n_μ is the number of possible different patterns. At this point, the calculation of the reduced-order basis $[\Psi(\mu)]$ can be carried out for $m_\mu < n_\mu$ judicious values of μ following for instance greedy strategies. Such parameterized reduced-order basis is then wisely merged for constructing an optimal global reduced-order basis $[\Psi]$, which is use for solving any pattern of interest. Otherwise, let us consider the case for which both detuning and mistuning phenomena are investigated for a given pattern. In such case, if the mistuning is implemented through the nonparametric probabilistic approach, an optimal reduced-order basis is required in order to solve the related stochastic nonlinear differential equations.

3 Numerical application

In this section, a numerical application concerning the nonlinear dynamical analysis of a bladed-disk structure is investigated in the detuning context.

3.1 Description of the finite element computational model

The geometric features of the generating sector are summarized in Table 1. Such given reference sector will be called the sector of type 1. The computational model of this reference sector and issued from the finite element method is provided with the commercial software ANSYS. This computational model is then used for constructing the computational model of the whole tuned bladed-disk with $N = 24$ blades, which will be taken as a reference. The structure is made of steel, and is assumed to be homogeneous and isotropic with Young modulus $E = 2 \times 10^{11}\, N \times m^{-2}$, Poisson ratio $\nu = 0.3$, and mass density $\rho = 7\,650\, Kg \times m^{-3}$. The structure is clamped at the inner radius of the disk sector. The numerical finite element mesh is constituted of tridimensional solid finite elements with 20 nodes (bricks element), tridimensional solid finite elements with 13 nodes (pyramidal elements) and tridimensional solid finite elements with 10 nodes (tetrahedral elements), corresponding to a quadratic interpolation. The numerical data related to the finite element model are summarized in Table 2. Figure 1 displays the 3D finite element mesh of the bladed-disk structure.

Inner disk Radius	19.8 mm
Outer disk Radius	100 mm
Disk width	20 mm
Blade thickness at root section	4.8 mm
Blade thickness at tip section	2 mm

Table 1: Geometric parameters of the generating sector

The detuned bladed-disk structure is then considered by defining another generating sector, which is obtained by decreasing the Young modulus E of the blade of the type-1 generating sector by $25\,\%$. Consequently, there is type-1 generating sector with Young modulus $E = 2 \times 10^{11}\, N \times m^{-2}$ for the blade and a type-2

Structure	Elements	Nodes	DOFs
Blade sector	2,714	6,896	20,688
Disk sector	836	4,554	13,662
Full structure	85,200	265,080	787,176

Table 2: Numerical finite element parameters for the generating sector and for the full structure

generating sector with Young modulus $E = 1.5 \times 10^{11}\, N \times m^{-2}$ for the blade, the Young modulus of the disk remaining to $E = 2 \times 10^{11}\, N \times m^{-2}$. In the following, it is assumed that there are 2 blades of type 2 and 22 blades of type 1, which defines many possible patterns. The assembly of the full detuned bladed-disk computational model is then performed according to a given pattern.

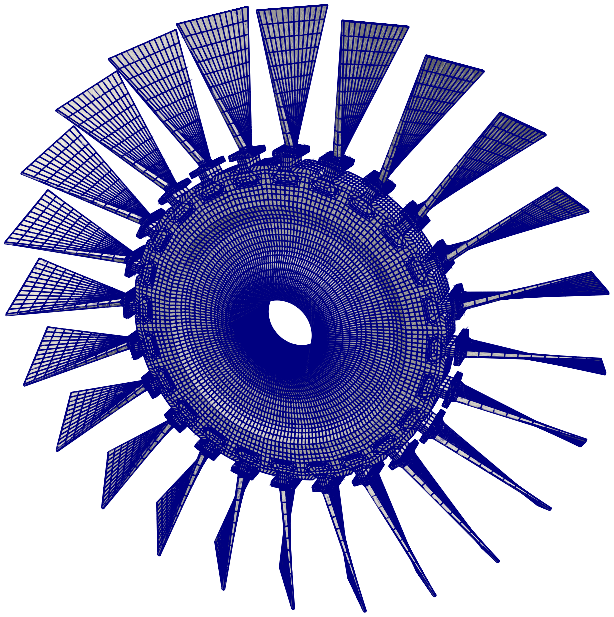


Figure 1: Finite element model of the bladed-disk.

The analysis is performed for two patterns. A cyclic pattern denoted as $\mathcal{P}_1$ that is defined by

$$\mathcal{P}_1 \;=\; [1\,1\,1\,1\,1\,1\,1\,1\,1\,1\,1\,1\,1\,1\,1\,1\,1\,1\,1\,1\,1\,1\,1\,1]\,, \tag{13}$$

and we consider a detuned pattern denoted by $\mathcal{P}_2$ and represented in Fig.2 such that

$$\mathcal{P}_2 \;=\; [1\,1\,1\,1\,1\,1\,1\,1\,2\,1\,1\,1\,2\,1\,1\,1\,1\,1\,1\,1\,1\,1\,1\,1] \quad . \tag{14}$$

3.2 Choice of the excitation force

Figure 3 represents the graph of the eigenfrequencies $\nu_\alpha = \sqrt{\lambda_\alpha}$, solution of Eq. (2) related to the tuned structure defined by $\mathcal{P}_1$ with a rotating velocity $\Omega = 465\, rad \times s^{-1}$ with respect to its circumferential wave number h.

This graph allows the excitation frequency band favorable to drastic mistuning effects to be defined. In the present case, a $h = 4$ engine-order excitation is chosen because there are two close eigenfrequencies issued from two different class of vibrational modes. In consequence, the time repartition of the load $g(t)$

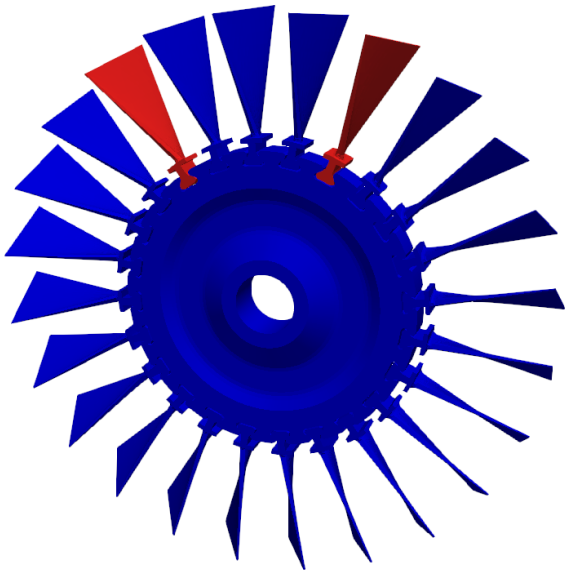


Figure 2: Pattern $\mathcal{P}_2$ for the detuned bladed-disk

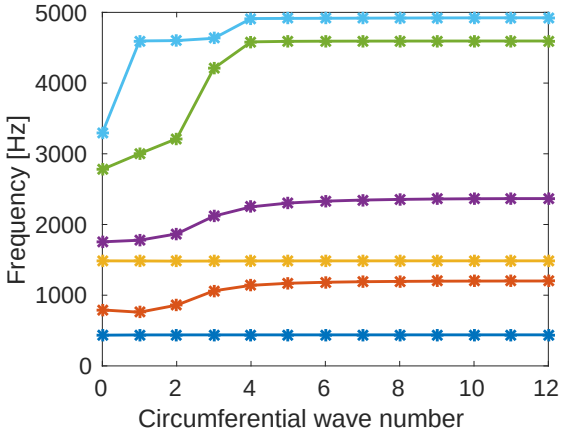


Figure 3: Graph $h \mapsto \nu_\alpha(h)$ of the eigenfrequencies ν_α related to the tuned pattern $\mathcal{P}_1$ of the rotating bladed-disk with respect to its corresponding circumferential wavenumber h.

is constructed so that an excitation frequency band $\mathbb{B}_e = [1000, 1600]\,Hz$ is uniformly excited. Let $\nu_{min} = 1\,000\,Hz$ and $\nu_{max} = 1\,600\,Hz$. We then have

$$g(t) = \sum_{i=1}^{Q} \frac{2}{\pi\, t} \sin(\pi\, \delta\nu\, t)\, \cos(2\pi s_i\, \delta\nu\, t)\,, \tag{15}$$

in which Q is chosen such that $Q = 10$. In Eq.(15), we have

$$\delta\nu = \frac{\nu_{max} - \nu_{min}}{Q} \quad , \quad s_i = \frac{\nu_{min}}{\delta\nu} + \left(i - \frac{1}{2}\right)\,. \tag{16}$$

As a consequence, the Fourier transform of function $g(t)$ is such that $|\hat{g}(2\pi\nu)| = 1$ on $\mathbb{B}_e$. Note that function $g(t)$ is theoretically defined for $t \in \mathbb{R}$ in order to consider in the time domain the problem of forced response. In the numerical process, the signal is truncated by choosing $t_{ini} = -0.065\,s$ such that $g(t_{ini}) = 0$ with a time duration $T = 0.35\,s$, ensuring the low frequencies located outside $\mathbb{B}_e$ to possibly be captured when

considering geometric nonlinear calculations. The sample frequency and the number of time steps are chosen as $\nu_e = 10\,000\,Hz$ and $n_t = 4\,096$ yielding a frequency resolution $\delta\nu_0 = 2.44\,Hz$. The dynamical analysis is carried out in the frequency band of analysis $\mathbb{B} = [0\,,\,4\,000]Hz$. Figure 4 shows the graph of the time repartition of the load $t \to g(t)$ and its Fourier transform $\nu \to |\widehat{g}(2\pi\nu)|$. The spatial repartition of the external load is a normalized vector $\mathbb{F}$ for which all directions related to the node located at the tip of each blade are simultaneously excited. The load intensity f_0 is given by $f_0 = 1.2\,N$ for which it will be shown below that geometrical nonlinear effects can be observed. The load vector $\mathbf{F}(t)$ is then defined in the time domain by

$$\mathbf{F}(t) = s_0\, g(t)\, \mathbb{F} \quad . \tag{17}$$

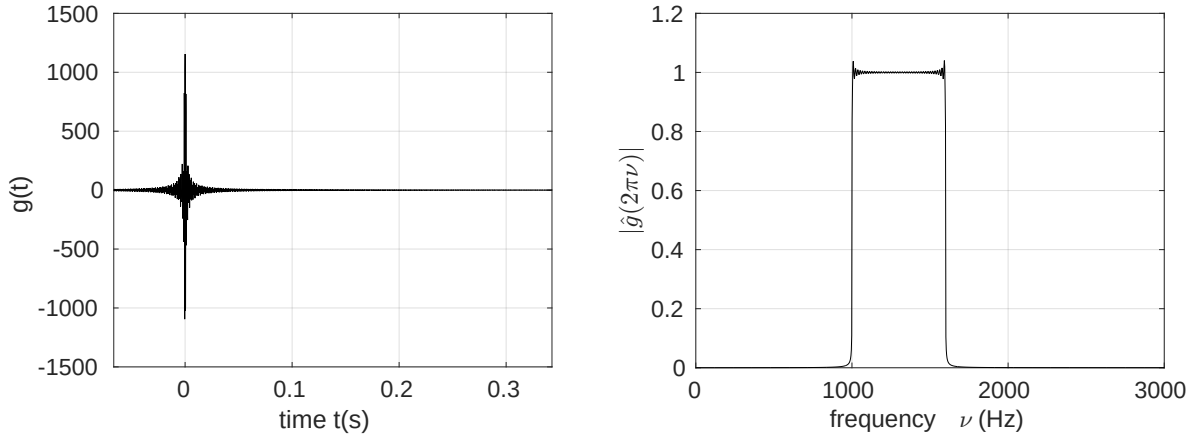


Figure 4: Representation of the external load in the time domain and in the frequency domain: graph of $t \mapsto g(t)$ (left graph) and $\nu \mapsto |\widehat{g}(2\pi\nu)|$ (right graph) for $\mathbb{B}_e = [1000\,,\,1600]\,Hz$.

3.3 Convergence analysis

Let $n_{obs} = N$ be the number of observation points located at the tip of each blade of the detuned bladed-disk. Let $\mathbf{U}_i^{obs,j}(t)$, with $j = 1, \ldots, n_{obs}$ and $i = 1, 2, 3$, be the displacement at observation node j according to dof i and let $\widehat{\mathbf{U}}_i^{obs,j}(2\pi\nu)$ be its Fourier Transform. We then define the scalar quantity W^{obs} such that

$$\widehat{W}^{obs}(2\pi\nu) = \sqrt{\sum_{j=1}^{n_{obs}} ||\hat{\mathbf{U}}^{obs,j}(2\pi\nu)||^2} \quad , \quad ||\hat{\mathbf{U}}^{obs,j}(2\pi\nu)||^2 = \sum_{i=1}^{3} |\hat{\mathbf{U}}_i^{obs,j}(2\pi\nu)|^2 \,. \tag{18}$$

Let $\widehat{W}_{LIN}^{obs,(m,p)}(2\pi\nu)$ or $\widehat{W}_{NONLIN}^{obs,(m,p)}(2\pi\nu)$ be the observation computed with the linear or with the nonlinear reduced-order model obtained with the first reduction, $p = m$, or with the second reduction, $p < m$. Subscript LIN and $NONLIN$ are omitted as soon as there is no possible confusion. A first convergence analysis is performed with respect to the number m of modes kept in the first reduced-order model. Let $Conv_1(m)$ be the function defined by

$$Conv_1(m) = \sqrt{\int_{\mathbb{B}} \left(\widehat{W}^{obs,(m,m)}(2\pi\nu)\right)^2 d\nu} \quad , \tag{19}$$

for which observation $\widehat{W}^{obs,(m,m)}(2\pi\nu)$ is constructed by solving Eq. (5). Figure 5 displays the graphs of functions $m \mapsto Conv_{1,LIN}(m)$ and $m \mapsto Conv_{1,NONLIN}(m)$. It can be seen that a good approximation is obtained for $m = 60$ for the linear case and for $m = 100$ for the nonlinear case. In the following, all the computations are carried out with $m = 100$.

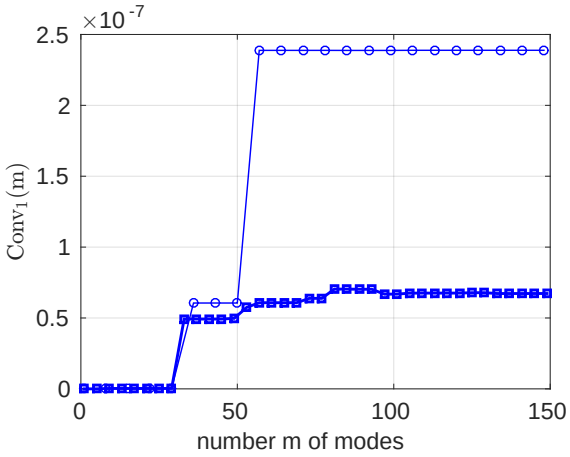


Figure 5: Convergence analysis related to the first reduced-order model: graphs of $m \mapsto Conv_{1,LIN}(m)$ related to the first linear reduced-order model (thin line, $\circ$ marker) and of $m \mapsto Conv_{1,NONLIN}(m)$ related to the first reduction (thick line, $\square$ marker).

For fixed m, a second convergence analysis is then carried out with respect to the number p of basis vectors calculated with Eqs. (9) and (10). Let $Conv_2(m,p)$ be the function defined by

$$Conv_2(m,p) = \sqrt{\int_{\mathbb{B}} \left(\widehat{W}^{obs,(m,p)}(2\pi\nu) \right)^2 d\nu} \quad , \tag{20}$$

for which observation $\widehat{W}^{obs,(m,p)}(2\pi\nu)$ is constructed by solving Eq. (12). Figure 6 displays the graph of functions $m \mapsto Conv_{2,NONLIN}(m = 100, p)$. It can be seen that a good approximation is obtained for $m = 100$ and $p = 20$, which proves the efficiency of this proposed second reduction method.

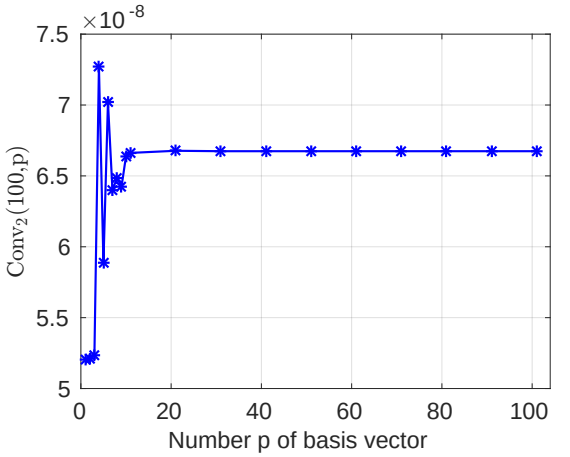


Figure 6: Convergence analysis related to the second nonlinear reduced-order model : graphs of $p \mapsto Conv_{2,NONLIN}(m,p)$ related to the second reduction (thick line, $\star$ marker).

3.4 Load sensitivity analysis

In this section, a load sensitivity is performed for pattern $\mathcal{P}_1$ in order to determine from which load intensity f_0, there are geometrical nonlinear effects in the dynamical response of the structure. Such analysis is performed by quantifying the energy outside the excitation frequency band $\mathbb{B}_e$ for f_0 belonging to $[0\,,\,1.9]\,N$.

We then define by $Conv_F(f_0)$ the quantity written as

$$Conv_F(f_0) = \frac{\sqrt{\int_{\mathbb{B}\setminus\mathbb{B}_e} \left(\widehat{W}^{obs,(m,m)}_{NONLIN}(2\pi\nu; f_0)\right)^2 d\nu}}{\sqrt{\int_{\mathbb{B}\setminus\mathbb{B}_e} \left(\widehat{W}^{obs,(m,m)}_{NONLIN}(2\pi\nu; 1.9)\right)^2 d\nu}} \quad . \tag{21}$$

Figure 7 displays the graph of $f_0 \mapsto Conv_F(f_0)$. It can be seen that geometrical nonlinear effects can be seen for $f_0 > 0.3\,N$. Figure 8 displays the graphs of $\nu \mapsto ||\widehat{\mathbf{U}}^{obs,10}_{NONLIN}(2\pi\nu)||$ corresponding to the nonlinear dynamical responses obtained with four different load intensities f_0. The yellow band represents excitation frequency band $\mathbb{B}_e$. The upper left figure clearly shows a dynamical response which remains in the linear domain since there is numerically a negligible response contribution. On the other hand, subsequent contributions with unexpected resonances appear below and beyond excitation frequency band $\mathbb{B}_e$ for larger load intensities.

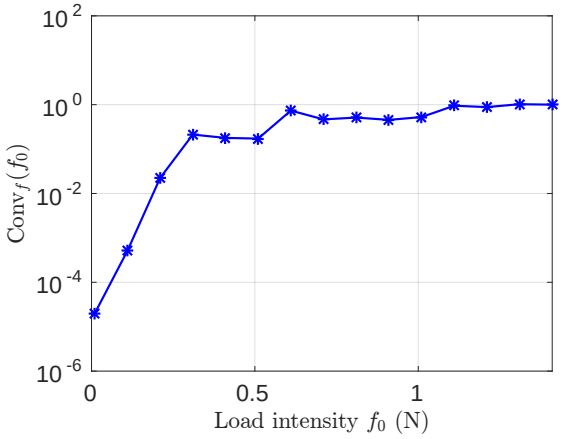


Figure 7: Sensitivity analysis with respect to the load intensity : graph of $f_0 \mapsto Conv_F(f_0)$.

3.5 Nonlinear dynamical response analysis

In this paragraph, a nonlinear dynamical analysis is performed for both tuned and detuned patterns $\mathcal{P}_1$ and $\mathcal{P}_2$. The time domain observation is chosen as $U_2^{obs,j_0}(t)$, which corresponds to the transverse dof expressed in the local frame related to observation node number j_0. The observation node is defined by

$$j_0 = \arg\left\{\max_j |||\mathbf{U}^{obs,j}|||\right\} \quad \text{with} \quad |||\mathbf{U}^{obs,j}||| = \max_t ||\mathbf{U}^{obs,j}(t)|| \quad , \tag{22}$$

in which $||\mathbf{U}^{obs,j}(t)||$ is defined similarly to Eq. (18). The frequency domain observation is then chosen as $||\widehat{\mathbf{U}}^{obs,j_0}(2\pi\nu)||$. The linear and the nonlinear analyses are presented with a load intensity $f_0 = 0.60\,N$ for both patterns $\mathcal{P}_1$ and $\mathcal{P}_2$, which correspond to moderate geometrical nonlinear effects. Figure 9 displays the graphs of $t \mapsto U^{obs,j_0}_{2,LIN}(t)$ for both patterns. It can be seen that both tuned and detuned structures yield different responses in the time domain. Figure10 displays the graphs of $t \mapsto U^{obs,j_0}_{2,NONLIN}(t)$ for both patterns. By comparing these figures, it can be seen that there are subsequent geometrical nonlinear effects. Furthermore, the observed nonlinear time response related to the considered detuned pattern $\mathcal{P}_2$ is clearly irregular, suggesting numerous resonances contributions outside $\mathbb{B}_e$. The nonlinear analysis is then carried out in the frequency domain by using a Fourier transform. Figure11 displays both graphs of $\nu \mapsto ||\widehat{\mathbf{U}}^{obs,j_0}_{LIN}(2\pi\nu)||$ and $\nu \mapsto ||\widehat{\mathbf{U}}^{obs,j_0}_{NONLIN}(2\pi\nu)||$ for both patterns. The main effect induced by the present detuning is to shift the

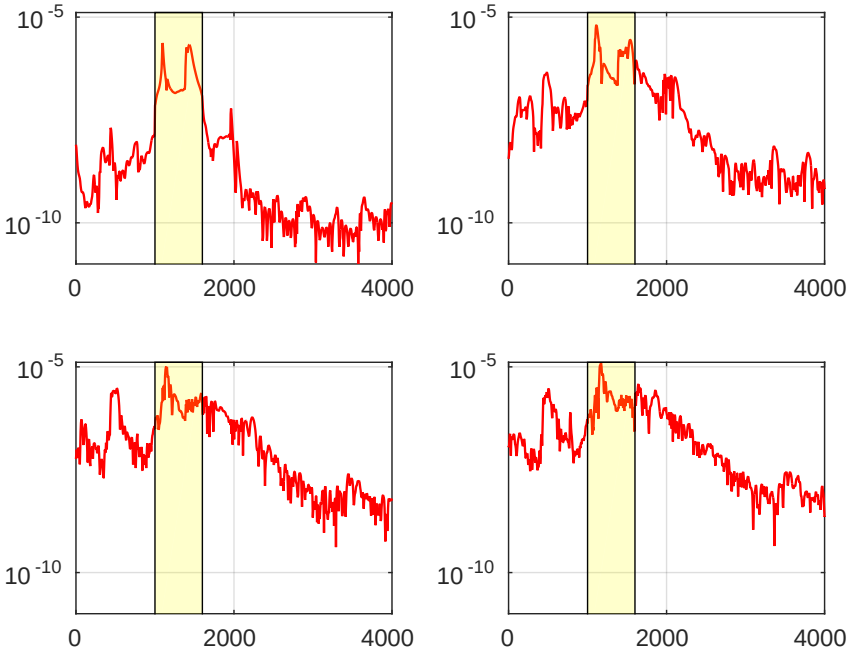


Figure 8: Sensitivity analysis with respect to the load intensity : representation of excitation frequency band $\mathbb{B}_e$ (light yellow zone), graphs of $\nu \mapsto ||\widehat{\mathbf{U}}^{obs,10}_{NONLIN}(2\pi\nu)||$ for $f_0 = 0.17\,N$ (upper left figure), $f_0 = 0.64\,N$ (upper right figure), $f_0 = 1.43\,N$ (lower left figure), $f_0 = 1.90\,N$ (lower right figure)

two main resonances related to the linear response to the left in the excitation frequency band. It is clearly observed that the geometrical nonlinear effects are stronger for the considered detuned pattern $\mathcal{P}_2$. For both patterns secondary resonances induced by the geometrical nonlinear effects appear below and above the excitation frequency band. This phenomenon is amplified for detuned pattern $\mathcal{P}_2$ and unexpected resonances with non negligible amplitudes exist for higher frequencies around $3\,000\,Hz$.

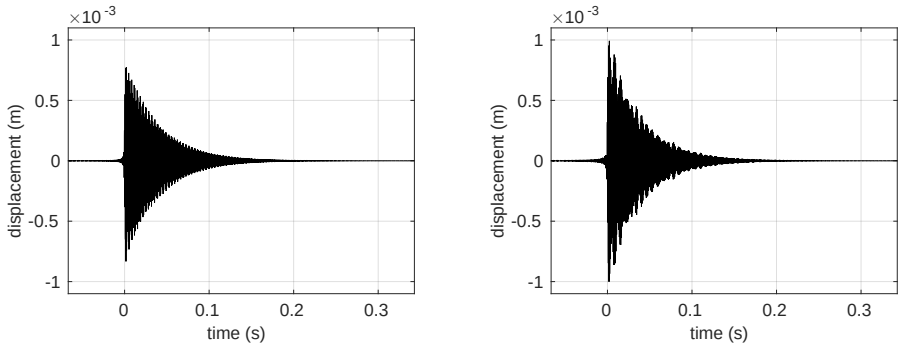


Figure 9: Linear dynamical analysis in the time domain: graphs of $t \mapsto U^{obs,j_0}_{2,LIN}(t)$ corresponding to patterns $\mathcal{P}_1$ (left figure) and $\mathcal{P}_2$ (right figure).

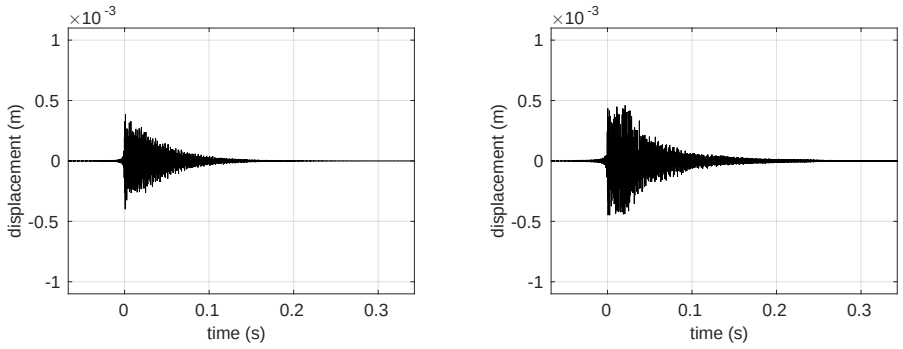


Figure 10: Nonlinear dynamical analysis in the time domain: graphs of $t \mapsto U^{obs,j_0}_{2,NONLIN}(t)$ corresponding to patterns $\mathcal{P}_1$ (left figure) and $\mathcal{P}_2$ (right figure).

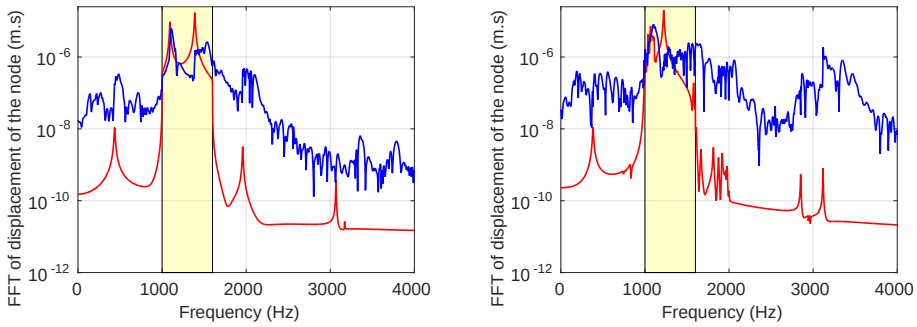


Figure 11: Nonlinear dynamical analysis in the frequency domain: graphs of $\nu \mapsto ||\widehat{\mathbf{U}}^{obs,j_0}_{LIN}(2\pi\nu)||$ (red line) and $\nu \mapsto ||\widehat{\mathbf{U}}^{obs,j_0}_{NONLIN}(2\pi\nu)||$ (blue line) corresponding to patterns $\mathcal{P}_1$ (left figure) and $\mathcal{P}_2$ (right figure).

4 Conclusions

A methodology that allows the nonlinear dynamical analysis of rotating detuned structures is proposed in the context of geometrical nonlinearities. It should be noted that the nonlinear reduced-order model presented in this work is also adapted for simultaneously modeling both detuning and mistuning.The results validate the numerical efficiency of the method and highlight the indirect excitation of the structure through the geometrical nonlinearities. Note that the numerical analysis is carried out on one tuned and one detuned pattern. The pattern optimization regarding the detuning is not considered in this work.

Acknowledgements

SafranTech is gratefully acknowledged for the permission to publish this work.

References

[1] D.J. Ewins. The effects of detuning upon the forced vibrations of bladed disks. *Journal of Sound and Vibration*, 9(1):65–79, 1969.

[2] D.S. Whitehead. The maximum factor by which forced vibration of blades can increase due to mistuning. *ASME Journal of Engineering for Gas Turbines and Power*, 120(1):115–119, 1998.

[3] M.P. Castanier, G. Ottarson, and C. Pierre. Reduced order modeling technique for mistuned bladed disks. *Journal of Vibration and Acoustics*, 119(3):439–447, 1997.

[4] M-T. Yang and J.H. Griffin. A reduced-order model of mistuning using a subset of nominal system modes. *ASME Journal of Engineering for Gas Turbines and Power*, 123(3):893–900, 2001.

[5] R. Bladh and M.P. Castanier. Component-mode-based reduced order modeling techniques for mistuned bladed disks-part 1: Theoretical models. *Journal of Engineering for Gas Turbines and Power*, 123(1):89–99, 2001.

[6] E. Capiez-Lernout, C. Soize, and M. Mbaye. Mistuning analysis and uncertainty quantification of an industrial bladed disk with geometrical nonlinearity. *Journal of Sound and Vibration*, 356:124–143, 2015.

[7] Aurelien Grolet and Fabrice Thouverez. Computing multiple periodic solutions of nonlinear vibration problems using the harmonic balance method and groebner bases. *Mechanical Systems and Signal Processing*, 52:529–547, 2015.

[8] C. Soize. A nonparametric model of random uncertainties for reduced matrix models in structural dynamics. *Probabilistic Engineering Mechanics*, 15(3):277–294, 2000.

[9] MP Mignolet and Christian Soize. Nonparametric stochastic modeling of linear systems with prescribed variance of several natural frequencies. *Probabilistic Engineering Mechanics*, 23(2-3):267–278, 2008.

[10] Matthew P Castanier and Christophe Pierre. Using intentional mistuning in the design of turbomachinery rotors. *AIAA journal*, 40(10):2077–2086, 2002.

[11] ByeongKeun Choi. Pattern optimization of intentional blade mistuning for the reduction of the forced response using genetic algorithm. *KSME international journal*, 17(7):966–977, 2003.

[12] M. Mbaye, C. Soize, J.-P. Ousty, and E. Capiez-Lernout. Robust analysis of design in vibration of turbomachines. *Journal of Turbomachinery*, 135(2):021008, 2013.

[13] C. Desceliers and C. Soize. Nonlinear viscoelastodynamic equations of three-dimensional rotating structures in finite displacement and finite element discretization. *International Journal of Nonlinear Mechanics*, 39:343–368, 2004.

[14] L. Sirovich. Turbulence and the dynamics of coherent structures. i. coherent structures. *Quarterly of applied mathematics*, 45(3):561–571, 1987.

[15] E. Capiez-Lernout, C. Soize, and M.-P. Mignolet. Computational stochastic statics of an uncertain curved structure with geometrical nonlinearity in three-dimensional elasticity. *Computational Mechanics*, 49(1):87–97, 2012.

[16] M.-P. Mignolet and C. Soize. Stochastic reduced order models for uncertain geometrically nonlinear dynamical systems. *Computer Methods in Applied Mechanics and Engineering*, 197(45-48):3951–3963, 2008.

A novel identification tool for rotors working under non-stationary conditions based on the IAS

E.Sghaier [1], **A.Bourdon** [1], **D.Remond** [1], **J-L.Dion**[2], **N.Peyret**[2]
[1] University of Lyon, LaMCoS, INSA-Lyon, CNRS UMR5259, F-69621, France
e-mail: **emna.sghaier@insa-lyon.fr**

[2] Laboratoire QUARTZ EA 7393 - SUPMECA Paris, 3 rue Fernand Hainaut, 93400 Saint Ouen, France

Abstract
The aim of this work is to provide a new model describing the dynamic behavior of the rotating machinery working under non-stationary conditions with no assumption on the IAS. This new model will provide an identification tool for the rotor parameters. An example of a simple rotor made of a flexible shaft, a rigid disk, bearings and a mass unbalance is considered. The model shows a coupling between the torsional and flexural behavior and it is proven that, owing to this coupled behavior, the signal of the IAS contains information about, not only the rotation frequency of the response of the rotor, but also about its flexural behavior, when operating under non-stationary conditions.

1 Introduction

Rotor dynamics are widely present in different engineering fields. In the automotive field for example, with the growing use of the electric motors rotating at very high speeds, it has become crucial to understand the dynamic behavior of rotors spinning at very high velocity especially when going through critical speeds. This critical working condition, as well as the presence of bearings or gears in the rotor structure, leads to a fluctuation of the instantaneous angular speed (IAS). However, conventional vibration-monitoring techniques are based on some assumptions on the IAS. The latter is often considered either constant or following a perfect linear or exponential law of variation [1]. Those assumptions lead to models which are not able to simulate rotating machinery under fluctuating load conditions.
Even though the major part of the scientific works on rotor dynamics focus on the study of the stationary working conditions, the transient response analysis is considered as the most inclusive analysis since it allows the study of different working conditions of the rotating machinery as the start up and shut down processes, stability, and impact [2].
Since many rotors operate above their critical speeds, a main interest was particularly given to the study of the behavior of rotating machinary when going through one or more critical speeds. Al-Bedoor [3] developed a model for the coupled torsional and lateral vibrations of unbalanced rotors that accounts for the rotor-to-stator rubbing. He showed that a split in resonance is observed due to the rubbing condition when the rotor torsional flexibility is considered. Zhou et Shi [4] gave an analytical solution for the unbalance response of the Jeffcott rotor during acceleration.They showed that, quantitatively, the motion consists of three parts: a transient vibration at damped natural frequency, a synchronous vibration with the frequency of instantaneous 'synchronous' frequency, and a suddenly occurring vibration at damped natural frequency. Li and Singh [5] studied also the analytical solutions of the transient response but focused on the envelopes of the lateral displacement, velocity and acceleration of a linear torsional oscillator excited by an instantaneous sinusoidal torque. They also gave a new analytical approximation to find the maximum amplifications and corresponding peak frequencies.

When the dynamic model takes as an input the induced driving torque and not the speed of rotation as a function of time, one must add an equation that describes how the energy source supplies the energy to the equations that govern the corresponding dynamical system. Mutual interaction between the driving source and the rotor motion is observed and we deal in this case with non-ideal problem of passage through resonance or what is also called sommerfeld effect [6]. This interaction manifests itself as a modification of the motor frequency or regime of operation near the resonance and changes in the stable-unstable portions of the dynamical system response [7].
In the following study, since we consider as a given of the dynamic problem the induced torque and as an unknown the speed of rotation (IAS), we will be dealing with a non-ideal system. A new dynamic model is then built to simulate the non-stationnary working conditions especially when going through one or more critical speeds. This model is developeed in order to serve as a tool for identification, based on the IAS, for certain parameters of the system as the mass unbalance and damping.

2 New model describing the rotordynamics

We consider a simple idealized rotor made of a flexible shaft, a rigid disk and supported by flexible damped bearings. The main excitation of the rotor is the mass unbalance (fig.3). In our approach we consider that a torque is induced to the rotating machinary and we make no preliminary assumption on the rotating speed.

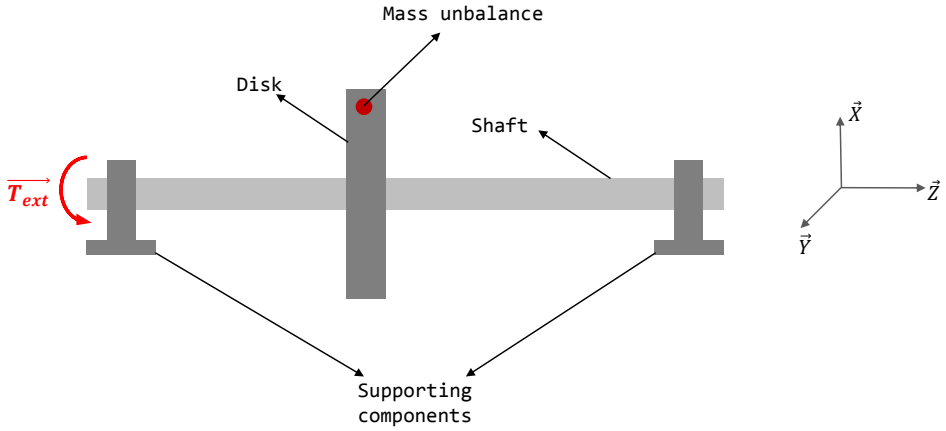


Figure 1: Rotor simplified model

Euler angles are used to discribe the motion of the rotor. The coordinate systems used in developing the model are shown in the following figure, wherein, (XYZ) is the fixed reference frame and (UVW) is the rotating reference frame which coincides with the principle axis of the cross section of the shaft. A first rotation by an angle Φ about the $Z-$axis is done then by an angle θ about the new X'-axis and finally by an angle Ψ about the final W'-axis. The latter, combined to the torsional deformation, is considered as an unknown of the dynamic problem.

The angular displacement about the X and Y axis as well as the spinning angle about the Z axis are calculated using Euler angles as follows:

$$\theta_x = \theta.cos(\phi) \tag{1a}$$

$$\theta_y = \theta.sin(\phi) \tag{1b}$$

$$\theta_z = \phi + \psi \tag{2}$$

It is very important to notice here that θ_z accounts for both the free body rotating motion as well as for the torsional deformation.

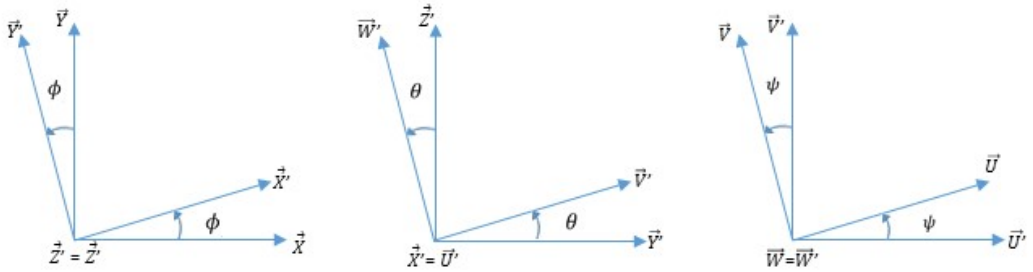


Figure 2: Euler angles

First the kinetic energy calculation is done. This energy is obtained by the sum of the contribution of the different components of the rotor, namely the disk, the shaft and the mass unbalance.

$$T = T_D + T_s + T_u \tag{3}$$

The finite element method is used and the dsiplacement fields are approximated using shape functions. We denote by $\{\delta\}$ the nodal displacement vector. Then the Lagrange equations are applied, which leads to the following matrix form:

$$\begin{aligned} \frac{d}{dt}\left(\frac{\partial T}{\partial \dot{\delta}}\right) - \frac{\partial T}{\partial \delta} = &([M_{Dconst}] + [M_{Dvar}(\{\delta_c\})])\left\{\ddot{\delta}\right\} + \left[C_D(\dot{\theta}_z)\right]\left\{\dot{\delta}\right\} \\ &+ [M_u(\theta_z)]\left\{\ddot{\delta}\right\} + \{F_{nl_u}(\theta_z)\} \\ &+ [M_s]\{\ddot{\delta}\} + [S_{gyr}(\{\delta\})]\{\ddot{\delta}\} + \{Fnl_{gyr}(\{\dot{\delta}\})\} \end{aligned} \tag{4}$$

where:

- $[M_{Dconst}]$ and $[M_s]$ are the classical mass matrices of the disk and the shaft respectively.
- $\left[C_D(\dot{\theta}_{z_c})\right]$ is the classical skew-matrix related to the gyroscopic effects of the disk.
- $\{F_{nl_u}(\theta_{z_c})\}$ is the centrifugal force resulting from the mass unbalance and proportional to the square of the spinning speed.

The two matrices $[M_{Dvar}]$ and $[M_u]$ respectively related to the disk and the mass unbalance result from the assumption of non-stationnary working condition where:

$$[M_{Dvar}(\{\delta\})] = \begin{bmatrix} 0 & 0 & 0 & 0 & 0 & 0 \\ 0 & 0 & 0 & 0 & 0 & 0 \\ 0 & 0 & 0 & 0 & 0 & 0 \\ 0 & 0 & 0 & 0 & 0 & \frac{I_{Dw}}{2}\theta_{y_c} \\ 0 & 0 & 0 & 0 & 0 & -\frac{I_{Dw}}{2}\theta_{x_c} \\ 0 & 0 & 0 & \frac{I_{Dw}}{2}\theta_{y_c} & -\frac{I_{Dw}}{2}\theta_{x_c} & 0 \end{bmatrix} \tag{5}$$

$$[M_u(\theta_z)] = d\, m_u \begin{bmatrix} 0 & 0 & 0 & 0 & 0 & cos(\theta_{z_c}) \\ 0 & 0 & 0 & 0 & 0 & -sin(\theta_{z_c}) \\ 0 & 0 & 0 & 0 & 0 & 0 \\ 0 & 0 & 0 & 0 & 0 & 0 \\ 0 & 0 & 0 & 0 & 0 & 0 \\ cos(\theta_{z_c}) & -sin(\theta_{z_c}) & 0 & 0 & 0 & d \end{bmatrix} \tag{6}$$

We notice that, by considering non-stationnary working conditions, matrices with extra-diagonal terms appear in the equation of dynamics of the rotor. Those terms clearly include coupling between the flexural and torsional degrees of freedom.
Finally, the matrix $[S_{gyr_e}]$ and the force vector $\{Fnl_{gyr_e}\}$ derive from the new formulation of the gyroscopic effect of the shaft under non-stationnary regime such as:

$$\begin{aligned} [S_{gyr_e}(\{\delta\})] = &- \langle N_3(l)\rangle^t \{\delta\}^t [M_{67}^g(l)]^t - [M_{67}^g(l)]\{\delta\}\langle N_3(l)\rangle \\ &+ \left\langle \frac{\partial N_3}{\partial z} \right\rangle^t \{\delta\}^t [M_{67}^{g*}(l)]^t + [M_{67}^{g*}(l)]\{\delta\} \left\langle \frac{\partial N_3}{\partial z} \right\rangle \end{aligned} \tag{7}$$

and,

$$\begin{aligned} \{Fnl_{gyr}(\{\dot\delta\},\{\dot\delta\})\} = &- \langle N_3(l)\rangle^t \left(\{\dot\delta\}^t [M_{67}^g(l)]\{\dot\delta\} \right) \\ &- 2\left(\langle N_3(l)\rangle \{\dot\delta\} \right) \left([M_{67}^g(l)]\{\dot\delta\} \right) \\ &+ \left\langle \frac{\partial N_3}{\partial z} \right\rangle^t \left(\{\dot\delta\}^t [M_{67}^{g*}(l)]\{\dot\delta\} \right) \\ &+ 2\left(\left\langle \frac{\partial N_3}{\partial z} \right\rangle \{\dot\delta\} \right) \left([M_{67}^{g*}(l)]\{\dot\delta\} \right) \end{aligned} \tag{8}$$

where $\langle N_3\rangle$ is a vector with polynomial shape functions of first order. $[M_{67}^g]$ and $[M_{67}^{g*}]$ are skew-symmetric matrices with constant terms obtained by the multiplication of shape function vectors.

Once the strain energy of the shaft and the virtual works of the bearings, assumed to be with linear stiffness and damping are calculated, the classical stiffness matrix is obtained and we finally write the equation of the dynamics of rotating shaft element such as:

$$\begin{aligned} ([M_s] + [M_{D_{const}}])\{\ddot\delta\} + [C_s]\{\dot\delta\} + [K_c]\{\delta\} = \\ - ([S_{gyr}(\{\delta\})] + [M_{D_{var}}(\{\delta\})] + [M_u(\theta_{z_c})])\{\ddot\delta\} \\ - \left[C_D(\dot\theta_{z_c})\right]\{\dot\delta\} \\ - \left(\{Fnl_{gyr}(\{\dot\delta\})\} + \{F_{nl_u}(\theta_{z_c})\} \right) \\ + \{F_{ext}\} \end{aligned} \tag{9}$$

3 Results and discussions

We consider an example of an idealized rotor with the properties detailed in table 1. The rotor is made of a flexible shaft, a rigid disk and is excited by the presence of a mass unbalance.

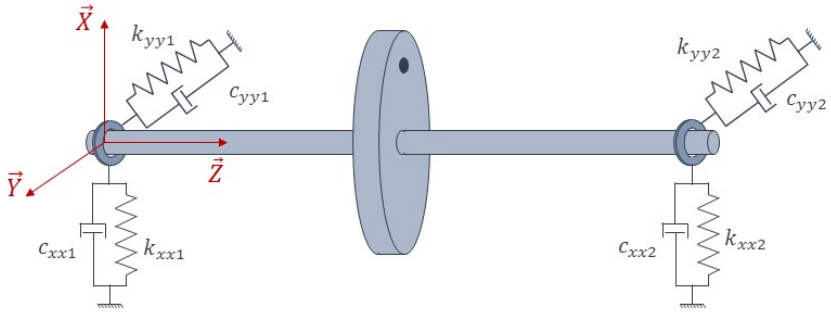


Figure 3: rotor exemple

Symbol	Quantity	Value
L	shaft length	$0.6\ m$
R_1	shaft radius	$0.01\ m$
R_2	disk radius	$0.08\ m$
h	thickness of the disk	$0.03\ m$
ρ	mass per unit volume	$7800\ kg.m^{-3}$
E	young modulus	$2.10^{11}\ N.m^{-2}$
m_u	mass unbalance	1% of the mass of the disk
d	eccentricity of the mass unbalance	0.1m
k_{xx1}, k_{xx2}	stiffness along x-axis of the left and right bearings	$1.e^8\ N.m^{-1}$
k_{yy1}, k_{yy2}	stiffness along y-axis of the left and right bearings	$1.e^8\ N.m^{-1}$
c_{xx1}, c_{xx2}	damping along x-axis of the left and right bearings	$2e2\ N.s.m^{-1}$
c_{yy1}, c_{yy2}	damping along y-axis of the left and right bearings	$2e2\ N.s.m^{-1}$

Table 1: Proprieties of the studied rotor

In this exemple we simulate the start up of a rotor. Therefore a driving torque following the law shown in figure 4 is induced to the system. The aim of applying a constant torque before the linear time-varying one is to better intialize the simulation for the non-stationary regime. It is important to mention that, for this exemple of rotor with the mentioned properties, the first critical speed is at 2527 rpm and the second one is at 26364 rpm. During the accelerarion period the rotor will go through the two mentioned critical speeds.

The simulation results are used for time-frequency analysis for both lateral displacement and instantaneous angular speed.
Figure 5 shows the results for the lateral displacement. As we can see, both the excitation frequency f_e and the first natural frequency f_1 contributes to the motion of the rotor. The results are qualitatively coherent with the analytical solution proposed by Zhou et Shi [4] saying that, during acceleration, the motion consists of three parts: a transient vibration at damped natural frequency, a synchronous vibration with the frequency of instantaneous 'synchronous' frequency, and a suddenly occurring vibration at damped natural frequency. We can see that the rotor has more difficulties crossing the second natural frequency than the first one.

The spectrogram of the instantaneous angular speed (fig.6) shows a coupling between the excitation frequency f_e and the first eigen frequency f_1. This simulation result proofs that the IAS, whose analyses is

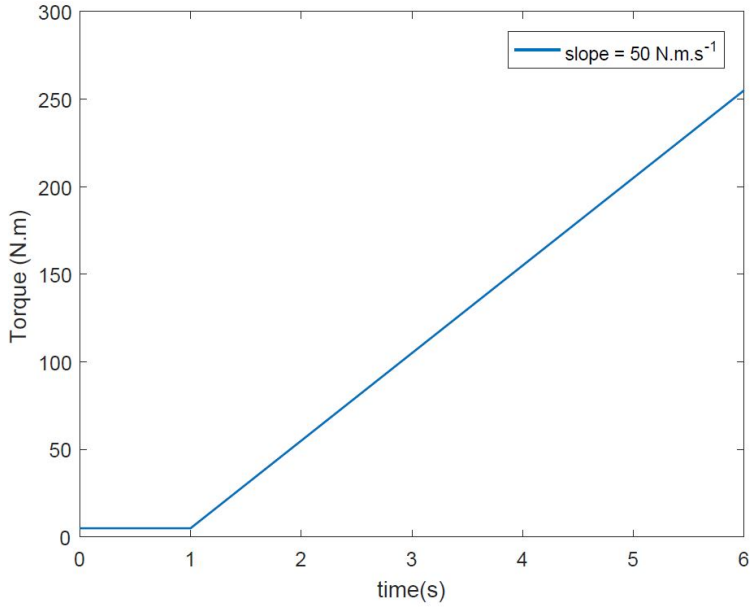


Figure 4: Torque law as a function of time

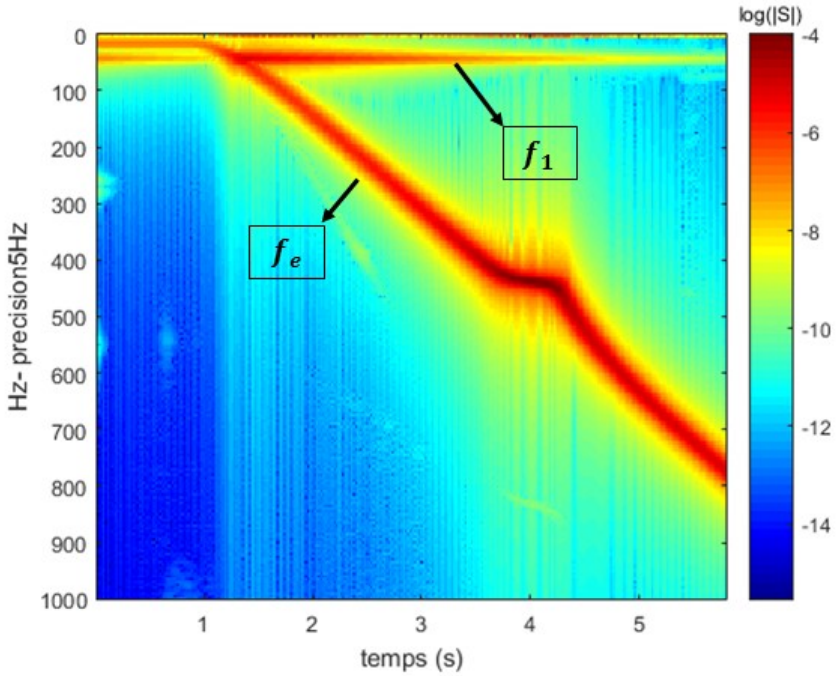


Figure 5: Spectrogram of the lateral displacement

neglected by previous research works, contains informations about the system dynamic properties. Considering the IAS as an unknown of the dynamic problem and not as a given law as a fonction of time provides us with a new source of informations about the rotor dynamics. Further analysis using Kalman filters will allow a better exploitation of the IAS in order to do a better tracking of the frequencies in the time-frequency

domain.

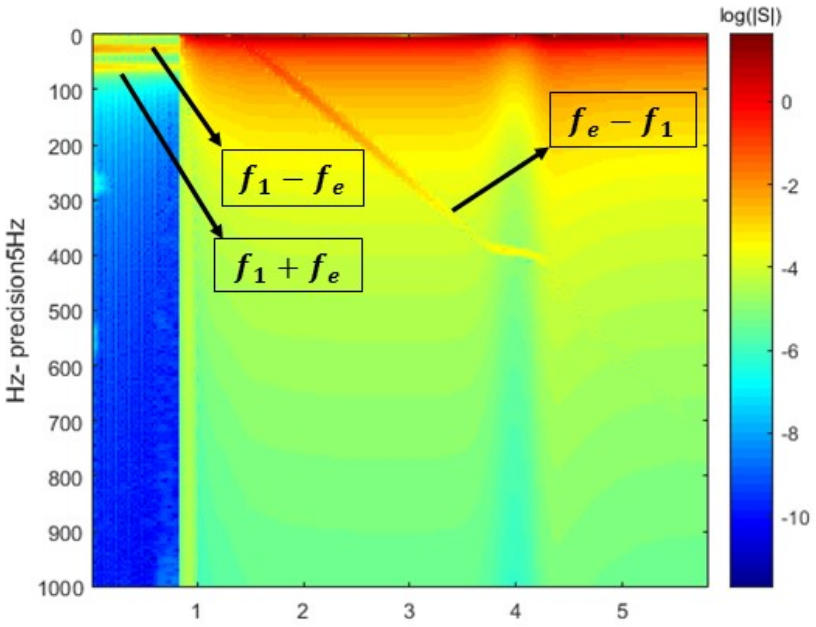


Figure 6: Spectrogram of the instantaneous angular speed

4 Conclusion

The big majority of previous works on the non-stationary rotordynamics were conducted under the assumption of a given law of the rotational speed. In our study, a new dynamic model is built considering no assumption on the IAS. It was shown, for a simple exemple of rotors, that when the IAS is considered as an unknown of the dynamic problem,it is highly influenced by the rotor dynmic properties. Based on the obtained results, we assume that the IAS is a physical quantity which is rich enough with informations about the studied system and that a better analysis using kalman filters is of big intesrest in order to identify the system parameters using the new proposed dynamic model for non-stationnary rotor dynamics.

References

[1] Michel Lalanne and Guy Ferraris. *Rotordynamics prediction in engineering*. Wiley, 1998.

[2] RG Kirk and EJ Gunter. Transient response of rotor-bearing systems. *Journal of Engineering for Industry*, 96(2):682–690, 1974.

[3] B O Al-bedoor. Transient torsional and lateral vibrations of unbalanced rotors with rotor-to-stator rubbing. *Journal of Sound and vibration*, 229(3):627–645, 2000.

[4] Shiyu Zhou and Jianjun Shi. The analytical imbalance response of jeffcott rotor during acceleration. *Journal of manufacturing science and engineering*, 123(2):299–302, 2001.

[5] Laihang Li and Rajendra Singh. Analysis of transient amplification for a torsional system passing through resonance. *Proceedings of the Institution of Mechanical Engineers, Part C: Journal of Mechanical Engineering Science*, 229(13):2341–2354, 2015.

[6] Arnold Sommerfeld. Beiträge zum dynamischen ausbau der festigkeitslehe. *Physikal Zeitschr*, 3:266–286, 1902.

[7] José Manoel Balthazar, Dean T Mook, Hans Ingo Weber, Reyolando MLRF Brasil, A Fenili, D Belato, and JLP Felix. An overview on non-ideal vibrations. *Meccanica*, 38(6):613–621, 2003.

Influence of internal friction dampers on global dynamics of discrete cyclic structure

M. Byrtus [1], **M. Hajžman** [1], **L.Pešek** [2], **L. Půst** [2]
[1] University of West Bohemia, Faculty of Applied Sciences,
NTIS – New Technologies for Information Society,
Technická 8, Plzeň, Czech Republic
e-mail: **mbyrtus@rice.zcu.cz**

[2] Institute of Thermomechanics of the CAS, v. v. i.,
Dolejškova 1402/5, Praha, Czech Republic

Abstract
This paper deals with vibration of a bladed disk containing internal friction dampers (FD). The disk is considered as a weakly coupled discrete cyclic structure where the blades are moreover mutually coupled by means of friction couplings. The global dynamics of the structure is studied. First, two limit cases are considered: unlocked FD and completely locked FD. Further, the behaviour of the structure is analysed with respect to time-dependent excitation (external force pulses). Different local behaviour is analysed along with discontinuity induced bifurcations like crossing-sliding and adding-sliding bifurcations. The stress is laid on the evaluation of dissipated power in FD per a defined time frame.

1 Introduction

Cyclic structures are commonly used in large number of mechanical and civil engineering applications. Typically, bladed disks assemblies represent such a system with cyclic symmetry. These structures usually involve small deviations from the idealized structural models and can show unexpected localized behaviour in the response of the system [3, 10, 11]. In turbomachinery and in other applications, these structures are subjected to non-stationary, high-amplitude external excitation which can exhibit unstable behaviour of the structure considering different bifurcation scenarios [6, 2, 4]. To capture dynamical properties of the structure more accurately, special reduced-order methods are employed [5, 1]. Such a large structural models need to be validated using experimental setups. To suppress large amplitude vibrations regimes, different damping mechanism are employed. Specifically, in turbomachinery, friction couplings by means of wedge or shrouding dampers are designed and their damping capability is studied in detail [8].

This paper deals with vibration of a bladed disk containing internal friction dampers (FD). The disk is considered as a weakly coupled discrete cyclic structure where the blades are moreover mutually coupled by means of friction couplings. The global dynamics of the structure is studied. First, two limit cases are considered: unlocked FD and completely locked FD. Further, the behaviour of the structure is analysed with respect to time-dependent excitation (external force pulses). The main goal is to study the behaviour of FD in dependence on amplitude of normal contact forces and on the shape of the excitation. There appear different phases of motion with locally either locked or unlocked friction dampers. The stress is laid on the evaluation of dissipated energy in FD per a defined time frame.

The main contribution of the work lays in the investigation of a cyclic symmetric structure with respect to resonance dynamical states which are undesirable from operational point of view and which can be suppressed by means of properly designed friction dampers. A case study is performed using a structural and

experimental data from an experimental set-up of a bladed wheel which has been designed installed at Institute of Thermomechanics of the Czech Academy of Sciences in Prague. All the analyses are performed using an in-house computational model created in MATLAB based on the developed mathematical models and corresponding modelling methodology.

2 Problem description

2.1 Motivation

In many engineering applications, especially in turbine bladed disk, the usage of damping elements is necessary. The friction dampers play a significant role and are often used. Their efficiency depends on complex tuning of the system for a particular application with respect to operational states. For the purpose to analyse the influence of friction dampers experimentally and to validate different computational models an experimental bladed disk has been designed and manufactured [9], see Fig. 1.

The experimental disk is equipped with thirty prismatic blades. Picture of a design of bladed wheels with so-called tie-boss couplings and additional weights is shown in Fig. 1. The tie-bosses are shoulders of blades whose ends are in a contact with shoulders of the neighbouring blades. The ends of the shoulders are cut so that its areas, i.e. contact areas, are parallel to a direction of the flexural vibration of a single blade.

Because of setting up the pre-stress in the contacts between the tie-bosses of the neighbouring blades, the tie-bosses were consisted of extensible shoulders screwed with left (right side) and right (left side shoulder) winding into the suspension bolt that was fixed to the blade by two nuts. By screwing the bolt in the nuts the shoulders extend simultaneously on both sides. The detail of the tie-boss structure is in Fig. 1, too. Each blade is fixed to the disk by the system of two small finger consoles. Bottom console is bolted down to the disk and upper console is bolted to the blade. The consoles are bolted together and their mutual position is set by angle 45° before their bolting together. At the end of the blades an additional mass is bolted to lower its first flexural eigen-frequency.

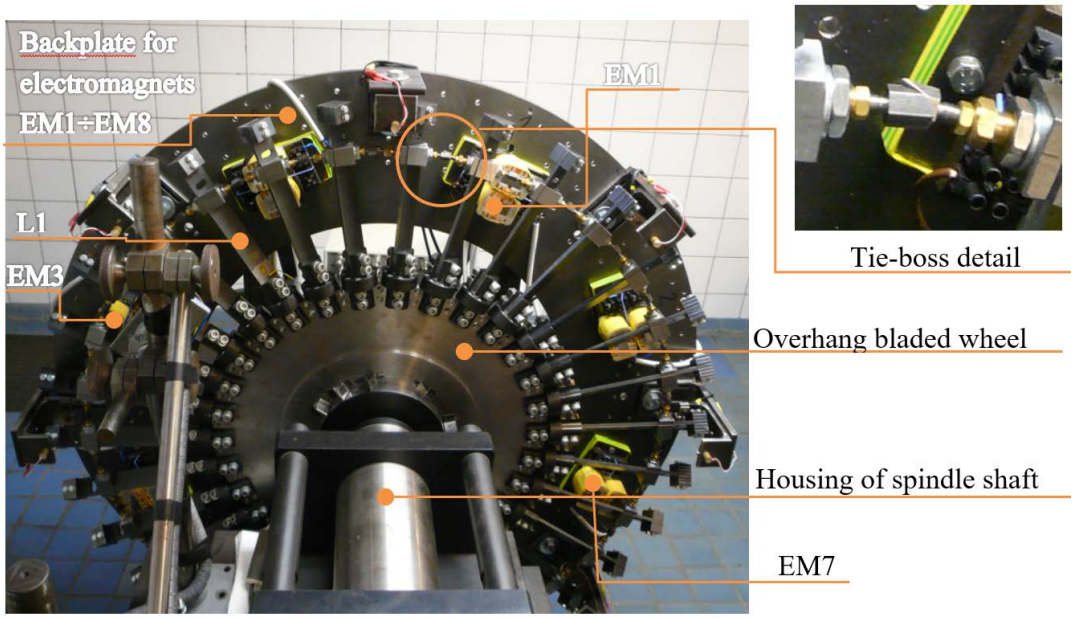


Figure 1: Experimental bladed disk

2.2 Dry friction force modelling

The way how is the dry friction modelled plays a key role in the dynamics which can be excited. The dry friction coupling allows two modes of motion: sticking and sliding. In the literature, there exist many approaches (models) which are capable to capture basic properties of the dry friction coupling [7, 2]. The models differ each other especially by the way how they can capture the sticking and sliding phases of the motion within the dry friction coupling. Three different models for unidirectional motion are depicted in Fig. 2.

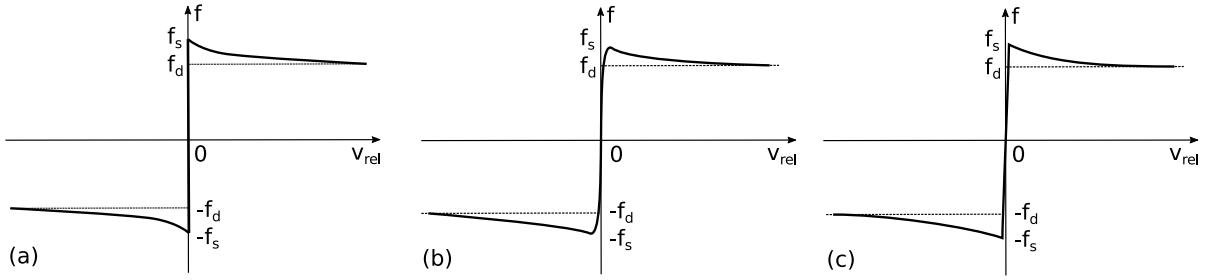


Figure 2: Friction characteristics

The model in Fig. 2 a can be managed by using the tools of non-smooth mechanics, one can express the friction coefficient by means of inclusions [2, 4]

$$f(v_{rel}) \in \begin{cases} -g(v_{rel}) & v_{rel} > 0, \\ [-f_s, f_s] & v_{rel} = 0, \\ g(v_{rel}) & v_{rel} < 0, \end{cases} \tag{1}$$

where $g(v_{rel})$ is a velocity-dependent function which can reproduce Coulomb and friction effect, v_{rel} is relative (sliding) velocity. Typically, one can express the velocity-dependent function as [7]

$$g(v_{rel}) = f_d + (f_s - f_d)\mathrm{e}^{-\left(\frac{|v_{rel}|}{v_{Stribeck}}\right)^{\alpha}}. \tag{2}$$

The Stribeck velocity $v_{Stribeck}$ defines the point at which the steady-state friction force starts decreasing. The real valued coefficient α has a value between 1 and 2.

The dry friction model (1) cannot be implemented into numerical simulations schemes directly because of the properties of the inclusion. The corresponding mathematical model of a dynamical systems with dry friction (1) is then formulated by means of differential inclusion. Such a dynamical system is discontinuous of Filippov-type [4].

The first approach how to deal (especially numerically) with the discontinuous function is to use its smoothening approximation, typically smoothening of the sign-function which is contained in the definition of the friction coefficient function. It is commonly used the arctangent approximation of (1)

$$f(v_{rel}) = \frac{2}{\pi}\arctan(\gamma v_{rel})g(v_{rel}), \quad \gamma \gg 1, \tag{3}$$

where γ is a coefficient which shapes the slope of the characteristic around zero sliding velocity. Based on the smoothed approximation, the sticking phases of the motion can not be captured with required accuracy. The sticking is then given by micro-slipping whose rate is given by the slope of the friction characteristic in the neighbourhood of the zero relative velocity, see Fig. 2b. The dynamical system which includes this approximation of dry friction suffers from stiff differential equation within the sliding mode.

A numerical technique for integrating differential inclusions with sliding modes without suffering from stiff differential equation is represented by *switch model* which is an improved version of the Karnopp model

[7, 4]. The switch model is based on the fact that it introduces a vector field in the stick band, such that the state of the system is pushed to the middle of the stick band. Therefore, the numerical instabilities can be avoided.

Another group of dry friction models is represented by so called *dynamic friction models*. These models are based on the Coulomb friction model with a lag in the change of the friction force during the switching the direction of motion. The models can reproduce Coulomb friction and Stribeck effect, e.g. Dahl model, LuGre model and their modifications like Gonthier model [7]. In the next, the attention will be paid at LuGre dry friction model where the coefficient of friction is formulated in following form [7]

$$f(z, v_{rel}) = \sigma_0 z + \sigma_1 \dot{z} + \sigma_2 v_{rel}, \tag{4}$$

where σ_0 is a stiffness, σ_1 corresponds to micro damping and σ_2 stands for viscous damping. The state variable z connected with the friction coupling satisfies following differential equation

$$\dot{z} = v_{rel}\left(1 - \frac{\sigma_0 z}{g(v_{rel})}\text{sign}(v_{rel})\right). \tag{5}$$

Other parameters used in (4) and (5) were defined above.

It is worthy to note, that there are some limitations of the mentioned dry friction models. Regarding multi-body systems, especially with cyclic structure, the switch model and simillar models, which assume set valued function philosophy, are not suitable. Within the switch model, in case of (almost) zero relative slip velocity, there is necessary to decide on the absolute value of the force transmitted by the friction coupling. The cyclic structure implies that the force transmitted e.g. by ith coupling is dependent even on forces transmitted by $(i-1)$th and $(i+1)$th couplings, i.e. the definition tends to be recursively defined which is not suitable for numerical integration scheme. While the smoothing models or dynamic friction models are suitable for cyclic structures because the friction models depend on relative velocity only, or an additional state variables are added.

In the next sections, switch model and LuGre model are chosen and some comparison of them will be provided. The LuGre model is then employed with formulation of mathematical model of a dynamical system with cyclic structure.

2.3 Friction damped and friction induced vibration

Dynamical system with dry friction couplings can exhibit different vibration regimes. Usually, the presence of dry friction in any mechanical system is understood as an element which dissipates energy. This holds for example in cases of non-autonomous systems, e.g. externally forced spring-mass oscillator, see Fig. 3a. Such a system represents friction damped vibration. On the other side, e.g. spring-mass model on a moving belt represents autonomous system, where the friction is a source of internal excitation. This case is designated as friction induced vibration, see Fig. 3 b.

Mathematical model of the spring-mass model displayed in Fig. 3a (upper friction coupling is neglected), completed by viscous damping can be written as follows

$$\ddot{x} + 2D\Omega\dot{x} + \Omega^2 x = \frac{1}{m}\left(f(v_{rel})N_0 + F(t)\right), \tag{6}$$

where D is damping ratio, $\Omega = \sqrt{k/m}$, k is spring stiffness, m is mass of the mass point, friction function $f(v_{rel})$ has been defined above, N_0 is normal contact force, $F(t)$ stands for external excitation and $v_{rel} = -\dot{x}$ is relative velocity between the mass and the frame.

Mathematical model of the spring-mass model with two belts displayed in Fig. 2 b, completed by viscous damping has following form

$$\ddot{x} + 2D\Omega\dot{x} + \Omega^2 x = \frac{N_0}{m}\left(f_1(v_{rel1}) + f_2(v_{rel2})\right). \tag{7}$$

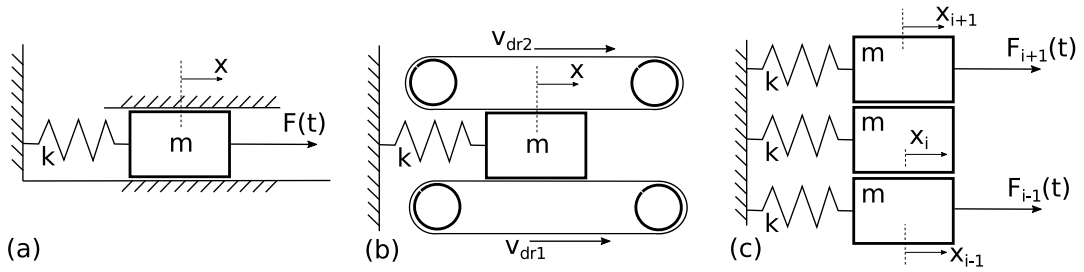


Figure 3: Spring-mass models: (a) friction damped vibration model, (b) friction induced vibration model, (c) combination of friction damped and induced vibration

where, comparing the previous model (6), friction functions $f_1(v_{rel})$ and $f_2(v_{rel})$ are defined for each friction coupling separately. The relative velocities between the mass and the belt are $v_{rel1} = -\dot{x} + v_{dr1}$, $v_{rel2} = -\dot{x} + v_{dr2}$.

Mathematical model of a single triplet of spring-masses taken out form a general cyclic structure displayed in Fig. 3c, where each spring is completed by viscous damping, has following form

$$\begin{aligned} \ddot{x}_{i-1} + 2D\Omega\dot{x}_{i-1} + \Omega^2 x_{i-1} &= \frac{1}{m}\left(f(v_{\mathrm{rel}(i-1)})N_0 + F_{i-1}(t)\right), \\ \ddot{x}_i + 2D\Omega\dot{x}_i + \Omega^2 x_i &= \frac{N_0}{m}\left(-f(v_{\mathrm{rel}(i-1)}) + f(v_{\mathrm{rel}(i)})\right), \\ \ddot{x}_{i+1} + 2D\Omega\dot{x}_{i+1} + \Omega^2 x_{i+1} &= -\frac{1}{m}\left(f(v_{\mathrm{rel}(i)})N_0 + F_{i+1}(t)\right). \end{aligned} \tag{8}$$

The vibrating masses are mutually interconnected by friction couplings only. The outer masses are forced externally, since the inner one not. This mechanical system can exhibit both friction damped and friction induced vibration. The relative velocities between two adjacent masses are defined as $v_{\mathrm{rel}(i)} = \dot{x}_i - \dot{x}_{i-1}$. For further usage, we will suppose three masses system and the indices will have values $i - 1 = 1$, $i = 2$ and $i + 1 = 3$.

2.4 Sliding bifurcations

The presented three mechanical systems can be classified as Filippov-type systems, as mentioned above. The approaches to modelling and analysing dynamical systems by the tools of non-smooth mechanics can help to understand their behaviour [2, 4]. Here, we try to focus on sliding bifurcations or adding-sliding bifurcations. It is convenient to define the sliding region locally with respect to particular dry friction coupling. Let us assume, we have a non-autonomous dynamical system with N_C friction couplings. With respect to a jth coupling, one can formulate the mathematical model on a local region $\mathcal{D} \in \mathbb{R}^n$ as follows

$$\dot{\mathbf{x}} = \begin{cases} \mathbf{F}_1(\mathbf{x}, \mu, t) & h_j(\mathbf{x}) > 0, \\ \mathbf{F}_2(\mathbf{x}, \mu, t) & h_j(\mathbf{x}) < 0. \end{cases} \tag{9}$$

The surface defined by the condition $h_j(\mathbf{x}) = 0$ defines a boundary

$$\Sigma_j = \{\mathbf{x} \in \mathcal{D} : h_j(\mathbf{x}) = 0\} \tag{10}$$

separates $\mathcal{D}$ locally with respect to Σ_j into two regions

$$\begin{aligned} S_{j1} &= \{\mathbf{x} \in \mathcal{D} : h_j(\mathbf{x}) < 0\}, \\ S_{j2} &= \{\mathbf{x} \in \mathcal{D} : h_j(\mathbf{x}) > 0\}. \end{aligned} \tag{11}$$

We consider Filippov systems for which $\mathbf{F}_1(\mathbf{x}, \mu, t) \neq \mathbf{F}_2(\mathbf{x}, \mu, t)$ for all $\mathbf{x} \in \Sigma_j$. The boundary Σ_j contains sliding region $\hat{\Sigma}_j$ with a boundary $\partial\hat{\Sigma}_j^{\pm}$. Based on the above terms, in general four different codimension-one

discontinuity induced bifurcations involving interaction with the boundary $\partial\hat{\Sigma}_j^{\pm}$ of a sliding region can be identified [2]. They are a crossing-sliding bifurcation, a grazing-sliding bifurcation, a switching sliding and adding-sliding bifurcation. During all the bifurcations, the topological change of the trajectories is observed. The trajectories which cross the boundary change after meeting the bifurcation point and they undergo a segment of sliding motion and then leave the switching manifold.

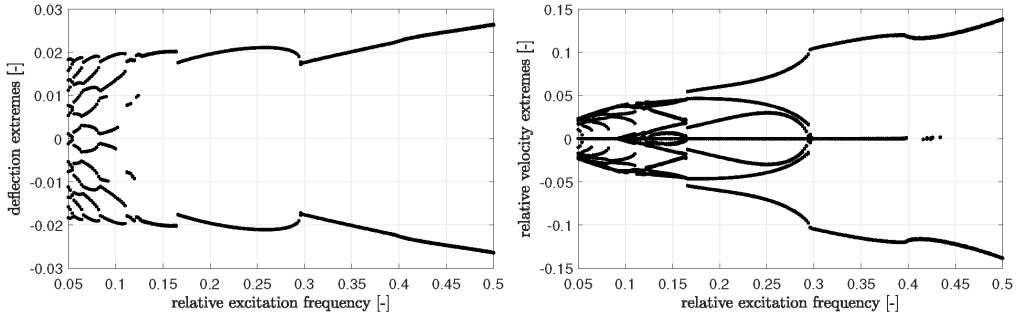


Figure 4: Spring-mass model (a): sliding bifurcation appear there where zero velocity points

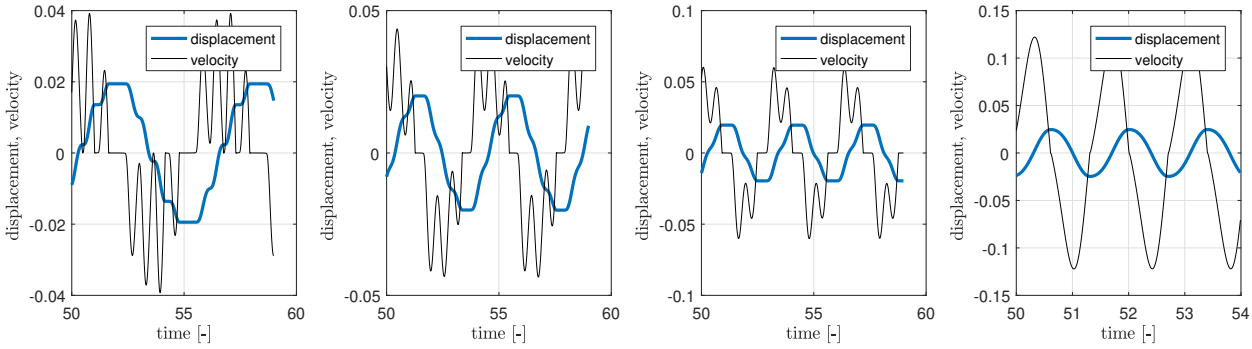


Figure 5: Spring-mass model (a): time courses of displacements and velocities for different values of relative excitation frequency: 0.1, 0.12, 0.2, 0.45. Sliding bifrcation appear there where zero velocity points.

As has been mentioned above, there are many ways to model the dry friction. The switch model (numerical scheme based on the approaches of non-smooth formulations) is numerically effective and can capture the sliding motions but its drawback lays in the impossibility to implement it in systems having two or more friction couplings acting at one body simultaneously. It has been shown that dynamics of a system with friction modelled by switch model and by LuGre model show good agreement. Therefore, all numerical simulations are performed using LuGre dry friction model and the evaluation of the results is carried out by means of formulations of non-smooth mechanics.

In case of friction damped model (Fig. 3 a) the (switching) boundary has a following form $h(\mathbf{x}) = v_{rel} = -\dot{x}_2 = 0$. The boundary is formed by by all points in state space of the system which correspond to zero velocity, i.e. the mass point is sticking. Because of the external excitation (we assume to be periodic) the system response is expected to be predominantly periodic as well. Let us assume the relative excitation frequency $\overline{\omega} = \omega/\Omega$ is a bifurcation parameter μ. At certain parameters of the friction coupling and under harmonic excitation with frequency $\overline{\omega} > 0.5$, the trajectory of the system crosses the switching boundary transversally. Decreasing the frequency $\overline{\omega}$ a *crossing-sliding* bifurcation appears at $\overline{\omega} \approx 0.4$ (see Fig. 5). Continuing the decreasing the frequency *adding-sliding* bifurcation occurs (the number of sliding regions during one period of the motion grows). Moreover, there are amplitude jumps in the response which are connected with interaction of excitation frequency, eigen-frequency of the linear spring-mass model and of the sliding motions.

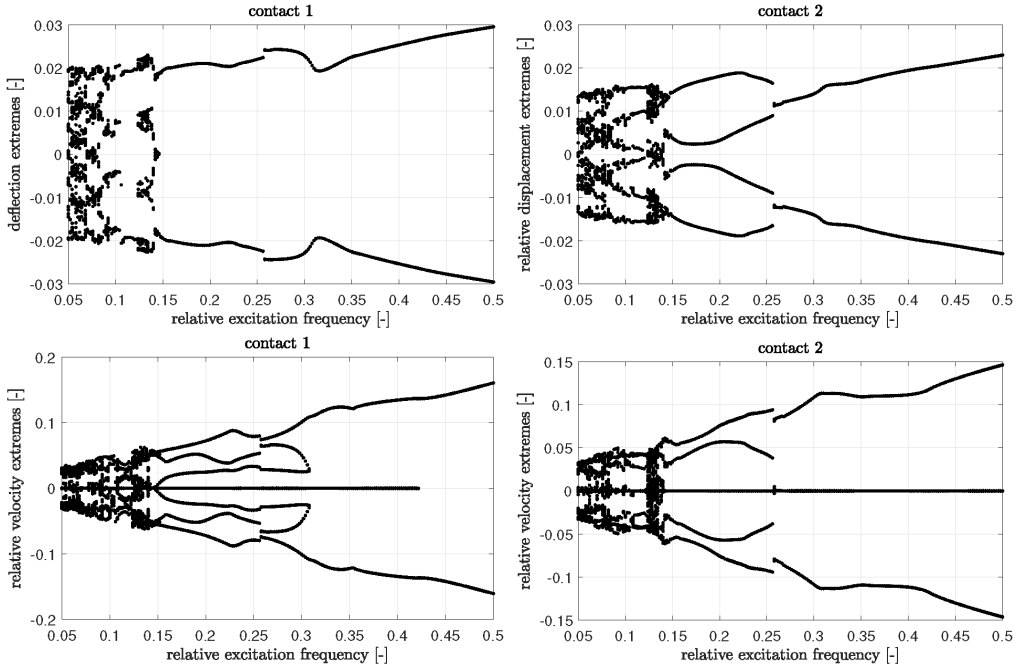


Figure 6: Spring-mass model (c): bifurcation diagram for displacements and velocities in both contacts, phase shift $\varphi = \pi/2$

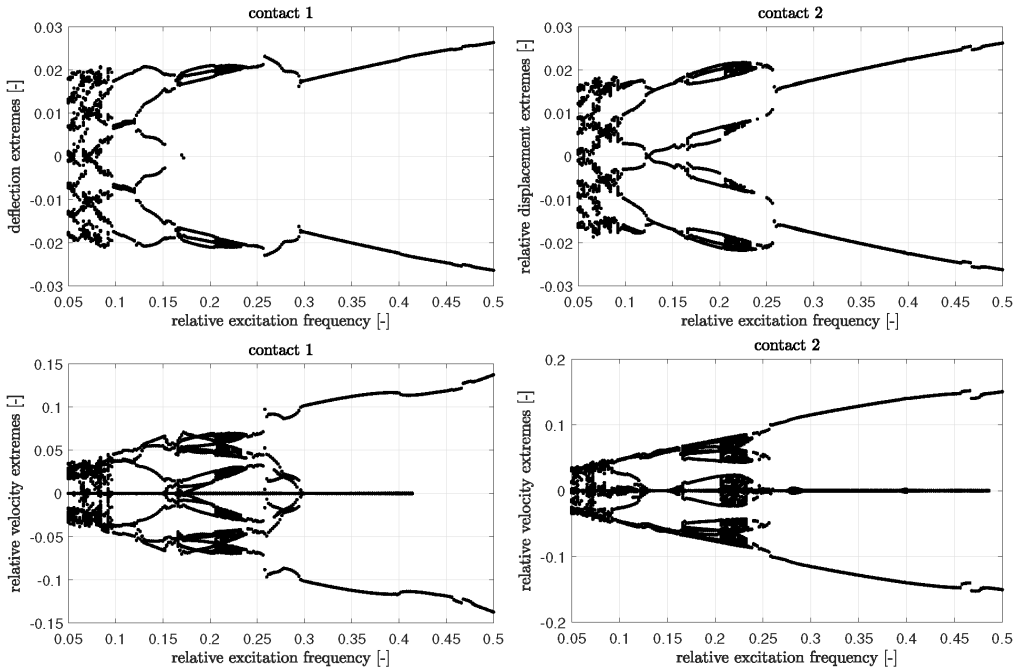


Figure 7: Spring-mass model (c): bifurcation diagram for displacements and velocities in both contacts, phase shift $\varphi = \pi$

To have a more insight in the dynamics, both displacement and velocity has been subjected to Monte-Carlo bifurcation diagrams which are displayed in Fig. 4 for subharmonic range of excitation frequency. The numerical simulations have shown that discontinuity induced bifurcations arise in the subharmonic range only. In case of the resonant and superharmonic response to harmonic excitation, the dry friction has a

damping influence only. There do not arise any nonlinear dynamical phenomena. Therefore, these areas are not studied. The presence of zero-valued velocities indicates sliding motions in the response. Based on the bifurcation diagrams, the adding-sliding bifurcation cannot be detected. Another maps has to be employed as presented in [3].

Similarly, the mechanical system from Fig. 3 c can be studied. Its dynamic is influenced by the presence of two dry friction couplings. The excitations are assumed to be harmonic (sine function) with a phase shift φ. Monte-Carlo bifurcation diagrams are plotted in Fig. 6 for phase shift $\varphi = \pi/2$ and Fig. 7 for phase shift $\varphi = \pi$.

3 Bladed disk as a cyclic structure

The bladed disc creates rotationally periodic structure where the basic structure is formed by a single blade structure. The structure studied here is equipped with 30 prismatic blades fixed to a rotating disc. Blade tips are designed with friction couplings between adjacent blades. The prismatic blades have a rectangular cross-section which influences the form of flexural vibration mode shapes. Moreover, the vibration modes fluctuate between two regimes. The first one corresponds to open friction contacts and the second one to locked friction couplings. In the next, we will focus only on the first flexural vibration mode of each blade including the dry friction coupling.

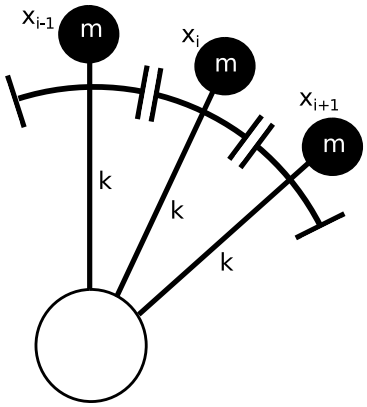


Figure 8: Scheme of a discrete cyclic structure with dry friction couplings

3.1 Simplification - cyclic structure (non-autonomous system)

In case of autonomous system, there exist boundary conditions induced vibration only. The dry friction couplings serve as friction dampers and the vibration vanishes. The dynamical behaviour will be investigated considering periodic excitation, i.e. non-autonomous system. The mathematical model of ith substructure of a discrete cyclic structure with N point masses displayed in Fig. 8 can be written as

$$\ddot{x}_i + 2D\Omega\dot{x}_i + \Omega^2 x_i = \frac{N_0}{m}\left(-f(v_{\mathrm{rel}(i-1)}) + f(v_{\mathrm{rel}(i)}) + F_i(t)\right), \tag{12}$$

where all used quantities were already generally defined in the text above. Particularly here, the stiffness k corresponds to flexural stiffness of the blade, x_i displays the displacement of the blade tip and m is mass of the blade concentrated into its tip.

3.2 Tuning of the model structural parameters based on modal properties

An experimental modal analysis of the experimental bladed wheel with dry friction couplings has been performed (see Fig. 1). Based on the results, parameters of the model (12) have been tuned. Especially, the natural frequency of a particular blade. During the experiment, two limit cases have been analysed. First, the bladed wheel with open contacts and second, the bladed wheel with closed (bonded) contacts. Simultaneously, a computational model has been created and compared with the experimental one [9]. To perform the modal analysis using the model (12), the dry friction couplings has been replaced by linear elastic couplings. The linearization enabled to model the two limit cases: open and bonded (closed) contact. The elastic coupling stiffness has non-zero values in both cases of open and bonded contact because, regarding the real experimental model, the contact geometry is geometrically complex and even in case of open contact some residual stiffness remains. In case of bonded contact, the modal properties depend on the structural stiffness of the coupling which is mostly given by normal contact force resulting from prestressing of the contact.

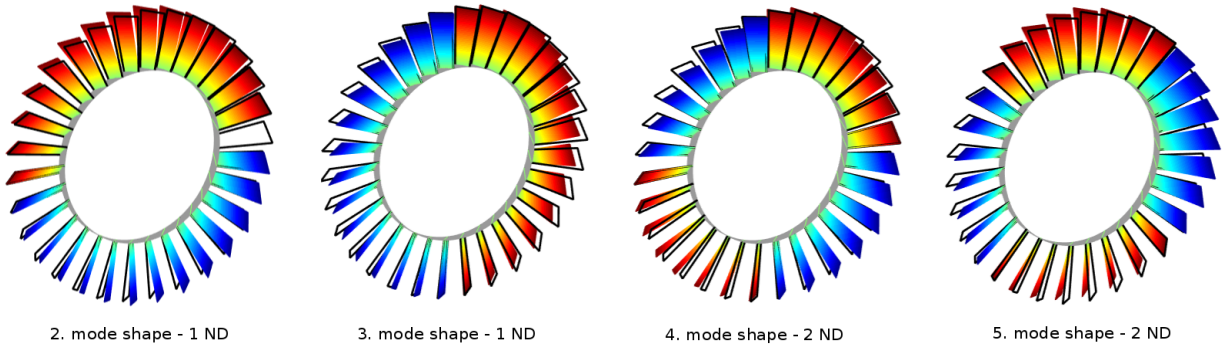


Figure 9: Mode shapes of a discrete cyclic structure with 1 and 2 nodal diameters (ND)

	open contacts		**bonded contacts**	
ND	experiment	discrete model	experiment	discrete model
0	—	43.00	—	43.00
1	37.34	43.28	43.66	47.47
1	37.71	43.28	46.85	47.47
2	43.51	43.10	62.51	58.72
2	—	43.10	66.92	58.72

Table 1: Modal analysis - overview of eigen-frequencies gained experimentally and couputationally

Here, we have chosen mode shapes which are characterized by one and two nodal diameters and are depicted in Fig. 9. Corresponding eigen-frequencies which were found out experimentally and numerically are presented in Tab. 1. The differences in eigen-frequencies for bonded contact are caused by the fact, that the computational model (12) takes into account the first flexural mode of each blade only, since the behaviour of the experimental model is more complex due to its geometry which influences the motion shapes with bonded contact.

4 Computational analysis

Based on the above presented mathematical model of the discrete cyclic structure, a computational model has been created. In many applications like steam turbines, the bladed disks are force by nozzle excitation

which is formed by stator bladed wheel. Generally, we consider following form of the excitation acting on the ith blade

$$F_i(t) = A_i(1 - \mathrm{e}^{-\beta t}) \sin(\omega t + (i-1)\Delta\varphi) H(\sin(\omega t + (i-1)\Delta\varphi)), \quad i = 1, \ldots, N_b. \tag{13}$$

A_i represents the amplitude, the function $(1 - \mathrm{e}^{-\beta t})$ constitutes exponential ramp of the excitation with coefficient β. $\Delta\varphi$ is a phase shift between blades and it enables to model running waves on the cyclic structure. H is standard Heaviside function which practically assures that the excitation simulates positive sine force pulses and N_b designates the number of blades.

Even if the model parameters are tuned based on the experiment data, the model is non-dimensionalised with respect to blade flexural eigen-frequency to perform simulations in time domain. The dynamic behaviour is investigated locally with respect to particular friction coupling, i.e. the attention is paid on time courses of relative displacements and velocities between adjacent blades. There are two significant parameters which influence the dynamics. The first one is the normalized excitation frequency $\overline{\omega}$ and the second one is the ration between normal contact force and the excitation amplitude N_0/A_i, $i = 1 \ldots N_b$. In all simulations, we assume $A_i = const. \forall i$.

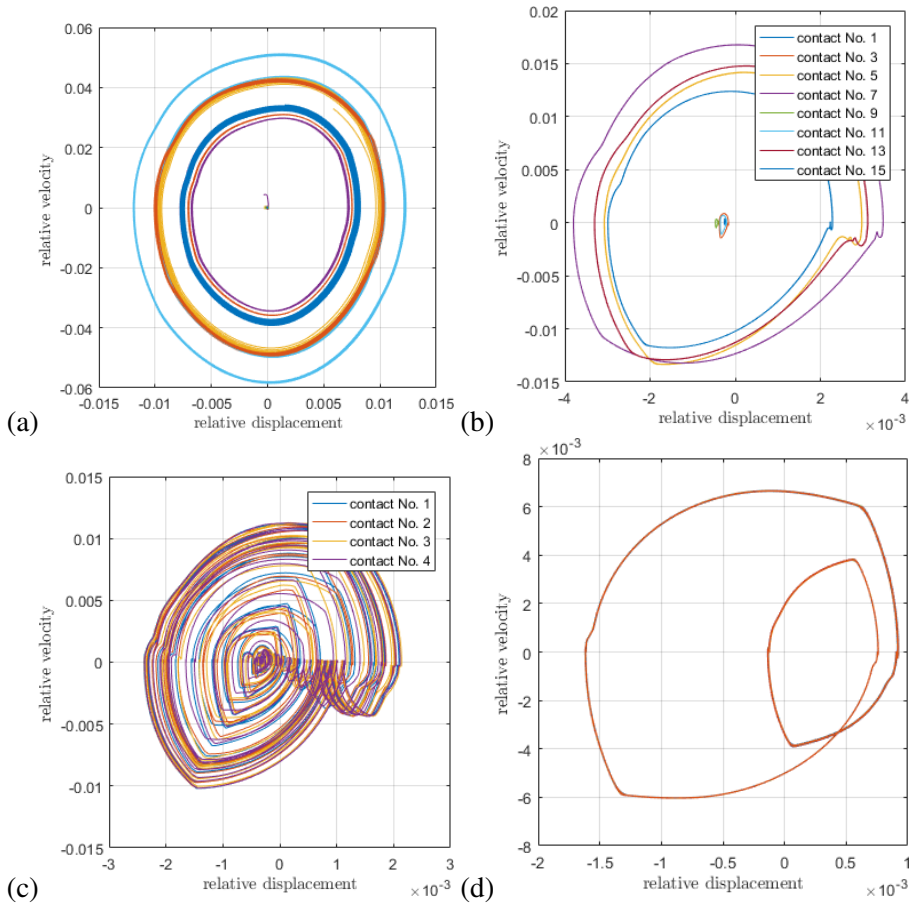


Figure 10: Phase trajectories on relative displacements and velocities of dry friction contact couplings caused by excitation with 1 nodal diameters (ND)

4.1 Running wave with 1ND

First, a running wave with a shape corresponding to eigen-mode with 1 ND is excited and the excitation frequency is chosen as a parameter. Four cases are presented: (a) the excitation frequency is close to the

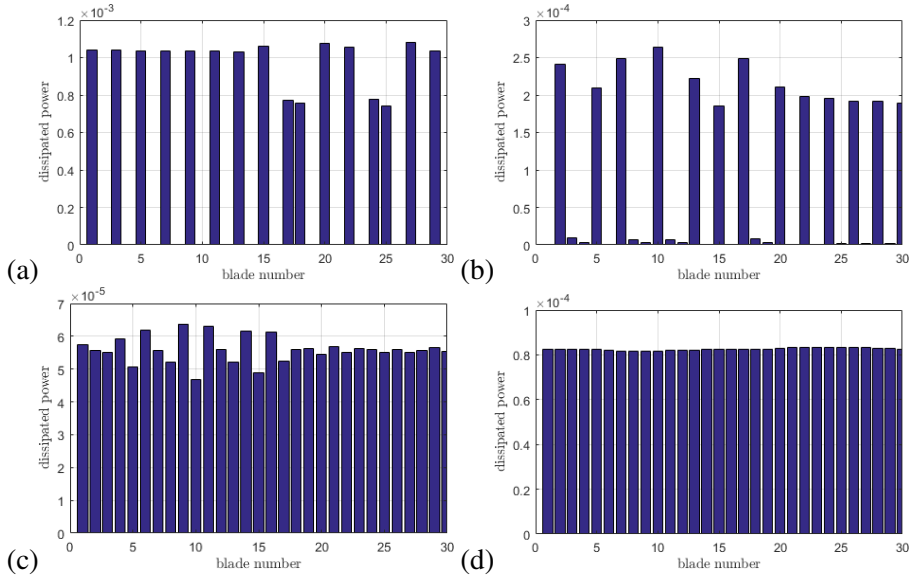


Figure 11: Normalised dissipated power of all frictionn couplings

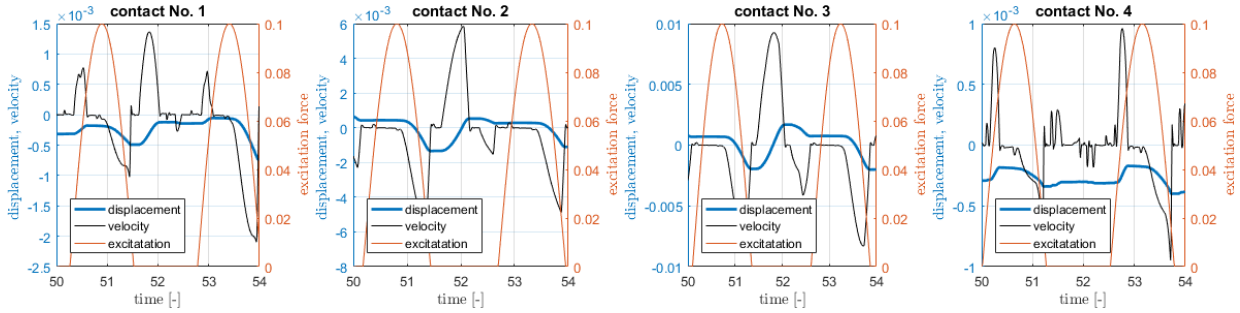


Figure 12: Chosen timespan of relative contact displacements, velocities and excitation of four neigbouring contacts for the case (c)

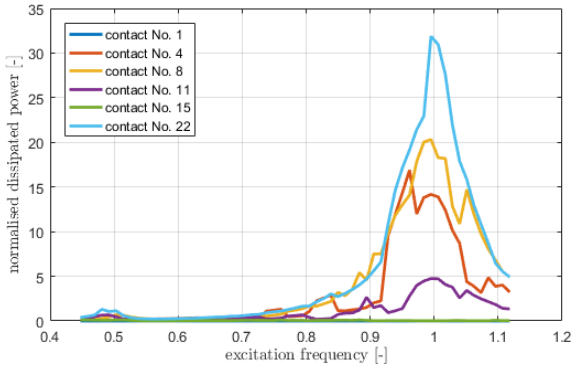


Figure 13: Dissipated normalised power in chosed dry friction contacts in dependence on excitation frequency

eigen-frequency of the 1 ND mode-shape Ω_{1ND}, i.e $\overline{\omega} = \omega/\Omega_{1ND} \approx 1$, (b) $\overline{\omega} = \omega/\Omega_{1ND} = 0.78$, (c) $\overline{\omega} = \omega/\Omega_{1ND} = 0.56$ and (d) $\overline{\omega} = \omega/\Omega_{1ND} = 0.49$.

Fig. 10 shows phase trajectories of steady-state of relative contact displacements and velocities for either all

or chosen contacts for excitation frequencies (a) – (d), respectively and the normalised dissipated power is shown in Fig. 11. The behaviours can be classified as follows:

(a) There are localised three different limit cycles in the coupling around the circumference, all contact show full slip motion.

(b) There are localised different limit cycles in the coupling around the circumference. Some contacts are sticking which corresponds to almost zero value of dissipated power; even if the vibration of blades follows the running wave excitation. The activity of contacts is not evenly distributed, some contact crossed the crossing-sliding bifurcation.

(c) Here, the behaviour shows a chaotic pattern with sticking and slipping motions. The dissipated power significantly decreased. Time courses of chosen contact displacement and velocities along with excitation force are plotted in Fig. 12.

(d) The phase trajectories of all contacts tend to a single limit cycle. The dissipated power is higher than in case (c).

Further, the so called normalised dissipated power which is related to the period of excitation can be evaluated. Fig. 13 clearly shows that the most energy is dissipated around the resonant state and the amount of the energy dissipated depends on the contact position on the bladed wheel circumference.

4.2 Running wave with 2ND

Secondly, a running wave with a shape corresponding to eigen-mode with 2 ND is excited. The same cases and quantities have been investigated as in previous case for 1 ND. Fig. 14 shows phase trajectories of steady-state of relative contact displacements and velocities for all contacts. The normalised dissipated power is plotted in Fig. 15.

Comparing to the previous case, the response in contacts is not described localised limit cycles, the behaviour is more complicated. On the other side, the normalised dissipated power in dry friction contacts is higher than in the case of 1ND running wave excitation.

To have a more insight into the response, contact kinematic properties for the case (a) are displayed in Fig. 16.

5 Conclusion

The work focuses on discrete mechanical systems with cyclic structure containing dry friction couplings. The motivation lays in designing of elements for vibration suppression of bladed wheels which are operated i.e. in steam turbines. In the first part, a short overview of dry friction couplings modelling and basic properties of friction induced and friction damped systems is presented. The 1 DoF spring-mass oscillators show discontinuity induced bifurcation in the subharmonic area with respect to its linear eigen-frequency. Especially, crossing-sliding and adding-sliding bifurcations are detected. The dynamics is influenced not only by the excitation frequency but also by dry friction coupling parameters (especially by friction characteristics, normal contact force). To analyse the system a hybrid approach is used. The conditions of discontinuity induced bifurcation are formulated analytically using the non-smooth approaches applied on Filippov's systems, since the computational implementation uses dynamic dry friction model. The results gained using LuGre model show very good agreement with results gained by switch model which cannot be easily implemented in systems with multiple dry friction couplings acting on one body.

The methodology is applied on a simplified model of an experimental bladed wheel with especially proposed design of blades with tunable friction couplings. The dynamics of the bladed wheel is investigated for two different excitations, for two running waves with 1 nodal diameter and with 2 nodal diameters. From the

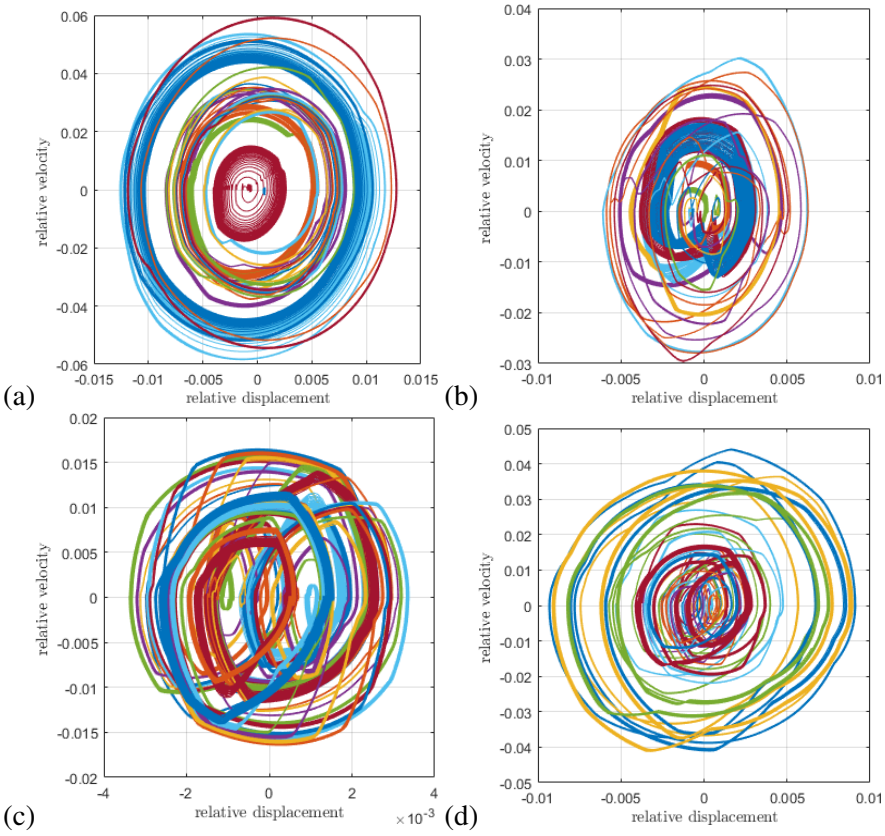


Figure 14: Phase trajectories on relative displacements and velocities of dry friction contact couplings caused by excitation with 2 nodal diameters (ND)

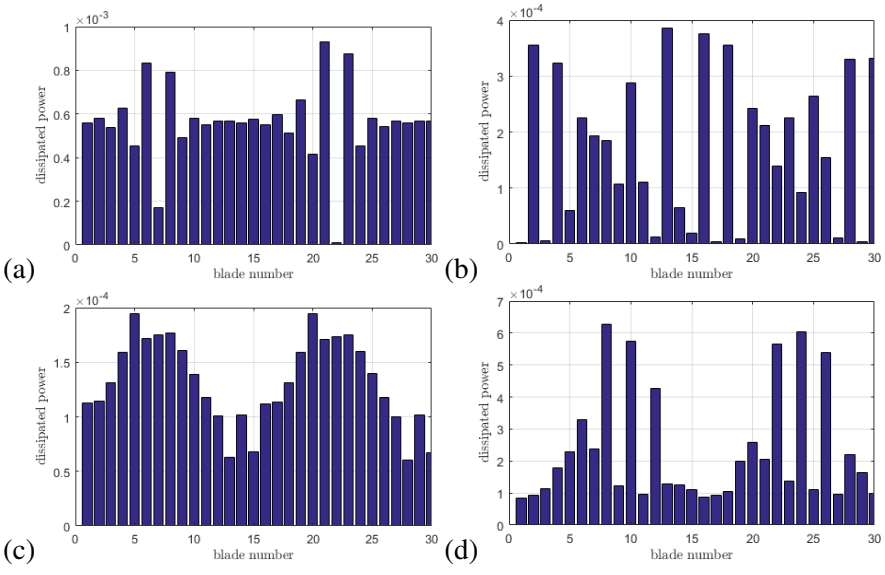


Figure 15: Normalised dissipated power of all frictionn couplings

dissipated power view, the most energy is dissipated around the resonance states when the blades vibrate with greatest amplitudes with no sticking phases. In subharmonic areas, the amount of dissipated energy is low but the vibration is accompanied by crossing-sliding and adding-sliding bifurcations.

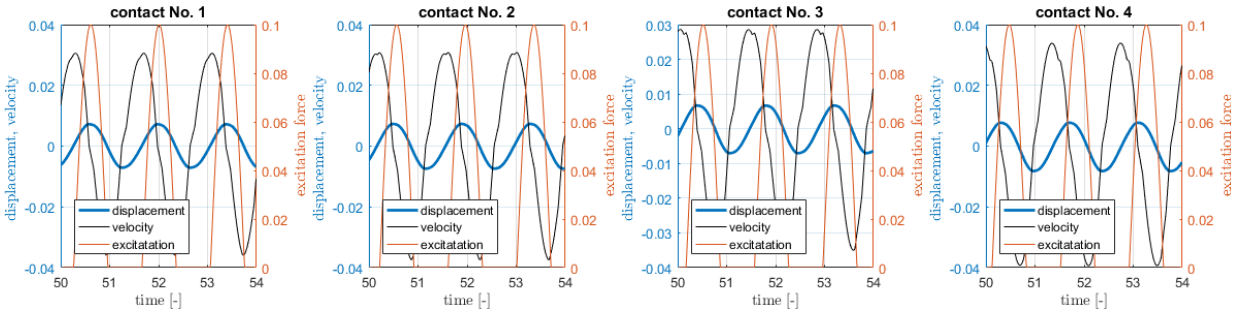


Figure 16: Chosen timespan of relative contact displacements, velocities and excitation of four neigbouring contacts, case (a)

Acknowledgements

This work was supported by the GA CR project No. 16-04546S "Aero-elastic couplings and dynamic behaviour of rotational periodic bodies".

References

[1] G. Battiato, C.M. Firrone, T.M. Berruti, and B.I. Epureanu. Reduced order modeling for multi-stage coupling of cyclic symmetric structures. In *Proceeding of the ISMA 2016 Conference*, pages 3447–3462, Leuven, 9 2016.

[2] M. di Bernardo, C.J. Budd, A.R. Champneys, and P. Kowalczyk. *Piecewise-smooth Dynamical Systems Theory and Applications*. Applied Mathematical Sciences. Springer, London, 1 edition, 2008.

[3] U. Galvanetto. Bifurcations and chaos in a four-dimensional mechanical system with dry friction. *Journal of Sound and Vibration*, 204(4):690 – 695, 1997.

[4] R. Leine and H. Nijmeijer. *Dynamics and Bifurcations of Non-Smooth Mechanical Systems*. Lecture Notes in Applied and Computational Mechanics. Springer, Berlin, 1 edition, 2004.

[5] M. Maurici, M.P. Salio, and L. Carassale. A method for reduced-order modelling of mistuned bladed disks. In *Proceeding of the ISMA 2016 Conference*, pages 887–889, Leuven, 9 2016.

[6] A. Papangelo, A. Grolet, L. Salles, N. Hoffmann, and M. Ciavarella. Snaking bifurcations in a self-excited oscillator chain with cyclic symmetry. *Communications in Nonlinear Science and Numerical Simulation*, 44:108 – 119, 2017.

[7] Ettore Pennestrì, Valerio Rossi, Pietro Salvini, and Pier Paolo Valentini. Review and comparison of dry friction force models. *Nonlinear Dynamics*, 83(4):1785–1801, Mar 2016.

[8] Luděk Pešek, Michal Hajžman, Ladislav Půst, Vladimír Zeman, Miroslav Byrtus, and Jan Brůha. Experimental and numerical investigation of friction element dissipative effects in blade shrouding. *Nonlinear Dynamics*, 79(3):1711–1726, Feb 2015.

[9] Ludek Pesek, Ladislav Pust, Vitezslav Bula, and Jan Cibulka. Numerical analysis of dry friction damping effect of tie-boss couplings on three blade bundle. In *ASME 2017 International design engineering technical conferences & computers and information in engineering conference. Cleveland, Ohio (US), 06.08.2017-09.08.2017*, pages 1 – 7, Washington, 7 2017. American Society of Mechanical Engineers (ASME).

[10] S. Samaranayake, G. Samaranayake, and A.K. Bajaj. Resonant vibrations in harmonically excited weakly coupled mechanical systems with cyclic symmetry. *Chaos, Solitons & Fractals*, 11(10):1519 – 1534, 2000.

[11] E. Sarrouy, A. Grolet, and F. Thouverez. Global and bifurcation analysis of a structure with cyclic symmetry. *International Journal of Non-Linear Mechanics*, 46(5):727 – 737, 2011.

Experimental investigation on timing belt drive dynamics with non-circular pulley

S. Passos[1,2], L. Manin[2], D. Remond[2], O. Sauvage[1], L. Rota[1], E. Besnier[2]
[1] Groupe PSA, Scientific & Future Technologies Department, OpenLab Vibro-Acoustic-Tribology @Lyon, F-78943, France.

[2] INSA-Lyon, CNRS UMR5259, LaMCoS, F-69621, France.

Abstract
The present work describes an experimental method that aims at providing a description of the dynamic and vibratory behavior involved by non-circular pulleys in timing belt drives. The experiments are carried out on an simple two-pulley transmission. The very simple architecture of this transmission offers an easy analysis of the phenomena. Two setups of the transmission are tested: one configuration comprising two circular pulleys (reference case) and the other one for which the driving pulley is substituted by an oval sprocket. The study focuses particularly on the pulley rotational vibrations by measuring rotational motion and torques. A comparative analysis is performed between experimental results obtained on the two setups enabling to point out the dynamic effect of the oval pulley. Finally, these results are compared with simulation results obtained from a numerical model developed in parallel of this work.

1 Introduction

In an automotive engine, the timing belt is a key component in charge of synchronizing the valve train system and the crankshaft (Figure 1). This synchronization constitutes one of the essential functions of the engine. It insures the correct timing of the valves opening and closing with respect to the piston movement and prevents the risk of piston-valve clash that can cause severe damages to the engine.

In running conditions, timing belt drives can be subjected to vibrations due to the belt elasticity and several excitation sources such as variable load torques and crankshaft velocity. Excessive vibrations can cause belt fatigue and wear, leading to a decrease of the belt life. These vibrations can also induce other undesirable phenomena such as noise, overconsumption, and instantaneous desynchronization of engine components that can degrade the global engine efficiency.

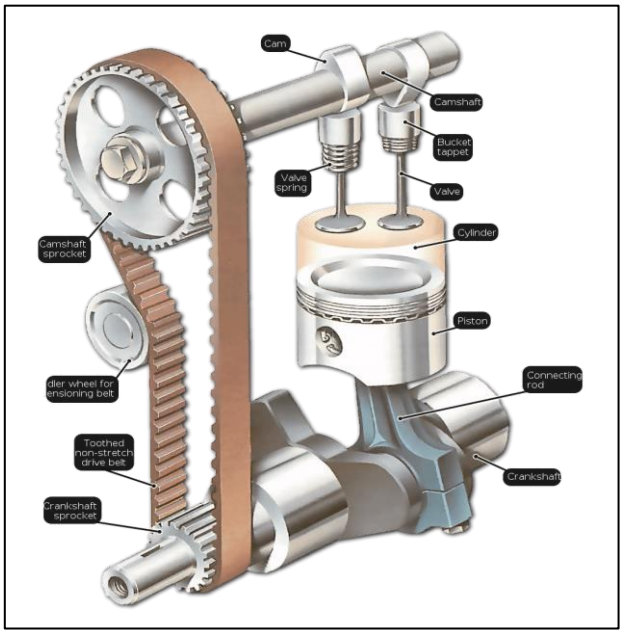


Figure 1 : Valve train system of a car engine with a timing belt drive

Within the objective of reducing these phenomena, car manufacturers have recently introduced non-circular pulleys in timing belt transmissions. When they rotate, such pulleys cause periodic elongation of their adjacent belt spans. According to a patent owned by the car equipment supplier Litens Automotive [1], this periodic elongation is assumed to generate a fluctuating corrective torque on the driven pulleys. Directly dependent on the pulley geometrical profile and its phasing in the transmission, this corrective torque can be set to counteract the excitation sources causing rotational vibrations of the driven pulleys. Thus, with optimal profiles and phasing, the non-circular pulleys may enable a significant reduction of these vibrations.

Determining the optimal design parameters of a non-circular pulley to obtain an efficient design of the transmission is not easy to accomplish. To achieve this, it is important to clearly understand and identify the impact of such pulleys on the dynamic behavior of a timing belt drive.

The literature concerning the use of non-circular pulleys and their dynamic impact is relatively poor. Most works focus only on kinematic and quasi-static analyses [2,3]. Recent papers referenced in [4] and [5], propose numerical models developed to predict the dynamic behavior of a transmission comprising non-circular pulleys. Using these models, the authors perform numerical studies that show how an oval crankshaft pulley can significantly reduce the rotational vibrations of a camshaft pulley in a four-cylinder engine (fourth order periodic load torque on the camshaft). The models are based on discrete approaches similar to that implemented by Hwang et al. [6] for poly-V belt transmissions comprising circular pulleys. In his model, Hwang considers the belt spans as linear spring-damper elements connected to the pulleys represented by rotational inertias.

The present work is an extension of the study presented in [5]. It aims at proposing an experimental method for characterizing and understanding the impact of a non-circular pulley on the dynamics of a timing belt transmission. Here, the study focuses on the effect of a marketed oval pulley. Nowadays, this kind of profile is commonly used in four-cylinder engines. The experiments are conducted for a simple two-pulley transmission offering an easy analysis of the system. The transmission is mounted on a test stand fully instrumented that is described in section 2. Two different setups of the transmission are studied:

- The **circular** setup (C-C): the driving and driven pulleys are both Circular (reference case),
- The **oval** setup (O-C): the driving pulley is Oval and the driven pulley is Circular.

In section 3, the results obtained for both setups are analyzed. In particular, a comparison analysis between the two considered transmission setups, points out the effect of the oval pulley on the dynamics of the system. Finally, in section 4, these experimental results are compared with some preliminary numerical

results obtained from the model developed in [5]. This comparison enables to assess the modelling validity and to interpret the phenomena observed experimentally.

2 Test stand

The experiments are conducted on a simple two-pulley transmission. The transmission is composed of one driving pulley (1) whose motion is imposed and one driven pulley (2) subject to a constant load torque.

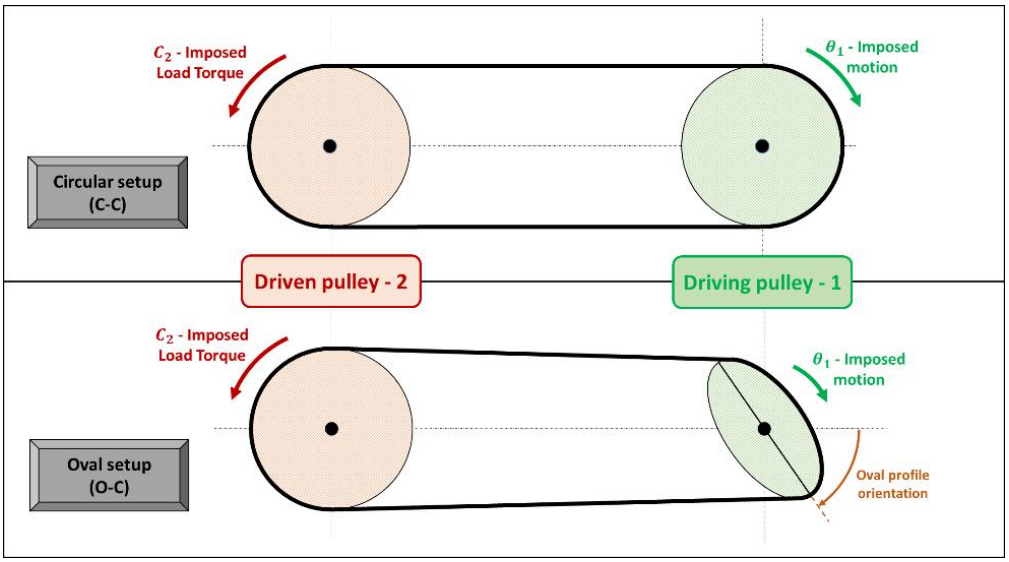


Figure 2: Test setups of the transmission.

As illustrated in Figure 2, two configurations of transmission are considered:

- The **circular** setup (C-C): pulley 1 Circular – pulley 2 Circular.
- The **oval** setup (O-C): pulley 1 Oval – pulley 2 Circular.

The oval profile has a geometrical periodicity of 0.5 over the pulley circumference. When the pulley is mounted on the transmission and rotates, this geometrical periodicity induces periodic length fluctuations of the belt spans with a frequency of 2 events per revolution of the oval pulley (see Figure 3). These fluctuations affect the dynamic behavior of the transmission.

For confidential reasons, the detailed characteristics of the transmission components (pulleys and belt) are not presented in this paper.

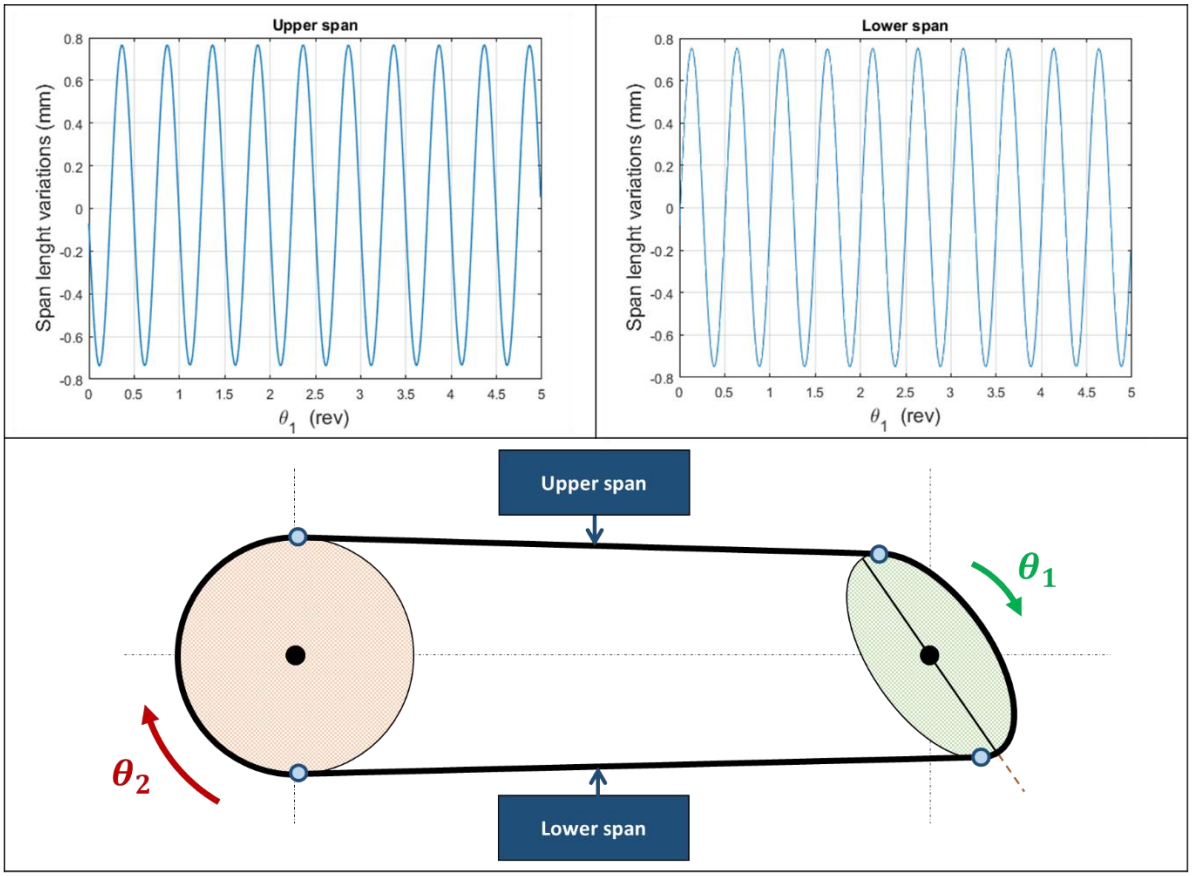


Figure 3: Length variations of belt spans caused by an oval profile (geometrical periodicity of second order).

2.1 Architecture

The global architecture of the test stand is illustrated in Figure 4 and Figure 5. The bench comprises two rotary shafts on which the pulleys of the test transmission are mounted:

- The driving shaft (1) is coupled with a speed-controlled electric brushless servomotor (51.3 kW) in charge of imposing the rotational motion of the driving pulley with a maximum speed of 2000 rpm.
- The driven shaft (2) is coupled with a torque-controlled electric brushless servomotor (11.03 kW) that applies the load torque on the driven pulley.

The center distance between the two shafts is adjustable, enabling a custom setting of the initial belt tension.

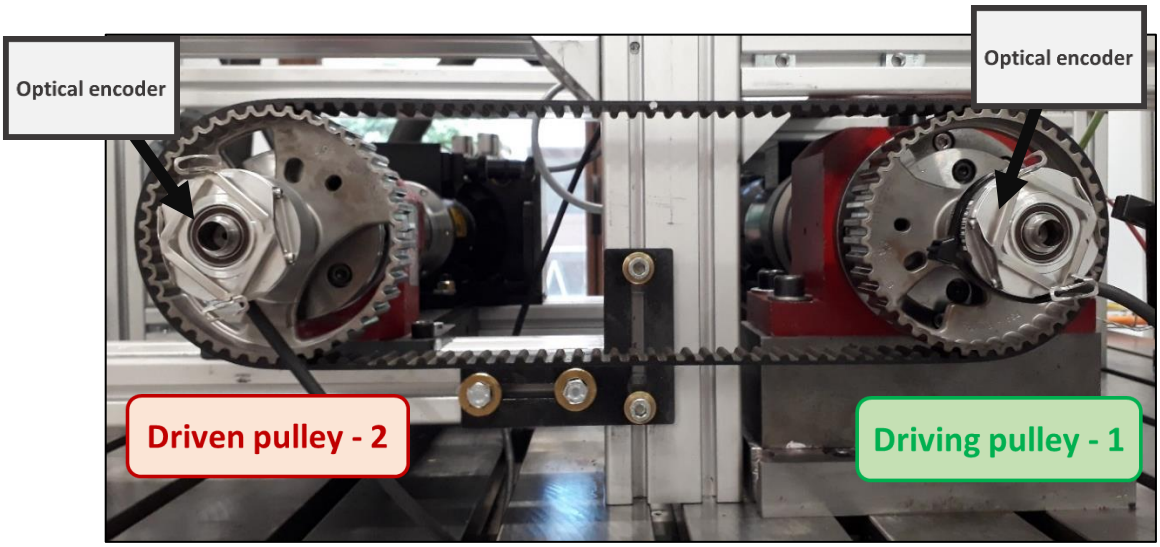


Figure 4: Face view of the test stand.

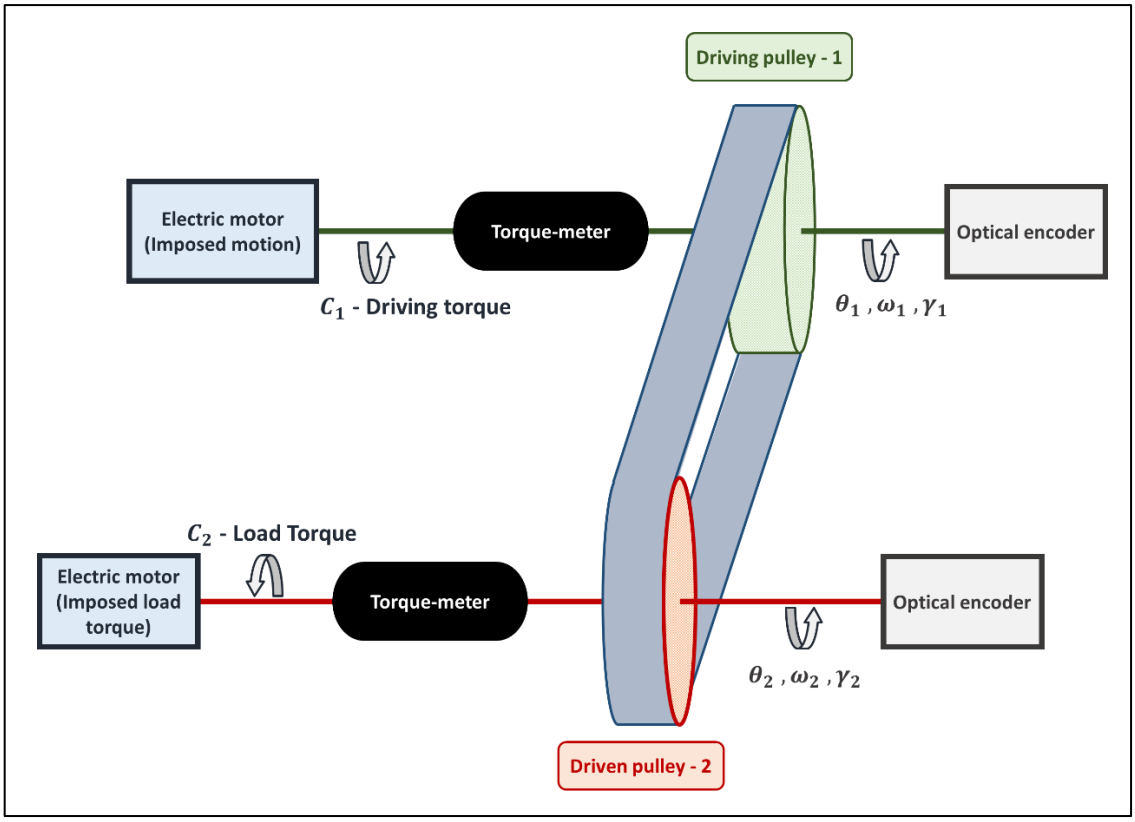


Figure 5: Diagram of the global test stand architecture.

2.2 Measurement devices

The instrumentation of the bench is similar to usual devices employed for experimental investigations on gear transmission error [7] and belt transmissions [8,9]. It enables measuring all the quantities depicting the transmission rotary dynamics. Pulley rotations are measured by means of optical encoders (2500 pulses/rev). Torque meters are mounted on both shafts (see Figure 6) to measure the driving and load torques with respective ranges of 20 and 50 N.m. When the driving pulley is oval, a laser proximity sensor (0.1 mm/V) is used to measure the variation of its pitch radius. The orientation of the non-circular pulley is deduced from this measurement (see Figure 7).

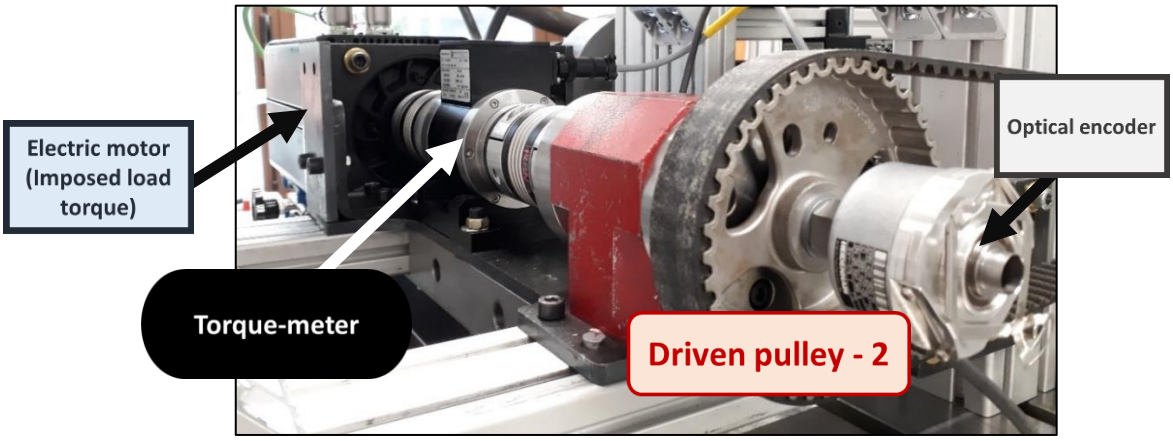


Figure 6: View of the driven shaft and its instrumentation.

The data acquisition system is custom made within a N.I. PXI frame including classical data acquisition boards and a four-channel counter board permitting the use of the pulse timing method [7]. Each optical encoder delivers a square signal (TTL) as it rotates. Between two rising edges of this signal, a counter records the number of pulses given by a high frequency clock (80 MHz), see Figure 9. For each encoder, it is therefore possible to build a time vector that contains the times of occurrence of the TTL signal's rising edges. Hence, the total rotation angle of each shaft is determined and instantaneous rotation speed and acceleration are deduced. In this application, the measurement is triggered on the reference encoder mounted on the driving shaft. The analog signals (torque meters and laser sensor) are recorded at a sampling frequency of 1 kHz.

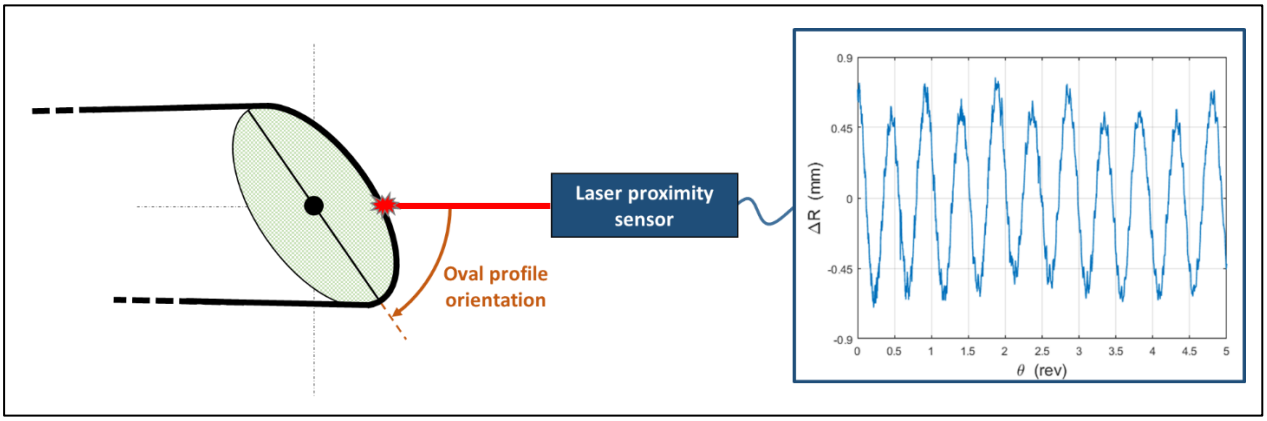


Figure 7: Principle of the measurement of the oval profile orientation.

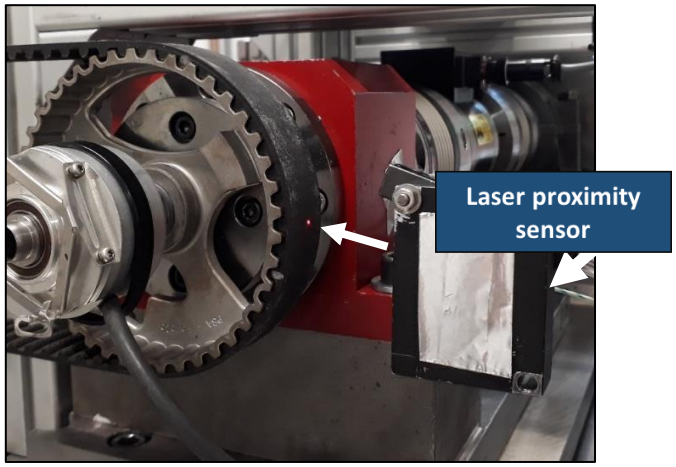


Figure 8: Laser proximity sensor.

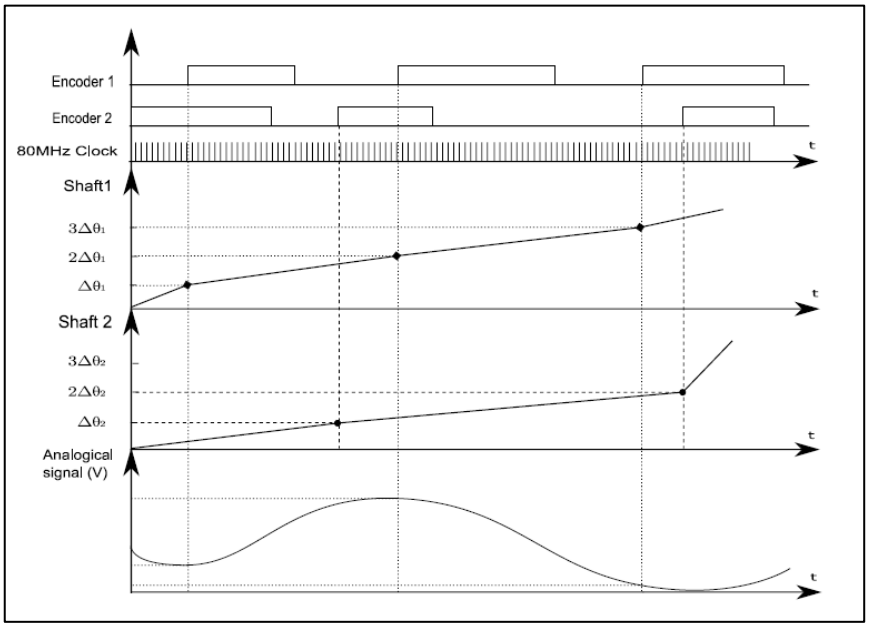


Figure 9: Pulley rotation measurement principle.

3 Experimental analysis

For both transmission configurations C-C and O-C, the following measured quantities are observed and compared:

- Instantaneous driven pulley rotation speed,
- Instantaneous driven pulley angular acceleration,
- Instantaneous Transmission Error (TE),
- Torque applied by the belt to the driven pulley.

The analysis is performed in the angular and angular frequency domains, where the reference is the driving pulley rotation angle. The comparison is made for constant average driving rotation speed (1000 rpm) and resisting torque (10 N.m).

3.1 Kinematic analysis

Instantaneous angular speed and acceleration variations of pulley 2 (driven) are plotted in Figure 10 and Figure 12 versus the pulley 1 (driving) number of revolutions for the two transmission configurations C-C and O-C. It can be seen that for the O-C transmission, the speed and acceleration fluctuation amplitudes for the driven pulley are amplified by a factor seven compared to the C-C configuration.

The spectral representations of the speed and acceleration fluctuations are plotted in Figure 11 and Figure 13. In the C-C case, the fluctuations are modulated by harmonics corresponding to the meshing frequency and disturbing excitation sources such as misalignments in the rotary assemblies or geometry faults on the pulleys. These harmonics are still present in the O-C configuration but are dominated by a second order harmonic with amplitude of 10 rpm. This harmonic corresponds to the oval profile effect.

Another important characteristic of timing belt drives is the Transmission Error (TE) that has to be minimum for efficient engine operation and synchronization of the valve train with the crankshaft. The use of non-circular pulley may affect the amplitude of the TE. The TE is plotted in Figure 14 for the C-C and O-C configurations. The fluctuation amplitude is multiplied by two with an oval pulley. The frequency content (see Figure 15) of the TE is dominated by the harmonic corresponding to the oval pulley in the O-C case.

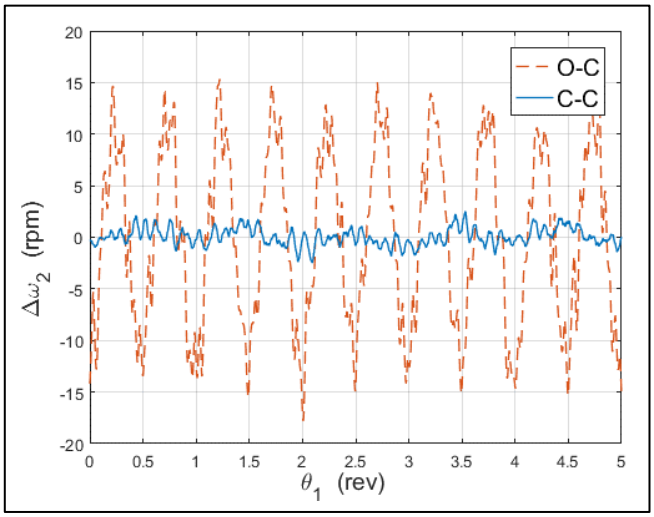


Figure 10: Instantaneous angular velocity fluctuations of pulley 2 vs. driving angle for C-C and O-C setups.

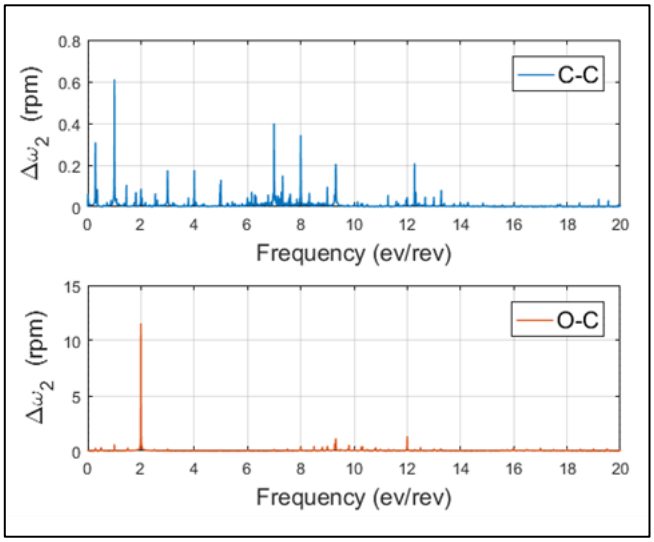


Figure 11: Frequency content of the instantaneous angular velocity fluctuations of pulley 2 for C-C and O-C setups.

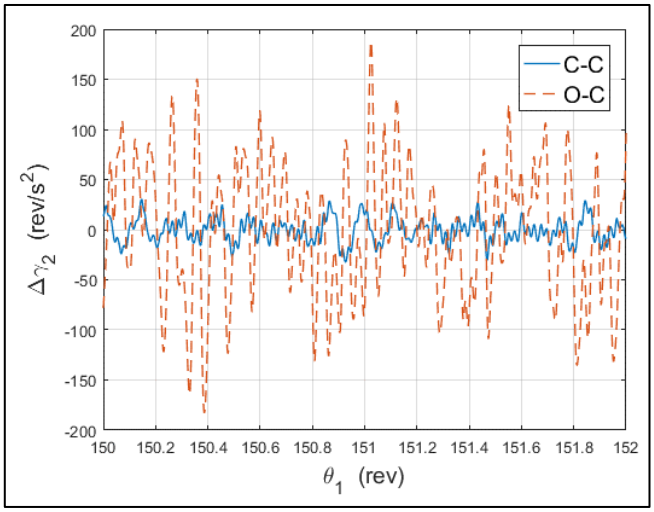


Figure 12: Instantaneous angular acceleration fluctuations of pulley 2 vs. driving angle for C-C and O-C setups.

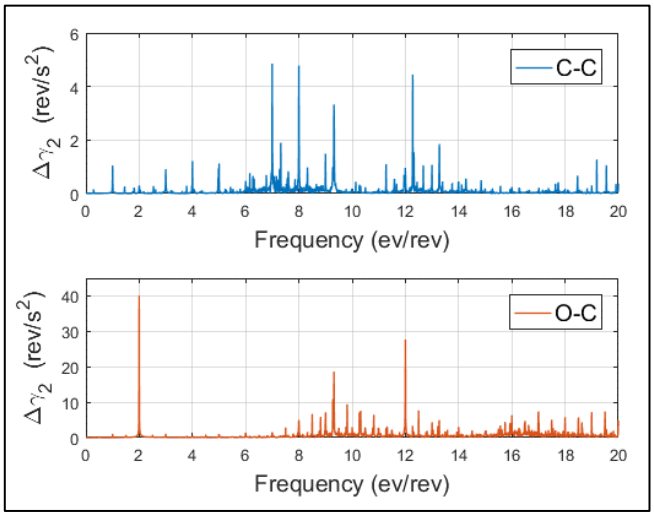


Figure 13: Frequency content of the instantaneous angular acceleration fluctuations of pulley 2 for C-C and O-C setups.

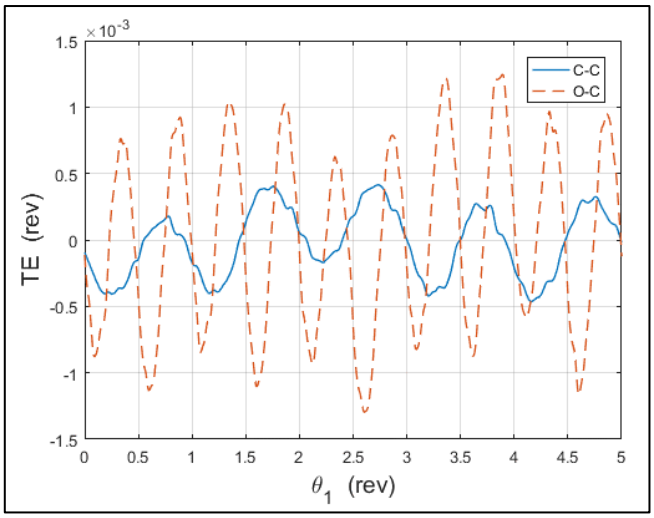


Figure 14: Transmission Error vs. driving angle for C-C and O-C setups.

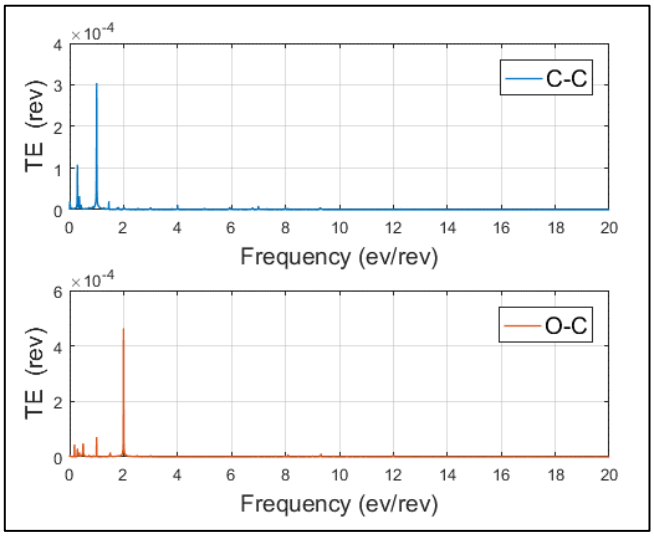


Figure 15: Frequency content of the Transmission Error for C-C and O-C setups

3.2 Driven pulley torque analysis

As shown in the previous section, the use of an oval driving pulley in a two-pulley transmission induces some second order angular oscillations of the driven pulley. These angular oscillations are related to fluctuations of the torque C_p generated by the belt span tensions applied to the driven pulley. This torque is deduced from the torque measured on the driving and driven axes of the test bench.

Figure 16 and Figure 17 show the torque C_p fluctuations and frequency content in both C-C and O-C cases. When using two circular pulleys, the fluctuations of the torque C_p are mainly governed by the harmonics corresponding to the tooth meshing and the disturbing excitation sources (misalignment, pulley geometrical faults …). In the O-C configuration, the torque is additionally modulated by a dominant harmonic of order 2 corresponding to periodic belt span length variations induced by the oval profile.

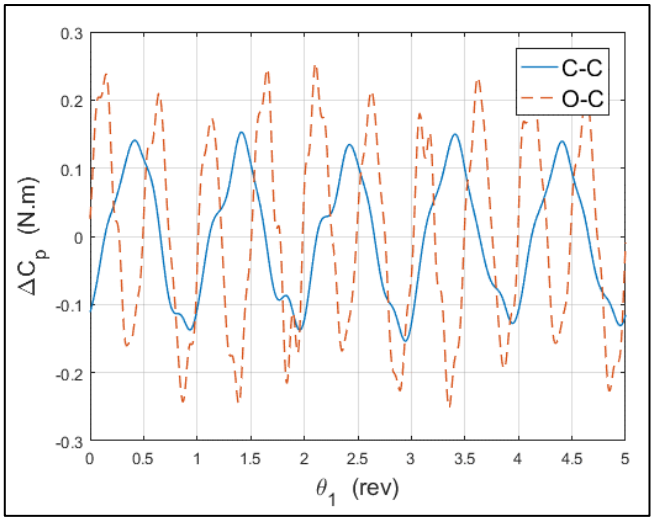


Figure 16: Fluctuations of the torque C_p for C-C and O-C transmissions.

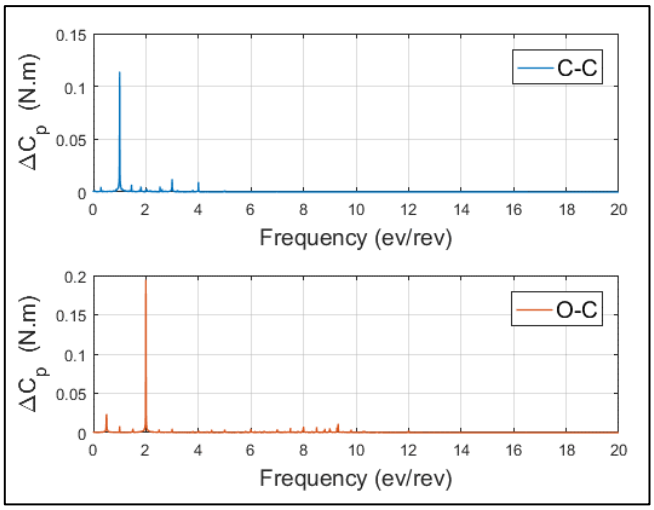


Figure 17: Frequency content of the torque C_p fluctuations for C-C and O-C transmissions.

4 Comparison with numerical results

In this section, the modeling method presented in [5] is applied to the O-C setup. The transmission is considered as a discrete 2D-system. The belt is represented by a linear elastic wire related to rotating rigid bodies representing the pulleys (see Figure 18).

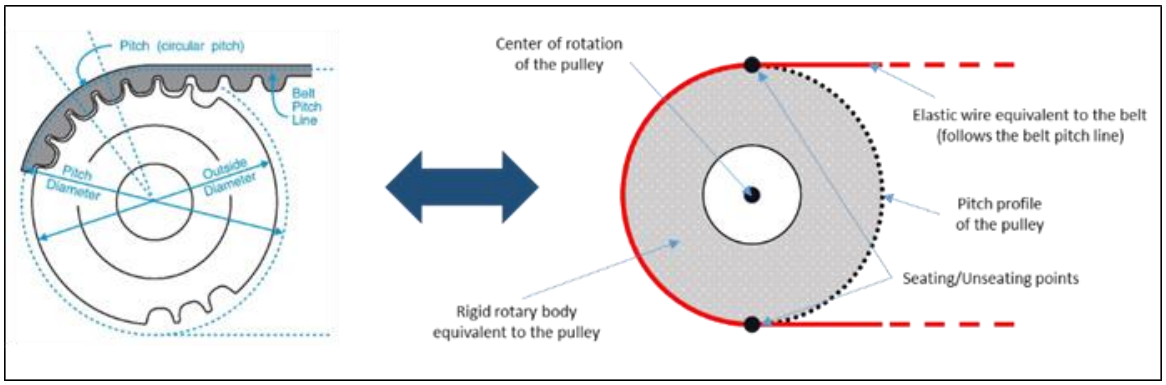


Figure 18: Modelling principle of a belt transmission.

The motion of the driving pulley θ_1 is imposed and the rotation of the driven pulley θ_2 is actuated by the effect of the belt span tensions T_a and T_b applied at the seating/unseating points (see Figure 19). The angle θ_2 is the degree of freedom of the system governed by the equation of motion (1) obtained by applying the fundamental principle of the dynamics on the driven pulley rotation:

$$I_2\ddot{\theta_2} = C_p - C_2 \tag{1}$$

Where I_2 is the rotational inertia of the pulley 2 and its shaft, C_2 is the constant load torque and C_p is the torque resulting from the belt tensions applied to the driven pulley given by:

$$C_p = R_2(T_a(t) - T_b(t)) \tag{2}$$

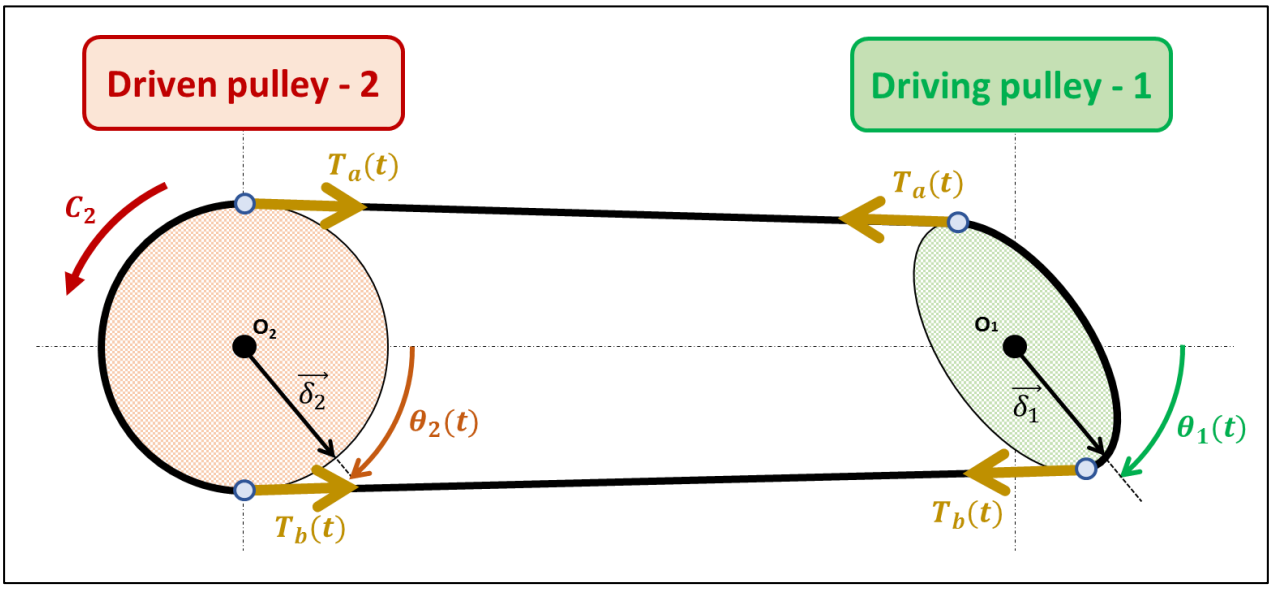


Figure 19: Modeling of the O-C setup.

Figure 20 shows a comparison of the instantaneous rotational speed variations of the driven pulley for the O-C transmission obtained from experiments and simulation. Second order variations due to the oval effect are present on both cases and have the same phase and amplitude. However, the fluctuations of other frequencies visible on the experiments (pulley eccentricity, meshing frequency, etc.) do not appear in the simulation results. Indeed, these phenomena are not taken into account in the current model. Similar comments can be made for the TE plot in Figure 21.

The simulated and experimental fluctuations of the torque C_p are plotted versus the driving angle in Figure 22. It can be seen again that the second order fluctuation caused by the oval pulley is well described by the model. From these observations, one can deduce that the model is able to predict rather well the dynamics of a two-pulley transmission comprising an oval pulley.

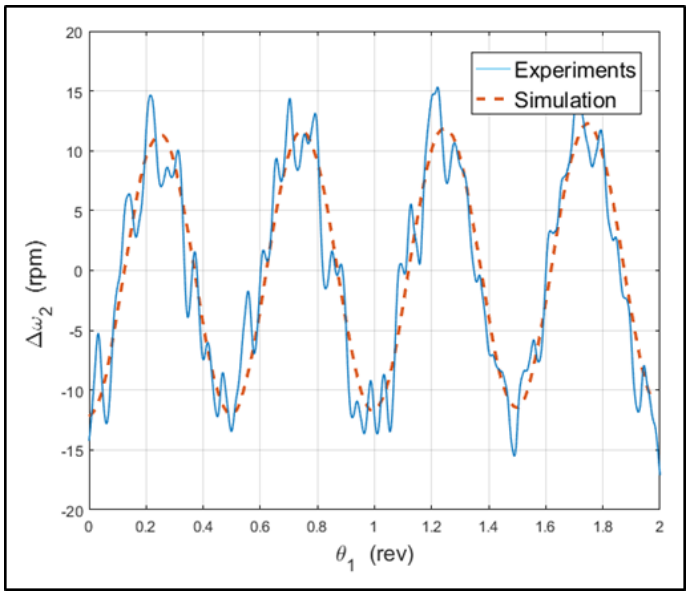


Figure 20: Simulated and experimental instantaneous angular velocity fluctuations of pulley 2 vs. driving angle (O-C transmission).

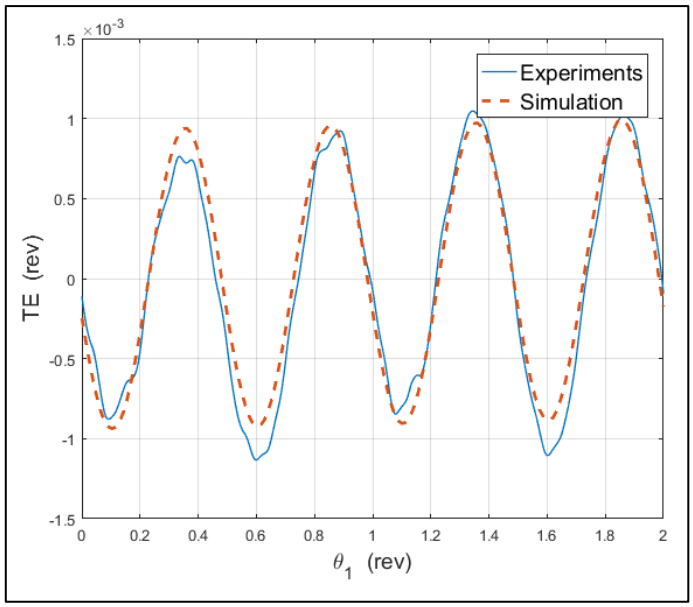


Figure 21: Simulated and experimental transmission error vs. driving angle (O-C transmission).

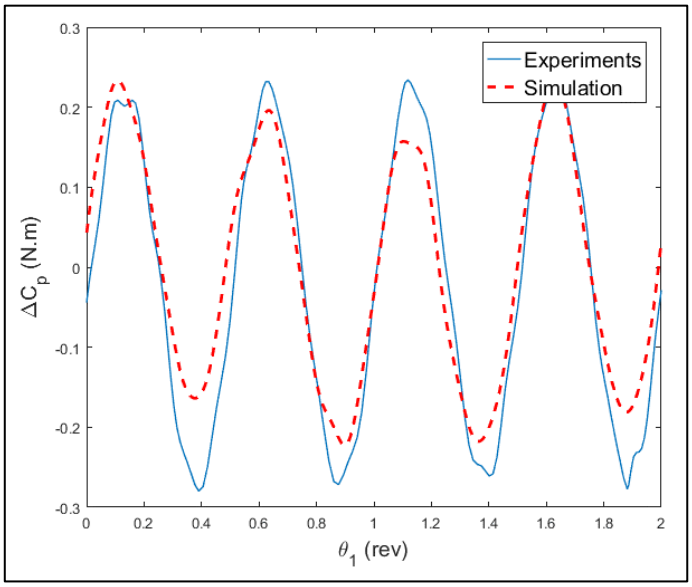


Figure 22: Simulated and experimental torque C_p (O-C transmission).

5 Conclusion

The experiments presented in this paper enable highlighting the effect of an oval pulley on a two-pulley transmission dynamics. The experimental analysis has been conducted for two transmission setups: one reference setup comprising circular pulleys only (C-C) and the other setup comprising an oval driving pulley (O-C). The comparison between the results obtained for the C-C and O-C setups clearly shows that the periodic belt span elongations generated by the oval profile, cause fluctuations of the torques applied to the pulleys. These torque variations induce rotational acceleration and speed fluctuations on the driven pulley with a frequency of two events per non-circular pulley revolution. These fluctuations lead to instantaneous desynchronization of the transmission quantified by periodic TE variations with the same angular frequency. These experiments have also confirmed the relevance of the model developed by Passos et al. [5].

Future works will concern the enrichment of the test stand in order to perform experiments on belt transmission setups fully representative of real running conditions encountered in a combustion engine. It is planned to study transmissions equipped with a dynamic tensioner pulley for higher rotational velocities (till ~5000 rpm on the driving pulley). Also, fluctuating load torque and driving speed acyclism will be introduced in order to test the non-circular pulley capability of counteracting these excitation sources.

References

[1] GAJEWSKI, W., *Synchronous drive apparatus and methods*. U.S. Patent No 7,044,875, Litens Automotive, 2006.

[2] ZHENG, E., JIA, F., SHA, H, WANG, S., *Non-circular belt transmission design of mechanical press,* Mechanism and Machine Theory, Volume 52, 2012, pp. 126-138.

[3] ENDO, G., YAMADA, H., YAJIMA, A., OGATA, M., HIROSE, S., *A passive weight compensation mechanism with a non-circular pulley and a spring, 2010 IEEE International Conference on Robotics and Automation (ICRA),* Anchorage, AK, 2010, pp. 3843-3848.

[4] ZHU, H., HU, Y., ZHU, W. D., *Dynamic response of a front end accessory drive system and parameter optimization for vibration reduction via a genetic algorithm*. Journal of Vibration and Control, Volume 25, Issue 11, 2018, pp. 2201-2220.

[5] PASSOS, S., MANIN. L., SAUVAGE, O., ROTA, L., DELATTRE, B. REMOND, D., *Investigation on the timing belt drive with a non-circular pulley, Proceedings of The 2018 International Gear Conference, Lyon - Villeurbanne, France, 27-29 august 2018*, Lyon-Villeurbanne, 2018.

[6] HWANG, S. J., PERKINS, N. C., ULSOY, A. G., MECKSTROTH, R. J., *Rotational Response and Slip Prediction of Serpentine Belt Drive Systems*, J. Vib. Acoust., Volume 116, Issue 1, 1994, pp. 71-78.

[7] REMOND, D., *Practical performances of high-speed measurement of gear Transmission Error or torsional vibrations with optical encoders*. Measurement Science and Technology, IOP Publishing, 1998, pp. 347-353

[8] MANIN, L., MICHON, G., REMOND, G., DUFOUR, R., *From transmission error measurement to pulley–belt slip determination in serpentine belt drives: Influence of tensioner and belt characteristics*, Mechanism and Machine Theory, Volume 44, Issue 4, 2009, pp. 813-821.

[9] MAKITA, K., KAGOTANI, M., UEDA, H., KOYAMA, T., *Influence of Idler on Transmission Error in Synchronous Belt Drives (Under Transmission Force),* ASME J. Mech. Des., Volume 125, Issue 2, 2003, pp. 404–410.

Improvement of instantaneous angular speed estimation based on frequency demodulation method under non stationary conditions

K. Lizoul [1], **H. André**[1], **F. Guillet** [1]
[1] Université de Lyon, Université Jean Monnet, LASPI EA3059, 42023 Saint-Etienne, France
20 Avenue de Paris, 42334 Roanne Cedex, France
e-mail: **k.lizoul@univ-st-etienne.fr**

Abstract
Instantaneous Angular Speed (IAS) has appeared to provide a new source of information on the rotating machine and the diagnosis of faults. Recently, different methods have been developed to estimate IAS, each method have attempted to improve the measurement using different techniques. In this study, we examine the precision of frequency demodulation, and we show that IAS spectral estimation depends on several parameters. The effect of temporal aliasing is studied. We show that under certain conditions, the aliasing phenomenon can be detrimental to IAS spectral estimate. For IAS estimation under non stationary conditions, a new approach is proposed and shown to yield good results.

1 Introduction

Nowadays, most of rotating machines are equipped with rotary encoders to track the angular position of the shaft. The information of speed can be then deducted from the variation of the position with regard to the time. The encoder is directly mounted on the shaft allowing a direct IAS measurement which makes it more robust to noise compared to vibration sensors. Besides its relatively low price, the incremental encoder doesn't need a periodic calibration. In certain cases, the environment of the machine,e.g cutting process, makes the use of vibration sensor more complicated. In this context, Lamraoui et al.[1] used IAS measurement to develop new indicators for the detection of chatter in high speed machining process. Yang et al.[2] proposed a new model based on IAS fluctuation ratio for fault detection in diesel engine. Gu et al.[3] carried out a study on IAS characteristics of engines and compressors, and used them for diagnosis. Ben Sasi et al.[4] demonstrated the effectiveness of IAS monitoring based for the diagnosis of broken bar failure in electrical motors. Recently, Zhao et al.[5] proposed a new method called Kurtosis-Guide Local Polynomial Differentiator (KLPD) to detect the weak speed jitters for the diagnosis of planetary gearbox. These investigations show why IAS has attracted many researchers in condition monitoring.

In the literature, direct IAS measurement methods are classified into two major groups : timer/counter based methods [6, 1, 7], and Analog to Digital Converter ADC-based methods[8, 9, 10]. The main difference between the two methods is the type of sampling (Angular sampling for timer/counter based methods and temporal sampling for ADC-based methods).

The accuracy of IAS measurement is a key point in early fault detection. Previous works showed that an increase of the counting frequency (high clock counter frequency) is definitely beneficial to IAS estimation [11, 7]. Meanwhile, this method provides low accuracy for high angular speeds [11]. Gu at al.[8] evaluated the influence of noise on IAS estimation using frequency demodulation method and showed that using higher encoder resolution improves the accuracy of IAS estimation. Frequency demodulation using Gabor's analytic signal is widely used for the estimation of the instantaneous frequency in different domains like reflection

seismology[12], communication engineering[13, 14], and vibration analysis[15, 16]. Meanwhile, the tools dedicated to IAS estimation were developed in the context of stationary conditions[8, 11, 10]. Feldman[15] proposed a new method for IF estimation under non stationary conditions for modal identification . The results have shown that this promising tool can be used for IAS estimation.

To overcome the limitation of timer/counter based methods in high speed applications, and the necessity to use higher encoder resolution to detect the different events related to machine operating and health conditions. Frequency demodulation using analytic signal provides a good alternative. Meanwhile, the influence of the different operating and acquisition parameters is not yet shown.

This paper will mainly focus on the precision of ADC-based method since any general-purpose board can be used for data collection. This analog approach is used to estimate IAS using signal processing techniques already developed in communication engineering. The results are compared to the original speed in frequency domain, since we are interested on IAS spectral estimation, via an appropriate comparison indicator.

This paper is organized into 5 sections. Section 2 presents the system modeling and the methods used for IAS estimation. Section 3 covers the influence of the different parameters on IAS estimates and shows the proposed algorithms for an appropriate selection of these parameters. In Section 4, an experimental study is performed for the detection of impulsive cyclic faults. The last section presents the major funding of this study and perspectives to improve the IAS accuracy for high angular speed.

2 System modeling and simulation setup

2.1 System modeling

A set of signals are simulated in order to evaluate the influence of the IAS acquisition technique on the precision of its spectral estimation. This simulation yields speed signal containing one cyclic train of impulses. the cyclic train can be seen as the repetition of a defect due to the angular movement of a shaft, while the impulse corresponds to the natural vibration of the structure when it is excited.

The impulse is defined through a linear Single Degree Of Freedom (SDOF) system represented by it's transfer function as following:

$$\theta(t) = Ae^{-\xi w_d t} sin(w_0 t) \tag{1}$$

where :

- ξ: damping factor
- $w_0 = 2\pi\nu_0$: natural angular frequency (ν_0 : resonance frequency)
- $w_d = \sqrt{1-\xi^2} w_0$: damped angular frequency
- A: constant

After setting the speed initial conditions, the angle/time function is constructed by integrating the speed signal. At each revolution traveled by the shaft, an impulse is added to the angle signal. The spectrum of the simulated speed is composed form a pulse train with a fundamental cyclic frequency corresponding to $1ev/rev$ in order domain. By integrating the resulting IAS, the encoder signal is generated from the angle/time function at the desired encoder resolution. An analog anti-aliasing filter is implemented, and it's cut-off frequency is set as a function of the number of harmonics allowed in the signal.

2.2 Frequency demodulation and instantaneous frequency

In this part, we are interested in estimating the instantaneous speed from a rotary encoder signal using frequency demodulation method which consists in calculating the instantaneous frequency considering the encoder signal as a Frequency Modulated (FM) signal.

2.2.1 Stationary conditions

In IAS condition based monitoring, angular speed is composed from two components:

$$f(t) = f_0 + \delta f(t) \tag{2}$$

where f_0 represents the average speed, and $\delta f(t)$ represents the time-varying component dependent on the dynamics of the mechanical system.

IAS signal is a FM signal [8, 9]:

$$s(t) = Acos[2\pi(F_c t + \varphi(t))] \tag{3}$$

where $F_c = Rf_0$ is the carrier frequency, and R refers to encoder resolution. $\varphi(t) = \int_0^t \delta f(\tau)\mathrm{d}\tau$ is the phase deviation where δf is the modulating signal containing the dynamic charcteristics of the system. The FM signal is conditioned further by a comparator to generate the TTL encoder signal[9]. Theoretically, the spectrum of a square FM signal is composed only from odd harmonics symmetrically surrounded by an infinite number of sidebands around the carrier frequency.

FM signals are widely analyzed by the scientific community and many techniques developed in communication engineering can be used for IAS estimation. This leads us to the concept of Instantaneous Frequency (IF) discussed in many works and different techniques were used to estimate it [14, 17, 13]. Vakman[17] showed that IF estimation using Gabor's [18] analytic signal is more accurate compared to local estimation methods.

The analytic representation of a signal s is defined as following :

$$S_a(t) = s(t) + iH[s(t)] \tag{4}$$

where H represents Hilbert Transform (HT) defined by :

$$H[s(t)] = \frac{1}{\pi}\int_{-\infty}^{+\infty} \frac{s(\tau)}{t-\tau}\,\mathrm{d}\tau \tag{5}$$

HT operator is a convolution integral of s with the impulse response $h(t) = 1/(\pi t)$. Physically, HT operator is a kind of a linear filtering process where all the amplitudes of spectral components are left unchanged, but their phases are shifted by $\pi/2$ for positive frequencies and by $-\pi/2$ for negative frequencies. The spectrum of the analytic signal is zero for negative frequencies, and two times the spectrum of the signal for positive frequencies.

HT operator attributes a unique Amplitude-Phase couple $(A(t), \phi(t))$ at each instant t to the analytic signal :

$$S_a(t) = A(t)e^{\phi(t)} \tag{6}$$

The instantaneous frequency is then calculated by the derivation of the instantaneous phase:

$$f(t) = \frac{d\phi(t)}{dt} = Im(\frac{\dot{S}_a}{S_a}) \tag{7}$$

In frequency domain, the first derivative of the analytic signal is obtained by multiplying the AS sequence by the frequency sequence. In the case of multi-component signals, a bandpass digital filtering should be performed before applying the HT operator. The filter bandwidth is determined by Carson's formula[19] :

$$B = 2(\Delta f + f_{max}) \tag{8}$$

where f_{max} is the highest frequency in the modulating signal, and $\Delta f = R\ max(|\delta f(t)|)$ is the peak frequency deviation where R refers to encoder resolution. This bandwidth requirement allows the extraction of at least 98% of the power of modulating signal with a limited number of sidebands. For chirp FM signal, Gaussian window filter has been demonstrated to give the best results[20]. In this study, a rectangular window is used. The influence of signal-to-noise ratio on IAS estimation is characterized in[8] and showed to be proportional to peak frequency deviation :

$$SNR \sim (\frac{\Delta f}{f_{max}})^2 \tag{9}$$

Finally, IAS estimation process is implemented using a frequency domain approach as following :

- Apply FFT to TTL encoder signal
- Apply rectangular window for bandpass filtering using the bandwidth according to **Eq.8**
- Set negative frequencies to zero to obtain the AS sequence
- Multiply the AS sequence by the frequency sequence to obtain the first derivative of the AS
- Apply IFFT to obtain both AS and it's first derivative
- Calculate IAS according to **Eq.7**

This FFT-based implementation provides the advantage of a high efficiency and reduces considerably the computation time compared to FIR filter implementation of HT operator. The frequency demodulation using HT developed in this section works only for stationary and narrowband signals . In the case where the signal is non stationary, a different scheme is proposed in the next part.

2.2.2 Non stationary conditions

In this section, we propose a method for IAS estimation under non stationary conditions. Let's consider a double component signal $x(t)$ composed of two signals as following :

$$x(t) = x_1(t) + x_2(t) \tag{10}$$

where $x_1(t) = A_1 cos(w_1 t)$, and $x_2(t) = A_2 cos(w_2 t)$ where $A_1 > A_2$.

Feldman[16] demonstrated that the IF $w(t)$ of the double component signal $x(t)$ is:

$$w(t) = w_1 + \frac{(w_2 - w_1)[A_2^2 + A_1 A_2 cos[(w_2 - w_1)t]}{A(t)^2} \tag{11}$$

where $A(t) = [A_1^2 + A_2^2 + 2A_1 A_2 cos[(w_2 - w_1)t]]$.

The IF $w(t)$ is composed from the largest energy component and a time-varying asymmetrical component. For $w_1 > w_2$, the IF exhibits negative frequencies. It is not the case for TTL encoder signal where the conditions $A_1 > A_2, w_1 < w_2$ are always verified. Assuming that $A_1 > A_2$, if we integrate the asymmetrical part with integration limits corresponding to one full cycle $T = \frac{2\pi}{w_2 - w_1}$, we will obtain a definite integral equals to zero[16]:

$$\int_0^T \frac{(w_2 - w_1)[A_2^2 + A_1 A_2 cos[(w_2 - w_1)t]}{A(t)^2} \mathrm{d}t = 0 \tag{12}$$

This averaging process allows the extraction of the frequency of the largest harmonic $\overline{w(t)} = \int_0^T w(t)\mathrm{d}t = w_1$. In the case of slow varying amplitude and frequency: $A_1(t)e^{i\int_0^t w_1(\tau)\mathrm{d}\tau} + A_2(t)e^{i\int_0^t w_2(\tau)\mathrm{d}\tau}$, the integration over one full cycle period is replaced by the convolution with a low pass filter[15]. The low pass filtering, instead of the integration, will cut down the fast asymmetrical oscillations and leave only a slow varying frequency of the main signal component $w_1(t)$ (Flowchart in **Fig.1**).

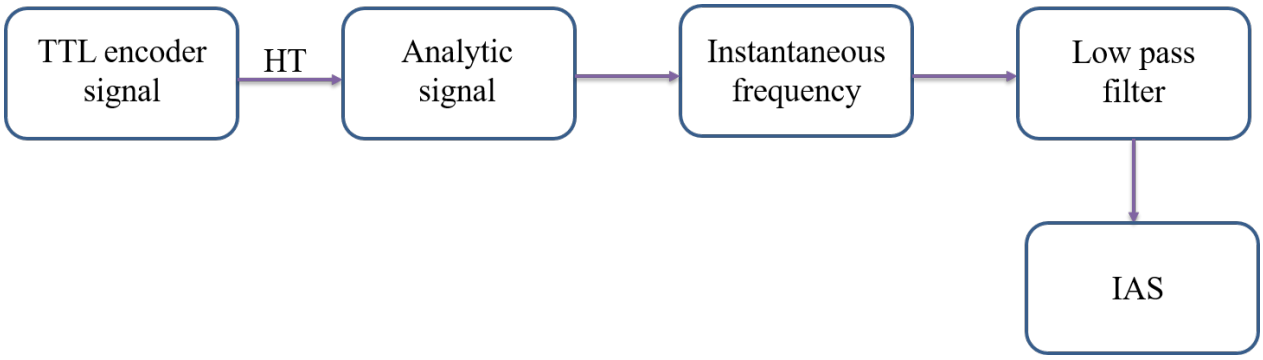


Figure 1: IAS estimation under non stationary conditions

2.3 Comparison indicator

To evaluate the influence of parameters on IAS estimation. The spectral components of each estimation method are compared to the spectrum of the original IAS via the Sum of Squared residuals (SSR) which is a second order distance :

$$L_2 = log_{10}(\sum_i (W_i - \overline{W_i})^2) \tag{13}$$

where W_i is the FT of the original speed, and $\overline{W_i}$ is the FT of the estimated speed.

Under non stationary conditions, the indicator is calculated in order domain where the frequency sequence is expressed in $Events/revolution$ instead of $Hertz$. For this purpose, IAS signal is resampled in the angular domain. The angular resampling process adopted in this work is described in[21]. By integrating the resulting IAS signal, the angle/time function returns the instants corresponding to every angle position where the IAS signal is sampled **Fig.2**. These instants are used to resample IAS signal using a cubic spline interpolation[22].

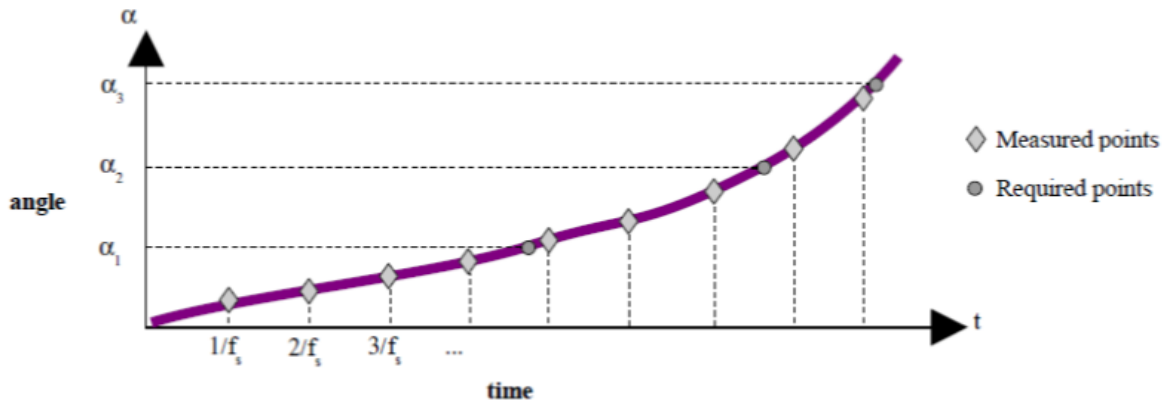


Figure 2: Angle/time function (André et al)

2.4 Selection of the sampling frequency

To evaluate the influence of the sampling frequency, an analog anti-aliasing filter is introduced before the data collection. The cut-off frequency is set as function of the number of the harmonics . This part is dedicated to stationary conditions where the carrier frequency is kept constant.

The alias frequency of each harmonic is calculated as a function of the sampling frequency as following :

$$Fa(F_k) = |E(\frac{F_k}{Fs})Fs - F_k| \tag{14}$$

where :

- $E(.)$: integer part function
- $F_k = kFc$: the frequency of the kth harmonic where Fc is the carrier frequency
- Fs : sampling frequency
- Fa : apparent frequency (i.e the position of the aliased harmonic)

In the case where the alias frequencies are located around the carrier frequency in the range of the bandpass filter bandwidth, they will be seen as modulating frequencies leading to a wrong interpretation of IAS spectral components as they could be associated to some real phenomenons. For this purpose, we propose new algorithms to calculate the optimal parameters for an accurate estimation. Therefore, these parameters will be used to control the sampling frequency and the bandwidth of the bandpass filter.

The algorithm consists in calculating the distance of the nearest alias frequencies from the carrier frequency Fc as following:

$$Dh(F_k) = |F_a(F_k) - Fc|; k > 1 \tag{15}$$

Where $D_h(F_k)$ is the distance of the kth aliased harmonic from the carrier frequency. $MinDh = \bigcap_{k>1} min(Dh(F_k))$ is the vector describing the nearest alias frequency as a function of F_s. The sampling rate is then selected so as $MinDh$ is maximal providing a large choice of the filter's bandwidth. If the ADC-board does not allow the selection of the sampling frequency, the algorithm allows also the selection of the optimal encoder resolution since Fa can be calculated as a function of the carrier frequency and it's harmonics.

3 Results and discussion

3.1 Influence of the average speed

In this part, we examine the impact of the average speed on IAS spectral components. Theoretically, the IAS spectrum is composed of an infinite number of harmonics amplified by the system's response around the natural frequency. Thus, the maximal frequency in the signal is infinite. **Figure 3.** shows IAS spectrum where the parameters are set as following :

- The natural frequency of the mechanical system $f_0 = 400Hz$
- The average speed is set to $20Hz$
- The filter's bandwidth is set to $4,000Hz$ which represents 10 times the natural frequency of the system.

In this case, the choice of the filter's bandwidth depends on: the natural frequency of the system since the fault detection is easier in this frequency range, and the average speed since 100 harmonics are considered. Different cases are considered:

- **Constant number of cycles**

Figure 4. illustrates the impact of the average speed on IAS estimation. As mentioned in **Eq 3.**, IAS accuracy depends on the peak frequency deviation. its value is set to $0.314\,Hz$ for all speeds and the number of cycles is set to $100\,revolutions$. Two configurations were tested:

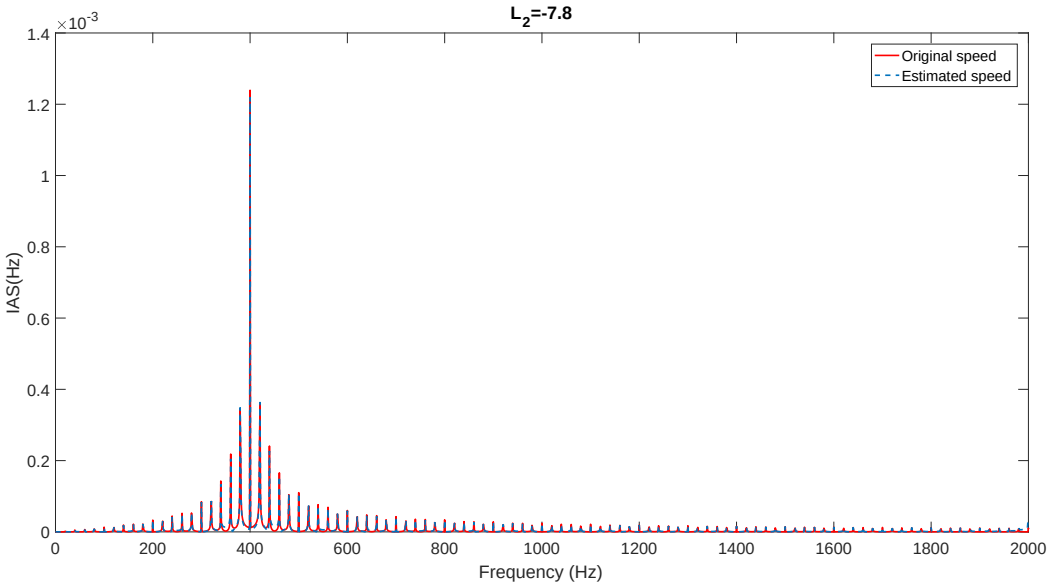


Figure 3: IAS spectrum

1. Constant filter's bandwidth : The number of harmonics contained in the bandwidth range decreases with the average speed due to the cyclicality of the fault. As a result, less energy is considered in the calculation of the indicator when the speed increases what explains the improvement of the estimation.
2. Constant number of harmonics: In this case, The filter's bandwidth depends on the average speed. Thus, the indicator shows no evolution with the average speed because the energy of the signal is kept constant.

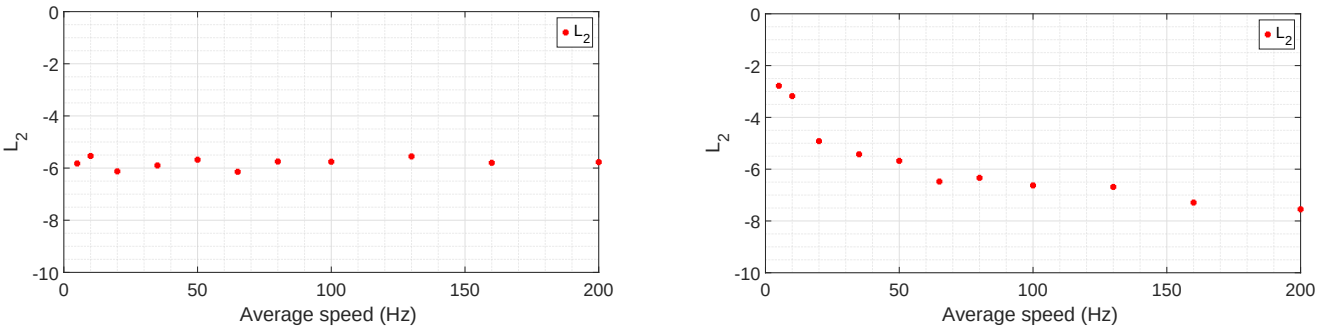


Figure 4: Influence of average speed on IAS estimation (duration=100 revolutions): $B = 100\ harmonics$ (left), $B = 5000\ Hz$ (right)

- **Constant acquisition duration**

In this part, the acquisition duration is set to $1\ second$ and the peak frequency deviation is kept constant. **Figure 5.** shows the influence of the average speed on IAS estimation. For both configurations tested in the previous part, similar behavior is observed.

These results show that the accuracy of frequency demodulation method using analytic signal does not depend on the average speed since the peak frequency deviation is kept constant. Compared to timer/counter based methods, this method is suitable to high speed applications and allows the use of high encoder resolutions. But, it is still limited by the properties of the acquisition system in terms of sampling rate.

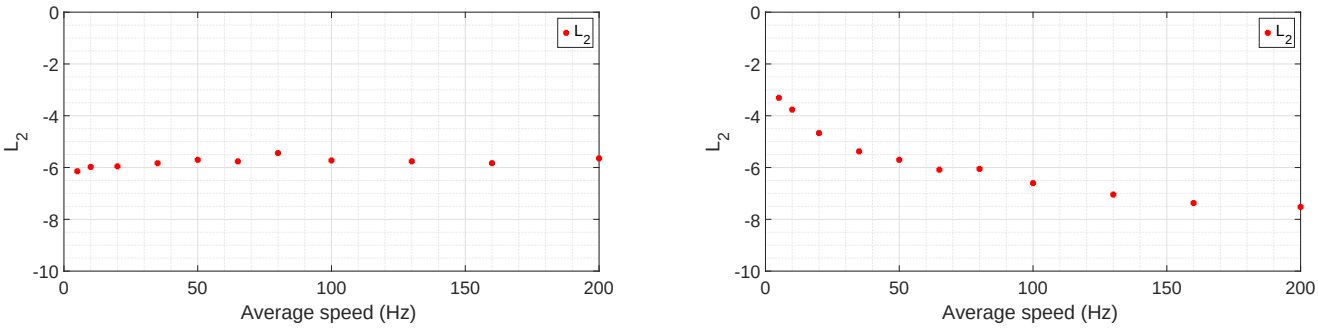


Figure 5: Influence of average speed on IAS estimation(duration=1 second): $B = 100\ harmonics$ (left), $B = 5000\ Hz$ (right)

3.2 Influence of encoder resolution

To evaluate the impact of the encoder resolution, The comparison indicator is calculated in the range of the filter's bandwidth since all the information is contained within this range.

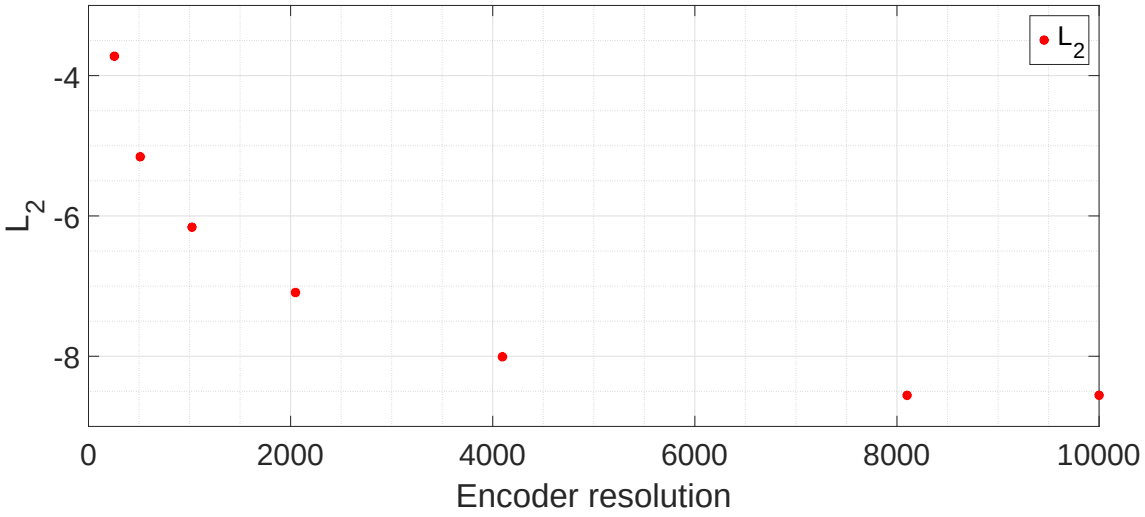


Figure 6: Influence of encoder resolution on IAS estimation

The results of the simulation show that IAS estimation can be improved by using a higher encoder resolution **Fig.6**. The study carried out in [8] showed similar results that using a higher encoder resolution improves the signal-to-noise ratio (SNR) as the frequency demodulation is very sensitive to noise due to the differentiation operator used to calculate the instantaneous frequency. Thus, a zero mean white Gaussian noise is added to examine the influence of SNR on IAS estimation. **Figure 7.** shows the influence of SNR on IAS estimation. These results show that using a higher encoder resolution is beneficial to IAS spectral estimation. Similarly to the average speed, this operation is only limited by the capability of the ADC-board to collect the data.

3.3 Influence of the sampling frequency

Figure 9 shows the aliasing diagram describing the evolution of the apparent frequency with the sampling frequency. As encoder signal is composed only from odd harmonics, the filter cut-off frequency is set to keep the $7th$ harmonic. The carrier frequency is set to $10kHz$.

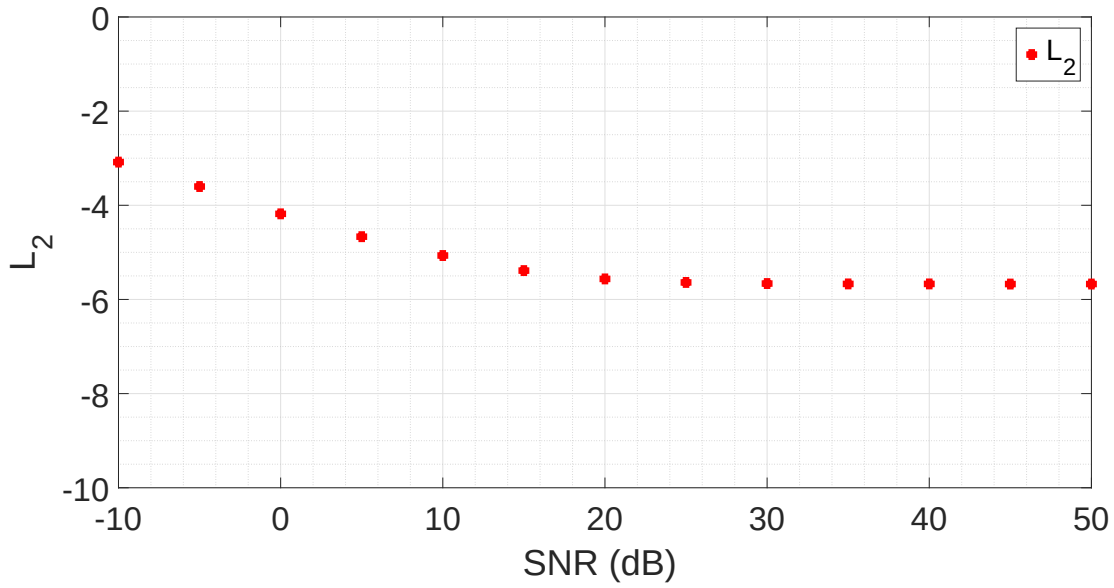


Figure 7: Influence of SNR on IAS estimation, $R = 1024 points/rev$

Under these conditions, sampling data at $F_s = 40kHz$ will result in aliasing all the harmonics at the same position $F_a = 10kHz$. Thus, it is nearly impossible to distinguish the alias frequencies from the carrier frequency **Fig 8.** Consequently, IAS estimation is corrupted by this phenomenon and provides higher estimation error.

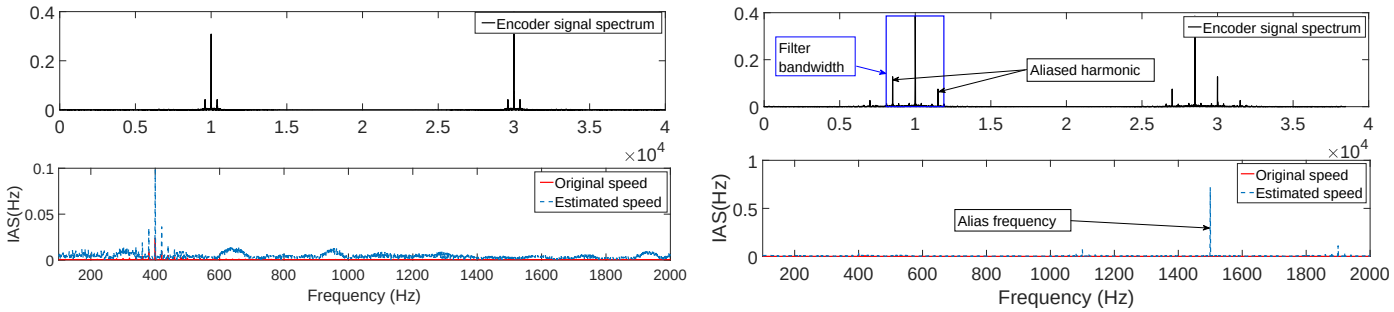


Figure 8: Effect of aliasing on IAS estimation, $F_s = 40kHz$ (left), $F_s = 38.5kHz$ (right)

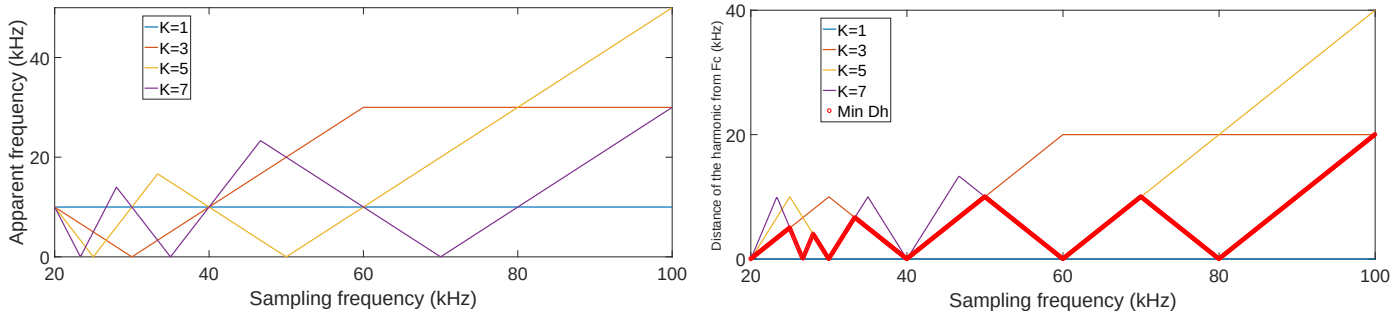


Figure 9: Aliasing diagram (left), Distance of each harmonic from the carrier frequency $F_c = 10kHz$ (right)

Figure 9. shows the evolution of the distance of aliased harmonics from the carrier frequency with the sampling rate. In the case where the ADC-board provides possible sampling rates from $20kHz$ to $80kHz$, the algorithm proposes two solutions : sampling with $50kHz$ or with $70kHz$. Both solutions guarantee that the nearest alias frequency is located at $10kHz$ from the carrier frequency. The bandwidth of the filter can be then selected within this range to avoid aliasing. Meanwhile, collecting data with $60kHz$ sampling rate is detrimental to IAS estimation as the $5th$ harmonic is aliased exactly at the carrier frequency.

3.4 Non stationary conditions

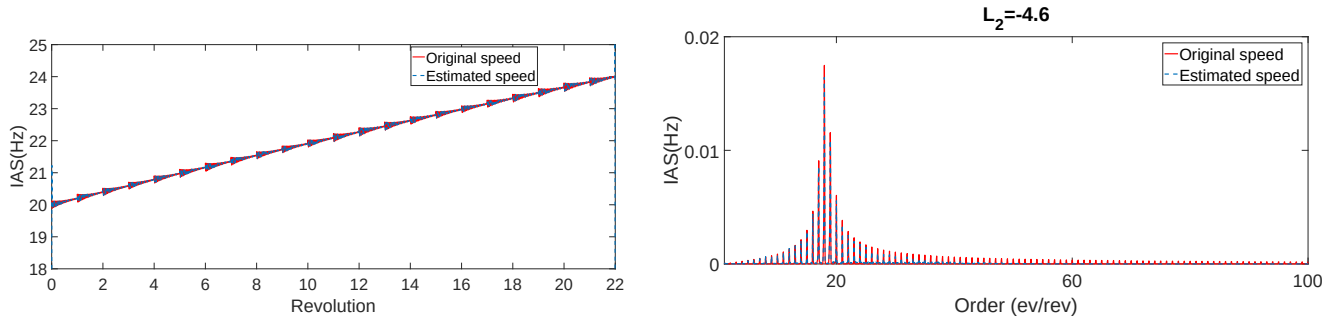


Figure 10: Linear varying speed: Generated IAS (left), IAS spectrum (right)

Generally, rotating machines are working under non stationary conditions where the speed variation is 10% up to 20% of the starting speed. **Figure 10.** illustrates a generated linear increasing speed where the starting speed is set to $20Hz$ with a variation rate of 20%. The IAS estimation is therefore resampled in angular domain and compared to the original speed. The sampling rate is set to $100kHz$ with an encoder resolution of $1024points/rev$.

The results show that IAS estimation exhibits slightly higher error compared to the stationary conditions **Fig.10**. This difference is due two factors : The angular sampling since IAS estimation is used to resample itself. As a result, the error estimation is accumulated through this operation. The other factor is that the comparison indicator is calculated for the whole spectrum instead of a limited interval since no bandpass filtering is used. We believe that using different resampling strategies can improve the accuracy of IAS estimation in non stationary conditions.

4 Experimental validation

4.1 Test bench description

The signals were acquired on one-stage gearbox where a shock is introduced in the output gear. To measure IAS, an optical encoder with a resolution of 4096 points/rev is mounted on the primary shaft via a flexible coupling to reduce the torsional forces. The gearbox is driven by 3-phase asynchronous motor controlled with a variable speed drive. A vibration sensor is mounted for the verification of the results **Fig.11**.

4.2 Data acquisition

The signals are acquired using two data acquisition systems. A frequency divider is used to acquire the signals with different resolutions. The sampling frequency is set to $51.2kHz$ for the ADC-based measurement where both vibration and speed signals are acquired synchronously. An 80Mhz counter is used for Elapsed Time (ET) measurement.

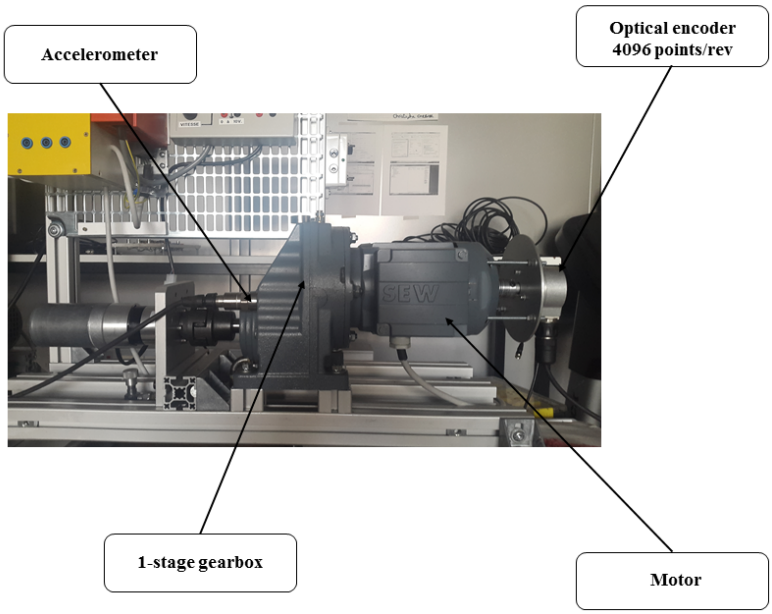


Figure 11: Gearbox test bench

4.3 Results and discussion

In the experimental study, the main goal is to examine the ability of the frequency demodulation method to detect the mechanical phenomenons particularly in non stationary conditions. ET measurement is taken as IAS reference since it's accuracy was already tested for low speed applications. The meshing ratio is $mesh_{ratio} = \frac{N_1}{N_2} = \frac{23}{38} = 0.6052$, where $N_1 = 23$ the number of the teeth of the input gear, and $N_2 = 38$ the number of teeth of the output gear.

The tests were performed under non stationary conditions where a low frequency generator to control the variable speed drive. A triangular wave is used to generate a linear varying speed and no load is applied **Fig. 12**. The encoder resolution is set to $R = 1024 points/rev$. Different speeds were also tested and the results showed no significant difference.

Figure 13. illustrates IAS spectrum with both ET method and frequency demodulation method. We can see that ADC-based method yields good results compared to ET based method. The meshing frequency $f_mesh = 23\, ev/rev$ is well detected by both methods as well as the sidebands at $0.6052\, ev/rev$. As it is explained in the simulation section, the difference is due to the resampling process in which a part of the information is lost.

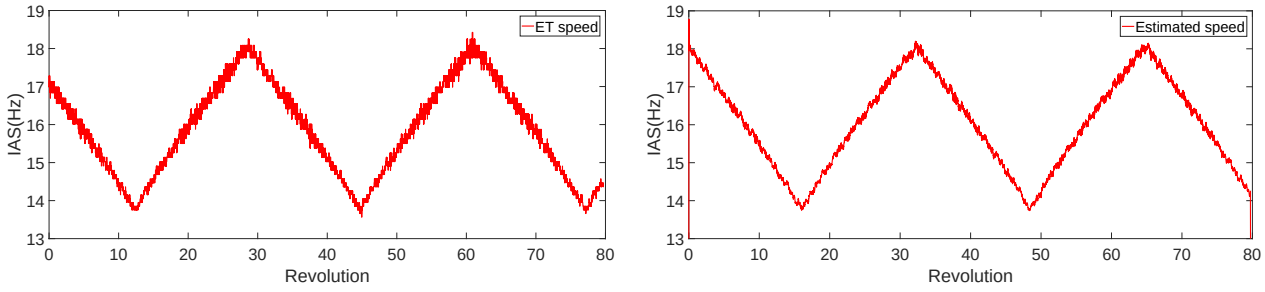


Figure 12: IAS estimation, ET measurement (left), frequency demodulation method (right)

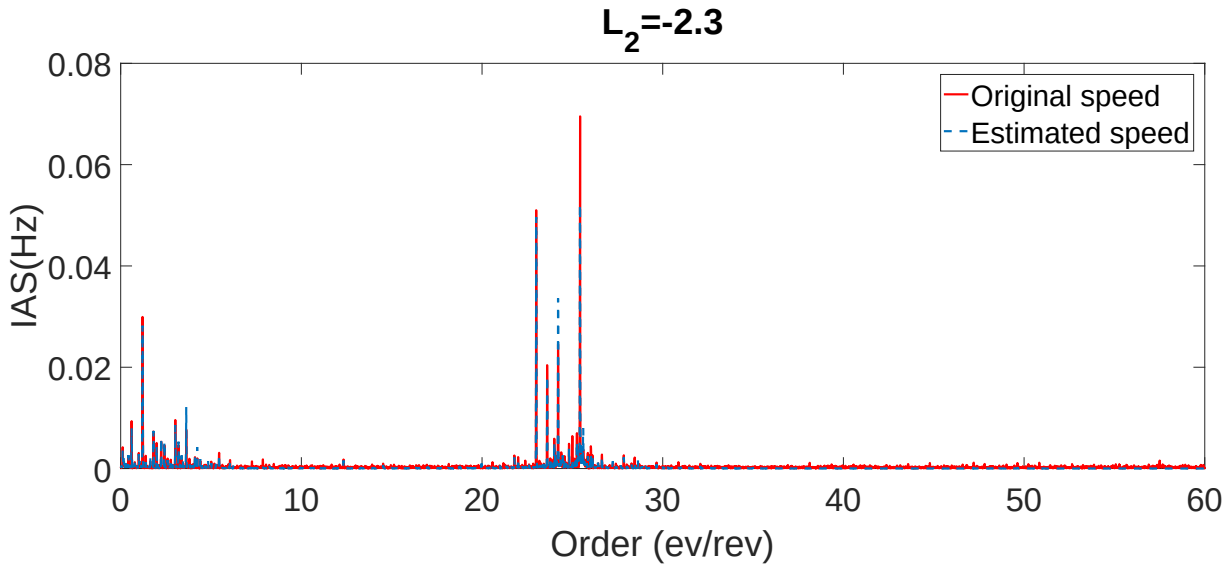


Figure 13: IAS spectrum of gearbox

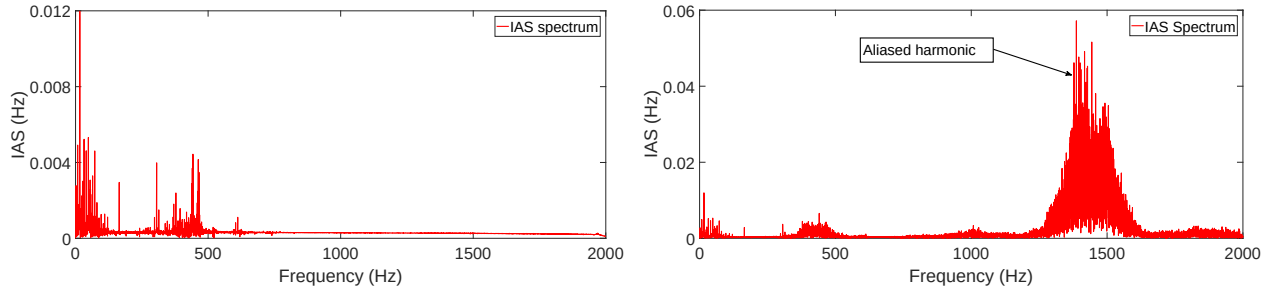


Figure 14: Effect of aliasing on IAS spectrum, $Fs = 51.2\,kHz$ (left), $Fs = 19\,kHz$ (right)

To examine the effect of aliasing, we perform a data acquisition under constant speed $f_0 = 800rpm$ and the encoder resolution is set to $256points/rev$. The acquisition board does not allow the control of the cut-off frequency of the anti-aliasing filter. The cut-off is set automatically to $F_s/2$. Therefore, the encoder signal is down-sampled with a sampling rate of $19kHz$. The nearest alias frequency is located at $1475Hz$ from the carrier frequency. The bandwidth of the bandpass filter is set to $4000Hz$.

Figure 14. illustrates the IAS spectrum using the frequency demodulation method. As it is expected, the largest energy component($f = 1475Hz$) is present in the spectrum due to the aliasing effect as the aliased harmonic is located within the filter bandwidth. This component could be considered as a local resonance leading to a misinterpretation of the spectral components. The results of this study can be extended to temporal resampling of angularily acquired signals for Blade Tip-timing (BTT) measurement for the identification of resonance frequencies[23]. The sampling rate and the cut-off frequency of the anti-aliasing filter can be controlled to avoid aliasing.

5 Conclusion

The accuracy of IAS estimation is key feature to ensure a better fault detection. The theoretical study performed in this paper show that the IAS measurement is influenced by different parameters. The results show that frequency demodulation is suitable for high speed application compared to timer/counter based methods

aliasing effect has been proved to be detrimental to IAS spectral estimation, and the proposed tools allow an optimal choice of these parameters.

The proposed approach in non stationary conditions has been shown to provide good results. Meanwhile, the accuracy of IAS estimation can be improved by revisiting angular sampling techniques. For high speed applications, a combined method can be used. These issues will be studied in future works.

References

[1] Mourad Lamraoui, Marc Thomas, Mohamed El Badaoui, and François Girardin. Indicators for monitoring chatter in milling based on instantaneous angular speeds. *Mechanical Systems and Signal Processing*, 44(1-2):72–85, 2014.

[2] Jianguo Yang, Lijun Pu, Zhihua Wang, Yichen Zhou, and Xinping Yan. Fault detection in a diesel engine by analysing the instantaneous angular speed. *Mechanical systems and signal processing*, 15(3):549–564, 2001.

[3] Fengshou Gu, PJ Jacob, and AD Ball. Non-parametric models in the monitoring of engine performance and condition: Part 2: Non-intrusive estimation of diesel engine cylinder pressure and its use in fault detection. *Proceedings of the Institution of Mechanical Engineers, Part D: Journal of Automobile Engineering*, 213(2):135–143, 1999.

[4] Ahmed Yousef Ben Sasi, Fengshou Gu, Bradley Payne, and Andrew Ball. Instantaneous angular speed monitoring of electric motors. *Journal of Quality in Maintenance Engineering*, 10(2):123–135, 2004.

[5] Ming Zhao, Xiaodong Jia, Jing Lin, Yaguo Lei, and Jay Lee. Instantaneous speed jitter detection via encoder signal and its application for the diagnosis of planetary gearbox. *Mechanical Systems and Signal Processing*, 98:16–31, 2018.

[6] Laurence Renaudin, Frédéric Bonnardot, Olivier Musy, JB Doray, and Didier Rémond. Natural roller bearing fault detection by angular measurement of true instantaneous angular speed. *Mechanical Systems and Signal Processing*, 24(7):1998–2011, 2010.

[7] Hugo Andre, François Girardin, A Bourdon, Jérôme Antoni, and Didier Rémond. Precision of the ias monitoring system based on the elapsed time method in the spectral domain. *Mechanical Systems and Signal Processing*, 44(1-2):14–30, 2014.

[8] Fengshou Gu, Isa Yesilyurt, Yuhua Li, Georgina Harris, and Andrew Ball. An investigation of the effects of measurement noise in the use of instantaneous angular speed for machine diagnosis. *Mechanical Systems and Signal Processing*, 20(6):1444–1460, 2006.

[9] Sankar K Roy, Amiya R Mohanty, and Cheruvu S Kumar. Fault detection in a multistage gearbox by time synchronous averaging of the instantaneous angular speed. *Journal of Vibration and Control*, 22(2):468–480, 2016.

[10] Bing Li and Xining Zhang. A new strategy of instantaneous angular speed extraction and its application to multistage gearbox fault diagnosis. *Journal of Sound and Vibration*, 396:340–355, 2017.

[11] Yuhua Li, Fengshou Gu, Georgina Harris, Andrew Ball, Nick Bennett, and Ken Travis. The measurement of instantaneous angular speed. *Mechanical Systems and Signal Processing*, 19(4):786–805, 2005.

[12] Arthur E Barnes. The calculation of instantaneous frequency and instantaneous bandwidth. *Geophysics*, 57(11):1520–1524, 1992.

[13] Boualem Boashash. Estimating and interpreting the instantaneous frequency of a signal. ii. algorithms and applications. *Proceedings of the IEEE*, 80(4):540–568, 1992.

[14] DE Vakman and Vaĭĭ. Amplitude, phase, frequencyfundamental concepts of oscillation theory.

[15] Michael Feldman. Time-varying vibration decomposition and analysis based on the hilbert transform. *Journal of Sound and Vibration*, 295(3-5):518–530, 2006.

[16] Michael Feldman. Hilbert transform in vibration analysis. *Mechanical systems and signal processing*, 25(3):735–802, 2011.

[17] David Vakman. On the analytic signal, the teager-kaiser energy algorithm, and other methods for defining amplitude and frequency. *IEEE Transactions on signal processing*, 44(4):791–797, 1996.

[18] Dennis Gabor. Theory of communication. part 1: The analysis of information. *Journal of the Institution of Electrical Engineers-Part III: Radio and Communication Engineering*, 93(26):429–441, 1946.

[19] John R Carson. Notes on the theory of modulation. *Proceedings of the Institute of Radio Engineers*, 10(1):57–64, 1922.

[20] D Vakman. Computer measuring of frequency stability and the analytic signal. *IEEE transactions on instrumentation and measurement*, 43(4):668–671, 1994.

[21] Hugo André, Z Daher, J Antoni, and Didier Rémond. Comparison between angular sampling and angular resampling methods applied on the vibration monitoring of a gear meshing in non stationary conditions. *Proceedings of ISMA2010 including USD2010*, pages 2727–2736, 2010.

[22] Mohamed El Badaoui, Jérôme Antoni, François Guillet, and J Daniere. Ré-échantillonnage angulaire par interpolation spline cubic des signaux d'engrenages. In *6ème Congrès Français d'Acoustique CFA*, page 0, 2002.

[23] G Battiato, CM Firrone, and TM Berruti. Forced response of rotating bladed disks: Blade tip-timing measurements. *Mechanical Systems and Signal Processing*, 85:912–926, 2017.

Nonlinear dynamical analysis of a fluid-structure computational model with sloshing and capillarity

Q. Akkaoui[1], **E. Capiez-Lernout**[1], **C. Soize**[1], **R. Ohayon**[2]
[1] Laboratoire Modélisation et Simulation Multi Echelle (MSME) UMR 8208 CNRS, 5 Boulevard Descartes 77454 Marne-La-Vallée, France
e-mail: **quentin.akkaoui@univ-paris-est.fr**

[2] Structural Mechanics and Coupled System Laboratory, Conservatoire National des Arts et Métiers (CNAM), 2 rue Conté, 75003, Paris , France

Abstract

This paper deals with a computational methodology for analyzing a fluid-structure system taking into account sloshing and capillarity phenomena. The fluid is assumed to be linear acoustic and the structure is assumed to undergo large displacements/deformations, which induce geometrical nonlinearities in the fluid-structure system. An adapted nonlinear reduced-order model is constructed using a modal characterization of each part of the coupled system. A numerical application is considered in order to study the effects of the geometrical nonlinearities on the dynamical forced response of the structural acoustic system.

1 Introduction

The understanding of fluid-structure dynamic interactions has always received a great attention and is of fundamental interest with respect to numerous applications (see for instance [2, 14, 10]). In particular, the sloshing phenomenon and the influence of the surface tension on the vibrational motion of the free surface of a fluid have been widely studied these last decades (see [10, **?**, 6, 12]). Note that the physics and modeling of surface tension can be found, for instance, in [7, 8]. The present work is devoted to a computational nonlinear dynamical analysis of a fluid-structure system, for which the fluid is a liquid is presence of a gravity field, taking into account both surface tension and sloshing effects. The structure is assumed to undergo large displacements and large deformations that could possibly influence the dynamical response of the fluid-structure system. Hence, the formulation used to analyze such fluid-structure system is the one recently proposed in [12, 13] that allows for considering the geometrical nonlinearities related to the structure through the use of an adapted computational nonlinear reduced-order model. This nonlinear reduced-order model relies on projecting the fluid-structure boundary value problem onto an adapted reduced-order basis that is constructed by considering several generalized eigenvalue problems related to the dynamics of the structure, of the acoustic fluid, and of the free surface. A detailed computational methodology for constructing this projection basis in the context of large scale fluid-structure systems has been proposed and validated in [1].

The computational model is constructed with the finite element method [15, 9] for which the unknowns of the problem are the nonlinear displacements of the elastic structure, the acoustic pressure in the liquid, and the free-surface normal elevation of the liquid. Furthermore, each reduced operator (linear or nonlinear) of the reduced-order computational model is explicitly calculated. The algorithm for solving the nonlinear reduced-order computational model uses simultaneously the arc-length algorithm (see [5]) and the fixed-point method.

The paper is organized as follows. Section 2 is dedicated to the formulation of the fluid-structure problem. In

particular, the construction of the nonlinear reduced-order model is explained in details. Section 3 is devoted to a numerical application that consists in a large scale computational model of an elastic cylindrical tank partially filled with the liquid (water). The nonlinear response of the fluid-structure system is analyzed in details.

2 Formulation of the fluid-structure problem

2.1 Notations and hypotheses

The equations of the fluid-structure system are written with a total Lagrange formulation and the related *reference configuration* is described in Figure 1. The structure, which is taken in its natural state without prestresses, occupies a bounded domain Ω_S and is assumed to be constituted of a homogeneous isotropic linear viscoelastic material without memory. The structure contains a linear dissipative acoustic fluid occupying a bounded domain Ω_F. Gravitational and surface tension effects are taken into account in the present formulation but internal gravity waves are neglected. It should be noted that the geometry of the free surface is obtained by a pre-computation allowing the static equilibrium to be found. The acoustic fluid is assumed to be dissipative. This dissipation is modeled by an equivalent damping term in the Helmholtz equation [11].

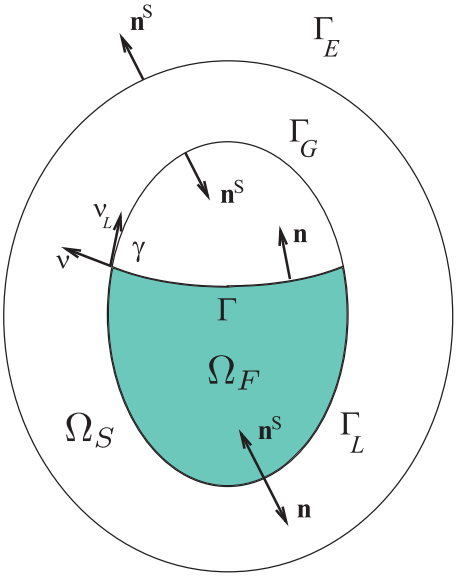


Figure 1: Reference configuration of the fluid-structure system (figure from [13])

The boundary of Ω_F is written as $\partial\Omega_F = \Gamma_L \cup \gamma \cup \Gamma$ (with $\Gamma_L \cap \gamma = \varnothing$, $\Gamma \cap \gamma = \varnothing$, $\Gamma_L \cap \Gamma = \varnothing$), where Γ_L is the fluid-structure interface, Γ is the free surface of the fluid and γ is the contact line between the structure and the fluid. The boundary of Ω_S is denoted by $\partial\Omega_S = \Gamma_E \cup \Gamma_L \cup \gamma \cup \Gamma_G$, where Γ_E and Γ_G are the external structural boundary of the structure and the part of the internal structural boundary that is not in contact with the fluid. The structure is submitted to a given body force field $\mathbf{b}$ in Ω_S and to a given surface force field $\mathbf{f}$ on Γ_E. The external unitary normals to $\partial\Omega_S$ and $\partial\Omega_F$ are denoted by $\mathbf{n}^S$ and $\mathbf{n}$. Let $\boldsymbol{\nu}$ and $\boldsymbol{\nu}_L$ be the external unit normals to γ belonging respectively to the tangent plane to Γ and to the tangent plane to Γ_L. The structure is assumed to be fixed on a part of its boundary Γ_E. We are then interested in analyzing the vibrations of the coupled fluid-structure system around its reference configuration.

Let $\mathbf{x} = (x_1, x_2, x_3)$ be the generic point in a Cartesian reference system $(\mathbf{O}, \mathbf{e}_1, \mathbf{e}_2, \mathbf{e}_3)$. The gravity vector is $\mathbf{g} = -g\,\mathbf{e}_3$ with $g = \| \mathbf{g} \|$. The boundary value problem is expressed in terms of the structural displacement

field $\mathbf{u}(\mathbf{x},t)$, of the internal pressure field $p(\mathbf{x},t)$, and of the normal displacement field of the free surface $\eta(\mathbf{x},t)$. In order to simplify the notations, the convention for summation over repeated Greek and Latin indices is considered and parameters $\mathbf{x}$ and t are removed if there is no possible confusion. Let $a(\mathbf{x},t)$ be a given function, the following notations are used : $a_{,j} = \partial a/\partial x_j$, $\dot{a} = \partial a/\partial t$ and $\ddot{a} = \partial^2 a/\partial t^2$.

2.2 Finite element computational model

In this work, the computational model is constructed with the finite element method. We are interested in analyzing the nonlinear forced response of the fluid-structure system and the equations are formulated in the time domain. Let $n_{PHS} = n_P + n_H + n_S$ be the total number of dof on the computational model, where n_P, n_H, and n_S correspond to the number of dofs of the fluid, of the free surface, and of the structure. We then denote by $\mathbb{P}$, $\mathbb{H}$, and $\mathbb{U}$ the $\mathbb{R}^{n_P}$-vector, $\mathbb{R}^{n_H}$-vector, and the $\mathbb{R}^{n_S}$-vector corresponding to the finite element discretization of the pressure field in the acoustic fluid, of the normal elevation of the free surface, and of the nonlinear structural displacement. The computational finite element model of the fluid-structure system is then described by the following set of nonlinear coupled differential equations,

$$[M]\,\ddot{\mathbb{P}} + [D]\,\dot{\mathbb{P}} + [K]\,\mathbb{P} - [C_{p\eta}]^T\,\ddot{\mathbb{H}} - [C_{pu}]^T\,\ddot{\mathbb{U}} = 0\,, \tag{1}$$

$$[C_{p\eta}]\,\mathbb{P} + [K_{gc}]\,\mathbb{H} + [C_{\eta u}]\,\mathbb{U} = 0\,, \tag{2}$$

$$[C_{pu}]\,\mathbb{P} + [C_{\eta u}]^T\,\mathbb{H} + [M_S]\,\ddot{\mathbb{U}} + [D_S]\,\dot{\mathbb{U}} + [K_S]\,\mathbb{U} + \mathbb{F}_{NL}(\mathbb{U}) = \mathbb{F}_S\,. \tag{3}$$

In Eq. (1), the $(n_P \times n_P)$ symmetric positive definite matrix $[M]$ is the fluid mass matrix. The $(n_P \times n_P)$ symmetric positive semidefinite matrices $[D] = \tau[K]$ and $[K]$ are the damping and stiffness matrices of the fluid, in which τ is the acoustic damping coefficient. In Eq. (2), the $(n_H \times n_H)$ symmetric positive definite matrix $[K_{gc}]$ is the matrix related to the sloshing/capillarity effects on the free surface. In Eq. (3), the $(n_S \times n_S)$ symmetric positive definite matrices $[M_S]$, $[D_S] = \tau_S[K_S]$, and $[K_S]$ are the mass, damping, and stiffness matrices of the structure with τ_S the elastic damping coefficient. The rectangular $(n_S \times n_P)$, $(n_H \times n_P)$, and $(n_H \times n_S)$ real matrices $[C_{pu}]$, $[C_{p\eta}]$, and $[C_{\eta u}]$ are the coupling matrices between the fluid and the structure, between the fluid and the free surface, and between the structure and the free surface. In Eq. (3) the $\mathbb{R}^{n_S}$-vectors $\mathbb{F}_S$ and $\mathbb{F}_{NL}(\mathbb{U})$ correspond to the discretization of the external force field applied to the structure and to the nonlinear internal forces in the structure induced by the geometrical nonlinearities.

The numerical resolution of the set of nonlinear coupled differential equations (Eqs.(1) to (3)) appears to be time consuming or even impossible when considering large finite element models. It is thus essential to introduce an efficient reduced-order model.

2.3 Nonlinear reduced-order computational model

The nonlinear reduced-order model is constructed by projecting the equations on an adapted reduced-order basis, whose basis vectors are represented by the $(n_{PHS} \times N_{PHS})$ real matrix $[\Psi]$. The corresponding approximated solution is denoted by the $\mathbb{R}^{n_{PHS}}$-vector $(\mathbf{P},\mathbf{H},\mathbf{U})$ that is written as follows

$$\begin{bmatrix}\mathbf{P}\\ \mathbf{H}\\ \mathbf{U}\end{bmatrix} = \begin{bmatrix}[\Phi_P] & [\Phi_{PH}] & 0\\ 0 & [\Phi_H] & 0\\ 0 & 0 & [\Phi_S]\end{bmatrix}\begin{bmatrix}\mathbf{q}^P\\ \mathbf{q}^H\\ \mathbf{q}^U\end{bmatrix} = [\Psi]\,\mathbf{Q}\,, \tag{4}$$

in which the $\mathbb{R}^{N_P}$-vector $\mathbf{q}^P$, the $\mathbb{R}^{N_H}$-vector $\mathbf{q}^H$, and the $\mathbb{R}^{N_S}$-vector $\mathbf{q}^U$ are the generalized coordinates. The total number of generalized coordinates is $N_{PHS} = N_P + N_H + N_S$. In Eq. (4), the $(n_P \times N_P)$ real matrix $[\Phi_P]$ is made up of the acoustic modes of the internal fluid, the $(n_H \times N_H)$ real matrix $[\Phi_H]$, of the sloshing modes of the free surface, and the $(n_S \times N_S)$ real matrix $[\Phi_S]$, the eigenmodes of the linearized structure for which the added mass matrix effect is taken into account [10]). It should be noted that the $(n_P \times N_H)$ real matrix $[\Phi_{PH}]$ is made up of the corresponding acoustic part associated with each sloshing modes. For

more details concerning the computational aspects of the construction of such proposed reduced-order basis, we refer the reader to [1]. The $\mathbb{R}^{N_{PHS}}$-vector $\mathbf{Q} = (\mathbf{q}^P, \mathbf{q}^H, \mathbf{q}^U)$ is then solution of the following set of N_{PHS} nonlinear coupled differential equations

$$[\mathscr{M}_{FSI}]\,\ddot{\mathbf{Q}}(t) + [\mathscr{D}_{FSI}]\,\dot{\mathbf{Q}}(t) + [\mathscr{K}_{FSI}]\,\mathbf{Q}(t) + \mathscr{F}_{NL}(\mathbf{Q}(t)) = \mathscr{F}(t)\,, \tag{5}$$

in which the $(N_{PHS} \times N_{PHS})$ matrices $[\mathscr{M}_{FSI}]$, $[\mathscr{D}_{FSI}]$, $[\mathscr{K}_{FSI}]$, and the $\mathbb{R}^{N_{PHS}}$ vectors $\mathscr{F}$ and $\mathscr{F}_{NL}$ are such that

$$[\mathscr{M}_{FSI}] = [\Psi]^T \begin{bmatrix} [M] & -[C_{p\eta}]^T & -[C_{pu}]^T \\ 0 & 0 & 0 \\ 0 & 0 & [M_S] \end{bmatrix} [\Psi]\,, \tag{6}$$

$$[\mathscr{D}_{FSI}] = [\Psi]^T \begin{bmatrix} [D] & 0 & 0 \\ 0 & 0 & 0 \\ 0 & 0 & [D_S] \end{bmatrix} [\Psi]\,, \tag{7}$$

$$[\mathscr{K}_{FSI}] = [\Psi]^T \begin{bmatrix} [K] & 0 & 0 \\ [C_{p\eta}] & [K_{gc}] & [C_{\eta u}] \\ [C_{pu}] & [C_{\eta u}]^T & [K_S] \end{bmatrix} [\Psi]\,, \tag{8}$$

$$\mathscr{F}(t) = [\Psi]^T \begin{bmatrix} 0 \\ 0 \\ \mathbb{F}_S(t) \end{bmatrix}\,, \tag{9}$$

$$\mathscr{F}_{NL}(\mathbf{Q}(t)) = [\Psi]^T \begin{bmatrix} 0 \\ 0 \\ \mathbb{F}_{NL}(\mathbf{Q}(t)) \end{bmatrix}\,. \tag{10}$$

In Eq. (5), vector $\mathscr{F}_{NL}(\mathbf{Q}(t))$ denotes the nonlinear internal forces induced by the geometrical nonlinearities of the structural part that are computationally constructed from the knowledge of the nonlinear reduced operators [4].

3 Numerical Application

3.1 Computational finite element model

The fluid-structure system is constituted of a thin circular cylindrical tank made up of aluminum. This cylinder is closed at both ends by a circular aluminum disk. Let $R_i = 0.03\,m$ and $e_{cyl} = 10^{-4}\,m$ be the internal radius of the cylinder and its thickness. Let $e_b = 2 \times 10^{-4}\,m$ be the thickness of the two circular aluminum disk at the top and at the bottom. The total height of the cylinder is $h = 0.1504\,m$. The Young modulus of aluminum is $E = 62 \times 10^9\,N.m^{-2}$, Poisson ratio $\nu = 0.33$, mass density $\rho_S = 2{,}700\,Kg.m^{-3}$, and damping coefficient $\tau_S = 10^{-6}\,s$. This tank is partially filled (at 30%) with water (see Figure 2)for which the sound velocity is $c_0 = 1{,}480\,m.s^{-1}$, mass density $\rho_0 = 1{,}000\,Kg.m^{-3}$, damping coefficient $\tau = 10^{-6}\,s$, surface tension coefficient $\sigma_\Gamma = 7.28 \times 10^{-2}\,N.m^{-1}$, and the contact angle between water and aluminum is $\alpha = 70^\circ$. The origin O of the Cartesian coordinates system $(O, \mathbf{e}_1, \mathbf{e}_2, \mathbf{e}_3)$ is located at the center of the bottom of the cylindrical tank. Axis $\mathbf{e}_3$ coincides with the revolution axis of the tank. The equilibrium position of the fluid in the cylindrical tank is precomputed using the software Surface Evolver [3]. The cylinder is clamped at its bottom. The finite element model of the fluid-structure requires to use high orders elements due to the slenderness of the cylinder wall and of the high flexibility of the free surface motion. The finite element discretization of the system is thus constructed using 27-nodes 3D-solid finite elements for the structure and for the acoustic fluid. The free surface of the liquid is meshed using 9-nodes 2D finite elements and the triple line is meshed using 3-nodes 1D finite elements. Table 1 summarizes the numerical data concerning the finite element mesh.

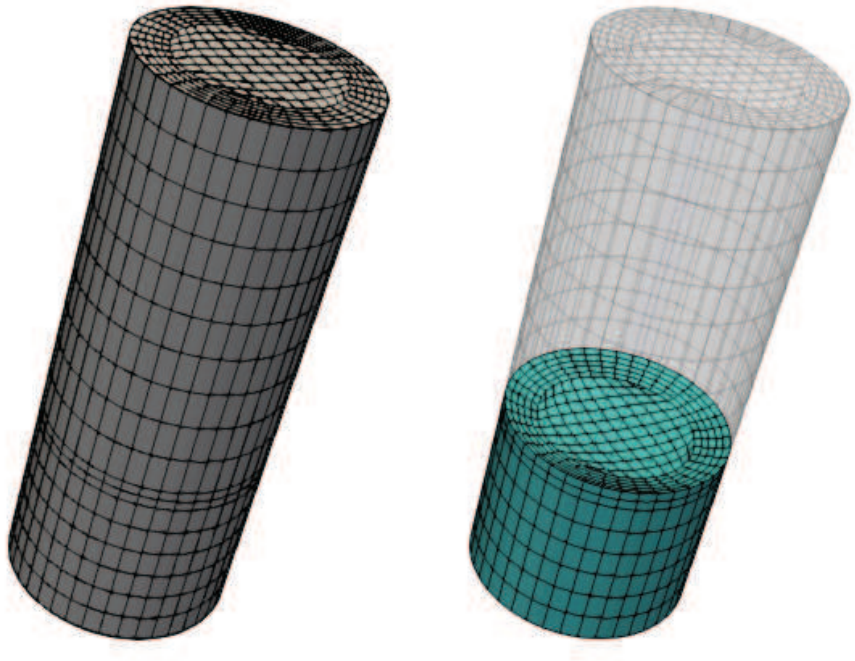


Figure 2: Finite element meshes of the structure (left) and of the liquid with its free surface (right).

	Nodes	**Dof**	**Elements**
Fluid	21,097	21,097	2,400
Free surface	1,241	1,241	300
Structure	16,806	50,418	1,400

Table 1: Table of the finite element mesh numerical data

3.1.1 Observation points

The dynamical response of the fluid-structure system is analyzed at different observation nodes. The first observation node is common to both structure and free surface, in order to see the coupling between the structural displacement and the elevation of the free surface. It is denoted by $\mathbf{x}_{H_1}^{obs}$ on the free surface and by $\mathbf{x}_{U}^{obs}$ on the structure. Then, two observation points denoted by $\mathbf{x}_{P_1}^{obs}$ and $\mathbf{x}_{P_2}^{obs}$, and corresponding to a node located at the fluid bottom and to a node located at mid-depth in the fluid are chosen. Finally, another observation node, denoted by $\mathbf{x}_{H_2}^{obs}$ and that is located at the center of the free surface is chosen. The coordinates of these observation points are summarized in Table 2. In the following, for the sake of clarity, the notations $\mathbf{P}_i$ and $\mathbf{H}_i$ are introduced for representing the pressure and the elevation of the free surface at the observation point $\mathbf{x}_{P_i}^{obs}$ and $\mathbf{x}_{H_i}^{obs}$ for $i = 1, 2$. The notation $\mathbf{U}_j$ is used for representing the component number j of the structural displacement observed at observation node $\mathbf{x}_{U}^{obs}$.

3.2 Computational reduced-order bases

The computational reduced-order basis $[\Psi]$ is constructed according to Section 2.3, by solving three generalized eigenvalue problems associated with $\mathbf{P}$, $\mathbf{H}$, and $\mathbf{U}$ [12, 1]. Some acoustic, sloshing, and elastic eigenmodes are represented with their respective eigenfrequencies denoted by ν_i^a, for $i = 1, \ldots, N_a$ with

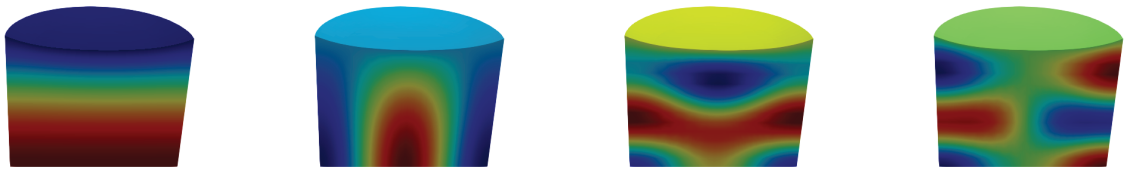
Location	Name	x coordinate	y coordinate	z coordinate
Fluid	$\mathbf{x}_{P_1}^{obs}$	0.0147	0	0.0002
	$\mathbf{x}_{P_2}^{obs}$	0.0147	0	0.0185
Free surface	$\mathbf{x}_{H_1}^{obs}$	0	0.03	0.0497
	$\mathbf{x}_{H_2}^{obs}$	0	0	0.0452
Structure	$\mathbf{x}_{U}^{obs}$	0.0168	−0.0168	0.0467

Table 2: Localization of the observation nodes for the fluid, the structure and the free surface

$a \in \{P, H, S\}$.

3.2.1 Acoustic eigenmodes of the internal fluid

Figure 3 displays some acoustic eigenmodes of the liquid computed with zero pressure on the free surface, and their respective eigenfrequencies. For the present numerical application, it should be noted that the resonance of the internal fluid is a high-frequency phenomenon since the fundamental frequency of the fluid is $\nu_1^P = 7{,}824\,Hz$.



$\nu_1^P = 7{,}824\,Hz$ $\nu_9^P = 30{,}718\,Hz$ $\nu_{15}^P = 39{,}279\,Hz$ $\nu_{18}^P = 41{,}226\,Hz$

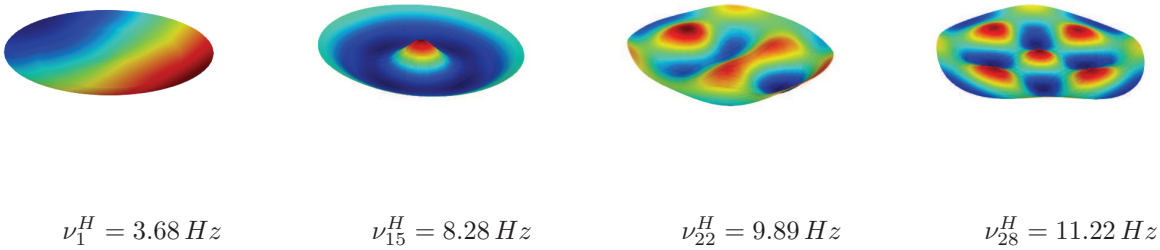
Figure 3: Example of acoustic modes of the internal fluid

3.2.2 Sloshing eigenmodes of the free surface

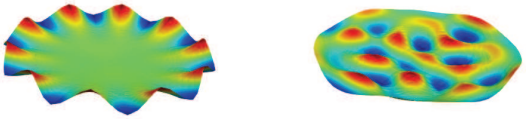
Figure 4 displays some sloshing modes of the free surface for which the fundamental eigenfrequency is $\nu_1^H = 3.68\,Hz$, which is of order 10^3 smaller than the fundamental frequency of the internal fluid. Moreover, it can be seen that the modal density of the sloshing is high since the 500-th eigenfrequency is $\nu_{500}^H = 56.38\,Hz$. The corresponding acoustic part of the sloshing modes $[\Phi_{PH}]$ is displayed in Figure 5. It can be seen that there is effectively an exponential decreasing of the pressure as function of the distance to the free surface.

3.2.3 Elastic eigenmodes of the structure

Figure 6 and 7 display some elastic eigenmodes of the structure related to the empty and the partially filled fluid-structure system. In particular, since these modes have been calculated by including the added mass effect induced by the fluid, this influence can be quantified regarding both modal shapes and relative eigenfrequencies. Note that the eigenmodes and the associated eigenfrequencies, whose modal contribution is concentrated at the top of the structure remain unchanged.

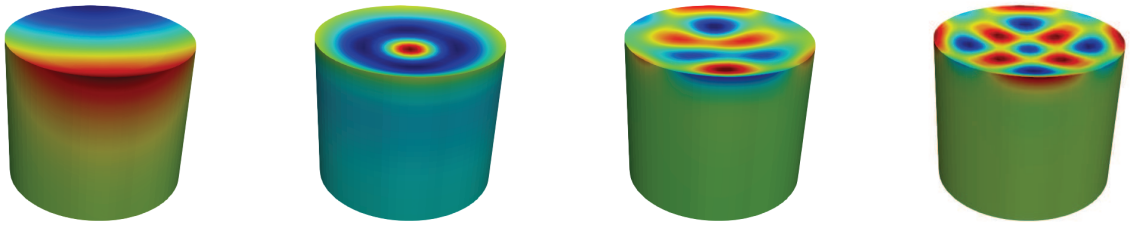


$\nu_1^H = 3.68\,Hz$ $\nu_{15}^H = 8.28\,Hz$ $\nu_{22}^H = 9.89\,Hz$ $\nu_{28}^H = 11.22\,Hz$

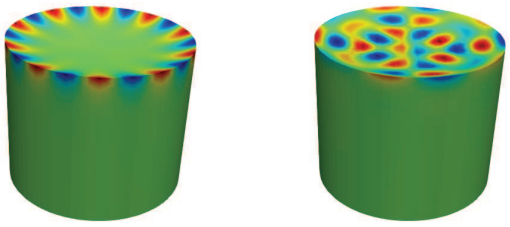


$\nu_{37}^H = 13.06\,Hz$ $\nu_{59}^H = 16.99\,Hz$

Figure 4: Example of sloshing modes of the free surface.



$\nu_1^H = 3.68\,Hz$ $\nu_{15}^H = 8.28\,Hz$ $\nu_{22}^H = 9.89\,Hz$ $\nu_{28}^H = 11.22\,Hz$

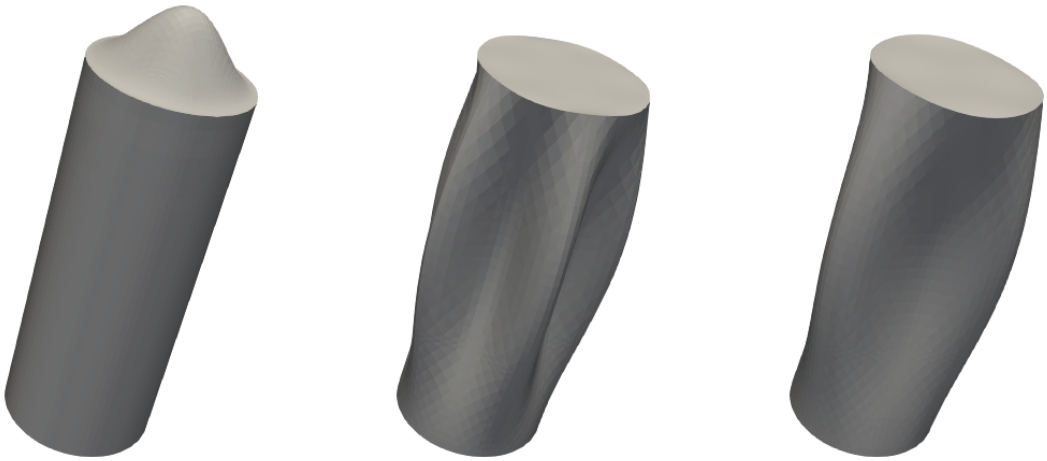


$\nu_{37}^H = 13.06\,Hz$ $\nu_{59}^H = 16.99\,Hz$

Figure 5: Example of corresponding acoustic part of the sloshing modes.

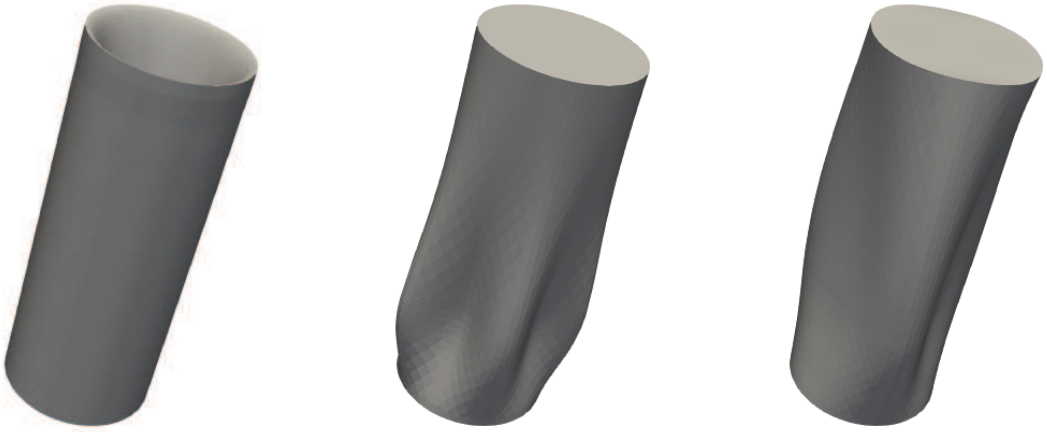
3.3 Dynamical excitation of the system

The dynamical excitation of the system is defined in the time domain and is chosen in order to uniformly excite a frequency band of interest that corresponds to some of the structural and sloshing resonances of the fluid-structure system. Since the fundamental sloshing eigenfrequency of the free surface is $\nu_1^H = 3.68\,Hz$ and since the fundamental frequency of the internal liquid is $\nu_1^P = 7{,}824\,Hz$, the time domain excitation is chosen such that the corresponding excitation frequency band is $\mathbb{B}_e = [\nu_{min}\,,\,\nu_{max}]\,Hz$, with $\nu_{min} = 15\,Hz$



$\nu_1^S = 510\,Hz$ $\nu_7^S = 1{,}461\,Hz$ $\nu_9^S = 1{,}514\,Hz$

Figure 6: Example of elastic modes of the empty structure.



$\nu_8^S = 510\,Hz$ $\nu_5^S = 530\,Hz$ $\nu_9^S = 639\,Hz$

Figure 7: Example of elastic modes of the structure when considering the influence of the liquid.

and $\nu_{max} = 1{,}550\,Hz$. In this frequency band, the first 9 eigenmodes of the structure are excited. The dynamical excitation is located on the surface zone defined by $r = R + e_{cyl}$, $\theta \in [-\pi/32, \pi/32]$ and $x_3 = [h/2-h_f, h/2+h_f]$ with $h_f = 0.02\,m$ in cylindrical coordinates. Figure 8 displays the graph $t \mapsto g(t)$ of the time repartition of the excitation (whose maximum over the time domain is set to 1) and of its corresponding Fourier transform. It can be seen that such a choice allows the frequencies between $15\,Hz$ and $1{,}550\,Hz$ to be excited. The maximum load intensity is given by $f_0 = 2{,}000\,N$ that corresponds to subsequent nonlinear geometrical effects. The computations is carried out with a sampling frequency $\nu_e = 15{,}500\,Hz$ and with $n_t = 10^6$ time steps. The initial time is chosen as $t_{ini} = -1.30\,s$ yielding a null initial load and the time duration is chosen as $T = 67\,s$. Consequently, these computational parameters are adapted for observing the resonances related to the sloshing motion, which is also known to be a low-frequency and weakly damped phenomenon in the present numerical application. It should be noted that the nonlinear dynamical response of the fluid-structure system is calculated in the time domain with a Newmark algorithm for which the

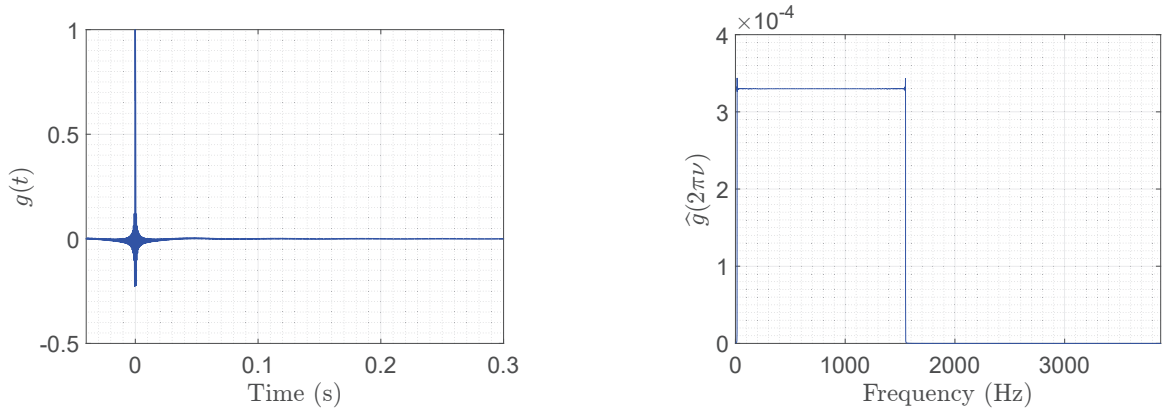


Figure 8: Graph of the dynamical excitation of the fluid-structure system (left) and its Fourier transform (right).

nonlinearity is solved using either the fixed point method or arc-length based algorithms. The nonlinear dynamical analysis is carried out *a posteriori* in the frequency domain by evaluating its Fourier transform from a FFT algorithm. The frequency band of analysis is given by $\mathbb{B}_a = [0\,,\,\nu_{max}]$ with $\nu_{max} = 5{,}000\,Hz$. In the following, the notation $\widehat{A}(2\pi\nu)$ denotes the Fourier transform of quantity $A(t)$.

3.4 Reduced-order model convergence

In order to construct an efficient reduced-order model, a convergence analysis is performed in order to determine the optimal number N_P, N_H, and N_S of bases vectors. Due to the large dimension of the finite element model, the computation of the solution $(\mathbb{P}, \mathbb{H}, \mathbb{U})$ of Eqs. (1) to (3) is not calculated. Thus, the solutions $(\mathbf{P}, \mathbf{H}, \mathbf{U})$ obtained by using the nonlinear reduced-order model cannot be compared to the reference solution. For circumventing this problem, we assume that the solution is converged for a high number of eigenmodes $N_P^{max} = 500$, $N_H^{max} = 500$, and $N_S^{max} = 200$. Then, three convergence analyses are performed with respect to N_P, N_H and N_S. In the following, the results presented are calculated using the optimal number of eigenmodes.

3.5 Linear and nonlinear dynamical responses of the fluid-structure system

The influence of the geometrical nonlinearities of the structure on the fluid-structure system is quantified by comparing the linear and the nonlinear dynamical responses of the fluid-structure system. The linear dynamical response of the system is calculated by solving the set of differential equations defined by Eq. (5) for which $\mathscr{F}_{NL}(\mathbf{Q}(t)) = 0$. These results are then compared to the nonlinear dynamical analysis of the fluid-structure system. For convenience, we denote by superscript L the quantities calculated for the linear system and by superscript *NL* the quantities calculated for the nonlinear system. Figure 9 displays the graphs of $\nu \mapsto |\widehat{P}_i^L(2\pi\nu)|$ (left figure) and of $\nu \mapsto |\widehat{P}_i^{NL}(2\pi\nu)|$ (right figure) for $i \in \{1, 2\}$. Figure 10 displays the graphs of $\nu \mapsto |\widehat{H}_i^L(2\pi\nu)|$ (left figure) and of $\nu \mapsto |\widehat{H}_i^{NL}(2\pi\nu)|$ (right figure) for $i \in \{1, 2\}$. Figure 11 displays the graphs of $\nu \mapsto |\widehat{U}_i^L(2\pi\nu)|$ (left figure) and of $\nu \mapsto |\widehat{U}_i^{NL}(2\pi\nu)|$ (right figure) for $i \in \{1, 2, 3\}$.

These results show that the geometrical nonlinearities that are taken into account in the computational modelling have a significant impact on the responses of the fluid-structure system. When considering the linear responses of the fluid-structure system, we clearly see that the resonances that are located in the excitation band $\mathbb{B}_e$ well match with the elastic and sloshing eigenfrequencies. The nonlinear responses of the fluid-structure system are more interesting. Unexpected resonances that are localized below and beyond $\mathbb{B}_e$ appear. Moreover, their contribution appear to be significative with resonance amplitudes of the same order as the resonance amplitudes that are localized in $\mathbb{B}_e$.

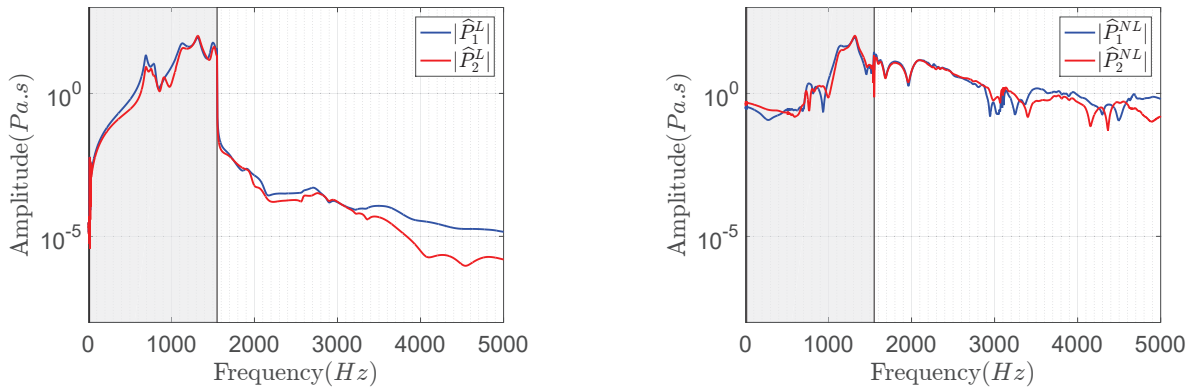


Figure 9: Graph of the linear (left) and nonlinear (right) FRF of the pressure in the internal liquid seen at the observation points.

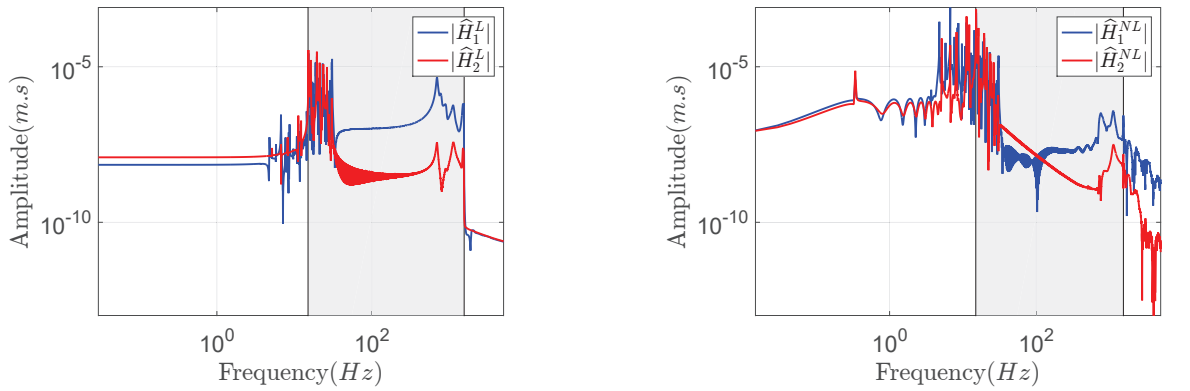


Figure 10: Graph of the linear (left) and nonlinear (right) FRF of the elevation of the free surface seen at the observation points.

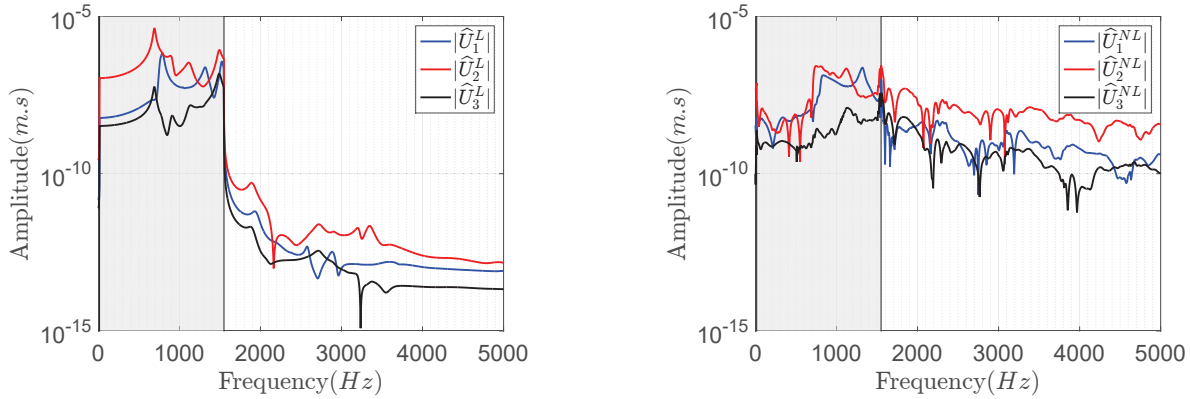


Figure 11: Graph of the linear (left) and nonlinear (right) FRF of the structural displacement seen at the observation point.

4 Conclusion

This paper proposes a computational methodology adapted to a fluid-structure system for which sloshing and capillarity effects are taken into account and for which the structure is assumed to undergo large displace-

ments/deformations. The construction of an adapted nonlinear reduced-order model is required for reducing the computational costs, mostly if large finite element models are considered. The formulation used for such nonlinear reduced-order model allows for constructing a projection basis for each part of the fluid-structure system in order to circumvent the possible gap between the eigenfrequencies of each sub-system. This means that if the eigenmodes of the coupled fluid-structure system were directly calculated, about ten thousands eigenmodes should be computed in the considered frequency band of analysis instead of the 500 that have been computed. In addition, the mesh should considerably be refined for computing this huge number of sloshing modes. The numerical application constituted of a cylindrical tank partially filled with a fluid demonstrate the efficiency of the proposed method. In particular, the results show that the responses are strongly modified by the presence of the geometrical nonlinearities.

Acknowledgements

This work has been supported by the DGA (French defence procurement agency) in the context of a PhD thesis.

References

[1] Q. Akkaoui, E. Capiez-Lernout, C. Soize, and R. Ohayon. Solving generalized eigenvalue problems for large scale fluid-structure computational models with mid-power computers. *Computers & Structures*, 205:45–54, 2018.

[2] H. Berger, R. Ohayon, and J. Boujot. On a spectral problem in vibration mechanics-computation of elastic tanks partially filled with liquids. *Journal of Mathematical analysis and applications*, 51:272–298, 1975.

[3] K. A. Brakke. The surface evolver. *Experimental mathematics*, 1(2):141–165, 1992.

[4] E. Capiez-Lernout, C. Soize, and M. Mignolet. Computational stochastic statics of an uncertain curved structure with geometrical nonlinearity in three-dimensional elasticity. *Computational Mechanics*, 49(1):87–97, 2012.

[5] M. A. Crisfield, J. J. Remmers, C. V. Verhoosel, et al. *Nonlinear finite element analysis of solids and structures*. John Wiley & Sons, 2012.

[6] C. Farhat, E. K.-Y. Chiu, D. Amsallem, J.-S. Schotté, and R. Ohayon. Modeling of fuel sloshing and its physical effects on flutter. *AIAA journal*, 51(9):2252–2265, 2013.

[7] R. Finn. The contact angle in capillarity. *Physics of Fluids*, 18(4):047102, 2006.

[8] R. Finn and G. K. Luli. On the capillary problem for compressible fluids. *Journal of Mathematical Fluid Mechanics*, 9(1):87–103, 2007.

[9] T. J. Hughes. *The finite element method: linear static and dynamic finite element analysis*. Courier Corporation, 2012.

[10] H. J. Morand and R. Ohayon. *Fluid Structure Interaction*. John Wiley & Sons, New York, 1995.

[11] R. Ohayon and C. Soize. Structural acoustic and vibration, 1998.

[12] R. Ohayon and C. Soize. Vibration of structures containing compressible liquids with surface tension and sloshing effects. Reduced-order model. *Computational Mechanics*, 55(6):1071–1078, 2015.

[13] R. Ohayon and C. Soize. Nonlinear model reduction for computational vibration analysis of structures with weak geometrical nonlinearity coupled with linear acoustic liquids in the presence of linear sloshing and capillarity. *Computers & Fluids*, 141:82 – 89, 2016.

[14] L. G. Olson and K. J. Bathe. Analysis of fluid-structure interactions - a direct symmetric coupled formulation based on a fluid velocity potential. *Computers & Structures*, 21:21–32, 1985.

[15] P. Wriggers. *Nonlinear finite element methods*. Springer Science & Business Media, 2008.

Energy dissipation due to sloshing in baffled fuel tanks

F. Buck [1], **H. Hetzler** [1], **E. Fruend** [2], **S. Oexl** [2]
[1] University of Kassel, Institute of Mechanics,
Engineering Dynamics Group, Mönchebergstraße 7, 34125 Kassel, Germany
e-mail: **hetzler@uni-kassel.de**

[2] Daimler AG, Commercial Vehicles,
Mercedesstraße 137, 70327 Stuttgart, Germany

Abstract
Sloshing in fuel tanks of commerical vehicles has to be considered for dynamic truck simulations. These tanks typcially possess perforated plates as baffles inside to reduce the sloshing amplitudes and the related forces. Besides the estimation of the eigenfrequencies and corresponding modes the dissipative effects have to be correctly described for simulating the sloshing forces using linear potential theory. The energy dissipation mechanisms - namely the viscous boundary layer damping, the bulk damping and the pressure drop at the baffles - are studied in detail. The calculated damping ratio as well as the simulated transfer function are validated with experimental findings. The results from simulations and experiments show only small deviations.

1 Introduction

Dynamic effects of a fluid with a free surface caused by the motion of the surrounding container, usually referred to as sloshing, have to be regarded in different applications. It is of crucial importance to know the occuring sloshing amplitudes and the corresponding forces in spacecrafts [1], liquid cargo ships [2] and tuned liquid dampers [3]. The focus of this contribution is set on fuel tanks of commercial vehicles. For an accurate simulation of the entire truck, the fluid behaviour and the resulting sloshing loads in the tanks with filling volumes up to 1000 liters have to be correctly depicted. Typical features of fuel tanks of commercial vehicles are a mainly translational excitation in all directions, many used variants regarding the size of the tanks and especially perforated plates used as baffles to subdivide the tank volume and to reduce the sloshing amplitudes.

Horizontal excitation causes vibrations of the fluid surface whereas parametric sloshing occurs for vertical excitation above a threshold when the fluid surface becomes unstable. To describe the observed fluid behaviour the eigenfrequencies and corresponding modes as well as the dissipative effects have to be determined. The eigenfrequencies and the free-surface shapes can be estimated using linear potential flow theory (see e.g. [2]). Extending the formulas enables the calculation of eigenfrequencies also for the baffled tank which agree well with measured values [4]. The reduction of the sloshing amplitudes is related to different dissipative effects: viscous boundary layer damping, bulk damping and especially the pressure drop at the holes of the baffles.

After introducing the test rig (section 2.1) and derivating the modal equations of motions based on linear potential theory (section 2.2), the influences of the baffles (section 2.3) and the possiblities to determine the eigenfrequencies and modes are given (section 2.4). The main part of this contribution focuses on the energy dissipation, including the descriptions of the different effects (section 3.1-3.3) and a semi-empirical

approach for the baffles used in truck tanks. The numerical results are discussed in section 4 in comparison with experimental values. This contribution closes with a conlusion and a short outlook (section 5).

2 Sloshing in rectangular tanks

2.1 Test rig

Besides analytical and numerical approaches to describe the sloshing behaviour for translational excitation, experiments have been used to understand the physical effects and to validate the numerical results. All investigations are conducted for a baffled rectangular tank (dimensions $317\,\mathrm{mm} \times 217\,\mathrm{mm} \times 188\,\mathrm{mm}$) which is the scaled simplification of a typical truck tank. Scaling the geometrical dimensions of the tank leads to modification of other physical quantities according to the dimensional analysis. The releveant fluid dynamic dimensionless parameter for gravity driven sloshing is the Froude number $\mathrm{Fr} = \frac{\rho v_c^2}{\rho g l_c} = \frac{\omega_c^2 l_c}{g}$ with characteristic velocity v_c, length l_c and eigenfrequency ω_c and density ρ and graviational constant g. The test rig is given in Figure 1. Silicone oil is used instead of diesel having the same viscous properties. The tank is horizontally excited by a shaker and the force, the accelerations and the displacement are measured. Investigated positions of the baffle dividing the tank at the ratio of 1/4 (A), 1/3 (B), 1/2 (C), 2/3 (D) und 3/4 (E) are noted with capital letters in Figure 1.

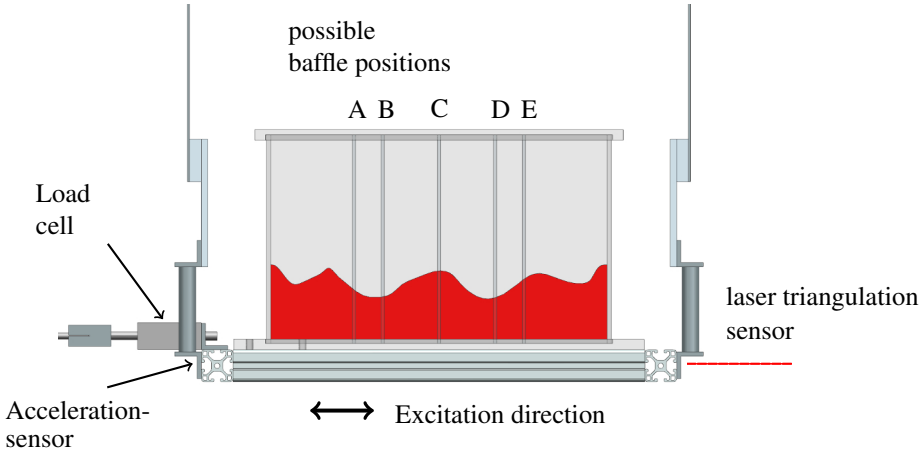


Figure 1: Side view of the tank including the investigated baffle positions and the sensor positions.

2.2 Derivation of modal equations of motions

Assuming an incompressible fluid ($\nabla \cdot \boldsymbol{v} = 0$), neglecting viscous stresses, surface tension effects and postulating an irrotational fluid motion allows for applying potential flow theory, i.e. $\boldsymbol{v} = \nabla\Phi$. With this, the field equations of linear sloshing read:

$$\Delta\Phi = 0, \qquad \frac{p}{\rho} + \frac{\partial\Phi}{\partial t} + \ddot{x}_0 x + (g + \ddot{z}_0)\,\zeta = 0. \tag{1}$$

The first equation represents the continuity equation and the second Bernoulli type equation the momentum balance. Φ denotes the velocity potential, p the pressure, g the gravitational constant and ζ the (small) surface elevation. For the sake of brevity, only translational excitations of the untilted tank in x- and z-direction with the related accelerations $\ddot{x}_0(t)$ and $\ddot{z}_0(t)$ are regarded.

Additionally, the kinematic boundary conditions at the solid walls (2) and the linearized kinematic and dynamic boundary conditions at the free surface ((3) and (4)) are (see also [4]):

$$0 = \frac{\partial \Phi}{\partial x}\Big|_{x=\pm\frac{b_x}{2}}, \quad 0 = \frac{\partial \Phi}{\partial y}\Big|_{y=\pm\frac{b_y}{2}}, \quad 0 = \frac{\partial \Phi}{\partial z}\Big|_{z=-h}, \tag{2}$$

$$0 = \frac{\partial \Phi}{\partial z}\Big|_{z=0} - \frac{\partial \zeta}{\partial t}, \tag{3}$$

$$0 = \frac{\partial \Phi}{\partial t}\Big|_{z=0} + \ddot{x}_0 x + (g + \ddot{z}_0)\,\zeta. \tag{4}$$

The rectangular tank and the relevant quantities are given in Figure 2.

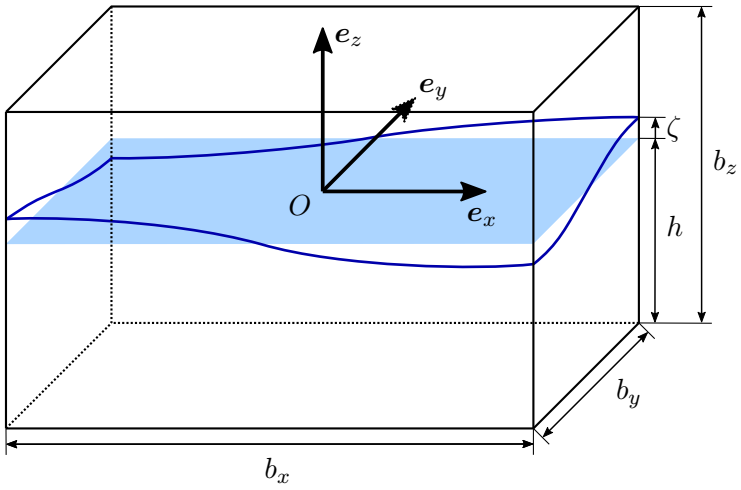


Figure 2: Rectangular tank of dimensions b_x, b_y, b_z, fill level h and free surface elevation ζ. The origin of the coordinate system is centered at the fluid surface at rest.

Using a modal approach, i.e.writing the elevation of the free surface as $\zeta(x,t) = \sum_{i=1}^{\infty} \beta_i(t)\varphi_i(x,0)$ and the velocity potential as $\Phi(x,z,t) = \dot{x}_0(t)x + \dot{z}_0(t)z + \sum_{i=1}^{\infty} R_i(t)\varphi_i(x,z)$ with $R_i(t) = \frac{g}{\omega_i^2}\dot{\beta}_i(t)$ and generalized coordinates $R_i(t)$ and $\beta_i(t)$, results in the following linear modal equations of motion

$$\ddot{\beta}_i(t) + 2\xi_i\omega_i\dot{\beta}_i(t) + \omega_i^2\left(1 + \frac{\ddot{z}_0(t)}{g}\right)\beta_i(t) = -\frac{\lambda_{xi}}{\mu_i}\ddot{x}_0(t) \tag{5}$$

with the hydrodynamic coefficients $\mu_i = \frac{\rho g}{\omega_i^2}\int_{\partial V_f}\varphi_i(x,y,0)^2\,\mathrm{d}x\,\mathrm{d}y$ and $\lambda_{xi} = \rho\int_{\partial V_f}\varphi_i(x,y,0)x\,\mathrm{d}x\,\mathrm{d}y$ as integrals over the fluid surface ∂V_f. ω_i are the eigenfrequencies and $\varphi_i(x,y,z)$ the corresponding eigenmodes.

For $\ddot{z}_0(t) = 0$ and $\ddot{x}_0(t) \neq 0$ equation (5) describes the known behaviour of a linear oscillator with force excitation, whereas for pure vertical exciation ($\ddot{x}_0(t) = 0, \ddot{z}_0(t) \neq 0$) we obtain a Mathieu equation and expect parametric instabilities.

The horizontal fluid force $F_{F,x}$ due to sloshing is the reaction force to the external force on the fluid $F = m_F\ddot{x}_{cog}$ with the acceleration of the center of gravity $\ddot{x}_{cog}$ and can be written as

$$F_{F,x} = -m_F\ddot{x}_0(t) - \sum_{k=1}^{\infty}\ddot{\beta}_k(t)\lambda_{xk}. \tag{6}$$

The transfer function between the acceleration $\ddot{x}_0$ of the tank and the corresponding force $F_{F,x}$ reads

$$\begin{aligned}\underline{\hat{F}}_{F,x} &= \underline{H}_{F_{F,x}\ddot{x}_0}(i\Omega)\left(-\Omega^2\underline{\hat{x}}_0\right)\\ \underline{H}_{F_{F,x}\ddot{x}_0}(i\Omega) &= -m_F - \sum_{k=1}^{\infty}\frac{\lambda_{xk}^2}{\mu_k}\frac{\Omega^2}{\omega_k^2 - \Omega^2 + i2\xi_k\omega_k\Omega},\end{aligned} \tag{7}$$

where underlines indicate complex quantities. It describes the so-called apparent mass and is used for validation with measured transfer function.

2.3 Influence of baffles

As already mentioned, the baffles as a characteristic feature of fuel tanks and their influence on the sloshing behaviour have to be investigated. Therefore, the measured transfer functions for different baffles and screens are plotted in Figure 3. For the tank without baffles (dark blue curve) the highest apparent mass along with strong amplification of the free surface occurs at the eigenfrequencies, especially for the first mode with the greatest movement of the center of gravity. Placing a solid wall (red curve) in the middle of the tank (position C) results in a shift of the eigenfrequencies to higher values (see also (8)). Dividing the tank by screens with low solidity ratios[1] (turquoise and light blue curve) - typically used in tuned liquid dampers - reduces the sloshing amplitudes and apparent mass [4, 5]. If perforated plates with high solidity ratios are applied as subdividing elements (orange and yellow curve) a shift of the eigenfrequencies beside the reduction of the sloshing amplitudes can be observed. Both effects depend on the specific geometry of the baffles [4, 6]. As these kinds of baffles are installed in truck tanks, the shift of the eigenfrequencies as well as the reduction of the sloshing amplitudes have to be regarded. The first part is addressed in [4] whereas this contribution focuses on the energy dissipation effects.

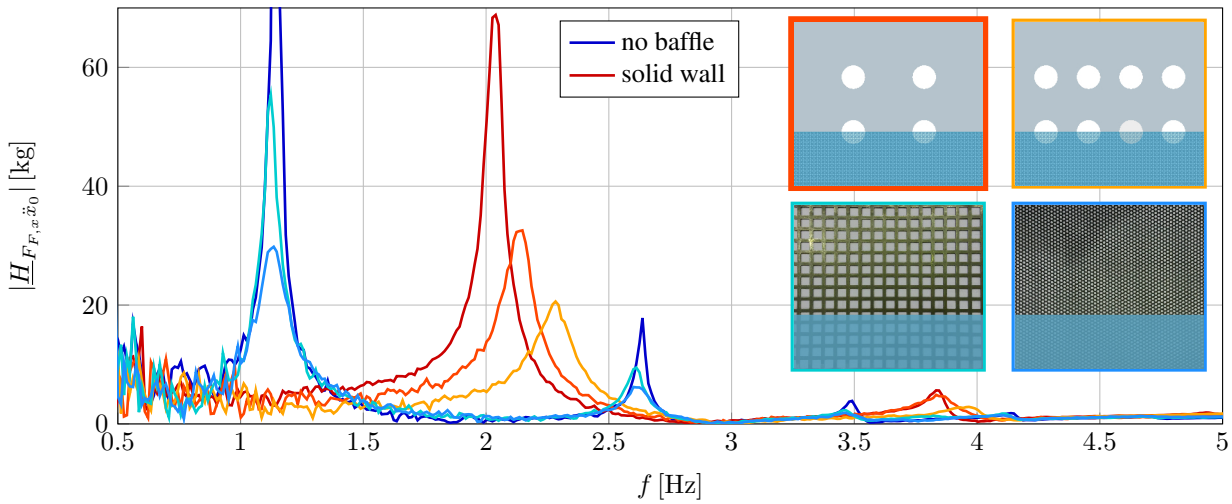


Figure 3: Influence of baffles and screens placed in the center of the tank on the transfer function (white noise excitation in x-direction, fill level 33.3 %).

2.4 Sloshing eigenfrequencies and modes

For a rectangular tank as depicted in Figure 2 the eigenfrequencies and eigenmodes can be given analytically [2] with the mode numbers n and m in x- and y-direction, respectively:

$$\omega_{mn}^2 = g\gamma_{mn}\tanh\left(\gamma_{mn}h\right) \quad \text{with} \quad \gamma_{mn} = \pi\sqrt{\left(\frac{m}{b_x}\right)^2 + \left(\frac{n}{b_y}\right)^2}, \tag{8}$$

$$\varphi_{mn}(x,y,0) = C_{mn}\cos\left(\frac{\pi m}{b_x}\left(x+\frac{b_x}{2}\right)\right)\cos\left(\frac{\pi n}{b_y}\left(y+\frac{b_y}{2}\right)\right). \tag{9}$$

Faltinsen and Timokha [5] show an analytical approach to describe the shift of the eigenfrequencies for a rectangular tank with a screen in the middle. These formulas can be extended to the case of a rectangular tank

[1] The solidity ratio is defined as the shadow area projected on a plane parallel to the baffle to the total cross sectional area of the tank.

with one or two perforated plates at arbitrary positions [4]. The simulated eigenfrequencies and modes agree reasonably with experimental ones. For complex tank shapes an eigenvalue analysis using finite elements is an appropriate possibility to obtain the eigenfrequencies and corresponding mode shapes, which can be used to calculate the hydrodynamic coefficients.

3 Energy dissipation

In addition to the eigenfrequencies and modes a correct description of the dissipative effects is crucial for the determination of the sloshing amplitudes and the resulting forces on the tank and the surrounding structure. Three different sources of energy dissipation can be identified: damping due to the viscous boundary layer, bulk damping (inner fluid damping) and the pressure drop resulting from the flow through holes and slits of the baffles. If baffles are present, the third dissipative effect will be the most important one. In general, the resulting reduction of the sloshing loads depends on the excitation frequency and amplitude, the examined fluid and especially on its viscosity and density as well as on the geometrical shape of the baffles.

3.1 Viscous boundary layer damping

Regarding the incompressible Navier-Stokes equations, the following term of viscous energy dissipation can be identified with the viscous stress tensor $\boldsymbol{\tau}$:

$$\dot{E}_{vb} = -\int_{V(t)} \boldsymbol{\tau} \cdot (\boldsymbol{v} \cdot \nabla) \, \mathrm{d}V. \tag{10}$$

Using the laminar boundary layer approximation and assuming an oscillating flow outside of the boundary layer of area A with small velocity amplitude $\hat{v}$ as well as a Newtonian fluid leads to

$$\langle \dot{E}_{vb} \rangle = -\frac{\eta}{2}\sqrt{\frac{\omega}{2\nu}} \int_{A(t)} \hat{v}^2 \, \mathrm{d}A \tag{11}$$

after averaging over one period T [2, chapter 6]. Following Keulegan [7], the energy disspation can be related to the total energy $E = E_{\text{pot}} + E_{\text{kin}}$ by

$$\langle \dot{E} \rangle = -2\frac{\delta}{T}E \tag{12}$$

and the modal damping ratio ξ is obtained as

$$\xi = \frac{\delta}{2\pi}. \tag{13}$$

For the rectangular tank (Figure 2) the total energy dissipation in the viscous boundary layer can be expressed as the sum

$$\langle \dot{E}_{vb} \rangle = \langle \dot{E}_{vb} \rangle\big|_{x=-\frac{b_x}{2}} + \langle \dot{E}_{vb} \rangle\big|_{x=\frac{b_x}{2}} + \langle \dot{E}_{vb} \rangle\big|_{y=-\frac{b_y}{2}} + \langle \dot{E}_{vb} \rangle\big|_{y=\frac{b_y}{2}} + \langle \dot{E}_{vb} \rangle\big|_{z=-h}. \tag{14}$$

The velocity amplitudes $\hat{v}$ are the corresponding derivatives of

$$\hat{\Phi}(x,z) = \frac{g}{\omega_m} C_m \cos\left(\frac{\pi m}{b_x}\left(x + \frac{b_x}{2}\right)\right) \frac{\cosh\left(\frac{m\pi}{b_x}(z+h)\right)}{\cosh\left(\frac{m\pi}{b_x}h\right)} \tag{15}$$

in parallel direction to the boundary layer with C_m being a constant. The given two-dimensional formulas can be extended to the third dimension. Baffles can be also included using the formulas in [4] neglecting holes and taking only the first order approximation into account.

The resulting damping ratio [8], which can be incorporated in equation (5),

$$\begin{aligned}\xi_{vb} = \frac{\delta_{vb}}{2\pi} &= -\frac{1}{2\pi}\frac{\langle \dot{E}_{vb}\rangle T_m}{2E} = -\frac{1}{2\omega_m}\frac{\langle \dot{E}_{vb}\rangle}{E} \\ &= \sqrt{\frac{\nu}{2\omega_m}}\left(\frac{\frac{1}{2}\sinh\left(\frac{2m\pi}{b_x}h\right) - \frac{m\pi}{b_x}h + \frac{1}{2}m\pi}{b_x \sinh\left(\frac{m\pi}{b_x}h\right)\cosh\left(\frac{m\pi}{b_x}h\right)} + \frac{1}{b_y}\right).\end{aligned} \tag{16}$$

is proportional to the square root of the kinematic viscosity ν.

3.2 Bulk damping

The energy dissipation in the bulk of the fluid with the dynamic viscosity η

$$\dot{E}_{bd} = -\eta \int_{V(t)} \left((\boldsymbol{v}\cdot\nabla) + (\boldsymbol{v}\cdot\nabla)^{\mathsf{T}}\right)\cdot(\boldsymbol{v}\cdot\nabla)\,\mathrm{d}V \tag{17}$$

can be formulated in the two-dimensional case with the given velocity potential in the previous subsection as

$$\begin{aligned}\langle \dot{E}_{bd}\rangle &= -\eta b_y \int_{x=-\frac{b_x}{2}}^{\frac{b_x}{2}} \int_{z=-h}^{0} \left(2\left(\frac{\partial^2\hat{\Phi}}{\partial x^2}\right) + 2\left(\frac{\partial^2\hat{\Phi}}{\partial z^2}\right) + 4\left(\frac{\partial^2\hat{\Phi}}{\partial x \partial z}\right)\right)\mathrm{d}z\,\mathrm{d}x \\ &= -\eta b_x b_y C_m^2 g \left(\frac{m\pi}{b_x}\right)^2.\end{aligned} \tag{18}$$

The corresponding damping ratio follows as

$$\xi_{bd} = \frac{\delta_{bd}}{2\pi} = -\frac{1}{2\omega_m}\frac{\langle \dot{E}_{bd}\rangle}{E} = 2\nu\left(\frac{m\pi}{b_x}\right)^2\frac{1}{\omega_m}, \tag{19}$$

which is proportional to the kinematic viscosity ν. As the values of ν are small for the investigated fluids, the bulk damping is only relevant for higher modes [9].

3.3 Pressure drop at the baffles

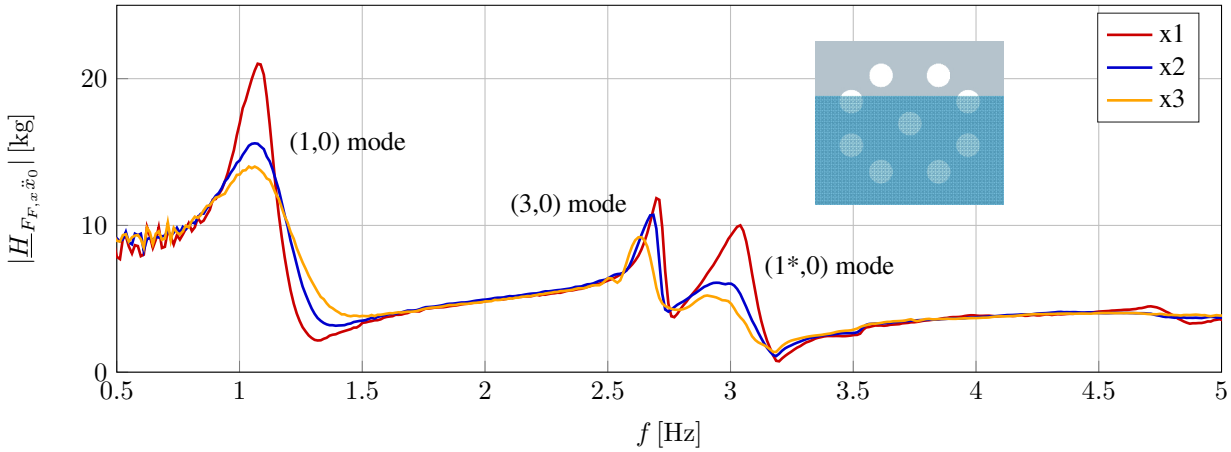
Baffles in commercial vehicle tanks normally divide the tank volume vertically in three compartments of similiar size. In Figure 4a the transfer function for this tank configuration being divided at position B and D with two baffles of the given shape is plotted. The corresponding mode shapes are given in Figures 4b-4d.

The excitation amplitude dependent reduction of the sloshing amplitudes due to the pressure drop at the baffles can be seen in Figure 4a. This pressure drop which is caused by jet flow, cross flow and flow separation at the baffle can be described by

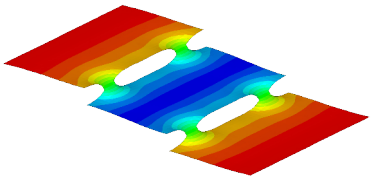
$$p^l - p^r = \frac{1}{2}\rho K_{\Delta p}|v_s|v_s \tag{20}$$

with the pressure p at the left (l) and right (r) side of the baffle, the approach velocity v_s and the pressure drop coefficient $K_{\Delta p}$. For most cases the higher the exicitation amplitudes the stronger the apparent mass is damped. Mode (3,0) is an exception, for which the damping ratio is nearly the same and much lower than for the other two modes. For this (3,0) mode the approach velocity at the baffles (tangent to the mode in 4c) is zero and only viscous boundary and bulk damping occur. The approach velocity can be written as

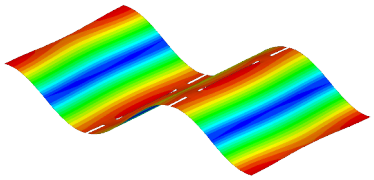
$$v_s(z,t) = \sum_{i=1}^{N_m} \frac{\dot{\beta}_i(t) g}{\omega_i^2}\left(\frac{\cosh(k_0(z+h))}{N_0}B_0\right) \tag{21}$$



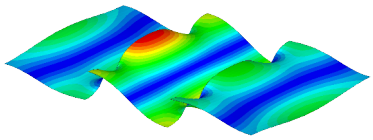
(a) Transfer function for different sine sweep excitation levels.



(b) (1,0) mode.



(c) (3,0) mode.



(d) (1*,0) mode.

Figure 4: Transfer function and mode shapes for the rectangular tank with baffles at position B and D at fill level 66.6 %.

with the number of regarded modes N_m and N_0 and B_0 being defined in [4]. The pressure drop can be integrated in the modal equations of motion [6, 10] and modified nonlinear modal equations of motion follow:

$$\begin{aligned} &\ddot{\beta}_i(t) + 2\xi_i\omega_i\dot{\beta}_i(t) + \omega_i^2\left(1 + \frac{\ddot{z}_0(t)}{g}\right)\beta_i(t) \\ &- \frac{K_{\Delta p}}{4h}\frac{\alpha_i^l + \alpha_i^r}{\mu_i}\int_{-h}^{0} v_s(z,t)|v_s(z,t)|\,\mathrm{d}z = -\frac{\lambda_{xi}}{\mu_i}\ddot{x}_0(t) \end{aligned} \tag{22}$$

with the terms $\alpha_i^l = \rho\int_{x=-\frac{b_x}{2}}^{x_s}\varphi_i(x,0)\,\mathrm{d}x$ and $\alpha_i^r = \rho\int_{x_s}^{x=\frac{b_x}{2}}\varphi_i(x,0)\,\mathrm{d}x$, the baffle position x_s and the already given hydrodynamic coefficients. An extension of the formulas to two baffles is also possible.

The empirical pressure drop coefficient $K_{\Delta p}$ depends on the solidity ratio, the Reynolds number and the Keulegan-Carpenter number. Different literature values for baffles are given in Table 1 including the value for the investigated baffle (Figure 4). The differences of the pressure drop coefficients are up to the value of 2 for the different applications and sources.

As there is no appropriate formula available for the pressure drop coefficient for the used perforated plates with few holes in truck tanks, a different, semi-empirical approach for tanks being equidistantly divided by two baffles is followed: Based on the known dependencies for a rectangular tank the formulas are fitted to experimental results using least-square approximation.

The total damping ratio $\xi = \xi_{vb} + \xi_{bd} + \xi_{\Delta p}$ consist of the viscous boundary and bulk damping part

$$\xi_{vb+bd,m} = C_1\sqrt{\frac{\nu}{f_m}}\left(\frac{\frac{1}{2}\sinh\left(\frac{2m\pi}{b_x}h\right) - \frac{m\pi}{b_x}h + \frac{1}{2}m\pi}{b_x\sinh\left(\frac{m\pi}{b_x}h\right)\cosh\left(\frac{m\pi}{b_x}h\right)} + \frac{1}{b_y}\right) + C_2\frac{\nu}{f_m}\frac{m^2}{b_x^2} \tag{23}$$

and the pressure drop at the baffles. The coefficients C_1 and C_2 are fitted to experimental damping ratios obtained by modal analysis for a clean rectangular tank and result in $C_1 = 0.3928$ and $C_2 = 7.3303$.

Formulation	Application	Reference	Example $K_{\Delta p}$
$K_{\Delta p} = \left(\frac{1}{\sqrt{D_c}(1-Sn)} - 1\right)^2$, $D_c = (0.405\exp(-\pi Sn) + 0.595)^2$	Plate with slits, $Sn \geq 0.3, KC \geq 15$	Tait [3]	145.79
$K_{\Delta p} = \frac{\left(0.707 Sn^{\frac{3}{8}} + Sn\right)^2}{(1-Sn)^2}$	Perforated sheet with sharp-edged orifices	Idelchik [11]	158.21
$K_{\Delta p} = \frac{Sn}{D_c(1-Sn)^2}$, $D_c = 0.78$	Screen made of metal wires	Idelchik [11]	73.93
$K_{\Delta p} = \frac{Sn}{D_c(1-Sn)^2}$, $D_c = 0.5$	Plate with holes	Molin [12]	115.51

Table 1: Different empirical formulas for the pressure drop coefficient $K_{\Delta p}$ for different applications and an example value for a baffle with a solidity ratio of $Sn = 0.8768$.

For the amplitude reduction due to the flow through baffles a linearization procedure according to Tait [14] is followed. The force due to the baffle is $F_{s,m}(x,z,t) = \int_{-h}^{0} f_{s,m}\,\mathrm{d}z = \Delta p\,\mathrm{d}A$ [15] with $f_{s,m}(x,t) = \frac{1}{2}\rho b_y K_{\Delta p} v_{s,m}|v_{s,m}|$ and the horizontal component of the velocity at the baffle $v_{s,m}$. Minimization of the error $\epsilon = \frac{1}{2}\rho b_y K_{\Delta p}\Xi_{s,m}\Xi_{g,m}\dot{\beta}_m|\dot{\beta}_m| - d_m\dot{\beta}_m$ with the terms

$$\Xi_{g,m} = \int_{z=-h}^{0} \frac{\cosh^3\left(\frac{\pi m}{b_x}(z+h)\right)}{\sinh^3\left(\frac{\pi m}{b_x}h\right)}\,\mathrm{d}z = \frac{b_x}{\pi m}\left(\frac{1}{3} + \frac{1}{\sinh^2\left(\frac{\pi m}{b_x}h\right)}\right) \tag{24}$$

and

$$\Xi_{s,m} = \sum_{j=1}^{N_s} \sin^3\left(\frac{\pi m}{b_x}\left(x_s^j + \frac{b_x}{2}\right)\right) \tag{25}$$

leads to the linear amplitude dependent damping term

$$\xi_{\Delta p,m} = \frac{K_{\Delta p}\Xi_{s,m}\Xi_{g,m}}{b_x}\left(\frac{1}{3}\tanh\left(\frac{\pi m}{b_x}h\right) + \frac{1}{\sinh\left(\frac{\pi m}{b_x}h\right)\cosh\left(\frac{\pi m}{b_x}h\right)}\right)\frac{4}{3\pi}\hat{\beta}. \tag{26}$$

The term $\Xi_{s,m}$ reflects the number of the baffles and their positions and has to be nonzero for all modes which are unsymmetric to the baffles. The obtained pressure drop coefficient after curve-fitting to experimental values is $K_{\Delta p} = 45.69$.

4 Results

4.1 Tank without baffles

The modal equations (5) are solved using the Dormand-Prince integration scheme and the measured displacement as excitation. For a rectangular tank without baffles only viscous boundary layer and bulk damping occur. Using the formulas in equations (16) and (19) the apparent masses in Figure 5 can be simulated.

The simulated damping values are too small and therefore the peak is too high. One possible reason could be the neglected sloshing amplitudes: Evaluating the integrals with the actual wetted area, i.e. replacing the undisturbed surface $z = 0$ by $z = \zeta_{\max}|\varphi(x,y,0)|$ results in a better approximation. However, the values are still too small.

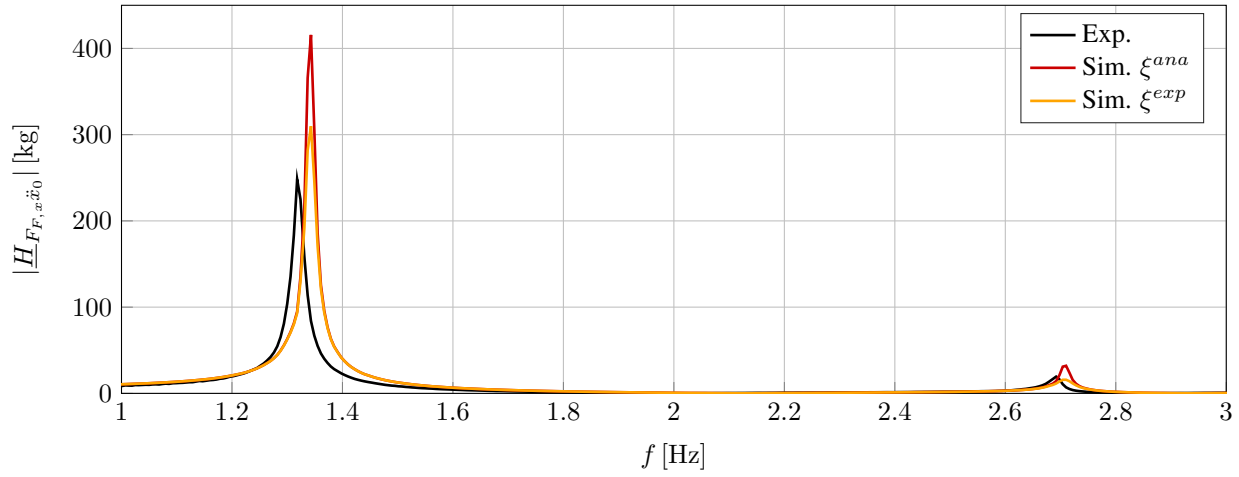


Figure 5: Comparison of measured and simulated transfer functions with experimental ξ^{exp} and analytical ξ^{ana} damping ratios for the unbaffled rectangular tank at sine sweep excitation and fill level 50.0 %.

4.2 Consideration of the pressure drop

In Figure 6 the numerical results using equation (22) and different values of $K_{\Delta p}$ for the given baffle being placed at position A (ratio 1:3) are compared to the test results.

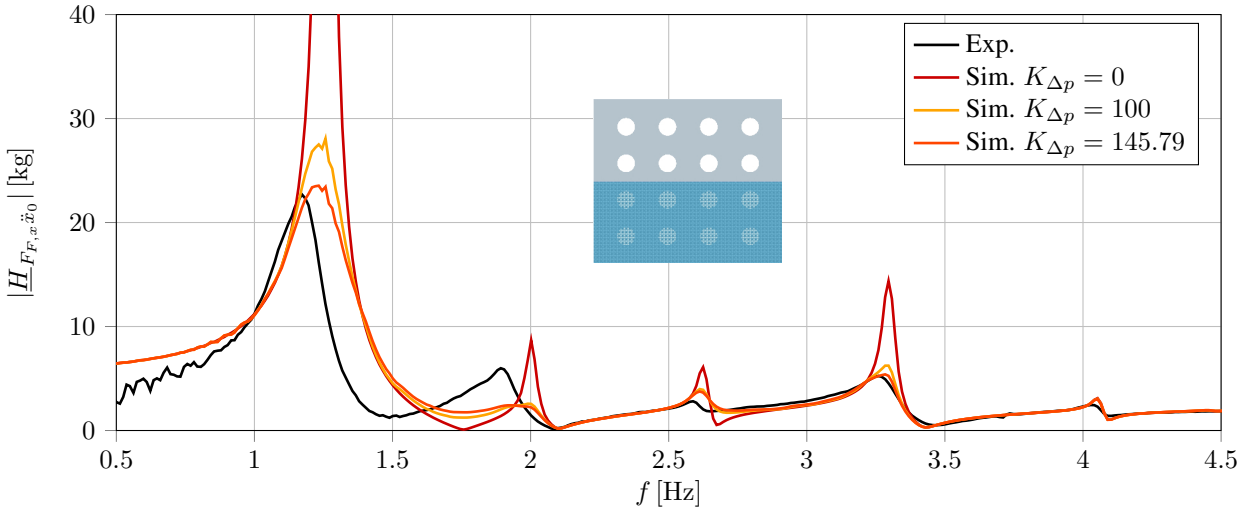


Figure 6: Comparison of experimental and simulated transfer functions for different values of $K_{\Delta p}$ (sine sweep excitation, fill level 50.0 %).

The measured transfer function can not be reproduced without accounting for the pressure drop ($K_{\Delta p} = 0$, red curve). Inserting higher values for $K_{\Delta p}$ reflects the measured curves.

4.3 Semi-empirical approach

The modal damping values due to viscous boundary layer and the material damping for the clean tank filled up to 33.3 % and 66.6 % are plotted in Figure 7 for the first five modes. The blank symbols are related to the modal analysis values of the measurements and the filled ones show the curve-fitting results. A very good approximation for the damping ratios, which are in general less than one percent, is obtained. For 66.6 % fill level, both dissipative contributions are plotted seperately. Whereas the viscous boundary layer damping decreases slowly with higher modes, the bulk damping becomes at all relevant only for higher frequencies.

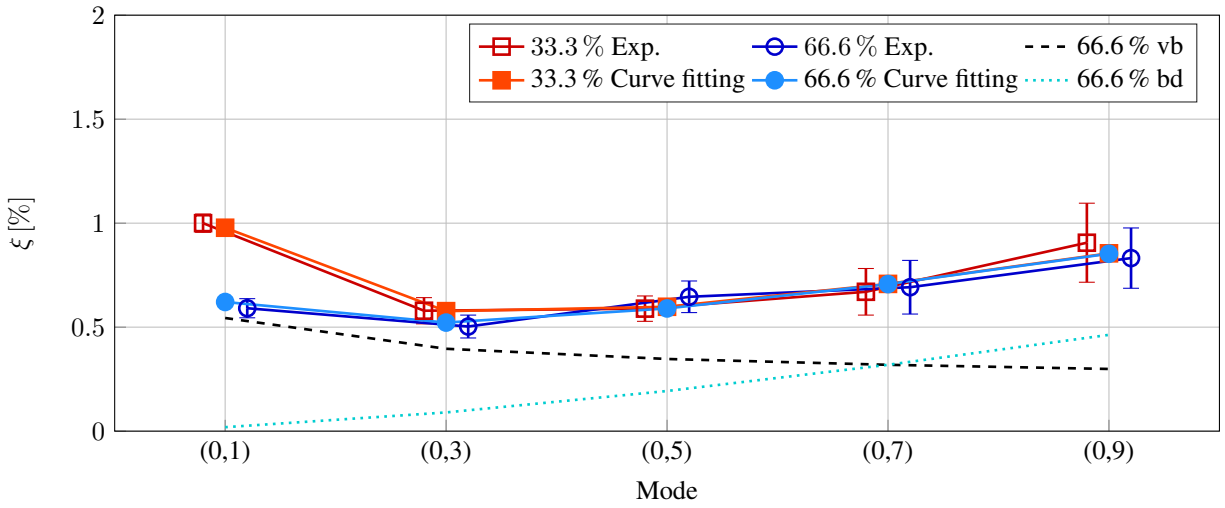


Figure 7: Experimentally determined modal damping ratios (blank symbols, mean value and standard deviation) for a clean tank with 33.3 % and 66.6 % fill level as well as the curve-fitting results (filled symbols, seperately for viscous boundary (vb) and bulk damping (bd) for 66.6 % fill level).

In the case of a tank equidistantly divided by two baffles, the damping ratios for the relevant first three modes are plotted in Figure 8 for three different excitation levels. The highest reduction of the sloshing amplitudes with damping ratios up to 15 % occur for the (1,0) mode. As already mentioned, there is no pressure drop for sloshing with the (3,0) mode and consequently the damping ratios are quite small. For the (1*,0) mode values up to roundabout 5 % can be measured. If the fluid moves through the openings at the baffle, the damping ratios increase strongly with the excitation amplitude. Again the curve-fitted values are plotted with filled symbols in comparison to the experimental blank marks. A satisfactory agreement is achieved, especially the amplitude dependent behaviour can be depicted correctly.

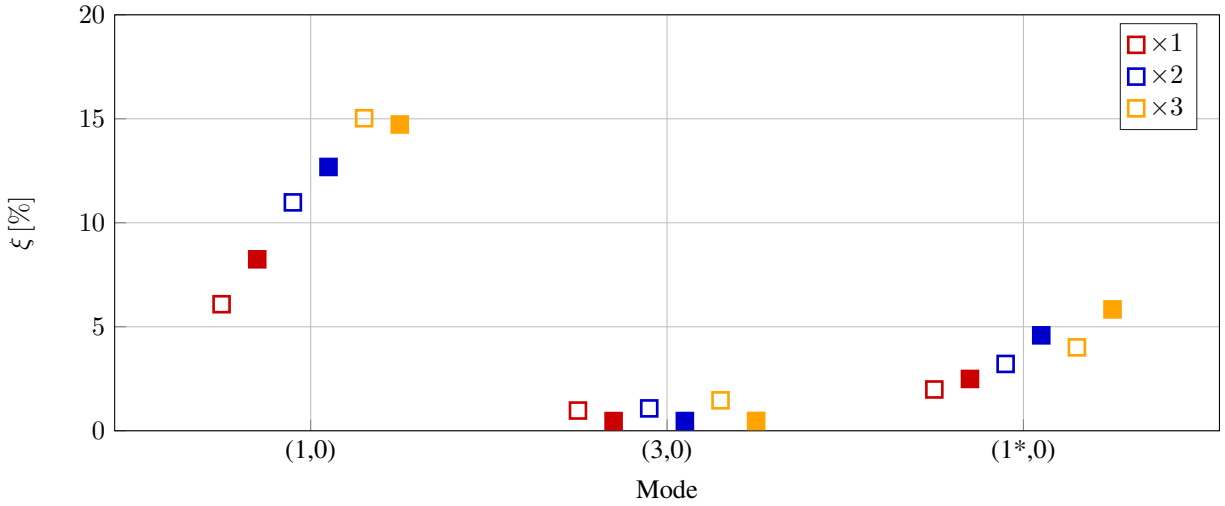


Figure 8: Experimentally determined modal damping ratios (blank symbols) and curve-fitted values (filled symbols) at different excitation amplitudes ($\times 1 \ldots \times 3$) for sine weep excitation at 66.6 % for the tank with two baffles (positions B and D).

Using the curve-fitted modal damping ratios and the numerical determined eigenfrequencies and modes with the finite element method in equation (5) results in the transfer function given in Figure 9. The comparison with the experiment shows a good depiction of the measured fluid behaviour.

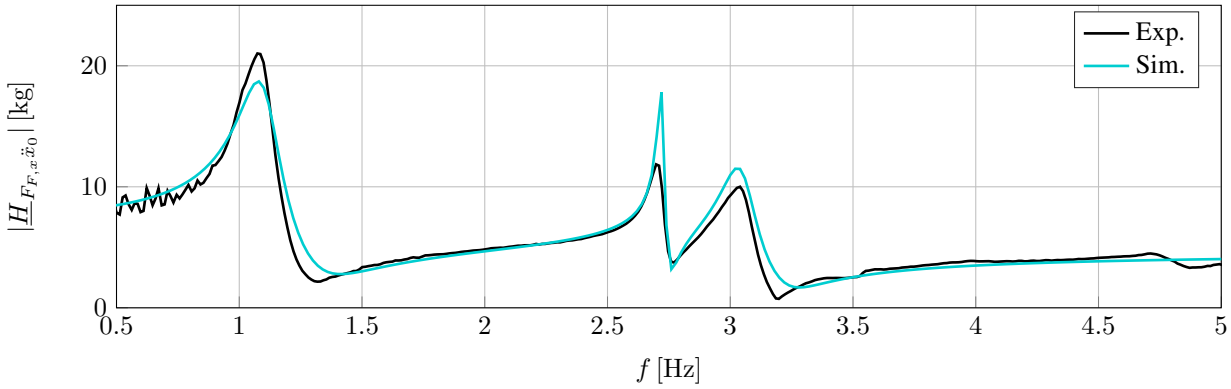


Figure 9: Experimental transfer function in comparison to simulated one using the curve-fitted damping ratios (sine sweep excitation, 66.6 % fill level, baffles at positions B and D).

5 Conclusion

The sloshing behaviour in rectangular tanks can be described with the linear potential theory for the investigated fluid. Besides the excitation which is normally known from the application case, the eigenfrequencies and corresponding modes as well as the dissipative effects have to be determined. This contribution focuses on the energy dissipation due to viscous boundary layer damping, bulk damping and especially the pressure drop at the baffles. Analytical formulas of all mentioned effects are given and the integration in the modal equations of motion is shown. For perforated plates, which are typically used in truck tanks, semi-empirical formulas are derived and validated with measurements resulting in good agreement.

It is shown how the dissipative effects due to sloshing can be modelled and simulated. The outlined procedure can be easily transfered to real-size truck tanks. Furthermore, the derived eigenfrequencies and modes in [4] and the calculated damping ratios given in this contribution can be utilized to parametrize an equivalent mechanical model, for example.

The consideration of nonlinear sloshing effects for higher amplitudes and the derivation of an optimal tank design using the given approaches could be part of further investigations.

References

[1] H. N. Abramson, *The dynamic behavior of liquids in moving containers*, NASA Special Publication 106 (1966).

[2] O. M. Faltinsen, A. N. Timokha, *Sloshing*, Cambridge University Press (2009).

[3] M. J. Tait, A. A. El Damatty, N. Isyumov, M.R. Siddique, *Numerical flow models to simulate tuned liquid dampers (TLD) with slat screens*, Journal of Fluids and Structures, Vol. 20, No. 8, Elsevier (2005), pp. 1007-1023.

[4] F. Buck, H. Hetzler, E. Fruend und S. Oexl, *Examination of the dynamic behavior of fuel tanks for different excitation directions*, Proceedings of ISMA 2016, KU Leuven (2016), pp. 3817-3828.

[5] O. M. Faltinsen, A. N. Timokha, *Natural sloshing frequencies and modes in a rectangular tank with a slat-type screen*, Journal of Sound and Vibration, Vol. 330, No. 7, Elsevier (2011), pp. 1490-1503.

[6] F. Buck, H. Hetzler, E. Fruend, S. Oexl, *Linear forced sloshing for a baffled rectangular fuel tank*, Proceedings in Applied Mathematics and Mechanics, Vol. 17, No. 1, Wiley (2017), pp. 673-674.

[7] G. H. Keulegan, *Energy dissipation in standing waves in rectangular basins*, Journal of Fluid Mechanics, Vol. 6, No. 1, Cambridge (1959), pp. 33-50.

[8] J.W. Miles, *Surface-wave damping in closed basins*, Proceedings of the Royal Society A: Mathematical, Physical and Engineering Sciences, Vol. 297, No. 1451, The Royal Society (1967), pp. 459-475.

[9] J. W. Miles, D. M. Henderson, *A note on interior vs. boundary-layer damping of surface waves in a circular cylinder*, Journal of Fluid Mechanics, Vol. 364, Cambridge (1998), pp. 319-323.

[10] O. M. Faltinsen, R. Firoozkoohi, A. N. Timokha, *Steady-state liquid sloshing in a rectangular tank with a slat-type screen in the middle: Quasilinear modal analysis and experiments*, Physics of Fluids, Vol. 23, No. 4, American Institute of Physics (2011), p. 042101.

[11] B. Molin, *Hydrodynamic modeling of perforated structures*, Applied Ocean Research, Vol. 33, No. 1, Elsevier (2011), pp. 1-11.

[12] B. Molin, F. Remy, *Experimental and numerical study of the sloshing motion in a rectangular tank with a perforated screen*, Journal of Fluids and Structures, Vol. 43, Elsevier (2013), pp. 463-480.

[13] B. Molin, F. Remy, *Inertia effects in TLD sloshing with perforated screens*, Journal of Fluids and Structures, Vol. 59, Elsevier (2015), pp. 165-177.

[14] M. J. Tait, *Modelling and preliminary design of a structure-TLD system*, Engineering Structures, Vol. 30, No. 10, Elsevier (2008), pp. 2644-2655.

[15] J. R. Morison, J.W. Johnson, S. A. Schaaf, *The force exerted by surface waves on piles*, Journal of Petroleum Technology, Vol. 2, No. 5, OnePetro (1950), pp. 149-154.

Efficient time-domain modeling of floating structures with fluid-structure interaction by reduced-order state-space approximations

Ø. W. Petersen [1], **O. Øiseth** [1]
[1] NTNU, Norwegian University of Science and Technology, Department of Structural Engineering
7491 Trondheim, Norway
e-mail: **oyvind.w.petersen@ntnu.no**

Abstract
High-fidelity dynamic models of floating structures must take into account the fluid-structure interaction, for example by considering frequency-dependent added mass and damping matrices. This translates to convolution integrals in the time-domain, which are computationally expensive. This paper shows how the convolution terms can be replaced with an approximate state-space representation to establish a time-invariant global system model, which also can be modally reduced. The state-space approximation is generated by fitting its input-output transfer function to the transfer function of the retardation forces from the added mass and damping. The methodology is numerically validated in a case-study of a long-span floating pontoon bridge, using first-order wave loads as input forces in a time-domain simulation. A time-invariant state-space model of the bridge is created using the mentioned approach. It is shown that both the calculated dynamic response and the retardation forces are highly accurate, when compared with a frequency-domain reference solution.

1 Introduction

The linear dynamic behavior of marine structures subjected to ambient loading is often analyzed in the frequency-domain, using a frequency-domain characterization of first-order wave loads and the wave-to-motion transfer function of the structure [1]. These transfer functions take into account the fluid-structure interaction (FSI) with the surrounding water. However, a frequency-domain solution it is not always possible or desired, e.g. in case of control systems design, cycle counting for fatigue in broadband vibration processes, long term extreme value estimation or non-linear wave loads. In time-domain analysis, the Cummins equation governs the dynamics of the system [2]. Due to the FSI, this equation contains convolution terms, which can be inconvenient in terms of computational efficiency.

The convolution terms can be approximated by equivalent state-space models, utilizing the property that the convolution is a linear operator [3–5]. This approach yields a time-invariant linear model of the system. The approximate state-space model can be established through either a time-domain or a frequency-domain identification [6]. The time-domain identification is based on fitting the input-output impulse response of the state-space model to the fluid-memory retardation function. In the frequency-domain identification, the input-output transfer function of the state-space model is fitted to the transfer function of the retardation forces, which is related to the so-called added mass and damping from the fluid, which is obtainable from commercial software such as WAMIT [7] or WADAM [8]. A thorough review of various methods that deals with the convolution in marine applications can be found in [9].

In this article, the frequency-domain identification approach is given attention. We show a framework for establishing of time-invariant linear models of floating structures, combined with a modal truncation to reduce the model order. The methodology is exemplified in a real case-study of the Bergsøysund Bridge,

a long-span floating bridge. A similar methodology has been tested before on the same structure, where a hydro-elastic element was developed for use in a (non-reduced) finite element (FE) model [10]. Using simulated wave loads as input forces, we evaluate the accuracy of the response obtained from the approximate model and compare it to a reference solution.

2 System formulation for the dynamic behavior of floating structures

2.1 Time-domain model and convolution replacement by parametric transfer functions

Consider a (stationary) floating structure modeled with $\mathrm{n_{DOF}}$ degrees of freedom (DOFs). The dynamic response $\mathbf{u}(t) \in \mathbb{R}^{\mathrm{n_{DOF}}}$ is governed by the equations of motion, which can be formulated in the frequency-domain as follows:

$$-\omega^2\big(\mathbf{M}_\mathrm{s} + \mathbf{M}_\mathrm{h}(\omega)\big)\mathbf{u}(\omega) + i\omega\big(\mathbf{C}_\mathrm{s} + \mathbf{C}_\mathrm{h}(\omega)\big)\mathbf{u}(\omega) + \big(\mathbf{K}_\mathrm{s} + \mathbf{K}_\mathrm{h}\big)\mathbf{u}(\omega) = \mathbf{S}_\mathrm{p}\mathbf{p}(\omega) \tag{1}$$

where $\mathbf{p} \in \mathbb{R}^{\mathrm{n_p}}$ is the vector of $\mathrm{n_p}$ external forces, and the boolean matrix $\mathbf{S}_\mathrm{p} \in \mathbb{R}^{\mathrm{n_{DOF}} \times \mathrm{n_p}}$ assigns these forces to the designated set of DOFs. The FSI is taken into account in Eq. 1 by the hydrodynamic mass $\mathbf{M}_\mathrm{h}(\omega)$ and damping $\mathbf{C}_\mathrm{h}(\omega) \in \mathbb{R}^{\mathrm{n_{DOF}} \times \mathrm{n_{DOF}}}$, which are frequency dependent, in addition to the hydrostatic restoring stiffness $\mathbf{K}_\mathrm{h} \in \mathbb{R}^{\mathrm{n_{DOF}} \times \mathrm{n_{DOF}}}$. The elements of these three matrices generally are zero except for the matrix elements corresponding to the wetted DOFs. $\mathbf{M}_\mathrm{s}$, $\mathbf{C}_\mathrm{s}$ and $\mathbf{K}_\mathrm{s} \in \mathbb{R}^{\mathrm{n_{DOF}} \times \mathrm{n_{DOF}}}$ represent the mass, damping and stiffness matrices of the structure.

By taking the inverse Fourier transform ($\mathcal{F}^{-1}$), Eq. 1 can be formulated in the time-domain as follows:

$$(\mathbf{M}_\mathrm{s} + \mathbf{M}_{\mathrm{h},\infty})\ddot{\mathbf{u}}(t) + \mathbf{C}_\mathrm{s}\dot{\mathbf{u}}(t) + (\mathbf{K}_\mathrm{s} + \mathbf{K}_\mathrm{h})\mathbf{u}(t) + \mathbf{p}_\mathrm{mi}(t) = \mathbf{S}_\mathrm{p}\mathbf{p}(t) \tag{2}$$

This formulation is commonly known as Cummins equation [2]. Here, we have defined the limit quantity $\mathbf{M}_{\mathrm{h},\infty} = \lim_{\omega\to\infty} \mathbf{M}_\mathrm{h}(\omega)$, which in practice converges for frequencies far less than infinity. Due to the frequency dependency of the hydrodynamic mass and damping the so-called radiation forces or motion-induced forces $\mathbf{p}_\mathrm{mi}(t) \in \mathbb{R}^{\mathrm{n_{DOF}}}$ become a convolution integral:

$$\mathbf{p}_\mathrm{mi}(t) = \int_0^t \mathbf{h}(t-\tau)\mathbf{u}(\tau)\,\mathrm{d}\tau \tag{3}$$

The impulse response $\mathbf{h}(t)$ is defined as $\mathcal{F}^{-1}(\mathbf{h}(\omega))$, where $\mathbf{h}(\omega)$ is the following transfer function:

$$\mathbf{h}(\omega) = i\omega\mathbf{C}_\mathrm{h}(\omega) - \omega^2\big(\mathbf{M}_\mathrm{h}(\omega) - \mathbf{M}_{\mathrm{h},\infty}\big) \tag{4}$$

The convolution term is not efficient in time-domain simulations. We therefore seek to replace it by first assuming $\mathbf{h}(\omega)$ can be approximated by the following parametric expression of order N_l:

$$\hat{\mathbf{h}}(\omega) = \sum_{l=1}^{N_l} \mathbf{a}_l \frac{i\omega}{i\omega + d_l} \tag{5}$$

This type of expression is common for parametric models of self-excited forces in wind engineering [11–13], and is sometimes referred to as Roger's approximation [14]. The applicability of Eq. 5 to model marine structures in particular is further elaborated in Section 2.2. Eq. 5 can be separated into the following real and imaginary parts:

$$\mathrm{Re}(\hat{\mathbf{h}}(\omega)) = \sum_{l=1}^{N} \mathbf{a}_l \frac{\omega^2}{d_l^2 + \omega^2} \tag{6}$$

$$\mathrm{Im}(\hat{\mathbf{h}}(\omega)) = \sum_{l=1}^{N} \mathbf{a}_l \frac{d_l \omega}{d_l^2 + \omega^2} \tag{7}$$

From the real and imaginary part of Eq. 4, we see that the mass and damping can be reconstructed in the parametric model by the following expressions:

$$\hat{\mathbf{M}}_{\mathrm{h}}(\omega) = \frac{\mathrm{Re}(\hat{\mathbf{h}}(\omega))}{-\omega^2} + \mathbf{M}_{\mathrm{h},\infty} = \sum_{l=1}^{N} \mathbf{a}_l \frac{-1}{d_l^2 + \omega^2} + \mathbf{M}_{\mathrm{h},\infty} \tag{8}$$

$$\hat{\mathbf{C}}_{\mathrm{h}}(\omega) = \frac{\mathrm{Im}(\hat{\mathbf{h}}(\omega))}{\omega} = \sum_{l=1}^{N} \mathbf{a}_l \frac{d_l}{d_l^2 + \omega^2} \tag{9}$$

Assuming that the hydrodynamic matrices are given at discrete frequencies ($\omega_r > 0$), the coefficients of $\mathbf{a}_l \in \mathbb{R}^{\mathrm{n_{DOF}} \times \mathrm{n_{DOF}}}$ and $d_l > 0$ ($l = 1 \ldots N_l$) can be found by minimizing the objective function:

$$\sum_{r \,\in\, \{\omega\}} \sum_{i,j} W(\omega_r) \Big(\big(\hat{M}_{\mathrm{h},ij}(\omega_r) - M_{\mathrm{h},ij}(\omega_r)\big)^2 + \big(\hat{C}_{\mathrm{h},ij}(\omega_r) - C_{\mathrm{h},ij}(\omega_r)\big)^2 \Big) \tag{10}$$

where the indexes ij now selects the non-zero matrix elements (i.e. the wetted DOFs). This fit is a weighted non-linear least squares problem where the objective is the parametric reconstruction of the hydrodynamic mass and damping by Eqs. 8 and 9. The weighting coefficients $W(\omega_r)$ are optional and can be used to emphasize a frequency range of interest.

Next, a modal truncation is performed by first solving the following eigenvalue problem:

$$[\mathbf{K}_{\mathrm{s}} + \mathbf{K}_{\mathrm{h}} - \omega_j^2 (\mathbf{M}_{\mathrm{s}} + \mathbf{M}_{\mathrm{h},\infty})]\boldsymbol{\phi}_j = \mathbf{0} \qquad (j = 1 \ldots \mathrm{n_m}) \tag{11}$$

We assume $\mathbf{u}(t) \approx \boldsymbol{\Phi}\mathbf{z}(t)$, where $\boldsymbol{\Phi} \in \mathbb{R}^{\mathrm{n_{DOF}} \times \mathrm{n_m}}$ contains $\mathrm{n_m}$ mass-normalized eigenvectors and $\mathbf{z}(t) \in \mathbb{R}^{\mathrm{n_m}}$ is the modal coordinate vector. From the truncation the following relations hold true:

$$\boldsymbol{\Phi}^{\mathrm{T}}(\mathbf{M}_{\mathrm{s}} + \mathbf{M}_{\mathrm{h},\infty})\boldsymbol{\Phi} = \mathbf{I} \tag{12}$$

$$\boldsymbol{\Phi}^{\mathrm{T}}(\mathbf{K}_{\mathrm{s}} + \mathbf{K}_{\mathrm{h}})\boldsymbol{\Phi} = \boldsymbol{\Omega}^2 \tag{13}$$

$$\boldsymbol{\Phi}^{\mathrm{T}}\mathbf{C}_{\mathrm{s}}\boldsymbol{\Phi} = 2\boldsymbol{\Omega}\boldsymbol{\Xi} \tag{14}$$

where $\boldsymbol{\Omega} = \mathrm{diag}(\omega_j) \in \mathbb{R}^{\mathrm{n_m} \times \mathrm{n_m}}$ and $\boldsymbol{\Xi} = \mathrm{diag}(\xi_j) \in \mathbb{R}^{\mathrm{n_m} \times \mathrm{n_m}}$. Proportional damping was also assumed in Eq. 14 so that $\boldsymbol{\Phi}$ diagonalizes $\mathbf{C}_{\mathrm{s}}$ and the damping from the structure only can be described by the modal damping ratio ξ_j. When Eq. 2 is premultiplied with $\boldsymbol{\Phi}^{\mathrm{T}}$, a modal equation of motion is obtained:

$$\ddot{\mathbf{z}}(t) + 2\boldsymbol{\Omega}\boldsymbol{\Xi}\dot{\mathbf{z}}(t) + \boldsymbol{\Omega}^2\mathbf{z}(t) + \boldsymbol{\Phi}^{\mathrm{T}}\mathbf{p}_{\mathrm{mi}}(t) = \boldsymbol{\Phi}^{\mathrm{T}}\mathbf{S}_{\mathrm{p}}\mathbf{p}(t) \tag{15}$$

Next we consider the parametric modeling of the (modal) motion-induced forces:

$$\boldsymbol{\Phi}^{\mathrm{T}}\mathbf{p}_{\mathrm{mi}}(\omega) = \boldsymbol{\Phi}^{\mathrm{T}}\mathbf{h}(\omega)\mathbf{u}(\omega) \approx \boldsymbol{\Phi}^{\mathrm{T}}\hat{\mathbf{h}}(\omega)\boldsymbol{\Phi}\mathbf{z}(\omega) = \sum_{l=1}^{N_l} \boldsymbol{\Phi}^{\mathrm{T}}\mathbf{a}_l\boldsymbol{\Phi}\frac{i\omega}{i\omega + d_l}\mathbf{z}(\omega) = \sum_{l=1}^{N_l} \boldsymbol{\Phi}^{\mathrm{T}}\mathbf{a}_l\boldsymbol{\Phi}\boldsymbol{\mu}_l(\omega) \tag{16}$$

where in the last step we introduced the definition:

$$\boldsymbol{\mu}_l(\omega) = \frac{i\omega}{i\omega + d_l}\mathbf{z}(\omega) \tag{17}$$

When the inverse Fourier transform is applied to Eq. 17, a first order time-domain differential equation is obtained:

$$\dot{\boldsymbol{\mu}}_l(t) = -d_l\boldsymbol{\mu}_l(t) + \dot{\mathbf{z}}(t) \tag{18}$$

Alternatively, this can be formulated for all terms $l = 1 \dots N_l$:

$$\begin{bmatrix} \dot{\boldsymbol{\mu}}_1(t) \\ \vdots \\ \dot{\boldsymbol{\mu}}_{N_l}(t) \end{bmatrix} = \begin{bmatrix} -d_1\mathbf{I} & & \\ & \ddots & \\ & & -d_{N_l}\mathbf{I} \end{bmatrix} \begin{bmatrix} \boldsymbol{\mu}_1(t) \\ \vdots \\ \boldsymbol{\mu}_{N_l}(t) \end{bmatrix} + \begin{bmatrix} \mathbf{I} \\ \vdots \\ \mathbf{I} \end{bmatrix} \dot{\mathbf{z}}(t) \tag{19}$$

or written in matrix state-space form:

$$\dot{\mathbf{q}}(t) = \hat{\mathbf{A}}\mathbf{q}(t) + \hat{\mathbf{B}}\dot{\mathbf{z}}(t) \tag{20}$$

where we define $\mathbf{q}(t) = [\boldsymbol{\mu}_1(t)^{\mathrm{T}} \ \dots \ \boldsymbol{\mu}_{N_l}(t)^{\mathrm{T}}]^{\mathrm{T}} \in \mathbb{R}^{N_l \mathrm{n_m}}$. Next, Eq. 16 can also be written in matrix form:

$$\boldsymbol{\Phi}^{\mathrm{T}}\mathbf{p}_{\mathrm{mi}}(t) = \begin{bmatrix} \boldsymbol{\Phi}^{\mathrm{T}}\mathbf{a}_1\boldsymbol{\Phi} & \dots & \boldsymbol{\Phi}^{\mathrm{T}}\mathbf{a}_{N_l}\boldsymbol{\Phi} \end{bmatrix} \begin{bmatrix} \boldsymbol{\mu}_1(t) \\ \vdots \\ \boldsymbol{\mu}_{N_l}(t) \end{bmatrix} = \hat{\mathbf{C}}\mathbf{q}(t) \tag{21}$$

The obtained matrices $\hat{\mathbf{A}} \in \mathbb{R}^{N_l \mathrm{n_m} \times N_l \mathrm{n_m}}$, $\hat{\mathbf{B}} \in \mathbb{R}^{N_l \mathrm{n_m} \times \mathrm{n_m}}$, and $\hat{\mathbf{C}} \in \mathbb{R}^{\mathrm{n_m} \times N_l \mathrm{n_m}}$ are now constant (time-invariant), which was desired in order to replace the convolution in Eq. 3. Eqs. 15, 20 and 21 can be combined to describe the total (coupled) system dynamics in state-space form:

$$\begin{bmatrix} \dot{\mathbf{z}}(t) \\ \ddot{\mathbf{z}}(t) \\ \dot{\mathbf{q}}(t) \end{bmatrix} = \begin{bmatrix} \mathbf{0} & \mathbf{I} & \mathbf{0} \\ -\boldsymbol{\Omega}^2 & -2\boldsymbol{\Omega}\boldsymbol{\Xi} & -\hat{\mathbf{C}} \\ \mathbf{0} & \hat{\mathbf{B}} & \hat{\mathbf{A}} \end{bmatrix} \begin{bmatrix} \mathbf{z}(t) \\ \dot{\mathbf{z}}(t) \\ \mathbf{q}(t) \end{bmatrix} + \begin{bmatrix} \mathbf{0} \\ \boldsymbol{\Phi}^{\mathrm{T}}\mathbf{S}_{\mathrm{p}} \\ \mathbf{0} \end{bmatrix} \mathbf{p}(t) \tag{22}$$

which finally is written in compact matrix form:

$$\dot{\mathbf{x}}(t) = \mathbf{A}_c\mathbf{x}(t) + \mathbf{B}_c\mathbf{p}(t) \tag{23}$$

The state vector is now $\mathbf{x}(t) = [\mathbf{z}(t)^{\mathrm{T}} \ \dot{\mathbf{z}}(t)^{\mathrm{T}} \ \mathbf{q}(t)^{\mathrm{T}}]^{\mathrm{T}} \in \mathbb{R}^{\mathrm{n_s}}$ with corresponding system matrices $\mathbf{A}_c \in \mathbb{R}^{\mathrm{n_s} \times \mathrm{n_s}}$ and $\mathbf{B}_c \in \mathbb{R}^{\mathrm{n_s} \times \mathrm{n_p}}$, where the state order is $\mathrm{n_s} = (2 + N_l)\mathrm{n_m}$.

Finally, the $\mathrm{n_y}$ linear response outputs are considered, which typically are displacements or accelerations. Using the boolean matrices $\mathbf{S}_{\mathrm{a}}$ and $\mathbf{S}_{\mathrm{d}} \in \mathbb{R}^{\mathrm{n_y} \times \mathrm{n_{DOF}}}$ to select the desired output DOFs, the output vector $\mathbf{y}(t) \in \mathbb{R}^{\mathrm{n_y}}$ is constructed as follows:

$$\begin{aligned} \mathbf{y}(t) &= \mathbf{S}_{\mathrm{a}}\ddot{\mathbf{u}}(t) + \mathbf{S}_{\mathrm{d}}\mathbf{u}(t) \approx \mathbf{S}_{\mathrm{a}}\boldsymbol{\Phi}\ddot{\mathbf{z}}(t) + \mathbf{S}_{\mathrm{d}}\boldsymbol{\Phi}\mathbf{z}(t) \\ &= \begin{bmatrix} \mathbf{S}_{\mathrm{d}}\boldsymbol{\Phi} - \mathbf{S}_{\mathrm{a}}\boldsymbol{\Phi}\boldsymbol{\Omega}^2 & -\mathbf{S}_{\mathrm{a}}\boldsymbol{\Phi}2\boldsymbol{\Omega}\boldsymbol{\Xi} & -\mathbf{S}_{\mathrm{a}}\boldsymbol{\Phi}\hat{\mathbf{C}} \end{bmatrix} \begin{bmatrix} \mathbf{z}(t) \\ \dot{\mathbf{z}}(t) \\ \mathbf{q}(t) \end{bmatrix} + \begin{bmatrix} \mathbf{S}_{\mathrm{a}}\boldsymbol{\Phi}\boldsymbol{\Phi}^{\mathrm{T}}\mathbf{S}_{\mathrm{p}} \end{bmatrix} \mathbf{p}(t) \end{aligned} \tag{24}$$

This equation can be written on compact matrix form, where $\mathbf{G}_c \in \mathbb{R}^{\mathrm{n_y} \times \mathrm{n_s}}$ and $\mathbf{J}_c \in \mathbb{R}^{\mathrm{n_y} \times \mathrm{n_p}}$:

$$\mathbf{y}(t) = \mathbf{G}_c \mathbf{x}(t) + \mathbf{J}_c \mathbf{p}(t) \tag{25}$$

Eqs. 23 and 25 together form the continuous state-space system. This formulation is an approximation of Eq. 2, and is efficient and easy to use in time-domain problems. In digital simulations, a formulation in discrete time is required. The continuous state-space model is discretized by a time step Δt such that $t_k = k\Delta t$ ($k = 0, 1 \ldots, N_t - 1$):

$$\mathbf{x}_{k+1} = \mathbf{A}\mathbf{x}_k + \mathbf{B}\mathbf{p}_k \tag{26}$$

$$\mathbf{y}_k = \mathbf{G}\mathbf{x}_k + \mathbf{J}\mathbf{p}_k \tag{27}$$

where $\mathbf{x}_k = \mathbf{x}(t_k)$, $\mathbf{y}_k = \mathbf{y}(t_k)$, and $\mathbf{p}_k = \mathbf{p}(t_k)$. The discrete time system matrices have the following definitions:

$$\mathbf{A} = \exp\Big(\mathbf{A}_c \Delta t\Big), \quad \mathbf{B} = (\mathbf{A} - \mathbf{I})\mathbf{A}_c^{-1}\mathbf{B}_c, \quad \mathbf{G} = \mathbf{G}_c, \quad \mathbf{J} = \mathbf{J}_c \tag{28}$$

2.2 Properties of the parametric transfer function

The focus is now directed to the chosen transfer function $\hat{\mathbf{h}}(\omega)$ in Eq. 5. In this section, we investigate if this parametric expression is adequate for modeling of floating structures, and also point out some of the similarities and differences to other approaches found in the literature. The inquiry is performed in terms of the transfer function $\mathbf{k}(\omega) = \mathbf{h}(\omega)/(i\omega)$ and its retardation impulse response $\mathbf{k}(t) = \mathcal{F}^{-1}(\mathbf{k}(\omega))$. This is analogue to a reformulation of Eq. 3 using velocity as the input in the convolution instead of the displacement, which is an equally possible choice.

In the general form, a matrix of rational transfer functions with relative degree 1, denoted $\hat{\mathbf{k}}'(\omega) \in \mathbb{C}^{\mathrm{n_{DOF}} \times \mathrm{n_{DOF}}}$, may be structured as follows:

$$\hat{\mathbf{k}}'(\omega) = \begin{bmatrix} \hat{k}'_{11}(\omega) & \ldots & \hat{k}'_{1\,\mathrm{n_{DOF}}}(\omega) \\ \vdots & \ddots & \vdots \\ \hat{k}'_{\mathrm{n_{DOF}}\,1}(\omega) & \ldots & \hat{k}'_{\mathrm{n_{DOF}}\,\mathrm{n_{DOF}}}(\omega) \end{bmatrix} \tag{29}$$

where an element of order n is given by:

$$\hat{k}'_{ij}(\omega) = \frac{b_{n-1}(i\omega)^{n-1} + \cdots + b_1(i\omega) + b_0}{(i\omega)^n + a_{n-1}(i\omega)^{n-1} + \cdots + a_1(i\omega) + a_0} \tag{30}$$

This form is a common starting point in parametric modeling of marine structures, as utilized by the authors in for example [5, 15]. Here, it is the individual element $\hat{k}'_{ij}(\omega)$ that is fitted by the polynomial coefficients $\{a_0, \ldots, a_{n-1}\}$ and $\{b_0, \ldots, b_{n-1}\}$. We now check how the formulation with basis in Eq. 5 differs from Eq. 29. It is clear that $\hat{\mathbf{k}}(\omega) = \hat{\mathbf{h}}(\omega)/(i\omega)$ from Eq. 5 is a partial fraction expansion, which can be factorized back into the full form:

$$\begin{aligned} \hat{\mathbf{k}}(\omega) &= \sum_{l=1}^{N_l} \mathbf{a}_l \frac{1}{i\omega + d_l} = \frac{\sum_{l=1}^{N_l} \left(\mathbf{a}_l \prod_{j=1, j\neq l}^{N_l} (i\omega + d_j)\right)}{\prod_{l=1}^{N_l} (i\omega + d_l)} \\ &= \frac{\sum_{l=1}^{N_l} \left(\mathbf{a}_l (b^{(l)}_{N_l-1}(i\omega)^{N_l-1} + \cdots + b^{(l)}_1(i\omega) + b^{(l)}_0)\right)}{(i\omega)^{N_l} + a_{N_l-1}(i\omega)^{N_l-1} + \cdots + a_1(i\omega) + a_0} \end{aligned} \tag{31}$$

We observe that Eq. 31 represents a special case of Eq. 29. In general, the poles of Eq. 30 appear as complex conjugate pairs, whereas Eq. 31 represents the special case where the poles $-d_l$ are strictly real. This is an advantage in terms of the stability properties. Since $d_l > 0$ is enforced, the poles $(-d_l)$ are always negative real, constraining $\hat{\mathbf{k}}(\omega)$ to be stable. This is not necessarily the case for Eq. 30, where unstable poles can occur in the identification when the polynomial coefficients are fitted. The instability can however usually be mended by reflecting the unstable poles about the imaginary axis [5].

Moreover, in the formulation presented in this paper, $\hat{\mathbf{h}}(\omega)$ is fitted for all wetted DOFs at once, and the the poles $(-d_l)$ are shared among all the wetted DOFs, as the denominator in Eq. 31 is the same for all matrix elements, also called a common-denominator model. This has the advantage that the size of the resulting system matrices ($\hat{\mathbf{A}}$, $\hat{\mathbf{B}}$, and $\hat{\mathbf{C}}$) can be reduced compared to the case where each DOF is fitted individually. This comes at the cost of having fever parameters to be fitted in total, which can make the fit less flexible. All the elements in Eq. 31 have the same polynomial order, this is not necessarily the case in Eq. 29.

From [6], it is known that the limit properties in Table 1 should be fulfilled to correctly represent the physics of the fluid memory:

No.	Property
(i)	$\lim_{\omega\to 0} \mathbf{k}(\omega) = \mathbf{0}$
(ii)	$\lim_{\omega\to \infty} \mathbf{k}(\omega) = \mathbf{0}$
(iii)	$\lim_{t\to 0} \mathbf{k}(t) \neq \mathbf{0}$
(iv)	$\lim_{t\to \infty} \mathbf{k}(t) = \mathbf{0}$
(v)	Passive mapping $\dot{\mathbf{x}} \to \mathbf{p}_{\text{mi}}$

Table 1: Properties of fluid memory models, from [6].

We now check whether the parametric expression for $\hat{\mathbf{h}}(\omega)$ in Eq. 5 can model these properties. With the help a similar inquiry in [15], and the initial/final value theorem from Laplace theory, we evaluate property (i)-(iv):

$$\lim_{\omega\to 0} \hat{\mathbf{k}}(\omega) = \lim_{\omega\to 0} \frac{\hat{\mathbf{h}}(\omega)}{i\omega} = \sum_{l=1}^{N_l} \mathbf{a}_l/d_l \tag{32}$$

$$\lim_{\omega\to \infty} \hat{\mathbf{k}}(\omega) = \lim_{\omega\to \infty} \frac{\hat{\mathbf{h}}(\omega)}{i\omega} = \mathbf{0} \tag{33}$$

$$\lim_{t\to 0} \hat{\mathbf{k}}(t) = \lim_{i\omega\to \infty} i\omega\hat{\mathbf{k}}(\omega) = \lim_{i\omega\to \infty} \hat{\mathbf{h}}(\omega) = \sum_{l=1}^{N_l} \mathbf{a}_l \tag{34}$$

$$\lim_{t\to \infty} \hat{\mathbf{k}}(t) = \lim_{i\omega\to 0} i\omega\hat{\mathbf{k}}(\omega) = \lim_{i\omega\to 0} \hat{\mathbf{h}}(\omega) = \mathbf{0} \tag{35}$$

We see that property (ii)-(iv) in Table 1 hold, while (i) is not explicitly fulfilled since in general $\sum_{l=1}^{N_l} \mathbf{a}_l/d_l \neq \mathbf{0}$. This means a small erroneous contribution can occur in the model at the zero-frequency. If instead the general form Eq. 30 was used with $b_0 = 0$, property (i) would be fulfilled [6], which is an advantage of that approach.

The passivity property (v) states that the diagonal elements $\hat{k}_{ii}(\omega)$ should be positive real [15], because negative potential damping is unphysical. $\text{Re}(\hat{k}_{ii}(\omega)) > 0$ is however not enforced in the parametric model, so it must be checked for every generated model that this condition holds.

2.3 Frequency-domain solution of the equations of motion

For completeness we also include a frequency-domain solution of the equations of motion, which will later be used as a reference solution for comparison with the solutions from the state-space model. The frequency-

domain solution is based on Eq. 1. The truncation $\mathbf{u}(t) \approx \mathbf{\Phi}\mathbf{z}(t)$ and Eq. 11 is still used, so that Eqs. 12-14 also hold.

We assume a temporal load history $\mathbf{p}(t)$ is available, which first is transformed into the frequency-domain:

$$\mathbf{p}(\omega) = \mathcal{F}(\mathbf{p}(t)) \tag{36}$$

Eq. 1 is pre-multiplied with $\mathbf{\Phi}^{\mathrm{T}}$:

$$\Big(-\omega^2\big(\mathbf{I} + \mathbf{\Phi}^{\mathrm{T}}(\mathbf{M}_{\mathrm{h}}(\omega) - \mathbf{M}_{\mathrm{h},\infty})\mathbf{\Phi}\big) - i\omega\big(2\mathbf{\Omega\Xi} + \mathbf{\Phi}^{\mathrm{T}}\mathbf{C}_{\mathrm{h}}(\omega)\mathbf{\Phi}\big) + \mathbf{\Omega}^2\Big)\mathbf{z}(\omega) = \mathbf{\Phi}^{\mathrm{T}}\mathbf{S}_{\mathrm{p}}\mathbf{p}(\omega) \tag{37}$$

We now define the force-to-motion (modal) transfer function $\mathbf{h}_{\mathrm{pz}}(\omega) \in \mathbb{C}^{\mathrm{n_m}\times\mathrm{n_m}}$ as follows:

$$\mathbf{h}_{\mathrm{pz}}(\omega) = \Big[-\omega^2\big(\mathbf{I} + \mathbf{\Phi}^{\mathrm{T}}(\mathbf{M}_{\mathrm{h}}(\omega) - \mathbf{M}_{\mathrm{h},\infty})\mathbf{\Phi}\big) - i\omega\big(2\mathbf{\Omega\Xi} + \mathbf{\Phi}^{\mathrm{T}}\mathbf{C}_{\mathrm{h}}(\omega)\mathbf{\Phi}\big) + \mathbf{\Omega}^2\Big]^{-1} \tag{38}$$

and obtain the following modal frequency response:

$$\mathbf{z}(\omega) = \mathbf{h}_{\mathrm{pz}}(\omega)\mathbf{\Phi}^{\mathrm{T}}\mathbf{S}_{\mathrm{p}}\mathbf{p}(\omega) \tag{39}$$

The temporal response $\mathbf{u}(t)$ is then recovered by the inverse Fourier transform:

$$\mathbf{u}(t) = \mathbf{\Phi}\mathbf{z}(t) = \mathbf{\Phi}\mathcal{F}^{-1}(\mathbf{z}(\omega)) \tag{40}$$

It can also be desired to obtain the resulting motion-induced forces, since these are the origin of the convolution term which was replaced in Section 2.1. The modal motion-induced forces then become:

$$\mathbf{\Phi}^{\mathrm{T}}\mathbf{p}_{\mathrm{mi}}(\omega) = \mathbf{\Phi}^{\mathrm{T}}\mathbf{h}(\omega)\mathbf{u}(\omega) = \mathbf{\Phi}^{\mathrm{T}}\mathbf{h}(\omega)\mathbf{\Phi}\mathbf{z}(\omega) \tag{41}$$

These forces can be recovered in the time-domain:

$$\mathbf{\Phi}^{\mathrm{T}}\mathbf{p}_{\mathrm{mi}}(t) = \mathcal{F}^{-1}(\mathbf{\Phi}^{\mathrm{T}}\mathbf{p}_{\mathrm{mi}}(\omega)) \tag{42}$$

The outlined solution method quite efficient when the Fast Fourier Transform (FFT) is used. Frequency-domain solutions are however not always desirable or possible.

3 Case study example

3.1 Description of the Bergsøysund Bridge

An example of the theory in Section 2 is now shown, with application to the Bergsøysund Bridge (Fig. 1). This bridge is located in Norway and is a floating pontoon-type bridge with end-anchoring only, making it very flexible. The bridge is is 840 m long, and consists of a steel superstructure supported by seven pontoons spaced approximately 100 m apart. For more information about the bridge under consideration, we refer to [16, 17].

Correct modeling of the motion-induced forces on floating bridges is critical, especially since the majority of the damping in the system is due to the fluid. As will be shown, the hydrodynamic mass in the system is highly frequency dependent, which is also important to take into account.



Figure 1: The Bergsøysund Bridge seen from the southwest end. Photo: K.A. Kvåle/NTNU.

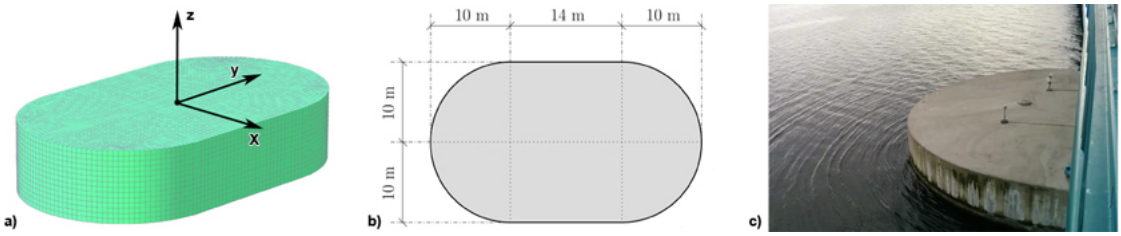


Figure 2: a) panel model of a pontoon; b) plan view of pontoon; c) pontoon seen from the bridge deck.

3.2 System model and parametric fit

The steel superstructure of the bridge is elastic and is modeled in the FE software Abaqus, see [18] for details. The concrete pontoons are very stiff, and are modeled as rigid bodies. The motion of each pontoon can therefore be described by six (wetted) DOFs in which the FSI occur. A panel model of the pontoons is made in the wave-structure interaction software HydroD WADAM [8] (Fig. 2 a), which is based on linearized potential theory. From the HydroD model, the non-parametric hydrodynamic mass ($\mathbf{M}_\mathrm{h}(\omega)$) and damping ($\mathbf{C}_\mathrm{h}(\omega)$) are obtained. The pontoons have two planes of symmetry (xz and yz, cf. Fig. 2), so that the hydrodynamic mass matrix has the following (local) structure for a single pontoon [15]:

$$\begin{bmatrix} M_{\mathrm{h},11}(\omega) & 0 & 0 & 0 & M_{\mathrm{h},15}(\omega) & 0 \\ 0 & M_{\mathrm{h},22}(\omega) & 0 & M_{\mathrm{h},24}(\omega) & 0 & 0 \\ 0 & 0 & M_{\mathrm{h},33}(\omega) & 0 & 0 & 0 \\ 0 & M_{\mathrm{h},24}(\omega) & 0 & M_{\mathrm{h},44}(\omega) & 0 & 0 \\ M_{\mathrm{h},15}(\omega) & 0 & 0 & 0 & M_{\mathrm{h},55}(\omega) & 0 \\ 0 & 0 & 0 & 0 & 0 & M_{\mathrm{h},66}(\omega) \end{bmatrix} \tag{43}$$

Here, DOFs 1-3 are the x, y and z translations, while DOFs 4-6 are the rotations about the x, y and z axes. The hydrodynamic damping matrix is populated in the same fashion as the hydrodynamic mass matrix.

The coefficients of $\mathbf{a}_l$ and d_l are now fitted by minimizing the term in Eq. 10. The weighting coefficients $W(\omega_r)$ are chosen as the curve in Fig. 3, showing $\log(\Sigma(\omega)/\omega^2) - \min(\log(\Sigma(\omega)/\omega^2))$ where $\Sigma(\omega)$ ($\omega \in (0, 15]$) is the largest singular value of an acceleration spectrum from measurements on the bridge during wave excitation. In practice this means that frequency range with highest response is emphasized, which is around 2 rad/s for the present case. The fit is made for the orders $N_l = 6$ and $N_l = 10$ to study the accuracy of the model approximation for different orders. Since non-linear optimization can be sensitive to initial parameter guesses, a three-step approach is used for the fit:

(i) Set d_l constant by the initial guess $d_l = d_0 + (l-1)\Delta d$. Fit $\mathbf{a}_l$ by linear least squares. Different values for d_0 and Δd may be tried here, in the order of $0.1 - 1$ and $0.1 - 0.2$ respectively.

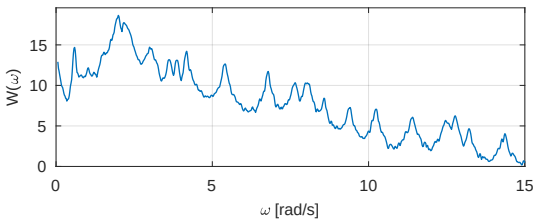


Figure 3: Weighting coefficients $W(\omega)$ in the non-linear least squares problem.

(ii) Use a non-linear least squares solver to fit d_l, but update $\mathbf{a}_l$ by linear least squares in all iterations. The initial guess for the coefficients in this step is taken from (i).

(iii) Use a non-linear least squares solver to fit both d_l and $\mathbf{a}_l$, with the initial guess taken from (ii).

Fig. 4 and 5 show the reconstructed hydrodynamic mass (Eq. 8) and damping (Eq. 9) compared to the non-parametric data from the HydroD model. In general the two orders give a quite similar fit, except for e.g. DOF 5 (Fig. 4 e) where there is a visible difference and the higher order ($N_l = 10$) clearly provides a better reconstruction. The lower order fit ($N_l = 6$) tend to give some unwanted oscillations, a common issue with fitting polynomial fractions.

It is seen in Fig. 5 e-f that the reconstructed damping can reach negative values, in particular for the lower order model. This indicates a non-passivity, and violates property (v) of Table 1. According to [19], this does not necessarily imply that the model is unstable. For the present case, we believe this small damping inaccuracy is insignificant. The structural damping, which is set to $\xi_j = 0.5\%$ for all modes, also contributes to the total damping of the system.

3.3 Response to simulated wave loads

The established state-space models are now tested in forward numerical simulations considering wave loads on the pontoons, generated from a (positive) wave load spectrum $\mathbf{\Lambda}_{\text{pp}}(\omega) \in \mathbb{R}^{\text{n}_\text{p} \times \text{n}_\text{p}}$. The sea state is described using a wave elevation spectrum measured at the bridge site (see [17]) with a peak period of 3 s, and $\mathbf{\Lambda}_{\text{pp}}(\omega) \in \mathbb{R}^{\text{n}_\text{p} \times \text{n}_\text{p}}$ is established using the approach in [20]. The load history is then generated by Monte Carlo simulations as follows:

$$p_m(t) = \sqrt{2\Delta\omega}\,\text{Re}\left(\sum_{l=1}^{m}\sum_{k=1}^{n} L_{ml}(\omega_k)\exp\left(i(\omega_k t + \alpha_{lk})\right)\right) \quad (m = 1 \ldots \text{n}_\text{p}) \tag{44}$$

where α_{lk} is a phase angle uniformly random in $[0, 2\pi)$ and L_{ml} are the elements of a Cholesky decomposition matrix $\mathbf{L}(\omega)$, defined as $\mathbf{\Lambda}_{\text{pp}}(\omega) = \mathbf{L}(\omega)\mathbf{L}^{\text{H}}(\omega)$. In the simulation there are six wave force components on each of the seven pontoons, so the total number of forces is $\text{n}_\text{p} = 42$. The sample time step is set to $\Delta t = 0.025$ s with a total simulation time of 1000 s.

Next, the dynamic response to the wave forces is solved using both the time-domain state-space approach (Section 2.1) and the frequency-domain approach (Section 2.3), which in this context is deemed an "exact" reference solution. The first 100 s of the time series are discarded to avoid the initial transient phase in the time-domain solution, dependent on the initial conditions ($\mathbf{x}_0 = \mathbf{0}$). For the two state-space models, $\text{n}_\text{m} = 26$ modes are included with natural frequencies in the range 0.6–11 rad/s. In the frequency-domain approach $\text{n}_\text{m} = 60$ modes are used to ensure that this method provides a precise reference solution.

Fig. 6 shows the response for the six DOFs of the pontoon in the middle on the bridge. By visible inspection both time-domain model responses matches very well with the response calculated by the frequency-domain approach. The following error metric is introduced to benchmark the error:

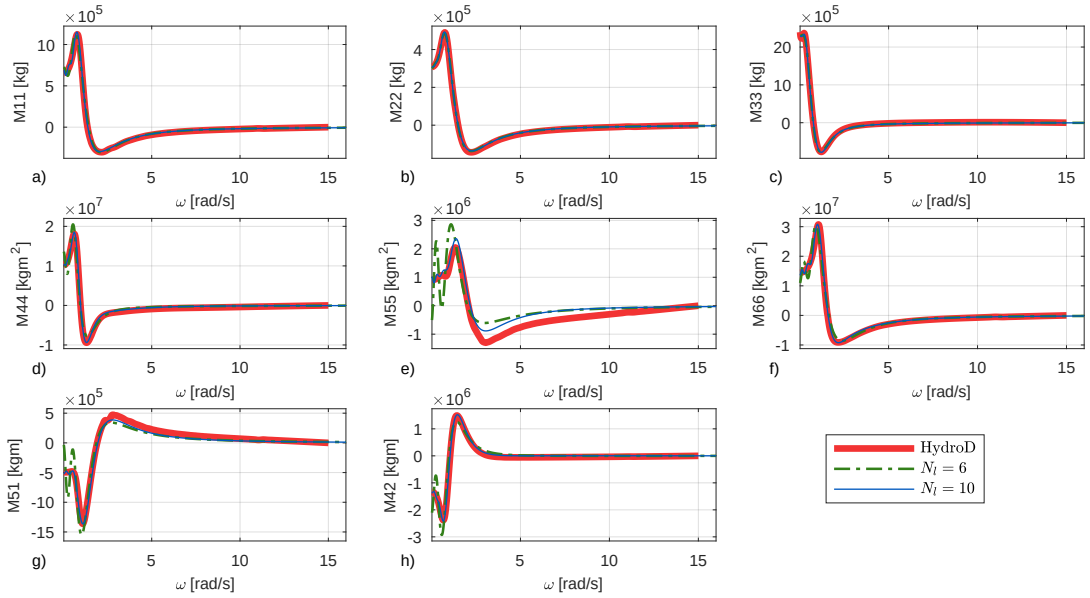


Figure 4: Hydrodynamic mass $(\mathbf{M}_{\mathrm{h}}(\omega) - \mathbf{M}_{\mathrm{h},\infty})$ for the middle pontoon. The figure shows both the non-parametric data from HydroD and the parametric reconstruction.

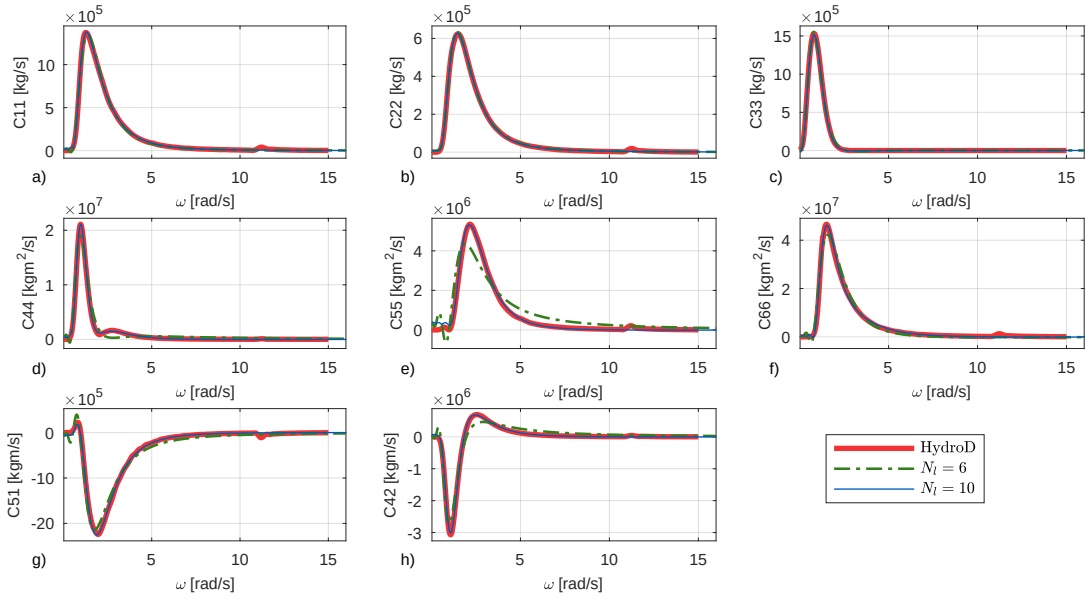


Figure 5: Hydrodynamic damping $(\mathbf{C}_{\mathrm{h}}(\omega))$ for the middle pontoon. The figure shows both the non-parametric data from HydroD and the parametric reconstruction.

$$\epsilon_u = \sqrt{\frac{1}{N_t}\sum_{k=0}^{N_t-1}(u_{FD}(t_k) - u_{TD}(t_k))^2} \tag{45}$$

Here, $u_{FD}(t)$ and $u_{TD}(t)$ represents the response solved by the frequency-domain and time-domain approaches, respectively. Tab. 2 shows the error ϵ_u of the six responses in Fig. 6. Overall, the higher order model ($N_l = 10$) performs better, although there is not is not a significantly difference for all six DOFs.

	DOF					
Order	1	2	3	4	5	6
$N_l = 6$	1.16e-4	3.90e-4	5.98e-4	4.86e-5	4.57e-6	5.98e-6
$N_l = 10$	1.15e-4	2.59e-4	4.68e-4	3.31e-5	3.36e-6	5.66e-6

Table 2: Standard deviation of the response error (ϵ_u) at the middle pontoon. DOFs 1-3 denote the x, y and z translation response, and DOFs 4-6 denote the rotation about the x, y, and z axes (cf. Fig. 2)

Lastly, a validation of the resulting modal motion-induced forces ($\mathbf{\Phi}^{\mathrm{T}}\mathbf{p}_{\mathrm{mi}}(t)$) from Eqs. 21 and 42 is shown in Fig. 7 for five selected modes. Also here a good agreement is seen, indicating that the convolution replacement by state-space models is a highly appropriate approximation.

4 Conclusion

This paper has presented a methodology for establishing reduced order time-invariant linear models of floating structures with FSI. The methodology is based on replacing the convolution integral in Cummins' equation with an approximate state-space model. The state-space model was identified by fitting a parametrized rational transfer function to a non-parametric hydrodynamic transfer function, which accounts for the added hydrodynamic mass and damping. This can be combined with a modal truncation to reduce the model order.

The modeling approach was validated in a case study of a floating bridge subjected to irregular wave forces. It was shown that approximate state-space models of low order can effectively solve the dynamic response of the bridge with high accuracy.

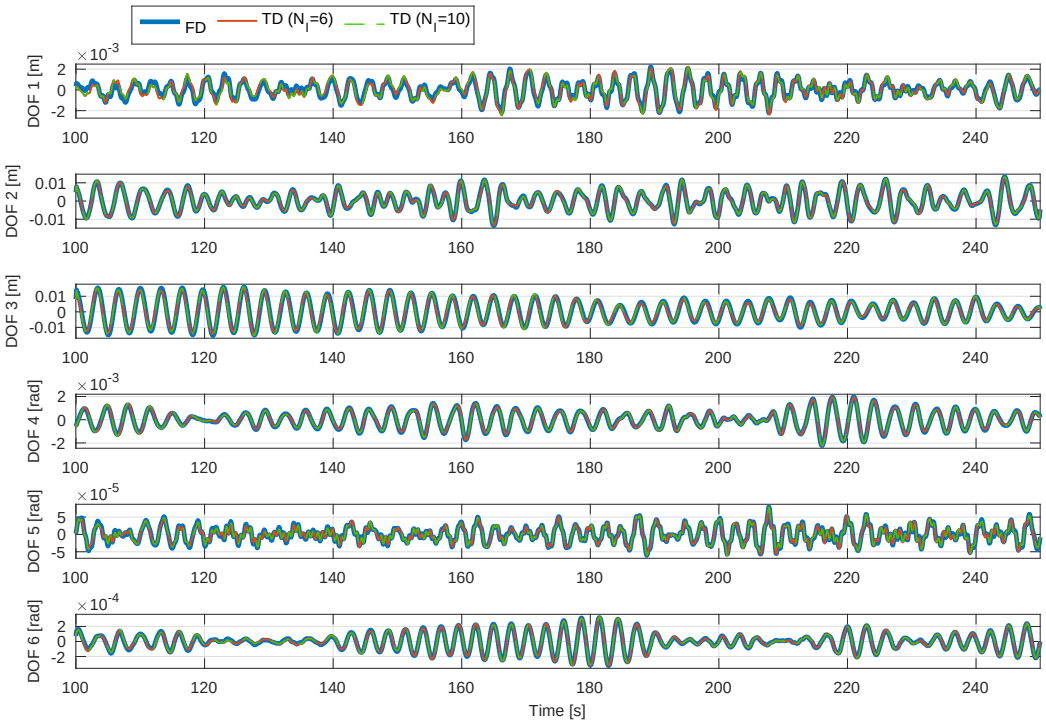


Figure 6: Displacement response at the middle pontoon, obtained both from the time-domain and frequency-domain solution methods. DOFs 1-3 denote the x, y and z translation response, and DOFs 4-6 denote the rotation about the x, y, and z axes (cf. Fig. 2)

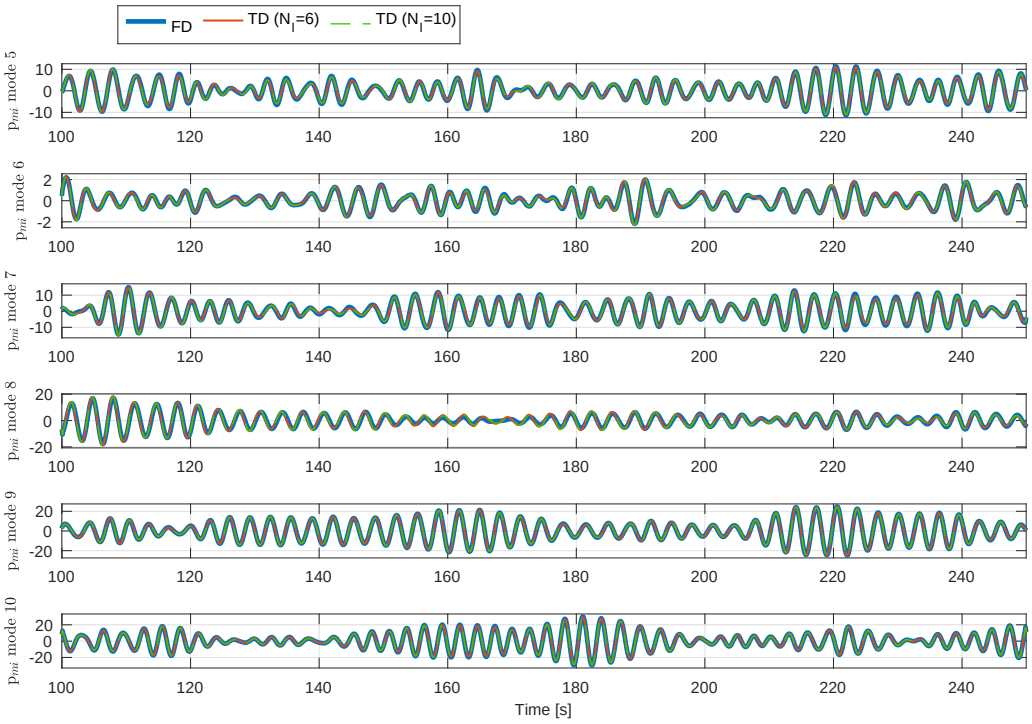


Figure 7: The modal motion-induced loads for mode 5-10.

References

[1] A. Naess, Torgeir Moan, *Stochastic dynamics of marine structures*, Cambridge University Press, (2012).

[2] W.E. Cummins, *The impulse response function and ship motions*, Technical report, DTIC Document, (1962), pp. 609-625.

[3] Z. Yu, J. Falnes, *State-space modelling of a vertical cylinder in heave*, Applied Ocean Research, Vol. 17, No. 5, (1995), pp. 265-275.

[4] E. Kristiansen, Å. Hjulstad, O. Egeland, *State-space representation of radiation forces in time-domain vessel models*, Ocean Engineering, Vol. 32, No. 17, (2005), pp. 2195-2216.

[5] R. Taghipour, T. Perez, T. Moan, *Hybrid frequency–time domain models for dynamic response analysis of marine structures*, Ocean Engineering, Vol. 35, No. 7, (2008), pp. 685-705.

[6] T. Pérez, T.I. Fossen, *Time-vs. frequency-domain identification of parametric radiation force models for marine structures at zero speed*, Modeling, Identification and Control, Vol. 29, No. 1, (2008), pp. 1-19.

[7] WAMIT, Inc., *WAMIT 7.2 User Manual*, MA, USA, (2016).

[8] DNV Software, *HydroD WADAM 9.1 User Manual*, Høvik, Norway, (2014).

[9] M. Folley, *Numerical Modelling of Wave Energy Converters: State-of-the-Art Techniques for Single Devices and Arrays*, Academic Press, (2016).

[10] O. Øiseth, A. Rönnquist, A. Naess, R. Sigbjörnsson, *Estimation of extreme response of floating bridges by Monte Carlo simulation*, in R. Boone, editor, *Proceedings of the 9th International Conference on Structural Dynamics, Porto, Portogal, 2014 June 30 - July 2*, Porto (2014).

[11] S.H. Tiffany, W.M. Adams Jr., *Nonlinear programming extensions to rational function approximation methods for unsteady aerodynamic forces*, Technical report NASA, (1988).

[12] X. Chen, M. Matsumoto, A. Kareem, *Time domain flutter and buffeting response analysis of bridges*, Journal of Engineering Mechanics, Vol. 126, No. 1, (2000), pp. 7-16.

[13] M. Lazzari, R.V. Vitaliani, A.V. Saetta, *Aeroelastic forces and dynamic response of long-span bridges*, International journal for numerical methods in engineering, Vol. 60, No. 6, (2004), pp. 1011-1048.

[14] K.L. Roger, *Airplane math modelling methods for active control design*, Technical report, Advisory Group for Aerodynamic Research and Development, Washington, DC (1977).

[15] K. Unneland, *Identification and order reduction of radiation force models of marine structures*, PhD thesis, Norwegian University of Science and Technology - Faculty of Information Technology, Mathematics and Electrical Engineering, (2007).

[16] Ø.W. Petersen, O. Øiseth, *Sensitivity-based finite element model updating of a pontoon bridge*, Engineering Structures, Vol. 150, (2017), pp. 573-584.

[17] K.A. Kvåle, O. Øiseth, *Structural monitoring of an end-supported pontoon bridge*, Marine Structures, Vol. 52, (2017), pp. 188-207.

[18] Ø.W. Petersen, O. Øiseth, T.S. Nord, E. Lourens, *Estimation of the full-field dynamic response of a floating bridge using Kalman-type filtering algorithms*, Mechanical Systems and Signal Processing, Vol. 107, (2018), pp. 12-28.

[19] T. Perez and T.I. Fossen, *Practical aspects of frequency-domain identification of dynamic models of marine structures from hydrodynamic data*, Ocean Engineering, Vol. 38, No. 2, (2011), pp. 426-435.

[20] F.I.G. Giske, B.J Leira, O. Øiseth, *Efficient computation of cross-spectral densities in the stochastic modelling of waves and wave loads*, Applied Ocean Research, Vol. 62, (2017), pp. 70-88.

High-speed 3D DIC random dynamic strain measurement of a panel subjected to Mach 2 flow

T. Beberniss [1], **D. Ehrhardt** [2]
[1] US Air Force Research Laboratory, Structural Sciences Center,
2790 D St, Building 64 Room 402W, WPAFB, OH, 45433
e-mail: **timothy.beberniss@us.af.mil**

[2] Ehrhardt Engineering,
2790 D St, Building 64 Room 402W, WPAFB, OH, 45433

Abstract
An ongoing experimental study of high-speed fluid structure interaction by the Structural Sciences Center of the United States Air Force Research Labs is presented. Previous work incorporated novel full field measurement techniques like high-speed 3D digital image correlation (DIC) and fast reaction pressure sensitive paint (PSP) for full field characterization of the phenomena. To further quantify the complex nature of the experiment, full field strains calculated from the DIC displacement results were included in the most recent analysis. Most recent tests also addressed thermal loading including buckling and resulting snap-through response. The real-time strain results from a single foil strain gauge indicated the level of strains at the panel edge were not sufficient to produce high cycle fatigue failure. However, full field DIC strain results showed that areas near the center of the panel experienced levels of dynamic strain that would cause panel cracking in relatively short order. Post test panel inspection revealed a 76mm crack along the spanwise trailing edge.

1 Introduction

High-speed air vehicles experienece a range of harsh conditions including high level fluctuating pressures from a turbulent boundary layer, large thermal gradients from panel skin friction, oscillating shock wave impingement, and snap-through buckling [1]. To withstand the high-speed fluctuating pressure and the 1000^{o}F heating from skin friction the lightweight skin stringer structure could be constructed from a lightweight high temperature metallic such as titanium. These more traditional structural designs and materials are fairly well understood, however certain phenomena such as shock impingement and panel thermal buckling combined with dynamic snap-through lack sufficient predictive capabilities and the experimental data to validate the required methods. The US Air Force Research Labs (AFRL) Structural Sciences Center (SSC) has been involved in a series of high-speed fluid-structure interaction experiments in a Mach 2 wind tunnel [2]. The experiments are intended to recreate an environment a high-speed aircraft structure would encounter but in a ground based testing environment as flight tests are either prohibitively expensive or simply not possible. Therefore, the experiments have been able to take advantage of many new and novel high-speed full-field measurement techniques. The desire for the full-field measurements stem from the complex nature of the loading and resulting nonlinear skin panel response. More traditional measurement techniques like accelerometers mass-load the lightly damped skin structure or if non-contact laser Doppler velocimetry is available there remains a limitation on the number of simultaneous measurement points. Various configurations of baseline, shock impingement, and thermal buckling load conditions were explored and displacement and specifically strain results will be presented. The ultimate goal of the experiment was to dynamically snap-through a buckled panel with an impinged shockwave to induce high cycle fatigue failure. This combined

loading environment was intended to represent and better understand a worst case scenario for a high-speed vehicle outer-mold-line structure.

2 Experimental Setup

The basic setup for the experiment did not significantly change from the previous work by the authors in the Mach 2 wind tunnel, research cell 19 (RC-19) at AFRL [3, 4, 5, 6]. The most significant changes include the upgrade to 4 SA-Z Photron high-speed cameras for the digital Image correlation (DIC) vibration measurement of the flexible panel from the back non-flow side, the pressure sensitive paint (PSP) and temperature sensitive paint (TSP) for full-field flexible panel pressure and temperature measurement from the front flow side, and the high-speed shadowgraph to measure the dynamic motion of the shock impingement as seen in figure 1. All experiments were run at a tunnel flow speed of Mach 2 and a stagnation pressure of 50 psi and a stagnation temperature on average of about 75^{o}F. Five shock impingement conditions were explored including no shock, panel 1/2 length point, 1/4 length point, 1/8 length point, and panel leading edge. The panel was machined out of a 304.8 x 152.4 x 12.7mm solid block of 4140 steel. The thin flexible region is 254 x 127 x 0.635mm. All high-speed cameras were synchronized and sampled at 5000 frames per second. The panel thermally buckled conditions were created by heating the flow with a furnace while diverted to atmosphere. Once the flow temperature stabilized at about 200^{o}F the flow was directed to the test section. The panel was thermally "shocked" causing very large temperature difference between the panel and its tunnel wall boundary and therefore a very high level of buckling. As the tunnel heat soaked the temperature difference between the two decreased until a suitable temperature difference between the tunnel and panel was achieved for panel snap-through. Data of the panel snap-through was acquired until the temperature difference became too low for panel buckling.

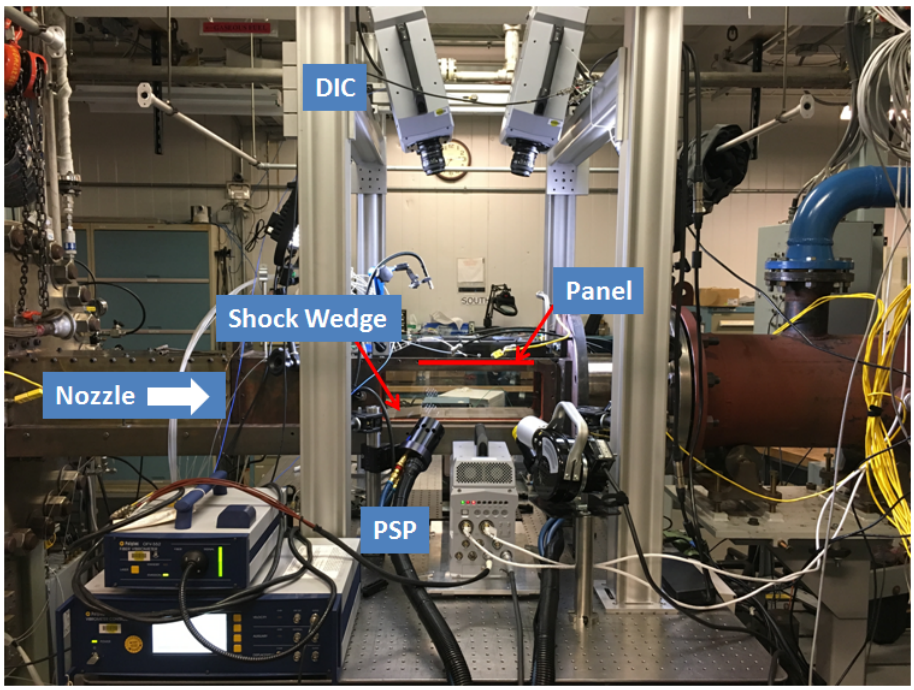


Figure 1: RC-19 fluid-structure Interaction general setup

3 Results

Unfortunately calculated strains from DIC displacements tend to be noisy. Typical vibration displacements are near the limit of DIC measurement sensitivity [5]. Calculating strains from measurements so near the noise tend to amplify that noise making adequate strain results difficult to achieve. In past FSI experiments the focus was largely on the displacements and any strain results were limited to the traditional foil strain gauge at the steamwise center edge of the panel. More recent FSI experiments in the RC-19 included thermal buckling with dynamic snap-through. Typically, buckled panel maximum displacements are more than twice as much as the unbuckled panel vibration displacements [7]. The fully buckled panel peak to peak displacements were on the order of 3mm. For reference the panel thickness is 0.635mm. Considering the buckled panel displacements were so large, DIC strain results of the FSI experiment were thoroughly explored for the first time. The most dynamic unheated panel response once again occurred with a shockwave impingement at approximately 1/8 the panel length from the leading edge. For reference figure 2 is a snapshot of the pressure distribution across the panel with the 1/8th panel length shock impingement. The x and y axes are pixels where a pixel covers approximately 0.4 x 0.4mm of the panel therefore about 270 x 127mm of the panel is represented.

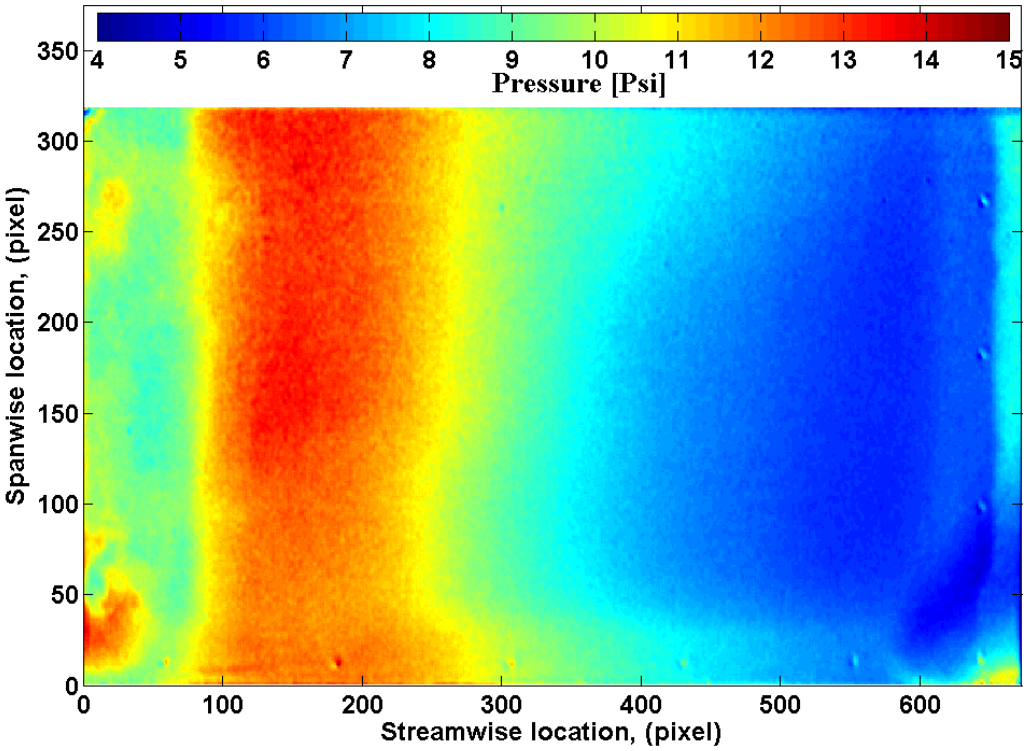
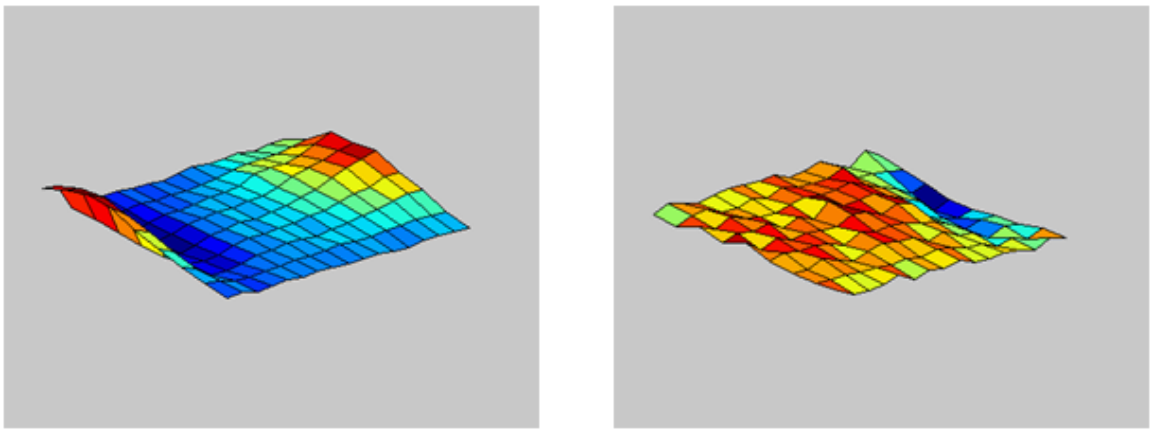


Figure 2: Panel pressure distribution at a moment in time with a 1/8th panel length shock impingement

Figure 3 shows a qualitative comparison of a single moment in time full field displacement and resulting strain of the panel with a shock impingement. It is perhaps immediately apparent the increase in noise between the displacement in figure 3a and the strain in figure3b. This panel response case is basically considered the lowest level random dynamic strain reasonably possible with high-speed DIC. Figure 4 shows the time history and power spectral density (PSD) of the panel strain along the streamwise centerline at discrete points near the leading edge, center line, and trailing edge. The root mean square (RMS) strains at the leading edge, center line, and trailing edge are 134$\mu\epsilon$, 302$\mu\epsilon$, and 398$\mu\epsilon$ respectively. It can be seen from

the PSD that the measurement noise floor was already beginning to limit the dynamic range at about 500 Hz resulting in only the panel first mode being fully characterized.



(a) Panel displacement (mm) (b) Panel strain ($\mu\epsilon$)

Figure 3: Contour of panel response from a shock impingement at 1/8th panel length from leading edge

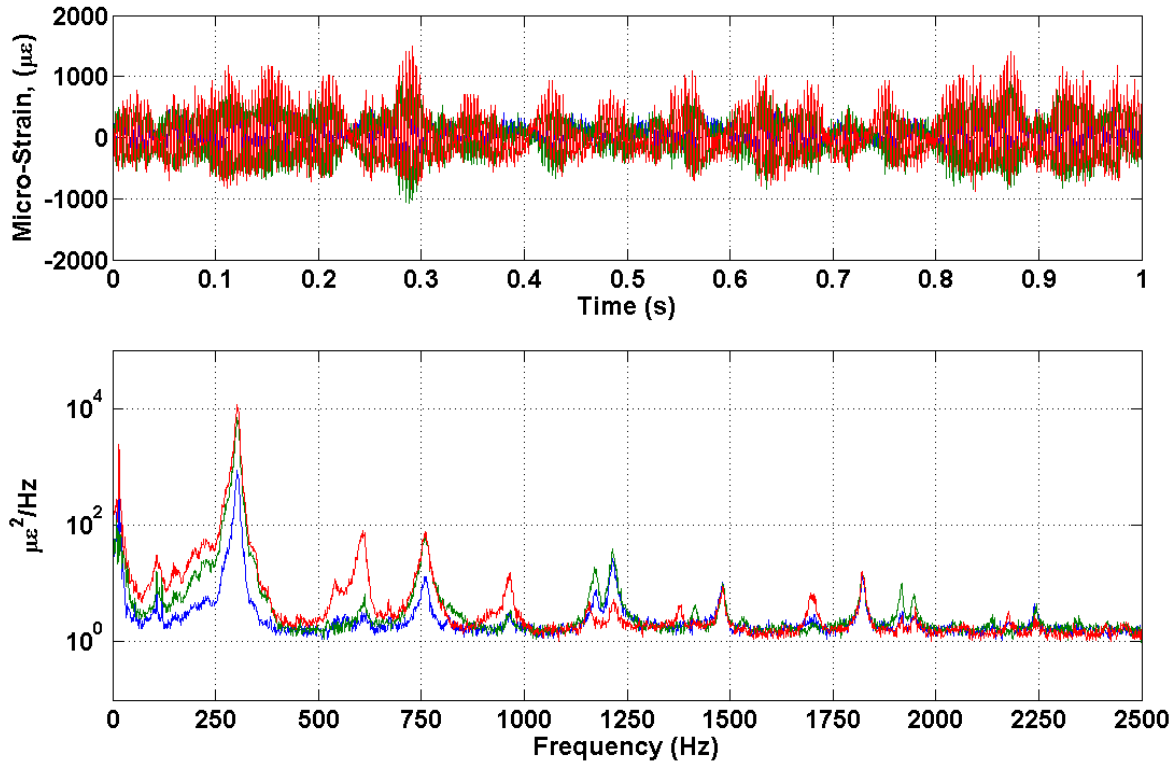


Figure 4: PSD panel streamwise direction strain of (-blue) leading edge, (-green) centerline, and (-red) trailing edge

Since the tunnel top wall consists of three separate pieces as described in Spottswood [4] the center top wall section was removed and used for panel system identification with the expected boundary conditions. Great care was taken to install the panel into the test frame (middle top wall section) during system identification

testing outside of the wind tunnel. Consistent boundary conditions were achieved across multiple panel installations following a set procedure including torquing bolts to a specified level in a consistent pattern. Unfortunately, despite great effort the panel was not in a nominal state once it was installed into the fully assembled wind tunnel test section. The state of the panel once installed into the wind tunnel can be seen in figure 5. The maximum deflection near the center of the panel was nearly 0.8mm which is considered quite large when compared to the panel nominal thickness of 0.635mm. Once again the initial deflection condition was unavoidable however, with the aid of DIC the initial shape of the panel was explicitly known. This bowed state of the panel combined with the panel being heated was what eventually led to the panel flutter condition discussed next. The temperature differential was not always sufficient for the panel to be completely buckled however, the thermal condition caused the panel to transition from one bowed state to the other which did not occur when the flow was not heated. Flutter is being defined as large panel deflections that are not attributed to a panel linear mode of vibration while also not technically being in a thermally buckled state.

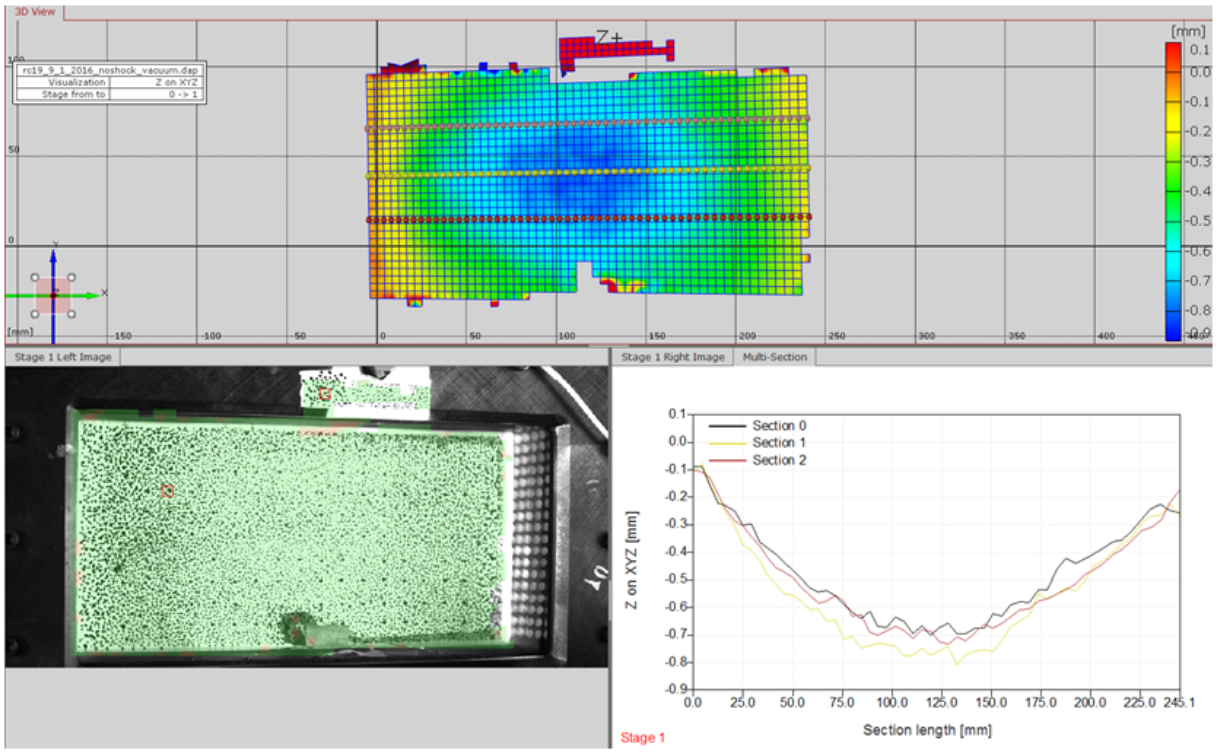
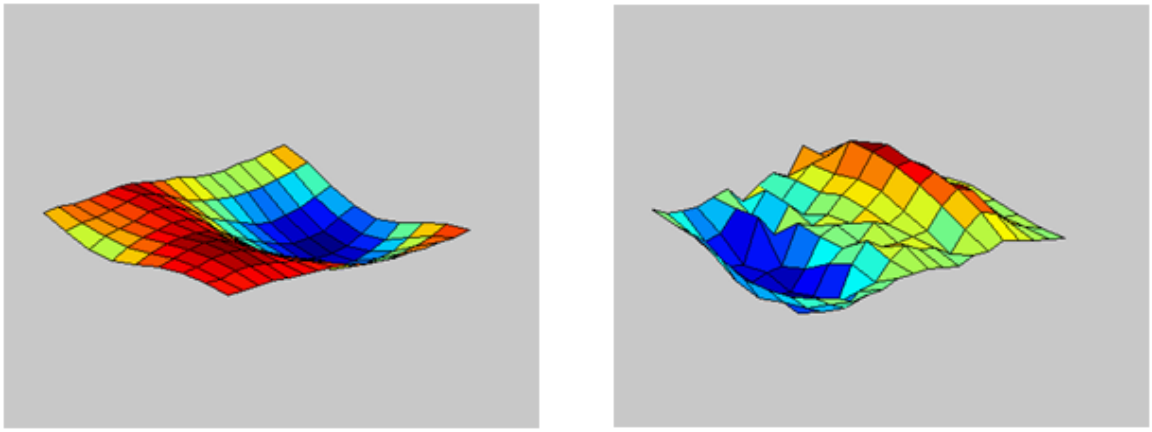


Figure 5: Static DIC displacement of the installed panel in the wind tunnel at atmosphere

The panel flutter condition displacement and strain contours can be seen in figure 6. Clearly the displacement levels are now at a level that make robust dynamic strain results possible. The strain PSD in figure 7 shows the strains are now above the measurement noise floor all the way out to the 2500 Hz Nyquist frequency. The strain RMS at the leading edge, centerline, and trailing edge are 2109$\mu\epsilon$, 1892$\mu\epsilon$, and 1491$\mu\epsilon$ respectively. These strain levels are quite large when compared to the unheated panel and highlight the effect thermal gradients can have on a thin constrained structure.



(a) Panel displacement (mm) (b) Panel strain ($\mu\epsilon$)

Figure 6: Contour of panel response from first thermal condition, panel flutter

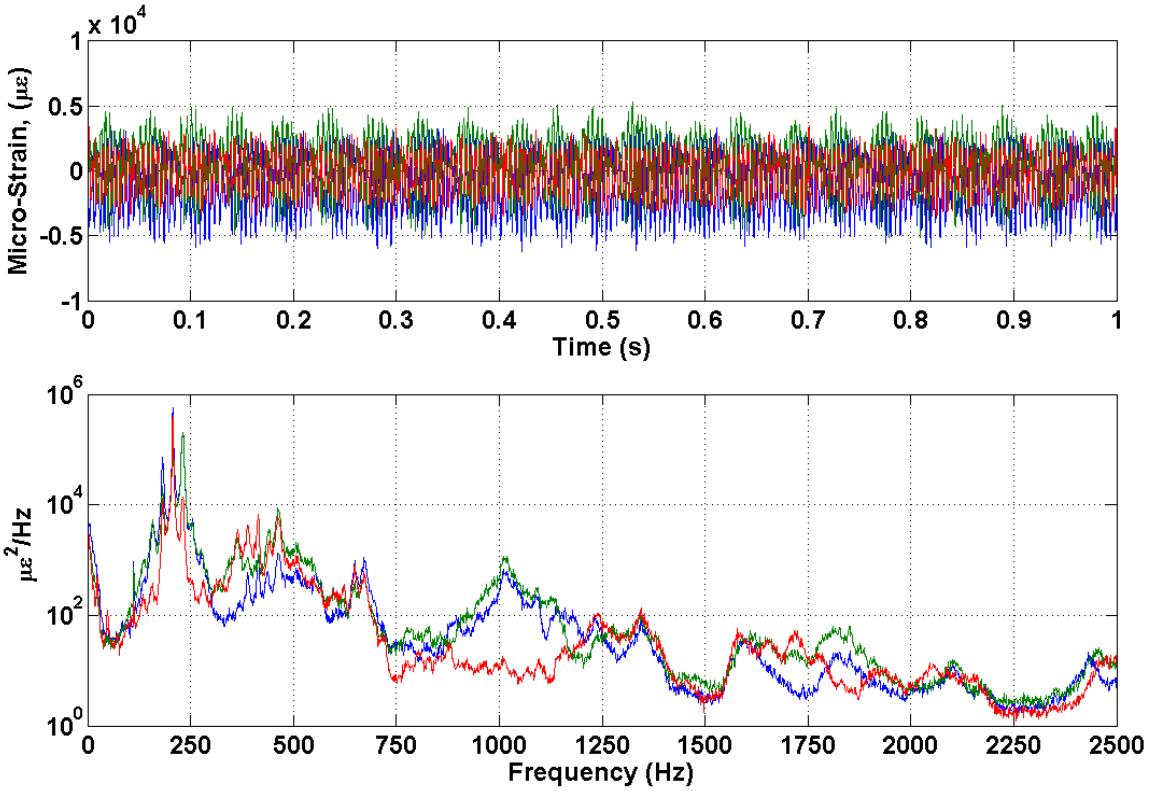


Figure 7: PSD panel streamwise direction strain of (-blue) leading edge, (-green) centerline, and (-red) trailing edge due to flutter

An example of the thermally buckled state can be seen in the time history of three points along the spanwise centerline of the panel in figure 8. The blue line is near the leading edge, the green line is near the streamwise centerline, and the red line is near the trailing edge. Between the 1.5 and 2.4 second region it can bee seen that the panel was in a buckle state. The preferred stable equilibria of the panel was the 3rd bending mode like shape depicted by the negative displacement on the leading and trailing edge and the positive displacement

at the streamwise centerline. The study of the panels buckled equilibria and quasi-static snap-through was investigated by Perez [7] prior to the wind tunnel tests. Dynamic snap-through can be seen prior to 1.5 seconds and after 2.4 seconds in figure 8 with the panel continuously snapping between the two equilibrium positions.

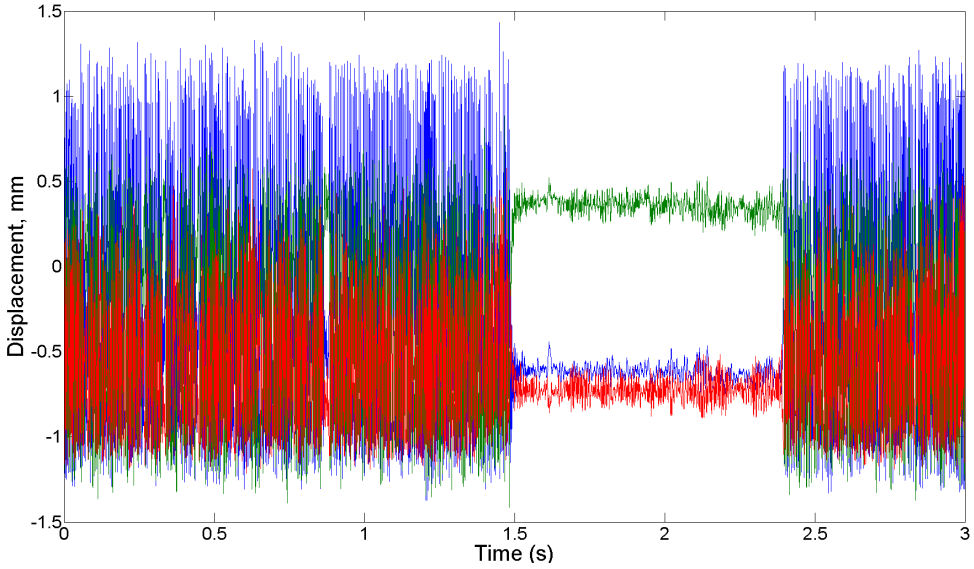
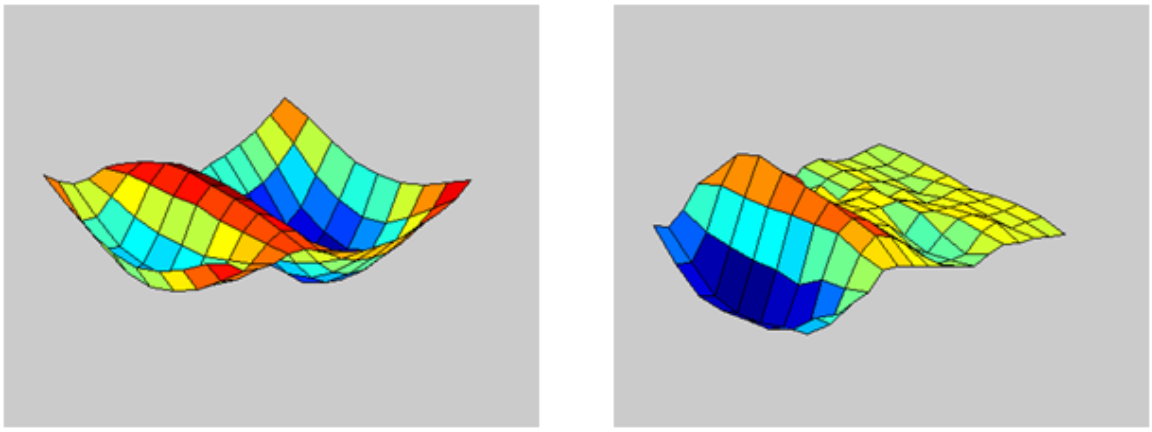


Figure 8: DIC displacement of buckled panel at discrete locations (-blue) leading edge, (-green) centerline, and (-red) trailing edge

The panel thermal buckling condition displacement and strain contours are pictured in figure 9 . Shown is the stable buckled configuration that resembles the panel third linear mode shape however, was skewed due to the high speed flow condition. Clearly the strain results are now well above the measurement noise floor. The strain PSD in figure 10 once again shows discrete point strain at the leading edge, centerline, and trailing edge. It should be noted that the buckled case PSD is 1/6th the time record of the previous cases in this study and hence the reduced number of ensemble averages. The RMS strains at the leading edge, centerline, and trailing edge are 2093$\mu\epsilon$, 2685$\mu\epsilon$, and 1332$\mu\epsilon$ respectively.



(a) Panel displacement (mm)

(b) Panel strain ($\mu\epsilon$)

Figure 9: Contour of panel response from thermal buckling

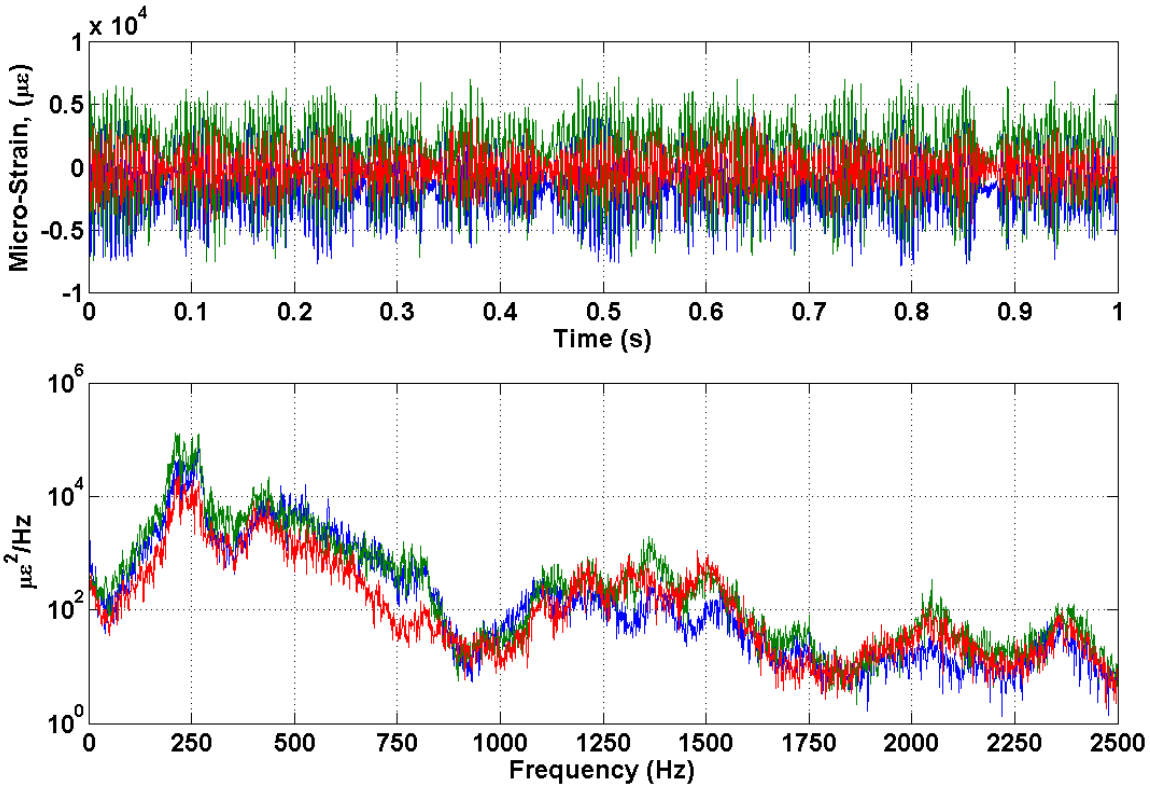


Figure 10: PSD panel streamwise direction strain of (-blue) leading edge, (-green) centerline, and (-red) trailing edge due to snap-through buckling

The RMS strains of both the flutter and buckled cases highlight a significant point. The strain levels experienced by the panel during the thermal cases are sufficient to result in high cycle fatigue. The panel material was 4140 steel which is the same material used in the wind tunnel test section. This panel specimen material was an attempt to avoid large coefficient of thermal expansion (CTE) differential between the tunnel walls and the panel. Unfortunately, steel 4140 is a particularly strong material with an ultimate strength of approximately 1034MPa. According to the DIC full field strain results the peak RMS strain experienced by the panel was equivalent to approximately 552MPa. However, the 552MPa loading experienced by the panel was accumulating cycles at about 250Hz. Approximations of panel life at these loading levels would indicate the panel would crack and thus fail in less than 30 minutes of test time under those conditions. To highlight the importance of the full field results obtained with high-speed 3D DIC, the discrete foil strain gauge at the panel edge streamwise centerline for the same buckled panel test conditions measured only $420\mu\epsilon$ as seen in figure 11. Unfortunately, as the panel was being initially installed into the wind tunnel the foil gauge bond to the panel failed. A new gauge was quickly applied to the panel however, it was not possible to properly reapply a DIC pattern therefore no direct comparison of DIC strain to gauge strain was possible. A qualitative comparison is instead shown in figure 12 where the DIC strain line is calculated using facets 130 and 147 further confirming the relatively low strain levels at that particular location. Based on the real-time foil gauge results during testing it was believed the strain the panel was experiencing was not of sufficient level and therefore it was decided the panel would not crack thus failure was not pursued further. However, once the panel was removed from the wind tunnel it was discovered that the panel had indeed experienced a 76mm crack along the trailing edge as seen in figure 13.

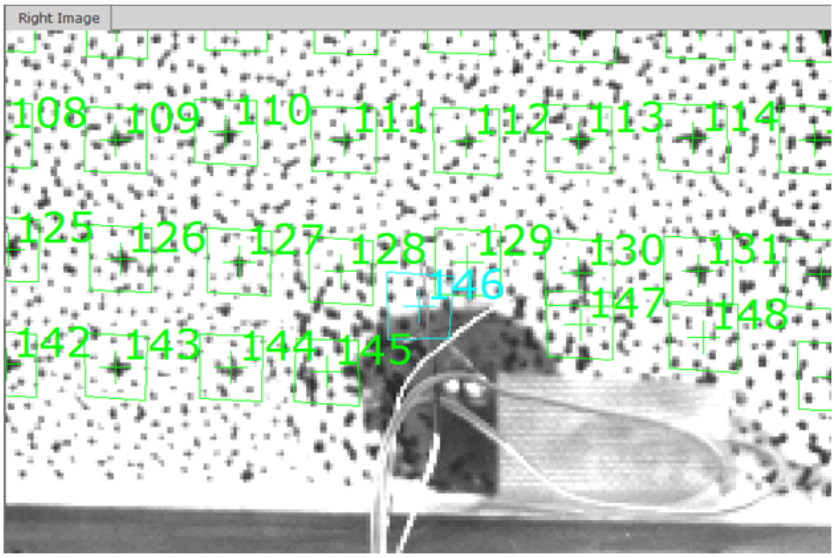


Figure 11: Digital zoom of panel foil strain gauge at streamwise panel centerline and surrounding DIC measurement points

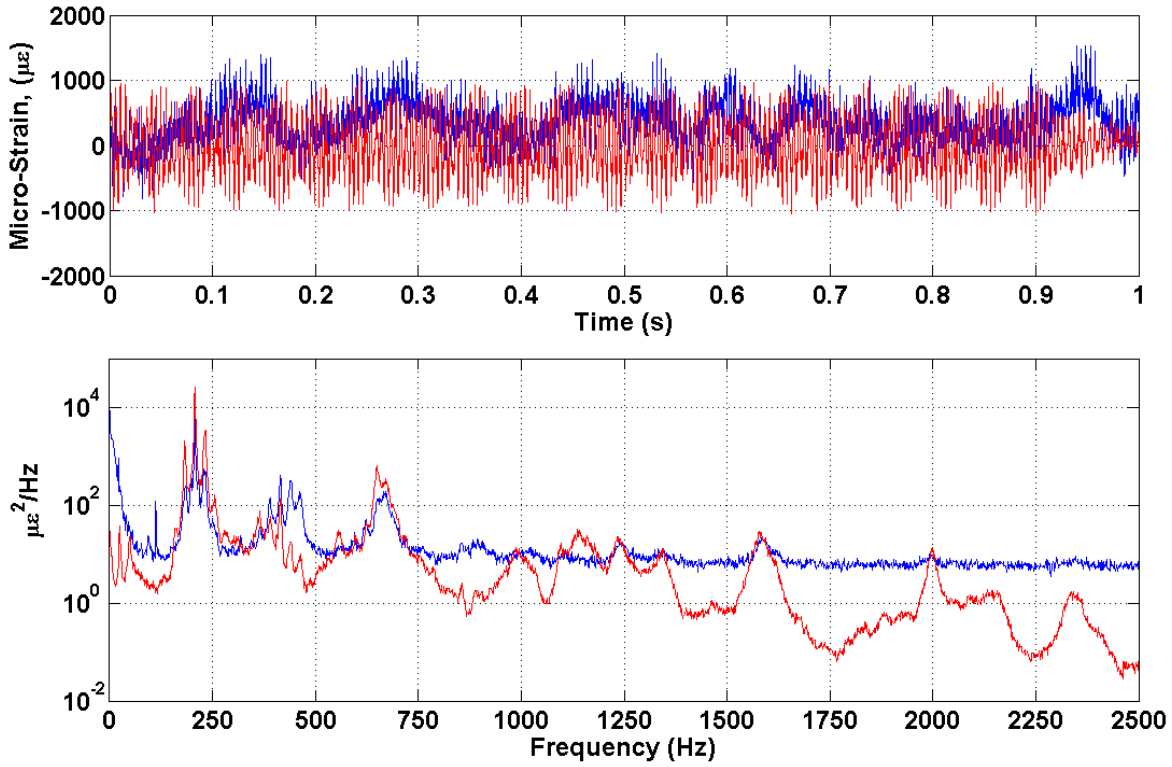


Figure 12: PSD of panel spanwise direction strain of (-blue) DIC strain line and (-red) foil gauge

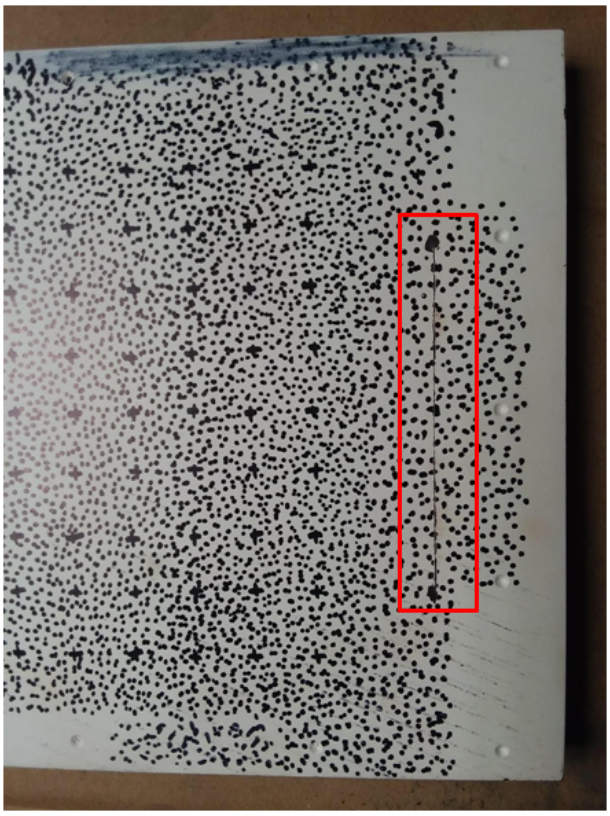


Figure 13: Panel specimen trailing edge post-test with highlight around crack

3.1 Conclusions

An extensive study of high-speed fluid-structure interaction on a flexible panel has been conducted in a Mach 2 wind tunnel. Most recently a study of the strain results from thermal buckling of the panel was undertaken. In previous tests the noise associated with the high-speed 3D DIC strain results made a study of the full field strain difficult if not unproductive. With the addition of thermal buckling to the test procedure sufficient levels of displacements and therefore strain were achieved to make a full field strain analysis feasible. Results indicate that not only were the random dynamic strain levels large enough to be quantified by DIC, but were of a sufficient level to induce high cycle fatigue failure. Initial fatigue predictions of the panel based on the maximum strains measured with DIC indicate that the panel would fail in a relatively short test time of approximately 30 minutes. However, due to the real-time foil gauge strain results further efforts to fail the panel were abandon. Ultimately, it was discovered during post-test inspection that the panel had indeed cracked just before testing was concluded achieving the final test goal of panel failure due to combined loading of turbulent boundary layer and thermal buckling with snap-through.

References

[1] B. Zuchowski, *Predictive Capability for Hypersonic Structural Response and Life Prediction: Phase I - Identification of Knowledge Gaps*, *Technical Report, AFRL-RB-WP-TR-2010-3069, August 2010.*,

[2] M. R. Gruber, A. S. Nejad, *Development of a Large-Scale Supersonic Combustion Research Facility*, *Proceedings of 32nd AIAA Aerospace Sciences Meeting and Exhibit, Reno, NV 1994*,

[3] T. Beberniss, S. Spottswood, T. Eason, *High-Speed Digital Image Correlation Measurements of Random Nonlinear Dynamic Response*, *Proceedings of The 2011 SEM Annual Conference, Uncasville, CT, 2011.*

[4] S. Spottswood, T. Eason, T. Beberniss, *Influence of Shock-Boundary Layer Interactions on the Dynamic Response of a Flexible Panel*, *Proceedings of The 2012 ISMA Biennial Conference on Noise and Vibration Engineering, Leuven, Belgium, 2012.*

[5] T. Beberniss, S. Spottswood, T. Eason, *High-Speed 3D digital image correlation measurements of long-duration random vibration; recent advancements and noted limitations*, *Proceedings of The 2012 ISMA Biennial Conference on Noise and Vibration Engineering, Leuven, Belgium, 2012.*

[6] T. Beberniss, S. Spottswood, D. Ehrhardt, R. Perez, *Dynamic Response of a Thin Panel Subjected to a Shock Wave Impingement and Thermal Buckling*, *Proceedings of The AIAA Aviation Conference, Denver, CO, 2017.*

[7] R. Perez, T. Beberniss, S. Spottswood *Nonlinear Dynamic Response Prediction of a Buckled Panel in Supersonic Flow*, *Proceedings of The 35th SEM International Modal Analysis Conference, Orlando, FL, 2017.*

Experimental and theoretical characterization of a dAFM cantilever dynamics

E. Pierro [1], **F. Bottiglione** [2], **G. Carbone** [2,3,4,5]
[1] Scuola di Ingegneria, Università degli Studi della Basilicata,
via dell'Ateneo Lucano 10, 85100 Potenza, Italy
e-mail: **elena.pierro@unibas.it**

[2] Department of Mechanics Mathematics and Management - Politecnico di Bari,
v.le Japigia 182, 70126 Bari, Italy

[3]Physics Department M. Merlin, CNR Institute for Photonics and Nanotechnologies U.O.S. Bari,
via Amendola 173, 70126 Bari, Italy

[4]Department of Mechanical Engineering, Imperial College London, South Kensington Campus,
Exhibition Road London SW7 2AZ, United Kingdom

[5]Center for Nonlinear Science, University of North Texas,
P. O. Box 311427, Denton, Texas 76203-1427, USA.

Abstract
In this paper we accurately describe the dynamics of a dAFM (dynamic atomic force microscope), by deeply investigating the relationship between the cantilever thermal fluctuations and its interactions with the surrounding liquid. To this end, we discuss the Brownian thermal noise, which affects the cantilever dynamics, both when it works in air and in presence of water. We present an analytical model of the drag of the liquid on the cantilever, which takes into account both the fluid inertia and diffusivity terms, whose crucial influence for the correct evaluation of the cantilever response to the thermal excitation is widely discussed. By fitting our analytical model with experimental or numerical data, the coefficients of the liquid response can be calculated, as a function of the distance of the beam from the substrate. Our analytical model is assessed by comparison with numerical and experimental results previously presented in literature, and with our experiments conducted with a dAFM working in air.

1 Introduction

The dynamic atomic force microscope (dAFM) consists of an oscillating microcantilever which holds a sharp nanoscale tip that intermittently interacts with the sample, close to its first resonance frequency. There are many fields of applications of dAFM, and ranges from measuring topography of organic and inorganic materials at nanometer length scales, to the accurate quantification of sample properties in materials science. Despite many years of investigations on dAFM dynamics [1], several aspects still demand further attention from the research community. Because of the complexity related to the small scales involved, where different physical effects coexist together, it is a very common approach to study each phenomenon separately, and to draw conclusions from each analysis [2, 3]. This is often a very good way to clarify aspects completely unknown before, but for more detailed insights, it is also necessary to analyze different effects together. This is the case of the dAFM research field, in which, in particular, it is extremely important to analyse both the tip-sample and the fluid-structure interactions. For such instruments a clear signal is one of the

utmost requirements in order to extract correct information from the measurement at so small length scales. However this is not a so straightforward task to be achieved because of the forces which act on the cantilever in operational conditions, especially when a liquid environment is required, e.g. in physiological buffer solutions [4, 5, 6, 7]. In such case, in particular, besides the tip-sample interaction, the presence of a liquid deeply modifies the response spectrum and is the origin of the so called Brownian thermal noise. Indeed, even though the molecular size of the fluid molecules is negligibly small in comparison to the size of the cantilever, the dynamics of the cantilever itself is strongly dependent on Brownian fluctuations, since the same molecular processes are responsible for both the dissipation and the fluctuations, due to the collisions between the fluid molecules and the cantilever. But to achieve a good AFM resolution, noise sources must be reduced as much as possible, since the lowest signal level that can be considered as a valid information must be not mixed up with external noise. In spite of this, the cantilever thermal motion is also utilized to calibrate the cantilever's spring constant [8] and to extract the resonance frequencies and quality factors of its resonances as well [9]. Therefore, a good understanding and theoretical modelling of this effect related to the equilibrium of the cantilever with the surrounding liquid is of paramount importance, whatever is the scope, i.e. either to study ad hoc control system to separate the signal from noise, or to obtain useful insights about the cantilever properties. With such an aim, several studies have been presented up to now [10, 11, 12], but the main difficulty for a proper description of the cantilever response to the thermal fluctuations is the fluid-structure interaction modelling. In order to overcome the complexity of the problem, some assumptions have been made in the previous studies, such as those of neglecting inertia [13] and the diffusivity [14, 15] terms, which, instead, become important from intermediate to high frequency range. In this paper the authors present an analytical model to describe the drag of the liquid on the cantilever which takes into account, in a relatively simple way, all the three mentioned contributions: (i) the fluid viscosity, (ii) fluid inertia, and (iii) the fluid vorticity diffusivity. It is shown, in particular, that the correct evaluation of the cantilever response to the thermal excitation cannot neglect the above mentioned effects. Moreover, experimental results of an AFM cantilever working in air are presented, which definitively assess the accuracy of the model.

2 Cantilever dynamics

We study the dynamics of a cantilever immersed in a viscous fluid (see Figure 1) near a rigid flat wall, with L, B, and H respectively the length, the width and the thickness of the rectangular cross section. We will assume that $L \gg B \gg H$, as well as that the transversal displacement $|w(x,t)| \ll L$. This enables us to use the Bernoulli theory of transversal vibrations and therefore neglect the influence of shear stress in the beam. The general motion equation of the cantilever is therefore:

$$EI\frac{\partial^4 w(x,t)}{\partial x^4} + \rho A\frac{\partial^2 w(x,t)}{\partial t^2} = f_B(x,t) + f_L(x,t) \tag{1}$$

where ρ is the bulk density of the material the cantilever is made of, E is the Young'modulus and A is the area of the cross section of the beam, i.e. $A = BH$. In the RHS of the above Eq. (1) we have introduced two terms. The first term $f_B(x,t)$ is the chaotic force per unit length acting on the beam as a consequence of the thermal fluctuation of the molecules constituting the liquid: we will refer to this type of excitation term as the Brownian force.

The term $f_L(x,t)$ is the force per unit length which the liquid, in a continuum sense, exerts on the cantilever, which is usually calculated by means of complex numerical simulations. However, under the hypothesis of small transversal displacements $|w(x,t)| \ll B$, we can assume that the response of the fluid is linear. Under this condition the force $f_L(x,t)$ can be expressed in terms of the response function $G(x,x',t)$:

$$f_L(x,t) = \int_{-\infty}^{t}\int_0^L dx' G\left(x,x',t-\tau\right)\frac{\partial v(x',\tau)}{\partial \tau}d\tau \tag{2}$$

where $v(x,\tau)$ is the transversal velocity of the generic cantilever section, i.e. $v(x,\tau) = w_t(x,t)$, where the subscript t denotes the partial time-derivative. Causality implies the linear response function of the liquid

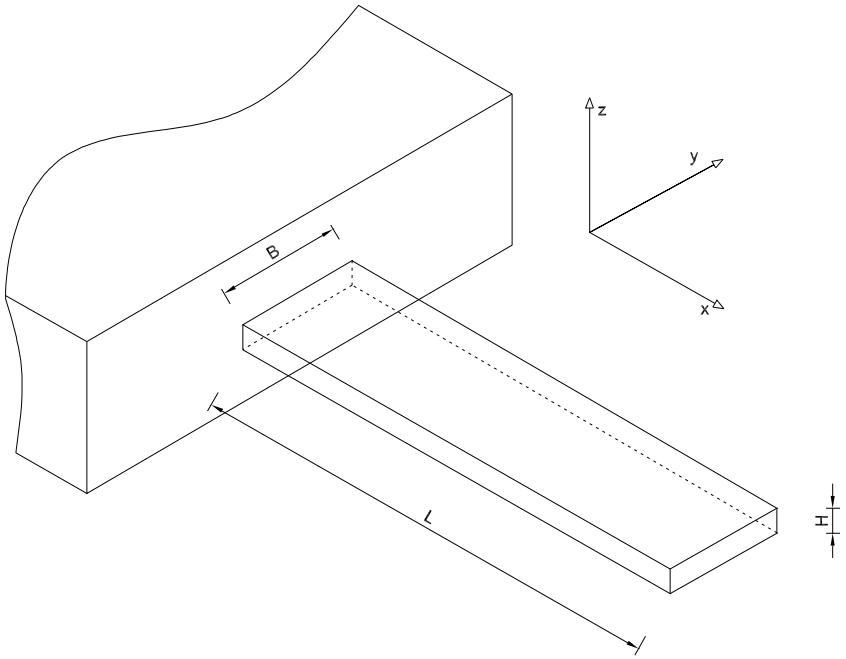


Figure 1: dAFM microcantilever.

must vanish for $t < 0$. This also implies that the quantity

$$G\left(x, x', \omega\right) = \int_{-\infty}^{+\infty} dt G\left(x, x', t\right) \exp\left(-i\omega t\right) \tag{3}$$

must be analytic in lower half-plane of the complex domain, and therefore must satisfy the Kramer-Kronig relations [21]. However, measurements or numerical calculations contain always some errors or approximations that do not guarantee the Kramer-Kroning relations to be exactly satisfied. This restriction in general leads to some difficulties in the calculations of the linear response function $G\left(x, x', t\right)$ of the liquid from the measured or numerically calculated frequency response, i.e. it is often not possible to determine the quantity $G\left(x, x', t\right)$ by simply taking the inverse Fourier transform of the measured frequency response of the system. However the task is much more simplified if the analytical form of this function is already known. For this reason, the authors have derived a new analytical model of the liquid response $G\left(x, x', t\right)$, that will be presented in the next section.

3 Fluid-cantilever interaction

We first observe that some hypothesis about the time dependence of the liquid response function $G\left(t\right)$ must be fulfilled. Indeed, the assumption that $L \gg B \gg H$ allows us to consider that the response of the fluid depends only on local quantities, i.e. the fluid motion is locally two dimensional [13, 15]. In such case we can write $G\left(x, x', t\right) = G\left(x, t\right) \delta\left(x' - x\right)$. Now, the leading-order incompressible flow generated by an isolated body oscillating at small amplitude is governed by the unsteady Stokes equation

$$\begin{gathered} \rho_L \frac{\partial \mathbf{v}}{\partial t} + \rho_L \left(\mathbf{v} \cdot \nabla\right) \mathbf{v} = -\nabla p + \eta \nabla^2 \mathbf{v} \\ \nabla \cdot \mathbf{v} = 0 \end{gathered} \tag{4}$$

where $\mathbf{v}$ is the velocity of the fluid, η is the liquid viscosity, ρ_L the liquid density. Observe that the non-linear term $\rho_L \left(\mathbf{v} \cdot \nabla\right) \mathbf{v}$ can be neglected in comparison with the time derivative of Eq.4. Indeed, by estimating

the two terms, we obtain that $\rho_L (\mathbf{v}\cdot\nabla)\mathbf{v} \sim (w_0\omega)^2/B$, and the time derivative $\rho_L \partial\mathbf{v}/\partial t \sim w_0\omega^2$, being B the characteristic dimensions of the moving bodies and w_0 the amplitude of the oscillations. Therefore the non linear convective term can be neglected if $w_0 \ll B$, which is indeed one of the hypotheses of our model. Moreover, Eq. (4) can be rephrased in terms of the vorticity $\mathbf{W}=\nabla\times\mathbf{v}$ as $\rho_L(\partial\mathbf{W}/\partial t) = \eta\nabla^2\mathbf{W}$, showing that the vorticity is governed by a diffusive-like equation which generates an exponential decay of the velocity as we move far from the walls of the bodies towards the interior of the liquid. The exponential decay allows to estimate the thickness h of the layer of fluid within which the flow is rotational and velocity diffusion is important. It is known [16] that $h \sim \omega^{-1/2}$ where ω is the characteristic frequency of the motion. Out of the layer the term $\nabla^2\mathbf{v}$ can be neglected in Eq. 4 so that we have potential flow. Since the value of h depends on the frequency ω, it follows that at large frequencies the thickness h will be very small and the response of the fluid will be then governed by inertia effects, i.e. it will depend proportionally on the acceleration $v_t(x,t)$ of the moving bodies. In this limiting case $G(x,t) = -\mu(x)\,\delta(t)$, where $\delta(t)$ is the Dirac delta function. If, on the contrary, the motion is sufficiently slow (low ω-values) then the term $\partial\mathbf{v}/\partial t$ can be neglected and the quantity h becomes larger than the characteristic dimensions of the moving bodies. The motion of the fluid becomes steady and the response of the fluid should depend linearly on the velocity v of the moving bodies, i.e. for $t \geq 0$, we have $G(x,t) = -c(x)$. At intermediate frequency the effect of diffusivity should be very important. It is known [16] that for the in-plane motion of flat plate the motion of the liquid is governed by a pure diffusive equation, and in this case $G(x,t)$ takes the form $G(x,t) = -\alpha(x)\,t^{-1/2}$ for $t \geq 0$, which represents the contribution to the fluid force coming from the diffusion of the tangential velocity of the plate into the interior of the liquid. Since Eqs. (4) are linear, the force the liquid exerts on the body will be given by the sum of the three contributions and we can heuristically give a general expression for $G(x,t)$ as

$$\begin{aligned} &G(x,t) = -c(x) - \frac{\alpha(x)}{\sqrt{t}} - \mu(x)\,\delta(t)\,; \qquad t \geq 0 \\ &G(x,t) = 0; \qquad t < 0 \end{aligned} \tag{5}$$

where $c(x)$ is the damping, $\alpha(x)$ is the diffusive coefficient, and $\mu(x)$ is the inertia term. Eq.(5), therefore, satisfies the causality principle. We observe, in particular, that for the case of a sphere moving in a liquid, the response of the fluid has exactly the form given by Eq. (5), see for example [16]. Moreover, by substituting Eq.(5) and Eq.(2) in Eq.(1), we get

$$\begin{aligned} &EI\frac{\partial^4 w(x,t)}{\partial x^4} + [\rho A + \mu(x)]\frac{\partial^2 w(x,t)}{\partial t^2} + c(x)\frac{\partial w(x,t)}{\partial t} + \\ &+\alpha(x)\int_{-\infty}^{t}\frac{1}{\sqrt{t-\tau}}\frac{\partial^2 w(x,\tau)}{\partial\tau^2}d\tau = f_B(x,t) \end{aligned} \tag{6}$$

and in particular, the linear response function $\chi(x,x',t)$ of this equation, also referred to as susceptibility, can be obtained by solving the fundamental problem (see [17]):

$$\begin{aligned} &EI\frac{\partial^4 \chi(x,x',t)}{\partial x^4} + [\rho A + \mu(x)]\frac{\partial^2 \chi(x,x',t)}{\partial t^2} + c(x)\frac{\partial \chi(x,x',t)}{\partial t} + \\ &+\alpha(x)\int_{-\infty}^{t}\frac{1}{\sqrt{t-\tau}}\frac{\partial^2 \chi(x,\tau)}{\partial\tau^2}d\tau = \delta\left(x-x'\right)\delta(t) \end{aligned} \tag{7}$$

Eq. (5) is, of course, approximated, but in what follows it will be shown that it works very well. In Eq. (5) the x-dependence can be present only as a consequence of the x- dependent distance of the cantilever cross sections from the wall, i.e. only when the beam is tilted, which is a case also covered by this study. Once the analytical form of the response function is known, the three coefficients can be determined by finding the best fitting with the existing accurate computational fluid dynamics non-dimensional solutions of a 2D fluid flowing around a vibrating rectangular cross-section, as reported in Ref. [15]. In Table1, the three

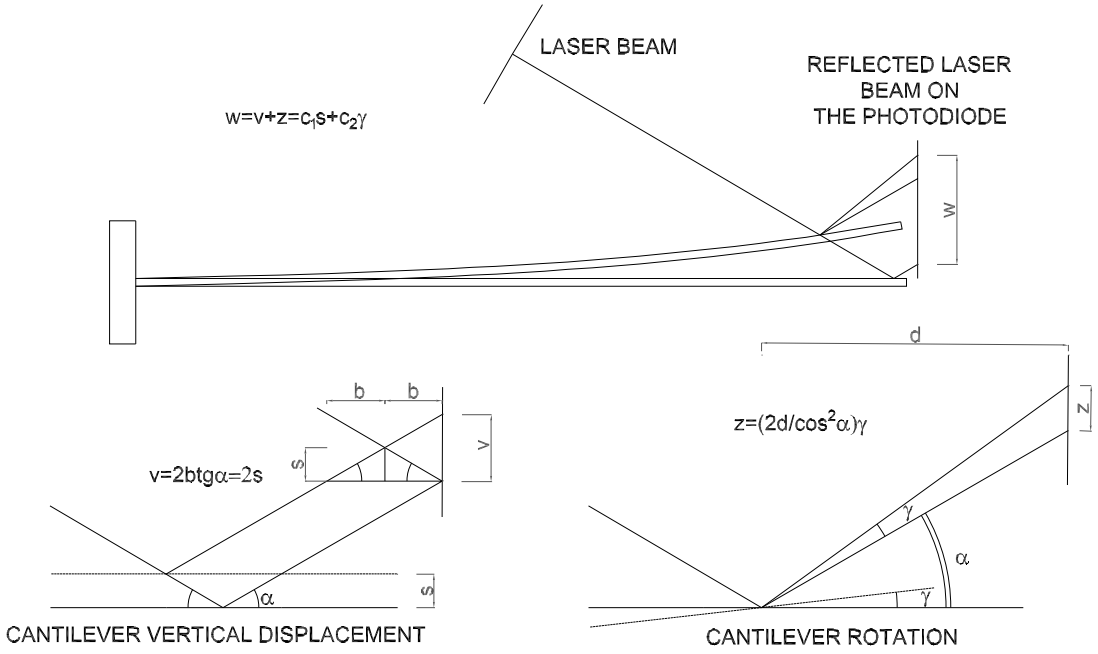


Figure 2: The total displacement w_{tot} of the laser beam on the photodiode is given by the weighted sum of both the vertical displacement $s\,(x,t)$ and the rotation $\gamma\,(x,t)$ of the cantilever.

coefficients are shown, calculated in correspondence of the cantilever free end $x = L$, for different values of $\Delta = 2d/B$, where d is the wall distance. Now, Fourier transforming Eq. (6) we obtain

$$\frac{\partial^4 w\,(x,\omega)}{\partial x^4} - B\,(x,\omega)^4\, w\,(x,\omega) = f_B\,(x,\omega) \tag{8}$$

where we define the function $B\,(x,\omega)$

$$B\,(x,\omega) = \sqrt[4]{-\frac{i\omega c\,(x) - [\rho A + \mu]\,\omega^2 + i\omega\,\alpha\,(x)\,\sqrt{i\omega\pi}}{EI}} \tag{9}$$

Δ	c [kg s^{-1}]	α [kg s$^{-1/2}$]	μ [kg]
0.5	0.157	8.32×10^{-6}	5.73×10^{-7}
1	0.042	1.25×10^{-5}	4.65×10^{-7}
2	0.016	2.13×10^{-5}	4.13×10^{-7}
4	8.6×10^{-3}	3.72×10^{-5}	3.81×10^{-7}
6	6.05×10^{-3}	4.91×10^{-5}	3.65×10^{-7}
8	4.91×10^{-3}	5.65×10^{-5}	3.56×10^{-7}
10	4.31×10^{-3}	6.1×10^{-5}	3.51×10^{-7}

Tab.1 - The three coefficients of the fluid response, at the free end of the cantilever $x = L$, for different values of the distance $\Delta = 2d/B$ of the cantilever from the substrate.

4 The fluctuation dissipation theorem

In AFM systems the micrometer size of the cantilever makes it particularly sensitive to Brownian fluctuations so that the thermal induced fluctuations of the cantilever displacement cannot be neglected, thus making the

measurement of the response function of the cantilever through its thermal fluctuations a viable technique. This is done by employing the Fluctuation Dissipation Theorem (FDT) (see [17]). The FDT states that the susceptibility function $\chi(x_1, x_2, t)$ of the cantilever, which is the displacement $w(x_1, \omega)$ at point x_1 due to the action of a concentrated unit force F at point x_2, is proportional to the time-derivative of the correlation function of the thermal fluctuations of the cantilever displacements [17], [18], that is

$$\chi(x_1, x_2, t) = -\beta H(t) \frac{\partial}{\partial t} \langle w(x_1, 0) w(x_2, t) \rangle \tag{10}$$

where $\beta = (k_B T)^{-1}$ and k_B is Boltzmann's constant, T the absolute temperature and $H(t)$ is the Heaviside unit step function. The susceptibility function can be used to rephrase the solution of Eq. (1) as

$$w(x_1, t) = \int_{-\infty}^{t} d\tau \int_0^L dx_2 \chi(x_1, x_2, t-\tau) f_B(x_2, \tau) \tag{11}$$

Moving from Eq.(10), the relation between the Cross Power Spectral Density (CPSD) $R(x_1, x_2, \omega) = \int dt \ \langle w(x_1, 0) w(x_2, t) \rangle \exp(-i\omega t)$ of the cantilever thermal fluctuations and the imaginary part of the time-Fourier transform of the susceptibility function, i.e. the imaginary part of the complex compliance $\chi(x_1, x_2, \omega) = \int dt \chi(x_1, x_2, t) \exp(-i\omega t)$, can be easily derived (see [17], [19]) as

$$R(x_1, x_2, \omega) = -\frac{2k_B T}{\omega} Im\chi(x_1, x_2, \omega) \tag{12}$$

Eq. (12) will be used to calculate the PSD of the thermal oscillations of the free end of the cantilever. We observe that the CPSD $R(x_1, x_2, \omega)$ is, in general, not ω-independent (as it should be in case of white noise), since, as we show later, the velocity-diffusive and the inertia terms of the liquid response, do not make $Im[\chi(x_1, x_2, \omega)]$ proportional to the radian frequency ω. Equation (12) shows that, in order to calculate the CPSD of the cantilever displacement fields, it is enough to measure or calculate the response function $\chi(x_1, x_2, \omega)$. However, this quantity is strongly affected by the presence of the liquid. By solving Eq. (8) it is possible to determine the complex compliance of the cantilever for the transversal displacement and therefore determine the CPSD $R(x_1, x_2, \omega)$. In order to define the correct signal information which is actually read by the AFM system, we point out that the angular rotation of the beam cross section gives a huge contribution to signal read by the photodiode. In Fig. 2, indeed, one can clearly observe that the total displacement $w_{\text{tot}}(t)$ of the reflected laser spot on the photodiode surface can be calculated as the weighted sum of both the vertical $s(x, t) = w(x, t)$ displacement and the angular $\gamma(x, t) = \dot{s}(x, t) = (\partial w / \partial x)_{l,t}$ rotation of the cantilever, i.e.

$$w_{\text{tot}}(x, t) = c_1 s(x, t) + c_2 \gamma(x, t) \tag{13}$$

Therefore we will assume in what follows that the CPSD of the quantity $w_{\text{tot}}(x, t)$ is $S_{\text{tot}}(x_1, x_2, \omega) = \int dt \langle w_{\text{tot}}(x_1, 0) w_{\text{tot}}(x_2, t) \rangle \exp(-i\omega t)$. So we get, at the cantilever free end $x_1 = x_2 = L$

$$\begin{aligned} \langle w_{\text{tot}}(L, 0) w_{\text{tot}}(L, t) \rangle = c_1^2 \ \langle w(L, 0) w(L, t) \rangle + \\ + c_1 c_2 \left[\langle w_x(L, 0) w(L, t) \rangle + \langle w(L, 0) w_x(L, t) \rangle \right] + c_2^2 \langle w_x(L, 0) w_x(L, t) \rangle \end{aligned} \tag{14}$$

Now recall that

$$\int dt \langle w(L, 0) w(L, t) \rangle e^{-i\omega t} = R(L, L, \omega) = -\frac{2k_B T}{\omega} Im\chi(L, L, \omega) \tag{15}$$

so taking the derivative we also obtain

$$\begin{aligned} \int dt \langle w_x(L, 0) w(L, t) \rangle e^{-i\omega t} &= R_1(L, L, \omega) = -\frac{2k_B T}{\omega} Im\chi_1(L, L, \omega) \\ \int dt \langle w(L, 0) w_x(L, t) \rangle e^{-i\omega t} &= R_2(L, L, \omega) = -\frac{2k_B T}{\omega} Im\chi_2(L, L, \omega) \\ \int dt \langle w_x(L, 0) w_x(L, t) \rangle e^{-i\omega t} &= R_{12}(L, L, \omega) = -\frac{2k_B T}{\omega} Im\chi_{12}(L, L, \omega) \end{aligned} \tag{16}$$

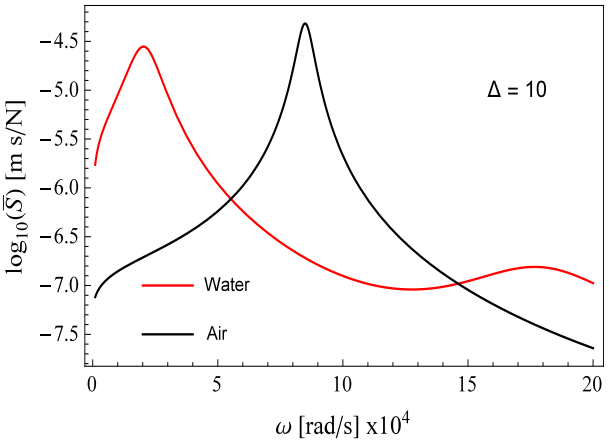


Figure 3: The cantilever thermal power spectrum in water (red curve) and in air (black curve), $\Delta = 2d/B = 10$.

where $(\cdot)_i = \partial(\cdot)/\partial x_i$ and $(\cdot)_{ij} = \partial^2(\cdot)/\partial x_i \partial x_j$. The power spectrum of the signal recorded by the photodiode is then

$$\begin{aligned} S(\omega) &= S_{\text{tot}}(L,L,\omega) = \int dt \, \langle w_{\text{tot}}(L,0) \, w_{\text{tot}}(L,t) \rangle \exp(-i\omega t) \\ &= c_1^2 R(L,L,\omega) + c_1 c_2 \left[R_1(L,L,\omega) + R_2(L,L,\omega) \right] + c_2^2 R_{12}(L,L,\omega) \\ &= -\frac{2k_B T}{\omega} Im \left\{ c_1^2 \chi(L,L,\omega) + c_1 c_2 \left[\chi_1(L,L,\omega) + \chi_2(L,L,\omega) \right] + c_2^2 \chi_{12}(L,L,\omega) \right\} \end{aligned} \tag{17}$$

5 Results

In this section we discuss the main results of our investigation. We compare the thermal response of the cantilever tip in air and in water, show how important is the influence of the diffusive-velocity term related to the parameter $\alpha(x)$, and also discuss the influence of the distance between the cantilever and the underlying substrate. The geometrical and mechanical properties of the cantilever, we have investigated, are listed in Tab.2. At first, we will focus on the PSD of the transversal displacement of the free end of the cantilever, i.e. we will focus on the quantity $S(\omega) = S(x_1 = L, x_2 = L, \omega)$.

Quantity	Value
L	$232.4\ \mu$m
B	$20.11\ \mu$m
H	$0.573\ \mu$m
Young Modulus	3.92×10^{11} Pa
Air density	1.2 kg/m^3
Air -dynamic viscosity	1.83×10^{-5} Pas
Water density	1000 kg/m^3
Water-dynamic viscosity	1.0×10^{-3} Pas

Tab.2 - The geometrical and physical quantities utilized to carry out the analysis.

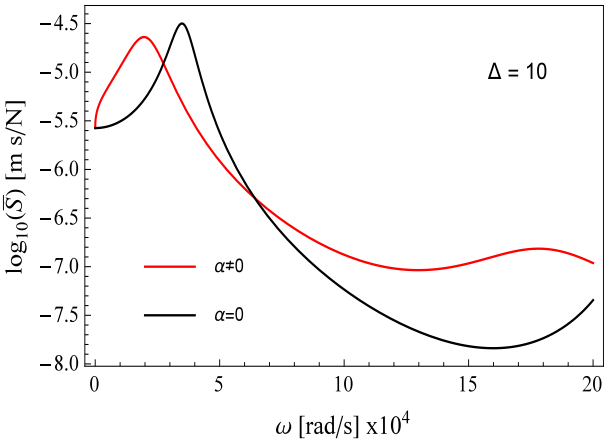


Figure 4: The influence of the velocity-diffusive term on the cantilever thermal power spectrum, for $\Delta = 2d/B = 10$.

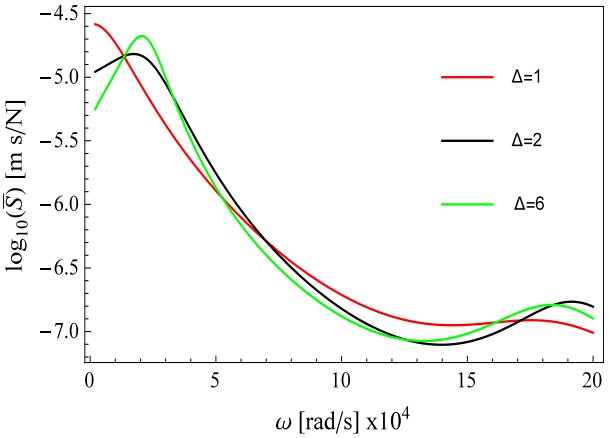


Figure 5: The thermal power spectrum for different values of the dimensionless distance $\Delta = 2d/B$.

Figure 3 shows the PSD of the cantilever tip deflection $\bar{S}(\omega) = S(\omega)/2k_BT$, when the dimensionless distance $\Delta = 2d/B$ of the cantilever from the substrate is constant and equal to $\Delta = 10$ (d is the distance in μm), for a cantilever thermally excited in water (red curve) and in air (black curve). Observe the large peak shifting towards the low frequency range when the system is in water. At a first sight one may be surprised to see that the heights of the two peaks for water and air are not significantly different. However this can be easily explained considering that, although the imaginary part of the complex compliance is larger in air if compared to water, the peak frequency is about 3 times larger in air than in water. Hence, these two opposite effects partially balance each-other when the quantity $\bar{S}(\omega)$ is calculated. Beside this, one should also consider that, even in air, the presence of the wall makes non negligible the viscous dissipation related to the term $c(x)$ in Eq.5. Thus, a blunted resonant peak is expected to be observed as indeed shown in Fig. 3. In Fig.4, the thermal power spectrum $\bar{S}(\omega)$ is shown, for $\alpha \neq 0$ as results from numerical fitting, and for $\alpha = 0$. Fig. 4 shows the very large influence of the velocity-diffusive parameter in terms of peak resonance position and the Q-factor values. This means that neglecting such effect can lead to a strong overestimation of the first resonance frequency and also to strongly underestimate the noise affecting the dAFM at larger frequencies. This error in the evaluation of the cantilever thermal response to Brownian forcing, can in turn lead to a wrong calibration of the instrument. In particular, a bad estimation of the cantilever resonances and damping properties, yields an invalid estimation of the system properties and therefore may result in a non-correct operation of the instrument. This means that our drag model can be an extremely useful tool in

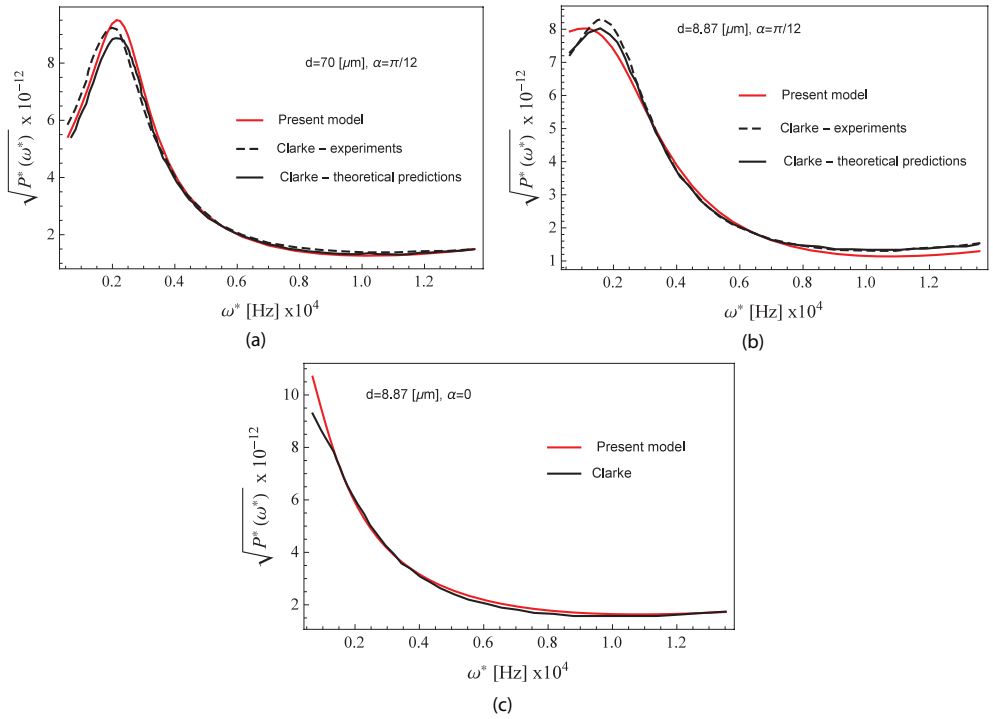


Figure 6: The thermal power spectrum $\sqrt{P^*(\omega^*)}$ in water near a wall. Comparison between experiments (dashed black curve) and theoretical predictions (solid black curve) presented in Ref.[14] with our analytical model (solid red curve) for a tilt angle $\pi/12$ to the wall and separations $d = 70\mu m$ (a) and $d = 8.87\mu m$ (b). Theoretical predictions from Ref.[14] (solid black curve) are also compared with our analytical model (solid red curve) for a tilt $\alpha = 0$ and separation $d = 8.87\mu m$ (c).

the calibration process of a dAFM.

In Fig. 5 the cantilever thermal power spectrum $\bar{S}(\omega)$ at different distances from the substrate is shown. Three beam-wall distances are considered. The figure shows that the closer the cantilever is to the wall, the more the spectrum is shifted toward lower frequencies, whereas the second resonance peak occurs at higher frequencies. In particular, for the lowest value of Δ here considered, i.e. $\Delta = 1$, the first resonant peaks almost disappears. The reason for such a strong influence of the substrate distance should be sought in the change of the viscous response of the liquid. Indeed at small beam-wall distances the viscous coefficient c increases with d^{-3} as the distance d is reduced.

Considering that in many applications the cantilever is slightly tilted along its length, the effect of the x-dependent distance of the beam cross section from the substrate should be accurately taken into account to correctly estimate the cantilever response. This is the case of the experimental data shown in Ref.[14], where a cantilever in water is moved close to the substrate, with a tilt $\alpha = \pi/12$ (geometrical and physical quantities are the same listed in Table 2), and the angular oscillations are measured. In order to compare our analytical model with the numerical and experimental thermal power spectra presented in [14], we have numerically calculated the interpolating functions of the three coefficients of the function $G(x,t)$ (Eq.5), i.e. $c(x)$, $m(x)$, and $\alpha(x)$, by means of the values reported in Table 1. Then we have calculated the PSD $S(\omega)$ (see Eq.17) given by both the vertical displacement and the angular rotation of the cantilever free end, and finally we have defined $P^*(\omega^*) = \left(\bar{A}^2/\omega_0\right) S(\omega)$, where $\bar{A} = \sqrt{k_B T L^3/(EJ)}$, $\omega^* = \omega_0 \omega$, and $\omega_0 = \sqrt{EJ/(\rho A L^4)}$. In Figure 6 we show the comparison of the quantity $\sqrt{P^*(\omega^*)}$ calculated by employing our analytical model (with $c_1 = 0$ and $c_2 = 0.86$ in Eq.17) and the experimental data and theoretical predictions presented in [14], conducted in water, using a molecular force probe with pyramidal tip. In Fig.6-a the cantilever is tilted at $\pi/12$ to the wall with a separation $d = 70\mu m$, in Fig.6-b the distance is reduced to $d = 8.87\mu m$

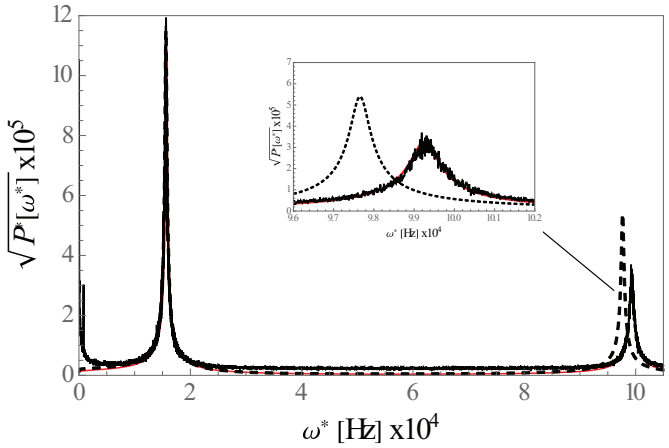


Figure 7: Our experimental thermal power spectrum $\sqrt{P^*(\omega^*)}$ in air (solid black curve), far from the wall, compared with our theoretical predictions (solid red curve) and the theoretical results presented in Ref.[14] (dashed black curve). Our analytical model perfectly fit the experimental curve, also at the second resonant peak, as shown in the inset.

(same tilt), in Fig. 6-c the cantilever has no tilt ($\alpha = 0$) and the separation is $d = 8.87\mu m$. In this last case no experimental data are presented in Ref. [14] and we show the comparison between our analytical model and the one utilized in [14], where the fluid - cantilever interaction is described considering the Stokes' expression for the drag on an oscillating circular cylinder. It is possible to observe a good agreement between our results (solid red lines), the experimental data (dashed black lines) and theoretical predictions (solid black lines) reported Ref.[14]. It is worth of being mentioned that our analytical model is able to fit very well the experimental data (see Fig. 6-a). When the tilted cantilever is much closer to the wall (i.e. for $\Delta < 1$) we expect to have a smaller degree of agreement, confirmed in Fig. 6-b, for the data presented in literature showed results for only a couple values of Δ. In particular, considering the near wall case, we have found data only for $\Delta = 0.5, 1$ (see Table 1) that are not sufficient for an accurate estimation of the damping coefficient c. To completely assess our analytical model, we have carried out experiments with an AFM NT-MDT Ntegra Aura (Tribolab, Politecnico di Bari, Bari, Italy) on a CSG01 rectangular silicon cantilever with tip, and dimensions $(L, B, H) = (350, 30, 1)\,\mu$m. The thermal oscillations of the free-end of the cantilever have been acquired, in the frequency range $0 < \omega^* < 105$ kHz, where the first and the second resonant peaks of the beam are present. In Figure 7 our experimentally measured thermal power spectrum $\sqrt{P^*(\omega^*)}$ is compared with our theoretically predicted response. An almost perfect agreement between the experimental data and our theoretical model is obtained. The inset shows, in particular, that this almost perfect matching still holds true for the second resonant peak, a condition not easy achievable with other techniques (see dashed black curve in Fig.7 corresponding to the model reported in Ref.[14]). Our results definitively show that the presented analytical model is able to accurately predict the dynamics of a dAFM cantilever in a wide frequency range, thus making it a possible tool for calibration procedures and high performance measurements.

6 Conclusions

The present study deals with the dAFM cantilever dynamics. The attention is focused on the interactions of the cantilever with the surrounding fluid. The impacts of the fluid molecules on the beam, indeed, generate the so called Brownian thermal noise, which is related to the macroscopic linear response of the system. We have presented an analytical model of the fluid-structure interactions, which takes into account of inertial, damping, and diffusive terms. In particular, the force the liquid exerts on the body has been heuristically

derived, and it is described as the sum of three contributions, which have been evaluated through the best fitting of accurate computational fluid dynamics (adimensionalized) data of a 2D fluid flowing around an oscillating rectangular cross section, found in the literature. Experiments have been also carried out, and the thermal oscillations of a dAFM cantilever operating in air have been acquired. The experimental data have been perfectly fitted by means of our analytic response of the beam, in a wide frequency range. Our results clearly demonstrate that the presented analytical model is an extremely useful and accurate tool to predict the cantilever dynamics, and therefore could be utilized to calculate the cantilever spring constants in the common calibration procedures, thus improving the quality of the measurements.

References

[1] A. Raman, J. Melcher, R. Tung, *Cantilever dynamics in atomic force microscopy*, Nanotoday 3, 20 , (2008), pp. 20-27.

[2] U. Rabe, J. Turner, W. Arnold, *Analysis of the high-frequency response of atomic force microscope cantilevers*, Appl. Phys. A - Materials Science & Processing 66, S277, (1998).

[3] T. R. Rodriguez, R. Garcia, *Tip motion in amplitude modulation (tapping-mode) atomic-force microscopy: Comparison between continuous and point-mass models*, Appl. Phys. Lett., 80, 1646, (2002).

[4] J. Legleiter, T. Kowalewskia, *Insights into fluid tapping-mode atomic force microscopy provided by numerical simulations*, Appl. Phys. Lett. 87, 163120, (2005).

[5] G. Y. Chen, R. J. Warmack, *Transient response of tapping scanning force microscopy in liquids*, J. Vac. Sci. Technol. B 14(2), 1313, (1996).

[6] C. A. J. Putman, K. O. Van der Wetf, B. G. De Grooth, N. F. Van Hulst, G. Greve, *Tapping mode atomic force microscopy in liquid*, Appl. Phys. Lett. 64, 2454, (1994).

[7] T. E. Schaffer, J. P. Cleveland, F. Ohnesorge, D. A. Walters, P. K. Hansma, *Studies of vibrating atomic force microscope cantilevers in liquid*, J. Appl. Phys. 80, 3622, (1996).

[8] J. L. Hutter, J. Bechhoefer, *Calibration of atomic-force microscope tips*, Rev. Sci. Instrum. 64, 1868, (1993).

[9] A. Gannepalli, A. Sebastian, J. Cleveland, M. Salapaka, *Thermally driven non-contact atomic force microscopy*, Appl. Phys. Lett. 87, 111901, (2005).

[10] A. Mehta, S. Cherian, S. Hedden, T. Thundat, *Manipulation and controlled amplification of Brownian motion of microcantilever sensors*, Appl. Phys. Lett. 78, 1637, (2001).

[11] H. J. Butt, M. Jaschke, *Calculation of thermal noise in atomic force microscopy*, Nanotechnology 6, 1, (1995).

[12] X. Xu, A. Raman, *Comparative dynamics of magnetically, acoustically, and Brownian motion driven microcantilevers in liquids*, J. Appl. Phys. 102, 034303, (2007).

[13] J. E. Sader, *Frequency response of cantilever beams immersed in viscous fluids with applications to the atomic force microscope*, J. Appl. Phys. 84, 64, (1998).

[14] R. J. Clarke, O. E. Jensen, J. Billingham, A. P. Pearson, P. M. Williams, *Stochastic Elastohydrodynamics of a Microcantilever Oscillating Near a Wall*, Phys. Rev. Lett. 96, 050801, (2006).

[15] R. J. Clarke, S. M. Cox, P. M. Williams, O. E. Jensen, *The drag on a microcantilever oscillating near a wall*, J. Fluid Mech. 545, 397, (2005).

[16] L. D. Landau, E. M. Lifshitz, *Fluid Mechanics*, (Pergamon Press, second edition, 1984).

[17] E. Pierro, F. Bottiglione, G. Carbone, *Thermal fluctuations and dynamic modelling of a dAFM cantilever*, Mechanical Systems and Signal Processing, under review, (2018).

[18] D. Chandler, *Introduction to Modern Statistical Mechanics* (Oxford University Press, New York, 1987).

[19] Forster D., *Hydrodynamic Fluctuations, Broken Symmetry, and Correlation Functions*, Advanced Book Classics , PERSEUS BOOKS, 1990, isbn 0-201-41049-4

[20] L. Onsager, *Reciprocal Relations in Irreversible Processes*, Phys. Rev. 37, (1931).

[21] Kronig R de L, *On the theory of dispersion of x-rays*, J. Opt. Soc. Am. Rev. Sci. Instrum. 12, 547, (1926)

[22] Kramers H A, *La diffusion de la lumiere par les atomes,* Atti del Congresso Internazionale dei Fisici, Como-Pavia-Roma, 2, 545, (1927)

[23] Callen, H.B. , *Thermodynamics and an Introduction to, Thermostatistics*, John Wiley & Sons Inc., USA . ISBN Q-471-86256-8, (1985).

Using wavelet deconvolution to determine the force applied by drops of water on dry plates and plates with a shallow water layer

Y. Yu[1], **C. Hopkins**[1]
[1] University of Liverpool, School of Architecture, Acoustic Research Unit
Liverpool L69 7ZN, UK
e-mail: **yicheng.yu@liverpool.ac.uk**

Abstract

Rain noise inside car cabins and buildings can be predicted with knowledge of the time-dependent impact force from individual raindrops. Previous experiments to measure the liquid drop impact force are based on the piezoelectric transducer with direct methods. This paper describes experimental work using both a wavelet deconvolution approach with a glass plate and a force transducer to quantify the force applied by 2 and 4.5 mm diameter drops with terminal velocity onto a dry surface and with a shallow water layer. The validity of the wavelet deconvolution approach is indicated by the close agreement with the force transducer measurements for the initial impact force. A particular advantage of the wavelet approach is that it is able to measure the forces that occur with a natural splash when a drop impacts upon a shallow water layer; these include the initial impact, formation of the crater and crown.

1 Introduction

Knowledge of the impact force applied by a liquid water drop on dry or wet surfaces is useful in many different areas of engineering including blade erosion in steam turbines, soil splash from raindrops, and rain noise in car cabin or buildings. For the latter the raindrop impact on windows and roofs in buildings or cars can generate high levels of re-radiated sound that has a negative effect on speech communication and comfort. To predict the sound and vibration resulting from raindrop impact, it is necessary to know the time-dependent force that is applied to a structure when it is dry or covered with a shallow surface layer of water.

The time-dependent force from liquid drops has previously been measured using a variety of direct approaches. Nearing et al [1] used pressure sensors and noted that the time-dependent force and average pressure were not adequately predicted by theory. Nearing and Bradford [2] used a pressure transducer to measure the force although the sensing area was sufficiently small that many drops did not fall on the sensor. Grinspan and Gnanamoorthy [3] used PVDF film to measure the impact force applied by a low velocity water drop on a solid surface and showed that impact force depends on drop velocity and liquid density. Soto et al [4] used two different approaches to measure the force from a water drop: piezoelectric quartz and a thin glass lamella. In general, the literature indicates problems with a piezoelectric transducer due to resonances of the transducer disc (e.g. [5]). For this reason an alternative inverse approach using wavelets is considered here.

Recent work by Yu and Hopkins [6] validated a wavelet deconvolution method to experimentally determine the force applied by liquid water drops on a dry and wet surface. In this paper, the initial impact force for 2 and 4.5 mm diameter drops travelling at terminal velocity is determined using Doyle's wavelet deconvolution method [7]. This is chosen because of its robustness to noise and the ability to use a glass plate which provides a realistic surface condition that is relevant to roof glazing on cars and in buildings. The wavelet approach is validated through comparison with measurements using a glass disc fixed to a force transducer. After the initial impact of the drop on a water layer, forces exerted from a range of

complex features can also be predicted by the wavelet method. This has been used to experimentally determine empirical formulae for the time-dependent force which can be used to assess prediction models based on an idealized drop shape. For the empirical formulae, the reader is referred to [6].

2 Experiment implementation

2.1 Wavelet approach

When an unknown force, **f**, excites a noiseless LTI system, a matrix of transfer accelerances, **X**, describes the acceleration, **e** , at points on this system by a linear convolution integral. Each transfer accelerance is the ratio of complex acceleration at a specified position to the complex force applied at another specified position. The discrete time domain acceleration can be expressed as [8]:

$$\mathbf{e} = \mathbf{X}\mathbf{f} \tag{1}$$

Wavelet deconvolution is used to determine the time-dependent force using an approach described by Doyle [7]. Doyle's theory assumes that there is no noise; hence, the unknown force is estimated according to [7]:

$$\mathbf{f} = \mathbf{\Phi}^{\mathrm{H}}\mathbf{f_w} = \mathbf{\Phi}^{\mathrm{H}}\left(\mathbf{\Psi}\mathbf{\Psi}^{\mathrm{H}}\right)^{-\mathbf{1}}\mathbf{\Psi}\mathbf{e} \tag{2}$$

where superscript H is the Hermitian, $\mathbf{\Phi}$ is an $M \times N$ matrix of wavelet functions with elements $\phi_m(t_n) = \exp\left[-\left(\frac{t_n - mt_0}{\alpha}\right)^2\right]$, t_n is the n^{th} sample in time (subscript w indicates wavelet), α is the scaling factor (which is dependent on the frequency range of analysis), m is the time shift integer, $\mathbf{f_w}$ is a vector with dimension M to replace the original unknown vector **f** with dimension, N, and $\mathbf{\Psi}$ is defined as

$$\mathbf{\Psi} = \mathbf{\Phi}\mathbf{X}^{\mathrm{H}} \tag{3}$$

where the elements are a matrix of functions $\psi_m(t_n) = \sum_{k=0}^{n-1} x(t_n - \tau_k)\phi_m(\tau_k)$.

In practice there will always be some unwanted noise. To consider the effect of additive noise in Eq. (1) requires the unknown force to be transformed to the wavelet domain, so it can be rewritten as:

$$\mathbf{e} = \mathbf{X}\mathbf{\Phi}^{\mathrm{H}}\mathbf{f_w} + \mathbf{n} = \mathbf{\Psi}^{\mathrm{H}}\mathbf{f_w} + \mathbf{n} \tag{4}$$

where **n** is the noise vector.

The aim is to estimate the M-dimensional vector $\mathbf{f_w}$ from an N-dimensional observation vector, **e**. Assuming that the matrix $\mathbf{\Psi}^{\mathrm{H}} = \mathbf{X}\mathbf{\Phi}^{\mathrm{H}}$ has been determined from measurements in the presence of noise, the likelihood function of the signal, **e**, given the parameter vector, $\mathbf{f_w}$:

$$f_{\mathbf{E}|\mathbf{F_w}}(\mathbf{e}|\mathbf{f_w}) = f_{\mathbf{n}}(\mathbf{n} = \mathbf{e} - \mathbf{\Psi}^{\mathrm{H}}\mathbf{f_w}) \tag{5}$$

Assuming that **n** is random noise with a Gaussian distribution of mean, $\boldsymbol{\mu}_{\mathbf{n}}$, and a covariance matrix, $\mathbf{\Sigma_{nn}}$, and that the parameter vector, $\mathbf{f_w}$, is also a Gaussian process with mean, $\boldsymbol{\mu}_{\mathbf{f_w}}$, and a covariance matrix, $\mathbf{\Sigma}_{\mathbf{f_w}\mathbf{f_w}}$ then the likelihood function is:

$$\begin{aligned} f_{\mathbf{E}|\mathbf{F_w}}(\mathbf{e}|\mathbf{f_w}) &= f_{\mathbf{n}}(\mathbf{n}) \\ &= \frac{1}{(2\pi)^{\frac{N}{2}}|\mathbf{\Sigma_{nn}}|^{\frac{1}{2}}}\exp[-\frac{1}{2}\left(\mathbf{e} - \mathbf{\Psi}^{\mathrm{H}}\mathbf{f_w} - \boldsymbol{\mu}_{\mathbf{n}}\right)^{\mathrm{H}}\mathbf{\Sigma_{nn}^{-1}}(\mathbf{e} - \mathbf{\Psi}^{\mathrm{H}}\mathbf{f_w} - \boldsymbol{\mu}_{\mathbf{n}})] \end{aligned} \tag{6}$$

The Maximum Likelihood Estimate (MLE) is obtained from maximization of the log-likelihood function, $\ln[f_{\mathbf{E}|\mathbf{F_w}}(\mathbf{e}|\mathbf{f_w})]$, with respect to $\mathbf{f_w}$ and is given by [8]:

$$\mathbf{\Psi}\mathbf{\Psi}^{\mathrm{H}}\mathbf{f_w} = \mathbf{\Psi}(\mathbf{e} - \boldsymbol{\mu}_{\mathbf{n}}) \tag{7}$$

and when $\mathbf{\Psi\Psi}^{\mathrm{H}}$ is well-posed,

$$\mathbf{f_w} = \left(\mathbf{\Psi\Psi}^{\mathrm{H}}\right)^{-1}\mathbf{\Psi}(\mathbf{e} - \boldsymbol{\mu}_{\mathbf{n}}) \tag{8}$$

The system impulse response is measured using force hammer with accelerometers at different positions. The unknown force applied by the real impact can then be related to the impact force, $\bar{\mathbf{f}}$, applied by the force hammer, and the associated acceleration signal, $\bar{\mathbf{e}}$, [9] by

$$\mathbf{e} * \bar{\mathbf{f}} = \bar{\mathbf{e}} * \mathbf{f} \tag{9}$$

Eqs. (7) or (8) can be solved by substituting $\mathbf{e} * \bar{\mathbf{f}}$ for $\mathbf{e}$ and $\bar{\mathbf{e}}$ for $\mathbf{X}$. When $\boldsymbol{\mu}_{\mathbf{n}} = \mathbf{0}$, the noise is defined as white Gaussian noise; Eq. (8) is the same as Eq. (2); and the wavelet approach is therefore robust against this form of noise. Depending on the experimental conditions, $\mathbf{X}$ can be sparse causing matrix $\mathbf{\Psi\Psi}^{\mathrm{H}}$ to be ill-conditioned which can lead to instability in the solution of Eq. (8); a solution to this problem is to solve Eq. (7) using the LSQR algorithm [10] to give $\mathrm{f_w}$.

In the experiment, an impact force is applied at the excitation position, p_{e}, using a force hammer with a 3 mm diameter steel tip (Brüel & Kjær Type 8203) to determine the matrix of transfer accelerances, $\mathbf{X}$. The acceleration at sensing positions, p_1, p_2 and p_3 was measured using three accelerometers (Brüel & Kjær Type 4375) fixed with cyanoacrylate glue to the underside of the glass plate at randomly located positions. Ten hits were averaged to give each transfer accelerance value.

When a liquid water drop hits the plate, Eqs. (2) and (8) are used to calculate the time-dependent forces from the acceleration measured at the same three accelerometer positions that are used to determine the matrix $\mathbf{X}$. Impacts from eight drops are averaged in the time-domain.

The wavelet approach requires measured transfer accelerances with point excitation at the same position as the drop impact. These measurements used a force hammer with a 3 mm diameter tip, which is approximately mid-way between the 2 and 4.5 mm drop diameters used in the experiments. For this reason the accelerance measurements are considered valid for the initial impact force because the excited areas are similar. It should be noted that forces which occur after the initial impact are not all applied at the exc position. The features that occur after the initial impact such as the formation of the crater apply forces over the perimeter of a circle with a diameter up to 7 mm, whereas the crown or vortex ring would apply forces over the perimeter of a circle with diameters between 15 and 31 mm. The jet emanates from a point that is close to the drop impact position; hence any forces associated with it should be reasonably estimated with point excitation. Some, but not all of the rebounding drops emanating from this jet will fall within the maximum crater diameter. To estimate the error in the forces applied after the initial impact it is assumed that in-phase forces are applied around the perimeter of a circle. Assuming an infinite plate, the driving-point accelerance with a response point at a distance, R_0, can be calculated for in-phase forces around the perimeter of a circle with radius, r_{c}, and for point excitation. The ratio of these two accelerances is given by

$$\frac{\int_0^{2\pi} H_0^{(1)}(k_{\mathrm{B}}R(\theta)) - H_0^{(1)}(ik_{\mathrm{B}}R(\theta))\,\mathrm{d}\theta}{2\pi\left[H_0^{(1)}(k_{\mathrm{B}}R_0) - H_0^{(1)}(ik_{\mathrm{B}}R_0)\right]} \tag{10}$$

where k_{B} is the wavenumber for bending waves, $H_0^{(1)}$ represents the Hankel function of the first kind and

$$R(\theta) = \sqrt{(R_0 + r_{\mathrm{c}}\cos\theta\,)^2 + r_{\mathrm{c}}^2\sin^2\theta} \tag{11}$$

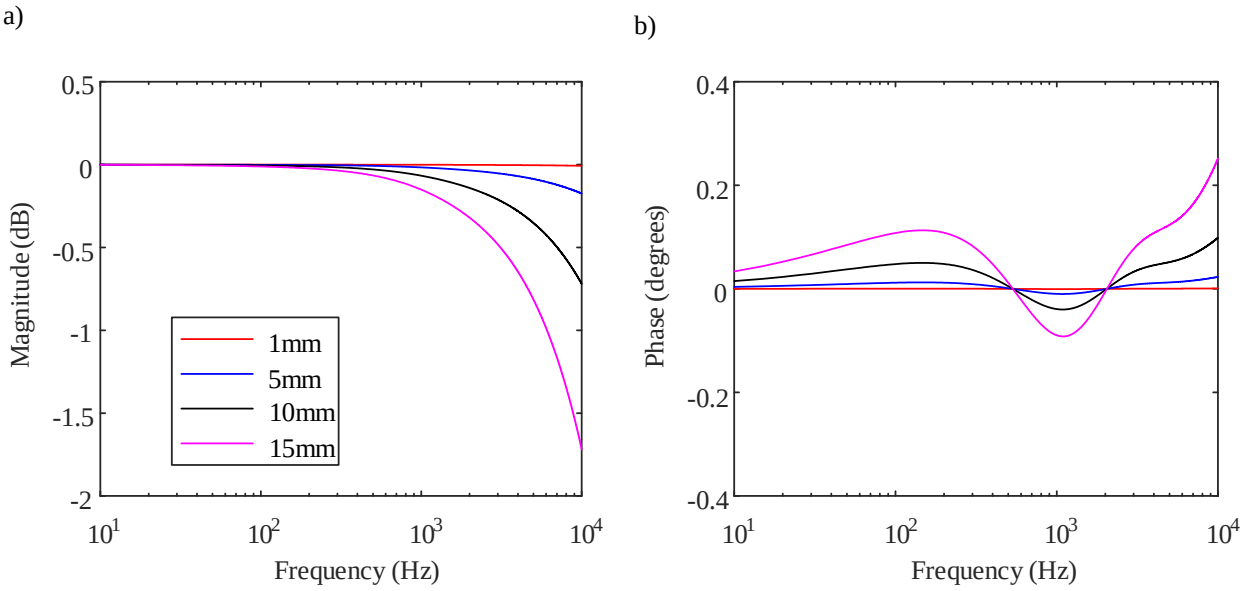


Figure 1. Ratio of accelerance for a circle of in-phase force with radius, *r*, to point excitation (a) magnitude and (b) phase.

Fig. 1 shows calculated values using Eq. (10). Below 6k Hz the error in the impact force is <1 dB in the magnitude and up to 0.2° in the phase. It is reasonable to assume that the maximum measurement uncertainty in narrow band accelerance would be 1 dB for the magnitude and that for the phase the variation between different accelerometers would be <0.4° [11]. Hence it is concluded that after the initial impact the wavelet approach can still be used to estimate the forces that are applied by the crater, crown, jet, vortex ring, or oscillating bubbles. However, rebounding drops can fall at many different positions on the plate and therefore it is difficult to assess the accuracy for these forces. Low-level forces applied by capillary waves propagating away from the crater will not be correctly estimated by the wavelet approach. For rebounding drops the forces tend to be negligible in comparison with the initial impact and the oscillating bubble, although this may not apply to the capillary waves.

2.2 Experimental set-up

The experimental set-up is shown in Fig. 2. Reverse osmosis water is used with a burette that produces 4.5 mm diameter drops. The velocity was 8.2 m/s for the 4.5mm drop (the velocity was the average of 10 measurements with the absolute error estimated to be <8%).

The drops impact upon a plate of 6 mm thick glass of dimensions 1.2 m × 1 m. Glass typically has an internal loss factor of 0.006; hence, to increase the overall damping of the plate (up to a loss factor of ≈0.05), 50 mm wide strips of 13 mm thick Sylomer SR55 are positioned on both sides of the glass around the entire perimeter with the upper layer of Sylomer compressed under a static load applied by 13 mm thick steel.

Water depths, *d*, of 1, 2, 4, 6, 8, and 10 mm (estimated variation over the surface is at ±0.5 mm) were used.

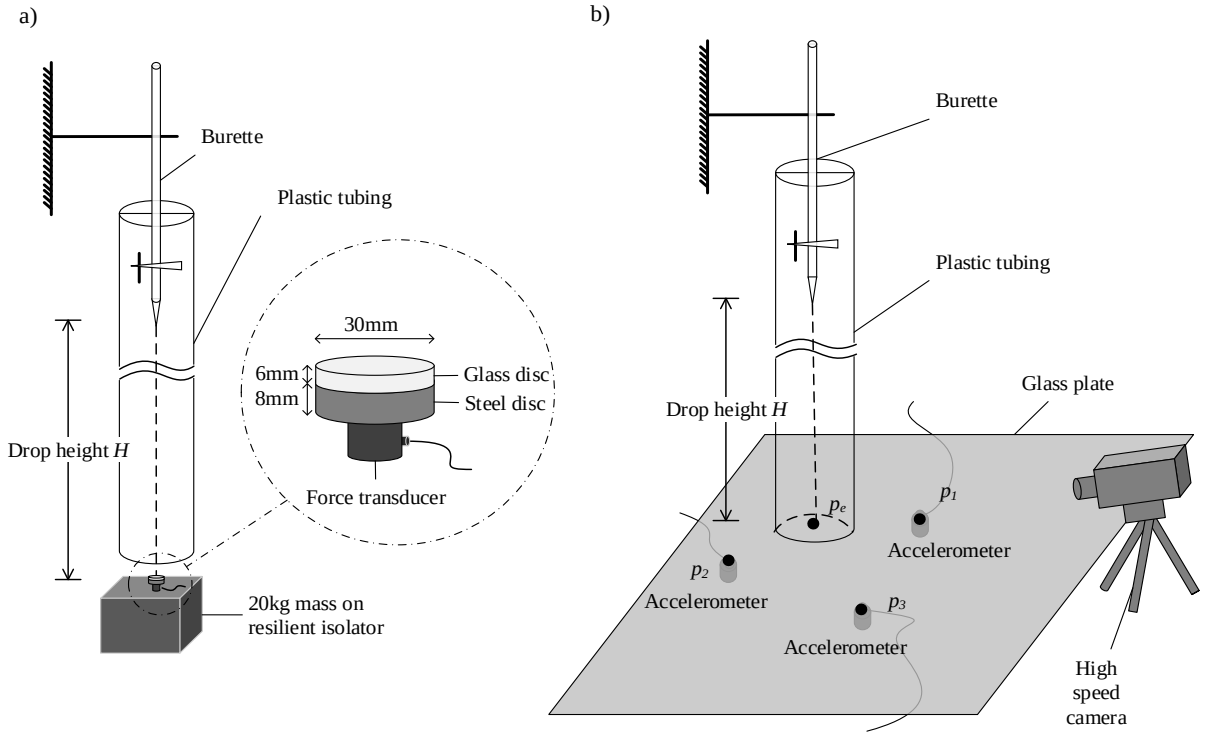
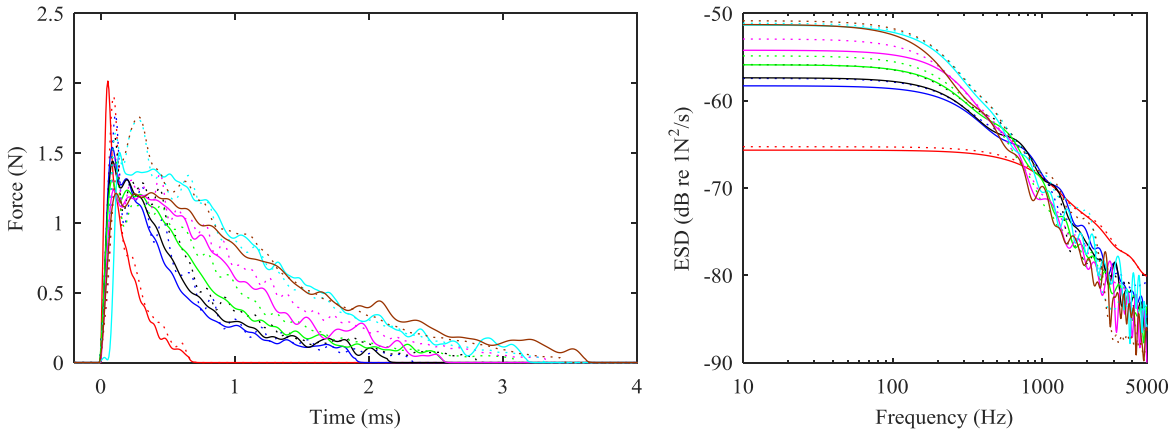


Figure 2. Experimental test rig: (a) force transducer disc, (b) glass plate used for wavelet deconvolution.

2.3 Results

Fig. 3 shows the initial impact force in the time and frequency domains to allow comparison of the wavelet deconvolution method and force transducer. All of the curves are carried out by zero padding the time signal before and after the initial impact. With a water layer, there are differences between the force transducer and wavelet approach in terms of the peak force and pulse width in the time domain but these only result in differences less than 3 dB between 10 and 2k Hz in the frequency domain. The differences between the force transducer and wavelet approach are more apparent with deeper water depths. Close agreement between the force transducer and wavelet deconvolution indicates that the latter could be used to overcome any errors due to the modal response of the force transducer-disc system and the effect of artificially constraining a water layer on the 30 mm disc. Hence the wavelet approach can now be used to assess impacts of drops on shallow water layers where forces are applied after the initial impact.



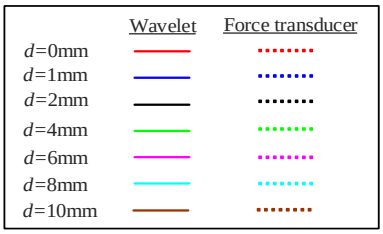


Figure 3. Measured force from the initial impact using the wavelet approach (solid line) and force transducer (dotted line). (a) time dependent force and (b) ESD for 4.5 mm drops with velocity 8.2 m/s impacting the dry glass surface (d=0 mm) and different water layer depths on the glass from d=1 mm to d=10 mm.

Fig. 4a shows the time domain impact force determined using wavelet deconvolution. For a dry surface, the estimated time-dependent force increases rapidly in the first 0.1ms, and decays within 1ms. For shallow water layers the peak force is reduced and the pulse width broadens compared to the dry surface.

Fig. 4b shows the energy density spectrum for the initial impact and features which occur after initial impact. With a shallow water layer, the force applied by the initial impact tends to increase below 200 Hz. In addition, forces applied by features such as the crater, crown, jet, vortex ring tend to increase with increasing water layer depth. As shown in Fig. 4b, the energy applied by these features is highest below 100 Hz.

Fig. 4c shows the distinct features relating to the splash, specifically the crown formation. During the formation of the raised crown-like perimeter after the initial impact, a negative force occurs as the water moves upwards, and drops detach from the tines around the perimeter of the crown (see Fig. 4c). The crown diameters are ≈31 mm for the 4.5 mm drops with impact velocity 8.2m/s.

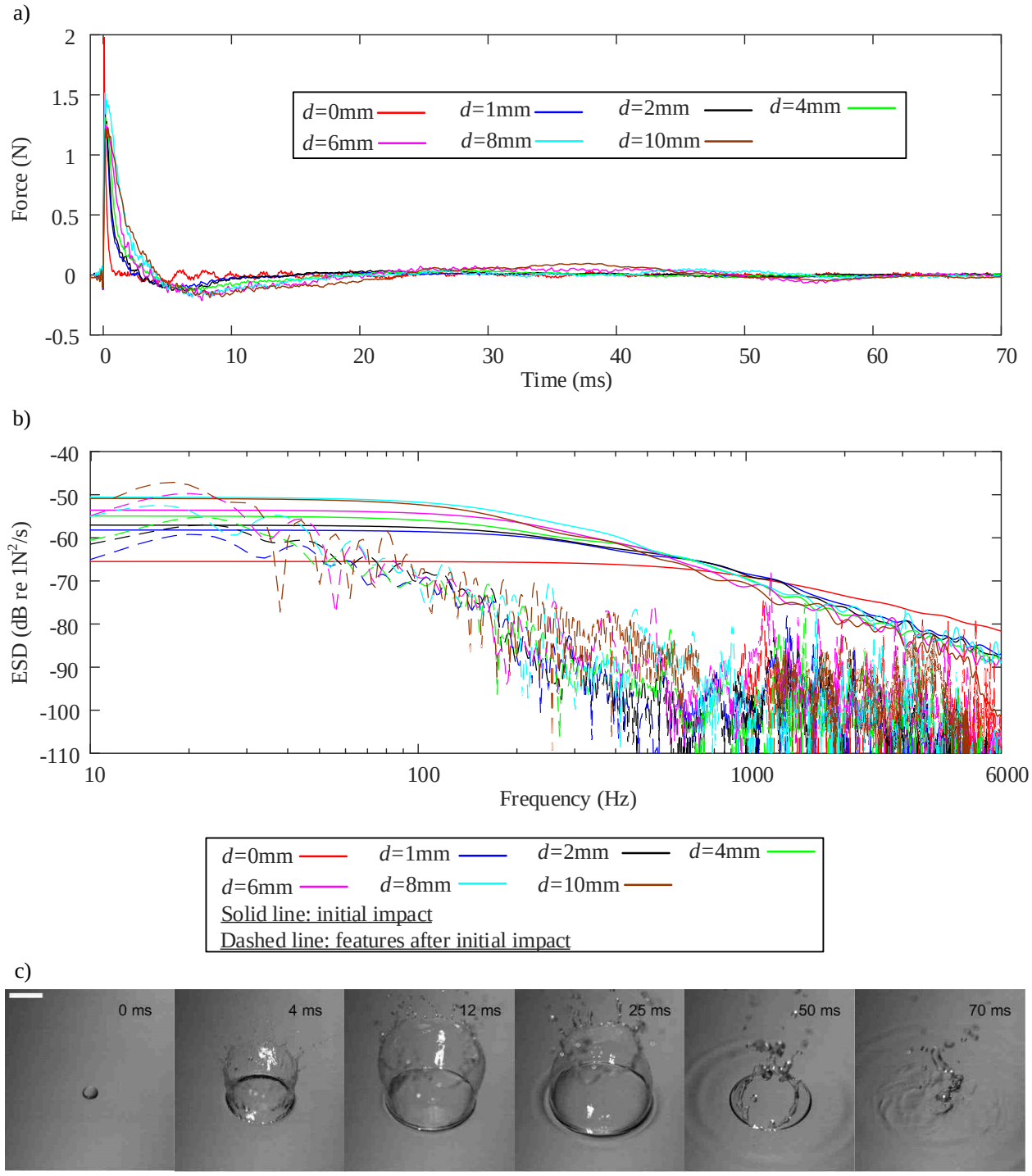


Figure 4. Impact from a 4.5 mm drop with a drop velocity of 8.2 m/s: (a) Force measurements in the time domain using the wavelet approach with different water layer depths on the glass ranging from d=1 to 10 mm (average of ten drops), (b) Energy Spectral Density for the initial impact and features after the initial impact, (c) High-speed camera images of a single example of a 4.5 mm drop impact on a water layer depth of 1 mm.

3 Conclusions

Wavelet deconvolution has been used to determine the force applied by a liquid water drop impact onto a dry glass plate and the same plate with shallow water layers. For the initial impact force there is agreement between measurements with the force transducer and wavelet deconvolution. However, only the latter approach is able to measure forces that naturally occur after the initial impact with water layers. With a shallow water layer, the force applied by the initial impact tends to increase below 200 Hz. In addition, forces applied by features such as the crater, crown, jet, vortex ring tend to increase with increasing water layer depth.

Acknowledgment

The authors are very grateful to Dr Gary Seiffert for all his help with designing and building the experimental set-up in the ARU laboratory.

References

1. M.A. Nearing, J.M. Bradford, R.D. Holtz, *Measurement of force vs. time relations for waterdrop impact.* Soil Sci. Soc. Am. J., (1986). **50**(6): p. 1532-1536.
2. M.A. Nearing, and J.M. Bradford, *Relationships between waterdrop properties and forces of impact.* Soil Sci. Soc. Am. J., (1987). **51**(2): p. 425-430.
3. A.S. Grinspan, and R. Gnanamoorthy, *Impact force of low velocity liquid droplets measured using piezoelectric PVDF film.* Colloids Surf. A (2010) **356**(1): p. 162-168.
4. D. Soto, A.B. De Lariviere, X. Boutillon, C. Clanet, D. Quéré, *The force of impacting rain.* Soft matter (2014). **10**(27): p. 4929-4934.
5. J. Li, B. Zhang, P. Guo, Q. Lv, *Impact force of a low speed water droplet colliding on a solid surface.* J. Appl. Phys., (2014). **116**: p. 214903.
6. Y. Yu, and C. Hopkins, *Experimental determination of forces applied by liquid water drops at high drop velocities impacting a glass plate with and without a shallow water layer using wavelet deconvolution.* Experiments in Fluids, 2018. **59**(5): p. 84.
7. J.F. Doyle, *A wavelet deconvolution method for impact force identification.* Exp. Mech., (1997). **37**(4): p. 403-408.
8. S.V. Vaseghi, *Advanced signal processing and digital noise reduction.* 2013, Springer-Verlag.
9. C. Chang, and C.T. Sun, *Determining transverse impact force on a composite laminate by signal deconvolution.* Experimental Mechanics, (1989). **29**(4): p. 414-419.
10. C.C. Paige, M.A. Saunders, *LSQR: An algorithm for sparse linear equations and sparse least squares.* . ACM Trans. Math. Softw. , (1982) **8**(1): p. 43-71.
11. C. Hopkins, *Sound Insulation*. (2007): Elsevier / Butterworth-Heinemann.

Localisation, characterisation and Identification of localised nonlinearity in structural dynamics using base excitation frequency response functions

J. Taghipour[1], H. Haddad Khodaparast[1], M.I. Friswell[1], H. Jalali[1], H. Madinei[1], X. Wang[2]
[1]Engineering Central, College of Engineering, Bay Campus, Swansea University, Swansea UK
e-mail: **h.haddadkhodaparast@swansea.ac.uk**

[2] Bristol University, Department of Mechanical Engineering, Queen's Building, University Walk, Clifton BS8 1TR, Bristol, UK

Abstract
Identification of structural nonlinearities has been of great interest over recent decades. In addition, due to high cost and time requirements, it is not practical to have complete experimental measurements. This study is initially focused on the localisation of structural nonlinearities using an approach based on spatially incomplete experimental frequency domain data from a structural vibration test. A cantilever beam with a nonlinear restoring force is considered under stepped-sine base excitation. An updated linear finite element model and the Craig-Bampton reduction method is used to obtain the reduced nonlinear forces (RNFs) in the measured region, leading to the location decision for nonlinear elements. Then, the Equivalent Dynamic Stiffness Mapping technique is used for characterization and mathematical modelling of the unknown nonlinearities. This technique utilizes the ratio of internal forces and the displacement response of the unknown elements (F/X) in the frequency domain as the Equivalent Dynamic Stiffness.

Key words: Nonlinear structural dynamics, Identification, Frequency response function, Finite element model updating, Equivalent Dynamic Stiffness Mapping, Base excitation.

1 Introduction

Nonlinear behaviour is very likely to occur in most practical structures due to the effects of material properties, structural joints and boundary conditions. In many cases, the nonlinearity of the structure is not small enough to be approximated as a linear structure. Therefore, nonlinear modal analysis has to be applied in order to localize, identify, and characterize the nonlinearities of the structure.

Nonlinear elements in practical engineering systems are often considered to be localized, and mostly the localization of such nonlinearities has to be performed before a parametric study in the nonlinear system identification process. There has been a wide range of studies in the literature focusing on location, identification and characterization of the nonlinear elements. One may find comprehensive reviews of system identification approaches in [1-4]. The following provides a brief literature review of localization and system identification methods for nonlinear dynamical structures.

To identify the position of the localized nonlinearities, methods are usually categorized in two groups. The first includes the methods which need complete coordinate measurements [5,6] and the second group are applicable with incomplete spatial measurements [7].

The force-state mapping method was used by Al-Hadid and Wright [5] to identify the nonlinearity of single- and multi-degree-of-freedom nonlinear systems. They presented an extension of force-state mapping to the location of nonlinear elements in a lumped-parameter system. Lin and Ewins [6] developed an approach to detect the location of a localized stiffness nonlinearity using a correlated

analytical model with measured vibration test data. It requires the data at no more than one mode with no need for complete coordinates of measurement. Wang et al. [7] presented a method for localization of the localized nonlinear elements in structural dynamics using frequency response data measured at incomplete coordinates from the vibration test.

The literature has an extensive range of identification approaches such as the force-state mapping technique, the restoring force surface method, the Hilbert transform, Bayesian system identification, Volterra series approximation, and the Equivalent Dynamic Stiffness Mapping technique [8-20]. Some methods assume the type of the nonlinearity is pre-known, and others don't rely on this assumption. Kerschen et al. [12] investigated the performance of the restoring force surface method in identifying nonlinear structural elements. In this regard, they considered the vibrations of a clamped beam with two different types of nonlinearities. Their method requires the displacement, velocity, acceleration and force of all degrees of freedom to be measured in the time domain. Feldman [13] recommended a nonparametric technique for identification of nonlinear elastic force functions based on the Hilbert transform. The method presented by Feldman does not require a priori information about the system structure or its parameters. Worden and Hensman [15] surveyed the benefits and limitations of using the Bayesian approach for identification of nonlinear structural systems. This approach is not limited to any assumption regarding the type and parameters of the system nonlinearity. Using a combination of time and frequency domain techniques, Haroon et al. [19] presented a method to identify nonlinear systems in the absence of input measurements. The Equivalent Dynamic Stiffness Mapping technique was proposed by Wang and Zheng [20] for identification of nonlinear structural elements in dynamical systems using steady-state primary harmonic frequency response functions (FRF). There is no need for the type and parameters of the system nonlinearity to be pre-known in this method, however having knowledge of the type of nonlinear element leads to a better parameter estimation and identification of the system.

In this study, a numerical simulation is used to examine the performance of the localization procedure introduced by Wang et al. [7]. However, because base excitation is used in this study instead of force, we introduce a method to evaluate the equivalent force. For this purpose, the assumed mode method and the complex averaging technique are used to obtain the response of the system under base excitation and the finite element method is used to estimate the equivalent force due to base excitation. After detecting the location of the nonlinear elements, the next step is to identify the nonlinearity of the system using the EDSM technique recommended by Wang and Zheng [17]. Finally, the results of the simulation are discussed and the conclusions of the study are made.

2 Localization and Identification

The equation of motion of an Euler-Bernoulli beam, subject to base excitation, is considered as

$$\mathbf{M}\ddot{\mathbf{z}} + \mathbf{C}\dot{\mathbf{z}} + \mathbf{K}\mathbf{z} + \boldsymbol{f}_{in}^{*}(\mathbf{z}, \dot{\mathbf{z}}) = 0, \tag{1}$$

where $\mathbf{M}, \mathbf{K}, \mathbf{C}$ denote the mass, stiffness, and damping matrices, respectively. $\mathbf{z}(t)$ is the vector of displacement, and $\dot{\mathbf{z}}, \ddot{\mathbf{z}}$ are its first and second time-derivatives, respectively. $\boldsymbol{f}_{in}^{*}(\mathbf{z}, \dot{\mathbf{z}})$ denotes the internal nonlinear force of the system excited by the base excitation. Replacing $\mathbf{z}(t)$ by relative displacement $\mathbf{w} = \mathbf{z} - z_0$, where z_0 denotes the base movement, the equation of motion of the system can be rewritten as

$$\mathbf{M}\ddot{\mathbf{w}} + \mathbf{C}\dot{\mathbf{w}} + \mathbf{K}\mathbf{w} + \boldsymbol{f}_{in}(\mathbf{w}, \dot{\mathbf{w}}) = \boldsymbol{f}_{b}(t), \tag{2}$$

where $\boldsymbol{f}_{b}(t)$ is the equivalent force vector due to base excitation.

The problem here is to detect the exact location of the localized nonlinear elements of the system, and then identify the nonlinearity. In the following paragraphs, the localization process and the Equivalent Dynamic Stiffness Mapping Technique for identification of the nonlinear elements are briefly explained.

In this study, the localization procedure introduced by Wang et al. [7] is developed for vibration tests with base excitation. To use this method, experimental data from two vibration tests is needed. One is a low-

amplitude excitation test to measure the response of the underlying linear system, and for the second test the excitation amplitude should be considered high enough to ensure that the system responds with nonlinear behaviour. The localisation method described in [7] does not require measurement at all coordinates.

For this purpose, displacement (or acceleration) and forces of the system need to be measured for two tests with low and high amplitude excitation, respectively, providing the response of the underlying linear and nonlinear systems. However, this measurement doesn't need to be spatially complete. Therefore, the system is separated into measured and unmeasured regions:

$$\mathbf{w} = \begin{Bmatrix} \mathbf{w}_m \\ \mathbf{w}_u \end{Bmatrix}, \tag{3}$$

where the indices m, u represent the measured and unmeasured DOFs, respectively.

Base excitation is the excitation method used in this study. The external force applied to the system is not directly measured in base excitation tests. Hence, the external force vector calculation step precedes the localization and identification processes in this study. Consequently, the whole identification process used in this study is described in three steps as below:

I. ***Updating the linear finite element model***:
Experimental data obtained from the low-amplitude test is used to update the linear finite element model of the system using well-developed updating methods [21-22]. The updated linear FE model is used for both localization and identification of nonlinear elements, described later in this section.

II. ***Finding the equivalent external force vector resulting from the base excitation***:
There have been approaches proposed to find the equivalent force of the base excitation. In this paper, the equivalent force vector of base excitation may be calculated as [23]:

$$\boldsymbol{f}_b(t) = -\ddot{z}_0[\mathbf{M}]\{\mathbf{g}\}, \tag{4}$$

where $\ddot{z}_0$ is the base acceleration and $g_i = 1$ if z_i and z_0 are in the same direction.
Here, in this study, by applying the Galerkin approach to a cantilever Euler-Bernoulli beam, the equivalent force for a single element of the beam is obtained as

$$\boldsymbol{f}_b^e = -\rho A\ddot{z}_0 \int_0^{l_e} \varphi_i(x)dx - \ddot{z}_0 \sum_0^{N_a} m_a\varphi_i(x_a), \tag{5}$$

where ρA is the mass per length of the beam, l_e is the length of a beam element, and $\varphi_i(x)$ denotes for the shape function in Galerkin method. Here it is assumed that N_a point masses with the mass of m_a are located at x_a along the beam.

III. ***Detecting the location of the localized nonlinearities*** [7]:
a) A criterion is defined to evaluate the difference between the underlying linear and nonlinear responses of the system. Accordingly, data selection is carried out to select the measured data for frequencies at which the criterion is satisfied.
b) As the measurement is not spatially complete, the updated linear model is separated into measured and unmeasured regions. Then, the Craig-Bampton reduction method is used to project the unmeasured DOFs onto the measured region. As a result, the reduced nonlinear force (RNF) is calculated as a summation of measured nonlinear forces and the projection of unmeasured nonlinear forces onto the measured region.

$$\mathbf{F}_{reduced} = \mathbf{F}_{eq_H} - \left(\overline{\mathbf{D}}_{mm} - \overline{\mathbf{D}}_{mk}\overline{\mathbf{D}}_{kk}^{-1}\overline{\mathbf{D}}_{km}\right)\mathbf{W}_m, \tag{6}$$

where $\overline{\mathbf{D}}_{mm}, \overline{\mathbf{D}}_{mk}, \overline{\mathbf{D}}_{kk}, \overline{\mathbf{D}}_{km}$ are dynamic stiffness sub-matrices [7]. The index of the reduced nonlinear force is calculated as a summation of the RNFs at the measured DOFs over a range of measured frequencies,

$$\mathbf{I}_{\mathbf{F}^*_{reduced}} = \sum_{\omega_i} |\mathbf{F}^*_{reduced}(\omega_i)|, \tag{7}$$

The suspect region for the location of the nonlinearity is determined using the resulting RNFs, the index of RNFs, and the phase of RNFs. Consequently, the preliminary decision for the location of nonlinear elements is made.

c) Finally, the result of the location is verified by comparing the nonlinear forces for the suspected region with the reduced nonlinear forces for the measured region.

IV. ***Identifying the nonlinear element using the Equivalent Dynamic Stiffness Mapping technique*** [17]:

The nonlinear dynamical system described by Eq. (1) is considered. Using the Fourier transform, the nonlinear internal force is obtained in the frequency domain as

$$\mathbf{F}_N = \mathbf{F}_{ex} - (\mathbf{K} + j\omega\mathbf{C} - \omega^2\mathbf{M})\mathbf{W}, \tag{8}$$

a) The nonlinear internal force $\mathbf{F}_N$ may be composed of both nonlinear damping and stiffness

$$\mathbf{F}_N = \left(\mathbf{K}_{eq} + j\omega\mathbf{C}_{eq}\right)\mathbf{W}, \tag{9}$$

where $\mathbf{K}_{eq}$ and $\mathbf{C}_{eq}$ are, respectively, the equivalent stiffness and damping elements of the system.

b) Define the Equivalent Dynamic Stiffness as the ratio of the nonlinear internal force to the displacement response of the system in the frequency domain,

$$\mathbf{D}_{stiff}(\omega, \mathbf{W}) = \frac{\mathbf{F}_N}{\mathbf{W}}, \tag{10}$$

The equivalent dynamic stiffness and damping is obtained as,

$$K_{eq} = \Re\left(D_{stiff}\right), \qquad C_{eq} = \frac{\Im\left(D_{stiff}\right)}{\omega}. \tag{11}$$

In the following section, an example of a cantilever beam is simulated numerically in MATLAB. The results of the numerical simulation are provided in Section 3.

3 Theoretical Simulation

The stainless-steel cantilever beam shown in Fig. 1 has a length of 0.30 m, a width of 30 mm, and a thickness of 1.5 mm and is considered for numerical simulation. The modulus of elasticity and the density of the beam are taken as $E = 205$ GPa and $\rho = 7800\ \mathrm{kg/m^3}$, respectively. The beam is assumed to have a damping coefficient per length of the beam as follows

$$\gamma = 0.2\,\frac{\mathrm{kg}}{\mathrm{m.\,s}}. \tag{12}$$

In order to consider the effect of the accelerometers' masses on the dynamics of the beam, point masses $p_m = \{6, 6, 6, 8\}$ g are located at positions $x_m = \left\{\frac{l}{6}, \frac{3l}{6}, \frac{5l}{6}, l\right\}$, respectively, where l is the beam length. The beam is attached to a grounded (to the base plate) nonlinear spring creating the nonlinear restoring force

$$F_N = k_l w\left(\frac{2l}{3}, t\right) + k_N w\left(\frac{2l}{3}, t\right)^3, \tag{13}$$

where

$$k_l = 20\,\frac{\mathrm{N}}{\mathrm{m}}, \qquad k_N = 1 \times 10^5\,\frac{\mathrm{N}}{\mathrm{m^3}}. \tag{14}$$

and $w\left(\frac{2l}{3}, t\right)$ denotes the deflection of the beam at the distance of $\frac{2l}{3}$ from the clamped end.

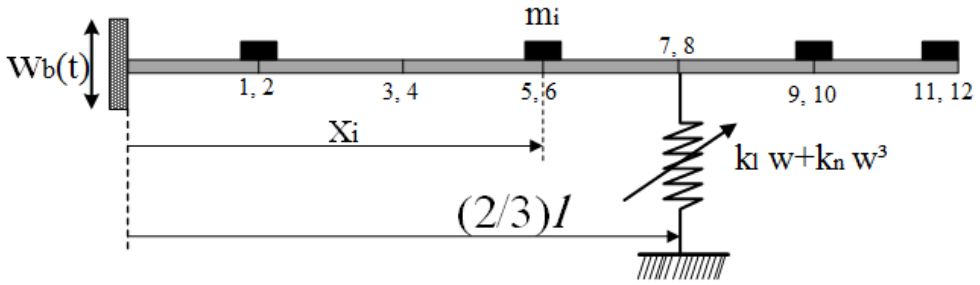


Figure 1: Base excitation of a cantilever beam attached to a grounded nonlinear spring at the distance of $\frac{2l}{3}$ from the clamped end.

Applying the assumed-mode method [24] and the semi-analytical complex-averaging technique [25] to the Euler-Bernoulli equation of the beam, the dynamics of the above-described cantilever beam has been studied under base excitation with constant acceleration. The amplitude of base acceleration is set to constant values of 0.025 and $2.5\ \mathrm{m/s^2}$ for low and high-amplitude tests respectively. For this purpose, three modes have been considered in the assumed-mode method in order to discretize the equation of motion of the beam. Then, complex-averaging and Arc-length continuation are applied to the discretized equations in order to obtain the steady state response of the system for the primary harmonic (dynamics of the system is dominated by the primary harmonic). The responses at DOFs 1, 5, and 9 (having distances of 5, 15, and 25 cm from the clamped end of the beam) are measured.

3.1 Results and Discussion

Figure 2 illustrates the measured frequency domain steady state responses of the beam at the three measured points, respectively. In fact, applying low amplitude base excitation led to the underlying linear system to be excited, as shown in Fig. 2 by blue dash-dot line. The high amplitude stepped-sine excitation resulted in the nonlinear behaviour of the system, shown by green triangles (stable solution) and red crosses (unstable solution) in Fig. 2.

The localisation process was applied to the simulated data and resulted in the reduced nonlinear forces of the three measured DOFs, shown in Fig. 3(a). Based on the difference between the linear and nonlinear responses of the beam, data within the frequency range of [11.5-14.75] (Hz) has been selected for further analysis.

Figure 4 shows the index of the RNFs of the measured DOFs. The magnitude of the indices of the three measured DOFs indicates that the nonlinearity of the system may be closer to DOF 5 and 9. However, there is a possibility that more than one nonlinearity exists.

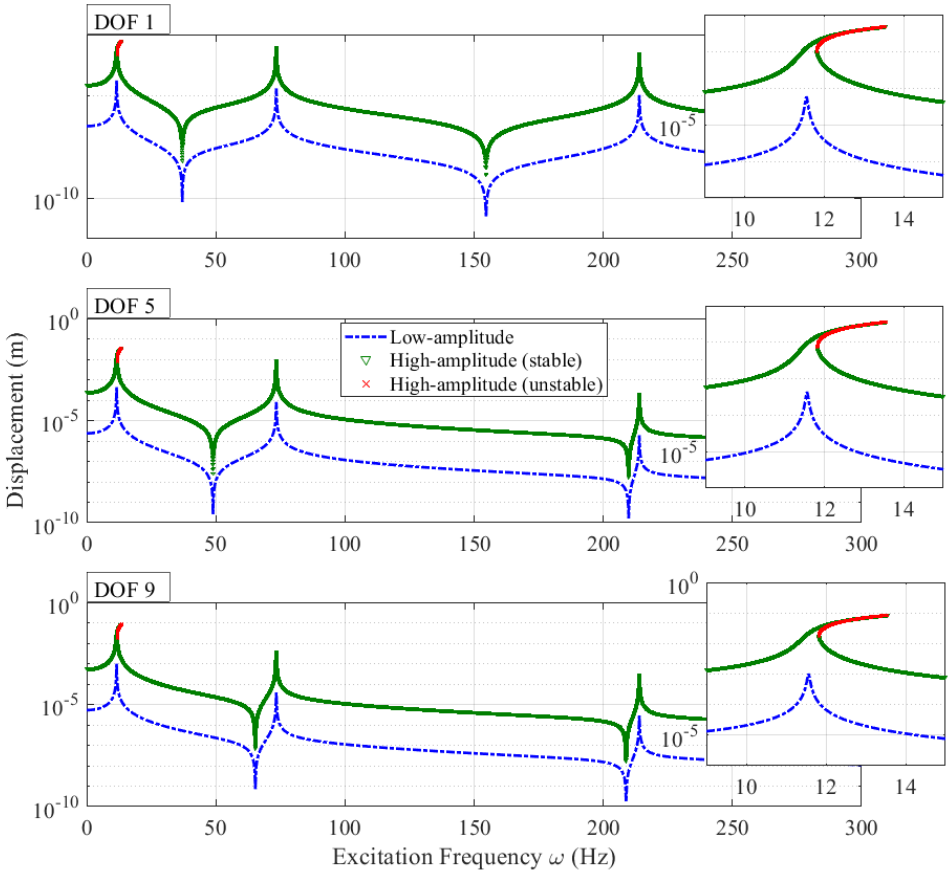


Figure 2: Response amplitude in terms of excitation frequency at DOFs 1, 5, and 9; blue dash-dot line: linear response (low amplitude excitation), green triangle: stable nonlinear response (high-amplitude excitation), red cross: unstable nonlinear response.

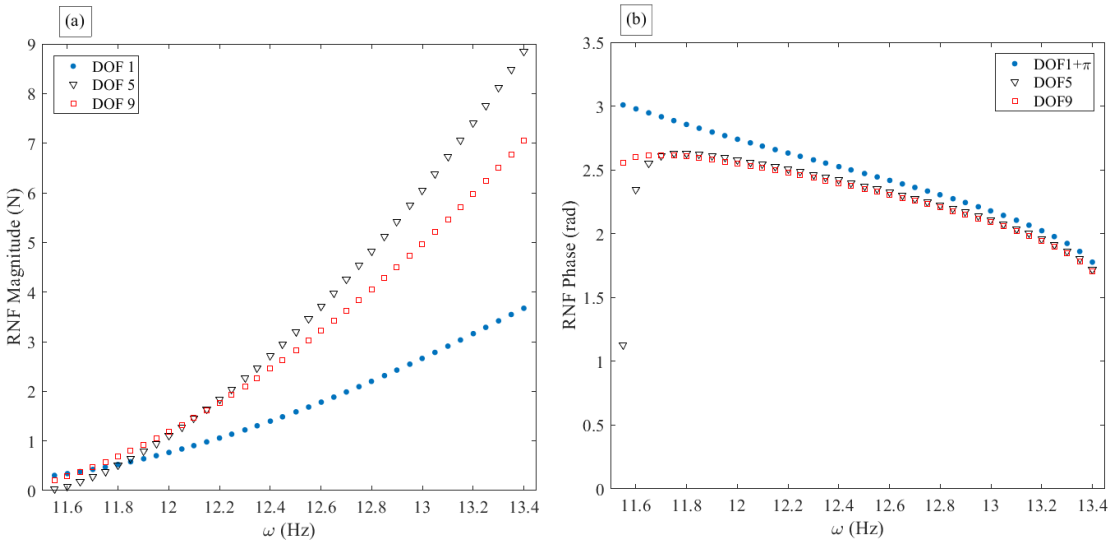


Figure 3: (a) Magnitude and (b) phase of the reduced nonlinear forces at the measured DOFs of the cantilever beam.

Looking at the phase diagram of the RNFs, one can see the same phase at DOFs 5 and 9, and π rad of phase difference at DOF 1 with respect to DOFs 5 and 9. Hence, it can be concluded that all these RNFs at DOFs 1, 5, and 9 arise because of a nonlinearity at an unmeasured DOF. Therefore, DOFs 1, 5, and 9 are discarded from the suspected regions. The RNFs are calculated at DOFs 3, 7, and 11, as suspected regions, using the linear constraint modes of the Craig-Bampton reduction method [7]. The indices of the calculated RNFs, shown in Fig. 6, indicates the existence of a nonlinear element at DOF-7.

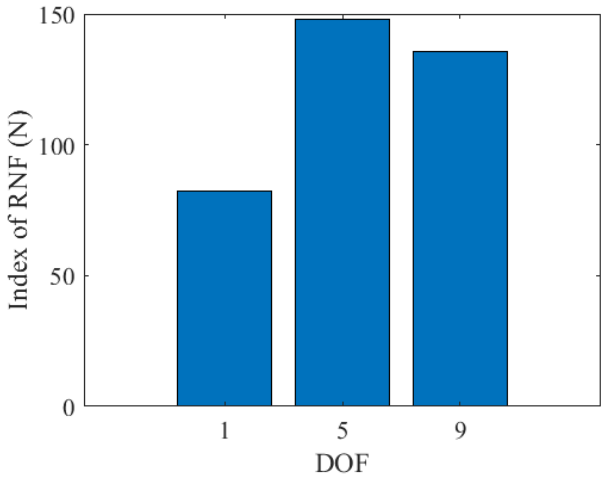


Figure 4: Indices of the reduced nonlinear forces at measured DOFs 1, 5, and 9.

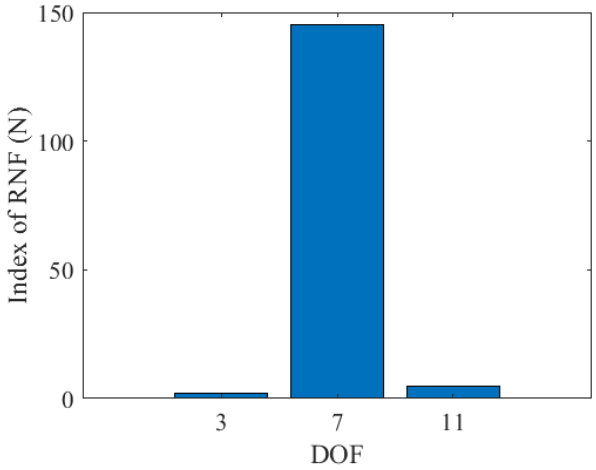


Figure 5: Indices of the RNFs in the suspect regions.

Figure 6 illustrates the indices of the RNFs at DOFs 1, 5, 7, and 9 with direct measurement at DOF7. This plot shows that the nonlinear element is truly located at DOF7, which is in accordance with the result of the preliminary location decision.

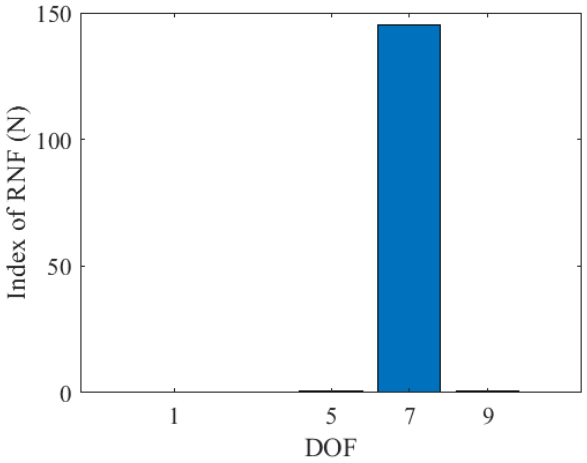


Figure 6: Indices of reduced nonlinear force including direct measurement at DOF7.

Subsequent to defining the exact location of nonlinearity, identification of the nonlinear element is carried out using the equivalent dynamic stiffness mapping method. To this end, direct measured data at the location/s of the nonlinear element is needed. However, in many practical engineering cases, direct measurement at some points such as joints is not possible or results in damaging the structure. Therefore, in this study, the aim is to find an identification approach with no need for direct measurement at the location of the nonlinearity. For this purpose, System Equivalent Reduction Expansion Process (SEREP) is used to expand the measured data to all required DOFs [21]. After expansion of the data, nonlinear identification of the system is carried out according to the identification process described in Section 2. Fig. 7(a) shows the 3D plot of the real part of the equivalent dynamic stiffness in terms of the excitation frequency and the amplitude of vibration at the location of the nonlinearity. In Fig. 7(b), the real part of the equivalent dynamic stiffness is shown in terms of the amplitude of the system.

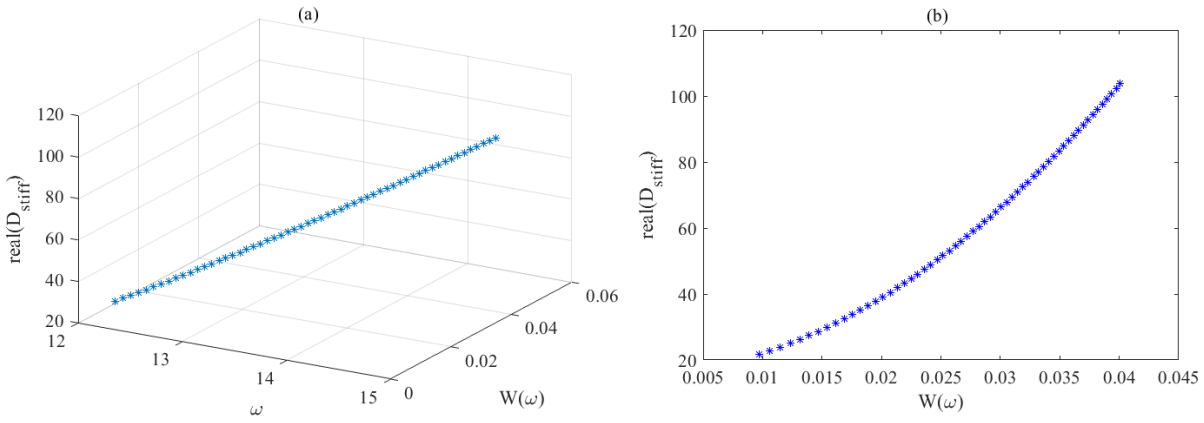


Figure 7- Mapping of the real part of the EDS in terms of excitation frequency and response amplitude at the location of the nonlinearity; (b) the equivalent stiffness is estimated by curve-fitting the real part of the EDS as a function of response amplitude.

In the results of the identification, in case of the nonlinear stiffness,

$$f_N = k_l W + k_n W^3, \tag{15}$$

the real part of the equivalent dynamic stiffness gives the nonlinear stiffness as [20],

$$real\left(D_{stiff}\right) = K_{eq} = k_l + \frac{3}{4} k_n W^2. \tag{16}$$

Figure 7 illustrates both linear and cubic nonlinear part of the spring attached to the beam.

4 Conclusion and future work

The location detection and identification of localised nonlinear structural elements of a base-excited dynamical system was carried out using an approach based on spatially incomplete experimental frequency domain data. Base-excited vibration of a cantilever beam attached to a grounded nonlinear spring near the tip has been numerically simulated and the results of the simulation were used to locate the nonlinear elements of the system using the frequency domain data. The results illustrate the acceptable performance of the localisation method used in this study. The identification method used in this study shows that the method is capable of identifying type of nonlinearity, i.e. cubic nonlinearity. However, there are errors in identified parameters of the model and further investigation is required to investigate this.

Also, an experimental set-up, shown in Fig. 8, is considered for experimental study. In this set-up, a stainless-steel cantilever beam is selected for the vibration tests. The beam is mounted on a shaker bed, and divided into six equal longitudinal elements. Figure 9 illustrates the finite element model of the experimental set-up. The acceleration of the base and the beam is measured using four accelerometers, one on the base and three on the beam, as shown in Figs. 8 and 9. Two permanent magnets, attached to the tip of the beam, along with two electromagnets placed on two sides of the permanent magnets, create and apply the nonlinear restoring force to the beam. Figure 10 shows the linear and nonlinear frequency response of the beam resulted from low and high amplitude tests, respectively. The results of the analysis of the experimental data will be presented at the conference.

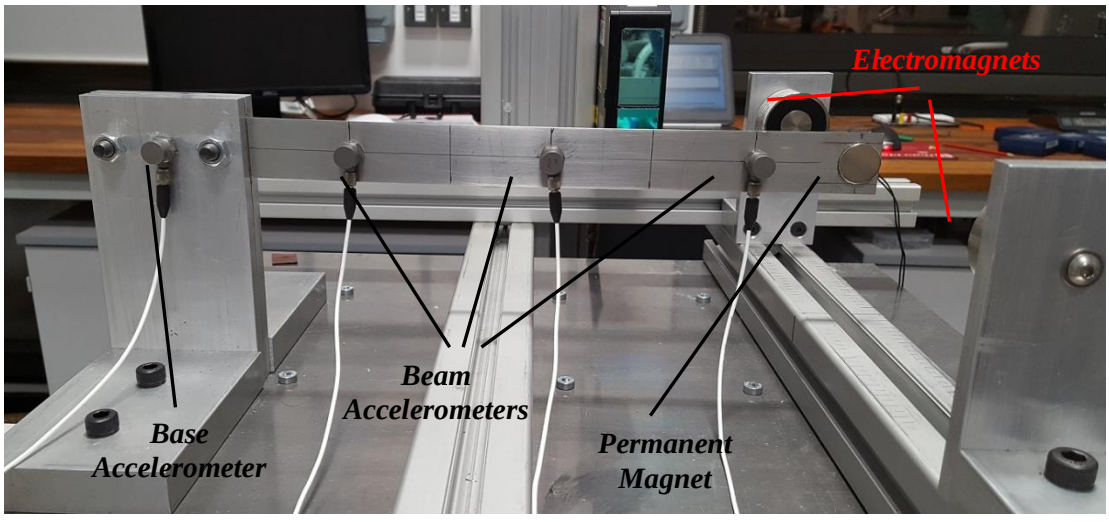


Figure 8: Experimental set-up for the base excitation vibration test of a cantilever beam.

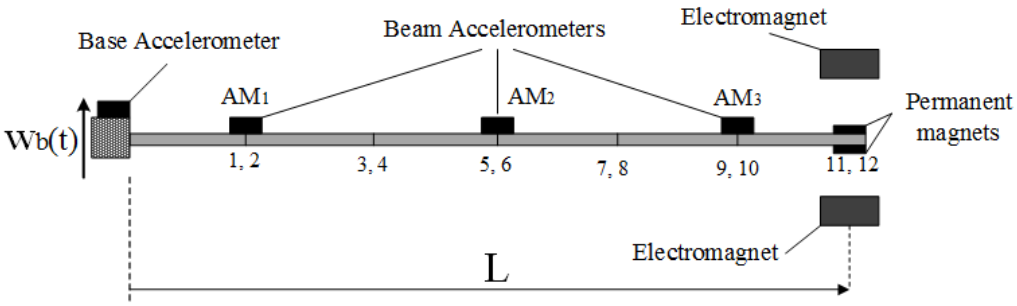


Figure 9: Finite element model of the experimental set-up.

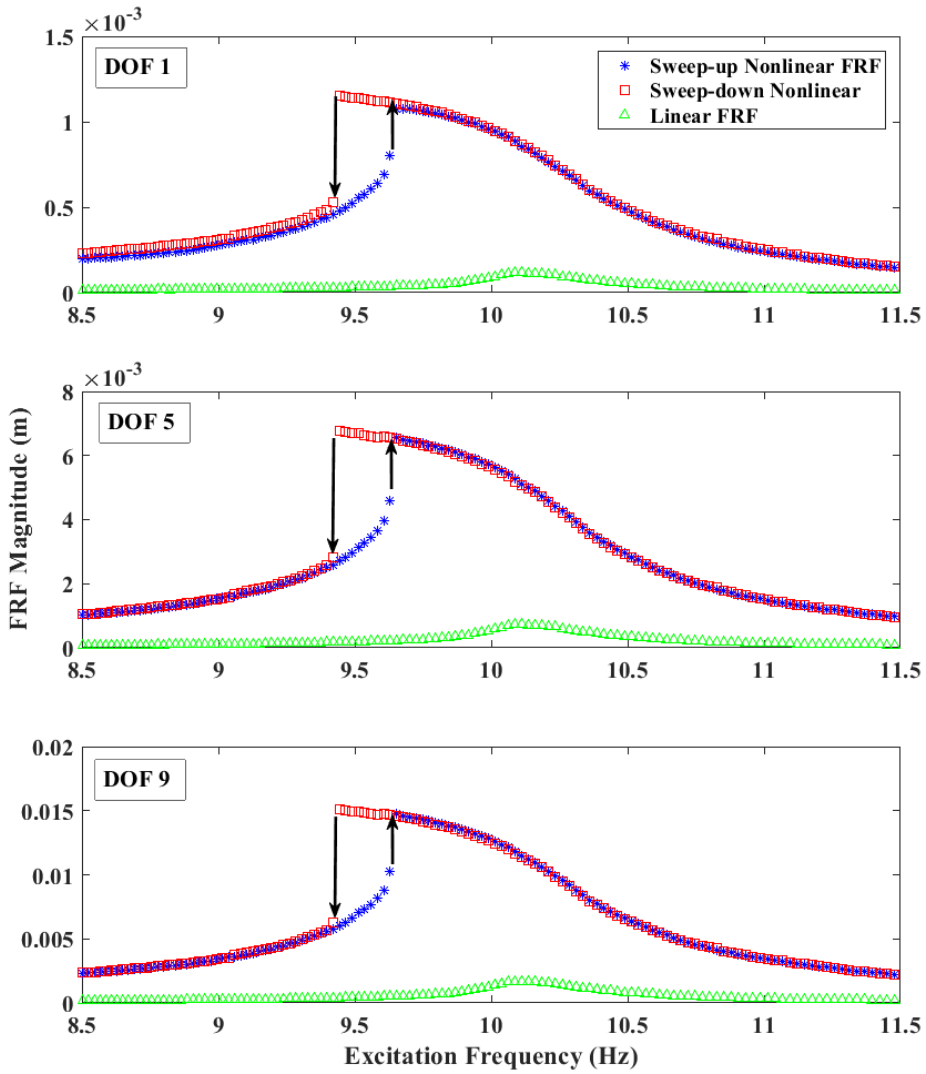


Figure 10- Linear and nonlinear frequency response of the beam resulted from low and high-amplitude test.

Acknowledgement

This research is funded by the Engineering and Physical Sciences Research Council through Grant no. EP/P01271X/1.

References

[1] K. Worden, G. Tomlinson, *Nonlinearity in Structural Dynamics: Detection, Identification and Modelling*, Philadelphia, IOP Publishing Ltd., Bristol (2001).
[2] G. Kerschen, K. Worden, A.F. Vakakis, J. Golinval, *Past, present and future of nonlinear system identification in structural dynamics*, Mechanical Systems and Signal Processing, Vol. 20, No. 3, (2006), pp. 505-592.
[3] J.P. Noël, G. Kerschen, *Nonlinear system identification in structural dynamics: 10 more years of progress*, Mechanical Systems and Signal Processing, Vol. 83, (2017), pp. 2-35.
[4] C.M. Cheng, Z.K. Peng, W.M. Zhang, G. Meng , *Volterra-series-based nonlinear system modeling and its engineering applications: A state-of-the-art review*, Mechanical Systems and Signal Processing, Vol. 87, (2017), pp. 340-364.
[5] M. Ajjan Al-Hadid, J.R. Wright, *Developments in the force-state mapping technique for non-linear systems and the extension to the location of non-linear elements in a lumped-parameter system*, Mechanical Systems and Signal Processing, Vol. 3, No. 3, (1989), pp. 269-290.
[6] R.M. Lin, D.J. Ewins, *Location of localised stiffness non-linearity using measured modal data*, Mechanical Systems and Signal Processing, Vol. 9, No. 3, (1995), pp. 329-339.
[7] X. Wang, H.H. Khodaparast, A.D. Shaw, M.I. Friswell, G. Zheng, *Localisation of local nonlinearities in structural dynamics using spatially incomplete measured data*, Mechanical Systems and Signal Processing, Vol. 99, (2018), pp. 364-383.
[8] A. Carrella, D.J. Ewins, *Identifying and quantifying structural nonlinearities in engineering applications from measured frequency response functions*, Mechanical Systems and Signal Processing, Vol. 25, No. 3, (2011), pp. 1011-1027.
[9] K. Yasuda, S. Kawamura, K. Watanabe, *Identification of Nonlinear Multi-Degree-of-Freedom Systems : Identification Under Noisy Measurements*, JSME international journal, Ser. 3, Vibration, control engineering, engineering for industry, Vol. 31, No. 3, (1988), pp. 502-509.
[10] E.F. Crawley, A.C. Aubert, *Identification of nonlinear structural elements by force-state mapping*, AIAA Journal, Vol. 24, No. 1, (1986), pp. 155-162.
[11] E.F. Crawley, K.J. O'Donnell, *Force-state mapping identification of nonlinear joints*, AIAA Journal, Vol. 25, No. 7, (1987), pp. 1003-1010.
[12] G. Kerschen, J.C. Golinval, K. Worden, *Theoretical and experimental identifcation of a nonlinear beam*, Journal of Sound and Vibration, Vol. 244, No. 4, (2001), pp. 597-613.
[13] M. Feldman, *Nonparametric identification of asymmetric nonlinear vibration systems with the Hilbert transform*, Journal of Sound and Vibration, Vol. 331, No. 14, (2012), pp. 3386-3396.
[14] M. Feldman, *Hilbert transform methods for nonparametric identification of nonlinear time varying vibration systems*, Mechanical Systems and Signal Processing, Vol. 47, No. 1, (2014), pp. 66-77.
[15] K. Worden, J.J. Hensman, *Parameter estimation and model selection for a class of hysteretic systems using Bayesian inference*, Mechanical Systems and Signal Processing, Vol. 32, (2012), pp. 153-169.
[16] P.L. Green, *Bayesian system identification of a nonlinear dynamical system using a novel variant of Simulated Annealing*, Mechanical Systems and Signal Processing, Vol. 52-53, (2015), pp. 133-146.
[17] A. Ben Abdessalem, N. Dervilis, D. Wagg, K. Worden, *Model selection and parameter estimation in structural dynamics using approximate Bayesian computation*, Mechanical Systems and Signal Processing, Vol. 99, (2018), pp. 306-325.
[18] J. Prawin, A.R.M. Rao, *Nonlinear identification of MDOF systems using Volterra series approximation*. Mechanical Systems and Signal Processing, Vol. 84, (2017), pp. 58-77.

[19] M. Haroon, D.E. Adams, Y.W. Luk, A.A. Ferri, *A time and frequency domain approach for identifying nonlinear mechanical system models in the absence of an input measurement*, Journal of Sound and Vibration, Vol 283, No. 3, (2005), pp. 1137-1155.

[20] X. Wang, G.T. Zheng, *Equivalent Dynamic Stiffness Mapping technique for identifying nonlinear structural elements from frequency response functions*, Mechanical Systems and Signal Processing, Vol. 68-69, (2016), pp. 394-415.

[21] M.I. Friswell, J.E. Mottershead, *Finite Element Model Updating in Structural Dynamics*, Springer Science & Business Media (1995).

[22] J.E. Mottershead, M. Link, M.I. Friswell, *The sensitivity method in finite element model updating: a tutorial*, Mechanical Systems and Signal Processing, Vol. 25, No. 7, (2011), pp. 2275–2296.

[23] D.J. Ewins, *Modal Testing: Theory, Practice.*, Research studies press, Letchworth (1995).

[24] M. Parseh, M. Dardel. M.H. Ghasemi, M.H. Pashaei, *Steady state dynamics of a non-linear beam coupled to a non-linear energy sink,* International Journal of Non-Linear Mechanics, Vol. 79, (2016), 99. 48-65.

[25] J. Taghipour, M. Dardel, *Steady state dynamics and robustness of a harmonically excited essentially nonlinear oscillator coupled with a two-DOF nonlinear energy sink*, Mechanical Systems and Signal Processing, Vol. 62-63, (2015), pp. 164-182.

Random force identification via Kalman filtering on a cantilevered structure

R. Álvarez-Briceño [1], **L. P. R. de Oliveira** [1]
[1] Mechanical Engineering Department, São Carlos School of Engineering, University of São Paulo,
Av. Trabalhador São Carlense, 400, Parque Arnold Schmidt,
São Carlos, São Paulo, CEP 13566-590, Brazil.
e-mail: **leopro@sc.usp.br**

Abstract
Several engineering applications demand in-operation dynamic forces exerted on structural component to be modeled. Although direct input measurements would be the first option to solve this lack, in many instances an appropriate and feasible instrumentation is hard to be accomplished due to reduced space, especial environment conditions, etc. New methods have to be explored to solve instrument limitations. In the field of virtual sensing, augmented-state Kalman Filter (AKF) based techniques have recently been introduced in the field of force estimation. The ability of the AKF for predicting a point force random in time, based only on accelerometer measurements, is evaluated experimentally in the present work. The present experimental approach features a cantilevered structure, instrumented with two pairs of accelerometers, mounted approximately at its mid-length and at its free tip. A force sensor is used to measure the actual input force on the beams free end. Measured and predicted force time histories show a good agreement.

1 Introduction

Shell-and-tube heat exchangers are the most common type of heat exchanger found in industrial processes [1]. These devices are also used in more complex systems, for example, in pressurized water reactors of nuclear power plants, which represent a critical application since a mechanical failure implies significant economical losses, unexpected shut downs, not to mention critical radioactive accidents. In this sense, design engineers must take care not only of thermohydraulic efficiency but also of the structural integrity of the heat exchanger. Flow-induced vibration (FIV) is the most important dynamic issue in the design of heat exchangers. Furthermore, almost half of all shell-and-tube heat exchangers in the industry operate under two-phase flow condition in the shell side [2, 3], which corresponds to a more critical condition for FIV if compared with the single-phase flow case. Therefore, the experimental database that can be obtained on FIV is key to understand the phenomena and develop design guidelines to avoid extreme conditions that may shorten the apparatus lifetime.

In two-phase crossflow conditions, there are four types of vibration mechanisms that may take place in the tube bundle, namely: (i) fluidelastic instability, (ii) vortex shedding, (iii) turbulence-induced excitation and (iv) acoustic resonance, their definitions are detailed in many references [4, 5, 6, 7, 8]. According to Pettigrew et al. [9], fluidelastic instability and turbulence-induced excitation are the most important vibration mechanisms in tube bundles during two-phase crossflow, while periodic shedding and acoustic resonance are unlikely to occur.

Although there are some design guidelines to estimate the vibration amplitude in turbulence-induced vibration [10, 11, 12], the database about this phenomenon is limited if compared to that available for fluidelastic instability mechanism. This is somewhat surprising since the turbulence-induced vibration mechanism in

tube bundles cannot be avoided, and can only be due to the challenges imposed by both, theoretical and experimental approaches, in tackling this problem. Further, this vibration mechanism is a *necessary evil* since it helps to improve heat transfer through the external fluid. On the other hand, turbulence-induced vibration without supervision may generate fretting wear between tubes and fatigue of structural components, thereby shortening heat exchanger lifetime. In this sense, a deeper knowledge on the turbulence-induced vibration mechanism would help in designing tasks, leading to enhanced heat exchanger performance and security. For this, further experimental studies on this vibration mechanism are required, mainly when it comes to identifying the nature of loads acting on such structures. However, an appropriate instrumentation is hard to be accomplished, mainly due to reduced spaces in tube bundles and because typical instruments are hardly liquid resistant.

In recent years, virtual sensing has arisen as a solution for determining forces when direct measurements are not feasible or present important technical challenges. Virtual sensors, based on a previously modeled system, take readings from real physical sensors to calculate the desired outputs by using some process models [13, 14]. Moreover, these readings are used to get the system model continuously updated, thus model imperfections or non considered in-operating modifications are taken into account for every time instant. This feature enables the assessment of uncertain parameters or variabilities within the system [15], which, with the present application in mind, could mean tracking dynamic changes in the tube bundles promoted by the surrounding fluid and flow conditions and flow - induced forces.

Recently, deterministic - stochastic methods have attracted more attention of researchers since these methods can be used to model the noise as stochastic processes and assume that noise is present not only on the measurements, but also on the state variables, which is a feature that set them apart from purely deterministic techniques. Furthermore, they differ from purely stochastic techniques because force values are still considered to be deterministic quantities [16]. In this context, Kalman filtering (KF) [17, 18] based techniques have been introduced in the field of force estimation. This method provides a particularly practical and efficient state estimation algorithm for linear systems which leads to an optimal result with respect to the expected error covariance [19]. In order to do that, the approach adopted by some authors [20, 16, 15, 19] is to implement a coupled state - disturbance - parameter estimator based on a state-augmented Kalman filter (AKF). In other words, the regular states are augmented with the unknown forces in order to estimate them together [16]. Such kind of estimator is needed in order to distinguish whether changes in time history result from inherent system dynamics or external excitation [14].

The AKF algorithm stability and methods to avoid divergence on estimates are currently being discussed [16, 19]. For instance, Naets et al. [19] propose the addition of displacement dummy measurements for all the degrees of freedom (DOF) in order to prevent drift on predictions. Moreover, one of the most important questions to be clarified in this matter is what type of forces can be estimated reasonably via AKF algorithm. In this context, Berg and Keith Miller [20] implemented the AKF algorithm to estimate random wind loads, while Lourens et al. [16] used the method to predict impulse and sine-sweep forces, showing acceptable results in both cases. Naets et al. [15] tested the AKF algorithm for the identification of an impulsive force applied on a beam free-end, showing good results. In this context, it is expected that the flow turbulence delivers a random in time force to the tube, therefore it is worth testing if the AKF-DM algorithm is able to predict this kind of force. Thus, a structure can be immersed in a two-phase flow aiming to estimate flow-induced forces based on its acceleration response.

The present work focuses on checking the validity of the AKF-DM algorithm to estimate a known point force, which is applied at the free end of a cantilever structure. The applied force is random in time, whose prediction represents a new challenge for this kind of approach. As the aim of this study is to validate a concept for turbulence-induced vibration under two-phase flow, the structure is mounted on a heat exchanger mock-up, which mimics the same boundary conditions that the structure will present in the actual test section. Moreover, the structure is designed so that future tests in two-phase flow can be performed. The remainder of this document is organized as such: the next section present the formulation of the Kalman filter and the necessary modifications to grant stability to the process. Next, a description of the test set-up is presented and the system's identification via Experimental Modal Analysis (EMA) is detailed. Finally, the AKF-DM

algorithm is implemented to estimate the input force, then the results are discussed and compared with measured data.

2 Augmented Kalman filter and dummy measurements for force estimation

This section is devoted to define the formulation used in the implementation of the AKF-DM algorithm. First, since the present analysis is performed on an existent physical system, the modeling equations are expressed in terms of the modal space representation. Subsequently, the discrete state space notation is introduced, which is helpful in the KF algorithm definition. After that, some modifications on KF formulation are proposed in order to obtain the AKF algorithm. Finally, the inclusion of displacement dummy measurements in the algorithm is explained and implemented.

2.1 State equations for the mechanical system

Mechanical systems can be formulated in several ways, including those based on experimental results, such as Experimental Modal Analysis (EMA) procedure. After the corresponding tests are performed, and under the assumptions that the system is Linear Time - Invariant (LTI) with proportional damping, related algorithms are used to obtain the system modal matrix $\mathbf{\Psi}$, undamped natural frequencies ω_n, and damping ratios ζ_n. This set of data enables the derivation of a completely defined modal model of the system.

In order to define the system in physical generalized coordinates [1], the following equations can be used to calculate the mass $\mathbf{M}$, stiffness $\mathbf{K}$, and damping $\mathbf{C}$ matrices, respectively [21]:

$$\mathbf{M} = \mathbf{\Psi}^{-T}\mathbf{\Psi}^{-1}, \tag{1}$$

$$\mathbf{K} = \mathbf{\Psi}^{-T}\begin{bmatrix} \ddots & & \\ & \omega_r^2 & \\ & & \ddots \end{bmatrix}\mathbf{\Psi}^{-1}, \tag{2}$$

$$\mathbf{C} = \mathbf{\Psi}^{-T}\begin{bmatrix} \ddots & & \\ & 2\zeta_r\omega_r & \\ & & \ddots \end{bmatrix}\mathbf{\Psi}^{-1}, \tag{3}$$

where r denotes the r-th vibration mode. Matrices $\mathbf{M}$, $\mathbf{C}$ and $\mathbf{K}$ characterize the system in its spatial model defined by the system of second - order differential equations

$$\mathbf{M}\ddot{\xi} + \mathbf{C}\dot{\xi} + \mathbf{K}\xi = \mathbf{b}\mathbf{f} + \mathbf{b_d}\mathbf{f_d}, \tag{4}$$

where ξ is the vector of physical generalized coordinates. The terms $\mathbf{f}$ and $\mathbf{f_d}$ represent the forces and unknown disturbances, which are applied on the system at positions coordinates described by the selection matrices $\mathbf{b}$ and $\mathbf{b_d}$, respectively.

Mechanical systems can also be represented as a system of first order differential equations, which is referred to as state space model [22]. In the same way, for a LTI system, Eq. 4 can be written as:

$$\dot{\mathbf{x}}(t) = \mathbf{A}\mathbf{x}(t) + \mathbf{B}\mathbf{u}(t) + \mathbf{B_1}\mathbf{w}(t), \tag{5}$$

with measurements

$$\mathbf{y}(t) = \mathbf{H}\mathbf{x}(t) + \mathbf{v}(t), \tag{6}$$

[1] In this case, physical generalized coordinates are preferred over modal coordinates since it facilitates the choose of displacement dummy measurements in further sections

where $\mathbf{x}(t)$ is the state vector, $\mathbf{u}(t)$ is the known control inputs vector, $\mathbf{y}(t)$ represent the sensor outputs vector, and $\mathbf{w}(t)$ and $\mathbf{v}(t)$ are the process and measurement noise, which are assumed as stochastic processes [16].

The state matrix $\mathbf{A}$, the input matrix $\mathbf{B}$ and input disturbance matrix $\mathbf{B_1}$ are formulated in terms of the system's mass, stiffness and damping as follows:

$$\mathbf{A} = \begin{bmatrix} 0 & \mathbf{I} \\ -\mathbf{M}^{-1}\mathbf{K} & -\mathbf{M}^{-1}\mathbf{C} \end{bmatrix} \qquad \mathbf{B} = \begin{bmatrix} 0 \\ \mathbf{M}^{-1}\mathbf{b} \end{bmatrix} \qquad \mathbf{B_1} = \begin{bmatrix} 0 \\ \mathbf{M}^{-1}\mathbf{b_d} \end{bmatrix} \tag{7}$$

The measurement matrix, $\mathbf{H}$, is used to theoretically formulate the measurements as a linear combination of the states at a given time. The measurement matrix will be formulated further for an augmented-state formulation.

The state space nomenclature given by Eqs. 5 and 6 is derived in continuous time domain. However, the simulation analysis using the KF algorithm is performed by sampling the system dynamics at regular time intervals, therefore it is convenient to define the system equations in the discrete time domain. In this manner, these differential equations can be expressed as recursive difference equations [23]

$$\mathbf{x}(k+1) = \mathbf{\Phi}\mathbf{x}(k) + \mathbf{\Gamma}\mathbf{u}(k) + \mathbf{\Gamma_1}\mathbf{w}(k), \tag{8}$$

with measurements

$$\mathbf{y}(k) = \mathbf{H}\mathbf{x}(k) + \mathbf{v}(k), \tag{9}$$

where $\mathbf{\Phi}$, $\mathbf{\Gamma}$ and $\mathbf{\Gamma_1}$ are the discrete versions of matrices $\mathbf{A}$, $\mathbf{B}$ and $\mathbf{B_1}$, respectively. There are some methods to convert continuous system matrices in their discrete - time versions that have already been implemented in MATLAB ®. In the present study, the zero-order hold (ZOH) method is adopted.

Regarding the properties of process and measurement noise, $\mathbf{w}(k)$ and $\mathbf{v}(k)$, respectively, it can be assumed that they are random stationary sequences, mutually uncorrelated, with zero mean, that is:

$$\mathbf{E}\left\{\mathbf{w}(k)\right\} = \mathbf{E}\left\{\mathbf{v}(k)\right\} = 0,$$

have no time correlation or are "white" noise, that is:

$$\mathbf{E}\left\{\mathbf{w}(i)\mathbf{w}^T(j)\right\} = \mathbf{E}\left\{\mathbf{v}(i)\mathbf{v}^T(j)\right\} = 0 \qquad \text{if} \quad i \neq j,$$

and their covariances or mean square "noise levels" are defined by

$$\mathbf{E}\left\{\mathbf{w}(k)\mathbf{w}^T(k)\right\} = \mathbf{R_w}, \qquad \mathbf{E}\left\{\mathbf{v}(k)\mathbf{v}^T(k)\right\} = \mathbf{R_v}.$$

as detailed in [23] and acknowledged in references [20, 16, 19].

2.2 Kalman filter equations

The Kalman filter [17, 18] can be defined as a recursive linear state estimator designed to be optimal in a minimum - variance unbiased sense [16].

The main feature of Kalman filtering is the propagation of the covariance of the state estimates, $\mathbf{P}$ [19]. The basic idea behind this algorithm is to calculate the best state estimate $\hat{\mathbf{x}}(k)$, by combining a previous estimate $\bar{\mathbf{x}}(k)$ with the current measurement $\bar{\mathbf{y}}(k)$, based on the relative accuracy of both, which is in terms of the covariance of the prior estimate, $\mathbf{G}(k)$, and the covariance of the current measurement $\mathbf{R_v}$. Furthermore, the other key idea is to use the known dynamics of $\mathbf{x}$ to predict its behavior in order to estimate $\bar{\mathbf{x}}(k)$ given $\hat{\mathbf{x}}(k-1)$ [23].

The discrete KF algorithm can be arranged in two-stages: measurement update and time update. Based on [23], a summary of the required relations is:

- At the measurement time (measurement update)

$$\hat{\mathbf{x}}(k) = \bar{\mathbf{x}}(k) + \mathbf{P}(k)\mathbf{H}^T\mathbf{R}_\mathbf{v}^{-1}\left(\mathbf{y}(k) - \mathbf{H}\bar{\mathbf{x}}(k)\right), \tag{10}$$

where

$$\mathbf{P}(k) = \mathbf{G}(k) - \mathbf{G}(k)\mathbf{H}^T\left(\mathbf{H}\mathbf{G}(k)\mathbf{H}^T + \mathbf{R}_\mathbf{v}\right)^{-1}\mathbf{H}\mathbf{G}(k). \tag{11}$$

- Between measurements (time update)

$$\bar{\mathbf{x}}(k+1) = \mathbf{\Phi}\hat{\mathbf{x}}(k) + \mathbf{\Gamma}\mathbf{u}(k), \tag{12}$$

and

$$\mathbf{G}(k+1) = \mathbf{\Phi}\mathbf{P}(k)\mathbf{\Phi}^T + \mathbf{\Gamma_1}\mathbf{R_w}{\mathbf{\Gamma_1}}^T, \tag{13}$$

where the initial conditions for $\bar{\mathbf{x}}(0)$ and $\mathbf{G}(0)$ must be assumed to be some value for initialization.

2.3 Augmented Kalman filter for input estimation

The discrete Kalman filter algorithm can be rearranged in order to allow the coupled state - disturbance estimation. For that purpose, the input vector is included in the state vector. However, as it was noted by Naets et al. [19] and Berg and Keith Miller [20], the dynamics relating $\dot{\mathbf{u}}$ to the new state vector, now composed by ξ, $\dot{\xi}$ and $\mathbf{u}$, are likely unknown. This lack of knowledge can be modeled setting:

$$\dot{\mathbf{u}}(t) = 0 + \mathbf{z}(t), \tag{14}$$

where $\mathbf{z}$ is a random vector, thus making $\mathbf{u}$ constant except for model uncertainty. In this manner, Eq. 8 can be rearranged as [20]:

$$\begin{bmatrix}\mathbf{x}(k+1)\\ \mathbf{u}(k+1)\end{bmatrix} = \begin{bmatrix}\mathbf{\Phi} & \mathbf{\Gamma}\\ 0 & \mathbf{L}\end{bmatrix}\begin{bmatrix}\mathbf{x}(k)\\ \mathbf{u}(k)\end{bmatrix} + \begin{bmatrix}\mathbf{\Gamma_1} & 0\\ 0 & \Delta t\mathbf{L}\end{bmatrix}\begin{bmatrix}\mathbf{w}(k)\\ \mathbf{z}(k)\end{bmatrix},$$
$$\begin{bmatrix}\mathbf{w}(k)\\ \mathbf{z}(k)\end{bmatrix} \sim N\left(0, \begin{bmatrix}\mathbf{R_w} & 0\\ 0 & \mathbf{R_z}\end{bmatrix}\right) \tag{15}$$

where Δt is the time step and $\mathbf{L}$ must be set according to the position where the force is applied. Furthermore, in the case of acceleration measurements on each DOF, the measurements equation is given by [19]

$$\mathbf{y}(k) = \begin{bmatrix}-\mathbf{M^{-1}K} & -\mathbf{M^{-1}C} & \mathbf{M^{-1}b}\end{bmatrix}\begin{bmatrix}\mathbf{x}(k)\\ \mathbf{u}(k)\end{bmatrix} + \mathbf{v}(k), \quad \mathbf{v}(k) \sim N\left(0, \mathbf{R_v}\right) \tag{16}$$

In this manner, the AKF for coupled state - disturbance excitation can be implemented by substituting the non-starred matrices by the starred ones in Eqs. 10 - 13:

$$\mathbf{\Phi}^\star = \begin{bmatrix}\mathbf{\Phi} & \mathbf{\Gamma}\\ 0 & \mathbf{L}\end{bmatrix}, \quad \mathbf{\Gamma}^\star = 0, \quad \mathbf{\Gamma_1}^\star = \begin{bmatrix}\mathbf{\Gamma_1} & 0\\ 0 & \Delta t\mathbf{L}\end{bmatrix},$$
$$\mathbf{R_w}^\star = \begin{bmatrix}\mathbf{R_w} & 0\\ 0 & \mathbf{R_z}\end{bmatrix}, \quad \mathbf{H}^\star = \begin{bmatrix}-\mathbf{M^{-1}K} & -\mathbf{M^{-1}C} & \mathbf{M^{-1}b}\end{bmatrix} \tag{17}$$

2.4 Dummy measurements implementation in augmented Kalman filter algorithm

Aiming at stable simulations and trying to maintain a generally applicable approach for coupled state/input force estimation, that relies only on acceleration measurements, Naets et al. [19] propose to add displacement dummy measurements for the positions in which the acceleration response is measured. This AKF-DM algorithm was validated via numerical and experimental procedures in [19]. It was found that the inclusion of such dummy measurements to the AKF algorithm (AKF-DM) present stable and consistent results on force predictions, while force estimation through regular AKF diverges from the real force values over longer estimation periods. This is a solution similar to that initially proposed by Chatzi and Fuggini [32] for civil structure monitoring purposes. They indicate that this artifice is plausible since, in structural systems, the deformation of the structure is bounded and it can typically be estimated a priori via analytical models or finite element models. In this way, the estimated deformation can then be considered as the uncertainty on a dummy measurement with an actual zero value [19].

The displacement dummy measurements have equations

$$\mathbf{H_{dm}x} + \mathbf{v_{dm}} = 0, \tag{18}$$

with

$$\mathbf{H_{dm}} = \begin{bmatrix} \mathbf{I}_n & 0 & 0 \end{bmatrix}. \tag{19}$$

Equation 18 states that the position of the DOF is zero with an uncertainty $\mathbf{v_{dm}}$ with covariance $\mathbf{R_{dm}}$. Moreover, the entries of $\mathbf{R_{dm}}$ can be used for the tuning of the KF. In this context, Naets et al. [19] suggest that displacement dummy values should be chosen an order of magnitude higher than the actual motion of the system. Furthermore, covariances smaller than the suggested will constrain the estimates too much and may lead to erroneous results. On the other hand, if too high covariances are set, the dummy measurement will not be able to properly restrict the drift on the estimates [19].

In order to include the displacement dummy measurements in the AKF algorithm, some definitions must be updated. The measurement matrix has to include information about displacement dummy measurements in Eq. 18,

$$\mathbf{H_T^\star} = \begin{bmatrix} \mathbf{H^\star} \\ \mathbf{H_{dm}} \end{bmatrix}. \tag{20}$$

Furthermore, the sensor outputs vector must contain the displacement dummy measurements values, $\mathbf{y_{dm}}$, which are zero displacement,

$$\mathbf{y_T} = \begin{Bmatrix} \mathbf{y} \\ \mathbf{y_{dm}} \end{Bmatrix} = \begin{Bmatrix} \mathbf{y} \\ 0 \end{Bmatrix}, \tag{21}$$

and the measurement covariance matrix must include the dummy measurements covariance, as follows,

$$\mathbf{R_T} = \begin{bmatrix} \mathbf{R_v} & 0 \\ 0 & \mathbf{R_{dm}} \end{bmatrix}. \tag{22}$$

Naets et al. [19] point out that, due to the relatively large uncertainty on these dummy measurements, they will not contribute considerably to the fast estimation, typically required in force estimation for on-line control tasks. However, they will prevent the long-term drift created by the force estimation based on only acceleration measurements. In fact, since the objective of the present work is to estimate a point force rather than control a system, a fast estimation is not required.

3 Validation

In the present work, the capacity of the AKF-DM algorithm to predict a random in time point force applied on a cantilevered mounted structure is tested. In the following subsections the test apparatus and the used

instrumentation are described. Furthermore, the results of the EMA procedure are presented and used to represent the system in the modal space. Subsequently, the values for the process noise covariance matrix and input covariance matrix are set, while the dummy measurements covariance values are tuned. Finally, results on force identification are presented.

3.1 Instrumentation and section - model

The stainless steel structure (386 mm length, 19 mm diameter), shown in Fig. 1, has been manufactured in order to allow the installation of the instruments that will sense the structure vibration which are, presently, due to the external point force. In this manner, the structure is instrumented with four piezolectric uniaxial accelerometers model 352A24 with broadband resolution of 0.002 m/s^2 RMS (0.0002 g RMS), from PCB Piezotronics. They are installed at positions A1 (185 mm from fixed end) and A2 (345 mm) with sensing axes perpendicular to each other so that they can measure vibration in x and y coordinates.

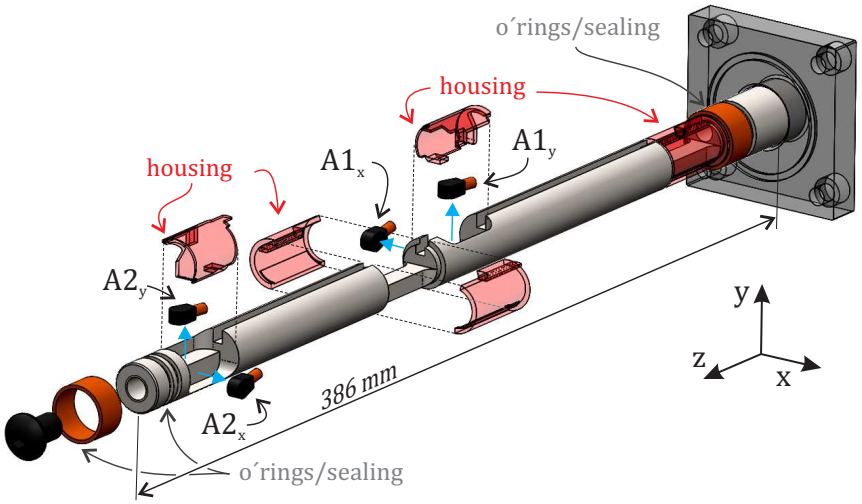


Figure 1: Instrumented cylinder.

After the sensors are installed, four 3D printed housing components are mounted on the structure, as shown in Fig. 1, in order to provide a uniform cylindrical profile. Furthermore, the structure is coated with a heat shrink tube, which is devoted to isolate the instruments from liquid when in-flow tests are performed. Although the present tests are performed in air, it was decided to maintain the heat shrink tube since it belongs to the actual structure design. It is worth mentioning that the inclusion of the mentioned coating must increase the system effective damping. Conversely, stiffness and inertia are expected to remain the same. Two aluminum rings are used to compress the o-rings mounted at the end and close to the clamping edge, and a stainless steel bolt is used to compress the heat shrink tube against the structure tip, adding some redundancy to the sealing of the instrumentation compartments.

The structure is mounted in cantilever on a section-model that represents an actual heat exchanger, whose dimensions (381 mm long and 95 mm width) and its lateral walls have been manufactured identical to the original test section. In this manner, the mounting and boundary conditions are as close as possible to those found in the actual tube bundle; the only difference being the absence of the remainder tubes that would prevent the shaker installation. Furthermore, this configuration facilitates tests with force aligned to y coordinate, however tests with force applied in x coordinate require the tube to be rotated 90° and reinstalled to allow the positioning of the shaker.

The structure is excited with an electrodynamic shaker model K2007E01 from Modal Shop, which is mounted at point A2 in order to allow collocated measurements since, as reported by Lourens et al. [16], more accurate results can be obtained with the AKF algorithm. Force is measured with a force transducer model Y208C01 from PCB Piezotronics, it is set next to the shaker (rather than the structure) in order to avoid contact with water in further experimental campaigns. The described set-up is shown in Fig. 2.

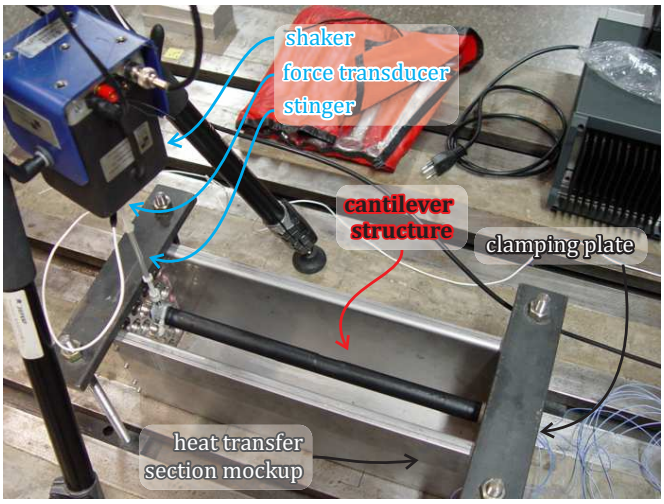


Figure 2: Experimental set-up for tests in water with electrodynamic shaker mounted at point A2.

Data is acquired with a SCADAS Mobile system running Siemens Test.Lab. The authors have devised the methodology for data acquisition and signal processing based on the form that these results are typically presented in the recent literature as well as the qualitative evolution of the data during the initial runs. Based on these criteria, acceleration and strain were measured in periods of 2 s, with a sampling frequency of 4096 Hz and a resolution of 0.5 Hz. Moreover, the obtained FRFs are the result of 30 linear averages.

3.2 System identification

The system dynamic behavior can be approximated via experimental identification. It is worth mentioning that a successful identification is very valuable since it can reduce the dependence of state estimation on the modeling of system (plant) uncertainties.

In the present study, EMA techniques are used to identify and represent the cantilevered structure described above. For this, the structure is excited at point A2 and responses are measured at points A1 and A2 since the structure design is intended to induce a 2 DOF behavior in the low frequency range, below 500 Hz. After acquiring the FRFs, the data post processing comprises two stages: (i) the poles and damping ratios are estimated via Least Squares Complex Exponential (LSCE) method, and (ii) residues and mode shapes coefficients are estimated via Least Squares Frequency Domain (LSFD) method.

This analysis is performed in the 0 - 500 Hz frequency bandwidth, which presents the two expected resonance frequencies, as seen in Fig. 3. This process is performed for x and y coordinates, according to the system coordinates in Fig. 1. The undamped natural frequencies, damping ratios and modal vectors are shown in Tab. 1. The modal vectors shown in these tables have been normalized according to the unity modal mass criterion.

As it can be seen from values in Tab. 1, the natural frequencies in x coordinate are distinct from those in y coordinate, which is intentional and due to the structure design, as discussed before. Moreover, in order to check the hypothesis of proportionally damped structure, mode complexity indicators such as Modal Phase Collinearity (MPC) and Mean Phase Deviation (MPD) are included in Tab. 1 for each calculated mode. Considering that for real modes MPC approaches to unity and MPD scatter value should be zero, it can be

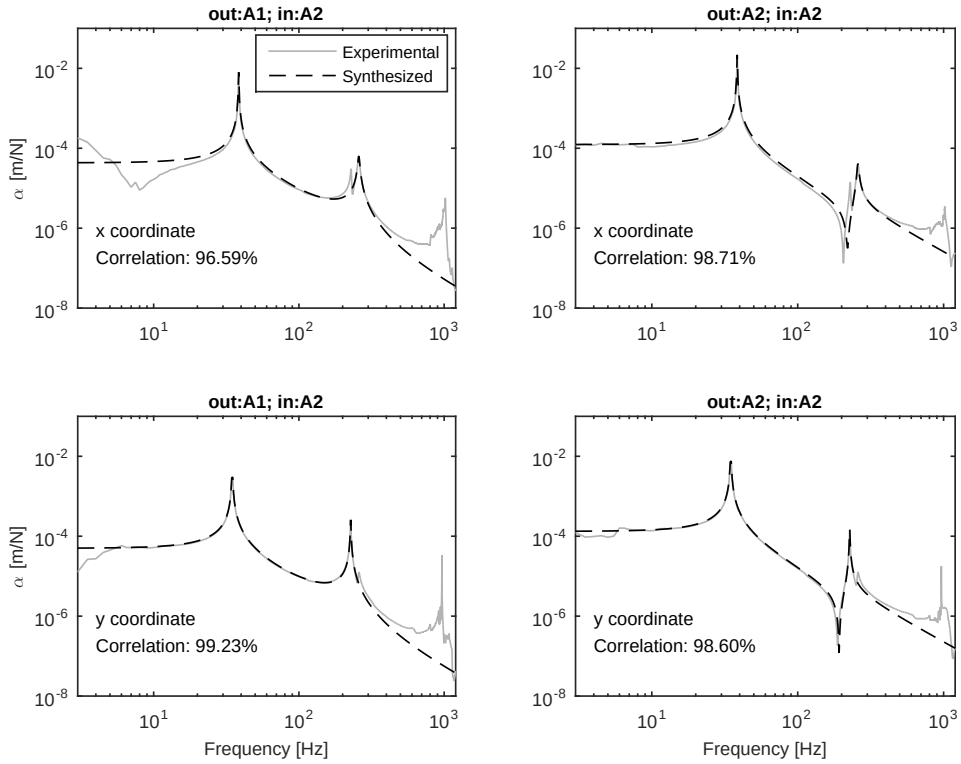


Figure 3: Experimental and synthesized receptance FRFs in x and y coordinates.

said that calculated mode shapes are normal modes, thus proportional damping is a good approximation for the present study.

The synthesized and experimental receptance FRFs are compared and shown in Fig. 3. As it can be seen from these FRFs, the models have been truncated to represent only the first two modes in each direction, since acceleration is measured only at two distinct points. Furthermore, as it can be noticed, there is some cross sensitivity, that is, the accelerometers in A1 and A2 in x coordinate are also sensing a little portion of the tube vibration in y coordinate and vice versa. This must be related to manufacturing imperfections in the surfaces where the accelerometers are installed as well as on the fixturing of the sensors themselves. This effect is more accentuated in x than in y coordinate. Despite this, the identified system, represented by the synthesized FRFs, presents high correlation with experimental data for the frequency bandwidth in which the EMA algorithms are implemented [2].

[2]Correlation values are obtained from LMS Test.Lab - Modal Analysis module.

Parameter		**x** coordinate		**y** coordinate	
		Mode 1	**Mode 2**	**Mode 1**	**Mode 2**
f [Hz]		38.4	258.4	34.7	227.1
ζ [%]		0.26	1.32	0.52	0.42
ψ	A1	9.81×10^{-1}	-2.61×10^{0}	9.96×10^{-1}	-2.78×10^{0}
	A2	2.67×10^{0}	1.68×10^{0}	2.50×10^{0}	1.60×10^{0}
MPC		1	1	1	1
MPD		$1 \times 10^{-14\circ}$	$3 \times 10^{-15\circ}$	$3 \times 10^{-15\circ}$	$3 \times 10^{-15\circ}$

Table 1: EMA results in x and y coordinates.

3.3 Covariance matrices

The present Kalman filtering implementation entails in tuning of process, input and dummy measurements covariances, whereas measurement covariance related to accelerometers is obtained from calibration tests or provided by the instrument manufacturer.

The process noise covariance matrix, $\mathbf{R}_{\mathbf{w}}^{\star}$, as defined in Eq. 17, contains information about the uncertainty on the proposed model for the system and input force. Since the system has been identified in situ via EMA techniques in section 3.2, it can be assumed as exact [19] in the analyzed frequency bandwidth even though the modal model was truncated for its first two vibration modes. Assuming an exact system model the tuning variables related to process covariance can be eliminated and all the uncertainty can be charged to the unknown covariance. This criterion agrees with that proposed by Berg and Keith Miller [20], who used very low covariance for the system in comparison to the input force covariance. On the other hand, the input force is totally unknown. Therefore, for tests in both coordinates, a very low covariance values in $\mathbf{R}_{\mathbf{w}}$ are assumed, given in the form:

$$\mathbf{R}_{\mathbf{w}} = \begin{bmatrix} R_{\dot{\xi}} & 0 \\ 0 & R_{\ddot{\xi}} \end{bmatrix}, \tag{23}$$

with

$$R_{\dot{\xi}} = 1(\text{m/s})^2, \qquad R_{\ddot{\xi}} = 1(\text{m/s}^2)^2. \tag{24}$$

Moreover, it is worth noting that all the covariance matrices in this section are assumed as diagonal matrices since disturbances are mutually uncorrelated. Furthermore, the input covariance matrix $\mathbf{R}_{\mathbf{z}}$ is defined as:

$$\mathbf{R}_{\mathbf{z}} = \begin{bmatrix} R_{\dot{u}1} & 0 \\ 0 & R_{\dot{u}2} \end{bmatrix}. \tag{25}$$

where $R_{\dot{u}1} = 0$ N^2 because no force was applied at point A1 and $R_{\dot{u}2}$ is tuned and set equal to 4×10^{10} N^2. According to Naets et al. [19], $R_{\dot{u}2}$ must be a high value in order to avoid inhibiting the estimation. This value has been used for both directions.

The instruments covariance, $\mathbf{R}_{\mathbf{T}}$, given by Eq. 22, contains information about the uncertainty on the dummy measurements, whose matrix covariance is defined by

$$\mathbf{R}_{\mathbf{dm}} = \begin{bmatrix} R_{dm1} & 0 \\ 0 & R_{dm2} \end{bmatrix}, \tag{26}$$

where R_{dm1} and R_{dm2} are tuning variables chosen an order of magnitude higher than the actual motion of the system [19]. In this sense, estimates for displacement are obtained by using the model identified in section 3.2 and simulating its time response to the measured force applied on A2. Thus, for the present study it is assumed that $R_{dm1} = R_{dm2} = 1 \times 10^{-5}$ m^2, which are maintained for tests in both coordinates.

Regarding the accelerometers covariance, $\mathbf{R}_{\mathbf{v}}$, it is given by

$$\mathbf{R}_{\mathbf{v}} = \begin{bmatrix} R_1 & 0 \\ 0 & R_2 \end{bmatrix}, \tag{27}$$

where R_1 and R_2 correspond to the covariance of accelerometers in A1 and A2, respectively, which were obtained via calibration and are detailed in Tab. 2.

Table 2: Accelerometers covariance in (m/s^2)^2.

Point	x **coordinate**	y **coordinate**
A1	40×10^{-4}	33×10^{-4}
A2	42×10^{-4}	22×10^{-4}

3.4 Results on force identification

The results on the prediction of a random in time point force via AKF-DM algorithm are discussed in this section. Since the force is predicted via a recursive type algorithm, which is based on actual acceleration measurements for its updating, it is necessary to define the time step for its implementation. It is convenient to define the same sampling time used for data acquisition as the time step for system discretization, this is $\Delta t = 2.4414 \times 10^{-4}$ s.

First, a comparison between the predicted and measured forces in the x coordinate is shown in Fig. 4. In order to do that, the results are presented in a time window of 2 s with detailed views in two time lapses of 0.04s. These time lapses are taken at the beginning and at the end of the complete window. As it can be noticed from these time lapses, the AKF-DM algorithm is able to predict the actual force in a relatively good manner based only on acceleration measurements and by introducing the displacement dummy measurements. In the same manner, as it can be noticed from Fig. 5, predicted forces for the y coordinate are in good agreement with measurements. For results in both coordinates, it can be seen that predicted forces differ slightly from the actual values at the beginning of the time window, however, these differences decrease rapidly.

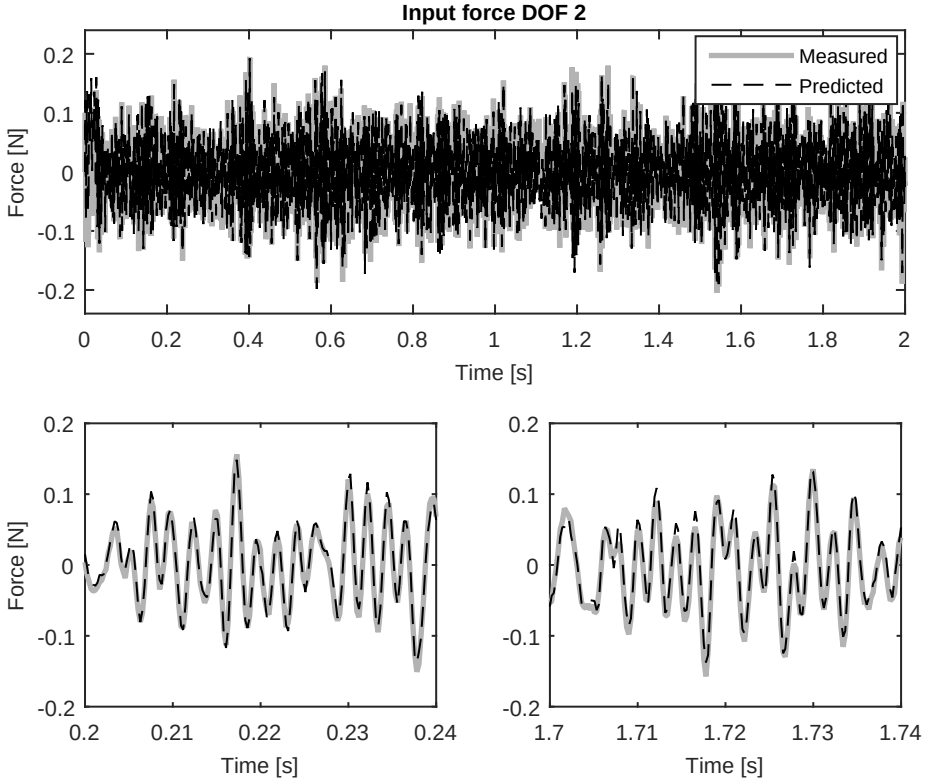


Figure 4: Measured and estimated force at DOF 2 in x coordinate shown for a complete time window and in detail for two distinct time lapses.

In general, it can be said that forces predicted via AKF-DM are in good agreement with the measurements. However, it must be noted that this result cannot be completely extrapolated for the other state variables. In other words, predicted ξ and $\dot{\xi}$ may present distinct behavior if compared with values estimated via numerical simulation in MATLAB ®, as shown, for example, for the x coordinate in Fig. 6. These differences can be better analyzed when comparing the Power Spectrum Densities (PSD) of displacement at each instrumented point, which is shown in Fig. 6. As it can be noticed, the main difference between simulated and predicted values is that the former presents a higher peak amplitude at the resonance frequency, which makes sense with the results presented in time domain.

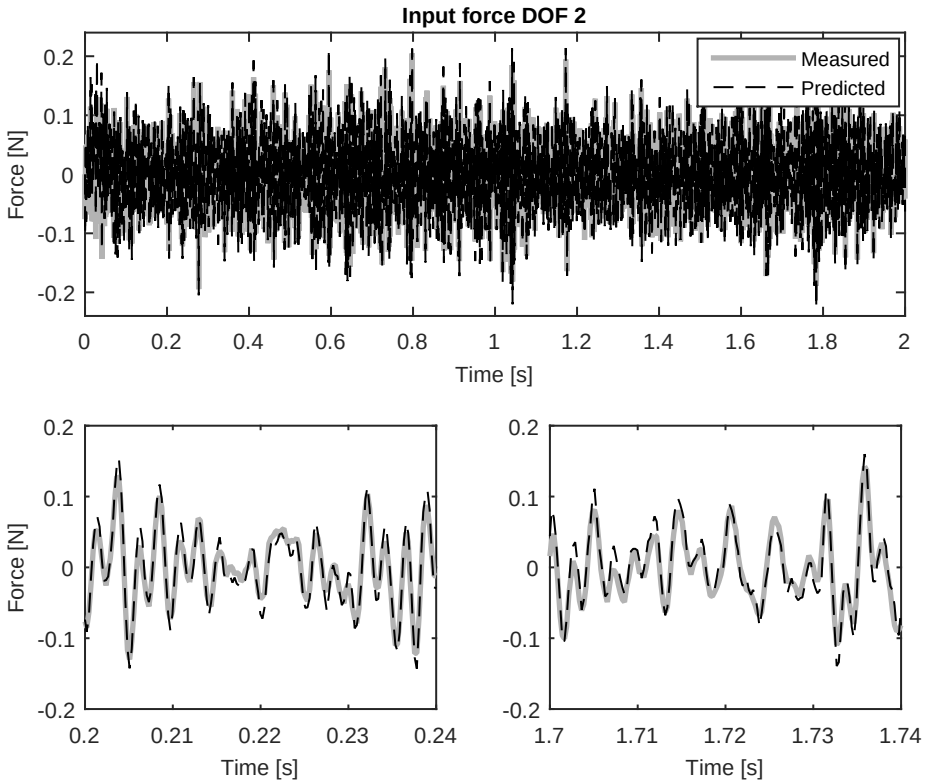


Figure 5: Measured and estimated force at DOF 2 in y coordinate shown for a complete time window and in detail for two distinct time lapses.

4 Conclusions

The ability of the AKF-DM algorithm for predicting a random in time, point force, applied on a cantilever structure was checked. For this, the KF was tuned at hand.

The comparison between experimental and predicted force time histories showed good agreement in x and y coordinates. Hence, it can be said that the AKF-DM algorithm is capable of predicting random point forces. However, it was seen that the AKF-DM algorithm fails to predict the other state variables; *i.e.* displacement and velocity.

Based on these results, further works can be proposed on the study of two-phase flow-induced forces via KF based techniques. These studies, currently under investigation, will present a set of more complex surrounding conditions, *e.g.* flow velocity and buffeting forces due to two-phase flow.

Acknowledgements

The authors acknowledge the financial assistance of the Brazilian National Council for Scientific and Technological Development - CNPq (grant numbers 481044/2010-8 and 307369/2013-7) and the doctoral scholarship awarded to the first author by CAPES Foundation.

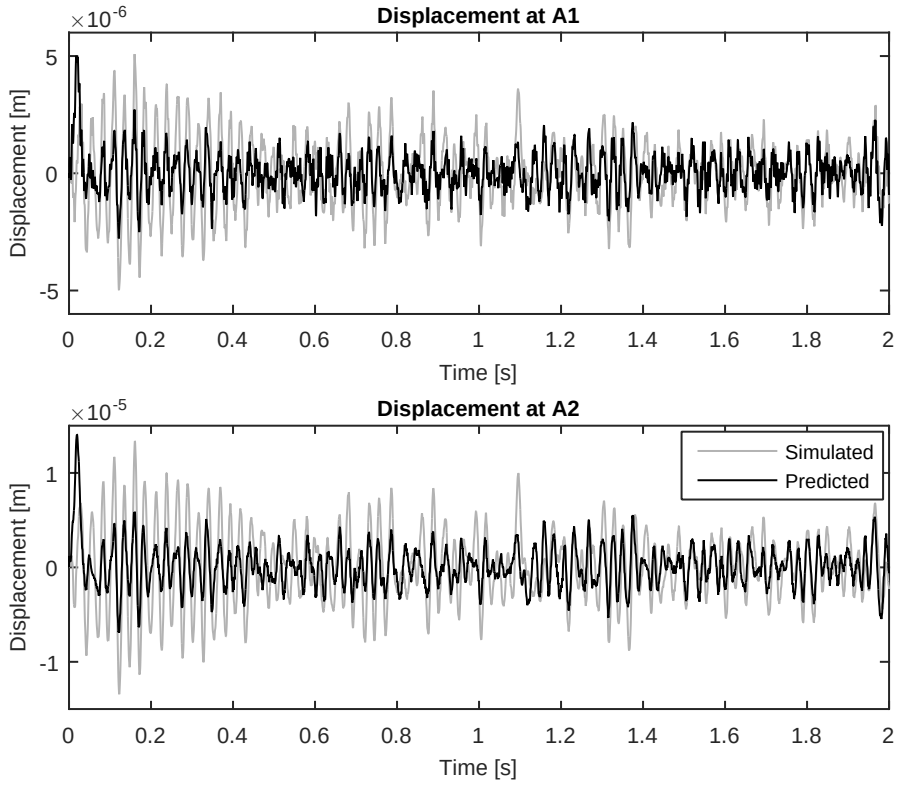


Figure 6: Simulated and predicted displacements in x coordinate

References

[1] F. T. Kanizawa, G. Ribatski, *Two-phase flow patterns across triangular tube bundles for air-water upward flow*, International Journal of Multiphase Flow, Vol. 80, Elsevier (2016), pp. 43-56.

[2] S. J. Green, G. Hetsroni, *PWR steam generators*, International Journal of Multiphase Flow, Vol. 21, No. 1, Pergamon (1995), pp. 1-97.

[3] G. Noghrehkar, M. Kawaji, A. Chan, *Investigation of two-phase flow regimes in tube bundles under cross-flows conditions*, International Journal of Multiphase Flow, Vol. 25, Pergamon (1999), pp. 857-874.

[4] M. J. Pettigrew, C. E. Taylor, *Vibration analysis of shell and tube heat exchangers: an overview - part 2. vibration response, fretting wear, guidelines*, Journal of Fluids and Structures, Vol. 18, Elsevier (2003), pp. 485-500.

[5] M. J. Pettigrew, C. E. Taylor, *Two-phase flow induced vibration: An overview*, Journal of Pressure Vessel Technology, Vol. 116, American Society of Mechanical Engineers (1994), pp. 233-253.

[6] M. J. Pettigrew, C. E. Taylor, *Vibration analysis of shell and tube heat exchangers: an overview - part 1. flow damping, fluidelastic instability*, Journal of Fluids and Structures, Vol. 18, Elsevier (2003), pp. 469-489.

[7] S. Kaneko, T. Nakamura, F. Inada, M. Kato, *Flow Induced Vibrations: Classifications and Lessons from Practical Experiences*, Elsevier (2008).

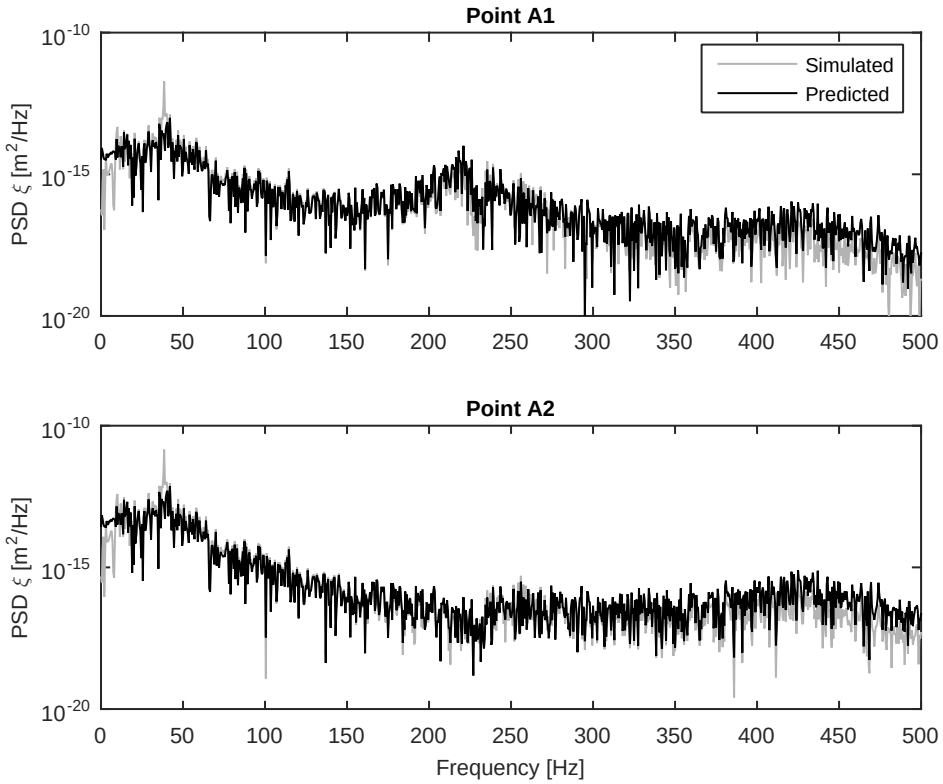


Figure 7: PSDs of simulated and predicted displacements in x coordinate

[8] M. J. Pettigrew, C. E. Taylor, V. P. Janzen, T. Whan, *Vibration behavior of rotated triangular tube bundles in two-phase cross flows*, Journal of Pressure Vessel Technology, Vol. 124, American Society of Mechanical Engineers (2002), pp. 144-153.

[9] M. J. Pettigrew, L. N. Carlucci, C. E. Taylor, N. Fisher, *Flow-induced vibration and related technologies in nuclear components*, Nuclear Engineering and Design, Vol. 131, Elsevier (1991), pp. 81-100.

[10] R. Álvarez - Briceño, F. T. Kanizawa, G. Ribatski, L. P. R. de Oliveira, *Updated results on hydrodynamic mass and damping estimations in tube bundles under two-phase crossflow*, International Journal of Multiphase Flow, Vol. 89, Elsevier (2017), pp. 150-162.

[11] R. Álvarez - Briceño, F. T. Kanizawa, G. Ribatski, L. P. R. de Oliveira, *Validation of turbulence induced vibration design guidelines in a normal triangular tube bundle during two-phase crossflow*, Journal of Fluids and Structures, Vol. 76, Elsevier (2018), pp. 301-318.

[12] R. Álvarez - Briceño, L. P. R. de Oliveira, F. T. Kanizawa, G. Ribatski, *Flow Induced Vibrations in Tube Bundles under Crossflow. Encyclopedia of Two-Phase Heat Transfer and Flow III: Macro and Micro Flow Boiling and Numerical Modeling Fundamentals. 1ed.*, World Scientific Publishing Co. Pte. Ltd., v. 4, p. 251-334 (2018).

[13] E. Wilson, *Virtual sensor technology for process optimization*, in *Proceedings of the Symposium on Computers and Controls in the Metals Industry in Iron and Steel Society, Baltimore, Maryland, 1997*, USA (2001).

[14] J. Croes, *Virtual sensing in mechatronic systems. State estimation using system level models*, PhD thesis, Katholieke Universiteit Leuven, Leuven (2017).

[15] F. Naets, J. Croes, W. Desmet *An online coupled state/input/parameter estimation approach for structural dynamics*, Computer methods in applied mechanics and engineering, Vol. 283, Elsevier (2015), pp. 1167-1188.

[16] E. Lourens, E. Reynders, G. De Roeck, G. Degrande, G. Lombaert, *An augmented Kalman filter for force identification in structural dynamics*, Mechanical Systems and Signal Processing, Vol. 27, Elsevier (2012), pp. 446-460.

[17] R. E. Kalman, *A new approach to linear filtering and prediction problems*, Journal of Basic Engineering, Vol. 82, American Society of Mechanical Engineers (1960), pp. 35-45.

[18] R. E. Kalman, R. S. Bucy, *New results in linear filtering and prediction theory*, Journal of Basic Engineering, Vol. 83, American Society of Mechanical Engineers (1961), pp. 95-108.

[19] F. Naets, J. Cuadrado, W. Desmet, *Stable force identification in structural dynamics using Kalman filtering and dummy measurements*, Mechanical Systems and Signal Processing, Vol. 50 - 51, Elsevier (2015), pp. 235-248.

[20] J. C. Berg, A. Keith Miller, *Force estimation via Kalman filtering for wind turbine blade control*, *Proceedings of the IMAC - XXVIII, Jacksonville, Florida, USA, 2010*, USA (2010).

[21] N. Maia, J. Silva, *Theoretical and Experimental Modal Analysis*, 1st ed., Research Studies Press LTD., Hertfordshire (1998).

[22] L. P. R. de Oliveira, P. S. Varoto, P. Sas, W. Desmet, *A state-space modeling approach for active structural acoustic control*, Shock and Vibration, Vol. 16 (6), Hindawi (2009), pp. 607-621.

[23] G. Franklin, J. D. Powell, M. Workman, *Digital control of dynamic systems*, Ellis - Kagle Press, Addison-wesley Menlo Park, CA (1998).

[24] M. L. J. Hautus, *Stabilization controllability and observability of linear autonomous systems*, *Proceedings of Indagationes Mathematicae, Eindhoven, The Netherlands, 1970*, Eindhoven (1970).

[25] C. -K. Ma, P. -C. Tuan, D. -C. Lin, C. -S. Liu, *A study of an inverse method for estimation of impulsive loads*, International Journal of Systems Science, Vol. 29, Taylor & Francis (1998), pp. 663-672.

[26] C. -K. Ma, J. -M. Chang, D. -C. Lin, *Input forces estimation of beam structures by an inverse method*, Journal of Sound and Vibration, Vol. 259 (3), Elsevier (2003), pp. 387-407.

[27] J. J. Liu, C. -K. Ma, I. C. Kung, D. -C. Lin *Input force estimation of a cantilever plate by using a system identification technique*, Computer Methods in Applied Mechanics and Engineering, Vol. 190, Elsevier (2000), pp. 1309-1322.

[28] J. -S. Hwang, A. Kareem, W. -J. Kim, *Estimation of modal loads using structural response*, Journal of Sound and Vibration, Vol. 326 (3-5), Elsevier (2009), pp. 522-539.

[29] D. Simon, *Optimal State Estimation: Kalman, H_∞ and Nonlinear Approaches*, John Wiley and Sons, New York (2006).

[30] W. M. Wonham, *On a matrix Riccati equation of stochastic control*, SIAM Journal on Control, Vol. 6 (4), SIAM (1968), pp. 681-697.

[31] V. Kucera, *A contribution to matrix quadratic equations*, IEEE Transactions on Automatic Control, Vol. 17 (3), IEEE (1972), pp. 344-347.

[32] E. N. Chatzi, C. Fuggini, *Structural identification of a super-tall tower by gps and accelerometer data fusion using a multi-rate kalman filter*, *Life-Cycle and Sustainability of Civil Infrastructure Systems: Proceedings of the Third International Symposium on Life-Cycle Civil Engineering (IALCCE12), Vienna, Austria, 2012*, Vienna (2012).

Inverse parameter estimation in resonant, coupled fluid-structure interaction problems

J. Cuenca[1,2], **P. Göransson**[2], **L. De Ryck**[1], **T. Lähivaara**[3]
[1] Siemens Industry Software, Interleuvenlaan 68, B-3001 Leuven, Belgium
email: **jacques.cuenca@siemens.com**

[2] Aeronautical and Vehicle Engineering, KTH Royal Institute of Technology, Teknikringen 8, SE-10044 Stockholm, Sweden

[3] Department of Applied Physics, University of Eastern Finland, Yliopistonranta 1, FIN-70211 Kuopio, Finland

Abstract
This work discusses the estimation of model parameters in resonant coupled systems over a wide frequency range. Such problems are known to be subjected to local minima, which represent a major obstacle in the field of parameter identification. This work evaluates various approaches to finding the global minimum, i.e. the true model parameters. The L2 norm between a target and a model frequency response function is used as the objective function. The estimation is performed through deterministic and statistical inversion frameworks, using both full-spectrum and step-wise approaches. The occurrence and the background of local minima are discussed and the performance of the different solution methods is evaluated. In particular, the correlation between different model parameters is analysed and observed to control the path towards the solution. Two illustrative examples are proposed, including the estimation of geometrical and material properties of an expansion chamber coupled to a limp porous material.

1 Introduction

Material and geometrical properties are observable individually by using direct methods. However, direct measurement requires dedicated setups for each individual parameter and such measurements are rarely practicable on a single material sample. An example of this is the case of porous media, where several separate setups are required for a direct observation of all acoustic and mechanical properties, e.g. [1–3]. In addition and most importantly, due to the mutual independence of individual parameter observations, the estimated material parameters are not guaranteed to satisfy a constitutive model.

As an alternative, inverse estimation methods rely on the ability for a model to describe an experimental observation. The material and geometrical properties are obtained indirectly as model parameters, as a result of a curve-fitting procedure. This guarantees that any set of trial parameters satisfies the constitutive model.

Typically the inversion procedure relies on optimisation algorithms, ensuring a low number of model evaluations. The most commonly used inversion frameworks rely on a gradient-based minimisation of an objective function. One of the major obstacles in such approaches is the presence of local minima, which can arise as a consequence of multiple factors. Recent work has shown that anisotropy in material properties leads to similarities in the behaviour of a structure for specific spatial orientations, which in turn results in local minima [4, 5]. In the case of inverse estimation of material or geometrical properties using frequency-dependent data, a major source of local minima is the presence of multiple resonances. Indeed, the inherent similarity among multiple resonances is a cause of wrong parameter estimations.

Other inversion paradigms do not suffer from local minima in the same manner, but generally require a large number of model evaluations. For instance, Bayesian inversion framework enables to investigate the inverse problem in a probabilistic sense. However, a significant number of model evaluations is required in order to provide a reliable estimate of the probability density function [6].

Effectively a trade-off exists between a low number of model evaluations and the assurance of finding the global minimum of the problem. Strategies to overcome the problem of multiple local minima in inverse estimation problems include, for instance, the use of multiple starting points with randomly distributed values [7], the use of neural networks or related paradigms [8], or the simultaneous use of different optimisation algorithms concurrently exploiting common evaluation points.

The present paper addresses the problem of inverse estimation of material and geometrical properties of structures exhibiting a non-monotonous behaviour with frequency. A strategy is here employed in order to overcome resulting local minima, based on physical principles governing the dynamic behaviour. The method, proposed in a recent paper [9], decomposes the broadband inverse estimation problem into a number of subsequent subproblems over increasingly broad frequency ranges. In the case of a coupled fluid-structure problem, a starting subproblem over a frequency band where the structure exhibits an asymptotic behaviour governed by a partial set of the unknowns has been shown to guide the solution towards the true solution. In the present paper, the method is presented and applied to problems of reduced complexity, thus allowing for analytical derivations to support the observations. A gradient-based framework is used as the underlying inversion method in the proposed method. This is used in combination with a Bayesian framework, which provides an insight into the nature of the multiple local minima, including the true solution of the problem. The combined use of deterministic and statistical approaches thus allows to benefit from a low number of model evaluations while gaining additional knowledge on the problem. The focus of the present paper is nonetheless on the physical aspects governing local minima rather than on the computational efficiency itself.

2 Inverse estimation problem

2.1 Observation model

This paragraph describes the general aspects of the inverse estimation problem, without a particular focus on a specific physical system. As described in the introduction, the goal is to measure material and/or geometrical properties of frequency-dependent systems. Accordingly, the system under consideration is characterised by an observation

$$g_0(\omega_m), \quad m \in [1, M], \tag{1}$$

where ω_m is a sequence of discrete circular frequencies at which the observation is performed.

It is assumed that a known model describes the behaviour of the system as a function of its material and geometrical parameters, in the additive form

$$g_0(\omega_m) = g(\mathbf{x}_0, \omega_m) + e, \tag{2}$$

where $\mathbf{x}_0$ is the set of unknown model parameters, considered as the true properties of the observed system, and e is a model of the measurement error (assumed to be Gaussian).

The primary goal is to find an estimate $\tilde{\mathbf{x}}_0$ of $\mathbf{x}_0$ by means of a suitable inversion framework for the available model. The focus of the present paper is on dynamic problems and in particular those exhibiting resonances which frequently lead to multiple wrong estimations.

2.2 Gradient-based inversion

The objective function is here defined as the 2-norm distance between the modelled response and the observed response, which can be written as

$$d(\mathbf{x}, M) = \sum_{m=1}^{M} |g(\mathbf{x}, \omega_m) - g_0(\omega_m)|^2 . \tag{3}$$

An estimate $\tilde{\mathbf{x}}_0$ of the unknown model parameters $\mathbf{x}_0$ is thus obtained by minimising the objective function, in the form

$$\tilde{\mathbf{x}}_0 = \text{argmin}\left(d(\mathbf{x}, M)\right). \tag{4}$$

In the present paper, the Globally Convergent Method of Moving Asymptotes (GCMMA) [10] is used.

In addition to the global minimum of Eq. (4), resonant problems often exhibit a series of local minima, which arise as a consequence of the similarity of the system's behaviour for different values of its properties. A direct inversion thus proves to be ineffective, as multiple starting points will lead to multiple solutions. Furthermore, in a general sense it is not guaranteed that the value of the objective function is strictly lower at the true solution, as shown in the first example below.

2.3 Bayesian inversion framework

In the Bayesian framework [11,12], all quantities are modelled as random variables. The Bayesian inference is based on the Bayes' rule and results in the conditional probability distribution of the unknowns $\mathbf{x}$ given the measurements g_0. This distribution is commonly called as the posterior probability distribution of the unknowns $\mathbf{x}$ and can further be used for computing not only point estimates for $\mathbf{x}$ but also spread estimates, such as credible intervals.

For the sampling of the posterior densities, we use the Metropolis-Hastings algorithm with an adaptive proposal distribution scheme [13, 14], referred to as MCMC (Markov chain Monte Carlo) in the following sections. The point estimate for the parameters we use in this work is the maximum a posteriori and as an indication of the uncertainty in the point estimates we use the narrowest 95% credible interval. For more detailed discussion of the Bayesian framework used in this work, we refer to [9].

2.4 Incremental-frequency inverse estimation

The method proposed in this paragraph consists of solving the inversion problem as a sequence of sub-problems where the solution to a given sub-problem is used as the starting point for the next sub-problem. By doing so, the aim is to guide the model parameters towards the true solution, without terminating at a local minimum.

The sequence of sub-problems is chosen following an a priori behaviour of dynamic systems, and as such is potentially suitable for a large number of problems. An initial sub-problem is defined by constraining Eq. (4) to a narrow frequency range in which the system can be expected to behave in an asymptotic manner, that is, with a dependence on a subset of the model variables and away from resonant behaviour. The solution to such sub-problem is used as the starting point for a second sub-problem, whose frequency range is wider. The process is continued until the frequency range is that of the original full problem. The strength of such a process lies in the fact that the solution to the first sub-problem lies in a subspace that contains the true solution.

The sub-problems can be formally stated as

$$\tilde{\mathbf{x}}_0^{(n)} = \text{argmin}\left(d(\mathbf{x}, M(n))\right), \quad n \in [1, N], \tag{5}$$

where $M(n)$ is the number of frequencies in sub-problem n. Accordingly, $\tilde{\mathbf{x}}_0^{(N)} = \tilde{\mathbf{x}}_0 \simeq \mathbf{x}_0$ is the final solution, expected to provide a good estimate of the true model parameters.

3 Application examples

3.1 General framework

The two examples considered in this section rely on the knowledge of the sound transmission loss (STL) of the studied component, for instance as measured in an impedance tube setup. A transfer matrix approach [15] is used, providing a relation between the acoustic pressure and particle flow at the inlet and outlet in the form

$$\begin{bmatrix} p_{\text{in}}(\omega) \\ S_{\text{in}} v_{\text{in}}(\omega) \end{bmatrix} = \mathbf{T}(\omega) \begin{bmatrix} p_{\text{out}}(\omega) \\ S_{\text{out}} v_{\text{out}}(\omega) \end{bmatrix}, \tag{6}$$

where p, v and S are respectively the acoustic pressure, particle velocity and tube cross-section area, at the inlet or outlet. By assuming that the studied component is composed of N equivalent homogeneous fluid layers. its transfer matrix may be written as the product

$$\mathbf{T}(\omega) = \prod_{n=1}^{N} \mathbf{T}_n(\omega). \tag{7}$$

The transfer matrix of layer n can be written in the form

$$\mathbf{T}_n(\omega) = \begin{bmatrix} \cos(k_n l_n) & \dfrac{-Z_n}{iS_n} \sin(k_n l_n) \\ \dfrac{iS_n}{Z_n} \sin(k_n l_n) & \cos(k_n l_n) \end{bmatrix}, \tag{8}$$

where l_n, S_n, k_n and Z_n respectively denote the layer's length, cross-section area, wavenumber and characteristic impedance. It is worth noting that equivalent fluid models of complex media will exhibit a dependence of the wavenumber and impedance on intrinsic material properties. The STL of the full component is given by

$$\text{STL} = 20 \log_{10} \left(\frac{1}{2} \left| T_{11} + T_{12} \frac{S_{\text{out}}}{Z_{\text{out}}} + T_{21} \frac{Z_{\text{in}}}{S_{\text{in}}} + T_{22} \frac{Z_{\text{in}}}{Z_{\text{out}}} \frac{S_{\text{out}}}{S_{\text{in}}} \right| \right). \tag{9}$$

3.2 Expansion chamber

3.2.1 Model

As a first application example, a simple expansion chamber is considered, as illustrated in Fig. 1. The measured quantity is chosen as the sound transmission loss within a plane-wave approximation, which may be written as

$$\text{STL}(\mathbf{x}) = 20 \log_{10} \left(\frac{1}{2} \left| 2\cos(kl) + \left(\frac{r^2}{R^2} + \frac{R^2}{r^2} \right) i \sin(kl) \right| \right), \tag{10}$$

where R is the radius of the inlet and outlet ducts and l and r are respectively the length and radius of the expansion chamber, considered as the two unknowns of the problem, denoted as

$$\mathbf{x} = \{l, r\}. \tag{11}$$

The true values of the model parameters are denoted

$$\mathbf{x}_0 = \{l_0, r_0\}. \tag{12}$$

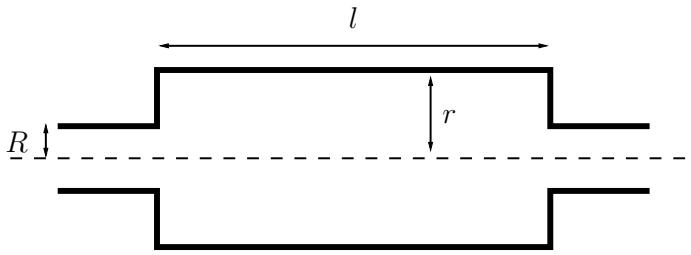


Figure 1: Expansion chamber with unknown length and radius.

The aim of the following is to retrieve arbitrarily chosen values for l_0 and r_0 from the knowledge of the sound transmission loss of the system. Following Eq. (2), the observation is here modelled as

$$\mathrm{STL}_0(\omega_m) = \mathrm{STL}(\mathbf{x}_0, \omega_m) + e, \tag{13}$$

where e is a normally distributed random variable, representing an additive noise. The objective function is defined as

$$d(\mathbf{x}) = \sum_m \left|\mathrm{STL}(\mathbf{x}, \omega_m) - \mathrm{STL}_0(\omega_m)\right|^2. \tag{14}$$

First, the gradient-based inversion is applied in the full frequency spectrum, defined as $f \in [1, 1200]$ Hz. The target values of the chamber length and radius are chosen as $l_0 = 0.5$ m and $r_0 = 0.12$ m and the inlet/outlet duct radius is set to $R = 0.04$ m.

3.2.2 Full-spectrum gradient-based inversion

This paragraph discusses the gradient-based inverse estimation of model parameters l and r. As a convergence criterion, the GCMMA algorithm is set to stop after 5 consecutive iterations where the variation in the objective function and design variable values is less than 10^{-4} relative to the previous iteration.

Figure 2 shows a map of the objective function as a function of (l, r) and the solutions found from running the gradient-based algorithm 1000 times using a random multi-start procedure. It shall be noted that e is chosen to be different for each run, in order to quantify the spread of the solution, rather than a solution bias. The standard deviation of the additive noise is set to 2 dB in this case.

The figure shows that the gradient-based algorithm terminates at multiple local minima, including the true solution. This allows to conclude that the solution of this inverse problem on the full available spectrum is not viable.

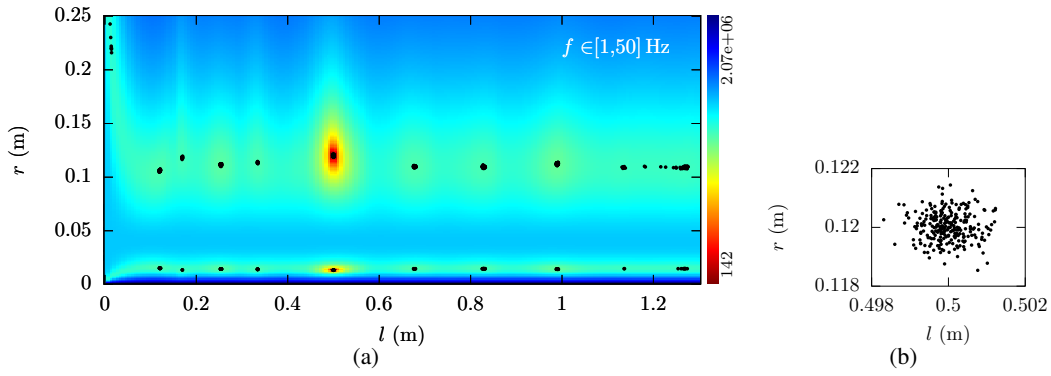


Figure 2: (a) Map of the full frequency range objective function (color) and local minima (dots); (b) closeup around the true solution.

An additional observation can be made on this simplified problem. In fact, Fig. 2 displays two sets of local minima, distributed horizontally. This is attributed to the dependence of the sound transmission loss on the expansion chamber radius, in the form $\left(r^2/R^2 + R^2/r^2\right)$. The expression is symmetric with respect to $r = R$, which implies that the objective function and its local minima within $r \leq R$ are a mirror image of those within $r \geq R$. Therefore the observation of the sound transmission loss does not allow to distinguish an expansion from a constriction, unless a constraint such as $r > R$ is imposed onto the inversion algorithm.

3.2.3 Incremental inverse estimation

The inverse estimation of the length and radius of the expansion chamber is here solved using the proposed incremental approach. As the starting sub-problem, a low-frequency narrow band where the system is non-resonant is chosen. An asymptotic expansion of the sound transmission loss for small kl yields

$$\mathrm{STL}(\mathbf{x}) \simeq 10 \log_{10} \left(1 + \left(\frac{r^2}{R^2} + \frac{R^2}{r^2} \right)^2 \frac{(kl)^2}{4} \right). \tag{15}$$

The behaviour of the system is thus monotonous in l and symmetric in r. The roots of the objective function, Eq. (14), at the limit $kl \ll 1$, can be derived as functions of l and r and expressed as

$$r_\pm = R \sqrt{\frac{r_0^2}{R^2} + \frac{R^2}{r_0^2}} \left(\frac{l_0}{l} \right)^{\pm 1/2} \tag{16}$$

as shown in Fig. 3. Therefore, by constraining the first sub-problem to a low frequency range, the corresponding estimate of $\mathbf{x}_0$ is expected to fall onto one of the curves.

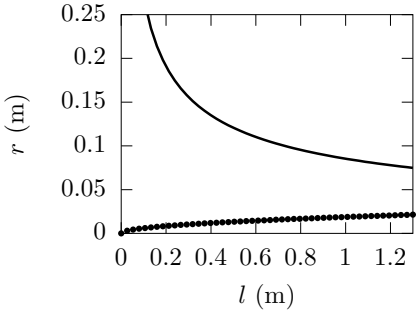


Figure 3: Roots of the objective function in the low frequency limit for the expansion chamber problem.

The sub-problem frequency ranges are chosen as

$$f \in [1\,\mathrm{Hz} - f_{\mathrm{max}}], \quad f_{\mathrm{max}} = \{50, 100, 200, 400, 700, 1200\}\,\mathrm{Hz}. \tag{17}$$

Each subproblem is solved using GCMMA with identical stabilisation criteria as for the full-range estimation.

An example of solution using the proposed approach is here presented in detail. Table 1 summarises the sub-problem frequency ranges, the final estimate per sub-problem and the deviation from the true solution for an arbitrary starting point. Figure 4 shows a map of the objective function for each sub-problem, together with the path of the design variables $\mathbf{x} = (l, r)$. It is worth noting that similar results are obtained by using different starting points. It has been observed for the present case that the procedure invariably converges to the true solution (l_0, r_0), or to its mirror image $(l_0, R^2/r_0)$.

Sub-problem	Stable estimate (l, r)	Absolute relative deviation
$f \in$[1,50] Hz	$(0.2663, 0.1601)$ m	$(46.74, 33.43)$ %
$f \in$[1,100] Hz	$(0.7709, 0.1011)$ m	$(54.18, 15.73)$ %
$f \in$[1,200] Hz	$(0.5088, 0.1202)$ m	$(1.75, 0.20)$ %
$f \in$[1,400] Hz	$(0.5003, 0.1202)$ m	$(0.06, 0.18)$ %
$f \in$[1,700] Hz	$(0.4992, 0.1196)$ m	$(0.16, 0.33)$ %
$f \in$[1,1200] Hz	$(0.4997, 0.1203)$ m	$(0.07, 0.27)$ %

Table 1: Sub-problem frequency ranges, final estimates and deviation from the target values $\mathbf{x}_0 = (0.5, 0.12)$ m.

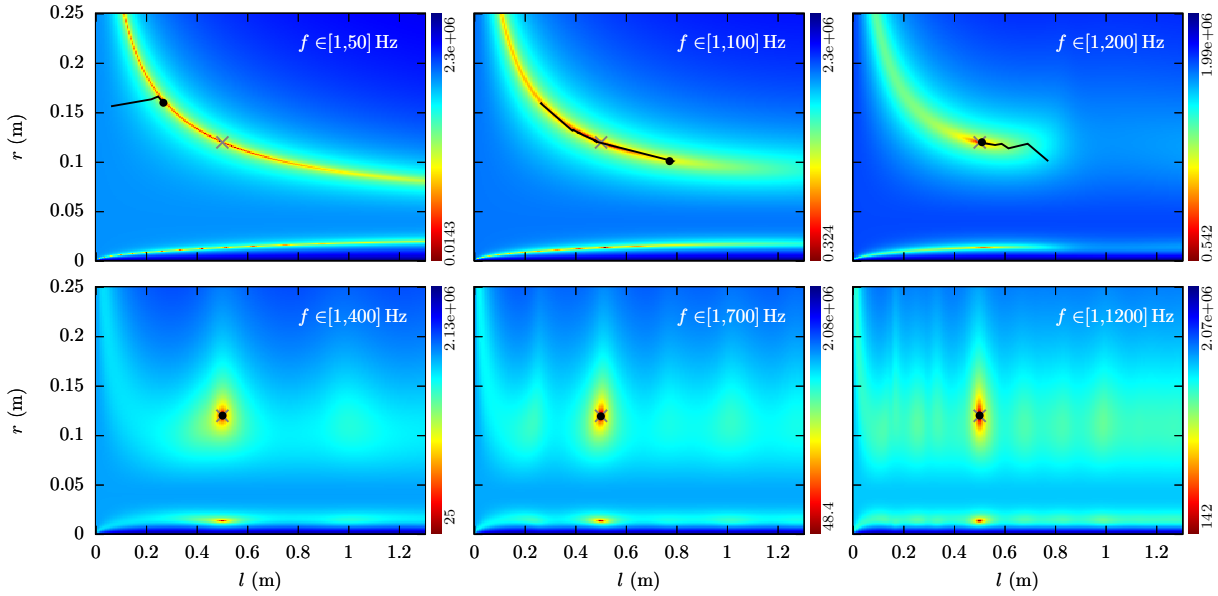


Figure 4: Objective function map and path of the design variables in the successive sub-problems. —● Path and final state of the design variables within a given sub-problem; × true solution. The frequency ranges of the sub-problems are indicated within the figures.

3.2.4 Bayesian inversion

The MCMC algorithm is here applied to the present problem and the solution for each of the frequency ranges is given in Fig. 5. The posterior densities are consistent with the maps of Fig. 4 and moreover allow for point estimates and credible intervals to be evaluated. These are given in Tab. 2, providing an increasingly accurate and narrow estimation as the frequency range is widened. It is worth noting that, due to the shape of the posterior density the proposal density is relatively wide, enabling the chain to jump between separate branches, e.g. local minima, of the solution. The existence of two solutions is thus apparent in the first sub-problem, as predicted in Eq. (16).

Sub-problem	MAP estimate (l, r)	$l_{95\%}$ (min, max)	$r_{95\%}$ (min, max)
$f \in$[1,50] Hz	$(0.1103, 0.2480)$ m	$(0.1025, 1.1631)$ m	$(0.0125, 0.2241)$ m
$f \in$[1,100] Hz	$(0.2648, 0.1599)$ m	$(0.1035, 0.5981)$ m	$(0.1033, 0.2361)$ m
$f \in$[1,200] Hz	$(0.4863, 0.1209)$ m	$(0.4268, 0.5352)$ m	$(0.1173, 0.1257)$ m
$f \in$[1,400] Hz	$(0.4995, 0.1194)$ m	$(0.4955, 0.5035)$ m	$(0.1176, 0.1213)$ m
$f \in$[1,700] Hz	$(0.4995, 0.1192)$ m	$(0.4973, 0.5017)$ m	$(0.1179, 0.1206)$ m
$f \in$[1,1200] Hz	$(0.5000, 0.1196)$ m	$(0.4990, 0.5009)$ m	$(0.1186, 0.1206)$ m

Table 2: Sub-problem frequency ranges, MAP estimates, and 95% credible intervals.

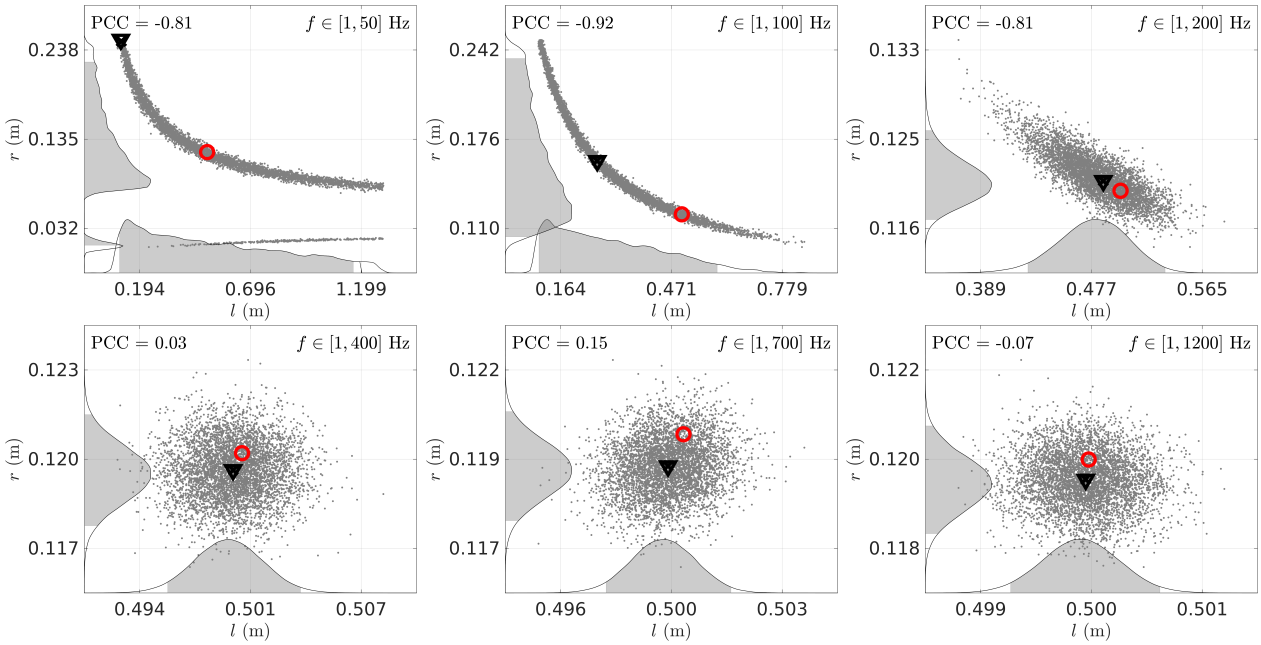


Figure 5: 2D posterior densities for sub-problems. The black cross denotes the maximum a posteriori (MAP) estimate, the black triangle is the initial condition (based on Matlab's *lsqnonlin* estimation), and the red circle is the true value. The dots represent a sample of the MCMC points, PCC is the Pearson correlation coefficient, and f indicates the frequency range of the corresponding sub-problem. The black curves on the bottom and left side of each plot are the 1D marginal densities. For the 1D densities, the light gray zone denotes the narrowest 95% credible interval (bounds are given in Table 2).

3.3 Expansion chamber coupled to a porous material

3.3.1 Model

As a second example, a coupled problem involving an expansion chamber and a porous material is considered, as illustrated in Fig. 6. The porous material is assumed to have a limp frame and is placed adjacent to the air expansion. Such a configuration is expected to ensure a strong coupling between the two components. The inverse estimation problem consists of 5 unknowns, namely the length and radius of the expansion chamber and the porosity, flow resistivity and tortuosity of the porous material. All other parameters are considered to be fixed.

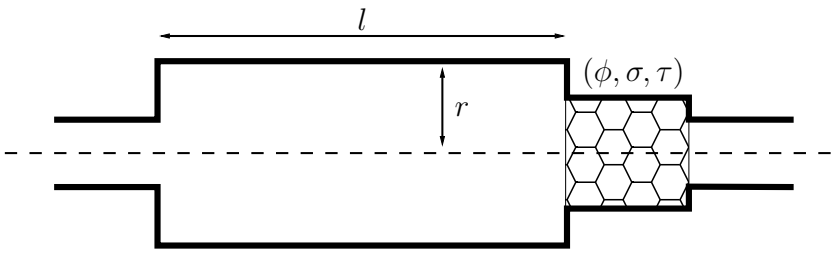


Figure 6: Expansion chamber coupled to a porous material. The unknown properties are the length and radius of the expansion chamber and the porosity, flow resistivity and tortuosity of the porous material.

The porous material is modelled by means of the Johnson-Champoux-Allard model [16, 17], providing the equivalent density $\tilde{\rho}(\omega)$ and bulk modulus $\tilde{K}(\omega)$ as

$$\tilde{\rho}(\omega) = \frac{\tau\rho_0}{\phi}\left(1 + \frac{\sigma\phi}{i\omega\rho_0\tau}\sqrt{1 + \frac{i\omega\rho_0 4\tau^2\eta}{\sigma^2\Lambda^2\phi^2}}\right) \tag{18}$$

and

$$\tilde{K}(\omega) = \frac{\gamma P_0}{\phi}\left(\gamma - (\gamma-1)\left[1 + \frac{\sigma\phi}{i\omega\rho_0\tau\mathrm{Pr}}\sqrt{1 + \frac{i\omega\rho_0 4\tau^2\eta\mathrm{Pr}}{\sigma^2\Lambda'^2\phi^2}}\right]^{-1}\right)^{-1}, \tag{19}$$

with the parameters of air defined as ρ_0 the mass density, η the viscosity, Pr Prandtl's number, P_0 the atmospheric pressure and γ the heat capacity ratio, and the parameters of the porous material defined as ϕ the porosity, σ the flow resistivity, τ the tortuosity, Λ the viscous characteristic length and Λ' the thermal characteristic length.

Under the assumption of a limp frame [17, 18], the equivalent density of the porous material can be approximated as

$$\tilde{\rho}_{\mathrm{limp}}(\omega) = \frac{\rho_t\tilde{\rho}(\omega) - \rho_0^2}{\rho_t + \tilde{\rho}(\omega) - 2\rho_0}, \tag{20}$$

where $\rho_t = \rho_s + \phi\rho_0$ is the total apparent mass density of the porous material, ρ_s being the mass density of the frame. For the purposes of the present model, the equivalent characteristic impedance $\tilde{Z}(\omega)$ and wavenumber $\tilde{k}(\omega)$ are used, defined as

$$\tilde{Z}(\omega) = \sqrt{\tilde{\rho}_{\mathrm{limp}}(\omega)\tilde{K}(\omega)}, \quad \tilde{k}(\omega) = \omega\sqrt{\frac{\tilde{\rho}_{\mathrm{limp}}(\omega)}{\tilde{K}(\omega)}}. \tag{21}$$

The unknowns of the problem are denoted

$$\mathbf{x} = \{l, r, \phi, \sigma, \tau\} \tag{22}$$

and the true values of the model parameters are denoted

$$\mathbf{x}_0 = \{l_0, r_0, \phi_0, \sigma_0, \tau_0\}. \tag{23}$$

Table 3 summarises the model parameters and their values, as well as those considered as unknown for the inverse estimation problem.

The full-spectrum estimation and the proposed approach are applied below, using the sound transmission loss of the coupled system as the data to be reproduced by the inverse estimation, with Eq. (14) as the objective function. The numerical experiments are performed with identical settings to the previous example on the single expansion chamber, with the exception of the additive noise, here set to $0.5\,\mathrm{dB}$.

3.3.2 Full-spectrum gradient-based inversion

The inverse estimation is here performed on the full frequency range of the problem. A multi-start scheme with 400 starting points with randomly generated values is used. Figure 7 shows the ensemble of solutions and the histogram of objective function residual values. The figure shows a high sparsity of the objective function residual values and a wide scattering of the model parameters, i.e. the appearance of multiple local minima. The model parameter values can be obtained as the solution exhibiting the lowest objective function residual value. However, such a full-spectrum multi-start procedure is only guaranteed to provide the true solution for a sufficiently large sample of starting points.

Property	Symbol	Target value	Unknown	Range
Geometry				
Expansion chamber length	l_0	0.5 m	l	$[0.01, 1]$ m
Expansion chamber radius	r_0	0.12 m	r	$[0.005, 0.25]$ m
Porous material length	l_p	0.15 m		
Porous material radius	r_p	0.09 m		
Inlet/outlet radius	R	0.04 m		
Air				
Mass density	ρ_0	1.2 kg·m^{-3}		
Viscosity	η	1.81·10^{-5} Pa·s		
Prandtl's number	Pr	0.71		
Atmospheric pressure	P_0	101325 Pa		
Heat capacity ratio	γ	1.4		
Porous material				
Frame density	ρ_s	10 kg·m^{-3}		
Porosity	ϕ_0	0.98	ϕ	$[0, 1]$
Flow resistivity	σ_0	10^4 N·s·m^{-4}	σ	$[10^3, 10^5]$ N·s·m^{-4}
Tortuosity	τ_0	3	τ	$[1, 4]$
Viscous characteristic length	Λ	180·10^{-6} m		
Thermal characteristic length	Λ'	270·10^{-6} m		

Table 3: Values used for air properties and porous material properties for the Johnson-Champoux-Allard model within the limp frame limit. The ranges used for the inversion procedures are specified.

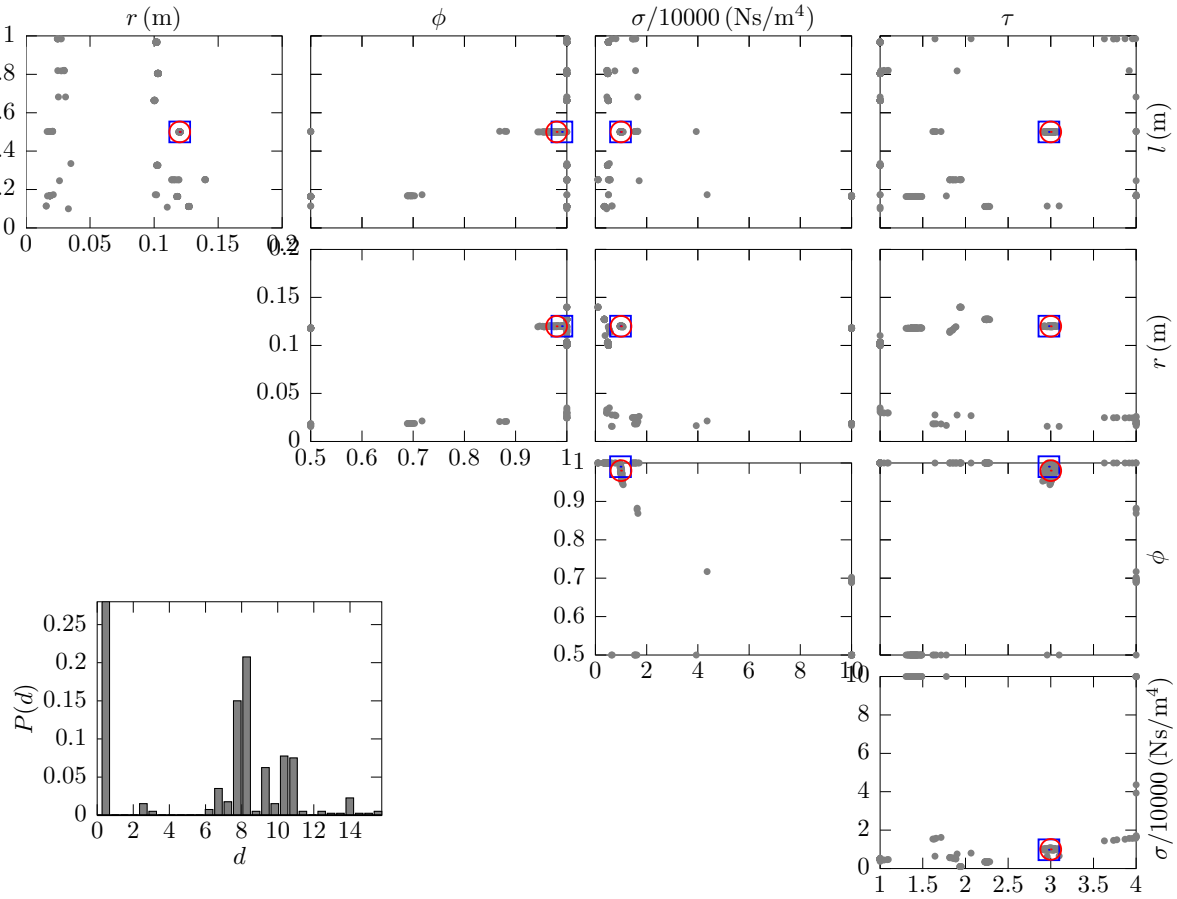


Figure 7: Parameter values obtained for 400 runs of the full-spectrum gradient-based inversion and histogram of objective function residual values. ◯ true solution, □ solution with the lowest objective function residual.

3.3.3 Low frequency asymptotic behaviour

An expression for the low-frequency asymptotic behaviour of the coupled system may be obtained by considering the limp Johnson-Champoux-Allard model at the limit $\omega \ll 1$, which yields

$$\tilde{Z}(\omega) \simeq \rho_t c_p, \quad \tilde{k}(\omega) \simeq \frac{\omega}{c_p}, \tag{24}$$

where $c_p = \sqrt{\dfrac{P_0}{\phi\rho_t}}$ is the low-frequency limit of the speed of sound in the limp porous medium. This in turn leads to a low-frequency approximation of the sound transmission loss,

$$\mathrm{STL}(\mathbf{x}) \simeq 10\log_{10}\left(1+\omega^2\left[\left(\frac{l}{2c}\psi\left(\frac{r^2}{R^2}\right)+\frac{l_p}{2c_p}\psi\left(\frac{\rho_0 c r_p^2}{\rho_t c_p R^2}\right)\right)^2-\frac{l_p l}{c_p c}\psi\left(\frac{\rho_0 c r_p^2}{\rho_t c_p r^2}\right)\right]\right), \tag{25}$$

where

$$\psi(x) = x + x^{-1}. \tag{26}$$

The expression is comparable to Eq. (15) in that it is monotonous in l and presents a similar dependence in r. The dependence on the porosity of the foam is weak, only appearing through its total mass density ρ_t. Furthermore, this low-frequency asymptotic expression does not depend on the flow resistivity or tortuosity of the foam.

The roots of the objective function, Eq. (14), are given by

$$l_\pm(r,\phi) = \frac{-\big(\alpha(r)\beta(\phi)-\gamma(r,\phi)\big) \pm \sqrt{\big(\alpha(r)\beta(\phi)-\gamma(r,\phi)\big)^2-\alpha(r)^2\big(\beta(\phi)^2-\delta^2\big)}}{\alpha(r)^2}, \tag{27}$$

where

$$\alpha(r) = \frac{1}{2c}\psi\left(\frac{r^2}{R^2}\right), \quad \beta(\phi) = \frac{l_p}{2c_p}\psi\left(\frac{\rho_0 c r_p^2}{\rho_t c_p R^2}\right), \quad \gamma(r,\phi) = \frac{l_p}{2c_p c}\psi\left(\frac{\rho_0 c r_p^2}{\rho_t c_p r^2}\right),$$
$$\delta^2 = \big(\alpha(r_0)l_0+\beta(\phi_0)\big)^2 - 2\gamma(r_0,\phi_0))l_0.$$

The root l_+ is positive and is shown in Fig. 8 for $\phi = 10^{-6}$ and $\phi = 1$. The figure shows that the behaviour of the coupled system in the low frequency range is governed by the parameters of the expansion chamber, while the dependence on the porosity is rather weak. The first step of the incremental estimation will thus provide the relation between l and r, the rest of the parameters being estimated in the subsequent steps.

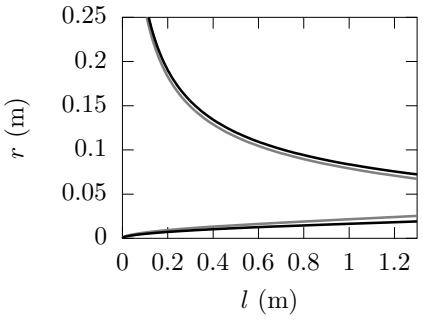


Figure 8: Root of the objective function in the low frequency limit for the coupled expansion-foam problem. ——— $\phi = 10^{-6}$, ——— $\phi = 1$.

3.3.4 Incremental inverse estimation

The proposed incremental approach is here applied to the case of a coupled expansion chamber and porous material. The inverse estimation is performed with identical incremental frequency ranges as in the previous example. Analogously to the full-spectrum estimation, a multi-start scheme with 400 randomly generated starting points is used here. Figure 9 shows the ensemble of solutions and the corresponding ensemble of values of the objective function, for the final substep of the method, $f \in [1, 1200]$ Hz. The figure shows that the proposed incremental frequency approach invariably converges to the true solution. Furthermore, the histogram of objective function residual values is densely distributed, its dispersion being consistent with the noise model.

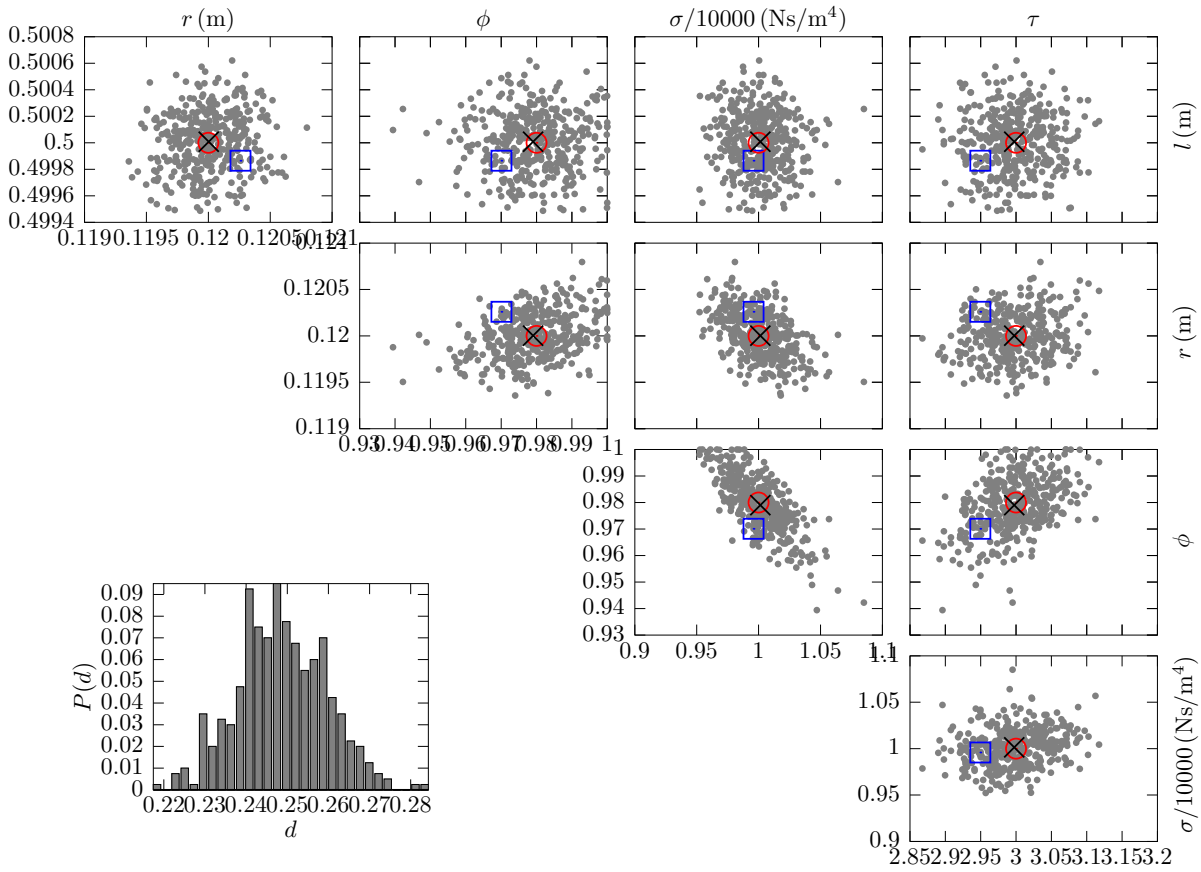


Figure 9: Parameter values obtained for 400 runs of the incremental-frequency gradient-based inversion and histogram of objective function residual values. ◯ true solution, □ solution with the lowest objective function residual, × mean value over the ensemble.

3.3.5 Bayesian inversion

The Bayesian inversion is here applied to the coupled problem. The solution for the first and last of the frequency ranges are given in Figs. 10 and 11. The marginal densities for the first frequency range exhibit a strong dependence on the length and radius of the expansion chamber, while the densities associated with the material properties of the porous material are close to the assumed uniform prior model. This result is consistent with the low-frequency asymptotic behaviour derived above, which predicts a strong dependence on the radius and length of the expansion, a weak dependence on the porosity of the foam, and no dependence on the flow resistivity and tortuosity. Furthermore, the point estimates and credible intervals evaluated in Fig. 11 are consistent with the solution using the incremental-frequency gradient-based inversion procedure.

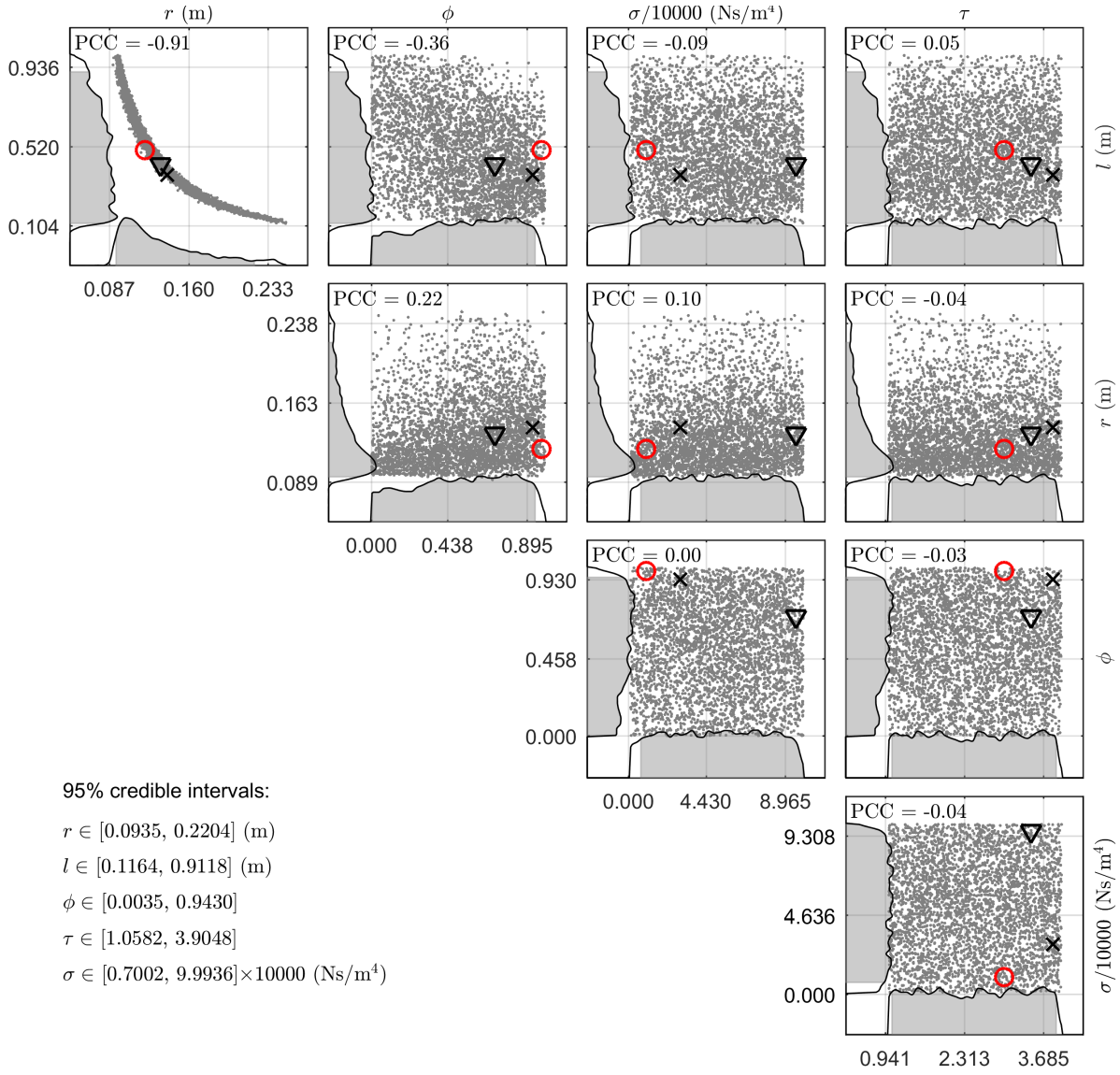


Figure 10: 2D marginal densities for the substep $f \leq 50$ Hz data. The black cross denotes the MAP estimate, the black triangle is the initial condition (based on Matlab's *lsqnonlin* estimation), and the red circle is the true value. The dots represent a sample of the MCMC points and PCC is the Pearson correlation coefficient. The black curves on the bottom and left side of each plot are the 1D marginal densities, for which the light gray zone denotes the narrowest 95% credible interval (bounds are given in the figure).

4 Conclusion

A method for the inverse estimation of material and geometrical properties of resonant coupled systems including duct components and porous media is proposed. The method consists in performing an inverse estimation procedure by steps over increasingly broader frequency ranges, in the present case starting from a low frequency limit. It has been shown, here and in a recent paper [9], that the proposed method allows to obtain the global solution of the inverse estimation problem in cases where the full spectrum inversion fails.

A crucial aspect is the availability of a frequency band where the system is non-resonant, as a starting point for the method. This ensures that the solution to the starting sub-problem belongs to a subspace containing the global solution. It is important to note that the method relies on the physical nature of resonant systems and therefore its success is in principle independent from the inversion algorithm used. In fact, both a

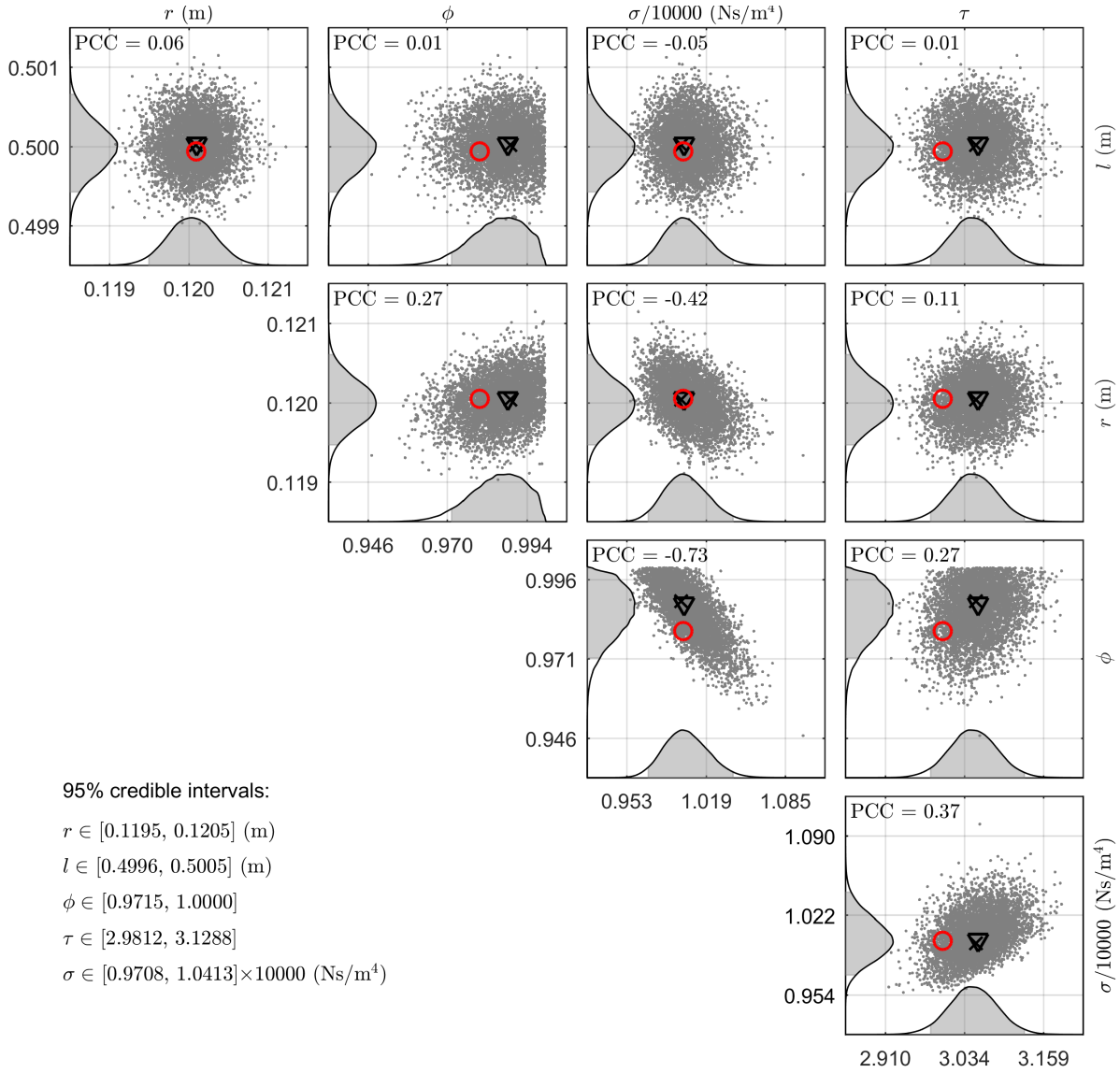


Figure 11: Results for the substep $f \leq 1200$ Hz. Otherwise same caption as in Fig. 10.

deterministic and a Bayesian framework have been implemented and shown to benefit from the robustness of the procedure for the cases under consideration.

Future work will focus on evaluating the performance of the proposed incremental frequency approach to experimental cases.

The gradient-based implementation of the method presented herein is used in another paper in this conference [19] for the purpose of identifying the geometrical properties of muffler components.

Acknowledgements

This paper is based upon work from COST Action DENORMS CA15125, supported by COST (European Cooperation in Science and Technology). The work has been supported by the strategic funding of the University of Eastern Finland and by the Academy of Finland (Finnish Centre of Excellence of Inverse Modelling and Imaging), and the Centre for ECO2 Vehicle Design at KTH.

References

[1] R. Panneton and X. Olny. Acoustical determination of the parameters governing viscous dissipation in porous media. *The Journal of the Acoustical Society of America*, 119(4):2027–2040, 2006.

[2] L. Jaouen, A. Renault, and M. Deverge. Elastic and damping characterizations of acoustical porous materials: Available experimental methods and applications to a melamine foam. *Applied Acoustics*, 69(12):1129–1140, 2008.

[3] P. Leclaire, O. Umnova, K.V. Horoshenkov, and L. Maillet. Porosity measurement by comparison of air volumes. *Review of Scientific Instruments*, 74(3):1366–1370, 2003.

[4] J. Cuenca, C. Van der Kelen, and P. Göransson. A general methodology for inverse estimation of the elastic and anelastic properties of anisotropic open-cell porous materials — with application to a melamine foam. *Journal of Applied Physics*, 115(8):084904, 2014.

[5] J.P. Parra Martínez, O. Dazel, P. Göransson, and J. Cuenca. Acoustic analysis of anisotropic poroelastic multilayered systems. *Journal of Applied Physics*, 119(8):084907, 2016.

[6] M. Niskanen, J.-P. Groby, A. Duclos, O. Dazel, J.C. Le Roux, N. Poulain, T. Huttunen, and T. Lähivaara. Deterministic and statistical characterization of rigid frame porous materials from impedance tube measurements. *The Journal of the Acoustical Society of America*, 142(4):2407–2418, 2017.

[7] W. Tu and R.W. Mayne. Studies of multi-start clustering for global optimization. *International Journal for Numerical Methods in Engineering*, 53(9):2239–2252, 2002.

[8] T. Lähivaara, L. Kärkkäinen, J.M.J. Huttunen, and J.S. Hesthaven. Deep convolutional neural networks for estimating porous material parameters with ultrasound tomography. *The Journal of the Acoustical Society of America*, 143(2):1148–1158, 2018.

[9] P. Göransson, J. Cuenca, and T. Lähivaara. Parameter estimation in modelling frequency response of coupled systems using a stepwise approach. ArXiv:1808.04985 [physics.comp–ph], 2018.

[10] K. Svanberg. A class of globally convergent optimization methods based on conservative convex separable approximations. *SIAM Journal on Optimization*, 12(2):555, 2002.

[11] J.P. Kaipio and E. Somersalo. *Statistical and Computational Inverse Problems*. Springer-Verlag, 2005.

[12] D. Calvetti and E. Somersalo. *Introduction to Bayesian Scientific Computing: Ten Lectures on Subjective Computing (Surveys and Tutorials in the Applied Mathematical Sciences)*. Springer-Verlag New York, Inc., 2007.

[13] H. Haario, E. Saksman, and J. Tamminen. Adaptive proposal distribution for random walk Metropolis algorithm. *Computational Statistics*, 14:375–396, 1999.

[14] H. Haario, E. Saksman, and J. Tamminen. An adaptive Metropolis algorithm. *Bernoulli*, 7:223–242, 2001.

[15] M.L. Munjal. *Acoustics of Ducts and Mufflers With Application to Exhaust and Ventilation System Design*. 1987.

[16] Y. Champoux and J.-F. Allard. Dynamic tortuosity and bulk modulus in air-saturated porous media. *Journal of Applied Physics*, 70(4):1975–1979, 1991.

[17] J.F. Allard and N. Atalla. *Propagation of Sound in Porous Media: Modelling Sound Absorbing Materials 2e*. Wiley, 2009.

[18] R. Panneton. Comments on the limp frame equivalent fluid model for porous media. *The Journal of the Acoustical Society of America*, 122(6):EL217–EL222, 2007.

[19] M.H. Alkmim, J. Cuenca, L. De Ryck, and P. Göransson. Model-based acoustic characterisation of duct components and extrapolation to inhomogeneous thermal conditions. In *ISMA/USD*, 2018/9/17-19.

Identification of wave forces on a floating bridge from acceleration and wave elevation data using inverse methods and wave field reconstruction

Ø. W. Petersen [1], **O. Øiseth** [1], **E.-M. Lourens** [2]
[1] NTNU, Norwegian University of Science and Technology, Department of Structural Engineering
7491 Trondheim, Norway
e-mail: **oyvind.w.petersen@ntnu.no**

[2] Delft University of Technology
2628 CN Delft, The Netherlands

Abstract
Knowledge of the loads on long-span bridges are important for assessing the dynamic behavior. To reduce the uncertainties in the adopted load models, full-scale studies of existing structures can be performed. Recently developed methods for inverse identification can estimate the unknown forces on a structure from a limited set of dynamic response measurements. In this contribution, a pilot study of full-scale force identification is performed in a practical case study of the Bergsøysund bridge, a floating pontoon bridge with a span of 840 m, that is also instrumented with accelerometers. A state of the art filtering technique is applied to identify the wave forces on the bridge. This article also presents a method for frequency-domain reconstruction of the wave forces, based on a parametric wave field model from measured wave elevation data. The obtained force estimates from the two approaches shows a reasonable agreement. The practical results are reviewed from the viewpoint of this case study and sources of uncertainties are discussed.

1 Introduction

Floating bridges with spans of 3-5 kilometers are currently being reviewed as a fjord-crossing solution in the infrastructural project Coastal Highway Route E39 in Norway. Suspension bridges with floating towers [1] or pontoon-type bridges [2] are two of the considered concepts. A good understanding of the dynamic behavior of such bridges is essential to ensure the structural safety through the life-time. However, the dynamic behavior is uncertain due to the complexity, novelty and operational environment of these structures. The floating bridges must endure large-amplitude vibrations since the natural frequencies occur in the super-low region (< 0.05 Hz) that is prone to wind and second-order wave forces, as well as in the frequency range of swell and wind sea ($\sim [0.05, 0.3]$ Hz).

In the design phase, established load models dictated by design codes are used to evaluate the dynamic response of the structure. One approach to better understand the true loading is to perform full-scale measurements. This can either be performed on the desired structure after it is built, or alternatively, on already existing similar structures to learn about the in-operation behavior. The dynamic loads are however not possible to measure directly in full-scale, which has lead to the development of inverse methods for identification of forces. These methods utilize response measurements together with a system model to estimate the input forces on a structure.

This article presents a case-study of full-scale force identification on the Bergsøysund bridge, an existing

pontoon-type bridge with a floating span of 840 m. The bridge has been monitored since 2013, and the extensive measurement data has been used in for example studies of response statistics [3], operational modal analysis [4], and full-field response estimation [5]. The force identification method used in the presented study is a joint input-state estimation algorithm [6, 7], a popular Kalman-type filtering method. In addition, separate method for frequency-domain reconstruction of the wave forces from wave elevation data is considered.

2 The Bergsøysund bridge

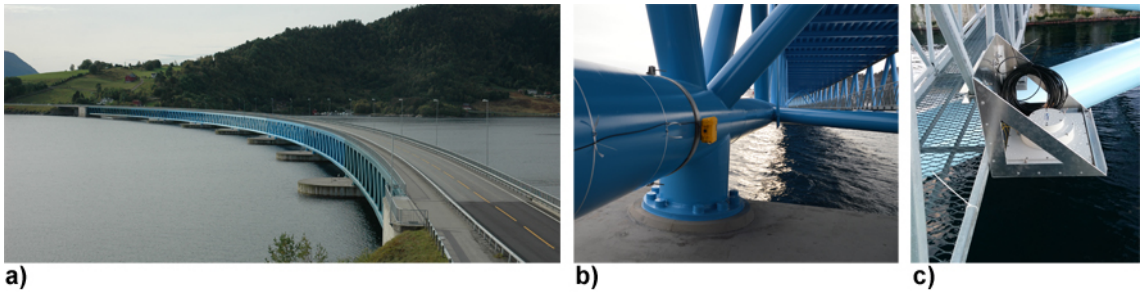
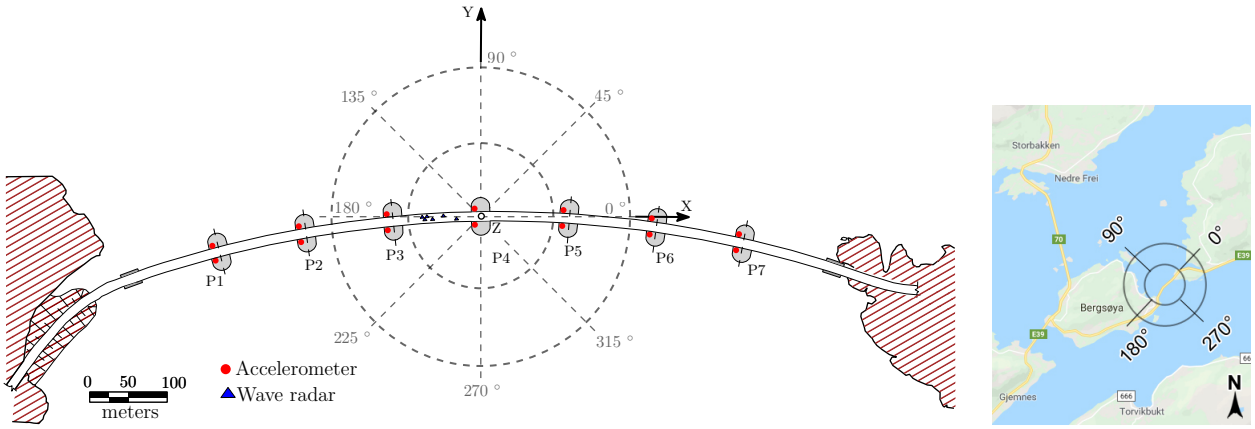


Figure 1: a) The Bergsøysund bridge seen from the northeast end; b) acceleration sensor mounted on the truss; c) wave radar mounted on the walkway.



(a) (b)

Figure 2: a) Overhead view of the Bergsøysund bridge showing the locations the accelerometers and wave radars. The compass indicates the definition of the wave direction; b) surrounding area of the bridge (Google maps, 2018).

2.1 Description of the bridge and monitoring system

The Bergsøysund bridge (Fig. 1 a) is located on the northwest coast of Norway. The bridge is 840 m long, and consists of a steel truss that is supported by seven pontoons. The structure is only anchored to the ground at the ends, which makes it very flexible and susceptible to dynamic excitation from wave actions on the pontoons. The bridge is surrounded by other islands and fjords (Fig. 2 b), causing the waves to mainly approach from the north sector ($\sim [30°, 90°]$) or the south sector ($\sim [220°, 320°]$).

A monitoring system at the site records the triaxial acceleration response in 14 locations (Fig. 1 b) and the wave elevation in six locations (Fig. 1 c). The positions of these sensors are shown in Fig. 2 a. More details about the monitoring system are given in [3].

2.2 State-space system model in the time-domain

This section gives a brief overview of how a time-domain state-space model of a floating bridge can be established. The bridge is discretized into n_{DOF} degrees of freedom (DOFs), and is assumed to be excited primarily by n_p wave forces. The governing equations of motion can be formulated in the frequency-domain as follows:

$$-\omega^2\big(\mathbf{M}_s+\mathbf{M}_h(\omega)\big)\mathbf{u}(\omega)+i\omega\big(\mathbf{C}_s+\mathbf{C}_h(\omega)\big)\mathbf{u}(\omega)+\big(\mathbf{K}_s+\mathbf{K}_h\big)\mathbf{u}(\omega)=\mathbf{L}_p\mathbf{p}_w(\omega) \tag{1}$$

The vectors and matrices and their respective sizes are summarized below:

- $\mathbf{u}\in\mathbb{R}^{n_{DOF}}$: response vector
- $\mathbf{p}_w\in\mathbb{R}^{n_p}$: wave force vector
- $\mathbf{L}_p\in\mathbb{R}^{n_{DOF}\times n_p}$: force selection matrix
- $\mathbf{M}_s\in\mathbb{R}^{n_{DOF}\times n_{DOF}}$: structural mass
- $\mathbf{C}_s\in\mathbb{R}^{n_{DOF}\times n_{DOF}}$: structural damping
- $\mathbf{K}_s\in\mathbb{R}^{n_{DOF}\times n_{DOF}}$: structural stiffness
- $\mathbf{M}_h(\omega)\in\mathbb{R}^{n_{DOF}\times n_{DOF}}$: hydrodynamic mass
- $\mathbf{C}_h(\omega)\in\mathbb{R}^{n_{DOF}\times n_{DOF}}$: hydrodynamic damping
- $\mathbf{K}_h\in\mathbb{R}^{n_{DOF}\times n_{DOF}}$: restoring stiffness

The mass, damping and stiffness matrices are obtained from a finite element model of the structure coupled with a fluid-structure interaction model of the pontoons [8].

For purposes of force identification using time-domain filter techniques, it is common to establish a reduced-order modal model [6]. Here, we use the modal base $\mathbf{\Phi}\in\mathbb{R}^{n_{DOF}\times n_m}$ obtained from the following eigenvalue problem:

$$[\mathbf{K}_s+\mathbf{K}_h-\omega_j^2(\mathbf{M}_s+\mathbf{M}_{h,\infty})]\boldsymbol{\phi}_j=\mathbf{0}\quad,\quad(\mathbf{M}_{h,\infty}=\lim_{\omega\to\infty}\mathbf{M}_h(\omega)) \tag{2}$$

$$\mathbf{\Phi}=\begin{bmatrix}\boldsymbol{\phi}_1 & \boldsymbol{\phi}_2 & \dots & \boldsymbol{\phi}_{n_m}\end{bmatrix} \tag{3}$$

However, the traditional mode-based reduction approach cannot directly be applied here due to the frequency-dependency of the hydrodynamic matrices $\mathbf{M}_h(\omega)$ and $\mathbf{C}_h(\omega)$ in Eq. 1, which give rise to so-called motion-induced forces or radiation forces that are represented by convolution integrals in the time-domain. However, Eq. 1 is still linear, and it is possible to create a high-fidelity state-space model approximation. The details behind this type of state-space modeling, and in particular the handling of the motion-induced forces, is given in [8] and is excluded here for brevity. The result is a time-invariant reduced-order state-space model based on n_m selected modes, given in continuous form as:

$$\dot{\mathbf{x}}(t)=\mathbf{A}_c\mathbf{x}(t)+\mathbf{B}_c\mathbf{p}(t) \tag{4}$$

where $\mathbf{p}(t)\in\mathbb{R}^{n_m}$ contain the *modal* wave forces ($\mathbf{\Phi}^T\mathbf{L}_p\mathbf{p}_w(t)$) and $\mathbf{x}(t)\in\mathbb{R}^{n_s}$ is a state vector that takes into account the vibration modes as well as the motion-induced forces.

The output equation considering n_y acceleration or displacement measurements in the vector $\mathbf{y}(t)\in\mathbb{R}^{n_y}$ can be established as:

$$\mathbf{y}(t)=\mathbf{S}_a\ddot{\mathbf{u}}(t)+\mathbf{S}_d\mathbf{u}(t)=\mathbf{G}_c\mathbf{x}(t)+\mathbf{J}_c\mathbf{p}(t) \tag{5}$$

where $\mathbf{S}_a$ and $\mathbf{S}_d\in\mathbb{R}^{n_y\times n_{DOF}}$ are used to select the measured DOFs. The special definition of the state-space system matrices $\mathbf{A}_c\in\mathbb{R}^{n_s\times n_s}$, $\mathbf{B}_c\in\mathbb{R}^{n_s\times n_m}$, $\mathbf{G}_c\in\mathbb{R}^{n_y\times n_m}$ and $\mathbf{J}_c\in\mathbb{R}^{n_y\times n_m}$ are given in [8]. In our case the state-space model of the Bergsøysund bridge is constructed using $n_m=18$ modes, with frequencies ω_j in the range $[0.6,4]$ rad/s. The total number of system states is $n_s=180$.

We now discretize the state-space formulation by a time step Δt such that $t_k = k\Delta t$ ($k = 0, 1, \ldots, N_t - 1$), and consider the presence of stochastic noise:

$$\mathbf{x}_{k+1} = \mathbf{A}\mathbf{x}_k + \mathbf{B}\mathbf{p}_k + \mathbf{w}_k \tag{6}$$

$$\mathbf{y}_k = \mathbf{G}\mathbf{x}_k + \mathbf{J}\mathbf{p}_k + \mathbf{v}_k \tag{7}$$

where $\mathbf{x}_k = \mathbf{x}(t_k)$, $\mathbf{p}_k = \mathbf{p}(t_k)$ and $\mathbf{y}_k = \mathbf{y}(t_k)$. Assuming the force is constant between the sample instants ($t_k < t < t_{k+1}$), the discrete time system matrices can be shown to have the following definition:

$$\mathbf{A} = \exp\Big(\mathbf{A}_\mathrm{c}\Delta t\Big), \quad \mathbf{B} = (\mathbf{A} - \mathbf{I})\mathbf{A}_\mathrm{c}^{-1}\mathbf{B}_\mathrm{c}, \quad \mathbf{G} = \mathbf{G}_\mathrm{c}, \quad \mathbf{J} = \mathbf{J}_\mathrm{c} \tag{8}$$

The following covariance relations are used to describe the white-noise processes $\mathbf{w}_k \in \mathbb{R}^{\mathrm{n_s}}$ and $\mathbf{v}_k \in \mathbb{R}^{\mathrm{n_y}}$:

$$\mathbb{E}[\mathbf{w}_k\mathbf{w}_l^\mathrm{T}] = \mathbf{Q}\delta_{kl}, \quad \mathbb{E}[\mathbf{v}_k\mathbf{v}_l^\mathrm{T}] = \mathbf{R}\delta_{kl}, \quad \mathbb{E}[\mathbf{w}_k\mathbf{v}_l^\mathrm{T}] = \mathbf{S}\delta_{kl} \tag{9}$$

3 Methods for estimation of wave forces

3.1 Estimation by inverse identification algorithms

In this study we apply a joint input-state estimation algorithm [6, 7], which is a stochastic-deterministic method utilizing the system description in Eq. 6 and 7. The algorithm is a Kalman-type filter, where the input is unknown and thus jointly estimated with the system states. The filter equations are omitted here; the reader is referred to the cited references for an explanation of the algorithm.

It is chosen to identify modal forces ($\mathbf{p}(t)$) rather than the physical pontoon wave forces directly ($\mathbf{p}_\mathrm{w}(t)$). This necessary due to theoretical limitations of the number of forces that can be identified, which generally cannot exceed the number of acceleration outputs or the number of modes in the model [9]. Note that for algorithms with time-delayed inversion rather than instantaneous inversion, this criterion can for certain cases be given some slack [10]. In addition, it is an advantage to use modal forces when the additional unknown excitation from wind and traffic cannot be neglected, since any unmodelled sources of excitation conflicts with a system description where only localized inputs are considered. The modal forces covers by definition any kind of external loading to the system. We expect that the modal forces that are identified still should be dominated by the wave force content, since in comparison the wind and traffic excitation are much smaller.

3.2 Frequency-domain reconstruction using wave radar data

This sections shows idea behind the frequency-domain reconstruction of the wave forces, using a parametric model of the sea state together with a panel model of the pontoons.

We assume the sea surface elevation $\eta(x, y, t)$ is a zero-mean, homogeneous and stationary stochastic process. The wave field is described by the directional wave spectral density $S_{\eta\eta}(\omega, \theta) \in \mathbb{R}$, where θ represents the wave direction, which here is defined as the polar angle shown in Fig. 2. The one-dimensional wave spectrum $S_{\eta\eta}(\omega)$ can be obtained by integration over the directions:

$$S_{\eta\eta}(\omega) = \int_0^{2\pi} S_{\eta\eta}(\omega, \theta)\,\mathrm{d}\theta \tag{10}$$

The directional wave spectrum can be estimated from wave elevation measurements, for example by using the DIWASP Toolbox for MATLAB [11]. This toolbox implements the Extended Maximum Entropy Principle (EMEP) [12], a robust estimation method which utilizes the cross-spectral density of wave elevation measurements from a distributed array of wave radars.

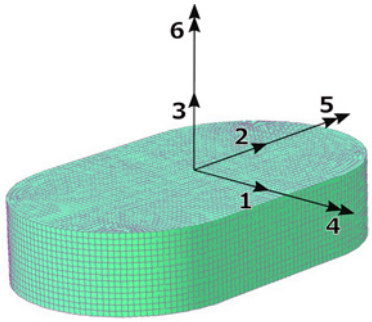


Figure 3: Panel model of the pontoon geometry. The numbers denotes the six local DOFs.

Provided that $S_{\eta\eta}(\omega,\theta)$ is known and equal at all the pontoon locations (homogenenous wave field), the cross-spectral density of the first-order wave forces on pontoon m can be calculated by the following integral:

$$S_{p_{\mathrm{w},i}^{(m)} p_{\mathrm{w},j}^{(m)}}(\omega) = \int_0^{2\pi} S_{\eta\eta}(\omega,\theta)\, Q_i^{(m)}(\omega,\theta-\alpha_m)\left(Q_j^{(m)}(\omega,\theta-\alpha_m)\right)^* \mathrm{d}\theta, \quad i,j=\{1\dots6\} \tag{11}$$

where the asterix denote the complex conjugate and $m \in \{1\dots7\}$ are indices for the seven pontoons. The subindexes i and j denote the six local DOFs, where $1-3$ are displacements and $4-6$ are rotations, see Fig. 3. $Q_i^{(m)}(\omega,\theta) \in \mathbb{C}$ is the directional transfer function relating wave elevation to the wave forces on pontoon number m, and depends on the incoming wave direction θ. α_m is the local rotation of the a pontoon with respect to the global xy-coordinate system ($\alpha_1 = 14°, \dots, \alpha_7 = -14°$). Finally, note that the formulation in Eq. 11 assumes the waves are fairly short-crested compared to the distance between two pontoons, which is reasonable since in this case the distance is ~ 105 m.

The transfer functions $Q_i^{(m)}(\omega,\theta)$ can be obtained by hydrodynamic codes. Here, we have created panel models of the pontoons in the software HydroD WADAM [13], with a geometry similar to the one shown in Fig. 3. The obtained transfer functions are shown in Fig. 4 and 5, using the middle pontoon ($m = 4$) as an example. The export resolution for the frequency and angle is set to 0.05 rad/s and $10°$, respectively.

To establish a global picture of wave loads, the power spectral density (PSD) matrix $\mathbf{S}_{\mathrm{p_w p_w}}(\omega) \in \mathbb{C}^{\mathrm{n_p}\times\mathrm{n_p}}$ containing all the wave forces ($\mathrm{n_p} = 7\times6 = 42$) is populated with the elements $S_{p_{\mathrm{w},i}^{(m)} p_{\mathrm{w},j}^{(m)}}(\omega)$ from Eq. 11. Since modal forces are identified with the inverse methods, $\mathbf{S}_{\mathrm{p_w p_w}}(\omega)$ can be transformed to the modal form $\mathbf{S}_{\mathrm{pp}}(\omega) \in \mathbb{C}^{\mathrm{n_m}\times\mathrm{n_m}}$ for a common basis of comparison:

$$\mathbf{S}_{\mathrm{pp}}(\omega) = \mathbf{\Phi}^{\mathrm{T}}\mathbf{L}_{\mathrm{p}}\mathbf{S}_{\mathrm{p_w p_w}}(\omega)(\mathbf{\Phi}^{\mathrm{T}}\mathbf{L}_{\mathrm{p}})^{\mathrm{T}} \tag{12}$$

4 Estimation of forces on the Bergsøysund bridge

4.1 Processing of the measurement data

A time series recorded 2017-10-29 12:39 with length 30 minutes is used in the full-scale identification. The acceleration and wave data is resampled to a sample rate of 10 Hz ($\Delta t = 0.1$ s), corresponding to $N_t = 1.8\cdot10^4$ time steps. In addition, the acceleration data is low-pass filtered to only include content below 4.5 rad/s. Above this limit, the contribution to the total response is negligible, and cannot be accounted for by the modal basis of the reduced-order state-space model. Sample time series from the wave radars and accelerometers are shown in Fig. 6 and 7, respectively. The peak wave frequency is 2.45 rad/s, which also leads to the highest dynamic response around this frequency.

For simplicity, only acceleration data and no displacement data is used in the inverse algorithms. In this case, this leads to a so-called marginally stable system inversion [9]. As will be shown, this mainly results

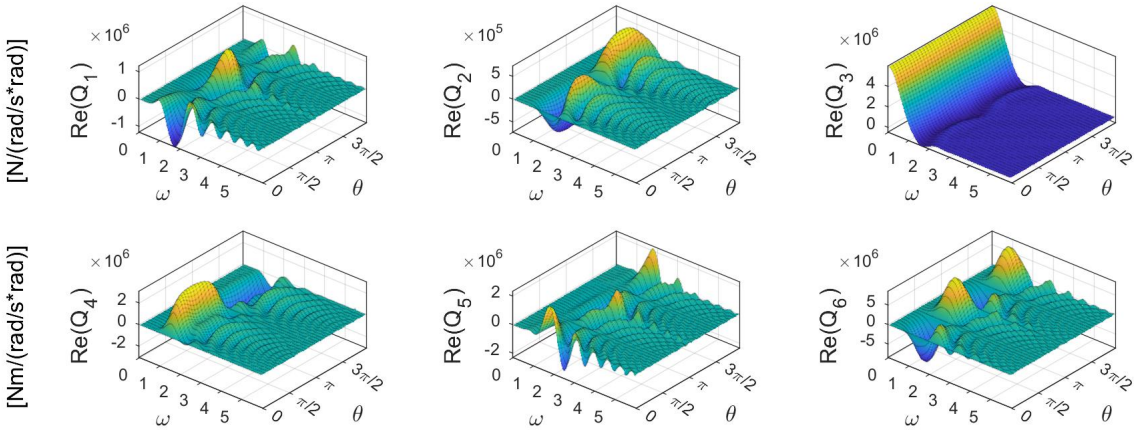


Figure 4: The real value of the transfer functions $Q_i(\omega, \theta)$ $(i = 1 \ldots 6)$ for the middle pontoon.

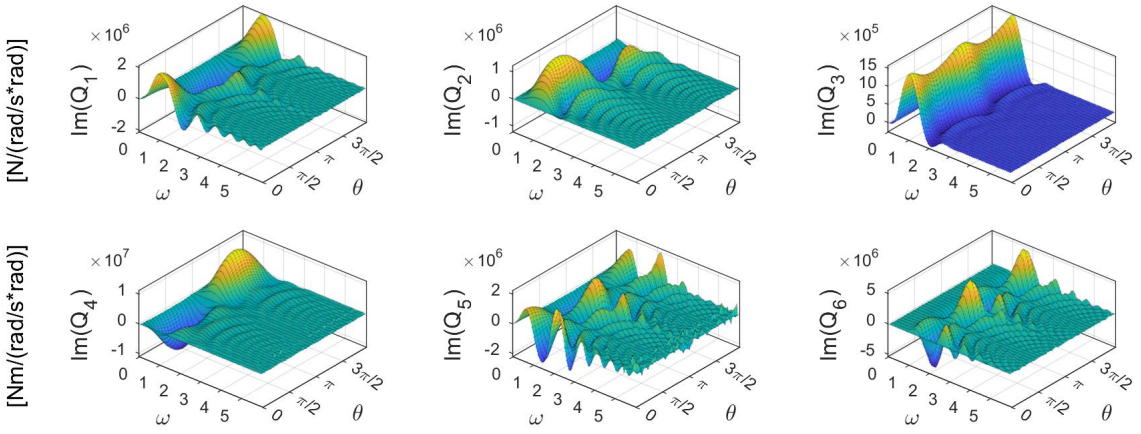


Figure 5: The imaginary value of the transfer functions $Q_i(\omega, \theta)$ $(i = 1 \ldots 6)$ for the middle pontoon.

in spurious low-frequent content in the input estimates due to the lack of static-sensitive data, which is necessary to stabilize the filter solution.

The cross-spectral density between all the six wave radar measurements, which goes into the EMEP estimation, are calculated using a Welch-estimate with a section division of 512 samples and no overlap.

4.2 Force estimation results and discussion

The wave forces are now estimated using the methods presented in Section 3.1 and 3.2, respectively driven by acceleration data and wave elevation data.

The resulting estimate of the directional wave spectrum is illustrated in Fig. 8. The waves mainly approach from a skew angle of $65°$, coming from the fjord north of the bridge. Using the estimated directional wave spectrum, the modal waves forces are predicted using Eq. 11 and 12, as shown in Fig. 9. The figure also shows the PSD of the modal forces identified using the inverse algorithms. The covariance matrices $\mathbf{Q} = 10^{-2} \cdot \mathbf{I}$, $\mathbf{S} = \mathbf{0}$, $\mathbf{R} = 10^{-6} \cdot \mathbf{I}$ have been prescribed as the tuning variables for the filter.

Neglecting the frequency range $[0, 1]$ rad/s, the force estimates obtained from the two approaches are similar. Overall, this indicates that estimates of the forces are reasonable. A direct comparison of the forces obtained from the two methods should be interpreted with caution, however, since the methods are based on different assumptions. Both approaches are expected to have sources of uncertainties or assumptions that in reality are violated. The most important can be summarized as:

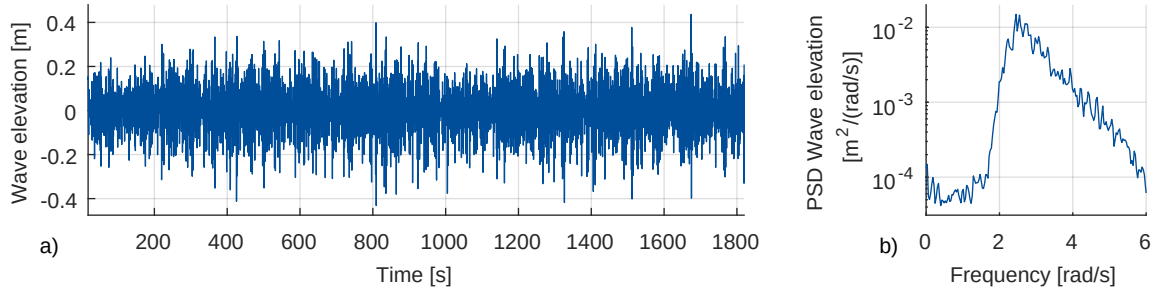


Figure 6: Sample wave elevation measurement from one of the wave radars.

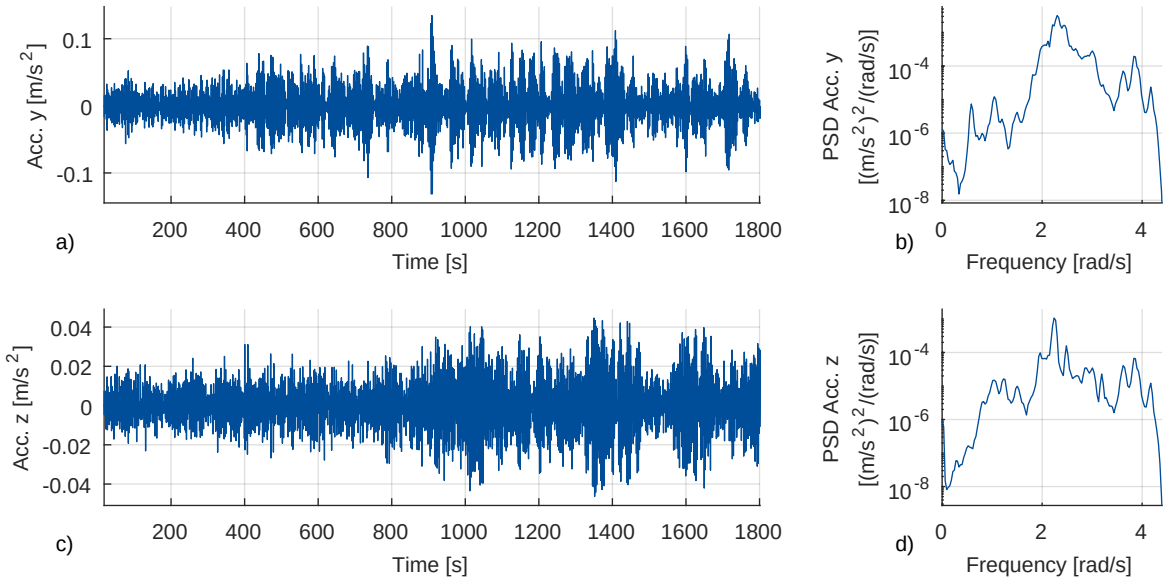


Figure 7: Sample acceleration measurements from pontoon number 3 in the horizontal (y) and vertical (z) direction. The data is low-pass filtered below 4.5 rad/s.

- Errors on the state-space model, coming from model errors in the structural finite element model or the model for the fluid-structure interaction.
- Sensor uncertainty in the accelerometers and wave radars, in particular for the low-frequent range below 1 rad/s.
- EMEP estimation errors of the directional wave field, leading to for example waves approaching from unlikely directions such as 180° in Fig. 8 a.
- Inhomogeneities of the global wave field in the strait cannot be detected when the wave radars are clustered closely together (cf. Fig. 2 a).
- Multibody pontoon interaction through the fluid is not considered here. This influences the transfer functions $Q_i^{(m)}(\omega, \theta)$, as well as $\mathbf{M}_\mathrm{h}(\omega)$ and $\mathbf{C}_\mathrm{h}(\omega)$ and so also the state-space model.
- Second-order sum and difference wave forces are not considered in the wave force reconstruction.
- Presence of additional excitation (wind or traffic) will show up in the identified forces, although their magnitude is small when compared to the wave loads.

Further work should consider more recordings from the measurement database with various ambient wave conditions, such as SWH, wave direction and peak frequency.

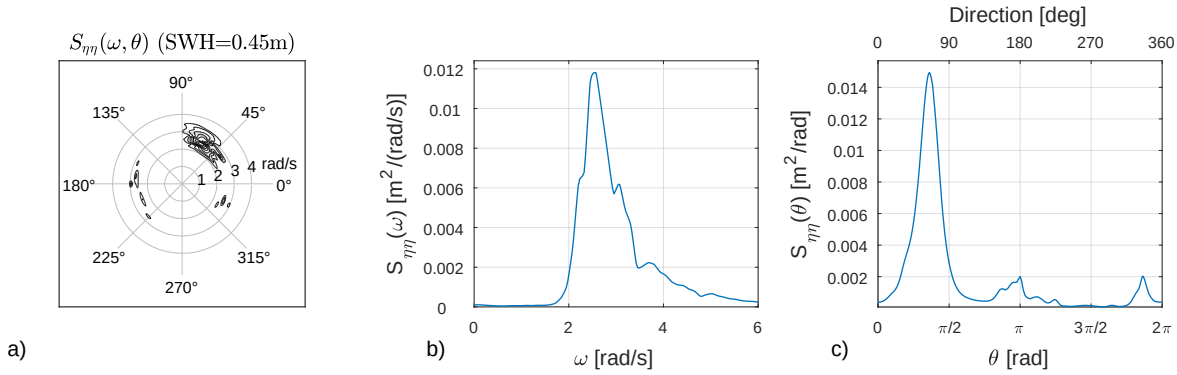


Figure 8: a) Estimated directional wave spectrum using EMEP in the DIWASP Toolbox; b) marginal wave spectrum for frequency only; c) marginal wave spectrum for direction only.

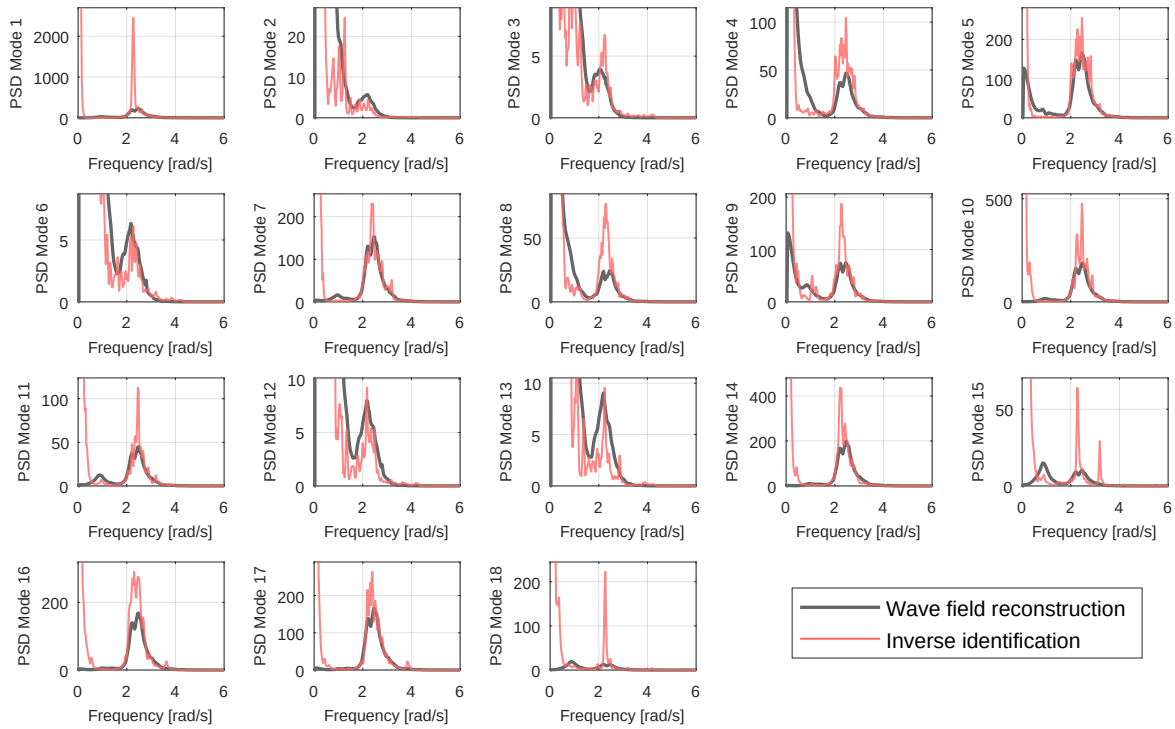


Figure 9: Auto PSD of the estimated modal forces for all the 18 modes. Both the force estimate from the wave field reconstruction and the input estimate from the inverse identification is shown.

5 Conclusion

This paper has presented has presented a case-study of the full-scale identification of wave forces on a floating bridge. Two different approaches was used: 1): force identification by a joint input-state estimation algorithm using measured acceleration data; 2): frequency-domain reconstruction of the forces using measured wave elevation data. The force estimates obtained from the two methods appear to have a reasonable agreement when compared in the frequency-domain. The discrepancies that occur can be explained by the different simplifications, modelling uncertainties and assumptions behind the two methods. The study shows that different approaches for obtaining the ambient forces have advantages and disadvantages, so that the methods can complement each other in the total assessment of the forces.

Acknowledgements

We gratefully acknowledge the financial support from the Norwegian Public Roads Administration.

References

[1] Y. Xu, O. Øiseth, T. Moan, *Time domain simulations of wind-and wave-induced load effects on a three-span suspension bridge with two floating pylons*, Marine Structures, Vol. 58, (2018), pp. 434-452.

[2] Z. Cheng, Z. Gao, T. Moan, *Wave load effect analysis of a floating bridge in a fjord considering inhomogeneous wave conditions*, Engineering Structures, Vol. 163, (2018), pp. 197-214.

[3] K. Kvåle, O. Øiseth, *Structural monitoring of an end-supported pontoon bridge*, Marine Structures, Vol. 52, (2017), pp. 188-207.

[4] K. Kvåle, O. Øiseth, A. Rønnquist, *Operational modal analysis of an end-supported pontoon bridge*, Engineering Structures, Vol. 148, (2017), pp. 410-423.

[5] Ø.W. Petersen, O. Øiseth, T.S. Nord, E. Lourens, *Estimation of the full-field dynamic response of a floating bridge using Kalman-type filtering algorithms*, Mechanical Systems and Signal Processing, Vol. 107, (2018), pp. 12-28.

[6] E. Lourens, C. Papadimitriou, S. Gillijns, E. Reynders, G. De Roeck, G. Lombaert, *Joint input-response estimation for structural systems based on reduced-order models and vibration data from a limited number of sensors*, Mechanical Systems and Signal Processing, Vol. 29, (2012), pp. 310-327.

[7] K. Maes, A.W. Smyth, G. De Roeck, G. Lombaert, *Joint input-state estimation in structural dynamics*, Mechanical Systems and Signal Processing, Vol. 70-71, (2012), pp. 445-466.

[8] Ø.W. Petersen, O. Øiseth, *Efficient time-domain modeling of floating structures with fluid-structure interaction by reduced order state-space approximations*, *Submitted to the 28th Conference on Noise and Vibration Engineering, Leuven, Belgium, 2018*.

[9] K. Maes, E. Lourens, K. Van Nimmen, E. Reynders, G. De Roeck, G. Lombaert, *Design of sensor networks for instantaneous inversion of modally reduced order models in structural dynamics*, Mechanical Systems and Signal Processing, Vol. 52, (2014), pp. 628-644.

[10] K. Maes, S. Gillijns, G. Lombaert, *A smoothing algorithm for joint input-state estimation in structural dynamics*, Mechanical Systems and Signal Processing, Vol. 98, (2018), pp. 292-309.

[11] D. Johnson, *DIWASP, a directional wave spectra toolbox for MATLAB: User manual*, Research Report WP-1601-DJ (V1.1), Centre for Water Research, University of Western Australia, (2012).

[12] N. Hashimoto, T. Nagai, T. Asai, *Extension of the maximum entropy principle method for directional wave spectrum estimation*, in B. Edge, editor, *Proceedings of 24th Conference on Coastal Engineering, 1994, Kobe, Japan*, Kobe (1994), pp. 232-246.

[13] DNV Software, *HydroD WADAM 9.1 User Manual*, Høvik, Norway, (2014).

Investigation of virtual sensing techniques on a rear twistbeam suspension by performing multiple-input/state estimation

R. Cumbo [1], **T. Tamarozzi** [1,2], **K. Janssens** [1], **W. Desmet** [2]
[1] Siemens Industry Software NV
Interleuvenlaan 68, B-3001, Leuven, Belgium
e-mail: **roberta.cumbo@siemens.com**

[2] KU Leuven, Department of Mechanical Engineering
Celestijnenlaan 300 B, B-3001, Heverlee, Belgium

Abstract
The identification of external loads acting on a mechanical system represents a challenging target for many applications. The knowledge of these forces in operational conditions represents a potential benefit for durability and NVH assessments. In this paper, two indirect load identification strategies are presented: i) a time-domain TPA approach based on matrix inversion, and ii) a Kalman approach combining operational measurement data with a system FE model. These two approaches are investigated on a complex twistbeam rear suspension application. The potential of the two techniques for multiple input/state estimation is discussed together with implementation hurdles that need to be overcome for both approaches. A measurement campaign on the twistbeam was performed by acquiring strain responses together with force measurements for validation purposes.

1 Introduction

The identification of loads acting on a mechanical component together with the estimation of full-field responses during its operational life is very active topic of research in structural dynamic applications. The input loads are often difficult to measure directly since dedicated sensors can be expensive, intrusive and can rarely be equipped during the operational life of the system. Within the last decades, inverse load identification strategies have been researched and developed to deal with these issues. Experimental-based and model-based techniques are available in literature. An experimental-based approach commonly used for industrial scale applications is the Transfer Path Analysis (TPA) Matrix Inversion (MI) [1,4]. The purely experimental nature of TPA MI and the low computational cost represents great advantages over other available inverse identification methods. However, several disadvantages might limit its usability. It results easily in ill-conditioned problems and leads to some erroneous estimation especially when stiffer load directions have to be estimated [2]. To guarantee the over-determination of the inversion, a large set of sensors is needed and thus big effort is required for the acquisition of a large amount of data. In the last years, some model-based approaches are developed by combining experimental and numerical data to improve the results. Estimators such as Kalman Filters have been used to approach the inverse load identification problem [5, 8], where the link between responses and loads is defined by the numerical model. The load estimation problem can be solved using a joint state-input estimation algorithm, giving the possibility to estimate full-field e.g. displacements, strains, accelerations concurrently with the unknown loads. An efficient algorithm is the Augmented Kalman Filter (AKF) [6] that was recently applied to structural dynamics [9, 11].
Within the present work, a comparison between the experimental-based TPA MI and the model-based AKF

is proposed to solve the load identification problem on an industrial test case, such as a rear twistbeam suspension [12]. The Optimal Sensor Placement (OSP) strategy, developed in [13], is adopted in this work to select the sensors location for a successful application of the AKF algorithm. The full-field strain estimation is also analyzed.
The paper is structured as follows: a theory section about TPA Matrix Inversion approach is proposed in Sec. 2, followed by the derivation of Augmented Kalman Filter algorithm applied on a dynamic system. After the description of the analyzed structure in Sec. 3, the comparison of loads and strain field estimation through both techniques is shown. Finally, in Sec. 4, conclusions and future development are discussed.

2 Theoretical Background

2.1 TPA Matrix Inversion

Transfer Path Analysis (TPA) is an experimental technique aimed to identify vibro-acoustic transfer paths. The external loads acting on a system are obtained by solving an inverse problem. In the analyzed system, the active i.e. source and passive i.e. receiver parts are defined. The energy is generated by the active part and transferred to the passive part through physical connections. One common example is a mechanical system as a car or an aircraft in which the engine represents the source of energy and it can be identified as active part. The main strong advantage of TPA is that it allows engineers perform simulation using only test data. Two main ways are available for TPA load identification: Mount Stiffness and Matrix Inversion. The first approach is adopted when active and passive parts are connected through flexible mounts. In this paper, only Matrix Inversion (MI) is analyzed. Its formulation requires the inversion of the FRFs matrix which has to be measured off-line, when the source is disconnected from the receiver. The so-called indicator responses are also measured on the receiver in operational conditions and they are usually located close to the source connection. The relationship in frequency domain between the FRFs matrix and the indicators data is the following:

$$\boldsymbol{y}(\omega) = \boldsymbol{H}(\omega)\boldsymbol{f}(\omega) \tag{1}$$

where $\boldsymbol{y}$ and $\boldsymbol{f}$ are the vector of the measured quantities (as accelerations or strains) and the vector of the loads acting on the receiver respectively, both functions of the spectral lines ω. By inverting the FRF matrix $\boldsymbol{H}$ and by multiplying this with the operational data $\boldsymbol{y}$, the load identification can be performed:

$$\boldsymbol{f}(\omega) = \boldsymbol{H}(\omega)^{-1}\boldsymbol{y}(\omega) \tag{2}$$

This equation is evaluated for each frequency line. In order to minimize the ill-conditioning of the problem, the number of responses must exceed the number of forces with a factor 2. This hence leads to the calculation of the pseudo-inverse matrix in Eq. 2. Inaccuracies in the measured FRFs data e.g. impact direction can results in large errors on the estimated loads. It is important to include responses that can give useful information: if, for example, two accelerations too close to each other are measured, the same transfer path is added in the FRFs matrix and it leads to noisy results.

2.2 Augmented Kalman Filter for joint state-input estimation

In this section, an overview of the Kalman Filter (KF) applied on a dynamic system and the following derivation of the Augmented Kalman Filter (AKF) are proposed. Lets start from the dynamic equation of motion:

$$\boldsymbol{M_z}\ddot{\boldsymbol{z}}(t) + \boldsymbol{C_z}\dot{\boldsymbol{z}}(t) + \boldsymbol{K_z}\boldsymbol{z}(t) = \boldsymbol{B_z}\boldsymbol{u}(t) \tag{3}$$

where $\boldsymbol{z}(t) \in \Re^{n_{dof}}$ is the Degrees of Freedom (DoF) vector (n_{dof} number of DoFs of the model), $\boldsymbol{M_z}$, $\boldsymbol{C_z}$, $\boldsymbol{K_z}$ denote the mass, damping and stiffness matrices respectively; $\boldsymbol{u}(t) \in \Re^{n_i}$ (n_i number of loads) is the input vector and $\boldsymbol{B_z} \in \Re^{n_{dof} \times n_i}$ is the Boolean input shape matrix that distributes the inputs over the DoFs

of the system.
Considering a mechanical system, the FE numerical model is used in the filter. In order to reduce the size of the problem and thus the computational costs needed for computing the Kalman Filter equations, a Model Order Reduction (MOR) has to be used. As in [11, 13, 14], the following reduction basis is used:

$$\boldsymbol{\Psi} = [\boldsymbol{\Psi}_{ram} \quad \boldsymbol{\Psi}_{nm}] \tag{4}$$

where $\boldsymbol{\Psi}_{ram} \in \Re^{n_{dof} \times n_{ram}}$ is the *residual attachment modes* [15] matrix and $\boldsymbol{\Psi}_{nm} \in \Re^{n_{dof} \times n_{nm}}$ is the *normal modes* matrix. The reduced FE model has a total of $n_{red} = n_{ram} + n_{nm}$ DoFs. From the model order reduction, the DoFs vector can be approximated as:

$$\boldsymbol{z} \simeq \boldsymbol{\Psi} \boldsymbol{q} \tag{5}$$

where $\boldsymbol{q} \in \Re^{n_{red}}$ contains the generalized coordinates of the system.
Since the Kalman Filter formulation is based on a space-state approach, the second-order equation of motion has to be formulated as a first-order equation. Coupling Eq. 3 (projected onto the reduction basis in Eq. 4) with the response equation, the state-space form is written as:

$$\begin{cases} \dot{\boldsymbol{x}}(t) = \boldsymbol{A}\boldsymbol{x}(t) + \boldsymbol{B}\boldsymbol{u}(t) \\ \boldsymbol{y}(t) = \boldsymbol{C}\boldsymbol{x}(t) + \boldsymbol{D}\boldsymbol{u}(t) \end{cases} \tag{6}$$

where $\boldsymbol{x} = [\boldsymbol{q} \quad \dot{\boldsymbol{q}}]^T$ defines the state vector. $\boldsymbol{A}$, $\boldsymbol{B}$, $\boldsymbol{C}$, and $\boldsymbol{D}$ are real matrices. The firsts two are functions of mass, stiffness and damping matrices [14], while $\boldsymbol{C}$ and $\boldsymbol{D}$ depend on the output response type $\boldsymbol{y}$. The latter defines the measurement vector containing the observed quantities. Detailed explanation on how to build $\boldsymbol{C}$ and $\boldsymbol{D}$ in relation with acceleration, strain or position measurements is reported in [14]. If both measurements and input are known, Eq. 6 is sufficient to define a linear Kalman Filter and a simple state estimation (i.e. full-field response) can be performed. Since the joint state-input estimation is of interest in this paper, the augmented state vector has to be defined as follows:

$$\boldsymbol{x}^* = [\boldsymbol{x} \quad \boldsymbol{u}]^T \tag{7}$$

The dynamics of the input has also to be modeled for the augmented filter. In this work, a zeroth-order random walk model is introduced for the input [10, 11, 13, 16]:

$$\dot{\boldsymbol{u}}(t) = \boldsymbol{0} + \boldsymbol{w}_{\boldsymbol{u}}(t) \tag{8}$$

with $\boldsymbol{w}_{\boldsymbol{u}}$ stochastic process associated to the covariance matrix $\boldsymbol{Q}_{\boldsymbol{u}}$.
Using a sampling time Δt, the time-discrete formulation of Eq. 6 in an augmented form is:

$$\begin{cases} \boldsymbol{x}_k^* = \boldsymbol{F}^* \boldsymbol{x}_{k-1}^* + \boldsymbol{w}_{k-1}^* \\ \boldsymbol{y}_k = \boldsymbol{H}^* \boldsymbol{x}_k^* + \boldsymbol{v}_k^* \end{cases} \tag{9}$$

where the symbol * is assigned to indicate all the augmented quantities. Vectors $\boldsymbol{w}^*$ and $\boldsymbol{v}^*$ are mutually uncorrelated Gaussian variables (process and measurement noise), not usually included in the equations of motion. They are now introduced to take into account model and measurement uncertainties, with associated covariance matrix $\boldsymbol{Q}^*$ and $\boldsymbol{R}$. $\boldsymbol{Q}^*$ is defined as a block diagonal matrix composed by $\boldsymbol{Q}$ and $\boldsymbol{Q}_{\boldsymbol{u}}$, that are the covariance matrices referred to the model and input uncertainties respectively. $\boldsymbol{F}^*$ and $\boldsymbol{G}^*$ are the discretized-time and augmented form of the matrices $\boldsymbol{A}$, $\boldsymbol{B}$, $\boldsymbol{C}$, $\boldsymbol{D}$. Their formulation depends on the discretization scheme (see [17] for more details). In this work, an exponential time integration is used [14]. The discrete-time version of the Augmented Kalman Filter can be formulated as following, by considering the time and measurement update. The a priori $\hat{\boldsymbol{x}}_k^{*-}$ (without taking into account the new measurement at time k) and a posteriori $\hat{\boldsymbol{x}}_k^{*+}$ augmented states are easily obtained:

Time update

$$\begin{aligned} \hat{\boldsymbol{x}}_k^{*-} &= \boldsymbol{F}^* \hat{\boldsymbol{x}}_{k-1}^{*+} \\ \boldsymbol{P}_k^- &= \boldsymbol{F}^* \boldsymbol{P}_{k-1}^+ \boldsymbol{F}^{*T} + \boldsymbol{Q}_{k-1}^* \end{aligned} \tag{10}$$

Measurement update

$$\begin{aligned} \boldsymbol{K}_k &= \boldsymbol{P}_k^- \boldsymbol{H}^{*T} \left(\boldsymbol{H}^* \boldsymbol{P}_k^- \boldsymbol{H}^{*T} + \boldsymbol{R}_k \right)^{-1} \\ \hat{\boldsymbol{x}}_k^{*+} &= \hat{\boldsymbol{x}}_k^{*-} + \boldsymbol{K}_k \left(\boldsymbol{y}_k - \boldsymbol{H}^* \hat{\boldsymbol{x}}_k^{*-} \right) \\ \boldsymbol{P}_k^+ &= \left(\boldsymbol{I} - \boldsymbol{K}_k \boldsymbol{H}^* \right) \boldsymbol{P}_k^- \end{aligned} \tag{11}$$

The estimator is designed to be optimal in the sense that it minimizes the trace of the error covariance $\boldsymbol{P}_k$, which is defined as:

$$\boldsymbol{P}_k = E \left[\left(\boldsymbol{x}_k^* - \hat{\boldsymbol{x}}_k^* \right) \left(\boldsymbol{x}_k^* - \hat{\boldsymbol{x}}_k^* \right)^T \right] \tag{12}$$

In order to have a stable estimator, the augmented system in Eq. 9 has to be observable. The requirements for guaranteeing the observability of a structural system can be summarized as following [8, 9]:

- the number of DoFs of the reduced model has to be equal or greater than the number of external loads to be estimated: $n_{red} \geq n_f$;
- the number of position/strain measurements has to be greater than the number of external loads to be estimated: $n_y \geq n_f$;
- in the case of full position measurement the AKF leads to a fully observable system and to a stable estimator. Performing only acceleration measurements will typically not lead to a stable AKF for structural systems.

In the following section, the Optimal Sensor Placement (OSP) criterion [13] is briefly described. It aims to select the optimal number, type and location of sensors for the loads identification, satisfying the observability requirement of the system.

2.2.1 OSP: theory and experimental validation

Experimental applications for inverse load identification often use to locate the sensors close to the interested input area or, more in general, in the areas that are more sensitive to the external excitation. This selection criterion is adopted for TPA MI identification analysis. The safety of the sensors is lower if they are installed in the loaded area. How to locate sensors is an open question also for numerical reasons, since inverse load identification methods results often in ill-conditioned and ill-posed problems. In [5], an Optimal Sensor Placement (OSP) strategy is developed to deal with these issues for Kalman-based load identification, by allowing a smart selection of optimal type, number and sensors location. Five steps are identified and schematically shown in Fig. 1:

- **Pool of sensors:** First large random selection of position/strain/acceleration over all the FE model. Choosing sensors located on all available nodes and elements is the optimal way, but a subset has to be selected for reducing the computational cost.
- **Training scenarios:** The FE model is simulated under loads with different direction, amplitude and frequencies. The excitation is applied on the known input location of the external loads to identify.
- **Coarse screening:** From the previous step, a data set of position/strain/acceleration responses is collected. This step removes all the sensors with lowest contribution for each training scenario. A second screening removes selected sensors too close to each other.

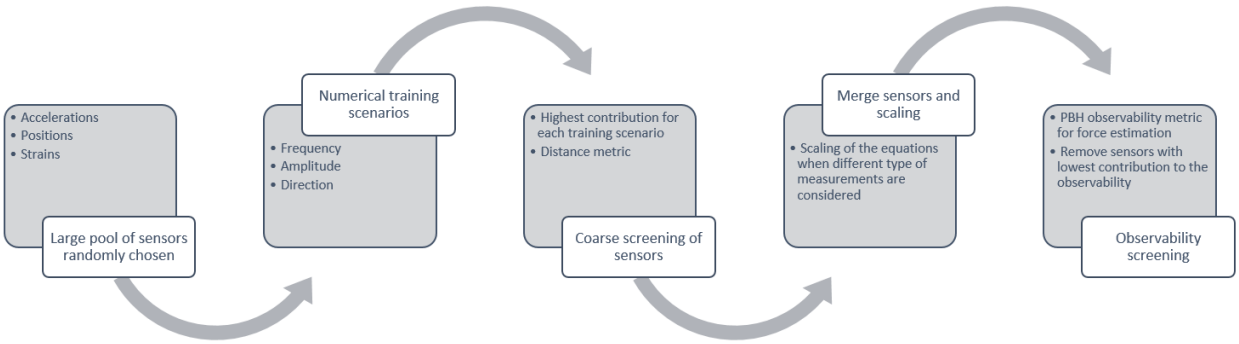


Figure 1: Optimal Sensor Placement strategy

- **Merge sensors and scaling:** All the measurements identify the C matrix of the state-space system. The rows of the matrix is scaled so that the following step doesn't take into account different type of sensors.

- **Observability screening:** a loop is performed by selecting the sensors with main contribution to force identification. The observability is quantified as follows [13]:

$$O_m = \frac{1}{n_i \cdot cond(\boldsymbol{PBH}(0))} \tag{13}$$

  where n_i is the number of loads to estimate and $\boldsymbol{PBH}$ is the observability matrix. The latter matrix is evaluated at 0Hz since that is the frequency related to the random walk eigenvector.

Some numerical results in [5] show the performance of this strategy. The experimental validation is proposed in [18] on the same twistbeam setup and it is used in this paper for the application of AKF.

3 Experimental investigation of a twistbeam rear suspension

The structure under investigation is a twistbeam rear suspension shown in Fig. 2. The physical setup in the picture consists of the twistbeam mounted on an ad-hoc built setup excited with a 6DoFs hydraulic shaker. The latter is a unique piece of equipment that allows to retain full control on the desired excitation spectrum up to high frequency (around 200Hz) and in 6 directions independently. All the following analysis are related to the setup shown in Fig. 2, consisting in clamped bushings and one clamped tyre. The right side tyre is in free condition and it is excited by the shaker. This setup is indicated in the following as *operational configuration*. A force cell is also used to collect experimental load data for validating the estimated results. Accelerometers and strain gages are installed all over the structure. The advantages of the presented methods are defined starting from the effort needed for instrumentation and measurement campaign, followed by the data-processing. In the following, these two tasks aimed to load identification are separately described for TPA MI and AKF. In the proposed analysis of this paper, only strain measurements are taken into account.

TPA Matrix Inversion

The MI load identification of Eq. 2 needs the knowledge of the full FRFs matrix and the indicator responses. The greater effort during the measurement campaign resides in the FRFs measurements. Firstly, active and passive parts have to be defined. In the operational configuration of Fig. 2, they can be easily identified by the twistbeam and the shaker respectively. The frequency domain data has to be acquired off-line, when the source is disconnected from the receiver. The excitation point is identified at the corresponding connection

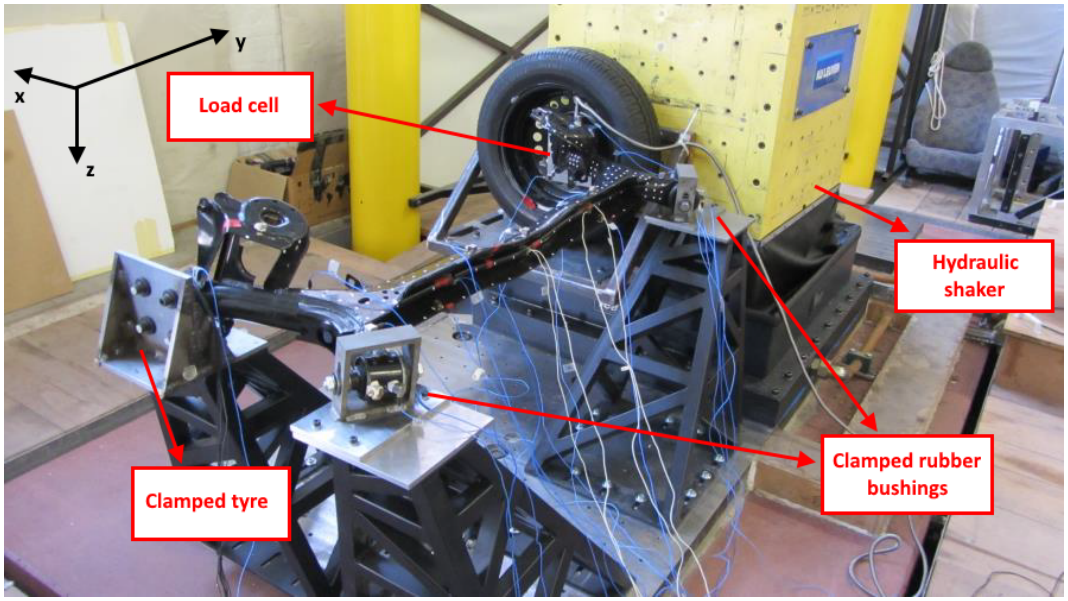


Figure 2: Twistbeam rear suspension setup - operational configuration

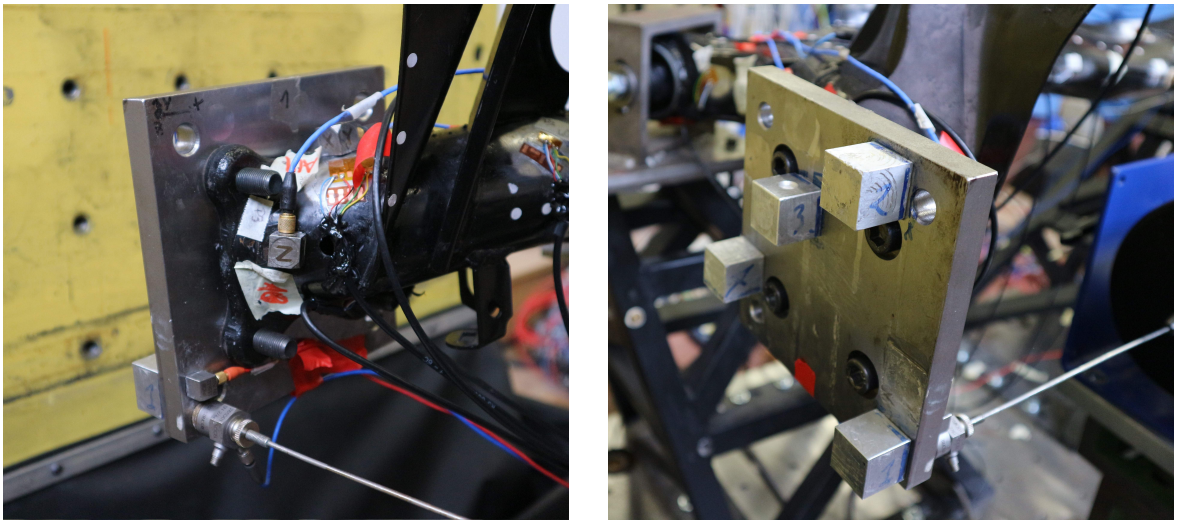
point of the source on the passive side, which is located at the free tyre. The point where the structure is excited is the one where the external loads are estimated in operational conditions. The main assumption that was made before performing FRFs data acquisition resides in the fact that transmission between the active and the passive part in off-line mode through the clamping supports of the twistbeam is negligible. This is a reasonable assumption because the clamping system is sufficiently isolated from the shaker. The Fig. 3a shows the loaded section of the tyre, where a plate is bolted: the loads are identified at the central point. Two sets of loads are acting on the tyre, identifiable in 3 forces and 3 torques in each direction. For effects overlapping, a general output response can be written as:

$$\boldsymbol{y} = \boldsymbol{y}_f + \boldsymbol{y}_t \tag{14}$$

where f and t are force and torque indices. As consequence, the full FRF matrix has the size $[n_y \times (n_f + n_t)]$. The disadvantage of the TPA MI method is thus that all forces acting in the interested input point need to be analyzed simultaneously, because all of them may cause motion and deformation throughout the structure. Even if the analyst could be interested in estimating only one force direction or more in general a subset of all 6 loads, the knowledge of the full FRFs matrix is still needed. Indeed Eq. 2 can be rewritten in a general form as:

$$\boldsymbol{f}_u(\omega) = \boldsymbol{H}_u(\omega)^+ \left(\boldsymbol{y}(\omega) - \boldsymbol{H}_k(\omega)\boldsymbol{f}_k(\omega)\right) \tag{15}$$

where the indices k and u are referred to known and unknown loads respectively. In this contribution, all the loads are estimated. Consequently $\boldsymbol{H}_k(\omega)$ is an empty matrix and Eq. 15 reverts into Eq. 2.
In order to collect a dataset of force and torque FRFs, a data reduction at the central point of the tyre section is needed. Four points are excited by a shaker in three directions, as shown in Fig. 3b (four aluminum blocks). Thus a total number of $[n_y \times 12]$ FRFs are acquired and then reduced on the central point to obtain a matrix with size $[n_y \times 6]$. The map of indicators is described later together with the ones used for AKF. The sensors are located both close to and far from the load area. This choice aims to verify which area is more sensitive in a clamped configuration of the system subject to the external excitation. The strain-based TPA MI is performed and compared against the results of AKF.



(a) (b)

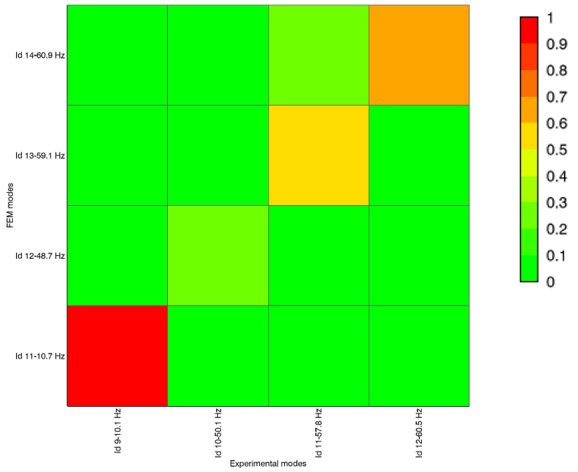
Figure 3: Free tyre which is subject to the external excitation

Augmented Kalman Filter

The adopted Kalman-based strategy needs the knowledge of a well validated FE model. In this paper, a linear model is used. A first validation was performed in free-free conditions, as reported in Ref. [12]. The operational configuration needs further validation that take into account the contribution of the two bushings. Under these boundary conditions, the following measures were recorded respectively for static and dynamic validation:

- 30 and 80 N (static load) along z direction at the free tyre
- FRFs measurements along the three directions, with input excitation at the free tyre (same dataset acquired for TPA)

The results of dynamic validation are shown in Fig. 4: the second mode represents the first mode of the torsional bar and it is not matched since no accelerometers were located in that area. Good validation can be reached till 60Hz. This four modes are included in the reduced space Ψ_{nm} of Eq.4.



	Exp. [Hz]	FEM [Hz]	|Err| %
1	10.1	10.7	5.9
2	50.1	48.7	2.8
3	57.8	59.1	2.2
4	60.5	60.9	0.6

Figure 4: MAC representation and natural frequencies comparison between experimental and FEM normal modes in the frequency range [0-60]Hz - operational configuration

The static validation requires matching between measured strain and FE model information. It is particularly challanging to match the exact location and direction of a strain gage and locate it on a finite element model. This issue has particular relevance for strain measurements that are located in areas with high stress gradient. After the instrumentation phase, the location and measurement direction of each sensor were acquired through the use of an optical device AICON ProCam camera [19]. This system comprises an active mobile probe with a high resolution camera. Thanks to this data acquisition, a sensors map of the experimental setup is available. Overlap the obtained map on the FE model is not a straightforward task. A common issue is the not exact geometry representation of the model, combined to the inaccuracies of the camera device. For this end, an optimal procedure for finding the exact location of the used sensors on the FE model was developed in [18] and briefly reported in the following. The results reached from this selection criterion are very useful for the application of a successful Kalman-based strategy.

Looking at the Fig.5, the following steps are performed in the optimization procedure:

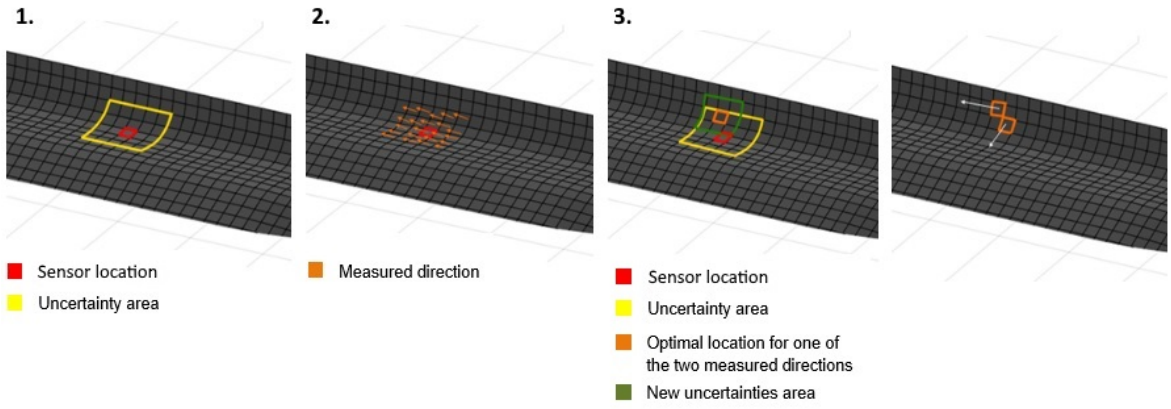


Figure 5: Optimization steps for matching measured and simulated strain

1. Starting from the location (red) identified by ProCam camera, it is possible to define an area of uncertainties (yellow) where the sensor could really take place. The size of the area is defined considering: geometry of the model and ProCam errors

2. Evaluation of strain value of each element in the considered grid: local rotation of strain quantities is needed on each element. Find the element that minimize the error between numerical and experimental data

3. If rosettes are considered, another step is needed: a new uncertainty area (green) is defined around the optimal location (orange) found by the previous steps (for one of the two measured directions). This area is smaller because takes into account only the size of the rosetta. The same previous steps can be performed on the green area for the remaining direction

The application of the proposed method needs to start from the knowledge of a strain dataset corresponding to a certain load case. Before performing the load identification through AKF, this preliminary step is hence introduced for a static load case.

3.1 Inverse load identification and full-field estimation: TPA MI vs AKF

In order to compare TPA MI and AKF, the operational data reported in Tab. 1, were collected under sine and pseudo-random excitations, covering a range of frequency up to 50Hz. A coupled state-input estimation is

Run	Type	Freq. [Hz]	Amplitude [mm]
1	sine	1	5
2	pseudo-random	5-50	30

Table 1: Excitation of operational data

performed for Kalman-based strategy and 12 optimal sensors selected in [18] are used for the estimation of 6 loads. It is worth to note that, even if the minimum requirement for the system observability is $n_y = n_f$, more measurements are needed for a good estimation to balance the inaccuracies occurring when experimental data are used, e.g. inaccuracies in the measurement data itself and in the matching on the FE model. The number of needed measurements is however case dependent. In [18], 18 sensors are proved to be the minimum number needed to obtain the best possible estimation through TPA MI. The sensors are distributed at the load and clamp area respectively, as shown in Fig. 6. Two analysis are proposed in the following:

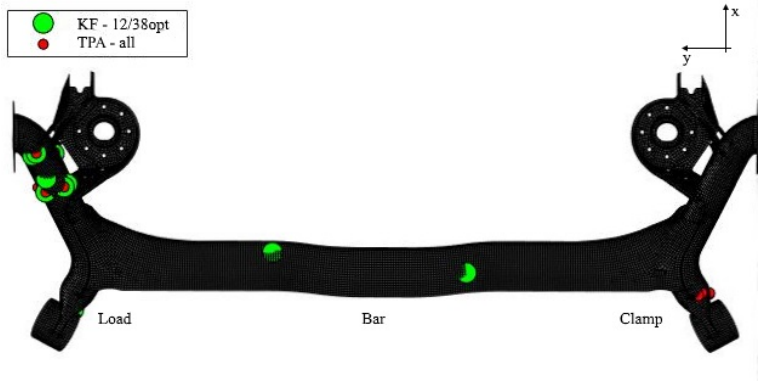


Figure 6: Location of selected sensors for load identification. KF: 12 optimal between 38 available sensors. TPA: all (18) available sensors.

1. **Load identification:** the estimation for run 1 and 2 are respectively reported in Fig. 7/8 and Fig. 9/10 (frame of reference shown in Fig. 2) both in time and frequency domain. In order to evaluate the quality of the estimation, the results are compared with the measured loads. Main attention is paid to the loads Y and Z that are referred to the stiffer and the more flexible directions respectively. In Fig. 7 and Fig. 9, a loss of accuracy occurs on the load Z estimated through TPA MI. A first explanation lies in the quality of the measured FRFs used for MI. Before applying the method, a correction of each strain FRFs at low frequencies had to be performed, since issues about noise, bridge settings and temperature drift occur on the static value. If the problem concerns a wide number of FRFs involved in the computation of the matrix inversion, a loss of accuracy can occur on the estimation. On the other hand, issues about quality of the measured FRFs occur also in high frequency range, where giving good excitation to the structure is always a challenging task. This observation is reflected on the results shown in Fig. 9/10, that are referred to pseudo-random excitation (run 2). Loss of accuracy occurs in the frequency range of interest for TPA MI estimation, with the exception of load X and torque Y. The direction of the stinger of the shaker used for FRFs acquisition is also a source of influence for the estimation.
   Regarding the performance of AKF, the results show the same trend of estimation from run 1 to run 2, even if worse prediction is given for load Z in Fig. 9. Looking at all the frequency range, some loss in accuracy is present also for AKF by increasing the frequency. The explanation resides in the dynamic validation of the model, that means the load prediction is also affected by model errors.
   The accuracy of the estimation of load Y needs further explanation since it regards the stiffer direction of the twistbeam, identified by the axial direction. The load Y results indeed in a wrong estimation from both techniques. The reason resides in the stiffness of the structure along Y direction which is definitely the stiffer one i.e. axial direction. The wrong order of magnitude estimated from TPA

is given by the ill-conditioning problem caused by the different stiffness distribution of the structure along the different directions of estimation. Indeed, applying a static load to the input location of the FE model along Y direction results in a much lower deformation as compared to the same static load applied along Z or X directions. Defining the static stiffness K for each direction as the ratio between the amplitude of the load and the displacement evaluated at the same input point, it results in large ratios K_y/K_z and K_y/K_y. That is directly translated into an ill-conditioned inverse problem. An improvement is obtained from AKF: it has to be noticed that in the model-based inverse problems, the only link between the estimated forces and the responses is the model itself. Contrarily, the link for TPA is given by measured FRFs which results in the issues mentioned above. Simultaneously estimation of 6 loads can be hence considered acceptable through AKF, both for run 1 and 2. Some parameters of the filter had to be set for the shown analysis. The initial state of the system was assumed to be known and equal to zero, that means $\boldsymbol{P}_0$ is set to be zero. The block-diagonal covariance matrix $\boldsymbol{Q}^*$ was chosen by considering that the higher source of uncertainty in the model is given by the unknown input, such that $\boldsymbol{Q}_u >> \boldsymbol{Q}$. The matrix $\boldsymbol{Q}$ is thus set to zero, as the extra-diagonal terms of $\boldsymbol{Q}_u$. The diagonal matrix $\boldsymbol{R}$ assumes the values of the covariance associated to each measurement. A noise acquisition data was performed during the test campaign for this purpose.

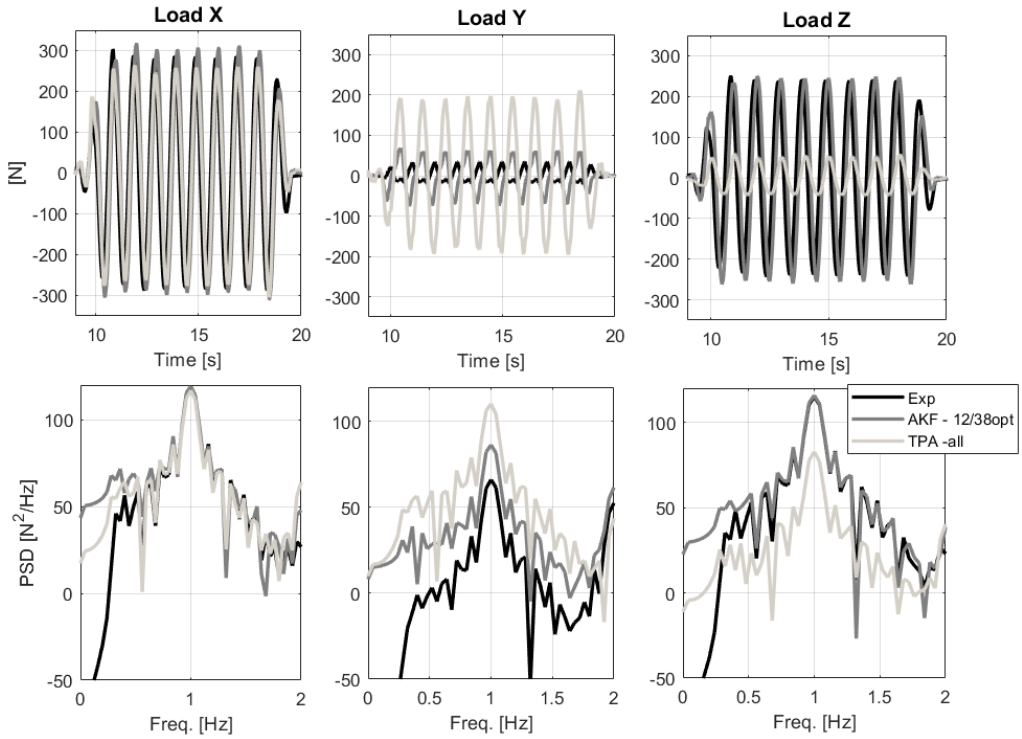


Figure 7: Run 1. Time histories of estimated loads. Comparison between AKF (12 optimal sensors), TPA MI (18 sensors) and measured data by load cell.

2. **Full-field strain estimation:** since coupled state-input estimation is performed, a coupled experimental and FE model approach is also proposed for TPA MI to compare the strain field estimation. That means the response of the FE model is simulated under the loads which are estimated by TPA MI. The strain comparison between AKF and TPA MI is shown in Fig. 11. The marked points in the picture are to indicate which sensors are used for both estimations. Even if Fig. 7 shows significant inaccuracies in the estimation of load Z through TPA MI, the strain estimation in Fig. 11 shows an accurate trend in according with the measured strain field. High RMSE values are instead obtained for the strain field of run 2 in Fig. 11 through TPA MI. Little discrepancies in the load estimation can result in high error on the FE simulation, since the model itself is well validated at relatively low frequen-

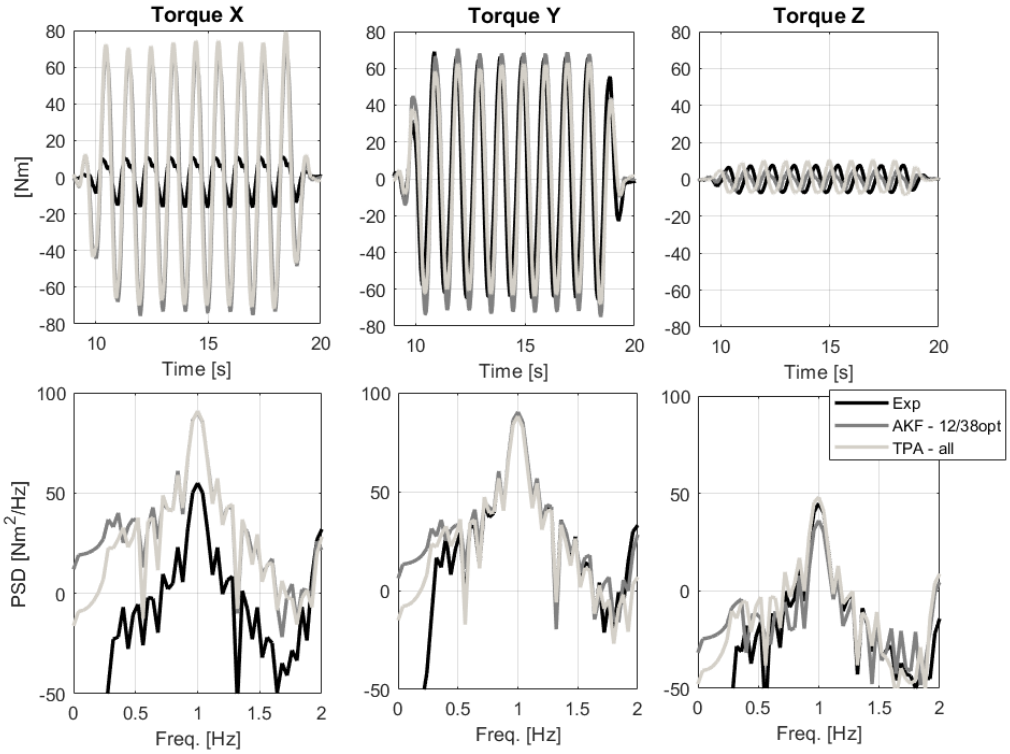


Figure 8: Run 1. Frequency content of estimated torques. Comparison between AKF (12 optimal sensors), TPA MI (18 sensors) and measured data by load cell.

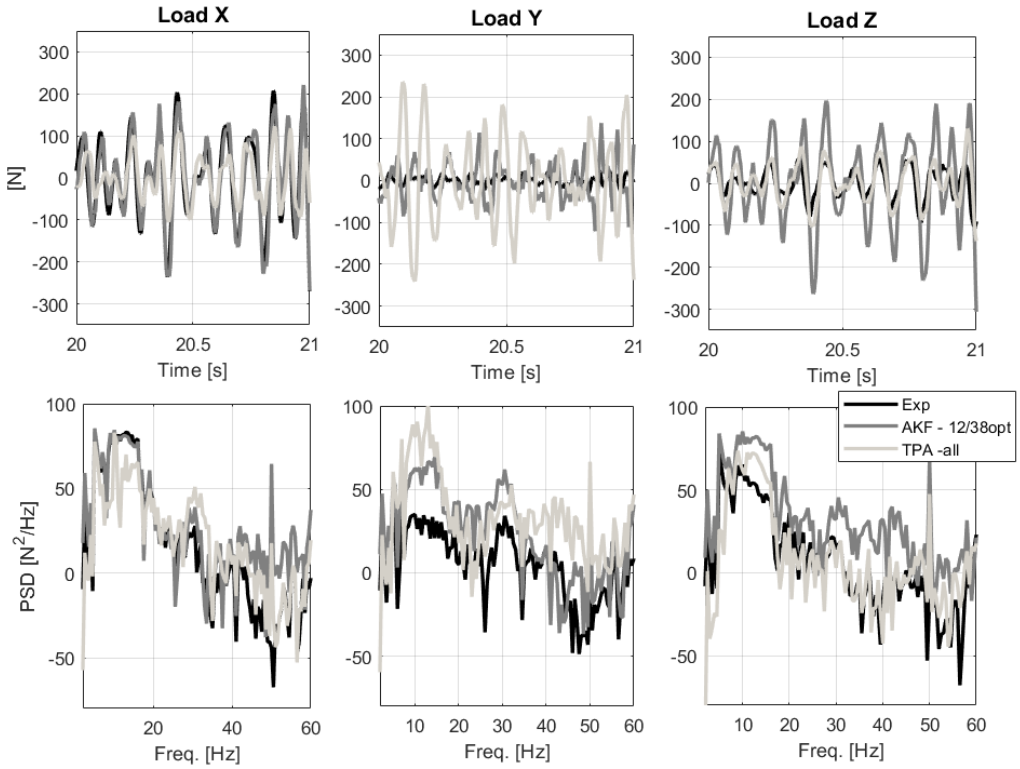


Figure 9: Run 2. Time histories (zoom) of estimated loads. Comparison between AKF (12 optimal sensors), TPA MI (18 sensors) and measured data by load cell.

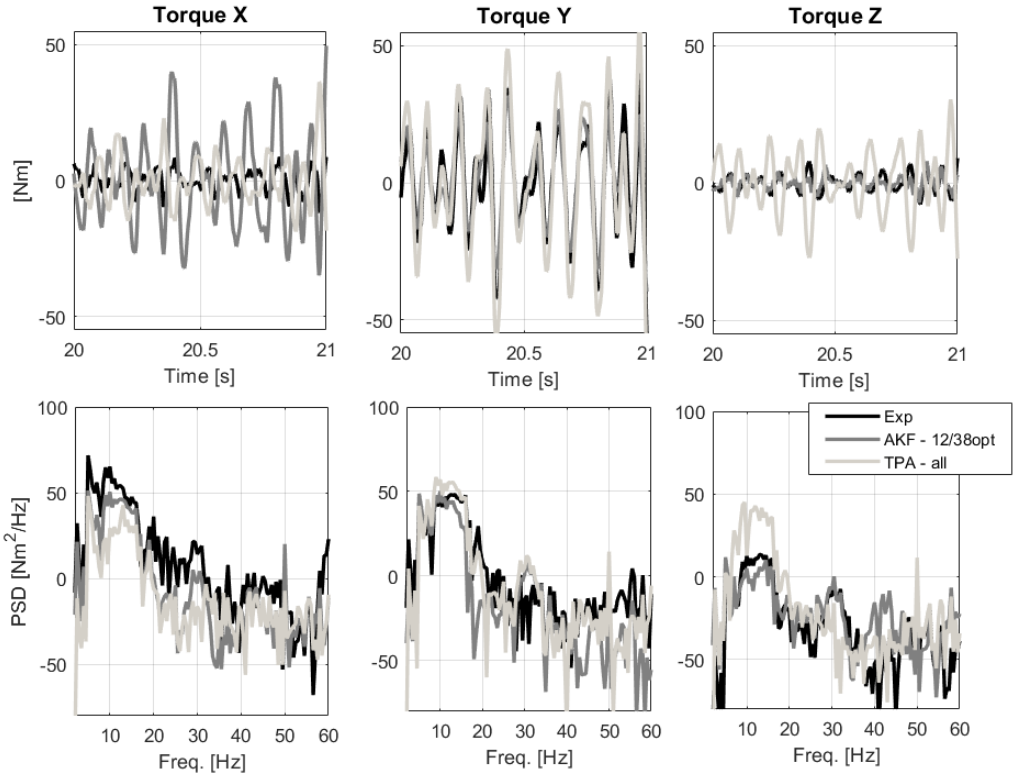


Figure 10: Run1. Frequency content of estimated torques. Comparison between AKF (12 optimal sensors), TPA MI (18 sensors) and measured data by load cell.

cies. The optimal but not exact position of the sensors on the FE model, where the strain responses are evaluated, has also high influence on the lost in accuracy on the strain estimation for run 2. Even if the location of the sensors is not exact or other inaccuracies in the model occur, better estimation is possible trough AKF because of the nature of the filter itself which can tune the model to match the measured data. The covariance matrix $\boldsymbol{Q}^*$ and $\boldsymbol{R}$ plays a significant rule in the joint state/input estimation through AKF. As mentioned before, the higher source of uncertainty in the model is given by the unknown input and it is considered in the $\boldsymbol{Q}^*$ matrix, such that $\boldsymbol{Q_u} >> \boldsymbol{Q}$. The effect of $\boldsymbol{Q}^*$ on the estimation can be then understood comparing its value with the one assumed by $\boldsymbol{R}$, which represents the response uncertainties. Since $\boldsymbol{Q_u} >> \boldsymbol{R}$, the model is considered to be less reliable and consequently the estimated response field follows the measured data. In Fig. 12, the quality of the estimation proposed in Fig. 11 is better quantified by showing the time-histories of strains Ind. Channel n. 38 and 29 related to both run 1 and 2.

4 Concluding remarks and future developments

Two strategies are compared in the paper regarding the problem of inverse load identification. A Kalman-based strategy and TPA Matrix Inversion techniques are proposed and applied on a real industrial case to identify the advantages with respect to the effort needed for the setup preparation, for the data-processing and the quality of the estimation. A setup of a rear twistbeam suspension is investigated by simulating the structure under different excitation scenarios. The results showed that better load estimation can be obtained through Augmented Kalman Filter. Less sensors are needed against the application of the Matrix Inversion technique. The effort needed for both applications is detailed compared starting by measurement acquisitions and data-processing. These preliminary analysis led to the conclusions that both proposed techniques need high effort in FRFs acquisition and FE modelling issues for TPA MI and Kalman Filter respectively. The

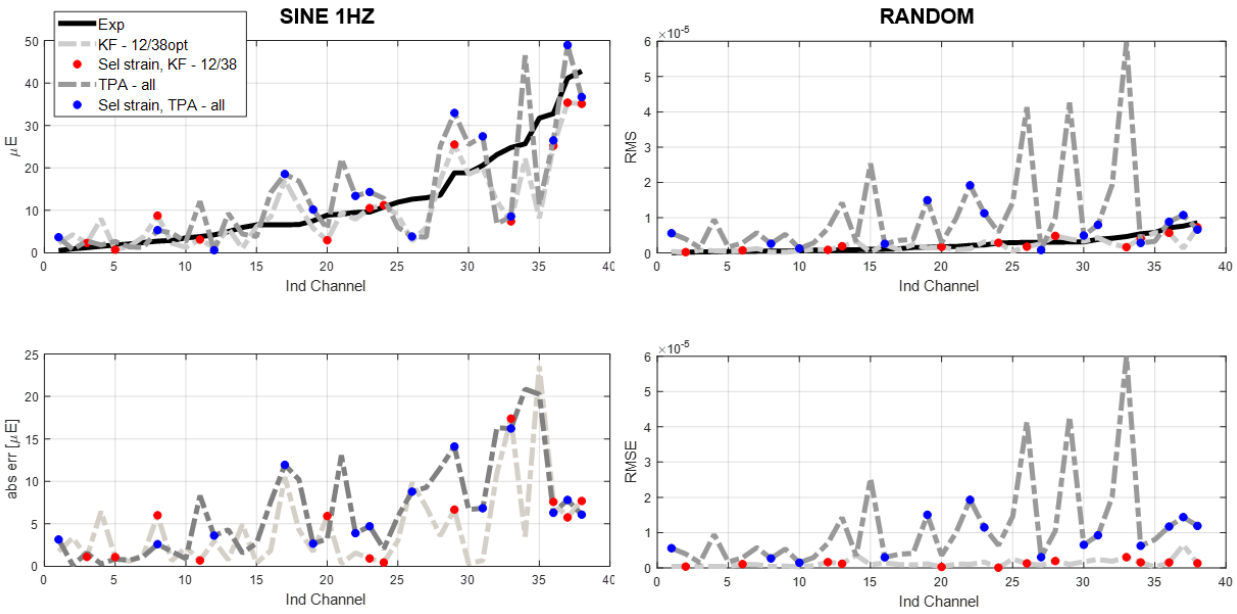


Figure 11: Left: run 1, amplitude value of strain. Right: run 6, RMS value of time histories. Comparison between AKF (12 optimal sensors), TPA MI (18 sensors) estimated strain and measured data.

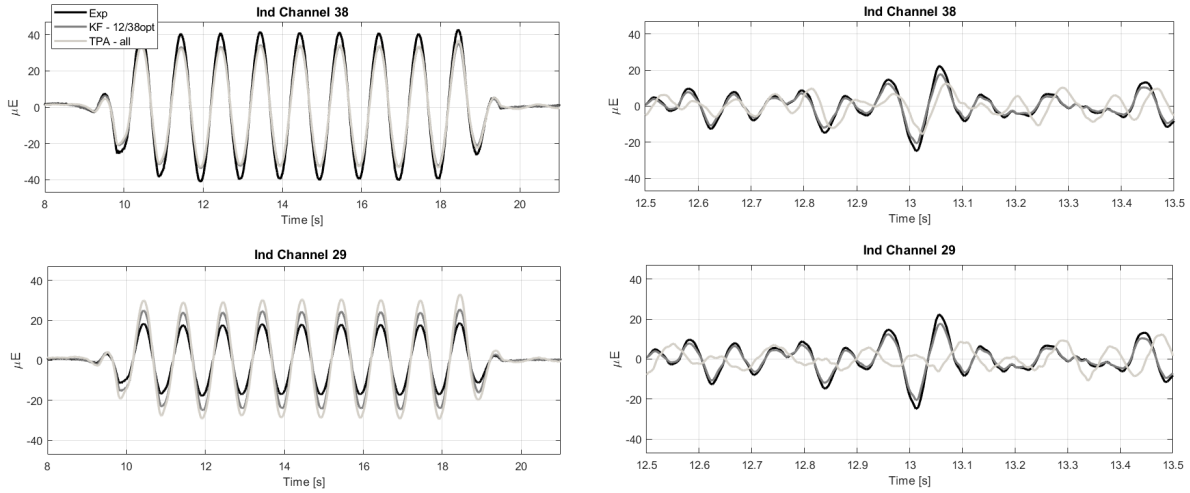


Figure 12: Run 1 (left) and run 2 (right). Time histories of two strains: comparison between AKF (12 optimal sensors), TPA MI (18 sensors) estimated strain and measured data.

quality of strain field (state) estimation over the structure is also tested through the knowledge of the FE model. The analysis showed that inaccuracies of the model combined with the ones of the estimated loads can lead to high errors in the state estimation. That is overcame through the application of a Kalman strategy which can tune the model finding a right compromise between load and state estimation. Future investigation aims to evaluate the improvement of the results combining strains and accelerations data. External excitation scenarios with different frequencies and amplitudes will be also explored in order to evaluate the consistency of the results.

Acknowledgements

The authors acknowledge the VLAIO (Flemish Innovation & Entrepreneurship) through the Innovation mandate IWT project VIRTUAL MATES (nr. 140778).

References

[1] Peter Gajdatsy *Advanced Transfer Path Analysis Methods*, PhD Dissertation, Katholieke Univeristeit Leuven, 2011

[2] P. Mas, P. Sas, and K. Wyckaert *Indirect force identification based on impedance matrix inversion: a study on statistical and deterministic accuracy*, Proceedings of 19th International Seminar on Modal Analysis, pp. 1049–1065, 1994

[3] J. Starkey, G. Merril *On the ill-conditioned nature of indirect force measurement techniques*, IJAEMA, Vol. 4, No. 3, (1989) 103–108

[4] P. Gajdatsy, K. Janssens, W. Desmet, H. Van Der Auweraer *Application of the transmissibility concept in transfer path analysis*, Mechanical Systems and Signal Processing, 24(7), 1963-1976

[5] R. E. Kalman, A new approach to linear filtering and prediction problems, Journal of Basic Engineering, 82(1):35-45 (1960).

[6] D. Simon, Optimal state estimation: Kalman, H_∞ and nonlinear approaches, John Wiley, New York, 2006

[7] M. I. Ribeiro, Kalman and extended kalman filters: Concept, derivation and properties, Institute for Systems and Robotics, 43 (2004)

[8] K. Maes, Filtering techniques for force identification and response estimation in structural dynamics, PhD Dissertation, Katholieke Univeristeit Leuven (2016)

[9] F. Naets, J. Cuadrado, W. Desmet *Stable force identification in structural dynamics using Kalman filtering and dummy-measurements*, Mechanical Systems and Signal Processing, 50-51:235-248 (2015).

[10] E. Lourens, E. Reynders, G. De Roeck, G. Degrande, G. Lombaert *An augmented Kalman filter for force identification in structural dynamics*, Mechanical Systems and Signal Processing, 27:446-460 (2012).

[11] E. Risaliti, J. Van Cauteren, T. Tamarozzi, B. Cornelis, W. Desmet, Virtual sensing of wheel center forces by means of a linear state estimator, in: Proceedings of International Conference on Noise and Vibration Engineering, ISMA 2016, Leuven, Belgium.

[12] F. Cosco, F. Naets, W. Desmet *Use of concept modelling for online input force estimation*, International Conference on Noise and Vibration Engineering (ISMA2014).

[13] T. Tamarozzi, E. Risaliti, W. Rottiers, K. Janssens, W. Desmet *Noise, ill-conditioning and sensor placement analysis for force estimation through virtual sensing*, International Conference on Noise and Vibration Engineering, ISMA 2016, (pp. 1741-1756).

[14] E. Risaliti, B. Cornelis, T. Tamarozzi, W. Desmet *A State-Input Estimation Approach for Force Identification on an Automotive Suspension Component*, Conference Proceedings of the Society for Experimental Mechanics Series, vol.3 IMAC-XXXIV (Orlando Florida USA, 2016).

[15] Roy R. Craig, Jr. *A review of time-domain and frequency-domain component mode synthesis method*, Journal of Modal Analysis 2, 2(2):59-72 (1987).

[16] F. Naets, J. Croes, W. Desmet *An online coupled state/input/parameter estimation approach for structural dynamics*, Computer Methods in Applied Mechanics and Engineering, 283:1167-1188 (2015)

[17] C. F. Van Loan, Computing integrals involving the matrix exponential, IEEE Transactions on Automatic Control, (1987) 23(3):395-404.

[18] R. Cumbo, T. Tamarozzi, J. Janssens, W. Desmet, *Kalman-based load identification and full-field estimation analysis on industrial test case*, Submitted to Mechanical Systems and Signal Processing Journal (May, 2018).

[19] AICON 3D System, Procam, http://aicon3d.com/products/vehicle-testing/procam, 2018.

Linking manufacturing simulation with functional performance engineering for composites applications

K. Vanclooster[1], L. Spina[2], S. Donders[1], R. Lombardi[3], R. D'Ippolito[3], L. Farkas[1] and D. Mundo[2]
[1] Siemens Industry Software NV
Interleuvenlaan 68, B-3000, Leuven, Belgium
e-mail: **kristof.vanclooster@siemens.com**

[2] Università della Calabria, DIMEG
Via Bucci Cubo 46C, 87036, Rende (Cs), Italy

[3] Noesis Solutions NV
Gaston Geenslaan, 11 B4, B-3000, Leuven, Belgium

Abstract
The study reported in this paper shows the importance for taking into account the manufacturing simulation on the performance of a composite component. First the different type of manufacturing simulations are discussed after which the influence of the draping on an omega shaped stiffener is assessed. The predicted response is compared to experimentally measured FRFs. It is concluded that for this components the influence of having the accurate local thickness distribution and material properties are crucial for predicting the correct response. In a final step an inverse identification of the local thickness profiled is attempted by evaluating the predicted and measured FRF and trying to match them by changing the local thickness.

1 Introduction

Composites are promising materials in terms of lightweight and structural performance, although their manufacturing is still posing some challenges and the prediction of their structural performance is not yet straightforward. Manufacturing of composites is often a cumbersome trial and error process, in which designers learn by doing and by designing variant after variant. First benefits can be achieved by virtually simulating the composites manufacturing process, so that designers can optimize and understand better the design process, and create corresponding tooling optimally for the specific process and application at hand. For a thermoset composite material, this includes draping simulations, i.e. to simulate the manufacturing step where the reinforcement is 'wrapped' onto a mould, infusion modelling to predict the resin flow during the composites impregnation process, and curing simulation to predict the densification of the composites matrix under thermal treatment (see Figure 1).

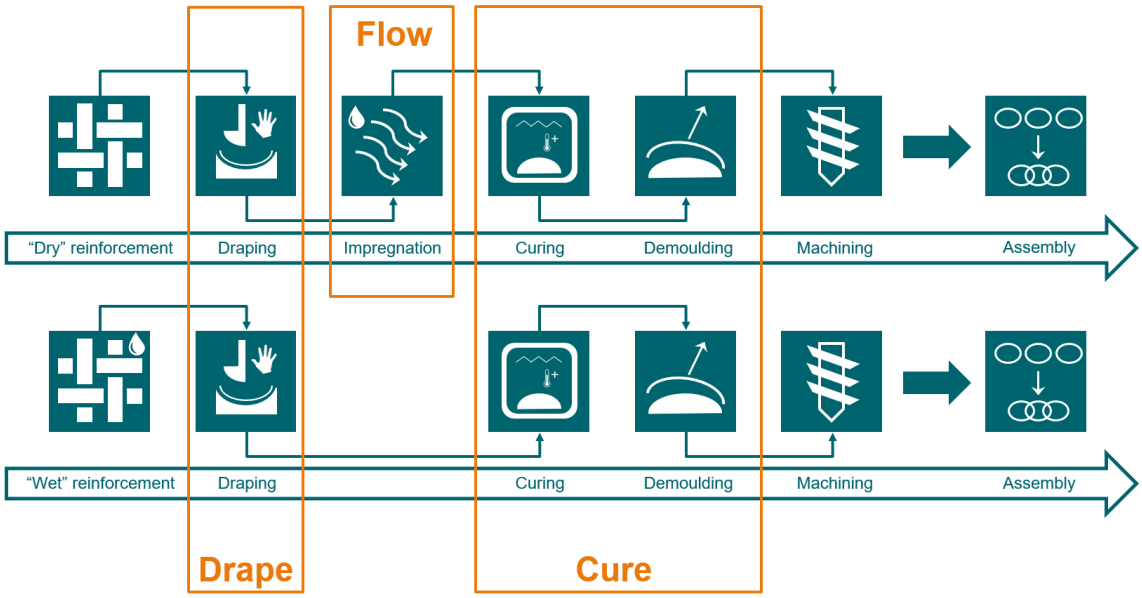


Figure 1. Typical thermoset composite manufacturing steps, enabled by simulations: drape, flow, cure.

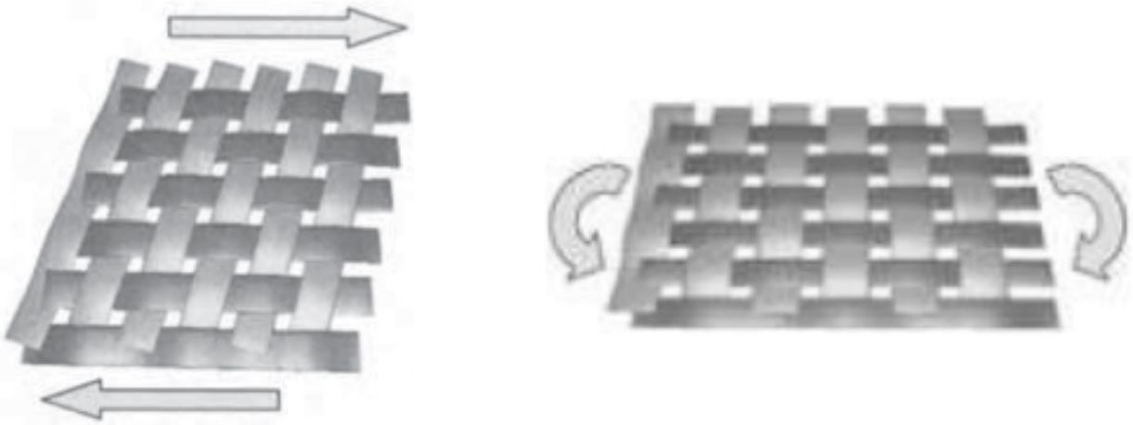
Using the manufacturing simulation tools and analysing their results are only a first step in understanding the virtual product. A second step must still be taken: predict the product performance (in terms of stiffness, noise and vibration, durability, etc.) and the impact that the manufacturing parameters have on this performance. Only then, one can virtually optimize the manufacturing process and simultaneously optimize the product performance. In reality, the properties of composites are highly dependent on the manufacturing process parameters and hence it is crucial to include the influence of manufacturing in the design process of composites structures. In addition, non-deterministic effects (variability in manufacturing tolerances, uncertainty in material properties …) influence the composites performance, and should therefore be characterized and included as well in the product design process. It will be shown in this paper how we enable to link the manufacturing simulation and the multi-attribute functional performance engineering (FPE) process loops for continuous fibre-reinforced composites.

1.1 Manufacturing simulation of composite components

In this section a general overview of several methodologies, all related to a specific aspect of composite manufacturing, will be given. First the prediction of draping the reinforcement onto the mould will be discussed, followed by an introduction to the simulation of the impregnation with the resin of a draped, but 'dry' reinforcement. The final section of this paragraph will show how to address the prediction of residual stresses and the associated distortion of the demoulded component due to the curing of the resin.

1.1.1 Simulation of the draping of composite materials

During the draping stage, an initially flat sheet, often referred to as the blank, will be forced to adjust to the desired configuration. The main deformation modes during the draping are (a) in-plane shear and (b) bending, which are indicated in Figure 2. The effect of in-plane shear is a local re-orientation of the fibres, while the low bending rigidity makes these type of material prone to the occurrence of wrinkles. In order to have a good product performance, it is necessary to be able to (i) predict correctly the local fibre orientation, as they determined the local stiffness and strength and (ii) to avoid the occurrence of wrinkles as these defects give rise to weak spots in the final product.



a b

Figure 2. Key deformation mechanisms during draping a composite reinforcement are (a) in-plane shear and (b) bending [1]

In the state of the art, there exist two different approaches for draping simulations:

- The Kinematic approach: an approximate approach that allows predicting the in-plane shear and bending (no stretching, no forces are calculated). Siemens Fibersim [2] can simulate the laminate composite layup by accounting for draping and avoid manufacturing-induced defects such as wrinkling by introducing darts or splits in the blank. With the kinematic approach, the material is allowed only to distort in the shear direction, while the bending resistance is considered negligible. Hence, no extensive material characterization routines are required.
- The Mechanical approach: a complex constitutive model is built, including exact boundary conditions also for shear forces / shear angles predictions. Leading tools for this are AniForm [3] and PAM-FORM [4]. A disadvantage of this approach is that you have to do an extensive material characterization routine, including picture frame or bias-extension, bending characterization, uni-axial or bi-axial tensile test [1] and even friction characterization [5] to get all the parameters you need, which is not straight-forward.

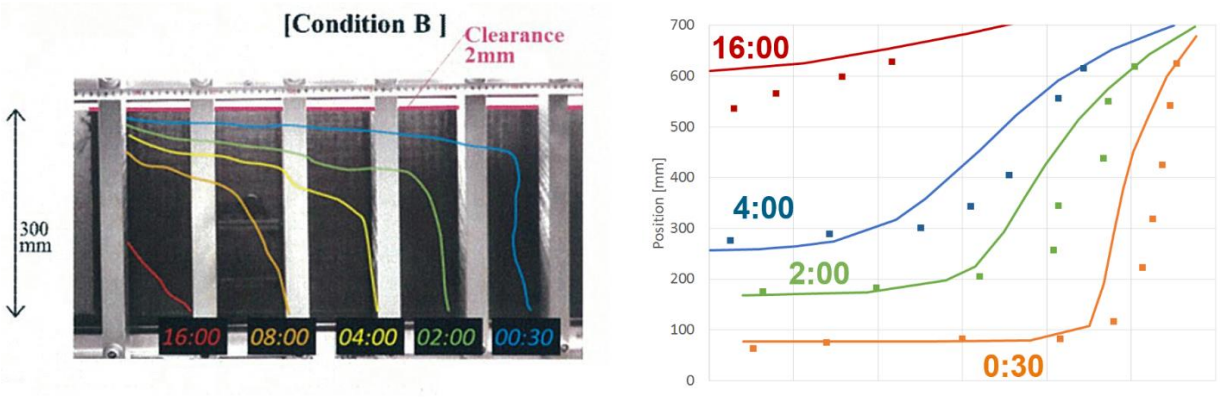
1.1.2 Infusion simulation of composite materials

During infusion, the dry and draped reinforcement is gradually impregnated with the uncured resin. The main goal is to obtain a fully impregnated structure. During the infusion, defects such as dry spots and voids can occur. Components with dry spots are scrapped, while excessive void content has an influence on the product performance. Therefore, the void content should be as low as possible (target is 1-2 % vol). Simulation-based predictions of the infusion process help in predicting where such defects can occur by tracking the flow front, and can enable improving the manufacturing process such that the defects are reduced.

Two different approaches exist for infusion simulations (see Figure 6):

- A general CFD solver [6]: solving the Navier-Stokes equation. This just assumes that the fluid is incompressible, and preserves a lot of the physics of the flow in the solution sequence, such that physical phenomena can be predicted more accurately.
- The CFD solver for Darcy's law [7]: This approach comes with a number of assumptions (assume steady flow, low Reynolds number (Stokes flow) and no external body forces). While this approach is computationally less demanding, certain aspects associated to typical high-volume composite production require a numerical identification, e.g. race-tracking.

Race-tracking occurs when there is a mismatch between the edge of the draped reinforcement and the mould, i.e. there is a small channel that does not contain reinforcing material. As been shown by Kobayashi et al. [8] (see Figure 3(a)), there is an important influence in the resulting filling profile. Using a general CFD solver, Siemens CD-ADAPCO Star-CCM+ [6], the resulting flow front could be predicted well, without any additional assumptions as shown in Figure 3(b).



a b

Figure 3. Development of the flow front with the presence of race-tracking (a) according to the experimental measurement by Kobayashi [8] and (b) the prediction of the flow front with CD-ADAPCO StarCCM+

1.1.3 Curing simulation of composite materials

When the polymer used has a thermoset nature, a curing reaction is needed to induce a continuous 3D molecular network which results in a solid structure. Due to the exothermic nature of this reaction the temperature control is crucial, a too fast rise in temperature might result in a (locally) degrade polymer as the (local) temperature has risen above the thermal degradation temperature [9].

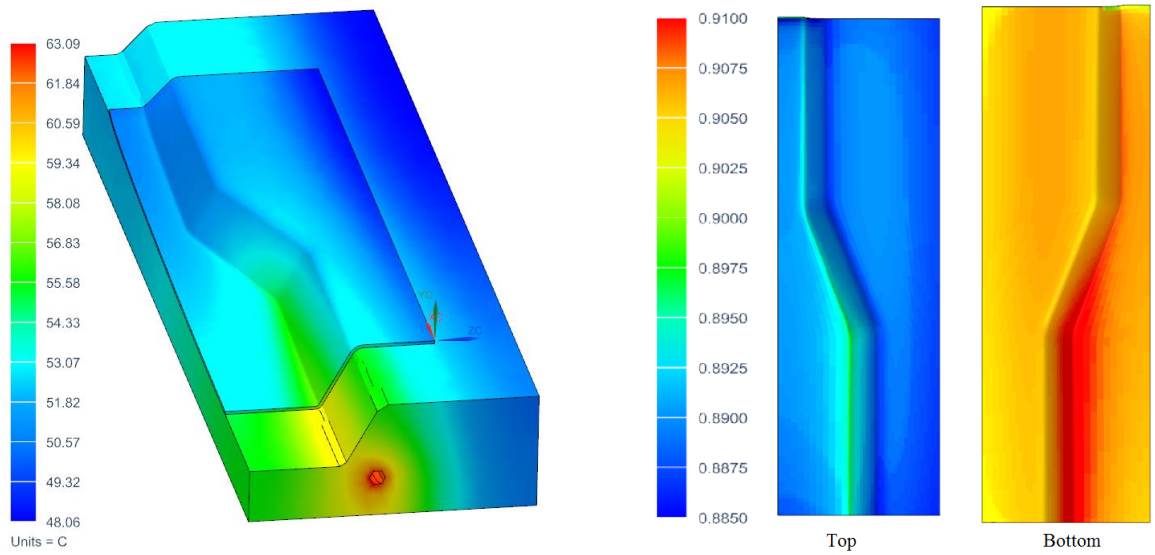
Additionally during curing and subsequent cooling, residual stresses are build-up within the composite material, the main cause of these stresses are (i) the densification of the matrix during curing, (ii) the shrinkage of the matrix during cooling, due to the thermal expansion mismatch between the fibres and matrix and (iii) the mismatch between the part and mould thermal expansion, which are coupled with a certain friction coefficient [10].

The effect of the residual stresses are two-fold, at first too high residual stresses lower the strength of the component as less externally applied stresses are required to reach the strength of the reinforced polymer. Second, during demoulding the residual stresses will cause the structure to achieve an equilibrium shape, where the residual stresses are in a local minimum. However, this will create a mismatch between the as-designed shaped and as-manufactured shape. Tolerances are often in the range of millimetres while typical part sizes are in the order of decimetres to metres [11], any unexpected deviations will create stresses in the structure or connections between different structures beyond what was originally planned.

Figure 4 shows an application of the method on a similar component that will be studied throughout this work. The local temperature profile (in combination with several material parameters) forms an input in order to predict the local degree of cure, which allows to predict the residual stress state inside the component.

1.2 Performance simulation of composite components

Composites performance is linked to the application domain of interest, and may cover several attributes (e.g. stiffness, strength, durability) that need its mechanical behaviour under various loading conditions [18]. This paper deals with the vibration behaviour of composites, which is driven by its stiffness, mass and damping properties. In the work presented here, the focus was to compare the resonance frequencies and associated mode-shapes. Therefore, in the simulated predictions, only the local equivalent homogenized elastic properties together with the local mass were considered. The different manufacturing process steps alter the local material micro-structure, hence influencing the performance of the material. In this work, the local fibre architecture changes due to the draping process was considered. The homogenization of the elastic properties are either done analytically (e.g. Chamis equation [12]) or numerically by FE calculations (e.g. using Virtual Materials Characterization (VMC) Toolkit [13]).



(a) (b)

Figure 4. Curing simulation uses as input (a) the local temperature profile applied to the component and gives as a result (b) the local degree of cure.

1.3 Production and experimental modal analysis of composite stiffeners

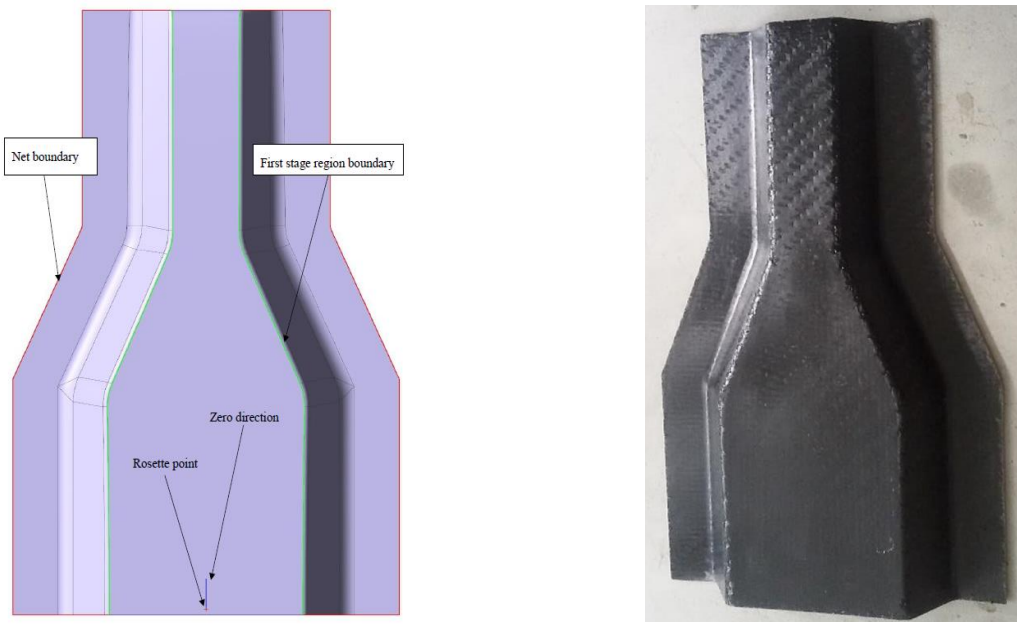
In the previous section both the different manufacturing and performance simulation tools for composite components have been introduced. The remaining part of this paper will describe a case study performed on an omega-shaped stiffener (Figure 5(a)), where the influence of certain simulation parameters, manufacturing induced aspects and material parameters on the modal behaviour is assessed.

The simulated results are compared with experimentally obtained Frequency Response Functions (FRFs), of which the set-up is described below.

1.3.1 Production of composite omega-shaped stiffeners

Two different types of omega-shaped stiffeners have been produced, namely a thermoplastic and thermoset. The thermoplastic fibre reinforced stiffener is made from glass fibre 2/2 twill woven reinforcement and polyamide matrix. The commercial name is Vizilon SB63G1 produced by DuPont [14]. The thermoset material is made using a dry non-crimp fabric (Carbon fibre UD 430g/m^2) with a lay-up of $[0/90]_s$ and an

epoxy resin system from Sicomin (Sicomin SR 8500 and Sicomin SA 8525). The weight ratio between the resin and the hardener is 100/25.



a b

Figure 5. Investigated omega-shaped stiffener with (a) the CAD model and (b) a produced thermoplastic stiffener

The thermoplastic component is made via thermoforming (Figure 6(a)), while for the thermoset component vacuum infusion has been chosen (Figure 6(b)). For both types of components the same mould has been used. After production of the components, they were trimmed using waterjet cutting.



a b

Figure 6. Production of the stiffener with (a) thermoforming for the thermoplastic stiffener and (b) the infusion of the thermoset component – see the flow front.

1.3.2 Modal analysis of the produced stiffeners

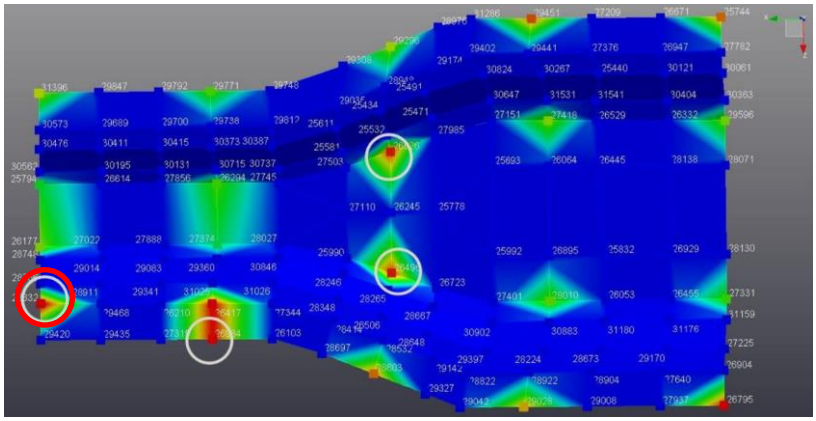
After production and machining of the stiffeners, the modal response has been experimentally measured. To excite the component, a small modal hammer (MODEL 086E89) was used. This serves to excite the component at a predetermined point, in order to make it vibrate and acquire the necessary information as displacement, speed or acceleration. This particular hammer is equipped with an accelerometer on the head that impacts on the component in order to measure the impact force with the specimen. The component response was measured using a laser vibrometer. The choice of excitation and response measurement is motivated by the lightweight properties of the structures. In Figure 7, you can see the tools used and the chosen measurement points.



Figure 7. Measurement tools and points of measurement on the sample [15]

To reproduce the free-free boundary conditions, the component was suspended using two thin rubber bands. Additionally to the hammer method, the mid frequency volume source method has also been used to excite the specimen. This type of excitation avoids the contact between the parts and combined with the laser vibrometer, it allows to obtain a contactless excitation.

In order to compare with the simulated results, it was chosen to not measure the full modal shapes of the stiffeners, instead FRF in the same points for different stiffeners has been identified. To determine the best points, a verification based on the coherence function was carried out. The average value of the coherence over the desired bandwidth was calculated for each measured point in a reference modal analysis from this measurement the point 28832 (see **Error! Reference source not found.**, indicated with the red circle) was then chosen based on the maximum achieved coherence values.



1.4 Linking manufacturing and performance simulation of composite components

In this study, the fibre orientation after draping are predicted using the geometrical approach (see section 1.2.1) is applied with the help of Fibersim, a Siemens software package. The first step to perform a draping simulation is to associate an initiation point on the component surface and associated to this point the fibre orientation in this point, this combination is typically called the rosette (see Figure 5(a)). The rosette defines the reference orientation for the part and all plies composing the part. Hence, the fibre orientations elsewhere in the part are calculated based on that rosette. When modifications are made to the rosette, the orientations of all plies referencing the rosette are updated automatically, so that subsequent producibility analyses reflect the change.

Besides the rosette, different draping strategies can be chosen, in this study we applied the 'traditional' simulation method combined with the geodesic approach, other approaches were assessed but no influence on the result has been identified.

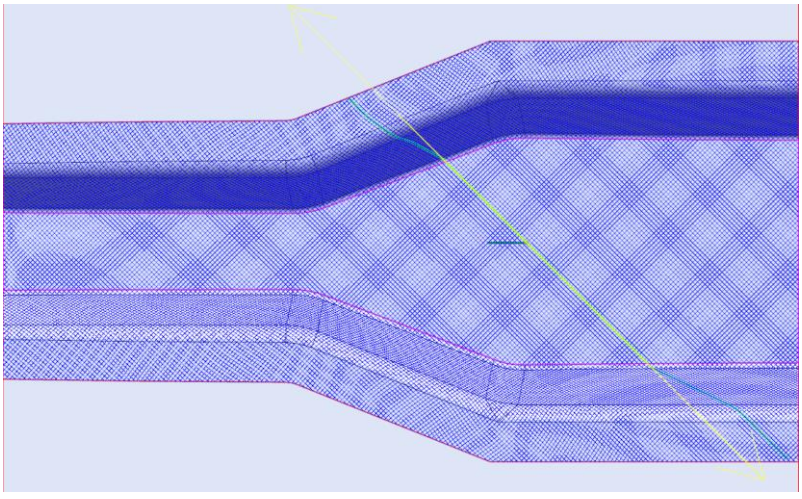
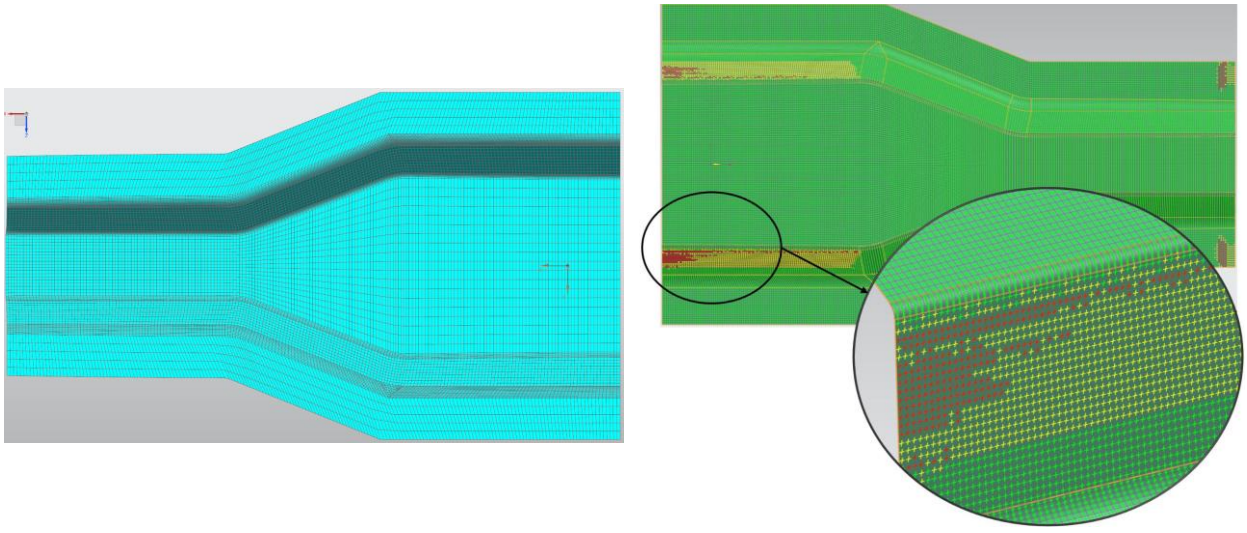


Figure 8. Typical result of a draping simulation using Siemens Fibersim (±45 fibre orientation) [15]

The resulting fiber orientation can be exported in different file formats and serve as an input in Siemens Simcenter 3D. In Simcenter 3D the CAD model is meshed using 2D elements (CQUAD4), see Figure 9(a). The fiber orientations from Fibersim are imported (Figure 9(b)) and automatically create the lay-up within Simcenter that was generated in Fibersim. Finally, the composite material properties are assigned to the plies in the lay-up. These properties are calculated from Chamis equation in case of the NCF material [12]

and they are determined using Virtual Materials Characterization (VMC) Toolkit with Simcenter in case of the woven reinforcement [13].



a b

Figure 9. Within Simcenter 3D the CAD is (a) meshed and (b) the Fibersim result is imported.

After the fibre orientation is imported and the material properties have been assigned, NX Nastran will be used to predict the modal behaviour of a structure (using the Simcenter 3D native SOL 103 - Response Dynamics). As the experimental measurement aimed to reproduce free-free conditions, there are no boundary conditions applied in the simulation. The obtained results can be seen in Figure 10, where some of the predicted modal shapes are depicted. The shape of the first mode is of the torsional type, while the second shape is bending, while at higher frequencies the modal shapes become more complex.

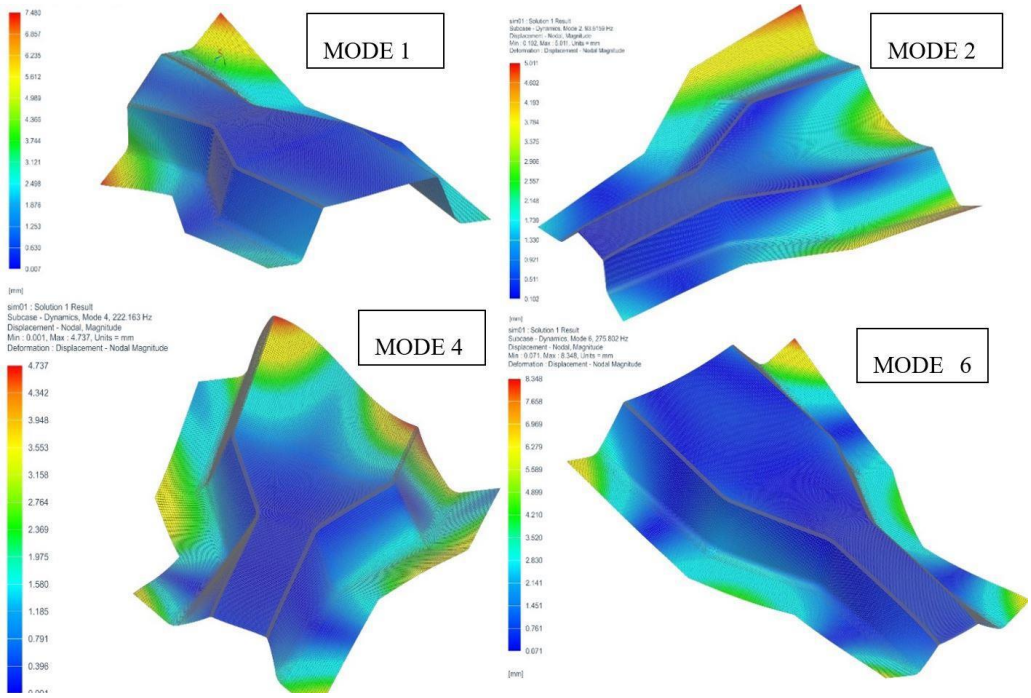


Figure 10. Indication of the different flexible mode shapes of the omega-shaped stiffener [15]

When comparing the measured flexible mode shapes (rigid ones are not considered) with the predicted ones by means of the Modal Assurance Criterion (MAC) matrix, it is noticed that the first six predicted flexible mode shapes agree well with the experimentally determined once. The mode shapes at higher frequencies however could not be captured well by the model. As seen in Figure 10, at higher mode shapes, local zones are contributing to the general mode shape, since manufacturing of composites and the material itself are prone to a mix of undeterministic effects, these start to play a role at higher frequencies.

1.4.1 Influence of the rosette on the modal behaviour

Using Siemens Fibersim, the fibre orientation after forming an omega-shaped component can be assessed. One of the key input parameters is the location of the 'Rosette point', i.e. the start point of the draping simulation.

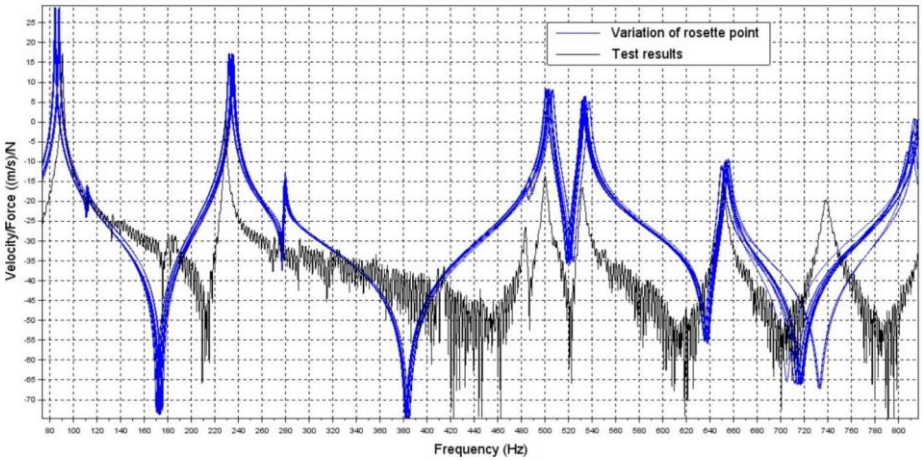
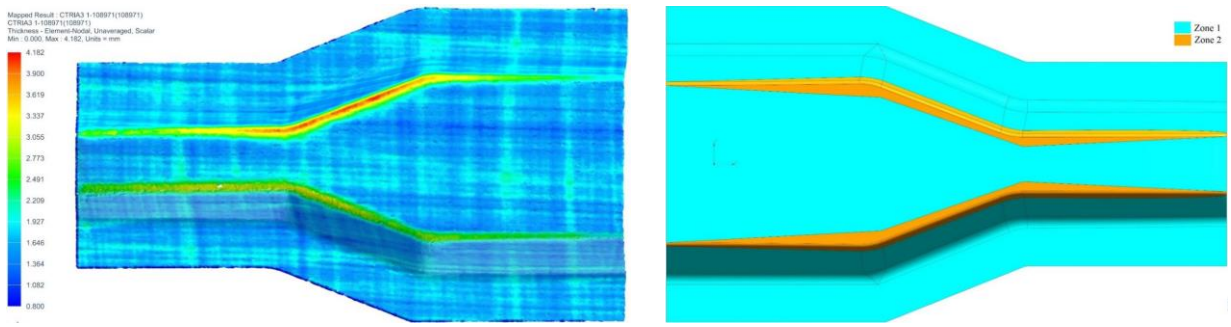


Figure 11. Influence of the variation of the rosette point on the frequency response function (FRF) of a thermoset composite omega shaped stiffener obtained using Simcenter and OPTIMUS. [15]

1.4.2 Influence of the local thickness on the modal behaviour

Additionally, the influence of the local thickness has been investigated, since during experimental measurements it is noticed that the thickness of the component is not constant as visualized in Figure 12(a). This thickness variation is introduced into the numerical model by defining 2 zones with a different thickness. One zone has a thickness of approximately 1.7 mm, represented by the vast blue area, while the orange area represented higher thickness area of the measured component, and is assigned a thickness of either 2.5mm or 3.0mm. The influence on the FRF can be seen in Figure 13, where it can be noticed that although only a relatively small area has a different thickness, the resulting FRF is affected throughout the whole frequency spectrum.



a b

Figure 12. Local thickness profile of the thermoset omega shaped stiffener (a) as measured and (b) simplified within Simcenter by defining 2 zones with different thickness. [15]

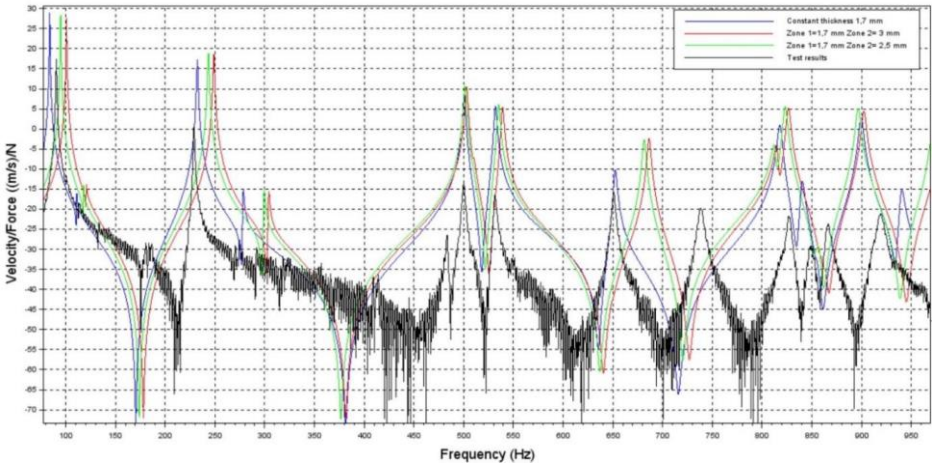


Figure 13. FRF obtained with the 2-zone model with variable thickness (red = 2.50mm and green = 3.00mm), compared to the test result and the constant thickness (1.70mm) model. [15]

A similar exercise was done for the thermoplastic case, with that difference that the thickness profile showed a more complex distribution. To mimic the real thickness distribution, the CAD shape was divide in 49 zones which are all assigned the average as-measured thickness zone.

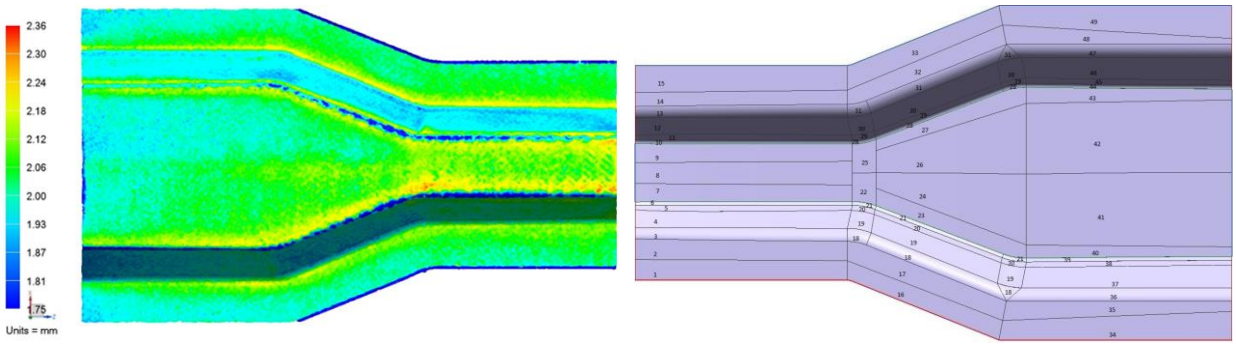


Figure 14. Local thickness profile of the thermoplastic omega shaped stiffener (a) as measured and (b) simplified within Simcenter by defining 49 zones with different thickness. [15]

Similar to the thermoset case, the change in thickness also affects the FRF of the thermoplastic case. The modal frequencies tend to be closer to the measured values at low frequency values, the high modal behaviour in the higher frequency range cannot be captured correctly in spite of having the correct geometry and thickness distribution.

1.4.1 Influence of the material properties on the modal behaviour

A third feature that causes uncertainty when dealing with composite material are the material properties. As been indicated before the properties of the woven reinforced thermoplastic were determined by VMC Toolkit [13], which makes use of an idealized woven unit cell representation. Since the representative unit cell is prone to variability, the influence of the material properties, namely density and elastic constants on

the FRF have been investigated. Figure 15 shows the resulting FRF with changing the density (-10%) and increasing the elastic properties (E11, E22, E33, G12, G13 and G23) with 15%.

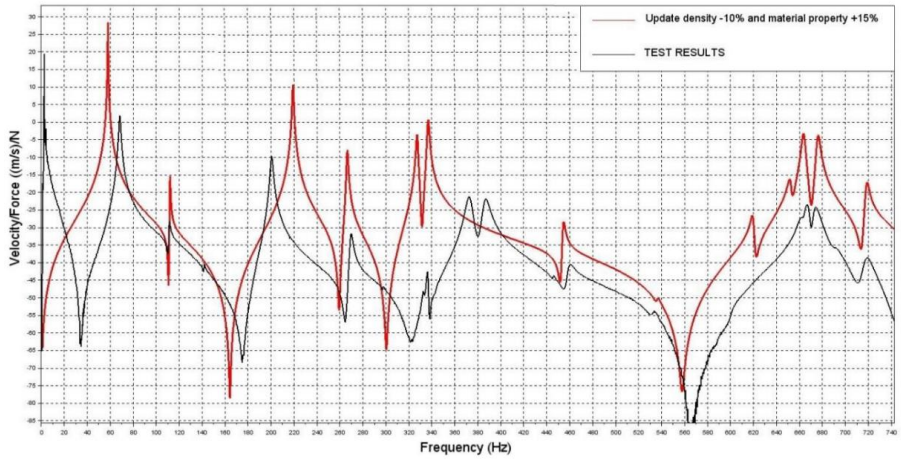


Figure 15. FRF obtained with the 49-zone model with variable thickness and adjusted density (-10%) and elastic material properties (+10%) [15]

1.4.1 Inverse identification of thickness profile

The availability of both a parameterized model of the omega shaped stiffener and the reference FRF have allowed creating a procedure that is aimed at the identification of the thickness distribution that ensures the best match between the numerical and experimental FRF. To this end, the 49 zones variable thickness model has been integrated into an automated input update and output evaluation schema as indicated in Figure 16.

The identification of the thickness in each area has been reformulated as an optimization problem, where the thicknesses are the design variables and the objective is the minimization of the difference between the numerical and experimental FRF. The depicted workflow has been implemented using the Product Integration and Design Optimization (PIDO) platform Optimus by Noesis Solutions. The operations performed within this workflow are:

- The mapping of the thickness on the omega shaped model.
- The analysis of the FEM model using Simcenter and the FRF extraction.
- The post-processing of the FRF and the evaluation of the total frequency shift

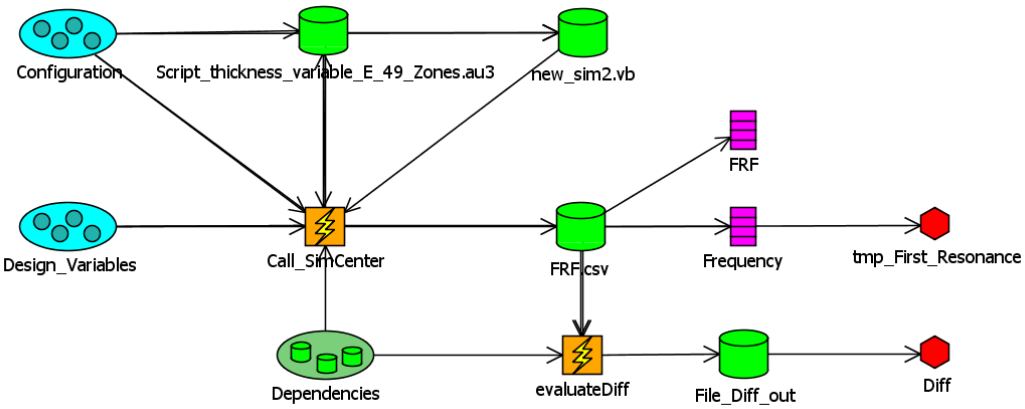


Figure 16. Optimus workflow for the evaluation of the local thickness.

The used performance indicator is the sum of the differences between the first 4 evaluated and measured resonances. The measurements taken on the build sample have indicated that the real thickness values were to be expected in the 1.5 to 2.5 mm range with a minimum step of 0.05 mm. The boundaries of the thickness design variables have been set accordingly.

The created structure, and the software that encompasses it, are suitable both to study how thickness influences the FRF and what are the areas that have a greater impact on it, and to determine the thickness distribution associated with the best match using a selection of optimization methods.

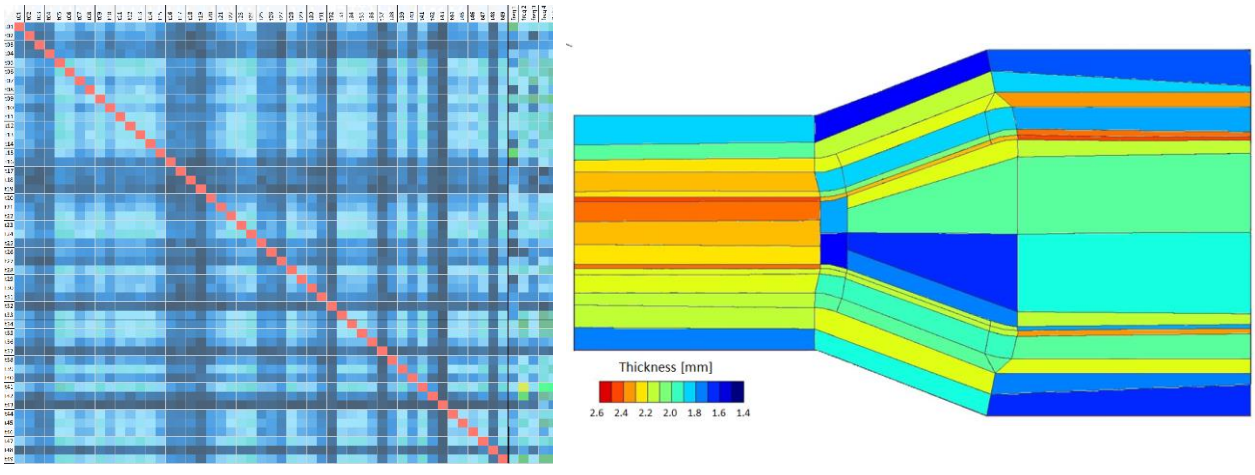
The first point is addressed by performing a design space exploration (DOE); due to the number of design variables (49) a Latin Hypercube Design (LHD) has been preferred over Factorial approaches, as in this methodology the number of experiments is not a function of the number of design variables [16] and at the same time ensures at least partial decoupling among them. The number of experiments has been set to 300.

A correlation analysis using the Pearson coefficient, which is a measure of the linear correlation between two variables between zonal thickness and total shift, is also performed. The chart, shown in Figure 17(a), highlights some aspects of the thickness-to-total-shift relationship: symmetry of the model is verified, thus right-side elements of the model have the same influence on the outputs as their left-side counterparts; the contribution of each area on the frequencies can be evaluated too, as an example 1 and 15 thicknesses (flat flanges of the narrow part of the component) have a strong linear correlation with the first mode whereas the reduction of 41 and 42, central panels of the wide side, would improve the match with the second mode.

The same analysis also confirmed the (at least partial) decoupling among inputs, as testified by the low correlation values, but still not zero due to the random component in the LHD behaviour.

The DOE has been used as entry point for the optimization; due to the time required by each computation (about 4 minutes), a surrogate model built on the DOE data has been used as replacement for the analysis. The interpolated cubic Radial Basis Function model has been cross-validated before the optimization resulting in a R^2_{press} value of .93, high enough to provide reliable global optimization results but predicted results still need validation by actual analysis [17].

Using Differential Evolution [18] as optimization method (better suited to problems with discrete or stepped variables) and the best configuration found from the DOE as starting point, the candidate solution has been found after 25 iterations, each composed of 250 experiments. The candidate design point has been validated with a dedicated run, the difference between the estimated and the actual frequency shift is 3 Hz



a b

Figure 17. The Pearson chart where (a) correlation values, zonal thickness to first modes and total shift. Blue indicates minimum (absolute) correlation and (b) thickness distribution for the thermoplastic omega shaped stiffener after numerical optimization.

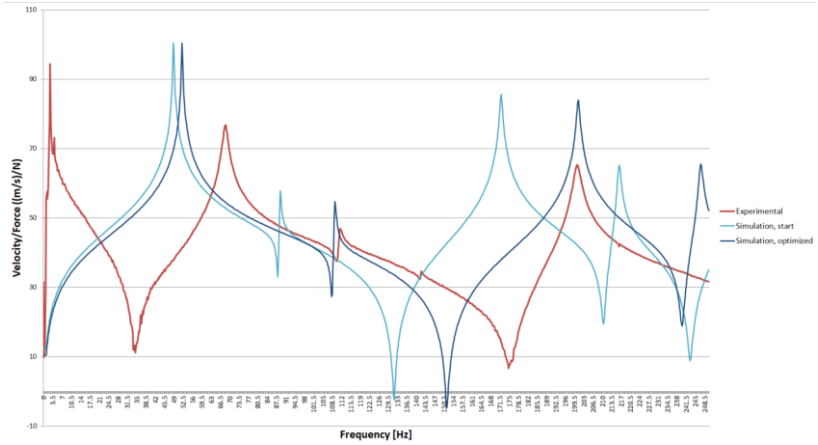


Figure 18. Thickness profile determination of the thermoplastic omega shaped stiffener through optimization.

The thickness profile of the optimized model depicted in Figure 17(b) has similarities with the real thickness profile of the omega shaped stiffener shown in Figure 14. The displayed thicknesses are only the result of a global optimization performed using a surrogate model; the achieved configuration could be further refined performing a local search based on actual analysis.

The results of the optimization, resumed in Figure 18, show a good match with the frequencies of the second and fourth mode whereas first and third are only partially influenced. As the previous analysis have suggested, the thickness is not the only parameter whose influence has to be accounted for in order to correctly model the modal behaviour.

Conclusions

The manufacturing process has a significant impact on the performance of modern industrial products, including lightweight composites components in automotive industry. Even if we can predict how a product's design should be and how it should be manufactured, the next step is to predict the product performance and its impact on the manufacturing parameters and vice versa. Only then, can you virtually and simultaneously optimize the manufacturing process and product performance, thus closing the loop.

In this paper, we have done a case study derived from an industrial context for which we closed this loop. There is some further investigation necessary on other sources of uncertainty that have not yet been modelled, but the analysis process showed its value in order to identify major parameters that are subject to uncertainty and improve model fidelity/confidence.

Acknowledgements

The authors would like to acknowledge KU Leuven for performing the thickness and shape measurements of the components. Additionally the authors also kindly acknowledge the support of Flanders Make and Flanders Innovation & Entrepreneurship (VLAIO) to support this study, which is part of an ICON project entitled "Virtual Design Platform for Sheet Material Products (VIDESPRO icon)"

References

[1] A. Long, Composites Forming Technologies, Woodhead Publishing, 2017.

[2] "Fibersim," Siemens PLM Software, [Online]. Available: https://www.plm.automation.siemens.com/global/en/products/nx/fibersim.html. [Accessed 15 5 2018].

[3] "AniForm," AniForm Engineering B.V., [Online]. Available: https://aniform.com/. [Accessed 15 5 2018].

[4] "PAM-FORM Composites Forming Simulation Software," ESI, [Online]. Available: https://www.esi-group.com/software-solutions/virtual-manufacturing/composites/pam-composites/pam-form-composites-forming-simulation-software. [Accessed 15 5 2018].

[5] K. Vanclooster, Forming of multilayered fabric reinforced thermoplastic composites, Leuven: KU Leuven, 2010.

[6] "Star-CCM+," Siemens PLM Software, [Online]. Available: https://mdx.plm.automation.siemens.com/star-ccm-plus. [Accessed 15 5 2018].

[7] "PAM-RTM - Composites Molding Simulation Software," ESI, [Online]. Available: https://www.esi-group.com/software-solutions/virtual-manufacturing/composites/pam-composites/pam-rtm-composites-molding-simulation-software. [Accessed 15 5 2018].

[8] M. Kobayashi, K. Dan, T. Baba, K. Yamakawa and R. Nakano, "Visualization experiment and numerical simulation of liquid impregnation with race-tracking for RTM process," in *Proceedings of ECCM17*, Munich, 2016.

[9] F. Pascon, T. van Eekelen, C. Brauner and M. Bach, "An integrated virtual tool chain for the simulation of thermoset composite manufacturing process," in *SAMPE Europe Conference*, Liege, 2016.

[10] J. Gilbert, Simulation of Thermoset Polymer Composite Curing, Leuven: KU Leuven, 2017.

[11] G. Fernlund and A. Poursatip, "Getting part dimensions right in composites molding," *Composites World*, vol. 1, no. 2, pp. 10-11, 2 2015.

[12] C. C. Chamis, "Simplified composite micromechanics equations for strength, fracture toughness, impact resistance and environmental effects," in *29th Annual Conference of the Society of the Plastics Industry*, Houston, Texas, 1984.

[13] L. Farkas, K. Vanclooster, H. Erdelyi, R. Sevenois, S. V. Lomov, T. Naito, Y. Urushiyama and W. Van Paepegem, "Virtual material characterization process for composite materials: an industrial solution," in *Proceedings of ECCM17*, Munich, 2016.

[14] DuPont, "Vizilon® Thermoplastic Composite Sheet," [Online]. Available: http://www.dupont.com/content/dam/dupont/products-and-services/plastics-polymers-and-resins/thermoplastics/documents/Vizilon/DPM17_22558_Vizilon_SB63G1_Series_Data_Sheet_me11.pdf. [Accessed 15 5 2018].

[15] L. Spina, Numerical assessment of the influence of manufacturing features on the modal behaviour of a composite structure, Rende: University of Calabria, 2018.

[16] R. L. Iman, Latin Hypercube Sampling, Wiley, 2008.

[17] T. Tarpey, "A Note on the Prediction Sum of Squares Statistic for Restricted Least Squares," *The American Statistician*, vol. 54, no. 2, pp. 166-118, 2000.

[18] R. Storn and K. Price, "Differential Evolution – A Simple and Efficient Heuristic for global Optimization over Continuous Spaces," *Journal of Global Optimization*, vol. 11, no. 4, pp. 341-359, 1997.

Mesoscale structure of periodic textile composites effect on wave propagation

V. Thierry [1], **L. Brown** [2]
[1] Institute for Aerospace Technology & The Composites Research Group, University of Nottingham, NG7 2RD, UK
e-mail: **victor.thierry@nottingham.ac.uk**

[2] The Composites Research Group, University of Nottingham, NG7 2RD, UK

Abstract
In this article, a method for wave propagation analysis of textile composites at a mesoscopic level is presented for the first time. This study is performed in the vibro-acoustic and ultrasonic frequency ranges. The presented method combines a mode-based reduction method, allowing for great CPU cost saving, and the Wave Finite Element Method (WFEM), which associates the Periodic Structure Theory (PST) and standard Finite Element Method (FEM). The PST allows to analyse the wave propagation properties of a periodic structure by modelling only a periodicity (unit cell) of it. A standard wave propagation analysis of textile composite structures is also performed, using homogenized properties in the unit cell, and used as a comparison. It is shown for different types of textiles that using the standard method results in errors in the dispersion curves.

1 Introduction

Textile composites are widely used for their excellent mechanical properties [1] in many industries. It is greatly applied in aerospace industry in particular thanks to a low weight and high strength when compared to metallic alloys. These composite structures are periodic and can be considered as an assembly of identical unit cells assembled in an identical manner. These periodic structures and their applications have attracted a lot of research for the past decades [2, 3, 4, 5, 6].

However, textile composites are subject to failure such as fibre breakages, cracks or delamination. In the aerospace industry, damage in the structure can lead to catastrophic scenarios, and that is why intensive research has been conducted on Non Destructive Testing (NDT) and Structural Health Monitoring (SHM), which would allow for safest flight while reducing the maintenance costs. One popular technique for 'on-line' inspection is ultrasound guided waves spectroscopy [7]. Guided wave propagation in thin plates is dispersive, and therefore the velocity of wave propagation depends on the frequency. For this reason it is of the upmost importance to know the dispersion relations for use in NDT and SHM.

As the behaviours of textile composite structures are complex, numerical simulations are more and more required for the design of inspection processes. When excited in the mid-frequency range, the material allows for the mechanical energy to propagate through the entire structure but wave localization in the periodic cell will also be produced. This makes this frequency range suitable for the detection of small cracks. In order to study this frequency range, the composite textile needs to be modelled at a mesoscopic scale, which means modelling the yarns and matrix.

The Wave Finite Element Method (WFEM) is an efficient tool to study wave propagation in periodic structures. The WFEM has been widely used in precedent research for various structure types such as beam-like structures [8, 9], cylinders [10, 11], plates [10, 12, 13], thin-walled structures [14]. It has also found applications in predicting the vibroacoustic and dynamic performance of composite panels and shells [15, 16, 17],

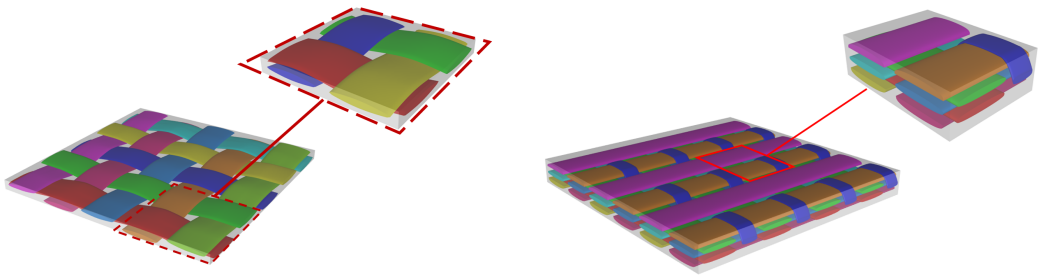
with pressurized shells [18] and complex periodic structures [19] having been investigated. The variability of vibroacoustic transmission through layered structures [20, 21, 22], as well as structural identification [23] and complex wave interaction phenomena in anisotropic composites [22, 24] have been modelled through the same methodology. However, applying the WFEM to textile composites means that a fine mesh is needed in order to describe the geometry precisely, which implies high computational expenses and that is why another model reduction method is applied to the model. This method is called the component mode synthesis (CMS) and it has been extensively used in the literature [25, 26, 6, 27].

The principal novelty of this work is the investigation of ultrasonic wave propagation analysis in anisotropic periodic structures such as textile composites. The mesoscopic properties of the material are taken into account for the first time for this type of analysis and it is shown that mesoscale models can successfully predict stop-band behaviour which is indispensable for guided wave inspection purposes. This paper is organised as follows.

In section 2, the method used to model the textile composite structure at a mesoscopic scale is presented. Then the Craig-Bampton reduction method is described. It will be coupled with the WFEM in the following section. Thus in order to perform ultrasound wave propagation analysis of a 2D weave textile composite structure. This results are presented in the last section.

2 Mesoscale modelling of textile composites

A mesoscale modelling suggests a detailed geometric representation of fabrics such as the yarns and the matrix. By opposition to a macroscale modelling which consists in homogenized mechanical properties along the unit cell. Mesoscale modelling of textile composites starts with the definition of the geometry of a unit cell using a specialist pre-processor such as TexGen [28, 29, 30, 31, 32]. This open source software is developed by the Composites Research Group at the University of Nottingham and is used for modelling the geometry of fabric such as 2D fabric weave or 3D woven textiles (see Fig.1). The model is then exported to a FE software and the M and K matrices of the unit cell are extracted.



(a) Unit cell of a periodic 2D weave (b) Unit cell of a periodic 3D weave

Figure 1: Periodic textile composite examples

A macroscale model, obtained through a homogenization process of the mechanical properties of the mesoscale model, is considered as well, allowing for comparison.

3 Model reduction using the Craig-Bampton Method

The equation of motion of the unit cell is written as:

$$\mathbf{M}\ddot{\mathbf{q}}(t) + \mathbf{C}\dot{\mathbf{q}}(t) + \mathbf{K}\mathbf{q}(\mathbf{t}) = \mathbf{f}(\mathbf{t}) \tag{1}$$

If a time-harmonic behavior is assumed and no damping is considered, Eq.1 can be rewritten as follows (Eq.2):

$$\left[\mathbf{K} - \omega^2 \mathbf{M}\right] \mathbf{q} = \mathbf{F} \tag{2}$$

The nodal DOFs of the unit cell are partitioned in the following way: boundary DOFs (themself partitioned as bottom, top, left, right, left-bottom corner, right-bottom corner, left-top corner, right-top corner) and internal DOFs (see Fig.2), which gives the following equation (subscript *bd* stands for boundary):

$$\mathbf{q} = \left\{\mathbf{q_{bd}^T} \quad \mathbf{q_I^T}\right\}^T = \left\{\mathbf{q_B^T} \quad \mathbf{q_T^T} \quad \mathbf{q_L^T} \quad \mathbf{q_R^T} \quad \mathbf{q_{LB}^T} \quad \mathbf{q_{RB}^T} \quad \mathbf{q_{LT}^T} \quad \mathbf{q_{RT}^T} \quad \mathbf{q_I^T}\right\}^T \tag{3}$$

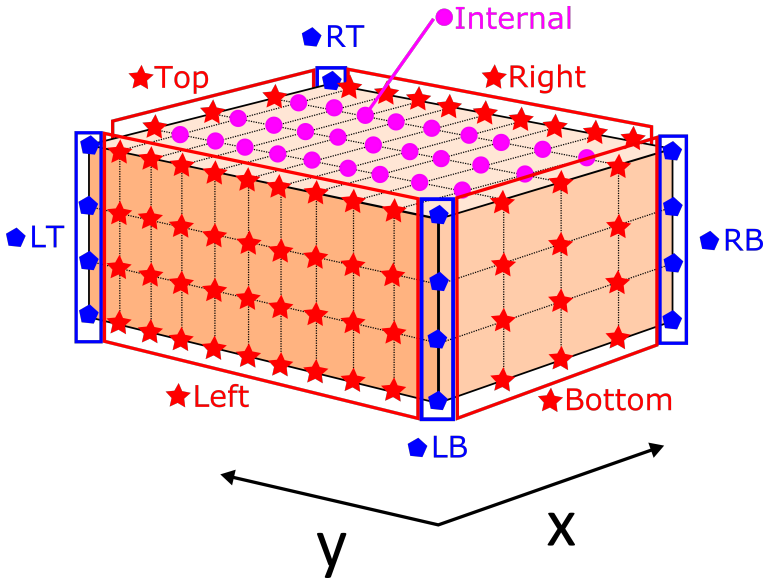


Figure 2: DOFs partitioning

Component Mode Synthesis (CMS) are methods used for reducing the complexity of structural dynamics models leading to a decrease in CPU time cost. The Craig-Bampton Method [33] is one of these approaches.

For free wave propagation, no external force acts on the internal nodes of the structure. This leads to $\mathbf{f_I} = \mathbf{0}$. The equation of motion of the unit cell (Eq.2) becomes:

$$\left(\begin{bmatrix} \mathbf{K_{bdbd}} & \mathbf{K_{bdI}} \\ \mathbf{K_{Ibd}} & \mathbf{K_{II}} \end{bmatrix} - \omega^2 \begin{bmatrix} \mathbf{M_{bdbd}} & \mathbf{M_{bdI}} \\ \mathbf{M_{Ibd}} & \mathbf{M_{II}} \end{bmatrix}\right) \begin{Bmatrix} \mathbf{q_{bd}} \\ \mathbf{q_I} \end{Bmatrix} = \begin{Bmatrix} \mathbf{f_{bd}} \\ \mathbf{0} \end{Bmatrix} \tag{4}$$

The key to this method is to reduce the number of internal DOFs by selecting component modes Φ_C among a subset of the local modes of the unit cell when the boundary DoFs are fixed. The boundary modes Φ_{bd} are calculated by static condensation. The projection matrix B is determined as shown in Eq.5, on which the M and K matrix are then projected (see Eq.6).

$$\begin{Bmatrix} \mathbf{q_{bd}} \\ \mathbf{q_I} \end{Bmatrix} = \begin{bmatrix} \mathbf{I} & \mathbf{0} \\ \mathbf{\Phi_{bd}} & \mathbf{\Phi_C} \end{bmatrix} \begin{Bmatrix} \mathbf{q_{bd}} \\ \mathbf{q_\Phi} \end{Bmatrix} = \mathbf{B} \begin{Bmatrix} \mathbf{q_{bd}} \\ \mathbf{q_\Phi} \end{Bmatrix} \tag{5}$$

$\mathbf{q_\Phi}$ is the reduced set of the physical internal DOFs $\mathbf{q_I}$, whereas the boundary DOFs are kept as physical coordinates [34].

$$\tilde{\mathbf{K}} = \mathbf{B^T K B}, \qquad \tilde{\mathbf{M}} = \mathbf{B^T M B} \tag{6}$$

4 Overview of the WFE method

The WFEM uses both the periodic structure theory (PST) developed in [35] and the finite element method. The advantage of that method is that only a period of the structure needs to be modelled to find the dispersion relations for the whole structure. The number of boundary DoFs from the unit cell (and thus unknown of the problem) can be reduced thanks to the PST. A reduction matrix $\mathbf{\Lambda_R}$ on which the reduced mass and stiffness matrix will be projected is created based on the relations from the PST.

For example for a two dimensional periodic composite plate-like structure, the wave motion is in the Oxy plane. This gives

$$\begin{Bmatrix} \mathbf{q_B} \\ \mathbf{q_T} \\ \mathbf{q_L} \\ \mathbf{q_R} \\ \mathbf{q_{LB}} \\ \mathbf{q_{RB}} \\ \mathbf{q_{LT}} \\ \mathbf{q_{RT}} \\ \mathbf{q_I} \end{Bmatrix} = \begin{bmatrix} \mathbf{I} & \mathbf{0} & \mathbf{0} & \mathbf{0} \\ \mathbf{I}\lambda_y & \mathbf{0} & \mathbf{0} & \mathbf{0} \\ \mathbf{0} & \mathbf{I} & \mathbf{0} & \mathbf{0} \\ \mathbf{0} & \mathbf{I}\lambda_x & \mathbf{0} & \mathbf{0} \\ \mathbf{0} & \mathbf{0} & \mathbf{I} & \mathbf{0} \\ \mathbf{0} & \mathbf{0} & \mathbf{I}\lambda_x & \mathbf{0} \\ \mathbf{0} & \mathbf{0} & \mathbf{I}\lambda_y & \mathbf{0} \\ \mathbf{0} & \mathbf{0} & \mathbf{I}\lambda_x\lambda_y & \mathbf{0} \\ \mathbf{0} & \mathbf{0} & \mathbf{0} & \mathbf{I} \end{bmatrix} \begin{Bmatrix} \mathbf{q_B} \\ \mathbf{q_L} \\ \mathbf{q_{LB}} \\ \mathbf{q_I} \end{Bmatrix} = \mathbf{\Lambda_R}(\lambda_x, \lambda_y) \begin{Bmatrix} \mathbf{q_B} \\ \mathbf{q_L} \\ \mathbf{q_{LB}} \\ \mathbf{q_I} \end{Bmatrix} \tag{7}$$

Equilibrium at the right-top corner nodes gives:

$$\mathbf{\Lambda_L}(\lambda_x, \lambda_y) \begin{Bmatrix} \mathbf{f_{bd}} \\ \mathbf{0} \end{Bmatrix} = \mathbf{0} \tag{8}$$

with $\mathbf{\Lambda_L}(\lambda_x, \lambda_y)$ the conjugate transpose of $\mathbf{\Lambda_R}(\lambda_x, \lambda_y)$.

The following eigenvalue problem appears

$$\mathbf{\Lambda_L}(\mathbf{K} - \omega^2\mathbf{M})\mathbf{\Lambda_R} \begin{Bmatrix} \mathbf{q_B} \\ \mathbf{q_L} \\ \mathbf{q_{LB}} \\ \mathbf{q_I} \end{Bmatrix} = 0 \tag{9}$$

5 Numerical investigation of a 2D weave fabric

A 2D weave fabric composite is presented as a case study. In this section, dispersion curves for the modelled textile composites are presented. Even though the WFE calculations are performed in 2D, the results will be displayed in the $\Theta = 0^o$ direction for the sake of clarity. A unit cell is extracted from the fabric as shown in

Fig.1(a), its dimensions are 2x2x0.2 mm, and the WFE/CMS method is performed on it as explained in the previous sections.

A macroscale model, containing the homogenized mechanical properties of the mesoscale model, is created; the aim being to compare both models. The modelled elements need to have the same dimensions as the ones of the mesoscale model. The WFE method is then performed on a model composed of one element in both the x and y directions and of ten elements in the z direction (1x1x10) to comply with the mesoscale model (composed of 6250 elements: 25x25x10).

The dispersion curve for the flexural mode of this model is displayed in Fig.3, as well as the one of the 6250 elements mesoscale model.

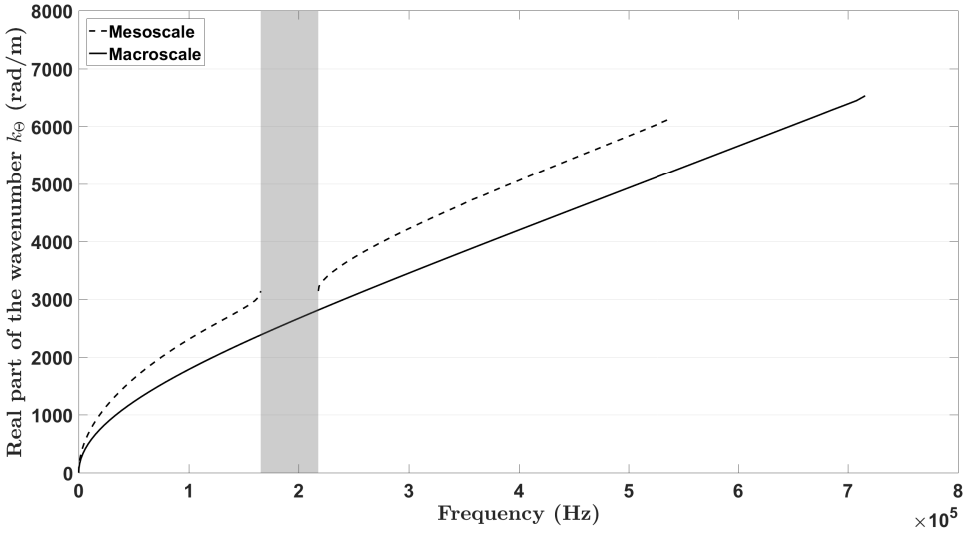


Figure 3: Dispersion curve of the flexural mode of the mesoscale model and the macroscale model; presenting a stop-band (grayed area) for the the mesoscale model; '- -' mesoscale model and '–' macroscale model

In Fig.3, we notice some important differences between the curves from the meso- and macroscale models. The mean relative frequency difference for the flexural mode (Fig.3) is of 30 %, and the dispersion curve present a stop-band when modelled at a mesoscopic scale.

It can be noted that stop-band occurs (Fig.3) when the wavenumber reaches $k_x = \dfrac{2\pi}{\Delta_x}$, which means when the wavelength is of the size of a periodicity of the structure. A stop-band means that the concerned wave (flexural in our case) will not propagate in this frequency range.

6 Conclusion

In this paper, a method for wave propagation analysis of textile composites at a mesoscopic level is presented for the first time. It is shown that mesoscopic scale design increases the computation accuracy. An example of a 2D fabric weave is presented and modelled.

- It can be seen that there are some significant differences in the dispersion relations between the different scales.
- It appears that when studied at a mesoscopic scale, the textile show stop-bands for certain ranges of frequency and modes.

- Computational times are feasible while modelling the entire textile with FE would be very costly.

Acknowledgements

This work is funded by the INNOVATIVE doctoral programme. The INNOVATIVE programme is partially funded by the Marie Curie Initial Training Networks (ITN) action (project number 665468) and partially by the Institute for Aerospace Technology (IAT) at the University of Nottingham.

Software engineering support was funded by the Engineering and Physical Sciences Research Council RSE Fellowship [Grant number: EP/N019040/1].

References

[1] C. Soutis, "Fibre reinforced composites in aircraft construction," *Progress in Aerospace Sciences*, vol. 41, no. 2, pp. 143–151, 2005.

[2] S. Mead, D. J.; Parthan, "Free wave propagation in two-dimensional periodic plates," *Journal of Sound and Vibration*, 1979.

[3] D. . J. Mead, "Wave propagation in continuous periodic structures: research contributions from southampton, 1964-1995," *Journal of Sound and Vibration*, 1996.

[4] L. Hinke, B. R. Mace, and M. J. Brennan, "Finite element analysis of waveguides," *Institute of Sound and Vibration Research*, 2004.

[5] C. Barbarosie and M. M. Neves, "Periodic structures for frequency filtering: analysis and optimization," *Computers & Structures*, vol. 82, no. 17-19, pp. 1399–1403, 2004.

[6] C. Droz, C. Zhou, M. N. Ichchou, and J. P. Lain, "A hybrid wave-mode formulation for the vibro-acoustic analysis of 2d periodic structures," *Journal of Sound and Vibration*, vol. 363, pp. 285–302, 2016.

[7] V. Giurgiutiu, *Structural Health Monitoring of Aerospace Composites*. Academic Press, 2015.

[8] J. M. Mencik and M. N. Ichchou, "Multi-mode propagation and diffusion in structures through finite elements," *European Journal of Mechanics - A/Solids*, vol. 24, no. 5, pp. 877–898, 2005.

[9] B. R. Mace, D. Duhamel, M. J. Brennan, and L. Hinke, "Finite element prediction of wave motion in structural waveguides," *The Journal of the Acoustical Society of America*, vol. 117, no. 5, pp. 2835–2843, 2005.

[10] E. Manconi and B. R. Mace, "Modelling wave propagation in two-dimensional structures using a wave/finite element technique," *Institute of Sound and Vibration Research*, 2007.

[11] E. Manconi and B. R. Mace, "Wave characterization of cylindrical and curved panels using a finite element method," *J Acoust Soc Am*, vol. 125, no. 1, pp. 154–63, 2009.

[12] M. N. Ichchou, J. Berthaut, and M. Collet, "Multi-mode wave propagation in ribbed plates: Part i, wavenumber-space characteristics," *International Journal of Solids and Structures*, vol. 45, no. 5, pp. 1179–1195, 2008.

[13] M. N. Ichchou, J. Berthaut, and M. Collet, "Multi-mode wave propagation in ribbed plates. part ii: Predictions and comparisons," *International Journal of Solids and Structures*, vol. 45, no. 5, pp. 1196–1216, 2008.

[14] L. Houillon, M. N. Ichchou, and L. Jezequel, "Wave motion in thin-walled structures," *Journal of Sound and Vibration*, vol. 281, no. 3-5, pp. 483–507, 2005.

[15] D. Chronopoulos, M. Ichchou, B. Troclet, and O. Bareille, "Predicting the broadband response of a layered cone-cylinder-cone shell," *Composite Structures*, vol. 107, pp. 149–159, 2014.

[16] D. Chronopoulos, M. Ichchou, B. Troclet, and O. Bareille, "Predicting the broadband vibroacoustic response of systems subject to aeroacoustic loads by a krylov subspace reduction," *Applied Acoustics*, vol. 74, no. 12, pp. 1394–1405, 2013.

[17] D. Chronopoulos, "Design optimization of composite structures operating in acoustic environments," *Journal of Sound and Vibration*, vol. 355, pp. 322–344, 2015.

[18] T. Ampatzidis and D. Chronopoulos, "Acoustic transmission properties of pressurised and pre-stressed composite structures," *Composite Structures*, vol. 152, pp. 900–912, 2016.

[19] D. Chronopoulos, I. Antoniadis, and T. Ampatzidis, "Enhanced acoustic insulation properties of composite metamaterials having embedded negative stiffness inclusions," *Extreme Mechanics Letters*, vol. 12, pp. 48–54, 2017.

[20] D. Chronopoulos, M. Ichchou, B. Troclet, and O. Bareille, "Thermal effects on the sound transmission through aerospace composite structures," *Aerospace Science and Technology*, vol. 30, no. 1, pp. 192–199, 2013.

[21] R. Apalowo, D. Chronopoulos, M. Ichchou, Y. Essa, and F. Martin De La Escalera, "The impact of temperature on wave interaction with damage in composite structures," *Proceedings of the Institution of Mechanical Engineers, Part C: Journal of Mechanical Engineering Science*, vol. 231, no. 16, pp. 3042–3056, 2017.

[22] D. Chronopoulos, D. Chronopoulos, M. Collet, M. Collet, M. Ichchou, and M. Ichchou, "Wave sensitivity analysis for periodic and arbitrarily complex composite structures," *Engineering Computations*, vol. 34, no. 5, pp. 1572–1597, 2017.

[23] D. Chronopoulos, C. Droz, R. Apalowo, M. Ichchou, and W. Yan, "Accurate structural identification for layered composite structures, through a wave and finite element scheme," *Composite Structures*, vol. 182, pp. 566–578, 2017.

[24] D. Chronopoulos, "Calculation of guided wave interaction with nonlinearities and generation of harmonics in composite structures through a wave finite element method," *Composite Structures*, 2017.

[25] V. Cotoni, R. S. Langley, and P. J. Shorter, "A statistical energy analysis subsystem formulation using finite element and periodic structure theory," *Journal of Sound and Vibration*, vol. 318, no. 4-5, pp. 1077–1108, 2008.

[26] C. W. Zhou, J. P. Lain, M. N. Ichchou, and A. M. Zine, "Multi-scale modelling for two-dimensional periodic structures using a combined mode/wave based approach," *Computers & Structures*, vol. 154, pp. 145–162, 2015.

[27] Y. Fan, M. Collet, M. Ichchou, L. Li, O. Bareille, and Z. Dimitrijevic, "Energy flow prediction in built-up structures through a hybrid finite element/wave and finite element approach," *Mechanical Systems and Signal Processing*, vol. 66-67, pp. 137–158, 2016.

[28] M. Sherburn, *Geometric and Mechanical Modelling of Textiles*. Thesis, 2007.

[29] H. Lin, L. P. Brown, and A. C. Long, "Modelling and simulating textile structures using texgen," *Advanced Materials Research*, vol. 331, pp. 44–47, 2011.

[30] H. Lin, X. Zeng, M. Sherburn, A. C. Long, and M. J. Clifford, "Automated geometric modelling of textile structures," *Textile Research Journal*, vol. 82, no. 16, pp. 1689–1702, 2012.

[31] S. D. Green, M. Y. Matveev, A. C. Long, D. Ivanov, and S. R. Hallett, "Mechanical modelling of 3d woven composites considering realistic unit cell geometry," *Composite Structures*, vol. 118, pp. 284–293, 2014.

[32] L. P. Brown and M. Sherburn, "Texgen v3.9.0," Feb. 2017. This software is currently funded by EPSRC Research Software Engineering Fellowship - Software for Textile Modelling and Simulation, EP/N019040/1.

[33] M. C. C. Bampton and R. R. Craig, Jr., "Coupling of substructures for dynamic analyses," *AIAA Journal*, vol. 6, pp. 1313–1319, July 1968.

[34] L. G. J. Becker, "Cms methods for efficient damping prediction for structures with friction," 2008.

[35] R. S. Langley, "A note on the force boundary conditions for two-dimensional periodic structures with corner freedoms," *Journal of Sound and Vibration*, 1992.

Modal frequency and damping analysis of tow steered CFRP composite plates

D.A. Pereira [1,3], **T. A. M. Guimarães** [2], **D. A. Rade** [1]
[1] ITA - Technological Institute of Aeronautics, Division of Mechanical Engineering,
São José dos Campos, Brazil
e-mail: **rade@ita.br**

[2] UFU - Federal University of Uberlândia, School of Mechanical Engineering,
Uberlândia, Brazil

[3] IPT - Institute for Technological Research, Lightweight Structures Laboratory,
São José dos Campos, Brazil

Abstract
In composite materials, previous studies show that carbon-fiber reinforced polymers (CFRP) can be designed in terms of damping characteristics by acting on its physical and geometric features. In recent years, the development of automatic fiber placement (AFP) allows the realization of variable stiffness composite laminates (VSCL), among which tow steered composites are considered very promising. Therefore, the objective of this paper is to present a numerical assessment of the influence of fiber steering on the modal damping of CFRP plates for different fiber trajectories. The dynamic model is derived by using a semi-analytical approach based on the combination of the Classical Lamination Theory with the Rayleigh-Ritz (Assumed-Modes) approach. The modal damping factors are calculated using the Strain Energy Method, which is based on the ratio between the stored and the dissipated energies, giving the specific damping capacity (SDC) for each vibration mode.

1 Introduction

It is widely recognized that composite materials, especially fiber-reinforced ones, have enormous potential for applications to lightweight structures. One of the main advantages of these materials is the possibility of being designed to comply with specific performance criteria by changing the relative fiber orientations of the plies. In addition, the current emergence of novel manufacturing techniques, such as automatic fiber placement, opens new possibilities for further improvement of composite structural components. In particular, it is currently possible to manufacture the so-called variable stiffness composite laminates (VSCL), which encompass those made with variable fiber spacing (VFSL) and those in which the fibers are deposited following curvilinear paths. These latter are known as tow-steered composites (TSCL) [1]. As compared to traditional composite laminates, VSCL provide the designer with a broader range of options to design composite plates considering multiple design goals, while minimizing weight penalties [2]. Under these motivations, various researchers have been investigating the vibrational work [3, 4], aeroelastic [5, 6, 7] and buckling behavior of tow-steered laminates [8, 9].

In terms of vibration behavior, damping of composite materials can be several orders of magnitude higher than that of traditional engineering materials, making them appealing for use in components undergoing dynamic loading [10]. Various authors have investigated the influence of layup on the damping levels of traditional composite plates [11, 12, 13, 14, 15, 16]. However, to the authors' best knowledge, studies on the damping characteristics of tow-steered composite laminates have not been reported in the literature hitherto.

The identification of modal damping can be achieved through experimental modal analysis. An alternative, more appropriate to be used in design phase, is the use of theoretical or hybrid theoretical/experimental models, which require few experimental analyses. Severals approaches have been proposed to model damping in composite materials. [14] uses the concept of specific damping capacity (SDC) [17] to predict the modal damping of thin unidirectional laminates. [13] presents damping analysis of unidirectional laminates with two different boundary conditions using the SDC method. The authors conclude that modal damping factors are determined by the corresponding vibration mode shapes.

Among the methodologies available for damping characterization, the SDC model represents an adequate approach to study the effect of fiber steering on the modal damping of composite laminates. Therefore, this method is adopted herein. Based on the hypotheses of Kirchhoff plate theory, a dynamic model is formulated by associating the Classical Lamination Theory with the Rayleigh–Ritz (Assumed-Modes) approach. The modeling approach duly accounts for the curvilinear trajectory of the fibers on each lamina. The modal damping factors are calculated using the Strain Energy Method, which is based on the ratio between the stored and the dissipated energies, giving the specific damping capacity (SDC) for each vibration mode. The values of natural frequencies and modal damping factors are evaluated for different fiber trajectories.

2 Theory

In this work, the procedure for the modeling of damping follows the approach proposed by [17], which is based on the assumption that the dissipated energy is associated to principal stress components at the ply level. The specific damping capacity (SDC) is defined as the ratio of the dissipated strain energy (ΔU) per cycle of vibration to the maximum strain energy (U) [14].

$$\Psi = \frac{\Delta U}{U} \tag{1}$$

When U and ΔU are computed for the displacement fields corresponding to a set of natural vibration modes, the SDC provides the modal damping factors associated to those modes. Hence, U and ΔU are formulated herein for the tow-steered laminate.

Considering a thin individual ply illustrated in Fig. 1, for which plane stress state is assumed, the strain energy is given by:

$$U = \frac{1}{2}\int_V \boldsymbol{\varepsilon}^{\mathrm{T}}_{(x,y)}\boldsymbol{\sigma}_{(x,y)}dV, \tag{2}$$

where:

$$\boldsymbol{\varepsilon}_{(x,y)} = \left\{ \begin{array}{c} \varepsilon_x \\ \varepsilon_y \\ \gamma_{xy} \end{array} \right\} \quad and \quad \boldsymbol{\sigma}_{(x,y)} = \left\{ \begin{array}{c} \sigma_x \\ \sigma_y \\ \tau_{xy} \end{array} \right\}. \tag{3}$$

The dissipated energy takes a form similar to Eq.3, being given by [18]:

$$\Delta U = \frac{1}{2}\int_V \boldsymbol{\varepsilon}^{\mathrm{T}}_{(x,y)}\boldsymbol{\psi}\boldsymbol{\sigma}_{(x,y)}dV, \tag{4}$$

where:

$$\boldsymbol{\psi} = \left[\begin{array}{ccc} \psi_{11} & 0 & 0 \\ 0 & \psi_{22} & 0 \\ 0 & 0 & \psi_{66} \end{array} \right]. \tag{5}$$

In the equations above, the subscripts (x, y) indicate that the stress and strain components are represented in terms of their components in the x, y axes shown in Fig. 1. In addition, the factors $\psi_{ii}, i = 1, 2, 6$ characterize the damping properties of the material [14].

The composite laminate is modeled according to the Classical Lamination Theory (CLT). For that purpose, the constitutive equations of each lamina are formulated in the principal coordinates $(1-2)$, shown in Figure 1. Then, rotation transformations are performed to obtain the constitutive equations in the global coordinate system $x - y$. It should be noticed that, in Fig.1 θ indicates the angle between both coordinate systems, and can also be interpreted as the angle defining the local fiber orientation with respect to the global coordinate system.

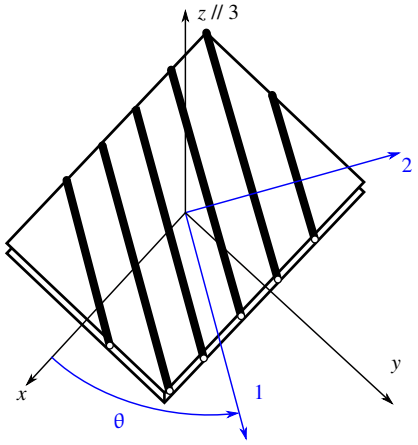


Figure 1: Lamina in the principal (1,2 and 3) and off-axis coordinates(x, y and z).

The constitutive equations of a lamina in its principal coordinate system are expressed as:

$$\left\{ \begin{array}{c} \sigma_1 \\ \sigma_2 \\ \tau_{12} \end{array} \right\} = \left[\begin{array}{ccc} Q_{11} & Q_{12} & 0 \\ Q_{12} & Q_{22} & 0 \\ 0 & 0 & Q_{66} \end{array} \right] \left\{ \begin{array}{c} \varepsilon_1 \\ \varepsilon_2 \\ \gamma_{12} \end{array} \right\}, \quad or \quad \boldsymbol{\sigma}_{(1,2)} = \mathbf{Q}\boldsymbol{\epsilon}_{(1,2)} \tag{6}$$

where the components of the stiffness matrix are given by:

$$Q_{11} = \frac{E_1}{1 - \nu_{12}\nu_{21}}, \quad Q_{22} = \frac{E_2}{1 - \nu_{12}\nu_{21}}, \quad Q_{12} = Q_{21} = \frac{\nu_{12}E_2}{1 - \nu_{12}\nu_{21}}, \quad Q_{66} = G_{12}. \tag{7}$$

The transformations of the stress and strain vectors from axes $x - y$ to axes $1 - 2$ are expressed as follows:

$$\left\{ \begin{array}{c} \sigma_1 \\ \sigma_2 \\ \tau_{12} \end{array} \right\} = \left[\begin{array}{ccc} c^2 & s^2 & 2cs \\ s^2 & c^2 & -2cs \\ -cs & cs & c^2 - s^2 \end{array} \right] \left\{ \begin{array}{c} \sigma_x \\ \sigma_y \\ \tau_{xy} \end{array} \right\} \quad or \quad \boldsymbol{\sigma}_{(1,2)} = \mathbf{T}_\sigma \boldsymbol{\sigma}_{(x,y)} \tag{8}$$

$$\left\{ \begin{array}{c} \varepsilon_1 \\ \varepsilon_2 \\ \gamma_{12} \end{array} \right\} = \left[\begin{array}{ccc} c^2 & s^2 & cs \\ s^2 & c^2 & -cs \\ -2cs & 2cs & c^2 - s^2 \end{array} \right] \left\{ \begin{array}{c} \varepsilon_x \\ \varepsilon_y \\ \gamma_{xy} \end{array} \right\} \quad or \quad \boldsymbol{\varepsilon}_{(1,2)} = \mathbf{T}_\varepsilon \boldsymbol{\varepsilon}_{(x,y)} \tag{9}$$

where $c = \cos\theta$, $s = \text{sen}\,\theta$:

Substituting Eq. 8 and Eq. 9 into Eq. 6, one obtains:

$$\mathbf{T}_\sigma \boldsymbol{\sigma}_{(x,y)} = \mathbf{Q}\mathbf{T}_\varepsilon \boldsymbol{\varepsilon}_{(x,y)}. \tag{10}$$

Multiplying both sides by $\mathbf{T}_\sigma^{-1}$, result in:

$$\boldsymbol{\sigma}_{(x,y)} = \mathbf{T}_{\sigma}^{-1}\mathbf{Q}\mathbf{T}_{\varepsilon}\boldsymbol{\varepsilon}_{(x,y)}. \tag{11}$$

The above equation can be recast as follows:

$$\boldsymbol{\sigma}_{(x,y)} = \bar{\mathbf{Q}}\boldsymbol{\varepsilon}_{(x,y)}. \tag{12}$$

where $\bar{\mathbf{Q}} = \mathbf{T}_{\sigma}^{-1}\mathbf{Q}\mathbf{T}_{\varepsilon}$.

At this point, it is worth noticing that for traditional composite plates all the fibers on a same ply have the same orientation angle, which makes matrix $\bar{\mathbf{Q}}$ independent of the coordinates x and y. However, for tow-steered composite plates, the fiber orientation angle changes as a function of coordinates x and y. In this case, matrix $\bar{\mathbf{Q}}$ is expressed as follows:

$$\bar{\mathbf{Q}}(x,y) = \begin{bmatrix} \bar{Q}_{11}(x,y) & \bar{Q}_{12}(x,y) & \bar{Q}_{16}(x,y) \\ \bar{Q}_{12}(x,y) & \bar{Q}_{22}(x,y) & \bar{Q}_{26}(x,y) \\ \bar{Q}_{16}(x,y) & \bar{Q}_{26}(x,y) & \bar{Q}_{66}(x,y) \end{bmatrix}. \tag{13}$$

Associating Eq.12 and Eq. 2, the strain energy is expressed as:

$$U = \frac{1}{2}\int_V \boldsymbol{\varepsilon}_{(x,y)}^{\mathrm{T}}\bar{\mathbf{Q}}(x,y)\boldsymbol{\varepsilon}_{(x,y)}dV. \tag{14}$$

Appying similar transformation to matrix $\boldsymbol{\psi}$, one gets $\mathbf{R} = \mathbf{T}_{\sigma}^{-1}\boldsymbol{\psi}\mathbf{Q}\mathbf{T}_{\varepsilon}$, and the dissipative strain energy is found to be expressed as:

$$\Delta U = \frac{1}{2}\int_V \boldsymbol{\varepsilon}_{(x,y)}^{\mathrm{T}}\mathbf{R}(x,y)\boldsymbol{\varepsilon}_{(x,y)}dV. \tag{15}$$

The strain vector is given by:

$$\begin{Bmatrix} \varepsilon_x \\ \varepsilon_y \\ \gamma_{xy} \end{Bmatrix} = \begin{Bmatrix} \varepsilon_x^0 \\ \varepsilon_y^0 \\ \gamma_{xy}^0 \end{Bmatrix} + z\begin{Bmatrix} \kappa_x \\ \kappa_y \\ \kappa_{xy} \end{Bmatrix} \quad or \quad \boldsymbol{\varepsilon}_{(x,y)} = \boldsymbol{\varepsilon}_{(x,y)}^0 + z\boldsymbol{\kappa}_{(x,y)} \tag{16}$$

where the first vector on the right-hand side is formed from the membrane strains, while the components of second vector are the bending strains, expressed in terms of the curvatures:

$$\kappa_x = -\frac{\partial^2 w}{\partial x^2}, \quad \kappa_y = -\frac{\partial^2 w}{\partial y^2}, \quad \kappa_{xy} = -2\frac{\partial^2 w}{\partial x \partial y}, \tag{17}$$

where $w = w(x,y,t)$ indicates the transverse displacement field.

Therefore, Eq.16 can be written as:

$$\boldsymbol{\varepsilon}_{(x,y)} = z\boldsymbol{\kappa}_{(x,y)} \tag{18}$$

Neglecting membrane strains, associating Eqs. 16, 15 and 14, the strain and dissipated energies as expressed as:

$$U = \frac{1}{2}\int_V z^2\boldsymbol{\kappa}_{(x,y)}^{\mathrm{T}}\bar{\mathbf{Q}}(x,y)\boldsymbol{\kappa}_{(x,y)}dV \tag{19}$$

$$\Delta U = \frac{1}{2}\int_V z^2\boldsymbol{\kappa}_{(x,y)}^{\mathrm{T}}\mathbf{R}(x,y)\boldsymbol{\kappa}_{(x,y)}dV \tag{20}$$

The strain and dissipated energies of the laminate are obtained by simply adding the corresponding contributions of each layer:

$$U = \frac{1}{2}\int_{-a/2}^{a/2}\int_{-b/2}^{b/2} \boldsymbol{\kappa}_{(x,y)}^{\mathrm{T}} \sum_{k=1}^{N}\left(\int_{z_{k-1}}^{z_k} \bar{\mathbf{Q}}_k(x,y) z^2 dz\right) \boldsymbol{\kappa}_{(x,y)} dxdy \tag{21}$$

$$\Delta U = \frac{1}{2}\int_{-a/2}^{a/2}\int_{-b/2}^{b/2} \boldsymbol{\kappa}_{(x,y)}^{\mathrm{T}} \sum_{k=1}^{N}\left(\int_{z_{k-1}}^{z_k} \mathbf{R}_k(x,y) z^2 dz\right) \boldsymbol{\kappa}_{(x,y)} dxdy \tag{22}$$

or

$$U = \frac{1}{2}\int_{-a/2}^{a/2}\int_{-b/2}^{b/2} \boldsymbol{\kappa}_{(x,y)}^{\mathrm{T}} \mathbf{D}\,(x,y) \boldsymbol{\kappa}_{(x,y)} dxdy \tag{23}$$

$$\Delta U = \frac{1}{2}\int_{-a/2}^{a/2}\int_{-b/2}^{b/2} \boldsymbol{\kappa}_{(x,y)}^{\mathrm{T}} \mathbf{d}\,(x,y) \boldsymbol{\kappa}_{(x,y)} dxdy \tag{24}$$

where

$$\mathbf{D}(x,y) = \sum_{k=1}^{N}\left(\int_{z_{k-1}}^{z_k} \bar{\mathbf{Q}}_k z^2 dz\right) = \sum_{k=1}^{N}\int_{z_{k-1}}^{z_k} \begin{bmatrix} \bar{Q}_{11} & \bar{Q}_{12} & \bar{Q}_{16} \\ \bar{Q}_{12} & \bar{Q}_{22} & \bar{Q}_{26} \\ \bar{Q}_{16} & \bar{Q}_{26} & \bar{Q}_{66} \end{bmatrix}_k z^2 dz = \frac{1}{3}\sum_{k=1}^{N}(z_k^3 - z_{k-1}^3)\bar{\mathbf{Q}}_k \tag{25}$$

$$\mathbf{d}(x,y) = \sum_{k=1}^{N}\left(\int_{z_{k-1}}^{z_k} \mathbf{R}_k z^2 dz\right) = \sum_{k=1}^{N}\int_{z_{k-1}}^{z_k} \begin{bmatrix} R_{11} & R_{12} & R_{16} \\ R_{21} & R_{22} & R_{26} \\ R_{61} & R_{62} & R_{66} \end{bmatrix}_k z^2 dz = \frac{1}{3}\sum_{k=1}^{N}(z_k^3 - z_{k-1}^3)\mathbf{R}_k \tag{26}$$

Finally, the strain and dissipated energies are expressed in terms of the components of matrices $\mathbf{D}(x,y)$ and $\mathbf{d}(x,y)$ as:

$$U = \frac{1}{2}\int_{-a/2}^{a/2}\int_{-b/2}^{b/2}\left\{D_{11}\left(\frac{\partial^2 w}{\partial x^2}\right)^2 + 2D_{12}\frac{\partial^2 w}{\partial x^2}\frac{\partial^2 w}{\partial y^2} + D_{22}\left(\frac{\partial^2 w}{\partial y^2}\right)^2 + 4D_{16}\frac{\partial^2 w}{\partial x^2}\frac{\partial^2 w}{\partial x \partial y} + 4D_{26}\frac{\partial^2 w}{\partial y^2}\frac{\partial^2 w}{\partial x \partial y} + 4D_{66}\left(\frac{\partial^2 w}{\partial x \partial y}\right)^2\right\} dxdy \tag{27}$$

$$\Delta U = \frac{1}{2}\int_{-a/2}^{a/2}\int_{-b/2}^{b/2}\left\{d_{11}\left(\frac{\partial^2 w}{\partial x^2}\right)^2 + (d_{12}+d_{21})\frac{\partial^2 w}{\partial x^2}\frac{\partial^2 w}{\partial y^2} + d_{22}\left(\frac{\partial^2 w}{\partial y^2}\right)^2 + 2(d_{16}+d_{61})\frac{\partial^2 w}{\partial x^2}\frac{\partial^2 w}{\partial x \partial y} + 2(d_{26}+d_{62})\frac{\partial^2 w}{\partial y^2}\frac{\partial^2 w}{\partial x \partial y} + 4d_{66}\left(\frac{\partial^2 w}{\partial x \partial y}\right)^2\right\} dxdy \tag{28}$$

The kinetic energy of the laminate is expressed as [19]:

$$T = \frac{1}{2}\int_{-a/2}^{a/2}\int_{-b/2}^{b/2}\int_{-h/2}^{h/2} \rho\left(\frac{\partial w}{\partial t}\right)^2 dxdydz. \tag{29}$$

According the Rayleigh-Ritz method, the transverse displacement field $w(x,y,t)$ is approximated as:

$$w(x,y,t) = \sum_{m=0}^{\mathrm{M}} \sum_{n=0}^{\mathrm{N}} X_m(x) Y_n(y) q_{mn}(t), \tag{30}$$

The functions $X_m(x)$ and $Y_n(y)$ must be differentiable, at least to the maximum order of the derivatives that appear in the expressions of strain energy, and must obey at least the geometric boundary conditions of the problem. Here, these functions $X_m(x)$ and $Y_n(y)$ have been chosen as Legendre polynomials, so that Eq. 30 is rewritten in terms of dimensionless coordinates ($\zeta = 2x/a$ and $\eta = 2y/b$) as follows [9]:

$$w(\zeta,\eta,t) = (1-\zeta^2)^c (1-\eta^2)^c \sum_{m=0}^{\mathrm{M}} \sum_{n=0}^{\mathrm{N}} X_m(\zeta) Y_n(\eta) q_{mn}(t), \tag{31}$$

where

$$\begin{aligned} X_m(\zeta) &= \frac{1}{2^m} \sum_{k=0}^{m} \left(\begin{array}{c} m \\ k \end{array} \right)^2 (\zeta-1)^{m-k} (\zeta+1)^k, \\ Y_n(\eta) &= \frac{1}{2^n} \sum_{k=0}^{n} \left(\begin{array}{c} n \\ k \end{array} \right)^2 (\eta-1)^{n-k} (\eta+1)^k. \end{aligned} \tag{32}$$

It should be noticed that the parameter c enables to account for different boundary conditions, c=0,1,2 corresponding to free, simply-supported and clamped edges, respectively. Equation 31 can be written in a compact form as:

$$w(\zeta,\eta,t) = \mathbf{\Phi}(\zeta,\eta)\mathbf{q}(t), \tag{33}$$

Then, considering the absence of external forces and applying Lagrange's equations, the equations of motion are found in the form:

$$\mathbf{M}\ddot{\mathbf{q}}(t) + \mathbf{K}\mathbf{q}(t) = \mathbf{0}, \tag{34}$$

with the following associated eigenvalue problem:

$$\left(\mathbf{K} - \omega_w^2 \mathbf{M}\right)\mathbf{q} = 0, \tag{35}$$

where

$$\begin{aligned} \mathbf{K} = \frac{ab}{4} \int_{-1}^{1}\int_{-1}^{1} \Bigg\{ & D_{11} \frac{\partial^2 \mathbf{\Phi}}{\partial x^2}^{\mathrm{T}} \frac{\partial^2 \mathbf{\Phi}}{\partial x^2} + 2D_{12} \frac{\partial^2 \mathbf{\Phi}}{\partial x^2}^{\mathrm{T}} \frac{\partial^2 \mathbf{\Phi}}{\partial y^2} + D_{22} \frac{\partial^2 \mathbf{\Phi}}{\partial y^2}^{\mathrm{T}} \frac{\partial^2 \mathbf{\Phi}}{\partial y^2} \\ & + 4D_{16} \frac{\partial^2 \mathbf{\Phi}}{\partial x^2}^{\mathrm{T}} \frac{\partial^2 \mathbf{\Phi}}{\partial x \partial y} + 4D_{26} \frac{\partial^2 \mathbf{\Phi}}{\partial y^2}^{\mathrm{T}} \frac{\partial^2 \mathbf{\Phi}}{\partial x \partial y} + 4D_{66} \frac{\partial^2 \mathbf{\Phi}}{\partial x \partial y}^{\mathrm{T}} \frac{\partial^2 \mathbf{\Phi}}{\partial x \partial y} \Bigg\} d\zeta d\eta, \end{aligned} \tag{36}$$

and

$$\mathbf{M} = h\rho \frac{ab}{4} \int_{-1}^{1}\int_{-1}^{1} \mathbf{\Phi}^{\mathrm{T}} \mathbf{\Phi} d\zeta d\eta, \tag{37}$$

such that

$$U = \frac{1}{2}\mathbf{q}^{\mathrm{T}}\mathbf{K}\mathbf{q}, \quad T = \frac{1}{2}\dot{\mathbf{q}}^{\mathrm{T}}\mathbf{M}\dot{\mathbf{q}}. \tag{38}$$

In addition,

$$\Delta U = \frac{1}{2}\mathbf{q}^{\mathrm{T}}\mathbf{K}_{\mathbf{d}}\mathbf{q}, \tag{39}$$

where

$$\mathbf{K_d} = \frac{ab}{4}\int_{-1}^{1}\int_{-1}^{1}\left\{d_{11}\frac{\partial^2\mathbf{\Phi}}{\partial x^2}^{\mathrm{T}}\frac{\partial^2\mathbf{\Phi}}{\partial x^2} + (d_{12}+d_{21})\frac{\partial^2\mathbf{\Phi}}{\partial x^2}^{\mathrm{T}}\frac{\partial^2\mathbf{\Phi}}{\partial y^2} + d_{22}\frac{\partial^2\mathbf{\Phi}}{\partial y^2}^{\mathrm{T}}\frac{\partial^2\mathbf{\Phi}}{\partial y^2}\right.$$
$$\left. +2(d_{16}+d_{61})\frac{\partial^2\mathbf{\Phi}}{\partial x^2}^{\mathrm{T}}\frac{\partial^2\mathbf{\Phi}}{\partial x\partial y} + 2(d_{26}+d_{62})\frac{\partial^2\mathbf{\Phi}}{\partial y^2}^{\mathrm{T}}\frac{\partial^2\mathbf{\Phi}}{\partial x\partial y} + 4d_{66}\frac{\partial^2\mathbf{\Phi}}{\partial x\partial y}^{\mathrm{T}}\frac{\partial^2\mathbf{\Phi}}{\partial x\partial y}\right\}d\zeta d\eta. \tag{40}$$

According to [20], the relation between the specific damping capacity and the modal damping factor of the laminate for the $r-$th mode is given by:

$$\zeta_r = \frac{\Psi_r}{4\pi} = \frac{1}{4\pi}\frac{\Delta U}{U} = \frac{1}{4\pi}\frac{\mathbf{q}^{\mathrm{T}}\mathbf{K_d}\mathbf{q}}{\mathbf{q}^{\mathrm{T}}\mathbf{K}\mathbf{q}} \tag{41}$$

3 Numerical results

In this section, the results of numerical simulations are first presented aiming at validating the Rayleigh-Ritz model by means of comparisons with finite element and experimental results reported in the literature [14] comprising natural frequency and damping factors of constant stiffness composite plates. Then, further model validation is carried-out by comparing the natural frequencies obtained from the Rayleigh-Ritz model with finite element and experimental counterparts found in the literature for a ten layer tow-steered composite laminate [21]. After the validations, the Rayleigh-Ritz model is then employed to assess the influence of fiber steering on the damping characteristics of laminates. As mentioned previously, this assessment had not been done before.

The material properties and geometric parameters of the laminates of dimensions $a \times b \times h$ (length $\times$ width $\times$ total laminate thickness, respectively), are presented in Table 1 and Table 2. All the simulations in this work considers the plates with the free-free boundary condition.

Table 1: Material properties of the laminates used in the simulations.

Material	E_1 (GPa)	E_2 (GPa)	G_{12} (GPa)	ν_{12}	ψ_1 (%)	ψ_2 (%)	ψ_{12} (%)	$\rho\ (kg/m^3)$
913C-TS[1]	110.0	9.0	3.9	0.34	0.75	5.95	6.79	1513
Hexply AS4/8552[2]	126.3	8.765	4.92	0.31	-	-	-	1600

[1] Data from [14]
[2] Data from [21]

3.1 Natural frequencies and damping factors of non-steered laminates

Table 3 shows the values of the first six natural frequencies and SDC's obtained from the Rayleigh-Ritz (R-R) model with $N = M = 9$, with the counterparts drawn from [14], for the non-steered laminate identified as Plate 1 in Tab. 2, made of eight layers using the material 913C-TS and the lay-up is $[0,0,0,0]_s$, with

Table 2: Geometrical properties of the plates used in the simulations

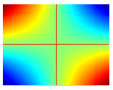
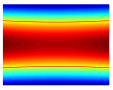
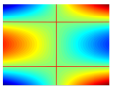
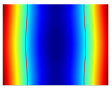
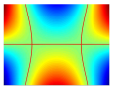
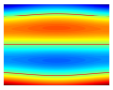
Name	Type	Lay-up	a (mm)	b (mm)	h (mm)
Plate 1[1]	non-steered	$[0,0,0,0]_s$	252	192	1.155
Plate 2[2]	steered	$[(<30,10>,<-30,-10>)_2,<90,90>]_s$	400	300	1.75

[1] Material 913C-TS
[2] Material Hexply AS4/8552

$a = 252$ mm and $b = 192$ mm, $h = 1.155$ mm. Also illustrated are the mode shapes corresponding to the six vibration modes considered.

It can be seen that the values of the three sets of results are very close to each other, which serves an indicator of the satisfactory accuracy of the Rayleigh-Ritz model developed in this study.

Table 3: Comparison between the Rayleigh-Ritz simulation results and those from [14] for **Plate 1**

Mode shapes							
Freq. (Hz)	**R-R**	**40.9**	**78.5**	**114.5**	**160.0**	**179.2**	**217.8**
	FEM[1]	41.0	83.4	118.0	161.1	180.3	234.6
	Exp.[1]	39.2	76.4	111.8	161.9	178.6	215.5
SDC (%)	**R-R**	**6.69**	**5.94**	**6.30**	**0.76**	**2.06**	**5.88**
	FEM[1]	6.69	5.94	6.31	0.76	2.06	5.88
	Exp.[1]	8.33	5.36	7.13	0.67	2.31	5.51

[1] Data from [14]

3.2 Natural frequencies of tow-steered laminates

Many strategies can be adopted to define the fiber trajectories in tow-steered laminates. In this paper, accounting for typical limitations of AFP machines, which precludes the use of complicated paths, especially those exhibiting small radii of curvature, the fiber course is chosen so as to vary only along one of the coordinates. Therefore, Figure 2 shows the fiber path and the two angles T_0 and T_1, which are used to define the curve indicated with thick line, according to:

$$\theta(x) = \frac{2(T_1 - T_0)}{a}|x| + T_0 \tag{42}$$

where T_0 and T_1 are fiber orientations at the center and on the left and right edges of the plate, the dimensions of which are b and a in directions x and y, respectively. The paths of the other fibers are obtained by shifting the one defined by Eq. 42 along the y-axis [23].

The tow-steered laminate is identified by the notation <T_0,T_1>, which has been used in Tab. 2 [22].

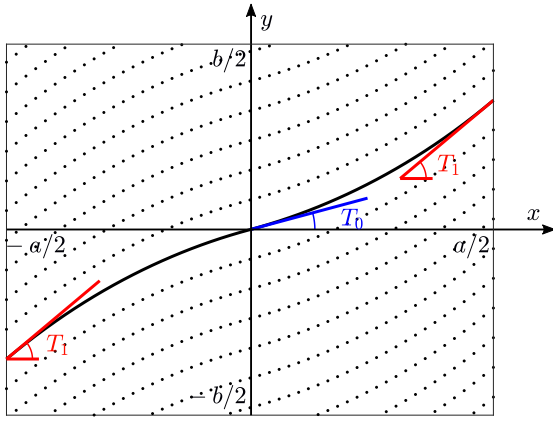
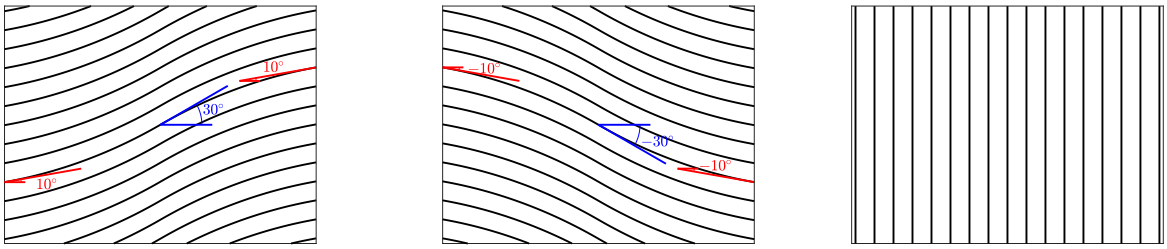


Figure 2: Fiber path of the tow-steered laminate.

The first objective is to compare the accuracy of Rayleigh-Ritz method in calculating the natural frequencies of the composite plate. Therefore, the results were compared to those from FE modeling and experimental data obtained from the literature. The composite plate is made of ten layers of the material Hexply AS4/8552. The lay-up is [(<30,10>,<-30,-10>)$_2$,<90,90>], with $a = 400$ mm and $b = 300$ mm, $h = 1.75$ mm. Fig. 3 depicts each type of layer of the laminate.



(a) ply <30,10> (b) ply <-30,-10> (c) ply <90,90>

Figure 3: Illustration of the fiber orientations of the three types of layers used in the ten-layer laminate with lay-up [(<30,10>,<-30,-10>)$_2$,<90,90>]$_s$ [21].

Table 4 shows the values of the first six natural frequencies obtained from the Rayleigh-Ritz (R-R) model with $N = M = 9$, with the counterparts provided by [21], for the tow-steered laminate. Also illustrated are the vibration mode shapes corresponding to the six vibration modes considered.

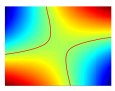
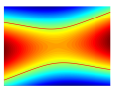
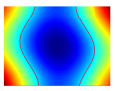
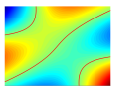
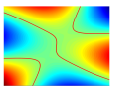
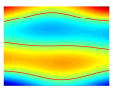
It can be seen that the values of the three sets of results are very close to each other, which serves an indicator of the satisfactory accuracy of the Rayleigh-Ritz model developed for modeling tow-steered composite laminates.

3.3 Natural frequencies and specific damping capacity of tow-steered laminates

The interest here is to examine the influence of various fiber paths on the undamped natural frequencies and specific damping capacities of a set of laminates obtained by changing the values of T_0 and T_1 appearing in 42. For this purpose, one considers a laminated made of 913-TS with lay-up $[(< T_0, T_1 >)_4]_s$ and dimensions $a = 252$ mm, $b = 192$ mm, $h = 1.155$ mm.

Figures 4 and 5 show, in color maps, the values of the first six natural frequencies and SDC obtained for combinations of T_0 and T_1 in the range $-90° - 90°$, with $5°$ increments. The values on the diagonal dashed

Table 4: Values of the natural frequencies obtained from Rayleigh-Ritz, FE and experimental analyses for the ten-layer tow-steered laminate

Mode shapes							
Freq. (Hz)	**R-R**	**47.193**	**49.421**	**84.318**	**106.34**	**115.88**	**158.57**
	FEM[2]	47.126	49.449	84.279	106.16	115.65	159.40
	Exp.[2]	50.897	57.522	85.777	109.28	120.14	162.36

[2] Data from [21]

lines correspond to non-steered composites, for which $T_0 = T_1$. In each graph, the circle markers indicate the maximum values of natural frequencies and SDC for the corresponding vibration mode, while the triangles indicate the corresponding minimum values.

Table 5 summarizes the results of Figs. 4 and 5, indicating the maximum and minimum values of the natural frequencies and SDC obtained for each vibration mode in the range of T_0 and T_1 considered. It can be seen that the range of variation of the natural frequencies and SDC vary considerably from one vibration mode to another. As, according to the formulation developed in Section 2, both the natural frequencies and SDC are determined by the modal strain energies, it can be concluded that the sensitivity of a given natural frequency or SDC depend on the corresponding vibration mode shape. However, a regular variation pattern cannot be identified. Fig.6 illustrates the fiber trajectories of some of the plies corresponding to maximum values of natural frequencies and SDC.

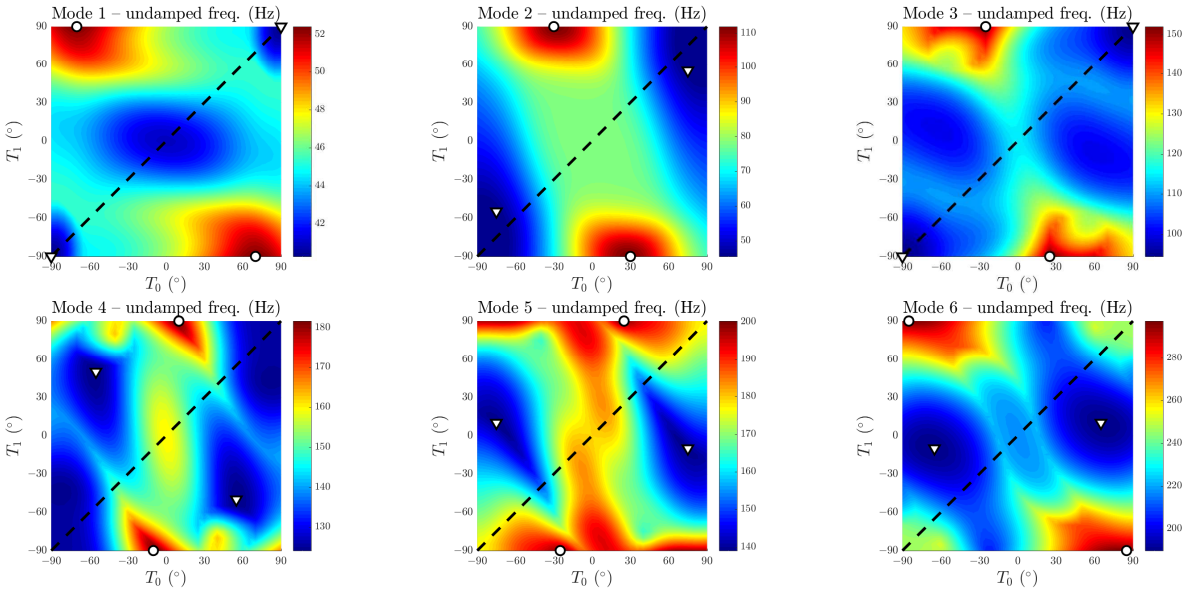


Figure 4: Influence of steering angles T_0 and T_1 on the undamped natural frequencies of the first six vibration modes.

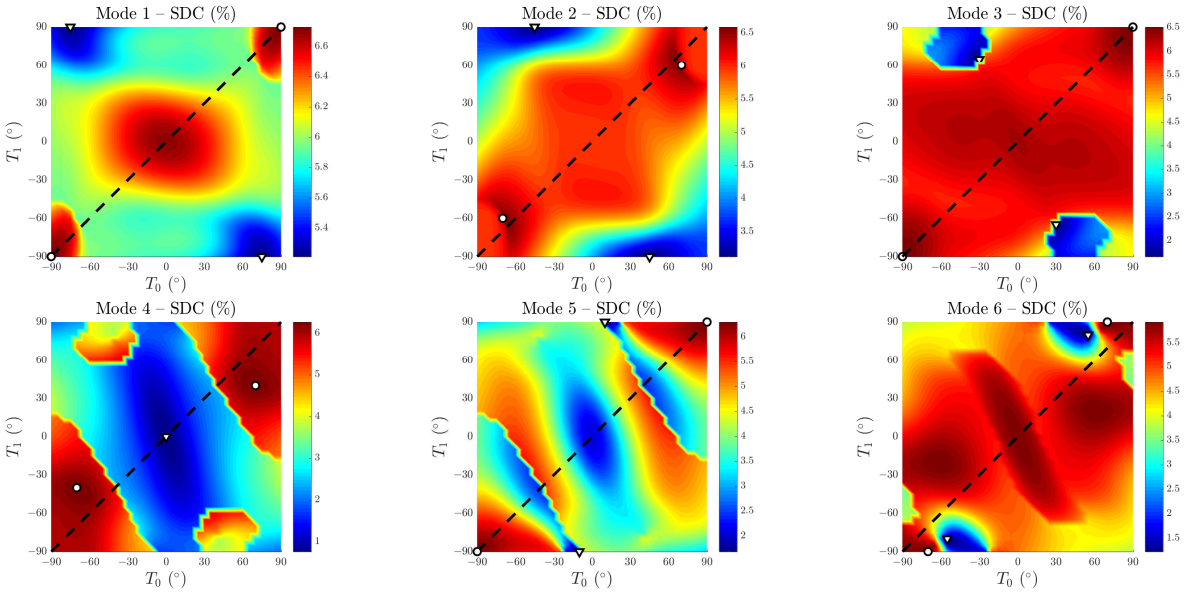
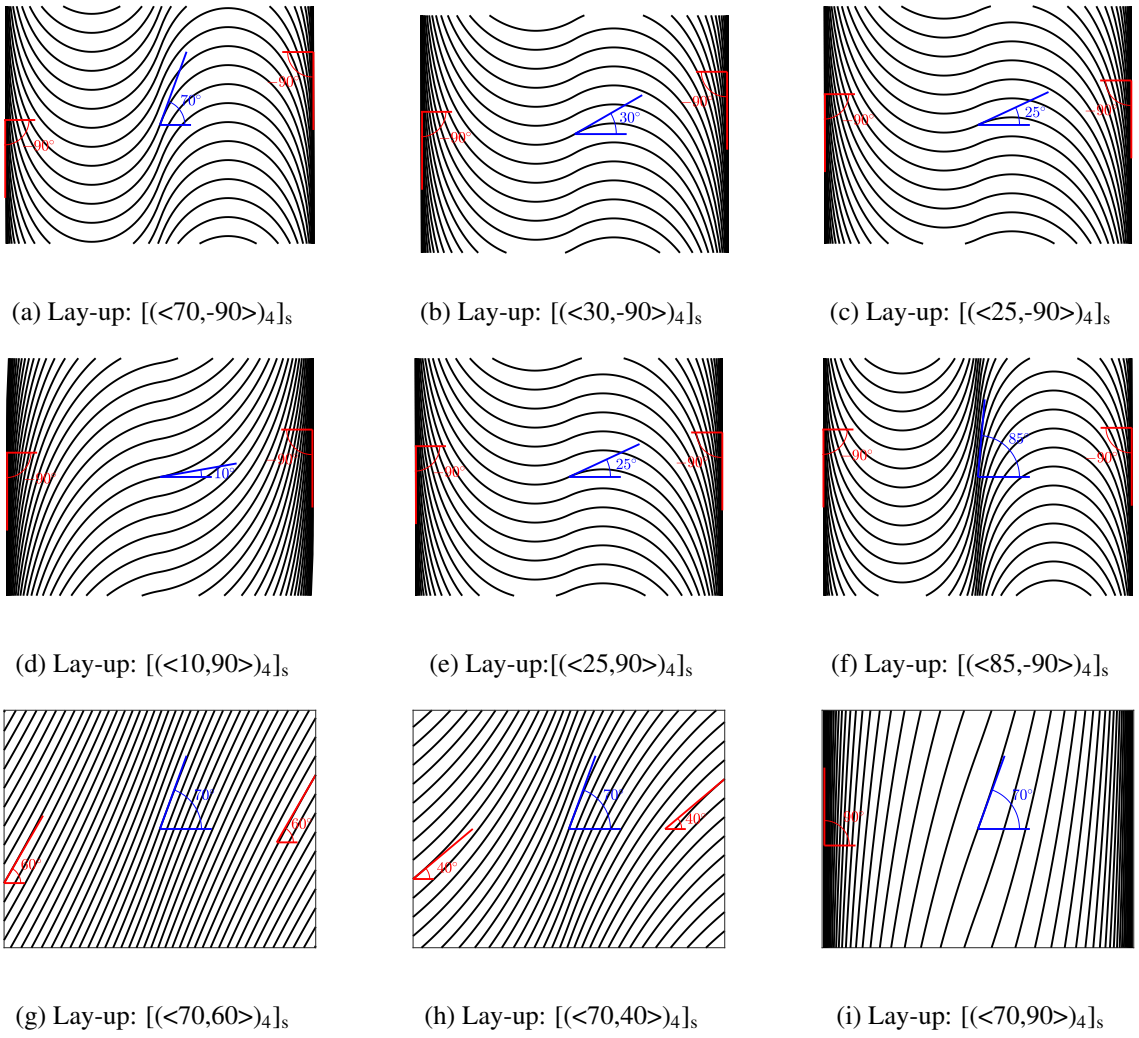


Figure 5: Influence of steering angles T_0 and T_1 on the SDC of the first six vibration modes.

Table 5: Summary of the influence of the steering angles T_0 and T_1 on the first six natural frequencies and specific damping capacities.

Freq. (Hz)	Max. (Hz)	Lay-up	Laminate	Min. (Hz)	Lay-up	Laminate	Diff.[1] (%)
f_1	52.42	$[(<70,-90>)_4]_s$	**steered**	40.27	$[(<90,90>)_4]_s$	non-steered	26.2
f_2	111.9	$[(<30,-90>)_4]_s$	**steered**	45.45	$[(<-75,-55>)_4]_s$	**steered**	84.5
f_3	152.0	$[(<25,-90>)_4]_s$	**steered**	94.41	$[(<90,90>)_4]_s$	non-steered	46.7
f_4	181.6	$[(<10,90>)_4]_s$	**steered**	124.14	$[(<-55,50>)_4]_s$	**steered**	37.6
f_5	200.2	$[(<25,90>)_4]_s$	**steered**	139.02	$[(<-75,10>)_4]_s$	**steered**	36.1
f_6	297.3	$[(<85,-90>)_4]_s$	**steered**	189.72	$[(<-65,-10>)_4]_s$	**steered**	44.2
Damp. (%)	Max. (%)	Lay-up	Laminate	Min. (%)	Lay-up	Laminate	Diff.[1] (%)
SDC_1	6.726	$[(<90,90>)_4]_s$	non-steered	5.210	$[(<-75,90>)_4]_s$	**steered**	25.4
SDC_2	6.589	$[(<70,60>)_4]_s$	**steered**	3.123	$[(<-45,90>)_4]_s$	**steered**	71.4
SDC_3	6.511	$[(<90,90>)_4]_s$	non-steered	1.663	$[(<-30,65>)_4]_s$	**steered**	118.6
SDC_4	6.269	$[(<70,40>)_4]_s$	**steered**	0.761	$[(<0,0>)_4]_s$	non-steered	156.7
SDC_5	6.294	$[(<90,90>)_4]_s$	non-steered	1.690	$[(<10,90>)_4]_s$	**steered**	115.3
SDC_6	5.921	$[(<70,90>)_4]_s$	**steered**	1.224	$[(<55,80>)_4]_s$	**steered**	131.5

[1] Relative difference computed as $2(\text{Max.} - \text{Min.})/(\text{Max.} + \text{Min.})$.



(a) Lay-up: $[(<70,-90>)_4]_s$ (b) Lay-up: $[(<30,-90>)_4]_s$ (c) Lay-up: $[(<25,-90>)_4]_s$

(d) Lay-up: $[(<10,90>)_4]_s$ (e) Lay-up:$[(<25,90>)_4]_s$ (f) Lay-up: $[(<85,-90>)_4]_s$

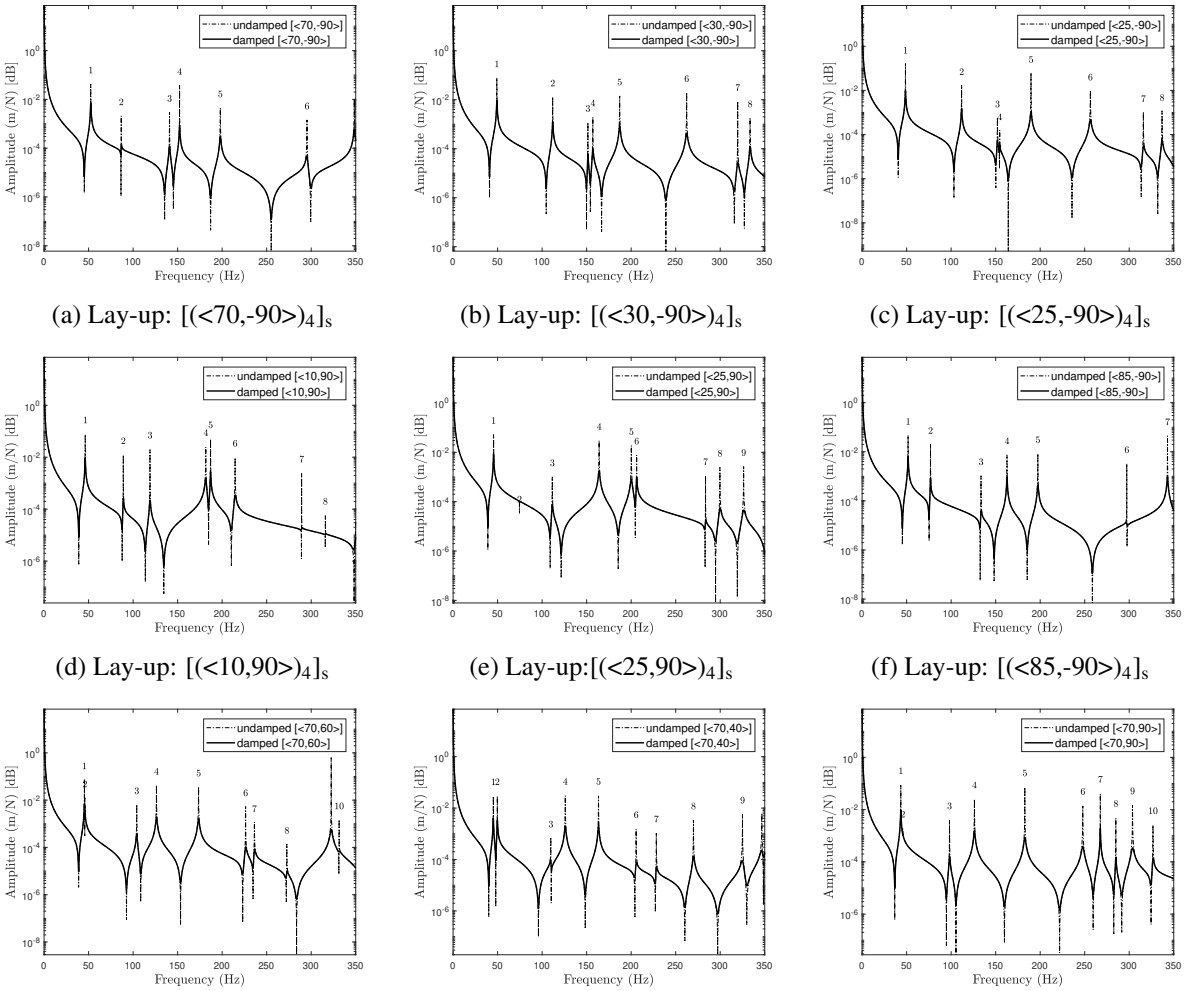
(g) Lay-up: $[(<70,60>)_4]_s$ (h) Lay-up: $[(<70,40>)_4]_s$ (i) Lay-up: $[(<70,90>)_4]_s$

Figure 6: Lay-up configurations of some steered plies corresponding to the maximum values of the natural frequencies and SDC given in Table 5.

Figure 7 shows the driving point frequency response functions (receptances corresponding to the point $x = a/4$ and $y = b/8$) for some of the lay-ups given in Table 5, compared to the associated undamped configurations. Table 6 shows the first six vibration mode shapes of the tow-steered plates. This results enable better evaluation of the influence of fiber steering on the natural frequencies, mode shapes and vibration amplitude levels. It can be seen that a large range of diversity in terms of dynamics characteristic is provided for the steered configurations.

4 Conclusion

This work presented a numerical assessment of the influence of fiber steering on the natural frequencies, specific damping capacities and natural vibration modes of CFRP plates, for different fiber trajectories. A numerical procedure has been developed to enable the calculation of specific damping capacities of tow steered composites. It has been shown that a semi-analytical Ritz-type modeling combined with the Classical Lamination Theory was capable of providing a sufficiently accurate dynamic model of tow steered plates and to capture the effect of fiber steering on damping. Due to the typical low number of degrees-of-freedom, such a model is very convenient to alleviate the computation cost involved in the analyses.



(a) Lay-up: $[(<70,-90>)_4]_s$ (b) Lay-up: $[(<30,-90>)_4]_s$ (c) Lay-up: $[(<25,-90>)_4]_s$

(d) Lay-up: $[(<10,90>)_4]_s$ (e) Lay-up:$[(<25,90>)_4]_s$ (f) Lay-up: $[(<85,-90>)_4]_s$

(g) Lay-up: $[(<70,60>)_4]_s$ (h) Lay-up: $[(<70,40>)_4]_s$ (i) Lay-up: $[(<70,90>)_4]_s$

Figure 7: Frequency response function (FRF) of the results presented in Table 5.

Table 6: Mode shapes of the non-steered and some steered composite plates presented in Table 5.

	Mode 1	Mode 2	Mode 3	Mode 4	Mode 5	Mode 6
$[(<0,0>)_4]_s$	40.97 Hz; 6.69%	78.54 Hz; 5.94%	114.5 Hz; 6.3%	160 Hz; 0.761%	179.2 Hz; 2.06%	217.8 Hz; 5.88%
$[(<70,-90>)_4]_s$	52.42 Hz; 5.23%	86.66 Hz; 3.46%	140.9 Hz; 4.38%	152.2 Hz; 2.24%	197.9 Hz; 3.42%	295.3 Hz; 3.95%
$[(<30,-90>)_4]_s$	49.16 Hz; 5.73%	111.9 Hz; 3.26%	151.4 Hz; 2.08%	156.9 Hz; 4.01%	187.1 Hz; 3.96%	262.3 Hz; 4.29%
$[(<25,-90>)_4]_s$	48.69 Hz; 5.77%	111.7 Hz; 3.37%	152 Hz; 4.24%	154.5 Hz; 2%	189.7 Hz; 3.93%	256.4 Hz; 4.37%
$[(<10,90>)_4]_s$	46.2 Hz; 5.86%	88.96 Hz; 4.5%	119 Hz; 5.42%	181.6 Hz; 4.41%	187 Hz; 1.69%	214.5 Hz; 4.98%
$[(<25,90>)_4]_s$	45.49 Hz; 5.88%	74.6 Hz; 5.02%	111.4 Hz; 5.66%	164 Hz; 4.76%	200.2 Hz; 5.28%	206.2 Hz; 1.73%
$[(<85,-90>)_4]_s$	51.64 Hz; 5.29%	76.81 Hz; 3.65%	133.5 Hz; 4.62%	162.7 Hz; 2.05%	197.4 Hz; 3.25%	297.3 Hz; 3.86%
$[(<70,60>)_4]_s$	45.31 Hz; 5.91%	45.83 Hz; 6.59%	104.1 Hz; 6.1%	126.2 Hz; 6.11%	173.5 Hz; 5.12%	226.3 Hz; 4.7%
$[(<70,40>)_4]_s$	45.17 Hz; 6%	49.67 Hz; 6.26%	109.8 Hz; 5.76%	126 Hz; 6.27%	163.3 Hz; 3.89%	205.6 Hz; 5.55%
$[(<70,90>)_4]_s$	43.47 Hz; 6.35%	45.69 Hz; 6.09%	98.2 Hz; 6.26%	126.2 Hz; 5.98%	182.8 Hz; 6.02%	247.9 Hz; 5.92%

In the present investigation, the steering configurations considered were defined by only two geometrical parameters, θ_0 and θ_1, whose values were extensively combined for the analyses of a large number of possible steering configurations. From those, the configurations presenting maximum and minimum values of natural frequencies and SDC for the first six vibration modes of the laminate were identified. It was possible to verify that broad ranges of values of these dynamic were covered by the steering configurations considered. This confirms that fiber steering can be an effective strategy for the design of composite laminates in terms of their dynamic behavior. In particular, it has been found that damping levels can be significantly increased by exploring fiber steering.

However, since the influence of fiber steering on the natural frequencies and modal damping factors are driven by the strain and dissipated energies associated to the vibration modes, the improvement of the dynamic behavior of laminates in a given frequency band encompassing various vibration modes certainly involves the concurrence of many candidate configurations, each of which favors a particular dynamic fea-

ture. Hence, in these cases, numerical multi-objective optimization must be used, and is being presently investigated by the authors.

Despite the existence of a number of technological and scientific issues to be tacked, it seems clear that the emergence of tow steered composites broadens the possibilities of achieving improved dynamic performance, as compared to traditional unidirectional composites.

Acknowledgements

The authors acknowledge the National Council for Scientific and Technological Development (CNPq) (grants #301633/2013-3, #402238/2013-3 and #145439/2015-1), the National Institute of Science and Technology of Smart Structures in Engineering (INCT − EIE), FAPEMIG, Fundação de Apoio ao Instituto de Pesquisas Tecnológicas (FIPT) and São Paulo State Research Agency (FAPESP) grant #2015/20363-6 for the financial support to their research work.

References

[1] P. Ribeiro, H. Akhavan, A. Teter, J. Warmiński, A review on the mechanical behaviour of curvilinear fibre composite laminated panels, Journal of Composite Materials 48 (22) (2014) 2761–2777.

[2] Z. Wu, P. M. Weaver, G. Raju, Postbuckling optimisation of variable angle tow composite plates, Composite Structures 103 (2013) 34–42.

[3] H. Akhavan, P. Ribeiro, Natural modes of vibration of variable stiffness composite laminates with curvilinear fibers, Composite Structures 93 (11) (2011) 3040 – 3047.

[4] T. Guimaraes, D. A. Pereira, D. A. Rade, Dynamic behavior and optimization of composite tow steered plates, in: A. T. Fleury, D. A. Rade, P. R. G. Kurka (Eds.), Proceedings of the XVII International Symposium on Dynamic Problems of Mechanics, ABCM, 2017.

[5] O. Stodieck, J. E. Cooper, P. M. Weaver, P. Kealy, Improved aeroelastic tailoring using tow-steered composites, Composite Structures 106 (2013) 703–715.

[6] B. K. Stanford, C. V. Jutte, K. Chauncey Wu, Aeroelastic benefits of tow steering for composite plates, Composite Structures 118 (2014) 416–422.

[7] T. A. Guimaraes, S. G. Castro, D. A. Rade, C. E. Cesnik, Panel flutter analysis and optimization of composite tow steered plates, in: 58th AIAA/ASCE/AHS/ASC Structures, Structural Dynamics, and Materials Conference, 2017, p. 1118.

[8] A. Marouene, R. Boukhili, J. Chen, A. Yousefpour, Effects of gaps and overlaps on the buckling behavior of an optimally designed variable-stiffness composite laminates - a numerical and experimental study, Composite Structures 140 (2016) 556–566, cited By 2.

[9] Z. Wu, P. M. Weaver, G. Raju, B. Chul Kim, Buckling analysis and optimisation of variable angle tow composite plates, Thin-Walled Structures 60 (2012) 163–172.

[10] A. Treviso, B. Van Genechten, D. Mundo, M. Tournour, Damping in composite materials: Properties and models, Composites Part B: Engineering 78 (2015) 144–152.

[11] D. A. Saravanos, C. C. Chamis, Unified micromechanics of damping for unidirectional and off-axis fiber composites, Journal of Composites, Technology and Research 12 (1) (1990) 31–40.

[12] S. Hwang, R. Gibson, J. Singh, Decomposition of coupling effects on damping of laminated composites under flexural vibration, Composites Science and Technology 43 (2) (1992) 159–169.

[13] J.-M. Berthelot, Damping analysis of laminated beams and plates using the ritz method, Composite Structures 74 (2) (2006) 186–201.

[14] M. R. Maheri, R. Adams, Modal vibration damping of anisotropic frp laminates using the rayleigh–ritz energy minimization scheme, Journal of sound and vibration 259 (1) (2003) 17–29.

[15] M. Maheri, The effect of layup and boundary conditions on the modal damping of frp composite panels, Journal of Composite Materials 45 (13) (2011) 1411–1422.

[16] A. Abbaslou, M. Maheri, Prediction of the damping properties of fiber-reinforced polymer composite panels with arbitrary geometries, Proceedings of the Institution of Mechanical Engineers, Part C: Journal of Mechanical Engineering Science 232 (2) (2016) 275–283.

[17] R. Adams, D. Bacon, Effect of fibre orientation and laminate geometry on the dynamic properties of cfrp, Journal of Composite Materials 7 (4) (1973) 402–428.

[18] M. Maheri, R. Adams, Finite-element prediction of modal response of damped layered composite panels, Composites science and technology 55 (1) (1995) 13–23.

[19] A. E. H. Love, The small free vibrations and deformation of a thin elastic shell, Philosophical Transactions of the Royal Society of London A: Mathematical, Physical and Engineering Sciences 179 (1888) 491–546.

[20] N. Zabaras, T. Pervez, Viscous damping approximation of laminated anisotropic composite plates using the finite element method, Computer methods in applied mechanics and engineering 81 (3) (1990) 291–316.

[21] J. Rodrigues, P. Ribeiro, H. Akhavan, Experimental and finite element modal analysis of variable stiffness composite laminated plates, in: Proceedings of the 11th Biennial International Conference on Vibration Problems (ICOVP-2013), 2013, p. 30.

[22] Z. Gurdal, R. Olmedo, In-plane response of laminates with spatially varying fiber orientations-variable stiffness concept, AIAA journal 31 (4) (1993) 751–758.

[23] C. Waldhart, Analysis of tow-placed, variable-stiffness laminates, Ph.D. thesis, Virginia Tech (1996).

Numerical and experimental investigation of prestress effect on natural frequencies of composite beams

A. Orlowska[1], C. Graczykowski[1], A. Galezia[2]
[1] Institute of Fundamental Technological Research of the Polish Academy of Sciences
Pawinskiego 5B, 02-106, Warsaw, Poland
e-mail: **cezary.graczykowski@ippt.pan.pl**

[2] Warsaw University of Technology, Institute of Vehicles
Narbutta 84, 02-524 Warsaw, Poland

Abstract
The paper analyzes the influence of prestressing force on the natural frequencies on Glass Fibre Reinforced Polymer (GFRP) composite beams. Prestress is introduced by applying initial tensile forces to the fibres embedded in selected layer of the composite material during the manufacturing process. Release of prestressing forces results in deformation and self-equilibrated state of stress of the entire composite which changes both its static properties and dynamic characteristics. The paper is focused on analysis of shifts in natural frequencies corresponding to initial bending modes of the composite beams of various fibre volume fraction and prestressed layer location. The problem is analyzed with the use of finite element simulations and experimental modal analysis. The conducted numerical and experimental work reveals that shifts in the natural frequencies caused by non-axial prestressing can be significant and they are important phenomenon which has to be taken into account during design of the composite material.

1 Introduction

Initial prestressing is effectively used in reinforced concrete structures, such as girders and slabs, in order to minimize tensile stresses generated during bending and to overcome low tensile strength and brittle behaviour of concrete. Large number of applications of prestressed concrete structures in civil engineering proves that such technique is efficient and allows to design lighter and more durable structures. In the recent years the concept of prestressing was generalized and applied to fibre reinforced laminates of polymeric matrix. In such case prestressing refers to initial pre-tensioning of the reinforcing fibres of selected layers of the laminate, which produces clamping load generating compressive stresses in the surrounding matrix and self-equilibrated state of stress of the entire laminate. Depending on the location and orientation of the layer the introduced prestress may evoke various state of deformation and state of stress of composite material. Therefore, prestressing provides wide possibilities for modifying initial state of composite elements and enables influencing their response to external loading.

From technological point of view the process of composite prestressing is relatively simple. The first step is pre-tensioning of the fibres, which is conducted after moulding but before curing of the matrix. In this stage the external tensile force is applied to the fibres of selected composite layer causing their elongation and corresponding tensile stresses. Since polymeric matrix remains in uncured state and it is not yet solidified, it is not affected by applied pre-load. Further, the laminate is cured in a standard manner, causing the matrix to harden, to adhere and bond to prestressing fibres. Once the composite is entirely cured and cooled down to room temperature the external tensile force is released. The pre-tensioned fibres tend to contract and static friction forces cause that compressive stresses are locally induced to the surrounding matrix. This results in generation of the initial state of deformation and initial state of stress in the entire composite specimen.

Most of the publications devoted to prestressed fibre reinforce polymer (FRP) composites analyze the influence of prestress on their static properties. The researchers had reported significant advantages of prestressing such as improvement of load-carrying capacity [1, 2, 3], reduction of thermally induced residual stresses and increased durability to fatigue [4], reduction of fibre misalignment [5] and increase of resistance to stiffness degradation [6]. The paper [7] presents simple analytic model of the prestressed laminated composite, which is verified by standard numerical model and experimental analysis of prestressed composites samples, and further used for optimization of the applied prestressing forces.

In contrast, the number of publications related to dynamic properties of prestressed structures is very limited. In particular, the influence of the prestress on modal characteristics and mode shapes is not well recognised. In fact, there seems to be certain contradiction in conclusions drawn by particular authors. Several researchers observe decrease in natural frequencies of prestressed concrete structures [8, 9, 10], which corresponds to "compression-softening" effect occurring in externally, axially loaded homogenous beams. Other researchers suggest that natural frequencies of prestressed concrete structures are unaffected by prestressing forces [11, 12]. Finally, there are papers reporting that prestressing causes increase of natural frequencies of the reinforced concrete structures [13, 14, 15]. The extensive experimental investigation of the natural frequencies of prestressed composites beams with various location of the prestressing strand and various magnitude of prestressing force is presented in [16]. Unfortunately, the analysis does not reveal any non-random, statistically relevant correlation between application of prestressing force and direction of the shift of natural frequencies. According to above discussion the problem of the influence of the prestressing force magnitude and location on the natural frequencies of the prestressed FRP composites remains an open question.

The paper attempts to fill the above gap in the theory of prestressed structures by detailed numerical and experimental analysis of fibre reinforced composite polymer beams of various fibre volume fraction, location and magnitude of the prestressing force. The remainder of the paper is organized as follows. The second section briefly describes fundamentals of the finite element modelling of prestressed composites. The third section presents results of finite element simulations aimed at determination of natural frequencies of composite beams subjected to non-axial prestressing. In the fourth section the modal characteristics of the same composite beams are analyzed with the use of Experimental Modal Analysis. Finally, the conclusion section attempts to identify two phenomena responsible for shifts in natural frequencies of prestressed structures and shed a new light on interpretation of the prestressing effect.

2 Finite element model of prestressed composite

The complete derivation of the equations governing the finite element model of the prestressed composites was presented in previous paper of the authors [17]. Therefore, herein we will discuss exclusively the basic assumptions of the analysis and final form of the equations describing small-displacement static model, large-displacement static model and large-displacement dynamic model of the composite structure. The proposed model will be based on layer-wise (LW) method, which utilizes three dimensional modeling of each layer of the composite and does not directly apply classical kinematic hypotheses of the plate theory.

In all considered problems the material will be assumed as linear elastic. We will apply standard constitutive equation for the prestressed material, which links the strain tensor $\boldsymbol{\varepsilon}-\boldsymbol{\varepsilon}^{\mathbf{o}}$ with the stress tensor $\boldsymbol{\sigma}-\boldsymbol{\sigma}^{\mathbf{o}}$. The upper index "zero" indicates initial strains and stresses.

In the case of assumption of small displacement theory the relation between strains and stress will be expressed in a standard manner, with the use of first order linear differential operator including derivatives with respect to subsequent space variables. The corresponding equation of the Finite Element Method describing static equilibrium of the composite takes the form:

$$\mathbf{K}_0\mathbf{q}+\mathbf{R}_0=\mathbf{P} \tag{1}$$

where $\mathbf{q}$ are nodal displacements, $\mathbf{P}$ are nodal forces, $\mathbf{K}_0$ is the global linear stiffness matrix composed of element matrices $\mathbf{K}^{(e)}$:

$$\mathbf{K}^{(e)} = \int_V \mathbf{B}^T \mathbf{D} \mathbf{B} \, dV \tag{2}$$

where $\mathbf{B}$ is the so-called strain matrix involving derivatives of elements' shape functions and V is the volume of the finite element. Finally $\mathbf{R_0}$ expresses internal elastic bonds resulting from prestress and is composed of element vectors $\mathbf{R_0^{(e)}}$ given in the form:

$$\mathbf{R}_0^{(e)} = \int_V \mathbf{B}^T \boldsymbol{\sigma}_0 \, dV \tag{3}$$

Eq.1 can be solved with the use of standard methods of linear statics in order to obtain displacement field caused by initial prestress and applied external loading.

In contrast, in the case of adopting the large displacement theory the relation between strains and stresses is expressed with the use of nonlinear differential operator, which includes the products of derivatives with respect to subsequent space variables. In this case, the equation of the Finite Element Method describing equilibrium of the composite takes the form:

$$\left(\mathbf{K}_{\mathbf{NL}} + \mathbf{K}_{\boldsymbol{\sigma}}\right)\mathbf{q} + \mathbf{R}_0 = \mathbf{P} \tag{4}$$

where $\mathbf{K_{NL}}$ is the "geometrically nonlinear" global stiffness matrix corresponding to current configuration of the structure, composed of elements' stiffness matrices $\mathbf{K_{NL}^{(e)}}$:

$$\mathbf{K}_{\mathbf{NL}}^{(e)} = \int_v \mathbf{B}^T \mathbf{D} \mathbf{B} \, dV \tag{5}$$

in which the integration is performed over actual (deformed) volume of the finite element, while $\mathbf{K_\sigma}$ is global stress stiffness matrix composed of elementary stress stiffness matrices $\mathbf{K_\sigma^{(e)}}$:

$$\mathbf{K}_{\boldsymbol{\sigma}}^{(e)} = \int_v \mathbf{B}^{\mathbf{T}} \boldsymbol{\sigma} \mathbf{B} \, dV \tag{6}$$

where $\boldsymbol{\sigma}$ is the tensor of Cauchy stresses and integration is also performed over actual volume of the finite element. Let us note that matrix $\mathbf{K_{NL}}$ reflects large deformation of the prestressed structure, while matrix $\mathbf{K_\sigma}$ describes the so-called "stress-stiffening" effect. Eq. 4 can be solved with the use of standard iterative methods of non-linear statics in order to obtain displacement field caused by initial prestress and applied external loading.

When large displacement theory is assumed the finite element equation governing the dynamics of prestressed structure takes the form:

$$\mathbf{M}\ddot{\mathbf{q}}(t) + \left(\mathbf{K}_{\mathbf{NL}} + \mathbf{K}_{\boldsymbol{\sigma}}\right)\mathbf{q}(t) + \mathbf{R}_0(t) = \mathbf{P}(t) \tag{7}$$

where $\mathbf{M}$ is the global mass matrix composed of elementary mass matrices $\mathbf{M^{(e)}}$:

$$\mathbf{M}^{(e)} = \int_v \mathbf{N}^T \rho \mathbf{N} \, dV \tag{8}$$

where ρ is material density, $\mathbf{N}$ is the shape functions matrix, whereas $\mathbf{K_{NL}}$, $\mathbf{K_\sigma}$ and $\mathbf{R_0}$ are defined in the same way as previously. By assuming that there are no external forces acting on the system, we obtain homogenous equation describing free vibrations of the structure. Further, by assuming that harmonic free vibrations in the form $\mathbf{q}(t) = \tilde{\mathbf{q}}\sin(\omega t + \phi)$, where $\tilde{\mathbf{q}}$ is vector of vibration amplitudes, we obtain system of linear homogeneous algebraic equations:

$$\left(\mathbf{K}_{\mathbf{NL}} + \mathbf{K}_{\boldsymbol{\sigma}} - \boldsymbol{\omega}^2 \mathbf{M}\right)\tilde{\mathbf{q}} = \mathbf{0} \tag{9}$$

which has non-zero solutions when:

$$\det\left(\mathbf{K}_{\mathrm{NL}}+\mathbf{K}_{\sigma}-\omega^{2}\mathbf{M}\right)=0 \tag{10}$$

We obtain a polynomial of degree *n* in respect of ω^2, where ω are natural frequencies of vibrations of the prestressed structure. The corresponding eigenvectors indicate its mode shapes.

Let us once again highlight the fact that components of the stiffness matrices $\mathbf{K}_{\mathrm{NL}}$ and $\mathbf{K}_{\sigma}$ depend on deformation of the structure and state of stress resulting from prestress. Therefore, the modal analysis of the prestressed structure has to be always preceded by nonlinear static analysis. Otherwise, the effect of prestress will not be observed.

3 Numerical simulations of prestress effect

The model of the prestressed composite analyzed the numerical tests was uni-directionally reinforced 5-layer composite beam with geometrical dimensions: length L=0.2 [m], height h=0.00131 [m] and width w=0.01 [m]. Each layer of the composite was constructed of the resin (ρ=1200 kg/m^3, E=3.5 GPa, v=0.35) and reinforcing fibres (ρ=2600 kg/m^3, E=60 GPa, v=0.22). The fibre volume fraction in the subsequent analysis was modified in the range between 20% to 90%. The finite element analysis always consisted of two separate steps:

- static prestressing of the lowest layer of simply supported composite beam by forces of a various magnitudes, aimed at determination of the stiffness matrix for further computations, Fig. 1a;
- modal analysis of prestressed composite with modified boundary conditions (static scheme of a cantilever), aimed at finding natural frequencies corresponding to initial bending modes and their change caused by prestressing, Fig. 1b.

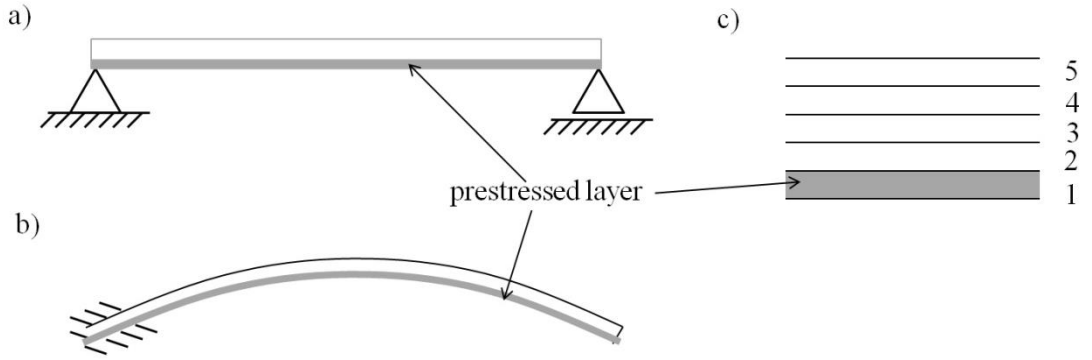


Figure 1: Boundary conditions applied in simulation: prestressing step (a), modal analysis step (b), scheme of the layers numbering (c)

The static analysis of the prestressing process enabled comparison of the deflection obtained with the use linear and nonlinear layer-wise (LW) model, as well as linear and nonlinear equivalent single layer (ESL) model. In all cases comparable values of maximal displacement were obtained (Fig. 2a). However, it was observed that both nonlinear model results in slightly smaller value of displacement.

Maximal deflection difference between linear and nonlinear LW models was analyzed for various fibre volume fractions and magnitudes of prestressing forces (Fig. 2b). The smallest difference was obtained for the highest fibre volume fraction (below 1% for prestressing force of 200N), while the largest discrepancy was observed for the smallest fibre volume fraction (above 8% for prestressing force of 200N). This confirms intuitive conclusion that linear model provides much better estimation of stiff prestressed structure with high volume fraction then compliant structure with small fibre volume fraction.

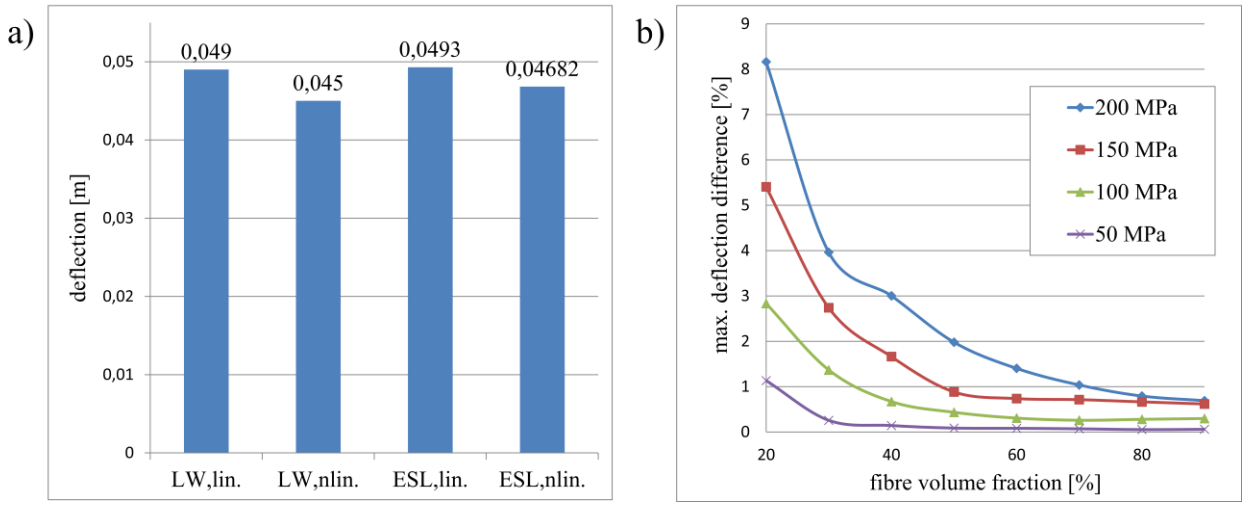


Figure 2: Comparison of deflection obtained from linear and nonlinear LW and ESL models (a), comparison of linear and nonlinear LW models for various FVF and magnitude of prestressing force (b)

The elaborated numerical model also allows to analyze change of longitudinal strains and stresses in prestressed beam. Fig. 3a shows that applied non-axial prestress being a superposition of compression and bending causes that maximal shortening of the lowest layer is significantly larger than maximal elongation of the upper one. Moreover, it reveals that dependence between the absolute values of the longitudinal strains and fibre volume fraction of the composite is nonlinear. In turn, Fig. 3b shows exemplary distribution of stresses which clearly corresponds to applied loading combining compression and bending. It includes transparent shift of stress at the boundary of the prestressed layer.

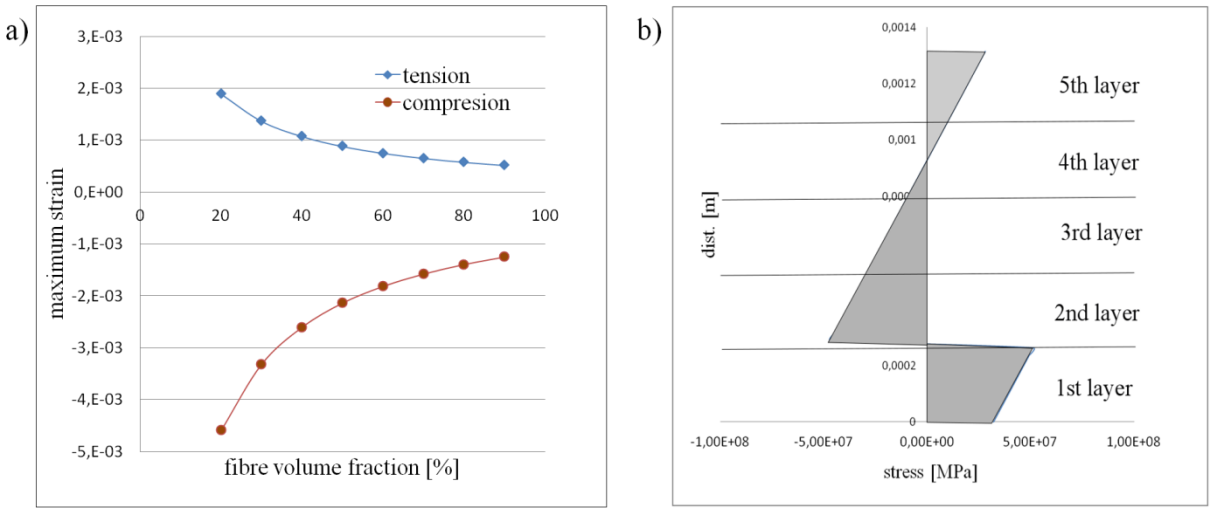


Figure 3: Comparison of maximum strain obtained for various fibre volume fractions (a), exemplary stress distribution in the middle cross section of the beam (b)

In the following stage of numerical simulations the modal analysis was used to compute natural frequencies and modal shapes of prestressed composite beams and their shifts caused by change of magnitude of the applied prestressing force. In order to observe the effect of prestress the stiffness matrix used in computations included both the effect of prestressing and structure deformation (cf. Eq.7, Sec.2). The analysis was focused exclusively on bending modes, which are the most sensitive to prestress. The initial bending modes of the prestressed structure are presented in Fig. 4. They appear to be qualitatively similar to the bending modes of straight non-prestressed beam, however they are imposed on deformed configuration of the structure.

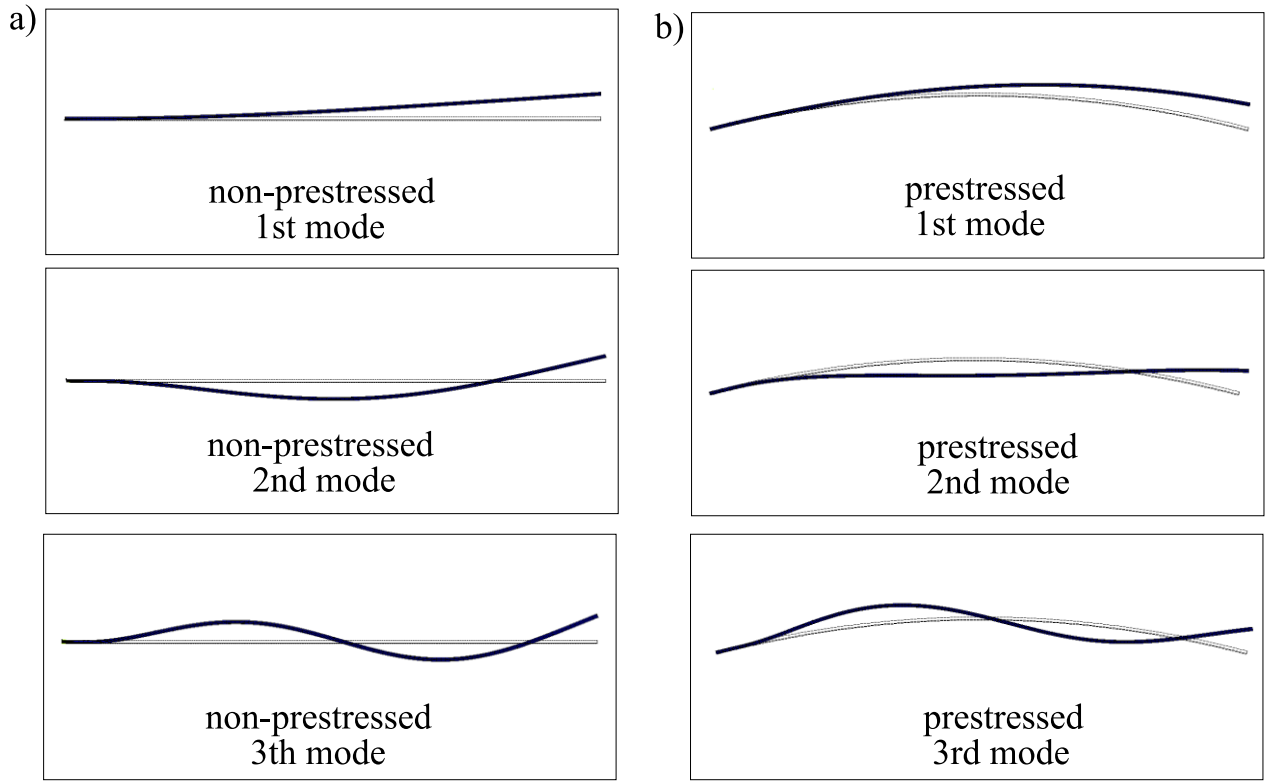


Figure 4: Three initial bending modes of the non-prestressed straight composite beam (a) and deformed prestressed composite beam (b)

The comparison of natural frequencies corresponding to three initial bending modes of prestressed composite beams with various fibre volume fraction is presented in Table 1. It is observed that for the first bending mode the applied prestressing force causes increase of the natural frequency. The effect is more transparent for the fibre volume fraction equal to 20%, which is associated with larger compliance and deformation of the composite structure. Moreover, the effect of increase of the first natural frequency gradually decreases when the prestressed layer is located closer to the natural axis of the beam, which corresponds to smaller flexural deformation caused by prestress.

The influence of prestress for the second and third bending mode is reversed, i.e. prestressing force causes decrease of the natural frequency of these modes. Similarly as in previous case, the effect is more transparent for smaller fibre volume fraction and it decreases when prestressed layer is located closer to the natural axis of the beam.

	0 MPa (20%)	100 MPa 1st layer (20 %)	100 MPa 2nd layer (20%)	100 MPa 3rd layer (20%)	0 MPa (50%)	100 MPa 1st layer (50 %)	100 MPa 2nd layer (50 %)	100 MPa 3rd layer (50 %)
1 mode	**18,62**	19,00	18,70	18,63	**24,07**	24,19	24,11	24,09
2 mode	**116,61**	106,94	114,20	117,06	**150,72**	147,72	150,16	150,99
3 mode	**326,25**	315,29	324,13	327,43	**421,50**	418,18	421,24	422,25

Table 1: Natural frequencies [Hz] of three initial bending modes for non-prestressed and prestressed composite beams of fibre volume fraction 20% and 50%.

The last investigated topic was detailed analysis of the influence of prestressing force of the same magnitude, applied to various layers of the beam. The conducted simulations confirm that the largest shift in natural frequency occurs in case of prestressing of the lowest layer of the composite (Fig. 5). The corresponding frequency shift is the largest in case of 20% fibre volume fraction. It exceeds 2% for the first mode, -8% for the second mode and -3,4% for the third mode. Although the frequency shifts corresponding to fibre volume fraction 50% are significantly smaller, they are also the largest in case of prestressing of the lowest layer. When prestressing is applied to the layer located closer to the middle surface of the composite the relative change in each natural frequency decreases. In particular, in the case of axial prestressing the shifts in frequency are almost negligible. An illustrative example can be the frequency shift observed in the most compliant, axially prestressed composite with FVF=20%, which does not exceed 0,4%. Therefore, it can be concluded that the factor which has the largest influence on modal characteristics of prestressed composite is the change of composite shape.

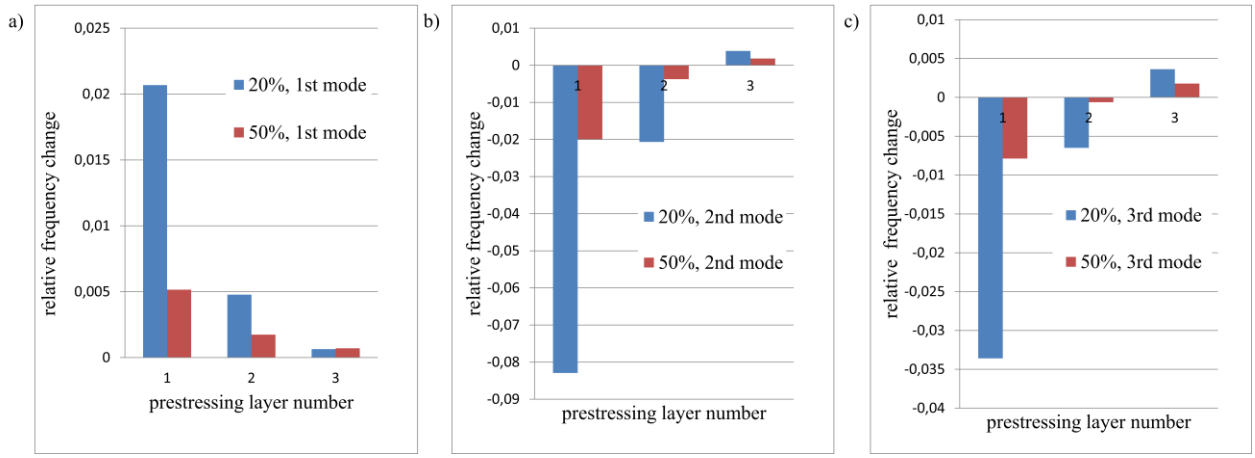


Figure 5: Relative change of frequency caused by prestressing force of magnitude 260 N applied to different layers of composite. Results presented for the first (a), second (b) and third (c) bending mode

4 Experimental verification

In order to identify influence of the prestress on the modal behaviour of the composite beams, two types of composite plates were prepared:

- one plate composed of 5-layer of bidirectional E-glass fabric and epoxy resin with no external force applied during fabrication,
- one plate composed of 5-layer of bidirectional E-glass fabric and epoxy resin with tension applied to the outer layer during fabrication.

Both plates were manufactured simultaneously by the vacuum bag technique and cured in identical conditions. The prestressed plate was manufactured using a so-called prestressing bed presented in Fig. 6a. Methodology of preparation the prestressed composite with the use of such device was described by Krishnamurthy in [4]. The main part of the prestressing bed was a plane table, made of two blocks: one of them was fixed to a base plate and the other one was movable. A load screw was installed in the moving block in that way, that the screw end was blocked in the fixed part of the prestressing bed and the movable part was shifted by the rotation of the screw. For the purpose of alignment of the moving and fixed blocks two guide bars were used. The glass fabric was mounted on the prestressing bed by the use of clamps placed at its opposite ends and prestress was applied by screw rotation. Prestressing force was measured by the load cell installed in the fixed part of the prestressing bed. The force acting on the sensor was a reaction force due to the tensioning of the fabric. After finishing the plates preparation, each plate

was cut into beam samples with 0.02 [m] width and 0.2 [m] length and tested by the use of experimental modal analysis procedure.

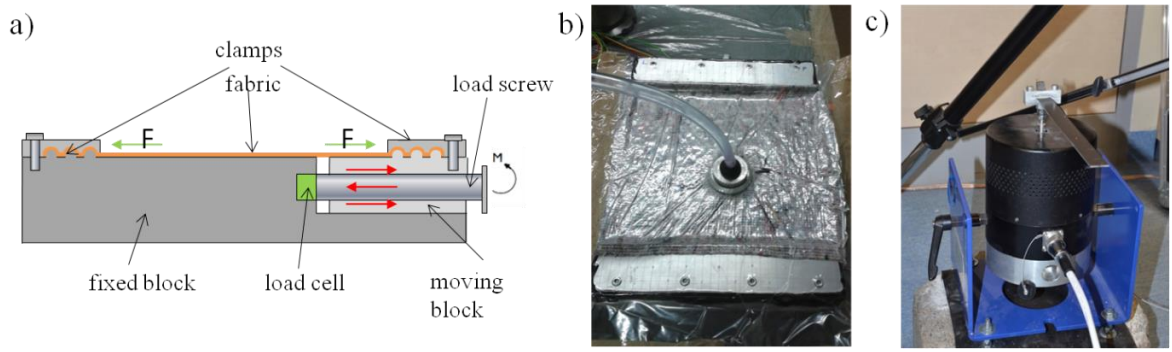


Figure 6: Prestressing bed scheme (a), view of the prestressing bed during samples preparation (b), view of the modal shaker with specimen during modal test experiment (c).

The experimental test-stand for modal analysis research was composed of modal shaker ModalShop 2100E11, Polytec Scanning Vibrometer PSV-400-3D and acceleration sensor B&K 4507 B 004. The modal shaker created wide band pseudorandom excitation according to control signal produced by Polytec PSV-400-3D internal signal generator. Velocity of vibrations of the specimen were measured by the Scanning Vibrometer in 1D configuration, in direction normal to surface of the specimen. The acceleration sensor B&K 4507 B 004 was used as a reference sensor measuring the vibrations in direction of shaker excitation. Signals from the scanning head and the accelerometer as well as from the generator were recorded by PSV-400-3D acquisition system for purpose of further analysis.

During modal experiments, the tested specimens were mounted in special mounting clamp, attached to the shaker, which allowed to create repetitive boundary conditions for all experiments. The reference sensor was constantly mounted on clamp not influencing vibrations of the specimens. It has been decided to focus only on identification of bending modes. Due to this, measurement points created a straight line on the surface of the specimen.

For each specimen the test procedure was repeated ten times. Between repeating measurement, the sample was removed from mounting clamp and mounted again before start of a test. This approach allowed to identify dispersion of experiment. The frequencies measured for successive tests of given beam did not differ more than 0,8%. Averaged values of identification of modal parameters as well as relative differences between frequencies measured for prestressed and non-prestressed sample are presented in Tab. 2. Fig. 7 shows Complex Mode Indicator Function for examined prestressed and non-prestressed composite beams.

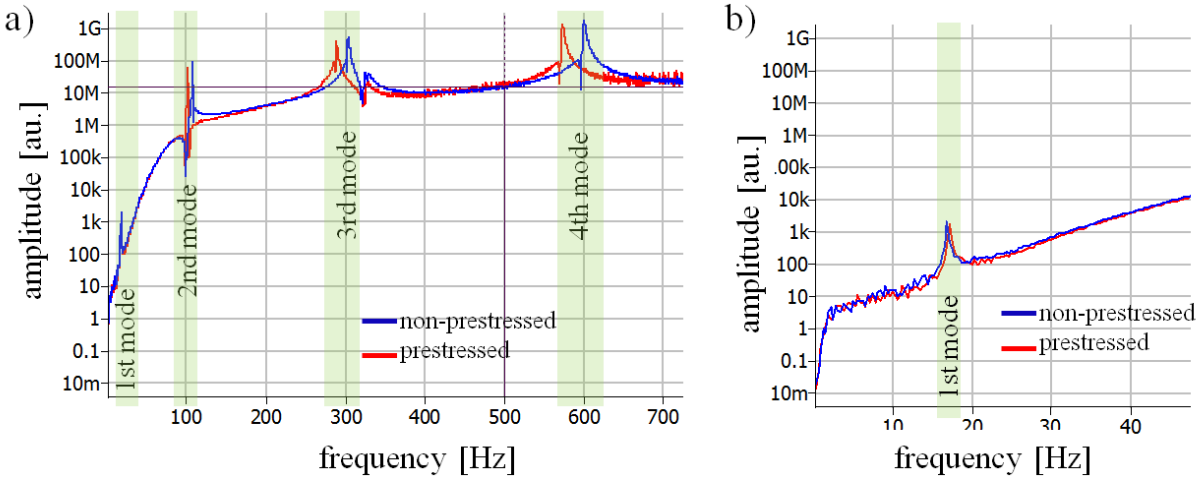


Figure 7: CMIF functions for examined prestressed and non-prestressed composite beams: for frequency range 0 -700 Hz (a), for frequency range 0-50 Hz (b).

Mode number	natural frequencies of non-prestressed sample [Hz]	natural frequencies of prestressed sample [Hz]	relative frequency change [%]
1st	17	17.3	1.8
2nd	107.5	101.5	-5.6
3rd	303.4	288.2	-5.0

Table 2: Results of experimental measurements.

The increase of fundamental frequency was observed for the prestressed samples of composite cantilever beam. In turn, the second and third bending frequency for those beam decreased with prestress application. Character of frequency change observed in the experiment reflect the overall character of frequency change revealed by numerical computations.

5 Conclusions

Prediction of changes of the natural frequencies of fibre reinforced polymer composites caused by applied prestressing force appeared to be relatively complex numerical and experimental problem. Conducting numerical simulation requires taking into account the effect of structure deformation and the effect of generated non-uniform state of stress, and their influence on stiffness matrix of the model. In turn, the challenging problems during experimental analysis include obtaining required thickness and stiffness of the specimens, as well as taking into account the processes such as relaxation and creep. The presented study clearly shows that non-axial prestressing of the fibre reinforced polymer beams significantly changes their dynamic characteristics including natural frequencies and mode shapes. The most important conclusions from above numerical and experimental work are as follows:

- the influence of prestress on natural frequencies of the composite beams is significant when prestressing causes their large flexural deformation;
- prestressing causes increase of the natural frequency associated with the first bending mode of the composite beam;
- prestressing causes decrease of the natural frequencies associated with the second and third bending mode of the composite beam (and probably the same holds for subsequent modes);

Conducted research indicates that shifts in the natural frequencies of prestressed composite beams are caused by two concurrent but counteracting effects: i) the stress-stiffening effect and ii) prestress-induced change of beam geometry. The following hypothesis can be drawn. In the case of the first bending mode the stress-stiffening effect prevails over the geometry-change effect and thus the natural frequency increases. In turn, for the subsequent bending modes the stress-stiffening effect gradually diminishes while geometry-change effect raises and thus the corresponding natural frequencies decrease.

The entire analysis reveals that in case of non-axial prestressing the resulting frequency changes can be significant. Therefore the observed frequency shift it is a practically relevant phenomenon, which has to be taken into account during potential application of prestressing technology in FRP composite structures.

Acknowledgements

The authors would like to gratefully acknowledge the financial support through the Grant No. 2012/07/D/ST8/02661 financed by the National Science Centre in Poland.

References

[1] A. S. Hadi, J. N. Ashton, *On the influence of pre-stress on the mechanical properties of a unidirectional GRE composite*, Composite Structures, Vol. 40, No. 3-4, (1998), pp. 305-311.

[2] S. Motahhari, J. Cameron, *Impact Strength of Fiber Pre-Stressed Composites*, Journal of Reinforced Plastics and Composites, Vol. 17, No. 2, (1998), pp. 123-130.

[3] S. Motahhari, J. Cameron, *Fibre prestressed composites: Improvement of flexural properties through fibre prestressing*, Journal of Reinf. Plast. and Compos. Vol. 18, No. 3, (1999), pp. 279-288.

[4] S. Krishnamurthy, *Prestressed advanced fibre reinforced composites fabrication and mechanical performance*, PhD Thesis, Cranfield University, (2006).

[5] G.J. Dvorak, *The effect of fibre prestress on residual stresses and the onset of damage in symmetric laminate plates*, Composites Science and Technology, Vol. 60, (2000), pp. 1129-1139

[6] B. Harris, *Fatigue and accumulation of damage in reinforced plastics*, Composites, Vol. 8, No. 4, (1977), pp. 214-220.

[7] C. Graczykowski, A. Orlowska, J. Holnicki-Szulc, *Prestressed composite structures – modeling, manufacturing, design*, Comp. Struct., Vol. 151, (2016), pp. 172-182.

[8] K. Dai, S. Chen, *Vibration of spun-cast prestressed concrete poles*, Proceedings of the Society for Experimental Mechanics Series, (2007).

[9] S. Law, Z. Lu, *Time domain responses of a prestressed beam and prestress identification*, Journal and Sound and Vibration, Vol. 288, No. 4-5, (2005), pp. 1011-1025.

[10] K. Raju, G. V. Rao, *Free vibration behavior of prestressed beams*, Journal of Structural Engineering, Vol. 112, (1986), pp. 433-437.

[11] E. Hamed, Y. Frostig, *Natural frequencies of bonded and unbounded prestressed beams – prestress force effects*, Journal of Sound and Vibration, Vol. 295, (2006), pp. 28-39.

[12] A. Kerr, *On the dynamic response of a prestressed beam*, Journal of Sound and Vibration, Vol. 49, No. 4, (1976), pp. 569-573.

[13] T. Hop, *The effect of degree of prestressing and age of concrete beams on frequency and damping of their free vibration*, Materials and Structures, Vol. 24, (1991), pp. 210-220.

[14] M. Saiidi, B. Douglas, S. Feng, *Prestress force effect on vibration frequency of concrete bridges*, Journal of Structural Engineering, Vol. 120, No. 7, (1994), pp. 2233-2241.

[15] Y. Zhang, R. Li, *Natural frequency of full prestressed concrete beam*, Transactions of Tianjin University, Vol. 13, No. 5, (2007), pp. 354-359.

[16] D. Noble, M. Nogal, A. O'Connor, V. Pakrashi, *The effect of prestress force magnitude and eccentricity on the natural bending frequencies of uncracked prestressed concrete beams*, Journal of Sound and Vibration, Vol. 365, (2016), pp. 22-44.

[17] A. Orlowska, C. Graczykowski, A. Galezia, *The effect of prestress force magnitude on the natural bending frequencies of the eccentrically prestressed glass fibre reinforced polymer composite beams*, Journal of Composite Materials, Vol. 52, No. 15 (2018), pp. 2115-2128

Multi-attribute evaluation of concept variants for lightweight structures

C. López [1], **M. Boucher** [2,4], **B. Van Doninck**[3], **F. Maurin** [2,4], **V. Iliopoulou** [1], **J. Stroobants** [1], **S. Jonckheere** [2,4], **E. Deckers** [2,4], **S. van Poppel** [1], **B. Pluymers** [2,4]

[1] Core lab CodesignS, Flanders Make
Celestijnenlaan 300, B-3001, Heverlee, Belgium
e-mail: **carlos.lopez@flandersmake.be**

[2] Core lab DMMS-D, Flanders Make
Celestijnenlaan 300, B-3001, Heverlee, Belgium

[3] Core lab ProductionS, Flanders Make
Celestijnenlaan 300, B-3001, Heverlee, Belgium

[4] Dept. Mechanical Engineering, KU Leuven
Celestijnenlaan 300, B-3001, Heverlee, Belgium

Abstract

The design and evaluation of lightweight structures is a multi-step process that involves several different attribute evaluations. In the early design phase, specific functions of the structure have to be decided, geometry may not yet be fixed and materials must be assigned. Only rough values of attributes such as mass, stiffness and Noise, Vibration & Harshness (NVH) behavior can be estimated. On the other hand, in the final design process, full finite element models predict detailed product performance. The links between early design decisions and final product performance are not always apparent. More importantly, the variation of different concept models, which are most efficiently evaluated in the early design stage, must also be correlated to final design specifications. This work aims at defining a work-flow for the multi-attribute evaluation of concept variants, using a lightweight car door as an example.

1 Introduction

Weight reduction is one of the cornerstones of structural design, however it needs to come together with a minimal impact on other key attributes such as cost, performance or robustness. Manufacturing industries such as aerospace or automotive look for lightweight designs since weight is one of the main factors influencing fuel consumption and vehicle emissions, so providing such designs represent a strong competitive advantage and a way to accomplish the more and more strict regulations on emissions. On top of being lightweight, these designs should be at the same time reliable, cost-competitive and easy to manufacture, among other characteristics.

This research aims to provide a tool to evaluate in an objective way the main attributes that are relevant in a conceptual design of a mechanical structure. For every attribute of every new concept, a metric value is calculated/assigned on which the evaluation of the concept will be assessed. In this sense, our approach is based on Concurrent Engineering (CE), since different attributes coming from different engineering fields (mechanical, manufacturing, design, ...) are integrated simultaneously in order to reduce the product's time-to-market [1]. The end goal is to determine which concept is the most promising to elaborate in the next

phases of the design process based exclusively on objective information on the metric values and therefore enriching the designers experience in unexplored yet design spaces.

Several tools have been developed in the past to assist during the concept phase of the development process, such as CDSTsped [2], AIDA [3], MODESSA [4], Schemebuilder [5], EFDEX [6], 2nd CAD [7], IDEA-INSPIRE [8], Concept Generator [9], DFX [10], DEE [11]. Some of these tools are designed for generating concepts from a database, whereas others cover the conceptual design process including an evaluation of the generated concepts. They all use varieties of approaches for representation and categorization of designer knowledge, however most of them are limited to specific domains. In general, the main focus of these tools is on concept generation, while the evaluation and scoring is still a manual process (based on knowledge and past experience) instead of using a model-based approach with metric values of the attributes.

Since this research focuses on application in the manufacturing industry for the transport sector, one of the most important attributes to evaluate in the design is the Noise, Vibration and Harshness (NVH) behavior. NVH affects decisively the comfort and user-experience of the passenger, being a key decision maker for potential customers when using or acquiring the product, and furthermore because NVH becomes one of the more complex attributes to master when considering the overall trend towards lighter structures and design.

Section 2 focuses on the flowchart and general way of working of the proposed methodology, while section 3 deepens on the implementation of the multi-attribute evaluation within the selected tools selected. Section 4 shows a preliminary strategy for filtering and ranking of the concepts, and section 5 presents an application example consisting of a door frame structure, for which five different concepts are ranked based on an objective multi-attribute evaluation. To end, section 6 draws some conclusions.

2 General methodology

Figure 1 shows the general flowchart of the proposed methodology. As a preliminary step, the user should provide a list of requirements that the product must fulfill (i.e. mass should be less than *10* kg, first vibration frequency must be above *50* Hz). A spreadsheet gathers this information.

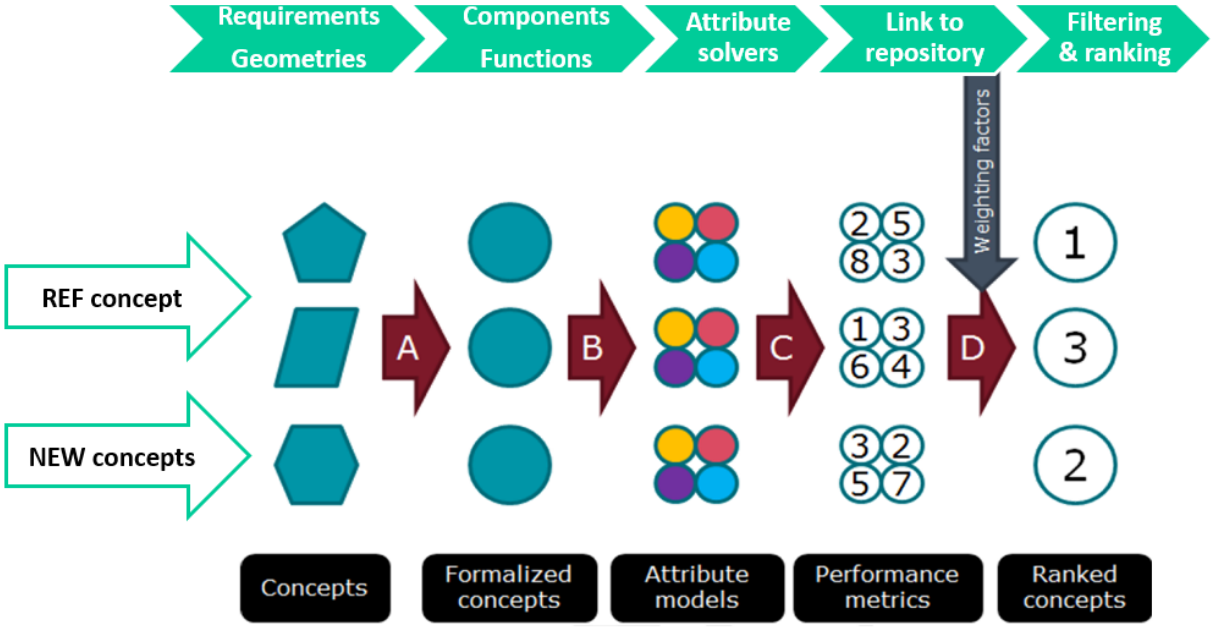


Figure 1: General flowchart of the methodology proposed

Since the goal is to compare different concepts (in geometry, functionality or any other characteristic), the

first step should be to represent them in a formal and consistent way (step A of Figure 1). Thus, an integrated concept model will encode all the information describing a concept from different viewpoints in a computer-readable form. This can be done by using basic spreadsheets [12], computer aided design (CAD) tools [13] and more abstract formalization languages, such as Systems Modelling Language (SysML, [14]).

To be able to objectively score each concept a number of attributes will be evaluated. The list of attributes evaluated may vary depending on the product, however those included in this research are more biased towards the conception of automotive or aerospace components. Therefore, attributes such as mass, stiffness, strength, fatigue, NVH, cost, manufacturability and robustness are considered. The approach is to create attribute models based on the formalized concept models, (step B in Figure 1) obtaining a unique performance metric for each attribute of the concepts (step C in Figure 1). This is straightforward in some cases (mass or cost), but may be more difficult for others (manufacturability or NVH). By doing so, the concept scoring (step D in Figure 1) is enriched with model-based input.

Special mention to NVH, since all the information regarding such an extensive and key discipline for automotive and aerospace design needs to be simplified to a value. Within this study, the following expressions are used to assess the NVH behavior: (i) the first dynamic eigenfrequency of the considered structure, (ii) the Sound Transmission Loss value and (iii) the Sound Absorption Loss value.

The framework selected to implement our methodology is FreeCAD [15], since it provides an open-source environment for CAD/CAE and FEA and it is based on Python, which eases the implementation of in-house codes within it. Consequently, a new workbench is created in FreeCAD, which includes all the capabilities of the methodology proposed. This workbench and the way of working proposed for the methodology is shown in Figure 2

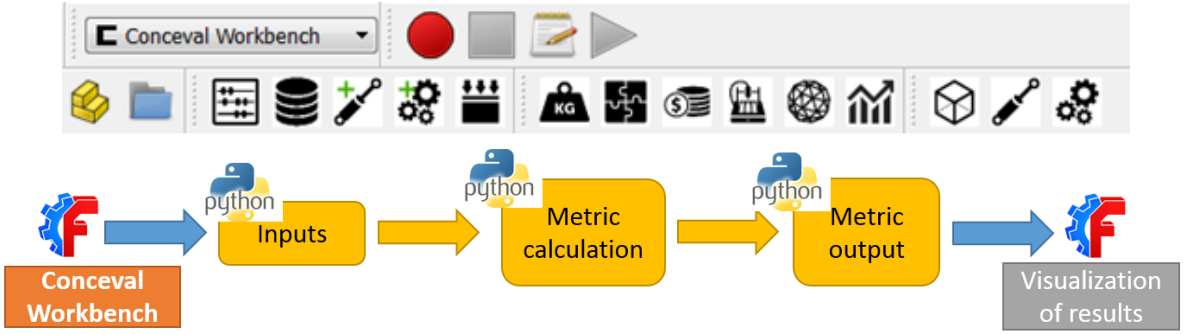


Figure 2: Workbench implementation based on python codes visualized in FreeCAD environment.

However, it has to be highlighted that this methodology is modular, flexible and easily transferable to other frameworks (Figure 3). For instance, attributes related to NVH or others that require complex FEA can be also obtained using external commercial software.

The specific steps required to use the workbench in the FreeCAD framework are stated below:

- Define the requirements of the product or import them from the reference product.
- Define or import the geometry of the concept.
- Decompose the geometry of the concept in different parts or components, extracting the connectivity between them.
- Define the materials and load cases existing in the concept.
- Perform the multi-attribute evaluation of the concept.
- Perform the filtering and ranking of the concepts.

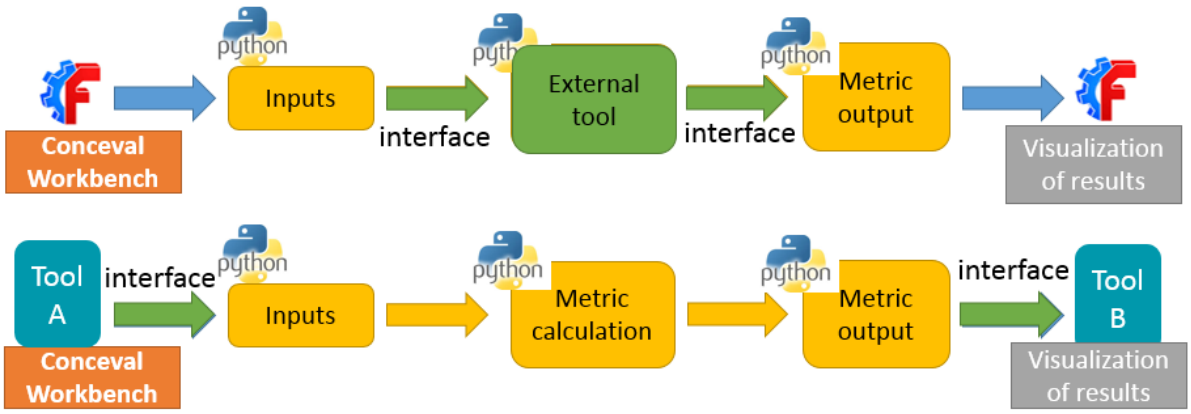


Figure 3: Workbench implementation based on python codes visualized in other environments and coupled with other conception tools.

3 Multi-attribute evaluation

This section describes in detail the implementation of the evaluation methods behind the attributes mentioned in Section 2. Most of the attributes are evaluated using in-house Python scripts that either directly perform the calculations or that link the FreeCAD framework with external software.

Attribute	**Metric**
Mass	Total mass [kg]
Strength	Stress ratio [-]
Stiffness	Stiffness [N/m]
Fatigues	Number of cycles [-]
Modal analysis	First eigenfrequency [Hz]
Sound absorption loss	Integrated SAL [dB]
Sound transmission loss	Integrated STL [dB]
Robustness	Robustness [%]

3.1 Mechanical attributes

The mechanical attributes that are considered in the framework of the research project are mass, stiffness, strength and fatigue. The magnitude of these attributes can already be estimated in the early design phase and therefore these attributes can be used as one of the key decision factor whether to further elaborate the concept or not.

Mass The mass calculation is based on the volume of the geometries within the concept and the density of the materials involved. The metric to be used in the filtering and ranking algorithms is the total mass of the concept.

Strength and stiffness The evaluation of strength and stiffness is based on Finite Element (FE) simulations that can be performed either directly within FreeCAD or by using an external software. The results of the FE analysis are further processed to extract the relevant information, such as maximum displacements and stresses for all the components of the assembled concepts. The information is then filled in in the table, as shown in Figure 4, where ”Beam” and ”Plate” refer to the individual components that together build up

the concept. These values will be reused in the fatigue estimation. The metric to be used in the filtering and ranking algorithms for strength is the maximum tensile and compression stress at each material, and for stiffness is the inverse of the structural compliance, which is calculated as:

$$C = \frac{1}{2} \cdot \mathbf{u}^T \cdot \mathbf{f} \tag{1}$$

where **u** is vector of displacements and **f** is the vector of forces (both in all nodes of the structure).

Results of FE Analysis

Calculation finished. Select the results to be loaded.

☑ Sxx ☑ Sxy ☑ Sxz
☑ Syy ☑ Syz ☑ Szz
☑ Fatigue ☑ Stiffness

Load results

Fatigue [# cycles]	4.386e+09
Stiffness [N/mm]	0.001

	Material	Yield Strength	Sxx [Min/Max]	Sxy [Min/Max]	Sxz [Min/Max]	Syy [Min/Max]	Syz [Min/Max]	Szz [Min/Max]	Fatigue
Joints	Joint material	?	-5.4/2.7	-2.7/3.3	-3.0/2.1	-1.3/1.3	-0.4/0.9	-0.4/0.6	
Beam4_01	AISI1015-Fatigue	255	-5.6/5.9	-3.9/3.9	-4.6/5.6	-3.2/2.0	-3.5/3.4	-2.7/2.6	5.786e+31
Beam3_02	AISI1015-Fatigue	255	-27.9/36.9	-11.4/11.1	-8.0/9.1	-7.5/5.7	-5.9/7.7	-7.5/6.2	1.041e+19
Beam1_01	AISI1015-Fatigue	255	-2.2/4.5	-2.0/2.3	-6.7/6.4	-1.0/1.1	-1.3/2.1	-1.8/1.4	7.557e+30
Plate1_01	Wood-Fatigue	63	-18.2/0.7	-5.9/5.0	-7.9/2.2	-3.7/3.7	-2.4/2.7	-1.4/1.0	4.386e+09
Beam3_01	AISI1015-Fatigue	255	-34.9/44.8	-13.9/10.0	-10.5/9.1	-13.1/7.3	-9.7/10.8	-8.1/9.5	4.663e+17
Beam5_01	AISI1015-Fatigue	255	-37.4/32.6	-13.8/13.9	-17.1/13.7	-11.0/12.0	-14.9/15.5	-6.6/6.6	8.39e+18
Beam2_01	AISI1015-Fatigue	255	-25.7/15.9	-5.0/9.0	-5.3/6.0	-3.6/5.5	-6.1/6.6	-2.8/3.2	3.405e+21

Figure 4: Overview of stiffness, strength and fatigue results in FreeCAD.

Fatigue For the assessment of fatigue in early design phases, when the geometry is not yet fixed, the designer cannot rely on detailed time-domain simulations because they are both time consuming and highly dependent on the geometry. Therefore, the approach followed in this project is based on S-N curves. However, since the methodology is flexible, fatigue results could be extracted from a specific external software as well. The S-N curves relate the cyclic stress (S) within a product to the number of cycles (N) to failure. These curves are commonly used to describe the material fatigue performance.

The implementation of the S-N curves within FreeCAD is based on information in CES Selector [16]. Once the S-N curves of the materials are incorporated to the workbench (see Figure 5), the number of cycles until failure is obtained by looking up the number of cycles corresponding to the maximum stress within each material. The results are shown in the results table in Figure 4). The table indicates whether the current concept fulfills the requirements defined by the designer. The metric to be used in the filtering and ranking algorithms for fatigue is the minimum amount of cycles that can be withstand by all the components within the concept.

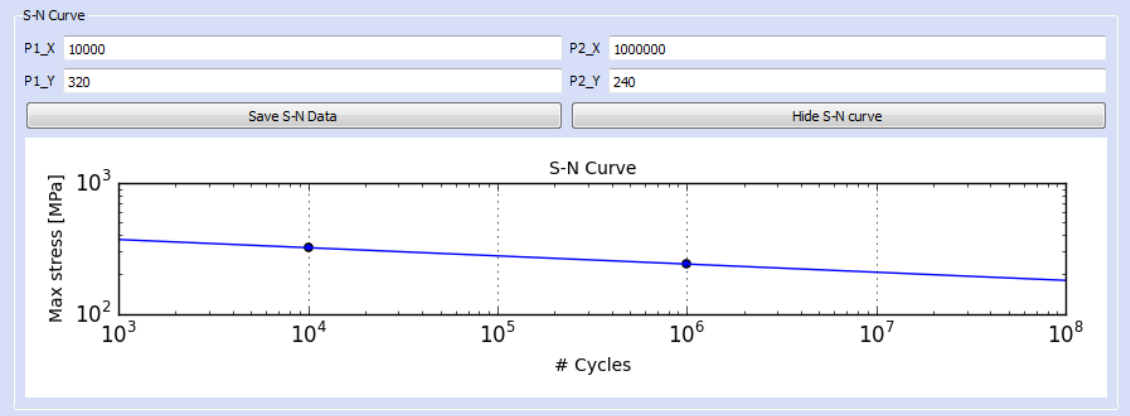


Figure 5: S-N curve defined for a specific material.

3.2 NVH attributes

Three descriptors, whose implementation can be seen in Figure 6, are used to assess the NVH behavior of the considered structures:

First eigenfrequency [Hz] The first resonant frequency ($f_1 = 2\pi w_1$) is automatically computed from the mass (M) and stiffness (K) matrices. It is defined by solving for the smallest value of w verifying the equation $det(K - w^2 M) = 0$.

Sound transmission loss (STL) Integrated [dB Hz] The sound transmission loss represents the amount of sound, in decibels (dB), that is isolated (not transmitted) by a layer. In the project, the layer is assumed infinitely large and can be a fluid, a plate or a mixt of both. It is computed using the transfer matrix method [17]. In order to get a metric, the STL is integrated over the frequency range of interest (frequency in log scale).

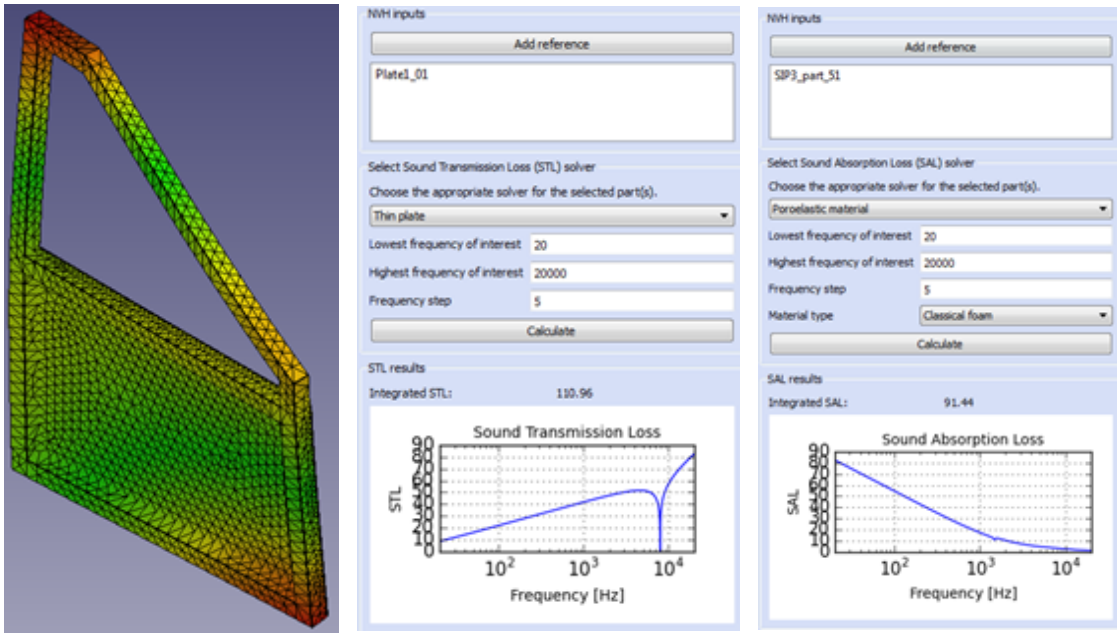
Sound absorption loss (SAL) Integrated [dB Hz] The sound absorption loss represents the amount of sound, in decibels (dB), that is absorbed by a layer. In the project the layer is assumed infinitely large and can be a viscoelastic or a poroelastic material. It is computed using the transfer matrix method [17]. In order to get a metric, the SAL is integrated over the frequency range of interest (frequency in log scale).

3.3 Non-functional attributes

The main non-functional attributes that are considered within this research are cost, manufacturability and robustness. Apart from these, there are also some use case dependent attributes such as thermal behavior, recyclability and paintability, but these will not be tackled within this paper.

Cost To evaluate the cost of a design, an external tool: the Eco Audit tool from CES Selector [16] will be coupled to the FreeCAD environment. The Eco Audit tool includes a broad set of information about material prices, but also about the cost of manufacturing and joining processes (including energy and labour costs). Basically, the cost model can be formulated as:

$$C_{product} = \sum_{components} C_c + \sum_{joints} C_j + \sum_{manuf} C_{mp} \tag{2}$$



(a) First vibration mode. (b) Interface for STL analysis. (c) Interface for SAL analysis.

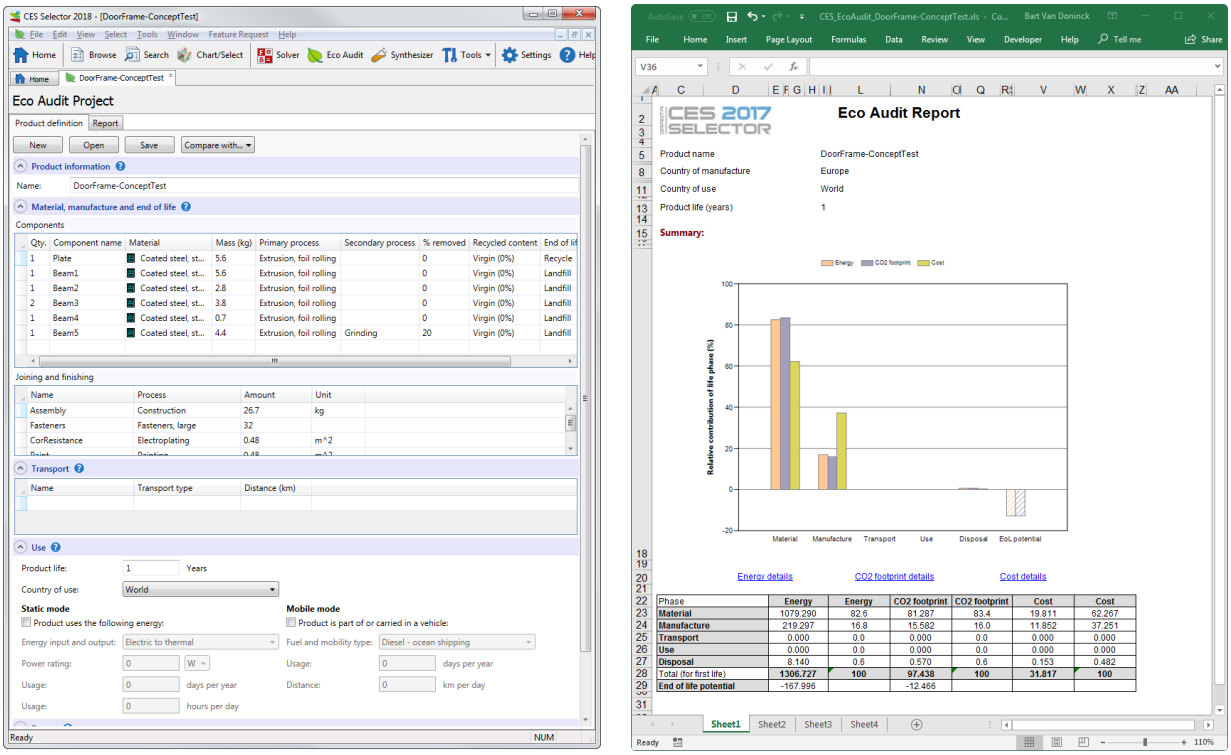
Figure 6: Implementation of the NVH attributes within FreeCAD.

where C_c, C_j and C_{mp} are respectively the cost of a component (material cost), the cost of a joint (labour cost, adhesive cost, process cost) and the cost of the manufacturing process (machining cost, labour cost, finishing cost, etc.). Figure 7a shows a view on the Eco Audit tool related to the cost of a product. For detailed information about the cost formulation, interested readers are referred to [18].

The Eco Audit tool will be coupled to the FreeCAD environment, which allows the designer to calculate the cost in the background without needing to know the details of the specific software. Eco Audit expects as input from the user the materials, the mass, the primary and secondary manufacturing process and some geometrical parameters of the concept. By extracting this information automatically from the design and passing it to the Eco Audit tool, the designer will not be burdened with the manual look up and entry of information. The total cost can be retrieved by FreeCAD from the exported cost report as shown in Figure 7b. The metric to be used in the filtering and ranking algorithms for cost is the total cost of the concept, from raw materials to assembled product, that includes the raw materials cost, the assembly cost of the production and the cost of the human labor.

Manufacturability The manufacturability information is obtained using the method developed by Flanders Make in the Design For Manufacturing and Assembly project(DFMA, [19]). Within this project, a generic scoring tool is developed to asses the manufacturability of both conceptual and detailed designs. The DFMA tool consists of a set of generic questions, derived from some best practices in manufacturing and design experience. Based on the answers on these questions, a relative score can be given to indicate how easy it is to manufacture the product.

The methodology of the DFMA tool is implemented within FreeCAD. Since both geometrical information of the concept, as well as additional information such as mass, joints, manufacturing processes, etc. is available within the CAD environment, the answers on several of these questions is extracted automatically and a metric value is calculated/assigned. For each metric value, a weighting factor and a reference needs to be specified. This can be for instance extracted from a reference design. By comparing the answers for the concept to the the answers for the reference case, a score can be given to indicate whether it is easier or more difficult to manufacture the concept. In the end, the scores for each metric values are weighted and combined,



(a) Cost calculation using Eco Audit tool.

(b) Cost report as interface to FreeCAD.

Figure 7: The use of the Eco Audit Tool by CES as external tool to calculate the cost.

to come to a final score on manufacturability. Figure 8 shows the implementation of the manufacturing tool in the workbench. The single value to be used in the filtering and ranking algorithms for manufacturability is the weighted sum of all the metric values of the manufacturability combined. It is a percentage score which indicates whether the concept is easier to manufacture (>100%) or more difficult (<100%).

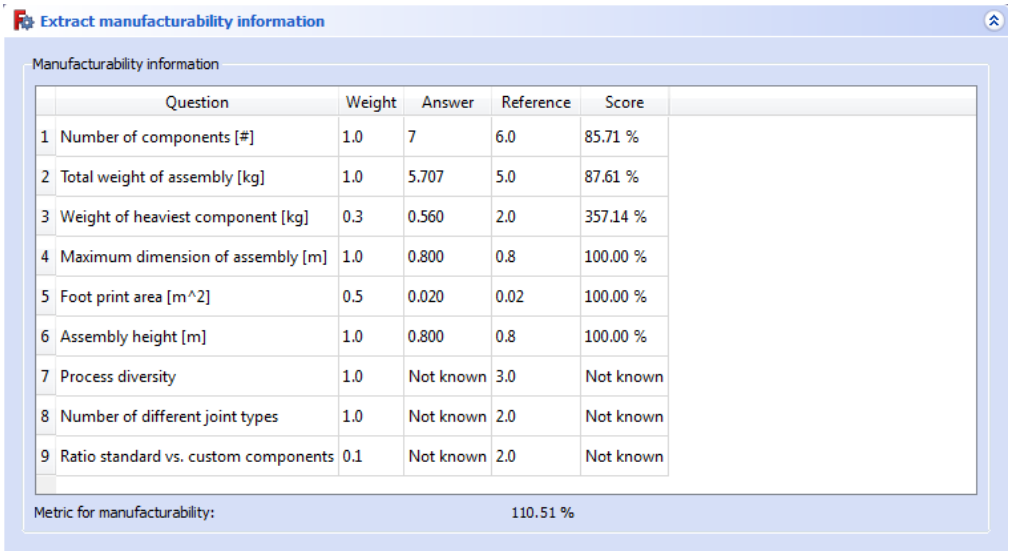


Figure 8: Manufacturing evaluation.

Robustness Robustness can be defined as *'reducing variation in a product without eliminating the causes of the variation'* [20]. In other words, a product is robust if it is insensitive to variation (i.e., replacing one of its components does not have an effect in the rest). In this project, the metric for robustness is obtained based on the study of [21], which defines R as follows:

$$R = 1 - \sum_{i=1}^{n} P_{X_i} \cdot I'_{X_i} \tag{3}$$

where P_{X_i} is the probability (that a change occurs at a certain component i) and I'_{X_i} the normalized impact (of a specific component i in the whole product), respectively. The value of R can go from 0 to 1, being 0 non-robust and 1 robust. The values of P_{X_i} and I'_{X_i} are derived based on the bi-directional dependencies that a component X_i has with respect to other components X_j. In this project, the relations or dependencies between components are based on geometrical connectivity. This information is extracted automatically from the workbench, and summarized in a table similar to the one of Figure 9. In this table, the value '1' means that there is a dependency between components X_i and X_j (geometrical connectivity), whereas '0' means no dependency between X_i and X_j.

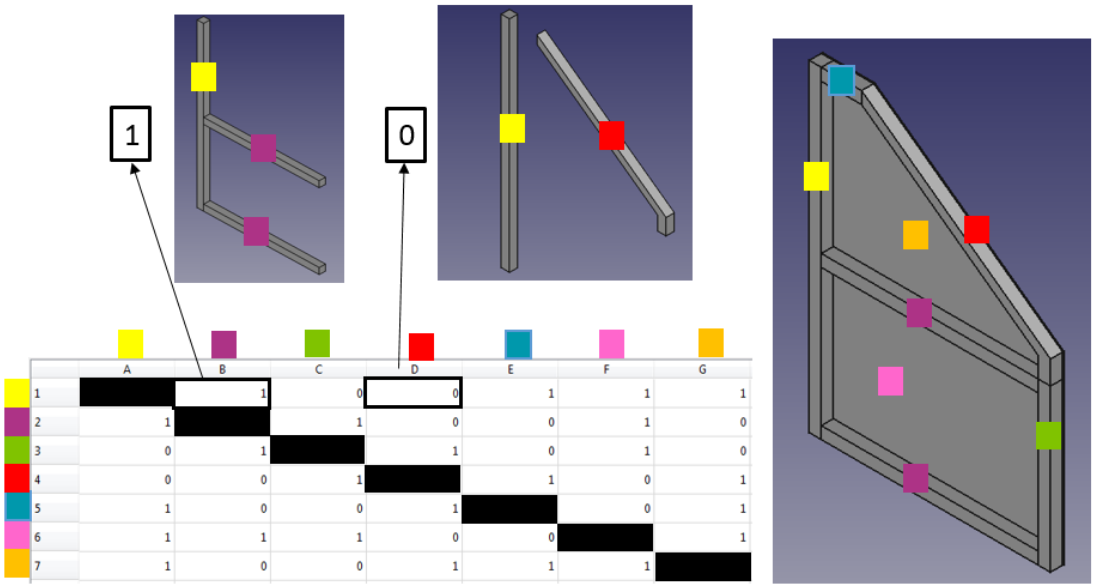


Figure 9: Table for definition of dependencies between the components of a concept.

The formulations required to obtain P_{X_i}, I'_{X_i} and R have been implemented in python codes that are included within the workbench. Weighting factors are added since there might be components that are more critical than others in a product design.

4 Filtering and Ranking of concepts

The end goal of performing a comprehensive multi-attribute evaluation in a vast variety of concepts is to be able to discard most of them based exclusively on their insufficient performance in any of the attributes, and later on rank the filtered concepts and determine in an objective way which one is the best candidate to pass to the next design phase (Figure 10).

The filtering of the concepts is based on the information provided by the designer in the requirements file. As an example, if the designer sets that the mass of the concept should be less than *10* kg, all the concepts with a mass above 10 kg will be discarded. Among the concepts that pass the filtering phase, a scoring of

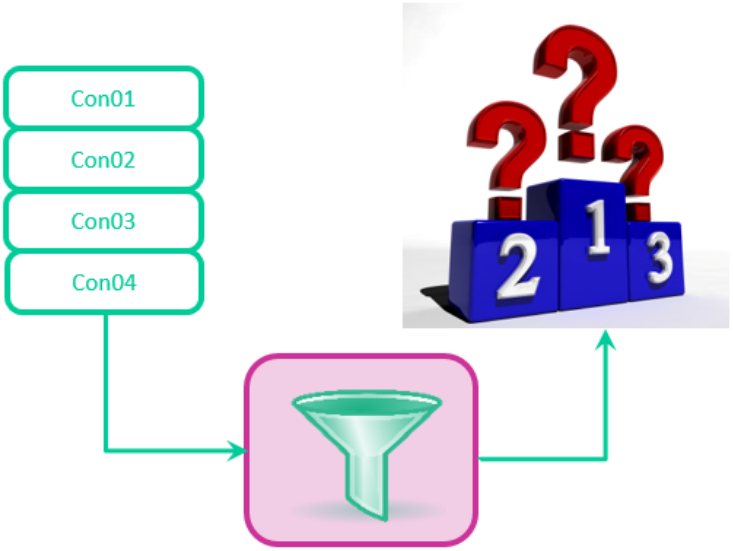


Figure 10: Filtering and Ranking

the attributes is assessed in order to rank them. To do so, decision matrix [22] techniques can be applied. These techniques are commonly used in design theory in different engineering/non-engineering domains. In such a decision matrix, there are a number of concepts to be assessed on a number of attributes, respectively the rows and columns of the decision matrix (Table 1). The relative importance of each attribute can be altered by applying weighting factors (WF), since the relevance of an attribute may change depending on the product. In this research, the acquisition of the required performance metrics from the models is automatic, whereas the choice of the WF is a manual process to be filled in by the designer (last row of Table 1).

	Mass	Stiffness	Strength	Fatigue	NVH	Cost	Manufact.	Robustness
Concept 1								
Concept 2								
...								
Concept n								
WF								

Table 1: Decision matrix for ranking of concepts

However, one can think that the concepts that the designer proposes are not always the best possible ones. Therefore, this methodology is able to generate automatically new feasible concepts based on the information gathered in the filtering and ranking phase, exploring the full design space available using algorithms and an architecture-based model synthesis methodology. Further information about the automatic concept generation in the framework of this research can be found in [23].

5 Application to a door frame structure

The methodology proposed in this research is applied to the design of an automotive door frame. Five different concepts were defined, being three of them identical in terms of geometry, but with different materials. Figure 11 shows the different concepts to be evaluated.

The attributes considered for evaluation are: mass [kg], stiffness [N/m], strength ratio (which is the relation between the maximum stress and the maximum stress allowed), fatigue [$\#cycles$], NVH (frequency of the first eigenmode in [Hz]), cost [eur], manufacturability [$\%$] and robustness [].

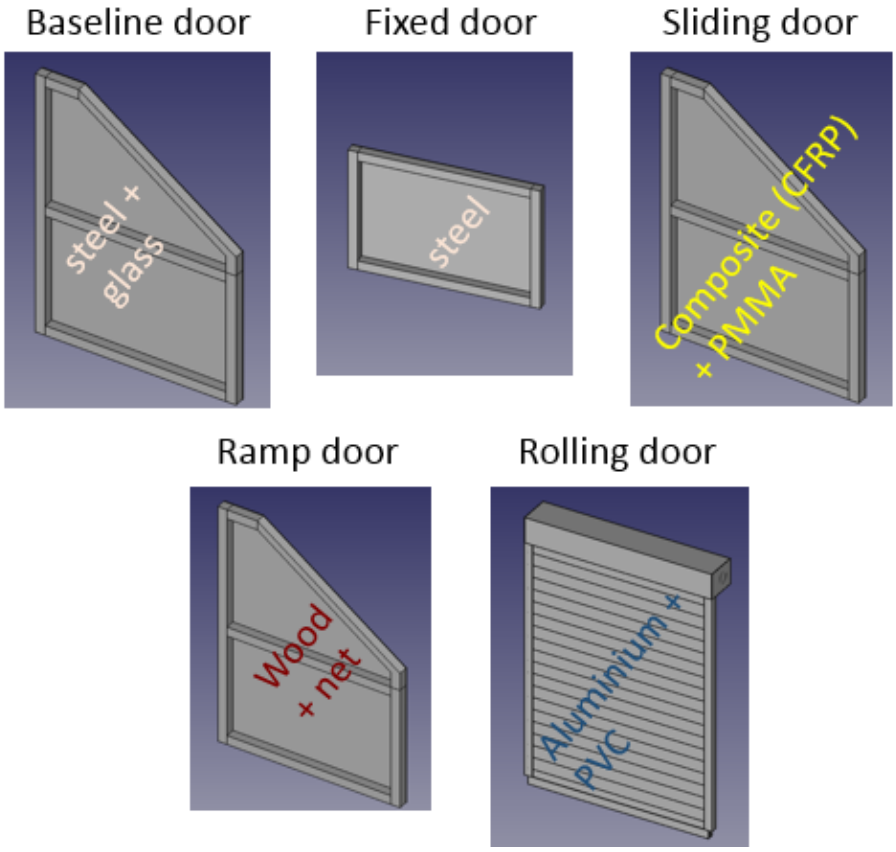


Figure 11: Different concepts for evaluation of an automotive door frame

Once the multi-attribute evaluation is completed using the tools and scripts implemented in the workbench, the upper part of the table of Figure 12 is automatically filled in. Moreover, the requirements set by the designer at the beginning of the process are also stored. Then the metrics obtained during the analyses for all attributes are compared against the corresponding requirements, and only the concepts that fulfill all the requirements are filtered for the upcoming scoring and ranking phase. As seen in Figure 12, Concept 4 (Ramp Door) and Concept 5 (Rolling door) do not fulfill the requirements related to strength and fatigue. This is reasonable since those concepts are built-in using weak materials such as net and PVC.

However, to continue with the explanation of the scoring and ranking strategy, let us filter all the concepts. The next step should be to define weighting factors for the different attributes and assess a preliminary ranking based exclusively on the objective performance of the concepts. The scoring of each attribute is directly linked to the weight defined for it, meaning that the concept with the best metric value will score the value defined as weighted factor, and the others will be scored proportionally. For instance, in the lower part of the table of Figure 13, one can see that the ramp door scores 9 in weight, since it is the lighter concept and the weighting factor defined for the attribute 'Weight' is 9. With this approach, it can be seen that all the values for the metrics lie in the range of [0,10]. The ranking is just a weighted sum of the normalized metrics, expressed as follows:

$$TOTAL = \sum_{i=1}^{n} WF_{AT_i} \cdot MET'_{AT_i} \tag{4}$$

where WF are the weighting factors, MET' are the normalized metrics and AT_i is the attribute i.

However, this first approach is not always pertinent, since it can happen that one concept scores much better than all the rest in one specific attribute, leading to a strong biasing towards that concept in the ranking.

	MASS [kg]	STIFFNESS [N/m]	STRENGTH [ ]	FATIGUE [cycles]	NVH [Hz]	COST [eur]	MANUF. [%]	ROBUSTNESS [ ]
BASELINE	27,1	0,666	0,20	9,2E+07	198	21	85	42
FIXED	18,8	4,069	0,16	1,2E+16	355	9	115	62
SLIDING	5,7	0,351	0,07	7,0E+08	232	144	111	42
RAMP	2,4	0,053	4186,36	7,1E+02	126	4	707	42
ROLLING	7,1	0,003	4,03	3,4E-01	73	23	94	44
REQUIREMENTS	50	1,000	1,00	1,0E+03	50	150	50	20
	FILTERING							
BASELINE	1	1	1	1	1	1	1	1
FIXED	1	1	1	1	1	1	1	1
SLIDING	1	1	1	1	1	1	1	1
RAMP	1	1	0	0	1	1	1	1
ROLLING	1	1	0	0	1	1	1	1

Figure 12: Filtering of the concepts

	MASS [kg]	STIFFNESS [N/m]	STRENGTH [ ]	FATIGUE [cycles]	NVH [Hz]	COST [eur]	MANUF. [%]	ROBUSTNESS [ ]	
BASELINE	27,1	0,666	0,20	9,2E+07	198	21	85	42	
FIXED	18,8	4,069	0,16	1,2E+16	355	9	115	62	
SLIDING	5,7	0,351	0,07	7,0E+08	232	144	111	42	
RAMP	2,4	0,053	4186,36	7,1E+02	126	4	707	42	
ROLLING	7,1	0,003	4,03	3,4E-01	73	23	94	44	
									TOTAL
WEIGHTS	9	7	9	5	5	5	7	9	
	WEIGHTED NORMALIZED ATTRIBUTES								
BASELINE	0,8	1,1	3,0	0,0	2,8	1,0	0,8	6,0	15,6
FIXED	1,2	7,0	3,7	5,0	5,0	2,4	1,1	9,0	34,4
SLIDING	3,8	0,6	9,0	0,0	3,3	0,2	1,1	6,0	24,0
RAMP	9,0	0,1	0,0	0,0	1,8	5,0	7,0	6,0	28,9
ROLLING	3,1	0,0	0,1	0,0	1,0	1,0	0,9	6,3	12,5

Figure 13: First approach for ranking of concepts

Focusing on Figure 13, one can see that the fixed door scores much better than the others in fatigue (at least one order of magnitude higher), meaning that in the normalized metrics, that concept will scores the maximum (5 in this case), whereas the others will scores 0. This gives an extra advantage in the ranking phase, although it might happen that the concept is not the best. Indeed, it can be seen that the ramp door is the 2^{nd} best ranked concept, even if it was discarded in the filtering phase. This is because this concept is light, cheap and easy to manufacture (the best in these 3 attributes), but it scores equally than the baseline and sliding door in fatigue (even though they are much better).

To correct this biasing, an extra correlation was added to the scoring for the second approach. It is reasonable to state that if the values of an attribute metrics for two different concepts are better than a qualified value, they will score equally in that specific attribute. In our case, for instance, different concepts will score equally in fatigue if the # of cycles are above $1e^7$. This method makes the values more comparable and takes engineering input into account, hence a more realistic comparison can be assessed (Figure 14).

The way to proceed now is to use the 'qualified requirements' as the reference values for scoring, instead of

	MASS [kg]	STIFFNESS [N/m]	STRENGTH [ ]	FATIGUE [cycles]	NVH [Hz]	COST [eur]	MANUF. [%]	ROBUSTNESS [ ]	
BASELINE	27,1	0,666	0,30	1,0E+07	198	21	85	42	
FIXED	18,8	1,000	0,30	1,0E+07	200	9	115	62	
SLIDING	5,7	0,351	0,30	1,0E+07	200	144	111	42	
RAMP	3,0	0,053	4186,36	7,1E+02	126	4	150	42	
ROLLING	7,1	0,003	4,03	3,4E-01	73	23	94	44	
WEIGHTS	9	7	9	5	5	5	7	9	TOTAL
QUALIFIED REQUIREMENTS	3	1,000	0,30	1,0E+07	200	20	150	80	
	IMPORTED ATTRIBUTES INTO THE DECISION MATRIX								
BASELINE	1,0	4,7	9,0	5,0	5,0	4,8	4,0	4,7	38,0
FIXED	1,4	7,0	9,0	5,0	5,0	5,0	5,4	7,0	44,8
SLIDING	4,7	2,5	9,0	5,0	5,0	0,7	5,2	4,7	36,7
RAMP	9,0	0,4	0,0	0,0	3,2	5,0	7,0	4,7	29,2
ROLLING	3,8	0,0	0,7	0,0	1,8	4,3	4,4	4,9	20,0

Figure 14: Second approach for ranking of concepts

the best metric. Therefore, in the upper part of the table of Figure 14 the metric values that perform better than the qualified requirements are directly replaced by these values (see numbers colored in blue).

If we look at the ranking results, now it is clear that the three concepts that pass the filtering phase are the best ranked, which is somehow expected. The best concept is still the fixed door, due to its superior stiffness, cost and robustness, as a result of being a concept with a small number of connections and made of a cheap and stiff material like steel. Having a deeper look at the table, we can think of further improvements to find an even better potential concept. We see that the worst attribute regarding the fixed door is the mass, and at the same time we see that the sliding door (made of CFRP + PMMA) is very light (but very expensive compared to the others due to the price of the CFRP). Therefore, if we replace the steel or the CFRP by other stiff (but much cheaper) composite, like GFRP, in the fixed and sliding door, these concepts may score even better.

6 Conclusions

This paper presents a methodology to objectively evaluate the general performance of a product based on a multi-attribute analysis. In this sense, different concept variants of the same product can be analyzed in order to determine which one should be used in later stages of the design phase. The methodology proposed has proven to be flexible since it can be combined with different external tools and solvers available. Moreover, details of the implementation for the calculation of attribute metrics, such as mass, stiffness, strength, NVH, cost, manufacturability and robustness are described. Afterwards, a first approach for filtering and ranking is proposed, providing information about automatic concept generation. Finally, an application example consisting of a door frame structure is studied, discussing the results of the filtering and ranking and proposing further enhancements for the ranking strategy, based on the results obtained. To end, two different concept variants are proposed based on the information provided by the decision matrix.

Acknowledgements

The research leading to these results is part of the ICON project '*Multi-attribute concept evaluation of lightweight structures*' (HBC.2016.0460). This research was supported by Flanders Make, the strategic

research centre for the manufacturing industry, and by VLAIO, the Flemish agency of innovation and business. The research of E. Deckers is funded by a grant from the Research Foundation - Flanders (FWO). The Research Fund KU Leuven is also gratefully acknowledged for its support.

References

[1] Prasad B., *Concurrent engineering fundamentals: Integrated product development, Vol. II.*, Prentice and Hall, Saddle River, New Jersey (1997).

[2] D. Woldemichael and F. Hashim, *Development of Conceptual Design Support Tool for Subsea Process Equipment Design*, (2009).

[3] D. Rentema and E. Jansen, *An AI tool for conceptual design of complex products*, Eindhoven University of Technology, Eindhoven, (2000).

[4] T. Kersten, *'Modessa' A Computer Based Conceptual Design Support System*, AI System Support for Conceptual Design pp. 241-259, (1995).

[5] R. Bracewell, D. Bradley, R. Chaplin, P. Langdon and J. Sharpe, *Schemebuilder: A design aid for the conceptual stages of product design*, in Proceedings of the 9th International Conference on Engineering Design, Prague, (1993).

[6] W. Zhang, S. Tor, G. Britton and Y.-M. Deng, *EFDEX: A knowledge-based expert system for functional design of engineering systems*, Engineering with Computers, vol. 17, pp. 339-353, (2001).

[7] N. Vargas-Hernandez and J. J. Shah, *2nd-CAD: A tool for conceptual systems design in electromechanical domain*, Journal of Computing and Information Science in Engineering, vol. 4, pp. 28-36, (2004).

[8] A. Chakrabarti, P. Sarkar, B. Leelavathamma and B. S. Nataraju, *A functional representation for aiding biomimetic and artificial inspiration of new ideas*, Artificial Intelligence for Engineering Design, Analysis and Manufacturing, vol. 19, pp. 113-132, (2005).

[9] C. R. Bryant, D. A. McAdams, R. B. Stone, T. Kurtoglu and M. I. Campbell, *A computational technique for concept generation*, in IDETC/CIE 2005, Long Beach, California USA, (2005).

[10] P. Boart, M. Sandberg, H. Nergrd and T. Larsson, *Multidisciplinary design tool for conceptual design and evaluation*, in Proceedings of 15th International Conference on Engineering Design,(2005).

[11] G. La Rocca and M. van Tooren, *A knowledge based engineering approach to support automatic generation of FE models in aircraft design*, in 45th AIAA Aerospace Sciences Meeting and Exhibit, Aerospace Sciences Meetings, (2007).

[12] K. Hurst, *Design concept selection using spreadsheet analysis*, Journal of Engineering Design, vol. 2, no. 4, pp. 291-302, (1991).

[13] M. Tovey and J. Owen, *Sketching and direct CAD modelling in automotive design*, Design Studies, vol. 21, no. 6, pp. 569-588, (2000).

[14] S. Wolkl and K. Shea, *A computational product model for conceptual design using SysML*, in ASME 2009 International Design Engineering Technical Conferences and Computers and Information in Engineering Conference, San Diego, (2009).

[15] FreeCAD *https://www.freecadweb.org/wiki/Main_Page*, visited on 20/06/2018.

[16] Granta CES Selector. *http://www.grantadesign.com/products/ces/index.htm*, visited on 19/06/2018.

[17] Allard, J.F. and Atalla, N., *Propagation of Sound in Porous Media: Modeling Sound Absorbing Materials*, John Wiley & Sons, West Sussex, United Kingdom, 2nd edition, (2009)

[18] Granta CES Selector. *http://support.grantadesign.com/resources/cesselector/2018/help/index.htm*, visited on 19/06/2018.

[19] Flanders Make. Manufacturability assessment of heavy duty, complex and low volume product design (DFMA). *http://www.flandersmake.be/en/projects/manufacturability-assessment-heavy-duty-complex-and-low-volume-product-design-dfma.* visited on 19/06/2018.

[20] K. Maurer, S. Lau, *Robust design*, Industrial Engineering 361, (2000).

[21] M. Kissel, D. Hellenbrand and U. Lindemann, *A methodology to evaluate the structural robustness of product concepts*, in Proceedings of the 18th International Conference on Engineering Design (ICED 11), Lyngby/Copenhagen, Denmark, (2011).

[22] Online *https://en.wikipedia.org/wiki/Decision_matrix*, visited on 21/06/2018.

[23] E. Allegaert, J. Menu, E. Ongut, Y. Lemmens and B. Verbeek *A mode-based design methodology for rapid preliminary landing gear design*, in NAFEMS18 UK Conference, Milton Keynes, UK, (2018).

The effect of the weaving architecture of periodic composite structures on structural damping

V. Thierry [1], **D. Chronopoulos** [1]
[1] Institute for Aerospace Technology & The Composites Research Group, University of Nottingham, NG7 2RD, UK
e-mail: **victor.thierry@nottingham.ac.uk**

Abstract
In this article, the structural damping induced by the weaving architecture of composite structures is studied at a mesoscale level. A method allowing to calculate the loss factor depending on the direction of a propagating wave and the frequency in any periodic woven architecture is proposed. The scheme associates two reduction methods, the Craig-Bampton method that reduces the size of the dynamic stiffness matrix of a periodicity is the first, while the second is the Wave and Finite Element Method (WFEM) that uses the Periodic Structure Theory (PST) to lower the size of the problem by allowing to model only a unit cell of a periodic structure. The presented methodology can be used to optimize the structural damping induced by the weave architecture. Predictions of the structural damping for complex architectures are shown.

1 Introduction

Textile composites are widely used for their excellent mechanical properties [1] in many industries. It is greatly applied in aerospace industry in particular thanks to a low weight and high strength when compared to metallic alloys. These composite structures are periodic and can be considered as an assembly of identical unit cells assembled in an identical manner. These periodic structures and their applications have attracted a lot of research for the past decades [2, 3, 4, 5, 6].

When it comes to the design of composite materials, damping is a very important factor as the dynamic response of an engineered structure often needs to be controlled. An extensive number of analytical models have been developed throughout the years for calculating this parameter in composites. The effect of the macroscopic lay-up sequence of a composite on the damping have been studied. However when considered at a mesoscopic scale, the yarns and matrix arrangements are of concern. The damping capacity of a composite is usually higher than of a traditional material, because of the viscoelastic properties of the matrix. This capacity can be used to enhance the uses of composite materials. Composites can be adjusted to fit particular mechanical properties, such as the strength or the damping properties by modifying parameters such as the lay-up, the mesoscale arrangement of the composite or the volume fraction of the matrix etc. [7]. Damping of the propagating guided wave modes results in a reduction in inspection ranges, and therefore knowing these properties for Non Destructive Evaluation (NDE) purposes and for Structural Health Monitoring (SHM) is very important.

The effect of the fibre properties on the damping has been investigated in early experimental work [8, 9]. Layup and fibers orientation are factors with a great effect on the damping as well and thus have been studied in numerous publications [10, 11, 12, 13, 14]. Theoretical models for predicting damping emerged at the same period [15, 16, 17, 18] and it was shown that the angle of the fibre has an influence on the modal damping. With the progress of numerical methods, the effect of the micromechanical arrangement of the fibers has been thoroughly investigated, using finite element methods (FEM) for example [19, 20, 21, 22]. FEM was used as well for establishing damping model at a macroscopic scale [23]. Finite element methods

were finally used to study the damping characteristics of woven fabric-reinforced for the first time in [24]. However, the effect of undulate fiber bundles on the damping properties is not considered in that study, this was investigated later in [25] and once again a correlation between the decreasing of the loss factor with an increasing fiber volume fraction was shown.

In this paper, the vibro-acoustic and ultrasonic wave propagation properties of the structure are studied using the Wave and Finite Element Method (WFEM). This is an efficient tool to study waves in periodic structures. The one-dimensional WFEM has been applied in numerous previous works and for various type of structures such as beams like structures [26, 27], plates [28, 29], thin-walled structures [30] and curved layered shells [31] and then extended to two-dimensional by [32]. In order to reduce the size of the problem and therefore the computation cost, the component mode synthesis (CMS) approach is used. This has been widely used in the literature [33, 34, 6, 35]. The textile composite is modelled at a mesoscopic scale which will allow for establishing the effects inherent to the micromechanics of the material. The mass and the stiffness matrix are computed using a FE software.

The principal novelty of this paper is the vibrational analysis of damped textile composites at a mesoscopic scale, taking into account the undulation of the fibers. The paper is organised as follows. In Sec.2 an overview of the used modelling approach is presented. In the following section (Sec.3), the damping modelling method is introduced: the model used in this paper is shown, as well as the loss factor calculation method. Finally a case study is displayed in Sec.4.

2 Modelling textile composites through a full FE approach

Mechanical modelling of textile composites can be achieved at different scales [36]. A macroscale modelling consists in homogenizing the mechanical properties along the unit cell, while a mesoscale modelling suggests a detailed geometric representation of fabrics such as the yarns and the matrix (here the assembly of fibre is homogenised). In this paper, the analysis is performed at a mesoscopic scale so that the effect of the fibers arrangement and volume fraction can be investigated.

The modelling of this textile composite is performed using an open source software developed by the Polymer Composites Group at the University of Nottingham and named TexGen [37, 38]. It is used for modelling the geometry of complex composite structures such as 3D woven textiles or braid fabric for example. The model is then exported on a FE software where the mass and stiffness matrices $\mathbf{M}$ and $\mathbf{K}$ of the unit cell will be extracted.

The nodal DOFs of the unit cell are partitioned in the following way: bottom, top, left, right, left-bottom corner, right-bottom corner, left-top corner, right-top corner and internal DOFs, which gives: $\mathbf{q} = \left\{\mathbf{q_B^T} \quad \mathbf{q_T^T} \quad \mathbf{q_L^T} \quad \mathbf{q_R^T} \quad \mathbf{q_{LB}^T} \quad \mathbf{q_{RB}^T} \quad \mathbf{q_{LT}^T} \quad \mathbf{q_{RT}^T} \quad \mathbf{q_I^T}\right\}^T$. Assuming time-harmonic behaviour leads to $\ddot{\mathbf{q}} = -\omega^2\mathbf{q}$, the equation of motion of the unit cell is written as:

$$\left[\mathbf{K} + \mathrm{i}\mathbf{C} - \omega^2\mathbf{M}\right]\mathbf{q} = \mathbf{F} \tag{1}$$

In order to reduce the size of the model, a Component Mode Synthesis (CMS) method named the Craig-Bampton reduction method is applied. It will allow for reducing the use of CPU time and memory. In this method, the internal DOFs are reduced, while the boundary DOFs are kept as physical coordinates [39]. A set of 'fixed boundary modes' are selected among the local modes of the unit cell when the boundary DOFs are clamped and no force is acting on the internal nodes.

After reduction of the problem, the periodic structure theory (PST) is employed. The PST states that when a free wave travels along a waveguide, the displacements between two opposite boundary sides of a cell differ only by a propagation factor. Combining those two methods allows us to reduce significantly the number

of unknown in the eigenvalue problem and thus the calculation time. In our case, the wave motion is in the Oxy plan, which gives the following relations

$$\begin{aligned} &\mathbf{q_R} = \lambda_x \mathbf{q_L}; \qquad \mathbf{q_T} = \lambda_y \mathbf{q_B} \\ &\mathbf{q_{RB}} = \lambda_x \mathbf{q_{LB}}; \quad \mathbf{q_{LT}} = \lambda_y \mathbf{q_{LB}}; \quad \mathbf{q_{RT}} = \lambda_x \lambda_y \mathbf{q_{LB}} \end{aligned} \tag{2}$$

λ_x and λ_y being respectively the propagation factors along the x and y axis.

The propagation factors are obtained through this relation:

$$\lambda_x = e^{-\mathrm{i}k_x \Delta}; \quad \lambda_y = e^{-\mathrm{i}k_y \Delta} \tag{3}$$

and the direction of propagation θ can be computed using the following equations

$$k_x = kcos(\theta); \quad k_y = ksin(\theta) \tag{4}$$

3 Damping calculation in composite structures using FE

There are several ways of modelling the damping using FE. In this paper, the complex modulus approach is used. It consists of introducing complex components in the material's stiffness matrix. The complex modulus approach is widely used for modelling the damping in FE codes [40, 41, 42, 43]. The 'i$\mathbf{C}$' term in Eq.1 is suppressed and the stiffness matrix $\mathbf{K}$ is treated as complex [44]. The real part of the newly formed matrix represents the storage modulus referring to the elastic behaviour of the material, while the imaginary part represent the loss modulus referring to the dissipative behaviour.

The global stiffness matrix K is then given as in Eq.5.

$$\mathbf{K} = \mathbf{K}' + \mathrm{i}\mathbf{K}'' = \sum_{k=1}^{n} (\mathbf{K'}_k + \mathrm{i}\mathbf{K''}_k) \tag{5}$$

Where n is the total number of solid elements used in the FE discretisation. $\mathbf{K'}_i$ and $\mathbf{K''}_i$ are respectively the real and imaginary stiffness matrix contributions to the i^{th} finite element to the global stiffness matrices $\mathbf{K}'$ and $\mathbf{K}''$.

In this paper, structural damping is assumed: the viscoelastic properties of each material involved are characterised by complex component in the stiffness matrix. The imaginary part $\mathbf{K}''$ of the global stiffness matrix $\mathbf{K}$ is inspired from the strain energy method, stating that the contributions of each component are divided based on the energy the constituent material stores, and thus we use

$$\mathbf{K}'' = \eta_{yarn} \mathbf{K'}_{yarn} + \eta_{mat} \mathbf{K'}_{mat} \tag{6}$$

With η_{yarn} and η_{mat} respectively the yarn and matrix loss factor. $\mathbf{K'}_{yarn}$ and $\mathbf{K'}_{mat}$ being respectively the stiffness matrix of the yarn and matrix elements.

Once the damping has been modelled, the CMS and WFE methods are applied to the problem.

In this paper, the eigenvalue problem formulation consists of choosing real and known wavenumbers and seeking for the frequencies of the propagating waves.

The equation of motion is thus solved for complex frequencies $\omega = \omega_r + \mathrm{i}\omega_i$. The loss factor associated with the i^{th} propagating wave can be calculated as proposed in [43, 45].

$$\eta_i(\omega, \theta) = 2 \frac{\omega_r \omega_i}{(\omega_r^2 - \omega_i^2)} \tag{7}$$

4 Case study: 2D weave fabric

As an example, a unit cell of a 2D weave fabric was modeled (Fig.1) and the loss factor has been calculated in function of the propagation angle and the frequency. This FE model is composed of 6250 elements (25x25x10) and has a fiber fraction volume of 0.5338. We use $\eta_{yarn} = 0.0001$ and $\eta_{mat} = 0.02$.

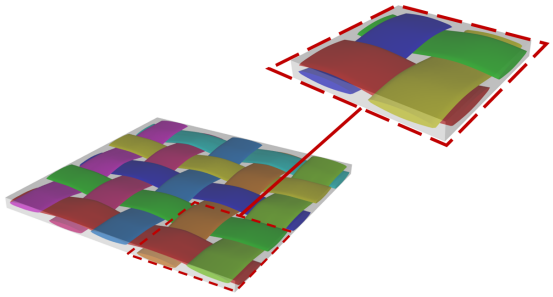


Figure 1: Unit cell of a 2D weave fabric

Using the method presented in section 3, the loss factor associated to any propagating wave can be calculated, in function of the wave direction of propagation and the frequency.

In Fig.2, the loss factor, associated to the flexural mode, as function of the frequency, propagating in the x direction is displayed for a larger frequency range. The dispersion curve for this mode is shown as well on the figure allowing for comparison. A stop-band is present in the dispersion curve, and the loss factor seem to have an asymptotic behavior next to it. This confirm that the first flexural wave will not propagate for this frequency range as the loss factor tends to infinity.

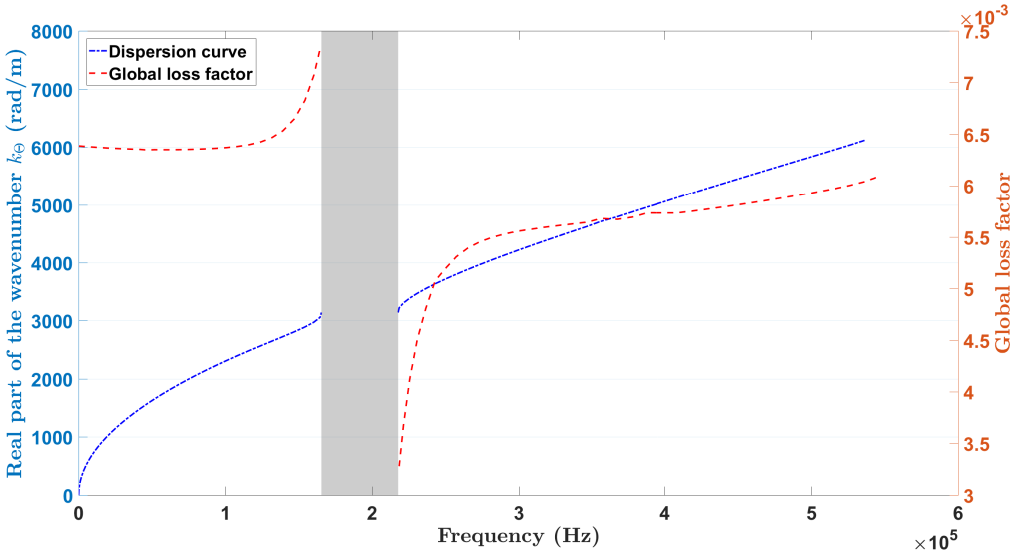


Figure 2: Loss factor in a 6250 elements model of a 2D weave fabric, function of the frequency, propagating in the x direction, associated to the flexural mode of the anisotropic plate

Parametric study 1: fiber volume fraction

Two new models have been created based on the one described above. The difference between these models is the width of the fibers, which has an impact on the fiber volume fraction (see Fig.3), and therefore on the structural damping performance. The external dimensions are the same for these three unit cells.

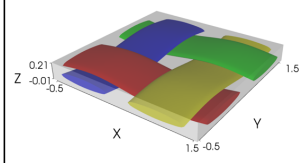
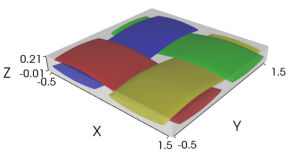
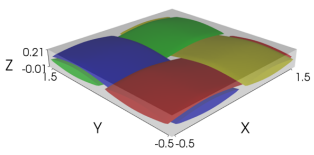
Textile geometry			
Fibre volume fraction	0.4813	0.5338	0.5709

Figure 3: Parametric study: change of the fibers width (the model in the middle of the figure is the reference model used in the previous part of the subsection)

The results of this study are displayed in Fig.4-5. As expected, the lower the fiber volume fraction is, the more effective the model is in dissipating energy, and this is true for the first flexural, shear and pressure modes. All three models present similar loss factor curve shapes for the three first modes.
The loss factor curves of the three models present an asymptotic behavior when the frequency reaches the stop-band for the first flexural mode (see Fig.4). The loss factor has a lower value on the higher frequency part of the figure when considering dividing the figure by its asymptote.
In Fig.5, the dissipative characteristics slightly decrease until reaching a frequency of around 300 kHz. The loss factor then increases until overcoming its initial value.

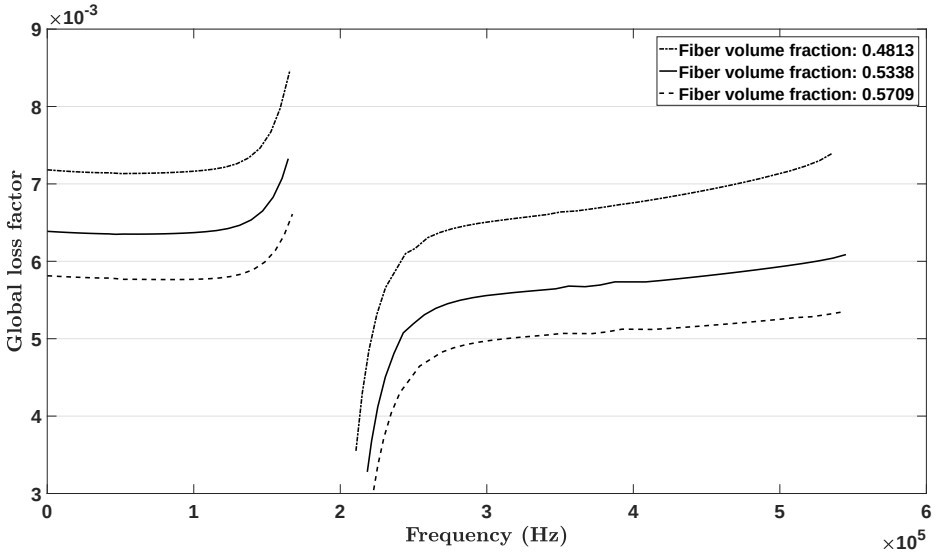


Figure 4: Loss factor displayed for three 6250 elements models of a 2D weave fabric as a function of the frequency, associated to the flexural mode of the anisotropic plate (angle of propagation null: x direction): structure with larger fibers (–), reference structure (_), thinner fibers (-.)

Parametric study 2: direction of propagation
The effect of the direction of propagation is studied. As the model presents a symmetry axis, the dispersion curves and loss factors are symmetric as well. The directions of propagation with an angle superior to 45^o will not be studied. However, directions of propagation such as $[30^o, 45^o]$ can be studied. The results of this study are displayed in Fig.6.

It can be observed in the left part of the figure that the first flexural wave is more attenuated for the highest

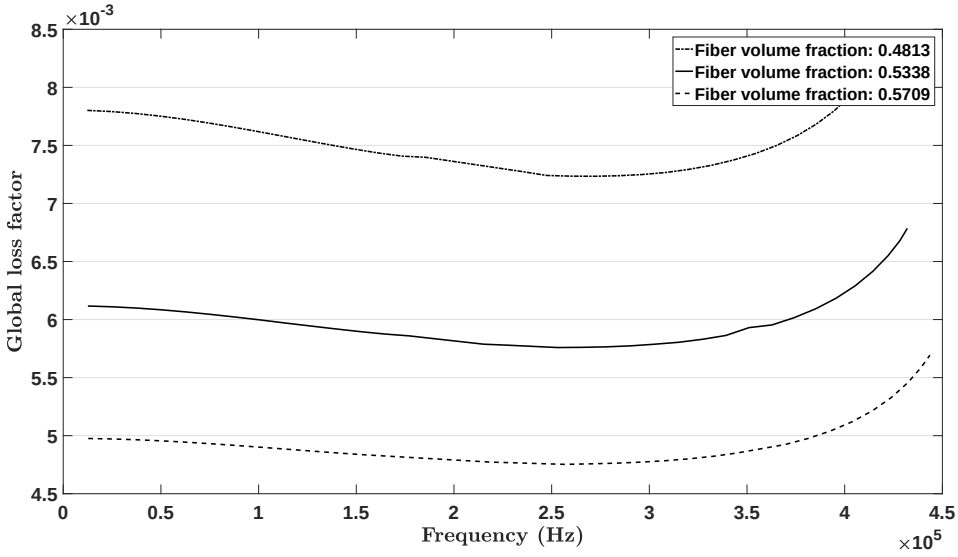


Figure 5: Loss factor displayed for three 6250 elements models of a 2D weave fabric as a function of the frequency, associated to the shear mode of the anisotropic plate (angle of propagation null: x direction): structure with larger fibers (–), reference structure (_), thinner fibers (-.)

angles of propagation, and yet, both values of the loss factor for the 30^o and 45^o angles of propagation start decreasing for a frequency around 100 kHz until reaching and following the curve representing an angle of propagation of 0^o. In the right part of the figure, after the asymptotic behavior, it seems that the angle of propagation with the most damping (among the studied ones) is of 30^o, followed by 45^o and then 0^o. It can be concluded from this paragraph that the damping is clearly affected by the direction of propagation.

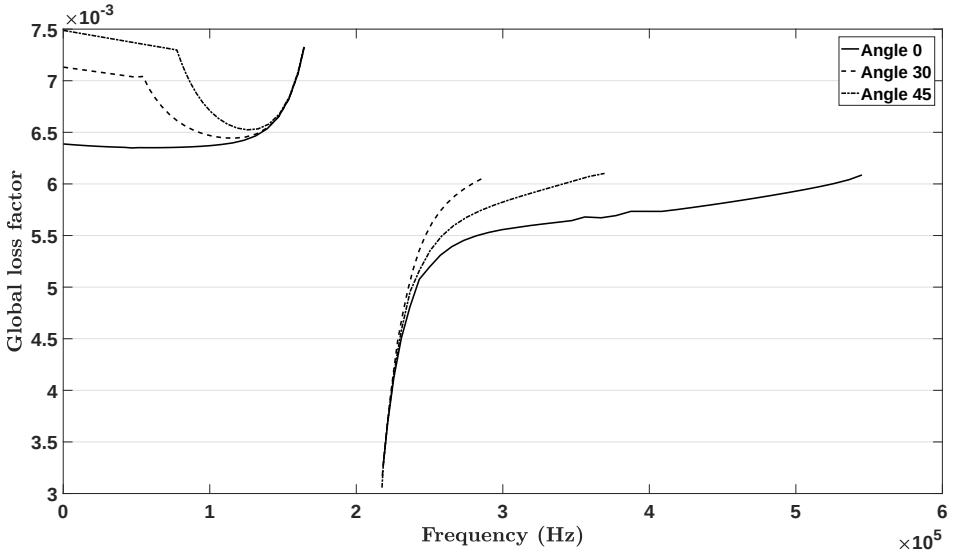


Figure 6: Loss factor displayed for a 6250 elements model of a 2D weave fabric (with changing direction of propagation), function of frequency, associated to the flexural mode of the anisotropic plate

5 Conclusions

In this paper a method allowing for prediction of the structural damping in textile composite at a mesoscopic scale is presented. A 2D weave textile is used as a case study, the dispersion relations are computed as well as the variation of the loss factor versus the frequency for the first modes.

- It can be seen that the damping is strongly affected by the direction of propagation of the waves in a textile composite.
- It appears that when the textiles show stop-bands, the damping loss factor tends toward infinity.
- It can be seen that the damping is affected by the fiber volume fraction of the textile. However the values of the damping loss factor change but the shapes remain quite similar.

Acknowledgements

This work is funded by the INNOVATIVE doctoral programme. The INNOVATIVE programme is partially funded by the Marie Curie Initial Training Networks (ITN) action (project number 665468) and partially by the Institute for Aerospace Technology (IAT) at the University of Nottingham.

References

[1] C. Soutis, "Fibre reinforced composites in aircraft construction," *Progress in Aerospace Sciences*, vol. 41, no. 2, pp. 143–151, 2005.

[2] S. Mead, D. J.; Parthan, "Free wave propagation in two-dimensional periodic plates," *Journal of Sound and Vibration*, 1979.

[3] D. . J. Mead, "Wave propagation in continuous periodic structures: research contributions from southampton, 1964-1995," *Journal of Sound and Vibration*, 1996.

[4] L. Hinke, B. R. Mace, and M. J. Brennan, "Finite element analysis of waveguides," *Institute of Sound and Vibration Research*, 2004.

[5] C. Barbarosie and M. M. Neves, "Periodic structures for frequency filtering: analysis and optimization," *Computers & Structures*, vol. 82, no. 17-19, pp. 1399–1403, 2004.

[6] C. Droz, C. Zhou, M. N. Ichchou, and J. P. Lain, "A hybrid wave-mode formulation for the vibro-acoustic analysis of 2d periodic structures," *Journal of Sound and Vibration*, vol. 363, pp. 285–302, 2016.

[7] A. Treviso, B. Van Genechten, D. Mundo, and M. Tournour, "Damping in composite materials: Properties and models," *Composites Part B: Engineering*, vol. 78, pp. 144–152.

[8] G. C. Wright, "The dynamic properties of glass and carbon fibre reinforced plastic beams," *Journal of Sound and Vibration*, vol. 21, no. 2, pp. 205–212, 1972.

[9] R. M. Crane and J. W. Gillespie, "Characterization of the vibration damping loss factor of glass and graphite fiber composites," *Composites Science and Technology*, vol. 40, no. 4, pp. 355–375, 1991.

[10] R. D. Adams and D. G. C. Bacon, "Effect of fibre orientation and laminate geometry on the dynamic properties of cfrp," *Journal of Composite Materials*, vol. 7, no. 4, pp. 402–428, 1973.

[11] R. D. Adams and M. R. Maheri, "Dynamic flexural properties of anisotropic fibrous composite beams," *Composites Science and Technology*, vol. 50, no. 4, pp. 497–514, 1994.

[12] R. D. Adams and M. R. Maheri, "Damping in advanced polymermatrix composites," *Journal of Alloys and Compounds*, vol. 355, no. 1, pp. 126–130, 2003.

[13] J.-M. Berthelot and Y. Sefrani, "Damping analysis of unidirectional glass and kevlar fibre composites," *Composites Science and Technology*, vol. 64, no. 9, pp. 1261–1278, 2004.

[14] S. Wray, J. N. Ashton, and H. El-Sobky, "An investigation of the influence of anisotropy and frequency on damping in short glass fibre reinforced polypropylene," *Composite Structures*, vol. 15, no. 1, pp. 43–60, 1990.

[15] R. G. Ni and R. Adams, "The damping and dynamic moduli of symmetric laminated composite beams-theoretical and experimental results," *Journal of Composite Materials*, vol. 18, no. 2, pp. 104–121, 1984.

[16] J. H. Yim, "A damping analysis of composite laminates using the closed form expression for the basic damping of poisson's ratio," *Composite Structures*, vol. 46, no. 4, pp. 405–411, 1999.

[17] J.-M. Berthelot, M. Assarar, Y. Sefrani, and A. E. Mahi, "Damping analysis of composite materials and structures," *Composite Structures*, vol. 85, no. 3, pp. 189–204, 2008.

[18] M. R. Maheri, "The effect of layup and boundary conditions on the modal damping of frp composite panels," *Journal of Composite Materials*, vol. 45, no. 13, pp. 1411–1422, 2010.

[19] S. J. Hwang and R. F. Gibson, "The effects of three-dimensional states of stress on damping of laminated composites," *Composites Science and Technology*, vol. 41, no. 4, pp. 379–393, 1991.

[20] S. J. Hwang and R. F. Gibson, "Contribution of interlaminar stresses to damping in thick laminated composites under uniaxial extension," *Composite Structures*, vol. 20, no. 1, pp. 29–35, 1992.

[21] J.-L. Tsai and Y.-K. Chi, "Effect of fiber array on damping behaviors of fiber composites," *Composites Part B: Engineering*, vol. 39, no. 7, pp. 1196–1204, 2008.

[22] R. Chandra, S. P. Singh, and K. Gupta, "Micromechanical damping models for fiber-reinforced composites: a comparative study," *Composites Part A: Applied Science and Manufacturing*, vol. 33, no. 6, pp. 787–796, 2002.

[23] A. E. Mahi, M. Assarar, Y. Sefrani, and J.-M. Berthelot, "Damping analysis of orthotropic composite materials and laminates," *Composites Part B: Engineering*, vol. 39, no. 7, pp. 1069–1076, 2008.

[24] H. Guan and R. F. Gibson, "Micromechanical models for damping in woven fabric-reinforced polymer matrix composites," *Journal of Composite Materials*, vol. 35, no. 16, pp. 1417–1434, 2001.

[25] H. Yu and C. Zhou, "Complex stiffness method for damping properties of woven composites," *Journal of Reinforced Plastics and Composites*, p. 0731684417709617, 2017.

[26] J. M. Mencik and M. N. Ichchou, "Multi-mode propagation and diffusion in structures through finite elements," *European Journal of Mechanics - A/Solids*, vol. 24, no. 5, pp. 877–898, 2005.

[27] B. R. Mace, D. Duhamel, M. J. Brennan, and L. Hinke, "Finite element prediction of wave motion in structural waveguides," *The Journal of the Acoustical Society of America*, vol. 117, no. 5, pp. 2835–2843, 2005.

[28] M. N. Ichchou, J. Berthaut, and M. Collet, "Multi-mode wave propagation in ribbed plates: Part i, wavenumber-space characteristics," *International Journal of Solids and Structures*, vol. 45, no. 5, pp. 1179–1195, 2008.

[29] M. N. Ichchou, J. Berthaut, and M. Collet, "Multi-mode wave propagation in ribbed plates. part ii: Predictions and comparisons," *International Journal of Solids and Structures*, vol. 45, no. 5, pp. 1196–1216, 2008.

[30] L. Houillon, M. N. Ichchou, and L. Jezequel, "Wave motion in thin-walled structures," *Journal of Sound and Vibration*, vol. 281, no. 3-5, pp. 483–507, 2005.

[31] D. Chronopoulos, M. Ichchou, B. Troclet, and O. Bareille, "Predicting the broadband response of a layered cone-cylinder-cone shell," *Composite Structures*, vol. 107, pp. 149–159, 2014.

[32] E. Manconi and B. R. Mace, "Modelling wave propagation in two-dimensional structures using a wave/finite element technique," *Institute of Sound and Vibration Research*, 2007.

[33] V. Cotoni, R. S. Langley, and P. J. Shorter, "A statistical energy analysis subsystem formulation using finite element and periodic structure theory," *Journal of Sound and Vibration*, vol. 318, no. 4-5, pp. 1077–1108, 2008.

[34] C. W. Zhou, J. P. Lain, M. N. Ichchou, and A. M. Zine, "Multi-scale modelling for two-dimensional periodic structures using a combined mode/wave based approach," *Computers & Structures*, vol. 154, pp. 145–162, 2015.

[35] Y. Fan, M. Collet, M. Ichchou, L. Li, O. Bareille, and Z. Dimitrijevic, "Energy flow prediction in built-up structures through a hybrid finite element/wave and finite element approach," *Mechanical Systems and Signal Processing*, vol. 66-67, pp. 137–158, 2016.

[36] Q. Pan, "Multi-scale modelling and material characterisation of textile composites for aerospace applications," 2016.

[37] M. Sherburn, *Geometric and Mechanical Modelling of Textiles*. Thesis, 2007.

[38] H. Lin, L. P. Brown, and A. C. Long, "Modelling and simulating textile structures using texgen," *Advanced Materials Research*, vol. 331, pp. 44–47, 2011.

[39] L. G. J. Becker, "Cms methods for efficient damping prediction for structures with friction," 2008.

[40] G. D. Gounaris and N. K. Anifantis, "Structural damping determination by finite element approach," *Computers & Structures*, vol. 73, no. 1, pp. 445–452, 1999.

[41] I. Bartoli, A. Marzani, F. Lanza di Scalea, and E. Viola, "Modeling wave propagation in damped waveguides of arbitrary cross-section," *Journal of Sound and Vibration*, vol. 295, no. 3, pp. 685–707, 2006.

[42] A. Marzani, E. Viola, I. Bartoli, F. Lanza di Scalea, and P. Rizzo, "A semi-analytical finite element formulation for modeling stress wave propagation in axisymmetric damped waveguides," *Journal of Sound and Vibration*, vol. 318, no. 3, pp. 488–505, 2008.

[43] E. Manconi and B. R. Mace, "Estimation of the loss factor of viscoelastic laminated panels from finite element analysis," *Journal of Sound and Vibration*, vol. 329, no. 19, pp. 3928–3939, 2010.

[44] C. D. Johnson and D. A. Kienholz, "Finite element prediction of damping in structures with constrained viscoelastic layers," *AIAA Journal*, vol. 20, no. 9, pp. 1284–1290, 1982.

[45] D. Chronopoulos, "Design optimization of composite structures operating in acoustic environments," *Journal of Sound and Vibration*, vol. 355, no. Supplement C, pp. 322–344, 2015.

Analysis of sound transmission loss of a rectangular plate with acoustic treatments

S. Zhang[1], X. Sheng[1]
[1]State Key Laboratory of Traction Power, Southwest Jiaotong University
111 Section One, North Second Ring Road, Chengdu, Sichuan, P. R. China
e-mail: **fxzhangshumin@163.com**

Abstract
A panel is often used with a layer of soft material applied on its 'interior' surface. Regarding sound insulation, the layer of soft material can improve the panel's acoustic performance by two mechanisms: (1) adding mass to the panel to enhance sound reflections; and (2) absorbing part of the otherwise transmitted sound power. To study the mechanism of the panel's acoustic performance, a more general predictive model is established in this paper. A comparison is made between the model established in this paper and models based on plane wave assumptions. Sound transmission loss (TL) of panels with different sound absorbing materials are calculated using this model. In the end, TLs of the plate considering the effects of sound absorbing and mass, separately and then combinedly, are given to explore which mechanism is dominant.

1 Introduction

Sound insulation performances of panels are important in many applications such as vehicle engineering and architectures. On the basis of the mass law, an effective way to increase a panel's acoustic performance is to increase the mass of the panel. For high speed trains, panels are often used with a layer of soft material applied on the 'interior' surface. The layer of soft material may serve different purposes, e.g. for usage safety and comfort, heat and sound insulations, and decorations. The soft material can also improve the acoustic performance of the panel either by increasing the mass or by sound absorption, and which way is dominant is yet to be explored. Nowadays, to be energy-efficient light-weight structures are commonly used in many engineering applications. However, light-weight and low-noise designs are often contradictory [1]. Therefore, exploring the sound transmission loss mechanism of a plate with absorbing material is very meaningful and may provide guidance for design.

Over the years, acoustic and vibrational characteristics of a panel has been studied extensively by a large number of researchers in past years [2-3]. For the radiation problem, Xie G et al [4] presented an approximate model for calculating the radiation efficiency of a strip using the Rayleigh integral equation and modal superposition method. Putra A et al [5] compared the radiation efficiencies of baffled and unbaffled plates for a single mode and for multi-modal responses. Wallace C E [6] used a simplified Rayleigh integral equation method to model the absorption of oblique incidence sound by a finite micro-perforated panel absorber. Davy J L et al [7] calculated the radiation impedance of the panel due to the combined effect of two different types of fields when the panel is excited by an incident diffuse sound field or by transverse point or line forces.

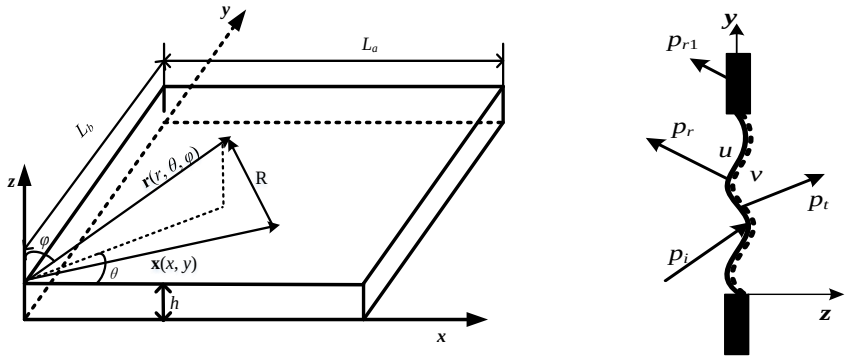
When coming to the sound field in an enclosure, sound transmission loss of a panel is normally investigated. Trevathan J W et al [8] studied the effect of angle of incidence on the apparent sound transmission loss of thin panels. In that paper, they suggested that a reconsideration of the traditional definition of the sound transmission should be made, but without specified how to revise it. Mana [9] pointed out that if the panel is set in a baffle, the power reflected by the baffle cannot be ignored, otherwise the TL may become negative at low frequencies. London A [10] calculated the sound transmission loss of a homogeneous single wall by assuming the reflected and transmitted pressures are

both plane waves, but this assumption may cause an inaccuracy in TL at low frequencies. Zhang Y et al [11] used the wave-based method and modal superposition method to model the sound transmission loss of high speed train windows and investigated parameters affecting TL.

In this paper, a panel with an absorbing layer hinged in an infinite baffle is considered. Equations which are required to calculate the transmission loss of the panel are derived in Section 2. Firstly, the Rayleigh integral equation is used to link the reflected and transmitted pressures with the vibration velocity of the panel. The vibration of the panel is expressed using modal superposition with modal participation parameters to be determined. Secondly, by dividing the plate into a number of small elements, and letting the above equations be satisfied at the centers of those elements, a set of linear algebraic equations are established from which the modal participation parameters can be solved. Then the sound transmission loss can be calculated. In Section 3, after validating the model, sound transmission loss of panels with different sound absorbing materials are calculated using this model. In the end, TLs of the plate considering sound absorbing and mass, separately and then combinedly, are given to explore which mechanism is dominant. And finally, this paper is concluded in Section 4.

2 TL model

2.1 Governing equations



(a) (b)

Fig. 1: Coordinate configuration of the plate hinged in an infinite baffle

Consider a finite rectangular thin plate which is simply supported in an infinite rigid baffle. The panel's dimensions are $L_a \times L_b \times h$, as shown in Fig. 1(a). One of the surfaces (the incident surface) of the plate is plain and smooth and the other is acoustic absorbent due to that absorbing material is applied. In Fig. 1(b), the solid-line curve represents the deformed bare panel and the dotted-line curve represents the absorbing material. The absorbing material layer is assumed to be thin and acoustically local, and therefore the acoustic property of the layer may be represented by impedance Z which is equal to sound pressure applied on the layer divided by the layer's compressional velocity.

Based on the classic thin-plate theory, the equation of motion governing the bending vibrations of the plate is given by

$$D\left(\frac{\partial^4 w(x,y,t)}{\partial x^4}+2\frac{\partial^4 w(x,y,t)}{\partial x^2\partial y^2}+\frac{\partial^4 w(x,y,t)}{\partial y^4}\right)+\rho h\frac{\partial^2 w(x,y,t)}{\partial t^2}=p_i+p_{r1}+p_{r2}-p_t \qquad (1)$$

where, $D=E(1+\mathrm{i}\eta)h^3/12(1-\upsilon^2)$ is the bending stiffness of the plate, E, h, η and υ are the Young's modulus, thickness, damping loss factor and Poisson's ratio of the plate, respectively. w is the displacement of the plate, p_i is the incident pressure, p_{r1} is the blocked pressure due to the reflection of

the baffle, and its amplitude is equal to the amplitude of the incident pressure. p_{r2} is the reflected pressure, and p_t is the transmitted pressure.

The incident pressure is assumed to be an obliquely incident travelling plane wave, given by

$$p_i(x,y,z,t) = \tilde{p}_i \mathrm{e}^{\mathrm{i}(\omega t - k_x x - k_y y - k_z z)} \tag{2}$$

where, $\tilde{p}_i$ is the amplitude of the incident pressure, ω is the angular frequency, $k_0 = \omega / c_0$ is the acoustic wavenumber, $k_x = k_0 \sin\varphi\cos\theta$, $k_y = k_0 \sin\varphi\sin\theta$, $k_z = k_0 \cos\varphi$ are the acoustic wavenumbers along the directions of *x*, *y*, *z* directions, c_0 is the sound speed in air, φ and θ are the angles of incidence.

The blocked acoustic pressure satisfies Snell's law [12], and therefore can be written to be

$$p_{r1}(x,y,z,t) = \tilde{p}_i \mathrm{e}^{\mathrm{i}(\omega t - k_x x - k_y y + k_z z)} \tag{3}$$

The reflected and transmitted acoustic pressures are related to the surface normal velocity via the Rayleigh's integral equation [12]

$$\tilde{p}_{r2}(\boldsymbol{r}) = -\frac{\mathrm{i}\omega\rho_0}{2\pi}\int_S \frac{\tilde{u}(\mathbf{x})}{R}\mathrm{e}^{-\mathrm{i}k_0 R}\mathrm{d}S \tag{4}$$

$$\tilde{p}_t(\mathbf{r}) = \frac{\mathrm{i}\omega\rho_0}{2\pi}\int_S \frac{\tilde{v}(\mathbf{x})}{R}\mathrm{e}^{-\mathrm{i}k_0 R}\mathrm{d}S \tag{5}$$

where, ρ_0 is the air density, $\tilde{u}(\mathbf{x})$ is the surface normal velocity amplitude of the plate at location $\mathbf{x} = (x, y)$, $\tilde{v}(\mathbf{x})$ is the surface normal velocity amplitude of the absorbing material. The integral is evaluated over the plate surface S . The distance between the source point and the acoustic response point is $R = |\mathbf{r} - \mathbf{x}|$, as shown in Fig. 1(a).

Applying the definition of the impedance, Eq. (4) can be written as

$$\tilde{p}_t(\mathbf{r}) = \frac{\mathrm{i}\omega\rho_0}{2\pi}\int_S \frac{\tilde{v}(\mathbf{x})}{R}\mathrm{e}^{-\mathrm{i}k_0 R}\mathrm{d}S = \frac{\mathrm{i}\omega\rho_0}{2\pi}\int_S (\tilde{u}(\mathbf{x}) - \frac{\tilde{p}(\mathbf{x})}{Z})\frac{\mathrm{e}^{-\mathrm{i}k_0 R}}{R}\mathrm{d}S \tag{6}$$

The surface normal velocity of the plate at any location **x** can be calculated by using the modal superposition method

$$u(\mathbf{x},t) = \tilde{u}(\mathbf{x})\mathrm{e}^{\mathrm{i}\omega t} = \mathrm{i}\omega\sum_{m,n}\alpha_{mn}\varphi_{mn}(x,y)\mathrm{e}^{\mathrm{i}\omega t} \tag{7}$$

where α_{mn} is the modal participation coefficient of the (*m*, *n*) mode, which depends on the form of the excitation as well as frequency, $\varphi_{mn}(x,y)$ is the associated mode shape function, which depends on the boundary conditions.

The mode shape function $\varphi_{mn}(x,y)$ for the simply supported rectangular plate can be expressed as

$$\varphi_{mn}(x,y) = \sin\frac{m\pi x}{L_a}\sin\frac{n\pi y}{L_b} \tag{8}$$

and the natural frequencies ω_{mn} are given by

$$\omega_{mn} = \sqrt{\frac{D}{\rho h}}[(\frac{m\pi}{L_a})^2 + (\frac{n\pi}{L_b})^2] \tag{9}$$

2.2 Discretization of the plate

In this section, the reflected and transmitted pressures are calculated by dividing the panel into a number of small elements and assuming a uniform pressure for each element, as shown in Fig.2. The spacings between the centers of adjacent cells are dx in the x direction and dy in the y direction. Each cell can be considered as a discrete monopole source. This requires that the size of the elemental source must be much smaller than half the acoustic wavelength ($k_0\mathrm{d}x \ll \pi, k_0\mathrm{d}y \ll \pi$) [13].

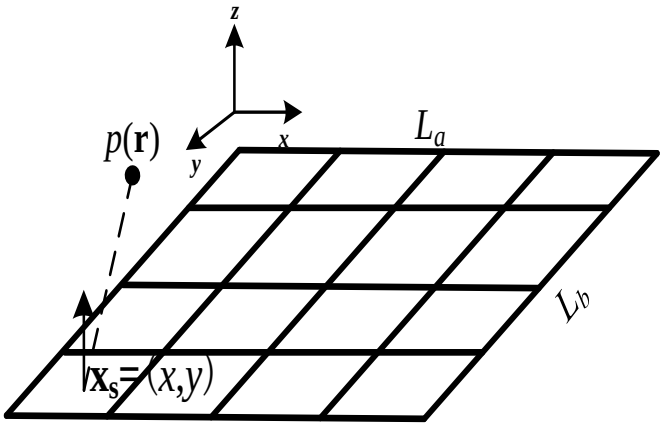


Fig. 2: Discretization of the plate

In Ref. [14], Morse and Ingard give the radiation impedance of a rectangle piston, so the impedance at a given cell generated by itself alone of the plate can be written as

$$\frac{p}{u}=\frac{\rho c k_0^2}{16}(\mathrm{d}x^2+\mathrm{d}y^2)+\frac{\mathrm{i}8\rho c k_0}{9\pi}\left(\frac{\mathrm{d}x^2+\mathrm{d}x\mathrm{d}y+\mathrm{d}y^2}{\mathrm{d}x+\mathrm{d}y}\right) \tag{10}$$

Rewriting the Rayleigh's integral equation into matrix form, the reflected sound pressure can be given

$$\mathbf{P}_\mathbf{r}=-\mathbf{M}\mathbf{u} \tag{11}$$

where $\mathbf{M}$ is an impedance matrix, and its elements are given as

$$M_{rs}=\begin{cases}\dfrac{\mathrm{i}\rho_0 c_0 k_0}{2\pi}\left(\dfrac{\mathrm{e}^{-\mathrm{i}k_0 R_{rs}}}{R_{rs}}\right)\mathrm{d}x\mathrm{d}y, & r\neq s\\ \dfrac{\rho_0 c_0 k_0^2}{16}(\mathrm{d}x^2+\mathrm{d}y^2)+\dfrac{\mathrm{i}8\rho_0 c_0 k_0}{9\pi}\left(\dfrac{\mathrm{d}x^2+\mathrm{d}x\mathrm{d}y+\mathrm{d}y^2}{\mathrm{d}x+\mathrm{d}y}\right), & r=s\end{cases} \tag{12}$$

Similarly, the transmitted pressure can be written as

$$\mathbf{P}_\mathbf{t}=\left[\mathbf{I}+\mathbf{N}\right]^{-1}\mathbf{M}\mathbf{u} \tag{13}$$

where, $\mathbf{I}$ represents the unit matrix, and the elements of $\mathbf{N}$ matrix are

$$N_{rs}=\begin{cases}\dfrac{\mathrm{i}\rho_0 c_0 k_0}{Z2\pi}\left(\dfrac{\mathrm{e}^{-\mathrm{i}k_0 R_{rs}}}{R_{rs}}\right)\mathrm{d}x\mathrm{d}y, & r\neq s\\ \dfrac{\rho_0 c_0 k_0^2}{16Z}(\mathrm{d}x^2+\mathrm{d}y^2)+\dfrac{\mathrm{i}8\rho_0 c_0 k_0}{9\pi Z}\left(\dfrac{\mathrm{d}x^2+\mathrm{d}x\mathrm{d}y+\mathrm{d}y^2}{\mathrm{d}x+\mathrm{d}y}\right), & r=s\end{cases} \tag{14}$$

Substituting Eq. (11) - $N_{rs}=\begin{cases}\dfrac{\mathrm{i}\rho_0 c_0 k_0}{Z2\pi}\left(\dfrac{\mathrm{e}^{-\mathrm{i}k_0 R_{rs}}}{R_{rs}}\right)\mathrm{d}x\mathrm{d}y, & r\neq s\\ \dfrac{\rho_0 c_0 k_0^2}{16Z}(\mathrm{d}x^2+\mathrm{d}y^2)+\dfrac{\mathrm{i}8\rho_0 c_0 k_0}{9\pi Z}\left(\dfrac{\mathrm{d}x^2+\mathrm{d}x\mathrm{d}y+\mathrm{d}y^2}{\mathrm{d}x+\mathrm{d}y}\right), & r=s\end{cases}$ (14) into Eq. (1), and written it into matrix form

$$\mathbf{Aw}+\mathbf{Mu}+\mathbf{[I+N]^{-1}Mu}=\mathbf{2P_i} \tag{15}$$

In relation with $\mathbf{u}=\mathrm{i}\omega\mathbf{w}=\mathbf{Bx}$, Eq. (14) can be written as

$$\left\{\mathbf{A}+\mathbf{MB}+\mathbf{[I+N]^{-1}MB}\right\}\boldsymbol{\alpha}=\mathbf{b} \tag{16}$$

where

$$\mathbf{A}=\begin{bmatrix}\rho h(\omega_{11}^2-\omega^2)\varphi_{11}(x_1,y_1) & \cdots & \rho h(\omega_{1N}^2-\omega^2)\varphi_{1N}(x_1,y_1) & \cdots & \rho h(\omega_{MN}^2-\omega^2)\varphi_{MN}(x_1,y_1)\\ \rho h(\omega_{11}^2-\omega^2)\varphi_{11}(x_1,y_2) & \cdots & \rho h(\omega_{1N}^2-\omega^2)\varphi_{1N}(x_1,y_2) & \cdots & \rho h(\omega_{MN}^2-\omega^2)\varphi_{MN}(x_1,y_2)\\ \vdots & \vdots & \vdots & \vdots & \vdots\\ \rho h(\omega_{11}^2-\omega^2)\varphi_{11}(x_M,y_N) & \cdots & \rho h(\omega_{1N}^2-\omega^2)\varphi_{1N}(x_M,y_N) & \cdots & \rho h(\omega_{MN}^2-\omega^2)\varphi_{MN}(x_M,y_N)\end{bmatrix} \tag{17}$$

$$\mathbf{B}=\mathrm{i}\omega\begin{bmatrix}\varphi_{11}(x_1,y_1) & \cdots & \varphi_{1N}(x_1,y_1) & \cdots & \varphi_{MN}(x_1,y_1)\\ \varphi_{11}(x_1,y_2) & \cdots & \varphi_{1N}(x_1,y_2) & \cdots & \varphi_{MN}(x_1,y_2)\\ \vdots & \vdots & \vdots & \vdots & \vdots\\ \varphi_{11}(x_M,y_N) & \cdots & \varphi_{1N}(x_M,y_N) & \cdots & \varphi_{MN}(x_M,y_N)\end{bmatrix} \tag{18}$$

$$\mathbf{b}=\begin{bmatrix}2\tilde{p}_i\mathrm{e}^{-\mathrm{i}(k_x x_1+k_y y_1)} & 2\tilde{p}_i\mathrm{e}^{-\mathrm{i}(k_x x_1+k_y y_2)} & \cdots & 2\tilde{p}_i\mathrm{e}^{-\mathrm{i}(k_x x_M+k_y y_N)}\end{bmatrix}^T \tag{19}$$

$$\boldsymbol{\alpha}=\begin{bmatrix}\alpha_{11} & \cdots & \alpha_{1N} & \cdots & \alpha_{MN}\end{bmatrix}^T \tag{20}$$

Taking $M \times N$ points on the plate, then the modal participation coefficient $\boldsymbol{\alpha}$ can be obtained by solving a set of linear algebraic equations.

2.3 TL under oblique incidence

Using the modal participation coefficient calculated in the previous sections, the transmitted pressure can be given by

$$\mathbf{P_t}=\left[\mathbf{I+N}\right]^{-1}\mathbf{MBx} \tag{21}$$

The normal velocity amplitude of the absorbing material surface is

$$\mathbf{v}=\mathbf{u}-\frac{\mathbf{p_t}}{\mathrm{Z}} \tag{22}$$

So, the transmitted sound power can be calculated by the following equation

$$W_{trans}=\mathrm{Re}\left(\sum_S p_t v^*(x,y)\mathrm{d}x\mathrm{d}y\right) \tag{23}$$

The incident sound power can be calculated by

$$W_{in}=\mathrm{Re}\left(\sum_S pu^*(x,y)dxdy\right) \tag{24}$$

And the sound transmission loss of the plate with sound absorbing materials under oblique incidence can be calculated [15]

$$TL(\varphi,\theta)=10\lg\frac{W_{in}}{W_{trans}} \tag{25}$$

where, φ and θ are the incident angles as defined in Fig. 1(a).

3 Results

3.1 Model validation

3.1.1 Convergence check

Dimensions and material parameters of the plate are listed in Table 1. The thickness of the plate is 2 or 8 mm. The air density is 1.21 kg/m^3, the sound speed in air is 343 m/s. The amplitude of the incident acoustic pressure is fixed at 1 N/m^2. Frequency resolution is taken to be 10 Hz.

Length (a)	Width (b)	Elastic modulus (E)	Density (ρ)	Passion ratio (υ)	Loss factor (η)	Incident angle ($\theta=\varphi$)
0.5 m	0.6 m	7.1×10^{10} Pa	2700 kg/m^3	0.33	0.04	45°

Table 1: Plate's dimensions and material parameters

To calculate the TL of the plate, the convergence of the solution is checked first. Since the vibration of the plate is calculated based on the modal superposition method, it needs to determine how many modes are required in the simulation. Only if enough modes are used can the convergence and accuracy of the result be assured.

The convergence check result is shown in Fig. 3. According to Ref. [13], the size of the elemental source must be much smaller than half the acoustic wavelength, so for 4000 Hz, the element size can be set to be 0.008 m in x and y directions. Two frequencies are checked by using different numbers of modes in the calculation. It can be seen that, for both of the frequencies, when the number of modes in each direction exceeds 6, the predicted TL almost remains unchanged, indicating convergence. Thus, up to 4000 Hz, the number of modes in each direction may be taken to be 15.

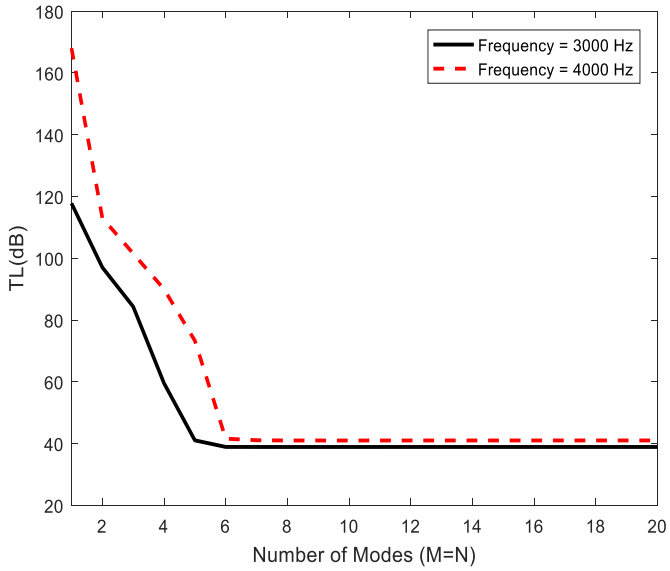


Fig. 3: Convergence check of the plate (h = 8 mm)

3.1.2 Model validation

In this section, model validation is made by using commercial software. The panel's material parameters, boundary conditions, incident angles, size of cells are the same as those in Section 3.1.1. Results are shown in Fig. 4. It can be seen that the results produced by this model agree well with those from the commercial software, showing the effectiveness of the model and the corresponding MATLAB program.

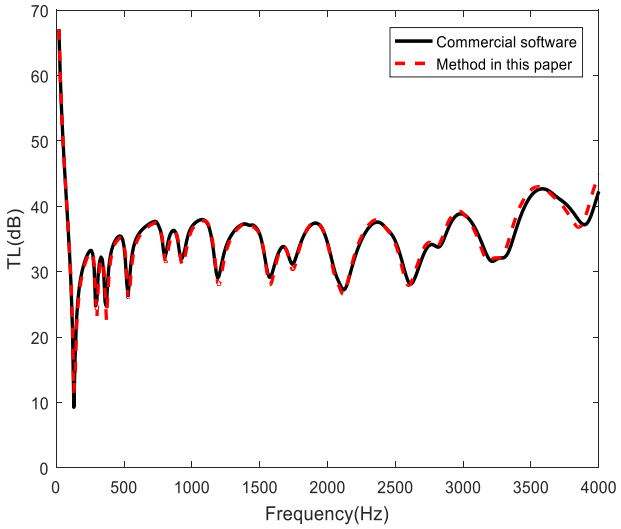


Fig. 4: Model validation (h = 8 mm)

Features of TL in the frequency range [100-1000] Hz are shown and explained in Fig. 5. It can be seen that, there are six dips at 133, 298, 370, 530, 800 and 930 Hz. Comparing these with the natural frequencies of the panel, it can be seen that both these frequencies are corresponds to the natural frequencies of the panel.

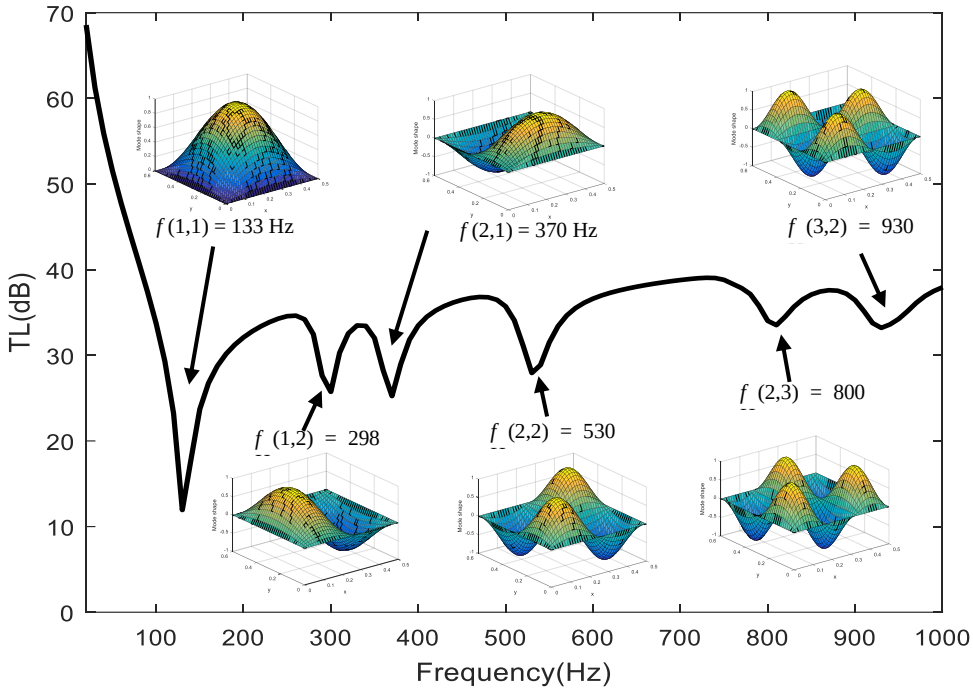


Fig. 5: TL of the bare plate

3.1.3 Limitation of the plane wave assumption for the transmitted and reflected waves

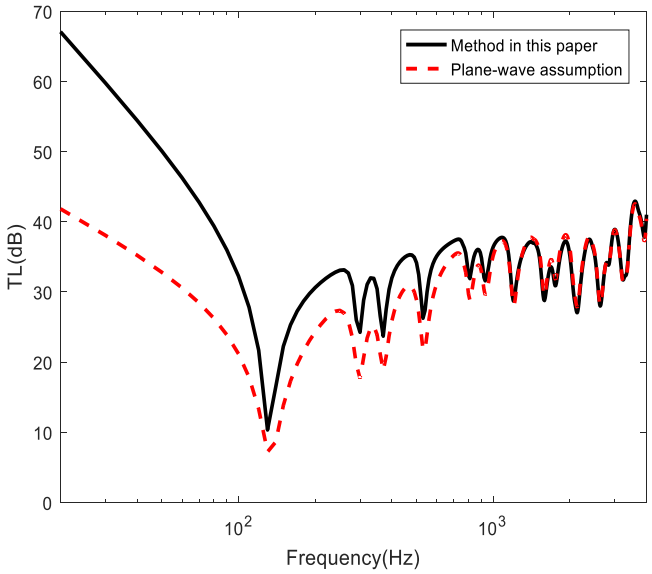


Fig. 6: TL predicted using different methods (h = 8 mm)

In the past, many researchers assumed the transmitted and reflected waves to be plane waves, without considering the effect of the baffle. To assess the validity of this assumption, the TL model established in this paper is compared with the model based on plane wave assumptions [10]. Results are shown in Fig. 6, from which it can be seen that there is significant difference below the critical frequency of the plate, which is given by $\omega_c = \sqrt{\rho h / D} c_0^2$, equal to 1490 Hz for the parameters considered here. When

frequency is higher than the critical frequency, results calculated from these two methods are agree well. In other words, the plane wave assumption is valid only when frequency is sufficiently high.

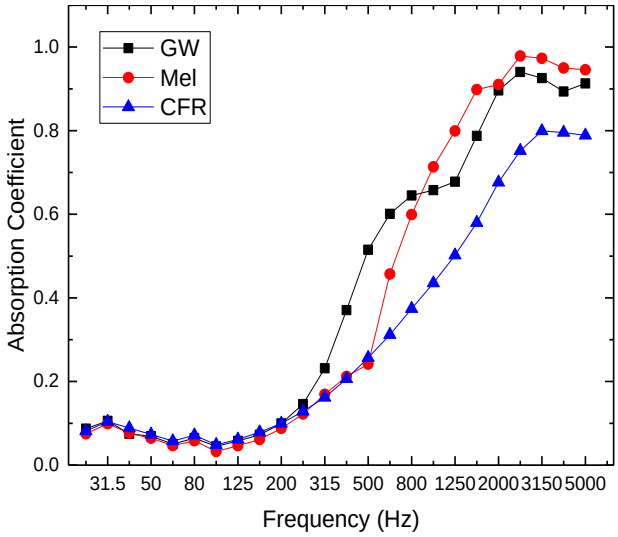
3.2 Plate with sound absorbing material

As demonstrated before, the layer of the absorbing material may increase the panel's acoustic performance by two mechanisms: (1) adding mass to the panel to enhance sound reflections; and (2) absorbing part of the otherwise transmitted sound power. In order to reveal which mechanism is dominant, three typical sound absorbing materials are considered in this paper: glass wool (GW), melamine (Mel), and carbon fiber (CFR). Experimental measurements are carried out to obtain the impedances of these materials in an impedance tube according to ISO standard 10534-2 "Acoustics - Determination of sound absorption coefficient and impedance in impedance tubes - Part 2: Transfer-function method".

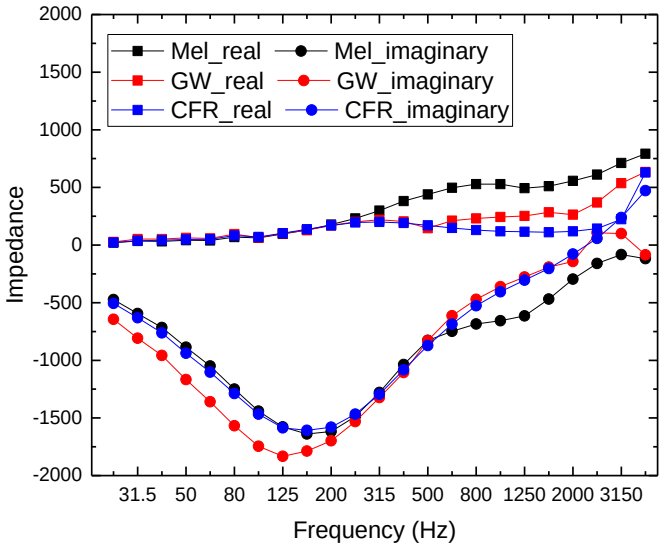
Material parameters of those three sound absorbing materials and the bare plate (BP) are listed in Table 2, the sound absorption coefficients and impedance of them are shown in Fig. 7(a) – (b). Fig. 7(a) illustrates that the sound absorption coefficients of the three materials increase with frequency. The sound absorption coefficients of the three materials are basically the same below about 250 Hz, but with frequency increases, the sound absorption coefficients of the GW and Mel are higher than that of the CFR. The average sound absorption coefficients of the Mel, GW and CFR are 0.51, 0.53 and 0.39, respectively.
From Fig. 7 (b) it can be seen that, the reactive part is much larger than the resistive part, which may lead to a decrease in TL.

Materials	Mel	GW	CFR	BP
Density (kg/m^3)	9.12	57.51	11.45	2700
Thickness (mm)	36.35	30.33	50.53	2
Mass per unit area (kg/m^2)	0.332	1.744	0.579	5.4

Table 2: Parameters of sound absorbing materials



(a) Sound absorption coefficients of the sound absorbing materials



(b) Impedance data of the sound absorbing materials

Fig. 7: Experimental data of the three sound absorbing materials

3.2.1 Comparison with bare plate

Taking the GW absorbing material for example, a comparison is made between the bare plate and plate with absorbing material. Results are shown in Fig. 8. It depicts that the sound absorbing material can largely improve the panel's acoustic performance at frequencies higher than 400 Hz. However, the transmission loss of the bare plate is higher than the plate with absorbing material at some low frequencies. This is due to that the surface density of the absorbing material is not too small compared to that of the bare plate, effectively shifting the resonance/anti-resonance frequencies to a lower value. Fig. 8 also gives the transmission loss of the classical infinite plate (see Ref. [13]). It can be seen that the transmission loss of the bare plate agrees well with the classical transmission loss at high frequencies.

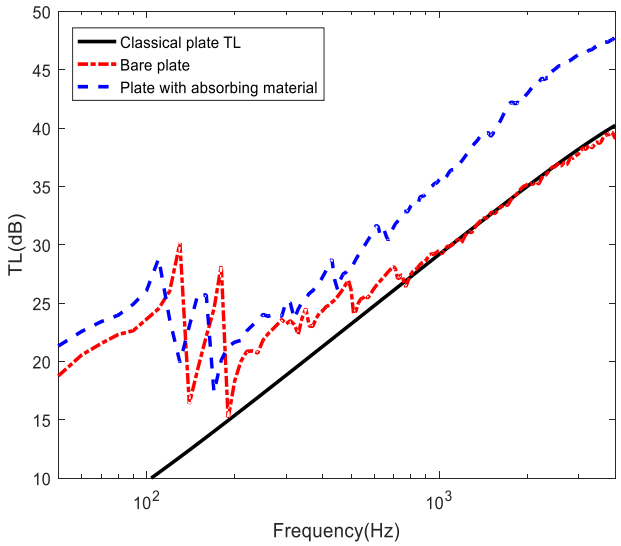
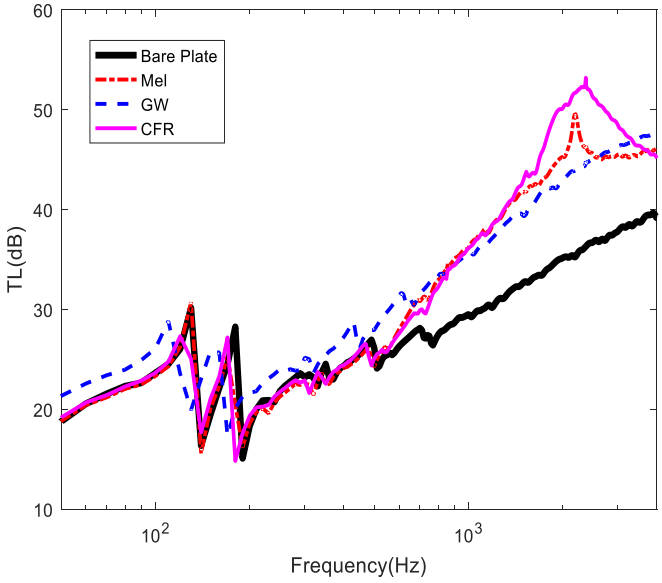


Fig. 8: Transmission loss of plate (h = 2 mm) with or without absorbing material GW

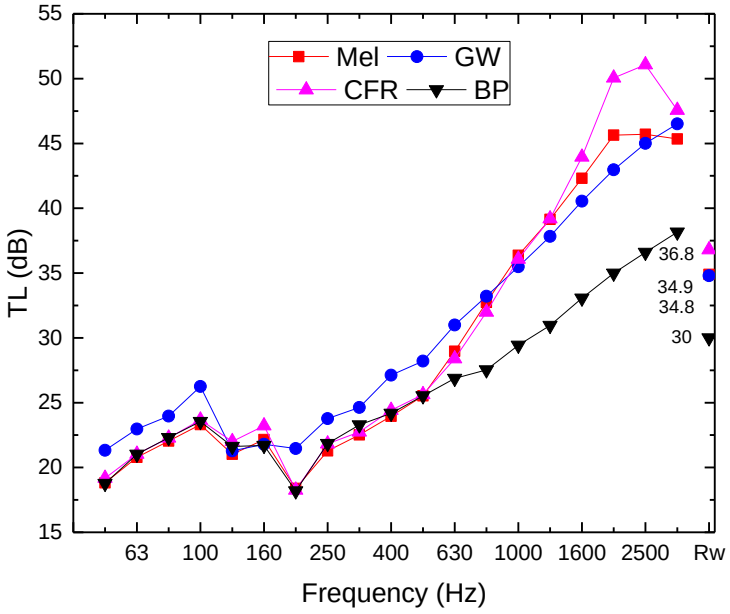
3.2.2 Comparison between different sound absorbing materials

Fig. 9 illustrates the transmission loss of the plate with different sound absorbing material layers (CFR, GW, Mel) from 50 to 4000 Hz in terms of narrow frequency band and one-third octave frequency band. From Fig. 9(a), it can be seen that the three absorbing materials can increase the transmission loss of the plate at high frequencies. Mel and CFR have no benefit to the transmission loss below 800 Hz, while the GW can increase the transmission loss below 100 Hz, which is because the mass of the Mel is larger than the other two materials, the sound transmission mechanism is mainly influenced by the mass law at low frequencies.

An important observation can be made by comparing Fig. 9(a) and Fig. 7(a) that the transmission loss has no specific correlation with the sound absorption coefficient. In other words, a higher sound absorption coefficient does not necessarily have a higher transmission loss. This is because sound transmission loss is affected by a combination of the impedance and the mass of the absorbing material, while sound absorption coefficient is a function of the impedance only. Therefore, care must be exercised when applying absorbing material to improve TL.



(a) Narrow frequency band



(b) One-third octave frequency band

Fig. 9: TL of the plate (h = 2 mm) with different sound absorbing materials

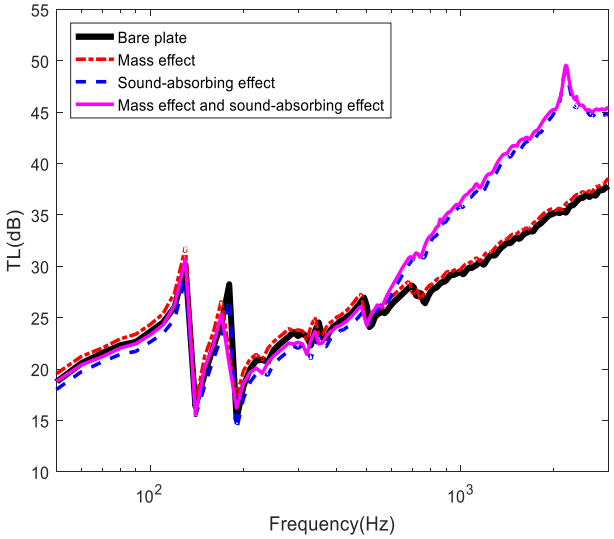
As has stated that, the layer of the sound absorbing material can increase the panel's acoustic performance by two mechanisms: (1) adding mass to the panel, and (2) absorbing part of the otherwise transmitted sound power. In order to illustrate which mechanism is dominant, Fig. 10 gives TL for the following four cases:

(1) just a bare plate;

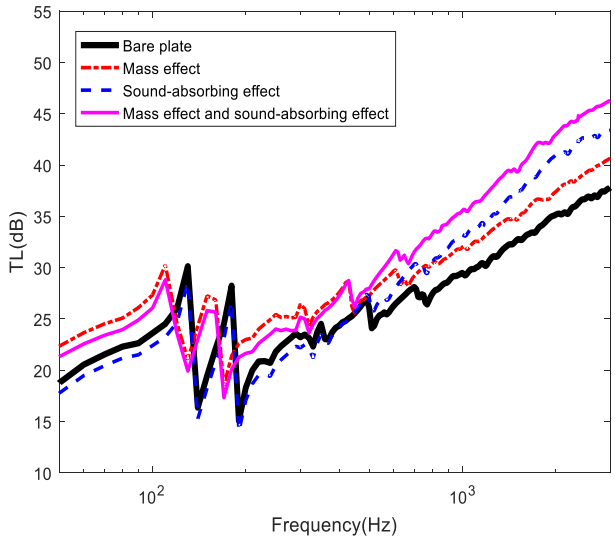
(2) plate with sound absorbing material but only the mass effect being considered, termed as the mass effect;

(3) plate with sound absorbing material but only the sound absorption coefficients being considered, termed as the sound absorbing effect;

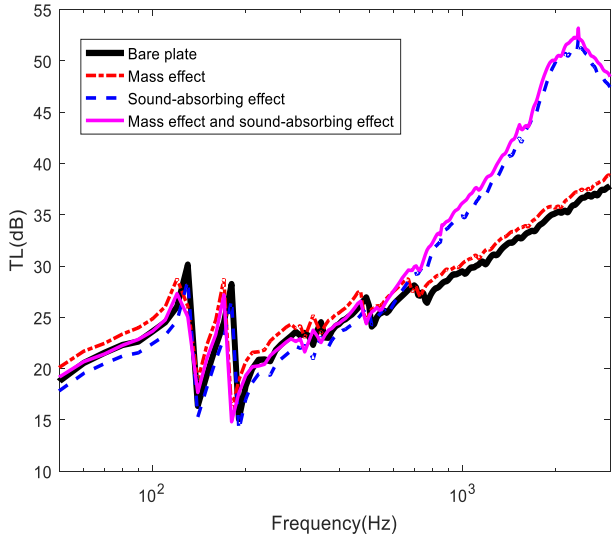
(4) plate with sound absorbing material and both the mass and sound absorbing effects being considered.



(a) Plate with Mel absorbing material



(b) Plate with GW absorbing material



(c) Plate with CFR absorbing material

Fig. 10: TL of the plate (h = 2 mm) with sound absorbing materials

Materials	Mass ratio (%)	Mass effect (%)	Sound absorbing effect (%)
Mel	6	6	94
GW	32	33	67
CFR	10	8	92

Table 3: Contribution of mass effect and sound-absorbing effect

Materials	Mel	GW	CFR	BP
R_w (dB）	34.8	34.9	36.8	R_{w0} = 30 dB
R_{wm} (dB)	30.5	32.4	31.3	
R_{wa} (dB)	34.3	32.5	35.5	

Table 4: Weighted TL of different sound absorbing materials

Results are shown in Fig. 10(a) - (c). Fig. 10(a) - (c) show that at low frequencies, sound absorbing effect has no benefit to the sound transmission loss, and the increased TL is mainly caused by the mass effect to enhance sound reflection.

To be more quantitative, contributions of the mass effect and sound absorbing effect in frequency range [800-3000] Hz of the three materials are listed in Table 3. In Table 3, the mass ratio is defined as the ratio of the mass of the sound absorbing material to that of the bare plate, the percentage of the mass effect is defined as the ratio of the average TL of case (2) to that of case (4), the percentage of the absorbing effect is defined as the ratio of the average TL of case (3) to that of case (4). Table 3 shows that in frequency range [800-3000] Hz, the increased TL of the plate is mainly influenced by the sound absorbing effect, Mel has the most excellent sound absorption performance compared with the other two materials. Interestingly, for those three types of absorbing materials, the percentage of mass effect is close to the mass ratio.

In engineering, the so-called weighted TL is often used to quantify a panel's sound insulation performance. As shown in Fig. 9(b), the weighted transmission loss R_w of Mel, GW, CFR and BP are 34.9, 34.8, 36.8 and 30 dB. According to the four cases defined before, the weighted benchmark TL of the bare panel, R_{w0}, the weighted mass effect TL, R_{wm}, and the weighted sound-absorbing effect TL, R_{wa}, can be calculated in one-third octave frequency band in [50-3150] Hz.

Results are shown in Table 4. It can be seen that, for the absorbing material of GW, R_{wm} is approximately equal to R_{wa}, while for the other two kinds of absorbing materials, R_{wm} is much lower than R_{wa}. So, it can be concluded that for Mel and CFR absorbing materials, the increased TLs are dominant by the sound absorption properties, but for GW, the increased TL is affected by a combination of its mass and sound absorption property.

It can also be seen that the sound absorption performance of CFR is better than the other two materials, although its mass per area is not the greatest and sound absorption coefficients are smallest at high frequencies. There seems to have an optimal combination of mass and impedance for panel sound transmission loss which is to be investigated in the future.

4 Conclusions

A sound transmission loss prediction model is established in this paper for a panel with sound absorbing materials set in a baffle. The vibration of the plate is obtained by the modal superposition method and the reflected and transmitted pressures are calculated by the Rayleigh's integral. A discretion is made to the plate to simplify the calculation. The following conclusions can be made:

(1) Models with the plane wave assumption are inaccurate below the critical frequency, and therefore a more general model like the one developed in this paper should be used;

(2) The sound transmission loss of the plate with sound absorbing material is dependent not only on its acoustic impedance but also on its mass. At low frequencies, the increased transmission loss is mainly dependent on the mass effect, while at high frequencies, the sound-absorbing effect is the main influence factor;

(3) However, a higher sound absorption coefficient does not necessarily have a higher transmission loss. Therefore, care must be exercised when applying absorbing material to improve transmission loss;

(4) The sound absorption performance of CFR is better than the GW and CFR in terms of the weighted transmission loss, but Mel and CFR are much better than GW at high frequencies if the average transmission loss is used;

(5) There seems to have an optimal combination of mass and absorbing coefficient for panel sound transmission loss which is to be investigated in the future.

Acknowledgements

This work described in this paper was financially supported by the Key Strategic International Collaborations on Scientific and Technologic Innovations project (2016YFE0205200).

References

[1] Thompson D J. *Railway noise and vibration: mechanisms, modelling and means of control*[M]. Elsevier, 2008.

[2] Fahy F, Gardonio P. *Sound and structural vibration: radiation, transmission and response: second edition*[M]. Academic Press, 2007.

[3] Qibo Mao, Stanislaw Pietrzko. *Vibration and Sound Radiation*[J]. Control of Noise & Structural Vibration, 2013:27-76.

[4] Xie G, Thompson D J, Jones C J C. *The radiation efficiency of baffled plates and strips*[J]. Journal of Sound and Vibration, 2005, 280(1-2): 181-209.

[5] Putra A, Thompson D J. *Sound radiation from rectangular baffled and unbaffled plates*[J]. Applied Acoustics, 2010, 71(12): 1113-1125.

[6] Wallace C E. *The Radiation Resistance of a Baffled Rectangular Panel*[J]. The Journal of the Acoustical Society of America, 1971, 49(1A): 128-129.

[7] Davy J L, Larner D J, Wareing R R, et al. *The acoustic radiation impedance of a rectangular panel*[J]. Building and Environment, 2015, 92: 743-755.

[8] Trevathan J W, Pearse J R. *The significance of the incident sound field on the sound transmission loss of a finite panel*[J]. Building Acoustics, 2005, 12(4): 225-235.

[9] Anoop Akkoorath Mana, Venkata R. Sonti. *Sound transmission through a finite perforated panel set in a rigid baffle: A fully coupled analysis*[J]. Journal of Sound and Vibration, 2018, 414: 126-156.

[10] London A. *Transmission of reverberant sound through single walls*[J]. J. Research Nat. Bur. of Stand, 1949, 42(605): 2.

[11] Zhang Y, Xiao X, Thompson D, et al. *Sound transmission loss of windows on high speed trains*[C]//Journal of Physics: Conference Series. IOP Publishing, 2016, 744(1): 012141.

[12] Rayleigh L, Nachtrieb N H. *The Theory of Sound*[J]. Physics Today, 1957, 10(1):32-34.

[13] Putra A, Thompson D J. *Sound radiation from perforated plates*[J]. Journal of Sound and Vibration, 2010, 329(20): 4227-4250.

[14] Morse P M, Ingard K U, Stumpf F B. *Theoretical acoustics*[M]. Princeton university press, 1968.

Narrow band analysis of structure borne noise in complex dynamical systems using energy methods

G. Borello[1], I. Abettan[2], T. Lambert[2], L. Gagliardini[2]
[1] InterAC
10 impasse Borde-Basse, 31240 L'Union, France
e-mail: **gerard.borello@interac.fr**

[2] PSA Group
4 Route de Gisy, 78943 Vélizy-Villacoublay cedex, France

Abstract
Vibroacoustic predictions of structure borne noise in cars/aircrafts are highly sensitive to modeling errors and input data uncertainties. Seriality of wave propagation paths cumulates errors, scattering predictions. In FEM, model and boundary conditions are idealized. Some fuzziness must be introduced for better simulation of dispersions observed between vehicles. In SEA, the partition in subsystems is unknown and may evolve when frequency increases due the simultaneous presence of global and local modes. The Virtual SEA (VSEA) method is a way of mixing FEM and SEA dynamical information in a single stochastic model with frequency-variable subdomains. Due to its dual nature (FEM & SEA) VSEA provides more accurate local predictions on narrower frequency analysis bandwidths than classical SEA models. After documenting how VSEA may handle narrowband vibration predictions, simple test cases are detailed for validating the concept. Measurement/prediction comparisons from industrial VSEA cars models are presented.

1 Introduction

Stochastic analysis is necessary in vibroacoustic predictions over the mid and high frequency range (200 Hz-10000 Hz for transport industry). The amplitude of distributed uncertainties in related models increases when wavelength decreases. This is a natural trend of field descriptors distributed over space when propagating in non-homogeneous supporting medium. Shannon [1] taught us that knowledge might be characterized by an information entropy function diminishing when information content grows. An engineering project developing a new type of vehicle carries a growing amount of information for its starts and the shared entropy function will be constantly decaying along with its realization. Acquiring expertise is interpreted as reducing his own entropy and gaining knowledge from projects. Vibroacoustic methods may then be scaled against the information content they carry.

Finite Element Methods (FEM), based on discretization, are generally qualified by the adjective "deterministic" while Statistical Energy Analysis (SEA) which works with random data inputs is intrinsically "stochastic". SEA and FEM are complementary both working as twins for efficiently reducing the project information entropy. SEA models are obviously defined by poor geometrical information and a few spectra in band-integrated format defining the subsystems. Nevertheless, the modeling tasks provide a global picture of the dynamics of the whole system. Instead, FEM details all aspects of heterogeneity at the local scale (the component) but cannot generally model the full system or at least up to some frequency limit. Working with SEA or FEM is like working on one hand with a large (global) picture but pixelated and on the other hand with smaller (local) detailed pictures without an overview of the total picture.

In the early 2000s, cooperation between SEA and FEM was reinforced by introducing the Virtual SEA method or VSEA [2]. The latter acts as a compressional algorithm of the informative content of any FEM model to fit with the pixelated system-level picture of the dynamics handled by SEA. Reducing the size of models may then make the engineering outputs more interpretable, inducing a gain in reducing entropy.

Compared to classical analytical SEA method, VSEA is providing extra information as the ability of working in narrow band format and retrieving some dynamic information at local scale. Next, an overview of VSEA method is presented, followed by application examples.

2 Virtual SEA for mid-frequency range

2.1 From structural FE model to Virtual SEA representation

Structural dynamic in non-homogeneous systems cannot be modelled accurately by analytically computed SEA parameters. Presence of global modes strongly coupling all parts of the system domain is also a limitation in using analytical formulas. Only FE models are currently able to describe these complex behaviors.

VSEA method is implemented in SEA+ software as a specific solver that reduces the dynamical information content of the FE model. Inputs of the solver are the real modes of the FE structural model. SEA+ is relying on NX-NASTRAN for extracting modal amplitudes exported at a limited set of reference nodes (typically 1000 to 2000 nodes) mapping the structure. Alternate FE-solver like ABAQUS are also supported.

From modal amplitude, the VSEA solver synthesizes a complex velocity FRF matrix of which elements are the transfer velocity, $v_{ij} = v_i/f_j$, between each pair *(i, j)* of the nodal set in the global x, y and z directions where a unitary force is applied at a turn.

The FE dynamical information may be equated to the synthesized transfer velocity matrix $\mathbf{V}$ made of v_{ij} elements.

The assumed global damping loss factor for modal synthesis is taken equal to some default value for all modes and generally decreasing with frequency to get a rather constant modal overlap factor over frequency i.e. a constant uncertainty vs. frequency [3]. V^2 matrix is compressed into a selected frequency band format (constant or 1/Nth octave bands) and projected in the direction n_i and n_j of maximal input/output conductances (real part of driving point mobility).

The conductance vector is given for at all nodes by

$$Y = \mathrm{Re}\{\mathrm{Diag}(\mathbf{V})\} \cdot n$$

$\bar{\mathbf{V}}^2$ is then reduced dividing v_{ij}^2 by 4 times the product of conductances at points *i* and *j*. The resulting reduced FRF has the dimension of modal energy as seen in equation (6).

The final FRF matrix $\bar{\mathbf{V}}^2$, further used in the SEA-parameter identification process, is expressed in band-averaged format at center radial frequency ω_c and bandwidth *B* with elements given by

$$\overline{v_{ij}^2}(\omega_c, B) = \frac{1}{B}\int_B v_{ij}^2(\omega) d\omega \tag{1}$$

The new transfer matrix is finally auto-partitioned by SEA+ peripheral algorithm, which groups nodes into a set of weakly coupled subsystems Ω_k as required by SEA for a clean inversion of the matrix.

The SEA transfer matrix $\langle \bar{\mathbf{V}}^2 \rangle$ is obtained from the previous by averaging response nodes over subdomains of Ω_k for each excitation nodes. The related compressed SEA matrix is rectangular with size equal to the number of reference node times the number of subsystems. Elements of the matrix are given by

$$\left\langle \overline{v_{kk'i}^2} \right\rangle = \frac{1}{N_k} \sum_{j \in \Omega_k} \bar{v}_{kk'ij}^2 \tag{2}$$

SEA parameter identification is performed by solving the SEA inverse problem relating $\langle \bar{\mathbf{V}}^2 \rangle$ to SEA loss matrix $\mathbf{L}$ through the normalized SEA power balanced equations:

$$\mathbf{I}Y/\omega_c = \mathbf{L}\cdot\left\langle m\bar{\mathbf{V}}^2\right\rangle \Rightarrow \mathbf{L} = \left[\left\langle m\bar{\mathbf{V}}^2\right\rangle\right]^{-1^*}\mathbf{I}Y/\omega_c \tag{3}$$

m is the subsystem mass vector; * indicates the pseudo-inverse introducing the unknown subsystem modal density $\mathcal{N}$, the following expression relates *m*, *Y* and $\mathcal{N}$

$$m = \mathcal{N}/4Y \tag{4}$$

Equation set (3) is reshaped for direct solve of modal density vector $\mathcal{N}$. It leads to the local modal energy matrix power balanced equations given by

$$\mathbf{I}/\omega = \mathbf{L}\mathcal{N}\boldsymbol{\varepsilon} = \boldsymbol{\mathcal{L}}\boldsymbol{\varepsilon} \tag{5}$$

with elements of $\boldsymbol{\varepsilon}$ given by

$$e_{kk'i} = \frac{1}{N_k}\sum_{j\in\Omega_k}\frac{\bar{v}^2_{kk'ij}}{4y_i y_j} \tag{6}$$

$$\boldsymbol{\mathcal{L}} = \begin{bmatrix} \eta_1\mathcal{N}_1 + \sum_{k'}\eta_{1k'}\mathcal{N}_{k'} & .. & -\eta_{N1}\mathcal{N}_N \\ .. & .. & .. \\ -\eta_{1N}\mathcal{N}_1 & .. & \eta_N\mathcal{N}_N + \sum_{k'}\eta_{k'N}\mathcal{N}_{k'} \end{bmatrix} \tag{7}$$

$\boldsymbol{\varepsilon}$ has dimension of modal energy and leads to accurate identification of $\boldsymbol{\mathcal{L}}$ thanks to SEA+ algorithm that performs auto-partitioning into weakly coupled regions.

In practice, with lossless junctions, system is solved for identifying separately modal density and coupling loss factors. Model quality is assessed by comparing $\left\langle\tilde{\mathbf{V}}^2\right\rangle = 4Y^T\boldsymbol{\mathcal{L}}^{-1^*}Y/\omega$ with direct $\left\langle\bar{\mathbf{V}}^2\right\rangle$ FRF input. Difference $\tilde{\mathbf{V}}^2 - \mathbf{V}^2$ gives the reconstruction error matrix plot as a reconstruction performance index useful in SEA+ for checking the quality and the global loss of information due to compression [4].

The MS-VSEA (MS for Multi-Scaled) patch method is a variant formulation of the inverse SEA problem where the auto-partition is applied to pre-defined group of nodes (the patch) instead of nodes. This method is thus providing a partition into subsystems per frequency band corresponding to specific groupings of patches into subsystems. Its main advantage is to accurately reconstruct FE transfers over the whole frequency range. Figure 1 shows the flow chart of the VSEA or MS-VSEA process.

If upper frequency limit of the VSEA model exceeds the frequency limit f_t of the modal extraction, it is complemented by dynamical analytical operators to derive SEA subsystem parameters in the high frequency domain. Interior fluid volumes and acoustic trims are treated by analytical modeling over entire frequency range due to their assumed homogeneity. Acoustic trims are located in subsystems and their insertion loss is used for filtering the radiated power of the un-trimmed structure and perturbing the mass and damping of the bare car body or Body-In-White (BIW).

Below f_t, VSEA or MS-VSEA subsystems are coupled to analytical SEA cavities through a specific statistical radiation integral calculated by spatial windowing of an elementary infinite structural wave [5]. The related structural VSEA wavenumber is estimated from ratio of rotational over translational nodal principal-direction conductances.

For a subsystem of domain Ω_k,

$$\langle k\rangle = \sqrt{\frac{Trace\left\{\left\langle\mathbf{Y}_R\right\rangle_{\Omega_k}\right\}}{\left\langle Y_T\right\rangle_{\Omega_k}}} \tag{8}$$

where $\left\langle\mathbf{Y}_R\right\rangle$ and $\left\langle Y_T\right\rangle$ are respectively the matrix of the local rotational conductances and the local maximal principal translational conductance, both averaged over nodes in domain Ω_k.

The transformation of FE into SEA has been progressively automated and now delivers the VSEA/MS-VSEA dynamic model within a few hours.

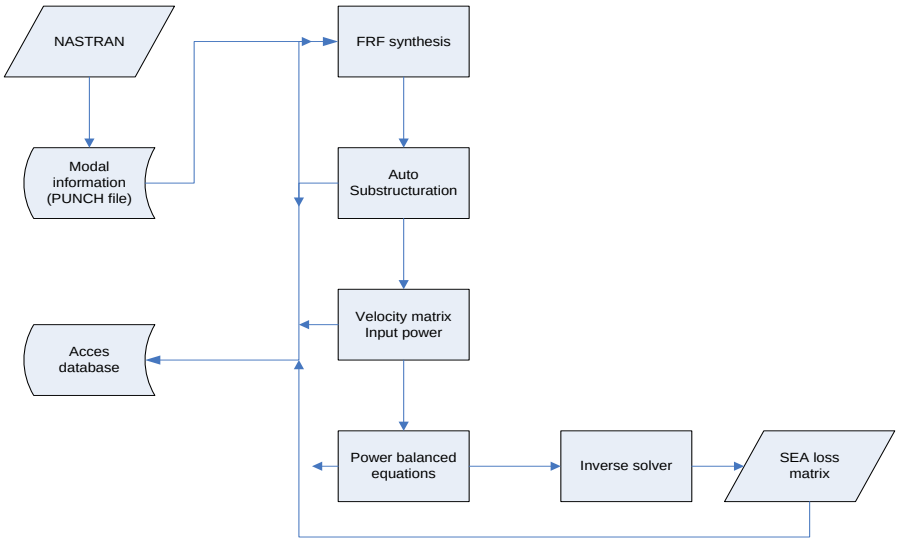


Figure 1: VSEA data flow

2.2 Narrow band reconstruction from VSEA model

At each reference node M_0 of a VSEA model, the local transfer conductance matrix can be reconstructed from real modal amplitudes. The translational conductance matrix of a thin shell provides three eigenvalue vectors $\varphi_{ix,y\ or\ z}$ corresponding to flexural, shear and extensional energy directions of oscillation.

$$\begin{bmatrix} Y_{xx} & Y_{xy} & Y_{xz} \\ Y_{yx} & Y_{yy} & Y_{yz} \\ Y_{zx} & Y_{zy} & Y_{zz} \end{bmatrix} \Rightarrow \boldsymbol{\varphi}_{T0}(i,\omega,\Delta\omega) = \begin{bmatrix} \varphi_{1x} & \varphi_{2x} & \varphi_{3x} \\ \varphi_{1y} & \varphi_{2y} & \varphi_{3y} \\ \varphi_{1z} & \varphi_{2z} & \varphi_{3z} \end{bmatrix} \tag{9}$$

The quadratic velocity computed at M_0 by the VSEA model depends on its total related subsystem energy from following reconstruction formula:

$$\bar{V}_0^2(M_0, f_c) = \frac{E}{m_0} = \frac{4Y_0 E}{\mathcal{N}} \tag{10}$$

Y_0 is the maximal principal conductance at M_0. A tensorial expression is deduced from (10).

$$\overline{\overline{V_0^2}}(M_0, f_c) = 4\overline{\overline{Y}}_0 \overline{\overline{(E/\mathcal{N})}} \tag{11}$$

From (11), the quadratic velocity is expressed in global axis from the SEA smooth energy response and from the local conductance tensor at selected response point. The latter can be expressed in narrow band using modal synthesis at M_0 from the global modes of the FE model stored within the SEA database of the model. From global modal amplitudes at reference nodes, stored in the SEA+ database, the nodal narrow band conductance matrix is interactively synthesized to weight the mean-spaced and frequency band averaged response of the VSEA model.

Formula (11) is not an exact formulation of the velocity but an approximation derived from (6): any point-to-point band-averaged transfer over a band B, $V_{kk'}{}^2(M_{ik}, M_{jk'}, f_c, B)$, may be approximated by the product of three quantities:

$$V_{kk'}{}^2(M_{ik}, M_{jk'}, f_c, B) \simeq 4 y_i y_j \langle e_{kk'} \rangle_{B,\Omega_{k'}} \tag{12}$$

where $\langle e_{kk'} \rangle_{B,\Omega_{k'}}$ is the mean energy transfer (per unit power) between two subsystems k and k' and y_i, y_j the driving point conductance at excitation and response points in the respective principal directions. When working in narrow band and applying a force at a given point of the SEA model and exporting the total energy transfer $E_{kk'}$, the response is then given by (11).

$\langle e_{kk'} \rangle_{B,\Omega_{k'}}$ is a smooth scalar function, low variant vs. frequency and space, at least within each subsystem domain and when its vibration state is governed by local modes. The local conductances contain the primary information of the local variability of response inside the subsystem domain. Their spectrum is including all resonance peaks of underlying modes and is not smooth at all. In short, $\langle e_{kk'} \rangle_{B,\Omega_{k'}}$ describes long distance drop of mean amplitude between subsystems and conductances terms describes local variability of responses inside subsystems. This explains that the system must be portioned in each frequency band into subdomains required to be weakly coupled i.e. showing a significant drop of energy between them when one is excited. Then the auto-substructuration process in the VSEA method conditions the accuracy of the resulting SEA model over the low and mid frequencies. Over the high frequency range, the SEA partition into weakly subsystems is performed by their natural boundary conditions and is no more an issue.

Therefore, due to (12), there is no lower limitation on the width of the frequency band of SEA computation.

When the external force vector contained a lot of peaky harmonics, it is then enough computing the injected power in narrow band for each x, y and z global directions and integrating it over the SEA frequency band, prior to the solve for robust estimates of responses after solving.

2.3 Applying VSEA to simple sandwich panel with mounted equipment

The supporting panel (1x1 m²) is a typical spacecraft sandwich made of two aluminum skins of 1 mm thickness maintained at a distance of 10 mm by honeycomb aluminum core.

A box equipment is mounted on the plate through four connecting points. The equipment bottom panel is meshed with solid elements. All other system parts are meshed with FE plate elements. For identifying the VSEA parameters from FE, 113 real modes of the FE model are extracted up to 2500 Hz. Modal amplitudes are exported at 746 reference nodes as shown in Figure 2 (left). For further comparisons, a pure analytical SEA model is built from scratch following intuitive partition of the model into subsystems (discontinuity at boundary) as also shown in Figure 2 (right).

In Figure 3, the 1/3rd octave band mean accelerations for the subsystems are given for a point force applied on Equipment Top panel. Responses, from classic analytical SEA and from VSEA, are compared in Figure 3 and as expected both models are given the same results above 2500 Hz. Below 500 Hz, the system behaves as a two-subsystem model (full Equipment and Supporting panel as two weakly coupled subsystems). Related PSD accelerations are lower than the predicted ones delivered by the analytical SEA model. In the latter, components are always weakly coupled (softer and liter) all over the frequency bands. In contrast, the VSEA model follows the FE-behavior; when frequency increases, the various parts of the equipment gradually decouple. It clearly shows the interest of VSEA modeling as in a single model are embedded at the same time the low, mid and high frequency behaviors.

FE-FRF synthesis is now performed per constant band of 20 Hz and the SEA parameters are identified over all bands up to from 50 to 2500 Hz. For comparing the 1/3rd octave and the 20 Hz-band results, a corresponding rms force spectrum is generated in both models. The excitation force is taken equal to 1 N rms over 20 Hz in the narrow band model and is taken equal to $F = \sqrt{\frac{0.23 f_c}{20}}$ in the 1/3rd octave one.

Comparisons between both models are given for excited Equipment Top and Supporting Sandwich Panel in Figure 4.

Working with VSEA in narrow band captures more dynamical features than in 1/3rd octave. It is worthwhile to note the two models are different in their intimate structure: SEA parameters are identified in each band by the VSEA inverse solver in both models. There is then much more SEA models in the 20 Hz-band one than in the third octave i.e. more information content.

The injected power at the selected node of Equipment Top panel is given for the two models in Figure 5 (left) and the various conductances (active power injected/N²) inside this small panel are seen on right picture over the band 50-2500 Hz.

The latter picture shows the potential high variability of the power vs. node given by direct excitation of local modes of the Top panel. Lower levels are found on nodes located on panel edges.

At all reference nodes, responses can be recover in the direction of global axis as well the nodal rotations, as shown in Figure 6. As expected the strongest response is found in the normal direction of the panel containing the reference node but at low frequency the direction of maximum response may not be the normal direction as observed around 400 Hz.

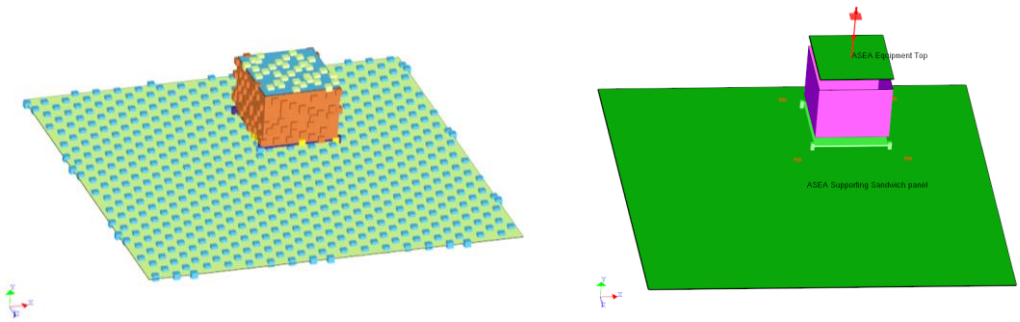


Figure 2: On left FE reference nodes of sandwich panel system and on right related ASEA model

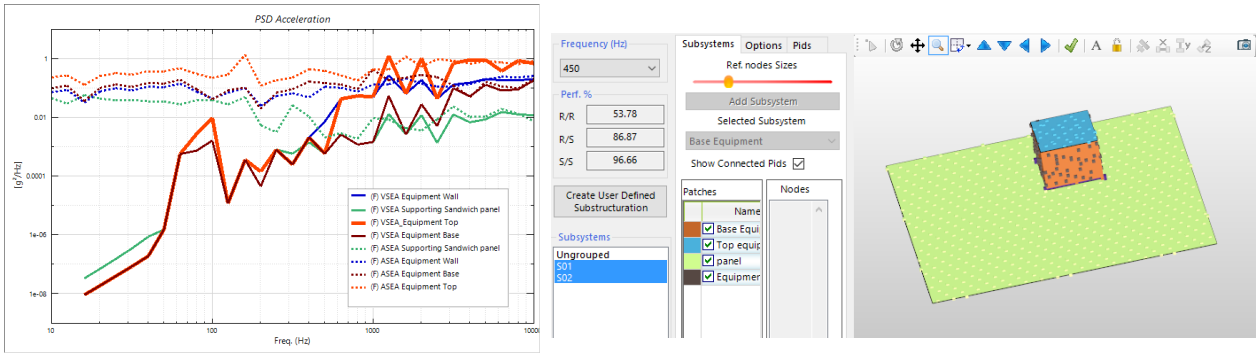


Figure 3: Comparison of acceleration PSD distribution in both VSEA (plain) and ASEA (dashed) models (left) and around 500 Hz grouping of patches into two effective subsystems

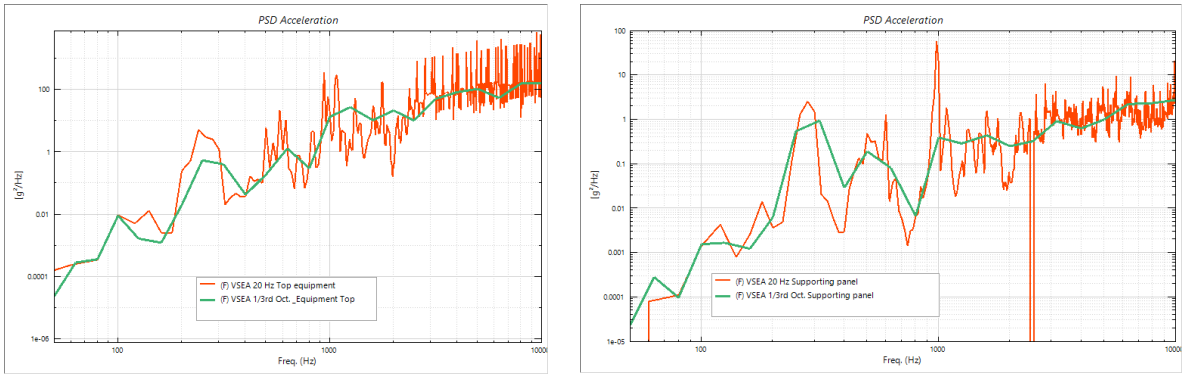


Figure 4: Comparison of Equipment Top (left) and Supporting panel (right) PSD mean acceleration responses in the 20 Hz-band model and the 13rd octave band model

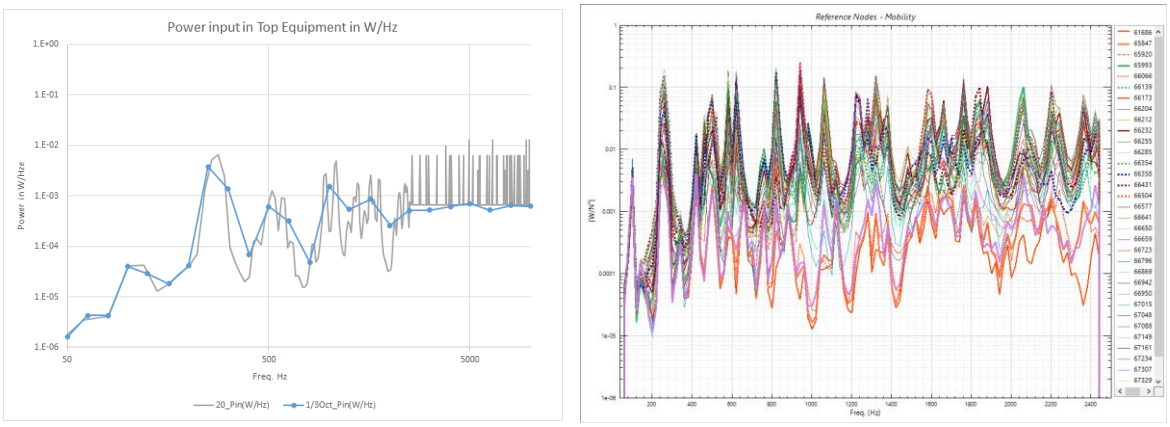


Figure 5: On left, injected power in vertical direction in Equipment Top at a particular node in the 20-Hz band model and in the 1/3rd octave-band model; on right, conductances at all reference nodes in Equipment Top panel

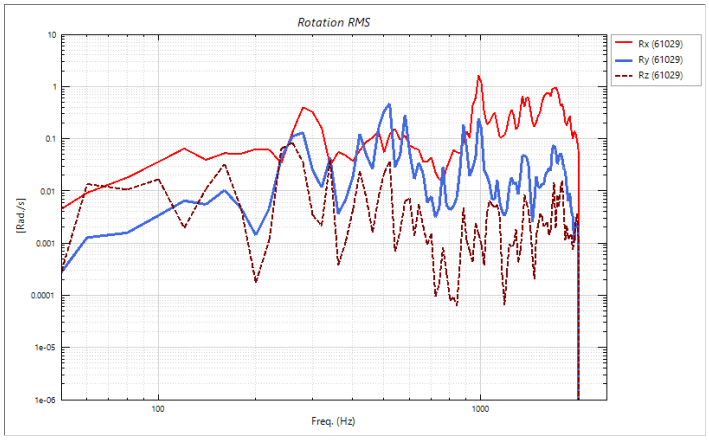


Figure 6: Output response in the global axis x, y and z of the VSEA model (here rotation at central node of equipment lateral X+ panel)

3 Structure borne sound prediction in a full-trimmed car

A BIW is complex (local curvatures and re-enforcements, spot welded points…). No analytical SEA representation provides, in the low and mid-frequency range, a sufficient accuracy of modal densities and coupling loss factor (CLF) spectra, required by the SEA modeling process. On the contrary a FE model of

the BIW with suitable mesh usable up to 1000 Hz (transition frequency, f_t) is more representative of the "true" dynamic of the system. Above 1000 Hz, due to progressive decoupling of the various BIW subparts, analytical SEA becomes appropriate.

The structural dynamic of the vehicle is then adequately represented by a VSEA model up to 1000 Hz and by ASEA above. ASEA subsystem description is embedded within the VSEA and the final VSEA model may then be run over the entire frequency range. A Peugeot 208 car (Figure 7) is modelled using SEA+, starting from a FEM of the car body, transformed into VSEA model. The VSEA model is expanded to high frequency and enriched by acoustic trims computed from transfer matrix approach. Only a fraction of trims is modeled deterministically due to availability of data, the other trim properties being inferred from similar trims on other vehicles.



Figure 7: Peugeot 208 vehicle

The full-trimmed VSEA model of Peugeot 208 is displayed within SEA+ modeling environment in Figure 8. The interior of car body is darker indicating the presence of acoustic trims mounted on inner faces, following requirement of the car manufacturer. Internal fluid volumes are seen on the Figure 8, right picture; five cavities for describing the fluid volume above seats, four cavities at seat level, one cavity for trunk and a few additional ones when necessary, such as the under-body cavity. The model has to cover the mid frequency range and its behavior is fully described by the VSEA parameters below 1200 Hz: modal density, wavenumber, mass, conductance and CLF. From 1200 Hz and above, model parameters are computed from analytical SEA+ operators by defining the subsystem type following its main topology: plate, singly or doubly curved shell, with or without rib distribution for better evolution of the dynamic stiffness vs. frequency.

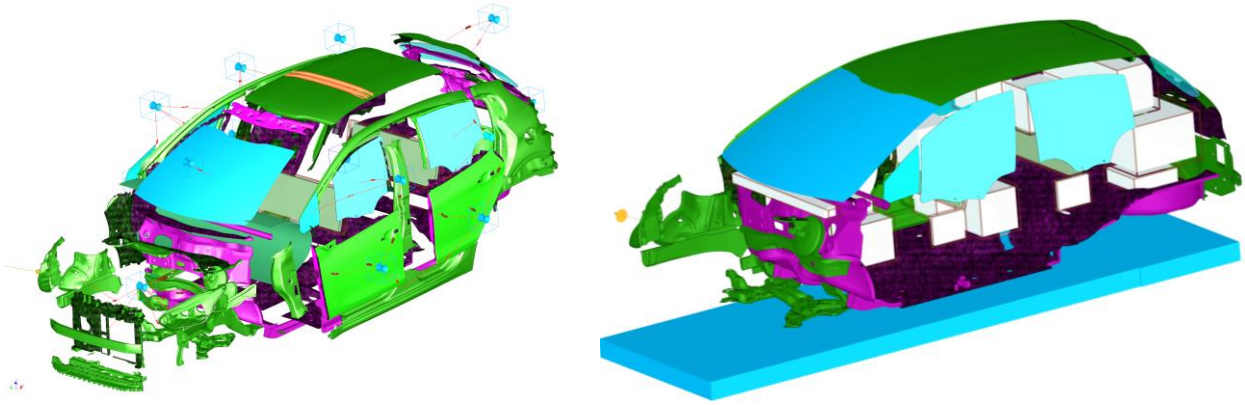


Figure 8: BIW coupled to acoustic trim in SEA+ modelling environment

The model was compared to reciprocal vibroacoustic test performed by the manufacturer. In the test, a point-acoustic source delivering a calibrated power is installed at driver's ear location while accelerations are measured at a set of locations over the body.

Transfer functions between acceleration response point and source is then predicted by the SEA model from reciprocity theorem: applying a unitary force in the direction of each measured acceleration and prediction of acoustic pressure level in the cavity containing the driver's ear source.

Damping of the bare BIW is assessed to a mean value as used in the FE-FRF modal synthesis. Applied acoustic trims interaction with BIW is also simulated in SEA+ model and may lead to damping change as porous material are efficient dampers of structural vibration around the breathing frequency of trims.

Acoustic cavities are inheriting of BIW trims and are damped by theoretical absorption they generate. All predictions are done in 10 Hz bandwidth, the resolution of the synthesized FE-FRF, for verifying the capability of reproducing detailed spectra of the vibroacoustic response over the range 0-800 Hz.

Figure 9 shows the acoustic pressure level (green curve) at passenger's ear predicted from the SEA model, force being applied in the X-direction (vehicle direction) on the pivot cross-beam. This pressure level is compared to the measured pressure (red curve) along with the manufacturer uncertainty bounds (blue curve). VSEA prediction is following the measured curve. Maximal deviation of about 5 dB is observed around 400 Hz, still staying within uncertainty bounds.

Figure 10 shows the comparison of predicted and measured windscreen-to-driver's ear sound pressure transfers. Predicted transfer is close to measurement except between 125 and 250 Hz. Windscreen has a sandwich cross section with PVB-like core and is mounted on joint and seems actually behaving in a softer way on first modes than its FE/VSEA-description, which may explain the 10 dB discrepancy in 125-250 Hz range.

At engine mounting points, results are similar to previous ones, despite the engine was present in measurement but not simulated in the model. Best results are obtained in the direction of principal conductance as seen in Figure 11.

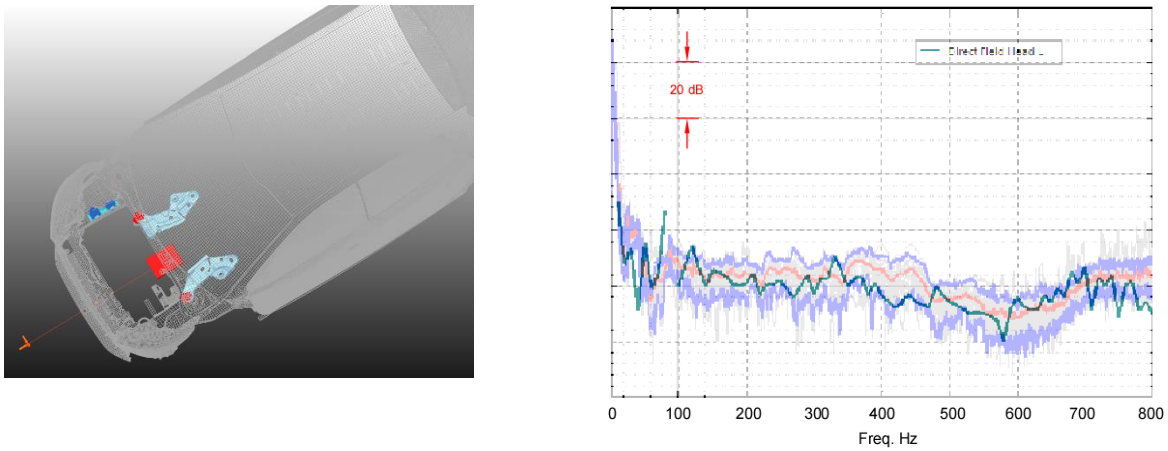


Figure 9: Excitation of pivot cross-beam in X axis and measured and predicted sound pressure level at driver's ear

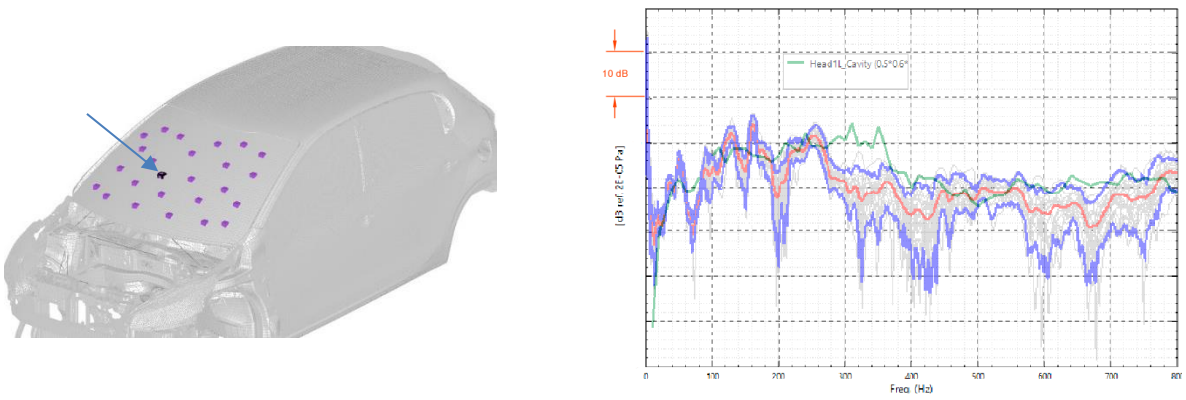


Figure 10: Excitation of windscreen in normal direction and measured and predicted sound pressure levels at driver's ear

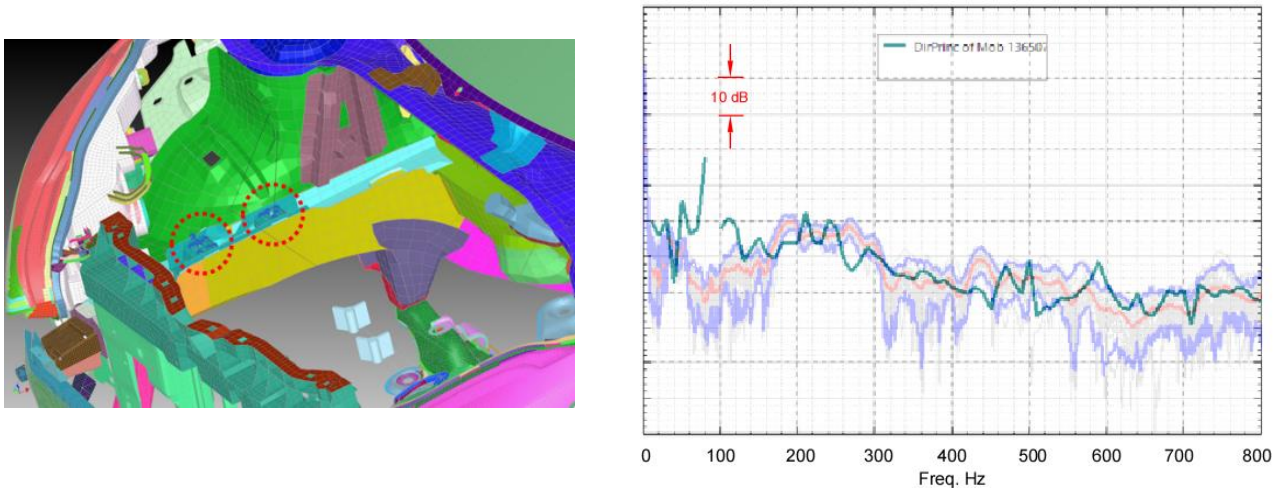


Figure 11: Excitation at engine mounting points in principal direction of point conductance and measured and predicted sound pressure levels at driver's ear

4 Conclusions

For structure-borne analysis, Virtual SEA method extends the applicability of SEA over the low and mid-frequency range thanks to the determination of all SEA structural parameters from a discretized FE model. Above FE limit of modal extraction (about 1000 to 2000 Hz for a car-body), the SEA parameters are computed from analytical operators and a user-defined typology (beam, plate, curved shell…). The model is based on the calculation of local modal energy transfers of which remarkable properties are observed: act as a smooth operator of frequency with low spatial variation from point to point. A Virtual SEA model has more locality than its analytical SEA counterpart: responses can be computed in narrow bands and decomposed in the global axis of the system at each reference nodes used for constructing the model from synthesized FE frequency response functions. Applied to the modeling of a full-trimmed car, the VSEA model is able to reproduce measured pressure-over-force transfers within their confidence intervals. The VSEA model of the car gives more accurate results in 10 Hz-frequency bands. This gain of information is due to the preservation of all local tensors of driving point mobility at model reference nodes.

VSEA acts as a compressor of the modal FE information and preserves the mean transfers between the subsystems with an accuracy similar to the original FE model. Interactive solves with randomly distributed sources or correlated sound pressure fields as used in SEA method can be then performed at no computational cost in an interactive way, leading to more understanding about dynamical behavior and system-level prediction.

Acknowledgements

The author acknowledges PSA Vibroacoustic Team for their kind support and their contribution to Virtual SEA development.

References

[1] C.E. Shannon, *A Mathematical Theory of Communication*, Bell System Technical Journal, 27, pp. 379-423 & 623-656, July & October, 1948.

[2] G. Borello, L. Gagliardini, L. Houillon, L. Petrinelli, *Virtual SEA: Mid-Frequency Structure-Borne Noise Modeling Based on Finite Element Analysis*, SAE Noise and Vibration Conference, May 6-8, 2003, Traverse City, Michigan, USA.

[3] F. Fahy, *Statistical Energy Analysis: A Critical Overview*, Philosophical Transactions: Physical Sciences and Engineering, Vol. 346, No. 1681, Statistical Energy Analysis (Mar. 15, 1994), pp. 431-447.

[4] G. Borello L. Gagliardini, D. Thenail, *Virtual SEA: Towards an Industrial Process*, SAE Noise and Vibration Conference, May 15-17, 2007, Saint Charles, Ill, USA.

[5] G. Borello, L. Gagliardini, D. Thenail, *Virtual SEA for Noise Prediction and Structure Borne Sound Modeling, Ri*eter Automotive Conference, June 14-15, 2007, Pfaffikon, Switzerland.

[6] G. Borello, *Simulation of Finite-Sized Dynamic Systems Using Wave Transmission Methods*, MEDYNA 2017 (2nd Euro-Mediterranean Conference on Structural Dynamics and Vibroacoustics), 2017 April 25-27, Sevilla, Spain.

Dynamical energy analysis modelling by using transfer path analysis

S. Morita[1], T. Hartmann[2] , G. Tanner[2]
[1] Yanmar R&D Europe, Viale Galileo 3/A 50125, Firenze, Italy

[2] University of Nottingham, University Park, Nottingham NG7 2RD, UK
e-mail: **satoshi_morita@yanmar.com**

Abstract
Dynamical Energy Analysis (DEA) has been introduced as a mesh-based high frequency method modelling structure borne sound for complex built-up structures. DEA has been used to calculate the structure borne sound of an assembled agricultural tractor and good agreement between measurements and DEA calculations has been shown. However, it is still difficult to model a solid structure because currently DEA is based on wave transmission calculations through plate/plate junctions. We propose here to integrate measurement data into DEA to improve the effectiveness of DEA modelling. Advanced Transfer Path Analysis (ATPA) is employed to extract energy transmission characteristics of a structure. DEA elements connecting interface points and representing energy transmission characteristics of the structure are created based on the ATPA result. The proposed method is verified with a finite element model of a simple structure.

1 Introduction

Simulations of the vibro-acoustic performance of cars, trains, airplanes as well as heavy goods vehicles such as lorries and tractors are routinely carried out at various design stages. To understand the transmission of structure-borne sound in such mechanical structures, it is necessary to have effective and efficient modelling tools to support the structural design process, ideally before a prototype vehicle is built. Numerical calculations are widely used to aid the understanding and estimation of noise and vibrations. In particular, the Finite Element Method (FEM) is used routinely for noise and vibration simulations in complex structures in the low frequency regime. It requires extremely fine meshes at high frequencies, however, to capture shorter wave lengths leading to large model sizes. Additionally, since the structural response at high frequencies is very sensitive to small variations in material properties and boundary conditions, the simulation result from FEM become less reliable. Statistical representations such as the Statistical Energy Analysis (SEA) [1] have been developed, leading to relatively small and simple models in comparison with FEM. SEA has found widespread applications in the automotive and aviation industry, as well as in architectural acoustics. However, SEA is based on a set of often hard to verify assumptions, which effectively require diffuse wave fields and quasi-equilibrium of wave energy within sub-systems. In addition, SEA gives results only on a relatively course scale and cannot deal with details of the structure [2,3,4].

Here, we start from a ray-tracing ansatz reformulated in terms of integral equations. This leads to linear flow equations for the mean vibrational energy density and forms the basis of the Dynamical Energy Analysis (DEA) method introduced first in [5]. DEA includes SEA as special case via a low order representation of the so-called transfer operator. Higher order implementations enrich the DEA model with information from the underlying ray dynamics, leading to a relaxation of SEA assumptions. In particular, DEA allows for more freedom in sub-structuring the total system and variations of the energy density across sub-structures can be modelled. Hence, DEA can resolve the full geometrical complexity of the structure. An efficient implementation of DEA on meshes has been presented in [6, 7]. Vibro-acoustic energy densities are computed for multi-modal propagation, including energy transport over curved surfaces. Connections at

material interfaces are described in terms of reflection/transmission matrices. DEA has been used to calculate the structure borne sound of an assembled agricultural tractor and good agreement between measurements and DEA calculations have been shown [8]. In particular, it has been demonstrated that DEA can model shell structures accurately. However, it is still difficult to model a solid structure because currently DEA is based on wave transmission calculations through plate/plate junctions. Additionally, it is often difficult to generate accurate FE meshes of assembled complex structures because of welds, bolts and rubber bushes between each of the components. To overcome these limitations, we suggest to integrate measurement data into DEA to improve the effectiveness of DEA modelling.

In this paper, we propose a novel method to generate DEA elements based on the Advanced Transfer Path Analysis (ATPA) [11]. ATPA is employed to extract energy transmission characteristics of a structure. Firstly, Frequency Response Functions (FRFs) are measured between interface points on a structure. Then the direct transfer functions between all interface points are calculated using ATPA. Finally, DEA elements connecting interface points and representing energy transmission characteristics of the structure are created based on the ATPA result. The proposed method is verified with a finite element model of a simple structure.

2 Theory

2.1 Dynamical Energy Analysis on complex meshes

We will give a brief account of the major ideas behind DEA here – for a detailed description of the theory and the implementation on 2D meshes, see [6, 8]. In the high frequency regime, the dynamics described by linear wave equations can be approximated using semi-classical or ray-tracing methods describing the transition from wave acoustics to ray acoustics; this serves as a starting point for DEA. By neglecting phase information, DEA approximates the transport of wave energy by a Hamiltonian flow [5] described by the *Liouville equation*. The flow is phase space volume preserving and can be formulated in terms of trajectories or *rays*. In contrast to ray tracing, DEA does not work with individual rays, but describes how ray densities are transported along the flow. In this work we are primarily interested in the stationary solution of transport problems corresponding to wave problems in the frequency domain with time-harmonic driving terms. Interference (or phase) effects are neglected.

The ray density can be related to a wave energy density and is defined on a phase space, that is, it depends both on position and direction. For two-dimensional systems (as considered in this work), the phase space is four dimensional and is parametrized by two position and two momentum coordinates. The momentum coordinates are equivalent to the wave vector. For fixed frequency ω and a given wave mode, the modulus of the wave vector, that is, the wavenumber, is fixed. Hence, there is only one free parameter necessary to describe the direction.

The transport problem can be conveniently solved on a mesh as described in [6, 8]. In particular, it is advantageous to restrict the Hamiltonian flow to sections on the union of all the edges of the mesh describing the two-dimensional structure in question. The coordinates used to describe this restricted two-dimensional phase space, the so-called Surface of Section (SoS), are the arc-length along each edge i, s_i, and the corresponding component of the wave vector along the direction of the edge, p_i. The continuous Hamiltonian flow is thus transformed into a discrete map, also called the Discrete Flow Map (DFM) [6].

DEA describes the transport of ray densities from the SoS to itself using a linear transfer operator which is now discretised and represented as a matrix with entries of the from [6, 8]

$$T_{(i,l',m')'(j,l,m)} = \frac{2m+1}{2\sqrt{A_{l'}\,A_l}} \int_0^{A_l} \int_{-c_j^{-1}}^{c_j^{-1}} w_{rt}(p_i')\, e^{-\nu L(s_j,s_i')}\, P_{m'}(p_i')\, P_m(p_j) dp_j\, ds_j,$$

where P_m is a scaled Legendre polynomial of order m as detailed in [8], and the energy is propagated along a trajectory through the mesh element j with propagation speed c_j. This trajectory starts at position s_j on edge

l of element j and is transported to position s'_i on the common edge l' of the boundary of element i. The tangential component of the momentum (or slowness) of the trajectory at s_j is denoted p_j and likewise for p'_i at s'_i. Note, that p'_i and s'_i are uniquely determined by p_j at s_j. Also $L(s_j,s'_i)$ is the length of the trajectory from s_j to s'_i, η is a (viscous) damping parameter. Furthermore, A_l is the length of edge l from element j, and likewise A'_l is the length of edge l' from element i. The weight function w_{rt} gives the reflection/transmission coefficients which are obtained from wave scattering theory [9]. Mode conversion between in-plane and flexural waves at boundaries can be included in the treatment. Shell effects leading to curved rays [10] are included by treating the meshed structure as set of plate-like elements, see [6-8] for details.

Once the matrix B has been constructed, the energy density on the boundary phase-space of each element is given by the solution of a linear system of the form

$$(\mathbf{I} - \mathbf{T})\rho_0 = \rho$$

where $\boldsymbol{I}$ is the identity matrix and T has entries as defined by equation (1). Here, ρ_0 is the initial density produced by a source term. Once ρ has been computed, the energy density at any location inside the structure can be computed in a post-processing step.

2.2 DEA-TPA modeling

In many practical applications, providing meshes for some parts of the structure may be very time-consuming and thus costly due the internal complexity of the parts. Typical examples are the engine, the gear-box or the drive train as a whole and adjacent parts. In these circumstances, it would be easier to do local measurements and include effective transmission parameters into the DEA calculation. In order to extract the energy transmission parameters, the Transfer Path Analysis (TPA) approach is taken here [11]. The DEA-TPA method is based on the same principle as the RBE-patch method introduced in [8]. The difference to the RBE-patch method is that we use frequency dependent transition rates obtained from measurements. Energy transitions are assumed to take place between connecting interfaces. Labelling the interfaces with k, k' = 1, n, we define a transition matrix $S_{k,k'}$ between these interfaces. An interface is normally made up of different edges of the mesh. Let us assume the edge $E_{b''}$ is part of interface k and the edge $E_{b'}$ is part of interface k' which is shown in Figure 1. We now allow a transition between E_b and $E_{b'}$ via the edge $E_{b''}$ using the equation,

$$\tilde{T}_{(b',\beta'),(b,\beta)} = \left[\sum_{\tilde{k}} S_{\tilde{k},k}\right] \frac{S_{k',k}\, A_{b'}}{\sum_{\tilde{k}} S_{\tilde{k},k} \sum_{\tilde{b}\in J_{\tilde{k}}} A_{\tilde{b}}}\, T_{(b',\beta'),(b,\beta)} \tag{1}$$

Here, A_b , $A_{b'}$ are the lengths of the edges E_b, $E_{b'}$, β, β', the indices for the momentum basis and $T_{(b',\beta'),(b,\beta)}$ is the transfer operator matrix element between two edges not including weighting factors. The first term in (1) represents overall damping, the fraction in the middle gives the relative transition rates for a single edge. The denominator represents the total outgoing energy flux from interface k.

In [8], the RBE-patch method was introduced to account for coupling between different sub-meshes provided by an FE-modeler. For combining measurement results with DEA, we determine the rates for the transition matrix S using the ATPA method which is ideal to derive local transition rates from global response functions. The basic theory of ATPA is described in the next session.

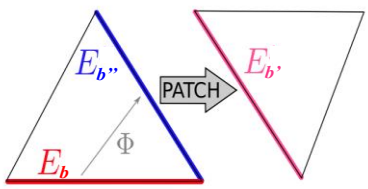


Figure 1: Schematic sketch of the connection between mesh edges using patch elements

2.3 Advanced Transfer Path Analysis

ATPA is a variant of the transmission path analysis method using so-called Direct Transfer Functions (DTFs) calculated from a Global Transfer Functions (GTFs) [11]. The GTFs correspond to the common concept of a measurable transfer function. The GTFs represent transitions between measured points via all transmission path. The DTF elements represent the quotient between two specific points where all the other paths remain blocked.

The GTF G^g_{ij} from point *i* to *j* is defined as the scenario where one applies an external excitation f^{ext} (for example a force) at point *i* and the external excitation at all other points is set to zero [11], that is,

$$G^g_{ij} = \frac{s_j}{s_i} \text{ with } f^{ext}\left(0,\cdots,0,f^{ext}_i,0,\cdots,0\right)^T \tag{2}$$

where s_i and s_j represent a measured signal which can describe quantities such as acceleration, velocity, displacement or energy. The DTF T^D_{ij} from *i* to *j* is defined as the scenario where one applies an external excitation at point *i* with vanishing external excitation at point *j* and vanishing displacements at any point other than *i* or *j*, that is

$$G^D_{ij} = \frac{s_j}{s_i} \text{with } S_k = 0, k \neq i, j. \tag{3}$$

As already mentioned, the DTF between two points gives the quotient of their signals when all the other points in the system are blocked. Consequently, the DTF is normally difficult to measured but it can be calculated by using the GTF as follows:

$$G^D_{kk} = \frac{1}{[(G^g)^{-1}]_{kk}} \tag{4}$$

$$G^D_{jk} = \frac{-[(G^g)^{-1}]_{jk}}{[(G^g)^{-1}]_{kk}} \quad \text{for} \quad j \neq k\ . \tag{5}$$

In this paper, an energetic approach of the ATPA is employed as we focus here on the mid-high frequency regime. In the energetic approach, the measured signal s_i represents the energy at point *i*. Therefore, the energy density is used which is calculated using

$$s_i = \rho h v_i^2 \tag{6}$$

where ρ is the material density, *h* is the thickness of the plate and v_i is the velocity at point *i*.

3 FE model for DEA-TPA

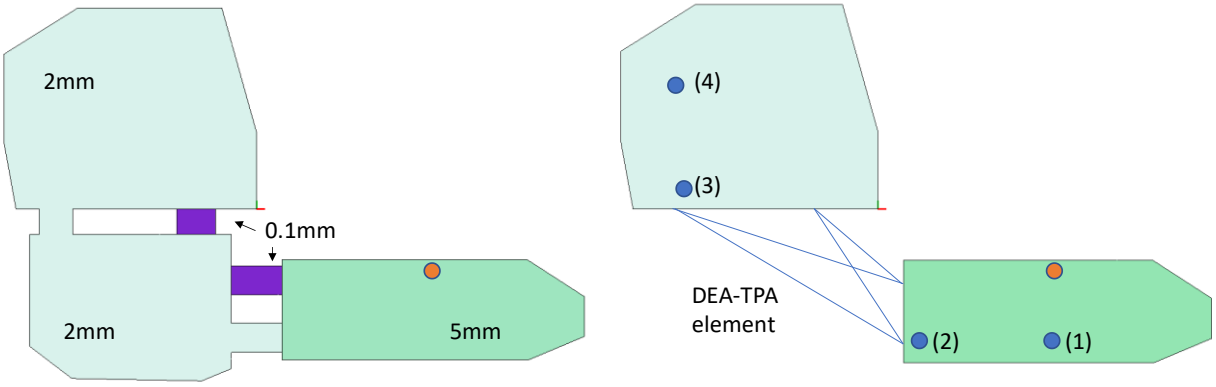
In order to validate the DEA-TPA approach, the method is tested with an FE model of a simple structure made up of three plates connected via 4 connecting beams. We assume that the middle plate, plate 2, represents the complicated part and is modelled as the DEA-TPA element. Four interface points are defined at the boundaries of the connecting beams as shown in Figure 2. The GTFs is calculated here using FEM instead of measuring a real structure, validation is also performed doing an FE calculation of the full structure. To define the transition matrix described in Eq. (1), several steps are introduced as follows:

- We first normalise the outgoing flow to 1, that is

$$\tilde{G}^D_{ij} = G^D_{ij} / \sum_j G^D_{ij}$$

- We then set $S_{ji} = \tilde{G}^D_{ij}$ in the case that interface *i* and *j* are not on the same plate.
- The diagonal terms correspond to reflection from the interface and we set $S_{ii} = \tilde{G}^D_{ii} + \tilde{G}^D_{ij}$ if *i* and *j* are on the same plate.
- We set $S_{ij} = 0$, if *i* and *j* are different points on the same plate.

The excitation point is on plate 1 (lower right plate) and shown in Figure 2.



(a) Original structure (b) DEA-TPA modelling

Figure 2: The FE models for the full structure and the TPA model. The thicknesses of the plates are shown in the left figure. The orange dot shows excitation point. The blue dots give measurement points, see the results in Figure 4.

4 Results

4.1 Energy distribution calculation

Entities of the transition matrix are calculated based on Eq. (4) and (5). However, for frequencies below 1000Hz negative value of the calculated GTFs have been observed. Therefore, here, we focus on the frequency above 1000Hz for the ATPA results. Figure 3 shows a comparison of the acceleration distributions between averaged FEM result over 1/3 frequency band, a full DEA calculation and DEA-TPA result for 2500 Hz. Figure 4 also shows results for the energy calculated at the points depicted in Figure 2 clearly demonstrating that both the DEA and the DEA-TPA capture the energy distributions accurately at 2500 Hz. A comparison between DEA, DEA-TPA results and FEM at selected points and over the full frequency range from 250Hz to 2500Hz are presented in Figure 5 showing good agreement over the whole available frequency range.

4.2 Vibrational energy flow calculation

The ray density $\rho(\mathbf{r},\mathbf{p})$ computed in DEA provides more information than just the energy density. In particular, it allows one to estimate the momentum density vector $\mathbf{I}(\mathbf{r})$ (sometimes called intensity vector) directly, and thus gives information about the direction of mean energy flow at each point on the structure. This can be done as a post-processing step by computing the vectoral quantity

$$\mathbf{I}(\mathbf{r}) \propto \int \mathbf{p}\, \varrho(\mathbf{r},\mathbf{p})\, \mathrm{d}\mathbf{p}$$

at each point on the structure. Here $\mathbf{r}$ is the position and $\mathbf{p}$ is the (two-dimensional) momentum variable. Figure 6 shows calculated result.

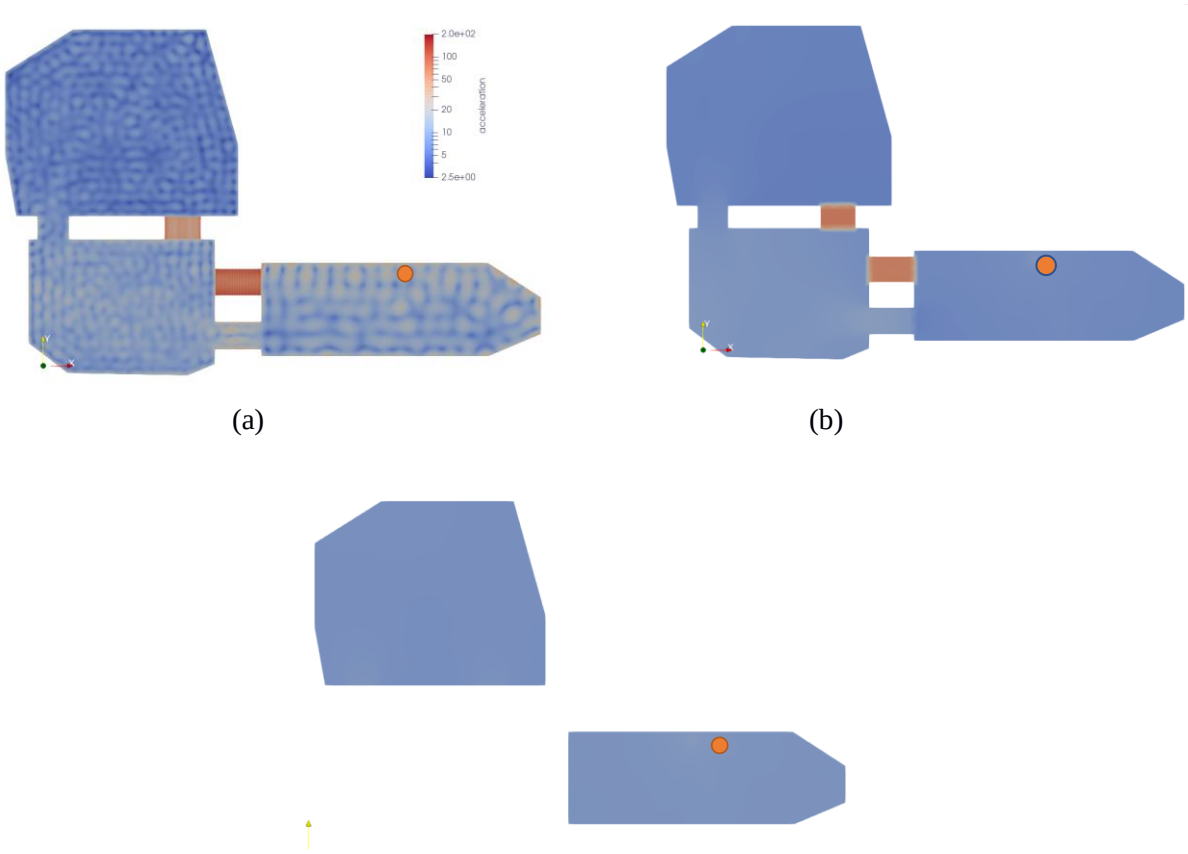


Figure 3: Comparison of FEM, DEA and DEA-TPA model at 2500Hz; (a) averaged FEM over 1/3 octave frequency region at 2500Hz, (b) DEA and (c) DEA - TPA

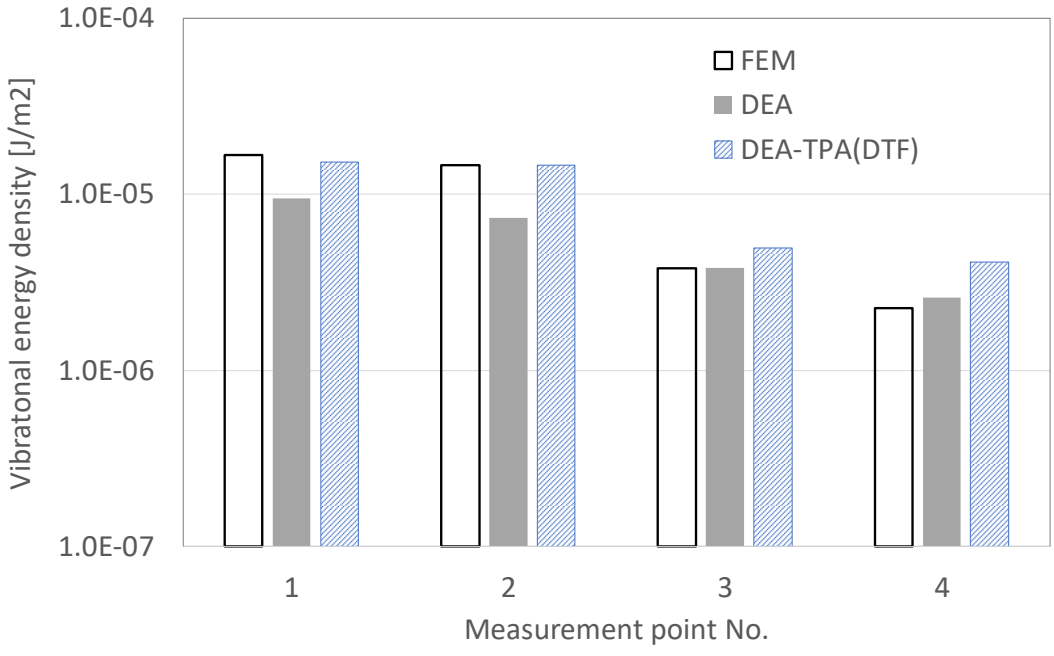


Figure 4: Comparison of FEM, DEA and DEA-TPA model at 2500Hz

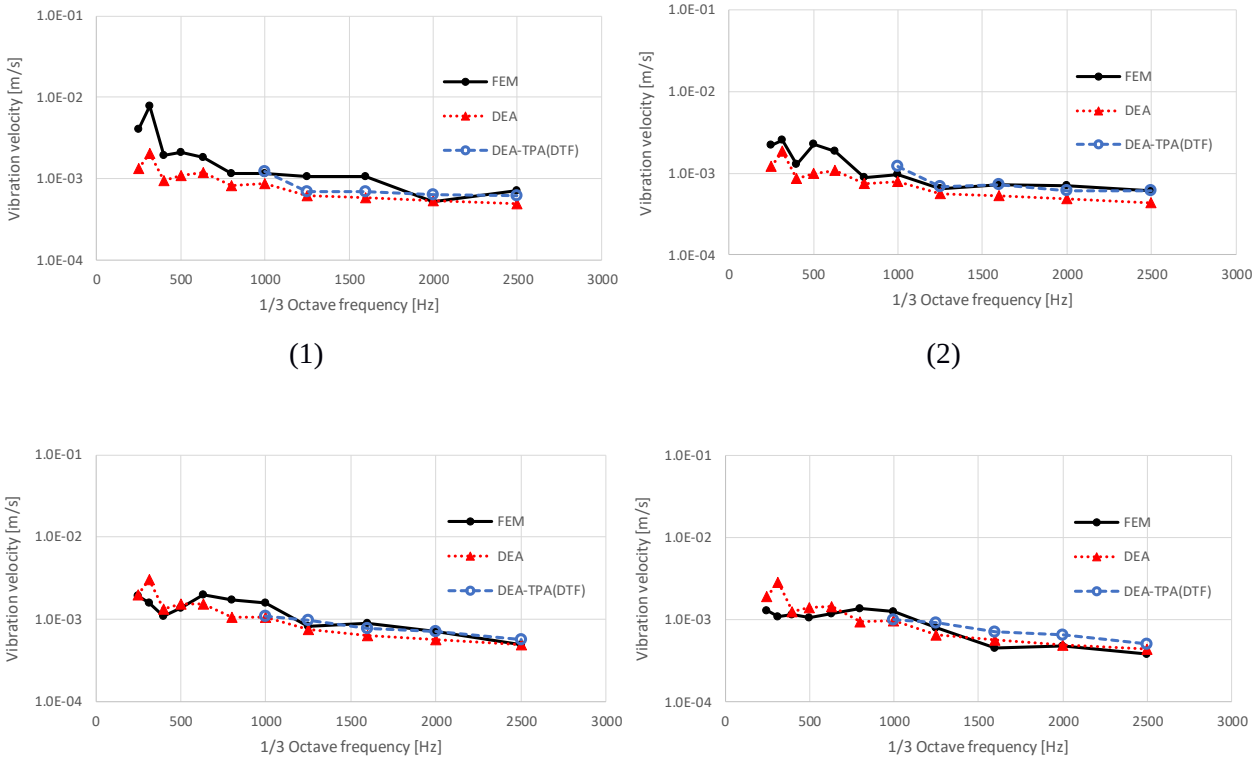


Figure 5: Comparison of FEM, DEA and DEA-TPA model over the frequency range 250Hz to 2500Hz

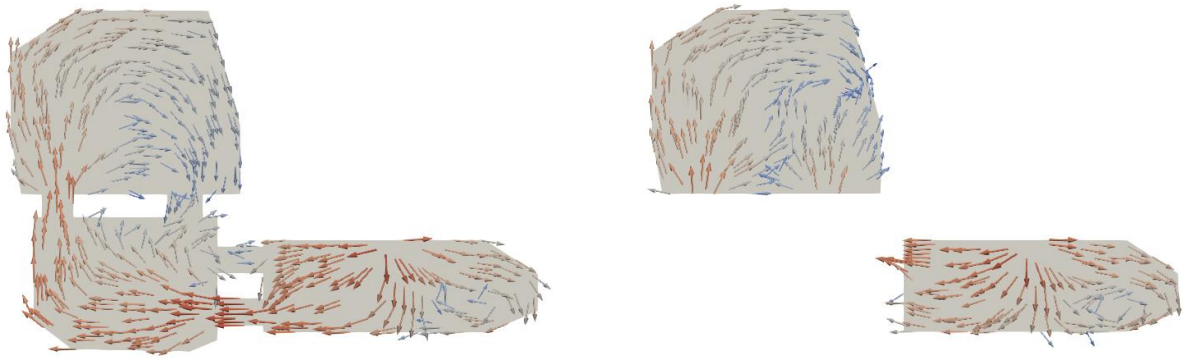


Figure 6: Comparison of calculated energy flow between DEA and DEA-TPA at 1600Hz

5 Conclusions

In this paper, the DEA-TPA modelling method was proposed and compared with an FEM calculation. It was shown how ATPA input can be integrated into a transition matrix calculation giving rise to a hybrid DEA-TPA method. Both the DEA-TPA modelling as well as a DEA computation compares favorably with the FEM results with DEA-TPA giving a slightly more accurate description as expected.

References

1. R. H. Lyon, and R. G. DeJong, Theory and Application of Statistical Energy Analysis, Butterworth-Heinemann, Boston ,1995.
2. P. J. Shorter and R. S. Langley, Vibro-acoustic analysis of complex systems, Journal Sound Vib., Vol. 288, 669-699, 2005.
3. V. Cotoni, P.J. Shorter, and R.S. Langley, Numerical and validation of a hybrid finite element-statistical energy analysis method, J. Acoust. Soc. Am., 122, 259-270, 2007.
4. G. Xie, L. Dunne, A. Secgin and A. Zoghaib, Mid-frequency modelling of a car floor structure with hybrid method and SEA, International Symposium on the Computational Modelling and Analysis of Vehicle Body Noise and Vibration, 2012, Sussex, UK.
5. G. Tanner, Dynamical energy analysis - Determining wave energy distributions in vibro-acoustical structures in the high-frequency regime, J. Sound Vib. 320, 1023-1038, 2009.
6. D. J. Chappell, G. Tanner, D. Lochel and N. Sondergaard, Discrete flow mapping: transport of phase space densities on triangulated surfaces, Proc. R. Soc. A, 469, 20130153, 2013.
7. D. J. Chappell, D. Lochel, N. Sondergaard and G. Tanner, Dynamical energy analysis on mesh grids: A new tool for describing the vibro-acoustic response of complex mechanical structures, Wave Motion 51, 589-597, 2014.
8. T. Hartmann, S. Morita, G. Tanner, and D. J. Chappell, High-frequency structure-borne sound transmission for a tractor model using Dynamical Energy Analysis, submitted to Wave Motion.
9. R. S. Langley and K. H. Heron, Elastic wave transmission through plate/beam junctions, J. Sound Vib. 143, 241, 1990.
10. A. N. Norris and D. A. Rebinsky, Membrane and Flexural Waves on Thin Shells, ASME J. Vib. Acoust. 116, 457-467, 1994.
11. O. Guasch, F. X. Magrans, The Global Transfer Direct Transfer method applied to a finite simply supported elastic beam, J. Sound Vib., 276, 335-359, 2004

A fast and efficient approach for simulating ultrasonic waves and their interaction with defects in periodic structures

M. K. Malik [1,2], **D. Chronopoulos** [1], **G. Tanner** [1], **Y. Essa** [2], **F. de la Escalera** [2]
[1] University of Nottingham, Nottingham, NG7 2RD, United Kingdom
e-mail: **Muhammad.Malik@nottingham.ac.uk**

[2] Aernnova Engineering Division S.A., Madrid, 28034, Spain

Abstract
An approach for simulating transient wave propagation in periodic waveguides is presented. Free and forced propagation of ultrasonic waves is modelled in one dimensional periodic structures. The interaction of ultrasonic waves with structural inhomogeneities is also studied. The approach is a combination of a hybrid Wave and Finite Element Method (WFEM) for free wave propagation, a coupling element for forced response and a time domain reconstruction technique. WFEM is used to obtain dispersion characteristics of the waveguide along with the basis functions for calculating the excitation response from the coupling element. The time domain response is obtained by taking an inverse Discrete Fourier Transform (DFT) of the frequency domain amplitudes. The results are compared with a full explicit FE simulation done in Abaqus. The presented approach is found to accurately simulate the excitation response of periodic waveguides as well as to drastically reduce the overall computation time.

1 Introduction

Ultrasonic guided waves are of particular importance for structural health monitoring (SHM). They can travel long distances without much energy loss and require minimal equipment. Hence, they have been the focus of the SHM community for decades. The transient wave propagation characteristics of a structural waveguide can give information about the health of the structure and the presence of potential defects. Usually this is done by comparing the signal with a database of possible responses and concluding the type of defect present. Generating a baseline experimentally is often not practical, hence simulations are used to generate a library of baseline states. From here arises the need for fast and efficient simulation tools. The most reliable and widely used method is explicit FE but due to very short wavelengths in the ultrasonic regime, a very high resolution in spatial and temporal domain is required. Hence, the approach quickly becomes computationally prohibitive. Over the years different methodologies have been developed to overcome this issue, the foremost being semi-analytical finite element method (SAFE) [1],[2]. It uses finite element method to describe wave behaviour in thickness direction whereas a complex exponential function to describe displacement field in direction of wave propagation is used [3]. There is also the scaled boundary finite element method (SBFEM) used for modelling guided waves and detecting damage in structures [4]. The dominant feature of these approaches is a combined analytical and numerical framework to reduce computational complexity. The hybrid wave and finite element method (WFEM) is one such methodology developed in the last decade [5]. It is used in a number of research areas like structural identification [6], damage detection [7], multiscale wave propagation [8] and wave steering in composites [9]. There have been efforts recently to develop a full transient simulation method based on WFEM [10],[11], but none addressing ultrasonic guided waves exists so far.

The main novelty introduced in this paper is a comprehensive transient analysis technique which can simulate ultrasonic guided wave propagation and their interaction with defects in period structures orders of magnitude faster than conventional methods. The organisation of this paper is as follows. After a brief introduction on the need to develop a new approach, the entire methodology is presented in Section 2. A brief overview of WFEM is given in Section 2.1 and its use in the transient analysis framework. This is followed by a frequency domain forced response analysis described in Section 2.2, scattering from defects in Section 2.3 and time domain reconstruction in Section 2.4. A comprehensive numerical example is presented in Section 3. That is followed by some conclusions as well as an outlook for possible future extensions.

2 Transient analysis

An approach for the modelling ultrasonic guided waves is presented in this section. The methodology is based on the hybrid wave and finite element method (WFEM), hence it brings all the benefits of this approach to model wave propagation in periodic structures. The wave solution obtained from the WFEM for the free wave propagation in frequency domain is used as basis for projecting the solution on the entire structure. The forced response is obtained by transforming transient excitation functions into the frequency domain and applying it to the dynamic equilibrium of coupling elements to obtain the outgoing amplitudes. A simplified illustration of the structure under consideration is shown in Figure 1. The entire approach is illustrated schematically in Figure 2.

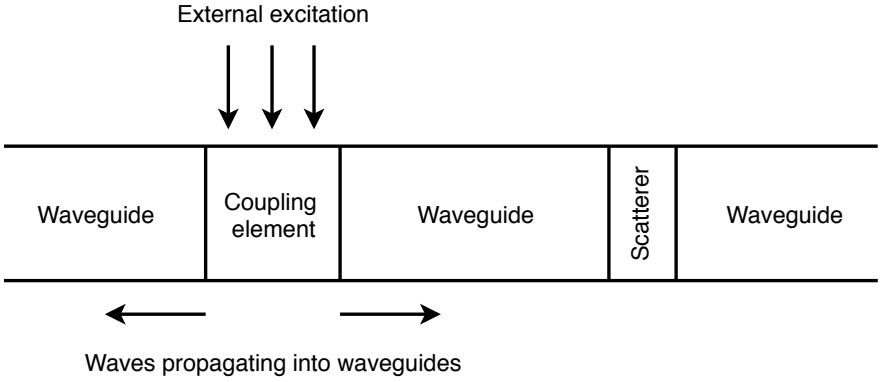


Figure 1: Wave propagation due to external excitation.

2.1 Hybrid wave and finite element method

The hybrid wave and finite element method is a technique to model wave propagation in periodic structures. It is presented in detail in [12] and [13]. This section closely follows the steps presented in these articles. The first step is to model a periodic section in FE software. The cross-section of the periodic element can be of arbitrary complexity. Hence, this approach is quite useful for modelling wave propagation in layered media. It is necessary for structure to be uniform in the direction of wave propagation and to have same number of degrees of freedom on the left and right side of the waveguide. The finite element model of the periodic section is used to obtain the stiffness $\mathbf{K}$, mass $\mathbf{M}$ and damping $\mathbf{C}$ matrices. These are used to establish the governing equations of motion as follows:

$$\left[\mathbf{K} + \mathrm{i}\omega\mathbf{C} - \omega^2\mathbf{M}\right]\mathbf{q} = \mathbf{f} + \mathbf{f}_p. \tag{1}$$

Here, $\mathbf{q}$ is the vector of nodal displacements and $\mathbf{f}$ and $\mathbf{f_p}$ are vectors of internal and external forces. For a system with n degrees of freedom on each side of the waveguide $\mathbf{K}$, $\mathbf{C}$ and $\mathbf{M}$ are $[2n \times 2n]$ matrices where $\mathbf{q}$, $\mathbf{f}$ and $\mathbf{f_p}$ are $[2n \times 1]$ vectors. There is a time harmonic dependence of the form $\mathrm{e}^{\mathrm{i}\omega t}$ assumed throughout this work which has been suppressed for brevity. Rearranging the degrees of freedom into left ($\mathbf{L}$), right ($\mathbf{R}$)

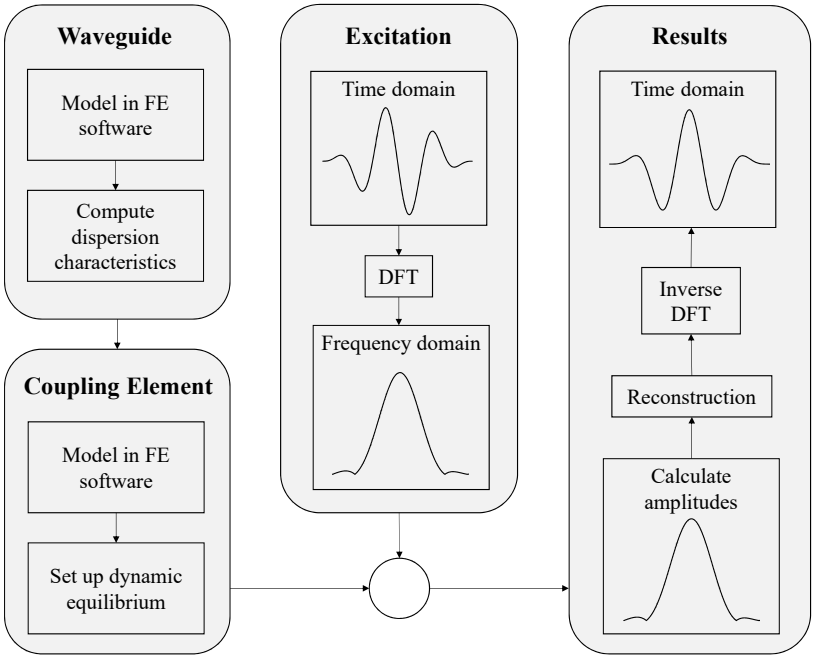


Figure 2: Schematic of approach.

and internal (**I**) leads to the following expression for Eq. (1):

$$\begin{bmatrix} \mathbf{D}_{LL} & \mathbf{D}_{LR} & \mathbf{D}_{LI} \\ \mathbf{D}_{RL} & \mathbf{D}_{RR} & \mathbf{D}_{RI} \\ \mathbf{D}_{IL} & \mathbf{D}_{IR} & \mathbf{D}_{II} \end{bmatrix} \begin{Bmatrix} \mathbf{q}_L \\ \mathbf{q}_R \\ \mathbf{q}_I \end{Bmatrix} = \begin{Bmatrix} \mathbf{f}_L \\ \mathbf{f}_R \\ \mathbf{f}_I \end{Bmatrix} + \begin{Bmatrix} \mathbf{f}_{pL} \\ \mathbf{f}_{pR} \\ \mathbf{f}_{pI} \end{Bmatrix} \tag{2}$$

or

$$\mathbf{D}(\omega)\mathbf{q} = \mathbf{f} + \mathbf{f}_p, \tag{3}$$

where $\mathbf{D}$ is a frequency dependent dynamic stiffness matrix of the waveguide. The free wave propagation characteristics are obtained by simplifying Eq. (2) with the knowledge that there are no forces on internal degrees of freedom and no external excitations. This helps in condensing the internal degrees of freedom and reducing Eq. (2) as follows:

$$\begin{bmatrix} \tilde{\mathbf{D}}_{LL} & \tilde{\mathbf{D}}_{LR} \\ \tilde{\mathbf{D}}_{RL} & \tilde{\mathbf{D}}_{RR} \end{bmatrix} \begin{Bmatrix} \mathbf{q}_L \\ \mathbf{q}_R \end{Bmatrix} = \begin{Bmatrix} \mathbf{f}_L \\ \mathbf{f}_R \end{Bmatrix}, \tag{4}$$

where

$$\begin{aligned} \tilde{\mathbf{D}}_{LL} &= \mathbf{D}_{LL} - \mathbf{D}_{LI}\mathbf{D}_{II}^{-1}\mathbf{D}_{IL} \\ \tilde{\mathbf{D}}_{LR} &= \mathbf{D}_{LR} - \mathbf{D}_{LI}\mathbf{D}_{II}^{-1}\mathbf{D}_{IR} \\ \tilde{\mathbf{D}}_{RL} &= \mathbf{D}_{RL} - \mathbf{D}_{RI}\mathbf{D}_{II}^{-1}\mathbf{D}_{IL} \\ \tilde{\mathbf{D}}_{RR} &= \mathbf{D}_{RR} - \mathbf{D}_{RI}\mathbf{D}_{II}^{-1}\mathbf{D}_{IR} \end{aligned}. \tag{5}$$

This condensation technique is the simplest of its kind, other methods are available for better accuracy and computational speed [14],[15]. According to Bloch's theorem for free wave propagation in waveguides of length l_x, the propagation constant $\lambda = \mathrm{e}^{\mathrm{i}kl_x}$ relates the nodal degrees of freedom on the left and right hand side by [13]

$$\mathbf{q}_R = \lambda \mathbf{q}_L, \quad \mathbf{f}_R = -\lambda \mathbf{f}_L. \tag{6}$$

An eigenvalue problem for λ is formulated by substituting Eq. (6) into Eq. (4) as follows

$$\lambda \left\{ \begin{array}{c} \mathbf{q}_L \\ \mathbf{f}_L \end{array} \right\} = \mathbf{T} \left\{ \begin{array}{c} \mathbf{q}_L \\ \mathbf{f}_L \end{array} \right\}, \tag{7}$$

where $\mathbf{T}$ is the transfer matrix given in Eq. (8). Based on eigenvalue problem in Eq. (7), the propagation constants λ are eigenvalues of the transfer matrix $\mathbf{T}$. They exist in pairs of $[\lambda^+, 1/\lambda^+]$ for the positive and negative travelling waves, respectively. The eigenvalue problem can be poorly conditioned leading to numerical issues. Different formulations are used to mitigate this effect which are mentioned in [16], that is,

$$\mathbf{T} = \left[\begin{array}{cc} -\tilde{\mathbf{D}}_{LR}^{-1}\tilde{\mathbf{D}}_{LL} & \tilde{\mathbf{D}}_{LR}^{-1} \\ -\tilde{\mathbf{D}}_{RL} + \tilde{\mathbf{D}}_{RR}\tilde{\mathbf{D}}_{LR}^{-1}\tilde{\mathbf{D}}_{LL} & -\tilde{\mathbf{D}}_{RR}\tilde{\mathbf{D}}_{LR}^{-1} \end{array} \right]. \tag{8}$$

The propagation constants for positive and negative going waves are used to obtain wavenumbers k_j^+ and k_j^- of propagating waves where $j = 1, ..., 2n$. The number of waves N retained to be used as basis functions are less than the total number of modes computed as many of these modes are numerical artefacts. Only the propagating modes and the least rapidly attenuating evanescent modes are retained, hence $N < 2n$. Actual basis functions are eigenvectors $\boldsymbol{\phi}_j$ accompanying the propagation constants. They exist for both positive $\boldsymbol{\phi}_j^+$ and negative $\boldsymbol{\phi}_j^-$ going waves and can internally be partitioned to represent displacement and forces as follows:

$$\boldsymbol{\phi}_j = \left\{ \begin{array}{c} \boldsymbol{\phi}_q \\ \boldsymbol{\phi}_f \end{array} \right\}, \quad \text{where } \boldsymbol{\phi}_j^+ = \left\{ \begin{array}{c} \boldsymbol{\phi}_q^+ \\ \boldsymbol{\phi}_f^+ \end{array} \right\}, \boldsymbol{\phi}_j^- = \left\{ \begin{array}{c} \boldsymbol{\phi}_q^- \\ \boldsymbol{\phi}_f^- \end{array} \right\}. \tag{9}$$

2.2 Coupling element

The section of the waveguide under influence of external excitation is modelled as a coupling element. This part can be of arbitrary complexity and is completely modelled using finite elements. An important consideration is to satisfy continuity and equilibrium conditions at the interface with the waveguide. The coupling element and the waveguide must therefore have consistent degrees of freedom at the interface. A finite element model of the coupling element is used to obtain the stiffness $\mathbf{K_c}$, mass $\mathbf{M_c}$ and damping $\mathbf{C_c}$ matrices. The dynamic equilibrium for the coupling element is established as follows:

$$\begin{aligned} \left[\mathbf{K_c} + \mathrm{i}\omega\mathbf{C_c} - \omega^2\mathbf{M_c}\right] \mathbf{q_c} &= \mathbf{f_c} + \mathbf{f_{cp}} \\ \text{or} \quad \mathbf{D_c}(\omega)\mathbf{q_c} &= \mathbf{f_c} + \mathbf{f_{cp}}, \end{aligned} \tag{10}$$

where $\mathbf{D_c}(\omega)$ is the frequency dependent dynamic stiffness matrix and $\mathbf{q_c}$ are the displacement degrees of

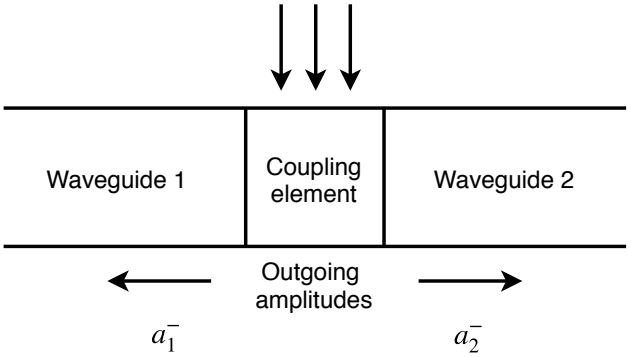


Figure 3: Amplitudes generated due to external excitation.

freedom for the coupling element while $\mathbf{f_c}$ and $\mathbf{f_{cp}}$ are internal and external forces acting on the coupling element. They are related to the waveguide degrees of freedom by using continuity and equilibrium conditions as shown in [17], that is,

$$\begin{aligned} \mathbf{q_c} &= \mathbf{R}\mathbf{q} \qquad \text{(continuity)} \\ \mathbf{f_c} - \mathbf{R}\mathbf{f} &= \mathbf{0} \qquad \text{(equilibrium)}, \end{aligned} \tag{11}$$

where $\mathbf{R}$ is a rotation matrix to transform the degrees of freedom of the waveguide from a local coordinate system to a global coordinate system assuming that the coupling element degrees of freedom are already in a global coordinate system. Based on the approach presented in [17], a wave solution is imposed on the equations of motion using the wavemodes of the waveguide as basis functions, that is,

$$\begin{aligned} \mathbf{q} &= \mathbf{R}\left[\boldsymbol{\phi}_q^+ \mathbf{a}^+ + \boldsymbol{\phi}_q^- \mathbf{a}^-\right] \\ \mathbf{f} &= \mathbf{R}\left[\boldsymbol{\phi}_f^+ \mathbf{a}^+ + \boldsymbol{\phi}_f^- \mathbf{a}^-\right]. \end{aligned} \tag{12}$$

Since the goal is to calculate wave propagation in a waveguide due to external excitation, it can safely be assumed that there are no amplitudes incident on the coupling element. This assumption leads to setting incident amplitudes $\mathbf{a}^+$ to zero. The external excitation applied to the coupling element is a transient force $\mathbf{f}(t)$ in the time domain. It is introduced in Eq. (10) by converting the force into the frequency domain using the discrete Fourier transform (DFT). The time domain signal is sampled at m points and converted into the frequency domain as follows:

$$\mathbf{F}_{cp}(\omega_j) = \sum_{i=1}^{m} \mathbf{f}_{cp}(t_i) \mathrm{e}^{-\mathrm{i}t_i\omega_j} \quad \text{where } j = 1, ..., m. \tag{13}$$

This step is also crucial because the resolution in the frequency domain influences the final result in the time domain and hence should be given special consideration. The result is a frequency dependent force vector. Equations (12) and (13) are used to establish a dynamic equilibrium for the coupling element in the frequency domain by substituting them into Eq. (10). The solution are frequency dependent outgoing amplitudes $\mathbf{a}^-$ from the coupling element.

2.3 Scattering from the defect

The wave propagates through the structure due to external excitation and is incident on a defect present in the structure. The incident wave is reflected and transmitted which is known as scattering. This is illustrated in Figure 4. The incident wave is represented as incoming amplitudes which have already been calculated in section 2.2. Once again, the degrees of freedom at the interface of the waveguide and the region encapsulating the defect must be consistent and must satisfy continuity and equilibrium conditions. The region containing the defect is modelled in finite element software from which the stiffness $\mathbf{K_J}$, mass $\mathbf{M_J}$ and damping $\mathbf{C_J}$ matrices are obtained to establish the dynamic equilibrium as follows

$$\begin{aligned} \left[\mathbf{K_J} + \mathrm{i}\omega\mathbf{C_J} - \omega^2\mathbf{M_J}\right]\mathbf{q_J} &= \mathbf{f_J} \\ \text{or} \quad \mathbf{D_J}(\omega)\mathbf{q_J} &= \mathbf{f_J}, \end{aligned} \tag{14}$$

where $\mathbf{q_J}$ and $\mathbf{f_J}$ are displacement and internal force vectors of the region containing the defect while $\mathbf{D_J}(\omega)$ is the frequency dependent dynamic stiffness matrix. The continuity and equilibrium conditions are applied to Eq. (14) similar as done for the coupling element. It is important to state here that the waveguides surrounding the region of the defect can be different from each other and can support different wavemodes. The formulation described here will still be able to obtain the amplitudes travelling into the structure as a result of scattering. We obtain

$$\begin{aligned} \mathbf{q_J} &= \mathbf{Rq} \qquad \text{(continuity)} \\ \mathbf{f_J} - \mathbf{Rf} &= \mathbf{0} \qquad \text{(equilibrium)}. \end{aligned} \tag{15}$$

$\mathbf{R}$ is once again used to transform all vectors into a global coordinate system. The wave solution is imposed on Eq. (14) using the relation shown in Eq. (12). As mentioned at the start of this section, amplitudes incident on the defect are known from section 2.2, hence the only unknowns are amplitudes scattered from the defect which are obtained as follows:

$$\mathbf{D_J R}\left[\boldsymbol{\phi}_q^+ \mathbf{a}^+ + \boldsymbol{\phi}_q^- \mathbf{a}^-\right] = \mathbf{R}\left[\boldsymbol{\phi}_f^+ \mathbf{a}^+ + \boldsymbol{\phi}_f^- \mathbf{a}^-\right]. \tag{16}$$

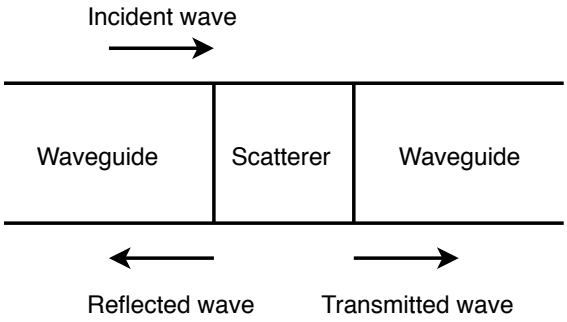


Figure 4: Scattering of waves from the defect.

2.4 Reconstruction in the time domain

The amplitudes are calculated with contribution factors for each wave over a range of frequencies. Hence these amplitudes are in the frequency domain and represent the wave motion of an entire cross-section instead of individual nodes. The nodal displacement is obtained by projecting amplitudes on individual degrees of freedom by means of basis functions, that is,

$$\mathbf{q}(\omega) = \boldsymbol{\phi}_q^+ \mathbf{a}^+ + \boldsymbol{\phi}_q^- \mathbf{a}^-, \tag{17}$$

where nodal displacements $\mathbf{q}$ of the waveguide are a function of frequency ω. The contribution of the wavemodes and their respective amplitude determines the nodal displacement in the time domain. This is achieved by performing an inverse DFT as follows:

$$\mathbf{q}(t_j) = \frac{1}{m} \sum_{i=1}^{m} \mathbf{q}(\omega_i) \mathrm{e}^{-\mathrm{i}\omega_i t_j} \quad \text{where } j = 1, ..., m. \tag{18}$$

The time domain result from this step gives the response at the point of excitation. In order to obtain the

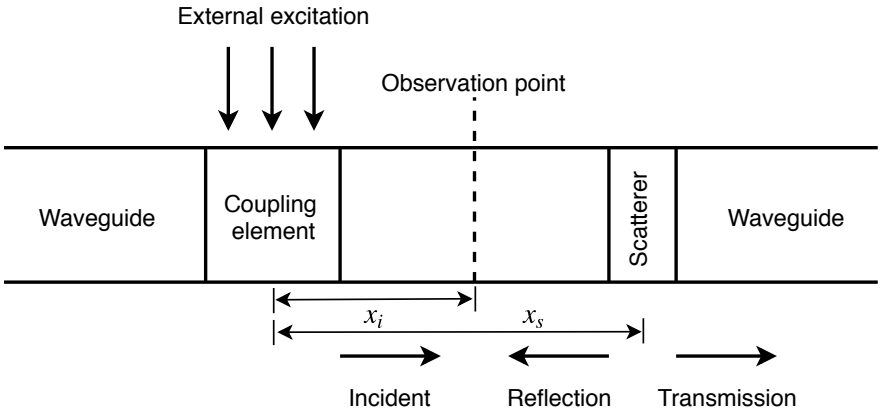


Figure 5: Wave propagation due to external excitation.

complete time history at some arbitrary point of observation in the structure, it is necessary to sum up all amplitudes arriving at that point. In Figure 5, we see the response at an observation point in the structure at some distance from the point of excitation showing the incident waves with displacement vector $\mathbf{q}_I$ passing through it, impinging on the defect and reflecting from it with displacement vector $\mathbf{q}_R$ and again passing through the observation point. Then total frequency domain displacement at the observation point is then given as

$$\mathbf{q}_O(\omega) = \mathbf{q}_I(\omega) + \mathbf{q}_R(\omega), \tag{19}$$

where $\mathbf{q}_O$ is the wave signal recorded at the observation point. There can be any number of waves passing through the observation point which will simply be added to the signal in Eq. (19) to obtain the final frequency domain response. Each of these signals will have a time of flight depending on the distance travelled by the wave to reach the observation point. This is calculated for each wave separately. The amplitudes arriving at the observation point for the first incident wave are obtained as

$$\mathbf{a}_I = \mathbf{a} \cdot \mathrm{e}^{\mathrm{i}kx_i}, \tag{20}$$

where $\mathbf{a}$ is the amplitude generated from the external excitation, k is the corresponding wavenumber of the mode, x_i is the distance the incident wave travels to reach the observation point and $\mathbf{a}_I$ the amplitudes of incident wave at the observation point. The same wave travels further and is scattered due to the defect. Obtaining reflected amplitudes from scattering at the observation point is done in three steps as shown in Eq. (21). The first step obtains the amplitudes reaching the scatterer, in second step describes scattering from the defect which acts as a new source with modified amplitudes going back into the waveguide and in a final step, we obtain the reflected amplitudes reaching the observation point. That is,

$$\begin{aligned} \mathbf{a}_1 &= \mathbf{a} \cdot \mathrm{e}^{\mathrm{i}kx_s} \\ \mathbf{a}_2 &= [S] \cdot \mathbf{a}_1 \\ \mathbf{a}_R &= \mathbf{a}_2 \cdot \mathrm{e}^{\mathrm{i}k(x_s - x_i)}, \end{aligned} \tag{21}$$

where $\mathbf{a}$ are the amplitudes generated in the waveguide due to the external excitation, x_s is the distance of the scatterer from the excitation point, $[S]$ is the scattering matrix which is intrinsic in the formulation presented in Section 2.3, $\mathbf{a}_2$ are reflected amplitudes due to scattering and $\mathbf{a}_R$ are reflected amplitudes reaching the point of observation. Once all amplitudes are obtained they can be projected onto individual degrees of freedom using Eq. (17) and added together as in Eq. (19). The final time domain response at the observation point is obtained by taking the inverse DFT of the complete signal using Eq. (18).

3 A numerical example

In this section, a numerical case study is presented and results are compared with those obtained from a full explicit finite element simulation performed in Abaqus. The entire methodology developed in this paper is coded in MATLAB. The waveguide under consideration is illustrated in Figure 6. The waveguide is made of steel with material properties shown in Table 1. The defect is simulated by inserting a single-element thick layer of aluminium in the waveguide which lead to reflection. The material properties of aluminium are also stated in Table 1. Dimensions of the structure are marked on Figure 6. The final goal is to obtain a complete transient response at the point of observation.

Material	Young's modulus (E, GPa)	Density $(\rho, kg/m^3)$	Posisson ratio (ν)
Steel	210	7800	0.3
Aluminium	70	2700	0.3

Table 1: Material properties

It is important to list all wave packets passing through observation point in order to make sense of the resulting displacement profile. The simulation is done for 150 microseconds and the external excitation is a 30 microsecond signal. Considering the time window being simulated, the following waves will pass through the observation point:

- Transmitted wave (w1) from scattering of first incident wave on the aluminium scatterer.
- Reflected wave (w2) generated from w1 reflecting from fixed boundary.
- Reflected wave (w3) generated from w2 reflecting from aluminium scatterer.

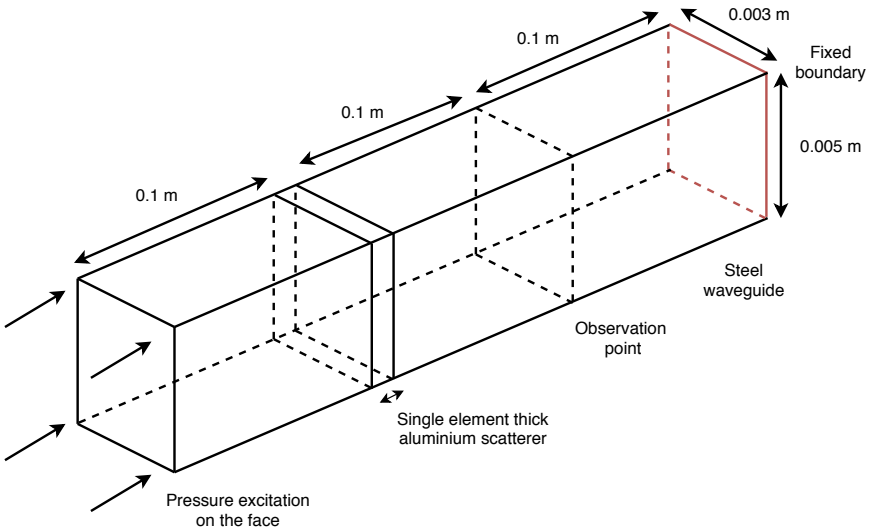
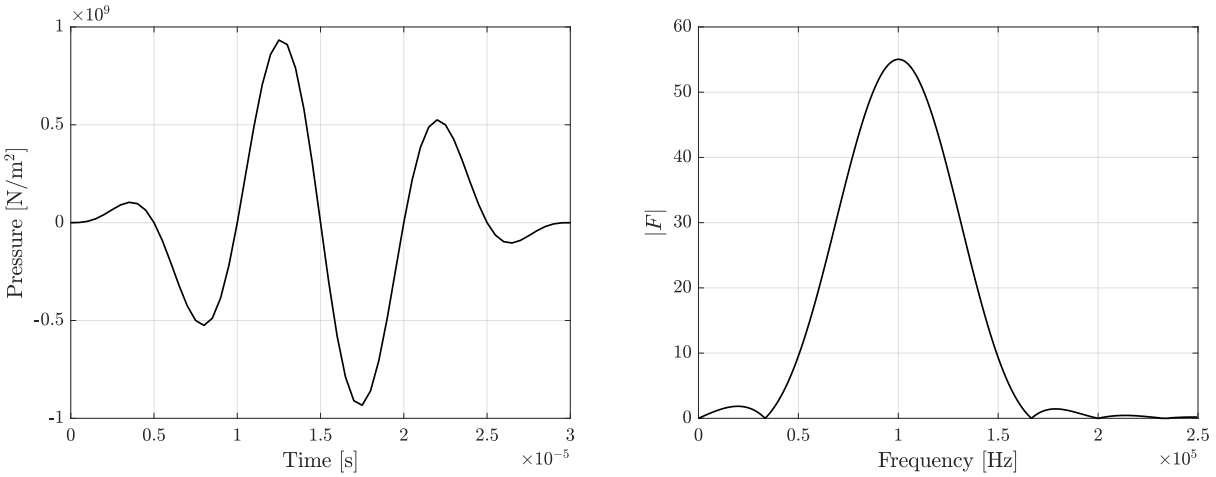


Figure 6: Illustration of the structure used in the numerical example.

- Transmitted wave (w4) generated from the initial reflected wave from the scatterer which travels back to the free end of the structure, gets reflected again and is incident again on the scatterer and is then transmitted.
- Reflected wave (w5) generated from w4 reflecting from fixed boundary.

The external excitation applied to the structure is a Hanning windowed sinusoid with central frequency at 100 kHz in the time domain. This signal is shown in Figure 7a and is used directly as input in Abaqus. For the approach developed in this paper, it is converted into nodal forces in the frequency domain using Eq. (13) as shown in Figure 7b.

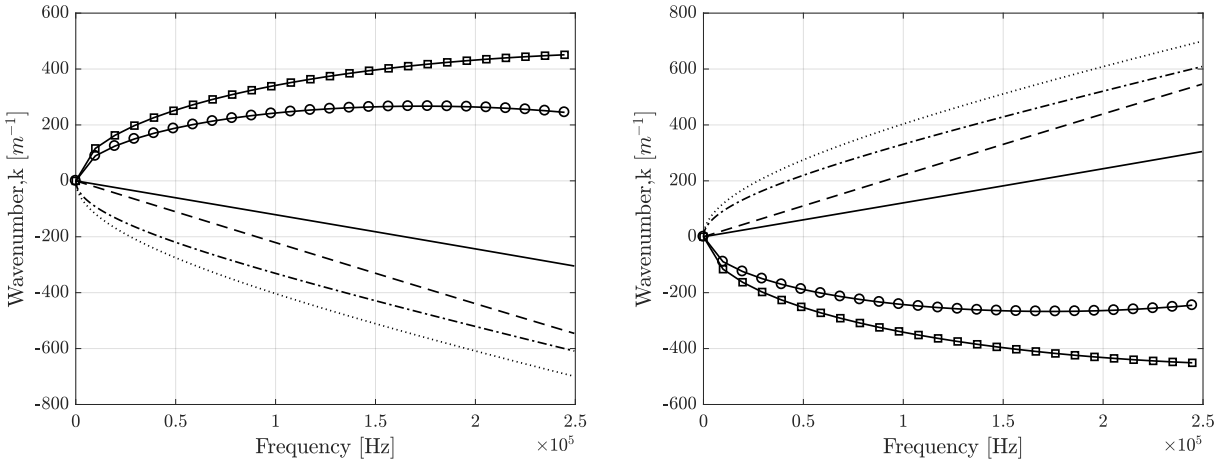


(a) Time domain (b) Frequency domain

Figure 7: Excitation signal used for exciting the symmetric Lamb wave mode in the waveguide.

The waveguide is modelled as single periodic element with dimensions $0.001\text{m}\times0.005\text{m}\times0.003\text{m}$ using the solid element C3D8R which is an 8-node linear brick element in Abaqus standard element library [18]. The mass and stiffness matrices are obtained for this single periodic element to compute the dispersion characteristics of the steel waveguide as explained in Section 2.1. The wavemodes obtained from the wave finite element method are then used as basis functions for the entire waveguide. The dispersion plots for waves retained to be used as basis are shown in Figures 8a and 8b.

Applying the methodology presented in Section 2.2, the amplitudes generated in the waveguide due to external excitation are calculated. A frequency domain resolution of 976 Hz is used with a total of 256 steps. After obtaining the amplitudes, the response at the point of observation is calculated using the technique presented in Sections 2.3 and 2.4. The resulting displacement of a single node in the direction of wave propagation is plotted in Figure 9 against values obtained from an Abaqus simulation. Abaqus simulation is carried out using 3500 elements. The element selected is the same as that used for modelling periodic waveguide element. Both simulations are performed on the same computer with a 7^{th} Generation Intel Core i3-7100U 2.50 GHz processor with 8 GB RAM. The simulation in Abaqus takes approximately 28 seconds whereas the same results are obtained using the developed approach in 5.365 seconds. It is important to mention here that the MATLAB codes are not optimised and the main goal of a full two-dimensional simulation with this approach coded in C environment is expected to be at least an order of magnitude faster than conventional FEM. Moreover the results plotted in Figure 9 are found to be in good agreement.



(a) Negative waves

(b) Positive waves

Figure 8: Dispersion curves for steel waveguide ——Pressure, - - - Shear, -·-·-Vertical bending, ·····Lateral bending, —o—Evanescent, —□—Evanescent

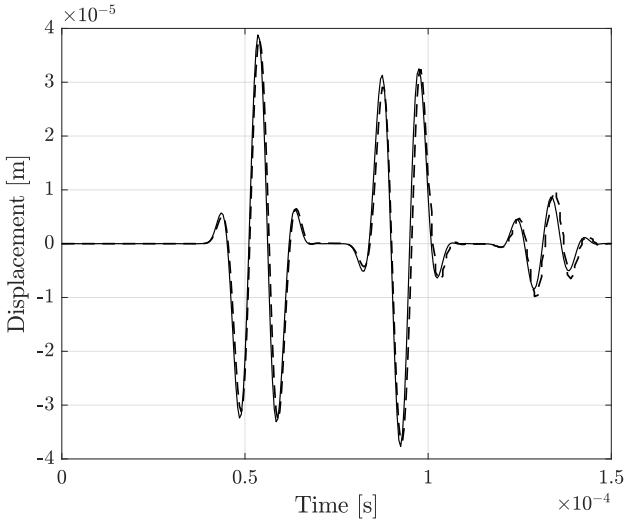


Figure 9: Displacement in direction of wave propagation of a node at observation point ——Matlab, - - - Abaqus.

4 Conclusions

The approach developed in this paper is capable of simulating ultrasonic wave propagation in periodic structures. The main objectives achieved are listed below

- Free wave propagation in one dimensional waveguides.
- Forced wave propagation in one dimensional waveguides.
- Reflection from boundaries and scattering from defects.
- Complete transient response.

It is observed that sorting of wavemodes is not necessary for time domain response which is a major strength of this method. Moreover a very high resolution in frequency domain is also not required to get sufficient resolution in the time domain. The computational complexity can further be reduced by only considering amplitudes in the vicinity of the central excitation frequency. The methodology can also be extended easily to simulate layered media because the base formulation in WFEM is capable of handling arbitrarily complex cross-sectional geometry. The approach developed in this paper will be used as groundwork to build a more comprehensive approach to simulate wave propagation in complex two dimensional waveguides.

Acknowledgements

This project has received funding from the European Union Horizon 2020 research and innovation programme under the Marie Sklodowska-Curie grant agreement No 721455.

References

[1] T. Hayashi, K. Kawashima and J.L.Rose *Calculation for guided waves in pipes and rails*, Key Engineering Materials, Vol. 270, 2004, pp. 410-415.

[2] I. Bartoli, A. Marzani, F. Lanza di Scalea and E. Viola *Modeling wave propagation in damped waveguides of arbitrary cross-section*, Journal of Sound and Vibration, Vol. 295, No. 3, 2006, pp. 685-707.

[3] Z. A. B. Ahmad, J. M. Vivar-Perez and U. Gabbert *Semi-analytical finite element method for modeling of lamb wave propagation*, CEAS Aeronautical Journal, Vol. 4, No. 1, 2013, pp. 21-33.

[4] H, Gravenkamp, C. Birk and C. Song *Simulation of elastic guided waves interacting with defects in arbitrarily long structures using the Scaled Boundary Finite Element Method*, Journal of Computational Physics, Vol. 295, 2015, pp. 438-455.

[5] Brian R. Mace and Elisabetta Manconi, *Modelling wave propagation in two-dimensional structures using finite element analysis*, Journal of Sound and Vibration, Vol. 318, No. 4, 2008, pp. 884-902.

[6] D. Chronopoulos, C. Droz, R. Apalowo, M. Ichchou and W.J. Yan *Accurate structural identification for layered composite structures, through a wave and finite element scheme*, Composite Structures, Vol. 182, 2017, pp. 566-568.

[7] R.K. Apalowo, D. Chronopoulos and G. Tanner, *Wave Interaction with Defects in Pressurised Composite Structures*, Journal of Nondestructive Evaluation, Vol. 37, No. 3, 2018, pp. 48.

[8] V. Thierry, L. Brown and D. Chronopoulos *Multi-scale wave propagation modelling for two-dimensional periodic textile composites*, Composites Part B: Engineering, Vol. 150, 2018, pp. 144-156.

[9] D. Chronopoulos, *Wave steering effects in anisotropic composite structures: Direct calculation of the energy skew angle through a finite element scheme*, Ultrasonics, Vol. 73, 2017, pp. 43-48.

[10] M. Mallouli, M.A. Ben Souf, O. Bareille, M.N. Ichchou, T. Fakhfakh and M. Haddar *Transient wave scattering and forced response analysis of damaged composite beams through a hybrid finite element-wave based method*, Finite Elements in Analysis and Design, Vol. 147, 2018, pp. 1-9.

[11] M. Mallouli, M.A. Ben Souf, O. Bareille, M.N. Ichchou, T. Fakhfakh and M. Haddar *Damage detection on composite beam under transverse impact using the Wave Finite Element method*, Applied Acoustics, 2018.

[12] Jamil M. Renno, Brian R. Mace, *Calculation of reflection and transmission coefficients of joints using a hybrid finite element/wave and finite element approach*, Journal of Sound and Vibration, Vol. 332, No. 9, 2013, pp. 2149-2164.

[13] Y.Waki, B.R.Mace,M.J. Brennan, *Numerical issues concerning the wave and finite element method for free and forced vibrations of waveguides*, Journal of Sound and Vibration, Vol. 327, No. 1-2, 2009, pp. 92-108.

[14] James F. Doyle, *Wave Propagation in Structures: spectral analysis using fast discrete Fourier transforms*, F.F.Ling.(Ed.), Mechanical Engineering Series, Springer-Verlag, New York, 2007.

[15] Y. Waki, *On the Application of Finite Element Analysis to Wave Motion in One-dimensional Waveguides*, ISVR, University of Southampton, Southampton, 2007.

[16] Zhong, WX and Williams, FW, *On the direct solution of wave propagation for repetitive structures*, Journal of Sound and Vibration, Vol. 181, No. 3, 1995, pp. 485-501.

[17] D. Chronopoulos, *Calculation of guided wave interaction with nonlinearities and generation of harmonics in composite structures through a wave finite element method*, Composite Structures, Vol. 186, 2018, pp. 375-384.

[18] Systèmes, Dassault, *Abaqus Analysis User's Guide*, 2014.

Band-averaged variance prediction in hybrid deterministic-statistical energy analysis of vibro-acoustic systems

E.P.B. Reynders [1], **R.S. Langley** [2]
[1] KU Leuven, Department of Civil Engineering,
Kasteelpark Arenberg 40, B-3001 Leuven, Belgium
e-mail: **edwin.reynders@kuleuven.be**

[2] University of Cambridge, Department of Engineering,
Trumpington Street, Cambridge CB2 1PZ, United Kingdom

Abstract
The hybrid deterministic - statistical energy analysis method is a versatile framework for vibro-acoustic analysis. Stiff system components are modelled deterministically, while the wave fields in flexible components are modelled as diffuse. In this paper, the hybrid method is extended such that the ensemble mean and variance of the band-averaged system response can be computed. The variance represents the uncertainty that is due to the assumption of a diffuse field in the flexible components of the hybrid system. After generalizing the diffuse field reciprocity relationship, explicit expressions are derived for the cross-frequency and band-averaged variance of the vibrational energies in the diffuse components and the cross spectrum of the response of the deterministic components. These expressions are extensively validated against detailed Monte Carlo analyses of coupled plate systems in which diffuse fields are simulated by randomly distributing small point masses across the flexible components, and good agreement is found.

1 Introduction

Effective vibro-acoustic analysis tools are essential for the design of engineering systems with adequate noise and vibration performance. Ideally such tools would be applicable over the entire frequency range of interest, but in practice, the workability of specific methods is restricted to a limited frequency region. Straightforward application of deterministic field-based analysis techniques such as finite element (FE) analysis is possible at low frequencies, where the wavelength of deformation is long in all system components and the response is dominated by a limited number of eigenmodes. However, as the frequency increases, the wavelength of deformation becomes short in the flexible components of the built-up system, resulting in refined meshes and a large computation cost. At the same time, the response at a specific location in such a flexible component becomes highly sensitive to the possible presence of small entities with a wave scattering effect, such as local inhomogeneities or small objects attached to the component.

In contrast to what might be initially expected, one can exploit the sensitivity of the local response of a flexible component to small wave scattering entities for setting up an effective high-frequency component model. This is achieved by modelling the wave field due to random wave scattering directly, rather than modelling the physical mechanisms behind the wave scattering. If the randomness of the wave scattering is sufficiently large such that a state of maximum uncertainty, termed maximum entropy, is reached, then the related wave field is called diffuse [9]. The notion of a diffuse field has evolved over time with increasing level of sophistication. The conventional definition of a diffuse field is a random field, composed of plane waves with statistically independent phases and statistically independent and uniformly distributed directions.

Such a model can only describe the behavior of a random system in an exact way when it has diffusely re-

flecting boundaries. In built-up systems where the mechanic interaction between different components needs to be analyzed, a generalization is therefore necessary. This is possible by establishing a harmonic linear relationship between the mean total energy in the diffuse field and the mean squared amplitude of the blocked interface reverberant forces, i.e., the forces that are caused by the diffuse field at the blocked deterministic interface degrees of freedom. This relationship is termed the diffuse field reciprocity relationship [9]. Its evaluation requires the computation of the radiation impedance matrix of the deterministic interface degrees of freedom at the considered frequency. A further generalization of the diffuse field concept has been driven by the search for an accurate quantification of the variance of the energetic response. Weaver [11] found that, in high-frequency regime, the statistics of the natural frequency spacings conform to those of the eigenvalues of a Gaussian Orthogonal Ensemble (GOE) random matrix. The GOE model is a substantial generalization of the conventional diffuse field model. The formal connection is that, in the GOE model, the mode shapes are independent Gaussian random fields. Assumptions other than on the nature of the statistics of the natural frequencies and mode shapes are not needed.

The analysis of the total vibrational energy of and the power flows between diffuse components of a built-up system is termed statistical energy analysis (SEA) [4]. The key to modern SEA is the diffuse field reciprocity relationship because it enables the computation of coupling loss factors in a rigorous and straightforward way, and therefore it resolves the problems related to ad hoc approaches that make a distinction between resonant and non-resonant transmission. It also allows combining reverberant system component models with other component models, such as finite element or boundary element models, within a single, hybrid framework of analysis. The resulting hybrid deterministic-SEA method [10] can therefore be also employed for the analysis of built-up systems in the medium frequency range, where the stiff components of the built-up system (e.g., the beam-column frames of a building) still exhibit long-wavelength deformation while the flexible components (e.g., the floors and walls of a building) already exhibit short-wavelength deformation.

The hybrid deterministic-SEA method has been extended such that not only mean energetic response quantities can be computed, but also their variance [3]. This variance represents the uncertainty that is due to the assumption of a diffuse field in the flexible components of the hybrid system. At present, only the variance of the harmonic energetic response can be computed. However in technical acoustics, energetic responses are usually averaged or integrated over frequency bands because such integration correlates well with human perception and because it results in a reduced uncertainty. Therefore, in the present paper, the hybrid method is extended such that also the ensemble variance of the band-averaged system response can be computed. *The present paper is an abbreviated version of a more detailed analysis to be found in reference* [7].

2 Hybrid deterministic-statistical energy analysis

2.1 Definitions and equations of motion

A built-up vibro-acoustic system is considered. It is decomposed into a set of deterministic components and a set of homogeneous random components. The random components carry a diffuse wave field. The deterministic components and all interfaces are referred to as the "master system", while each random component is referred to as a "subsystem". When the displacement degrees of freedom of the master system are grouped in a vector $\mathbf{q}$, its equations of motion at a given frequency ω can be written as

$$\mathbf{D}_{\mathrm{d}}(\omega)\mathbf{q}(\omega) = \mathbf{f}(\omega) + \sum_k \mathbf{f}_k(\omega) \tag{1}$$

where $\mathbf{D}_{\mathrm{d}}$ is the dynamic stiffness matrix of the master system, $\mathbf{f}$ the vector with external forces and $\mathbf{f}_k$ the vector of forces that are exerted onto the master system by subsystem k. Phasor notation is being employed, so the time history of the master system's response, for example, is obtained as $\mathbf{q}(t) = \mathrm{Re}\left(\mathbf{q}(\omega)e^{i\omega t}\right)$. In what follows, the dependence on frequency is omitted for ease of notation, e.g., $\mathbf{q}(\omega)$ is denoted simply as $\mathbf{q}$. The equation of motion of subsystem k is

$$\mathbf{D}_k\mathbf{q} = -\mathbf{f}_k \tag{2}$$

where $\mathbf{D}_k$ is the dynamic stiffness matrix of the subsystem. This is a random matrix, which can be decomposed into a deterministic (mean) part and a random part with zero mean:

$$\mathbf{D}_k = \mathbf{D}_{\mathrm{dir}}^{(k)} + \mathbf{D}_{\mathrm{ran}}^{(k)}, \qquad \text{where} \qquad \mathbf{D}_{\mathrm{dir}}^{(k)} := \mathbb{E}\left[\mathbf{D}_k\right] \tag{3}$$

so that (2) can be re-written as

$$\mathbf{D}_{\mathrm{dir}}^{(k)}\mathbf{q} = -\mathbf{f}_k + \mathbf{f}_{\mathrm{rev}}^{(k)}, \qquad \text{where} \qquad \mathbf{f}_{\mathrm{rev}}^{(k)} := -\mathbf{D}_{\mathrm{ran}}^{(k)}\mathbf{q} \tag{4}$$

This subsystem equation of motion can be interpreted in the following way [9]. When a known displacement $\mathbf{q}$ is applied to the subsystem at the interface degrees of freedom, waves travel into the subsystem. If these waves would never be reflected back to the interface, the reaction force $-\mathbf{f}_k$ would be deterministic and equivalent to the reaction force of the unbounded system without any wave scattering, $\mathbf{D}_{\mathrm{dir}}^{(k)}\mathbf{q}$. The corresponding wave field is called the "direct field" of the subsystem. The reflections back to the interface are accounted for by means of a "blocked reverberant force" $-\mathbf{f}_{\mathrm{rev}}^{(k)}$ in order to yield the correct value for $\mathbf{f}_k$. Substitution of (4) into (1) yields

$$\mathbf{D}_{\mathrm{tot}}\mathbf{q} = \mathbf{f} + \sum_k \mathbf{f}_{\mathrm{rev}}^{(k)} \qquad \text{where} \qquad \mathbf{D}_{\mathrm{tot}} := \mathbf{D}_{\mathrm{d}} + \mathbf{D}_{\mathrm{dir}}^{(k)} \tag{5}$$

The dynamic stiffness matrix $\mathbf{D}_{\mathrm{tot}}$ is deterministic. It can be computed as the deterministic stiffness matrix of the master system with unbounded subsystems attached. This implies that, for a known external loading $\mathbf{f}$, the master system response $\mathbf{q}$ can be computed as soon as the blocked reverberant subsystem forces $\mathbf{f}_{\mathrm{rev}}^{(k)}$ are known. There are stochastic quantities which by definition have zero mean, so the ensemble average of the master system displacement $\mathbf{q}$ follows directly from (5). However, in many applications the energetic responses of the master system and the subsystems are of interest, and these require the knowledge of the higher order statistics of $\mathbf{f}_{\mathrm{rev}}^{(k)}$.

2.2 Ensemble average of the harmonic energetic response

In order to compute these statistics, the following assumptions are needed.

Assumption 1. *The random wave scattering in each subsystem is statistically independent from the random wave scattering in the other subsystems and independent from the external loading.*

Assumption 2. *The response of each random subsystem, when viewed across the ensemble of random structures, constitutes a diffuse wave field, in the sense that the random wave scattering is such that a state of maximum entropy is reached.*

When assumption 1 is valid, it follows directly from (5) that the cross-frequency correlation matrix of the complex response amplitudes at angular frequencies ω_1 and ω_2 is given by

$$\mathbb{E}\left[\underbrace{\mathbf{q}(\omega_1)\mathbf{q}^{\mathrm{H}}(\omega_2)}_{:=\mathbf{S}_{q_1q_2}}\right] = \mathbf{D}_{\mathrm{tot}}^{-1}(\omega_1)\left(\mathbb{E}\left[\underbrace{\mathbf{f}(\omega_1)\mathbf{f}^{\mathrm{H}}(\omega_2)}_{:=\mathbf{S}_{f_1f_2}}\right] + \sum_k \mathbb{E}\left[\mathbf{f}_{\mathrm{rev}}^{(k)}(\omega_1)\mathbf{f}_{\mathrm{rev}}^{(k)\mathrm{H}}(\omega_2)\right]\right)\mathbf{D}_{\mathrm{tot}}^{-\mathrm{H}}(\omega_2) \tag{6}$$

For the auto-frequency response, $\omega_1 = \omega_2 = \omega$, and in this case it has been demonstrated [9] that when assumption 2 is valid,

$$\mathbb{E}\left[\mathbf{f}_{\mathrm{rev}}^{(k)}\mathbf{f}_{\mathrm{rev}}^{(s)\mathrm{H}}\right] = \delta_{ks}\frac{4a_k}{\omega\pi n_k}\mathbb{E}\left[E_k\right]\mathrm{Im}\left(\mathbf{D}_{\mathrm{dir}}^{(k)}\right) \qquad \text{and} \qquad \mathbb{E}\left[\mathbf{f}_{\mathrm{rev}}^{(k)}\mathbf{f}_{\mathrm{rev}}^{(s)\mathrm{T}}\right] = 0 \tag{7}$$

where n_k denotes the modal density (i.e., the number of modes per radial bandwidth) of subsystem k and δ_{ks} the Kronecker delta (so $\delta_{ks} = 1$ when $k = s$, and $\delta_{ks} = 1$ when $k \neq s$). The factor a_k is the diffuse field

correction factor that has been introduced in [3]. In most cases a_k will be close to unity, which means that the conventional definition of a diffuse field and the GOE definition lead to approximately the same result. Eq. (7) is the field reciprocity relationship; it is the basis for computing the ensemble average harmonic energetic response. Substitution into (6) yields

$$\hat{\mathbf{S}}_{qq} = \mathbf{D}_{\mathrm{tot}}^{-1} \left(\hat{\mathbf{S}}_{ff} + \sum_k \frac{4\hat{E}_k a_k}{\omega \pi n_k} \tilde{\mathbf{D}}_{\mathrm{dir}}^{(k)} \right) \mathbf{D}_{\mathrm{tot}}^{-\mathrm{H}} \tag{8}$$

where ensemble averages are noted by a hat and imaginary parts by a tilde. This shorthand notation will be employed throughout the remainder of this work. From this result, the ensemble average of the harmonic energetic response of the master system can be computed, once the ensemble averaged total energies of the subsystems are known.

In order to compute the mean subsystem energies, one may write a time-averaged power balance for each subsystem in stationary conditions [10]:

$$P_{\mathrm{in,dir}}^{(k)} + P_k = P_{\mathrm{out,rev}}^{(k)} + P_{\mathrm{diss}}^{(k)} \tag{9}$$

where $P_{\mathrm{in,dir}}^{(k)}$ denotes the power injected into subsystem k by the master system, P_k the power that is directly injected into the reverberant field of subsystem k, $P_{\mathrm{out,rev}}^{(k)}$ the power output, and $P_{\mathrm{diss}}^{(k)}$ the dissipated power, all in a time and ensemble averaged sense. Following the physical interpretation of (4), the excitation coming from the master system acts onto the direct field of the subsystem (before scattering), while the output power comes from the reverberant field (after scattering). In principle, all interfaces belong to the master system and therefore all input power is contained within $P_{\mathrm{in,dir}}^{(k)}$, leaving P_k equal to zero. However, an excitation source with known power may act directly onto a subsystem at a location remote from other interfaces, and in such case it is more convenient to describe that excitation via P_k when the subsystems are weakly coupled through the master system, such that the power P_k that is directly injected into a subsystem by external loading can be approximated to that obtained from a decoupled subsystem. In such case, P_k can be readily computed with conventional SEA procedures [4].

Shorter and Langley [10] have shown that, in an ensemble averaged sense, the power balance (9) can be written as

$$\omega(\eta_k + \eta_{\mathrm{d},k})\hat{E}_k + \sum_j \omega \eta_{jk} \frac{n_k}{a_k} \left(\frac{a_k \hat{E}_k}{n_k} - \frac{a_j \hat{E}_j}{n_j} \right) = \hat{P}_k + \hat{P}_{\mathrm{in},k}^{\mathrm{ext}} \tag{10}$$

where

$$\eta_{\mathrm{d},k} := \frac{2a_k}{\pi n_k} \sum_{r,s} \tilde{D}_{\mathrm{d},rs} \left(\mathbf{D}_{\mathrm{tot}}^{-1} \tilde{\mathbf{D}}_{\mathrm{dir}}^{(k)} \mathbf{D}_{\mathrm{tot}}^{-\mathrm{H}} \right)_{rs} \qquad \eta_{jk} := \frac{2a_k}{\pi n_k} \sum_{r,s} \tilde{D}_{\mathrm{dir},rs}^{(k)} \left(\mathbf{D}_{\mathrm{tot}}^{-1} \tilde{\mathbf{D}}_{\mathrm{dir}}^{(j)} \mathbf{D}_{\mathrm{tot}}^{-\mathrm{H}} \right)_{rs} \tag{11}$$

$$\hat{P}_{\mathrm{in},k}^{\mathrm{ext}} := \frac{\omega}{2} \sum_{r,s} \tilde{D}_{\mathrm{dir},rs}^{(k)} \left(\mathbf{D}_{\mathrm{tot}}^{-1} \mathbf{S}_{ff} \mathbf{D}_{\mathrm{tot}}^{-\mathrm{H}} \right)_{rs} \tag{12}$$

Note that (10) has the same structure as a power balance in conventional statistical energy analysis [4], so η_{jk} has the physical meaning of a coupling loss factor between subsystems j and k. $P_{\mathrm{in},k}^{\mathrm{ext}}$ represents the power input into the direct field of subsystem k due to external loading on the master system only; obviously it is a part of $P_{\mathrm{in,dir}}^{(k)}$. A power balance of the form of Eq. (10) can be constructed for all random subsystems, i.e., for $k = 1, \ldots, N_{\mathrm{r}}$. This leads to the following linear system of equations, which can be solved for the mean subsystem energies:

$$\mathbf{C}_0 \hat{\mathbf{E}} = \hat{\mathbf{P}} + \hat{\mathbf{P}}_{\mathrm{in}}^{\mathrm{ext}} \qquad \text{where} \qquad C_{0,jk} := \delta_{jk}\omega \left(\eta_k + \eta_{\mathrm{d},k} + \sum_j \eta_{jk} \right) - \omega \frac{n_k}{a_k} \sum_j \eta_{jk} \frac{a_j}{n_j} \tag{13}$$

Once $\hat{\mathbf{E}}$ is known, Eq. (8) can be solved for the master system energetic response.

3 Cross-frequency response of a single diffuse subsystem

In the previous section, it was discussed how the ensemble mean of the harmonic energetic response of a combined deterministic-stochastic model of a built-up vibro-acoustic system, the stochastic parts of which carry a diffuse field, can be obtained. The ensemble variance of the harmonic response can also be computed [3], however, for computing the variance of the band-averaged response which is the aim of the present work, a cross-frequency generalization of the diffuse-field reciprocity relationship (7) is needed. Since the correlation between the energetic response at different frequencies is known to decrease in amplitude with increasing frequency separation, it is reasonable to invoke the following assumption.

Assumption 3. *The considered frequency band is sufficiently narrow such that, within this band, both the external loading and the mean random properties of the built-up system are constant.*

From (4), one has that

$$\mathbf{f}_{\text{rev}}^{(k)} = \mathbf{D}_{\text{dir}}^{(k)}\mathbf{q} - \mathbf{f}_k = \mathbf{D}_{\text{dir}}^{(k)}\left(\mathbf{H}_k - \hat{\mathbf{H}}_k\right)\mathbf{f}_k \tag{14}$$

where

$$\mathbf{H}_k := \mathbf{D}_k^{-1} \qquad \text{and} \qquad \hat{\mathbf{H}}_k = {\mathbf{D}_{\text{dir}}^{(k)}}^{-1} \tag{15}$$

The last equality was proven in [1]. If assumption 1 is valid, the external loading onto subsystem k is statistically independent from the properties of that subsystem. From assumption 3, both the external loading on the subsystem and the mean random properties of the subsystem itself are constant. Application of both assumptions leads to

$$\mathbb{E}\left[f_{\text{rev},r}^{(k)}(\omega_1) f_{\text{rev},s}^{(k)}(\omega_2)\right] = \sum_{t,u,\alpha,\beta} D_{\text{dir},rt}^{(k)} D_{\text{dir},su}^{(k)*} \text{Cov}\left[H_{t\alpha}^{(k)}(\omega_1) H_{u\beta}^{(k)*}(\omega_2)\right] \mathbb{E}\left[f_{k,\alpha} f_{k,\beta}^*\right] \tag{16}$$

From this expression, it is clear that the cross-frequency covariance of the reverberant forces of subsystem k can be computed as soon as the cross-frequency covariance between the elements of the frequency response function (FRF) matrix of that subsystem are known.

Therefore, an explicit relationship between a cross-frequency FRF covariance function of a diffuse subsystem and the corresponding auto-frequency FRF covariance function is now derived. This is achieved by generalizing Schroeder's work on the cross-frequency correlation of diffuse field FRF's [8] to arbitrary source and receiver positions. Consider first the impulse response functions $h_{t\alpha}^{(k)}(t)$ and $h_{u\beta}^{(k)}(t)$. They are, respectively, the inverse Fourier transforms of the frequency response functions $H_{t\alpha}^{(k)}(\omega)$ and $H_{u\beta}^{(k)}(\omega)$ which appear in Eq. (16). Since the considered subsystem carries a diffuse field (assumption 2), the joint ensemble average of these impulse response functions satisfies

$$\mathbb{E}\left[h_{t\alpha}^{(k)}(t) h_{u\beta}^{(k)}(t)\right] = \mathbb{E}\left[h_{t\alpha}^{(k)}(0) h_{u\beta}^{(k)}(0)\right] e^{-t/\tau_k}, \quad t \geq 0 \tag{17}$$

where τ_k is the time constant of subsystem k. It relates to the damping loss factor η_k as

$$\tau_k = \frac{1}{\omega \eta_k} \tag{18}$$

In practice, both η_k and τ_k vary slowly and smoothly with frequency, so they can be considered as constant in a limited frequency range. When Eq. (17) is extended to negative values of t as an even function, it represents a cross-power spectral density (in the time domain). This power spectral density is related to the correlation function of the real or imaginary part of the FRF (in the frequency domain) via a Fourier transform. Applying the Fourier transform then results in the following covariance functions in the frequency domain:

$$\text{Cov}\left[\text{Re}\left(H_{t\alpha}^{(k)}(\omega_1)\right), \text{Re}\left(H_{u\beta}^{(k)}(\omega_2)\right)\right] = \text{Cov}\left[\tilde{H}_{t\alpha}^{(k)}(\omega_1), \tilde{H}_{u\beta}^{(k)}(\omega_2)\right] = \frac{C}{1 + \left(\tau_k(\omega_2 - \omega_1)\right)^2} \tag{19}$$

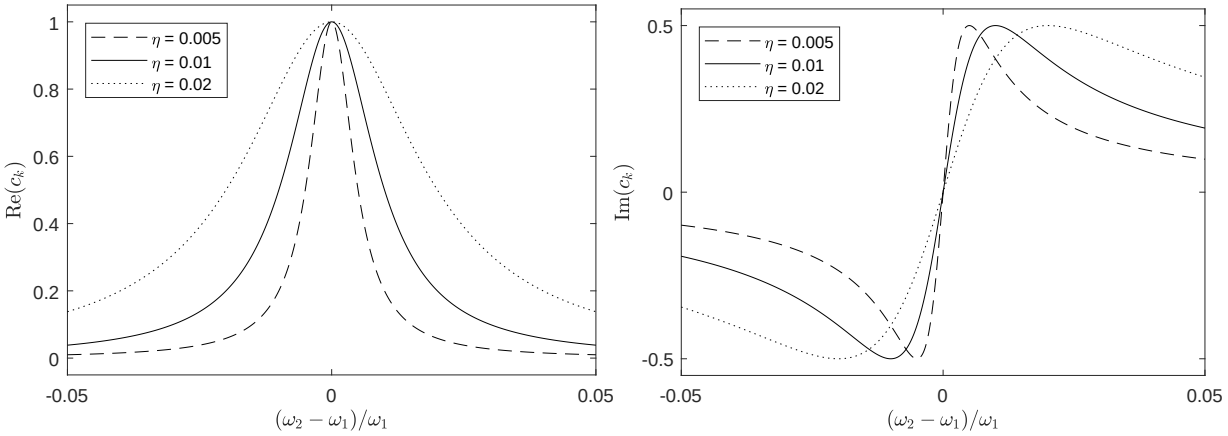


Figure 1: Real and imaginary part of c_k, which represents the ratio between the cross-and auto-frequency spectrum of the reverberant forces of subsystem k, for different values of damping.

where C is a normalization constant, equal to the auto-frequency covariance. Following the lines of [8], one can make use of the fact that the FRF is a causal function and show that

$$\mathrm{Cov}\left[\mathrm{Re}\left(H_{t\alpha}^{(k)}(\omega_1)\right), \tilde{H}_{u\beta}^{(k)}(\omega_2)\right] = \frac{C\tau_k(\omega_2-\omega_1)}{1+\left(\tau_k(\omega_2-\omega_1)\right)^2}. \tag{20}$$

Combining (19) and (20) results in

$$\begin{aligned}\mathrm{Cov}\left(H_{t\alpha}^{(k)}(\omega_1)H_{u\beta}^{(k)*}(\omega_2)\right) &= \mathrm{Cov}\left[\mathrm{Re}\left(H_{t\alpha}^{(k)}(\omega_1)\right), \mathrm{Re}\left(H_{u\beta}^{(k)}(\omega_2)\right)\right] + \mathrm{Cov}\left[\tilde{H}_{t\alpha}^{(k)}(\omega_1), \tilde{H}_{u\beta}^{(k)}(\omega_2)\right] \\ &\quad + \mathrm{i}\left(-\mathrm{Cov}\left[\mathrm{Re}\left(H_{t\alpha}^{(k)}(\omega_1)\right), \tilde{H}_{u\beta}^{(k)}(\omega_2)\right] + \mathrm{Cov}\left[\tilde{H}_{t\alpha}^{(k)}(\omega_1), \mathrm{Re}\left(H_{u\beta}^{(k)}(\omega_2)\right)\right]\right) \qquad (21) \\ &= \frac{1+\mathrm{i}\tau_k(\omega_2-\omega_1)}{1+\left(\tau_k(\omega_2-\omega_1)\right)^2}\mathrm{Cov}\left(H_{t\alpha}^{(k)}(\omega)H_{u\beta}^{(k)*}(\omega)\right), \qquad \omega\in[\omega_1,\omega_2] \qquad (22)\end{aligned}$$

This expression provides an explicit relationship between the cross-frequency FRF covariance function and the auto-frequency FRF covariance function.

Substitution of the cross-frequency FRF covariance expression (22) into the cross-frequency reverberant force covariance expression (16) and application of the auto-frequency diffuse field reciprocity relationship (7) results in

$$\mathbb{E}\left[f_{\mathrm{rev},i}^{(k)}(\omega_1)f_{\mathrm{rev},j}^{(s)*}(\omega_2)\right] = c_k(\omega_1,\omega_2)\delta_{ks}\frac{4\hat{E}_k a_k}{\omega\pi n_k}\left(\tilde{\mathbf{D}}_{\mathrm{dir}}^{(k)}\right)_{ij} \quad \text{where} \quad c_k(\omega_1,\omega_2) := \frac{1+\mathrm{i}\tau_k(\omega_2-\omega_1)}{1+\left(\tau_k(\omega_2-\omega_1)\right)^2} \tag{23}$$

This implies that, under the stated assumptions, the diffuse field reciprocity relationship can be generalized to the cross-frequency spectrum of the reverberant forces by multiplying the auto-spectrum with a factor $c_k(\omega_1,\omega_2)$, which depends only on the relative difference between both frequencies and the subsystem damping. This factor is displayed in Fig. 1 for different values of damping. It can be observed that c_k decays to zero when the relative frequency difference increases, and it does more rapidly so for low values of damping. This can be understood from the modal structure of the FRF (see, e.g., [6]): when the damping is low, individual modes only contribute significantly to the FRF in the immediate vicinity of the corresponding natural frequency.

4 Ensemble cross-frequency covariance of the energetic response

A power balance of the form (13) can also be written for each individual member of the random ensemble of the hybrid deterministic-nonparametric random system:

$$\mathbf{C}(\omega)\mathbf{E}(\omega) = \mathbf{P}(\omega) + \mathbf{P}_{\text{in}}^{\text{ext}}(\omega). \tag{24}$$

From assumption 3, one has that the average loading and system quantities that appear in (13) are constant within the considered narrow frequency band. A first-order perturbation of (24) then results in the following expression for the covariance of the subsystem energies:

$$\begin{aligned}\text{Cov}[E_i(\omega_1), E_j(\omega_2)] = &\sum_{k=1}^{N_r}\sum_{s=1}^{N_r} C_{0,ik}^{-1}C_{0,js}^{-1}\left(\delta_{ks}\text{Cov}[P_k(\omega_1), P_s(\omega_2)] + \text{Cov}[P_{\text{in},k}^{\text{ext}}(\omega_1), P_{\text{in},s}^{\text{ext}}(\omega_2)]\right)\\ &+ \sum_{k=1}^{N_r}\sum_{s=1}^{N_r}\sum_{\substack{r=1\\r\neq k}}^{N_r}\left(\left(C_{0,ik}^{-1} - C_{0,ir}^{-1}\right)C_{0,js}^{-1} + \left(C_{0,jk}^{-1} - C_{0,jr}^{-1}\right)C_{0,is}^{-1}\right)\hat{E}_r\text{Cov}[C_{kr}(\omega_1), P_{\text{in},s}^{\text{ext}}(\omega_2)]\\ &+ \sum_{k=1}^{N_r}\sum_{p=1}^{N_r}\sum_{\substack{s=1\\s\neq k}}^{N_r}\sum_{\substack{r=1\\r\neq p}}^{N_r}\left(C_{0,ik}^{-1} - C_{0,is}^{-1}\right)\left(C_{0,jp}^{-1} - C_{0,jr}^{-1}\right)\hat{E}_s\hat{E}_r\text{Cov}[C_{ks}(\omega_1), C_{pr}(\omega 2)].\end{aligned} \tag{25}$$

where $C_{0,ik}^{-1}$ represents element ik of matrix $\mathbf{C}_0^{-1}$. All terms on the right-hand side arise also in the computation of the mean response, except for the covariance terms. These terms can be derived by generalizing the single-frequency approach of [3] with the results of section 3. The results of this derivation are provided in the remainder of this section. The interested reader is referred to [7] for the detailed derivation.

Under assumptions 1, 2 and 3, the relative cross-frequency covariance of the power input into two subsystems k and r due to external loading on the master system satisfies the following expression:

$$\text{Relcov}\left[P_{\text{in},k}^{\text{ext}}(\omega_1), P_{\text{in},r}^{\text{ext}}(\omega_2)\right] := \frac{\text{Cov}\left[P_{\text{in},k}^{\text{ext}}(\omega_1), P_{\text{in},r}^{\text{ext}}(\omega_2)\right]}{\mathbb{E}\left[P_{\text{in},k}^{\text{ext}}\right]\mathbb{E}\left[P_{\text{in},r}^{\text{ext}}\right]} \tag{26}$$

$$= \sum_s \frac{a_s}{\pi m_s'}\frac{\text{Re}\left(c_s(\omega_1,\omega_2)\mathbf{q}^{(0)\text{H}}\mathbf{H}_{ksr}\mathbf{q}^{(0)}\right)\left(\mathbf{q}^{(0)\text{H}}\tilde{\mathbf{D}}_{\text{dir}}^{(s)}\mathbf{q}^{(0)}\right)}{\left(\mathbf{q}^{(0)\text{H}}\tilde{\mathbf{D}}_{\text{dir}}^{(k)}\mathbf{q}^{(0)}\right)\left(\mathbf{q}^{(0)\text{H}}\tilde{\mathbf{D}}_{\text{dir}}^{(r)}\mathbf{q}^{(0)}\right)} \tag{27}$$

where

$$\mathbf{H}_{ksr} := 4\tilde{\mathbf{D}}_{\text{dir}}^{(k)}\mathbf{D}_{\text{tot}}^{-1}\tilde{\mathbf{D}}_{\text{dir}}^{(s)}\mathbf{D}_{\text{tot}}^{-\text{H}}\tilde{\mathbf{D}}_{\text{dir}}^{(r)} + \delta_{kr}\delta_{ks}\tilde{\mathbf{D}}_{\text{dir}}^{(k)} - 2\delta_{rs}i\tilde{\mathbf{D}}_{\text{dir}}^{(k)}\mathbf{D}_{\text{tot}}^{-1}\tilde{\mathbf{D}}_{\text{dir}}^{(r)} + 2\delta_{ks}i\tilde{\mathbf{D}}_{\text{dir}}^{(k)}\mathbf{D}_{\text{tot}}^{-\text{H}}\tilde{\mathbf{D}}_{\text{dir}}^{(r)} \tag{28}$$

$$\mathbf{q}^{(0)} := \mathbf{D}_{\text{tot}}^{-1}\mathbf{f}. \tag{29}$$

and m_k' represents the effective modal overlap factor of subsystem k, which is defined as [4]

$$m_k' := \omega\eta_k' n_k, \qquad \text{where} \qquad \eta_k' := \frac{1}{\omega n_k C_{0,kk}^{-1}}, \tag{30}$$

Again under assumptions 1, 2 and 3, the relative cross-frequency covariance between any two entries of the power balance matrix $\mathbf{C}$ satisfies the following expression:

$$\text{Relcov}[C_{km}(\omega_1), C_{rp}(\omega_2)] = \delta_{mp}|c_m(\omega_1,\omega_2)|^2\frac{\text{Tr}\left(\tilde{\mathbf{D}}_{\text{dir}}^{(k)}\mathbf{G}^{(m)}\tilde{\mathbf{D}}_{\text{dir}}^{(r)}\mathbf{G}^{(m)}\right)}{\text{Tr}\left(\mathbf{G}^{(m)}\tilde{\mathbf{D}}_{\text{dir}}^{(k)}\right)\text{Tr}\left(\mathbf{G}^{(m)}\tilde{\mathbf{D}}_{\text{dir}}^{(r)}\right)} \tag{31}$$

$$+ \sum_s \frac{a_s}{\pi m_s'}\text{Re}\left(c_s(\omega_1,\omega_2)\frac{\delta_{mp}|c_m(\omega_1,\omega_2)|^2\text{Tr}\left(\mathbf{H}_{ksr}\mathbf{G}^{(m)}\right)\text{Tr}\left(\tilde{\mathbf{D}}_{\text{dir}}^{(s)}\mathbf{G}^{(m)}\right) + \text{Tr}\left(\mathbf{H}_{ksr}\mathbf{G}^{(p)}\tilde{\mathbf{D}}_{\text{dir}}^{(s)}\mathbf{G}^{(m)}\right)}{\text{Tr}\left(\mathbf{G}^{(m)}\tilde{\mathbf{D}}_{\text{dir}}^{(k)}\right)\text{Tr}\left(\mathbf{G}^{(p)}\tilde{\mathbf{D}}_{\text{dir}}^{(r)}\right)}\right)$$

where

$$\mathbf{G}^{(m)} := \frac{4a_m}{\omega\pi n_m}\mathbf{D}_{\mathrm{tot}}^{-1}\tilde{\mathbf{D}}_{\mathrm{dir}}^{(m)}\mathbf{D}_{\mathrm{tot}}^{-\mathrm{H}} \tag{32}$$

Still under assumptions 1, 2 and 3, the relative cross-frequency covariance between the power input into subsystems k due to external loading on the master system and any two entries of the power balance matrix $\mathbf{C}$ satisfies the following expression:

$$\mathrm{Relcov}\left[P_{\mathrm{in},k}^{\mathrm{ext}}, C_{rp}\right] = \sum_s \frac{a_s}{\pi m_s'} \frac{\mathrm{Re}\left(c_s(\omega_1,\omega_2)\mathbf{q}^{(0)\,\mathrm{H}}\mathbf{H}_{ksr}\mathbf{G}^{(p)}\tilde{\mathbf{D}}_{\mathrm{dir}}^{(s)}\mathbf{q}^{(0)}\right)}{\left(\mathbf{q}^{(0)\,\mathrm{H}}\tilde{\mathbf{D}}_{\mathrm{dir}}^{(k)}\mathbf{q}^{(0)}\right)\mathrm{Tr}\left(\mathbf{G}^{(p)}\tilde{\mathbf{D}}_{\mathrm{dir}}^{(r)}\right)} \tag{33}$$

Once the cross-frequency covariance of the subsystem energies has been obtained, the cross-frequency covariance of the master system can be computed as follows. Under assumptions 1, 2 and 3, the relative cross-frequency covariance between any two elements of the master system's cross-spectral response matrix satisfies the following expression:

$$\begin{aligned}\mathrm{Cov}\left[\left(\mathbf{q}\mathbf{q}^{\mathrm{H}}(\omega_1)\right)_{ij}, \left(\mathbf{q}\mathbf{q}^{\mathrm{H}}(\omega_2)\right)_{ij}\right] &= 2\left(\mathbf{D}_{\mathrm{tot}}^{-1}\mathbf{f}\mathbf{f}^{\mathrm{H}}\mathbf{D}_{\mathrm{tot}}^{-\mathrm{H}}\right)_{ij}\sum_k \mathrm{Re}\left(c_k(\omega_1,\omega_2)\right)\hat{E}_k G_{ij}^{(k)} \\ &+ \sum_k\sum_s G_{ij}^{(k)}G_{ij}^{(s)}\left(\mathrm{Cov}\left[E_k(\omega_1), E_s(\omega_2)\right]\left(1 + c_k(\omega_1,\omega_2)c_s(\omega_2,\omega_1)\right) + \hat{E}_k\hat{E}_s c_k(\omega_1,\omega_2)c_s(\omega_2,\omega_1)\right)\end{aligned} \tag{34}$$

5 Band-averaged hybrid deterministic-statistical energy analysis

The band-averaged mean energetic response quantities can be directly obtained from the related harmonic quantities by integration over the considered frequency band. For example, the band-averaged energy of subsystem k over frequency band $\Delta = \omega_{\mathrm{u}} - \omega_{\mathrm{l}}$ is defined as

$$E_{k\Delta} := \frac{1}{\Delta}\int_{\omega_{\mathrm{l}}}^{\omega_{\mathrm{u}}} E_k(\omega)d\omega \tag{35}$$

It follows immediately that for relatively narrow bands, in which the external loading and the system statistics are approximately constant, the mean band-averaged energetic response quantities are approximately equal to the corresponding harmonic ones. The mean band-averaged master system response, $\hat{\mathbf{S}}_{qq\Delta}$, is obtained in the same way.

Evaluation of the variance of the band-averaged energetic response quantities requires the computation and integration of the cross-frequency covariances. For example, one has for the variance of the band-averaged energies that

$$\mathrm{Cov}\left(E_{i\Delta}, E_{j\Delta}\right) = \frac{1}{\Delta^2}\int_{\omega_1=\omega_{\mathrm{l}}}^{\omega_{\mathrm{u}}}\int_{\omega_2=\omega_{\mathrm{l}}}^{\omega_{\mathrm{u}}}\mathrm{Cov}\left(E_i(\omega_1), E_j(\omega_2)\right)d\omega_1 d\omega_2 \tag{36}$$

Application of (25) results in

$$\begin{aligned}\mathrm{Cov}[E_{i\Delta}, E_{j\Delta}] &= \sum_{k=1}^{N_r}\sum_{s=1}^{N_r} C_{0,ik}^{-1}C_{0,js}^{-1}\left(\delta_{ks}\mathrm{Var}[P_{k\Delta}] + \mathrm{Cov}[P_{\mathrm{in},k\Delta}^{\mathrm{ext}}, P_{\mathrm{in},s\Delta}^{\mathrm{ext}}]\right) \\ &+ \sum_{k=1}^{N_r}\sum_{s=1}^{N_r}\sum_{\substack{r=1\\r\neq k}}^{N_r}\left(\left(C_{0,ik}^{-1} - C_{0,ir}^{-1}\right)C_{0,js}^{-1} + \left(C_{0,jk}^{-1} - C_{0,jr}^{-1}\right)C_{0,is}^{-1}\right)\hat{E}_r\mathrm{Cov}[C_{kr\Delta}, P_{\mathrm{in},s\Delta}^{\mathrm{ext}}] \\ &+ \sum_{k=1}^{N_r}\sum_{p=1}^{N_r}\sum_{\substack{s=1\\s\neq k}}^{N_r}\sum_{\substack{r=1\\r\neq p}}^{N_r}\left(C_{0,ik}^{-1} - C_{0,is}^{-1}\right)\left(C_{0,jp}^{-1} - C_{0,jr}^{-1}\right)\hat{E}_s\hat{E}_r\mathrm{Cov}[C_{ks\Delta}, C_{pr\Delta}].\end{aligned} \tag{37}$$

The relative covariance of the band-averaged external power inputs follows from the integration of the cross-frequency relative covariance expression (27), leading to

$$\mathrm{Relcov}[P^{\mathrm{ext}}_{\mathrm{in},k\Delta}, P^{\mathrm{ext}}_{\mathrm{in},r\Delta}] = \sum_{s=1}^{N_r} \frac{a_s b_s(\Delta)}{\pi m'_s} \cdot \frac{\mathrm{Re}\left(\mathbf{q}^{(0)H}\mathbf{H}_{ksr}\mathbf{q}^{(0)}\right)\left(\mathbf{q}^{(0)H}\tilde{\mathbf{D}}^{(s)}_{\mathrm{dir}}\mathbf{q}^{(0)}\right)}{\left(\mathbf{q}^{(0)H}\tilde{\mathbf{D}}^{(k)}_{\mathrm{dir}}\mathbf{q}^{(0)}\right)\left(\mathbf{q}^{(0)H}\tilde{\mathbf{D}}^{(s)}_{\mathrm{dir}}\mathbf{r}^{(0)}\right)} \tag{38}$$

where

$$b_s(\Delta) := \frac{1}{\Delta^2}\int_{\omega_1=\omega_{\mathrm{l}}}^{\omega_{\mathrm{u}}}\int_{\omega_2=\omega_{\mathrm{l}}}^{\omega_{\mathrm{u}}} c_s(\omega_1,\omega_2)d\omega_1 d\omega_2 = \frac{1}{\Delta^2}\int_{\omega_1=\omega_{\mathrm{l}}}^{\omega_{\mathrm{u}}}\int_{\omega_2=\omega_{\mathrm{l}}}^{\omega_{\mathrm{u}}} \frac{1+\mathrm{i}\tau_s(\omega_2-\omega_1)}{1+\left(\tau_s(\omega_2-\omega_1)\right)^2}d\omega_1 d\omega_2 \tag{39}$$

$$= \frac{-1}{\tau_s^2\Delta^2}\ln\left(1+\tau_s^2\Delta^2\right) + \frac{2}{\tau_s\Delta}\arctan\left(\tau_s\Delta\right) \tag{40}$$

The relative covariance of the band-averaged entries of the power balance matrix follows from the integration of the cross-frequency relative covariance expression (31):

$$\mathrm{Relcov}[C_{km\Delta}, C_{rp\Delta}] = \sum_s \frac{a_s b_s(\Delta)}{\pi m'_s}\frac{\mathrm{Re}\left(\mathrm{Tr}\left(\mathbf{H}_{ksr}\mathbf{G}^{(p)}\tilde{\mathbf{D}}^{(s)}_{\mathrm{dir}}\mathbf{G}^{(m)}\right)\right)}{\mathrm{Tr}\left(\mathbf{G}^{(m)}\tilde{\mathbf{D}}^{(k)}_{\mathrm{dir}}\right)\mathrm{Tr}\left(\mathbf{G}^{(p)}\tilde{\mathbf{D}}^{(r)}_{\mathrm{dir}}\right)} \tag{41}$$

$$+ \delta_{mp}\mathrm{Re}\left(\frac{\sum_s b_{s\mathrm{R}m}(\Delta)\frac{a_s}{\pi m'_s}\mathrm{Tr}\left(\mathbf{H}_{ksr}\mathbf{G}^{(m)}\right)\mathrm{Tr}\left(\tilde{\mathbf{D}}^{(s)}_{\mathrm{dir}}\mathbf{G}^{(m)}\right) + b_m(\Delta)\mathrm{Tr}\left(\tilde{\mathbf{D}}^{(k)}_{\mathrm{dir}}\mathbf{G}^{(m)}\tilde{\mathbf{D}}^{(r)}_{\mathrm{dir}}\mathbf{G}^{(m)}\right)}{\mathrm{Tr}\left(\mathbf{G}^{(m)}\tilde{\mathbf{D}}^{(k)}_{\mathrm{dir}}\right)\mathrm{Tr}\left(\mathbf{G}^{(p)}\tilde{\mathbf{D}}^{(r)}_{\mathrm{dir}}\right)}\right)$$

where

$$b_{s\mathrm{R}m}(\Delta) := \frac{1}{\Delta^2}\int_{\omega_{\mathrm{l}}}^{\omega_{\mathrm{u}}}\int_{\omega_{\mathrm{l}}}^{\omega_{\mathrm{u}}} c_s(\omega_1,\omega_2)\mathrm{Re}\left(c_m(\omega_1,\omega_2)\right)d\omega_1 d\omega_2 \tag{42}$$

$$= \frac{1}{\Delta^2}\int_{\omega_{\mathrm{l}}}^{\omega_{\mathrm{u}}}\int_{\omega_{\mathrm{l}}}^{\omega_{\mathrm{u}}} \frac{1+\mathrm{i}\tau_s(\omega_2-\omega_1)}{\left(1+\left(\tau_s(\omega_2-\omega_1)\right)^2\right)\left(1+\left(\tau_m(\omega_2-\omega_1)\right)^2\right)}d\omega_1 d\omega_2 \tag{43}$$

$$= \delta_{ms}\frac{\arctan\left(\tau_s\Delta\right)}{\tau_s\Delta} + (1-\delta_{ms})\frac{\beta\left(m,\Delta\right)-\beta\left(s,\Delta\right)}{(\tau_m-\tau_s)(\tau_m+\tau_s)\Delta^2} \tag{44}$$

$$\beta(t,\Delta) := 2\Delta\tau_t\arctan\left(\tau_t\Delta\right) - \ln\left(1+\tau_t^2\Delta^2\right) \tag{45}$$

The relative cross-covariance between the external power inputs and the energy matrix entries follows from the integration of the cross-frequency relative covariance expression (33), leading to

$$\mathrm{Relcov}\left[P^{\mathrm{ext}}_{\mathrm{in},k\Delta}, C_{rp\Delta}\right] = \sum_s \frac{a_s b_s(\Delta)}{\pi m'_s}\frac{\mathrm{Re}\left(\mathbf{q}^{(0)\mathrm{H}}\mathbf{H}_{ksr}\mathbf{G}^{(p)}\tilde{\mathbf{D}}^{(s)}_{\mathrm{dir}}\mathbf{q}^{(0)}\right)}{\left(\mathbf{q}^{(0)\mathrm{H}}\tilde{\mathbf{D}}^{(k)}_{\mathrm{dir}}\mathbf{q}^{(0)}\right)\mathrm{Tr}\left(\mathbf{G}^{(p)}\tilde{\mathbf{D}}^{(r)}_{\mathrm{dir}}\right)} \tag{46}$$

The factors $b_s(\Delta)$ which appear in this expression are the same as in the expression for the power inputs, Eq. (38), so band averaging has the same effect here. As discussed in section 2.2, when a subsystem is loaded directly at a location that is remote from the master system, then the resulting power input may be described via P_k instead of via $P^{\mathrm{ext}}_{\mathrm{in},k}$. A corresponding band-averaged variance expression has already been derived in the literature, yet with a more sophisticated diffuse field model than the one of assumption 2. The interested reader is referred to [2] for details.

Evaluation of the variance of the band-averaged energetic master system response requires, just as for the subsystems, the computation and integration of the cross-frequency covariances:

$$\mathrm{Var}\left[\left(\mathbf{q}\mathbf{q}^{\mathrm{H}}\right)_{ij,\Delta}\right] = \frac{1}{\Delta^2}\int_{\omega_1=\omega_{\mathrm{l}}}^{\omega_{\mathrm{u}}}\int_{\omega_2=\omega_{\mathrm{l}}}^{\omega_{\mathrm{u}}} \mathrm{Cov}\left(\left(\mathbf{q}\mathbf{q}^{\mathrm{H}}(\omega_1)\right)_{ij}, \left(\mathbf{q}\mathbf{q}^{\mathrm{H}}(\omega_2)\right)_{ij}\right)d\omega_1 d\omega_2 \tag{47}$$

After substituting the cross-frequency master system covariance expression (34), one has that

$$\mathrm{Var}\left[\left(\mathbf{q}\mathbf{q}^{\mathrm{H}}\right)_{ij,\Delta}\right] = 2\left(\mathbf{D}_{\mathrm{tot}}^{-1}\mathbf{f}\mathbf{f}^{\mathrm{H}}\mathbf{D}_{\mathrm{tot}}^{-\mathrm{H}}\right)_{ij}\sum_k b_k(\Delta)\hat{E}_k G_{ij}^{(k)} \tag{48}$$
$$+\sum_k\sum_t G_{ij}^{(k)}G_{ij}^{(t)}\left(\mathrm{Cov}\left[E_{k\Delta},E_{t\Delta}\right]+\mathrm{Covm}\left[E_{k\Delta},E_{t\Delta}\right]+\hat{E}_k\hat{E}_t b_{kt}(\Delta)\right)$$

where $b_k(\Delta)$ has been defined in (39),

$$b_{kt}(\Delta) := \frac{1}{\Delta^2}\int_{\omega_1=\omega_\mathrm{l}}^{\omega_\mathrm{u}}\int_{\omega_2=\omega_\mathrm{l}}^{\omega_\mathrm{u}} c_k(\omega_1,\omega_2)c_t(\omega_2,\omega_1)d\omega_1 d\omega_2 \tag{49}$$

$$= \frac{1}{\tau_k\tau_t(\tau_k+\tau_t)\Delta^2}\left(2\tau_k\tau_t\Delta\left(\arctan\left(\tau_k\Delta\right)+\arctan\left(\tau_t\Delta\right)\right)-\tau_t\ln\left(1+(\tau_k\Delta)^2\right)-\tau_k\ln\left(1+(\tau_t\Delta)^2\right)\right) \tag{50}$$

and

$$\mathrm{Covm}\left[E_{k\Delta},E_{t\Delta}\right] := \frac{1}{\Delta^2}\int_{\omega_1=\omega_\mathrm{l}}^{\omega_\mathrm{u}}\int_{\omega_2=\omega_\mathrm{l}}^{\omega_\mathrm{u}}\mathrm{Cov}\left[E_k(\omega_1),E_t(\omega_2)\right]c_k(\omega_1,\omega_2)c_t(\omega_2,\omega_1)d\omega_1 d\omega_2 \tag{51}$$

Note that $b_{kk}(\Delta) = b_k(\Delta)$ and that $\mathrm{Covm}\left[E_{k\Delta},E_{t\Delta}\right]$ can be computed in the same way as $\mathrm{Cov}\left[E_{k\Delta},E_{t\Delta}\right]$, but with the following substitutions:

$$b_s(\Delta)\rightarrow b_{skt}(\omega_l,\omega_u) := \frac{1}{\Delta^2}\int_{\omega_1=\omega_\mathrm{l}}^{\omega_\mathrm{u}}\int_{\omega_2=\omega_\mathrm{l}}^{\omega_\mathrm{u}} c_s(\omega_1,\omega_2)c_k(\omega_1,\omega_2)c_t(\omega_2,\omega_1)d\omega_1 d\omega_2 \tag{52}$$

$$b_{s\mathrm{R}m}(\Delta)\rightarrow b_{s\mathrm{R}mkt}(\omega_l,\omega_u) := \frac{1}{\Delta^2}\int_{\omega_\mathrm{l}}^{\omega_\mathrm{u}}\int_{\omega_\mathrm{l}}^{\omega_\mathrm{u}} c_s(\omega_1,\omega_2)\mathrm{Re}\left(c_m(\omega_1,\omega_2)\right)c_k(\omega_1,\omega_2)c_t(\omega_2,\omega_1)d\omega_1 d\omega_2 \tag{53}$$

These integrals can be analytically evaluated but the related expressions are unwieldy. In the special case where the time constants of all subsystems take the same value, the following concise expressions are obtained:

$$b_{skk}(\Delta) = b_{s\mathrm{R}k}(\Delta) \tag{54}$$

$$b_{s\mathrm{R}sss}(\Delta) = \frac{1}{4(1+\tau_s^2\Delta^2)}+\frac{3}{4\tau_s\Delta}\arctan(\tau_s\Delta) \tag{55}$$

The functions $b_s(\Delta)$, $b_{s\mathrm{R}s}(\Delta)$ and $b_{s\mathrm{R}sss}(\Delta)$ are displayed in Fig. **??** for different values of damping. They are quantitatively different but the differences are relatively small.

6 Numerical example

In this section, the proposed method is verified in a numerical example involving a stiff, simply supported master plate connected to two flexible, simply supported plates with 20 point masses attached at random locations, see Fig. 2. Each of these point masses has 0.75 % of the total mass of the plat.e In the mid-frequency range, the stiff plate exhibits long-wavelength deformation and it are modeled as deterministic, while the thin plates show short-wavelength deformation, and they are modeled as nonparametric random subsystems. The considered assembly is sufficiently simple in order to allow a comparison of the hybrid deterministic-SEA model with an 'exact' model, in which the attached point masses are modeled in detail. The exact model is constructed with the assumed-modes method [5], in which the location of the attached point masses is varied randomly in a total of 1000 Monte Carlo realizations.

The dimensions of the master plate are $1.05\,\mathrm{m}\times 0.95\,\mathrm{m}\times 5\,\mathrm{mm}$, those of the first and second randomized plate are $1.9\,\mathrm{m}\times 2.1\,\mathrm{m}\times 1.25\,\mathrm{mm}$ and $2.625\,\mathrm{m}\times 2.375\,\mathrm{m}\times 1.67\,\mathrm{mm}$, respectively. The randomized

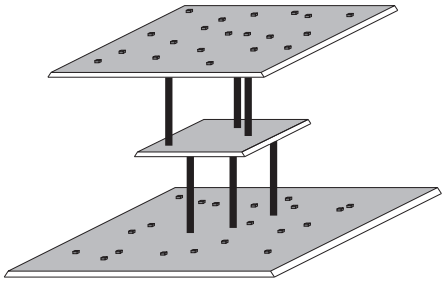


Figure 2: Built-up structure with two flexible plates with point masses attached at random locations, rigidly connected to a common stiff plate.

plates are rigidly connected to the master plate, the first one at the coordinates (0.464,0.762), (0.832,0.525), and (0.161,0.268), which are in meters relative to one corner of the master plate, and the second one at (0.809,0.209), (0.402,0.181), and (0.764,0.723). The material properties of all plates are the same: a density of $\rho = 2800\ \frac{\mathrm{kg}}{\mathrm{m}^3}$, a Young's modulus of $E = 7.2 \cdot 10^{10}\ \frac{\mathrm{N}}{\mathrm{m}^2}$, a Poisson's ratio of $\nu = 0.3$ and a damping loss factor of $\eta = 0.01$. The considered loading consists of a single point force applied to the first random plate at a location that is fixed across the random ensemble. The force has an amplitude of $1\ \mathrm{N}$ at all frequencies.

The mean and relative variance of the plate energy and the master plate's squared amplitude are plotted in Figs. 3 and 4. Fig. 3 displays results for the entire frequency range and two fixed bandwidths, $0\,\mathrm{Hz}$ and $10\,\mathrm{Hz}$. Fig. 4 displays results for a single frequency ($200\,\mathrm{Hz}$) and a range of bandwidths. The hybrid deterministic-SEA predictions are compared with the 'exact' results from a Monte Carlo analysis with the Lagrange-Rayleigh-Ritz model that captures the wave scattering and modal behavior of the random plates in detail. Very good agreement between the hybrid method and the Monte Carlo simulation is obtained.

Averaging over the relatively narrow frequency band of $10\,\mathrm{Hz}$ does not significantly affect the mean energetic response quantities. This indicates that assumption 3 is satisfied in the present example. However, band averaging results in a clear and substantial decrease of the relative variance that is well predicted by the present theory. As seen in Fig. 4, the relative variance predictions remain accurate even when the bandwidth is increased to relatively large values.

7 Conclusions

The hybrid deterministic-SEA method for vibro-acoustic analysis has been extended to predict the variance of band-averaged energetic response quantities. This variance represents the uncertainty caused by the assumption of a diffuse field in the SEA subsystems. The main results are Eq. (37), Eq. (47) and the related expressions. They have a similar structure as the harmonic variance expressions of Langley and Cotoni [3], but additional band-averaging factors are present. An important theoretical result in underpinning the band-averaged variance expressions is the cross-frequency diffuse field reciprocity relationship, Eq. (23). The accuracy of the band-averaged variance expressions has been investigated in a numerical validations against Monte Carlo simulations involving a built-up plate assembly. A very good prediction accuracy has been found. Further details are given in reference [7].

Acknowledgments

This research was funded by the European Research Council (ERC) Executive Agency, in the form of an ERC Starting Grant provided to Edwin Reynders under the Horizon 2020 framework program, project 714591 VirBAcous. The financial support is gratefully acknowledged.

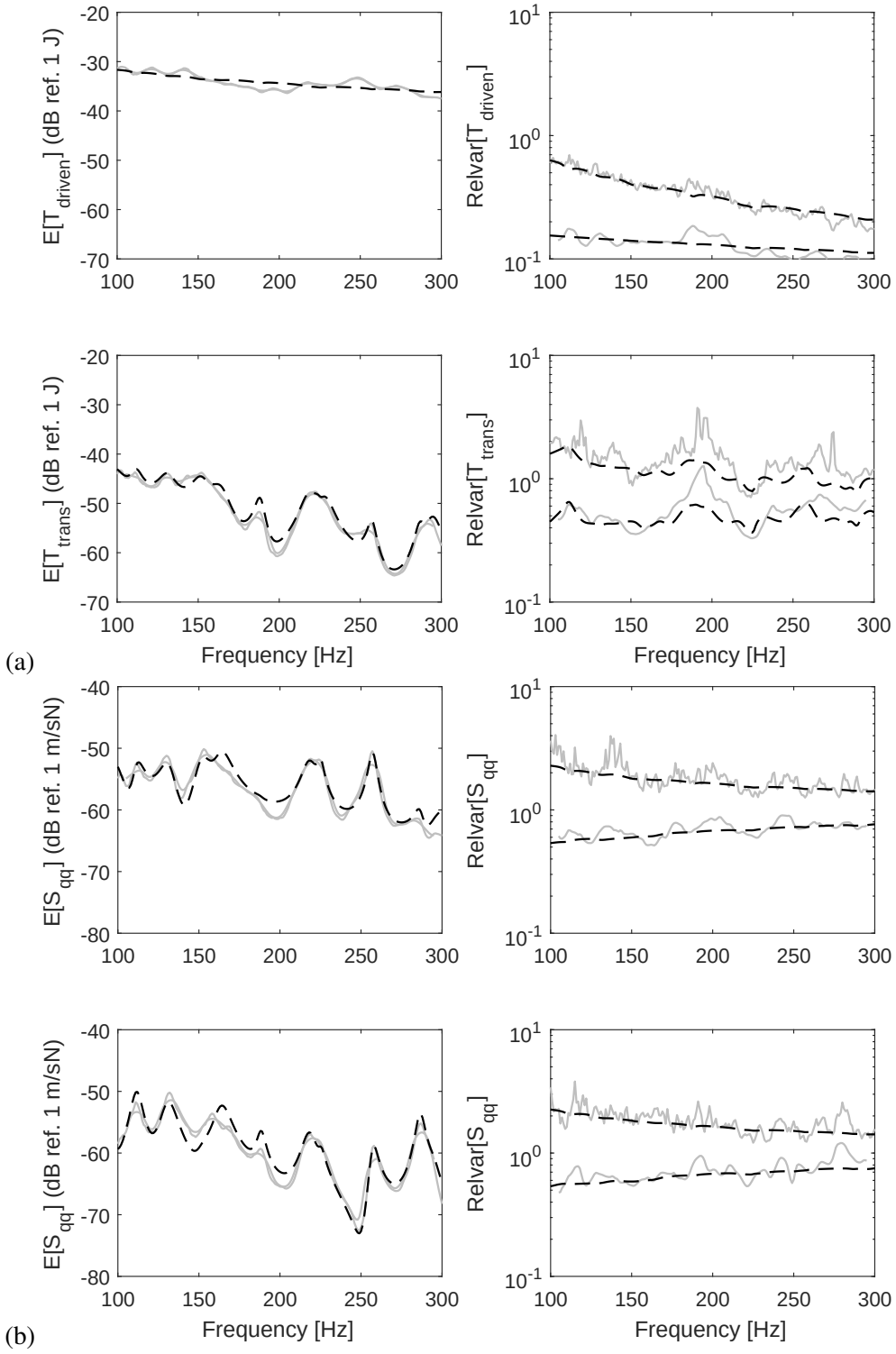


Figure 3: Mean and relative variance of (a) total energies of the driven and nondriven subsystems and (b) squared velocity amplitude of the master plate response at coordinates (0.255,0.142) and (0.760,0.503). Dashed lines: hybrid predictions; solid lines: Monte Carlo simulations. Upper curves: harmonic response, lower curves: band-averaged response for a 10 Hz bandwidth.

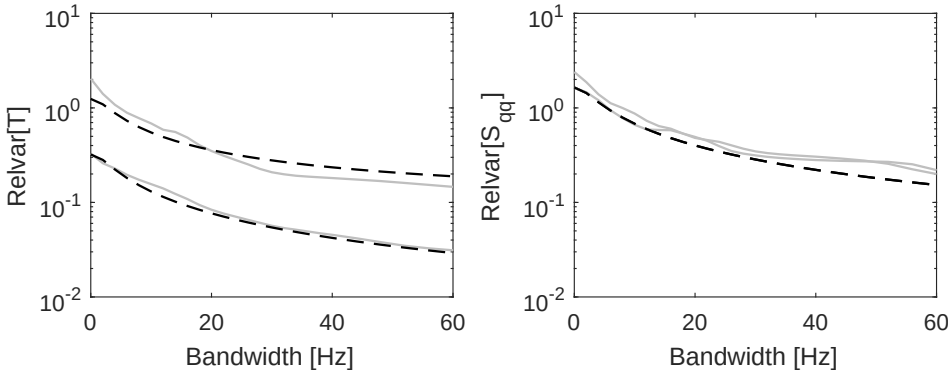


Figure 4: Relative variance of the total energies of the random plates (top line: nondriven subsystem, bottom line: driven subsystem) and relative variance of the squared velocity amplitude of the master plate response at coordinates (0.255,0.142) and (0.760,0.503), for a center frequency of 200 Hz. Dashed lines: hybrid predictions; solid lines: Monte Carlo simulations.

References

[1] R.S. Langley. On the diffuse field reciprocity relationship and vibrational energy variance in a random subsystem at high frequencies. *Journal of the Acoustical Society of America*, 121(2):913–921, 2007.

[2] R.S. Langley and A.W.M. Brown. The ensemble statistics of the band-averaged energy of a random system. *Journal of Sound and Vibration*, 275(3–5):847–857, 2004.

[3] R.S. Langley and V. Cotoni. Response variance prediction for uncertain vibro-acoustic systems using a hybrid deterministic-statistical method. *Journal of the Acoustical Society of America*, 122(6):3445–3463, 2007.

[4] R.H. Lyon and R.G. DeJong. *Theory and application of statistical energy analysis*. Butterworth-Heinemann, Newton, MA, second edition, 1995.

[5] L. Meirovitch. *Elements of vibration analysis*. McGraw-Hill, New York, NY, 1975.

[6] E. Reynders. System identification methods for (operational) modal analysis: review and comparison. *Archives of Computational Methods in Engineering*, 19(1):51–124, 2012.

[7] E.P.B. Reynders and R.S. Langley. Cross-frequency and band-averaged response variance prediction in the hybrid deterministic-statistical energy analysis method. *Journal of Sound and Vibration*, 428:19–146, 2018. Open access.

[8] M. Schroeder. Frequency-correlation functions of frequency responses in rooms. *Journal of the Acoustical Society of America*, 34(12):1819–1823, 1962.

[9] P.J. Shorter and R.S. Langley. On the reciprocity relationship between direct field radiation and diffuse reverberant loading. *Journal of the Acoustical Society of America*, 117(1):85–95, 2005.

[10] P.J. Shorter and R.S. Langley. Vibro-acoustic analysis of complex systems. *Journal of Sound and Vibration*, 288(3):669–699, 2005.

[11] R.L. Weaver. On the ensemble variance of reverberation room transmission functions, the effect of spectral rigidity. *Journal of Sound and Vibration*, 130(3):487–491, 1989.

An experimental investigation of the three-dimensional vibration characteristics of ultrasonic irrigation tips

M. Dannemann [1], **M. Kucher** [1], **M.-T. Weber** [2], **N. Modler**[1]
[1] TU Dresden, Institute of Lightweight Engineering and Polymer Technology (ILK), Faculty of Mechanical Engineering, Holbeinstraße 3, D-01307, Dresden, Germany
e-mail: **martin.dannemann@tu-dresden.de**

[2] TU Dresden, Clinic of Restorative and Pediatric Dentistry, Faculty of Medicine Carl Gustav Carus, Fetscherstraße 74, D-01307, Dresden, Germany

Abstract
During a root canal treatment, fluid streaming and acoustic effects generated by irrigation tip's oscillation, in combination with root canal irrigant dissolve tissue and kill microbes effectively. For a gentle passive ultrasonic irrigation, the frequencies and displacement amplitudes as well as the tip's temperature increase are required to predict streaming effects and the device's fatigue behaviour. As an initial step an operating deflection shape analysis was performed to understand the free vibration behaviour of irrigation tips. The operating frequency and the three-dimensional displacement of two specimens of irrigation tips (IRRI S 21/25, VDW) driven by an ultrasonic irrigation device were measured by means of scanning laser vibrometry. Both irrigation tips oscillated sinusoidally at a frequency of 30 kHz. With growing power level the maximum deflection increased up to 30 µm at the tip's free end. This study can be seen as preliminary investigations of the vibration characteristic of a metallic endodontic tip and will be used to design further experiments under realistic conditions.

1 Introduction

Ultrasonic tips driven by a piezoelectric ultrasonic generator are widespread for dental treatments, especially for effective root canal treatments [1]. Passive ultrasonic irrigation (compare [2, 3]) is the cleaning of root canal systems by means of irrigants and a small tip or wire. The passive ultrasonic irrigation tipes oscillates freely in the root canal and induces acoustic microstreaming. Collis et al. describe, that the effects of cavitation and microstreaming as well as shear stress fields are introduced by microbubbles [4]. The irrigant sodium hypochlorite (NaOCl) reduces friction between the instrument and dentine to prevent the dentine's removal during the dental treatment, dissolves tissue and kills microbes effectively [5]. Ultrasonic vibrations move the irrigant to hard reachable areas, such as lateral canals, isthmi and ramifications [5]. In this way, the impact to root canal walls not touched by mechanical instrumentation is significantly improved by means of irrigant. The deformation of the irrigation tip generates a temperature increase, which can influence the tissue dissolving properties of root canal irrigants [3]. An extensive literature review about ultrasonic irrigation was given by van der Sluis et al. in 2007 [3]. The intensity of the acoustic streaming is directly related to the driving frequency, the diameter of the instrument and the displacement amplitude [3]. The understanding of the ultrasonic irrigation tip's vibration characteristics helps to improve the efficacy of root canal treatments. The investigated ultrasonic irrigation tips operate at frequencies between 28 and 36 kHz and have a displacement amplitude from 4 to 200 µm [6]. Endodontic instruments' oscillations have a high impact, especially the load cycling, on material fatigue and the prediction of canal perforations or instrument fractures [7, 8, 9]. Preliminary investigation of endodontic instruments made of fibre-reinforced polymer composites show that the usage of non-metal irrigation tips has a great potential [10]. Another important

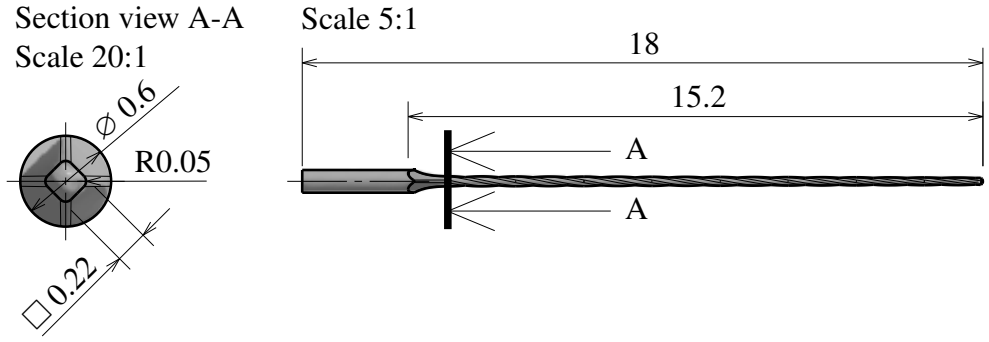


Figure 1: Cross-sectional and longitudinal dimensions of ultrasonic endodontic tip (Irri S 21/25).

aspect to design new dental instruments is the shaping ability of the tip in curved root canals of human teeth. Therefore an assessment and a statistical evaluation of the root canal geometry, especially root canal's curvature and cross-sectional dimensions, is required [11].

There are several studies considering the displacement amplitude of ultrasonic endodontic instruments. Walmsley et al. [12] investigated the effects of constraint on the oscillatory pattern of endosonic irrigation tips compared to the free oscillations in air by means of photomicrograph. Lea et al. measured the vibration characteristic of ultrasonic scalers [13] and endosonic tips using scanning laser vibrometry (SLV) [14]. Similar studies are carried out by Verhaagen et al. [15]; simulating the oscillation characteristics of endodontic tips and validate their numerical results by SLV measurements. Compared to earlier studies [12, 15], the new approach in this study provides the benefit to examine all velocity components and not only an one-dimensional deflection of the transverse bending vibration by means of simultaneously three-dimensional SLV. The employed SLV is an established vibration measurement method and applied on various applications, such as experimental characterisation of sensor-actuator arrays for ultrasonic applications [16] or novel developed sandwich structures for adaptive vibration control [17] and is particularly suitable for measurements of small and light objects.

The aim of this study is the accurate and non-invasive measurement of the temperature development and the three-dimensional operational deflection shapes (ODS) of two ultrasonic irrigation tips for different power levels. The temperature variation of the instrument's active parts and their deflection with the beginning and the operating at driving frequency were determined by means of infrared thermography (IR) and SLV. This study can be seen as a preliminary investigation for further experiments on ultrasonic oscillating endodontic instruments.Using the non-surface-contacting method , the three-dimensional of were measured.

2 Materials and methods

2.1 Specimens and geometrical dimensions

For this study a commercially available ultrasonic irrigation tip (IRRI S 21/25, VDW) was selected. The investigation was carried out for two specimens; in the following denoted as irrigation tip A and irrigation tip B. A high resolution 3D scanner (ATOS SO 4M, GOM) was used to measure the dimensions of these ultrasonic irrigation tips. Resembling the real tip, a CAD geometrical model was created to visualise the tip's dimensions (Figure 1). The instrument's active parts were divided into the sonotrode of the ultrasonic handpiece, and the ultrasonic irrigation tip. The irrigation tip was connected by an angle adapter with the sonotrode. The tip had a blade, a shaft and a transition section between these parts. The total length of the tip's free end was 18 mm with a 15.2 mm long working part, which was made of stainless steel. The shaft's diameter amounted 0.6 mm. The blade had the shape of a right-hand helix with a pitch length of each helix of 3.6 mm and a taper of approximately 0.25 percent. From Figure 1 it can be seen, that the blade had a

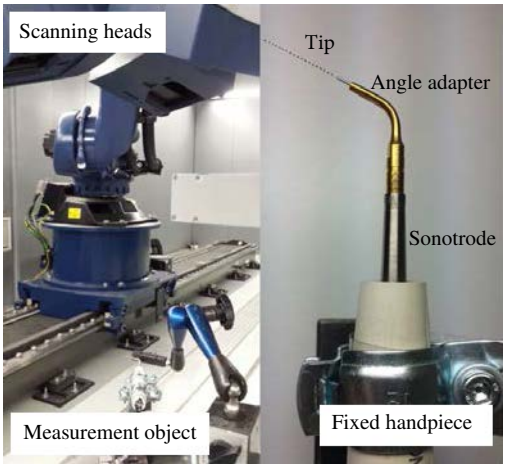


Figure 2: Measurement of the vibration characteristic of ultrasonic irrigation tips using three-dimensional scanning laser vibrometry.

square cross-section with an edge length of 0.22 mm at the beginning of the helix. The edges of the square were rounded and had a corner radius of 0.05 mm.

2.2 Measurement equipment

Due to the irrigation tip's visibility, both measurements were performed for the free oscillation of the ultrasonic irrigation devices in air at a relative air humidity of 52.8 $\pm$ 4.2 percent and a temperature T = 22.8 °C $\pm$ 0.7 K. The operating tip's temperature development was measured for a period of 200 s at a frame rate of 2 Hz by means of an infrared camera (Variocam, Jenoptik). The camera system had a temperature resolution at 30°C up to 0.04 K with a measurement accuracy of $\pm$ 1°C for a temperature measuring range of -40...1,200°C. The temperature measurements were performed with different power settings.

A high voltages generator delivered the power supply of the ultrasonic device (ultrasonic handpiece, VDW); driving the ultrasonic irrigation tip by means of piezoelectric elements at a constant driving frequency. For this excitation, an operating deflection shape analysis was carried out. The ultrasonic tip's vibration characteristics were investigated using a SLV (PSV 500 3D Xtra, Polytec). The SLV consisted of three scanning heads and allowed the measurement of a three-dimensional velocity vector at different measurement positions at the device to obtain the velocity field of the visible measured objects. The vibrometer operated at a velocity range up to 30 m/s with a maximum sampling frequency of 2 MHz. This measurement set-up had the benefit, that all relevant velocity amplitudes of the ultrasonic irrigation tip's oscillating parts were accurately measured and thus the main amplitude can be securely derived.

Using an industrial robot systems, the scanning heads with the integrated video camera were placed perpendicular above the ultrasonic tip at a distance of approximately 450 mm (Figure 2). The camera was used for the alignment and the spatial calibration of the scanning heads. The three scanners of the SLV covered a common area with a diameter of approximately 50...100 µm. A virtual measurement grid was adjusted at the sonotrode, the angle adapter and along a line upon the working part. Using the manufactures original software, a fast Fourier transform (FFT) was performed for a bandwidth from 0...50 kHz for 400 data point, which yielded an frequency resolution of 125 Hz. For the evaluation, a flat top window function with 75 percent overlap and the average of 200 frequency spectra was used. This approach allowed the measurement of all fundamental frequencies as well as higher harmonics.

The operating deflection shape analysis was performed for two new and previously unused ultrasonic tips. Using the oscillation pattern, the displacement u_i at the antinodes (points of maximum oscillation) and half wavelength λ, which represent the distance between two consecutive nodes (points of minimum oscillation), were calculated. For three different power settings P (10 percent power, 20 percent power, 30 percent power)

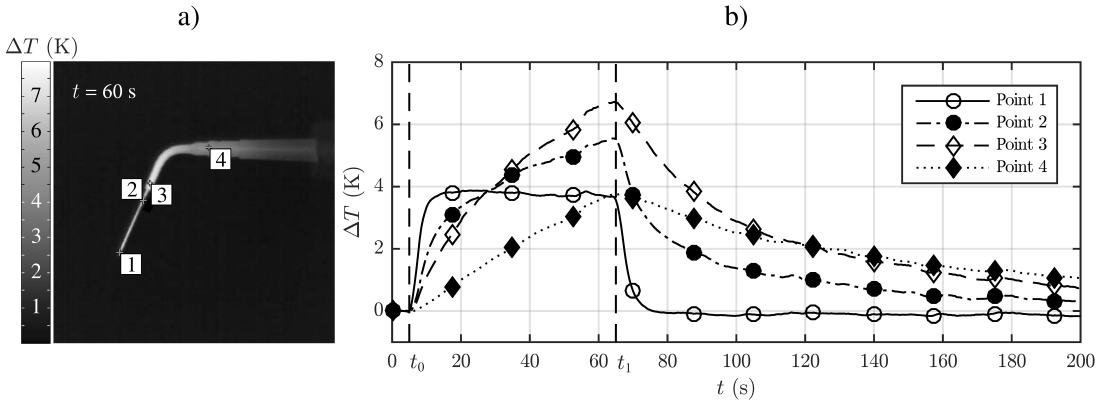


Figure 3: (a) Temperature distribution of ultrasonic irrigation tip A after an operating time of 60 s (between dashed vertical lines at t_0 and t_1) and (b) curve of temperature variation with 30 percent generator power setting at different measurement positions denoted as point 1 to point 4.

Power level (%)	Temperature increase ΔT (K) at different measuring positions			
	Free end (1)	Shaft (2)	Connection (3)	Thread (4)
10	0.1	0.1	0.2	0.1
20	1.6	1.5	1.7	1.1
30	3.8	5.5	6.7	3.8

Table 1: Temperature increase of a ultrasonic irrigation tip A with different generator power levels at the measurement positions illustrated in Figure 3

according to the manufacture's original control dial; markings ensured a repeatable adjustability. During the measurement the irrigation device was mounted to an optical table. The displacement was measured after a setting time of 10 s due to the transient change of the velocity amplitude of the excitation after starting the ultrasonic device. Between each measurement, there was a interruption of 300 s. The oscillation of the ultrasonic tip was damped due to interaction with the surrounding air and material damping. For the estimation of the damping behaviour of the irrigation tip, the velocity's decay curve of one tip was measured and hence the logarithmic decrement Λ was calculated for all investigated power settings and all velocity components.

3 Results

3.1 Temperature development

Due to dissipation effects during the operating of piezoelectric driven generator, the device's active parts warm up. The dashed vertical lines at t_0 and t_1 in Figure 3 represent the generator's operating time interval $t_1 - t_0$ = 60 s. For all power setting, the highest temperatures were reached at the connection between working part and the angle adapter. As expected, it can be seen that with increasing power level the maximum temperature increased (Table 1). The temperature of the irrigation tip's free end quickly grew to a maximum value in less than 10 s and cooled down fast to ambient temperature $T_0 = T(t = t_0)$ when the generator was switched off (Figure 3, b). The heating process of the tip had a proportional transfer function with first order time-delay. This yields the following temperature variation

$$\Delta T(t) = T_\infty - T_0 \left(1 - e^{-\frac{t}{\tau_1}}\right) \quad \text{for} \quad t_0 \leq t < t_1, \tag{1}$$

where $T_\infty = T(t \to \infty)$ is the maximum temperature and τ_1 is the time constant. For 30 percent power level, an evaluation of the time signal of the tip obtained a time constant of T_1 = 1.1 $\pm$ 0.1 s. The temperature

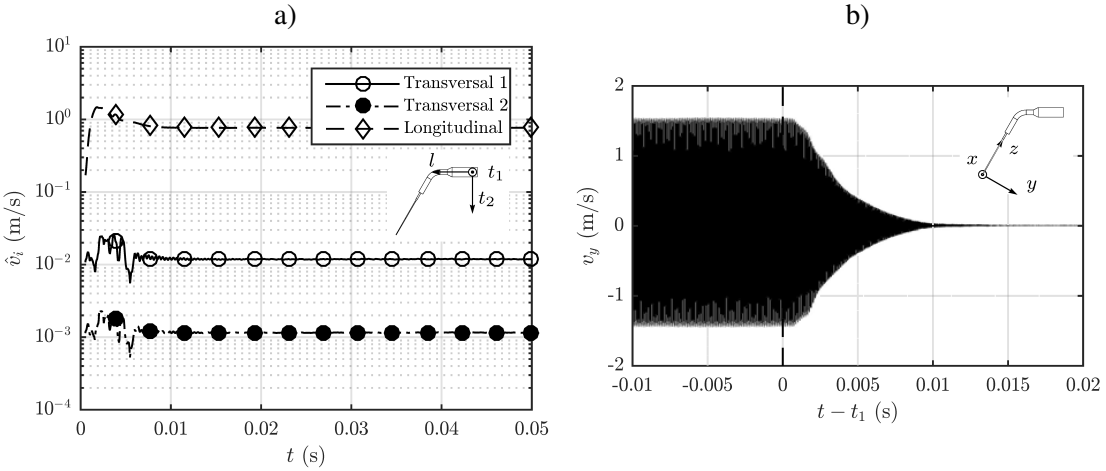


Figure 4: a) Velocity amplitude of the angle adapter of irrigation tip B with 30 percent generator power setting, b) Measured velocity in y-direction after the ultrasonic device's operating (dashed vertical line at $t - t_1 = 0$) and its exponential decay curve

Direction i	Logarithmic decrement Λ at different generator power levels		
	10 %	20 %	30 %
x	0.011	0.011	0.012
y	0.011	0.01	0.013
z	0.01	0.011	0.01

Table 2: Estimation of logarithmic decrement using the free vibrations method of ultrasonic irrigation tip A at different power settings

increased to $T_\infty - T_0 = 0.1$ K for the smallest power level and 3.8 K for 30 percent power. After operating, the temperature rapidly decreased to ambient temperature with according to the time curve of an transient cooling process

$$\Delta T(t) = T_\infty - T_0 \left(e^{-\frac{t}{\tau_2}}\right) \quad \text{for} \quad t \geq t_1. \tag{2}$$

The temperature delay time τ_2 was 3.1 ± 0.14 s for the highest investigated power level. Considering the other investigated positions, the temperature did not reach their maximum value and it decreased much more slowly than the tip's blade.

3.2 Excitation and damping of the endodontic irrigation tip

The piezoelectric driven sonotrode induced vibrations of the angle adapter. For a period of 10 ms, the angle adapter was excited with a transient changing velocity amplitude. The velocity in each direction was up to three times higher than in steady-state condition. After this transient period, the velocity amplitude $\hat{v}_i$ became stationary over the measured time period. The angle adapter's velocity reached values of $v_l = 7.7 \cdot 10^{-1}$ m/s in longitudinal direction and velocities from $v_{t1} = 1.1 \cdot 10^{-2}$ m/s to $v_{t1} = 1.2 \cdot 10^{-3}$ m/s in transversal direction (Figure 4a). The time signals of the angle adapter in longitudinal and transversal directions can be approximated by sine curves and oscillated in a frequency of $f = 1/T = 30.6$ kHz. Taking into consideration the displacement amplitudes, there was, as expected, an almost longitudinal movement of the sonotrode which excited the angle adapter.

Using the time signal after the piezoelectric generator's operating, an exponential decay curve with a decay time of less than 10 ms was determined for irrigation tip A at 30 percent power (Figure 4b). The logarithmic decrement

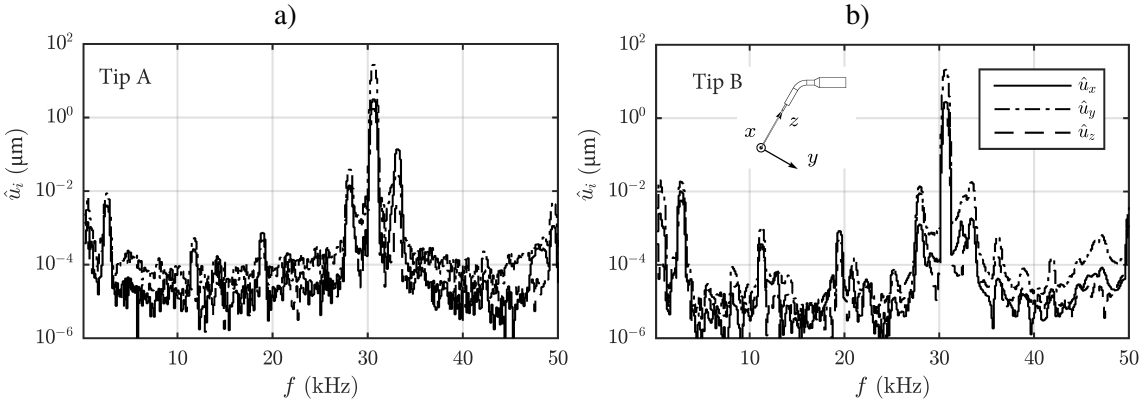


Figure 5: (a) Frequency spectrum of the displacement amplitude with 30 percent generator power setting at the free end of irrigation tip A and (b) of irrigation tip B.

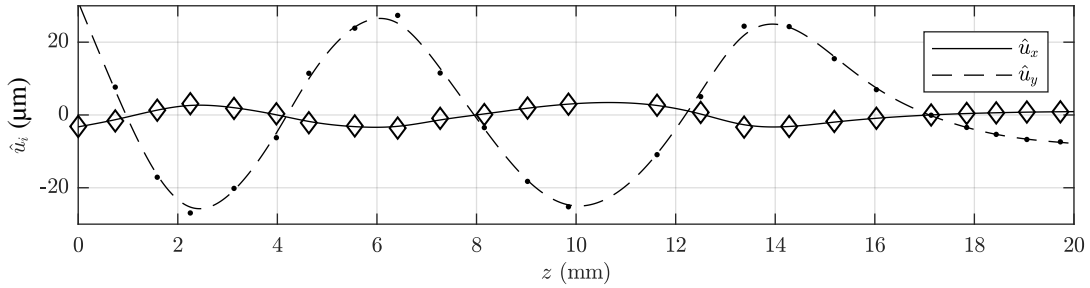


Figure 6: Comparison of displacement amplitude $\hat{u}_i$ of irrigation tip A with 30 percent generator power setting.

Direction i	Specimen	Displacement amplitude $\hat{u}_i$ with different generator power levels (µm)		
		10 %	20 %	30 %
x	Tip A	0.8 ± 0.003	2.5 ± 0.014	5 ± 0.046
	Tip B	0.4 ± 0.052	1.5 ± 0.100	3 ± 0.469
y	Tip A	4.7 ± 0.012	14.7 ± 0.023	28.4 ± 0.430
	Tip B	4.9 ± 0.054	15.6 ± 0.548	30.8 ± 1.490
z	Tip A	0.1 ± 0.010	0.2 ± 0.018	0.6 ± 0.134
	Tip B	0.4 ± 0.068	1.4 ± 0.313	2.3 ± 0.190
$\lvert(\hat{u}_i\rvert$	Tip A	4.8	14.9	28.8
	Tip B	4.9	15.7	31

Table 3: Mean and standard deviation of the maximum measured displacement amplitude of the top end of two ultrasonic irrigation tips at different power settings (f = 30,6 kHz)

$$\Lambda_i = \frac{1}{k} ln \left| \frac{\hat{v}_i(t_0)}{\hat{v}_i(t_0 + kT)} \right|, \tag{3}$$

where k is the number of investigated periods T. The value differed between $1.0{\cdot}10^{-2}$ and $1.3{\cdot}10^{-2}$ for the different power settings and the different three-dimensional direction (Table 2). Averaging all logarithmic decrements, a mean value of $\Lambda = 1.1{\cdot}10^{-2} \pm 9{\cdot}10^{-4}$ was obtained.

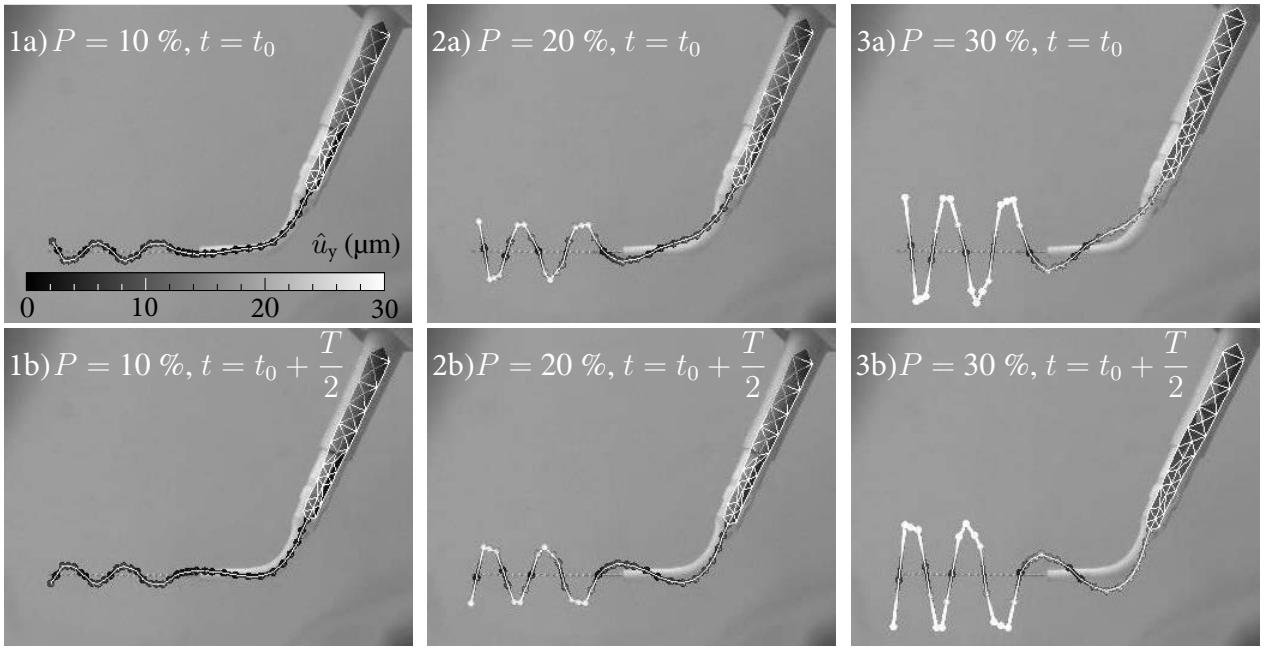


Figure 7: Operating deflection shapes of the ultrasonic irrigation tip A with increasing generator power setting illustrate at both reversal point of the oscillation: (1a, b) P = 10 percent, (2a, b) P = 20 percent,(3a, b) P = 30 percent.

3.3 Vibration characteristics and oscillation pattern

As expected, the irrigation tip's ODS analysis obtained a operating frequency of f = 30.6 kHz; both tips oscillated at the same frequency as the angle adapter (Figure 5). During the steady state oscillation, the highest amplitudes could be seen at driving frequency. Vibrations at other frequencies were excited as well, however theirs amplitudes were very small. The highest displacement amplitude was measured at the irrigation tip's free end at $z = 0$ (Figure 6). With increasing power level, the displacement components increased (Table 3). Considering magnitude of the displacement vector it can be seen that the results differed for the investigated irrigation tips. The tip showed a three-dimensional deflection. The main deflection was in transversal x- and y-direction; the transversal displacement amplitude $\hat{u}_y$ achieved the highest values. There was a axial elongation as well which can be mainly seen as the result of the angle adapter's bending. The bending resulted in a longitudinal displacement of the irrigation tip (compare Figure 7). The axial amplitudes $\hat{u}_y$ were smaller compared to transversal amplitude.

Both irrigation tips had the transverse oscillating pattern of a standing wave (Figure 7) with five nodes and five antinodes. Denoting the antinodes and nodes, starting from the tip's free end, the displacement amplitudes decrease whereas the wavelength simultaneously increased (Figure 8). The nodes and antinodes in x- and y-direction had similar positions (Figure 6). The irrigation tip's displacement amplitudes follow an exponential trend, comparable to Verhaagen et al. [15]

$$\hat{u}_{i,n} = \hat{u}_{i,0} e^{\alpha_i n} \quad \text{for} \quad n \in \mathbb{N}, 0 \leq n \leq n_{\max}, \tag{4}$$

where n is counted from the tip's free end, $\hat{u}_{i,0}$ is the displacement amplitude of the antinode and α_i is the exponential component. Analogously, the wavelength increases linearly and can be approximated by [15]

$$\lambda_{i,n} = \lambda_{i,0} + n\Delta\lambda_i. \tag{5}$$

The wavelength $\lambda_{i,0}$ represented the distance between the first and the second node. Using (4), (5), the maximum number of nodes $n_{\max}$ and the driving frequency of the irrigation tip can be characterised. The resulting parameters are listed in Table 4.

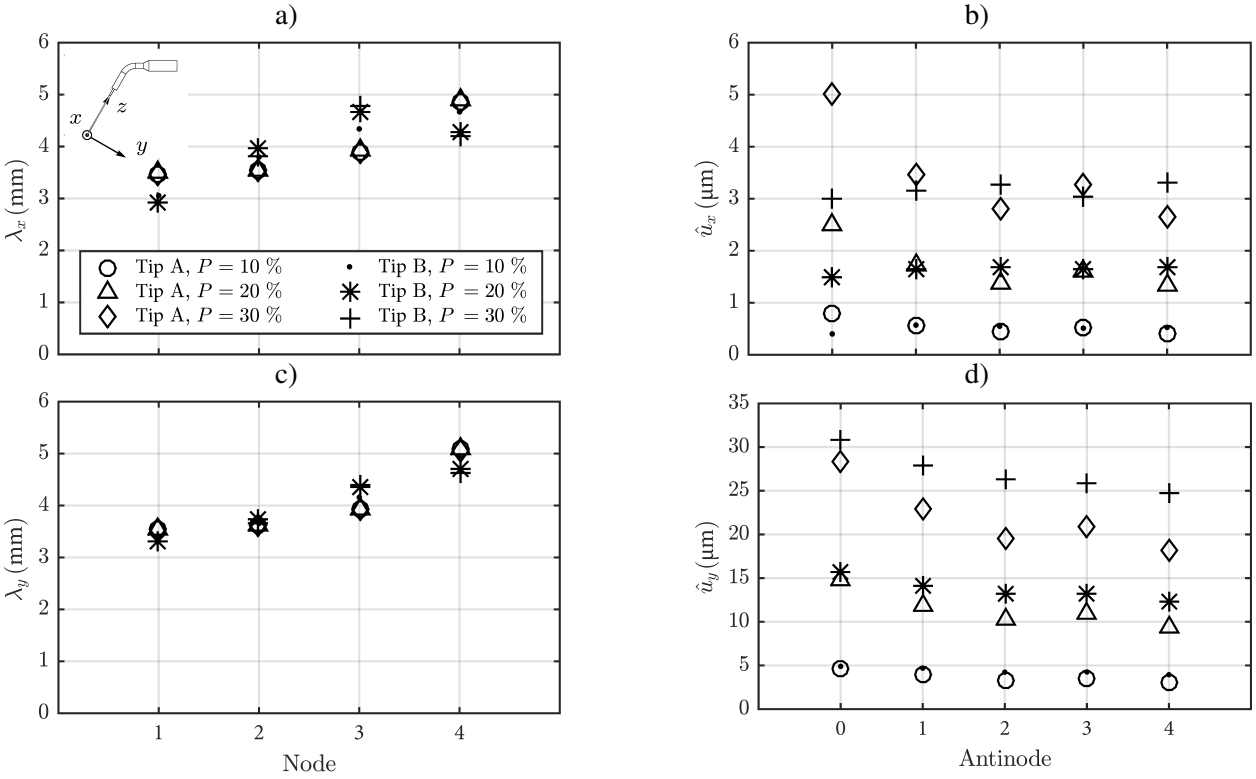


Figure 8: Experimental results of wave pattern characteristics of ultrasonic irrigation tips (Irri S 21/25) starting from the tip's free end: (a) x-component's wavelength and (b) displacement amplitude of the of the transverse wave, (c) y-component's wavelength and (d) displacement amplitude of the transverse wave.

4 Discussion

The characterisation of the ultrasonic irrigation tip's vibration shapes placed high demands on the applied measurement technology due to the small dimensions and design as well as the oscillations at high frequencies. The quantification of the vibration pattern by means of SLV enabled an accurate and non-contacting measurement method of the ultrasonic oscillations. Furthermore, the usage of IRT allowed to measure the temperature variation during the tips sinusoidal oscillation.

The irrigation tip's helical shape consisted of only a few areas approximately perpendicular to beam direction, which allow a correct focusing of the laser beams and ensure a high reflection. Upon the blade this areas restricted the number of measurement positions and thus spatial resolution of the operational deflection shape analysis. However, the number of scanning points allowed the determination of the occurring bending vibration mode. Furthermore, a minimal gradual displacement of the irrigation device was not avoidable and yielded a minimal shifting of the scanning points' position during the measurement. Both effects influenced the results of deflection amplitude and could justify the different measured displacement amplitudes of both investigated specimens. Similar studies on ultrasonic driven endodontic instruments had shown that the deflections differed for structurally identical tips as well [13]. The alignment of the scanning heads to the measured object influences the individual components of the deflection vector. This results in the demand for a subsequent transformation of the coordinate directions according to the irrigation tip's orientation. However, the analysis of the magnitude of the displacement vector allowed a comparison of the vibration characteristics of the measured specimens.

The measurement of vibration characteristic at driving frequency showed that there were lower as well as higher order harmonics, which are around three to four orders smaller than the amplitude at operating frequency and thus were neglected. The longitudinal oscillation of the sonotrode and the angle adapter resulted in bending vibration of the irrigation tip. Comparable to [12, 15], the oscillation pattern had the form of a

Direction i	Specimen	Generator Power level (%)	$\hat{u}_{i,0}$ (µm)	$-\alpha_i$	$\lambda_{i,0}$ (mm)	$\Delta\lambda_i$ (mm)
x	Tip A	10	0.8	0.16	2.77	0.45
	Tip B*		-	-	2.64	0.54
	Tip A	20	2.5	0.16	2.77	0.45
	Tip B*		-	-	2.78	0.5
	Tip A	30	5	0.16	2.78	0.45
	Tip B*		-	-	2.74	0.5
y	Tip A	10	4.7	0.11	2.78	0.49
	Tip B		4.9	0.05	2.71	0.51
	Tip A	20	14.7	0.11	2.78	0.49
	Tip B		15.6	0.06	2.82	0.47
	Tip A	30	28.4	0.11	2.78	0.48
	Tip B		30.8	0.06	2.87	0.44

* The measured displacement amplitudes did not shown an exponential trend.

Table 4: Oscillation pattern characteristic of endodontic tip (Irri S 21/25)

standing wave with five nodes and five antinodes. Counted from the tip's free end, the wavelength increased linearly whereas the displacement amplitude at the antinodes showed an exponential decrease. The discrepancy of this trend, especially for the amplitudes in x-direction could be justified by the finite resolutions of the measuring grid and the lower signal-to-noise ratio. The antinode's and node's position did not change; the deflection amplitude at the antinodes increased with growing power level (Figure 8). In this way it can be seen that the different power settings did not influence the operational deflection shape, though the displacement amplitudes. The highest displacement amplitude was measurable at the free end in transversal direction with an amount of 5 µm (10 percent power), 15 µm (20 percent power) and 30 µm (30 percent power), which represent y-direction in Figure 8. These results were similar to the results of Lea et al. [14] and Verhaagen [15]. Walmsley et al. [12] and Verhaagen et al. [15] considered a transverse oscillation of the irrigation tip. Verhaagen et al. [15] measured the vibrations perpendicular to main direction and identified a sinusoidal oscillation pattern but did not investigate this effect for all endodontic tips. The measurements in this study showed that there were vibrations in all directions (Table 3). According to the coordinate directions in Figure 8, the displacement amplitudes $\hat{u}_x$ and $\hat{u}_z$ differed between almost 0.1 µm and 5 µm. Compared to this investigation, which was performed in air, the majority of the irrigation tip is immersed in irrigant and interacts with the solution in practical use. Taking into consideration the three-dimensional motion of the tip, the fluid-structure interaction (FSI), as argued by Verhaagen et al. [15], had to be considered as three-dimensional as well. This results in more complex relation between the displacement amplitude and the streaming velocity in the irrigant [3]. Further investigations are required, which quantify the three-dimensional FSI of the acoustic microstreaming and the caused shear flow. Especially at the beginning of the irrigation tip's excitation an increase of displacement amplitude was measured. This transient behaviour have to take into consideration for practical use of the endodontic tips. The risk of a fatigue fracture is most probable during this time. To prevent the fracture due to fatigue, the irrigation tip should be replaced after a certain operating time which is not quantified in this study.

The investigation had shown a temperature increase of oscillating parts and obtained the highest value at the connection between the angle adapter and the irrigation tip. This can be seen as dissipation due to friction in the clamping. Further dissipative processes were the transformation of deformation energy into thermal energy, especially at the angle adapter. Both effects causes the damping of the system and obtained an averaged damping ratio of $1.1{\cdot}10^{-2}$. Compared with the damping in a liquid, the influence of the damping effected by FSI decreases in air [15]. Due to the small tip's front-facing area, a small volume, small displacements amplitudes and the low density of air, the interaction with the surrounding air had a neglectable influence [18].

It has to be admitted that the measured temperatures are not completely comparable to the temperature distribution and development in practical use. The boundary conditions, mainly of the irrigation tip's immersed part, differ from a freely oscillating tip in air. However, even in practical use, most vibrating components are surrounded by air and therefore the thermal behaviour, apart from the irrigation tip's behaviour, differs only slightly.

At this stage it should be noted that the deflection shape and the displacement amplitudes will change depending on effects such as the contact pressure, the form and the condition of the contact surface, dentine's material properties and the surrounding fluid. As Walmsley described [12], different constraints influence the irrigation device's oscillations. However this investigation of ultrasonic oscillating irrigation tips can help to quantify the structural-dynamic and thermal FSI related to the movement of ultrasonic irrigation tips.

5 Conclusions

The usage of non-contacting measurement technique enabled the determination of the oscillation characteristics, geometry and operating temperature of ultrasonically driven low mass passive ultrasonic irrigation tips. Using scanning laser vibrometry, the transient, as well as the steady state conditions of the irrigation tip was measured successfully. The sonotrode's longitudinal excitation results in three-dimensional bending vibrations of the irrigation tip; having the highest displacement amplitudes in transversal direction at the tip's free end. The amplitude grows with increasing power level and obtains much higher values when operation starts than in steady-state condition. The irrigation tip's oscillation pattern at steady-state conditions is a sinusoidal wave with antinodes and nodes. During operating, the irrigation tip's temperature increase and reaches the highest values in the clamping due to friction between the irrigation tip and the angle adapter. With increasing power level, the temperature rise grows. The temperature development and operational deflection shape are both different compared to measurements of an immersed instrument. Permanent changing boundary conditions influence the temperature variation as well as the vibration characteristic and are difficult to quantify. Further research is required to investigate the temperature distribution and vibration of immersed irrigation devices within natural root canals and the interaction with the irrigant during a root canal treatment. Nevertheless this study shows the three-dimensional deflection shape and the influence of different power levels on the operating of an ultrasonic irrigation tip and can be used for further investigation in the field of endodontic research.

Acknowledgements

This work was supported by a project grant from the German Research Foundation (grant no. DA 1701/1-1, WE 5838/1-1). We are thankful to the company Polytec GmbH (Polytec-Platz 1-7, D-76337 Waldbronn) for the technical support and assistance with the SLV measurements. The authors deny any conflicts of interest related to this study.

References

[1] M. Dannemann, M. Kucher, R. Gottwald, N. Modler, M.-T. Weber, *Numerical modeling of ultrasonic excited instrument tips made of fibre-reinforced polymers for irrigation in the root canal*, *Proceedings of The 23rd International Congress on Sound and Vibration, Athens, Greece, 2016 July 10-14*, No. 634, Athens (2016), pp. 1-8.

[2] R. N. Weller, J. M. Brady, W. E. Bernier, *Efficacy of ultrasonic cleaning* Journal of Endodontics, Vol. 6, No. 9, Elsevier (1980), pp. 740-743.

[3] L. W. van der Sluis, M. Versluis, M. K. Wu, P. R. Wesselink, *Passive ultrasonic irrigation of the root canal: a review of the literature* International Endodontic Journal, Vol. 40, No. 6, John Wiley & Sons (2007), pp. 415-426.

[4] J. Collis, R. Manasseh, P. Liovic, P. Tho, A. Ooi, K. Petkovic-Duran, Y. Zhu, *Cavitation microstreaming and stress fields created by microbubbles*, Ultrasonics, Vol. 50, No. 2, Elsevier (2010), pp. 273-279.

[5] M. Haapasalo, Y. Shen, Z. Wang, Y. Gao, *Irrigation in endodontics*, British Dental Journal, Vol. 216, No. 6, Springer Nature (2014), pp. 299-303.

[6] F. Engel, M. Böhringer, R. Winters, *Powerful, dedicated endo ultrasonic device with optimal endo tips [online]*. URL http://www.vdw-dental.com/produkte/ultraschall.html [accessed on 11 November 2016], vdw (2015).

[7] J. P. Pruett, D. J. Clement, D. L. Carnes Jr., *Cyclic fatigue testing of nickel-titanium endodontic instruments*, Journal of Endodontics, Vol. 23, No. 2, Elsevier (1997), pp. 77-85.

[8] H. P. Lopes, M. V. Vieira, C. N. Elias, L. S. Gonçalves, J. F. Siqueira Jr., E. J. Moreira, V. T. Vieira, L. C. Souza, *Influence of the geometry of curved artificial canals on the fracture of rotary nickel-titanium instruments subjected to cyclic fatigue tests*, Journal of Endodontics, Vol. 39, No. 5, Elsevier (2013), pp. 704-707.

[9] D. Montalvão, Q. Shengwen, M. Freitas, *A study on the influence of Ni-Ti M-Wire in the flexural fatigue life of endodontic rotary files by using finite element analysis*, Materials Science and Engineering: C, Vol. 40, Elsevier (2014), pp. 172-179.

[10] N. Modler, W. A. Hufenbach, S. Gäbler, R. Gottwald, F. Schubert, M. Dannemann, *Endodontic instuments made of fibre-reinforced polymer composites - preliminary FEM and experimental investigations*, Composites Theory and Practice, Vol. 15, No. 2, The Polish Society of Composite Materials (2015), pp. 95-100.

[11] M. Dannemann, M. Kucher, J. Kirsch, A. Binkowski, N. Modler, C. Hannig, M.-T. Weber, *An approach for a mathematical description of human root canals by means of elementary Parameters* Journal of Endodondics, Vol. 43, No. 4, Elsevier (2017), pp. 536-543.

[12] A. D. Walmsley, A. R. Williams, *Effects of constraint on the oscillatory pattern of endosonic files*, Journal of Endodontics, Vol. 15, No. 5, Elsevier (1989), pp. 189-194.

[13] S. C. Lea, G. Landini, A. D. Walmsley, *Vibration characteristics of ultrasonic scalers assessed with scanning laser vibrometry*, Journal of Dentistry, Vol. 30, No. 4, Elsevier (2002), pp. 147-151.

[14] S. C. Lea, A. D. Walmsley, P. J. Lumley, G. Landini, *A new insight into the oscillation characteristics of endosonic files used in dentistry*, Physics in Medicine and Biology, Vol. 49, No. 10, IOP Science (2004), pp. 2095-2102.

[15] B. Verhaagen, S. C. Lea, G. J. de Bruin, L. W. van der Sluis, A. D. Walmsley AD, M. Versluis, *Oscillation characteristics of endodontic files: numerical model and its validation*, IEEE Transactions on Ultrasonics, Ferroelectrics, and Frequency Control, Vol. 59, No. 11, IEEE (2012), pp. 2448-2459.

[16] K. Holeczek, E. Starke, A. Winkler, M. Dannemann, N. Modler, *Numerical and experimental characterization of fiber-reinforced thermoplastic composite structures with embedded piezoelectric sensor-actuator arrays for ultrasonic applications*, Applied Sciences, Vol. 6, No. 3, MDPI (2016), pp. 1-13.

[17] J. Kozlowska, A. Boczkowska, A. Czulak, B. Przybyszewski, K. Holeczek, R. Stanik, M. Gude, *Novel MRE/CFRP sandwich structures for adaptive vibration control*, Smart Materials and Structures, Vol. 25, IOP Publishing (2016), pp. 1-14.

[18] M. Wesolowski, E. Barkanov, *Air damping influence on dynamic parameters of laminated composite plates*, Measurements, Vol. 85, Elsevier (2016), pp. 239-248.

Tunnelling corrections to wave transmissions on shell structures

N. M. Mohammed [1,3], **S. C. Creagh** [1], **G. Tanner**[1], **D. J. Chappell** [2]
[1] University of Nottingham, School of Mathematics, Nottingham, United Kingdom
e-mail: **pmxnm3@nottingham.ac.uk**

[2] Nottingham Trent University, Nottingham, United Kingdom

[3] University of Sulaimani, Iraq

Abstract
In this paper mid-frequency effects below the ring frequency of curved plates for a cylindrical region smoothly connected to two flat plates using Donnell shell theory has been analysed. We perform ray tracing based on Hamilton's equations derived in the short wavelength regime for bending incident waves. Simple ray tracing gives either total reflection or total transmission; the numerical solution of the full wave equations shows in contrast a smooth transition and exhibits resonant states. In this paper a method that captures wave effects in a ray-tracing treatment on curved plates is presented. We use graph models to account for resonant tunnelling in such curved plates. We successfully find a theoretical expression for the scattering matrix for such bending rays which accounts for tunnelling mediated by resonant states. Our model agrees well with the full wave solution.

1 Introduction

Studying the vibration of mechanical systems and waves in solids especially for very large curved complex structures in the mid-high frequency range is necessary for understanding mechanical waves in structures and how they interact with and radiate into adjacent media. This plays an important role in noise control. Furthermore standard modelling tools, such as finite and boundary element methods for predicting vibrational properties are not scalable to higher frequencies due to the prohibitive increase in model size. One approximation which is well suited for capturing such propagation is ray tracing.

To model the vibro-acoustic response of complex curved solid structures, we want to use the Dynamical Energy Analysis (DEA) method to work on meshed shell structures [1]. DEA is based on local ray tracing approximations with ray trajectories moving along straight lines in each mesh segment and can estimate the flow of vibrational energy in complex structures [2]. DEA describes the ray dynamics well in homogeneous, isotropic, flat plates or on curved shells at high frequencies in the geodesic ray limit. In the case that the curvature of the shell being considered is of the same size of the wavelength, the situation will change as the underlying equations of motion for the curved rays depend on the local radii of curvature. Equations of ray dynamics for energy transport on arbitrarily curved and homogeneous smooth thin shells can be derived from the equations of motion. One of the conventional approaches to describe ray theories for bending waves and in-plane waves (longitudinal and shear) on thin shells has been done by Pierce [3], starting from the general equations for thin shells of arbitrary curvature. Pierce has shown that one can find a local dispersion relation for short wavelength disturbances that includes both bending and in-plane waves. Later, Norris and Rebinsky [4] also derived separate dispersion relations for in-plane and bending waves on arbitrarily shaped shells, which is a simpler form of Pierce's equation. In this work we will use the dispersion relation presented in Norris and Rebinsky [4] for short wavelength that includes both bending and in-plane waves.

We consider wave propagation and the dispersion relation in isotropic complex curved structures. For the sake of simplicity, we start with cylindrical shells. Søndergaard *et al.* [5, 6] studied the ray dynamics for a particular example of two plates joined to a segment of a cylindrical shell below the ring frequeny. This is an important parameter used to indicate the range in which curvature effects are important. They analyzed mid-frequency effects on the dispersion curves in curved plates and their effect on the ray dynamics. Their result depended on a threshold incident wave direction which separates waves that exhibit total reflection and total transmission.

A classical ray incident on a bend can either reflect or pass over it, depending on the angle between the incident ray and the position axis. Therefore, classical ray tracing gives total reflection or total transmission, but the solution of the full wave equations has smooth transition. This smooth transition in one-dimension can be treated using the Wentzel-Kramers-Brillouin (WKB) approximation. Thus to describe the WKB approximation, rays must be extended to complex rays, analogous to tunnelling in quantum mechanics. Complex rays can be found by assuming that time is complex $t = -i\tau$ and changing the position and momentum to complex values: $x = x_r + ix_i$ and $k = k_r + ik_i$ in the equations of motion. For systems with many degrees of freedom, tunnelling is more complicated and this simple picture of tunnelling is no longer valid (see Refs. [7, 8] for more discussions). This work is intended to improve a calculation described in [5] by accounting for tunnelling. In addition to gaining insight into the underlying tunnelling phenomena, we wish to implement these features of ray tracing on curved shell in a DEA treatment.

We will present a thin shell theory on two flat plates joined by a segment of a cylindrical shell below the ring frequency with smooth Gaussian curvature profile in Section 2, an approach similar to [5, 6]. In section 3, we will analyze the dispersion curves in curved plates and their effect on the ray dynamics for bending and in-plane wave propagation. In Section 4, we will derive the ray dynamics for waves propagating on shell from Hamilton's equations of motion which we considered in the Section 3. We will analysis the dynamics in phase space plane for bending rays. Next, we will interpret resonant states in the system in term of resonance condition using a graph model. We will also present a theoretical expression for calculating the scattering matrix for bending rays which accounts for tunnelling mediated by resonant states. We will find complex trajectories for bending incident rays. In the last section, we compare our result with the solution for the full wave equations.

2 Thin Shell Theory

The shell equations employed here are discussed in more detail by Pierce [3], and Norris and Rebinsky [4]. Both [3, 4], use Donnell shell theory, one of the most widely adopted shell theories. Here, the transverse forces and moments are expressed by the displacement w of the middle surface as known from the theory of laterally loaded plates. For a special case of a shell being curved only along the x direction as shown in Fig. 1, the theory is discussed in more detail by Søndergaard *et al.* [5, 6]. Following Søndergaard *et al.* [5, 6], we start from an isotropic cylindrical shell with radius of curvature R, density ρ, thickness h, Youngs modulus E and Poisson ratio ν. It is assumed that the shell is thin, i.e. $h \ll R$. The coordinate system representing the position on the shell with respect to the direction perpendicular to and tangential to the ridge, shown in Fig. 1, is denoted by $\mathbf{X} = (X, Y)$. The corresponding curvilinear coordinates on the shell are (x, y), where $\mathbf{X} = \mathbf{X}(x, y)$. We consider a Gaussian curvature profile defining smoothly varying curvature along x to interpolates the curvature between zero (flat) and constant (cylinder):

$$\kappa(x) = \kappa_{\text{max}} \ \exp\left(\frac{-1}{2}\left(\frac{x}{\sigma_x}\right)^2\right), \tag{1}$$

where σ_x is the width of the transition region, and κ_{max} is a constant corresponding to the maximum curvature in the cylindrical region. The PDE system in [5] can be reduced here to a set of ordinary differential equations (ODEs). We will use this to extract scattering properties that are independent of the position along the ridge

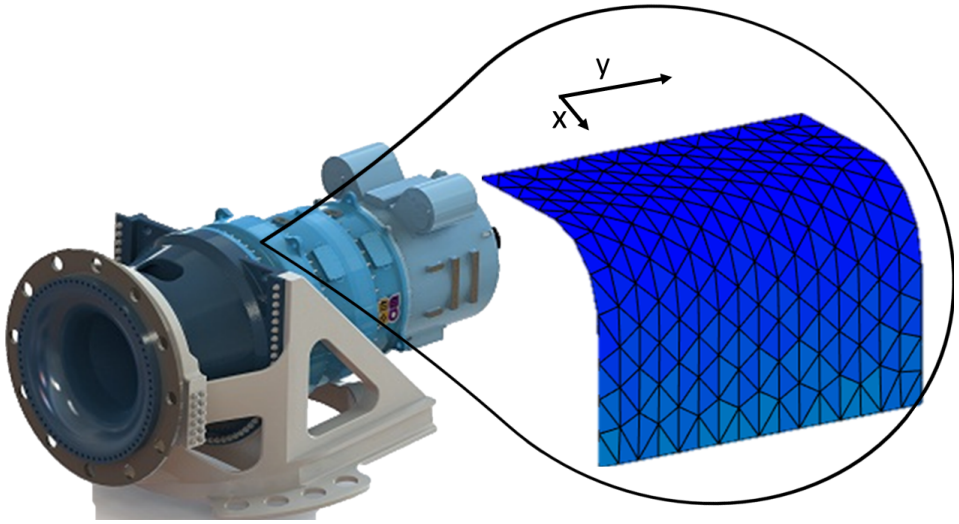


Figure 1: A model of a wind turbine gearbox from Romax Technology; A quarter cylindrical ridge connected to flat plates on either side.

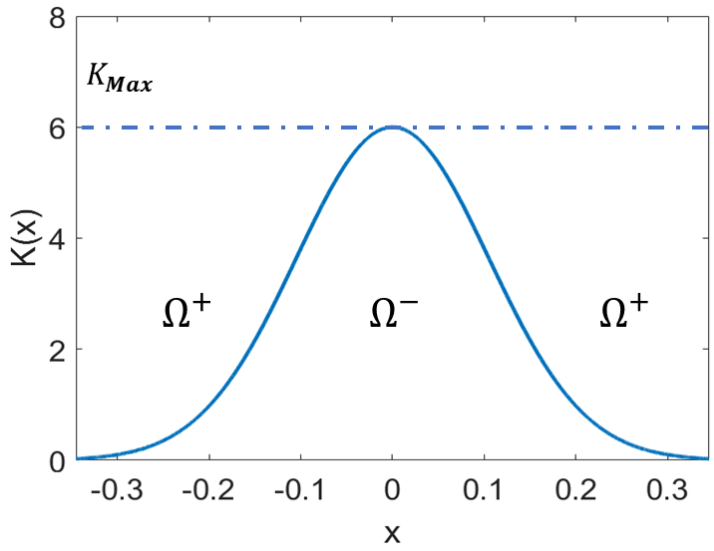


Figure 2: The curvature profile for the problem setting: a cylindrical ridge with the maximum curvature $\kappa_{\max}$ connected to flat plates on either side.The subdivision of the cylindrical ridge geometry into interior Ω^- and exterior Ω^+ regions for the scattering problem. The interfaces between Ω^+ and Ω^- lie with the flat regions where $\kappa(x) = 0$. The curvature increases smoothly to $\kappa(0) = \kappa_{\max}$ for $x \in \Omega^-$.

by exploiting the translational symmetry and assuming that the ridge is of infinite extent in the y- direction. Under these assumptions we may write

$$\mathbf{u}(x,y,t) = \hat{\mathbf{u}}(x)e^{ik_y y - i\omega t}, \tag{2}$$

where $\hat{\mathbf{u}} = [\hat{u}\ \hat{v}\ \hat{w}]^T$ are the coefficients of (2) in the in-plane directions x and y, and the normal direction, respectively; furthermore k_y is the component of the wavenumber in the y-direction and ω is frequency. Substituting the ansatz (2) into the PDE system yields the following fourth-order ODE system in the variable x:

$$c_p^2\frac{d^2\hat{u}}{d^2x} + \left(\omega^2 - c_s^2k_y^2\right)\hat{u} + ik_y\left(c_p^2 - c_s^2\right)\frac{d\hat{v}}{dx} + c_p^2\frac{d}{dx}\left(\kappa\hat{w}\right) = 0, \tag{3a}$$

$$c_s^2\frac{d^2\hat{v}}{d^2x} + \left(\omega^2 - c_p^2k_y^2\right)\hat{v} + ik_y\left(\left(c_p^2 - c_s^2\right)\frac{d\hat{u}}{dx} + \nu c_p^2\kappa\hat{w}\right) = 0, \tag{3b}$$

$$\frac{B}{\rho h}\left(\frac{d^4\hat{w}}{dx^4} - 2k_y^2\frac{d^2\hat{w}}{dx^2} + k_y^4\hat{w}\right) + \left(c_p^2\kappa^2 - \omega^2\right)\hat{w} + c_p^2\kappa\left(\frac{d\hat{u}}{dx} + i\nu k_y\hat{v}\right) = 0, \tag{3c}$$

$$B = \frac{Eh^3}{12(1-\nu^2)}\ ,\ C = \frac{Eh}{1-\nu^2},$$

are the bending and extensional stiffnesses; and the system has been simplified by writing the constants in terms of pressure and shear wave velocities,

$$c_p = \sqrt{\frac{E}{\rho(1-\upsilon^2)}}\ \text{ and }\ c_s = \sqrt{\frac{E}{2\rho(1+\upsilon)}},$$

respectively. We used the following relations

$$c_p^2 = \frac{C}{\rho h},\ \ \frac{c_s^2}{c_p^2} = \frac{(1-\upsilon)}{2}\ \text{ and }\ c_p^2 - c_s^2 = \frac{(1+\upsilon)c_p^2}{2}.$$

The numerical solution of the full wave equations (3) using finite difference methods is discussed in detail in Ref. [6]. The solution typically exhibit a smooth transition between reflective and transmissive behaviour and show anti-resonances (see Fig. 3), which we interpret using a graph model later on.

3 Dispersion Relation in Short Wavelength Asymptotics

Furthermore, we can obtain a dispersion relation which relates the wavelength or wavenumber of a wave to its frequency by assuming:

$$u(x) = a(x)e^{ikS(x)},\ v(x) = b(x)e^{ikS(x)}\ \text{ and }\ \hat{w}(x) = c(x)e^{ikS(x)}, \tag{4}$$

where $S(x)$ is a phase function and $k = \sqrt{k_x^2 + k_y^2}$. Substituting (4) into the equations of motion (3), and choosing the leading order terms regarding the wave number, we can obtain the full dispersion relation for waves propagating over the shell below the ring frequency. For the configuration in Fig. 1 with zero curvature in the y direction we obtain:

$$\begin{aligned} H(x,k,\omega,t) = \left(\Omega^2 - \frac{1}{2}k^2(1-\nu)\right)\left(\left(\Omega^2 - k^2\right)\left(\Omega^2 - \frac{h^2k^4}{12}\right) - \Omega^2\Omega_{\text{ring}}^2\right) \\ +(1-\upsilon^2)\left(\Omega^2\kappa^2k_y^2 - \frac{1}{2}(1-\nu)\kappa^2k_y^4\right), \end{aligned} \tag{5}$$

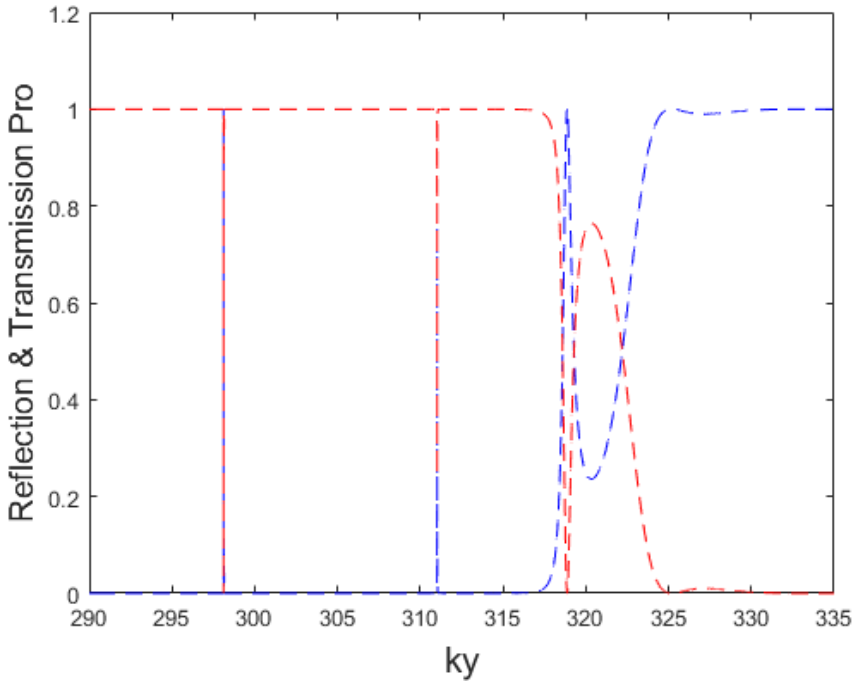


Figure 3: Reflection and transmission probabilities for the bending mode, by solving the full wave equations Eq. (3), as a function of k_y plotted on a linear scale. The plot shows anti-resonances close to $k_y = 318.9$, $k_y = 311$ and $k_y = 298$. There is a switch in the dominant behaviour from transmission to reflection close to $k_y = 319.5$.

where $\Omega = \omega/c_p$ is a wavenumber, and Ω_{ring} denote the wave number at the ring frequency. This dispersion relation includes both bending and in-plane wave. This asymptotic is obtained under the assumption that the wavelength of interest are much shorter than R. For the configuration shown in Fig. 1, Søndergaard *et al.* [5, 6] set $\Omega_{\text{ring}} = \kappa(x)$. The parameters of this work are listed in the appendix. We depicted the dispersion curve at zero curvature see Fig. 4a, i.e. at the flat plates, and at maximum curvature see Fig. 4b, i.e in the cylindrical region. These figures show that in the flat and cylindrical regions we have three different type of modes: bending modes, shear modes and pressure modes. In the cylindrical, region the dispersion surface changes character, the bending mode sheet has a peanut shape which has also been observed experimentally in [9].

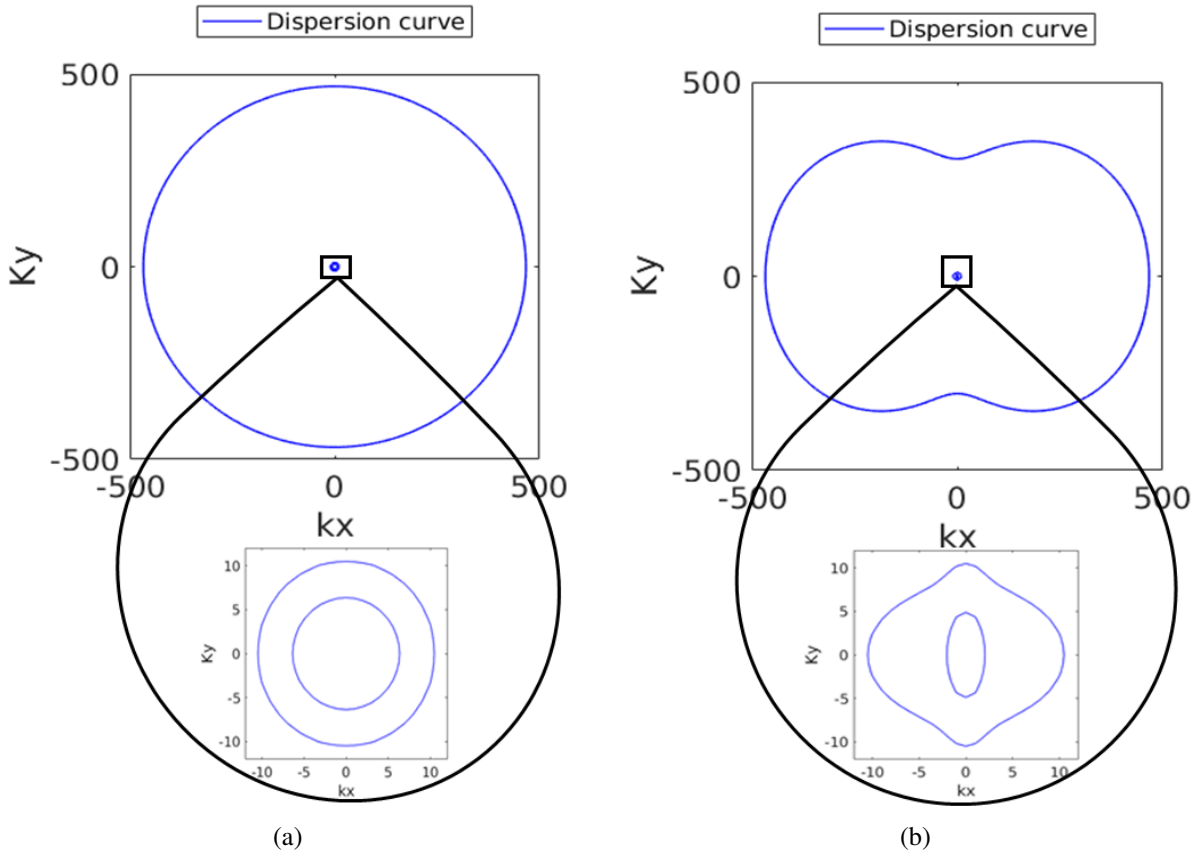
4 Ray Dynamics

The ray equations for energy transport on arbitrary curved and homogeneous smooth thin shells can be derived from the dispersion relation (5) in terms of the Hamilton's equations of motion, that is

$$\dot{x} = \frac{\partial H}{\partial k_x}, \; \dot{k_x} = -\frac{\partial H}{\partial x},$$

$$\dot{y} = \frac{\partial H}{\partial k_y}, \; \dot{k_y} = -\frac{\partial H}{\partial y},$$

$$\dot{t} = -\frac{\partial H}{\partial \omega}, \; \dot{\omega} = \frac{\partial H}{\partial t}.$$



(a) (b)

Figure 4: Dispersion relations represented by plotting $\Omega(k_x, k_y)$ at zeros of the Hamiltonian H; (a) Isotropic dispersion relation at flat plate; the outer circle correspond to bending modes, the middle circle is shear modes and the smallest circle represent pressure modes (b) Anisotropic dispersion relation at cylinder region.

It is clear from Eq. (5) that the Hamiltonian does not depend on t and y explicitly. Thus k_y and ω are constants, i.e. $H(x, k, \omega, t) = \tilde{H}(x, k_x)$. It suffices to study the above Hamiltonian system in the (x, k_x) phase-plane only. The remaining coordinates are suppressed due to the translaional invariance of the cylinder. Fig. 5 shows the bending phase-space; one can see that rays are reflected until they cross the stable manifold (red line) of the fixed points (the blue stars). Those classical trapped rays in the waist of the cylindrical curve are oscillating along the ridge $x = 0$ and form interior resonances. Above the red line the rays transmit. To find the fixed points whose stable and unstable manifolds separate transmission from reflection, we solve for:

$$H(x = 0, k_x, k_y) = 0, \frac{\partial H}{\partial k_x}(x = 0, k_x, k_y) = 0.$$

This gives the threshold value for k_x and k_y in the cylinder region. We find solution numerically, $(k_x, k_y) = (196.8, 320)$ that coincides with the fixed point $(x, k_x) = (0, 196.8)$, see the blue star above the central island region in Fig. 5.

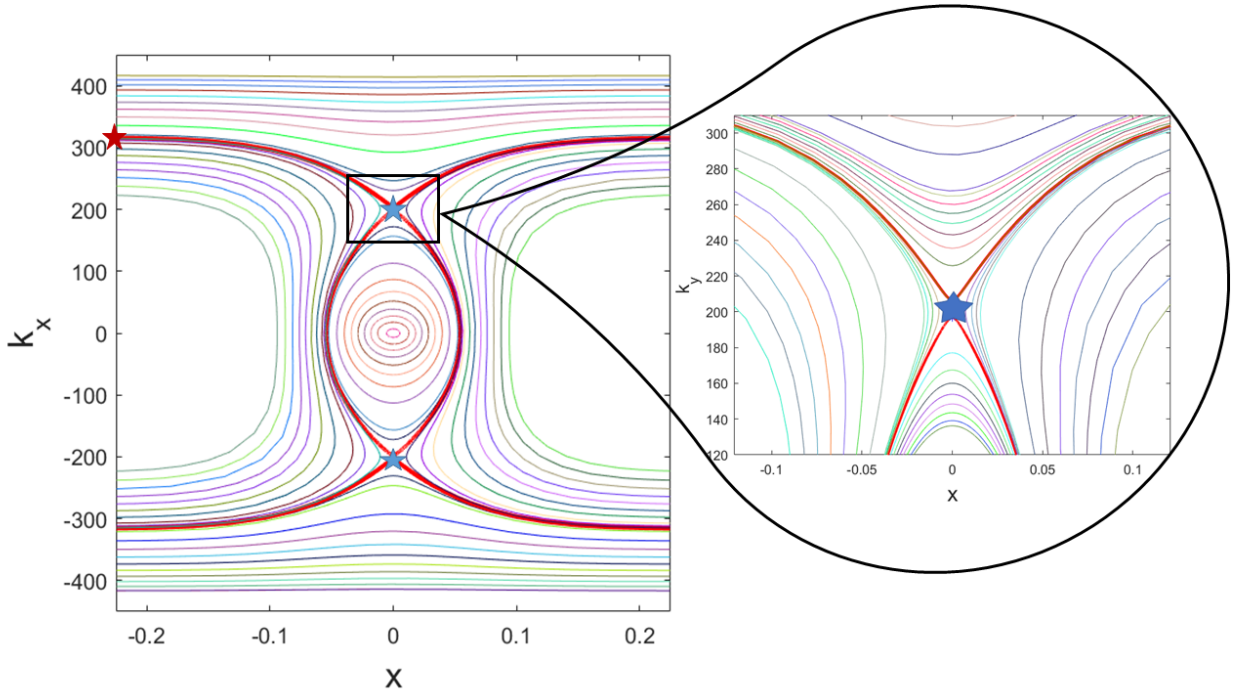


Figure 5: Phase-space plot for bending rays for Gaussian curvature profile; the red star $(k_x, k_y) = (315.7, 320)$ indicate the threshold value at $x = -2.86x^*$; the blue stars below and above the central island region are the fixed points $(0, 196.8)$ and $(0, -196.8)$ respectively; (b) is a close-up plot of the fixed point $(0, 196.8)$.

The next step is for this threshold value of k_y to find the corresponding value k_x in the flat region for rays starting in the left region. For practical purposes, we take $x = -2.86x^*$, where $\pm x^*$ denote the centres of the transition regions. For $k_y = 320$, we solve:

$$H(x = -2.86x^*, k_x, k_y = 320) = 0.$$

These results are similar to those found by Søndergaard *et al.* [5]. We see that for almost normal incidence rays are totally transmitted and for oblique incidence the rays are totally reflected. Thus the smooth transition and anti-resonances in the full wave solution (see Fig. 3) can not be interpreting using simple ray tracing. Next we interpret the phase-space as a graph model to find theoretical expressions for the scattering matrix accounting for resonant tunnelling mediated by resonant states.

5 Graph Model for Resonant Tunnelling

As shown in the phase space for bending incident rays, we have two types of classical rays, see Fig. 5: those with classically transmission behaviour and with classically reflective behaviour and also some rays oscillating in the waist of cylindrical regime which can lead to resonant states. These resonant states can be found using a graph model. We treat the curvature profile as we would a quadratic real potential barrier. We have an explicit formula for the reflection and transmission coefficients following Berry [10] for a potential barrier with quadratic top which has two real classical turning points, given by:

$$r = \frac{-i\exp(-i\delta)}{\sqrt{1+\exp(-2I)}}, \tag{6}$$

$$t = \frac{\exp(-I)\exp(-i\delta)}{\sqrt{1+\exp(-2I)}}, \tag{7}$$

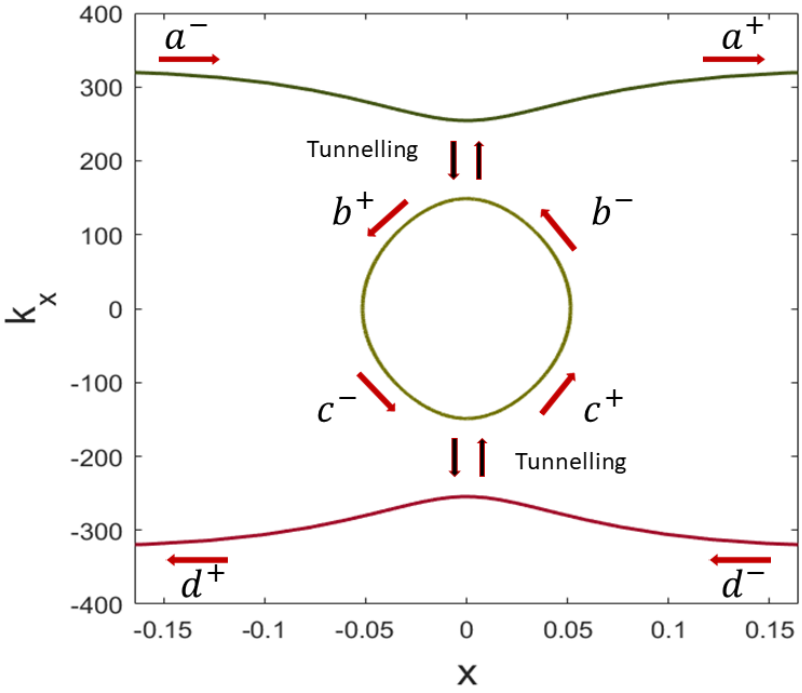


Figure 6: Graph model for resonant tunnelling for ray with classically transmission behavior.

where I is the action along complex orbits and is real valued, which we will discuss in the next section, and the action is defined by

$$I = -i \int_{x_-}^{x+} k_x dx, \tag{8}$$

where x_-, x_+ are the classical turning points and δ is defined as

$$\delta(I) = \frac{I}{\pi} ln \left| \frac{I}{\pi e} \right| + \arg \Gamma \left(\frac{1}{2} - \frac{iI}{\pi} \right), \tag{9}$$

where e is the exponential number. We find the scattering matrix for this problem setting as follows: first, we focus on those rays that are classically transmitting and how they are connected to those rays that are oscillating in the waist of cylindrical regime, Fig. 6. We define a^-, b^-, c^- and d^- as amplitudes of incoming rays, and a^+, b^+, c^+ and d^+ represent outgoing rays from the turning points. We describe the relation between incoming and outgoing ray amplitudes from the turning points as:

$$\begin{bmatrix} a^+ \\ b^+ \end{bmatrix} = \begin{bmatrix} r & t \\ t & r \end{bmatrix} = \begin{bmatrix} a^- \\ b^- \end{bmatrix}, \tag{10}$$

$$\begin{bmatrix} b^- \\ c^- \end{bmatrix} = \begin{bmatrix} 0 & e^{iS} \\ e^{iS} & 0 \end{bmatrix} = \begin{bmatrix} b^+ \\ c^+ \end{bmatrix}, \tag{11}$$

where $S = \frac{1}{2} \oint k_x dx$ is the action along closed real rays trapped in the central island. Furthermore, due to symmetry

$$\begin{bmatrix} d^+ \\ c^+ \end{bmatrix} = \begin{bmatrix} r & t \\ t & r \end{bmatrix} = \begin{bmatrix} d^- \\ c^- \end{bmatrix}. \tag{12}$$

By solving (10), (11) and (12) for a^+ and d^+ as a function of a^- and d^-, we obtain the scattering matrix:

$$\begin{bmatrix} a^+ \\ d^+ \end{bmatrix} = \begin{bmatrix} T & R \\ R & T \end{bmatrix} = \begin{bmatrix} a^- \\ d^- \end{bmatrix}, \tag{13}$$

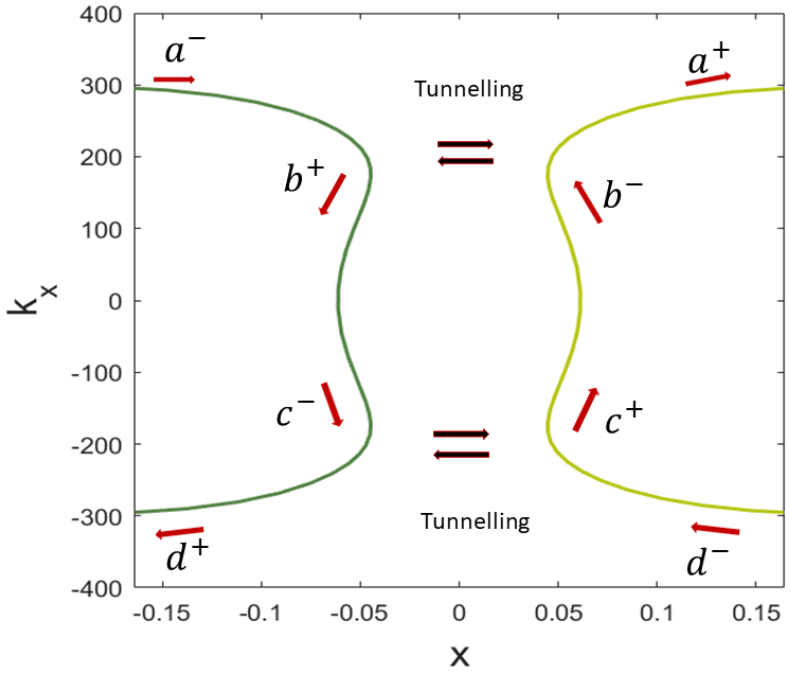


Figure 7: Graph model for resonant tunnelling for ray with classically reflective behavior.

where

$$T = r\left[\frac{1+e^{2iS}(t^2-r^2)}{1-r^2e^{2iS}}\right], \tag{14}$$

$$R = \frac{t^2e^{iS}}{(1-r^2e^{2iS})}, \tag{15}$$

are the transmission and reflection coefficients. Note that both T and R include the term

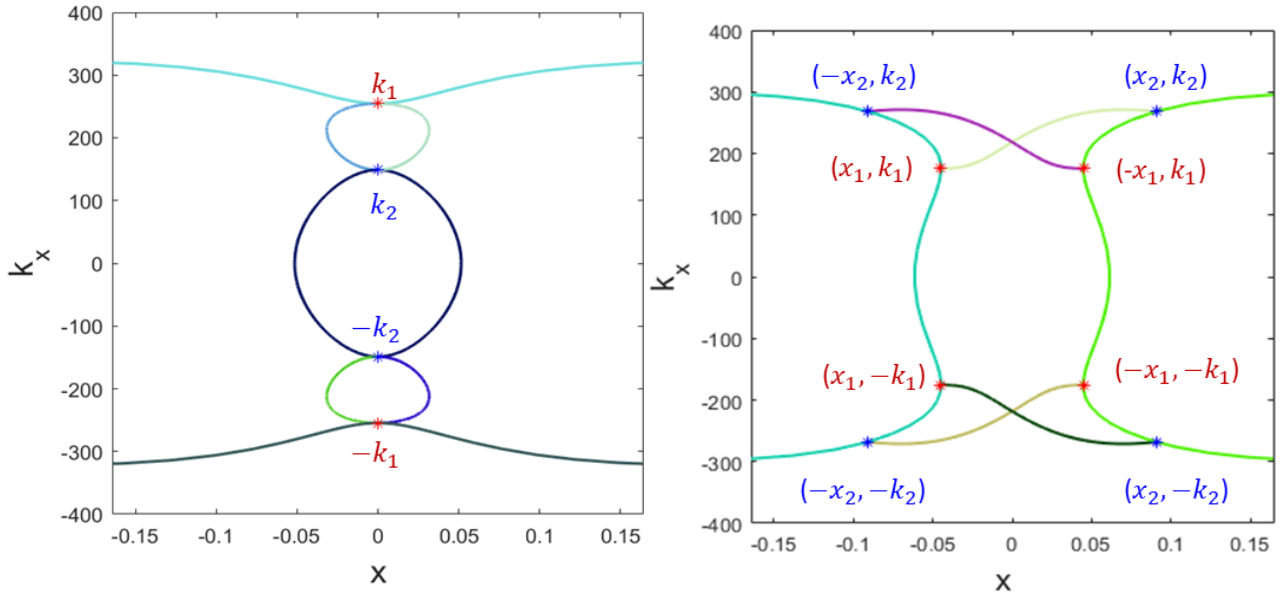
$$\frac{1}{1-r^2e^{2iS}} \simeq \frac{1}{1+e^{2iS}} \text{ if } r \simeq -i,$$

which diverges when $\frac{1}{\pi}S = n + \frac{1}{2}$, where $n = 0, 1, 2, ...$ (resonance condition). That means each time the resonance condition is satisfied a resonance state can form. By a process of analytical continuation that is also valid for the classical rays with reflective behaviour case, Fig. 7. In the next section we will present the method used to find the complex trajectories and then calculate the action along them.

6 The complex method for treating classical turning points (Tunnelling phenomena)

The smooth transition and resonant states in the solution of the full wave equations shown in Fig. 3, in one-dimension can be described using the Wentzel-Kramers-Brillouin (WKB) approximation. To describe the WKB approximation, rays must be extended to complex rays. We want to find the complex trajectories for rays starting at the left interface with the initial position $x_0 = -2.86x^*$ and an initial wave number $k_x = k_{x_0}$, $k_y = k_{y_0}$. First, we transform the equation of motions for the same rays into a new real valued system by substituting $t = -i\tau$, $x = x_r + ix_i$ and $k_x = k_r + ik_i$ as:

$$\frac{dx_r}{d\tau} + i\frac{dx_i}{d\tau} = \frac{dx}{idt} = -i\frac{dx}{dt}, \tag{16a}$$



(a) (b)

Figure 8: Ray trajectories in complex (x, k_x) plane.

$$\frac{dk_r}{d\tau} + i\frac{dk_i}{d\tau} = -i\frac{dk_x}{idt} = -i\frac{dk_x}{dt}. \tag{16b}$$

$$\int_{x_-}^{x+} k_x dx = \int_{x_-}^{x+} (k_r dx_r - k_i dx_i) + i(k_r dx_i + k_i dx_r) = I_r - iI_i. \tag{16c}$$

Next step, we find the classical turning points by fixing $k_y = k_{y_0}$, first for rays with classically transmission behavior, by imposing $x = 0$ and solving

$$H(x = 0, k_x, k_y = k_{y_0}) = 0 \Rightarrow (x, k_x) = (0, k_\alpha),$$

where $\alpha = 1, 2$. For rays with the classically reflective behavior, we solve

$$\begin{aligned} &H(x, k_x, k_y = k_{y_0}) = 0 \\ &\frac{dx}{dt}(x, k_x, k_y = k_{y_0}) = 0 \end{aligned} \quad \Rightarrow (x, k_x) = (x_\alpha, k_\alpha).$$

We calculate reflection and transmission coefficients by solving this new real valued system (16) to find the action $I = I_i$ which is a path integral along complex trajectories from one turning point until it hits the classical trajectories at another turning point. For example from $(0, k_1)$ to $(0, k_2)$ for rays with classical transmission behavior starting at the left interface, and for rays with classical reflective behavior from $(x_1, -k_1)$ to $(x_2, -k_2)$. Calculating the action along the real trajectories S which is area under the classical ray, for example from $(0, k_2)$ to $(0, -k_2)$ for rays with classical transmission behavior, and for rays with classical reflective behavior from $(x_1, -k_1)$ to $(x_2, -k_2)$, plus I_r. $I_r = 0$ for classical transmitted rays. In the next section we show a comparison between our model and the full wave solution.

7 Result

We compare our result with the numerical solution of the full wave equation Fig. 3 for the Gaussian curvature profile. Our model agrees well with the full wave solution see Fig. 9. We find two more resonant states at

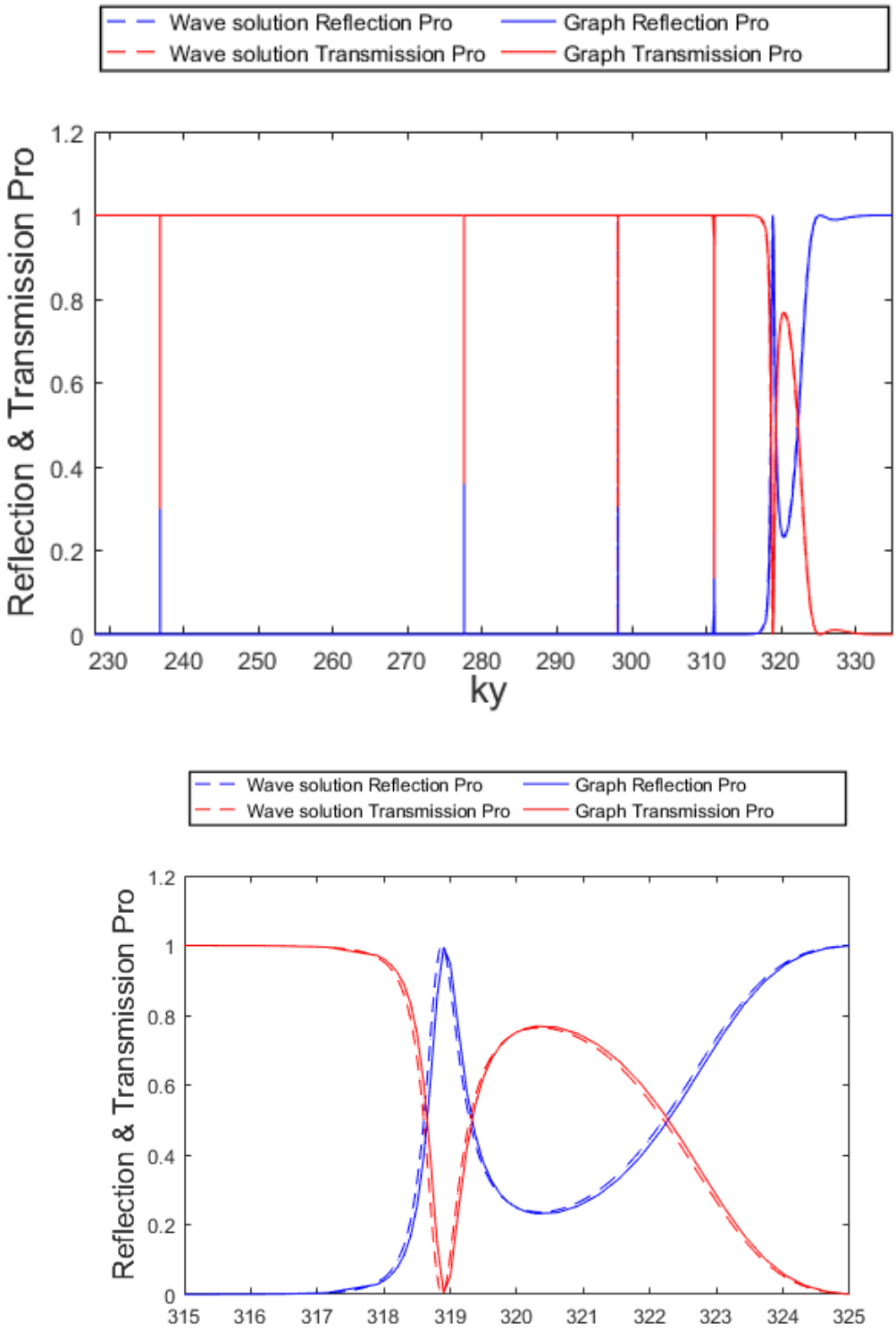


Figure 9: Reflection and transmission probabilities for the bending mode, by solving the full wave equations vs our graph model for resonant tunnelling for Gaussian curvature profile, as a function of k_y. The plot shows anti-resonances close to $k_y = 318.9$, $k_y = 311$, $k_y = 298$, $k_y = 277.5$, $k_y = 237$. There is a switch in the dominant behaviour from transmission to reflection close to $k_y = 319.5$.

$k_y = 277.5$ and $k_y = 237$. These resonances are extremely narrow and and required a very small step size in the k_y initial condition. Our model provides the location of resonances using the condition described in section 5. The local reflection and transmission coefficients given in equations (7) and (6) assume generic hyperbolic fixed points as produced by a quadratic maximum in the curvature profile, but may break down for very flat maxima.

8 Conclusion

We analyse the dispersion curves for both in-plane and bending waves for a cylindrical ridge smoothly connecting to two flat plates using Donnell shell theory. We perform ray tracing from Hamilton's equations of motion in the short wavelength regime for bending incident rays with a Gaussian curvature profile. When waves propagate over the shell structure, this gives rise to tunneling due to the fact that varying curvature from one point to other behaves as a potential barrier in quantum mechanics. These tunnelling correction alter the reflection and transmission coefficient from those obtained by a ray tracing analysis only. There is a smooth transition and resonant states in the solution of the full wave equations which can not be interpreted using classical ray tracing. Tunnelling for this one-dimensional structure can be treated by the WKB methods. We find the scattering matrix and an analytical formula for refection and transmission coefficients for such bending waves by presenting a graph model for resonant tunnelling.Then we compare our results with the numerical solution of the full wave equations. Our model agrees well. Furthermore, we can successfully predict the locations of resonant states occurring in term of a resonance condition from our formula for refection and transmission coefficients.

Acknowledgement

We thank Dr.Sharad Jain for helpful discussion and Romax Technology for financial support.

Parameter values

- $R = 0.1666m.$
- $h = 1 \times 10^{-4}m.$
- $\sigma_x = 0.047m.$
- $x^* = 0.121m.$
- $E = 1.95 \times 10^{11}Pa.$
- $\rho = 7700\frac{kg}{m^3}.$
- $\nu = 0.28.$
- $\omega = 9742\pi\frac{Rad}{s}.$

References

[1] G. Tanner. Dynamical energy analysisdetermining wave energy distributions in vibro-acoustical structures in the high-frequency regime. *Journal of Sound and Vibration*, 320(4):1023–1038, 2009.

[2] D. J. Chappell, D. Loechel, N. Søndergaard, and G. Tanner. Dynamical energy analysis on mesh grids: a new tool for describing the vibro-acoustic response of complex mechanical structures. *Wave Motion*, 51(4):589–597, 2014.

[3] A. D. Pierce. Waves on fluid-loaded inhomogeneous elastic shells of arbitrary shape. *Journal of vibration and acoustics*, 115(4):384–390, 1993.

[4] A. N. Norris and D. A. Rebinsky. Membrane and flexural waves on thin shells. *Journal of vibration and acoustics*, 116(4):457–467, 1994.

[5] N. Søndergaard, D. J. Chappell, and G. Tanner. Tracking vibrational energy on curved shell structures in the mid-high frequency limit-a ray-tracing approach. *Proceedings of Noise and Vibration-Emerging Technologies (NOVEM)*, 251(1):195–204, 2015.

[6] N. Søndergaard and D. J. Chappell. Ray and wave scattering in smoothly curved thin shell cylindrical ridges. *Journal of Sound and Vibration*, 377:155–168, 2016.

[7] Z. H. Huang, T. E. Feuchtwang, P. H. Cutler, and E. Kazes. Wentze-Kramers-Brillouin method in multidimensional tunnelling. *Physical Review A*, 41(1):32–41, 1990.

[8] S. Takada and H. Nakamura. Wentzel-Kramers-Brillouin theory of multidimensional tunnelling: General theory for energy splitting. *The Journal of Chemical Physics*, 100(1):98–113, 1994.

[9] E. G. Williams, B. H. Houston, and J. A. Bucaro. Experimental investigation of the wave propagation on a point-driven, submerged capped cylinder using k-space analysis. *The Journal of the Acoustical Society of America*, 87(2):513–522, 1990.

[10] M. V. Berry and K. E. Mount. Semiclassical approximations in wave mechanics. *Reports on Progress in Physics*, 35(1):315, 1972.

Connectivity in waves and vibrations: one-to-six, one-to-all, all-to-all and random connections

A. Carcaterra[1], N. Roveri[1], A. Akay[2]
[1] Dep. of Mechanical and Aerospace Engineering, Sapienza University of Rome
e-mail: **antonio.carcaterra@uniroma1.it**

[2] Bilkent University, Ankara, Turkey

Abstract
This paper develops a theory of propagation based on connectivity templates. Connectivity describes how the elastic connections distribute. A visual counterpart is the structure of the stiffness matrix. D'Alembert equation refers to classical elasticity based on closest neighbors connectivity and is characterized by propagation of waves, which can be classified as *one-to-six*, since each particle of the scheme is connected only with two other particles for each direction. However, very different connectivity schemes can be introduced, e.g. a *one-to-all connectivity* scheme, in which one particle can be connected with a cluster of particles, or *all-to-all* where each particle is connected with any other. Moreover, connections are not instantaneous: the information flows is delayed due to the connection length. Waves exhibit unbelievable behaviour changing the system connectivity. Nondissipative structures shows damping. Energy can propagate backwards in respect to wave direction. Waves can stop or localize at some points. Negative mass effect can emerge. These effects will be discussed in the present paper.

1 Introduction

This paper has its focus in synthesizing new results in the field of vibrations and waves the authors and the group of structural dynamics of Sapienza introduced in some recent works [1-37]. The dominant concept is that of topological connectivity and its effect on wave propagation, vibration characteristics, damping, modal behavior.

The connectivity in a vibrating system (or more in general, in a dynamical system) is the attribute that indicates the topology of the force exchange among the degrees of freedom of the system under investigation. Thinking to linear systems, interactions can be reduced to displacement proportional force, and the concept of connectivity becomes, for discrete systems, a characteristic of the stiffness matrix. For continuous systems, a general connectivity scheme is represented by integral-differential equations of motion and the connective topology is characterized by the properties of the integral kernel.

Conventional vibrating systems, especially continuous elastic structures, are characterized by closest neighbors interactions: each mass interacts only with its adjacent masses. This connectivity paradigm, denominated here *short-range* interaction, is the basis of the traditional theory of local elasticity. This way to build the connectivity texture in a three-dimensional space and in a regular cubic lattice, includes a six-connection topology: each particle in the lattice is elastically connected to 6 other particles, namely the preceding and the following particles along the three axes x, y, z, respectively. It appears clearly a more arbitrary topological connectivity can be introduced, deeply different from the standard local elasticity, since many others connective schemes can be proposed. Broadly speaking, any other connective template that is more general than the paradigm of the six-connection topology, implies to connect particles in the lattice that not adjacent, but located at distant positions. The reason to indicate these connective schemes as *long-range* [3-5].

This paper makes the point on some fundamental differences that can be expected when passing from a purely *short-range* connectivity to a *long-range* type in vibration characteristics. Correspondently, we highlight some structural differences between the dynamics of *local-elasticity* and *nonlocal-elasticity*. However, our previous investigations show that, in the family of long-range interactions, the emergence of a wide class of different behaviors is observed [3-5, 8, 10, 16-18]. Note, in fact, the *long-range* interaction textures can be deeply different, including many different topologies of connections [3-5].

In this paper we analyze three main types of *long-range* connectivity to compare to *short-range* or closest neighbors: all-all full-range, , all-all limited range , all-all randomly and sparsely connected, one-all. The general mathematical framework is given, but the focus is to outline only the general scenario, and any mathematical detail can be found in the references.

The particles of the scheme behave as individuals of a population, and our investigation represents an attempt to classify the collective behavior of these individuals depending on their freedom to communicate. Implications of this point of view are in vibration properties of the populations as a collective behavior that can affect wave propagation, synchronization, decoherence, damping properties, mode shapes, modal density and localization. These implications can be of practical use in the analysis of microscopical vibrations of lattices (thermal baths) in design of new metamaterials, design of new vibration absorbing devices and waves at interface between two different media [1, 6, 7, 10, 12-14, 16-20, 24-27, 30].

2 Connectivity topology scenarios and properties

In this paper we analyze four main types of *long-range* connectivity to compare to *short-range* or closest neighbors: one-all, all-all full-range, all-all randomly and sparsely connected, all-all limited range.

A set of individuals in a population of masses are connected in a circle (the representation is useful graphically, the system has not to be mechanically connected necessarily in a closed chain), called *ring*. Figure 1 represents the typical connections in a *short-range* interaction fashion, where individuals can communicate, i.e. exchange forces, only with those individuals that are adjacent (red connecting line represent the *short-range* interactions). This is the typical connectivity that mechanically represent the world of *local-elasticity*. The behaviour of such a connected system is well known. One of the main characteristic is the chance of having travelling disturbances we call waves. Energy travels across the ring and two typical speeds can be introduced: phase and group. The spectral properties of theses kind of systems are associated to eigenvectors the shape of which is typically an oscillating space function that involves the whole ring. The characteristic correlation expressed by the waves is the motion of the particles is strongly correlated at a given distance, depending on the propagation velocity (phase or group, depending on the characteristic we desire to correlate).

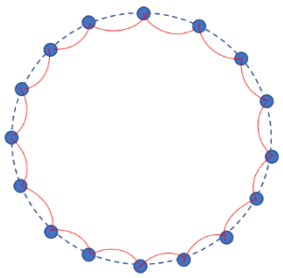


Figure 1. Connectivity based on neighbors interaction, short-range classical case

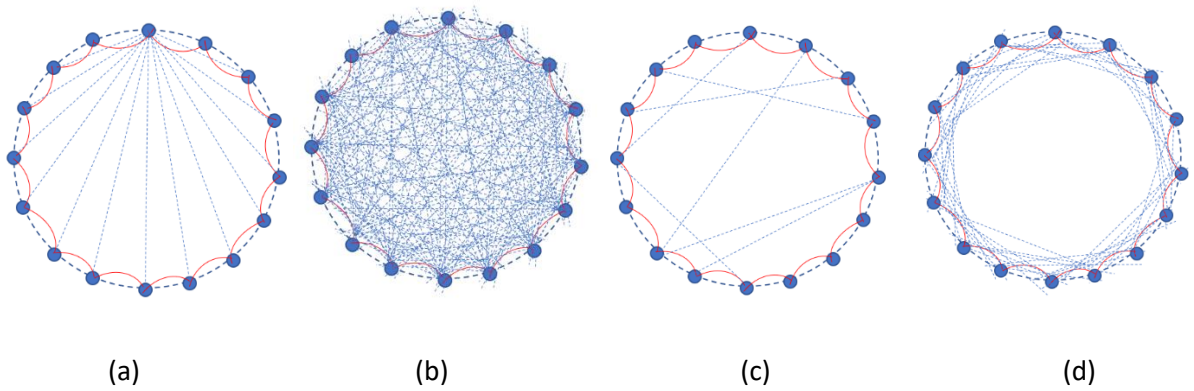


Figure 2.

Different kind of connectivity: (a) one-all, (b) all-all, (c) all-all random sparse, (d) all-all limited range

However, very different topology of connections can be introduced and each characterized by the common fact the interaction is *long-range* in the sense that, along the ring, the connectivity is not only between neighbors, but among distant individuals along the ring. In particular, we would like to describe four basic connectivity templates, that emerge form a previous experience in detailing the dynamics of such systems [3-8, 11, 17, 18, 25, 26, 29] that enter the domain of the propagation in *nonlocal elasticity*.

The one-all scheme is the case in which only a single mass, we call *leader*, generally larger with respect to the other in the ring, communicates with all the individuals of the ring. The short-range connections are general of smaller intensity with respect to the long-range, or they can be even completely absent. This kind of system has been investigated for a long time by the authors and exhibits completely new characteristics with respect to the short-range properties [7, 8, 11, 17-19, 25, 26, 29, 31, 32, 36, 37].

We observed, using mathematical models, simulations and experiments the following:

(i) Waves propagate along the ring, and this happens even in the absence of the short-range forces(!); the propagation speed depends on the distribution law of the intensity of the connections of the scheme.

(ii) For some particular distribution of the interaction forces, one-all connectivity produces a phenomenon of wave stopping: the energy transported along the ring when exciting the connected mass, can stop and the excited mass does not receive any echo from the ring; this means the group velocity along the ring exhibits frequencies at which it vanishes.

(iii) Modes of the ring are localized, and the leader location is never the place at which the modes localize;

(iv) The energy initially stored in the leader tends to be very fast transferred to the ring and it is possible to modulate the intensity of the connections in a way this process is irreversible.

(v) The modes of the ring tend to group at a special frequency, where they are accumulated producing a singularity in the modal density.

The all-all scheme full-range is realized in such systems in which any possible connection between any arbitrariy pair of individuals in the ring is promoted. A recent analysis carried on in [3-5], shows the following remarkable results:

(i) All-all full-range produces a phenomenon of wave stopping along the ring;

(ii) Moreover, at some frequencies, an anomalous propagation phenomenon appears: superluminal propagation of waves along the ring can be observed, meaning the waves transported along the ring itself reach an infinite group velocity.

(iii) Modes of the ring are localized.

(iv) Singularity in the modal density are observed at those frequencies at which the wave stopping is produced.

For the case (d), all-all limited range, the same phenomena, under a qualitative point of view, are identical to those observed in the all-all full-range.

The case (c), in which a small number of connections are present, randomly involving pair of individuals along the ring, i.e. the connections are randomly sparse, exhibits additional effects [41], that are based on the small world theory, originally proposed in social sciences [38-40]:

(i) The number of long-range connections to be introduced to deeply depart from the short-range characteristic propagation is very small. Even a few percent of activated long-range connections permit to observe the following phenomena:

(ii) Strong synchronization of the individual motion, meaning the motion of a large group of masses along the ring move in-phase, and no phase-delay is observed as it happens in the propagation of conventional waves.

(iii) Very high speed of propagation of the disturbance along the ring, with amplification of the group velocity of the system, in part analogous the case observed for limited range and full-range long-distance interaction.

3 *Long-range* effects general modelling

The mathematical model to which we can reduce all the examined cases has a common root into integral-differential equations. Differential equations, both in space and time, is the typical ground on which the local-elasticity operates. A theory of long-range connections includes in general integral convolution terms, analogously in space and time. All the previous cases can be included in the same general model, but with different definition of the kernel of the convolutional part. This kind of model are certainly claimed in the new generation of metamaterials, where the connections can be built up by using, for example, adding manufacturing techniques. The field of vibration absorbers based on new concepts is also part of the possibilities of these methods. The investigation of thermodynamic systems, as the thermal bath used in physics to model Brownian motion for the meso-scale analysis is presented in [6, 14, 16, 20]. In the next section, as an example of more conventional system, generally investigated by coupled differential equations, is considered: the case of a fluid-loaded plate. We show that, even these kind of coupled problems, can be reduced to an integral-differential model governed by topological connectivity features.

The general structure of the cases (a), (b), (c), (d) is kept by the general integral-differential equation:

$$L_x^{(n)}\{w(x,t)\} + m'(x)\frac{\partial^2 w(x,t)}{\partial\, t^2} + K(x,t) ** w(x,t) = 0$$

*wh*ere double convolution indicates, in general, space and time are involved. Differential terms involve $L_x^{(n)}$, a *n-th* order differential operator with respect to space *x*, and an inertia term second-order in time $\frac{\partial^2 w(x,t)}{\partial\, t^2}$. The nature of the kernel *K* is the key to describe the kind of connections. If the connections are simple elastic elements, then the convolution is only space-based and the time *t* does not play any role and the term can be reduced to:

$$K(x,t) ** w(x,t) = \int_{-\infty}^{-\infty} K(x,\xi)\, w(x-\xi,t)d\xi$$

However, if the channel of communication between the pair of individuals of the ring implies delayed information transport itself (or also waves mechanisms), then the double convolution $K(x,t) ** w(x,t)$ brings both space and time effects:

$$K(x,t) ** w(x,t) = \int_{-\infty}^{+\infty} \int_{-\infty}^{-\infty} K(x,\xi,t,\tau)\, w(x-\xi, t-\tau) d\xi\, d\tau$$

The general physical interpretation of the double convolution term is simple: it brings at the place *x* all the information that is coming from other locations of the ring that are distant $x-\xi$ in space and of which the flight time to reach *x* from the place $x-\xi$ is $\tau = x-\xi/c(x-\xi)$.

Most of the propagation properties that are involved in the previous schemes can be determined in the frequency and wavenumber counterpart of this equation:

$$P^{(n)}(k) - m'\omega^2 + K(k,\omega) = 0$$

where P is a polynomial of order *n* in the wavenumber *k* and $K(k,\omega)$ is in general a complicated expression depending on both the wavenumber and the frequency.

This is the basis to investigate the wave dispersion relationship, that because of the highly unconventional term $K(k,\omega)$, produces very new and characteristic effects that are related to propagation in the field of nonlocal elasticity.

4 *An example: interface waves as a long-range connectivity problem*

Propagation of waves at the interface between two different media is an example that can be approached with the connectivity analysis presented in section 2. The case of a fluid-loaded flexural elastic plate is considered. The most frequent modelling of this system is made by coupling the differential equation of the plate (simplified in a beam for a two dimensional problem in the *x*,*y* plane), governed by its displacement *w(x.t)* and the differential equation of the compressible fluid, governed by the potential *φ(x,y,t)*:

$$EI\frac{\partial^4 w(x,t)}{\partial\, x^4} + \rho A\frac{\partial^2 w(x,t)}{\partial\, t^2} = p, \quad \nabla^2\varphi(x,y,t) - \frac{1}{c^2}\frac{\partial^2}{\partial\, t^2}\varphi(x,y,t) = 0$$

where the coupling condition, relating the potential and the pressure, is:

$$p(x,y,t) = -\rho\frac{\partial}{\partial t}\varphi(x,y,t)$$

Therefore, the two partial differential equations can be solved with the help of the coupling condition, that is the conventional way to formulate the problem.

Let us try to bring the problem on the ground of the connectivity explained in section 2. We can consider that the sections of the beam are the nodes of the network, connected by *short-length* interactions represented by the differential term $EI\frac{\partial^4 w(x,t)}{\partial\, x^4}$, but there is a further channel of communication among them represented by the waves that propagate in the compressible fluid. Therefore, the effect of the displacement signal of the beam connects distant sections, providing the *long-range* channel among the nodes of the network.

The last condition implies that along the plate surface, one can write:

$$p(x,y,t) = -\rho \frac{\partial}{\partial t}\varphi(x,y,t) \quad \rightarrow \quad \frac{\partial}{\partial x}\, p(x,y,t) = -\rho \frac{\partial}{\partial t}\frac{\partial}{\partial x}\varphi(x,y,t) = -\rho \frac{\partial}{\partial t} v(x,y,t)$$

i.e.:

$$\frac{\partial}{\partial y}\, p(x,0,t) = -\rho \frac{\partial^2}{\partial t^2} w(x,t)$$

$$\nabla^2 \varphi(x,y,t) - \frac{1}{c^2}\frac{\partial^2}{\partial\, t^2}\varphi(x,y,t) = 0 \quad \rightarrow \quad \nabla^2 p(x,y,t) - \frac{1}{c^2}\frac{\partial^2}{\partial\, t^2} p(x,y,t) = 0$$

Transforming into the Fourier domain the beam equation and the last two pressure equations (space and time):

$$EI{k_x}^4 W - \rho A\omega^2 W = P, \quad jk_y P = \rho\omega^2 W, \quad {k_x}^2 + {k_y}^2 = \frac{\omega^2}{c^2}$$

and after substitution:

$$EI{k_x}^4 W - \rho A\omega^2 W = \pm j\omega W G$$

$$G\left(\frac{ck_x}{\omega}\right) = \frac{\rho c}{\sqrt{1 - \left(\frac{ck_x}{\omega}\right)^2}}, \quad \frac{\omega}{c} H_0^{(1)}\left(\left|\frac{\omega}{c}x\right|\right) = {F_{k_x}}^{-1}\left\{G\left(\frac{ck_x}{\omega}\right)\right\}$$

and finally:

$$EI\frac{\partial^4 w(x,t)}{\partial\, x^4} + \rho A\frac{\partial^2 w(x,t)}{\partial\, t^2} = \pm\frac{1}{x} h_0^{(1)}\left(\frac{ct}{x}\right) ** w(x,t)$$

$$\text{where: } h_0^{(1)}(t) = {F_\omega}^{-1}\left\{H_0^{(1)}(\omega)\right\}$$

revealing the convolution long-range nature of the phenomenon described in the previous section.

Concluding Remarks

This paper highlights some effects that are disclosed in a series of researches, some very recent, developed by the authors. The point considered here is related to characteristic response that a population of oscillators, connected through communication channels of given topology that bring force information, exhibits as a collective behavior. The problem is based on consideration of long-range interaction forces, opposed to the short-range, characteristic of the classical local-elasticity. Relevant effects, in this field of non-local elasticity propagation, emerge as synchronization, wave stopping, superluminal group velocity, mode localization and singularity in the modal density.

Different scenarios are considered, and the mathematical framework is based on the theory of integral-differential equations. It put the basis for the analysis of dispersion relationship of unconventional form that is responsible of the investigated effects.

Acknowledgements

This work was carried out with funds of the Department of Mechanical and Aerospace Engineering, Sapienza, University of Rome.

References

[1] A. Carcaterra, General thermodynamics of vibrating systems, The Journal of the Acoustical Society of America 141 (5), 3696-3696.

[2] A Culla, G Pepe, A Carcaterra, Nonlinear unsteady energy analysis of structural systems, The Journal of the Acoustical Society of America 141 (5), 3745-3746.

[3] A Carcaterra, F Coppo, F Mezzani, S Pensalfini, Long-range elastic metamaterials, The Journal of the Acoustical Society of America 141 (5), 3744-3744.

[4] S Pensalfini, F Coppo, F Mezzani, G Pepe, A Carcaterra, Optimal control theory based design of elasto-magnetic metamaterial, Procedia Engineering 199 (2017), 1761-1766.

[5] F Mezzani, F Coppo, S Pensalfini, N Roveri, A Carcaterra, Twin-waves propagation phenomena in magnetically-coupled structures, Procedia Engineering 199, 711-716.

[6] A Carcaterra, A Akay, Fluctuation-dissipation and energy properties of a finite bath, Physical Review E 93 (3), 032142.

[7] A Carcaterra, G Pepe, N Roveri, Energy exchange between nonlinear oscillators: an entropy foundation, ISMA 2016 - International Conference on Noise and Vibration Engineering.

[8] A Carcaterra, F Dell'Isola, R Esposito, M Pulvirenti, Macroscopic description of microscopically strongly inhomogenous systems: A mathematical basis for the synthesis of higher gradients metamaterials, Archive for Rational Mechanics and Analysis 218 (3), 1239-1262.

[9] A Carcaterra, N Roveri, G Pepe, Fractional dissipation generated by hidden wave-fields, Mathematics and Mechanics of Solids 20 (10), 1251-1262.

[10] R Rojas, A Carcaterra, Vibration energy harvesting and optimal control theory: an investigation on physical limitations in capturing the environmental energy. INTER-NOISE and NOISE-CON Congress and Conference Proceedings 251 (1), 984-994.

[11] N Roveri, A Carcaterra, A Akay, Frequency intermittency and energy pumping by linear attachments, Journal of Sound and Vibration 333 (18), 4281-4294.

[12] A Carcaterra, Thermodynamic temperature in linear and nonlinear Hamiltonian Systems, International Journal of Engineering Science 80, 189-208.

[13] A Carcaterra, Quantum Euler Beam - QUEB: modeling nanobeams vibration, Continuum Mechanics and Thermodynamics, 1-12.

[14] A Akay, A Carcaterra, Damping Mechanisms, Active and Passive Vibration Control of Structures, 259-299.

[15] A Sestieri, A Carcaterra, Vibroacoustic: The challenges of a mission impossible?Mechanical Systems and Signal Processing 34 (1-2), 1-18.

[16] A Carcaterra, A Akay, Uncertainty and dissipation, International Conference on Noise and Vibration Engineering 2012, ISMA 2012.

[17] N Roveri, A Carcaterra, A Akay, Targeted energy pumping using a linear complex attachment, Proceedings of ISMA 2012.

[18] A Carcaterra, N Roveri, Energy distribution in impulsively excited structures, Shock and Vibration 19 (5), 1143-1163.

[19] A Carcaterra, A Akay, C Bernardini, Trapping of vibration energy into a set of resonators: Theory and application to aerospace structures, Mechanical Systems and Signal Processing 26, 1-14.

[20] A Carcaterra, A Akay, Dissipation in a finite-size bath, Physical Review E 84 (1), 011121.

[21] A Carcaterra, A Sestieri, T Svaton, High-frequency transient vibration: time-space complex envelope vectorization, Proceedings of ICEDyn2011 International Conference on Structural Engineering.

[22] A Carcaterra, Minimum-variance-response and irreversible energy confinement, IUTAM Symposium on the Vibration Analysis of Structures with Uncertainties 2011.
[23] A Carcaterra, New concepts in damping generation and control: theoretical formulation and industrial applications. Variational Models and Methods in Solid and Fluid Mechanics, 249-313.
[24] A Le Bot, A Carcaterra, D Mazuyer, Statistical vibroacoustics and entropy concept, Entropy 12 (12), 2418-2435.
[25] N Roveri, A Carcaterra, A Akay, Vibration absorption using non-dissipative complex attachments with impacts and parametric stiffness, The Journal of the Acoustical Society of America 126 (5), 2306-2314 27, 2009.
[26] N Roveri, A Carcaterra, A Akay, Energy equipartition and frequency distribution in complex attachments, The Journal of the Acoustical Society of America 126 (1), 122-128, 2009.
[27] F Magionesi, A Carcaterra, Insights into the energy equipartition principle in large undamped structures, Journal of Sound and Vibration 322 (4-5), 851-869.
[28] A Carcaterra, A Aknay, A novel shock absorber based on complex resonators: Theory and application to aerospace structures, INTER-NOISE and NOISE-CON Congress and Conference Proceedings 2009 (8), 941-951.
[29] N Roveri, A Carcaterra, A Aknay, Nonlinear dynamics of complex attachments, INTER-NOISE and NOISE-CON Congress and Conference Proceedings 2009 (8), 933-940.
[30] A Carcaterra, A Akay, Vibration damping device, US Patent App. 11/887,138.
[31] A Akay, A Carcaterra, Theory and application of pseudo-damping in structures, The Journal of the Acoustical Society of America 123 (5), 3058-3058, 2008.
[32] O Giannini, A Carcaterra, A Akay, Tailored Damping Induced by a Cluster of Resonators, ISMA2008 conference, Leuven (BE).
[33] O Giannini, A Sestieri, Complex envelope vectorization for the solution of external acoustical problems, Proceedings of ISMA 2008.
[34] F Magionesi, A Carcaterra, Insights into the energy equipartition principle in undamped engineering structures, J. Sound Vib 322 (4-5), 851-869.
[35] F Magionesi, A Carcaterra, A new energy approach to the analysis of complex and uncertain systems. INTER-NOISE and NOISE-CON Congress and Conference Proceedings 2007 (1), 1297.
[36] IM Koc, A Akay, A Carcaterra, Characteristics of optimized frequencies in nearly irreversible linear energy sinks, INTER-NOISE and NOISE-CON Congress and Conference Proceedings 2007 (7), 573-582.
[37] A Carcaterra, A Akay, F Lenti, Pseudo-damping in undamped plates and shells, The Journal of the Acoustical Society of America 122 (2), 804-813.
[38] S Milgram, The Small-World Problem, Psychology Today, vol. 1, no. 1, pp. 61-67, 1967.
[39] A Barrat, M. Barthélemy, A Vespignani, Dynamical processes on complex networks, Cambridge University Press, 2008.
[40] D J Watts, S H Strogatz, "Collective dynamics of ‘small-world’ networks," Nature magazine, vol. 393, pp. 440-442, 1998.
[41] N Roveri, S Pensalfini, A Carcaterra, Small-world based interactions in mechanical systems, ISMA 2018, sent for publication.

Waves path in an elastic membrane with selective nonlocality

F. Coppo[1], A. S. Rezaei[1], F. Mezzani[1], S. Pensalfini[1], A. Carcaterra[1]
[1] Department of Mechanical and Aerospace Engineering
Sapienza, University of Rome
Via Eudossiana 18, 00184, Roma
e-mail: **antonio.carcaterra@uniroma1.it**

Abstract
Nonlocal long-range effects are at the base of new phenomena investigated by the authors. In one dimensional systems, this permits the chance of modifying the phase and group velocity of the waveguide, even producing waves transporting energy backwards. In the two-dimensional case a richer scenario is opened. This paper investigates the chance of transporting the energy over a two-dimensional domain through vibrations that can follow a given path. The relationship between the path and the connection template is investigated. This directional effect is shown presenting the theoretical analysis and corroborating its results through numerical simulations.

1 Introduction

Tailoring and combining different geometries with not necessarily identical elastic properties may give rise to a certain type of materials, which are called metamaterials, that can be used in wide range of applications such as noise cancelling and acoustic cloaking [1-9]. On the other hand, the nonlocal interactions have attracted many researchers' attention in different areas of science and engineering. Several studies have shown how the introduction of unconventional connection leads to a more complicated wave propagation behavior, as those investigated in [10-18]. The present paper is an attempt to investigate the way that waves travel in an unbounded rectangular membrane made of linearly elastic materials with long-range interactions. Such materials induce some propagation regimes that have not been in typical elastic solids. It is not the first time that unconventional effects are discussed for plates and membranes [19-22], but not even in these cases the correlation between nonlocality and waves is directly appreciated.

Very recently, Carcaterra and co-authors [23-25] have studied the characteristics of plane waves travelling in one-dimensional elastic media with long-range interaction and their related propagation regimes. Their research has been often carried out by linearizing the force in order to achieve closed form solutions which can shed light on the propagation of waves in such media. Their approach has been applied on both continuous systems and their discrete counterparts, and it unveil the existence of peculiar propagation regimes, as for instance the backward energy flow.

This paper has a double nature. Indeed, it combines the linearized long-range approach developed by Carcaterra et al. [26] to the membrane theory, extending what so far determined for one-dimensional structures. In the present paper, the equation of motion for an elastic membrane, containing a region of interaction in which each point is connected to nonadjacent counterparts by spring-like connection is formulated. In order to provide an insight into the wave propagation characteristics, the plane wave solution is considered and, the nondimensional form of the dispersion relation is derived. Using this, purely dispersive modes are identified. The numerical results illustrate how the propagation regimes are dependent upon the value of the nondimensional regulator parameter χ and some discontinuities may be found in the modal density function if the aforementioned parameter is large enough. It implies that the envelope of the wave pocket tends to move in the opposite direction.

2 Mathematical description

The equation of motion for linear free vibration of a rectangular membrane is

$$\rho\ddot{W} - P\,\nabla^2 W = 0 \tag{1}$$

where $W(x,y,t)$ is the deflection of the membrane, ρ is the mass per unit area and P denotes the tension per unit length. A wave equation which is typical of a topological structure of elastic connections that involve only the closest neighbors. New advances in additive manufacturing open the chance to include into this systems elastic connections that involve points of the membrane at far distance. To fit their presence into the previous equation, an additional integral term is added:

$$\rho\ddot{W} - P\,\nabla^2 W - \iint \tilde{k}\,[W(x,y) - W(\xi,\eta)]d\xi d\eta = 0 \tag{2}$$

where $\tilde{k}$ represents the spatial stiffness modulation of the elastic connections. Indeed, $\iint \tilde{k}\,[W(x,y) - W(\xi,\eta)]$ mechanically resembles simple springs, which connect each point to nonadjacent counterparts in a defined region. This mathematical model carries two distinct elastic behavior: the short-range interaction, described by the differential term $\nabla^2 W$, and the long-range interaction described by $\iint \tilde{k}\,[W(x,y) - W(\xi,\eta)]$.

Introducing in the plane the axis-symmetric rectangular window function $H(r) = H\left(\sqrt{x^2+y^2}\right)$ (Figure 1) in order to control the region of interaction, equation (2) reads into:

$$\rho\ddot{W} - P\,\nabla^2 W - \tilde{k}SW + k\,H(r) * W = 0 \tag{3}$$

where S is the area of the region of interaction and $*$ denotes the convolution operation.

(r) can be chosen as follows:

$$H(r) = \begin{cases} 1, & |r| \le a \\ 0, & |r| > a \end{cases} \tag{4}$$

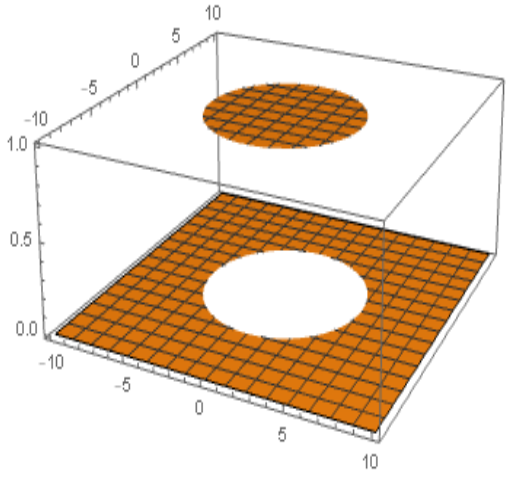


Figure 1: Two-dimensional circularly symmetric window

where a is a positive quantity representing the interaction radius. In order to determine the dispersion relationship, the Fourier transform with respect to time and space variables is applied, and the following dispersion relationship is obtained:

$$\rho\omega^2 = P\left(k_x^2 + k_y^2\right) + \tilde{k}S - \frac{\tilde{k}a}{\sqrt{k_x^2+k_y^2}} J_1\left(a\sqrt{k_x^2 + k_y^2}\right) \tag{5}$$

Here J_1 is the Bessel function of first kind. This equation is fundamentally different with respect to the conventional short-range interaction equation that leads trivially to $\rho\omega^2 = P\left(k_x^2 + k_y^2\right)$.

For the sake of simplicity, the dispersion relation is rewritten in nondimensional form, as follows:

$$\Omega^2 = \left(K_x^2 + K_y^2\right) + \chi\left[\pi - \frac{J_1\left(\sqrt{K_x^2+K_y^2}\right)}{\sqrt{K_x^2+K_y^2}}\right] \tag{6}$$

where the nondimensional parameters are:

$$\begin{aligned} \Omega^2 &= a\sqrt{\frac{\rho}{P}}\,\omega \\ K_{x,y} &= a\,k_{x,y} \\ \chi &= \frac{\tilde{k}a^4}{P} \end{aligned} \tag{7}$$

The parameter χ, which stems from the physical and geometrical parameters, regulates the relation between the nondimensional frequency Ω and the nondimensional wavenumbers (K_x , K_y); moreover it contains information on the ratio between the long-range interaction and the short-range elasticity. The nondimensional dispersion relation reveals that the frequencies are always real, assuming positive χ. This fact is shown in Figure 2, where the variations of the nondimensional frequency is plotted against $K = \sqrt{K_x^2 + K_y^2}$. One should also note that the horizontal axis does not intersect the curves, demonstrating that there is no region in the $K_x - K_y$ plane in which the system's frequencies are imaginary.

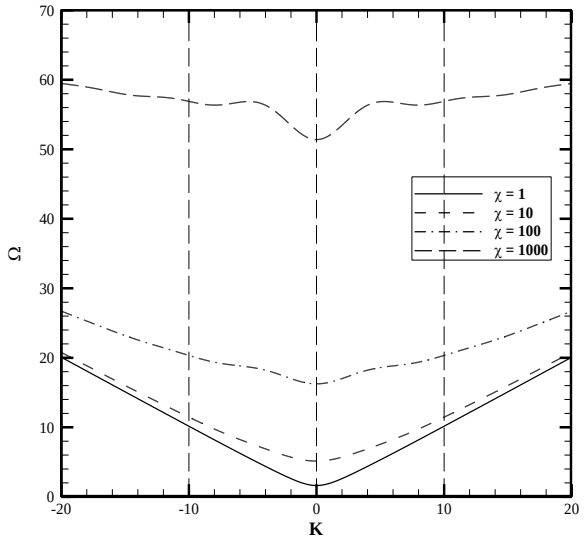


Figure 2: Dispersion relationship for the long-range membrane

3 Numerical results

The solution to equation (6) is represented as dispersion surfaces in Figure 3. This figure shows the trend of Ω versus K_x and K_y. Since $C_g = \partial\Omega/\partial\mathrm{K}$, a direct measure of group velocity is the surfaces' slope, and its variation discloses the chance to achieve particular trends of the group velocity itself, by changing the frequency. Namely, the presence of multiple crests for each surface, at which the group velocity vanishes, implies potential wave-stopping phenomenon.

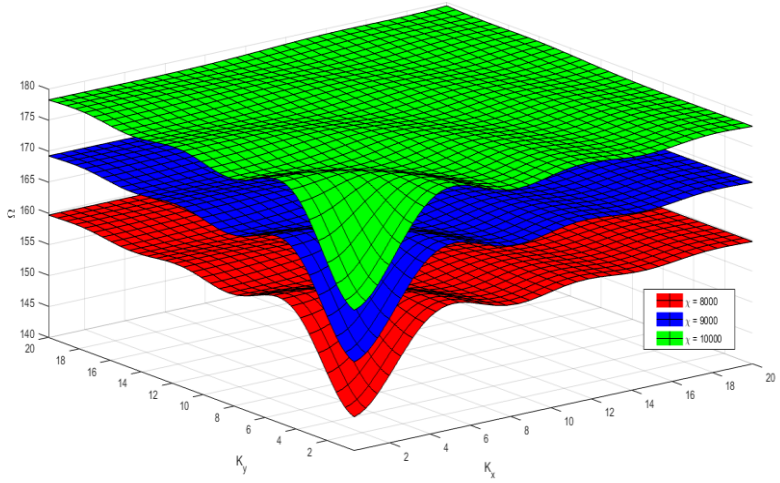


Figure 3: Dispersion surface for different values the nondimensional parameter χ

The phase and group velocities as well as the modal density [27] are as follows:

$$\begin{aligned} C_{\varphi_x} &= \frac{\Omega}{K_x} \\ C_{\varphi_y} &= \frac{\Omega}{K_y} \\ C_{g_x} &= \frac{\partial \Omega}{\partial K_x} \\ C_{gy} &= \frac{\partial \Omega}{\partial K_y} \\ \mathrm{n}(\Omega) &\propto \int_{\theta_1}^{\theta_2} K \frac{\partial K}{\partial \Omega}\, d\theta \end{aligned} \tag{8}$$

Figure 4 shows the variations of C_{φ_x} as a function of the wavenumbers. The phase velocity in the x-direction grows rapidly as K_x approaches zero, because of the presence of K_x in the denominator. Plotting C_{φ_y} against the wavenumber along K_x and K_y generates surfaces like those presented in Figure 4. However, in this case the frequency grows rapidly as K_y becomes smaller.

Figure 5 demonstrates the changes in the group velocity and modal density for a long-range membrane with fairly small long-range interactions. As depicted, the group velocity is always positive, showing that no wave-stopping phenomenon appears, when χ is small enough. These surfaces are in good agreement with those of modal density where no singularity could be observed.

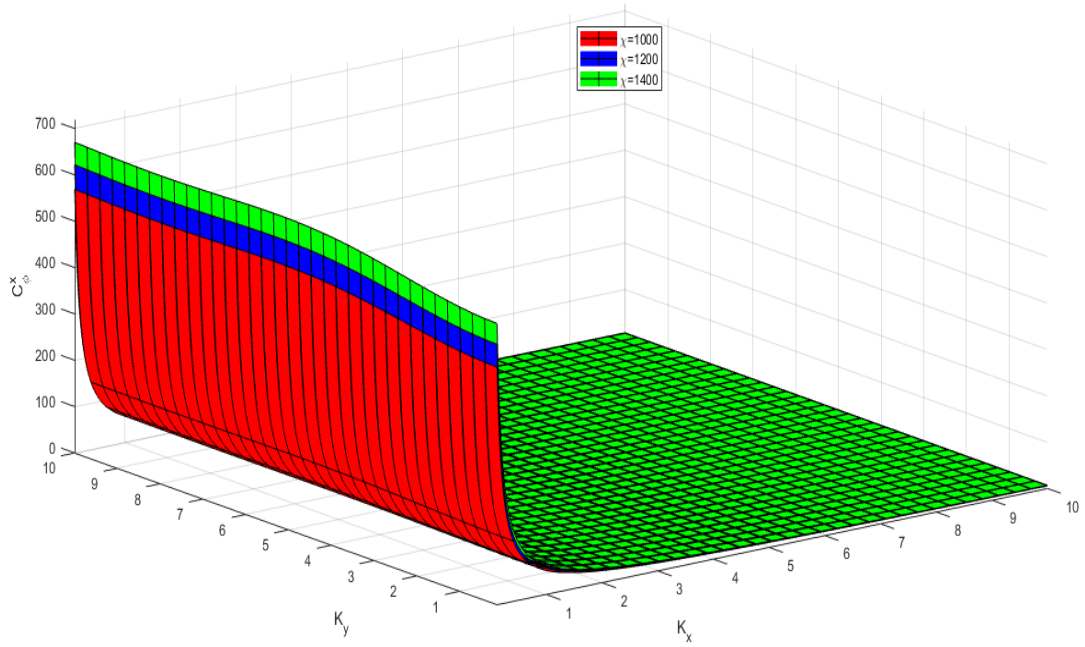
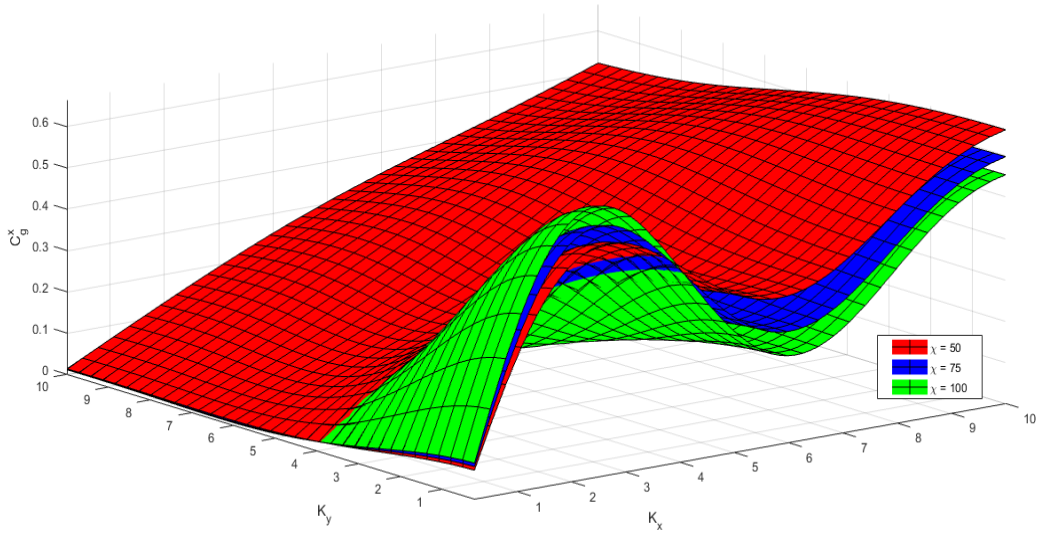
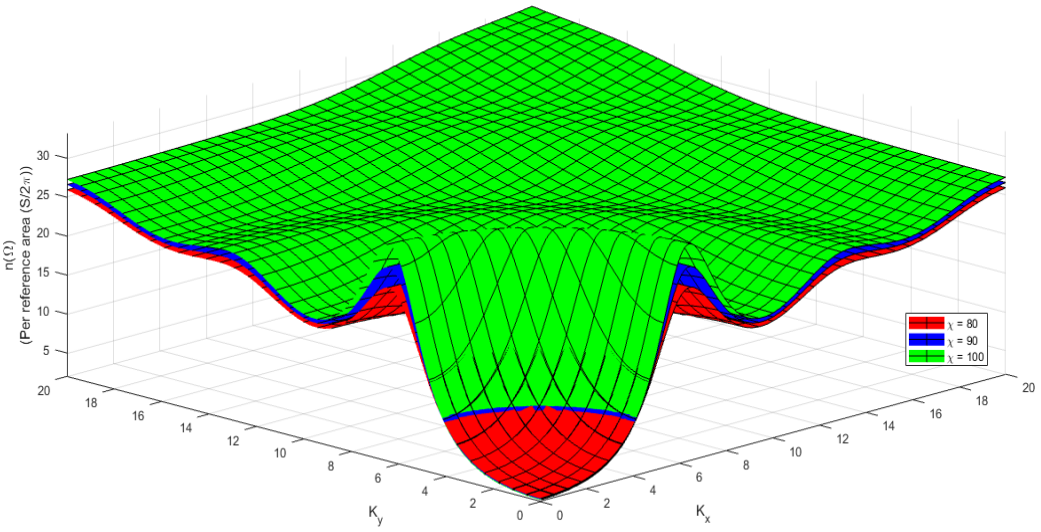


Figure 4: Phase velocity for long-range membranes for different values of χ



(a)



(b)

Figure 5: Different low values of : (a) Group velocity, (b) modal density

For larger values of χ, which indicate stronger long-range interactions (Figure 6), the negative terms in group velocity relation overcome the positive ones for some sets of (K_x, K_y), leading to negative group velocity. This identifies the wave-stopping phenomenon when the group velocity vanishes. Hence, this interesting propagation regime occurs only when the long-range interactions are strong enough.

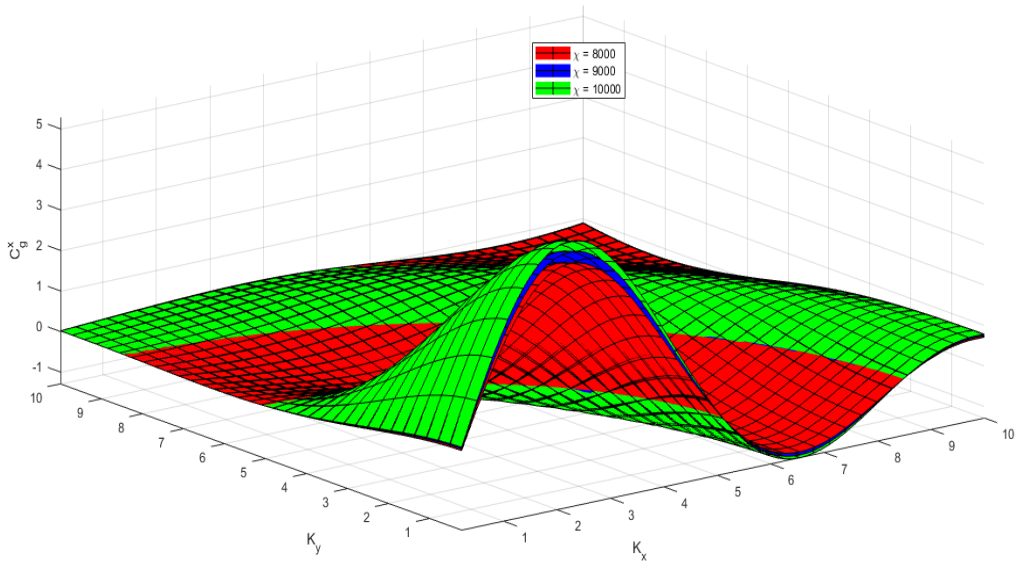


Figure 6: Group velocity for long-range membranes for different values of χ (High values)

Figure 7 shows the modal density in case of stronger long-range interaction, for which two discontinuity rings appear, where wave-stopping phenomena occurs [14].

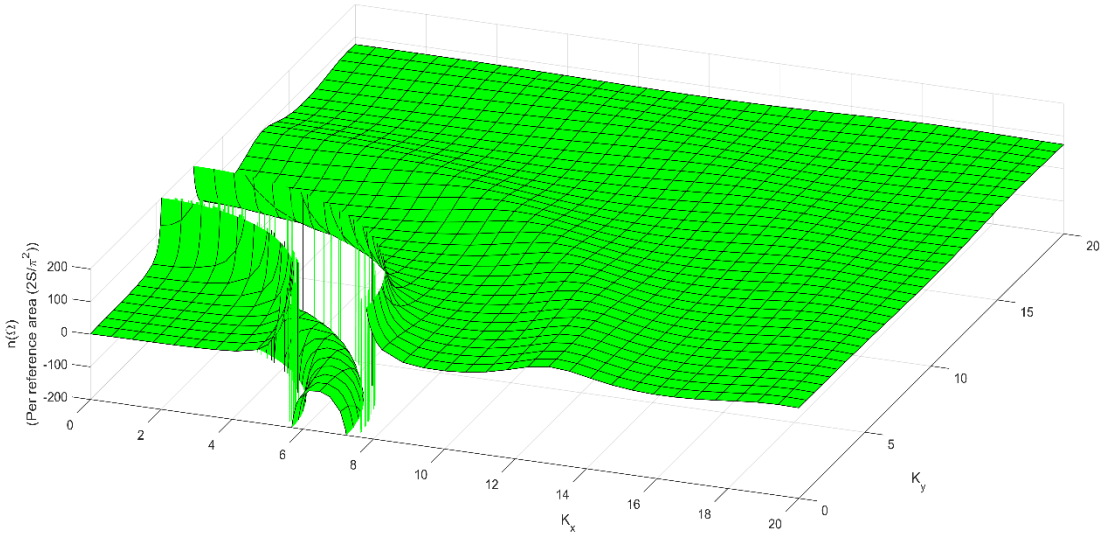


Figure 7: Modal density for long-range membranes (χ=500).

4 Conclusions

This paper analyzes the plane wave dispersion characteristics of an elastic membrane. The configuration consists of a finite area in which there are spring-like connections with similar stiffness between nonadjacent points. The solution for plane waves is analytically obtained in the wavenumber domain for the medium under investigation. Note that the mechanisms contributing to wave attenuation are disregarded in this study. Since this paper is an attempt to identify the purely propagating modes, complex-valued wavenumbers are not taken into account. Such modes are found by solving the dispersion equation for real frequencies. The main effects observed in this study are as follow:

- Relatively small values of the regulator parameter do not cause any significant effect on the group velocity surface of the system, since the group velocity is always positive and the waves propagate normally along the membrane.
- As the crests of group velocity surface become larger by increasing the regulator parameter, we are able to observe some sectorial areas in which the group velocity is negative, indicating wave-stopping phenomena.

References

[1] A. Carcaterra and A. Akay, "Dissipation in a finite-size bath," *Physical Review E*, vol. 84, no. 1, p. 011121, 2011.

[2] A. Carcaterra and A. Akay, "Theoretical foundations of apparent-damping phenomena and nearly irreversible energy exchange in linear conservative systems," *The Journal of the Acoustical Society of America*, vol. 121, no. 4, pp. 1971-1982, 2007.

[3] S. A. Cummer, J. Christensen, and A. Alù, "Controlling sound with acoustic metamaterials," *Nature Reviews Materials*, vol. 1, p. 16001, 2016.

[4] S. Zhang, C. Xia, and N. Fang, "Broadband acoustic cloak for ultrasound waves," *Physical Review Letters*, vol. 106, no. 2, p. 024301, 2011.

[5] N. Roveri, A. Carcaterra, and A. Akay, "Vibration absorption using non-dissipative complex attachments with impacts and parametric stiffness," *The Journal of the Acoustical Society of America,* vol. 126, no. 5, pp. 2306-2314, 2009.
[6] A. Carcaterra, A. Akay, and I. Koc, "Near-irreversibility in a conservative linear structure with singularity points in its modal density," *The Journal of the Acoustical Society of America,* vol. 119, no. 4, pp. 2141-2149, 2006.
[7] A. Akay, Z. Xu, A. Carcaterra, and I. M. Koç, "Experiments on vibration absorption using energy sinks," *The Journal of the Acoustical Society of America,* vol. 118, no. 5, pp. 3043-3049, 2005.
[8] A. Carcaterra and A. Akay, "Transient energy exchange between a primary structure and a set of oscillators: Return time and apparent damping," *The Journal of the Acoustical Society of America,* vol. 115, no. 2, pp. 683-696, 2004.
[9] A. Carcaterra, "An entropy formulation for the analysis of energy flow between mechanical resonators," *Mechanical systems and signal processing,* vol. 16, no. 5, pp. 905-920, 2002.
[10] A. Carcaterra and A. Akay, "Fluctuation-dissipation and energy properties of a finite bath," *Physical Review E,* vol. 93, no. 3, p. 032142, 2016.
[11] A. Carcaterra, F. Dell'Isola, R. Esposito, and M. Pulvirenti, "Macroscopic description of microscopically strongly inhomogenous systems: A mathematical basis for the synthesis of higher gradients metamaterials," *Archive for Rational Mechanics and Analysis,* vol. 218, no. 3, pp. 1239-1262, 2015.
[12] A. C. Eringen, "Linear theory of nonlocal elasticity and dispersion of plane waves," *International Journal of Engineering Science,* vol. 10, no. 5, pp. 425-435, 1972.
[13] V. E. Tarasov and G. M. Zaslavsky, "Fractional dynamics of coupled oscillators with long-range interaction," *Chaos: An Interdisciplinary Journal of Nonlinear Science,* vol. 16, no. 2, p. 023110, 2006.
[14] V. E. Tarasov, "Lattice model of fractional gradient and integral elasticity: long-range interaction of Grünwald–Letnikov–Riesz type," *Mechanics of Materials,* vol. 70, pp. 106-114, 2014.
[15] M. Zingales, "Wave propagation in 1D elastic solids in presence of long-range central interactions," *Journal of Sound and Vibration,* vol. 330, no. 16, pp. 3973-3989, 2011.
[16] A. Madeo, G. Barbagallo, M. V. d'Agostino, L. Placidi, and P. Neff, "First evidence of non-locality in real band-gap metamaterials: determining parameters in the relaxed micromorphic model," *Proc. R. Soc. A,* vol. 472, no. 2190, p. 20160169, 2016.
[17] N. Roveri, A. Carcaterra, and A. Akay, "Energy equipartition and frequency distribution in complex attachments," *The Journal of the Acoustical Society of America,* vol. 126, no. 1, pp. 122-128, 2009.
[18] A. Carcaterra, "Ensemble energy average and energy flow relationships for nonstationary vibrating systems," *Journal of Sound and Vibration,* vol. 288, no. 3, pp. 751-790, 2005.
[19] H. Cohen, "Wave propagation in elastic plates," *Journal of Elasticity,* vol. 6, no. 3, pp. 245-259, 1976.
[20] L. Solie and B. Auld, "Elastic waves in free anisotropic plates," *The Journal of the Acoustical Society of America,* vol. 54, no. 1, pp. 50-65, 1973.
[21] I. Tolstoy and E. Usdin, "Wave propagation in elastic plates: low and high mode dispersion," *The Journal of the Acoustical Society of America,* vol. 29, no. 1, pp. 37-42, 1957.
[22] H. Lamb, "On waves in an elastic plate," *Proceedings of the Royal Society of London. Series A,* vol. 93, no. 648, pp. 114-128, 1917.
[23] A. Carcaterra, F. Coppo, F. Mezzani, and S. Pensalfini, "Metamaterials: wave propagation control," *Proceedings of Isma2016 International Conference on Noise and Vibration Engineering and Usd2016 International Conference on Uncertainty in Structural Dynamics,* pp. 1995-2009, 2016 2016.
[24] F. Mezzani, F. Coppo, S. Pensalfini, N. Roveri, and A. Carcaterra, "Twin-waves propagation phenomena in magnetically-coupled structures," *Procedia Engineering,* vol. 199, pp. 711-716, 2017.
[25] S. Pensalfini, F. Coppo, F. Mezzani, G. Pepe, and A. Carcaterra, "Optimal control theory based design of elasto-magnetic metamaterial," *Procedia Engineering,* vol. 199, pp. 1761-1766, 2017.
[26] A. Carcaterra, F. Coppo, F. Mezzani, and S. Pensalfini, "*Long-range retarded elastic metamaterials: wave-stopping, negative and hypersonic group velocity*," 2018 (Submitted, under review).
[27] A. Carcaterra, A. Akay, and F. Lenti, "Pseudo-damping in undamped plates and shells," *The Journal of the Acoustical Society of America,* vol. 122, no. 2, pp. 804-813, 2007.

Model order reduction of large stroke flexure hinges using modal derivatives

J.P. Schilder, F.M. Segeth, M.H.M. Ellenbroek, M. van den Belt, A. de Boer
University of Twente, Faculty of Engineering Technology
P.O. Box 217, 7500AE Enschede, The Netherlands
e-mail: **j.p.schilder@utwente.nl**

Abstract
In this work, a strategy for the model order reduction of large stroke flexure mechanisms is presented. In this, geometrically nonlinear finite element models of each flexible body within the mechanism are projected onto a reduction basis. This basis consists of the body's Craig-Bampton modes and corresponding modal derivatives. Validation simulations that are performed on commonly used flexure mechanisms show good accuracy of the reduced order models. Therefore, the proposed reduction strategy can be efficiently applied to reduce computational costs of structural optimizations that are required to improve the design of flexure mechanisms.

1 Introduction

Flexure hinges are commonly used in precision engineering because of the absence of friction, hysteresis and backlash [1]. Typically, these hinges are designed such that they have high compliance in their driving directions and high stiffness in supporting directions. Many modern applications require the flexure hinges to be well-behaved in a large range of motion. In particular, this means that the hinge should maintain its support stiffness for deformations outside of the driving direction's linear range. Because the support stiffness of standard hinges dramatically drops with deflection, more sophisticated flexure hinges are required to meet the stiffness requirement.

Due to the geometrical nonlinear nature of large stroke flexure hinges, the use of nonlinear finite element models is typically required for their design, as expressions for stiffness as a function of deflection are difficult to obtain analytically. In order to further increase the performance of flexure hinges, shape and topology optimization is used, which requires many finite element calculations. Moreover, in order to study the dynamic behavior or stability of an entire mechanism, larger finite element models or flexible multibody models are required. The high computational costs of such advanced analyses, ask for model order reduction techniques that can deal with geometric nonlinearities.

In this work, a model order reduction technique based on modal derivatives is proposed. The modal derivatives can be interpreted as the sensitivity of a structure's vibration modes to a deflection in the generalized direction of any vibration mode. The success of adding modal derivatives to a reduction basis of vibration modes in order to reduce geometrical nonlinear flexible multibody problems was demonstrated before [2]. In previous work, the authors have demonstrated that this technique can also be used to compute so-called frequency derivatives [3]. It was explained that in this way, a flexure hinge's first parasitic frequency can be determined for the large range of motion with great computational efficiency. Because the first parasitic frequency is an often-used measure for the performance of a flexure hinge, this has the potential to significantly speed-up optimization procedures.

In this work, the efficient reduction of the geometrical nonlinear models of large stroke flexure hinges will be explained. To this end, a reduction basis consisting of Craig-Bampton modes and their corresponding modal derivatives is used to reduce the model of a single flexible body. In contrast to vibration modes, the use of Craig-Bampton modes does not require any a priori knowledge of how the body is constrained, which makes the method generally applicable. This strategy is validated with the equilibrium analysis of a number of compound flexure mechanisms.

The remainder of this work is organized as follows: Chapter 2 describes how the modal derivatives of vibration modes can be determined by differentiation of the appropriate eigenvalue problem. This summarizes the essentials from the method as it is reported in literature. Chapter 3 describes how the modal derivatives of Craig-Bampton modes can be determined by differentiation of the appropriate equation of equilibrium. This summarizes the general strategy for the model order reduction of a flexible body that may undergo large deformations. Chapter 4 describes the model order reduction of a flexible multibody system based on Craig-Bampton modes and their modal derivatives. Relevant simulation results are presented and discussed. The paper is finalized by the most important conclusions.

2 Modal derivatives of vibration modes

Consider a structure that is constrained to the fixed world. It is assumed that a nonlinear finite element model is available from which the mass matrix $\mathbf{M}$ and a configuration dependent tangent stiffness matrix $\mathbf{K}(\mathbf{q})$ can be extracted. When the geometric nonlinearities are described using the nonlinear Green-Lagrange strain definition, the sensitivities of the tangent stiffness matrix with respect to the generalized coordinates can be determined analytically. Alternatively, when for instance a corotational finite element formulation is used, these sensitivities can be determined numerically.

Free vibrations about the system's equilibrium configuration are considered. From the relevant eigenvalue problem, the natural frequencies ω_i and corresponding vibrations modes $\boldsymbol{\phi}_i$ can be determined, which satisfy:

$$\left(\mathbf{K} - \omega_i^2 \mathbf{M}\right)\boldsymbol{\phi}_i = \mathbf{0} \tag{1}$$

In linear modal expansion, the generalized coordinates are expressed as a linear combination of the system's vibration modes. The response of the system is expressed in terms of the modal coordinates η_i that describe the contribution of vibration mode $\boldsymbol{\phi}_i$ to the response:

$$\mathbf{q} = \sum \boldsymbol{\phi}_i \eta_i \tag{2}$$

The modal derivatives $\boldsymbol{\theta}_{ij}$ are defined as the sensitivity of vibration mode $\boldsymbol{\phi}_i$ with respect to modal coordinate η_j [2]. To this end, the eigenvalue problem (1) is differentiated with respect to the modal coordinates η_j:

$$\left(\frac{\partial \mathbf{K}}{\partial \eta_j} - \frac{\partial \omega_i^2}{\partial \eta_j}\mathbf{M}\right)\boldsymbol{\phi}_i + \left(\mathbf{K} - \omega_i^2 \mathbf{M}\right)\boldsymbol{\theta}_{ij} = \mathbf{0} \tag{3}$$

From literature, it is known that the influence of the inertia terms on this sensitivity can in general be neglected [4]. Therefore, the following expression for the modal derivatives is obtained:

$$\boldsymbol{\theta}_{ij} = -\mathbf{K}^{-1}\frac{\partial \mathbf{K}}{\partial \eta_j}\boldsymbol{\phi}_i \tag{4}$$

In this way, it is possible to determine the modal derivatives of any structure of which a nonlinear finite element model is available. As an example, Figure 1 shows a cantilever beam's lowest 2 vibration modes (ϕ_1, ϕ_2) and the related modal derivatives $(\theta_{11}, \theta_{12}, \theta_{22})$. Note that the vibration modes describe a deformation in the transverse direction $v(x)$, whereas the modal derivatives describe a deformation in the axial direction $u(x)$. In fact the modal derivatives describe the shortening of the beam, that occurs when it is subjected to bending.

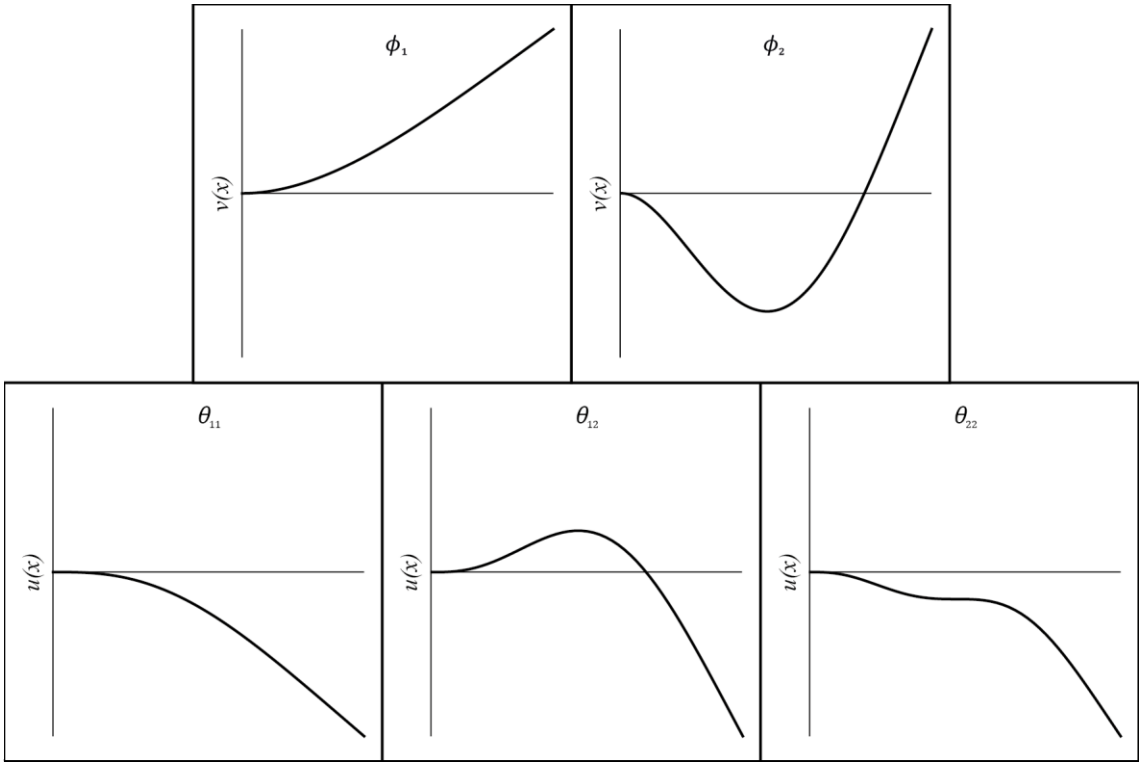


Figure 1: Vibration modes and modal derivatives of a cantilever beam

As soon as the modal derivatives are determined, it is possible to express the generalized coordinates as a combination of the vibration modes and the modal derivatives, which spans a quadratic manifold [5]:

$$\mathbf{q} = \sum \boldsymbol{\Phi}_i \eta_i + \sum \sum \boldsymbol{\Theta}_{ij}\, \eta_i \eta_j \tag{5}$$

3 Modal derivatives of Craig-Bampton modes

Consider a flexible multibody system in which multiple flexible bodies are coupled together or to the fixed world by joints located at the bodies' interface points. In general these joints may allow for large rigid body motions in between bodies. Unfortunately, the possibility for the system to move in these rigid body motions is the reason that modal derivatives cannot be computed for the multibody system as a whole. To explain this, note that for determining the modal derivatives, the inverse of the stiffness matrix is required in Eq. (4). Because systems that allow for rigid body motions have a singular stiffness matrix, this inverse does not exist. Hence, modal derivatives can only be computed for systems that do not allow for rigid body motions.

In order to allow for the efficient study of such flexible multibody systems as well, it is proposed to apply model order reduction to each individual flexible body within the multibody system. To keep this solution strategy as general as possible, no constraints may be imposed on the interface points of individual bodies. Hence, a strategy is developed that works without any pre-knowledge about how a certain body is constrained to the rest.

For this purpose, Craig-Bampton modes [6] are used for the model order reduction of a body's linear elastic behavior. The Craig-Bampton modes consist of so-called boundary modes and internal vibration modes. A Craig-Bampton boundary mode is determined by fixing all-but-one boundary degrees of freedom and prescribing the remaining interface degree of freedom a unit displacement. The Craig-Bampton internal vibration modes are the vibration modes of the structure with all boundary degrees of freedom fixed. Without loss of generalization, only the boundary modes are considered in this work. Let $\mathbf{q}_i$ and $\mathbf{q}_b$ denote the internal and boundary degrees of freedom, respectively. Then the body's equation of equilibrium can be partitioned as follows:

$$\begin{bmatrix} \mathbf{K}_{ii} & \mathbf{K}_{ib} \\ \mathbf{K}_{bi} & \mathbf{K}_{bb} \end{bmatrix} \begin{bmatrix} \mathbf{q}_i \\ \mathbf{q}_b \end{bmatrix} = \begin{bmatrix} \mathbf{0} \\ \mathbf{F}_b \end{bmatrix} \tag{6}$$

The Craig-Bampton modes $\mathbf{\Phi}_{CB}$ are obtained from static condensation to the boundary degrees of freedom:

$$\begin{bmatrix} \mathbf{q}_i \\ \mathbf{q}_b \end{bmatrix} = \begin{bmatrix} -\mathbf{K}_{ii}^{-1}\mathbf{K}_{ib} \\ \mathbf{1} \end{bmatrix} \mathbf{q}_b = \mathbf{\Phi}_{CB}\mathbf{q}_b, \qquad \mathbf{\Phi}_{CB} \equiv \begin{bmatrix} -\mathbf{K}_{ii}^{-1}\mathbf{K}_{ib} \\ \mathbf{1} \end{bmatrix} \tag{7}$$

Next, the modal derivative $\mathbf{\theta}_{ij}$ related to a Craig-Bampton mode $\mathbf{\phi}_i$ is determined from a modified version of Eq. (4) as follows:

$$\mathbf{\theta}_{ij} = -\mathbf{K}^{-1}\frac{\partial \mathbf{K}}{\partial q_j}\mathbf{\phi}_i \tag{8}$$

where **K** should be interpreted as the stiffness matrix of the body with all boundary degrees of freedom fixed, except for the degrees of freedom of the boundary node of which q_i is a degree of freedom. As an example, Figure 2 shows the Craig-Bampton bending modes of a beam's right boundary node and the corresponding modal derivatives.

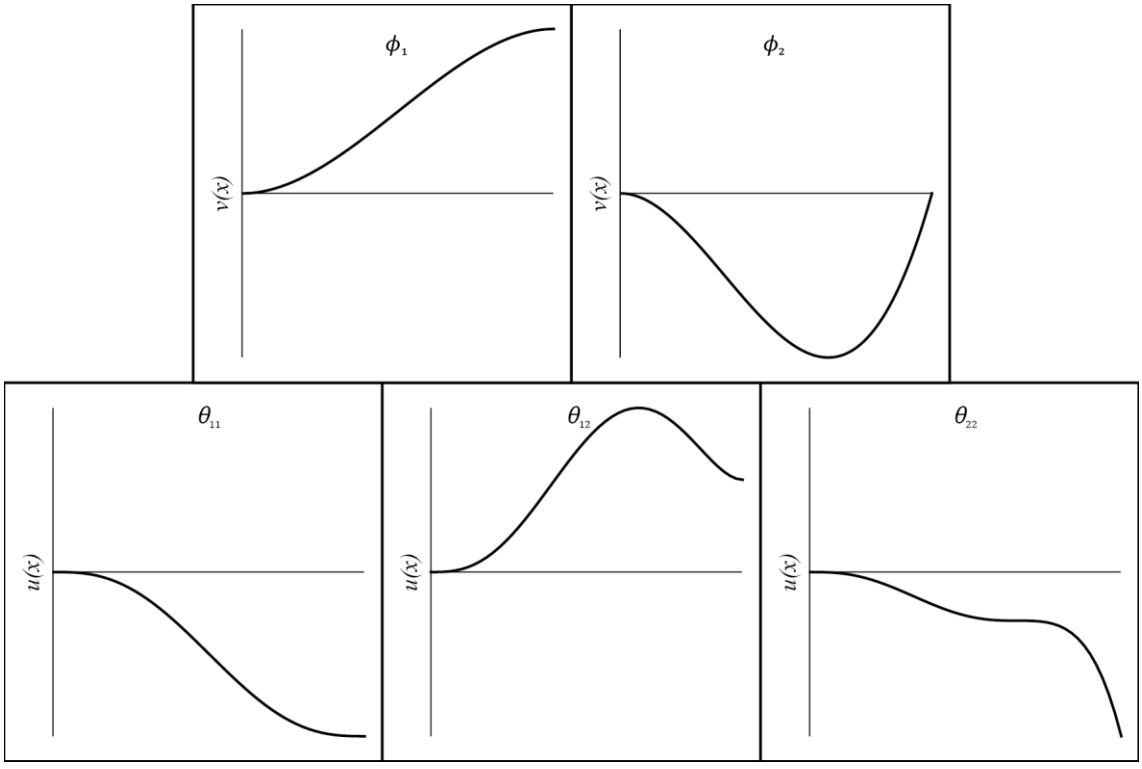


Figure 2: Craig-Bampton modes and modal derivatives related to a beam's right boundary point

For the comparison between a reduction basis of vibration modes and their modal derivatives and a reduction basis of Craig-Bampton modes and their modal derivatives, the equilibrium analysis of a cantilever beam is considered as an example. The nonlinear equations of equilibrium can be formulated in the following form:

$$\mathbf{Kq} = \mathbf{F} \tag{9}$$

where it should be understood that $\mathbf{K} = \mathbf{K}(\mathbf{q})$ is the nonlinear stiffness matrix and $\mathbf{F}$ are the applied external forces. Let $\mathbf{R}$ denote the reduction basis consisting of a set of mode shapes and modal derivatives, then the reduced form of (9) can be written as:

$$\mathbf{R}^T\mathbf{K}\mathbf{R}\bar{\mathbf{q}} = \mathbf{R}^T\mathbf{F}, \qquad \mathbf{R} \equiv [\boldsymbol{\Phi} \quad \boldsymbol{\Theta}] \tag{10}$$

where $\bar{\mathbf{q}}$ is the set of reduced generalized coordinates. Figure 3 shows the deflected shape of a cantilever beam that is subjected to a vertical tip load. The load is such that the beam is deformed slightly beyond its linear range, such that a geometrical nonlinear analysis is required. It can be seen that the solution of the unreduced model is the same as the solution by nonlinear finite element package Ansys. Model order reduction is applied using 2 vibration modes and the 3 corresponding modal derivatives or using 2 Craig-Bampton bending modes and the 3 corresponding modal derivatives. It is observed that both reduced models produce similar results, but that they are slightly stiffer than the exact solution.

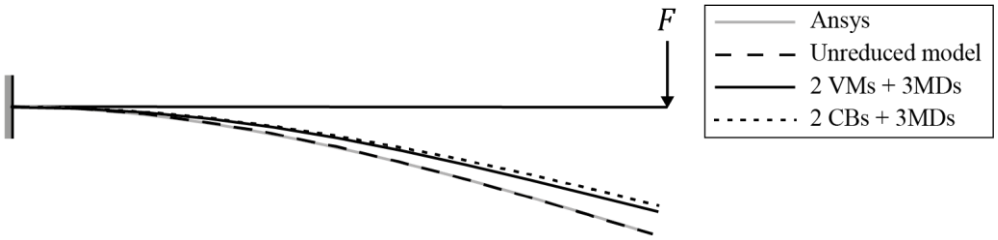


Figure 3: Equilibrium analysis of a cantilever beam subjected to a tip load

4 Model order reduction of a flexible multibody system

For simulating flexible multibody dynamics, the floating frame formulation is a commonly used and well-developed formulation. In the floating frame formulation, the rigid body motion is described by the position and orientation of the body's floating frame relative to the inertial frame. Elastic deformation is described locally, relative to the floating frame. When this elastic deformation is small, linear theory can be applied and model order reduction techniques, such as the Craig-Bampton method, can be applied locally. For our present purposes, a nonlinear finite element model is used for describing local elastic deformations and it is not demanded that these remain small. The local mass and configuration dependent stiffness matrices of each body are reduced using the Craig-Bampton boundary modes and associated modal derivatives.

For equilibrium analysis of a multibody system, the equations of equilibrium for each flexible body need to be solved simultaneously with the kinematic constraint equations that connect different bodies together. This forms a set of combined differential-algebraic equations of the following form:

$$\begin{bmatrix} \mathbf{K}_{sys} & \boldsymbol{\Psi}_{\mathbf{q}}^T \\ \boldsymbol{\Psi}_{\mathbf{q}} & \mathbf{0} \end{bmatrix} \begin{bmatrix} \mathbf{q} \\ \boldsymbol{\lambda} \end{bmatrix} = \begin{bmatrix} \mathbf{Q}_a \\ \mathbf{0} \end{bmatrix} \tag{11}$$

In this, $\mathbf{K}_{sys}$ is the assembly of the reduced stiffness matrices of all flexible bodies, $\boldsymbol{\Psi}_{\mathbf{q}}$ is the Jacobian of the kinematic constraint equations $\boldsymbol{\Psi} = \mathbf{0}$, $\mathbf{Q}_a$ is the vector of externally applied generalized forces and $\boldsymbol{\lambda}$ is the vector of Lagrange multipliers used to enforce the constraints.

For geometrically large deformations, the constrained equations of equilibrium (11) need to be solved numerically with an incremental method. To this end, the tangent stiffness matrix is derived, which consists of both the material stiffness matrix and geometrical stiffness matrix. The externally applied generalized forces are applied in increments. For each load increment, Newton-Raphson iterations are applied until the solution is converged with sufficient accuracy.

As validation of this solution strategy, an equilibrium analysis is performed on two flexure mechanisms that are commonly used in precision engineering: a parallel leaf spring mechanism and a cross flexure mechanism. These mechanisms are subjected to a static load that deforms the mechanisms beyond the linear range. A nonlinear finite element model of each leaf spring is created using 10 beam elements and is reduced subsequently using Craig-Bampton modes and their model derivatives. As a comparison, an equilibrium analysis of both flexure hinges is performed using the nonlinear finite element formulation of Ansys. Figures 4 and 5 show the deformed configuration of the parallel leaf spring mechanism and cross flexure, respectively. It can be seen that the proposed reduction basis again produces results that are slightly stiffer than the exact solution.

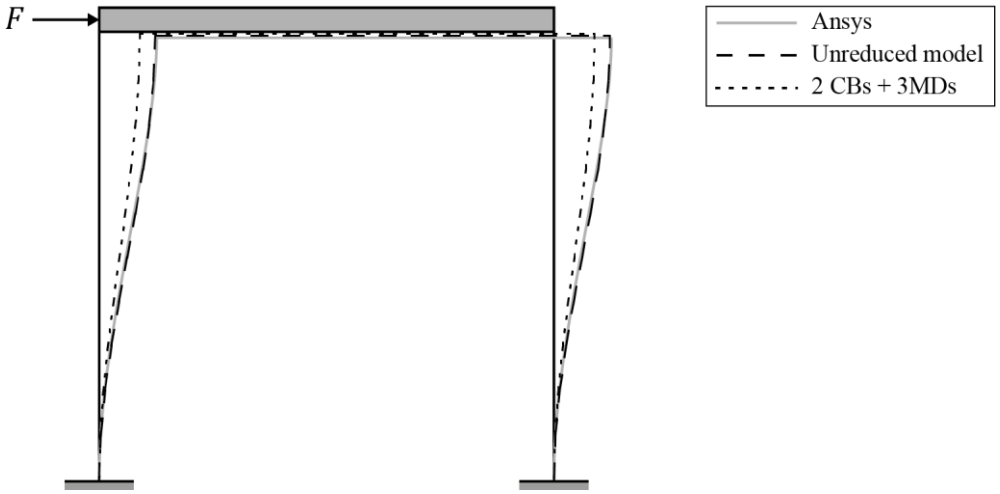


Figure 4: Equilibrium analysis of a parallel leaf spring mechanism subjected to a horizontal load

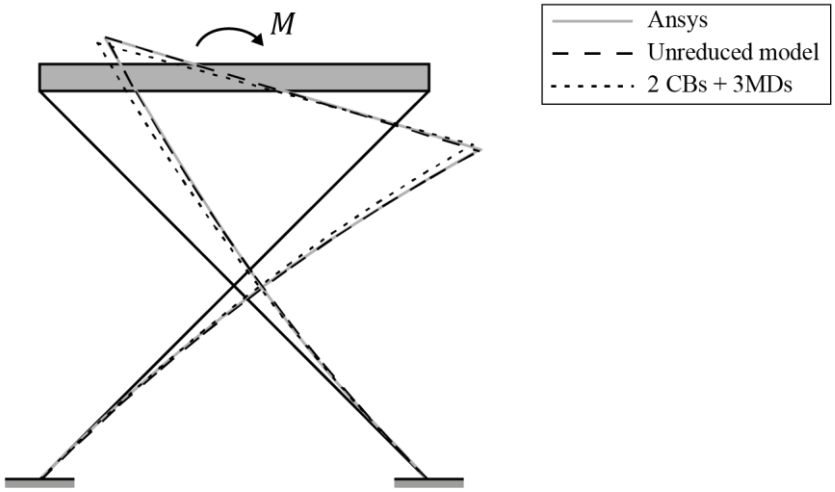


Figure 5: Equilibrium analysis of a cross flexure mechanism subjected to a bending moment

It is observed that when the applied external load increases such that the mechanism's deformation becomes exceedingly large, the reduction basis is no longer successful. To demonstrate this, Figure 6 shows the results of the equilibrium analysis of the parallel leaf spring mechanism for increased loading. It is concluded that for such large deformations, additional higher order terms should be included. Taking only first order changes of the linear basis into account is clearly not sufficient.

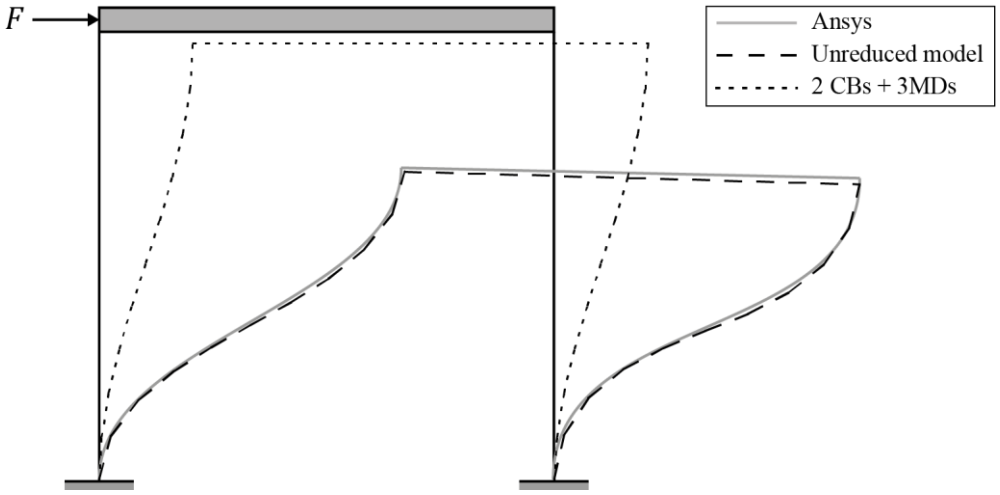


Figure 6: Equilibrium analysis of a parallel leaf spring mechanism subjected to an increased load

5 Conclusions

It is found that the equilibrium analysis of flexible multibody models of large stroke flexure hinges can be reduced successfully by the proposed model order reduction strategy. For each flexible body of which the elastic deformations may become large, its nonlinear finite element model is projected onto a reduction basis consisting of a limited number of Craig-Bampton modes and related modal derivatives. Comparison between the full and reduced simulations of a number of standard flexure hinges shows the high potential of this strategy. In future work, the method will be applied to reduce computational costs of shape and topology optimization of large stroke mechanisms. This potentially leads to more sophisticated designs with improved performance. Additional research is required for determining a reduction basis for situations in which the deformations become exceedingly large.

References

[1] K. Gunnink, R.G.K.M. Aarts, D.M. Brouwer, *Performance optimization of large stroke flexure hinges for high stiffness and eigenfrequency, Proceedings of the 28th Annual Meeting of the American Society for Precision Engineering (ASPE), 2013 October 20-25,* Saint Paul, Minnesota, USA.

[2] L. Wu, P. Tiso, *Modal derivatives based reduction method for finite deflections in floating frame, Proceedings of the 11th World Congress on Computational Mechanics, 2014 July 20-25,* Barcelona, Spain.

[3] M. van den Belt, J.P. Schilder, *The use of modal derivatives in determining stroke-dependent frequencies of large stroke flexure hinges, Proceedings of the ECCOMAS Thematic Conference on Multibody Dynamics, 2017 June 19-22*, Prague, Czech Republic.

[4] P.M.A. Slaats, J. de Jongh and A.A.H.J. Sauren, *Model reduction tools for nonlinear structural dynamics*, Computers & Structures, Vol. 54 (1995), pp 1155-1171.

[5] L. Wu, P. Tiso, A. van Keulen, *Quadratic manifolds for reduced order modelling of highly flexible multibody systems, Proceedings of the ECCOMAS Thematic Conference on Multibody Dynamics, 2015 July 19-22,* Barcelona, Spain.

[6] R.R. Craig, M.C.C. Bampton. *Coupling of substructures for dynamic analysis,* AIAA Journal, Vol. 6, No. 7 (1968), pp. 1313-1319.

A full PGD/HBM-based algorithm for a low-dimensional NNM continuation with modal enrichment

L. Meyrand[1], **E. Sarrouy**[1], **B. Cochelin**[1], **G. Ricciardi**[2]
[1] Aix Marseille Univ, CNRS, Centrale Marseille, LMA, Marseille, France
e-mail: **meyrand@lma.cnrs-mrs.fr**

[2] DEN/DTN/STRI/LHC, CEA Cadarache, France

Abstract

This work proposes a full algorithm to compute Nonlinear Normal Modes (NNMs) using a Proper Generalized Decomposition (PGD) approach combined to a continuation method. Because periodic solutions are sought, a harmonic balance method (HBM) is implemented to process the time-dependent functions. The interest of this study is first to couple this approach to a continuation method with a progressive enrichment of the PGD modes family and second to improve some of the PGD steps to get a robust algorithm. In particular, the initializations of solvers are chosen consistently with the available physical data through the use of LNMs shapes. The reduced basis is kept as small as possible since it is computed with on the fly enrichment, possibly from a unique mode. No particular assumptions on the non linearity have been made and hence a wide class of mechanical problems can be processed. The resulting method is applied on several beam models with localized nonlinearities which allows for an accurate analysis of its performance.

1 Introduction

The computing power currently achieved allows to take into account nonlinear effects in physical models and allows to deal with systems with a very large number of degrees of freedom. As systems became more and more realistic and sophisticated, model reduction techniques had to be developed in order to save digital resources while obtaining a physically satisfactory result.

Nonlinear Normal Modes (NMMs) are objects that can be exploited as part of modal reduction methods, similar as with Linear Normal Modes (LNMs). Their properties are studied to estimate and interpret more precisely the dynamics of mechanical systems [1, 2]. In this paper, only the Rosenberg's definition of NNMs [3] will be considered, *i.e.* a family of periodic solutions of the underlying free and conservative mechanical system. The reader can refer to the work of Shaw and Pierre [4, 5] or Kerschen and Renson [6, 7, 8] for more information about NNMs.

From a numerical point of view, the algorithms used to compute the NNMs of high-dimensional structures do not have yet reached maturity [9, 8] and the nonlinear effects causes convergence issues. NNMs require large sets of variables to be properly described which make them hard to compute in short times and hard to reuse even if some work still take advantage of their computations [10]. This remark serves as a starting point for the work presented in this article.

The reducted model developed in this paper falls within the framework of Proper Generalized Decomposition (PGD) methods. This class of reduction techniques is based on the separation of the unknowns and a fixed point algorithm which allows to deal with smaller systems in order to reduce the computation times. PGD was already used by Grolet and Thouverez [11] to compute free and forced responses of nonlinear systems. The reader can refers to Chinesta and Nouy [12, 13, 14, 15] to learn more about the possibilities offered by this approach.

In this work, a full algorithm is proposed in order to compute NNMs using a combination of a PGD approach and classical continuation schemes. A quick reminder of the NNM framework investigated here is given in Sec. 2. Then the PGD method is detailed in Sec. 3, including the use of a harmonic balance method (HBM) to deal with temporal aspects of the problem. The contributions of this work are highlighted in this section: first the PGD approach is coupled with a continuation method and a progressive enrichment of the PGD modes family is made and second some of the PGD steps are improved to get a robust algorithm. The PGD/HBM-based continuation scheme is described in Sec. 4. The last section, Sec. 5, is dedicated to illustrative cases to show some possibilities introduced by this algorithm.

2 Mechanical framework and Nonlinear Normal Modes (NNMs)

The equations of dynamics describing the behavior of a set of general coordinates can be obtained after a spatial discretization process using for example the Finite Elements method. It usually takes the following form:

$$\boldsymbol{M}\ddot{\boldsymbol{u}} + \boldsymbol{C}\dot{\boldsymbol{u}} + \boldsymbol{K}\boldsymbol{u} + \boldsymbol{f}_{\text{nl}}(\boldsymbol{u}, \dot{\boldsymbol{u}}) = \boldsymbol{f}(t) \tag{1}$$

Eq. (1) is a set of N second order nonlinear differential equations, the vector of the unknowns $\boldsymbol{u}$ – or vector of the degrees of freedom (dof) – is a vector of $\mathbb{R}^N$. $\boldsymbol{M}$, $\boldsymbol{C}$ and $\boldsymbol{K}$ are respectively the linear mass, damping and stiffness matrices, with $\{\boldsymbol{M}, \boldsymbol{C}, \boldsymbol{K}\} \in \mathcal{M}_N(\mathbb{R})^3$. $\boldsymbol{f}(t)$ is the vector of excitation forces and lies in $\mathbb{R}^N$ too. Finally $\boldsymbol{f}_{\text{nl}}(\boldsymbol{u}, \dot{\boldsymbol{u}})$ is the vector of non linear forces and belongs to $\mathbb{R}^N$. The general system described by Eq. (1) represents a very wide class of mechanical problems. Indeed, the $\boldsymbol{f}_{\text{nl}}$ term can be any nonlinear expression (*e.g.* cosine function, polynomial terms like $u_i u_j^3$, non smooth function, etc.).

This paper focuses on the particular study of NNMs, which will be considered as the periodic solutions of Eq. (1) in the particular case when no forcing neither damping is considered, or as an extension of the definition of LNMs which takes into account the nonlinear vector $\boldsymbol{f}_{\text{nl}}$. In this framework, introduced by Rosenberg, a NNM is a set of limit cycles – or periodic solutions – of the following system:

$$\boldsymbol{R}(\boldsymbol{u}(t)) = \boldsymbol{M}\ddot{\boldsymbol{u}} + \boldsymbol{K}\boldsymbol{u} + \boldsymbol{f}_{\text{nl}}(\boldsymbol{u}, \dot{\boldsymbol{u}}) = \boldsymbol{0} \tag{2}$$

Unlike LNMs, NNMs do not decouple the equations, and there exists a frequency-amplitude dependency. However, they take into account non linear effects and can be useful to investigate modal interaction between widely spaced modes or modal bifurcations [7, 8]. Numerically, building a NNM branch requires a large number of descriptors and consequent computation times [8]. This observation motivates the developments described in this work.

3 PGD and HBM combination to describe periodic solutions

3.1 Harmonic Balance Method

As NNMs are periodic solutions, a HBM framework is used. It does not require a time integration scheme as in shooting methods [16, 9]. Detailed explanations about this method and its advantages are given in works [17, 18, 19, 20]. Dealing with algebraic equations in the frequency domain has the disadvantages first to introduce a truncation order dependence and second to become costly as the number of dof increases and more harmonics are involved in the underlying physics of the system. A combination with a PGD reduction technique will permit to compute smaller systems without losing HBM advantages.

Some notations used later are here introduced. We are looking for a T-periodic signal $\boldsymbol{u}(t)$, with $T = 2\pi/\omega$:

$$\boldsymbol{u}(t) = \frac{\boldsymbol{a}_0}{\sqrt{2}} + \sum_{k=1}^{H} \left(\boldsymbol{a}_k \cos(k\omega t) + \boldsymbol{b}_k \sin(k\omega t)\right) \tag{3}$$

where $\boldsymbol{a}_k$ and $\boldsymbol{b}_k$ are respectively the cosine and sine coefficients of the Fourier series. A compact way to write $\boldsymbol{u}(t)$ is then:

$$\boldsymbol{u}(t) = \boldsymbol{U}_H \boldsymbol{h}_H(t,\omega), \text{ where } \begin{cases} \boldsymbol{U}_H = [\boldsymbol{a}_0, \boldsymbol{a}_1, \boldsymbol{b}_1, \dots] \\ \boldsymbol{h}_H = [1/\sqrt{2}, \cos(\omega t), \sin(\omega t), \dots]^{\mathrm{T}} \end{cases} \tag{4}$$

This formalism first shows computing $\boldsymbol{u}(t)$ is equivalent to compute both $\boldsymbol{U}_H$ and ω, second allows to link the Fourier coefficient of $\boldsymbol{u}(t)$ to those of its temporal derivative $\dot{\boldsymbol{u}}(t)$ via a matrix $\boldsymbol{D}$:

$$\boldsymbol{D} = \mathrm{diag}\left(0, \begin{bmatrix} 0 & 1 \\ -1 & 0 \end{bmatrix}, \dots, H \begin{bmatrix} 0 & 1 \\ -1 & 0 \end{bmatrix}\right) \tag{5}$$

As HBM is a Galerkine method, this decomposition is injected in Eq. (2) and the equations are projected on each element of the Fourier basis $\boldsymbol{h}_H$ using the inner product:

$$< f, g >_T = \frac{2}{T}\int_0^T f(t)g(t)dt \tag{6}$$

This leads to a set of $N(2H+1)$ equations with $N(2H+1)+1$ unknowns, where N is the number of dofs. As there is no external forcing in Eq. (2), ω is also an unknown, and the final problem can be written:

$$\boldsymbol{H}(\boldsymbol{a}_0, \boldsymbol{a}_1, \boldsymbol{b}_1, \dots, \omega) = \boldsymbol{0} \tag{7}$$

Whether a HBM is applied on the forced equation Eq. (1), ω is taken equal to the forcing frequency, and the system described by Eq. (7) is square. In the case of NNMs computation, an extra equation usually called *phase condition* [21] is needed. Indeed, no "initial time" exists for a given periodic solution $\boldsymbol{u}(t)$ so the phase condition allows to define the Fourier coefficients uniquely. Here are given some possibilities of equations: to lock the amplitude or the velocity of a given dof at $t = 0$ in Eq. (3) [21], or to nullify one of the Fourier coefficient components [22]. Considering a conservative system, please note that nullifying one sine coefficient implies that all sine coefficients are null, hence only (H+1) $\boldsymbol{a}_k$ coefficients must be computed.

Considering Eq. (7) again, it is possible to analytically establish the expression of the projection of the linear part $\boldsymbol{H}_1(\omega)\,\boldsymbol{u}_H$ of Eq. (2), where $\boldsymbol{u}_H = \{\boldsymbol{a}_0^{\mathrm{T}}, \dots, \boldsymbol{a}_k^{\mathrm{T}}, \boldsymbol{b}_k^{\mathrm{T}}, \dots\}^{\mathrm{T}}$. Hence, Eq. (7) is rewritten $\boldsymbol{H}_1(\omega)\,\boldsymbol{u}_H + \boldsymbol{H}_{\mathrm{nl}}(\boldsymbol{u}_H, \omega) = \boldsymbol{0}$, with:

$$\begin{cases} \boldsymbol{H}_1(\omega) = \mathrm{diag}(\boldsymbol{\Lambda}_0, \boldsymbol{\Lambda}_1, \dots, \boldsymbol{\Lambda}_H) \\ \boldsymbol{\Lambda}_0 = \boldsymbol{K}, \ \boldsymbol{\Lambda}_k = \mathrm{diag}(\boldsymbol{K} - (k\omega)^2\boldsymbol{M}, \boldsymbol{K} - (k\omega)^2\boldsymbol{M}) \end{cases} \tag{8}$$

The term $\boldsymbol{H}_{\mathrm{nl}}(\boldsymbol{u}_H, \omega)$ corresponds to the projections of nonlinear forces $\boldsymbol{f}_{\mathrm{nl}}(\boldsymbol{u}, \dot{\boldsymbol{u}})$ onto the Fourier basis. Evaluating this nonlinear contribution is time consuming as analytical expressions can scarcely be derived. The most commun approach to deal with this term is to use the Alternating Frequency/Time (AFT) method introduced by Cameron and Griffin [23]. Basically, $\boldsymbol{u}(t_k)$ and $\dot{\boldsymbol{u}}(t_k)$ are evaluated for specific t_k values in $[0, T]$ using an Inverse Fast Fourier Transform (IFFT) based on $\boldsymbol{a}_k$ and $\boldsymbol{b}_k$ coefficients. Then, $\boldsymbol{f}_{\mathrm{nl}}(\boldsymbol{u}(t_k), \dot{\boldsymbol{u}}(t_k))$ is computed for each time t_k; finally, a Fast Fourier Transform (FFT) is used to evaluate the projections, that is the coefficients of the Fourier series of $\boldsymbol{f}_{\mathrm{nl}}(\boldsymbol{u}, \dot{\boldsymbol{u}})$.

3.2 PGD combined to HBM

For the purpose of this work, the PGD process is divided in three main steps, which are separating variables (space and time here), obtaining as many subproblems as there are variables (time and space problems here), and run an alternated directions fixed point loop which solves each subproblem with the other variables fixed, for a given loop iteration. Here both subproblems are coupled with HBM features introduced in Sec. 3.1 to

produce a global PGD/HBM algorithm. Many variants of the PGD method exist and we chose to describe the one usually called *optimized PGD* (oPGD) [11, 15] in the following theoretical developments. A lighter adaptation of the oPGD from a computational point of view and called *progressive PGD* (pPGD) is detailed in Sec. 4.1.3.

Given a positive integer $m << N$, we look for a space-time separated solution $\boldsymbol{u}(t)$ of Eq. (2) such as:

$$\boldsymbol{u}(t) \approx \sum_{j=1}^{m} \boldsymbol{p}_j q_j(t) \Leftrightarrow \boldsymbol{u}(t) \approx \boldsymbol{P}\boldsymbol{q}(t) \text{ with } \boldsymbol{P} = [\boldsymbol{p}_1, \dots, \boldsymbol{p}_m] \in \mathcal{M}_{N,m} \tag{9}$$

Assuming this notation, the m *PGD modes* are defined by their PGD mode shapes $\boldsymbol{p}_j$ and their time dependences $q_j(t)$, assembled in a vector $\boldsymbol{q}(t) \in \mathbb{R}^m$. In this two-term product, the amplitude information is chosen to be given by $q_j(t)$ only so the $\boldsymbol{p}_j$ PGD mode shapes are normalized to 1.

This decomposition will to split the problem into two smaller problems (*cf.* Sec. 3.2.1 and Sec. 3.2.2) whose sizes depend on m. As NNMs are periodic solutions of Eq. (2), the temporal part $\boldsymbol{q}(t)$ will be decomposed using HBM:

$$\boldsymbol{q}(t) = \boldsymbol{Q}_H \boldsymbol{h}_H(t,\omega), \text{ where } \begin{cases} \boldsymbol{Q}_H = [\boldsymbol{a}_0, \boldsymbol{a}_1, \boldsymbol{b}_1, \dots] \\ \boldsymbol{h}_H = [1/\sqrt{2}, \cos(\omega t), \sin(\omega t), \dots]^{\mathrm{T}} \end{cases} \tag{10}$$

Computing a NNM point by a combined PGD/HBM approach is then equivalent to compute a $\{\boldsymbol{P}, \boldsymbol{Q}_H, \omega\}$ set.

3.2.1 Temporal problem $\mathcal{T}_m$

The objective of this section is to compute the temporal part – *i.e* $\boldsymbol{Q}_H$ and ω – knowing the PGD mode shapes – *i.e.* the matrix $\boldsymbol{P}$. A weak formulation is written on an oscillation period $I_T = [0, 2\pi/\omega]$, with the test function $\boldsymbol{u}^\star(t) = \boldsymbol{P}\,\boldsymbol{q}^\star(t)$:

$$\forall t \in I_T \;\; \forall \boldsymbol{q}^\star(t) \int_{I_T} \boldsymbol{q}^{\star T}(t) \boldsymbol{P}^T \boldsymbol{R}(\boldsymbol{P}\boldsymbol{q}(t)) dt = 0 \tag{11}$$

The final temporal problem is established from the weak formulation Eq. (11):

$$\forall t \in I_T \;\; \mathbf{M_r}\ddot{\mathbf{q}}(t) + \mathbf{K_r}\boldsymbol{q}(t) + \boldsymbol{f}_{\mathrm{nl}r}(\boldsymbol{P}\boldsymbol{q}(t), \boldsymbol{P}\dot{\boldsymbol{q}}(t)) = \mathbf{0} \tag{12}$$

where $\{\mathbf{M_r} = \boldsymbol{P}^T\boldsymbol{M}\boldsymbol{P}, \mathbf{K_r} = \boldsymbol{P}^T\boldsymbol{K}\boldsymbol{P}\} \in \mathcal{M}_m(\mathbb{R})^2$ and $\boldsymbol{f}_{\mathrm{nl}r} = \boldsymbol{P}^T\boldsymbol{f}_{\mathrm{nl}} \in \mathbb{R}^m$. This system of m second order nonlinear ODEs is solved by HBM. Using the same notations as in Sec. 3.1, the temporal problem $\mathcal{T}_m$ is defined as a square algebraic system with $m(2H+1)+1$ unknowns in the following manner:

$$\mathcal{T}_m(\boldsymbol{Q}_H, \omega | \boldsymbol{P}) = \mathbf{0} \Leftrightarrow \begin{cases} \boldsymbol{H}_{\mathrm{l}}(\omega)\boldsymbol{q}_H + \boldsymbol{H}_{\mathrm{nl}}(\boldsymbol{q}_H, \omega) = \mathbf{0} \\ c(\boldsymbol{q}_H, \omega) = 0 \end{cases} \tag{13}$$

where $\boldsymbol{q}_H = \{\boldsymbol{a}_0^{\mathrm{T}}, \dots, \boldsymbol{a}_k^{\mathrm{T}}, \boldsymbol{b}_k^{\mathrm{T}}, \dots\}^{\mathrm{T}}$ are the Fourier coefficients put into a vectorial form, $\boldsymbol{H}_{\mathrm{l}}$ is the linear contribution, $\boldsymbol{H}_{\mathrm{nl}}$ is the vector of Fourier coefficients of the nonlinear contribution of Eq. (12), and $c(\boldsymbol{q}_H, \omega) \in \mathbb{R}$ is an arbitrary constraint equation which allows to get a square system. $c(\boldsymbol{q}_H, \omega)$ will be specified in Sec. 4.1 as a continuation criterion.

3.2.2 Spatial problem $\mathcal{S}_m$

The objective of this section is to compute the spatial part – *i.e* the matrix $\boldsymbol{P}$ – knowing the temporal part – *i.e.* $\boldsymbol{Q}_H$ and ω. This time, a weak formulation is obtained with the test function $\boldsymbol{u}^\star = \sum_{k=1}^{m} \mathbf{p}_k^\star q_k$, leading to a set of m systems with N equations:

$$\forall k \in [\![1;m]\!],\ \sum_{j=1}^{m} \left(\int_{I_T} q_k \ddot{q}_j \, dt \, \boldsymbol{M} + \int_{I_T} q_k q_j \, dt \, \boldsymbol{K} \right) \boldsymbol{p}_j + \int_{I_T} q_k \boldsymbol{f}_{\text{nl}}(\boldsymbol{P}\boldsymbol{q}(t)) \, dt = \mathbf{0} \tag{14}$$

Finally, these equations can be condensed in a $N \times m$ algebraic system denoted $\mathcal{S}_m$:

$$\mathcal{S}_m(\boldsymbol{P}|\boldsymbol{Q}_H, \omega) = \mathbf{0} \Leftrightarrow \boldsymbol{S}_{\text{l}} \, \tilde{\mathbf{p}} + \boldsymbol{S}_{\text{nl}}(\tilde{\mathbf{p}}) = \mathbf{0} \tag{15}$$

where $\tilde{\mathbf{p}} = \{\boldsymbol{p}_1^{\text{T}}, \ldots, \boldsymbol{p}_m^{\text{T}}\}^{\text{T}} \in \mathbb{R}^{N \times m}$ contains the columns of $\boldsymbol{P}$, $\boldsymbol{S}_{\text{l}}$ is the linear contribution with respect to $\tilde{\mathbf{p}}$, and $\boldsymbol{S}_{\text{nl}}(\tilde{\boldsymbol{p}}) = [\int_{I_T} q_k \boldsymbol{f}_{\text{nl}}(\boldsymbol{P}\boldsymbol{q}(t)) \, dt]_{1 \leq k \leq m}$ the nonlinear one. $\boldsymbol{S}_{\text{nl}}$ is computed using the AFT approach, and $\boldsymbol{S}_{\text{l}}$ can be established analitically:

$$\boldsymbol{S}_{\text{l}} = \boldsymbol{I}_2 \otimes \boldsymbol{M} + \boldsymbol{I}_0 \otimes \boldsymbol{K} \text{ , with } \boldsymbol{I}_k = \pi \omega^{k-1} \boldsymbol{Q}_H \boldsymbol{D}^{k^{\text{T}}} \boldsymbol{Q}_H^{\text{T}} \tag{16}$$

The spatial subproblem $\mathcal{S}_m$ is more expensive to solve than $\mathcal{T}_m$ as its size depends on $N >> m$.

3.2.3 PGD/HBM fixed point algorithm

The last step of the PGD process consists in integrating both temporal and spatial subproblems into a fixed point algorithm. The full fixed point loop is detailed in Algorithm 1. The subproblems resolution lies at lines 6 and 7. Two main issues have to be adressed: the choice of an error measure ε and the way in which potential additional PGD modes are initialized.

The error measure ε, defined at lines 1 and 11, compares the norm of the residue vector $\boldsymbol{R}(\boldsymbol{u}(t))$ – where $\boldsymbol{u}(t) = \boldsymbol{P}\boldsymbol{Q}_H \boldsymbol{h}_H(t, \omega)$ – to $||\boldsymbol{K}\boldsymbol{u}(t)||$ over a period I_T. Unlike in Grolet and Thouverez work [11] in which $k < k_{max} = 3$ was the only stopping criterion of the loop, here the convergence is checked by the use of this physical criterion, introduced at line 4. Moreover the fixed point loop is broken when $k > k_{max}$ or if the current iteration does not reduce ε enough, that is, when ε is greater than $r_{\text{fp}} \varepsilon_{\text{prev}}$ where $r_{\text{fp}} < 1$ and $\varepsilon_{\text{prev}}$ denotes the error measured at the end of the previous iteration.

If the convergence criterion $\varepsilon \leq \varepsilon_{\text{max}}$ is not fulfilled at the end of the fixed point loop, the choice is made to add a new PGD mode (from line 13): a new column $\boldsymbol{p}_j$ is added to $\boldsymbol{P}$ and the associated row is added to the $\boldsymbol{Q}_H$ matrix. In previous works [11], random values were used to fill these new vectors, and the order in which subproblems are dealt with in the algorithm did not seem to be important. Here, the initial observation is that it is difficult to initialize $\boldsymbol{Q}_H$ with new temporal information. Hence, the temporal problem is computed first into the fixed point loop, with a new row filled with zeros. The new column $\boldsymbol{p}_j$ is initialized with the shape of the $(n_0 + m)$-th LNM, with n_0 being the index of the n_0-th NNM being computed. Indeed, this spatial data is easily computable and it seems relevant to add new shapes from the LNMs as they form a basis. Moreover, avoiding random initializations makes the algorithm more robust and results reproducible.

4 NNM continuation using PGD/HBM modes enrichment

In this section, a full NNM computation algorithm combining PGD/HBM and continuation schemes is detailed. Near the n_0-th LNM, first NNM points are searched using a single PGD mode ($m = 1$) which initially has the shape of the n_0-th LNM. When the mechanical energy is growing, new PGD modes are included to

Algorithm 1: PGD/HBM global algorithm

Parameters: Values for m_{max}, k_{max}, ε_{max} and r_{fp};
Definition of $c(\boldsymbol{q}_H, \omega)$ used in $\mathcal{T}_m$;
LNMs: $\boldsymbol{\Phi} = [\boldsymbol{\phi}_{n_0}, \ldots, \boldsymbol{\phi}_n]$.
Data: Initial values for m, $\boldsymbol{P}$, $\boldsymbol{Q}_H$ and ω.

$\varepsilon \leftarrow \max_{t\in I_T}(||\boldsymbol{R}(\boldsymbol{u}(t))||/||\boldsymbol{K}\boldsymbol{u}(t)||)$;
while $m \leq m_{\text{max}}$ **and** $\varepsilon > \varepsilon_{\text{max}}$ **do**
  $k \leftarrow 0$, $\varepsilon_{\text{prev}} \leftarrow 2\,\varepsilon$;
  while $k \leq k_{\text{max}}$ **and** $\varepsilon \geq \varepsilon_{\text{max}}$ **and** $\varepsilon \leq r_{\text{fp}}\varepsilon_{\text{prev}}$ **do** /* FP loop */
    $k \leftarrow k + 1$, $\varepsilon_{\text{prev}} \leftarrow \varepsilon$;
    $\boldsymbol{Q}_H, \omega \leftarrow$ solutions of $\mathcal{T}_m(\boldsymbol{Q}_H, \omega|\boldsymbol{P}) = \boldsymbol{0}$;
    $\boldsymbol{P} \leftarrow$ solution of $\mathcal{S}_m(\boldsymbol{P}|\boldsymbol{Q}_H, \omega) = \boldsymbol{0}$;
    for $j \leftarrow 1$ **to** m **do** /* Mode normalization */
      $\boldsymbol{p}_j \leftarrow \boldsymbol{p}_j/||\boldsymbol{p}_j||$;
    end
    $\varepsilon \leftarrow \max_{t\in I_T}(||\boldsymbol{R}(\boldsymbol{u}(t))||/||\boldsymbol{K}\boldsymbol{u}(t)||)$;
  end
  if $\varepsilon \geq \varepsilon_{\text{max}}$ **then** /* Next mode initialization */
    $\boldsymbol{P} \leftarrow [\boldsymbol{P}, \boldsymbol{\phi}_{n_0+m}]$, $\boldsymbol{Q}_H \leftarrow \begin{bmatrix} \boldsymbol{Q}_H \\ \boldsymbol{0}_{1,2H+1} \end{bmatrix}$;
    $m \leftarrow m + 1$;
  end
end
Return m, $\boldsymbol{P}$, $\boldsymbol{Q}_H$, ω and ε;

the decomposition only when it is necessary along the path. The hightlights of the method are a dimension varying continuation scheme which keeps the number of NNM descriptors as small as possible and with an on the fly enrichment of the PGD modes set as the system behavior becomes more complex.

Before giving some details about the continuation scheme, we will define $\boldsymbol{y}_n$ as the the n-th point on the current path. As explained in Sec. 3.2, a point of the NNM is fully determined by its $\{\boldsymbol{P}, \boldsymbol{Q}_H, \omega\}$ set. Hence we will note:

$$\boldsymbol{y}_n \equiv \{\boldsymbol{P}_n, \boldsymbol{Q}_{Hn}, \omega_n\} \quad \text{(size: } N\,m + (2H+1)\,m + 1\text{)} \tag{17}$$

A distance d between two consecutive points $\boldsymbol{y}_{n-1}$ and $\boldsymbol{y}_n$ is also defined. It is weighted by a set of positive constants $\{\alpha_P, \alpha_Q, \alpha_\omega\}$ which are arbitrary continuation control parameters, such as:

$$d(\boldsymbol{y}_{n-1}, \boldsymbol{y}_n) = \sqrt{\alpha_P^2||\boldsymbol{P}_n - \boldsymbol{P}_{n-1}||^2 + \alpha_Q^2||\boldsymbol{Q}_{Hn} - \boldsymbol{Q}_{Hn-1}||^2 + \alpha_\omega^2|\omega_n - \omega_{n-1}|^2} \tag{18}$$

The prediction and correction equations used in Sec. 4.1 both rely on this choice of distance.

4.1 Prediction/Correction continuation process

Although more complex continuation procedures exist [24], the algorithm presented in this work can be used with a choice of simple predictor and correctors. The next point sought, denoted $\boldsymbol{y}_\star$, is computed from a predicted point $\boldsymbol{y}_\star^{pred}$ obtained with a secant method whose the arclength is set by Δs. This predictor is chosen because of its simplicity. The correction step relies on the PGD/HBM solver described previously in Sec. 3.2 with a specific choice of constraint equation $c(\boldsymbol{q}_H, \omega) = 0$, linked to a classical correction method (*e.g.* arclength, pseudo-arclength, etc.). The global algorithm is depicted in Algorithm 2.

Algorithm 2: Continuation with on the fly PGD enrichment algorithm

Parameters: Values for Δm, $m_{\text{max tot}}$, r_ε, r_s^{mult}, r_s^{div} and Δs;
Values for Algorithm 1:
- k_{max}, ε_{max} and r_{fp};
- LNMs: $\boldsymbol{\Phi} = [\boldsymbol{\phi}_{n_0}, \dots, \boldsymbol{\phi}_n]$;
- Constraint equations: $c_2(\boldsymbol{q}_H, \omega)$ and $c_p(\boldsymbol{q}_H, \omega)$.

Data: Circular frequency of n_0-th mode ω_{n_0}.

1 $\boldsymbol{y}_1 \leftarrow \{\boldsymbol{\phi}_{n_0}, \mathbf{0}_{1,2H+1}, \omega_{n_0}\}$; // First point
2 $c(\boldsymbol{q}_H, \omega) \leftarrow c_2(\boldsymbol{q}_H, \omega)$, $m_{\text{max}} \leftarrow m_{\text{max tot}}$; // Second point
3 Compute $\boldsymbol{y}_2$ using Algorithm 1 with $\boldsymbol{y}_1$ as initial value;
4 $c(\boldsymbol{q}_H, \omega) \leftarrow c_p(\boldsymbol{q}_H, \omega)$; // Continuation loop
5 $p \leftarrow 2$;
6 **while** $m \leq m_{\text{max tot}}$ **do**
7 $\quad m_{\text{max}} \leftarrow m + \Delta m$;
8 $\quad$ Compute $\boldsymbol{y}_\star$ using secant method with $\boldsymbol{y}_p$, $\boldsymbol{y}_{p-1}$ and Δs; // Prediction
9 $\quad$ Compute $\boldsymbol{y}_\star$ using Algorithm 1 with $\boldsymbol{y}_\star$ as initial value; // Correction
10 $\quad$ **if** $\varepsilon < \varepsilon_{\text{max}}$ **then**
11 $\quad\quad \boldsymbol{y}_{p+1} \leftarrow \boldsymbol{y}_\star$;
12 $\quad\quad p \leftarrow p + 1$;
13 $\quad\quad$ **if** $\varepsilon < r_\varepsilon \varepsilon_{\text{max}}$ **then**
14 $\quad\quad\quad \Delta s \leftarrow r_s^{mult} \Delta s$;
15 $\quad\quad$ **end**
16 $\quad$ **else**
17 $\quad\quad \Delta s \leftarrow r_s^{div} \Delta s$;
18 $\quad$ **end**
19 **end**

4.1.1 Prediction step features

The prediction arclength Δs is managed in a classical way, as follows: if the error ε measured after a correction step is too large (see Algorithm 1 in Sec. 3.2.3), Δs is decreased by multiplying it by $r_s^{div} < 1$ (see line 17) leading to a closer prediction point $\boldsymbol{y}_\star^{pred}$. On the contrary, if $\varepsilon < r_\varepsilon \varepsilon_{max}$ with $r_\varepsilon < 1$, Δs is multiplied by $r_s^{mult} > 1$ (see lines 13 and 14). Else Δs is kept constant for the next prediction step.

A secant prediction needs two solution points computed beforehand. The first point of the n_0-th NNM is already known: $\boldsymbol{y}_1 \equiv \{\boldsymbol{\phi}_{n_0}, \mathbf{0}_{1,2H+1}, \omega_{n_0}\}$. An amplitude condition imposed on the j-th dof at $t = 0$ is chosen to compute $\boldsymbol{y}_2$: $u_j(t = 0) = u_{j0}$ with $u_{j0} \neq 0$. This particular constraint, denoted $c_2(\boldsymbol{q}_H, \omega)$ in Algorithm 2, is injected into Algorithm 1 to find $\boldsymbol{y}_2$ starting from $\boldsymbol{y}_1$.

The reader could remark that during the prediction step, $\boldsymbol{y}_n$ can have a greater size than $\boldsymbol{y}_{n-1}$ because of the possibility to get different problem dimensions m along the path. The distance given by Eq. (18) need summations of matrices that do not have the same sizes, and the choice of padding $\boldsymbol{y}_{n-1}$ missing components with zeros instead of truncating $\boldsymbol{y}_n$ is made. Hence, all computed data are taken into account to reach a better prediction.

4.1.2 Correction step features

The startpoint of the correction step is $\boldsymbol{y}_\star^{pred}$. It is injected in the PGD/HBM solver described in Algorithm 1, in which the constraint equation involved in the temporal problem $\mathcal{T}_m$ is set to $c_p(\boldsymbol{q}_H, \omega)$, as denoted in Algorithm 2. $c_p(\boldsymbol{q}_H, \omega)$ defines the correction method and can be freely chosen among the classical possibilities

[19]. Here an arclength correction is used: $c_p(\boldsymbol{q}_{H\star}, \omega_\star) = d(\boldsymbol{y}_n, \boldsymbol{y}_\star)^2 - \Delta s^2$. This condition involves $\boldsymbol{P}_\star$ which is the last value of the spatial modes returned after the spatial problem $\mathcal{S}_m$ when processing the current temporal problem $\mathcal{T}_m$.

A remarkable point of this continuation scheme is the ability to increase the size of the problem when a new point $\boldsymbol{y}_{n+1}$ is computed from $\boldsymbol{y}_n$. At line 7 in Algorithm 2, the highest difference of size between $\boldsymbol{y}_n$ and $\boldsymbol{y}_{n+1}$ is defined as Δm. Consequently, two consecutive points can have different sizes, which has to be taken into account when $c_p(\boldsymbol{q}_H, \omega)$ is evaluated. Indeed, an arclength condition requires $d(\boldsymbol{y}_n, \boldsymbol{y}_\star)$. This time, a truncation is applied for the current point $\boldsymbol{y}_\star$ so the arclength condition is evaluated in a space which has the size of $\boldsymbol{y}_n$. Thus, no geometrical condition is imposed on the new component introduced in $\boldsymbol{y}_\star$.

4.1.3 Progressive PGD – a lighter variant

As said in Sec. 3.2.2, considering the oPGD method, $\mathcal{S}_m$ is more expensive to solve than $\mathcal{T}_m$ as its size is $N \times m$. This observation motivates the use of a variant of the oPGD approach developed before, in which $\mathcal{S}_m$ is solved as few times as possible, and in which only a few number of $\mathcal{S}_m$ equations is solved. In order to reach these goals, severals choices are made:

- During the correction step, the spatial problem is only solved when a new PGD mode is added, *i.e.* when the condition at line 13 in Algorithm 1 is fulfilled. Hence, most of the fixed point loops only solve the temporal problem. The matrix $\boldsymbol{P}_\star$ is put as the initialization of $\mathcal{T}_m$. This is consistent with the fact that in practice, the nature of many points close together in the NNM branch is not sufficiently different to require the introduction of a new PGD mode shape.
- In addition to that, in order to deal with the case when $\mathcal{S}_m$ has to be solved, a new lighter spatial problem is defined. The PGD mode shapes contained in $\boldsymbol{P}$ are definitively locked once computed, and only the new $\boldsymbol{p}_j$ added at line 13 in Algorithm 1 is updated by the spatial solver. This constitutes a gain in algorithmic complexity since the new size of the spatial problem is only N. The procedure leading to the analytical expression of the spatial problem is analogous to the Galerkine process described in Sec. 3.2.2, except that this time the projection is only made on the new PGD mode shape $\boldsymbol{p}_j$. The expression of this N-sized system can be found in [11].

This variant is usually called *progressive PGD* (pPGD). It allows to improve the numerical performance of the algorithm described before. However, its main disavantage is the lack of flexibility of the PGD mode shapes, which can finally generate NNM branches of higher dimension m_{max} because more spatial information is needed when the system behavior becomes more complex.

5 Numerical application on two beam models

The main branch of the first NNM of a beam model with a cubic nonlinearity described in Sec. 5.1 is built using the full PGD/HBM continuation algorithm. The main results proper to the presented approach are given in Sec. 5.2. This numerical study has been performed for the presented oPGD/HBM method and its pPGD/HBM variant, but for the sake of clarity only the pPGD results are presented on the figures of this section. Finally in Sec. 5.3 some numerical considerations are made for the presented example and another similar beam model with a localized contact. Hence, two different classes of conservative nonlinearities are adressed in this paper.

5.1 Description of the beam models

The considered system is an Euler-Bernouilli bending beam with one end clamped and a spring at its free end; it is spatially discretized by FEM, as illustrated in Fig. 1. The beam properties are: Young modulus

$E = 210$ GPa, density $\rho = 7800$ kg.m^{-3}, area of the square section $S = 9\ 10^{-4}$ m^2, second area moment $I = 6.71\ 10^{-8}$ m^4 for an in-plane bending and length $L = 1$ m. The linear stiffness of the spring is $k = 4\ 10^4$ N.m^{-1}. The first eigenvalues of the underlying linear system consisting of the beam plus the linear spring are $\{\omega_1, \omega_2, \omega_3, \omega_4, \omega_5\} = \{217, 999, 2769, 5420, 8960\}$ rad.s^{-1}. There are $N_e = 20$ elements with two dof per node: a transverse displacement u and a rotation θ, so there are $N = 40$ dof.

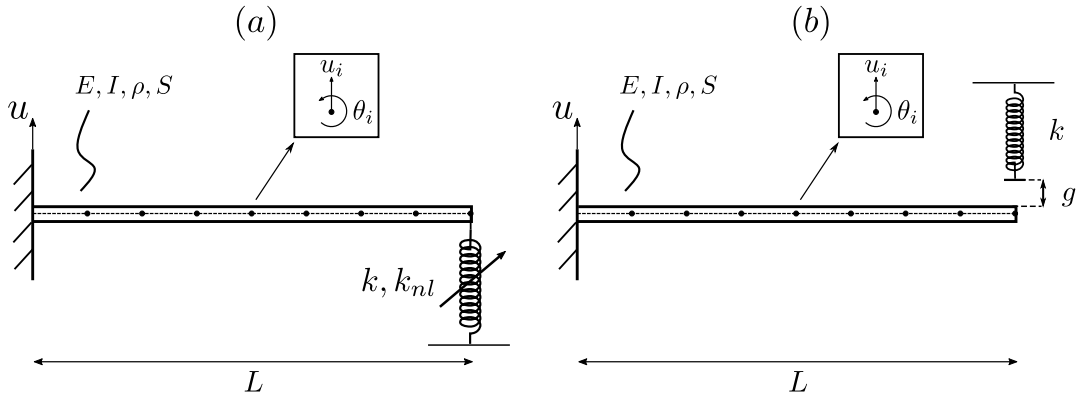


Figure 1: Euler-Bernouilli cantilever beam (a) with a transverse cubic spring at dof 1 (b) with a transverse gap between dof 1 and the linear spring.

- On the left in Fig. 1, a polynomial non linearity is chosen by introducing a cubic stiffness k_{nl} to the spring. The nonlinear contribution is $\boldsymbol{f}_{\text{nl}}(t) = [k_{nl} u_1^3(t)\ \mathbf{0}_{N-1}]^T$ with $k_{nl} = 9.2\ 10^5$ N.m^{-3}. Otherwise, we consider an underlying linear system made of the mass and stiffness matrices of the beam plus the linear stiffness of the spring – *i.e.* $K_{11} = K_{11beam} + k$. $H = 50$ harmonics are considered on an exploratory basis, in particular because the algorithmic complexity stays reasonable. Indeed, about twenty harmonics would be enough to deal with the involved physics.

- On the right in Fig. 1, a one-sided contact problem is also described: a gap $g = 2$ cm is introduced between the free end of the beam and the linear spring. The underlying linear system is the Euler-Bernouilli cantilever beam. The unilateral contact is modelled as follows:

$$\boldsymbol{f}_{\text{nl}}(t) = \begin{cases} [k(u_1(t) - g)\ \ \mathbf{0}_{N-1}]^T, & \text{if } u_1(t) > g \\ \mathbf{0}_N, & \text{otherwise} \end{cases} \tag{19}$$

  This unsmoothed contact is quite hard as $k/\dfrac{3EI}{L^3} = 94.56\%$ with $\dfrac{3EI}{L^3}$ the equivalent stiffness of the cantilever beam taken alone. A contact problem between two identical beams would be similar from the stiffness point of view. Consistently with this class of problem, the arbitrary value $H = 70$ is chosen.

  The results obtained for this second model will not be detailed in this paper. However, some numerical values will be given in Sec. 5.3 to extend some conclusions to this class of nonlinearities.

Parameters required by Algorithm 2 are given in Table 1. As both problems are conservative, a cosine basis is sufficient to describe the harmonic behavior of the system, so only $(H + 1)$ Fourier coefficients have to be computed instead of $(2H + 1)$.

5.2 Bending beam with a cubic spring at its free end

A convenient way to present the NNM branches is a Frequency-Energy plot (FEP) [1, 8], E being the mechanical energy of the NNM. The cubic spring case NNM1 (tangent to $\boldsymbol{\phi}_1$ at almost null amplitudes) is

Δm	$m_{\text{max tot}}$	r_ε	r_s^{mult}	r_s^{div}	Δs	k_{max}	ε_{max}	r_{fp}	$\boldsymbol{y}_2 : u_1(t=0)$	$\{\alpha_P, \alpha_q, \alpha_\omega\}$
1	10	0.1	1	0.5	1.5	10	10^{-3}	0.8	10^{-3} m	$\{10^{-6}, 10^{-1}, 10^{-4}\}$
(5)		(0.5)	(1.2)		(1)				(5 10^{-4} m)	$(\{0, 10^{-6}, 1\})$

Table 1: Algorithm 2 required parameters for the cubic spring case. The contact case parameters are given in parentheses on the second line, only when they differ from the previous ones.

displayed in a FEP given in Fig. 2. N_{pt} is the index of converged solution points through the 131 points computed during this pPGD/HBM continuation. Only 7 PGD modes are required by the pPGD algorithm (*cf.* Fig. 3) to build this branch which reaches about $E_{max} = 2.25\ 10^5$ J. The same branch can be computed with only 6 PGD modes using oPGD. Indeed the shapes of the PGD modes are always the same through a pPGD/HBM continuation process because the method involves blocking the shapes once they are integrated into the $\boldsymbol{P}$ matrix. This lack of flexibility can lead to the introduction of more PGD modes than with oPGD. Both variants obviously give identical FEP.

The interpretation of the modal interactions drawn in Fig. 2 (interaction tongue and final internal resonance) are deliberately limited in order to focus on the aspects specific to the numerical method developed.

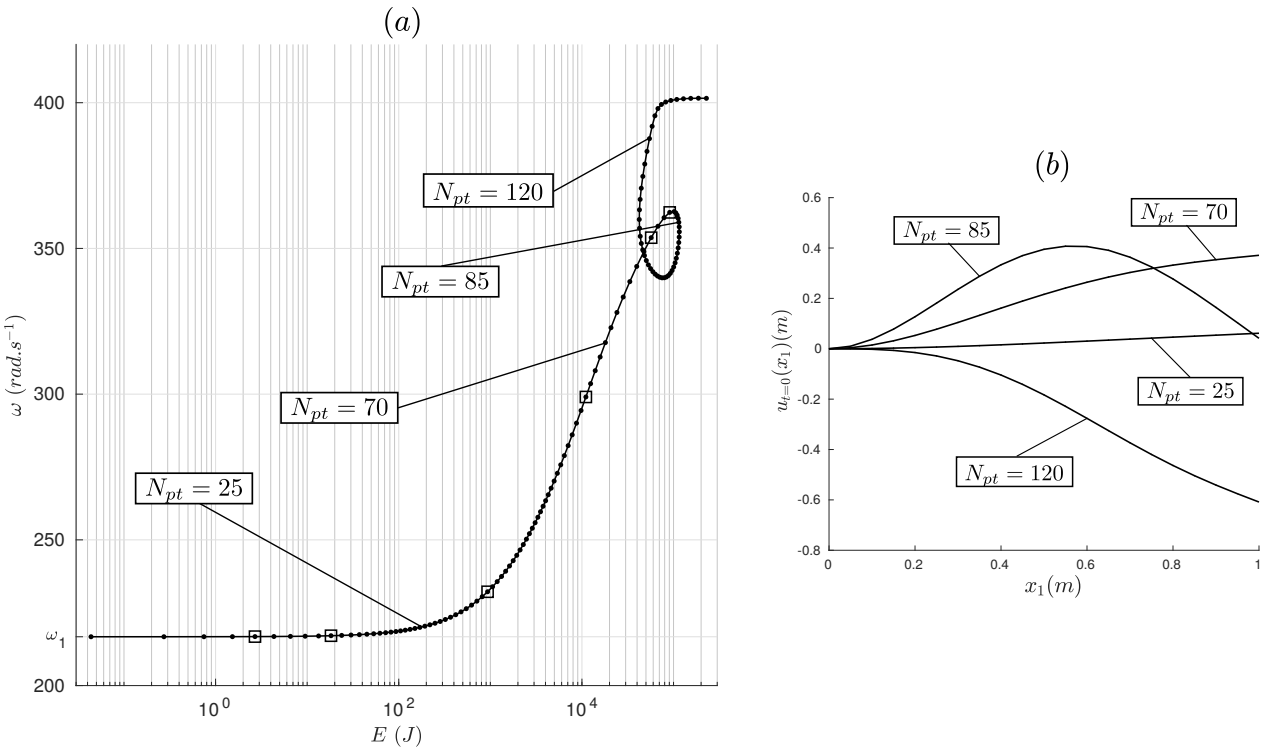


Figure 2: (a) Main branch of NNM1 in a FEP and (b) its mode shape at null velocity points for four continuation points. Squares: solution points where a PGD mode is added.

It is recalled that the NNM framework used in this paper is the Rosenberg's one [3]. In particular, all dofs reach their maximum at the same time, hence the NNM shapes at null velocity plotted in Fig. 2 gives interesting physical data. The more energy grows the more the nonlinear spring takes importance against the bending inertia of the beam, generating localized curvature inversions near the free end. Qualitatively similar results are obtained by Kerschen for another cantilever beam with cubic spring in [25].

On Fig. 3, the error measure ε along the path is depicted along with the number of PGD modes. The process for adding PGD modes is clearly identified: ε reaches the limit value ε_{max} then a new PGD mode is embedded in the calculations leading to a decrease of the error. Fig. 2 shows that the PGD modes are gradually added along the branch as expected with a smooth cubic nonlinearity. Please note that the error

for the first point $N_{pt} = 1$ is not displayed as it is null and cannot appear in a logarithmic scale. All these interpretations are retrieved in oPGD results.

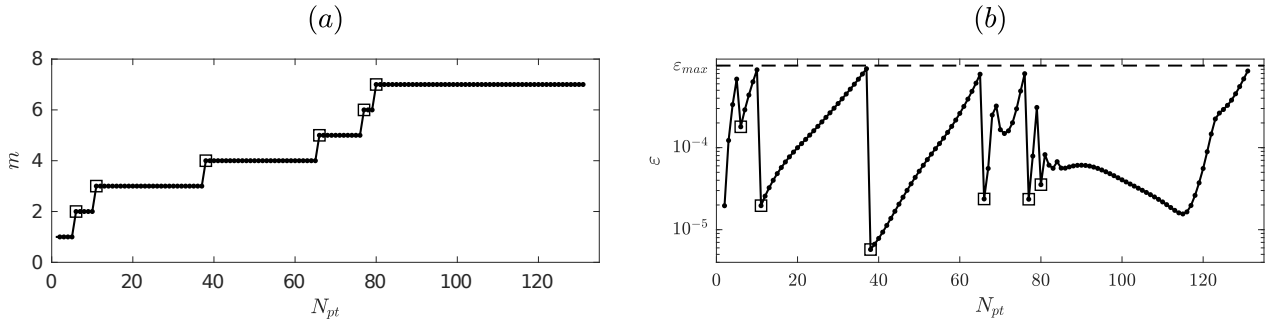


Figure 3: (a) Number of PGD modes m and (b) error measure ε against point index N_{pt}. Squares: solution points where a PGD mode is added.

An analysis of the seven PGD mode shapes $\boldsymbol{p}_j$ is provided on Fig. 4. An interesting feature proper to both pPGD and oPGD approaches is the presence of PGD modes which involve the participation of several LNMs. For instance such "combined mode" is here the PGD mode 3, which gathers contributions of the first 6 LNMs. With such an approach, high order LNMs can be taken into account in a reduced range of PGD mode shapes: here 5 PGD modes are sufficient to describe the system behavior until the interaction tongue and they involve the contributions of at least the first ten LNMs. Analoguously only 4 PGD modes are required to build the same area using oPGD, with the contributions of the first 6 LNMs.

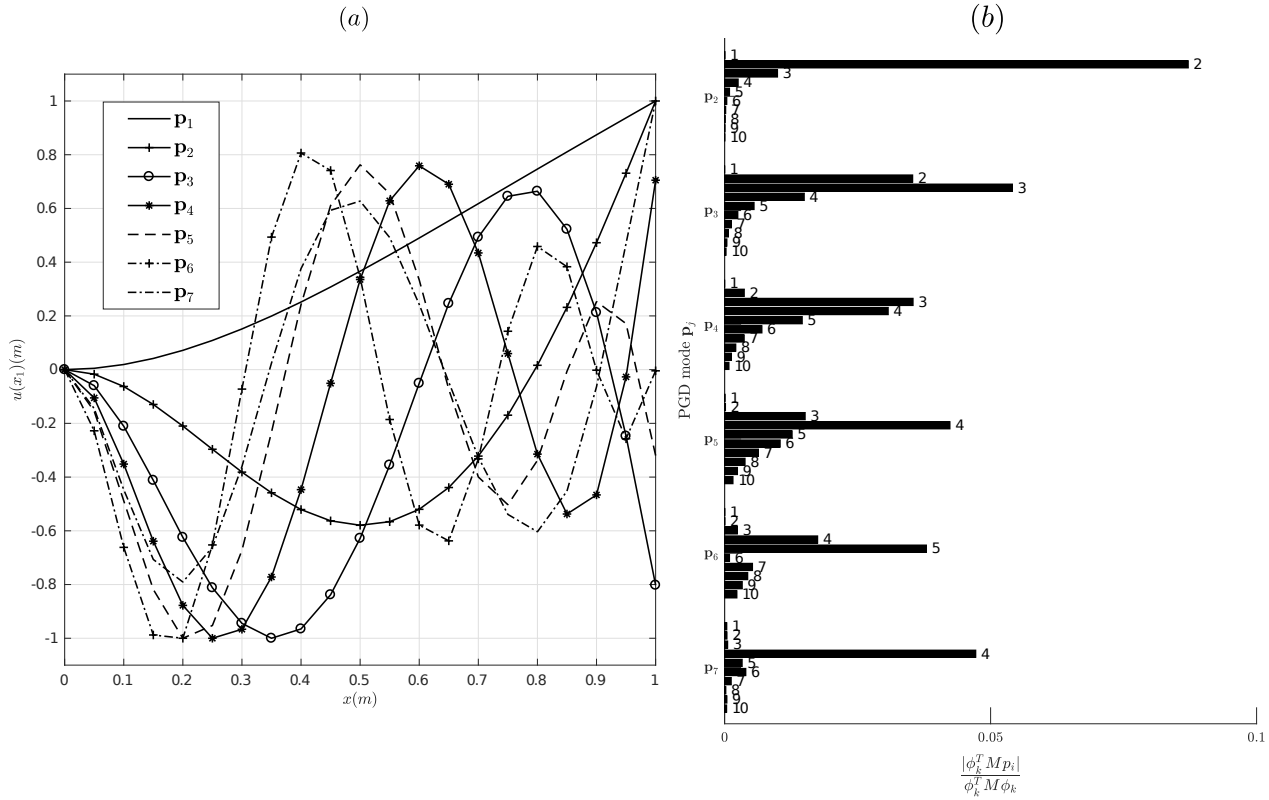


Figure 4: Analysis of PGD spatial modes. (a) PGD mode shapes. Normalization is made at the maximum deflection point. (b) Participation factors of LNMs in each PGD mode. In each bar group, LNMs participations are numbered in ascending order until the tenth linear mode. $\boldsymbol{p}_1$ is not displayed as it is LNM1 shape.

The temporal information associated with each PGD mode shape is plotted on Fig. 5. The significant variations of the temporal part through the NNM branch are expected as the previously described spatial part does not change through the pPGD/HBM continuation and the temporal part contains all the amplitude information. Only odd harmonics are plotted as all the even ones are null because of the cubic nature of the nonlinearity. As a global trend high order harmonics have less influence: at the higest energy point, all the amplitudes $|a_k|$ are sub-millimetric from $k = 23$, for all the PGD modes.

The PGD mode 1 has the simplest behavior as it stays mainly led by the fundamental cosine $|a_1|$ all along the continuation. Other PGD modes have a richer harmonic behavior with shared influences of the cosine coefficients. For example at the end of the branch, the fifteen first odd harmonics are predominant in PGD modes 2–4 and the highest harmonics are more represented by PGD modes 5–7. PGD mode shapes are combination of LNMs, as shown on Fig. 4, and this partly explains why the harmonics spectrum is complex on Fig. 5. All these qualitative interpretations also highlight the growing complexification of the beam behavior and the growing influence of high harmonics as energy grows. Here also similar results and interpretations about the temporal information are found with oPGD.

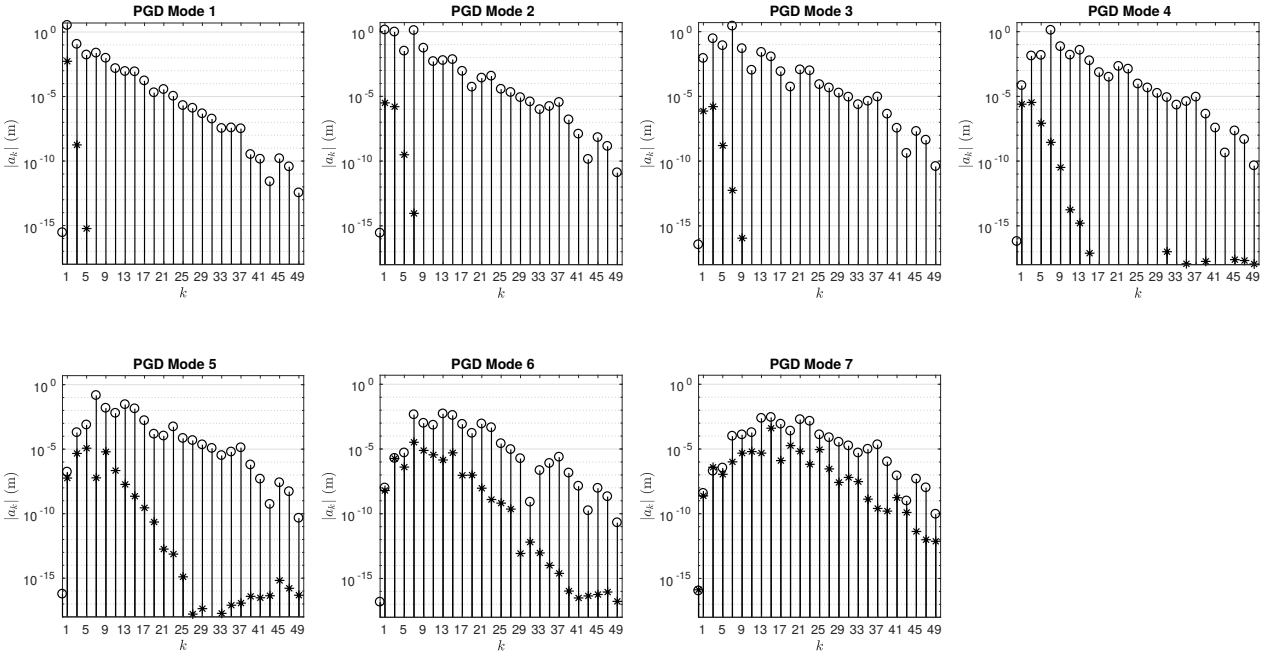


Figure 5: Amplitudes of (cosine) Fourier coefficients of PGD modes. Crosses: coefficients when the PGD mode is first introduced; Circles: coefficients at the end of the branch ($N_{pt} = 131$).

Finally the main objectives of the method are met: a NNM branch is built with a few variables, the number of PGD modes is kept as small as possible by incrementing m only when the convergence criterion $\varepsilon \leq \varepsilon_{max}$ is not fulfilled, and all physical data belonging to the case under study is retrieved. In the next section some details about the algorithmic performance are detailed. The presented oPGD algorithm is compared with its pPGD variant. Not only information about the the cubic spring case is given but also about the contact model described in Sec. 5.1.

5.3 Numerical considerations

Few descriptors are stored to describe the NNM branch so the main objective of reduced model approaches is reached. Table 2 shows this improvement for both PGD/HBM algorithms.

Please note that the first NNM of the contact problem has been obtained with the parameters given in Table 1 until a mechanical energy $E \approx 6.3\ 10^4$ J. Succintly, 8 PGD modes and 115 points were required to compute

the whole branch and setting $\Delta m = 5$ allowed to directly add 3 PGD modes in a single solution point (that is when the beam first hits the spring). This shows that describing sharp or gradual changes of the system behavior by the PGD/HBM continuation scheme with on the fly enrichment is feasible.

	pPGD/HBM $\Sigma_m\{N_{pt}^m \times (m(H+1)+1) + N\Delta m\}$	**oPGD/HBM** $N_{pt} m(N+H+1)$	**HBM** $N_{pt}\ (N(H+1)+1)$
Cubic Spring case	**33266**	**58695**	**267371**
Contact case	**39161**	**60606**	**326715**

Table 2: Comparison between the number of descriptors needed by pPGD/HBM, oPGD/HBM and classical HBM for both examples. The reference for the N_{pt}^m values are the ones provided by pPGD/HBM computation.

Only $m \times (N + H + 1)$ descriptors by solution point are required by the oPGD/HBM continuation whereas a classical HBM continuation needs $N(H + 1) + 1$ ones. In the case of the pPGD implementation, a single spatial problem of size $N \times \Delta m$ is solved for a whole NNM segment with m PGD modes: the total number of required descriptors is further reduced to reach $\Sigma_m\{N_{pt}^m \times (m(H + 1) + 1) + N\Delta m\}$, where N_{pt}^m is the number of solution points in the NNM segment with m PGD modes.

Obviously calculating a solution point via PGD/HBM is relevant if and only if $m \times (N + H + 1) < N \times (H + 1)$. An easy proof gives the necessary condition for the PGD/HBM method to be more interesting than a classical HBM approach: $m < H + 1$. In other words, the PGD/HBM method is useful for problems which require a large number of harmonics.

In both examples the saving of variables with respect to a classical HBM can be assessed with the following ratios: $1 - \frac{m\times(N+H+1)}{N\times(H+1)}$ for oPGD, and $1 - \frac{m\times(H+1)}{N\times(H+1)}$ or $1 - \frac{m\times(H+1)+N\Delta m}{N\times(H+1)}$ for a pPGD solution point. The oPGD reduction is very efficient, with 78% and 81% less variables than HBM for the cubic spring and the contact cases respectively. The pPGD reduction goes further with about 88% less variables than HBM for both examples.

We focus now on the underlying trust-region solver and its iteration data used to solve the subproblems. This algorithm requires function and abscissa tolerances – set on 10^{-12} here – and allows to set a maximum number of iterations $N_{\text{ite max}}$. The values $N_{\text{ite max}} = 100$ and $N_{\text{ite max}} = 25$ are set respectively for the cubic spring and the contact cases but this limit is reached for only very few points (maxima reached when a PGD mode is about to be added or at the first turning point of the interaction tongue). In Table. 3 are given mean and maximum numbers of solver iterations for temporal and spatial problems through the continuation, for both examples and both PGD approaches. The oPGD iteration data is obtained with the same values than with pPGD (*cf.* Table 1) except the following ones to improve the continuation: $\alpha_P = 10^{-6}$ and $\boldsymbol{y}_2 : u_1(t = 0) = 10^{-3}\ m$ for the cubic spring case, and $r_s^{mult} = 1.2$ for the contact case.

			Mean iteration number	Standard deviation	Maximum iteration number
Cubic spring case	oPGD	$\mathcal{T}_m$	6.23	4.89	22
		$\mathcal{S}_m$	16	10.92	54
	pPGD	$\mathcal{T}_m$	6.56	17.96	206
		$\mathcal{S}_m$	1.29	6.23	46
Contact case	oPGD	$\mathcal{T}_m$	2.18	1.53	16
		$\mathcal{S}_m$	9.77	8.68	49
	pPGD	$\mathcal{T}_m$	3.56	5.52	42
		$\mathcal{S}_m$	0.35	1.92	14

Table 3: Mean, standard deviation and maximum of iteration numbers for $\mathcal{T}_m$ and $\mathcal{S}_m$ problems, through the continuation.

In a oPGD framework the spatial problem is heavier as expected. The pPGD allows to compute less spatial subproblems so many solution points include a zero iteration number for the spatial problem in the mean and

standard deviation calculation. The cost of the space problem is thus well bypassed by this variant. Otherwise $N_{\text{ite max}}$ could be an interesting control parameter for bigger problems as one can keep it very small and save computation time by "converting" convergence issues into new PGD modes or a reduced arclength Δs.

6 Conclusion

A full PGD/HBM-based continuation technique with on the fly enrichment is presented in this paper. It is applied to two examples of beam models representing different classes of nonlinearies. These examples show that a highly reduced description of the NNMs branches can numerically be obtained. It is to be noted that spatial initializations rely on the LNMs of the system, which gives to the PGD mode shapes a physical meaning that a classical PGD approach provide *a priori*. As many parameters are let free (*cf.* Table 1), this algorithm has a certain flexibility.

The presented approach can be used to compute bigger structures with different kinds of nonlinearities. In order to exploit the physical potential of NNMs, future prospects could include the computation of damped NNMs or forced responses of a structure.

References

[1] G. Kerschen, M. Peeters, J. Golinval, A. Vakakis, *Nonlinear normal modes, part i: A useful framework for the structural dynamicist*, Mechanical Systems and Signal Processing, Vol. 23, No. 1, (2009), pp. 170-194.

[2] D. Laxalde, F. Thouverez, J.-J. Sinou, *Dynamics of a linear oscillator connected to a small strongly non-linear hysteretic absorber*, International Journal of Non-Linear Mechanics, Vol. 41, No. 8, (2006), pp. 969-978.

[3] R. Rosenberg, *On nonlinear vibrations of systems with many degrees of freedom*, Advances in Applied Mechanics, Vol. 9, Elsevier, (1966), pp. 155-242.

[4] S. Shaw, C. Pierre, *Non-linear normal modes and invariant manifolds*, Journal of Sound and Vibration, Vol. 150, No. 1, (1991), pp. 170-173.

[5] S. Shaw, C. Pierre, *Normal modes for non-linear vibratory systems*, Journal of Sound and Vibration, Vol. 164, No. 1, (1993), pp. 85-124.

[6] G. Kerschen, J.-C. Golinval, A. F. Vakakis, L. A. Bergman, *The method of proper orthogonal decomposition for dynamical characterization and order reduction of mechanical systems: An overview*, Nonlinear Dynamics, Vol. 41, No. 1, (2005), pp. 147-169.

[7] L. Renson, G. Kerschen, *Nonlinear Normal Modes of Nonconservative Systems*, in G. Kerschen, D. Adams, A. Carrella, editors, *Topics in Nonlinear Dynamics, Volume 1. Conference Proceedings of the Society for Experimental Mechanics Series*, Vol 35, Springer, New York, NY, (2013), pp. 189-202.

[8] L. Renson, G. Kerschen, B. Cochelin, *Numerical computation of nonlinear normal modes in mechanical engineering*, Journal of Sound and Vibration, Vol. 364, (2016), pp. 177-206.

[9] M. Peeters, R. Vigui, G. Srandour, G. Kerschen, J.-C. Golinval, *Nonlinear normal modes, part ii: Toward a practical computation using numerical continuation techniques*, Mechanical Systems and Signal Processing, Vol. 23, No. 1, (2009), pp. 195-216.

[10] C. Joannin, B. Chouvion, F. Thouverez, J.-P. Ousty, M. Mbaye, *A nonlinear component mode synthesis method for the computation of steady-state vibrations in non-conservative systems*, Mechanical Systems and Signal Processing, Vol. 83, (2017), pp. 75-92.

[11] A. Grolet, F. Thouverez, *On the use of the proper generalised decomposition for solving nonlinear vibration problems*, in ASME 2012 International Mechanical Engineering Congress and Exposition, Vol. 4, pp. 913-920.

[12] F. Chinesta, P. Ladeveze, E. Cueto, *A short review on model order reduction based on proper generalized decomposition*, Archives of Computational Methods in Engineering, Vol. 18, No. 4, (2011), pp. 395-404.

[13] F. Chinesta, A. Ammar, E. Cueto, *Recent advances and new challenges in the use of the proper generalized decomposition for solving multidimensional models*, Archives of Computational Methods in Engineering, Vol. 17, No. 4, (2010), pp. 327-350.

[14] F. Chinesta, A. Leygue, F. Bordeu, J. V. Aguado, E. Cueto, D. Gonzalez, I. Alfaro, A. Ammar, A. Huerta, *Pgd-based computational vademecum for efficient design, optimization and control*, Archives of Computational Methods in Engineering, Vol. 20, No. 1, (2013), pp. 31-59.

[15] A. Nouy, *A priori model reduction through proper generalized decomposition for solving time-dependent partial differential equations*, Computer Methods in Applied Mechanics and Engineering, Vol. 199, No. 2324, (2010), pp. 1603-1626.

[16] P. Sundararajan, S. T. Noah, *Dynamics of forced nonlinear systems using shooting/arc-length continuation method — application to rotor systems*, Journal of Vibration and Acoustics, Vol. 119, No. 1, (1997), pp. 9-20.

[17] M. Urabe, *Galerkin's procedure for nonlinear periodic systems*, Archive for Rational Mechanics and Analysis, Vol. 20, No. 2, (1965), pp. 120-152.

[18] M. Urabe, A. Reiter, *Numerical computation of nonlinear forced oscillations by galerkin's procedure*, Journal of Mathematical Analysis and Applications, Vol. 14, No.1, (1966), pp. 107-140.

[19] A. H. Nayfeh, D. T. Mook, *Nonlinear Oscillations*, Wiley, (1995).

[20] E. Sarrouy, J.-J. Sinou, *Non-linear periodic and quasi-periodic vibrations in mechanical systems - on the use of the harmonic balance methods*, in Advances in Vibration Analysis Research, InTech, (2011).

[21] R. Seydel, *From Equilibrium to Chaos, Practical Bifurcation and Stability Analysis*, Elsevier, (1988).

[22] E. Sarrouy, O. Dessombz, J.-J. Sinou, *Stochastic study of a non-linear self-excited system with friction*, European Journal of Mechanics - A/Solids, Vol. 40, (2013), pp. 1-10.

[23] T. M. Cameron, J. H. Griffin, *An alternating frequency/time domain method for calculating the steady-state response of nonlinear dynamic systems*, Journal of Applied Mechanics, Vol. 56, No. 1, (1989), pp. 149-154.

[24] E. L. Allgower, K. Georg, *Introduction to Numerical Continuation Methods*, Springer-Verlag, 2003.

[25] G. Kerschen, *Computation of Nonlinear Normal Modes through Shooting and Pseudo-Arclength Computation*, Springer Vienna, Vienna, 2014, pp. 215-250.

A multivariate, well-conditioned asymptotic waveform evaluation for finite element solutions with complex parametric dependence

R. Rumpler [1], **R. Rodríguez Sánchez** [2], **P. Göransson** [1]
[1] MWL/Centre for ECO2 Vehicle Design, Department of Aeronautical and Vehicle Engineering, KTH Royal Institute of Technology, Stockholm, Sweden
e-mail: **rumpler@kth.se**

[2] Chair of Structural Mechanics, Technical University of Munich, Arcisstraße, Munich, 80333, Germany

Abstract
Most engineering applications involving solutions by numerical methods are dependent on several parameters, whose impact on the solution may significantly vary from one to the other. At times an evaluation of these multivariate solutions may be required at the expense of a prohibitively high computational cost. In the present work, a multivariate finite element approach is proposed, allowing for a fast evaluation of parametric responses. It is based on the construction of a reduced basis spanning a subspace able to capture rough variations of the response. The method consists in an extension of the Well-Conditioned Asymptotic Waveform Evaluation (WCAWE) to multivariate problems, by an appropriate choice of derivative sequences, and a selection of the most relevant basis components. It is validated and demonstrated for its potential on a semi-industrial sized 3D application involving coupled poroelastic and internal acoustic domains.

1 Introduction

In order to limit the high computational burden associated with the evaluation of multivariate Finite Element (FE) solutions, an approach based on a Reduced-Order-Model (ROM), derived after a univariate moment-matching method, is proposed. This univariate method, namely the Well-Conditioned Asymptotic Waveform Evaluation (WCAWE) method, proposed by Slone *et al.* [1], is shown to allow for a robust generation of basis components with good convergence properties of the associated reduced systems [1–3]. It relies on a sequence of successive derivatives of the system of interest, leading to multiple Right-Hand-Side (RHS) problems to be solved sequentially, with intermediate orthonormalization steps and correction terms ensuring the robustness of the procedure and the good conditioning of the resulting transformation matrix. This univariate basis generation procedure may be extended to a multivariate procedure. However, the cost associated with the orthonormalization and correction steps, may lead to a computationally prohibitive cost, particularly as the dimension of the variable space increases [3]. Additionally, not all cross-derivative terms may contribute significantly to the convergence of the ROM, and it may be critical to be able to reduce them to a minimum. In this contribution, an effort is made to bring the WCAWE to multivariate problems, starting with a bivariate illustration, and attempting to limit the transformation bases to a minimum in view of higher dimensionality applications. The foundation for a multi-interval strategy is also presented in view of the reconstruction of wide parametric ranges. The approach is shown to benefit from the superior robustness of the WCAWE compared to the so-called component-wise Padé approximants [3–6], previously used to derive the Nested Padé approximant method [7, 8].

In the following Section, reminders are made about the WCAWE, the details of its procedure, and the proposed extension to multivariate problems. Then, the basis for a multi-interval strategy relying on error estimation following contours of convergence intervals is introduced. Finally, the accuracy and potential of the method are presented on a 3D poro-acoustic problem.

2 The WCAWE, a moment-matching, projection-based ROM

2.1 Generic multivariate problem and associated transformation

The starting point of the WCAWE-based parametric sweep is given by a linear system of the following form,

$$\mathbf{Z}(\mathbf{x})\mathbf{U}(\mathbf{x}) = \mathbf{F}(\mathbf{x}), \tag{1}$$

where $\mathbf{x}$ may be a vector of N_x independent variables corresponding to the parametric problem of interest, e.g. including the angular frequency ω, material parameters, ... For the original univariate case [1], the vector reduces to a scalar such that $\mathbf{x} = [x]$. In an FE problem, $\mathbf{Z}(\mathbf{x})$, $\mathbf{U}(\mathbf{x})$, and $\mathbf{F}(\mathbf{x})$ respectively represent the system matrix of the discretized problem, the solution vector and the vector of externally applied loads.

The projection-based approach, allowing to solve for a reduced set of equations associated with Eq. (1), relies on the construction of a transformation basis emerging from successive derivatives of the solution vector in Eq. (1) at a specific point $\mathbf{x}_0$ in the parameter space. The WCAWE algorithm provides a robust generation of this sequence of successive derivatives, overcoming the inherently ill-conditioned transformation matrix emerging from the direct approach used in the component-wise Padé approximants [3, 4], also used for the generation of Nested Padé approximants [7, 8]. The resulting well-conditioned transformation matrix $\mathbf{V}_\mathrm{N}$, consisting of N orthonormalized basis vectors, allows for a robust, non-stagnating convergence upon increasing the size of the subspace spanned. The associated approximation of the solution in Eq. (1), to the order N, is such that

$$\widehat{\mathbf{U}}_\mathrm{N}(\mathbf{x}) = \mathbf{V}_\mathrm{N}\, \boldsymbol{\alpha}(\mathbf{x}) \approx \mathbf{U}(\mathbf{x}), \tag{2}$$

$\boldsymbol{\alpha}$ being a vector of N generalized coordinates. This transformation leads to a reduced system corresponding to Eq. (1), solving for the generalized coordinates in $\boldsymbol{\alpha}(\mathbf{x})$,

$$\mathbf{V}_\mathrm{N}{}^T\mathbf{Z}(\mathbf{x})\mathbf{V}_\mathrm{N}\boldsymbol{\alpha}(\mathbf{x}) = \mathbf{V}_\mathrm{N}{}^T\mathbf{F}(\mathbf{x}). \tag{3}$$

2.2 A multivariate WCAWE basis generation procedure

A generic expression of the multivariate WCAWE algorithm, as proposed in this contribution, may be given in $\mathbf{x} = \mathbf{x}_0$ by the following multiple right-hand-side procedure,

$$\begin{cases} \mathbf{Z}^{(0)}\overline{\mathbf{v}}_1 = \mathbf{F}^{(0)} \\ \qquad Normalization \;\; \overline{\mathbf{v}}_1 \longrightarrow \mathbf{v}_1 \\ \mathbf{Z}^{(0)}\overline{\mathbf{v}}_2 = \mathbf{F}^{(1)}\mathbf{e}_1^T\mathbf{P}_{\mathbf{Q_1}}(2,1)\mathbf{e}_1 - \mathbf{Z}^{(1)}\mathbf{v}_1 \\ \qquad Othonormalization \;\; \overline{\mathbf{v}}_2 \longrightarrow \mathbf{v}_2 \\ \qquad \vdots \\ \mathbf{Z}^{(0)}\overline{\mathbf{v}}_n = \left(\sum\limits_{j=1}^{(n-1)} \left(\mathbf{F}^{(n)}\mathbf{e}_1^T\mathbf{P}_{\mathbf{Q_1}}(n,j)\mathbf{e}_{n-j} \right) - \mathbf{Z}^{(1)}\mathbf{v}_{n-1} \right. \\ \qquad\qquad \left. - \sum\limits_{j=2}^{(n-1)} \left(\mathbf{Z}^{(j)}\mathbf{v}_{n-j}\mathbf{P}_{\mathbf{Q_2}}(n,j)\mathbf{e}_{n-j} \right) \right) \\ \qquad Othonormalization \;\; \overline{\mathbf{v}}_n \longrightarrow \mathbf{v}_n \\ \qquad \vdots \\ \mathbf{Z}^{(0)}\overline{\mathbf{v}}_{\mathrm{N}} = \left(\sum\limits_{j=1}^{(\mathrm{N}-1)} \left(\mathbf{F}^{(\mathrm{N})}\mathbf{e}_1^T\mathbf{P}_{\mathbf{Q_1}}(\mathrm{N},j)\mathbf{e}_{\mathrm{N}-j} \right) - \mathbf{Z}^{(1)}\mathbf{v}_{\mathrm{N}-1} \right. \\ \qquad\qquad \left. - \sum\limits_{j=2}^{(\mathrm{N}-1)} \left(\mathbf{Z}^{(j)}\mathbf{v}_{\mathrm{N}-j}\mathbf{P}_{\mathbf{Q_2}}(\mathrm{N},j)\mathbf{e}_{\mathrm{N}-j} \right) \right) \\ \qquad Othonormalization \;\; \overline{\mathbf{v}}_{\mathrm{N}} \longrightarrow \mathbf{v}_{\mathrm{N}} \end{cases} \tag{4}$$

where a modified Gram-Schmidt orthonormalization step is performed between each vector generation by the multiple RHS systems in Eq. (4), and where

- $\mathbf{Z}^{(k)}$ stands for the differentiation of the system matrix $\mathbf{Z}$, in $\mathbf{x} = \mathbf{x}_0$, to the "cumulative" order k, regardless of the distribution of the differentiation between the independent variables x_i. In other words, given the notation $\partial_{x_j}^{i_j}(\cdot)$ for the partial derivative with respect to x_j at order i_j, and the convention $\partial_{x_j}^{0}(\cdot) = (\cdot)$, then $\mathbf{Z}^{(k)}$ results from the partial derivative orders summation such that

$$\mathbf{Z}^{\left(\sum\limits_{j=1}^{\mathrm{N}_x} i_j\right)} = \left(\prod_{j=1}^{\mathrm{N}_x} \partial_{x_j}^{i_j} \right) \mathbf{Z}, \tag{5}$$

  with the aforementioned convention implying that $\mathbf{Z}^{(0)} = \mathbf{Z}$.

- $\mathbf{e}_k$ is a unitary standard basis vector associated with the k^{th} component of the solution vector,

- $\overline{\mathbf{v}}_k$ is the non-orthonormalized vector generated in the k^{th} iteration of the procedure,

- $\mathbf{v}_k$ is the basis vector orthonormalized against $\mathbf{v}_{k-1}$, generated after the k^{th} iteration of the procedure,

- $\mathbf{P}_{\mathbf{Q}_\omega}(\alpha,\beta)$, $\omega = 1, 2$, corresponds to the RHS correction terms, chosen to be associated with the modified Gram-Schmidt orthonormalisation process [1].

The orthonormalized and non-orthonormalized bases, $\mathbf{V}_{\mathrm{N}}$ and $\overline{\mathbf{V}}_{\mathrm{N}}$ respectively, are related by

$$\mathbf{V}_{\mathrm{N}} = \overline{\mathbf{V}}_{\mathrm{N}}\mathbf{Q}^{-1}, \tag{6}$$

where $\mathbf{Q}$ is an N×N upper triangular, nonsingular matrix containing the modified Gram-Schmidt coefficients. More precisely, column k of $\mathbf{Q}$ contains the successive coefficients resulting from the projection of partially orthonormalized $\overline{\mathbf{v}}_k$ on the orthnormalized vectors $\mathbf{v}_j$, $j < k$, and Q_{kk} corresponds to the norm of $\mathbf{v}_k$ before its normalization. The correction terms $\mathbf{P}_{\mathbf{Q}_\omega}(\alpha, \beta)$, $\omega = 1, 2$, are given by the following product of block matrices extracted from $\mathbf{Q}$,

$$\mathbf{P}_{\mathbf{Q}_\omega}(\alpha, \beta) = \prod_{t=\omega}^{\beta} \mathbf{Q}^{-1}_{[t:\alpha-\beta+t-1, t:\alpha-\beta+t-1]} \tag{7}$$

Further discussions on the choice of the RHS correction coefficients other than associated with the Gram-Schmidt coefficients, may be found in Ref. [1].

The approximated solution is evaluated at all DOFs from the generalized coordinates vector $\boldsymbol{\alpha}$, after Eq. (2).

Adapting the WCAWE algorithm from univariate problems to multivariate ones lies in the generation of sequences of RHS vectors, emerging from sequences of iteratively differentiated matrices $\mathbf{Z}^{(k)}$. The choice adopted here is to generate such sequences independently, thus generating a set of $\mathrm{N_V}$ bases $\left\{\mathbf{V}_\mathrm{N}^1, \cdots, \mathbf{V}_\mathrm{N}^{\mathrm{N_V}}\right\}$ associated with $\mathrm{N_V}$ sequences of iteratively differentiated matrices $\mathbf{Z}^{(k)}$. These bases, in principle all of the same size N, each consist of orthonormalized basis vectors, but these are naturally not mutually orthonormalized from one to the next basis. These are not even guaranteed to produce linearly independent subsets of vectors upon merging these bases. A simple way to ensure this, as well as to reduce the basis to a minimum number of basis vectors is to proceed to a compression, or a component selection, via a Singular Value Decomposition (SVD) of the merged set of bases. Either way, the initial step consists in an SVD of the merged basis after concatenation, $\mathbf{V}_\mathrm{N}^\mathrm{mer} = \left[\mathbf{V}_\mathrm{N}^1 \cdots \mathbf{V}_\mathrm{N}^{\mathrm{N_V}}\right]$, resulting in

$$\mathbf{V}_\mathrm{N}^\mathrm{mer} = \sum_{i=1}^{\mathrm{N_{mer}}} \sigma_i \mathbf{w}_i^\mathrm{l} \mathbf{w}_i^{\mathrm{r}T}, \tag{8}$$

where $\mathrm{N_{mer}}$ corresponds to the total number of basis vectors in $\mathbf{V}_\mathrm{N}^\mathrm{mer}$, *i.e.* $\mathrm{N_{mer}} = \mathrm{N} \cdot \mathrm{N_V}$; σ_i, $\mathbf{w}_i^\mathrm{l}$, and $\mathbf{w}_i^\mathrm{r}$ correspond to the singular values, left and right singular vectors respectively.

From the SVD, either the (left) singular vectors associated with the highest singular values are selected as the components of the reduced merged basis, or the compression of the merged basis associated with the highest singular values is performed from the selected left singular vectors, right singular vectors and their corresponding singular values. Here the former approach is used, such that assuming a descending-ordered sequence of singular values $(\sigma_1 \cdots \sigma_{\mathrm{N_{mer}}})$, the reduced, merged basis $\mathbf{V}^*$ is

$$\mathbf{V}^* = \left\{\mathbf{w}_i^\mathrm{l} \mid i \in (1, \mathrm{N_{mer}}) \wedge \sigma_i \geq \sigma_\mathrm{thresh}\right\}, \tag{9}$$

where σ_thresh corresponds to the empirically chosen threshold value for the selection of the singular values resulting from the decomposition in Eq. (8).

The resulting reduced basis $\mathbf{V}^*$, consisting of $\mathrm{N_{V^*}}$ vectors, is then used in place of the univariate transformations corresponding to Eq. (2) and Eq. (3), in order to solve a reduced set of equations at most involving $\mathrm{N_{mer}}$ DOFs.

2.3 Sequences of multivariate differentiation

The sequential WCAWE procedure above depends on the generation of sequences of differentiated system matrices to successive "cumulated multivariate orders" k, i.e. $\mathbf{Z}^{(k)}$. The choice of these sequences is addressed empirically in this contribution, and illustrated for the case of bivariate problems. For the bivariate case, the cumulated differentiation orders and the associated differentiation paths may be represented in a matrix form, see Fig. 1.

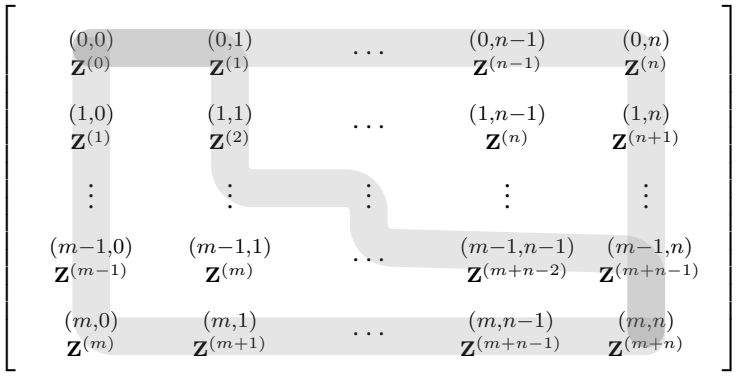


Figure 1: Illustration of three possible bivariate derivation paths for the system matrix $\mathbf{Z}$ up to the "cumulated order" $(m+n)$.

The matrix sequences obtained from these differentiation paths of the system matrix subsequently feed the procedure presented in Eq. (4).

The rationale behind choosing a limited number of derivation paths is connected to the potential inefficiency resulting from the attempt to calculate all multivariate derivatives for a given set of maximum orders. Preliminary tests based on the methodology introduced in the previous section rapidly confirm the emergence of quasi-linearly dependent basis vectors associated with different differentiation orders from distinct sequences. In practice, it is estimated that a number of sequences of the order of the dimensionality of the multivariate problem may be sufficient in order to provide good convergence properties of the ROM. For instance, 2 sequences may be sufficient for a bivariate problem. Note that this observation addresses in part the issue of dimensionality and the associated efficiency of the approach: the number of successive derivatives necessary grows linearly with the dimensionality as opposed to an exponential growth if all cross-derivatives are calculated in a fully multivariate approach.

3 Multi-interval, multivariate WCAWE approach

In practice, the size of the reduction basis may be limited due to the increase of the computational cost of the procedure in Eq. (4) [3]. This implies that there may be a tradeoff between increasing the order of approximation, reflected in the size of the basis for a given reference point, and a multi-interval strategy. In order to proceed with an approximation based on multiple intervals, an error estimator is first necessary.

3.1 Error estimation

A Cauchy-type of convergence test is chosen in order to estimate the accuracy of the approximation without having to calculate the full solution. Provided an approximated output (scalar) quantity of interest, to the order N, in point $\mathbf{x}$, of the form

$$\widehat{S}_{\mathrm{N}}(\mathbf{x}) = 10\ \log\left(\frac{\widehat{U}_{\mathrm{N}}(\mathbf{x})^2}{U_{\mathrm{ref}}(\mathbf{x})^2}\right), \tag{10}$$

the convergence is estimated in a given point $\mathbf{x}$ with the Cauchy convergence test associated with the relative error $\epsilon^{(\mathrm{N})}(\mathbf{x}) = \widehat{S}_{(\mathrm{N}+2)}(\mathbf{x}) - \widehat{S}_{(\mathrm{N})}(\mathbf{x})$, such that

$$\epsilon^{(\mathrm{N})}(\mathbf{x}) \leq \epsilon_{\max}, \quad \forall \mathbf{x} \in [\mathbf{x}_{\min}, \mathbf{x}_{\max}]\,. \tag{11}$$

Note that the convergence test involves the solutions associated with several orders of difference. Two orders of difference is suggested here for examples associated with bivariate problems; more may be required for

higher dimensionality. Despite a slight reduction of the convergence range achieved, a sufficiently enriched basis reduces the possibility of an erroneous estimate to occur, and leads to a conservative measure of the actual approximation error.

A Cauchy-type of convergence test however requires an evaluation of two solutions in each point of interest. It is consequently necessary to limit the number of evaluations of the relative error for each interval in order to limit the extra cost associated with the error estimation.

3.2 Contour-following and multi-interval strategy

In order to reduce the number of points at which the error estimation needs to be made, a contour-following strategy is implemented. Starting from the reference point for each interval, an isocontour is determined (Moore-Neighbour Tracing algorithm), associated with the max error ϵ_{max} in Eq. (11). This contour subsequently allows to fit a regular shape (e.g. a rectangle for a bivariate problem) providing a simplified measure of the interval of convergence. The successive dimensions of the intervals of convergence may further be used in order to anticipate the choice of subsequent reference points for approximation of the solution on neighbour intervals.

There are several simple strategies possible in order to fill an entire parametric solution space with smaller intervals of convergence. One may iteratively choose reference points in direct connection with the range of convergence of the previously calculated intervals, as adopted for instance in Ref. [8]. Another possibility is to successively choose the reference points such that they are the furthest away from any boundary of the parametric space or the converged contours.

4 Application: poro-acoustic parametric sweep

The proposed multivariate approach is tested on an average-sized problem consisting of the interior cavity of a passenger train, treated with a 15-cm layer of sound absorbing porous material on the top surface. A time-harmonic point source is defined at a corner of the cavity, and parametric sweeps with respect to both the frequency and the static airflow resistivity of the porous layer are performed. All boundary walls are considered as rigid walls, except from the porous boundary. The porous boundary is modelled by an equivalent fluid formulation, consisting of a modified Helmholtz equation where the equivalent speed of sound is complex and frequency-dependent, given by

$$\tilde{c_{\text{p}}} = \frac{c_0}{\sqrt{\dfrac{1 - i\Phi}{\rho_0 \omega}}}, \tag{12}$$

where $\tilde{(\cdot)}$ denotes a complex-valued quantity, $\rho_0 = 1.21$ kg.m^{-3} is the ambient density of the air saturating the pores and $c_0 = 343$ m.s^{-1} the speed of sound in the air. $\omega = 2\pi f$ is the angular frequency associated with the time-harmonic excitation, and Φ is the static flow resistivity, associated with the viscous dissipation in the porous material.

After a standard expression of the problem in its weak form and subsequent discretization by a Galerkin method, the finite element problem has the general form

$$\left(\mathbf{K_a} - \frac{\omega^2}{c_0^2} \mathbf{M_a} + \mathbf{K_p} - \frac{\omega^2}{\tilde{c_{\text{p}}}^2} \mathbf{M_p} \right) \tilde{\mathbf{U}} = \mathbf{F}, \tag{13}$$

where $\square_{\mathbf{a}}$ correspond to air cavity global matrices, and $\square_{\mathbf{p}}$ to porous global matrices. $\tilde{\mathbf{U}}$ is the vector of nodal unknowns (acoustic pressure fluctuation here). The right-hand-side vector $\mathbf{F}$, associated with the time-harmonic acoustic excitation is in practice only non-zero at a few DOFs. The FE problem in Eq. (13) is

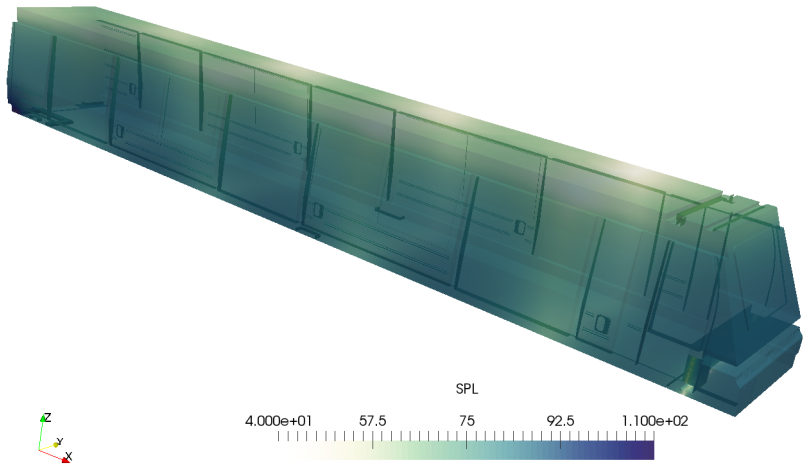


Figure 2: Sound pressure level of the damped solution at 63 Hz, $\Phi = 25000$ N.s.m^{-4}, scale $40 - 110$ dB.

evidently of the form of the generic problem in Eq. (1), thus suitable for the multivariate approach proposed. The discretized problem consists of around 300000 acoustic pressure DOFs.

Fig. 2 illustrates the solution at a given point of the parametric sweep, for a frequency of 63 Hz, and a flow resistivity of 25000 N.s.m^{-4}.

The reference solution for the bivariate parametric sweep, where $f \in [50, 150]$ Hz and $\Phi \in [3000, 50000]$ N.s.m^{-4}, at a point in the cavity, is plotted in Fig. 3.

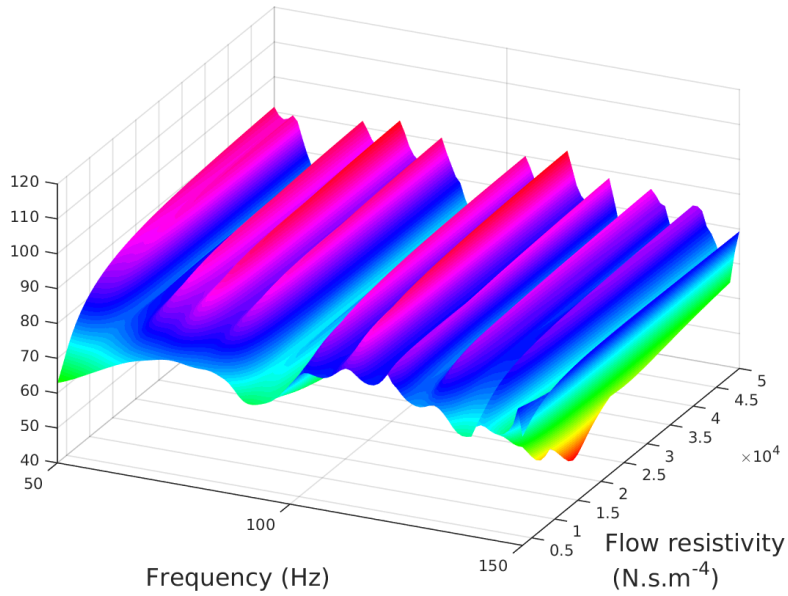


Figure 3: Reference solution. Sound pressure level at a point in the acoustic cavity, parametric solution, in dB.

The multivariate WCAWE procedure proposed here is applied for an approximated solution based on one reference point in the parametric space for the construction of the transformation basis.

Two configurations are tested regarding the number of sequences necessary in order to produce the reduced merged basis $\mathbf{V}^*$ of Eq. (9). The first configuration includes 3 sequences: the 2 "outer" sequences, and one "diagonal" sequence, as presented in Fig. 1. Given that in this configuration, some components added by the third sequence are not selected by the SVD, and that the increased size of the reduced basis $\mathbf{V}^*$ does not noticeably improve the accuracy of the approximation, the second configuration includes only the two "outer" sequences. The singular value threshold σ_{thresh}, used for the selection of the main components for the reduced basis $\mathbf{V}^*$, is chosen to be such that $\sigma_{\text{thresh}} = \sigma_{\text{max}} \cdot 10^{-15}$, where σ_{max} corresponds to the largest singular value in the decomposition of Eq. (8).

In Fig. 4, the convergence of the approximated bivariate solution is illustrated for three different orders of approximation, for a reduced basis $\mathbf{V}^*$ based on the two "outer" sequences.

Given the smooth variation of the solution with respect to the static flow resistivity, it is natural that a lower order of approximation is required than for the frequency. In this illustration, the order of differentiation for the static flow resistivity is set to 9. Three increasing orders of differentiation are plotted for the frequency, from order 19 to order 55. The degree of accuracy reached for the latter case, although using one point only at $f = 88$ Hz and $\Phi = 25000$ N.s.m^{-4} for the construction of the basis, highlights the potential of the method.

Table 1 provides a brief comparison of the size of the bases obtained from the proposed procedure when 2 or 3 sequences of differentiation are used prior to the SVD. A combination of the facts that some vectors added

	N vec/basis	N_{mer}	N_{V^*}
2-sequence	29 (9+19+1)	56 (29+27)	56
3-sequence	29 (9+19+1)	83 (29+27+27)	79
2-sequence	41 (9+31+1)	80 (41+39)	80
3-sequence	41 (9+31+1)	119 (41+39+39)	112
2-sequence	65 (9+55+1)	128 (65+63)	128

Table 1: Overview of the size of the reduced basis $\mathbf{V}^*$ emerging from the 2- and 3-sequence procedure associated with the results in Fig.4.

by the 3rd sequence are filtered out by the SVD, while all vectors emerging from the combination of the 2 "outer" sequences are kept, indicates that a 2-sequence approach may be sufficient for the bivariate case. In particular, no improvement of convergence and accuracy was observed by adding the third sequence, thus indicating a minor contribution from the basis vectors emerging from this additional sequence. This also reflects a conservative threshold value for σ_{thresh}. Finally, the fact that no basis vector is filtered out by the SVD, when all vectors emerging from the combination of the 2 "outer" sequences are kept, implies that the SVD is in this case not associated with a selection of the basis components, but rather with a re-orthogonalization of the reduced basis $\mathbf{V}^*$.

Limiting the expansion to derivative orders 20/12 for the frequency and flow resistivity, respectively, Fig. 5 illustrates the contour-following, filling and shape-fitting approach in order to define sub-intervals of convergence. The error estimation is calculated along the contours only, in Figs. 5a and 5c, assuming a monotonous increase of the relative error inside the contours around the reference point of expansion, and a tolerance of $\epsilon_{\text{max}} = 0.02$ dB. These contours may subsequently be fitted, as plotted in grey in Figs. 5b and 5d, with a regular shape connected to the shape of the parametric space, i.e. a rectangle for this bivariate example.

A first attempt for a multi-interval approximation of the full bivariate parametric space is plotted in Figs. 6. This approach is based on a surface-fitting matching the surface area of the estimated contour, augmented by an overestimation factor, here set to 1.5. This over-estimation factor is justified by the slow increase of the error beyond the convergence contours, provided that the error tolerance is low enough (here 0.02 dB). The first reference point, associated with the first interval in Fig. 6a, is chosen following a preliminary step testing the convergence range associated with a reference point in the center of the parametric space. Then, subsequent intervals are chosen based on the dimensions of the last 2 calculated intervals, in the

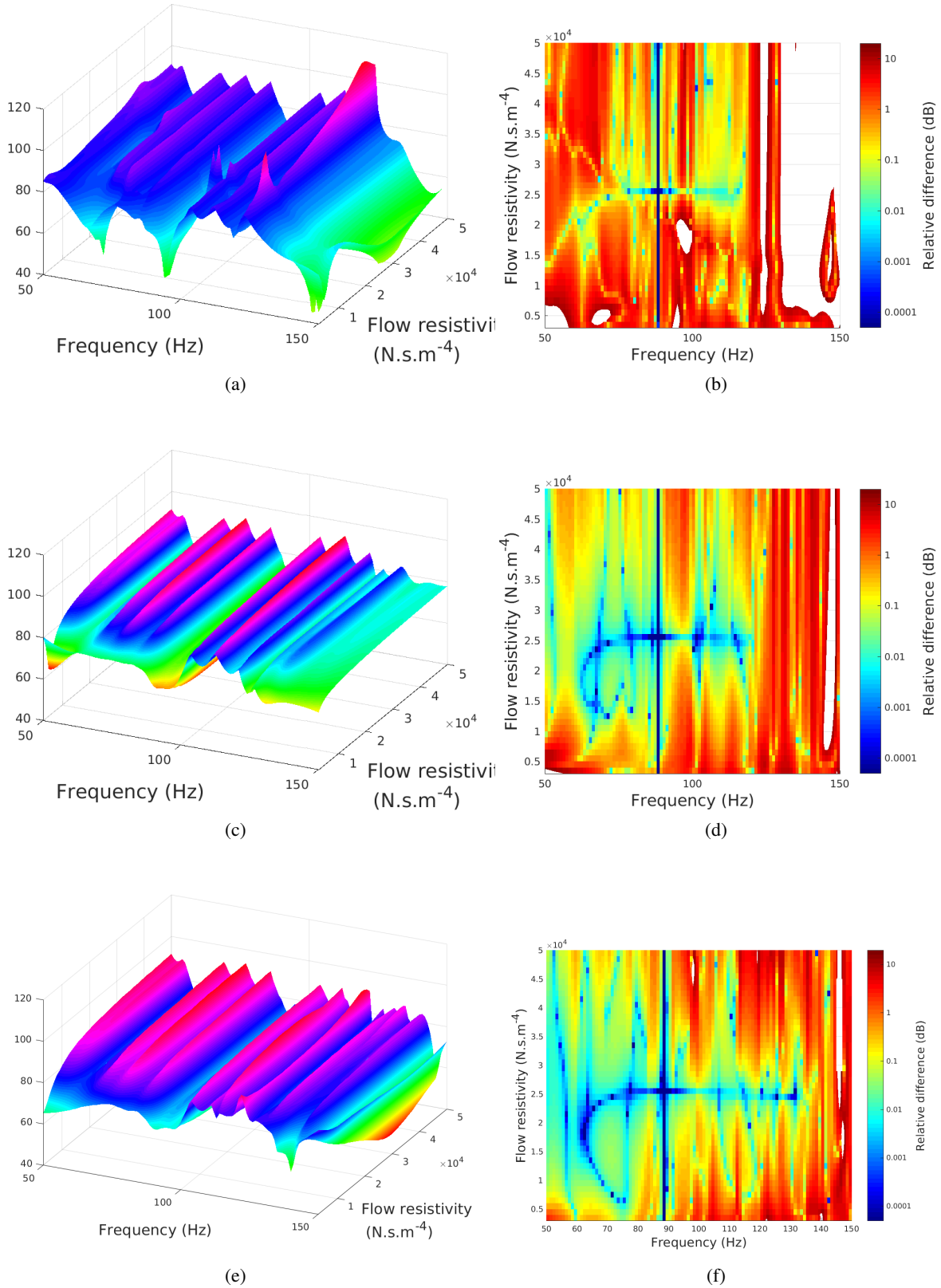


Figure 4: Convergence of the one-point WCAWE-approximated solution. SPL at a single point, in dB. Reference parametric point for the WCAWE basis procedure: $f = 88$ Hz and $\Phi = 25000$ N.s.m^{-4}. (a)-(b) Derivative orders 19/9 for frequency/resistivity; (c)-(d) Derivative orders 31/9 for frequency/resistivity; (e)-(f) Derivative orders 55/9 for frequency/resistivity. Approximation (left) and relative difference to the reference solution (right).

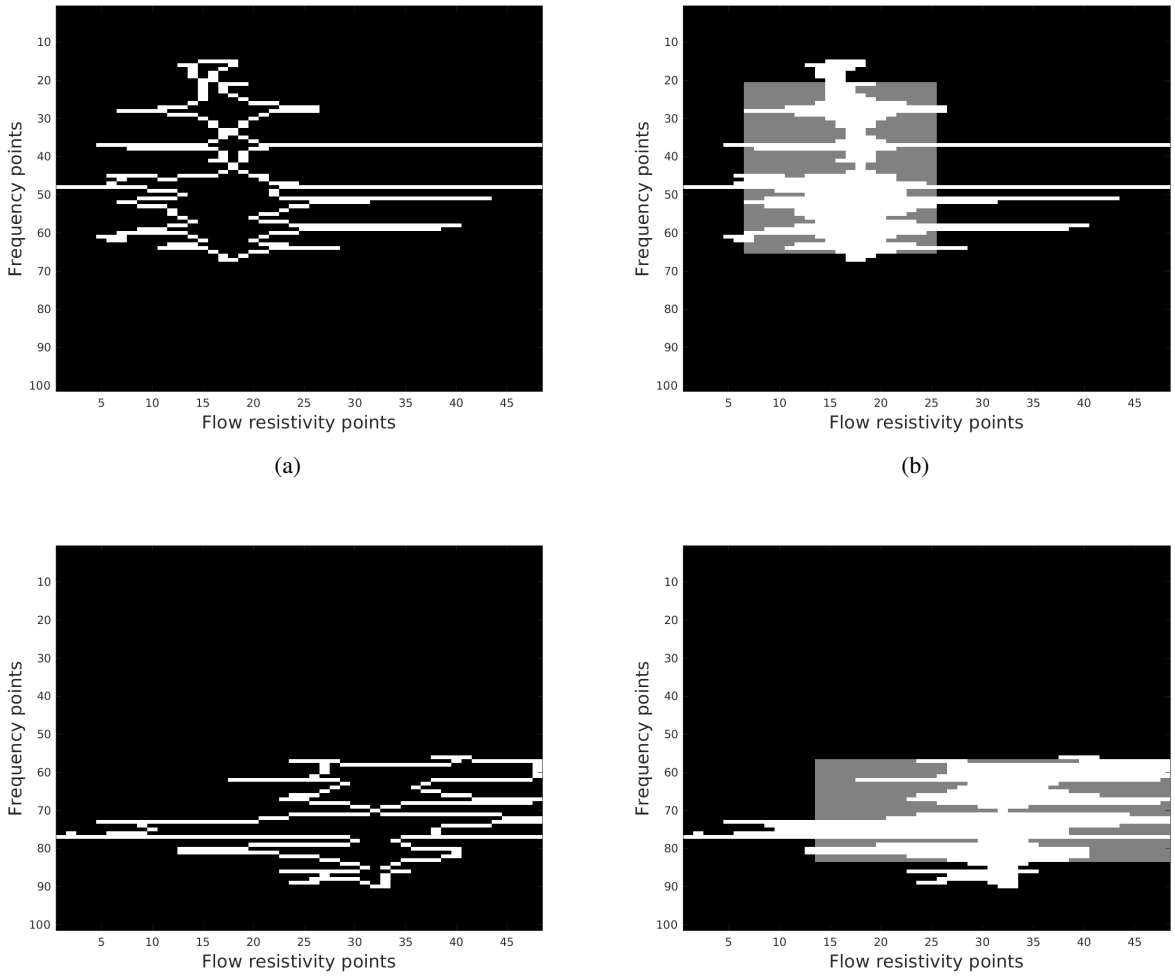


Figure 5: Illustration of the contour-following and shape fitting strategy for a single interval associated with the poro-acoustic bivariate problem. (a) and (c) Isocontour following of the max relative error; (b) and (d) Isocontour filling and fitting with a regular shape (rectangle).

closest neighbourhood possible to the last calculated interval. When the parametric space has been entirely covered, the algorithm attempts to bridge the largest gaps, based on the dimension of the smallest interval of convergence. Fig. 6b shows in white the estimated range of convergence after 3 intervals (starting from the low frequency and low flow resistivity ranges). Fig. 6c shows the estimated range of convergence after 9 intervals, after which the entire parametric range is ”covered”. Finally, Fig. 6d plots the estimated range of convergence after the largest gaps have been added extra reference points, including 16 intervals in total. This implies the calculation of 16 multiple RHS problems consisting of 33 RHS vectors in order to build the complete set of reduced bases, to be contrasted with the full solution to be calculated at $101 \times 48 = 4848$ points for the reference solution.

The proposed approach is currently being tested for its robustness with respect to a wide range of problems, starting, as done here, with bi-parametric problems.

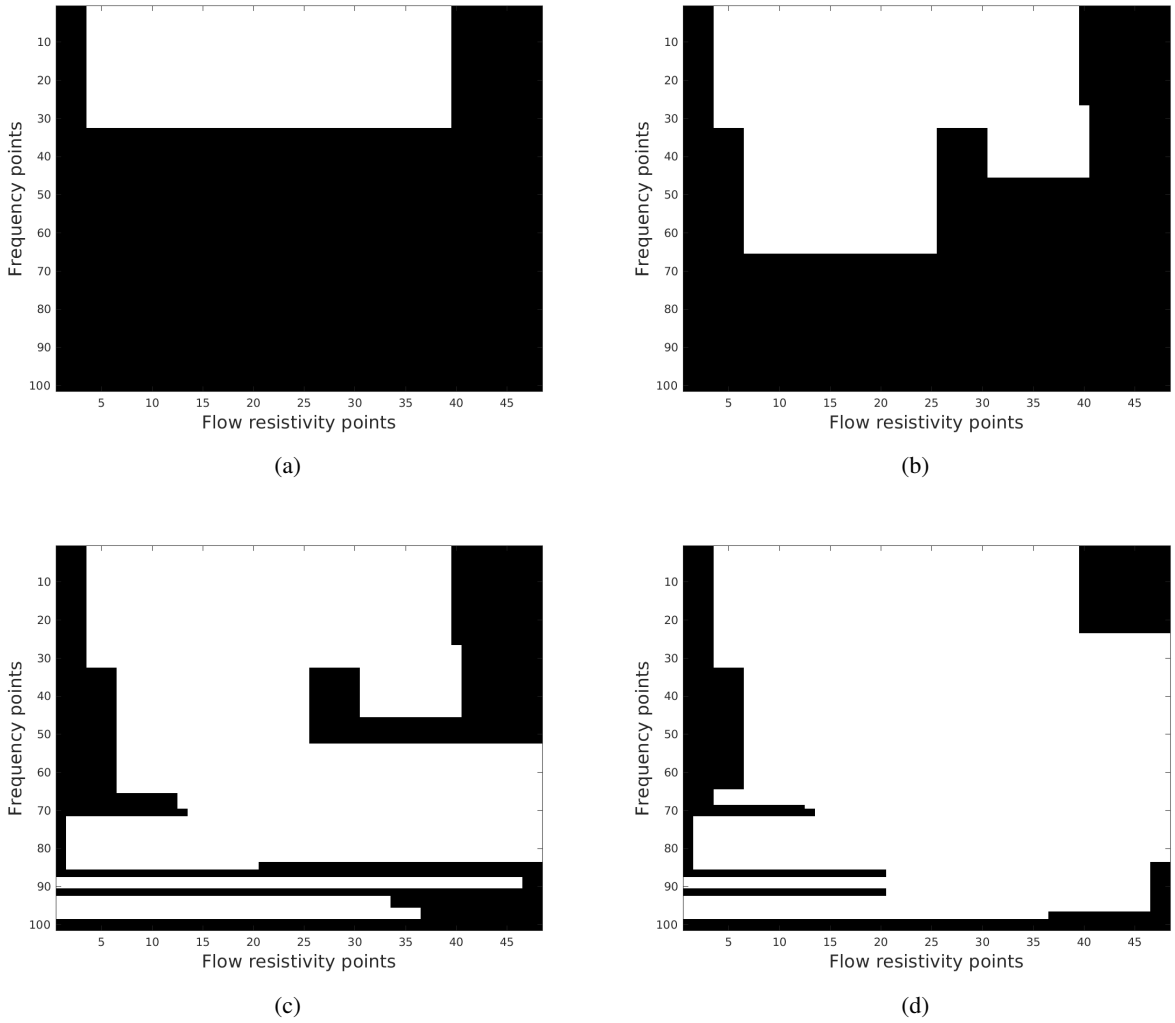


Figure 6: Convergence of a multi-interval approach for bases with fixed derivative orders 20/12, with a tolerance of $\epsilon_{\max} = 0.02$ dB. (a): 1 convergence interval, (b): 3 convergence intervals, (c): 9 convergence intervals, (d): 16 convergence intervals.

5 CONCLUSIONS

In this contribution, a multivariate approach based on the Well-Conditioned Asymptotic Waveform Evaluation algorithm is proposed. It relies on the generation of basis vectors emerging from sequences of incrementally differentiated system matrices at parametric points of expansion. These sequences, efficiently generated by a multiple right-hand-side type of problem, are subsequently merged and further reduced via a singular value decomposition.

The convergence of the approach is illustrated on a bivariate poro-acoustic application of about 300000 degrees of freedom. The limitation to a reduced set of sequences is promising in the scope of using the proposed approach for higher dimensionality. An extension to a multi-interval approximation strategy, based on the efficient use of error estimator is also tested and currently under further developments in connection with its robustness.

Acknowledgements

The financial support from the Swedish Research Council (Vetenskapsrådet VR Grant 2015-04925 for the first author) and the Centre for ECO2 Vehicle Design (VINNOVA Grant 2016-05195) are gratefully acknowledged.

References

[1] R. D. Slone, R. Lee, and J.-F. Lee. Well-conditioned asymptotic waveform evaluation for finite elements. *IEEE Transactions on Antennas and Propagation*, 51(9):2442–2447, 2003.

[2] M. S. Lenzi, S. Lefteriu, H. Beriot, and W. Desmet. A fast frequency sweep approach using Padé approximations for solving Helmholtz finite element models. *Journal of Sound and Vibration*, 332(8):1897–1917, 2013.

[3] R. Rumpler, and P. Göransson. An assessment of two popular Padé-based approaches for fast frequency sweeps of time-harmonic finite element problems. *Proceedings of Meetings on Acoustics*, 30(1):022003, 2017. DOI: 10.1121/2.0000649

[4] G.A. Baker and P.R. Graves-Morris. *Padé approximants*, volume 59. Cambridge University Press, 1996.

[5] R. Djellouli, C. Farhat, and R. Tezaur. A fast method for solving acoustic scattering problems in frequency bands. *Journal of Computational Physics*, 168(2):412–432, 2001.

[6] R. Rumpler, P. Göransson, and J.-F. Deü. A finite element approach combining a reduced-order system, padé approximants, and an adaptive frequency windowing for fast multi-frequency solution of poro-acoustic problems. *International Journal for Numerical Methods in Engineering*, 97(10):759–784, 2014.

[7] P. Guillaume. Nested multivariate padé approximants. *Journal of computational and applied mathematics*, 82(1):149–158, 1997.

[8] R. Rumpler, P. Göransson, and H.J. Rice. An adaptive strategy for the bivariate solution of finite element problems using multivariate nested Padé approximants. *International Journal for Numerical Methods in Engineering*, 100(9):689–710, 2014.

[9] R. Rumpler. Padé approximants and the modal connection: towards increased robustness for fast parametric sweeps. *International Journal for Numerical Methods in Engineering*, 113(1):65–81, 2018.

Model order reduction for nonlinear dynamics engineering applications

F. Naets [1,2], **T. Tamarozzi** [1,3], **W. Rottiers** [1,2], **S. Donders** [3], **H. Van der Auweraer** [3], **W. Desmet** [1,2]
[1] KU Leuven, Department of Mechanical Engineering, Division PMA,
Celestijnenlaan 300 B, B-3001, Leuven, Belgium
e-mail: **frank.naets@kuleuven.be**

[2] DMMS Lab, Flanders Make

[3] Siemens Industry Software NV,
Interleuvenlaan 68, B-3001 Leuven, Belgium

Abstract
In order to fully exploit available computer aided engineering (CAE) models for modern mechatronic systems they need to be merged with measurement data in order to obtain reliable Digital Twins. These Digital Twins are evolving to become instrumental assets that accompany the product throughout its lifetime, enabling virtual quality assurance, virtual sensing and model-based control.
However, in mechatronics, the typical CAE design models are relatively expensive physics based models which cannot be directly used throughout the entire lifecycle as Digital Twins. Model order reduction approaches for these nonlinear dynamic applications allow to reduce the computational cost sufficiently for use in a Digital Twin setting.
This work gives an overview of nonlinear dynamics engineering applications in modern mechatronics products design, and demonstrates the role of (novel) MOR techniques in the design engineering process.

1 Introduction

Over the past decades, the design of mechatronic systems has relied more and more on model driven design cycles. Where initial efforts, starting from the ‘50s, were mainly focused on component level design analysis, recent efforts show a strong tendency towards model based system engineering (MBSE). In these approaches, component models are not evaluated in isolation, but in their dynamic interaction with other components in the mechatronic system. Typical examples include the dynamic structural component interaction included in flexible multibody models, or the control-system interaction typically described with lumped-parameter models.

Up until recently, these efforts were rooted in a pure modeling framework, with only limited touch point with experimental data through e.g. finite-element model updating based on modal analysis. However, in the current internet-of-things (IoT) and connected machine context prescribed by Industry 4.0, much more data is becoming continuously available. A novel trend is therefore arising to combine both models and data to enable predictive engineering analytics. This leads to the concept of *Digital Twins*. This concept entails the continuous *synchronization* of models with reality to better understand and predict the behavior of complex machinery.

Even though the concept of Digital Twins has been around for about two decades [1], the concept of fully exploiting engineering design models in this concepts is rather recent [2, 3]. The reason for this is simple: these models require relatively large computational effort, which is difficult to introduce in the online requirements pose on Digital Twins.

This work discusses how the KU Leuven Noise and Vibration Research group and Siemens Industry Software (SISW) develop and exploit physics based models to construct robust digital twins for mechatronic applications. Through the introduction of novel model order reduction techniques, the computational load of these models can be brought down sufficiently such that they serve purposes far beyond their initial design analysis purpose.

In section 2 it is discussed how different types of models are exploited through different stages of the mechatronic product lifecycle. Section 3 then provides an overview of different reduced order modeling (ROM) techniques for mechatronic systems.

2 Digital Twin to couple engineering with data driven models

A Digital Twin is a digital replica of a physical asset, process or system. The digital representation can be exploited for a range of different purposes. In the context of mechatronic systems, these purposes can be the evaluation of dynamic system quantities, monitoring of the condition of the system, the evaluation of new (optimized) control strategies, etc. A reliable replica can be obtained by combining both physics based models of the system with (operational) measurements on the same (nominal) real-life system [4].

Depending on the stage of use, a distinction can be made between three different Digital Twin categories for mechatronic systems [2], as shown in figure 1.



Figure 1: Mechatronic digital twins from system ideation to realization and utilization.

During the ideation and design stage, a Digital Product Twin can be exploited to evaluate the dynamic system behavior before the full physical system is available. As measurement data becomes available during the physical prototyping, these Digital Twins can be updated and refined to better match the physical behavior. Digital Production Twins allow to evaluate and optimize the realization of the designed products. The applications range from production process control to supply chain management. Finally, during the utilization of the system, a Digital Performance Twin allows to continuously monitor the performance of performance of the physical asset and to test different product updates without interrupting regular operation.

These different digital twins manifest themselves during different stages of the product lifecycle. Whereas classically the use of models was limited to the first ‘leg’ of the V-cycle design process, the paradigm as shifted to a *square-root cycle* [5], as shown in figure 2.

As many companies in the mechatronic domain are shifting to new business models like product-service-systems and X-as-a-service, enabled by new building blocks as Big Data [6] and the Internet of Things, they remain responsible for (and make profits from) their product further along their lifecycle, beyond the point-of-sale. It therefore becomes key to monitor and evaluate the products beyond their design and into their general operation. Digital Twins provide an essential tool to perform this product tracking during this entire process.

A particular challenge encountered in mechatronic system design and deployment are the different types of models used during the different stages of the design, as shown in figure 2. During the initial stages

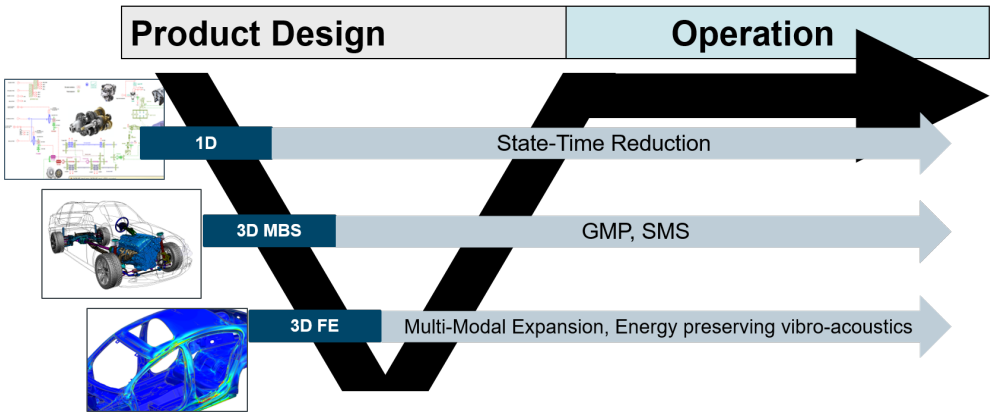


Figure 2: Square-root product cycle with different model categories.

of the model based design, lumped parameter models which roughly describe the overall system behavior are typically employed. These models have as main benefit that no detailed design information on specific components is required yet. As the design progresses, more detailed information becomes available and (flexible) multibody models can be used to assess the dynamic machine behavior with an accurate assessment of e.g. component loads. In the final model based design phase, a highly detailed analysis can be performed by exploiting (multi-physical/nonlinear) finite element models, which allows a detailed assessment of e.g. component stresses and fatigue. In the frame of the square-root cycle and the development of Digital Twins, the aim is now to exploit these models to obtain more and more reliable information on the product during the physical prototyping and operational stage of the product [4, 7]. During these stages, each of these models offers a unique value proposition and the potential to obtain dedicated information for specific applications. However, a direct application of these models during the latter stages of the square-root cycle is practically infeasible due to their computational load.

In order to enable the exploitation of these different design models during the physical prototyping and operation, model order reduction (MOR) techniques are key. These approaches allow to construct low-cost models which preserve the dominant dynamic phenomena of the original models. As the mathematical model structures of the different approaches used during the design span a wide range of methods, the approaches for model order reduction need to be equally diverse. The specific model order reduction approach depends both on the original model structure and final application of the reduced order model. In the following section, several approaches are discussed which have been developed with the aim of generating practical Digital Twins for (diverse aspects of) mechatronic systems in the square-root cycle.

3 Model order reduction for dynamic mecha(tro)nic models

In this section we provide an overview of the range of model order reduction techniques which are being developed (collaboratively) at the Noise and Vibration research group and Siemens Industry Software with the aim of tackling different challenges encountered in the Digital Twin setup for mecha(tro)nic systems. These approaches span the entire spectrum for low order lumped-parameter models to high-fidelity nonlinear finite-element models and their use through the square-root cycle shown in figure 2.

3.1 State-time reduction for low-order models

3.1.1 Methodology

During the early design stages and for mechatronic system integrators, 1D or lumped parameter simulation present a suite of tools to effectively assess the full system behavior. These models are typically based on idealized components with clearly defined interface ports which enable an effective graphical representation of their connection on the full system level. A particular example of this type of software is Simcenter Amesim from SISW [8]. This software is based on a causal bond-graph approach, which enables a highly efficient model representation which allows to include a wide range of elements from different physical domains. A typical graphical representation of a Simcenter Amesim model is shown in figure 3.

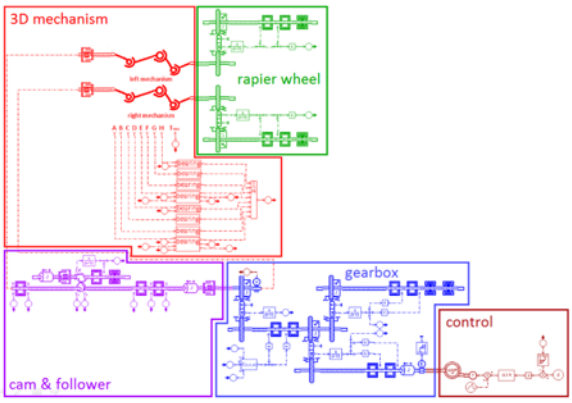


Figure 3: Example of the graphical representation of a Simcenter Amesim model.

Even though these models are directly translated to C-code and compiled, the computational load during multi-query applications can still become considerable and hence requires model order reduction.

However, regular state-projection based model order reduction schemes do not offer a good solution for these models. The key issue here is the typically limited number of states (fewer than 100 states), such that there is limited margin for state-reduction. Moreover, as each model block with limited states has to be added manually, the model developer typically already selects only the most relevant states. On the other hand, these models are typically solved through explicit time integrators over relatively large time horizons. This opens up the possibility to use MOR to limit the time dimension and hence reduce the computational burden for a model evaluation.

In this framework, the state-time reduction order modeling (ST-MOR) scheme has recently been proposed [9]. In this approach, the full response over the simulation horizon is considered to set up a reduced order basis which spans the states and their time variations. For the reduced evaluation of the model equations, the sequential time problem is concatenated and projected as a fully coupled problem. In order to prevent a back-transformation to the original time-dependent model size, a hyper-reduction scheme is applied which selects only the most significant time-steps for evaluation.

3.1.2 Application

The proposed state-time reduction scheme for low order models can be applied in a range of settings. The presented approach is mainly valuable in multi-query settings where the same model topology is evaluated repeatedly for different parameter values. This is encountered amongst others in design parameter optimization and parameter identification problems. An example is the parameterized evaluation of a mechatronic drivetrain, for which a conceptual sketch is shown in figure 4.

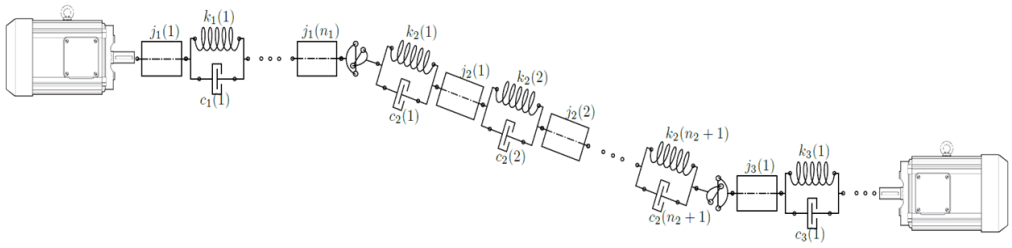


Figure 4: Mechatronic powertrain model.

For this system, an evaluation of the model states for different system parameters can be performed, as shown in figure 5.

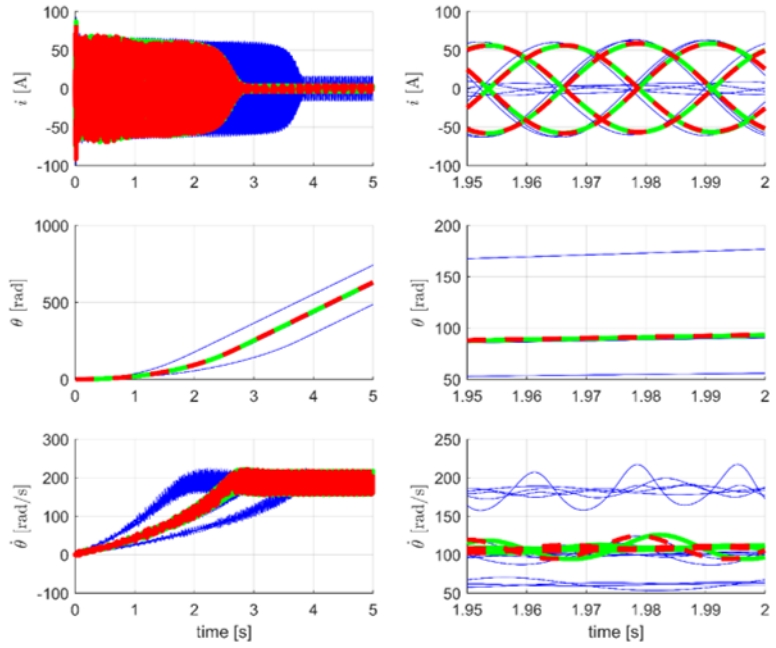


Figure 5: Mechatronic powertrain model response (full time response and zoom).

This figure shows the response for different training parameters in blue, the full order response for a certain design parameter in red and the response for the ST-ROM in green. Even though this model is limited in size (only double-digit states), a speed-up of an order of magnitude is obtained through the proposed approach.

3.2 Efficient geartrain simulation through MOR

3.2.1 Methodology

One of the key components in mechatronic drivetrains are gears. These classical mechanical components have become the target of a large body of numerical analysis techniques due to their large impact on the efficiency, reliability/durability, and dynamic performance of many modern applications, ranging from precision mechanics to efficient vehicles and wind turbines. However, the numerical assessment of these systems has always been very challenging due to the high importance of small geometrical alterations and complex contact dynamics between the gears. In classical approaches the full gears and their contact conditions are either modelled through analytical approaches, which often lack the accuracy required for detailed dynamic anal-

ysis, or through full nonlinear finite element models, which present an enormous computational load. In more recent years many researchers have started using (flexible) multibody approaches in order to describe the gear dynamics. However, due to the inherent nature and complexity of the contact conditions, even these models often lead to excessive computational loads when e.g. accurate stress evaluations are required.

In order to offer solutions for efficient gear simulation in a range of applications, a comprehensive set of model order reduction schemes has been developed. As outlined in figure 6, these methods focus on each step involved in the gear modeling:

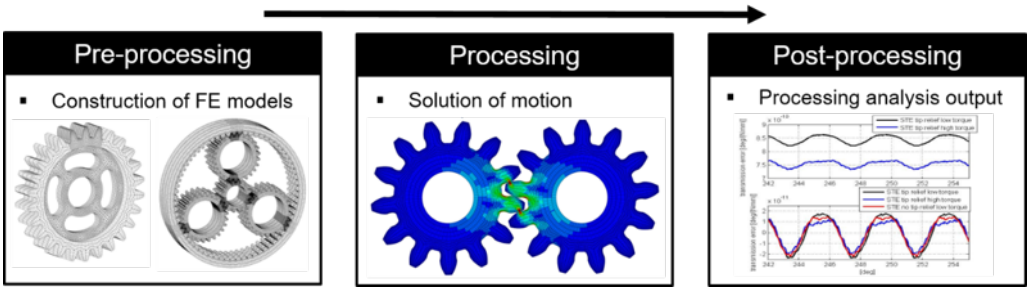


Figure 6: Gear simulation workflow.

- **Pre-processing:** Tools have been developed to effectively set up the meshes for different gear configurations and accounting for specific micro-geometries. Moreover, the controlled mesh setup allows to exploit e.g. symmetry properties in the model order reduction. These methods will be brought to market in the Simcenter 3D [10] product offering of SISW, as the "Advanced FE-preprocessor" technique [11], an innovative method that combines the advantages of FE methods, model order reduction schemes and analytical formulas, while offering significantly reduced computation time.

- **Processing:** During the solution of the motion, a range of different aspects are exploited to reduce the model size and limit the contact evaluation cost. On the one hand the reduced order basis to describe the model deformations is dependent on the gear angle θ and hence optimized to resolve a certain configuration [11, 12]:

$$\mathbf{u}_d = \mathbf{V}(\theta)\delta, \tag{1}$$

  and on the other hand parametric model order reduction techniques are further exploited to construct robust bases for different contact conditions such as misalignment [13]. Moreover, in order to reduce the contact evaluation cost, the discrete empirical interpolation method (DEIM) is used for hyper-reduction such that the full contact conditions do not need to be evaluated for each time step [13, 14]. The resulting model is time-integrated through an optimized integration scheme for gear-contact simulation.

- **Post-processing:** During the post-processing, the results of the simulations are transformed back to the original model space such that detailed analyses of local stresses and gear transmission errors can be evaluated.

Further speed-ups of the developed models are possible through the use of stiffness maps and quasi-analytic contact conditions. Through the developed suite of approaches, accurate gear models can be incorporated in detailed mechatronic model simulations, enabling a reliable digital twin assessment of geared systems.

3.2.2 Application

For gear applications, the reduced order models are employed in a range of applications. A first step in this research track was to perform experimental validation of the developed gear models, which was previously

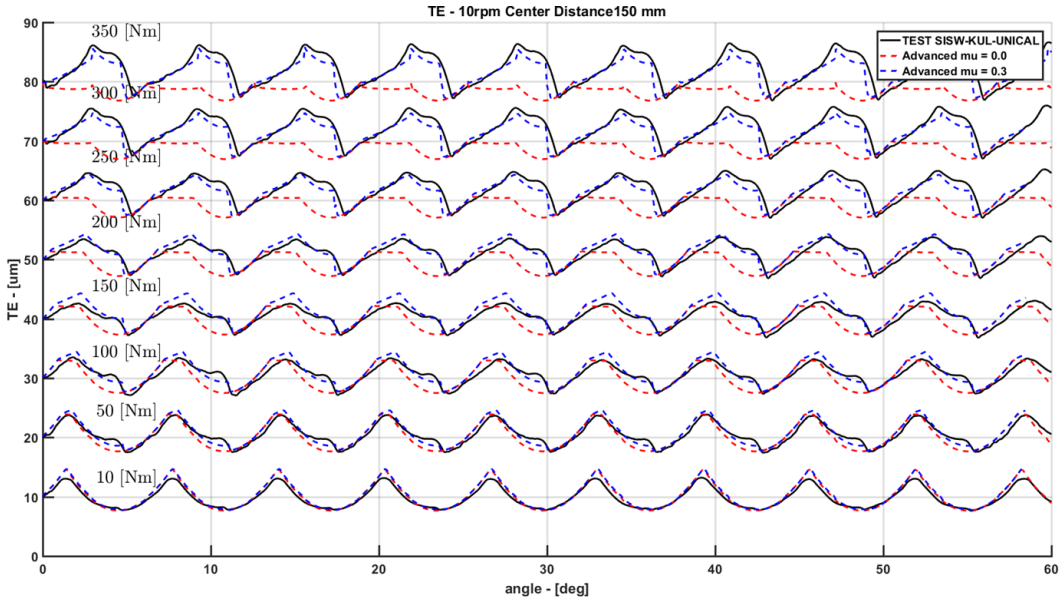


Figure 7: Gear model validation for different load torques and different friction conditions.

difficult due to the very high cost of these models. A comparison of measured and simulated transmission error is shown in figure 7.

These validated models are then exploited in an automated toolbox for transmission model creation. By exploiting the stiffness map approach, these models can be made highly efficient for rapid design evaluation on the Digital Twin [15]. Through these developments the impact of teeth coupling and lightweight gear design on the transmission dynamics and NVH can be effectively evaluated [13].

3.3 Reduced flexible multibody towards real-time performance

3.3.1 Methodology

Over the past decades, flexible multibody simulation has become a key tool for evaluating system level dynamic interaction between different structural components in mecha(tro)nic systems. In these approaches, since the seventies, each component is already represented in a reduced fashion by projecting each (linear) body deformation on a modal basis in a floating-frame-of-reference component-mode-synthesis (FFR-CMS) approach. Overall this provides a very general formalism to describe (flexible) mechanisms, leading to a set of equations of motion in the form:

$$\mathbf{M}(\mathbf{q})\ddot{\mathbf{q}} + \mathbf{f}^{gyr}(\mathbf{q},\dot{\mathbf{q}}) + \mathbf{K}\mathbf{q} - \mathbf{C}^T\lambda = \mathbf{f}^{ext} \tag{2}$$

$$\mathbf{c}(\mathbf{q}) = 0 \tag{3}$$

Even though highly efficient formulations exist to solve these equations of motion, as implemented in VirtualLab Motion, the differential algebraic (DAE) nature of these equations often makes them not particularly suitable for a range of applications. These general DAE's can typically not be solved effectively through explicit integrators, which are required for hard real-time applications and state-estimators.

In order to circumvent these issues, a range of model order reduction schemes have been developed to reformulate the (flexible) multibody models as a set of low-order ordinary differential equations (ODEs):

$$\mathbf{M}^r(\mathbf{q})\ddot{\mathbf{q}} + \mathbf{f}^{gyr,r}(\mathbf{q},\dot{\mathbf{q}}) + \mathbf{f}^{int,r}(\mathbf{q}) = \mathbf{f}^{ext,r}. \tag{4}$$

A range of different approaches have been developed to enable this model reduction and transformation. On the one hand, methodologies have been developed which approximate the nonlinear (flexible) multibody dynamics by setting up an approximation through a set of locally linear models which fit the motion manifold. A first effort in this respect was the introduction of the Global Modal Parameterization (GMP) [16, 17]. In order to further solidify this concept in a more generalized setting, more recently a strongly data-driven approach has been proposed for multibody model order reduction [18]. These approaches lead to a set of equations in the form of:

$$\mathbf{M}^r(\mathbf{q})\ddot{\mathbf{q}} + \mathbf{f}^{gyr,r}(\mathbf{q},\dot{\mathbf{q}}) + \mathbf{K}(\mathbf{q})\mathbf{q} = \mathbf{f}^{ext,r} \tag{5}$$

On the other hand, a novel approach based on global nodal coordinate reduction has been developed which allows to describe the nodal coordinates as an affine projection from the reduced degrees-of-freedom, denoted as the System-Level Affine Approximation (SLAP) [19]. The main benefit of this approach is the resulting constant mass matrix, lack of gyroscopic contributions, and the avoidance of setting up a piecewise approximation of the motion manifold. The resulting equations of motion take the form:

$$\mathbf{M}^r\ddot{\mathbf{q}} + \mathbf{f}^{int,r}(\mathbf{q}) = \mathbf{f}^{ext,r}. \tag{6}$$

3.3.2 Application

A typical application of explicit (flexible) multibody models is found in the analysis of vehicle suspension components under dynamic loading. The aim is often to track the loads, deformations and stresses in these components on test-rigs and operational conditions. The multibody model for a quarter car suspension system is shown in figure 8 on the left. For the motion, a clustering can be set up to construct the different linearized models, as shown in figure 8 on the right.

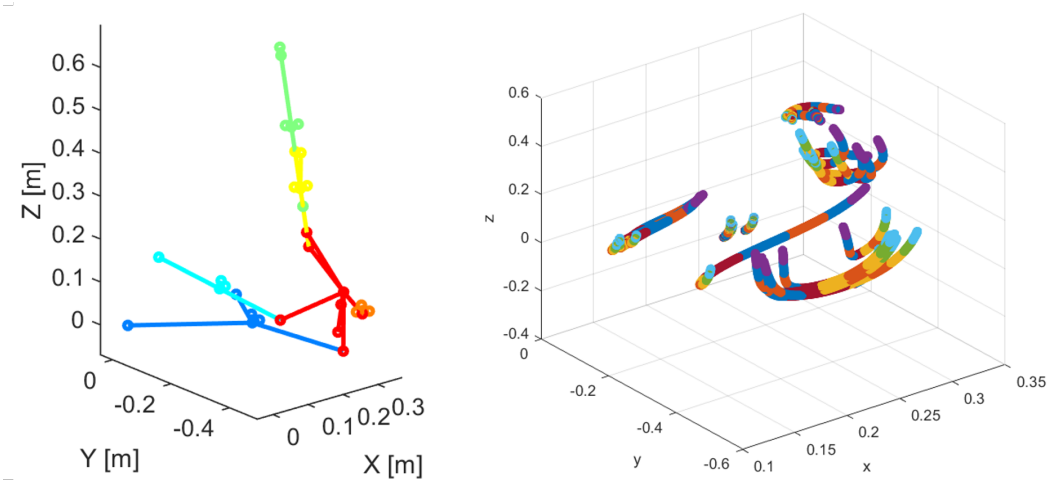


Figure 8: Quarter-car suspension multibody model (left) and motion clustering (right).

Through the proposed model order reduction approaches, these general multibody models are converted in a very low order model with a simple ODE structure, while maintaining accurate results, as shown in figure 9.

In the future, these model order reduction approaches will be deployed in real-time systems and state-estimators for Digital Twin purposes.

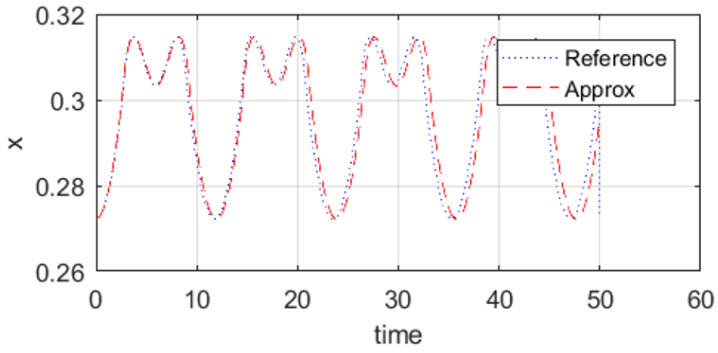


Figure 9: Data-driven model order reduction results on quarter car model.

3.4 Reduced order linear finite element models for real-time estimation

3.4.1 Methodology

State and load identification are key in a range of mechatronic systems. This is required both for control purposes and for monitoring the system condition. However, direct instrumentation is often not feasible due to costs or practical constraints. In these applications (coupled) state(-input) estimation offers a powerful solution to obtain a wide range of measurement signals. However, in order to exploit these approaches, accurate low cost models are required which allow to fuse data coming from a number of distributed sensors. Finite-element models offer the perfect framework for these applications. For these models, the dynamics are described through the mass and stiffness matrices $\mathbf{M}, \mathbf{K} \in \mathbb{R}^{n \times n}$:

$$\mathbf{M}\ddot{\mathbf{u}} + \mathbf{C}\dot{\mathbf{u}} + \mathbf{K}\mathbf{u} = \mathbf{f}^{ext}, \tag{7}$$

with $\mathbf{u} \in \mathbb{R}^n$ the finite element degrees-of-freedom. In regular structural models, these are typically nodal displacements, but in vibro-acoustic models these can be generalized to nodal displacement, pressures and fluid velocities. However, as typical estimators rely on the time-discretized equations of motion, these models needs to be explicitly integrated in time. Due to the high (spurious) frequencies present in these full order FE models, the explicit integration is practically infeasible as the required time steps would be unacceptably small. In order to circumvent this issue, projection based model order reduction can be applied [20]:

$$\mathbf{u} \approx \mathbf{V}\mathbf{q} \tag{8}$$

with $\mathbf{V} \in \mathbb{R}^{n \times m}$ the reduced order basis and $\mathbf{q} \in \mathbb{R}^m$ the reduced DOFs. The resulting reduced order model is then evaluated as:

$$\mathbf{M}^r\ddot{\mathbf{q}} + \mathbf{C}^r\dot{\mathbf{q}} + \mathbf{K}^r\mathbf{q}, \tag{9}$$

with the reduced order matrices obtained from a Galerkin projection:

$$\mathbf{M}^r = \mathbf{V}^T\mathbf{M}\mathbf{V}, \quad \mathbf{C}^r = \mathbf{V}^T\mathbf{C}\mathbf{V}, \quad \mathbf{K}^r = \mathbf{V}^T\mathbf{K}\mathbf{V}. \tag{10}$$

For these estimation applications, the main aim of the model order reduction is not only to reduce the model size, but particularly also to limit the highest frequencies and numerical conditioning of the model such that a range of explicit integrators can be effectively applied. The reduced model size also allows to reliably apply an exponential integration scheme, such that large time steps are possible in an explicit integration scheme.

3.4.2 Application

The linear reduced order modeling approach for state and input estimation can be applied in a wide range of applications. One important application is the load estimation on e.g. vehicle suspension [21]. A vehicle rear suspension system is shown in figure 10.

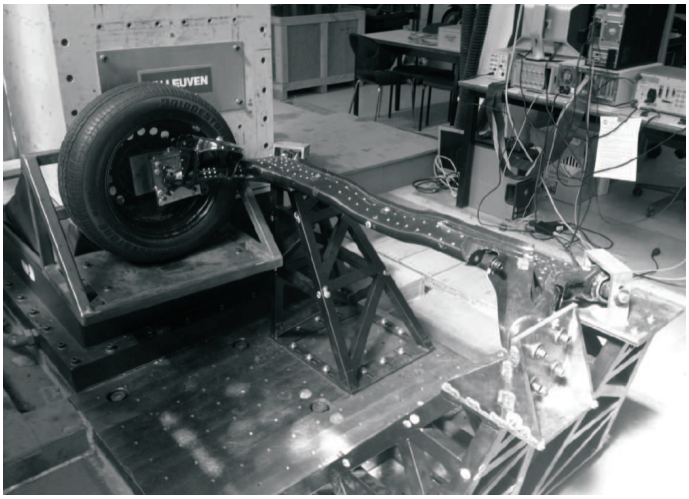


Figure 10: Loaded vehicle suspension.

Using the reduced order finite element model, the vertical input load can be accurately estimated, in contrast to approaches based on alternative simplified models. These estimation results are shown in figure 11.

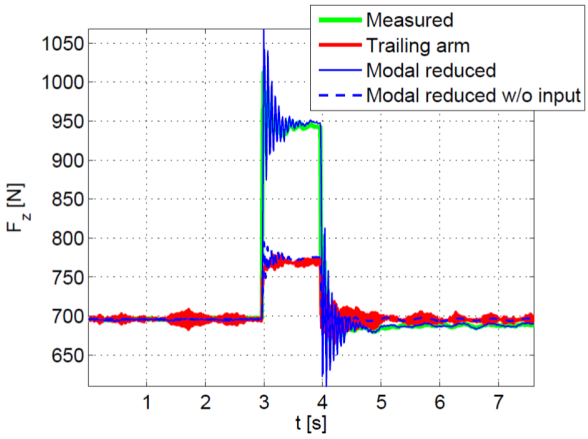


Figure 11: Input load estimation on vehicle suspension.

Using the appropriate model order reduction schemes [22], these estimation approaches can also be applied to a vibro-acoustic model, where the full sound field can be accurately reproduced from a limited number of accelerometer and microphone measurements, as shown in figure 12.

3.5 Reduced order nonlinear finite element models for vision based estimation

3.5.1 Methodology

For highly dynamical and large deformation mechatronic application, nonlinear finite element models are required to accurately describe the system motion. This is also true when optical (camera based) measurements are used to evaluate the system state, as these measurement can be particularly sensitive to geometric nonlinear effects. Even though these nonlinear finite elements models have proven highly valuable for high fidelity applications over the past decades, they are also associated with (very) high computational loads and are often run on cluster computers. This high computational load is the result of the fine semi-discretization

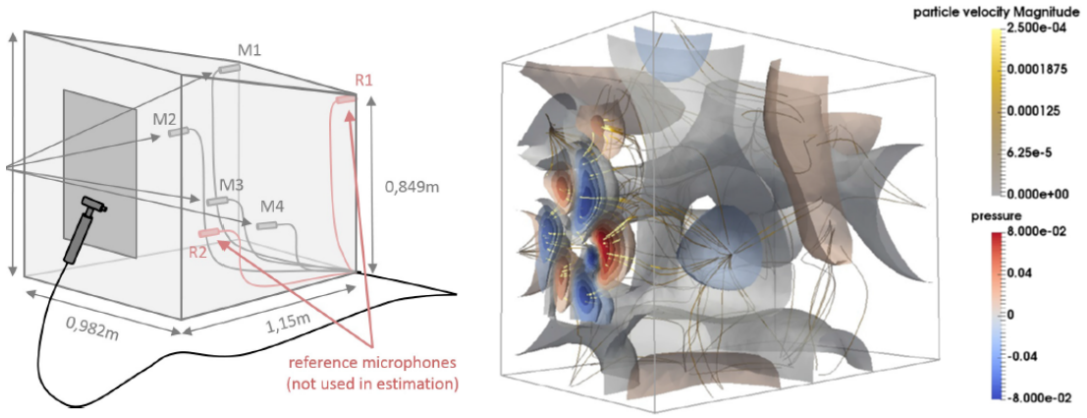


Figure 12: Vibro-acoustic test setup (left) and estimated sound field (right).

required for the spatial domain, resulting in a high number of degrees-of-freedom $\mathbf{u} \in \mathbb{R}^n$ and large number n_e of finite elements. The resulting equations of motion take the form:

$$\mathbf{M}\ddot{\mathbf{u}} + \mathbf{f}^{int}(u) = \mathbf{f}^{ext}. \tag{11}$$

Contrary to linear finite-elements, each element needs to be re-evaluated at every time step to evaluate the internal forces:

$$\mathbf{f}^{int} = \sum_{i=1}^{n_e} \mathbf{f}_i^{int}(u_e), \tag{12}$$

which rapidly leads to large computational loads. Combined with the large system of equations to solve for each time step, this leads to unacceptable computational loads in anything but large scale offline design evaluations.

In order to enable the use of these models in multi-query, online and Digital Twin applications, model order reduction techniques have been developed which reduce the model size and limit the evaluation cost of the elements. In common nonlinear model order reduction schemes like discrete empirical interpolation (DEIM) [14] or energy conserving sampling and weighting (ECSW) [23], the reduced order model is set up by first performing a (number of) reference simulation(s). However in many practical applications, these reference simulation might already pose an unacceptable computational load. For these applications we therefore propose a semi a-priori approach which allows to set up the reduced order model based on a limited set of static analyses, rather than full time domain analyses. The reduction scheme is based on two aspects [24]:

- First a reduced order basis $\mathbf{V} \in \mathbb{R}^{n \times m}$ is constructed together with a reference configuration $\rho \in \mathbb{R}^n$ to approximate the full model state:

  $$\mathbf{u} \approx \rho + \mathbf{V}\mathbf{q}, \tag{13}$$

  with the reduced order DOFs $\mathbf{q} \in \mathbb{R}^m$. The reduced order basis $\mathbf{V}$ results from a truncated singular value decomposition on a set of nonlinear static deformation shapes and a set of linearized eigenmodes around these static deformation shapes.

- Next a reduced number of elements is selected to approximate the internal forces, in correspondence to the ECSW approach:

  $$\mathbf{V}^T\mathbf{f}^{int} \approx \sum_{i \in s_e} \mathbf{w}_i \mathbf{f}_i^{int}(u_e), \tag{14}$$

  with s_e a subset of the full element set and w_i a set of corresponding nonlinear weights. In order to avoid the necessity of training forces, the elements and weights are selected from a nonnegative L1

optimization problem on the undeformed stiffness matrix $\mathbf{K}$:

$$\min |\mathbf{w}|_1 \mathbf{w} \in \mathbb{R}_+^{n_e} s.t. \mathbf{V}^T\mathbf{K}\mathbf{V} - \mathbf{w}_i\mathbf{V}^T\mathbf{K}_i(\rho)\mathbf{V} \tag{15}$$

This approximation is the hyper-reduction which also reduces the evaluation cost of the model.

Through this multi-expansion modal (MEM) approach the computational load for high-fidelity mecha(tro)nic model can be brought down sufficiently for a range of new applications.

3.5.2 Application

A typical application encountered in automotive mechatronic systems is the assessment of wheel loads. This is possible by combining flexible suspension models with appropriate measurements from strain gauges and/or optical sensors. It was shown by means of virtual exercises in [25] that an optimal sensor placement strategy can be very beneficial in achieving a reliable force estimation by using a very limited set of well-chosen and well-positioned sensors.

However, the inclusion of a flexible suspension model becomes very challenging in the case of the common twistbeam rear suspension. In this case a geometrically nonlinear finite element model is required to describe the dynamics. As shown in figure 13, a typical finite element model for this system consists of around 100k elements and DOFs.

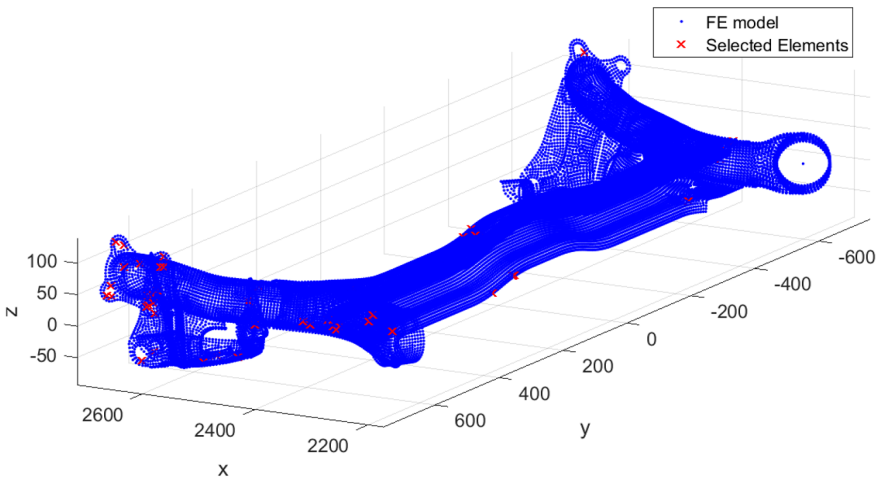


Figure 13: Twistbeam finite element mesh.

Through the MEM approach this model can be brought down to a model with 16 reduced order DOFs and 129 elements (as shown in figure 13). This allows to make the model sufficiently low cost to run full analyses such that the response can be shown over long timeframes, as shown in figure 14.

4 Conclusion

In recent years, it has become clear that Digital Twins offer an important added value throughout the mechatronic product development and exploitation. Preferably, these Digital Twins exploit all information available in the physics based engineering models used during the initial design V-cycle. However, these models' high computational load limit their direct applicability in an extended square-root cycle for the product. Model order reduction has therefore proven to be a key technique in (automatically) transforming different design

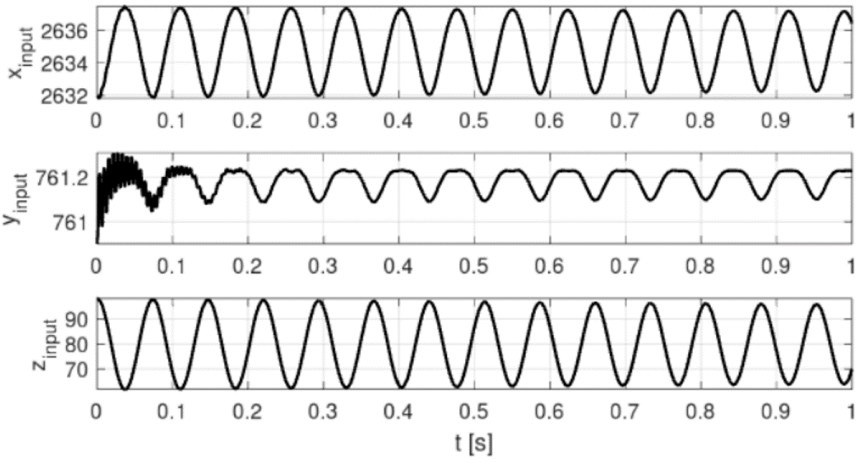


Figure 14: Twistbeam response from nonlinear reduced order model.

models into lower cost counterparts that maintain the required accuracy.
Given the wide range of models encountered in mechatronic system design, an equally wide range of model order reduction techniques has been developed tailored to the different model structures and applications. These techniques result from a close collaboration between Siemens Industry Software and the KU Leuven Noise and Vibration research group. The developed techniques allow high efficiency by actively exploiting the key physical properties of the different models and allow to be exploited in virtual sensor applications to extend classical measurement with the available model data.

Acknowledgements

The Research Fund KU Leuven is gratefully acknowledged for its support.

The research of Frank Naets and Ward Rottiers is funded by a grant from the Research Foundation – Flanders (FWO). This research was also partially supported by Flanders Make, the strategic research centre for the manufacturing industry.

VLAIO is gratefully acknowledged for funding the project “EfficieNt DURability testing ANd vehiCle usage Evaluation” (ENDURANCE, 2017-2019). The research of T. Tamarozzi is funded by the VLAIO Innovation Mandate 160343, “Virtual Mates”. The authors also gratefully acknowledge the Marie Sklodowska-Curie ITN project “Advanced Training and Research in Energy Efficient Smart Structures” (ANTARES, 2014-2018).

References

[1] M. Grieves, *Virtually Perfect: Driving Innovative and Lean Products through Product Lifecycle Management*, Space Coast Press, Cocoa Beach, Florida (2011).

[2] J. Bohman, J. Leuridan, M. O’Brien, *Ideation*, Siemens PLM Software Annual Industry Analyst Conference, Boston, USA (2017).

[3] H. Van der Auweraer, S. Donders, D. Hartmann, W. Desmet, *Simulation and Digital Twin for Mechatronic Product Design*, in W. Desmet, B. Pluymers, D. Moens, W. Rottiers, editor, *Proceedings of the*

International Conference on Noise and Vibration Engineering (ISMA2018) and the International Conference on Uncertainty in Structural Dynamics (USD2018), Leuven, Belgium (2018).

[4] S. Boschert, R. Rosen, *Digital Twin – The Simulation Aspect*, in P. Hehenberger, D. Bradley, editor, *Mechatronic Futures, Springer*, Cham (2016), pp. 59–74.

[5] S. Donders, M. Luczak, B. Peeters, D. von Werne, D. Kading, H. Van der Auweraer, *Innovative Simulation and Testing Methodologies for Optimized Design and Operation of Wind Turbine Systems*, Proceedings of Recent Advances in Structural Dynamics Conference 2010 (RASD2010), Southampton, UK (2010).

[6] J. Lee, E. Lapira, B. Bagheri, H. Kao, *Recent advances and trends in predictive manufacturing systems in big data environment*, Manufacturing Letters (2013), pp. 38-41.

[7] CIMdata, *Digital Twins – Changing the Way We Engineer, Validate, Market, and Operate our Products*, eBook (2018).

[8] Siemens PLM Software, *Simcenter Amesim*, Version 16.1 (2018).

[9] W. Rottiers, F. Naets, W. Desmet, *Parametric state-time reduction for the transient analysis of multiphysical systems*, ScienceOpen Posters (2018).

[10] Siemens PLM Software, *Simcenter 3D*, 13 (2019).

[11] A. Rezayat, S. Shweiki, D. Park, M. Vivet, S. Donders, S. Flock, P. Jiranek, T. Tamarozzi, *A novel efficient high fidelity approach to gear contact simulation in multibody systems*, Proceedings of the International Gear Conference, Lyon Villeurbanne, France (2018).

[12] N. Cappellini, T. Tamarozzi, B. Blockmans, J. Fiszer, F. Cosco, W. Desmet, *Semi-analytic contact technique in a non-linear parametric model order reduction method for gear simulations*, Meccanica, Vol. 53, Springer (2018), pp. 49-75.

[13] B. Blockmans, *Model reduction of contact problems in flexible multibody dynamics: With emphasis on dynamic gear contact problems*, Phd Dissertation, KU Leuven (2018).

[14] S. Chaturantabut, D. Sorensen, *Nonlinear model reduction via discrete empirical interpolation*, SIAM Journal on Scientific Computing, Volume 32, Issue 5 (2010), pp. 2737-2764.

[15] T. Tamarozzi, P. Jiranek, D. Park, M. Vivet, S. Donders, S. Flock, *Democratization of simulation in the design engineering of gear boxes*, Proceedings of NAFEMS Seminar "Simulation Driven Engineering", Neuendettelsau, Germany (2017).

[16] F. Naets, G. Heirman, D. Vandepitte, W. Desmet, *Inertial force term approximations for the use of global modal parameterization for planar mechanisms*, International Journal for Numerical Methods in Engineering, Volume 85, Issue 4 (2011), pp. 518-536.

[17] F. Naets, T. Tamarozzi, G. Heirman, W. Desmet, *Real-time flexible multibody simulation with Global Modal Parameterization*, Multibody System Dynamics, Volume 27, Issue 3 (2012), pp. 267-284.

[18] A. Angeli, F. Naets, W. Desmet, *Data-Driven Model Order Reduction for real-time multibody simulations*, International conference on multibody system dynamics, Lisbon, Portugal (2018).

[19] F. Naets, T. Devos, A. Humer, J. Gerstmayr, *A non-invasive system-level model order reduction scheme for flexible multibody simulation*, International Journal for Numerical Methods in Engineering (Submitted).

[20] F. Naets, J. Croes, W. Desmet, *An online coupled state/input/parameter estimation approach for structural dynamics*, Computer Methods in Applied Mechanics and Engineering, Volume 283 (2015), pp. 1167-1188.

[21] F. Cosco, F. Naets, W. Desmet, *Use of concept modelling for online input force estimation*, in P. Sas, H. Denayer, editor, *Proceedings of the International Conference on Noise and Vibration Engineering (ISMA2014) and the International Conference on Uncertainty in Structural Dynamics (USD2014)*, Leuven, Belgium (2014).

[22] A. van de Walle, F. Naets, W. Desmet, *Virtual microphone sensing through vibro-acoustic modelling and Kalman filtering*, Mechanical Systems and Signal Processing, Volume 104 (2018), pp. 120-133.

[23] C. Farhat, P. Avery, T. Chapman, J.Cortial, *Dimensional reduction of nonlinear finite element dynamic models with finite rotations and energy-based mesh sampling and weighting for computational efficiency*, International Journal for Numerical Methods in Engineering, Volume 98, Issue 9 (2014), pp. 625-662.

[24] F. Naets, D. De Gregoriis, W. Desmet, *Multi-expansion modal reduction: a pragmatic semi-a-priori model order reduction approach for nonlinear structural dynamics*, International Journal for Numerical Methods in Engineering (Submitted).

[25] T. Tamarozzi, E. Risaliti, W. Rottiers, K. Janssens, W. Desmet, *Noise, ill-conditioning and sensor placement analysis for force estimation through virtual sensing*, in P. Sas, A. van de Walle, editor, *Proceedings of the International Conference on Noise and Vibration Engineering (ISMA2016) and the International Conference on Uncertainty in Structural Dynamics (USD2016)*, Leuven, Belgium (2016).

The application of artificial neural networks in mechatronics system development

P. Mas[1], S. B. Maddina[2], F. L.M. dos Santos[3], C. Sobie[3], H. Van der Auweraer[3]
[1]Siemens Industry Software SAS, 84 Quai Charles de Gaulle, 69006 Lyon, France

[2]Siemens Industry Software Priv. Ltd, C-28 Cipet Rd., 600032 Chennai, India

[3]Siemens Industry Software NV, Interleuvenlaan 68, 3001 Leuven, Belgium
e-mail: **herman.vanderauweraer@siemens.com**

Abstract
Artificial neural networks, currently a backbone behind many data driven artificial intelligence applications, have been growing in popularity in different domains, from speech recognition over image processing to control tasks with complex sensory inputs and multiple outputs. Mechatronic systems have in the meantime been growing in complexity requiring a dedicated model based systems development process to assure the functional and performance design attributes. A complex mixture of 1D and 3D multi-physics models and test based characterization is used to design the hardware as well as the controls. In this paper the aid of artificial neural networks in mechatronics system development is demonstrated based on examples from the different phases of the development cycle of vehicle systems. The applicability of various types of neural networks (DNN, CNN, RNN) is explored for the different engineering tasks. The work fits into a broader context of merging data driven and model based approaches, a topic attracting major interest today [1].

1 Introduction

Different terms are used in the addressed field. Artificial Intelligence (AI) covers a very broad domain and range of technologies, which in general try to enable the growing intelligence of machines, which means to have them execute tasks that are typically done by humans. It started in the 60's with the game computers like chess. This involves complex programming of rules and sequences. Machine learning is a subdomain of AI (or a way to realize AI) where during the process of usage of the algorithm, the algorithm itself becomes smarter. The algorithm "learns". One of the first examples is the sorting of the spam mails which came up in the 90's.

Neural Networks are one way to achieve machine learning next to other methods such as for example inductive logic programming, support vector machines, clustering, reinforcement learning, and Bayesian networks. Although neural networks have been around for a long time, only recently from 2010 onwards their usage has come into an acceleration phase mainly due to 3 reasons:

- The availability of training data based on the Internet of Things (IoT) boom but also based on the abundance of simulation data.
- The constant improvement of computer speed and the usage of GPUs instead of CPUs as calculation servers.
- The improvement of the neural network training algorithms and the variety of neural network architectures.

Today artificial neural networks are the main driver behind the artificial intelligence technology growth and are typically seen as a subcategory of machine learning. They can generally be used for 3 types of learning [2, 3]:

- Supervised learning where labelled data is used for inputs and their connected outputs.
- Unsupervised learning where only inputs are known (for example feature extraction).
- Reinforcement learning where actions need to be decided based on a reward/penalty (for example in optimal control algorithms).

In this paper only the supervised learning is addressed while also unsupervised learning and reinforcement learning are finding their way into the mechatronic systems development process. In supervised learning a collection of inputs and outputs of a system are known and the learning process allows to find the best possible correlation between the inputs and the outputs by adapting parameters of the neural network in a smart iterative way. Different type of learning algorithms are available but the Levenberg-Marquardt optimization [4, 5] is the most widely applied in connection with neural networks.

2 Neural network architectures

Artificial Neural Networks (ANN) come today in many different architectures but essentially, they can be classified in 3 main categories:

- Feedforward neural networks (FNN) which make a direct connection between input and output data through one or more combinatorial layers [6].
- Recurrent neural networks (RNN) which have a memory that allows to remember previous inputs and store data in "context nodes" [7].
- Convolutional neural networks (CNN) which keep in mind a spatial relation between the inputs [8-10].

Feedforward neural networks can be used for the correlation of inputs and outputs without any relationship between the current inputs or outputs in function of time nor space. The word "deep" learning [6] is used if the neural network has many hidden layers between inputs and outputs. A recurrent neural network with one hidden layer can in that context also be seen as a deep neural net since the training process to perform it uses an unwrapped version of the recurrent neural net.

In case there is a correlation between the inputs in terms of their spatial arrangement, convolutional neural networks (CNN) are a more appropriate architecture since during training the proximity between the inputs in the architecture is already a-priori taken into consideration by optimizing filter values. This is for example useful for extracting signal features, analyzing 2 dimensional pictures or spatially correlated multisensory data. Also in condition monitoring, CNN can be applied to detect if a given vibration signal can lead to faulty or correct operation.

In case there is a time historical relationship between the current inputs and their past values, a recurrent neural network is a more appropriate architecture since it contains memory that allows to make relationships between past values and the current value. This is in particular very useful for time data, for sequences (as in text) or for describing system-like behavior. This time dependency can however lead to difficulties in training the network as large variations of the weights lead to small changes in the gradients. This is known as the "vanishing gradient problem". As a consequence, several innovative approaches have been made over the last few years to the RNN architecture to improve the learning for particular relationships between inputs and outputs. Some best known forms are:

- Layered Recurrent Nets (LRNN) [11].
- Long Short Term Memory (LSTM) [12].
- Gated Recurrent Unit (GRU) [13].

In case of an LRNN, the hidden layer neuron outputs are artificially delayed during a pre-defined amount of time steps to maintain a longer memory.

In case of an LSTM, the hidden layer neuron outputs are kept artificially based on thresholds which are also variables during the training process. This allows to combine slowly varying phenomena with dynamically changing phenomena in the identification process.

3 Neural networks and system identification

LRNN have proven to be particularly useful to identify low damped resonances in non-linear systems as shown in the example of figure 1. LSTM have proven to be particularly useful to understand speech since it can recognize sentences and words in the same learning process. In this paper the application of the LSTM to model data has not been handled yet and will be the subject of future research.

A neural network in supervised learning can be used directly as a model identification method using input and output time data to train an RNN. However the training might not always be successful because the starting values of the neural network coefficients cannot always easily be iteratively updated towards a global optimum.

Figure 1 shows the concept of training a neural network based on simulation data. The upper right picture shows the model in Simcenter Amesim. It is a mass-spring-damper system with 5 masses and thus 10 states. The model input is a force on 1 mass, either a random excitation or a swept sine. A random excitation is used to train the neural network. A swept sine signal is used to validate if the neural network can deal also with other input arrangements in function of time. The outputs of the neural network are the accelerometer sensors on each mass. The system has 5 resonances below 100Hz and the excitation signals are defined up to 100Hz.

A layered recurrent neural network in Matlab is used as architecture to train the data. An optimal size of 6 neurons in the hidden layer and 6 delayed neuron values in the feedback loop are used for training. This gives 36 states in total (6x6) when the model is linearized but it is the experience of the authors that an under-determination is needed for a neural network to arrive to a stable minimum.

The inputs and outputs of the random excitation are used to train the neural network. In the upper right figure the accuracy performance of the network after every epoch is shown. It can be seen that the network stabilizes after 100 Epochs and does not improve further visually. In the bottom left, the result in frequency domain of the predicted accelerometer signals is given for the 5 accelerometers, on the upper part for the training data and on the lower part for the swept sine data for which the neural network was not trained. It can be seen that in both cases the neural network gives a good correlation when using the trained neural network after 100 Epochs. When linearizing the neural network it could also be observed that the major modes of the linearized system are identical to the modes of the actual system but also additional modes are present which have no impact on the result. This proves that the neural network finds the unique solution to the problem after 100 Epochs but still has additional parameters for further improvement.

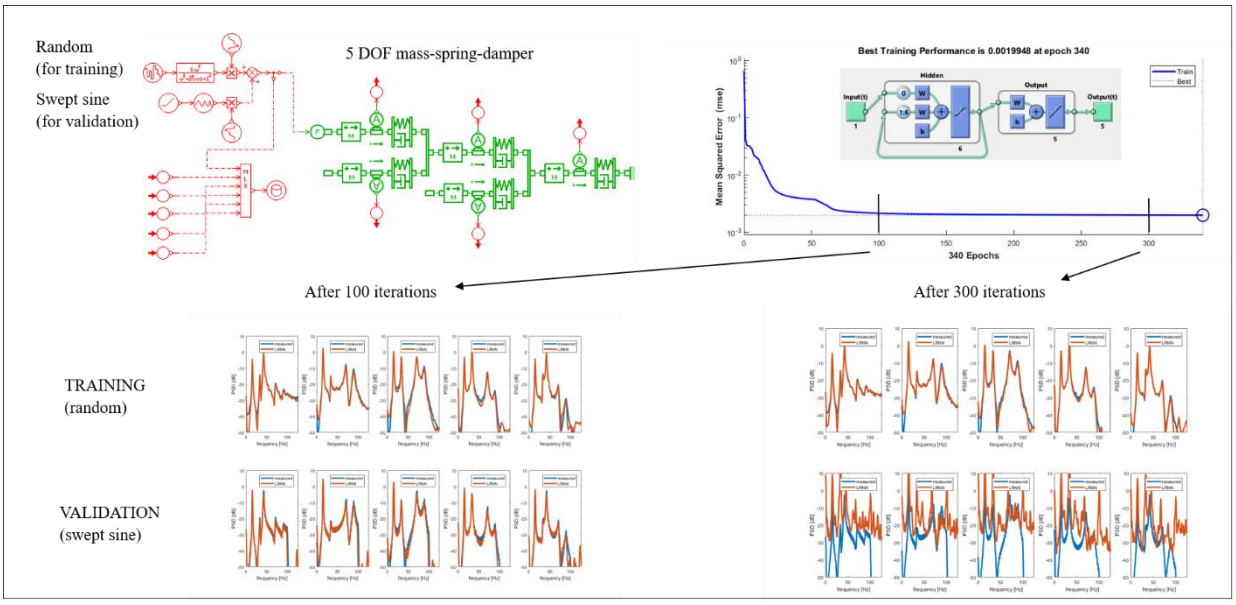


Figure 1: Identification of a 5 DOF mass-spring-damper system

In the bottom right the neural network that stabilizes after 300 Epochs is applied to the same validation data. In this case however it can be seen that the neural network works even better on the training data but at the cost of a very limited extrapolation capability of the network outside the domain of the training data. It also shows that the observability of the states in the training data will determine the success of the training.

The above example shows the importance of making the right choices, on the one hand related to the network architecture and size, its inputs and outputs and related to the time to stop the training. Further research is needed to give the user the right indications on the extrapolation capabilities of the neural network.

One of the major difficulties in the development cycle of a system is the identification of the right parameters for a systems model since those parameters are often a simplification of reality. In the R&D phase this is often done through dedicated test benches defined for the component to be characterized. With the upcoming technologies around Internet of Things (IoT), the identification of parameters based on operational data is a question that also can be addressed by the use of neural networks. The problem statement is addressed in figure 2 by a simplified example.

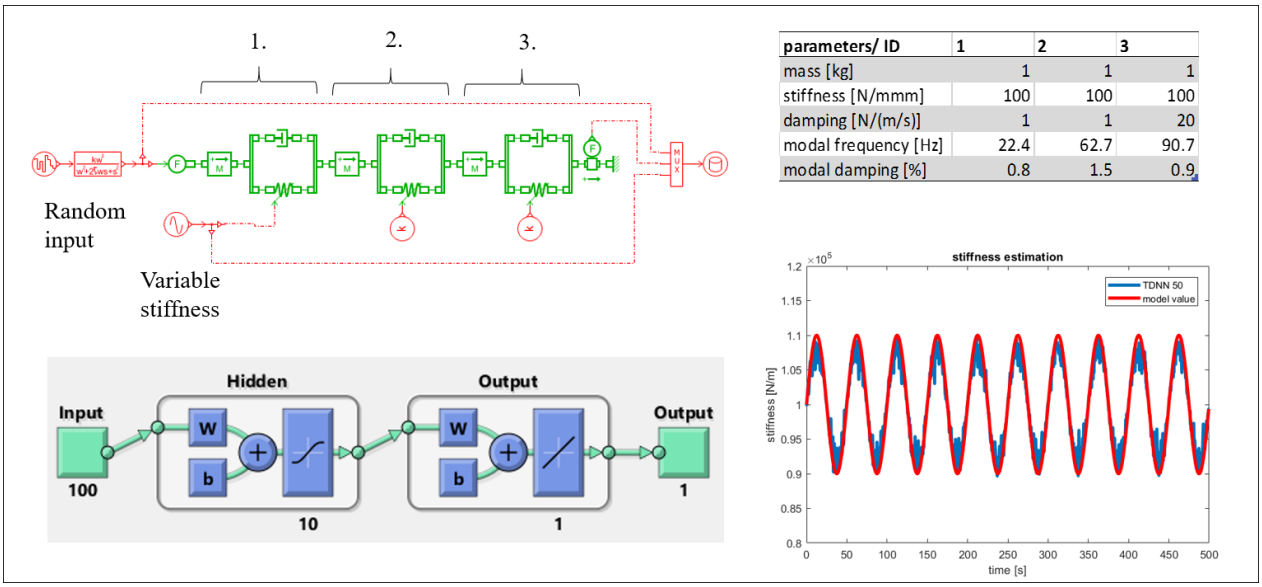


Figure 2: Parameter estimation using neural networks

In the upper part of figure 2, a 3 degree of freedom mass-spring damper system is indicated. The system is excited by random noise on the most left hand side mass in the frequency band between 0Hz and 100Hz. The resonance frequencies and damping of the nominal system are indicated on the right hand side of the picture. The stiffness of the most left hand side spring is varying in function of time following a sinusoidal shape at a frequency of 0.02Hz. The time data of the clamping force on the right hand side of the system is stored together with the varying stiffness. Both signals are used to train a neural network. Several network architectures have been verified but the most successful network has been a simple feedforward network with 10 neurons in the single hidden layer. The inputs are segmented into 2500 segments of 100 samples without overlap as can be seen in the representation of the neural network architecture in the bottom left of the picture. The bottom right of the picture gives in blue the result of the network prediction using the training data versus the original stiffness variation which can be considered as quite impressive for only a 10% peak to peak variation, considering the fact that as a user it will be very difficult to find a rule based algorithm that can give the same results. Obviously is speaks for itself that the currently trained network is not yet able to deal with excitations that are very different from the excitation used to train the network. To be able to secure this, a more reasonable representation of the actual inputs will be needed.

In the next sections different applications of neural networks in the field of mechatronic model based system development are brought forward and discussed. The application cases are projected on the mechatronic system development cycle, typically used for the automotive industry as shown in figure 3.

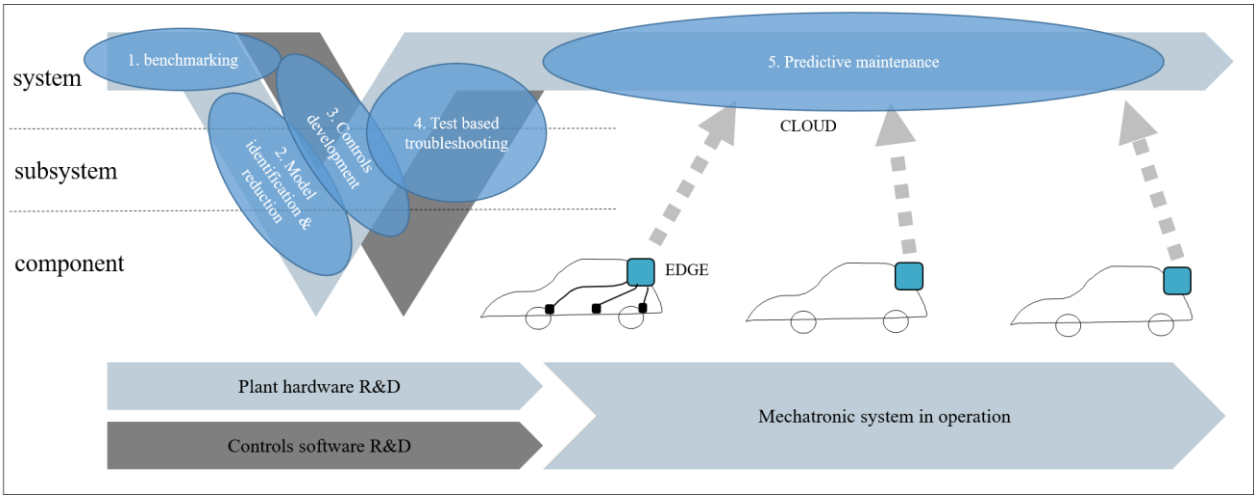


Figure 3: Selected application cases, projected on the automotive development cycle

4 Neural network application cases in model based engineering

Over the last decade, mechatronic systems have grown strongly in complexity and in many industries a dedicated model based systems development process has been put in place to assure the mechatronic system under development fulfils the functional and performance attributes for which the system is designed. The automotive industry is one of such industries that today is heavily changing their development processes to be able to have models driving the development of the cars. While the car evolved from a mechanical system to a mechatronic multi-physics system, the model development methodology became a complex mixture of 1D multi-physics models, 3D multi-physics models & test based analysis & characterization, to design the hardware as well as the controls of the hardware. The concept of the Digital Twin as backbone for the design, production and operation is becoming commonplace [14, 15]. In this paper the aid of artificial neural networks in supporting or enhancing the mechatronics system development will be demonstrated based on several examples out of the different phases of the development cycle of such a system.

4.1 Reverse engineering of controls during the benchmarking phase

During the benchmarking phase, many industries try to set targets for their subsystems based on a competitor analysis. Typically test data is acquired of the subsystems of a vehicle and this data is converted into a test based model that is assembled at system level to predict the system performance. Figure 4 shows this process in the case of fuel economy evaluation of a vehicle.

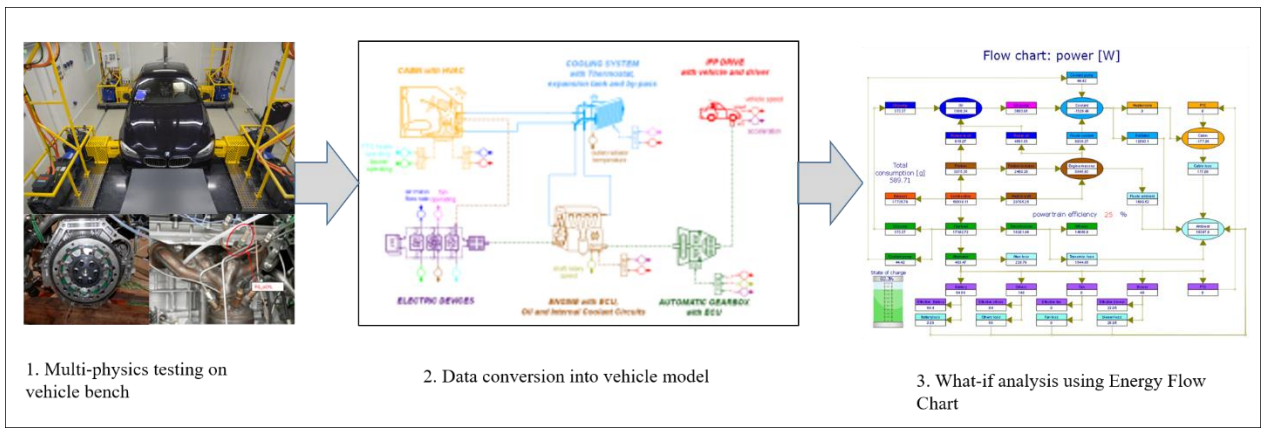


Figure 4: Process to analyze an existing vehicle for fuel economy performance

The resulting energy flow chart allows to analyze the consumption of each subsystem in the operational case that is measured. In case of a hybrid vehicle, there is however 1 component that often is most difficult to identify as a test model, while it is often having the highest potential improvement on the fuel economy performance: the supervisory control. This control determines when the different actuators need to come into action and is often not easily converted into a model since its operation is hidden in software. This leaves the physical model only to be operated in open loop, which limits the analysis that can be done with the model. A neural network can however be used to convert the existing measurements into a controller to close the loop for the model. The following steps can be performed to create such a controller:

1. Selection of all the operational conditions to train the network.
2. Selection of the different sub-controller inputs and outputs based on experience.
3. Selection of the network architecture and size for each sub-controller.
4. Training of each network and cross validation with an unknown scenario.
5. Export of the neural network coefficients to a system simulation environment & close the loop with the plant model.

In figure 5 some of the steps are visualized for a controls reverse engineering of a hybrid vehicle architecture including some typical results that can be obtained.

The figure shows the results of the sub-controller performance using the measured operational input data of 3 drive cycles based on a normal feedforward network and a recurrent neural net. It can be seen that in both cases the correlation is quite good, indicating that the temporal aspects are most likely not important for this sub-controller. When applying the complete controller to the full vehicle model, in both cases satisfactory results could be obtained.

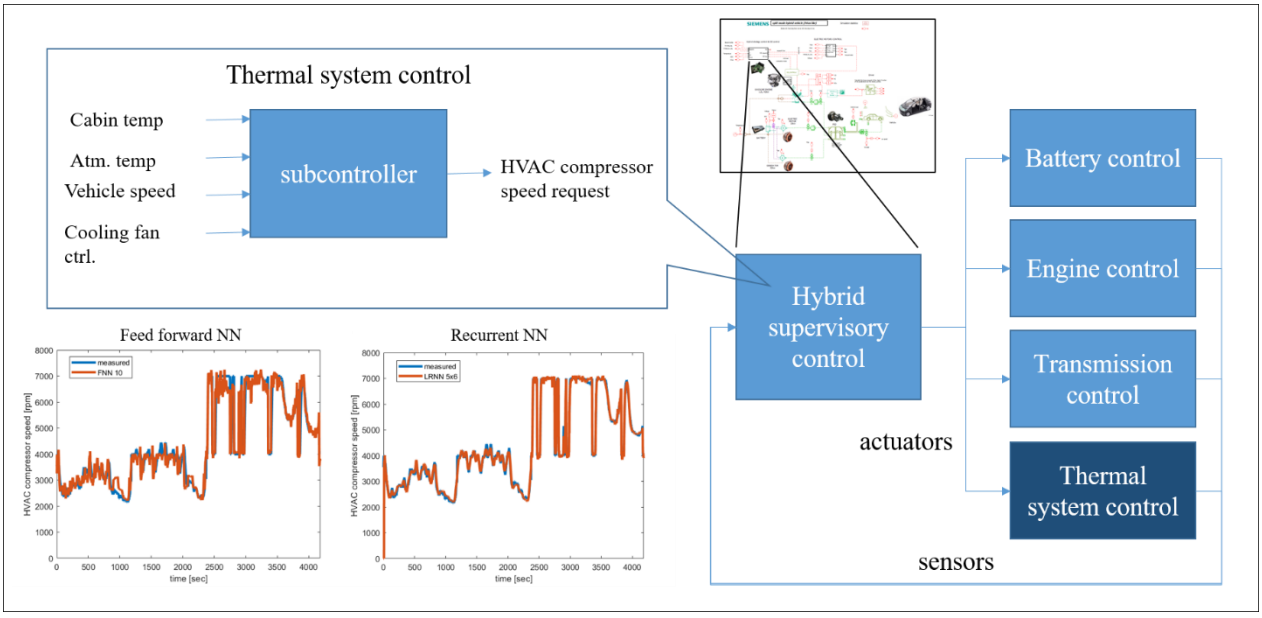


Figure 5: Results obtained by using a neural network to reverse-engineer a controls model for closed loop fuel economy simulations

4.2 Concept phase subsystem model reduction for faster system calculations

Figure 6 shows an application case for model reduction. A neural network can quite easily be implemented into a time domain based modelling environment since it is based on simple matrix calculations. In this figure the application of mount stiffness identification is shown. In a first step the mount stiffness is measured on a dedicated machine that allows to measure the static stiffness and the dynamic stiffness for

different amplitudes. To convert this into a time domain modelling environment is not straightforward and typically an equivalent modelling approach is used based on multiple mass-spring-damper elements.

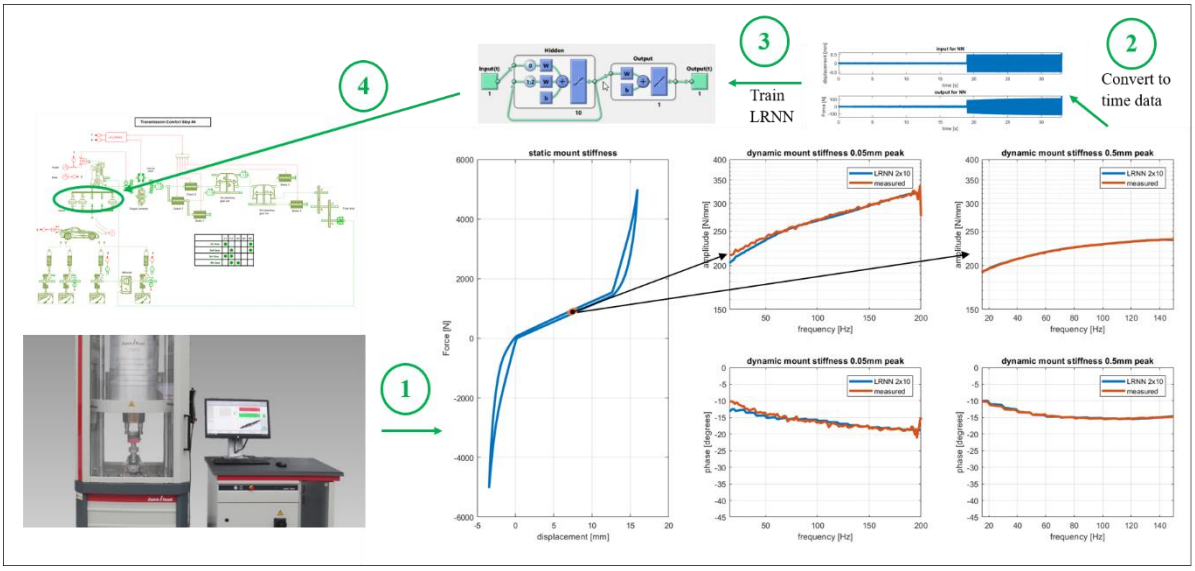


Figure 6: Mount stiffness identification for usage in a system model

With a neural network the dynamic stiffness curves in frequency domain can be converted into 1 set of training time data (upper right). In this example this time data is fed into a layered recurrent net with 10 hidden layer neurons and 2 delays. The result of the trained network is validated again in frequency domain (red curve for the 2 different excitation amplitudes) and gives excellent correlation with the measured data.

Afterwards this neural network can be combined with the static curve by placing both models in parallel to obtain the total stiffness and implemented in a vehicle model (upper left).

4.3 Model driven controls development during detailed design stage

The development of the control of mechatronic systems becomes more complex when multiple actuators and sensors are interfacing with a highly dynamic system, often not having the sensors available to develop an optimal control. In the automotive industry, controls have mostly been developed using rule based methods, first by directly writing code, later using a model based approach with tools like Simulink from Mathworks or the Embedded Software Designer from Siemens [16]. In the automotive industry, the complex balancing of multiple performances of the combustion engine such as emissions, fuel economy and acceleration performance have increased the complexity of the engine actuators. To develop the controls for such complex mechatronic systems, new methods are required. Optimal control such as Model Predictive Control (MPC) in combination with technologies to predict virtual controllable quantities using state estimation technologies in combination with Kalman filtering, are examples of such new technologies that start to find their entry in the automotive world. MPC and Kalman filtering based state estimation require however models that run fast while keeping a certain level of accuracy.

The simulation models for designing mechatronic systems are often created based on a combination of detailed 3D models and test data and have a high level of accuracy but have a too slow calculation time to be used in MPC or state estimation methodologies in real time on an ECU. To be able to convert such system models into the context of optimal control in combination with virtual sensing, neural networks can be the ideal methodology to develop a controls model directly from the detailed plant model to be controlled. Figure 7 explains the different steps in the process, showing the reduction of the detailed engine model to a neural network based model for as well the virtual sensor as the optimal controller. Initial results using the controls model in closed loop with the detailed plant model for tracking purposes indicate that the

performance, for scenarios that the neural network is not trained for, remains within good accuracy as long as the important states of the model are kept observable. Further results in this field will bring more clarity in how broad this technology can be used for the engine controls or other advanced vehicle controllers.

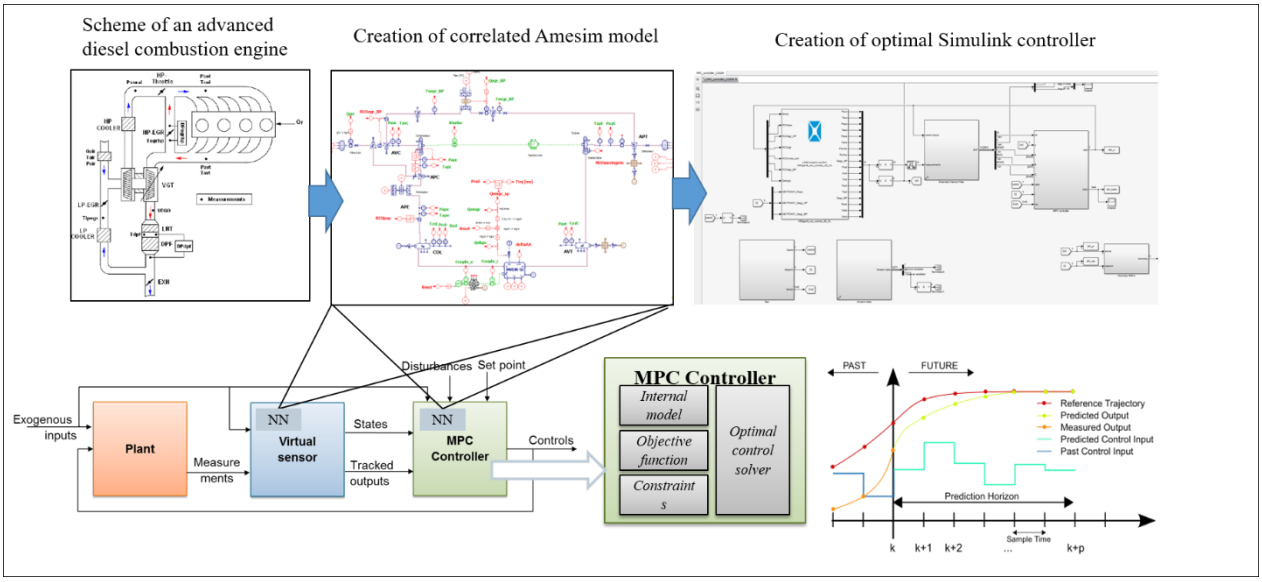


Figure 7: Different steps in the automatic generation of optimal controls models using a Simcenter Amesim plant model in combination with neural networks

4.4 Test based troubleshooting during prototype stage

Noise, Vibration and Harshness (NVH) is an important attribute of the vehicle and it is very difficult to frontload NVH issues into the simulation based development of the vehicle. Typically during the first prototype stage, the road induced and engine induced low frequency NVH issues become visible and NVH test engineers use methodologies like Transfer Path Analysis (TPA) or Acoustic Source Quantification (ASQ) to separate the noise problem into its contributing paths and afterwards focus on the major contributing paths with effective countermeasures [17].

The methodology of TPA is however a time consuming activity that can be separated in 2 major components:

- In the first step the paths need to be instrumented with sensors and operational data needs to be acquired on the full system.
- In a second step the active system (driveline and/or suspension) needs to be removed and the contributions from unity loads at each path to the interior noise need to be quantified using dedicated excitation techniques.

Even in this context of test based troubleshooting, neural networks have proven to be useful to direct the NVH engineer even faster to useful countermeasures. In this approach only the potentially contributing paths needs to be instrumented for which only operational conditions need to be acquired. During a first phase a layered recurrent neural network is trained based on the path sensors as inputs and the noise as output. In a second phase the trained neural network is fed with each sensor individually to be able to calculate the contributions of each path. Figure 8 shows the results of the neural network based approach versus the result of a classical TPA approach. It can be seen that in both cases the major paths come out identical while the neural network based approach can be realized in a fraction of the total time needed for the full TPA approach.

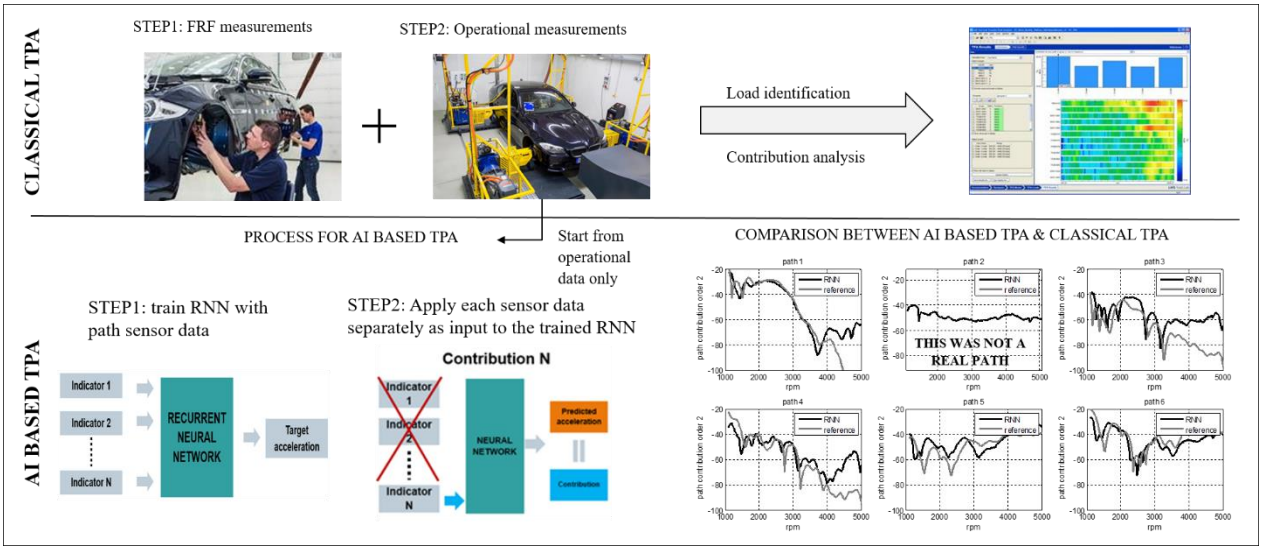


Figure 8: Process and results of using neural networks for Transfer Path Analysis

4.5 Predictive maintenance during operations phase

Predictive maintenance is the capability to predict an upcoming failure of the system based on operational sensors. Typically statistics based techniques were used in the past to predict such failure occurrence based on data from the past. Obviously it would be more interesting to not have to wait for failures to have occurred before being able to do predictive maintenance. In this context a simulation model can as well be used to convert the available operational sensors into variables that represent a failure. This methodology is typically called the "*digital twin in operation*". In this section 2 examples are given of how models can improve the predictive capabilities of a maintenance activity, both with the help of neural networks. More details can be found in [18, 19].

A first example concerns the failures of bearings in large gas-turbine based energy conversion (Figure 9).

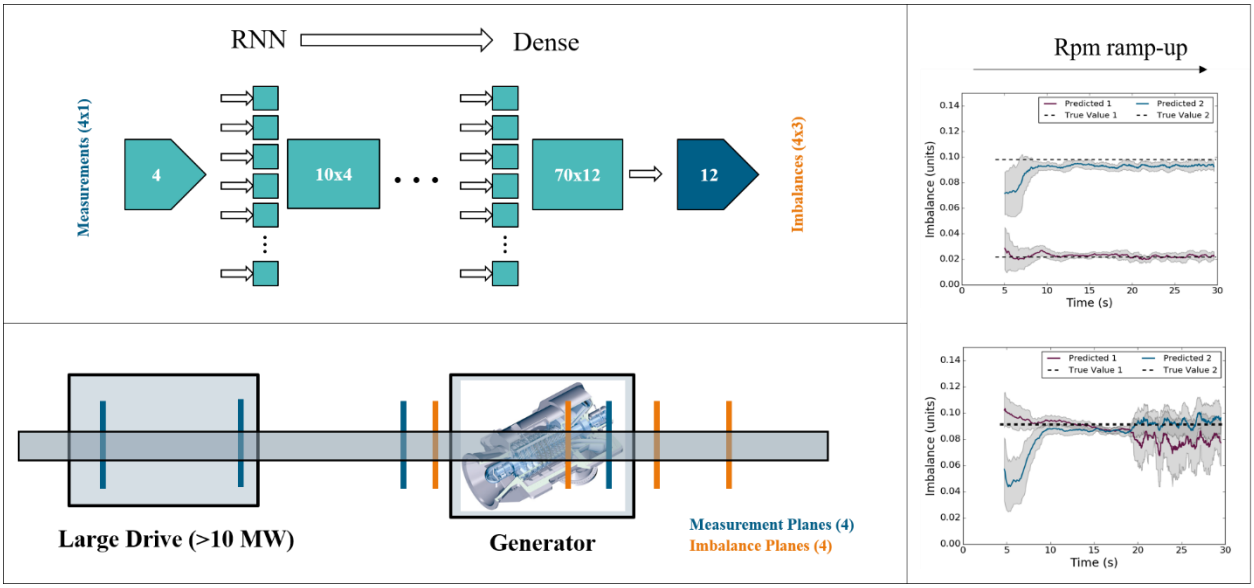


Figure 9: Identification of shaft unbalance of gas turbines using dynamic signals and a simple RNN

Such turbines have high speed shafts to transmit the torque and an increased unbalance on the shaft will cause the shaft bearings to age rapidly until they break down, which on their turn will cause expensive downtime that needs to be avoided. Such an unbalance cannot be measured directly but through accelerometers at the bearing positions the ideal observers can be measured in relation to the unbalance. Since the relationship between the time signals measured and the unbalance causing it, is too difficult to derive in a robust way, a recurrent neural network is used to identify the relationships.The neural network can potentially be trained using only simulation models and can afterwards be applied on real life signals in operation. Figure 9 shows the output of the induced unbalances in a model versus the prediction of the unbalance by the neural network. The results are currently only based on virtual test data, generated by a model.

A second example also concerns the failure of bearings but in this case mainly caused by built up wear or damage in the bearing of a wind-turbine. Off shore wind turbines are difficult to access and therefor the predictive maintenance is an important aspect to be able to limit the maintenance costs. In this application the bearing is modelled as a simple source of vibrations, caused by defects in the bearings. The vibrations can be measured by operational sensors in the real wind-turbine. To be able to improve the realism of the signals, different manipulations are done to the ideal time signals coming from the model:

- Addition of measurement noise
- Gaussian broadening & introduction of half-normal distribution to introduce the effect of slippage from the roller defect

In principle these time signals could be fed to an RNN to find the relationships between the signature of the signal and the status of the defect. To be able to help the neural network find the relationship more easily an additional pre-processing is done based on the knowledge of the recurrence of the vibration. The post-processing that is done to facilitate the neural network in finding the relationship are the following 2 steps:

- Synchronous averaging at expected defect periods
- Averaging to improve the signal to noise ratio

This will result in time invariant data that can be used to train a CNN rather than an RNN. The complete sensor processing to create the data for the neural network to be trained on is given in figure 10.

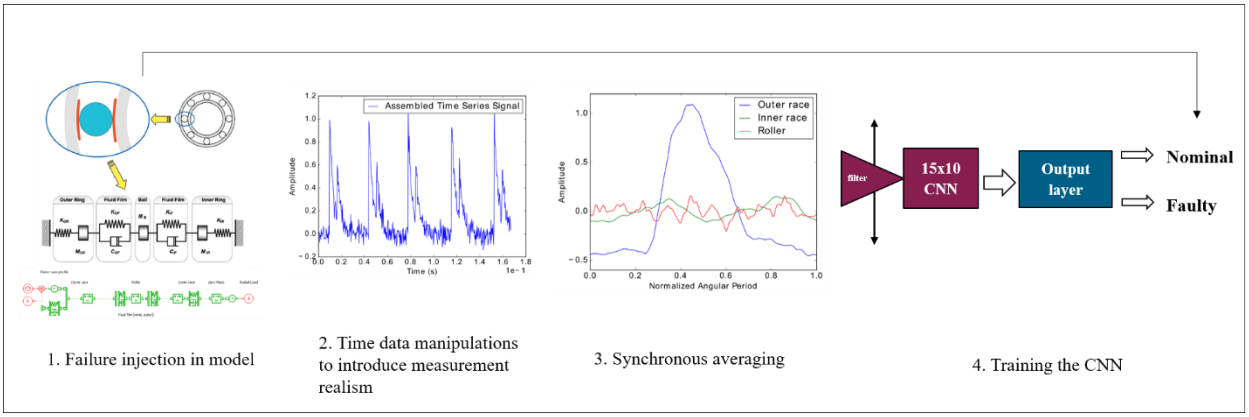


Figure 10: Post-processing from the raw measurement data to the neural network training data

The CNN is chosen as the neural network architecture for this learning since the proximity relationship of the samples in the time averaged signal are of importance. The CNN is used in a regression context where a value is given between fully nominal (0) or fully faulty (1). This allows the network to predict the time to failure if enough knowledge is available between the gravity of the defect and the risk to fail.

Figure 11 shows the result of the constant monitoring during 50 days until failure using a trained CNN with only simulation data for a bearing inner ring as well as outer ring failure. More information on the results and the other methods that are used can be found in reference [18, 19].

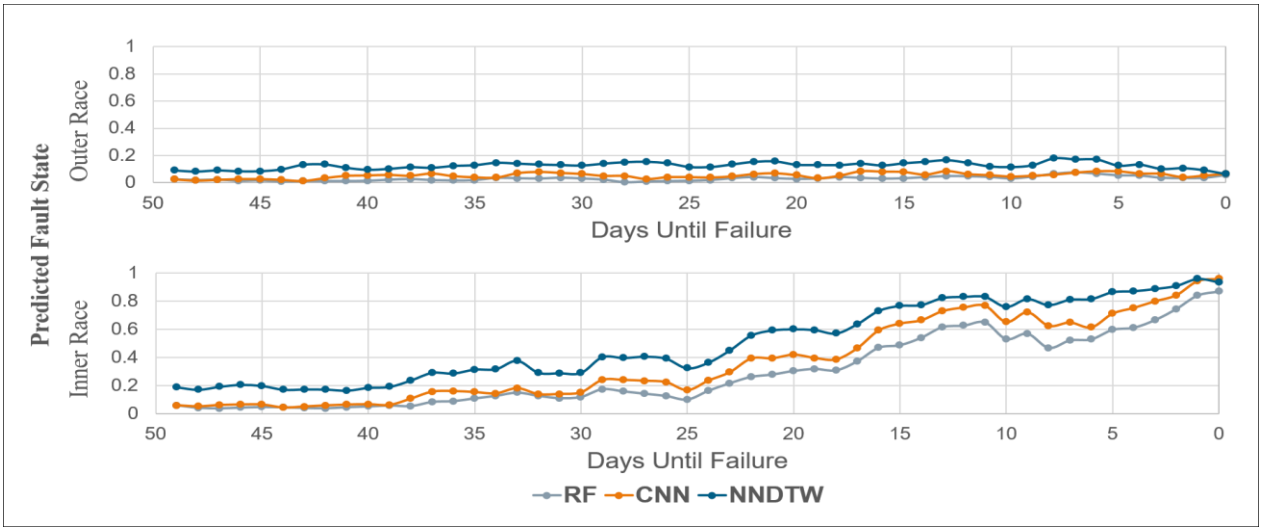


Figure 11: Simulation model based bearing failure prediction for a wind-turbine comparing neural networks with traditional machine learning methods

5 Conclusions

Neural networks are a core technology behind the increasing importance of Artificial Intelligence applied to design engineering, validation and verification. A significant progress has been made in terms of network architectures and training methodologies. Most of the applications have currently been found in the world of sensor interpretation (speech, vision). In general however, supervised learning has made from the neural network technology an ideal capability to also be used in the mechatronics system design. In this paper some successfully applied applications have been shown throughout the complete development cycle of a product. The authors anticipate that the amount and range of applications will grow at a rapid pace in the upcoming years and next to identification using supervised learning, also other applications of neural networks will find its place in the system development cycle such as the identification of the physical equations of a system based on operational data [20-22] or the automated design of counter measures based on system models or the continuous improvement of the system controls using reinforcement learning.

Acknowledgements

The authors would like to thank the RTD teams of the Siemens PLM Simulation and Test Solutions segment together with the Siemens PLM Engineering Services engineers, contributing to the presented work by sharing their application cases and applying the neural network technology to it. Some of application cases were executed as part of the RTD projects ITEA2-Reflexion and Eco-Powertrain, the support of the Flemish funding agency VLAIO hereto is gratefully acknowledged. The global research theme is also part of the Siemens Core Technology Simulation and Digital Twin.

References

[1] D. Hartmann, Y. Kevrekidis, M. Reiterer, L. White, K. Willcox (org.), *Integrating Machine Learning and Predictive Simulation: From Uncertainty Quantification to Digital Twins*, Institute for Mathematics and its Applications, Minneapolis (MN, USA), March 06 - 08, 2018, **https://www.ima.umn.edu/2017-2018/SW3.6-8.18**.

[2] M.I. Jordan, Ch.M. Bishop, *Neural Networks*. In Allen B. Tucker, *Computer Science Handbook, Second Edition (Section VII: Intelligent Systems)*. Boca Raton, Florida: Chapman & Hall/CRC Press, (2004). LLC. **ISBN 1-58488-360-X**.

[3] O. Bousquet, U. von Luxburg, G. Raetsch, (Eds.), *Advanced Lectures on Machine Learning*. Springer-Verlag, (2004). **ISBN 978-3540231226**.

[4] Ch. Kanzow, N. Yamashita, M. Fukushima, *Levenberg-Marquardt methods with strong local convergence properties for solving nonlinear equations with convex constraints*, JCAM, 172(2):375-97, Dec. 2004, doi:10.1016/j.cam.2004.02.013.

[5] B.M. Wilamowski, H. Yu, *Improved computation for Levenberg–Marquardt training*, IEEE Transactions on Neural Networks, Vol. 21, Issue 6 (2010).

[6] Y. LeCun, Y. Bengio, G. Hinton, *Deep Learning*, Nature 521.7553 (2015): 436.

[7] K. Funahashi, Y. Nakamura, *Approximation of dynamical systems by continuous time recurrent neural networks*. Neural networks 6.6 (1993): 801-806.

[8] A. Krizhevsky, I. Sutskever, G.E. Hinton, *Imagenet classification with deep convolutional neural networks*. In NIPS'12 *Proc. 25th* International Conference on Neural Information Processing Systems Vol. 1: 1097-1105.

[9] Y. LeCun, Y. Bengio, *Convolutional networks for images, speech, and time series*. The handbook of brain theory and neural networks. (1995)

[10] O. Janssens, V. Slavkovikj, B. Vervisch, K. Stockman, M. Loccufier, S. Verstockt, S. Van Hoecke, *Convolutional neural network based fault detection for rotating machinery*. Journal of Sound and Vibration, 331-345. (2016)

[11] W. Xie, A. Noble, A. Zisserman, *Layer Recurrent Neural Networks*, Under review for Proc. ICLR 2017, 5th International Conference on Learning Representations.

[12] S. Hochreiter, J. Schmidhuber, *Long short-term memory*, Neural computation 9.8 (1997): 1735-1780.

[13] J. Chung, et al., *Empirical evaluation of gated recurrent neural networks on sequence modeling*, arXiv preprint arXiv:1412.3555. (2014)

[14] H. Van der Auweraer, J. Anthonis, S. De Bruyne, J. Leuridan, *Virtual engineering at work: the challenges for designing mechatronic products*, *Engineering with Computers*, July 2013, Vol. 29 (3): 389-408, DOI 10.1007/s00366-012-0286-6.

[15] H. Van der Auweraer, S. Donders, D. Hartmann, W. Desmet, *Simulation and digital twin for mechatronic product design*, Proc. ISMA 2018, Leuven, Belgium, September 17-19, 2018.

[16] https://www.plm.automation.siemens.com/es/products/lms/imagine-lab/embedded-software-designer.shtml.

[17] H. Van der Auweraer, P. Mas, S. Dom, A. Vecchio, K. Janssens, P. Van de Ponseele, *Transfer Path Analysis in the critical path of vehicle refinement: the role of fast, hybrid and operational path analysis*, In *Proc. SAE Noise and Vibration Conf.*, May 14-17, 2007, paper no. 2007-01-2352.

[18] C. Sobie, C. Freitas, M. Nicolai, *Bearing Race Faults Classification using Simulation-generated Training Data and Feature Free Methods*, In *Proc. Asia Pacific Conference of the Prognostics and Health Management Society*, (2017).

[19] C. Sobie, C. Freitas, M. Nicolai, *Simulation-Driven Machine Learning: Bearing Fault Classification*, Submitted to Mechanical Systems and Signal Processing (2018).

[20] S.H. Rudy, S.L. Brunton, J.L. Proctor, J.N. Kutz, *Data-driven discovery of partial differential equations*, (2016) arXiv:1609.06401.

[21] V. Austel, S. Dash, O. Gunluk, L. Horesh, L. Liberti, G. Nannicini, B. Schieber, *Globally Optimal Symbolic Regression*, In *Proc. Interpretable ML Symposium, 31st Conference on Neural Information Processing Systems* (NIPS 2017), Long Beach, CA, USA, (2017), arXiv:1710.10720.

[22] R.R. Lama, L. Horesh, H. Avron, K.E. Willcox, *Should You Derive, Or Let the Data Drive? An Optimization Framework for Hybrid First-Principles Data-Driven Modeling*, (2017) arXiv:1711.04374v1.

Non-intrusive model-order reduction of geometrically nonlinear finite elements: enhancement with static augmentation

M. Karamooz Mahdiabadi [1], **D. J. Rixen** [1]
[1] TU Munich, Department of Mechanical Engineering, Chair of Applied Mechanics
Boltzmannstr. 15, D-85748 Garching, Germany
e-mail: **m.karamooz@tum.de**

Abstract
This paper improves the accuracy of the non-intrusively developed nonlinear reduced order models (NLROM) using two methods which are novel to the nonlinear Model Order Reduction (MOR) field. Non-intrusive MOR techniques have the advantage compared to intrusive methods that they can be implemented in any FE package which has nonlinear static solution capability, without having to handle closed form nonlinear FE formulation. In the first method, which is called Mode Acceleration Correction, quasi-static contribution of truncated modes due to forced excitation is added to the NLROM response. In the second method, known as Modal Truncation Augmentation, Ritz vectors, which compensate the mode truncation inaccuracies on the spatial distribution of the applied loads, are used to determine modal truncation (MT) vectors. The MT vectors are then appended to the linear basis for input generation to accurately construct the NLROM. The proposed approaches are examined on a numerical example and the results show an improvement compared to the classical non-intrusive method.
***Keywods**: Modal Truncation Augmentation, Residual Flexibility, Model Reduction, Geometric Nonlinearity, Mode Acceleration*

1 Introduction

Model order reduction (MOR) has become an important topic in many industrial applications which deal with nonlinear finite element (FE) models. This is due to the fact that prediction of the structural response of large nonlinear FEs to static and dynamic loads is extremely time consuming. Therefore, the full order FE model in MOR techniques are transformed to a reduced number of generalized coordinates, to increase the computational efficiency. The number of reduced coordinates is generally much smaller than the number of the full-order FE model. Accordingly, the structural response to different load cases (acoustic, thermal, etc.) can be computed much faster using the reduced order model (ROM).

There are generally two different approaches in the literature to developing the nonlinear reduced order model (NLROM) from large nonlinear finite element models: direct and indirect methods. Direct (or intrusive) methods [2, 17, 18] are usually based on the Galerkin projection method which transforms the full physical coordinates to a reduced set of generalized (or modal) coordinates. To perform MOR with direct methods, it is necessary to deal with the full-order nonlinear finite element formulation in closed form. In other words, NLROM is developed by direct projection of the nonlinear internal force by a chosen reduction basis matrix. This limitation

does not allow an engineer to reduce the nonlinear FE models which are constructed in FE packages provided by third parties who don't share their nonlinear element formulations (e.g. commercial software). Alternatively, an NLROM can be developed using an indirect (or non-intrusive) approach [8, 11, 14], which need no directly access the full-order nonlinear element formulation. The linear part of the NLROM is reduced using a proper projection basis which usually consists of a truncated number of linear normal modes of the structure. The reduced nonlinear internal force (or nonlinear stiffness vector) is written as a summation of quadratic and cubic multiplication of generalized coordinates. Each term is multiplied by its corresponding unknown coefficient. A series of nonlinear static solutions are then performed to identify the unknown Nonlinear Stiffness Coefficients (NSCs) of the quadratic and cubic terms. Consequently, the only requirement for developing an NLROM from the FE package, is to be capable of performing nonlinear static analysis.

In order to identify the NSCs, appropriate inputs have to be assigned to the FE packages, which also capture nonlinear interactions between the nonlinear modes. E.g., for beam-like structures (i.e. beams, shells and plates) the input has to trigger the coupling between bending and membrane (in-plane) displacement (also called stretching effects). Two approaches have been considered in the literature to determine the unknown parameters. In the first approach which is introduced in [11] and further developed in [8], the procedure of fitting the NLROM to the full-order FE model is conducted by prescribing series of selected static loads to the FE package to be solved for the corresponding displacements. This method is here referred to as *Applied Force (AF) or Implicit Condensation (IC) Method*). In the second class of approaches which is outlined in [14], a set of pre-processed displacements are statically prescribed to the FE package to obtain the corresponding reaction forces to identify the NSCs (which is referred to as the *Enforced Displacement (ED) Method*).

When using the ED Method for coefficient identification, the bending and in-plane modes have to be explicitly imposed to achieve a reasonably accurate response for transverse displacements. Whereas, in the AF method, the prescribed forces which are generated using only the bending modes, suffice for accurate response prediction of transverse displacements [13].

For identification of the NSCs in a non-intrusive approach, linear modes are often used to generate the inputs to be prescribed to the FE package. However, we know from linear structural dynamics that taking a few modes in the modal response of a linear system for linear model reduction without considering the static deflection of the truncated modes due to spatial distribution of external loads will cause inaccuracies in the system. The Mode Acceleration (MA) [1, 5, 16] and Modal Truncation Augmentation (MTA) [6, 5, 16] methods have been widely studied to best approximate the effect of modal truncation on the spatial distribution of applied loads in the linear systems.

This paper proposes two ways to extend the MA and MTA methods for nonlinear response prediction. In the first approach, the contribution of the truncated modes are assumed linear and quasi-statically affect the response of the system. Consequently, theses quasi-static deflections due to applied load are computed from the linear flexibility matrix of the FE model and added to the dynamic response of the NLROM which is developed from the AF method. In the second approach, Modal Truncation (MT) vectors are first computes using the Reileygh-Ritz method. Afterwards, these vectors are appended to the reduced mode basis and the stiffness coefficient identification of the AF method is performed with the new reduction basis.

2 Nonlinear Model Order Reduction

The governing Equations of Motion (EoM) for a discretized finite element problem with large deflections and linear elastic material can be written as [3]

$$\boldsymbol{M}\ddot{\boldsymbol{u}}(t) + \boldsymbol{C}\dot{\boldsymbol{u}}(t) + \boldsymbol{K}\boldsymbol{u}(t) + \boldsymbol{f_{nl}}(\boldsymbol{u}(t)) = \boldsymbol{f}(t) \tag{1}$$

Where $\boldsymbol{M}$ ($n \times n$, where n is the number of full-order DOFs), $\boldsymbol{C}$ ($n \times n$), $\boldsymbol{K}$ ($n \times n$), and $\boldsymbol{f_{nl}}$ ($n \times 1$) are the mass, damping and stiffness matrices and nonlinear internal force vector, respectively; $\boldsymbol{u}(t)$ ($n \times 1$) is the physical displacement vector and the overdots denote the derivations with respect to time. The vector $\boldsymbol{f}(t)$ ($n \times 1$) denotes the applied loads on the structure. For the sake of simplicity, the dependency of the parameters in Equation (Eq.) (1) on time, t, is omitted in the remainder of this paper, unless it is required.

To obtain a reduced order model for Eq. (1), a transformation matrix $\boldsymbol{T}$ is constructed, which projects the full-order physical DOFs, n, on to a reduced number of generalized coordinates, m ($m << n$):

$$\boldsymbol{u} = \boldsymbol{T}\,\boldsymbol{q} \tag{2}$$

Here, $\boldsymbol{q}$ is the reduced generalized coordinate vector, and $\boldsymbol{T}$ is the transformation matrix, projecting the physical DOFs on to a set of reduced generalized coordinate of the system. By substituting Eq. (2) in (1) and applying the Galerkin projection method, the EoM for the NLROM is obtained:

$$\hat{\boldsymbol{M}}\ddot{\boldsymbol{q}} + \hat{\boldsymbol{C}}\dot{\boldsymbol{q}} + \hat{\boldsymbol{K}}\boldsymbol{q} + \hat{\boldsymbol{f}}_{\boldsymbol{nl}}(\boldsymbol{q}) = \hat{\boldsymbol{f}} \tag{3}$$

with

$$\hat{\boldsymbol{M}} = \boldsymbol{T}^T\boldsymbol{M}\boldsymbol{T} \tag{4}$$

$$\hat{\boldsymbol{C}} = \boldsymbol{T}^T\boldsymbol{C}\boldsymbol{T} \tag{5}$$

$$\hat{\boldsymbol{K}} = \boldsymbol{T}^T\boldsymbol{K}\boldsymbol{T} \tag{6}$$

$$\hat{\boldsymbol{f}}_{\boldsymbol{nl}}(\boldsymbol{q}) = \boldsymbol{T}^T\boldsymbol{f}_{\boldsymbol{nl}}(\boldsymbol{T}\boldsymbol{q}) \tag{7}$$

$$\hat{\boldsymbol{f}} = \boldsymbol{T}^T\boldsymbol{f} \tag{8}$$

If the relationship between the strain and displacement for a FE problem is quadratic, the nonlinear internal force for the reduced (and full-order) model can be written in a polynomial form with quadratic and cubic terms [3, 15]. Therefore, the i^{th} element of the nonlinear reduced internal force vector is written as

$$\hat{f}_{nl_i} = \hat{K}^{(2)}_{ijl}\,q_j q_l + \hat{K}^{(3)}_{ijlp}\,q_j q_l q_p \tag{9}$$

where, $\hat{K}^{(2)}_{ijl}$ and $\hat{K}^{(3)}_{ijlp}$ are the components of the third-and-fourth-order stiffness tensors, respectively. One way to compute the Nonlinear Stiffness Coefficients (NSCs) of Eq. (9) is to project directly the full-order nonlinear internal force on to the reduced space. However, the challenge here is that the full-order nonlinear internal force is not accessible in many commercial FE packages. Alternatively, one can estimate the unknown tensors in an indirect way, namely, based on assignment of inputs to the FE package and fitting the NLROM to the static solution from that [13]. The *Implicit Condensation* (IC) method [8] is an indirect nonlinear coefficient estimation method which is based on application of a set of static forces as input to the FE package. The IC method has the advantage that it allows for the coupling between the generalized coordinates in nonlinear form (e.g. stretching effects) by just applying the transverse modes as input forces. As a result, this paper investigates the enhancement of the IC method, which will be explained in section (2.1).

The transformation matrix for the IC method contains a truncated number of (transverse) linear modes. However, the problem with taking a truncated number of linear modes as projection basis is that it fails to accurately approximate the spatial distribution of the applied loads. Accordingly, in this paper we propose two augmentation methods to compensate for the effect of modal truncation on applied loads (see sections (3.2) and (3.3)).

2.1 Applied Load or Implicit Condensation

The applied load method was first developed by McEwan et al. [11] and later extended by Hollcamp and Gordon [8] to improve the approximation of in-plane motions. This method attempts to identify the unknown NSCs based on prescription of selected static forces to the nonlinear FE-EoM to solve for the corresponding displacements. The procedure can be employed in any FE package which is capable of performing nonlinear static FE analysis. Since the load in the applied load method is enforced statically, the velocity and acceleration in Eq. (3) are equal to zero, giving

$$\hat{\boldsymbol{K}}\boldsymbol{q} + \hat{\boldsymbol{f}}_{\boldsymbol{nl}}(\boldsymbol{q}) = \hat{\boldsymbol{f}} \tag{10}$$

or

$$\hat{K}_{ij}q_j + \hat{K}^{(2)}_{ijl}q_jq_l + \hat{K}^{(3)}_{ijlp}q_jq_lq_p = \hat{f}_i \tag{11}$$

for the i^{th} component of Eq. (10). By applying a set of static loads to solve Eq. (10) for their corresponding displacements, the NSCs can be obtained using any regression analysis method. One of the most critical points in all non-intrusive MOR methods is the appropriate generation of the prescribing inputs which can trigger all the essential nonlinear properties in the full-order FE model. This will be studied in section (3). Let us assume that the static loads are formed from a combination of weighted basis vectors, $\boldsymbol{V}_i$, which results in fulfillment of the properties that are discussed in section (3) for the applied loads, namely:

$$\boldsymbol{f} = s_1\boldsymbol{V}_1 + s_2\boldsymbol{V}_2 + ... + s_m\boldsymbol{V}_m = \sum_{i=1}^{m} s_i\boldsymbol{V}_i \tag{12}$$

where, s_i are the scalar weighting factors corresponding to their vectors, $\boldsymbol{V}_i$. The most common choice for the basis vectors, $\boldsymbol{V}_i$, is a truncated number of eigenmodes of the linearized Eq. (1), as used by McEwan et al. [11] in the original IC method. This choice is based on the idea of the Mode Displacement method (see section (3.1)). Additionally, for the case that the basis vectors are the truncated linear (transverse) eigenmodes, Gordon and Hollcamp [7] have proposed a physically meaningful value for the scaling factor. In other words, they have defined a scaling factor for each mode as the force which is required to linearly obtain the maximum desired displacement as

$$s_i = \frac{W_{i_{\max}}}{V_{i_{\max}}}\omega_i^2 \tag{13}$$

where, $W_{i_{\max}}$, $V_{i_{\max}}$, and ω_i denote the maximum desired displacement for the linearized EoM, the maximum (transnational) eigenmode component and the eigenfrequency, respectively, all for the i^{th} mode. The eigenmodes, $V_{i_{\max}}$, are usually normalized with respect to the mass matrix. The maximum desired displacement is usually chosen in the order of the thickness of the structure. The computed scaling factors from Eq. (13) are used in both positive and negative signs to generate the prescribing forces.

A certain number of such static loads are generated and assigned to the FE code to obtain the corresponding displacements. These forces are afterwards projected onto the modal domain to be substituted in Eq. (11).

$$\hat{\boldsymbol{f}} = \boldsymbol{T}^T\boldsymbol{f} \tag{14}$$

Likewise, the displacement is projected onto the reduced set of generalized coordinates by solving

$$\boldsymbol{u} = \boldsymbol{T}\boldsymbol{q} \tag{15}$$

for $\boldsymbol{q}$. The linear stiffness of the FE model is usually available in FE packages. Therefore, the reduced linear stiffness matrix in (11) can be calculated directly from Eq. (6) without performing a regression procedure. The number of NSCs which dominantly contribute in the nonlinear behavior of a structure can be drastically reduced depending on the type of the model, nonlinearity, loading condition, etc. For instance, if a structure is symmetric with respect to transverse modes, initially flat and geometric nonlinear, one can neglect all quadratic terms as well as those cubic terms which contain the multiplication of more than two generalized coordinates, as shown by McEwan et al. [12]. In other words, the NSCs consisting of more than three unequal indices are zero:

$$\hat{K}^{(3)}_{ijlp} = 0 \quad for \quad i \neq j \neq l \neq p \tag{16}$$

Consequently, in this case, the nonlinear restoring force in Eq. (10) for the r^{th} EoM is reduced to

$$f_r = \hat{K}^{(3)}_{ijjp} {q_j}^2 q_p + \hat{K}^{(3)}_{ippj} {q_p}^2 q_i + \hat{K}^{(3)}_{ijjj} {q_j}^3 + \hat{K}^{(3)}_{ippp} {q_p}^3 \tag{17}$$

However, it has been shown in the literature (e.g. see [9, 7]) that for many structures such as cantilevered or curved FE models, the truncated form of the nonlinear restoring force (Eq. 17) no longer applies. In this paper, the full form of the quadratic and cubic terms with the presence of all NSCs is investigated, for the sake of generality.

For the case of a geometrical nonlinear FE problem, it is sufficient to generate the required loads for IC using permutations of one, two and three basis vectors. One usual possibility to choose the basis vectors for the static loads is to set them equal to the columns of the reduction basis matrix, $\boldsymbol{T}$ times the stiffness matrix as

$$\boldsymbol{f} = \boldsymbol{K}(\boldsymbol{T}_i s_i + \boldsymbol{T}_j s_j + \boldsymbol{T}_k s_k) \qquad i, j, k = 0, 1, 2, ..., m \tag{18}$$

In this case, the scaling factor to obtain the required force for the linear maximum desired displacement defined by [7] in Eq. (13) is

$$s_i = \frac{W_{i_{\max}}}{T_{i_{\max}}} \tag{19}$$

Finally, recalling that each scaling factor is used with both signs, the total number of required prescribing forces [7] is given by

$$2m + 4_m C_2 + 8_m C_2 \tag{20}$$

where

$${}_m C_r = \frac{m!}{(m-r)!\, r!} \tag{21}$$

Once all the prescribed loads and their corresponding displacements are calculated from the nonlinear static analysis, the NCSs are computed from a regression analysis procedure, e.g. as explained in [11]. The next section discusses the possible basis vectors for the projection basis, $\boldsymbol{T}$.

3 Basis Selection Methods

The accuracy of the developed NLROM by IC method, strongly depends on the "correct" selection of the basis vectors in Eq. (18). Generally, the prescribing load sets have to be constructed based on the following properties:

- They have to be large enough to trigger the essential nonlinear effects and the coupling between the modes.

- They have to contain the required modes corresponding to the desired frequency range of excitation as well as the modes which have strong modal interaction between them.
- They have to consider the spatial distribution of the external loads in operational condition
- They have to be easy to compute.

The original IC method selects the load bases using the idea of Mode Displacement (MD) method for linear FE models. The projection in MD method contains a truncated number of linear modes based on mode superposition [4, 1, 19]. When using the MD method, the applied loads on the system will also be projected by the reduction basis which can then change the spatial shape of these loads. This is because it is usual to choose the truncated modes that only contain the excitation frequencies of the applied loads. However, these modes do not necessarily represent the spatial shape of the applied loads accurately. To solve this problem for the linear elastic FE model, Mode Acceleration (MA) [1, 5, 16] and Modal Truncation Augmentation (MTA) methods [6, 5, 16] have been developed in the literature.
In this paper, we aim to extend these methods to the nonlinear FE structures. First, we give an overview of the classical MD method, in order to further explain why this method can cause inaccuracies in the dynamic response of systems.

3.1 Mode Displacement

Let us define the governing EoM for the linearized finite element Eq. (1) as

$$\boldsymbol{M}\ddot{\boldsymbol{u}}(t) + \boldsymbol{C}\dot{\boldsymbol{u}}(t) + \boldsymbol{K}\boldsymbol{u}(t) = \boldsymbol{f}(t) = \boldsymbol{F}_0\,\boldsymbol{g}(t) \tag{22}$$

where, the applied loads, $\boldsymbol{f}(t)$, are decomposed into a constant matrix, $\boldsymbol{F}_0$ ($n \times k$, where k is the number of spatial distribution vectors), which represents its spatial distribution, and a time varying vector, $\boldsymbol{g}(t)$ ($k \times 1$).

According to the MD method, to reduce the dimension of the system, the displacement of the system is approximated by a superposition of a truncated number of modes multiplied by their corresponding coordinates:

$$\boldsymbol{u} = \boldsymbol{\Phi}\boldsymbol{q} = \sum_{i=1}^{m} q_i \boldsymbol{\varphi}_i \tag{23}$$

here, $\boldsymbol{\Phi}$ ($n \times k$, where k is the number of kept modes in the superposition) is the reduction basis matrix containing the kept eigenmodes of the system in its columns and $\boldsymbol{q}$ is the vector of the reduced number of modal coordinates. The i^{th} modal coordinate and eigenmodes of the system are denoted by q_i and $\boldsymbol{\varphi}_i$, respectively. The eigenvalue problem for obtaining the i^{th} eigenmode of Eq. (22) is given as

$$(\boldsymbol{K} - \omega_i^2 \boldsymbol{M})\boldsymbol{\varphi}_i = 0 \tag{24}$$

where, the i^{th} eigenfrequency of the system is denoted by ω_i^2. The eigenmodes of the system are usually mass normalized such that:

$$\begin{aligned} &\boldsymbol{\Phi}^T \boldsymbol{M} \boldsymbol{\Phi} = \boldsymbol{I} \\ &\boldsymbol{\Phi}^T \boldsymbol{K} \boldsymbol{\Phi} = \boldsymbol{\Omega} = \text{Diag}(\omega_1^2, \omega_2^2, ..., \omega_k^2) \end{aligned} \tag{25}$$

the matrix $\boldsymbol{\Omega}$ here is a diagonal matrix that contains the square of the eigenfrequencies of the system in its diagonals, and $\boldsymbol{I}$ is the identity matrix. The set of k uncoupled equations of motion is obtained by substituting eq. (23) in (22) and premultiplying (22) by $\boldsymbol{\Phi}^T$:

$$\ddot{\boldsymbol{q}} + \boldsymbol{\Omega q} = \hat{\boldsymbol{F}}_{\mathbf{0}} \boldsymbol{g} \tag{26}$$

where

$$\hat{\boldsymbol{F}}_{\mathbf{0}} = \boldsymbol{\Phi}^T \boldsymbol{F}_{\mathbf{0}} \tag{27}$$

McEwan et al. [11] took the MD projection basis also for the nonlinear FE-EoM, namely

$$\boldsymbol{T} = \begin{bmatrix} \boldsymbol{\varphi}_1 & \boldsymbol{\varphi}_2 & \dots & \boldsymbol{\varphi}_m \end{bmatrix} \tag{28}$$

therefore, the NLROM can then be written in the following form

$$\ddot{\boldsymbol{q}} + \boldsymbol{\Omega q} + \hat{\boldsymbol{f}}_{\boldsymbol{nl}}(\boldsymbol{q}) = \hat{\boldsymbol{F}}_{\mathbf{0}} \boldsymbol{g} \tag{29}$$

The prescribing static forces are computed from Eq. (18) to be further employed in the IC method (section (2.1)) and identify the NSCs. After development of the (nonlinear) ROM, the velocity and acceleration vector of the physical DOFs can be obtained from the corresponding ones in the ROM

$$\dot{\boldsymbol{u}} = \boldsymbol{\Phi} \dot{\boldsymbol{q}} = \sum_{i=1}^{k} \dot{q}_i \boldsymbol{\varphi}_i \tag{30}$$

$$\ddot{\boldsymbol{u}} = \boldsymbol{\Phi} \ddot{\boldsymbol{q}} = \sum_{i=1}^{k} \ddot{q}_i \boldsymbol{\varphi}_i \tag{31}$$

In the procedure for choosing the number of kept modes in the reduction basis, it is usually the case that the eigenvectors are kept such that their corresponding eigenfrequencies cover the excitation frequencies imposed by the time varying part of the applied load, $\boldsymbol{g}(t)$, with a predefined margin. However, choosing the modes in this way can cause inaccuracies due to the poor approximation of the spatial distribution of the applied loads by the chosen reduction basis. To quantify the error of the spatial distribution approximation caused by truncation of the eigenmodes in the reduction basis, let us define the residual spatial distribution matrix, $\boldsymbol{F}_r$, which is the portion of the full spatial distribution matrix not represented by the superposition of the kept modes. The residual spatial distribution matrix is obtained by subtracting the spatial distribution represented by the truncated eigenmodes from the full spatial distribution matrix, $\boldsymbol{F}_0$:

$$\boldsymbol{F_r} = \boldsymbol{F_0} - \boldsymbol{F_t} \tag{32}$$

where the spatial distribution represented by the truncated eigenmodes is given by

$$\boldsymbol{F}_t = \boldsymbol{M \Phi \Phi^T F_0} \tag{33}$$

The residual spatial distribution, $\boldsymbol{F}_r$, is in fact the part of the full spatial distribution which is lost due to the use of its truncated mode representation. Accordingly, the more the number of modes in the reduction basis are taken, the less $\boldsymbol{F}_r$ becomes. However, choosing too many modes in the reduction basis which can reasonably reduce $\boldsymbol{F}_r$, may lose the advantage of computational efficiency achieved by the MD method. To reduce the loss of spatial distribution of the applied load and simultaneously take the advantage of dealing with just a few sets of equation of motions, Mode Acceleration [1, 5, 16] and Modal Truncation Augmentation [6, 5, 16] methods have been developed. These will be explained next.

3.2 Mode Acceleration Correction

The mode acceleration method [1, 5, 16] is proposed to minimize the error of spatial distribution of the applied loads induced by modal representation of them in linear FE analysis. The idea of the MA method is based on the definition that the kept modes in the MD method span all the frequency content which is imposed by the applied loads. Therefore, the response of the system due to the truncated modes is quasi-static and contains no dynamics. In other words, the truncated modes do not make any appreciable contribution to the velocity and acceleration of the system and the acceleration, for example, can be computed using Eq. (31). The truncated modes affect only the displacement of the system, and therefore, the only parameter which has to be modified is the displacement.

To compute the modified displacement from the MA method, let us consider the governing equations of motion (22) and rewrite it in the following form:

$$\boldsymbol{K}\boldsymbol{u} = \boldsymbol{f} - \boldsymbol{M}\ddot{\boldsymbol{u}} \tag{34}$$

since by definition the truncated modes quasi-statically affect the response of the system, the acceleration of Eq. (34) can be directly substituted by Eq. (31), and Eq. (34) is solved for the displacement:

$$\boldsymbol{u} = \boldsymbol{K}^{(-1)}\boldsymbol{f} - \boldsymbol{K}^{(-1)}\boldsymbol{M}\sum_{i=1}^{k}\ddot{q}_i\boldsymbol{\varphi}_i \tag{35}$$

From Eq. (26) the acceleration for the i^{th} generalized coordinate is written as

$$\ddot{q}_i = {\boldsymbol{\varphi}_i}^T\boldsymbol{f} - {\omega_i}^2 q_i \tag{36}$$

Substituting eq. (36) in (35) and rearranging (35) gives

$$\boldsymbol{u} = \boldsymbol{K}^{(-1)}\boldsymbol{f} - \boldsymbol{K}^{(-1)}\boldsymbol{M}\sum_{i=1}^{k}({\boldsymbol{\varphi}_i}^T\boldsymbol{f} - {\omega_i}^2 q_i)\boldsymbol{\varphi}_i \tag{37}$$

Finally, from eq. (37), the displacement achieved by the MA method is derived:

$$\boldsymbol{u} = \sum_{i=1}^{k} q_i\boldsymbol{\varphi}_i + (\boldsymbol{K}^{(-1)} - \sum_{i=1}^{k}\frac{\boldsymbol{\varphi}_i\boldsymbol{\varphi}_i^T}{\omega_i^2})\boldsymbol{f} \tag{38}$$

If a structure contains rigid body modes, the linear stiffness matrix is singular and the generalized inverse methods have to be used. In this paper, the generalized coordinates, $\boldsymbol{q}$, are first computed from the NLROM Eq. (29) and substituted in Eq. (38) instead of (23) to correct, in a post-processing step, the linear quasi-static effect of the truncated modes on the external loads.

3.3 Modal Truncation Augmentation

The method of Modal Truncation augmentation [6, 5, 16] compensates for the inaccuracies in the modal representation of the spatial distribution of the applied loads by appending some correction vectors to the reduction basis. The MTA method employs the Rayleigh-Ritz method to compute the modal truncation (MT) vectors, which has the advantage of being mathematically consistent. First, Ritz vectors are obtained as a static deformation due to residual spatial force distribution, $\boldsymbol{F}_r$,(defined in Eq. (32)). Afterwards, an eigenvalue problem is

solved from the mass and stiffness matrices which are projected by Ritz vectors and the MT vectors are obtained from them. The MT vectors are orthogonal to the kept modes in the reduction basis, since the residual spatial distribution of the applied loads does not by definition comprise the contribution of the kept modes, by definition (see eq. (32)).

To compute the MT vectors, we start from the computation of the Ritz vectors by a static problem under the residual force distribution:

$$\boldsymbol{K}\boldsymbol{X} = \boldsymbol{F}_r \tag{39}$$

where, $\boldsymbol{X}$ is the static displacement matrix which comprises the static displacement (Ritz) vectors in its columns. Afterwards, the reduced mass matrix, $\bar{\boldsymbol{M}}$, and stiffness matrix, $\bar{\boldsymbol{K}}$ are obtained using these Ritz vectors.

$$\bar{\boldsymbol{K}} = \boldsymbol{X}^T\boldsymbol{K}\boldsymbol{X} \tag{40}$$

$$\bar{\boldsymbol{M}} = \boldsymbol{X}^T\boldsymbol{M}\boldsymbol{X} \tag{41}$$

The reduced eigenvalue problem is then given by

$$(\bar{\boldsymbol{K}} - \omega_i^2\bar{\boldsymbol{M}})\boldsymbol{v}_i \tag{42}$$

here, the i^{th} eigenvector and eigenfrequency of the reduced eigenvalue problem are denoted by ω_i and $\boldsymbol{v}_i$, respectively. The MT vectors are consequently defined by

$$\boldsymbol{\Phi}_{mt} = \boldsymbol{X}\boldsymbol{V} \tag{43}$$

where, the matrix $\boldsymbol{V}$ contains the reduced eigenvectors, $\boldsymbol{v}_i$, in its columns. Finally, the new reduction basis according to the MTA method is constructed by appending the MT vector to the set of kept modes, $\boldsymbol{\Phi}$, namely

$$\boldsymbol{\Psi} = \begin{bmatrix} \boldsymbol{\Phi} & \boldsymbol{\Phi_{mt}} \end{bmatrix} \tag{44}$$

Now, the procedure of model reduction is exactly the same as the MD method, except that the new reduction basis, $\boldsymbol{\Psi}$, is used as the reduction basis.

$$\boldsymbol{u} = \boldsymbol{\Psi}\ \boldsymbol{q} \tag{45}$$

$$\ddot{\boldsymbol{u}} = \boldsymbol{\Psi}\ \ddot{\boldsymbol{q}} \tag{46}$$

The novelty of this paper is that we propose to use the MT vectors in addition to the linear modes as the basis vectors in the identification procedure of the IC method, namely

$$\boldsymbol{T} = \begin{bmatrix} \boldsymbol{\Phi} & \boldsymbol{\Phi_{mt}} \end{bmatrix} \tag{47}$$

to compensate for the spatial representation of the external loads in the nonlinear restoring forces, which was constructed using only linear modes in the original IC method.

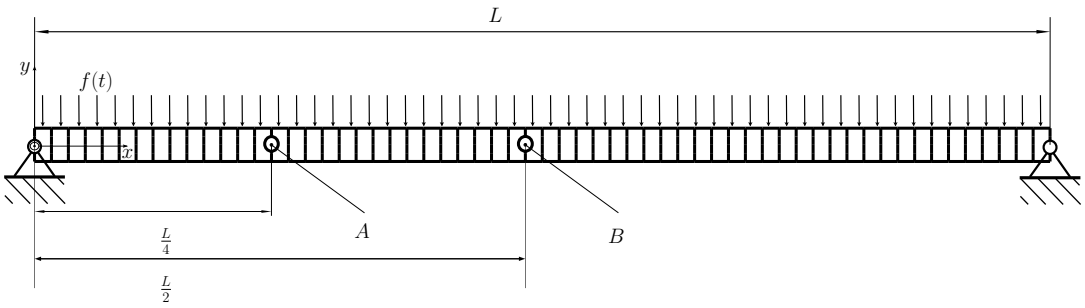


Figure 1: Schematic of the simply-supported beam

4 Numerical Example

A simply-supported beam (figure (1)) made from linear elastic material and with a geometric nonlinear effect is investigated in this study to examine the performance of the proposed methods. The material, geometry and mesh properties of the beam are outlined in table (1). The beam has 179 active DOFs in total. There are a few important parameters for the development of a NLROM in any non-intrusive approach that have to be carefully selected, because of their possibly huge effect on the accuracy of the NLROM. The scaling factor and basis vectors for generating the static forces (in IC) are two of these parameters. Previous research, e.g. in [10, 7], has discussed some of the possibilities to choose or compute such parameters. For the beam investigated in this paper, Eq. (19) is used to calculate the required scaling factors. As soon as the basis vectors are selected, the only unknown parameter in Eq. (19) is the maximum desired displacement, $W_{i_{\max}}$. Most of the researchers have reported good results, when this parameter is chosen to have the order of the thickness of the structure. Here, we have performed a comparative study for different proportion of the thickness of the beam, and $W_{i_{\max}}$ is chosen as

$$W_{i_{\max}} = \tfrac{1}{2}t \tag{48}$$

where, t is the thickness of the beam. Two types of error measures have been use in this work. The first measure is called the relative error

$$\boldsymbol{\epsilon} = \frac{\|\boldsymbol{u}_{full} - \boldsymbol{u}_{rom}\|}{\boldsymbol{u}_{average}} \tag{49}$$

with $\boldsymbol{u}_{full}$, $\boldsymbol{u}_{rom}$ as the displacements of the full-and-reduced-order solutions, respectively, and $\boldsymbol{u}_{average}$ as the average value of the full-order solution displacement, $\|\boldsymbol{u}_{full}\|$. The second error is the Global Relative Error (GRE), defined by

$$GRE = \frac{\sqrt{\sum_{t\in T}(\boldsymbol{u}_{full} - \boldsymbol{u}_{rom})'(\boldsymbol{u}_{full} - \boldsymbol{u}_{rom})}}{\sqrt{\sum_{t\in T}(\boldsymbol{u}_{full})'(\boldsymbol{u}_{full})}} \tag{50}$$

which is a scalar value. The summation in both numerator and denominator is over the whole time period. the sign ($'$) denotes the transpose of the matrices. The relative error, $\boldsymbol{\epsilon}$ represents the change of NLROM's error over time for all or a set of DOFs, while the global relative error, GRE, represents the quality of the NLROM approximation for all DOFs and over the whole time period. An acoustic pressure which is uniform in space and random in time is applied to the beam. The time history of the acoustic pressure is shown in figure (2) which has the average level of 149.6 dB. The NLROM is developed using the IC method (section (2.1)). The NLROM is developed in MATLAB® using the IC method with three different bases as force basis vectors:

Table 1: Properties of the investigated clamped-clamped beam

Property	Value	Property	Value
Length,	0.3 m	Density	7870 kg/m^3
Width	0.013 m	E modulus	$2.05\times10^{11}Pa$
Thickness	$1.5\times10^{-3}m$	Poisson's ratio	0.28
No. of elements	60	Element type	Abaqus, B21

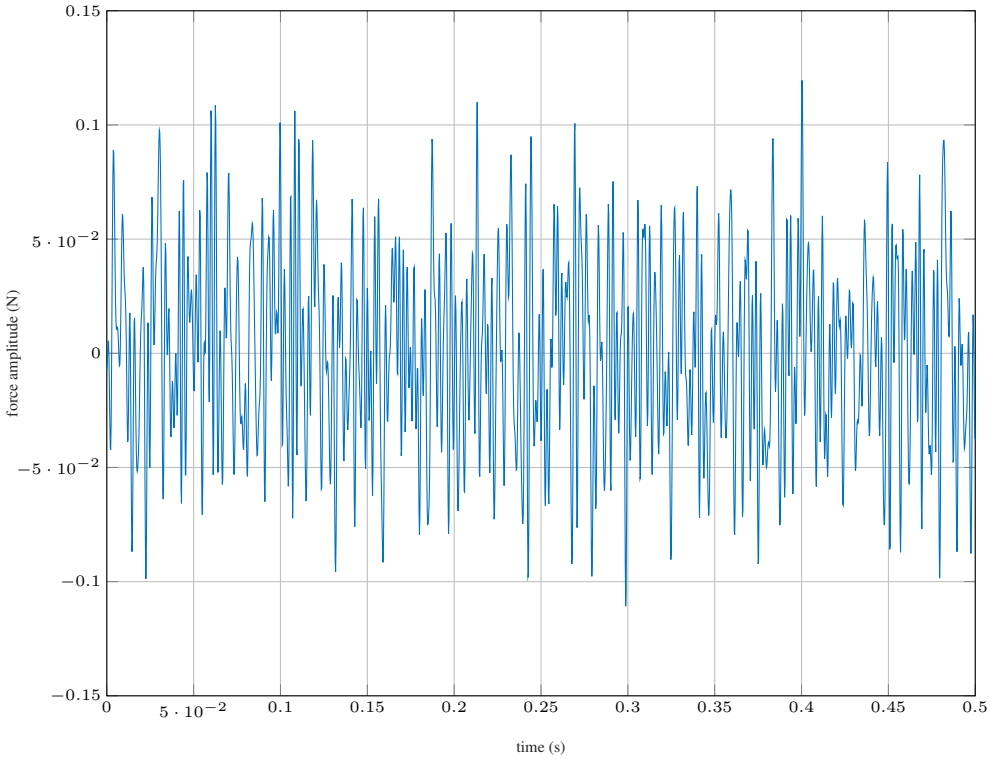


Figure 2: Time history of the uniformly distributed random sound pressure excitation. The average level is 149.6 dB and the frequency band is [0, 500] Hz.

- NLROM: the first five linear (transverse) modes.
- NLROMMA: the NLROM obtained using the first five modes is augmented with the MA method explained in section (3.2).
- NLROMMT: the first five modes in companion with one MT vector proposed in section (3.3).

Abaqus® is used as the FE package to develop the full-order model and perform the nonlinear static analysis required for IC. Furthermore, to validate the accuracy of different NLROMs, the time responses of the mentioned NLROMs are compared with those of the full-order model which was computed in Abaqus. The Newmark-β method is used to obtain the time response of the NLROMs. A constant time increment of $2.5\times10^{-4}s$ is chosen for all time integration studies.

Figure (3) shows the relative error for all transverse displacements with respect to the full-order model (the in-plane motion is not studied in this paper). In this figure, the NLROM error is relatively much smaller than the

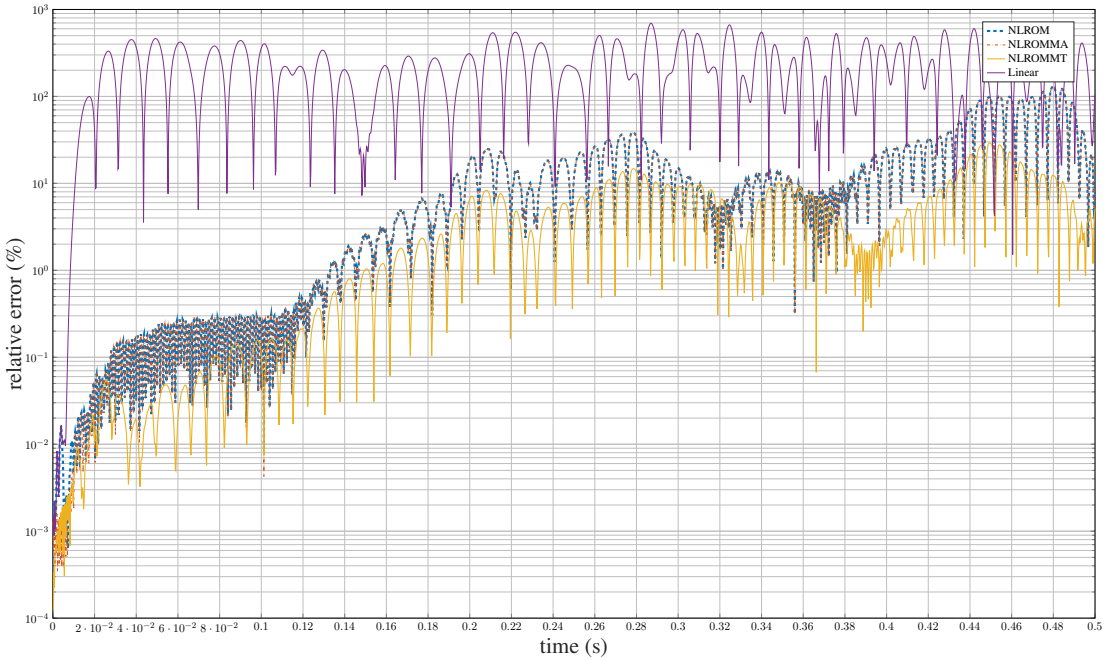


Figure 3: Relative error (in percent), for all transverse displacements of the simply-supported beam over time for different NLROM strategies.

linear response; however, the augmentation of the MT vector (NLROMMT) has apparently reduced the relative error of NLROM. Moreover, it can be seen that the static augmentation with the MA method has no improvement in the accuracy of the NLROM. This is due to the fact that for nonlinear structures with large vibrations, the error induced by the truncation of the linearized internal forces is negligible compared to the error induced by the nonlinear terms in the internal force vector.

Figures (4) and (5) depict the Power Spectral Density (PSD) of the mid-point (shown by point A in figure (1)) and quarter-point (shown by point B in figure (1)) displacement of the beam in the transverse direction, respectively. While the PSD of NLROM and NLROMMA responses have the same accuracy to follow the PSD of the full-model response, the PSD of the NLROMMT response improves this accuracy significantly.

Finally, the GRE of the beam's reduced order model compared to the full-order nonlinear response is calculated for Linear ROM (LROM), NLROM, NLROMMA and NLROMMT, respectively, as shown in table (2). The GREs of the NLROM and NLROMMA in this case are the same in this case and 9 times better than LROM. Whereas, NLROMMT is 39 times better than LROM and 4 times better than both NLROM and NLROMMA. It is concluded that among all the three different developed NLROMs in this paper, the best result has been delivered by the NLROMMT. The NLROMMT includes the Modal Truncation vectors in addition to the linear modes to generate force basis vectors in the identification procedure of the Nonlinear Stiffness Coefficients using the Implicit Condensation method.

In this work, the expansion procedure of the in-plane displacement explained in [8] is not investigated, is to be studied in future studies. Furthermore, the effect of higher order terms of the MT vectors considered in [16] will be investigated for the nonlinear model order reduction in further studies.

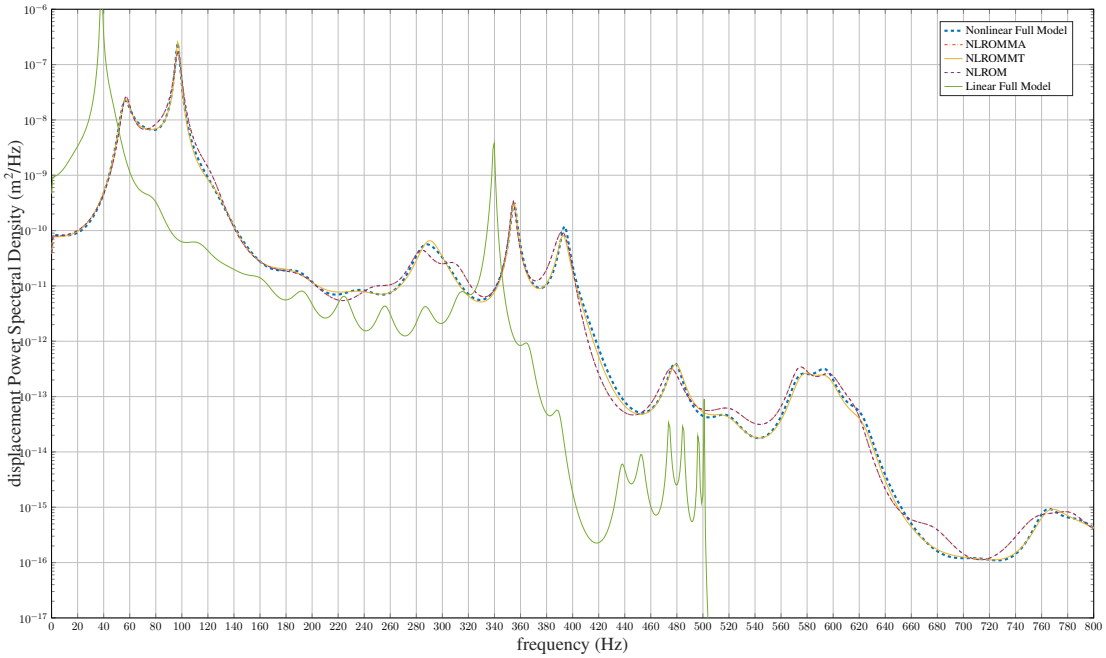


Figure 4: Displacement power spectral density of the beam's mid-point (node 30) in transverse direction. Comparison for different NLROM strategies compared with the full-order linear and nonlinear models.

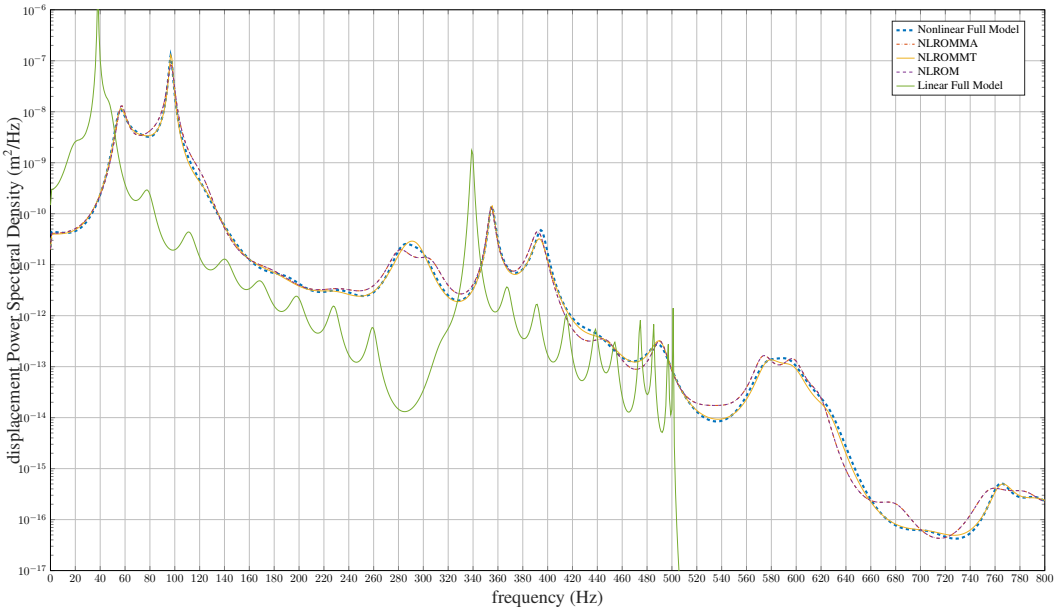


Figure 5: Displacement power spectral density of the beam's mid-point (node 15) in transverse direction. Comparison for different NLROM strategies compared with the full-order linear and nonlinear models.

Table 2: Global Relative Error (GRE) for different model order reduction strategies

Method	LROM	NLROM	NLROMMA	NLROMMT
GRE	2.2978	0.2544	0.2544	0.0591

5 Conclusion

This paper is the first step in extending the Mode Acceleration Correction (MA) and Modal Truncation Augmentation (MTA) methods in nonlinear model order reduction. To develop the nonlinear reduced order model (NLROM), a force-based non-intrusive approach has been employed. This has the advantage that the model order reduction procedure can be performed in any FE package without requiring direct access to the nonlinear finite element equations of motion of the full-order model. In this way, a set of static loads has to be generated and applied to the nonlinear FE formulation, which is called Implicit Condensation (IC) method. In the original IC method, the static loads are constructed using a truncated number of linear (transverse) eigenmodes which are in the frequency range of interest with a margin and a scaling factor which can trigger the nonlinear restoring force. However, these modes are not able to accurately approximate the spatial distribution of the external excitation. Therefore, in this paper we extended the classical force bases with two new methods in nonlinear model order reduction field.

In the MA method, the displacements computed from the original IC method are augmented by linear static contribution of truncated modes due to external loads, whereas in the MTA method, the quasi-static contribution of truncated modes is obtained using the Rayleigh-Ritz method, as Modal Truncation (MT) vectors. These vectors are afterwards employed as new basis vectors to generate the static loads required for the identification of the Nonlinear Stiffness Coefficients (NSC) in the IC method.

The two proposed methods are implemented for a simply-supported beam example with geometric nonlinear effects. A random excitation is imposed on the structure to check the accuracy of the proposed methods. It has been shown that the MA method does not improve the time response of the NLROM when the response is in the nonlinear regime. However, the proposed nonlinear MTA method significantly enhances the accuracy of the NLROM for both linear an nonlinear regimes. In the next step, the effect of higher order terms of the MT method can be investigated.

References

[1] M. Akguen. “A New Family Of Mode-Superposition Methods For Response Calculations”. In: *Journal of Sound and Vibration* 167.2 (1993), pp. 289–302. ISSN: 0022-460X. DOI: https://doi.org/10.1006/jsvi.1993.1336. URL: http://www.sciencedirect.com/science/article/pii/S0022460X83713362.

[2] Z. Bai. “Krylov subspace techniques for reduced-order modeling of large-scale dynamical systems”. In: *Applied Numerical Mathematics* 43.1-2 (2002), pp. 9–44. ISSN: 01689274. DOI: 10.1016/S0168-9274(02)00116-2.

[3] R. de Borst, M. Crisfield, J. Remmers, and C. Verhoosel. *Non-Linear Finite Element Analysis of Solids and Structures: Second Edition*. 2012. DOI: 10.1002/9781118375938.

[4] R. R. Craig and A. J. Kurdila. *Fundamentals of Structural Dynamics*. New Jersey: Wiley, 2006, p. 744. ISBN: 978-0-471-43044-5.

[5] J. Dickens, J. Nakagawa, and M. Wittbrodt. “A critique of mode acceleration and modal truncation augmentation methods for modal response analysis”. In: *Computers and Structures* 62.6 (1997), pp. 985–998. ISSN: 0045-7949. DOI: https://doi.org/10.1016/S0045-7949(96)00315-X.

[6] J. Dickens and K. Pool. “Modal truncation vectors and periodic time domain analysis applied to a cyclic symmetry structure”. In: *Computers & Structures* 45.4 (Nov. 1992), pp. 685–696. ISSN: 0045-7949. DOI: 10.1016/0045-7949(92)90487-K. URL: https://www.sciencedirect.com/science/article/pii/004579499290487K.

[7] R. W. Gordon and J. J. Hollkamp. *Reduced-Order Models for Acoustic Response Prediction*. Tech. rep. July. AFRL-RB-WP-TR-2011-3040, 2011.

[8] J. J. Hollkamp and R. W. Gordon. "Reduced-order models for nonlinear response prediction: Implicit condensation and expansion". In: *Journal of Sound and Vibration* 318.4-5 (2008), pp. 1139–1153. DOI: 10.1016/j.jsv.2008.04.035.

[9] K. Kim, V. Khanna, X. Q. Wang, and M. P. Mignolet. "Nonlinear Reduced Order Modeling of Flat Cantilevered Structures". In: *Proceedings of the 50th Structures, Structural Dynamics, and Materials Conference, Palm Springs, California, May*. May. 2009, pp. 4–7. ISBN: 9781563479731.

[10] R. J. Kuether. "Nonlinear Modal Substructuring of Geometrically Nonlinear Finite Element Models". PhD thesis. Wisconsin-Madison, 2014, p. 181.

[11] M. I. McEwan, J. R. Wright, J. E. Cooper, and A. Y. Leung. "A combined modal/finite element analysis technique for the dynamic response of a non-linear beam to harmonic excitation". In: *Journal of Sound and Vibration* 243.4 (2001), pp. 601–624. ISSN: 0022460X. DOI: 10.1006/jsvi.2000.3434.

[12] M. McEwan, J. Wright, J. Cooper, and A. Leung. "A finite element/modal technique for nonlinear plate and stiffened panel response prediction". In: vol. 5. cited By 20. 2001, pp. 3061–3070. URL: https://www.scopus.com/inward/record.uri?eid=2-s2.0-0035001805&partnerID=40&md5=47b17bf9c2030657236bee15065bb6e9.

[13] M. P. Mignolet, A. Przekop, S. A. Rizzi, and S. M. Spottswood. "A review of indirect/non-intrusive reduced order modeling of nonlinear geometric structures". In: *Journal of Sound and Vibration* 332.10 (2013), pp. 2437–2460. ISSN: 0022-460X. DOI: https://doi.org/10.1016/j.jsv.2012.10.017. URL: http://www.sciencedirect.com/science/article/pii/S0022460X12008188.

[14] A. A. Muravyov and S. A. Rizzi. "Determination of nonlinear stiffness with application to random vibration of geometrically nonlinear structures". In: *Computers and Structures* 81.15 (2003), pp. 1513–1523. ISSN: 00457949. DOI: 10.1016/S0045-7949(03)00145-7.

[15] M. Nash. "Nonlinear Structure Dynamics by Finite Element Modal Synthesis". PhD thesis. Imperial College London, 1977.

[16] D. Rixen. "Generalized Mode Acceleration methods and Modal Truncation Augmentation". In: *Structures, Structural Dynamics and Material Conference and Exhibit*. 42st AIAA/ASME/ASCE/AHS/ASC. Seattle, WA, USA, Apr. 2001.

[17] P. M. A. Slaats, J. de Jongh, and A. Sauren. "Model Reduction Tools for Nonlinear Structural Dynamics". In: *Computers & Structures* 54.6 (1995), pp. 1155–1171.

[18] K. Willcox and J. Peraire. "Balanced Model Reduction via the Proper Orthogonal Decomposition". In: *AIAA Journal* 40.11 (2002), pp. 2323–2330. ISSN: 0001-1452. DOI: 10.2514/2.1570. URL: http://arc.aiaa.org/doi/10.2514/2.1570.

[19] E. L. Wilson. "Dynamic Analysis By Direct Superposition of Ritz Vectors". In: *Earthquake Engineering and Structural Dynamics* 10.October 1981 (1982), pp. 813–821. DOI: 10.1002/eqe.4290100606.

Parametric model order reduction for efficient frequency response evaluation

V. Cool [1], **F. Naets** [1,2], **W. Rottiers** [1,2], **W. Desmet** [1,2]
[1] KU Leuven, Department of Mechanical Engineering,
Celestijnenlaan 300 B, B-3001, Heverlee, Belgium
e-mail: **frank.naets@kuleuven.be**

[2] DMMS Lab, Flanders Make

Abstract

In many mechanical applications, a design optimization is performed on the frequency response functions of the mechanical system. In this work, a novel model reduction technique is explored for the parametric analysis of the frequency response functions of dynamical mechanical systems. This approach entails two novel aspects. First, a super-local reduced order basis is introduced which allows models of much lower order compared to models obtained with single, frequency independent reduced order basis approaches. Secondly, a novel hyper-reduction scheme is introduced which selects a subset of the considered, discrete frequency domain and computes the corresponding interpolation matrix. During the online phase, the full frequency domain response is reconstructed by interpolating between these sampled frequency lines. The proposed approach is validated numerically on an academic mass-spring-damper system and shows promising results.

1 Introduction

In many mechanical applications, a design optimization is performed on the frequency response functions (FRFs) of the mechanical system in order to limit the vibration, sound, ... transmission. These FRFs are the result of a system inversion performed on the large scale (and often frequency dependent) dynamic stiffness, which comprises the mass, damping and stiffness matrix. During manual and automatic design studies, the evaluation of these FRFs leads to high computational loads due to a large number of degrees-of-freedom (DOFs) in the underlying finite element models for these problems and the large number of frequency lines to evaluate.

Over the past decades, a range of methods for parametric model order reduction have been proposed which allow to accelerate the (online) evaluation of these types of models. Classically only order reduction was considered, and an excellent overview of different projection approaches employed in mechanical applications is given by Besselink *et al.* [1]. In these approaches, a method is selected to identify a low(er) rank reduced order basis (ROB) which is exploited over the full frequency range of interest. However, these traditional projection methods suffer from a very important issue: they typically require to set up a new reduced order basis for every new parameter set which is encountered. The computational load of setting up this ROB is often on par with a full order model (FOM) evaluation such that little gains can be made in practical parametric applications. More recently, there has been more focus on dedicated parametric model order reduction (pMOR) techniques. Benner *et al.* [2] discuss a range of parametric model order reduction methods, such that a new basis does not need to be constructed for every new parameter set. Still, a single basis is employed over the full frequency range. For mechanical applications however, which often exhibit high modal densities, the single basis approach can often lead to large resulting reduced order bases. Moreover, the

hyper-reduction methods typically used in these approaches assume an affine parameter dependency, which typically does not exist in mechanical FRF evaluations.

In this work, we therefore explore a novel model reduction technique for parametric analysis of the frequency response of dynamic, mechanical systems.
The proposed approach first consists of the definition of a local reduced order basis (LROB) in the frequency range. In classical approaches, a computed reduced order basis (ROB) which accounts for the parameter variations is exploited over the full frequency range. However, for systems with high modal densities, this often leads to a limited reduction ratio. In this work, we propose to exploit a number of training responses at each frequency line to set up an ROB which is only employed at that specific frequency line. As each local basis only has to be valid at a specific frequency, this basis can be drastically smaller compared to the general case. As this reduced order basis is only valid at a single frequency line, we denote it here as a *super-local* ROB, to highlight the contrast with other local reduced order modeling approach, as e.g. proposed by Amsallem *et al.* [3], where the ROB is used in a wider region.
Secondly, a hyper-reduction is proposed through sampling in the frequency range. In order to reduce the total number of frequency line evaluations, a greedy sampling algorithm is deployed in order to determine a limited set of dominant frequency lines for the considered parametric variations. A corresponding interpolation matrix is defined to reconstruct the full frequency range from the limited number of obtained samples. In order to limit the initial setup cost of the reduced order model, the LROB setup and hyper-reduction steps are reversed in the practical implementation, such that the LROBs only need to be computed for the retained frequency lines.

The proposed scheme is set up with the aim of interacting with external (commercial) software for extracting the parameterized model matrices. The non-intrusive property of the proposed model order reduction scheme is an important benefit, since it allows the usage of existing finite-element software for which interfaces are typically available to extract system matrices for different frequencies.

The proposed super-local model order reduction method is validated numerically on an academic parameterized mass-spring-damper system. This validation demonstrates the potential of the novel scheme to provide an accelerated mechanical frequency response evaluation with high accuracy.

2 Problem statement

In this work, parameterized mechanical models are considered. The semi-discretized, continuous-time equations for these models are:

$$\mathbf{M}(\mathbf{p},\omega)\ddot{\mathbf{x}} + \mathbf{C}(\mathbf{p},\omega)\dot{\mathbf{x}} + \mathbf{K}(\mathbf{p},\omega)\mathbf{x} = \mathbf{f}^{ext}, \tag{1}$$

for spatially discretized DOFs $\mathbf{x} \in \mathbb{R}^n$, where the mass $\mathbf{M} \in \mathbb{R}^{n\times n}$, damping $\mathbf{C} \in \mathbb{R}^{n\times n}$ and stiffness matrix $\mathbf{K} \in \mathbb{R}^{n\times n}$ are generally both dependent on the parameters $\mathbf{p} \in \mathbb{R}^{n_p}$ and the pulsation $\omega \in \mathbb{R}$. In many applications, these type of models are evaluated in the frequency domain, and the frequency response can be computed as:

$$\mathbf{H}(\mathbf{p},\omega) = \left(-\mathbf{M}(\mathbf{p},\omega)\omega^2 + j\mathbf{C}(\mathbf{p},\omega)\omega + \mathbf{K}(\mathbf{p},\omega)\right)^{-1}\mathbf{b}, \tag{2}$$

for which $\mathbf{b} \in \mathbb{R}^n$ respresents an input selection vector. In many inverse problems, this frequency domain characteristic is used either to evaluated a desired system behavior at the design stage or to match a model response to an experimentally measured response.

However, the repeated evaluation of the inverse of a large system in equation (2) for a large number of pulsations $\boldsymbol{\omega} \in \mathbb{R}^{n_\omega}$ over a number of parameter combinations typically leads to large computational loads. In this work, a novel model order reduction scheme is proposed which allows for an accelerated FRF evaluation in these multi-query settings.

3 Super-Local Model Order Reduction

This section discusses the proposed super-local model order reduction approach in detail. First the idea behind the approach is discussed. Then the construction of the super-local reduced order basis and hyper-reduction are discussed. Finally, several aspects of the practical implementation are discussed.

3.1 Method overview

The proposed approach consists of two aspects: a projection based reduction to limit the model size and a hyper-reduction to limit the number of model inversions to compute an FRF.

In the first stage, a Galerkin projection is employed with a reduced order basis $\mathbf{V} \in \mathbb{R}^{n \times m}$ to reduce the size of the to be inverted dynamic stiffness matrix:

$$\mathbf{H}^r(\mathbf{p}, \omega) = \left(-\mathbf{V}^T\mathbf{M}(\mathbf{p}, \omega)\mathbf{V}\omega^2 + j\mathbf{V}^T\mathbf{C}(\mathbf{p}, \omega)\mathbf{V}\omega + \mathbf{V}^T\mathbf{K}(\mathbf{p}, \omega)\mathbf{V}\right)^{-1}. \tag{3}$$

In classical model order reduction, the ROB $\mathbf{V}$ is set up to be valid over the full frequency range of interest. In practice, this can still lead to a relatively large reduced order basis which limits the performance of the reduced order model. This is typically the case in systems with high modal density, like mechanical systems, where many eigenmodes are closely spaced in a certain frequency range. As an alternative, this work proposes to set up a basis for each frequency line separately which is valid over the parameter range of interest. This reduced order basis is denoted as the super-local reduced order basis $\mathbf{V}_i$ which is assumed to only be relevant at a specific pulsation ω_i. The construction of this basis will be discussed in section 3.2.

However, at this point, still a large number of frequency lines need to be evaluated. This is particularly problematic in the case of frequency dependent model matrices, which require a reconstructions of the model matrices for each frequency line leading to a considerable computational load. In order to mitigate this cost, a novel hyper-reduction scheme is proposed. This scheme is based on the selection of a limited set of dominant frequency lines for the parameter range of interest. The remaining frequency lines of interest are then obtained through an interpolation of the evaluated dominant frequency lines. This aspect is further discussed in section 3.3.

3.2 Frequency-dependent reduced order basis

For the super-local reduced order basis, a new reduced order basis $\mathbf{V}_i \in \mathbb{R}^{n \times m}$ is constructed for all n_ω pulsations ω_i in the frequency domain evaluation range:

$$\omega \in [\omega_1, \ldots, \omega_{n_\omega}]. \tag{4}$$

The reduced order basis for each frequency needs to be representative for the full parameter domain Ω_p of interest. This is achieved by evaluating the full order response for a representative set of training samples $\mathbf{p}^{tr}$ on this parameter domain. For each of these n_{tr} training samples $\mathbf{p}_k^{tr}$, training FRFs $\mathbf{H}_i^{tr,k}$ are computed for each pulsation ω_i:

$$\mathbf{H}_i^{tr,k} = \mathbf{H}(\mathbf{p}_k^{tr}, \omega_i). \tag{5}$$

The FRFs for the different parameter sets are concatenated per pulsation ω_i in the training set $\mathbf{H}_i^{tr}$:

$$\mathbf{H}_i^{tr} = \left[\mathbf{H}(\mathbf{p}_1^{tr}, \omega_i), \quad \ldots, \quad \mathbf{H}(\mathbf{p}_{n_{tr}}^{tr}, \omega_i)\right]. \tag{6}$$

The ROB for a certain frequency line $\mathbf{V}_i$ is then obtained through a proper orthogonal decomposition (POD) of the training set $\mathbf{H}_i^{tr}$. In practice, this POD is obtained by performing a thin singular value decomposition, only retaining the m singular vectors belonging to the largest singular values:

$$\mathbf{V}_i = \text{svd}(\mathbf{H}_i^{tr}, m) \tag{7}$$

This reduction space is computed for every relevant pulsation ω_i from their respective training results. In a practical implementation, these singular value decompositions for all relevant frequency lines can be performed in parallel in order to limit the offline computational time.

Note moreover that m is not necessarily the same for all frequency lines. When using an error driven criterion to determine the ROM size for example, the proposed methodology allows to have a different model size for every frequency line. However, in the remainder of this work, this property is not explicitly exploited.

With these reduced order bases, the approximate FRFs $\bar{\mathbf{H}}$ from equation (3) at pulsation ω_i is evaluated as:

$$\bar{\mathbf{H}}(\mathbf{p},\omega_i) = \mathbf{V}_i \left(-\mathbf{V}_i^T\mathbf{M}(\mathbf{p},\omega_i)\mathbf{V}_i\omega_i^2 + j\mathbf{V}_i^T\mathbf{C}(\mathbf{p},\omega_i)\mathbf{V}_i\omega_i + \mathbf{V}_i^T\mathbf{K}(\mathbf{p},\omega_i)\mathbf{V}_i\right)^{-1}\mathbf{V}_i^T\mathbf{b}, \tag{8}$$

such that only low order $m \times m$ systems needs to be solved for each frequency line. In short hand form, this is written as:

$$\bar{\mathbf{H}}(\mathbf{p},\omega_i) = \mathbf{V}_i \left(-\bar{\mathbf{M}}(\mathbf{p},\omega_i)\omega_i^2 + j\bar{\mathbf{C}}(\mathbf{p},\omega_i)\omega_i + \bar{\mathbf{K}}(\mathbf{p},\omega_i)\right)^{-1}\mathbf{V}_i^T\mathbf{b}, \tag{9}$$

with

$$\bar{\mathbf{M}}(\mathbf{p},\omega_i) = \mathbf{V}_i^T\mathbf{M}(\mathbf{p},\omega_i)\mathbf{V}_i, \tag{10}$$

$$\bar{\mathbf{C}}(\mathbf{p},\omega_i) = \mathbf{V}_i^T\mathbf{C}(\mathbf{p},\omega_i)\mathbf{V}_i, \tag{11}$$

$$\bar{\mathbf{K}}(\mathbf{p},\omega_i) = \mathbf{V}_i^T\mathbf{K}(\mathbf{p},\omega_i)\mathbf{V}_i. \tag{12}$$

However, this projection based reduction scheme still involves a large number of evaluations as often a large number of pulsations ω_i need to be evaluated. In order to reduce this computational load further, a frequency sampling hyper-reduction is introduced in the next section.

3.3 Frequency sampling and interpolation for hyper-reduction

This section describes the hyper-reduction which allows to reduce the number of frequency lines which need to be evaluated.

In contrast to other works on hyper-reduction, the aim is not to reduce the evaluation cost of the reduced model system matrices, e.g. through an affine decomposition [2]. The aim in this work is to set up a procedure which can be conveniently exploited in interaction with commercial finite-element software from which the model system matrices are extracted. For the considered mechanical systems, it is often very difficult, if not impossible, to employ rather intrusive affine reduction schemes. Therefore, the assumption is made that the FOM system matrices can be extracted for different frequencies, as is typically foreseen in the interfaces of commercial software.

The proposed hyper-reduction schemes starts from the training sets $\mathbf{H}^{tr}$ used for the reduced order basis setup. The aim of the procedure is to identify a minimal number of sampled pulsations $\boldsymbol{\omega}^s \in \mathbb{R}^{n_s}$ which allow to accurately evaluate the response at other pulsations ω_i through interpolation of the evaluated frequency responses.

The proposed approach searches for a hyper-reduced approximation of the FRFs as:

$$\mathbf{H}(\mathbf{p},\omega_i) \approx \mathbf{H}^{hr}(\mathbf{p},\omega_i) = \sum_{\omega_j \in \boldsymbol{\omega}^s} \mathbf{W}_{ij}^* \left(-\bar{\mathbf{M}}(\mathbf{p},\omega_j)\omega_j^2 + j\bar{\mathbf{C}}(\mathbf{p},\omega_j)\omega_j + \bar{\mathbf{K}}(\mathbf{p},\omega_j)\right)^{-1}\mathbf{V}_j^T\mathbf{b}, \tag{13}$$

where $\boldsymbol{\omega}^s$ represents a set of n_s pulsation samples with $n_s < n_\omega$ and $\mathbf{W}_{ij}^* \in \mathbb{C}^{n\times m}$ is the interpolation matrix which determines the contribution from the response at pulsation ω_j to the response at pulsation ω_i. However, in order to reliably identify the full optimal interpolation matrices $\mathbf{W}_{ij}^*$, a large amount of training data is required. In order to resolve this issue, an approximation is performed where all contributions from a certain frequency are interpolated together as:

$$\mathbf{H}(\mathbf{p},\omega_i) \approx \mathbf{H}^{hr}(\mathbf{p},\omega_i) = \sum_{\omega_j \in \boldsymbol{\omega}^s} w_{ji}\mathbf{V}_j \left(-\bar{\mathbf{M}}(\mathbf{p},\omega_j)\omega_j^2 + j\bar{\mathbf{C}}(\mathbf{p},\omega_j)\omega_j + \bar{\mathbf{K}}(\mathbf{p},\omega_j)\right)^{-1}\mathbf{V}_j^T\mathbf{b}, \tag{14}$$

where $w_{ji} \in \mathbb{C}$ is a scalar and the super-local basis $\mathbf{V}_j$ are reused to perform the interpolation between the different reduced DOFs.

The challenge in setting up the hyper-reduction is to determine the frequency samples such that a minimal number of samples is required to obtain a certain accuracy ϵ for the frequency response over the desired frequency range and training parameters:

$$\left|\mathbf{H}(\mathbf{p},\omega_i) - \mathbf{H}^{hr}(\mathbf{p},\omega_i)\right|_F \leq \epsilon \qquad \forall \quad \omega_i \in \boldsymbol{\omega}, \quad \mathbf{p} \in \mathbf{p}^{tr}. \tag{15}$$

The selection of the frequency samples can then be written as an L_0 optimization problem (which minimizes the number of selected frequencies):

$$\begin{aligned} \min_{\boldsymbol{\omega}^s \in \boldsymbol{\omega}} \quad & |\boldsymbol{\omega}^s|_0 \\ \text{s.t.} \quad & \left|\mathbf{H}(\mathbf{p},\omega_i) - \mathbf{H}^{hr}(\mathbf{p},\omega_i)\right|_F \leq \epsilon, \qquad \forall \quad \omega_i \in \boldsymbol{\omega}, \quad \mathbf{p} \in \mathbf{p}^{tr}. \end{aligned} \tag{16}$$

However, in practice it is typically infeasible to solve these L_0 optimization problems exactly as this generally require a combinatorial solution search. Therefore, this work proposes a sub-optimal greedy procedure to compute a good set of frequency samples and corresponding interpolation matrices which enables a practical computational scheme. This greedy procedure is summarized in algorithm 1.

3.4 Practical implementation

For the practical implementation of the approach, an offline and an online phase are present. During the offline phase the reduced order model is set up and during the online phase this reduced order model is used to rapidly evaluate the design response.

The reduced order model is set up based on a number of training runs on the FOM during the offline phase. These training parameter sets $\mathbf{p}^{tr}$ can be chosen in a number of ways, and for simplicity's sake this work selects an equidistant grid on the parameter space. In the practical implementation, first the frequency sampling and interpolation is set up. This allows to forgo the singular value decomposition of each frequency line and only for the sampled frequencies. The sampling and interpolation is conducted according to the algorithm outlined in algorithm 1. The outputs of this greedy sampling are the sampled pulsations ω^s and the corresponding interpolation matrix $\mathbf{W}$ where:

$$\mathbf{W} = \begin{bmatrix} w_{11} & \dots & w_{1n_\omega} \\ \vdots & \ddots & \vdots \\ w_{n_s 1} & \dots & w_{n_s n_\omega} \end{bmatrix} \tag{17}$$

During the online phase, the model is revisited for new parameter sets $\mathbf{p}$ for which the system response is of interest. This can for example be the case in a numerical design optimization where a certain frequency response is desired. The different steps of the online evaluation are outlined in algorithm 2. This scheme aims to enable an accelerated evaluation of the model during the online phase in contrast to the FOM approach. The gains are expected on the one hand from the smaller system solves due to the projection and on the other hand from the smaller number of system solves due to the hyper-reduction.

4 Numerical validation

This section discusses a proof-of-concept for the proposed approach with a specific aim on evaluating the potential accuracy for a low order ROM.

Algorithm 1 Greedy sampling for frequency line selection and interpolation weights.

In: $\mathbf{H}^{tr}$, ϵ

Restructure inputs: $\mathbf{R} = \begin{bmatrix} \mathbf{H}_1^{tr,1} & \dots & \mathbf{H}_{n_\omega}^{tr,1} \\ \vdots & \ddots & \vdots \\ \mathbf{H}_1^{tr,n_{tr}} & \dots & \mathbf{H}_{n_\omega}^{tr,n_{tr}} \end{bmatrix}$

Initialize outputs: $\boldsymbol{\omega}^s = [\quad]$, $\mathbf{W} = [\quad]$, $\mathbf{R}^{\boldsymbol{\omega}^s} = [\quad]$

$\mathbf{R}^{error} = \mathbf{R}$

while $max\left(|\mathbf{R}^{error}|\right) > \epsilon$ **do**

$j = \underset{i \in [1, n_\omega] \subset \mathbb{N}}{\operatorname{argmax}} \left\| \mathbf{R}^{error}|_{:,i} \right\|_2$

$\boldsymbol{\omega}^s = \left[\boldsymbol{\omega}^s, \quad \omega_j\right]$; $\mathbf{R}^{\boldsymbol{\omega}^s} = \left[\mathbf{R}^{\boldsymbol{\omega}^s}, \quad \mathbf{R}|_{:,j}\right]$

$\mathbf{W} = \left(\mathbf{R}^{\boldsymbol{\omega}^s}\right)^+ \mathbf{R}$

$\mathbf{R}^{error} = \mathbf{R} - \mathbf{R}^{\boldsymbol{\omega}^s}\mathbf{W}$

end while

Out: $\boldsymbol{\omega}^s$, $\mathbf{W}$

Algorithm 2 SL-MOR online computation.

1: For the desired parameter set $\mathbf{p}$: evaluate FOM system matrices $\mathbf{M}, \mathbf{C}, \mathbf{K}$ at pulsation samples $\boldsymbol{\omega}^s$
2: Project FOM system matrices on SL-ROB according to equations (10)-(12)
3: Use the hyper-reduced frequency response to extract the full frequency domain response according to equation (14).

4.1 Analysis description

For the initial validation of the proposed model order reduction scheme, a 1D mass-spring-damper system is considered as shown in figure 1. For this example, the masses, stiffnesses and dampers are all uniform – except the parametrized values – over the length of the mass-spring-damper chain and are 1 kg, 10^5 $^N/_m$ and 10^{-2} $\frac{N}{m/s}$, respectively.



Figure 1: Mass-spring-damper system

The reduced, parametric frequency domain analysis is computed for the case where:

- the parameter set contains the mass of the first and last mass;
- the training parameter sets $\mathbf{p}_k^{tr}$ are sampled in a full factorial manner and each parameter is sampled 7 times in an equidistant manner between the bounds of 5 and 10 kg;
- the nominal parameter for the analysis $\mathbf{p}$ is 8.3 kg for the first mass and 7 kg for the last mass;
- the frequency range of interest goes from 1 $\frac{rad}{s}$ to 30 $\frac{rad}{s}$, with an equidistant sampling of 10^{-1} $\frac{rad}{s}$;
- the force input is equally distributed over all masses;
- the output is the displacement at the first mass.

4.2 Results

The reduced order model is set up based on training data, which contains the FRFs computed by the inversion of the FOM, as described by equation (2), for each parameter set of the training. Figure 2 compares the FRF for the nominal parameter set $\mathbf{p}$. The three lines on the graph represent:

- the FRF computed via equation (2) employing the Full Order Model (FOM) for parameter set $\mathbf{p}$;
- the FRF for parameter set $\mathbf{p}$ employing the newly proposed super-local ROB and hyper-reduction;
- the FRF from training $\mathbf{H}(\mathbf{p}_k^{tr}, \omega)$ for which $k = \underset{k \in [1, n_{tr}] \subset \mathbb{N}}{\operatorname{argmin}} \left\| \mathbf{p} - \mathbf{p}_k^{tr} \right\|_2$.

The ROM uses super-local reduced order bases of order $m = 5$, and hence leads to very low order models. The hyper-reduction sampling has an error tolerance of $\epsilon = 10^{-4}$, leading to 83 selected frequency lines which are also shown in figure 2 as vertical dashed lines.

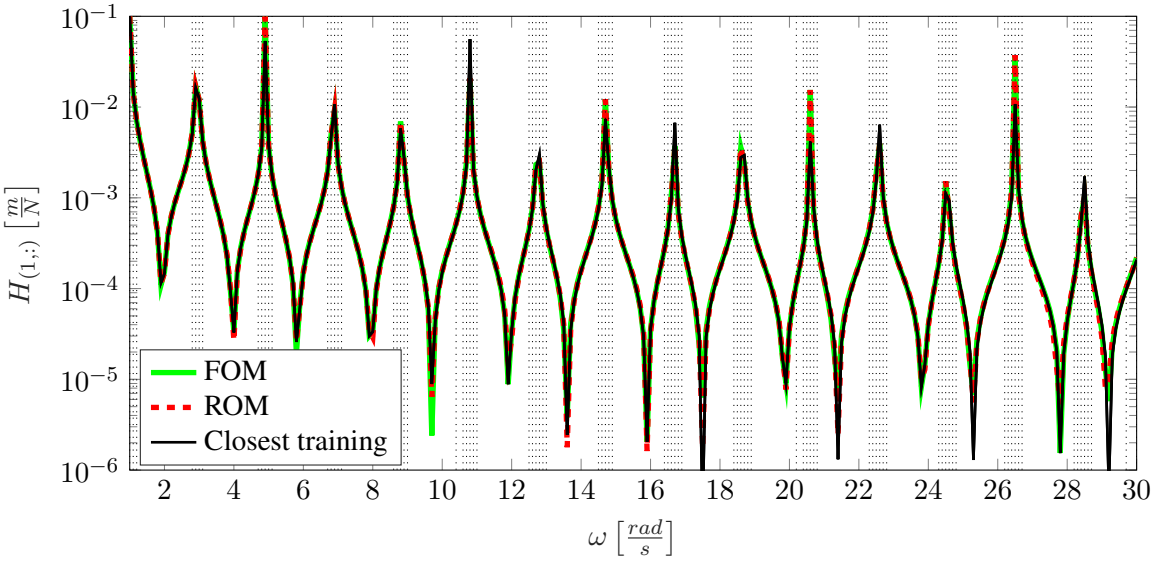


Figure 2: Approximation for frequency-response function for mass-spring-damper model

This figure clearly shows the good accuracy obtained with the proposed approach for a very low order model. Even though a simple response is expected, an improvement is obtained through the proposed approach with respect to the closest response in the training set, which indicates potential for predictive applications. Even though it is not shown in the figure, an approach with a constant reduced order basis over the full frequency domain of interest required an order of one up to two orders of magnitude more than the super-local approach in order to achieve a similar accuracy as the presented approach.

5 Conclusion

This work proposes a novel model order reduction scheme for accelerated parameterized frequency response function evaluation. This approach entails two novel aspects. The first aspect is the application of a super-local reduced order basis. Rather than setting up a single basis which is exploited over the full frequency range, a separate basis is set up for each frequency line separately. This enables the use of a very low order model, which is often not possible when using a single reduced order basis. Secondly, a novel hyper-reduction scheme is introduced which allows to evaluate only a subset of the evaluated frequency lines of

the full order model for the reduced order model. The response for this subset is then interpolated in order to reconstruct the full frequency domain response. This novel approach is validated numerically on a proof-of-concept mass-spring-damper model for which promising results are obtained. Future work focuses on validation of the proposed approach on large-scale industrial mechanical models and further robustification of the reduced order model setup.

Acknowledgements

The research of Frank Naets and Ward Rottiers is funded by a grant from the Research Foundation – Flanders (FWO). This research was also partially supported by Flanders Make, the strategic research center for the manufacturing industry.

References

[1] B. Besselink, U. Tabak, A. Lutowska, N. van de Wouw, H. Nijmeijer, D. Rixen, M. Hochstenbach, W. Schilders, *A comparison of model reduction techniques from structural dynamics, numerical mathematics and systems and control*, Journal of Sound and Vibration, Vol. 332, (2013), pp. 4403-4422.

[2] P. Benner, S. Gugercin, K. Willcox, *A Survey of Model Reduction Methods for Parametric Systems*, Max Planck Institute Magdeburg Preprint, MPIMD/13-14 (2013).

[3] D. Amsallem, M.J. Zahr, C. Farhat, *Nonlinear model order reduction based on local reduced-order bases*, International Journal for Numerical Methods in Engineering, Vol. 92, (2012), pp. 891-916

Application of the wave finite element method to the analysis of locally resonant band gaps in periodic structures with viscoelastic properties

J.-M. Mencik [1], **V. Denis** [1], **M. Caliez** [1], **S. Méo** [2]

[1] INSA Centre Val de Loire, Université d'Orléans, Université de Tours, Laboratoire de Mécanique Gabriel Lamé, 3 Rue de la Chocolaterie, 41034 Blois, France

[2] Université de Tours, Université d'Orléans, INSA Centre Val de Loire, Laboratoire de Mécanique Gabriel Lamé, Polytech Tours, 7 avenue Marcel Dassault, 37200 Tours, France

e-mail: **jean-mathieu.mencik@insa-cvl.fr**

Abstract

This paper investigates the wave propagation in one-dimensional periodic structures made up of cells/substructures with inclusions of viscoelastic materials and heavy materials. Such structures are referred to as locally resonant metamaterials where local stiffness/damping effects and mass effects occur due to the viscoelastic and heavy materials. Emphasis is placed on the analysis of the band gap phenomena — i.e., the fact that waves do not propagate on certain frequency bands — in such metamaterials, and on their capability to reduce the vibration levels of periodic structures. For this purpose, the wave finite element method is used. It provides an efficient means to compute the wave propagation and the forced response of periodic structures. Numerical experiments are carried out on periodic structures with viscoelastic properties and assemblies made up of these periodic structures. 2D substructures with single and double viscoelastic (rubber) layers are dealt with. It is shown that, compared to the purely elastic case, the use of viscoelastic materials yields wider band gaps as well as improved reduction of the vibration levels of periodic structures.

1 Introduction

Metamaterials in structural vibration usually refer to periodic structures which are made up of cells/substructures whose shape is designed to enhance certain phenomena. Among these are band gaps (stop bands) which involve frequency regions in which waves do not propagate. These appear interesting in passive vibration control of engineering structures, especially in the aeronautical industry. Usually, band gaps are strongly linked to Bragg scattering phenomena, i.e., they occur when the wavelengths of the traveling waves become twice the length of the substructures. For this reason, band gaps tend to occur at high frequencies in most engineering structures. Another way to create band gaps is to use locally resonant metamaterials, in which band gaps are induced by a periodic array of resonant devices (see for instance [1, 2, 3, 4, 5]). In this framework, band gaps typically occur at lower frequencies, i.e., about half the frequencies involved in Bragg scattering phenomena. The shortcoming with this approach, however, is that locally resonant band gaps tend to have smaller frequency ranges over which they are effective.

The present work aims at investigating periodic structures with periodic inclusion of viscoelastic layers (spring and damping effects) and heavy parts (mass effect). Periodic structures with one-dimensional periodicity, i.e., with substructures arranged along a straight direction, are specifically dealt with. The goal is to see whether periodic structures with viscoelastic properties can be used to create band gaps with larger bandwidths, to make them useful for a wider range of engineering applications. Passive vibration control of

periodic structures, and assemblies of periodic structures, is also explored.

The effect of the viscoelasticity on the wave propagation behavior of periodic structures has been analyzed in various ways in the literature (see for instance [6, 7, 8]). However, the impact of using viscoelastic layers on the reduction of the vibration levels of periodic structures, like those made up of a finite number of substructures, and assemblies of periodic structures having different geometrical properties, is not well mastered nowadays. One key issue, when assemblies of periodic structures are dealt with, is to see whether the band gaps of the periodic structures can be combined together to yield large reduction of the global vibration levels on wide frequency bands.

To address these issues, the wave finite element (WFE) method is used. It provides an efficient numerical means to compute waves in periodic structures, and assess their forced response. The periodic structures under concern can be composed of 2D or 3D substructures with complex geometrical and material properties, which are described using finite element (FE) models [9, 10]. Hence, substructures that combine elastic and viscoelastic components can be easily taken into account, where a generalized Maxwell model can be used to describe the viscoelastic part. The key advantage of the WFE method is that the wave (modes) of periodic structures can be computed in an accurate way by using appropriate eigensolvers [10], whatever the complexity of the substructures. Also, the analysis of the forced response of periodic structures, and assemblies of these structures, can be undertaken efficiently over wide frequency bands (not only at low frequencies).

The rest of the paper is organized as follows. In Section 2, the FE model of a substructure which contains elastic and viscoelastic parts is presented. In Section 3, the basics of the WFE method are recalled. The strategy to compute the wave modes of periodic structures is presented along with the strategy to compute the forced response of periodic structures and assemblies of periodic structures. Numerical experiments are finally brought in Section 4. Single periodic structures made up of 2D substructures with one or two viscoelastic (rubber) layers surrounding one or two tungsten parts are dealt with. Also, an assembly composed of two periodic structures with different substructure designs is analyzed. For each case, locally resonant band gaps are highlighted along with their capability to reduce the vibration levels of the structure. The effectiveness of the viscoelasticity for creating band gaps with large bandwidths is studied.

2 Substructure modeling

Let us consider a one-dimensional periodic structure made up of several identical substructures as shown in Figure 1, which is subject to harmonic boundary conditions at frequency $\omega/2\pi$ (ω being the pulsation). Here, the substructures are supposed to be linear and composed of elastic and viscoelastic parts. For the sake of clarity, a substructure incorporating two elastic parts (including heavy materials) and one viscoelastic part (layer) is shown in Figure 1.

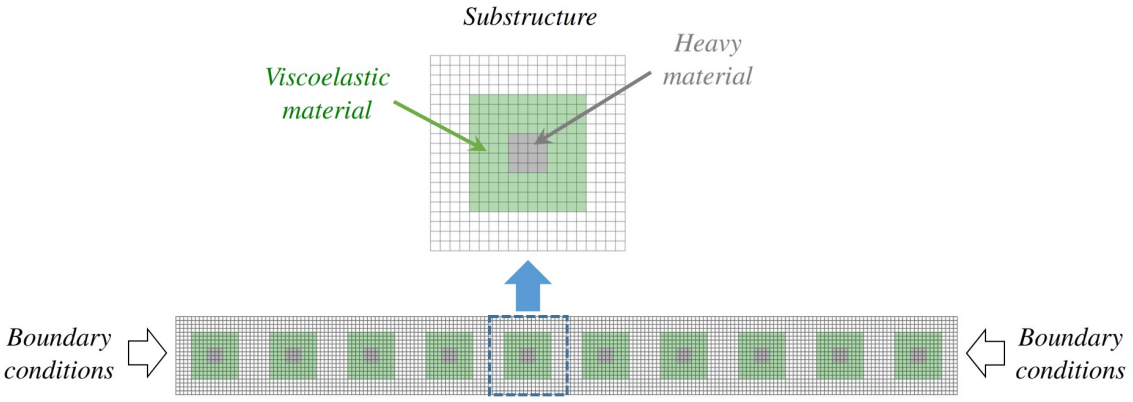


Figure 1: FE mesh of a periodic structure with viscoelastic properties.

Assume that each elastic part — say, e ($e = 1, 2, \ldots, N^{\mathtt{el}}$) — is homogeneous and isotropic, and described with a Young's modulus $E_e^{\mathtt{el}}$, a Poisson's ratio $\nu_e^{\mathtt{el}}$, a loss factor $\eta_e^{\mathtt{el}}$ and a mass density $\rho_e^{\mathtt{el}}$. Also assume that each viscoelastic part — say, v ($v = 1, 2, \ldots, N^{\mathtt{vel}}$) — is homogeneous and isotropic, and described with a generalized Maxwell model. In this case, a frequency-dependent Young's modulus $E_v^{\mathtt{vel}}(\omega)$ is considered, which can be split into an in-phase part $E_v^{'}(\omega)$ related to the storage modulus, and an out-phase part $E_v^{''}(\omega)$ related to the loss modulus. These moduli are related to the long term Young's modulus — namely, $E_{v\infty}$ — and the viscoelastic parameters as follows [11]:

$$E_v^{\mathtt{vel}}(\omega) = E_v^{'}(\omega) + \mathtt{i}E_v^{''}(\omega), \tag{1}$$

where

$$E_v^{'}(\omega) = E_{v\infty} + \sum_{i=1}^{n_v} E_{vi}\frac{\omega^2\tau_i^2}{1+\omega^2\tau_i^2}, \tag{2}$$

and

$$E_v^{''}(\omega) = \sum_{i=1}^{n_v} E_{vi}\frac{\omega\tau_i}{1+\omega^2\tau_i^2}, \tag{3}$$

where τ_i have the meaning of relaxation times, defined so that $\tau_i = 10^{-i}$ s for $i = 1, 2, \cdots, n_v$. Note that the Poisson's ratio and the density of each viscoelastic part v are supposed to be non-frequency dependent and real, and are denoted as $\nu_v^{\mathtt{vel}}$ and $\rho_v^{\mathtt{vel}}$, respectively.

Within the framework of the FE method, the elastic parts of the substructures are modeled by means of complex stiffness matrices $(1 + \mathtt{i}\eta_e^{\mathtt{el}})\mathbf{K}_e^{\mathtt{el}}$ — $\mathbf{K}_e^{\mathtt{el}}$ being real-valued — and mass matrices $\mathbf{M}_e^{\mathtt{el}}$. Also, the mass matrices of the viscoelastic parts do not depend on the frequency and are denoted by $\mathbf{M}_v^{\mathtt{vel}}$. In contrast, their stiffness matrices are frequency-dependent and complex. Their expression follows from Eqs. (1)-(3), i.e.

$$\mathbf{K}_v^{\mathtt{vel}}(\omega) = \mathbf{K}_{v\infty} + \sum_{i=1}^{n_v} \mathbf{K}_{vi}\left(\frac{\omega^2\tau_i^2}{1+\omega^2\tau_i^2} + \mathtt{i}\frac{\omega\tau_i}{1+\omega^2\tau_i^2}\right). \tag{4}$$

Within the framework of the FE assembly procedure, the global mass matrix of the substructure can be built from the local mass matrices of the elastic and viscoelastic parts:

$$\mathbf{M} = \sum_{e=1}^{N^{\mathtt{el}}} (\mathcal{L}_e^{\mathtt{el}})^T \mathbf{M}_e^{\mathtt{el}} \mathcal{L}_e^{\mathtt{el}} + \sum_{v=1}^{N^{\mathtt{vel}}} (\mathcal{L}_v^{\mathtt{vel}})^T \mathbf{M}_v^{\mathtt{vel}} \mathcal{L}_v^{\mathtt{vel}}, \tag{5}$$

where $\mathcal{L}_e^{\mathtt{el}}$ and $\mathcal{L}_v^{\mathtt{vel}}$ are localization (Boolean) matrices. Also, the complex, frequency-dependent, global stiffness matrix of the substructure is given by:

$$\mathbf{K}(\omega) = \mathbf{K}_1 + \mathbf{K}_2(\omega), \tag{6}$$

where

$$\mathbf{K}_1 = \sum_{e=1}^{N^{\mathtt{el}}} (1 + \mathtt{i}\eta_e^{\mathtt{el}})(\mathcal{L}_e^{\mathtt{el}})^T \mathbf{K}_e^{\mathtt{el}} \mathcal{L}_e^{\mathtt{el}} + \sum_{v=1}^{N^{\mathtt{vel}}} (\mathcal{L}_v^{\mathtt{vel}})^T \mathbf{K}_{v\infty} \mathcal{L}_v^{\mathtt{vel}}, \tag{7}$$

and

$$\mathbf{K}_2(\omega) = \sum_{v=1}^{N^{\mathtt{vel}}} \sum_{i=1}^{n_v} (\mathcal{L}_v^{\mathtt{vel}})^T \mathbf{K}_{vi} \mathcal{L}_v^{\mathtt{vel}} \left(\frac{\omega^2\tau_i^2}{1+\omega^2\tau_i^2} + \mathtt{i}\frac{\omega\tau_i}{1+\omega^2\tau_i^2}\right). \tag{8}$$

Let us denote by $\mathbf{D}$ the dynamic stiffness matrix (DSM) of the substructure, defined by $\mathbf{D}(\omega) = \omega^2\mathbf{M} + \mathbf{K}(\omega)$, i.e.

$$\mathbf{D} = -\omega^2\mathbf{M} + \mathbf{K}_1 + \mathbf{K}_2(\omega). \tag{9}$$

As a requirement of the WFE method (see Section 3), the DSM has to be condensed on the left and right boundaries of the substructure (see Figure 2). The condensed DSM — namely, $\mathbf{D}^*$ — is defined by $\mathbf{D}^* =$

$\mathbf{D}_{\mathtt{BB}} - \mathbf{D}_{\mathtt{BI}}\mathbf{D}_{\mathtt{II}}^{-1}\mathbf{D}_{\mathtt{IB}}$ where subscripts B and I refer to the boundary degrees of freedom (DOFs) — i.e., those on the left and right boundaries — and the internal/remaining DOFs, respectively. Note that the computation of the condensed DSM is to be done at each frequency ω analyzed which is usually cumbersome due to the inversion of the matrix $\mathbf{D}_{\mathtt{II}}$. To solve this issue, the Craig-Bampton (CB) method can be used which consists in projecting the DSM onto the subspace spanned by the static modes of the substructure, and a small number of fixed interface modes [9]. The matrices of static modes and fixed interface modes are denoted by $\mathbf{X}_{\mathtt{st}}$ and $\widetilde{\mathbf{X}}_{\mathtt{el}}$, respectively, and are defined by $\mathbf{X}_{\mathtt{st}} = -\mathbf{K}_{\mathtt{II}}^{-1}\mathbf{K}_{\mathtt{IB}}$ and $\widetilde{\mathbf{X}}_{\mathtt{el}} = [\boldsymbol{\xi}_1 \cdots \boldsymbol{\xi}_{m_{\mathtt{el}}}]$ where $m_{\mathtt{el}}$ is the number of fixed interface modes retained, and $\boldsymbol{\xi}_j$ are the eigenvectors of the matrix pencil $(\mathbf{K}_{\mathtt{II}}, \mathbf{M}_{\mathtt{II}})$, i.e., which are solutions of the generalized eigenproblem $\mathbf{K}_{\mathtt{II}}\boldsymbol{\xi}_j = \lambda_j \mathbf{M}_{\mathtt{II}}\boldsymbol{\xi}_j$.

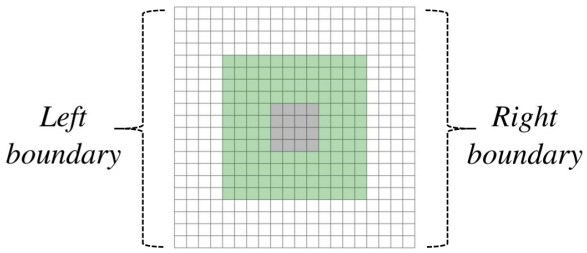


Figure 2: Schematic of the FE mesh of a substructure with left (L) and right (R) boundaries.

It should be recalled that the stiffness matrix of the substructure depends on the frequency, see Eqs. (6) and (8). Therefore, the matrices of static modes and fixed interface modes depend on the frequency, i.e., they should be computed at each frequency analyzed. To overcome this issue, a strategy can been proposed which consists in considering the matrices of static modes and fixed interface modes defined at one single frequency only, e.g., the maximum eigenpulsation $\omega = \omega_{\mathtt{max}}$ within the frequency band analyzed. Such an idea has been proposed in [12] where fixed interface modes at both the minimum and maximum frequencies are considered. In the present work however, the fixed interface modes at the maximum frequency are only considered. Such a strategy will be proven relevant for modeling the substructures involved in Section 4. The space spanned by those vectors of static modes and fixed interface modes appears to be well suited for describing the high-frequency behavior of the substructure, i.e., where the number of contributing vibration modes is likely to be much higher than at low frequency. In other words, this space is supposed to be rich enough to accurately describe the low-frequency dynamics of the substructure. Hence, the following projection matrix $\mathbf{T}_{\mathtt{CB}}$ can be defined:

$$\mathbf{T}_{\mathtt{CB}} = \begin{bmatrix} \widetilde{\mathbf{X}}_{\mathtt{el}}(\omega_{\mathtt{max}}) & \mathbf{X}_{\mathtt{st}}(\omega_{\mathtt{max}}) \\ \mathbf{0} & \mathbf{I} \end{bmatrix}. \tag{10}$$

Let us write the DSM of the substructure as follows:

$$\mathbf{D} = \begin{bmatrix} \mathbf{D}_{\mathtt{II}} & \mathbf{D}_{\mathtt{IB}} \\ \mathbf{D}_{\mathtt{BI}} & \mathbf{D}_{\mathtt{BB}} \end{bmatrix}. \tag{11}$$

Hence, a reduced DSM can be defined as follows:

$$\mathbf{T}_{\mathtt{CB}}^T \mathbf{D} \mathbf{T}_{\mathtt{CB}} = \begin{bmatrix} \widetilde{\mathbf{D}}_{\mathtt{el-el}} & \widetilde{\mathbf{D}}_{\mathtt{el-st}} \\ \widetilde{\mathbf{D}}_{\mathtt{st-el}} & \mathbf{D}_{\mathtt{st-st}} \end{bmatrix}, \tag{12}$$

where

$$\widetilde{\mathbf{D}}_{\mathtt{el-el}} = \widetilde{\mathbf{X}}_{\mathtt{el}}(\omega_{\mathtt{max}})^T \mathbf{D}_{\mathtt{II}} \widetilde{\mathbf{X}}_{\mathtt{el}}(\omega_{\mathtt{max}}), \tag{13}$$

$$\widetilde{\mathbf{D}}_{\mathtt{el-st}} = \widetilde{\mathbf{D}}_{\mathtt{st-el}}^T = \widetilde{\mathbf{X}}_{\mathtt{el}}(\omega_{\mathtt{max}})^T \left(\mathbf{D}_{\mathtt{II}} \mathbf{X}_{\mathtt{st}}(\omega_{\mathtt{max}}) + \mathbf{D}_{\mathtt{IB}} \right), \tag{14}$$

$$\mathbf{D}_{\mathtt{st-st}} = \mathbf{D}_{\mathtt{BB}} + \mathbf{D}_{\mathtt{BI}} \mathbf{X}_{\mathtt{st}}(\omega_{\mathtt{max}}) + \mathbf{X}_{\mathtt{st}}(\omega_{\mathtt{max}})^T \mathbf{D}_{\mathtt{IB}} + \mathbf{X}_{\mathtt{st}}(\omega_{\mathtt{max}})^T \mathbf{D}_{\mathtt{II}} \mathbf{X}_{\mathtt{st}}(\omega_{\mathtt{max}}). \tag{15}$$

As a result, the condensed DSM of the substructure can be approximated as follows:

$$\mathbf{D}^* \approx \mathbf{D}_{\mathtt{st-st}} - \widetilde{\mathbf{D}}_{\mathtt{st-el}} \widetilde{\mathbf{D}}^{-1}_{\mathtt{el-el}} \widetilde{\mathbf{D}}_{\mathtt{el-st}}. \tag{16}$$

In this case, the computation of the right hand side term of Eq. (16) can be quickly achieved, which is explained by the fact that the size of the matrix $\widetilde{\mathbf{D}}_{\mathtt{el-el}}$ is small.

3 WFE method

3.1 Wave propagation

Let us denote by $\mathbf{q}_{\mathtt{L}}$ and $\mathbf{q}_{\mathtt{R}}$ (resp. $\mathbf{F}_{\mathtt{L}}$ and $\mathbf{F}_{\mathtt{R}}$) the displacement (resp. force) vectors at the the left ($\mathtt{L}$) and right ($\mathtt{R}$) boundaries of the substructure, respectively (see Figure 2). The dynamic equilibrium equation of the substructure can be written as follows:

$$\mathbf{D}^* \begin{bmatrix} \mathbf{q}_{\mathtt{L}} \\ \mathbf{q}_{\mathtt{R}} \end{bmatrix} = \begin{bmatrix} \mathbf{F}_{\mathtt{L}} \\ \mathbf{F}_{\mathtt{R}} \end{bmatrix} \quad \Rightarrow \quad \begin{bmatrix} \mathbf{D}^*_{\mathtt{LL}} & \mathbf{D}^*_{\mathtt{LR}} \\ \mathbf{D}^*_{\mathtt{RL}} & \mathbf{D}^*_{\mathtt{RR}} \end{bmatrix} \begin{bmatrix} \mathbf{q}_{\mathtt{L}} \\ \mathbf{q}_{\mathtt{R}} \end{bmatrix} = \begin{bmatrix} \mathbf{F}_{\mathtt{L}} \\ \mathbf{F}_{\mathtt{R}} \end{bmatrix}. \tag{17}$$

Assume that the left and right boundaries of the substructure are meshed in the same way with the same number n of DOFs. This particularly means that the vectors $\mathbf{q}_{\mathtt{L}}$, $\mathbf{q}_{\mathtt{R}}$, $\mathbf{F}_{\mathtt{L}}$ and $\mathbf{F}_{\mathtt{R}}$ have the same size of $n \times 1$, and that $\mathbf{D}^*_{\mathtt{LR}}$ and $\mathbf{D}^*_{\mathtt{RL}}$ in Eq. (17) are square matrices of size $n \times n$. Let us introduce the transfer matrix of the substructure — namely, $\mathbf{S}$, of size $2n \times 2n$ —, given by [13, 14]:

$$\mathbf{S} = \begin{bmatrix} -\mathbf{D}^{*-1}_{\mathtt{LR}} \mathbf{D}^*_{\mathtt{LL}} & -\mathbf{D}^{*-1}_{\mathtt{LR}} \\ \mathbf{D}^*_{\mathtt{RL}} - \mathbf{D}^*_{\mathtt{RR}} \mathbf{D}^{*-1}_{\mathtt{LR}} \mathbf{D}^*_{\mathtt{LL}} & -\mathbf{D}^*_{\mathtt{RR}} \mathbf{D}^{*-1}_{\mathtt{LR}} \end{bmatrix}. \tag{18}$$

Clearly speaking, the transfer matrix $\mathbf{S}$ links the displacement/force vectors between two consecutive substructures, i.e., between two consecutive interfaces (k) and $(k+1)$, as follows:

$$\begin{bmatrix} \mathbf{q}^{(k+1)}_{\mathtt{L}} \\ -\mathbf{F}^{(k+1)}_{\mathtt{L}} \end{bmatrix} = \mathbf{S} \begin{bmatrix} \mathbf{q}^{(k)}_{\mathtt{L}} \\ -\mathbf{F}^{(k)}_{\mathtt{L}} \end{bmatrix} \qquad \text{and} \qquad \begin{bmatrix} \mathbf{q}^{(k+1)}_{\mathtt{R}} \\ \mathbf{F}^{(k+1)}_{\mathtt{R}} \end{bmatrix} = \mathbf{S} \begin{bmatrix} \mathbf{q}^{(k)}_{\mathtt{R}} \\ \mathbf{F}^{(k)}_{\mathtt{R}} \end{bmatrix}, \tag{19}$$

where $\mathbf{q}^{(k)}_{\mathtt{R}} = \mathbf{q}^{(k)}_{\mathtt{L}}$ (resp. $\mathbf{q}^{(k+1)}_{\mathtt{R}} = \mathbf{q}^{(k+1)}_{\mathtt{L}}$) denotes the displacement vector at substructure interface (k) (resp. $(k+1)$) which corresponds either to the right side of the first substructure or the left side of the subsequent substructure. Also, $\mathbf{F}^{(k)}_{\mathtt{R}}$ and $\mathbf{F}^{(k)}_{\mathtt{L}}$ (resp. $\mathbf{F}^{(k+1)}_{\mathtt{R}}$ and $\mathbf{F}^{(k+1)}_{\mathtt{L}}$) are the force vectors at substructure interface (k) (resp. $(k+1)$), which are defined so that $\mathbf{F}^{(k)}_{\mathtt{R}} = -\mathbf{F}^{(k)}_{\mathtt{L}}$ (resp. $\mathbf{F}^{(k+1)}_{\mathtt{R}} = -\mathbf{F}^{(k+1)}_{\mathtt{L}}$) due to the action-reaction principle.

The eigenvalues and eigenvectors of the transfer matrix $\mathbf{S}$ are the so-called wave modes of the periodic structure, i.e., the one resulting from a one-dimensional periodic array of identical substructures as previously explained. The eigenvalues are denoted by μ_j which refer to the wave parameters, with the property that $\mu_j = \mathtt{exp}(-\mathtt{i}\beta_j d)$ where β_j and d have the meaning of wave numbers and substructure length. Also, the eigenvectors are denoted by $\boldsymbol{\phi}_j$ and refer to the wave shapes which are usually partitioned into displacement and force components as $\boldsymbol{\phi}_j = [\boldsymbol{\phi}^T_{\mathtt{q}j}\ \boldsymbol{\phi}^T_{\mathtt{F}j}]^T$.

Note that the transfer matrix $\mathbf{S}$ is symplectic [14], which means that the eigenvalues come in pairs, say, n eigenvalues μ_j defined so that $|\mu_j| < 1$ and which reflect right-going wave modes, and n eigenvalues $\mu^\star_j$ defined so that $\mu^\star_j = 1/\mu_j$ ($|\mu^\star_j| > 1$) which reflect left-going wave modes. The wave shapes can be partitioned accordingly into n right-going wave modes $\boldsymbol{\phi}_j$ and n left-going wave modes $\boldsymbol{\phi}^\star_j$.

Finally note that the computation of the eigenvalues and eigenvectors of the matrix $\mathbf{S}$ is usually undertaken using well-conditioned and accurate eigensolvers like the $\mathbf{S} + \mathbf{S}^{-1}$ transformation technique [10].

3.2 Forced response

Let us consider a finite-length periodic structure as shown in Figure 1, with a finite number N of substructures, and denote by (k) $(k = 1, \ldots, N+1)$ the interfaces between the substructures, starting from the left end until the right end of the periodic structure. Let us express the displacement and force vectors at a substructure boundary (k) using the basis of wave shapes. This yields [9]:

$$\mathbf{q}_{\mathtt{L}}^{(k)} = \mathbf{q}_{\mathtt{R}}^{(k)} = \boldsymbol{\Phi}_{\mathtt{q}} \boldsymbol{\mu}^{k-1} \mathbf{Q} + \boldsymbol{\Phi}_{\mathtt{q}}^{\star} \boldsymbol{\mu}^{N+1-k} \mathbf{Q}^{\star}, \tag{20}$$

$$-\mathbf{F}_{\mathtt{L}}^{(k)} = \mathbf{F}_{\mathtt{R}}^{(k)} = \boldsymbol{\Phi}_{\mathtt{F}} \boldsymbol{\mu}^{k-1} \mathbf{Q} + \boldsymbol{\Phi}_{\mathtt{F}}^{\star} \boldsymbol{\mu}^{N+1-k} \mathbf{Q}^{\star}, \tag{21}$$

where $\boldsymbol{\Phi}_{\mathtt{q}}$, $\boldsymbol{\Phi}_{\mathtt{q}}^{\star}$, $\boldsymbol{\Phi}_{\mathtt{F}}$ and $\boldsymbol{\Phi}_{\mathtt{F}}^{\star}$ are square $n \times n$ matrices defined by $\boldsymbol{\Phi}_{\mathtt{q}} = [\boldsymbol{\phi}_{\mathtt{q}1} \cdots \boldsymbol{\phi}_{\mathtt{q}n}]$, $\boldsymbol{\Phi}_{\mathtt{q}}^{\star} = [\boldsymbol{\phi}_{\mathtt{q}1}^{\star} \cdots \boldsymbol{\phi}_{\mathtt{q}n}^{\star}]$, $\boldsymbol{\Phi}_{\mathtt{F}} = [\boldsymbol{\phi}_{\mathtt{F}1} \cdots \boldsymbol{\phi}_{\mathtt{F}n}]$ and $\boldsymbol{\Phi}_{\mathtt{F}}^{\star} = [\boldsymbol{\phi}_{\mathtt{F}1}^{\star} \cdots \boldsymbol{\phi}_{\mathtt{F}n}^{\star}]$; also, $\boldsymbol{\mu} = \mathtt{diag}\{\mu_j\}_{j=1,\ldots,n}$ is the $n \times n$ diagonal matrix of the eigenvalues μ_j which are associated to the right-going wave modes, i.e., those for which $|\mu_j| < 1$; finally, $\mathbf{Q}$ and $\mathbf{Q}^{\star}$ are $n \times 1$ vectors of wave amplitudes.

The strategy to determine the displacement and force vectors of the periodic structure consists in computing the vectors of wave amplitudes $\mathbf{Q}$ and $\mathbf{Q}^{\star}$. This is achieved through the analysis of the boundary conditions (BCs), as explained hereafter.

For instance, consider the case of a periodic structure subject to known BCs such as two vectors $\mathbf{F}_0$ and $\mathbf{q}_0$ (prescribed forces and displacements) at the left and right ends, respectively. Remark that the left and right ends of the structure correspond to the substructure interfaces (1) and $(N+1)$, respectively. By considering Eqs. (20) and (21), the BCs can be expressed in wave-based form as follows:

$$-\mathbf{F}_0 = -\mathbf{F}_{\mathtt{L}}^{(1)} = \boldsymbol{\Phi}_{\mathtt{F}} \mathbf{Q} + \boldsymbol{\Phi}_{\mathtt{F}}^{\star} \boldsymbol{\mu}^{N} \mathbf{Q}^{\star} \qquad \text{(left end)}, \tag{22}$$

$$\mathbf{q}_0 = \mathbf{q}_{\mathtt{R}}^{(N+1)} = \boldsymbol{\Phi}_{\mathtt{q}} \boldsymbol{\mu}^{N} \mathbf{Q} + \boldsymbol{\Phi}_{\mathtt{q}}^{\star} \mathbf{Q}^{\star} \qquad \text{(right end)}. \tag{23}$$

As a result of Eqs. (22) and (23), the following $2n \times 2n$ wave-based matrix equation can be derived [15, 9]:

$$\begin{bmatrix} \mathbf{I}_n & \boldsymbol{\Phi}_{\mathtt{F}}^{-1} \boldsymbol{\Phi}_{\mathtt{F}}^{\star} \boldsymbol{\mu}^{N} \\ \boldsymbol{\Phi}_{\mathtt{q}}^{\star -1} \boldsymbol{\Phi}_{\mathtt{q}} \boldsymbol{\mu}^{N} & \mathbf{I}_n \end{bmatrix} \begin{bmatrix} \mathbf{Q} \\ \mathbf{Q}^{\star} \end{bmatrix} = \begin{bmatrix} -\boldsymbol{\Phi}_{\mathtt{F}}^{-1} \mathbf{F}_0 \\ \boldsymbol{\Phi}_{\mathtt{q}}^{\star -1} \mathbf{q}_0 \end{bmatrix}. \tag{24}$$

It can be proven that the matrix on the left-hand side of Eq. (24) is well-conditioned [15, 9], i.e., it can be inverted without difficulty. Also, the size of this matrix is $2n \times 2n$, i.e., it is small and can be quickly inverted.

As a second example, consider two periodic structures labeled 1 and 2, with N_1 and N_2 substructures (respectively), which are connected together on a coupling interface where the right end of structure 1 (substructure interface (N_1+1)) perfectly matches the left end of structure 2 (substructure interface (1)) (see for instance Figure 8). Also, consider two vectors of prescribed forces $\mathbf{F}_0$ and displacements $\mathbf{q}_0$ applied to the left end of structure 1 and the right end of structure 2, respectively. In this case, the BCs (including coupling conditions) of the structures are given by:

$$-\mathbf{F}_0 = -\mathbf{F}_{\mathtt{L}1}^{(1)} = \boldsymbol{\Phi}_{\mathtt{F}1} \mathbf{Q}_1 + \boldsymbol{\Phi}_{\mathtt{F}1}^{\star} \boldsymbol{\mu}_1^{N_1} \mathbf{Q}_1^{\star} \qquad \text{(left end of structure 1)}, \tag{25}$$

$$\mathbf{q}_0 = \mathbf{q}_{\mathtt{R}2}^{(N_2+1)} = \boldsymbol{\Phi}_{\mathtt{q}2} \boldsymbol{\mu}_2^{N_2} \mathbf{Q}_2 + \boldsymbol{\Phi}_{\mathtt{q}2}^{\star} \mathbf{Q}_2^{\star} \qquad \text{(right end of structure 2)}. \tag{26}$$

$$\mathbf{F}_{\mathtt{R}1}^{(N_1+1)} = -\mathbf{F}_{\mathtt{L}2}^{(1)} \quad \Rightarrow \quad \boldsymbol{\Phi}_{\mathtt{F}1} \boldsymbol{\mu}_1^{N_1} \mathbf{Q}_1 + \boldsymbol{\Phi}_{\mathtt{F}1}^{\star} \mathbf{Q}_1^{\star} = \boldsymbol{\Phi}_{\mathtt{F}2} \mathbf{Q}_2 + \boldsymbol{\Phi}_{\mathtt{F}2}^{\star} \boldsymbol{\mu}_2^{N_2} \mathbf{Q}_2^{\star} \qquad \text{(coupling condition)}, \tag{27}$$

$$\mathbf{q}_{\mathtt{R}1}^{(N_1+1)} = \mathbf{q}_{\mathtt{L}2}^{(1)} \quad \Rightarrow \quad \boldsymbol{\Phi}_{\mathtt{q}1} \boldsymbol{\mu}_1^{N_1} \mathbf{Q}_1 + \boldsymbol{\Phi}_{\mathtt{q}1}^{\star} \mathbf{Q}_1^{\star} = \boldsymbol{\Phi}_{\mathtt{q}2} \mathbf{Q}_2 + \boldsymbol{\Phi}_{\mathtt{q}2}^{\star} \boldsymbol{\mu}_2^{N_2} \mathbf{Q}_2^{\star} \qquad \text{(coupling condition)}. \tag{28}$$

Eqs. (27) and (28) yield:

$$\begin{bmatrix} \boldsymbol{\Phi}_{\mathtt{F}1}^{\star} & -\boldsymbol{\Phi}_{\mathtt{F}2} \\ \boldsymbol{\Phi}_{\mathtt{q}1}^{\star} & -\boldsymbol{\Phi}_{\mathtt{q}2} \end{bmatrix} \begin{bmatrix} \mathbf{Q}_1^{\star} \\ \mathbf{Q}_2 \end{bmatrix} = - \begin{bmatrix} \boldsymbol{\Phi}_{\mathtt{F}1} & -\boldsymbol{\Phi}_{\mathtt{F}2}^{\star} \\ \boldsymbol{\Phi}_{\mathtt{q}1} & -\boldsymbol{\Phi}_{\mathtt{q}2}^{\star} \end{bmatrix} \begin{bmatrix} \boldsymbol{\mu}_1^{N_1} \mathbf{Q}_1 \\ \boldsymbol{\mu}_2^{N_2} \mathbf{Q}_2^{\star} \end{bmatrix}, \tag{29}$$

i.e.,

$$\begin{bmatrix}\mathbf{Q}_1^\star\\ \mathbf{Q}_2\end{bmatrix} = \mathbb{C}\begin{bmatrix}\boldsymbol{\mu}_1^{N_1}\mathbf{Q}_1\\ \boldsymbol{\mu}_2^{N_2}\mathbf{Q}_2^\star\end{bmatrix} = \begin{bmatrix}\mathbb{C}_{11} & \mathbb{C}_{12}\\ \mathbb{C}_{21} & \mathbb{C}_{22}\end{bmatrix}\begin{bmatrix}\boldsymbol{\mu}_1^{N_1}\mathbf{Q}_1\\ \boldsymbol{\mu}_2^{N_2}\mathbf{Q}_2^\star\end{bmatrix}, \tag{30}$$

where $\mathbb{C}$ is the so-called scattering matrix, which in the present case is expressed by:

$$\mathbb{C} = -\begin{bmatrix}\boldsymbol{\Phi}_{\mathtt{F}1}^\star & -\boldsymbol{\Phi}_{\mathtt{F}2}\\ \boldsymbol{\Phi}_{\mathtt{q}1}^\star & -\boldsymbol{\Phi}_{\mathtt{q}2}\end{bmatrix}^{-1}\begin{bmatrix}\boldsymbol{\Phi}_{\mathtt{F}1} & -\boldsymbol{\Phi}_{\mathtt{F}2}^\star\\ \boldsymbol{\Phi}_{\mathtt{q}1} & -\boldsymbol{\Phi}_{\mathtt{q}2}^\star\end{bmatrix}. \tag{31}$$

Eqs. (25), (26) and (30) lead to:

$$\mathbf{Q}_1 + \boldsymbol{\Phi}_{\mathtt{F}1}^{-1}\boldsymbol{\Phi}_{\mathtt{F}1}^\star\boldsymbol{\mu}_1^{N_1}\mathbf{Q}_1^\star = -\boldsymbol{\Phi}_{\mathtt{F}1}^{-1}\mathbf{F}_0, \tag{32}$$

$$\mathbf{Q}_2^\star + \boldsymbol{\Phi}_{\mathtt{q}2}^{\star-1}\boldsymbol{\Phi}_{\mathtt{q}2}\boldsymbol{\mu}_2^{N_2}\mathbf{Q}_2 = \boldsymbol{\Phi}_{\mathtt{q}2}^{\star-1}\mathbf{q}_0, \tag{33}$$

$$\mathbf{Q}_1^\star - \mathbb{C}_{11}\boldsymbol{\mu}_1^{N_1}\mathbf{Q}_1 - \mathbb{C}_{12}\boldsymbol{\mu}_2^{N_2}\mathbf{Q}_2^\star = \mathbf{0}, \tag{34}$$

$$\mathbf{Q}_2 - \mathbb{C}_{21}\boldsymbol{\mu}_1^{N_1}\mathbf{Q}_1 - \mathbb{C}_{22}\boldsymbol{\mu}_2^{N_2}\mathbf{Q}_2^\star = \mathbf{0}. \tag{35}$$

In matrix form, this yields:

$$\begin{bmatrix}\mathbf{I}_n & \boldsymbol{\Phi}_{\mathtt{F}1}^{-1}\boldsymbol{\Phi}_{\mathtt{F}1}^\star\boldsymbol{\mu}_1^N & \mathbf{0} & \mathbf{0}\\ -\mathbb{C}_{11}\boldsymbol{\mu}_1^{N_1} & \mathbf{I}_n & \mathbf{0} & -\mathbb{C}_{12}\boldsymbol{\mu}_2^{N_2}\\ -\mathbb{C}_{21}\boldsymbol{\mu}_1^{N_1} & \mathbf{0} & \mathbf{I}_n & -\mathbb{C}_{22}\boldsymbol{\mu}_2^{N_2}\\ \mathbf{0} & \mathbf{0} & \boldsymbol{\Phi}_{\mathtt{q}2}^{\star-1}\boldsymbol{\Phi}_{\mathtt{q}2}\boldsymbol{\mu}^{N_2} & \mathbf{I}_n\end{bmatrix}\begin{bmatrix}\mathbf{Q}_1\\ \mathbf{Q}_1^\star\\ \mathbf{Q}_2\\ \mathbf{Q}_2^\star\end{bmatrix} = \begin{bmatrix}-\boldsymbol{\Phi}_{\mathtt{F}1}^{-1}\mathbf{F}_0\\ \mathbf{0}\\ \mathbf{0}\\ \boldsymbol{\Phi}_{\mathtt{q}2}^{\star-1}\mathbf{q}_0\end{bmatrix}. \tag{36}$$

Eq. (36) is a wave-based matrix equation, well-conditioned [15], whose size is small ($4n \times 4n$ in this case). Solving the wave-based matrix equation yields the vectors of wave amplitudes $\mathbf{Q}_1$, $\mathbf{Q}_1^\star$, $\mathbf{Q}_2$ and $\mathbf{Q}_2^\star$. The computation of the displacement and force vectors, for each structure, follows from the wave expansions (20) and (21).

The modeling of assemblies made up of several periodic structures (i.e., more than two), and other non-periodic components, can be assessed on the same way using the aforementioned strategy. This involves expressing the boundary/coupling conditions in wave-based forms (see [16] for further details), and expressing a whole wave-based matrix equation to compute the vectors of wave amplitudes of the periodic structures.

4 Numerical results

Numerical simulations are carried out to analyze the wave propagation behavior and dynamic response of periodic structures with viscoelastic properties. The substructures analyzed are square 2D cells with a small thickness of 0.002 m, which are made of aluminum material with inclusions of one or two tungsten parts (heavy material) surrounded by one or two rubber layers (viscoelastic material) as shown in Figures 3 and 6. The related material properties are listed in Table 1. Those substructures are meshed using 20×20 eight-node quadratic plane stress rectangular elements, leading to $n = 82$ interface DOFs. Within the framework of the CB method, 100 fixed interface modes are used to model the substructures (see before Eq. (10)). Single periodic structures, and assemblies made up of two periodic structures connected on their right/left ends, are studied. For each test case, the right end of the structure/assembly is assumed to be clamped and subject to a transverse support motion (vector $\mathbf{q}_0$).

The viscoelastic (rubber) layers are modeled with the generalized Maxwell model where $E_\infty = 0.15$ GPa and $n_v = 5$, see Eqs. (1)-(3). Here, the terms E_{vi} are defined such that $E_{vi} = cE_\infty\ \forall i$, where c is a proportionality coefficient (in percent). For each test case, the dispersion curves of the bending wave mode — i.e., the frequency evolutions of the real and imaginary parts of the wave number — are computed on a frequency band of $[0 - 5000]$ Hz, say, using 2500 discrete frequencies with a frequency step of 2 Hz. Also,

Table 1: Material properties.

Material	Young's modulus (GPa)	Density (kg/m^3)	Poisson's ratio	Loss factor
Aluminum	70	2700	0.3	0.005
Rubber	0.15 (E_∞)	950	0.48	0.005 (elastic case)
Tungsten	340	19250	0.27	0.005

the frequency response function (FRF) is assessed. In this case, the frequency evolution of the quadratic velocity $\|\mathtt{i}\omega\mathbf{q}\|^2$ at the left end of the structures/assembly is analyzed.

The structures with viscoelastic properties (rubber layers) are compared to purely elastic structures when the rubber layers are modeled with an equivalent Young's modulus of $E_\infty + \sum_{i=1}^{n_v} E_{vi} = E_\infty(1+5c)$, and a loss factor of 0.005.

4.1 Single periodic structures

4.1.1 One rubber layer

Let us start with a periodic structure with $N = 10$ substructures, as shown in Figure 3, which incorporate one rubber layer with a weak viscoelastic behavior, e.g., when the proportionality coefficient c in $E_{vi} = cE_\infty$ is equal to 2%. The dispersion curves of the bending wave mode are plotted along with the FRF of the structure as shown in Figure 4, where the solutions obtained from the purely elastic structure are compared to those obtained with a viscoelastic rubber layer.

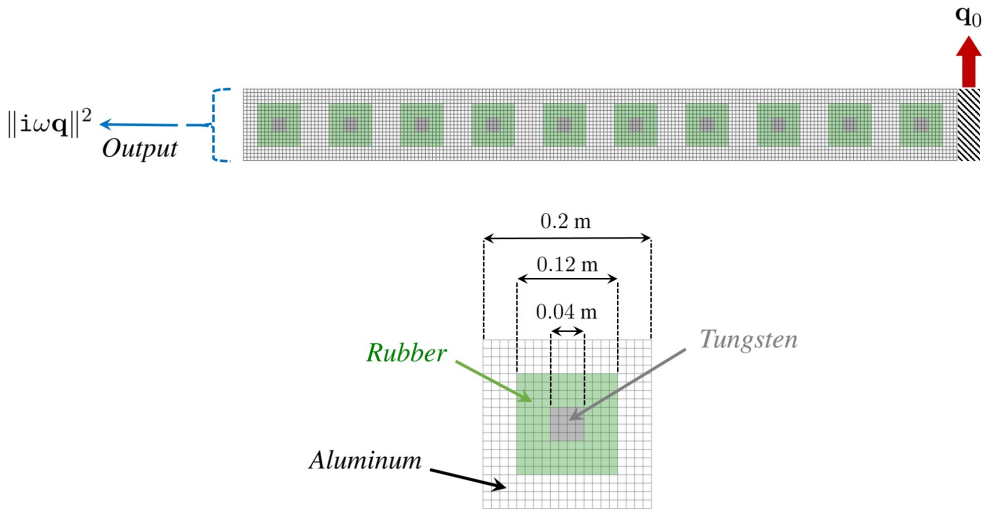


Figure 3: Single periodic structure with one rubber layer.

It is seen in Figure 4 that several locally resonant band gaps occur for the elastic and viscoelastic cases. They are localized around the resonance frequencies of the system tungsten-rubber parts, and represent frequency regions in which the quadratic velocity admits sudden and local decreases. Associated to this behavior are local increases of the magnitude of the imaginary part of the wave number, which means that the bending mode is becoming evanescent. Wide spread band gaps also occur due to Bragg scattering phenomena, e.g., between 2000 Hz and 3200 Hz when the real part of the wave number reaches 0 or π/d. However, their influence on the reduction of the vibration levels of the structure is less pronounced compared to locally resonant band gaps.

As for the locally resonant bang gaps, it is seen that, when compared to the elastic case, the viscoelastic case yields wider band gaps occurring at lower frequencies. Although not significant at low frequency (first band

gap), these trends appear to be magnified at high frequencies, e.g., with an increase of about 33% of the width of the fourth band gaps (around 3800 Hz) in favor of the viscoelastic case.

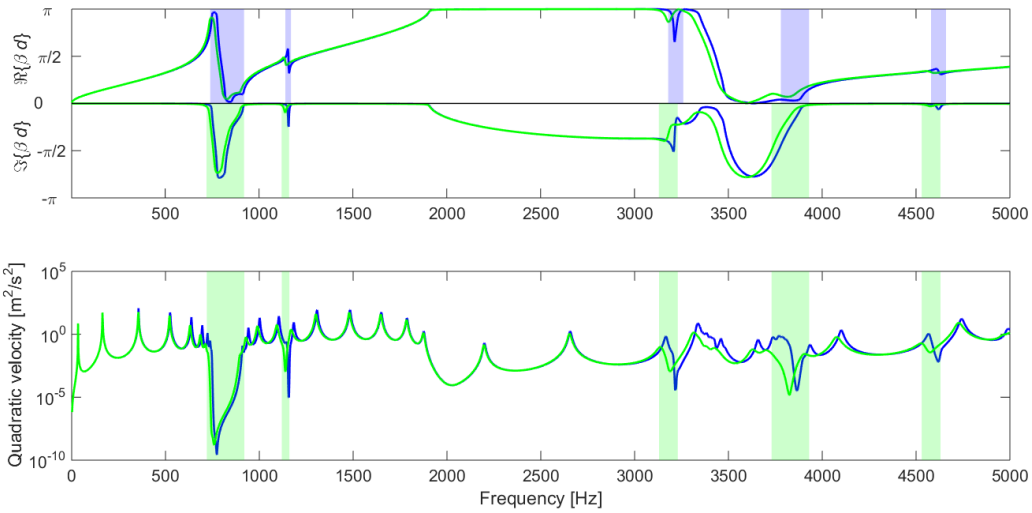


Figure 4: Dispersion curves and FRF for the structure shown in Figure 3, for the elastic case (blue line) and viscoelastic case (green line) when $c = 2\%$. (Blue shaded area) band gaps for the elastic case; (Green shaded area) band gaps for the viscoelastic case.

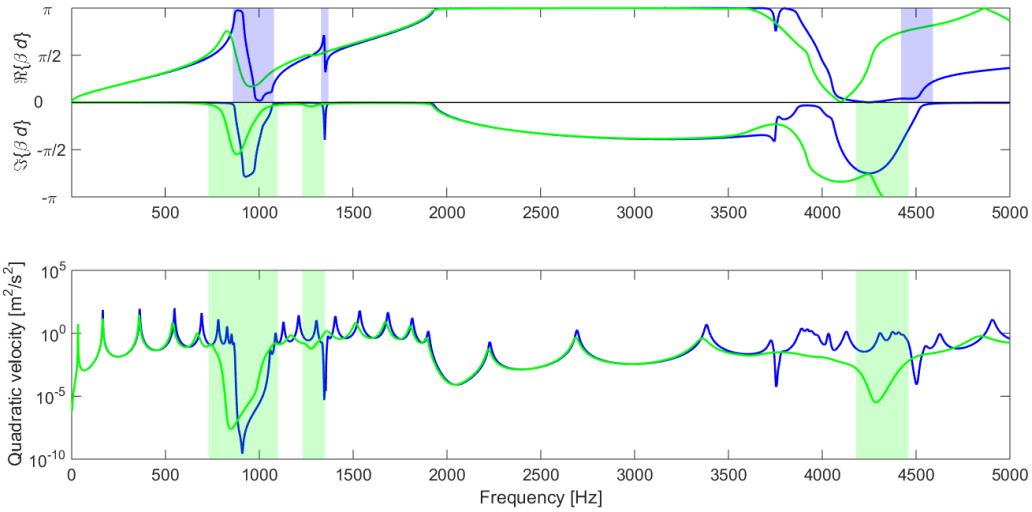


Figure 5: Dispersion curves and FRF for the structure shown in Figure 3, for the elastic case (blue line) and viscoelastic case (green line) when $c = 10\%$. (Blue shaded area) band gaps for the elastic case; (Green shaded area) band gaps for the viscoelastic case.

To further highlight the advantages of periodic structures with viscoelastic properties, a rubber layer with a strong viscoelastic behavior is considered, e.g., when $c = 10\%$. Again, the dispersion curves of the bending wave mode are plotted along with the FRF of the structure (see Figure 5). Three band gaps can be well identified for the viscoelastic case (green shaded area), which correspond to local decreases of the vibration levels of the structure. The corresponding band gaps, for the elastic case, are highlighted in blue shaded area in Figure 5. As expected, the structure with viscoelastic properties yields wide spread band gaps, with an increase of about 65% of the widths of the first and third band gaps, and 200% of the width the second band gap, compared to the purely elastic case. Also, they occur at lower frequencies.

4.1.2 Two rubber layers

The band gap effect can be improved by considering substructures with multiple local resonators. The design of such substructures may involve two rubber layers, one tungsten layer and one tungsten core as shown in Figure 6. Hence, a two masses-springs system tungsten-rubber can be considered which exhibits two low-frequency local resonances, and therefore, two locally resonant band gaps. Other band gaps are likely to occur at high frequencies at other resonance frequencies of the system tungsten-rubber. As for the rubber layers, a proportionality coefficient of 5% is considered which is midway between the two previous test cases. Again, a periodic structure with $N = 10$ substructures is considered. The related dispersion curves and FRF are shown in Figure 7.

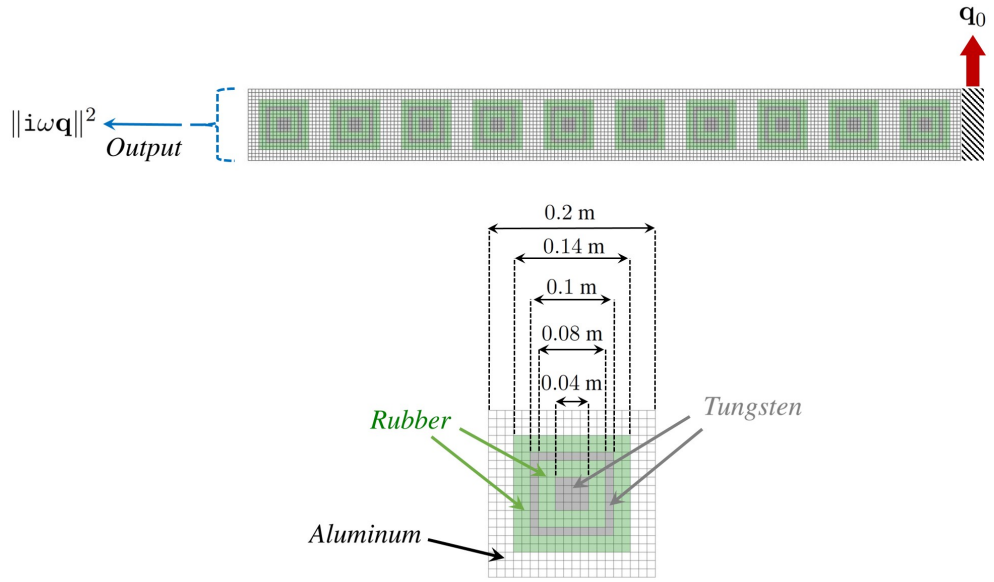


Figure 6: Single periodic structure with two rubber layers.

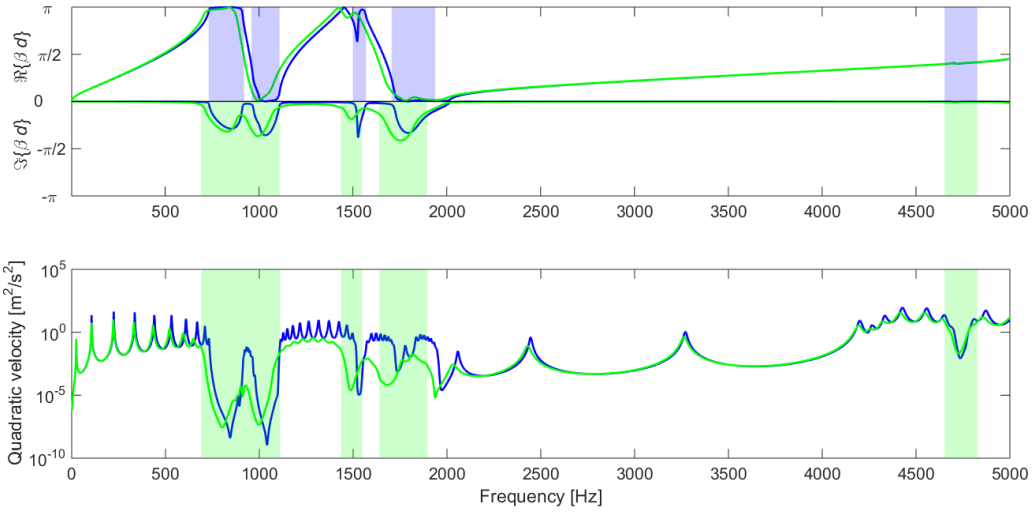


Figure 7: Dispersion curves and FRF for the structure shown in Figure 6, for the elastic case (blue line) and viscoelastic case (green line) when $c = 5\%$. (Blue shaded area) band gaps for the elastic case; (Green shaded area) band gaps for the viscoelastic case.

As expected, two locally resonant band gaps appear around 850 Hz and 1050 Hz which are close to each

other. In the purely elastic case, the FRF shows two local minima at these frequencies which appear to be well separated to each other. The interesting feature in the viscoelastic case is that these locally resonant band gaps can be merged together to yield a wide frequency band on which the vibration levels of the structure are well reduced, i.e., between 700 Hz and 1100 Hz (see Figure 7). Other band gaps also occur around 1500 Hz and 1750 Hz which appear to be wide compared to the elastic case. Finally note that a fourth band gap occurs around 4750 Hz where the FRF undergoes a sudden decrease. This is mostly linked to the behavior of the shearing wave mode, whose dispersion curves are not represented here.

4.2 Assembly of two periodic structures

A question which is often raised is whether the consideration of assemblies of different periodic structures can produce an added effect, i.e., when the band gaps of the structures overlap to generate wide attenuation zones of the FRF. To address this issue, an assembly made up of two periodic structures with different substructure properties is considered as shown in Figure 8. Here, a periodic structure 1 with $N_1 = 10$ single (rubber)-layered substructures (Figure 3) is considered which is connected to a second periodic structure 2 with $N_2 = 5$ two-layered substructures (Figure 6). In this case, a moderate proportionality coefficient $c = 5\%$ is used to describe the rubber layers of both structures.

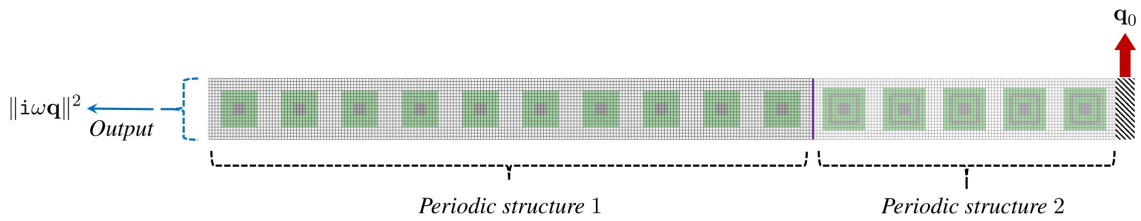


Figure 8: Assembly involving a first periodic structure with one rubber layer and a second periodic structure with two rubber layers.

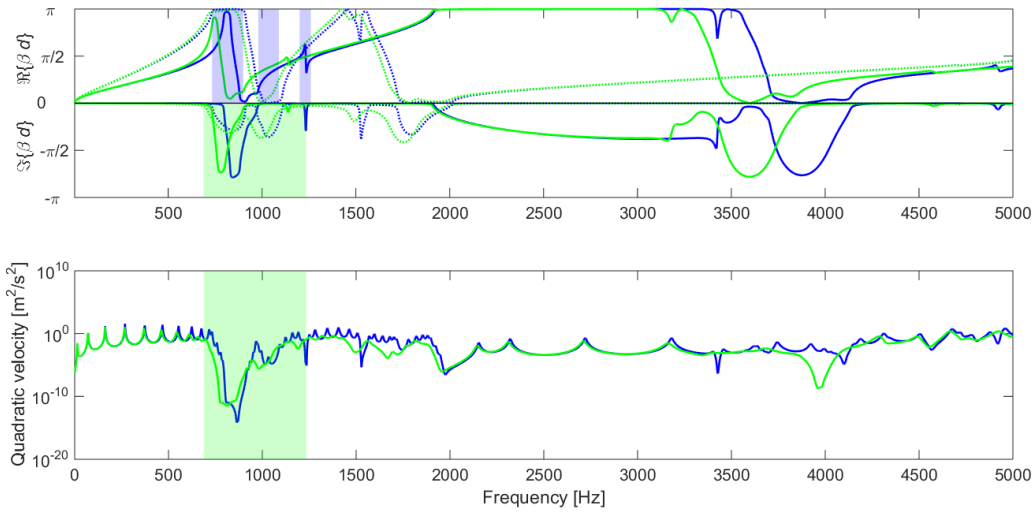


Figure 9: Dispersion curves for the structures shown in Figure 8 when $c = 5\%$: (Blue solid line) structure 1, elastic case, (Blue dotted line) structure 2, elastic case, (Green solid line) structure 1, viscoelastic case, (Green dotted line) structure 2, viscoelastic case. FRF of the assembly made up of structures 1 and 2: (Blue line) elastic case, (Green line) viscoelastic case.

The dispersion curves of the two structures are displayed in Figure 9 for the elastic and viscoelastic cases, along with the FRF of the structural assembly. Several band gaps occur at low frequencies for both structures,

e.g., between 700 Hz and 1250 Hz. These band gaps have been highlighted in the previous subsections. The key point here is that the vibration levels of the assembly can be highly reduced where the band gaps of the two structures coexist, e.g., around 850 Hz. The added effects of band gaps appear to be much more pronounced in the viscoelastic case with a wide attenuation zone between 700 Hz and 1250 Hz. Here, the first and second band gaps of the structure 1 overlap with the first band gap of structure 2 (see Figure 7). In contrast, the band gap effects issued from the purely elastic case appears to be localized as shown in Figure 9.

5 Conclusion

The WFE method has been applied to describe the wave propagation in periodic structures with viscoelastic properties. The harmonic forced response of periodic structures with a finite number of substructures, and assemblies composed of periodic structures with different substructure designs, has been analyzed. Several WFE strategies have been recalled and adapted to structures with viscoelastic properties, with a view to efficiently computing the wave modes and the FRFs. Several test cases have been considered which involve 2D substructures with one or two viscoelastic (rubber) layers and tungsten parts. Such structures exhibit locally resonant band gaps due to the consideration of resonant systems tungsten-rubber. It has been shown that, compared to the purely elastic case, the consideration of rubber layers with viscoelastic properties yields wide band gaps. This effect can be magnified for assemblies of periodic structures with different substructure designs, in which case the band gaps of the periodic structures overlap to generate a strong reduction of the vibration levels on wide frequency bands.

Acknowledgements

The authors express their thanks for the financial support provided by “Le Commissariat à l’énergie atomique et aux énergies alternatives (CEA)” and “La Région Centre”.

References

[1] W.-W. L. T.-M. Huang, J. Qian, *Structure-preserving algorithms for palindromic quadratic eigenvalue problems arising from vibration of fast trains*, SIAM Journal on Matrix Analysis and Applications, vol. 30, no. 4, (2009) pp. 1566–1592.

[2] Y. Xiao, B.R.Mace, J. Wen, X. Wen, *Formation and coupling of band gaps in a locally resonant elastic system comprising a string with attached resonators*, Physics Letters A, vol. 375, (2011) p. 14851491.

[3] Z. Wang, P. Zhang, Y. Zhang, *Locally Resonant Band Gaps in Flexural Vibrations of a Timoshenko Beam with Periodically Attached Multioscillators*, Mathematical Problems in Engineering, vol. Article ID 146975, (2013) p. 104110.

[4] A. Krushynska, V. Kouznetsova, M. Geers, *Towards optimal design of locally resonant acoustic metamaterials*, Journal of the Mechanics and Physics of Solids, vol. 71, (2014) pp. 179–196.

[5] P. Silva, J.-M. Mencik, J. Arruda, *On the use of the wave finite element method for passive vibration control of periodic structures*, Advances in Aircraft and Spacecraft Science, vol. 3, no. 3, (2016) pp. 299–315.

[6] Y.-F. Wang, Y.-S. Wang, V. Laude, *Wave propagation in two-dimensional viscoelastic metamaterials*, Physical Review B, vol. 92, (2015) p. 104110.

[7] B. Merheb, P. Deymier, M. Jain, M. Aloshyna-Lesuffleur, S. Mohanty, A. Berker, , R. W. Greger, *Elastic and viscoelastic effects in rubber/air acoustic band gap structures: A theoretical and experimental study*, Journal of Applied Physics, vol. 104, (2008) p. 064913.

[8] M. Lewinska, V. Kouznetsova, J. van Dommelen, A. Krushynska, *The attenuation performance of locally resonant acoustic metamaterials based on generalised viscoelastic modelling*, International Journal of Solids and Structures, vol. 126-127, (2017) pp. 163–174.

[9] J.-M. Mencik, *New advances in the forced response computation of periodic structures using the wave finite element (WFE) method*, Computational Mechanics, vol. 54, no. 3, (2014) pp. 789–801.

[10] J.-M. Mencik, D. Duhamel, *A wave-based model reduction technique for the description of the dynamic behavior of periodic structures involving arbitrary-shaped substructures and large-sized finite element models*, Finite Elements in Analysis and Design, vol. 101, (2015) pp. 1–14.

[11] J. Ferry, *Viscoelastic Properties of Polymers, 3rd ed., Chap. 5*, Wiley, New York (1980).

[12] L. Rouleau, J.-F. Deu, A. Legay, J.-F. Sigrist, F. L. Lay, P. Marin-Curtoud, *A component mode synthesis approach for dynamic analysis of viscoelastically damped structures*, Proceedings of the 10th World Congress on Computational Mechanics, Sao Paulo, Brazil.

[13] W. X. Zhong, F. W. Williams, *On the direct solution of wave propagation for repetitive structures*, Journal of Sound and Vibration, vol. 181, no. 3, (1995) pp. 485–501.

[14] J.-M. Mencik, M. N. Ichchou, *Multi-mode propagation and diffusion in structures through finite elements*, European Journal of Mechanics - A/Solids, vol. 24, no. 5, (2005) pp. 877–898.

[15] J.-M. Mencik, *On the low- and mid-frequency forced response of elastic systems using wave finite elements with one-dimensional propagation*, Computers and Structures, vol. 88, no. 11-12, (2010) pp. 674–689.

[16] J.-M. Mencik, *A wave finite element-based formulation for computing the forced response of structures involving rectangular flat shells*, International Journal for Numerical Methods in Engineering, vol. 95, no. 2, (2013) pp. 91–120.

Investigating simple designs of phononic crystal plates and their influence on the wave propagation properties

E.D. Nobrega[1 2], **M.-L. Gobert** [3], **J.M.C. Dos Santos** [1], **J.-M. Mencik** [3]
[1] Department of Computational Mechanics, Faculty of Mechanical Engineering, State University of Campinas
Cidade Universitria "Zeferino Vaz", Rua Mendeleyev, 200, 13083-860, Campinas-SP, Brazil
e-mail: **edilson.dantas@ufma.br**

[2] Federal University of Maranhão,
Bacanga, Av. dos Portugueses, 1966, 65080-805, São Luis-MA, Brazil

[3] INSA Centre Val de Loire, Université d'Orléans, Université de Tours, Laboratoire de Mécanique Gabriel Lamé, 3 rue de la Chocolaterie, F-41034 Blois, France

Abstract
Phononic crystals (PCs) are periodic structures whose shapes and material properties can be designed to enhance certain phenomena including band gaps, i.e., frequency regions in which waves do not propagate. This work focuses on periodic structures consisting of PC flat plates arranged along a triangular shaped pattern, each plate containing a periodic distribution of two material strips along its length. The structures hence present two levels of periodic variations, related respectively to the material properties of the strips and to the angle between the plates, which may generate band gaps. The coupling angle may create in particular wide attenuation zones due to wave mode conversion. In this paper, a parametric analysis is proposed to highlight its influence on the vibration levels of the above periodic structures. The computations of the wave modes and the frequency response functions of the structures are achieved using the Wave Finite Element method. The accuracy and efficiency of the approach are discussed through numerical comparisons with the Finite Element method.

1 Introduction

The engineering studies of periodic structures using wave propagation began to spread in the mid-70 with Mead's works [1, 2, 3, 4]. In recent decades, new methods have been developed that use the same basic concepts of periodicity together with approximated solutions as a way to reduce computational costs and to solve complex engineering models that cannot be solved analytically neither numerically using traditional methods [5, 6, 7, 14, 8]. One of them is the Wave Finite Element method (WFE), which consists of modeling a small slice of the elastic waveguide by FEM, to apply periodicity condition with Floquet-Bloch's theorem to obtain a transfer matrix eigenproblem. The solution provides complex wavenumbers and wave modes, from where wave motion amplitudes are obtained. The method has been applied successfully to various types of structures, such as beams, thin plates, cylindrical shells, including different material properties, couplings, and mediums.

Phononic crystals (PCs) constitute an example of periodic structures; they are made up of identical substructures/patterns arranged along a straight direction, whose shapes and material properties can be properly designed to enhance certain phenomena. Among these are band gaps which concern frequency regions on which waves do not propagate. In [10], the wave propagation in the audio frequency range within rod-shaped PCs and the dynamic response of the structure are investigated using analytical spectral elements for

periodic rods. The existence of band gaps in the dynamic responses is observed. An experimental test is performed to compare the numerical results. In [11], the wave propagation and vibration transmission in metamaterial-based elastic rods containing periodically attached multi-degree-of-freedom springmass resonators are investigated. For this purpose a methodology based on a combination of the spectral element method and the Bloch theorem is developed, yielding an explicit formulation for the complex band structure calculation. Recently, in the context of band gaps studies in PCs, those methods have been applied to beams and plates. For instance in [12], the vibration band gaps in a PC Euler beam on two-parameter foundation are investigated theoretically by the combination of the transfer matrix (TM) method and the Bloch theorem.

In this paper, we intend to investigate the wave propagation along periodic structures consisting of several PC flat plates arranged through a triangular shaped pattern, each rectangular plate being itself made of a periodic distribution of different material strips. In such structures involving two levels of periodic variations (related respectively to the variation of material properties in each plate, and to the angle variation between the plates), two-scale band gaps are expected to occur on different frequency bands. At a first level, band gaps are produced by the Bragg scattering effect when wavelengths of traveling waves become of the same order of magnitude than the width of a material strip. At a second level, wider attenuation zones might be achieved for appropriate angles between two PC flat plates, exploiting in particular the conversion mode phenomenon linked to the change of orientation between the plates. The aim of the paper is to study the influence of the coupling angle between the PC flat plates and of the periodicity pattern in each plate on the dispersion curves of the propagating modes and the frequency response functions (FRFs) of structures composed of a finite number of PC flat plates. The WFE method constitutes an efficient tool to perform this analysis.

The rest of the paper is organized as follows: in section 2, the WFE method is briefly recalled, and the coupling conditions between two strips of different materials and two plates of varying directions are specified. Numerical experiments are carried out in section 3, highlighting the efficiency of the proposed approach.

2 WFE modeling of the PC structure

The WFE method is applied to analyze a PC structure composed of several rectangular connected plates, each plate consisting in a periodic assembly of strips. Within the FE framework, a single strip may be viewed itself as a periodic structure, providing that it is meshed periodically in the direction of propagation. The strip is therefore equivalent to an assembly of N identical substructures having a same number of degrees of freedom (DOF) n on their left and right edges, as shown for instance in Figure 1.

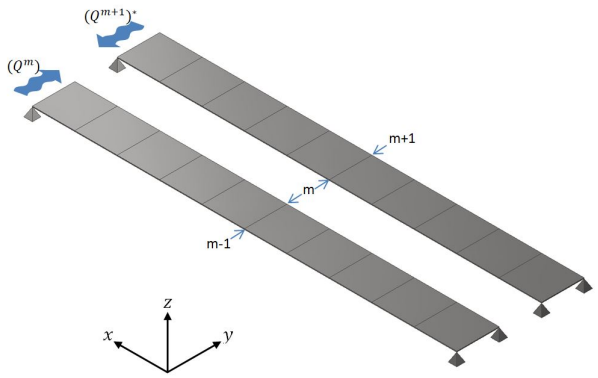


Figure 1: Example of two consecutive elementary substructures of a strip

The WFE method uses the dynamic stiffness matrix $\mathbf{D} = \mathbf{K} - \omega^2\mathbf{M}$ of the elementary substructure, where $\mathbf{K}$ and $\mathbf{M}$ are respectively the stiffness and mass matrices of the substructure, built from the classical plate

theory [9, 13].

The dynamic equilibrium equation of the substructure is then

$$\mathbf{D}\mathbf{q} = \mathbf{F}, \tag{1}$$

where $\mathbf{u}$ and $\mathbf{F}$ are respectively the vectors of DOFs and forces applied to the substructure. Assuming that there are no internal forces and partitioning the DOFS between the left and right edges and the internal domain of the substructure, Eq. (1) may be rewritten as follows:

$$\begin{bmatrix} \mathbf{D}_{ii} & \mathbf{D}_{il} & \mathbf{D}_{ir} \\ \mathbf{D}_{li} & \mathbf{D}_{ll} & \mathbf{D}_{lr} \\ \mathbf{D}_{ri} & \mathbf{D}_{rl} & \mathbf{D}_{rr} \end{bmatrix} \begin{Bmatrix} \mathbf{q}_i \\ \mathbf{q}_l \\ \mathbf{q}_r \end{Bmatrix} = \begin{Bmatrix} \mathbf{0} \\ \mathbf{F}_l \\ \mathbf{F}_r \end{Bmatrix}. \tag{2}$$

Expressing the internal DOFs as:

$$\mathbf{q}_i = \mathbf{D}_{ii}^{-1}(\mathbf{D}_{il}\mathbf{q}_l + \mathbf{D}_{ir}\mathbf{q}_r), \tag{3}$$

Eq. (2) may be condensed in the following form:

$$\begin{bmatrix} \mathbf{D}_{ll}^* & \mathbf{D}_{lr}^* \\ \mathbf{D}_{rl}^* & \mathbf{D}_{rr}^* \end{bmatrix} \begin{Bmatrix} \mathbf{q}_l \\ \mathbf{q}_r \end{Bmatrix} = \begin{Bmatrix} \mathbf{F}_l \\ \mathbf{F}_r \end{Bmatrix} \tag{4}$$

where the terms of the condensed dynamic stiffness $\mathbf{D}^*$ are respectively defined as $\mathbf{D}_{ll}^* = \mathbf{D}_{ll} - \mathbf{D}_{li}\mathbf{D}_{ii}^{-1}\mathbf{D}_{il}$, $\mathbf{D}_{rl}^* = \mathbf{D}_{rl} - \mathbf{D}_{ri}\mathbf{D}_{ii}^{-1}\mathbf{D}_{il}$, $\mathbf{D}_{lr}^* = \mathbf{D}_{lr} - \mathbf{D}_{li}\mathbf{D}_{ii}^{-1}\mathbf{D}_{ir}$, and $\mathbf{D}_{rr}^* = \mathbf{D}_{rr} - \mathbf{D}_{ri}\mathbf{D}_{ii}^{-1}\mathbf{D}_{ir}$.

Eq. (4) may finally be rearranged in a state vector form:

$$\underbrace{\begin{Bmatrix} \mathbf{q}_r \\ \mathbf{F}_r \end{Bmatrix}}_{\mathbf{u}_r} = \underbrace{\begin{bmatrix} -\mathbf{D}_{lr}^{*\,-1}\mathbf{D}_{ll}^* & -\mathbf{D}_{lr}^{*\,-1} \\ \mathbf{D}_{rl}^* - \mathbf{D}_{rr}^*\mathbf{D}_{lr}^{*\,-1}\mathbf{D}_{ll}^* & -\mathbf{D}_{rr}^*\mathbf{D}_{lr}^{*\,-1} \end{bmatrix}}_{\mathbf{T}} \underbrace{\begin{Bmatrix} \mathbf{q}_l \\ -\mathbf{F}_l \end{Bmatrix}}_{\mathbf{u}_l} \tag{5}$$

where $\mathbf{T}$ is the transfer matrix that relates the left state vector $\mathbf{u}_l$ to the right state vector $\mathbf{u}_r$ of the substructure.

2.1 Local periodicity condition

Let's now consider two consecutive substructures, numbered respectively m and $m+1$, within a single strip. The displacement continuity condition ${\mathbf{q}_r}^{(m)} = {\mathbf{q}_l}^{(m+1)}$ and the force balance ${\mathbf{F}_r}^{(m)} = -{\mathbf{F}_l}^{(m+1)}$ produce the condition ${\mathbf{u}_r}^{(m)} = {\mathbf{u}_l}^{(m+1)}$. Substituting this relation in Eq. (5), we obtain the following condition

$${\mathbf{u}_l}^{(m+1)} = \mathbf{T}{\mathbf{u}_l}^{(m)}. \tag{6}$$

The Floquet-Bloch's theorem for wave propagation in an infinite periodic system [2] applied to consecutive substructures gives

$$\begin{aligned} \mathbf{q}_l^{(m+1)} &= \mu\, \mathbf{q}_l^{(m)} \\ \mathbf{F}_l^{(m+1)} &= \mu\, \mathbf{F}_l^{(m)} \end{aligned} \tag{7}$$

where $\mu = e^{-i\beta d}$ is the attenuation constant, β the wavenumber and d the width of the substructure in the direction of propagation [11]. The periodic condition (6) may therefore be finally written as:

$$\mathbf{T}\mathbf{u}_l = \mu\, \mathbf{u}_l. \tag{8}$$

From Eq. (5) it is observed that $\mathbf{T}$ depends on the term $\mathbf{D}_{lr}^{*\,-1}$. However, even if the matrix $\mathbf{D}_{lr}^*$ is invertible, numerical ill-conditioning is likely to occur. To avoid this issue, a representation by displacement/rotation

vector alone is preferable [15]. By rewriting the state vectors as functions of the left and right displacement/rotation vectors:

$$\mathbf{u}_l = \underbrace{\begin{bmatrix} \mathbf{I}_n & \mathbf{0} \\ -\mathbf{D}^*_{ll} & -\mathbf{D}^*_{lr} \end{bmatrix}}_{\mathbf{L}} \underbrace{\begin{Bmatrix} \mathbf{q}_l \\ \mathbf{q}_r \end{Bmatrix}}_{\mathbf{w}} \quad \text{and} \quad \mathbf{u}_r = \underbrace{\begin{bmatrix} \mathbf{0} & \mathbf{I}_n \\ \mathbf{D}^*_{rl} & \mathbf{D}^*_{rr} \end{bmatrix}}_{\mathbf{N}} \underbrace{\begin{Bmatrix} \mathbf{q}_l \\ \mathbf{q}_r \end{Bmatrix}}_{\mathbf{w}}, \tag{9}$$

the transfer matrix can be expressed as $\mathbf{T} = \mathbf{N}\mathbf{L}^{-1}$, where the matrices $\mathbf{L}$ and $\mathbf{N}$ are invertible if $\mathbf{D}^*_{lr}$ is invertible. Thus, Eq. (8) leads to the generalized eigenequation

$$\mu \mathbf{L}\mathbf{w} = \mathbf{N}\mathbf{w}, \tag{10}$$

admitting $2n$ eigenvalues $\mu_j = e^{-i\beta_j d}$ and eigenvectors $\mathbf{w}_j$. The eigenvectors of the initial problem (8) are then computed as $\mathbf{\Phi}_j = \mathbf{L}\mathbf{w}_j$. In the above equations, β_j represents the wavenumber, and $\mathbf{\Phi}_j$ the corresponding wave mode. It can also be shown that the eigenvalues come in pairs $\{\mu_j, \mu_j^\star\}$ for $j = 1, \dots n$, with $\mu_j^\star = 1/\mu_j$; the first set of eigenvalues verify the property $|\mu_j| \leq 1$ and correspond to waves traveling towards the right direction, while for the second set $|\mu_j^\star| \geq 1$, which corresponds to waves traveling towards the left direction. The corresponding eigenvectors are denoted respectively as $\mathbf{\Phi}_j$ and $\mathbf{\Phi}_j^\star$, $j = 1, \dots, n$. Defining matrices $\boldsymbol{\mu} = \text{diag}\{\mu_j\}_{j=1,\dots,n}$, $\boldsymbol{\mu}^\star = \text{diag}\{\mu_j^\star\}_{j=1,\dots,n}$, $\mathbf{\Phi} = \{\mathbf{\Phi}_j\}_{j=1,\dots,n}$ and $\mathbf{\Phi}^\star = \{\mathbf{\Phi}_j^\star\}_{j=1,\dots,n}$, the state vector $\mathbf{u}_l^{(m)}$ of the m^{th} substructure can be finally expressed as [16]:

$$\mathbf{u}_l^{(m)} = \mathbf{\Phi}\, \mathbf{Q}^{(m)} + \mathbf{\Phi}^\star\, \mathbf{Q}^{\star(m)}, \quad m = 1 \dots N+1, \tag{11}$$

where $\mathbf{Q}^{(m)}$ and $\mathbf{Q}^{\star\,(m)}$ are the $n \times 1$ vectors of wave amplitudes at the left boundary of the m^{th} substructure and depend on the boundary conditions at the extremities of the whole structure. They satisfy the following properties: $\mathbf{Q}^{(m+1)} = \boldsymbol{\mu}\mathbf{Q}^{(m)}$ and $\mathbf{Q}^{\star(m)} = \boldsymbol{\mu}\mathbf{Q}^{\star(m+1)}$. Defining the amplitude vectors $\mathbf{Q} = \mathbf{Q}^{(1)}$ and $\mathbf{Q}^\star = \mathbf{Q}^{\star(N+1)}$ at the extremities of a strip (N being the number of substructures composing the strip), as illustrated in Figure 2, Eq. (11) may be rewritten as follows:

$$\mathbf{u}_l^{(m)} = \mathbf{\Phi}\, \boldsymbol{\mu}^{m-1}\, \mathbf{Q} + \mathbf{\Phi}^\star\, \boldsymbol{\mu}^{N+1-m}\, \mathbf{Q}^\star, \quad m = 1 \dots N+1. \tag{12}$$

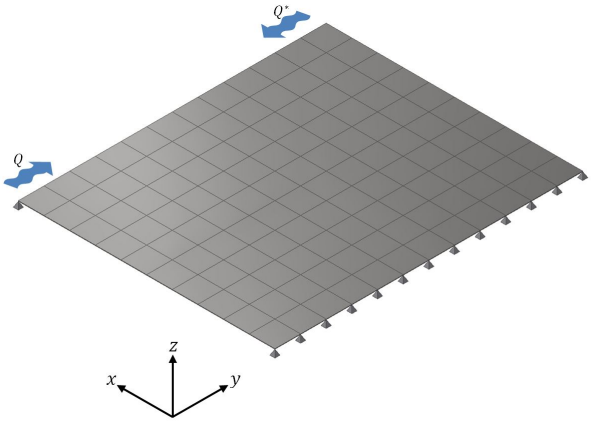


Figure 2: Example of a strip containing 12 substructures where $\mathbf{Q} = \mathbf{Q}^{(1)}$ and $\mathbf{Q}^\star = \mathbf{Q}^{\star\,(N+1)}$.

For a single isolated strip with prescribed boundary conditions, the unknown amplitude vectors $\mathbf{Q}$ and $\mathbf{Q}^\star$ are computed by solving a matrix system that expresses the boundary conditions in matrix form. As an illustration, we consider the case of a strip which is subject to a force vector $\mathbf{F}_0$ on its left end and prescribed

displacements/rotations $\mathbf{q}_0$ on its right end. Further partitioning the eigenvector matrices as $\mathbf{\Phi} = \left[\mathbf{\Phi}_{\mathrm{q}}^T \; \mathbf{\Phi}_{\mathrm{F}}^T\right]^T$ and $\mathbf{\Phi}^\star = \left[\mathbf{\Phi}_{\mathrm{q}}^{\star T} \; \mathbf{\Phi}_{\mathrm{F}}^T\right]^{\star T}$, the boundary conditions may be written as

$$\mathbf{\Phi}_{\mathrm{F}}\,\mathbf{Q} + \mathbf{\Phi}_{\mathrm{F}}^\star\,\boldsymbol{\mu}^N\,\mathbf{Q}^\star = -\mathbf{F}_0, \tag{13}$$

$$\mathbf{\Phi}_{\mathrm{q}}\,\boldsymbol{\mu}^N\,\mathbf{Q} + \mathbf{\Phi}_{\mathrm{q}}^\star\,\mathbf{Q}^\star = \mathbf{q}_0. \tag{14}$$

The computation of $\mathbf{Q}$ and $\mathbf{Q}^\star$ follows from the inversion of the resulting matrix system

$$\begin{bmatrix} \mathbf{I}_n & \mathbf{\Phi}_{\mathrm{F}}^{-1}\,\mathbf{\Phi}_{\mathrm{F}}^\star\boldsymbol{\mu}^N \\ \mathbf{\Phi}_{\mathrm{q}}^{\star\,-1}\,\mathbf{\Phi}_{\mathrm{q}}\,\boldsymbol{\mu}^N & \mathbf{I}_n \end{bmatrix} \begin{bmatrix} \mathbf{Q} \\ \mathbf{Q}^\star \end{bmatrix} = \begin{bmatrix} -\mathbf{\Phi}_{\mathrm{F}}^{-1}\,\mathbf{F}_0 \\ \mathbf{\Phi}_{\mathrm{q}}^{\star\,-1}\,\mathbf{q}_0 \end{bmatrix}, \tag{15}$$

where $\mathbf{I}_n$ is the identity matrix of rank n.

2.2 Coupling conditions

Within the PC structure, several strips of different materials are connected in a periodic way, and coupling conditions apply at the interfaces between two consecutive strips. According to Eq. (12), for any strip (i) composed of N_i substructures having n_i DOFs on each left/right boundary, the state vector at the m^{th} substructure is now given by the following expression:

$$\mathbf{u}_{l,i}^{(m)} = \mathbf{\Phi}_i\,\boldsymbol{\mu}_i^{m-1}\,\mathbf{Q}_i + \mathbf{\Phi}_i^\star\,\boldsymbol{\mu}_i^{N_i+1-m}\,\mathbf{Q}_i^\star, \tag{16}$$

with again $\mathbf{Q}_i = \mathbf{Q}_i^{(1)}$ and $\mathbf{Q}_i^\star = \mathbf{Q}_i^{\star\,(N_i+1)}$ (as illustrated in Figure 3).

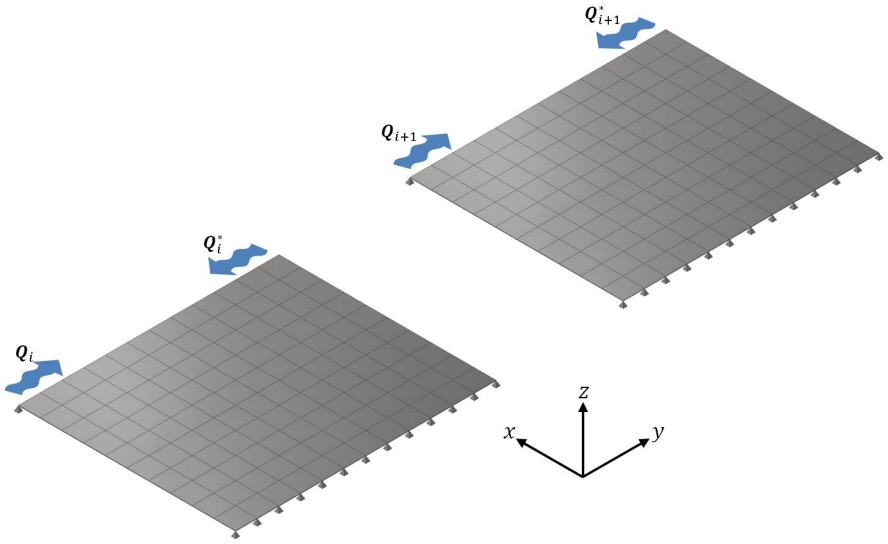


Figure 3: Coupling of two consecutive strips.

At the interface between two consecutive strips (i) and $(i+1)$ where an external excitation $\mathbf{F}_{ex}$ may apply, the coupling conditions are written:

$$\mathbf{q}_i^{(N_i+1)} = \mathbf{q}_{i+1}^{(1)} \tag{17}$$

$$\mathbf{F}_{L,i}^{(N_i+1)} + \mathbf{F}_{ex} = \mathbf{F}_{L,i+1}^{(1)}, \tag{18}$$

that is, in matrix form,

$$\mathbf{\Phi}_{\mathrm{q},i}\,\boldsymbol{\mu}^{N_i}\,\mathbf{Q}_i + \mathbf{\Phi}_{\mathrm{q},i}^\star\,\mathbf{Q}_i^\star = \mathbf{\Phi}_{\mathrm{q},i+1}\,\mathbf{Q}_{i+1} + \mathbf{\Phi}_{\mathrm{q},i+1}^\star\,\boldsymbol{\mu}_{i+1}^{N_{i+1}}\,\mathbf{Q}_{i+1}^\star \tag{19}$$

$$-\mathbf{\Phi}_{\mathrm{F},i}\,\boldsymbol{\mu}^{N_i}\,\mathbf{Q}_i - \mathbf{\Phi}_{\mathrm{F},i}^\star\,\mathbf{Q}_i^\star + \mathbf{F}_{ex} = -\mathbf{\Phi}_{\mathrm{F},i+1}\,\mathbf{Q}_{i+1} - \mathbf{\Phi}_{\mathrm{F},i+1}^\star\,\boldsymbol{\mu}_{i+1}^{N_{i+1}}\,\mathbf{Q}_{i+1}^\star. \tag{20}$$

Taking into account that in our case $n_i = n_{i+1} = n$ (the case $n_i \neq n_{i+1}$ may be considered by using Lagrange multipliers, as developed for instance in [17]), the above equations may be simplified into the following matrix system:

$$\mathbf{A} \left[\begin{array}{c} \mathbf{Q}_i^\star \\ \mathbf{Q}_{i+1} \end{array} \right] = \mathbf{B} \left[\begin{array}{c} \boldsymbol{\mu}_i^{N_i} \mathbf{Q}_i \\ \boldsymbol{\mu}_{i+1}^{N_{i+1}} \mathbf{Q}_{i+1}^\star \end{array} \right] + \left[\begin{array}{c} \mathbf{0} \\ -(\boldsymbol{\Phi}_{\mathrm{F}\,i+1})^{-1} \mathbf{F}_{ex} \end{array} \right] \quad \text{where} \tag{21}$$

$$\mathbf{A} = \left[\begin{array}{cc} \mathbf{I}_n & -(\boldsymbol{\Phi}_{\mathrm{q},i}^\star)^{-1} \boldsymbol{\Phi}_{\mathrm{q},i+1} \\ -(\boldsymbol{\Phi}_{\mathrm{F},i+1})^{-1} \boldsymbol{\Phi}_{\mathrm{F},i}^\star & \mathbf{I}_n \end{array} \right] \quad \mathbf{B} = \left[\begin{array}{cc} -(\boldsymbol{\Phi}_{\mathrm{q},i}^\star)^{-1} \boldsymbol{\Phi}_{\mathrm{q},i} & (\boldsymbol{\Phi}_{\mathrm{q},i}^\star)^{-1} \boldsymbol{\Phi}_{\mathrm{q},i+1}^\star \\ (\boldsymbol{\Phi}_{\mathrm{F},i+1})^{-1} \boldsymbol{\Phi}_{\mathrm{F},i} & -(\boldsymbol{\Phi}_{\mathrm{F},i+1})^{-1} \boldsymbol{\Phi}_{\mathrm{F},i+1}^\star \end{array} \right].$$

As in [17] the latter matrix system may be finally put in the following form:

$$\left[\begin{array}{c} \mathbf{Q}_i^\star \\ \mathbf{Q}_{i+1} \end{array} \right] = \mathbb{C} \left[\begin{array}{c} \boldsymbol{\mu}_i^{N_i} \mathbf{Q}_i \\ \boldsymbol{\mu}_{i+1}^{N_{i+1}} \mathbf{Q}_{i+1}^\star \end{array} \right] + \mathbb{F} \quad \text{with} \tag{22}$$

$$\mathbb{C} = \left[\begin{array}{cc} \mathbb{C}_{i,i}^\star & \mathbb{C}_{i,i+1}^\star \\ \mathbb{C}_{i+1,i} & \mathbb{C}_{i+1,i+1} \end{array} \right] = \mathbf{A}^{-1} \mathbf{B} \quad \text{and} \quad \mathbb{F} = \left[\begin{array}{c} \mathbb{F}_i^\star \\ \mathbb{F}_{i+1} \end{array} \right] = \mathbf{A}^{-1} \left[\begin{array}{c} \mathbf{0} \\ -(\boldsymbol{\Phi}_{\mathrm{F},i+1})^{-1} \mathbf{F}_{ex} \end{array} \right].$$

In the above equation, $\mathbb{C}_{i,i}$ and $\mathbb{C}_{i+1,i+1}$) are square matrices of size $n \times n$ that express the reflection coefficients of the wave modes of the strips respectively (i) and $(i+1)$ at the interface. The $n \times n$ matrices $\mathbb{C}_{i,i+1}^\star$ and $\mathbb{C}_{i+1,i}$ contain the transmission coefficients between the wave modes of the two strips at the interface. Finally, the vector $\mathbb{F}$ takes into account possible excitation sources at the interface.

For p strips connected to each other, a complete matrix system may be built by applying Eq. (22) at all the interfaces between strip (i) and $(i+1)$ for $i = 1 \ldots p-1$, and boundary conditions at the left end of strip (1) and the right end of strip (p). As an example, if the same Newmann / Dirichlet boundary conditions as in the previous section apply, Eqs. (13) and (14) become

$$\mathbf{Q}_1 + (\boldsymbol{\Phi}_{\mathrm{F},1})^{-1} \boldsymbol{\Phi}_{\mathrm{F},1}^\star \, \boldsymbol{\mu}_1^{N_1} \, \mathbf{Q}_1^\star = -(\boldsymbol{\Phi}_{\mathrm{F},1})^{-1} \mathbf{F}_0, \tag{23}$$

$$(\boldsymbol{\Phi}_{\mathrm{q},p}^\star)^{-1} \, \boldsymbol{\Phi}_{\mathrm{q},p} \, \boldsymbol{\mu}_p^{N_p} \, \mathbf{Q}_p + \mathbf{Q}_p^\star = (\boldsymbol{\Phi}_{\mathrm{q},p}^\star)^{-1} \, \mathbf{q}_0. \tag{24}$$

In the latter case, the computation of the unknown wave amplitudes for the set of p strips follows from the inversion of the final system

$$\boldsymbol{\Psi} \, \mathcal{Q} = \mathcal{F} \quad \text{where} \quad \mathcal{Q} = \left[\begin{array}{c} \mathbf{Q}_1 \\ \mathbf{Q}_1^\star \\ \mathbf{Q}_2 \\ \mathbf{Q}_2^\star \\ \vdots \\ \mathbf{Q}_p \\ \mathbf{Q}_p^\star \end{array} \right], \quad \mathcal{F} = \left[\begin{array}{c} -(\boldsymbol{\Phi}_{\mathrm{F},1})^{-1} \mathbf{F}_0 \\ \mathbb{F}_1^\star \\ \mathbb{F}_2 \\ \mathbb{F}_2^\star \\ \vdots \\ \mathbb{F}_p \\ (\boldsymbol{\Phi}_{\mathrm{q},p}^\star)^{-1} \, \mathbf{q}_0 \end{array} \right], \quad \text{and} \tag{25}$$

$$\boldsymbol{\Psi} = \left[\begin{array}{ccccccc} \mathbf{I_n} & (\boldsymbol{\Phi}_{\mathrm{F},1})^{-1} \boldsymbol{\Phi}_{\mathrm{F},1}^\star \, \boldsymbol{\mu}_1^{N_1} & \mathbf{0} & \mathbf{0} & \ldots & \mathbf{0} & \mathbf{0} \\ -\mathbb{C}_{1,1}^\star \, \boldsymbol{\mu}_1^{N_1} & \mathbf{I_n} & \mathbf{0} & -\mathbb{C}_{1,2}^\star \, \boldsymbol{\mu}_2^{N_2} & \ldots & \mathbf{0} & \mathbf{0} \\ -\mathbb{C}_{2,1} \, \boldsymbol{\mu}_1^{N_1} & \mathbf{0} & \mathbf{I_n} & -\mathbb{C}_{2,2} \, \boldsymbol{\mu}_2^{N_2} & \ldots & \mathbf{0} & \mathbf{0} \\ \mathbf{0} & \mathbf{0} & -\mathbb{C}_{2,2}^\star \, \boldsymbol{\mu}_2^{N_2} & \mathbf{I_n} & \ldots & \mathbf{0} & \mathbf{0} \\ \vdots & \vdots & \vdots & \vdots & \ddots & \vdots & \vdots \\ \mathbf{0} & \mathbf{0} & \mathbf{0} & \mathbf{0} & \ldots & \mathbf{I_n} & -\mathbb{C}_{p,p} \, \boldsymbol{\mu}_p^{N_p} \\ \mathbf{0} & \mathbf{0} & \mathbf{0} & \mathbf{0} & \ldots & (\boldsymbol{\Phi}_{\mathrm{q},p}^\star)^{-1} \, \boldsymbol{\Phi}_{\mathrm{q},p} \, \boldsymbol{\mu}_p^{N_p} & \mathbf{I_n} \end{array} \right].$$

The displacements/rotations and forces at any location of any strip are then computed from Eq. (16).

The same kind of formulation applies when modifying the orientation of a strip by introducing a θ angle between the strip and the horizontal direction, but the wave modes matrices $\boldsymbol{\Phi}_i$ and $\boldsymbol{\Phi}_i^\star$ are multiplied by rotation matrices depending on θ.

3 Numerical results

Numerical experiments are performed for various PC structures made up of an assembly of 6 plates arranged along a triangular pattern. Each plate is composed of an alternation of 3 strips (either two steel strips and one aluminum strip, or two aluminum strip and one steel strip), as depicted in Figure 4. The dimensions

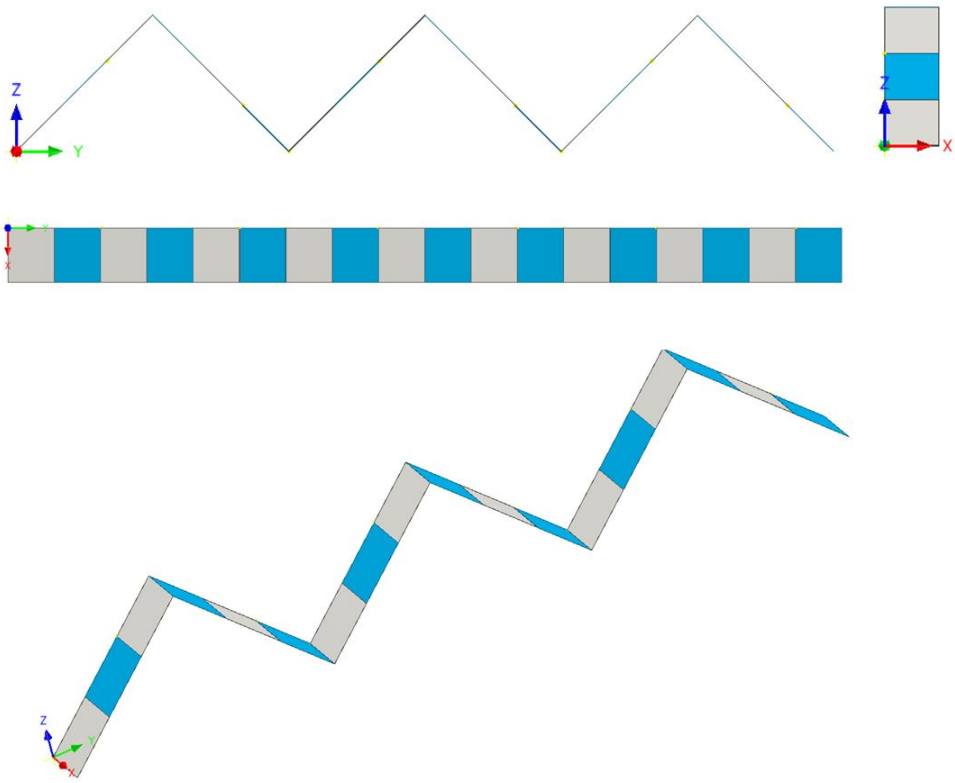


Figure 4: PC structure composed of 18 alternate strips made of steel (grey color) and aluminum (blue color).

(specified in Table 1) and meshing properties of the different strips are chosen similar, each strip being composed of 12 identical substructures of width $d = 0.05$ in the direction of propagation (y for $\theta = 0°$). The mesh of each substructure contains 1 shell element in the direction of propagation and 10 elements in the $x-$direction. The differences between the strips are linked to the properties of the chosen materials, which are also detailed in Table 1; for both materials, a damping is considered through a loss factor $\eta = 0.005$. The influence of the coupling angle between the plates on the responses of the PC structures is investigated by making the angle θ (between the first plate direction and the horizontal axis) varying from $0°$ to $60°$ with a step of $15°$.

Material and geometrical properties of the strips	Steel	Aluminum
$E\,[Pa]$	$210e9$	$70e9$
$\rho\,[kg/m^3]$	7800	2700
η	0.005	0.005
ν	0.3	0.3
$h\,[m]$	0.001	0.001
$L_x\,[m]$	0.5	0.5
$L_y\,[m]$	0.6	0.6

Table 1: Strip configurations

The 18 strips involved in the PC structure are supposed simply supported along their longitudinal edges. The whole PC structure is free on its left end ($y = 0$) and clamped on its right extremity ($y = y_{end}$ which depends

on the θ value). A punctual harmonic excitation is applied at the node of coordinates $(0.05, 0, 0)$ located on the free end, with a magnitude of $1N$ in the z direction. The frequency range considered in this study is $[0; 100]$ Hz with a frequency step of 0.2 Hz.

For comparison purposes, the case of a structure composed of a single material (chosen as steel) is also presented, for the same angle configurations ($\theta = 0°$ to $\theta = 45°$ by $15°$).

The frequency responses of the structures are computed using the WFE formulations described above, and compared to the reference solution obtained with the classic FE method. In the following, two quantities are considered to analyze the results obtained in the different configurations: the displacement in the $z-$direction at the forcing position (node of coordinates $(0.05, 0, 0)$ on the left end), and the transmittance, defined as the ratio of the reaction force in the $z-$direction at the node of coordinates $(0.05, y_{end}, 0)$ located on the right end to the excitation force.

The results obtained for the steel structure with $\theta = 0°$ are first presented in Figures 5 (displacement) and 6 (transmittance). A good agreement can be found in Figure 5 between the WFE results (solid line in blue color) and the FEM results (dotted line in red color), throughout the frequency range, with error levels far below 1%. In terms of computational times, the elapsed time obtained in Matlab for the WFE method is 607s, while the FE computation requires $2e4$s. The gain of computational time in this case reaches here about 97%, hence highlighting the efficiency of the proposed approach.

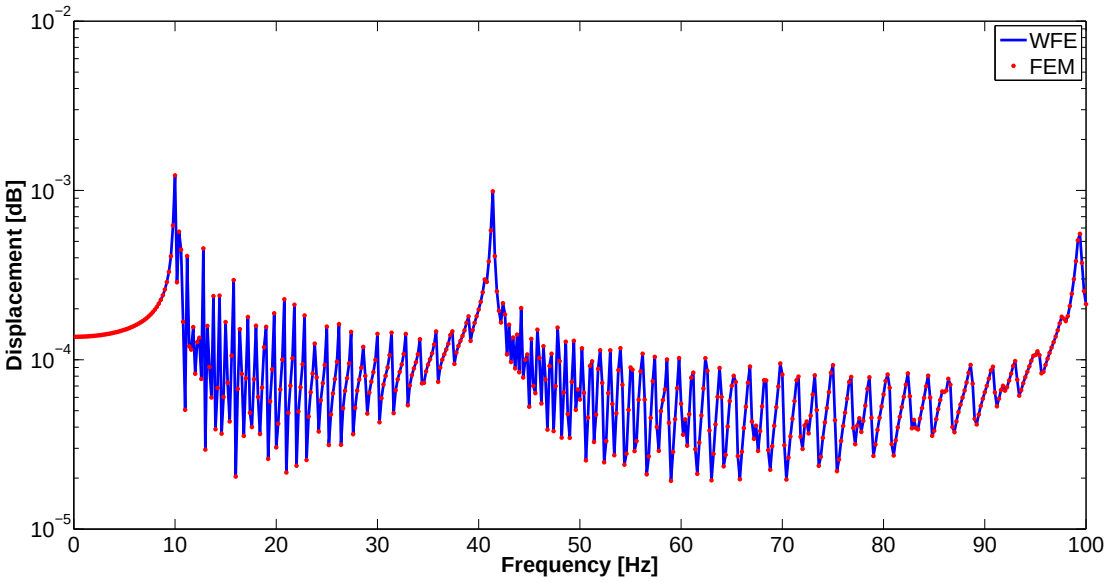


Figure 5: Displacement of the steel structure with $\theta = 0°$ obtained from the WFE method (solid blue line) and the FE method (dotted red line)

The corresponding results for the case $\theta = 45°$ are displayed in Figures 7 and 8. The diplacement curves obtained with the WFE and the FE methods are seen again perfectly superimposed on Figure 7. The distribution of resonance frequencies on the displacement curves are seen strongly affected by the coupling angle between the plates compared to the case $\theta = 0°$, as well as the vibration levels. The transmittance patterns between the two cases vary accordingly. The variations of transmittance visible for $\theta = 45°$ (Figure 8) are representative of bandgap effects, hence validating the hypothesis that the triangular shape of a structure might enhance the efficiency of a PC structure.

The effects of alternating materials between the strips are illustrated in Figures 9 and 10 for the case $\theta = 0°$: the periodic change of properties is seen to create extra resonance peaks on the displacement curves and attenuation areas on the transmittance levels. Those variations appear however moderate compared to the effect of a change of orientation of the plates, which is probably due to the relative proximity of material

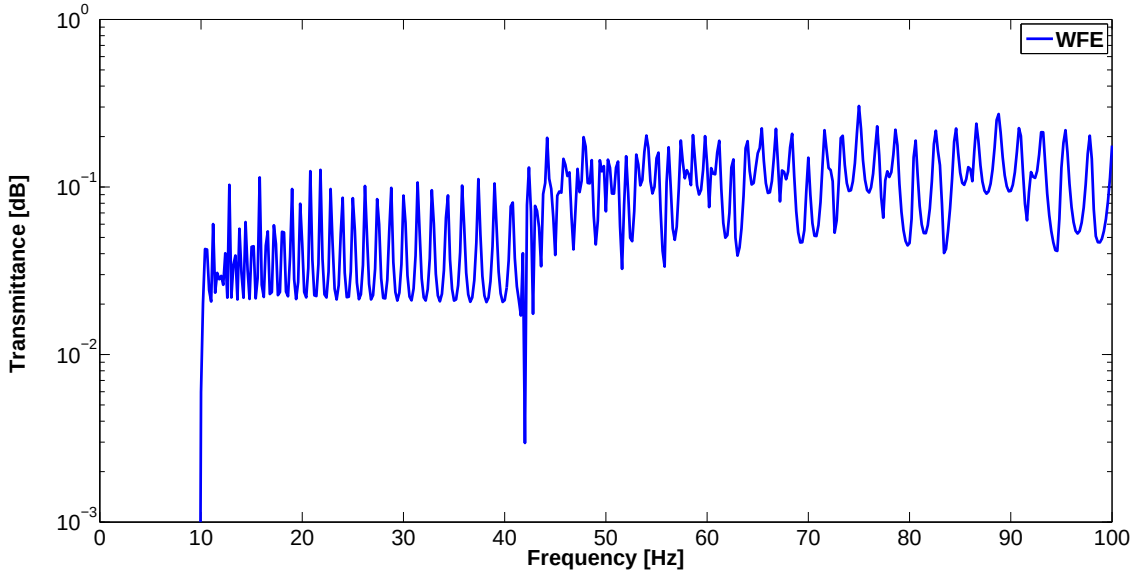


Figure 6: Transmittance of the steel structure with $\theta = 0°$ obtained from the WFE method

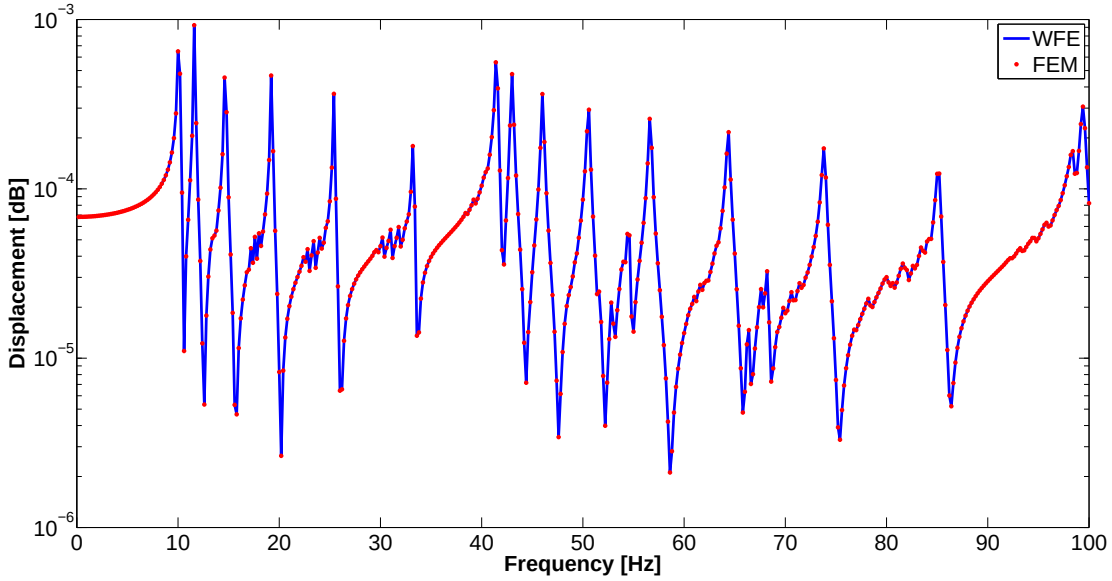


Figure 7: Displacement of the steel structure with $\theta = 45°$ obtained from the WFE method (solid blue line) and the FE method (dotted red line)

properties between steel and aluminum. It can again be noticed in Figure 9 that the WFE and FE results are perfectly matching.

Those trends are confirmed when displaying the results for all the plate angles considered ($\theta = 0°$ to $60°$) and for the two retained configurations, that is the structure made of steel only and the structure involving alternate steel and aluminum strips. Regarding the displacement levels, it is clear from Figures 11 and 12 that they are primarily affected by the introduction of a nonzero angle between the plates, which creates additional resonance and anti-resonance peaks throughout the frequency range, as compared to the case $\theta = 0°$. The value of the chosen θ angle (between the first plate and the horizontal direction) is seen to be of moderate importance, as it only affects the displacement magnitudes but not the positions of those peaks. The lowest

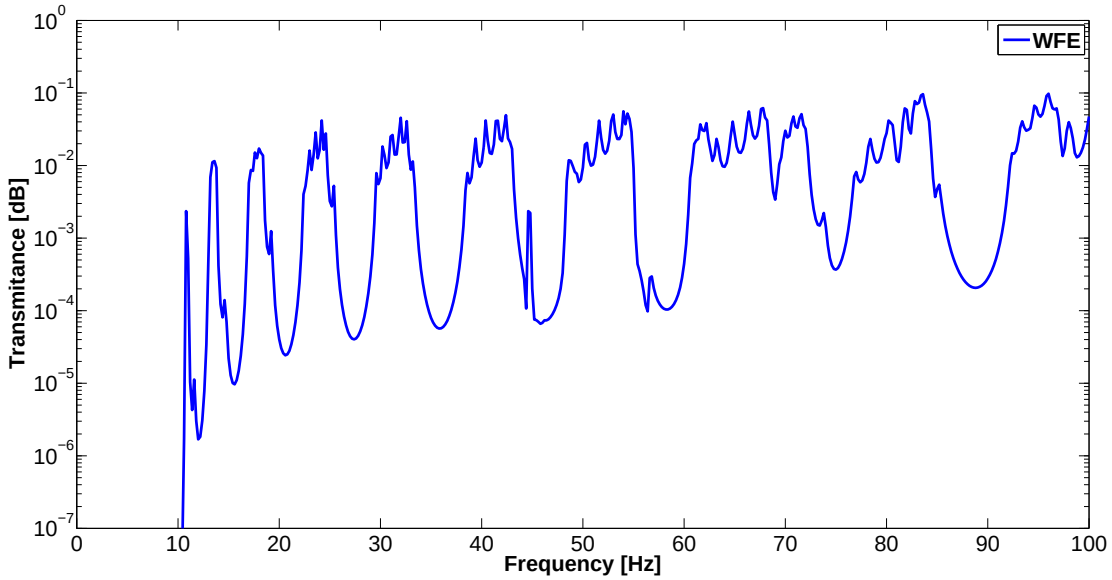


Figure 8: Transmittance of the steel structure with $\theta = 45°$ obtained with the WFE method

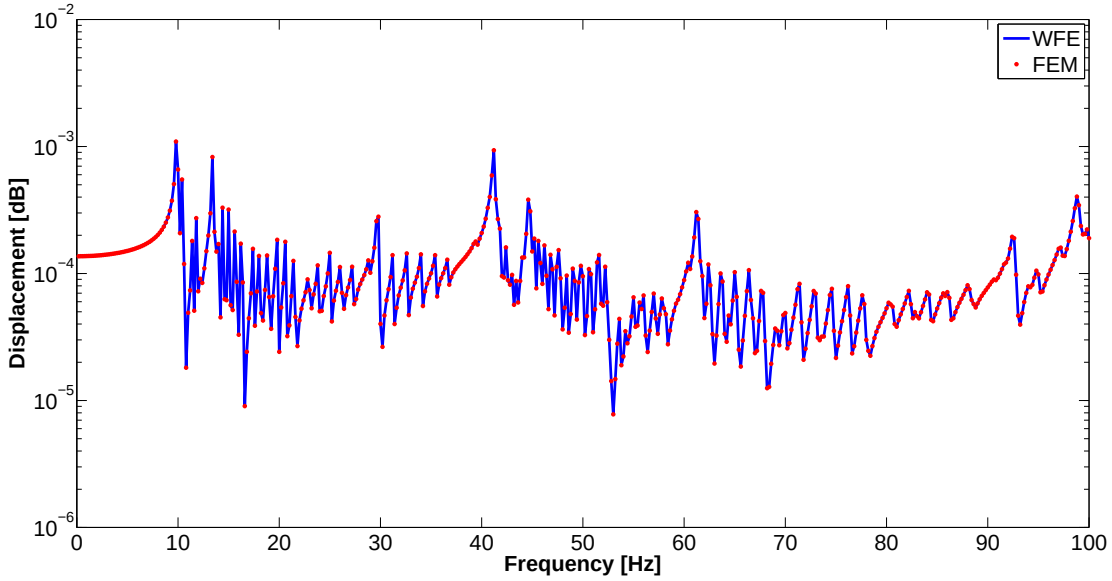


Figure 9: Displacement of the structure with alternate steel and aluminum strips and $\theta = 0°$ obtained from the WFE method (solid blue line) and the FE method (dotted red line)

vibration levels are obtained for the highest θ value, that is $\theta = 60°$, which corresponds to the configuration with the strongest change of orientation between the plates. As mentioned previously, the introduction of alternate material strips also has a moderate effect; the local variations (with extra resonance frequencies) that could be seen at $\theta = 0°$ are less visible in the presence of the additional peaks for nonzero θ angles which dominate the displacement behavior. The vibration levels at the resonance and anti-resonance frequencies are however modified as compared to the case of the purely steel structure.

The transmittance levels are affected in accordance with the prior observations on the vibration levels. A band gap effect is created as soon as a nonzero θ angle is introduced; the efficiency of the band gaps may be improved by increasing the value of the θ angle, the lowest levels of transmittance being in both cases

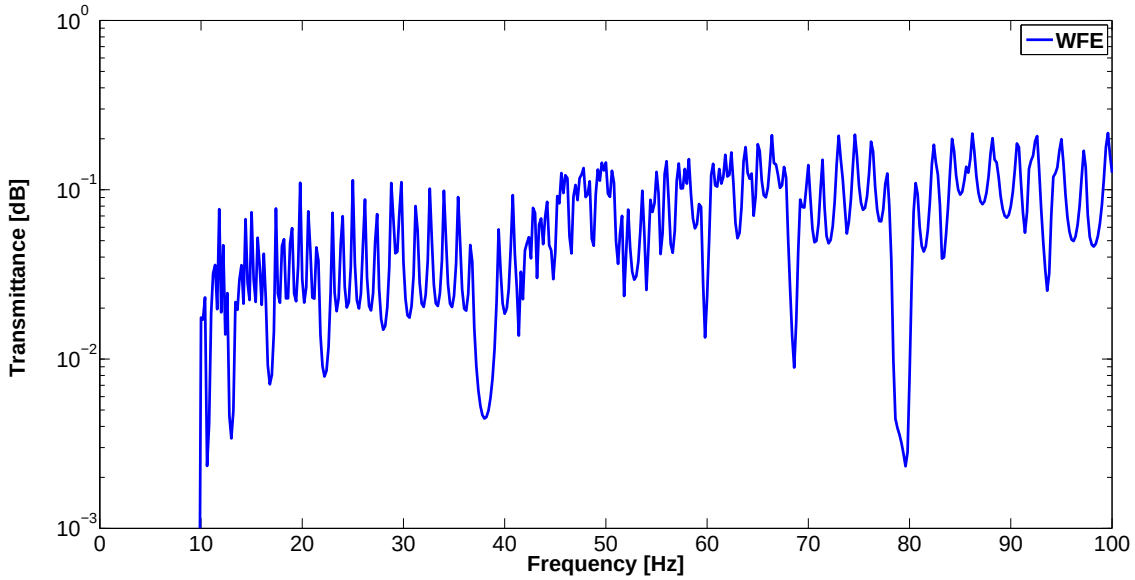


Figure 10: Transmittance of the structure with alternate steel and aluminum strips and $\theta = 0°$ obtained from the WFE method

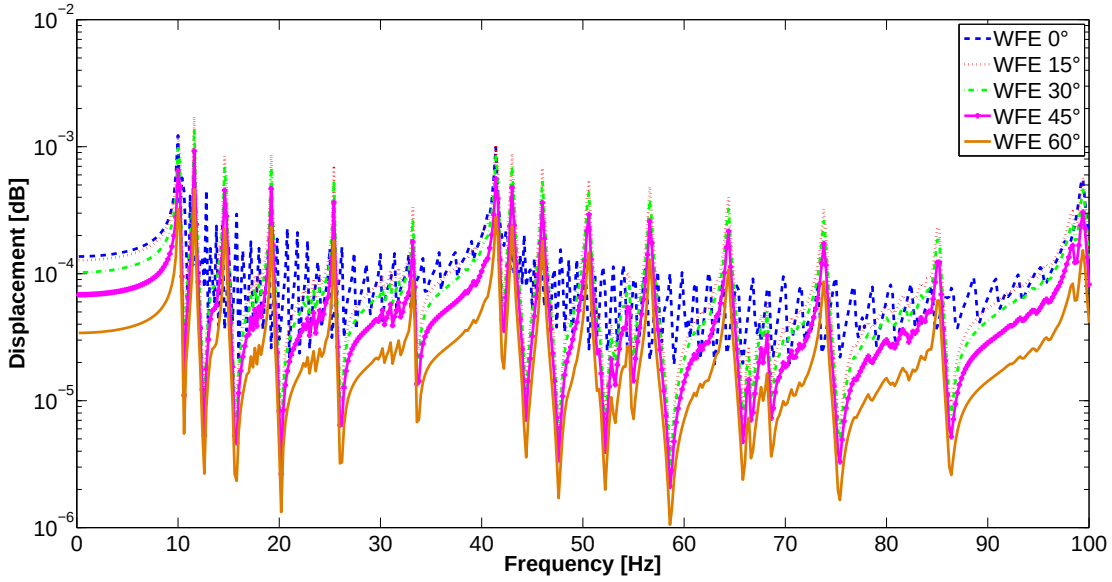


Figure 11: Displacements of the steel structure with angles θ of $0°$, $15°$, $30°$, $45°$ and $60°$ obtained from the WFE method

obtained for $\theta = 60°$. The presence of alternate steel and aluminum strips affects locally the transmittance levels as compared to purely steel PC structure by lowering the transmittance levels at some frequencies, for instance between 30 and 40Hz, or around 68Hz. Choosing materials with even larger discrepancies in their properties could therefore enable to increase the band gap effects within multi-material PC structures.

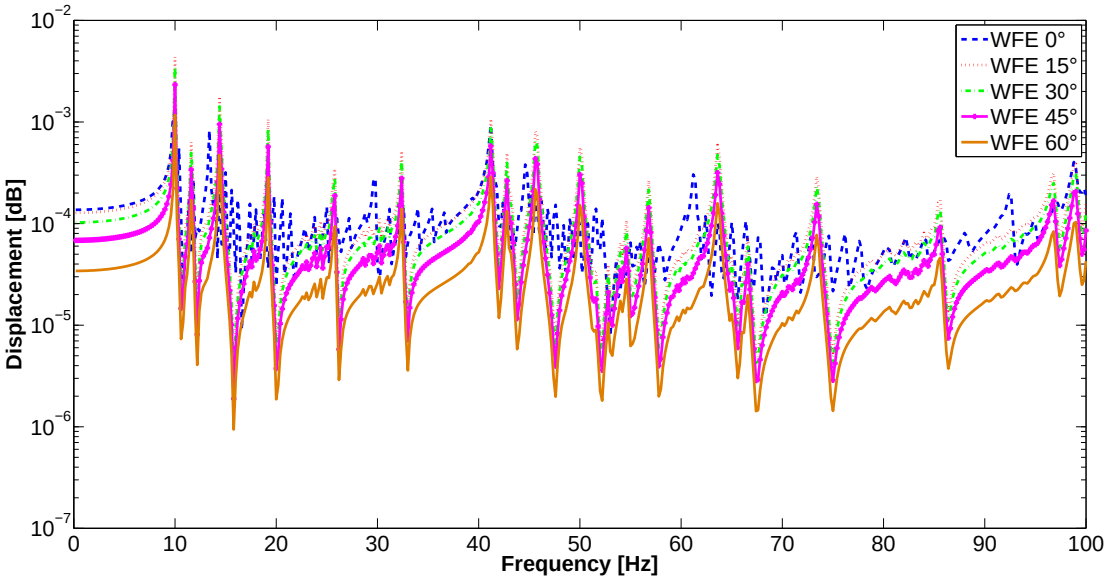


Figure 12: Displacements of the structure with alternate steel and aluminum strips and angles θ of $0°$, $15°$, $30°$, $45°$ and $60°$ obtained from the WFE method

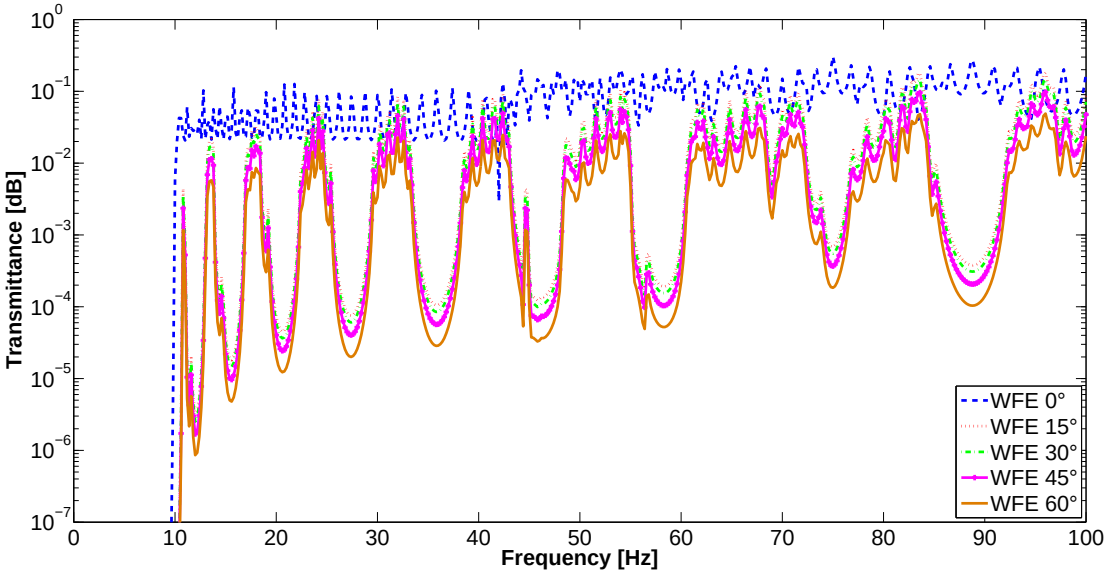


Figure 13: Transmittances of the steel structure with angles θ of $0°$, $15°$, $30°$, $45°$ and $60°$ obtained from the WFE method

4 Conclusion

In this paper, two level PC structures composed of multi-material plates arranged along a triangular pattern have been investigated using the WFE method. The developed approach has proved efficient, in terms of accuracy and computational time, to compute the frequency responses of such structures as compared to the classic FE method. The numerical experiments carried out have shown that the triangular shape of the PC structure favors the expected band gap effect, which is all the more efficient when the structure is sharp, i.e. for small angle values between the plates. The use of alternate steel / aluminum strips on each plate is seen

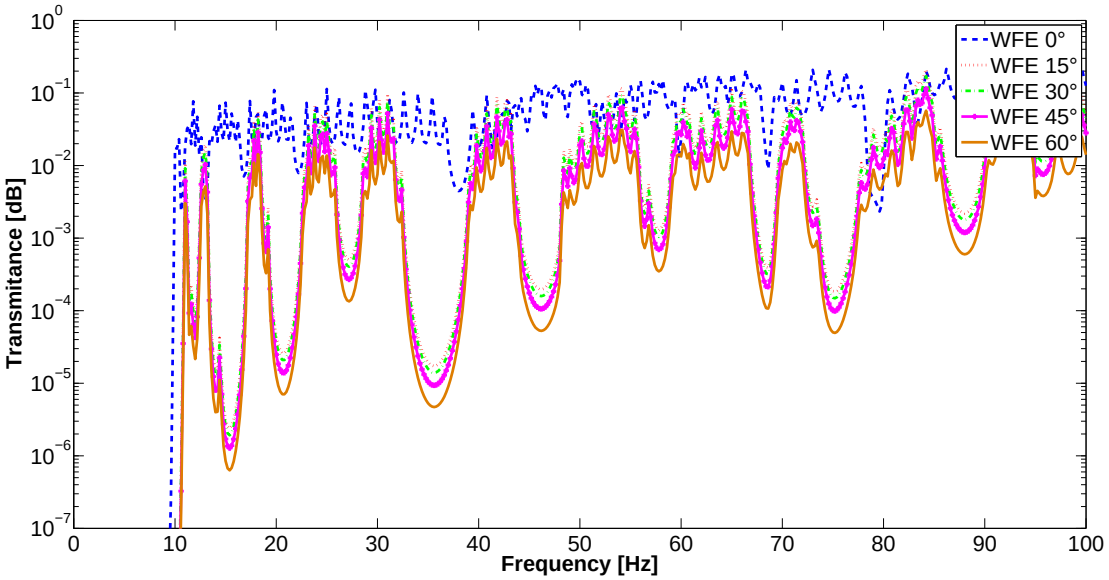


Figure 14: Transmittances of the structure with alternate steel and aluminum strips and angles θ of $0°$, $15°$, $30°$, $45°$ and $60°$ obtained from the WFE method

to modify locally the vibration and transmittance levels in limited frequency ranges. Choosing materials with more discrepant properties could therefore enable to improve the efficiency of the band gaps in desired frequency regions.

Acknowledgements

The authors of this article would like to thank FAPEMA, FAPESP, CNPq, CAPES, DEMM, INSA, UFMA and DMC / FEMUNICAMP for their support.

References

[1] D. Mead, *Free wave propagation in periodically supported, infinite beams*, Journal of Sound and Vibration, Vol. 11, No. 2 (1970), pp. 181-197.

[2] D. Mead, *A general theory of harmonic wave propagation in linear periodic systems with multiple coupling*, Journal of Sound and Vibration, Vol. 27, No. 2 (1973), pp. 235-260.

[3] D. Mead, *Wave propagation and natural modes in periodic systems: I. mono-coupled systems*, Journal of Sound and Vibration, Vol. 40, No. 1 (1975), pp. 118.

[4] D. Mead, *Wave propagation and natural modes in periodic systems: II. multi-coupled systems, with and without damping*, Journal of Sound and Vibration, Vol. 40, No. 1 (1975), pp. 1939.

[5] J.-M. Mencik, M. Ichchou, *Multi-mode propagation and diffusion in structures through finite elements*, European Journal of Mechanics - A/Solids, Vol. 24, No. 5 (2005), pp. 877898.

[6] D. Duhamel, B. Mace, M. Brennan, *Finite element analysis of the vibrations of waveguides and periodic structures*, Journal of Sound and Vibration, Vol. 294, No. 12 (2006), pp. 205220.

[7] B. R. Mace, E. Manconi, *Modelling wave propagation in two-dimensional structures using finite element analysis*, Journal of Sound and Vibration, Vol. 318, No. 45 (2008), pp. 884902.

[8] Y. Waki, B. Mace, M. Brennan, *Free and forced vibrations of a tyre using a wave/finite element approach*, Journal of Sound and Vibration, Vol. 323, No. 35 (2009), pp. 737756.

[9] M. Petyt, *Introduction to finite element vibration analysis*, Cambridge University Press, New York, USA (2010).

[10] P. B. Silva, J.R.F. Arruda, A.L. Goldstein, *Study of Elastic Band-Gaps in Finite Periodic Structure Using Finite Element Models*, Proceedings of the XIV International Symposium on Dynamic Problems of Mechanics - DINAME (2011).

[11] Y. Xiao, J. Wen, X. Wen, *Longitudinal wave band gaps in metamaterial-based elastic rods containing multi-degree-of-freedom resonators*, New Journal of Physics, Vol. 14, No. 3 (2012), p. 033042.

[12] Y. Zhang, J. He, L.-H. Jiang, *Flexural Vibration Band Gaps Characteristics in Phononic Crystal Euler Beams on Two-Parameter Foundation*, Advances in Mechanical Engineering, Vol. 2013, No. 935258 (2013), pp. 1-7.

[13] R. Szilard, *Theories and applications of plate analysis: classical, numerical and engineering methods*, Wiley and Sons, Inc., Hoboken, New Jersey (2004).

[14] J.-M. Mencik, *Approche numérique pour la propagation multi-modale guidée*, Université François Rabelais de Tours (2008).

[15] W. Zhong, F. Williams, *On the direct solution of wave propagation for repetitive structures*, Journal of Sound and Vibration, Vol. 181, No. 3 (1995), pp. 485-501.

[16] P.B. Silva, J.-M. Mencik, J.R.F. Arruda, *On the forced harmonic response of coupled systems via a wfe-based super-element approach*, Vol. 1 (2014), pp. 1-13.

[17] J.-M. Mencik, *A wave finite element-based formulation for computing the forced response of structures involving rectangular flat shells*, International Journal For Numerical Methods In Engineering, Vol. 95 (2013), pp. 91-120.

Computing the dispersion diagram and the forced response of periodic elastic structures using a state-space formulation

G. F. C. A. Assis[1], **E. J. P. Miranda Jr.**[2], **D. Beli**[1], **J. F. Camino**[1], **J. M. C. Dos Santos**[1], **J. R. F. Arruda**[1]

[1] University of Campinas - UNICAMP
Rua Mendeleyev, 200, CEP-13083-970, Campinas, SP, Brazil.
e-mail: **arruda@fem.unicamp.br**

[2] Federal Institute of Maranhão - IFMA
Rua Afonso Pena, 174, 65010030, São Luís, MA, Brazil.

Abstract

In the context of acoustic black hole investigations, recent works have proposed the use of a spatial state-space formulation for one-dimensional elastic waveguides. The boundary value problem is thus transformed into an initial value problem. Given that the state (displacements and forces) cannot be known *a priori* at any given boundary, but the impedance can, the state-space problem is recast into an impedance formulation, in the form of a Riccati equation. In this paper, this formulation is extended to compute the transfer matrix of a periodic cell of a one-dimensional elastic waveguide. With this transfer matrix, not only can the dispersion diagram be computed, but also the forced response of the finite structure. The simple case of an elastic rod is used to illustrate the proposed method. The dispersion diagram is verified with the plane wave expansion method, and the forced response is verified with the spectral element method. Numerical results show that the proposed method is an efficient way to characterize wave propagation in period elastic structures.

1 Introduction

Linear elastodynamic problems are usually formulated as boundary value problems, which may be solved analytically or numerically [1]. Analytical solutions are often derived in the frequency domain, which can be referred to as spectral solutions. For simple structures, it is straightforward to derive solutions in the form of finite elements in the frequency domain. This semi analytical approach is known as spectral element method (SEM) [2]. In SEM, a global dynamic stiffness matrix can be assembled via the direct stiffness method, commonly used in finite element analysis [1].

Deriving a spectral element for a straight homogeneous rod with constant material and geometrical properties along its length is a straightforward process. However, this task can be awkward for rods with varying properties. Analytical solutions exist for only a few cases, such as rods with linearly varying (tapered) and exponentially varying geometrical properties.

Some authors have proposed a solution method (see [3] and references therein) for acoustic waveguides (Helmholtz spectral equation), in which the problem is reformulated in the state-space framework, where the state consists of the pressure and the particle velocity along the tube. This approach transforms the boundary value problem into an initial value problem. Given that one does not known the initial condition, i.e. the state at one end of the waveguide, the authors in [3] have reformulated the problem in terms of the impedance, the ratio between pressure and velocity.

The problem stated in terms of the impedance yields a Riccati matrix equation that can be solved analytically, for simple problems, or numerically, for more complex problems. The Riccati differential equation (RDE) plays an important role in many engineering science applications [4]. This type of equation [5, 6], which is quadratic and, thus, nonlinear, can be reduced to a linear system of twice its size that can be efficiently solved using numerical algorithms [7, 8].

Georgiev et al. [9] recently used this method to solve the problem of a beam with a varying cross-section. The thickness, which decreases with a power law profile, can be tailored to minimize wave reflection by slowing the propagation speed and eventually stopping the propagation. This creates an anechoic termination, which is called an acoustic black hole (ABH). The authors in [9] have only computed the impedance of the beam. The solution technique consists of writing the elastodynamic equations as a state-space equation in the frequency domain, as a function of the spatial variable only. Restating the problem for an impedance variable, a Riccati equation is formulated and numerically solved.

In this paper, this method is complemented by a back propagation of the force and displacement (state) at one end of the rod, to compute the full state at the other end. From the relations between these states, it is shown how to compute the dynamic stiffness or the transfer matrix of a finite rod with arbitrarily varying geometrical and material properties. With these matrices, the forced responses may be computed.

The proposed method is particularly interesting for periodic waveguides. Given a periodic rod cell, the dispersion relation (also known as dispersion diagram) can be computed using the transfer matrix by applying the Floquet-Bloch periodicity condition [10]. The dispersion relation shows the frequency bands where the wavenumber becomes complex, which indicates a band gap, where there is no propagation and, therefore, no normal modes can exist. Furthermore, given the dynamic stiffness matrix of the rod cell, the global dynamic stiffness of the built up structure can be easily assembled, allowing the computation of the forced response.

With the proposed technique, it is straightforward to analyze rods with varying cross-section, which is useful, for instance, to optimize the waveguide shape aiming at creating band gaps to reduce or enhance vibration energy propagation. The proposed method can be extended to treat other structural one-dimensional waveguides, such as beams.

2 Modeling Methods

This section presents the proposed method. The elementary rod theory is used, but the technique can be extended to other one-dimensional structures. The problem is written in the state-space form, leading to a Riccati differential equation in terms of the mechanical impedance. Starting from a known impedance at one end, the impedance at the other end is obtained. For a given input force, the state can be obtained for the whole periodic rod cell, using the computed impedance. With the obtained state, the transfer matrix and the dynamic stiffness matrix are derived.

The proposed method is numerically verified using the dispersion diagram of a periodic rod cell with varying properties, and also the forced response of a finite periodic rod. The PWE method [11] is used to compute the dispersion diagram, while the SEM [12] is used for the computation of both the dispersion relation and the forced response.

Given a periodic one dimensional structure, the SEM computes a frequency-dependent dynamic stiffness matrix of one element, which can be assembled as a global stiffness matrix. Using the dynamic stiffness matrix of one periodic element, the transfer matrix is obtained, whose eigenvalues yield the dispersion relation. However, the SEM is limited to simple geometries such as the homogeneous rod and the linearly tapered rod, while the PWE method allows the computation of the dispersion relation for more complex geometries. First, the SEM and the PWE method are briefly reviewed. Then, the proposed approach is presented. All the methods in this paper can be applied to symmetric and to nonsymmetric cells as well.

2.1 Spectral Element Method

This section derives the spectral elements for homogeneous and linearly tapered rods. Using these spectral elements, one with a trapezoidal and the other with a rectangular profile, two types of periodic rods are modeled, as illustrated in Figure 1. The trapezoidal profile is generated with two coupled tapered elements, and the rectangular profile with homogeneous elements with different cross-sections.

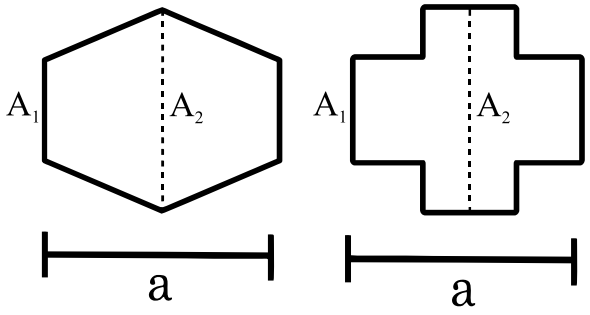


Figure 1: Symmetric cell shapes built with rectangular and tapered spectral elements.

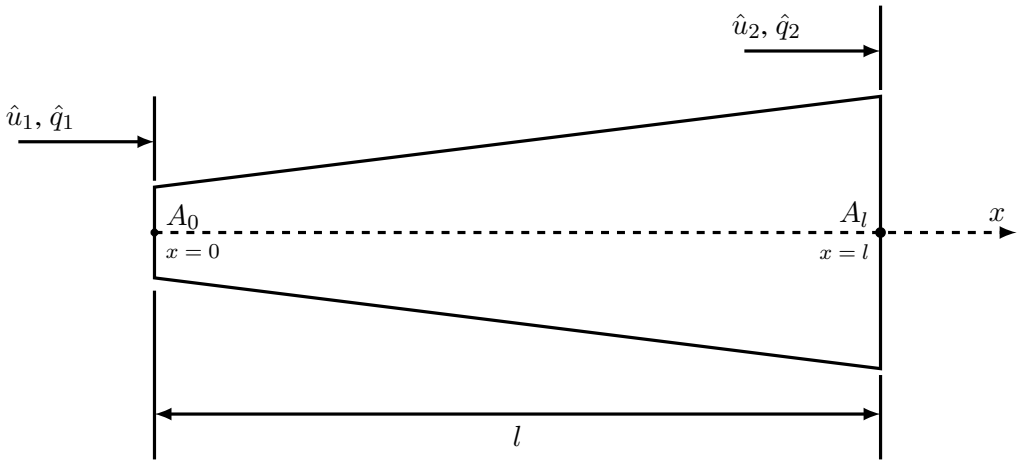


Figure 2: Two-node tapered rod spectral element with linearly varying cross-sectional area.

Figure 2 shows a two-node tapered rod spectral element with linearly varying cross-sectional area. In the trapezoidal case, the tapered spectral element developed by [13], for acoustic duct element, was used in [14]. The homogeneous case can be found in [2]. The tapered element is described by the following equation

$$A(x) = \epsilon(x + \xi) \qquad \text{with} \qquad \xi = \frac{l\, A_0}{A_l - A_0} \qquad \text{and} \qquad \epsilon = \frac{A_0}{\xi} \tag{1}$$

where l is the length of the element, $A(x)$ is the varying cross-sectional area, in which A_0 and A_l are the areas at the positions $x = 0$ (the smaller edge) and $x = l$ (the larger edge), respectively. The elementary rod theory considers a slender structure that supports only axial stresses, neglecting the lateral contraction (Poisson's effect). As shown in [10], the equation of motion for a tapered rod is given by

$$\frac{\partial}{\partial x}\left[EA(x)\frac{\partial u(x,t)}{\partial x}\right] = \rho A(x)\frac{\partial^2 u(x,t)}{\partial t^2} \tag{2}$$

with $u(x,t)$ the axial displacement, ρ the mass density, and $E = \bar{E}(1 + j\eta)$ the complex (or dynamic) Young's modulus, to account for energy dissipation, where $\bar{E}$ is the Young's modulus, η is the loss factor, and $j = \sqrt{-1}$.

Using the expression for $A(x)$ given by (1), the elastodynamic equation (2) becomes

$$(x+\xi)\frac{\partial^2 u(x,t)}{\partial x^2} + \frac{\partial u(x,t)}{\partial x} - \frac{\rho}{E}(x+\xi)\frac{\partial^2 u(x,t)}{\partial t^2} = 0 \tag{3}$$

The general form of the solution $u(x,t)$, for the elastodynamic equation (3), is assumed to be expressed as

$$u(x,t) = \hat{u}(x)e^{j\omega t} \tag{4}$$

where $\hat{u}(x) := \hat{u}(x,\omega)$ is the displacement in the frequency domain. Thus, substituting (4) in (3), one obtains, after some manipulation

$$\frac{d^2\hat{u}(x,\omega)}{dx^2} + \frac{1}{(x+\xi)}\frac{d\hat{u}(x,\omega)}{dx} + k^2\hat{u}(x,\omega) = 0 \tag{5}$$

where $k = \omega\sqrt{\rho/E}$ is the wavenumber. As shown in [15], a Bessel type solution for (5) is given by

$$\hat{u}(x) = \alpha_1 J_0(\gamma) + \alpha_2 Y_0(\gamma), \qquad \gamma = k(x+\xi)$$

where γ, α_1, and α_2 are constants determined from the boundary conditions, J_0 and Y_0 are, respectively, Bessel functions of first and second kind, both of order zero. The displacement boundary conditions for the two-node element, shown in Figure 2, are

$$\hat{u}_1 = \hat{u}(0) = \alpha_1 J_0(k\xi) + \alpha_2 Y_0(k\xi)$$

$$\hat{u}_2 = \hat{u}(l) = \alpha_1 J_0(kl + k\xi) + \alpha_2 Y_0(kl + k\xi)$$

where, $\hat{u}_1$ and $\hat{u}_2$ are the nodal displacements. This equation can be rewritten in matrix form as

$$\hat{u} = \Phi\alpha, \quad \text{with} \quad \hat{u} = \begin{bmatrix}\hat{u}_1\\ \hat{u}_2\end{bmatrix}, \quad \Phi = \begin{bmatrix}J_0(k\xi) & Y_0(k\xi)\\ J_0(kl+k\xi) & Y_0(kl+k\xi)\end{bmatrix}, \quad \alpha = \begin{bmatrix}\alpha_1\\ \alpha_2\end{bmatrix} \tag{6}$$

Noting that the rod axial force is given by

$$\hat{q}(x) = EA(x)\frac{\partial\hat{u}(x)}{\partial x} \tag{7}$$

and evaluating $\hat{q}(x)$ at the element boundaries, the following equations are obtained

$$\hat{q}_1 = \hat{q}(0) = EA_0\frac{\partial\hat{u}(x)}{\partial x}\bigg|_{x=0} = -kEA_0\left[\alpha_1 J_1(k\xi) + \alpha_2 Y_1(k\xi)\right]$$

$$\hat{q}_2 = \hat{q}(l) = EA_l\frac{\partial\hat{u}(x)}{\partial x}\bigg|_{x=l} = -kEA_l\left[\alpha_1 J_1(kl+k\xi) + \alpha_2 Y_1(kl+\xi)\right]$$

where J_1 and Y_1 are, respectively, Bessel functions of first and second kind, both of first order. The above equation in matrix form is given by

$$\hat{q} = \Psi\alpha \qquad \text{with} \qquad \Psi = -kE\begin{bmatrix}A_0J_1(k\xi) & A_0Y_1(k\xi)\\ A_lJ_1(kl+k\xi) & A_lY_1(kl+k\xi)\end{bmatrix} \tag{8}$$

Now, solving (6) for α and substituting the result in (8), one obtains

$$\hat{q} = \hat{K}(\omega)\hat{u}, \qquad \hat{K}(\omega) = \Psi\Phi^{-1}$$

where $\hat{K}(\omega)$ is a dynamic stiffness matrix of the two-node element with linearly varying cross-sectional area.

The trapezoidal element can now be assembled by interchanging the terms of the principal diagonal of the dynamic stiffness matrix of one element and coupling it with a regular element, condensing the internal node.

As shown in [10], the transfer matrix can be evaluated from the dynamic stiffness matrix as follows

$$\hat{T}(\omega) = \begin{bmatrix}-K_{12}^{-1}K_{11} & -K_{12}^{-1}\\ K_{21} - K_{22}K_{12}^{-1}K_{11} & -K_{22}K_{12}^{-1}\end{bmatrix} \tag{9}$$

where K_{ij}, for $i,j = 1,2$, are the entries of the 2×2 stiffness matrix $\hat{K}(\omega)$.

2.2 Plane Wave Expansion Method

The sinusoidally varying element is modeled by the plane wave expansion (PWE) method. Figure 3 illustrates the geometry of a symmetric cell shape with sinusoidal cross-sectional area. The rod width is constant in the direction perpendicular to the figure, so that the cross-sectional area varies sinusoidally.

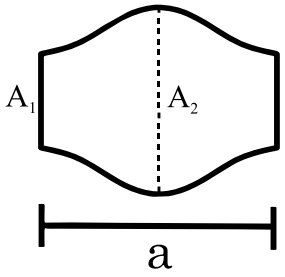


Figure 3: Symmetric cell shape with sinusoidal cross-sectional area.

Applying the Fourier transform on (2), which is the governing equation for longitudinal vibrations of a straight rod, one obtains

$$\frac{\partial}{\partial x}\left[EA(x)\frac{\partial \hat{u}(x,\omega)}{\partial x}\right] + \omega^2 \rho A(x)\hat{u}(x,\omega) = 0 \tag{10}$$

It is assumed that the rod has a periodic cross-sectional area variation given by $A(x) = A(x+a)$, where a is the lattice parameter, i.e., the unit cell length.

Applying the Floquet-Bloch periodicity condition of the solution in x, and considering one-dimensional wave propagation, one obtains

$$\hat{u}(x) = \tilde{u}(x)e^{jkx}$$

with the Bloch wave amplitude $\tilde{u}(x)$ periodic of period a, i.e., $\tilde{u}(x+a) = \tilde{u}(x)$. k is the Bloch wave vector (here being scalar), also known as wavenumber. The wave vector has its value within the first irreducible Brillouin zone (FIBZ), in the reciprocal space, $[0, \pi/a]$, or within the first Brillouin zone (FBZ), $[-\pi/a, \pi/a]$.

Expanding the Bloch wave amplitude $\tilde{u}(x)$ as a Fourier series in the reciprocal space, yields

$$\hat{u}(x) = \left(\sum_{m=-\infty}^{+\infty} u_m e^{jg_m x}\right) e^{jkx} = \sum_{m=-\infty}^{+\infty} u_m e^{j(k+g_m)x} \tag{11}$$

where u_m are the coefficients of the Fourier series of $\tilde{u}(x)$ and $g_m = 2\pi m/a$ is the reciprocal lattice vector. Note that g_m is a constant, since a one-dimensional periodicity is considered. Furthermore, the cross-sectional area can also be expanded as Fourier series in the reciprocal space as

$$A(x) = \sum_{n=-\infty}^{+\infty} A_n e^{jg_n x} \tag{12}$$

where $g_n = 2\pi n/a$. Note that Fourier series coefficients A_n in (12) can be computed using

$$A_n = \frac{1}{a}\int_{-a/2}^{a/2} A(x)e^{-jg_n x}\,\mathrm{d}x$$

Substituting (11) and (12) in (10), gives

$$\sum_{m=-\infty}^{+\infty}\sum_{n=-\infty}^{+\infty}\left(EA_n(k+g_m)(k+g_m+g_n) - \omega^2\rho A_n\right)u_m e^{j(k+g_m+g_n)x} = 0 \tag{13}$$

Multiplying (13) by $e^{-j(k+g_r)x}$, with $g_r = 2\pi r/a$, and integrating from $-a/2$ to $a/2$, yields

$$\sum_{m=-\infty}^{+\infty}\sum_{n=-\infty}^{+\infty}\left(EA_n(k+g_m)(k+g_m+g_n)-\omega^2\rho A_n\right)u_m\frac{1}{a}\int_{-a/2}^{a/2}e^{j(g_m+g_n-g_r)x}\,\mathrm{d}x=0 \qquad (14)$$

Given that

$$\frac{1}{a}\int_{-a/2}^{a/2}e^{j(g_m+g_n-g_r)x}\,\mathrm{d}x=\frac{1}{a}\int_{-a/2}^{a/2}e^{j2\pi/a(m+n-r)x}\,\mathrm{d}x=\begin{cases}1 & ,\text{if } n=r-m\\ 0 & ,\text{otherwise}\end{cases}$$

one can rewrite (14) as

$$\sum_{m=-\infty}^{+\infty}\left(EA_{r-m}(k+g_m)(k+g_r)-\omega^2\rho A_{r-m}\right)u_m=0$$

Equivalently

$$\sum_{m=-\infty}^{+\infty}EA_{r-m}(k+g_m)(k+g_r)u_m=\lambda\sum_{r=-\infty}^{+\infty}\rho A_{r-m}u_m,\qquad \lambda=\omega^2 \qquad (15)$$

which is a system with an infinite amount of equations. Thus, to solve this system, one can truncate the Fourier series to the first M terms, i.e., $r, m \in [-M,\ldots,M] \in \mathbb{Z}$, such that (15) can be rewritten as

$$\mathbf{Bu}=\lambda\mathbf{Cu} \qquad (16)$$

where the coefficients of vector $\mathbf{u}$ are u_m and the coefficients of matrices $\mathbf{B}$ and $\mathbf{C}$ are given by

$$\mathbf{B}_{rm}=EA_{r-m}(k+g_m)(k+g_r),\qquad \mathbf{C}_{rm}=\rho A_{r-m}$$

Notice that (16) represents a generalized eigenvalue problem on λ and should be solved for each k, within FBZ or FIBZ.

2.3 State-Space Formulation

This section presents the proposed method. It shows how to write the elastodynamic equations for a rod in a state-space formulation, to rewrite the problem in terms of the mechanical impedance and to solve a Riccati equation to obtain the impedance at one end, given a zero impedance at the other end (free end). It also illustrates how to obtain the transfer matrix and the dynamic stiffness matrix from the impedance. The results obtained with this method will be referred to as state-space formulation (SSF) in the numerical section.

Using (10) and (7), one can write the set of state-space equations

$$\frac{\partial\hat{q}(x)}{\partial x}=-\omega^2\rho A(x)\hat{u}(x)\qquad\text{and}\qquad\frac{\partial\hat{u}(x)}{\partial x}=\frac{\hat{q}(x)}{EA(x)}$$

which can be written in matrix form as

$$\frac{\partial\hat{p}}{\partial x}=H\hat{p} \qquad (17)$$

with the state $\hat{p}(x):=\hat{p}(x,\omega)$ and $H(x,\omega)$ having the following expressions

$$\hat{p}(x)=\begin{bmatrix}\hat{u}(x)\\ \hat{q}(x)\end{bmatrix}\qquad\text{and}\qquad H(x,\omega)=\begin{bmatrix}H_{11}&H_{12}\\ H_{21}&H_{22}\end{bmatrix}=\begin{bmatrix}0&\dfrac{1}{EA(x)}\\ -\omega^2\rho A(x)&0\end{bmatrix}$$

Note that this is a system of linear ordinary differential equations of the first order, where the system parameters may vary along x. It is straightforward to solve this system numerically for any type of parameter variation along x, if the state initial condition is known. However, the initial condition is not known, since the boundary condition at any edge of the structure is given by either the force (Neumann condition), the displacement (Dirichlet condition), or the mechanical impedance (mixed condition). Thus, to overcome this issue, one can rewrite the problem (see [9]) in terms of the mechanical impedance $\hat{z}(x)$, which is the relation between the state variables $\hat{u}$ and $\hat{q}$ given by

$$\hat{q}(x) = j\omega\hat{z}(x)\hat{u}(x) \tag{18}$$

Substituting (18) into (17), one obtains the following set of equations

$$\frac{\partial\hat{u}(x)}{\partial x} = H_{11}\hat{u}(x) + H_{12}\hat{q}(x) \qquad \text{and} \qquad j\omega\frac{\partial\hat{z}(x)\hat{u}(x)}{\partial x} = H_{21}\hat{u}(x) + H_{22}\hat{q}(x)$$

which leads to

$$j\omega\left(\frac{\partial\hat{z}(x)}{\partial x}\hat{u}(x) + \hat{z}(x)H_{11}\hat{u}(x) + \hat{z}(x)H_{12}j\omega\hat{z}(x)\hat{u}(x)\right) = H_{21}\hat{u}(x) + H_{22}j\omega\hat{z}(x)\hat{u}(x)$$

Since $\hat{u}(x)$ cannot be identically zero, one finally obtains the following Riccati equation

$$\frac{\partial\hat{z}(x)}{\partial x} + \hat{z}(x)H_{11} - H_{22}\hat{z}(x) + j\omega\hat{z}(x)H_{12}\hat{z}(x) = (j\omega)^{-1}H_{21}$$

To solve the above Riccati differential equation, it is necessary an initial condition, which can be taken to be $\hat{z}(0) = 0$. This condition on a free end of the structure corresponds to the force $\hat{q}_0 = 0$, and a displacement $\hat{u}_0$ unknown but different from zero. Once the impedance $\hat{z}(L)$, the solution of the Riccati equation at the terminal position $x = L$, is computed using the initial condition $\hat{z}(0) = 0$, the displacement $\hat{u}(L)$ can be computed by considering that the external force in (18) is given by $\hat{q}(L) = 1$.

With $\hat{q}(L)$ and $\hat{u}(L)$ computed, the state $\hat{p}(L)$ can be used as the initial condition in (17) so that the state $\hat{p}(0)$ can be obtained by a backward integration of the state equations (17). Then, using the states at both ends, given by $\hat{p}(0)$ and $\hat{p}(L)$, it is possible to compute the transfer matrix, which relates the states at the extremes of a finite rod, as follows

$$\hat{p}(L) = \hat{T}(\omega)\hat{p}(0)$$

where $\hat{T}(\omega)$ is the transfer matrix of size 2×2. Using the boundary conditions $\hat{q}(L) = 1$, $\hat{q}(0) = 0$, $\hat{u}(L) = \hat{u}_L$, and $\hat{u}(0) = \hat{u}_0$, ones obtains

$$\begin{bmatrix}\hat{u}_L \\ 1\end{bmatrix} = \begin{bmatrix}T_{11} & T_{12} \\ T_{21} & T_{22}\end{bmatrix}\begin{bmatrix}\hat{u}_0 \\ 0\end{bmatrix}$$

Solving this algebraic system of equations leads to

$$T_{11} = \hat{u}_L/\hat{u}_0, \qquad T_{21} = \hat{u}_0^{-1}$$
$$T_{22} = T_{11}, \quad \text{(due to the rod cell symmetry)}$$

The relation between the off diagonal terms of matrix $\hat{T}$ can be evaluated using the relation between the transfer matrix and the symmetric (due to reciprocity) dynamic stiffness matrix, given by (9), and imposing $T_{11} = T_{22}$ for a symmetric cell. It can be shown that

$$T_{12} = (T_{11}^2 - I)T_{21}^{-1}$$

Once the transfer matrix $\hat{T}(\omega)$ is computed, the dynamic stiffness matrix is readily obtained using (9).

If the structure cell is not symmetric, $T_{11} \neq T_{22}$, the above formulation is unable to compute T_{12}. In order to overcome this issue, the initial condition is applied at the other end, $x = L$ and the impedance is integrated in the opposite direction up to $x = 0$. Repeating the procedure done earlier, one obtains $\hat{p}(0)$ and $\hat{p}(L)$. Applying the new boundary conditions, given by $\hat{q}(L) = 0$ and $\hat{q}(0) = 1$, the transfer matrix relation becomes

$$\begin{bmatrix} \hat{u}_L^* \\ 0 \end{bmatrix} = \begin{bmatrix} T_{11} & T_{12} \\ T_{21} & T_{22} \end{bmatrix} \begin{bmatrix} \hat{u}_0^* \\ 1 \end{bmatrix}$$

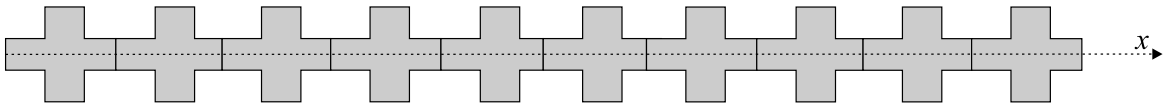
Writing T_{12} and T_{22} in terms of T_{11} and T_{21}, gives

$$T_{12} = \hat{u}_L^* - T_{11}\hat{u}_0^*, \qquad T_{22} = -T_{21}\hat{u}_0^*$$

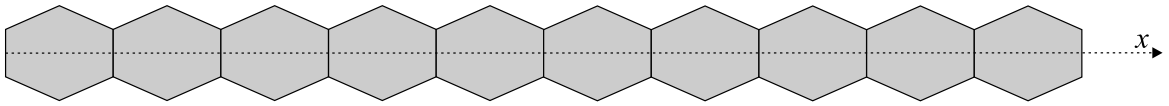
where $\hat{u}_L^*$ and $\hat{u}_0^*$ are the new displacement terms obtained. Now, with T_{11} and T_{21} previously obtained, the transfer matrix and, consequently, the dynamic stiffness matrix, are obtained.

3 Numerical Results

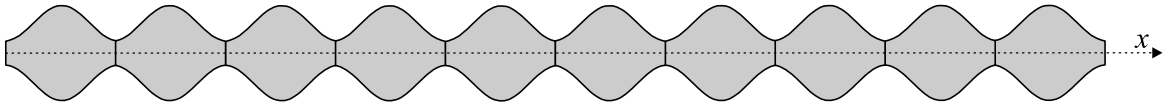
In this section, the proposed method is verified for three different structural models by comparison with conventional methods. In these examples, only the variation of the cross-sectional area is considered. The material is homogeneous steel with structural loss factor $\eta = 0.01$, incorporated as a complex Young's modulus $E = \bar{E}(1 + j\eta)$. The material and geometrical properties used for all the examples are: $L = 0.5$ [m], $\bar{E} = 210$ [GPa], and $\rho = 7800$ [kg/m^3]. Besides the trapezoidal and rectangular cases shown in Figure 1, a case with sinusoidally varying cross-sectional area, shown in Figure 3, is treated. In the latter case, the Fourier series has only 3 nonzero plane waves.



(a) Rectangular profile.



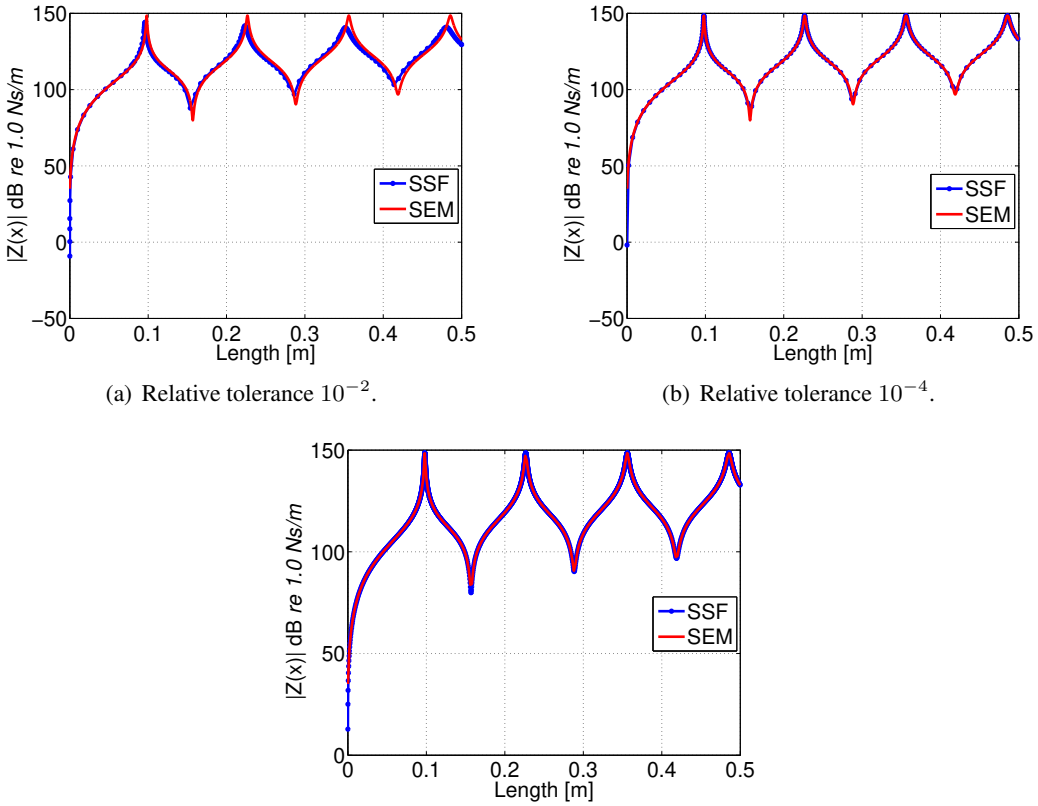
(b) Trapezoidal profile.



(c) Sinusoidal profile.

Figure 4: Three different variations of the cross-sectional area.

The three examples are shown in Figure 4. In the sinusoidal profile: $A_1 = 1 \times 10^{-2}$ [m^2] and $A_2 = 2 \times 10^{-2}$ [m^2]. In the rectangular profile: $A_1 = 1 \times 10^{-2}$ [m^2] and $A_2 = 2 \times 10^{-2}$ [m^2]. In the trapezoidal profile: $A_1 = 1 \times 10^{-4}$ [m^2] and $A_2 = 3 \times 10^{-2}$ [m^2].



(a) Relative tolerance 10^{-2}.

(b) Relative tolerance 10^{-4}.

(c) Relative tolerance 10^{-9}.

Figure 5: Impedance evaluated at 20 kHz.

The first verification consists in comparing the impedance obtained by solving the Riccati equation using an algorithm based on the Runge-Kutta method with the analytical solution obtained using SEM for rectangular case. The convergence for decreasing integration step sizes is verified by the mechanical impedance, with relative tolerances: 10^{-2}, 10^{-4}, and 10^{-9} in Figure 5(a), Figure 5(b), and Figure 5(c), respectively.

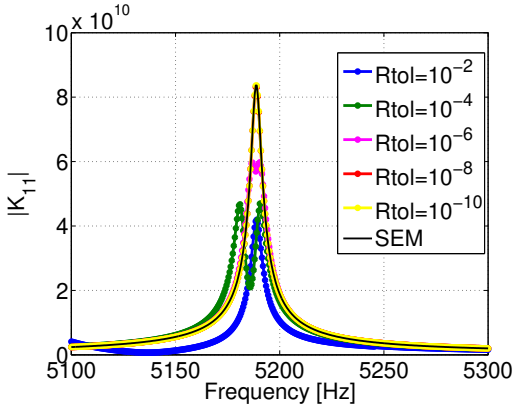
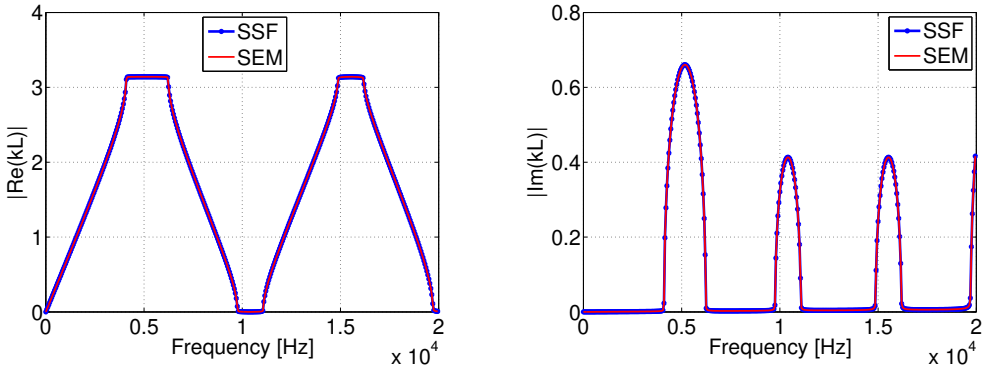


Figure 6: Absolute value of element K_{11}.

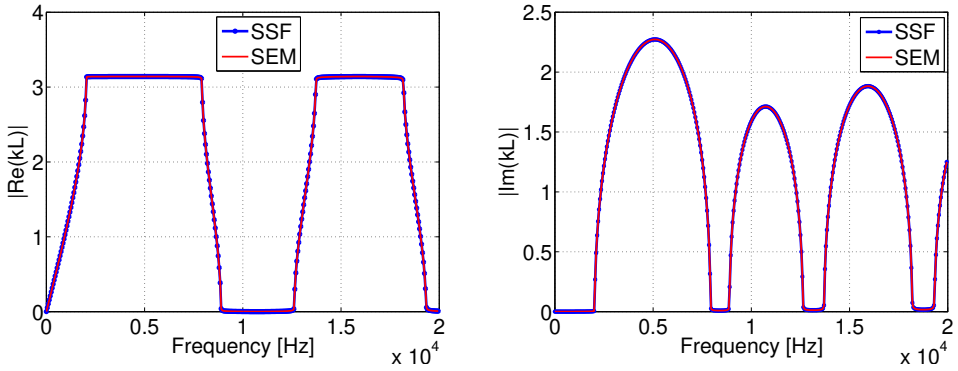
The convergence is also verified in Figure 6, which presents the absolute value of element K_{11} of the dynamic stiffness matrix, obtained using the SSF method with different relative tolerances, compared to the analytical solution (in black) obtained with SEM.

The dispersion curve for one periodic cell is verified by comparison with both the PWE method and SEM for the rectangular and trapezoidal profiles. For the sinusoidal case, only the PWE is used for comparison, since

there is no spectral element available in the literature for this cross-sectional area variation. The agreement is very good in all cases, see Figure 7, provided the integration step is chosen appropriately.



(a) Real part. (b) Imaginary part.



(c) Real part. (d) Imaginary part.

Figure 7: Dispersion diagram for the rectangular (a,b) and trapezoidal (c,d) profiles.

The presence of band gaps can be observed in both models in Figure 7. It is noticeable that the band gap is larger for the tapered profile, suggesting that the smoother variation of area can increase the band gap size.

Figure 8 shows the comparison between PWE and the proposed SSF method for the sinusoidally varying cross-section.

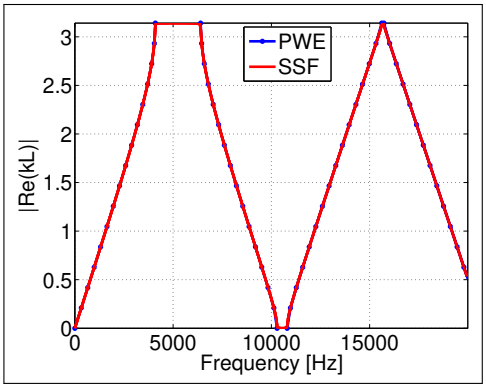
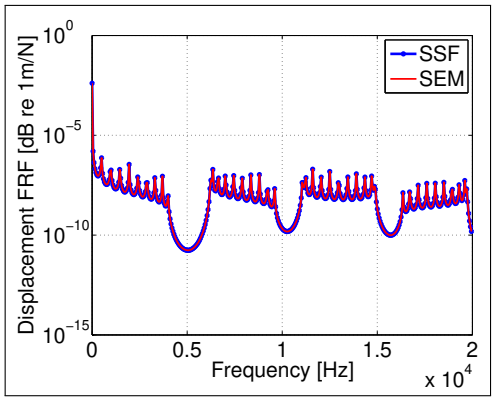
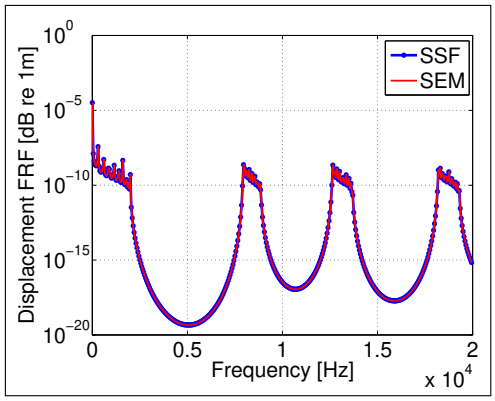


Figure 8: Real part of dispersion diagram evaluated by SSF and PWE for the sinusoidal rod.

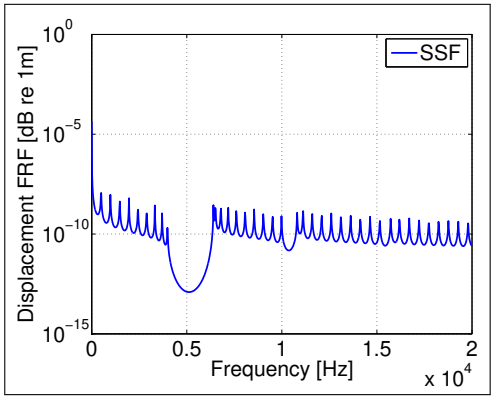
The forced response of a finite rod with ten cells is analyzed in Figure 9, considering the free-free boundary condition and a harmonic force $F = 1$ [N] as excitation at the one end, at $x = L$. The response is measured at the other end, at $x = 0$, avoiding the antiresonance and making it easier to observe the band-gap effect.



(a) Rectangular profile.



(b) Trapezoidal profile.



(c) Sinusoidal profile.

Figure 9: Rod displacement at $x = 0$ evaluated using SEM and SSF method.

4 Conclusion

A new solution method for computing the band diagram and forced response of one-dimensional structures using a state-space formulation and the solution of a Riccati equation with impedance as variable was proposed and verified by comparison with existing methods. The band diagrams obtained with the proposed method showed good agreement with results obtained by the traditional PWE method. The forced response obtained with the proposed method showed good agreement with results computed using a SEM formulation.

A previous works [9] showed the formulation of the one-dimensional problem of a straight beam with varying cross-section as a state-space problem reformulated into a Riccati equation. The present work extended this approach to compute the transfer matrix and the dynamic stiffness matrix, with which both the dispersion diagram (with real and imaginary parts) and the forced response of a periodic finite structure can be computed. Results were shown for a rod, but can be extended for a beam.

Examples of elastic phononic crystal rods with different geometries were computed to illustrate the proposed method and verify it by comparison with the conventional methods SEM and PWE. All the numerical results obtained with the proposed method were shown to be in agreement with the conventional methods.

The proposed method is an efficient way to characterize the wave propagation in periodic one-dimensional elastic structures, and can be used in shape optimization aiming at designing band gaps for passive vibration control.

Acknowledgments

The authors gratefully acknowledge the support of the Brazilian funding agencies CAPES, CNPq, FAPEMA, and FAPESP Grant Number 14/19054-6.

References

[1] Roy R. Craig. *Structural Dynamics: An Introduction to Computer Methods*. John Wiley & Sons, New York, 1981.

[2] James F. Doyle. *Wave Propagation in Structures*. Springer, New York, 1989.

[3] Jacques Cuenca. *Wave models for the flexural vibrations of thin plates*. PhD thesis, Université du Maine, 2009.

[4] Peter Lancaster and Leiba Rodman. *Algebraic Riccati Equations*. Oxford Science Publications. Clarendon Press, 1st edition edition, 1995.

[5] J. J. Levin. On the matrix Riccati equation. *Proceedings of the American Mathematical Society*, 10(4): 519–524, 1959.

[6] William T. Reid. A matrix differential equation of Riccati type. *American Journal of Mathematics*, 68 (2):237–246, 1946.

[7] E. Davison and M. Maki. The numerical solution of the matrix Riccati differential equation. *IEEE Transactions on Automatic Control*, 18(1):71–73, 1973.

[8] Charles S . Kenney and Roy B. Lepnik. Numerical integration of the differential matrix Riccati equation. *IEEE Transactions on Automatic Control*, 30(10):962–970, 1985.

[9] V. B. Georgiev, J. Cuenca, F. Gautier, L. Simon, and V. V. Krylov. Damping of structural vibrations in beams and elliptical plates using the acoustic black hole effect. *Journal of Sound and Vibration*, 330 (11):2497–2508, 2011.

[10] P. B. Silva, J. M. Mencik, and J. R. F. Arruda. Wave finite element-based superelements for forced response analysis of coupled systems via dynamic substructuring. *International Journal for Numerical Methods in Engineering*, 107(6):453–476, 2016.

[11] M. M. Sigalas and E. N. Economou. Elastic waves in plates with periodically placed inclusions. *Journal of Applied Physics*, 75(6):2845–2850, 1994.

[12] Usik Lee. *Spectral Element Method in Structural Dynamics*. John Wiley & Sons, New York, 2009.

[13] Khaled M. Ahmida, José Roberto F. Arruda, and Luiz Otávio F. Ferreira. A tapered acoustic duct spectral element. In *Proceedings of the Tenth International Congress on Sound and Vibration*, 2003.

[14] G. F. C. A. Assis, J. M. C. Dos Santos, J. F. Camino, and J. R. F. Arruda. Impedance computation using the spectral element method and the Riccati equation. In *Proceedings of the 2017 CILAMCE*, pages 1–9, Florianópolis, SC, Brazil, November 2017.

[15] Norman William McLachlan. *Bessel Functions for Engineers*. Clarendon Press Oxford, 1955.

Increasing the threshold of vibration stability of soft mounted induction motors with elastic rotors and sleeve bearings using active motor foot mounts

U. Werner
University of Applied Sciences Georg Simon Ohm Nuremberg
Keßlerplatz 12, 90489, Nuremberg, Germany
e-mail: **ulrich.werner@th-nuernberg.de**

Abstract
In the paper, the threshold of vibration stability of induction motors with flexible shafts and sleeve bearings, mounted on soft steel frame foundations with active motor foot mounts, is analyzed. The developed model is based on a multibody model, considering electromagnetic influence, stiffness and internal damping of the rotor, stiffness and damping of the bearing housings and end shields, stiffness and damping of the foundation and stiffness and damping of the oil film of the sleeve bearings. Additionally the stiffness and damping of the motor foot mounts – which are positioned between the motor feet the soft steel frame foundation – are considered, as well as the controlled forces which are applied in the vibration system by the motor foot mounts, using PD-controllers. The aim of the paper is to unite all these influences in a mathematical model and to derive a procedure for calculating the threshold of vibration stability. Based on a numerical example it can be shown, that the threshold of stability can be pushed to very high rotor speeds, using active motor foot mounts.

1 Introduction

Nowadays, in many applications induction motors and load machines (e.g. pumps or compressors) are mounted together on a steel frame foundation, which is often designed soft, because of economic reasons. The advantage is that all components can be mounted together and can be delivered together to the end customer, where the complete unit is then mounted on a base frame. The disadvantage is that the soft steel frame foundation influences the vibration behaviour clearly [1]-[5]. The natural frequencies are changed completely, compared to the natural frequencies, when the motor is mounted on a massive foundation, which is usually the case for large induction motors (power rating > 1MW), when the motor is tested in the motor factory, according to international motor standards (e.g. EN 60034-14). The consequence is that critical speeds may occur in the operation speed range, because nowadays applications are often converter driven to generate an optimal operation speed range to increase the efficiency. But not only critical speeds are influenced by the foundation, also self-excited vibrations, leading to vibration instability [1]-[5]. Therefore, it is important to know, at which rotor speed the threshold of vibration stability lies. Large induction motors (power rating > 1MW) with high rotor speeds (> 3000 rpm) are often designed with sleeve bearings and elastic rotors, operating above the first critical bending speed. However, the oil film characteristic – especially for sleeve bearings with cylindrical shells –, the internal damping of the rotor and the electromagnetic field damping may cause vibration instability. The aim of the paper is to analyze the use of active control, which is a very powerful instrument [6]-[11], to increase the threshold of stability. The idea is, to place actuators – active motor foot mounts – between the motor feet and the steel frame foundation and to use active control to influence the vibration system (Figure 1). The actuators here only operate in vertical direction (*z*-direction). By controlling each vertical motor foot displacement, the vibration system can be influenced, and therefore also the threshold of stability, which is the focus of the paper.

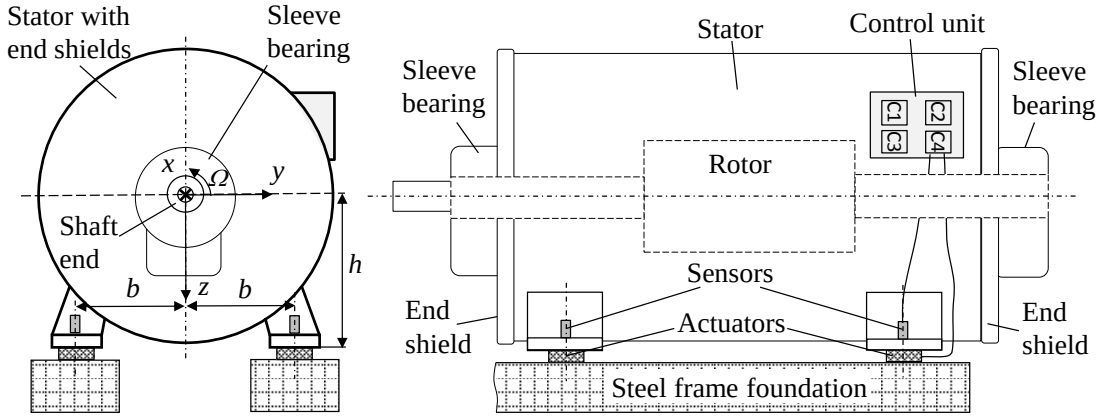


Figure 1: Induction motor with active motor foot mounts

2 Electromagnetic field damping

In induction motors a radial magnetic force $\hat{F}_{\mathrm{mr}}$ and a tangential magnetic force $\hat{F}_{\mathrm{mt}}$ is caused due to eccentricity $\hat{e}$ (Figure 2) [12]-[14].

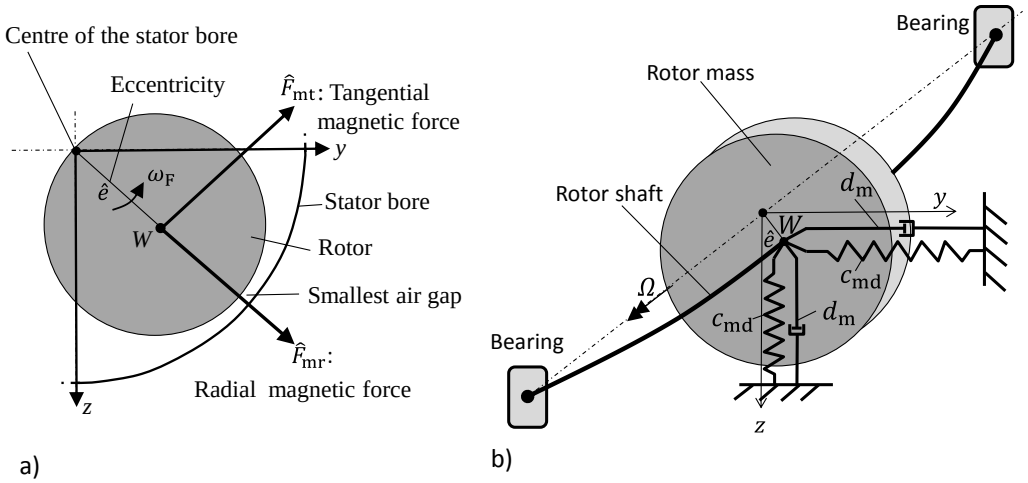


Figure 2: a) Electromagnetic forces; b) Magnetic spring and magnetic damper [12]-[14]

The radial magnetic force can be described by an electromagnetic spring element c_{md} [12]-[14]:

$$p > 1: \quad c_{\mathrm{md}} = \frac{c_{\mathrm{m}}}{2} \cdot \left(\alpha_{\mathrm{p+1}} + \alpha_{\mathrm{p-1}}\right); \qquad p = 1: \quad c_{\mathrm{md}} = c_{\mathrm{m}} \cdot \alpha_{\mathrm{p+1}} \tag{1}$$

$$\text{with: } c_{\mathrm{m}} = \frac{\pi \cdot R \cdot l}{2 \cdot \mu_0 \cdot \delta''} \cdot \hat{B}_{\mathrm{p}}^2; \qquad \text{with: } c_{\mathrm{m}} = \frac{1}{2} \cdot \frac{\pi \cdot R \cdot l}{2 \cdot \mu_0 \cdot \delta''} \cdot \hat{B}_{\mathrm{p}}^2$$

With *p:* Number of pole pairs of the motor; c_{m}: Electromagnetic spring element without electromagnetic field damping; $\alpha_{\mathrm{p+1}}$ and $\alpha_{\mathrm{p-1}}$: Real parts of the complex field damping value. Without electromagnetic field damping, the real parts of the field damping coefficients get $\alpha_{\mathrm{p+1}} = \alpha_{\mathrm{p-1}} = 1$. For 2-pole motors ($p$ =1) the component $\alpha_{\mathrm{p-1}}$ gets zero, neglecting the homopolar flux; *R:* Radius of the stator bore; l: Length of the core; μ_0: Permeability of air; δ'': Equivalent magnetic air gap width; $\hat{B}_{\mathrm{p}}$: Amplitude of fundamental air gap field; The tangential magnetic force can be described by the electromagnetic damper element d_{m} (with $\omega_{\mathrm{F}} \neq 0$) [12]-[14]:

$$p > 1: d_{\mathrm{m}} = -\frac{1}{\omega_{\mathrm{F}}} \cdot \frac{c_{\mathrm{m}}}{2} \cdot \left(\delta_{\mathrm{p+1}} - \delta_{\mathrm{p-1}}\right); \qquad p = 1: \; d_{\mathrm{m}} = -\frac{1}{\omega_{\mathrm{F}}} \cdot c_{\mathrm{m}} \cdot \delta_{\mathrm{p+1}} \tag{2}$$

With: ω_{F}: Whirling angular frequency of the rotor; $\delta_{\mathrm{p+1}}$ and $\delta_{\mathrm{p-1}}$: Imaginary parts of the complex field damping value. For 2-pole motors (p=1) the component $\delta_{\mathrm{p-1}}$ gets also zero, neglecting the homopolar flux; If electromagnetic field damping has to be considered, the electromagnetic field damping coefficients $\alpha_{\mathrm{p+1}}, \alpha_{\mathrm{p-1}}, \delta_{\mathrm{p+1}}, \delta_{\mathrm{p-1}}$ have to be derived. With the ordinal number $\nu = p \pm 1$ for an eccentricity field wave, the electromagnetic field damping coefficients can be calculated [12]-[14]:

$$\alpha_{\nu} = 1 - K_{\nu} \cdot s_{\nu}^2 \;\; ; \quad \delta_{\nu} = -K_{\nu} \cdot \beta_{\nu} \cdot \mathrm{s}_{\nu} \tag{3}$$

$$\text{with: } \beta_{\nu} = \frac{R_{2,\nu}}{\omega_1 (L_{2\mathrm{h},\nu} + L_{2\sigma,\nu})} \quad \text{and} \quad K_{\nu} = \frac{1}{\beta_{\nu}^2 + s_{\nu}^2} \cdot \frac{\xi_{\mathrm{Schr},\nu}^2 \cdot \zeta_{\mathrm{K},\nu}^2}{1 + \frac{L_{2\sigma,\nu}}{L_{2\mathrm{h},\nu}}}$$

With: $R_{2,\nu}$: Resistance of a rotor bar and ring segment; ω_1: Electrical stator angular frequency; $L_{2\mathrm{h},\nu}$: Main field inductance of a rotor mesh; $L_{2\sigma,\nu}$: Leakage inductance of a bar and ring segment; $\xi_{\mathrm{Schr},\nu}$: Screwing factor; $\zeta_{\mathrm{K},\nu}$: Coupling factor;

The harmonic slip s_{ν} can be described by [12]-[14]:

$$s_{\nu} = \frac{\frac{\omega_{\nu}}{\nu} - \Omega}{\frac{\omega_1}{\nu}} \qquad \text{with: } \Omega = \frac{\omega_1}{p}(1 - s) \tag{4}$$

With: s: Fundamental slip of the induction motor; Ω: Rotor angular frequency; ω_{ν}/ν: Angular frequencies of the eccentricity fields, depending on the kind of eccentricity:

- Static eccentricity: $\omega_{\nu} = \omega_1$
- Dynamic eccentricity as a circular forward whirl: $\omega_{\nu} = \omega_1 \pm \omega_{\mathrm{F}}$
- Dynamic eccentricity as a circular backward whirl: $\omega_{\nu} = \omega_1 \mp \omega_{\mathrm{F}}$

In order to consider the electromagnetic field damping effect by a simple magnetic spring element c_{md} and by a simple magnetic damper element d_{m}, the simplification has to be made, that the calculation of c_{md} and d_{m} is only based on circular forward whirls. So, the electromagnetic influence is supposed to be higher than it maybe in reality. If the absolute value of the harmonic slip $|s_{\nu}|$ is high – as it is for a circular backward whirl in conjunction with a small fundamental slip s – which is usual for steady state operation – the damped magnetic spring c_{md} gets very small as well as the magnetic damper d_{m}. In this case, the eccentricity fields induce strongly in the rotor cage and so the eccentricity fields get clearly reduced due to the harmonic rotor currents. Therefore, calculating c_{md} and d_{m} based on circular forward whirls is the worst case regarding the height of the electromagnetic influence, when considering electromagnetic field damping [14].

3 Vibration model

The vibration model is a plane multibody model (Figure 3), generally based on [15], but important enhancements and modifications are now implemented. The most important enhancement is that now a feedback control system is implemented and that only actuators acting in vertical direction are used. Additionally bearing housing damping, rotating damping of the rotor shaft and electromagnetic damping is now implemented in the model. In [15] the focus was on forced vibrations, but here the focus is on the analysis of the threshold of vibration stability. The model consists of two main masses, the rotor mass m_{w}, concentrated in the shaft centre point *W*, and the stator mass m_{s}, which has the inertia θ_{sx} and is concentrated in the centre of gravity *S*. The mass of the shaft journal m_{v} and the mass of the bearing housing m_{b} are accounted separately. The rotor rotates with the rotary angular frequency Ω. The inertia moments of the rotor are not considered and therefore also no gyroscopic effects. The shaft journal centre point *V* describes the movement of the shaft journals. The point *B* describes the movement of the bearing housing. The rotor mass is linked to the stator mass by the stiffness and damping (rotating damping) of the rotor c and d_{i}, the stiffness and the damping matrices of the oil film in the sleeve bearings $\mathbf{C_v}$ and $\mathbf{D_v}$ and the stiffness and damping matrix of the end-shield and bearing housing stiffness $\mathbf{C_b}$ and $\mathbf{D_b}$. Sleeve bearings and bearing housings and end-shields are here identical for drive side and non-drive side. The electromagnetism is

considered by the electromagnetic spring and damper matrix $\mathbf{C_m}$ and $\mathbf{D_m}$ – described by the damped magnetic spring value c_{md} and the electromagnetic damper value d_{m} [14]. The stator structure is assumed to be rigid, compared to the soft foundation.

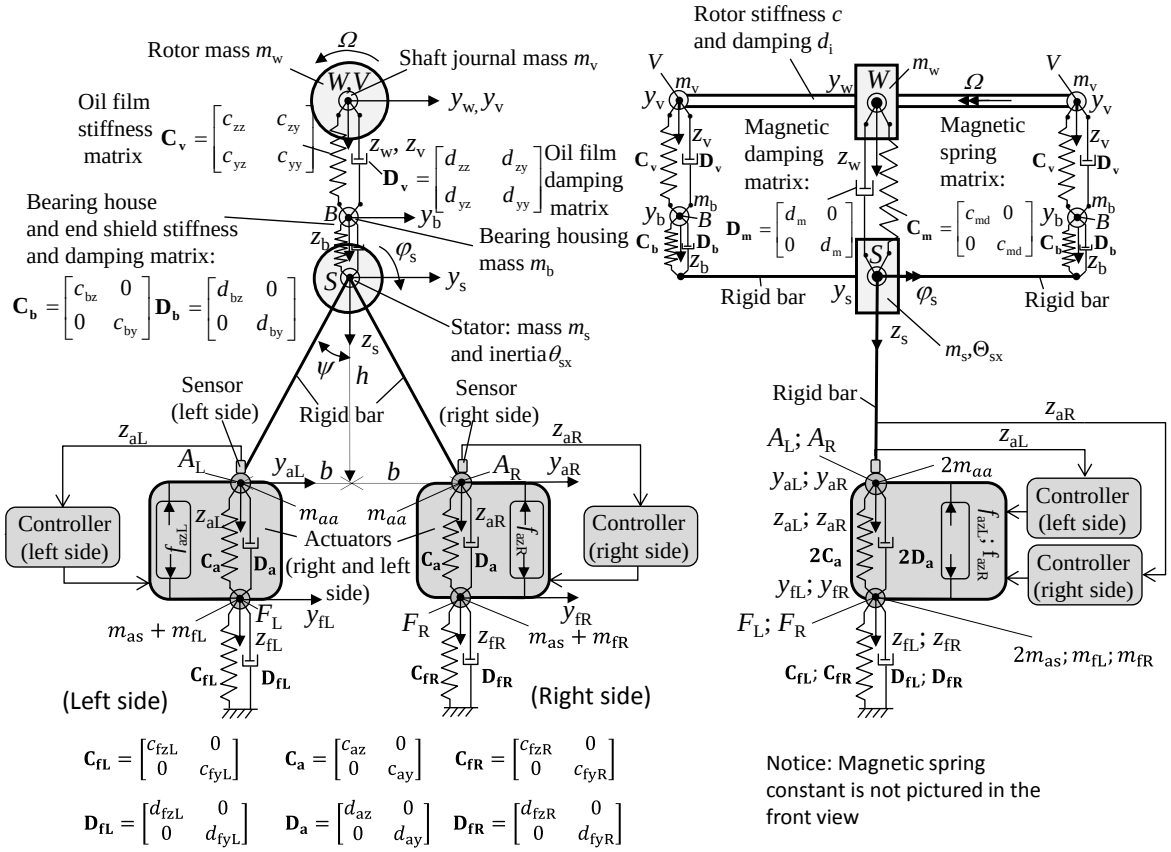


Figure 3: Vibration model of induction motor with active motor foot mounts on a soft foundation

The actuators are described by the actuator stiffness matrix $\mathbf{C_a}$ and actuator damping matrix $\mathbf{D_a}$, with the stiffness constants c_{ay} and c_{az} and the actuator damping constants d_{ay} and d_{az}.The mass of the actuator is split into mass of the stator (m_{as}) and mass of the armature (m_{aa}). The active forces of the actuators are described by f_{azL} and f_{azR}. All this values for the actuators are related on one motor side. On each motor side one sensor is positioned so, that the vertical displacement of the left side and of the right side of the motor feet can be detected and processed in the controllers. In the model only two controllers are necessary – one for the right side and one for the left side of the motor, because of the planarity of the model. The foundation is simplified described by the masses m_{fL} and m_{fR} and by the foundation stiffness matrices $\mathbf{C_{fL}}$ and $\mathbf{C_{fR}}$ and the foundation damping matrices $\mathbf{D_{fL}}$ and $\mathbf{D_{fR}}$. For deriving the damping coefficients, it is important to consider here, that natural vibrations with the angular natural frequency ω_{stab} of the critical mode at the limit of stability with the rotary angular frequency Ω_{stab} has to be analyzed. Therefore the whirling angular frequency ω_{F} becomes ω_{stab}:

$$\omega_{\mathrm{F}} = \omega_{\mathrm{stab}} \tag{5}$$

The oil film stiffness and damping coefficients c_{ij} and d_{ij} $(i,j = z,y)$ of the sleeve bearing are calculated by solving the Reynolds differential equation[16] and [17]:

$$c_{\mathrm{ij}} = c_{\mathrm{ij}}(\Omega) \text{ and } d_{\mathrm{ij}} = d_{\mathrm{ij}}(\Omega) \tag{6}$$

Referring to [2], the internal material damping of the rotor d_{i} is described here by the mechanical loss factor $\tan\delta_{\mathrm{i}}$ of the rotor, depending on the whirling angular frequency ω_{F}.

$$d_{\mathrm{i}}(\omega_{\mathrm{F}}) = \frac{c \cdot \tan \delta_{\mathrm{i}}}{\omega_{\mathrm{F}}} \tag{7}$$

With the stiffness of the bearing housing and end shield (c_{bz}; c_{by}), the damping of the bearing housing and end shield (d_{bz};d_{by}) is here also described by the mechanical loss factor $\tan \delta_{\mathrm{b}}$:

$$d_{\mathrm{bz}}(\omega_{\mathrm{F}}) = \frac{c_{\mathrm{bz}} \cdot \tan \delta_{\mathrm{b}}}{\omega_{\mathrm{F}}} \; ; \quad d_{\mathrm{by}}(\omega_{\mathrm{F}}) = \frac{c_{\mathrm{by}} \cdot \tan \delta_{\mathrm{b}}}{\omega_{\mathrm{F}}} \tag{8}$$

Also the damping of the actuators is described by the mechanical loss factor $\tan \delta_a$:

$$d_{\mathrm{az}}(\omega_{\mathrm{F}}) = \frac{c_{\mathrm{az}} \cdot \tan \delta_{\mathrm{a}}}{\omega_{\mathrm{F}}} \; ; \quad d_{\mathrm{ay}}(\omega_{\mathrm{F}}) = \frac{c_{\mathrm{ay}} \cdot \tan \delta_{\mathrm{a}}}{\omega_{\mathrm{F}}} \tag{9}$$

as well as the damping of the foundation, by the mechanical loss factor $\tan \delta_{\mathrm{f}}$:

$$d_{\mathrm{fzL}}(\omega_{\mathrm{F}}) = \frac{c_{\mathrm{fzL}} \cdot \tan \delta_{\mathrm{f}}}{\omega_{\mathrm{F}}} \; ; \; d_{\mathrm{fyL}}(\omega_{\mathrm{F}}) = \frac{c_{\mathrm{fyL}} \cdot \tan \delta_{\mathrm{f}}}{\omega_{\mathrm{F}}} ; d_{\mathrm{fzR}}(\omega_{\mathrm{F}}) = \frac{c_{\mathrm{fzR}} \cdot \tan \delta_{\mathrm{f}}}{\omega_{\mathrm{F}}} \; ; \; d_{\mathrm{fyR}}(\omega_{\mathrm{F}}) = \frac{c_{\mathrm{fyR}} \cdot \tan \delta_{\mathrm{f}}}{\omega_{\mathrm{F}}} \tag{10}$$

The electromagnetic stiffness coefficient c_{md} and damping coefficient d_{m} are depending on the harmonic slip s_{ν}, and therefore also depending on the whirling angular frequency ω_{F} [14].

$$c_{\mathrm{md}} = c_{\mathrm{md}}(\omega_{\mathrm{F}}) \text{ and } d_{\mathrm{m}} = d_{\mathrm{m}}(\omega_{\mathrm{F}}) \tag{11}$$

4 Mathematical description

To derive the mathematical description, the vibration system is split into subsystems (Figure 4). The displacements of the stator mass z_{s}, y_{s}, φ_{s} are much smaller compared to the dimensions of the motor h, b, Ψ, therefore following linearization is possible [15]:

$$z_{\mathrm{aL}} = z_{\mathrm{s}} - \varphi_{\mathrm{s}} \cdot b; \; z_{\mathrm{aR}} = z_{\mathrm{s}} + \varphi_{\mathrm{s}} \cdot b; \; y_{\mathrm{aL}} = y_{\mathrm{aR}} = y_{\mathrm{s}} - \varphi_{\mathrm{s}} \cdot h \tag{12}$$

Now, a linear inhomogeneous differential equation system can be derived, described by mass matrix **M,** damping matrix **D**, stiffness matrix **C**, coordinate vector **q**, and vector for actuator forces $\mathbf{f_a}$.

$$\mathbf{M} \cdot \ddot{\mathbf{q}} + \mathbf{D} \cdot \dot{\mathbf{q}} + \mathbf{C} \cdot \mathbf{q} = \mathbf{f_a} \tag{13}$$

The coordinate vector **q** can be described by:

$$\mathbf{q} = [z_{\mathrm{s}}; z_{\mathrm{w}}; y_{\mathrm{s}}; y_{\mathrm{w}}; \varphi_{\mathrm{s}}; z_{\nu}; z_{\mathrm{b}}; z_{\mathrm{fL}}; z_{\mathrm{fR}}; y_{\nu}; y_{\mathrm{b}}; y_{\mathrm{fL}}; y_{\mathrm{fR}}]^T \tag{14}$$

The actuator forces can be split into the actuator forces on the left side and on the right side:

$$\begin{aligned} \mathbf{f_a} = \mathbf{f_{azL}} + \mathbf{f_{azR}} = & \underbrace{[1 \;\; 0 \;\; 0 \;\; 0 \;\; -b \;\; 0 \;\; 0 \;\; -1 \;\; 0 \;\; 0 \;\; 0 \;\; 0 \;\; 0]^T}_{\mathbf{P_{azL}}} \cdot f_{\mathrm{azL}} \\ & + \underbrace{[1 \;\; 0 \;\; 0 \;\; 0 \;\; b \;\; 0 \;\; 0 \;\; 0 \;\; -1 \;\; 0 \;\; 0 \;\; 0 \;\; 0]^T}_{\mathbf{P_{azR}}} \cdot f_{\mathrm{azR}} \end{aligned} \tag{15}$$

For an ideal PD-controller – K_{PL}, K_{PR} proportional coefficients (left side and right side) and K_{DL}, K_{DR} derivative coefficients (left side and right side) – with a negative feedback loop for the vertical motor feet displacements z_{aL} and z_{aR}, the actuator forces can described by:

$$\mathbf{f_a} = -\mathbf{P_{azL}} \left(K_{\mathrm{PL}} \cdot z_{\mathrm{aL}} + K_{\mathrm{DL}} \frac{dz_{\mathrm{aL}}}{dt} \right) - \mathbf{P_{azR}} \left(K_{\mathrm{PR}} \cdot z_{\mathrm{aR}} + K_{\mathrm{DR}} \frac{dz_{\mathrm{aR}}}{dt} \right) \tag{16}$$

With the cinematic constrains (12), follows:

$$\mathbf{f_a} = -\mathbf{P_{azL}} \left[K_{\mathrm{PL}} (z_{\mathrm{s}} - \varphi_{\mathrm{s}} \cdot b) + K_{\mathrm{DL}} \left(\frac{dz_{\mathrm{s}}}{dt} - \frac{d\varphi_{\mathrm{s}}}{dt} \cdot b \right) \right] - \mathbf{P_{azR}} \left[K_{\mathrm{PR}} (z_{\mathrm{s}} + \varphi_{\mathrm{s}} \cdot b) + K_{\mathrm{DR}} \left(\frac{dz_{\mathrm{s}}}{dt} + \frac{d\varphi_{\mathrm{s}}}{dt} \cdot b \right) \right] \tag{17}$$

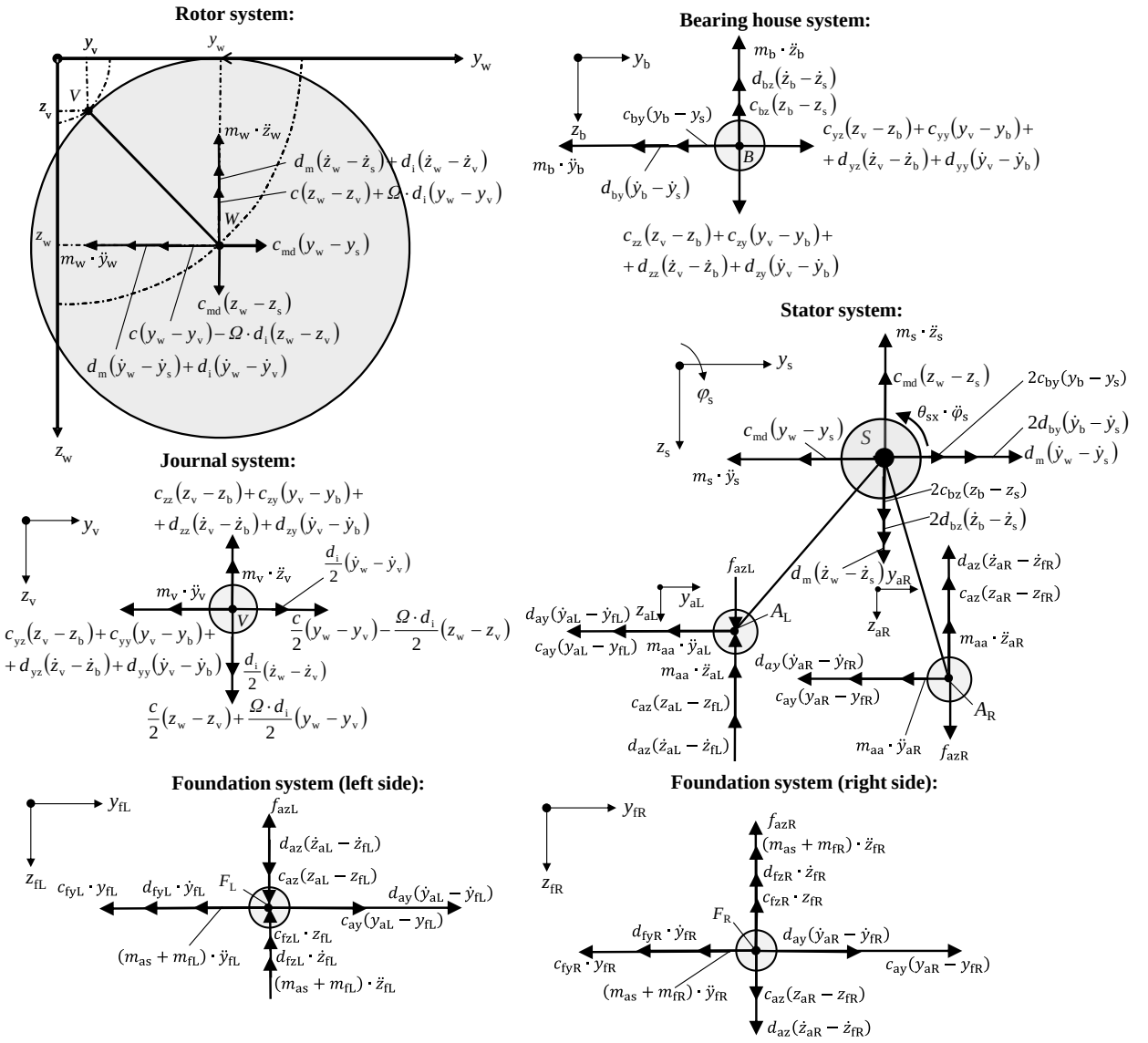


Figure 4: Vibration model split into subsystems

So the differential equation system can be described by:

$$\begin{aligned}&\mathbf{M}\cdot\ddot{\mathbf{q}}+\mathbf{D}\cdot\dot{\mathbf{q}}+\mathbf{C}\cdot\mathbf{q}\\&+\mathbf{P}_{\mathbf{azL}}\left[K_{\mathrm{PL}}\left(z_{\mathrm{s}}-\varphi_{\mathrm{s}}\cdot b\right)+K_{\mathrm{DL}}\left(\frac{dz_{\mathrm{s}}}{dt}-\frac{d\varphi_{\mathrm{s}}}{dt}\cdot b\right)\right]\\&+\mathbf{P}_{\mathbf{azR}}\left[K_{\mathrm{PR}}\left(z_{\mathrm{s}}+\varphi_{\mathrm{s}}\cdot b\right)+K_{\mathrm{DR}}\left(\frac{dz_{\mathrm{s}}}{dt}+\frac{d\varphi_{\mathrm{s}}}{dt}\cdot b\right)\right]=\mathbf{0}\end{aligned}\tag{18}$$

The control coefficients K_{PL}, K_{PR}, K_{DL}, K_{DR} can now be integrated into the damping matrix and stiffness matrix leading to a controlled system stiffness matrix $\tilde{\mathbf{C}}$ and a controlled system damping matrix $\tilde{\mathbf{D}}$. The new differential equation system can now be described by:

$$\mathbf{M}\cdot\ddot{\mathbf{q}}+\tilde{\mathbf{D}}\cdot\dot{\mathbf{q}}+\tilde{\mathbf{C}}\cdot\mathbf{q}=\mathbf{0}\tag{19}$$

The mass matrix **M:** (20)

$$\mathbf{M}=\begin{bmatrix}
m_s+2m_{aa} & 0 & 0 & 0 & 0 & 0 & 0\\
0 & m_w & 0 & 0 & 0 & 0 & 0\\
0 & 0 & m_s+2m_{aa} & 0 & -2h\cdot m_{aa} & 0 & 0\\
0 & 0 & 0 & m_w & 0 & 0 & 0\\
0 & 0 & -2h\cdot m_{aa} & 0 & \theta_{sx}+2m_{aa}\left(b^2+h^2\right) & 0 & 0\\
0 & 0 & 0 & 0 & 0 & 2m_v & 0\\
0 & 0 & 0 & 0 & 0 & 0 & 2m_b\\
0 & 0 & 0 & 0 & 0 & 0 & 0\\
0 & 0 & 0 & 0 & 0 & 0 & 0\\
0 & 0 & 0 & 0 & 0 & 0 & 0\\
0 & 0 & 0 & 0 & 0 & 0 & 0\\
0 & 0 & 0 & 0 & 0 & 0 & 0\\
0 & 0 & 0 & 0 & 0 & 0 & 0
\end{bmatrix}$$

$$\begin{bmatrix}
0 & 0 & 0 & 0 & 0 & 0\\
0 & 0 & 0 & 0 & 0 & 0\\
0 & 0 & 0 & 0 & 0 & 0\\
0 & 0 & 0 & 0 & 0 & 0\\
0 & 0 & 0 & 0 & 0 & 0\\
0 & 0 & 0 & 0 & 0 & 0\\
0 & 0 & 0 & 0 & 0 & 0\\
m_{as}+m_{fL} & 0 & 0 & 0 & 0 & 0\\
0 & m_{as}+m_{fR} & 0 & 0 & 0 & 0\\
0 & 0 & 2m_v & 0 & 0 & 0\\
0 & 0 & 0 & 2m_b & 0 & 0\\
0 & 0 & 0 & 0 & m_{as}+m_{fL} & 0\\
0 & 0 & 0 & 0 & 0 & m_{as}+m_{fR}
\end{bmatrix}$$

The damping matrix $\widetilde{\mathbf{D}}$: (21)

$$\widetilde{\mathbf{D}}=\begin{bmatrix}
2\left(d_{az}+d_{bz}\right)+d_m+K_{DL}+K_{DR} & -d_m & 0 & 0 & b\left(K_{DR}-K_{DL}\right)\\
-d_m & d_m+d_i & 0 & 0 & 0\\
0 & 0 & 2\left(d_{ay}+d_{by}\right)+d_m & -d_m & -2d_{ay}\cdot h\\
0 & 0 & -d_m & d_m+d_i & 0\\
b\left(K_{DR}-K_{DL}\right) & 0 & -2d_{ay}\cdot h & 0 & 2\left(d_{ay}h^2+d_{az}b^2\right)+b^2\left(K_{DL}+K_{DR}\right)\\
0 & -d_i & 0 & 0 & 0\\
-2d_{bz} & 0 & 0 & 0 & 0\\
-d_{az}-K_{DL} & 0 & 0 & 0 & b\left(d_{az}+K_{DL}\right)\\
-d_{az}-K_{DR} & 0 & 0 & 0 & -b\left(d_{az}+K_{DR}\right)\\
0 & 0 & 0 & -d_i & 0\\
0 & 0 & -2d_{by} & 0 & 0\\
0 & 0 & -d_{ay} & 0 & d_{ay}\cdot h\\
0 & 0 & -d_{ay} & 0 & d_{ay}\cdot h
\end{bmatrix}$$

$$\begin{bmatrix}
0 & -2d_{bz} & -d_{az} & -d_{az} & 0 & 0 & 0 & 0\\
-d_i & 0 & 0 & 0 & 0 & 0 & 0 & 0\\
0 & 0 & 0 & 0 & 0 & -2d_{by} & -d_{ay} & -d_{ay}\\
0 & 0 & 0 & 0 & -d_i & 0 & 0 & 0\\
0 & 0 & d_{az}\cdot b & -d_{az}\cdot b & 0 & 0 & d_{ay}\cdot h & d_{ay}\cdot h\\
2d_{zz}+d_i & -2d_{zz} & 0 & 0 & 2d_{zy} & -2d_{zy} & 0 & 0\\
-2d_{zz} & 2\left(d_{zz}+d_{bz}\right) & 0 & 0 & -2d_{zy} & 2d_{zy} & 0 & 0\\
0 & 0 & d_{az}+d_{fzL} & 0 & 0 & 0 & 0 & 0\\
0 & 0 & 0 & d_{az}+d_{fzR} & 0 & 0 & 0 & 0\\
2d_{yz} & -2d_{yz} & 0 & 0 & 2d_{yy}+d_i & -2d_{yy} & 0 & 0\\
-2d_{yz} & 2d_{yz} & 0 & 0 & -2d_{yy} & 2\left(d_{yy}+d_{by}\right) & 0 & 0\\
0 & 0 & 0 & 0 & 0 & 0 & d_{ay}+d_{fyL} & 0\\
0 & 0 & 0 & 0 & 0 & 0 & 0 & d_{ay}+d_{fyR}
\end{bmatrix}$$

The stiffness matrix $\tilde{\mathbf{C}}$: (22)

$$\tilde{\mathbf{C}} = \begin{bmatrix}
2(c_{\mathrm{bz}}+c_{\mathrm{az}})-c_{\mathrm{md}}+K_{\mathrm{PR}}+K_{\mathrm{PL}} & c_{\mathrm{md}} & 0 & 0 & b\left(K_{\mathrm{PR}}-K_{\mathrm{PL}}\right) \\
c_{\mathrm{md}} & c-c_{\mathrm{md}} & 0 & \Omega\cdot d_{\mathrm{i}} & 0 \\
0 & 0 & 2(c_{\mathrm{by}}+c_{\mathrm{ay}})-c_{\mathrm{md}} & c_{\mathrm{md}} & -2c_{\mathrm{ay}}\cdot h \\
0 & -\Omega\cdot d_{\mathrm{i}} & c_{\mathrm{md}} & c-c_{\mathrm{md}} & 0 \\
b\left(K_{\mathrm{PR}}-K_{\mathrm{PL}}\right) & 0 & -2c_{\mathrm{ay}}\cdot h & 0 & 2\left(c_{\mathrm{ay}}h^2+c_{\mathrm{az}}b^2\right)+b^2\left(K_{\mathrm{PL}}+K_{\mathrm{PR}}\right) \\
0 & -c & 0 & -\Omega\cdot d_{\mathrm{i}} & 0 \\
-2c_{\mathrm{bz}} & 0 & 0 & 0 & 0 \\
-c_{\mathrm{az}}-K_{\mathrm{PL}} & 0 & 0 & 0 & b\left(c_{\mathrm{az}}+K_{\mathrm{PL}}\right) \\
-c_{\mathrm{az}}-K_{\mathrm{PR}} & 0 & 0 & 0 & -b\left(c_{\mathrm{az}}+K_{\mathrm{PR}}\right) \\
0 & \Omega\cdot d_{\mathrm{i}} & 0 & -c & 0 \\
0 & 0 & -2c_{\mathrm{by}} & 0 & 0 \\
0 & 0 & -c_{\mathrm{ay}} & 0 & c_{\mathrm{ay}}\cdot h \\
0 & 0 & -c_{\mathrm{ay}} & 0 & c_{\mathrm{ay}}\cdot h
\end{bmatrix}$$

$$\begin{bmatrix}
0 & -2c_{\mathrm{bz}} & -c_{\mathrm{az}} & -c_{\mathrm{az}} & 0 & 0 & 0 & 0 \\
-c & 0 & 0 & 0 & -\Omega\cdot d_{\mathrm{i}} & 0 & 0 & 0 \\
0 & 0 & 0 & 0 & 0 & -2c_{\mathrm{by}} & -c_{\mathrm{ay}} & -c_{\mathrm{ay}} \\
\Omega\cdot d_{\mathrm{i}} & 0 & 0 & 0 & -c & 0 & 0 & 0 \\
0 & 0 & c_{\mathrm{az}}\cdot b & -c_{\mathrm{az}}\cdot b & 0 & 0 & c_{\mathrm{ay}}\cdot h & c_{\mathrm{ay}}\cdot h \\
2c_{zz}+c & -2c_{zz} & 0 & 0 & 2c_{zy}+\Omega\cdot d_{\mathrm{i}} & -2c_{zy} & 0 & 0 \\
-2c_{zz} & 2(c_{zz}+c_{\mathrm{bz}}) & 0 & 0 & -2c_{zy} & 2c_{zy} & 0 & 0 \\
0 & 0 & c_{\mathrm{az}}+c_{\mathrm{fzL}} & 0 & 0 & 0 & 0 & 0 \\
0 & 0 & 0 & c_{\mathrm{az}}+c_{\mathrm{fzR}} & 0 & 0 & 0 & 0 \\
2c_{\mathrm{yz}}-\Omega\cdot d_{\mathrm{i}} & -2c_{\mathrm{yz}} & 0 & 0 & 2c_{\mathrm{yy}}+c & -2c_{\mathrm{yy}} & 0 & 0 \\
-2c_{\mathrm{yz}} & 2c_{\mathrm{yz}} & 0 & 0 & -2c_{\mathrm{yy}} & 2(c_{\mathrm{yy}}+c_{\mathrm{by}}) & 0 & 0 \\
0 & 0 & 0 & 0 & 0 & 0 & c_{\mathrm{ay}}+c_{\mathrm{fyL}} & 0 \\
0 & 0 & 0 & 0 & 0 & 0 & 0 & c_{\mathrm{ay}}+c_{\mathrm{fyR}}
\end{bmatrix}$$

Referring to [14], the state-space formulation can be described by:

$$\underbrace{\begin{bmatrix}\dot{\mathbf{q}}\\ \ddot{\mathbf{q}}\end{bmatrix}}_{\dot{\mathbf{x}}} = \underbrace{\begin{bmatrix}\mathbf{0} & \mathbf{I}\\ -\mathbf{M}^{-1}\cdot\tilde{\mathbf{C}} & -\mathbf{M}^{-1}\cdot\tilde{\mathbf{D}}\end{bmatrix}}_{\tilde{\mathbf{A}}_{\mathbf{z}}} \cdot \underbrace{\begin{bmatrix}\mathbf{q}\\ \dot{\mathbf{q}}\end{bmatrix}}_{\mathbf{x}} \tag{23}$$

Where $\mathbf{0}$ is the zero-matrix and $\mathbf{I}$ is the unit matrix, $\tilde{\mathbf{A}}_{\mathbf{z}}$ is the system matrix. With:

$$\mathbf{x} = \hat{\mathbf{x}}\cdot e^{\lambda t} \rightarrow \tilde{\mathbf{A}}_{\mathbf{z}}\cdot\hat{\mathbf{x}} = \lambda\cdot\hat{\mathbf{x}} \tag{24}$$

the eigenvalue equation is described:

$$[\tilde{\mathbf{A}}_{\mathbf{z}} - \lambda\cdot\mathbf{I}]\cdot\hat{\mathbf{x}} = \mathbf{0} \tag{25}$$

The eigenvalues λ can be calculated by:

$$\det[\tilde{\mathbf{A}}_{\mathbf{z}} - \lambda\cdot\mathbf{I}] = 0 \tag{26}$$

According to (25) the eigenvectors $\hat{\mathbf{x}}$ can be calculated. If the eigenvalues λ and the eigenvectors $\hat{\mathbf{x}}$ shall be calculated without control system, the controller parameters have to set to zero (K_{PL}= K_{PR} = K_{DL}= $K_{\mathrm{DR}} = 0$) in the damping matrix $\tilde{\mathbf{D}}$ and in the stiffness matrix $\tilde{\mathbf{C}}$.

5 Threshold of vibration stability

At the threshold of stability, the eigenvalue λ of the critical mode gets:

$$\lambda = \lambda_{\mathrm{stab}} = \pm j \cdot \omega_{\mathrm{stab}} \tag{27}$$

Knowing the eigenvalue λ_{stab}, the critical mode shape at the limit of stability can be derived. The real part of the critical eigenvalue λ_{stab} is zero and the whirling angular frequency ω_{F} is then identical to ω_{stab}, while the rotor is rotating with Ω_{stab}. It has to be considered, that the coefficients d_{i}, d_{bz}, d_{by}, d_{fzL}, d_{fyL}, d_{fzR}, d_{fyR}, d_{az}, d_{ay}, d_{m}, c_{md} are depending on the whirling angular frequency ω_{F}, which has to be determined. Referring to [14] an iterative solution has to be deduced, according to Figure 5. First, the coefficients d_{i}, d_{bz}, d_{by}, d_{fzL}, d_{fyL}, d_{fzR}, d_{fyR}, d_{az}, d_{ay}, d_{m}, c_{md} , which depend on the whirling angular frequency ω_{F}, are set to zero, so that only the non-symmetric stiffness matrix of the oil film will cause instability. The eigenvalues are calculated according to (26), depending on the rotary angular frequency Ω.

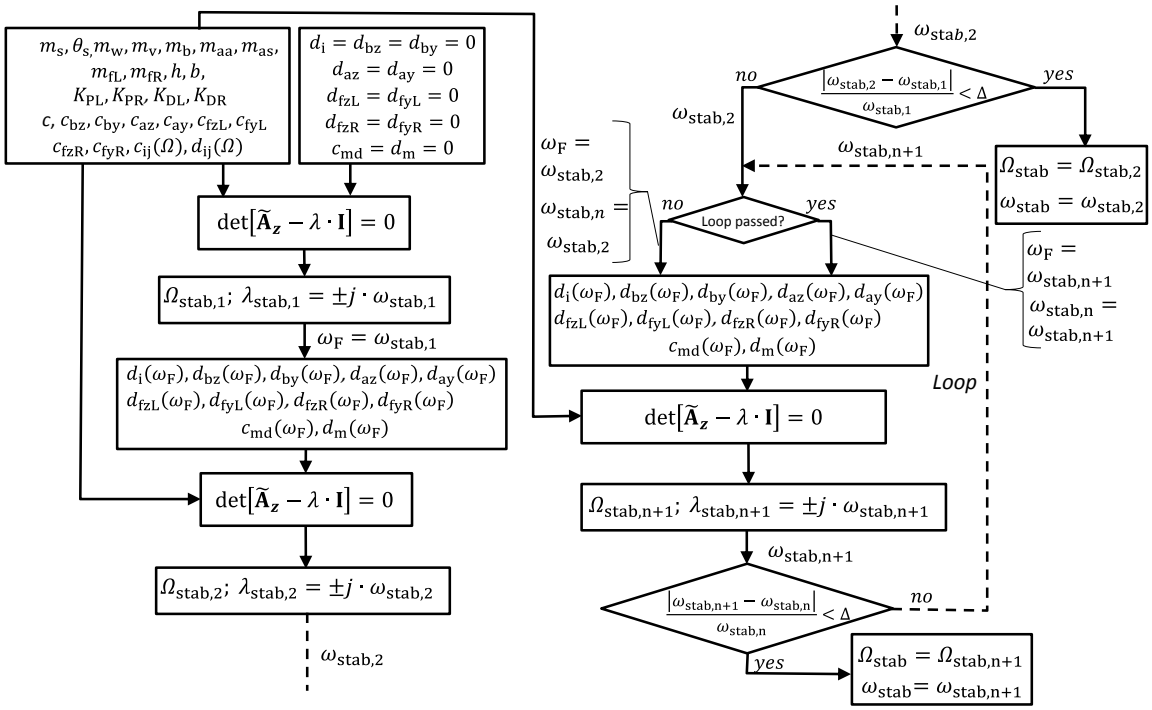


Figure 5: Flow diagram to derive the limit of stability

To derive the limit of stability, the rotary angular frequency Ω is increased, till the real part of an eigenvalue gets zero. At this limit, the rotary angular frequency is $\Omega_{\mathrm{stab},1}$ – index "1" for the first calculation – and the natural angular frequency of the critical mode $\omega_{stab,1}$ can be derived from the eigenvalue. Afterwards the coefficients d_{i}, d_{bz}, d_{by}, d_{fzL}, d_{fyL}, d_{fzR}, d_{fyR}, d_{az}, d_{ay}, d_{m}, c_{md} are calculated with $\omega_{\mathrm{F}} = \omega_{\mathrm{stab},1}$, and the limit of stability and the natural angular frequency are calculated again, leading to $\Omega_{\mathrm{stab},2}$ and $\omega_{\mathrm{stab},2}$. Then the new calculated natural angular frequency $\omega_{\mathrm{stab},2}$ will be compared to the origin natural angular frequency $\omega_{\mathrm{stab},1}$. If the ratio is less than Δ – an arbitrarily chosen value –, the calculation is finished and $\Omega_{\mathrm{stab}} = \Omega_{\mathrm{stab},2}$ and $\omega_{\mathrm{stab}} = \omega_{\mathrm{stab},2}$. If the ration is larger as the chosen value Δ, a new calculation is deduced and the coefficients d_{i}, d_{bz}, d_{by}, d_{fzL}, d_{fyL}, d_{fzR}, d_{fyR}, d_{az}, d_{ay}, d_{m}, c_{md} are now calculated with $\omega_{\mathrm{F}} = \omega_{\mathrm{stab},2}$. With these new coefficients, the new limit of stability $\Omega_{\mathrm{stab,n+1}}$ and the natural angular frequency $\omega_{\mathrm{stab,n+1}}$ are derived. Then again the new value $\omega_{\mathrm{stab,n+1}}$ is compared to the previous value $\omega_{\mathrm{stab},2}$. If the deviation is still too large, the loop will run through, till the deviation is less than Δ. With this iterative process the limit of stability Ω_{stab} can be derived, as well as the corresponding natural angular frequency ω_{stab} of the critical mode.

6 Example

In this section the threshold of stability is analysed for a 2-pole induction motor (Table 1), with sleeve bearings and flexible rotor. The induction motor is mounted on a soft foundation with active motor mounts between the motor feet and foundation and is driven by a converter with constant magnetization in the whole speed rang, operating without load ($s = 0$). The investigated speed range is from 1000 rpm up to 10000 rpm. Mechanical damping of the actuators is neglected here ($\tan \delta_\mathrm{a} = 0$).

6.1 Basic data

The basic data are described in Table 1.

Data of the motor:	
- Masse of the stator	$m_\mathrm{s} = 7040\ kg$
- Mass inertia of the stator at the *x*-axis	$\theta_\mathrm{sx} = 1550\ kgm^2$
- Mass of the rotor	$m_\mathrm{w} = 1900\ kg$
- Mass of the rotor shaft journal	$m_\mathrm{v} = 10\ kg$
- Mass of the bearing housing	$m_\mathrm{b} = 80\ kg$
- Stiffness of the rotor	$c = 1.0 \cdot 10^8\ kg/s^2$
- Undamped magnetic spring constant	$c_\mathrm{m} = 7.0 \cdot 10^6\ kg/s^2$
- Height of the centre of gravity *S*	$h = 560\ mm$
- Distance between motor feet	$2b = 1060\ mm$
- Horizontal stiffness of bearing housing and end shield	$c_\mathrm{by} = 4.8 \cdot 10^8\ kg/s^2$
- Vertical stiffness of bearing housing and end shield	$c_\mathrm{bz} = 5.7 \cdot 10^8\ kg/s^2$
- Mechanical loss factor of the bearing housing and end shield	$\tan \delta_\mathrm{b} = 0.04$
- Mechanical loss factor of the rotor	$\tan \delta_\mathrm{i} = 0.03$
Data of the sleeve bearings:	
- Bearing shell	Cylindrical
- Lubricant viscosity grade	ISO VG 32
- Nominal bore diameter / Bearing width	d_b = 110 mm / b_b = 81.4 mm
- Ambient temperature / Supply oil temperature	T_amb = 20°C / T_in = 40°C
- Mean relative bearing clearance (DIN 31698)	Ψ_m = 1.6 ‰
Data of the actuators (for each motor side):	
- Mass of the stator	$m_\mathrm{as} = 10$ kg
- Mass of the armature	$m_\mathrm{aa} = 3$ kg
- Vertical stiffness for each motor side	$c_\mathrm{az} = 6.0 \cdot 10^8\ kg/s^2$
- Horizontal stiffness for each motor side	$c_\mathrm{ay} = 3.0 \cdot 10^8\ kg/s^2$
- Mechanical loss factor of the actuators	$\tan \delta_a = 0$
Data of the foundation (for each motor side):	
- Mass left side	$m_\mathrm{fL} = 30$ kg
- Mass right side	$m_\mathrm{fR} = 30$ kg
- Vertical stiffness for each motor side	$c_\mathrm{fzL} = c_\mathrm{fzR} = 1.5 \cdot 10^8\ kg/s^2$
- Horizontal stiffness for each motor side	$c_\mathrm{fyL} = c_\mathrm{fyL} = 1.0 \cdot 10^8\ kg/s^2$
- Mechanical loss factor of the foundation	$\tan \delta_\mathrm{f} = 0.04$

Table 1: Data 2-pole induction motor (2 MW), bearings, actuators and foundation

The oil film stiffness and damping coefficients of the sleeve bearings are calculated for each rotor speed in steady state operation (Figure 5). Therefore the program SBCALC from RENK AG is used.

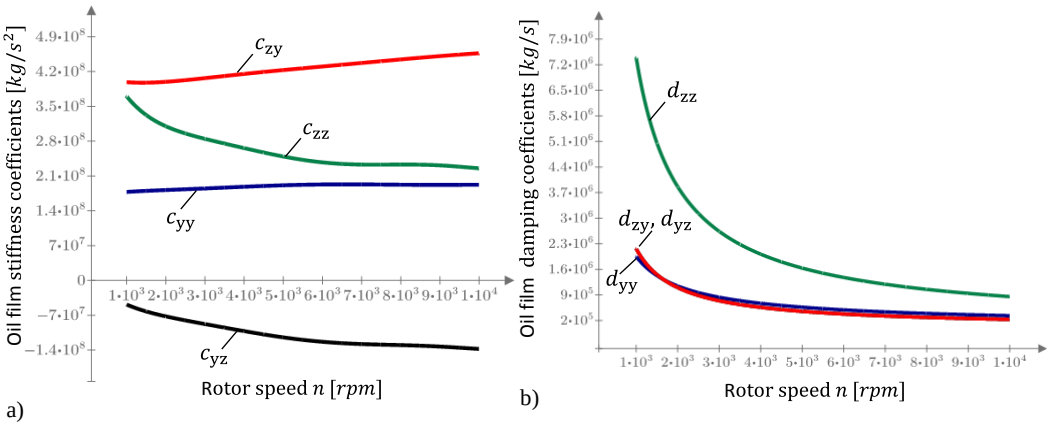


Figure 6: Oil film stiffness coefficients (a)) and damping coefficients (b)), for different rotor speeds

The electromagnetic spring value c_{md} and the electromagnetic damper value d_{m} are calculated according to section 2, depending on rotor angular frequency Ω and on whirling angular frequency ω_{F} (Figure 7).

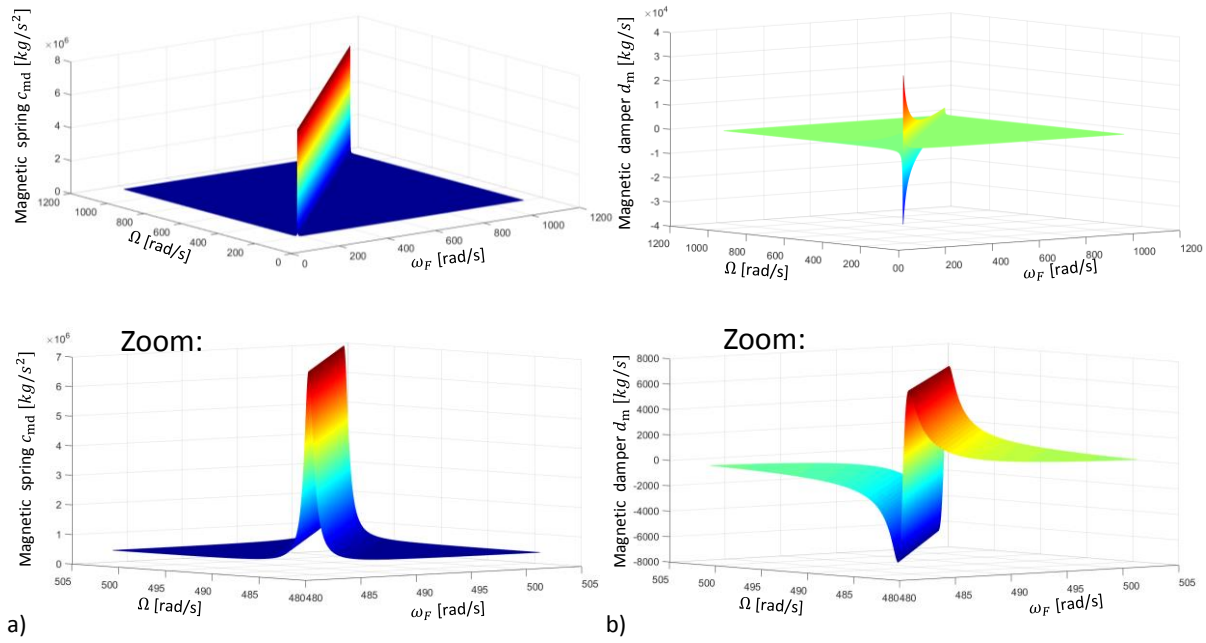


Figure 7: Electromagnetic spring value c_{md} (a)) and electromagnetic damper value d_{m} (b)), depending on the rotor angular frequency Ω and the whirling angular frequency ω_{F}, operating at no load ($s = 0$)

Figure 7 shows that the highest magnetic spring value c_{md} occurs, if the rotor angular frequency Ω and the whirling angular frequency ω_{F} are identical. So no electromagnetic damping occurs, and the magnetic spring value c_{md} is equal to the undamped magnetic spring value c_{m}. In this case the electromagnetic damper d_{m} is zero. If there is a difference between Ω and ω_{F}, electromagnetic damping occurs, and c_{md} will be reduced. For a specific difference, d_{m} reaches its maximum value. With increasing difference, d_{m} tends to zero. If the rotor angular frequency Ω is higher as the whirling angular frequency ω_{F}, the electromagnetic damper d_{m} is negative, which forwards instability. When analyzing vibration instability of rotating machines with sleeve bearings, the rotor angular frequency Ω at the threshold of stability is mostly much higher as the whirling angular frequency ($\Omega \gg \omega_{\mathrm{F}}$), leading to a strong electromagnetic field damping and so to a very high harmonic slip s_{ν}. So the electromagnetic spring c_{md} is strongly reduced and the electromagnetic damper d_{m} is negative, but so small, that d_{m} can be mostly neglected.

6.2 Controller parameter

For the simulation an ideal PD-Controller is used – identical for the left side and for the right side of the motor – controlling the motor feet displacements z_{aL} and z_{aR}.

- Rated proportional coefficient (right and left controller)	$K_{\mathrm{PN}} = K_{\mathrm{PR}} = K_{\mathrm{PL}} = 1 \cdot 10^9\ \mathrm{kg/s^2}$
- Rated derivative coefficient (right and left controller)	$K_{\mathrm{DN}} = K_{\mathrm{DR}} = K_{\mathrm{DL}} = 1 \cdot 10^7\ \mathrm{kg/s}$

Table 2: Basic (rated) controller parameter

The ratio between K_{DN} and K_{PN} is here chosen to be: $\frac{K_{\mathrm{DN}}}{K_{\mathrm{PN}}} = 0.01$ (28)

6.3 Threshold of stability for different mounting conditions

Now the threshold of stability is calculated for different mounting conditions:

a) Motor mounted on a rigid foundation
b) Motor directly mounted on the soft steel frame foundation
c) Motor mounted on the soft steel frame foundation with actuators between the motor feet and foundation. Actuators acting only passively.
d) Motor mounted on the soft steel frame foundation with actuators between the motor feet and foundation. Actuators acting actively, controlled by ideal PD-controllers.

For each case, the eigenvalues were calculated for different rotor speeds (Figure 5). The real part and the imaginary part of the eigenvalues are analyzed for the critical mode, which becomes instable (Figure 8). When the real part gets zero, the threshold of stability is reached, which is presented by the rotor angular frequency Ω_{stab}, respectively by the rotor speed n_{stab}. The whirling angular frequency of the critical mode is then $\omega_{\mathrm{F}} = \omega_{\mathrm{stab}}$, which can be seen in Figure 8.

Case	Threshold of stability n_{stab} [rpm]	Whirling angular frequency $\omega_{\mathrm{F}} = \omega_{\mathrm{stab}}$ [rad/s]
a) Motor on rigid foundation	3417	190.4
b) Motor on soft foundation, directly mounted	4807	223.0
c) Motor on soft foundation with actuators (passive)	4450	218.7
d) Motor on soft foundation with actuators (active)	7760	220.8

Table 3: Threshold of stability n_{stab} and whirling angular frequency $\omega_{\mathrm{F}} = \omega_{\mathrm{stab}}$ of the critical mode

Figure 8 and Table 3 shows that the lowest threshold of stability occurs for the rigid mounted motor ($n_{\mathrm{stab}} = 3417\ rpm$). When the motor is directly mounted on the soft steel frame foundation, the threshold of stability is increased to 4807 rpm. If actuators are mounted between motor feet and the soft foundation, operating passively, the threshold of stability drops to 4450 rpm. If the actuators are active controlled, the threshold of stability can be pushed up to 7760 rpm. Figure 9 shows the critical mode shape – where the real part of the eigenvalue gets zero – for each case, when the motor is operated at the threshold of stability n_{stab}. For case a) only orbits of the rotor centre, the shaft journal centres and the bearing housing centres occur, because the motor is here rigid mounted. If the motor is directly mounted on the soft foundation (case b)) the mode shapes changes clearly. The ellipse of the rotor orbit gets thinner and the angle changes. Also the orbits of the shaft journals changes clearly. Additionally, now orbits of the motor feet occur, which are here identically with the orbits of the foundation points, because the motor is directly mounted on the foundation. If actuators are positioned between motor and soft foundation, acting only passively, the orbits of the foundation points are different to the orbits of the motor feet points (case c)). The critical mode shapes of case b) and c) look very similar. If the actuators are active controlled (case

d)), the critical mode shape changes clearly, which can be seen when looking at the rotor orbit. Also the orbits of the motor feet and of the foundation points have changed clearly.

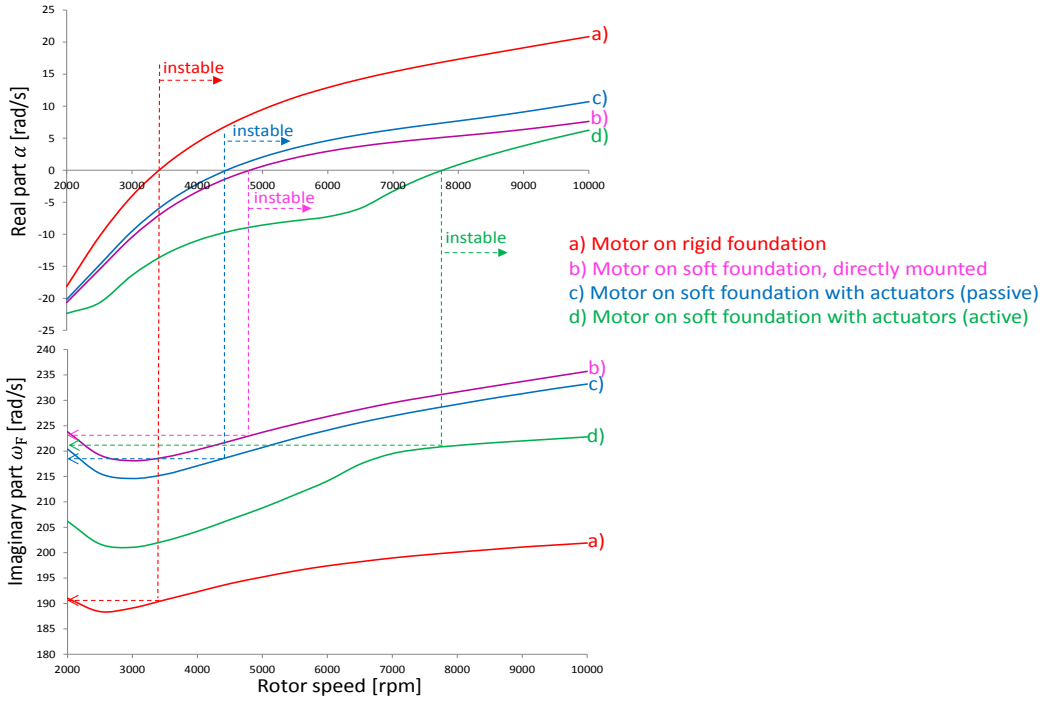


Figure 8: Real part and imaginary part of the eigenvalue belonging to the critical mode, which becomes instable, depending on the rotor speed, for different cases.

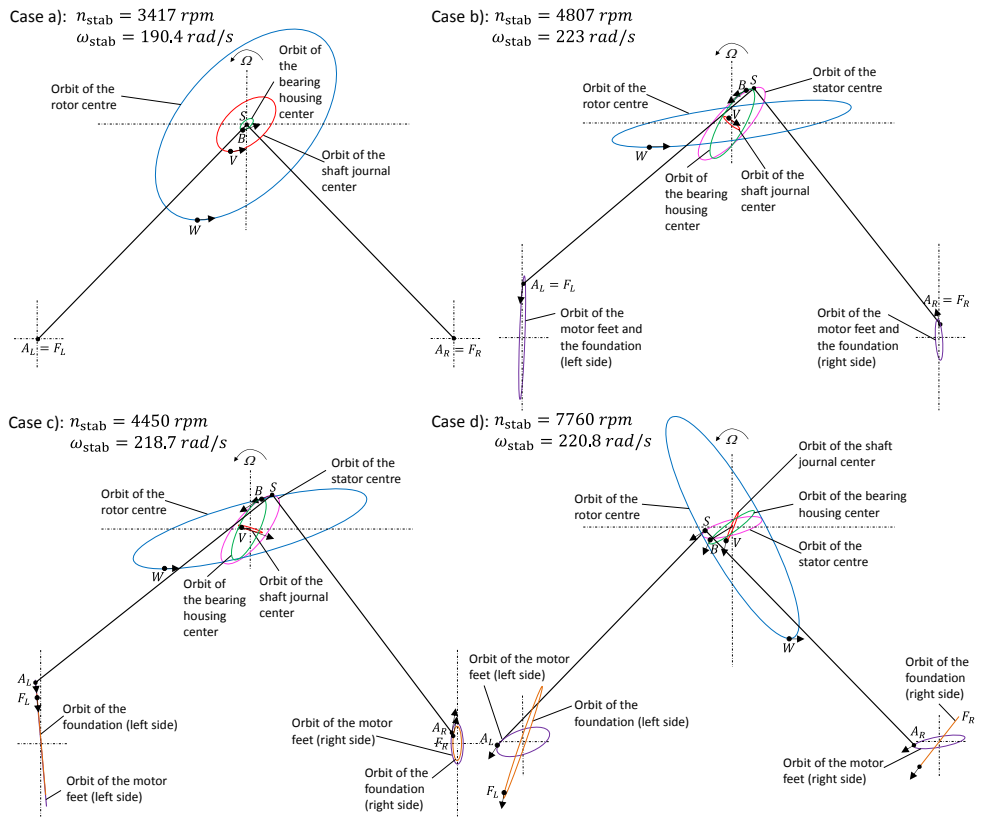


Figure 9: Critical mode shapes for the different cases at the threshold of stability

6.4 Threshold of stability for different controller parameter and actuators

6.4.1 For the rated actuators

For the rated actuators and for an arbitrary ration between K_P and K_D – which is only possible in a theoretical analysis – the threshold of stability is calculated and pictured in Figure 10. The rotor speed is limited to 10000 rpm, because above this rotor speed, the calculation of the oil film coefficients reaches its validation**.** Parameter K_P is varied in the range of $1 \cdot 10^3 \ldots 5 \cdot 10^9$ kg/s^2 and parameter K_D in the range of $1 \cdot 10^2 \ldots 3 \cdot 10^7$ kg/s. The maximum threshold of stability is reached in the range where K_P lies between $0.6 \cdot 10^9 \ldots 1.8 \cdot 10^9$ kg/s^2 and K_D between $1 \cdot 10^2 \ldots 4 \cdot 10^6$ kg/s.

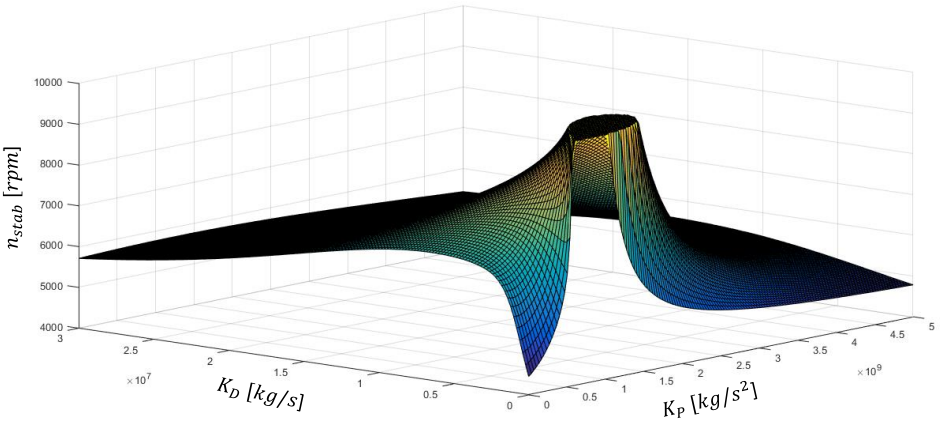


Figure 10: Threshold of stability n_{stab}, depending on the controller data K_P and K_D, for the rated actuators (actuator stiffness: $c_{az} = 6{\cdot}10^8$ kg/s^2; $c_{ay} = 3{\cdot}10^8$ kg/s^2)

6.4.2 For soft actuators

For soft actuators, which have here the same masse but only 1/10 of the stiffness of the rated actuators, and also no mechanical damping ($\tan \delta_a = 0$), the threshold of stability is calculated, for different values of K_P and K_D. The maximum threshold of stability is reached in the range, where K_P lies between $2.6 \cdot 10^8 \ldots 4.5 \cdot 10^8$ kg/s^2 and K_D between $1 \times 10^1 \ldots 4.3 \times 10^5$ kg/s. Additionally a local maximum occurs, where K_P is about $1 \cdot 10^8$ kg/s^2 and K_D is about $5.4 \cdot 10^4$ kg/s.

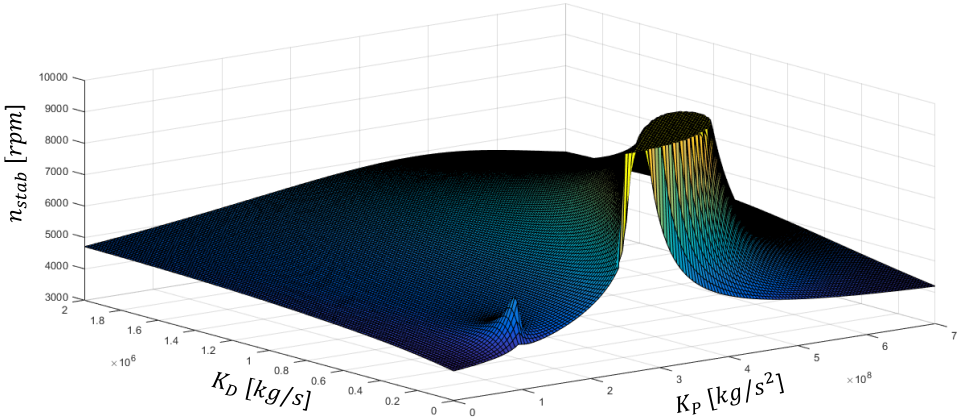


Figure 11: Threshold of stability n_{stab}, depending on the controller data K_P and K_D, for soft actuators (actuator stiffness: $c_{az} = 6{\cdot}10^7$ kg/s^2; $c_{ay} = 3{\cdot}10^7$ kg/s^2)

7 Conclusion

In the paper the threshold of vibration stability of induction motors with flexible shafts and sleeve bearings, mounted on soft steel frame foundations with active motor foot mounts, was analyzed. Therefore a multibody model was developed, considering electromagnetic influence, stiffness and internal damping of the rotor, stiffness and damping of the bearing housings and end shields, stiffness and damping of the foundation, stiffness and damping of the oil film of the sleeve bearings and the stiffness and damping of the motor foot mounts, as well as the controlled forces, which are applied in the vibration system by the motor foot mounts, using PD-controllers. The aim of the paper is to unite all these influences in a model and to derive a procedure for calculating the threshold of vibration stability. Based on a numerical example, different mountings of a large 2-pole induction motor (2MW) were investigated. It could be shown, that the threshold of stability can be pushed to very high rotor speeds, using active motor foot mounts.

References

[1] G. Genta, *Dynamics of Rotating Systems*, Springer Science & Business Media (2005).

[2] R. Gasch, R.Nordmann, H. Pfützner, *Rotordynamik*, Springer-Verlag, Berlin Heidelberg (2002).

[3] J. S. Rao, *Rotor Dynamics*, Wiley Eastern Limited, New Dehli (1991).

[4] R.G. Kirk, P. DeChowdhury, E.J. Gunter, *The effect of support flexibility on the stability of rotors mounted in plain cylindrical bearings*, IUTAM Symposium Dynamics of Rotors (1974), pp. 244.

[5] R. Gasch, J. Maurer, W. Sarfeld, *The influence of the elastic half space on stability and unbalance of a simple rotor-bearing foundation system*, in Proc. Conference Vibration in Rotating Machinery, C300/84, IMechE, Edinburg (1984).

[6] A. Preumont, *Vibration Control of Active Structures: An Introduction*, Springer (2011).

[7] C.R. Fuller, S.J. Elliot, P.A. Nelson, *Active control of vibration*, Academic Press Limited (1996).

[8] K. Janschek, *Mechatronic Systems Design: Methods, Models, Concepts*, Springer (2012).

[9] C. Ehmann, R. Nordmann, *Comparison of control strategies for active vibration control of flexible Structures*, Archives of Control Sciences, 13(3), (2012), pp. 303-312.

[10] H. Ulbrich, *A comparison of different actuator concepts for applications in rotating machinery*, *International Journal of Rotating Machinery*, Volume 1, Issue 1 (1994) pp.61-71.

[11] F. Dohnal, H. Ecker, A. Tondl, *Vibration Control of Self-Excited Oscillations by Parametric Stiffness Excitation*, Eleventh International Congress of Sound and Vibration (2004), pp. 339 – 346.

[12] H.-O. Seinsch, Oberfelderscheinungen in Drehfeldmaschinen. Teubner-Verlag, Stuttgart (1992).

[13] J. Früchtenicht, H. Jordan, H.O. Seinsch, *Exzentrizitätsfelder als Ursache von Laufinstabilitäten bei Asynchronmaschinen.* Archiv für Elektrotechnik, Vol. 65, Issue 4, Part 1, pp. 271-281, Part 2,(1982) pp. *283-292*.

[14] U. Werner, *Influence of electromagnetic field damping on the vibration stability of soft mounted induction motors with sleeve bearings, based on a multibody model*, SIRM-12th International Conference on Vibrations in Rotating Machines, Graz, Austria, (2017).

[15] U. Werner, *Analysis of Active Vibration Reduction for Soft Mounted Electrical Machines Based on a Multibody Model*, Int. J. Appl. Mechanics, 08 (2017).

[16] J. Lund, K. Thomsen, *A calculation method and data for the dynamics of oil lubricated journal bearings in fluid film bearings and rotor bearings system design and optimization*, ASME, New York (1978) pp.1-28.

[17] J. Glienicke, *Feder- und Dämfpungskonstanten von Gleitlagern für Turbomaschinen und deren Einfluss auf das Schwingungsverhalten eines einfachen Rotors*. Dissertation TH Karlsruhe (1966).

Separation of structural response and excitation characteristics in planetary gearboxes

D. F. Plöger[1], **J. Jungblut**[1], **P. Zech**[1], **S. Rinderknecht**[1]
[1] TU Darmstadt, Mechatronic Systems in Mechanical Engineering,
Otto-Berndt-Straße 2, 64287 Darmstadt, Germany
e-mail: **ploeger@ims.tu-darmstadt.de**

Abstract
The vibration recorded from planetary gearboxes is not only modulated, but also exhibits resonances. These two phenomena are separated using a technique derived from operational modal analysis (OMA). The modulation can be represented by a Fourier series, as shown previously. A non-parametric estimate of the frequency response function (FRF) is obtained from run-up experiments without the use of order tracking. While this is mainly advantageous, the PolyMax algorithm is no longer applicable. Nevertheless, a parametric fit of the non-parametric estimate of the FRF can still be computed using non-linear optimization. Stationary measurements obtained with order tracking are used for validation.

1 Introduction

Planetary gearboxes play a vital role in many applications. They feature high power densities in comparison to parallel shaft gear boxes which is enabled by load sharing among the planets. In many cases, such as servo drives, the coaxial shafts further support lightweight and efficient design. Their vibration behavior however is more complicated than that of gearboxes in which the axes of the gears do not revolve. The excitation is highly modulated, which is well known from the classic article by McFadden [1]. In addition, Ericson and Parker [2] report clusters of natural frequencies in the frequency response function (FRF) of planetary gearboxes.

For a better understanding of planetary gearbox vibrations it is desirable to separate the excitation and the dynamic behavior of the structure, which is described by the FRF. This will be attempted in this contribution. The approach used in this contribution may be summarized as follows: First, measured data will be analyzed. From this initial analysis it becomes clear that a linear frequency response model should be combined with a Fourier series as input. While the Fourier series approach has previously shown to accurately reflect the excitation of the structure by the gear meshing in [3], resonances have not been included in this model. In this contribution, operational modal analysis (OMA) techniques will be combined with the existing Fourier series approach. The reason for this choice is the difficulty in measuring the excitation forces resulting from the meshing gears. In larger gearboxes strain gauges may be applied to the ring gear, which still do not account for the meshing of planets and sun. OMA provides a non-invasive, less elaborate and therefore more flexible alternative. The chosen output-only method however causes the concept of the FRF to be not as precisely defined as in an input-output framework, as the true input can never be known.

Peeters and Roeck [4] provide a comprehensive, if not quite up to date, overview for the topic of OMA. Since then, techniques more specific to rotating machinery have been developed [5, 6, 7] which rely on order tracking. This approach is not effective for planetary gearboxes for two reasons: First, relevant orders may be as high as 500 which causes a high slew rate in the frequencies associated with these high orders. This makes order tracking unreliable. Second, tracking a high number of orders at high frequencies produces a very high amount of intermediate data and thus complicates the approach. Instead a simplified method of estimating the

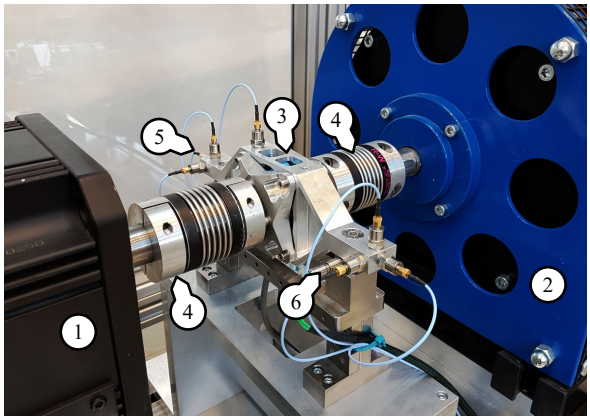


Figure 1: Experimental setup. The gearbox can be driven at arbitrary speed and load.

frequency response function will be developed. In addition, a parametric fit of the non-parametric estimate will be obtained.

In a first step, the modulation of the recorded vibration needs to be discussed. The vibration is modulated because the gear meshing takes place in a rotating reference frame. Therefore the lines of action of the gear mesh forces rotate. In addition, there is a movement of the contact points at which the planet gears mesh with sun and ring gears. The effect of the motion of the contact points has been first discussed by McFadden [1]. Further notable contributions have been made by McNames [8] and by Inalpolat and Kahraman [9]. Morikawa et al. [10, 11] present a different view on the topic. While the first group of authors focus on the moving contact points in the gearbox, the latter examines the effect of forces with rotating lines of action.

Experiments conducted on our test-rig (see [3]) generally agree with the phenomena reported by these authors. Therefore any vibration signal x excited by a planetary gearbox may be modeled as a Fourier series.

$$x = \sum_{k=-\infty}^{\infty} c_k e^{ik\varphi} = \frac{a_0}{2} + \sum_{k=1}^{\infty} (a_k \cos k\varphi + b_k \sin k\varphi) \tag{1}$$

Here, the argument of the series is not the time t, but the instantaneous angle of the planet carrier φ. As the angle $\varphi(t)$ of the planet carrier is time dependent, the vibration x may be either understood as a function of time or as a function of the reference angle φ. The real coefficients a_k, b_k and the complex coefficients c_k are linked by

$$c_k = \begin{cases} a_0 & \text{for } k = 0 \\ \frac{1}{2}(a_k - ib_k) & \text{for } k > 0 \\ \frac{1}{2}(a_{-k} + ib_{-k}) & \text{for } k < 0 \end{cases} . \tag{2}$$

This yields that any vibration signal recorded from a planetary gearbox may be decomposed into orders. Any order can be conveniently addressed by the index k and is represented by its magnitude $|c_k|$ and its phase angle $\angle c_k$. The extraction of the Fourier coefficients c_k from recorded data is called computational order tracking (COT). For stationary operation, COT may be implemented in a straightforward manner using the fast discrete Fourier transform (FFT). For more sophisticated methods see the classic paper by Fyfe and Munck [12].

2 Experiments

Figure 1 depicts the rest-rig used in this investigation. It primarily consists of an asynchronous motor (1), an eddy current brake (2) and the planetary gearbox (3). The gearbox cannot be seen well in the photograph as it is mounted inside the assembly. Metal bellow couplings (4) transfer mechanical power. Accelerometers (5) and force transducers (6) acquire vibration data. An incremental encoder also captures the angle of the

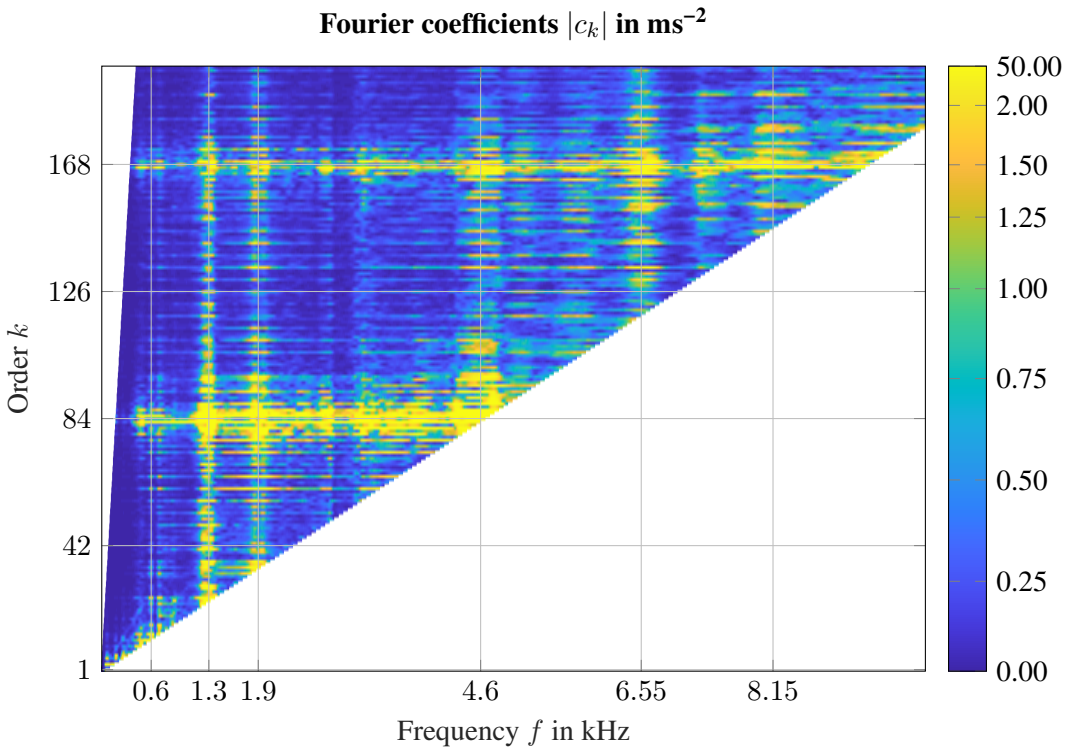


Figure 2: Magnitudes of the first 200 orders. The colormap is compressed non-linearly for better visibility.

planet carrier. The data is recorded at a sampling rate of 80 kHz. In this contribution the data obtained from the accelerometers is primarily used as the vibration signal x.

Figure 2 relates the magnitude of the Fourier coefficients $|c_k|$ to the corresponding frequency of each order when the gearbox runs at different speeds. This order chart is related to the more common Campbell diagram by transformation of the axes. In comparison, the order chart displays the individual orders more precisely. The empty areas represent the boundaries set by the minimal and maximal speed used in the experiments. The data has been obtained by tracking the orders of 500 stationary measurements at different frequencies and equal load. Afterwards a Bayesian interpolation (see [13]) has been performed. The mapping of the colors to the magnitudes of the Fourier coefficients $|c_k|$ uses a sigmoid characteristic to improve visibility of resonances. This however makes it harder to judge the magnitude of individual orders.

Figure 2 yields two major observations: First, only some orders contribute significantly to the overall vibration level. They are found in the vicinity of the nominal gear mesh order at $k = 84$ and its integer multiples. This is in good agreement with the theory explained in Section 1. The second observation is that at certain frequencies resonances are visible for all orders. This suggests that an accurate linear model may be found for these structural modes.

3 Structural model

In order to identify a linear model, vibration data is needed. Here, two approaches are possible: First, the test-rig may be operated at different, but stationary speeds. Alternatively, a run-up may be performed. Performing multiple stationary measurements is time consuming. In addition, it may not be feasible at speeds where resonances occur if imbalances are too big. During a run-up, the vibration will remain within the safety limits, if an appropriate angular acceleration is chosen. The main advantage of a run-up experiment however lies in its ability to excite a continuous range of frequencies within a short execution time. All estimates will be made based on run-up data. Stationary operation will only serve as a reference for validation purposes.

In the first step, a non-parametric estimate of the FRF is obtained from run-up experiments. An operational modal analysis (OMA) based approach is necessary because it is not possible to apply an external excitation accurately representing the excitation by the gearbox at operation. The non-linear gear mesh effects cause different dynamic behavior in operation and stand-still.

OMA typically assumes white noise as input or at least an evenly distributed excitation in the frequency domain [4]. This is approximately true for a run-up excitation comprised of a single order. However, the experimental data contains multiple orders. This causes the assumption of an evenly distributed excitation spectrum to be not entirely true. The excitation spectrum is not constant for all frequencies. Instead, it fluctuates around an approximately constant value. Thus, the cross-correlation cannot be used to estimate the FRF. In many cases, this problem can be overcome by performing order tracking on the acquired data as shown in [5, 6, 7]. An individual order of a run-up provides the required constant spectrum. In the case of planetary gearboxes, the relevant orders are considerably higher than in other applications. Also, the number of relevant orders is higher than in most systems. While the extraction of individual orders has been shown for planetary gearboxes in [3], the high angular acceleration at high orders causes the results to be not sufficiently accurate for system identification.

However, the magnitude of the excitation can be made approximately constant for all frequencies using a smoothing algorithm. Here, a moving average (MA) filter is applied to the magnitude of the spectrum. This eliminates the unwanted fluctuation which result from the presence of more than one order in the excitation but removes the phase information in the process. Once the requirement of a constant excitation spectrum is sufficiently satisfied, the measured response spectrum is approximately proportional to the FRF due to

$$X\left(\Omega\right) = F\left(\Omega\right) H\left(\Omega\right) \approx a\tilde{H}\left(\Omega\right), \tag{3}$$

were $X(\Omega)$ is the spectrum of the recorded vibration $x(t)$, $H(\Omega)$ the ideal FRF, $\tilde{H}(\Omega)$ the estimated FRF and a a scalar factor. $F(\Omega)$ denotes the spectrum of the unknown excitation which is assumed constant for all frequencies interest.

In comparison to the usual approach using order tracking, only the magnitude of the FRF can be estimated. From a strictly theoretical standpoint, "end-of-orders" effects would need to be considered. They occur because each order has a different maximum frequency which can be excited by a given maximum speed of the gearbox. This effect will be neglected because this effect is not observable from the recorded data. Most likely this is due to the high amount of orders and the fact that not all orders contribute equally to the spectrum. The experimental data meets the assumption of a constant moving average of the excitation spectra. This can be concluded from the absence of artifacts associated with "end-of-orders" effects. Excitation caused by unbalance forces can be neglected because only frequencies exceeding 200 Hz will be considered. The maximum frequency of the 3th order, which corresponds to the unbalance at the drive shaft is 165 Hz.

The FRF is obtained by transforming the measured response into the frequency domain, calculating its magnitude and computing the moving average of the spectrum. An a-causal MA filter has been used which increases the bandwidth with rising frequencies. The estimated FRF is shown in Figure 3 along with the Fourier transform of the run-up response X. The computation of the moving average introduces a bias to the estimated FRF due to attenuation of the maxima and thus increases spectral leakage. Because the magnitude of the excitation is unknown the scalar factor a cannot be calculated by principle. Hence the estimated FRF $\tilde{H}$ is arbitrarily scaled.

Furthermore the modal parameters have been estimated. As only the magnitude of the estimated non-parametric FRF is known, standard algorithms such as PolyMax cannot be applied. A method has been developed which uses the magnitude of the FRF and non-linear regression to find the modal parameters. The FRF is usually given in standard form

$$H\left(\Omega\right) = \sum_{n=1}^{N} \left(\frac{R_n}{i\Omega - \lambda_n} + \frac{R_n^*}{i\Omega - \lambda_n^*} \right) = \sum_{n=1}^{N} R_n \frac{2D\omega_n + 2i\Omega}{\omega_n^2 - \Omega + 2iD\omega_n\Omega} \tag{4}$$

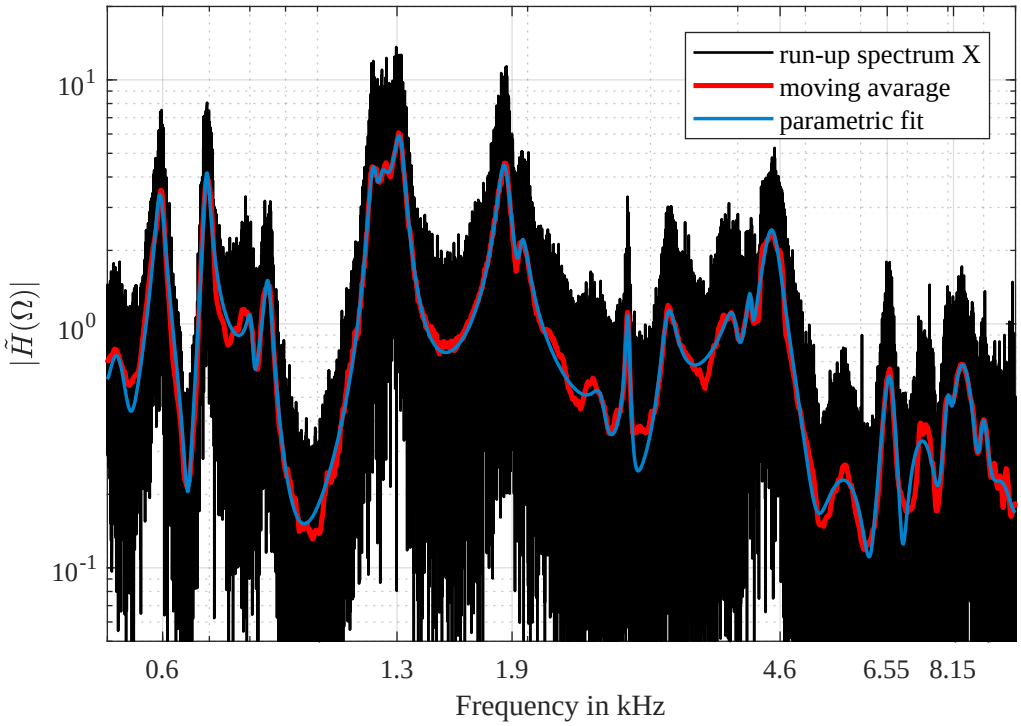


Figure 3: Estimated FRF and intermediate results for one accelerometer. The marked frequencies are the same as found in Figure 2.

where λ_n are the eigenvalues, D_n are the damping ratios and ω_n the natural frequencies. R_n denotes the amplitudes, also called residuals, which are assumed to be real in the following. The complex eigenvalues are related to the modal parameters by $\lambda_n = D\omega_n + i\omega_n\sqrt{1-D^2}$.

This notation is not suited for non-linear optimization. Graphically explained, any change of the damping ratio will alter the height of the corresponding pole. This causes bad numerical condition. To solve this problem, height and width of each pole are made independent by introducing a new Amplitude parameter A_n. The parametric form

$$H(\Omega) = \sum_{n=1}^{N} A_n \frac{2iD\Omega\omega_n}{\omega_n^2 - \Omega^2 + 2iD_n\Omega\omega_n} \tag{5}$$

implements the idea, as the peak value at $\Omega = \omega_n$ is independent of the damping ratio D_n for a given Amplitude A_n. The parametric form (5) enables a numerically stable solution of the non-linear least-squares problem. The results of the method are also shown in Figure 3. The method is capable to identify closely spaced modes as well as modes which do not form distinguished peaks. However the method does not perform a separation of numerical modes and physical modes. It is able to obtain an arbitrarily close fit by introducing numerical modes. Therefore a manual selection of the system modes has been performed were only the relevant resonances have been taken into account.

The FRF which has been obtained with a run-up measurement can now be compared with the stationary measurements. Therefor the 85th order of the stationary measurements is shown in Figure 4 along with the approximated FRF. One can see a high correlation between 0.9 kHz and 3 kHz. The diagram also shows a notable amount of uncertainty in the stationary measurements. The uncertainty does not result from numerical artifacts. Further, as the temperature and the load have been tightly controlled, it must be concluded that the observed uncertainty is inherent to the gearbox. In comparison to the FRF estimate, the Fourier coefficient $|c_{85}|$ raises with higher frequencies. This indicates that not all excitation orders contribute evenly to the total excitation at all speeds of the gearbox. The advantage of the run-up approach over stationary measurements becomes clear by the fact that it yields continuous information, where the stationary measurements only

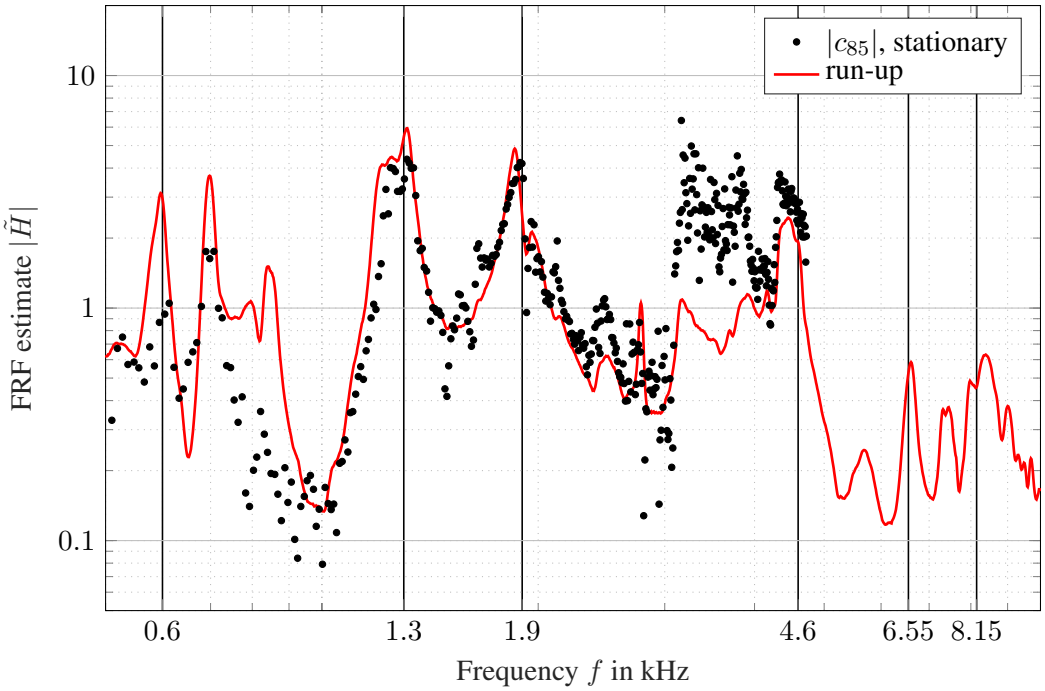


Figure 4: Estimated FRF. Please note the arbitrary scale. The marked frequencies are the same as found in Figure 2.

provide individual points.

The advantage of the non-linear optimization is that it is possible to identify closely spaced modes due to the consideration of all nearby modes. This results in a better approximation of the modal parameters compared to other methods which are neglecting these. The simplest of these other methods is peak-picking were a single pole-pair is optimized for a narrow frequency range. This methods yields good results for isolated modes like the Peak at 0.6 kHz. The results in this case are $f_0 = 596\,\text{Hz}$ for the natural frequency and $D = 0.016$ for the damping ratio. This is a good approximation given the results of the non-linear optimization with $f_0 = 595\,\text{Hz}$ and $D = 0.015$. However if multiple modes are present the results show a higher difference form each other. For the peak at 8.3 kHz, which is surrounded by two closely spaced modes, peak-picking yields $f_0 = 8.38\,\text{kHz}$, $D = 0.03$ and the non-linear fit $f_0 = 8.38\,\text{kHz}$, $D = 0.043$. More importantly, peak-picking cannot identify modes, if they do not exhibit distinct peaks.

4 Conclusion

The method presented in this contribution can successfully identify the dynamics of the gearbox and the surrounding test-rig. Therefor run-up experiments have been conducted which only require limited effort. Despite that only the magnitude of the non-parametric FRF can be estimated, a set of modal parameters could be obtained. This was achieved by non-linear optimization, for which the parametric form of the FRF had to be slightly modified. While the results of stationary measurement agree with the estimated FRF, they also show certain deviations. In addition, the inherent uncertainty of the system seems to be rather high. In summary, the method provides useful insights in the propagation of the gear mesh vibration through the dynamics of the test-rig. In the future, the method will be applied to vibration signature analysis.

References

[1] P. McFadden and J. Smith, *"An Explanation for the Asymmetry of the Modulation Sidebands about the Tooth Meshing Frequency in Epicyclic Gear Vibration,"* Proceedings of the Institution of Mechanical Engineers, Part C: Journal of Mechanical Engineering Science, Vol. 199, No. 1, pp. 65–70, 1985.

[2] T. M. Ericson and R. G. Parker, *"Natural Frequency Clusters in Planetary Gear Vibration,"* Journal of Vibration and Acoustics, Vol. 135, pp. 061002–061002–13, June 2013.

[3] D. F. Plöger, P. Zech, and S. Rinderknecht, *"Experimental identification of high-frequency gear mesh vibrations in a planetary gearbox,"* in *Proceedings of ISMA2016 International Conference on Noise and Vibration Engineering*, (Leuven, Belgium), pp. 911–924, Sept. 2016.

[4] B. Peeters and G. Roeck, *"Stochastic system identification for operational modal analysis: A Review,"* Journal of Dynamic Systems, Measurement and Control, Transactions of the ASME, Vol. 123, No. 4, pp. 659–667, 2001.

[5] K. Janssens, Z. Kollar, B. Peeters, S. Pauwels, and D. A. Van, *"Order-based resonance identification using operational polyMAX,"* in *Proceedings of 24th IMAC Conference on Structural Dynamics*, (St Louis, Missouri, USA), 2006.

[6] B. Peter, P. Gajdatsy, P. Aarnoutse, K. Janssens, and W. Desmet, *"Vibro-acoustic operational modal analysis using engine run-up data,"* in *Proceedings of 3rd International Operational Modal Analysis Conference*, (Portonovo, AN, Italy), pp. 447–455, 2009.

[7] L. Di, S. Manzato, A. Dabizzi, B. Peeters, F. Marulo, and W. Desmet, *"Industrial applications of advanced modal identification on operational rotating machineries,"* in *Proceedings of ISMA2016 International Conference on Noise and Vibration Engineering*, (Leuven, Belgium), pp. 2833–2847, 2016.

[8] J. McNames, *"Fourier Series Analysis of Epicyclic Gearbox Vibration,"* Journal of Vibration and Acoustics, Vol. 124, pp. 150–153, June 2001.

[9] M. Inalpolat and A. Kahraman, *"A Theoretical and Experimental Investigation of Modulation Sidebands of Planetary Gear Sets,"* Journal of Sound and Vibration, Vol. 323, No. 3-5, pp. 677–696, 2009.

[10] K. Morikawa, K. Kumagai, and R. Nishihara, *"A Study on the Sideband Phenomenon of Planetary Gears,"* Transactions of the JSME (in Japanese), Vol. 80, No. 815, pp. DSM0212–DSM0212, 2014.

[11] K. Morikawa, K. Kumagai, R. Nishihara, and J. Nemoto, *"Vibration Behaviour of Stepped Pinion Type Planetary Gears,"* Transactions of the JSME (in Japanese), pp. 15–00310, Sept. 2015.

[12] K. R. Fyfe and E. D. S. Munck, *"Analysis of Computed Order Tracking,"* Mechanical Systems and Signal Processing, Vol. 11, pp. 187–205, Mar. 1997.

[13] C. E. Rasmussen and C. K. I. Williams, *Gaussian Processes for Machine Learning (Adaptive Computation and Machine Learning)*. The MIT Press, 2005.

Full model multibody approach for the sound calculation of gearboxes

D. Werner [1], S. Falkenberger [2], B. Graf [1], F. Wegerer [3], J. Neher [4], B. Wender [1]
[1] University of Applied Sciences of Ulm, Department of Structural Mechanics and Acoustics, Prittwitzstr. 10, 89075 Ulm, Germany
e-mail: **d.werner@hs-ulm.de**

[2] Continental AG, ADC Automotive Distance Control Systems GmbH, Lise-Meitner-Str. 10, 89081 Ulm, Germany

[3] Hensoldt Sensors GmbH, Wörthstraße 85, 89077 Ulm, Germany

[4] MAN Diesel & Turbo SE, Department Mechanics Engine Structure, Stadtbachstr. 1, 86153 Augsburg, Germany

Abstract
The project described in this paper aims to validate a full model multibody approach for the sound calculation of vehicle gearboxes. A complex gearbox housing with a customized two-stage gear train inside is used as test object. It is equipped with special devices for the direct and indirect measurement of the operational bearing forces. This setup mounted on a test rig in a reverberation chamber delivers all the data necessary in order to validate the state of the art approach for the sound calculation of vehicle gearboxes. Within that approach the gearbox is completely modelled in a multibody simulation software. The housing typically is included as a reduced flexible body. Using the results of several modal analyses the modelling techniques for the bolted joint connections are evaluated. Gears and bearings are modelled in a simplified yet accurate way with stiffness maps. The implementation of this new simulation and measurement techniques requires thorough preliminary investigations.

1 Introduction

Although it is often claimed that in the medium term transmissions will disappear from vehicles assuming that electrical engines do not require them, current developments imply a different tendency. As some experts suggest the market for low cost vehicles will continue growing especially in third world countries and it is highly unlikely that they will be realized as electrical cars [1]. Consequently there is no doubt that transmissions cannot be removed completely from new designs. In [2] it is stated that even electrical cars might rely on transmissions in order to meet basic customer requirements such as efficiency or range and maximum speed. Furthermore, hybrid cars that are considered a medium term solution are equipped with silent engines that still need transmissions. Taking this into account the need for acoustically optimized vehicle transmissions appears even higher. Modern combustion engines were continuously improved so that the engine sound often cannot “mask” other sounds anymore. As a further result of the engine optimization the sound pressure level in the passenger cell of vehicles dropped from around 75 dB (A) in the year 1980 to values around 60 dB (A) in 2010 [3]. Nevertheless, the increasing traffic volume leads to a stagnation of the overall sound pollution. In addition, psychoacoustic effects have to be considered. For instance, the perceived loudness stays equal for a single tone compared to the same tone with added harmonics [3]. Consequently tonal sounds are evaluated as much more disturbing than sounds that contain a broader range of frequency components. Especially in transmissions there are only few characteristic excitation frequencies such as the meshing and bearing frequencies and their harmonics. Besides, the housing eigenfrequencies tend to be low damped which leads to sharp resonances. All these aspects

account for the tonal character of the sound radiated by the gearbox and eventually justify the effort to resolve the target conflict between costs, lightweight demands and NVH comfort. However, the use of gears is additionally widespread in mechanical industry where safety requirements demand a limit of noise exposure. As every radiating source contributes to the overall sound pressure level it is crucial for noise minimization to reduce the noise of the main source and of every other radiating object if possible.

Without doubt, acoustically optimized transmissions lower the noise emission in the public and industrial environment. This optimization has to take place in an early stage of the product development in order to avoid expensive changes later on. Reviewing the literature reveals the large effort already invested into the elaboration of reliable and validated simulation methods for the sound calculation of gearboxes. In the earlier publications one can observe a division into three systems according to their different roles in the noise generation:

1. The inner parts such as shafts, gears and bearings
2. The gearbox housing
3. The radiating housing surface and the surrounding fluid

The first system is mainly responsible for the excitation of the structure vibrations of the second system. Those vibrations, in turn, cause the propagation of sound waves through the surrounding fluid which is described by the third system. Usually the first system was examined separately from the housing and the fluid. The largest noise reduction can be achieved by optimizing the gears as thereby the excitation decreases. Regarding the excitation behavior of the shafts, bearings and gears various publications are present, e.g. [4], [5], [6]. Here the systems are mostly modelled with systems of linear differential equations. As demonstrated in [7] it is also possible to use nonlinear multibody systems (MBS) although the computation time increases drastically. On the other side, many research projects focused on the sound radiation of housings exist. In [8] and [9] the authors describe the validation of the sound calculation of complex ribbed housing structures. In this case the Finite Element Method (FEM) is used for the calculation of the structural vibrations whereas the sound radiation is calculated with the Boundary Element Method (BEM). Those investigations lead to design guidelines that enable the design engineer to consider acoustic requirements early in the design phase. However, normally gearbox housings consist of several parts that interact with each other. This circumstance required further investigations regarding the modelling of joints for the sound radiation simulation. In [10] and [11] validated solutions are presented and likewise result in modelling guidelines. Furthermore, it is clearly demonstrated that the inclusion of bearings and shafts into the FE Model does not lead to meaningful results. The main reason is the nonlinear behavior of the bearings that change their stiffness with the rotation angle and the applied load and therefore cannot be linearized properly. This underlines the necessity for nonlinear MB models in the acoustic calculation chain. As shown in [7] and [12] the exciting bearing forces can be calculated with a MB model containing the gears, bearings and shafts. As the model uses contact definitions for the bearing and gear models, the calculation times are very high with up to ten days [7]. The bearing forces are transferred into the frequency domain and thereby represent the input for a frequency response analysis of the gearbox housing. The results are the surface velocities that are the boundary condition for the acoustic model for the calculation of the sound radiated by the housing. In order to validate this approach, a gearbox test rig which is operated in a reverberation chamber was used by Falkenberger. The gearbox has a special bearing force measurement device which directly measures the excitation forces at one bearing via piezo-electric sensors. The evaluation of the bearing force measurements, sound power and the simulation results from [7] indicates the need for further extensions:

1. Consideration of the interaction between the inner parts and the gearbox housing in the simulation.
2. A simplified modelling of the bearings and gears is required due to the long calculation times.
3. The obtainment of proper damping values for the assembled gearbox.
4. The measurement of all bearing forces.

The following chapters expound in which manners the named aspects shall be considered in the simulation and measurement of the sound radiation of a customized two-staged transmission with a series-production

housing. The main goal of the project is to provide a validated calculation procedure that enables a quicker generation of reliable simulation results for the sound radiation of gearboxes.

2 Workflow for the validation of the sound calculation

In order to identify possible sources for deviations each step of the calculation has to be validated with measurements. Figure 1 illustrates the workflow of the planned calculations and the according experimental investigations. Concerning the dynamic behavior of the gearbox the applied strategy is bottom-up like, meaning that the single parts are investigated separately before the assembly.

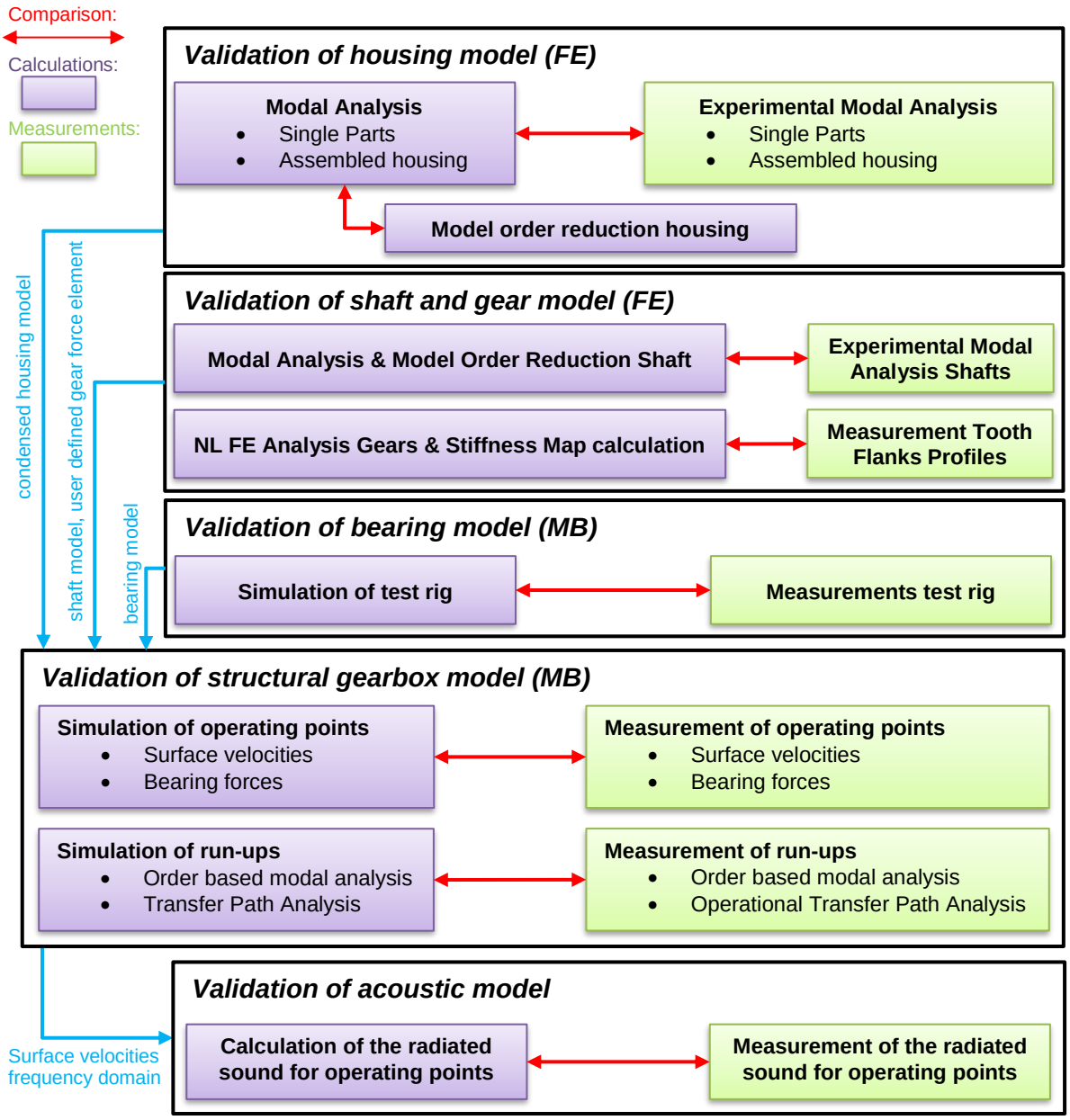


Figure 1: Validation of the gearbox sound calculation with a full model multibody approach

The validated parts of the gearbox are assembled in one multibody structural model. This enables the consideration of a shaft-housing interaction. Due to their dimension the FE models of the shafts and the

housing have to be imported as condensed models into the multibody model. As the investigations conducted in [7] imply, the usage of contact models leads to unpractical long computation times. Therefore the bearings and gears are modelled with user defined force elements. The stiffness values for these elements have to be obtained by pre-calculations or measurements. Usually the manufacturer, e.g. Schaeffler AG, provides the bearing stiffness maps [13]. If the stiffness map has to be obtained manually, one can either use the formulations provided in [14] or nonlinear FE-models. Although time consuming those pre-calculations have to be conducted only once. For the gears usually no stiffness maps exist. If the gear wheel body deformations are negligible then usually the analytical approach from [15] is used. More accurate, but also much more time consuming is the calculation of the stiffness values with nonlinear FE-models. In [16] e.g. the researchers conduct analyses for 50 angular positions of the gear pairs.

The two experimental options for the investigation of the dynamic behavior of the assembled gearbox are run-ups and constant operating points. With run-ups critical operating points can be identified as well as the eigenfrequencies, -shapes and damping values of the assembled gearbox. For this the order based modal analysis (OBMA) is used as it was developed for rotating machineries [17] and avoids the necessity of an artificial excitation. In addition, an operational transfer path analysis (OTPA) can be conducted given that the exciting bearing forces can be measured [18]. It is aimed to derive the contributions of the bearing forces to the surface velocities over the excited frequency range. Simulations and measurements will be conducted at several operating points. Comparing the measured and calculated bearing forces reveals whether the excitation was calculated correctly. With the comparison of the surface velocities, the impact of possible deviations on the sound radiation can be detected. Furthermore the calculated velocities, transferred into the frequency domain, are the input for the acoustic analysis. For the validation of this last step the radiated sound power can be used as it is a quantity that is comparatively simple to obtain. The only limitation from the experimental side is that the measurements have to be carried out in a reverberation chamber with a diffuse sound field.

Although the proposed modelling of the gearbox was already applied in a similar way (e.g. [19], [20]), new insights can be expected regarding the interaction of the housing with the bearings and shafts. Besides this, the results of the sound radiation calculation will be evaluated at each step from the excitation to the radiation using a unique test setup.

3 Test rig for the validation of the sound calculation

Two test rig designs were elaborated, one for the bearing force measurement device with a mounted bearing and another for the actual gearbox assembly.

3.1 Bearing test rig and bearing force measurement devices

Due to space limitations usually occurring in transmissions, sensors for the measurement of operational bearing forces have to be compact, but also robust as they are used in an harsh and oily environment. In this project two kinds of force sensors will be used. The first sensor works with four triaxial piezoelectric force sensors that are mounted between two parts with a respective pre-load of 10 kN [7]. One part contains the bearing whereas the other part is pressed into the original bearing seat. The sensors in between measure the transmitted force within a range of ± 2 kN radially, resp. ± 1kN axially. The second type of sensor uses strain gauges that are mounted on radial bars that connect two coaxial rings and detect transmitted forces in three directions. The bearing sits in the inner ring and the outer ring is pressed into the original bearing seat in the housing. As this kind of sensor is not available on the market it had to be purchased as a single-item production from the HBM GmbH. The sensor has to be properly calibrated because of the crosstalk between the channels. This results in a compensation matrix that has to be multiplied with the raw signals $\vec{U}$ in order to obtain the corrected force in kN, see (1). The range of ± 2 kN in each direction is similar to the piezo sensor device. Figure 2 provides illustrations of the two bearing force measurement devices.

$$\vec{F} = K\vec{U} = \begin{bmatrix} F_X \\ F_Y \\ F_Z \end{bmatrix} \; with \; K = \begin{bmatrix} 1.3303 & 0.0095 & -0.0109 \\ -0.0054 & 1.3087 & -0.0079 \\ 0.0056 & 0.0374 & 1.6275 \end{bmatrix} in \; \frac{kN \cdot V}{mV} \tag{1}$$

The advantage of the strain gauge system is the low space requirement and weight. However, the piezo sensors are more sensitive and can detect smaller forces more accurately.

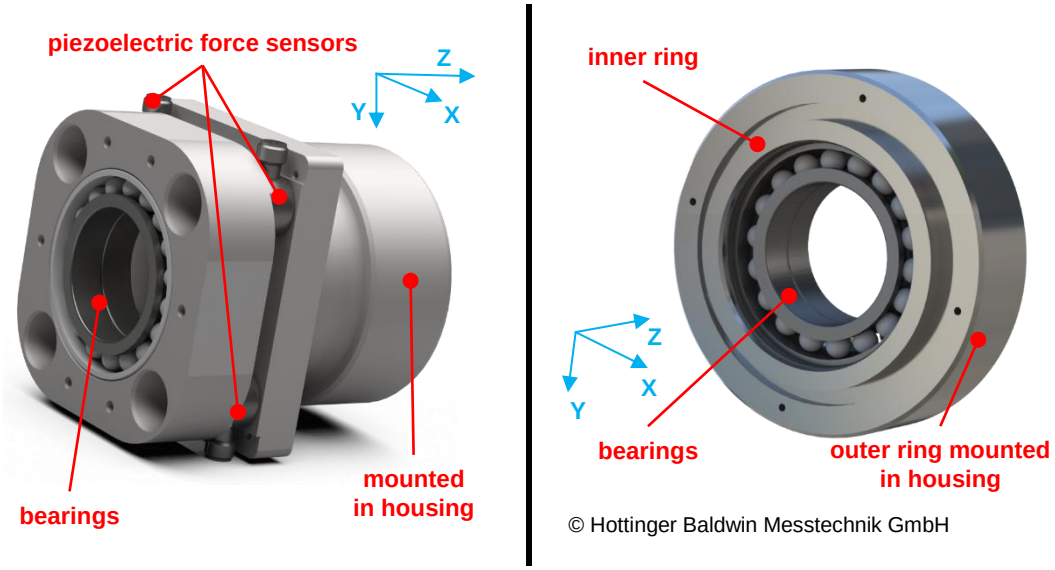


Figure 2: Bearing force measurement devices: with piezoelectric senors (left) and strain gauges (right)

Tests for the sensor with the piezoelectric force measurement are already documented in [12]. For this reason only the new strain gauge sensor is tested. The test rig created for this purpose consists of a simple shaft with two bearings of which one is mounted in the sensor. Furthermore dynamic forces can be introduced by mounting an unbalance mass or a shaker to an additional slider bearing. Figure 3 illustrates the set up.

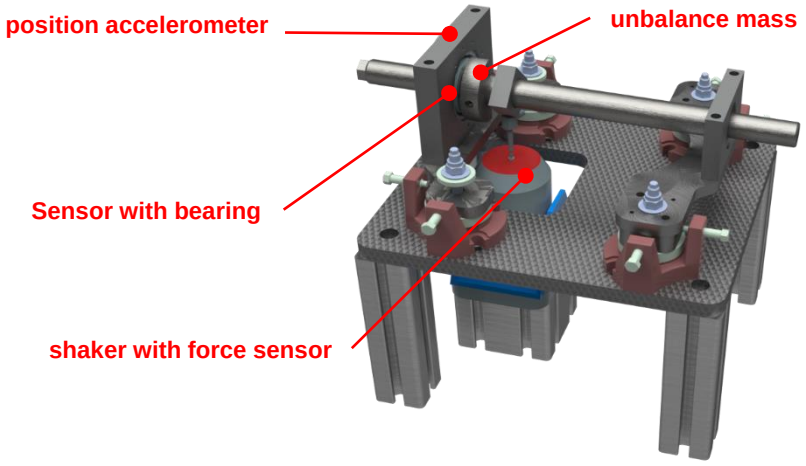


Figure 3 : Test rig for the bearing force measurement device with strain gauges

As the sensor came with a calibration certificate for static loads, only dynamic loads will be considered in the testing. The shaker is mounted with a piezoelectric uniaxial force sensor for the measurement of the excitation force. For all force measurement devices the bearing B71907-E-T-P4S-DUM is used. It consists of two single row angular ball bearings mounted in an O arrangement with an axial preload. Thus, there is no clearance which is important for the modelling. FRF Measurements with a small modal hammer (max.

420 N) from the shaft to the y-component of the strain gauge sensor and to the accelerometer on the bracket reveal the suitability for dynamic measurements. Up to 3000 Hz the quality of the FRF of the strain gauge is comparable to that of the accelerometer. For higher frequencies the noise of the amplifier is too high with an equivalent of ± 2 N. However, in the gearbox setup the excitation forces are expected to be much higher. If FRF have to be recorded for a wider frequency range, either a shaker or a larger modal hammer has to be used.

3.2 Gearbox test rig

The actual investigations are conducted with a gearbox test rig that is placed in a reverberation chamber that complies with the requirements from [21]. Those are e.g. the reverberation time which characterizes the degree of the diffusivity of the sound field. In such fields, the radiated sound power is proportional to the sound pressure and therefore can be measured directly with microphones. Usually in manually shifted gearboxes only two stages are transmitting torque simultaneously so that the original shafts, gears and bearings will be replaced by a two-staged gear train. The housing comes from the series-production gearbox ZF S 6-53 and has already been used in previous investigations [7], [12]. It is mounted on a steel bracket that simulates the mass of the combustion engine the gearbox normally is attached to. The supporting hollow rods are designed to isolate oscillations of the machine bed above 250 Hz from the gearbox. For the measurement of the bearing forces both measurement devices (see Figure 2) are used, the strain gauge sensor twice. At the smallest bearing there is no space for any direct force measurement. As stated in [18], different types of load quantities can be used at the same time in the OTPA. Hence, two accelerometers are placed orthogonally inside the gearbox near the smallest bearing. Figure 4 depicts this setup in a schematic and a more detailed illustration. Overall, this setup allows the measurement of all excitation forces transmitted through the bearing seats of the housing. Two identical asynchronous motors are used as engine at the pinion shaft and as generator at the outlet shaft. The operating points lie in a range of 800 to 3500 rpm and up to 120 Nm of maximum torque. By mounting the engine to the countershaft, furthermore effects of idler gears (stage 1) turning simultaneously to loaded gears (stage 2) on the gearbox acoustics can be investigated.

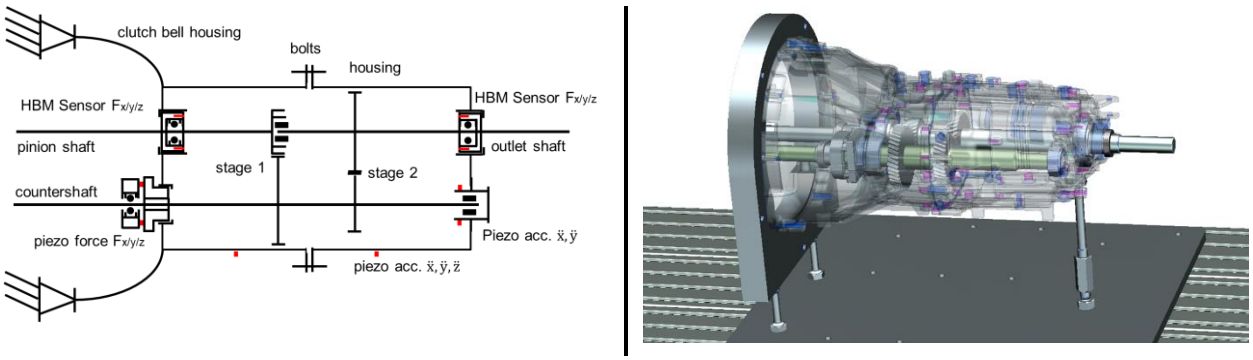


Figure 4: Gearbox assembly with measurement devices

Table 1 summarizes the basic data of the gear wheels of the two stages. The center distance between the wheels is 95 mm. All gear wheels have a normal module of 2.5 mm and a helix angle of 20 degrees. These values are chosen similarly to the original gears. The overall gear ratio is 1.768 (43/28 x 38/33).

helical gear stage 1	helical gear stage 2
pinion: number of teeth: 28, width: 22 mm, profile shift coefficient: - 0.0054	***pinion:*** number of teeth: 33, width: 22 mm, profile shift coefficient: 0
gear wheel: number of teeth: 43, width: 20 mm, profile shift coefficient: 0.2314	***gear wheel:*** number of teeth: 38, width: 20 mm, profile shift coefficient: 0.2259

Table 1: Gear wheels and bearings used in the gearbox assembly

4 Modelling of the drivetrain

4.1 Bearing model

The bearing model used is based on pre-calculated stiffness maps that consider axial and radial displacement as well as tilting around the radial axes. Therewith the dof of the bearing are fully coupled. The stiffness maps are used for the interpolation of the stiffness values of an user defined six dimensional force element depending on the relative displacements between the inner and outer ring. When using Schaeffler bearings the stiffness maps can be obtained directly from the manufacturer [13] (BEARINX-MAP). However, an interface with the MB software has to be installed beforehand. According to [22] the quality of the results is comparable to contact based bearing models. The excitation through the rolling elements is considered as well. In addition, a significant reduction of calculation time can be achieved. First simulations with simplified bearing models performed approximately more than 10 times faster compared to models of similar complexity and step size.

4.2 Modelling of the shafts

The best modeling of the shafts depends on their geometrical complexity and influence on the dynamic behavior. Rigid shafts with a simpler geometry can be modelled with Timoshenko beams that consist of rigid cylinders whose central nodes are coupled with six-dimensional beam elements [7], [23]. The rigid cylinders represent the mass properties of the shaft whereas the massless beam element defines the stiffness.

Unfortunately this approach requires many cylinders when the shaft has a more complex geometry (e.g. many radii etc.). Then the modelling effort is high and the result quality not necessarily satisfying. In this case a condensed model of the shaft can be used. For the condensation resp. model order reduction the Craig Bampton method can be used as described in chapter 5.3. Therewith a FE based model can be used in the MB model without the disadvantage of large dof numbers.

4.3 Modelling of the gears

In [7] a contact based modelling approach is used for the gears. There the gears are rigid bodies with tooth flank tessellation which is needed as discretization for the calculation of the contact normal force according to (2) [23]. The stiffness coefficient k and the damping coefficient c influence together with the corresponding exponents m_1, m_2, m_3 the contact force that is generated through the penetration δ at the teeth flanks and its time derivative $\dot{\delta}$.

$$F_n = k \cdot \delta^{m_1} + c \cdot \dot{\delta} \cdot \left|\dot{\delta}\right|^{m_2-1} \cdot \delta^{m_3} \tag{2}$$

Although this modelling approach requires long computation times it is used for comparison purposes. A less time consuming approach is described in [24]. It relies on pre-calculated static transmission errors (STE) that are used as lookup tables for the dynamic transmission error (DTE) in the actual MB model. Thereby changes to the position of the gears due to the dynamics of the assembly are accounted for. The lookup tables for the DTE are generated with nonlinear static FE analyses applying discrete torque values and displacements to the gears. The DTE is calculated at each time step using the central markers of the gears and has a radial and a translational part. Next, the resulting normal contact force vector between the gears at the contact point is obtained with the DTE and its time derivative, see equation (3) [24] (α_n: $normal\ pressure\ angle, \beta$: $helix\ angle$). The meshing stiffness k is determined with the actual DTE. It is used to interpolate a tangential force from the inverted lookup table. The ratio of the interpolated force to DTE equals the meshing stiffness. This approach will be implemented as a user subroutine in the MB software. Note that the STE based lookup tables can also be generated with analytical formulations (e.g. [15]) or other special software. The dimension of the lookup table depends on

the considered variables such as position on the mesh cycle, transmitted load, center distance variations, misalignment in the plain of action and shuttling [24].

$$\overrightarrow{F_n} = \left(k \cdot DTE + c \cdot \frac{dDTE}{dt}\right) \cdot \begin{Bmatrix} \tan \alpha_n / \cos \beta \\ 1 \\ -\tan \beta \end{Bmatrix} = \begin{Bmatrix} F_{radial} \\ F_{tangential} \\ F_{axial} \end{Bmatrix} \tag{3}$$

5 Structural gearbox housing model

As depicted in Figure 1 the condensed model of the gearbox housing usually is compared with the results of a modal analysis. When no experimental results are available, this is the only criterion left for evaluating the quality of the condensed model. However, in this case the modal analysis results are verified by measurements in order to exclude a source of error. The approach used is the bottom-up strategy that starts with the correlation of the experimental and calculated modal analysis of the single parts. In this case, the single parts of the housing show satisfying average MAC values of around 0.87 and 0.92 over the first 40 modes. The next step is the assembly of the two housing parts.

5.1 Empty housing without bracket

The used housing consists of two bolted parts that are assembled with a screw torque M_A of 23 Nm that results in an exerted screw force approximately 16.3 kN to 16.9 kN [25]. The friction values and the loss of pretension are the main sources for uncertainties. However, nonlinear static FE simulations showed only tiny differences between the contact areas when 15 kN, 16 kN or 17 kN pretension force were applied. In general two ways exist for the modeling of bolted joints for FE modal analysis. The first is described in [10] and [11] and is illustrated by Figure 5.

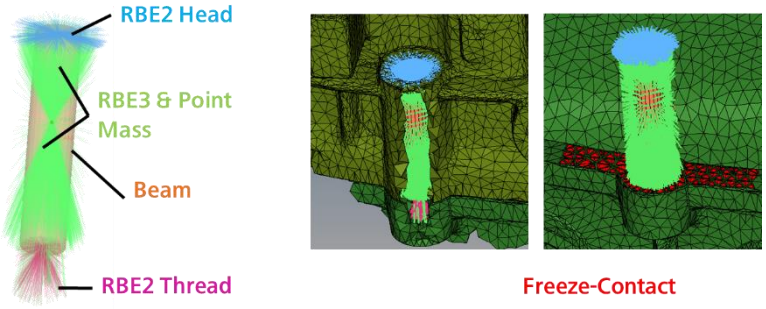


Figure 5: Modelling of the bolted joints according to [11]

The screws are modeled as beams that connect rigid elements in the area of the thread and the screw head. The mass of the screw is attached to a center node that is connected to the housing parts with RBE3 elements that do not increase stiffness. In a diameter approximately three times the screw diameter around the hole, the elements of the two parts are assigned to fixed contact formulation (“Freeze Contact”). In order to correctly identify the best coupling diameter it was varied in steps of 5 mm from 20 mm to 55 mm. In addition a variant with a fully coupled flange area is calculated. Alternatively, a similar approach can be used where the elements for the fixed contact are determined with a static nonlinear FE-analysis. This approach is described in more detail in [11] and [20]. Falkenberger used the same housing for his investigations. However, it was based on a 3D Scan model and therefore had much more DOF. The average MAC value with 95 % is very satisfying though [7]. Therefore it is used as a reference for the CAD based FE model that allows more mesh manipulations and therewith a reduction of DOF. The model illustrated in Figure 6 has 1.53 Mio. DOF. According to [26] an FE model should have at least 6 elements per wavelength (airborne sound). The aimed element size is 7 mm, although complex curvatures require lower sizes in certain areas. To verify the results of the static nonlinear contact analysis a pressure

measurement with a special foil that reacts on pressures above 10 MPa was conducted. Figure 7 illustrates the measured and calculated pressure distribution in the flange (red: above 10 MPa) and the extracted contact status elements (red: contact closed) that are used for the coupling. Without doubt the pressure distributions coincide very well.

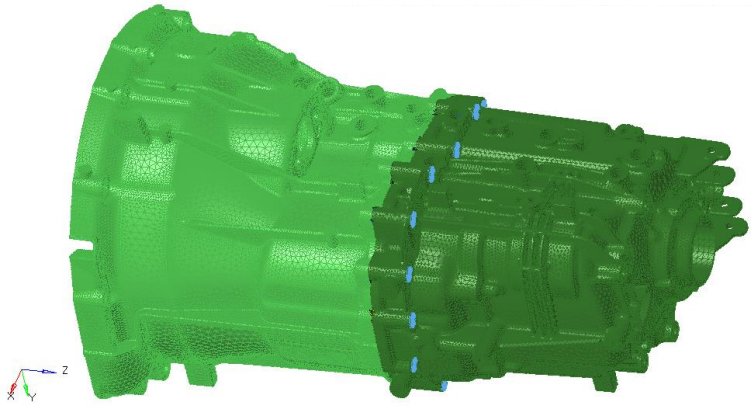


Figure 6: CAD based FE model

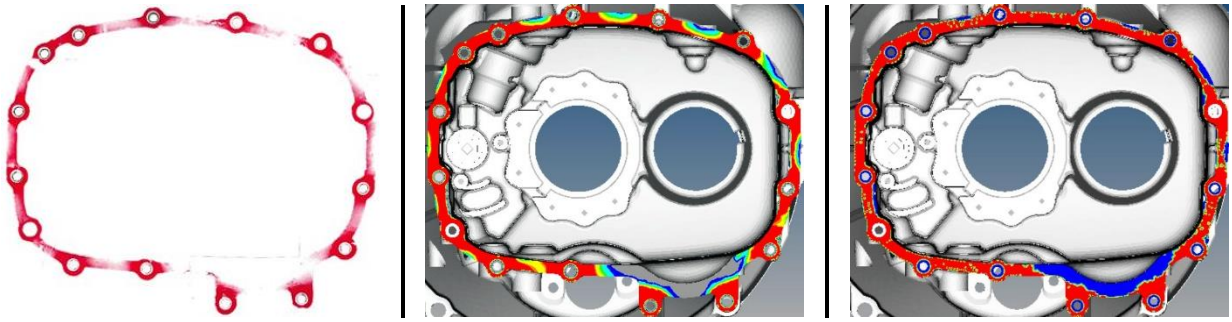


Figure 7: Flange pressure distribution (left: measured, middle: calculated) and contact status (right)

Next, the results of the modal analyses were correlated with experimentally obtained mode shapes. For the evaluation, the average of the first 40 diagonal MAC values is used as listed in Table 2.

Variant	D20	D25	D30	D35	D40	D45	D50	D55	Complete	Contact	Reference
Ø MAC	80.9	82.0	82.8	82.8	82.4	81.6	81.0	80.5	68.4	81.1	94.7

Table 2: Average diagonal MAC values of the empty gearbox housing models in %

There is no doubt that simply coupling the whole flange leads to unsatisfying results whereas coupling the contact elements respectively the elements within a diameter around the holes generates good results. Geometry deviations between the CAD model and the scanned reference model explain the overall lower MAC values. This effect is also documented for many other casted structures (e.g. [8]) and therewith appears plausible. Especially for close eigenfrequencies some parts of the mode shapes appear to shift to neighbored modes. However, it is not clear in which way the MAC value represents the sound radiation properties of the model. Therefore the estimated radiated power is calculated with the normal component of the surface velocities $\hat{v}_k$ (4) according to (5) [27]. For this estimation the radiation loss factor σ is set to 1. The unit excitation forces $\hat{F}_Z$ were applied in every translational direction to the center nodes of rigid elements in the bearing seats. Modal damping values D_i were taken from the measurement. The calculated frequencies Ω were the eigenfrequencies and 20 frequencies in between.

$$\hat{v}_k e^{j\Omega t} = j\Omega \sum_{i=1}^{n} \frac{\psi_{ki}^* \cdot \sum_{z=1}^{l} \psi_{zi}^* \cdot \hat{F}_z}{\omega_i^2 - \Omega^2 + j2D_i\omega_i\Omega} \, e^{j\Omega t} \tag{4}$$

$$P_{ERP} = \frac{1}{2} \cdot \sigma \cdot c \cdot \rho \cdot \sum A_i \cdot v_i^2 \tag{5}$$

Figure 8 clearly shows that the variants show a similar behavior except for the completely coupled model. Especially the highest peak at 950 Hz differs significantly. The D30 variant appears to model the modes in the middle frequency area too softly as the ERP is comparatively high. In general the accordance to the reference model is acceptable since the evaluation of the sound power normally uses third-octave bands.

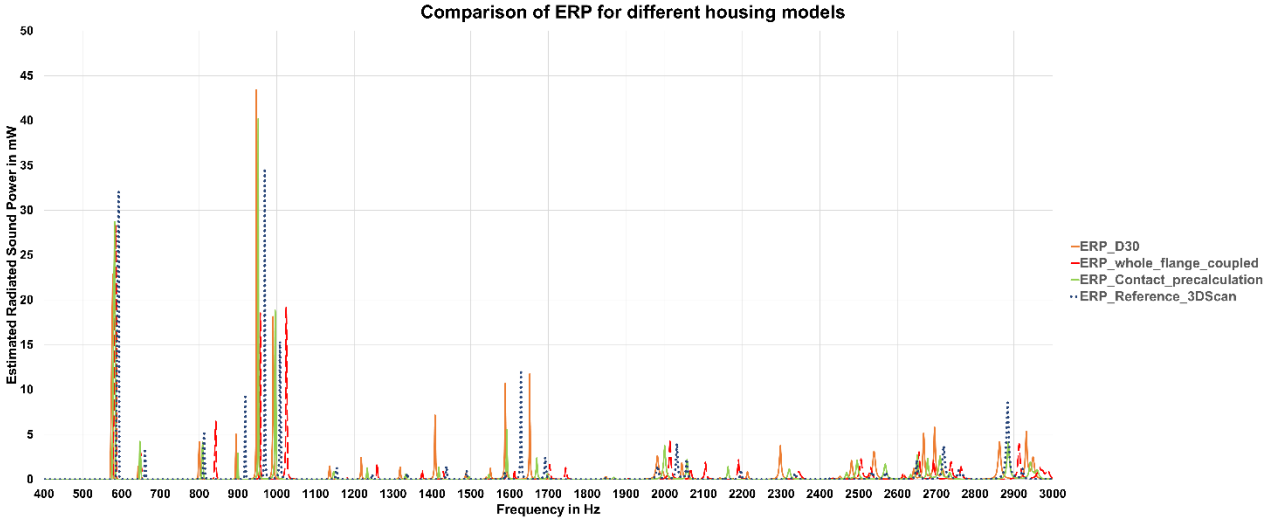


Figure 8: ERP of the different housing models

5.2 Empty housing with bracket

As shown in Figure 4 the gearbox housing is mounted on a steel bracket. For this reason the model of the housing with the bracket had to be validated. Due to the weight of the steel bracket, ensuring free-free boundary conditions is difficult. Figure 9 shows the experimental modal analysis test setup with the bracket attached to a frame with rubber elements and the FE model for the calculated modal analysis.

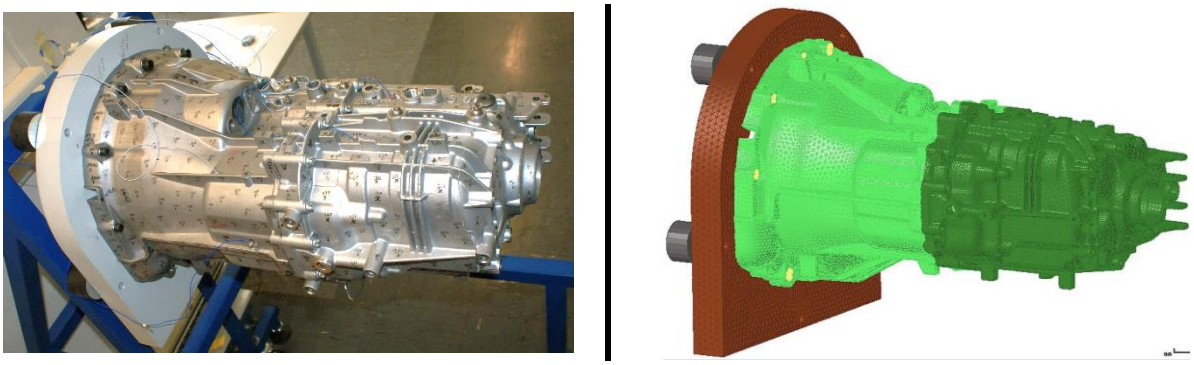


Figure 9: Modal analysis setup for the housing with bracket and FE model

For the FE model a contact pre-calculation between the bracket and the clutch bell housing with a pretension of 12 kN per screw is applied. The resulting contact elements are the coupled in the modal analysis. Due to the nonlinearity of the rubber elements, some modes correlate with very low MAC values. Nevertheless the average of the first 24 diagonal MAC values lies at 83.6 % which is very satisfying given the average MAC value of the housing without bracket of 82.8 %. For higher modes the mode shapes seem to be “polluted” with those of the frame and therefore were not evaluated.

5.3 Model order reduction

In conclusion, the described FE model of the housing with bracket can be used as a reference for the evaluation of condensed models, e.g. by correlating the mode shapes. The condensed model for a MB model can be generated in various ways of which the Craig Bampton based approach is commonly used. According to [23] the generation includes two steps:

- Calculation of the normal and static modes with the Craig Bampton method [28]
- Orthonormalization of the normal and static modes in a residual run

In the first run the housing is regarded as a complete substructure. Each point where loads of the other parts of the assembled MB model can be transmitted into the housing has to be declared as an interface point. For the housing these are the central points of rigid elements with the bearing seat nodes as dependent nodes. Note that fixed boundary conditions with the ground should be set as such and not as interface nodes in order to keep the number of static modes low. Within the Craig Bampton reduction the static modes are calculated by applying unit deflections at the interface nodes. However, the normal modes that are also calculated are not orthogonal to the static modes which would lead to non-diagonal mass and stiffness matrices. Therefore a second modal solution (orthonormalization) is performed on the reduced system. The resulting final modes capture the global dynamics and local stiffness characteristics of the flexible MB model. The number of modes of the reduced system equals the number of the normal modes and the fixed interface static modes. In order to further reduce the number of static modes not every dof of the interface nodes has to be considered, especially when only small forces occur (e.g. axial direction for roller bearings). The influence on the number of considered normal modes is restricted as it depends on the frequency range.

5.4 Sound radiation calculation

For the sound calculation several methods have been investigated in [7], [8] and [11]. Comparing the different methods the so-called Automatically Matched Layer Method performed best regarding the ratio of accuracy to computation time [7]. This FE based method has the specialty that the solver automatically creates an absorbing layer around the fluid elements in order to prevent reflections. In [7] the input surface velocities for the sound calculation were computed with a frequency response analysis. For the further investigations those velocities will be calculated for constant operating points using the full MB model of the gearbox. As they are calculated in the time domain, a transfer into the frequency domain has to follow due to the much higher efficiency of the sound calculation. Within that process only the frequencies with the highest peaks can be considered. Usually this is not problematic due to the tonal characteristic of the gear excitation. Another method not yet applied to the currently used gearbox housing are the so-called Trefftz methods. One of these methods is the Wave Based Technique which is implemented in the software AVL EXCITE™ Acoustics [26]. First investigations with simpler structures generated promising results. The main advantage of this method is its very short calculation time. This is mainly achieved by employing approximate solutions that satisfy the governing Helmholtz equation, but not necessarily the boundary conditions [26].

6 Preliminary investigations

6.1 Simulation and measurement of the bearing force with the bearing test rig

First tests with rotating shaft were conducted at 1000 rpm with a simultaneously applied shaker force. A sine wave generator created by Wegerer [29] generated a user defined excitation force at 350 Hz and the six first multiples which approximates a tooth meshing frequency of a gear wheel with 21 teeth. The test rig (Figure 3) was also modelled as a MB model using BEARINX MAP bearings and condensed models

for the shaft and brackets. The measured excitation force of the shaker was also applied to the MB model. As depicted by Figure 10 the frequency peaks are calculated with the correct tendency although the peak values are higher in the simulation. This indicates too low damping values in the model as only default values were used. Only at 1750 Hz the MB model does not show any significant peak which may be due to a missing eigenfrequency of the test rig parts not modelled. Despite the high excitation at 2100 Hz both the measurement and the calculation show a small response at the bearing.

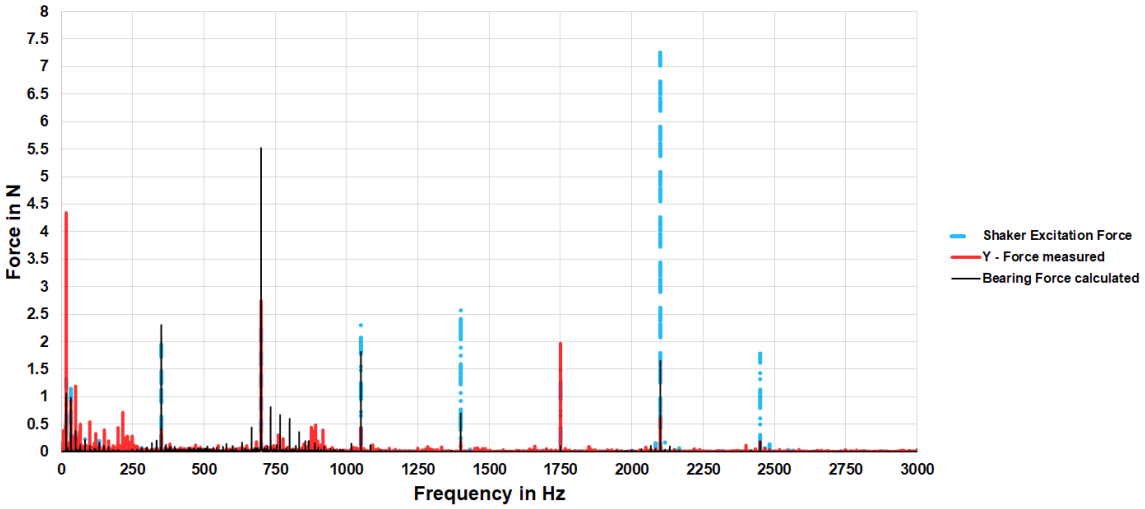


Figure 10: Excitation of the bearing test rig and the measured and calculated bearing force

6.2 Order based modal analysis and Operational transfer path analysis

The gearbox assembly as it is illustrated in Figure 4 is not assembled yet. Consequently, only preliminary investigations with a single gear stage setup could be conducted.

6.2.1 Order based modal analysis

With only eight channels available, the tacho signal and the accelerations had to be recorded sequentially. The run-ups began at 1000 rpm and ended at 3500 rpm after 20 s. After each run-up the set of accelerometers was transitioned to the next group of surface nodes. Overall 81 run-ups were recorded. With that approximately half of the housing surface was covered, enough to get a proper impression of the extracted modes. The recorded data is then transferred into the frequency domain which typically is illustrated with waterfall diagrams. There the most significant orders can be identified for the order tracking process that extracts the frequency domain based acceleration signals along the chosen orders. More details regarding the order tracking techniques can be found in [17]. The Time Variant Discrete Fourier Transform is one of the commonly used methods and claimed to generate good results. In this case the number of teeth of the gear wheel mounted on the shaft for the tacho signal is 21 which determines the orders to track as illustrated in Figure 11.

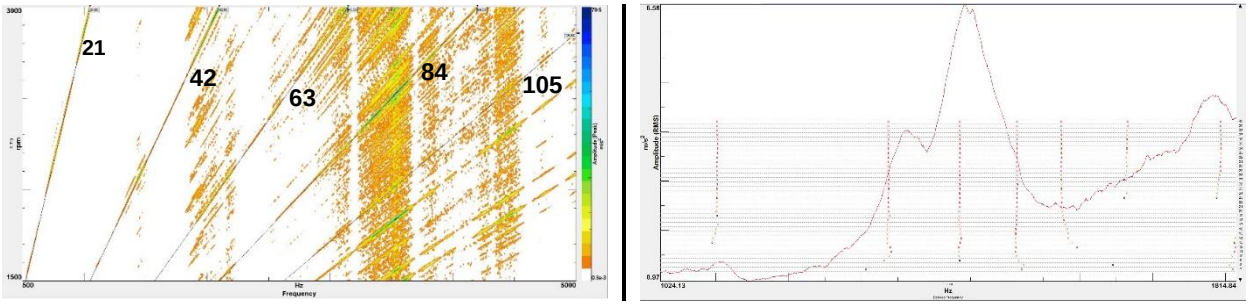


Figure 11: Colormap display of tracked orders and derived order 42 in stability diagram

Next, the tracked orders are used for the identification of the modal parameters with the polymax method. Figure 11 exemplarily illustrates the quality of the extracted order 42 that contains very stable poles. The calculated mode shapes are also plausible and reveal the influence of the shafts, bearings and gears on the modes of the housing. As expected some damping values are quite high. The damping of the majority of modes is higher by the factor of approximately 10 compared to the empty housing.

In conclusion, these investigations clearly show that the OBMA is suitable for the identification of the modal parameters of gearboxes and can be seen as the last step of the bottom-up approach. Regarding the measurements with the new two staged gearbox the following aspects are of special interest:

- Excitation behavior of the two stages and quality of the extracted orders
- Derivation of realistic damping values
- Identification of the acoustically most relevant mode shapes by simultaneous measurement of the sound power

However, the test setup depicted in Figure 4 furthermore allows the application of the OTPA. In fact, the run-up measurements can be both used for the OBMA and the OTPA as long as the operational bearing forces are recorded.

6.2.2 Operational transfer path analysis

Wegerer conducted first preparatory investigations for the application of the OTPA [29]. More accurate, an extended version of the OTPA, the so called operational path analysis with exogenous inputs (OPAX) is used. The main goal of the OTPA or OPAX is to determine path contributions y_{ki} to the response at a target location k. If every path $i = 1 \dots n$ is identified correctly, the sum of the contributions equals the measured target response y_k. However, in reality often only the main paths can be identified which causes deviations between those quantities. The partial contributions are calculated with the path loads $F_i(\omega)$ and the corresponding frequency response functions (FRF) $H_{ki}(\omega)$. Neglecting the acoustic loads, this is described by equation (6). The left side is the measured response and the right side the synthesized response from the path loads and FRFs.

$$y_k = \sum_{i=1}^{n} y_{ki}(\omega) = \sum_{i=1}^{n} H_{ki}(\omega) \cdot F_i(\omega) \tag{6}$$

The key extension compared to the OTPA consists in using parametric models for the calculation of operational loads using measured mount accelerations [30]. Those calculated loads can be used together with directly measured path loads, in this case the bearing forces. Therewith the number of unknown parameters is reduced, leading to results that are more reliable. Typically for all TPA techniques is the division into an active side (source) and a passive side (receiver) with a stiff or elastic connection between them. In the case of gearboxes the active side consists of gears and shafts that transmit an excitation force through bearings to the housing which is the passive side. Indicator points that are close to the input points can be added to the measurement e.g. when no measurements are possible on the active side. The five basic steps of the OPAX are [30]:

- Operational measurements: Recording of path inputs, targets and indicator responses. This data can be collected with the run-ups for the OBMA. Consequently order tracking techniques are applied to extract the relevant orders. The more orders available the more reliable the results are, assumed that no weak orders with high noise levels are used.
- FRF measurements: Measurement of FRFs between inputs and targets. If indicator points are considered, the FRFs from the inputs to the indicators are also required.
- Identification of parametric load models: In principle, any load model can be used and its parameters can be calculated with the data from the first two steps. This is only necessary when the direct loads are not available. In this case three of the four excitation loads can be measured directly. As depicted in Figure 4, the bearing force at the small roller bearing is measured indirectly. One possibility is to derive the load via simulations where the input acceleration is applied to the model in order to calculate the bearing load. A pure experimental approach would

be mounting further accelerometers as indicators close to the input location and use them for a bandwise approximation of the housing stiffness in the area of the bearing.
- Calculation of the model based operational loads with the measured path inputs.
- Computation of path contributions: Multiplying the operational loads with the measured FRFs equals the path contributions, see equation (6).

Investigations conducted by Wegerer with two shakers that were mounted to the gearbox with force sensors and excited with virtual multi-order run-ups show that the best results can be obtained with directly measured loads. However, the combined usage of direct loads and calculated loads with additional indicator points leads to similar results [29]. In general the deviations between the sum of contributions and the measured response were small using direct loads and indirect loads.

7 Conclusions

Stated briefly, the goal of the presented research project is to determine the contributions of the gear stages to the housing oscillations through measurements and calculations. This paper describes a new way for the validation of the state of the art sound calculation approach for gearboxes. It combines methods for the reduced modelling of gears, bearings, shafts and housings to one holistic approach. As the complex gearbox housing is the main radiating element, its model was validated applying a bottom-up strategy. On the system level the validation relies on the measurement of the bearing forces, the surface accelerations and the radiated sound power. For the measurement of the bearing forces a newly developed sensor with strain gauges is presented. First measurements demonstrate its capability to measure the dynamic bearing force up to several kHz. Consequently, it can be used in the OBMA and OPAX of the gearbox. Preliminary investigations demonstrate the suitability of those methods for experimental investigations of the sound generation in gearboxes.

References

[1] M. Ersoy and S. Gies, Fahrwerkhandbuch, Wiesbaden: Springer Vieweg, 2017.

[2] T. Resch, "NVH Simulation und Optimierung," in *AVL Getriebe Tech Day 2016*, Neu-Ulm, 2016.

[3] P. Zeller, Handbuch Fahrzeugakustik, Wiesbaden: Springer Vieweg, 2018.

[4] F. A. Thoma, Lastübertragung im verformten System Lager-Welle-Zahnrad, PhD thesis, München: FZG, 2011.

[5] M. K. Heider, Schwingungsverhalten von Zahnradgetrieben - Beurteilung und Optimierung des Schwingungsverhaltens von Stirnrad- und Planetengetrieben, PhD thesis, München: Dr. Hut, 2012.

[6] J. H. Bihr, Untersuchung des Schwingungsverhaltens von mehrstufigenStirnradgetrieben unter besonderer Berücksichtigung des Welle-Lager-Systems, PhD thesis, München: Dr. Hut, 2016.

[7] S. Falkenberger, Optimierung der Berechnung der Schallabstrahlung von Getriebegehäusen, PhD thesis, TU Ilmenau: Universitätsverlag Ilmenau, 2018.

[8] B. Graf, Validierung von Methoden zur Berechnung und Reduzierung der Schallabstrahlung von Getriebegehäusen, PhD thesis, TU Ilmenau: Universitätsverlag Ilmenau, 2007.

[9] B. Graf and J. Neher, "Frequency-specific parametric studies for the reduction of the sound radiation of gearbox housings," in *ISMA 2008*, Leuven, 2008.

[10] J. Neher and B. Wender, "Validated modelling of joints for the sound radiation simulation of

gearboxes," in *ISMA 2010*, Leuven, 2010.

[11] J. Neher, Rechnerische und experimentelle Untersuchungen der Schallabstrahlung bei Fahrzeuggetrieben, PhD thesis, TU Ilmenau: Universitätsverlag Ilmenau, 2011.

[12] S. Falkenberger, "Sound radiation of gearboxes – Investigation of the measured and calculated dynamic bearing force in gearboxes," in *ISMA 2016*, Leuven, 2016.

[13] "BEARINX-MAP – Wälzlagermodellierung für MKS," Schaeffler AG, [Online]. Available: https://www.schaeffler.de/content.schaeffler.de/de/produkte-und-loesungen/industrie/berechnung-und-beratung/berechnung/bearinx_map/index.jsp. [Accessed 2018].

[14] T. C. Lim and R. Signh, "Vibration transmission through rolling element bearings, Part I: Bearing stiffness formulation," *Journal of Sound and Vibration 139 (2)*, pp. 179-199, 1990.

[15] C. Weber and K. Banaschek, "Formänderung und Profilrücknahme bei gerad- und schrägverzahnten Rädern," in *Schriftenreihe Antriebstechnik Bd. 11*, Braunschweig, Vieweg-Verlag, 1955.

[16] S. Shweiki, D. Mundo and e. al., "Investigation of mesh phasing in a planetary gear train using combined FE and Multibody simulations," in *ISMA 2016*, Leuven, 2016.

[17] E. Di Lorenzo, S. Manzato and e. al., "Order based modal analysis: a modal parameter estimation technique for rotating machineries," in *IOMAC 2015*, Gijón, 2015.

[18] D. De Klerk, M. Lohrmann and e. al., "Application of operational transfer path analysis on a classic car," in *NAG/DAGA*, Rotterdam, 2009.

[19] V. Kirsch, M. Wegerhoff and e. al., "Prognosemethodik für die Schaltleistung von Getrieben während der Konstruktionsphase," *FVA 587 II Prognose der Luftschallabstrahlung in Getrieben*, 2015.

[20] S. Sanzenbacher, Reduzierung von Getriebegeräuschen durch Körperschallminderungsmaßnahmen, PhD thesis, Stuttgart: Institut für Maschinenelemente, 2016.

[21] Deutsches Institut für Normung e.V., *DIN EN ISO 3743-1*, Berlin: Beuth Verlag, 2011.

[22] T. Giese and T. Hahn, "Modelling of Rolling Bearings in MBS - Choose the Best Model for Your System Simulation with RECURDYN," in *RecurDyn TecDays 2017*, München, 2017.

[23] "RecurDyn Online help," Functionbay, 2018. [Online]. Available: http://www.functionbay.co.kr/documentation/onlinehelp/default.htm. [Accessed 2018].

[24] A. Palermo, D. Mundo and e. al., "Multibody element for spur and helical gear meshing based on detailed three-dimensional contact calculations," *Mechanism and Machine Theory 62*, pp. 13-30, 28 12 2012.

[25] H. Wittel, D. Muhs and e. al., *Roloff/Matek Maschinenelemente*, Wiesbaden: Springer Vieweg, 2015.

[26] AVL, "AVL Excite™ Acoustics User Manual," Chapter 5. Theory, 2018.

[27] "Altair Connect," Altair, [Online]. Available: https://connect.altair.com/CP/kb-view.html?kb=166197. [Accessed 2018].

[28] R. Craig and M. Bampton, "Coupling of Substructures for Dynamic Analyses," *AIAA JOURNAL Vol. 6, No. 7*, pp. 1313-1319, 07 1968.

[29] F. Wegerer, Theoretische und experimentelle Einführung sowie Validierung der Operational Transfer Path Analysis, Master thesis, University of Applied Sciences of Ulm, 2018.

[30] K. Janssens, P. Gajdatsy, L. Gielen, P. Mas and L. Britte, "OPAX: A new transfer path analysis method based on parametric load models," *Mechanical Systems and Signal Processing 25*, pp. 1321-1338, 3 11 2010.

Comparison of finite-element methods to compute the transmission error to noise transfer function of a simple gear box.

Y. Goth [1]
[1] CETIM, Pole Simulation
52 av. Felix Louat, Senlis, France
e-mail: **yvon.goth@cetim.fr**

Abstract

The work presented here focus on the numerical techniques used to compute the transfer function between the vibrations generated in a gear box by the transmission error and the noise power that results in the surrounding. Finite element method is used to compute the vibration and acoustic components of the transfer function, in the frequency domain or time domain.

The numerical results have been compared to an experimental dataset.

1 Introduction

Noise becomes a major concern for gear box makers. The main source of the noise radiated by the gearbox is known for long to be related to the transmission error (TE) [1]. TE is defined as the existing offset between the ideal angular position of the driven pinion and its actual position regarding a homocinetic transmission.

Literature on the computation of the transmission error and to the transmission of vibrations through a gearbox is wide, but only a few papers deals with the complete vibro-acoustic chain, from the transmission error to the computation of the noise radiated by the system[2]. The vibration transfer function is, in general, computed in time domain, and the extension to the acoustic domain is not straightforward and seldom done.

This works aims at comparing the different methods that allows computing the noise radiated by a gearbox mainly excited by the transmission error. Here, the concern is the transfer function between the transmission error, taken as an input of the model, and the external noise.

In the present study, three approaches have been used and compared for the vibration computation, direct harmonic, harmonic on modal base, and temporal on modal base, while the acoustic part is computed with the direct harmonic or harmonic on modal base approach.

The numerical results have been compared to an experimental dataset, where transmission error, gearbox accelerations and acoustic data have been recorded.

2 Comparison of different numerical approaches

Vibration calculations can be made in four quadrants (Table 1)

Time domain	Frequency domain
direct $u = g(x,t)$	direct $u = g(x,f)$
modal base	modal base

$u = \sum \Phi_k(x)\eta(t)$	$u = \sum \phi_k(x)\,\eta(f)$

Table 1- Possible approaches for vibrations computation

The three following approaches have been used and compared: Computation in the time domain on a modal base, and in the frequency domain, both direct and modal. The direct time domain approach, while being the standard way of approach for this type of computation, was not used here, because it implies a large computing time, and the transfer of data from the vibration problem to the acoustic one, treated in the frequency domain, is not easy: it would imply to do a Fourier transform on each point of the external mesh of the gearbox.

The time domain approach is less suitable than the frequency domain approach to analyze a periodic dynamic phenomenon. It requires computing the transient phase that precedes the stabilized phase of interest. Its use is justified when non-linearities are to be taken into account, what is not possible in the frequency domain.

Acoustic calculations are made in all cases in the frequency domain.

The transmission error spectrum is taken as an input, defined upstream. No feedback mechanism from vibration to the TE is taken into account here.

Vibration and acoustic computations are chained: vibrations of the gearbox are computed first, and the noise is computed in a second step using the vibration data as input.

3 Numerical models

3.1 General structure

The test setup used to get the experimental data compared to the numerical results is shown Figure 1. It has been described in details elsewhere [3], and only the main characteristics are given here.

The modeled and tested structure is a single stage reducer. The pinion has 32 teeth, and the gear 43 teeth. The module is 1.75 mm.

The angular error between the two shafts is measured by using optical encoders on the free ends of the shafts, with respectively 2000 top/rev and 2500 top/rev.

Several accelerometers are set on the casing and close to the bearings to get the vibration response of the system.

The sound power radiated by the gearbox is measured by an intensity probe for the stabilized measurement, and deduce from the sound pressure given by a microphone over the structure, previously calibrated on the intensity sound power measurements, for the transient measurements.

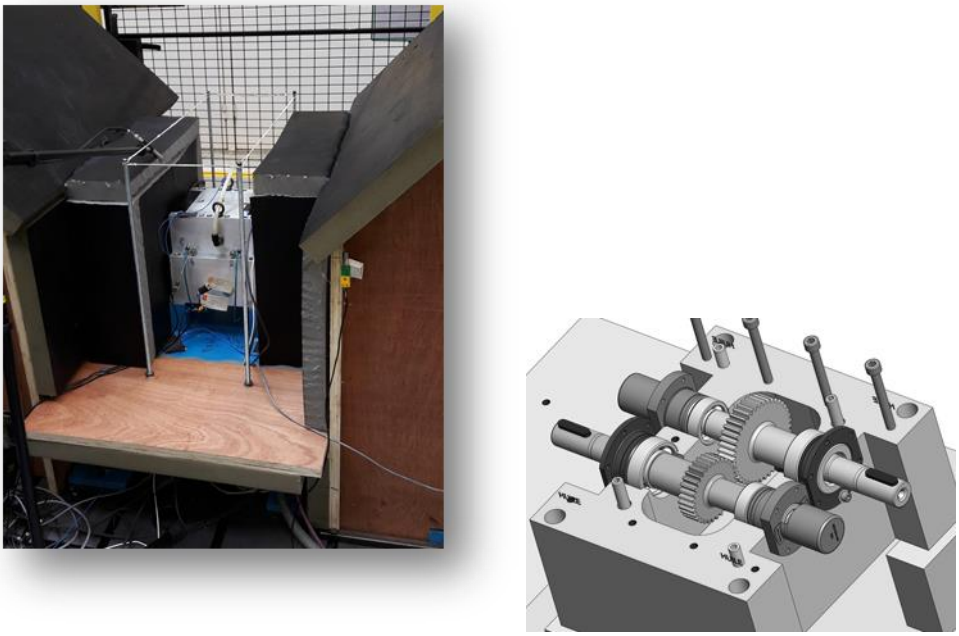


Figure 1 – Picture of the test bench (left) and CAD view of the reducer (right)

3.2 Components models

The model is composed of three components, defined in separate meshes: The shafts and wheels, the gearbox, and the acoustic medium.

3.2.1 Shafts models

In a compromise between computation efficiency and accuracy, the shafts and gears are modeled as beams and disks assemblies (Figure 2). Bearings are taken into account by their equivalent stiffness. Couplings at the shafts ends are taken into account by inertia matrix associated to their end points.

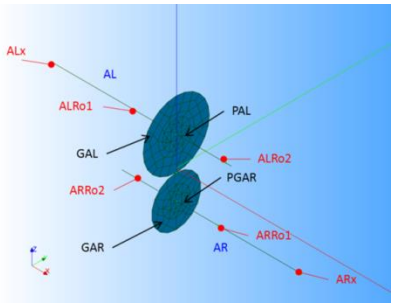


Figure 2 – Shafts numerical models.

As shown in Figure 3, the contact between teeth is modeled by a link composed of stiffness elements representing the teeth stiffness (KAL, KAR) and a stiffness element where the transmission error is applied (KET).

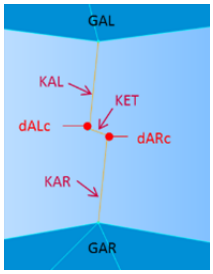


Figure 3 – Model for the teeth contact

The transmission error is:

- either imposed as a kinematic relation between the displacements of the two nodal points at the end of the KAR, KAL stiffness:

  displacement(dALc) - displacement(dARc)= TE. (1)

  This approach is used in the calculation in the frequency domain on physical base

- or imposed by two antagonist forces on the stiffness KET. In that case, the stiffness has to be given a value far larger than the stiffness of the components of the model (here, 10^{12} N/m). The amplitude of the forces is given by

  $$F = K_{ET}.TE/2 \quad (2)$$

  and the direction of application is normal to the teeth contact faces.

  This is the model used for the calculations on modal base, in the frequency and time domains.

The two approaches have been compared, and it has been shown that, for the given value of the stiffness KET, they give the same results.

3.2.2 Gearbox model

The gearbox is composed of five thick faces, the top face being thinner. A simplified model has been used. The mesh use coarse 3D elements on the thick faces, while a finer mesh is used on the top face. The shafts are linked to the gearbox by the stiffness representing the bearings (Figure 4). As no detailed data were available for the bearing stiffness, they have been assumed to be stiff (10^{10} N.m).

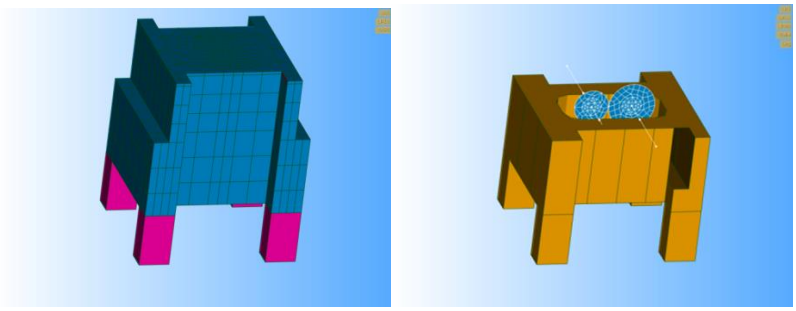


Figure 4- Gearbox mesh and linking between the shafts and the gearbox

3.2.3 Acoustic domain model

In order to use one unique software for all the computations, the acoustic radiation around the gearbox is computed using the finite element method too. So the air volume surrounding the system has to be meshed. This volume is delimited by a spherical surface, on which an impedance boundary conditions is imposed to simulate the radiation in an infinite domain (Figure 5).

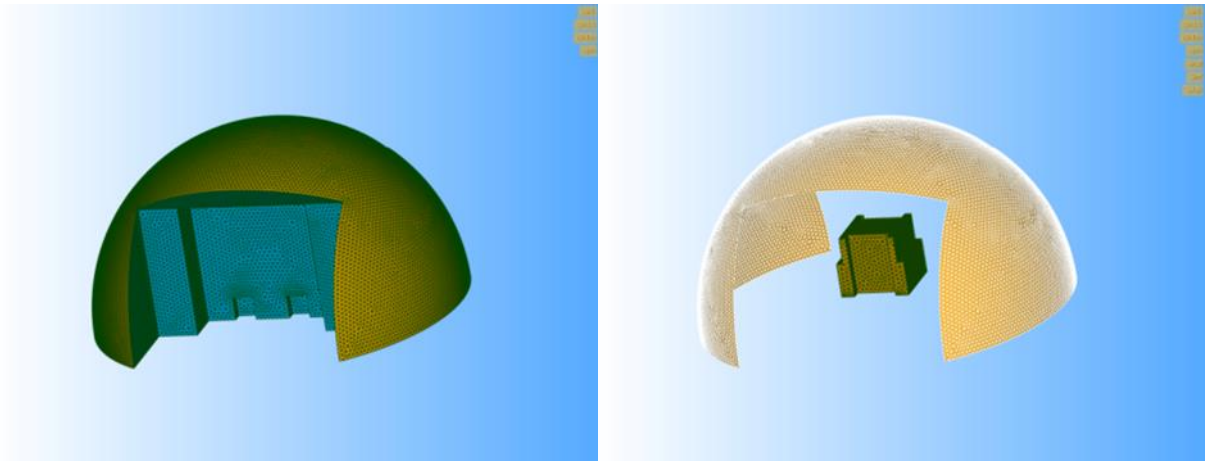


Figure 5- Air volume mesh (left) and spherical surface where non-reflecting boundary condition is applied (right)

The other external surfaces, representing the walls around the test gearbox setup, are considered as rigid.

The vibration velocity field issued from the vibration analysis is projected on the gearbox surface and used as the acoustic loading.

4 Results

4.1 Finite elements solver

The solver used in all calculations is Code_Aster, version 13.3. This open-source code created by EDF [4] is a generic finite element mechanical solver with acoustic capabilities. The vibration computations, either in time or frequency domain, used the native functionalities of the software, while the acoustic computations have required some specific developments [5].

4.2 Vibration calculations

4.2.1 Frequency domain, direct approach

The vibration transfer functions are computed by calculating the vibration spectra resulting from an imposed TE of constant amplitude 1µm. The transmission error is directly imposed as a relative displacement between the two teeth.

The direct approach doesn't introduce any shortcomings in the model, but the calculation times are high on complex models. Here, on this simple model, the computation time is 780s on a laptop for 300 frequencies, being 2.6 s/frequency.

Figures 6 to 7 show some examples of the results got.

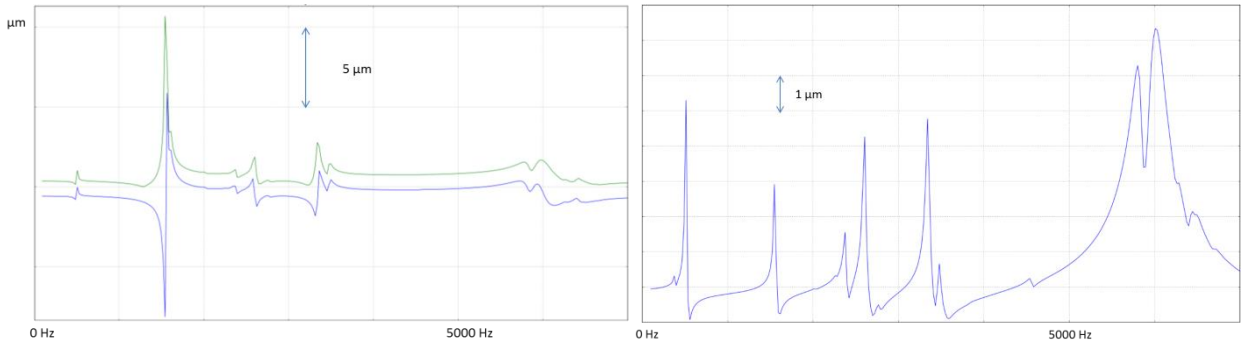


Figure 6 – Calculated teeth angular displacement (left) and TE deduced from the angular displacements at the encoder position (right) for an imposed TE of 1µm

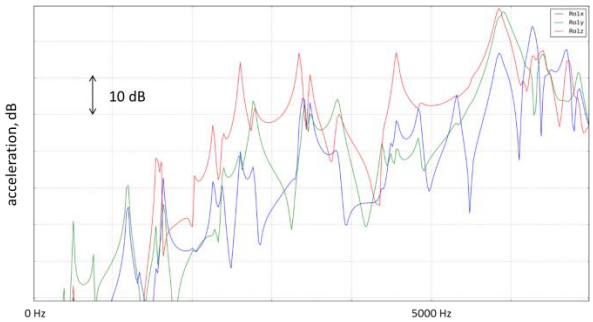


Figure 7 – Calculated acceleration of the bearings for an imposed TE of 1µm

It can be notice that over 300 Hz, the TE deduced from the angular displacement read at the encoders positions is very different from the imposed constant TE. This is due to the presence of shafts torsional modes, that decouple the rotation of the ends of the shafts from the rotations of the wheels. So, in that experimental setup, encoders measurements, while very useful to validate the finite element model, can't be taken as an accurate measurement of the TE over some hundreds of Hertz.

4.2.2 Frequency domain – Modal base

Frequency computation on a modal base that uses an imposed displacement as load (Dirichlet conditions) is not compatible with a standard approach. For this reason, the TE load is imposed here by using two antagonist forces acting on a high stiffness between the teeth.

This approach presents some technical difficulties. Due to the high value used to connect the two teeth, the mode that support the TE load is rejected at a frequency that is too high to extend the computation of the modal base up to that frequency. To overcome this problem, we use an approach similar to the one used to define Craig-Bampton type superelements: The modal base is computed with the teeth nodal point blocked, and is completed with the static modes linked to those points. The static modes allow to fix the modal troncation error.

The results are very close to the ones got with the direct method, as can be seen on Figure 8, compared to results shown Figure 6.

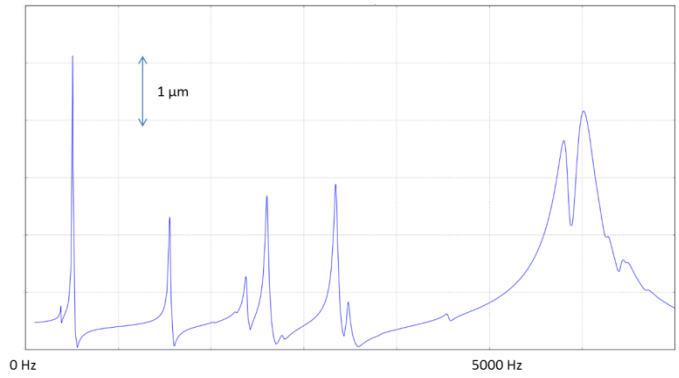


Figure 8 - Calculated TE deduced from the angular displacements at the encoder position (right) for an imposed TE of 1µm - Calculation on modal base

The computation time is 25s for 60 modes and 360 frequencies, being 0.07 s/frequency. The gain against the direct approach is close to 40, which largely justify the added complexity of this later approach.

4.2.3 Time domain, modal base

The time domain approach is justified when one has to take into account non-linearities (choc, variable stiffness, ...). Here, the time domain approach on a modal base is used. The modal base is the base completed with the static modes formerly used in the frequency domain.

The hysteretic damping used for frequency calculations has no equivalent in the time domain approach. In that case, a Rayleigh damping is used instead.

The integration algorithm must be explicit to take non-linearities into account. Tests have shown that the time step needed to get convergence was very short: 10^{-7} to 10^{-8} s. It is probably the high stiffness used to define the TE load that is the cause of this short time step.

One example of the results got is shown in Figure 9. One computes the response to a transmission error of amplitude 1µm, in swept sine, for a frequency ramp ranging linearly from 900 rpm to 6300 rpm.

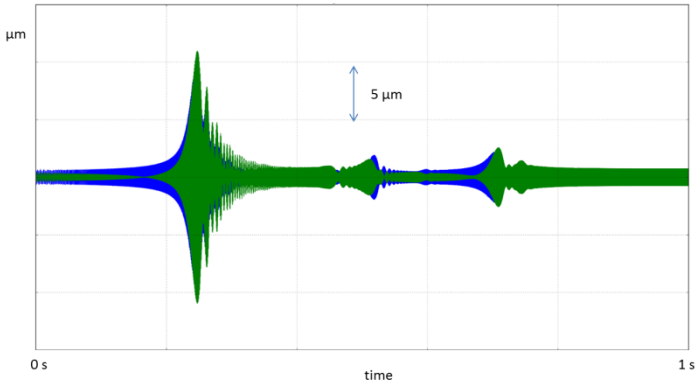


Figure 9 – Calculated Teeth angular displacement for a given TE of 1µm. Swept sine between 900 rpm and 6300 rpm

The amplitudes and frequencies of the peaks are in agreement with the calculations in the frequency domain. But the computation time is much longer: time to compute 1 s is 250 s.

4.3 Acoustic calculations

A simplified approach has been used to compute the acoustic response of the structure. The acoustic radiation is computed only at the modal frequencies of the structure, using the modal shapes projected on the gearbox surface as acoustic loads. The acoustic pressure is interpolated between the modal frequencies of the structure. The calculation is exact for each modal frequency, and only approximated in between, but, as the contribution of the modal peaks is dominant, the approximation leads only to an acceptable error.

The acoustic power radiated for an imposed TE of amplitude 1 µm is shown Figure 10.



Figure 10 – Acoustic power radiated for an imposed TE of 1µm

Some examples of the acoustic fields calculated on noteworthy points are given Figure 11.

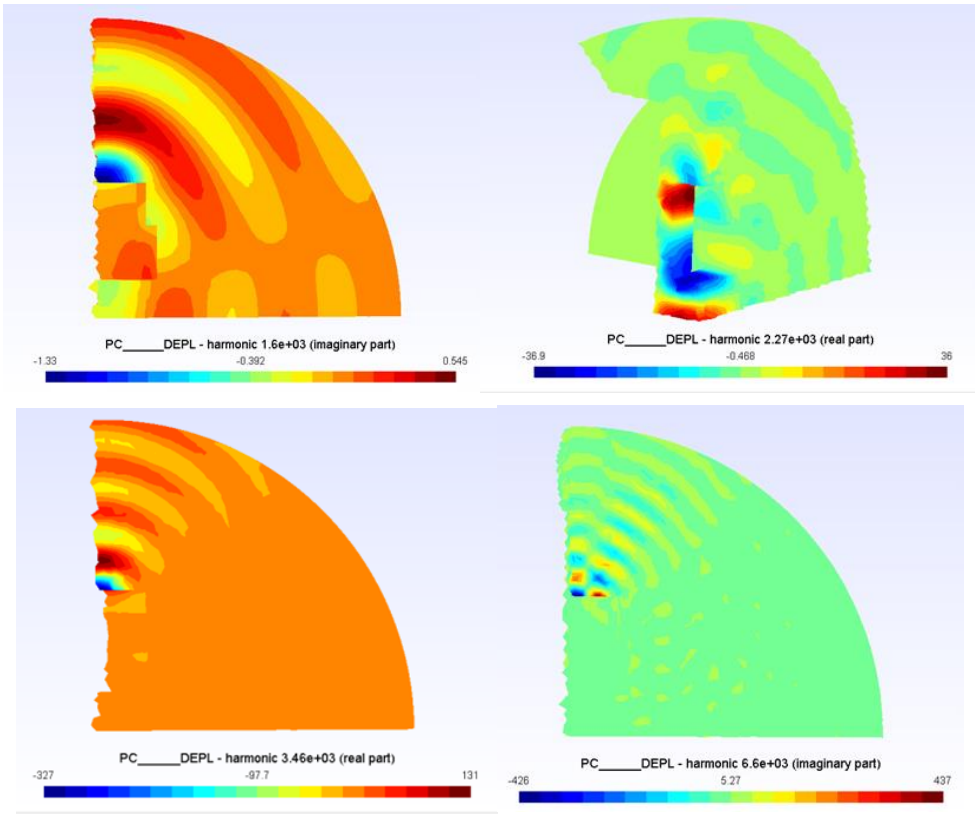


Figure 11 – From top left to bottom right, Acoustic field radiated at 1600 Hz, 2270 Hz, 3450 Hz, and 6600 Hz

5 Comparison with test results

The noise powers radiated for 1 µm TE got from measurements in stabilized regime are compared with the computed results in Figure 11. The test results are given by markers for the frequency band around the harmonics of the mesh frequency.

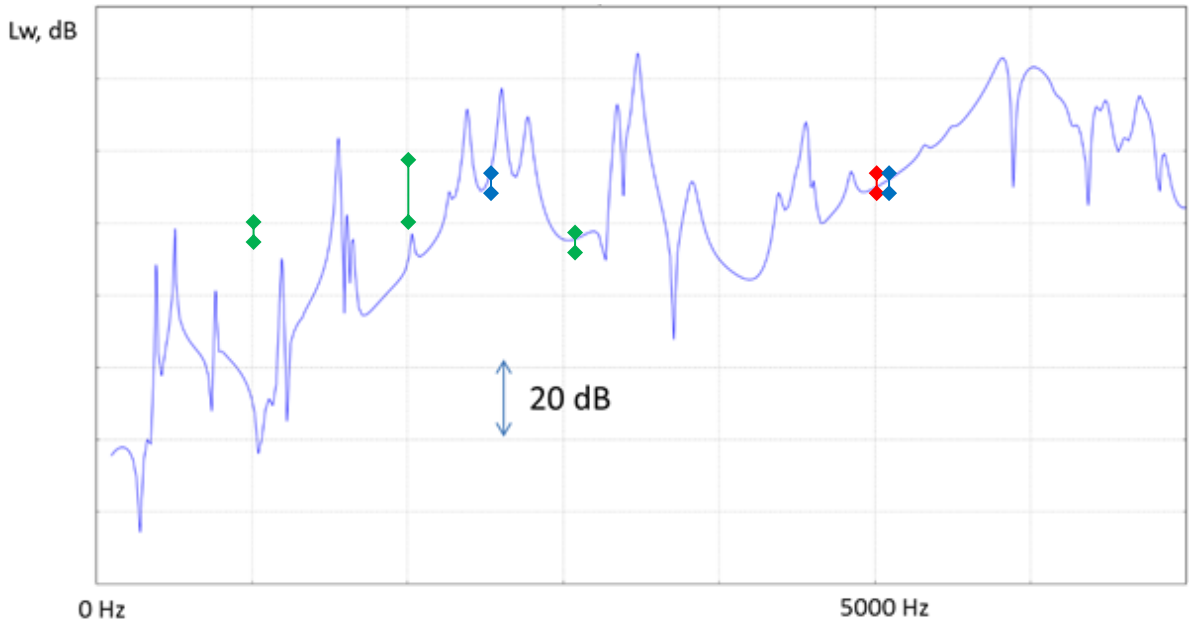


Figure 12 – Comparison calculation-test. Acoustic power radiated for 1µm TE. Markers are the test points, green: 1490 rpm, H1, H2, H3, blue: 3550 rpm, H1, H2, red: 6550 rpm, H1

The agreement between the computed and measured transfer functions is correct for frequencies above 2000 Hz. Due to the high complexity of the transfer function, a small error in frequency can results in a large error in the amplitude at a given frequency, and the comparison is not easy at fixed velocity .

A better estimation of the quality of the model would be obtained by using transient velocity tests (runup). The experimental runup data are currently post-processed to allow this comparison.

5.1 Conclusions

The comparison of the calculation methods for the transfer function between the transmission error and the noise radiated by gearboxes leads to recommend the approach based on the computation in the frequency domain on a modal base. The modal base must be completed with the static modes associated to the link between the teeth.

The model agrees with the experimental data for frequencies above 2 kHz. The agreement is poorer at lower frequencies. A deeper analysis, based on transient measurements, is needed to better understand and correct the mismatches.

Acknowledgements

This study has been founded by the technical committee “Transmissions mécaniques” of the CETIM.

References

[1] J. D. Smith , *The Uses and Limitations of transmission Error*, Gear technology July/August 1988 (1988).

[2] A. Caillet, Y. Gargouri, W. Van Hal, *From gears dynamic to noise radiation, end to end simulation of a gear box*, Aachen Acoustic Colloquium (2016), pp. 49-59

[3] J. Champain, S. Dalle, M. Octrue, *Simultaneous experimental characterization of dynamic transmission error to noise and vibration behavior of a gear system under load*, International Conference on Gears, München (2017)

[4] Code_Aster Open Source – general FEA sofware, **www.code-aster.org**.

[5] D. Leray, Y. Goth, *Acoustic calculation with the free solver Code_Aster*, International Compressor Engineering Conference, Purdue (2012).

An absolute interface coordinates floating frame of reference formulation for plates

M. van den Belt[1], J.P. Schilder[1], D.M. Brouwer[1]
[1] University of Twente, Faculty of Engineering Technology
P.O. Box 217, 7500AE Enschede, The Netherlands
e-mail: **m.vandenbelt@utwente.nl**

Abstract
In this work, a recently developed superelement formulation in the floating frame of reference is implemented for plates. By using Craig-Bampton modes, a coordinate transformation from the absolute floating frame coordinates and local elastic coordinates to the absolute interface coordinates is established. Several benchmark problems are considered to validate the formulation for plates. Results from the superelement formulation for plates are in good agreement with other formulations, meaning that the formulation can successfully be used for the efficient description of plates in flexible multibody systems, such as flexure mechanisms that can no longer be modelled as beam elements because of their unbeamlike dimensions.

1 Introduction

In precision engineering, flexure hinges are frequently used for their deterministic behavior, due to the absence of friction, hysteresis, and backlash [2]. Flexure hinges allow motion by being compliant in driving directions, while constraining motion in other directions, as shown in Figure 1. Generally, as the support stiffness rapidly decreases with deflection, flexure hinges have a reduced performance in their deflected state [2]. Shape and topology optimization is used to design sophisticated mechanisms to minimize this performance reduction. This requires modelling the flexure mechanisms with computer simulations.

As these forms of optimization require many design evaluations, reduction of computational costs is desired. To decrease the computational costs, flexures are often simplified as flexible multibody systems using nonlinear beam elements. This is a valid assumption as long as the flexures are long and slender, and thus have a high aspect ratio (defined as length/height).

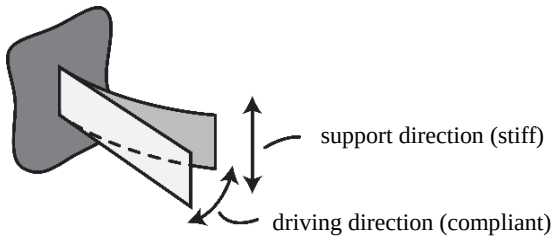


Figure 1 Single leaf spring flexure.

Flexible multibody dynamics concerns the study of mechanisms that consist of multiple deformable bodies. These deformable bodies are attached to each other or to the fixed world at their interface points. The problem is geometrically nonlinear as the joints at the interface points allow for large rigid body rotations. However, because the elastic deformations within a body are considered to remain small, linear elasticity

theory can be used. For the simulations of such systems, general suitable formulations can be classified into three categories: the inertial frame formulation, the corotational formulation, and the floating frame formulation. In each formulation, kinematics and kinematic constraints are described differently. The kinematics of a body represent its motion, which is described by the motion of coordinate frames that are rigidly attached to different material points on the body. Kinematic constraints represent the connections between bodies, and relate the motions of the coordinate frames at the interface points of different bodies.

The inertial frame formulation is a nonlinear finite element formulation, using the nonlinear Green-Lagrange strain definition [3]. By using global interpolation functions, each body is discretized into finite elements. The degrees of freedom in this formulation are the absolute nodal coordinates. Kinematic constraints are easily enforced by equating nodal coordinates of the interface points between the different bodies. The inertial frame formulation does not make a distinction between large rigid body rotations and small elastic deformations.

The corotational frame formulation can be regarded as an extension of the linear finite element formulation [4, 5]. A corotational coordinate frame describes large rigid body motions of elements with respect to an inertial frame. Small deformations are then superimposed using linear finite element matrices, based on the Cauchy strain definition [6]. Nonlinear finite element models are obtained by pre- and post-multiplying element matrices with rotation matrices based on the corotational frame. As in the inertial frame formulation, absolute nodal coordinates are the degrees of freedom, and as such, constraints are obtained in the same way. The corotational frame formulation does not distinguish between flexible and rigid bodies, which makes the simulation of models containing rigid bodies less efficient.

The floating frame formulation can be interpreted as a flexible extension on rigid multibody formulations [7]. In this formulation a floating frame describes a body's large rigid body motions and a linear combination of mode shapes is used to describe local elastic deformations. Since the local deformations remain small, these mode shapes can be obtained by applying powerful model order reduction techniques on a body's linear finite element model [7]. The absolute floating frame coordinates and the local generalized coordinates corresponding to the mode shapes are the degrees of freedom of the system. As the interface points are not part of the degrees of freedom, the kinematic constrains are in general nonlinear. Therefore, Lagrange multipliers are required to enforce the kinematic constraints, increasing the number of degrees of freedom and subsequently the computational costs.

As the floating frame formulation allows for well-developed model order reduction techniques, this is the preferred formulation in many multibody systems where the elastic deformation within a body remains small. Recent research presented a method that overcomes the disadvantage of having to introduce Lagrange multipliers [1]. By using Craig-Bampton modes [8], a coordinate transformation from the absolute floating frame coordinates and local elastic coordinates to the absolute interface coordinates is established. The coordinate transformation is used to create so-called superelements in the floating frame formulation. This way, the Lagrange multipliers are eliminated and as the interface coordinates are now part of the degrees of freedom, kinematic constraints can be enforced in the same straightforward way as in inertial frame formulation. In this way, the new superelement formulation combines the advantages of the different formulations mentioned above.

Within precision engineering, recent developments of flexure mechanisms are aimed at the optimization of mechanisms with a high support stiffness while heavily loaded in supporting directions; whereas, state-of-the-art optimizations are mostly aimed at high support stiffness during a large range of motion [9]. In the latter case, flexure mechanisms can often be simplified as beam elements. However, flexure mechanisms that are loaded in their supporting direction typically are short and wide instead of long and slender, meaning that they have a low aspect-ratio instead of a high one. This implies that the mechanisms can no longer be simplified as beam elements, as they do not provide sufficient accuracy. Plate elements should be used instead of beam elements to obtain sufficient accuracy; however, this increases the number of degrees of freedom and therefore computational costs significantly.

The method presented by Ellenbroek and Schilder offers a promising reduction method for these types of problems [1]. The method is applicable for the reduction of arbitrarily shaped bodies, although the original work only presented validation problems with beams. In this work, superelements are implemented in the floating frame formulation for plates. Benchmark problems for plates are considered to extend this

validation. To this end, a cantilever and a clamped square plate are modelled. The cantilever is loaded at the free tip, whereas the clamped square plate is loaded with a point load on the centerline of the plate. Simulation results are compared to results obtained using both the corotational frame formulation and the inertial frame formulation. This way, validity of the superelements in the floating frame formulation are validated against other formulations as well.

The paper is structured as follows: Chapter 2 of this paper presents an overview of the essentials of the method presented by Ellenbroek and Schilder [1]. In Chapter 3, this method will be applied to plates; kinematics for plates in the floating frame are discussed, as well as its implementation in the new superelement method. In Chapter 4, two validation examples are considered: a cantilever and a clamped square plate. These examples are adapted from Izzuddin [10]. Conclusions are discussed in Chapter 5 and this paper is concluded with recommendations for further research in Chapter 6.

2 Absolute interface coordinates in the floating frame formulation

To describe the kinematics of a plate in the regular floating frame formulation, the coordinates of each interface point are expressed in terms of the absolute floating frame coordinates and the local interface coordinates. This is shown graphically in Figure 2.

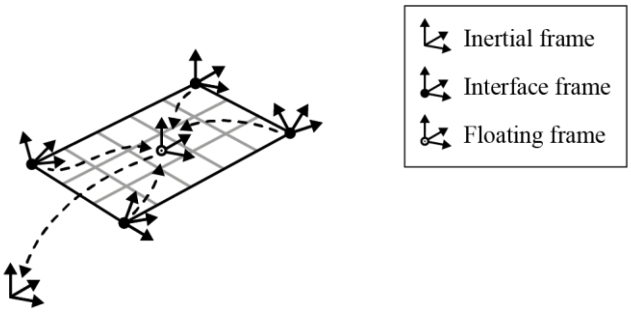


Figure 2 Floating frame formulation for a plate.

Different choices can be made for the set of deformation shapes that describe the local elastic deformations. However, as the local interface coordinates are in fact the generalized coordinates corresponding to static Craig-Bampton modes, it is natural to choose these as the deformation shapes. This way, the coordinate transformation towards absolute interface coordinates can be established. However, since both the Craig-Bampton modes and the floating frame coordinates are able to describe rigid body modes, these modes need to be eliminated from the Craig-Bampton modes. This is realized by defining the floating frame such that there is zero elastic deformation at its location. Both the coordinate transformation and the way the constraints are satisfied are described in detail in [1]. Using the coordinate transformation, the equation of motion and the equilibrium equation can be rewritten from the standard floating frame to the new coordinate set. As Chapter 3 only addresses static examples, the equilibrium equations are of more relevance here. The equilibrium equation in standard floating frame form is given by:

$$\mathbf{Kq} = \mathbf{F}, \tag{1}$$

where $\mathbf{K}$ is the global stiffness matrix according to the floating frame formulation, $\mathbf{q}$ is the vector of generalized coordinates and $\mathbf{F}$ contains the generalized forces that are externally applied or due to kinematic constraints. The equilibrium equation after the coordinate transformation is given by:

$$[\mathbf{R}][\mathbf{T}]^T\mathbf{K}_{CB}\mathbf{q}_{LI} = \mathbf{F}, \tag{2}$$

where [**R**] contains the rotation matrices that relate the floating frame to the inertial frame. $\mathbf{K}_{CB}$ is the stiffness matrix that is obtained by model order reduction of the body's finite element model, using the Craig-Bampton modes and $\mathbf{q}_{LI}$ are the local interface coordinates. Finally, [**T**] is a transformation matrix that removes the rigid body motion of the floating frame from the expression. [**T**] is given by:

$$[\mathbf{T}] = \mathbf{1} - \left[\mathbf{\Phi}_{rig}\right][\mathbf{Z}], \tag{3}$$

in which $\left[\mathbf{\Phi}_{rig}\right]$ contains the displacement of all interface coordinates when the body is subjected to a rigid body motion with respect to the floating frame. The matrix [**Z**] is given by:

$$[\mathbf{Z}] = \left([\mathbf{\Phi}_{CB}]\left[\mathbf{\Phi}_{rig}\right]\right)^{-1}[\mathbf{\Phi}_{CB}], \tag{4}$$

where $[\mathbf{\Phi}_{CB}]$ consists of the Craig-Bampton mode shapes evaluated at the floating frame. This equilibrium equation is the basis of the examples discussed in Chapter 3. Further details of the coordinate transformation and derivations are presented in [1].

3 Validation

To verify validity of the proposed formulation for plates, two static problems are modelled. First, a cantilever that is loaded out-of-plane is considered. Its dimensions are such that beam theory is still valid and therefore the results are also compared to formulations for beams. Second, a square plate is considered that is clamped on two opposite sides. Both examples are adapted from [10].

3.1 Cantilever

In the first example, a cantilever is modelled. The cantilever, shown in Figure 3, is loaded in positive transverse (z-)direction. The cantilever has length $L = 10\ m$, width $w = 1\ m$, and thickness $t = 0.1\ m$. It has a Young's modules of $E = 12\ GPa$ and a Poisson ratio of $\nu = 0.3$. A mesh of 10 elements is used for all simulations and the load is modelled as two equal point loads at the two nodes at the cantilever tip. The response of the tip in both x- and z-direction is measured.

The problem is modelled using the superelement formulation for plates and is compared to three other formulations. The results for the superelement formulation implemented for plates are represented by the black solid line in Figure 4. The grey solid line represents the problem modelled in Ansys (shell181 elements), using a nonlinear finite element formulation based on the full nonlinear Green-Lagrange strain expression [3]. As the cantilever is long and slender, and thus has a high aspect-ratio, simplifying it as beam elements is allowed. To this end, the superelement formulation for beams is also used for validation, as well as the corotational formulation using nonlinear beam elements from software package Spacar. The latter two are represented by, respectively, black and grey dashed lines. The detailed formulation of Spacar can be found in [11].

Figure 4 shows the normalized transverse (w/L) and axial ($-u/L$) displacements. This figure shows that there is a favorable comparison between the four methods. Maximum deviations from Ansys are in the range of approximately 1 to 3%. Furthermore, there is a clear resemblance between Figure 4 and the results from Izzuddin (Figure 8 from [10]).

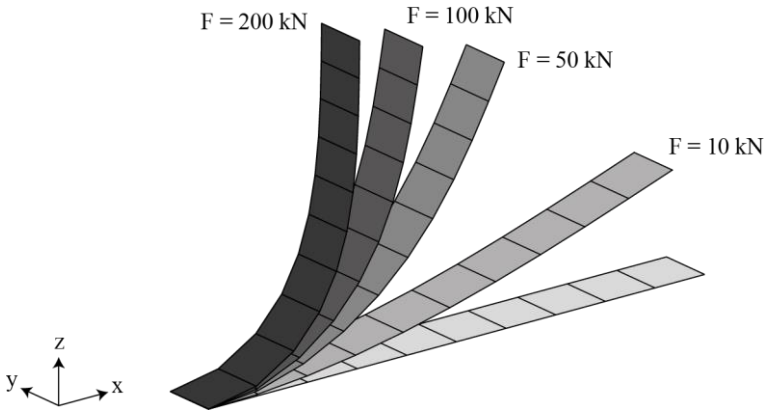


Figure 3 Deflected shapes of cantilever for different loads.

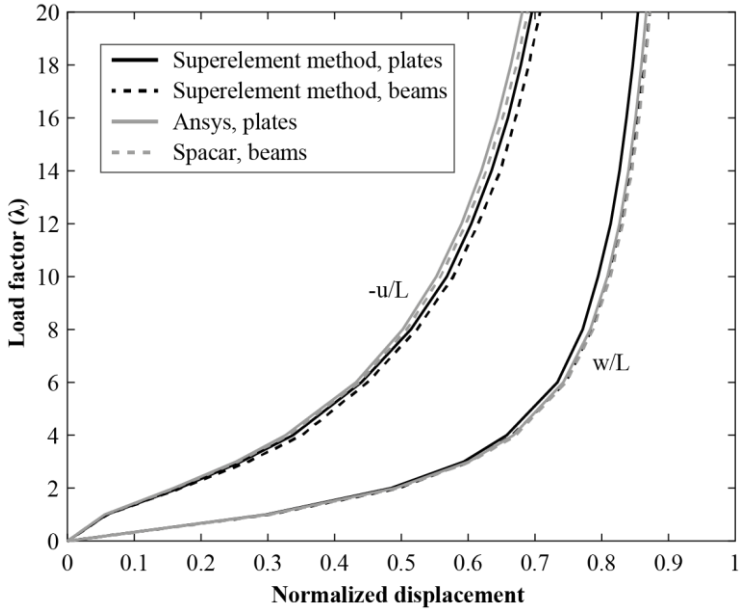


Figure 4 Response of cantilever to tip point loading.

3.2 Clamped square plate

In the second example, a square plate is modelled and loaded by a point load P. The plate has length and width $L = w = 400\,mm$ and thickness $t = 1.98\,mm$. Its Young's modulus is $E = 21.5\,GPa$ and its Poisson ratio is $\nu = 0.3$. The plate is clamped on two opposite edges. Figure 5 shows the plate (left) as well as shows the deflected shape (right). For clarity reasons, only half of the deflected plate is shown and displacements are scaled with a factor 10. A mesh of 10 x 10 elements is used. The point load is applied at node A (Figure 5) which lies on the center line, at the third node from the free edge. The z-displacement at this node, as well as at node B, is measured. As this problem cannot be modelled using beam elements, the results are compared with software package Ansys only.

Figure 6 shows the results for displacements in the order of the thickness of the plate (P = [0, 25] N). As can be seen, both methods correspond very well. For a point load of 25 N, the deviation is approximately 1 to 2%. If the load is increased up to 250 N, the deviation also slightly increases, with a maximum deviation of slightly over 3% for the displacement of node B. The results for the load range P = [0, 250] N are presented in Figure 7. Results for both load ranges are also in close agreement with the results from Izzuddin (Figures 10 and 11 from [10]).

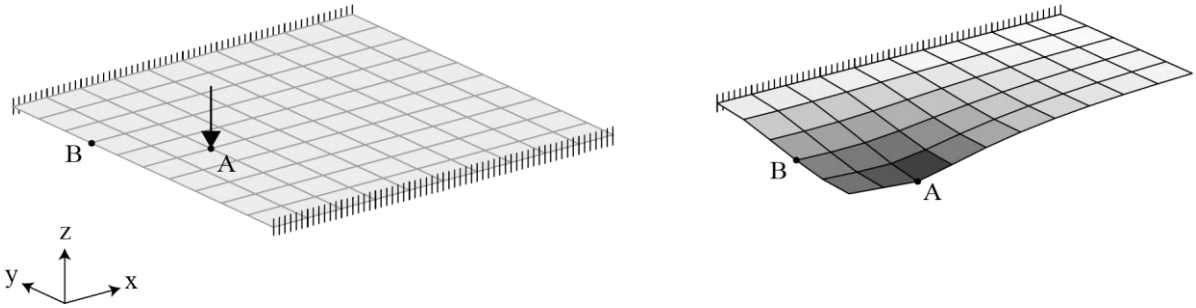


Figure 5 Clamped square plate (left) and deflected shape for P = 250 N (right, displacement scale = 10).

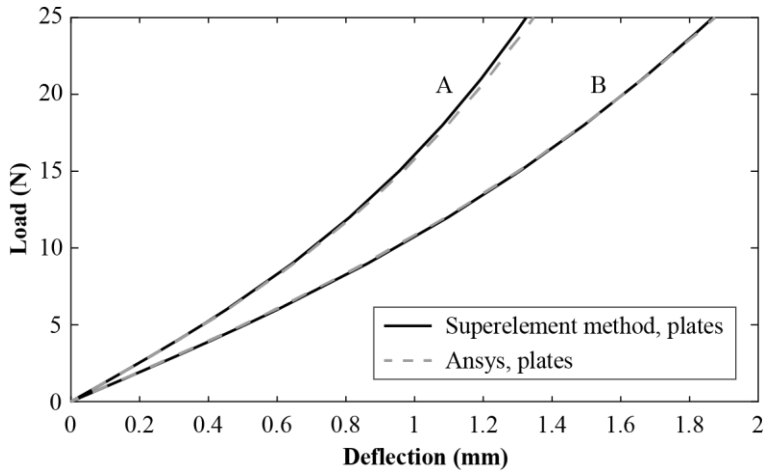


Figure 6 Response of nodes A and B on clamped square plate for P = [0, 25] N.

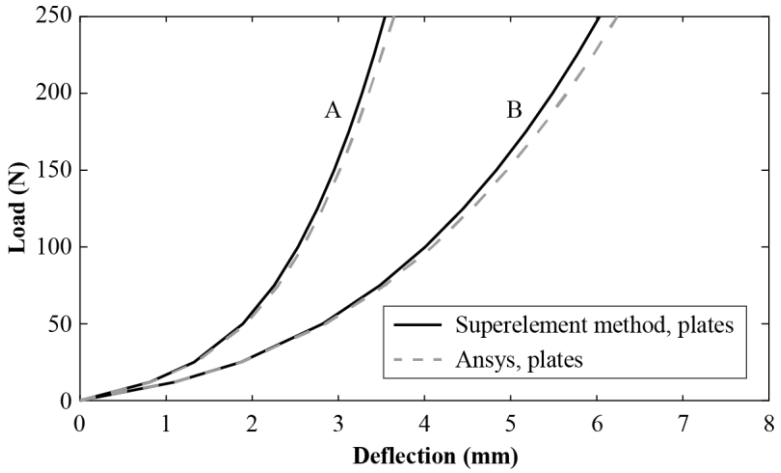


Figure 7 Response of nodes A and B on clamped square plate for P = [0, 250] N.

4 Discussion

Examples in Chapter 3 showed that the results from the superelement formulation for plates are in good agreement with the other formulations. This means that the method can successfully be used for the efficient description of plates in flexible multibody dynamics. However, some small deviations of around 1 to 3% still occur.

The small deviation is probably caused by the way the location of the floating frame is determined. It is known that the elastic displacements in the interface coordinates, multiplied by the Craig-Bampton mode shapes, should always equal zero at the location of the floating frame. However, a numerical error may cause this relation to be non-zero, and thus cause the floating frame to drift away. Therefore the location becomes slightly inaccurate after a while. This problem is expected be solved by determining the location of the floating frame using a Newton-Raphson procedure. The Newton-Raphson procedure should be applied on the multiplication of the elastic displacements in the interface coordinates and the Craig-Bampton mode shapes, which should finally equal zero. The position of the floating frame at the current time step can be used as an initial estimate. In future work, this Newton-Raphson procedure will be implemented.

As the method is successfully implemented for plates, the method offers a promising reduction method for flexure mechanisms. Flexures that can no longer be simplified as beam elements, because of their low aspect-ratio, can be modelled in an accurate way using superelements.

Acknowledgements

This research was funded by the Netherlands Organisation for Scientific Research (14665 NWO TTW) of the Ministry of Education, Culture and Science of the Netherlands.

References

[1] M.H.M. Ellenbroek, J.P. Schilder. *On the use of absolute interface coordinates in the floating frame of reference formulation for flexible multibody dynamics.* Multibody System Dynamics (2017). https://doi.org/10.1007/s11044-017-9606-3

[2] K. Gunnink, R.G.K.M. Aarts, D.M. Brouwer. *Performance optimization of large stroke flexure hinges for high stiffness and eigenfrequency,* in *Proceedings of the 28th Annual Meeting of the American Society for Precision Engineering (ASPE), 2013 October 20-25*, Saint Paul, Minnesota, USA: American Society for Precision Engineering.

[3] R. de Borst, M.A. Crisfield, J.J.C. Remmers, C.V. Verhoosel. *Non-Linear Finite Element Analysis of Solids and Structures, 2nd edn*, John Wiley & Sons, Ltd, New York (2012).

[4] C.C. Rankin, F.A. Brogan. *An Element Independent Corotational Procedure for the Treatment of Large Rotations.* J. Pressure Vessel Technol, Vol. 108, No. 2 (1986), pp. 165-174.

[5] M.A. Crisfield. *A consistent co-rotational formulation for non-linear, three-dimensional, beam elements.* Computer Methods in Applied Mechanics and Engineering, Vol. 81, Issue 2 (1990), pp. 131-150.

[6] A. Kaye, R.F.T. Stepto, W.J. Work, J.V. Alemán, A. Ya. Malkin. *Definition of terms relation to the non-ultimate mechanical properties of polymers.* Pure and Applied Chemistry, Vol. 70, Issue 3 (1998), pp 701-754.

[7] A.A. Nada, B.A. Hussein, S.M. Megahed, A.A. Shabana. *Use of the floating frame of reference formulation in large deformation analysis: experimental and numerical validation*. Proceedings of the Institution of Mechanical Engineers, Part K: Journal of Multi-body Dynamics, Vol. 224, Issue 1 (2010), pp. 45-58.

[8] R.R. Craig, M.C.C. Bampton. *Coupling of substructures for dynamic analysis,* AIAA Journal, Vol. 6, No. 7 (1968), pp. 1313-1319.

[9] M. Naves, D.M. Brouwer, R.G.K.M. Aarts. *Building block based spatial topology synthesis method for large stroke flexure hinges,* Journal of mechanisms and robotics, Vol 9, Issue 4 (2017), [041006].

[10] B.A. Izzuddin, *An enhanced co-rotational approach for large displacement analysis of plates.* International Journal for Numerical Methods in Engineering, Vol 64, Issue 10, John Wiley & Sons, Ltd (2005), pp. 1350-1374.

[11] J.B. Jonker, J.P. Meijaard. *A geometrically non-linear formulation of a three-dimensional beam element for solving large deflection multibody system problems,* International journal of non-linear mechanics, Vol. 53 (2013), pp. 63-74.

Topology optimization of a high-speed cutting mechanism

K. Asrih [1], **M.Vermaut** [1,2], **F. Naets** [1,2], **W. Desmet** [1,2]
[1] KU Leuven, Department of Mechanical Engineering,
Celestijnenlaan 300 B, B-3001, Heverlee, Belgium
e-mail: **karim.asrih@kuleuven.be**

[2] DMMS Lab, Flanders Make, Belgium

Abstract

Topology optimization is used to find the optimized components of a flexible mechanism. Over the past decades topology optimization has gained large interest in structural design since it allows fast development of optimized complex geometries. In this work we exploit the Flexible Natural Coordinate Formulation (FNCF) to describe the flexible multibody dynamics. This formulation is used due to its simple description of the dynamic equations of motion (linear equations of motion with quadratic constraint equations) which limits the computational load and thus allows a fast evaluation of the dynamic multibody simulation. Finally we discuss the results of a numerical validation. In particular we look at a design problem which concerns the tip deflection of a high-speed cutting mechanism. This application is particularly interesting since the flexibility of the whole system is considered in order to find the component with the lowest rotational inertia whilst minimizing the tip deflection with respect to the prescribed motion.

1 Introduction

Over the past decades structural topology optimization has gained large interest in structural design as it enables fast development of optimized complex geometries. These designs will often lead to superior properties compared to classical human designs [1, 2, 3].

Although topology optimization was originally developed for optimizing single components rather than full mechanical system assemblies, several methods have been proposed in literature to account for the dynamic behavior of multibody systems[4, 5, 6]. Most notably Kang proposed the method of Equivalent Static Loads (ESL)[7], which remains the standard method for these applications.

The ESL approach transforms the dynamic loads obtained from a multibody simulation into a static optimization problem consisting of multiple critical load cases for a single body. In this weakly coupled approach the optimizer does not explicitly take the multibody interaction into account, but only re-evaluates the component loads from the multibody model after a full topology optimization run on the statically loaded component.

This decoupling is convenient as it enables the exploitation of off-the-shelf multibody software and structural topology optimizers, but also has several drawbacks: the ESL approach for example makes it particularly challenging to introduce constraints directly based on the dynamic response of the component.

In this work we therefore propose a fully-coupled approach for component topology optimization in a flexible multibody system (MBS). In this approach, a full flexible multibody simulation is performed for each topology iteration. The design goal and constraints are then evaluated on the body response directly from this MBS simulation. This resolves the issue of imposing artificial constraints to the body to eliminate the rigid body motion as required for ESL based approaches [4].

The computation of the response derivatives with respect to the topology parameters, as required for the optimization iterations, is enabled through the use of a recently proposed flexible multibody formulation,

namely the *flexible natural coordinate formulation* (FNCF) [8, 9].

The overall topology optimization scheme is discussed in Sec. 2 and the application on the high-speed cutting mechanism is discussed in Sec. 3.

2 Optimization Framework

This work focuses on the geometric optimization of the components of mechanisms for industrial mechatronic applications. For these applications the flexible deformation is typically assumed to be small in comparison with the rigid motion of the components. However they can have an important impact on the functional behaviour and operational lifetime of the machine.

These deformations are assumed to be sufficiently small in this work such that a small-deformation flexible multibody model can be used, rather than a fully geometricall nonlinear finite element model. The latter would lead to unacceptable computational loads for system level optimization for most practical applications.

This section presents an approach for structural topology optimization based on flexible multibody responses. First the overall scheme is discussed in Sec. 2.1, the specific FMBS approach used is briefly summarized in Sec. 2.3 and the optimizer is discussed in Sec. 2.4.

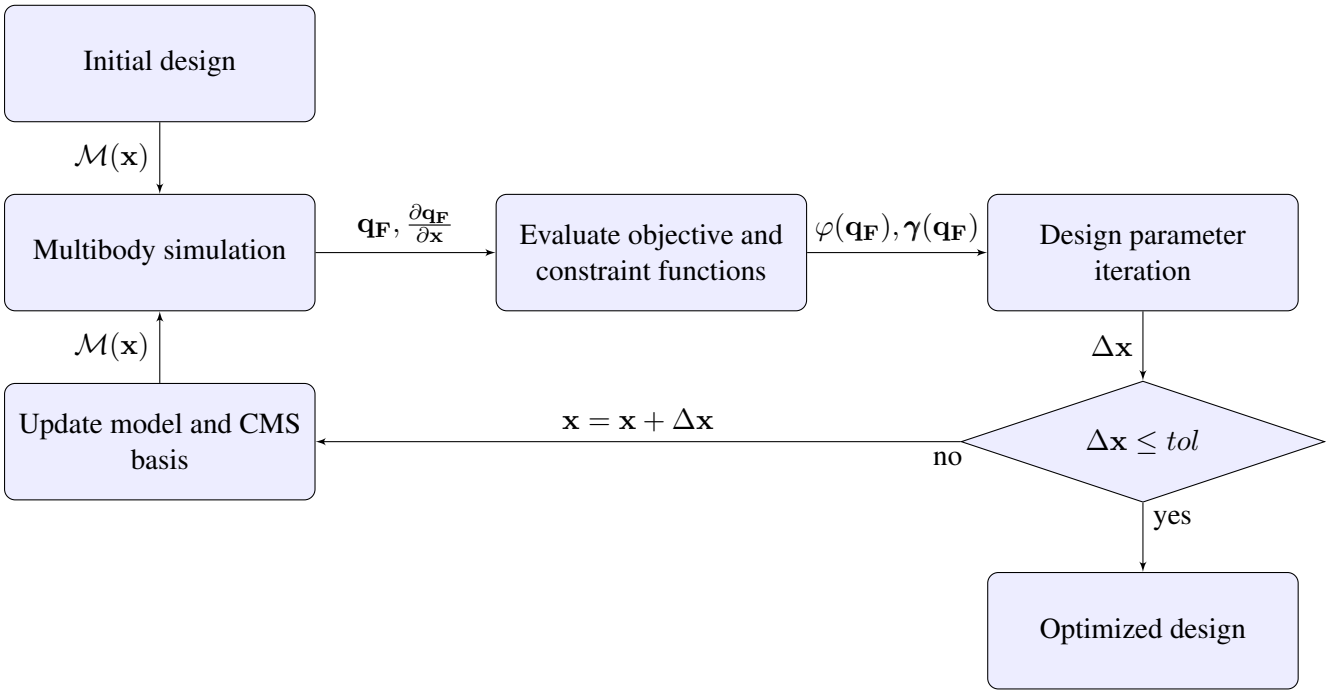


Fig. 1: Schematic of multibody based component structural topology optimization

2.1 Fully-coupled topology optimization

The overall scheme for the structural topology of a component in a flexible multibody system proposed in this work, is summarized in Fig. 1. The initial design paremeters, gathered in $\mathbf{x} \in \mathbb{R}^{1\times n_e}$, represent the available design space for the novel component, bounded by the physical space available in the machine. These parameters are connected to the *density* of the elements in a Finite Element (FE) discretization of the design space [1]. With these parameters and component FE model, there is an associated multibody model $\mathcal{M}(\mathbf{x})$ which is simulated to evaluate the system and body response $\mathbf{q}$. The topology parameterized body description and associated FMBS model are discussed in Sec. 2.2-2.3.

The corresponding flexible response $\mathbf{q_F}$ is then used for evaluating the design objective $\varphi(\mathbf{q_F}, \mathbf{x})$ and design constraints $\boldsymbol{\gamma}(\mathbf{q_F}, \mathbf{x})$. Next the topology design update $\Delta\mathbf{x}$ is computed and the convergence is evaluated on the magnitude of this update (the optimizer stops if this update is smaller than a prescribed tolerance tol). The optimizer and constraints are discussed in Sec. 2.4.

2.2 Topology parameterized flexible body description

For small deformation problems, as discussed here, the global finite element (lumped) mass $\mathbf{M_{FE}}$ and stiffness $\mathbf{K_{FE}}$ matrices can be described as a function of the *density* parameter x_i for element i:

$$\mathbf{M_{FE}} = \sum_{i=1}^{n_e} \mathbf{M^0_{FE,i}} g(x_i), \tag{1}$$

$$\mathbf{K_{FE}} = \sum_{i=1}^{n_e} \mathbf{K^0_{FE,i}} g(x_i). \tag{2}$$

Here $\mathbf{M^0_{FE,i}}$ and $\mathbf{K^0_{FE,i}}$ represent the contribution to the full body mass and stiffness matrix from element i for the full design domain finite element discretization and $g(x)$ is a scalar function to describe the dependency on the density parameter. The parameter x_i then indicates how much each element contributes to the optimized model. Essentially the design variable indicates whether the domain represented by the finite element should be filled with material or be void. To obtain a practical solution the final values for the design parameters should be as close as possible to either 1 or 0.

A fundamental issue when including a finite element model in a multibody model is the large model size. The small deformation assumption partially eliminates this issue as it allows the use of linear model order reduction (MOR) techniques. In this work, we exploit the well-known Component Mode Synthesis technique [10] to approximate the local displacement field of the FE model $\mathbf{u} \in \mathbb{R}^{n_{DOF}}$ by projecting an appropriate set of n_m assumed modes gathered in $\boldsymbol{\Psi} \in \mathbb{R}^{n_{DOF} \times n_m}$ such that

$$\mathbf{u} \cong \mathbf{u_0} + \boldsymbol{\Psi}\mathbf{q_F} \tag{3}$$

where $n_m \ll n_{DOF}$. Due to the MOR-approach the computational cost of the MBS simulation is not affected by the number of elements but rather by the amount of assumed modes. This reduction basis $\boldsymbol{\Psi}$ is computed from the body mass and stiffness matrices and is therefore also a function of the topology parameters $\mathbf{x}$. It is important to highlight that this implies that the reduction basis needs to be recomputed for every topology parameter update, which can also lead to considerable computational loads for large scale problems.

The original nodal mesh positions $\mathbf{u_0}$, reduction basis $\boldsymbol{\Psi}$, mass and stiffness matrices are the body information which is passed to set up the multibody model, as discussed in the next section.

2.3 Flexible Natural Coordinate formulation for system and body dynamics

To model the flexible multibody dynamics, we exploit the Flexible Natural Coordinate Formulation (FNCF) as originally suggested by Vermaut [8]. This FNCF approach allows a fast and easy evaluation of the dynamic multibody simulation which is important due to the iterative nature of optimization routines. The formulation is based on a small deformation assumption. A particularly desirable property of this approach is the simple structure of the resulting equations of motion: the dynamic balance equations reduce to a set of (bi)linear equations and the constraint equations are a set of quadratic equations. Here, we briefly summarize the linear structure of the dynamic balance in the equations of motion. For the full derivation of the formulation we refer the reader to Vermaut *et al.* [8].

The generalized multibody coordinates $\mathbf{q}$ are

$$\mathbf{q} = \begin{bmatrix} \mathbf{q_P} \\ \mathbf{q_R} \\ \mathbf{q_G} \\ \mathbf{q_F} \end{bmatrix}, \tag{4}$$

which holds a set of displacement $\mathbf{q_P}$ and redundant orientation $\mathbf{q_R}$ coordinates for each body followed by a set of redundant modal participation factors expressed in the inertial $\mathbf{q_G}$ and body attached $\mathbf{q_F}$ reference frame. It is important to note that a set of intra-body constraints are necessary due to the redundant flexible description:

$$\mathbf{q_G} = \mathbf{q_F} \otimes \mathbf{q_R} \tag{5}$$

where $\otimes$ represented the Kronecker product.

The equations of motion are derived from the Lagrangian which yields

$$\mathcal{L}(\mathbf{q}, \dot{\mathbf{q}}, \boldsymbol{\lambda}) = E_{kin}(\mathbf{q}, \dot{\mathbf{q}}) - E_{ela}(\mathbf{q}) - \boldsymbol{\lambda}^T \boldsymbol{\phi}(\mathbf{q}) \tag{6}$$

where $\boldsymbol{\phi}$ holds a set of intra- and inter-body constraint equations accompanied by their Lagrangian multipliers $\boldsymbol{\lambda}$. The equation of motion are then obtained by applying Hamilton's principle to the Lagrangian:

$$\begin{cases} \frac{\mathrm{d}}{\mathrm{d}t}\left(\frac{\partial \mathcal{L}(\mathbf{q},\dot{\mathbf{q}},\boldsymbol{\lambda})}{\partial \dot{\mathbf{q}}}\right) - \frac{\partial \mathcal{L}(\mathbf{q},\dot{\mathbf{q}},\boldsymbol{\lambda})}{\partial \mathbf{q}} = 0 \\ -\frac{\partial \mathcal{L}(\mathbf{q},\dot{\mathbf{q}},\boldsymbol{\lambda})}{\partial \boldsymbol{\lambda}} = 0 \end{cases} \tag{7}$$

This leads to the following set of equations of motion in the generalized coordinates $\mathbf{q}$:

$$\begin{cases} \mathbf{M}_{qq}(\ddot{\mathbf{q}}) + \mathbf{K}_{qq}(\mathbf{q}) + \frac{\partial \boldsymbol{\phi}^T}{\partial q}\boldsymbol{\lambda} = \mathbf{f}_{ext}(\mathbf{q}, \dot{\mathbf{q}}, t) \\ \boldsymbol{\phi}(\mathbf{q}) = 0 \end{cases} \tag{8}$$

where an optional external force term ($\mathbf{f}_{ext}$) has been included.

For the FNCF description, in contrast to the classical floating-frame-of-reference (FFR) approach, the generalized mass matrix is configuration independent and has the following structure for a given body with nodal mesh coordinates $\mathbf{u_0}$ and reduction basis $\boldsymbol{\Psi}$:

$$\mathbf{M}_{qq} = \begin{bmatrix} \begin{bmatrix} \sum_{i=1}^{N} m_i & \bar{u}_0\vec{m} & \bar{\Psi}\vec{m} \\ & \bar{u}_0\tilde{M}\bar{u}_0^T & \bar{\Psi}\tilde{M}\bar{u}_0^T \\ symm & & \bar{\Psi}\tilde{M}\bar{\Psi}^T \end{bmatrix} \otimes I_3 & 0_{(12+9n_m)\times n_m} \\ 0_{n_m\times(12+9n_m)} & 0_{n_m\times n_m} \end{bmatrix} \tag{9}$$

where $\tilde{M}$ is the lumped diagonal mass matrix for the FE body, $\vec{m}$ is a vector containing all the lumped mass values of the finite element model, m_i is the i-th lumped mass contribution. The operator $\bar{\cdot}$ represent the split of a vector along the nine components of a rotation matrix for obtaining the global contribution of local components under any rotation [11, 8]. It is important to note that a mass matrix consisting of only uncoupled translational components is invariant for rotation, as has been discussed by Gerstmayr & Ambrosio [11]. The resulting mass matrix for the FNCF approach is therefore also constant.

Under the proposed FNCF approach, the generalized body stiffness matrix becomes:

$$\mathbf{K}_{qq} = \begin{bmatrix} 0_{(12+9n_m)\times n_m} \\ \Psi^T \end{bmatrix} K_{FE} \begin{bmatrix} 0_{n_m\times(12+9n_m)} & \Psi \end{bmatrix} \tag{10}$$

Note from the brief discussion of FNCF that the method has both a constant mass and stiffness matrix at the cost of a larger set of generalized coordinates in comparison to the FFR approach. Furthermore if viscous damping, such as Rayleigh or modal damping, is assumed the resulting damping matrix will also be constant. This structure contributes to the computational efficiency of the FNCF methodology and makes it particularly easy to obtain derivatives with respect to the topology design parameters.

2.4 Optimization scheme

Starting from the FNCF multibody formulation presented above, the general topology optimization problem for the *density* parameters $\mathbf{x}$ of a body can be summarized as:

$$\begin{aligned} &\min_{\mathbf{x}} \quad \varphi(\mathbf{x}) \\ &\text{s.t.} \quad \begin{cases} \mathbf{M_{qq}}\ddot{\mathbf{q}} + \mathbf{K_{qq}}\mathbf{q} + \frac{\partial \boldsymbol{\phi}^T}{\partial \mathbf{q}}\boldsymbol{\lambda} - \mathbf{f}_{ext} = \mathbf{0} \\ \boldsymbol{\phi}(\mathbf{q}) = \mathbf{0} \\ x_{min} \leq x_i \leq x_{max}, \; i = 1, \ldots, n_e \\ \gamma_j(x) \leq \gamma_{jmax}, \quad j = 1, \ldots, n_{con} \end{cases} \end{aligned} \tag{11}$$

where n_e is the number of design variables and n_{con} is the number of optimization constraints. The first two constraint equations account for the dynamic behavior of the multibody system. The third constraint equation represents the bounds for the i-th density variable x_i and the last set of constraint equations can include general design constraints like the maximum deviation of a prescribed trajectory, a maximum value for Von-Misses stresses or many other limitations.

For this topology optimization approach with *density* parameters, the problem is essentially a binary programming problem: the design variables should either be 0 or 1 indicating that the domain represented by the element is a void or solid material. In order to avoid expensive combinatorial searches, the binary problem is relaxed in the sense that intermediate values are allowed during optimization. However, in order to prevent physically unsensible designs, the parameters are penalized such that when convergence is reached a close to *black-and-white design* is obtained.

To asses the convergence of the proposed design we use the so called *grayness* value G [12, 5]. This is a scalar value indicating the discreteness of the design. If G equals 1 this indicates a fully gray design meaning that all elements i have $x_i = 0.5$. On the other hand if $G = 0$, it indicates a fully black-and-white design, meaning that all elements have either $x = 0$ or $x = 1$. Hence near-zero values of G are an indication of a converged design:

$$G(x) = \frac{4}{n_e} \sum_{i=1}^{n_e} x_i(1 - x_i) \tag{12}$$

In this work, we utilize the solid isotropic material with penalization method (SIMP) as suggested by Sigmund to penalize the intermediate density values in order to obtain a near black-and-white solution [1]. With the SIMP approach the material properties can expressed as:

$$E_i(x) = x_i^p E_0 \tag{13}$$

where E_0 is the Young's Modulus of the isotropic material and $p \leq 1$ is the penalization power. If the penalization factor is larger then 1, the intermediate design variables are penalized. The full body stiffness matrix can then be found from:

$$\mathbf{K}_{FE}(x) = \sum_{i=1}^{n_e} x_i^p \mathbf{K}_{FE,i}^0, \tag{14}$$

where $\mathbf{K}_{FE,i}^0$ is the initial element stiffness matrix assembled with E_0, and which fits the framework presented in Sec. 2.2.

Several optimization routines can be used to solve equation (11). Both heuristic schemes and numerical programming methods are readily available from literature. Examples include: ConLin [13], GCM [14], Sequential Quadratic Programming (SQP) [15], Surrogate Based Optimization (SBO) [16] and Method of Moving Asymptotes (MMA) [17]. The selection of a suitable optimizer depends on the characteristics of the problem and the available information e.g. existence of gradient.

3 Numerical example

This work focuses on a reduction on the tip deflection of a high-speed cutting mechanism. The mechanism is depicted in Fig. 2. Whilst no problems occur at lower operational speeds an increased tip deflection is noticeable at higher speeds resulting in increased wear of the cutting blades and reduced cutting performance. To remedy this, the current design was revisited and optimized. The optimization was done in two phases: firstly the trajectory is optimized by improving the cam-profile. However due to the required tip-motion, which is needed for the cutting process, and several geometric constraints on the system due to a lack of physical space on the machine, the tip-motion still shows undesired vibrational behaviour even after the optimization of the cam profile. The next step involves the optimization of the geometry of the cutting arm in order to minimize the tip deflection as well as the rotational inertia of the arm. The geometric optimization is realized by means op toplogy optimization using an in house developed code. The framework used to perform the optimization was discussed in Sec. 2.1.

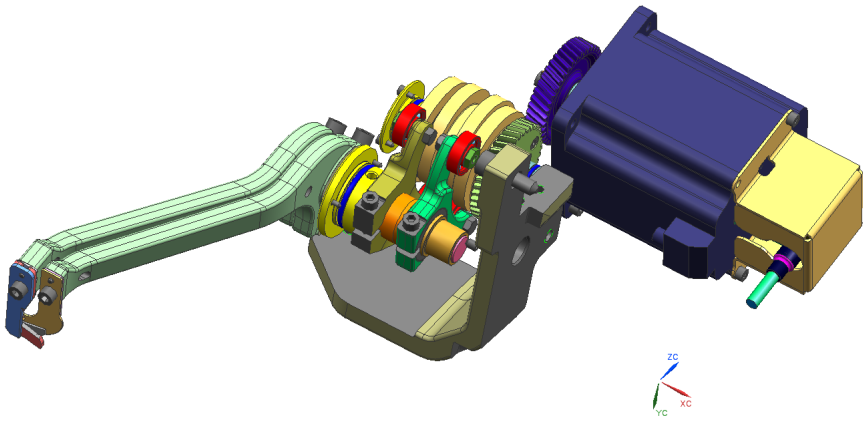


Fig. 2: Inital design of the cutting-mechanism

The component discussed in this example was discretized with 120000 higher order tetrahedral elements, the mesh is shown in Fig. 3, resulting in the same number of design variables for the optimization. Note that this type of mesh is not ideal for topology optimization. Hexahedral elements are preferred since they are more efficient space fillers with a lower computational cost: to fill 1 hexahedron one needs 5 to 7 terahedrons. Unfortunaly meshing complex shapes with hexhedral elements is not supported by most commercial meshers.

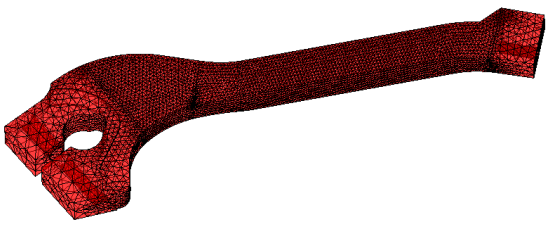


Fig. 3: Initial design space meshed with quadratic tetraherdal elements.

The trajectory of the tip should follow the newly optimized cam motion as close as possible to obtain the best cutting performance. Indeed in the ideal case of rigid body motion of the mechanism no undesired wear

of the cutting blades occur. It is due to the flexible motion of the mechanism that the cutting blades may collide and/or being exposed to additional and undesired slip. Consequently the lifetime can be improved by minimizing the flexible deformation of the mechanism. In this work the objective functions is formulated as a minimization of the strain energy of the system. Since rigid body motion can be seen as the optimal case where no flexible deformation occurs and hence no strain energy is present. The objective function described in (11) takes the form of

$$\varphi(\mathbf{x}) = \mathbf{q}_F^T \mathbf{\Psi}^T \mathbf{K}_{FE}(\mathbf{x}) \mathbf{\Psi} \mathbf{q}_F \tag{15}$$

As shown in Fig. 4 the optimization requires less than 20 iterations to converge and a few additional iterations were used to improve the grayness as discussed in Sec. 2.4.

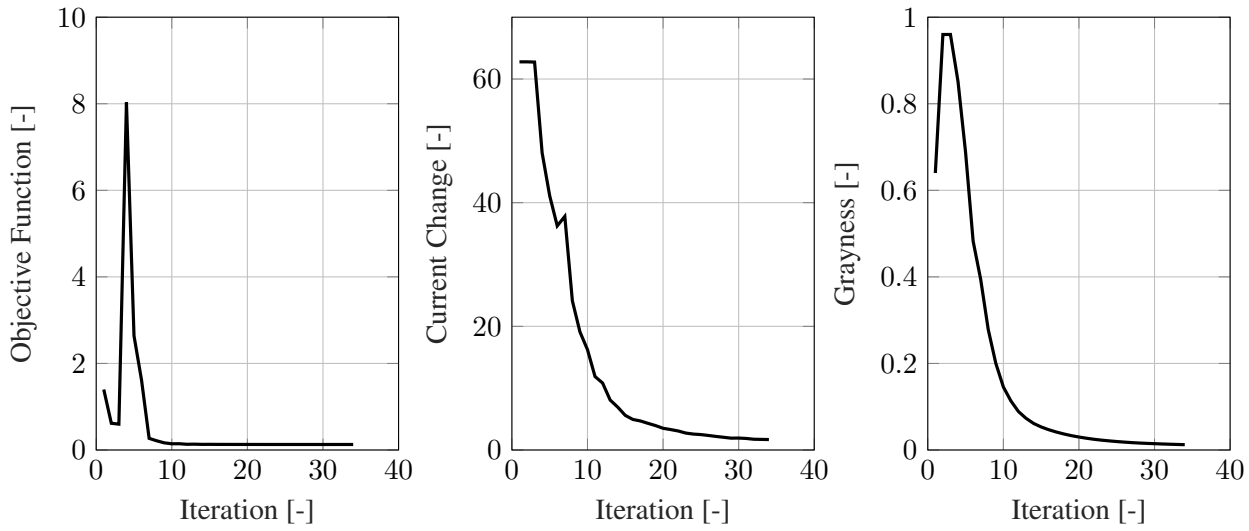


Fig. 4: Convergence history

4 Conclusions

This work investigated the use of topology optimization to reduce undesired deviation from a trajectory and simultaneously reducing the inertia of the component. The proposed methodology has been successfully applied to the mechanism, presented in Sec. 3, where the maximum Y deflection is reduced with 49,5% and the Z deflection is reduced by 71%. The components of the resulting tip motion can be seen in Fig. 5. The rotational inertia of the optimized component is 46% lower than the original structure whilst showing better performance for the presented case study. Moreover due to the reduced inertia, the driving torque also decreases. Since the cam and the followers were kept fixed during the topology optimization the pressure angles did not change and consequently the reduced forces between the cam and follower result in a longer lifetime of the mechanism. Whilst the resulting component is structurally feasible, it is not straightforward to manufacture it using classical manufacturing tools. Further work will focus on a comparison between the minimization of the compliance of the structure and placing a constraint on deviation of the trajectory.

Acknowledgements

The research of K. Asrih is funded by a grant from the Flanders Innovation & Entrepreneurship Agency. The research of F. Naets is funded by a grant from the Research Foundation - Flanders (FWO).

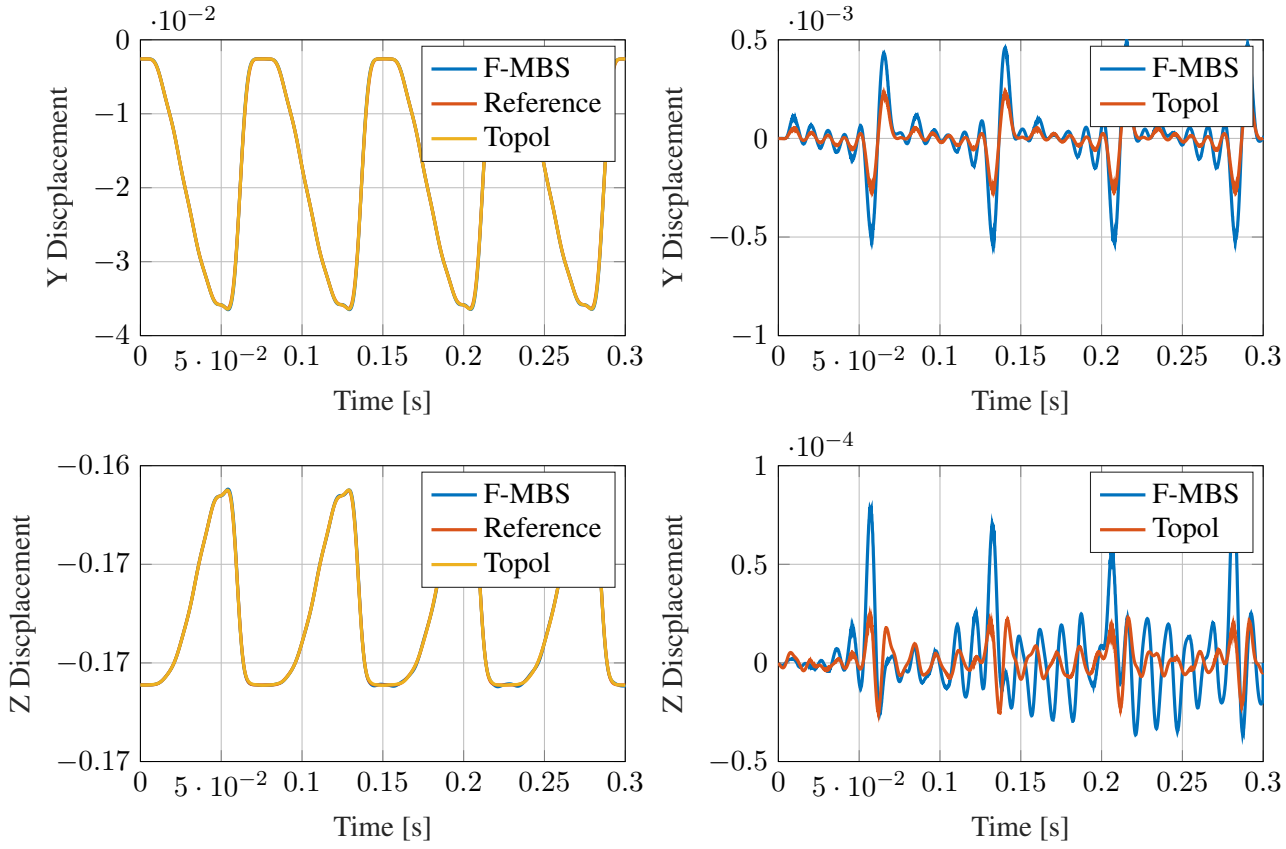


Fig. 5: Comparison of the tip trajectory

References

[1] M. P. Bendsøe and O. Sigmund, *Topology optimization by distribution of isotropic material*. Springer, 2004.

[2] E. Tromme, A. Held, P. Duysinx, and O. Brüls, "System-based approaches for structural optimization of flexible mechanisms," *Archives of Computational Methods in Engineering*, pp. 1–28, 2017.

[3] O. Brüls, E. Lemaire, P. Duysinx, and P. Eberhard, "Optimization of multibody systems and their structural components," in *Multibody Dynamics*, pp. 49–68, Springer, 2011.

[4] E. Tromme, V. Sonneville, J. K. Guest, and O. Brüls, "System-wise equivalent static loads for the design of flexible mechanisms," *Computer Methods in Applied Mechanics and Engineering*, vol. 329, pp. 312–331, 2018.

[5] A. Moghadasi, A. Held, and R. Seifried, "Topology optimization of members of flexible multibody systems under dominant inertia loading," *Multibody System Dynamics*, vol. 42, no. 4, pp. 431–446, 2018.

[6] K. Asrih, F. Cosco, F. Naets, and W. Desmet, "Multibody based topology optimization including manufacturing constraints," in *The Fifth Joint International Conference on Multibody System Dynamics - IMSD 2018, Técnico Lisboa, Lisboa, Portugal*, 2018.

[7] B. Kang, W. Choi, and G. Park, "Structural optimization under equivalent static loads transformed from dynamic loads based on displacement," *Computers & Structures*, vol. 79, no. 2, pp. 145–154, 2001.

[8] M. Vermaut, F. Naets, and W. Desmet, "A flexible natural coordinates formulation (fncf) for the efficient simulation of small-deformation multibody systems," *International Journal for Numerical Methods in Engineering*, 2018.

[9] S. Vanpaemel, M. Vermaut, F. Naets, and W. Desmet, "A system-level bushing joint parameter identification approach using flexible multibody models," in *The Fifth Joint International Conference on Multibody System Dynamics - IMSD 2018, Técnico Lisboa, Lisboa, Portugal*, 2018.

[10] R. R. Craig Jr, "A review of time-domain and frequency-domain component mode synthesis method," 1985.

[11] J. Gerstmayr and J. A. C. Ambrosio, "Component mode synthesis with constant mass and stiffness matrices applied to flexible multibody systems," *International journal for numerical methods in engineering*, vol. 73, pp. 1518–1546, 2008.

[12] O. Sigmund, "Morphology-based black and white filters for topology optimization," *Structural and Multidisciplinary Optimization*, vol. 33, no. 4-5, pp. 401–424, 2007.

[13] C. Fleury, "Conlin: an efficient dual optimizer based on convex approximation concepts," *Structural optimization*, vol. 1, no. 2, pp. 81–89, 1989.

[14] M. Bruyneel, P. Duysinx, and C. Fleury, "A family of mma approximations for structural optimization," *Structural and Multidisciplinary Optimization*, vol. 24, no. 4, pp. 263–276, 2002.

[15] K. Schittkowski, "Nlpql: A fortran subroutine solving constrained nonlinear programming problems," *Annals of operations research*, vol. 5, no. 2, pp. 485–500, 1986.

[16] B. Colson, M. Bruyneel, S. Grihon, C. Raick, and A. Remouchamps, "Optimization methods for advanced design of aircraft panels: a comparison," *Optimization and Engineering*, vol. 11, no. 4, pp. 583–596, 2010.

[17] K. Svanberg, "The method of moving asymptotesa new method for structural optimization," *International journal for numerical methods in engineering*, vol. 24, no. 2, pp. 359–373, 1987.

Modal behavior and transient dynamic analysis of a planetary gear train with time-varying mesh stiffness using a multibody model

C. Alessio [1], **D. Park** [2,*], **D. Mundo** [1], **T. Tamarozzi** [2], **A. Rezayat** [2]
[1] University of Calabria, Department of Mechanical, Energy and Management Engineering, Via Bucci, Cubo 46C, 87036 Rende, Italy

[2] Siemens Industry Software NV,
Interleuvenlaan 68, B-3001 Leuven, Belgium
e-mail: **daehyun.park@siemens.com**

Abstract
An approach to estimate the natural modes and dynamic responses of a planetary gear train with spur gears is proposed by using a general purpose multibody simulation tool with a gear contact model that allowed to include time-varying mesh stiffness. The numerical model is two dimensional and takes into account the component motions in torsional and transverse directions. The modal behavior of the gear set was firstly investigated in terms of natural frequencies and mode shapes in a stationary condition. These natural modes were predicted and compared with experimental results available in the literature. Furthermore, a dynamic response in terms of dynamic transmission error at a spinning condition with in-phase or sequentially phase planetary configurations were carried out and concluded that the natural frequency range varies in gear mesh stiffness associated modes.

1 Introduction

Mechanical power transmissions that comprise planetary gears are widely used in many industrial applications, e.g., in the automotive and aerospace sectors due to the fact that component durability increases by load sharing from the multiple load paths with high levels of transmitted power within a confined design space. Moreover, a combination of the central members (sun, carrier, and ring) with planet gears enables to achieve various gear ratios in a single design. However, planetary gear trains may exhibit undesirable dynamic behavior resulting in high noise and vibration. It is due to the fact that complexity of the planetary gear train having multiple gear meshes is higher than the one of simpler counter-shaft gear drives. Therefore, a detailed understanding of the system parameters that influence the dynamic characteristics is crucial to solving various performance issues in dynamics.

A significant amount of dynamic analyses concerning the planetary gear systems are found in the literature in various aspects. Kahraman [1] described the natural modes of planetary gear trains and their sensitivity to the system parameters through a pure torsional model. Inalpolat and Kahraman [2] developed a torsional dynamic model to study single and double-planet or complex compound configurations. They [3] also developed a simplified mathematical model to investigate a planetary gear sideband with various planetary gear configurations. Subsequently, They [4] studied sideband phenomena in a planetary gear train from manufacturing errors by using a two dimensional nonlinear time-varying model they developed. A large part of the literature about the planetary gears was published by Parker whose works are the major references for this work, especially for the studies on the planetary gears dynamic modal behaviors. Lin and Parker [5] investigated modal energy distribution and analyzed the sensitivity of the planetary gear systems to the system

parameters such as tooth mesh stiffness and component inertia. The authors [6] also described the modes that are typical for a planetary gear system describing them in terms of kinetic energy distribution among the various components. Parker and Lin [7] reported formulae to determine the mesh phasing relationships to inspect the different dynamic behavior in different categories of the system configuration. Parker [8], and Parker and Ambarisha [9] analyzed the effects of the mesh phasing in the planet modes on planetary gear transmission error suppression. Regarding an experimental study for planetary gear systems, Ericson and Parker [10, 11] performed experimental modal analyses including planetary gear vibration measurement and compared with the results of the analytical model they developed. They are perhaps the first researchers conducting the planetary gear experimental modal analysis with an inclusion of the measurement of the planet gear modes by installing a set of linear accelerometers on the planet bodies. Their successive work [12] investigated load dependent system dynamics by an experimental study.

2 Experimental study in the literature

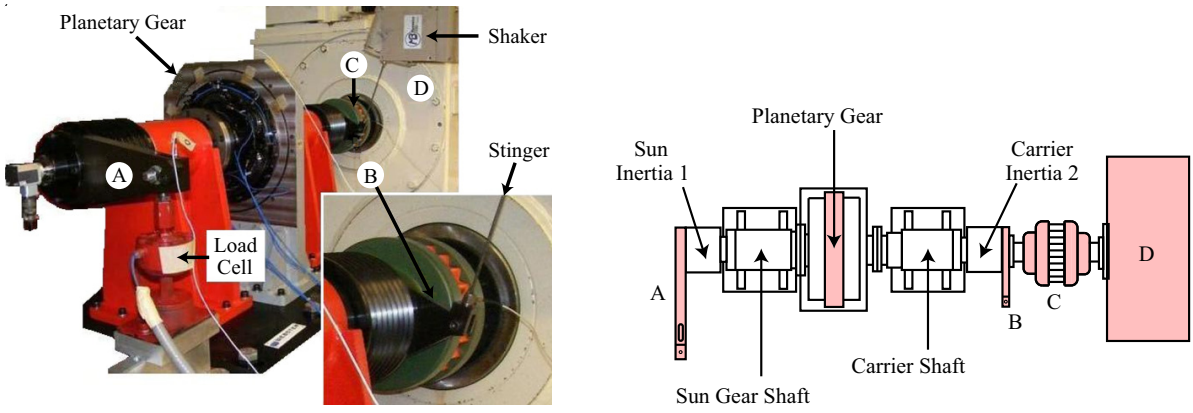
The experimental investigation by Ericson and Parker [10] of the planetary gear modal behavior includes low frequency fixture modes, where high strain and kinetic energy are concentrated in the central members (shaft, sun, carrier, ring) and high frequency gear modes, where high kinetic energy is focused on the gear tooth meshes and planet bearings. The test results explained throughout this section are all based on the work by Ericson and Parker [10].

2.1 Experimental setup

Ericson and Parker conducted a planetary gear system experimental modal analysis at stationary condition by applying both impact hammers and modal shaker in various directions depending on the mode of interest. The planetary gearbox originally used in industry has been modified to make the gear tooth stiffness more compliant resulting in the richer frequency spectrum to be measured.

2.1.1 Test rig

The test rig and its schematic are presented in Figure 1.



(a) Test rig

(b) Test rig schematic

Figure 1: Planetary gear train test rig [10]

All members marked in Figure 1 are described in the list below:

- A (radial arm): it fixes the sun gear shaft to a bedplate to measure the applied static torque from the actuator by the load cell connected to it.
- Sun inertia 1: it is a shaft having a relatively large inertia compared to the sun gear shaft to isolate the gear vibration, and connected to the arm A and sun gear shaft.
- Sun gear shaft: it is a shaft that supports the sun gear in the bearing block supported by spherical thrust roller bearings.
- Planetary gear: it comprises sun, ring, carrier and three planets, and the ring gear is bolted to a housing.
- Carrier shaft: it is a shaft that supports the carrier in the bearing block supported by spherical thrust roller bearings.
- Carrier inertia 2: similar to sun inertia 1, it is a shaft having a relatively large inertia compared to the carrier shaft to isolate the gear vibration, and connected to the arm B and carrier shaft.
- B (excitation arm): it is connected to the carrier shaft and excitation is applied to it by using an impact hammer or vibration shaker.
- C (coupling): it isolates the planetary gear from the torque actuator with a compliant torsional stiffness.
- D (torque actuator): it generates the torque as a preload to the system at a stationary condition.

2.1.2 Gear geometry

There were two planetary gear sets ("Gear set A" and "Gear set B") described in the work of Ericson and Parker [10] and "Gear set B" has been taken in this study as a benchmark system because it has been modified from "Gear set A" acquired from a production helicopter transmission to make the mesh stiffness more compliant by reducing facewidth and pressure angles to achieve the measurable frequency ranges of high frequency gear mode. This gear set comprises spur gears without profile modification but flank line modifications of 4 μm lead crowning in order to avoid edge contact conditions. The geometrical parameters of these gears are listed in Table 1.

Parameters	Sun gear	Planets gears	Ring gear
Number of teeth	65	55	175
Module (mm)	1.609	1.609	1.609
Tooth thickness (mm)	2	2	2
Facewidth (mm)	10	8	10
Pressure angle (deg)		15.97	
Center distance (mm)		96.52	
Base diameter (mm)	100.6	85.08	270.7
Root diameter (mm)	97.91	81.78	288.0
Tip diameter (mm)	107.8	91.69	278.9

Table 1: Gear basic dimensions

2.1.3 Modal testing

Ericson and Parker conducted experimental modal analysis with non-rotating gears: the rotational degree of freedom of the test rig is constrained by the load cell that is jointed to the sun inertia 1, and preload 150 Nm measured on the sun gear shaft is applied by the torque actuator. In these experiments, two different types

of force excitation methods were used by an impact hammer and modal shaker. The impact testing excites the system at a design point, i.e. the arm A (radial arm) or arms B (excitation arm) illustrated in Figure 1 to detect mainly rotational modes in a low frequency range with a plastic tip at the impact hammer. In addition, to detect the translation modes better, impacts to the sun gear, carrier and ring gear housing in the vertical and horizontal directions were applied. Lastly, the modal shaker was directly applied to a planet gear in the line of action direction of the gear mesh to effectively obtain the tooth stiffness associated high frequency modes.

2.2 Experimental results

Performing modal analysis experiments, Ericson and Parker [10, 11] have been able to fully define the modal behavior of the planetary gear system. The modes can be clearly distinguished into two frequency ranges, one below and one above 1500 Hz. Depending on the range that they belong to, the modes are defined as:

- Fixture modes:
  these are characterized by high kinetic energy in the central members, i.e. sun inertia 1 and carrier inertia 2, sun gear, carrier, and ring. The definition of "fixture modes" comes from the deflection concentrated in these fixture components, while the components of the planetary system move as a single rigid body. The frequency ranges of these modes are found at below 1500 Hz.
- Gear modes:
  these are characterized by high kinetic energy in the planets and planet bearings, all gear mode natural frequencies are detected as clusters that are exhibited as three groups, where each of radial, rotational and tangential direction of planet deflection is dominant at each of cluster. The gear modes are nine in total, grouped in clusters of three each. The frequency ranges of these modes are found at above 1500 Hz.

2.2.1 Low frequency fixture modes

Impulse testing results detected eleven natural frequencies of four rotational and seven translational modes. As compared with the results from their analytical model, one translational mode associated with the x translational deflection in sun inertia 1 was not excited well, therefore not reported. Since there are two translational modes at sun and carrier appearing as a degenerate pair (repeated natural frequency), it can be said that fourteen modes in total are explained.

It is noted that anisotropic bearing stiffnesses are associated with sun inertia 1 and carrier inertia 2 due to the fact that they are connected to the arm A and B respectively under the applied load or excitation on them. Therefore, instead of having repeated natural frequencies, the separate ones exhibiting the coupled modes of rotation and translation were examined. On the other hand, repeated natural frequencies in a translation direction on sun and carrier were examined due to the nature of isotropic bearing stiffnesses associated with these components. The 14 modes including repeated modes (mode 7 and 9) are illustrated in the literature [10] and summarized in Table 2.

2.2.2 High frequency gear modes

Gear modes in a high frequency range can be considered as the most important ones in practice because they can be excited by the gear tooth meshing harmonics and can be a major source of high noise or elevated bearing loads. These modes are mainly associated with planet gears, and the coupling of these modes with central members such as shafts, and fixtures are weak. It is noteworthy that planet bearings should be in condition to have anisotropic stiffness values under load resulting in higher stiffness in the tangential direction and lower one in the radial direction. This is caused by the fact that forces are applied in the line

Mode	Freq. (Hz)	Description
1	124	Trans. mode in x-dir. of inertia 2
2	140	Trans. mode in y-dir. of inertia 2
3	180	Rot. mode coupled with y-dir. of inertia 1
4	200	Trans. mode in x-dir. of inertia 1 (only detected by analytical model)
5	217	Trans. mode in x-dir. coupled with rot. of inertia 1
6	254	Rot. mode of inertia 1 and inertia 2
7	333	Trans. mode (in-phase) of sun and carrier (repeated)
8	404	Rot. mode (in-phase) of sun and carrier
9	582	Trans. mode (out-of-phase) of sun and carrier (repeated)
10	604	Rot. mode (out-of-phase) of sun and carrier
11	648	Trans. mode in x-dir. of ring
12	1465	Trans. mode in y-dir. of ring

Table 2: Fixture modes measured by an experiment

of action direction of each sun-planet and planet-ring mesh generating a higher reaction force in tangential directions. Therefore, special care needs to be taken when a numerical model is created for correlation related to gear modes. In addition, gear mesh stiffnesses in planet angular position, equally spaced three planets, are not identical due to the mesh stiffness at each contact are different due to the nature of the sequentially phased planet configuration in the mesh. In this sense, averaged mesh stiffness assumption made in the model may mislead the judgment of the result correlation. The nine gear modes (each translation modes has a multiplicity of two) are summarized in Table 3

Mode	Freq. (Hz)	Description
13	1420	Rot. mode of central members with planet deflection in radial dir.
14	1600	Trans. mode of central members with planet deflection in radial dir. (repeated)
15	2735	Rot. mode of central members with planet deflection in rotational dir.
16	2832	Trans. mode of central members with planet deflection in rotational dir. (repeated)
17	3380	Trans. mode of central members with planet deflection in tangential dir. (repeated)
18	3430	Rot. mode of central members with planet deflection in tangential dir.

Table 3: Gear modes measured by an experiment

3 Multibody modeling of a planetary gear system

In order to understand the dependency of the dynamic behavior of a planetary gear system on its geometrical characteristics, the use of a multibody model that combines gear contact analysis solver representing all structures, rotating elements and gear geometrical configuration is appropriate. The main objectives in this study are to validate the multibody simulation results against the experimental results in Section 2 and extend this multibody model to investigate the dynamic behavior in high frequency gear modes with respect to the different planetary gear configurations, i.e., in-phase or sequentially phase planets at stationary and spinning conditions. This multibody model relied on the test rig configurations with the degrees of freedom and the given geometrical parameters reported in the literature [10].

3.1 Multibody simulation tool for a transmission system

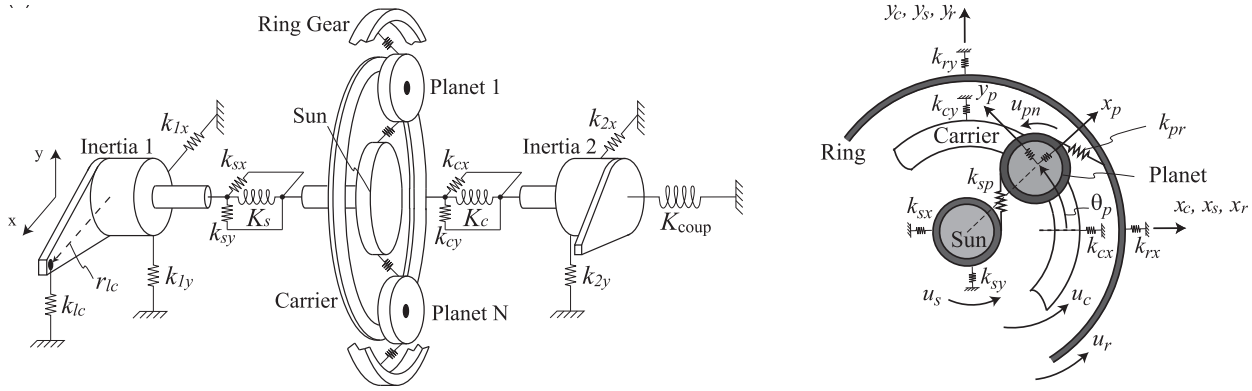
To create and solve a multibody model of an example planetary gear system, a general purpose commercial multibody software, “Simcenter 3D Motion” (hereafter, also called “Motion”) from Siemens Industry

Software NV was employed in conjunction with a gear train multibody model creation tool, "Transmission Builder" [13]. Transmission Builder is a vertical application to set up the multibody simulation model of the transmission enabling the workflow to be simplified reducing time when 3D CAD geometries and multibody elements are created. It creates the initial and boundary conditions such as component positions, orientations, gear mesh phases, rigid joints and bushing elements for flexible joints.

Furthermore, the multibody research team of Siemens Industry Software NV has put considerable effort in revisiting their gear contact numerical approach to drivetrain simulation. This gear contact solver architecture is designed to allow the user to perform a dynamic multibody simulation with different levels of fidelity with measured transmission error values or FE method for gear contact according to the required computation time and desired level of predictive capacity. Constant stiffness computation is implemented as per ISO 6336 [14] and time-varying mesh stiffness is computed with the combined method of ISO [14] and Cai [15]. FE method has a hybrid scheme combining nonlinear FE computation for tooth bending including gear body deflection with an analytical formula to compute local tooth contact deformation by using Herztian formula, which accelerates the computation speed without compromising the accuracy. The details of these individual methods were explained in the literature by Tamarozzi et al. [16]. This tool can also deal with microgeometry of a tooth profile and flank line to predict gear dynamics precisely.

3.2 Degrees of freedom for a multibody model

Regarding the test rig configuration and planetary gear system that are referenced to create the multibody model in this study, the literature [10] does not describe all detailed geometries for fixtures, shafts, and gears, but lists lumped parameter masses, moments of inertia, and stiffness values used in creating their analytical model. It is a two dimensional model including rotational and transverse DOFs by neglecting axial DOF, which is a feasible approximation in a sense that only spur gears, not generating axial reaction forces from the gear mesh, are used in the planetary gear system. The lumped parameter models for test rig and planetary gear are illustrated in Figure 2.



(a) Model for test rig

(b) Planetary gear model

Figure 2: Lumpled parameter models [10]

Each inertia and mass of the shafts connected to the sun gear shaft and carrier shaft is not taken into account because those values are minor compared with the inertia 1 and 2, whereas their bending and torsional stiffness values are included. Since experimental results did not show the rotational mode on the ring gear, the rotational degrees of freedom is not considered; however, translational degrees of freedom from the housing structure were considered. These corresponding values of the housing stiffness are calculated with FE software. The transverse stiffness values of sun and carrier bearings are experimentally obtained and the bearings of inertia 1 shaft and inertia 2 shaft are calculated with commercial software. The mesh stiffness values are firstly calculated with an FE based gear contact software evaluating different values of mesh stiffness for different steps during the mesh cycle and the average value are subsequently used. With these

assumptions, a lumped-parameter model comprises 23 degrees of freedom in total, i.e., transverse (x and y) and rotational (z) for inertia 1, inertia 2, sun, carrier, three planets, and transverse (x and y) for the ring. All parameters characterized by Ericson and Parker [10] are summarized in Table 4:

	Sun	Planet	Ring	Carrier
Mass (kg)	12.44	1.433	110.2	28.38
Moment of inertia (kg m^2)	64.04×10^{-3}	1.606×10^{-3}	–	398.7×10^{-3}
Bearing stiffness (N/m)	98.0×10^6	x: 146×10^6 y: 427×10^6	x: 1.72×10^9 y: 10.2×10^9	10.1×10^6
Mesh stiffness (N/m)	89.1×10^6		120×10^6	

(c) Experimental fixtures

	Inertia 1 (sun)	Inertia 2 (carrier)
Mass (kg)	29.72	36.49
Moment of Inertia (kg m^2)	259.9×10^{-3}	145.2×10^{-3}
Radius (m)	91.44×10^{-3}	
Bearing stiffness (N/m)	x: 46.3×10^6 y: 45.8×10^6	x: 22.2×10^6 y: 28.3×10^6
Load cell arm radius r_{lc} (m)	266.8×10^{-3}	
Load cell arm stiffness k_{lc} (N/m)	17.8×10^6	
Compliant coupling stiffness K_{coup} (N m/rad)	20.3×10^3	

Shaft stiffness	Torsional (N m/rad)	Flexural (N/m)	
Sun gear	316×10^3	x: 316×10^3	y: 423×10^3
Carrier	231×10^3	x: 392×10^3	y: 470×10^3

Table 4: Lumped system parameters [10]

3.3 Multibody modeling

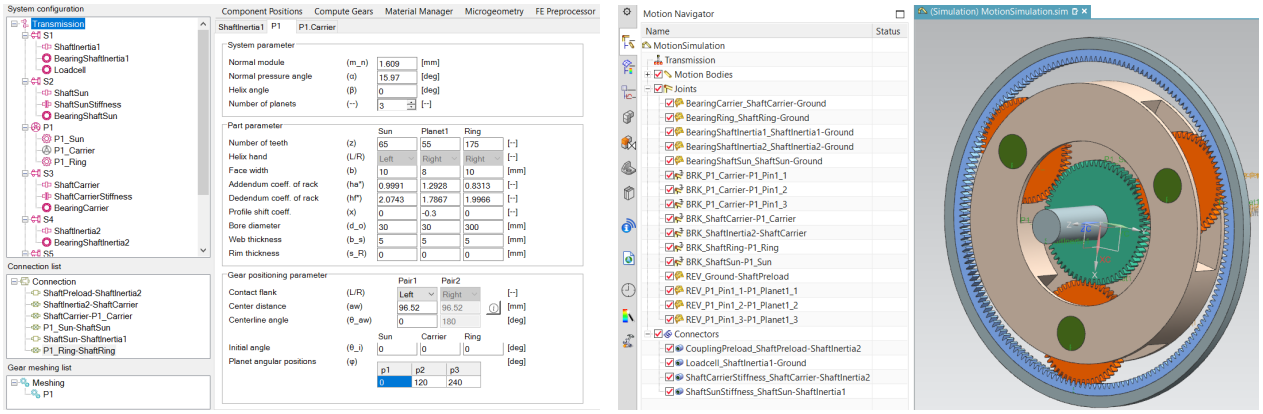
Each component of test rig is firstly required to be added in Transmission Builder as seen in Figure 3a, then connections between components are defined according to the schemes in Figure 2 followed by defining gear meshings as per the values listed in Table 1. To consider the gear geometry with accuracy, the geometry parameters such as profile shift coefficients, addendum and dedendum of the standard basic rack tooth profiles, which was not reported in Ericson's work has been calculated as per ISO 21771 [17] based on the reported value of contact ratio, 2.07 for all meshes informed in the literature [10]. A profile shift coefficient of -0.3 mm has been added in order to reach the contact ratio of 2.07. Afterwards, addendum h_{aP} and dedendum h_{fP} were calculated from the following equations [17]:

$$d_a = d + 2\frac{z}{|z|}(xm_n + h_{aP} + km_n) \tag{1}$$

$$d_f = d - 2\frac{z}{|z|}(h_{fP} - xm_n) \tag{2}$$

where d is the reference diameter, z the number of teeth, x the profile shift coefficient, m_n the normal module, h_{aP} the addendum of the standard basic rack tooth profile, and k the tip alteration coefficient which is assumed to be zero in these example gears.

Bearing and coupling definition set up at Transmission Builder create bushing elements to represent the corresponding degrees of freedom with stiffnesses and damping coefficients. For these component properties, Table 4 was referred with an assumption of damping coefficients. Figure 3b shows the multibody model created with Simcenter 3D Motion with the work flow mentioned above.



(a) Transmission Builder (b) Multibody model created in Simcenter 3D Motion

Figure 3: Multibody model creation software tools

Once multibody model is created in Motion, preload of 150 Nm was added to the arm A. Motion has a functionality to compute the eigenvalues and eigenvectors from the multibody model created by using a process, “linearization”, which enable all the nonlinear varying parameter in each step to be linearized that reduces the system to a set of first order linear equations, whose matrices are then used to obtain natural frequencies and modal matrix.

4 Result comparison

The modes falling into the two categories of low frequency fixture mode and high frequency gear mode are to be separately discussed in this section as modal behaviors are distinct at each mode.

4.1 Fixture mode results

All fixture modes observed in the results from Motion exhibit correspondence with experimental results. A comparison of Motion results against experimental ones in terms of natural frequencies is listed in Table 5.

Mode	Type	Exp. (Hz)	Motion (Hz)	Deviation (%)
1	Trans.	124	125	0.81
2	Trans.	140	141	0.71
3	Rot.	180	169	6.11
4	Trans.	-	193	
5	Trans.	217	199	8.29
6	Rot.	254	281	10.63
7	Trans.	333	299	10.21
8	Trans.	333	301	9.61
9	Rot.	404	416	2.97
10	Trans.	582	590	1.37
11	Trans.	582	648	11.34
12	Rot.	604	651	7.78
13	Trans.	648	692	6.79
14	Trans.	1465	1533	4.64

Table 5: Natural frequency comparisons in fixture modes (experiment vs. Motion)

As mentioned in Section 2.2.1, the fourth mode is not present in the experiment but at an analytical model due to the weak excitation of that mode, but it is also detected from the Motion model. Some modes are closely aligned with the experimental results, but also some are deviated up to 12%. It can be said that there are various reasons for this deviations. Since their analytical model is 2D lumped-parameter one (transverse and torsional DOFs) and component flexibility such as shafts, carrier, and fixtures are not modeled with finite elements. There would be some measurement errors when mass and inertia values were experimentally obtained.

Ericson and Parker [10] showed responses in the sun rotation, carrier rotation, planet rotation, and planet translation obtained from the experiment in a range below 700 Hz. In order to obtain a better match of the response peaks, it is necessary that the damping ratios for each mode from the Motion model would be aligned with the experimentally obtained values. The damping coefficients were iteratively attempted to be obtained for each degree of freedom of the system until a good match was reached. However, any complex approach for this estimation was not performed because the natural frequency correlations are of major interest in this study. Figure 4 shows the frequency response functions (FRFs) for the selective modes.

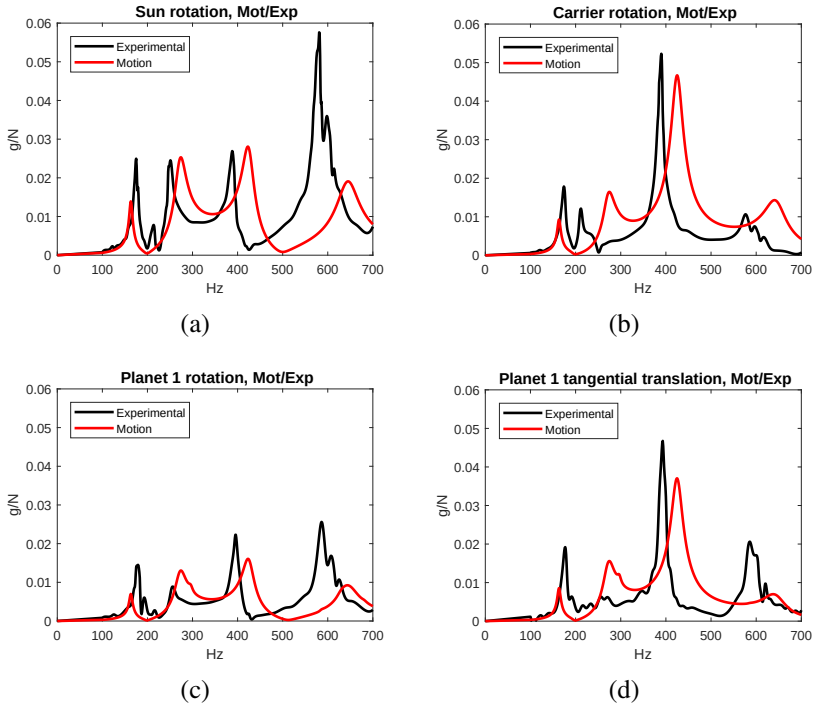


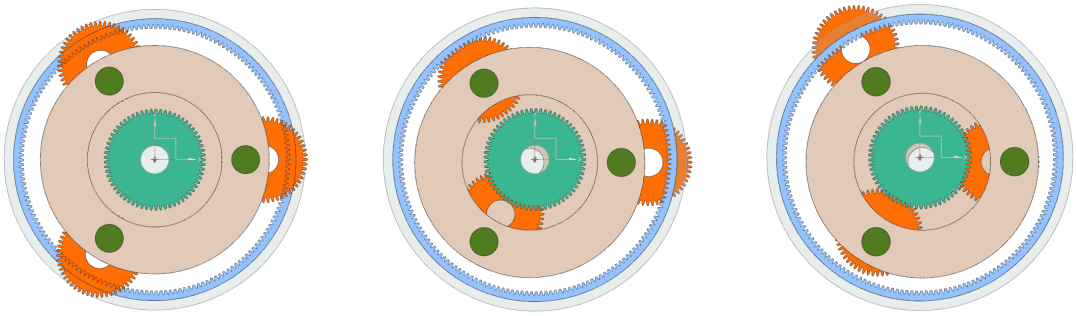
Figure 4: Response comparison of selective modes (experiment vs. Motion)

4.2 Gear mode results

In this gear mode, kinetic energies are concentrated in the planet gears, which leads planet radial, rotational and tangential mode at each of three clusters in order, and at the same time, rotational and translational modes of central members are exhibited. While planet deflections are distinguished for all clusters, the modes from central members are also detected as a single rotational and two translational modes. The rotational mode associated natural frequency is distinct while the translations of sun, carrier and ring are zero, and all the planets have identical deflections. The translational mode associated natural frequency has a multiplicity of two, especially in the case that mesh stiffnesses are identical to meshes with all planets, while the rotations of sun, carrier, and ring are zero.

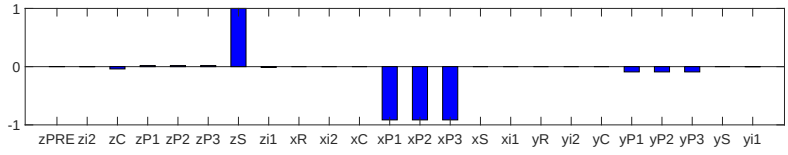
As an example, Figure 5 shows three modes in cluster 1 and Figure 6 shows the corresponding mode shapes associated with each natural mode in a 1st cluster, where radial modes (x dir.) of planets are predominated with mixture of a single rotational and two translational modes (y dir.) of central members. The acronyms

used on the x-axis of the plot in Figure 6 are as follows: i1 (inertia 1), i2 (inertia2), S(sun), P1 (planet 1), P2 (planet 2), P3 (planet 3), C (carrier), R (ring), PRE (preloading). They are used with the prefix indicating the direction vectors (x, y, z).

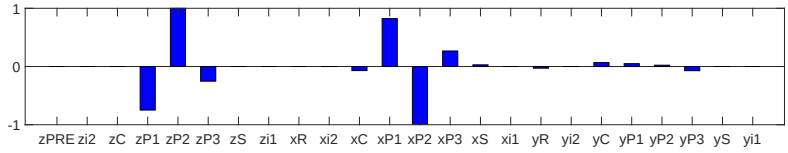


(a) Rotational mode (b) 1st translational mode (c) 2nd translational mode

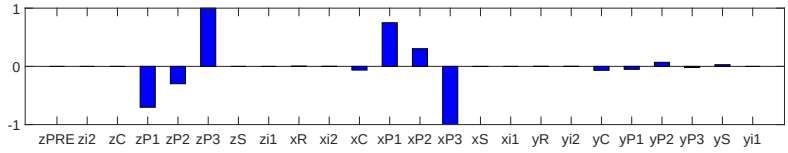
Figure 5: Gear mode in cluster 1



(a) Rotational mode



(b) 1st translational mode



(c) 2nd translational mode

Figure 6: Eigenvectors of gear modes in cluster 1

From Figures 5 and 6, it is observed that radial modes in planets are predominant in all three natural frequencies in a 1st cluster, which is aligned with what the Ericson and Parker reported [10]. Especially, for the rotational mode in this cluster, all three planets are in-phase and equal magnitude of eigenvectors in radial (x) and tangential (y) directions. In addition, sun and carrier are in pure rotational modes without translation. From Figure 6b and c, it is visible that the radial translations of the planets are still predominant deflections in the 2nd and 3rd natural frequencies in a 1st cluster. Having described all characteristics of the gear modes, the comparisons between the results of experiment and Motion model are listed in Table 6. It is noted that average mesh stiffness according to ISO [14] is used for this simulation because no information was found about gear phase at impulse testing [10].

The natural frequencies obtained from the Motion model agrees well in general, showing that the largest deviation is within 10%. There might be various reasons to explain these differences. Gear mesh stiffness computation under load with numerical software tool is a challenging task considering the manufacturing or assembly errors of the real gears of the system. Also, gear phases in a stationary condition at the experimental

Mode	Type	Exp. (Hz)	Motion (Hz)	Deviation (%)
Cluster 1				
1	Rot.	1420	1566	9.58
2	Trans.	1600	1620	1.25
3	Trans.	1600	1621	1.31
Cluster 2				
4	Rot.	2735	2860	4.57
5	Trans.	2832	2867	1.24
6	Trans.	2832	2868	1.27
Cluster 3				
7	Trans.	3380	3506	3.73
8	Trans.	3380	3506	3.73
9	Rot.	3430	3521	2.65

Table 6: Natural frequency comparisons in gear modes (experiment vs. Motion)

set would not be easily measurable. Under these circumstances, the Motion model can only assume a certain meshing position even if mesh stiffness varies at a certain rotational position. Lastly, the measured values of the planet bearing stiffnesses having anisotropic properties under load are not found in the literature except for the estimated value from numerical analyses.

5 Time-varying mesh stiffness influence on gear mode

Gear mesh stiffness for any gear pair varies in time, and the amount of variation and shapes depends on the number of teeth in contact at each time instance and geometry itself. In a planetary gear system, gear meshes also go through a phase relationship, i.e., in-phase and sequentially phase. *In-phase* is referred to as the condition that all meshes (sun-planet and planet-ring) of each planet have identical stiffnesses with other planet at each instance. On the other hand, *Sequentially phase* is referenced with the condition that mesh stiffness per each planet at each instance has a different value in a planetary system. Referring to the literature [6], the orthogonality of the eigenvectors are described in translational modes depending on the symmetry of the mesh stiffness values. In the system of in-phase condition, two translational modes (multiplicity of two) are detected whereas this two modes will veer if there are differences among the mesh stiffness values. Moreover, it is explained that the larger the stiffness differences are, the wider the frequency bands of the clusters becomes [11].

5.1 Gear mode changes with meshing condition

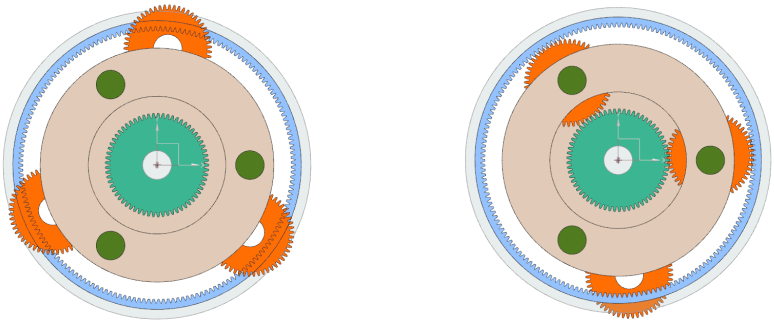
The natural frequency investigation with two different mesh stiffness assumptions having a constant stiffness and time-varying mesh stiffness with sequentially phase condition will differ. The multibody simulation in section 3 used the constant averaged stiffness because of the experimental setup gear orientation is not measurable. If time-varying stiffness is taken, the variations and differences among the mesh stiffness values at each planet will be captured in the sequentially phased planetary system, which is the case of the example gear set in this study. The first piece of evidence for the natural frequency changes in a gear mode is listed in Table 7.

The multiplicities of the translational modes in each cluster listed in the column associated with constant stiffness are recognized in Table 7; however, it is not the case anymore when it comes to the results with the time-varying stiffness. It is noted that those translational modes are still close to having a repeated mode in cluster 1. This can be explained that the mesh stiffness influence is minimal when the radial mode of a planet is predominant in cluster 1, where the projection of the forces along the line of action to the radial

Mode	Type	Const. stiff. (Hz)	Time-varying stiff. (Hz)
Cluster 1			
1	Rot.	1556	1563
2	Trans.	1620	1625
3	Trans.	1621	1626
Cluster 2			
4	Rot.	2860	2771
5	Trans.	2867	2833
6	Trans.	2868	2876
Cluster 3			
7	Trans.	3506	3473
8	Trans.	3506	3501
9	Rot.	3521	3518

Table 7: Gear mode comparison (constant vs. time-varying stiffness)

direction is relatively small. Moreover, the differences are present not only in terms of multiplicity but also of mode shapes: the rotational and translational mode shapes in cluster 2 and cluster 3 do not coincide anymore between two different mesh stiffness assumptions. These differences are presented in Figure 7.



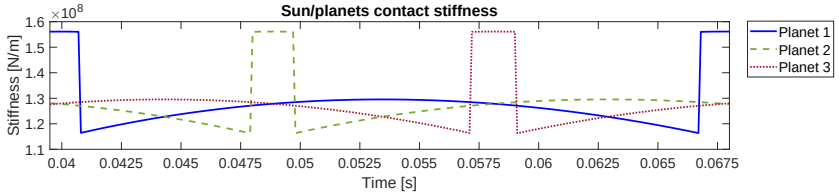
(a) Constant (b) Time-varying

Figure 7: Mode shape comparison with two different mesh stiffnesses at Mode 9 in Table 7

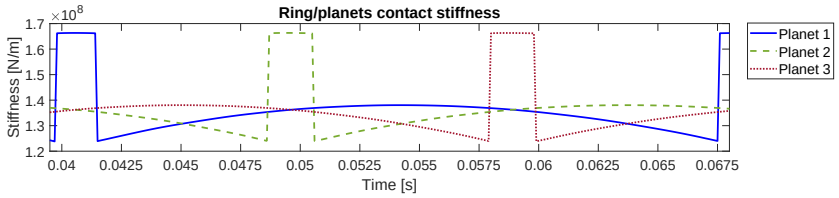
Therefore, these two different mesh stiffness assumption in the Motion model needs to be taken into account if a distinction between the in-phase and sequentially phased configurations has to be analyzed.

5.2 Gear mode variation on gear spinning

Mesh stiffness continuously changes in gear spinning condition both with in-phase or sequentially phase planetary gear systems. To investigate the gear mode variation in time while the example planetary gear system is spinning, the Motion model has been modified by removing the fixture constraints to allow the model to rotate under a certain amount of load. A subsequent linearization was performed at each time step in Motion to obtain the natural frequencies, especially of the gear modes. Torque ($T = 1500$ Nm) and input speed ($\Omega_{input} = 200$ rpm) are applied at sun shaft side. Figure 8 shows the stiffness variation between sun-planet and planet-ring in time, respectively. From Figure 8, the system configuration of sequentially phase condition were visually observed from the stiffness variation curves in time. It is noted that the phase between sun-planet and planet-ring are also different in this example system. In this case, more complex phase relationship would be analyzed to capture the combined effect of the mesh stiffness at sun-planet and planet-ring contacting interfaces for each planet in time. As a result, the natural frequency variation types and magnitude would defer with planetary gear configuration.



(a) Sun - planet



(b) Ring - planet

Figure 8: Time-varying mesh stiffness computed

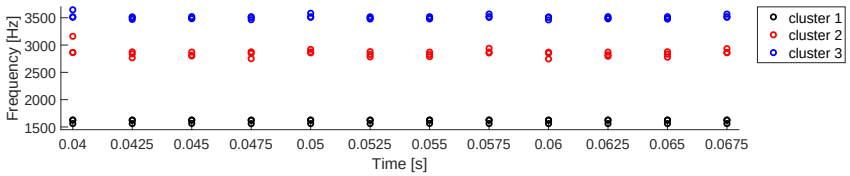


Figure 9: Frequency variation with time-varying mesh stiffness

5.3 Speed sweep simulation

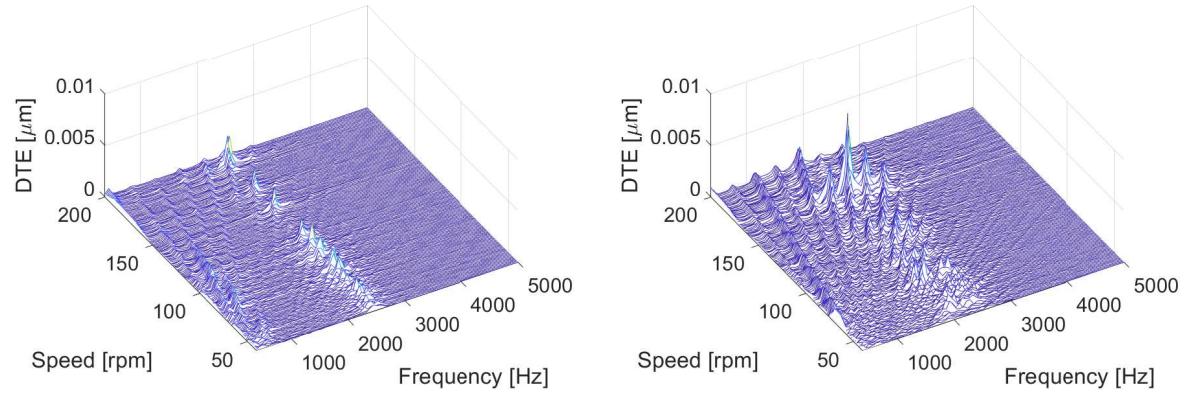
To further investigate the time-varying mesh stiffness influences on system dynamics, a transient dynamic simulation was conducted by speed sweeping. Two system configurations were simulated, i.e., one for a sequentially phase and the other for an in-phase condition. To make an in-phase configuration, a small adjustment was made on the number of teeth from the original system (sequentially phase) by maintaining the stiffness variation level as similar as possible. Table 8 shows two configurations of planetary systems used for the speed sweep simulations.

	Sun (z_s)	Planet (z_p)	Ring (z_r)
Original system	65	55	175
In-phase system	66	54	174

Table 8: Number of teeth

To focus on the high frequency gear mode study, the multibody model described in Section 3 were modified accordingly. The transverse degrees of freedom was removed to make the system to be a pure torsional model with time-varying mesh stiffness consideration. In addition, the gear parameters have been modified to obtain lower contact ratios to make more prominent values of mesh stiffness variation. For speed sweep simulation, a constant acceleration in the system is applied by inserting a torque imbalance between sun and carrier side. The rotating speed reached 200 rpm in 5.2 seconds to avoid any abrupt transition. Figure 10 shows two waterfall plots to compare the dynamic amplitude in DTE (dynamic transmission error) between two different gear sets having in-phase and sequentially phase.

From both cases, the dynamic amplitudes at mesh orders of transmission error were captured, which are caused by the mesh excitation forces in time. Integer number of mesh harmonics pass by the high frequency gear mode ranges (1500 to 3500 Hz) and resonated. By comparing the results obtained from these two configurations, it is observed that there are differences in terms of natural frequency bands where the resonance



(a) In-phase

(b) Sequentially phase

Figure 10: Dynamic transmission error from a speed sweep simulation with two different planet phases; (a) in-phase and (b) sequentially phase

peaks were examined: in both cases, the peaks are caused by the excitation at three natural frequencies at each cluster in the gear mode; however, in the case of the sequentially phased planets, the resulting peak becomes wider whereas in the case of in-phase planets, the frequency band gets very narrow.

6 Conclusion and future work

To examine a dynamic behavior of a planetary gear system by multibody software tools (Simcenter 3D Motion and Transmission Builder with a gear contact solver), this multibody model validation step was firstly conducted against experiments available in the literature. The experimental modal test configurations, results, and system parameters except for gear mesh stiffness were referred from Ericson and Parker's work [10]. The multibody model with an average mesh stiffness value successfully demonstrated that its results were well aligned with all natural modes experimentally obtained: showing maximum deviation in natural frequency in low frequency fixture mode (below 1500 Hz) within 12% and in high frequency gear mode (above 1500 Hz) within 10%.

Subsequently, an investigation of natural modes influenced by time-varying mesh stiffness at different phase conditions in both quasi-static and dynamic conditions are conducted. In a stationary condition, it was examined that there were differences in natural modes when the mesh stiffness was assumed to be either constant or time-varying in sequentially phase planetary gear system. On the other hand, in a spinning condition, it was concluded that the time-varying mesh stiffness consideration in the multibody models are crucial both for in-phase and sequentially phase planetary gear system to capture the ranges of natural frequency variations in time, especially in the gear modes.

Lastly, a speed sweep simulations under a constant load were performed to examine the dynamic transient effect on the natural modes between in-phase and sequentially phase configurations. Waterfall plots for the gear modes (above 1500 Hz) were generated to emphasize a clear distinction regarding the variation of the gear mode cluster ranges. As a result, sequentially phase planetary gear system exhibited a wider range of the natural frequencies in the gear modes than those of the counterpart.

In order to increase the model accuracy, the inclusion of finite element based models for shafts, gear bodies, pins, carrier, and fixtures would be necessary with FE based gear mesh stiffness computation. To simulate the spinning gearbox with higher fidelity, the lubrication influence that alters the contact stiffness and damping with load and speed on bearing and gear contacting interfaces has to be taken into account, which are to be the future work of this study.

References

[1] A. Kahraman, *Planetary Gear Train Dynamics*, Journal of Mechanical Design, Vol. 116, No. 3, ASME (1994), pp. 713-720.

[2] M. Inalpolat, A. Kahraman, *Dynamic Modelling of Planetary Gears of Automatic Transmissions*, Proceedings of the Institution of Mechanical Engineers, Part K: Journal of Multi-body Dynamics, Vol. 222, No. 3, 2008, pp. 229-242.

[3] M. Inalpolat, A. Kahraman, *A Theoretical and Experimental Investigation of Modulation Sidebands of Planetary Gear Sets*, Journal of Sound and Vibration, Vol. 323, No. 3-5, 2009, pp. 677-696.

[4] M. Inalpolat, A. Kahraman, *A Dynamic Model to Predict Modulation Sidebands of a Planetary Gear Set Having Manufacturing Errors*, Journal of Sound and Vibration, Vol. 329, No. 4, 2010, pp. 371-393.

[5] J. Lin, R. G. Parker, *Sensitivity of Planetary Gear Natural Frequencies and Vibration Modes to Model Parameters*, Journal of sound and vibration, Vol. 228, No. 1, 1999, pp. 109-128.

[6] J. Lin, R. G.. Parker, *Analytical Characterization of the Unique Properties of Planetary Gear Free Vibration*, Journal of vibration and acoustics, Vol. 121, No. 3, 1999, pp. 316-321.

[7] R. G. Parker, J. Lin, *Mesh Phasing Relationships in Planetary and Epicyclic Gears*, Journal of Mechanical Design, Vol. 126, No. 2, 2004, pp. 365-370.

[8] R. G. Parker, *A Physical Explanation for the Effectiveness of Planet Phasing to Suppress Planetary Gear Vibration*, Journal of sound and vibration, Vol. 236, No. 4, 2000, pp. 561-573.

[9] V. K. Ambarisha, R. G. Parker, *Suppression of Planet Mode Response in Planetary Gear Dynamics through Mesh Phasing*, Journal of Vibration and Acoustics, Vol. 128, No. 2, 2006, pp. 133-142.

[10] T. M. Ericson, R. G. Parker, *Planetary Gear Modal Vibration Experiments and Correlation against Lumped-parameter and Finite Element Models*, Journal of sound and vibration, Vol. 332, No. 9, 2013, pp. 2350-2375.

[11] T. M. Ericson, R. G. Parker, *Natural Frequency Clusters in Planetary Gear Vibration*, Journal of Vibration and Acoustics, Vol. 135, No. 6, 2013, pp. 061002 (1-13).

[12] T. M. Ericson, R. G. Parker, *Experimental Measurement of the Effects of Torque on the Dynamic Behavior and System Parameters of Planetary Gears*, Mechanism and Machine Theory, Vol 74, 2014, pp. 370-389.

[13] D. Park, A. Toso, G. Heirman, and S. Popescu, *A User Friendly Process to Build Up High-fidelity Models of Gear Transmissions for Multibody Dynamic Simulation*, ISMA 2016 (International Conference on Noise and Vibration Engineering), pp. 1391-1405.

[14] International Standard ISO 6336/1, *Calculation of Load Capacity of Spur and Helical Gears Part 1: Basic Principle, Introduction and General Influence Factors*, 2006.

[15] Y. Cai, T. Hayashi, *The Linear Approximated Equation of Vibration of a Pair of Spur Gears (theory and experiment)*, Journal of Mechanical Design, Vol. 116, No. 2, ASME (1994), pp. 558-564.

[16] T. Tamarozzi, P. Jiranek, D. Park, M. Vivet, S. Donders, S. Flock, *Democratization of simulation in the design engineering of gear boxes*, Proceedings of NAFEMS Seminar Simulation Driven Engineering, NAFEMS Seminar, 2017.

[17] International Standard ISO 21771, *Gears - Cylindrical Involute Gears and Gear Pairs - Concepts and Geometry*, 2007.

A nonlinear energy harvester for torsional oscillations

B. E. Gunn, S. Theodossiades, S. J. Rothberg
Loughborough University, Wolfson School of Mechanical, Electrical and Manufacturing Engineering
Loughborough, Leicestershire, LE11 3TU
e-mail: **S.Theodossiades@lboro.ac.uk**

Abstract
Torsional fluctuations around the mean speed of a rotating shaft represent a typical source of undesirable energy losses in many industrial applications. Furthermore, many control and structural health monitoring systems in rotordynamics require an ever-increasing number of sensors. Currently, powering a wireless sensor mounted on a rotating shaft is feasible using either slip rings or batteries, both of which often incur high maintenance costs in applications with difficult access or when idle due to malfunction. In this paper, an electromagnetic energy harvester prototype is manufactured by adapting a commercially available permanent magnet DC motor. The energy harvesting capabilities of the device are preliminary tested and compared to theoretical predictions.

1 Introduction

Vibration energy harvesters are becoming increasingly widespread as a means of powering small, low power electronic wireless sensors for control and system health monitoring systems. Due to the often unavoidable, undesirable and ubiquitous nature of vibrations in engineering applications, vibration energy harvesters can provide a virtually endless supply of energy for such sensors without the need for regular maintenance or complicated wiring harnesses. This is ideal for applications where servicing such a system could be tedious or cause severe costs due to machine down time.

One such environment is that of rotating shafts which exhibit torsional speed fluctuations. Such rotordynamics are hard to avoid in industrial applications; however, often these speed fluctuations are undesirable and can lead to durability issues if not suitably addressed. Typically, these vibrations are absorbed by mechanical vibration dampers which ultimately dissipate this energy as heat, representing an energy loss from the system.

Past research involving energy harvesters in rotordynamics include Kim [1] and Trimble et al [2]. Kim implemented a piezoelectric cantilever beam which protruded radially from a rotating shaft connected to an internal combustion engine. The aim was to harness energy excess from the second order speed fluctuations of the shaft. Due to centripetal acceleration effects, the beam stiffens as the shaft speed increases, which allowed the harvester to remain at resonance throughout the operating speed range of the engine. However, it was concluded that little power could be scavenged from this device.

Trimble et al [2] used an electromagnetic energy harvester to extract torsional vibration energy from an oil well drill to power a wireless sensor. Their device was capable of harvesting 205mW at resonance and 74 mW when excited using real world random vibrations measured from the drill. However, by using an energy harvester that operates away from resonance, a larger proof mass is needed compared to when the energy harvester is resonating. In the present work, where the shaft has a clear second order speed fluctuation about its mean speed ranging from around 800 rpm to 4000 rpm, such an approach is not ideal; hence some method of maintaining resonance is sought.

Other researchers have investigated harvesters which extract energy from the mean speed of rotating components for applications, such as automotive tyre pressure monitoring systems. Roundy et al [3] used a self-tuning pendulum arrangement to ensure their device was at resonance at any tyre speed. It employed a

frequency up converting mechanism to pluck piezoelectric beams that were able to resonate. Such a device has benefits at low speeds where the piezoelectric components cause bistable response whereas at high speeds the centripetal acceleration dominates and allows the harvester to resonate at speed.

Gu and Livermore [4], [5] developed self-tuning energy harvesters which were tuned using the centripetal acceleration to resonate at a wide speed range. Meanwhile, other researchers such as Mann and Sims [6] and Liu and Yuan [7] have employed a cubic nonlinear stiffness to increase the operating frequency range of their axial harvesters.

To the authors' knowledge, the present work is the first cubic nonlinear energy harvester application for torsional shaft speed fluctuations. An electromagnetic energy harvester is used to generate electricity from torsional oscillations. The device uses a cubic nonlinear spring and has, in a previous work, shown potential to work across the full operating range of the shaft. In this paper, preliminary experimental results of a tested physical prototype are presented. An introduction to the experimental set up is followed by a description of the physical device. A typical frequency response function follows. Then, the experimental results are presented and the main conclusions are drawn.

2 Nomenclature

A	Dimensionless constant of acceleration
c_{mech}	Mechanical damping coefficient
I	Electric current
J	Mass moment of inertia
k_1	Linear coefficient of stiffness
k_3	Cubic coefficient of stiffness
t	Time
$\dot{\alpha}_1$	Angular velocity of the driving shaft
$\dot{\alpha}_2$	Angular velocity of the driven shaft
$\dot{\beta}$	Angular velocity of the energy harvester rotor
γ	Angle between driving and driven shaft
$\hat{\theta}$	Electromagnetic coupling factor

3 Description of the device

In this section, the experimental test rig is presented followed by a brief description of the energy harvester itself. The key characteristics of a typical nonlinear energy harvester are then discussed.

3.1 Excitation environment

To emulate the torsional speed fluctuations often present in rotordynamics, the energy harvester is mounted on the end of an unloaded shaft. The latter is driven by an electric motor through a universal joint that is

intentionally set at an angle in order to induce second order speed fluctuations from which the energy harvester will extract its power. Figure 1 shows a schematic depiction of the test rig.

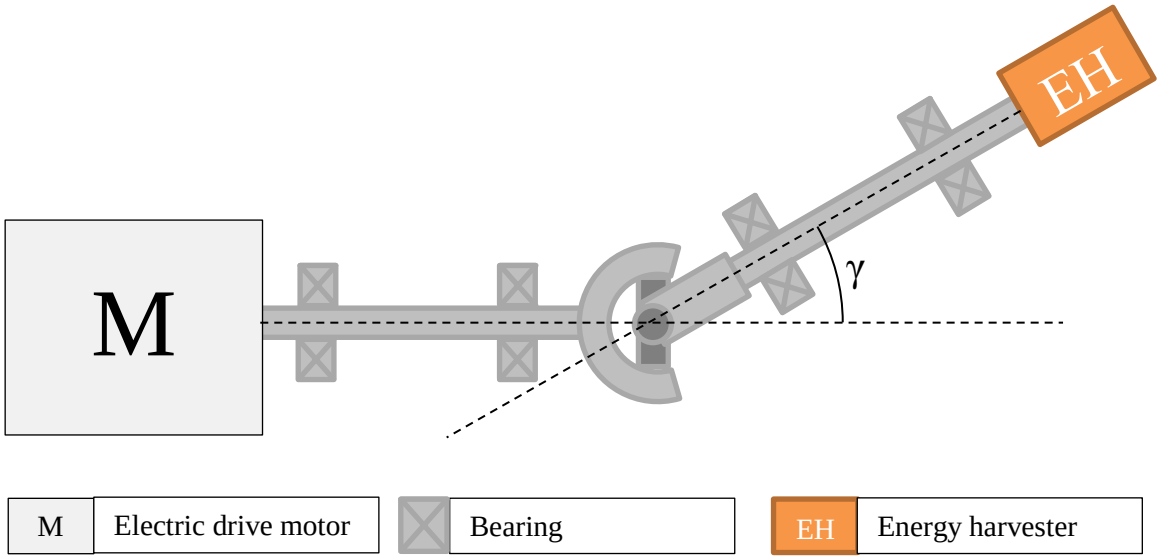


Figure 1: Schematic diagram of the energy harvester test rig

The angular velocity of the driven shaft, α_2, is calculated using the angular velocity of the driving shaft, α_1, using Eqn. (1) [8]:

$$\dot{\alpha}_2 = \frac{\dot{\alpha}_1 cos\gamma}{1 - \sin^2\gamma\cos^2\alpha_1} \tag{1}$$

Differentiating Eqn. (1) with respect to time yields the acceleration of the driven shaft:

$$\ddot{\alpha}_2 = \frac{\ddot{\alpha}_1 cos\gamma}{1 - \sin^2\gamma\cos^2\alpha_1} - \frac{\dot{\alpha}_1^2 cos\gamma \sin^2\gamma\, sin2\alpha_1}{(1 - \sin^2\gamma\cos^2\alpha_1)^2} \tag{2}$$

Where γ denotes the angle between the rotating axes of the two shafts.

Assuming the inertia of the driving shaft is significantly larger than that of the driven shaft, the acceleration of the driving shaft will not be affected by the universal joint, thus the first term of Eqn. (2) can be neglected. The resulting acceleration with a constant drive speed is therefore approximated by

$$\ddot{\alpha}_2 = -A\dot{\alpha}_1^2 \sin(2\dot{\alpha}_1 t) \tag{3}$$

Where A is a dimensionless constant which depends on the angle of the universal joint, γ.

3.2 Energy harvester

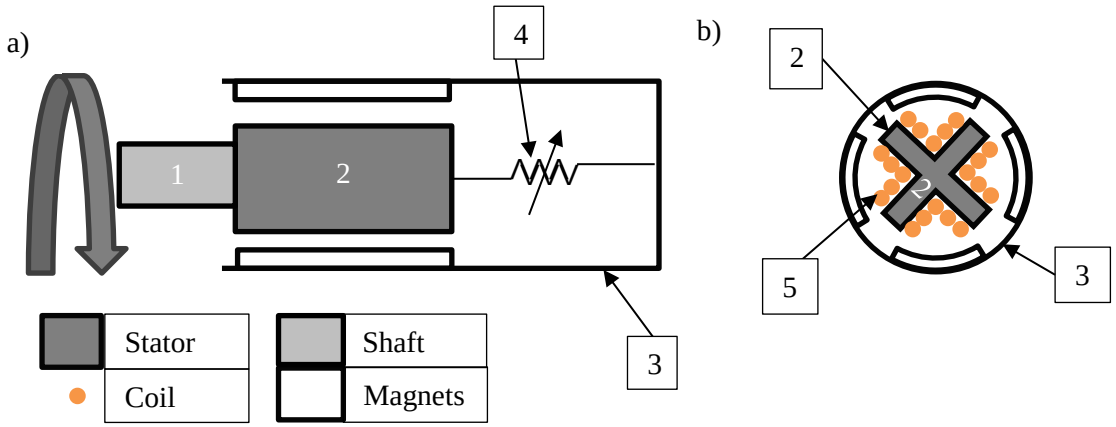


Figure 2: Schematic representation of the energy harvester: a) Side view and b) End view

An off-the-shelf external rotor brushless DC permanent magnet motor has been adapted to build the energy harvester. With reference to Figure 2, the stator (2) is made of a laminated iron core with series wound copper windings (5). The stator is mounted to the rotating shaft (1) and rotates with it. The rotor (3) comprises a housing with radially magnetized permanent magnets fixed to its inner surface. The rotor (3) is free to rotate around the stator (1) except for the cubic nonlinear torsional spring (4) whose torque is calculated as a function of the angular displacement:

$$T = k_1(\alpha_2 - \beta) + k_3(\alpha_2 - \beta)^3 \tag{4}$$

This nonlinear spring setting restricts the rotation of the rotor and allows for the rotor to oscillate torsionally with respect to the stator. When the rotor moves relative to the stator, the relative velocity induces an electromotive force in the coils which can power a load. In the present work, the electrical power is simply dissipated through a resistor with resistance matching the internal resistance of the coil. This introduces a damping effect on the mechanical system. The motion of the energy harvester is given by:

$$J\ddot{\beta} = k_1(\alpha_2 - \beta) + k_3(\alpha_2 - \beta)^3 + c_{mech}\left(\dot{\alpha}_2 - \dot{\beta}\right) + \hat{\theta}I \tag{5}$$

Where J denotes the mass moment of inertia of the rotor; β denotes the angular position of the rotor; α_2 is the angular position of the stator. An over dot denotes differentiation with respect to time. The linear component of the stiffness is denoted by k_1 and the cubic nonlinear stiffness coefficient is denoted by k_3. c_{mech} is the linear mechanical damping coefficient of the system and $\hat{\theta}I$ represents the power extracted by the electrical circuit with $\hat{\theta}$ being the nonlinear electromechanical coupling factor and I, the electric current in the load circuit.

A derivation of $\hat{\theta}$ can be found in Gunn et al [9], which is based on the work of Markovic and Perriard [10]. However, due to a malfunction in the physical prototype, the electrical load was disconnected during the tests, thus the $\hat{\theta}I$ term plays no role in the following experiments. The aim of this work is therefore to assess the dynamics of the system and its potential to generate power, neglecting any electrical effects.

3.3 Numerical model results

The AUTO 07p bifurcation analysis software [11] was used to perform numerical continuation of the energy harvester equation of motion (Eqn. (5)). Figure 3 shows a typical frequency response graph of the energy harvester. The response is similar to that of a Duffing oscillator; however, due to the frequency dependent amplitude of the excitation acceleration, there exists a condition where the jump down frequency is unattainable [9]. In the figure, the solid lines represent stable solutions and the dashed lines are unstable response that cannot be realised in a physical prototype. Below around 2800 rpm there is only one stable solution to the equations of motion. However, as the excitation frequency increases, the three-coinciding solutions region begins, where two responses are stable. The higher of the two stable solutions is the desired operating zone of the energy harvester, where naturally more power will be generated.

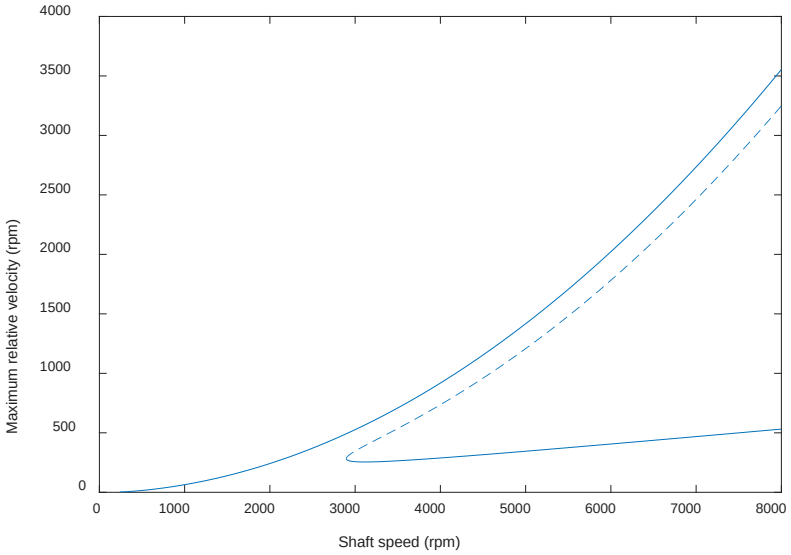


Figure 3: Typical frequency response graph of the energy harvester.

4 Experimental results

This section presents the results of tests conducted on a physical prototype. Typical time histories of the harvester's response are shown followed by the corresponding plot of the frequency response. The energy harvester behaves in a similar fashion to the numerical model presented in the previous section. Throughout this experiment, the universal joint is set at 20°, which induces sinusoidal speed fluctuations with $A = 0.0311$, which when substituted in Eqn. (3) yields:

$$\ddot{\alpha}_2 = -0.0311\dot{\alpha}_1^2 \sin(2\dot{\alpha}_1 t) \tag{6}$$

4.1 Time histories

Figure 4 shows the velocity time histories of the oscillating shaft (labelled "stator shaft") and the rotor of the energy harvester (labelled "energy harvester"). These velocities were measured using two-beam laser vibrometers to provide accurate measurements without contacting the device under test. The relative velocity of the energy harvester is calculated by subtracting the energy harvester velocity from the stator

shaft velocity. In Figure 4, the steady state response of the energy harvester is shown at around 1150 rpm mean shaft speed.

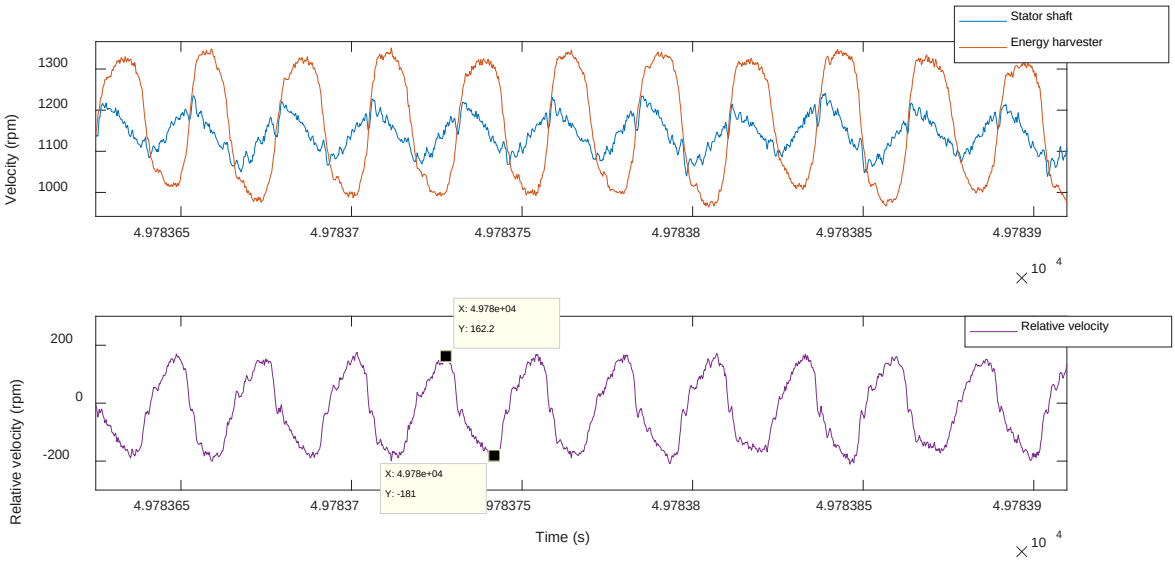


Figure 4: Steady state velocity time histories at 1150 rpm: top – raw shaft speed and energy harvester speed; bottom – relative velocity of the energy harvester.

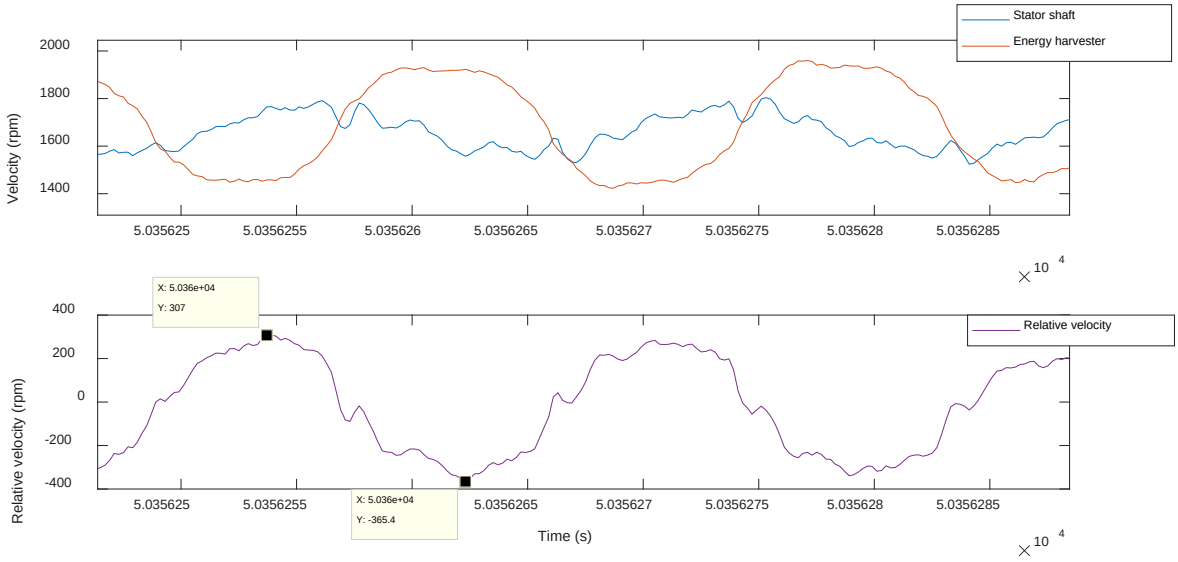


Figure 5: High energy branch solution at 1700 rpm: top – raw shaft speed and energy harvester speed; bottom – relative velocity of the energy harvester.

Figure 5 shows the higher energy stable branch solution at approximately 1700 rpm mean driving shaft speed. The amplitude of the relative velocity is approximately 336.2 rpm as indicated by the insets of the bottom half of Figure 5. The lower stable branch solution at 1700 rpm mean driving speed is depicted in Figure 6. For the same driving conditions as in Figure 5, much lower response amplitude is observed with a relative velocity of approximately 127 rpm. Furthermore, the energy harvester is 180° out of phase with the shaft velocity in the lower energy branch response compared to about 90° out of phase in the higher energy branch response shown in Figure 5. Thus, it can be clearly seen that two distinct stable solutions exist when the driving shaft operates at 1700 rpm with corresponding speed fluctuations as calculated using Eqn. (3).

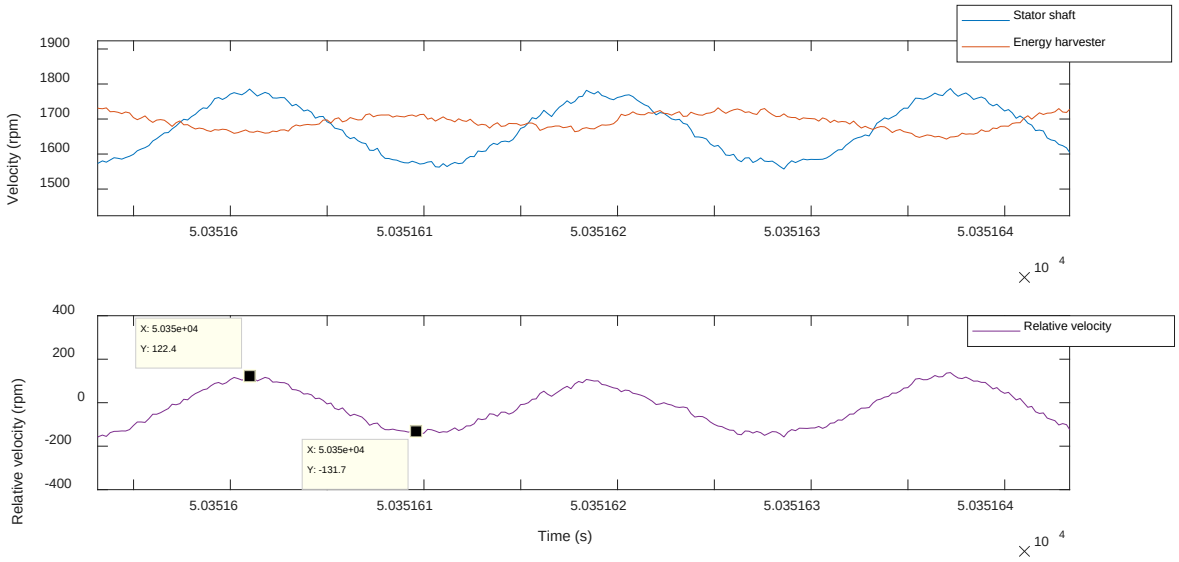


Figure 6: Low energy branch solution at 1700 rpm: top – raw shaft speed and energy harvester speed; bottom – relative velocity of the energy harvester.

4.2 Frequency response diagram

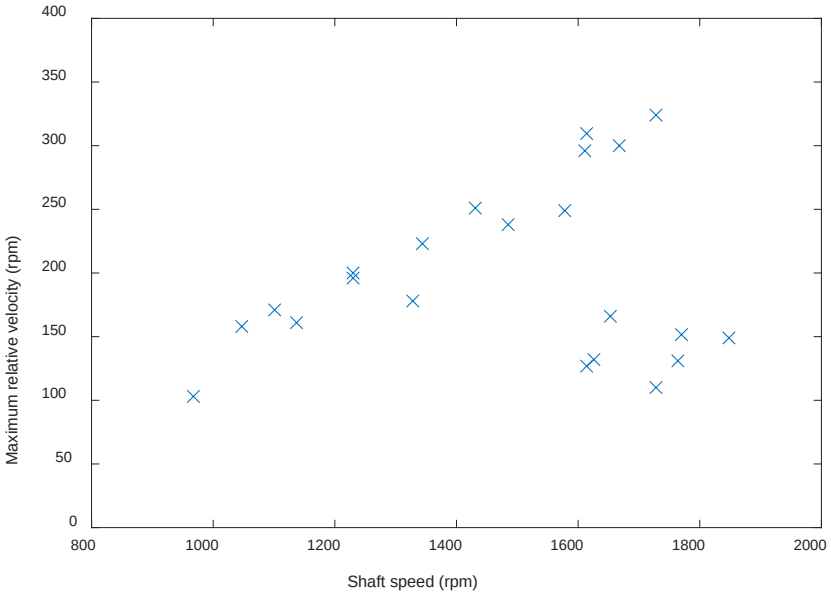


Figure 7: Experimental frequency response graph of the relative velocity

Figure 7 depicts the frequency response graph of the experimental energy harvester. The drive motor was accelerated gradually by manually adjusting the speed control dial of the inverter. At each speed the shaft was allowed to run for at least 30 s to ensure that any transients have faded. From the measured data, the relative velocity was calculated as stated above at each test point. These values are then plotted against the mean shaft speed. Figure 7 follows the same general trend as in Figure 3. At low speeds (<1600rpm in Figure 7, <2800 rpm in Figure 3) there exists only one stable solution. Above this speed threshold, two stable solutions appear. In Figure 7, the high energy branch is maintained until around 1730 rpm however, unlike Figure 3, where the upper stable branch was unattainable above 1730 rpm. This is due to the need for system identification in order to use the right data in the numerical calculations.

5 Conclusions

A physical prototype of a torsional electromagnetic energy harvester has been presented. The experimental results exhibit similar trend as in the predicted model response. A lower energy branch solution region exists at low speeds, followed by a higher energy region, where stable solutions coexist. Further work is required in order to identify the accurate system features and to separate further the upper stable branch from the unstable solution in order to decrease the likelihood of dropping to the lower energy stable branch (and increase the power output potential of the device).

6 References

[1] G. W. Kim, "Piezoelectric energy harvesting from torsional vibration in internal combustion engines," *Int. J. Automot. Technol.*, vol. 16, no. 4, pp. 645–651, Aug. 2015.

[2] A. Z. Trimble, J. H. Lang, J. Pabon, and A. Slocum, "A Device for Harvesting Energy From Rotational Vibrations," *J. Mech. Des.*, vol. 132, no. 9, p. 091001, 2010.

[3] S. Roundy and J. Tola, "Energy harvester for rotating environments using offset pendulum and nonlinear dynamics," *Smart Mater. Struct.*, vol. 23, no. 10, p. 105004, 2014.

[4] L. Gu and C. Livermore, "Passive self-tuning energy harvester for extracting energy from rotational motion," *Appl. Phys. Lett.*, vol. 97, no. 8, 2010.

[5] L. Gu and C. Livermore, "Compact passively self-tuning energy harvesting for rotating applications," *Smart Mater. Struct.*, vol. 21, no. 1, p. 015002, 2012.

[6] B. P. Mann and N. D. Sims, "Energy harvesting from the nonlinear oscillations of magnetic levitation," *J. Sound Vib.*, vol. 319, no. 1–2, pp. 515–530, 2009.

[7] L. Liu and F. G. Yuan, "Nonlinear vibration energy harvester using diamagnetic levitation," *Appl. Phys. Lett.*, vol. 98, no. 20, pp. 2009–2012, 2011.

[8] F. Schmelz, C. H.-C. Seherr-Thoss, and E. Aucktor, *Universal Joints and Driveshafts*, English Ed. Berlin: Springer-Verlag, 1992.

[9] B. Gunn, S. Theodossiades, S. Rothberg, and T. Saunders, "An electromagnetic energy harvester for rotational applications," *Proc. ASME Des. Eng. Tech. Conf.*, vol. 8, 2017.

[10] M. Markovic and Y. Perriard, "An analytical formula for the back emf of a slotted BLDC motor," *Proc. IEEE Int. Electr. Mach. Drives Conf. IEMDC 2007*, vol. 2, pp. 1534–1539, 2007.

[11] E. J. . Doedel, T. F. . Fairgrieve, B. Sandstede, A. R. . Champneys, Y. A. ; Kuznetsov, and X. Wang, "AUTO-07P: Continuation and bifurcation software for ordinary differential equations (2007)." 2007.

On selecting appropriate training data to model an autonomous oscillator

J. Decuyper [1], **T. De Troyer** [1], **M.C. Runacres** [1], **K. Tiels** [2] **and J. Schoukens** [1]
[1] Vrije Universiteit Brussel (VUB), Department of Engineering Technology,
Pleinlaan 2, 1050, Brussels, Belgium
e-mail: **jan.decuyper@vub.be**

[2] Uppsala University (UU), Department of Information Technology,
PO Box 337, SE-75105 Uppsala, Sweden

Abstract
In this work we study the effect of using different types of excitation signals as training data when constructing black box nonlinear models. We focus in particular on the class of nonlinear systems which exhibit autonomous oscillations. Three type of excitation signals are considered: random-phase multisines, filtered white noise and swept sines. It is shown that depending on the excitation signal, the resulting model can fail to reproduce the autonomous output. Results are presented for the forced Van der Pol oscillator and the oscillatory wake of an submerged circular cylinder in a flow. It is moreover shown that broadband excitations such as multisines or noise, are appropriate signals when intending to capture the synchronisation principle observed for autonomous oscillators. The latter is shown on computational fluid dynamic data of a submerged cylinder in a flow.

1 Introduction

An autonomous oscillator is a system that in the absence of an excitation maintains a steady oscillation. The oscillator is in other words 'self-sustained' or 'self-oscillatory'. In order for an oscillation to persist, a constant transformation of internal energy, compensating for all dissipation, takes place. Self-sustained oscillation is encountered in a variety of fields ranging from the chirps of neurons [20] to self-exciting transmitters. It is known that such systems can be described by the class of nonlinear dynamic models [15].

A much studied autonomous oscillator is the flow about a bluff body, e.g. a circular cylinder, submerged in a uniform flow. For a wide range of Reynolds numbers, defined by the diameter of the object, the unperturbed flow speed and the viscosity of the flow, an alternating vortex shedding pattern forms in the wake. The wake oscillates periodically, resulting in a periodic change of the pressure distribution on the surface of the body, eventually resulting in fluctuating forces [22]. If the body is allowed some degree of freedom, a dynamical fluid-structure interaction called vortex-induced vibrations (VIV) arises. VIV are potentially large amplitude vibrations which may be harmful to the structure. Especially chimneys exposed to wind and slender bodies exposed to ocean currents are known to suffer from accelerated fatigue and even failure, following from VIV [21]. An accurate model, enabling simulation and prediction of VIV is therefore vital in the design phase of such structures. So far, no analytical formulation of the dynamics has been found, though some empirical models exist. What is evident is that the model will necessarily need to be nonlinear [1].

An effective approach, in particular when the structure of the underlying system is unknown, is black-box modelling. During black-box modelling a model is built solely from data. The technique relies on a proper selection of the model structure, flexible enough to be able to describe the observed data, and proper selection

of the data itself, which should be a sufficiently rich description of the regime of interest of the system. In [2] accurate results where presented of a nonlinear model able to describe the forces acting on an oscillating circular cylinder in a uniform flow. It was shown that the polynomial nonlinear state-space (PNLSS) model class is a sufficiently flexible model class in order to describe the considered fluid system. An important question which remains is how the operating regime of interest can be described in an efficient way by the data. Here efficient refers to the number of data points required. In other words, what excitation signals should the training data be made of to ensure that the features of the system are captured and effectively encoded into the model.

Experiment design, for the purpose of nonlinear system identification, remains an open problem. Nonlinear models in particular tend to be highly conditioned on the training data, making them vulnerable for extrapolation and in some cases even interpolation (illustrated in Section 1.2). Assembling an appropriate training data set therefore continues to be an ad hoc procedure, tailored to the specifics of the system and to the intended application of the model.

In this work we compare black-box models (of the PNLSS type) obtained from seemingly similar excitation signals, i.e. exciting the same frequency band and of the same root-mean-square amplitude level, but of different kinds. Three types of signals are considered: random-phase multisines, filtered noise and swept-sine excitation. We focus on systems that, similar to the fluid system previously discussed, exhibit autonomous oscillations. As a case study the well known Van der Pol equation is studied.

The layout of the paper is as follows: in Section 1.1 the Van der Pol system and its key features are introduced. Section 1.2 illustrates why nonlinear models become conditioned upon their training data. In Section 2 the polynomial nonlinear state-space model class is introduced. Section 3 comprises a case study on the Van der Pol equation. In Section 4 the usage of multisine excitation on the true fluid system is illustrated. Section 5 provides the conclusions.

1.1 The Van der Pol system

The Van der Pol equation is a nonlinear oscillator which has been the starting point of a great number of wake oscillator models [4, 8, 14]. It is a second order ordinary differential equation (ODE) with a nonlinear damping term. In reduced form it reads

$$\ddot{\mathbf{y}} + \varepsilon(\mathbf{y}^2 - 1)\dot{\mathbf{y}} + \omega_0^2\mathbf{y} = \mathbf{u}, \tag{1}$$

where $\mathbf{u}$ is a forcing term which we will refer to as the input and $\mathbf{y}$ is regarded as the output. Bold lower case letters denote vectors while regular lower case letters are used for constants. A weight on the nonlinear term is provided through the Van der Pol parameter ε. The linear stiffness parameter is denoted by ω_0^2 such that the angular natural frequency of the underlying linear system equals ω_0. When used as a wake oscillator model, $\mathbf{u}$ is generally considered as the displacement of the body while $\mathbf{y}$ represents the nonlinear force acting on the structure. In order to model the fluid-structure interaction VIV, Eq. (1) is often coupled to a second linear ODE in $\mathbf{u}$ which then incorporates the linear dynamics of the structure [6].

At any given time the state of the system described by Eq. (1) is defined by the set of state variables $\mathbf{x} = [\dot{\mathbf{y}} \quad \mathbf{y}]^T$. One can study the stability of Eq. (1) from a linearisation at its fixed points, i.e. the points which satisfy the autonomous equation $\dot{\mathbf{x}} = 0$. It can be seen that the origin, where $\mathbf{y} = 0$ and $\dot{\mathbf{y}} = 0$, is the only fixed point. Evaluating the Jacobian in the origin gives

$$\mathbf{J}_0 = \begin{pmatrix} \varepsilon & -\omega_0^2 \\ 1 & 0 \end{pmatrix}. \tag{2}$$

We hence have a set of complex conjugate eigenvalues with positive real parts for $\varepsilon > 0$ and in that case an unstable oscillatory fixed point at the origin. For increasing amplitude of $\mathbf{y}$, positive damping will appear for $|\mathbf{y}| > 1$, eventually leading to a limit cycle oscillation [3].

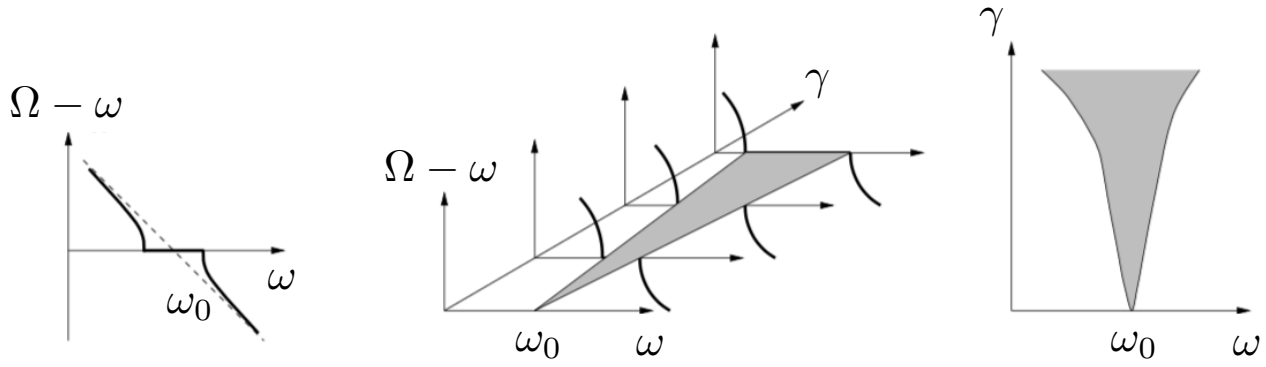


Figure 1: Illustration of the lock-in region. The frequency of **y** is given by ω, the frequency of the forcing **u** is denoted Ω and γ is the amplitude of forcing. Figure was taken from [15].

For the forced case, $\mathbf{u} \neq 0$, periodic forcing can draw the frequency of the output away from ω_0, thereby synchronising to the input frequency (denoted Ω). The latter is referred to as lock-in or entrainment. The region of parameter space for which synchronisation is observed is known as the lock-in region. Figure 1 illustrates the typical v-shaped lock-in region in the frequency-amplitude plane of the forcing [15].

1.2 Phase-space trajectories

One can track the evolution of a system by visualising its so-called trajectory through phase space. At any given moment of time, t, the evolution of the state of the system depends on the current state, $\mathbf{x}(t)$, and the input $\mathbf{u}(t)$. Connecting the triplet of coordinates $(\mathbf{x}_1(t), \mathbf{x}_2(t), \mathbf{u}(t))$, in the case of a second order system, reveals the trajectory.

To illustrate the key difference between linear and nonlinear systems and discuss its implications concerning modelling, the phase-space trajectories of the Van der Pol system and a classical linear mass-spring-damper system are shown in Figure 2. To reduce the dimensions, the input **u** is set to zero. Along the trajectories the functions are evaluated in terms of $\ddot{\mathbf{y}}$. To explore the phase space, the trajectories corresponding to a range of initial states are shown. The expressions are given by

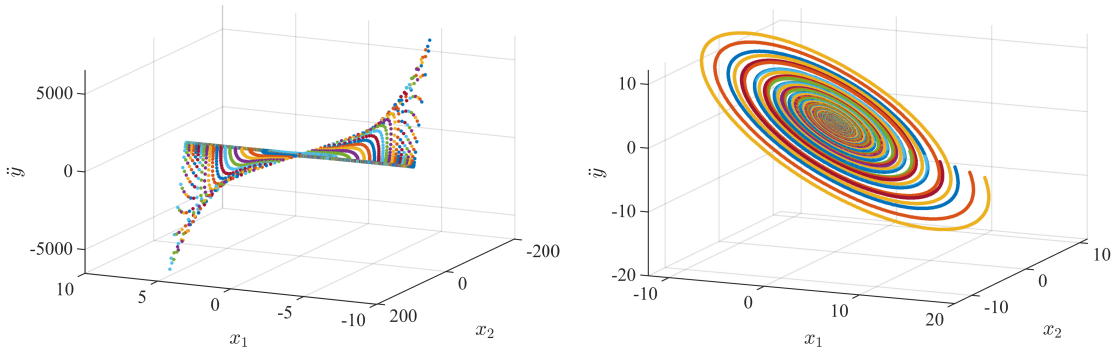
$$\ddot{\mathbf{y}} = -\varepsilon(\mathbf{y}^2 - 1)\dot{\mathbf{y}} - \omega_0^2\mathbf{y}, \tag{3}$$

for the Van der Pol system and

$$\ddot{\mathbf{y}} = -\frac{d}{m}\dot{\mathbf{y}} - \frac{k}{m}\mathbf{y}, \tag{4}$$

for the linear system. Here m is the mass, d the damping coefficient and k the stiffness constant ($m, d, k \in \mathbb{R}^+$). What can be observed from Figure 2 is that linear systems evolve along a hyperplane wheras nonlinear systems describe a manifold. This difference constitutes the fundamental reason why nonlinear models become conditioned upon the training data used during the identification step. A model which approximates well the true system within the region of the phase space covered during training might perform poorly when evaluated in another region.

Given that the internal state variables are generally not accessible through measurement one cannot a priori know whether certain inputs will lead to an extrapolation of the model to unexplored regions of the phase space. In Section 3 it will moreover be shown that such extrapolations might occur for input signals which are very similar in terms of frequency band and amplitude but differ in kind.



(a) (b)

Figure 2: (a) Manifold described by the nonlinear Van der Pol equation when evaluated from a range of initial states and in the absence of an input. (b) Hyperplane described by a linear second order system when evaluated from a range of initial states and in the absence of an input. Different colours indicate a different initial state with the states being $\mathbf{x} = [\mathbf{y} \quad \dot{\mathbf{y}}]^T$.

2 Black-box nonlinear state-space modelling

The conditioning upon training data of nonlinear data-driven models is present for all model classes. In this work polynomial nonlinear state-space (PNLSS) models are used to illustrate the matter. PNLSS is a very generic model class, intuitively obtained by extending the linear state-space equations with nonlinear functions (i.e. polynomials):

$$\begin{cases} \mathbf{x}(k+1) = \mathbf{A}\mathbf{x}(k) + \mathbf{B}\mathbf{u}(k) + \mathbf{E}\zeta(t) & \text{(5a)} \\ \mathbf{y}(k) = \mathbf{C}\mathbf{x}(k) + \mathbf{D}\mathbf{u}(k) + \mathbf{F}\eta(k), & \text{(5b)} \end{cases}$$

where bold upper case letters denote matrices of coefficients and ζ and η contain monomial crossproducts between the states and the input raised to a user defined total power [13].

Given the nonlinear feedback, introduced by the state equation (Eq. (5a)), a wide class of nonlinear systems is covered by this model structure. Noël et al. [12] showed that hysteretic systems can be modelled using PNLSS models and in [2] both autonomous and forced oscillations of the forces arising from vortex shedding on a submerged cylinder were modelled.

Identifying a PNLSS model is a three step procedure:

1. Identify a parametric linear approximation of the system.
2. Use the parametric linear model as initialisation of the PNLSS model. Initialise the nonlinear coefficients in **E** and **F** with zeros and run a nonlinear optimisation routine to tune all the coefficients of the model on the basis of the training data set.
3. Assess the performance of the model on validation data.

Typically the best linear approximation (BLA) is used as an initial linear model [17]. Using frequency-domain subspace identification a parametric estimate is obtained [11, 16]. To tune the full nonlinear model, a least-squares cost function is minimised using a Levenberg-Marquardt algorithm. The identification procedure is made available in the Polynomial Nonlinear State-Space toolbox for MATLAB [19] and can be found online at `http://homepages.vub.ac.be/~jschouk/`.

3 A Van der Pol case study on selecting training data

In this section we create PNLSS models that approximate the forced Van der Pol oscillator. The models differ only on the basis of the data from which they are built. As training data, three types are considered: random-phase multisine realisations, filtered noise and swept sines. All three signals are designed such that they cover the same frequency band $(0-4\omega_0)$ and that they are of equal rms amplitude level ($\text{rms}(\mathbf{u}) = 200$). Choosing $\varepsilon = 1.5$ ensures strong nonlinear effects, ω_0 is set equal to π. This places the excitation entirely in the lock-in region.

3.1 Acquiring data of the Van der Pol system

To obtain data of the forced Van der Pol oscillator a discretised state-space formulation is used. Choosing as state vector $\mathbf{x} = [\mathbf{y} \quad \dot{\mathbf{y}}]^T$ and implementing a first order Euler discretisation one can rewrite Eq. (1) as

$$\begin{cases} \mathbf{x}(k+1) = \begin{bmatrix} 1 & T_s \\ -\omega_0^2 T_s & \varepsilon T_s + 1 \end{bmatrix} \mathbf{x}(k) + \begin{bmatrix} 0 \\ T_s \end{bmatrix} \mathbf{u}(k) \\ \qquad\qquad\qquad\qquad + \begin{bmatrix} 0 \\ -\varepsilon T_s \end{bmatrix} \mathbf{x}_1^2(k)\mathbf{x}_2(k) \qquad (6a) \\ \mathbf{y}(k) = [1 \quad 0]\mathbf{x}(k). \qquad (6b) \end{cases}$$

with T_s indicating the sample period and k a sample index such that $t_k = kT_s$. Note that the Van der Pol oscillator is indeed covered by the PNLSS model class (the nonlinearity is described by a polynomial cross product of state variables) and that Eq. (6) approximates Eq. (1) only for sufficiently small T_s. A detailed discussion on the discretisation error of nonlinear state-space models is given in [7, 18].

As input signal $\mathbf{u}(t)$ three types are considered: random-phase multisines, filtered white Gaussian noise and swept sine singals.

- **Random-phase multisine excitations** are periodic signals obtained from a sum of harmonically related sines with a user-defined amplitude spectrum and a set of independent random phases

$$\mathbf{u}(t) = \sum_{n=1}^{N} A_n \sin(2\pi n f_b t + \phi_n), \qquad (7)$$

  with f_b the base frequency, N the number of excited harmonics and A_n the amplitude associated to the n^{th} harmonic. The phases are independently drawn from a uniform distribution on the interval $(0, 2\pi]$.

- **Filtered white noise excitation** is sampled from a zero-mean normal distribution and low-pass filtered using a Butterworth filter of 6^{th} order.

- **Swept-sine excitation.** A linear frequency sweep given by

$$\mathbf{u}(t) = A \sin((\alpha t + \beta)t), \qquad (8)$$

  with $\beta = 2\pi f_1$, $\alpha = \pi \frac{f_2 - f_1}{T_{\text{SWS}}}$, f_1 and f_2 being the start and the cut-off frequencies respectively. The sweep period, T_{SWS}, was set equal to $1/f_b$.

In Fig. 3 the spectra of the three excitation signals are shown. All signals have been scaled such that $\text{rms}(\mathbf{u}) = 200$. The probability density functions highlight the fact that both the multisine realisation and the noise are asymptotically normally distributed while the swept sine signal is not.

Fig. 4 depicts the phase-space trajectories corresponding to the 3 input signals. It is clear that different regions of the phase-space are covered, depending on the type of excitation signal. For this configuration of

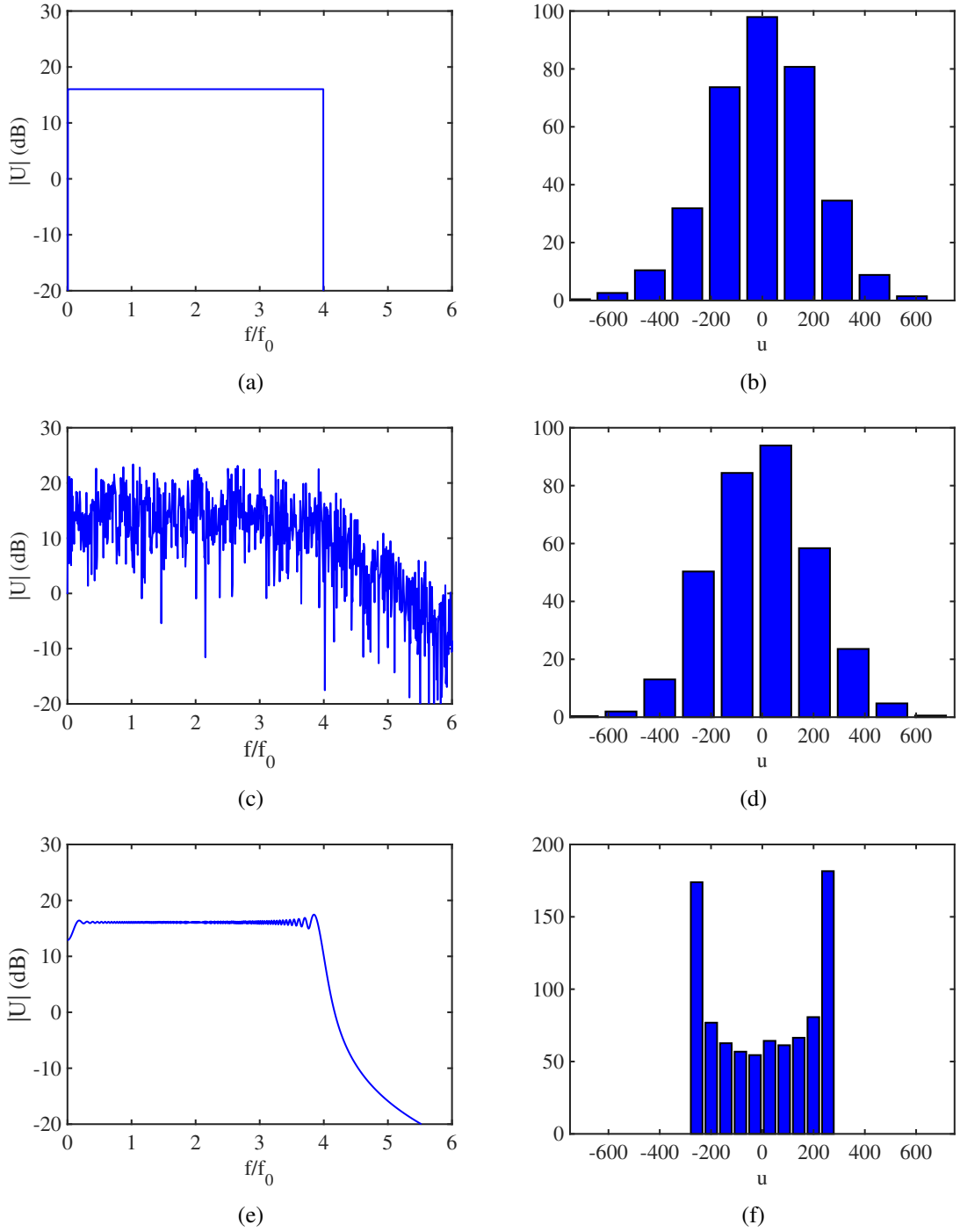


Figure 3: The left column are the spectra of a random-phase multisine realisation, a low-pass filtered noise signal and a swept sine respectively. On the right the histograms of the signals are shown. Frequency axes are normalised with respect to $f_0 = \omega_0/(2\pi)$.

$\{\varepsilon, \omega_0, \text{rms}(\mathbf{u}), f_1, f_2\}$ the swept sine covers a thin shell with, apart from a transient path leading away from the initial condition, no coverage of the region around the origin. The multisine and the noise excitation do however cover a much denser region around the origin. This is highlighted by studying the intersections of the trajectories with the plane $\mathbf{x}_1 = 0$ (Fig. 7c, 7d, 4f). Notice that for this particular swept sine, the covered region does not include the limit cycle trajectory of the autonomous solution (shown in red).

3.2 Approximating the Van der Pol system with a nonlinear state-space model

We now apply the identification procedure of Section 2 to the 3 training datasets introduced in Section 3.1. To initialise the nonlinear model the best linear approximation is used. For the nonlinear optimisation to to run, the initialised model should be able to simulate the training data. Hence the model should remain stable on the training data. A BLA obtained at a higher amplitude level, $\text{rms}(\mathbf{u}) = 300$, was found to provide a stable initialisation as apposed to using the training data level of $\text{rms}(\mathbf{u}) = 300$.

From the frequency-domain subspace identification, second order parametric BLAs are obtained. As nonlinear basis functions, the monomial crossproduct between the states and input raised to the power 3 are used in the state equation and no nonlinearity is introduced in the output equation. Hence all nonlinear contributions in the data are approximated using the following set of basis functions:

$$\eta(t) = \begin{bmatrix} \mathbf{x}_1^3 \\ \mathbf{x}_1^2\mathbf{x}_2 \\ \mathbf{x}_1^2\mathbf{u} \\ \mathbf{x}_1\mathbf{x}_2^2 \\ \mathbf{x}_1\mathbf{x}_2\mathbf{u} \\ \mathbf{x}_1\mathbf{u}^2 \\ \mathbf{x}_2^3 \\ \mathbf{x}_2^2\mathbf{u} \\ \mathbf{x}_2\mathbf{u}^2 \\ \mathbf{u}^3 \end{bmatrix}. \tag{9}$$

Table 1 shows the estimation results, expressed in terms of relative root-mean-square error:

$$e_{\text{rms}} = \frac{\sqrt{\frac{1}{N}\sum_{k=1}^{N}(\mathbf{y}(k) - \mathbf{y}_{\text{sim}}(k))^2}}{\sqrt{\frac{1}{N}\sum_{k=1}^{N}\mathbf{y}(k)^2}}, \tag{10}$$

with N the number of data ponts, $\mathbf{y}$ the true output and $\mathbf{y}_{\text{sim}}$ the output simulated by the PNLSS model. The left column indicates the type of data to which the model has been trained.

Table 1: Estimation results (relative errors) on the training data of the PNLSS models tuned to multisine, noise and swept sine data respectively. 'R' denotes the number of realisations used.

	e_{rms} BLA	e_{rms} PNLSS
3 R multisine	0.36	1.7e-5
3 R noise	0.35	2.3e-6
swept sine (sweep up)	0.62	8e-4

The results of Table 1 indicate that all 3 PNLSS models could be tuned well and approximate the provided training data very accurately. Notice that no measurement noise was added to the data and that hence the 3 models are indeed accurate approximations of Eq. (6) within their trained domains.

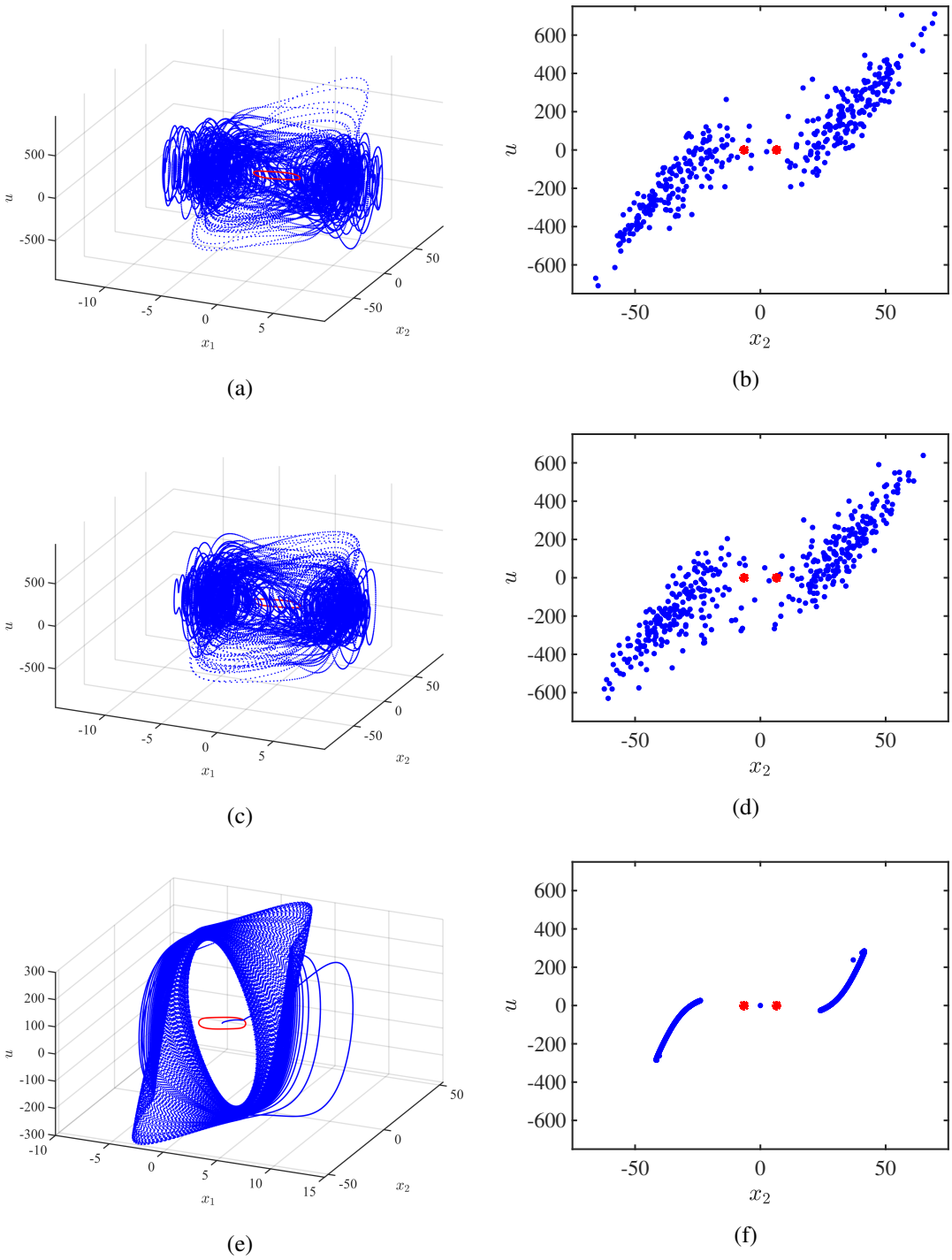


Figure 4: Phase-space trajectories of (a) 3 random-phase multisine realisations (c) 3 filtered noise realisations (e) a swept-sine excitation (sweep up). The column on the right shows the linearly interpolated intersections with the plane $\mathbf{x}_1 = 0$. Red markers indicate the limit cycle described by the autonomous solution.

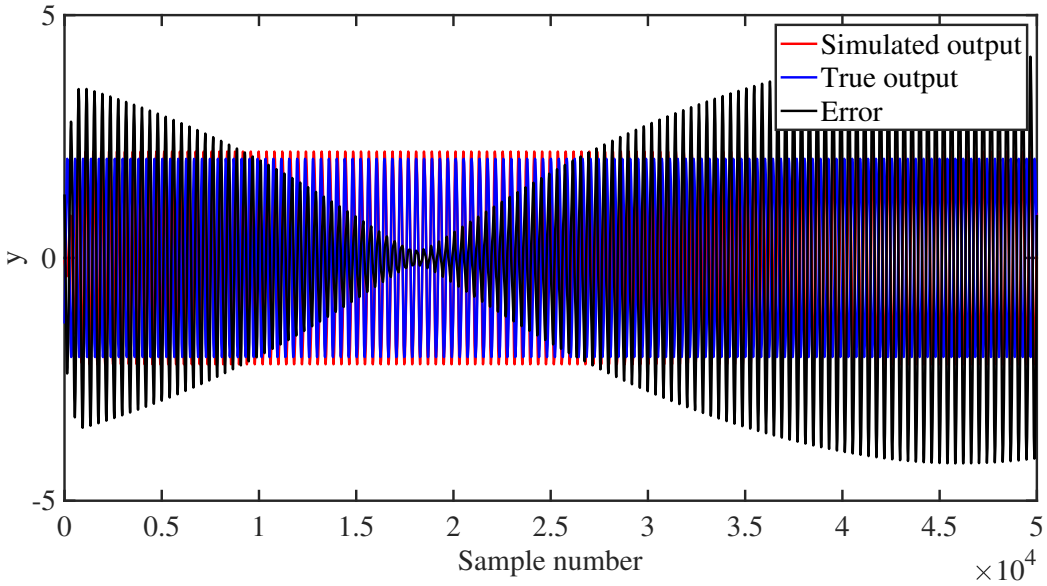


Figure 5: The autonomous output of Eq. 6 simulated using model PNLSS$_S$. PNLSS$_S$ was obtained from training on a swept sine training data set. Since the training data did not cover the autonomous trajectory in phase space, the model performs poorly.

3.3 Validating the nonlinear state-space approximations

In this section the PNLSS models trained on the basis of the different training sets are cross-validated on the remaining data types. The model tuned to multisine data will be denoted PNLSS$_M$, the one tuned to the swept sine PNLSS$_S$ and the one tuned to noise PNLSS$_N$. For validation on the basis of the same data type as the training data a new realisation is used in case of the multisine and the noise and the opposite sweep direction, i.e. sweep down, in case of the swept sine model. Als the autonomous output is used for validation.The validation results are shown in Table 2.

Table 2: Validation results (relative errors) of the PNLSS models tuned to multisine, swept sine and noise data respectively.

	e_{rms} aut.	e_{rms} multisine	e_{rms} swept sine	e_{rms} noise
PNLSS$_M$	0.01	1.9e-5	1.4e-4	2.3e-5
PNLSS$_N$	0.003	2.4e-6	1.2e-5	2.6e-6
PNLSS$_S$	1.39	0.02	6e-3	0.07

From Table 2 it is observed that the models which were trained to data that includes the region of the autonomous solution in phase space, i.e. PNLSS$_M$ and PNLSS$_N$, were indeed able to reproduce the limit cycle output. The simulated output of PNLSS$_S$ along with the error is depicted in Fig. 5. Also notice how extrapolating PNLSS$_S$ to the wider regions covered by the validation multisine and the validation noise realisation results in considerably lower errors than the error on the autonomous output. This illustrates how an extrapolation does not necessarily lead to poor results.

In practice, the estimated models are likely to show larger errors on the training data than the ones shown in Table 1, e.g. the data might be of lesser quality or the system might not belong to the selected model class. To study the effect of larger estimation errors, PNLSS models with a relative error in the order of 1% are validated in Table 3. The models are obtained by deliberately ending the optimisation procedure when the error has dropped to the 1%-level.

Table 3: Validation results (relative errors) of the 1% PNLSS models tuned to multisine, swept sine and noise data respectively.

	e_{rms} aut.	e_{rms} multisine	e_{rms} swept sine	e_{rms} noise
PNLSS$_M$	1.11	0.01	0.04	0.01
PNLSS$_N$	1.19	0.01	0.05	0.01
PNLSS$_S$	1.71	0.12	0.02	0.28

The 1%-error models of Table 3 show that also PNLSS$_M$ and PNLSS$_N$ fail to reproduce the correct autonomous output when their fit to the training data is less accurate. Recalling the cross-section plots of Fig. 4 it is concluded that the coverage of the region where the autonomous solution exists was not dense enough with higher concentrations of data lying away from the origin. Having increased model errors adds to the sensitivity for extrapolation in those regions.

It is concluded from this section that excitation signals of equal amplitude level and frequency band but different in kind can cover different regions of the phase-space. Data-driven models, built upon different signals are hence only good approximations of the underlying system in their distinct regions. We have seen that swept sine signals tend to provide a less dense coverage of the region around the origin compared to Gaussian signals. This can result in models obtained from swept sine signals to fail in reproducing the autonomous solution, typically found in a region around the origin. Also randomness of phases has shown to improve the uniformity of covering the phase space [5].

4 A fluid oscillator example

In Section 3 it was shown that broadband excitation such as random-phase multisines are appropriate signals to model an autonomous oscillator. In this section we study the response of a true autonomous oscillator, i.e. the oscillatory wake behind a submerged cylinder, when applying multisine excitations.

The input to the system is the imposed motion of the cylinder, transverse to the incoming flow, the output is the force coefficient measured on the cylinder along the axis of motion:

$$c_y = \frac{F_y}{\frac{1}{2}\rho D U^2}, \tag{11}$$

with F_y begin the resulting force acting in the y-direction, ρ the density of the fluid D the diameter of the cylinder and U the unperturbed velocity of the flow. Data is obtained from a computational fluid dynamic simulation at Re $= 100$. Validation of the CFD models can be consulted in [2]. Fig. 6 shows the set up. The flow is considered uniform and travelling parallel to the x-axis for increasing x.

It is known that there exists a v-shaped lock-in region, similar to the one of Fig 1, centred around the so-called Strouhal frequency:

$$f_{\text{St}} = \frac{U\text{St}}{D}, \tag{12}$$

where St is the Strouhal number, which was observed to be 0.168 for Re $= 100$ in the present study [2]. We will examine the response of the system for two random-phase multisine signals: one overlapping with the presumed lock-in region and one covering a frequency band outside lock-in. The objective is to determine whether the key feature of the fluid system, being the synchronisation of the vortex shedding, and hence c_y, to frequency components in the lock-in region is still observed when excited with a random-phase multisine.

In order to establish whether the wake is locked we can no longer use the existing definitions of lock-in [9] which explicitly rely on the excitation being a single harmonic sine. We therefore introduce a **lock-in test based on initial conditions:**

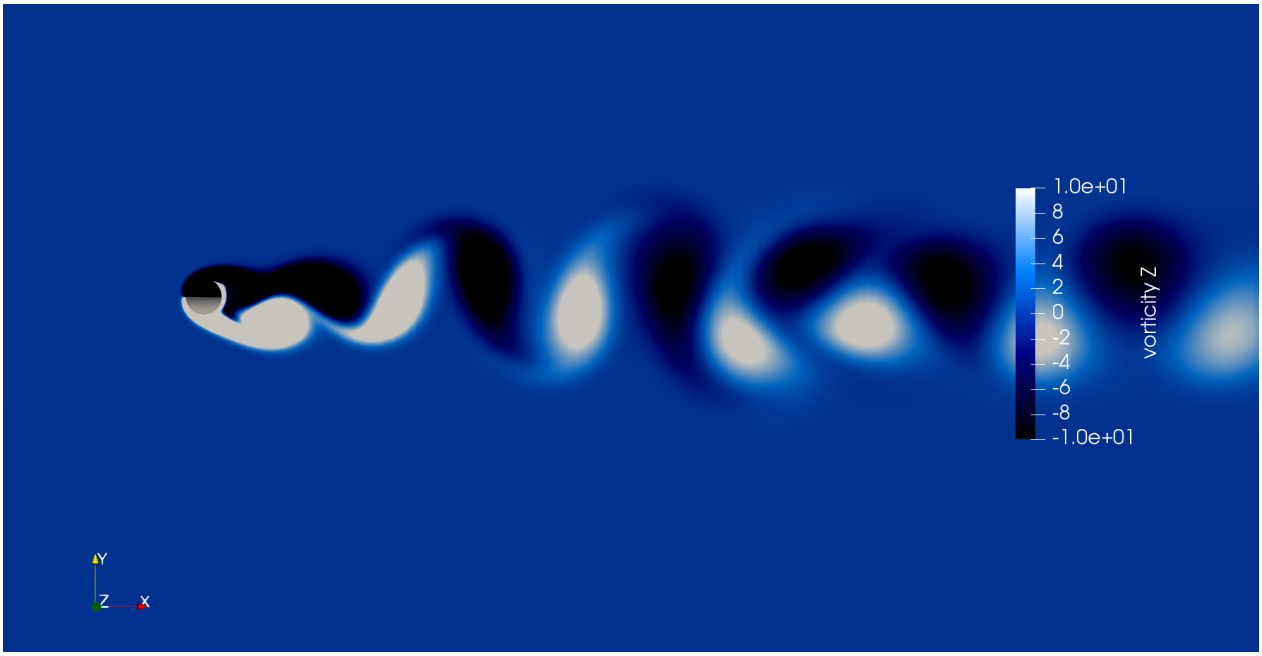


Figure 6: Snapshot of a CFD simulation of a cylinder submerged in a $\mathrm{Re} = 100$ uniform flow. The cylinder is following an imposed random-phase multisine trajectory in the y-direction with a relative amplitude $y/D = 0.30$ and a frequency band ranging from 0.10 up to 4.5 Hz with a resolution of 0.10 Hz. The Strouhal frequency is equal to 3 Hz. Flow is from left to right.

1. Apply the broadband excitation signal twice starting from different initial conditions. In practice the input is initiated at different instances of the autonomous cycle.
2. Subtract both outputs.
3. The oscillator is only considered to be locked if the difference in output signals dies out over time, indicating that the influence of the initial condition is lost.

Two random-phase multisines with the following specifications were applied:

- $f_{\mathrm{ex}}/f_{\mathrm{St}} \in [{}^{1}/_{30}, 1.5]$ with a step of ${}^{1}/_{30}$ and a relative amplitude of $A/D = 0.20$.
- $f_{\mathrm{ex}}/f_{\mathrm{St}} \in [{}^{1}/_{30}, 0.6]$ with a step of ${}^{1}/_{30}$ and a relative amplitude of $A/D = 0.20$.

The results are shown in Fig. 7. The proposed initial condition test clearly distinguishes the locked from the non-locked wake. Based on the conclusions from Section 3 and the fact that the fluid system continues to exhibit the key feature of synchronisation, we propose that random-phase multisine excitation is an appropriate input signal for data-driven modelling of an autonomous oscillator.

5 Conclusion

In this work the intrinsic dependence upon the choice of training data in nonlinear black-box modelling is highlighted. In particular systems which exhibit autonomous oscillations were studied. The impact of using three different kinds of excitation signals as training data: random-phase multisine excitation, filtered white noise and swept sine signals was studied for the forced Van der Pol oscillator. Nonlinear state-space models were built from the data. It was found that swept-sine excitation results in a less dense coverage of the phase

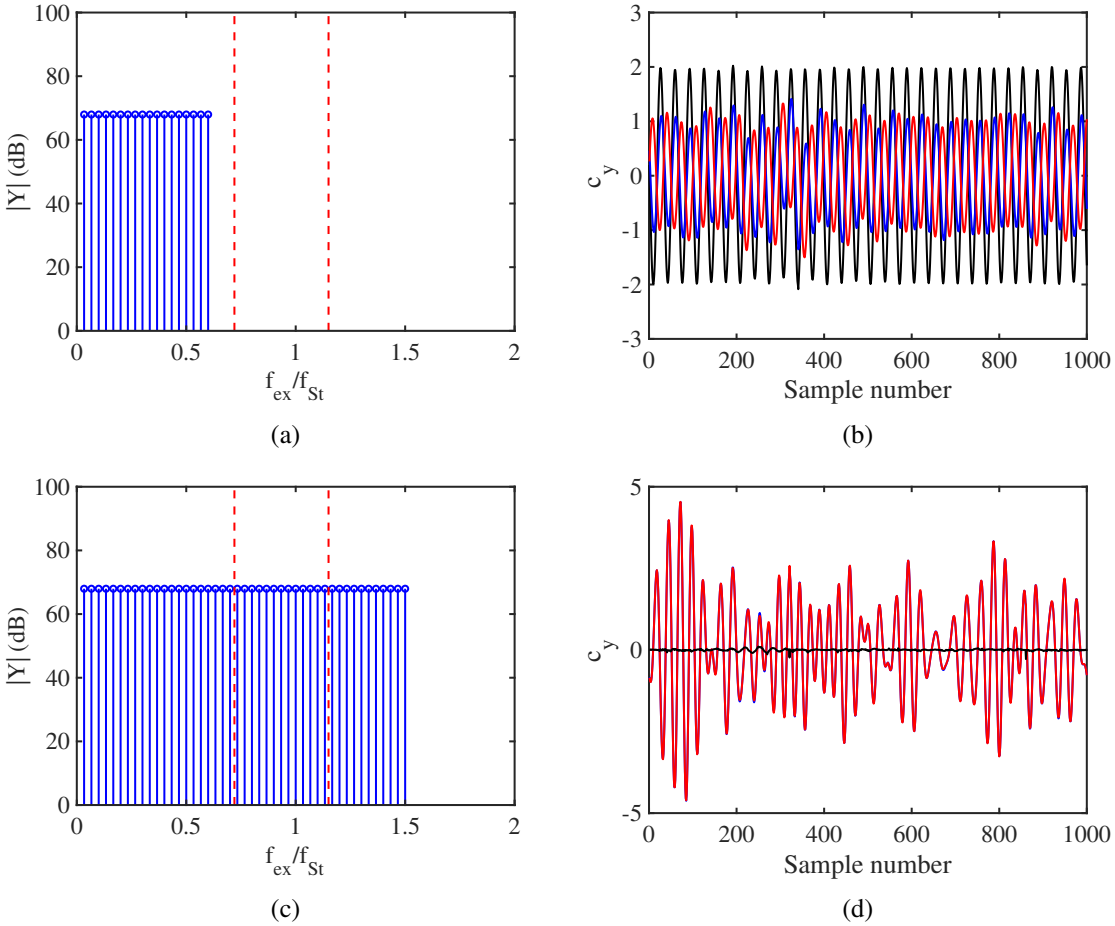


Figure 7: (a) Frequency spectrum of the imposed motion multisine not overlapping with the lock-in region. (b) One period of transient-free c_y starting from two different initial conditions (blue and red) and the difference between both (black) for an excitation not overlapping with the lock-in region. (c) Frequency spectrum of the imposed motion multisine overlapping with the lock-in region. (d) One period of transient-free c_y starting from two different initial conditions (blue and red) and the difference between both (black) for an excitation overlapping with the lock-in region. The boundaries of the lock-in region for $A/D = 0.20$ are indicated with dashed red lines [10].

space compared to multisine or filtered noise, for the studied regimes. As a result, the model obtained from swept sine signals was not able to reproduce the autonomous output while the models trained to multisine excitation or filtered noise were. It was also shown that even the models based on the more dense covered data suffer from extrapolation errors when model errors are introduced into the training step. Additionally the use of multisine excitation on an autonomous fluid oscillator was studied. A new lock-in test, on the basis of the dependence on the initial condition was proposed.

It would be interesting to study how general the present observations are on Monte Carlo simulations of the Van der Pol equation.

Acknowledgements

This work was supported in part by the Fund for Scientific Research (FWO-Vlaanderen), and the ERC advanced grant SNLSID, under contract 320378.

References

[1] R. E. D. Bishop and A. Y. Hassan. The lift and drag forces on a circular cylinder oscillating in a flowing fluid. In *Proceedings of the Royal Society of London A*, volume 227, pages 51–75, 1963.

[2] J. Decuyper, T. De Troyer, M. Runacres, K. Tiels, and J. Schoukens. Nonlinear state-space modelling of the kinematics of an oscillating circular cylinder in a fluid flow. *Mechanical Systems and Signal Processing*, 98:209–230, 2018.

[3] G. Dimitriadis. *Introduction to Nonlinear Aeroelasticity*. Wiley, 2017.

[4] E. H. Dowell. Non-linear oscilltor models in bluff body aero-elasticity. *Journal of Sound and Vibration*, 75(2):251–264, 1981.

[5] S. Duym and J. Schoukens. Design of excitation signals for the restoring force surface method. *Mechanical Systems And Signal Processing*, 9(2):139–158, 1995.

[6] M. L. Facchinetti, E. de Langre, and F. Biolley. Coupling of structure and wake oscillators in vortex-induced vibrations. *Journal of Fluids And Structures*, 19:123–140, 2004.

[7] G. C. Goodwin, A. J. C., G. M. E. C., S. M. E., and J. I. Yuz. Sampling and sampled-data models. *IEEE Control systems magazine*, October 2013.

[8] R. T. Hartlen and I. G. Currie. Lift-oscillator model of vortex-induced vibration. *Journal of Engineering Mechanics Division*, 96(5):577–591, 1970.

[9] S. Kumar, Navrose, and S. Mittal. Lock-in in forced vibration of a circular cylinder. *Physics of Fluids*, 28:113605, 2016.

[10] J. S. Leontini, B. E. Stewart, M. C. Thompson, and K. Hourigan. Wake state and energy transitions of an oscillating cylinder at low Reynolds number. *Physics of Fluids*, 18(067101):10.1063/1.2204632, 2006.

[11] T. McKelvey, H. Akcay, and L. Ljung. Subspace-based multivariable system identification from frequency response data. *Transactions on Automatic Control*, 41(7):960–979, 1996.

[12] J. P. Noël, A. F. Esfahani, G. Kerschen, and J. Schoukens. A nonlinear state-space approach to hysteresis identification. *Mechanical Systems and Signal Processing*, 84:171–184, 2017.

[13] J. Paduart, L. Lauwers, J. Swevers, K. Smolders, J. Schoukens, and R. Pintelon. Identification of nonlinear systems using polynomial nonlinear state space models. *Automatica*, 46:647–657, 2010.

[14] G. V. Parkinson. *Mathematical models of fluid-induced vibrations of bluff bodies*. Flow-induced structural vibrations. Springer, 1974.

[15] A. Pikovsky, M. Rosenblum, and J. Kurths. *Synchronization, A universal concept in nonlinear sciences*. Cambridge University Press, New York, 2001.

[16] R. Pintelon. Frequency-domain subspace system identificaton using non-parametric noise models. *Automatica*, 38(8):1296–1311, 2002.

[17] R. Pintelon and J. Schoukens. *System Identification: A Frequency Domain Approach.* IEEE Press, 2001.

[18] J. Schoukens, R. Relan, and M. Schoukens. Discrete time approximation of continuois time nonlinear state space models. *IFAC PaersOnline*, 50(1):8339–8346, 2017.

[19] K. Tiels. *PNLSS 1.0 A polynomial nonlinear state-space toolbox for MATLAB*. Vrije Universiteit Brussel, 1st ed. edition, 2016.

[20] T. Wigren. Model order and identifiability of non-linear biological systems in stable oscillation. *Transactions on Computational Biology and Bioinformatics*, 2015.

[21] C. H. K. Williamson. Vortex dynamics in the cylinder wake. *Annual Review of Fluid Mechanics*, 28:477–539, 1996.

[22] M. M. Zdravkovich. *Flow around circular cylinders, Volume 1: Fundamentals*, volume 1. Oxford University Press, 1991.

Unsteady aerodynamics and nonlinear dynamics of free-falling rotating seeds

B. A. Roccia[1,2], M. L. Verstraete[1], G. Dimitriadis[2], O. Brüls[2], S. Preidikman[1]
[1] CONICET – National Council of Scientific and Technological Research
Godoy Cruz 2290, C1425FQB CABA, Argentina
e-mail: **bruno.roccia@gmail.com**

[2] University of Liège, Aerospace and Mechanical Engineering Department
Allée de la Découverte 9 (B52/3), B-4000 Liège, Belgium

Abstract
This work presents a three-dimensional numerical tool that is suitable for studying the aerodynamics and nonlinear dynamics of free-falling rotating seeds like samaras. The proposed simulation framework consists of a modified version of the unsteady vortex-lattice method (enhanced by including a diffusion model and the leading-edge vortex contribution by means of the Polhamus analogy) coupled with a multibody rigid dynamic model for the whole seed. The numerical scheme adopted by the aerodynamic subsystem is based on an explicit low-order integrator (Euler's explicit first-order method). On the other hand, the equations of motion associated with the structural part are integrated in the time domain using a second-order Lie group integrator based on an extension of the classical generalized-α method for dynamical systems. Among the main results obtained, it is found that the predicted terminal descending velocity and angular velocity (around the vertical axis) are in close agreement with experimental results reported in the literature.

1 Introduction

In recent decades, different research groups around the world have addressed the difficult task of studying and understanding the underlying physics that characterizes flight at small scales. Despite the constant advances in this area, many of them attributed to Dickinson's team (Caltech, USA) and the Group of Animal Flight led by Ellington, there are still many unanswered questions [1]. The development of micro-air-vehicles (MAVs) with similar capabilities to those shown by flying creatures is, nowadays, a very active research area. An alternative to MAV-like flapping wings is based on the simple way in which almost all plants and trees disperse their seeds over large distances ([2],[3]). Among the dispersal modes exhibited by seeds and flying fruits, the most interesting one, from an engineering point of view, is spinning flight [4]. The seeds that execute a rotary motion as they descend to the ground are known as samaras, and they are perhaps, the simplest, most stable and efficient "flyers" conceived by nature. Moreover, this kind of flight is an example of elegance and balance whereby gravitational potential energy becomes rotational kinetic energy that perpetuates an aerodynamically stable helical descent.

Early studies related to rotating seeds date back to the 50s and were oriented towards analyzing the autorotation mechanism. Subsequently, several works about morphological features (e.g., roughness, airfoil shape, etc.) of samaras were published ([5]-[8]). However, none of these works provide detailed information on the inertial properties of the samaras (e.g. mass center, mass distribution, and first and second moment of inertia).

On aerodynamics, Isaac Newton was the first to describe the falling free motion of a body immersed in a fluid medium in *Philosophiae Naturalis Principia Mathematica*. Nevertheless, it was Maxwell, who led the first systematic study about the autorotation mechanism [9]. He observed that a flat plate under gravitational and aerodynamic forces will start rotating even when there is no initial angular velocity, deducing that the center of pressure (CoP) and the center of mass (CoM) do not coincide during the descent movement. This

discrepancy in the positions between the CoP and CoM produces a torque that finally triggers a rotary motion. However, it was not until the second half of the 20th century that the autorotation phenomenon received the attention of the scientific community. In particular, maple seeds were extensively used for experimentation because their Ω_V / V_D ratio is relatively high (Ω_V being the rotation speed and V_D the sinking velocity). Norberg [5], conducted the first scientific study on a winged seed by using the momentum theory. Burrows [10] and McCutchen [11] used results derived from helicopter theory to investigate the autorotation transition in the flight of samaras. At the same time, Green [12] found a high correlation between the sinking velocity and the square root of the wing loading.

Later, Lentink *et al*. [13] used a dynamically scaled model of a maple seed in order to study the three-dimensional flow around it. They found that the presence of a leading-edge vortex (LEV) is one of the main mechanisms of lift production. In addition, it should be noted that the LEV is an underlying feature of animal flight, which explains the large lifting forces produced by insects, bats and birds [14]. On this basis, Lentink's team pointed out that the LEV is a convergent solution in the context of natural flight, both in animals and insects as well as in plants. By using digital particle image velocimetry (DPIV), Salcedo *et al*. [15] obtained a detailed three-dimensional structure of the LEV on a samara, in close agreement with the results reported by Lentink. Several subsequent research efforts attempted to characterize the kinematics and aerodynamics of rotating seeds ([16]-[20]).

Due to the great promises of the autorotation phenomenon in the context of MAVs, several numerical studies were published, aiming to understand the underlying physics behind this aerodynamic mechanism: flat plates undergoing an autorotation motion ([21],[22]), aerodynamics of freely falling plates and thin disks ([23],[24]), and fluttering and tumbling of falling cards [25], among others. Despite these efforts, there are still several questions related to the unsteady aerodynamic, dynamic stability, and falling/autorotation transition associated with these flying structures.

2 Kinematics of rotating seeds

The computational model adopted in this work to study the aerodynamics/dynamics of rotating seeds is based on the maple seed (*Acer Platanoides*) morphology [5]. For reasons concerning the aerodynamic model, the surfaces that define the pod as well as the blade (lifting surface) of the seed were discretized using simple quadrilateral elements with four nodes (see Fig. 1*a*).

Unlike other types of flying seeds, those that exhibit a rotating motion present two special features: *i*) the center of mass of the whole seed is located at one end; and *ii*) the blade area S_b is small, but the swept disk area generated by the rotation of the blade is large (see Table 1). The first characteristic promotes a rapid onset of autorotation, while the second allows the seed a stable descent on its way to the ground.

Numerous experiments have shown that, in a quiet atmosphere, certain samaras can follow two different trajectories. The most frequent flight mode is characterized by a center of rotation (CoR) describing a straight vertical line. A second, more complex, flight mode is characterized by a compound motion, whereby the CoR also experiences an oscillation in the horizontal plane (normal to the rotation axis) leading to a helical motion of the CoR [26]. Table 1 presents the values of the main morphological and kinematic parameters for the maple seed used as a study case in this work.

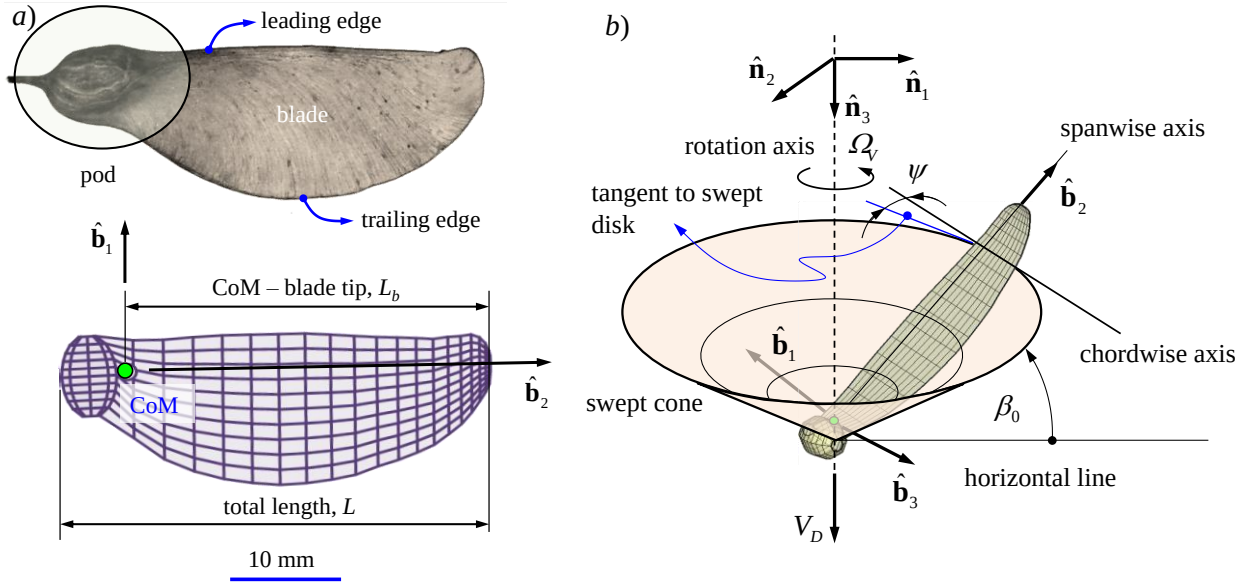


Figure 1: *a*) Spatial geometry of seed; *b*) definition of the kinematical parameters for a samara

In its descending motion, the samara does not adopt a perfectly horizontal blade plane, but the wing tip has an elevation with respect to the seed pod (see Figure 1*b*). Specifically, the coning angle β_0, is defined as the angle between the longitudinal axis of the samara and the horizontal plane (being positive when the wingtip lies above the seed pod). This angle is a consequence of an equilibrium condition, whereby the torque due to the inertial forces (which tends to rotate the wing about its overall center of mass decreasing the coning angle) is balanced by the torque arising from the aerodynamic forces (which tends to increase the coning angle) [26]. If the wing is deflected into a different coning angle, these torques bring it back to the proper angle.

Another important kinematic parameter is the pitch angle ψ, which is defined relative to the plane tangent to the swept cone, as depicted in Figure 1*b*. Equilibrium pitch angles tend to lie between 0º and –3º ([13],[27]).

Parameters value (*Acer Platanoides*)		
L	Total length (cm)	4.70
L_b	Blade length (from CM to blade tip) (cm)	3.70
β_0	Coning angle	20º
C_{max}	Maximal width (max chord) (cm)	1.70
S_b	Blade area (cm^2)	4.52
A_d	Swept disk area (projected on the tip path plane) (cm^2)	38.50
m	Mass (g)	0.11
W	Weight (N)	0.00107
B_W	Blade loading (N/m^2)	2.83
D_W	Disk loading W/A_d (N/m^2)	0.332
Ω_V	Spinning velocity (rad/s)	81.6
V_D	Sinking velocity (m/s)	0.90

Table 1: Morphological and kinematical parameters of the *Acer Platanoides* (extracted from [5])

3 Aerodynamic model

The Unsteady Vortex Lattice model employed for this work is similar to the one used by Preidikman [28] and Roccia *et al.* [29], but it incorporates two major additions: *i*) a vortex-core growth model; and *ii*) a LEV model based on the Polhamus analogy. The UVLM can be applied to three-dimensional lifting and non-

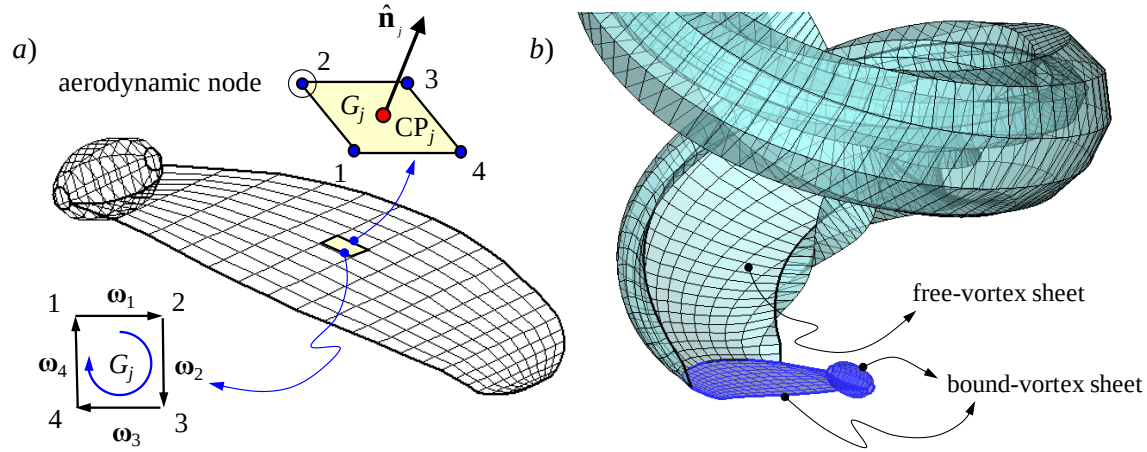


Figure 2: *a*) Discretization of the bound-vortex sheets representing the seed; *b*) arrangement of vortex rings on the bound- and free-vortex sheets

lifting flows. The surface of the body may undergo arbitrary time-dependent deformation, and it can execute any type of maneuver in the space surrounded by moving air. The flow around the full body, i.e. the pod and the blade, is assumed to be irrotational and incompressible over the entire flowfield, except in the regions surrounding the solid boundaries of the body and wakes. As a result of the relative motion between the body and fluid, vorticity is generated in a thin region surrounding the surface of the body (the boundary layer). Part of this vorticity is shed from the sharp edges and forms the wakes. We consider the boundary layers and wakes as zero-thickness sheets of vorticity.

In the unsteady vortex-lattice method, the bound vortex sheet is replaced by a lattice of short, straight vortex segments of circulation $\Gamma_i(t)$. These segments divide the surface of the seed's pod and blade into a number of surface elements (panels) (see Figure 2*a*). The model is completed by joining free vortex lines, representing the free vortex sheets, to the bound vortex lattice along the edges of separation, such as the trailing edge and wing tip of the lifting surface (see Figure 2*b*).

The velocity induced by a finite straight vortex segment of circulation $\Gamma(t)$ can be computed using the following discrete version of the Biot-Savart law:

$$\mathbf{V}(\mathbf{r};t)=\frac{\Gamma(t)}{4\pi}\frac{(\mathbf{r}_1\times\mathbf{r}_2)(\|\mathbf{r}_1\|+\|\mathbf{r}_2\|)}{\|\mathbf{r}_1\|\|\mathbf{r}_2\|(\|\mathbf{r}_1\|\|\mathbf{r}_2\|+\mathbf{r}_1\cdot\mathbf{r}_2)+(\delta_c\|\boldsymbol{\omega}\|)^2}, \tag{1}$$

where $\mathbf{r}$ is the field point where the velocity is being computed, $\mathbf{r}_1$ and $\mathbf{r}_2$ are position vectors of the point where the velocity is being computed relative to the ends of the straight vortex segment, $\boldsymbol{\omega} = \mathbf{r}_1 - \mathbf{r}_2$, and δ_c is the cutoff radius ([29],[30]) used to eliminate the singularity at points on the vortex line. Standard procedures use a range for the cutoff radius between 10% and 25% of the vortex segment length [30].

The governing equation of the problem is complemented with a set of boundary conditions: the regularity at infinity condition and the non-penetration (or impermeability) condition. For imposing these conditions, it is necessary to recall that the position of the solid surface is known, as a function of time, and the normal component of the fluid velocity is prescribed at the boundary. The former condition requires that the velocity field associated with the disturbance decays away from the body and their wakes. Hence,

$$\lim_{\|\mathbf{r}\|\to\infty}\|\mathbf{V}_B(\mathbf{r},t)+\mathbf{V}_W(\mathbf{r},t)\|=0, \tag{2}$$

where $\mathbf{V}_B$ is the velocity associated with the bound vortex lattice, and $\mathbf{V}_W$ is the velocity associated with the free vortex lattice being shed from the wing's trailing edge and tip. The velocity field obtained from Eq. (1) satisfies this condition.

The non-penetration condition requires that, over the entire surface of the seed, the normal component of the fluid velocity relative to the body's surface must be zero:

$$(\mathbf{V}_\infty+\mathbf{V}_B+\mathbf{V}_W-\mathbf{V}_p)\cdot\hat{\mathbf{n}}=0, \tag{3}$$

where $\mathbf{V}_\infty$ is the free-stream velocity, $\mathbf{V}_P$ is the velocity of the solid (seed's pod and blade), and $\hat{\mathbf{n}}$ is the unit vector normal to the body surface.

Because the vortex sheets are replaced by vortex lattices, the non-penetration condition given by Eq. (3) is only satisfied at one point in each panel; these are called control points (CPs), and they are located at the centroid of area of each panel (see Figure 2*b*). The specification of this condition at each control point of the body results in a linear system of algebraic equations (generally with variable coefficients) in terms of the unknown vortex ring circulations $G_j(t)$ and the aerodynamic influence coefficients $A_{ij}(t)$ ([28],[31]),

$$\sum_{j=1}^{NP} A_{ij}\, G_j + \left(\mathbf{V}_\infty + \mathbf{V}_W - \mathbf{V}_p\right)\cdot \hat{\mathbf{n}}_i = 0 \qquad \text{for} \quad i = 1,2,...,NP. \tag{4}$$

where NP is the number of aerodynamic panels. The system of equations (4) is solved for the $G_j(t)$ by using either a direct procedure, such as *LU* decomposition, or an iterative procedure, such as the Jacobi or Gauss Seidel methods.

Once the circulations $G_j(t)$ are calculated, the wake is propagated, at the local velocity of the fluid, using a simple first order numerical scheme such as,

$$\mathbf{r}_{node}\left(t+\Delta t\right) = \mathbf{r}_{node}\left(t\right) + \mathbf{V}_{node}\left(t\right)\Delta t, \tag{5}$$

where $\mathbf{r}_{node}(t)$ is the vector position of a straight vortex segment node at time t, $\mathbf{V}_{node}(t)$ is the velocity of the node at time t, and Δt is the time step.

3.1 Growth vortex-core model

The UVLM is based on a potential flow model and therefore does not consider viscous effects. This fact implies that each vortex segment shed and convected away from the sharp edges maintains its intensity regardless of its "age". However, because of both viscosity and vortex-core growth effects, its circulation intensity decreases with time until it eventually disappears [32]. In addition, the inclusion of a viscous vortex core has proven to be an efficient mechanism to handle situations where two vortex lines are in close proximity or when the wing cuts through its own wake. This treatment has been used to overcome the difficulties when simulating blade-vortex interactions for helicopter rotors [33], and wing-wake interaction for flapping wings ([34],[35]), among others.

Each row of vortex segments in the wake is labeled with a different age, and thus, the core radius of the segments shed at t_0 is bigger than the radii of the segments shed into the wake at the latest time step. Although there exist several vortex-core growth models, in this work we adopted a modified version of the viscous Lamb-Ossen model (which includes the viscosity effect) [36] and initially proposed by Squire [37]. On this basis, the cutoff radius in Eq. (1) is replaced by,

$$\delta_c\left(t\right) = \sqrt{4\alpha_v \delta_v \nu \left(t+t_0\right)}, \qquad \text{and} \qquad t_0 = \frac{r_{c0}^2}{4\alpha_v \delta_v \nu}, \tag{6}$$

where $\alpha_v = 1.25643$ is the Ossen parameter, ν is the kinematic viscosity of air, t is the time elapsed since the vortex segment was shed into the wake, r_{c0} is usually set to 10% of the vortex segment length, and δ_v represents the additional dissipation due to viscosity, which is defined in term of the vortex segment circulation Γ as,

$$\delta_v = 1 + a_1 \frac{\Gamma}{\nu}, \tag{7}$$

where a_1 is the Squire's parameter. The choice of Squire's parameter is directly related to the core growth rate and is important for maintaining the stability of the solution [38].

3.2 Leading-edge model

Because the motion of natural flyers such as winged insects and rotating seeds is quite complex, vortex shedding from the leading edge depends on the angle between the local fluid velocity and the wing/blade plane (effective angle of attack). As mentioned earlier, the LEV plays a crucial role in enhancing the lift generated by insect wings. Several experiments, mostly due to Ellington's group ([39],[40]) and Dickinson's team ([14],[41],[42]), have shown that the separated sheet near the leading-edge reattaches, leading to a stable LEV. This phenomenon depends partly on a strong spanwise flow that drains vorticity from the LEV toward the wing-tip vortex (analogous to the LEV on delta wings). These findings allowed the use of Polhamus's leading-edge suction analogy to take into account the extra lifting force due to the presence of an attached and stable LEV on insect wings ([34],[41],[43],[44]). Other techniques can be used to calculate the LEV contribution to the lift, such as the Leishman-Beddoes model [35] and a leading-edge wake shed from the bound leading-edge panels [29].

In the context of rotating seeds, Lentink *et al*. [13] carried out a series of experiments on a dynamically scaled robot to test whether this natural autorotating phenomenon generates a LEV. For all tested seed models, Lentink's team found that a prominent LEV is generated near the blade root, which is markedly similar to the LEVs produced by insect wings. Because the seed rotation introduces a radial velocity distribution while it descends, the geometrical angle of attack, α_G, increases towards the blade root, taking its minimum value at the blade tip (see Figure 3*a*). According to results reported by Lentink *et al*., this trend explains in part why the LEV remains well attached to the seed's surface.

According to Polhamus [45], it is possible to estimate the additional lifting force associate with the presence of a LEV from the suction force (predicted by potential flow theory), provided that the vortex travels with the wing. Thanks to the important similarity between the LEV in insects and seeds, together with the reasoning pointed out by [34], it is possible to estimate the leading edge vortex contribution on these natural flyers using the analogy proposed by Polhamus. It assumes that the vortex force in a separated flow has a magnitude equal to that of the suction force predicted in attached flow conditions. However, the force direction is rotated by 90º (when the flow is separated) in order to be normal to the lifting surface. In this work, the force calculated by means of the leading-edge suction analogy is applied at the control points of the panels located along the leading edge of the seed´s blade. To determine the flow condition, we implemented a scheme based on an on/off mechanism [29]. The mechanism consists mainly of computing the value of the effective angle of attack α at each time step and comparing it with a reference value; in the present examples, the reference is $\alpha_c = 12^o$. If $\alpha \geq \alpha_c$, the flow is separated, and the suction force is rotated by 90º to be perpendicular to the blade's surface; conversely, if $\alpha < \alpha_c$, the suction force remains parallel to the blade's surface (see Figure 3*b*). The angle of attack is computed at each panel located along the leading edge by considering the freestream velocity (if it exists), the instantaneous wing velocity, and the velocity induced by all the vortex segments belonging to the bound and wake vortex sheets.

According to Lan and Roskam [46], the leading edge suction force per unit length of the leading edge is,

$$F_s = \frac{\pi}{8\cos\Lambda_{LE}} q_\infty \Delta C_p^2 \left(\eta - \eta_{LE}\right), \tag{8}$$

where q_∞ is the freestream dynamic pressure, Λ_{LE} is the leading edge sweep angle, ΔC_p is the pressure jump coefficient, η_{LE} is the position of the leading edge and η is a spatial coordinate along the chordwise direction. Following the procedure detailed by Nguyen *et al*. [34], the final, quasi-steady, expression for the leading edge suction force, adapted for the UVLM, is given by,

$$\left(F_s\right)_j = \eta_s \frac{\pi}{16} \frac{\rho \Gamma_{LE_j}^2}{\Delta\eta_{LE_j} \cos\Lambda_{LE_j}}, \tag{9}$$

where Γ_{LE_j} is the circulation of the vortex segment placed at the leading edge of the *jth* aerodynamic panel along the leading edge, $\Delta\eta_{LE_j}$ is the length of the *jth* leading-edge panel in the chordwise direction, ρ is the

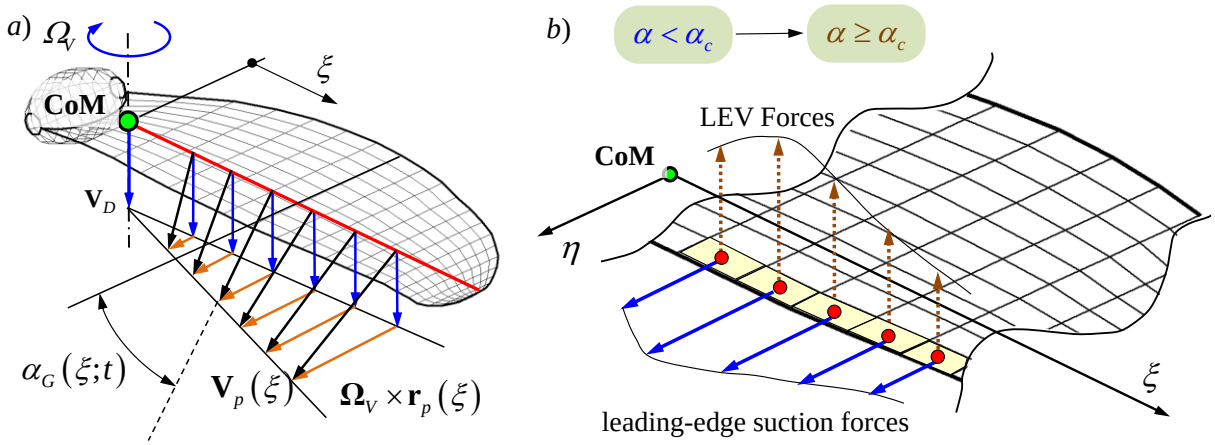


Figure 3: *a*) Geometrical angle of attack, where ξ is the spatial coordinate along the spanwise direction (adapted from [13]); *b*) leading-edge suction force and LEV force sketch

constant density of the fluid, and η_s is the leading-edge suction efficiency coefficient (which can range from 0 to 1). The efficiency coefficient is introduced because the value of the real suction force can be less than the one predicted by Eq. (9) due to viscous effects and the leading-edge shape, among other reasons ([34],[47]).

3.3 Aerodynamic loads

The aerodynamic loads acting on the lifting surfaces are computed as follows: 1) for each element, the pressure jump at the control point is computed by applying the unsteady Bernoulli equation; 2) the force on each element is calculated as the product of the pressure jump, the element area, and the unit vector normal to each aerodynamic panel; 3) the resultant forces and moments are computed as the (vector) summation of the forces and moments produced by each element. The unsteady Bernoulli equation is given by

$$\partial_t \boldsymbol{\varphi}(\mathbf{r};t) + \frac{1}{2}\mathbf{V}(\mathbf{r};t)\cdot\mathbf{V}(\mathbf{r};t) + \frac{1}{\rho}p(\mathbf{r};t) = H(t), \tag{10}$$

where ∂_t denotes the partial time derivative at a fixed space location in an inertial reference frame, $\mathbf{V}(\mathbf{r};t)$ is the spatial gradient of the velocity potential $\boldsymbol{\varphi}(\mathbf{r};t)$, $p(\mathbf{r};t)$ is the unknown pressure, $H(t)$ is the total energy per unit mass, which only depends on time and has a unique value at every point of the whole fluid domain, and $\mathbf{r}$ is the position vector of a fluid particle at the instance t.

In its present form, the evaluation of $\partial_t \boldsymbol{\varphi}$ is troublesome, but this term can be stated so as to make its evaluation relatively easy. Detailed explanations of the treatment of each term in Eq. (10), as well as a full formulation of the unsteady vortex lattice method are given by Preidikman [28], Preidikman and Mook [48] and Roccia *et al.* [29]. It should be noted that the leading edge suction forces (if $\alpha < \alpha_c$) or LEV forces (if $\alpha \geq \alpha_c$) computed by Eq. (9) are added to those calculated by Eq. (10).

4 Rigid body dynamic model

In this work, the complete seed is modeled as a rigid body, whose equations of motion are described on the Lie group defined as the Cartesian product of the translations group $\mathbb{R}^3$ (Euclidean space) and the special orthogonal group $SO(3)$ (proper rotations) [49]. In this formulation, the configuration of the seed is represented by an element $Q(\mathbf{x}_0, \mathbf{R})$, where $\mathbf{x}_0 \in \mathbb{R}^3$ is the position vector of the mass center of the seed (translation) and $\mathbf{R} \in SO(3)$ is a rotation matrix that characterizes the orientation of the fixed-body frame (denoted here by $\boldsymbol{B} = \{\hat{\mathbf{b}}_1, \hat{\mathbf{b}}_2, \hat{\mathbf{b}}_3\}$) with respect to the inertial frame $\boldsymbol{N} = \{\hat{\mathbf{n}}_1, \hat{\mathbf{n}}_2, \hat{\mathbf{n}}_3\}$. The set $\mathbb{R}^3 \times SO(3)$ is a six-dimensional Lie group whose composition is given by the direct product, i.e, if $Q_1(\mathbf{x}_1, \mathbf{R}_1)$ and $Q_2(\mathbf{x}_2, \mathbf{R}_2) \in \mathbb{R}^3 \times SO(3)$, then the group operation is simply $Q_1 \circ Q_2 = (\mathbf{x}_1 + \mathbf{x}_2, \mathbf{R}_1\mathbf{R}_2)$.

This composition can be expressed as matrix product provided that Q is represented by the following 7×7 matrix,

$$\mathbf{Q}(\mathbf{x}_0, \mathbf{R}) = \begin{bmatrix} \mathbf{R} & \mathbf{0}_{3\times3} & \mathbf{0}_{3\times1} \\ \mathbf{0}_{3\times3} & \mathbf{I}_3 & \mathbf{x}_0 \\ \mathbf{0}_{1\times3} & \mathbf{0}_{1\times3} & 1 \end{bmatrix}. \tag{11}$$

Its Lie algebra, denoted by $\mathbb{R}^3 \times \mathfrak{so}(3)$, is given by the following set of matrices,

$$\tilde{\mathbf{v}} = \begin{bmatrix} \tilde{\boldsymbol{\Omega}} & \mathbf{0}_{3\times3} & \mathbf{0}_{3\times1} \\ \mathbf{0}_{3\times3} & \mathbf{0}_{3\times3} & \mathbf{u}_0 \\ \mathbf{0}_{1\times3} & \mathbf{0}_{1\times3} & 0 \end{bmatrix}. \tag{12}$$

where $\widetilde{\boldsymbol{\Omega}}$ is a skew-symmetric matrix. As $\mathbb{R}^3 \times \mathfrak{so}(3)$ is isomorphic to $\mathbb{R}^6$, through the invertible mapping $\widetilde{(\cdot)}$, each $\tilde{\mathbf{v}}$ can be expressed as a six-dimensional vector $\mathbf{v} = (\mathbf{u}_0^T, \boldsymbol{\Omega}^T)^T$ with $\boldsymbol{\Omega} = \mathrm{vect}(\widetilde{\boldsymbol{\Omega}})$. By using a left invariant representation for derivatives and assuming $\mathbf{v}$ as the velocity, $\mathbf{u}_0$ is interpreted as the vector of translation velocities in the inertial frame and $\boldsymbol{\Omega}$ is the vector of angular velocities in the body-fixed frame.

In this work, we consider two different models for the seed: *i*) a full six degree-of-freedom model (6-DOFs), and *ii*) a five degree-of-freedom model (5-DOFs) where the coning angle is set at a constant value throughout the simulation. Due to the constant coning angle condition, the rotation matrix $\mathbf{R}$ has to satisfy some kinematic constraint.

Following the procedure exposed in [49] and after some algebraic manipulations, the index-3 differential-algebraic equations that govern the temporal evolution of the rotating seed under gravitational and aerodynamic forces are given by,

$$\begin{aligned} \dot{\mathbf{Q}} &= \mathbf{Q}(\mathbf{x}_0, \mathbf{R})\tilde{\mathbf{v}}, \\ m\dot{\mathbf{u}}_0 - \mathbf{F}_g - \mathbf{F}_a &= \mathbf{0}_{3\times1}, \\ \mathbf{J}\dot{\boldsymbol{\Omega}} + \tilde{\boldsymbol{\Omega}}\mathbf{J}\boldsymbol{\Omega} - \mathbf{R}^T\mathbf{m}_a + \mathbf{B}^T\lambda &= \mathbf{0}_{3\times1}, \\ \phi(\mathbf{Q}) = \hat{\mathbf{b}}_2^T\left(\mathbf{R}^T\hat{\mathbf{n}}_3\right) - a_\beta &= 0, \end{aligned} \tag{13}$$

where $\mathbf{J}$ is the inertia tensor of the seed with respect to the center of mass in the body-fixed frame, $\mathbf{F}_g$ is the force due to the gravitational field, $\mathbf{F}_a$ is the force vector that accounts for the aerodynamic force distribution on the seed's blade, $\mathbf{m}_a$ is the aerodynamic moment with respect to the center of mass of the seed, a_β is the cosine of the coning angle formed between vector $\hat{\mathbf{b}}_2$ (pointing along the span direction of the seed) and vector $\hat{\mathbf{n}}_3$ (aligned with the vertical axis), λ is the Lagrange multiplier associated with the constraint ϕ, and $\mathbf{B}$ is the Jacobian matrix due to the constraint, written as,

$$\mathbf{B} = \hat{\mathbf{b}}_2^T\widetilde{\mathbf{R}^T\hat{\mathbf{n}}_3}. \tag{14}$$

If the constraint equation as well as the Jacobian matrix are removed from the formulation in Eq. (13), we obtain the equations of motion for the unconstrained system (six degrees of freedom).

4.1 Computational implementation

The approach followed in this work treats the rigid body dynamic model (called Simulator 1) and the airflow model (called Simulator 2) as different subsystems of a single dynamical system. These two simulator engines exchange information bi-directionally in an iterative sequence in order to continuously improve the estimation of the structure's response and the aerodynamic loads, respectively ([50],[51]). On the one hand, the numerical scheme used by Simulator 2 utilizes a simple first order scheme (Euler method) ([28],[29]). On the other hand, the numerical procedure adopted for Simulator 1 to solve the equations of motion of the seed is a second order Lie group integrator [49] based on an index-3 formulation of the generalized-α time integration scheme [52]. As the adopted numerical procedure in Simulator 1 performs Newton-Raphson

iterations, it requires the linearization of the equations of motion expressed in Eq. (13). After some algebraic manipulations, the iteration matrices associated with the dynamical equations (13) for the 5 and 6 degree-of-freedom models are,

$$\mathbf{S}_{5-DOF} = \begin{bmatrix} m\beta'\mathbf{I}_3 & \mathbf{0}_{3\times3} & \mathbf{0}_{3\times1} \\ \mathbf{0}_{3\times3} & \beta'\mathbf{J} + \gamma'\mathbf{C}_T - \mathbf{K}_{T_1}\mathbf{T}_{SO3} & \mathbf{B}^T \\ \mathbf{0}_{1\times3} & \mathbf{B}\mathbf{T}_{SO3} & 0 \end{bmatrix},$$
$$\mathbf{S}_{6-DOF} = \begin{bmatrix} m\beta'\mathbf{I}_3 & \mathbf{0}_{3\times3} \\ \mathbf{0}_{3\times3} & \beta'\mathbf{J} + \gamma'\mathbf{C}_T - \mathbf{K}_{T_2}\mathbf{T}_{SO3} \end{bmatrix}, \tag{15}$$

where $\mathbf{C}_T$ is the damping tangent matrix, $\mathbf{K}_{T_1}$ and $\mathbf{K}_{T_2}$ are the stiffness tangent matrices, $\mathbf{T}_{SO3}$ is the tangent operator associated with the exponential map in $SO(3)$, and β' and γ' are algorithmic parameters,

$$\mathbf{C}_T = \widetilde{\mathbf{\Omega}}\,\mathbf{J} - \widetilde{\mathbf{J}\,\mathbf{\Omega}},$$
$$\mathbf{K}_{T_1} = \widetilde{\mathbf{R}^T\mathbf{m}_a} - \widetilde{\hat{\mathbf{b}}_2}\widetilde{\mathbf{R}^T\hat{\mathbf{n}}_3}\boldsymbol{\lambda},$$
$$\mathbf{K}_{T_2} = \widetilde{\mathbf{R}^T\mathbf{m}_a}, \tag{16}$$
$$\mathbf{T}_{SO3} = I_3 + \frac{\cos\sigma - 1}{\sigma^2}\tilde{\boldsymbol{\psi}} + \left(1 - \frac{\sin\sigma}{\sigma}\right)\frac{\tilde{\boldsymbol{\psi}}\tilde{\boldsymbol{\psi}}}{\sigma^2},$$
$$\beta' = \frac{(1-\alpha_m)}{\beta h^2(1-\alpha_f)}, \quad \text{and} \quad \gamma' = \frac{\gamma}{\beta h}.$$

In Eq. (16), h is the time-step, $\boldsymbol{\psi}$ is the Cartesian rotation vector [53], $\sigma = \|\boldsymbol{\psi}\|$, and β, γ, α_f and α_m are numerical parameters associated with the integrator. Let us note that the generalized-α method is equivalent to the Hilber-Hughes-Taylor method if $\alpha_m = 0$ and to the Newmark method if $\alpha_m = \alpha_f = 0$. Here, their values are selected according to

$$\alpha_f = \frac{\rho_\infty}{\rho_\infty + 1}, \quad \alpha_m = \frac{2\rho_\infty - 1}{\rho_\infty + 1}, \quad \beta = \frac{1}{4}\left(1 + \alpha_f - \alpha_m\right)^2, \text{ and } \quad \gamma = \frac{1}{2} + \alpha_f - \alpha_m, \tag{17}$$

where ρ_∞ represents the desired value of the spectral radius at infinite frequencies. For a detailed integration algorithm and a full explanation of the derivation and linearization of the equations of motion of a rigid multibody system, the reader can consult ([49],[54]).

Sequence of steps during a typical time-step

1	Simulator 2 is used to convect the wakes to their new positions through Eq. (5)
2	Simulator 1 uses the current loads computed by Simulator 2 to predict the response of the seed's structure.
3	The current state of the seed is used as input to Simulator 2 and the loads are recalculated, but the wake remains frozen. Then, these loads are used as input to Simulator 1 and the state of the seed is updated. This step is repeated until convergence.
4	Then, the final position and velocity of the seed are evaluated by Simulator 1, and these values are used by Simulator 2 to recalculate the flow field and obtain the final estimate for the aerodynamic loads.

Table 2: Co-simulation strategy

In the context of this paper, simulation refers to a numerical solution of a continuous system, whereas co-simulation describes the concept of simultaneous executions of multiple interacting subsystem simulators.

During a time-step h, the wakes are consistently convected to their new positions with the requirement that vorticity moves with the fluid particles, while, simultaneously, the structure of the seed moves to its new position as a result of the applied forces and constraint equations. This concept is implemented by performing a sequence of steps to calculate the solution at time $t_{n+1} = t_n + h$ (see Table 2). At each time step, Newton-Raphson iterations are performed until the absolute error in the residue (motion equations) and the iteration error (in the increments) are both less than a prescribed error tolerance. Usually, in step 3, seven to twelve iterations are required to reduce the error to less than 10^{-10}.

Although Simulator 1 and Simulator 2 are computational implementations of physical fields independently modeled as the aerodynamics and the seed structure, the coupling procedure is indeed strong because information is exchanged bi-directionally until convergence of the coupled problem, and the chosen step, which advances the solution in time, is unique for the two simulation environments.

5 Numerical results

In this section, results obtained from the implementation of the proposed methodology written in Fortran 90 are presented. This implementation is highly structured in a modular organization; each component can be individually removed and replaced. Furthermore, new modules can be added without modifying the general structure of the program. The morphological data of the rotating seed analyzed in this section were already presented in Table 1. The rest of the parameters are: aerodynamic coefficient $a_1 = 0.1$, leading-edge suction efficiency coefficient $\eta_s = 0.7$, spectral radius $\rho_\infty = 0.8$, critical angle of attack $\alpha_c = 12^o$, and a fully spatial discretization of the seed of 280 aerodynamic panels (80 for the pod and 200 for the blade). The time-step is $h = 1.06766 \times 10^{-3}$ s and is determined as the ratio between a characteristic length and a characteristic velocity. The former is the typical length of a panel on the aerodynamic mesh ($L_c = 1.4736$ mm). The latter is a representative velocity of the problem, in this case the linear velocity of a point at 50% of the blade's span once the seed has achieved a steady motion ($V_c = 1380.22$ mm/s).

Finally, the initial conditions are: initial position of the center of mass $\mathbf{x}_0 = 0.0$, initial velocity of the center of mass $\mathbf{u}_0 = 0.0$, initial angular velocity $\Omega_V = -50.0$ rad/s, coning angle $\beta_0 = 20^o$, and pitch angle $\psi = -0.5^o$. Four thousand time steps (equivalent to 4.27 seconds of physical time) were used to perform numerical simulations of the descent of a samara, since its initial configuration until it reaches a steady motion. The total computational cost per simulation was, on average, four hours.

When the model is released from this initial condition, the constrained model (constant coning angle) predicts a final steady motion in close agreement with the data reported by biologists. After 0.5 s of simulation, the seed starts to stabilize its motion by achieving a terminal sinking velocity of $V_D = 1021.00$ mm/s, a terminal angular velocity $\Omega_V = -74.14$ rad/s and a pitch angle $\psi = -2.74^o$ (see Figures 4*c*, 4*d* and 4*e*). The predicted values of the sinking and angular velocities exhibit relative percentage errors of 13% and 9.17%, respectively, when compared to typical measured values for this kind of seed. Although there is no detailed information in the literature about the pitch angle of the seed studied here, the value obtained is within the expected range according to Lentink *et al*. [13] and Azuma and Yasuda [27]. In steady motion, the aerodynamic force cancels the weight of the samara, preventing it from accelerating downwards (see Figure 5*a*). A steady descending motion necessarily implies, at least, three stable characteristics: the effective angle of attack of the blade, the coning angle, and the sideways motion. In this analysis, while the coning angle is forced to a constant value of 20º, the pitch angle is allowed to change, reaching a constant value in steady motion (see Figure 4*e*). This means that the effective angle of attack also achieves a constant distribution along the blade's span. This stability condition occurs whenever the center of pressure coincides with the center of mass of the samara. In figure 5*b*, we can observe that the effective angle of attack is high near the seed's pod, which means that the CoP is shifted toward the trailing-edge. However, towards the tip where most of the lift is generated, the angle of attack is lower and the center of pressure lies near the quarter-chord point, leading to a nose-up pitch moment. Although there is no data for the angle of attack of the seed studied, the distribution obtained is similar (in both trend and magnitude) to other seeds analyzed by Lentink *et al*. In addition, it should be noted from Figures 4*a* and 4*b* that the seed's mass center describes a sort of helical path while falling to the ground, also in agreement with experimental observations [55].

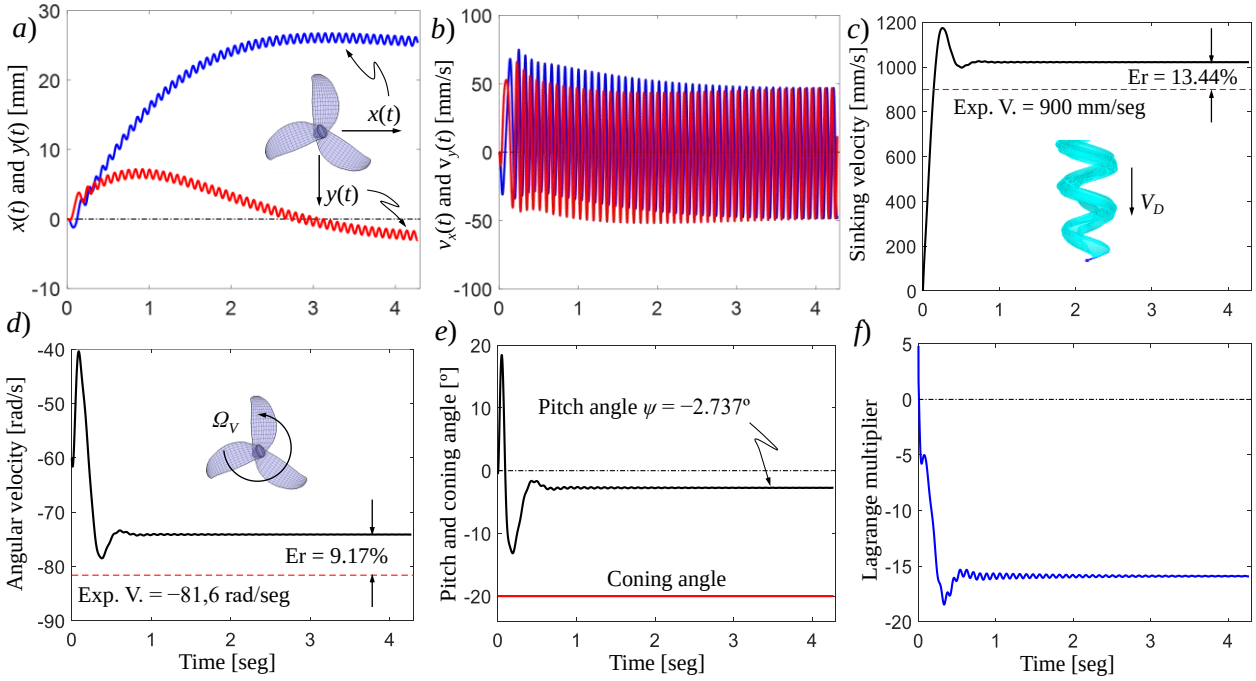


Figure 4: *a*) Sideway displacement; *b*) sideway velocity; *c*) sinking velocity; *d*) angular velocity around the vertical axis; *e*) pitch and coning angles; *e*) Lagrange multiplier

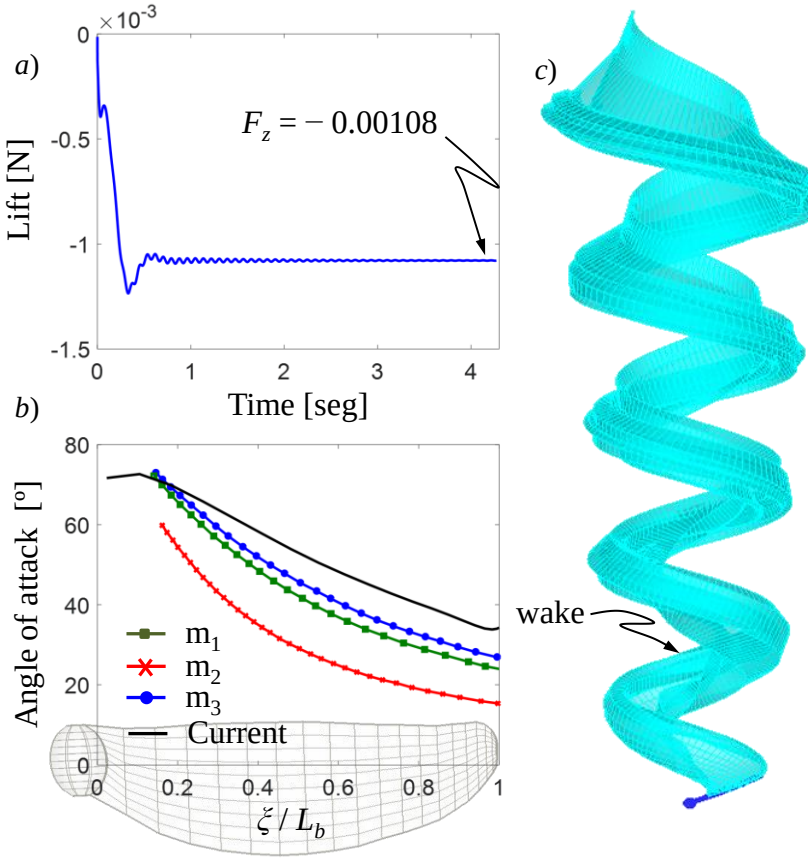


Figure 5: *a*) Lift force; *b*) effective angle of attack distribution (m_1: *Acer palmatum*, m_2: *Acer diabolicum Blume*, m_3: *Carpinus ischonoskii*, extracted from [13]); *c*) wake pattern in steady motion

Finally, results for the Lagrange multiplier associated with the coning angle constraint are presented in Figure 4*f*. As can be observed, its magnitude is different from zero in steady motion. Despite the very encouraging results obtained, this fact implies that there exists some kind of unbalance between the inertialforces and the aerodynamic forces. Numerical simulations performed with the six degrees of freedom model showed that removing the coning angle constraint leads to another stable configuration characterized by: *i*) a sinking velocity V_D = 2500 mm/s, *ii*) angular velocity Ω_V = –158.7 rad/s, *iii*) pitch angle ψ = –23º, and *iv*) coning angle β_0 = –63º. In this configuration, the angle of attack along the blade showed a similar distribution as the one presented in Figure 5*b*.

It is necessary to highlight the lack of data related to the inertial properties (mass center and inertia tensor), which necessitated some gross estimations of these parameters, based on approximate measurements reported by Norberg [5]. In addition, Azuma and Yasuda [8] found several reasons why their prototypes reached a stable motion in a very different configuration from that exhibited by the real samaras, or even worse, the transition to autorotation never happened. Among the most important reasons, they mentioned that the blade should have a negative camber, at least at the inboard portion (but recall it is the tip of the blade that contributes most to lift). In other words, it should be convex downwards; this causes the airfoil to settle at a stable and suitable angle of attack.

6 Conclusions

This paper presented the development of a numerical tool for studying the dynamics and unsteady aerodynamics of rotating seeds. The subsystem involving the rigid body dynamic model was built using a formalism based on matrix Lie groups. This dynamic model has been successfully coupled in a strong way to the subsystem that models the aerodynamics, which is based on an enhanced version of the unsteady vortex lattice method. The numerical integration of the dynamical equations was performed successfully in the time domain using a specially modified generalized-α scheme to handle index-3 differential-algebraic equations formulated in a Lie group setting.

Some important preliminary conclusions can be drawn from the work. The five degree-of-freedom model (constrained coning angle) results in accurate predictions for the response of rotating seeds, including the aerodynamic forces, terminal sinking velocity, terminal angular velocity, terminal pitch angle, and angle of attack distribution, among others. These variables are crucial for understanding the seed dispersion and for the development of micro air vehicles based on the autorotation phenomenon. However, the 5-DOFs model does not fully reflect the real behavior of these natural flyers because of a non-zero torque arising from an unbalance between the inertial and aerodynamic forces. In this regard, more studies (using the 6-DOFs model) are needed in order to fully identify the causes of this unbalance.

Despite the limitations outlined above, the co-simulation framework presented in this article is an excellent starting point for studying rotating seeds as well as samara-like MAVs.

Acknowledgements

The authors gratefully acknowledge the partial support received from the Consejo Nacional de Investigaciones Científicas y Técnicas (CONICET), Argentina and the International Wallonie-Bruxelles Federation (WBI), Belgium.

References

[1] D. J. Pines, F. Bohorquez, *Challenges facing future micro-air-vehicle development*, Journal of Aircraft, Vol. 43, No. 2, (2006), pp. 290-305.

[2] H. S. Horn, R. Nathan, S. R. Kaplan, *Long distance dispersal of tree seeds by wind*, Ecological Research, Vol. 16, (2001), pp. 877-885.

[3] R. Nathan, *Long-distance of dispersal plants*, Science, Vol. 313, (2006), pp. 786-788.

[4] C. Pandolfi, D. Izzo, *Biomimetic on seed dispersal: survey and insights for space exploration*, Bioinspiration & Biomimetics, Vol. 8, (2013), 025003 - 9pp.

[5] R. A. Norberg, *Autorotation, self-stability, and structure of single-winged fruits and seeds (samaras) with comparative remarks on animal flight*, Biological Review, Vol. 48, (1973), pp. 561-596.

[6] D. Seter, A. Rosen, *Stability of the vertical autorotation of a single-winged samara*, Journal of Applied Mechanics, Vol. 59, (1992), pp. 1000-1008.

[7] T. W. Sipe, A. R. Linnerooth, *Intraspecific variation in samara morphology and flight behavior in acer saccharinum (aceraceae)*, American Journal of Botanic, Vol. 82, No. 11, (1995), pp. 1412-1419.

[8] A. Azuma, K. Yasuda, *The autorotation boundary of the flight of samaras*, Journal of Theoretical Biology, Vol. 185, (1997), pp. 313-20.

[9] J. C. Maxwell, *On a particular case of the descent of a heavy body in a resisting medium*, Cambridge Dublin Mathematical Journal, Vol. 9, (1894), pp. 145-148.

[10] F. M. Burrows, *Wind-borne seed and fruit movement*, New Phytol., Vol. 75, (1975), pp. 405-418.

[11] C. W. McCutchen, *The spinning rotation of ash and tulip tree samaras*, Science, Vol. 197, (1977), pp. 691-692.

[12] D. S. Green, *The terminal velocity and dispersal of spinning samaras*, American Journal of Botanic, Vol. 67, No. 8, (1980), pp. 1218-1224.

[13] D. Lentink, W. B. Dickson, J. L. van Leeuwen, M. H. Dickinson, *Leading-edge vortices elevate lift of autorotating plant seeds*, Science, Vol. 324, (2009), pp. 1440-1438.

[14] J. M. Birch, M. H. Dickinson, *Spanwise flow and the attachment of the leading-edge vortex on insect wings*, Nature, Vol. 412, (2001), pp. 729-733.

[15] E. Salcedo, C. Treviño, R. O. Vargas, L. Martínez-Suástegui, *Stereoscopic particle image velocimetry measurements of the three-dimensional flow field of a descending autorotating mahogany seed (Swietenia macrophylla)*, The Journal of Experimental Biology, Vol. 216, (2013), pp. 2017-2030.

[16] K. Varshney, C. Chang, Z. J., Wang, *The kinematics of falling maple seeds and the initial transition to helical motion*, Nonlinearity, Vol. 25, (2012), pp. C1-C8.

[17] S. J. Lee, E. J. Lee, M. H. Sohn, *Mechanism of autorotation flight of maple samaras (Acer palmatum)*, Experimental Fluids, Vol. 55, No. 4, (2014), pp. 1-9.

[18] V. M. Ortega-Jimenez, A. Martín-Alcántara, R. Fernandez-Feria, R. Dudley, *On the autorotation of animal wings*, Interface, Vol. 14, (2017), pp. 1-10.

[19] A. Rosen, D. Seter, *Vertical autorotation of a single-winged samara*, Transactions of the ASME, Vol. 58, (1991), pp. 1064-1071.

[20] I. Hernández Arroyo, D. Rezgui, R. Theunissen, *Analytical model for leading-edge vortex lift on rotating samara seeds: development and validation*, *Proceedings of Applied Aerodynamics Conference, Bristol, Inited Kingdom, 2016 July 19-21*, Bristol (2016).

[21] P. R. Andronov, D. A. Grigorenko, S. V. Guvernyuk, G. Y. Dynnikova, *Numerical simulation of plate autorotation in a viscous fluid flow*, Journal of Fluid Dynamics, Vol. 42, No. 5, (2007), pp. 719-731.

[22] R. Mittal, V. Seshadri, H. S. Udaykumar, *Flutter, tumble and vortex induced autorotation*, Journal of Theoretical and Computational Fluid Dynamics, Vol. 17, (2004), pp. 165-170.

[23] C. Jin, K, Xu, *Numerical study of the unsteady aerodynamics of freely falling plates*, Comunications in Computational Physics, Vol. 3, No. 4, (2008), pp. 834-851.

[24] H. Zhong, S. Chen, C. Lee, *Experimental study of freely falling thin disks: Transition from planar zigzag to spiral*, Phisics of Fluids, Vol. 23, (2011), 011702 pp. 1-4.

[25] A. Andersen, U. Pesavento, Z. J. Wang, *Analysis of transitions between fluttering, tumbling and steady descent of falling cards*, Journal of Fluid Mechanics, Vol. 541, (2005), pp. 91-104.

[26] A. J. Ward-Smith, *Biophysical Aerodynamics and the Natural Environment*. John Wiley & Sons, New York (1984).

[27] A. Azuma, and K. Yasuda, *Flight performance of rotary seeds*, Journal of Theoretical Biology, Vol. 138, (1989), pp. 23-53.

[28] S. Preidikman, *Numerical Simulations of Interactions Among Aerodynamics, Structural Dynamics, and Control Systems*, Ph.D. Dissertation, Dept. of Engineering Science and Mechanics, Virginia Polytechnic Inst. and State Univ., Blacksburg, VA, (1998).

[29] B. A. Roccia, S. Preidikman, J. C. Massa, and D. T. Mook, *A modified unsteady vortex-lattice method to study flapping wings in hover flight*, AIAA Journal, Vol. 51, No. 11, (2013), pp. 2628-2642.

[30] A. Van Garrel, *The development of a wind turbine aerodynamics simulation module*, ECN Rep. ECN-C-03-079, Delft University of Technology, Delft, Netherlands, (2003).

[31] J. Katz J., A. Plotkin, *Low-Speed Aerodynamics*, 2nd Ed., Cambridge University Press, (2001).

[32] J. Han, Y. Lin, S. P. Arya, *Numerical study of the wake vortex decay and descent in homogeneous atmospheric turbulence*, AIAA Journal, Vol. 38, No. 4, (2000), pp. 643-656.

[33] S. Y. Wie, S. K. Lee, D. J. Lee, *Potential panel and time-marching free-wake coupling analysis for helicopter rotor*," Journal of Aircraft, Vol. 46, No. 3, (2009), pp. 1030-1041.

[34] A. T. Nguyen, J. K. Kim, J. S. Han, J. H. Han, *Extended unsteady vortex-lattice method for insect flapping wings*, Journal of Aircraft, Vol. 53, No. 6, (2016), pp. 1709-1718.

[35] T. Lambert, N. A. Razak, G. Dimitriadis, *Vortex lattice simulations of attached and separated flows around flapping wings*, Aerospace, Vol. 4, No. 22, (2017), pp. 1-20.

[36] M. J. Bhagwat, J. G. Leishman, *Generalized viscous vortex core models for application to free-vortex wake and aeroacoustic calculations*, American Helicopter Society 58th Annual Forum Proceedings, Montreal, Canada, June 11-13, (2002).

[37] H. B. Squire, *The growth of a vortex in turbulent flow*, Aeronautical Quarterly, Vol. 16, (1965), pp. 302-306.

[38] S. Ananthan, J. G. Leishman, *Role of filament strain in the free-vortex modeling of rotor wakes*, Journal of American Helicopter Soc., Vol. 49, (2004), pp. 176-191.

[39] C. P. Ellington, C. Van Den Berg, A. P. Willmott, L. R. Thomas, *Leading-edge vortices in insect flight*, Nature, Vol. 384, No. 6610, (1996), pp. 626-630.

[40] C. Van den Berg, C. P. Ellington, *The three-dimensional leading-edge vortex of a 'hovering' model hawkmoth*, Philosophical Transactions B, Vol. 352, No. 1351, (1997), pp. 329-340.

[41] M. H. Dickinson, K. G. Gotz, *Unsteady Aerodynamic Performance of Model Wings at Low Reynolds Numbers*. Journal of Experimental Biology, Vol. 174, No. 1, (1993), pp. 45-64.

[42] M. H. Dickinson, F. -O. Lehmann, S. P. Sane, *Wing Rotation and the Aerodynamic Basis of Insect Flight*, Science, Vol. 284, No. 5422, (1999), pp. 1954-1960.

[43] S. P. Sane, *The aerodynamics of insect flight*, Journal of Experimental Biology, Vol. 206, No. 23, (2003), pp. 4191-4208.

[44] L. W. Traub, *Analysis and estimation of the lift components of hovering insects*, Journal of Aircraft, Vol. 41, No. 2, (2004), pp. 284-289.

[45] E. C. Polhamus, *Predictions of vortex-lift characteristics by a leading-edge suction analogy*, Journal of Aircraft, Vol. 8, No. 4, (1971), pp. 193-199.

[46] C. T. Lan, J. Roskam, *Leading-edge force features of the aerodynamic finite element method*, Journal of Aircraft, Vol. 9, No. 12, (1972), pp. 864-867.

[47] G. E. Bartlett, R. J. Vidal, *Experimental investigation of influence of edge shape on the aerodynamic characteristics of lowaspect ratio wings at low speeds*, Journal of the Aeronautical Sciences, Vol. 22, No. 8, (1955), pp. 517-533.

[48] S. Preidikman, S., and D. T. Mook, *Time domain simulations of linear and nonlinear aeroelastic behavior*, Journal of Vibrations and Control, Vol. 6, No. 8, (2000), pp. 1135-1175.

[49] O. Brüls, A. Cardona, *On the use of Lie group time integrators in multibody dynamics*, ASME Journal of Computational and Nonlinear Dynamics, Vol. 5, No. 3, (2010), p. 031002.

[50] B. Roccia, S. Preidikman, B. Balachandran, *Computational dynamics of flapping wings in hover flight: A co-Simulation strategy*, AIAA Journal, Vol. 55, No. 6, (2017), pp. 1806-1822.

[51] C. S. Prasad, Q-z. Chen, G. Dimitriadis, O. Brüls, *Advanced Aeroservoelastic Modeling for Horizontal axisWind Turbines*, Proceedings of the 9th International Conference on Structural Dynamics, EURODYN 2014, Porto, Portugal, June 30 – July 2, (2014).

[52] M. Arnold, O. Brüls, *Convergence of the generalized-a scheme for constrained mechanical systems*, Multibody System Dynamics, Vol. 18, No. 2, (2007), pp. 185-202.

[53] M. Géradin, A. Cardona, *Flexible Multibody Dynamics: A Finite Element Approach*. Wiley: New York, (2001).

[54] O. Brüls, M. Arnold, A. Cardona, *Two Lie group formulations for dynamic multibody systems with large rotations*, In Proceedings of the IDETC/MSNDC Conference, Washington D.C., U.S., August (2011).

[55] R. D. Lorentz, *Spinning Flight: Dynamics of Frisbees, Boomerangs, Samaras, and Skipping Stones*, Springer, New York, (2006).

Predicting nonlinear system responses without a single simulation

G. Manson[1]
[1] Dynamics Research Group, Department of Mechanical Engineering
University of Sheffield, Mappin Street, Sheffield, S1 3JD, United Kingdom
e-mail: **graeme.manson@sheffield.ac.uk**

Abstract

This paper extends the work presented at the previous ISMA conference which introduced a completely novel approach for the understanding of nonlinear system behaviour. The idea was simply that all nonlinear systems can be represented as a combination of linear systems between which information is exchanged. The full range of nonlinear behaviour was able to be exactly represented via a combination of linear transient and steady-state expressions. The current work demonstrates that the technique may be used to predict all periodic responses of a harmonically excited nonlinear system without any recourse to simulation of the system. The initial system of interest was the bilinear system but an extension of the work to continuous nonlinear systems was also discussed.

1 Motivation

The environmental and economic pressures of the last couple of decades have resulted in an unprecedented effort on the part of structural design engineers to design structures that are more lightweight than, yet are at least as strong as, their structural ancestors. Three major factors have enabled this transformation: (1) the relatively recent advent of structurally-advantageous materials, including carbon- and glass-fibre reinforced polymers, syntactic foams and viscoelastic materials, (2) the revolution in manufacturing techniques, including a host of Additive Manufacturing methods and (3) the computational capability to efficiently apply optimisation techniques for real, complex structures. This is typified by the nature-inspired design of aerospace components currently being developed by Airbus [1].

Whilst this drive for strong, lightweight structures is clearly desirable, in many cases this may also result in greater complexity in the structural response. The source of such complexity is nonlinearity. Whereas an assumption of linearity would often be reasonable in traditional, relatively-stiff structures, manufactured using linear-elastic materials, this will generally not be the case for the new generation of optimized structures. Increased structural flexibility in such structures will lead to the growing likelihood of geometric nonlinearities whilst these new structurally-advantageous materials tend to behave in a manner far-removed from the linear elastic behaviour associated with metals.

In order to have a full understanding of how this new generation of structures will behave dynamically, it will be necessary to have, not only a thorough understanding of the wide range of possible nonlinear behaviour that may arise, but also the ability to predict such behaviour in a computationally efficient manner. Whilst research has been conducted into nonlinear system behaviour for centuries, the current situation appears to be, as Worden and Tomlinson wrote in their monograph 'Nonlinearity in Structural Dynamics' [2] that "there is no unique approach to dealing with the problem of nonlinearity either analytically or experimentally and thus we must be prepared to experiment with several approaches". The primary aim of this monograph was to introduce and explain a number of these approaches that would belong in a 'toolbox' for the analysis of nonlinear structural systems and included Harmonic Balance [3], Hilbert Transform [4], NARMAX modelling [5], the Masri-Caughey Restoring Force Surface method [6],

Direct Parameter Estimation [7] and the Volterra Series approximation [8]. Approaches not considered in the monograph included perturbation methods [9], multiple scales [10] and nonlinear normal modes [11]. The research conducted using the aforementioned approaches over the last five or so decades have undoubtedly led to much greater understanding of the behaviour of nonlinear systems and has resulted in countless applications. That said, it is fair to say that all approaches are not without their limitations. These limitations are often associated with the need for approximation or, where infinite series are being employed, are associated with the related issues of series convergence and truncation. Another limitation with the bulk of these approaches is that they are only capable of representing what is often termed "weak nonlinearity".

The current work follows on from work presented at the previous ISMA conference [12] where the author presented a completely novel approach to understanding how nonlinear behaviour arises. The technique, which will be discussed in the upcoming sections, does not rely on approximations and is not limited to particular nonlinear behaviour regimes but rather is capable of explaining the full spectrum of nonlinear behaviour. The previous work demonstrated that this new approach was capable of replicating superharmonic, subharmonic and even chaotic behaviour from a harmonically-excited, single-degree-of-freedom (SDOF) bilinear stiffness system.

The first aim of this current work is to demonstrate that it is possible to predict all possible periodic solutions from a bilinear system for a given harmonic input. It will be shown that this is possible without recourse to even a single simulation – the traditional approach would be that a number of simulations with different initial conditions would be required to achieve the same result.

One potential criticism of the previous work could be that it focussed on a system that may easily be considered as the amalgamation of two linear systems and therefore the findings of the paper may only be applicable to such systems. The second aim of this paper is to address these concerns by showing the progress that the author has made in applying this approach to arguably the nonlinear system of greatest interest, namely the Duffing oscillator [13]. The motivation of this entire body of work is the desire to develop a framework that is capable of explaining and predicting the full richness of responses that are observed in systems such as the Duffing oscillator.

The layout of the paper is as follows: Section 2 summarises the work of the previous paper by discussing the idea of switching between different linear systems to show that it is capable of replicating the full range of nonlinear behaviour exhibited by a bilinear system. Section 3 extends this work by showing that it is possible to predict what periodic responses are possible from a bilinear system, without resorting to numerical simulations. Section 4 introduces a pathway that may allow this method to be extended to continuous nonlinear systems such as the Duffing oscillator. Section 5 rounds off with some discussion.

2 Switching between linear systems

The overall concept offered in this paper and the previous paper [12] is an incredibly simple one: namely, that the response of a nonlinear system will be the same as the response obtained by switching between a series of linear systems. The benefits of such an approach will be that linear techniques will be employed throughout and all response components will be either linear transient response components or linear steady-state response components. The primary nonlinear vehicle for this work will be the simplest nonlinear system which can be considered as a combination of linear systems: namely, a bilinear system.

This section will recap the findings of the previous paper before demonstrating how this work may be extended to predict all possible periodic solutions from a bilinear system for a given harmonic input.

In the current section, the concept of switching will be introduced and shown how it can be applied to a bilinear system. First, however, to set the scene and introduce the notation, the response of a linear single-degree-of-freedom (SDOF) oscillator to sinusoidal forcing will be considered.

2.1 Response of a linear SDOF system to sinusoidal forcing

Figure 1 shows a linear single degree-of-freedom mass-spring-damper system.

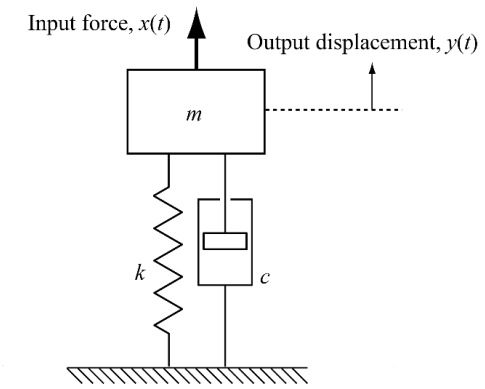


Figure 1: Single degree-of-freedom linear system

The equation of motion of the above system is given by:

$$m\ddot{y}(t) + c\dot{y}(t) + ky(t) = x(t) \tag{1}$$

The work will be concerned with the response of systems to a sinusoidal input. Let the input be given by:

$$x(t) = X\cos(\Omega t) \tag{2}$$

The total output response is written as the sum of steady-state and transient parts, i.e.

$$y(t) = y_{ss}(t) + y_{tr}(t) \tag{3}$$

The steady-state part of the response will be:

$$y_{ss}(t) = X\left|H(\Omega)\right|\cos\left(\Omega t + \angle H(\Omega)\right) \tag{4}$$

where $H(\Omega)$, the frequency response function (FRF) of the linear system, is given by:

$$H(\Omega) = \frac{1}{k - m\Omega^2 + i\Omega c} \tag{5}$$

The transient part of the response will be:

$$y_{tr}(t) = \exp\left(-\zeta\omega_n t\right)\left[A\cos\left(\omega_d t\right) + B\sin\left(\omega_d t\right)\right] \tag{6}$$

where ζ, ω_n and ω_d are the damping ratio, undamped natural frequency and damped natural frequency respectively and A and B are calculated to satisfy the initial conditions. If the initial displacement and velocity are denoted $y(0)$ and $\dot{y}(0)$ respectively, the values of A and B will be:

$$\begin{aligned} A &= y(0) - X\,\mathrm{Re}\left(H(\Omega)\right) \\ B &= \frac{\dot{y}(0) - \Omega X\left|H(\Omega)\right|\cos\left(\angle H(\Omega) + \frac{\pi}{2}\right) + \zeta\omega_n A}{\omega_d} \end{aligned} \tag{7}$$

A simple numerical example will now be introduced and will be revisited throughout the paper. The linear system described in equation (1) will be investigated using the following parameters: mass, $m = 1$ kg, damping, $c = 20$ N/(m/s) and stiffness, $k = 1\times10^4$ N/m. The system will therefore have an undamped

natural frequency $\omega_n = 100$ rad/s and a damping ratio $\zeta = 0.1$. This will give a damped natural frequency $\omega_d = 99.5$ rad/s. The chosen input parameters were $X = 10$ N and $\Omega = 50$ rad/s and the initial conditions were set to zero i.e. $y(0) = \dot{y}(0) = 0$.

The above parameters were inserted into equations (1) to (7) to give the steady-state and transient response components of the system. These two components were then summed to give the total system response. Figure 2 shows the two individual components of the response along with the total response of the linear system. The total response was validated against a system response generated using Simulink.

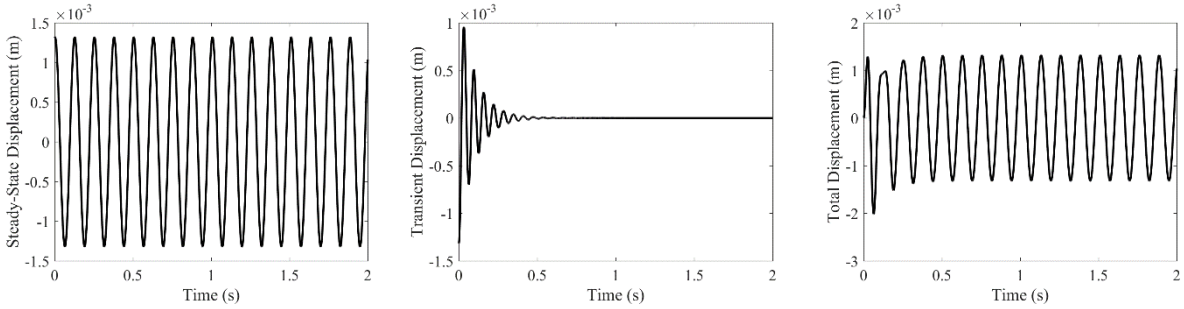


Figure 2: Displacement time history for $X = 10$ N and $\Omega = 50$ rad/s. Left plot shows steady-state response, middle plot shows transient response and right plot shows total response (sum of steady-state and transient responses).

2.2 Response of a bilinear SDOF system to sinusoidal forcing

In the previous paper [12], the concept of switching between linear systems was developed slowly. First, the idea of changing the value of a system parameter (stiffness in this case) at some point in time was presented – this simply resulted in the generation of a new transient response component at the point of switching before the system settled down to its new linear steady-state behaviour. This concept was then extended to consider the idea of switching the parameter back and forth between two values with the switching being conducted at periodic time intervals. When the switching time intervals were sufficiently large, the transient component produced at switching had sufficient time to decay before the next transient component was generated at the next switch point. As the time interval between switches become shorter however, the transient components did not have sufficient to decay and the system did not have sufficient time to settle down to its linear steady-state behaviour. When this switching frequency was the same as the input forcing frequency, the resulting system response settled down into a pattern of periodic behaviour that looked like a typical nonlinear response yet this response was simply constructed from linear steady-state components and linear transient components.

The final stage of the previous paper was to move to the more realistic scenario of a system which switched parameters when it reached a certain displacement value rather than at a pre-determined time. The same approach was employed but with the slightly more involved calculation of ascertaining when a switch had occurred.

The bilinear system that was investigated had the following parameters: mass, $m = 1$ kg, damping, $c = 20$ N/(m/s) and linear stiffness that switched between $k = 1\times10^4$ N/m and 2×10^4 N/m. The switching displacement chosen was $y_{switch} = 0$m meaning that the bilinear system was homogeneous. When the displacement was negative, the lower stiffness value was applied and, when the displacement was positive, the higher stiffness value was applied.

Two different forcing frequencies were investigated and it was shown that the approach of simply considering the response as a sum of two linear steady-state and two linear transient components was capable of reproducing superharmonic behaviour and subharmonic behaviour.

The first example considered the same sinusoidal forcing amplitude and frequency as used in the previous section (i.e. $X = 10$ N and $\Omega = 50$ rad/s). Figure 3 shows the steady-state, transient and total displacement

responses. It may be seen that the total system response settles down to periodic nonlinear steady-state behaviour – this response was constructed only by summing the two linear steady-state components and the two linear transient components but was validated by comparing against simulation results. Figure 4 shows the phase plane plot which has a single red Poincaré section point indicating that the response repeats with every excitation period. The middle plot shows the frequency domain content of the displacement signal for the nonlinear steady-state response. Peaks may be observed at the forcing frequency of 50 rad/s and its superharmonics. The final plot in Figure 4 shows the plot of the bilinear spring restoring force against the displacement.

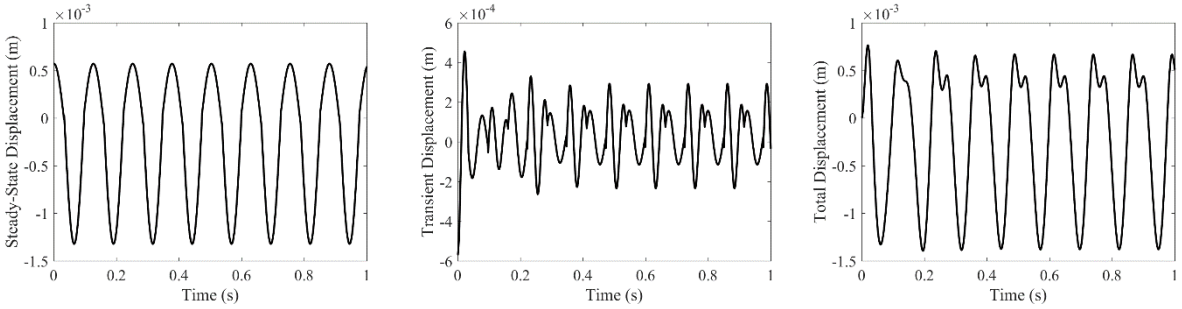


Figure 3: Displacement time history for $X = 10$ N and $\Omega = 50$ rad/s. Left plot shows steady-state response, middle plot shows transient response and right plot shows total response. The linear spring stiffness had a value of 1×10^4 N/m when the displacement was negative and a value of 2×10^4 N/m when the displacement was positive.

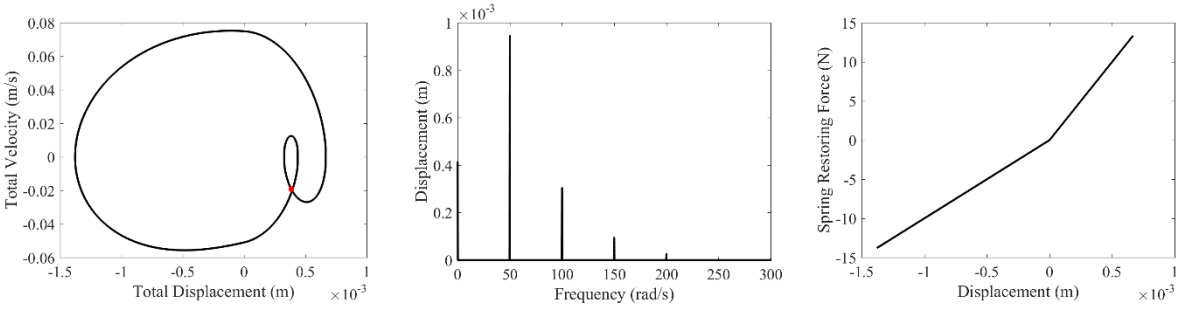


Figure 4: Further results for $X = 10$ N and $\Omega = 50$ rad/s. Left plot shows the phase plane plot of the nonlinear steady-state response, the middle plot shows the frequency domain content of the nonlinear steady-state response and the right plot shows the bilinear spring restoring force behaviour.

The second example was the same as the first in all respects other than the sinusoidal forcing frequency was now $\Omega = 240$ rad/s. Figure 5 shows the steady-state, transient and total displacement responses. A scaled force excitation time history is superimposed on these plots (red dotted line) and it can be seen that, whilst the system settles down to periodic steady-state behaviour, the response only repeats after two forcing cycles. This is known as a period 2 response. Period 2 behaviour is usually considered as being indicative of stronger nonlinear behaviour than the presence of superharmonics alone yet, it was shown that this behaviour could also be constructed using the same four linear response components as before (two steady-state and two transient components). The first plot in Figure 6 shows the phase plane plot which also shows two red Poincaré section points indicating the period 2 response. The middle plot shows the frequency domain content of the displacement signal for the nonlinear steady-state response. Peaks may be observed at the forcing frequency of 240 rad/s and also at 120 rad/s (1/2 subharmonic) and 360 rad/s (3/2 subharmonic) along with a DC peak at zero. The final plot in Figure 6 shows the plot of the bilinear spring restoring force against the displacement.

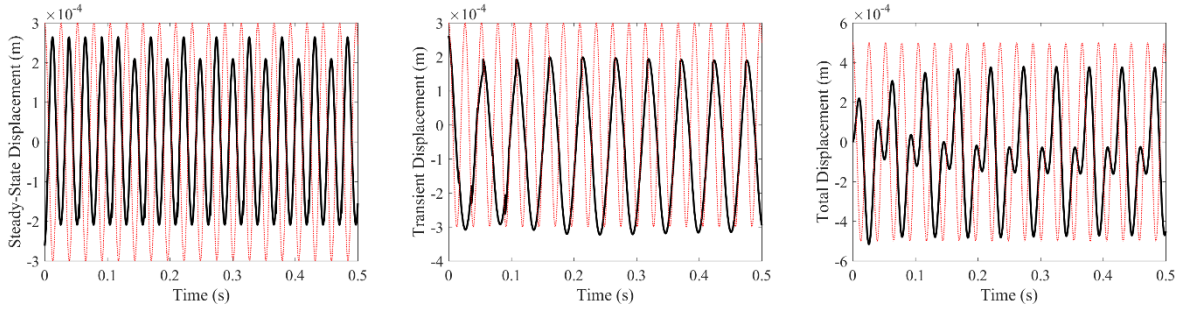


Figure 5: Displacement time history for $X = 10$ N and $\Omega = 240$ rad/s. Left plot shows steady-state response, middle plot shows transient response and right plot shows total response. The linear spring stiffness had a value of 1×10^4 N/m when the displacement was negative and a value of 2×10^4 N/m when the displacement was positive. Scaled input excitation shown as red dotted line.

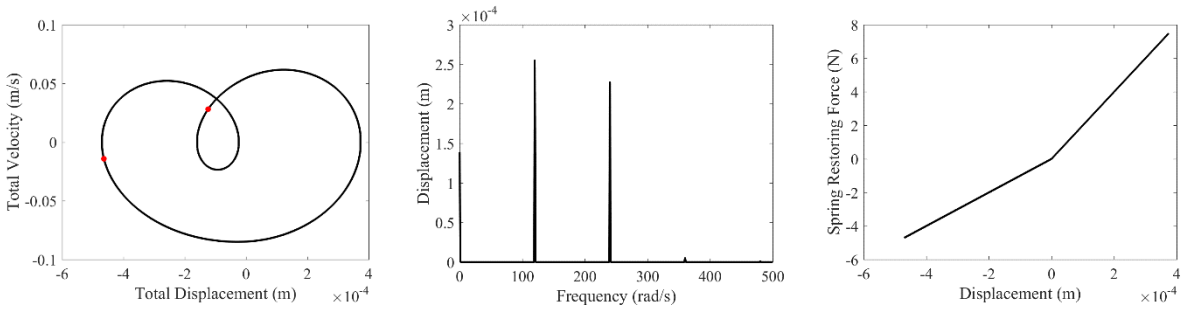


Figure 6: Further results for $X = 10$ N and $\Omega = 240$ rad/s. Left plot shows the phase plane plot of the nonlinear steady-state response, the middle plot shows the frequency domain content of the nonlinear steady-state response and the right plot shows the bilinear spring restoring force behaviour.

In the paper, it was stated that the bilinear system was not capable of generating chaotic behaviour. During the conference presentation, it was shown that the approach was capable of representing the chaotic response of a different bilinear system. It was found that increasing the larger stiffness value from 2×10^4 to 25×10^4 N/m and using a forcing amplitude and frequency of $X = 1$ N and $\Omega = 436$ rad/s respectively, resulted in a chaotic response. All other parameter values were as before. Figure 7 shows the resulting displacement time history and phase plane plot. Once again, this response was generated using only the linear steady-state and linear transient components of the two constituent linear systems and was validated by simulation. Whilst the superharmonic and subharmonic behaviour depicted in Figure 3 to Figure 6 resulted in switching times that quickly settled down into periodic behaviour, for the chaotic response, the times at which the system switched from one linear system to the other never settles into a periodic pattern.

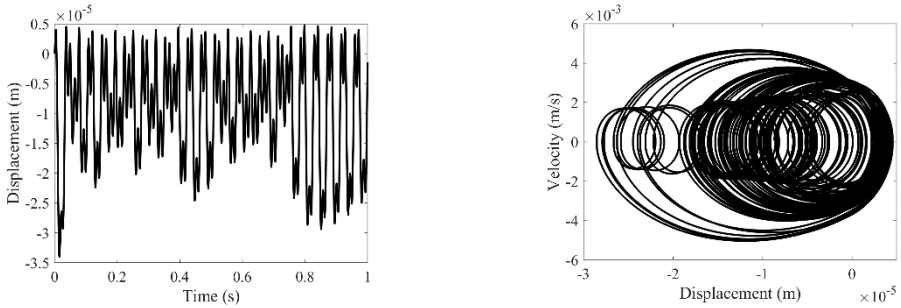


Figure 7: Displacement time history for $X = 1$ N and $\Omega = 436$ rad/s. Left plot total displacement response and right plot shows the phase plane plot. The linear spring stiffness had a value of 1×10^4 N/m when the displacement was negative and a value of 25×10^4 N/m when the displacement was positive.

3 Identifying Periodic Responses in a Bilinear System

This section and the next seeks to extend the work presented in the previous ISMA paper. The driver for this work is the desire to be able to take a nonlinear system, with known parameters and a specified harmonic input frequency and amplitude, and be able to state the full range of steady-state nonlinear behaviour that may be exhibited by the system, all without conducting any simulations via numerical integration. The current section will provide definitive proof that this is possible for a bilinear system whilst the following section will be more speculative in offering a potential pathway describing how this work may also be applicable to systems with continuous, rather than discretised, nonlinearities, such as the Duffing Oscillator.

3.1 Matching Bilinear System Responses at the Switch Point

As discussed in the previous section, the choice of using a bilinear system for demonstrating this novel approach was due to it being the simplest nonlinear system that could be considered as a combination of linear systems. The response of the bilinear system to a harmonic excitation will be given by a slight variation of the linear equations introduced at the start of the previous section. It will be useful to label the two linear systems. Linear System 1 will arbitrarily be denoted as the linear system with the lower stiffness (active when the system displacement is less than the switch displacement) whilst Linear System 2 will be the higher stiffness system (active when the system displacement is greater than the switch displacement). The lower stiffness will be denoted k_1 and the higher stiffness as k_2.

When Linear System 1 is active, the total displacement and total velocity responses of the system will be given by the sum of the Linear System 1 steady-state and transient displacement and velocity components respectively, i.e.

$$\begin{aligned} y(t) &= y_{ss}^{(1)}(t) + y_{tr}^{(1)}(t) \\ \dot{y}(t) &= \dot{y}_{ss}^{(1)}(t) + \dot{y}_{tr}^{(1)}(t) \end{aligned} \tag{8}$$

The Linear System 1 steady-state components of the displacement and velocity responses will be:

$$\begin{aligned} y_{ss}^{(1)}(t) &= X\left|H_1(\Omega)\right|\cos\left(\Omega t + \angle H_1(\Omega)\right) \\ \dot{y}_{ss}^{(1)}(t) &= X\Omega\left|H_1(\Omega)\right|\cos\left(\Omega t + \angle H_1(\Omega) + \frac{\pi}{2}\right) \end{aligned} \tag{9}$$

where $H_1(\Omega)$, the frequency response function (FRF) of Linear System 1, is given by:

$$H_1(\Omega) = \frac{1}{k_1 - m\Omega^2 + i\Omega c} \tag{10}$$

There are a number of ways that the Linear System 1 transient components of the displacement and velocity responses could be considered but the following form will be used:

$$\begin{aligned} y_{tr}^{(1)}(t) &= \exp\left(-\zeta_1\omega_{n1}\Delta t\right)\left[A_1\cos\left(\omega_{d1}\Delta t\right) + B_1\sin\left(\omega_{d1}\Delta t\right)\right] \\ \dot{y}_{tr}^{(1)}(t) &= \exp\left(-\zeta_1\omega_{n1}\Delta t\right)\left[\left(\omega_{d1}B_1 - \zeta_1\omega_{n1}A_1\right)\cos\left(\omega_{d1}\Delta t\right) + \left(-\omega_{d1}A_1 - \zeta_1\omega_{n1}B_1\right)\sin\left(\omega_{d1}\Delta t\right)\right] \end{aligned} \tag{11}$$

where ζ_1, ω_{n1} and ω_{d1} are the damping ratio, undamped natural frequency and damped natural frequency of Linear System 1 respectively. Δt refers to the time interval from the time point at which the system displacement crossed the switch displacement value into the Linear System 1 domain. The transient parameters A_1 and B_1 are calculated in order to ensure that the total displacement and velocity values match the system displacement and velocity values at the point of switching.

When Linear System 2 is active, there will be a corresponding set of equations to equations (8) to (11) but with all the 1 subscripts and superscripts changed to 2.

As stated earlier, the aim of this part of the work is to identify all possible periodic nonlinear responses that can arise for a particular bilinear system for a given harmonic input. The key to identifying these periodic responses lies in the identification of the switch points that result in the Linear System 1 displacement matching the Linear System 2 displacement and the Linear System 1 velocity matching the Linear System 2 velocity at the point of switching. These switch points cannot be identified in isolation but rather as pairs of switch points. $t_{switch1}$ will be designated as the switch point for the system switching from Linear System 1 to Linear System 2 (i.e. with the system displacement increasing due to its positive velocity) whilst $t_{switch2}$ will be designated as the switch point for the system switching from Linear System 2 to Linear System 1 (i.e. with the system displacement decreasing due to its negative velocity).

The process for identifying these pairs of switch points is as follows:

1. Create grid of $t_{switch1}$ and $t_{switch2}$ pairs where each switch is between the start and end of the forcing cycle – this was done using a resolution of 1000 time points per forcing cycle resulting in a grid of 1000 x 1000 pairs of switch points.
2. For each switch point, calculate the steady-state displacement and steady-state velocity for Linear System 1 and Linear System 2 using expressions of the form given in equation (9).
3. For each $t_{switch1}$, calculate the required value of A_2, the first of the Linear System 2 transient parameters – this is calculated through the knowledge of the switch displacement, y_{switch}, the steady-state displacement for Linear System 2 at $t_{switch1}$, $y_{ss}^{(2)}(t_{switch1})$, and from the knowledge that $y_{ss}^{(2)}(t_{switch1}) + y_{tr}^{(2)}(t_{switch1}) = y_{switch}$. This leads to the required value of A_2.
4. Repeat above process to calculate required value of A_1, the first of the Linear System 1 transient parameters for each $t_{switch2}$.
5. For each pair of switch points, using equations of the form of the first equation in equation (11), calculate the required values of B_1 and B_2 to ensure that the Linear System 1 displacement will match the Linear System 2 displacement at both switch points.
6. For each pair of switch points, use the values of A_1, A_2, B_1 and B_2 in equations of the form of the second equation in equation (11) to calculate the transient velocity at each of the switch points for both Linear System 1 and Linear System 2. These are added to the steady-state velocities to give the total velocities for each Linear System for each switch point.
7. Identify pairs of switch points that result in sufficiently close match between Linear System 1 velocity and Linear System 2 velocity – repeat for switch point from Linear System 1 to Linear System 2 and vice versa. Identify which of these result in valid responses.
8. Combine information from step 7 to identify the pairs of switch points which result in complete periodic behaviour.

The above process may sound involved but it is relatively straightforward to implement in the MATLAB environment and runs very efficiently. It will be best illustrated by considering a a couple of numerical examples.

3.2 Illustrative Examples of Periodic Response Identification for Bilinear Systems

The process described in the previous subsection will now be illustrated via two numerical examples. The first example will be that introduced in the previous ISMA paper [12] and revisited in Section 2 of this paper. To recap, the bilinear system that was investigated had the following parameters: mass, $m = 1$ kg, damping, $c = 20$ N/(m/s) and linear stiffness that switched between $k_1 = 1\times10^4$ N/m and $k_2 = 2\times10^4$

N/m at a switching displacement of $y_{switch} = 0$m. Linear System 1 is the system with the lower stiffness value and was active when the displacement was positive. The sinusoidal forcing amplitude and frequency were $X = 10$ N and $\Omega = 50$ rad/s respectively.

As explained previously, a resolution of 1000 time points per forcing cycle was used – this resulted in a grid of 1000 x 1000 pairs of switch points. Steps 1 to 7 of the above process were conducted and this resulted in the plots shown in Figure 8. The white regions on these plots depict combinations of switch points that result in the Linear System 1 and Linear System 2 velocities being close (an arbitrary threshold of within 10% of the maximum steady-state velocity was used). The leftmost plot depicts combinations that result in the velocities at $t_{switch1}$ (System 1 to System 2) being close and the rightmost plot depicts combinations that result in the velocities at $t_{switch2}$ (System 2 to System 1) being close.

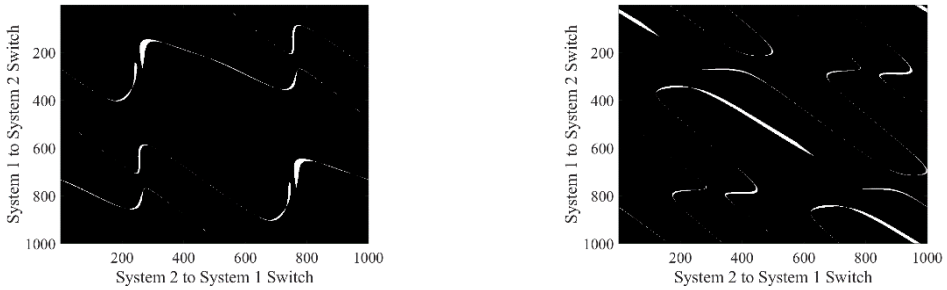


Figure 8: Plots showing pairs of switch points that result in the Linear System 1 velocity and Linear System 2 velocity being very similar (within 10% of the maximum steady-state velocity) – these are depicted as white regions. Left plot refers to $t_{switch1}$ comparison and right plot shows $t_{switch2}$ comparison.

The plots shown in Figure 8 only compare similarity of velocities and therefore include combinations that result in invalid responses – it is a simple matter to remove the combinations that result in negative velocities at $t_{switch1}$ or positive velocities at $t_{switch2}$. This results in the reduced plot of valid combinations shown in Figure 9.

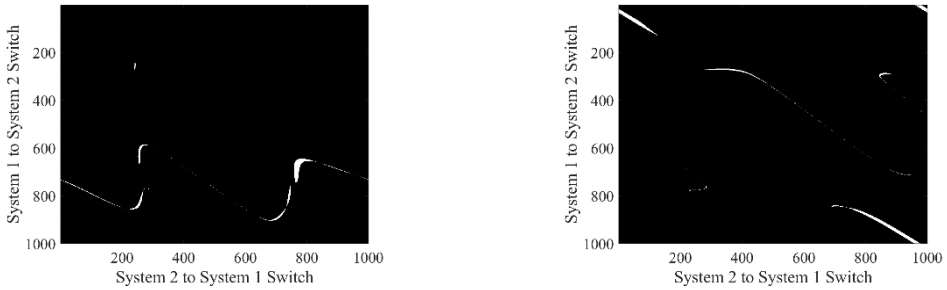


Figure 9: Same as Figure 8 but only includes valid switch combinations (positive velocities for $t_{switch1}$ and negative velocities for $t_{switch2}$).

The two plots of Figure 9 can now be examined to see if there are switch combinations that result in matching velocities for both $t_{switch1}$ and $t_{switch2}$. It transpires that there are just two pixels that give matching velocities (below the threshold) for both switches. This occurred for System 1 to System 2 Switch at point 769 and System 2 to System 1 Switch at points 281 and 282. The area immediately around this area of interest was further explored with a zoomed-in version (resolution of 100000 points per forcing cycle) of the previous analysis. This identified the best overall match to be point 76818 for the System 1 to System 2 Switch and point 28009 for the System 2 to System 1 Switch. This was identified as the only periodic response which could occur for these forcing conditions. The overall Linear System 1 part of the response and overall Linear System 2 part of the response for this identified switch combination was plotted and is shown in Figure 10. It may be seen to be the same as that shown in Figure

4 – the difference is that, using the current process, no initial conditions were expressed and the response was shown to be the only possible periodic response for these forcing conditions.

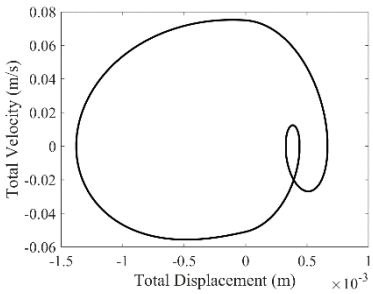


Figure 10: Phase plane of the only nonlinear steady-state response identified without recourse to simulation for the homogeneous bilinear system discussed in Section 2.

The second numerical example considers a bilinear system whose switch point is not at 0 and so the system is not homogeneous. The bilinear system had the following parameters: mass, $m = 1$ kg, damping, $c = 20$ N/(m/s) and linear stiffness that switched between $k_1 = 1\times10^4$ N/m and $k_2 = 10\times10^4$ N/m at a switching displacement of $y_{switch} = 1.5\times10^{-3}$ m. As before, Linear System 1 is the system with the lower stiffness value. The sinusoidal forcing amplitude and frequency were $X = 10$ N and $\Omega = 128$ rad/s respectively.

The same process as was outlined above was followed but the full range of figures produced will not be included here. It transpired that, for this system with this forcing input, two possible steady-state solutions were identified. These are shown in Figure 11 where it may be seen that the inner steady-state response is elliptical due to the steady-state response being linear. It may be observed that the maximum displacement response remains just below the switch displacement. The outer steady-state response is definitely not elliptical in nature and the portions of the response when Linear System 1 was active and when Linear System 2 was active may clearly be discerned. What is clearly being portrayed by Figure 11 is the jump phenomenon whereby two different steady-state responses are possible depending upon the system's initial conditions. The important point for the current work is that these two responses have been identified as the only two possible responses for this forcing input and they have been identified without any need for numerical simulations. The one thing that is missing is that the process identifies all possible periodic responses but does not furnish any information about the initial conditions that may result in a particular response. If this information were important, it would be a straightforward matter to conduct an initial condition sweep via numerical simulation.

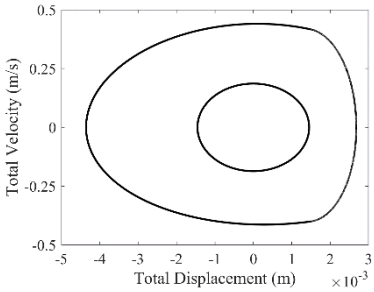


Figure 11: Phase plane of the two steady-state responses identified without recourse to simulation for the bilinear system with m=1kg, c=20N/(m/s), $k_1 = 1\times10^4$ N/m and $k_2 = 10\times10^4$ N/m. The switch displacement was $y_{switch} = 1.5\times10^{-3}$ m and the forcing input amplitude and frequency were $X = 10$ N and $\Omega = 128$ rad/s respectively.

4 A Potential Pathway for Identifying Periodic Responses in Continuous Nonlinear Systems

Whilst the previous section presented an approach for identifying periodic steady-state responses for bilinear systems, the real aim of this overall body of work is to develop an approach that is capable of doing similar with continuous nonlinear systems. The initial system of interest is the most-investigated of all nonlinear systems, namely the Duffing oscillator. The current section seeks to demonstrate that this concept of considering nonlinear system responses in terms of linear steady-state and transient components is not only limited to nonlinear systems with discrete nonlinearities such as the bilinear system. It is hoped that this section will show that this approach may also have the potential to consider systems with continuous nonlinearities. The work being included is very much a work in progress but it is hoped that there will be sufficient material to convince the reader that the ambition for this new approach extends well beyond one particular type of nonlinear system.

Figure 12 shows a schematic of the single degree-of-freedom Duffing oscillator – the only difference from the linear system shown in Figure 1 is the addition of a cubic spring stiffness element, k_3, to the linear spring stiffness element, k_1.

The equation of motion of the above system is given by:

$$m\ddot{y}(t) + c\dot{y}(t) + k_1 y(t) + k_3 y(t)^3 = x(t) \tag{12}$$

As before, the work will be concerned with the response of systems to a harmonic input. Let the input be given by:

$$x(t) = X\cos(\Omega t) \tag{13}$$

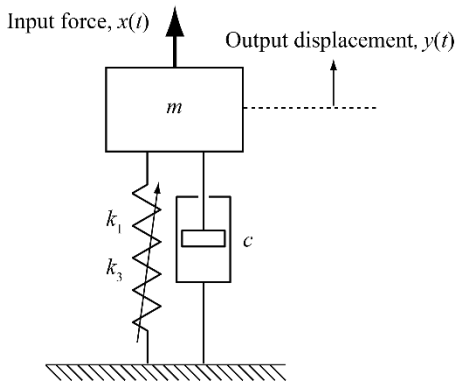


Figure 12: Single degree-of-freedom classical Duffing oscillator system.

The simple concept that has been exploited in the previously-described bilinear system investigations will once again be used for the Duffing oscillator. At any point in time, the total output response will be equal to the sum of a linear steady-state component and a linear transient component. The big difference between applying this approach to the bilinear system and the Duffing system relates to the amount of time that the system spends in an active Linear System. With the bilinear system, there were only two Linear Systems and one Linear System remained active until the response crossed the switch displacement at which point the second Linear System became active. The case is very different for a continuous system like the Duffing oscillator whereby the concepts of a single switch displacement and a finite number of Linear Systems are no longer valid. The concept can still be applied but, rather than a particular Linear System being active for a finite amount of time, a particular Linear System will only be active for an infinitesimal amount of time and then the Linear System will have changed. The same displacement expression used in Section 2 may be applied with the use of an asterisk to denote that the response and response components are instantaneous:

$$y^*(t) = y^*_{ss}(t) + y^*_{tr}(t) \tag{14}$$

A similar expression depicts the decomposition of the instantaneous velocity into an instantaneous linear steady-state velocity component and an instantaneous linear transient velocity component:

$$\dot{y}^*(t) = \dot{y}^*_{ss}(t) + \dot{y}^*_{tr}(t) \tag{15}$$

It is the author's opinion that knowledge of the instantaneous steady-state displacement and velocity components for all possible values of the overall system displacement may lead to a breakthrough regarding what behaviour is possible for a given nonlinear system with a given force input. The nature of these instantaneous steady-state components will now be discussed.

The approach will be best illustrated with a numerical example. A Duffing oscillator with the following parameters shall be considered: mass, $m = 1$ kg, damping, $c = 20$ N/(m/s), linear stiffness, $k = 1\times10^4$ N/m and cubic stiffness, $k_3 = 5\times10^9$ N/m^3.

The key to calculating the instantaneous steady-state displacement and velocity components is the calculation of the instantaneous linear stiffness and its associated instantaneous offset displacement term. Figure 13 shows the Spring Force vs. Displacement plot for the nonlinear spring stiffness with the linear and cubic stiffness parameters given above. Depicted on the plot is some arbitrary value of displacement y^*. Also shown as the solid red line is the gradient of the black curve at displacement y^* – this gradient will be equal to the instantaneous linear stiffness, k^*. The point at which this gradient crosses the displacement axis will be the instantaneous offset displacement term, y^*_{offset}.

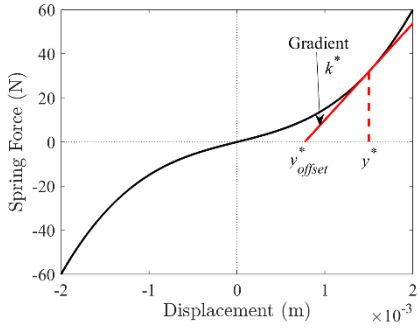


Figure 13: Displacement vs. Spring Force plot depicting equivalent stiffness k^* and offset displacement y^*_{offset} for a given system displacement y^*.

The instantaneous linear stiffness, k^*, is simply the derivative of the spring force with respect to displacement at displacement y^*:

$$k^* = k_1 + 3k_3 y^{*2} \tag{16}$$

whilst the instantaneous offset displacement y^*_{offset} is given by:

$$y^*_{offset} = y^* - \frac{k_1 + k_3 y^{*3}}{k^*} \tag{17}$$

These expressions may then be used in the calculation of equations for the instantaneous steady-state displacement and velocity components for the given system displacement y^*. The instantaneous steady-state displacement will be:

$$y^*_{ss}(t) = y^*_{offset} + X\left|H^*(\Omega)\right|\cos\left(\Omega t + \angle H^*(\Omega)\right) \tag{18}$$

and the instantaneous steady-state velocity will be:

$$\dot{y}_{ss}^{*}(t) = \Omega X \left| H^{*}(\Omega) \right| \cos\left(\Omega t + \angle H^{*}(\Omega) + \frac{\pi}{2} \right) \tag{19}$$

$H^{*}(\Omega)$ is the instantaneous frequency response function (FRF) of the equivalent linear system for the given system displacement y^{*} and is given by:

$$H^{*}(\Omega) = \frac{1}{k^{*} - m\Omega^{2} + i\Omega c} \tag{20}$$

This instantaneous steady-state behaviour will now be illustrated for the Duffing system with the previously-stated parameters and a forcing amplitude and frequency of $X = 10$ N and $\Omega = 50$ rad/s respectively. The plots shown below in Figure 14 shows the instantaneous steady-state behaviour from equations (18) and (19) for a number of different values of actual system displacement y^{*}. The plot on the left is simply the steady-state phase plane of the underlying linear system – the reason for this is due to the instantaneous linear stiffness for a displacement value of 0 being equal to the linear stiffness k_1. Also shown on the figure are a series of coloured time points that show the displacement and velocity response for forcing cycle with the red point indicating the response at the start of the forcing cycle. The plot on the right shows a series of steady-state phase planes for overall system displacement values from 0 to 1×10^{-3} m in steps of 2.5×10^{-4} m. It may be seen that the ellipses diminish in size and shift to the right – this is due to the decrease in the magnitude of $H^{*}(\Omega)$ (due to the increase in k^{*}) and the increase in the instantaneous offset displacement y_{offset}^{*} as the system displacement increases.

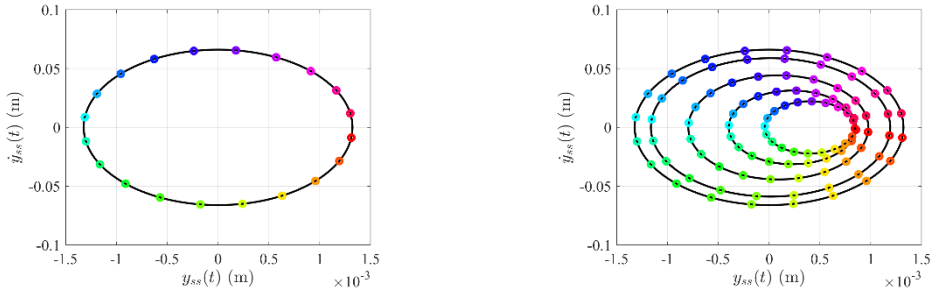


Figure 14: Plots showing phase plane of instantaneous steady-state displacement vs. velocity for Duffing oscillator system with forcing amplitude and frequency of $X = 10$ N and $\Omega = 50$ rad/s respectively. Left plot shows instantaneous steady-state phase plane for when system displacement passes through 0. Right plot shows instantaneous steady-state phase plane for when system displacement is 0 to 1×10^{-3} m in steps of 2.5×10^{-4} m.

The reader may well be asking the importance of the above plots – it is the author's opinion that these instantaneous steady-state plots may well hold the key to understanding the full range of responses that are possible for a given nonlinear system and a given forcing input – this would clearly be a significant step forward for the field of nonlinear dynamics.

If one has a response from a nonlinear system with known parameters and a known forcing input, it is a straightforward matter to decompose this total response into what the author would term an amalgamated linear steady-state response and an amalgamated linear transient response. For a continuous nonlinearity, the total response and the two amalgamated linear responses will be continuous and smooth. If this amalgamated linear steady-state response were plotted against the series of instantaneous steady-state phase planes of the type shown in Figure 14, it would be found that the amalgamated linear steady-state response would be bound by a strict set of rules regarding its trajectory – it would have to cross the appropriate instantaneous steady-state phase plane at the appropriate time point and the trajectory would only be able to travel in a direction of positive time flow. The way that the next phase of this work will

progress will be to take actual nonlinear responses, decompose them and plot the amalgamated linear steady-state responses against the instantaneous linear steady-state phase planes – it is believed that this approach will provide much illumination regarding what types of amalgamated linear steady-state responses are permissible. It would then be a straightforward matter to state which nonlinear responses were permissible for a given nonlinear system and input.

The real goal of this work is to be in a position whereby it would be possible to state all possible responses that could arise from a nonlinear system with a continuous nonlinearity for a given input, purely through the extremely computationally-efficient plotting a series of instantaneous linear steady-state phase planes.

The author will close the main part of this paper by briefly introducing some interesting and, in the author's opinion, beautiful plots that have arisen from this work. As the reader can imagine, plots of the type shown in Figure 14 can quickly become quite cluttered and difficult to interpret as the number of instantaneous phase planes increases. This can be alleviated somewhat by the realisation that a third dimension can be introduced in the form of the actual system displacement – this would mean that each of the ellipses shown in the right plot of Figure 14 would exist in a different plane in the z-axis direction. This is shown in the leftmost plot of Figure 15. The middle plot extends this first plot by depicting instantaneous steady-state phase planes from system displacement values from -2×10^{-3} m to 2×10^{-3} m in steps of 1×10^{-4} m. Common time points are connected together as coloured lines. The rightmost plot shows the manifold that arises when the forcing amplitude and frequency were set to $X = 10$ N and $\Omega =$ 120 rad/s respectively. The twin bulges arise due to the forcing frequency being greater than the natural frequency of the underlying linear system (100 rad/s) – the bulges will occur at system displacements that have an instantaneous stiffness that result in a natural frequency of 120 rad/s.

It is anticipated that the plotting of amalgamated linear steady-state responses (derived by decomposing a nonlinear response) against these manifolds will reveal much about what their trajectories are allowed to do, within the rules. This will then reveal what nonlinear responses are possible.

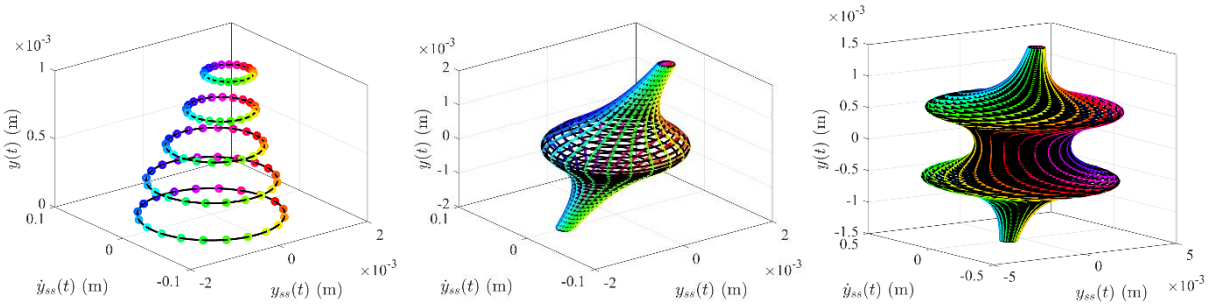


Figure 15: Series of manifolds showing instantaneous linear steady-state displacement vs. instantaneous linear steady-state velocity vs. actual system displacement for a Duffing oscillator system. Left plot shows 3D version of the Figure 14 right plot. The middle plot shows this extended for a greater actual displacement range and the right plot shows the manifold that arises when the forcing frequency is greater than the natural frequency of the underlying linear system.

5 Discussion

The paper that the author presented at the previous ISMA conference introduced a completely novel approach to considering nonlinear behaviour. The current paper has extended that idea to show how it may be useful. It was shown that it was possible to predict all periodic nonlinear responses of which a bilinear system was capable, for a given harmonic input, without recourse to numerical simulations. Whilst real-life uses of the bilinear system model are limited, it is the perfectly initial vehicle for demonstrating the power of this approach.

It will be a relatively straightforward matter to extend the approach to other piecewise linear systems – this could include systems whereby nonlinear damping (e.g. combinations of friction and viscous damping) is represented via a number of linear systems.

Whilst the approach was not computationally intensive, it is believed that there is significant scope to further streamline the process.

In this work, only periodic responses were identified – no investigation was conducted to try to understand what happens with this approach when a chaotic response is a possibility- it would clearly be very desirable to be able to predict when this was the case.

The really exciting work, in the author's view, was left to the last section, whereby early results were presented regarding investigations into applying this novel approach to continuous nonlinear systems.

As scientists, we often operate on instinct and, whilst I have been convinced that this was an area worth exploring since the first day I had the idea, this conviction has only become stronger since seeking to try to get the ever-surprising Duffing oscillator to reveal its secrets using my approach. The wonderful manifolds that have arisen from this much-studied system lead me to believe that I am on the right track and, if I'm wrong, at least I will have these lovely sculptures upon which to dwell.

References

[1] C. Emmelman, P. Sander, J. Kranz, E. Wycisk, *Laser Additive Manufacturing and Bionics: Redefining Lightweight Design*, Physics Procedia, Vol. 12, (2011), pp. 364-368.

[2] K. Worden, G. Tomlinson, *Nonlinearity in Structural Dynamics: Detection, Identification and Modelling*, IoP Publishing, Bristol and Philidelphia (2001).

[3] S. Maas, *Nonlinear Microwave and RF Circuits, 2nd Edition,* Artech House (2003).

[4] J. Peters, *A beginner's guide to the Hilbert transform*, Int. J. Math. Education Sci. Technol., Vol. 1, (1995), pp. 89-106.

[5] S. Chen, S. Billings, *Representation of non-linear systems: the NARMAX model*, Int. J. Control, Vol. 49, (1989), pp. 1013-1032.

[6] S. Masri, T. Caughey, *A nonparametric identification technique for nonlinear dynamical problems*, J. Appl. Mech., Vol. 46, (1979), pp. 433-447.

[7] K. Mohammad, K. Worden, G. Tomlinson, *Direct parameter estimation for linear and nonlinear structures*, J. Sound Vibration, Vol. 152, (1991), pp. 471-499.

[8] V. Volterra, *Theory of Functionals and Integral equations*, New York: Dover (1959).

[9] A. Nayfeh, *Perturbation Methods*, New York: Wiley (1973).

[10] A. Nayfeh, D. Mook, *Nonlinear Oscillations*, New York: Wiley (1979).

[11] A. Vakakis, L Manevitch, Y. Mikhlin, V. Pilipchuk, A. Zevin, *Normal Modes and Localization in Nonlinear Systems*, New York: Wiley-Interscience (1996).

[12] G. Manson, *A Forward-Looking Approach to Nonlinear Systems*, in *Proceedings of ISMA 2016 - International Conference on Noise and Vibration Engineering and USD2016 - International Conference on Uncertainty in Structural Dynamics, Leuven, Belgium*, (2016), pp. 2697-2708.

[13] I. Kovacic, M. Brennan, *The Duffing Equation: Nonlinear Oscillators and their Behaviour*, Wiley-Blackwell (2011).

Experiments and simulations of an industrial assembly with nonlinear joints subjected to harmonic and random vibrations

T. Roncen [1,2]**, J.-J. Sinou** [2,3]**, J.-P. Lambelin** [1]
[1] CEA DAM CESTA,
F-33114 Le Barp, France

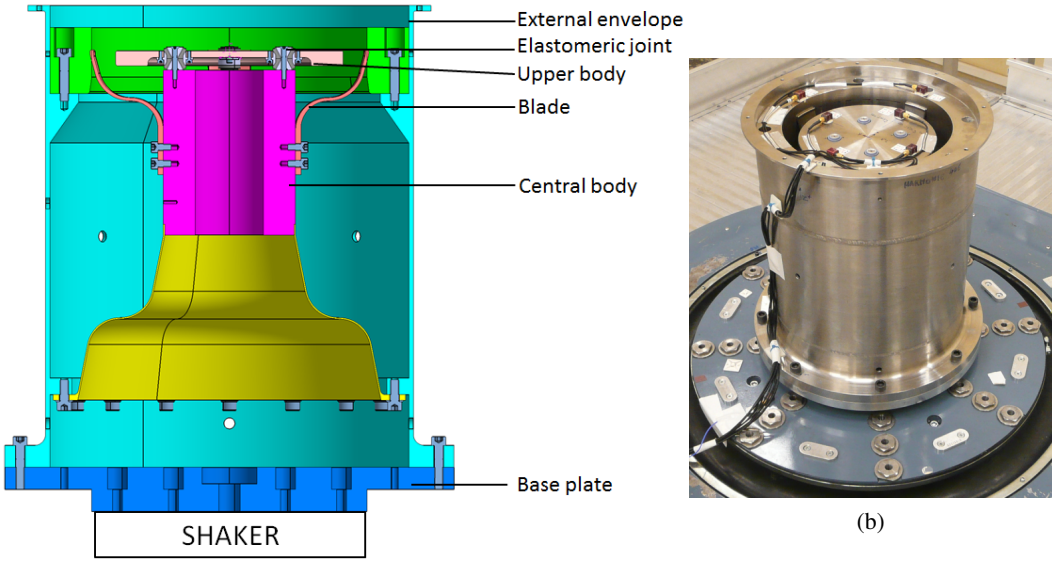
[2] Laboratoire de Tribologie et Dynamique des Systmes,
UMR CNRS 5513, Ecole Centrale de Lyon, France
e-mail: **jean-jacques.sinou@ec-lyon.fr**

[3] Institut Universitaire de France,
75005 Paris, France

Abstract
The "Harmony-Gamma" test structure is an industrial assembly that presents a nonlinear behavior. The nonlinearities have two distinct origins. First, a set of four blades creates friction at the interfaces. Second, a set of four elastomeric compounds subjected to the Payne effect. Both types of nonlinearities induce energy dissipation and local stiffness softening in the test structure. In the present study, random vibration experiments are performed to investigate the nonlinear behavior of the system at higher excitation levels. Concerning the numerical part, a classical complete methodology from the finite element and friction/elastomer modeling to the prediction of the nonlinear vibration responses is implemented. The well-known Harmonic Balance Method (HBM) with a specific condensation process on the nonlinear elements is achieved. Secondly, the HBM is extended for the case of random vibrations, while keeping the global methodology intact. Third, comparisons between experiments and simulations are conducted.

1 Introduction

The vibration response of mechanical systems used to be mainly studied by means of a linear analysis. Indeed, numerical simulations for both the modal analysis and frequency response function of linear systems are implemented in every Finite Element software package and are widely used in industry. However, experimentally, the dynamical system can experience nonlinear behavior with a frequency response that strongly depends on the excitation level. The nonlinearities may be caused by large displacements, contact, friction in the joints, or non-elastic compounds. The consequences of such nonlinearities are a dependency of eigenfrequencies and dissipation with input amplitude, discontinuities in the frequency response and a multi-harmonic response to a mono-harmonic excitation.
Including the set of nonlinear elements that play a predominant role in the dynamic behavior of structures proves essential to studying the dynamic behavior of systems. It requires both an efficient modeling of the nonlinearity and the development of nonlinear computational techniques in order to correctly assess the nonlinear dynamics of the structure. The present study concerns the modeling and simulation of nonlinear phenomena in an industrial assembly subjected to random excitation.
Concerning the computational method, the Harmonic Balance Method is one of the most popular for approximating the stationary nonlinear responses of mechanical systems. It has been used in various nonlinear applications involving dry frictions [1, 2] or rotatory machines [3]. More recently, Claeys et al. [4] presented



(a) (b)

Figure 1: Cross-section schema and picture of the structure "Harmony-Gamma".

an application of nonlinear vibration simulations using the HBM on an industrial finite element model. The application was limited to harmonic excitations, but could have been extended to multi-harmonic excitations, as showed in [5] with the example of a Duffing oscillator. In the present application, the HBM is extended for the case of random excitations. A key element of the study is the decomposition of a random signal into a suitable multi-harmonic periodic equivalent signal, used alongside a Periodogram strategy to properly estimate the Power Spectral Density (PSD) of the response.
In the following section, the experimental assembly and the experimentally observed effects of friction and elastomer are described. The corresponding finite element model and the reduction method are detailed in Sections 3 and 4. The modeling of friction and the elastomer, the Harmonic Balance Method and the nonlinear simulation results are then presented and compared to the experiments for random vibrations.

2 Experiments

The structure studied, named "Harmony-Gamma", is presented in Figure 1. This structure was previously used in [4] without the upper body, that is linked to the central body by the means of four elastomeric joints. The experimental setup is quite similar between the two structures. The central body is bolted to the external envelope at the bottom and is also in contact with this envelope through 4 blades at the top. During the assembly, the central body is inserted in the envelope from the bottom. The blades are compressed, so that the contact is never broken, even during vibration experiments. This structure is designed to have two distinct axial modes, the first one stressing the contact between the four blades and the external envelope and that initiates friction at high excitation level, and the second one stressing the elastomeric compounds. The structure is tested with the base plate bolted to the shaker. Experimental frequency response functions are plotted in Figure 2 for random vibrations with increasing levels. The friction phenomenon is characterized by an increasing dissipation in the vicinity of the first resonance, while the elastomer phenomenon mostly affects the decreasing resonance frequency of the first two modes. The third mode is a structural mode that is weakly affected by the nonlinearities. For the random excitations at high levels, oscillations are observed in the output PSD around the second mode of resonance.

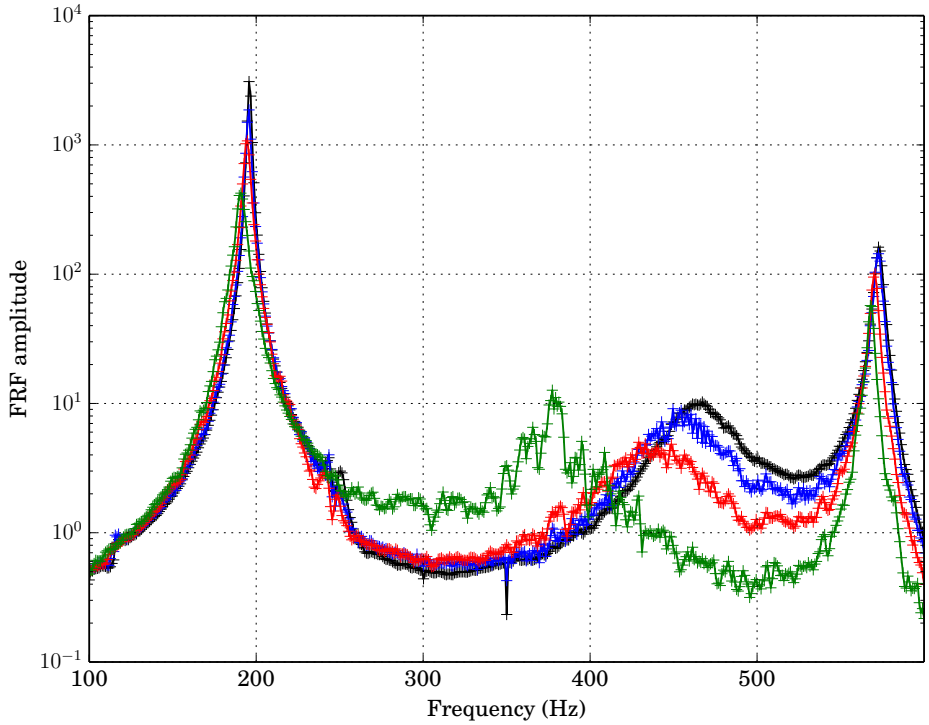


Figure 2: Experimental results for random excitations.

3 Modeling

3.1 Finite element model

The structure is modeled using the finite element software Abaqus CAE. Figure 3 presents the finite element model, focusing on the two kinds of interface. The model only includes solid elements, either linear or quadratic. As the experiments are made with constant input intensity amplitude, a model of the shaker is necessary. The moving part of the shaker is a coil attached to the table where the structure is mounted. Its transverse displacements and rotations are inhibited by strong springs and its axial displacement is possible and only limited by a soft spring. The shaker is modeled by a punctual mass, coupled to the base of "Harmony-Gamma" and to the ground with a soft spring ($K_{soft} = 22800\,N.m$ according to the shaker manufacturer). The model is excited by a force applied on the inertial mass. As a first approximation, this force is proportional to the current delivered to the shaker.
Each of the 4 joints where the friction slides happen at high excitation levels is modeled by a connector linking 2 nodes. One node is coupled with the contact zone of the blade, the other one is coupled with the surface of contact of the external envelope. The four elastomeric joints are similarly modeled, using 2-points connectors. The upper node is linked to the circular contact surface between the elastomer and the upper body, while the lower node is linked to the contact surface between the elastomer and the central body. The two nodes of a same joint can be at the same position. Reducing the total number of nodes involved in the joints relationships is an important step that will combine well with the model reduction step.

3.2 Modal analysis and model validation

The prerequisite for nonlinear studies is the validation of the linear model. Figure 4 compares finite element simulations to experimental measures at low excitation levels, when the nonlinearities are not active. Simulation and experimental resonance and anti-resonance frequencies match with less than 0.1% errors. Moreover, the good agreement between experimental and simulation results on various sensors validate the

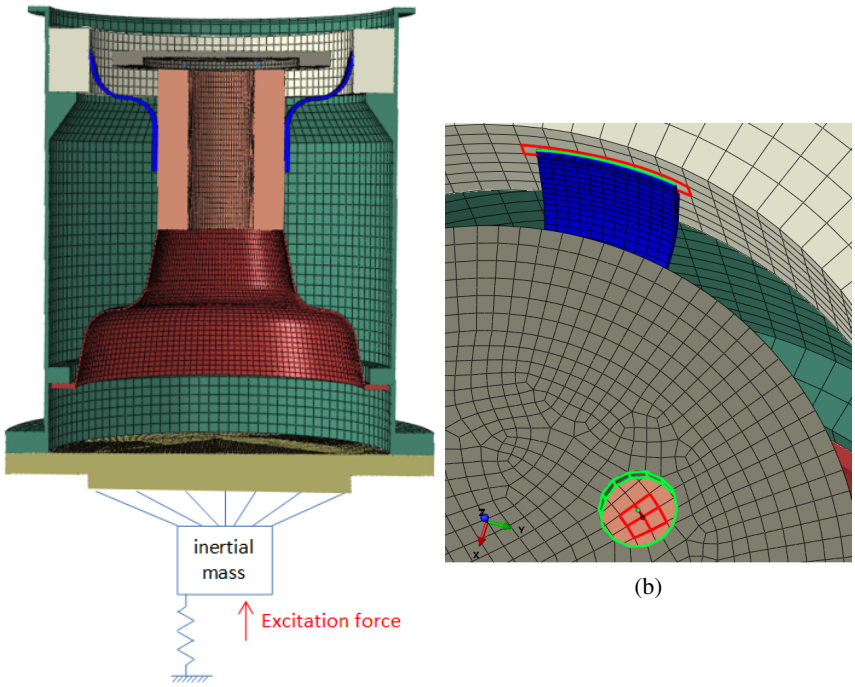


Figure 3: Cross-section schema of the finite element model (a) and focus on the contact zone model (b).

assumption of a linear relation between the intensity and the force over the frequency range considered. To process the experimental data into an experimental modal analysis, the software LMS was used. The experimental modal damping is automatically computed along the experimental modal analysis. We obtained a set of three modal damping coefficients for the three axial modes that are studied. These coefficients were then implemented in the devoted place in the finite element software. The deformed shapes are plotted in Figure 5.

3.3 Model reduction

The "Harmony-Gamma" finite element model has more than 300000 degrees of freedom. The resulting matrices of the problem would be too big to be treated with nonlinear simulations. To pally this difficulty, a reduction model is proposed. This reduction model is implemented in the finite element software ABAQUS and is very close to a Craig-Bampton reduction. This method allows to keep the physical degrees of freedom of the structure (the accelerometers) while keeping its modal behavior. It was successfully used in the previous work of [4]. For the elastomers, the DOFs of the connectors are retained in the reduction. The case is more complex for the blades, because of the nonlinear behavior of the friction. A solution was brought in [4], but is not detailed in the present paper. Before the implementation of the nonlinear joints, the equation of dynamics is written in the reduced basis as :

$$\mathbf{M}\ddot{\mathbf{x}} + \mathbf{D}\dot{\mathbf{x}} + \mathbf{K}\mathbf{x} = \mathbf{F}_{\mathbf{excit}}(t) \tag{1}$$

$\mathbf{x}$ is the displacement vector in the reduced basis. $\mathbf{M}$, $\mathbf{D}$ and $\mathbf{K}$ are respectively the reduced matrices of mass, damping and stiffness, and $\mathbf{F}_{\mathbf{excit}}$ is the projection of the excitation on the reduced basis.
The matrix $\mathbf{D}$ is generated from the Rayleigh method, i.e. $\mathbf{D} = \alpha\mathbf{K} + \beta\mathbf{M}$, with α and β chosen to represent an equivalent modal damping for the first and the third modes of the structure. Experimentally their modal damping are $\xi_1 = 0.71\%$ and $\xi_3 = 0.54\%$ respectively. The equation that links ξ_i to α and β is :

$$\xi_i = \frac{1}{2}(\alpha\Omega_i + \frac{\beta}{\Omega_i})\,. \tag{2}$$

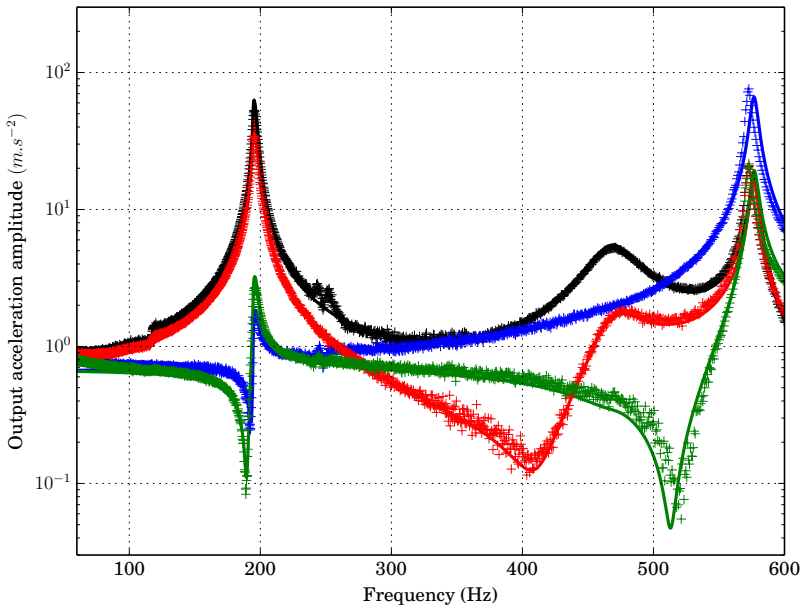


Figure 4: Comparison between experimental (crosses) and finite element simulation (plain curves) results on 4 experimental points : top of the upper body (black), top of the central body (red), bottom edge of the envelope (green) and table (blue).

The solving of the previous equation gives the values of α and β, and thus the matrix $\mathbf{D}$.
The next step consists in implementing the nonlinear joints. This step is detailed in [4]. The result is a change in the form of the dynamical equation, that is now given by the following relation :

$$\mathbf{M}\ddot{\mathbf{x}} + \mathbf{D}(\mathbf{x})\dot{\mathbf{x}} + \mathbf{K}(\mathbf{x})\mathbf{x} = \mathbf{F_{excit}}(t) \tag{3}$$

with $\mathbf{D}$ and $\mathbf{K}$ functions of $\mathbf{x}$. The constant part is separated from the non constant parts for matrices $\mathbf{D}$ and $\mathbf{K}$, this leads to :

$$\mathbf{M}\ddot{\mathbf{x}} + \mathbf{D}\dot{\mathbf{x}} + \mathbf{K}\mathbf{x} = \mathbf{F_{excit}}(t) + \mathbf{F_{nl}}(\mathbf{x}) \tag{4}$$

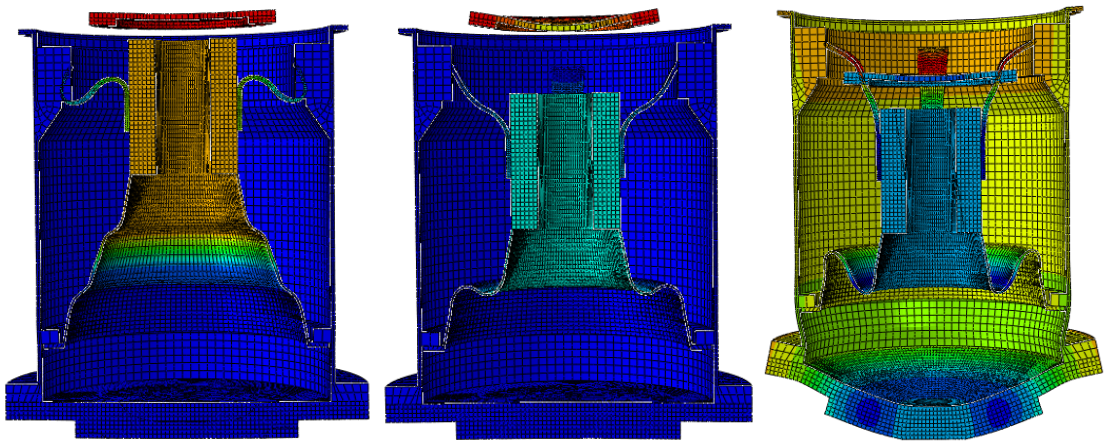
with $\mathbf{F_{nl}}(\mathbf{x}) = (\mathbf{D} - \mathbf{D}(\mathbf{x}))\dot{\mathbf{x}} + (\mathbf{K} - \mathbf{K}(\mathbf{x}))\mathbf{x}$ the nonlinear source term. The form of $\mathbf{F_{nl}}$ depends on the type of nonlinearity.

3.4 Friction modeling

Many friction models have been developed to represent the nonlinear force induced by friction. Some of the most used are the models of Coulomb, Dahl [6], Iwan [7], Valanis [8] or LuGre [9, 10]. Concerning the friction observed in our structure of interest, a Jenkins model [11] gave good results in the work of Claeys [4] for a very similar structure, so the same model is used in our application. This model is schematically presented in Figure 6, and consists in adding a linear spring in series with a Coulomb friction model. The slider remains in the stuck position until the force in the spring reaches the friction force when slipping begins. This force threshold $F_{Coulomb}$ is the only parameter of the model. The sliding of the blade is such that the internal force of the joint stays equal to the threshold.
The algorithm to calculate the nonlinear force in the joint was first proposed by Guillen and Pierre [12]. For each time iteration i of the temporal signal, in a first step, a trial force is estimated assuming that the friction slider remains in the stuck position between the iteration $i-1$ and i :

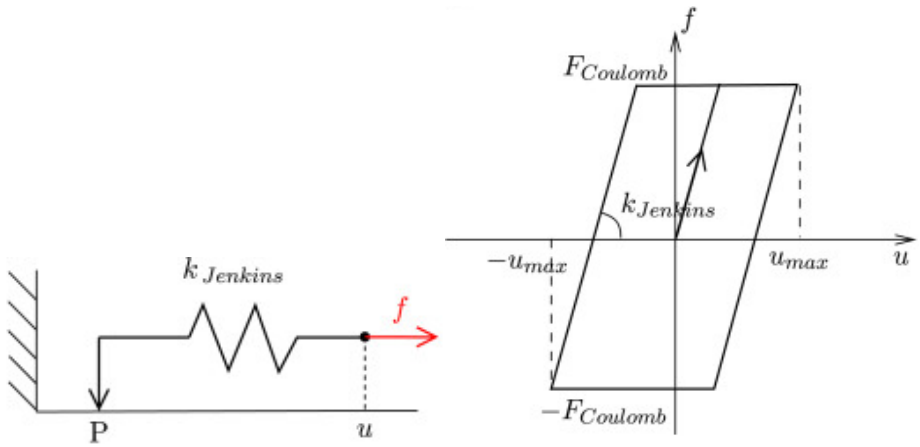
$$^{tr}f = f_{i-1} + k_{Jenkins}(u_i - u_{i-1}) \tag{5}$$

Then the friction threshold $F_{Coulomb}$ is applied to calculate the force in the Jenkins element at the iteration i. This threshold creates 2 states : slip and stick. When the slip threshold is reached, a classical friction



(a) (b) (c)

Figure 5: Cross-section view of the three first axial modes.



(a) (b)

Figure 6: Schema (a) and forcedisplacement diagram (b) of a Jenkins friction model.

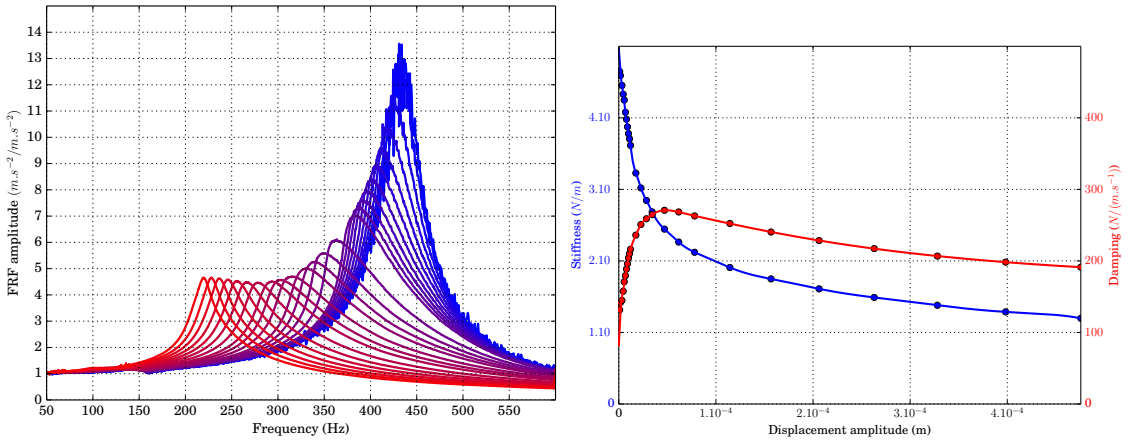
behavior is assumed. In the reverse case, no energy is dissipated and the contact behavior is purely elastic :

$$f_i = \begin{cases} {}^{tr}f & \text{if } |{}^{tr}f| < F_{Coulomb} \text{ (stick)} \\ sign({}^{tr}f)F_{Coulomb} & \text{if } |{}^{tr}f| \geq F_{Coulomb} \text{ (slip)} \end{cases} \tag{6}$$

This algorithm only works when applied to periodic motions.

3.5 Elastomer modeling

In the present study we are interested in the modeling of an elastomeric joint in the structural dynamics frame, and the validation of this model by test-simulation comparisons. These joints are vibration isolators and have a nonlinear behavior, exhibiting a dependency of eigenfrequencies and dissipation with input amplitude (Payne effect), hysteresis in the frequency response (Mullins effect) and multi-harmonic response to a mono-harmonic excitation. The joints are subjected to harmonic and random excitations. The harmonic excitations are used to create the model, while the random excitations are used to validate the latter.
Many methods have been developed in the literature to study the dynamic behavior of filled rubber isolators. First, methods based on the modeling of the mechanical laws of the elastomer, using physical models such as the Kelvin-Voigt or Maxwell model [13], fractional derivatives [14] or Berg model [15] to name just a few.



(a) (b)

Figure 7: Sine-swept experiments (a) and resulting model (b) for the elastomeric joint.

These methods are accurate but require a complex modeling of the joint, generally using a finite element discretisation of the later [16, 17]. The second class of methods is based on phenomenological modelings integrated at the scale of the mechanism. They usually take the form of a one degree-of-freedom system whom stiffness and damping are polynomials [18] or exponentials [19] of the relative displacement of the mechanism. The approach used in the present work is close to the later. The uniaxial behavior of the joint is identified using sine-swept experiments with increasing levels of excitation. The choice of modeling consists in a dependency of the stiffness and the damping of the joint with respect to the amplitude of the relative displacement.
Sine-swept experiments were conducted with various levels of excitation in the vicinity of the first resonance peak of a mass-spring system. The spring is the elastomer, with a mass attached to it. The spring is linked to the shaker. Results of the experiments are shown in Figure 7. The softening of the elastomer with the excitation level is characteristic. For every excitation level, the frequency of the resonance and the peak amplitude are measured. By approximating the system with a linear one DOF system, it is possible to assume the stiffness and the damping of the latter for each peak :

$$K_{Elastomer} = m_{System} \times \Omega^2_{Resonance} \tag{7}$$

$$D_{Elastomer} = \frac{\sqrt{m_{System} \times K_{Elastomer}}}{Q_{Resonance}} \tag{8}$$

Therefore, a set of N duos $(K_{Elastomer}, D_{Elastomer})$ is obtained, with N the number of sine-swept experiments. These couples are only valid at the specific resonance they were calculated. The main nonlinearity in an elastomer is the Payne effect, which is the dependency of the properties of the elastomer towards its internal deformation. Therefore, the duos $(K_{Elastomer}, D_{Elastomer})$ are assumed to be functions of the amplitude of deformation. The other nonlinear effects (dependency with the temperature, the frequency, the loads...) are neglected.

3.6 Modeling of the signal

Many mechanical problems can be considered as stochastic nonlinear problems. A few examples are structures subjected to wind or vehicles on irregular roads. In these cases, the excitation is random and in general, only the statistical quanta (moments, spectra) are known.
Several methods allow for the resolution of these mechanical problems : the Fokker-Planck method [20, 21], the perturbation method [22] and the stochastic linearisation [23]. However, these techniques are limited to

weak nonlinearities. A broader approach consists in numerically solving the nonlinear equations by using a trajectory of the excitation. In this paper, we use the work of Shinozuka [24, 25] that employs trigonometrical series to describe a random signal.
Let $x(t)$ be a second order, stationary, centered and Gaussian process. $x(t)$ has a PSD $S_x(f)$, with a compact support, meaning that there is a frequency $f_m > 0$ for which $S_x(f) = 0$ for $|f| > f_m$.
To simulate $x(t)$, a series of process $x^N(t)$ is build and indexed by N, converging toward $x(t)$. For N fixed, the process $x^N(t)$ is simulated from the knowledge of the PSD $S_x(f)$. For N big enough, the obtained trajectories are seen as good approximations of the trajectories of the process $x(t)$. According to Shinozuka [25], the process $x^N(t)$ is defined as a series of cosinus with frequencies divided equally on the interval $[-f_m, f_m]$, with random phases uniformly distributed on $[0, 2\pi]$ and with amplitudes function of $S_x(f)$. We write :

$$x^N(t) = \sqrt{\frac{1}{T}} \sum_{k=0}^{N-1} \sqrt{S_x(f_k)} \cos(2\pi f_k t + \Phi_k) \,. \tag{9}$$

When N is big, the computational time of the series (9) can be high. To overcome this issue, Eq. (9) is written for times t, equidistant and with a frequency discretisation chosen in order to use Fast Fourier Transform algorithms. Using the previous formalism alongside a FFT algorithm in Eq. (9), one obtains

$$x^N(t_n) = \sqrt{\frac{1}{T}} \left(FFT^{-1}(e^{i\Phi_k} \sqrt{S_x(f_k)}) \right) \,. \tag{10}$$

By construction of the family Φ_k, $x^N(t_n)$ should be a series of real values, however round-off errors can occur from the FFT, so we write :

$$x^N(t_n) = \sqrt{\frac{1}{T}} Re \left(FFT^{-1}(e^{i\Phi_k} \sqrt{S_x[f_k]}) \right) \,. \tag{11}$$

On one hand, one can simulate a random time series $x^N(t_n)$ with computational efficiency provided that the PSD is known at the frequencies f_k and that a random family of phases is generated. On the other hand, one can estimate a PSD from a time series evenly spaced in time. The estimate has a lower variance when the signal is split into K signals of the same duration.
In this paper, the input data is the Power Spectral Density of the excitation, while the desired data is the Power Spectral Density of the output acceleration at a given point of a structure. To solve the nonlinear equations, temporal representations of the signal are necessary. The procedure is then as follow :

1. First, K signals are generated from the input PSD using the procedure developed previously. These signals will be the input of the Harmonic Balance Method (in a Fourier form).

2. Secondly, K deterministic simulations are conducted using an HBM. These simulations are detailed in next Section 4. The results are K output signals in a Fourier form.

3. Then, the output PSD is estimate by averaging the K PSD of the output signals, in order to reduce the variance of the estimate.

3.7 Updating of the signal parameters

A few parameters need to be updated in order to simulate the system. The two main constraints are the frequency bandwidth and the frequency resolution.
The PSD is of interest in the bandwidth $[10, 600]$ Hz, so the Nyquist's frequency impose that the time step is $dt = \dfrac{1}{2 \cdot 600} = 8.33 \cdot 10^{-4} s$ or inferior.
Now, regarding the frequency resolution, the resolution needs to be high enough in order to capture the resonance of the structure. With a small resolution, it is possible to jump over the peak, with a consequence

in the prediction of the response. This behavior tends to be of even more importance with nonlinear systems as a bad representation of the signal on certain frequencies will affect the whole bandwidth and not only the concerned frequency. In order to have a high enough resolution, a criterion is to have 8 points in the mid-power interval of the peak. This corresponds to a resolution Δf that verifies :

$$\Delta f = f_0 \left(1 - \sqrt{1 - 2\xi \tan\left(\frac{\pi}{16}\right)}\right), \tag{12}$$

where $\xi = \frac{1}{2Q}$ is the modal damping (and Q is the Quality factor, i.e. the maximum of the FRF) and f_0 is the frequency of the peak. Experimentally we measure approximately a Quality factor of $Q = 100$ with a resonance frequency $f_0 = 200$ Hz. This leads to $\Delta f = 0.2\,Hz$.
With a Nyquist's frequency $f_n = 1200Hz$, this leads to $N = \frac{f_n}{\Delta f} = 6000$. N is chosen as the closest power of 2 to simplify the use of the FFT, so $N = 2^{13}$.

4 Nonlinear simulation

4.1 Description of the method

First of all, the deterministic nonlinear problem is solved with the Harmonic Balance Method [26]. This method seeks the stationary solution in the form of truncated Fourier series. Both the nonlinear dynamical response and the force vector are approximated by finite Fourier series with df (the frequency resolution) as fundamental frequency. Let $\Omega = 2 \cdot \pi \cdot df$ be the fundamental pulsation. $(\mathbf{A}_k, \mathbf{B}_k)_{k\in[1,p]}$, $(\mathbf{S}_k, \mathbf{C}_k)_{k\in[1,p]}$, $(\mathbf{S}_{k,excit}, \mathbf{C}_{k,excit})_{k\in[1,p]}$ are respectively the Fourier coefficients of the solution $\mathbf{W}$, the nonlinear force $\mathbf{F_{NL}}$ and the excitation $\mathbf{F}$.

$$\mathbf{x}(t) = \mathbf{B}_0 + \sum_{k=1}^{p} \left(\mathbf{B}_k \cos(k\Omega t) + \mathbf{A}_k \sin(k\Omega t)\right) \tag{13}$$

$$\mathbf{F_{nl}}(t) = \mathbf{C}_0 + \sum_{k=1}^{p} \left(\mathbf{C}_k \cos(k\Omega t) + \mathbf{S}_k \sin(k\Omega t)\right) \tag{14}$$

$$\mathbf{F}(t) = \sum_{k=1}^{p} \left(\mathbf{C}_{k,\mathbf{excit}} \cos(k\Omega t) + \mathbf{S}_{k,\mathbf{excit}} \sin(k\Omega t)\right) \tag{15}$$

p, the order of the truncated Fourier series is selected on the basis of the number of significant harmonics required in the dynamical response. For our application, p is chosen to be equal to N (where $N = 2^{13}$ has been calculated in Section 3.7). Equation (4) is rewritten in the Fourier basis :

$$\begin{bmatrix} \mathbf{K} - (k\Omega)^2\mathbf{I} & -k\Omega\mathbf{D} \\ k\Omega\mathbf{D} & \mathbf{K} - (k\Omega)^2\boldsymbol{I} \end{bmatrix} \begin{bmatrix} \mathbf{A}_k \\ \mathbf{B}_k \end{bmatrix} = \begin{bmatrix} \mathbf{S}_k \\ \mathbf{C}_k \end{bmatrix} + \begin{bmatrix} \mathbf{S}_{k,\mathbf{excit}} \\ \mathbf{C}_{k,\mathbf{excit}} \end{bmatrix} \quad \forall k \in [0, p] \tag{16}$$

where $\mathbf{I}$ is the identity. The coefficients $\mathbf{S}_k$ and $\mathbf{C}_k$ depend on the coefficients $\mathbf{A}_k$ and $\mathbf{B}_k$. They are calculated through an Alternate Frequency Time domain method (AFT-method) [27]. Usually this method deals with a small number of harmonics which makes the Discrete Fourier Transform (DFT) a suitable method to go from the temporal representation to the frequency representation of the signal, and inversely. However in this paper, the number of harmonics is extremely high. The AFT is adapted by using the FFT algorithm instead of the classic DFT. Using the FFT, one can calculate the non-linearity in the temporal space before switching back to the Fourier domain, as summed up by the following scheme :

$$\mathbf{X} = [\mathbf{A}_0\mathbf{B}_0\mathbf{A}_1\mathbf{B}_1...\mathbf{A}_p\mathbf{B}_p] \overset{FFT^{-1}}{\longrightarrow} \mathbf{x}(t) \overset{Eq.\ (4)}{\longrightarrow} \mathbf{F_{nl}}(\mathbf{x}) \overset{FFT}{\longrightarrow} [\mathbf{S}_0\mathbf{C}_0\mathbf{S}_1\mathbf{C}_1...\mathbf{S}_p\mathbf{C}_p] \tag{17}$$

This equation creates a direct link between the Fourier coefficients of $\mathbf{W}$ and $\mathbf{F_{nl}}$ which enables a nonlinear solving of problem (4) that can be written as :

$$\mathbf{H}(\mathbf{X}, \Omega, \mathbf{F}) = \mathbf{AX} - \mathbf{B} - \mathbf{B_{NL}}(\mathbf{X}) = \mathbf{0} \tag{18}$$

with :

$$\mathbf{A} = \begin{bmatrix} \mathbf{K} & & & & & & & & \\ & \mathbf{K} & & & & & & & \\ & & \mathbf{K} - \Omega^2\mathbf{M} & -\Omega\mathbf{D} & & & & & \\ & & \Omega\mathbf{D} & \mathbf{K} - \Omega^2\mathbf{M} & & & & & \\ & & & & \ddots & & & & \\ & & & & & \mathbf{K} - (k\Omega)^2\mathbf{M} & -k\Omega\mathbf{D} & & \\ & & & & & k\Omega\mathbf{D} & \mathbf{K} - (k\Omega)^2\mathbf{M} & & \\ & & & & & & & \ddots & \end{bmatrix}, \tag{19}$$

and $\mathbf{B}$ and $\mathbf{B_{NL}}$ the Fourier series of $\mathbf{F}$ and $\mathbf{F_{nl}}$ respectively.
The solution $\mathbf{X}$ is a discrete response curve in the frequency-amplitude domain. It represents the Fourier Transform of the solution over the entire frequency bandwidth, and can be used to estimate the PSD of the solution. However, it might not be possible to find a solution $\mathbf{X}$ that verifies Equation (18), especially for strong nonlinearities. Therefore, a Newton-Raphson continuation method has been used. The input PSD of $\mathbf{F}$ is considered as a variable as well as the Fourier coefficients $\mathbf{X}$ of the solution.
The continuation starts with a prediction step. Considering two points that are already computed ($\mathbf{Y}_{n-1}$ and $\mathbf{Y}_n$, where $\mathbf{Y}_n = [\mathbf{X}^{(n)}, \mathbf{F}^{(n)}]$), the next point belongs to the secant generated by the two later points. The distance between $\mathbf{Y}_n$ and $\mathbf{Y}^0_{n+1}$ is the step-length Δs, so that the prediction point is :

$$\mathbf{Y}^0_{n+1} = \mathbf{Y}_n + \Delta s.(\mathbf{Y}_n - Y_{n-1}) \tag{20}$$

The second part of the continuation is the correction. The Newton-Raphson correction is such that at the i^{th} iteration, $\mathbf{X}_i$ needs to be a zero of $\mathbf{H}$, so the correction is written :

$$\mathbf{X}^i_{n+1} = \mathbf{X}^{i-1}_{n+1} + \begin{bmatrix} \mathbf{\Delta X} \\ \mathbf{\Delta F} \end{bmatrix} \quad \text{with} \quad \begin{bmatrix} \mathbf{\Delta X} \\ \mathbf{\Delta F} \end{bmatrix} = -\mathbf{J}^+_{\mathbf{y}}\mathbf{H}(\mathbf{x}^{(i)}_{n+1})\mathbf{H}(\mathbf{x}^{(i)}_{n+1}) \tag{21}$$

Once the Fourier coefficients $\mathbf{X}$ are calculated, the n^{th} harmonic of $\mathbf{x}$ is given by the formula $H^n = \sqrt{\|A_n\|^2 + \|B_n\|^2}$ so that the frequency response can be plotted for each harmonic.

4.2 Changes in the Jacobian

The previous algorithm does not scale well with the dimension of the problem. With N being the number of harmonics, the size of the Jacobian of the system is $(2N, 2N)$. The first source of computation time is in the inversion of the Jacobian that scale in $O(N^3)$. The second source of computation time is in the making of the Jacobian. Each column needs the calculation of a nonlinear force $\mathbf{F_{nl}}(t)$, and the later is based on the use of one FFT and one inverse FFT with signals of size N. The result is that the making of the Jacobian scales in $O(N^2 log(N))$ as one FFT scales in $O(N log(N))$.
Let $\mathbf{J_f}(\mathbf{X})$ be the Jacobian of a function $\mathbf{f}$ depending on $\mathbf{X}$. For a random excitation, the optimization problem requires the calculation of the Jacobian :

$$\mathbf{J_H}(\mathbf{X}) = \mathbf{J_{AX+B+B_{NL}(X)}}(\mathbf{X}) = \mathbf{A} + \mathbf{J_{B_{NL}}}(\mathbf{X})\,. \tag{22}$$

The matrix A is block-diagonal by construction and represents the linear part of the equation. In most cases, the nonlinearity acts as a perturbation of the nonlinear system so we can assume that the full Jacobian is block-diagonal dominant. Based on the method developed in [28], we choose to solve our optimization

problem using an approximation of the Jacobian, that is the block-diagonal part of the full Jacobian. The new Jacobian is much more easier to inverse. The solving of one linear system of size $(2N)$ is changed to the solving of N linear systems of size 2.
Another possible speed-up can be actuated in the making of the Jacobian. Now, only the block-diagonal part of the Jacobian is of interest, so there is no need to calculate the full Jacobian. Indeed, for each column of the matrix, only two rows are used for the inversion of the Jacobian matrix. To provide a simple explanation of the speed-up, we take the example of the k^{th} block of matrix $\mathbf{A}$, that is written :

$$\begin{bmatrix} \mathbf{K} - (k\Omega)^2\mathbf{M} & -k\Omega\mathbf{D} \\ k\Omega\mathbf{D} & \mathbf{K} - (k\Omega)^2\mathbf{M} \end{bmatrix}. \tag{23}$$

This block is positioned at the indices $(2k, 2k)$,$(2k, 2k+1)$,$(2k+1, 2k)$ and $(2k+1, 2k+1)$ of matrix $\mathbf{A}$. One wants to calculate the components $2k$ and $2k+1$ for the nonlinear vectors $\mathbf{B_{NL}}(\mathbf{X} + \mathbf{dX}_{2k})$ and $\mathbf{B_{NL}}(\mathbf{X} + \mathbf{dX}_{2k+1})$, the other components being irrelevant with the block-diagonal assumption on the Jacobian.
Firstly, the calculation of the temporal signals of $\mathbf{X} + \mathbf{dX}_{2k}$ and $\mathbf{X} + \mathbf{dX}_{2k+1}$ do not require the use of an inverse FFT. This fact is actually independent of the assumption on the Jacobian. Indeed, as the inverse FFT operator is linear and since and inverse FFT was conducted once on the vector $\mathbf{X}$, one just needs to add the cosine and sinusoidal compounds to the output signal :

$$\mathbf{x}_{2k}(t) = FFT^{-1}(\mathbf{X} + \mathbf{dX}_{2k}) = FFT^{-1}(\mathbf{X}) - \frac{1}{N}\|\mathbf{dX}_{2k}\| \sin(k\Omega t)\,, \tag{24}$$

$$\mathbf{x}_{2k+1}(t) = FFT^{-1}(\mathbf{X} + \mathbf{dX}_{2k+1}) = FFT^{-1}(\mathbf{X}) + \frac{1}{N}\|\mathbf{dX}_{2k+1}\| \cos(k\Omega t)\,, \tag{25}$$

which requires $O(N)$ operations instead of $O(Nlog(N))$.
Once these two temporal signals are computed, one can calculate the two resulting temporal nonlinear source terms. With the assumption on the Jacobian, we are only interested in two components for each of these signals. Instead of using an FFT, a Galerkin projection on the desired frequencies, in order to calculate the necessary nonlinear source terms :

$$\mathbf{B_{NL}}(\mathbf{X} + \mathbf{dX}_{2k})_{2k} = -\sum_t (\mathbf{F}_{\mathbf{nl}_{2k}}(t).\sin(k\Omega t))\,, \tag{26}$$

$$\mathbf{B_{NL}}(\mathbf{X} + \mathbf{dX}_{2k})_{2k+1} = +\sum_t (\mathbf{F}_{\mathbf{nl}_{2k}}(t).\cos(k\Omega t))\,, \tag{27}$$

$$\mathbf{B_{NL}}(\mathbf{X} + \mathbf{dX}_{2k+1})_{2k} = -\sum_t (\mathbf{F}_{\mathbf{nl}_{2k+1}}(t).\sin(k\Omega t))\,, \tag{28}$$

$$\mathbf{B_{NL}}(\mathbf{X} + \mathbf{dX}_{2k+1})_{2k+1} = +\sum_t (\mathbf{F}_{\mathbf{nl}_{2k+1}}(t).\cos(k\Omega t))\,, \tag{29}$$

which requires $O(N)$ operations instead of $O\left(Nlog(N)\right)$.
In the end, this procedure changes the scaling of our algorithm to a small factor, from $O\left(N^2log(N)\right)$ to $O\left(N^2\right)$.
It is of paramount importance to note that the speed-up of the algorithm per iteration does not necessary mean a speed-up in the overall calculation time. Indeed, the assumption made on the Jacobian deteriorates the latter and can slow down the convergence of the algorithm. However, there is always a gain in term of memory.

5 Results

Simulated and experimental frequency response functions for random vibrations of increasing excitation levels are plotted in Figure 8 for "Harmony-Gamma". Similar behaviors are observed between the simulations

and the experiments. In the vicinity of the first mode, there is a decreasing of the frequency and the resonance amplitude starts decreasing. This is due to a combination of the two nonlinear joints. For the second mode, there is a significant decrease of the frequency, due to the elastomer joint only. The third mode is only impacted in its amplitude peak due to the increasing distance with the second mode.

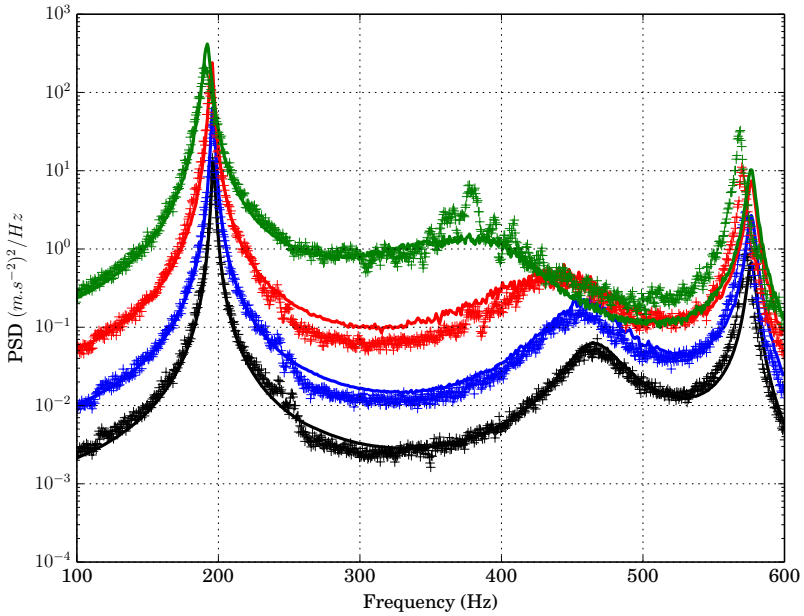


Figure 8: Cross-section schema and picture of the structure "Harmony-Gamma".

6 Conclusion

A nonlinear vibration simulation method is applied to an assembly with friction and elastomeric joints. The presented method is based on 4 main steps: finite element modeling, model reduction, nonlinear simulation and comparison with experimental results. The nonlinear simulation process uses the Harmonic Balance Method adapted to random vibrations and coupled with condensation algorithms. It is observed that simulations reproduce the experimental flattening and shifting of the resonance peaks when increasing the excitation level.
This study demonstrates that the presented nonlinear simulation method is relevant in simulating the evolution of the frequency response due to nonlinear joints in assemblies subjected to random excitations. It is an important step toward the actual use of such nonlinear simulation methods in industry.

Acknowledgement

J.-J. Sinou acknowledges the support of the Institut Universitaire de France.

References

[1] C. Pierre, A. Ferri, E. Dowell, Multi-harmonic analysis of dry friction damped systems using an incremental harmonic balance method, Journal of applied mechanics 52 (4) (1985) 958–964.

[2] K. Sanliturk, D. Ewins, Modelling two-dimensional friction contact and its application using harmonic balance method, Journal of sound and vibration 193 (2) (1996) 511–523.

[3] G. Von Groll, D. J. Ewins, The harmonic balance method with arc-length continuation in rotor/stator contact problems, Journal of sound and vibration 241 (2) (2001) 223–233.

[4] M. Claeys, J. Sinou, J. Lambelin, R. Todeschini, Experiments and numerical simulations of nonlinear vibration responses of an assembly with friction joints–application on a test structure named harmony, Mechanical Systems and Signal Processing 70 (2016) 1097–1116.

[5] M. Claeys, J.-J. Sinou, J.-P. Lambelin, B. Alcoverro, Multi-harmonic measurements and numerical simulations of nonlinear vibrations of a beam with non-ideal boundary conditions, Communications in Nonlinear Science and Numerical Simulation 19 (12) (2014) 4196–4212.

[6] P. R. Dahl, A solid friction model, Tech. rep., Aerospace Corp El Segundo Ca (1968).

[7] D. J. Segalman, An initial overview of iwan modeling for mechanical joints, Tech. rep., Tech. Rep. SAND2001-0811, Sandia National Laboratories (2001).

[8] K. C. Valanis, Fundamental consequences of a new intrinsic time measure. plasticity as a limit of the endochronic theory, Tech. rep., IOWA UNIV IOWA CITY (1978).

[9] C. C. De Wit, H. Olsson, K. Astrom, P. Lischinsky, Dynamic friction models and control design, in: American Control Conference, 1993, IEEE, 1993, pp. 1920–1926.

[10] C. C. De Wit, H. Olsson, K. J. Astrom, P. Lischinsky, A new model for control of systems with friction, IEEE Transactions on automatic control 40 (3) (1995) 419–425.

[11] G. Masing, Zur heynschen theorie der verfestigung der metalle durch verborgen elastische spannungen, in: Wissenschaftliche Veröffentlichungen aus dem Siemens-Konzern, Springer, 1923, pp. 231–239.

[12] J. Guillen, C. Pierre, An efficient, hybrid, frequency-time domain method for the dynamics of large-scale dry-friction damped structural systems., in: IUTAM Symposium on Unilateral Multibody Contacts, Springer, 1999, pp. 169–178.

[13] R. Lewandowski, B. Chorazyczewski, Identification of the parameters of the kelvinvoigt and the maxwell fractional models, used to modeling of viscoelastic dampers, Computers and Structures 88 (1) (2010) 1 – 17.

[14] M. M. Sjberg, L. Kari, Non-linear behavior of a rubber isolator system using fractional derivatives, Vehicle System Dynamics 37 (3) (2002) 217–236.

[15] M. BERG, A non-linear rubber spring model for rail vehicle dynamics analysis, Vehicle System Dynamics 30 (3-4) (1998) 197–212.

[16] N. Gil-Negrete, J. Vinolas, L. Kari, A simplified methodology to predict the dynamic stiffness of carbon-black filled rubber isolators using a finite element code, Journal of Sound and vibration 296 (4-5) (2006) 757–776.

[17] V. Jaumouillé, J.-J. Sinou, B. Petitjean, Simulation of payne effect of elastomeric isolators with a harmonic balance method, Shock and Vibration 19 (6) (2012) 1281–1295.

[18] C. Xueqian, S. Zhanpeng, H. Qinshu, D. Qiang, L. Xinen, Influence of uncertainty and excitation amplitude on the vibration characteristics of rubber isolators, Journal of Sound and Vibration 377 (2016) 216–225.

[19] D.-w. Sun, Z.-g. Chen, G.-y. Zhang, P. Eberhard, Modeling and parameter identification of amplitude- and frequency-dependent rubber isolator, Journal of Central South University of Technology 18 (3) (2011) 672.

[20] H. Risken, Fokker-planck equation, in: The Fokker-Planck Equation, Springer, 1996, pp. 63–95.

[21] B. Spencer, L. Bergman, On the numerical solution of the fokker-planck equation for nonlinear stochastic systems, Nonlinear Dynamics 4 (4) (1993) 357–372.

[22] J.-H. He, The homotopy perturbation method for nonlinear oscillators with discontinuities, Applied mathematics and computation 151 (1) (2004) 287–292.

[23] J. Roberts, P. Spanos, Stochastic averaging: an approximate method of solving random vibration problems, International Journal of Non-Linear Mechanics 21 (2) (1986) 111–134.

[24] M. Shinozuka, Simulation of multivariate and multidimensional random processes, The Journal of the Acoustical Society of America 49 (1B) (1971) 357–368.

[25] M. Shinozuka, C.-M. Jan, Digital simulation of random processes and its applications, Journal of sound and vibration 25 (1) (1972) 111–128.

[26] E. Sarrouy, J.-J. Sinou, Non-linear periodic and quasi-periodic vibrations in mechanical systems – on the use of the harmonic balance methods, INTECH Open Access Publisher, 2011.

[27] T. Cameron, J. Griffin, An alternating frequency time domain method for calculating the steady state response of nonlinear dynamic systems, Journal of Applied Mechanics 56 (1989) 149–154.

[28] R. Bouc, M. Defilippi, A galerkin multiharmonic procedure for nonlinear multidimensional random vibration, Int. J. Engng Sci. 25 (6) (1987) 723–733.

Modal analysis of an isolated nonlinear response mode using the Nyquist circle properties: numerical case.

D. Di Maio[1]
[1] University of Twente, Department of Applied Mechanics
De Horst 2, 7522 LW, Enschede, the Netherlands
e-mail: **d.dimaio@utwente.nl**

Abstract
Modal testing practitioners are well accustomed to FRFs which, nowadays, can be measured and analysed by a large variety of methods and tools. However, most of the tools for linear modal analysis are practically unusable when the frequency response is amplitude dependent. Hence, the methods based on the properties of the Nyquist circle become unavailable because of the loss of its circularity and completeness. Nevertheless, FRFs of well-isolated modes can still be processed by calculating the modal parameters for every pair of receptance points taken at equal amplitude either side the maximum response peak. The major limitation of this method is the absence of one branch of the response function due to unstable dynamics. The objective of this work is to show that incomplete FRF functions can be still processed to obtain the modal parameters. The method is benchmarked against a single degree of freedom both for linear and nonlinear response conditions.

1 Introduction

Modal testing is today a well-established practice for measuring and analysing frequency response functions. The modal parameters can be both used to generate a simple mathematical model (few degrees of freedom) or to validate a model generated by Finite Element (a large number of degrees of freedom). The groundwork was carried out by several scholars, who delivered several methods now packaged in high levels of technology readiness software suites [1], [2], [3]. However, experimental measurements showed that the linear modal analysis tools were unusable when the frequency responses presented a skewness typical of the nonlinear systems. Experimental methods, for analysing nonlinear vibrations, have to rely on measurements carried out by controlling the vibration amplitude of the response, which means "*linearize*" the FRF for a given constant response amplitude. By doing so, single DoF analysis methods can be used for processing FRFs and evaluate both natural frequency and damping nonlinear curves. This approach can be accurate, but its implementation is highly time consuming and therefore limited to some selected nonlinear responses[4]. The analysis was improved by using a method still based on single DoF approach, but which enabled fast nonlinear modal analysis. In fact, it analyses two pairs of frequency points at equal vibration amplitude either side the response peak to compute the four modal parameters. By sweeping pairs of frequency points from low up to high vibration amplitude, both the frequency and damping nonlinear curves were estimated [5]. Despite the intelligent approach to the data analysis, the method failed when one branch of the FRF was not present due to the unstable dynamic behaviour of the system, or commonly known as response jump. Furthermore, the analysis revealed poor accuracy in the identification of the damping nonlinear curve. Some minor issues were also observed on the constructed backbone that presented discontinuities when two modes were too close to each other. Many scholars investigated and successfully identified several methods based on direct analysis of time responses or frequency spectra, but no references in this work mainly based on steady-state measurements.

The objective of this research is to develop an identification method which can process FRFs measured under steady-state conditions when the vibration response becomes nonlinear. This method will start from the shortfalls of the method presented by Carrella [5] and aim to overcome those in the attempt to offer a

valuable tool to modal analysis practitioners. The paper is divided into two parts; the first one explains the basic idea developed to overcome analysis issues due to the frequency jump. Moreover, it proves that the method can intelligently calculate the system parameters of a linear single DoF system. The second part will present examples of a single DoF system included with stiffness and damping nonlinearity.

2 Theoretical background

This section will deal with the theoretical background which leads to the development of a novel method for performing the identification of nonlinear modal parameters. The case regards all those frequency response functions which present a response jump from high to low vibration amplitude, or the other way around. As already explained in section 1, the complex FRF analysis method, presented by Lin and Carrella [5], is unable to resolve the modal parameters when one branch of the frequency response curve is absent. However, the method paved the way to a simple approach to unbundling features from nonlinear system dynamics without going through expensive experiments or complex signal processing. This paper will show that it is possible to overcome the existing limitations and to derive the modal properties form an incomplete Nyquist dataset. The novel analysis method will be attempted by using a single degree of freedom system (SDOF).

The mobility FRF of an SDOF is described by equation (1), which by post-multiplying the numerator and denominator by the conjugate of the denominator will decouple the equation is the Real and Imaginary parts, in equations (2) and (3).

$$H(\omega) = Y(\omega) = i\omega\alpha(\omega) = \frac{i\omega}{\left(k - \omega^2 m\right) + i\omega c} = \frac{\omega^2 c}{\left(k - \omega^2 m\right) + \omega^2 c^2} + i\frac{\omega\left(k - \omega^2 m\right)}{\left(k - \omega^2 m\right) + \omega^2 c^2} \tag{1}$$

$$\mathrm{RE}\left(Y\left(\omega\right)\right) = \frac{\omega^2 c}{\left(k - \omega^2 m\right)^2 + \omega^2 c^2} \tag{2}$$

$$\mathrm{IM}\left(Y\left(\omega\right)\right) = \frac{\omega\left(k - \omega^2 m\right)}{\left(k - \omega^2 m\right)^2 + \omega^2 c^2} \tag{3}$$

The choice of using the mobility FRF for developing this new methodology is due to the circularity of the Nyquist circle whereby the viscous damping is the inverse of the diameter of the circle. Furthermore, the simulation of nonlinear FRFs is performed by ODE methods, where the use of viscous damping makes the solution of the equation of motion more practical than using other types of damping models. One should immediately notice from equations (2) and (3) three unknown parameters *m*, *c* and *k* are present But, the parameter *c* can be quickly determined by measuring the circle diameter in a single DoF system. Therefore, two equations are now necessary to resolve both *m* and *k*. The solution to this problem is sought from the fundamental principle of the geometry of the circle, which can be defined by a minimum of three points. To understand how to exploit this principle, one should look at Figure 1 which shows two Nyquist circles for linear (black trace) and nonlinear (red trace) systems, respectively. By first focussing on the linear system, one can notice that every three frequency points taken from the Nyquist dataset will always resolve the same circle, in fact, the circle parameters are unique. The explanation is sensible since the system is linear and, therefore, all the frequency points are equally spaced from the centre of such a circle. By switching the attention to the nonlinear system, described by the Nyquist dataset in red, one should notice that every three frequency points will define an amplitude dependent circle. It means that the circle parameters will depend

on the magnitudes of the three selected frequency points. How to exploit this feature will depend on how these three frequency points are selected.

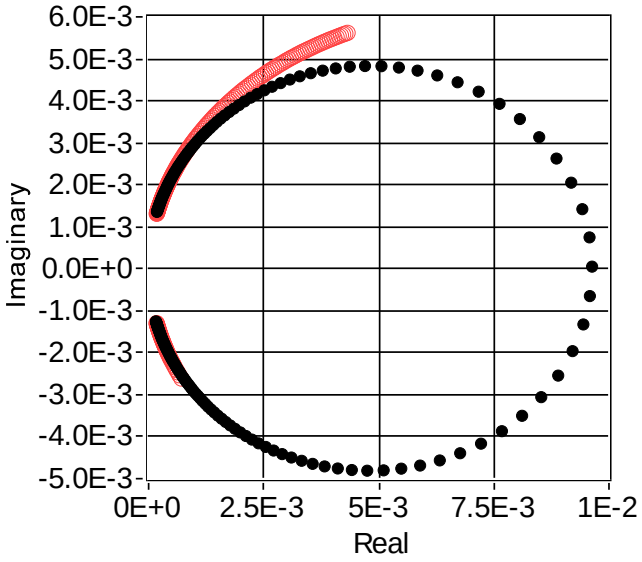


Figure 1 Nyquist circle for linear (in black) and nonlinear (in red) system

Mechanical structures are known to exhibit a degree of nonlinearity depending on the material, geometrical and boundary condition properties and the level of vibration amplitude to which such systems are exposed to. However, in all cases, mechanical systems will always show an underlining linear behaviour for low levels of vibration amplitude. This behaviour is somewhat essential for understanding how to perform the selection of the frequency points from a Nyquist dataset. It means that to observe the evolution of the circle parameters depending on the vibration amplitude; one should select three frequency points two of which are references and let the last one sweeping the frequency range measured for the FRF. In practice, two frequency points are selected as references at the lowest vibration amplitude, at which the mechanical system is assumed to present an underlying linear behaviour. The third frequency point can be called the sweeper and used to sweep all, but the two references, data points forming the FRF. It is now possible to determine the circle's parameters at the vibration amplitude of the sweeper. It is now possible to write a system of equations based on the equation (2) and (3). The system of equations (4) is defined by fixing two references at ω_s (start frequency) and ω_e (end frequency) typically at very low vibration amplitude and ω_i which is the sweeping frequency. One can notice that the system parameter *c*, the inverse of the diameter of the circle, depends on the point selected (the sweeper).

$$\begin{cases} \mathrm{Re}\left(Y\left(\omega_s\right)\right) = \dfrac{\omega_s^2 c_i}{\left(k-\omega_s^2 m\right)^2 + \omega_s^2 c_i^2} \\ \mathrm{Im}\left(Y\left(\omega_s\right)\right) = \dfrac{\omega_s^2\left(k-\omega_s^2 m\right)}{\left(k-\omega_s^2 m\right)^2 + \omega_s^2 c_i^2} \\ \mathrm{Re}\left(Y\left(\omega_i\right)\right) = \dfrac{\omega_i^2 c_i}{\left(k-\omega_i^2 m\right)^2 + \omega_i^2 c_i^2} \\ \mathrm{Im}\left(Y\left(\omega_i\right)\right) = \dfrac{\omega_i^2\left(k-\omega_i^2 m\right)}{\left(k-\omega_i^2 m\right)^2 + \omega_i^2 c_i^2} \\ \mathrm{Re}\left(Y\left(\omega_e\right)\right) = \dfrac{\omega_e^2 c_i}{\left(k-\omega_e^2 m\right)^2 + \omega_e^2 c_i^2} \\ \mathrm{Im}\left(Y\left(\omega_e\right)\right) = \dfrac{\omega_e^2\left(k-\omega_e^2 m\right)}{\left(k-\omega_e^2 m\right)^2 + \omega_e^2 c_i^2} \end{cases} \tag{4}$$

It is trivial to note that only two of the equations in (4) are necessary for resolving the system parameters *m* and *k*. Another simple approach which will not require to measure the circle diameter is based on the use of the imaginary part of the inverse of the mobility as expressed in equations (5). By taking two equations of the three available in the system of equations (5), both *m* and *k* can be resolved for every set of three frequency points.

$$\begin{cases} IM\left(\dfrac{1}{Y(\omega_s)}\right) = \dfrac{\left(k-\omega_s^2 m\right)}{\omega_e} \\ IM\left(\dfrac{1}{Y(\omega_i)}\right) = \dfrac{\left(k-\omega_i^2 m\right)}{\omega_i} \\ IM\left(\dfrac{1}{Y(\omega_e)}\right) = \dfrac{\left(k-\omega_e^2 m\right)}{\omega_e} \end{cases} \tag{5}$$

2.1 Numerical simulations and system identification

This section is focussed on the numerical simulation, and the definition of the nonlinear systems developed for studying the newly developed identification method. A single degree of freedom system is initially attempted to prove that the approach can identify the system parameters correctly. However, before the system is integrated with nonlinear terms, a mobility FRF is calculated from equation 1 and solved by using two of the equations of the system in (4) and (5).

2.1.1 Evaluation of system parameters from linear vibrations

Figure 2 shows the Nyquist circle of equation (1) calculated with the following system parameters, m = 6 kg, c = 100 Ns/m and k = 1e^8 Nm in a frequency range between 600 (0.1) 700 Hz. The natural frequency of such a system is $\omega_n = 649.75$ Hz.

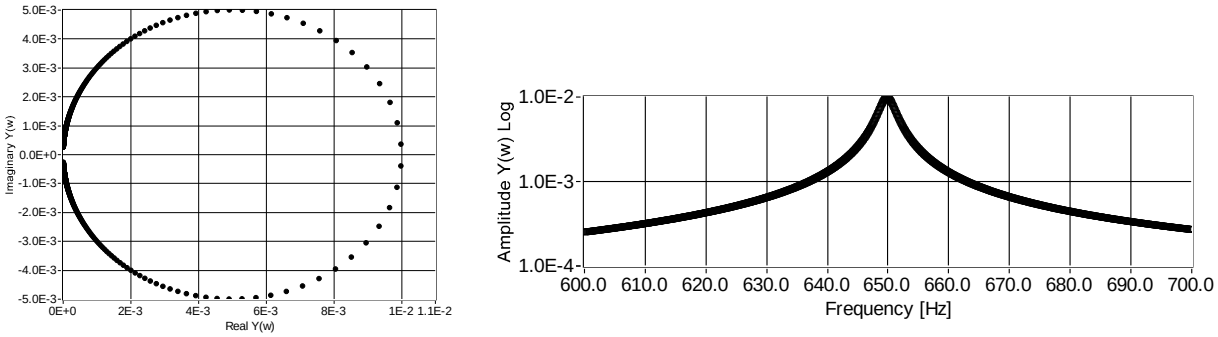
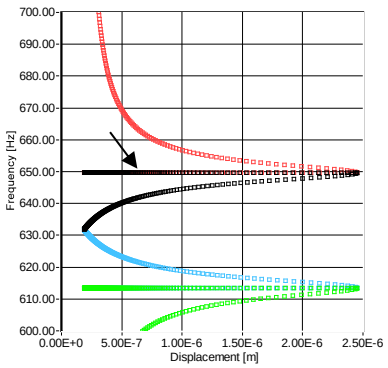
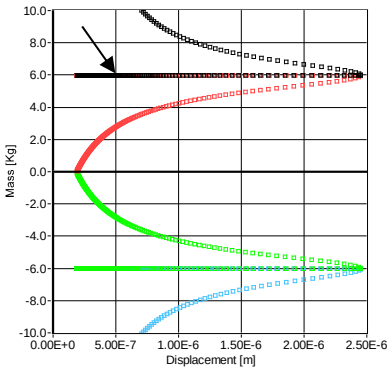


Figure 2 Nyquist circle (left) and magnitude (right) of mobility for a linear system

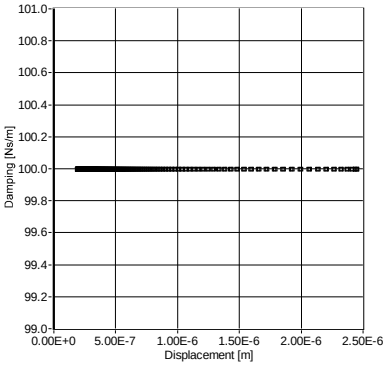
Using two of the equations in the system (4) it is possible to calculate the modal parameters; these are shown in Figure 3. The plots of Figure 3 a, b, c and d only report the partial solutions calculated for the frequency range between 600 and 700 Hz using the real part of the system of equations (4). The damping value *c* is directly calculated from the measurement of the circle diameter. The other two parameters *m* and *k* are calculated by using two equations which, when resolved, will give four sets of solutions. These are visible from the colours (red, black, blue and green) used to describe the curves in Figure 3. Two of the four set of solutions are meaningful, and one part of these two (see the black arrows in Figure 3) describes the correct system parameters *m* and *k*. Hence, the method to fix two references and sweep the entire Nyquist mobility dataset enables the recovery of the system parameters, which match the initial ones used for simulating the mobility FRF. The result should have been evident at the outset since whichever selection of three frequency points would fit the same circle. Nevertheless, the nonlinear system will present a *quasi*-linear response for low vibration amplitude which will change to nonlinear as the amplitude is increased. Therefore, given two references the sweeper will determine a new circle the parameters of which can be calculated. Finally, by tracking the behaviour of the system parameters against the vibration amplitude one can determine the full dynamics of a nonlinear single degree of freedom system.

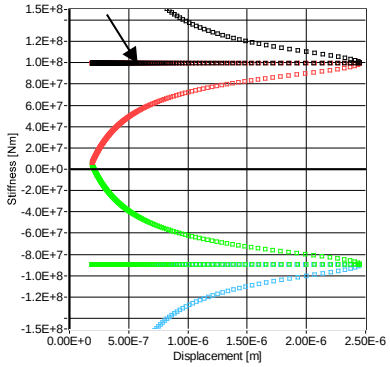


(a) Solutions calculated for the natural frequency



(b) Solutions calculated for the mass *m*





(c) Solutions calculated for the damping *c* (d) Solutions calculated for the stiffness *k*

Figure 3 Calculation of the system parameters and natural frequency

Instead, by using the equation in (5) one can notice that the parameter *c* is not necessary for resolving the equations and the parameters *m* and *k* are easy to find. Figure 4 shows the natural frequency of the single DoF system, which is a straight line because every three sets of frequency points will always resolve the same circle parameters.

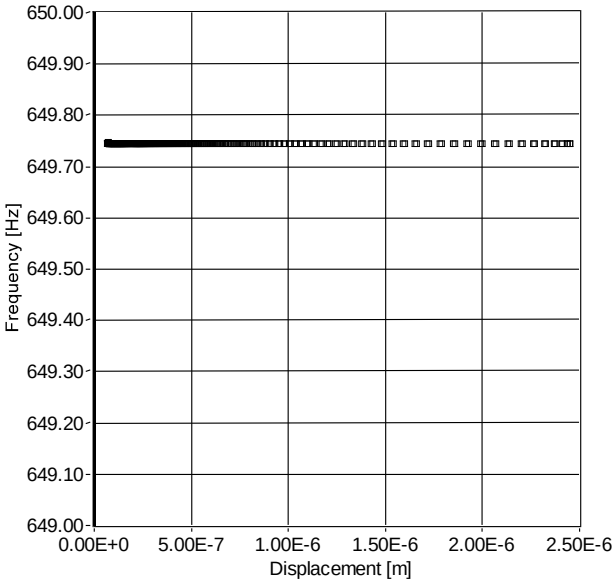


Figure 4 Calculation of the natural frequency by using the system of equation (5)

2.1.2 Evaluation of system parameters from nonlinear vibrations

This section deals with the identification of the system parameters which are amplitude dependent. As already explained a set of three frequency points would define a circle from which the system parameters can be calculated. Repeating this calculation for as many circles as defined by the set of Nyquist data, it is possible to track the evolution of the system parameters over the vibration amplitude. Two nonlinear systems were created to carry out the validation of the proposed identification method, such as one with a cubic stiffness nonlinearity and one with both cubic stiffness and quadratic damping nonlinearity.

Equation (6) represents a nonlinear single DoF with cubic nonlinearity. The parameter *m*, *c*, and *k* are the same already used for the linear system. Instead, the k_{nl} = 1e18N/m^3 is the coefficient of the stiffness nonlinearity. Equation (7) represents a single DoF system with a quadratic damping and cubic stiffness nonlinearity. The nonlinear stiffness coefficient is the same used for equation (6) instead the damping nonlinear coefficient is c_{nl} = 10000N(s/m)^2.

$$m\ddot{x} + c\dot{x} + kx + k_{nl}x^3 = f\sin(\Omega t) \tag{6}$$

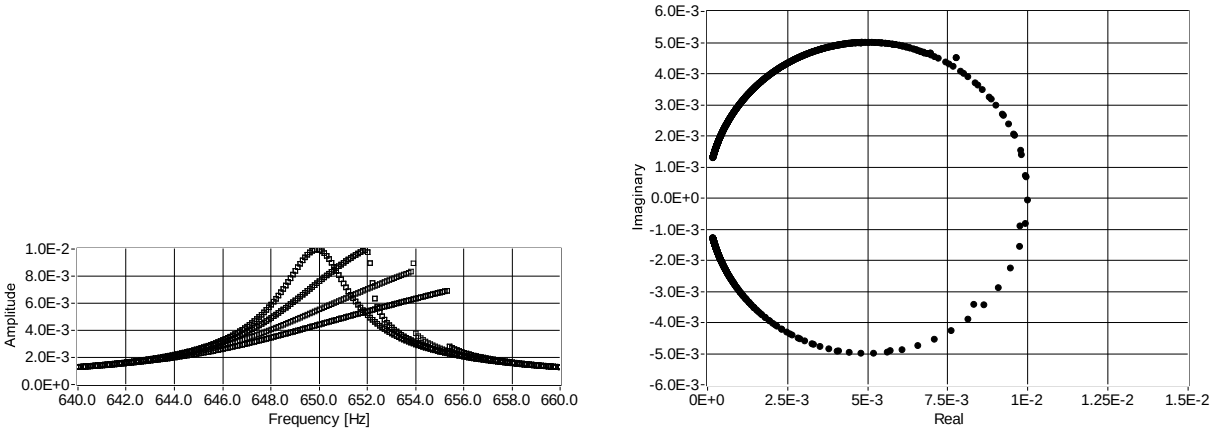
$$m\ddot{x} + c\dot{x} + c_{nl}\dot{x}|\dot{x}| + kx + k_{nl}x^3 = f\sin(\Omega t) \tag{7}$$

Equations (6) and (7) were calculated by integration method and hundred cycles of steady-state vibration were used for the analysis. The frequency range simulated was between 640Hz and 660Hz with a frequency spacing of 0.1Hz. The sample rate and the length of the time vector were 30kHz and 2 seconds, respectively. The FRF was calculated by the ratio between the response and the excitation force of the first fundamental component. The higher order harmonics from the response were neglected because their very tiny magnitudes.

2.1.3 Stiffness nonlinearity case study

Figure 5 shows the four FRFs, both Magnitude and Nyquist format, of a single DoF system with stiffness nonlinearity. These FRFs were simulated with excitation forces of 0.1N, 0.4N, 0.7N and 1N, respectively. The system presents hardening behaviour with typical jump caused by its unstable dynamic behaviour, and with the Nyquist circles presenting no loss of circularity due to the sole inclusion of stiffness nonlinearity. By closer inspection, one can notice that the frequency points rotate clockwise concerning a reference, such as a frequency point measured at the lowest forcing. This supports the ideas that by selecting two references and sweeping the third point, one can observe the nonlinear properties of the system as the vibration amplitude is increased. The primary objective is to trace the natural frequency of the system against the vibration amplitude. The analysis can be done by using two of the equations presented in the system of equation (6), which require the calculation of the damping, *c*. This parameter can be calculated merely because of a mobility FRF of a single DoF system would correspond to the inverse of the diameter of the circle. This diameter is calculated by fixing two frequency points at the lowest vibration amplitude and sweeping the third point over the number of points measured for the Nyquist.

Figure 6 shows that the diameter is approximately constant for the four FRFs simulated (alternated black-red) and it matches the original value set for the simulation (c = 100Ns/m). One would notice a numerical error of approx. 5% for the lowest vibration amplitudes.



(a) FRF magnitude (b) FRF Nyquist

Figure 5 FRF of a single DoF with stiffness nonlinearity

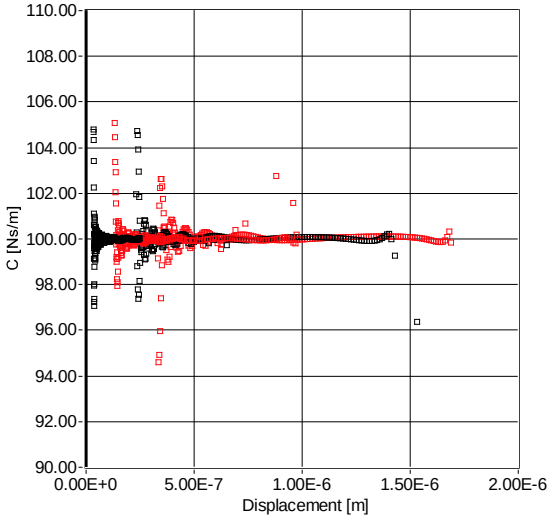
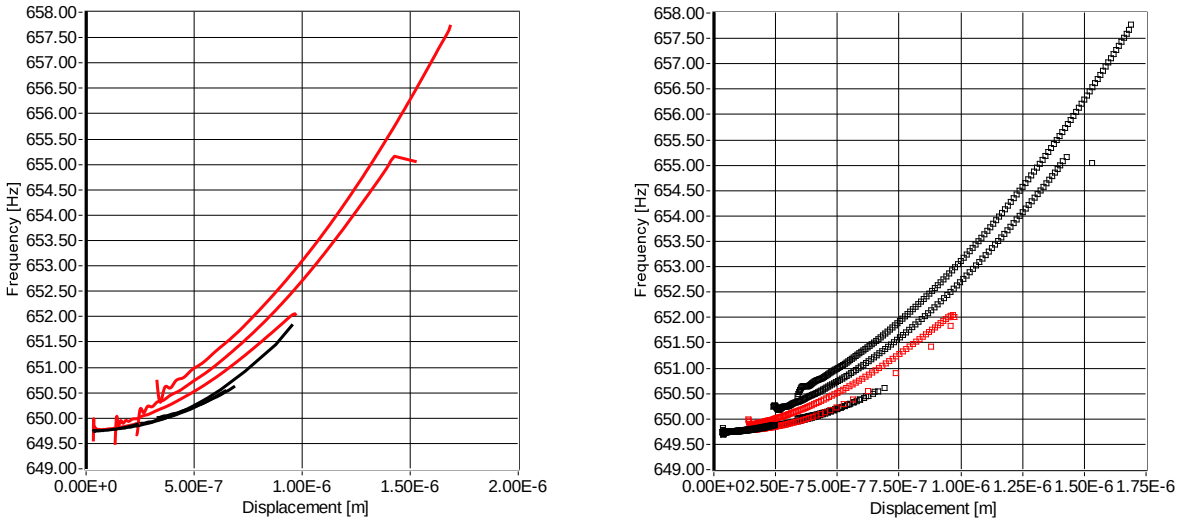


Figure 6 Damping, *c*, of the single DoF system

It is possible to use two of the system of equation (4) to calculate both *m* and *k* and therefore possible to calculate a natural frequency for the equivalent linear system. By repeating this calculation for ever set of three frequency points, as explained earlier, it is possible to track the natural frequency against the vibration amplitude. Figure 7a shows the four traces of the natural frequency of the system. The red branch refers to the natural frequencies calculated by sweeping the FRF branch before the jump, from low to high frequency. The black branch refers to the frequency points after the jump, from high to low amplitude. Figure 7b shows a similar behaviour of the natural frequency, but the curves were calculated using equation (5). The difference between the two plots is about the way the curves are constructed, which requires to isolate the meaningful solution from the results of equation (4) and, therefore, the curve is built by composition of the upper and lower branch. The use of equation (5) leads to the complete calculation of the natural frequency curve. One can observe in Figure 7b the red curve. Interestingly, this curve also shows that by sweeping the data points the two branches before and after the jump do not overlap but create a kind of hysteresis. This behaviour will be more evident during the analysis of the single DoF system including both stiffness and damping nonlinearity.



(a) Analysis carried out by using equation (6) (b) Analysis carried out by using equation (7)

Figure 7 Natural frequency traces

The data of the natural frequency from the graph in Figure 7b was curve-fitted by a polynomial function to identify if the natural frequency of the underlying linear system was correctly identified and if the nonlinearity was also adequately identified. Figure 8 shows the four natural frequency curves fitted by a polynomial function, depicted in red colour. The nonlinear polynomial function identifying the nonlinearity is:

$$\omega_{nl}(x) = -2.97e^{18}x^3 + 5.75e^{12}x^2 - 2.8e^5x + 649.75 \tag{8}$$

The polynomial function of equation (8) captures the underlying linear natural frequency of the system correctly, 649.75Hz. It also identifies the cubic nonlinearity as initially used for the simulating the FRFs of the single DoF system but with an overestimated coefficient, $-2.97e^{18}x^3$ instead of $1e^{18}x^3$.

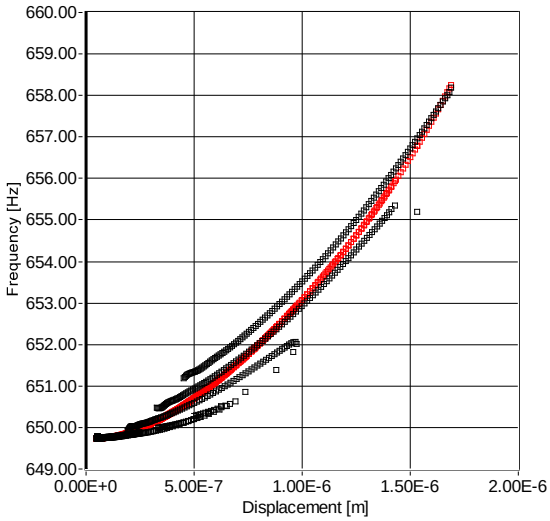
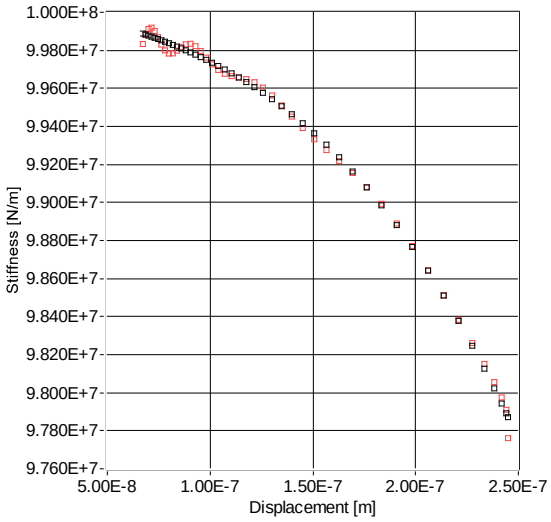
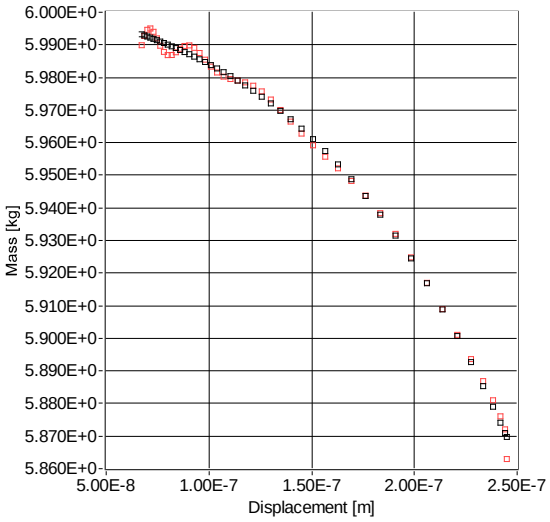


Figure 8 Natural frequency traces fitted by polynomial function in red colour

The functions of the stiffness and the mass, which are used to generate the natural frequency of the system, present some interesting features. For instance, the mass function would be assumed constant for all the vibration amplitudes, but this is not the case. Furthermore, being a hardening nonlinearity, one would suppose that the stiffness function would also present higher stiffness for higher vibration amplitudes. Again, this is not the case either and Figure 9a&b show what was just explained. Both behaviours are presented for an FRF measured with an input force of 0.1N. Both stiffness and mass functions tend to converge to the underlying linear system properties, such as m = 6kg and k = 1e^8 N/m. In principle, the method identifies the nature of the nonlinearity correctly, but it is yet to understand why the mass is not a constant function and the stiffness presents an opposite behaviour than expected for a hardening nonlinearity.



(a) Stiffness function



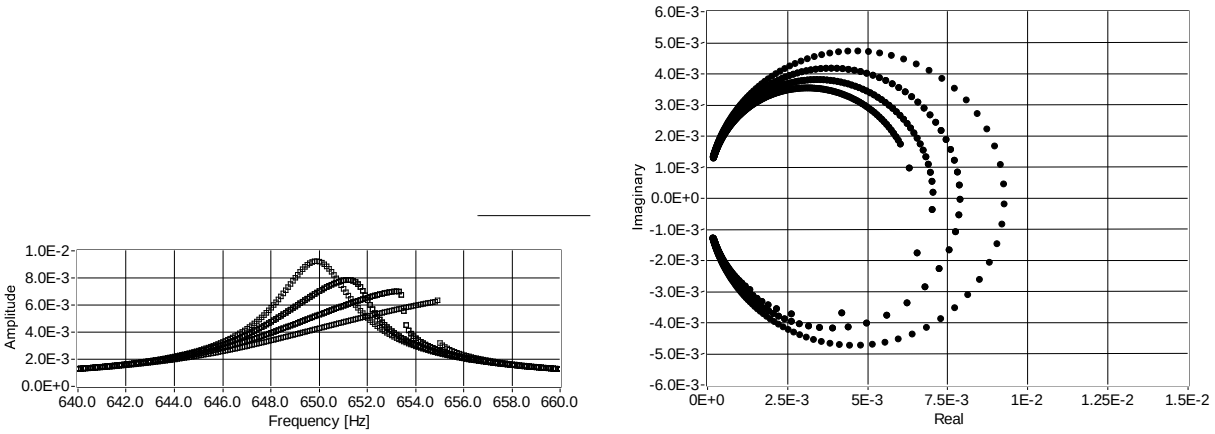
(b) Mass function

Figure 9 Stiffness and mass functions obtained from equation (4)

2.1.4 Stiffness and damping nonlinearity case study

The second case presented in this paper is the inclusion of both stiffness and damping nonlinearity in the single DoF system. Figure 10 shows both the FRF magnitudes in (a) and the Nyquist circles in (b). The inclusion of damping nonlinearity determines the change of the circle diameter for every excitation force, but it does not rotate the frequency points on the Argand diagram. The combination of stiffness and damping

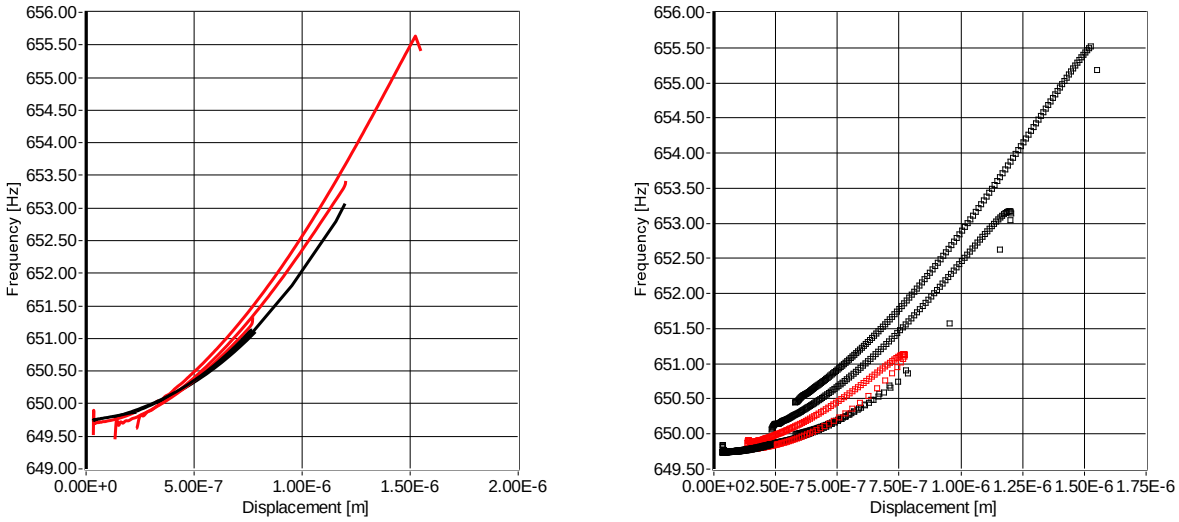
will rotate the circles and change its diameters. The procedure for analysing the frequency points is precisely performed as described in the previous case, and both equations (4) and (5) can be used for this.



(a) FRF magnitudes (b) Nyquist circles

Figure 10 FRF of a single DoF with stiffness and damping nonlinearity nonlinearity

The results for this stiffness and damping nonlinear system are presented in Figure 11 a&b. The observation should be drawn on the "hysteresis" feature of the curves as the sweeper inspects the frequency points of the FRF. One possible explanation is that the energy of the nonlinear response is not concentrated in its first fundamental frequency but spread across multiple harmonics. By neglecting the high order harmonics when generating the FRF one could claim that an energy loss is artificially created. Figure 11a is created by using the real part of equation (4). Instead, the Figure 11b shows the results obtained by using equation (5), which takes into account both real and imaginary part of the frequency points. The red curve in Figure 11b shows the analysis carried out on FRF simulated with excitation force 0.4N. This behaviour is understandable since the imaginary part which carries information about the damping is not included in the analysis. One could argue that for frequency identification the system of equation (4) could be sufficient.



(a) Analysis carried out by using equation 4 (b) Analysis carried out by using equation 5

Figure 11 Natural frequency traces

Finally, the viscous damping is calculated by measuring the circle diameter for every three frequency points selected. Such a calculation is possible because of the single DoF system analysis whereby the parameter *c* is:

$$c = 1/D \tag{9}$$

where D is the circle diameter. Figure 12 shows the damping behaviour against the vibration displacement. This paper will not go through the simulation of a nonlinear FRF based on the nonlinear parameters so far identified. Instead, it will select three values from the mass, damping and stiffness nonlinear functions and use them to calculate the regenerated FRF. The analysis is carried out on the assumption of linearity, which means that every three frequency points define a linear single DoF system for the given m_i, c_i, and k_i. Therefore, by using equation (1) to regenerate the FRF, the match with the nonlinear FRF will be at the extremes and one frequency point, as it is showed in Figure 13 for nonlinear FRF simulated with 0.4N excitation force. One can observe that such a match is qualitatively poor, but here the aim is to evaluate the peak response at any point of the natural frequency and nonlinear damping function.

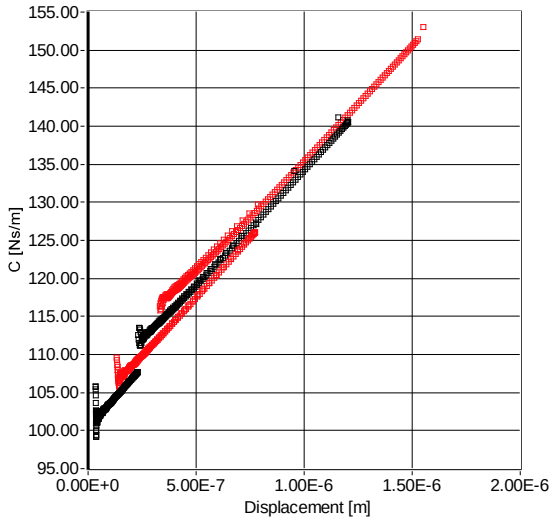


Figure 12 Viscous damping trace

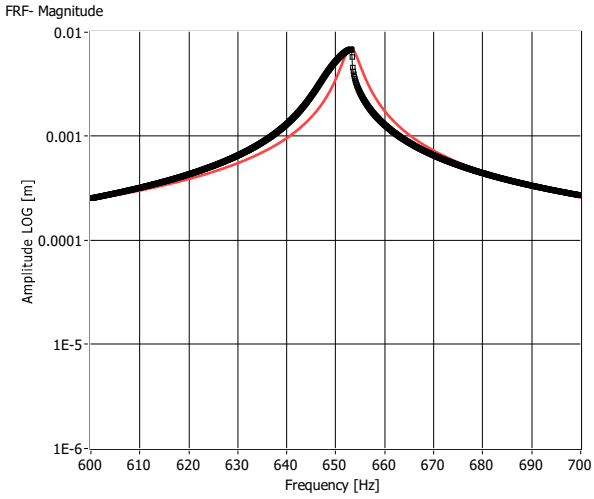


Figure 13 Comparison between simulated nonlinear FRF and a regenerated linear one

3 Conclusions and future work

This paper shows for the first time how to overcome the issue of the vibration response jump in the analysis of FRF Nyquist data. The method proposed is relatively simple, it is based on the idea that both the natural frequency and damping can be observed when two references and one sweeper are selected from the data set. Hence, three frequency points will always be available to define Nyquist circle of a linear system, from

which the modal parameters can be extracted. This new methodology is applied to two numerical cases of a single DoF system which was included with stiffness and damping nonlinearity. The results from the analysis revealed that the nonlinear functions describing the natural frequency and the damping could be retrieved from the simulated data. The method based on the proposed equations work adequately, but these are not sufficiently accurate. A forthcoming publication will present a new algorithm which will resolve both the frequency and nonlinear damping functions as well as the modal constant.

References

[1] D. J. Ewins, *Modal Testing: theory, practice and application*, no. 2000. 1970.
[2] P. Avitabile, "Insight into Modal Parameter Estimation," *Modal Test. A Pract. Guid.*, pp. 327–364.
[3] "ICATS." ICON Suite, 58 Prince's Gate Exhibition Road, London SW7 2PG.
[4] D. Göge, M. Sinapius, U. Füllekrug, and M. Link, "Detection and description of non-linear phenomena in experimental modal analysis via linearity plots," *Int. J. Non. Linear. Mech.*, vol. 40, no. 1, pp. 27–48, Jan. 2005.
[5] A. Carrella and D. J. Ewins, "Identifying and quantifying structural nonlinearities in engineering applications from measured frequency response functions," *Mech. Syst. Signal Process.*, vol. 25, pp. 1011–1027, 2011.

Linearization of modal parameters in Duffing oscillator using the random decrement technique

K. K. Vesterholm [1,*], **R. Brincker** [2] , **A. Brandt** [1]
[1] University of Southern Demark, Department of Technology and Innovation
Campusvej 55, DK-5230 Odense M, Denmark
[*] Corresponding author e-mail: **kav@iti.sdu.dk**

[2] Technical University of Denmark, Danish Hydrocarbon Research and Technology Centre
Anker Engelunds Vej 1, DK-2800 Kgs. Lyngby, Denmark

Abstract
In this study, it is investigated how the random decrement (RD) technique can be used to linearize the nonlinear stiffness of a single degree of freedom system with a hardening spring, known as a Duffing oscillator. The linearization is implemented by using a set of trigger levels in the response signal to define RD signatures. The modal parameters are estimated at the same response level for various excitation force levels, from the RD signatures describing the system at that specific level, and extracting the modal parameters using time domain parameter extraction methods. The system described by the RD signature is assumed to behave as a linear system with an equivalent stiffness depending on the trigger level. Various triggering conditions for the RD technique are investigated, to study their applicability in linearizing the nonlinear system. The results of the study show that, with the Local Extremum, and Envelope triggering condition, the RD technique can be successfully used to linearize the modal parameters of the Duffing oscillator.

1 Introduction

The random decrement (RD) technique is an established method for evaluating modal parameters of structures under random force inputs. Since the RD technique can be applied at a specific response level, it is an obvious step to apply it on multiple levels in the same signal, to investigate the response for amplitude dependent nonlinearities. Using this approach, it should be possible to examine if, and how the modal parameters vary at different response amplitudes, and thereby linearizing the nonlinearity. The idea of analyzing systems with amplitude dependent nonlinearities has been part of the RD technique since H. A. Cole introduced it in 1968 [1], where he showed that the technique is promising regarding the detection of amplitude dependent nonlinearities. The results from this study can be used in any application where a nonlinear dynamic system is excited by a random force, and the amplitude dependent properties need to be identified.

S. R. Ibrahim et. al. introduced multi-triggering in 1987 [2] to identify amplitude dependent nonlinearities, and investigated various triggering conditions including the level crossing (LC) condition. The modal parameters were identified with the Ibrahim Time Domain (ITD) method. In 1992 A. P. Jeary [3] also used multiple triggering levels with the LC triggering condition and suggested that a nonlinearity in the natural frequency can appear as a decay function. A new triggering condition was proposed in 1996 by Tamura and Suganuma [4], which in the present paper is referred to as local extremum (LE), to identify amplitude dependent nonlinearities. A numerical study was performed, where the system parameters were simulated to be dependent on the previous peak in the response, and constant between peaks. The RD technique with LE was then applied to a wind-induced response of various buildings. The amplitude envelope RD technique

was introduced in 2016 by Huang and Gu [5]. RD was used here under the assumption that the dynamic parameters of the system do not change within the individual signal segments, and that the system parameters, corresponding to the triggering level, is contained within the corresponding segment. The numerical study in [5] introduces a new iterative computing method that uses the Newmark method, and the system is modelled such that the stiffness and damping are functions of the amplitude envelope of the response. A review of various implementations of the RD technique was performed in 2017 by T. Reynolds [6], who compares the level crossing, local extremum, envelope, and positive point (see Section 2.2). The review was done by performing a Monte-Carlo simulation with the computation method introduced in [5] with amplitude dependent damping in an SDOF system. The review concludes that local extremum, envelope, and positive point give good estimates of the nonlinear parameters compared to level crossing, but have higher variability.

In the present paper we study the duffing oscillator, which has a nonlinear restoring force, see Figure 1. It is investigated how accurately the RD technique can identify the linear and nonlinear parts of the restoring force, by testing various triggering conditions.

In a linear system, the modal parameters are the same, regardless of the level of excitation force, because the principle of superposition is valid. For a nonlinear system, like the Duffing oscillator, the principle of superposition no longer applies, and modal parameters are dependent on the level of excitation force. For the linearization of modal parameters to be successful, investigating a specific response level of the system being excited by one level of force, should reveal the same modal parameters when investigating the same specific response level, where the system is excited by another level of force. I.e. the linearization of the system should only be dependent on the system parameters and not the excitation force.

In the present work, several numerical examples are analyzed with various triggering conditions. From the RD signatures, modal parameters are extracted and the natural frequencies are then used to calculate the linearized restoring force.

2 Theory

In this section the theory for the linearization of the Duffing oscillator, and the RD technique is described.

2.1 Duffing oscillator

The Duffing oscillator is described by Duffing's equation [7]

$$m\ddot{x}(t) + c\dot{x}(t) + kx(t) + k_3x^3(t) = F(t) \tag{1}$$

where m, c and k are the linear mass, damping, and stiffness respectively, k_3 is the nonlinear stiffness, x is displacement, and F is the applied force. The Duffing oscillator can be described as a single degree of freedom (SDOF) system, with a cubic spring attached, see Figure 1. When the nonlinear stiffness k_3 is positive it is interpreted as a hardening spring.

The nonlinear part of Equation (1) is included in the total restoring force

$$F_{rest}(t) = kx(t) + k_3x^3(t). \tag{2}$$

It is assumed that the total restoring force can be reformulated as

$$F^*_{rest}(\alpha, t) = k^*(\alpha) \cdot x(t) \tag{3}$$

where the equivalent stiffness k^* is dependent on some amplitude α. This assumption results in a linearized form of Duffing's equation

$$m\ddot{x}(t) + c\dot{x}(t) + k^*(\alpha)x(t) = F(t), \tag{4}$$

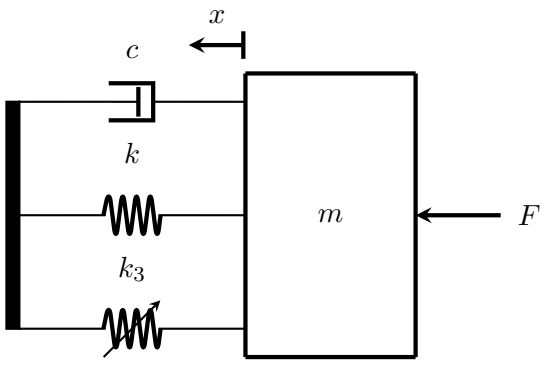


Figure 1: Single degree of freedom system with cubic spring, also called Duffing oscillator

where the system is interpreted as being linear for a specific amplitude α.

With the introduction of an amplitude dependent stiffness, the relative damping also changes with amplitude. The amplitude dependent relative damping is described by [8]

$$\zeta(\alpha) = \frac{c}{2\sqrt{mk^*(\alpha)}} \tag{5}$$

which means ζ will decrease when k^* increases.

2.2 Random Decrement

This section will explain how the RD technique is performed, and specify the triggering conditions used in the present study.

The RD technique is the method of obtaining the RD signature, which is calculated as an average of N signal segments extracted from $x(t)$ [9]

$$\hat{D}_{X,Y}(\tau) = \frac{1}{N}\sum_{i=1}^{N} x(t_i + \tau)|T_{y(t_i)} \tag{6}$$

where x and y are realizations of the stochastic processes X and Y. N is the number of time points in process y that satisfies the triggering condition $T_{y(t_i)}$ at the time points t_i. τ is the lag of the RD signature, which extends from $-M$ to M. In Figure 2, the algorithm to perform this calculation is illustrated, where the level crossing (LC) triggering condition is used. The algorithm is explained stepwise by following the steps 1 - 4:

1) The triggering condition LC is applied to signal $y(t)$ to find the time point t_i. Four triggering points are found, which are marked by dots.

2) The triggering points t_i, found in signal $y(t)$ are transferred to $x(t)$ to mark the centers of the segments, that are extracted from the signal $x(t)$. The segments are symmetrical around the triggering points.

3) The four individual segments, extracted from signal $x(t)$, are illustrated on top of each other in the lag domain.

4) The average of the four segments results in the RD signature. Since only four segments are extracted the RD signature is not complete and it has a large random error, but the general outline is quite clear.

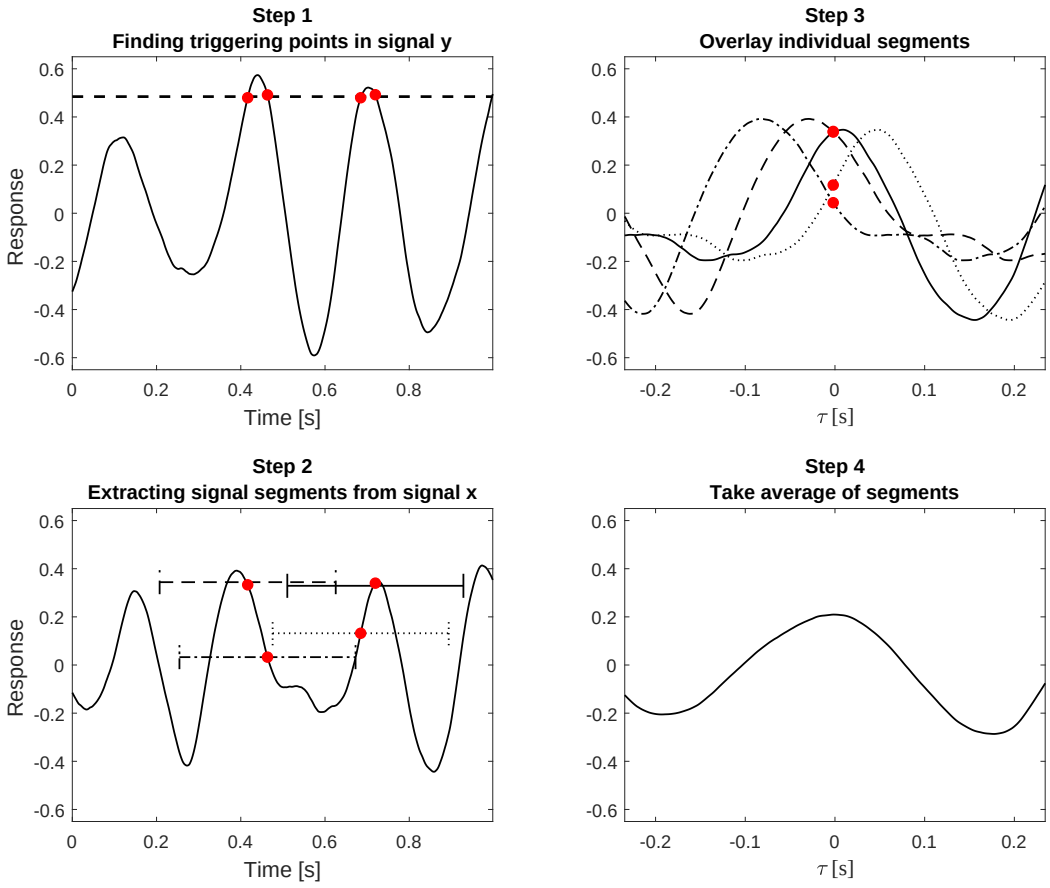


Figure 2: By following steps 1-4, it is illustrated of how the random decrement technique is performed, according to Equation (6). Here, the level crossing triggering condition is applied

There are two forms of RD signatures. Auto RD signature $\hat{D}_{X,X}(\tau)$, where both the triggering condition is applied to, and the segments extracted from, signal $x(t)$. Cross RD signature $\hat{D}_{X,Y}(\tau)$, where the triggering condition is applied to signal $y(t)$ and the segments are extracted from signal $x(t)$, as shown in Equation (6) and illustrated in Figure 2.

There are many triggering conditions, and this study will be investigating how four of them perform when analyzing the Duffing oscillator, namely level crossing (LC), positive point (PP), local extremum (LE), and envelope (ENV). There is a confusion in the naming of triggering conditions, and for consistency the triggering conditions PP, LE, and LC are named to correspond with [9]. This study presents a modified version of the envelope triggering condition presented in [5].

The LC triggering condition is the one H. A. Cole used when he introduced the RD technique [1]. The condition states, that a triggering point is detected if the signal is equal to a triggering level a

$$T^{LC}_{y(t)} = \{y(t) = a\}. \tag{7}$$

In the PP triggering condition, a triggering point is detected when the signal is between two triggering bounds a_1 and a_2

$$T^{PP}_{y(t)} = \{a_1 \leq y(t) < a_2\}. \tag{8}$$

For LE a triggering point is detected when the signal satisfies two conditions. It has to be between the two triggering bounds, a_1 and a_2, and the derivative of the signal has to be equal to zero, which is equivalent to

a local maximum or minimum

$$T_{y(t)}^{LE} = \{a_1 \leq y(t) < a_2, \dot{y}(t) = 0\}. \tag{9}$$

The ENV triggering condition uses the same principle as PP, but instead of using signal $y(t)$ to find the triggering points, the amplitude envelope of $y(t)$ is used. The amplitude envelope is calculated as the magnitude of the analytical signal

$$A(t) = |y(t) + j\tilde{y}(t)| \tag{10}$$

where $\tilde{y}(t)$ is the Hilbert transform of $y(t)$ [11]. The triggering condition is defined as

$$T_{y(t)}^{ENV} = \{a_1 \leq A(t) < a_2\}. \tag{11}$$

ENV is not as well understood as the other triggering conditions, and exactly how it works leaves room for discussion in another study. An interpretation of ENV could be that the amplitude envelope $A(t)$ represents equivalent peaks in the signal, and using it to find triggering points is equivalent to LE. The difference is that the triggering points found are not restricted to a response with zero slope, that is the case for LE, but the extracted segments have the same properties. With the triggering condition ENV, the identified triggering points are not located neatly around the triggering level, as is the case for the other triggering conditions, but spread out in both the positive and negative part of the response.

In [10] it is shown that the RD signature is proportional to the correlation function in the following way

$$D_{X,Y} = \frac{R_{X,Y}(\tau)}{\sigma_X^2} \cdot \tilde{a} - \frac{\dot{R}_{X,Y}}{\sigma_{\dot{X}}^2} \cdot \tilde{b} \tag{12}$$

where σ^2 is the variance and $\tilde{a}$ is a function of the triggering bound and the signals' probability density function, and is related to the part of $T_{y(t)}$ that is applied to the response. $\tilde{b}$ is a function of the triggering bound and the signals' probability density function, and is related to the part of $T_{y(t)}$ that is applied to the derivative of the response[9].

One of the assumptions for the RD technique is that a response signal can be decomposed into three parts; the response due to initial displacement, the response due to initial velocity, and response due to the excitation force. When averaging the segments, the excitation force averages out, since it is assumed to have zero mean. The velocity part is removed by making sure that if a triggering point is on a positive slope, another triggering point is on the negative part of a slope, so they cancel out, and in most cases this is what happens around a peak with PP and LC, as can be seen in Figure 2. Another way to eliminate the velocity part is by only triggering on samples that have no velocity, which is the principle for LE.

For this study, the RD technique is applied, by first identifying the triggering points in the positive part of the response, calculating the RD signature from the extracted segments, then identifying the triggering points in the negative part of the response by multiplying the triggering level with -1, calculating the RD signature from these extracted segments as well. The RD signature from the negative part of the response is multiplied by -1, and an average is taken of the RD signatures from the positive and negative parts of the response. The final step is to flip the part of the RD signature with negative lags over to the positive side, and again taking an average of the two. The RD signature is now finalized and ready for the next step in the analysis.

3 Numerical tests and analyses

The numerical tests are performed by simulating the forced response of mechanical systems in the time domain using a digital filter based method [12], and is done with a sampling frequency of $f_s = 1024$ Hz. The excitation force is a normal distributed signal with different variances, representing various force levels. The force is low pass filtered at 100 Hz with a 4th order Butterworth filter before exciting the system. All time history responses are 81.2 minutes resulting in 4990000 samples, and no noise is added in the

System	Mass	Damping	Linear Stiffness	Nonlinear Stiffness
#	[kg]	$[\mathrm{Nsm}^{-1}]$	$[\mathrm{Nm}^{-1}]$	$[\mathrm{Nm}^{-3}]$
1	0.50	0.4	1000	0
2	0.50	0.4	1000	500
3	0.50	0.4	1000	2000
4	0.50	0.4	1000	4000

System	Mass	Damping	Linear Stiffness	Nonlinear Stiffness
#	[kg]	$[\mathrm{Nsm}^{-1}]$	$[\mathrm{Nm}^{-1}]$	$[\mathrm{Nm}^{-3}]$
5	0.65	0.8	1500	0
6	0.65	0.8	1500	750
7	0.65	0.8	1500	1500
8	0.65	0.8	1500	3500

System	Mass	Damping	Linear Stiffness	Nonlinear Stiffness
#	[kg]	$[\mathrm{Nsm}^{-1}]$	$[\mathrm{Nm}^{-1}]$	$[\mathrm{Nm}^{-3}]$
9	350	400	1.5e6	0
10	350	400	1.5e6	1.7e15
11	350	400	1.5e6	1.7e14

Table 1: Mechanical systems that are investigated

simulations. In the present study, the simulated response is a displacement signal. Several mechanical systems are investigated to conduct a thorough analysis, and are presented in Table 1. Each system is excited by 11 different force levels.

After the responses have been simulated the next step is to set up the RD analysis.

In [9], it is recommended that the triggering level should not be below the standard deviation of the response signal σ_y, and not above $2\sigma_y$. This recommendation is made on the basis of an analysis of linear systems. The triggering levels in the present study is chosen with two things in consideration; the recommendation from [9], and a desire to investigate a large range in the response signal. These considerations results in triggering levels in the interval $[\sigma_y, 2.5\sigma_y]$ for the present analysis.

The triggering levels are defined for each system as 75 logarithmically spaced levels, where the lowest triggering level is the standard deviation of the response for the case where the system is excited by the lowest force level, and the highest triggering level is 2.5 times the standard deviation of the response when the system is excited by the highest force level. When the system is then analyzed, the response can be divided to approximately 16 levels in the interval $[\sigma_y, 2.5\sigma_y]$ for each case with a different force level. This allows for an easy comparison between cases of different force levels, because the triggering levels are at the same specific response levels.

For the triggering conditions PP, LE, and ENV, where two levels are needed to define a triggering point, the levels $[a_1, a_2]$ form a triggering band. When using a triggering band, and analyzing amplitude dependencies, there are a few things to consider. It is desired to calculate an accurate RD signature using Equation (6), meaning that N should be large, which can be realized by having a wide triggering band. However, the analysis is desired to reveal information about a specific amplitude, meaning that the band should be narrow, and thereby having a well defined amplitude. The triggering band is defined as a_2 being the level specified above, and a_1 is tweaked such that an amplitude is well defined, while also having a large N to calculate an accurate RD signature. For PP a_1 is chosen to find approximately 10000 triggering points in the response signal, and for LE, there are found approximately 3500 triggering points. For ENV the band is in the amplitude envelope $A(t)$, and a_2 is still as defined above, but a_1 is now defined such that the band $[a_1, a_2]$ represents 0.1% of the range of $A(t)$.

The number of lags in the RD signature must be defined through the number M, and for all analyses performed in the present study $M = 1024$. This is a very large M, and only the first 110 lags are involved in the further analysis, but this allows the analyst to visually inspect the RD signatures during the investigations, with a lot of information available.

With these settings, the RD analysis can be performed on all systems, and an example of RD signatures with three triggering levels, from a linear and a nonlinear system is presented in Figure 3. The case illustrated,

is for systems 1 and 3, both excited with an rms force of 89 N. It is very clear that for the linear system, only the scaling of the RD signature changes with triggering levels high, middle or low. The signatures from the nonlinear systems experience other changes as well as scaling of the RD signature, an indicator that this system is in fact amplitude dependent.

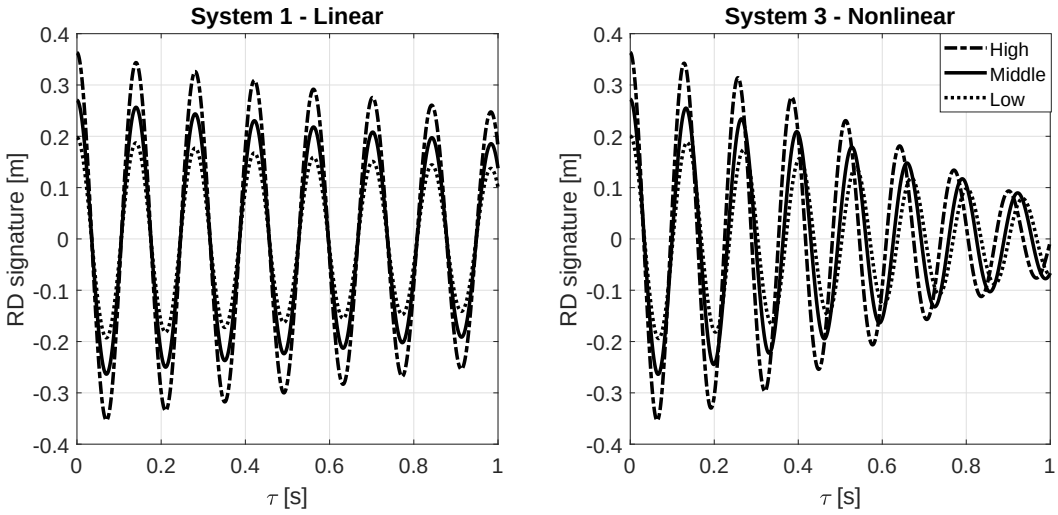


Figure 3: Comparison of 3 RD signatures from a linear an a nonlinear system. The systems 1, and 3, are both excited by a force with rms level of 89 N, and analyzed with the LE triggering condition

Once the RD signatures are obtained, they are treated as correlation functions, and the modal parameters are extracted using time domain methods. In the present study, three methods are compared, Prony [13], Least Squares Complex Exponential (LSCE) [14], and Ibrahim Time Domain (ITD) [15]. The modal parameter extraction methods are all applied using the ABRAVIBE toolbox [16], where the methods are implemented using stabilization diagrams. The first 10 lags are excluded from the RD signatures, and the following 100 lags are used in all the modal parameter extraction methods.

4 Results and Discussion

There are two main results presented and discussed in this section. First, results concerning the question whether it is possible to linearize the modal parameters independently of the excitation force level. And second, how accurately the nonlinearity is identified.

In the investigation, the deviations between the parameter estimation methods is minimal, and only results for Prony are presented.

The four different triggering conditions are compared, to evaluate whether they can be used to linearize the nonlinear systems independently of the excitation force level. The results presented here are from the analysis of system 4, as these are representing the general results from all the systems very well.

In Figure 4, the estimated frequencies are given as a function of triggering level for the four triggering conditions, each line in the plots represents a case of the system being excited by a specific rms force level. The different ranges in triggering levels for the different cases, stems from the fact that the variance of the response gets large when the system is excited by a larger force, and the triggering levels are logarithmically spaced in the interval $[\sigma_y, 2.5\sigma_y]$ for the individual case.

When comparing the four triggering conditions in Figure 4, it is easy to see that PP and LC behaves differently from LE and ENV. Focusing on the triggering level around 0.3 m, the 4 cases with the rms forces 66.9 N, 89.3 N, 112 N, and 134 N are represented. Triggering conditions PP and LC do not identify the same frequency for the four cases at this triggering level, instead the frequency increases with the applied force. If

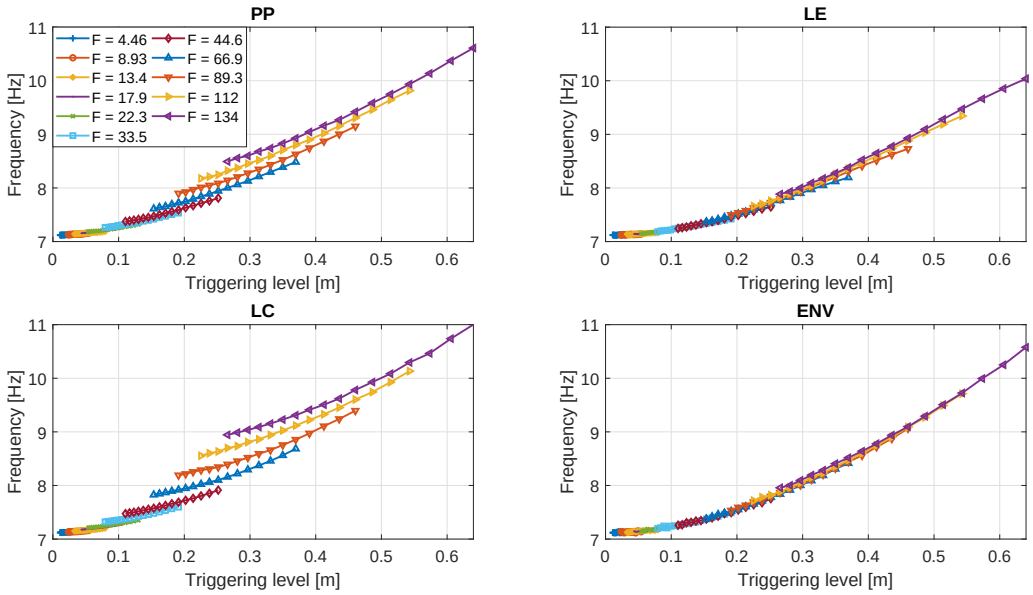


Figure 4: Example of estimated eigenfrequencies as a function of triggering level. The present analysis is done on system 4. The various curves represent cases with different rms force applied to the system

the curves in PP and LC, for the rms force of 134 N, would be described by a function, it would not be the same function that described the other curves. For LE and ENV, the frequency estimates are nearly the same for the various rms force levels, and a single function could describe all the curves, since they all overlap.

From this comparison, the triggering conditions PP and LC cannot linearize the eigenfrequencies independently of the excitation force, while LE and ENV can. This pattern repeats for all systems, and all modal parameter extraction methods.

The exact reason why PP and LC are not capable of the desired linearization is unknown. It is however known that it is not because PP and LC triggers on samples with a slope and LE does not, because ENV finds most triggering points on a slope.

According to Equation (5), the relative damping decreases as a function of triggering level. In Figure 5 the damping estimates are presented as a function of triggering level. As in Figure 4, each line in the plots represents a case of the system being excited by a specific rms force level. Again the triggering conditions PP and LC behave in a comparable way, while differing from LE and ENV. For rms force levels below 44.6 N, all triggering conditions result in an acceptable damping estimate, but PP and LC give an erroneous amplitude dependent damping estimate when the excitation force is increased. LE and ENV lead to acceptable damping estimates for a larger range of rms force levels. When the force exceeds 89.3 N, the estimates have a slight increasing trend, while the true relative damping is decreasing, resulting in up to 100 % difference between the true, and the estimated damping for the highest triggering levels. The damping estimates when using LE and ENV are quite poor, but the error is similar for the various force levels.

At the triggering level of 0.33 m, four cases with the rms forces 66.9 N, 89.3 N, 112 N, and 134 N, are represented. If the linearization is independent of the force level, it is expected that the RD signatures, from this triggering level, will have the same appearance. A comparison of the RD signatures at that triggering level is done in Figure 6, and here the trend continues, where the PP and LC look very similar, but differing from LE and ENV. It should be noted that LE and ENV also are very similar, except for the scaling. The RD signatures of LE and ENV for the different force levels are very similar in the first part, and as the lags increase, the RD signatures appear to be increasing slightly in frequency and damping, when the force level increases. For PP and LC, the increase in frequency and damping, as the force level increases, is significant, and the RD signatures do not appear to be describing the same system. These observations from the RD

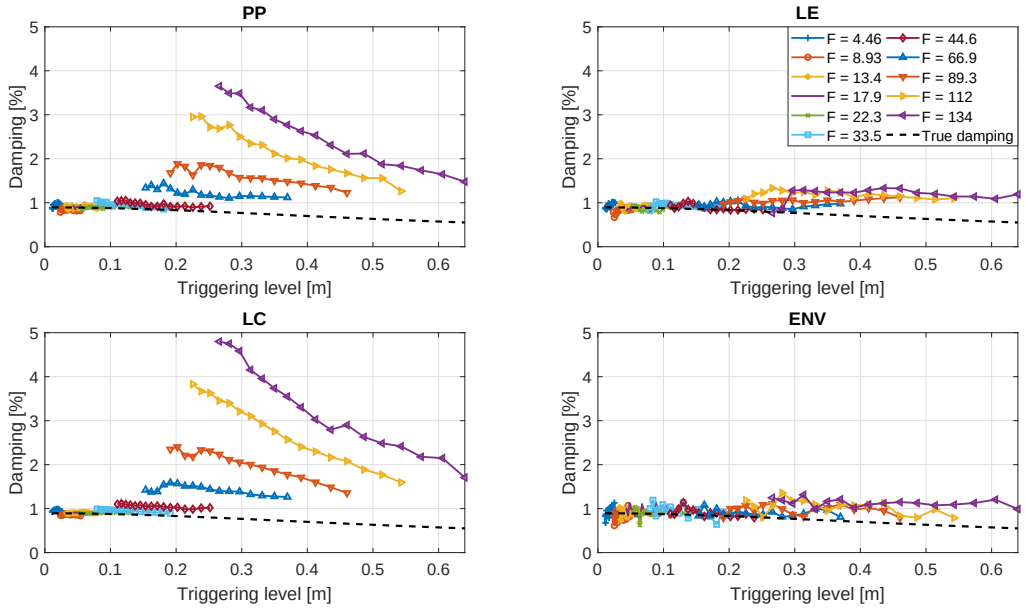


Figure 5: Example of estimated damping as a function of triggering level. The present analysis is done on system 4. The various curves represent cases with different rms force applied to the system. The true damping is calculated with Equation (5), using the triggering level as α

signatures are corresponding very well with the estimated eigenfrequencies and damping factors in Figures 4 and 5.

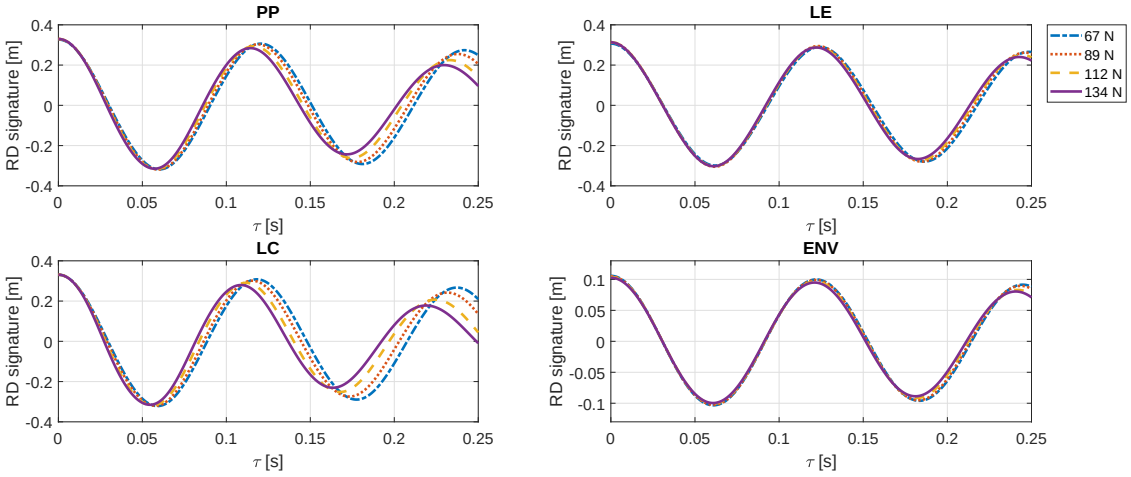


Figure 6: RD signatures for system 4, with four different levels of force, all at the triggering level 0.33 m

The accuracy, with which the nonlinearity is identified, is evaluated on the basis of how well Equation (3) can be fitted to Equation (2). This means that the equivalent stiffness must be calculated for each triggering level (Tl_i)

$$k^*(Tl_i) = m\left(2\pi f(Tl_i)\right)^2 \tag{13}$$

where $f(Tl_i)$ is the estimated eigenfrequency as a function of the triggering level as presented in Figure 4. With the equivalent stiffness, the equivalent restoring force is calculated, using the triggering levels as the displacement term

$$F^*_{rest}(Tl_i) = k^*(Tl_i) \cdot Tl_i. \tag{14}$$

This interpretation of the restoring force says that the system- and modal parameters are both extracted from, and describing the system, at that specific triggering level.

As mentioned above, PP and LC cannot linearize the eigenfrequency independently of the excitation force, and it does not make sense to describe the corresponding restoring force with a single function. Therefore, PP and LC are excluded for the next part of the discussion.

In order to evaluate how well the linearization describes the nonlinear restoring force, an average is taken of the restoring forces, calculated for the individual cases of various excitation force levels, producing a single curve with which to perform the fit. The RD signatures are calculated by applying the technique to both the positive and negative parts of the response, as mentioned in Section 2.2. Because the RD signatures are calculated from both the positive and negative parts of the response, both the negative and positive parts of the restoring force can be used in the fitting. A duplicate of the average restoring force is therefore rotated 180° representing the negative parts of the restoring force. A combination of the positive and negative parts, forms the antisymmetric curve that is the restoring force as a function of the triggering level, see Figure 7.

In Figure 7, the estimated restoring force of system 10 for both ENV and LE is compared with a reference restoring force, which is calculated with Equation (15) where the stiffness coefficients for the system, and the triggering level as the displacement term is inserted. Both ENV and LE fails to fit completely with the true restoring force of the system, as the cubic part of the function is underestimated in both cases. When focusing on the linear part, around zero, both ENV and LE fit very well.

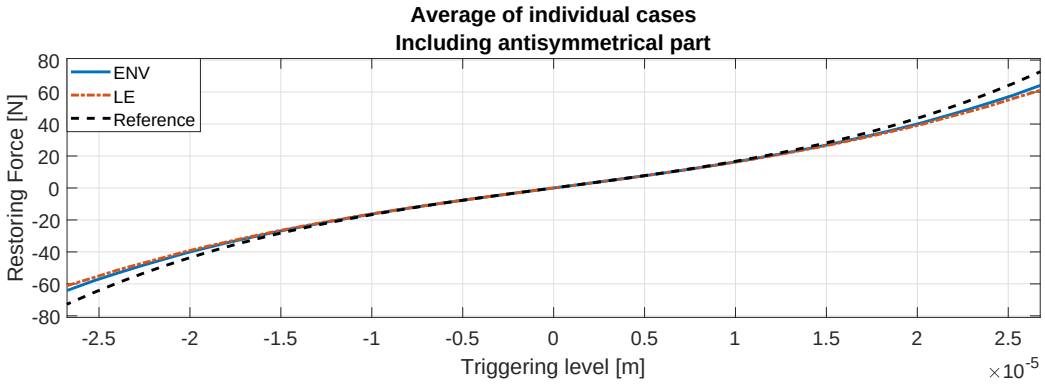


Figure 7: The estimated restoring forces are compared to a reference, calculated by Equation (15). The investigated system, is number 10

The evaluation of the accuracy is done by fitting the restoring force to a function in the form

$$F_{rest} = k_3 x^3 + kx \tag{15}$$

and calculating the error of the coefficients, in relation to the system parameters as given in Table 1. The fitting errors for systems with a nonlinearity are presented in Figure 8. The linear coefficient in the restoring force k, is identified very well, below 2.5 % error for all systems. For both LE and ENV, there is a negative bias of approximately -39 % and -28 % respectively, in the identification of the cubic coefficient in the restoring force k_3. What is really interesting here is that the bias is the same, regardless of system parameters.

For the purely linear systems 1, 5, and 9, the linear stiffness coefficient k is determined within ± 0.1 %, with all triggering conditions investigated here, PP, LC, LE, ENV.

Due to the bias being the same for systems with a nonlinearity, a correction factor β is introduced in the calculation of the restoring force

$$F^{\dagger}_{rest}(Tl_i) = k^*(Tl_i) \cdot \frac{Tl_i}{\beta}. \tag{16}$$

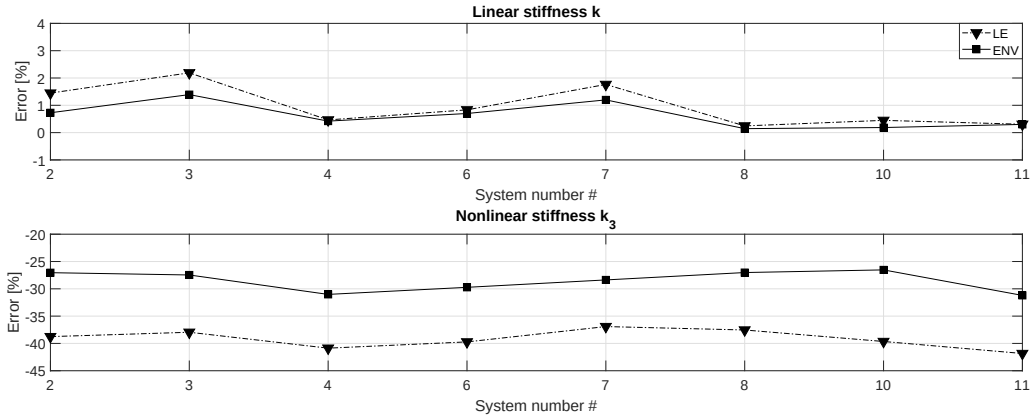


Figure 8: Error in fitted stiffness coefficients for both linear and nonlinear terms, plotted against system number

The displacement term is now proportional to the triggering level. Interpreting the restoring force now, leads to the modal parameters being extracted at the triggering level, but the system parameters are extracted at a response level proportional to the triggering level.

The correction factor is found empirically for the triggering conditions, to be $\beta_{LE} = 1.28$ and $\beta_{ENV} = 1.19$. The restoring force, for both LE and ENV, calculated with the corrected displacement term, is compared in Figure 9, where the reference force is calculated by inserting the stiffness coefficients and the corrected displacement term in Equation (15). β corrected the estimated restoring force to fit with the reference very effectively, as can be seen in Figure 10, where the fitting errors for the cubic coefficient is presented. The error is within $\pm 5\%$ for all nonlinear systems, which is considered an excellent result. The estimation of the linear term remains unchanged with the correction factor.

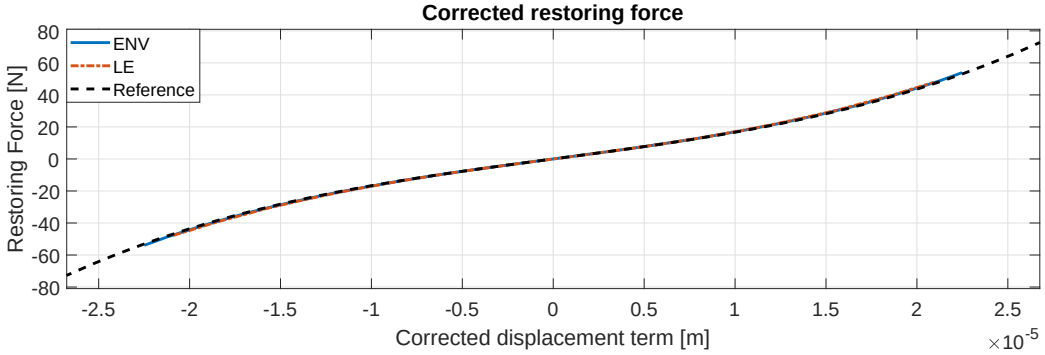


Figure 9: Estimated restoring forces, calculated with the corrected displacement term $\frac{Tl_i}{\beta}$ using Equation (16), compared to a reference calculated with Equation (15). The investigated system, is number 10

It is also investigated how good the fitting of the restoring forces is, calculated from only one case. System 8 is excited by a force with rms level of 33.5 N, and there are 16 triggering levels in the interval $[\sigma_y, 2.5\sigma_y]$, ultimately resulting in 16 points on the curve representing the restoring force as a function of the corrected displacement term. The fitting is a success and the errors for the linear term k, are 0.8 % and 0.1 % for LE and ENV respectively, the errors for the cubic term k_3 is -14.5 % and 0.4 % for LE and ENV, respectively. This means that a single case, where the excitation force is large enough to excite the system beyond the linear regime, is enough to identify the nonlinearity quite well.

The exact nature of β is not well understood at this point, and the present study shows only a dependence of triggering condition. The need for a correction factor stems from the triggering level being a poor substitute for $x(t)$ in Equation (2). The triggering level is a fixed number, while $x(t)$ is a random process, and in

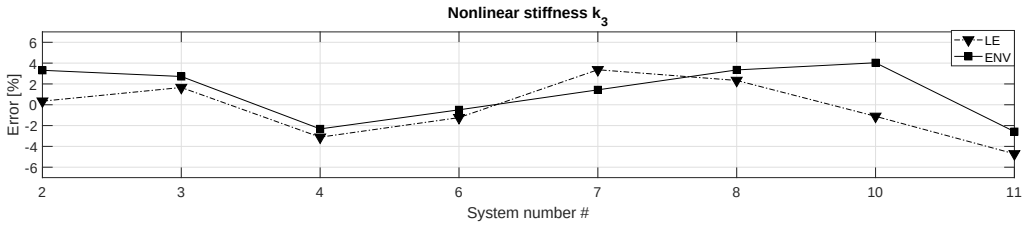


Figure 10: Fitting error for the cubic coefficient in the corrected restoring force

Equation (2), these will cause different outcomes, due to its nonlinearity. In the present study, the excitation force $F(t)$ is normally distributed, and it is expected that a different β will be found for other statistical distributions.

During the investigations, it was discovered that the parameter identification methods had greater difficulty finding stable poles in the stabilization diagrams when the nonlinear systems were excited by a greater force. This phenomenon is illustrated in Figure 11, where system 4 is excited by a medium force level, and a high force level. The RD signatures illustrated are with the same triggering level, and are the 100 lags used in the parameter estimation, the two are almost indistinguishable. The parameter estimation method is Prony, and the difference between the stabilization diagrams is clear. The top one, for the medium force level, has a very clear column of stable pole, represented by green $+$-symbols around 10 Hz. Note how, once the poles are stable, they stay stable as the model order increases, as is expected. For the high force level, the column is now a mix of stable and unstable poles. This is not usual behavior, and is attributed to the nonlinearity, but the exact cause is unknown. This phenomenon is consistent to a varying degree for all systems and parameter estimation methods tested.

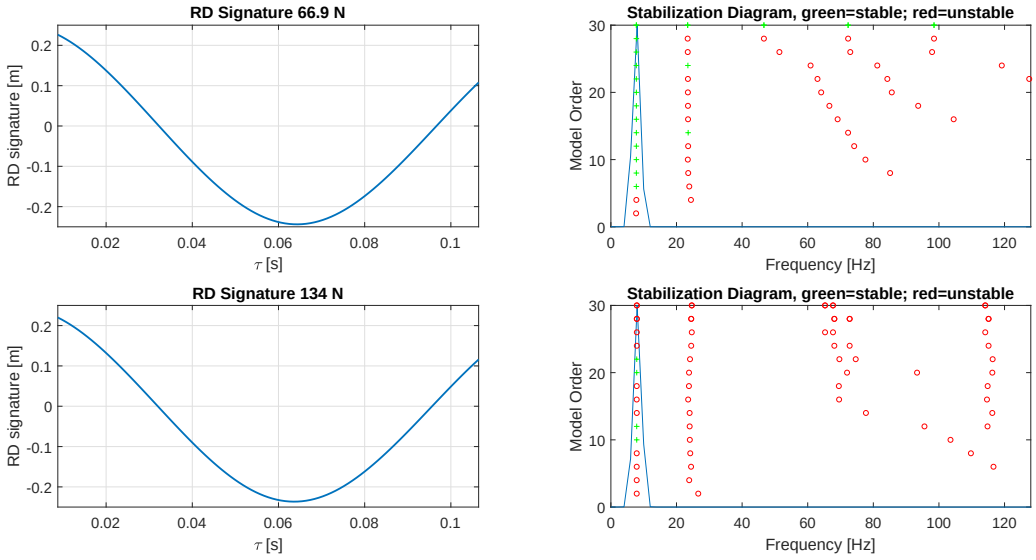


Figure 11: Application of Prony on RD signature found with LE of system 4 with a triggering level of 0.2658 m. The top row shows a medium force excitation, and the bottom row shows a high force excitation

5 Conclusions

The presence of a nonlinearity in the restoring force can be detected in a single response time history, by applying the RD technique at multiple triggering levels, and inspecting the RD signatures to see that properties,

in addition to the scaling, are changing with the triggering level. Of the four RD technique triggering conditions investigated in the present study, PP and LC have been found unable to linearize the modal parameters of the Duffing oscillator independently of the excitation force. The frequency is increasingly overestimated and the damping estimates becomes completely unreliable, when an increasing force excites the system. LE and ENV can successfully linearize the modal parameters, and, when introducing the correction factor β, identify the nonlinear system parameter k_3 with ± 5 % accuracy. The linear stiffness parameter k has been identified with approximately ± 2 % accuracy regardless if the restoring force is linear or nonlinear. For low excitation levels, the damping is accurately estimated using LE and ENV. When the level of excitation force gets large enough, there is a positive bias in the damping estimation method, while the true relative damping is decreasing. These two factors leads to high errors in damping estimates for high levels of excitation force.

Acknowledgements

The authors acknowledge the funding received from Centre for Oil and Gas - DTU/Danish Hydrocarbon Research and Technology Centre (DHRTC).

References

[1] H. A. Cole *On-the-line Analysis of Random Vibrations* AIAA/ASME 9th Structural Dynamics Materials Conference (1968)

[2] S. R. Ibrahim, K. R. Wentz, J. Lee *Damping Identification From Non-Linear Random Responses Using a Multi-Triggering Random Decrement Technique* Mechanical Systems and Signal Processing (1987)

[3] A. P. Jeary *Establishing non-linear damping characteristics of structures from non-stationary response time-histories* The Structural Engineer, Volume 70 (1992)

[4] Y. Tamura, S. Suganuma *Evaluation of amplitude-dependent damping and natural frequency of buildings during strong winds* Journal of Wind Engineering and Industrial Aerodynamics (1996)

[5] Z. Huang, M. Gu *Envelope Random Decrement Technique for Identification of Nonlinear Damping of Tall Buildings* Journal of Structural Engineering, Volume 142 issue 11 (2016)

[6] T. Reynolds *Amplitude Dependence of Modal Properties in Lateral Vibration of Timber Buildings* Proceedings of 24th International Congress on Sound and Vibration (2017)

[7] S. S. Rao *Mechanical Vibrations* Prentice Hall Upper Saddle River (2011)

[8] A. Brandt *Noise and vibration analysis: signal analysis and experimental procedures* John Wiley & Sons (2011)

[9] J. C. Asmussen *Modal Analysis Based on the Random Decrement Technique*, University of Aalborg, Department Building Technology and Structural Engineering, Denmark (1997).

[10] R. Brincker, C. Ventura *Introduction to Operational Modal Analysis* John Wiley & Sons (2015)

[11] J. S. Bendat, A. G. Piersol *Random data: analysis and measurement procedures* John Wiley & Sons (2011)

[12] K. Ahlin, M. Magnevall, A. Josefsson *Simulation of force response in linear and nonlinear mechanical systems using digital filters*, International Conference on Noise and Vibration Engineering (2006)

[13] R. Prony *Essai Expérimental et analytique: sur les lois de la dilatabilité de fluides élastique et sur celles de la Force expansive de la vapeur de l'eau et de la vapeur de l'alkool, à différentes températures.*, Journal de l'École Polytechnique Floréal et Plairial (1795)

[14] Allemang, Randall J. and Brown, David L. *Experimental Modal Analysis and Dynamic Component Synthesis. Volume 3. Modal Parameter Estimation* University of Cincinnati, Department of Mechanical and Industrial Engineering (1987)

[15] S. R. Ibraham, E. C. Mikulcik *A method for the direct identification of vibration parameter from the free responses* Shock and Vibration Bulletin (1977)

[16] A. Brandt *ABRAVIBE - A MATLAB toolbox for noise and vibration analysis and teaching* University of Southern Demark, Department of Technology and Innovation (2018)

Computation of nonlinear modes of non-conservative mechanical systems

M. Jahn *, **S. Tatzko, L. Panning-von Scheidt, J. Wallaschek**
Leibniz Universität Hannover, Institute of Dynamics and Vibration Research,
Appelstrasse 11, 30167 Hannover, Germany
* e-mail: **jahn@ids.uni-hannover.de**

Abstract
The motion of autonomous nonlinear non-conservative mechanical systems is in general non-periodic which contradicts the computation of their nonlinear modes as natural periodic solutions. Utilizing the harmonic balance method (HBM) two approaches for nonlinear mode computation of non-conservative systems exist - the damped motion concept (DMC) and the extended periodic motion concept (E-PMC). Each nonlinear mode computed using one of these methods is then described by its frequency, damping, the harmonics, and the corresponding phase angles of each degree of freedom as functions of the generalized amplitude. Applying averaging methods transient system responses of the system can be efficiently computed regarding one nonlinear mode. In this work differences between the damped motion concept and the extended periodic motion concept as well as corresponding results will be addressed.

1 Introduction

For autonomous nonlinear mechanical systems periodic solutions exist like the normal modes of autonomous linear mechanical systems. One major difference between these nonlinear modes and their linear counterpart is that they may not be designated normal as they may not be described by a set of vectors that span an orthonormal base in the state-space of the systems displacements. For this reason it is impossible to perform a modal reduction of a nonlinear mechanical system using the corresponding nonlinear modes. A common property of normal modes and nonlinear modes is that for weakly damped systems the system response shows maxima in the regions of the modes of the corresponding systems, although for nonlinear modes the frequency of the corresponding periodic motion usually depends on the amplitude of the vibration. In general the motion of autonomous damped systems is not periodic, so for linear systems normal modes are computed for the underlying conservative system first and damping will be added afterwards. For general nonlinear systems there is no counterpart for this procedure as the underlying conservative system might be linear, so that the corresponding normal modes had to be expanded by nonlinear damping which contradicts to the existence of normal modes. To overcome this conflict and compute periodic solutions for damped nonlinear mechanical systems two methods based on harmonic balance exist – the damped motion concept and the extended periodic motion concept — which are also suitable for non-modal damped linear systems. Using one of these methods the nonlinear modes of damped nonlinear systems can be computed. Existing averaging methods like the decomposition of the systems dynamics into its slow and fast dynamics might be applied to this description of a damped nonlinear mode to efficiently compute stationary or transient system responses. The focus of this work is on the differences between the methods to compute nonlinear modes for non-conservative nonlinear systems. Computational effort or certain phenomena occurring at nonlinear modes are not adressed.

2 Modes of nonlinear systems

Linear dynamic systems can be analyzed by their vibration eigenmodes. These modes are obtained by a modal analysis of the undamped and unforced conservative equation of motion where every mode is characterized by a synchronous motion of all material points. Rosenberg [1] proposed a similar definition for nonlinear conservative systems. All material points of a nonlinear mode should reach simultaneously their maximum and zero displacement, respectively. In contrast to the linear case, Rosenberg's idea of nonlinear modes includes an energy-dependent relationship between displacements of material points to each other. Kerschen et al. [2] adapted Rosenberg's synchronous motion condition by a *nonnecessarily synchronous motion condition* to consider internal resonances. At high energy levels free vibrations of nonlinear conservative systems can exhibit different frequencies within one structure. One material point can e.g. vibrate with a multiple of the frequency of another point. The overall motion at these internal resonances is still periodic and allows for numerical approximation methods developed for finding periodic solutions.

The general equation of motion of a nonlinear autonomous system reads

$$\underline{M}\ddot{\vec{x}} + \underline{C}\dot{\vec{x}} + \underline{K}\vec{x} + \vec{f}_{\mathrm{nl}}(\dot{\vec{x}}, \vec{x}) = \vec{0} \tag{1}$$

with the structural matrices $\underline{M}, \underline{C}$ and $\underline{K}$ of the underlying linear system and the nonlinear forces gathered in $\vec{f}_{\mathrm{nl}}(\dot{\vec{x}}, \vec{x})$. Rosenberg's definiton is not compatible with non-conservative nonlinearities which are buried in the nonlinear force vector and cannot be switched off for a separate analysis like linear damping. Periodic solutions to eq. 1 only exist either for the undamped system with conservative nonlinearity or for limit cycles of self-excited systems where self-excitation and damping are cancelling each other out.

Given that a periodic solution exists it can be computed by the HBM. The motion is approximated by a fourier series of the form

$$\vec{x}(t) = \sum_{n=-N}^{N} \hat{\vec{x}}_n \mathrm{e}^{\mathrm{j}n\omega t} \tag{2}$$

using a truncated set of N harmonics with fourier coefficients $\hat{\vec{x}}_n$. Inserting eq. 2 into eq. 1 and balancing out the harmonic components yields a system of nonlinear equations for each harmonic n

$$\left(-(n\omega)^2\underline{M} + \mathrm{j}n\omega\underline{C} + \underline{K}\right)\hat{\vec{x}}_n + \hat{\vec{F}}_{\mathrm{AFT},n}(\hat{\vec{x}}_{(-N\ldots N)}) = \vec{0} \quad ; \quad n = -N, ..., N \quad . \tag{3}$$

The nonlinear forces are assumed to be periodic and can be evaluated by the alternating frequency time method (AFT) [3]. Within the AFT-procedure the nonlinear signal is computed in the time domain and its harmonic content is extracted by the fourier transform. In the following the general form in eq. 3 representing multiple degree of freedom (MDOF) systems is reduced to the single degree of freedom (SDOF) case

$$\left(-(n\omega)^2 m + \mathrm{j}n\omega c + k\right)\hat{x}_n + \hat{F}_{\mathrm{AFT},n}(\hat{x}_{(-N\ldots N)}) = 0 \quad ; \quad n = -N, ..., N \quad . \tag{4}$$

The SDOF equation retains all necessary information and raises the possibility of describing each nonlinear equation by its complex pointer representation.

2.1 Conservative Systems

In the case of pure conservative systems there is no linear damping and nonlinear forces are not dissipative. Eq. 4 turns into

$$\left(-(n\omega)^2 m + k\right)\hat{x}_n + \hat{F}_{\mathrm{AFT},n}(\hat{x}_{(-N\ldots N)}) = 0 \quad ; \quad n = -N, ..., N \tag{5}$$

and fig. 1 (a) shows the corresponding complex pointer diagram. For each harmonic component of the approximation the nonlinear amplitude $\hat{F}_{\mathrm{AFT},n}$ is balanced by the system dynamics. The oscillation frequency ω generally changes with the energy level of the system.

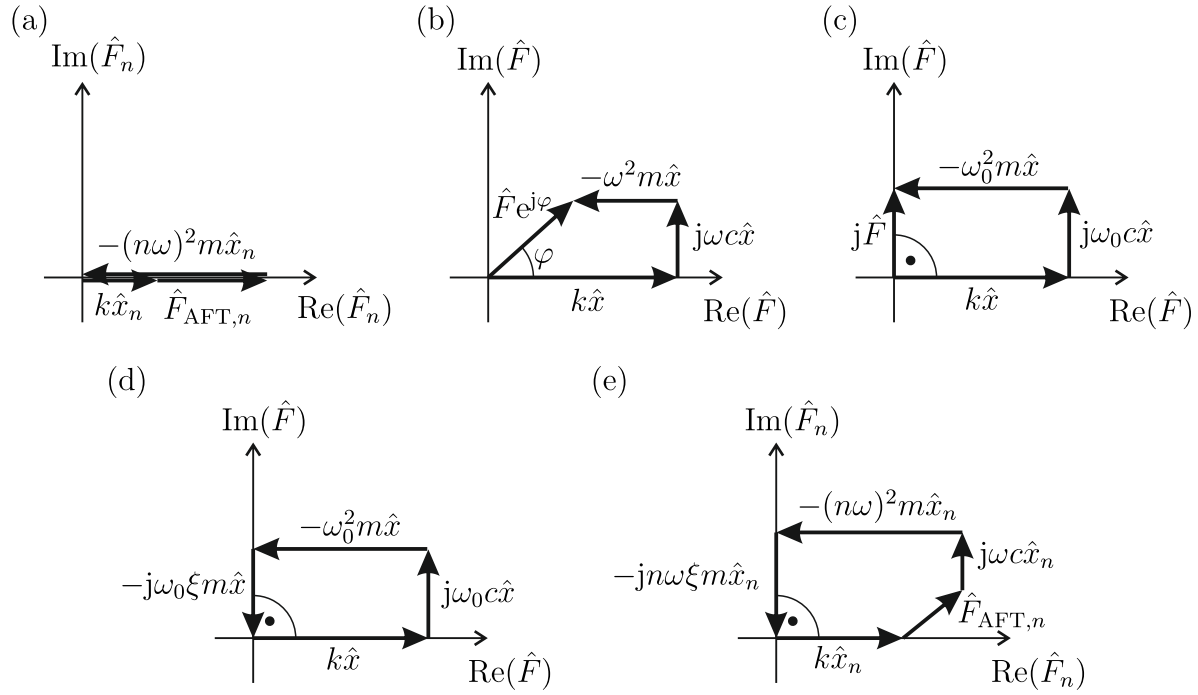


Figure 1: Complex pointer diagrams of the SDOF system; (a) harmonic component of a conservative nonlinear system; (b) linear system with external excitation; (c) linear system with external excitation in resonance; (d) self-excited linear system; (e) harmonic component ($n > 0$) of self-excited nonlinear system (extended periodic motion concept)

2.2 Non-conservative Systems

Non-conservative systems do not vibrate in a periodic manner by their own. If the nonlinearity has a dissipative character energy is reduced during vibratory motion. When nonlinear damping is neglected the computed modes of the conservative nonlinear system are in general not suitable to describe the dynamics of the non-conservative system. To overcome this restriction in the computation of nonlinear modes two approaches have been developed, the *extended periodic motion concept* [4] and the *damped motion concept* [5], which is also known as *complex modes*. Both existing approaches will be derived and compared in this work.

2.2.1 Extension of the Periodic Motion Concept - Linear SDOF System

Starting with a linear SDOF system including damping the complex pointer diagram is given in fig. 1 (b). Due to the damping term the chain of pointers is expanded into the complex plane and can only be closed by an external force to realize periodic motion. The corresponding equation is given by

$$\left(-\omega^2 m + \mathrm{j}\omega c + k\right)\hat{x} = \hat{F}\mathrm{e}^{\mathrm{j}\varphi} \quad . \tag{6}$$

The disadvantage in using an external signal $F(t) = \hat{F}\mathrm{e}^{\mathrm{j}(\Omega t+\varphi)}$ for enforcing periodic motion is that the resulting vibration frequency ω always equals the imposed excitation frequency Ω. The solution is not connected to the dynamic of the autonomous system. However, in resonance when $\varphi = \frac{\pi}{2}$ and $\omega = \Omega = \omega_0$ a pure imaginary excitation pointer follows. The corresponding complex pointer diagram is shown in fig. 1 (c) representing the following equation

$$\left(-\omega_0^2 m + \mathrm{j}\omega_0 c + k\right)\hat{x} = \hat{F}\mathrm{e}^{\mathrm{j}\frac{\pi}{2}} = \mathrm{j}\hat{F} \tag{7}$$

where the excitation is only working against the damping term. This particular configuration can be achieved by self-excitation and an appropriated force term proportional to the mass is chosen by $\hat{F} = \omega_0 \xi m \hat{x}$, cp. fig. 1 (d). The factor ξ is a measure for balancing the damping term of the linear system and the equation

$$\left(-\omega_0^2 m + \mathrm{j}\omega_0(c - \xi m) + k\right)\hat{x} = 0 \tag{8}$$

can be solved when $c = \xi m$. The linear damping ratio $2D\omega_0 = \frac{c}{m}$ is connected to the factor ξ by

$$D = \frac{\xi}{2\omega_0} \quad . \tag{9}$$

2.2.2 Extension of the Periodic Motion Concept - Nonlinear SDOF System

Mass proportional self-excitation as explained in the previous section can be used to calculate periodic solutions of non-conservative nonlinear systems using the HBM. The fourier series approximation yields a nonlinear system of equations for the harmonic coefficients where nonlinear forces are evaluated by the AFT method in the time domain. Each harmonic component is obtained by solving the corresponding equation

$$\left(-(n\omega)^2 m + \mathrm{j}n\omega(c - \xi m) + k\right)\hat{x}_n + \hat{F}_{\mathrm{AFT},n}(\hat{x}_{(-N\ldots N)}) = 0 \quad ; \quad n = -N, ..., N \tag{10}$$

which can be solved due to the ξm-term. The artificial damping term is the key to calculate the energy dependent nonlinear eigenfrequency and nonlinear damping. In fig. 1 (e) the corresponding complex pointer diagram is shown ($n > 0$). The factor ξ cannot be calculated in advance but is part of the argument of the harmonic balance residual function. As a result the self-excitation is balancing both the linear and nonlinear damping of the system. The nonlinear damping can be computed afterwards from the obtained values of ξ and ω similar to eq. 9. Although the damping ratio D is not defined for nonlinear systems this methodology provides a way to evaluate the energy dependent damping of nonlinear non-conservative systems.

2.2.3 Extension of the Periodic Motion Concept - Nonlinear MDOF Systems

Considering MDOF systems eq. 10 turns into

$$\left(-(n\omega)^2 \underline{M} + \mathrm{j}n\omega(\underline{C} - \xi\underline{M}) + \underline{K}\right)\hat{\vec{x}}_n + \hat{\vec{F}}_{\mathrm{AFT},n}(\hat{\vec{x}}_{(-N\ldots N)}) = \vec{0} \quad ; \quad n = -N, ..., N \quad . \tag{11}$$

For each solution the damping ratio is computed from the obtained values of ξ and ω similar to eq. 9 as done for the SDOF system. In eq. 11 the reason for choosing a mass proportional self-excitation can be seen as the mass matrix in $\xi\underline{M}$ distributes the artificial damping force over all degrees of freedom. The advantage of using the mass matrix is that at least one of its entrys is unequal to zero so that the method works even if the considered system only consists of masses and exclusively nonlinear restoring elements.

2.2.4 Damped Motion Concept - Linear SDOF System

For the damped motion concept a linear SDOF system is considered first. The damped autonomous differential equation is given by

$$m\ddot{x} + c\dot{x} + kx = 0 \tag{12}$$

and its general solution is composed of a harmonic oscillation with a decay term

$$x(t) = \hat{x}\frac{\mathrm{e}^{(\mathrm{j}\omega-\beta)t} + \mathrm{e}^{(-\mathrm{j}\omega-\beta)t}}{2} \quad . \tag{13}$$

Inserting eq. 13 into eq. 12 results in two complex algebraic equations for each of the two counter rotating pointers of eq. 13. Starting at $t = 0$ the first complex equation reads

$$(\mathrm{j}\omega - \beta)^2 m\hat{x} + (\mathrm{j}\omega - \beta)c\hat{x} + k\hat{x} = 0 \tag{14}$$

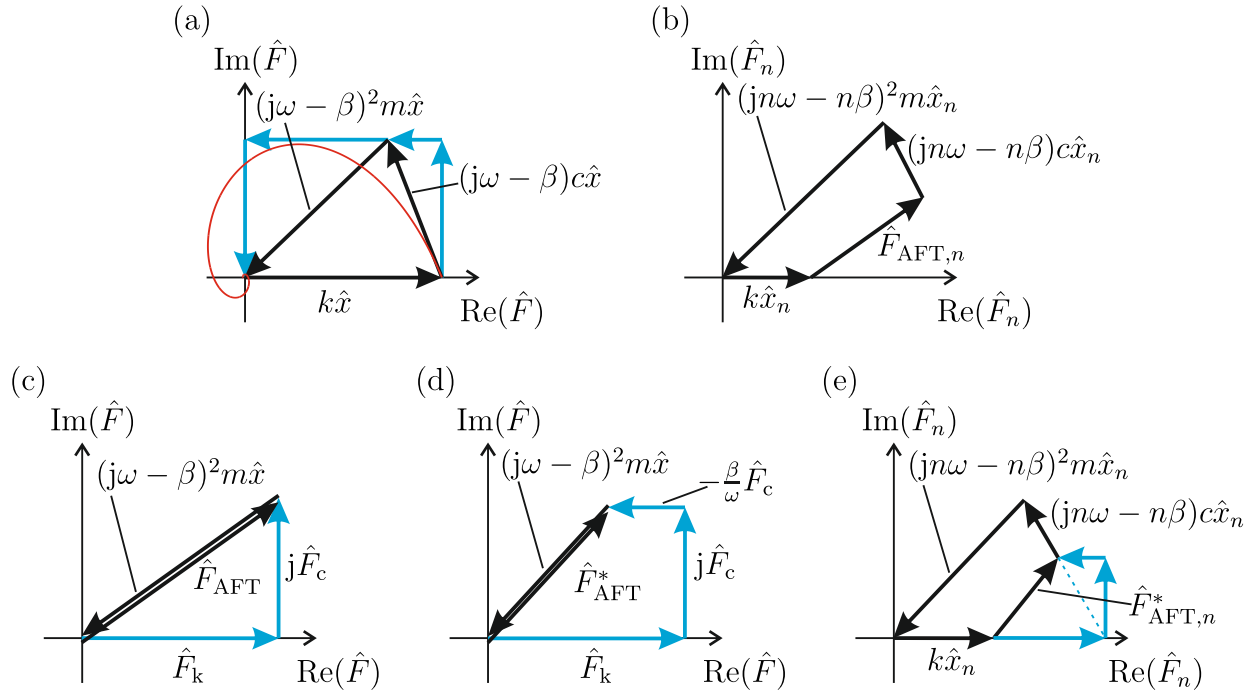


Figure 2: Complex pointer diagrams of the damped SDOF system, (a) autonomous linear system (black arrows), real and imaginary components (blue), with free decay curve; (b) harmonic component ($n > 0$) of autonomous nonlinear system (damped motion concept); (c) autonomous linear system (damped motion concept, restoring force computed with AFT); (d) like previous fig. with phase correction of $\hat{F}_{\mathrm{AFT}}$; (e) harmonic component ($n > 0$) with phase correction (phase corrected damped motion concept)

and describes the free decay vibration of a damped SDOF oscillator. The complex pointer diagram in fig. 2 (a) shows a closed loop of the three components and the free decay curve is added. Attention should be paid to the fact that ω in eq. 13 is the damped frequency $\omega = \sqrt{1-D^2}\omega_0$. From $\mathrm{j}\omega - \beta = \mathrm{j}\sqrt{1-D^2}\omega_0 - D\omega_0$ the systems eigenfrequency ω_0 and the damping ratio D can be computed depending on ω und β in the form

$$\omega_0 = \sqrt{\omega^2 + \beta^2} \quad , \tag{15}$$

$$D = \frac{\beta}{\sqrt{\omega^2 + \beta^2}} \quad . \tag{16}$$

2.2.5 Damped Motion Concept - Nonlinear SDOF System

Following eq. 13 the damped motion concept for nonlinear SDOF systems is based on the multiharmonic ansatz

$$x(t) = \sum_{n=-N}^{N} \hat{x}_n \mathrm{e}^{(\mathrm{j}n\omega - |n|\beta)t} \quad . \tag{17}$$

The solution to the non-conservative system consists of a set of complex pointers for the harmonic components each of which describing a free decay curve in the complex plane shown examplarily in fig. 2 (a). Considering a nonlinear system and applying the harmonic balance method the resulting algebraic system of equations is solved only for the initial state of the beginning decay motion. The phase angles between arrows within a chain of complex pointers is the same for each harmonic component. Nonlinear forces are evaluated again using the AFT method, however the undamped ansatz from eq. 2 is used. This is due to the

need of periodic functions to perform the Fourier transform [5]. For each harmonic component an equation of the form

$$(\mathrm{j}n\omega - |n|\beta)^2 m\hat{x}_n + (\mathrm{j}n\omega - |n|\beta)c\hat{x}_n + k\hat{x}_n + \hat{F}_{\mathrm{AFT},n}(\hat{x}_{(-N\ldots N)}) = 0 \quad ; \quad n = -N, ..., N \tag{18}$$

is obtained. Components with $n > 0$ can be illustrated by fig. 2 (b). The complex pointer resulting from the nonlinear force is added to the chain of pointers of the linear system. With this method even for the non-conservative nonlinear system a solution can be found, since β causes the needed tilt in the pointers of the linear components $c\dot{x}$ and $m\ddot{x}$. Eigenfrequency ω_0 and damping ratio D are obtained from ω and β similar to eq. 15 and eq. 16, respectively.

2.2.6 Damped Motion Concept - Nonlinear MDOF System

For multiple DOF systems eq. 18 is changed to

$$(\mathrm{j}n\omega - |n|\beta)^2 \underline{M}\hat{\vec{x}}_n + (\mathrm{j}n\omega - |n|\beta)\underline{C}\hat{\vec{x}}_n + \underline{K}\hat{\vec{x}}_n + \hat{\vec{F}}_{\mathrm{AFT},n}(\hat{\vec{x}}_{(-N\ldots N)}) = \vec{0} \quad ; \quad n = -N, ..., N \quad . \tag{19}$$

Here, still eigenfrequency ω_0 and damping ratio D can be calculated similar to eq. 15 and eq. 16. If linear problems with modal damping are considered eq. 19 yields the exact solution to the problem. Furthermore if linear non modal damped problems are considered eq. 19 still yields solutions with an evaluation of the present damping as will be shown in the numerical examples. The same holds for eq. 11 and the E-PMC regarding non modal damped systems.

2.2.7 Phase correction of Damped Motion Concept

The damped motion concept is based on a damped description of the linear part and the conventional evaluation of the nonlinear forces within the HBM. This can be a problem with respect to accuracy as shown in the following.

We consider the following linear SDOF system of the form

$$m\ddot{x} + f_{\mathrm{rf}}(\dot{x}, x) = 0 \tag{20}$$

whose linear restoring forces are gathered in the force $f_{\mathrm{rf}}(\dot{x}, x)$. Even though the system is linear we apply the damped motion concept and assume a possible nonlinearity in the mixed linear/nonlinear restoring forces. As a reference solution the same damped motion procedure is applied to the system definition given in eq. 12 where the linear system is defined explicitly and nonlinear forces are zero. Exemplarily, the parameters are set to $m = 1$, $c = 1$ und $k = 1$. The general description with separate linear and nonlinear parts yields the correct values $\omega_0 = 1$ und $D = 0.5$ which are found analytically from eq. 14.

However, applying the damped motion concept on the mixed linear/nonlinear restoring force which is purely linear in this case the HBM approach from eq. 2 yields

$$(\mathrm{j}\omega - \beta)^2 m\hat{x} + \hat{F}_{\mathrm{AFT}}(\hat{x}) = 0 \tag{21}$$

and fails to cover the correct decay behavior. The resulting components

$$\hat{F}_{\mathrm{k}} = k\hat{x} \quad ; \quad \mathrm{j}\hat{F}_{\mathrm{c}} = \mathrm{j}\omega c\hat{x} \tag{22}$$

are shown in the diagram in fig. 2 (c). Comparing fig. 2 (c) and fig. 2 (a) makes clear that the component $-\beta c\hat{x}$ is missing which causes incorrect values $\omega_0 = 1.225$ und $D = 0.408$ obtained by the damped motion concept considering the system definition given in eq. 20. The present definition of the damped motion concept thus yields different values for ω_0 and D depending on whether the non-conservative linear parts are included in the nonlinear forces and evaluated by the AFT method or described separately from the nonlinear

forces. We deduce that the computed nonlinear modes of non-conservative nonlinear systems are affected in the same way and the damped motion concept should be adjusted accordingly.

We propose a phase correction of the complex amplitude obtained from the AFT method. A component $-\frac{\beta}{\omega}\hat{F}_{\mathrm{c}}$ is added to the complex amplitude $\hat{F}_{\mathrm{AFT}}$ as follows

$$\hat{F}^{*}_{\mathrm{AFT}} = \hat{F}_{\mathrm{k}} + \mathrm{j}\hat{F}_{\mathrm{c}} \cdot (1 + \mathrm{j}\frac{\beta}{\omega}) = \hat{F}_{\mathrm{k}} + \mathrm{j}\hat{F}_{\mathrm{c}} - \frac{\beta}{\omega}\hat{F}_{\mathrm{c}} \quad . \tag{23}$$

The additional component is aligned in parallel to $\hat{F}_{\mathrm{k}}$, see fig. 2 (d). Consequently, the adjusted version of the aforementioned mixed linear/nonlinear problem from eq. 21 is given by

$$(\mathrm{j}\omega - \beta)^2 m\hat{x} + \hat{F}^{*}_{\mathrm{AFT}}(\hat{x}) = 0 \tag{24}$$

and yields the exact values $\omega_0 = 1$ and $D = 0.5$. Fig. 2 (d) shows the corresponding chain of complex pointers.

As far as higher harmonics are concerned the phase correction needs to be applied to the $\hat{F}_{\mathrm{AFT},n}$ of each harmonic n individually. We thus obtain an equation for each harmonic given in eq. 18 but with phase corrected $\hat{F}^{*}_{\mathrm{AFT}}(\hat{x})$. The corresponding complex pointer diagram for harmonic components with $n > 0$ is given in fig. 2 (e).

Due to the HBM approximation we are not able to quantify for MDOF systems how the complex amplitudes of individual DOF's affect the values of the vector $\hat{\vec{F}}_{\mathrm{AFT},n}$. The phase correction can still be applied in a first approximation for each entry in $\hat{\vec{F}}_{\mathrm{AFT},n}$ with respect to the corresponding entry in $\hat{\vec{x}}_n$. The effectiveness of the phase correction for MDOF systems as explained above can not be estimated yet and is part of ongoing research.

3 Numerical examples

In the following section numerical examples are presented to show differences and similarities of the explained methods. To keep it clear each method is abbreviated by E-PMC (extended periodic motion concept), DMC (damped motion concept), and PC-DMC (phase corrected damped motion concept), respectively.

3.1 Linear two DOF System

In a first example a linear two DOF oscillator is considered which can be solved analytically.

3.1.1 System with Modal Damping

The equation of motion for free vibrations is the known differential equation system

$$\underline{M}\ddot{\vec{x}} + \underline{C}\dot{\vec{x}} + \underline{K}\vec{x} = \vec{0} \tag{25}$$

with the chosen matrices

$$\underline{M} = \begin{bmatrix} 1 & 0 \\ 0 & 1 \end{bmatrix} \quad ; \quad \underline{C} = \begin{bmatrix} 1 & 0 \\ 0 & 1 \end{bmatrix} \quad ; \quad \underline{K} = \begin{bmatrix} 4 & -3 \\ -3 & 3 \end{bmatrix} \quad . \tag{26}$$

The structure of the damping matrix is similar to the mass matrix to easily achieve modal damping. We compare the results of the different methods with the analytical result obtained from the eingenproblem

$$\left(\underline{K} - \omega_0^2 \underline{M}\right) \vec{\Phi} = \vec{0} \quad . \tag{27}$$

In tab. 1 eigenfrequency ω_0, damping ratio D, and the entries of the first eigenvector are given. As all of the considered methods are derived from linear modal analysis they all yield the exact solution for this linear modal damped problem. Since no AFT evaluation is executed the numerical procedure performed evaluating the DMC and the PC-DMC are identical. This example is trivial but provides a good reference for the next test case with mixed linear/nonlinear parts. Similar to eq. 20 the linear stiffness and damping components of the system description are gathered in the potential nonlinear force vector

$$\underline{M}\ddot{\vec{x}} + \vec{f}_{\mathrm{rf}}(\dot{\vec{x}}, \vec{x}) = \vec{0} \quad \text{with} \quad \vec{f}_{\mathrm{rf}}(\dot{\vec{x}}, \vec{x}) = \underline{C}\dot{\vec{x}} + \underline{K}\vec{x} \quad . \tag{28}$$

When the AFT method is applied to the actually linear force vector we end up with the results given in tab. 2. Like for the SDOF case in section 2.2.7 eigenfrequency and damping values are inaccurate in the DMC computation even though its a linear problem. However, the eigenvector is computed correctly.

	ω_0	D	$\Phi_{1,1}$	$\Phi_{2,1}$
analytic	0.6772	0.1477	0.6464	0.7630
E-PMC	0.6772	0.1477	0.6464	0.7630
DMC; PC-DMC	0.6772	0.1477	0.6464	0.7630

Table 1: Parameters of first mode of the modal damped linear system computed with different methods without utilization of the AFT procedure

	ω_0	D	$\Phi_{1,1}$	$\Phi_{2,1}$
analytic	0.6772	0.1477	0.6464	0.7630
E-PMC	0.6772	0.1477	0.6464	0.7630
DMC	0.6918	0.1445	0.6464	0.7630
PC-DMC	0.6772	0.1477	0.6464	0.7630

Table 2: Parameters of first mode of the modal damped linear system computed with different methods utilizing AFT procedure for restoring forces

3.1.2 System with non modal Damping

The next example is still the linear system given in eq. 25 but with a different damping matrix

$$\underline{M} = \begin{bmatrix} 1 & 0 \\ 0 & 1 \end{bmatrix} \quad ; \quad \underline{C} = \begin{bmatrix} 0 & 0 \\ 0 & 1 \end{bmatrix} \quad ; \quad \underline{K} = \begin{bmatrix} 4 & -3 \\ -3 & 3 \end{bmatrix} \quad . \tag{29}$$

The system is characterized by non modal damping which prohibits a modal decoupling and makes the given problem an interesting test case even though it is linear. An analytical solution is available but it does not allow for an evaluation of ω_0 and D. Results from the E-PMC, DMC, and PC-DMC are presented in tab. 3. The non-modal damping causes complex valued eigenvectors. In general, nonlinear systems can have non-modal damping like this as well and it is noteworthy that even when nonlinearities are absent the results vary with the selected method.

	ω_0	D	$\Phi_{1,1}$	$\Phi_{2,1}$
E-PMC	0.6912	0.4215	$0.6460\mathrm{e}^{\mathrm{j}0\pi}$	$0.7634\mathrm{e}^{-\mathrm{j}0.036\pi}$
DMC; PC-DMC	0.6909	0.4390	$0.6272\mathrm{e}^{\mathrm{j}0\pi}$	$0.7789\mathrm{e}^{-\mathrm{j}0.032\pi}$

Table 3: Parameters of first mode of the non modal damped linear system computed with different methods without utilization of the AFT procedure

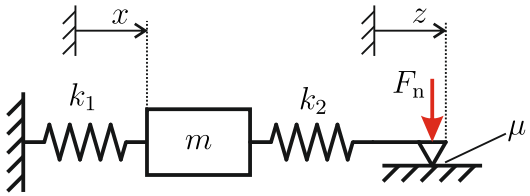


Figure 3: Friction damped single mass vibrating system

3.2 Nonlinear Systems

Each result of the nonlinear mode computation is represented by an energy dependent eigenfrequency and modal damping ratio. To be able to condense the energy dependency into only one parameter the fundamental harmonic denoted by the index $(\,)_{\mathrm{h1}}$ of the solution is considered. The generalized amplitude a of the solution is defined as the ratio between the vector representing the fundamental harmonic $\hat{\vec{x}}_{\mathrm{h1}}$ and its normalization with respect to the mass matrix $\hat{\vec{x}}_{\mathrm{M,h1}}$

$$\hat{\vec{x}}_{\mathrm{h1}} = a\hat{\vec{x}}_{\mathrm{M,h1}} \quad \text{with} \quad \hat{\vec{x}}^{\mathrm{T}}_{\mathrm{M,h1}}\underline{M}\hat{\vec{x}}_{\mathrm{M,h1}} = 1 \quad . \tag{30}$$

The solutions of the nonlinear equations are computed utilizing a predictor corrector continuation scheme with analytically determined jacobian of the residual function.

It should be mentioned that the results presented in the following sections cannot be assessed right or wrong as the compared parameters eigenfrequency and damping ratio are not defined for nonlinear systems. As the approaches compared in this work were derived from relations within linear systems they provide these parameters with similar meaning to characterize nonlinear systems.

3.2.1 Friction Damped SDOF System

The first considered nonlinear system consists of a single vibrating mass with elastic coupling to a dry friction element. The corresponding set of differential equations of the autonomous system reads

$$\begin{bmatrix} m & 0 \\ 0 & 0 \end{bmatrix} \begin{bmatrix} \ddot{x} \\ \ddot{z} \end{bmatrix} + \begin{bmatrix} k_1 + k_2 & -k_2 \\ -k_2 & k_2 \end{bmatrix} \begin{bmatrix} x \\ z \end{bmatrix} + \begin{bmatrix} 0 \\ \mu F_{\mathrm{n}} \mathrm{sgn}(\dot{z}) \end{bmatrix} = \vec{0} \quad . \tag{31}$$

The degree of freedom z describes the displacement of the friction element which is needed as an internal state of the system ending up in a second line of the set of differential equations. The entrys of the solutions describing the dynamics of z are a byproduct of the computation and will not be considered. For the computation of the nonlinear mode of the system the parameters $m = 1$, $k_1 = 1$, $k_2 = 3$ and $\mu F_{\mathrm{n}} = 1$ are chosen. The $\mathrm{sgn}(\,)$ function is approximated by the differentiable function

$$\mathrm{sgn}(z) \approx \frac{2}{\pi}\mathrm{atan}(1000 \cdot z) \quad . \tag{32}$$

which allows for a straight forward computation of the analytical Jacobian of the residual function. The eigenfrequencies ω_0 and damping ratios D were computed utilizing the three approaches mentioned before using 49 harmonincs which were chosen after a convergence study that was carried out in advance. The results are depicted with respect to the corresponding generalized amplitude a in fig. 4. The amplitude dependent eigenfrequency of the systems mode in fig. 4 (a) shows the characteristic frequency drop of friction damped systems with constant eigenfrequencies besides the drop. The results of the E-PMC and the PC-DMC are in excellent agreement to each other while a slight deviation of the DMC-result is present in the region of the frequency drop. The damping ratio in fig. 4 (b) shows the characteristic maximum in the amplitude range of the frequency drop for all the results. The magnitudes of the damping ratios computed with the different approaches differ from each other while the results are in good agreement apart from that again.

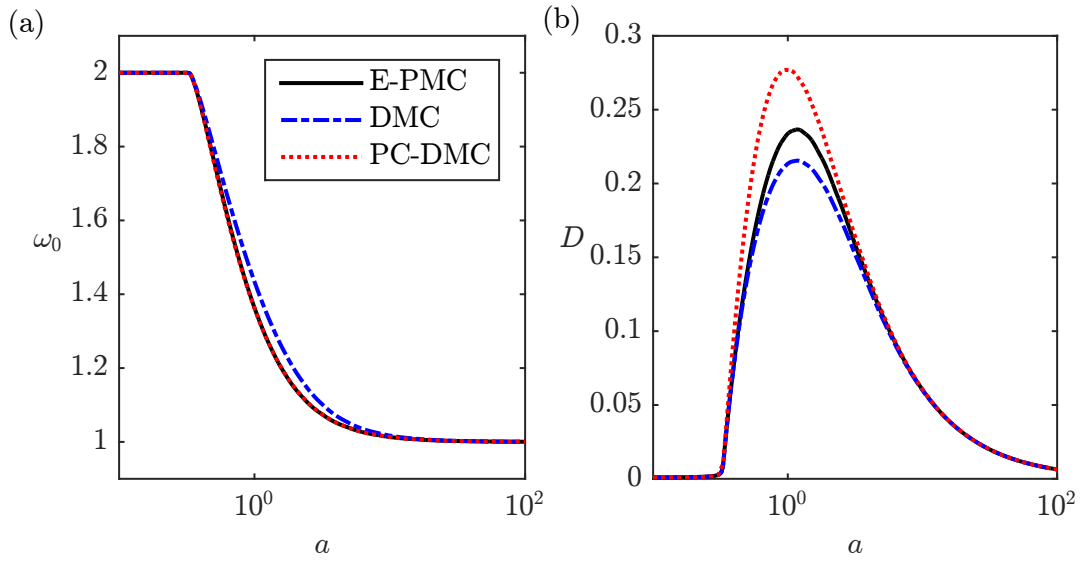


Figure 4: (a) Eigenfrequency and (b) damping ratio of friction damped single mass vibrating system over generalized amplitude computed with different approaches for non conservative nonlinear systems

3.2.2 Van der Pol Oscillator

The second nonlinear system investigated in this work is the self excited Van der Pol oscillator with the nonlinear differential equation

$$\ddot{x} + \left(\frac{1}{10}x^2 - \frac{2}{5}\right)\dot{x} + x = 0 \quad . \tag{33}$$

The corresponding eigenfrequencies and damping ratios computed with the three different approaches are depicted in fig. 5 over the generalized amplitude using 11 harmonics which were chosen after investigating the convergence in advance. The qualitative courses of the eigenfrequency curves resulting from the E-PMC and PC-DMC in fig. 5 (a) are in good agreement again, even if slight deviations are present. The eigenfrequency computed with the DMC deviates from the others and shows a different qualitative trend. The damping ratios in fig. 5 (b) are in good agreement for the results of all of the three approaches. Slight deviations occur for the result of the DMC from the other two results in the amplitude range $1 < a < 6$ and for the result of the PC-DMC from the corresponding other two results in the amplitude range $a > 7$. A certain condition is reached for the system at an amplitude level around $a = 6.37$ where the damping ratio is zero. This condition describes the limit cycle of the system. As mentioned before in the case of a limit cycle the system vibrates like a conservative system so that eq. 3 can be solved with the HBM without the need of extensions for nonconservative systems. For this reason the damping parameters ξ for the E-PMC and β for the DMC and PC-DMC are zero at this amplitude so that the corresponding numerical problems of the E-PMC in eq. 11 and the DMC (and corresponding PC-DMC) in eq. 19 degenerate to the classic harmonic balance problem for autonomous systems in eq. 3. Since the three approaches lead to the same numerical problem at this amplitude, the results for the eigenfrequencies are the same, too. This can be seen in fig. 5 (a) where the three curves cross at about $a = 6.37$.

Although the computational effort is not investigated in this work the authors would like to point out that the phase correction of the PC-DMC introduced in section 2.2.7 ends up in a significant increase of the computation time. Furthermore solving the PC-DMC requires increased solution tolerances in some cases to find a solution at all.

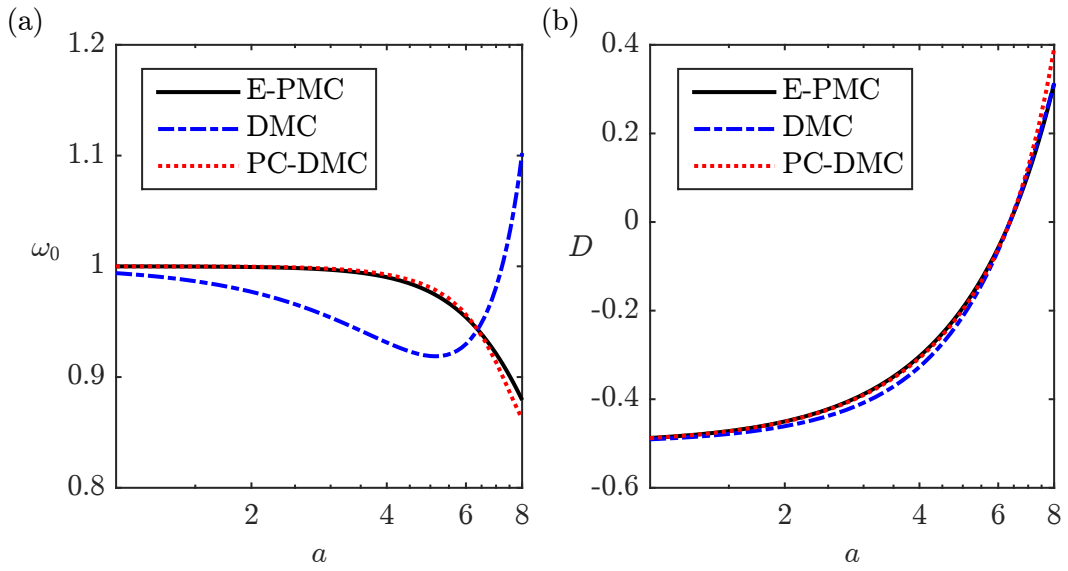


Figure 5: (a) Eigenfrequency and (b) damping ratio of Van der Pol oscillator over generalized amplitude computed with different approaches for non conservative nonlinear systems

3.3 Averaged System Response

In section 3.2 the parameters eigenfrequency and damping ratio of nonlinear modes have been compared for different approaches. Since no reference solution exists it was not possible to assess the quality of the different results. In the following sections the results for free vibrations of the considered systems determined from the nonlinear modal parameters from the previous sections will be compared with each other and with a reference solution computed by time step integration. The computation of the dynamics of nonlinear systems from parameters of a nonlinear mode is carried out utilizing a *slow dynamics decomposition* as described in [6]. For free vibrations the dynamics of the generalized amplitude is given as

$$\dot{a} = -D(a)\omega_0(a)a \quad , \tag{34}$$

and can be computed utilizing time step integration. With the result of the so called *slow dynamics* $a(t)$ and the parameters of the nonlinear mode the *fast dynamics* of the system can be reconstructed by

$$x(t) = a(t) \sum_{n=0}^{N} \left[\hat{x}_{\mathrm{M,n}}(a(t)) \cdot \cos\left(\int_0^t n\omega_0(a(\tau))\, \mathrm{d}\tau + \varphi_n(a(t)) \right) \right] \tag{35}$$

with the normalized real amplitudes of the harmonics $\hat{x}_{\mathrm{M,n}}(a)$ and their corresponding phase angles $\varphi_n(a)$.

3.3.1 Friction Damped SDOF System

For the friction damped single mass vibrating system from section 3.2.1 free vibrations have been computed with the slow dynamics decomposition mentioned in section 3.3 using the nonlinear modal parameters in fig. 4 and with time step integration of eq. 31 with the approximation of the $\mathrm{sgn}(\,)$ function in eq. 32 to provide a reference solution. In fig. 6 (a) the results for free vibration is depicted over time. It can be seen that the vibration computed from the nonlinear modes are in good agreement with each other and deviate slightly from the reference solution. The decay at the beginning of the simulation is in good agreement with the reference solution as well as the doubling of the frequency after the decay. The deviation of the results computed from the nonlinear modes occure at the end of the decay of the vibration resulting in a phase

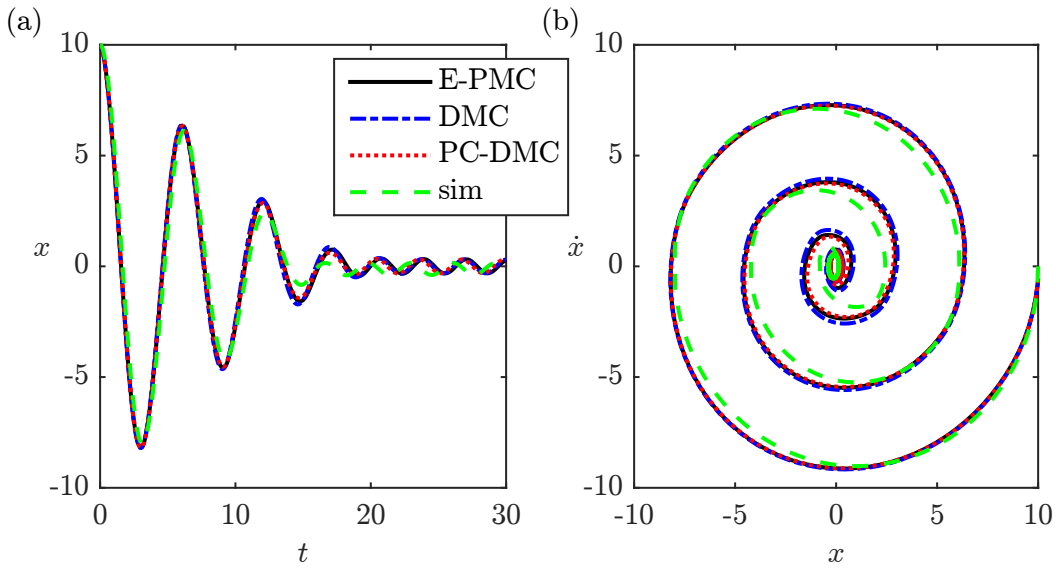


Figure 6: Free decay of friction damped single mass vibrating system, comparison of results of different computation approaches; (a) displacement over time; (b) phase curve

difference to the reference solution at the end. In fig. 6 (b) the corresponding phase curves are shown. It can be seen that all of the curves reach the same periodic condition at the end while the decay of the results from the nonlinear modes are a bit too slow compared to the reference solution. The small differences between the free vibration results show how comperatively small the effect of the deviations between the damping ratios in fig. 4 (b) are.

3.3.2 Van der Pol Oscillator

The same comparison as in the previous section was done for the free vibration of the Van der Pol oscillator and the corresponding modal parameters from fig. 5. The vibration is depicted over time in fig. 7 (a). The results computed from the nonlinear modes E-PMC and PC-DMC are in good agreement with each other and with the reference solution. The DMC result deviates in the beginning of the vibration resulting in a phase difference to the other results when the limit cycle is reached. In fig. 7 (b) the corresponding phase curves are depicted. It can be seen that the E-PMC und PC-DMC results are in excellent agreement with each other while they are closer to the reference solution than the DMC result at most of the time until all of the results reach the same limit cycle.

4 Summary

In this work methods to compute nonlinear modes of non-conservative nonlinear systems within the harmonic balance method have been addressed. The E-PMC and the DMC have been explained in the complex plain regarding their corresponding main ideas derived from linear system relations. Investigating linear systems a deviation of the results yielded by the DMC depending on the linear system formalism was pointed out and an enhancement in form of a phase correction was proposed, the PC-DMC. The eigenfrequency and the damping ratio of different linear and nonliner systems provided by the mentioned methods were compared. Investigation of a linear modal damped system showed correct results for the E-PMC and PC-DMC while the accuracy of the DMC results depend on the linear system formalism. For a linear system with non modal damping the first eigenfrequency, corresponding damping ratio and eigenvector have been determined with the different methods. The results slightly differ from each other since the applied methods approximate

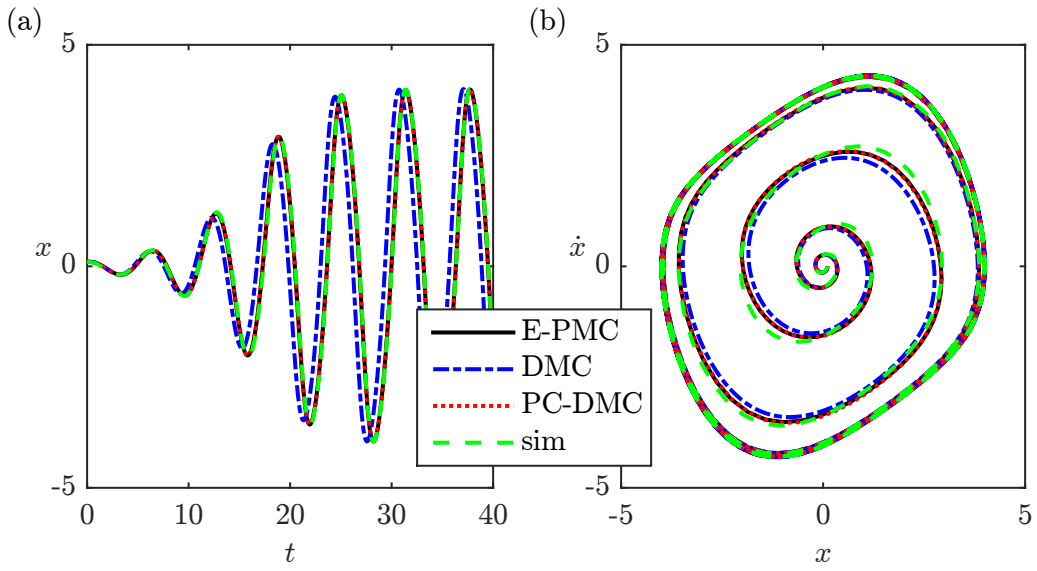


Figure 7: Free vibration of Van der Pol oscillator, comparison of results of different computation approaches; (a) displacement over time; (b) phase curve

these parameters which are only defined for modal damped linear systems. Two non-conservative nonlinear single mass vibrating systems have been adressed to compare eigenfrequencies and damping ratios of nonlinear systems obtained by the different methods. For a friction damped single mass vibrating system the eigenfrequency results from the E-PMC and PC-DMC show the same amplitude dependency while the result of the DMC slightly differs. The corresponding damping ratios show a similar qualitative behavior. Investigating a Van der Pol oscillator the eigenfrequencies provided by the E-PMC and PC-DMC show a similar amplitude dependency while the amplitude dependency of the DMC differs again. The damping ratios provided by all of the three methods were in good agreement in this case. To be able to compare the nonlinear modal parameters with a reference solution free vibrations were computed applying a slow- and fast-dynamics decomposition to the nonlinear modal parameters of the mentioned systems provided by the different approaches. For the friction damped system the deviations between the free vibrations computed from the nonliner modal parameters were smaller than their deviation to the reference solution. The free vibration of the Van der Pol oscillator showed a good agreement of the E-PMC and PC-DMC results and the reference solution. The free vibration computed from the modal parameters provided by the DMC showed a slight deviation from the other solutions while all solutions reach the same limit cycle. Concluding the comparison of the three mentioned methods for computing nonlinear modes for non-conservative nonlinear systems the authors would prefer the E-PMC as it didn't show disadvantages compared to the other two methods. Considering problems where a reference solution was available the DMC showed stronger deviations than the other methods. The introduced PC-DMC showed a reduced deviation to reference solutions compared to the DMC. However, the disadvantage of the PC-DMC is that the computational effort of its usage is much higher since the phase correction may cause numerical inaccuracies.

Acknowledgements

The authors thank the German Research Foundation (DFG) for the support within the priority program SPP 1897 "Calm, Smooth and Smart"

References

[1] R. M., Rosenberg *Normal modes of nonlinear dual-mode systems.* Journal of Applied Mechanics 27.2 (1960): 263-268.

[2] G. Kerschen, M. Peeters, J. C. Golinval, A. F. Vakakis *Nonlinear normal modes, Part I: A useful framework for the structural dynamicist.* Mechanical Systems and Signal Processing 23.1 (2009): 170-194.

[3] T. M. Cameron, J. H. Griffin. *An alternating frequency/time domain method for calculating the steady-state response of nonlinear dynamic systems.* Journal of applied mechanics 56.1 (1989): 149-154.

[4] M. Krack *Nonlinear modal analysis of nonconservative systems: extension of the periodic motion concept.* Computers & Structures 154 (2015): 59-71.

[5] D. Laxalde, F. Thouverez, *Complex non-linear modal analysis for mechanical systems: Application to turbomachinery bladings with friction interfaces.* Journal of sound and vibration 322.4-5 (2009): 1009-1025.

[6] M. Krack, L. Panning-von Scheidt, J. Wallaschek, *On the computation of the slow dynamics of nonlinear modes of mechanical systems.* Mechanical Systems and Signal Processing 42.1-2 (2014): 71-87.

Using the harmonic balance method to directly compute NNMs of geometrically nonlinear finite element models

C. I. Van Damme [1], **A. E. Madrid** [1], **M. S. Allen** [1]
[1] University of Wisconsin - Madison, Department of Engineering Physics,
1500 Engineering Drive, 544 ERB, Madison, Wisconsin, US
e-mail: **cvandamme@wisc.edu**

Abstract
Nonlinear Normal Modes (NNMs) have gained attention over the past few decades as a versatile tool for analyzing nonlinear dynamical systems. They have been used to analyze systems with both smooth and non-smooth nonlinearities, but most studies have limited their scope to low-order systems. For more complex systems it becomes too expensive to repeatedly evaluate the nonlinear function and nonlinear Jacobian that are required at each iteration in most continuation routines. This paper presents a numerical study of using the Multi Harmonic Balance as a tool to compute NNMs of large geometrically nonlinear finite element models. In particular, emphasis will be placed on the complexity and parallelization of the algorithm for large scale problems. It is shown that MHB method can be applied efficiently to compute NNMs of large scale problems.

1 Introduction

Normal modes provide a conceptual and mathematical framework for studying vibrations of dynamic systems. A normal mode of vibration is as a periodic orbit of a system about a stable equilibrium point [1, 2]. The linear normal modes of a system can be found by solving a generalized eigenvalue problem based on the linear equations of motion, a capability that is frequently used in commercial finite element (FE) packages. However, real dynamical systems are inherently nonlinear, and in some cases it is critical to consider how the dynamics described by the linear modes evolve at high amplitudes. For example, structures such as the skin panels on concept hypersonic aircraft and space reentry vehicles experience high acoustic and thermal loading, which can result in highly nonlinear behavior including modal coupling, internal resonances, and bifurcations.

In this work Nonlinear Normal Modes (NNMs) are defined as not necessarily synchronous periodic orbits of a nonlinear system about a stable equilibrium point [1, 2]. They originate from the linear system as nonlinear extensions of the underlying linear normal modes. Just as linear normal modes provide insight into the dynamics of a linear system, NNMs provide insight into the dynamics of complex nonlinear systems, though certain properties of linear normal modes, such as orthogonality and superposition, do not apply. NNMs have a variety of applications including sub-structuring and model updating [3, 4, 5, 6].

Even though NNMs provide important information about nonlinear dynamical systems, routines for computing them are not available in commercial finite element software and the high computational cost associated with computing NNMs from detailed FE models prevents them from being used in many cases. They are generally computed by tracing branches of periodic orbits originating from the underlying linear modes. There are many known methods for numerically computing NNMs, but the most popular for both general and complex nonlinear systems is to combine a routine that computes periodic orbits of the nonlinear system with a numerical continuation routine. The continuation routine is not a focus of this work, for more

information see [7]. Two popular approaches to the identification of periodic orbits are shooting methods and discretization routines.

Shooting methods rely on solving a two-point boundary value problem in which the period and initial conditions of the orbit are identified. The advantage of shooting routines lies in the ability to rigorously identify a periodic orbit and maintain a minimal Jacobian size. Shooting methods require integrating the nonlinear equation of motion to evaluate the periodicity and the Jacobian. As the nonlinear equations of motion are generally not known in closed form, generating the Jacobian typically requires the use of finite difference schemes, although the algorithm in [8] provides an attractive alternative. Even then, as the dimensionality of the system increases so does the computational demand required to generate the nonlinear Jacobian, making this approach unfeasible for large scale finite element models.

Discretization approaches, on the other hand, express the periodic orbit as a sum of time varying functions (i.e. Fourier series, Legendre Polynomials, etc...) and then transform the nonlinear partial differential equations into nonlinear algebraic equations. The two general subclasses of discretization techniques are collocation methods (for example the algorithm used in AUTO [9]) and the harmonic balance (HB) method. This work will focus on the harmonic balance method for two reasons. First, geometrically nonlinear structures typically only require a small number of harmonics to obtain an accurate solution [10, 11, 12], and second, the Jacobian needed for this algorithm can be found analytically at relatively low computational cost, even for large finite element models.

The HB method has been applied to geometrically nonlinear finite element models in previous studies [10, 11], but most works have used relatively simple models with a small number of degrees of freedom. This work will demonstrate the ability to significantly decrease the time of NNM computation for large scale mechanical systems by coupling a HB algorithm with parallelized high performance computing. Multiple numerical examples will demonstrate the ease with which HB is parallelized and the significant computational benefit therein.

This paper is organized in the following manner. §2 will cover background theory related to geometric nonlinearities of the finite element method, the HB method and the parallelization of computations. §3 will demonstrate the application of the HB method using high performance computing to multiple geometrically nonlinear finite element models and the conclusions will be presented in §4.

2 Theory

2.1 Geometric Nonlinear Finite Element Method

The undamped and unforced equations of motion for a n degree-of-freedom (DOF) geometrically nonlinear elastic finite element model can be written as

$$\mathbf{M}\ddot{\mathbf{x}} + \mathbf{K}\mathbf{x} + \mathbf{f}_{\mathrm{NL}}(\mathbf{x}) = 0 \tag{1}$$

where $\ddot{\mathbf{x}}$ and $\mathbf{x}$ are $n \times 1$ vectors and the nonlinear restoring force $\mathbf{f}_{NL}$ is a function of the displacement. The nonlinear normal modes of a structure are the periodic solutions to Eq 1. For geometric nonlinearities, in particular those of thin-structural panels undergoing large deformation, the internal force vector can be decomposed into a matrix vector product of the nonlinear portion of the tangent stiffness and the imposed displacement field.

$$\mathbf{f}_{NL}(\mathbf{x}) = \mathbf{K}_T(\mathbf{x})\mathbf{x} \tag{2}$$

Generation of the nonlinear portion of the tangent stiffness matrix in Equation 2 requires looping through all elements of the FE model. This computation cost is thus linearly proportional to the product of the number of elements and the number of integration points required for each element.

2.2 Harmonic Balance Method

The HB method is a powerful tool for studying a large variety of nonlinear problems. Specifically, it provides a method for approximating nonlinear differential equations without a known analytical solution. Assuming that the displacement $\mathbf{x}(t)$ and nonlinear force $\mathbf{f}(t)$ are periodic they can be approximated by a truncated Fourier series as follows:

$$\mathbf{x}(t) = \mathbf{c}_0^x + \sum_{k=1}^{N_H} (\mathbf{s}_k^x sin(k\omega t) + \mathbf{c}_k^x cos(k\omega t)) \tag{3}$$

$$\mathbf{f}(t) = \mathbf{c}_0^f + \sum_{k=1}^{N_H} (\mathbf{s}_k^f sin(k\omega t) + \mathbf{c}_k^f cos(k\omega t)) \tag{4}$$

Expressing the nonlinear equations of motion in the frequency domain gives the following $2n(2N_H + 1) \times 2n(2N_H + 1)$ algebraic system of equations:

$$\mathbf{h}(\mathbf{z}, \omega) = \mathbf{A}(\omega)\mathbf{z} - \mathbf{b}(\mathbf{z}) = 0 \tag{5}$$

where $\mathbf{b}$ is the Fourier approximation of the nonlinear force vector $\mathbf{f}_{NL}(\mathbf{x})$, which will be discussed in the next section, and $\mathbf{A}(\omega)$ is the matrix describing the linear dynamics of the system.

$$\mathbf{A}(\omega) = \begin{bmatrix} \mathbf{K} & & & & & & \\ & \mathbf{K} - \omega^2\mathbf{M} & & & & & \\ & & \mathbf{K} - \omega^2\mathbf{M} & & & & \\ & & & \cdot & & & \\ & & & & \cdot & & \\ & & & & & \cdot & \\ & & & & & \mathbf{K} - (N_H\omega^2\mathbf{M}) & \\ & & & & & & \mathbf{K} - (N_H\omega^2\mathbf{M}) \end{bmatrix} \tag{6}$$

For the full derivation of Equation 5 from Equation 1 see [13]. The linear dynamic matrix is a function of the mass matrix, linear stiffness matrix, and the current frequency. The next section will discuss the nonlinear internal force vector.

2.2.1 Nonlinear Internal Force and Jacobian Evaluation

A common approach for solving the nonlinear system of equations obtained in the HB method is the second-order Newton-Raphson method. The Newton-Raphson method uses an iterative shooting routine to find successive solutions. This requires calculating gradients of the harmonic balance equation with respect to the state variables of the system. A commonly used approach for constructing the frequency domain Jacobian is to use the alternating frequency/time-domain procedure. This approach uses alternating inverse FFTs (IFFT) and FFTs to switch between the time and frequency domain and compute $F_{NL}(z)$ and the nonlinear Jacobian using finite differences. In the best case each IFFT/FFT takes $\mathcal{O}(NlogN)$ operations, where N is the number of time steps used to discretize the period for each DOF, resulting in a significant computational cost for large finite element models.

In contrast, this paper builds on the work of [14] which presented an alternative method, known as *trigonometric collocation*, for computing the $2n(2N_H+1)$ Fourier coefficients. In this method the truncated inverse Fourier transform is represented by an $Nn \times (2N_H + 1)n$ linear operator as follows:

$$\Gamma(\omega) = \left[\mathbf{I}_n \otimes \begin{bmatrix} 1/\sqrt{2} \\ 1/\sqrt{2} \\ \vdots \\ 1/\sqrt{2} \end{bmatrix} \mathbf{I}_n \otimes \begin{bmatrix} sin\left(\omega t_1\right) \\ sin\left(\omega t_2\right) \\ \vdots \\ sin\left(\omega t_N\right) \end{bmatrix} \mathbf{I}_n \otimes \begin{bmatrix} cos\left(\omega t_1\right) \\ cos\left(\omega t_2\right) \\ \vdots \\ cos\left(\omega t_N\right) \end{bmatrix} \cdots \right. \tag{7}$$
$$\left. \mathbf{I}_n \otimes \begin{bmatrix} sin\left(N_H \omega t_1\right) \\ sin\left(N_H \omega t_2\right) \\ \vdots \\ sin\left(N_H \omega t_N\right) \end{bmatrix} \mathbf{I}_n \otimes \begin{bmatrix} cos\left(N_H \omega t_1\right) \\ cos\left(N_H \omega t_2\right) \\ \vdots \\ cos\left(N_H \omega t_N\right) \end{bmatrix} \right]$$

where $\otimes$ is the Kronecker product and $\mathbf{I}_n$ is a $n \times n$ identity matrix. Rewriting both the displacement and internal force in terms of the linear operator gives

$$\tilde{\mathbf{x}} = \mathbf{\Gamma}(\omega)\mathbf{z} \tag{8}$$

and

$$\tilde{\mathbf{f}} = \mathbf{\Gamma}(\omega)\mathbf{b}(\mathbf{z}). \tag{9}$$

where each is expressed in terms of nN discrete samples for all N time samples across the period.

$$\tilde{\mathbf{x}} = \begin{bmatrix} x_1(t_1) & x_2(t_1) & \cdots & x_N(t_1) & \cdots & x_1(t_n) & x_2(t_n) & \cdots x_N(t_n) \end{bmatrix}^T \tag{10}$$

$$\tilde{\mathbf{f}} = \begin{bmatrix} f_1(t_1) & f_2(t_1) & \cdots & f_N(t_1) & \cdots & f_1(t_n) & f_2(t_n) & \cdots f_N(t_n) \end{bmatrix}^T \tag{11}$$

Hence, the Fourier transform from the time domain to the frequency domain is performed using

$$\mathbf{z} = \mathbf{\Gamma}(\omega)^\dagger \tilde{\mathbf{x}} \tag{12}$$

$$\mathbf{b}(\mathbf{z}) = \mathbf{\Gamma}(\omega)^\dagger \tilde{\mathbf{f}} \tag{13}$$

where the Fourier transform can be calculated using the Moore-Penrose pseudo-inverse $\mathbf{\Gamma}^\dagger = (\mathbf{\Gamma}\mathbf{\Gamma}^T)^{-1}\mathbf{\Gamma}$. For small systems it is not expensive to compute the Moore-Penrose pseudo-inverse. However, as the size of the nonlinear system increases the size of $\mathbf{\Gamma}\mathbf{\Gamma}^T$ scales with nN and the computational complexity for back substitution scales with $\mathcal{O}((nN)^3)$ making this procedure a major bottleneck for large models. A more computationally efficient approach utilizes the properties of the Kronecker product. First, its possible to express the inverse Fourier transformation for the system as the Kronecker product of the sine and cosine terms with a $n \times n$ identity matrix as follows:

$$\mathbf{x}(t) = (\mathbf{Q}(t) \otimes \mathbf{I}_n)\mathbf{z} \tag{14}$$

$$\mathbf{f}(t) = (\mathbf{Q}(t) \otimes \mathbf{I}_n)\mathbf{b} \tag{15}$$

where the $\mathbf{Q}(t)$ term is a $N \times 2N_H + 1$ matrix containing the sine and cosine terms of the truncated Fourier series such that

$$\mathbf{Q}(t) = \left[\begin{bmatrix} 1/\sqrt{2} \\ 1/\sqrt{2} \\ \vdots \\ 1/\sqrt{2} \end{bmatrix} \begin{bmatrix} sin\,(\omega t_1) \\ sin\,(\omega t_2) \\ \vdots \\ sin\,(\omega t_N) \end{bmatrix} \begin{bmatrix} cos\,(\omega t_1) \\ cos\,(\omega t_2) \\ \vdots \\ cos\,(\omega t_N) \end{bmatrix} \cdots \begin{bmatrix} sin\,(N_H \omega t_1) \\ sin\,(N_H \omega t_2) \\ \vdots \\ sin\,(N_H \omega t_N) \end{bmatrix} \begin{bmatrix} cos\,(N_H \omega t_1) \\ cos\,(N_H \omega t_2) \\ \vdots \\ cos\,(N_H \omega t_N) \end{bmatrix} \right] \tag{16}$$

The Fourier transform can then be calculated using the properties of the Kronecker product as

$$\mathbf{\Gamma}(\omega)^\dagger = \begin{bmatrix} \mathbf{I}_n \otimes \mathbf{Q}_1^\dagger \\ \mathbf{I}_n \otimes \mathbf{Q}_2^\dagger \\ \mathbf{I}_n \otimes \mathbf{Q}_3^\dagger \\ \vdots \\ \mathbf{I}_n \otimes \mathbf{Q}_{(2N_H+1)}^\dagger \end{bmatrix} \tag{17}$$

Not only does the Kronecker product avoid costly matrix inversions, but the matrices $\mathbf{Q}_i$ are independent of the number of DOF. As a result the Kronecker product scales with $\mathcal{O}((nN))$ a significant savings over the $\mathcal{O}((nN)^3)$ of the normal equations. This allows the HB method to be efficiently applied to large models with many DOF.

The Jacobian of the nonlinear system with respect to the Fourier coefficients from [14] can be found analytically as

$$\mathbf{h_z} = \frac{\partial \mathbf{h}}{\partial \mathbf{z}} = \mathbf{A} - \frac{\partial \mathbf{b}}{\partial \mathbf{z}} = \mathbf{A} - \mathbf{\Gamma}^\dagger \frac{\partial \tilde{\mathbf{f}}}{\partial \tilde{\mathbf{x}}} \mathbf{\Gamma} \tag{18}$$

where $\frac{\partial \tilde{\mathbf{f}}}{\partial \tilde{\mathbf{x}}}$ represents the derivatives of the nonlinear internal forces with respect to the displacements at each instant within the periodic orbit. This form provides an efficient approach to generating the Jacobian matrix and can be efficiently solved when the system consists of solely geometric nonlinearities. This only requires generating the nonlinear portion of the tangent stiffness matrix at each point along the period orbit.

$$\frac{\partial \tilde{\mathbf{f}}}{\partial \tilde{\mathbf{x}}} = \tilde{\mathbf{K}}_T \tag{19}$$

Furthermore, to obtain the nonlinear internal force vector, $\tilde{\mathbf{f}}$, only a matrix-vector product of the nonlinear portion of tangent stiffness matrix with the imposed displacements across the orbit is required.

$$\tilde{\mathbf{f}} = \tilde{\mathbf{K}}_T \tilde{\mathbf{x}} \tag{20}$$

2.3 Parallelization

The implementation of the HB method can be further improved using high-performance computing techniques. Below, the internal force and nonlinear Jacobian are shown to be independent operations, and can thus be perfectly parallelized resulting in significant time savings, up to the number of time steps. The assumed deformation across the periodic orbit is as follows:

$$\tilde{x} = \left[\begin{array}{cccccccc} x_1(t_1) & x_2(t_1) & \cdots & x_n(t_1) & \cdots & x_1(t_N) & x_2(t_N) & \cdots x_n(t_N) \end{array} \right] \tag{21}$$

which can also be written as

$$\bar{x} = \left[\begin{array}{cccc} \mathbf{x}(t_1)^T & \mathbf{x}(t_2)^T & \cdots & \mathbf{x}(t_N)^T \end{array} \right] \tag{22}$$

Each solution for the internal force and the tangent stiffness matrices can be performed in parallel and assembled to obtain the nonlinear force vector as follows.

$$\bar{f} = \left[\begin{array}{cccc} f\left(\mathbf{x}(t_1)\right) & f\left(\mathbf{x}(t_2)\right) & \cdots & f\left(\mathbf{x}(t_N)\right) \end{array} \right] \tag{23}$$

Since the nonlinear internal force at time step, i, is simply the matrix-vector product of the displacement and nonlinear portion of the tangent stiffness, $\mathbf{K}_{T_i}$, at step i as $\mathbf{f}_i = \mathbf{K}_{T_i}\mathbf{x}_i$, the tangent stiffness matrices can be obtained in parallel with marginal extra cost. The nonlinear portion of the tangent stiffness matrix can be generated at each individual time point as follows.

$$\bar{\mathbf{K}}_T = \left[\begin{array}{cccc} \mathbf{K}_T\left(\mathbf{x}(t_1)\right) & \mathbf{K}_T\left(\mathbf{x}(t_2)\right) & \cdots & \mathbf{K}_T\left(\mathbf{x}(t_N)\right) \end{array} \right] \tag{24}$$

However, this matrix does not match the order of the entries required in Eq. 19, and when reordering the entries some special attention is needed when dealing with the sparse matrices. An efficient solution is to find relative local entries within the sparse tangent stiffness matrix at each point along the periodic orbit and map using the permutation operation, $\mathbf{P}$, to the tangent stiffness definition in Eq. 19.

$$\tilde{\mathbf{K}}_T = \mathbf{P}\left(\bar{\mathbf{K}}_T\right) \tag{25}$$

There are typically tens or a few hundred time steps per cycle, so this can provide significant speedup. If further parallelization is needed, then each individual solution can be spread across multiple processors. However, those algorithms are known to be imperfect so doubling the number of processors does not cut the solution time in half.

3 Numerical Studies

Three numerical studies were conducted and presented here to explore the feasibility of computing NNMs of full finite element models. The computations were performed on a 2.3 GHz AMD Opteron Processor P6376 with 128 GB of available RAM and 32 cores. The computations were performed with an in house finite element code and multi-harmonic balance code coupled with a continuation routine. All code development was done in Matlab®. The FE code was validated with simulations against Abaqus®.

3.1 Flat Plate

The first example is a flat plate with clamped edges at each end. The geometry is depicted in Figure 1. The flat plate is square with an edge length of 250mm (9.84in) and a thickness of 1.5mm (0.059 in). The plate is made of aluminum with a modulus of elasticity $E = 71000\frac{N}{mm^2}$, a density $\rho = 2.79e^{-9}\frac{kg}{mm^3}$, and Poisson's ratio $\nu = 0.33$. The mesh used in this section comprised a 25 by 25 grid of elements.

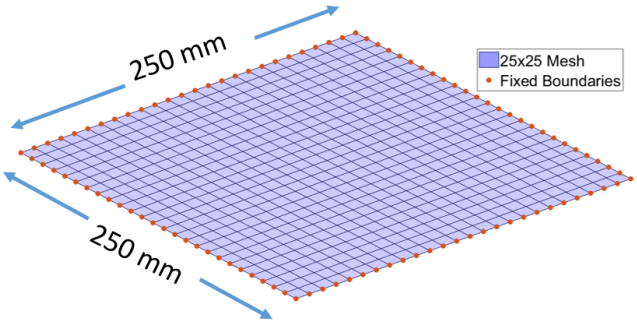


Figure 1: Flat Plate Finite Element Model

The first 6 linear normal modes of the flat plate are presented in Figure 2 for reference. The first NNM solution branch was initiated from the first linear normal mode of the flat plate, which is also the primary bending mode.

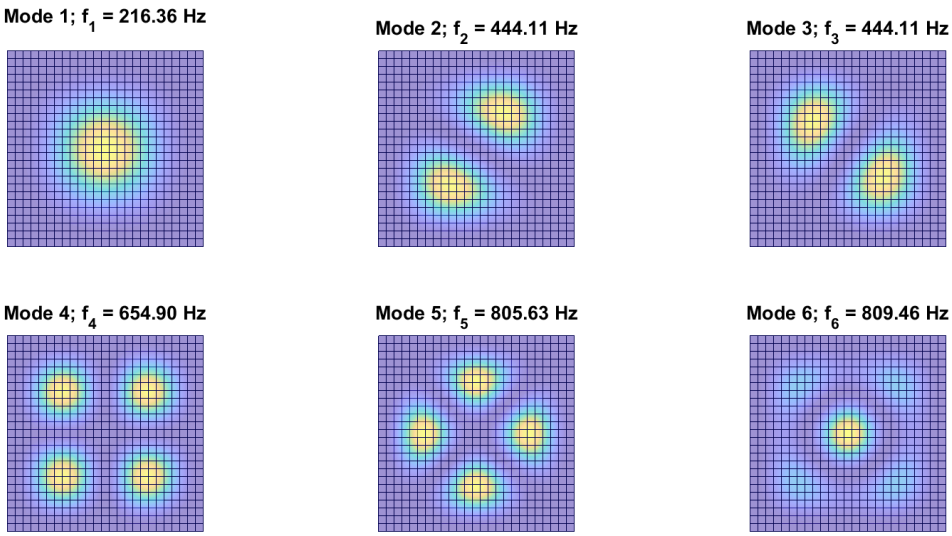


Figure 2: First 6 linear normal modes of the 25x25 flat plate finite element model

Prior works such as [10, 11] showed that a large number of harmonics are not required for simple structures such as flat plates and beams. Figure 3 plots the NNMs of the flat plate, each computed using a different number of harmonics. The left hand side of Figure 3 depicts the frequency-energy plot of the structure. This provides a general graphical representation of the frequency-amplitude dependence of each NNM solution. The right hand side of Figure 3 plots the vertical displacement of the center node versus frequency. The single harmonic solution is slightly although visibly different from the other two solutions for both the frequency versus energy and displacement versus frequency relationship. All of the higher harmonic models predict consistent solutions up to 260 Hz or a displacement equal to 1x thickness of the beam. Above 260 Hz the solution branches deviate from the main NNM backbones in favor of internal resonance branches. Prior works have shown that the internal resonances are not likely to be excited in the random environments that are the focus of this work [15], so the accurate identification of internal resonance branches is not explored further.

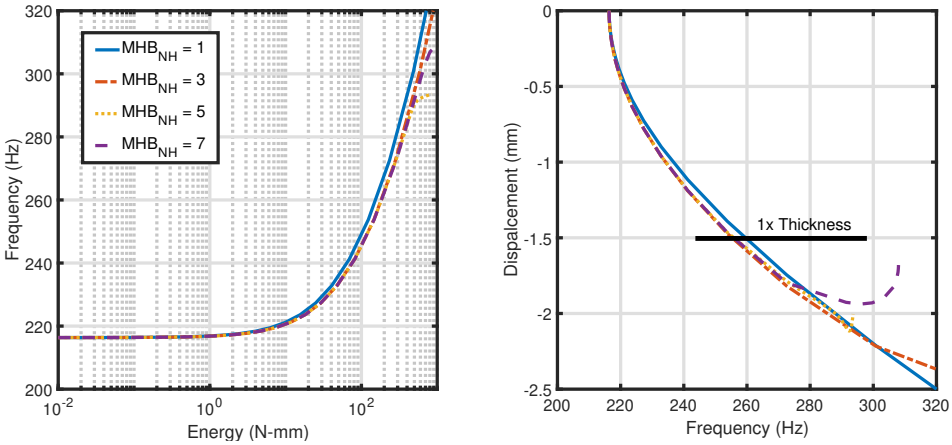


Figure 3: Nonlinear Normal Modes of flat plate FE model with increasing number of harmonics; (a) Frequency-energy plot. (b) Vertical displacement of center node versus frequency.

The validity of the harmonic balance solutions was further examined by integrating the FE model using the NNM solutions obtained with the HB method at which the displacement was approximately 1x the plate thickness. The error in the periodicity over one cycle, defined as

$$\epsilon = \frac{||\mathbf{x}(T) - \mathbf{x}(0)||}{||\mathbf{x}(0)||} \tag{26}$$

was computed for each model and are given in Table 1. This gives a rigorous measure of how well the computed NNM satisfies the full FE model and was also the convergence metric used in [3]. The single harmonic solution contains a 4.5% error in periodicity, which decreases to about 1% when three harmonics are used. As the number of harmonics increases to five and seven the solutions converge further. For this case a small number of harmonics was required to achieve quite accurate period solutions.

N_H	ϵ
1	0.045
3	0.011
5	0.003
7	0.00035

Table 1: Periodicity of the NNM solutions for the plate model at displacements equal to 1x the thickness for various numbers of harmonics.

3.2 Baseline Comparison of Shooting Method and Harmonic Balance

The time required to evaluate the residual for a shooting method (e.g. the AMF algorithm [3]) and this new harmonic balance method is presented in Table 2. The shooting method integrates the equation of motion over one period to evaluate the residual, and once more for each state in order to compute the Jacobian using finite differences. The number of states for that algorithm [3] is the number of active modes in the solution, which is typically between 1 and 10. Hence, the time for each iteration is a multiple of the time required to integrate over one period. To quantify this, an implicit integration scheme was used with 100 time steps to compute the response over one period and the time needed for the computation was recorded. For the results presented in Table 2 the methods were not parallelized and so this simply gives a baseline comparison. One can see that implicit integration over a single period is already more costly than the corresponding operation in the Harmonic Balance algorithm.

Mesh Size	#DOF	Implicit Integration	Harmonic Balance
10×10	486	17.51	6.22
25×25	3456	92.65	37.98
50×50	14408	358.93	155.31

Table 2: Comparison of time (seconds) to a.) evaluate the residual in the proposed Harmonic Balance method and b.) integrate the equation of motion for the shooting method [3]. Each method used a 100 time samples and serial execution.

3.3 Scaling Analysis

This section presents the reduction in computation time obtained by parallelizing the evaluation of the non-linear internal force and the generation of the nonlinear Jacobian. In both cases the computational cost scales independent of the number of harmonics used within the solution. Furthermore, the scaling is governed only by the cost associated with the discretization of the periodic orbit. While it is typically not a concern for models with smooth linearities and a small number of harmonics, it is important to note that the number of time samples must satisfy the Nyquist condition as the number of harmonics is increased.

As described in the theory section, in this work the harmonic balance method was parallelized only by simultaneously evaluating the nonlinear force vector and the Jacobian (tangent stiffness matrix) at each point in time. Hence, since 100 timesteps were used to describe the periodic orbit then at most 100 cores could be used simultaneously. The scaling computations were repeated while computing the NNMs for three different size models: a model with a 10x10 element mesh, a 25x25 mesh model and a 50x50 mesh model. Figure 4 plots the total simulation time required to compute the NNM up to a 2x frequency shift. The time required for the computations was found to fit a similar scaling law for each FE model, and these were compared by fitting a second order power law of the form $y = ax^b + c$ where y is the simulation time, x is the number of cores and the parameters a, b, and c are coefficients estimated from the fit. The primary coefficient of interest is the power law exponent coefficient, b, which dictates the scaling law as the number of cores increases. For the 10×10 mesh the reduction when doubling the cores used from 2 to 4 provided only a 30% reduction in computation time. This is due to the low work to communication ratio of the problem. For the largest model the computational time was able to be reduced by 40%.

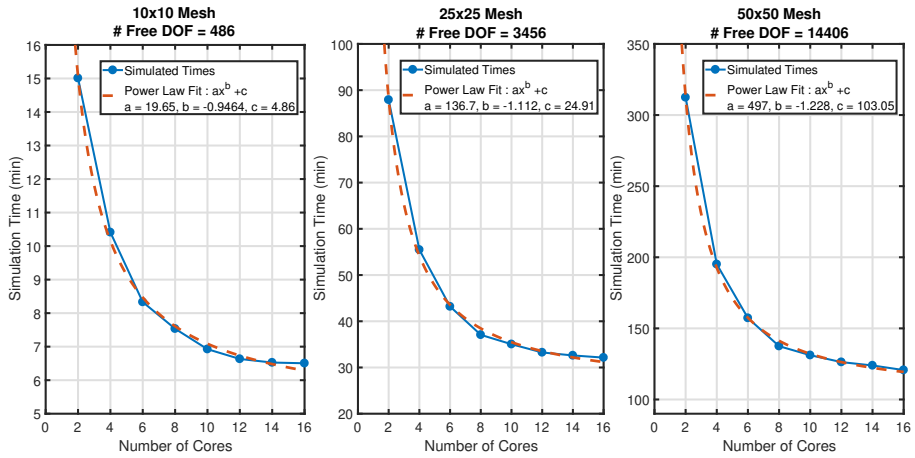


Figure 4: Scaling of total computational time with number of cores for calculation of the NNM up to a 2x frequency shift. Three models are presented: 10x10 mesh, 25x25 mesh, and a 50x50 mesh.

As has been noted in prior works [12] the major disadvantage of the harmonic balance method is that the

system size, and thus the Jacobian, increases linearly with the number of harmonics. This has negligible effect on the nonlinear force and nonlinear Jacobian generation but does indeed have a significant affect during the Newton-Rhapson routine, which requires the solution of a system of linear equations. The time required for the solution of the linear system that is solved at each step of the Newton-Rhapson routine is presented in Table 3. For reference, the time required to generate the nonlinear internal force using a serial execution, denoted NL_{Fun}, is also presented. As the number of harmonics increases the solution of the system starts to dominate the total computational time of the procedure. The method utilized to solve the linear system was back substitution on the sparse matrices, and no parallelization was utilized to accelerate this portion of the algorithm.

Mesh Size	#DOF	NL_{Fun}	$N_H = 1$	$N_H = 3$	$N_H = 5$	$N_H = 7$
$10x10$	486	6.22	0.21	0.81	2.60	5.94
$25x25$	3456	37.98	2.70	14.92	56.54	106.50
$50x50$	14408	155.31	21.44	89.92	522.29	1208.6

Table 3: Comparison of time (seconds) required to solve the linear system of equations generated for the three different sized models versus the number of harmonics included in the solution. The time required to compute nonlinear internal force vector in serial, denoted NL_{Fun}, is also presented for reference.

Even though the efficiency of the harmonic balance method is burdened by the increase in Jacobian size with the number of harmonics, the method still proves more efficient for large scale problems than shooting methods, in particular the AMF Algorithm [3]. This is demonstrated by comparing the unparallelized computational time to trace a $2\times$ frequency shift of the flat plate's first NNM between the AMF algorithm and the harmonic balance method with increasing number of harmonics. For each model size the harmonic balance method significantly outperforms the shooting method approach when including up to seven harmonics.

Mesh Size	#DOF	AMF	$N_H = 1$	$N_H = 3$	$N_H = 5$	$N_H = 7$
$10x10$	486	1202.02	15.01	15.56	17.20	20.26
$25x25$	3456	8801.45	87.91	98.30	133.67	176.14
$50x50$	14408	30050*	312.4	361.47	671.34	1163.20

Table 4: Comparison of time (minutes) required to compute the NNM backbone using the AMF Algorithm [3] and the harmonic balance method for the three different models and as the number of harmonics included in the solution is varied. Entries with the symbol $()^*$ denotes an estimated time of simulation.

3.4 Complex Systems : Curved Beams

Calculating the NNMs of curved beams has been previously studied in [16, 17] and those works have shown that it can prove difficult to obtain the NNMs. Two variants of a curved beam were investigated. The general geometric dimensions are presented in Figure 3.4. The shallow beam has a radius of curvature, R, of 22860 mm (900 inches) resulting in a maximum rise, h, of 1.016 mm (0.04 inches). The higher curved beam has radius of curvature of 3048 mm (120 inches) giving a maximum rise of 3.81 mm (0.15 inches). Each beam has a slight asymmetry in the curvature to avoid the singularity that can arise when seeking to buckle a perfectly symmetric beam.

Each beam has a length, A, of 304.8 mm (12 in) , a width of 12.7 mm (0.5 in), a thickness of 0.508 mm (0.02 in), a modulus of elasticity of E = 2.0684×10^5 $\frac{N}{mm^2}$ ($2.97 \times 10^7 \frac{lb}{in^2}$), a density of ρ = 7.8×10^{-6} $\frac{kg}{mm^3}$ ($7.36 \times 10^{-4} \frac{lb \cdot s^2}{in^4}$), and Poisson's ratio ν = 0.29. The beam was modeled with 400 shell elements resulting in a total of 3030 DOF. The beams are clamped on both ends as depicted in Figure 3.4 resulting in a total of 2970 free DOF.

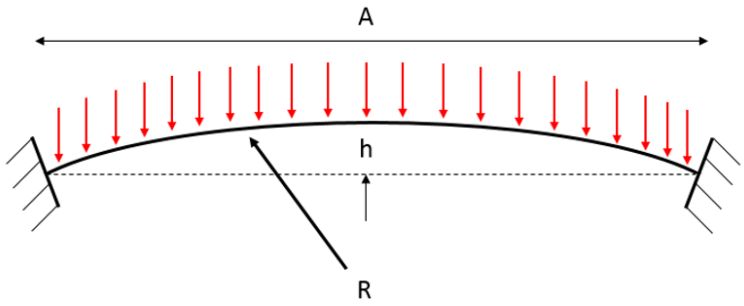


Figure 5: Curved Beam Geometry

3.4.1 Shallow Curved Beam

The first four linear modes of the shallowed curved beam are shown in Figure 6 for reference.

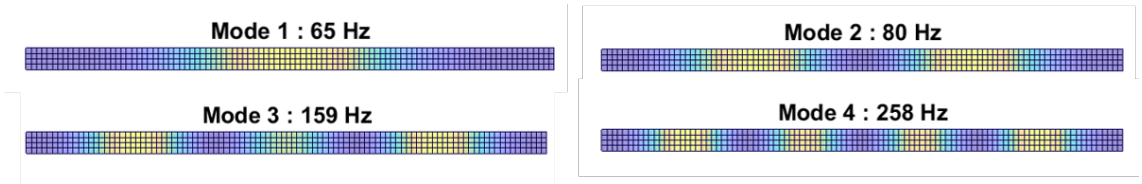


Figure 6: First four linear modes of the shallow curved beam.

The first nonlinear normal mode of the curved beam is depicted in Figure 7 for various numbers of harmonics included within the solution. All of the NNMs depict an initial softening of the system, a decrease in frequency with amplitude, followed by hardening. The single harmonic solution evolves smoothly due to its filtering property which eliminates the prediction of any internal resonance branches. As the number of harmonics included within the solution increases the branch becomes more difficult to compute because more internal resonance branches are identified.

All of the solutions contain similar predictions up to approximately 58 Hz, or prior to the identification of an internal resonance branch. Following the internal resonance branch the solutions with 3 or more harmonics deviate from the single harmonic during the softening. Further down the path during softening the higher harmonic solutions deviate from each other near the turning point. As the NNM starts to harden again the harmonic balance solutions start to coincide again near the point labeled C in Figure 7.

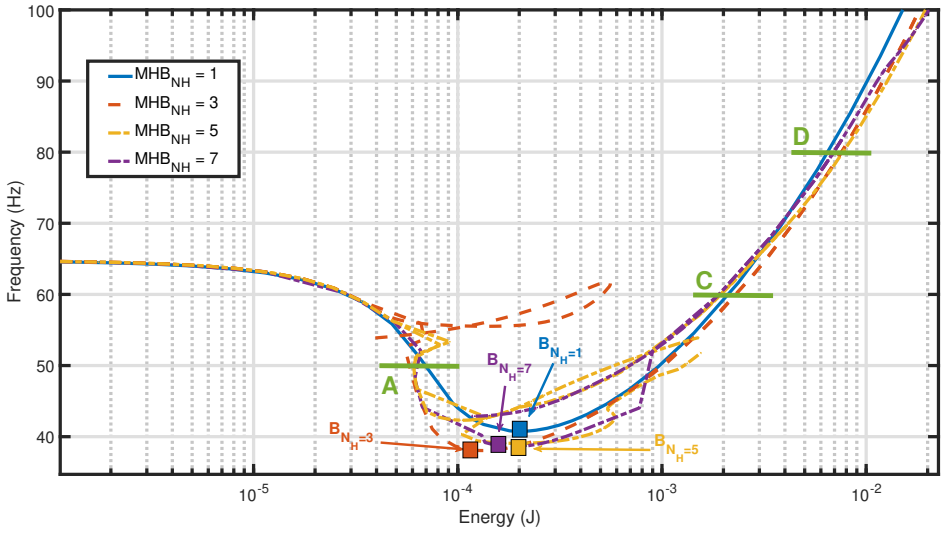


Figure 7: Nonlinear Normal Mode frequency-energy plot for the Shallow Curved Beam, computing using the harmonic balance method with varying number of harmonics. The NNM was originated from the first linear mode of the curved beam.

The initial displacements of the structure at each of the points marked by letters in Figure 7 are plotted in Figure 8 along with the undeformed geometry of the beam. At point A each solution has a similar deformation and a peak displacement near 1.5x the thickness of the beam. The one, three and five harmonic solutions at point B show an un-snapped state of deformation while the seven harmonic solution is snapped through. Moving to point C all the of the solutions are at the snapped state, although the shape found evolves significantly as the number of harmonics increased. This is true for point D as well.

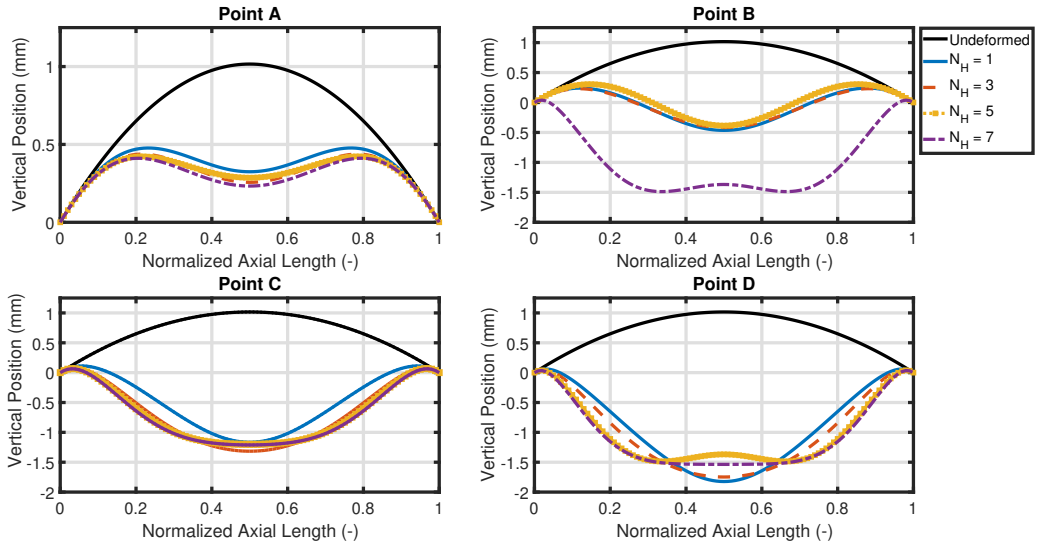


Figure 8: Initial deformation of the Shallow Curved Beam at the points along the NNM branch designated A, B, C and D in Figure 7.

To quantify these results, the accuracy of the harmonic balance solutions was evaluated at each of these points. Using the initial deformations shown in Fig. 8, the NNM solutions were integrated over the period

and the periodicity was calculated using Eq. 26. The results are presented in Table 5. At point A, approximately a displacement of 1.5× the thickness of the beam, each of the harmonic balance solutions has a marginally periodic response with max error of 0.055 for the single harmonic model. At the turning point of the branch the single harmonic and three harmonic solutions show considerable error. Increasing the solution to include five harmonics increases the accuracy of the solution. The five and seven harmonic solutions maintain periodicity at point C wherein the displacement reaches 4× the beam thickness at a value of 2.03 mm. Up to a displacement of approximately 2.54 mm, the five and seven harmonic solutions maintain a fairly periodic response. Interestingly, the solution with three harmonics is once again quite adequate at point D, or beyond the snap through point.

Pt	Approx. Displacement (×Thk)	$N_H = 1$	$N_H = 3$	$N_H = 5$	$N_H = 7$
A	1.5	0.055	0.049	0.006	0.004
B	3	0.127	0.191	0.062	0.008
C	4	0.255	0.128	0.009	0.002
D	5	0.280	0.074	0.048	0.037

Table 5: Comparison of periodicity (values of ϵ) of harmonic balance solutions from NNM solution points depicted in Figure 7.

To understand why the various models show errors in periodicity, the difference between the vertical displacement at the initial state, $\mathbf{x}(0)$, and final state $\mathbf{x}(T)$ is plotted in Figure 9 for the points extracted from the NNM plot. The plots coincide with those presented in Table 5 in which the seven harmonic solution is able to maintain a strong periodicity for each point.

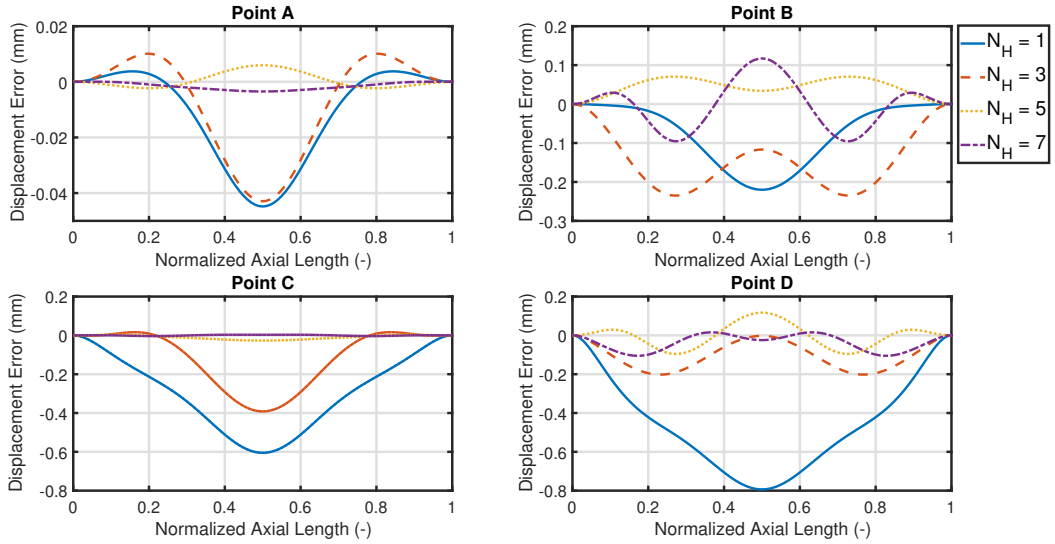


Figure 9: Difference in vertical displacement between the initial displacement of the NNM solutions from Figure 7 and the final displacement after numerically integrating the FE model over the period.

3.4.2 Deep Curved Beam

The last numerical example presented in this work is the clamped-clamped steel beam with a higher curvature, whose properties were given earlier. The first four linear modes and their natural frequencies are depicted in Figure 10.

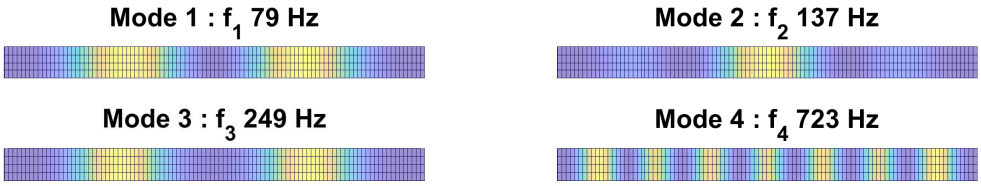


Figure 10: The first four linear modes of the Deep Curved Beam finite element model.

The second NNM of the Deep Curved Beam was initiated from the second linear normal mode at 137 Hz. Figure 11 shows an attempt to calculate the second NNM using one, three, five, and seven harmonics. Multiple points (labeled A-D in Figure 11) along each NNM branch were integrated to determine the periodicity of the specific solution. The corresponding periodicity values and approximate displacement are presented in Table 6.

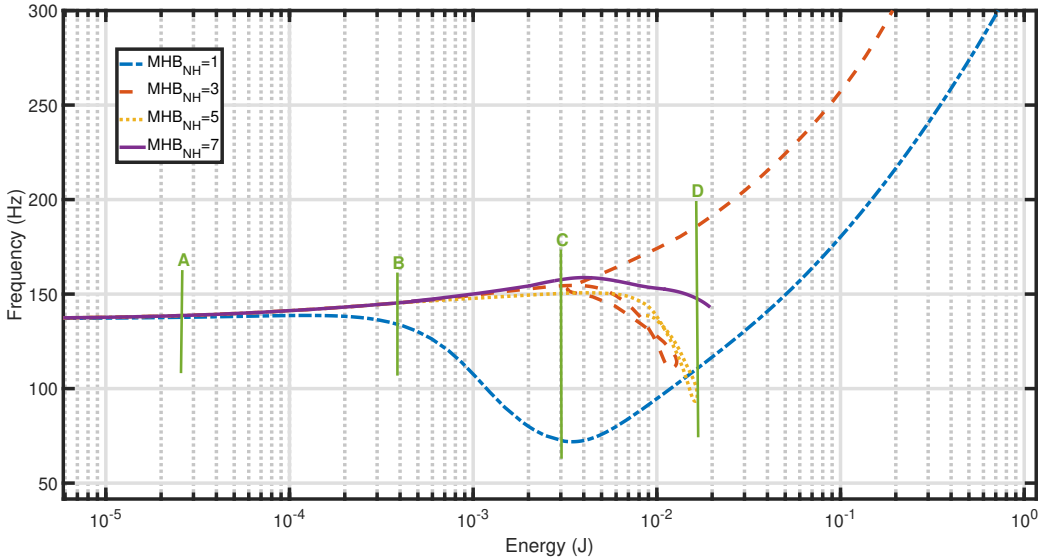


Figure 11: The NNM of the Deep Curved Beam originating from the second linear mode for increasing number of harmonics included within the solution.

The one harmonic solution branch exhibits softening between 2×10^{-4} and 2×10^{-2} J, reaching a minimum response frequency of approximately 70 Hz at about 3×10^{-3} J. The one-harmonic case is smooth throughout the full solution branch, but the values in Table 6 clearly show that none of the solutions from the single harmonic model have good periodicity when they are used as initial conditions in the full FE model. The three and five harmonic solution branches do not demonstrate the same softening behavior that is observed in the one harmonic case. Instead, both solution branches begin hardening at about 10^{-4} J before jumping to the internal resonance branches at about 3×10^{-3} J. The periodicity values at points A and B for three and five harmonics confirm that these solutions are accurate; this case underscores the importance of considering higher harmonics for curved structures. The three harmonic branch becomes smooth again following the internal resonance, but as shown by its periodicity at point D in Table 6, it is not a harmonic solution. Similar to the three and five harmonic solutions, the seven harmonic branch exhibits initial hardening behavior just before 10^{-4} J. Table 6 shows that the seven harmonic branch is similarly only accurate through point C.

Pt	Approx. Displacement (×Thk)	N_H=1	N_H=3	N_H=5	N_H=7
A	0.25	0.12	0.00	0.00	0.00
B	0.5	0.18	0.04	0.02	0.01
C	1	1.35	0.79	0.82	0.03
D	1.5	6.82	1.35	5.04	1.67

Table 6: Comparison of periodicity of harmonic balance solutions from NNM solution points depicted in Figure 11

The initial displacement for each of the NNM solutions at the four points in Figure 11 are shown in Figure 12. All four solutions at points A and B have a displacement close to 0.25 and 0.5× the thickness of the beam respectively with similar deformation shapes. At point C all four solutions have a displacement close to the thickness of the beam, but there is a clear deviation in the deformation shape as the one harmonic solution begins to soften and the other three begin to harden. At point D all four solutions have a displacement of approximately 1.5× the thickness of the beam. The one and three harmonic solutions have similar deformation shapes as both solution branches begin to harden while the five and seven harmonic solutions are both on an internal resonance branch.

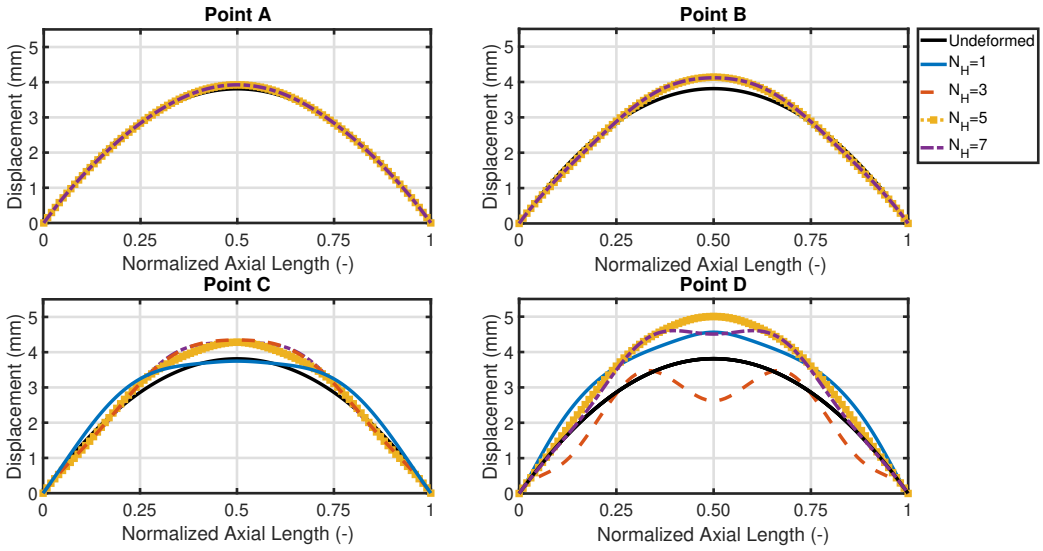


Figure 12: Initial deformation of the Deep Curved Beam at the points along the NNM branch designated A, B, C and D in Fig. 11

The high curvature beam demonstrates several important features of the HB method in its application to structures with complex nonlinear behavior. First, as was observed in the previous examples, in regimes where higher harmonics are needed, there is a clear correlation between the number of harmonics and the periodicity of the NNM solution. As the number of harmonics increases, the accuracy of the solution generally does as well but with a larger computational cost. Second, as the energy of the NNM solution increases, the accuracy of the solution generally decreases. As can be seen in the deformation plots in Figure 12, large amplitudes result in complex behavior such as internal resonances making it difficult to calculate accurate solutions using a small number of harmonics.

4 Conclusion

This work demonstrates an extension of the harmonic balance method that makes it possible to compute the nonlinear normal modes of geometrically nonlinear finite element models. The efficiency of the HB method was improved by using parallelization to significantly reduce the time required to evaluate the nonlinear internal force and generate the nonlinear Jacobian. These improvements made it possible to directly compute the NNMs of moderately sized finite element models. Basic scaling analysis showed that the scaling actually becomes more favorable as the size of the system increases, presumably due to reduction of overhead communication or parallel worker ratio.

The method was found to be an efficient means for computing NNMs of complex structures such as the Shallow Curved Beam. For the Shallow Curved Beam a periodic response was obtained with only a few harmonics for displacements up to 10x the thickness of the structure. The Deep Curved Beam, on the other hand, posed a more challenging task in which periodicity was not obtained at higher vibration amplitudes.

Despite the improvements presented in this work, there is still significant room for improving the algorithm. The system of equations to be solved in the harmonic balance method scales linearly with the number of harmonics, which eventually produces a large system of linear equations that must be solved at every iteration of the Newton-Rhapson method. This eventually becomes the computational bottleneck. Future investigations will look into iterative sparse solvers (which can be parallelized) rather than the back substitution algorithm that was used here to reduce the time required to solve this linear system. Alternatively, first order optimization methods could be used to resolve the correction phase of the continuation routine such as conjugate gradient methods or some other first order procedure.

Acknowledgements

This work was supported by the Air Force Office of Scientific Research, Award # FA9550-17-1-0009, under the Multi-Scale Structural Mechanics and Prognosis program managed by Dr. Jaimie Tiley. The authors gratefully acknowledge the input provided by Joseph Hollkamp and other collaborators in the Structural Sciences Center at the United States Air Force Research Laboratory.

References

[1] R. Rosenberg, *Normal Modes of Nonlinear Dual-Mode Systems*, ASME. J. Appl. Mech. 1960;27(2):263-268. doi:10.1115/1.3643948.

[2] R. Rosenberg, *The Normal Modes of Nonlinear n-Degree-of-Freedom Systems*, ASME. J. Appl. Mech. 1962;29(1):7-14. doi:10.1115/1.3636501.

[3] R. Kuether, M. Allen, *A numerical approach to directly compute nonlinear normal modes of geometrically nonlinear finite element models*, Journal of Sound and Vibration, Vol. 46, No. 1, 2014, pp. 1-15.

[4] R. Kuether, B. Deaner, J. Hollkamp, M. Allen, *Evaluation of Geometrically Nonlinear Reduced-Order Models with Nonlinear Normal Modes* AIAA Journal, Vol. 53, No. 11 (2015), pp. 3273-3285.

[5] R.J. Kuether, L. Renson, T. Detroux, C. Grappasonni, G. Kerschen, M. Allen, *Nonlinear normal modes, modal interactions and isolated resonance curves* Journal of Sound and Vibration, Vol. 351, 2015, pp. 299 - 310.

[6] David A. Ehrhardt, Matthew S. Allen, *Measurement of nonlinear normal modes using multi-harmonic stepped force appropriation and free decay* Mechanical Systems and Signal Processing, Vol. 76–77, 2016, pp. 612-633.

[7] Eugene L. Allgower, and Georg. Kurt, *Introduction to numerical continuation methods* SIAM Classics in Applied Mathematics (2003).

[8] M. Peeters, R. Viguie, G. Serandour, G. Kerschen, J. Golinval, *Nonlinear normal modes, part II: toward a practical computation using numerical continuation techniques* Mechanical Systems and Signal Processing, Vol. 23, 2008, pp. 195-216

[9] E. Doedel, A. Champneys, T. Fairgrieve, Y. Kuznetsov, B. Sandstede, X. Wang, *AUTO97: Continuation and Bifurcation Software for Ordinary Differential Equations*, 1998

[10] R. Lewandowski, *Computational Formulation for Periodic Vibration of Geometrically Nonlinear Structures-Part 2: Numerical Strategy and Examples*, Int. Journal of Solids and Structures, Vol. 34, No. 15, Elsevier (1997), pp. 1949-1964.

[11] R. Langley, *Harmonic Linearisation of Geometrically Non-linear Finite Element Models*, Computers and Structures, Vol. 28, No. 2, Pergamon (1988), pp. 165-172.

[12] L. Renson, G. Kerschen, B. Cochelin, *Numerical computation of nonlinear normal modes in mechanical engineering*, Journal of Sound and Vibration, Vol. 364, No. 3, Elsevier (2016), pp. 177-206.

[13] T. Detroux, L. Renson, L. Masset, G. Kerschen, *The Harmonic Balance Method for Bifurcation Analysis of Large-Scale Nonlinear Mechanical Systems*, Computer Methods in Applied Mechanics and Engineering, Vol. 296, No. 1, Elsevier (2015), pp. 18-38.

[14] J. Hwang, T. Shiau, *An application of the generalized polynomial expansion method to nonlinear rotor bearing systems*, Journal of Vibration and Acoustics, Vol. 113, No. 3, 1991, pp. 299–308.

[15] J. Schoneman, M. Allen, R. Kuether, *Relationships between Nonlinear Normal Modes and Response to Random Inputs*, Mechanical Systems and Signal Processing, Vol. 84, 2017, pp. 184-199

[16] C. Van Damme and M. Allen, *Using NNMs to Evaluate Reduced Order Models of Curved Beam*, *Proceedings in 34th International Modal Analysis Conference* (IMAC XXXIV) Orlando, Florida, 2016.

[17] C. Van Damme and M. Allen, *Nonlinear Normal Modes of a Curved Beam and its Response to Random Loading Proceedings in 35th International Modal Analysis Conference (IMAC XXXV)*, Garden Grove, California, 2017.

Nonlinear time series analysis of drillstring lateral vibrations

T. Kasper [1], **S. Tatzko** [1], **J. Wallaschek** [1]
[1] Institute of Dynamics and Vibration Research
Leibniz University of Hanover,
Appelstr. 11, 30167, Hannover, Germany
e-mail: **kasper@ids.uni-hannover.de**

Abstract
During oilwell drilling operations, downhole tools experience inevitable harmful shocks and vibrations. In this paper modern methods for nonlinear time series analysis are applied to investigate drillstring dynamics. The attractor is the subset of the phase space covering the characteristic dynamic behaviour. From a single time series an attractor can be reconstructed by applying delay embedding. Transitions in the system dynamics can be effectively detected using the recurrence quantification analysis. It is employed on a Laval rotor with contact as a simple drillstring model for different friction coefficients, which have significant influence on the solution behaviour.

1 Introduction

The dynamics of deep drilling operations are characterized by non-linearities, some of which are of course necessary for the drilling process. While friction and material removal at the drill bit are inevitable for drilling progress, contact between the drill string and the borehole wall can lead to undesirable effects. The classification of drillstring vibrations usually is conducted according to their direction of motion, which results in three different types: axial, torsional and lateral vibrations.

The interaction of the drillstring with the borehole wall during lateral vibrations may lead to several motion patterns, named forward or backward whirl and snaking [1]. Unfortunately, these known periodic processes are only parts of the drill string dynamics. Irregular vibrations are more common due to the unilateral contact with friction in the bore hole. Motion patterns like the backward whirl (drill string kinematically rolling on the borehole wall) cause high frequency bending cycles which are considered to be the most significant cause of inefficient drilling, poor borehole quality and premature tools failure [2]. Altogether, these factors result in prolonged well construction time and thus increased costs. Therefore, the design of downhole tools and the choice of the operational parameters need to be optimized to mitigate vibrations and improve drilling performance. Consequently, a better understanding of downhole tool dynamics and their interaction with the downhole environment is a key issue in optimizing the drilling performance.

In this context, dynamics and vibrations measurement tools have been developed to acquire, process, and record a comprehensive suite of data, including downhole loads, accelerations, pressures, and temperatures. Compiling this information and subsequently combining it with surface data will allow for an accurate investigation of drilling performance.

Due to non-linearities, analysis methods for linear systems as the modal analysis is not enough. Sophisticated methods such as the harmonic balance method for calculating nonlinear forced responses require periodicity. However, periodicity is not always given in the drilling process and more general methods are needed to analyse possible chaotic motion. A promising alternative is the attractor reconstruction of a time series of

a nonlinear dynamic system. Qilong Xue [4] has successfully applied attractor reconstruction on a drill string to investigate stability of torsional vibrations. The attractor allows the evaluation of various indicators for stability analysis. Both simulated data and measurements can be used for time series analysis. The embedding theorem of TAKEN [3] provides the reconstruction of a multidimensional phase space on the basis of a single scalar quantity. In the context of this work the embedding and attractor reconstruction is shown using the example of a lateral oscillator with contact, whereby the focus is on simulated time series.

The future goal is an improved vibration monitoring of drillstring processes by real-time data analysis. This enables the prediction of critical conditions and forms the basis for process control reducing harmful vibrations.

2 Laval rotor rodel with contact

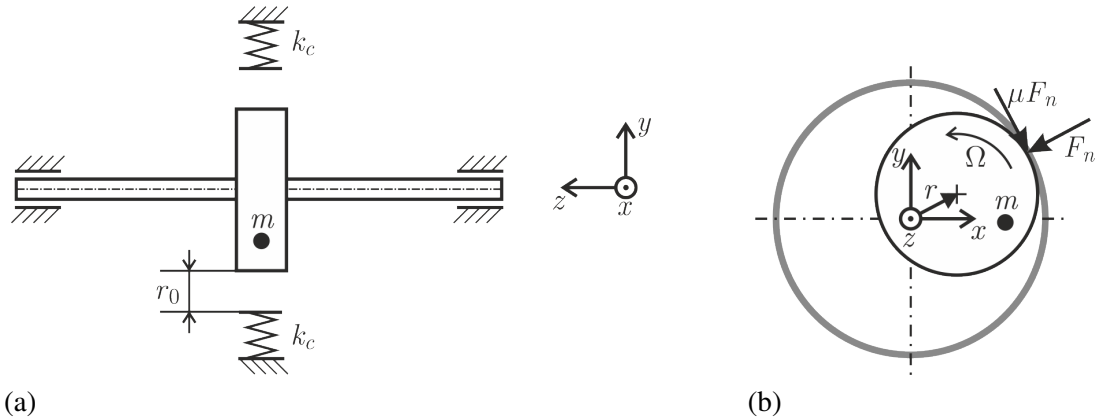
To investigate drilling dynamics a lumped parameter Laval rotor with unilateral constraint is observed. The rotor mass is concentrated in a disc mounted on a simply supported flexible shaft, see fig. 1(a). Fig. 1(b) shows the eccentricity of the center of gravity (black dot) and the disks centre of rotation. Shaft dynamics are approximated by stiffness k and damping c, respectively. Applying COULOMB'S Law the equations of motion in the $x-y-$plane are given by

$$m\ddot{x} + c\dot{x} + kx + \Theta k_c \left(1 - \frac{r_0}{r}\right)\left[x - \mu\ \mathrm{sgn}(v_{\mathrm{rel}})y\right] = me\Omega^2 \cos\Omega t \tag{1}$$

$$m\ddot{y} + c\dot{y} + ky + \Theta k_c \left(1 - \frac{r_0}{r}\right)\left[y + \mu\ \mathrm{sgn}(v_{\mathrm{rel}})x\right] = me\Omega^2 \sin\Omega t \tag{2}$$

$$v_{\mathrm{rel}} = \Omega r_{\mathrm{disk}} + \Omega_{\mathrm{w}} r \tag{3}$$

When the rotor contacts the borehole wall a unilateral penalty spring is activated and causes a repulsing normal contact force. The force value is computed with penalty stiffness k_c as well as friction forces due to relative motion in the contact point. The activation of the unilateral contact is controlled by the Heavyside function Θ in eq. (1) and eq. (2). As long as $r < r_0$ there is no contact and $\Theta = 0$. For $r \geq r_0$ the gap between rotor and stator vanishes and $\Theta = 1$ allowing contact forces to contribute to the equation system.



(a) (b)

Figure 1: Laval-Rotor Model

3 Methods

Continuous dynamical systems are usually defined by a set of first-order ordinary differential equations (ODE)

$$\frac{\mathrm{d}\mathbf{x}(t)}{\mathrm{d}t} = \mathbf{F}(\mathbf{x}(t)) \tag{4}$$

with the state vector $\mathbf{x} \in \mathbb{R}^m$. The ODE can also be written in time discrete form

$$\mathbf{x}_n \to \mathbf{F}(\mathbf{x}_n) = \mathbf{x}_{n+1}. \tag{5}$$

Under certain conditions (PAENO existence theorem, PICARD-LINDELÖF theorem, e. g.), the mathematical theory of ODE's ensures the existence and uniqueness of trajectories. These are the basic principles and requirements for the following method.

3.1 Phase Space Reconstruction

TAKENS theorem [3] allows the reconstruction of the phase space from a scalar observation $s_n = s(\mathbf{x}_n)$. The reconstructed phase space of the time series $s_0, s_1, \ldots, s_{n-1}$ is a diffeomorphism in the m-dimensional phase space, which can be built from time delay vectors

$$\tilde{\mathbf{x}}_i = \left[s_i, s_{i-\tau}, \ldots, s_{i-(m-1)\tau}\right] \tag{6}$$

of the present scalar time series (e. g. Fig. 4), where τ is the delay time.

An embedding can also be reconstructed by deriving the time series m times. This is a more intuitive way, because e. g. in mechanics it is unambiguous, that the derivation of the spatial coordinate gives the velocity coordinate. It is obvious, that one can reconstruct the phase-space of a SDOF-oscillator while measuring one state and calculate the other by deriving it. The disadvantage at higher derivatives is the increased smoothness requirements on the original signal. Moreover, approximating the derivatives by finite differences is nothing more than linear combinations of time delayed quantities.

In practical application we have to determine the delay time τ as well as the embedding dimension m. At first we look at the delay time. TAKENS makes no statement about the choice of τ, since it is irrelevant in theory. But using high-resolution time data, where the successive elements are strongly correlated in combination with small τ compared to the internal time scales of the dynamical system, yields to a clustered attractor around the diagonal in the $\mathbb{R}^m$.[5]

$$s_i \approx s_{i+1} \approx \cdots \approx s_{i+n-1} \approx s_{i+n} \quad \Rightarrow \quad \overbrace{(s_i, \ldots, s_{i+n-1})}^{\tilde{\mathbf{x}}_i} \approx \overbrace{(s_{i+1}, \ldots, s_{i+n})}^{\tilde{\mathbf{x}}_{i+1}} \tag{7}$$

Choosing τ to large, successive elements are already almost independent. Furthermore, real time-series are not infinitely long and the length is reduced by the factor $m\tau$. A good estimation for τ can be the first minimum on the autocorrelation function. This corresponds to a $\pi/2$ shift of the highest frequency, which is very similar to the first derivation in case of simple harmonic motion. While the autocorrelation function captures only linear correlation, the *average mutual information* (AMI) [6] uses the idea of the SHANNON-entropy [7], which attempts to characterize the unpredictability of a random state.

In terms of the embedding dimension m TAKENS states that the embedding is generally possible if $m > 2d$, with the *boxcounting-dimension* d of the attractor. "Roughly speaking, larger than twice the number of active degrees of freedom, regardless of how high the dimensionality of the true state space is. Depending on the application, even smaller m values satisfying $m > 2d$ can be sufficient."[5]

In our case it is obvious that the embedding should have the same dimension as the underlying attractor, which is $m = 4$ for the simulation model. Nevertheless, using this method with experimental time series

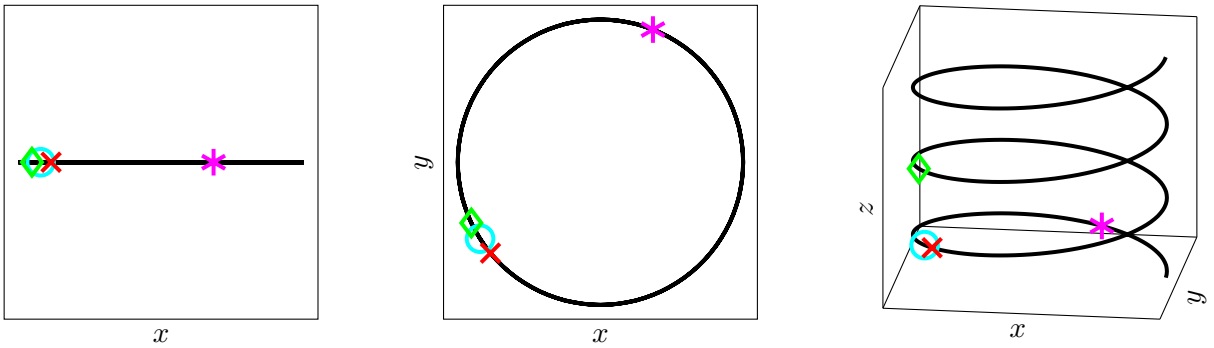
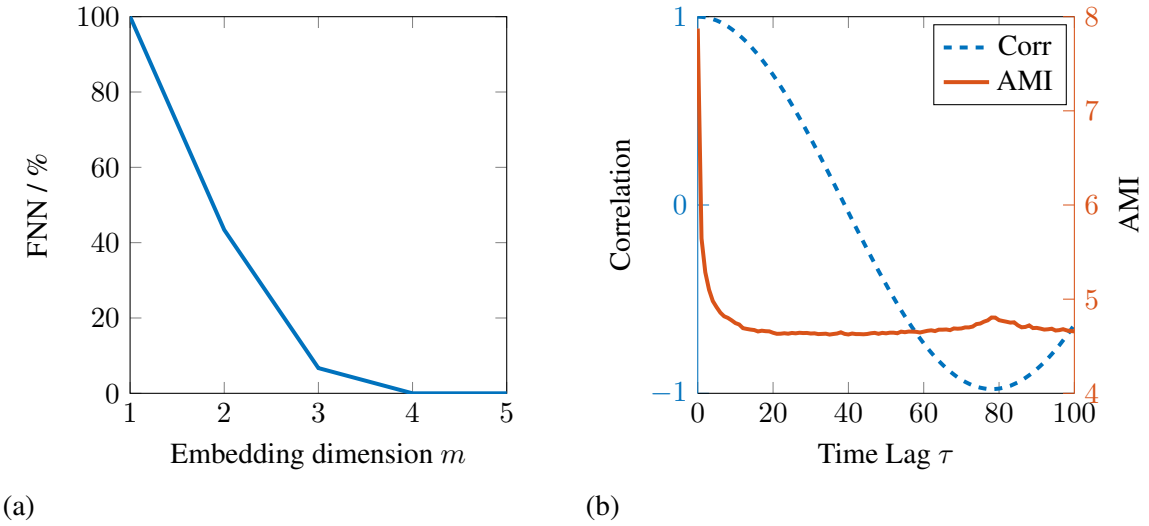


Figure 2: Simple example to illustrate false neighbours due to projection



(a) (b)

Figure 3: (a) Determine embedding dimension m with the method of false-nearest-neighbours and (b) time lag τ with the average-mutual-information

where the boxcounting-dimension d is not known, it is necessary to make an estimation. Therefore, the concept of *false nearest neighbours* (FNN)[8] will be used. Due to unsatisfactory embedding dimension, some not adjacent state vectors (e.g. same spatial but different velocity coordinate) become false neighbours as a result of subspace projection. An example is illustrated in Fig. 2 where the green diamond ◇ is a false neighbour till the dimension was unfolded to $\mathbb{R}^3$. By considering how the number of false neighbours relatively changes with increasing dimension (Fig. 3(a)), an appropriate embedding can be determined.

With the embedding parameters τ and m the attractor

$$\tilde{X} = [\tilde{\mathbf{x}}_1, \ldots, \tilde{\mathbf{x}}_m] \in \mathbb{R}^m \tag{8}$$

can be reconstructed from the time delayed scalar vectors $\tilde{\mathbf{x}}_i$ of Eq. (6).

3.2 Recurrence Analysis

After the attractor has been reconstructed, the recurrence matrix

$$\mathbf{R}_{i,j} = \Theta(\varepsilon - ||\tilde{X}(i) - \tilde{X}(j)||) \in \{0,1\} \quad \forall i,j = (1,\ldots,N) \in \mathbb{N} \tag{9}$$

can be setup. Here, $\mathbf{R}_{i,j}$ stands for one single element in the recurrence matrix, Θ describes the HEAVYSIDE function and ε the neighbourhood size. In this paper the euclidean norm for distance calculation was applied.

The corresponding recurrence plot (RP) visualizes similar states of the dynamic system (up to an error ε)

$$\mathbf{R}_{i,j} = \begin{cases} 1 : \tilde{\mathbf{x}}_i \approx \tilde{\mathbf{x}}_j \\ 0 : \tilde{\mathbf{x}}_i \not\approx \tilde{\mathbf{x}}_j \end{cases} \qquad \forall i,j = (1,\ldots,N) \in \mathbb{N} \tag{10}$$

as illustrated in Fig. 5. The diagonal oriented periodic recurrent lines parallel to the line-of-identity (LOI) are characteristic for oscillating systems, while single points in white areas occur if states are rare.

Although conclusions can be drawn on system behaviour on the RPs, this requires a bit of experience. However, scalar indicators that quantify the plot are much easier to interpret. In this paper the focus is on the most common indicators of the *recurrence quantification analysis* (RQA). They are based on the point density and line structures of the RP and described in detail in [12].

One of them is the *recurrence rate*

$$RR = \frac{1}{N^2} \sum_{i,j \in W} \mathbf{R}_{i,j} \tag{11}$$

which describes the density of recurrence points within the window W of the RP (LOI excluded).

Stochastic or weakly correlated processes cause none or very short diagonals, whereas deterministic processes cause longer diagonals. To quantify these information, we use the *determinism*

$$DET = \frac{\sum_{l=l_{\min}}^{N} lP(l)}{\sum_{l=1}^{N} lP(l)}, \tag{12}$$

which is the ratio of recurrence points that form a diagonal line $l > l_{\min}$ to all recurrence points. It is based on the histogram

$$P(l) = \sum_{i,j \in W} (1 - \mathbf{R}_{i-1,j-1})(1 - \mathbf{R}_{i+l,j+l}) \prod_{k=0}^{l-1} \mathbf{R}_{i+k,j+k} \tag{13}$$

of diagonal lines of length l.

The last measure is the inverse of the maximum diagonal length, called *divergence*

$$DIV = \frac{1}{L_{\max}}, \qquad L_{\max} = \max\left(\{l_i\}_{i=1}^{N_t}\right) \tag{14}$$

with N_t as the total number of diagonal lines. It is related to the largest positive Lyapunov exponent [13].

Since we are interested in analysing the changes in systems behaviour, we do not compute these measures for the hole RP. Instead we use a moving window with N_{win} points ($i,j \in W \subset (1,\ldots,N) \in \mathbb{N}\}$) to capture deviations in the solution behaviour.

4 Results and discussion

After computing the model from Chap. 2 for various friction parameters $\mu = \{0.1, 0.2, 0.3\}$. The different dynamical behaviour can be seen in Fig. 6(a), as well as the original and reconstructed phase-space. The initial conditions remain constant, so that every case starts with forward whirl. With increasing the friction μ the rotor drifts from stable forward whirl ($\mu = 0.1$) to chaotic motion ($\mu = 0.2$). Depending on the friction, chaotic motion can be transient and lead to stable backward whirl ($\mu = 0.3$).

Since the method will also be applied to measurement data in the future, where not all state variables are known, we extract only one single scalar times series, e. g. the spatial coordinate x as seen Fig. 4.

Then the embedding parameters can be determined (Fig. 3.1) and the attractor can be reconstructed. For the neighbourhood size $\varepsilon = 0.3\sigma$ has been chosen, where σ is the statistically expected value (normal

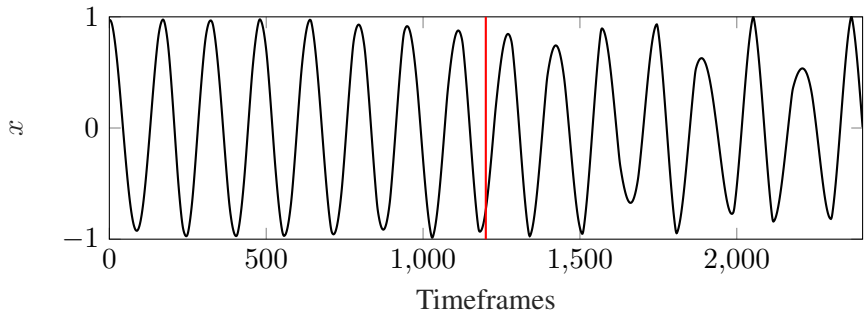


Figure 4: Time series of spatial coordinate x. Red line marks detected point in time for instability by RQA

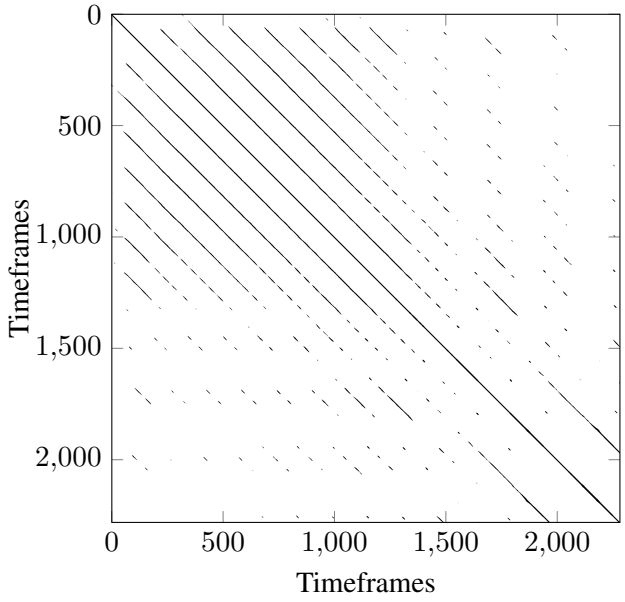


Figure 5: Recurrence plot of the time series from fig. 4 with embedding parameter $m = 4$, $\tau = 38$, $\varepsilon = 0.3\sigma$

distribution). The original phase-space of the state vectors (Fig. 6(b)) are of course not absolutely identical with the reconstructed phase-space (Fig. 6(c)) since they are only similar in the sense of a diffeomorphism. Furthermore, the 2D-projection distorts the structure, as the transient chaotic motion is not in the plane of stable periodic circles.

Already in the RP (Fig. 5) one can see that the periodicity is disturbed from about 1200 time frames, which can be seen by the interruptions of the diagonal lines. The RQA-measures clearly indicate the system behaviour, as seen in Fig. 6(e). Stable periodic oscillations reflected in constant recurrence rate (RR) and determinism (DET) while the divergence (DIV) is very low. They turn significantly as soon as the solution becomes unstable. This can happen even before an instability can be detected by looking at the time series itself (red line in Fig. 4).

Using the method for recurrence analysis, it was possible to separate areas of transient and periodic solutions of a nonlinear system by a single scalar time series. This method, can give additional information to the FOURIER-Transform, which is made for linear, time invariant systems. By taking further RQA-measures into account, the information value can be further increased. In the future, the influence of noisy signals will be investigated, as well as the application to real measurement data.

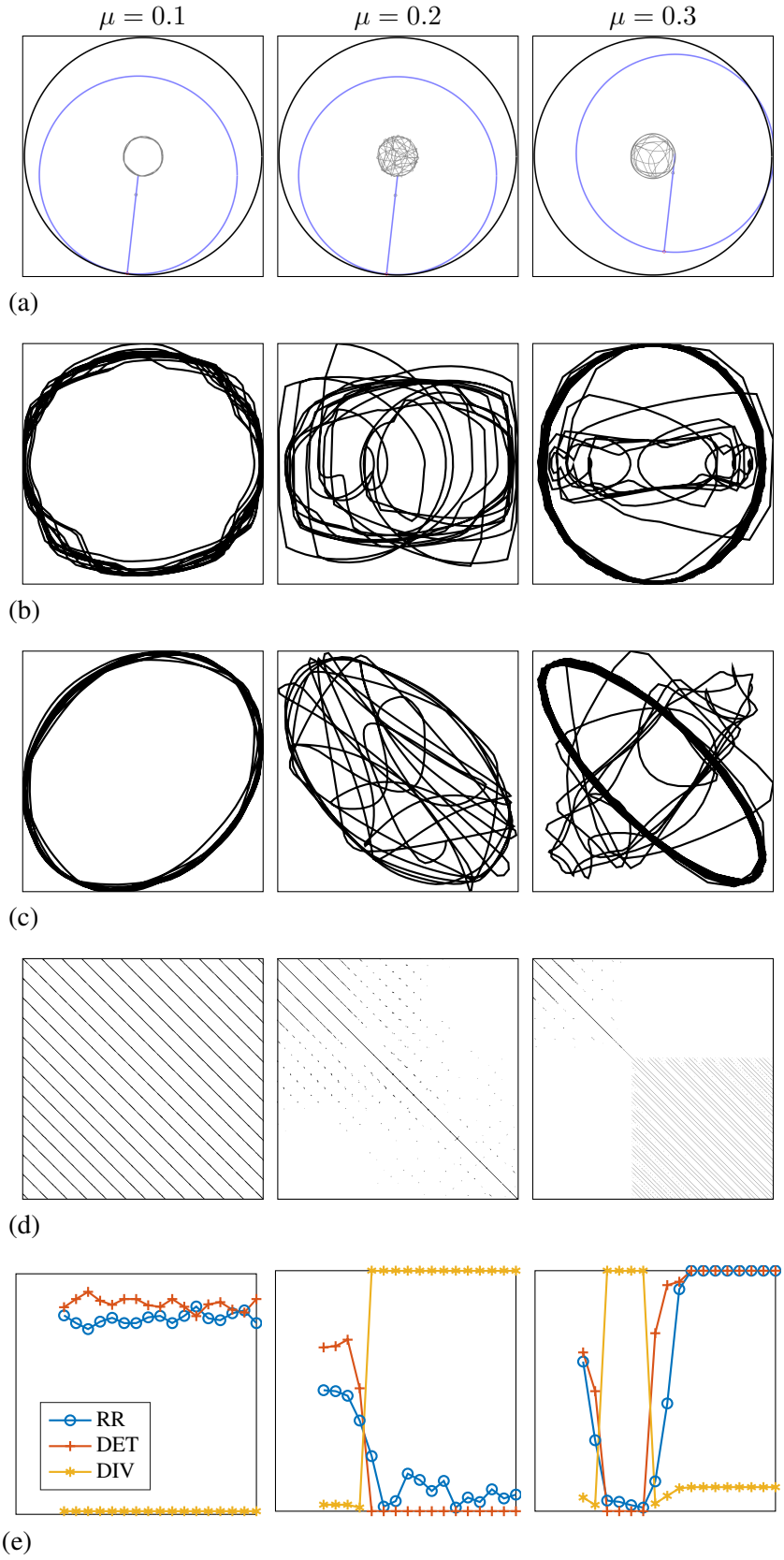


Figure 6: Stable forward whirl (left), chaotic motion (middle) which can evolve to stable backward whirl (right) (a) Black circle: borehole, blue circle: rotor. Inner lines shows trajectory of rotors centre point. (b) Phase-space of state vectors, (c) Reconstructed phase-space, (d) Recurrence plot of reconstruction, (e) Normalized measures: Recurrence rate (RR), determinism (DET), divergence (DIV)

References

[1] J. D. Jansen, *Nonlinear dynamics of oilwell drillstrings*, Delft University Press, (1993).

[2] V. A. Dunayevsky, F. Abbassian, A. Judzis, *Dynamic Stability of Drillstrings Under Fluctuating Weight on Bit*, Society of Petroleum Engineers, (1993).

[3] F. Takens, *Detecting strange attractors in turbulence*, Dynamical Systems and Turbulence. Lecture Notes in Mathematics, vol 898. Springer, Berlin, Heidelberg, pp. 366-381, (1981).

[4] Q. Xue, H. Leung, R. Wang et al., *The chaotic dynamics of drilling*, Nonlinear Dynamics , vol 83, no. 4, (2016).

[5] H. Kantz, T. Schreiber, *Nonlinear Time Series Analysis*, Cambridge University Press, New York, USA (2003).

[6] A. M. Fraser, H. L. Swinney, *Independent coordinates for strange attractors frommutual information*, Physical Review A, vol. 33, no. 1-2, pp. 1134-1140, (1986).

[7] C.E. Shannon, W. Weaver, *The Mathematical Theory of Communication*, University of Illinois Press, (1998).

[8] M. B. Kennel, R. Brown, H. D. I. Abarbanel, *Determining embedding dimension for phase-space reconstruction using a geometrical construction*, Phys. Rev. A, 45, (1992).

[9] W. Heylen, S. Lammens, P. Sas, *Modal Analysis Theory and Testing*, Katholieke Universiteit Leuven, Departement Werktuigkunde, Leuven (1997).

[10] P. Sas, C. Bao, F. Augusztinovicz, W. Desmet, *Active control of sound transmission through a double panel partition*, Journal of Sound and Vibration, Vol. 180, No. 4, Academic Press, pp. 609-625, (1995).

[11] R. Boonen, P. Sas, *Modified Smith Compensation for Feedback Active Noise Control in Ducts*, Proceedings of The 2001 International Congress and Exhibition on Noise Control Engineering, The Hague, pp. 619-624, (2001).

[12] N. Marwan, C Romano, M. Thiel, J. Kurths, *Recurrence plots for the analysis of complex systems*, Physics Reports, pp. 237-329, (2007).

[13] J.-P. Eckmann, S.O. Kamphorst, D. Ruelle, *Recurrence plots of dynamical systems*, Europhys. Lett. 5, pp. 973-977, (1987).

Investigating the bi-stable behavior of a lumped system with frictional contact

J. Brunetti [1a], **W. D'Ambrogio** [1], **N. Hoffmann** [2], **F. Massi** [3]
[1] Università dell'Aquila, Dipartimento di Ingegneria Industriale e dell'Informazione e di Economia,
Via G. Gronchi 18, I-67100, L'Aquila (AQ), Italy
[a] e-mail: **jacopo.brunetti@univaq.it**

[2] Department of Mechanical Engineering, Hamburg University of Technology, 21073 Hamburg, Germany

[3] Università di Roma La Sapienza, Dipartimento di Ingegneria Meccanica e Aerospaziale,
Via Eudossiana, 18, I-00184, Roma, Italy

Abstract
In non-conservative systems with frictional contact interfaces, the complex eigenvalue analysis is widely used to detect the instabilities of the system and it is generally performed on a linearized model around the equilibrium position. The change of contact status, due to the apparent negative damping, modifies the system dynamics and in certain condition it can induce instabilities. For instance, an equilibrium position that is stable in uniform sliding conditions can become a limit cycle when a portion of the contact interface passes from sliding to sticking condition, due to the action of an external perturbation force. In this paper this bi-stable behavior, that is typical of mechanical system with subcritical Hopf bifurcations, is investigated by a lumped parameter model with frictional contact. The effect of the friction on the system eigenvalues is analyzed not only for the uniform sliding condition but also for the other possible contact states, finding the ranges of the friction coefficient value that could lead to a bi-stable behavior.

1 Introduction

In the study of mechanical system composed by bodies in frictional contact, the coupling between the contact behavior and the vibrational response is definitely an essential point for the understanding of the system dynamics [1, 2]. In fact, the frictional contact forces can excite the system dynamics in different ways, leading to different contact instabilities phenomena as a function of system parameters (sliding velocity, contact pressure or material damping) [3]. The Complex Eigenvalue Analysis (CEA) is widely used to detect the instabilities of the system, and the analysis of the locus plot of the eigenvalues, with respect to the friction coefficient, is generally performed on a linearized model around the equilibrium position (a uniform sliding condition at the interface is generally chosen) [4]. This approach allows to investigate the effects of friction forces on the stability of the system [5]. In unstable systems, the increase of vibration amplitude due to the apparent negative damping reaches a saturation level given by the presence of material damping [6] or by the change of contact status (i.e. sliding, sticking and detachment transitions) [7]. The change of contact status modifies the system dynamics and in certain conditions it can induce instabilities. For instance, an equilibrium position that is stable in uniform sliding conditions can become a limit cycle when a portion of the contact interface passes from sliding to sticking condition. The initial condition (i.e. initial position and perturbation force) or external applied forces can lead the system from the stable equilibrium position to the

limit cycle. It is typical of bi-stable systems with subcritical Hopf bifurcations [8].

In this paper a lumped parameter model with frictional contact, previously developed by the authors [7, 9], has been exploited to investigate the bi-stable behavior on a mechanical system. The model is composed of both masses directly involved in the contact dynamic and masses that are not in contact but are linked to one other and to the contacting masses to represent the bulk. The system is basically a cyclic chain of nonlinear oscillators with a frictional contact point and the symmetries could be at the origin of localization phenomena of high interest within vibration engineering community [10, 11]. For the model under study, the effects of the friction on the system eigenvalues have been investigated not only for the starting equilibrium condition (i.e. uniform sliding at the interface) but also for the other possible contact states. To investigate the nonlinear behavior of the mechanical system, the forward increment Lagrange multiplier method is implemented [12, 13] and several analyses have been carried out in order to identify the ranges of the friction coefficient that could lead to a bi-stable behavior.

2 Method

2.1 Stability assessment

For a multi Degrees of Freedom (DoF's) mechanical system with frictional contact surfaces the equation of motion can be expressed as:

$$[M]\{\ddot{x}\} + [C]\{\dot{x}\} + [K]\{x\} = \{F_e\} + \{F_c\} \tag{1}$$

where, $[M]$, $[C]$ and $[K]$ are respectively the mass, the viscous damping and the stiffness matrix of the system; $\{x\}$ is the displacement vector and $\{F_e\}$ and $\{F_c\}$ are respectively the vectors of external forces and of contact forces acting on the mechanical system.

The contact forces $\{F_c\}$ can be expressed as a function of positions $\{x\}$ and velocities $\{\dot{x}\}$ of the system. The contact condition acts as unilateral constraint in the direction normal to the contact, the normal contact force $N \leq 0$ and the contact can be closed or open. If the normal contact force N is negative a compression force is exchanged between the contacting bodies and the contact is closed. Conversely if N is nil, no forces are exchanged at the interface and the contact is open.

Moreover, in the direction tangential to the contact, the friction force T opposes to the relative motion v_r between the two contacting bodies and is proportional to the normal contact force N. The proportionality factor between N and T is the friction coefficient μ.

$$T = -\text{sign}\,(v_r)\,\mu N \tag{2}$$

Several laws exist to express the friction coefficient as function of local contact quantities [14]. In this work the Amonton-Coulomb model is adopted for the friction force and a constant value of the friction coefficient μ is considered [7].

The contact forces represent a nonlinear boundary condition for the mechanical system. And each contact point can assume four contact state, i.e. sliding, reverse sliding, sticking or detachment. Hence, for a system with n contact points, 4^n possible configuration exist [9].

A very common approach to analyse the dynamic behavior of system with frictional interface is the Complex Eigenvalue Analysis (CEA) of the system linearized in uniform sliding condition. In this case, the contact forces $\{F_c\}$ add an asymmetric term to the stiffness matrix and the Equation (1) can be expressed as:

$$[\tilde{M}]\{\ddot{u}\} + [\tilde{C}]\{\dot{u}\} + \left[[\tilde{K}] + [\tilde{K_c}]\right]\{u\} = \{\tilde{F}_e\} \tag{3}$$

where $\{u\}$ represents the set of DoFs accounting for the assumed contact conditions, the $\tilde{\cdot}$ mark indicates that the system matrices and the external forces are expressed in the $\{u\}$ set of DoFs and the $[\tilde{K_c}]$ is the asymmetric term that makes the system not self-adjoint.

The Equation (3) can be recast in state space coordinate $\{Y\} = \left\{\{u\}^T \quad \{\dot{u}\}^T\right\}^T$:

$$[A]\{\dot{Y}\} + [B]\{Y\} = \{Q\} \tag{4}$$

where:

$$[A] = \begin{bmatrix} [\tilde{C}] & [\tilde{M}] \\ [\tilde{M}] & [0] \end{bmatrix}, \quad [B] = \begin{bmatrix} [\tilde{K}] + [\tilde{K}_c] & [0] \\ [0] & -[\tilde{M}] \end{bmatrix} \text{ and } \quad \{Q\} = \begin{Bmatrix} \{\tilde{F}_e\} \\ \{0\} \end{Bmatrix}. \tag{5}$$

The solutions of the right complex eigenvalue problem

$$\lambda_r\ [A]\{\xi\}_r = -\,[B]\ \{\xi\}_r \tag{6}$$

are the complex eigenvalues λ and the right complex eigenvectors ξ. The sign of the real part of the complex eigenvalues is a stability indicator of the mechanical system in Equation (3). If at least one eigenvalue real part is positive the system is unstable.

Nevertheless, the solutions of (6) refer to the uniform sliding condition, but if any of the contacting points is not in sliding, the linearization of contact could lead to a significantly different result. This is one of the main limitations on the use of CEA on linearized system to describe the nonlinear behavior. In fact, when the system is unstable it can exhibit very large amplitude vibrations with a relevant impact of contact nonlinearities. Typically, frictional unstable systems reach a limit cycle (stable orbit) that can be described as a dynamic energy equilibrium, where the contact nonlinearities bound the power absorbed by the system in sliding condition [4].

In this context, the stability of the system can be investigated also when the contact interface is not in uniform sliding condition [9]. For example, the system can be stable when in uniform sliding condition and exhibit some instabilities in states that are different from the uniform sliding. This could be associated to the presence of sub-critical instabilities, characterized by the coexistence of a static equilibrium position and a stable orbit, separated by an unstable orbit. In this case, the system is also called bi-stable and an external perturbation can move the system form one stable solution to the other.

2.2 Transient response

The time response of the system in Equation (1) can be obtained by explicit time integration using the forward increment Lagrange multiplier method [12, 13]. The contact conditions can be considered by constraint equation such as:

$$[G](\{x\} + \{X\}) = \{0\} \tag{7}$$

where $\{X\}$ is the vector of nodal coordinates at equilibrium, $(\{x\} + \{X\})$ is the current vector of nodal coordinates and $[G]$ is an a-priori unknown time-varying contact displacement constraint matrix. Hence, in Equation (1), the contact forces $\{F_c\}$ can be expressed using Lagrange multipliers $\{F_c\} = -[G]^T\{\lambda\}$. Equations (1) and (7) lead to a singular form that cannot be solved in the time domain. Therefore, to overcome this singularity the Forward increment Lagrange multipliers method can be used.

This formulation relates constraints at time $t_{n+1} = t_n + h$ with Lagrange multipliers at time t_n, and the equation of motion becomes:

$$\begin{cases} [M]\{\ddot{x}\}_n + [C]\{\dot{x}\}_n + [K]\{x\}_n + [G]^T_{n+1}\{\lambda\}_n = \{F_e\}_n \\ [G]_{n+1}\left(\{x\}_{n+1} + \{X\}\right) = \{0\} \end{cases} \tag{8}$$

For explicit integration of the equation, the Newmark β_2 scheme can be used, that for $\beta_2 = 0.5$ reduces to the central difference scheme:

$$\{\dot{x}\}_n = \frac{1}{2h}\left(\{x\}_{n+1} - \{x\}_{n-1}\right) \tag{9}$$

$$\{\ddot{x}\}_n = \frac{1}{h^2}\left(\{x\}_{n+1} - 2\{x\}_n + \{x\}_{n-1}\right) \tag{10}$$

The equation of motion can be rewritten as:

$$\{\ddot{x}\}_n = [M]^{-1}\left[\{F_e\}_n - [C]\{\dot{x}\}_n - [K]\{x\}_n - [G]_{n+1}^T\{\lambda\}_n\right] \tag{11}$$

By substituting the central difference expression of $\{\ddot{x}\}_n$ in the equation of motion, and by using $\{\dot{x}\}_n = \left(\{x\}_n - \{x\}_{n-1}\right)/h$ one obtains:

$$\{x\}_{n+1} = h^2[M]^{-1}\left[\{F_e\}_n - \frac{1}{h}[C]\left(\{x\}_n - \{x\}_{n-1}\right) - K\{x\}_n\right] + 2\{x\}_n - \{x\}_{n-1} - h^2[M]^{-1}[G]_{n+1}^T\{\lambda\}_n \tag{12}$$

By defining the predictor of displacement $\{x\}_{n+1}^\star$ as:

$$\{x\}_{n+1}^\star = h^2[M]^{-1}\left(\{F_e\}_n - [C]\{\dot{x}\}_n - [K]\{x\}_n\right) + 2\{x\}_n - \{x\}_{n-1} \tag{13}$$

the displacement at time t_{n+1} is:

$$\{x\}_{n+1} = \{x\}_{n+1}^\star - h^2[M]^{-1}[G]_{n+1}^T\{\lambda\}_n \tag{14}$$

Therefore, by substituting Eq. (14) in the second line of Eq. (8) one obtains:

$$[G]_{n+1}\left(\{x\}_{n+1}^\star + \{X\}\right) = h^2[G]_{n+1}[M]^{-1}[G]_{n+1}^T\{\lambda\}_n \tag{15}$$

Hence, an estimate of the contact forces $\{\lambda\}_n$ can be computed from the predictor $\{x\}_{n+1}^\star$:

$$\{\lambda\}_n = \left(h^2[G]_{n+1}[M]^{-1}[G]_{n+1}^T\right)^{-1}[G]_{n+1}\left(\{x\}_{n+1}^\star + \{X\}\right) \tag{16}$$

Finally, the corrector of the displacement $\{x\}_{n+1}^c$ is defined as:

$$\{x\}_{n+1}^c = -h^2[M]^{-1}[G]_{n+1}^T\{\lambda\}_n \tag{17}$$

and the displacement at time t_{n+1} is expressed as:

$$\{x\}_{n+1} = \{x\}_{n+1}^\star + \{x\}_{n+1}^c \tag{18}$$

For problems with M contact points the Equations (16) and (17) are solved together using a Gauss-Seidel iteration method. The i to $i+1$ Gauss-Seidel iteration for $I = 1, 2, \ldots, M$ can be expressed as follows omitting the step indexes:

$$^{i+1}\{p\}_I = [G]_I\left\{^{i+1}\{x\}^c + \{x\}^\star + \{X\}\right\} \tag{19}$$

$$\{\Delta\lambda\}_I = \left[h^2[G]_I[M]^{-1}[G]_I^T\right]^{-1}\ ^{i+1}\{p\}_I \tag{20}$$

$$^{i+1}\{\lambda\}_I = {}^{i}\{\lambda\}_I + \{\Delta\lambda\}_I \tag{21}$$

$$\{\Delta x\}_I^c = -h^2[M]^{-1}[G]_I^T\{\Delta\lambda\}_I \tag{22}$$

$$^{i+1}\{x\}^c \leftarrow {}^{i+1}\{x\}^c + \{\Delta x\}_I^c \tag{23}$$

The Gauss-Seidel iteration preceeds by simple element level calculations, until is satisfied the following convergence check:

$$|\{\Delta\lambda\}| < \text{tol}|^{i+1}\{\lambda\}|. \tag{24}$$

3 Model

The model considered in this work is shown in Figure 1, it is a lumped parameter model composed by masses m connected by springs k. The presence of both masses that are directly involved in the contact and masses that are not in contact allows to represent both the bulk and surface dynamic behavior of a system with frictional contact [7]. The circularity condition allows to account for the double modes that are generally due to the symmetry of a system [15, 10]. Finally, the presence of several contact points can reproduce in a discrete way the distribution of contact stresses and tangential velocity over an extended contact surface [5].

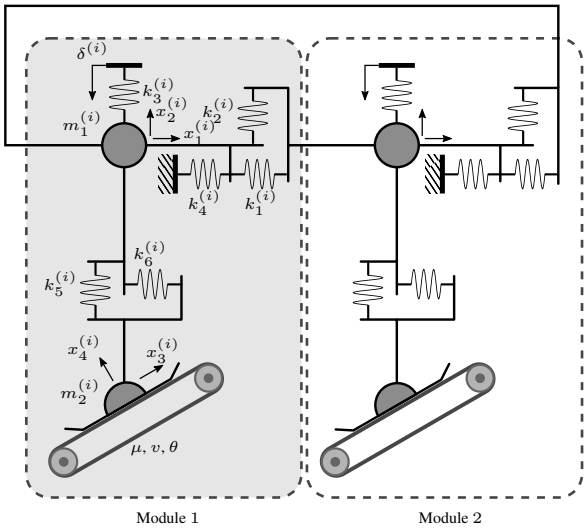


Figure 1: Lumped parameter model with frictional contact.

The system is composed by 2 modules circularly linked. Each module i is made of 2 masses and characterized by 4 DoFs ($x_1^{(i)}$, $x_2^{(i)}$, $x_3^{(i)}$ and $x_4^{(i)}$). The mass $m_2^{(i)}$ is in frictional contact (μ) with a rigid slider and is able to switch among the different contact states (Sliding, Sticking and Detachment). The slider moves with a tangential speed v and is inclined of an angle θ. The mass $m_1^{(i)}$ is simply linked to the adjacent masses. A static pre-load displacement $\delta^{(i)}$ can be applied on each module.

Two set of parameters will be considered for the model represented in Figure 1, the numerical values of the "Set 1" are shown in Table 1.

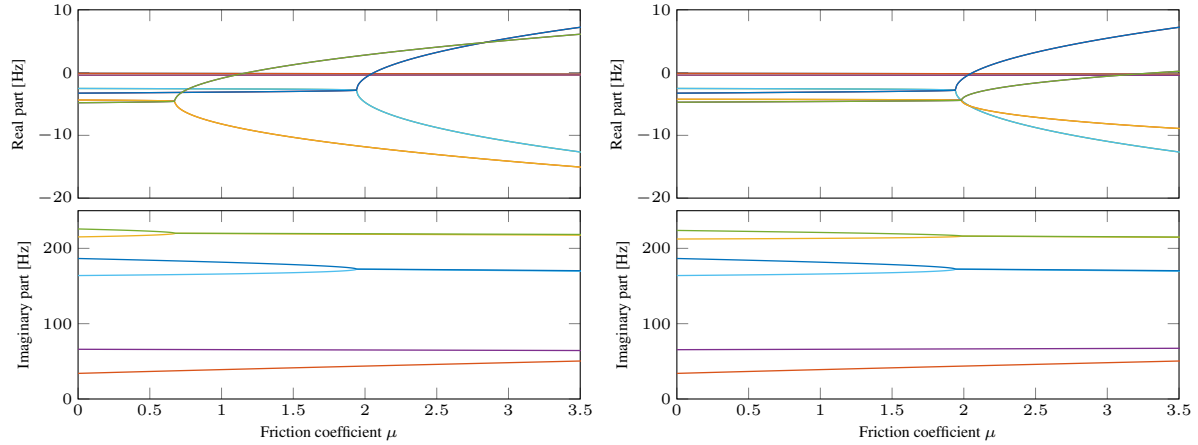
Parameter	**Set 1**	**Unity**
$m_{1:2}^{(i)}$	$\{0.3 \quad 0.7\}$	kg
$k_{1:6}^{(i)}$	$\{55 \quad 60 \quad 22 \quad 60 \quad 300 \quad 250\}$	kN/m
θ	0.5	rad
δ	$5.0\text{E}-3$	m
v	2.5E-2	m/s
β	$3.0\text{E}-5$	s

Table 1: Parameters of the lumped model.

Values of the "Set 2" are the same as the Set 1 except for the value of the stiffness $k_2^{(i)} = 53$ kN/m. The viscous damping C in Equation (1) is defined as proportional to the stiffness matrix $[C] = \beta[K]$.

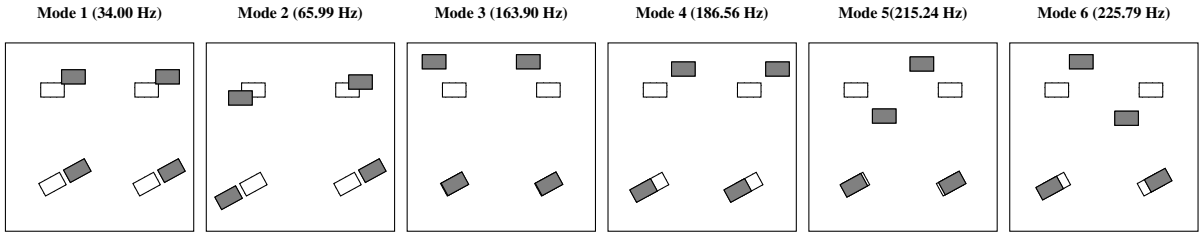
4 Results

In this section the dynamic behavior of the lumped parameter system described in the previous section has been analyzed using both the CEA for the stability assessment and the transient simulation to observe the time history response.



(a) Parametric CEA for the parameters in the Set 1

(b) Parametric CEA for the parameters in the Set 2



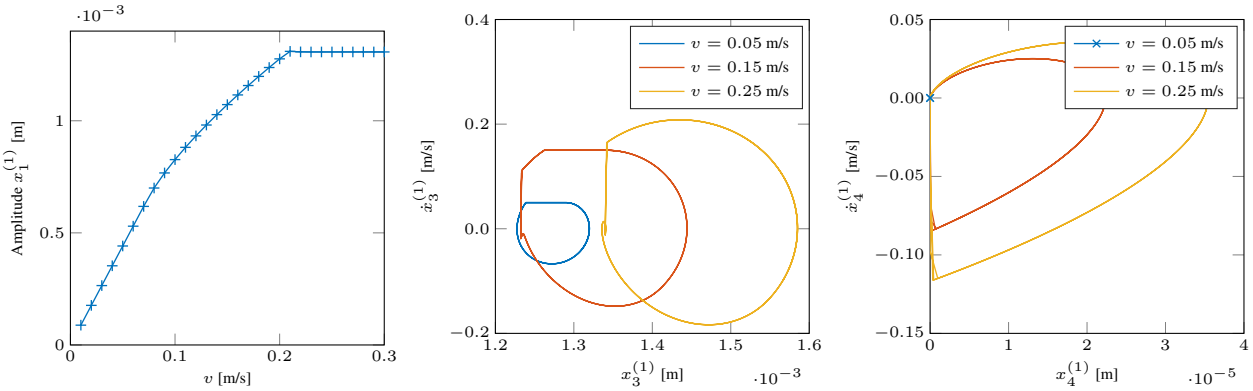
(c) Real mode shapes ($\mu = 0$) for the parameters of the Set 1

Figure 2: Complex eigenvalue analysis results

Figures 2(a) and (b) show the real and imaginary part of the complex eigenvalues, respectively for the parameters of the Set 1 and Set 2, with the friction coefficient in the range $0 \leq \mu \leq 3.5$. Figure 2(c) shows the real mode shapes of the system eigenvalues obtained for the parameters of Set 1 and a nil friction coefficient. Mode shapes for the Set 2 are not shown because they are very similar to mode shapes obtained for the Set 1.

For both sets of parameters the system exhibits two modal coupling in the considered range of the friction coefficient. The mode 3 coalesces with the mode 4 while the mode 5 coalesces with the mode 6. The two coalescences give rise to two unstable modes at frequencies of approximately 170 [Hz] and 215 [Hz]. For the parameters in the Set 1 the modes 5 and 6 coalesce for lower friction coefficient than modes 3 and 4 (cf. Figure 2(a)). The opposite occurs using the parameters in the Set 2 (see Figure 2(b)). In fact, the decrease of the stiffness k_2, connecting the vertical displacements of masses $m_1^{(i)}$ of adjacent subsystems, produces a relevant variation of the frequencies of modes 5 and 6, that are characterized by out of phase displacements of the upper masses $m_1^{(i)}$, without modifying the frequencies of modes 3 and 4 that are characterized by in phase displacements. Consequently, for the Set 2 of parameters the mode coupling between modes 5 and 6 occurs for higher values of friction coefficient than for the Set 1.

For a friction coefficient $\mu = 1.5$ the system with Set 1 of parameters is unstable since the real part of the mode 6 is positive (see Figure 2(a)). Figure 3 shows the limit cycle for different values of the slider velocity v. Figure 3(a) shows the amplitude of the limit cycle measured along the $x_1^{(i)}$ direction, the plot can be decomposed into three quasi-linear portions with different slopes. The slope variations are located at a slider velocity $v \simeq 0.1$ m/s and $v \simeq 0.2$ m/s. In the first range ($0 < v < 0.1$ [m/s]) the limit cycle is



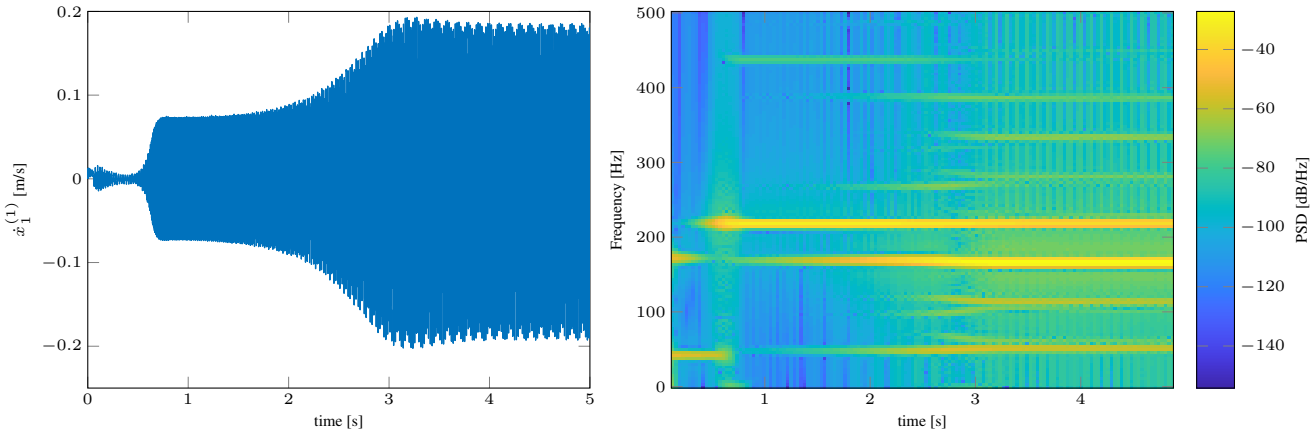
(a) Limit cycle amplitude on $x_1^{(i)}$.

(b) Limit cycle plots on the state plane of the tangential contact dof $x_3^{(i)}$.

(c) Limit cycle plots on the state plane of the normal contact dof $x_4^{(i)}$.

Figure 3: Unstable response of the system with the first set of parameters for $\mu = 1.5$. Effect of the slider velocity v on the limit cycle.

characterized by only stick-slip motion of the contacting masses $m_2^{(i)}$ (see the plots in Figures 3(b) and (c) for $v = 0.05$ m/s). The presence of horizontal portion for $\dot{x}_3^{(1)} = 0.05$ [m/s] in Figure 3(b) indicates the sticking motion and the point-wise plot in Figure 3(c) indicates that no detachment occurs ($x_4^{(1)} = 0$ and $\dot{x}_4^{(1)} = 0$). In the second range ($0.1 < v < 0.2$ [m/s]) the limit cycle is composed by stick slip and detachment of the contacting masses $m_2^{(i)}$ (see the plots in Figures 3(b) and (c) for $v = 0.15$ m/s). In Figure 3(b) the horizontal portion for $\dot{x}_3^{(1)} = 0.15$ [m/s] indicates the sticking motion and the plot in Figure 3(c) shows the detachment motion during the limit cycle ($x_4^{(1)} \neq 0$ and $\dot{x}_4^{(1)} \neq 0$). In the third range ($v > 0.2$ [m/s]) the limit cycle is composed by only slip and detachment motion of the contacting masses $m_2^{(i)}$ (see the plots in Figures 3(b) and (c) for $v = 0.25$ m/s). The absence of horizontal portion in Figure 3(b) indicates the absence of sticking. Furthermore, in absence of sticking and for a constant friction coefficient μ the limit cycle is independent from the slider velocity v (horizontal portion of Figure 3(a)).



(a) Time history response for DoF $x_1^{(i)}$

(b) Spectrogram of the response

Figure 4: System response of the system with the Set 1 of parameters and $\mu = 1.96$.

In Figure 4 the response of the system with the Set 1 of parameters for a friction coefficient $\mu = 1.96$ is shown. The system is unstable (see Figure 2(a)) and the time history response to a small initial perturbation is shown in Figure 4(a). Table 2 shows the eigenvalues of the system in all the possible contact statuses for $\mu = 1.96$. Observing the results in Figure 4(a) it is worth noting that the initial exponential increase of the amplitude moves the system form unstable equilibrium position to an orbit at about 1 s. Nevertheless,

Module 1 / Module 2	Sl	R-Sl	St	Dt
Sl	$-0.18 \pm 43.52i$ $-0.40 \pm 65.10i$ $-3.90 \pm 172.34i$ $-1.70 \pm 172.41i$ $-11.72 \pm 218.79i$ $2.68 \pm 219.38i$ - -	$-0.11 \pm 34.59i$ $-0.41 \pm 65.75i$ $-2.53 \pm 163.96i$ $-3.28 \pm 186.41i$ $-4.32 \pm 214.00i$ $-4.85 \pm 226.89i$ - -	$-0.28 \pm 54.57i$ $-7.04 \pm 167.53i$ $1.74 \pm 167.81i$ $-9.89 \pm 217.00i$ $1.00 \pm 217.45i$ - - -	$-7.29 \pm 44.65i$ $6.92 \pm 44.77i$ $-0.40 \pm 65.07i$ $-10.36 \pm 179.83i$ $4.25 \pm 180.32i$ $-8.81 \pm 224.02i$ $-0.66 \pm 224.37i$ -
R-Sl	$-0.11 \pm 34.59i$ $-0.41 \pm 65.75i$ $-2.53 \pm 163.96i$ $-3.28 \pm 186.41i$ $-4.32 \pm 214.00i$ $-4.85 \pm 226.89i$ - -	$-0.05 \pm 22.27i$ $-0.42 \pm 66.83i$ $-2.46 \pm 161.66i$ $-3.55 \pm 194.09i$ $-4.21 \pm 211.32i$ $-5.09 \pm 232.35i$	$-0.21 \pm 47.62i$ $-2.46 \pm 161.67i$ $-3.01 \pm 178.58i$ $-4.21 \pm 211.34i$ $-4.86 \pm 226.94i$ - - -	$-0.05 \pm 22.47i$ $-0.26 \pm 52.15i$ $-0.42 \pm 66.83i$ $-2.79 \pm 172.17i$ $-3.55 \pm 194.01i$ $-4.47 \pm 217.85i$ $-5.08 \pm 232.22i$ -
St	$-0.28 \pm 54.57i$ $-7.04 \pm 167.53i$ $1.74 \pm 167.81i$ $-9.89 \pm 217.00i$ $1.00 \pm 217.45i$ - - -	$-0.21 \pm 47.62i$ $-2.46 \pm 161.67i$ $-3.01 \pm 178.58i$ $-4.21 \pm 211.34i$ $-4.86 \pm 226.94i$ - - -	$-2.47 \pm 161.77i$ $-2.56 \pm 164.87i$ $-4.22 \pm 211.50i$ $-4.47 \pm 217.79i$ - - - -	$-0.22 \pm 47.85i$ $-0.26 \pm 52.03i$ $-2.80 \pm 172.34i$ $-3.00 \pm 178.33i$ $-4.48 \pm 218.02i$ $-4.84 \pm 226.65i$ - -
Dt	$-7.29 \pm 44.65i$ $6.92 \pm 44.77i$ $-0.40 \pm 65.07i$ $-10.36 \pm 179.83i$ $4.25 \pm 180.32i$ $-8.81 \pm 224.02i$ $-0.66 \pm 224.37i$ -	$-0.05 \pm 22.47i$ $-0.26 \pm 52.15i$ $-0.42 \pm 66.83i$ $-2.79 \pm 172.17i$ $-3.55 \pm 194.01i$ $-4.47 \pm 217.85i$ $-5.08 \pm 232.22i$ -	$-0.22 \pm 47.85i$ $-0.26 \pm 52.03i$ $-2.80 \pm 172.34i$ $-3.00 \pm 178.33i$ $-4.48 \pm 218.02i$ $-4.84 \pm 226.65i$ - -	$-0.05 \pm 23.19i$ $-0.13 \pm 36.79i$ $-0.41 \pm 65.75i$ $-0.42 \pm 66.78i$ $-3.19 \pm 184.00i$ $-3.53 \pm 193.63i$ $-4.66 \pm 222.38i$ $-5.08 \pm 232.00i$

Table 2: Complex eigenvalues in [Hz] in all the possible contact configurations for $\mu = 1.96$ for the parameters in Set 1.

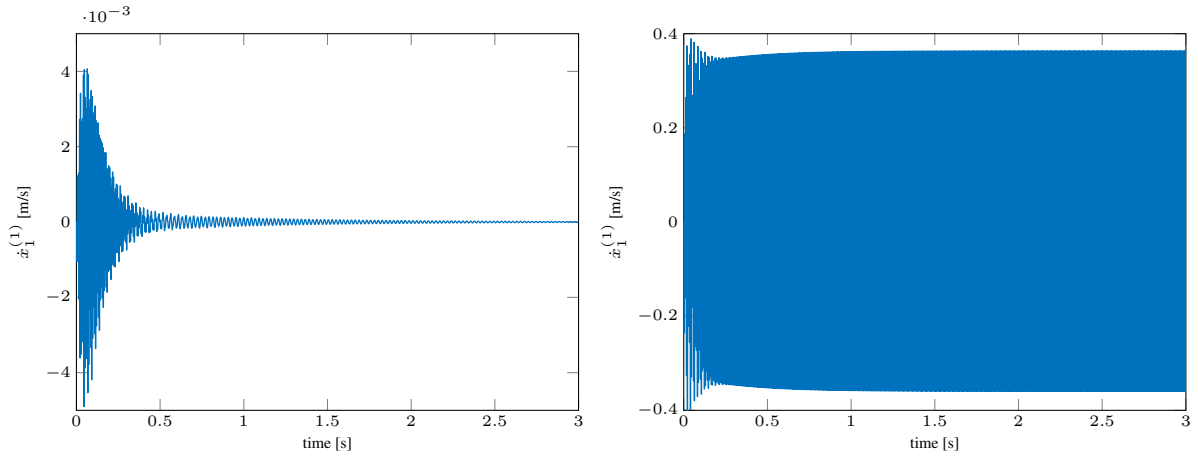
this orbit does not represent a stable condition and a second exponential increase of the amplitude leads the system to another orbit that this time is stable. This is because the system presents one instability at about 219 Hz, as shown in Table 2 when both the contact points are in sliding (Sl-Sl configuration). The coupled modes 5 and 6 are characterized by out of phase displacements of the two modules, hence, the two modules reach alternatively the sticking condition. When one of the two contact points is in sticking condition (configurations Sl-St or St-Sl) the system presents two unstable modes at about 168 Hz and 217 Hz. This is at the origin of the second exponential increase of the amplitude shown in Figure 4(a). The spectrogram in Figure 4(b) confirms the previous observations showing the presence of a band at about 220 Hz that begins at 0.6 s and a second band at about 180 Hz that increases its intensity between 1 and 3 s. Finally, during the limit cycle, both the frequencies at about 170 and 215 Hz appear in the spectrogram, even if the mode at the lowest frequency is stable in Sl-Sl configuration (see Figure 2(a) and Table 2).

As previously shown, the Set 2 of parameters allows to move the coalescence between modes 5 and 6 towards higher friction coefficients. Figure 2(b) highlights that for the friction coefficient adopted in the previous simulations ($\mu = 1.96$) the system is still stable in uniform sliding condition, since all the modes have negative real part (see Table 3 in Sl-Sl configuration). However, the system becomes unstable if one of the two masses is in sticking status (see eigenvalues in Table 3 in Sl-St or St-Sl conditions). Therefore the system in this conditions exhibits a bistable behavior. If the initial perturbation is small the system oscillates around the static equilibrium position as shown in Figure 5(a). If a large perturbation is imposed, that leads one of the two contact points in the sticking condition, the system reaches a stable orbit as shown in Figure 5(b).

Figure 6 shows the results of a "pseudo-continuation" analysis performed to investigate the effects of the friction coefficient on the presence and on the amplitude of the limit cycle for the system with the Set 2 of parameters. To obtain the curve for decreasing values of μ, the transient simulation is performed initially with a friction coefficient $\mu = 2.5$ and a small perturbation. Once that the system has reached the limit cycle, the transient simulation is arrested and restarted with a lower value of the friction coefficient $\mu^\star = \mu - \Delta\mu$ adopting as initial condition the ending state (displacement and velocity) of the previous simulation. This restart procedure is repeated to span the desired range of the friction coefficient. To obtain the curve for increasing values of μ the procedure is very similar, except for the small perturbation that is applied for each

Module 2 \ Module 1	Sl	R-Sl	St	Dt
Sl	$-0.18 \pm 43.52i$ $-0.42 \pm 66.48i$ $-3.90 \pm 172.34i$ $-1.70 \pm 172.41i$ $-4.39 \pm 215.67i$ $-4.44 \pm 216.90i$ - -	$-0.11 \pm 33.91i$ $-0.41 \pm 65.75i$ $-2.54 \pm 164.11i$ $-3.25 \pm 185.73i$ $-4.24 \pm 212.09i$ $-4.75 \pm 224.49i$ - -	$-0.29 \pm 55.29i$ $-7.05 \pm 167.61i$ $1.75 \pm 167.89i$ $-6.27 \pm 214.44i$ $-2.40 \pm 214.60i$ - - -	$-7.43 \pm 43.62i$ $7.08 \pm 43.74i$ $-0.42 \pm 66.46i$ $-10.25 \pm 179.40i$ $4.18 \pm 179.88i$ $-8.02 \pm 221.98i$ $-1.28 \pm 222.27i$ -
R-Sl	$-0.11 \pm 33.91i$ $-0.41 \pm 65.75i$ $-2.54 \pm 164.11i$ $-3.25 \pm 185.73i$ $-4.24 \pm 212.09i$ $-4.75 \pm 224.49i$ - -	$-0.05 \pm 22.27i$ $-0.39 \pm 64.51i$ $-2.46 \pm 161.66i$ $-3.55 \pm 194.09i$ $-4.22 \pm 211.45i$ $-4.91 \pm 228.22i$	$-0.20 \pm 46.30i$ $-2.46 \pm 161.67i$ $-2.99 \pm 178.08i$ $-4.22 \pm 211.46i$ $-4.68 \pm 222.72i$ - - -	$-0.05 \pm 22.47i$ $-0.26 \pm 52.21i$ $-0.39 \pm 64.51i$ $-2.80 \pm 172.19i$ $-3.55 \pm 194.00i$ $-4.48 \pm 217.90i$ $-4.91 \pm 228.13i$ -
St	$-0.29 \pm 55.29i$ $-7.05 \pm 167.61i$ $1.75 \pm 167.89i$ $-6.27 \pm 214.44i$ $-2.40 \pm 214.60i$ - - -	$-0.20 \pm 46.30i$ $-2.46 \pm 161.67i$ $-2.99 \pm 178.08i$ $-4.22 \pm 211.46i$ $-4.68 \pm 222.72i$ - - -	$-2.47 \pm 161.77i$ $-2.56 \pm 164.87i$ $-4.22 \pm 211.50i$ $-4.27 \pm 212.79i$ - - - -	$-0.20 \pm 46.60i$ $-0.26 \pm 52.03i$ $-2.80 \pm 172.34i$ $-2.98 \pm 177.86i$ $-4.48 \pm 218.02i$ $-4.67 \pm 222.49i$ - -
Dt	$-7.43 \pm 43.62i$ $7.08 \pm 43.74i$ $-0.42 \pm 66.46i$ $-10.25 \pm 179.40i$ $4.18 \pm 179.88i$ $-8.02 \pm 221.98i$ $-1.28 \pm 222.27i$ -	$-0.05 \pm 22.47i$ $-0.26 \pm 52.21i$ $-0.39 \pm 64.51i$ $-2.79 \pm 172.19i$ $-3.55 \pm 194.00i$ $-4.48 \pm 217.90i$ $-4.91 \pm 228.13i$ -	$-0.20 \pm 46.60i$ $-0.26 \pm 52.03i$ $-2.80 \pm 172.34i$ $-2.98 \pm 177.86i$ $-4.48 \pm 218.02i$ $-4.67 \pm 222.49i$ - -	$-0.05 \pm 23.19i$ $-0.13 \pm 36.79i$ $-0.39 \pm 64.57i$ $-0.41 \pm 65.75i$ $-3.19 \pm 184.00i$ $-3.53 \pm 193.63i$ $-4.66 \pm 222.38i$ $-4.90 \pm 227.94i$

Table 3: Complex eigenvalues in [Hz] in all the possible contact configurations for $\mu = 1.96$ for the parameters in Set 2.



(a) Time history response for a small perturbation.

(b) Time history response for a large perturbation.

Figure 5: System response of the system with the Set 2 of parameters and $\mu = 1.96$ for different values of the initial perturbation.

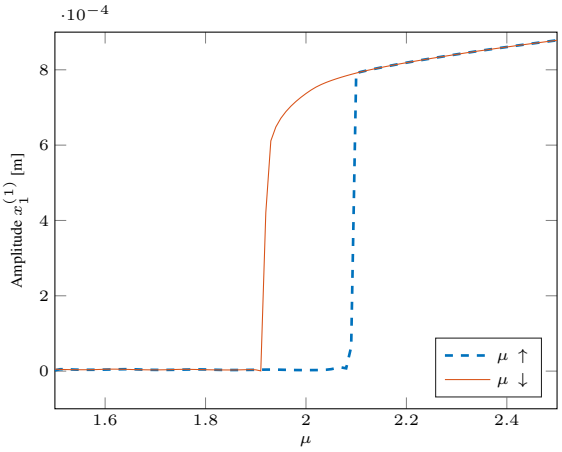


Figure 6: Amplitude of the limit cycle for increasing and decreasing values of the friction coefficient μ (with $\Delta\mu = 0.01$) for the Set 2 of parameters.

restart analysis. In this case, in fact the initial value of the friction coefficient $\mu = 1.5$ corresponds to a stable equilibrium position of the system in steady sliding and the small perturbation pushes the system away form the equilibrium position once it becomes unstable. Results in Figure 6 allows to clearly identify the bistable region.

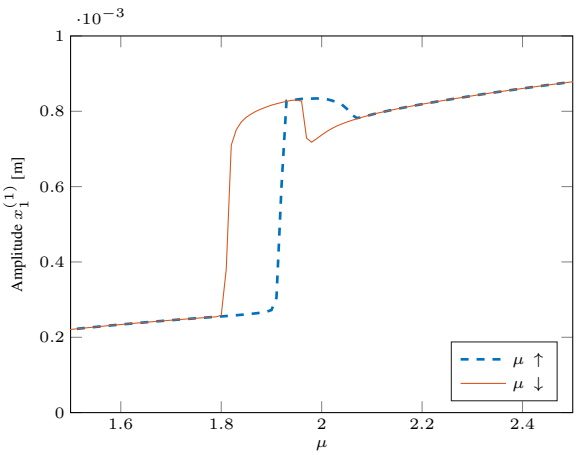


Figure 7: Amplitude of the limit cycle for increasing and decreasing values of the friction coefficient μ (with $\Delta\mu = 0.01$) for the Set 1 of parameters.

The same analysis approach can be applied to the system with the Set 1 of parameters. In this case the results in Figure 7 show the transition between two unstable branches at $\mu \simeq 2$. This transition occurs in different ways for increasing and decreasing values of the friction coefficient μ, highlighting the presence of a range of μ where the obtained solution is not unique but depends on boundary conditions.

Conclusions

In this paper a lumped parameter model with frictional contact has been exploited to investigate the bi-stable behavior of a mechanical system. The effects of the friction coefficient on the system stability have been investigated not only for the uniform sliding condition at the interface but also for different contact statuses. The results of transient simulations highlighted that the changes of contact status affect the system dynamics and in certain conditions they can induce instabilities. Subcritical instabilities have been related to the change

of contact status showing how a system that is stable in uniform sliding conditions can become unstable if an external perturbation modifies the contact status. Moreover, the same approach has been applied to a system with multiple instabilities showing the co-existence of multiple limit cycles depending on the initial conditions.

References

[1] D. Tonazzi, F. Massi, L. Baillet, J. Brunetti, Y. Berthier, *Interaction between contact behaviour and vibrational response for dry contact system*, Mechanical Systems and Signal Processing, Vol. 110, 2018, pp. 110-121.

[2] D. Tonazzi, F. Massi, L. Baillet, A. Culla, M. Di Bartolomeo, Y. Berthier, *Experimental and numerical analysis of frictional contact scenarios: from macro stick-slip to continuous sliding*, Meccanica, Vol. 50, No. 3, 2015, pp. 649-664.

[3] D. Tonazzi, F. Massi, L. Baillet, A. Culla, A. Fregolent, E. Regis, M. Lambert, *Experimental and numerical characterization of system response under dry frictional contact*, in *Proceedings of ISMA 2014 - International Conference on Noise and Vibration Engineering and USD 2014 - International Conference on Uncertainty in Structural Dynamics*, 2014.

[4] J. Brunetti, F. Massi, W. D'Ambrogio, L. Baillet, *Steady state of modal coupling instabilities as a dynamic energy equilibrium*, in *Proceedings of ISMA 2014 - International Conference on Noise and Vibration Engineering and USD 2014 - International Conference on Uncertainty in Structural Dynamics*, 2014.

[5] J. Brunetti, F. Massi, L. Baillet, W. D'Ambrogio, *Application of the modal absorption index (mai) to reduce the cea instability over-prediction on a complex frictional system*, in *Proceedings of ISMA 2016 - International Conference on Noise and Vibration Engineering and USD2016 - International Conference on Uncertainty in Structural Dynamics*, 2016.

[6] D. Tonazzi, F. Massi, A. Culla, A. Fregolent, Y. Berthier, *Role of damping on contact instability scenarios*, in *5th World Tribology Congress, WTC 2013*, volume 1, 2013.

[7] J. Brunetti, F. Massi, W. D'Ambrogio, Y. Berthier, *Dynamic and energy analysis of frictional contact instabilities on a lumped system*, Meccanica, Vol. 50, No. 3, 2015, pp. 633-647.

[8] A. Papangelo, M. Ciavarella, N. Hoffmann, *Subcritical bifurcation in a self-excited single-degree-of-freedom system with velocity weakening-strengthening friction law: analytical results and comparison with experiments*, Nonlinear Dynamics, Vol. 90, No. 3, 2017, pp. 2037-2046.

[9] J. Brunetti, F. Massi, W. D'Ambrogio, Y. Berthier, *A new instability index for unstable mode selection in squeal prediction by complex eigenvalue analysis*, Journal of Sound and Vibration, Vol. 377, 2016, pp. 106-122.

[10] F. Fontanela, A. Grolet, L. Salles, A. Chabchoub, N. Hoffmann, *Dark solitons, modulation instability and breathers in a chain of weakly nonlinear oscillators with cyclic symmetry*, Journal of Sound and Vibration, Vol. 413, 2018, pp. 467-481.

[11] A. Papangelo, N. Hoffmann, A. Grolet, M. Stender, M. Ciavarella, *Multiple spatially localized dynamical states in friction-excited oscillator chains*, Journal of Sound and Vibration, Vol. 417, 2018, pp. 56-64.

[12] N. J. Carpenter, R. L. Taylor, M. G. Katona, *Lagrange constraints for transient finite element surface contact*, International Journal for Numerical Methods in Engineering, Vol. 32, No. 1, 1991, pp. 103–128.

[13] L. Baillet, V. Linck, S. D'Errico, B. Laulagnet, Y. Berthier, *Finite element simulation of dynamic instabilities in frictional sliding contact*, Journal of Tribology, Vol. 127, No. 3, 2005, pp. 652–657.

[14] S. Andersson, A. Söderberg, S. Björklund, *Friction models for sliding dry, boundary and mixed lubricated contacts*, Tribology international, Vol. 40, No. 4, 2007, pp. 580–587.

[15] A. Papangelo, A. Grolet, L. Salles, N. Hoffmann, M. Ciavarella, *Snaking bifurcations in a self-excited oscillator chain with cyclic symmetry*, Communications in Nonlinear Science and Numerical Simulation, Vol. 44, 2017, pp. 108-119.

Investigating a mechanism which causes divergence of a resonant decay from the backbone curve

A. K. M. Brown [1], **T. L. Hill** [1], **S. A. Neild** [1], **I. Tartaruga** [2]
[1] Department of Mechanical Engineering, University of Bristol
University Walk, Bristol, BS8 1TR, UK
e-mail: **alice.brown@bristol.ac.uk**

[2] Department of Engineering Mathematics, University of Bristol
University Walk, Bristol, BS8 1TR, UK

Abstract
Backbone curves describe the unforced, undamped periodic responses of nonlinear structures. They represent valuable information about the fundamental behaviour of nonlinear systems and measuring them is a key challenge in experimental nonlinear dynamics. An approach that is commonly used to measure backbone curves is the resonant decay method, which relies on the free vibration response of a system following the backbone curve as it decays due to damping. However, here we show that some portions of the backbone curve cannot be followed using the resonant decay method and that under certain conditions the structural response may suddenly diverge from the backbone curve during a resonant decay. An energy-based method is then used to describe the mechanism that prevents the decaying system from following the backbone curves. It is shown that a phase shift between the modes is required to transfer energy internally to enable the resonant decay to follow the backbone curve.

1 Introduction

Nonlinear systems can often exhibit very complex behaviours which can make predicting and presenting their behaviour difficult [1]. A common way of understanding nonlinearities in structures is by using backbone curves [2]. Backbone curves describe the unforced, undamped periodic responses of nonlinear structures. They are also known as Nonlinear Normal Modes (NNM) [1] as they are analogous to the linear modes of a system and a lot of work has been done on predicting them numerically. Predicting the backbone curves experimentally, however, can be challenging as often the system will only follow certain parts of the backbone curve, due to stability changes and other effects, but one possible method is through resonant decay [3].

The resonant decay method can be used to measure the backbone curves of a system [4]. It relies on the assumption that when a system is released on or near the backbone curve, the response will follow the curve. However, to perform such a test requires some knowledge of where the backbone curve lies to ensure that the initial displacements are sufficiently close to the backbone curve for the response to find it. If the system isn't sufficiently close to the backbone curve, the response may not converge onto the backbone curve and could follow a different path. Another issue with this method is that response may 'jump' off its own backbone curve and oscillate around a different curve. This often happens when there is a change of stability, or when the response nears the linear system one or more of the modes may switch or 'jump' to their corresponding linear natural frequency. This can make it difficult to plot the backbone curve experimentally, especially at low amplitudes. The precise reason for this is where the focus of this paper will be. A potential mechanism for the modes 'jumping', which in this paper is referred to as the switching phenomenon, will be discussed.

An explanation could be due to the energy in the system and the internal energy transfer between the different modes [5, 6, 7].

This paper starts with a description of the structure being used to demonstrate the phenomenon. The backbone curves and resonant decay simulations are then produced using a nonlinear reduced order model. An energy based method is then presented to explain the effect seen in the simulation results. Finally, the paper ends with conclusions and ideas for future work.

2 The structure

A clear interaction between the first two modes was desired to show the switching phenomenon of the modes changing backbone curves. A structure was chosen such that the first two modes consisted primarily of bending and torsion and a picture of the structure can be found in Figure 1. The structure consists of a beam that is clamped at either end. In the centre a cross beam has been welded with two masses that can be moved along the cross beam in order to tune the linear natural frequencies. A smaller cross beam is used as the point of contact for the input force when measuring the natural frequencies and mode shapes. A picture of the rig can be found in Figure 1. The main beam is approximately 1m in length and 12mm thick. The cross beam is situated in the centre of the main beam, extends 216mm either side and has a diameter of 12mm. The tuneable masses along the cross beam have a mass of 218g each. This structure has also been considered in [8] and [9].

The system is designed such that the linear natural frequencies of the first bending and first torsional modes have a ratio of approximately 1:1, i.e. $\omega_{n1} \approx \omega_{n2}$, this is achieved by moving the masses to tune the frequencies. To ensure coupling between the modes the masses were positioned asymmetrically [8].

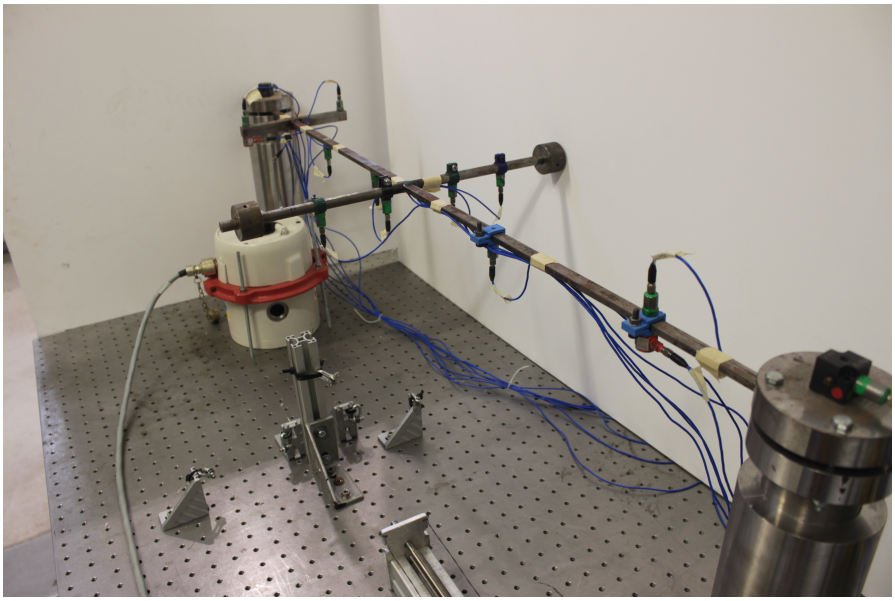


Figure 1: The crossbeam structure

3 Simulation results

3.1 Reduced order model

This system was first modelled in Abaqus, in a manner similar to [8] and [9]. From this, a nonlinear reduced order model (NLROM) was calculated from the finite element model using the Implicit Condensation and

Expansion technique (ICE) [10, 11]. This produces an N DoF system in modal coordinates in the form

$$\ddot{\mathbf{q}} + \Lambda\dot{\mathbf{q}} + \mathbf{N}_q(\mathbf{q}) = 0 \tag{1}$$

where $\mathbf{q}$ is the vector of modal coordinates, $\mathbf{\Lambda}$ is a diagonal matrix of the linear natural frequencies of each mode, and $\mathbf{N}_q(\mathbf{q})$ are the nonlinear terms in the equation. This paper is only interested in the interactions between the first two modes so a 2 DoF system was created using the ICE method and the full equations of this model are

$$\begin{aligned} \ddot{q_1} + 2\zeta\omega_{n1}\dot{q_1} + \omega_{n1}^2 q_1 + \gamma_1 q_1^3 + 3\gamma_2 q_1^2 q_2 + \gamma_3 q_1 q_2^2 + \gamma_4 q_2^3 = 0 \\ \ddot{q_1} + 2\zeta\omega_{n2}\dot{q_2} + \omega_{n2}^2 q_2 + \gamma_2 q_1^3 + \gamma_3 q_1^2 q_2 + 3\gamma_4 q_1 q_2^2 + \gamma_5 q_2^3 = 0 \end{aligned} \tag{2}$$

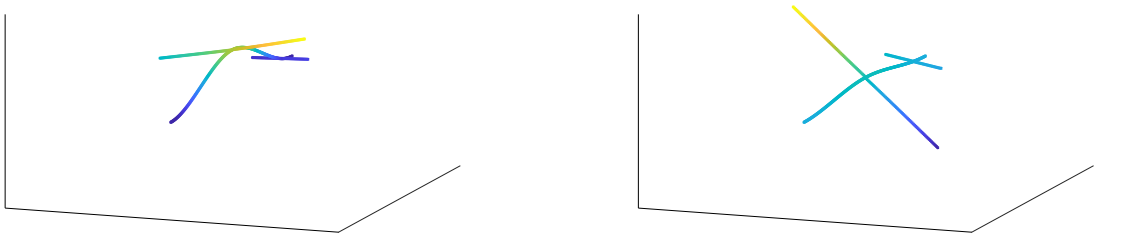
where ζ is the damping coefficient and γ_i the nonlinear coefficients. The reduced order model doesn't provide the damping term $2\zeta\omega_{ni}\dot{q}_i$, this has been added in order to perform the resonant decay simulation in Section 3.3.

The system was modified until the desired ratio between the second and the first natural frequencies was reached, i.e. $\omega_{n2}/\omega_{n1} = 1.12$, with the first torsional mode having a higher natural frequency than the first bending mode to ensure an interaction between the two. The nonlinear coefficients and the natural frequencies for Equation 2 can be found in Table 1. It should be noted that the NLROM did provide quadratic and cubic terms, but as the quadratic coefficients are very small (of the order 10^{-15}), they were neglected.

Coefficients	ω_{n1} (rad/s)	ω_{n2} (rad/s)	γ_1	γ_2	γ_3	γ_4	γ_5
	77.22	86.79	4.15×10^6	1.18×10^6	1.13×10^6	9.84×10^4	2.32×10^5

Table 1: Coefficients for Equation 2

The finite element analysis also provided the linear mode shapes of the system. These can be found in Figure 2. As the structure is asymmetric (due to the position of the masses) the mode shapes aren't purely bending and torsion. However it can be seen that the first mode is dominated by bending and the second mode dominated by torsion.



(a) Bending-dominated mode shape

(b) Torsion-dominated mode shape

Figure 2: First two mode shapes

3.2 Backbone curves

The backbone curves for the first two modes were calculated using the harmonic balance method [2]. It's assumed that the response, q, is in the form of Equation 3.

$$q_i \approx u_i = U_i \cos\left(\omega_r t - \phi_i\right) \tag{3}$$

where u_i represents the single-harmonic approximation of q_i. U_i is the amplitude, ϕ_i the phase of u_i and ω_r is the response frequency.

The next step in the harmonic balance method is to substitute Equation 3 into the original equations of motion (Equation 2). After some algebraic manipulation and removing the non-resonant terms (any term that doesn't resonate at $1\omega_r$) the following equations are calculated.

$$\begin{aligned}(\omega_{n1}^2-\omega_r^2)U_1\cos(\omega_r t-\phi_1)+\frac{3}{4}\gamma_1 U_1^3\cos(\phi_1-\omega_r t)+\frac{3}{4}\gamma_2 U_1^2U_2\cos(2\phi_1-\phi_2-\omega_r t)\\ +\frac{3}{2}\gamma_2 U_1^2U_2\cos(\phi_2-\omega_r t)+\frac{1}{4}\gamma_3 U_1U_2^2\cos(\phi_1-2\phi_2+\omega_r t)\\ +\frac{1}{2}\gamma_3 U_1U_2^2\cos(\phi_1-\omega_r t)+\frac{3}{4}\gamma_4 U_2^3\cos(\phi_2-\omega_r t)=0\end{aligned} \tag{4}$$

$$\begin{aligned}(\omega_{n2}^2-\omega_r^2)U_2\cos(\omega_r t-\phi_2)+\frac{3}{4}\gamma_2 U_1^3\cos(\phi_1-\omega_r t)+\frac{1}{4}\gamma_3 U_1^2U_2\cos(2\phi_1-\phi_2-\omega_r t)\\ +\frac{1}{2}\gamma_3 U_1^2U_2\cos(\phi_2-\omega_r t)+\frac{3}{4}\gamma_4 U_1U_2^2\cos(\phi_1-2\phi_2+\omega_r t)\\ +\frac{3}{2}\gamma_4 U_1U_2^2\cos(\phi_1-\omega_r t)+\frac{3}{4}\gamma_5 U_2^3\cos(\phi_2-\omega_r t)=0\end{aligned} \tag{5}$$

where ω_{ni} is the i^{th} linear natural frequency. To calculate the backbone curves of the system it is easiest to carry on in the exponential form. Later in this paper however, the trigonometric is needed to compute the phase difference and so is the form presented here. From the exponential form of Equations 4 and 5 and by following the method found in [8] and [2] the following relationships for the response frequency are calculated.

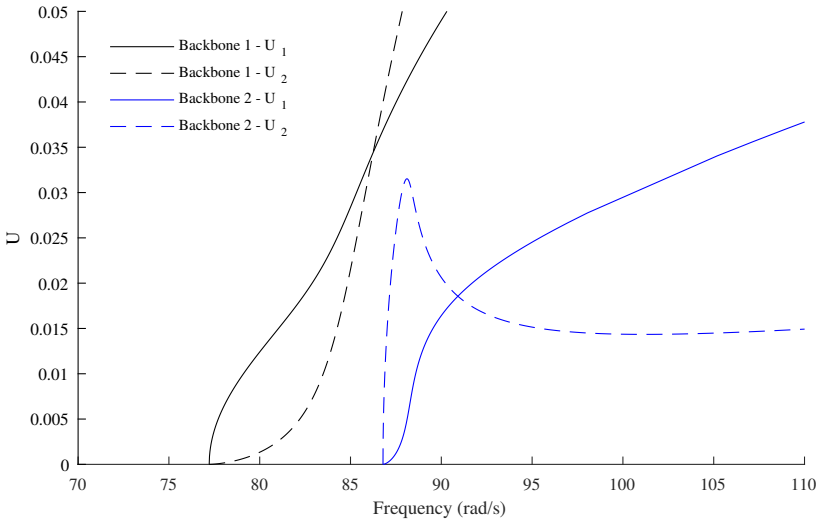


Figure 3: Backbone curves; U_1 corresponds to the bending-dominated mode shape and U_2 the torsion-dominated mode shape

$$\begin{aligned}\omega_r^2&=\omega_{n1}^2+\frac{1}{4}[3\gamma_1U_1^2+9p\gamma_2U_1U_2+3\gamma_3U_2^2+3p\gamma_4U_1^{-1}U_2^3]\\ \omega_r^2&=\omega_{n2}^2+\frac{1}{4}[3p\gamma_2U_1^3U_2^{-1}+3\gamma_3U_1^2+9p\gamma_4U_1U_2+3\gamma_5U_2^2]\end{aligned} \tag{6}$$

The response can either be in phase or anti-phase which is defined by p as

$$p=\cos(\phi_1-\phi_2)=\begin{cases}+1, & \text{when } (\phi_1-\phi_2)=0\\ -1, & \text{when } (\phi_1-\phi_2)=\pi\end{cases} \tag{7}$$

Equation 6 is used to plot the backbone curves of this system. These are shown in Figure 3.

3.3 Resonant decay

To measure backbone curves experimentally, the resonant decay method [3, 8, 12] is often used. This method involves displacing the system on or near the backbone curve and releasing the system allowing the response to decay down the backbone curve to the linear natural frequency. A numerical ode solver in MATLAB was used to simulate the decay, and the initial displacements were chosen directly from the backbone curve in Figure 3 to ensure the decay started on the curve. The equations of motion in Equation 2 were used with a damping coefficient $\zeta = 0.005$.

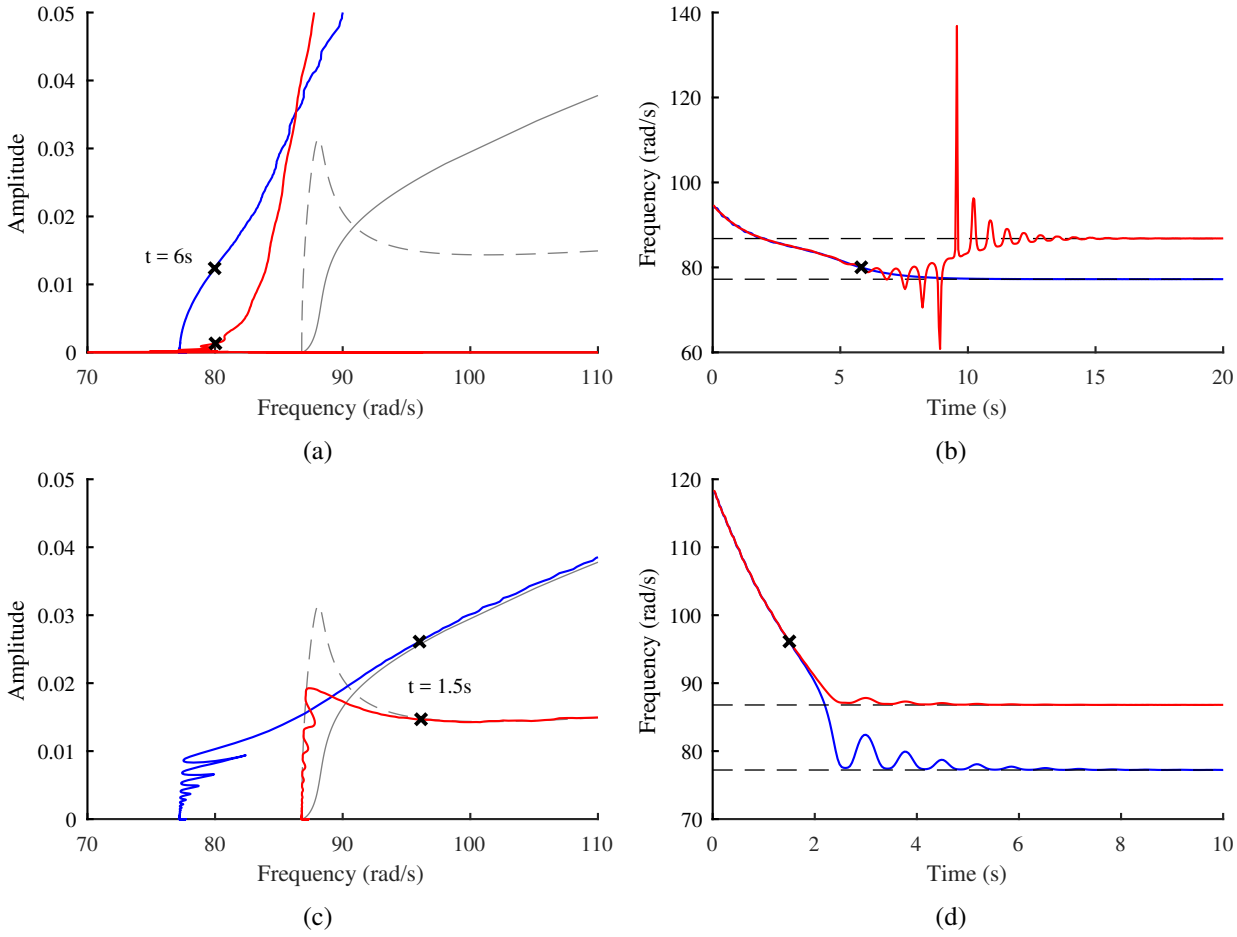


Figure 4: Resonant decay simulation; (a) and (b) starting on the first backbone curve, (c) and (d) starting on the second backbone curve. The point x corresponds to a time of 6 and 1.5 seconds for the first and second backbone curve respectively, when the frequencies start to diverge off the backbone curve.

The resonant decay for the first backbone curve is shown in Figure 4a and the corresponding plot of the frequency vs time in 4b. It can be seen that the decay follows the backbone curve mostly all the way and it's only at the very low amplitudes where the second mode splits off to the 2nd natural frequency (around 6 seconds in Figure 4b represented with an 'x'). However, by this point the majority of the backbone curve can be estimated and hence the resonant decay method is effective.

Performing a resonant decay starting on the second backbone curve (Figure 4c) doesn't have the same result. After about 1.5 seconds of the decay (again represented with an 'x' in Figure 4c) the first mode starts to diverge off the second backbone curve and onto the first instead of continuing down the backbone curve. Both modes then oscillate around and converge onto the two natural frequencies. This can also be seen in the

plot of frequency versus time (Figure 4d). This switching of the backbone curves occurs at a much higher amplitude than the first simulation and it doesn't leave enough information to estimate the 2nd backbone curve at the lower amplitudes.

The reasons for this divergence and the mechanisms that enable the system to follow the backbone curve will be examined next in Section 4.

4 Energy transfer

To understand the mechanisms that are causing the resonant decay to split and oscillate as seen in Figures 4c and 4d, the energy transfer between the two modes of the system will be investigated.

4.1 Energy on the backbone curve

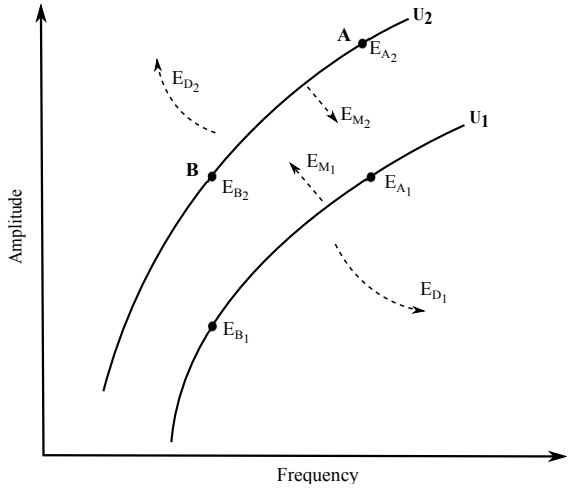


Figure 5: Schematic showing how energy moves between the modes

If a point A is chosen on a backbone curve (see Figure 5), and this point is used as the initial condition for a resonant decay, it can be assumed that the response will travel down the backbone curve and after one oscillation will arrive at another point, B. The energy in the system at both points are called E_A and E_B respectively. If the system is lightly damped then the energy in the system at point B must be less than the energy in the system at point A, and the energy lost between them must be $E_A - E_B$. The energy lost from the system then must be due to the damping from each mode and therefore

$$E_A - E_B = E_{D1} + E_{D2} \tag{8}$$

where E_{Di} is the energy lost from modal damping from the i^{th} mode.

The energy lost from modal damping from the i^{th} mode is not necessarily equal to the total energy lost from the i^{th} mode when transitioning from A to B. It is also possible for energy to be transferred between modes as, in nonlinear systems, the modes may be coupled together. So another term must be added to denote the energy lost from each mode due to modal coupling (E_{Mi}). It should be noted that E_{Mi} is not the energy lost from the system, but is the energy transferred internally from the i^{th} mode such that $\sum_i E_{Mi} = 0$, and Equation 8 still holds true.

The energy lost from the i^{th} mode can now be written as:

$$E_{Ai} - E_{Bi} = E_{Di} + E_{Mi} \tag{9}$$

A phase shift is required to transfer energy between modes [6], and so the next step is to calculate the phase difference between modes as the response travels down the backbone curve.

4.2 Internal energy transfer

Rearranging Equation 9 the internal energy transfer from mode i is

$$E_{Mi} = E_{Ai} - E_{Bi} - E_{Di} \tag{10}$$

The following sections will go through each term in this equation and how it is calculated.

$\mathbf{E_{Ai}}$: The backbone curves for this system have been calculated assuming that the modes are either in phase or in anti-phase (0° or 180° phase shift from each other). Therefore, at point A both modes must past through 0 at the same time and the energy will be purely kinetic. Assuming that the harmonics are negligible, this leads to

$$E_{Ai} = \frac{1}{2} U_{iA}^2 \omega_{rA}^2 \tag{11}$$

where ω_r is the response frequency.

$\mathbf{E_{Di}}$: Assuming a steady state solution, the external energy transfer from the i^{th} mode over one period may be written as

$$E_{Ei,k} = \int_0^T f_{Eik}(t)\dot{q}_i(t)dt \tag{12}$$

where $\dot{q}(t)$ is the velocity of the i^{th} mode, T is the period of the response, and f_{Eik} is the external transfer term in the modal equations of motion of the i^{th} mode. In the case of damping this term would be equal to $2\zeta w_{ni}\dot{u}_i$. Using also $T = 2\pi/\omega_r$, the energy lost due to damping from the i^{th} mode is

$$E_{Di} = 2\zeta\omega_{ni}\int_0^T \dot{u}_i^2 dt = 2\pi\zeta\omega_{ni}\omega_r U_i^2 \tag{13}$$

However, a resonant decay is transient and not steady state, so the average value between points A and B of E_{Di} will be taken into account. This leads to the energy lost due to damping as

$$E_{Di} = \pi\zeta\omega_{ni}(\omega_{rA}U_{iA}^2 + \omega_{rB}U_{iB}^2) \tag{14}$$

$\mathbf{E_{Bi}}$: E_B may be calculated by combining Equations 8, 11, 14 and by recognising that the total energy at A is the sum of the energy at the two modes, i.e. $E_A = E_{A1} + E_{A2}$.

$$E_B = \frac{\bar{\omega}_A^2}{2}(U_{1A}^2 + U_{2A}^2) - \pi\zeta\left[\omega_{n1}(\omega_{rA}U_{1A}^2 + \omega_{rB}U_{1B}^2) + \omega_{n2}(\omega_{rA}U_{2A}^2 + \omega_{rB}U_{2B}^2)\right] \tag{15}$$

From this and by using Equation 11, the energy at point B can be found as a function of its position on the backbone curve. The position of B can then be found numerically and now all the terms have been calculated in order to calculate E_{Mi} from Equation 10.

4.3 Phase-shift prediction

It is now considered how E_M can be related to the phase difference $\phi_1 - \phi_2$. This relationship can then be used along with Equation 10 to calculate the phase shift required for the internal energy transfer.

In a manner similar to Equation 12, assuming a steady state solution, the internal energy transfer for the k^{th} nonlinear term from the i^{th} mode over one period may be written as

$$E_{Mi,k} = \int_0^T f_{Mi,k}(t)\dot{q}_i(t)dt \tag{16}$$

where $f_{Mi,k}$ is the internal transfer term in the modal equations of motion of the i^{th} mode. It can be assumed that the terms in Equation 16 can be written as [5]

$$f_{Mi,k}(t) = \sum_{s=0}^{\infty} F_{Mi,k,s} \cos\left(s\bar{\omega}t - \theta_{i,k,s}\right) \tag{17}$$

$$q_i(t) = \sum_{j=0}^{\infty} Q_{i,j} \cos\left(j\bar{\omega}t - \phi_{i,j}\right) \tag{18}$$

where $F_{Mi,k,s}$ is the amplitude, $\theta_{i,k,s}$ the phase, and $s\bar{\omega}$ the frequency of $f_{Mi,k}$. $Q_{i,j}$ is the amplitude, $\phi_{i,j}$ the phase, and $j\bar{\omega}$ the frequency of q_i.

Integrating Equation 16 after substituting in Equations 17 and 18 results in

$$E_{Mi,k} = \pi\Big[\sum_{s=0}^{\infty} sF_{Mi,k,s}Q_{i,s} \sin\left(\phi_{i,s} - \theta_{i,k,s}\right)\Big] \tag{19}$$

Assuming a steady state response and a conservative system the energy can only be transferred internally, so the total net internal energy transfer must be zero and therefore

$$E_{Mi} = \sum_{k=1}^{K_{Mi}} E_{Mi,k} = \pi \sum_{k=1}^{K_{Mi}} \Big[\sum_{s=0}^{\infty} sF_{Mi,k,s}Q_{i,s} \sin\left(\phi_{i,s} - \theta_{i,k,s}\right)\Big] = 0 \tag{20}$$

where K_{Mi} is the number of nonlinear terms in the equation of motion.

From this, the total energy transfer over one period for mode i can be written as

$$E_{Mi,k} = \int_0^T \Big[\sum_{k=1}^{K_{Mi}} f_{Mi,k}\Big]\dot{q}_i(t)dt \tag{21}$$

When calculating the harmonic balance, Equations 4 and 5 were calculated which were in terms of $\phi_1 - \phi_2$. Only the internal transfer terms are needed which for the first mode is

$$\begin{aligned}\sum_{k=1}^{K_{M1}} f_{M1,k} = &\Big[\frac{3}{4}\gamma_1 U_1^3 + \frac{1}{2}\gamma_3 U_1 U_2^2\Big]\cos(\omega_r t - \phi_1) + \Big[\frac{3}{2}\gamma_2 U_1^2 U_2 + \frac{3}{4}\gamma_4 U_2^3\Big]\cos(\omega_r t - \phi_2) \\ &+\frac{3}{4}\gamma_2 U_1^2 U_2 \cos(\omega_r t - 2\phi_1 + \phi_2) + \frac{1}{4}\gamma_3 U_1 U_2^2 \cos(\omega_r t + \phi_1 - 2\phi_2)\end{aligned} \tag{22}$$

Substituting these terms and the equivalent for the second mode into Equation 21 results in

$$E_{M1} = \frac{1}{4}\pi U_1 U_2 \sin(\phi_1 - \phi_2)\left[3\gamma_2 U_1^2 + 2\gamma_3 U_1 U_2 \cos(\phi_1 - \phi_2) + 3\gamma_4 U_2^2\right]$$
$$E_{M2} = -\frac{1}{4}\pi U_1 U_2 \sin(\phi_1 - \phi_2)\left[3\gamma_2 U_1^2 + 2\gamma_3 U_1 U_2 \cos(\phi_1 - \phi_2) + 3\gamma_4 U_2^2\right] \quad (23)$$

Which can then be equated to Equation 10. The resulting expression can be used to calculate the phase difference required for the internal energy transfer to stay on the backbone curve.

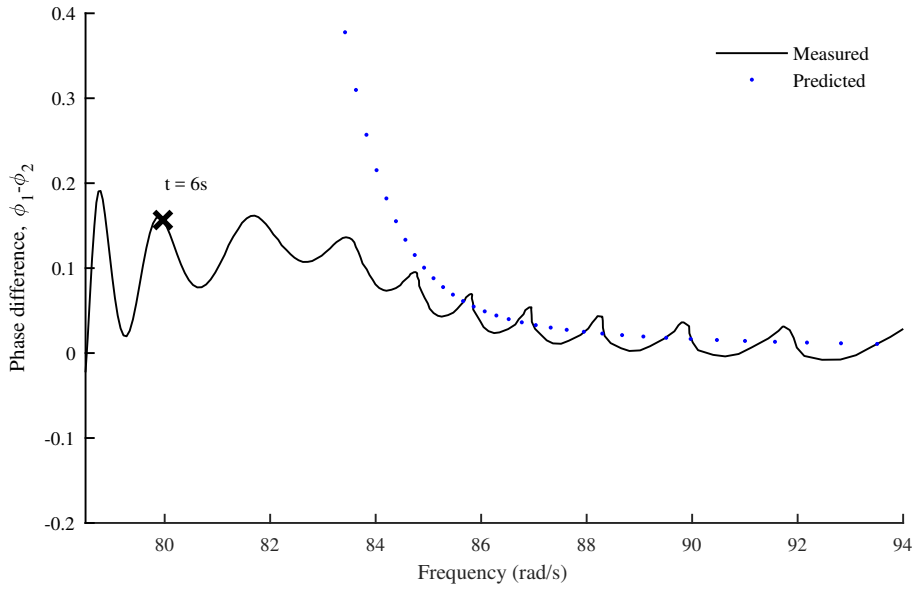


Figure 6: Phase difference between the two modes with respect to the fundamental response frequency for the first backbone curve.

Figure 6 is a plot of the phase difference with respect to the response frequency when starting on the first backbone curve (Figures 4a and 4b). It shows the measured phase difference from the simulation results and the predicted phase difference. The 'x' once again corresponds to a time of 6 seconds when the decay starts to diverge from the backbone curve. Figure 6 has been zoomed in to show the predicted phase difference before the decay diverges. After this point the two responses are responding at two different frequencies so the predicted phase difference is inaccurate. It can be seen that the the predicted phase difference remains close to zero and agrees with the measured phase difference up until 85 rad/s. After that point the phase difference starts to increase suggesting that the amount of energy needed to remain on the backbone curve is too much to be transferred internally, hence the response transitions to a combination of two responses at the two modal frequencies.

5 Conclusions

This paper described the process of resonant decay and a potential mechanism required to enable the decay to follow the backbone curve. The difference in phase between the two modes is what provides the ability to transfer energy between the modes in order to keep the decay on the backbone curve. When the phase difference increases, the energy transfer becomes too much to sustain and the decay may diverge off the backbone curve. Simulated results from the reduced order model were produced to demonstrate this. These

results show that due to the difference in phase it may not be possible to find all of the backbone curve just by using resonant decay.

Going forward experimental results using the rig in Figure 1 will be produced to show the switching phenomenon in an experiment. The energy transfer between the modes will also be calculated for both the simulation and experiment in order to be compared.

Acknowledgements

A.K.M.B gratefully acknowledges the support of EPSRC with an EPSRC studentship grant.

References

[1] G. Kerschen, M. Peeters, J.C. Golinval, A.F. Vakakis, *Nonlinear normal modes, Part I: a useful framework for the structural dynamicist*, Mechanical Systems and Signal Processing, Vol. 23, 2009.

[2] D. Wagg, S. A. Neild, *Nonlinear Vibration with Control*, 2nd ed. Springer International Publishing, Switzerland, 2015.

[3] J. M. Londono, S. A. Neild, J. E. Cooper, *Identification of backbone curves of nonlinear systems from resonance decay responses* Journal of Sound and Vibration, Vol. 348, 2015.

[4] S. Naylor, M.F. Platten, J.R. Wright, J.E. Cooper, *Identification of multi-degree of freedom systems with nonproportional damping using the resonant decay method*, Journal of Vibration and Acoustics, Vol. 126 (2), 2004.

[5] T. L. Hill, *Modal Interactions in Nonlinear Systems*, PhD Thesis, University of Bristol, 2016.

[6] T. L. Hill, A. Cammarano, S. A. Neild, D. J. Wagg, *Interpreting the forced responses of a two-degree-of-freedom nonlinear oscillator using backbone curves* Journal of Sound and Vibration, Vol. 349, 2015.

[7] D. E. Newland, *Energy sharing in the random vibration of non-linearly coupled modes*, Journal of the Institute of Mathematics and its Applications, Vol. 1, 1965.

[8] D. A. Ehrhardt, T. L. Hill, S. A. Neild, J. E. Cooper, *Veering and Nonlinear Interactions of a Clamped Beam in Bending and Torsion*, Journal of Sound and Vibration, Vol. 416, 2018.

[9] L. Renson, D. A. Ehrhardt, D. A. W. Barton, S. A. Neild, J. E. Cooper, *Connecting nonlinear normal modes to the forced response of a geometric nonlinear structure with closely spaced modes*, *in Proceedings of ISMA2016 including USD2016*, 2016.

[10] R. W. Gordon, J. J. Hollkamp, *Reduced Order Models for Acoustic Response Prediction*, Air Force Research Laboratory, 2011.

[11] J. J. Hollkamp, R. W. Gordon, *Reduced-order models for nonlinear reponse prediction: Implicit condensation and expansion*, Journal of Sound and Vibration, Vol. 318, 2008.

[12] D. J. Ewins, *Modal Testing: theory, practice and application*, 2nd edition, Research Studies Press Ltd., Hertfordshire, 2000.

Manuscript preparation instructions

A.J. Elliott[1], **I. Tartaruga**[2], **A. Cammarano**[1], **P.S. Dobson**[1], **S.A. Neild**[2]
[1] School of Engineering, University of Glasgow, Glasgow, G12 8QQ, UK
Email: **A.Elliott.1@research.gla.ac.uk**

[2] Department of Mechanical Engineering, University of Bristol, Queen's Building, University Walk, Bristol, BS8 1TR,UK

Abstract
The process of developing micro- and nanoscale structures is costly and time-consuming, so it is important that their dynamic behaviour is fully understood to prevent unexpected system failures. Given the greater influence of atomic forces at this scale, as well as inherently slender components and low damping, such systems can very easily exhibit nonlinear behaviour, including modal interactions. In this paper, a cantilever microbeam with a charged tip placed between two point charges is modelled analytically. Further, the implicit condensation method is applied to create reduced-order models, the accuracy of which is assessed through comparison with the free and forced responses of the full system.

1 Introduction

Recent developments in structural engineering, driven by an increasing demand for more efficient mechanical systems, have resulted in a marked increase into the production and refinement of lightweight, flexible structures. With this comes a need to address nonlinearities that arise in the resultant dynamics, as a failure to capture this behaviour has the potential to do irreversible damage to the system in question.

The slender nature of nanoscale structures, combined with the increased influence of atomic forces and inherently low damping, results in a system which is likely to encounter this nonlinear behaviour, often to a greater extent than similar systems at the macroscale. A notable example of such a phenomenon was presented in [1]. In this study, five parametric resonances of a microelectromechanical system (MEMS), governed by the Mathieu equation, are experimentally observed, whereas only the first can typically be achieved in macroscale systems with governing equations of the same form. Given that it is possible for MEMS and nanoelectromechanical systems (NEMS) to exhibit nonlinear behaviour which is not seen in their macroscale counterparts, it is important that dynamical models are able to capture such phenomena, particularly due to the expense and difficulty associated with their manufacture. As such, there have been a number of studies into the nonlinear dynamics of MEMS and NEMS, a more extensive summary of which is given in [2].

Of particular relevance to this paper are those studies which apply an analytical approach to investigate these nonlinear MEMS and NEMS. Nayfeh and collaborators [3–8] model a number of Euler-Bernoulli microbeams and microplates with a range of supports and electromagnetic configurations. In particular, the Galerkin method is applied to an electrically loaded clamped-clamped microbeam [5, 8] and microplate [6] to investigate nonlinear phenomena such as amplitude-dependent natural frequencies and internal resonance. The authors of [5] further investigate the extent to which the size of a Galerkin reduced-order model (ROM) influences its accuracy in terms of the modeshapes and natural, though they did not extend this investigation to include the effect had on the ability of the model to capture

internal resonances. A Galerkin model has been employed in [9] to investigate such resonances in an array of nonlinearly coupled microbeams; however, due to the symmetry of the system considered, a single-mode model was sufficient.

In recent years, the development of ROMs has been a key interest when exploring macroscale structures; these developments have been summarised in [10]. This work will apply the implicit condensation (IC) method to a Galerkin model to investigate its applicability for a microstructure. This technique has been widely applied in the literature and further reading on the subject can be found in [11–13].

In this paper, the internal resonances of a cantilever microbeam with a nonlinear electrostatic boundary condition (BC) at the free end are considered through use of a nonlinear spring support BC approximation; this is defined in Section 2. In Section 3, the backbone curves of the system are presented for the system. First, the magnitude of the electrostatic interaction is varied, with consideration given to the point at which such behaviour arises. Then, for a selection of illustrative cases, the aforementioned ROM techniques will be applied to investigate their ability to capture this behaviour. Conclusions are drawn in Section 4.

2 System definition and reduced-order modelling

2.1 Galerkin model

MEMS and NEMS can exhibit nonlinear behaviour and two of the key reasons for this are the naturally slim nature of such systems, and the increased influence of electrostatic forces due to their scale. This paper investigates a system which exhibits both of these characteristics, which takes the form of a cantilever microbeam with a charged tip placed between two point charges. This configuration is presented in Fig. 1 and provides a more general example of the electrostatic behaviour exhibited in an atomic force microscope.

In this system, the microbeam has length L, Young's modulus E, cross-sectional area $\hat{A}$, and density ρ. The tip of the beam has charge Q_{tip} and is placed equidistantly between two point charges of magnitude Q_1 and Q_2. All three of these charges have the same sign, so that, as the tip of the beam approaches one of the point charges, it is repelled towards its equilibrium position. In the following discussion, these point charges will be taken to be equal - i.e. $Q_1 = Q_2 = Q$.

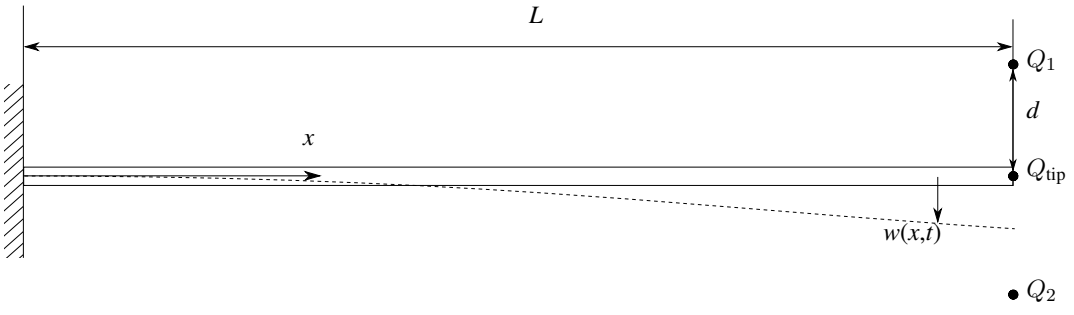


Figure 1: Schematic for a cantilever microbeam with a charged tip placed between two point charges.

This electrostatic interaction is modelled by Coulomb's law, so the force exerted on the tip of the beam is given by

$$F_{\text{tip}}(L) = k_0 Q_{\text{tip}} Q \left(\frac{1}{(d - w(L))^2} - \frac{1}{(d + w(L))^2} \right), \tag{1}$$

where $k_0 \approx 8.988 \times 10^9$ N m^2 C$^{-}2$ denotes Coulomb's constant and w represents a vertical perturbation of the beam tip. Note that the symmetry of the point charges has been implemented in Eq. (1). This model assumes that the interaction only occurs at the right hand end of the beam and, therefore, it can be treated as a boundary condition. Further, if a Taylor expansion of F_{tip} is taken about the point $w = 0$, this force can be approximated as

$$F_{\text{tip}}(w) = 4k_0 Q_{\text{tip}} Q \left(\frac{w}{d^3} + \frac{2w^3}{d^5} \right) = k_L w + k_{NL} w^3. \tag{2}$$

Here, it has been noted that this approximation is analogous to a cantilever beam supported by a nonlinear spring at the free end. The boundary conditions for such a system can be written as.

The unforced, undamped equations of motion for an Euler-Bernoulli beam are written as

$$EI \frac{\partial^4 w}{\partial x^4} - \frac{E\hat{A}}{2L} \int_0^L \left(\frac{\partial w}{\partial x} \right)^2 \mathrm{d}x \left(\frac{\partial^2 w}{\partial x^2} \right) + \rho \hat{A} \frac{\partial^2 w}{\partial t^2} = 0, \tag{3}$$

where I is the second moment of area.

At this point, a Galerkin decomposition can be applied, taking the form

$$w(x,t) = \sum_{j=1}^{\infty} \phi_j(x) q_j(t). \tag{4}$$

Here, ϕ_j and q_j denote the j^{th} mode shape and modal displacement, respectively. The former is defined by

$$\phi(y) = \cosh \kappa y - \cos \kappa y - \lambda(\sinh \kappa y - \sin \kappa y), \tag{5}$$

Applying the decomposition in Eq. (4) to Eq. (3), the modal equations of motion are written

$$EI \sum_{j=1}^{\infty} \frac{d^4 \phi_j}{dx^4} q_j - \frac{E\hat{A}}{2L} \sum_{k=1}^{\infty} \int_0^L \left(\frac{d\phi_k}{dx} \right)^2 \mathrm{d}x \left(\frac{d^2 \phi_j}{dx^2} \right) q_j q_k^2 + \rho \hat{A} \sum_{j=1}^{\infty} \ddot{q}_j \phi_j = 0. \tag{6}$$

For the configuration shown above, the boundary conditions are given by

$$\phi(0) = \phi'(0) = \phi''(L) = 0,\ \phi'''(L) = \hat{K}_L \phi(L) + \hat{K}_{NL} \phi(L)^3, \quad \text{where } \hat{K}_L = \frac{k_L L^3}{EI} \text{ and } \hat{K}_{NL} = \frac{k_{NL} L^5}{EI}. \tag{7}$$

Here, the final boundary condition arises as a result of the tip force given in Eq. (2). It is possible to decouple the equations in Eq. (6) by multiplying by an arbitrary modeshape and then integrating across the length of the beam. As such, the j^{th} equation of motion can be written as

$$EI \sum_{j=1}^{\infty} \int_0^L \frac{d^4 \phi_j}{dx^4} \phi_n \mathrm{d}x q_j - \frac{E\hat{A}}{2L} \sum_{j=1}^{\infty} \int_0^L \left[\sum_{k=1}^{\infty} \left(\int_0^L \left(\frac{d\phi_k}{dx} \right)^2 \mathrm{d}x q_k^2 \right) \times \left(\frac{d^2 \phi_j}{dx^2} \right) q_j \phi_n \right] \mathrm{d}x + \rho \hat{A} \int_0^L \sum_{j=1}^{\infty} \phi_j \phi_n \mathrm{d}x \ddot{q}_j = 0. \tag{8}$$

The integral terms in Eq. (8) define the orthogonality conditions between the linear modal basis, as well as the coefficients of the nonlinear terms. These are calculated as follows

$$\begin{aligned}
\int_0^L \phi_n \phi_j \mathrm{d}x &= \begin{cases} \alpha_{1,j}, & \text{if } n = j, \\ 0, & \text{otherwise,} \end{cases} \\
\int_0^L \phi_n \frac{d^2\phi_j}{dx^2} \mathrm{d}x &= \begin{cases} \alpha_{2,j}, & \text{if } n = k, \\ 0, & \text{otherwise,} \end{cases} \\
\int_0^L \phi_n \frac{d^4\phi_j}{dx^4} \mathrm{d}x &= \begin{cases} \alpha_{4,j}, & \text{if } n = k, \\ 0, & \text{otherwise,} \end{cases}
\end{aligned} \tag{9}$$

where

$$\begin{aligned}
\alpha_{1,j} =& 1 + \frac{1}{4\kappa}\Big(2\lambda(4\cos(\kappa)\cosh(\kappa) - \cos(2\kappa) - \cosh(2\kappa) - 2) + (\lambda^2 - 1)(4\cosh(\kappa)\sin(\kappa) - \sin(2\kappa)) \\
&+ (\lambda^2 + 1)(\sinh(2\kappa) - 4\cos(\kappa)\sinh(\kappa))\Big), \\
\alpha_{4,j} =& \frac{\kappa^4}{L^4}\alpha_{1,j}. \\
\alpha_{2,j} =& \frac{\kappa}{4L}\Big(4\lambda(\sin^2(\kappa) - \sinh^2(\kappa)) + (\lambda^2 - 1)\sin(2\kappa) + (\lambda^2 + 1)\sinh(2\kappa)\Big).
\end{aligned} \tag{10}$$

Note that the parameters κ and λ are calculated numerically. It is useful to introduce the additional notation

$$\beta_{i,k} = \int_0^L \left(\frac{d\phi_i}{dx}\right)\left(\frac{d\phi_k}{dx}\right)\mathrm{d}x. \tag{11}$$

Implementing the aforementioned conditions and notation, Eq. (8) can be written as

$$\ddot{q}_n + \frac{EI\kappa^4}{\rho\hat{A}L^4}q_n + \frac{E}{2\rho\alpha_{1,n}L}\sum_{i=1}^{\infty}\sum_{j=1}^{\infty}\sum_{k=1}^{\infty}\alpha_{2,i}\beta_{j,k}q_i q_j q_k = 0. \tag{12}$$

Note that, although the spring constants, k_L and k_{NL} are not seen explicitly in Eq. (12), they are captured by the nonlinear terms, due to their role in the definition of the modeshapes.

Up to this point, the micro-/nanoscale nature of the structure has had little influence on the development of the model. In fact, the only implicit reference to this is the assumption that w^3 is not negligible in the spring support approximation. As such, these spring constants are not explicitly written in Eq. (12). However, their influence is captured by the nonlinear coefficients $\alpha_{2,i}$ and $\beta_{j,k}$, which are defined by the boundary conditions. The impacts these have on the behaviour of the system are investigated in the following section.

2.2 Implicit condensation method

The system of equations written in Eq. (12) now define a nonlinear systems of equation that can be considered as a "full" model to be reduced by the IC method. This method is briefly outlined here.

Table 1:

Case	Q (C)	d (nm)	$\hat{K}_L$	$\hat{K}_{NL}$
1	1e-19	100	0	1e+3
2	4e-19	10	1	1e+9

Initially, it is assumed that the nonlinear part of the ROM can be written as a cubic polynomial, with the n^{th} component denoted

$$\theta_n(q_1, ..., q_M) = \sum_{i=1}^{M}\sum_{j=i}^{M} A_{ij}^{(n)} q_i q_j + \sum_{i=1}^{M}\sum_{j=i}^{M}\sum_{k=j}^{M} B_{ijk}^{(n)} q_i q_j q_k, \tag{13}$$

where M denotes the number of modes retained in the ROM. The procedure then applies a number of static load cases, which take the form

$$\mathbf{\Lambda q} + \mathbf{\Theta}_q(\mathbf{q}) = \mathbf{F}, \tag{14}$$

where $\mathbf{F}$ represents a statically applied force. In Eq. (14), the nonlinear coefficients are the only unknowns. Therefore, by implementing enough static cases, it is possible to perform a least-squares regression analysis to approximate $A_{ij}^{(n)}$ and $B_{ijk}^{(n)}$. Further details on the implementation of this method are given in [11, 12].

3 Results

3.1 Backbone curves

Although the the small nature of the system has been implicit thus far, naturally, this becomes explicit with the introduction of the dimensions of the beam, which will be 200μm long, 10μm wide, and 0.4μm thick. The beam will have a Young's modulus of 310 GPa and a density of 3170 kg/m^3. The two charges will be equal to one another. Two cases will be considered, in which the charge, distance d, and, hence, the approximating spring constants will be varied. The two cases are given in Table 1.

As alluded to in the previous section, the unforced, undamped response of the system will be considered initially. To investigate this, the backbone curves of both the full model, as well as a number of ROMs developed using the IC method, are presented. Fig. 2 displays the first backbone curve of the full Galerkin model for the two cases; both the first and second modal displacement are presented. It can be seen that, for both of these cases, there is a 1:3 modal interaction between the first and second mode, though the exact nature of these differs between the two backbone curves.

It is clear that, should a ROM fail to capture such an interaction, it is very possible that the MEMS or NEMS device could be damaged in a potentially irreversible way. As such, the IC method is applied to both of these systems to investigate the extent to which a model can be reduced at this scale.

The first modal coordinate of the Case 1 backbone curve is given in Fig. 3. In the single-mode model, as one might expect, the modal interaction is not captured at all. However, away from the modal interaction tongue, the backbone curve is captured well. This phenomenon persists across all of the ROMs, and the interaction can be seen in all of these except the first. Interestingly, although there is some movement toward the full model as more modes are added, the nature of the internal resonance is not correctly capture in any case. In the full model, the curve does not cross itself at any point, though this is true for all of the ROMs. The reason for this is likely to come from the 1:5 resonance which is present between the second and fifth modes. Since the fifth mode is not included in these ROMs, this behaviour can not be properly captured.

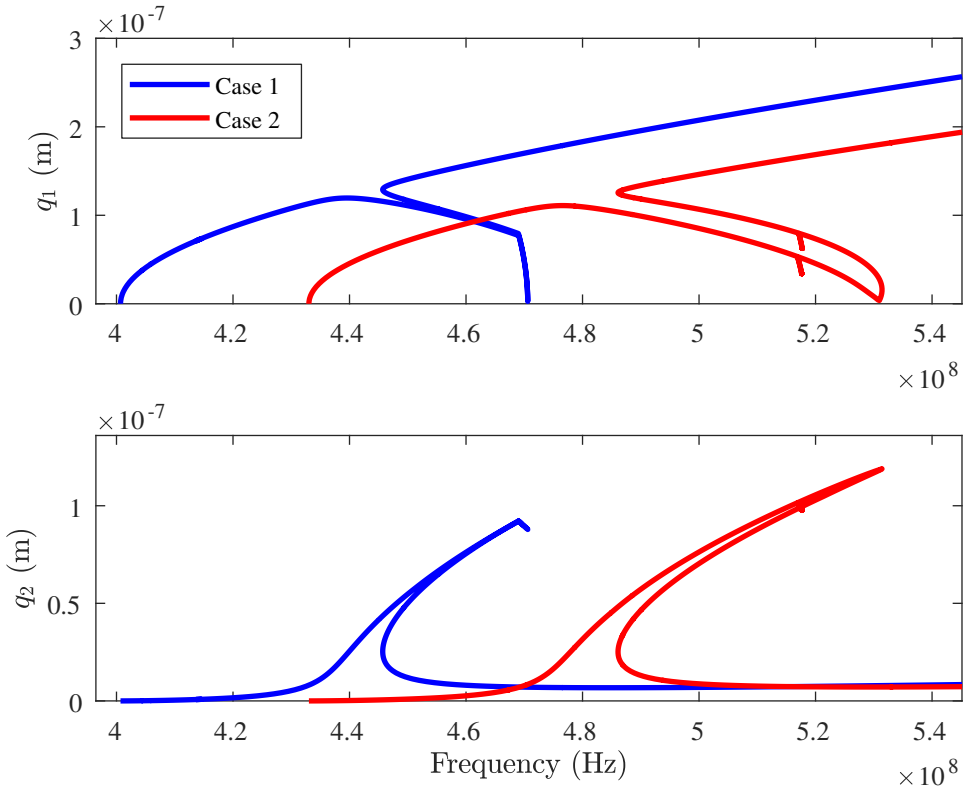


Figure 2: Modal contributions for modes 1 and 2 for the first backbone curve for Cases 1 and 2.

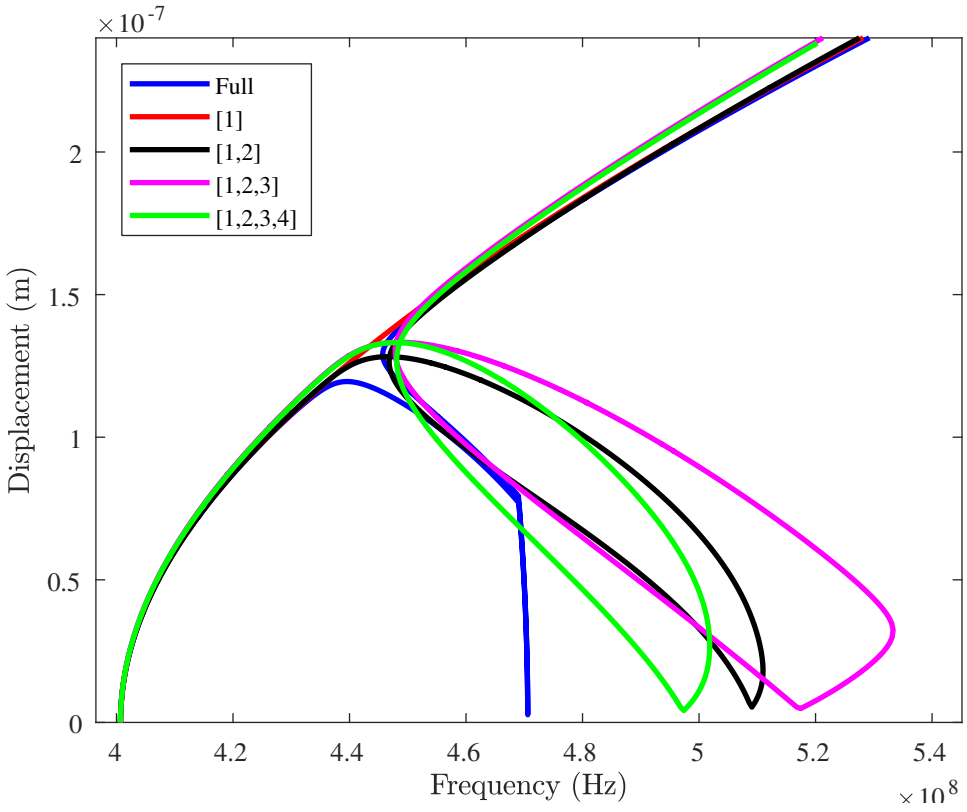


Figure 3: Comparison of ROMs with the full model in producing the first backbone for Case 1.

Similar behaviour can be seen in Case 2, as presented in Fig. 4. The resonance loops are noticeably close to the full model than in Case 1, even for the two-mode case. This implies that, as the charge at the tip increases and/or the distance between the tip and point charge decreases, the 1:3 internal resonance becomes more important to capture and relatively accurate results can be captured without the fifth mode being included in the modal basis.

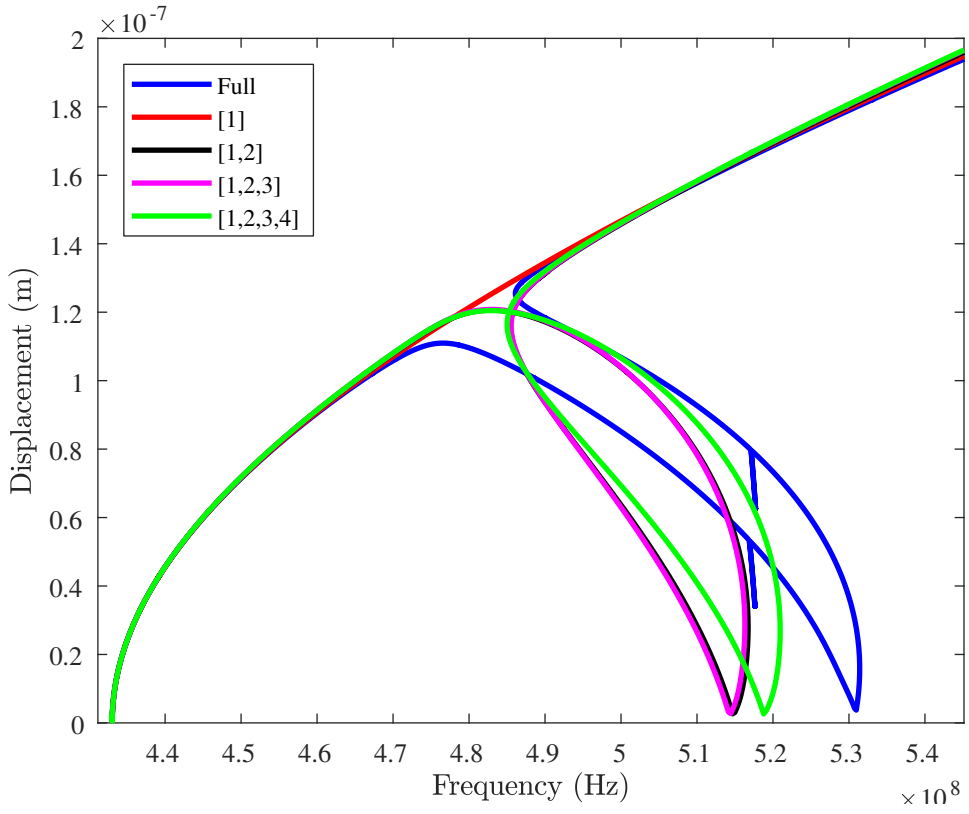


Figure 4: Comparison of ROMs with the full model in producing the first backbone for Case 2.

3.2 Forced responses

Although the backbone curves represent a somewhat idealised behaviour of the system, they can still provide a great deal of information regarding its nonlinear dynamics. This holds particularly true for systems with low damping and, as mentioned previously, this is inherent to MEMS and NEMS. The reason for this is related to the Q factor or quality factor of the system, a parameter that characterises the relationship between bandwidth and centre frequency (see, for instance, [14]).

The damping in a system is inversely proportional to its Q factor. This means that higher Q factors, such as those found in microscale systems, result in very low damping. In fact, in [15], values of up to 1550 were obtained experimentally. In this study, a representative value of 1000 will be used.

The relationship between damping and Q factor is characterised by

$$\zeta = \frac{1}{2Q_0}, \tag{15}$$

where ζ is the damping factor and Q_0 denotes the Q factor. Therefore, in the forced responses presented in this section, the damping ratio will be set to $\zeta =$ 5e-4. This can be implemented in the forced equations

of motion, given by

$$\ddot{q}_n + 2\omega_n \dot{q}_n + \omega_n^2 q_n + \frac{E}{2\rho\alpha_{1,n}L}\sum_{i=1}^{\infty}\sum_{j=1}^{\infty}\sum_{k=1}^{\infty}\alpha_{2,i}\beta_{j,k}q_i q_j q_k = \frac{P_n\cos(\Omega t)}{2\rho\alpha_{1,n}L}, \tag{16}$$

where P_n represents the forcing coefficient of the n^{th} modal coordinate. In this investigation, it is sufficient to force only the first mode; i.e., $P_n = 0$ for $n \neq 1$. Two forcing cases will be considered: $P_1 = $ 1e-3 and $P_1 = $ 2e-3.

Figs. 5 and 6 presents the forced responses, along with the previously displayed backbone curves, both for the full Galerkin model and the ROMs. The impact of having such a low Q factor is immediately clear. That is, in MEMS and NEMS systems, the forced response is very close to the free response and the backbone curves can give a great deal of insight into how the forced system will behave.

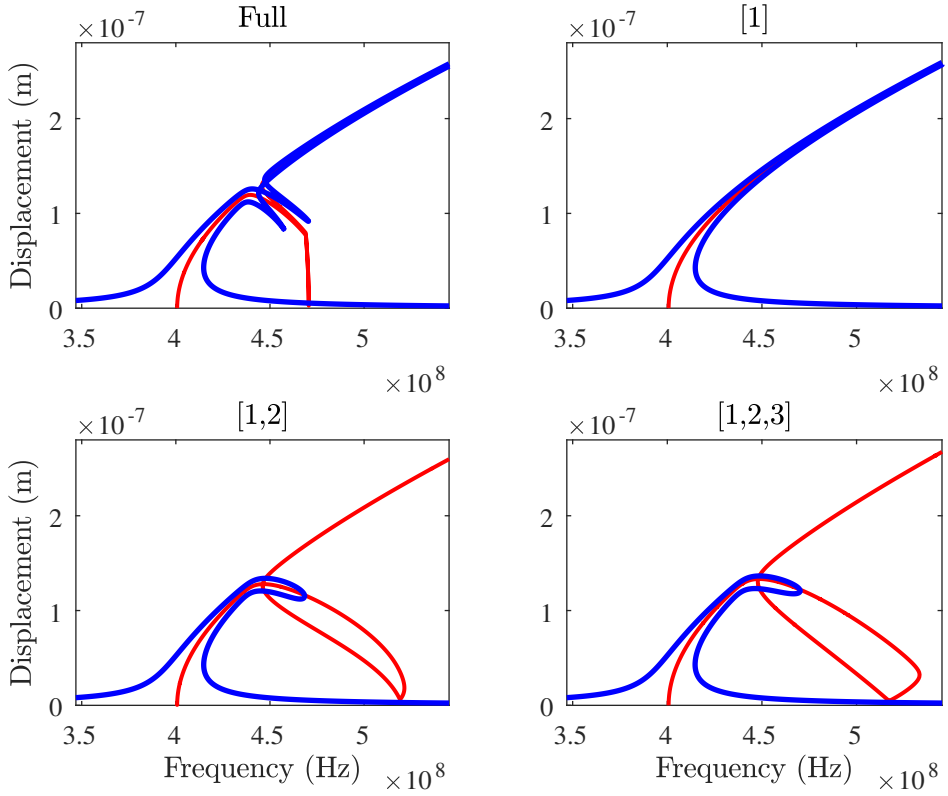


Figure 5: Comparison of the first backbone curve and forced response for the full model and first three ROMs in Case 1.

In the lower forcing case (Case 1), displayed in Fig. 5, it is immediately clear that the forced case stays close to the backbone curve, particularly at higher frequencies. However, where the full model increases in displacement after the modal interaction, this is not true for the two- and three-mode models; the behaviour is qualitatively similar for the four-mode model, so this is not shown here. In these two ROMs, the modal interaction loop is significantly larger than in the full model. This corresponds to the forced response, in which the greater influence of the interaction causes a more substantial change in curvature.

If the forcing level is increased, as can be seen in Fig. 6, the two- and three-mode models do capture this looping behaviour. Similarly to the backbone curve, the loops are greater than those in the full model, though they do occur at approximately the same point. This suggests that, even with only a two-mode model, it is possible to accurately capture modal interactions in microscale structures.

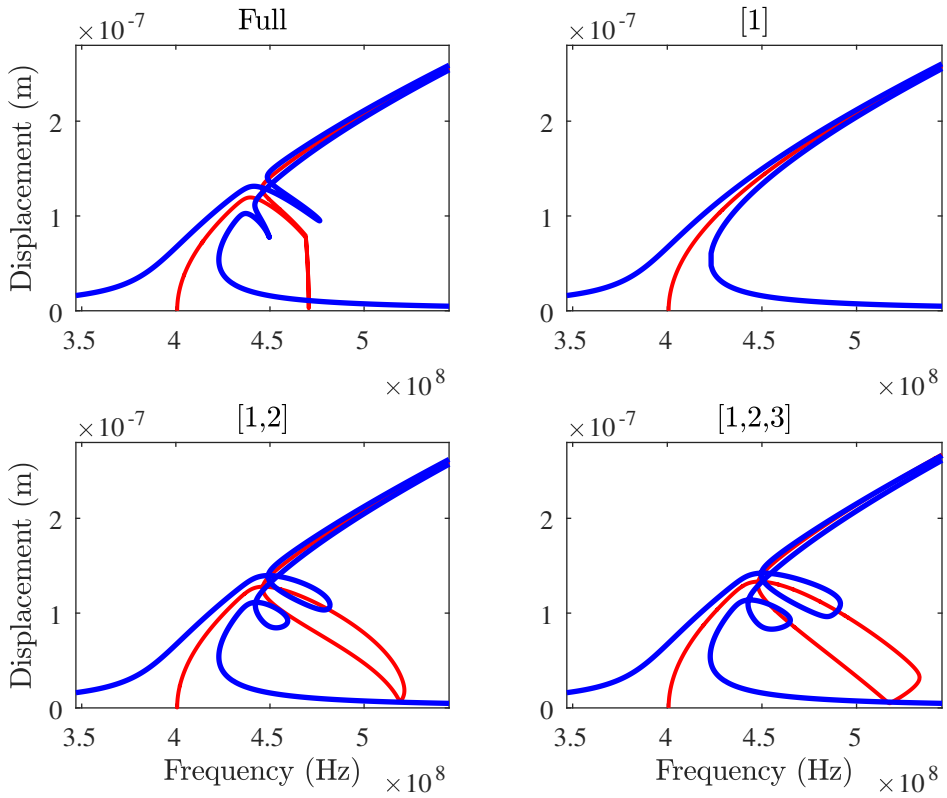


Figure 6: Comparison of the first backbone curve and forced response for the full model and first three ROMs in Case 2.

4 Conclusion

In this paper, an analytical model has been used to investigate the extent to which MEMS and NEMS model can be reduced. The physical structure in question is a cantilever microbeam with its tip equidistantly between to point charges. In taking a Taylor expansion of this nonlinearity, it is seen that this can be closely approximated by a cantilever beam model with a cubic nonlinear spring support at the tip. Treating a Galerkin model of this configuration as a full nonlinear model, reduced-order models have been computed using the implicit condensation method. These ROMs have been compared with the Galerkin model, both in terms of the free and forced response of the system.

Two variations of this beam have been considered, the more nonlinear of which includes a greater charge of the tip and a shorter distance between the tip and the point charges. In both cases, a 1:3 internal resonance between the first and second is clearly visible in the backbone curves. Although less noticeable, a 1:5 resonance exists between the second and fifth modes. Across all of the ROMs, the fundamental section of the backbone curve is well approximated, and it is only the single-mode model which fails to capture the interaction between modes. While these other models recognise that such an interaction takes place, the position and form of the tongue is never exactly captured, which is accounted for by the fact that the fifth mode is not included.

In terms of the forced responses, it is clear that, in all cases, the backbone curves act as a close approximation of these. This phenomenon arises due to the fact that the high Q factor found in MEMS and NEMS devices corresponds to a very low damping level. This suggests that the calculation of backbone curves may be sufficient for understanding forced dynamics of microscale systems, even though forcing is not explicitly included in the equations of motion. This is of particular interest for this system, as the internal resonances seen in the backbone curves have a noticeable influence on the forced response of the structure. For the case considered here, it was possible to obtain a close approximation of the modal

interaction using just two modes in the ROM.

References

[1] K. L. Turner, S. A. Miller, P. G. Hartwell, N. C. MacDonald, S. H. Strogatz, and S. G. Adams. Five parametric resonances in a microelectromechanical system. *Letters to Nature*, 396, 1998.

[2] J. R. Rhoads, S. W. Shaw, and K. L. Turner. Nonlinear dynamics and its applications in micro- and nanoresonators. *Journal of Dynamic Systems, Measurement, and Control*, 132, 2010.

[3] E. M. Abdel-Rahman, M. I. Younis, and A. H. Nayfeh. Characterization of the mechanical behavior of an electrically actuated microbeam. *Journal of Micromechanics and Microengineering*, 12:759–766, 2002.

[4] E. M. Abdel-Rahman and A. H. Nayfeh. Secondary resonances of electrically actuated resonant microsensors. *Journal of Micromechanics and Microengineering*, 13:491–501, 2003.

[5] M. I. Younis, E. M. Abdel-Rahman, and A. H. Nayfeh. A reduced-order model for electrically actuated microbeam-based mems. *Journal of Microelectromechanical Systems*, 12:672–680, 2003.

[6] X. Zhao, E. M. Abdel-Rahman, and A. H. Nayfeh. A reduced-order model for electrically actuated microplates. *Journal of Micromechanics and Microengineering*, 14:900–906, 2004.

[7] F. Najar, S. Choura, S. El-Borgi, E. M. Abdel-Rahman, and A. H. Nayfeh. Modeling and design of variable-geometry electrostatic microactuators. *Journal of Micromechanics and Microengineering*, 15:419–429, 2005.

[8] A. H. Nayfeh and M. I. Younis. Dynamics of mems resonators under superharmonic and subharmonic excitations. *Journal of Micromechanics and Microengineering*, 15:1840–1847, 2005.

[9] S. Gutschmidt. Internal resonances and bifurcation of an array below the first pull-in instability. *International Journal of Bifurcation and Chaos*, 20:605–618, 2010.

[10] M. P. Mignolet, A. Przekop, S. A. Rizzi, and S. M. Spottswood. A review of indirect/non-intrusive reduced order modeling of nonlinear geometric structures. *Journal of Sound and Vibration*, 332:2437–2460, 2013.

[11] M.I. McEwan, J.R. Wright, J.E. Cooper, and A.Y.Y Leung. A combined modal/finite element analysis technique for the dynamic response of a non-linear beam to harmonic excitation. *Journal of Sound and Vibration*, 243:601–624, 2001.

[12] J.J. Hollkamp and R.W. Gordon. Reduced-order models for nonlinear response prediction: Implicit condensation and expansion. *Journal of Sound and Vibration*, 318:1139–1153, 2008.

[13] R. J. Kuether, B. J. Deaner, J. J. Hollkamp, and M. S. Allen. Evaluation of geometrically nonlinear reduced order models with nonlinear normal modes. *AIAA Journal*, 53:1–13, 2015.

[14] J. H. Harlow. *Electric Power Transformer Engineering*. CRC Press, 2004.

[15] T. Ikehara, J. Lu, M. Konno, R. Maeda, and T. Mihara. A high quality-factor silicon cantilever for a low detection-limit resonant mass sensor operated in air. *Journal of Micromechanics and Microengineering*, 17:2491–2494, 2007.

On the identification of model error through observations of time-varying parameters

P.L. Green [1], **E. Chodora** [2], **S. Atamturktur** [2]
[1] Institute for Risk and Uncertainty, School of Engineering,
University of Liverpool, Liverpool, United Kingdom, L69 7ZF

[2] Department of Mechanical Engineering, Clemson University,
Clemson, United States, SC 29634

Abstract

When performing system identification, it can be possible to realise a deficient model (i.e. one that will make low fidelity predictions) that is able to closely represent a set of training data. For example, the parameters of linear dynamical models can often be tuned to realise a close match to training data that was generated from a system with strong nonlinearities. Despite this close match to available data, these same models may make very poor-quality predictions when shifted even slightly from the 'validation domain' (which could, for example, be a specific time window). In this paper we investigate the hypothesis that, by treating our model's parameters as being time-varying, we can identify key weaknesses in a model that would have been difficult to establish using other identification methods that do not consider the potentially time-varying nature of the model's parameters. Specifically, we use an Extended Kalman Filter to 'track' the parameters of a dynamical system, as a time history of training data is analysed. We then illustrate that this approach can reveal important information about the potential deficiencies of a model.

1 Introduction

Computational models are crucial to many fields of science and engineering. Before being used to influence decision-making, such models must be validated; it must be established that the model can represent the real world with a level of accuracy sufficient for its intended purpose. Model validation is, as a result, an active research area.

In a broad sense, the current paper considers the situation where:

1. our chosen model structure features a set of parameters that will need to be 'tuned' during the validation process.
2. a set of observations, from the system of interest, are available to the user (such that this data can be used to help infer parameter estimates).

While such scenarios are considered by much of the literature, the current paper differs from most in that it explicitly considers the issues associated with *extrapolation*. Specifically, by 'extrapolation' we are referring to a situation where a model will be used to make predictions in a region that is 'very far' from current experimental observations - a region where there is no observation data (and it may be difficult to collect data in the future). Using the terminology given in [1], we are essentially considering the situation where a model must be applied outside of its 'domain of applicability'. Inevitably then, we must ask the question:

will the model make valid extrapolations?

Answering such a question is extremely difficult. Furthermore the problem is often confounded by the fact that, in the regions where measurements are available, calibration can mask model error. In other words, a model's parameters can often be tuned such that the model appears to be sufficiently valid compared to the available data, even if the model will be a poor extrapolator (we show an illustrative example of this in section 4.2 of the current paper). The current work presents an approach that can, in such a scenario, illustrate the flaws in a model; warning us that the model should not be used for extrapolative predictions.

Briefly, our approach is as follows. Firstly, we limit ourselves to situations where we believe our model of interest's parameters should be time-invariant. We then adopt a calibration procedure that *deliberately treats these parameters as being time-varying, even though we believe this is not the case*. It is by observing that a model's parameters must vary with time if it is to replicate a set of measurements with a high level of fidelity that we aim to identify key discrepancies in the model that may be hidden by other calibration procedures. We believe that, for future work, the approach can form part of validation frameworks such as those described in [2] [3].

2 Literature Review

The idea that statistical models can be used to emulate *model discrepancy* (see [4] and [5] for example) has influenced a large body of work. This approach accepts that there will always be a discrepancy between a model that is formulated on our best understanding of the system of interest (a model that is based on physical laws, for example) and the system's true response. A purely data-based model is then trained and used to realise predictions of this discrepancy. Subsequent to calibration, then, predictions are made using a combination of the model that is based on our best understanding of the system and the data-based discrepancy model[1].

One of the best-known implementations of this approach is that of Kennedy and O'Hagan [4], where Gaussian Processes (GPs) were used to create statistical models of model discrepancy (as well as emulators, for the cases where simulations of the system of interest are expensive). This idea has contributed to many works in the field of model validation. These include generalised validation frameworks [6] [7] [8], model validation metrics that consider model discrepancy [1], metrics to establish when sufficient experimental data has been gathered in the model validation process [9] and approaches for resource allocation (between code development and experimental testing [10] or the development of substructures within a model [11]).

While undoubtedly a useful contribution, employing data-based models of discrepancy cannot help improve extrapolations that are far from the training data (GPs, for example, will return very quickly to predictions based only on prior knowledge of the discrepancy if used in a region where there is no data). This issue is highlighted by a number of authors. In [12] it is stated that 'the primary use of engineering models is to extrapolate to a system with new nominals when there are no new field data' but that extrapolation, using the approach described in [4], can only be performed if there is a 'modest' change in the inputs. The authors of [2] note that 'such a statistically adjusted engineering model lacks predictive power in the sense that it can be used only in the experimental conditions identical or very similar to those under which the statistical model was fitted' and in [3] it is stated that '...the discrepancy representation ... is highly dependent on calibration against observables and, hence, should not be used in situations in which it cannot be trained and

[1]This type of approach is sometimes called grey-box modelling, as it utilises a combination of a 'white box model' (model based on our understanding of the system) and a 'black box model' (a model that is purely data-based).

tested'.

At this point it is important to note that the above discussion isn't a direct critisism of [4] - the authors did not claim that the method will provide reliable extrapolations. In fact, an interesting discussion of the Kennedy and O'Hagan approach is given by Brynjarsdóttir and O'Hagan in [13], which considers how the use of GP emulators of model discrepancy can (1) aid the identification of a system's 'true' parameter values and (2) aid extrapolations. It is concluded that true parameter values can only be uncovered if realistic prior information about the model discrepancy is available and that, even if realistic prior information is available, extrapolation is not advisable. [13] highlights these two issues nicely using a simple case study.

To further clarify the position of our paper in current literature, it is stressed that we are considering the situation where, in the region we wish to make predictions, there is no data (and we don't expect there to be any data in the future). This consideration separates the current paper from [1] and [9] that (respectively) describe a 'predictive maturity index' and a 'forecasting metric', as these approaches utilise hold-out experiments (experimental observations, in the application domain, that are deliberately removed from the training data so that they can be used to aid validation at a later stage). Instead, we propose a method that can, potentially, be used to reveal additional *engineering knowledge* about a particular system. For future work, we aim to utilise this method as part of the frameworks described in [2] and [3], both of which specifically consider extrapolation.

3 Methodology

3.1 General Framework

As stated previously, the current work specifically concerns the analysis of dynamical systems. Using $\boldsymbol{x}_i$ to represent a system's state at time $i\Delta t$ then, generally, we propose that the system's state evolves according to

$$\boldsymbol{x}_i = \boldsymbol{f}(\boldsymbol{x}_{i-1}, \boldsymbol{u}_i) + \boldsymbol{v}_{i-1}, \qquad \boldsymbol{v}_{i-1} \sim \mathcal{N}(\boldsymbol{v}_{i-1}; \boldsymbol{0}, \boldsymbol{Q}_{i-1}) \tag{1}$$

where Δt is a fixed time increment, $\boldsymbol{u}_i$ is a system input, $\boldsymbol{f}$ is a model that predicts the next system state given $(\boldsymbol{x}_{i-1}, \boldsymbol{u}_i)$ and $\boldsymbol{v}_{i-1}$ is a 'noise term' that reflects the uncertainties in our predictions of the system's next state (arising because $\boldsymbol{f}$ is an approximation of the true system). Equation (1) is typically referred to as the 'prediction equation'.

Likewise, using $\boldsymbol{z}_i$ to represent an observation of some aspect of our system at time $i\Delta t$, we also suppose that measurements are made according to

$$\boldsymbol{z}_i = \boldsymbol{h}_i(\boldsymbol{x}_i) + \boldsymbol{n}_i, \qquad \boldsymbol{n}_i \sim \mathcal{N}(\boldsymbol{n}_i; \boldsymbol{0}, \boldsymbol{R}_i) \tag{2}$$

where $\boldsymbol{h}$ is a (potentially nonlinear) function of the system's state and $\boldsymbol{n}_i$ is used to capture uncertainty in the observation process (measurement noise). Equation (2) is typically referred to as the 'observation equation'. We note that, in the literature, the prediction and observation equations are often written as potentially nonlinear functions of their noise terms ($\boldsymbol{v}_{i-1}$ and $\boldsymbol{n}_i$ respectively) - we have neglected to do so here for notational simplicity later in the paper.

3.2 Extended Kalman Filter

Now consider the situation where the aim is to probabilistically 'track' how the state of our system changes with time, as more observations arrive over time. If, in our prediction and observation equations, $\boldsymbol{f}$ and $\boldsymbol{h}$ are linear functions of $\boldsymbol{x}_{i-1}$ and $\boldsymbol{x}_i$ respectively then it is possible to realise closed-form solutions for this problem. These solutions form the well-known Kalman filter.

If $\boldsymbol{f}$ and $\boldsymbol{h}$ are nonlinear then, generally, such closed-form solutions are unavailable. One way to address this is to approximate $\boldsymbol{f}$ and $\boldsymbol{h}$ using linear functions (via first-order Taylor series expansions), before applying the 'standard' Kalman filter equations to the new, linearised relationships. This approach is called the Extended Kalman Filter (EKF)[2].

Here we give a brief description of an extended Kalman filter, to establish notation used later in the paper. Firstly we define:

$$\boldsymbol{F}_{\hat{\boldsymbol{x}}} \equiv \left[\frac{\partial \boldsymbol{f}}{\partial \boldsymbol{x}}\right]_{\boldsymbol{x}=\hat{\boldsymbol{x}}} \tag{3}$$

and

$$\boldsymbol{H}_{\hat{\boldsymbol{x}}} \equiv \left[\frac{\partial \boldsymbol{h}}{\partial \boldsymbol{x}}\right]_{\boldsymbol{x}=\hat{\boldsymbol{x}}} \tag{4}$$

Now, say it is currently assumed that

$$p(\boldsymbol{x}_{i-1} \mid \boldsymbol{z}_{1:i-1}) = \mathcal{N}(\boldsymbol{x}_{i-1}; \boldsymbol{m}_{i-1|i-1}, \boldsymbol{P}_{i-1|i-1}) \tag{5}$$

such that the probability density function (PDF) of $\boldsymbol{x}_{i-1}$ given $\boldsymbol{z}_{1:i-1}$ is Gaussian with mean $\boldsymbol{m}_{i-1|i-1}$ and covariance matrix $\boldsymbol{P}_{i-1|i-1}$. With an EKF we first use our linearised prediction equation to predict the next system state. This yields the PDF

$$p(\boldsymbol{x}_i \mid \boldsymbol{z}_{1:i-1}) = \mathcal{N}(\boldsymbol{x}_i; \boldsymbol{m}_{i|i-1}, \boldsymbol{P}_{i|i-1}) \tag{6}$$

Once a new observation arrives ($\boldsymbol{z}_i$) then, through our observation equation, we can update our estimate of the system state to obtain:

$$p(\boldsymbol{x}_i \mid \boldsymbol{z}_{1:i}) = \mathcal{N}(\boldsymbol{x}_i; \boldsymbol{m}_{i|i}, \boldsymbol{P}_{i|i}) \tag{7}$$

where the parameters of the PDFs in equations (5), (6) and (7) are as follows:

$$\boldsymbol{m}_{i|i-1} = \boldsymbol{f}(\boldsymbol{m}_{i-1|i-1}) \tag{8}$$

$$\boldsymbol{P}_{i|i-1} = \boldsymbol{Q}_{i-1} + \boldsymbol{F}_{m_{i-1|i-1}} \boldsymbol{P}_{i-1|i-1} \boldsymbol{F}^T_{m_{i-1|i-1}} \tag{9}$$

$$\boldsymbol{m}_{i|i} = \boldsymbol{m}_{i|i-1} + \boldsymbol{K}_i(\boldsymbol{z}_i - \boldsymbol{h}(\boldsymbol{m}_{i|i-1})) \tag{10}$$

[2]There are many other ways in which this problem could be tackled. One of the most well-known is the *particle filter* - a numerical method that is fundamentally based on importance sampling (see [14] for a tutorial). Here, however, we found that an extended Kalman filter performed acceptably well and that our prediction and measurement equations were not sufficiently nonlinear to warrant use of a particle filter.

$$\boldsymbol{P}_{i|i} = \boldsymbol{P}_{i|i-1} - \boldsymbol{K}_i \boldsymbol{H}_{m_{i|i-1}} \boldsymbol{P}_{i|i-1} \tag{11}$$

and

$$\boldsymbol{K}_i = \boldsymbol{P}_{i|i-1} \boldsymbol{H}^T_{m_{i|i-1}} \boldsymbol{S}_i^{-1} \tag{12}$$

$$\boldsymbol{S}_i = \boldsymbol{H}_{m_{i|i-1}} \boldsymbol{P}_{i|i-1} \boldsymbol{H}^T_{m_{i|i-1}} + \boldsymbol{R}_i \tag{13}$$

3.3 Application to the 4th order Runge-Kutta integration scheme

In the following we consider a dynamical system that may be subjected to a time history of known excitations: $\boldsymbol{\delta}_1, \boldsymbol{\delta}_2, ...$ The state of these systems is calculated recursively using the 4th order Runge-Kutta numerical integration scheme. To help us relate this scheme back to the general 'prediction equation' shown in equation (1), we must make some additional notation. Firstly, we write

$$\boldsymbol{u}_i = \begin{pmatrix} \boldsymbol{\delta}_{i-1} \\ \boldsymbol{\delta}_i \end{pmatrix} \tag{14}$$

Secondly, we establish the notation

$$\dot{\boldsymbol{x}}(\boldsymbol{x}_i, \boldsymbol{\delta}_i) \equiv \left[\frac{\partial \boldsymbol{x}}{\partial t} \right]_{\boldsymbol{x}=\boldsymbol{x}_i, \boldsymbol{\delta}=\boldsymbol{\delta}_i} \tag{15}$$

and define

$$\boldsymbol{k}_1 = \dot{\boldsymbol{x}}(\boldsymbol{x}_{i-1}, \boldsymbol{\delta}_{i-1}) \tag{16}$$

$$\boldsymbol{k}_2 = \dot{\boldsymbol{x}} \left(\boldsymbol{x}_{i-1} + \frac{\Delta t}{2} \boldsymbol{k}_1, \boldsymbol{\delta}_{\text{int}} \right) \tag{17}$$

$$\boldsymbol{k}_3 = \dot{\boldsymbol{x}} \left(\boldsymbol{x}_{i-1} + \frac{\Delta t}{2} \boldsymbol{k}_2, \boldsymbol{\delta}_{\text{int}} \right) \tag{18}$$

$$\boldsymbol{k}_4 = \dot{\boldsymbol{x}} \left(\boldsymbol{x}_{i-1} + \Delta t \, \boldsymbol{k}_3, \boldsymbol{\delta}_i \right) \tag{19}$$

where Δt is the time-step of our integration scheme and $\boldsymbol{\delta}_{\text{int}} = \frac{1}{2}(\boldsymbol{\delta}_{i-1} + \boldsymbol{\delta}_i)$. Using this notation, the function $\boldsymbol{f}$ that maps $\boldsymbol{x}_{i-1}$ to $\boldsymbol{x}_i$ can be written as

$$\boldsymbol{x}_i = \boldsymbol{x}_{i-1} + \frac{\Delta t}{6} \left(\boldsymbol{k}_1 + 2\,\boldsymbol{k}_2 + 2\,\boldsymbol{k}_3 + \boldsymbol{k}_4 \right) \tag{20}$$

We now need to find an expression for $\boldsymbol{F}_{\hat{\boldsymbol{x}}}$ (equation (3)). We note that

$$\boldsymbol{F}_{\hat{\boldsymbol{x}}} = \boldsymbol{I} + \frac{\Delta t}{6} \left(\underbrace{\left[\frac{\partial \boldsymbol{k}_1}{\partial \boldsymbol{x}_{i-1}} \right]_{\boldsymbol{x}_{i-1}=\hat{\boldsymbol{x}}}}_{\text{Term 1}} + 2 \underbrace{\left[\frac{\partial \boldsymbol{k}_2}{\partial \boldsymbol{x}_{i-1}} \right]_{\boldsymbol{x}_{i-1}=\hat{\boldsymbol{x}}}}_{\text{Term 2}} + 2 \underbrace{\left[\frac{\partial \boldsymbol{k}_3}{\partial \boldsymbol{x}_{i-1}} \right]_{\boldsymbol{x}_{i-1}=\hat{\boldsymbol{x}}}}_{\text{Term 3}} + \underbrace{\left[\frac{\partial \boldsymbol{k}_4}{\partial \boldsymbol{x}_{i-1}} \right]_{\boldsymbol{x}_{i-1}=\hat{\boldsymbol{x}}}}_{\text{Term 4}} \right) \tag{21}$$

Evaluation of terms 1-4 in equation (21) essentially requires the application of some straightforward vector calculus. For the sake of completeness, the required derivatives are shown in detail in Appendix A. Ultimately, we find that

$$\left[\frac{\partial \boldsymbol{k}_1}{\partial \boldsymbol{x}_{i-1}}\right]_{\boldsymbol{x}_{i-1}=\hat{\boldsymbol{x}}} = \tilde{\boldsymbol{F}}(\hat{\boldsymbol{x}}, \boldsymbol{\delta}_{i-1}) \tag{22}$$

$$\left[\frac{\partial \boldsymbol{k}_2}{\partial \boldsymbol{x}_{i-1}}\right]_{\boldsymbol{x}_{i-1}=\hat{\boldsymbol{x}}} = \tilde{\boldsymbol{F}}\left(\hat{\boldsymbol{x}} + \frac{\Delta t}{2}\boldsymbol{k}_1(\hat{\boldsymbol{x}}, \boldsymbol{\delta}_{i-1}), \boldsymbol{\delta}_{\text{int}}\right)\left(\boldsymbol{I} + \frac{\Delta t}{2}\left[\frac{\partial \boldsymbol{k}_1}{\partial \boldsymbol{x}_{i-1}}\right]_{\boldsymbol{x}_{i-1}=\hat{\boldsymbol{x}}}\right) \tag{23}$$

$$\left[\frac{\partial \boldsymbol{k}_3}{\partial \boldsymbol{x}_{i-1}}\right]_{\boldsymbol{x}_{i-1}=\hat{\boldsymbol{x}}} = \tilde{\boldsymbol{F}}\left(\hat{\boldsymbol{x}} + \frac{\Delta t}{2}\boldsymbol{k}_2(\hat{\boldsymbol{x}}, \boldsymbol{\delta}_{\text{int}}), \boldsymbol{\delta}_{\text{int}}\right)\left(\boldsymbol{I} + \frac{\Delta t}{2}\left[\frac{\partial \boldsymbol{k}_2}{\partial \boldsymbol{x}_{i-1}}\right]_{\boldsymbol{x}_{i-1}=\hat{\boldsymbol{x}}}\right) \tag{24}$$

$$\left[\frac{\partial \boldsymbol{k}_4}{\partial \boldsymbol{x}_{i-1}}\right]_{\boldsymbol{x}_{i-1}=\hat{\boldsymbol{x}}} = \tilde{\boldsymbol{F}}\left(\hat{\boldsymbol{x}} + \Delta t\,\boldsymbol{k}_3(\hat{\boldsymbol{x}}, \boldsymbol{\delta}_{\text{int}}), \boldsymbol{\delta}_i\right)\left(\boldsymbol{I} + \Delta t\left[\frac{\partial \boldsymbol{k}_3}{\partial \boldsymbol{x}_{i-1}}\right]_{\boldsymbol{x}_{i-1}=\hat{\boldsymbol{x}}}\right) \tag{25}$$

where we have used $\tilde{\boldsymbol{F}}(\boldsymbol{x}, \boldsymbol{\delta})$ to represent the Jacobian of $\dot{\boldsymbol{x}}$, with respect to $\boldsymbol{x}_{i-1}$, evaluated at the points $\boldsymbol{x}$ and $\boldsymbol{\delta}$.

4 Numerical Case Study

4.1 Description

We consider modelling a single degree of freedom nonlinear dynamic system whose equation of motion is

$$\ddot{x} + c\dot{x} + kx + k^* x^3 = \delta(t) \tag{26}$$

In equation (26) x is displacement, c is a linear damping coefficient, k is a linear stiffness coefficient and k^* is a nonlinear stiffness coefficient that controls the strength of the system's 'hardening' stiffness nonlinearity. $\delta(t)$ is a random excitation that, in this case, consists of samples drawn from a zero-mean unit-variance Gaussian.

To generate a set of 'observation data' the nonlinear system was simulated using a time step of $\Delta t = 0.01$s. Observations were created by taking the resulting displacement time history and corrupting it with Gaussian noise (variance 1×10^{-5}). The model's parameters were $k = 10$ N/m, $c = 0.1$ Ns/m and $k^* = 50$ N/m^3. Observation data was generated over a time period of 200 seconds. The full set of observation data is shown in Figure 1 while a zoomed-in portion is shown in Figure 2.

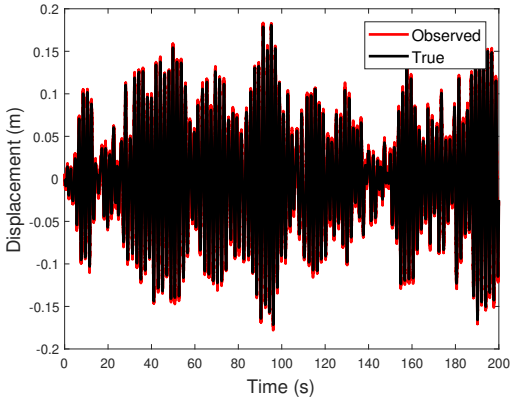


Figure 1: 200 seconds of displacement time history observations from the numerical case study. Black shows the true response of the system while red shows noisy observations.

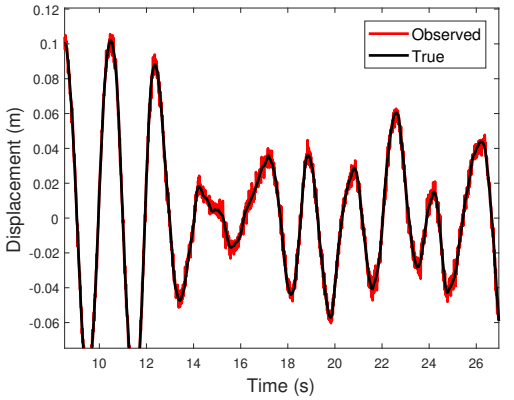


Figure 2: Numerical case study. A close-up view of the data shown in Figure 1.

In the following we will first consider the case where we are incorrectly attempting to fit a linear model to data that is obtained from the nonlinear system. We will also consider that, after calibration, the model will be used to predict the response of the system to a much greater amplitude excitation than that used to generate the data in Figure 1.

We have deliberately considered a situation where the excitation used to generate the observation data is relatively low, such that the nonlinearity is difficult to detect. Before exploring our methodology for detecting model deficiencies we will illustrate that, by tuning its parameters, this is a situation where we can make our linear model represent the data from the nonlinear system fairly accurately (Section 4.2), potentially giving false confidence in the model's ability to extrapolate. Our potential solution is then demonstrated in Section 4.3.

4.2 Highlighting the Problem

Here we adapt a common Bayesian approach to the calibration of the model, where it is assumed that the model's parameters are time-invariant. The results highlight some of the issues that can arise when the model is required for extrapolation. The approach begins with Bayes' theorem:

$$p(\boldsymbol{\theta}\,|\mathcal{D}) \propto p(\mathcal{D}|\,\boldsymbol{\theta})p(\boldsymbol{\theta}) \tag{27}$$

where $\boldsymbol{\theta}$ is the vector of parameters to be calibrated and $\mathcal{D}$ represents training data (in this case $\mathcal{D}$ is a time history of the excitation and the observed displacement response of our system). The likelihood, $p(\mathcal{D}|\,\boldsymbol{\theta})$, is defined based on the assumption that each of our observations are equal to the response of the model, corrupted by the addition of Gaussian noise. This noise is assumed to be zero-mean, have variance R and be independent of the noise that corrupted previous observations. Furthermore, we treat R as a time-invariant parameter that also requires calibration. Consequently, we have $\boldsymbol{\theta} = (k, c, R)^T$.

By defining the likelihood in this way we are treating any differences between what we observe and what the model predicts (i.e. errors that arise because of both measurement noise and model discrepancy) as independent Gaussian noise[3]. Moreover, by allowing R to be calibrated, we are also tuning the variance of this noise while simultaneously tuning the model's stiffness and damping parameters. This framework means that the maximum likelihood set of model parameters are those that make the discrepancy between the model and the observations most closely approximate a Gaussian distribution with variance R. This way of treating uncertainty in the calibration procedure has been applied by many (including the author's of the current manuscript) and is referred to in [13] as a 'traditional approach'.

In the academic example discussed herein, prior distributions over the calibration parameters were chosen to be

$$p(k) = \mathcal{N}(k; 10, 3^2), \quad p(c) = \mathcal{N}(c; 0.1, 0.1^2), \quad p(R) = \text{Gamma}(R; 1, 100) \tag{28}$$

(such that the prior over R is a Gamma distribution whose shape and rate parameters are equal to 1 and 100 respectively). Using the first 50 seconds of data for training, the Markov chain Monte Carlo (MCMC) algorithm detailed in [17] was used to generate 1000 samples from the posterior, $p(\boldsymbol{\theta}\,|\mathcal{D})$.

Histograms of the resulting samples are shown 'close up' in Figure 3 while, in Figure 4, histograms are plotted alongside the true parameter values. These results highlight two things. Firstly the posterior distribution over k is concentrated over values that are larger than the true stiffness. This illustrates how k has been calibrated to overcome the model discrepancy (the lack of the nonlinear term). Secondly, the distribution over R is also concentrated on values that are larger than the true measurement noise variance. From these results we can see that this particular approach has attempted to describe the model discrepancy present in the problem as additional noise on our observations (in other words, the errors present in the model has increased the most probable value of R).

[3]This assumption is often justified by the principle of maximum entropy [15], although [16] highlights examples where prediction errors can be spatially and/or temporally correlated.

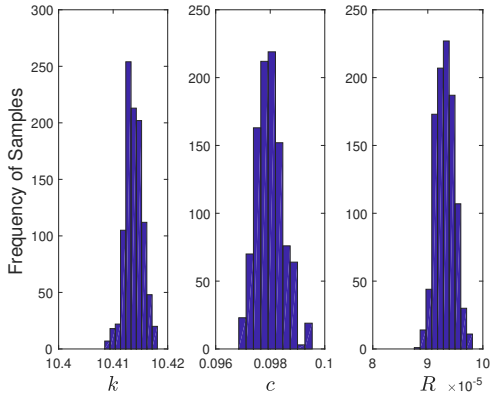


Figure 3: Histograms of samples from the posterior parameter distribution of the linear model in the numerical case study. All parameters in SI units.

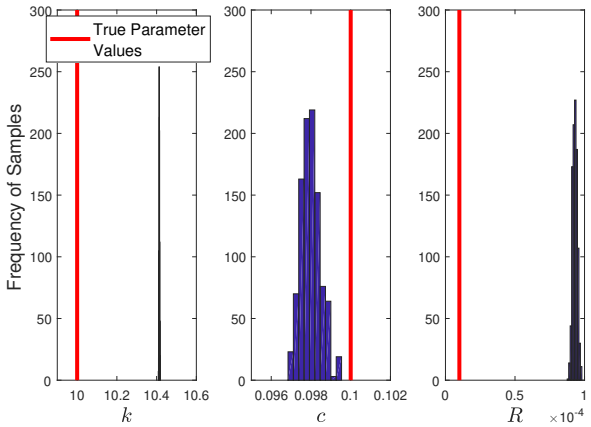


Figure 4: Histograms of samples from the posterior parameter distribution of the linear model in the numerical case study. True parameter values are marked by red lines. All parameters in SI units.

An illustration of the problem that motivates the current paper comes when the MCMC samples are used to propagate our parameter uncertainties into future model predictions. Recalling that we only have data in a relatively low amplitude regime, Figure 5 shows the model's predictions relative to (1) the training data and (2) data that was 'held back' for validation purposes. Figure 6 shows a close-up of the model's ability to replicate previously unseen data. These results illustrate that, for low amplitude excitations, the model is able to closely replicate data that was not used in training. This then, highlights the problem: the model has been tuned to work effectively in the region where we have data, however, because we have not included the hardening-stiffness nonlinearity, it will perform badly if used to predict the system's response at high amplitudes. To demonstrate this degradation in performance, the model was used to predict the response of the system to a higher amplitude excitation, whereby $\delta(t)$ consisted of samples drawn from a zero-mean Gaussian whose standard deviation was equal to 2. Figure 7 illustrates that, for this higher amplitude excitation, the model is not able to accurately replicate the response of the system (or accurately quantify the uncertainties involved in the predictions). Our main argument here is that, without the high amplitude response data, it is difficult to diagnose the errors in the model and infer that this model would be a poor extrapolator.

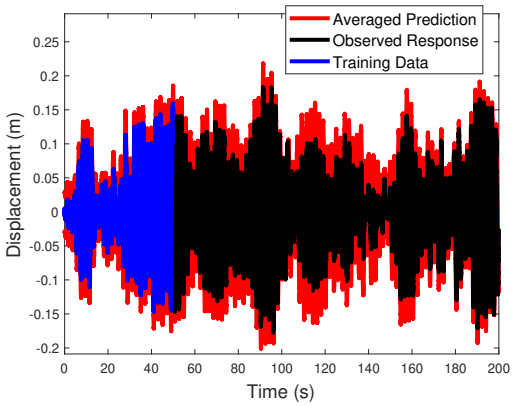


Figure 5: Propagating parameter uncertainties of the linear model into predictions (numerical case study). Blue represents training data, black represents previously unseen data and red represents the average model predictions. Bounds on model predictions are 3 standard deviations from the mean.

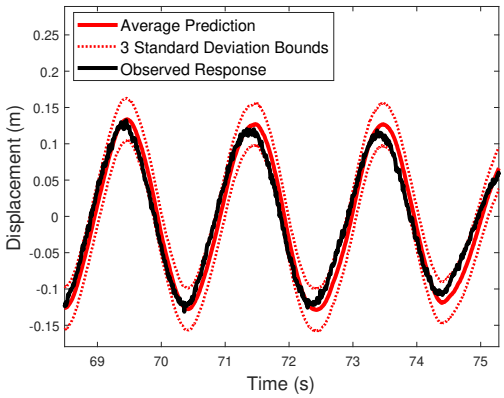


Figure 6: Propagating parameter uncertainties of the linear model into predictions of previously unseen, 'low amplitude' data. Bounds on model predictions are 3 standard deviations from the mean.

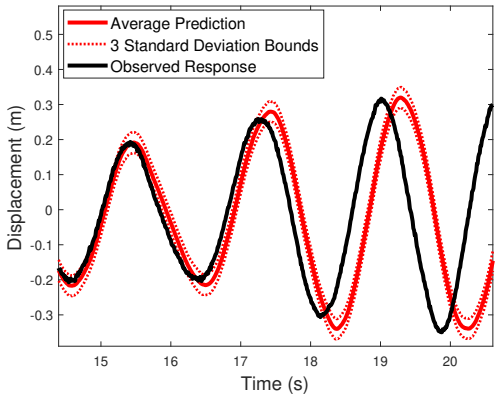


Figure 7: Propagating parameter uncertainties of the linear model into predictions of previously unseen, 'high amplitude' data. Bounds on model predictions are 3 standard deviations from the mean.

Below, we outline our proposed approach to the same situation, using the same observation data.

4.3 Proposed Approach

We now consider two separate model structures: $\mathcal{M}_1$ and $\mathcal{M}_2$. $\mathcal{M}_1$ represents the linear model i.e. the model discussed in the previous section. $\mathcal{M}_2$ includes the nonlinear stiffness term - it has the same structure as equation (26) and so, by considering $\mathcal{M}_2$, we are deliberately addressing a situation where there is no model error. The calibration parameters of $\mathcal{M}_1$ and $\mathcal{M}_2$ are now written as $\boldsymbol{\theta}_1$ and $\boldsymbol{\theta}_2$ respectively, such that

$$\boldsymbol{\theta}_1 = (k, c, R)^T, \qquad \boldsymbol{\theta}_2 = (k, c, k^*, R)^T \tag{29}$$

To treat our model's parameters as being time-varying, we include them in the definition of the system's state. This allows them to be 'tracked', alongside the system's displacement and velocity, using the EKF (see [18] for a similar approach that utilised particle filtering techniques). Here we illustrate how the approach can be implemented for $\mathcal{M}_2$ (the model that includes the nonlinear stiffness term), where the state at time $i\Delta t$ would be $\boldsymbol{x}_i = (x_i, \dot{x}_i, k_i, c_i, k_i^*)^T$. Implementation of this approach to $\mathcal{M}_1$ is very similar and, as such, is not discussed in detail here.

In order to implement the EKF, we must define a model that predicts how our parameters may vary through time i.e. we need to define $\boldsymbol{f}$ in equation (1). As with [18], we assume that each system parameter is equal to its preceeding value, such that

$$\dot{\boldsymbol{x}} = \begin{pmatrix} \dot{x} \\ \delta - kx - c\dot{x} - k^*x^3 \\ 0 \\ 0 \\ 0 \end{pmatrix} \tag{30}$$

Consequently, the Jacobian $\tilde{\boldsymbol{F}}$ is given by

$$\tilde{\boldsymbol{F}}(\boldsymbol{x}, \delta) = \begin{bmatrix} 0 & 1 & 0 & 0 & 0 \\ -(k + 3k^*x^2) & -c & -x & -\dot{x} & -x^3 \\ 0 & 0 & 0 & 0 & 0 \\ 0 & 0 & 0 & 0 & 0 \\ 0 & 0 & 0 & 0 & 0 \end{bmatrix} \tag{31}$$

We must also quantify the uncertainty in this predictive model (in other words we must define the covariance matrix $\boldsymbol{Q}_{i-1}$ in equation (1)). Here, we select

$$\boldsymbol{Q}_{i-1} = \begin{bmatrix} \mathbf{0}_{2\times 2} & \mathbf{0}_{2\times 3} \\ \mathbf{0}_{3\times 2} & \boldsymbol{G}_{i-1} \end{bmatrix} \tag{32}$$

where $\boldsymbol{G}_{i-1}$ is a diagonal matrix that, for model $\mathcal{M}_2$, is of size 3×3. Our approach assumes that there is zero uncertainty associated in the prediction of displacement and velocity, and that all of the uncertainty manifests itself in the prediction of how our parameter estimates vary through time. This is deliberate - it is the tracking of these parameter estimates that, we hope, will give us subtle indications of model error. Following on from [18], we choose the diagonal elements of $\boldsymbol{G}$ such that the coefficient of variation in the drift of each parameter is fixed. For the numerical case study shown here the coefficient of variation was set equal to 0.1 %.

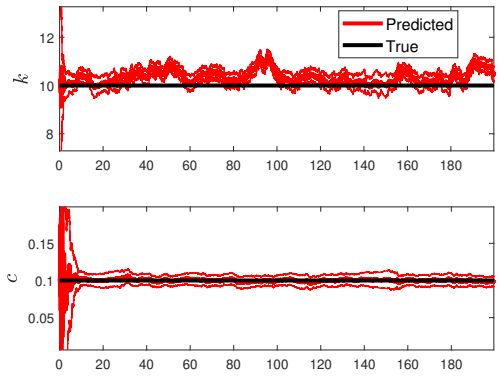


Figure 8: Tracking time varying parameters for the linear model. Black lines show true parameter values, red lines show estimated parameter values. Bounds on parameter estimates are 3 standard deviations from the mean.

Figure 8 shows the results that were obtained when the parameters of the linear model were treated as time varying, and tracked using the EKF. As we would expect, this method allows the displacement and velocity to be tracked very accurately - a comparison between the observed and predicted is not shown here because the two are essentially indistinguishable. Figure 8 shows that, relatively speaking, the system's damping value converges while the linear stiffness varies with time.

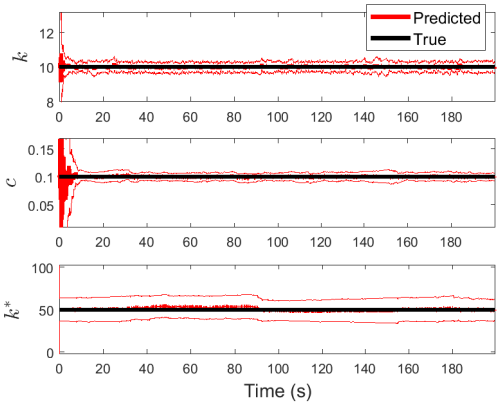


Figure 9: Tracking time varying parameters for the nonlinear model. Black lines show true parameter values, red lines show estimated parameter values. Bounds on parameter estimates are 3 standard deviations from the mean.

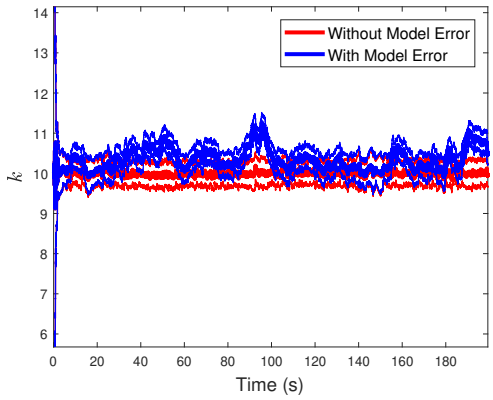


Figure 10: Tracking the stiffness for the nonlinear model (red) and linear model (blue). Bounds on parameter estimates are 3 standard deviations from the mean.

To aid comparison this analysis was repeated for the nonlinear model. These results are shown in Figure 9 while Figure 10 shows the comparison between the stiffness values that were identified, as a function of time, for both the linear and nonlinear models. To achieve an excellent fit to the observation data we can see that the stiffness of the linear model had to vary significantly more than the stiffness of the nonlinear model. Recall that we are deliberately studying systems whose parameters, we believe, should not be varying with time.

5 Discussion and future work

The question is: do the results in Figure 10 tell us that the linear model would extrapolate poorly if used at high amplitudes? The answer is not straightforward and it is clear that these results would require a significant amount of interpretation. However, we argue that allowing the parameters to vary with time provides a different type of information relative to the more traditional approach shown in Section 4.2. We believe it is conceivable that, by studying the results in Section 4.3, a practitioner may lead to a different set of conclusions about the suitability of the linear model for extrapolations compared to if they had studied the results in Section 4.2 (i.e. the more traditional approach). For future work it seems sensible to combine the proposed approach with a sensitivity analysis. This would help to establish, in a more rigorous manner, whether the witnessed variations in parameter values are truly significant. In particular, combining our approach with a sensitivity analysis of the model in the region where it is to be extrapolated could be an important part of an overall validation framework.

A Evaluating terms 1-4 in equation (21)

$$\left[\frac{\partial\, \boldsymbol{k}_1}{\partial\, \boldsymbol{x}_{i-1}}\right]_{\boldsymbol{x}_{i-1}=\hat{\boldsymbol{x}}} = \left[\frac{\partial \dot{\boldsymbol{x}}(\boldsymbol{x}_{i-1}, \boldsymbol{\delta}_{i-1})}{\partial\, \boldsymbol{x}_{i-1}}\right]_{\boldsymbol{x}_{i-1}=\hat{\boldsymbol{x}}} \equiv \tilde{\boldsymbol{F}}(\hat{\boldsymbol{x}}, \boldsymbol{\delta}_{i-1}) \tag{33}$$

Defining

$$\boldsymbol{s}_2 = \boldsymbol{x}_{i-1} + \frac{\Delta t}{2}\, \boldsymbol{k}_1(\boldsymbol{x}_{i-1}, \boldsymbol{\delta}_{i-1}) \tag{34}$$

then

$$\left[\frac{\partial \boldsymbol{k}_2}{\partial \boldsymbol{x}_{i-1}}\right]_{\boldsymbol{x}_{i-1}=\hat{\boldsymbol{x}}} = \left[\frac{\partial \dot{\boldsymbol{x}}(\boldsymbol{s}_2, \boldsymbol{\delta}_{\text{int}})}{\partial \boldsymbol{s}_2}\frac{\partial \boldsymbol{s}_2}{\partial \boldsymbol{x}_{i-1}}\right]_{\boldsymbol{x}_{i-1}=\hat{\boldsymbol{x}}} \tag{35}$$

$$= \left[\frac{\partial \dot{\boldsymbol{x}}(\boldsymbol{s}_2, \boldsymbol{\delta}_{\text{int}})}{\partial \boldsymbol{s}_2}\right]_{\boldsymbol{s}_2=\hat{\boldsymbol{x}}+\frac{\Delta t}{2}\boldsymbol{k}_1(\hat{\boldsymbol{x}},\boldsymbol{\delta}_{i-1})} \left(\boldsymbol{I} + \frac{\Delta t}{2}\left[\frac{\partial \boldsymbol{k}_1}{\partial \boldsymbol{x}_{i-1}}\right]_{\boldsymbol{x}_{i-1}=\hat{\boldsymbol{x}}}\right) \tag{36}$$

$$= \tilde{\boldsymbol{F}}\left(\hat{\boldsymbol{x}} + \frac{\Delta t}{2}\boldsymbol{k}_1(\hat{\boldsymbol{x}}, \boldsymbol{\delta}_{i-1}), \boldsymbol{\delta}_{\text{int}}\right)\left(\boldsymbol{I} + \frac{\Delta t}{2}\left[\frac{\partial \boldsymbol{k}_1}{\partial \boldsymbol{x}_{i-1}}\right]_{\boldsymbol{x}_{i-1}=\hat{\boldsymbol{x}}}\right) \tag{37}$$

Likewise, defining

$$\boldsymbol{s}_3 = \boldsymbol{x}_{i-1} + \frac{\Delta t}{2}\boldsymbol{k}_2(\boldsymbol{x}_{i-1}, \boldsymbol{\delta}_{\text{int}}) \tag{38}$$

allows us to write

$$\left[\frac{\partial \boldsymbol{k}_3}{\partial \boldsymbol{x}_{i-1}}\right]_{\boldsymbol{x}_{i-1}=\hat{\boldsymbol{x}}} = \left[\frac{\partial \dot{\boldsymbol{x}}(\boldsymbol{s}_3, \boldsymbol{\delta}_{\text{int}})}{\partial \boldsymbol{s}_3}\frac{\partial \boldsymbol{s}_3}{\partial \boldsymbol{x}_{i-1}}\right]_{\boldsymbol{x}_{i-1}=\hat{\boldsymbol{x}}} \tag{39}$$

$$= \left[\frac{\partial \dot{\boldsymbol{x}}(\boldsymbol{s}_3, \boldsymbol{\delta}_{\text{int}})}{\partial \boldsymbol{s}_3}\right]_{\boldsymbol{s}_3=\hat{\boldsymbol{x}}+\frac{\Delta t}{2}\boldsymbol{k}_2(\hat{\boldsymbol{x}},\boldsymbol{\delta}_{\text{int}})} \left(\boldsymbol{I} + \frac{\Delta t}{2}\left[\frac{\partial \boldsymbol{k}_2}{\partial \boldsymbol{x}_{i-1}}\right]_{\boldsymbol{x}_{i-1}=\hat{\boldsymbol{x}}}\right) \tag{40}$$

$$= \tilde{\boldsymbol{F}}\left(\hat{\boldsymbol{x}} + \frac{\Delta t}{2}\boldsymbol{k}_2(\hat{\boldsymbol{x}}, \boldsymbol{\delta}_{\text{int}}), \boldsymbol{\delta}_{\text{int}}\right)\left(\boldsymbol{I} + \frac{\Delta t}{2}\left[\frac{\partial \boldsymbol{k}_2}{\partial \boldsymbol{x}_{i-1}}\right]_{\boldsymbol{x}_{i-1}=\hat{\boldsymbol{x}}}\right) \tag{41}$$

Finally, writing

$$\boldsymbol{s}_4 = \boldsymbol{x}_{i-1} + \Delta t\,\boldsymbol{k}_3(\boldsymbol{x}_{i-1}, \boldsymbol{\delta}_{\text{int}}) \tag{42}$$

we have

$$\left[\frac{\partial \boldsymbol{k}_4}{\partial \boldsymbol{x}_{i-1}}\right]_{\boldsymbol{x}_{i-1}=\hat{\boldsymbol{x}}} = \left[\frac{\partial \dot{\boldsymbol{x}}(\boldsymbol{s}_4, \boldsymbol{\delta}_i)}{\partial \boldsymbol{s}_4}\frac{\partial \boldsymbol{s}_4}{\partial \boldsymbol{x}_{i-1}}\right]_{\boldsymbol{x}_{i-1}=\hat{\boldsymbol{x}}} \tag{43}$$

$$= \left[\frac{\partial \dot{\boldsymbol{x}}(\boldsymbol{s}_4, \boldsymbol{\delta}_i)}{\partial \boldsymbol{s}_4}\right]_{\boldsymbol{s}_4=\hat{\boldsymbol{x}}+\Delta t\,\boldsymbol{k}_3(\hat{\boldsymbol{x}},\boldsymbol{\delta}_{\text{int}})} \left(\boldsymbol{I} + \Delta t\left[\frac{\partial \boldsymbol{k}_3}{\partial \boldsymbol{x}_{i-1}}\right]_{\boldsymbol{x}_{i-1}=\hat{\boldsymbol{x}}}\right) \tag{44}$$

$$= \tilde{\boldsymbol{F}}\left(\hat{\boldsymbol{x}} + \Delta t\,\boldsymbol{k}_3(\hat{\boldsymbol{x}}, \boldsymbol{\delta}_{\text{int}}), \boldsymbol{\delta}_i\right)\left(\boldsymbol{I} + \Delta t\left[\frac{\partial \boldsymbol{k}_3}{\partial \boldsymbol{x}_{i-1}}\right]_{\boldsymbol{x}_{i-1}=\hat{\boldsymbol{x}}}\right) \tag{45}$$

References

[1] F. Hemez, H.S. Atamturktur, and C. Unal. Defining predictive maturity for validated numerical simulations. *Computers & structures*, 88(7-8):497–505, 2010.

[2] V.R. Joseph and H. Yan. Engineering-driven statistical adjustment and calibration. *Technometrics*, 57(2):257–267, 2015.

[3] T.A. Oliver, G. Terejanu, C.S. Simmons, and R.D. Moser. Validating predictions of unobserved quantities. *Computer Methods in Applied Mechanics and Engineering*, 283:1310–1335, 2015.

[4] M.C. Kennedy and A. O'Hagan. Bayesian calibration of computer models. *Journal of the Royal Statistical Society: Series B (Statistical Methodology)*, 63(3):425–464, 2001.

[5] M. Goldstein and J. Rougier. Probabilistic formulations for transferring inferences from mathematical models to physical systems. *SIAM journal on scientific computing*, 26(2):467–487, 2004.

[6] M.J. Bayarri, J.O. Berger, R. Paulo, J. Sacks, J.A. Cafeo, J. Cavendish, C.H. Lin, and J. Tu. A framework for validation of computer models. *Technometrics*, 49(2):138–154, 2007.

[7] M.J. Bayarri, J.O. Berger, M.C. Kennedy, A. Kottas, R. Paulo, J. Sacks, J.A. Cafeo, C.H. Lin, and J. Tu. Predicting vehicle crashworthiness: Validation of computer models for functional and hierarchical data. *Journal of the American Statistical Association*, 104(487):929–943, 2009.

[8] C. Unal, B. Williams, F. Hemez, S.H. Atamturktur, and P. McClure. Improved best estimate plus uncertainty methodology, including advanced validation concepts, to license evolving nuclear reactors. *Nuclear Engineering and Design*, 241(5):1813–1833, 2011.

[9] S. Atamturktur, F. Hemez, B. Williams, C. Tome, and C. Unal. A forecasting metric for predictive modeling. *Computers & Structures*, 89(23-24):2377–2387, 2011.

[10] S. Atamturktur, J. Hegenderfer, B. Williams, M. Egeberg, R.A. Lebensohn, and C. Unal. A resource allocation framework for experiment-based validation of numerical models. *Mechanics of Advanced Materials and Structures*, 22(8):641–654, 2015.

[11] J. Hegenderfer and S. Atamturktur. Prioritization of code development efforts in partitioned analysis. *Computer-Aided Civil and Infrastructure Engineering*, 28(4):289–306, 2013.

[12] M.J. Bayarri, J.O. Berger, J. Cafeo, G. Garcia-Donato, F. Liu, J. Palomo, R.J. Parthasarathy, R. Paulo, J. Sacks, and D. Walsh. Computer model validation with functional output. *The Annals of Statistics*, pages 1874–1906, 2007.

[13] J. Brynjarsdóttir and A. O'Hagan. Learning about physical parameters: The importance of model discrepancy. *Inverse Problems*, 30(11):114007, 2014.

[14] M.S. Arulampalam, S. Maskell, N. Gordon, and T. Clapp. A tutorial on particle filters for online nonlinear/non-Gaussian Bayesian tracking. *IEEE Transactions on signal processing*, 50(2):174–188, 2002.

[15] E.T. Jaynes. *Probability theory: the logic of science*. Cambridge university press, 2003.

[16] E. Simoen, C. Papadimitriou, and G. Lombaert. On prediction error correlation in Bayesian model updating. *Journal of Sound and Vibration*, 332(18):4136–4152, 2013.

[17] P.L. Green. Bayesian system identification of dynamical systems using large sets of training data: A MCMC solution. *Probabilistic Engineering Mechanics*, 42:54–63, 2015.

[18] J. Ching, J.L. Beck, and K.A. Porter. Bayesian state and parameter estimation of uncertain dynamical systems. *Probabilistic engineering mechanics*, 21(1):81–96, 2006.

On NARX models using treed Gaussian processes

T. Zhang, R.J. Barthorpe, K. Worden
Dynamics Research Group, Dept. of Mechanical Engineering, University of Sheffield, Mappin Street, Sheffield, S1 3JD, UK
e-mail: **k.worden@sheffield.ac.uk**

Abstract

Recent work in nonlinear system identification has considered the use of Gaussian processes (GPs) as a basis for forming nonlinear time-series models — NARX models. The two main advantages of the GP formulation are that the structure detection problem is avoided (i.e. there is no need to specify which model terms are included) and that natural confidence intervals on predictions are provided. The main disadvantage of the GP approach is that a global smoothness criterion is applied and this raises issues for the identification of piecewise-linear systems, or regime-switching systems in general. The aim of the current work is to show that the problems can be removed by using a Treed Gaussian process (TGP) in order to formulate the NARX model. Not only does this allow local smoothness criteria, but it also determines the relevant boundary points of the switching regimes. The method is illustrated using simulated data from a Duffing oscillator system.

1 Introduction

In the domain of time-series analysis, the *Nonlinear Auto-Regressive Moving Average eXogenous* (NARMAX) model is a popular data inferencing framework offering great versatility and adaptability [1]. The NARMAX model possesses a high degree of generality for taking a bipartite consideration of both the auto-regressive and the moving average natures of the signal. To achieve a more parsimonious improvement, the NARX (Nonlinear Autoregressive eXogenous) model is often used, which is a special case derived from the NARMAX model, when the model noise is assumed to be white Gaussian. This paper presents a study of the NARX modelling of the Duffing oscillator system using the *Treed Gaussian Process* (TGP).

The NARX model naturally inherits the character of the NAR (Nonlinear AutoRegressive) model, where the current prediction of the system output is a function of the previous inputs and outputs. The NARX model is distinguished for its inclusion of the eXogenous term, which accommodates a separate input from outside of the system, thus such an external input is naturally independent of the development of the system output. Such a configuration can be expressed in mathematical form by the following equation,

$$y_i = F(y_{i-1}, y_{i-2}..., y_{i-n_y}; x_{i-1}, x_{i-2}...x_{i-n_x}) + \epsilon_i \tag{1}$$

where y_i is the system output at the i^{th} step; x_i is the eXogenous input; n_y and n_x are the numbers of lags w.r.t. y and x and ϵ_i represents the noise or *residual* sequence.

There are various forms for the NARX modelling function F. The common choice, in a certain sense of tradition, describes the internal mechanism of the NARX system with a multivariate polynomial function. As being a member of the family of parametric modelling, the polynomial approach to the NARX system requires a two-step procedure to initialise. The first is to determine the specific model structure (e.g. what terms to include in the polynomial function) – which is known as the *model detection*. The second step is to determine the corresponding expansion parameters (e.g. polynomial coefficients) based on the result of the model detection. However, the procedure of model detection can be rather troublesome, as an inappropriate

establishment of the polynomial terms can lead to either poor prediction or overfitting issues. Therefore, in recent years, the nonparametric treatment of the modelling of the NARX system has gradually gained some increasing attentions, as it features a major advantage over the tradition parametric models. Nonparametric models such as neural networks [1] or Gaussian Processes (GP) [2], require no step for the model detection. Instead, since nonparametric models have a fixed group of system parameters which establish a general conformity to the data space, the user can simply specify all these parameters without reluctantly making selections on them. For example, Gaussian Processes as a nonparametric modelling paradigm, only have three hyperparameters to define once a Squared-Exponential (SE) kernel is selected for it to use [2]. Despite such an advantage, the nonparametric models do suffer from higher computational cost in terms of parameter estimation, especially when handling large dataset containing thousands of data points, as the computational cost is associated with N^3 (N is the number of data points).

In this paper, the authors present an advanced NARX model based on the nonparametric framework provided by the Chipman-based Treed Gaussian Processes (CTGP) [3], and this model will be applied to studying the behaviour of the Duffing Oscillator. Fundamentally, any GP-based model is, in general, considered to be nonparametric, because the GP commonly uses a distance-based-kernel function to specify the rule of inference resulting in a predictive profile in no compliance to a fixed form. However, the GP can also use non-distance based kernels to establish regular parametric models. In this paper, a simple linear kernel is selected for the GP, thereby the GP discussed here essentially is equivalent to a simple Bayesian linear model. Using the linear kernel GP in coalescence with the decision tree ultimately will produce a piecewise linear prediction of the training data space. It is common knowledge that curvatures can be approximated by multiple straight lines.

The *Linear-Kernel Chipman-based Treed Gaussian Process* (LK-CTGP) takes advantages from both the simple linear regression and the decision tree model in countering the nonlinearity of the NARX system. The model detection for the LK-CTGP model is rather simple, as it only requires a full specification of a simple multivariate linear regression formulation based on the model lag defined by the user. The lag specified does not necessarily need to be accurate (although in a completely principled formulation, the lag numbers are hyperparameters), but needs to be large enough so that all the effective lags are covered. The partitions produced under the decision tree framework, will generate regions where a fair linearity is guaranteed.

2 Chipman-based Treed Gaussian Processes

A Treed Gaussian Process, in mathematical terms, is an amalgamation of a Binary Decision Tree (BDT) and Gaussian Processes (GP)[4]. A decision tree is a logical mapping process through which the elements of a given input space will be assigned into different groups represented by leaves of the tree based on a series of criteria [5]. A binary tree basically means the criteria take the form of a simple choice of YES/NO, thus branching the underlying space into two subgroups. Through repeated application of this splitting process, a treed structure will be established. Figure 1 shows a typical BDT. In brief, the BDT may be thought of as a tangible representative framework for partitioning a set of data.

A Gaussian Process is an extensively applied statistical inference method based on the concept of Bayesian inference. It may be applied to either regression or classification problems. In the context of regression, the traditional GP offers a nonparametric prediction to the data space of interest [6] if a distance-based kernel function is chosen. The distance here refers to the distance between any pair of data points in the data space. Under the traditional GP setting with distance-based kernel functions, the inference is based on the argument that predictions at any point in space are latently influenced by all other data points in the training space. To quantify the extent of this influence, a covariance matrix is constructed which contains all the weight of the influence between any pair of data points in the training space. If the covariance function is non-distance based, the GP can also simply become a parametric model.

Gramacy introduced one type of TGP model [4] which has seen application in numerous contexts. More strictly say, Gramacy's TGP (GTGP) is the very first attempt to amalgamate the GP model with the decision

tree. Therefore Gramacy is indubitably recognised as the founder of the TGP. The closest predecessor of the TGP is the well-known Bayesian Classification and Regression Tree (BCART) by Chipman et al [7], where the idea of a Bayesian stochastic tree was first introduced. This paper discusses another type of TGP which will be referred to as the 'simplified TGP' or 'Chipman-based TGP'. The CTGP suggests a TGP model completely springs from the raw ideas of Chipman's BCART model. In order to prevent any confusion between these two TGP models, one should know that the Gramacy-based TGP also borrows ideas from Chipman's theory, but only in terms of how to alter the structure of the tree. The current paper sets complete reliance on Chipman's idea, which will be illustrated subsequently.

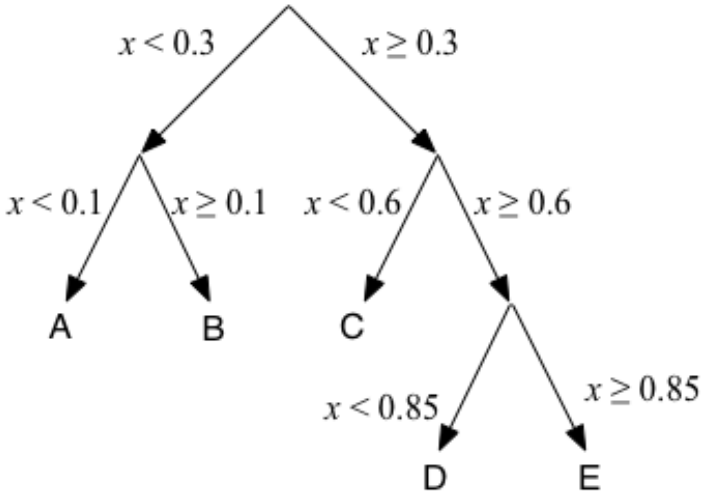


Figure 1: Typical Binary Decision Tree.

The CTGP samples the partitions in the training space as in a form of growing a tree. The tree is to be treated as a state in a Markov Chain, thus the holistic sampling process manifests itself as a manner of Markov Chain Monte Carlo (MCMC). The most crucial aim of sampling in the MCMC space is to arrive at those trees with high posterior probability which is the total product of local posteriors from all the leaves. The posterior of the tree can be expressed mathematically by equation (2).

$$\begin{aligned} p(T|X,Y) &\propto p(Y|X,T)p(T) \\ p(Y|X,T) &= \prod_{i=1}^{b} p(Y_i|X_i) \end{aligned} \tag{2}$$

where T represents the tree; X and Y are the training input and output respectively; b is the number of leaves.

To achieve suitably rapid convergence to appropriate trees, a Metropolis-Hastings (MH) algorithm with a complement of four tree structure alteration operations is adopted. Each step of the Markov Chain features a proposal stage and evaluation stage. The proposal stage involves the proposition of a new tree through one of four operations; these are GROW, PRUNE, CHANGE and ROTATE. Each of these operations possesses a high similarity to the ones described in Chipman's paper regarding BCART under the exact same names, except for the ROTATE; whilst Chipman used the idea of SWAP, the ROTATE execution derives its originality from Gramacy.

In simple terms, the four operations have the following effect on the structure of the tree:

- GROW: add one partition by split one leaf node of the tree

- PRUNE: remove one partition by joining two sibling child nodes
- CHANGE: relocate an existent partition by changing splitting rule in the tree
- ROTATE: maintain the partitions but change their 'staging' sequence by rearrangement of the tree structure

The evaluation stage involves evaluating the *Maximum A Posteriori* (MAP) estimate of the newly proposed tree, and then setting forth a comparison against the posterior from the last accepted tree. The residual that results from the subtraction between the logarithm of these two posteriors will be taken as a metric to decide on the probability that the proposal should be accepted. Through a large number of MCMC samples, the process will eventually explore the MCMC state space for high posterior trees, spending more time in regions of high posterior probability. In a little more detail, the evaluation of the MAP tree normally features an optimisation of the marginal likelihood function of each individual GP in terms of all its covariance hyperparameters, if a distance-based kernel function is chosen. To find the extrema of a given function, suggested optimisation approaches include either a gradient-based line search or a sampling-based search. In this particular application on the NARX model, the only parameter that requires the optimisation is the noise level, and it is treated as known here. The linear function parameters can be analytically obtained through Bayes' rule with the knowledge of the noise level.

Following the completion of the MAP evaluation, the MAP estimate is used for the Metropolis-Hastings evaluation, in which the MAP estimates of the current and last-accepted tree are compared in order to decide whether to accept the newly proposed tree. The rule of the Metropolis-Hasting algorithm is stated in the equation,

$$A = \min(1, \frac{P(T')}{P(T^*)} \frac{Q(T^*;T')}{Q(T';T^*)}) \tag{3}$$

where $*$ denotes the proposed tree, $'$ denotes the current tree state, Q is the transition probability which depicts the probability of jump between states in the Markov space, P is the MAP of the tree. The proposed state will be accepted with probability of A.

3 Model Performance Assessment Criteria

The prediction from the LK-CTGP on the NARX data can be assessed in various ways. The common basic metric is the *One-Step-Ahead* (OSA) predictions of the model. The OSA prediction only uses the training data as the reference for making the prediction at a given time, which is described by the equation,

$$y_i^* = f(y_{i-1}, ..., y_{i-n_y}; x_i, ..., x_{i-n_x+1}) \tag{4}$$

where the $*$ now denotes a predicted value.

It is rather arguable that the OSA prediction is a rigorous and descriptive metric to evaluate the model prediction performance. First, the OSA prediction completely depends on the training data, thus obviously it has problems with overfitting issues. Secondly, the NARX system is a self-generative or self-developing time series system, where once the initial condition is given, the subsequent process is largely deterministic. Therefore, a good metric should provide a measure on the generative performance of the model when given the same initial conditions as the training data. This leads to the *Model Predicted Output* (MPO) predictions as shown in equation (5), where the prediction at a certain time is computed based on the predictions made up to that time.

$$y_i^* = f(y_{i-1}^*, ..., y_{i-n_y}^*; x_i, ..., x_{i-n_x+1}) \tag{5}$$

Once the MPO predictions are made, the Normalised Mean Square Error (NMSE) of the model can be computed:

$$NMSE(\hat{y}) = \frac{100}{N\sigma_y^2}\sum_{i=1}^{N}(y_i - \hat{y}_i)^2 \tag{6}$$

According to previous experience, it is known that an NMSE less than 5.0 shows a good fit to the data, while an NMSE less than 1.0 shows an excellent fit.

4 Case Study: The Duffing Oscillator

The basic generative function for the Duffing oscillator NARX system is given as follows,

$$y_i = ay_{i-1} + by_{i-2} + cy_{i-1}^3 + du_{i-1} + \epsilon_i \tag{7}$$

where y is the output response variable, displacement; u is the eXogenous input variable, the external force; ϵ is the residual noise; a,b,c,d are all constants.

The generative function in equation (7) shows the true relation between the input and output to produce a sequence of responses y in terms of time is a 3D cubic function with input variables y_{i-1}, y_{i-2} and u_{i-1}. Therefore, a simple linear regression model is supposed to be inept at comprehensively describing the behaviour of the data. Naturally the cubic behaviour can be approximated by a piecewise-linear model, when given the correct partitioning locations to reasonably accommodate each individual linear model. The LK-CTGP offers a binary process to recursively partition the input space into regions, which is considered to be efficient and effective.

Before delving into the performance of the CTGP on the data, it is worthwhile to study the generative function theoretically. From Equation 7, it is clear that the nonlinearity is introduced by the cubic term associated with the first lag of y. from the partial differentiation with respect to each of the input variables, it can be found that only in the dimension of y_{i-1}, does the function have non-constant slope. Such a fact manifests that the entire input space has no gradient change in either dimension of y_{i-2} or u_{i-1}, therefore, the reasonable partitions are exclusive to taking in the dimension of y_{i-1}, where once the other two input variables are held fixed, the curve simplifies to a visualisable classic one-dimensional cubic function. Through performing the partial differentiation on Equation 7 with respect to y_{n-1} and equate it to zero, one can obtain the two roots,

$$r_{1,2} = \pm\sqrt{\frac{-b}{3c}} \tag{8}$$

Naturally these two roots represent the local peak and trough of the cubic function. The 3D cubic surface under the current Duffing setup can naturally be approximated as a piecewise-trilinear system by putting partitions at these two roots if the y set contains both roots. However, the nonlinearity of the NARX system has one extra influencing factor other than the coefficients associated with the cubic input terms here. Such a factor is the eXogenous input. Although the eXogenous input does not affect the surface profile of the generative function, it does affect the effective area in the function space. In the AR-based models (inc. ARX and NARX), since the current state of the response variable is a function of its previous states, the dynamical updating process in the training input space can naturally be periodic based on the property of the function. When the function value is greater than the unit linear function in terms of absolute value ($|y_i| > |y_{i-1}|$), the y value increases; if $|y_i| < |y_{i-1}|$, y decreases. Therefore, based on such relations, periodicity in y values can form for a cubic AR function. Figure 2 shows an example where the periodicity covers both the proximity of the maximum and minimum values (AR periodicity of y forms approximately in [-1.2,1.2]).

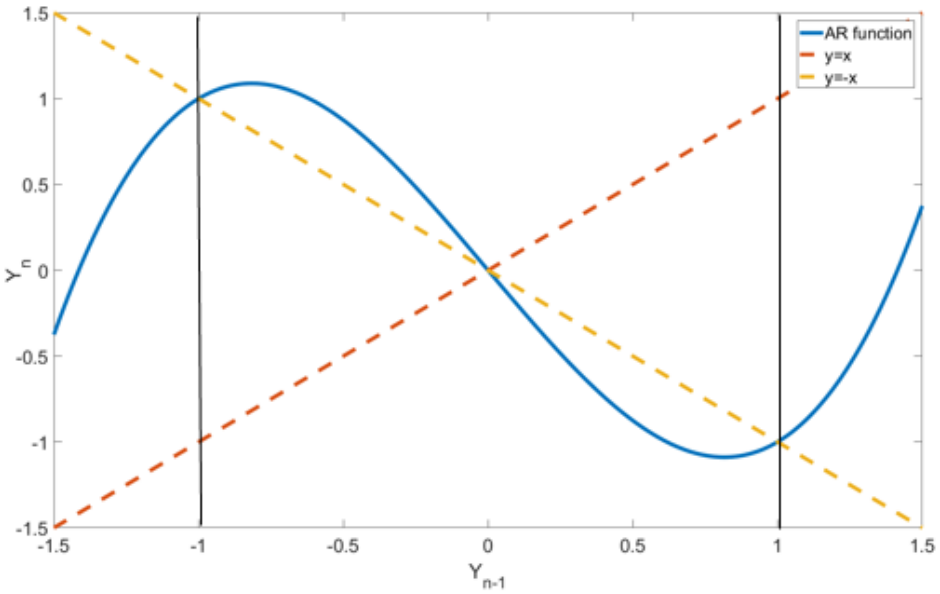


Figure 2: Illustration of the AR periodicity.

The level of the eXogenous input does affect the span of the periodicity, thus the local nonlinearity within the span will change accordingly, though the general cubic function profile remains unchanged.

The parameter value set-up for equation (7) is taken here as $a = -0.98$, $b = 1.97$, $c = -5000$, $d = 1e-6$ and $\epsilon = 0.0001 * \sigma_y$ (0.001% of RMS value). The eXogenous input is uniformly drawn from [-100,100]. 4000 points are generated. Under such a set-up, the y values are bounded in [-0.004,0.004], while the two roots are ± 0.114. The y values do not contain both peak and trough of the NARX generative function Equation 7. Since the y values concentrate in the small centre interval between ± 0.114, a weak effect of the nonlinearity in the system is to be expected. Figure 3 shows the original time series data of y.

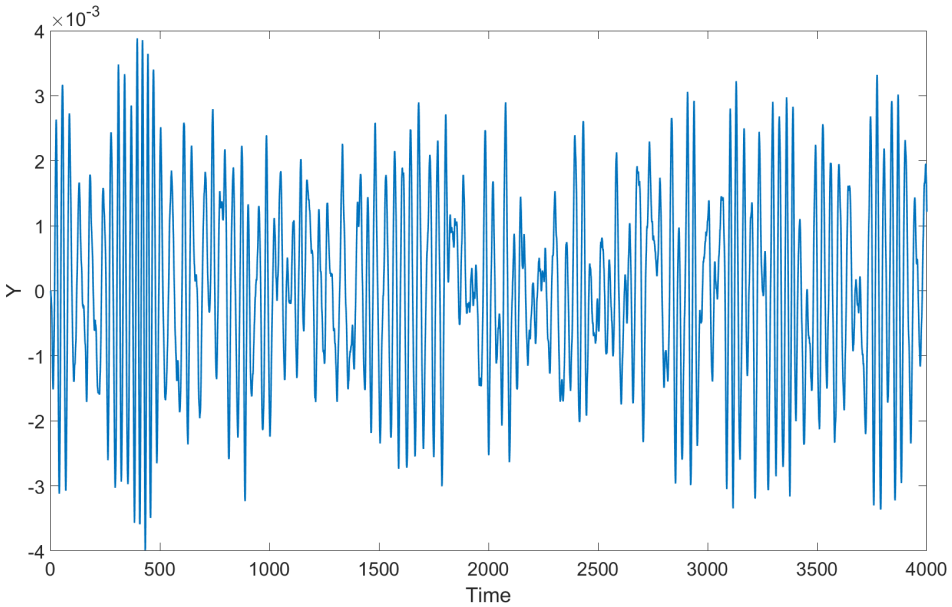


Figure 3: Original Time Series data.

Through applying the simple Least Square (LS) Model to the data space constructed by input variable $[y_{n-1}, y_{n-2}, u_{n-1}]$ and output y_n, the OSA prediction gives an extremely good fit to the original data by producing an NMSE value of 0.02 which is much less than 1.0. However, as has been addressed before, the OSA prediction is a rather rough metric to assess the NARX model. The MPO predictions of the first 1500 data points from the LS model are shown in Figure 4.

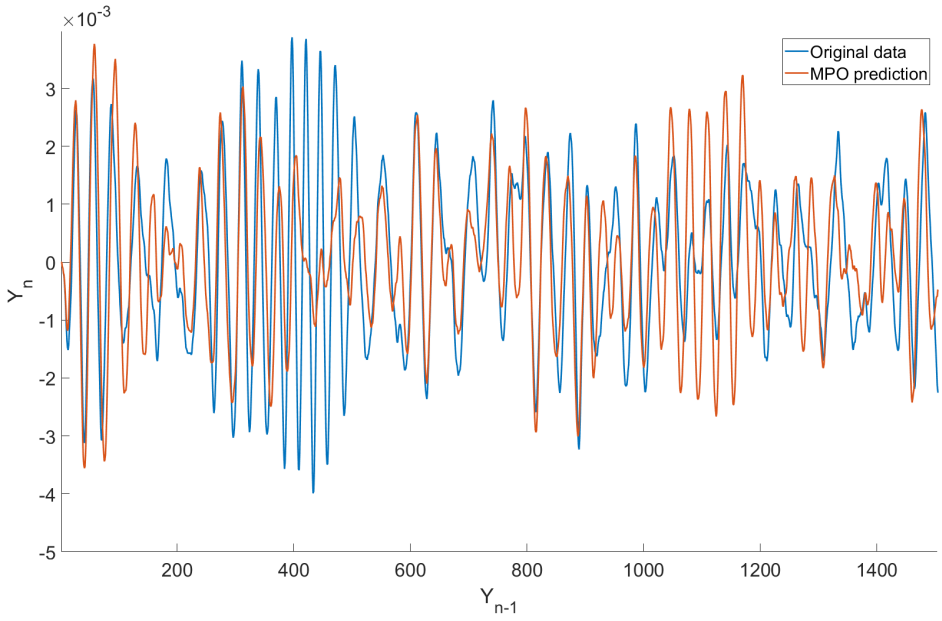


Figure 4: MPO predictions of LS model against original data.

Figure 4 shows that, even though the OSA predictions of the LS model show exceedingly good agreement to the original data at low level of nonlinearity, the small nonlinearity in the system can be large enough to cause significant departures from the original data in the MPO predictions; here the NMSE for the MPO predictions of the LS model is 69.5.

If the LK-CTGP is applied, the MPO predictions for the first 1500 data points are as shown in Figure 5.

The LK-CTGP produced 6 leaves to accommodate the nonlinearity in the system. All the leaves are generated from partitions concentrated in the dimension of y_{i-1} as expected, therefore, these partitions are reasonably placed. Figure 5 shows a good agreement between the MPO predictions of the LK-CTGP model and the original data. The NMSE here is decreased to 1.26. For clarity, the confidence intervals of the predictions are omitted.

5 Concluding Remarks

This paper presented a preliminary and trial study of the NARX system with the LK-CTGP model. The LK-CTGP model is easy to specify in terms of its parameters and counters nonlinearity by producing partitions. It has been found that the MPO predictions are strongly sensitive to the nonlinearity in the system, which caused the simple linear least-squares model to produce large MPO errors, even though the nonlinearity is thought to be low. The LK-CTGP successfully produced a piecewise-linear model, which broke down the nonlinearity by minimising the local nonlinearity in each generated region. The concentration of the partitions in the dimension of y_{i-1} proves that, these partitions are reasonably placed rather than merely by chance. The problem with the current LK-CTGP model for the NARX system is that the model requires an accurate input of the noise parameter, which in this study is treated as known. However, the direct access to the accurate noise in practice is rather idealistic. More fundamentally, the piecewise linear model might

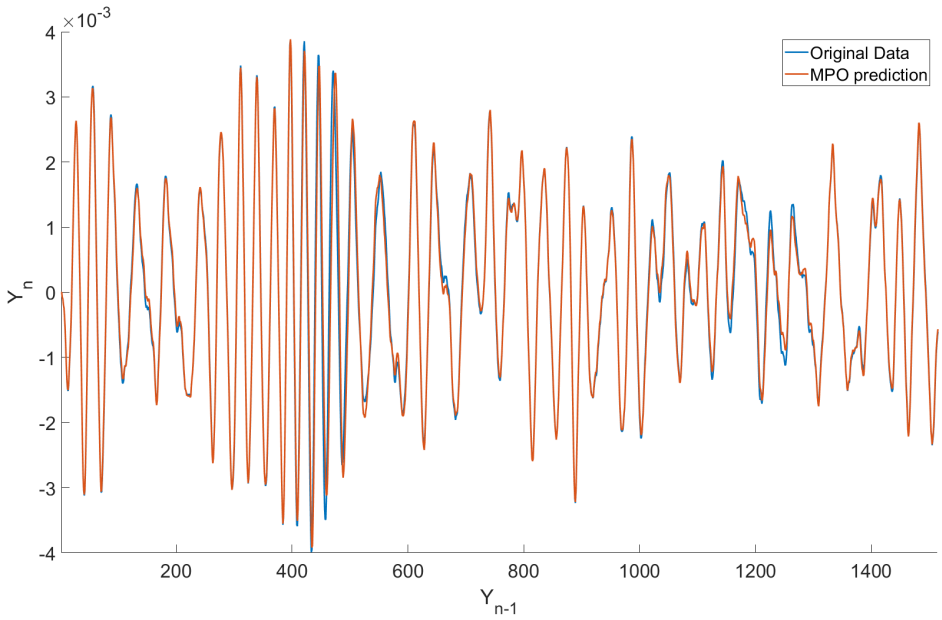


Figure 5: MPO predictions of LK-CTGP model against original data.

not be the best piecewise model for the NARX system, because too many regions are required to ensure a good linearity in each region. The general CTGP undoubtedly has more potential in studying the NARX model. Those distance-based kernels can offer smoother curve fittings for the TGP model, which seems to promising. However, the computational cost will drastically increase.

References

[1] S.A. Billings *Nonlinear System Identification: NARMAX, Methods in the Time, Frequency, and Spatio-Temporal Domains* Wiley-Blackwell, (2013).

[2] K. Worden, W.E. Becker, T.R. Rogers, E.J. Cross, *On the confidence bounds of Gaussian Process NARX models and their higher-order frequency response functions* Mechanical Systems and Signal Processing, Vol. 104, (2018), pp.188–223

[3] T. Zhang, *On Treed Gaussian Processes for Modelling Structural Dynamic Systems*, PhD Thesis, University of Sheffield, (2018).

[4] R.B. Gramacy, H.K.H. Lee, *Bayesian treed Gaussian process models with an application to computer modeling* Journal of the American Statistical Association, Vol. 103, (2008), pp.1119–1130.

[5] P. Chaudhuri, W.-D. Lo, W.-Y. Loh, C.-C. Yang, *Generalized regression trees* Statistica Sinica, (1995), pp.641–666.

[6] C. Rasmussen, C. Williams, *Gaussian Processes for Machine Learning*, MIT press, (2006)

[7] H.A. Chipman, E.I. George, R.E. McCulloch, *Bayesian CART model search* Journal of the American Statistical Association, Vol. 93, (1998), pp.935-948.

Optimal parameters in Data-driven stochastic subspace identification in Operational Modal Analysis

Chun-Yu Tsai[1], Yum Ji Chan[1], Jau-Liang Chen[1], Ching-Ling Chao[1], Shih-Yin Chien[1]
[1] National Chung Hsing University, Department Mechanical Engineering
145 Xing-da Road, Taichung 40227, Taiwan
e-mail: **yjchan@nchu.edu.tw**

Abstract
Stochastic subspace identification operational modal analysis is a recently-developed method in modal testing. In this method, determining the dimensions of the Hankel matrix in the projection procedure is an important step. In this paper, the number of rows of the Hankel matrix is recommended to be larger than a half period of Toeplitz matrix. There is no need to adopt excessive number of rows in the Hankel matrix, because the projection results would not vary significantly under high number of the matrix rows. Also, if computational power is limited, the projection results stabilize more quickly if the number of rows, number of columns and the sampling frequency are decreased as the same time.

1 Introduction

Traditionally, modal parameters including natural frequencies, damping ratios and mode shapes are identified by experimental modal analysis (EMA) [1]. However, EMA has some limitations [2], such as (i) difficulties in exciting large structures or structures in field testing, such as wind turbines, bridges or towers, and (ii) testing of structures under real conditions (such as machines under movement), which are different from laboratory conditions.

Operational modal analysis (OMA), also known as output-only modal analysis, has been developed to tackle the issues above [3]. In this method, only the responses of the structure under ambient or natural excitation are required to identify modal parameters. OMA has been used in many applications. For civil engineering structures, OMA has been applied to determine the dynamic properties of truss railway bridge [4], culvert for high speed train lines [5] and a statue [6]. OMA has also been applied to mechanical structures such as CNC machine tools [7], antenna reflector of spacecraft [8] and laminated glasses [9].

Stochastic subspace identification (SSI) and frequency domain decomposition (FDD) are two popular algorithms in OMA. Stochastic subspace identification is a time-domain identification method. This algorithm was developed since 1990s [10], and used to identify the dynamic parameters in civil engineering [11, 12]. Although SSI is often used in modal parameter identification, this algorithm has uncertainty caused by model order and stabilization diagram [13] and spurious poles [14].

Choosing a suitable dimension of Hankel matrix is an important step in the SSI algorithm [16]. Priori et al. show how the user-defined parameters in SSI effect the identification results [15]. Reynders et al. indicate that the number of columns of Hankel matrix (denoted N in the discussion below) should be as large as possible [17], while Brincker and Ventura propose a minimum value of N as a function of system damping ratio and lowest frequency of interest [3]. On the number of rows of the Hankel matrix, it has been proposed the number of rows should be larger than $f_s/2f$, where f_s is the sampling frequency and f is the lowest frequency of interest [17]. While large matrix sizes generally help statistical methods such as the SSI, this can lead to memory wasted and long computing time. Therefore, the objective of the current study is to determine the optimal values of the Hankel matrix, if these exist.

In this study, the projection procedure which is used to filter noise in measured data of the Hankel matrix is analyzed by covariance estimate. Variation of the projection results under different matrix sizes is discussed.

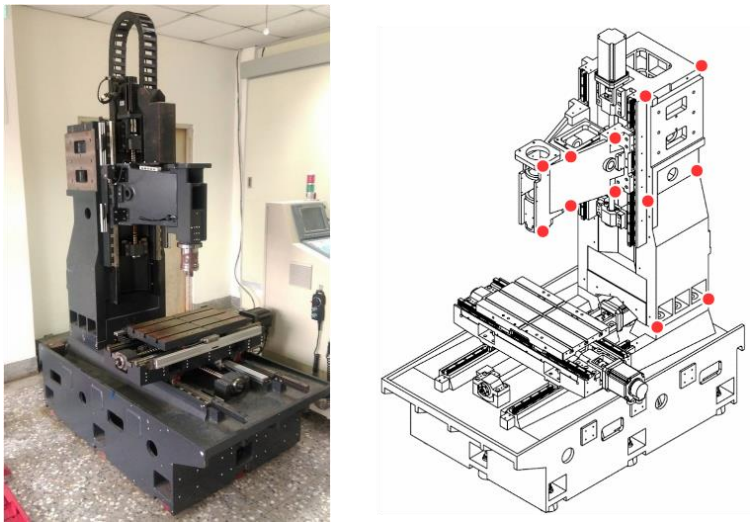


Figure 1 Vertical milling machine to be tested: (left) actual object (right) arrangement of measurement points [7]

2 Operational modal analysis and stochastic subspace identification

In OMA, the structure is assumed to be excited by white noise, and subsequent mathematical treatment is based on this assumption. However, in real-world OMA tests, the excitation is not white noise. In OMA theory, the nonwhite input is assumed that the output from the imaginary filter which is loaded by white noise. The OMA system estimates a combined system including the physical structure and a loading filter (Figure 2).

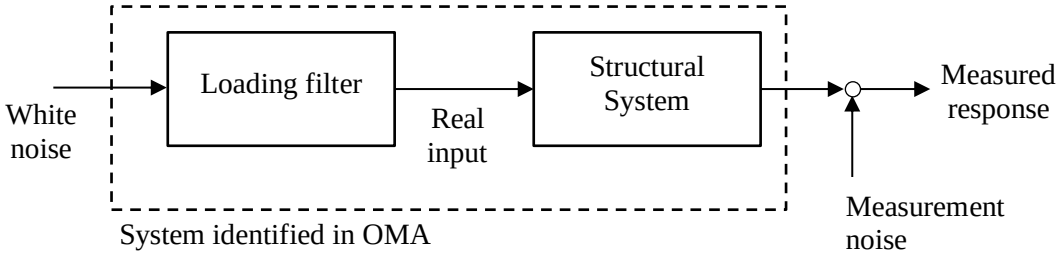


Figure 2 System identification in OMA

2.1 State space model

The governing equation of a n_0 degrees of freedom system is given by

$$\mathbf{M}\ddot{\mathbf{q}}(t) + \mathbf{C}^*\dot{\mathbf{q}}(t) + \mathbf{K}\mathbf{q}(t) = \mathbf{f}(t) \tag{1}$$

where $\mathbf{M}$, $\mathbf{C}^*$ and $\mathbf{K} \in \mathbb{R}^{n_0 \times n_0}$ represent mass, damping and stiffness matrix of the system. $\ddot{\mathbf{q}}(t)$, $\dot{\mathbf{q}}(t)$ and $\mathbf{q}(t) \in \mathbb{R}^{n_0 \times 1}$ are the acceleration, velocity and displacement of the system. $\mathbf{f}(t) \in \mathbb{R}^{n_0 \times 1}$ is the external force.

Define two state variables $\mathbf{x_1}$ and $\mathbf{x_2}$, where

$$\begin{aligned} \mathbf{x}_1(t) &= \mathbf{q}(t) \\ \mathbf{x}_2(t) &= \dot{\mathbf{x}}_1(t) \end{aligned} \tag{2}$$

The derivatives of the state variables are calculated using state differential equation.

$$\begin{Bmatrix}\dot{\mathbf{x}}_1(t)\\ \dot{\mathbf{x}}_2(t)\end{Bmatrix} = \mathbf{A}\begin{Bmatrix}\mathbf{x}_1(t)\\ \mathbf{x}_2(t)\end{Bmatrix} + \mathbf{B}\mathbf{f}(t)$$
$$\mathbf{y}(t) = \mathbf{C}\begin{Bmatrix}\mathbf{x}_1(t)\\ \mathbf{x}_2(t)\end{Bmatrix} \tag{3}$$

where $\mathbf{y}(t) \in \mathbb{R}^{M\times 1}$ is the output vector at M measured degrees of freedom:

$$\mathbf{y}(t) = \begin{Bmatrix} y_1(t)\\ y_2(t)\\ \vdots\\ y_M(t)\end{Bmatrix} \tag{4}$$

and

$$\mathbf{A} = \begin{bmatrix} 0 & \mathbf{I}\\ -\mathbf{M}^{-1}\mathbf{K} & -\mathbf{M}^{-1}\mathbf{C}^*\end{bmatrix}, \qquad \mathbf{B} = \begin{bmatrix} 0\\ \mathbf{M}^{-1}\end{bmatrix}, \qquad \mathbf{C} = [-\mathbf{M}^{-1}\mathbf{K} \quad -\mathbf{M}^{-1}\mathbf{C}^*] \tag{5}$$

The natural frequencies and viscous damping ratios of the system (denoted ω_i and ξ_i, respectively) can be sought from eigenvalues of matrix **A**. Matrix **C** called output matrix, and it is related to the mode shapes of the system.

2.2 Stochastic subspace identification

To determine the modal parameters of the system, matrices **A** and **C** are determined from the measured responses [18]. Firstly, data matrix **Y** is constructed based on lumping the output vector at N_T samples:

$$\mathbf{Y}_{1:N_T} = [\mathbf{y}_1 \quad \mathbf{y}_2 \quad \cdots \quad \mathbf{y}_{N_T}] \tag{6}$$

A block Hankel matrix $\mathbf{H} \in \mathbb{R}^{2IM\times N}$ is created by shifting the output vector.

$$\mathbf{H} = \frac{1}{\sqrt{N}}\begin{bmatrix}\mathbf{y}_1 & \mathbf{y}_2 & \cdots & \mathbf{y}_N\\ \mathbf{y}_2 & \mathbf{y}_3 & \cdots & \mathbf{y}_{N+1}\\ \vdots & \vdots & & \vdots\\ \mathbf{y}_{2I} & \mathbf{y}_{2I+1} & \cdots & \mathbf{y}_{2I+N-1}\end{bmatrix} = \begin{bmatrix}\mathbf{H}_p\\ \mathbf{H}_f\end{bmatrix} \tag{7}$$

The Hankel matrix is split into two block Hankel matrices of equal sizes. The upper half part of the Hankel matrix is called "the past" and denoted $\mathbf{H}_p$. the lower half part of the Hankel matrix is called "the future" and denoted $\mathbf{H}_f$. The total data shift in the Hankel matrix is $2I$ which is denoted "the number of block rows". Based on the defined block Hankel matrices, the projection matrix of "future" data unto "past" data is defined as [18]

$$\mathbf{O} = \mathbf{T}_{fp}\mathbf{T}_{pp}^{+}\mathbf{H}_p \tag{8}$$

where $\mathbf{T}_{fp}$ and $\mathbf{T}_{pp}$ are block Toeplitz matrices defined as

$$\mathbf{T}_{fp} = \mathbf{H}_f\mathbf{H}_p^T, \qquad \mathbf{T}_{pp} = \mathbf{H}_p\mathbf{H}_p^T \tag{9}$$

$\mathbf{T}_{fp}$ and $\mathbf{T}_{pp}$ are also called covariance matrices, which are discussed in the next section in detail. The values in these two matrices are represented the correlation of the output vectors with different time delay. The matrix **O** is the response matrix of the system in lower noise level. In SSI theory, the projection matrix can be expressed by

$$\mathbf{O} = \mathbf{\Gamma}_s\mathbf{X}_0 \tag{10}$$

where $\mathbf{\Gamma}_s$ and $\mathbf{X}_0$ are observability matrix and Kalman states matrix. To determine observability matrix, the singular value decomposition is used on matrix $\mathbf{O}$

$$\mathbf{O} = \mathbf{U}_n \mathbf{S}_n \mathbf{V}_n^T \tag{11}$$

The first n singular values in the diagonal matrix $\mathbf{S}$ is corresponding to $n/2$ modes. The estimate of the matrix $\mathbf{\Gamma}_s$ and the matrix $\mathbf{X}_0$ is defined by

$$\hat{\mathbf{\Gamma}} = \mathbf{U}_n \sqrt{\mathbf{S}_n}, \qquad \hat{\mathbf{X}}_0 = \sqrt{\mathbf{S}_n} \mathbf{V}_n^T \tag{12}$$

After the matrix $\hat{\mathbf{\Gamma}}_s$ is sought, the system matrix $\mathbf{A}$ can be found by solving a least squares problem. Natural frequencies and damping ratios can be found by calculating the eigenvalues of $\mathbf{A}$ [3]. output matrix $\mathbf{C}$ can be found by taking the first block row of the matrix $\hat{\mathbf{\Gamma}}_s$. The mode shapes are found by

$$\mathbf{\Phi} = \mathbf{C}\mathbf{\Psi} \tag{13}$$

where the matrix $\mathbf{\Psi}$ is the eigenvector of the matrix $\mathbf{A}$.

3 Variation of the projection results in data-driven SSI under different matrix sizes

In OMA, the system is assumed to be excited by white noise. Therefore, removing noise in responses is an important step before the modal parameters identification. In data-driven SSI, the projection is used to filter noise in system responses. However, the efficacy of filter is influenced obviously by dimensions of the Hankel matrix. In this section, the Hankel matrix would be projected by true random method and theoretical method. In theoretical method, length of response signals is assumed approaching to infinity. Therefore, projection procedure would not be influenced by number of columns of the Hankel matrix. The variation of projection results under different number of rows of the Hankel matrix can be found. In true random method, projection procedure is carried out by Equation (8). Under limited length of response signals, noise cannot be filtered perfectly. This method is used to analyzed the stability of the projection procedure under different number of columns of the Hankel matrix.

3.1 Random variables and signals

If the system is excited by random input, the measured responses are also random numbers. In the SSI algorithm, the projection procedure is based on probability processing.

Assume a stochastic vector $x(t)$. The mean value of μ_x is denoted as the expectation of $x(t)$

$$\mathrm{E}[x(t)] = \int_{-\infty}^{\infty} x p(x) dx = \mu_x \tag{14}$$

where $p(x)$ is the probability density function of $x(t)$. By time average assumption [3], $p(x)$ is assumed as $1/T$, where T is the time length of the vector. The expectation of $x(t)$ can be expressed by

$$\mathrm{E}[x(t)] = \frac{1}{T} \int_0^T x(t) dt \tag{15}$$

In random vibration, the measured signals are assumed as zero mean. Therefore, the variance is defined as

$$\sigma_x = \mathrm{E}\left[\left(x(t)\right)^2\right] = \frac{1}{T} \int_0^T \left(x(t)\right)^2 dt \tag{16}$$

Considering another stochastic vector $y(t)$, the covariance between $x(t)$ and $y(t)$ is given by

$$cov[x(t), y(t)] = \mathrm{E}[x(t)y(t)] = \frac{1}{T}\int_0^T x(t)y(t)dt \tag{17}$$

3.2 Analysis of Hankel matrix projection

In the SSI algorithm, the projection of future data unto past data is sought using Eq. (8). In the ideal situation where measurement noise is absent (that is, $v(n) = 0$) and the value of I being sufficiently high, $\mathbf{O} = \mathbf{H}_\mathrm{f}$ and $\mathbf{T}_{fp}\mathbf{T}_{pp}^{+}$ becomes a predictive filter:

$$\mathbf{y}(I + k - 1 + l) = (\mathbf{H}_\mathrm{f})_{kl} = \sum_{j=1}^{I}\left(\mathbf{T}_{fp}\mathbf{T}_{pp}^{+}\right)_{kj}\left(\mathbf{H}_p\right)_{jl} = \sum_{j=1}^{I}\left(\mathbf{T}_{fp}\mathbf{T}_{pp}^{+}\right)_{kj}\mathbf{y}(j - 1 + l) \tag{18}$$

Therefore, any difference, hence variability of the projection matrix $\mathbf{O}$ is a result of measurement noise $v(n)$.

Apparently, number of the rows of the Hankel matrix I should be as large as possible, because more period of the response vector can be covered in Toeplitz matrices. The period in Toeplitz matrix depends on natural and sampling frequency of the response vector. To determine the variability of the projection matrix under different dimensions. Matrices $\mathbf{T}_{pp}$ and $\mathbf{T}_{fp}$ are analyzed by probability processing. The measured response (denoted $\hat{y}$) is the sum of system response y and measurement noise:

$$\hat{\mathbf{y}}(n) = \mathbf{y}(n) + \mathbf{v}(n) \tag{19}$$

From Equation (17), the correlation function is defined as

$$\mathbf{R}(\tau) = \mathrm{E}[\hat{y}(t)\hat{y}(t + \tau)] = \frac{1}{T}\int_0^T \hat{y}(t)\hat{y}(t + \tau)dt \tag{20}$$

In discrete-time domain with multiple measurement points, Equation (20) can be expressed as

$$\mathbf{R}(k) = \frac{1}{N}\sum_{n=1}^{N}\hat{\mathbf{y}}(n)\hat{\mathbf{y}}^T(n + k) = \mathrm{E}[\hat{\mathbf{y}}(n)\hat{\mathbf{y}}^T(n + k)] \tag{21}$$

By Equation (7) and (21), matrix $\mathbf{T}_{pp}$ and $\mathbf{T}_{fp}$ can be expressed in terms of expected values:

$$\mathbf{T}_{pp} = \begin{bmatrix} \mathrm{E}[\hat{\mathbf{y}}_0\hat{\mathbf{y}}_0^T] & \mathrm{E}[\hat{\mathbf{y}}_0\hat{\mathbf{y}}_1^T] & \cdots & \mathrm{E}[\hat{\mathbf{y}}_0\hat{\mathbf{y}}_{I-1}^T] \\ \mathrm{E}[\hat{\mathbf{y}}_1\hat{\mathbf{y}}_0^T] & \mathrm{E}[\hat{\mathbf{y}}_1\hat{\mathbf{y}}_1^T] & & \vdots \\ \vdots & & \ddots & \vdots \\ \mathrm{E}[\hat{\mathbf{y}}_{I-1}\hat{\mathbf{y}}_0^T] & \cdots & \cdots & \mathrm{E}[\hat{\mathbf{y}}_{I-1}\hat{\mathbf{y}}_{I-1}^T] \end{bmatrix}, \quad \mathbf{T}_{fp} = \begin{bmatrix} \mathrm{E}[\hat{\mathbf{y}}_I\hat{\mathbf{y}}_0^T] & \mathrm{E}[\hat{\mathbf{y}}_I\hat{\mathbf{y}}_1^T] & \cdots & \mathrm{E}[\hat{\mathbf{y}}_I\hat{\mathbf{y}}_{I-1}^T] \\ \mathrm{E}[\hat{\mathbf{y}}_{I+1}\hat{\mathbf{y}}_0^T] & \mathrm{E}[\hat{\mathbf{y}}_{I+1}\hat{\mathbf{y}}_1^T] & & \vdots \\ \vdots & & \ddots & \vdots \\ \mathrm{E}[\hat{\mathbf{y}}_{2I-1}\hat{\mathbf{y}}_0^T] & \cdots & \cdots & \mathrm{E}[\hat{\mathbf{y}}_{2I-1}\hat{\mathbf{y}}_{I-1}^T] \end{bmatrix} \tag{22}$$

where $\hat{\mathbf{y}}_j$ means $\hat{\mathbf{y}}(n)$ with time delay of j samples. Combining Eq. (19) and (21), the correlation function $\mathbf{R}$ is calculated as

$$\mathbf{R}(k) = \mathrm{E}[\mathbf{y}(n)\mathbf{y}^T(n + k)] + \mathrm{E}[\mathbf{y}(n)\mathbf{v}^T(n + k)] + \mathrm{E}[\mathbf{v}(n)\mathbf{y}^T(n + k)] + \mathrm{E}[\mathbf{v}(n)\mathbf{v}^T(n + k)] \tag{23}$$

The correlation matrix is related with the number of columns of the Hankel matrix. In the current study, the correlation function is calculated using two approaches, and they are used to evaluate the influence of different parameters:

- In the first approach, Eq. (23) is determined analytically assuming $\mathbf{y}(n)$ and $\mathbf{v}(n)$ being independent of each other, and the number of matrix columns $N \to \infty$. This approach is used to study the variability of matrix projection on I and the sampling frequency (denoted f_s).
- In the second approach, a finite amount of pseudorandom values $\mathbf{v}(n)$ are taken to calculate the predictive filter $\mathbf{T}_{fp}\mathbf{T}_{pp}^{+}$. The approach is used to calculate the variability of matrix projection on N.

3.2.1 Projection matrix assuming independent random signals

Assuming $\mathbf{y}(n)$ and $\mathbf{v}(n)$ are independent random variables, the cross-covariance between the two variables vanishes:

$$\mathrm{E}[\mathbf{y}(n)\mathbf{v}^T(n+k)] = \mathrm{E}[\mathbf{v}(n)\mathbf{y}^T(n+k)] = 0 \tag{24}$$

Additionally, if $\mathbf{v}(n)$ is assumed to be a normally-distributed random variable, Eq. (25) holds:

$$\mathrm{E}[\mathbf{v}(n)\mathbf{v}^T(n+k)] = \begin{cases} \sigma^2, & k = 0 \\ 0, & k \neq 0 \end{cases} \tag{25}$$

Therefore, the block Toeplitz matrices $\widehat{\mathbf{T}}_{pp}$ and $\widehat{\mathbf{T}}_{fp}$ can be expressed as

$$\begin{aligned} \widehat{\mathbf{T}}_{pp} &= \mathbf{T}_{pp} + \sigma^2(\mathbf{v}(n))\mathbf{I} \\ \widehat{\mathbf{T}}_{fp} &= \mathbf{T}_{fp} \end{aligned} \tag{26}$$

4 Numerical studies and results

To find the variation of the projection result under different values of I, three response vectors including white noise are assumed by Equation (19), and

$$\hat{\mathbf{y}}(n) = \sin\left(f\frac{2\pi n}{f_s}\right) + \mathbf{v}(n) \tag{27}$$

Measurement noise vector is given by 'randn' in MATLAB® where $\sigma^2(\mathbf{v}(n)) = 1$. This signal simulates the response of a veryly-lightly-damped system.

4.1 Projection assuming independent random signals

Dependence of projection variability on sampling frequencies is first studied assuming $N \to \infty$ in determining matrices $\widehat{\mathbf{T}}_{pp}$ and $\widehat{\mathbf{T}}_{fp}$, which are constructed according to Eq. (26). The *N*-sample measured signal is generated according to Eq. (27), and quality of projection is defined as the correlation coefficient ($0 \leq \alpha \leq 1$) between the first row of matrices $\mathbf{O}$ and the counterpart in $\mathbf{Y}_F$. In a noiseless measurement, $\mathbf{O} = \mathbf{H}_\mathrm{f}$ and the coefficient is equal to 1. Therefore, a higher correlation coefficient means better projection performance.

In the simulations below, $f = 5$ Hz and f_s = 100 Hz. Although $\hat{\mathbf{y}}(n)$ is a finite-length signal with a pseudorandom component, the correlation coefficient does not vary significantly on *N* (Figure 3). The correlation coefficient increases monotonically with *I*, but the rate of increment is periodic. It is found that the periodic of increment variation depends on the period of the signal, in terms of number of samples. By testing the projection performance using three other frequencies $f = \{10, 20, 25\}$ Hz, Table 1 shows that correlation coefficient variation under different values of I has a period of $f_s/2f_0$. In practice, it means there are "sweet spots" of values taken in SSI-OMA: for example, under $f = 5$ Hz, a value of *I*=30 has to be taken if the identification results of *I*=20 are found to be unsatisfactory.

The next parameter to be studied is sampling frequency. In the simulations, f_s ={100, 300, 500} Hz. Under a higher value of *I* where $I/f_s > 1/f$, Figure 4 shows that the performance of projection improves with higher sampling frequency. However, if the value of *I* is constrained (for example, due to insufficient computing power to calculate pseudoinverse $\widehat{\mathbf{T}}_{fp}$) it may be beneficial to use a low sampling frequency.

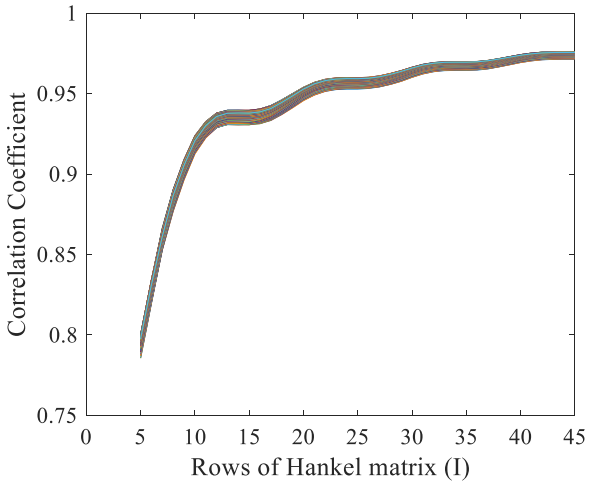


Figure 3 Correlation coefficient under different values of N, $f_s = 100$ Hz

Signal frequency f_s (Hz)	Period of the Toeplitz matrix (samples)	Period of correlation coefficient (samples)
5	20	10
10	10	5
20	5	2.5 (2 or 3)
25	4	2

Table 1 Period of correlation coefficient variation

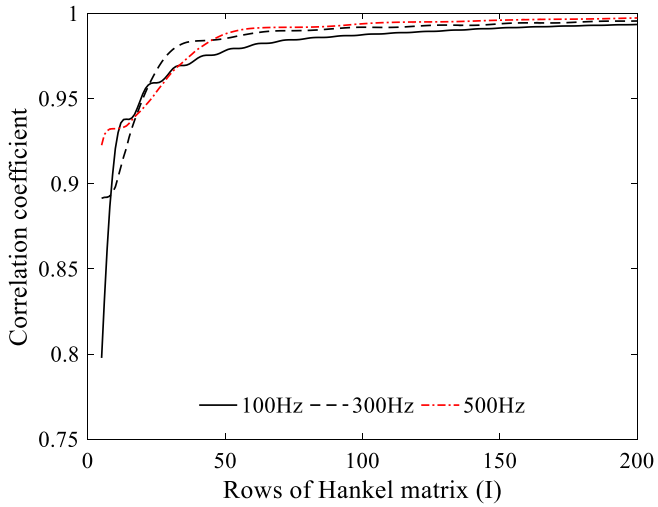


Figure 4 Correlation coefficient under different sampling frequencies

4.2 Hankel matrix projection with real noise signal

In SSI theory [17], the number of columns of Hankel matrix N is preferably approaching infinity. Because the correlation between response and noise would approach to zero. In practice, the length of response data is always finite, thus sampled covariances (Eq. (21)) are used to determine $\mathbf{T}_{fp}$ and $\mathbf{T}_{pp}$ (Eq. (22)). To determinate the variation of the projection result under various values of N, a response vector is constructed

using Equation (19) and (27), with f = 5 Hz and f_s = 100 Hz. Figure 5 shows the first and last rows of $\mathbf{T}_{fp}\mathbf{T}_{pp}^{+}$ in Equation (8). It is found that $\mathbf{T}_{fp}\mathbf{T}_{pp}^{+}$ gradually converge to the analytical counterpart if the value of N is increased. However, the entries would still be perturbed by noise for N as high as 10000.

To find the dependence of stability of $\mathbf{T}_{fp}\mathbf{T}_{pp}^{+}$ under joint variation of N, I and f_s, correlation coefficient of $\mathbf{T}_{fp}\mathbf{T}_{pp}^{+}$ under $4000 \leq N \leq 15000$ and $20 \leq I \leq 100$ are calculated. Stabilization diagram is shown as Figure 6. It is found that $\mathbf{T}_{fp}\mathbf{T}_{pp}^{+}$ would be stable if value of N is increased under the same value of I. Figure 6 also shows that stability would not vary significantly under different sampling frequencies. Because sampling frequency influences the period of Toeplitz matrices $\mathbf{T}_{pp}$ and $\mathbf{T}_{fp}$. Therefore, the dimensions of the Toeplitz matrices are related to sampling frequency. However, the values in the Toeplitz matrices are the correlation of the signals. The similarity of the signals would not be influenced by sampling frequency.

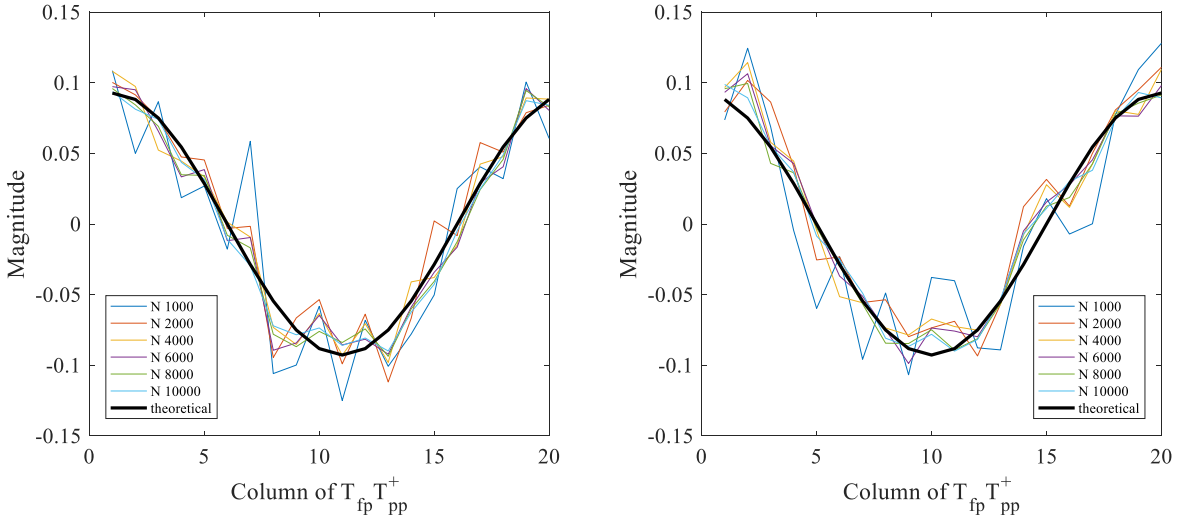


Figure 5 Entries of first (left) and last (right) rows of $\mathbf{T}_{fp}\mathbf{T}_{pp}^{+}$ under I = 20 and various values of N, compared with analytical counterpart (Eq. (27))

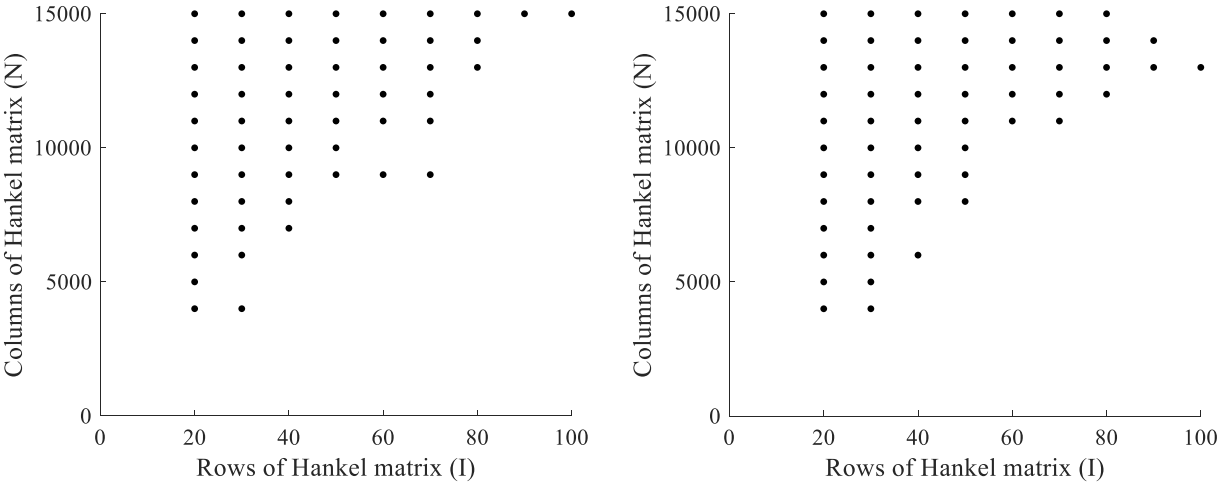


Figure 6 Stabilization diagram of $\mathbf{T}_{fp}\mathbf{T}_{pp}^{+}$ under sampling frequencies (a) 100 (b) 500 Hz. Red dots indicates the correlation coefficient is higher than 0.99

5 Conclusions

In this study, it is found that projection results would not vary significantly if the value of $I \geq f_s/2f_0$. Because longest response period be covered in Toeplitz matrices. Also, if computational resources are limited, it is beneficial to reduce both the number of rows (N) and the sampling frequency such that the projection results can be stabilized. It is also found that the matrix $\mathbf{T}_{fp}\mathbf{T}_{pp}^{+}$ in projection procedure would be gradually stabilize if the value of N is increased, but the results are still affected by noise.

Acknowledgements

This research is funded by Ministry of Science and Technology Project 105-2221-E-005 -030 -MY2.

References

[1] D. Ewins, Modal testing, theory, practice and application. 2nd edition, Research Studies Rress Ltd, 2000.

[2] L. Zhang, R. Brincker and P. Andersen, "An overview of operational modal analysis: Major development and issues," in *Proceedings of the 1st International Operational Modal Analysis Conference*, 2005.

[3] R. Brincker and C. Ventura, Introduction to operational modal analysis, Wiley, 2015.

[4] G. Poprawa, M. Salamak, S. Pradelok and P. Łaziński, "Operational modal analysis in model updating of a truss railway bridge," in *Proceedings of the 7th International Operational Modal Analysis Conference*, 2017.

[5] J. Fernández, M. Báez, A. Fraile, L. Hermanns and E. Alarcón, "Dynamic study of a culvert for high speed train lines," in *Proceedings of the 7th International Operational Modal Analysis Conference*, 2017.

[6] J. Grosel, W. Sawicki, J. Marcinowski and Z. Wójcicki, "OMA post-renovation study of the Christ the King monument preparation for wind-load analysis," in *Proceedings of the 7th International Operational Modal Analysis Conference*, 2017.

[7] Y. J. Chan and J.-W. Huang, "Time-Domain Operational Modal Analysis in Machine tools: optimal parameters and practical issues," *International Journal Of Precision Engineering And Manufacturing,* vol. 19, no. 6, pp. 889-897, 2018.

[8] B. Peeters, M. G. Alvarez Blanco, U. Musella, S. Waimer, E. Di Lorenzo and A. Carrella, "Identifying the structural behaviour of a specimen during spacecraft acoustic testing by operational modal analysis," in *Proceedings of the 7th International Operational Modal Analysis Conference*, 2017.

[9] M. Aenlle, F. Pelayo and G. Ismael, "Damping ratio of monolithic glass using operational modal analysis," in *Proceedings of the 7th International Operational Modal Analysis Conference*, 2017.

[10] P. V. Overschee and B. De Moor, "Subspace algorithm for the stochastic identification problem," *Automatica,* pp. 649-660, 5 1993.

[11] B. Peeters, G. De Roeck, T. Pollet and L. Schueremans, "Stochastic subspace techniques applied to parameter identification of civil engineering structures," in *Proceedings of the international conference MV2 on New Advances in modal synthesis of large structures: non-linear, damped and non-deterministic cases*, France, 1995.

[12] B. Peeters, "System identification and damage detection in civil engineering," Ph,D thesis, Faculteit Toegepaste Wetenschappen, Katholieke Universiteir (in Dutch), Leuven, 2000.

[13] M. Döhler, X.-B. Lam and L. Mevel, "Uncertainty quantification for modal parameters from

stochastic subspace identification on multi-setup measurements," *Mechanical Systems and Signal Processing,* vol. 36, no. 2, pp. 562-581, 2013.

[14] V. Kuts, S. Nikolaev and S. Voronov, "The procedure for subspace identification optimal parameters selection in application to the turbine blade modal analysis," *Procedia Engineering,* vol. 176, pp. 56-65, 2017.

[15] C. Priori, M. De Angelis and R. Betti, "On the selection of user-defined parameters in data-driven stochastic subspace identification," *Mechanical Systems and Signal Processing,* vol. 100, pp. 501-523, 2018.

[16] P. V. Overschee and B. De Moor, Subspace identification for linear system, theory, implementation, applications, Kluwer Academic Publishers, 1996.

[17] E. Reynders and G. De Roeck, "Reference-based combined deterministic–stochastic subspace identification for experimental and operational modal analysis," *Mechanical Systems and Signal Processing,* vol. 22, pp. 617-637, 2008.

[18] R. Brincker and P. Andersen, "Understanding stochastic subspace identification," in *IMAC-XXIV : A Conference & Exposition on Structural Dynamics*, 2006.

Operational modal analysis and fluid-structure interaction

M. Vigsø [1], **T. Kabel** [1], **M. Tarpø** [1], **R. Brincker**[2] **and C. Georgakis** [1]
[1] Aarhus University, Department of Engineering,
Inge Lehmanns Gade 10, 8000 Aarhus, Denmark
e-mail: **mvigso@eng.au.dk**

[2] Technical University of Denmark, Department of Civil Engineering,
Brovej Building 118, 2800 Kgs. Lyngby, Denmark

Abstract
Operational modal analysis (OMA) has in the last decade shown its potential in the field of offshore structures such as oilrigs and wind turbines etc. Typically, the estimated modal parameters will be used in conjunction with a finite element (FE) model. However since bottom-fixed offshore structures typically will be semi-submerged this affects the modal parameters by fluid-structure interaction. Fluid surrounding a structure is known to retard the response and locally introduce an increase in mass and damping. These local changes yield a complex alteration of the modal parameters and this paper highlights these effects by a wave flume experiment conducted on a cantilever structure. The structure is a scaled offshore structure and its modal parameters are examined at different water levels ranging from dry state to 60 % submerged.

1 Introduction

Modal analysis is an effective tool in describing the dynamic behaviour of a structure. When dealing with civil engineering structures, traditional experimental modal analysis (EMA) has some shortcomings and hence opens the playground for its cousin named operational modal analysis (OMA). OMA utilizes the operational conditions in providing the excitation of the structure and if the loading is approximating white noise, the modal parameters can elegantly be extracted from the structural response. The application of OMA is gaining ground and is becoming the preferred approach when evaluating modal properties of offshore structures [16]. The motivation for making modal analysis may be multiple; for instance in the field of structural health monitoring (SHM), model updating, fatigue estimation or indirect load estimation. Most of these disciplines use an FE model (updated to insitu conditions) as a basis.

There will always be some natural variations in the estimated modal parameters; besides estimation- or statistical error also environmental changes such as wind speed, scour or other seabed changes, structural degradation, mass loading, temperature or even tidal variations can cause the modal parameters to fluctuate. This paper will focus on how variations in the surrounding water may alter the dynamics of the structure.

The fluid-structure interaction is a complex topic and existing research in this area is plentiful. Both analytical, experimental and numerical work has been done in the past, e.g. [8, 12, 15, 18]. The content of this paper does not intend to challenge these works, instead it will demonstrate an application in the field of operational modal analysis conducted on a miniature offshore model. The results shown in this paper are preliminary findings which will be the basis for a later study, where an accurate model update is required. The model design does not descend from any actual physical structure, but is constructed as a simple cantilever with a topside in order to better monitor the torsional modes.

2 Experiment setup

The experimental campaign is conducted at Luminy University at Marseille, France in 2018. A cantilever structure made from plexiglass will be the scope for this study. The structure is a cylindrical mono tower with a truss box topside. The columnar part of the model is constructed by segments bolted together through an internal flange. Each segment is 200 mm in length and has an outer diameter of 150 mm. The structure is dry on the inside at all times during the tests. The topside has an outer geometry of $l \times b \times h$ of $400 \times 200 \times 200$ mm. The entire model is situated on a load cell connected to an aluminium base plate, which yields a total height of the model to be 1485 mm. The maximum water level, which can be applied in the flume, is 900 mm as indicated by Figure 1 a) and b). The sizing of the segments is primarily based on accessibility concerns regarding sensor installation. The joints between the circular sections are waterproofed through a gasket which may be seen in Figure 1 c).

The model is equipped with 16 uni-axial accelerometers; nine of which are positioned inside the pile and the remaining seven are distributed to the corners of the topside. The position and measuring direction are indicated in Figure 1 b). The accelerometers used are Brüel & Kjær TYPE 4508-002 1000 mV/g and the sampling rate is 2 kHz.

The scope of the test is to monitor the structure during water filling of the flume and track the changes in modal parameters due to the influence of water. The test will begin at zero water level (referred to as dry state) and the water level will be increased to a maximum of 900 mm. Intermediate tests are conducted at 150 mm, 400 mm, 670 mm, 800 mm and 850 mm respectively. For each of these water levels, 3-4 individual tests are performed. The tests are conducted by introducing some random loading to the structure and record the response for approximately 300 seconds. The concepts of operational modal analysis are then applied on the response data from the accelerometers and modal parameters (natural frequencies, damping ratios and mode shapes) are extracted [6].

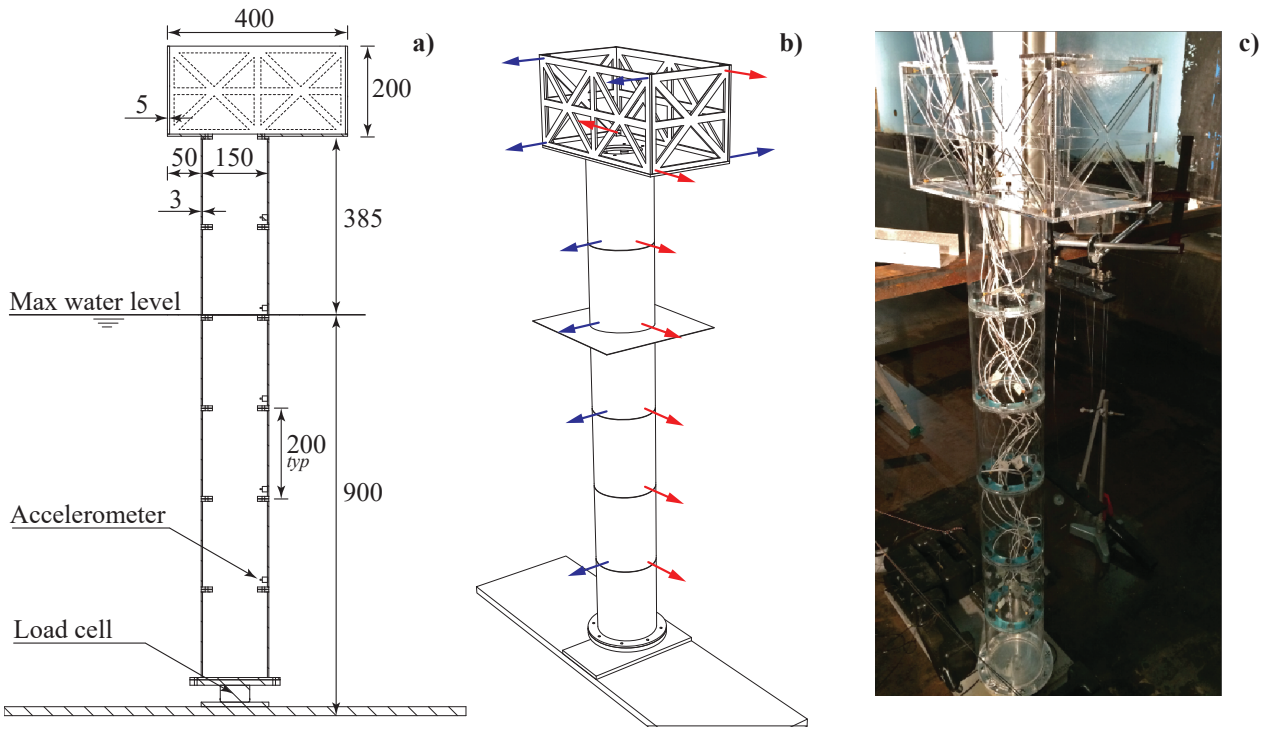


Figure 1: Experimental setup. a) shows the sideview cross section including the overall dimensions of the model, b) indicates the sensor position and direction, c) shows a picture from the test. Dimensions in mm.

In order for OMA to be successfully applied, the loading of the structure should be approximately white noise i.e. random in time and space [6]. The excitation medium utilized in this case is a soft brush swept over the structure along with disturbance to the surrounding water.

Additional instrumentation not relevant for the topic of this paper includes: ATI 6 DOF load cell, Wave gauges, 8 pcs kulite pressure transducers. These are installed for a later purpose in the test campaign.

3 ID algorithm

A total of 22 tests are conducted and though of different quality, each of these will yield an estimate on a number of modes. The frequency band of interest is 0 - 160 Hz as anything above this is too inflicted by noise and the sensor resolution not capable of spanning the modes shapes. Nine modes are identified in this frequency band and these nine modes will be examined in greater detail.

Now, several different identification methods are available both in the time domain and in the frequency domain. The identification algorithm selected is the Time Domain Poly Reference (TDPR) [17]. Although it was developed for impulse response functions, it can easily be adopted in OMA by using the correlation functions instead [5, 11]. Note that this section is not intended to go into details on the algorithm, however a brief overview of the method is outlined. For further details, the reader may find use of literature such as [6, 9].

Basically the response data of the structure are used to calculate the correlation functions. The transposed correlation function matrix is then considered as free decays of the system and the concepts of the TDPR can be applied; A Hankel matrix is constructed and the polynomial coefficients are solved by a least square approach. Then, the coefficients are stored in a companion matrix and by making an eigenvalue decomposition, the modal parameters can be found.

Now, in order to get the best conditions for the modal identification, filtering and DOF condensation are applied as a pre-step to the TDPR. This is exercised in the frequency domain by reducing the number of DOFs and amplifying the remaining principal components. The details on condensation can be found in [13].

The data is examined by looking at one frequency band at a time. While moving the frequency band and shifting the model order in the TDPR, stable poles are extracted from the signal. Typically these are represented by stabilization diagrams, but in order to limit the data flow in the figures of this paper, only the single picked modes are shown.

4 Modal parameter tracking

To give an indication of the quality of the data, a compilation of spectres are shown in Figure 2. The data series for each water level are merged into a single file and the spectra are averaged using the Welsh technique with a block size of 2^{13} samples corresponding to four seconds. A singular value decomposition of the spectral density is made and the figure shows the first three singular lines. The modes in Figure 2 are identified by peak picking and tracked by colour coding.

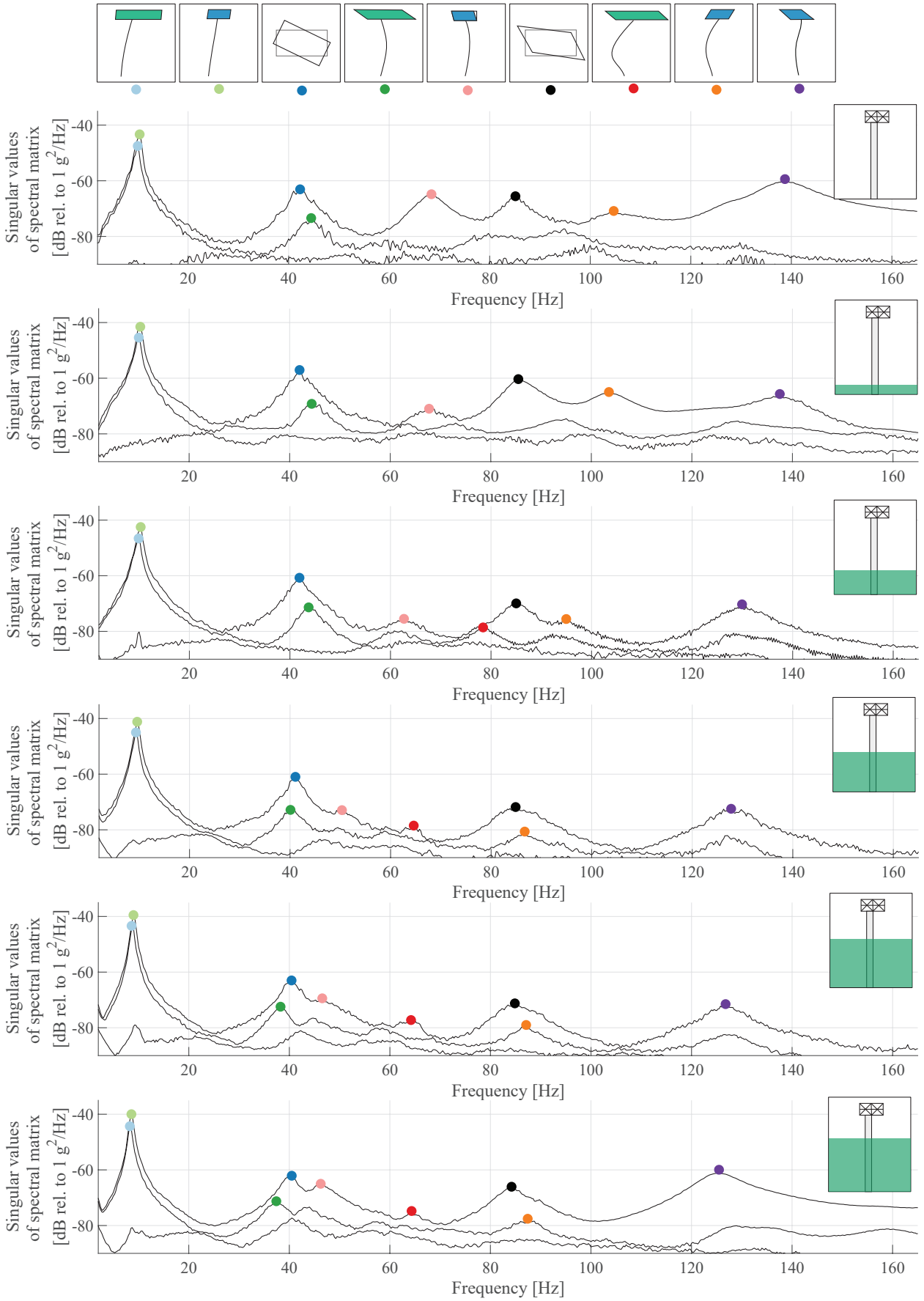


Figure 2: Singular values of the spectral density. The 3 first singular values are shown for different water levels. The water levels shown are 0, 150, 400, 670, 800 and 900 mm respectively. The different mode shapes identified are sketched in the top of the figure in ascending order and indicated by a coloured dot.

5 Results

For the seven different water levels ranging from 0 to 900 mm, modal identification is conducted using the TDPR technique outlined in Section 3. For each water level, 3-4 separate tests are made and the modal parameters are shown along with the average of the estimates. Figure 3 and Figure 4 show the identified modes in the frequency band of 0-160 Hz. The natural frequency, damping ratio and mode shape complexity are all given as a function of the water level. The individual mode shapes (1-9) are sketched in Figure 2 for reference.

The data in Figure 4 are merely the same as given in Figure 3, but normalized with respect to the average dry conditions to show the relative development in modal parameters.

As seen in Figure 3 and 4, the scatter in the estimates are significantly higher on the damping ratios and complexity indicators than for the frequencies. This is not uncommon when engaging in modal analysis on experimental data (especially when dealing with closely spaced modes), yet it masks the conclusion on the fluid influence on these parameters - more about this in the following.

First, looking at the frequencies; it is seen that in general the natural frequencies drop with the increase in water level due to the hydrodynamic added mass. Yet, mode 3 and mode 6 are nearly unaffected by the water. The mode shapes for these are characterized by predominant deformation to the topside and nearly no subsea deformation, see Figure 2. Literature such as [3, 4] states that one may encounter these effects when fluid-structure interaction is present. Since all modes, but the ones concerning only the topside, have a decrease in frequency, this yield an interesting phenomena as the modes start to cross each other by frequency. This is seen in Figure 3 a) at a water level of 670 mm for mode 3 and at a water level of 250 mm for mode 6.

Next looking at the damping estimates; the scatter from test to test is high compared to the average changes due to the influence of water. However, there is a tendency of an increase in damping for all modes. The higher modes (with exemption to mode 6) seems to be affected the most with respect to the damping with relative changes > 30 % whereas the the changes on the first two bending modes and the two topside modes are less significant, see Figure 4 b).

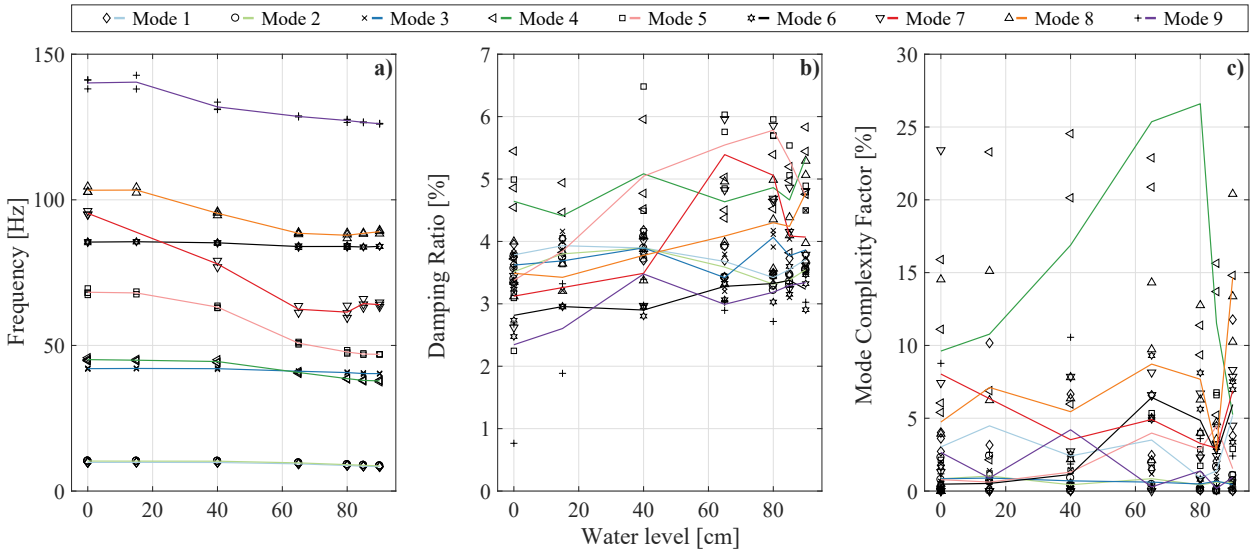


Figure 3: Estimated modal parameters at different water levels. Each mark represents an estimate from a data series and the solid lines are the water level averages. a) shows the development in natural frequency for each mode. b) shows the development in damping ratio for each mode. c) shows the development in mode shape complexity of each mode.

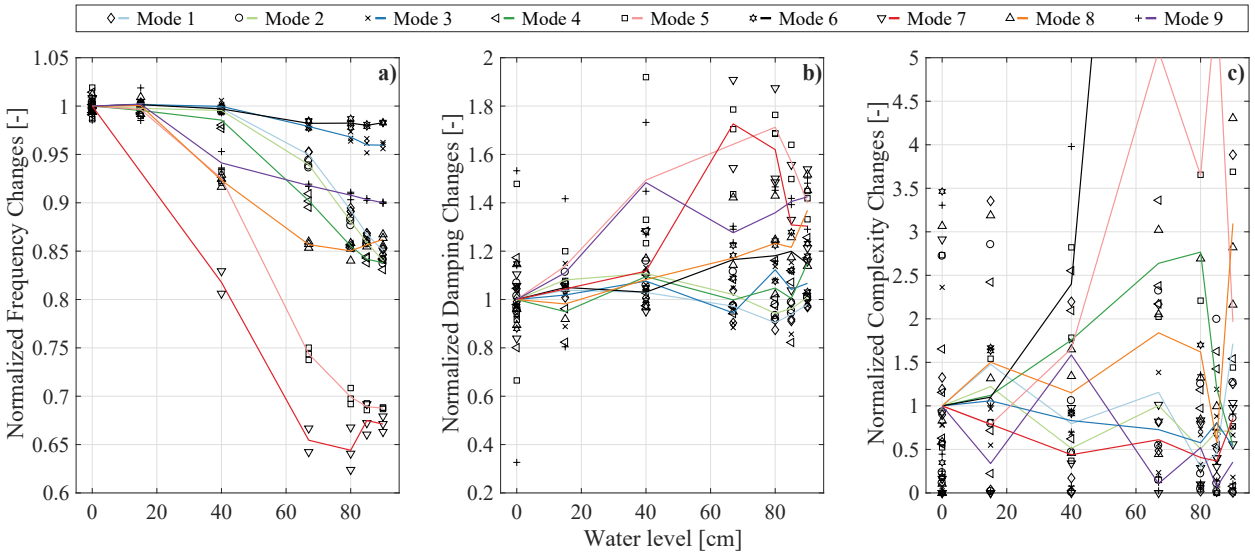


Figure 4: Relative changes in modal parameters due to shift in water level. Each mark represents an estimate from a data series and the solid lines are the water level averages and normalized with respect to the dry state. a) shows the relative development in natural frequency for each mode. b) shows the relative development in damping ratio for each mode. c) shows the relative development in mode shape complexity of each mode.

Finally, the complexity of the mode shapes are shown in Figure 3 c) and Figure 4 c). The details on how the mode complexity factor is calculated is described in Section 6.1. In general there is a considerable level of complexity in the mode shapes ranging between 1 and up to 30 %. However, given the level of scatter in the estimates it is inconcludable whether the complexity originates from the influence of water or rather non-linearities in the model. The latter is anticipated to be the main reason for the complexity considering the number of structural joints, material selection etc.

6 Mode shape alteration

6.1 Complex mode shapes

When identifying mode shapes from experimental data, often the identified mode shapes tend to have a imaginary part. This may be due to ID algorithm, non-linearities or cases of non proportional damping. The complex part is often considered as noise and disregarded, but it may indicate some physical properties of the system [10]. If the purpose of the modal analysis is to link the experimental mode shapes to ones obtained from an FE model, the most natural choice would be to disregard the imaginary part or use the absolute value.

Several different indicators can be used to quantify the complexity in a mode shape. For this case the mode complexity factor (MCF) will be utilized. The MCF is calculated for mode r as

$$\mathrm{MCF}_r = 1 - \frac{(S_{xx} - S_{yy})^2 + 4S_{xy}^2}{(S_{xx} + S_{yy}^2)} \tag{1}$$

where

$$S_{xx} = \Re\{\psi_r\}^T \Re\{\psi_r\} \qquad S_{yy} = \Im\{\psi_r\}^T \Im\{\psi_r\} \qquad S_{xy} = \Re\{\psi_r\}^T \Im\{\psi_r\} \tag{2}$$

Here $\{\psi_r\}$ is the mode shape vector for mode r. The MCF value is real and ranging between 0 and 1.

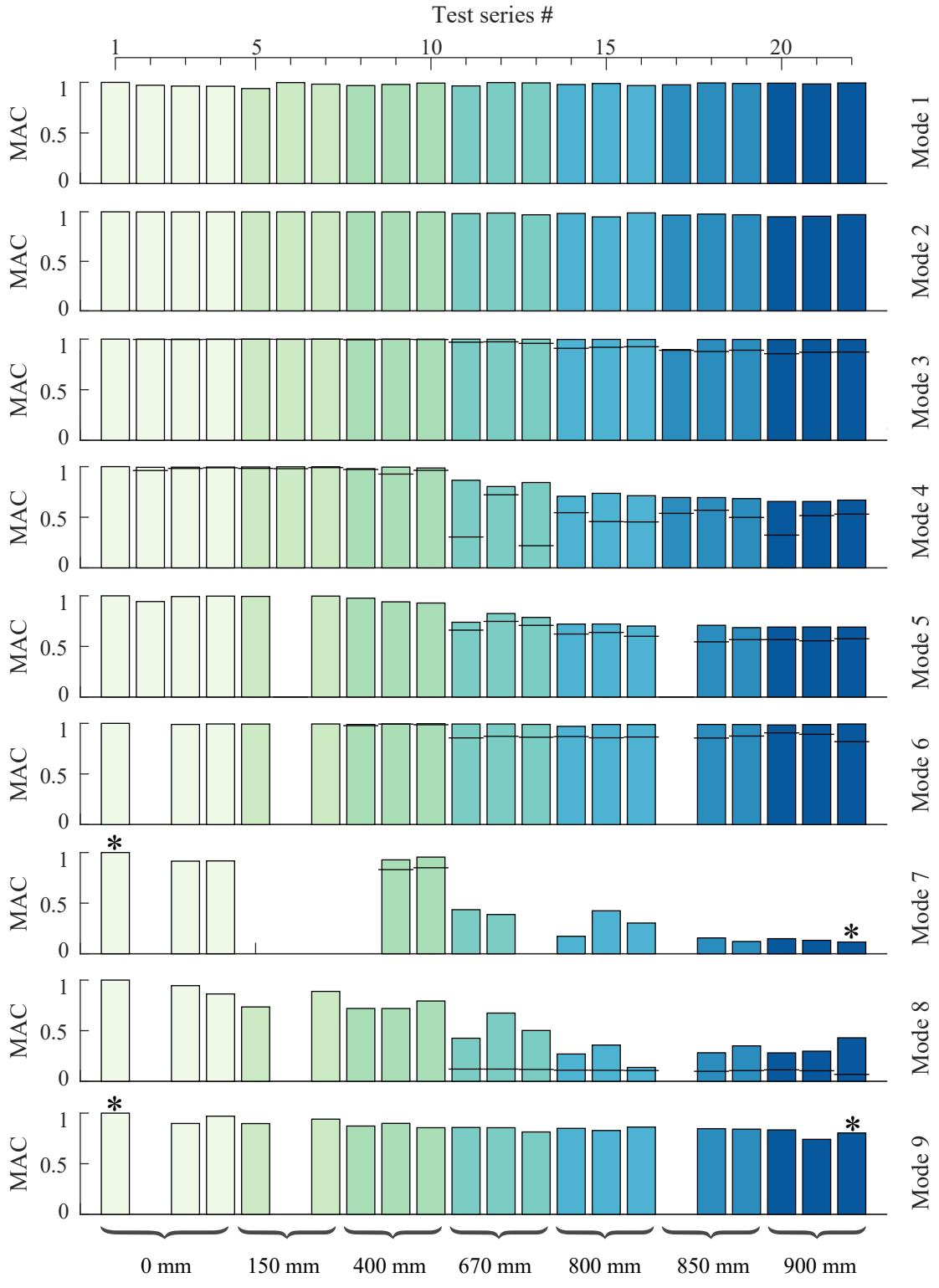


Figure 5: Modal assurance criterion (MAC). Every column corresponds to a test series while every row corresponds to a mode. The columns are grouped according to water level during the test. The black line splitting a single bar indicates the MAC value prior to rotating the mode shapes within their subspace. The four estimates marked by an asterisk (*) are shown in Figure 6 and Figure 7.

6.2 Mode shape

For complex modes, the MAC value between two mode shape vectors $\{\psi_a\}$ and $\{\psi_b\}$ can be calculated from [1, 14] as

$$\text{MAC}(\{\psi_a\},\{\psi_b\}) = \frac{|\{\psi_a\}^T\{\psi_b\}^*|^2}{(\{\psi_a\}^T\{\psi_a\}^*)\,(\{\psi_b\}^T\{\psi_b\}^*)} \tag{3}$$

In order to quantify the changes in mode shapes the MAC value is calculated for every mode compared to a reference mode shape. The reference mode shape is the mode shape at dry state identified by the first test series - i.e. the first column in Figure 5. The MAC values depicted are hence the same mode for all successive tests compared to the reference test.

When modes are closely spaced in frequencies, their associated modes shapes may be rotated within the subspace spanned by the modes engaged [2]. For instance, this can be observed in the case of mode 3, 4 and 5 whose mode shapes start to mix at a water level of 670 mm, see Figure 3 a) or Figure 2. How much the mode shapes will blend among the conjointly modes depends on ID algorithm used and its fitting parameters. Surely it is more convenient if this rotation does not occur, but it does not pose a problem as they can be reorientated to fit the reference modes better. This is done by assuming a linear combination of the mode engaged and making a least square fit to the reference modes.

Test series 2, 6 and 17 showed poor results due to improper excitation. As a result of this, only the first 4 modes were extractable from the data, hence the missing bars in Figure 5. Although a true random excitation was attempted also mode 7 was not greatly engaged in several tests as seen from the spectra in Figure 2, this may be the reason for increased fluctuations in the estimates.

6.3 Mode shapes in details

In this section, a close-up on two selected mode shapes is presented. The mode shapes displayed are mode 7 and mode 9 which are highlighted by an asterisk (*) in Figure 5. The mode shapes have been normalized to a maximum deflection of 0.15 m i.e. 10 % of the total height of the model.

Note that the mode shapes presented by Figure 6 and 7 are shown by utilizing some assumptions on the behaviour of the structure. By looking at Figure 7 a), it is clear that the nodal value for the 4th node from bottom is incorrect. Since no sensor is positioned at this node in this direction the nodal value depicted is simply an interpolation value between the adjacent nodes. These assumptions are just for visualization purposes and do not influence the MAC values presented earlier. Same applies to the topside.

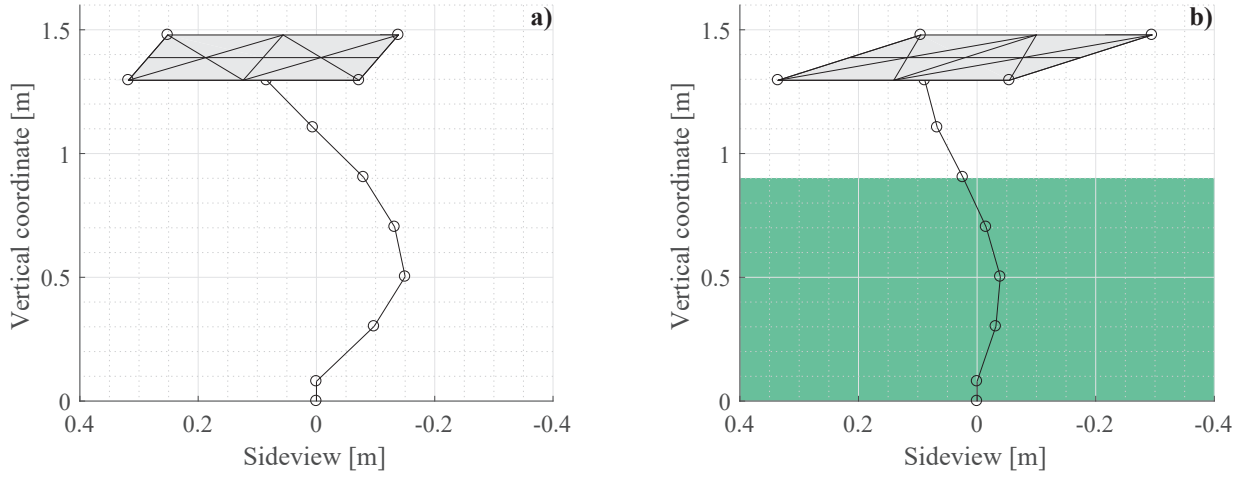


Figure 6: Mode shape 7 before and after water filling. MAC value between the two modes is 0.12.

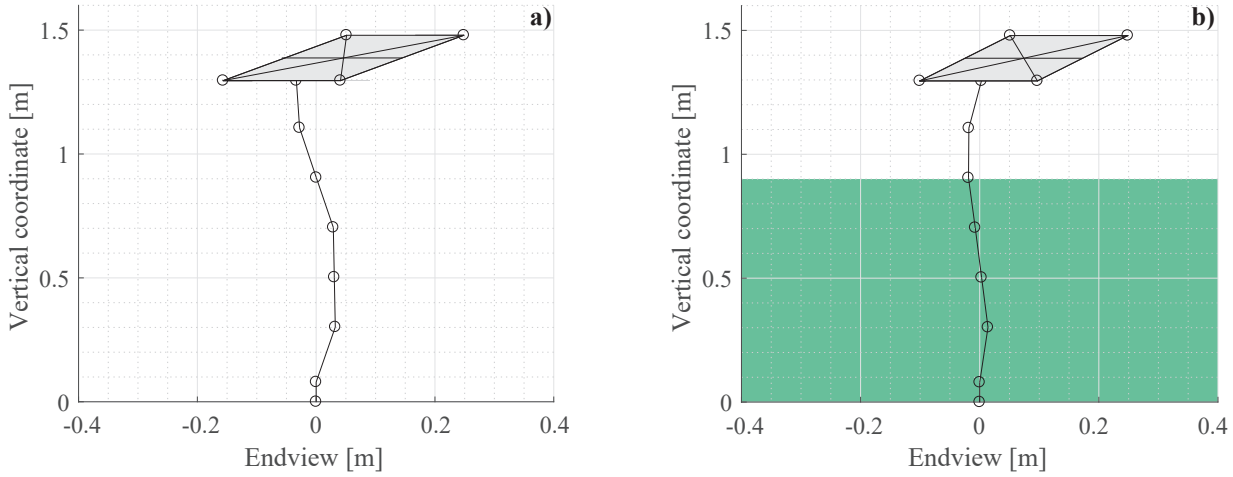


Figure 7: Mode shape 9 before and after water filling. MAC value between the two modes is 0.80.

Looking at these two modes shown by Figure 6 and Figure 7, the changes in mode shape are predominant subsea where the bending amplitude of the pile is reduced. The nodal point (zero vibration amplitude) for the pile is moved down for both cases.

7 Full scale perspective

The model considered in this paper is constituted as a hollow plexiglass model with a fairly large diameter to water depth ratio. This yields a large volume of water to be displaced by the structure and hence a large amount of added mass. Since the model itself is made from light weight material and air filled, the ratio of added mass versus the mass of the structure is also large. In the full scale perspective, the mass of the displaced water compared to the structural mass is likely to be a different ratio.

Now, if the structure is considered as an idealized SDOF system, the natural angular frequency is found as

$$\omega_{dry} = \sqrt{\frac{K_{dry}}{M_{dry}}} \tag{4}$$

where the K_{dry} is the generalized stiffness of the structure and M_{dry} is the generalized mass both at a dry state for a mode of vibration. If it is assumed that the stiffness of the structure is unchanged by the presence of water, the equation for the wet conditions becomes:

$$\omega_{wet} = \sqrt{\frac{K_{wet}}{M_{wet}}} = \sqrt{\frac{K_{dry}}{M_{dry} + M_{added}}} \tag{5}$$

Here, M_{added} symbolizes the added mass from the fluid- structure interaction [4, 12, 18]. Now, this is strictly only valid if the mode shape of interest is unchanged by the influence of water. This is a fair assumption for the first few modes in this case, see Figure 5. The change in frequency from the influence of water is hence seen as

$$\frac{\omega_{wet}}{\omega_{dry}} = \frac{1}{\sqrt{\left(1 + \frac{M_{added}}{M_{dry}}\right)}} \tag{6}$$

From equation (6) it is evident that the change in frequency depends on the ratio between the mass of the structure and the added mass from the fluid. Since the cross section of the model in this case is circular, there is no cross coupling and the added mass is somewhat proportional to the mass of the fluid displaced

by the structure: $M_{added} \propto V, \rho_w$, where V is the displaced volume and ρ_w is the fluid density. However other aspects such as boundary conditions for the fluid, viscosity, vibration amplitude and frequency can also influence the effect of added mass [4, 7]. Since the fluid density in this scaled experiment is larger than in full scale the effect from the fluid- structure interaction is amplified. This means that the relative changes in modal parameters shown by Figure 3 and Figure 4 may be less for the full scale scenario.

The model considered in this paper is dry on the inside (concerning the sensors). Offshore mono tower structures may be constructed as dry or wet on the inside where the latter is the most common. Water inside the structure will yield a different alteration of the structure as the internal water will further increase the added mass. This effect is not studied additionally but is worth mentioning.

8 Conclusion

This paper has outlined the changes in modal parameters from the influence of surrounding water on a small scale model. The model is a bottom fixed, surface piercing mono tower made from plexiglass. It was through operational modal analysis demonstrated how the modal parameters changes by the presence of water. Most significant finding was that the order of the modes were changing as the flume was filled with water. This was due to the nature of the individual mode shapes; mode shapes, where deflection is predominant ascribed to rotation and not bending of the tower will yield little or no changes from the water whereas especially higher order bending of the tower will experience great influence from the added mass. If modes are closely spaced this may cause them to change order.

Damping estimates were examined and found to increase with water level as expected. For semi-submerged structures, where fluid-structure interaction is present, it might be expected that non-proportional damping could cause the mode shapes to become complex. However it was not possible to show a decisive relation for this due to the scatter in the estimates. The mode shapes, however, were examined in details and it was seen that especially for higher modes; the deflection subsea were reduced.

The development in modal parameters are based on averages from different tests, where it was assumed that the water yields a constant alteration of the modal parameters. The conclusions from this study are hence based on small vibration amplitudes as different levels of excitation force is not examined.

8.1 Further work

As mentioned by the introduction, the work shown in this paper will be the basis for a successive study in indirect load estimation. The knowledge gained will feed the updating process of a finite element model needed for the dynamic analysis of wave action.

Acknowledgements

The authors acknowledge the funding received from Centre for Oil and Gas – DTU/Danish Hydrocarbon Research and Technology Centre (DHRTC). Also assistance from the staff at Luminy University, Marseille, during the experimental campaign needs to be acknowledged.

References

[1] R. Allemang. The modal assurance criterion (MAC): Twenty years of use and abuse. *Journal of Sound and Vibration*, Vol. 37(8):pp. 14–23, 2003.

[2] P. Avitabile. Modal space - back to basics. *Society of experimental mechanics Journal compilation*, December:pp. 1–2, 2007.

[3] N. Barltrop and A. Adams. *Dynamics of fixed marine structures*. Butterworth-Heinemann, UK, 3 edition, 1991.

[4] B. Blevins. *Formulas for natural frequency and mode shape*. Krieger Publishing Company, Malabar, Florida, USA, 1984.

[5] R. Brincker. On the application of correlation function matrices in OMA. *Mechanical Systems and Signal Processing*, 87:pp. 17–22, 2017.

[6] R. Brincker and C. Ventura. *Introduction to Operational Modal Analysis*. John Wiley and Sons, Ltd, UK, 2015.

[7] S. Chakrabarti. *Offshore structure modeling, Advanced series on ocean engineering*, volume 9. World Scientific Publishing Co. Pte. Ltd., 1994.

[8] R. Han and H. Xu. A simpled and accurate added mass model for hydrodynamic fluid-structure interaction analysis. *Journal of the Franklin Institute, Volume 333, Issue 6*, 1996.

[9] A. Harvey. *Time series models*. Phillip Allan Publisher Ltd, 1981.

[10] M. Imregun and D. Ewins. Complex modes - origins and limits. *Proceedings of the International Modal Analysis Conference, IMAC*, 1:pp. 496 – 506, 1995.

[11] G. C. James, T. G. Carne, and J. P. Lauffer. The natural excitation technique (NExT) for modal parameter extraction. *The International Journal of Analytical and Experimental Modal Analysis*, 10(4):pp. 260–277, 1995.

[12] M. Maheri and R. Severn. Experimental added-mass in modal vibration of cylindrical structures. *Engineering Structures*, 14 (3):pp. 163 – 175, 1992.

[13] P. Olsen, M. Juul, and R. Brincker. Condensation of the correlation functions in modal testing. *Submitted to Mechanical Systems and Signal Processing*, 2017.

[14] M. Pastor, M. Binda, and T. Harcarik. Modal assurance criterion. *Procedia Engineering 48*, 2012.

[15] M. Rahman and D. Bhatta. Evaluation of added mass and damping coefficient of an oscillating circular cylinder. *Applied Mathematical Modelling*, 17 (2):pp. 70–79, 1993.

[16] U. Tygesen, K. Worden, T. Rogers, G. Manson, and E. Cross. State-of-the-art and future directions for predictive modelling of offshore structure dynamics using machine learning. *Proceedings of the International Modal Analysis Conference, IMAC*, 2018.

[17] H. Vold, J. Knudrat, G. Rocklin, and R. Russell. A multi-input modal estimation algorithm for minicomputers. *SAE International Congress and Exposition*, Technical Paper 820194, 1982.

[18] V. Vu, M. Thomas, A. Lakis, and L. Marcouiller. Effect of added mass on submerged vibrated plates. *25th Seminar on machinery vibration, Canadian Machinery Vibration Association*, 2007.

Fatigue damage prediction based on strain field estimates using a smoothed Kalman filter and sparse measurements

U. Lagerblad[1,2], H. Wentzel[2], A. Kulachenko[1]
[1] KTH Royal Institute of Technology, Department of Solid Mechanics
SE-100 44, Stockholm, Sweden
e-mail: **ulag@kth.se**

[2] Scania AB, Truck Chassis Development
SE-151 87, Södertälje, Sweden

Abstract
In this work, we address the problem of fatigue damage prediction in a truck component excited by road induced vibrations. The damage is computed from strains estimated from sparse measurements of the dynamic response. Two different fixed-lag smoothing algorithm are employed, an augmented Kalman filter extended with a fixed-lag smoother and a smoothed joint input-state estimation algorithm. The system is described with a finite element model, and due to the complexity of reproducing the system by the model, the resulting representation may contain a number of discrepancies. Nevertheless, both smoothing algorithms succeed in capturing the dynamic behaviour of the component, although the estimated strains are affected more by the large model error than the estimated acceleration are. Furthermore, it is shown that the proposed methodology of strain estimation and fatigue damage calculations correlate well with the observed failure of a component when tested in a full-scale fatigue test of a truck chassis.

1 Introduction

In the development and maintenance of engineering structures it is often important to estimate the fatigue damage that is likely to occur due to a certain loading or use conditions. Fatigue damage estimates can be based on knowledge of the strain history in the critical points of the structure; in general the critical points are not exactly known *a priori*. To continuously measure the entire strain field is impractical and, therefore, it is proposed to estimate the strain history in all critical points from a limited number of discretely positioned sensors (accelerometers and strain gauges) and a finite element model of the structure.

This is a kind of inverse problem that has been extensively studied over the last decades [1-7]. Increased computing power enabled the use of more complex methods where larger arrays of data are used as inputs to the estimation algorithms, resulting in increased accuracy of the result. A high accuracy of the estimated strains is a prerequisite for damage calculations [8, 9]. In this work a specific problem is addressed, that of fatigue damage prediction based on strain history estimated from sparse measurements in a dynamic system with unknown inputs for which a finite element model exists. It is assumed that the dynamic system is well described as linear, and the model errors and the measurement noise are described as Gaussian white noise.

It is investigated to perform the damage estimates using a recursive non-causal adaptive filter to estimate the strain field. This methodology has the potential to overcome both modelling errors and measurement noise inevitably present in the system. Two similar algorithms are employed in this work, an experimentally validated augmented Kalman filter extended with a fixed-lag smoother (AKF-FLS), and a smoothed algorithm for joint input-state estimations (SJISE) [10]. The accuracy and the computational cost of the algorithms are compared.

An experimental setup is used for the investigation. The structure subjected to strain field identification and subsequent fatigue estimation is a truck side skirt, which serves to reduce the aerodynamic resistance of the vehicle. Components attached to the chassis are in general excited by road-induced vibrations but the loads that act on the side skirt are not readily available for measurement because there are several attachment points with complex geometry.

In-service vibration responses, both accelerations and strains, were measured in laboratory conditions in a test rig. The dynamic properties of the system were obtained from a finite element model. The finite element model was tuned so that the modal properties of the model were matching the modal properties of the experimental setup. This comparison was based on an operational modal analysis of the studied system.

Both algorithms were first verified and tuned by estimating discretely measured acceleration and strain signals. The smoothers were then used to estimate the strain in several other positions on the component. These estimated strains were used to compute the damage and the result was compared to the outcome of a full-scale vibration fatigue test of the component.

2 Method

In order to estimate the response in a complex component, a model of the system is needed. It needs not only to be accurate, but also to efficiently describe the dynamic behaviour of the system without getting to large. A minimized model complexity is essential for the computational cost of filtering algorithms. Here, a detailed finite element model is reduced and described by its modal parameters in a well-defined frequency interval. The finite element model is tuned to match the modal parameters with those from an operational modal analysis. Accelerations and strains were measured during a laboratory experiments of a truck side skirt simulating road induced vibrations from realistic driving conditions. The measured response was then used as input to the two smoothing algorithms estimating the strain in the structure from which the fatigue damage could be calculated.

2.1 System state-space description

Consider a linear time invariant system described by the discrete time modally reduced equation of motion

$$\ddot{\mathbf{q}}_k + \boldsymbol{\Gamma}\dot{\mathbf{q}}_k + \boldsymbol{\Omega}\mathbf{q}_k = \boldsymbol{\Phi}\mathbf{S}_\mathrm{f}\mathbf{f}_k \tag{1}$$

where $\mathbf{q}_k$ is a vector of n_N modal displacements where n_N denotes the number of participating modes. The matrix $\boldsymbol{\Omega} \in \mathbb{R}^{n_\mathrm{N} \times n_N}$ contains the eigenfrequencies ω_i arranged diagonally in ascending order and the mass normalized eigenvectors are arranged as columns in $\boldsymbol{\Phi} \in \mathbb{R}^{n_{dof} \times n_N}$ where n_{dof} is the number of degrees of freedom of the system. In addition, assuming proportional damping, the matrix $\boldsymbol{\Gamma} \in \mathbb{R}^{n_N \times n_N}$ contains the diagonal elements $2\omega_i\xi_i$ where ξ_i is the modal damping ratio for mode i. The system is excited by n_f external forces $\mathbf{f}_k$ acting in positions described by $\mathbf{S}_\mathrm{f} \in \mathbb{R}^{n_{dof} \times n_f}$. Furthermore, let the n_z measured responses $\mathbf{z}_k$ be connected to the modal parameters as

$$\mathbf{z}_k = \mathbf{S}_a\boldsymbol{\Phi}\ddot{\mathbf{q}}_k + \mathbf{S}_v\boldsymbol{\Phi}\dot{\mathbf{q}}_k + \mathbf{S}_d\boldsymbol{\Phi}\mathbf{q}_k. \tag{2}$$

By collecting the modal displacements and velocities into the state vector $\mathbf{x}_k$

$$\mathbf{x}_k = \begin{bmatrix}\mathbf{q}_k \\ \dot{\mathbf{q}}_k\end{bmatrix} \tag{3}$$

the equation of motion (1) and the measurement equation (2) can be reformulated to a state-space description of the system as

$$\begin{aligned}\mathbf{x}_{k+1} &= \mathbf{A}\mathbf{x}_k + \mathbf{B}\mathbf{f}_k + \mathbf{w}_k \\ \mathbf{z}_k &= \mathbf{C}\mathbf{x}_k + \mathbf{D}\mathbf{f}_k + \mathbf{v}_k.\end{aligned} \tag{4}$$

The time invariant state matrices **A** and **B** are calculated as

$$\begin{aligned}\mathbf{A} &= \exp\left(\begin{bmatrix}\mathbf{0} & \mathbf{I}\\ -\mathbf{\Omega^2} & -\mathbf{\Gamma}\end{bmatrix}\Delta t\right)\\ \mathbf{B} &= (\mathbf{A}-\mathbf{I})\begin{bmatrix}\mathbf{0} & \mathbf{I}\\ -\mathbf{\Omega^2} & -\mathbf{\Gamma}\end{bmatrix}^{-1}\begin{bmatrix}\mathbf{0}\\ \mathbf{\Phi}^{\mathrm{T}}\mathbf{S}_{\mathrm{f}}\end{bmatrix}\end{aligned} \tag{5}$$

whereas the measurement matrix $\mathbf{C}$ is defined as

$$\mathbf{C} = [\mathbf{S}_d\mathbf{\Phi} - \mathbf{S}_a\mathbf{\Phi}\mathbf{\Omega}^2 \quad \mathbf{S}_v\mathbf{\Phi} - \mathbf{S}_a\mathbf{\Phi}\mathbf{\Gamma}] \tag{6}$$

and the direct feed-through matrix $\mathbf{D}$ is given by

$$\mathbf{D} = [\mathbf{S}_a\mathbf{\Phi}\mathbf{\Phi}^{\mathrm{T}}\mathbf{S}_{\mathrm{f}}]. \tag{7}$$

The noise processes $\mathbf{w}_k$ and $\mathbf{v}_k$ which accounts for model errors and measurement noise, respectively, are assumed to be zero mean and white with known covariance according to

$$\mathbf{E}\left[\begin{pmatrix}\mathbf{w}_k\\ \mathbf{v}_k\end{pmatrix}(\mathbf{w}_k^{\mathrm{T}} \quad \mathbf{v}_k^{\mathrm{T}})\right] = \begin{bmatrix}\mathbf{Q}_{\mathrm{x}} & \mathbf{S}\\ \mathbf{S} & \mathbf{R}_v\end{bmatrix}\delta_{k-l}\,. \tag{8}$$

2.1.1 Augmented state-space description

Instead of using the state vector (3), an augmented state vector $\mathbf{x}_k^{\mathrm{a}} = [\mathbf{q}_k \quad \dot{\mathbf{q}}_k \quad \mathbf{f}_k]^{\mathrm{T}}$ can be used. This result in the augmented state and measurement equations as

$$\begin{aligned}\mathbf{x}_{k+1}^{\mathrm{a}} &= \mathbf{A}^{\mathrm{a}}\mathbf{x}_k^{\mathrm{a}} + \mathbf{w}_k^{\mathrm{a}}\\ \mathbf{z}_k &= \mathbf{C}^{\mathrm{a}}\mathbf{x}_k^{\mathrm{a}} + \mathbf{v}_k\end{aligned} \tag{9}$$

where the augmented state and measurement matrix are formulated as

$$\mathbf{A}^{\mathrm{a}} = \begin{bmatrix}\mathbf{A} & \mathbf{B}\\ \mathbf{0} & \mathbf{I}\end{bmatrix}, \qquad \mathbf{C}^{\mathrm{a}} = [\mathbf{C} \quad \mathbf{D}]. \tag{10}$$

It is assumed that the process noise $\mathbf{w}_k^{\mathrm{a}}$ is described by its covariance $\mathbf{Q}^{\mathrm{a}} = \begin{bmatrix}\mathbf{Q}_{\mathrm{x}} & \mathbf{0}\\ \mathbf{0} & \mathbf{Q}_{\mathrm{f}}\end{bmatrix}$.

2.2 Smoothing algorithms

Two different smoothing algorithms are employed, an augmented Kalman filter extended with a fixed lag smoother and a smoothed joint input-state estimation algorithm.

2.2.1 The augmented Kalman filter extended with a fixed-lag smoother

The augmented Kalman filter extended with a fixed-lag smoother (AKF-FLS) consists of two steps. First, a regular Kalman filter is applied to the augmented system described by Equation (9), which is then followed by the fixed-lag smoothing algorithm. The Kalman filter needs to be initialized with an initial augmented state estimate vector $\hat{\mathbf{x}}_{0|-1}^{\mathrm{a}}$ and its error covariance $\mathbf{P}_{0|-1}^{(0)}$. Here, the Kalman filter is formulated as a one-step *a priori* filter

$$\begin{aligned}\mathbf{K}_k^{(0)} &= \mathbf{A}^{\mathrm{a}}\mathbf{P}_{k|k-1}^{(0)}\mathbf{C}^{\mathrm{a}\mathrm{T}}\left(\mathbf{C}^{\mathrm{a}}\mathbf{P}_{k|k-1}^{(0)}\mathbf{C}^{\mathrm{a}\mathrm{T}} + \mathbf{R}_v\right)^{-1}\\ \mathbf{P}_{k+1|k}^{(0)} &= \mathbf{A}^{\mathrm{a}}\mathbf{P}_{k|k-1}^{(0)}\left(\mathbf{A}^{\mathrm{a}} - \mathbf{K}_k^{(0)}\mathbf{C}^{\mathrm{a}}\right)^{\mathrm{T}} + \mathbf{Q}^{\mathrm{a}}\\ \hat{\mathbf{x}}_{k+1|k}^{\mathrm{a}} &= \mathbf{A}^{\mathrm{a}}\hat{\mathbf{x}}_{k|k-1}^{\mathrm{a}} + \mathbf{K}_k^{(0)}\left(\mathbf{z}_k - \mathbf{C}^{\mathrm{a}}\hat{\mathbf{x}}_{k|k-1}^{\mathrm{a}}\right).\end{aligned} \tag{11}$$

This initialize the smoothing algorithm with Kalman gain $\mathbf{K}_k^0$ and error covariance $\mathbf{P}_k^0$. For a predefined time lag L, the smoothing algorithm is repeated for $i = [1: L+1]$:

$$\begin{aligned} \mathbf{K}_k^{(i)} &= \mathbf{P}_{k|k-1}^{(i-1)}\mathbf{C}^{\mathrm{aT}}\left(\mathbf{C}^{\mathrm{a}}\mathbf{P}_{k|k-1}^{(0)}\mathbf{C}^{\mathrm{aT}} + \mathbf{R}_v\right)^{-1} \\ \mathbf{P}_{k+1|k}^{(i)} &= \mathbf{P}_{k|k-1}^{(i-1)}\left(\mathbf{A}^{\mathrm{a}} - \mathbf{K}_k^{(0)}\mathbf{C}^{\mathrm{a}}\right)^{\mathrm{T}} \\ \hat{\mathbf{x}}_{k+1-i|k}^{\mathrm{a}} &= \hat{\mathbf{x}}_{k+1-i|k-1}^{\mathrm{a}} + \mathbf{K}_k^{(i)}\left(\mathbf{z}_k - \mathbf{C}^{\mathrm{a}}\hat{\mathbf{x}}_{k|k-1}^{\mathrm{a}}\right). \end{aligned} \tag{12}$$

This gives, in the last step, the estimated augmented state vector $\hat{\mathbf{x}}_{k-L|k}^{\mathrm{a}}$, containing both estimated states and forces.

2.2.2 The smoothed algorithm for joint input-state estimations

The smoothed algorithm for joint input-state estimations (SJISE) consist of two steps: input estimation and state estimation. The algorithm is based on the state-space formulation of Equation (4). The smoother is described in detail in Maes et al. [10], and is here only outlined in brief. The algorithm is initialized using an initial state $\hat{\mathbf{x}}_{[0|L-1]}$ and its error covariance $\mathbf{P}_{\mathrm{x}[0|L-1]}$.

Input estimation: (13)

$$\mathbf{P}_{\mathrm{xw}[k]} = \sum_{i=1}^{\min(k,L)}\left(\left(\prod_{j=1}^{i-1}\left(\mathbf{A} - \mathbf{K}_{L[k-j]}\mathcal{O}_L\right)\right)\left(\left(\check{\mathbf{I}}_{2n_N} - \mathbf{K}_{L[k-i]}\mathcal{N}_L\right)\mathbf{Q}_L^i - \mathbf{K}_{L[k-i]}\mathbf{S}_L^{-i^{\mathrm{T}}}\right)\right)$$

$$\mathbf{P}_{\mathrm{xv}[k]} = \sum_{i=1}^{\min(k,L)}\left(\left(\prod_{j=1}^{i-1}\left(\mathbf{A} - \mathbf{K}_{L[k-j]}\mathcal{O}_L\right)\right)\left(\left(\check{\mathbf{I}}_{2n_N} - \mathbf{K}_{L[k-i]}\mathcal{N}_L\right)\mathbf{S}_L^i - \mathbf{K}_{L[k-i]}\mathbf{R}_{L-1}^i\right)\right)$$

$$\begin{aligned} \overline{\mathbf{R}}_{[k]} = {} & \mathcal{O}_L\mathbf{P}_{\mathrm{x}[k|k+L-1]}\mathcal{O}_L^{\mathrm{T}} + \mathbf{R}_{L+1}^0 + \mathcal{N}_L\mathbf{Q}_L^0\mathcal{N}_L^{\mathrm{T}} + \mathcal{N}_L\mathbf{S}_L^0 + \mathbf{S}_L^{0^{\mathrm{T}}}\mathcal{N}_L^{\mathrm{T}} + \mathcal{O}_L\mathbf{P}_{\mathrm{xw}[k]}\mathcal{N}_L^{\mathrm{T}} + \mathcal{N}_L\mathbf{P}_{\mathrm{xw}[k]}^{\mathrm{T}}\mathcal{O}_L^{\mathrm{T}} \\ & + \mathcal{O}_L\mathbf{P}_{\mathrm{xv}[k]} + \mathbf{P}_{\mathrm{xv}[k]}^{\mathrm{T}}\mathcal{O}_L^{\mathrm{T}} \end{aligned}$$

$$\mathbf{M}_{\mathrm{L}[k]} = \check{\mathbf{I}}_{n_f}\left(\boldsymbol{\mathcal{H}}_L^{\mathrm{T}}\overline{\mathbf{R}}_{[k]}^{-1}\mathcal{H}_L\right)^{\dagger}\boldsymbol{\mathcal{H}}_L^{\mathrm{T}}\overline{\mathbf{R}}_{[k]}^{-1}$$

$$\hat{\mathbf{f}}_{[k|k+L]} = \mathbf{M}_{L[k]}\left(\mathbf{z}_{L[k]} - \mathcal{O}_L\hat{\mathbf{x}}_{[k|k+L-1]}\right)$$

$$\mathbf{P}_{\mathrm{p}[k|k+L]} = \mathbf{M}_{L[k]}\overline{\mathbf{R}}_{[k]}\mathbf{M}_{L[k]}^{\mathrm{T}}$$

State estimation: (14)

$$\overline{\mathbf{S}}_{[k]} = \mathbf{A}\mathbf{P}_{\mathrm{x}[k|k+L-1]}\mathcal{O}_L^{\mathrm{T}} + \check{\mathbf{I}}_{2n_N}\mathbf{Q}_L^0\mathcal{N}_L^{\mathrm{T}} + \check{\mathbf{I}}_{2n_N}\mathbf{S}_L^0 + \mathbf{A}\mathbf{P}_{\mathrm{xw}[k]}\mathcal{N}_L^{\mathrm{T}} + \check{\mathbf{I}}_{2n_N}\mathbf{P}_{\mathrm{xw}[k]}^{\mathrm{T}}\mathcal{O}_L^{\mathrm{T}} + \mathbf{A}\mathbf{P}_{\mathrm{xv}[k]}$$

$$\overline{\mathbf{T}}_{[k]} = \mathbf{A}\mathbf{P}_{\mathrm{x}[k|k+L-1]}\mathbf{A}^{\mathrm{T}} + \mathbf{Q} + \mathbf{A}\mathbf{P}_{\mathrm{xw}[k]}\check{\mathbf{I}}_{2n_N}^{\mathrm{T}} + \check{\mathbf{I}}_{2n_N}\mathbf{P}_{\mathrm{xw}[k]}^{\mathrm{T}}\mathbf{A}^{\mathrm{T}}$$

$$\mathbf{K}_{L[k]} = \overline{\mathbf{S}}_{[k]}\overline{\mathbf{R}}_{[k]}^{-1} - \left(\overline{\mathbf{S}}_{[k]}\overline{\mathbf{R}}_{[k]}^{-1}\mathcal{H}_L - \check{\mathbf{B}}\right)\left(\boldsymbol{\mathcal{H}}_L^{\mathrm{T}}\overline{\mathbf{R}}_{[k]}^{-1}\mathcal{H}_L\right)^{\dagger}\boldsymbol{\mathcal{H}}_L^{\mathrm{T}}\overline{\mathbf{R}}_{[k]}^{-1}$$

$$\hat{\mathbf{x}}_{[k+1|k+L]} = \mathbf{A}\hat{\mathbf{x}}_{[k|k+L-1]} + \mathbf{K}_{L[k]}\left(\mathbf{z}_{L[k]} - \mathcal{O}_L\hat{\mathbf{x}}_{[k|k+L-1]}\right)$$

$$\mathbf{P}_{\mathrm{x}[k+1|k+L]} = \mathbf{K}_{L[k]}\overline{\mathbf{R}}_{[k]}\mathbf{K}_{L[k]}^{\mathrm{T}} - \mathbf{K}_{L[k]}\overline{\mathbf{S}}_{[k]}^{\mathrm{T}} - \overline{\mathbf{S}}_{[k]}\mathbf{K}_{L[k]}^{\mathrm{T}} + \overline{\mathbf{T}}_{[k]}$$

For the definition of gain matrices and extended noise covariances, the reader is referred to [10]. The SJISE gives the smoothed input force estimate $\hat{\mathbf{f}}_{[k|k+L]}$ and state estimate $\hat{\mathbf{x}}_{[k+1|k+L]}$ separately.

2.3 Experiments

The dynamic system studied in this work is the load carrying structure of a truck side skirt, see Figure 1. Accelerometers and strain gauges were mounted on the component and the accelerations and the strains were measured on the Scania test track in Södertälje, Sweden.



Figure 1: A truck side skirt and an illustration of the global coordinate system.

Due to the slender shape of the side skirt, the vibrations in the y-direction are dominant. These accelerations were reproduced on the load carrying structure of a side skirt mounted in the vibration test rig presented in Figure 2. The response was measured with a sample rate of 1000 Hz. Due to prior knowledge of the dynamic behaviour of the side skirt, it is known that vibrations over 50 Hz give only a very small contribution to the motion and, consequently, to the strain in the component. Hence, for the frequency interval of interest, 1000 Hz gives a sufficient resolution of the participating modes. Acceleration was measured at five positions and strain at four positions, these are visualized in Figure 3.

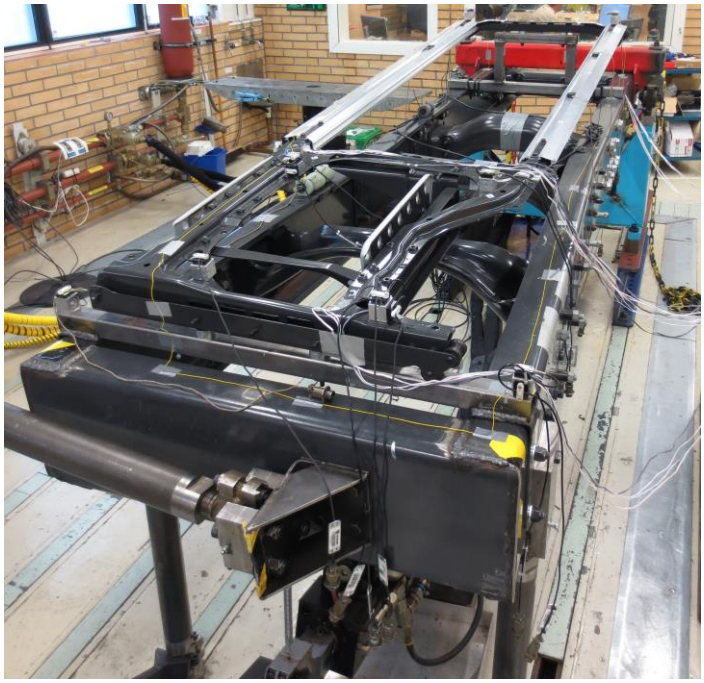


Figure 2: The side skirt mounted in the test rig.

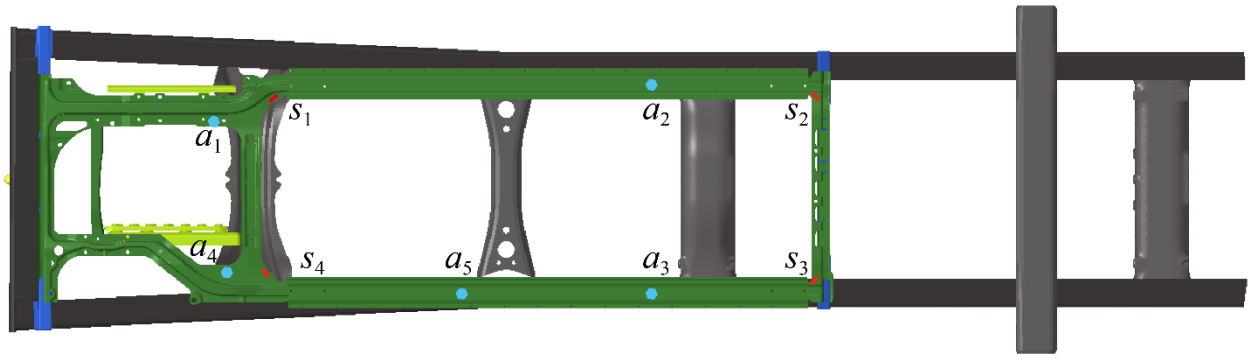


Figure 3: Position of the 5 accelerometers (marked with blue dots) and the 4 strain gauges (marked with red lines).

2.4 Finite element model

The rig structure and the side skirt were modelled in the finite element pre-processor HyperMesh 2017, and the modal parameters up to 50 Hz were then calculated with Abaqus CAE 2017. The stiffness of the finite element model was modified in order to make the computed modes match those of an operational modal analysis (OMA) [11] of the test rig and side skirt structure. The OMA was performed by exciting the test rig with a noise signal with evenly distributed power in the interval 0.2-60 Hz. The measured acceleration response was imported into the software LMS TestLab. The eigenmodes, frequencies and damping were computed using the PolyMAX method, a poly-reference least-squares complex frequency-domain method [12, 13]. Both the computed modes and the modes from the OMA are presented in Table 1. The comparison of modes were done by studying the modal assurance criterion [14] and the eigenfrequencies. There is a rather big difference between the two simulations as can be seen when comparing the modes from the finite element model and the OMA. Mode 1-2 and 5-6 show a decent correlation, both when it comes to frequency and shape of the modes. However, mode 3 and 4 shows very poor conformance. While the finite element simulation shows a combined motion in *y* and *z*, does the OMA catch a joint motion of the rig structure and the side skirt. This results in response estimations being performed with a large model error. The correctness of the model is also affected if a strain gauge is placed where the strain gradient is high since it is difficult to exactly match its position in the finite element model.

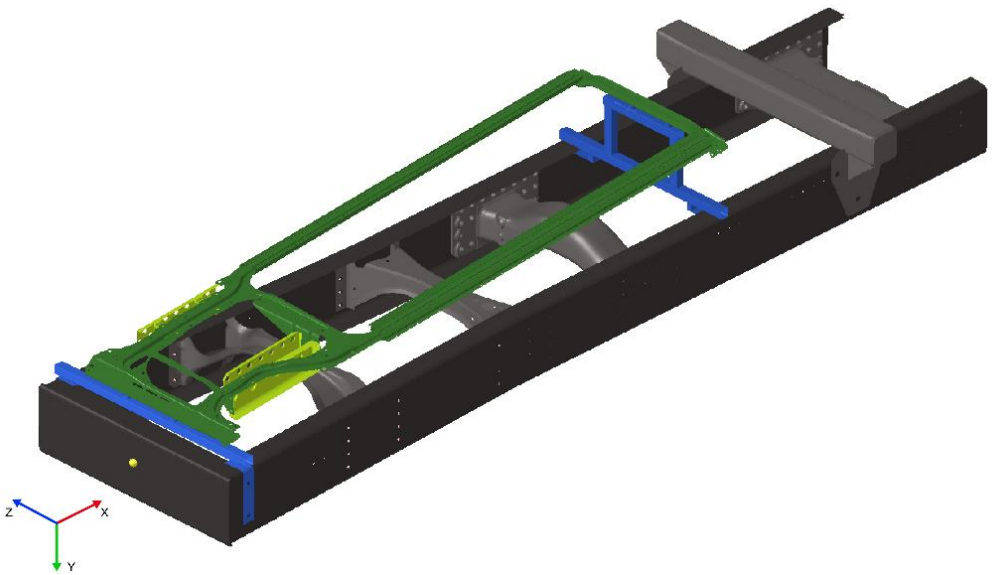


Figure 4: The finite element model of the test rig and side skirt.

Mode	Finite element model		OMA		
no.	Frequency	Shape	Frequency	Shape	Damping
1	11.27 Hz	1st bending mode *y* of side skirt	10.65 Hz	1st bending mode *y* of side skirt	0.7%
2	16.64 Hz	1st twisting mode *y* of side skirt	17.80 Hz	1st twisting mode *y* of side skirt	1.3%
3	32.98 Hz	Simultaneous 1st bending mode *y*, 1st bending mode *z*	26.20 Hz	1st bending mode *y* of side skirt together with oppositely directed motion of rig structure	1.5%
4	34.16 Hz	Simultaneous 2nd bending mode *y*, 1st bending mode *z*	32.47 Hz	1st bending mode *y* of side skirt together longitudinal *x* motion of rig structure	1.2%
5	39.17 Hz	2nd bending mode *y* of side skirt	38.35 Hz	2nd bending mode *y* of side skirt	0.9%
6	44.25 Hz	2nd twisting mode *y* of side skirt	44.76 Hz	2nd twisting mode *y* of side skirt	0.4%

Table 1: To the left, modes from finite element computations of the system up to 50 Hz. To the right, modes from an operational modal analysis up to 50 Hz.

3 Results

With a system model obtained from the finite element calculations and measured dynamic response from the test rig, the smoothers were first verified by estimating acceleration a_5 and strain s_2 based on the other sensors described in Figure 3. After that, the smoothers are challenged to estimate the strains in positions on the side skirt structure where strain measurements were not possible. These strains are then used to calculate the fatigue damage in the structure and the result is compared to the outcome from a full-scale vibration rig test of the structure.

3.1 Tuning of filters

In order to adapt the two smoothers to each specific model and measurement setup, they need to be tuned. That means assigning values to $\mathbf{Q}_\mathrm{x}$ and $\mathbf{Q}_\mathrm{f}$ in the AKF-FLS, and to $\mathbf{Q}_\mathrm{x}$ in the SJISE. The measurement noise covariance $\mathbf{R}_v$ is assumed to be known and to be diagonal, here $\mathbf{R}_v = \mathbf{I}$. No other input forces other than those in $\mathbf{f}_k$ are present, the process noise and the measurement noise are therefore assumed to be uncorrelated resulting in $\mathbf{S} = \mathbf{0}$ (see Equation (8)). Both $\mathbf{Q}_\mathrm{x}$ and $\mathbf{Q}_\mathrm{f}$ are assumed to be constant and to be diagonal. The tuning process can be seen as an optimization process to find the best trade-off between filter adaptability and noise sensitivity. The AKF-FLS is tuned by studying the smoothing norm $\left\|\hat{\mathbf{f}}\right\|_2$ and the error norm $\|\mathbf{z} - \hat{\mathbf{z}}\|_2$. These two quantities are calculated off-line for a wide range of values on $\mathbf{Q}_\mathrm{x}$ and $\mathbf{Q}_\mathrm{f}$. A generalized L-curve method [15] is then utilized where first the minimum error norm for each value of $\mathbf{Q}_\mathrm{x}$ is plotted, see Figure 5 (a). The $\mathbf{Q}_\mathrm{x}$ which gives the best trade-off between adaptability and stability is found in the L-corner, this value is marked with a red circle. Secondly, the smoothing norm is plotted versus the error norm for the selected value of $\mathbf{Q}_\mathrm{x}$, see Figure 5 (b). In this figure some of the values of $\mathbf{Q}_\mathrm{f}$ are marked with numbers. It can be seen that both the smoothing norm and the error norm are relatively unaffected by changes in $\mathbf{Q}_\mathrm{f}$ in the range of $10^{14} - 10^{16}$, resulting in the assigned value $\mathbf{Q}_\mathrm{f} = \mathbf{I} \cdot 10^{16}$.

The SJISE only needs to be assigned a value on $\mathbf{Q}_\mathrm{x}$. Again, both the smoothing norm and the error norm are computed for a wide range of values on $\mathbf{Q}_\mathrm{x}$. The smoothing norm and the error norm are plotted separately versus $\mathbf{Q}_\mathrm{x}$, see Figure 6, and the encircled covariance, $\mathbf{Q}_\mathrm{x} = \mathbf{I} \cdot 10^{-6}$, in the L-corner has been selected.

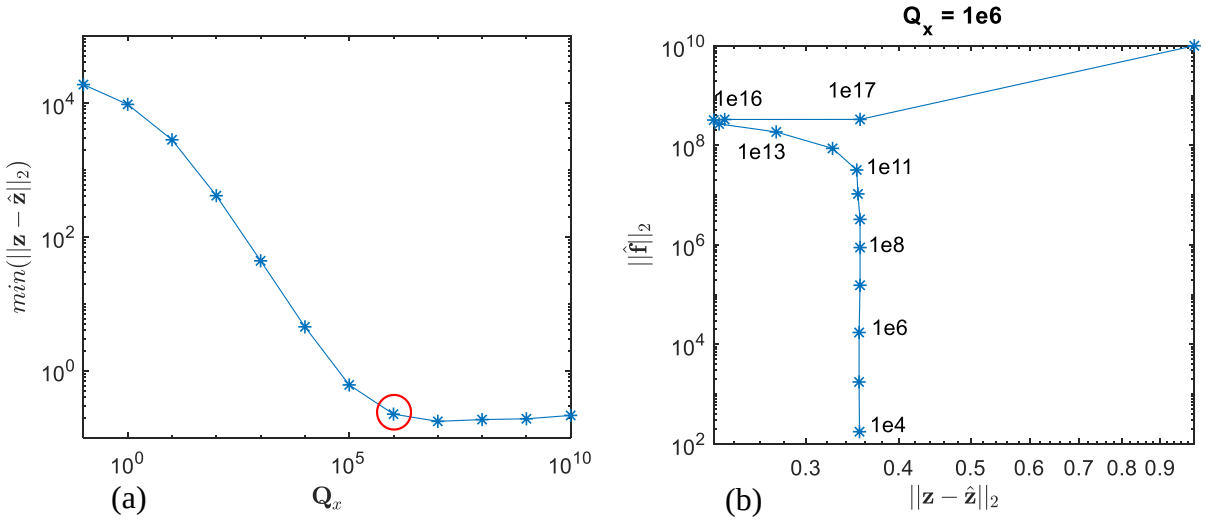


Figure 5: Tuning of AKF-FLS. In (a) the minimum error norm versus $\mathbf{Q}_x$ and in (b) the smoothing norm versus the error norm for the encircled value of $\mathbf{Q}_x$ where some of the values of $\mathbf{Q}_f$ are marked with numbers.

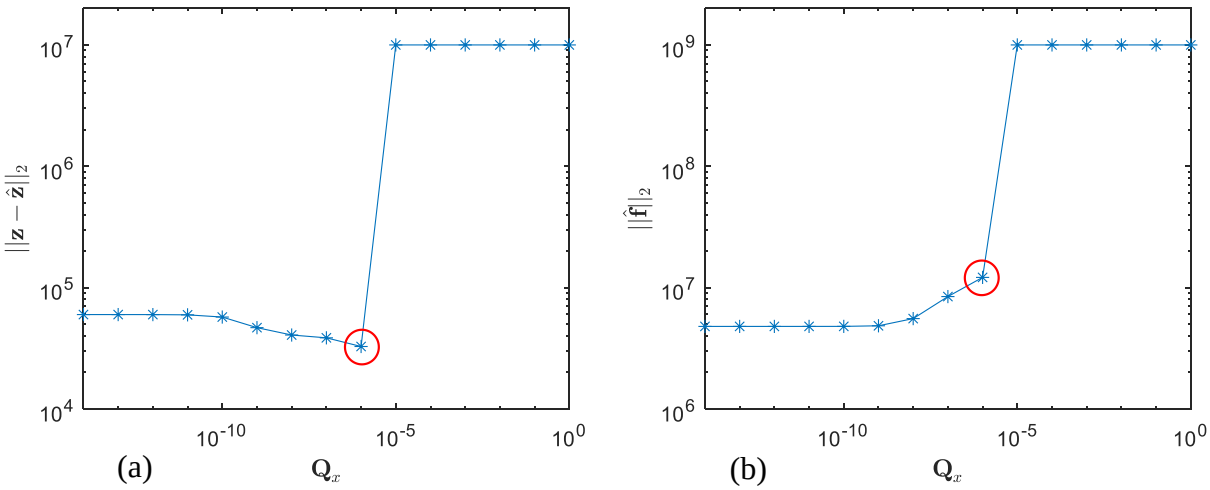


Figure 6: Tuning of SJISE. In (a) the error norm for different values of $\mathbf{Q}_x$ and in (b) the smoothing norm for different values of $\mathbf{Q}_x$. An upper cut-off value of 10^7 and 10^9, respectively, has been used in order to visualize the result.

3.2 Acceleration and strain estimation

With filter parameters as described in Section 3.1, acceleration a_5 and strain s_2 were estimated by the two smoothers. The test signal was 77 seconds long using the time step $\Delta t = 10^{-3}$ s. A time lag of $L = 30$ was used in both estimations. The estimated signals are compared to the actual measured quantities in the frequency domain as a power spectral density (PSD), see Figure 7. Here it can be seen that the acceleration is estimated with high accuracy in the entire studied frequency domain, except at the highest eigenfrequency $\omega_6 = 44.25$ Hz and above. However, it is worth noting that the power ratio drops significantly over 40 Hz. Acceleration estimates from the AKF-FLS and from the SJISE are similar.

The strain estimates differ more, both between the two filters and between the filters and the measured strain. The large model error, especially in the frequency range $20 - 35$ Hz, affects the accuracy of the estimated strains negatively. Figure 7 clearly shows that the strains are poorly estimated between 20 and 30 Hz.

A detail of one second of the estimated time signals is shown in Figure 8. As with the PSD, it can be seen that the acceleration estimates are very accurate while the strain estimated does not really capture the right dynamic behaviour. The difference between estimates from the smoothers appears to arise from the non-optimal tuning of the filters. The relation between measurement noise $\mathbf{R}_v$ and model error $\mathbf{Q}_x$ establish how much the smoothers should trust the measurements versus the model. Since $\mathbf{Q}_x$ is not chosen the same for both algorithms, the estimates may differ.

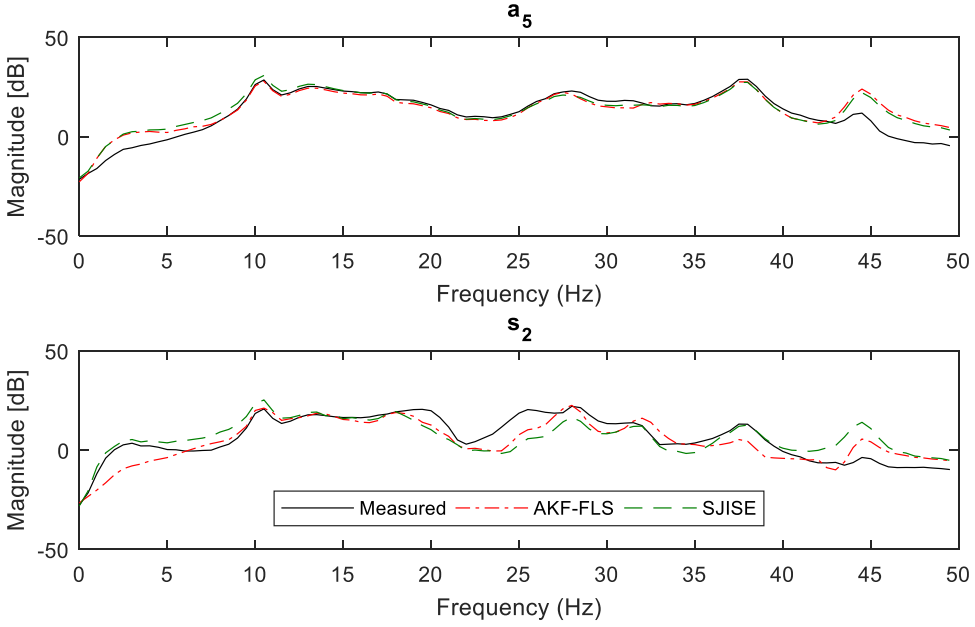


Figure 7: Comparison of measurements and estimates from AKF-FLS and SJISE in the frequency domain.

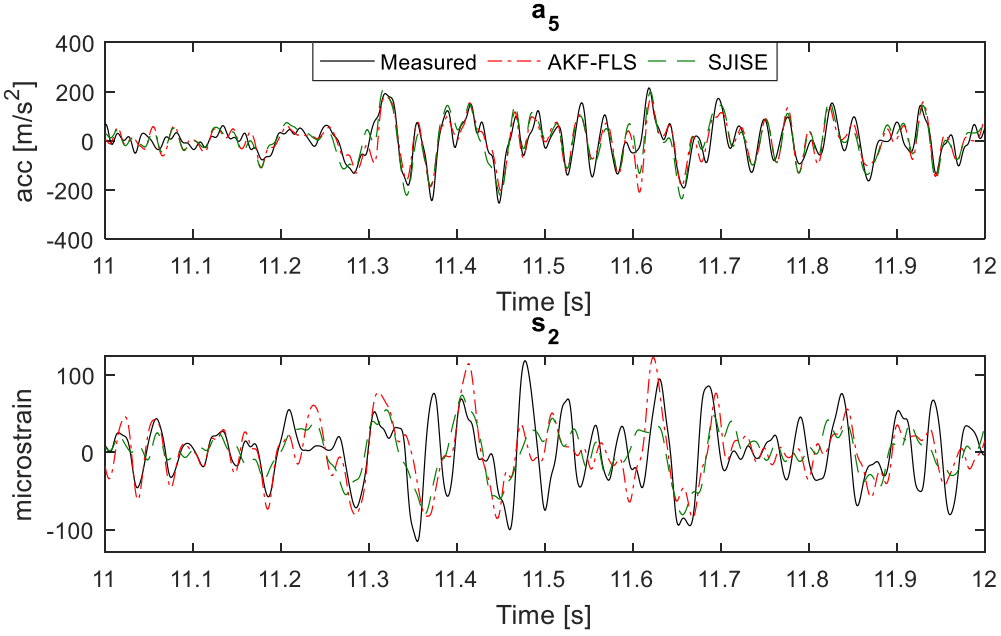


Figure 8: Detail of measured and estimated acceleration and strain time signals.

3.2.1 Fatigue damage calculation

To further evaluate the accuracy of the strain estimates, the corresponding fatigue damage was calculated. The Palmgren-Miner linear damage hypothesis [16] is a frequently used method to calculate the fatigue damage accumulation for structures subjected to variable amplitude stress time histories. The linear damage accumulation law

$$\sum_{i=1}^{k} \frac{n_i}{N_i} \tag{15}$$

is assumed, where n_i is the number of cycles at stress level σ_i and N_i is the number of cycles to failure at this stress level. The relation between σ_i and N_i is described by an S-N curve, typically generated from laboratory testing of simple specimens subjected to uniaxial loading. For small amplitudes, the fatigue life is often very large and the number of cycles to failure is set to infinity. The stress amplitude below which the fatigue life is endless is called the endurance limit σ_∞. In this work, the simple S-N curve described by Equation (16) is used.

$$N(\sigma) = \begin{cases} K^{-1}\sigma^{-\beta}, & \sigma > \sigma_\infty \\ \infty, & \sigma \leq \sigma_\infty \end{cases} \tag{16}$$

Here, K and β are material parameters and depends on both the material and geometry of the object studied. To count the numbers of cycles at each stress level, n_i, the rainflow counting algorithm included in the open access MATLAB toolbox WAFO2017 [17] has been used. The strain is transformed into stress using Hooke's law with Young's modulus $E = 207$ GPa and Poisson's ratio $\nu = 0.3$. The mean stress is set to zero. The computed damage D is presented in Table 2. The damage was calculated from only one test cycle of 77 seconds, which makes the actual number irrelevant. The damages were therefore normalized so that the measured strain equals $D_{Measured} = 1$, in order to facilitate a comparison of the estimated strain signals. Both smoothers underestimate the damage by about 25%. The cause of this is most likely the large model error discussed in Section 2.4.

	$D_{Measured}$	$D_{AKF-FLS}$	D_{SJISE}
Relative damage	1	0.75	0.73

Table 2: Damage computed from measured and estimated strain in sensor s_2.

3.2.2 Computational cost of the acceleration and strain estimations

The acceleration and strain responses were estimated using a range of values on the time lag L and the calculation time was recorded. Calculations were performed in MATLAB using a workstation with Intel® Xeon® E5-1650 v3 3.5 GHz, 1 thread. The calculation time were then averaged over the 77000 time steps, and the result is presented in Figure 9. The calculation time increases linearly with the lag L for the AKF-FLS, but has a quadratic growth for the SJISE, which is also shown in [10]. Figure 9 visualizes that it is possible to run the AKF-FLS online even for a lag of $L = 40$ since the calculation time for each time step is smaller than the simulation time step Δt. In contrast, the SJISE passes this limit already at a lag of $L = 7$.

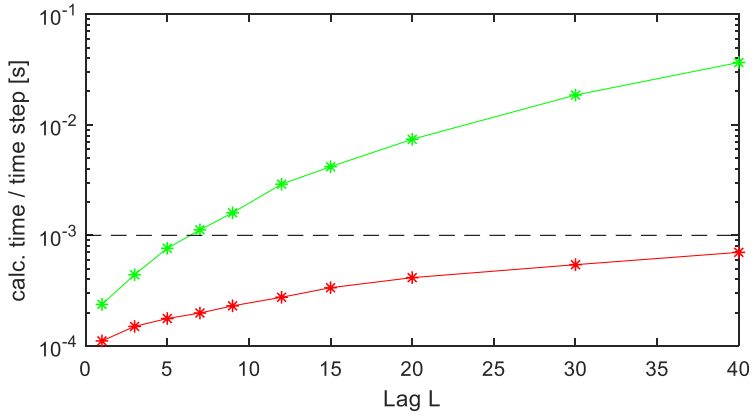


Figure 9: The calculation time per time step as a function of the lag L. The AKF-FLS is shown in red, the SJISE in green and Δt as a dashed black line.

3.3 Damage calculation and comparison to failures

The side skirt structure studied was fatigue tested in a vibration test rig simulating the entire truck chassis. This test simulated the entire life of the side skirt with a test signal measured on the Scania test track. In addition to the load carrying structure of the side skirt shown in Figure 2, the plastic covering was also included. During the test, a fatigue crack was initiated at the bottom of the upper hole in the vertical member of the steel front structure, see Figure 10. The crack grew until the vertical member was completely broken. However, the lower hole remained unaffected during this fatigue test. Since the failure occurred in the vicinity of a hole where another part was mounted onto the component, a measurement of the strain with a strain gauge was not possible. It would therefore beneficial if the strains could be estimated at these locations when designing for fatigue .

With measurements from the sensors $a_1 - a_4$ and $s_1 - s_4$ (see Figure 3), the complete strain tensor in four different nodes around the holes marked in Figure 10 was estimated, see Figure 11. The smoothers were run with the same covariances as described in Section 3.1, and with the same time lag $L = 30$.



Figure 10: The front structure of a side skirt after a completed vibration shake rig test. The vertical structural member is broken at the upper hole but unaffected at the lower one, both marked with red rectangles.

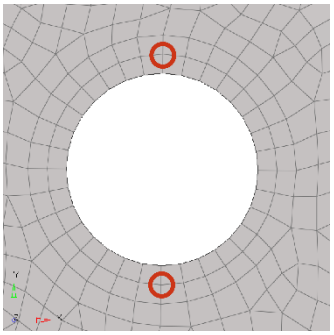


Figure 11: The mesh around the upper hole with the two nodes where strain is estimated marked with red circles. The bottom hole looks very much the same and the two nodes are located correspondingly.

The equivalent von Mises stress was calculated from the estimated strain tensors. The damage was then computed following the methodology described in Section 3.2.1. The damages computed from estimates by both the AKF-FLS and the SJISE are presented in Table 3.

Position	$D_{AKF-FLS}$	D_{SJISE}
Upper hole, top	0.82	0.79
Upper hole, bottom	0.65	0. 67
Lower hole, top	0.24	0.18
Lower hole, bottom	0.09	0.10

Table 3: The damage calculated in four different nodes from strains estimated by the AKF-FLS and the SJISE.

The result shows a clear distinction between the damage accumulated around the upper and the lower hole. However, a higher damage is estimated at the top of the upper hole rather than in the bottom of the hole where the crack initiated. In comparison with the accuracy of the strains and damages estimated in Section 3.2; this difference lies within the expected precision of the proposed method. The exact number is also influenced by both the tuning parameters of the filters and by the material parameters following the damage calculations. Nevertheless, this result indicates that both smoothing algorithms are useful when estimating the total strain state in a complex component from a limited number of sensors with an accuracy good enough to use for fatigue damage calculations, when compared to observed failure of a component tested in a full-scale fatigue test.

4 Conclusion

In this paper we present fatigue damage estimations in a truck component excited by road induced vibrations. The damage is computed from strains estimated from sparse dynamic response measurements, accelerations and strains. The system is assumed to be linear in the frequency range of interest and the model parameters are obtained from a finite element model. The strains are estimated with two different smoothing algorithms; an augmented Kalman filter extended with a fixed-lag smoother and a smoothed joint input-state estimator. The first simulation showed a comparison between estimated response and the actual measured quantities, and both algorithms succeeds equally well in estimating the strains. The damage computed from the estimated strain differs about 25% from the measured one, likely due to a large model error. Both algorithms perform well when predicting the damage in a side skirt subjected to a full-scale fatigue life vibration test. The result indicates that both smoothing algorithms are useful when estimating the total strain state in a complex component from a limited number of sensors with an accuracy good enough to use for fatigue damage calculations.

We also studied the calculation time needed for the two algorithms. The AKF-FLS shows a linear increase in calculation time with respect to the time lag L, while the computational time for the SJISE grows quadratically.

References

[1] J. Sanchez, H. Benaroya *Review of force reconstruction techniques*, Journal of Sound and Vibration, Vol. 333 (2014), pp. 2999- 3018.

[2] C-K. Ma, J-M. Chang, D-C. Lin, *Input forces estimation of beam structures by an inverse method*, Journal of Sound and Vibration, Vol. 259 (2003), pp. 387-407.

[3] L. Nordström, *A dynamic programming algorithm for input estimation on linear time-variant systems,* Computer Methods in Applied Mechanics and Engineering, Vol. 195 (2006), pp. 6407-6427.

[4] S. Gillijns, B. De Moor, *Unbiased minimum-variance input and state estimation for linear discrete-time systems,* Automatica, Vol. 43 (2007), pp. 111-116.

[5] E. Lourens, E. Reynders, G. De Roeck, et al. *An augmented Kalman filter for force identification in structural dynamics*, Mechanical Systems and Signal Processing. Vol. 27 (2012), pp. 446-460.

[6] E. Lourens, C. Papadimitriou, S. Gillijns, et al. *Joint input-response estimation for structural systems based on reduced-order models and vibration data from a limited number of sensors*, Mechanical Systems and Signal Processing, Vol. 29 (2012), pp. 310-327.

[7] K. Maes, A. Smyth, G. De Roeck, et al. *Joint input-state estimation in structural dynamics*, Mechanical systems and Signal Processing, Vol. 70-71 (2016), pp. 445-466.

[8] C. Papadimitriou, E. Lourens, G. Lombaert, G. De Roeck, K. Liu, *Prediction of fatigue damage accumulation in metallic structures by the estimation of strains from operational vibrations*, in A. Strauss, D. Frangopol, K. Bergmeister, editors, *Proceedings of 3rd International symposium on Life-Cycle Civil Engineering Vienna, Austria,3-6 October* (2012) pp. 304-310

[9] K. Tatsis, E. Chatzi, S. Thons, E. Lourens, *Reliability prediction of fatigue damage accumulation on wind turbine support structures*, in M. Papadrakakis, V. Papadopoulos, G. Stefanou, editors, *Proceedings of The 2nd ECCOMAS Thematic Conference on Uncertainty Quantification in Computational Sciences and Engineering*, *Rhodes Island, Greece, 15–17 June* (2017), pp. 76-89.

[10] K. Maes, S. Gillijns, G. Lombaert, *A smoothing algorithm for joint input-state estimation in structural dynamics*, Mechanical Systems and Signal Processing, Vol. 98 (2018), pp. 292-309.

[11] R. Brincker and C. E. Ventura, *Introduction to Operational Modal Analysis*, John Wiley & Sons, Chichester, UK, (2015).

[12] B. Peeters, H. Van der Auweraer, P. Guillaume, J. Leuridan, *The Poly-MAX frequency-domain method: A new standard for modal parameter estimation?*, Shock and Vibration 11 (2004), pp. 395-409.

[13] B. Peeters, H. Van der Auweraer, F. Vanhollebeke, P. Guillaume, *Operational modal analysis for estimating the dynamic properties of a stadium structure during a football game*, Shock and Vibration 14 (2007), pp. 283-303.

[14] R. J. Allemang, *The modal assurance criterion - Twenty years of use and abuse*, Sound and Vibration, Vol. 37 (2003), pp. 14-23.

[15] P. C. Hansen, *Analysis of discrete ill-posed problems by means of the L-curve*, SIAM 34 (1992), pp. 561-580.

[16] C. Bathias, A. Pineau, *Fatigue of Materials and Structures: Fundamentals*, Wiley-ISTE, (2013)

[17] WAFO. Wave Analysis for Fatigue and Oceanography, Centre for Mathematical Science, Lund University, (2017), <http://www.maths.lth.se/matstat/wafo/>, Accessed 31 May 2018.

Dealing with harmonics in continuous modal analysis

N. Gioia [1]**,C. Peeters** [1]**, P.J. Daems** [1]**, P. Guillaume** [1]**, J. Helsen** [1]
[1] Vrije Universiteit Brussel, Acoustic and Vibration Research Group,
Pleinlaan 2, 1050, Brussel (Belgium)
e-mail: **ngioia@vub.be**

Abstract
Noise, vibration and harshness (NVH) problems are critical issues to be tackled in case of rotating machineries. At this purpose, operational modal analysis (OMA) represents a powerful tool. OMA methods can be applied under the assumption that the excitation acting on the system under analysis is white noise. This requirement is not met in case of rotating machines, due the presence of excitations related to rotating elements. For this reason, harmonics need to be dealt with. This work focuses on two techniques for dealing with harmonics: the use of a cepstrum signal editing procedure and the use of order based modal analysis (OBMA). This paper shows the potential of these two methodologies when processing a continuous stream of real data coming from an offshore wind turbine drive train.

1 Introduction

In the field of mechanics, design values such as the modal parameters are essential: they are governing the system response to vibration sources. To avoid problems such as the transmission of undesired vibrations and the generation of tonalities, the design values must be optimized. Since in non-linear systems working at highly variable loads, modal parameters (and in particular damping values) strongly depend on the operating conditions, the experimental verification of prototypes is necessary for guaranteeing the reliability and the safety of the structure [1]. To this purpose Operational Modal Analysis (OMA) represents a powerful approach: it allows to extract the modal parameters from the dynamic response of the structure to unmeasured operational forces. The industrial design process currently comprises component-level testing and full-scale-machine testing both in laboratory environment and in the field. However, these tests are generally performed over short periods, trying to catch specific operating conditions to be tested. With this work, we want to propose an innovative approach for long-term operational modal analysis (OMA) testing of machines operating in the field or in a laboratory environment. The goal, is to give the designers information that allow to take decisions on how to improve the subsequent design variants based on what can be learnt in real operating conditions, i.e. with the machine running through every possible scenario that it could meet during its operating life. Coupling the modal parameters with the state of the machine allows to analyse how the environmental and operating conditions influence the modal behavior of the structure. The scope of this research is to make OMA suitable for processing a continuous stream of data coming from the operating machines. To do so, state-of-the-art vibration processing techniques are combined with methodologies coming from big data analysis and machine learning disciplines. As already mentioned, OMA is a highly capable methodology to extract modal parameters from operating machines [2]. What is missing to employ OMA as an approach for the proposed design methodology is the availability of reliable modal estimators capable of automatically processing the data received from the sensors, send the needed information to the cloud and provide a continuous view of the design values evolution. OMA is a technique that estimates the modal parameters from the dynamic response of the analysed system by fitting the data with parametric models and solving an optimization problem. The procedure is performed iteratively, using at each iteration a model with increased order (model order). However, the classical algorithms make use of the so-called stabilization

diagram: a graph where the poles are plotted for each model order allowing to observe the stabilization of the poles and distinguish the mathematical from the spurious ones. Description of algorithms that automatically select the physical poles from the stabilization diagram can be found in literature [3, 4, 5]. Starting from these ideas we want to move to the next step in order to achieve a methodology that is able to continuously process a stream of data, selecting the parameters needed for the analysis in an automatic way based on the operating conditions and the physical characteristics that can be extracted from the signals. This implies the implementation of automatic procedure also for both the pre- and post-processing steps. In case of rotating systems, a main challenge for the use of classical OMA is the problem of the harmonics. OMA is based on the assumption that the excitation to the system is a white noise signals, indeed, if this assumption is not satisfied, the output of the parameter estimators is a combination of structural modes and components already present into the excitation signal (e.g. harmonics), giving erroneous results [6, 7]. Unfortunately, this problem affects most of the cases in which the use of OMA would be useful for the designing purposes explained above, so finding a solution for dealing with the presence of harmonics is of high interest.

2 State of the Art

2.1 Operational Modal Analysis

OMA techniques aim at obtaining modal parameters characterizing the dynamics of the systems based only on the knowledge of the response (i.e. output) of the structure to various ambient excitations, which are not measured (e.g. wind, rain, traffic..). The greatest advantage of OMA techniques is in providing the dynamic model of the structure under actual operating conditions and real boundary conditions. For this research the poly-reference Least-Square Complex Frequency-Domain (pLSCF) algorithm has been selected as starting point of the work. This method consists in a frequency-domain Modal analysis method that requires as primary data the output spectra of the system under analysis [8]. This method is based on the assumption that the excitation to the system is a white noise spectrum signal. Under this assumption is indeed possible to model the output spectra exactly in the same way used for the frequency response functions (FRFs) H(ω):

$$H(\omega) = \sum_{i=1}^{n} \frac{\{v_i\} \left\langle l_i^T \right\rangle}{j\omega - \lambda_i} + \frac{\{v_i^*\} \left\langle l_i^H \right\rangle}{j\omega - \lambda_i^*} \tag{1}$$

Where n is the number of complex conjugate mode pairs, $*$ is the complex conjugate operator, ^{T} is the transpose of a matrix, H is the complex conjugate transpose (Hermitian) of a matrix, v_i is the mode shape vector of the mode i, l_i^T the modal participation factors of the mode i and λ_i are the poles of the system (occurring in complex conjugate pairs). The poles are linked to the resonance frequencies and the damping ratios of the system by means of the following relation:

$$\lambda i, \lambda_i^* = \xi_i \omega_i \pm j\sqrt{1 - \xi_i^2}\omega_i \tag{2}$$

The relationship between the input spectra $[S_{UU}(\omega)]$ and the output spectra $[S_{yy}(\omega)]$ of a system represented by the FRF $H(\omega)$ is described by:

$$[S_{YY}] = [H(\omega)][S_{UU}(\omega)][H(\omega)]^H \tag{3}$$

In case of output-only analysis, the auto-spectra are the only available information. The most important consequence of assuming the input signal as a white noise excitation is that the power spectrum of the input signal is constant; therefore $S_{UU}(\omega) = S_{UU}$ [8]. Considering this assumption and combining equation (1) and (3) it is possible to write the modal decomposition of the output spectrum matrix as following:

$$S_{YY}(\omega) = \sum_{i=1}^{n} \frac{\{v_i\}\langle g_i\rangle}{j\omega - \lambda_i} + \frac{\{v_i^*\}\langle g_i^*\rangle}{j\omega - \lambda_i^*} + \frac{\{g_i\}\langle v_i\rangle}{-j\omega - \lambda_i} + \frac{\{g_i^*\}\langle v_i^*\rangle}{j\omega - \lambda_i^*} \tag{4}$$

Where g_i are the operational reference factors, which replace the participation factors in case of output-only analysis. A right matrix model (equation 5) is then used to fit the measured FRFs data. The use of the right matrix model as parametric model has the advantage that the participation factors are available when constructing the stabilization diagram, thus a clearer stabilization diagram is generated, on which closely spaced modes are separated.

$$[H(\omega)] = [B(\omega)][A(\omega)]^{-1} \tag{5}$$

Where $H(\omega) \in \mathbb{C}^{l\times m}$ is the FRF matrix containing the FRFs between the m inputs and the l outputs, $B(\omega) \in \mathbb{C}^{l\times m}$ is the numerator matrix polynomial and $A(\omega) \in \mathbb{C}^{m\times m}$is the denominator matrix polynomial.

The results of the fitting of the measured FRFs data by means of a parametric model, are represented in the stabilization diagram [9]. The measured FRFs data are fitted with increasing model order models and the poles estimated for a certain model order are compared to the poles estimated for the lower model order. If their differences are within pre-set limits, the pole is labelled as stable one. The spurious numerical modes will not stabilize at all during this iteration procedure and they can be then easily sorted out of the modal parameter estimates. The stabilization diagram shows how the poles stabilize for increasing model orders and it allows the analyst to distinguish the physical modes from the spurious ones.

2.2 Cepstrum editing procedure

As already stated, OMA does not require input force information but it makes assumptions about the nature of the input excitation forces: 1) the excitation must be represented by a flat white noise spectrum in the frequency band of interest and 2) the forces acting on the structure must be uniformly distributed and uncorrelated temporally and spatially [10]. Both these assumptions imply that excitation is considered stochastic in time and space. Unfortunately, most of the time these assumptions are not fulfilled in case of complex rotating mechanical systems due to the presence of discrete components (i.e. harmonics) coming from internal sources (e.g. gear meshing phenomena) and aeroelastic forces. From the vibration analysis point of view, this research focuses mainly on dealing with the problems of harmonics. In literature there are several examples of extended OMA techniques tailored to deal with harmonics disturbances. These methods either assume that the frequency of the harmonic disturbances is known or identify the harmonics frequency from the data via noise poles on the unitary circles [11]. These methods are based on the assumption that the harmonic frequencies are stationary (i.e they are constant in amplitude, frequency and phase). However, this assumption is violated in most of the practical application such as turbines, diesel motors and helicopters. Indeed, in these machines the speed can not be assumed constant and therefore the harmonics are smeared in the spectrum of the signals and they influence broader frequency bands. As a consequence, the harmonic components in the signal can not be modeled accurately with the methods used in case of stationary harmonics and the extended OMA techniques fail whenever the time varying frequency is close to a resonance frequency of the structure [11]. One possibility for dealing with this problem is to use classical OMA algorithms after having filtered the harmonic components from the raw data during a pre-processing step. A list of basic signal processing techniques for removing harmonics from the vibration signals is given in [12]. In this work cepstrum-based time-domain signal editing procedure is adopted to reduce the in influence of the harmonics from the raw data. Cepstrum analysis is a procedure that through the double application of the Fourier algorithm brings the signal from the time domain in the quefrency domain, as shown in equation 6:

$$c_c(\tau) = log(\mathscr{F}(X(t))) = \mathscr{F}^{-1} ln(A(f)) + j\phi(f) \tag{6}$$

Where (X(t)) is the original signal in the time domain, A(f) and ϕ(f) are respectively the amplitude and phase of the frequency domain signal. By setting the phase to zero in equation 6, the formulation of the real cepstrum can be obtained (eq. 7):

$$C_r(\tau) = \mathscr{F}^{-1} ln(A(f)) \tag{7}$$

Ensuring the possibility of going back to the time domain. After that it has been realized that there are many situations in which the editing can be carried out by modifying the amplitude only, the cepstrum started to be considered a powerful signal editing tool: in the quefrency domain, families of harmonics are concentrated in single lines called rhamonics, setting to zero a line in the quefrency domain automatically smooth the corresponding family of harmonics in the time domain. The success of the use of cepstrum for OMA applications finds its reason in the fact that the information about the modes are concentrated at low quefrency values [13]. The application of a low-pass lifter (an exponential window) on the real cepstrum greatly enhances the modal information with respect to anything else: it allows to remove all the components at higher quefrencies keeping the modal information of the signal. The only distortion introduced at lower quefrency (thus on the interesting part of the signal) is the addition of a known amount of damping, that can be easily removed from the damping value estimated by an OMA procedure by means of the following equation:

$$\xi_r = \xi_m - \frac{1}{2\pi f_r \tau} \tag{8}$$

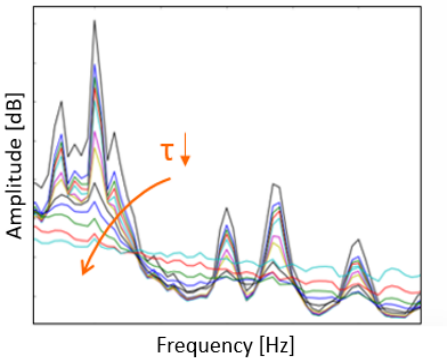
Where for each estimated mode, ξ_r is the real damping [%], ξ_m is the measured damping [%], f_r is the real frequency [Hz] and τ is the time constant of the exponential window [s]. Since it has been shown that the cepstrum lifter works better for narrow harmonics [13], speed correction has been performed before editing the acceleration signals: a virtual resampling of the signal allows the samples to correspond to fixed angular positions rather than being temporally equi-spaced. In this way it is possible to compensate for speed fluctuations narrowing the frequency bands excited by the harmonics. However, resampling the signal, one alters the resonance phenomena, that are not tied to the speed of the shaft [14]. For this reason, after having used the cepstrum lifter to reduce the influence of the harmonics on the raw signal, the latter is brought back to the time domain (i.e. samples every Δt seconds). This step is not necessary fr stand still data, since in this case harmonics present in the signal are narrow for nature (small speed variation in case of harmonics due to the gear meshing and differentf origin of the harmonics).

3 Methodology

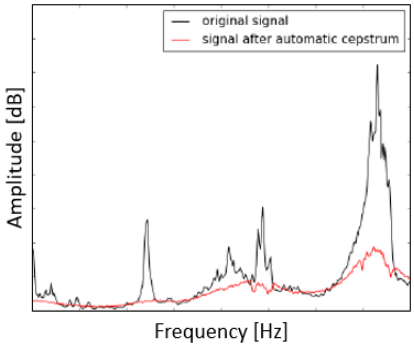
3.1 Automation of the procedure

The two procedures described in the previous section must be combined and improved in order to achieve a valuable methodology for performing OMA on a continuous stream of data acquired on rotating machines. The automation of the modal parameter estimator can be divided in two sub-steps. First the p-LSCF algorithm is made automatic eliminating the analyst-algorithm interaction by introducing a clustering method that autonomously interprets the information collected in the stabilization diagram. Clustering analysis is used to group poles that show stable characteristics. The physical poles are then selected automatically by considering statistical features for each cluster. The algorithm used to estimate the modal model of the analysed system is then coupled with an automatic tracking algorithm that shows how the modal parameters evolve along different datasets (i.e. for longer periods) [15]. The comparison amongst the estimates of each dataset is performed using MAC and poles values, in order to measure in which extend the estimates are coherent in terms of mode shapes (represented by the MAC value) and frequency/damping values (represented by the poles values). In this work, a completely automatic procedure that does not require the

definition of the reference dataset is implemented. Concerning the cepstrum editing procedure, an algorithm that automatically select the parameter required by the analysis is implemented. The mentioned parameter is the cutoff-quefrency, i.e. the time constant of the exponential window applied to the signal in the quefrency domain. The idea is to exploit the mechanical characteristic of the system to have knowledge of the frequency bands at which the harmonics are introduced in the signal: the method is based on the reduction of the energy introduced by harmonics consequent to the use of the cepstrum procedure. The method is iterative and a representative example of it is shown in figure 1. The iterative application of a cepstrum lifter with decreasing cutoff quefrency is stopped when the desired energy reduction is achieved. In figure 1a it is possible to observe the effect of the subsequent iterations, while in figure 1b it is possible to see how the use of the cepstrum lifter smears the energy of the peaks in the frequency band around them, producing a spectrum with a better energy distribution.



(a) Effects of a decreasing cutoff quefrency



(b) Signal before and after the use of cepstral editing procedure

Figure 1: Use of the automatic cesptrum procedure.

To apply automatic OMA on a continuous stream of data, it is also needed an automatic distinction between steady state data conditions (data acquired with the turbine in idling conditions or running at almost constant speed) and run-up/coast-down events. This is necessary due to the different pre-processing procedure that has to be used depending on the type of data analyzed. The implementation of an algorithm able to automatically detects event in the signal is implemented, allowing to complete the scheme represented in the block diagram in figure 2. In figure 2 it is also possible to notice that an additional step is introduced: data validation. This allows to assess the validity of the signal and avoid processing corrupted signals (for example erroneous acquisition due to the detachment of the sensor from the structure to be analyzed).

Since the automatic modal parameter estimation has already been showed and validated in previous works [16], the missing step to make this analysis running continuously over a significant amount of time is the introduction of the automatic classification of the data. The methodology investigated in this work makes use of a machine learning approach that is based on the fact that turbine run-up and coast-down events are controlled events. It is thus expected that a similar pattern in speed and power can be seen across several of these events. Based on this observation, machine learning algorithms can be used in the following way: standard run-up and coast-down events are learned such that subsequent similar repetitions can be detected automatically. Since in this work the focus is on the use of cepstrum-based preprocessing of the data to reduce the influence of the harmonics from steady state data, at this stage the detected events are simply removed from the set of data that will be analyzed. However, as it can be seen in figure 2, within the steady state data a further distinction must be made between stand still data (rotating speed approaching zero value) and rotating data. A threshold value on the average speed is then introduced in order to distinguish these two cases.

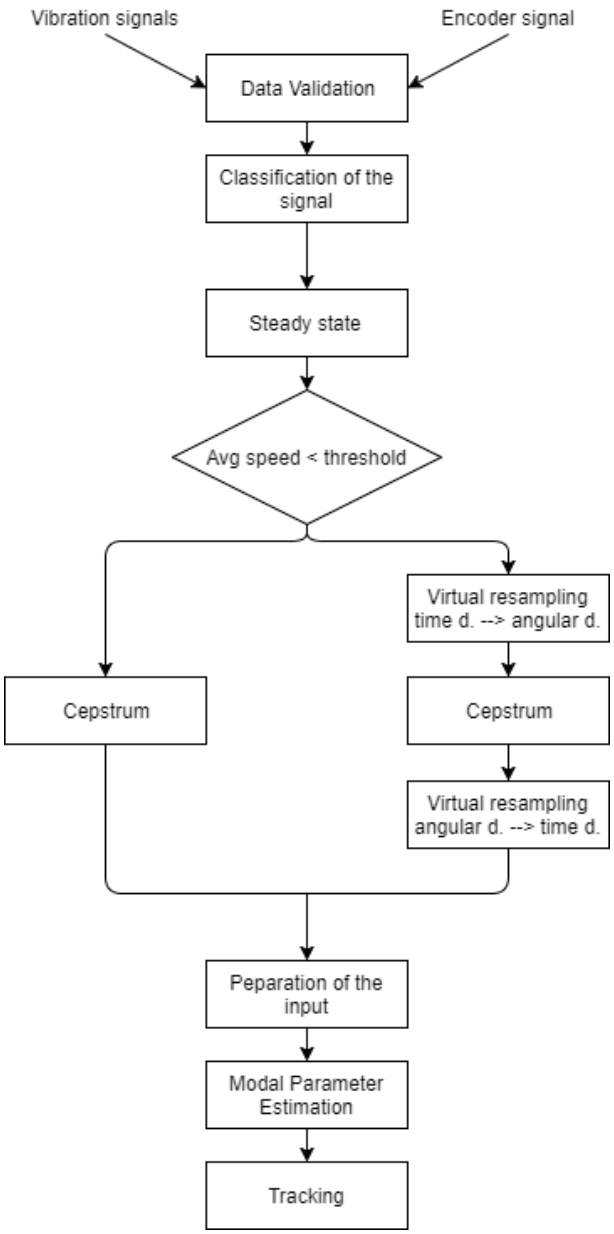


Figure 2: Block diagram of the automatic procedure implemented to autonomously and continuously track the modal parameters.

3.2 Use of big data analysis and tailored database

Due to the variability of the wind, the turbine is not always operating at nominal conditions. Several transient events occur during the control action, and several important loading cases act on the wind turbine (start-up, shut down, emergency stop and grid loss related events). The load cases cover different operating conditions, and the most unfavourable load effects govern the design of the machine. However, during the design process, it is important to observe how the machines globally respond to the different loading conditions. In this way it is possible to optimize the design of future prototypes and predict which is the modal behaviour of the machine in case of critical loads. Long-term analysis and monitoring of the turbines, leads to the need of dealing with a huge amount of data. It requires then an automatic approach able to tackle the described challenges. In addition to the implementation of autonomous algorithms for advanced signal processing, the key is having a system able to deal with such a big amount of data. Our integrated approach comprises three main steps [17]. 1) Data-acquisition system that allows to capture all the data within one consistent dataset:

each machine has its own sensor and data acquisition network consisting of machine embedded sensors and custom monitoring system. 2) Scalable data-warehouse in order to be able to deal with large amount of data non-equally sampled and heterogeneous for nature: a no-SQL database is used to tackle problems of scalability and to increase the reliability in case of node failure. 3) Distributed computing since the analysis of large amount of data is computationally intensive. No-SQL architectures distribute the data across the cluster; it is possible to couple it with parallelized querying and data analysis using Apache Spark (Spark). Our algorithms are written using Python as coding language. This architecture allows to combine machine learning algorithms with advanced vibration signal processing techniques. This allows to gather new insights in the modal behavior of the machine in different operating conditions and make prevision on how it will respond in the future using data-driven prognostic techniques. This allows the designers constructing data-driven models and improving the new prototypes based on physical system knowledge and experimental information.

4 Results

In order to validate the implemented procedure, a period of time in which several events are present has been selected. This allows to test the automatic event detection and to have a sufficient amount of rotating a standstill datasets to compare. In figure 3 it is possible to observe the speed variation of the turbine in the selected period.

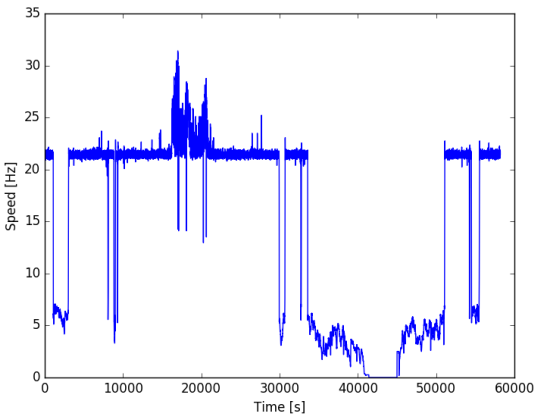


Figure 3: Profile of the speed of the machine in the period selected for the analysis.

By means of the event detection algorithm used to identify presence of run-up or coast-down in the signal, the events have been eliminated from the set of data analyzed. The remaining datasets have been divided in sub-signals and automatically clustered as rotating data or stand still data, using as discriminant the average value of the speed. The variation of the speed is also considered in a next step for the post processing of the data.

The output of the tracking procedure, it is shown in figure 4 concerning rotating data and in figure 5 concerning the stand still data.

At a first sight to figure 4 and 5, it can be noticed how, in both the cases, the damping presents a much higher variation, indication of the fat that the damping ratio is a modal parameter highly dependent on the operating conditions of the machine. On the opposite, frequency values present more consistent values along all the datasets.

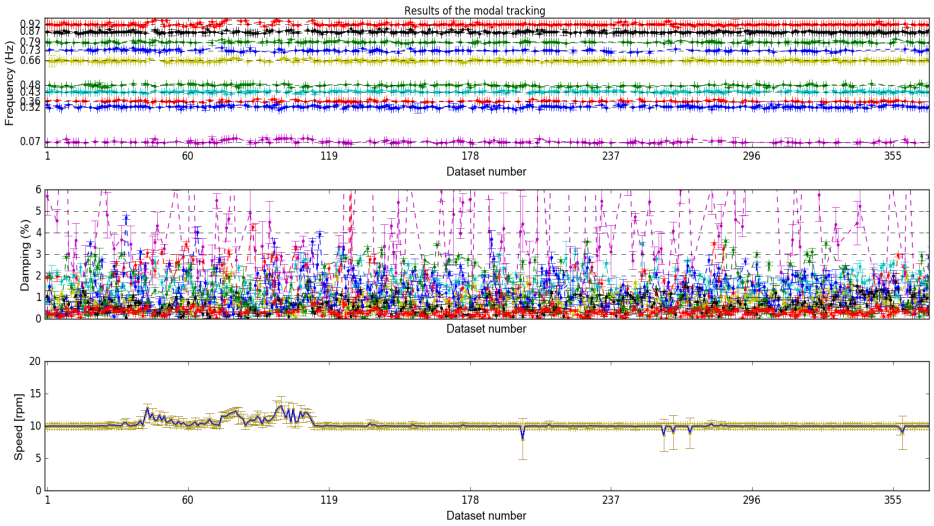


Figure 4: Results on the tracking on rotating data.

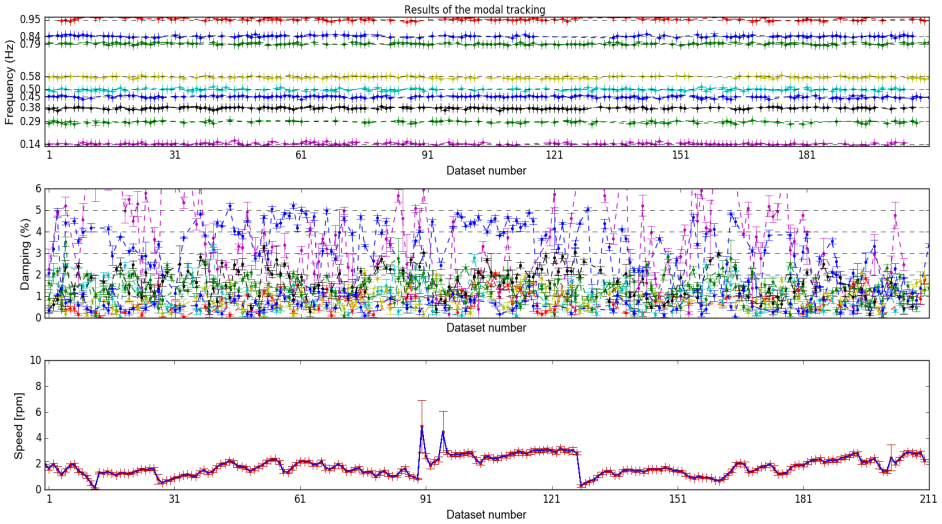


Figure 5: Results of the tracking on stand still data.

5 Conclusions

This paper has investigated a completely automated operational modal parameter estimation scheme, tackling the main challenges in applying OMA on complex systems like wind turbine gearboxes. The approach has been verified by processing real data coming from the drive train of an off-shore wind turbine.

The main challenges posed by the methodology used for the parameter estimation have been already investigated in previous works. With this research emphasis has been given to the automation of the procedure and the implementation of it in an ambient that allows to parallelize the needed steps and save computational power and analysis time. It has been shown that the automatic procedure gives promising results, consistent with the ones obtained with a manual procedure and shown in previous works. This will ensure the results to be objective and less dependent on the analyst decisions, opening the doors to further investigations.

The results obtained, confirm the variation of the modal behavior of a machine with the speed. What it is interesting to investigate, is then the presence of possible correlations between the evolution of the modal

parameters and other operating and environmental conditions than using the speed only. Parameters that are generally available through SCADA data.

Acknowledgements

SB PhD fellow at FWO.

This research was performed in the framework of the ongoing research project HYMOP funded by VLAIO Vlaanderen, furthermore we want to acknowledge our partners in acquiring the data.

References

[1] E. Reynders *System identification methods for (operational) modal analysis: review and comparison* Archives of computational methods in Engineering 19(1), pp.51-124, 2012

[2] F. Magalhaes and A. Cunha *Explaining Operational Modal Analysis with the data from an arch bridge*, Mechanical Systems and Signal Processing, vol. 25.5 pp. 1431-1450, July 2011

[3] C. Devriendt, M. El-kafafy, G. D. Sitter and P. Guillaume *Continuous dynamic monitoring of an offshore wind turbine on a monopile foundation*, International Conference on noise and vibration engineering (ISMA), Leuven, Sep 2012.

[4] F. Magalhaes and A. Cunha, *Online automatic identification of the modal parameters of a long span bridge*, Mechanical System and Signal Processing, vol. 25, pp. 316-319, 2010.

[5] E. Reynders, J. Houbrechts and G. D. Roeck *Fully automated (operational) modal analysis*, Mechanical System and Signal Processing, vol. 29, pp. 228-250, 2012.

[6] B. Peeters, B. Cornelis, K. Janssens and H. V. d. Auwaraer, *Removing disturbing harmonics in operational modal analysis*, Proccedings of International Operational Modal Analysis Conference (IOMAC), Copenhagen, April 2007.

[7] S. Gade, R. Schlombs, C. Hndeck and C. Fenselau, *Operational Modal Analysis on a wind turbine gearbox*, Conference and Exposition on Structural Dynamics, 2009.

[8] B. Peeters, H. Van der Auweraer, *PolyMAX: a revolution in operational modal analysis*, 1st International Operational Modal Analysis Conference (IOMAC), Copenhagen, Apr 2005.

[9] B. Peeters, G. Lowet, H. Van der Auweraer, J. Leuridan, *A new procedure for modal parameter estimation*, Sound and vibration, vol. 38(1), pp. 24-29, 2004.

[10] J. Houben F. Vanhollebeke S. Goris B. Peeters E. Di Lorenzo S. Manzato. *Wind Turbine Gearbox Dynamic Characterization using Operational Modal Analysis.*

[11] Pintelon, R., Peeters, B. and Guillaume, P., *Continuous-time operational modal analysis in the presence of harmonic disturbances*, Mechanical Systems and Signal Processing, 22(5), pp.1017-1035. 2008.

[12] Randall, R.B., Sawalhi, N. and Coats, M., *A comparison of methods for separation of deterministic and random signals*, International Journal of Condition Monitoring, 1(1), pp.11-19, 2011

[13] Randall, R.B., *A history of cepstrum analysis and its application to mechanical problems*. Mechanical Systems and Signal Processing, 97, pp.3-19. 2017.

[14] Roussel, J., Haritopoulos, M., Sekko, E., Capdessus, C. and Antoni, J., *Application of Speed Transform to the diagnosis of a roller bearing in variable speed* In Proceeding of the conference Surveillance (Vol. 7, pp. 29-30).

[15] El-Kafafy, M., Colanero, L., Gioia, N., Devriendt, C., Guillaume, P. and Helsen, J., *Modal Parameters Estimation of an Offshore Wind Turbine Using Measured Acceleration Signals from the Drive Train*, In Structural Health Monitoring and Damage Detection, Volume 7 (pp. 41-48). Springer, Cham. 2017.

[16] Gioia N., Daems P.J., Peeters C., El-Kafafy M., Guillaume P., Helsen J. *Influence of the Harmonics on the Modal Behavior of Wind Turbine Drivetrains*, 2018 International Modal Analysis Conference (IMAC), Orlando, Feb. 2018

[17] Helsen J, Peeters C, Doro P, Ververs E, Jordaens PJ, *Wind Farm Operation and Maintenance Optimization Using Big Data*, Big Data Computing Service and Applications (BigDataService), 2017 IEEE Third International Conference on 2017 Apr 6 (pp. 179-184). IEEE.

Output-only recursive identification of time-varying systems subject to gross errors

Z.-S. Ma[1,2], Q. Ding[1,2], B. Wang[1,2]
[1] Tianjin University, School of Mechanical Engineering
Yaguan Road 135, Jinnan District, 300350, Tianjin, China
e-mail: **zhisai.ma@tju.edu.cn**

[2] Tianjin Key Laboratory of Nonlinear Dynamics and Control
Yaguan Road 135, Jinnan District, 300350, Tianjin, China

Abstract
Gross errors are generally used to model intermittent sensor failures and occasional data packet losses or corruption, which arise in many engineering communities. This paper focuses on the problem of output-only recursive identification of time-varying systems subject to gross errors. Under the assumption that gross errors are unknown and can be of arbitrarily large magnitude, an adaptive recursive pseudo-linear regression time-dependent autoregressive moving average (TARMA) method is proposed by minimizing the sum of norm errors and achieving a sparse prediction error sequence. The proposed method is employed to identify a time-varying system and assessed against the existing recursive pseudo-linear regression TARMA method. The comparison demonstrates the superior achievable accuracy of the proposed method in extremely challenging circumstances.

1 Introduction

This paper focuses on the problem of output-only recursive identification of time-varying systems due to the following two reasons: Firstly, in many cases controlled testing may not be feasible or the excitation may be unobservable under realistic operating conditions. Hence, there exists a need to identify time-varying systems by exclusively using the available measured response signals, without measuring the excitation forces. Secondly, in many problems not all response signals are known in advance and the solution has to be recalculated as new observations become available. Hence, there also exists a need to identify time-varying systems in a recursive instead of batch manner.

In recent years, the problem of output-only recursive identification of time-varying systems has been considered and many identification methods have been proposed [1-4]. However, these methods are not able to accurately track the dynamics of time-varying systems by using measurements contaminated by unknown gross errors. Gross errors are generally used to model intermittent sensor failures and occasional data packet losses or corruption, which arise in many engineering communities. If the measurements were completely collected in a batch manner, the problem of time-varying system identification could be tackled by nonsmooth optimization-based estimators [5]. Unfortunately, in many real-time applications in which the data observations are arriving in a continuous stream, the system has to be identified before all of the response measurements are known [6]. As a consequence, the available batch data-based identification methods do not apply any more.

Obviously, the effects of gross errors could be minimized, if we could remove those data observations contaminated by gross errors. In this paper the weighting strategy is considered to deemphasize the data observations contaminated by gross errors. Under the assumption that gross errors are unknown and can be of arbitrarily large magnitude, an adaptive time-varying system identification method with the ability to remove the undesirable effects of gross errors is proposed by minimizing the sum of norm errors and achieving a sparse prediction error sequence.

The rest of this paper is structured as follows. Section 2 briefly introduces the vector TARMA model and its pseudo-linear regression form. The existing exponentially weighted recursive pseudo-linear regression TARMA (EWRPLR-TARMA) method is reviewed in Section 3. Section 4 proposes an adaptive EWRPLR-TARMA method with a relative insensitivity to gross errors by using the weighting strategy. To illustrate the behavior of the proposed adaptive method in extremely challenging circumstances, the proposed method is, along with the existing EWRPLR-TARMA method, numerically tested and comparatively assessed in Section 5. Section 6 summarizes the study.

2 Pseudo-linear regression form of vector TARMA model

The TARMA representation resembles its stationary counterparts, with the significant difference being that it allows its parameters to depend upon time [7, 8]. A TARMA (n_a, n_c) model, with n_a, n_c designating respectively its autoregressive (AR) and moving average (MA) orders, is of the form [1]

$$\boldsymbol{x}[t]+\sum_{i=1}^{n_a}\boldsymbol{A}_i[t]\boldsymbol{x}[t-i]=\boldsymbol{e}[t]+\sum_{i=1}^{n_c}\boldsymbol{C}_i[t]\boldsymbol{e}[t-i],\quad \boldsymbol{e}[t]\sim\mathcal{N}(\boldsymbol{0},\boldsymbol{\Sigma}[t]) \tag{1}$$

with t designating normalized discrete time, $\boldsymbol{x}[t]\in\mathbb{R}^{k\times 1}$ the discrete-time non-stationary vibration signal modeled, $\boldsymbol{e}[t]\in\mathbb{R}^{k\times 1}$ an unobservable uncorrelated innovations (residual) sequence with zero mean and time-varying non-singular covariance matrix $\boldsymbol{\Sigma}[t]\in\mathbb{R}^{k\times k}$. $\boldsymbol{A}_i[t]$ and $\boldsymbol{C}_i[t]$ are respectively the model's time-dependent AR and MA parameter matrices. $\mathcal{N}(\cdot,\cdot)$ stands for normally independently distributed random variables with the indicated mean and covariance.

As the multiple vibration response (vector or multivariate) case is much more important from a practical standpoint, the recursive pseudo-linear regression scheme has been extended from the simple single vibration response (univariate) case [7, 9] to its multivariate case [1]. In order to reduce the computational complexity of TARMA based recursive identification methods, we propose to rewrite the vector TARMA model in an improved pseudo-linear regression form [6]

$$\boldsymbol{x}[t]=\boldsymbol{w}[t]^{\mathrm{T}}\boldsymbol{\Psi}[t]+\boldsymbol{e}[t] \tag{2}$$

with

$$\boldsymbol{w}[t]^{\mathrm{T}}\triangleq\left[\boldsymbol{A}_1[t],\ldots,\boldsymbol{A}_{n_a}[t],\boldsymbol{C}_1[t],\ldots,\boldsymbol{C}_{n_c}[t]\right]\in\mathbb{R}^{k\times k(n_a+n_c)} \tag{3}$$

being the time-dependent parameter matrix, and

$$\boldsymbol{\Psi}[t]\triangleq\begin{bmatrix}-\boldsymbol{x}[t-1]\\ \vdots\\ -\boldsymbol{x}[t-n_a]\\ \boldsymbol{e}[t-1]\\ \vdots\\ \boldsymbol{e}[t-n_c]\end{bmatrix}\in\mathbb{R}^{k(n_a+n_c)\times 1} \tag{4}$$

the corresponding regression vector. The unknown prediction errors in this expression are approximated as $\boldsymbol{e}[t-i]\approx\hat{\boldsymbol{e}}[t,\hat{\boldsymbol{w}}[t-i-1]]$.

3 Existing EWRPLR-TARMA method

In order to track time-varying dynamics, more weight should be given to more recent data. The exponentially weighted mechanism is first used to put more emphasis on recent data and to deemphasize data from the remote past. Given the forgetting factor $0<\lambda\leq 1$ (a positive scalar, usually close to one), the weighted least squares cost function is defined as

$$\min_{\boldsymbol{w}[t]}\left[\frac{1}{2}\sum_{\tau=1}^{t}\lambda^{t-\tau}\left\|\boldsymbol{x}[\tau]-\boldsymbol{w}[t]^{\mathrm{T}}\boldsymbol{\Psi}[\tau]\right\|^{2}\right] \tag{5}$$

with $\|\cdot\|$ designating the Euclidean norm. The term $\lambda^{t-\tau}$ is a weight function that assigns more weight to more recent errors. It may be also rewritten as follows

$$\lambda^{t-\tau}=\left(e^{\ln\lambda}\right)^{t-\tau}=e^{(t-\tau)\cdot\ln\lambda}\approx e^{-(t-\tau)\cdot(1-\lambda)} \tag{6}$$

This means that measurements that are older than $(1-\lambda)^{-1}$ samples are included in the criterion with a weight that is $e^{-1}\approx 36\%$ of that of the most recent measurement [9]. The smaller the value of λ, the faster older values of the error (and thus the measurement) are forgotten, thus increasing the estimator's ability to track the evolution in the dynamics. Yet, at the same time, the accuracy of the estimator decreases, as its covariance increases. Therefore, the selection of λ is critical and represents the basic tradeoff between time-varying tracking ability in dynamics and achievable parameter accuracy [8, 9].

The exponentially weighted recursive pseudo-linear regression TARMA (EWRPLR-TARMA) method [1, 6] is summarized as

$$\begin{aligned}
&\hat{\boldsymbol{w}}[t]^{\mathrm{T}}=\hat{\boldsymbol{w}}[t-1]^{\mathrm{T}}+\hat{\boldsymbol{e}}[t|t-1]\boldsymbol{K}[t]^{\mathrm{T}}\\
&\hat{\boldsymbol{e}}[t|t-1]=\boldsymbol{x}[t]-\hat{\boldsymbol{x}}[t|t-1]=\boldsymbol{x}[t]-\hat{\boldsymbol{w}}[t-1]^{\mathrm{T}}\boldsymbol{\Psi}[t]\\
&\boldsymbol{K}[t]=\boldsymbol{P}[t-1]\boldsymbol{\Psi}[t]\left(\lambda+\boldsymbol{\Psi}[t]^{\mathrm{T}}\boldsymbol{P}[t-1]\boldsymbol{\Psi}[t]\right)^{-1}\\
&\boldsymbol{P}[t]=\lambda^{-1}\left(\boldsymbol{P}[t-1]-\boldsymbol{K}[t]\boldsymbol{\Psi}[t]^{\mathrm{T}}\boldsymbol{P}[t-1]\right)
\end{aligned} \tag{7}$$

with $\boldsymbol{K}[t]\in\mathbb{R}^{k(n_a+n_c)\times 1}$ designating the gain matrix, $\boldsymbol{P}[t]\in\mathbb{R}^{k(n_a+n_c)\times k(n_a+n_c)}$ the covariance matrix, $\hat{\boldsymbol{x}}[t|t-1]$ the one-step-ahead prediction of the signal, and $\hat{\boldsymbol{e}}[t|t-1]=\hat{\boldsymbol{e}}[t,\hat{\boldsymbol{w}}[t-1]]$ the corresponding prediction error. For the initialization of the method it is customary to set $\hat{\boldsymbol{w}}[0]=\boldsymbol{0}$, $\boldsymbol{P}[0]=\alpha\boldsymbol{I}$, with $\boldsymbol{I}$ designating the identity matrix of appropriate order, α a "large" positive number (for example, $\alpha=10^4$ [1]) whose influence on the estimate will gradually disappear due to the forgetting mechanism.

4 Adaptive EWRPLR-TARMA method under gross errors

The existing EWRPLR-TARMA method is not able to accurately track the dynamics of time-varying systems by using measurements contaminated by unknown gross errors. Hence, a TARMA model parameter recursive estimation method with the ability to remove the undesirable effects of gross errors is proposed in this section.

4.1 TARMA model with gross errors

Consider a TARMA model with gross errors defined by

$$\boldsymbol{x}[t]=\boldsymbol{w}[t]^{\mathrm{T}}\boldsymbol{\Psi}[t]+\boldsymbol{e}[t]+\boldsymbol{g}[t] \tag{8}$$

where $\boldsymbol{g}[t]$ is a disturbance of impulsive nature. $\boldsymbol{g}[t](t=1,2,\ldots)$ is also called a sparse sequence, as the elements of this sequence are nonzero only occasionally [5]. However, whenever the elements are nonzero, they can take on values of arbitrarily large magnitudes. The time instants for which $\boldsymbol{g}[t]\neq 0$ are denoted by $t_1<t_2<\ldots<t_i<\ldots$ and the set of these time instants is denoted by $T=\{t_1,t_2,\ldots,t_i,\ldots\}$. Hence for any $t\in T$, $\boldsymbol{g}[t]\neq\boldsymbol{0}$ and for any $t\notin T$, $\boldsymbol{g}[t]=\boldsymbol{0}$. Let $t_{\max}=\max\{t_{i+1}-t_i\}$ denote the maximum time between consecutive impulse times, by assuming $t_{\max}<\infty$ we have that the sequence $\boldsymbol{g}[t](t=1,2,\ldots)$ is persistent and does not vanish when $t\to\infty$.

4.2 Adaptive EWRPLR-TARMA method

Obviously, if we could choose a weight function $h[t]=0$ for any $t\in T$ and $h[t]=1$ for any $t\notin T$, then the effects of impulsive errors could be completely removed [5]. Unfortunately, the sequence $\boldsymbol{g}[t](t=1,2,\ldots)$ is sparse, but the values of the sequence are unknown and can be arbitrarily large, and the impulse times $T=\{t_1,t_2,\ldots,t_i,\ldots\}$ are not available. In order to propose an adaptive method with a relative insensitivity to the impulsive noise sequence, the weighting strategy is considered in this section.

We propose to define an adaptive weight function as

$$h[t]=\exp\left(-\left\|\boldsymbol{x}[t]-\hat{\boldsymbol{w}}[t-1]^{\mathrm{T}}\boldsymbol{\Psi}[t]\right\|\right),\ h[t]\in(0,1] \tag{9}$$

Then we have $h[t]\to 0$ if $\boldsymbol{g}[t]\neq 0$ and takes on value of large magnitude, and $h[t]\to 1$ if $\boldsymbol{g}[t]=\boldsymbol{0}$ holds.

Given the forgetting factor $0<\lambda\leq 1$ and the weight function $h[\tau]$, the weighted least squares cost function is defined as

$$\min_{\boldsymbol{w}[t]}\left[\frac{1}{2}\sum_{\tau=1}^{t}\lambda^{t-\tau}h[\tau]\left\|\boldsymbol{x}[\tau]-\boldsymbol{w}[t]^{\mathrm{T}}\boldsymbol{\Psi}[\tau]\right\|^2\right] \tag{10}$$

The solution to (10) is given by

$$\boldsymbol{w}[t]=\left(\tilde{\boldsymbol{\Psi}}[t]\boldsymbol{\Lambda}[t]\tilde{\boldsymbol{\Psi}}[t]^{\mathrm{T}}\right)^{-1}\tilde{\boldsymbol{\Psi}}[t]\boldsymbol{\Lambda}[t]\tilde{\boldsymbol{x}}[t] \tag{11}$$

where $\tilde{\boldsymbol{\Psi}}[t]\triangleq\left[\boldsymbol{\Psi}[1],\boldsymbol{\Psi}[2],\ldots,\boldsymbol{\Psi}[t]\right]$, $\tilde{\boldsymbol{x}}[t]\triangleq\left[\boldsymbol{x}[1],\boldsymbol{x}[2],\ldots,\boldsymbol{x}[t]\right]^{\mathrm{T}}$, $\boldsymbol{\Lambda}[t]\triangleq\mathrm{diag}\{\lambda^{t-1}h[1],\lambda^{t-2}h[2],\ldots,h[t]\}$, $\mathrm{diag}\{\cdot\}$ stands for diagonal matrices with the indicated diagonal elements.

Defining the covariance matrix $\boldsymbol{P}[t]$ by

$$\boldsymbol{P}[t]\triangleq\left(\tilde{\boldsymbol{\Psi}}[t]\boldsymbol{\Lambda}[t]\tilde{\boldsymbol{\Psi}}[t]^{\mathrm{T}}\right)^{-1} \tag{12}$$

We have

$$\boldsymbol{P}[t]^{-1}=\lambda\boldsymbol{P}[t-1]^{-1}+\boldsymbol{\Psi}[t]h[t]\boldsymbol{\Psi}[t]^{\mathrm{T}} \tag{13}$$

By using the matrix inversion lemma, we can write

$$\boldsymbol{P}[t]=\lambda^{-1}\left(\boldsymbol{P}[t-1]-\frac{\boldsymbol{P}[t-1]\boldsymbol{\Psi}[t]\boldsymbol{\Psi}[t]^{\mathrm{T}}\boldsymbol{P}[t-1]}{\lambda h[t]^{-1}+\boldsymbol{\Psi}[t]^{\mathrm{T}}\boldsymbol{P}[t-1]\boldsymbol{\Psi}[t]}\right) \tag{14}$$

Substituting (14) into (11), the time-dependent parameter matrix at instant of time t can be estimated by

$$\hat{\boldsymbol{w}}[t]=\hat{\boldsymbol{w}}[t-1]+\frac{\boldsymbol{P}[t-1]\boldsymbol{\Psi}[t]}{\lambda h[t]^{-1}+\boldsymbol{\Psi}[t]^{\mathrm{T}}\boldsymbol{P}[t-1]\boldsymbol{\Psi}[t]}\left(\boldsymbol{x}[t]^{\mathrm{T}}-\boldsymbol{\Psi}[t]^{\mathrm{T}}\boldsymbol{w}[t-1]\right) \tag{15}$$

Defining the gain matrix $\boldsymbol{K}[t]$, the one-step-ahead prediction of the signal $\hat{\boldsymbol{x}}[t|t-1]$ and the corresponding prediction error $\hat{\boldsymbol{e}}[t|t-1]$ respectively by

$$\boldsymbol{K}[t]\triangleq\frac{\boldsymbol{P}[t-1]\boldsymbol{\Psi}[t]}{\lambda h[t]^{-1}+\boldsymbol{\Psi}[t]^{\mathrm{T}}\boldsymbol{P}[t-1]\boldsymbol{\Psi}[t]} \tag{16}$$

$$\hat{\boldsymbol{x}}[t|t-1]\triangleq\hat{\boldsymbol{w}}[t-1]^{\mathrm{T}}\boldsymbol{\Psi}[t] \tag{17}$$

$$\hat{\boldsymbol{e}}[t|t-1]\triangleq\boldsymbol{x}[t]-\hat{\boldsymbol{x}}[t|t-1] \tag{18}$$

We can rewrite (15) as

$$\hat{\boldsymbol{w}}[t]^{\mathrm{T}}=\hat{\boldsymbol{w}}[t-1]^{\mathrm{T}}+\hat{\boldsymbol{e}}[t|t-1]\boldsymbol{K}[t]^{\mathrm{T}} \tag{19}$$

Furthermore, by combining (14), (16), (17), (18) and (19), we have the adaptive EWRPLR-TARMA method with the ability to remove the undesirable effects of gross errors, as follows

$$\begin{aligned}
&\hat{\boldsymbol{w}}[t]^{\mathrm{T}} = \hat{\boldsymbol{w}}[t-1]^{\mathrm{T}} + \hat{\boldsymbol{e}}[t|t-1]\boldsymbol{K}[t]^{\mathrm{T}} \\
&\hat{\boldsymbol{e}}[t|t-1] = \boldsymbol{x}[t] - \hat{\boldsymbol{x}}[t|t-1] = \boldsymbol{x}[t] - \hat{\boldsymbol{w}}[t-1]^{\mathrm{T}}\boldsymbol{\Psi}[t] \\
&\boldsymbol{K}[t] = \boldsymbol{P}[t-1]\boldsymbol{\Psi}[t]\left(\lambda h[t]^{-1} + \boldsymbol{\Psi}[t]^{\mathrm{T}}\boldsymbol{P}[t-1]\boldsymbol{\Psi}[t]\right)^{-1} \\
&\boldsymbol{P}[t] = \lambda^{-1}\left(\boldsymbol{P}[t-1] - \boldsymbol{K}[t]\boldsymbol{\Psi}[t]^{\mathrm{T}}\boldsymbol{P}[t-1]\right)
\end{aligned} \tag{20}$$

4.3 Adaptive weight functions

In addition to the adaptive weight function defined by (9), other weight functions [5] can be also used, for example

$$h[t] = \frac{1}{\left\|\boldsymbol{x}[t] - \hat{\boldsymbol{w}}[t-1]^{\mathrm{T}}\boldsymbol{\Psi}[t]\right\|^2 + \varepsilon},\ \varepsilon > 0,\ h[t] \in (0, \varepsilon^{-1}] \tag{21}$$

with ε designating a "small" positive number which is intended essentially for avoiding division by zero. Then we have $h[t] \to 0$ if $\boldsymbol{g}[t] \neq 0$ and takes on value of large magnitude, and $h[t] \to \varepsilon^{-1}$ if $\boldsymbol{g}[t] = \boldsymbol{0}$ holds.

Furthermore, we can have some extensions of (9) and (21), as follows

$$h[t] = \exp\left(-\sigma\left\|\boldsymbol{x}[t] - \hat{\boldsymbol{w}}[t-1]^{\mathrm{T}}\boldsymbol{\Psi}[t]\right\|^{\gamma}\right),\ \sigma > 0,\ h[t] \in (0,1] \tag{22}$$

$$h[t] = \frac{1}{\sigma\left\|\boldsymbol{x}[t] - \hat{\boldsymbol{w}}[t-1]^{\mathrm{T}}\boldsymbol{\Psi}[t]\right\|^{\gamma} + \varepsilon},\ \varepsilon > 0,\ h[t] \in (0, \varepsilon^{-1}] \tag{23}$$

with σ designating the adjustable parameter, γ the indicator of the type of norm.

Generally, σ and γ should be tuned to different problems. The suitable selection of σ and γ improves achievable accuracy. However, it does this at the expense of increasing the difficulty of model structure selection. In this work, only weight functions defined by (9) and (21) are considered in the subsequent part. A detailed weight function selection scheme is beyond the scope of the current paper and will be dealt with in the future research.

5 Numerical validation

5.1 Numerical example

The performance characteristics of the proposed adaptive EWRPLR-TARMA method, along with the existing EWRPLR-TARMA method, are examined via a comparative study focused on the identification of a TARMA(4,0) model with gradual parameter evolution, as follows

$$\boldsymbol{x}[t] + \boldsymbol{A}_1[t]\boldsymbol{x}[t-1] + \boldsymbol{A}_2[t]\boldsymbol{x}[t-2] + \boldsymbol{A}_3[t]\boldsymbol{x}[t-3] + \boldsymbol{A}_4[t]\boldsymbol{x}[t-4] = \boldsymbol{e}[t],\quad \boldsymbol{e}[t] \sim \mathcal{N}(\boldsymbol{0}, \boldsymbol{I}) \tag{24}$$

The mean of the innovations sequence is zero, while its covariance is constant and equal to unity, i.e. $\boldsymbol{e}[t] \sim \mathcal{N}(\boldsymbol{0}, \boldsymbol{I})$. The numerical values of the true AR parameters are given by

$$\begin{aligned}
\boldsymbol{A}_1[t] &= \begin{bmatrix} -0.5 & 0.2 + 0.2\sin(0.003\pi t) \\ 0.2 + 0.2\sin(0.003\pi t) & -0.5 \end{bmatrix}, \quad \boldsymbol{A}_3[t] = \begin{bmatrix} 0.3 & -0.1 \\ -0.1 & 0.3 \end{bmatrix} \\
\boldsymbol{A}_2[t] &= \begin{bmatrix} -0.4 & 0.2 + 0.2\cos(0.002\pi t) \\ 0.2 + 0.2\cos(0.002\pi t) & -0.4 \end{bmatrix}, \quad \boldsymbol{A}_4[t] = \begin{bmatrix} 0.2 & -0.1 \\ -0.1 & 0.2 \end{bmatrix}
\end{aligned} \tag{25}$$

A realization with signal length $L = 2000$ is generated and shown in Figure 1. An impulsive noise sequence is generated and shown in Figure 2. The sequence $\boldsymbol{g}[t](t = 1,2,\ldots 20)$ is sparse, but the values of the sequence and the impulse times $T = \{t_1, t_2, \ldots, t_{20}\}$ are random and unknown. By adding the impulsive errors of Figure 2 to the signals of Figure 1, we have the signals contaminated by unknown gross errors, as shown in Figure 3.

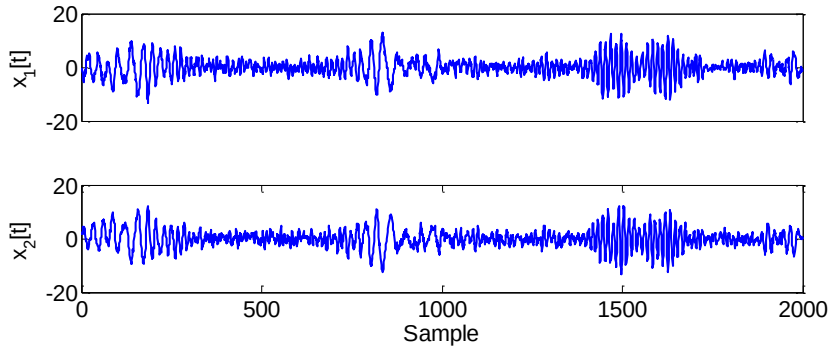


Figure 1: Signal realization of the TARMA(4,0) model.

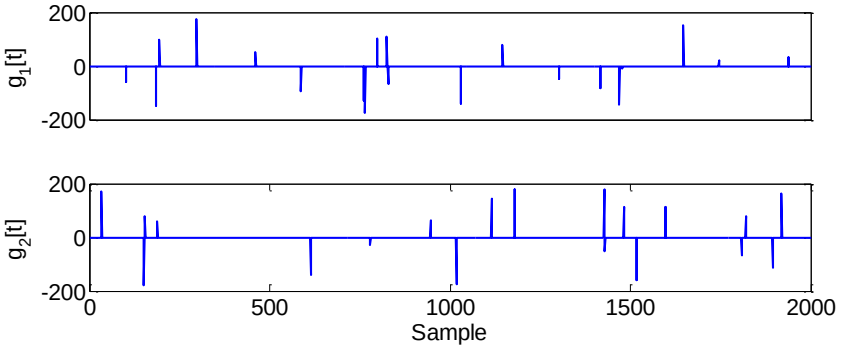


Figure 2: Impulsive errors with unknown values and random impulse times.

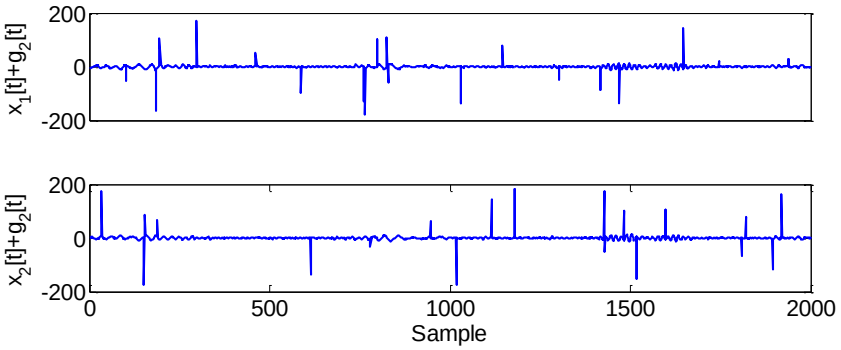


Figure 3: Signal realization of the TARMA(4,0) model subject to gross errors.

5.2 Identification results

Based on the signals without gross errors, as shown in Figure 1, the TARMA(4,0) model parameters are respectively estimated by the existing EWRPLR-TARMA method and the proposed adaptive EWRPLR-TARMA method here. Regarding the existing EWRPLR-TARMA method, the value of the forgetting factor is optimized based on minimization of the residual sum of squares (RSS) criterion [1, 2, 8] with the search space $[0.970, 0.971, \ldots, 0.999]$, which suggests $\lambda = 0.985$. Figure 4 illustrates the existing EWRPLR-

TARMA based model parameter estimates $\boldsymbol{A}_i(1,2)(i=1,2,3,4)$, along with their true counterparts. The red dots notate the model parameter estimates, and the green dashed lines notate the true model parameters given by (25).

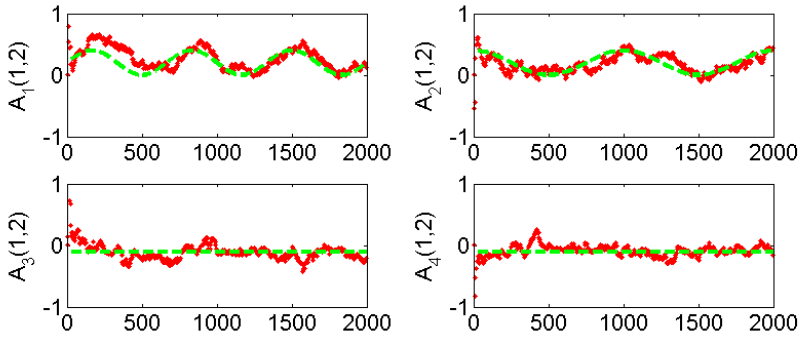


Figure 4: Existing EWRPLR-TARMA model parameter estimates based on signals without gross errors.

Regarding the adaptive EWRPLR-TARMA method, the value of the forgetting factor is optimized based on minimization of the RSS criterion and the suggested value is $\lambda = 0.976$. Figure 5(a) and 5(b) illustrate respectively the adaptive EWRPLR-TARMA based model parameter estimates with different weight functions given by (9) and (21), along with their true counterparts.

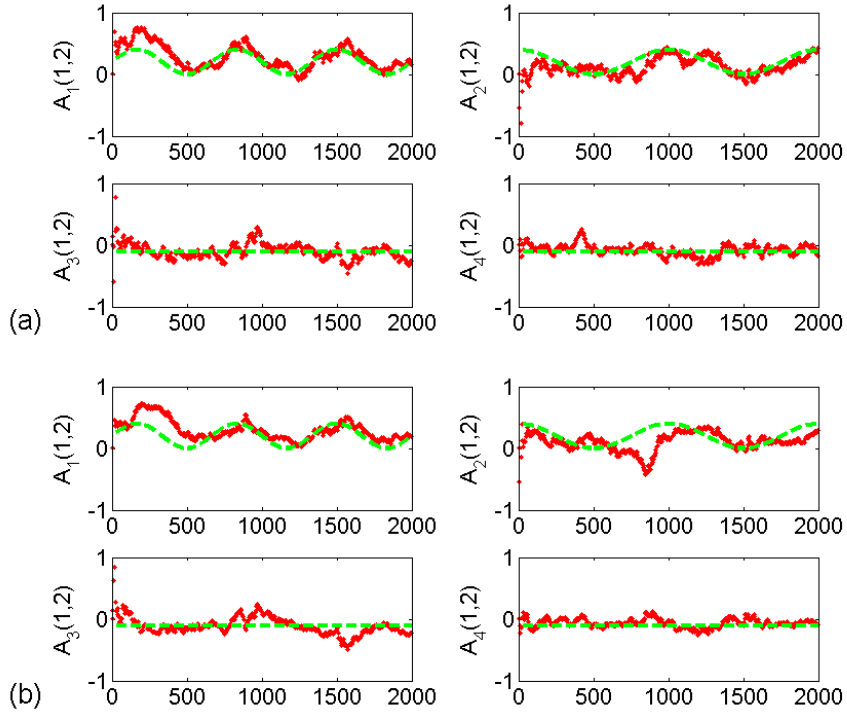


Figure 5: Adaptive EWRPLR-TARMA model parameter estimates based on signals without gross errors.

Compared to its counterparts of Figure 5, the existing EWRPLR-TARMA based model parameter estimates exhibit better tracking and superior accuracy, as shown in Figure 4. However, this is no longer true for the cases in which the measurements are contaminated by unknown gross errors.

Based on the signals contaminated by unknown gross errors, as shown in Figure 3, the TARMA(4,0) model parameters are respectively estimated by the existing EWRPLR-TARMA method and the proposed adaptive EWRPLR-TARMA method in the following part. Regarding the existing EWRPLR-TARMA method, the value of the forgetting factor is still $\lambda = 0.985$. Figure 6 illustrates the existing EWRPLR-TARMA based model parameter estimates, along with their true counterparts. Evidently, the existing

EWRPLR-TARMA method is not able to accurately track the dynamics of time-varying systems by using measurements contaminated by unknown gross errors.

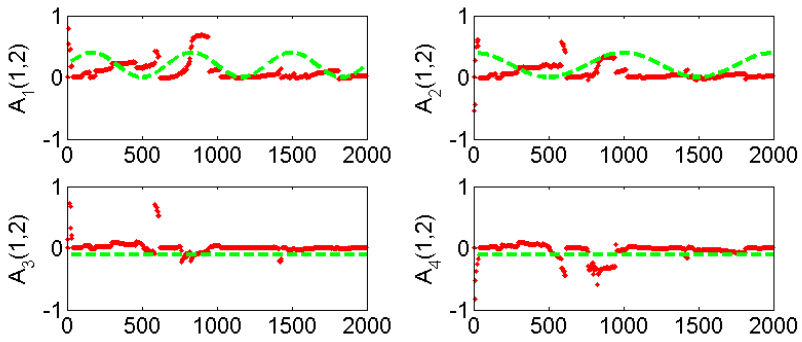


Figure 6: Existing EWRPLR-TARMA model parameter estimates based on signals with gross errors.

Regarding the adaptive EWRPLR-TARMA method, the value of the forgetting factor is still $\lambda = 0.976$. Figure 7(a) and 7(b) illustrate respectively the adaptive EWRPLR-TARMA based model parameter estimates with different weight functions given by (9) and (21), along with their true counterparts. Figure 7 demonstrates the superior achievable accuracy of the proposed adaptive EWRPLR-TARMA method in extremely challenging circumstances.

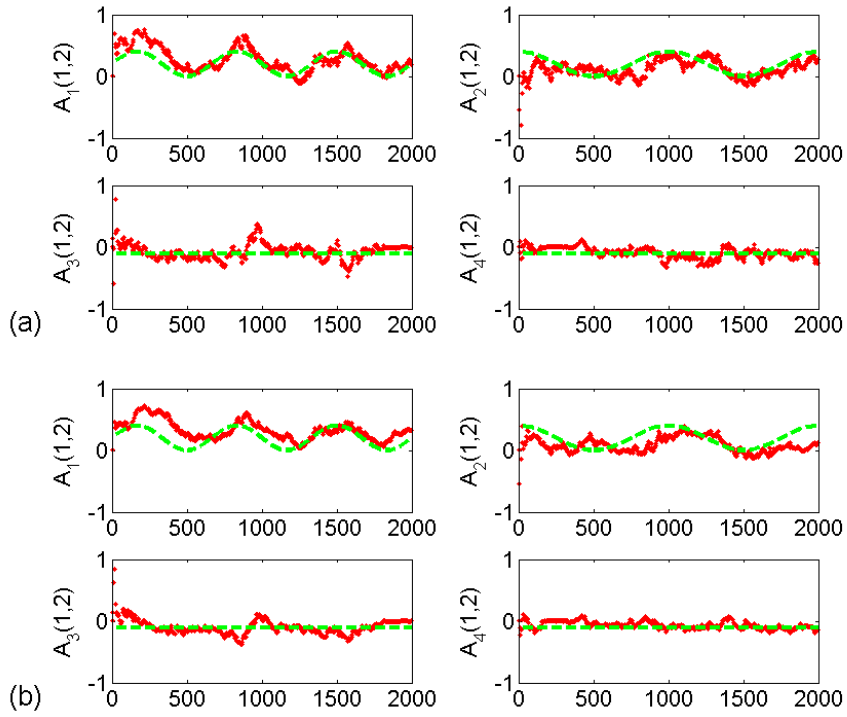


Figure 7: Adaptive EWRPLR-TARMA model parameter estimates based on signals with gross errors.

5.3 Comparative results

In order to effectively and reliably assess the proposed method, the study in this section is carried out based on Monte Carlo runs (number of runs: 30). In the same manner as previously introduced, 30 tests are repeatedly carried out. The output-only recursive identification of the numerical example is now considered based on the proposed adaptive EWRPLR-TARMA method with different weight functions given by (9) and (21).

Based on the signals without gross errors, Figure 8 illustrates the adaptive EWRPLR-TARMA based model parameter estimates from the 30 Monte Carlo tests, along with their true counterparts. The red dots notate the model parameter estimates from the single test given by Figure 5, the blue dots notate the model parameter estimates from the 30 tests, and the green dashed lines notate the true model parameters.

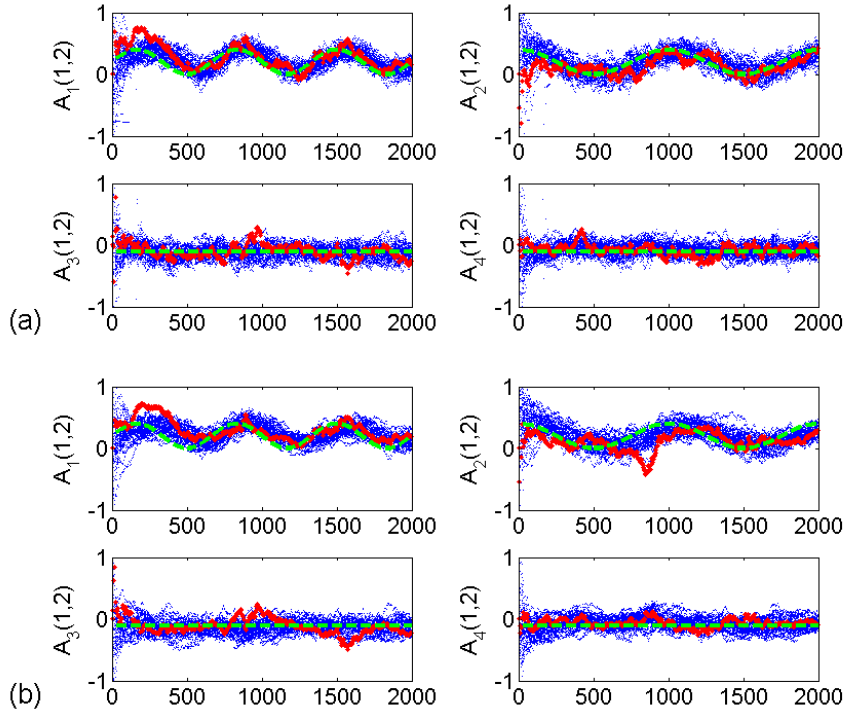


Figure 8: Adaptive EWRPLR-TARMA model parameter estimates based on signals without gross errors.

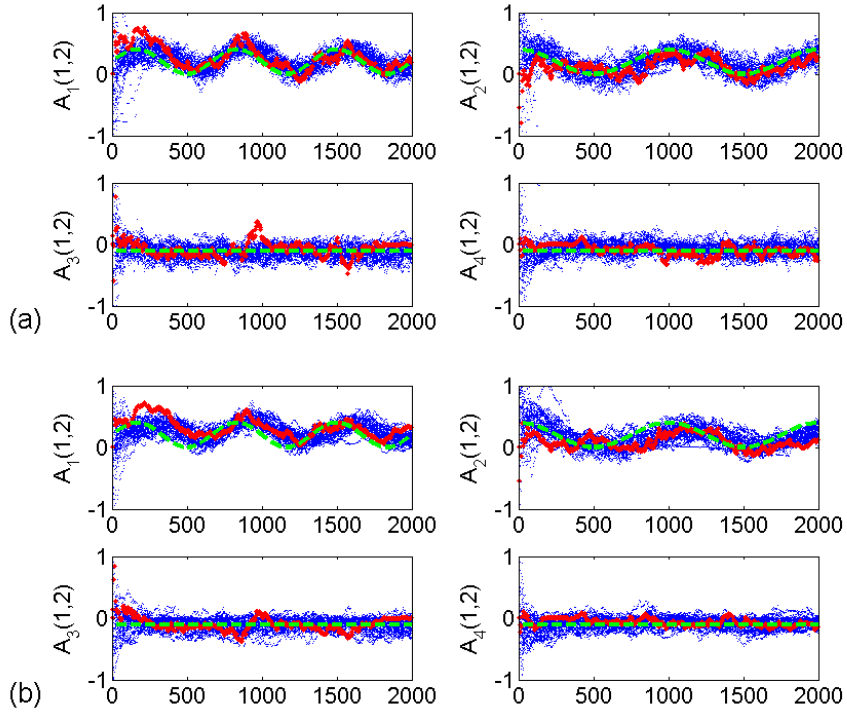


Figure 9: Adaptive EWRPLR-TARMA model parameter estimates based on signals with gross errors.

Based on the signals contaminated by unknown gross errors, Figure 9 illustrates the adaptive EWRPLR-TARMA based model parameter estimates from the 30 Monte Carlo tests, along with their true counterparts. The red dots notate the model parameter estimates from the single test given by Figure 7. As shown in Figure 8 and Figure 9, the proposed adaptive EWRPLR-TARMA method is able to track the time-varying dynamics of the numerical system, no matter the data is contaminated by unknown gross errors or not.

6 Conclusions

This paper focuses on the problem of output-only recursive identification of time-varying systems subject to gross errors. By using the weighting strategy to deemphasize the data observations contaminated by gross errors, an adaptive time-varying system identification method with the ability to remove the undesirable effects of gross errors was proposed. The proposed method was employed to identify a numerical time-varying system with gradual parameter evolution by exclusively using the non-stationary responses. The superior achievable accuracy of the proposed adaptive method in extremely challenging circumstances was finally demonstrated by comparing with the existing identification method.

Acknowledgements

The authors acknowledge the support from National Natural Science Foundation of China (Grant No. 11802201) and China Postdoctoral Science Foundation (Grant No. 2017M621075).

References

[1] M.D. Spiridonakos, S.D. Fassois, *Parametric identification of a time-varying structure based on vector vibration response measurements*, Mechanical Systems and Signal Processing, Vol. 23, No. 6 (2009), pp 2029-2048.

[2] Z.-S. Ma, L. Liu, S.-D. Zhou, L. Yu, F. Naets, W. Heylen, W. Desmet, *Parametric output-only identification of time-varying structures using a kernel recursive extended least squares TARMA approach*, Mechanical Systems and Signal Processing, Vol. 98 (2018), pp 684-701.

[3] Z.-S. Ma, L. Liu, S.-D. Zhou, L. Yu, *Output-only modal parameter recursive estimation of time-varying structures via a kernel ridge regression FS-TARMA approach*, Shock and Vibration, Vol. 2017, No. ID8176593 (2017), pp 1-14.

[4] Z.-S. Ma, L. Liu, S.-D. Zhou, F. Naets, W. Heylen, W. Desmet, *Output-only recursive identification of time-varying structures using a Gaussian process regression TARMA approach*, *Proceedings of ISMA2016 International Conference on Noise and Vibration Engineering, Leuven, 2016 September 19-21*, Leuven (2016), pp. 2859-2872.

[5] L. Bako, *Adaptive identification of linear systems subject to gross errors*, Automatica, Vol. 67, (2016), pp 192-199.

[6] Z.-S. Ma, *Output-only Modal Parameter Recursive Estimation for Linear Time-varying Structures*, Beijing Institute of Technology, Beijing (2017).

[7] M. Niedzwiecki, *Identification of Time-varying Processes*, John Wiley & Sons, New York (2000).

[8] A.G. Poulimenos, S.D. Fassois, *Parametric time-domain methods for non-stationary random vibration modelling and analysis - a critical survey and comparison*, Mechanical Systems and Signal Processing, Vol. 20, No. 4 (2006), pp 763-816.

[9] L. Ljung, *System identification - Theory for the User (Second Edition)*, Prentice Hall, Upper Saddle River, New Jersey (1999).

Operational modal analysis of a turbine in big noise environment

M. Zhao[1], L. Yue[1]
[1]Nanjing University of Aeronautics and Astronautics, College of Mechanical and Electronic Engineering
29 Yudao Street, Nanjing, P.R China
e-mail: **yuelinme@nuaa.edu.cn**

Abstract.
The testing of the dynamic behaviors of rotating machinery is important during its design and using process. Order based modal analysis (OBMA) is a novel modal analysis method of rotor systems under harmonic excitation. This paper utilizes OBMA to identify the resonances from the noise polluted operational data in a turbine's run-up process. First, stationary wavelet transform (SWT) is employed to filter out the uncorrelated noise. Then, an order tracking method is utilized to achieve the accurate harmonic response known as engine orders. Finally, the PolyMAX modal parameter estimation algorithm is applied to identify the resonance frequency, damping and modal shapes. The method simulation was constructed with both big noise and harmonic response during a run-up process. Afterwards, this method was verified by a rotor rig experiment using the run-up data of a laboratory turbine model.

1 Introduction

An operational modal analysis (OMA) is valuable for analyzing the dynamic behaviors of rotating machinery, first because the vibration characteristics in static and rotational state are quite different. Secondly, large structures are hard to excite artificially by hamming or shaker.

In operational modal analysis, the excitation force cannot be measured so the frequency response function (FRF) is unavailable. Therefore, OMA methods create different kinds of pseudo-Frequency Response Functions (pseudo-FRF) based on the assumption of the environmental excitation. For example, the power spectrum density function (PSD) is preferred, if the environmental excitation is assumed to be white noise with a wide frequency band. PSD based OMA method is widely used in modal analysis of large structure such as bridge or football stadium [1].

However in cases of rotating machinery, the external excitation contains the harmonics with frequency multiples of its rotational speed, the assumption of wide-band white noise excitation doesn't establish any more. Traditional OMA method based on PSD is no more valid, because harmonic peaks in PSD will be wrongly identified as resonance frequency. Even if the engine sweeps across a wide frequency band, "end of order" effect will become the main problem [2]. "End of order" means the highest frequency of each engine order, which may be wrongly identified as physical poles of the system.

To overcome the restriction on traditional white noise based OMA methods for rotating machinery, generally two different approaches has been taken into consideration. Firstly, varieties of methods have been proposed to diminish the influence of harmonics on the modal identification results [3]. Secondly, besides harmonic elimination, a new order based modal analysis method (OBMA), first proposed by Janssens [4][5] in 2006, utilizes the forced vibration response under sweeping harmonics for resonance identification. The order tracking method is used to extract the amplitude and phase response of forced vibration under different rotational speed. The response curves of different orders, which correlated amplitude/phase response with excitation frequency, are taken as the pseudo-FRF curve for further resonance identification. The OBMA method has been validated by some industrial examples, such as the dynamic characterization analysis of a

gear test rig [2][6]. Because harmonic excitation is usually dominating in rotating machinery, the OBMA method is more applicable than traditional white noise based OMA methods.

The vibration signal is usually measured via several piezoelectric accelerometers, which brings about a problem of big measurement noise especially in high frequency band. Broad band noise has a bad influence on the accuracy of order tracking result. In the present paper, Stationary Wavelet Transform (SWT) is employed to eliminate the noise outside the concerned frequency band.

The aim of the present paper is to validate an order based modal analysis method during an engine run-up process and the SWT noise suppression method. The theory background about forced vibration under harmonic excitation is described in section 2.1.1. Computed order tracking method and stationary wavelet transform are introduced in section 2.2. The problem of sweep rate selection in OBMA method is discussed in section 2.3. Section 3 illustrates the method via a simulated forced vibration signal under sweeping harmonic excitation, and a big white Gaussian noise is added in the signal simulated. In section 4, an experiment is carried out on a turbine rig to validate the introduced methods.

2 Theoretical background

2.1 Order based modal analysis

The excitation in many rotating machineries are periodical with its frequencies composed of multiples of the rotational frequency, which is known as Engine Orders (EO). As shown in Figure 1, the rotation of residue unbalance gives rise to two orthogonal excitations $f_X(t)$ and $f_Y(t)$ along the *x* and *y* axis. *c* is the engine order of harmonics, A_{cx}, A_{cy} and φ_c are the amplitude and phase of the orthogonal excitation of engine order *c* respectively [5].

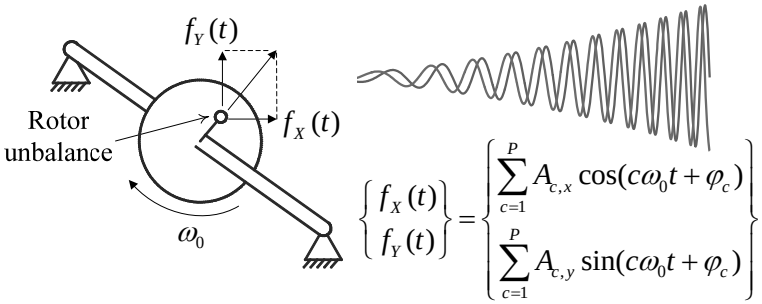


Figure 1: Forced vibration of rotating machinery under sweeping harmonic excitation

$$\begin{Bmatrix} F_X(\omega) \\ F_Y(\omega) \end{Bmatrix} = \begin{Bmatrix} \sum_{c=1}^{P} e^{j\varphi_c} A_{c,x}\delta(\omega - c\omega_0) \\ \sum_{c=1}^{P} je^{j\varphi_c} A_{c,y}\delta(\omega - c\omega_0) \end{Bmatrix} \tag{1}$$

$F_X(\omega)$ and $F_Y(\omega)$ in equation (1) are the frequency domain expression of $f_X(t)$ and $f_Y(t)$, while $\delta(\cdot)$ presents unit pulse function.

Forced vibration of a linear structure can be expressed in the frequency domain as:

$$X(\omega) = H(\omega)F(\omega) \tag{2}$$

Where, $H(\omega)$ is the FRF matrix of the rotor system, $F(\omega)$ is the external excitation. The FRF matrix can be expressed in the form of modal poles, shapes and participation factors [7].

$$H(\omega) = V(j\omega I - \Lambda)^{-1} L + \frac{1}{\omega^2} LR + LU \tag{3}$$

Where, Λ is the diagonal matrix of modal poles, which can be written in the combination of modal frequencies and dampings. V is the matrix of modal shapes and L is the matrix of modal participation factors. Λ, V and L are all complex valued. LR and LU are the real-valued lower and upper modal residuals.

Substituting equation (3) into equation (2), the forced vibration of a rotor system is shown as follow:

$$X(\omega) = V(j\omega I - \Lambda)^{-1}(L \cdot F(\omega)) + \frac{1}{\omega^2}(LR \cdot F(\omega)) + (LU \cdot F(\omega)) \tag{4}$$

As shown in equation (1), $F(\omega)$ is made up of multiple orders of rotational frequency ω_0. Separate $F(\omega)$ in x and y direction, equation (4) can be written into the following form.

$$X(\omega) \propto \omega^2 \left(V(j\omega I - \Lambda)^{-1}(L_x - jL_y) + \frac{1}{\omega^2}(LR_x - jLR_y) + (UR_x - jUR_y) \right) \tag{5}$$

It is assumed that the amplitude of external excitation $F(\omega)$ is proportional to the squared rotational frequency ω_0^2. In order to make equation (5) has the same form as FRF, equation (5) needs to be divided by ω_0^2. Furthermore, if the response measured is the acceleration response, the amplitude response needs to be divided by the fourth power of rational frequency, ω_0^4.

Equation (5) has the similar form as equation (3), also contains the information of poles and modal shapes. It means that the response curve during a run-up process can be used for modal parameter identification. In the present paper, the response curve is fitted by the least-squares complex frequency-domain (LSCF) estimation method, which is known as operational PolyMAX [8].

The range of frequency ω is related to the sweeping range of ω_0 and the engine order c extracted. Modes of higher frequency will be identified, if the rotating machinery runs up through a wider rpm range or higher engine orders are extracted from the signal measured.

2.2 Signal processing

The signal processing technologies used in the present paper are stationary wavelet transform and order tracking. The former one is used to suppress the measurement noise in the original signal and the latter one is used to extract the forced vibration amplitude $|X(c\omega_0)|$ and phase $\angle X(c\omega_0)$ of engine orders c during run-up process.

The order tracking method utilized in the present paper is called Computed Order Tracking (COT) [9]. COT is based on the concept of angle domain resample, which first converts a time domain signal to a homogeneous angle domain signal. Angle domain resample is based on high accuracy estimation of shaft angle, thus a tacho is necessary to measure the rotational angle of the shaft. After the signal resampled, Fast Fourier Transform (FFT) will be exercised on the angle domain signal to get the order spectrum. Order spectrum resolution and highest analysis order are two main parameters of order tracking. The highest analysis order is determined by the number of resample points per round and order spectrum resolution is determined by the block size of FFT. In this section, the order resolution is 1/16 and the highest analysis order is 32.

Vibration signal measured in practical environment is often masked by big noise. During the resample process, the wide band noise will lead to a problem of aliasing if the highest instantaneous frequency of the original signal exceeds the resample frequency. To avoid this, the angle domain resample frequency must double the highest frequency of the original time domain signal (Shannon's sampling theorem). Therefore, when an additive broad band noise is introduced, the original time domain signal must be filtered before resample to lower its frequency band.

Stationary wavelet transform (SWT) is applied in the present paper to filter out signal exceeding Nyquist frequency [10]. SWT is a kind of undecimated discrete wavelet transform, whose wavelet coefficients have

the same length as the original signal. Meanwhile, SWT keeps the signal filtered the same phase as the original signal, which is important for further modal parameters estimation. As a kind of orthogonal wavelet transform, SWT first pass the signal through a series of quadratic mirror filters and get the approximate coefficients and detail coefficients respectively.

Another problem in OBMA method is the selection of engine sweep rate. The sweep rate of rotating machinery will affect the accuracy of order tracking, which will finally affect parameter identification result of OBMA. A quasi-steady state response is needed to make the response close to the steady harmonic response $X(c\omega_0)$, thus the sweep rate shouldn't be too fast.

The amplitude response of a SDOF system of 4Hz natural frequency and 2% damping ratio is shown in Figure 2 and Figure 3. Figure 2 and Figure 3 represent logarithmic and linear sweeping process respectively. Obviously, high sweep rate makes the amplitude response deviate from the exact value X_{exact}. This is because if the sweep rate of a rotating machinery is too high, the transient response can't be neglected, which will lower the estimation accuracy of pseudo-FRF.

It has been discovered that the distortion of amplitude response has something to do with the system's damping ratio. Smaller damping leads to more severe distortion of the estimated pseudo-FRF. For a common small damping structure, the sweep rate could be determined by experience. For example, according to the recommendation of ISO standard, in order to meet a satisfying accuracy, the sweeping velocity should be less than 0.5 oct/min [11]. It means that for a logarithmic sweep case, the rotational speed is not allowed to double in every two minutes, and for a linear sweep case, the sweep rate is related to the initial rotational speed.

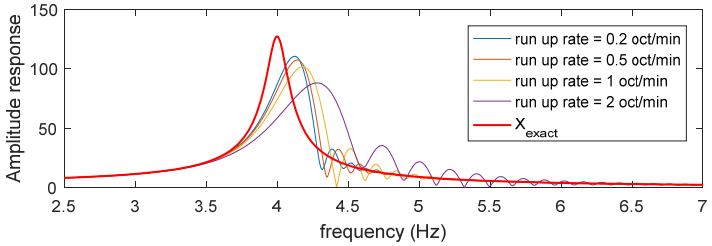


Figure 2: Amplitude distortion for a logarithmic sweep process

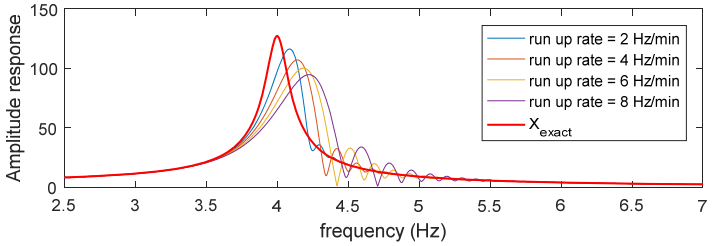


Figure 3: Amplitude distortion for a linear sweep process

3 Numerical Simulation

As shown in Figure 4, a rotor was mounted on a plate-shape foundation of size 300×800 mm. The modal frequencies and dampings of the plate calculated by finite element method are shown in the first column of Table 1. The rotor on two excitation points was assumed to run up from 400rpm to 1600rpm in four minutes with a linear sweep rate of 400 rpm/min. The acceleration responses at 26 homogeneously distributed points were simulated by Duhamel integral and modal superposition method.

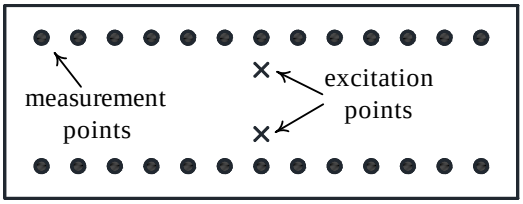
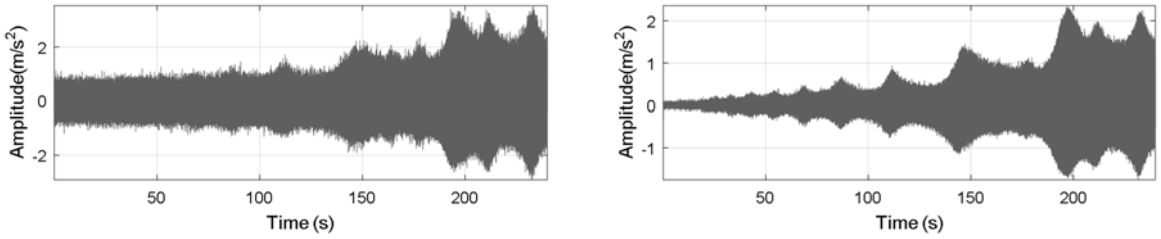


Figure 4: Excitation points and measurement points of a plate

The simulate time domain vibration signal is shown in Figure 5 (a). The signal was polluted by additive white Gaussian noise, whose S/N ratio is 10 dB. As shown in Figure 5 (b), after passing through an SWT filter of 10 levels as introduced in section 2.2, the noise was alleviated, and obviously harmonic resonance phenomenon was more explicit in the signal filtered. The waterfall plot in Figure 6 shows the amplitude response varying with the instantaneous rotational speed obtained at point 8. The peaks of red curves indicate harmonic resonance during sweeping process.



(a) *Original vibration signal with 10dB additive white Gaussian noise*

(b) *Signal filtered by SWT*

Figure 5: Original time domain signal and signal filtered

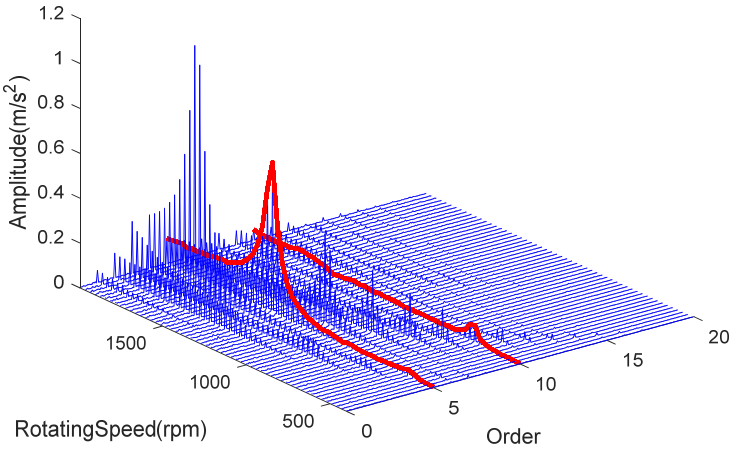
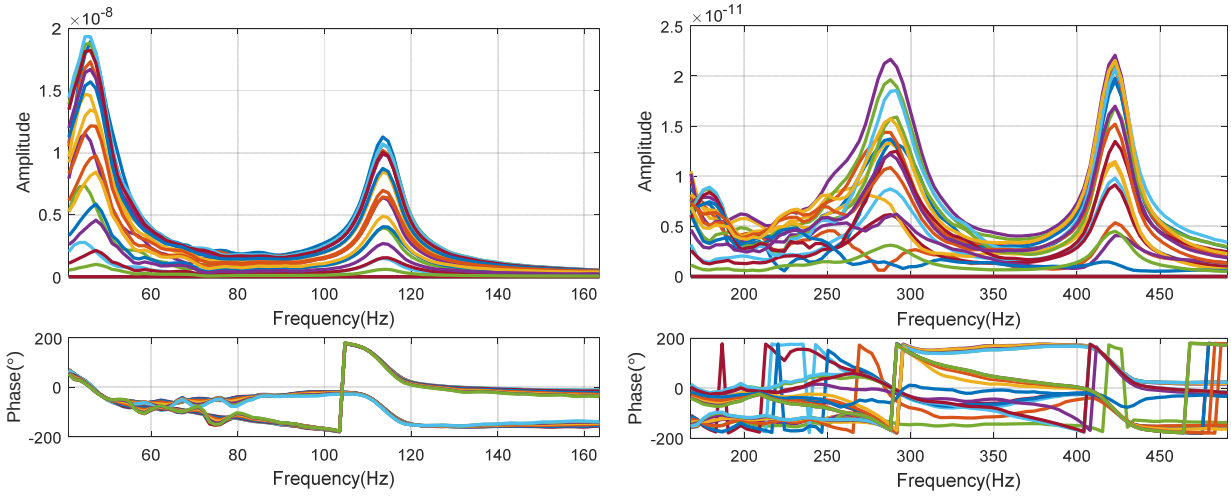


Figure 6: Waterfall plot in the order domain of measurement point 5

The response curves extracted from engine order 5 and 15 are shown in Figure 7, which has been divided by the fourth power of rotational frequency ω_0^4 as introduced in section 2.3. Figure 8 shows the stabilization diagrams of order 5 and order 15, after applying the LSCF modal parameter estimation method to the orders extracted. The vertical lines of 's' indicates the physical poles, 'f' represents modal frequency unstable, 'd' represents damping unstable and 'v' represents modal vector unstable.

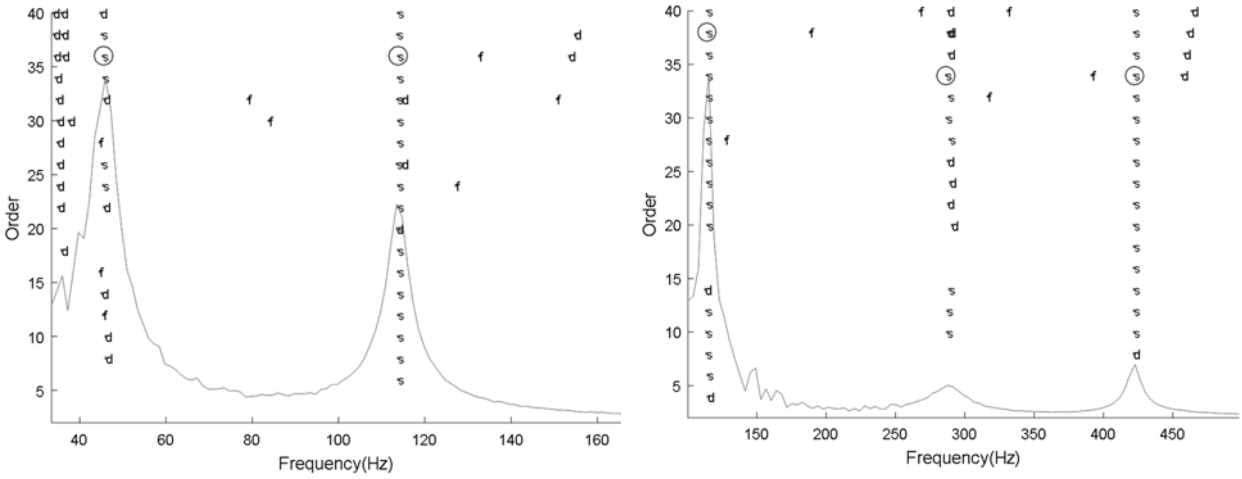
The modal parameters identified using order 5, order 10 and order 15 are shown in Table 1. There are 6 modes superposed in the simulate signal and totally 5 modes are identified using the OBMA method and SWT filter introduced previously. Mode 3 with natural frequency 116.26Hz cannot be identified. One

possible reason is that two natural frequencies are too close and masked by the noise. The modal shapes identified from mode 1 to mode 6 are shown in Figure 9. Two bending modes and three torsional modes are exhibited.



(a) *Order* 5 *of the* 26th *measurement points* (b) *Order* 15 *of the* 26th *measurement points*

Figure 7: Amplitude and phase of order 5 and order 15 extracted from the simulate signal

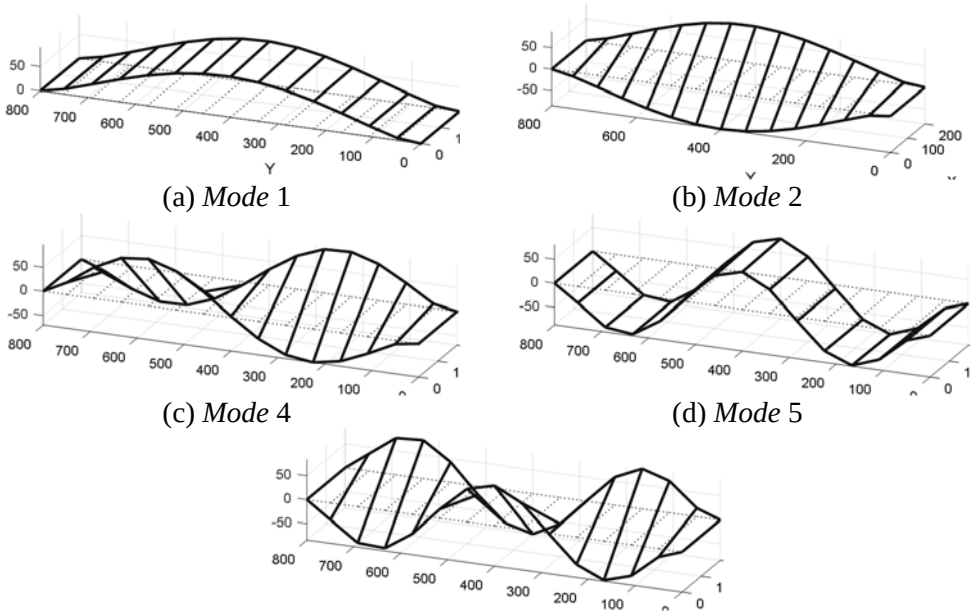


(a) *Order* 5 (b) *Order* 15

Figure 8: Stabilization plot of order 5 and order 15

Exact value		Order 5		Order 10		Order 15	
Frequency (Hz)	Damping (%)	Frequency (Hz)	Damping (%)	Frequency (Hz)	Damping (%)	Frequency (Hz)	Damping (%)
45.85	6.00	45.39	5.34	-	-	-	-
113.77	2.00	113.88	1.94	113.74	2.12	114.19	2.11
116.26	2.00	-	-	-	-	-	-
257.44	4.00	-	-	257.69	1.90	-	-
288.55	4.00	-	-	289.09	3.97	288.62	3.42
422.07	1.00	-	-	-	-	422.17	1.00

Table 1: Comparison of identified modal parameters and simulate modal parameters



(a) *Mode* 1 (b) *Mode* 2

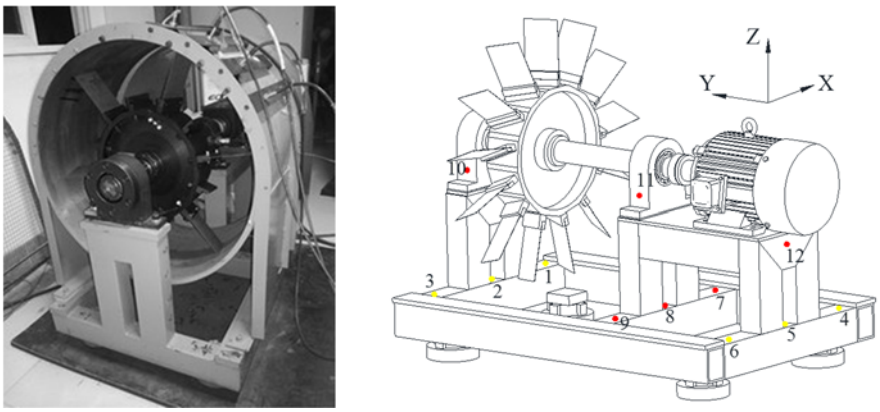
(c) *Mode* 4 (d) *Mode* 5

(e) *Mode* 6

Figure 9: Shapes of modes identified

4 Experimental validation

In order to validate the method described in the present paper, an experiment was carried out on an turbine rig. As shown in Figure 10, one blade disk was supported by a pair of ball bearings on two pedestals. Measurement points are presented by yellow and red points on the pedestals and foundation. The turbine model ran up from 200 rpm to 1200 rpm in 120 seconds, with a linear sweep rate of 8.3 rpm/s. Six piezoelectric accelerometers with 100 mV/g sensitivity were placed at point 1 to 12. 12 measurement points were divided into two groups represented by different colors. Each group contained 3 runs and the order spectrums of different runs in one group were averaged to further alleviate measurement error.

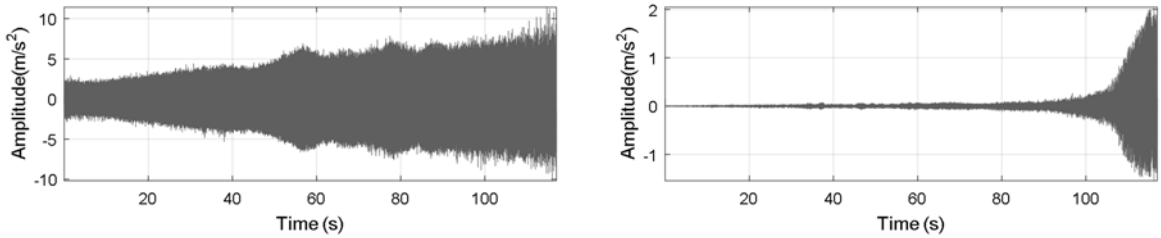


(a) *Turbine rig* (b) *Measurement points*

Figure 10: Turbine rig and the measurement points

As the unbalance mass remain the same in each measurement, the amplitude response under certain rotational speed was repeatable. The phase responses were calculated with reference to the tacho pulse. As the position of unbalance mass remained unchanged, the phase response was repeatable in each measurement either. Therefore, the order spectrum of different measurement groups can be directly combined for parameter estimation.

The acceleration along three orthogonal directions x, y and z was measured. In addition, one tacho was placed besides the shaft for angular speed estimation and order tracking. The signal was synchronously sampled by a 32-channels parallel data acquisition system, with a sampling rate of 12800Hz.



(a) *Original time domain signal* (b) *Signal filtered by SWT*

Figure 11: Original acceleration signal measured and signal filtered by SWT

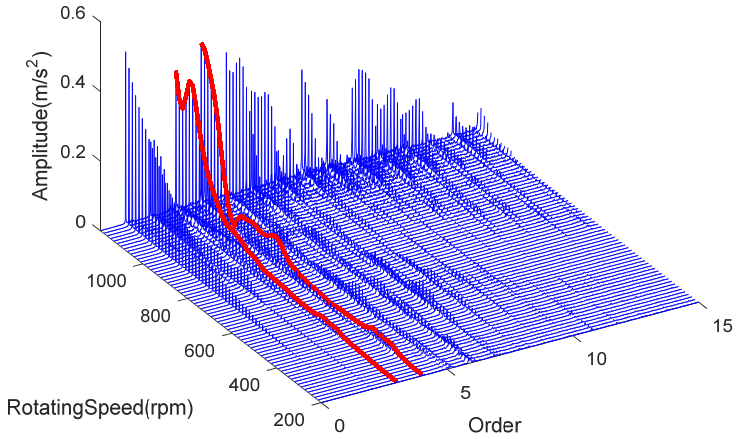
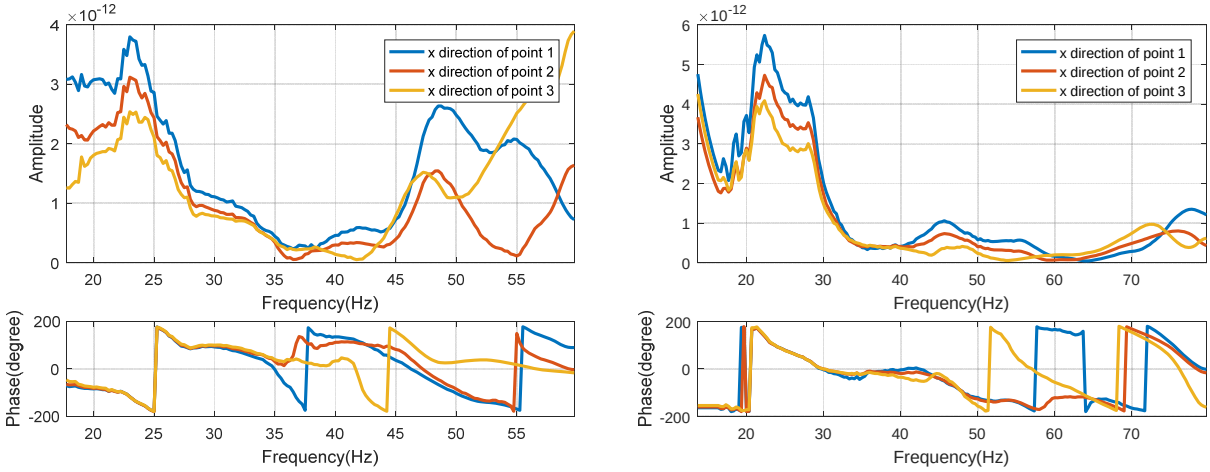


Figure 12: Waterfall plot for the averaged result of three runs



(a) *Order* 3 (b) *Order* 4

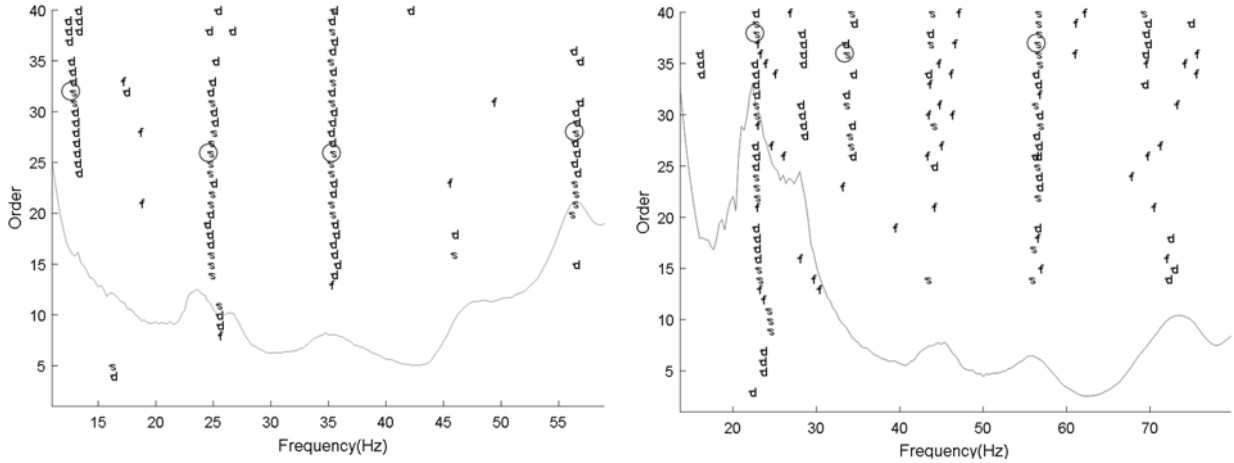
Figure 13: Amplitude and phase responses of order 3 and order 4

The original time domain signal measured in z direction of point 5 is shown in Figure 11 (a). The original signal was mainly polluted by the electrical oscillation of the three-phase asynchronous motor with

frequency around 4000Hz. The SWT filtered result is shown in Figure 11 (b). The signal is divided into 10 levels and the components out of frequency band concerned are filtered. After passing through the SWT filter, the noise is suppressed, and the vibration amplitude has an explicit increment in the run-up process due to the increase of the centrifugal excitation aroused by residue unbalance.

The computed order tracking result of vibration signal in z direction of point 6 is shown in Figure 12 in the form of a waterfall plot. The order resolution is 1/64 and highest analysis order is 32. The red curves in the waterfall plot indicate the amplitude responses under sweep excitation. Figure 13 (a) (b) are amplitude and phase responses of engine order 3 and 4 extracted from x direction of point 1 to 3.

The LSCF parameter estimation method has been applied to order 3 and order 4 to estimate modal parameters. The stabilization diagrams are shown in Figure 14. Modal parameters identified from order 2 to order 4 are shown in Table 2. The modal shapes of mode 2 and 3 are exhibited in Figure 15.

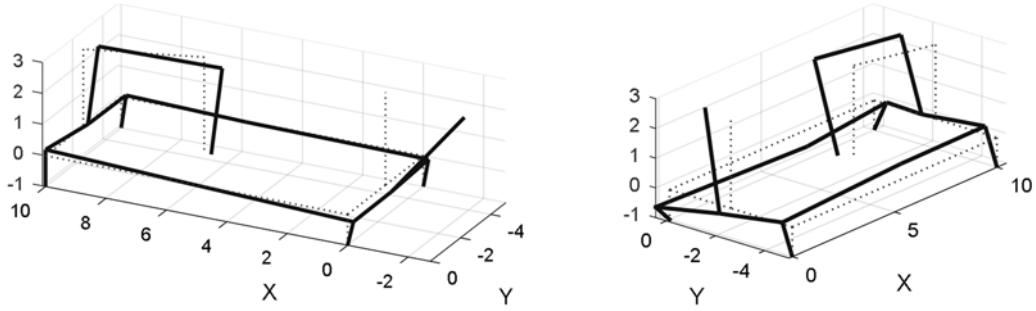


(a) *Stabilization diagram of order* 3 (b) *Stabilization diagram of order* 4

Figure 14: Comparison between stabilization diagram of order 3 and order 4

	Engine Order 2		Engine Order 3		Engine Order 4	
	Frequency (Hz)	Damping (%)	Frequency (Hz)	Damping (%)	Frequency (Hz)	Damping (%)
Mode 1	-	-	12.6	1.2	-	-
Mode 2	25.9	3.9	24.6	8.1	22.5	7.5
Mode 3	32.2	8.5	35.3	6.3	33.4	8.9
Mode 4	-	-	56.3	4.4	56.3	3.9

Table 2: Comparison of natural frequency and damping ratio identified from order 2 to 4



(a) *Shape of mode* 2 (b) *Shape of mode* 3

Figure 15: Shapes of mode 2 and mode 3 obtained by the OBMA method

5 Discussion

The experiment and the result introduced in section 4 are discussed from following three aspects:

(1) For safety concerns, the rpm range of the experimental rig was restricted under 1200, thus only modes of frequency less than 100Hz can be identified.

(2) The accuracy of estimation result is affected by the accuracy of order tracking. To improve the accuracy of order tracking, suitable sweep rate and order resolution are necessary. In the experiment above, a relatively low sweep rate and high order resolution is selected.

(3) To combine the experiment result, the unbalance mass should remain the same during each measurement. If the unbalance mass changes, there should be one reference point remain at the same position in each measurement to scale the unbalance change.

Acknowledgements

This research program was jointly funded by Jiangsu Six Talent Peaks program, announced by Education Department of Jiangsu Province and by National key research and development program of Ministry of science and technology(2016YFF0203300).

References

[1] B. Peeters, H. Van der Auweraer, F. Vanhollebeke, P. Guillaume, *Operational modal analysis for estimating the dynamic properties of a stadium during a football game*, Journal of Shock and Vibration, Vol.11 (2004), pp. 395-409.

[2] E. Di Lorenzo, S. Manzato, A. Dabizzi, *Industrial applications of advanced modal identification on operational rotating machineries*, Proceedings of International Conference on Noise and Vibration Engineering (ISMA) ,Leuven, Belgium (2016).

[3] S. Manzato, D. Moccia, B. Peeters, K. Janssens, J. R. White, *A review of harmonic removal methods for improved operational modal analysis of wind turbines*. Proceedings of International Conference on Noise and Vibration Engineering (ISMA) ,Leuven, Belgium (2012).

[4] K. Janssens, Z. Kollar, B. Peeters, S. Pauwels, H. Van der Auweraer, *Order-based resonance identification using operational PolyMAX*, Proceedings of 24th International Modal Analysis Conference (IMAC), Saint Louis, MO, USA (2006).

[5] B. Peeters, P. Gajdatsy, P. Aarnoutse, K. Janssens, *Vibro-acoustic operational modal analysis using engine run-up data*. Proceedings of the 3rd International Operational Modal Analysis Conference (IOMAC), Ancona, Italy (2009).

[6] E. Di Lorenzo, S. Manzato, F. Vanhollebeke, S. Goris, B. Peeters, W. Desmet, F. Marulo, *Dynamic characterization of wind turbine gearboxes using Order-Based Modal Analysis*, Proceedings of 26th International Conference on Noise and Vibration Engineering (ISMA), Leuven, Belgium (2014).

[7] Heylen, W., Sas, P, *Modal analysis theory and testing,* Dept. Mech. Eng., K.U.Leuven, Belgium (2006).

[8] B. Peeters, H. Van der Auweraer, P. Guillaume, J. Leuridan, *The PolyMAX frequency-domain method: a new standard for modal parameter estimation*, Shock and Vibration, Vol.11(3-4) (2004), pp. 395-409.

[9] K. R. Fyfe, E. D. S. Munck, *Analysis of computed order tracking. Mechanical Systems and Signal Processing,* Vol.11(2) (1997), pp. 187-205.

[10] G. P. Nason, B. W. Silverman, *The stationary wavelet transform and some statistical applications. In Wavelets and statistics,* Springer, New York, NY (1995), pp. 281-299.

[11] G. Gloth, & M. Sinapius, *Analysis of swept-sine runs during modal identification. Mechanical systems and signal processing*, Vol.18.6 (2004), pp. 1421-1441.

Statistical error reduction for correlation-driven operational modal analysis

M. Tarpø [1], **P. Olsen** [1], **M. Juul** [1], **S. Amador** [2], **T. Friis**[2], **R. Brincker** [2]
[1] Aarhus University, Department of Engineering,
Inge Lehmanns Gade 10, Aarhus, Denmark
e-mail: **martar@eng.au.dk**

[2] Technical Univeristy of Denmark, Department of Civil Engineering,
Brovej, Bldg. 118, Kgs. Lyngby, Denmark

Abstract
Statistical errors effect the estimated correlation function matrix in Operational Modal Analysis due to the finite time length of the sampled data. When these errors start to dominate the correlation functions, an erratic behaviour appears without any physics – this phenomenon is known as the Noise Tail. This tail region should be disregarded in an identification of modal parameters and it is possible to estimate the location of the Noise Tail for each structural mode. In this paper, an automated removal of the Noise Tail is introduced and studied and the paper finds that this removal reduces bias and random errors in identification of modal parameters for Operational Modal Analysis.

1 Introduction

In Operational Modal Analysis, we can treat the transposed correlation function matrix as free decays, which we can extract modal parameters from [1, 2]. This assumption is based on the properties of ambient vibrations from a linear and ergodic system excited by white Gaussian noise. However, the analytical correlation function matrix is still based on the properties of random vibrations from the system but these exact properties are indeterminable from sample data. This introduces statistical errors when we estimate the correlation function matrix by sample data with a finite time length [3]. Orlowitz and Brandt demonstrated the statistical errors for Operational Modal Analysis in regards to estimation of the modal damping [4]. Giampellegrini derived an expression for the statistical error of the estimated auto-correlation functions for Operational Modal Analysis. Tarpø et al. briefly explained the erratic behaviour in the tail region - the *Noise Tail* - and introduced an algorithm to detect the beginning of the Noise Tail based on the envelope of the modal correlation function [6]. Pridham and Wilson found that the tail region of correlation functions introduces bias in the identification of modal parameters in a numerical study [7]. They found that highly damped modes only need few time lags from the correlation function to get valid results. However, a similar truncation of a correlation function result in errors for modes with low damping and low frequency.

In the literature, we see that the statistical error is related to the finite time length and it creates a bias tail region of the correlation function matrix. Each mode has an individual position of this region in the matrix that will provide the ideal identification of the modal parameters. However, we should not truncate the correlation function matrix too much since this results in errors in the identification of other modes. In this paper, we present an automatic algorithm that reduces the statistical errors while it avoids a heavy truncation of the correlation function matrix. Based on a numerical study, the algorithm reduces bias and random errors of the identification of modal parameters.

2 Theory

We are considering a linear system that is excited by white Gaussian noise and we measure a spatial limited system response, $\mathbf{y}(t)$. In Operational Modal Analysis, we can calculate the correlation function matrix for the system response and use this matrix as free decays that corresponds to the system parameters, [1, 2].

$$\mathbf{R}_y(\tau) \quad = \quad \mathrm{E}\left[\mathbf{y}(t)\mathbf{y}^T(t+\tau)\right] \tag{1}$$

We use time averaging instead of ensemble averaging since the response is ergodic. However, the time length must tend toward infinite for this to be true [3].

$$\mathbf{R}_y(\tau) \quad = \quad \lim_{T\to\infty} \frac{1}{T} \int_0^{T-\tau} \mathbf{y}(t)\mathbf{y}^T(t+\tau)\, dt \tag{2}$$

where T is the time length of the measured data. However, properties of random variables cannot be precisely determined from sample data. In reality, a measured system response has a finite time length and this introduces statistical errors since we must estimate the correlation function matrix instead [3].

$$\widetilde{\mathbf{R}}_y(\tau) \quad = \quad \frac{1}{T-\tau} \int_0^{T-\tau} \mathbf{y}(t)\mathbf{y}^T(t+\tau)\, dt, \quad 0 \leq \tau < T \tag{3}$$

This means that the estimated correlation function matrix is a stochastic process due to the statistical errors. The expected values equal the analytic correlation functions (the free decay) and the variance is the statistical errors caused by the finite time length of the recorded signal [3]. By increasing the time length of recording, the variance of the estimated modal correlation functions decreases, see figure 1.

$$\lim_{T\to\infty} \widetilde{\mathbf{R}}_y(\tau) \quad \to \quad \mathbf{R}_y(\tau) \tag{4}$$

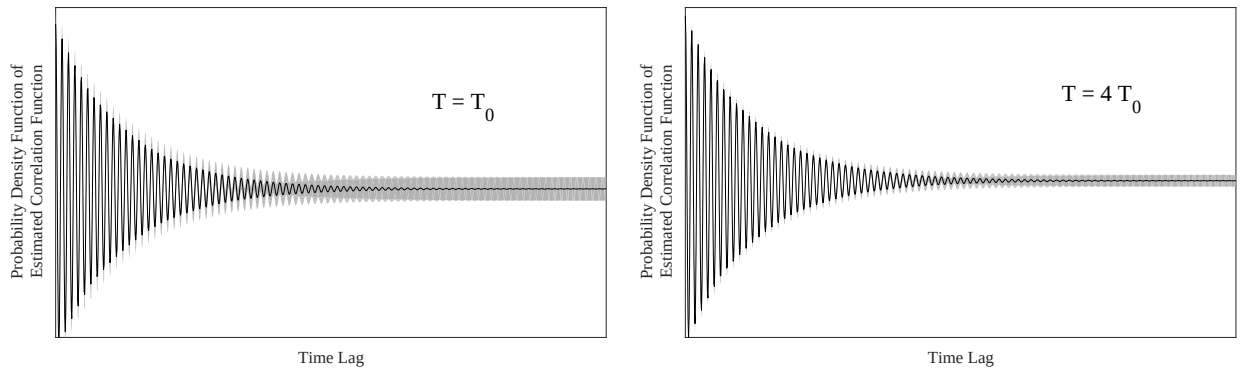


Figure 1: Probability Density Function of the estimated correlation function for an arbitrary system plotted for two different time lengths, the expected value (*black line*) and 2 standard deviations (*gray fill*)

The correlation function matrix has erratic behaviour in the tail region [5, 6], see figure 2. In this part of the correlation functions, the statistical errors dominate and the basic assumption, that the correlation function is a free decay, is invalid. By increasing the time length of the data, the statistical errors decrease, which means that the Noise Tail moves further into the tail region, see figure 3 & 4. This part of the correlation function is biased and its envelope is approximately constant in the Noise Tail as illustrated in figure 4. Therefore the Noise Tail should be excluded from any identification of modal parameters.

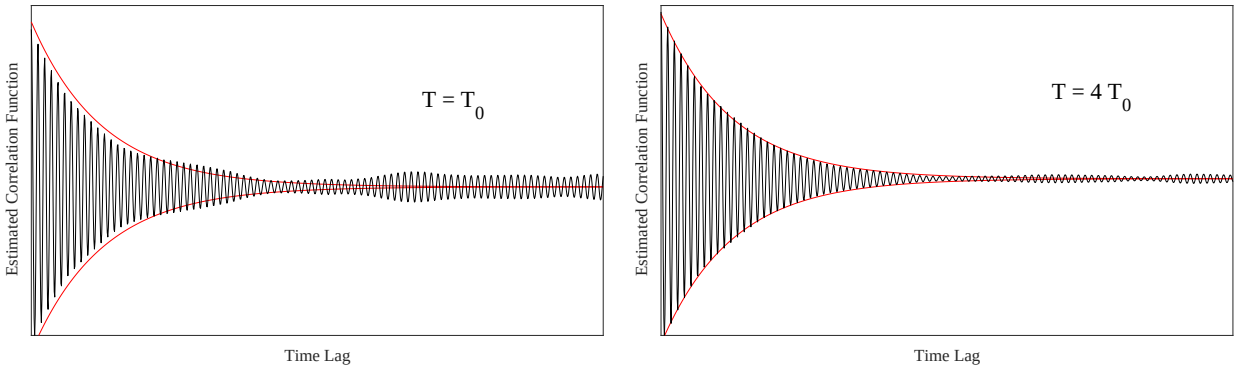


Figure 2: The analytical envelope of the correlation function and the estimated correlation function for an arbitrary system plotted for two different time lengths

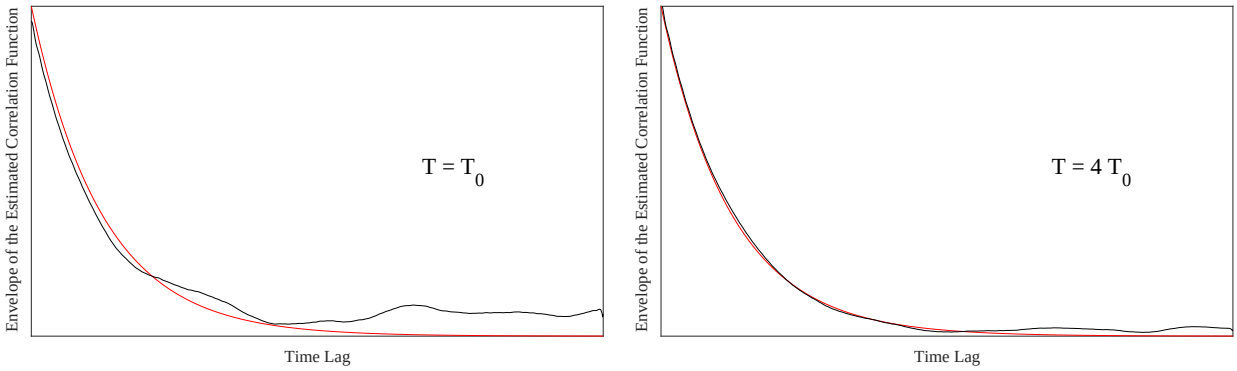


Figure 3: The envelopes of the analytical correlation function and the estimated correlation function for an arbitrary system plotted for two different time lengths

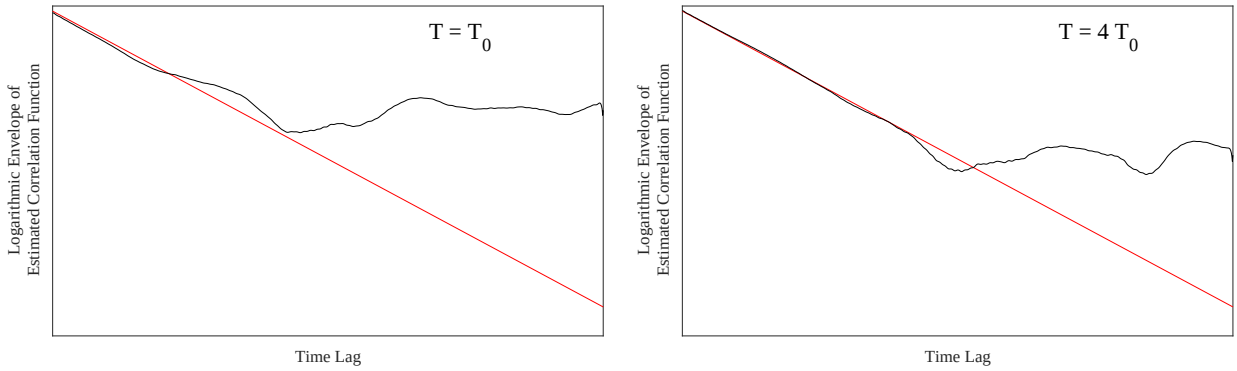


Figure 4: The logarithmic envelopes of the analytical correlation function and the estimated correlation function for an arbitrary system plotted for two different time lengths

For system with N degrees-of-freedom, we can use the modal decomposition to transform the estimated correlation function to the estimated modal correlation functions, which is the estimated auto-correlation function for the modal coordinates [6, 8].

$$\widetilde{\mathbf{R}}_y(\tau) = \sum_{i=1}^{N} \boldsymbol{\Phi}_i \left[\widetilde{R_{q_i}}(\tau)\right] \boldsymbol{\Phi}_i^H \tag{5}$$

where $\boldsymbol{\Phi}_i$ is the mode shape for i^{th} mode. By assuming the statistical errors on the mode shapes are small then this enables us to access the statistical errors on the correlation function matrix as the sum of statistical errors on the modal auto-correlation functions, $\widetilde{R_{q_i}}(\tau)$. We know that the variance of the estimated auto-correlation function is dependent of the excitation, modal parameters, time length and the time lags [5]. This means that the Noise Tail starts at different points for each modal coordinate. This poses a problem when we need to truncate the correlation function matrix to reduce the bias from the statistical errors. In the case, we truncate the correlation function in order to remove the noise tail from a certain mode then we might have too little left of the correlation function to get proper identification for other modes. We especially have this problem when we deal with combinations of modes with low frequencies and modes with high frequencies and high damping ratios. Here the noise tail begins at a much lower time lag for these modes with high frequency and damping than the modes with lower frequency. However, we need (ideally) a few periods of the modes with low frequency to get good estimation of the modal parameters.

3 Algorithm

In this section, we introduce the general idea behind an automated algorithm for detection and reduction of the Noise Tails in the correlation function matrix for Operational Modal Analysis.

We need to decorrelate the correlation function into the modal correlation function, eq. (5). For this we use a combination of principle component analysis [9] and an eigenvalue decomposition to estimate a transformation matrix that decorrelate the correlation function matrix.

We use the algorithm by Tarpø et al. to identify the start of each Noise Tail [6]. This algorithm utilises that the physical part of the correlation function has a sloping logarithmic envelope while the envelope of the Noise Tail is an approximated constant value, see figure 4. It fits two mathematical models to the envelope (a sloping line and a constant value) and the optimal fit indicates the beginning of the Noise Tail.

When we know the position of the Noise Tail for each modal correlation function, $\widetilde{R_{q_i}}(\tau)$, then we modify the envelope in the Noise Tail region. We change the envelope to mimic that of the physical correlation function by using a the least square fit of a negative exponential from the physical part of the modal correlation function.

Finally, we obtain an modified correlation function matrix where we reduced the statistical errors and we can use this in the identification of modal parameters.

4 Case Study

We will use a numerical system with 3 degree-of-freedom to illustrate the algorithm, see the modal parameters in table 1 and the spectral density matrix in figure 5. For this study, we ran $10,000$ simulations where we excited the system by white noise. The system response was simulated for 253.77 s (10240 data points) at a sampling frequency of 40.35 Hz (3.1 times the highest natural frequency). We calculated the correlation functions based on the simulated response using the discrete version of eq. (3) with 1025 time lags. In order to simulate the response of the linear system, we utilised the Fourier transformed superposition [8]. For the same simulation, we used the original correlation function matrices and the modified correlation function matrix from the algorithm in the identification of modal parameters. We utilise the Time Domain

Poly-reference technique to identify the modal parameters [10] and the results are plotted in figures 6 & 7 for the original and modified correlation function matrix.

Table 1: Modal parameters of numerical system

	Mode 1	Mode 2	Mode 3
Frequency [Hz]	3.39	10.0	13.0
Damping Ratio [%]	1.49	1.34	1.53

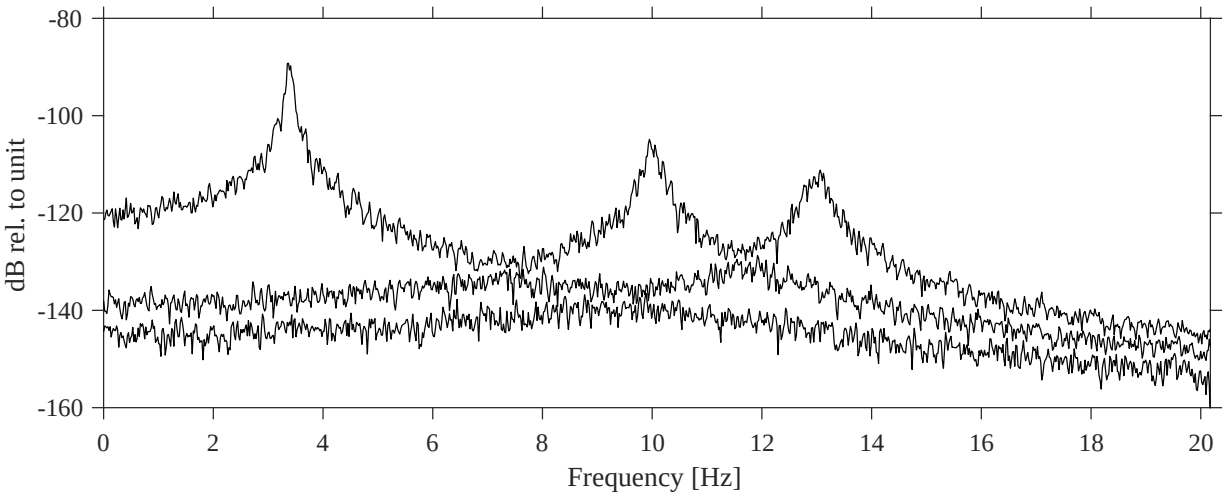


Figure 5: Singular values of the spectral density matrix using the Welch averaging technique [8]

Based on figure 6 & 7, the automated algorithm reduces both the bias and random error in the estimation of modal parameters. Furthermore, the distribution of the modal parameter changes from non-Gaussian to approximately Gaussian distributed.

5 Conclusion

We found that the properties of random data cannot be precisely determined from sample data. In other words, the finite time length introduces statistical errors in the correlation function matrix for Operational Modal Analysis and this results in a bias region of the correlation function matrix.

In this paper, we applied an new automatic algorithm for reduction of the statistical errors in the estimated correlation function by removing the noise tail. We found that the algorithm reduces estimation bias while reducing the variance of the modal parameters in this numerical study. For further research, the algorithm will be tested on real data.

Acknowledgements

The authors acknowledge the funding received from Centre for Oil and Gas - DTU/Danish Hydrocarbon Research and Technology Centre (DHRTC).

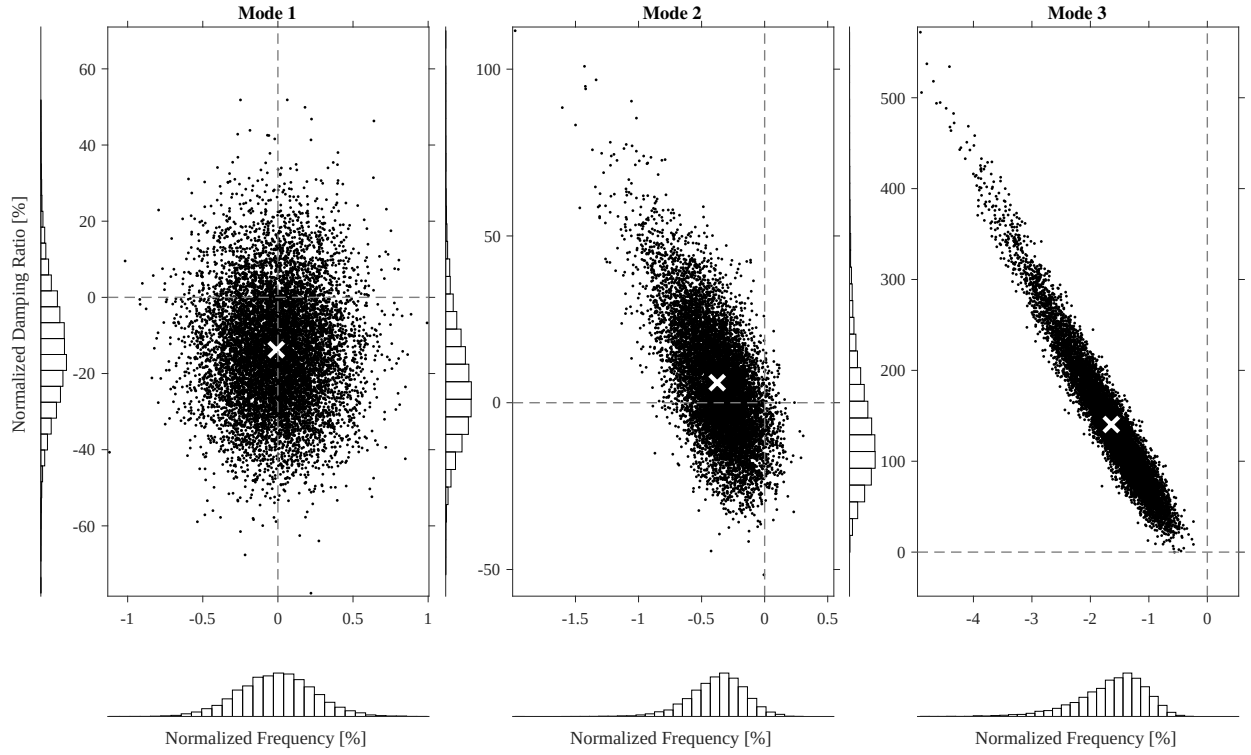


Figure 6: Identification of modal parameters from the original correlation function matrix and their distribution

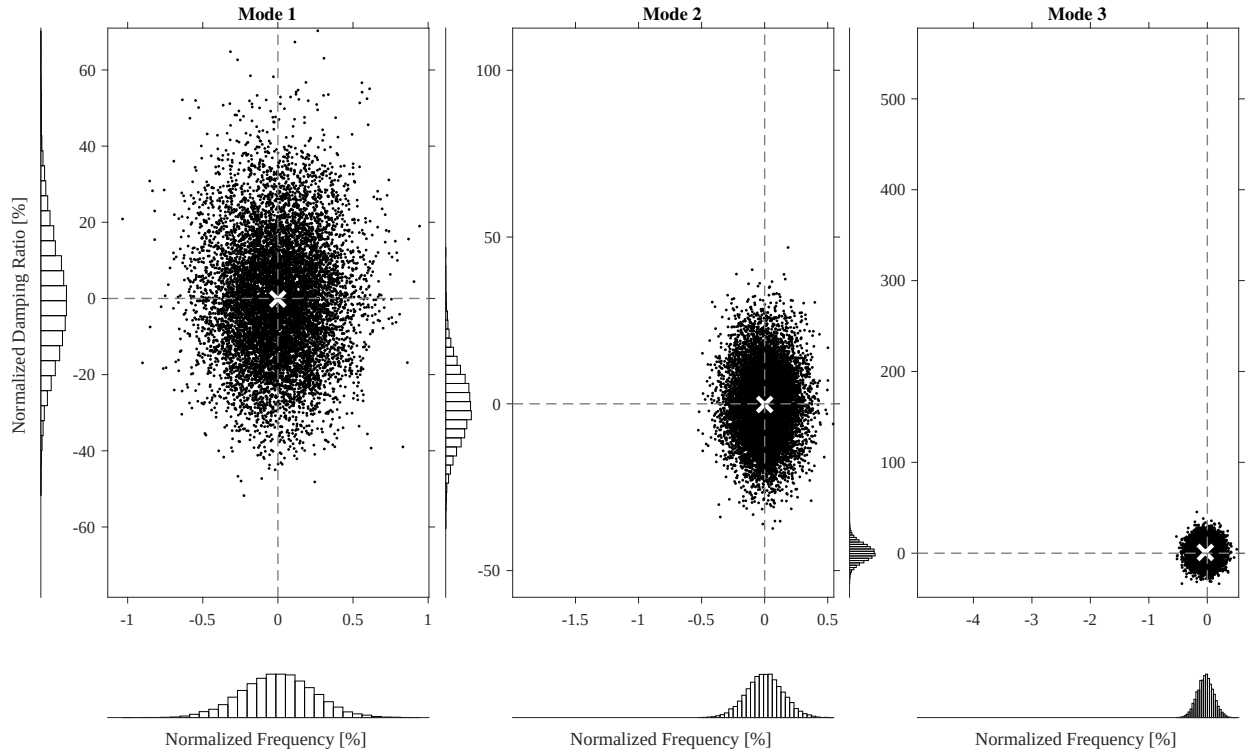


Figure 7: Identification of modal parameters from the modified correlation function matrix and their distribution

References

[1] G. C. James, T. G. Carne, J. P. Lauffer, The natural excitation technique (next) for modal parameter extraction, The International Journal of Analytical and Experimental Modal Analysis 10 (1995) 260–277.

[2] R. Brincker, On the application of correlation function matrices in oma, Mechanical Systems and Signal Processing 87 (2017) 17–22.

[3] J. S. Bendat, A. G. Piersol, Random data : analysis and measurement procedures, 4th ed., Wiley-Blackwell, Hoboken, N.J., USA, 2010.

[4] E. Orlowitz, A. Brandt, Influence of correlation estimation methods on damping estimates, 5th International Operational Modal Analysis Conference (2013).

[5] L. Giampellegrini, Uncertainty in correlation-driven operational modal analysis, Ph.D. thesis, University College London, UK, 2007. 64-74.

[6] M. Tarpø, P. Olsen, S. Amador, M. Juul, R. Brincker, On minimizing the influence of the noise tail of correlation functions in operational modal analysis, 2017. ID: 278653.

[7] B. A. Pridham, J. C. Wilson, A study of damping errors in correlation-driven stochastic realizations using short data sets, Probabilistic Engineering Mechanics 18 (2003) 61 – 77.

[8] R. Brincker, C. Ventura, Introduction to operational modal analysis, John Wiley and Sons, Inc., Chichester, West Sussex,UK, 2015.

[9] P. Olsen, M. Juul, R. Brincker, Condensation of the correlation functions in modal testing, Submitted to Mechanical Systems and Signal Processing, Currently in 2^{nd} review (2018).

[10] H. Vold, J. Kundrat, G. Rocklin, R. Russell, A multi-input modal estimation algorithm for minicomputers, SAE Technical Paper 820194 (1982) 10.

Regularized time-varying operational modal analysis illustrated on a wind tunnel testing measurement

P. Z. Csurcsia[1,2]**, B. Peeters**[1]**, J. Schoukens**[2]
[1] Siemens Industry Software NV.
Interleuvenlaan 68, 3001 Leuven, Belgium
e-mail: **peter.zoltan_csurcsia@siemens.com**

[2] Vrije Universiteit Brussel, Department of Engineering Technology
Pleinlaan 2, B-1050 Elsene, Belgium

Abstract
This paper presents an efficient nonparametric time-varying (TV) system identification method for the Operational Modal Analysis (OMA) framework. OMA tackles industrial measurements of vibrating structures in real-life operating conditions without the exact knowledge of the excitation signal. The main issue is that the dynamics of underlying systems may vary significantly when operating in real-life conditions. In this case it is desired to carefully verify and track the vibration behavior, since during flutter appearance, system destruction can occur.

In this work the first results of a regularized time domain based TV OMA method are presented to estimate the linear TV output autocorrelation function of the observed system. The method is illustrated on the measurement of wind tunnel test of an airplane model. Using the proposed methodology, the estimated TV 2D output autocorrelation model provides a good data-fit with respect to tracking of varying resonances.

1 Introduction

The goal of this paper is to present the first results of a new estimation technique developed to deal with time-varying (TV) mechanical and civil structures measured in an Operational Modal Analysis (OMA) framework. OMA is a special identification technique for estimating the modal properties of structures based on vibration data collected when the structures are under real operating conditions without having access to the excitation signals. Such modal parameters are, for instance, the natural frequencies, mode shapes, damping ratios. The OMA framework can provide the engineers with useful information to understand the dynamic behavior of the underlying structure in real-life usage scenarios, and it can be used to validate and update the numerical models developed in the design phase [1] [2].

OMA is a very important tool because in the case of vibrating structures it is common that the real operating conditions differ significantly from dynamic measurements performed in laboratory conditions and the unmodelled or wrongly modelled modes might lead to instability and structural failures. Contrary to the classical identification frameworks, a further challenge with the OMA framework is that the excitation signal is not known exactly, but it is assumed to be (nearly) white noise [2]. Methods for linear time-invariant (LTI) OMA have hence been developed and they are widely used also in the industrial environment, interested readers are referred to the detailed surveys [2] [3].

The dynamics of underlying systems may vary significantly when operating in real-life conditions. In this case, a TV modelling framework is needed because ignoring time variations might lead to instability and structural failures. A good example of a time-varying structure can be, for instance, an airplane. The time-varying behavior originates, for instance, from the decreasing weight due to the fuel consumption, and from different surface configurations during take-off, cruise and landing. Moreover, the resonance frequency and damping of most vibrating parts (for instance the wings) of a plane vary as a function of the flight speed and

height. The proposed LTV OMA method is illustrated on a wind tunnel testing measurement of a scaled aircraft model.

It is a common practice in system identification to use different types of short-time Fourier transform (SFT) techniques that describes slowly time-varying systems as a series of linear-time invariant (LTI) systems [4] [5] [6] [7] [8]. These SFT based models can describe the time-varying behavior quite well, when the time-variations are very smooth (i.e. the system varies very slowly). The drawback of these methods is that such an LTI model is not sufficient to describe the behavior of the underlying system, if the time variations are fast, or when a significant (sudden) variation occurs. A further issue is that in case of TV OMA, advanced system identification techniques have a limited applicability due to lack of knowledge of the excitation.

The proposed method is intended to overcome the issues with the classical SFT based methods, and it is based on the regularization methods that have been developed for nonparametric modelling of LTI systems [9] [10]. The main novelty of this work compared to classical regularization framework is to formulate the regularization for the special case of the estimation of LTV systems in an industrial OMA framework. Because this type of identification technique is relatively new and many ISMA readers are not familiar with the nonparametric regularization technique, a practical overview of the technique is provided in this paper.

This paper is organized as follows: in Section 2 the basic concepts of this work are summarized, and the problem formulation is given. Section 3 provides the model structure and the cost function of the underlying problem. Section 4 summarizes the practical considerations of the regularization technique, the LTV OMA estimation method, and addresses the implementation procedure. Section 5 shows a measurement example where the results of the classical SFT framework are shown to compare to the results proposed method. Finally, the conclusions are provided in Section 6.

2 Basics

In this section, a brief overview of the LTV OMA identification problem is presented from different aspects where we explain 1) the assumptions on the system and measurement used in the proposed framework, 2) the issues related to the nonparametric identification of LTV systems in general, and 3) the issues related to the OMA framework w.r.t. the classical identification framework.

2.1 Assumptions on the underlying system and measurement

In this paper a nonparametric description of (discrete) time-varying systems is considered. An LTV system can be characterized by its 2D impulse response function (IRF) $h[t,\tau]$. The steady-state output response to an arbitrary signal $u[t]$, measured with an $e[t]$ error, is given by [7] [11] [12] [13]:

$$y_m[t] = y[t] + e[t] = \sum_{\tau=-\infty}^{+\infty} h[t,\tau]u[t-\tau] + e[t] \quad (1)$$

where the parameter t is the global time (the time when the system is measured) and τ is the system time (the direction of the impulse responses/lags). An illustration of a TV IRF is shown in Figure 1.a.

In the proposed estimation framework the following assumptions are imposed:

Assumption 1 The true output ($y[t]$) is measured with additive, independent and identically distributed Gaussian noise ($e[t]$) with a zero mean and a finite variance (this assumption can be generalized to include colored noise).

Assumption 2 The TV IRF is smooth i.e. the spectral content of the LTV system is concentrated at the low frequencies. A more precise definition is out of the scope of this article, for a detailed study we refer to [14].

Assumption 3 The considered discrete system is causal (i.e. $h[t,\tau] = 0, \tau < 0$ [7]) and BIBO stable [15].

Assumption 4 The length of the IRFs (L+1) is much shorter than the measurement length (N).

Assumption 5 In case of the OMA framework, the excitation signal $u[t]$ is not known, but in the frequency band of interest it is assumed to be (nearly) white noise with a finite variance [2].

2.2 Nonparametric identification of LTV systems

The challenge with nonparametric time-varying system identification is that the TV IRF is not uniquely determined from a single set of input and output signal– unlike LTI IRF case. Consider the model defined in (1). Imposing *Assumptions 1–4*, the following measured output $y_m[t]$ is given at time t:

$$y_m[t] = \sum_{\tau=0}^{L} h[t,\tau]u[t-\tau] + e[t] \tag{2}$$

where $t = 0 \dots N-1$. Hence only N measured points are available to identify NL parameters.

Equation (2) can be written in vector form as $Y_m = UH + E$. This equation allows us to use the Maximum Likelihood (ML) framework [15] to estimate the time-varying IRF. Because the measurement noise is independent and white (*Assumption 1*) this estimation problem boils down to a Least Squares (LS) problem such that the LS cost function (V_{LS}) and IRF estimate ($\widehat{H}$) are given by the well-known expressions:

$$V_{LS} = \|Y_m - UH\|_2^2 \tag{3}$$

$$\widehat{H} = (U^T U)^{-1} U^T Y_m \tag{4}$$

To illustrate the difficulties of LS problem, a steady state simulation example is shown in Figure 1.c. The simulation is based on the time-varying system shown in Figure 1.a. This system is excited by white noise. To simplify this simulation, no observation noise has been added.

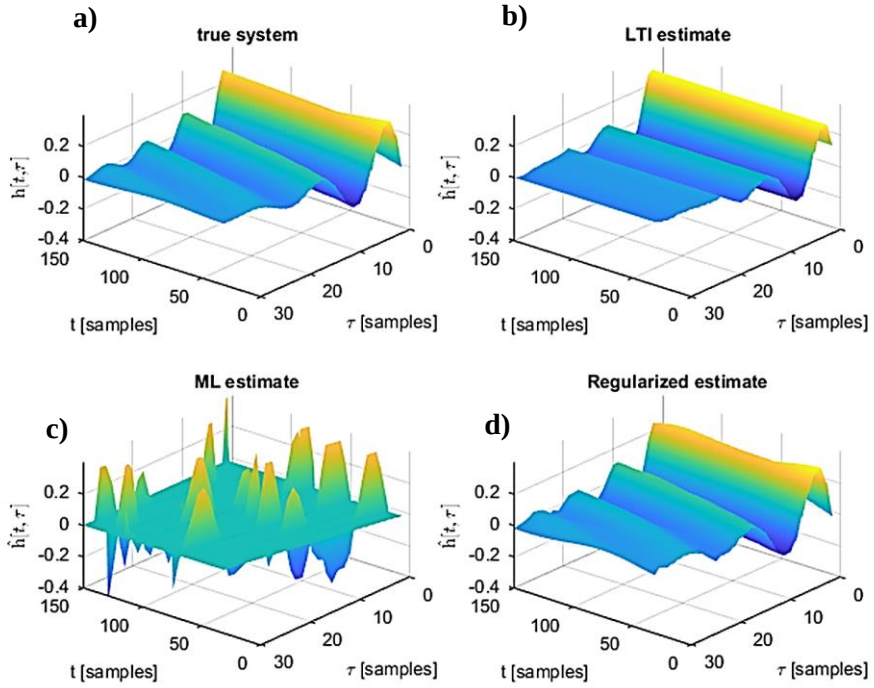


Figure 1 a) the TV IRF of the observed system b) the LTI estimate c) the ML estimate d) the regularized estimate. The system is excited by white noise. No observation noise is present.

The LTI, the LS and the proposed regularized based estimates are shown in Figure 1.b–d. When the time-varying nature of the underlying system is ignored, one can obtain the LTI estimate shown in Figure 1.b. In this case the issue is that all the changes in the dynamics are completely lost.

Figure 1.c. shows the time-varying LS (ML) solution which differs a lot from the true system and it does not correspond to our expectation: only few impulse responses are present, not all impulse responses are decaying, and the time variations are not smooth. The problem lies in the fact that there is a nonuniqeness issue. There are only N measured samples to estimate the nonparametric model containing NL samples. This underdetermined system of linear equations (i.e. $U^T U$ in (4) is not full rank) results in a situation where the nonparametric TV model that relates the input to the output is not unique.

In order to achieve a more reliable and unique solution (see Figure 1.d. for the proposed method) some prior information shall be taken into account as well. This will be explained in the following sections.

2.3 Operational Modal Analysis Framework

In case of industrial measurements of large mechanical and civil structures (e.g. airplanes, bridges, wind turbines), the excitation signal is most of the time not measurable, or it would be too difficult and complex to measure [2] [3]. In this case the OMA framework can provide the engineers with useful information to understand the dynamic behavior of the underlying structure. Because the excitation signal is not known (see *Assumption 5*) an impulse or frequency response function estimate cannot be directly obtained. Instead, the output autocorrelation function (ACF) and/or its Fourier transform are used in practice.

In this paper LTV systems are considered in OMA setup (see Figure 2). The goal of this work is to nonparametrically identify the 2D TV ACF of the underlying system. In practice, after this stage, there is typically a parametric estimation procedure where the resonance frequencies and damping ratios are estimated, for instance, with the help of PolyMAX method [16]. Due the limited scope of this paper, this stage of analysis is not elaborated.

For the sake of simplicity, the proposed methodology is explained on single output systems, but using advanced linear algebra it can be easily extended to systems with multiple outputs.

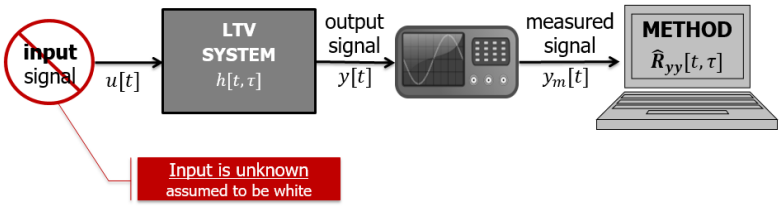


Figure 2 Schematic of the TV OMA. The excitation signal is not known but it is assumed to be (nearly) white in the frequency band of interest. The model obtained is based on the noisy output measurements of the underlying LTV system.

3 The nonparametric identification method

3.1 The model structure

In the OMA framework, the underlying time-varying systems are represented by their 2D ACF. When *Assumption 1–5* are satisfied, the expected value of 2D TV ACF would provide the convolved 2D LTV IRF in time-domain ($\sum_{\tau=0}^{L} h[t,\tau]h[t,t+\tau]$). The proof is out of scope of this paper, details for the LTI case can be found in [3].

The 2D TV ACF R_{yy} centered around the measurement (global) time t, at time lag τ is estimated with the measured output signal y_m (see (2)) by smoothing over a window with a length of $L+1$:

$$\hat{R}_{y_m y_m}[t,\tau] = \frac{1}{L+1}\sum_{k=-\frac{L}{2}}^{\frac{L}{2}} y_m[t+\tau+k]y_m[t+k] \tag{5}$$

It is important to remark that depending upon the application and the measurement, different weightings of the ACF is possible, for more technical details see [17].

Next, the double time indices $[t,\tau]$ will be omitted in order to make the text more accessible. The key idea of this work is to extend the existing nonparametric regularization methods such that some advanced prior information – elaborated in Section 4 – can be taken into account.

3.2 The cost function

The basic idea of the LTI regularization technique is that by using some reasonable prior knowledge on the system dynamics (formalized later on), and by introducing some bias error (a systematic model error), the variance of the estimate can be significantly reduced such that a lower mean square error (MSE, [18]) error is achieved, see Figure 3.

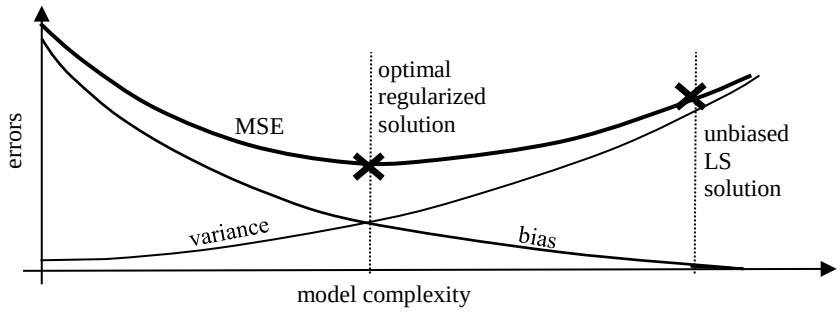


Figure 3 Illustration of the concept of the regularization technique with respect to the classical LS solution. The goal is to find the minimum MSE. The bias error represents the quantity of unmodelled data. The variance error represents the quantity of the modeled noise.

In order to include the prior knowledge in the nonparametric representation, an augmented cost function (V) must be defined. This cost function consists of two parts.

The first part is the LS cost function (V_{LS}) which is now defined for the 2D LTV ACF case as

$$V_{LS} = \left\| vect(R_{yy}) - vect(\hat{R}_{y_m y_m}) \right\|_2^2 \tag{6}$$

and the second part is the regularization cost function (V_r):

$$V_r = \sigma^2 vect(R_{yy}^T) P^{-1} vect(R_{yy}) \tag{7}$$

The new, combined cost function is given by:

$$V = V_{LS} + V_r \tag{8}$$

where P is a covariance matrix of the prior ACF, and σ^2 is the amount of regularization (prior) applied. By making a proper choice for P, smoothness and stability can be imposed on the estimated model (see Section 4). Minimizing (8) – with respect to R_{yy} – gives the 2D LTV ACF estimate:

$$vect(\hat{R}_{yy,reg}) = (I + \sigma^2 P^{-1})^{-1} vect(\hat{R}_{y_m y_m}) \tag{9}$$

where I denotes the identity matrix.

Note that σ^2 is usually (proportional to) the noise variance of the measurement. In the (persistently excited) LTI case, σ^2 tends to zero when the measurement length increases. However, in the LTV case, the σ^2 must always be greater than 0, because it is required to circumvent the non-uniqueness problem of LTV estimation (highlighted in Section 2.2). To simplify the model and computational complexity, σ^2 is kept constant but in general it can be time-varying.

4 Regularization

In the first part of this section the practical implementation of the inclusion of the prior knowledge into the covariance matrix is addressed and illustrated on the classical LTI impulse response estimation problem. In the second part the proposed method of LTV extension to ACFs is detailed. The last part of this section deals with the proposed parameter tuning technique.

4.1 Considered kernel functions

The covariance matrix P is constructed by using kernel functions. P introduces the prior knowledge into the cost function as (a prior) correlation between the elements of the IRFs/ACFs. The specific choice of the kernels, and the resulting covariance matrix has a major effect on the quality of the estimate. An illustration of different covariance matrix choices on an IRF estimation problem is given in Figure 4 . In this subsection, the most relevant kernels are shortly discussed. It is important to remark that – in principle – any kind of kernel can be used as long as the kernel function encodes the appropriate prior information. A strategy to achieve the exact numerical values of the kernel function parameters is explained in Section 4.3.

4.1.1 Radial Basis Functions

One of the simplest and widely used kernel is the radial basis function (RBF) [19]. It is a function whose values depend only on the distance between different points, and it is defined as:

$$P_{RBF}(i,j) = e^{-\frac{(i-j)^2}{\gamma}} \tag{10}$$

where $\gamma > 0$ is a parameter representing the length scale, and i, j are the two time points (sample indices). This type of RBF kernel is called Gaussian RBF kernel [19]. By using this kernel, the smoothness assumption can be imposed on the system to be estimated. The larger the length scale γ, the smoother the resulting estimated function is. This kernel is illustrated in Figure 4 a–c.

4.1.2 Diagonal Correlated kernel function

In most of the cases of stable IRF estimation, apart from smoothness, an exponential decaying can be imposed as well – as a stronger assumption on stability. Same properties can be applied to the ACF estimate as well. To satisfy these assumptions, the diagonal correlated (DC) kernel function gives a perfect solution [10] as it has the flexibility to tune independently the smoothness and the exponential decay. The diagonal correlated kernel function P_{DC} is defined as:

$$P_{DC}(i,j) = e^{-\alpha|i-j|}e^{-\frac{\beta(i+j)}{2}} \tag{11}$$

where α gives a scaling to the correlation between neighboring IRF/ACF coefficients, β scales the exponential decaying, $\alpha, \beta \geq 0$.

In other words, α controls the smoothness: the smaller its value, the smoother the estimation is, and β controls the length of the IRF/ACF. This kernel function is illustrated in the Figure 4 f.

4.1.3 Tuned-Correlated kernel function

While DC provides a very nice flexibility to tune the model behavior, unfortunately it can lead to a very high computational complexity. In many cases Tuned-Correlated (TC) kernels can provide a good balance between the flexibility and the computational load. TC kernel is widely used in different regularization toolboxes (e.g. *ident* [18]). When in the DC structure α is set to $\beta/2$ then it leads to the TC form [20]:

$$\mathrm{P_{TC}}(i,j) = \min\left(\mathrm{e}^{-\beta i}, \mathrm{e}^{-\beta j}\right) \tag{12}$$

where β is a scaling parameter, and $\beta \geq 0$.

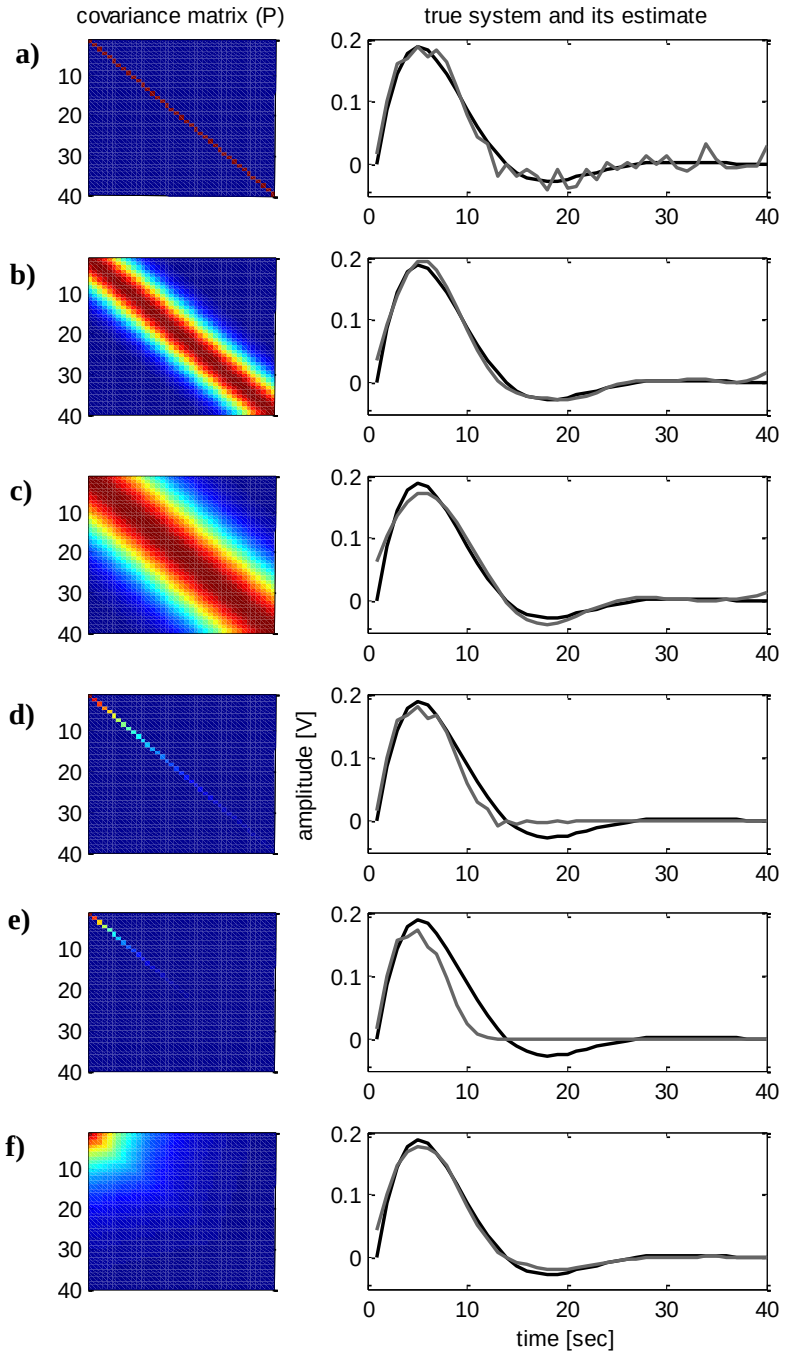


Figure 4 An example of different covariance matrices and regularized impulse response estimates. On the left different covariance matrices are shown. On the right, in black the true system and in gray its estimates are shown. The output is observed with an SNR of 20 dB. In figures (a)–(c) the smoothing is increased. In figures (d)–(e) the exponential decaying is increased. In figure (f) the optimal – w.r.t. MSE – smoothing and decaying is shown.

4.2 The LTV covariance matrix

In order to overview the properties of the TV ACF, an illustration is shown in Figure 5. This TV ACF correspond to the LTV system shown in Figure 1.a. By looking at this 2D ACF, several properties can be used to incorporate prior information to the TV covariance matrix – similarly to the concept of the classical 2D LTV IRF identification case [7] with known input.

The first prior knowledge is that the considered ACFs are smooth. This smoothing is applied once over the system time τ which refers to "classical" evolution of IRF/ACF, and once over the global time t which gives a support to handle the time-varying behavior.

In addition to smoothing properties, another assumption can be imposed and incorporated in the covariance matrix by applying a more strict definition of stability: the IRFs and therefore the ACFs are exponentially decaying. Note, that most of the stable mechanical systems exploit this behaviour. When this is not the case other kernels might be used.

In the proposed approach, every point of the 2D ACF surface is connected to each other. It means that all the elements in the covariance matrix are non-zero, therefore the number of constraints is high, and the degrees of freedom of the system of linear equations (see Section 2.2) are significantly decreased resulting in a unique solution.

The connections in the surface are defined for every possible pair of t and τ points, see Figure 5. The elements in the τ direction of the autocorrelations (horizontal blue direction) are linked by DC or TC kernels. Elements in the global time t direction (vertical red direction) are linked by RBF kernels. A graphical illustration is shown in Figure 5. The time-varying covariance matrix is then formulated as follows:

$$\mathrm{P}_{\{t_1,t_2\},\{\tau_1,\tau_2\}} = \mathrm{P}_{RBF}(t_1,t_2)\cdot \mathrm{P}_{DC}(\tau_1,\tau_2) \tag{13}$$

or

$$\mathrm{P}_{\{t_1,t_2\},\{\tau_1,\tau_2\}} = \mathrm{P}_{RBF}(t_1,t_2)\cdot \mathrm{P}_{TC}(\tau_1,\tau_2) \tag{14}$$

for every possible pair of t and τ.

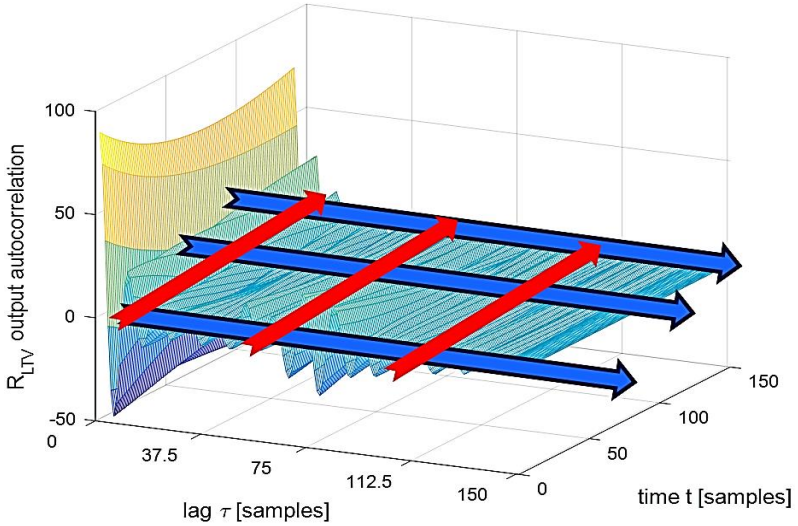


Figure 5 The TV output ACF of the system given in Figure 1.a. The arrows show the visualization of the possible regularization directions. The blue arrow refers to the τ system time where decaying and smoothness of the adjacent elements can be imposed. The red arrow refers to the direction of time variations (t axis) where the smoothness of the adjacent autocorrelation functions can be imposed.

4.3 Tuning of the model complexity

$\gamma, \alpha,\ \beta, \sigma^2$ parameters in (7),(9)–(12) are the so called hyperparameters. The nonparametric system identification method presented in this work consists essentially of two steps: 1) optimization of the hyperparameters to tune the matrix P, and 2) computation of the model parameters using (9).

All the hyperparameters are tuned with the use of measured output data only. The hyperparameters are optimized in this case by maximizing the marginal likelihood of the observed output [9]:

$$\hat{\theta}_{hp} = \arg\min_{R_{yy}} \hat{R}_{y_m y_m}{}^{T} \Sigma_Y^{-1} \hat{R}_{y_m y_m} + logdet\, \Sigma_R \tag{15}$$

where θ_{hp} is a vector containing all the hyperparameters $(\gamma, \alpha, \beta, \sigma^2)$ and $\Sigma_R = (P + \sigma^2 I)$ represents the covariance matrix of the output autocorrelation $\hat{R}_{y_m y_m}$.

Practically speaking, the optimal set of hyperparameters given the measured output data determines the covariance matrix which is most likely to have generated the observed output autocorrelation.

This objective function is non-convex in θ_{hp}, therefore to minimize the risk of resulting in a local minimum, it is advised that multi-start optimization of the hyperparameters is performed. In this work, a nonlinear gradient based Matlab solver is used (fmincon) for the optimization of the marginal likelihood of the observed output autocorrelation with reasonable constraints on smoothness and decaying of the 2D ACF. The interested reader can refer to [14], [21], [22] for more techniques for the tuning of the hyperparameters.

5 Results on a wind tunnel testing measurement

5.1 The measurement setup

This section presents an industrial example of the in-line flutter assessment of the wind tunnel testing of a scaled airplane model detailed in [5].

The measurement time is 424 sec , the sampling frequency (f_s) is 500 Hz, the number of data samples (N) is 212000. The segmented window size ($L+1$) is 500 samples (which corresponds to 1 sec, 1 Hz resolution). The Mach number (proportional to the airflow i.e. wind speed w.r.t. sound speed) is varying between 0.07 and 0.79. An illustration of the measurement setup is given in Fig 2.

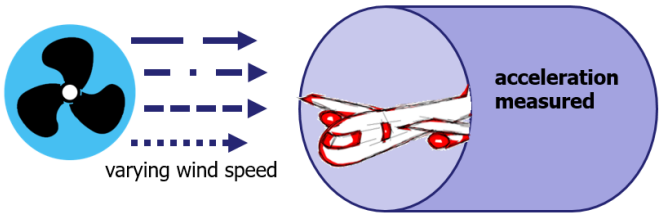


Figure 6 The measurement setup is shown. The airflow (wind speed) is varying while the airplanes acceleration is measured in the wind tunnel.

In this type of testing, it is desired to carefully verify and track the vibration behavior, since during flutter appearance, system destruction can occur. In this paper, wind tunnel data at various flow conditions are used to validate the approach for tracking the evolution of the resonance frequencies, damping ratios.

Further details on the measurement procedure can be found in [5]. Exact specifications on the airplane are omitted due to the confidentiality of the industrial project.

5.2 Results

In this section the time and frequency domain results of the traditional SFT approach [4] are compared to results of the proposed 2D regularization method.

In case of SFT the output measurement is split into short subrecords, and each time the output ACF is calculated. This results in a series of ACFs which represents the classical TV ACF estimate. The power spectrum estimate is then given by the discrete Fourier transform of the ACFs.

When the proposed method is considered, the ACF estimates are normalized and regularized as it is detailed in Section 3 and 4.

Figure 7 shows the magnified time domain results of the classical SFT and regularization based TV ACF estimation. Observe that the SFT approach has issues with the decaying of ACFs (see between 300-400 secs), and the transitions between the adjacent ACFs are non-smooth. In case of regularized approach all the ACFs are interconnected resulting in 1) smooth transitions between the normalized adjacent ACFs 2) automatic decaying of ACFs.

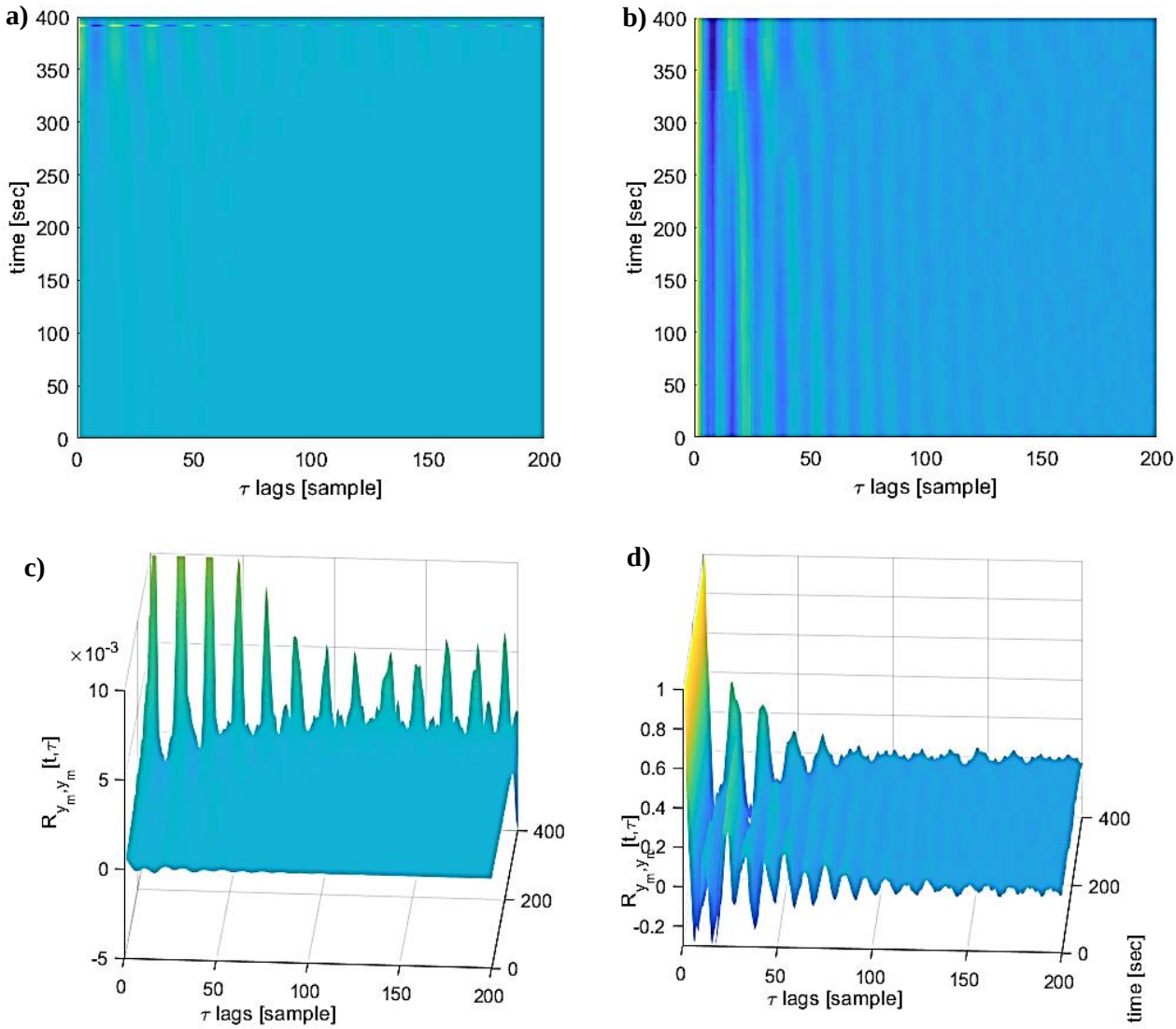


Figure 7 The time-varying output autocorrelation estimates of observed system are shown. On the left the classical SFT method is shown from the top (figure a) and from the front (figure c) views. On the right the proposed method is shown from the top (figure b) and from the front (figure d) views.

Figure 8 shows the frequency domain results of the SFT and regularized approach. The most important part is the evolution the resonances and it can be best seen on the top view of the 2D power spectrum estimates. Observe that the traditional approach is very noisy where the regularized solution is smooth and more details can be captured.

It is important to remark that the classical SFT results can also be post filtered/smoothened – even with regularization or with other approaches (e.g. B-spline techniques) – but in this case the accuracy of the result will be between the classical and proposed approach.

Numerical analysis and further (simulation examples) are out of the scope of this paper.

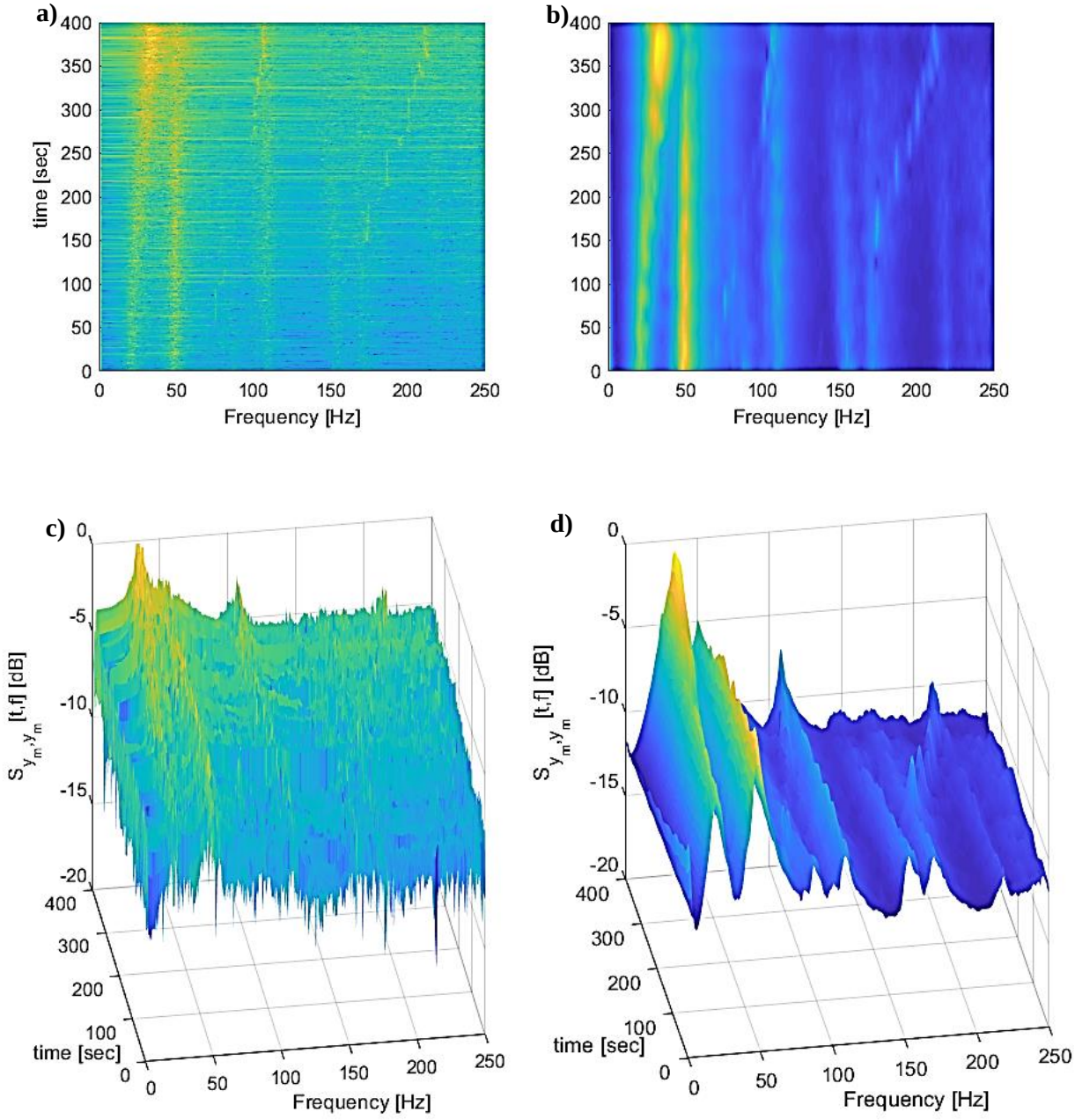


Figure 8 The time-varying output power spectrum estimates of observed system are shown. On the left the classical SFT method is shown from the top (figure a) and from the front (figure c) views. On the right the proposed method is shown from the top (figure b) and from the front (figure d) views.

5.3 Computational complexity

At this point we comment on the computational complexity. The considered matrix sizes have a negative impact on the computational load which increases with total number of the parameters i.e.: 1) with number of measured points (window segments, N), and 2) with the resolution of the window ($L+1$).

In case of the classical SFT techniques, the memory needs and computational complexity are linear in terms of parameters ($O(N(L+1))$), whereas the regularization approach is more demanding, which is the main drawback of the technique.

In the proposed method, the 2D ACF is regularized, such that each point of the 2D ACF is connected. This results in a quadratic function of complexity ($O((N(L+1))^2$)).

In this particular measurement, the time and memory needed for a classical SFT solution are in the order of minutes/megabytes, whereas the regularized solution has a much higher computational time and memory needs in the magnitude of hours/gigabytes. There is an ongoing research how to decrease the resources necessary in order to use it for online tracking of modal parameters.

The exact computational time depends on many parameters such as the model complexity, the initial values of the hyperparameters and the technique used to tune the hyperparameters.

6 Conclusions

The main idea of the proposed time-varying regularized OMA framework is to provide more accurate and smoother estimates which are suitable for simulation, design and – indirectly – control. This will improve the overall quality and safety of products, and speed up the design process. Using the proposed advanced 2D regularization techniques it is possible:

- to reduce the noise influence such that the measurement quality will be significantly better
- to gain a better insight into the details of the time-variations

Further, a nonparametric TV OMA model can be used:

- to capture and to track the time-varying resonance frequencies and damping ratios
- to simulate and validate during the design phases

When it is necessary, the nonparametric TV OMA model can be used to estimate a parametric OMA model by cleaning up the data and allowing direct access to the mode shapes and making the control possible.

The drawback of the proposed method is that the computational load and memory need are significantly higher but this is negligible in the applications where 1) the preparation of the measurement setup takes days, and 2) the safety of the product and its intended users is concerned.

Acknowledgements

This work was funded by the Fund for Scientific Research (FWO-Vlaanderen), by the ERC advanced grant SNLSID, under contract 320378, and by the VLAIO Innovation Mandate project number HBC.2016.0235.

References

[1] D. Edwins, Modal Testing: Theory, Practice and Applications (2nd edition), Research Studies Press L, 2000.

[2] B. Peeters and G. De Roeck, "Stochastic system identification for operational modal analysis: a review," *ASME Journal of Dynamic Systems, Measurement, and Control*, vol. 123, no. 4, pp. 659-667, 2001.

[3] E. Reynders, "System Identification Methods for (Operational) Modal Analysis: Review and Comparison," *Archives of Computational Methods in Engineering*, vol. 19, no. 1, pp. 51-124, 2012.

[4] Jont A. B., "Short Time Spectral Analysis, Synthesis, and Modification by Discrete Fourier Transform," *IEEE Transactions on Acoustics, Speech, and Signal Processing*, vol. 25, no. 3, pp. 235-238, 1977.

[5] B. Peeters, P. Karkle, M. Pronin and R. Van der Vorst, "Operational Modal Analysis for in-line flutter assessment during wind tunnel testing," in *15th International Forum on Aeroelasticity and Structural Dynamic*, 2011.

[6] P. Z. Csurcsia, J. Schoukens, "Nonparametric Estimation of a Time-variant System: An Experimental Study of B-splines and the Regularization Based Smoothing," in *IEEE International Instrumentation and Measurement Technology Conference*, Pisa, Italy, 2015.

[7] P. Z. Csurcsia, J. Lataire, "Nonparametric Estimation of Time-variant Systems Using 2D Regularization," *IEEE Transactions on Instrumentation & Measurement*, no. special issue, p. accepted, May 2016.

[8] P. Z. Csurcsia, J. Schoukens, J. Lataire, "Identification of Linear Time Varying Systems using 2D regularization," in *34th Benelux Meeting on Systems and Control*, Lommel, Belgium, 2015.

[9] G. Pillonetto, F. Dinuzzo, T. Chen , G. De Nicolao, L. Ljung, "Kernel methods in system identification, machine learning and function estimation: A survey," *Automatica*, vol. 50, no. 3, pp. 657-682, March 2014.

[10] G. Pillonetto, G. De Nicolao, "A new kernel-based approach for linear system identification," *Automatica*, vol. 46, no. 1, pp. 81-93, January 2010.

[11] L. A. Zadeh, J. R. Ragazzini, "Frequency analysis of variable networks," *Proceedings of the IRE*, vol. 38, no. 3, pp. 291-299, March 1950.

[12] L.A. Zadeh, "A general theory of linear signal transmission systems," *Journal of the Franklin Institute*, vol. 253, no. 4, p. 293–312, April 1952.

[13] L. A. Zadeh, "Time-Varying Networks I," *Proceedings of the IRE* , vol. 49, no. 10, pp. 1488-1503, Oct 1961.

[14] C. E. Rasmussen, C. K. I. Williams, Gaussian Processes for Machine Learning, The MIT Press, ISBN: 0-262-18253-X, 2006.

[15] R. Pintelon, J. Schoukens, System Identification: A Frequency Domain Approach, 2nd ed., New Jersey: Wiley-IEEE Press, ISBN: 978-0470640371, 2012.

[16] B. Peeters, H. Van der Auweraer, P. Guillaume, J. Leuridan, "The PolyMAX Frequency-Domain Method: A New Standard for Modal Parameter Estimation?," *Shock and Vibration*, vol. 11, no. 3-4, pp. 359-409, 2004.

[17] R. Priemer, Introductory Signal Processing, World Scientific, ISBN: 9971509199, 1991.

[18] L. Ljung, "System identification toolbox," 1988-2012.

[19] M. D. Buhmann, Radial Basis Functions: Theory and Implementations, New York: Cambridge University Press, ISBN: 9780521101332, 2009.

[20] G. Pillonetto, A. Chiuso, G. De Nicolao, "Regularized estimation of sums of exponentials in spaced generated by stable spline kernels," in *American Control Conference*, Baltimore, 2010.

[21] P. Z. Csurcsia, Nonparametric identification of linear time-varying systems (Phd thesis), University Press, Zelzate, 2015.

[22] G. Birpoutsoukis, P. Z. Csurcsia, J. Schoukens, "Efficient Multidimensional Regularization for Volterra Series Estimation," *Mechanical Systems and Signal Processing*, vol. 104, pp. 896-914, 2017.

[23] R. G. Lyons, Understanding Digital Signal Processing, 3rd ed., Prentice Hal, ISBN: 9780137027415, 2010.

[24] A. Oktay, Signals and Systems: A MATLAB® Integrated Approach, CRC Press, 2014.

Automated modal identification in operational conditions using 3D stabilization diagrams

G. Marrongelli[1], F. Magalhães[2], C. Gentile[1], Á. Cunha[2]
[1] Politecnico di Milano, Department ABC, Piazza Leonardo da Vinci 32, 20133, Milan, Italy
e-mail: **gabriele.marrongelli@polimi.it**

[2] CONSTRUCT-ViBest University of Porto, FEUP, Rua Dr. Roberto Frias, 4200-465 Porto, Portugal

Abstract
The development of efficient vibration-based Structural Health Monitoring (SHM) methodologies capable to timely detecting the onset of anomalies and possible damage in structures is still a challenging task, especially for large infrastructures, complex constructions and historic buildings. SHM strategies are often based on the automated extraction of the modal parameters from the signals collected during normal (operational) conditions and different approaches have been proposed in the literature for the automation of Operational Modal Analysis (OMA).Within this context, the paper focuses on the development of a new automated OMA procedure, which involves the construction and the automated interpretation of tri-dimensional stabilization diagrams, avoiding the initial tuning of the input parameters characterizing the SSI techniques and resulting in modal estimates with improved accuracy. The algorithm is exemplified through its application to data collected by continuous dynamic monitoring of two different bridges.

1 Introduction

Structural Health Monitoring (SHM) is generally defined as a multistage approach that interests several disciplines, mainly developed to identify the structural performance and the health state of structures, providing useful information about their structural conditions. The main goals of SHM procedures are also aimed at defining the tracking and the continuous assessment of those characteristics that tend to degrade during life-cycle in order to evaluate the vulnerability and to plan a strategy of minimal intervention and maintenance especially for Cultural Heritage structures. Among the different approaches for SHM, one of the most popular is based on Operational Modal Analysis (OMA) techniques. In fact, in the last decades, several techniques of SHM based on vibration monitoring and operational modal analysis have received an increasing attention in the field of Civil Engineering structures, because the extracted features (i.e. natural frequencies and mode shapes) are particularly suitable for damage detection strategies [1]. This could be mainly due to the recently technological advances that make easier and faster the installation of simple monitoring systems on strategic structures, such as large infrastructures, complex constructions and historic buildings. However, it is essential to create robust routines aiming at managing huge quantity of data, performing a continuous monitoring of collected records and making an automated detection of possible anomalies in the structural behavior. All these tasks still require many efforts to be reached in automatic way. Thus, the implementation of efficient tools apt to avoid the human interaction and mimic the user's choice is still a challenge task [2]. Still, some important goals have been achieved through the continuous analysis of modal parameters. In fact, the continuous extraction of modal parameters represents the base-step for the success of damage detection algorithm based on OMA procedure. One of

the available techniques is the well-known non-parametric method described in Brinker et al. [3], the Frequency Domain Decomposition (FDD) method. Nowadays, it still remains one of the more used methods for the identification problems. This probably depends on the fact that its easy interpretation of results maintains a straightforward physical meaning. Along the time, many applications were developed using this technique providing good results in terms of natural frequencies and mode shapes. Notwithstanding, few limitations concerning practical applications affect this method, as the strongly dependency of the estimates on the used frequency resolution, its inadequacy in the estimation of the modal damping ratios and the difficulty to easily detect closely space modes. These reasons have led to the development of further complex approaches based on more sophisticated algorithms that solve such limitations, such as the parametric methods based on the fitting of a numerical models based on experimental data [4,5]. In this work, the focus is on one of the most used methods that involves a discrete state-space model obtained through correlation and cross-correlation functions of the collected signals: the Covariance-driven Stochastic Subspace Identification (SSI-Cov) method. As well known, the application of a parametric method requires the definition of initial input parameters that need to be tuned in the initial phase, in order to obtain a good performance of the algorithm and provide satisfactory results [6]. The present work wants to provide a further improvement in the automation of the SHM approach based on the use of SSI-Cov method avoiding the choice of the time-lag parameter used to construct the correlation matrix. Following this way, the developed methodology consists of a further step to make fully automated the identification process, eliminating the expert user's interaction in the initial phase and introducing the concept of tri-dimensional stabilization diagrams.

The organization of this paper is as follows: in Section 2, the SSI method and the concept of tri-dimensional stabilization diagrams, as well as the main issues associated to the interpretation of stable planes are described. In Section 3, the proposed procedure of automated modal identification is presented in detail highlighting the cleaning action performed by each check of the developed methodology. In Section 4, after a brief description of the Infante D. Henrique Bridge, the modal parameters are firstly extracted from a single data-set and subsequently analyzing one month long period of continuously collected data. In Section 5, the methodology is used to extract the modal parameter of an important Cultural Heritage structure located in the neighbors of Milan: the San Michele Bridge and to track the evolution in time of the most relevant modes. Finally, some conclusions and observations are discussed in the last Section.

2 Covariance-driven subspace identification method and construction of tri-dimensional stabilization diagrams

The SSI-Cov method is a robust identification technique generally chosen because of its stability and convergence. As shown in Fig. 1 the set of modal parameters are extracted from collected data following several steps. Exemplifying, starting from equations of a discrete-time deterministic-stochastic state space model for a general case (see Fig 1), a simpler set of equations is used for output-only technique, assuming the excitation is modelled as a white noise. The method is aimed at identifying the state matrix A, which contains all the dynamic properties of the system, and the output matrix C. These matrices are obtained through a series of operations that begin with the construction of the correlation matrix of the measured responses. Then, the resulting data is consecutively organized in a Toeplitz matrix [5], which it is decomposed by the Singular Value Decomposition (SVD) procedure and the so-called observability matrix is extracted from its factorization. Adopting some properties concerning the stochastic linear system and through the resolution of a least-square equation (using the Moore-Penrose pseudo-inverse procedure) is possible to define the matrices A and C. Finally, after the identification of the state-space model, the modal parameters can be easily extracted from matrices A and C. But, it is worth mentioning that the identification of the state-space model requires *a-priori* definition of the time-lag value and the order of the model used to characterize the dynamics of the structure under analysis. For simple academic structures or numerical models both values can be easily selected to fit the experimental data and obtain a realistic characterization of the dynamic properties. In fact, the model order can be fixed equal to the double of the degrees of freedom of the structure, and the minimum time-lag value can be defined

respecting an appropriate combination between order of the model and the number of reference channels, as well described in [7]. On other hand, in case of real structure it is not possible to fix *a-priori* these parameters; thus an initial "tuning" becomes mandatory to find the best pair of them that characterize the dynamic behavior of the investigated system. The definition of both parameters to detect the state-space model is not straightforward and it is difficult, or even impossible, to define the combination that provides the best solution to the identification problem.

In fact, in common practice, it is common to explore a wide interval of both input parameters and the most appropriate way to overcome this problem is to fix the time-lag value and overestimate the model order. Normally, the estimation is carried out for increasing model order fixing the maximum order much higher than the double number of the expected modes. But, the use of very high model orders leads to the introduction of spurious poles (also called numerical modes) that do not have a physical meaning and that are directly associated to the noise content in the collected signals. For these reason, the spurious modes should be detected and removed before delivering a consistent set of modal parameters. Otherwise, the use of an incorrect time-lag value can affect the estimation of the modal parameters, leading to an incorrect characterization of the structural behavior. In common practice, this important parameter is initially adjusted in order to obtain consistent estimates of the expected modes. More specifically, the time-lag parameter is used to define the length of the covariance and cross-covariance functions of the collected signals to construct the covariance matrix, then it is subsequently used to define the dimensions of the Toeplitz matrix involved to estimate the matrices A and C. So, an initial "tuning" of both input parameters is mandatory. But, there is no certainty that the "tuned" pair is the best set for all data-sets collected during the continuous monitoring process. For this reason, in order to provide a solution to this uncertainty, in the proposed methodology the construction of tri dimensional stabilization diagrams is involved. This work wants to provide a further contribution in the context of OMA applications, avoiding the characterization of the time-lag and model order and overcoming the uncertainty related to the ad hoc selection of these parameters.

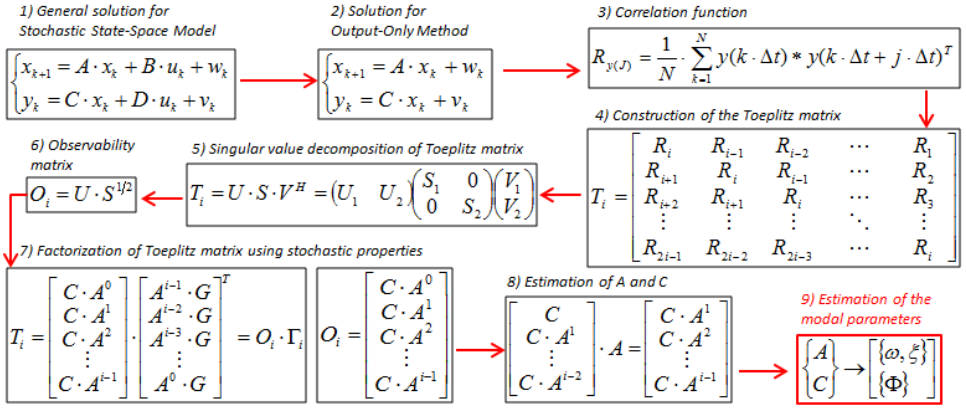


Figure 1: Flowchart of the SSI-Cov method

3 Proposed methodology for automated modal parameters estimation

As previously stated, the main objective of this paper is to present an efficient methodology to perform the automatic identification of the modal parameters, avoiding the initial tuning of the input parameters of the parametric method. To reach this task, increasing model order and increasing time-lag values were chosen in a conservative way and the automated procedure, composed by four different steps aimed at mimicking the choice of an expert user during the identification process, was applied. Each step is described in the following:

1. Application of SSI-Cov method (or other parametric method with similar outputs) to collected structural responses and construction of the tri-dimensional stabilization diagram.

2. Removal of spurious poles applying three threshold criteria based on modal damping ratio value and on the complexity degree of the mode shapes associated to each estimates.
3. Interpretation of the clearer 3D stabilization diagram through an innovative clustering procedure generalized to the complex modes.
4. Removal of possible replications of the structural modes and outliers values in order to deliver an accurate set of modal estimate.

Once the SSI method is performed for increasing time-lags and increasing model orders, the consecutive step consists of a series of checks aimed at detecting and removing spurious poles from the 3D stabilization diagram. First discrimination between spurious and physical poles was performed using a pre-selected damping ratio threshold. In fact, in normal operating conditions, current civil engineering structures are slightly damped. For this reason highly damped modes (i.e. modes with damping ratio larger than 10%) are conceivably associated to the noise content and removed. Furthermore, estimates exhibiting negative damping are also removed. Further, single-mode validation criteria were adopted to detect noise modes, using the Modal Phase Collinearity (MPC) index and the Mean Phase Deviation (MPD) index. Both indices are based on the quantification of the complexity degree of the mode shapes. As known, when the structural system is proportionally damped, the mode shapes are real and the components lie on a straight line in the complex plane, this means that the covariance between the imaginary and real part of each component can be used as a measure of the complexity degree, through the MPC index; in addition, the distance between the best straight line associated to the mean component of mode shape and every single (weighted) component can also be used as single-criterion check, with the MPD index, as shown in [2]. Once most of spurious poles are removed from the diagram, the third step of the proposed methodology is the clustering procedure. This procedure is inspired by the contribution firstly proposed by Magalhaes et al. [8] and modified in the recent publishing by Cabboi at al. [9]. Furthermore, in order to generalize the procedure extending the approach to all possible cases such as modes with relevant complex components, the limitation related to the MAC index was removed using the MACX index [10]. Using this metric, the clustering process has been developed with the objective of grouping all poles that share same characteristics in terms of natural frequencies and mode shapes.

$$d_{i,ref} = \frac{\left| f_{i,ref} - f_{i,j} \right|}{f_{i,ref}} + 1 - MACX\left(\phi_{i,ref}; \phi_{i,j}\right) \tag{1}$$

where $d_{i,ref}$ represents the inter-cluster distance, obtained by the distance between each candidate pole and the reference pole of the cluster, $f_{i,ref}$ and $\phi_{i,ref}$ represent the mean frequency and mean mode shape of the reference pole updated for increasing model order, whereas $f_{i,j}$ and $\phi_{i,j}$ are the same modal parameters corresponding to *j-th* "current pole". The procedure is repeated in order to scan all available poles and it is stopped only when all poles are grouped into the clusters. As demonstrated in several works present in literature [2,8,11] the noise modes do not have consistency in terms of modal parameters and they are spread inside many small clusters, then all those clusters with dimensions less of one third of the tallest cluster are considered as numerical modes and then deleted. In current application, this condition could be really restricted, therefore in a conservative perspective this value has been halved, reducing this limit to *n/6*, where *n* is the number of elements belongs to the biggest cluster. The last step of the proposed methodology is composed by three subsections, where each one is aimed at improving the accuracy of the final modes estimations. The first check consists of a further clustering procedure based on agglomerative approach. The procedure consists of an application of a k-mean cluster algorithm in which the centroids of the clusters are known and they have been already defined by the mean frequencies and mean mode shapes provided by the previous cluster procedure. This operation is performed in order to recovering any possible estimates lost during the initial association phase and removing others that fall inside the defined threshold due to continuous updating of the reference cluster pole. The second check is aimed at removing any possible replication of the physical modes in the stabilization diagram. In fact, as also mentioned in [9], for high value of time-lag a stable alignment that represents a structural mode could splits into two close alignments providing an incorrect association during the clustering procedure. This check tends to avoid this possibility recognizing possible replication and deleting that one with higher complexity component. The last accuracy check is aimed at reducing the scatter that could affect the estimates. The removal of the outliers is performed by applying simple rules based on the so called "box-plot" tool, as

described in [12]. In case of 3D diagram this check was carried out on both distributions of natural frequencies and damping ratios, separately. Finally, the delivered outputs obtained by the application of developed methodology are: mean natural frequency, mean mode shape and median modal damping ratio belonging to each detected cluster. The efficiency of the proposed algorithm was initially tested using a single dataset collected on Infant D. Henrique Bridge. For the initial test, the time-lag value was fixed at 50 and model order interval was chosen in conservative way between 20 and 100, as already done in previously published papers [1,8].

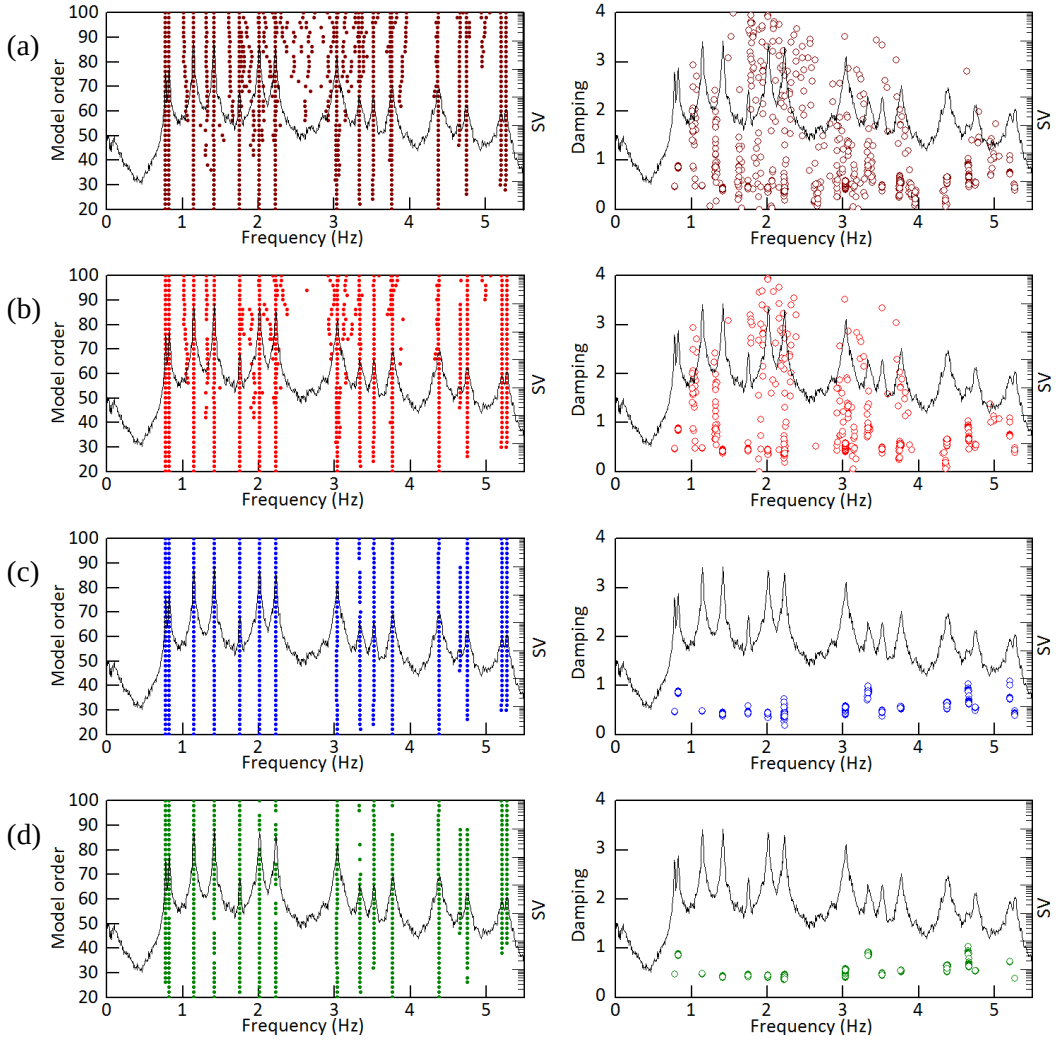


Figure 2: Stabilization diagram: (a) obtained SSI-Cov outputs; (b) after check on damping and modal complexity; (c) after clustering process; (d) after post processing check.

Fig. 2 shows the 2D stabilization diagrams and the corresponding frequency vs damping diagrams obtained after the cleaning action exerted by the main checks of the methodology previously described. In details: i) Fig. 2(a) shows all output poles obtained by the SSI-Cov method, ii) Fig. 2(b) shows the remain poles after the checks on modal damping ratio and on mode shape complexity, iii) Fig. 2(c) highlights the performance of the clustering process and iv) finally Fig. 2(d) contains the stable alignments and damping values after the removal of the outliers. It is worth mentioning that there is a very good correspondence between all 16 stable alignments that stand on in the stabilization diagram and well-defined spectral peaks obtained using the non-parametric FFD method. Furthermore, the extension of the investigated frequency interval to 5.5 Hz, with regard to previously published results, shows 4 further modes of the bridge that deserve a deeper investigation. To compete the first test of the developed procedure using a fix time-lag value, the automatically identified modal parameters of the bridge (in term of natural frequencies, modal

damping ratio and standard deviations of the estimates) together with the complexity indices associated to the obtained mode shapes estimates, are summarized in Table 1. Moreover, the mode shapes associated to the identified modes are shown in Fig. 3.

n°	*Mode*	*f [Hz]*	*σ(f)* [Hz]*	*ξ [%]*	*σ(ξ)* [%]*	*MPC*	*MPD*
1	L1	**0.777**	0.0001	**0.47**	0.0007	0.994	2.75
2	V1	**0.823**	0.0004	**0.87**	0.0079	1.000	0.72
3	V2	**1.145**	0.0001	**0.48**	0.0056	1.000	0.56
4	V3	**1.414**	0.0003	**0.42**	0.0134	1.000	0.42
5	L2	**1.751**	0.0001	**0.44**	0.0103	0.989	3.64
6	V4	**2.013**	0.0003	**0.42**	0.0164	1.000	0.37
7	T1	**2.228**	0.0015	**0.42**	0.0229	1.000	0.45
8	V5	**3.035**	0.0024	**0.51**	0.0571	1.000	0.51
9	T2	**3.340**	0.0016	**0.86**	0.0145	0.997	1.60
10	V6	**3.519**	0.0002	**0.44**	0.0115	0.996	2.36
11	T3	**3.766**	0.0005	**0.53**	0.0088	0.990	2.36
12	V7	**4.379**	0.0029	**0.65**	0.0626	0.999	1.57
13	V8	**4.659**	0.0061	**0.70**	0.1737	0.857	15.99
14	T4	**4.752**	0.0004	**0.53**	0.0042	0.992	2.15
15	T5	**5.207**	0.0002	**0.72**	0.0034	0.975	4.01
16	V9	**5.273**	0.0002	**0.39**	0.0025	0.999	0.94

Table 1: Modal parameters, standard deviations and complexity indices of modes shapes obtained. *calculated from the estimates included in the same cluster

It should be noticed that: a) an excellent correspondence between the obtained results and those already published in literature, in terms of natural frequency mode shapes and also modal damping ratio is shown, b) the standard deviation of the natural frequency estimates and also of the damping ratios are lower than those obtained with other OMA techniques, c) extending the investigated frequency range to 5.5 Hz, the proposed automatic algorithm detects four further modes not identified in the previous works.

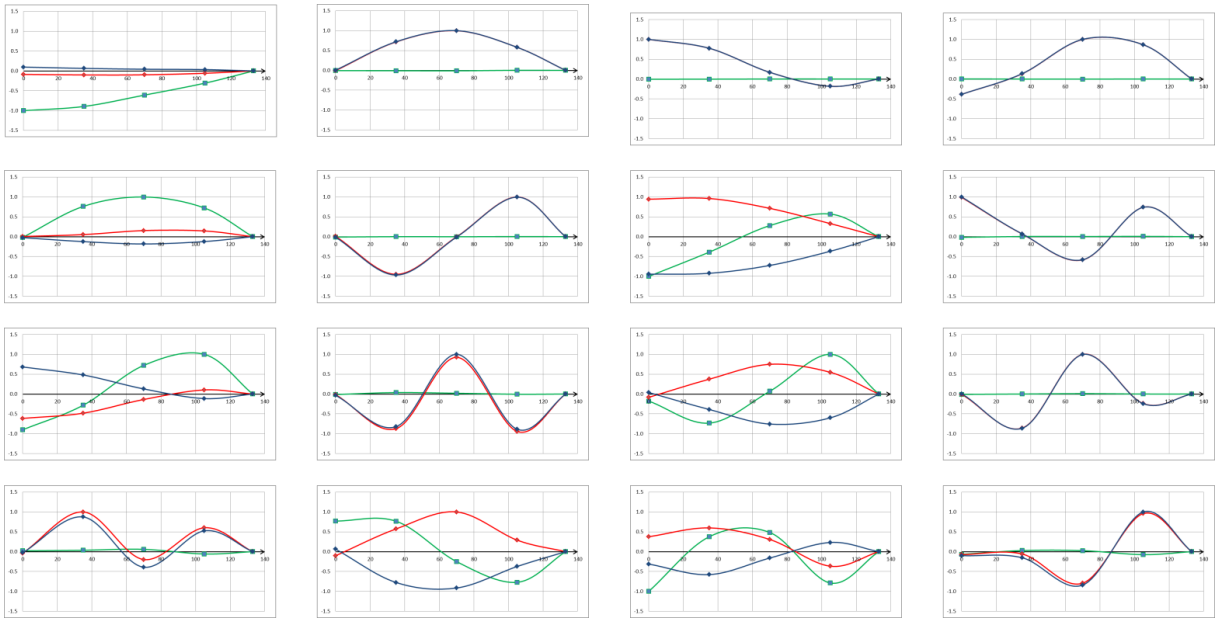


Figure 3: Vibration modes automatically identified by the proposed methodology (green line, blue line, red line are referred to lateral, vertical upstream and vertical downstream components, respectively). See Fig. 4 for location of the sensors.

4 First case of study: Infante D. Henrique bridge

The first real structure herein considered to demonstrate the robust performance of the developed methodology is the Infante D. Henrique Bridge. It crosses the Duoro River and connects the city of Porto to Gaia.

4.1 Description of the bridge

The Infante D. Henrique Bridge is composed of two mutually interacting fundamental elements: a very rigid pre-stressed concrete box beam supported by a reinforced concrete arch with a span of 280m that rises 25m from abutments and crown. After its construction, a dynamic monitoring system was installed in the bridge. This is essentially composed by 12 force balance accelerometers and 2 digitizers. Due to its symmetry, the mode shapes are approximately symmetric, therefore it was decided to instrument just one-half of the bridge. So, the accelerometers were distributed along four sections between mid-span and the abutment at Porto bank with three sensors for each section: one to measure the lateral acceleration and other for vertical acceleration at downstream and upstream sides.

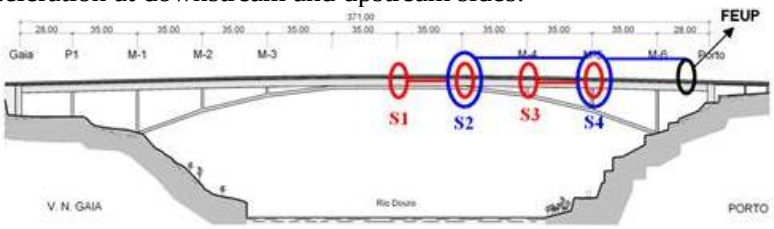


Figure 4: Scheme of the monitoring system

4.2 Application of automated procedure to single collected data-set

The developed procedure was used to perform the automatic identification of the modal parameters adopting a wide range of time-lag parameter to fit the operational responses of the bridge. In the current application the minimum value of time-lag was set equal to 10, with an increasing step of 10 units until reach the maximum value of 100. Meanwhile the model order interval was set in conservative way between 20 and 100.

As mentioned before, the methodology is based on the construction and on the automatic interpretation of a tri-dimensional stabilization diagram composed by all outputs obtained by each run of the parametric method. This means that SSI-Cov method was performed for increasing the model order and increasing the time-lag, providing a huge quantity of estimates composed by physical and spurious poles that need to be separated (see Fig. 5(a)). Thus, when the first step of the developed procedure is achieved, the removal of spurious poles was performed adopting three selected criterion based on application of thresholds. Such values were not very restrictive because the bridge may have complex modes but they were fixed ensuring the elimination of noise modes with very high complexity and damping: 5% for damping, and 0.75 and 20° for MPC and MPD respectively. As already stated in several works, the clustering procedure could also be performed by avoiding the removal of spurious poles, because consistency of noise modes dramatically change for different model orders and does not affect the correct classification. This second option is strongly discouraged in the herein application, because the non-elimination of spurious modes leads to a very high waste of time during the clustering process that makes the procedure inefficient due to its high time-consuming. The results obtained after removing of noise modes are shown in Fig. 5(b). The clustering procedure herein proposed consists on the application of the formula (1) to all remaining poles belong to the diagram. Its application is based on the similarity between all stable poles with the reference one that is constantly updated when one estimates is linked into the cluster. The success of the clustering procedure is dependent of a distance threshold value that allows the correct grouping of poles that share the same characteristics; such distance was set equal to 0.03. Following this way, the distance between the

reference pole (defined in terms of mean frequency and mean mode shape of all poles previously grouped into the cluster) and candidate pole must be shorter than such prefixed distance. If the distance is shorter, the current pole presents similar natural frequency and mode shape of the reference pole and probably belongs to the group that represents the same physical mode and should be included into the cluster. The metric described in the formula (1) is used to scan all available poles until all estimates have been grouped. Moreover, in this procedure the single-linkage is used, this ensures that only one estimate can be introduced into the cluster for every model order and every time-lag value. In other words, two different estimates obtained with the same model order cannot be included in the same cluster. An application of the developed algorithm with the construction of the tri-dimensional diagram is shown in Fig. 5. All SSI outputs and the obtained estimates after the pre-filtering check are shown in Figs 5a and 5b. The clusters associated to the structural modes are shown in Fig. 5(c). To conclude this first validation, the final "stable planes" after the removal of possible replication and outliers, are shown in Fig. 5(d).

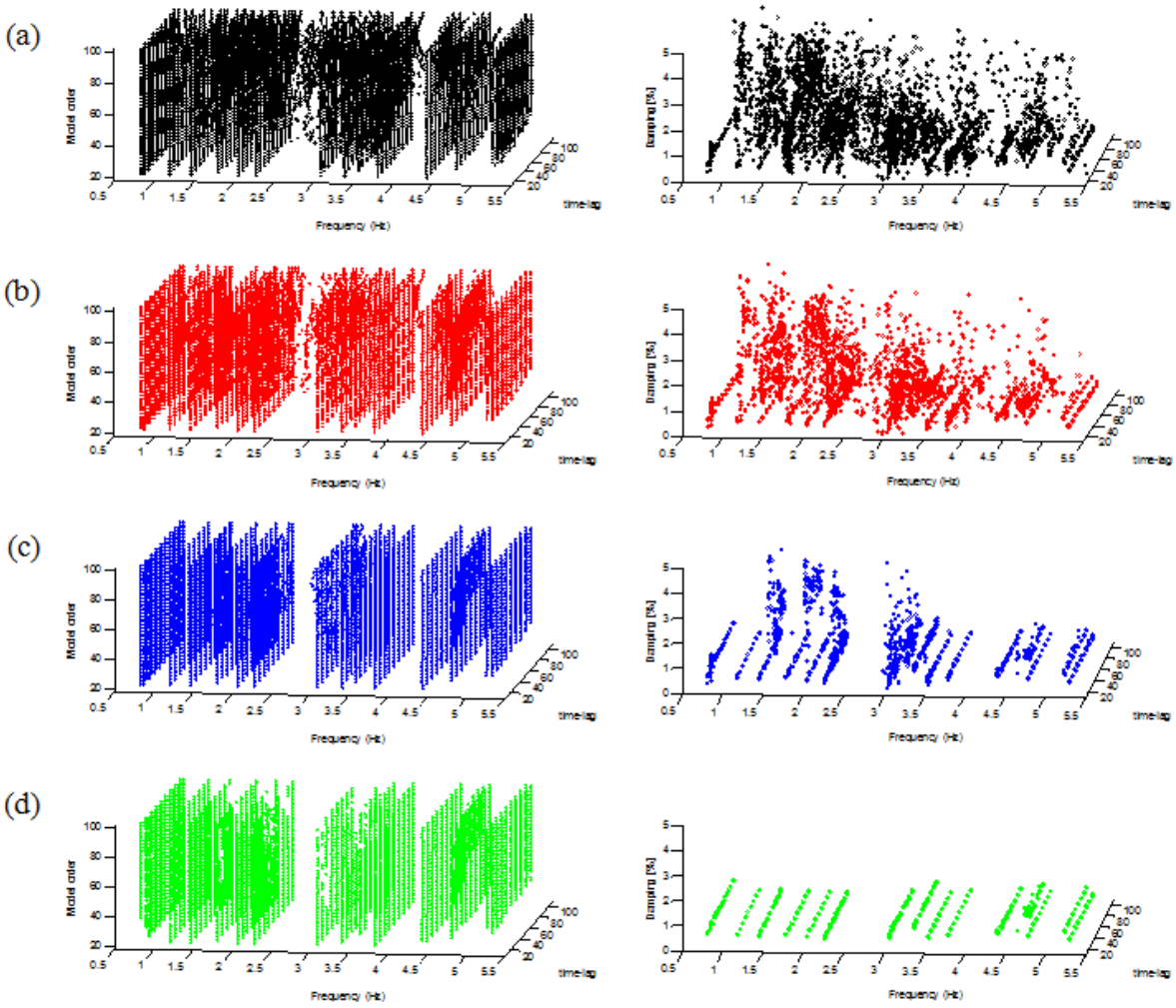


Figure 5: Tri-dimensional stabilization diagram: (a) SSI-Cov outputs; (b) after pre-filtering check; (c) after application of cluster procedure; (d) after removal of possible modes replications and outliers.

4.3 Application of the proposed methodology to continuous dynamic monitoring

The proposed methodology for automated modal parameter estimation was associated with a simple modal tracking procedure and both used to automatically process data continuously collected by the monitoring system installed on Infante D. Henrique Bridge. As shown in the previous paragraph, the

investigated frequency interval was extended to 5.5 Hz and four further structural modes were identified in addition to the 12 modes reported in previous publications. Thus, the new set of all 16 identified modes was used as reference parameters in the tracking process. In the context of continuous dynamic monitoring, the most representative features are normally plotted over the time in order to study their evolution and detect any possible anomalies. To reach this task, every set of obtained estimates is linked to the reference baseline list through a comparison among modal estimates. There are several approaches to perform a correct tracking process [2,8,9], the most successful procedures are usually based on the use of a fix baseline (associated to pre-defined structural modes) or based on adaptive baseline (continuously updated after the analysis of each data-set). In this work, a fixed reference list associated to the modes extracted from the data-set collected on the 1st of November 2017 was used. Then, continuous monitoring process was achieved comparing each new set with the 16 selected modes, and their evolution are shown in Fig.6. Moreover, the zoom of the two lower identified modes highlights the robust performance of the developed methodology, capable to correctly identified closely spaced modes also subjected to the effects of the environmental and operational conditions (i.e. temperature and traffic).

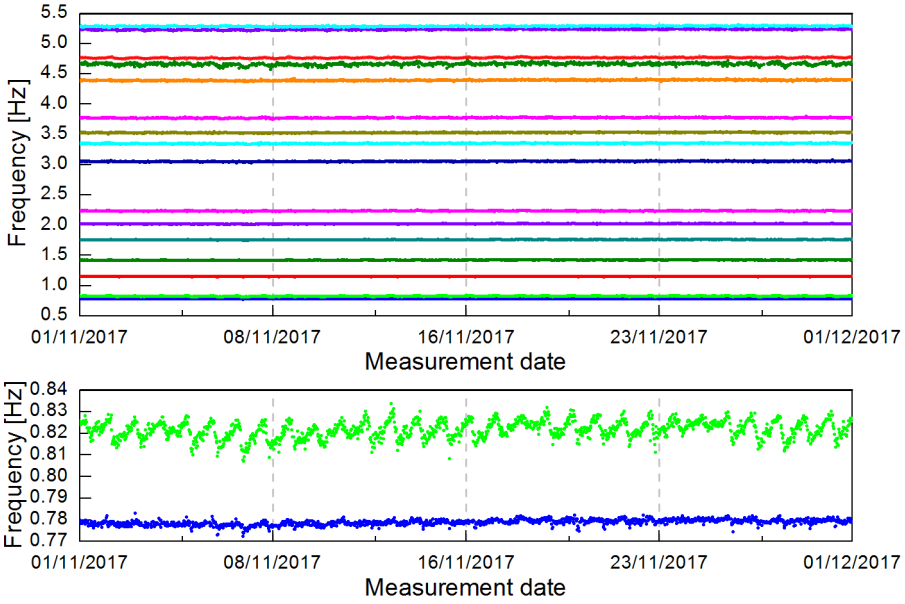


Figure 6: Evolution of the natural frequencies of the modes automatically identified during the period from 01/11/2017 to 30/11/2017. Overview of all natural frequencies and zoom of the frequencies fluctuation of the first two modes

Mode	Success	f_{mean}[Hz]	σ (f) [Hz]	ξ_{median} [%]	σ (ξ) [%]	MAC_{mean}	MAC_{min}	MPC_{mean}	MPD_{mean}
L1	100.00	0.78	0.001	0.43	0.104	1.00	0.94	1.00	1.51
V1	100.00	0.82	0.004	1.16	0.389	1.00	0.98	1.00	1.31
V2	100.00	1.15	0.002	0.45	0.086	1.00	1.00	1.00	0.30
V3	100.00	1.42	0.002	0.45	0.106	1.00	0.99	1.00	0.41
L2	100.00	1.75	0.003	0.47	0.096	0.99	0.92	0.99	3.09
V4	100.00	2.02	0.003	0.49	0.146	1.00	0.98	1.00	0.90
T1	100.00	2.23	0.004	0.47	0.141	1.00	0.98	1.00	0.50
V5	100.00	3.05	0.006	0.48	0.132	1.00	0.98	1.00	0.63
T2	99.86	3.34	0.006	0.50	0.110	0.99	0.94	0.99	2.22
V6	99.79	3.52	0.005	0.41	0.100	0.99	0.92	0.99	3.12
T3	96.46	3.77	0.006	0.47	0.107	0.98	0.84	0.96	3.20
V7	99.93	4.39	0.008	0.57	0.145	1.00	0.98	1.00	2.10
V8	83.61	4.66	0.020	1.18	0.311	0.91	0.73	0.93	8.31
T4	99.44	4.76	0.009	0.63	0.115	0.99	0.90	0.99	2.50
T5	96.32	5.23	0.008	0.55	0.094	0.98	0.85	0.97	3.09
V9	97.22	5.28	0.006	0.46	0.070	0.98	0.87	0.97	5.18

Table 2: Results of the continuous monitoring

Table 2 summarizes the most relevant results obtained by the application of the algorithm to data collected in one-month period long. Detailing, in the first column the type of the investigated modes is described. In the second column the success rate associated to each mode is quantified; as shown 10 modes were identified in all analyzed data-sets (success rate of 100%), just one mode with relative low success rate (equal 83%) is identified, while for the others 5 modes the success rate is higher than 96%. Columns 3-6 presents the mean values and the standard deviations of the natural frequencies and the median values and standard deviation of the modal damping ratios associated to each identified mode, respectively. In the columns 7-8, the mean and the minimum value of the MAC index obtained during the monitoring are reported, meanwhile in the columns 9-10 the mean values of the two complex indices, MPC and MPD, are also reported. The last two columns provide relevant information about the structural modes behavior; in fact all identified modes are strictly real, except for the 8th vertical bending mode, which complex component is not negligible, such information is confirmed by both complex indices.

5 Second case of study: San Michele bridge

In order to demonstrate the robustness of the proposed methodology, the current approach was exemplified also using data continuously collected on an important Italian Cultural Heritage structure: the San Michele Bridge [13,14].

5.1 Description of the bridge

San Michele Bridge is one of the most important Italian Cultural Heritage monuments of the 19th century. It was built in 1889 and it consists of an iron arch that supports a box girder to links the small town of Paderno to Carlusco d'Adda in the north of Italy (about 50 km far from the city of Milan). It is characterized by the main parabolic iron arch with span of 150m long that rises 37.5m. The upper girder is 266m long and it is supported by nine equally spaced bearing, Due to the difficulty of performing a regular maintenance, the state of preservation of the bridge is quite poor and several structural components are significantly damaged by corrosion. Moreover, the increase in traffic in the last decades is gradually worsening the maintenance of its security status; for these reasons, it was decided to carry out several ambient vibration tests in order to understand the dynamic behavior of the bridge and to plan some damage mitigation strategies to preserve the historic bridge [14]. Furthermore, test results highlighted some issues in the behavior of the bridge that need to be deeper analyzed. For these reasons, a permanent dynamic monitoring system was installed for SHM purposes.

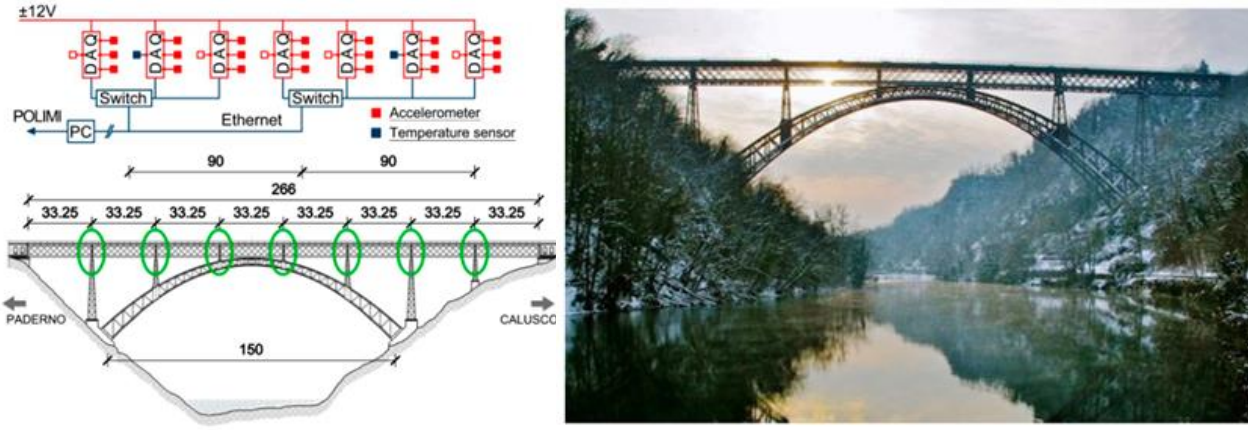


Figure 7: Layout of the monitoring system and view of the San Michele iron arch bridge (1889).

5.2 Application of the automated procedure to single collected data-set

Also for this case of study, the proposed methodology was initially applied to several single data-set in order to extract the best set of modal estimates used as reference baseline for continuous dynamic monitoring process. The acceleration time series collected during the monitoring process were processed separately. In this work, only the main results related to lateral modes are reported. It is wort mentioning that collected data were initially pre-processed to remove parts of the responses that do not comply with the basic assumptions of OMA applications (e.g. [13]) and then filtered, decimated and re-sampling at 20 Hz.

n°	*f [Hz]*	*σ(f) [Hz]*	*ξ [%]*	*σ(ξ) [%]*	*MPC*	*MPD*
1	0.991	0.0001	0.33	0.0137	0.999	0.83
2	1.345	0.0001	0.56	0.0269	0.997	1.59
3	1.646	0.0002	0.60	0.0132	0.992	2.03
4	2.014	0.0004	0.55	0.0076	0.983	3.60
5	2.160	0.0004	0.78	0.0101	0.980	3.75
6	2.508	0.0002	0.75	0.0021	0.895	8.70
7	2.802	0.0002	0.89	0.0208	0.972	4.92
8	3.122	0.0006	0.53	0.0051	0.895	11.26
9	3.530	0.0013	1.12	0.0231	0.974	5.17
10	3.800	0.0006	0.63	0.0122	0.919	8.21
11	4.020	0.0117	0.42	0.3688	0.846	10.77
12	4.078	0.0029	0.25	0.0321	0.898	10.96
13	4.126	0.0014	0.35	0.0069	0.981	4.55
14	4.383	0.0004	0.41	0.0056	0.909	6.74
15	4.789	0.0007	0.40	0.0130	0.933	8.53

Table 3: Modal parameters, standard deviations and complexity indices of modes shapes obtained

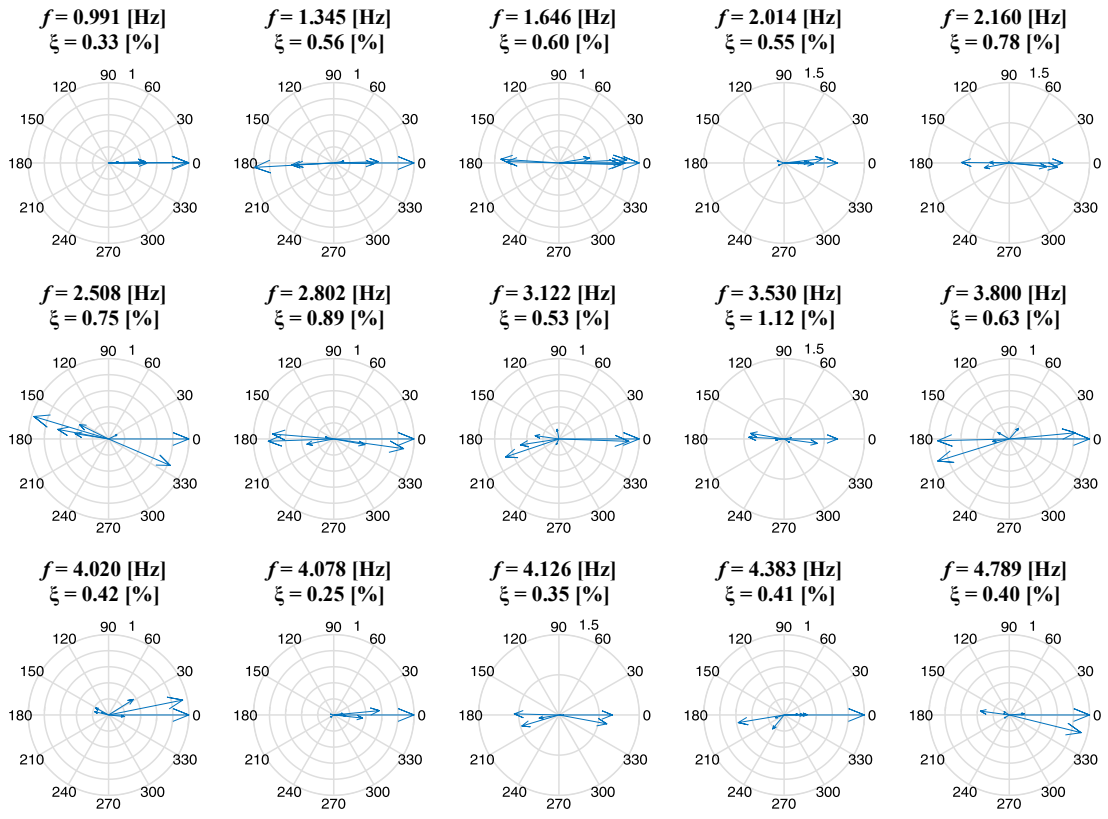


Figure 8: Reference parameters of the first 8 modes: natural frequency, modal damping ratio and mode shapes represented in a polar plot

As described in previous publications [10,13] 15 lateral modes of the bridge were expected. Hence, the proposed methodology was used to extract the evolution of these features during a winter period, setting the initial parametric inputs as follows: time-lag interval from 20 to 100 (increasing value equal to 10) and model's order interval as 30-150 (step equal to 2). Table 3 shows the results automatically obtained by structural responses collected during the 19th of February 2012 at 9 a.m., where 15 different modes were detected. Fig. 8 provides a graphical representation of the modes of the bridge. Moreover, the polar plot representation highlights the strong complexity associated to the investigated modes. As described in [15], the complexity of the modes shapes could depends on various factors (i.e. linkage, synchronization problem, high noise ratio) and non-linear behaviour of the structure (generally related to non-proportional damping or hysteretic factors). Therefore, the choice of the thresholds used to remove most of spurious poles is still related to the expected characteristics of investigated structure and it is required some trial tests to define them. For this case of study, the single criterion thresholds used to remove spurious poles from the tri-dimensional stabilization diagram were set equal to 0.5 and 25° for MPC and MPD respectively. So all estimates obtained by SSI-Cov method with MPC value lower than 0.5 and MPD upper than 25° were considered as noise modes and removed.

5.3 Application to the proposed methodology to continuous collected data

Once the baseline list was set, the developed algorithm was applied to one-month of data collected on San Michele Bridge in order to track the natural frequencies evolution and to find any possible anomalies in the normal behaviour of the bridge. Despite modal tracking is a well-known problem for permanent monitoring purposes, its application is not always straightforward. The tracking process herein proposed exploits the similarity measurements already presented in [7,13], involving the frequency variation and the MAC index (necessary to separate the close spaced modes). Instead the short period of monitoring, the linking process was performed using static rejection thresholds applied to frequency variation and MAC index separately, such threshold were fixed to 0,20 Hz and 30%, respectively. The results of the automated identification of the natural frequencies of the bridge, based on SSI-Cov method, are shown in Fig. 9. Moreover, main statistical information of the obtained results is shown in Table 4. Also in this case, the robust performance of the proposed methodology is confirmed by the high success rate of all structural modes. Columns 3-4 present the mean values of natural frequencies and standard deviations associated to the natural frequencies, the mean values of the standard deviations highlight the low scatter of the obtained estimates during the tracking process, as well as same trend is seen for the damping ratios (columns 5 and 6). Finally, in columns 7-8 are shown the mean values, MPC and MPD associated to all modes during the one-month monitoring period. It is worth mentioning the relative high values associated to the complexity indices, demonstrating the high complex component related to almost all structural modes.

n°	*Success*	*f [Hz]*	*σ(f) [Hz]*	*ξ [%]*	*σ(ξ) [%]*	*MPD*	*MPD*
1	100.00	0.995	0.0095	0.257	0.0875	0.999	1.05
2	100.00	1.356	0.0251	0.497	0.1885	0.990	2.24
3	100.00	1.662	0.0327	0.538	0.2088	0.973	3.73
4	100.00	2.032	0.0409	0.509	0.2009	0.926	4.56
5	99.80	2.201	0.0650	0.634	0.1958	0.905	6.82
6	97.43	2.545	0.0737	0.731	0.2019	0.894	8.49
7	99.93	2.865	0.0883	0.644	0.2143	0.869	7.90
8	99.86	3.161	0.1003	0.526	0.2060	0.855	11.80
9	100.00	3.623	0.1092	0.695	0.2861	0.929	5.51
10	100.00	3.841	0.0898	0.553	0.1692	0.916	8.31
11	100.00	4.105	0.0654	0.375	0.2215	0.838	9.72
12	99.93	4.154	0.0331	0.277	0.1473	0.780	12.93
13	96.75	4.405	0.0501	0.350	0.0857	0.909	12.48
14	99.59	4.580	0.0566	0.486	0.1280	0.933	15.57
15	92.79	4.812	0.0264	0.350	0.1378	0.999	6.77

Table 4: Results of the continuous monitoring of San Michele Bridge

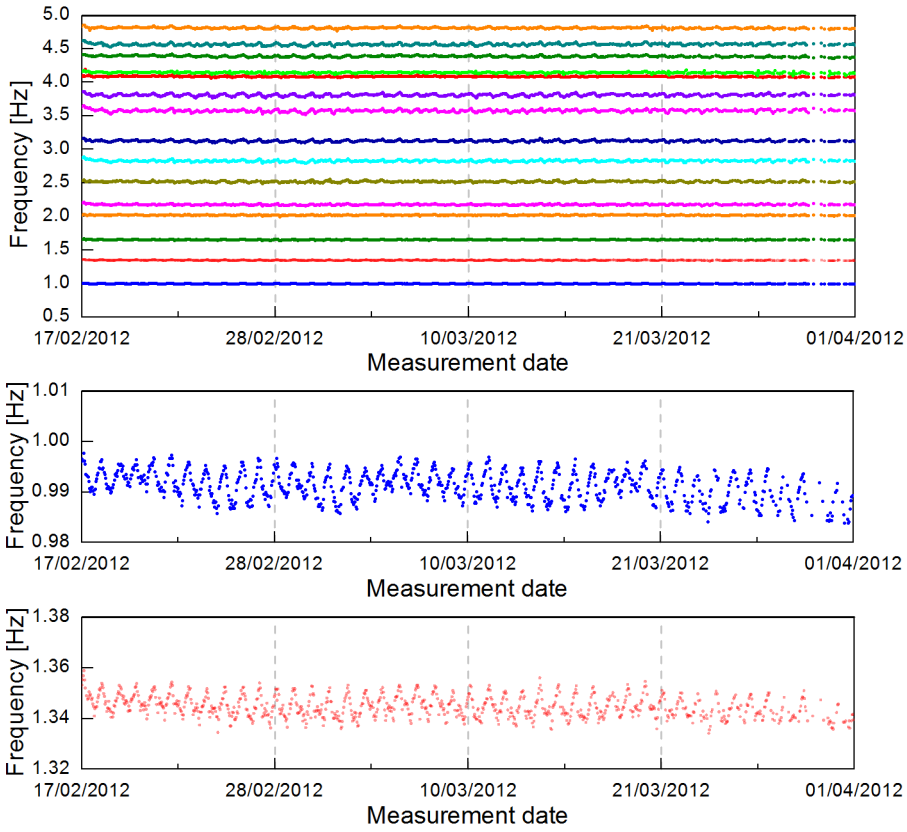


Figure 9: Evolution of the natural frequencies of the lateral modes of the bridge identified during the period from 17/02/2012 to31/03/2012, zoom of the first and second natural frequency

6 Conclusions

The paper presents two applications of a recently developed methodology for automated modal parameter estimation based on the construction and interpretation of tri-dimensional stabilization diagrams, suitable for continuous dynamic monitoring.

The goal of the proposed methodology is based on two different aspects apt to provide a more generalized automated procedure for the identification problems. The first aspect is related to the human interaction in a very primary stage of the identification process. In detail, the new methodology provides a further effort in the automation of the process avoiding the user choice in the definition of the input parameter of SSI-Cov method (i.e. time-lag) used to construct the correlation matrix. The second aspect is related to a further generalization of the developed procedure to complex cases through a new clustering approach based on the use of MACX index.

The proposed algorithm was used to analyze data collected on two different cases of studies: Infante D. Henrique Bridge located in Porto (Portugal) and San Michele Bridge located in the neighborhood of Milan (Italy). In both cases the robust performance of the developed algorithm is proven by the high success rate in the identification of the structural modes. In the former, 16 structural modes were identified with a success rate generally higher than 97%. Moreover, the obtained results also show the ability of the implemented algorithm in the identification of closely spaced modes, the first lateral mode and the first vertical mode with frequencies of 0.78 Hz and 0.82 Hz, respectively. The results also show very coherent mode shapes that maintain a very high consistence during the investigated period. In the latter, 15 lateral modes of the bridge were successfully identified and tracked. Also in this case, the robustness of the algorithm allows the high success rate in the tracking of the bridge modes. Furthermore, the high complexity of some mode shapes highlights the effects of the improvement in the cluster procedure; in fact, the generalization of the clustering procedure to complex modes through the use of the MACX index allows an efficient generation of the clusters and consequently a better performance of the tracking

process. In the resulting outputs of both cases, the evolution over time of the modal parameters (i.e. natural frequencies) confirms the influence of the environmental conditions on the dynamic behavior of both bridges. Concluding, the application of the developed automated procedure could be of great interest in the context of continuous dynamic monitoring of real scale structures. In particular a deeper analysis of the uncertainty related to obtained estimations will be very useful to understand and quantify the robustness and the flexibility of the implemented methodology to deliver coherent sets of structural modes, completely avoiding the initial tuning of the most important input parameters (i.e. time-lag and model order) of parametric methods.

References

[1] F. Magalhães, Á. Cunha, E. Caetano, *Vibration based structural health monitoring of an arch bridge: from automated OMA to damage detection*, Mechanical Systems and Signal Processing Vol. 28, (2012), pp. 212-228.

[2] E. Reynders, J. Houbrechts, G. De Roeck, *Fully automated (operational) modal analysis*, Mechanical Systems and Signal Processing, Vol. 29, (2012), pp. 228-250.

[3] R. Brincker, L. Zhang, P. Andersen, *Modal identification of output-only systems using Frequency Domain Decomposition*, Smart Materials and Structures, Vol. 10, (2001), pp. 441-445.

[4] B. Peeters, G. De Roeck, *Reference-based Stochastic Subspace Identification for output-only modal analysis*, Mechanical Systems and Signal Processing, Vol. 13, (1999), pp. 855-878.

[5] P. Van Overschee, B. De Moor, *Subspace Identification for Linear System: Theory - Implementation - Applications*, Springer, 161-196 (1996).

[6] V. Zabel, F. Magalhães, C. Bucher, *The influence of parameter choice in Operational Modal Analysis: a case study*, IMAC, In M. Mains, editor, Topics in Modal Analysis & Testing, Vol. 10, Conference Proceedings of SEM Series, Springer, (2016).

[7] F. Magalhães, *Operational modal analysis for testing and monitoring of Bridge and special structure*, PhD Thesis, Porto, (2010).

[8] F. Magalhães, Á. Cunha, E. Caetano, *Online automatic identification of the modal parameters of a long span arch bridge*, Mechanical Systems and Signal Processing, Vol. 23, (2009), pp. 316-329.

[9] A. Cabboi, F. Magalhães, C. Gentile, Á. Cunha, *Automated modal identification and tracking: application to an iron arch bridge*, Structural Control and Health Monitoring, Vol. 24(1), e1854 (2017).

[10] P. Vacher, B. Jacquier, A. Bucharles, *Extensions of the MAC criterion to complex modes*, in *Proceedings of ISMA 2010 - International Conference on Noise and Vibration Engineering, Leuven , Belgium, 2010 September 20-22*, Leuven (2010), pp. 2713-2725.

[11] F. Ubertini, C. Gentile, A. L. Materazzi, *Automated modal identification in operational conditions and its application to bridges*. Engineering Structures, Vol. 46, (2013), pp. 264-278.

[12] G. Marrongelli, F. Magalhães, Á. Cunha, *Automated operational modal analysis of an arch bridge considering the influence of the parametric methods inputs*, Procedia Engineering 199, (2017), pp. 2172-2177.

[13] C. Gentile, A. Saisi, *Continuous dynamic monitoring of a centenary iron bridge for structural modification assessment*, Frontiers of Structural and Civil Engineering., Vol. 9, No. 1, (2015), pp 26-41.

[14] C. Gentile, A. Saisi, *Ambient vibration testing and condition assessment of the Paderno iron arch bridge (1889)*, Construction Building Materials, Vol. 25, No. 9, (2011), pp. 3709–3720.

[15] M. Imregun, D.J. Ewins, *Complex modes – origin and limit*, *Proceedings of The 13th International Modal Analysis Conference*, Nashville, Tennessee (1995).

Operational modal analysis based on time-domain expansion of transmissibility

J. Kang[1], L. Liu[1,2,3], S. D. Zhou[1,2,3], L. Yu[1]
[1] School of Aerospace Engineering, Beijing Institute of Technology, China, People's Republic of

[2] Key Laboratory of Dynamics and Control of Flight Vehicle, Ministry of Education, 100081 Beijing, China;

[3] Key Laboratory of Autonomous Navigation and Control for Deep Space Exploration, Ministry of Industry and Information Technology, 100081 Beijing, China
e-mail: **kangjie@bit.edu.cn**

Abstract
Transmissibility based operational modal analysis (TOMA) can estimate the modal parameters under non-white excitations. The transmissibility functions defined in frequency-domain require the Fourier transformation of time-domain responses into frequency-domain data, which leads to problems of leakage errors and selection of window function. This paper presents a novel time-domain expansion of transmissibility (TDET) to avoid the Fourier transformation. This expansion implies the definition of Auto-Regressive with eXogenous excitation (ARX) model, by using time-domain reference responses and non-reference responses to replace the eXogenous and Auto-Regressive part, respectively. The comparative results from two simulation examples show that the TDET-based operational modal analysis method presents overall better performance than the TOMA method in terms of the modal parameters estimation accuracy and the spurious modes suppression.

1 Introduction

The last decades have seen great progress in modal analysis. Early research in modal analysis constructs an approach later described as Experimental Modal Analysis (EMA), which has found its wide use in studying the dynamic behaviors of mechanic structures [1]. This classical method measures both excitations and responses of the structure. Based on these input and output data, a modal model representing the dynamic properties of structure can be estimated. Modal analysis then focuses on the extraction of physical information (often modal parameters) from the modal model [2]. Ward Heylen et al. [3] and D. J. Ewins [4] comprehensively summarized the theory and practical testing of EMA.

An alternative method is operational modal analysis (OMA) based on output-only vibration responses [5, 6]. Because the ambient excitations acting on the structures in operation are always random and can't be measured precisely, the EMA method based on both the excitations and responses is not appropriate [5, 7].

However, the OMA method usually takes the assumption that the excitations are white noise, whose frequency spectrum is plat. This assumption is not strictly satisfied in practice. For example, the rotating parts of turbines, and the sloshing liquids of rocket can characterize the excitations by harmonic components [8, 9]. The harmonic components in excitations hamper the application of traditional OMA method. The harmonic frequencies may be identified as spurious resonance modes when harmonic components are well separated from system poles. If the harmonic components are close to the structural resonance modes, they can affect the estimation of modal parameters, especially resulting in poor damping ratios estimation [5, 10].

Originally, the concept of transmissibility was given by a relationship between only two responses in the frequency-domain for single-degree-of-freedom system (SDOF) [11]. The work of Liu et al. [12] and Varoto et al. [13] generalized the scalar transmissibility to multivariable transmissibility, but the proposed notations have limitations in practice. The more practical multivariable transmissibility matrix was reported in Ref. [11], which showed that it can be calculated by the frequency response functions (FRF). Fontul et al. [14] proved that the transmissibility does not depend on the applied type of forces exciting the system, but only on the chosen sets of co-ordinates for the applied forces and for the 'unknown' and 'known' responses.

In this sense, C. Devriendt et al. [15-17] firstly presented TOMA method, which obtains system poles by combining the transmissibility functions determined by different load cases. When the frequency being close to poles of the given system, the subtraction between two scalar transmissibility functions of different load cases equals to zero, so the system poles are also poles of the reciprocal of subtraction functions. C. Devriendt et al. [18] combined all the measured single-reference transmissibility functions in a unique matrix formulation to identify system poles, hence reduced the risk of missing system poles and identifying extra mathematical poles. C. Devriendt et al. [19] successfully generalized scalar transmissibility to multivariable one and utilized the subtraction of pseudo scalar transmissibility functions of two different load cases to obtain system poles. Weijtjens et al. [20, 21]presented poly-reference transmissibility based operational modal analysis (pTOMA) associated with different loading conditions to obtain the system eigenvalues using output-only data. Wang-Ji Yan et al. [22] presented the power spectrum density transmissibility (PSDT) to extract the modal parameters through combining the PSDTs with different transferring outputs instead of different load conditions. Iván Gómez Araújo et al. [23] presented the singular value decomposition of PSDT matrices with different references (PSDTM-SVD), which reduces the risk of identifying the spurious poles compared to PSDT. Iván Gómez Araújo et al. [24]extended the scalar PSDT to multivariable PSDT by relating multiple responses instead of only two, providing greater reliability during modal parameters estimation.

Aforementioned TOMA methods utilize frequency-domain data of structural responses, thus the data transformation from time-domain to frequency-domain is required. This transformation may result in a series of problems, such as leakage errors and the selection of window function [25]. The leakage errors resulted from the finite length of signals can be reduced by two methods [4, 25]. One is that the spectrum of periodic signals measured over an integer number of periods is perfectly calculated, and this method can thoroughly eliminate leakage errors. The compromise is to use random burst excitations. However, these two conditions are usually impossible in practice. The alternative method is to use, for example, a Hanning window, instead of a rectangular window to reshape the response signals. The main lobe of Hanning window is two times wider than that of rectangular window, hence the interference between the components that are close to each other may increase [25].

This paper presents the time-domain expansion of transmissibility, which directly permits the time-domain responses instead of frequency-domain data. The TDET links the traditional transmissibility with time-domain ARX model, whose auto-regressive part (AR part) and exogenous excitation part (X part) are non-reference responses and reference responses in time-domain, respectively. Combining the TDET in different load cases enables the extraction of modal parameters including modal frequencies, mode shapes and damping ratios. The novel method can not only successfully estimate modal parameters under non-white excitations, but also can thoroughly eliminate the leakage errors and avoid the selection of window function.

The remainder of this paper is organized as follows. The concepts of transmissibility and TOMA method are introduced in Section 2. The formulation of the proposed TDET, as well as the calculation approach of modal parameters through the TDET are presented in Section 3. To validate the proposed method and its advantages, a numerical dynamic system and a finite element example under excitations with predominant frequencies are set up in Section 4. Finally, Section 5 gives the remarkable conclusions.

2 Multivariable transmissibility

This section recaps the properties of multivariable transmissibility, and then introduces the method of multivariable transmissibility estimation.

2.1 Properties of multivariable transmissibility

Transmissibility functions are defined as the function that relates reference outputs to non-reference outputs as opposed to frequency response function. For multiple inputs and multivariable outputs (MIMO) system, the relationship between inputs and outputs can be formulated as:

$$\boldsymbol{X}(s)=\boldsymbol{H}(s)\boldsymbol{U}(s) \tag{1}$$

where, $\boldsymbol{X}(s)\in \mathrm{C}^{N_o\times 1}$ and $\boldsymbol{U}(s)\in \mathrm{C}^{N_i\times 1}$ are the frequency-domain output signals and input signals, respectively. $\boldsymbol{H}(s)\in \mathrm{C}^{N_o\times N_i}$ is the transfer function matrix, in which N_o and N_i are output channels and input channels, respectively.

Dividing the output signals into reference and non-reference subsets:

$$\begin{bmatrix}\boldsymbol{X}_r(s)\\ \boldsymbol{X}_l(s)\end{bmatrix}=\begin{bmatrix}\boldsymbol{H}_r(s)\\ \boldsymbol{H}_l(s)\end{bmatrix}\boldsymbol{U}(s) \tag{2}$$

where, the subscript r and l denote reference and non-reference subsets, respectively. $\boldsymbol{X}_r(s)\in \mathrm{C}^{N_r\times 1}$ and $\boldsymbol{X}_l(s)\in \mathrm{C}^{(N_o-N_r)\times 1}$ are reference and non-reference responses, respectively. $\boldsymbol{H}_r(s)\in \mathrm{C}^{N_r\times N_i}$ and $\boldsymbol{H}_l(s)\in \mathrm{C}^{(N_o-N_r)\times N_i}$ are the rows of $\boldsymbol{H}(s)$ that relate respectively the elements of $\boldsymbol{X}_r(s)$ and $\boldsymbol{X}_l(s)$ to $\boldsymbol{U}(s)$. $N_r<N_o$ is reference channel.

According to Ref. [21], the input signals $\boldsymbol{U}(s)$ can be viewed as the linear combination of N_i independent forces distributed over all input locations. Therefore, the input forces are written as

$$\boldsymbol{U}(s)=\begin{bmatrix}\boldsymbol{f}_1 & \boldsymbol{f}_2 & \cdots & \boldsymbol{f}_{N_s}\end{bmatrix}\begin{bmatrix}\beta_1(s)\\ \beta_2(s)\\ \vdots\\ \beta_{N_s}(s)\end{bmatrix}=\boldsymbol{F}\boldsymbol{\beta}(s) \tag{3}$$

in which $\boldsymbol{F}$ including N_s independent input sources describes the spatial distribution, indicating how the N_s sources ($\beta_1(s)$ to $\beta_{N_s}(s)$) are distributed over the N_i input locations.

Substituting Eq.(3) into Eq.(2) yields

$$\begin{bmatrix}\boldsymbol{X}_r(s)\\ \boldsymbol{X}_l(s)\end{bmatrix}=\begin{bmatrix}\boldsymbol{H}_r(s)\boldsymbol{F}\\ \boldsymbol{H}_l(s)\boldsymbol{F}\end{bmatrix}\boldsymbol{\beta}(s) \tag{4}$$

so

$$\boldsymbol{X}_l(s)=\boldsymbol{H}_l(s)\boldsymbol{F}\left[\boldsymbol{H}_r(s)\boldsymbol{F}\right]^{-1}\boldsymbol{X}_r(s) \tag{5}$$

According to Ref. [11], the multivariable transmissibility can be reformulated as

$$\boldsymbol{X}_l(s)=\boldsymbol{T}(s)\boldsymbol{X}_r(s) \tag{6}$$

where, $\boldsymbol{T}(s)\in \mathrm{C}^{(N_o-N_r)\times N_r}$ designates the multivariable transmissibility functions.

Combining Eq.(5) and Eq.(6) yields

$$\boldsymbol{T}(s)=\boldsymbol{H}_l(s)\boldsymbol{F}\left[\boldsymbol{H}_r(s)\boldsymbol{F}\right]^{-1} \tag{7}$$

If the inverse in Eq.(7) does not exist, the pseudo-inverse is alternated as

$$\boldsymbol{T}(s)=\boldsymbol{H}_l(s)\boldsymbol{F}\left[\boldsymbol{H}_r(s)\boldsymbol{F}\right]^{+} \tag{8}$$

where superscript "+" designates pseudo-inverse of matrix. According to Eq.(7) and Eq.(8), poly-reference transmissibility functions are independent of the input spectrum $\boldsymbol{\beta}(s)$, and solely depend on the transfer function $\boldsymbol{H}(s)$ and the spatial distribution matrix $\boldsymbol{F}$.

Under sufficiently different load cases, the transmissibility functions are different because of changes in spatial distribution matrix $\boldsymbol{F}$. By using a subscript "k" to designate different load cases, the transmissibility functions in Eq.(7) and Eq.(8) are written as

$$\begin{aligned} \boldsymbol{T}_k(s) &= \boldsymbol{H}_l(s)\boldsymbol{F}_k\left[\boldsymbol{H}_r(s)\boldsymbol{F}_k\right]^{-1}, \text{ or} \\ \boldsymbol{T}_k(s) &= \boldsymbol{H}_l(s)\boldsymbol{F}_k\left[\boldsymbol{H}_r(s)\boldsymbol{F}_k\right]^{+}, \quad k=1,2,\cdots,N_k \end{aligned} \tag{9}$$

where N_k is the number of all load cases.

2.2 Multivariable transmissibility estimation

For each load case k, multivariable transmissibility can be parameterized by using left matrix-fractional model as

$$\hat{\boldsymbol{T}}_k(s) = \boldsymbol{A}_k^{-1}(s)\boldsymbol{B}_k(s) \tag{10}$$

where $\hat{\boldsymbol{T}}_k(s)$ is the estimated $\boldsymbol{T}_k(s)$. s equals $j\omega$ in Laplace-domain and $\mathrm{e}^{-j\omega\cdot\Delta T}$ in z-domain, respectively, where ΔT is the sampling period. The denominator matrix polynomial $\boldsymbol{A}_k(s)\in \mathrm{C}^{(N_o-N_r)\times(N_o-N_r)}$ and the numerator matrix polynomial $\boldsymbol{B}_k(s)\in \mathrm{C}^{(N_o-N_r)\times N_r}$ can be written as

$$\boldsymbol{A}_k(s)=\sum_{m=0}^{n_A}\boldsymbol{A}_{k,m}s^m, \quad \boldsymbol{B}_k(s)=\sum_{n=0}^{n_B}\boldsymbol{B}_{k,n}s^n \tag{11}$$

where n_A and n_B are polynomial orders. $\boldsymbol{A}_{k,m}$ and $\boldsymbol{B}_{k,n}$ are coefficients matrices to be estimated.

Substituting Eq.(11) to Eq.(10) yields

$$\sum_{m=0}^{n_A}\boldsymbol{A}_{k,m}s^m\boldsymbol{X}_{k,l}(s)=\sum_{n=0}^{n_B}\boldsymbol{B}_{k,n}s^n\boldsymbol{X}_{k,r}(s) \tag{12}$$

For each load case with n_f considered frequency points, the equation error of Eq.(12) is

$$\boldsymbol{e}_{k,i}(\boldsymbol{\Theta}_k,s_i)=\sum_{m=0}^{n_A}\boldsymbol{A}_{k,m}s_i^m\boldsymbol{X}_{k,l}(s_i)-\sum_{n=0}^{n_B}\boldsymbol{B}_{k,n}s_i^n\boldsymbol{X}_{k,r}(s_i) \tag{13}$$

where $\boldsymbol{e}_{k,i}\in \mathrm{C}^{(N_o-N_r)\times 1}$ is the equation error in i-th frequency point for load case k. The transpose of Eq.(13) is

$$\boldsymbol{e}_{k,i}^T(\boldsymbol{\Theta}_k,s_i)=\sum_{m=0}^{n_A}s_i^m\boldsymbol{X}_{k,l}^T(s_i)\boldsymbol{A}_{k,m}^T-\sum_{n=0}^{n_B}s_i^n\boldsymbol{X}_{k,r}^T(s_i)\boldsymbol{B}_{k,n}^T \tag{14}$$

Combining all n_f considered frequency points yields

$$\boldsymbol{E}_k(\boldsymbol{\Theta})=\begin{bmatrix}\boldsymbol{\Phi}_{k,l} & \boldsymbol{\Phi}_{k,r}\end{bmatrix}\begin{bmatrix}\boldsymbol{A}_k\\ \boldsymbol{B}_k\end{bmatrix} \tag{15}$$

For ease of notation, the equation errors matrix $\boldsymbol{E}_k\in \mathrm{C}^{n_f\times(N_o-N_r)}$ in Eq.(15) can be simplified as

$$\boldsymbol{E}_k(\boldsymbol{\Theta})=\boldsymbol{\Phi}_k\boldsymbol{\Theta}_k \tag{16}$$

where $\boldsymbol{\Phi}_k=\begin{bmatrix}\boldsymbol{\Phi}_{k,l} & \boldsymbol{\Phi}_{k,r}\end{bmatrix}$ and $\boldsymbol{\Theta}_k=\begin{bmatrix}\boldsymbol{A}_k^T & \boldsymbol{B}_k^T\end{bmatrix}^T$ are

$$\boldsymbol{\Phi}_{k,l}=\begin{bmatrix}\boldsymbol{X}_{k,l}^T(s_1) & s_1\boldsymbol{X}_{k,l}^T(s_1) & \cdots & s_1^{n_A}\boldsymbol{X}_{k,l}^T(s_1)\\ \boldsymbol{X}_{k,l}^T(s_2) & s_2\boldsymbol{X}_{k,l}^T(s_2) & \cdots & s_2^{n_A}\boldsymbol{X}_{k,l}^T(s_2)\\ \vdots & \vdots & \ddots & \vdots\\ \boldsymbol{X}_{k,l}^T(s_{n_f}) & s_{n_f}\boldsymbol{X}_{k,l}^T(s_{n_f}) & \cdots & s_{n_f}^{n_A}\boldsymbol{X}_{k,l}^T(s_{n_f})\end{bmatrix},\boldsymbol{\Phi}_{k,r}=-\begin{bmatrix}\boldsymbol{X}_{k,r}^T(s_1) & s_1\boldsymbol{X}_{k,r}^T(s_1) & \cdots & s_1^{n_B}\boldsymbol{X}_{k,r}^T(s_1)\\ \boldsymbol{X}_{k,r}^T(s_2) & s_2\boldsymbol{X}_{k,r}^T(s_2) & \cdots & s_2^{n_B}\boldsymbol{X}_{k,r}^T(s_2)\\ \vdots & \vdots & \ddots & \vdots\\ \boldsymbol{X}_{k,r}^T(s_{n_f}) & s_{n_f}\boldsymbol{X}_{k,r}^T(s_{n_f}) & \cdots & s_{n_f}^{n_B}\boldsymbol{X}_{k,r}^T(s_{n_f})\end{bmatrix} \tag{17}$$

$$\begin{aligned}\boldsymbol{A}_k&=\begin{bmatrix}\boldsymbol{A}_{k,0} & \boldsymbol{A}_{k,1} & \cdots & \boldsymbol{A}_{k,n_A}\end{bmatrix}^T,\\ \boldsymbol{B}_k&=\begin{bmatrix}\boldsymbol{B}_{k,0} & \boldsymbol{B}_{k,1} & \cdots & \boldsymbol{B}_{k,n_B}\end{bmatrix}^T\end{aligned} \tag{18}$$

Based on Eq.(16), via ordinary least square approach, the parameter matrices $\boldsymbol{A}_k$ and $\boldsymbol{B}_k$ can be obtained directly.

3 Time-domain expansion of multivariable transmissibility

3.1 Description of TDET

The conventional $\mathrm{ARX}(n_A,n_X)$ model, with n_A and n_X designating AR part and X part orders, respectively, is defined by [2]

$$\sum_{i=0}^{n_A}\boldsymbol{A}_i\boldsymbol{x}(\kappa-i)=\sum_{j=0}^{n_X}\boldsymbol{B}_j\boldsymbol{u}(\kappa-j)+\boldsymbol{e}(\kappa) \tag{19}$$

Using the backshift operator $z(z^i\cdot\boldsymbol{x}(\kappa)\ \boldsymbol{x}(\kappa-i))$, the ARX model in Eq.(19) can be rewritten as

$$\sum_{i=0}^{n_A}\boldsymbol{A}_i z^i\cdot\boldsymbol{x}(\kappa)=\sum_{j=0}^{n_X}\boldsymbol{B}_j z^j\cdot\boldsymbol{u}(\kappa)+\boldsymbol{e}(\kappa) \tag{20}$$

where $\boldsymbol{A}_i$ and $\boldsymbol{B}_j$ are parameter matrices. $\boldsymbol{x}(\kappa)$ and $\boldsymbol{u}(\kappa)$ are structural responses and input signals, respectively. $\boldsymbol{e}(\kappa)$ is the innovation sequence, and κ designates the κ-th discrete time.

If $\boldsymbol{x}(\kappa)$ and $\boldsymbol{u}(\kappa)$ in Eq.(20) are replaced by structural reference responses $\boldsymbol{x}_r(\kappa)$ and non-reference responses $\boldsymbol{x}_l(\kappa)$, respectively, the form of Eq.(20) is same as Eq.(12), and the $\boldsymbol{e}(\kappa)$ in Eq.(20) can be viewed as equation errors. Consequently, the TDET in load case *k* is defined as

$$\sum_{i=0}^{n_A}\tilde{\boldsymbol{A}}_{k,i}\boldsymbol{x}_{k,l}(\kappa-i)=\sum_{j=0}^{n_X}\tilde{\boldsymbol{B}}_{k,j}\boldsymbol{x}_{k,r}(\kappa-j) \tag{21}$$

Using the backshift operator z, the TDET in Eq.(21) can be rewritten as

$$\left(\sum_{i=0}^{n_A}\tilde{\boldsymbol{A}}_{k,i}z^i\right)\boldsymbol{x}_{k.l}(\kappa)=\left(\sum_{j=0}^{n_X}\tilde{\boldsymbol{B}}_{k,j}z^j\right)\boldsymbol{x}_{k.r}(\kappa) \tag{22}$$

Based on Eq.(21), the $\tilde{\boldsymbol{A}}_{k,i}$ and $\tilde{\boldsymbol{B}}_{k,j}$ can be estimated by ordinary least square method same as Section 2.2. The normalized equation is

$$\tilde{\boldsymbol{\Phi}}_k^T\tilde{\boldsymbol{\Phi}}_k\tilde{\boldsymbol{\Theta}}_k=\boldsymbol{0} \tag{23}$$

where $\tilde{\boldsymbol{\Phi}}_k=\begin{bmatrix}\tilde{\boldsymbol{\Phi}}_{k,l} & \tilde{\boldsymbol{\Phi}}_{k,r}\end{bmatrix}$ and $\tilde{\boldsymbol{\Theta}}_k=\begin{bmatrix}\tilde{\boldsymbol{A}}_k^T & \tilde{\boldsymbol{B}}_k^T\end{bmatrix}^T$ are given as

$$\tilde{\boldsymbol{\Phi}}_{k,l}=\begin{bmatrix}\boldsymbol{x}_{k,l}^T(n_A+1) & \boldsymbol{x}_{k,l}^T(n_A) & \cdots & \boldsymbol{x}_{k,l}^T(1)\\ \boldsymbol{x}_{k,l}^T(n_A+2) & \boldsymbol{x}_{k,l}^T(n_A+1) & \cdots & \boldsymbol{x}_{k,l}^T(2)\\ \vdots & \vdots & \ddots & \vdots\\ \boldsymbol{x}_{k,l}^T(N) & \boldsymbol{x}_{k,l}^T(N-1) & \cdots & \boldsymbol{x}_{k,l}^T(N-n_A)\end{bmatrix},\tilde{\boldsymbol{\Phi}}_{k,r}=-\begin{bmatrix}\boldsymbol{x}_{k,r}^T(n_X+1) & \boldsymbol{x}_{k,r}^T(n_X) & \cdots & \boldsymbol{x}_{k,r}^T(1)\\ \boldsymbol{x}_{k,r}^T(n_X+2) & \boldsymbol{x}_{k,r}^T(n_X+1) & \cdots & \boldsymbol{x}_{k,r}^T(2)\\ \vdots & \vdots & \ddots & \vdots\\ \boldsymbol{x}_{k,r}^T(N) & \boldsymbol{x}_{k,r}^T(N-1) & \cdots & \boldsymbol{x}_{k,r}^T(N-n_X)\end{bmatrix} \tag{24}$$

$$\begin{aligned}\tilde{\boldsymbol{A}}_k &= \begin{bmatrix}\tilde{\boldsymbol{A}}_{k,0} & \tilde{\boldsymbol{A}}_{k,1} & \cdots & \tilde{\boldsymbol{A}}_{k,n_A}\end{bmatrix}^T, \\ \tilde{\boldsymbol{B}}_k &= \begin{bmatrix}\tilde{\boldsymbol{B}}_{k,0} & \tilde{\boldsymbol{B}}_{k,1} & \cdots & \tilde{\boldsymbol{B}}_{k,n_X}\end{bmatrix}^T\end{aligned} \tag{25}$$

where N is the length of responses.

As shown in Eq.(21), TDET implies the ARX model, whose AR part and X part are replaced with non-reference and reference time-domain responses, respectively. This property avoids the data transformation from time-domain responses to frequency-domain data, hence thoroughly eliminates the leakage errors, which will be illustrated by numerical example in Section 4.1. Furthermore, the TDET reduces the computational complexity of Jacobi matrix by removing the multiply operations in Eq.(17).

3.2 TDET-based modal parameters estimation

Based on Eq.(22), the multivariable transmissibility can also be formulated as

$$\tilde{\boldsymbol{T}}(s) = \left(\sum_{i=0}^{n_A} \tilde{\boldsymbol{A}}_{k,i} s^i\right)^{-1} \sum_{j=0}^{n_X} \tilde{\boldsymbol{B}}_{k,j} s^j \tag{26}$$

where s equals $\mathrm{i}\omega$ in Laplace-domain and $\mathrm{e}^{-\mathrm{i}\omega\cdot\Delta T}$ in z-domain, respectively. $\tilde{\boldsymbol{T}}(s)$ designates the estimated multivariable transmissibility based on the proposed TDET.

Combining Eq.(26) and Eq.(9) yields

$$\tilde{\boldsymbol{B}}_k(s)\boldsymbol{H}_r(s)\boldsymbol{F}_k = \tilde{\boldsymbol{A}}_k(s)\boldsymbol{H}_l(s)\boldsymbol{F}_k \tag{27}$$

where $\tilde{\boldsymbol{A}}_k(s) = \sum_{i=0}^{n_A} \tilde{\boldsymbol{A}}_{k,i} s^i$, $\tilde{\boldsymbol{B}}_k(s) = \sum_{j=0}^{n_X} \tilde{\boldsymbol{B}}_{k,j} s^j$.

The Eq.(27) can be written as

$$\begin{bmatrix}\tilde{\boldsymbol{B}}_k(s) & -\tilde{\boldsymbol{A}}_k(s)\end{bmatrix}\begin{bmatrix}\boldsymbol{H}_r(s) \\ \boldsymbol{H}_l(s)\end{bmatrix}\boldsymbol{F}_k = \bar{\boldsymbol{T}}_k(s)\boldsymbol{H}(s)\boldsymbol{F}_k = 0 \tag{28}$$

This means $\bar{\boldsymbol{T}}_k(s)$ matrix to be estimated is independent of input spectrum, but depends on their spatial distribution. Noting that all column vectors of the transfer functions matrix for linear time invariant (LTI) MIMO system are proportional with corresponding mode shape vector $\boldsymbol{\phi}_m$ when the frequency being close to system pole λ_m [3]. So the simplified form of Eq.(28) when $s \to \lambda_m$ becomes

$$\bar{\boldsymbol{T}}_k(\lambda_m)\boldsymbol{\phi}_m = 0 \tag{29}$$

where m means m-th system pole, $m = 1, 2, \cdots, N_m$. Combine all N_k different load cases into one matrix, namely

$$\begin{bmatrix}\bar{\boldsymbol{T}}_1(\lambda_m) \\ \bar{\boldsymbol{T}}_2(\lambda_m) \\ \vdots \\ \bar{\boldsymbol{T}}_{N_k}(\lambda_m)\end{bmatrix}\boldsymbol{\phi}_m = \left(\sum_{j=0}^{\max(n_A,n_X)} \begin{bmatrix}\tilde{\boldsymbol{B}}_{1,j} & -\tilde{\boldsymbol{A}}_{1,j} \\ \tilde{\boldsymbol{B}}_{2,j} & -\tilde{\boldsymbol{A}}_{2,j} \\ \vdots & \vdots \\ \tilde{\boldsymbol{B}}_{N_k,j} & -\tilde{\boldsymbol{A}}_{N_k,j}\end{bmatrix}\lambda_m^j\right)\boldsymbol{\phi}_m = 0 \tag{30}$$

For ease of notation, Eq.(30) can be rewritten as

$$\left(\sum_{j=0}^{\max(n_A,n_X)} \boldsymbol{C}_j \lambda_m^j\right)\boldsymbol{\phi}_m = 0 \tag{31}$$

where

$$\boldsymbol{C}_j = \begin{bmatrix} \tilde{\boldsymbol{B}}_{1,j} & -\tilde{\boldsymbol{A}}_{1,j} \\ \tilde{\boldsymbol{B}}_{2,j} & -\tilde{\boldsymbol{A}}_{2,j} \\ \vdots & \vdots \\ \tilde{\boldsymbol{B}}_{N_k,j} & -\tilde{\boldsymbol{A}}_{N_k,j} \end{bmatrix} \tag{32}$$

The generalized eigenvalues problem of Eq.(31) can be transformed into the eigenvalue problem

$$(\boldsymbol{\Gamma} - \lambda_m \boldsymbol{I})\boldsymbol{\varphi}_m = 0 \tag{33}$$

where

$$\boldsymbol{\Gamma} = \begin{bmatrix} \boldsymbol{C}'_{n-1} & \cdots & \boldsymbol{C}'_1 & \boldsymbol{C}'_0 \\ \boldsymbol{I} & \cdots & \boldsymbol{0} & \boldsymbol{0} \\ \vdots & \boldsymbol{I} & \vdots & \boldsymbol{0} \\ \boldsymbol{0} & \boldsymbol{0} & \boldsymbol{I} & \boldsymbol{0} \end{bmatrix}, \quad \boldsymbol{\varphi}_m = \begin{bmatrix} \lambda_m^{n-1}\boldsymbol{\phi}_m \\ \vdots \\ \lambda_m^1 \boldsymbol{\phi}_m \\ \boldsymbol{\phi}_m \end{bmatrix} \tag{34}$$

in which $n = \max(n_A, n_X)$. $\boldsymbol{\Gamma}$ is commonly named high dimensional adjoint matrix, and its submatrices should be square, but the matrix $\boldsymbol{C}_j$ in Eq.(32) may be not square because the load case number N_k does not satisfy the condition $N_k = N_o/(N_o - N_r)$. To remove this constraint, the pseudo-inverse can be used as

$$\boldsymbol{C}'_{i-1} = \boldsymbol{C}_n^+ \boldsymbol{C}_{i-1}, \quad i = 1, 2, \cdots, n \tag{35}$$

The modal frequency ω_m and corresponding damping ratio ξ_m can be calculated from λ_m.

Two important things should be noted. Firstly, when only one same freedom of the structural system is excited in all different load cases, the transfer functions matrix becomes a column vector and the Eq.(30) always holds for all *s* values. Therefore, we have to adopt a series of different load cases in which the excitation locations are different from each other to obtain the system poles. Secondly, to obtain a finite deterministic solution of Eq.(31), the rank of matrix $\boldsymbol{C}_j$ should be N_o, i.e. $N_k(N_o - N_r) \geq N_o$, which means the number of different load cases should satisfy $N_k \geq N_o/(N_o - N_r)$.

4 Numerical example

To investigate the performances of presented TDET method, this method was used to process the simulation data from a 4-degree-of-freedom (DOF) viscous damped mechanical system and a finite element beam example, respectively.

4.1 4-DOF mechanical system

4.1.1 Description of simulated system

The 4-DOF mechanical system is shown in Figure 1. The dynamic equation of this system is given by

$$\boldsymbol{M}\ddot{\boldsymbol{x}}(t) + \boldsymbol{C}\dot{\boldsymbol{x}}(t) + \boldsymbol{K}\boldsymbol{x}(t) = \boldsymbol{F}(t) \tag{36}$$

where $\ddot{\boldsymbol{x}}(t)$, $\dot{\boldsymbol{x}}(t)$, $\boldsymbol{x}(t)$ are acceleration, velocity, and displacement responses, respectively. $\boldsymbol{F}(t)$ is excitation force vector acting on the system. $\boldsymbol{M}$, $\boldsymbol{C}$, $\boldsymbol{K}$ are mass matrix, damping matrix, and stiffness matrix, respectively.

The parameters defined in Figure 1 are listed in Table 1, with the theoretical resonance frequencies and damping ratios of the modelled system exhibited in Table 2.

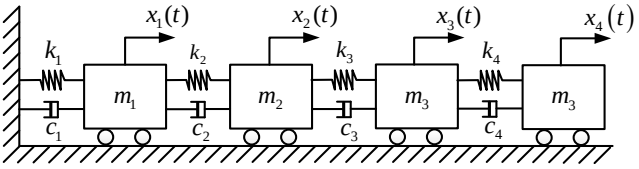


Figure 1 Schematic diagram of a 4-DOF mechanical system

Parameters	Value
Mass(kg)	$m_1 = m_2 = m_3 = m_4 = 10$
Damping($\mathrm{N \cdot m^{-1} \cdot s}$)	$k_1 = 4 \times 10^3$,
	$k_2 = k_3 = k_4 = 3.0 \times 10^3$
Stiffness($\mathrm{N \cdot m^{-1}}$)	$c_1 = c_3 = 5$, $c_2 = 8$, $c_4 = 3$

Table 1 Property parameters of the 4-DOF system

No.	1	2	3	4
Frequency (Hz)	1.01	2.89	4.35	5.23
Damping ratio (%)	0.59	1.18	2.09	3.12

Table 2 Resonance frequencies and damping ratios of the 4-DOF system

The system is excited by $F_k(t) = \mu_{k,1} f_1(t) + \mu_{k,2} f_2(t)$ on each degree of freedom. $f_1(t)$ and $f_2(t)$ are two uncorrelated excitation signals. $f_1(t)$ is Gaussian white noise, and $f_2(t)$ is the response of an SDOF system to Gaussian white noise. Modal parameters estimation based on transmissibility necessitates sufficiently different load cases. In this example, two different load cases were adopted, i.e. $N_k = 2$, which was realized by changing the load distribution factors, namely, $\mu_{k,1}$ and $\mu_{k,2}$, as illustrated in Table 3.

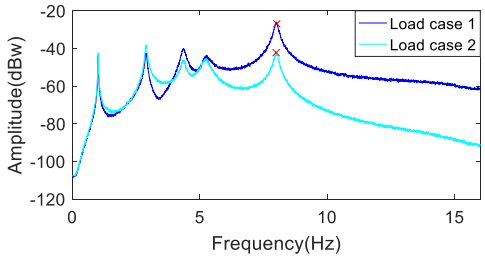


Figure 2 The averaged auto-power spectrum of $x_1(t)$ (×: predominant frequency)

The acceleration responses of modelled system were obtained by Newmark-β method with $\Delta t = 1/1024$ s, $\beta = 0.5, \gamma = 0.25$ and then resampled at 32 Hz, and the record time was 150 s. As shown in Figure 2, the responses are characterized by a predominant frequency, which indicates that the excitations are non-white. The model order $n_A = n_B = 4$ was chosen according to Ref. [20, 21].

4.1.2 Results and discussion

The summary results of 150 Monte Carlo runs are presented in Figure 3, where the modal frequencies and damping ratios derived by TDET method and TOMA method are compared with their theoretical counterparts. One can evidently observe that the TDET method outperforms the TOMA method in accuracy, in terms of both modal frequency and damping ratio of each mode. This can be verified by the fact that the results estimated by TOMA method significantly scatter, especially the damping ratios. Furthermore, the TOMA method leads to a number of spurious modes and performs poorly in terms of the first mode, which can only works for 68 times of 150 Monte Carlo runs.

No.	First case(k=1)		Second case(k=2)	
	$\mu_{1,1}$	$\mu_{1,2}$	$\mu_{2,1}$	$\mu_{2,2}$
1	0.1	0.1	0	0
2	0	0	0.1	0.1
3	0.1	0.1	0	0
4	0	0	0.1	0.1

Table 3 Load distribution factors of two different load cases

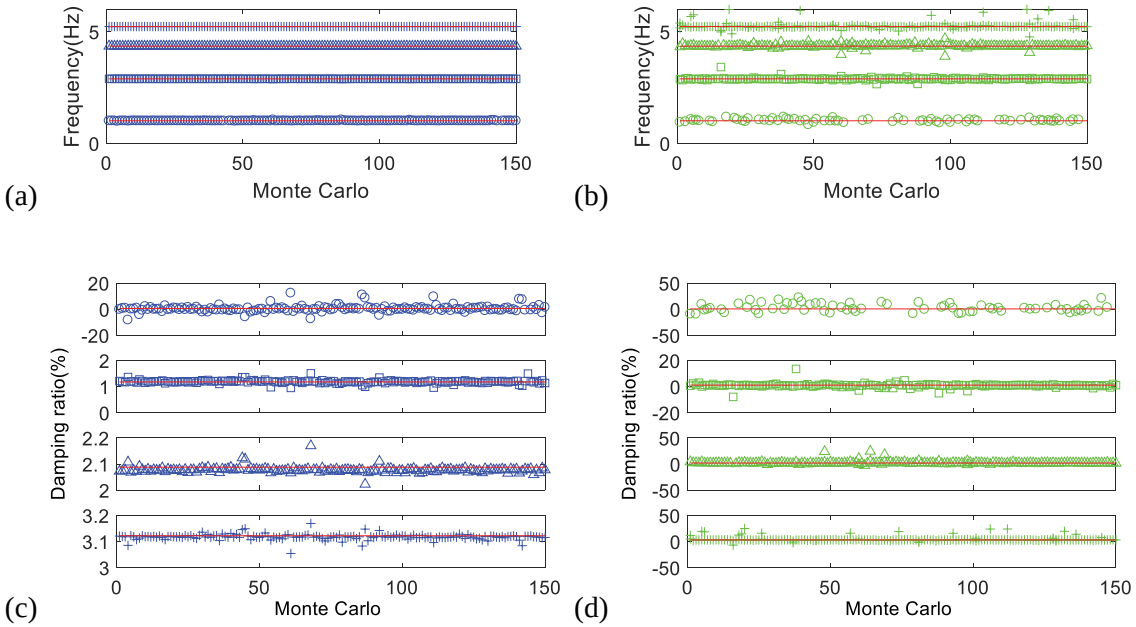


Figure 3 Summary results obtained by 150 Monte Carlo runs for 4-DOF system: (a) and (c): TDET method; (b) and (d): TOMA method (red line: theoretical value; circle: first mode; square: second mode; triangle: third mode; plus: fourth mode)

The modal assurance criterion (MAC) values of four natural normalized mode shapes are shown in Figure 4. The better overall performance of TDET method than TOMA method can also be observed, especially for the third mode.

To directly quantify the achievable accuracy of two methods, an averaged relative error (ARE) and a standard deviation (SD) are defined as

$$\mathrm{ARE}_r = \frac{1}{N}\sum_{i=1}^{N}\frac{\left|\hat{p}_{r,i} - p_r^o\right|}{p_r^o}\times 100\% \quad , \quad \mathrm{SD}_r = \sqrt{\frac{\sum_{i=1}^{N}\left(\frac{\left|\hat{p}_{r,i} - p_r^o\right|}{p_r^o} - ARE_r\right)^2}{N-1}} \tag{37}$$

where, p_r^o designates the theoretical values of r-th mode, $\hat{p}_{r,i}$ corresponding estimated values of r-th mode obtained by i-th Monte Carlo run. N is the number of Monte Carlo runs.

The ARE and SD values of each mode obtained by two methods are directly depicted in Figure 5. Note that the errors of modal frequencies estimated by the TDET method are less than 2% on average with variability less than 1%, which significantly surpasses the traditional TOMA method. The damping ratios are much less accurate, which results from the fact that the damping ratio highly depends on the discrete-to-continuous transformation, particularly for light damping [26], but the TDET method can still provide proper magnitude.

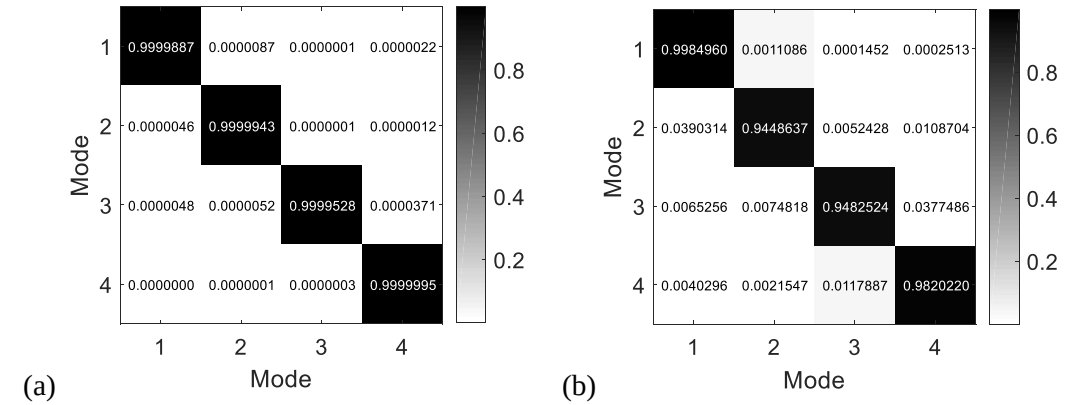


Figure 4 Averaged MAC matrices estimated by 150 Monte Carlo runs for 4-DOF system: (a) TDET method; (b) TOMA method

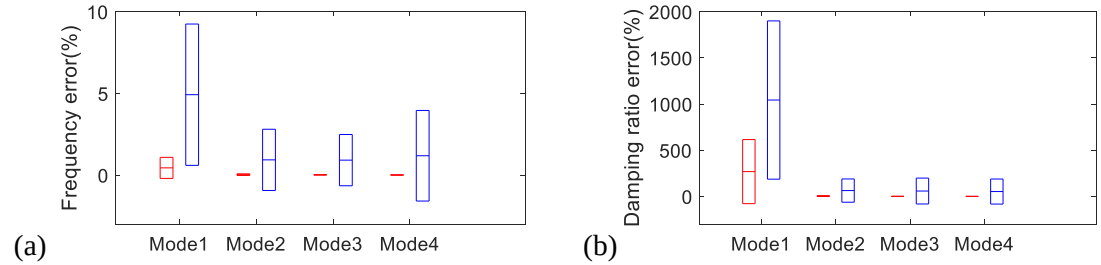


Figure 5 Averaged relative error and standard deviation of two methods: (a) modal frequency and (b) damping ratio (red: TDET method; blue: TOMA method; $\mathrm{ARE} \pm \mathrm{SD}$ values are shown with box)

Section 2 introduces that the TOMA method is based on the frequency-domain data of structural responses, thus the time-domain acceleration responses should be transformed into frequency-domain data, by using discrete Fourier transform. It should be noted that this transformation leads to leakage errors, resulting from the finite length of the measured signals. Leakage errors can be reduced by two methods. The first one is that the spectrum of periodic signals measured over an integer number of periods is perfectly calculated, and this method can thoroughly eliminate this error. Another method is to use, for example, a Hanning window, instead of a rectangular window to reshape the response signals. It is impossible to measure an integer number periodic acceleration signals of the structure under the Gaussian white noise excitations. The second method will lead to a typical effect that these window functions minimize the leakage effects at the

cost of a loss in the frequency resolution, and different window functions also affect the noise sensitivity. The interested readers are recommended to refer the Ref. [3] and the Ref. [27].

To study the influences of leakage errors on the TOMA method, burst random excitations is used for this example. The burst random excitation is defined as

$$u(t)=w(t)r(t),\ \ 0\le t\le T \tag{38}$$

In this expression, $r(t)$ is an excitation signal. $w(t)$ is window function, defined by

$$w(t)=\begin{cases}1, & 0\le t\le T_1\\ 0, & T_1\le t\le T\end{cases} \tag{39}$$

The selection of T_1 and T should allow the responses to decay to zero before the end of the observation time window. This paper used burst random excitations with $T=150$ s, $T_1=100$ s. $r(t)$ is same with the aforementioned $F_k(t)$ in Section 4.1.1, so the burst random excitations acting on the modelled system are characterized by a predominant frequency. Other properties of the excitations, including spatial distribution, are same with Section 4.1.1. One typical excitation and acceleration response are presented in Figure 6. The acceleration responses become negligible at the end of the measurement window.

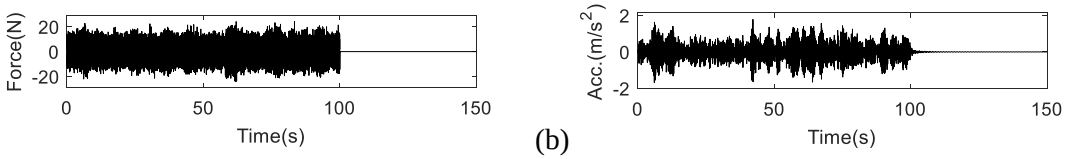
As indicated in Figure 7, the TOMA method is comparable with the TDET method when the system is under burst random excitations with a predominant frequency. This conclusion can be verified by several facts: one is that less spurious modes compared with Figure 3(b) are observed, and the estimated frequencies obtained by TOMA method are well separated, gathering densely around the four modes; The another is that the accuracy of damping ratios obtained by TOMA method is drastically improved, showing much lower variability of relative errors compared with those in Figure 3. Furthermore, the TOMA method can estimate the first mode well under burst random excitations, as presented in Figure 7(b).

To obtain a directly view on the quantities of errors, the ARE and SD values are depicted in Figure 8. Under the burst random excitations with a predominant frequency, the TOMA method and the TDET method are in fact comparable, with the latter slightly better than the former for all estimation results.

4.2 Finite element example

As shown in Figure 9, this model considered a simply supported beam, whose parameters are as follows: length along *x* axis 2 m, square cross-section $0.05\times 0.005m^2$, material Young Modulus 220 GPa, material Poisson's ratio 0.30, material density $7.85\times 10^3 \text{kg}/\text{m}^3$. The beam was uniformly divided into 10 elements, with the node labeled as 1 to 11, respectively. The proportional damping matrix was adopted. To simplify the simulation, only the vertical translation freedoms and the first four order modes were considered.

The required two different load cases were realized by changing the location point of excitations, node 5 and node 8, respectively. The input signals were constructed similarly to $F_k(t)$ in Section 4.1.1. The colored part $f_2(t)$ was the response of an SDOF system, which is characterized by a natural frequency of 10 Hz, 50 Hz and a damping ratio 2%, 1% in two load cases, respectively. The averaged auto-power spectrums of excitation forces and acceleration responses are shown in Figure 10.



(a) (b)

Figure 6 Typical realization of signals: (a) burst random excitation signal and (b) response signal

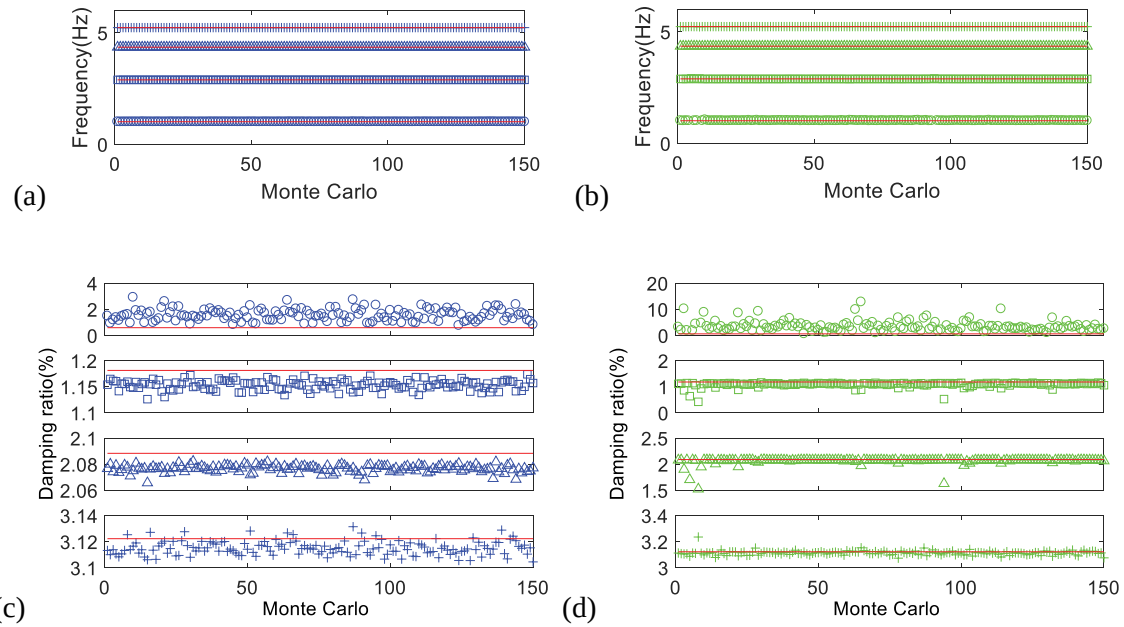


Figure 7 Summary results obtained under burst random excitations with 150 Monte Carlo runs for 4-DOF system: (a) and (c): TDET method; (b) and (d): TOMA method (red line: theoretical value; circle: first mode; square: second mode; triangle: third mode; plus: fourth mode)

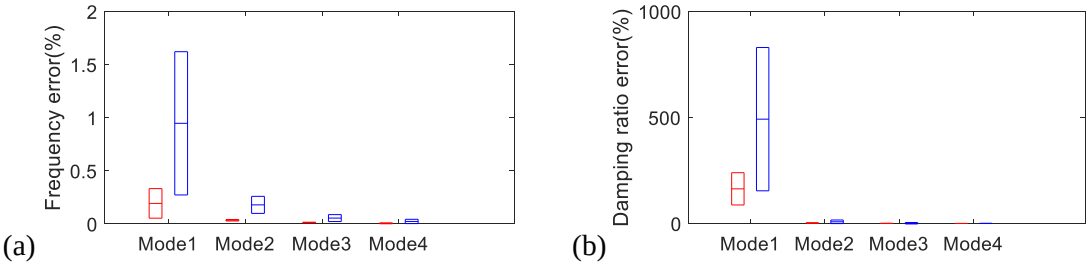


Figure 8 Averaged relative error and standard deviation under Hanning window: (a) modal frequency and (b) damping ratio (red: TDET method; blue: TOMA method; ARE $\pm$ SD values are shown with box)

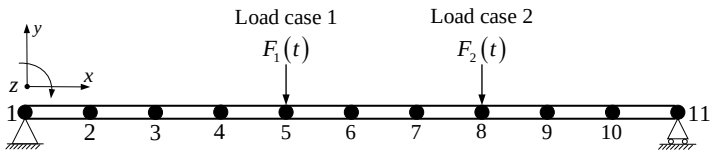


Figure 9 Schematic diagram of the finite element beam model

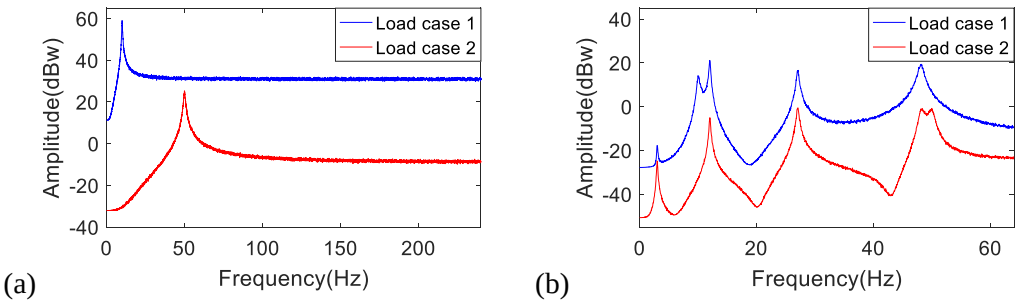


Figure 10 Averaged auto-power spectrum of excitation forces (a) and responses of node 10 (b) over 150 Monte Carlo runs

The acceleration responses were calculated by Newmark-β method with $\Delta t = 0.00025\,\text{s}$, $\beta = 0.5$, $\gamma = 0.25$ and then resampled with a frequency 256 Hz over a period of 20 s. The responses of node 2, 3, 4, and 5 were selected as reference signals, and the other 5 channels of node 6 to node 10 were non-reference responses. In this case $n_A = n_B$ was chosen for simplicity, and the value $n_A = n_B = 5$ was determined by BIC (Bayesian Information Criterion) [26], shown in Figure 11.

To further assess the performance of TDET method, the Hanning window was used for the frequency spectrum estimation in TOMA method. The summary results obtained with 150 Monte Carlo runs are presented in Figure 12 and Figure 13. Evidently, when the Hanning window is used, the TOMA method can achieve good frequency estimates, but the results of damping ratios are much worse than the proposed TDET method. The damping ratios derived by TDET method are less accurate than the frequency estimates, but the averaged relative errors are still smaller than 10%.

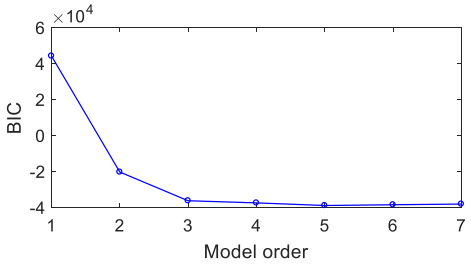
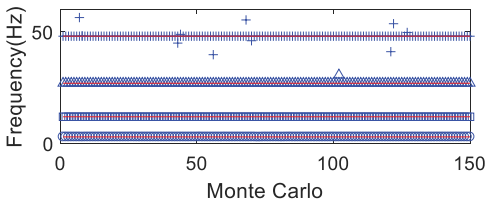


Figure 11 BIC based model order selection

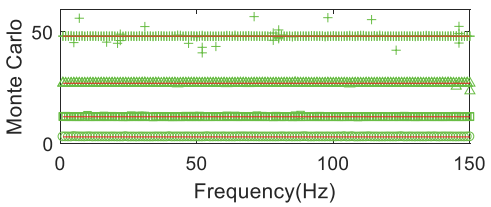
5 Conclusion

The TDET method proposed in this paper is able to estimate the modal parameters of a system under non-white excitations. The TDET method links the multivariable transmissibility with the ARX model in time-domain, by using time-domain reference and non-reference responses to replace the exogenous excitation part and auto-regressive part, respectively. This property enables the proposed TDET method to avoid the data transformation from time-domain responses into frequency-domain data, which thoroughly eliminates the leakage errors and avoids the selection of window function. Therefore, the TDET method is easier to use in practice than TOMA method.

The results of the 4-DOF system under the random and burst random excitations characterized by a predominant frequency show the fact that the leakage errors resulting from the finite length of the measurements will reduce the accuracy of TOMA method, especially for the damping ratios estimation. Contrarily, the TDET method directly permits time-domain responses, hence thoroughly eliminates the leakage errors. This property enables the TDET method to achieve overall better performance than TOMA method, especially in terms of the estimation accuracy of low-frequency modes. This method was also used to analyze the vibration data of a finite element beam example. The results of this application demonstrate that the Hanning window can improve frequency estimates of the TOMA method, but the damping ratio estimates are much worse than those of the proposed TDET model.



(a)



(b)

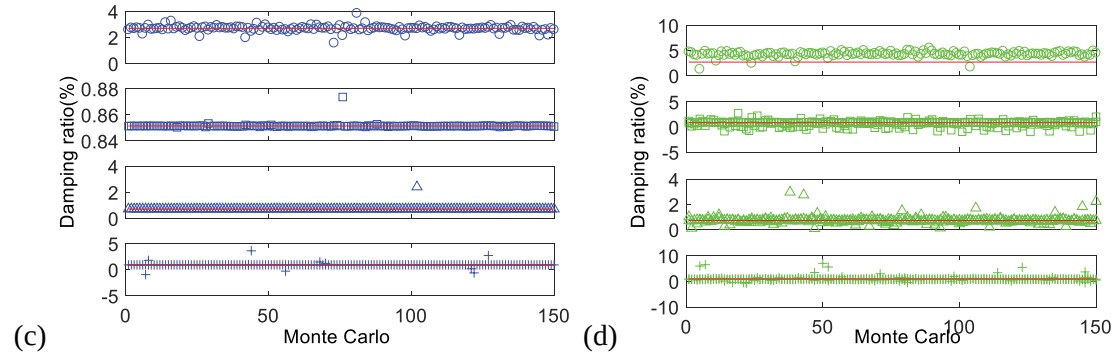


Figure 12 Summary results obtained by 150 Monte Carlo runs for beam model: (a) and (c): TDET method; (b) and (d): TOMA method (red line: theoretical value; circle: first mode; square: second mode; triangle: third mode; plus: fourth mode)

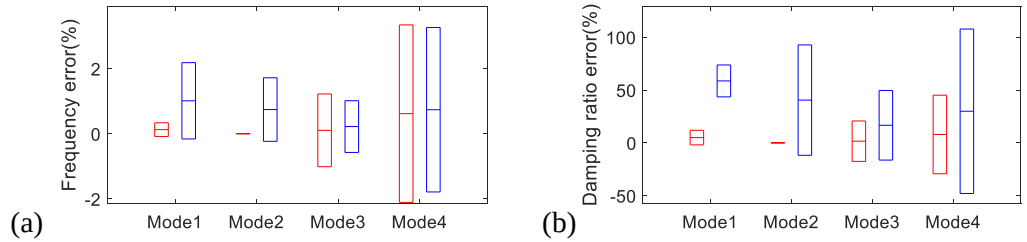


Figure 13 Averaged relative error and standard deviation: (a) modal frequency and (b) damping ratio (red: TDET method; blue: TOMA method with Hanning window; $\mathrm{ARE} \pm \mathrm{SD}$ values are shown with box)

References

[1] Á. Cunha, E. Caetano, Experimental Modal Analysis of Civil Engineering Structures, Sound and Vibration, 40 (2006) 269-279.

[2] K.A. PETSOUNIS, S.D. FASSOIS, Pamametric time-domain methods for the identification of vibrating structures—A critical comparison and assessment, Mechanical Systems & Signal Processing, 15 (2001) 1031-1060.

[3] W. Heylen, S. Lammens, P. Sas, Modal analysis theory and testing, Leuvem, belgium, Katholieke Universiteit Leuven, 1997.

[4] D.J. Ewins, Modal testing: theory and practice, Research Studies Press LTD, London,England, 2000.

[5] B. Peeters, G.D. Roeck, Stochastic System Identification for Operational Modal Analysis: A Review, Journal of Dynamic Systems Measurement & Control, 123 (2001) 659-667.

[6] M.S. Allen, M.W. Sracic, S. Chauhan, M.H. Hansen, Output-only modal analysis of linear time-periodic systems with application to wind turbine simulation data, Mechanical Systems & Signal Processing, 25 (2011) 1174-1191.

[7] C. Devriendt, G.D. Sitter, S. Vanlanduit, P. Guillaume, Operational modal analysis in the presence of harmonic excitations by the use of transmissibility measurements, Machanical Systems and Signal Processing, 23 (2009) 621-635.

[8] Y. Yang, X.J.Dong, Z.K.Peng, W.M.Zhang, G.Meng, Vibration signal analysis using parameterized time–frequency method forfeaturesextractionofvarying-speed rotarymachinery, Journal of Sound and Vibration, 335 (2015) 350-366.

[9] P. Mohanty, D.J. Rixen, Operational modal analysis in the presence of harmonic excitation, Journal of Sound and Vibration, 270 (2004) 93-109.

[10] K. Motte, W. Weijtjens, C. Devriendt, P. Guillaume, Operational Modal Analysis in the Presence of Harmonic Excitations: A Review, in: Conference Proceedings of the Society for Experimental Mechanics Series, Springer, Cham, Caicedo J., Pakzad S., 2015.

[11] A.M.R. RIBEIRO, J.M.M. SILVA, N.M.M. MAIA, On the generalisation of the transmissibility concept, Mechanical Systems and Signal Processing, 14 (2000) 29-35.

[12] W. Liu, D.J. Ewins, Transmissibility Properties of MDOF Systems, in: Proceedings of the 16th International Modal Analysis Conference, Proceedings of SPIE Santa Barbara,CA, 1998.

[13] P. Varoto, K. Mcconnell, Single Point vs Multi Point Acceleration Transmissibility Concepts in Vibration Testing, in: Proceedings of the 16th International Modal Analysis Conference, Proceedings of SPIE, Santa Barbara,CA, 1998, pp. 83-90.

[14] M. Fontul, A.M.R. Ribeiro, J.M.M. Silva, N.M.M. Maia, Transmissibility matrix in harmonic and random processes, Shock & Vibration, 11 (2004) 563-571.

[15] P. Guillaume, C. Devriendt, G.D. Sitter, Identification of modal parameters from transmissibility measurements, in: 1st International Operational Modal Analysis Conference, Copenhagen, Denmark, April 2005.

[16] C. Devriendt, P. Guillaume, The use of transmissibility measurements in output-only modal analysis, Mechanical Systems & Signal Processing, 21 (2007) 2689-2696.

[17] C. Devriendt, P. Guillaume, Identification of modal parameters from transmissibility measurements, Journal of Sound and Vibration, 314 (2008) 343-356.

[18] C. Devriendt, W.Weijtjens, G.DeSitter, P.Guillaume, Combining multiple single-reference transmissibility functions in a unique matrix formulation for operational modal analysis, MechanicalSystemsandSignalProcessing, 40 (2013) 278-287.

[19] P. Guillaume, C. Devriendt, G.D. Sitter, An operational modal analysis approach based on parametrically identified multivariable transmissibilities, Mechanical Systems and Signal Processing, 24 (2010) 1250-1259.

[20] WoutWeijtjens, G.d. Sitter, C. Devriendt, P. Guillaume, Operational Modal Analysis Based on Multivariable Transmissibility Functions: Revisited, in: Conference Proceedings of the Society for Experimental Mechanics Series, 2013, pp. 317-326.

[21] W. Weijtjens, G.D. Sitter, C. Devriendt, P. Guillaume, Operational modal parameter estimation of MIMO systems using transmissibility functions☆, Automatica, 50 (2014) 559-564.

[22] W.-J. Yan, W.-X. Ren, Operational Modal Parameter Identification from Power Spectrum Density Transmissibility, Computer-Aided Civil and Infrastructure Engineering, 27 (2012) 202-217.

[23] I.G. Araújo, J.E. Laier, Operational modal analysis using SVD of power spectral density transmissibility matrices, Mechanical Systems and Signal Processing, 46 (2014) 129-145.

[24] I.G. Araújo, J.E. Laier, Operational modal analysis approach based on multivariable transmissibility with different transferring outputs, Journal of Sound and Vibration, 351 (2015) 90-105.

[25] R. Pintelon, J. Schoukens, System identification-A frequency domain approach, IEEE Press, New York, 2001.

[26] A. Poulimenos, S. Fassois, Parametric time-domain methods for non-stationary random vibration modelling and analysis — A critical survey and comparison, Machanical Systems and Signal Processing, 20 (2006) 763-816.

[27] F.J. HARRIS, On the Use of Windows for Harmonic Analysis with the Discrete Fourier Transform, PROCEEDINGS OF THE IEEE, 66 (1978) 51-83.

Output-only modal parameter estimator of time-varying structures based on maximum correntropy criterion and kernelized TARMA model

L. Yu[1], L. Liu[1,2,3], J. Kang[1]
[1] Beijing Institute of Technology, School of Aerospace Engineering

[2] Ministry of Education, Key Laboratory of Dynamics and Control of Flight Vehicle

[3] Ministry of Industry and Information Technology, Key Laboratory of Autonomous Navigation and Control for Deep Space Exploration

Abstract
The problem of output-only identification of a Time-Varying structure under non-Gaussian impulsive noise is considered. A novel estimator is proposed based on maximum correntropy criterion and kernelized time-dependent autoregressive moving average model (TARMA), and a sliding-window technique is applied to fix the computational complexity. The steps of the identification procedure and model selection are presented, and for modelling non-Gaussian impulsive noise, a class of alpha-stable distribution is introduced. The proposed approach is comparatively assessed against the classical recursive pseudo-linear regression TARMA method. The results of the study demonstrate the superior achievable accuracy, higher computation efficiency and enhanced robustness to non-Gaussian impulsive noise of the proposed approach.

1 Introduction

Most of the mechanical structures in the real world are characterized by time-dependent characteristics, such as traffic-excited bridges with varying mass [1], airplanes with varying additional aerodynamic effects in flight [2], rotating machinery [3], robotic devices and so on. With the development in industry and engineering, more and more such time-varying structures are appeared.

The problem of time-varying structures identification involving exclusively available response signals is referred as output-only time-varying identification problem [4], due to the excitation is hard to obtain in practical cases. The identification methods of linear time-varying structural can be classified as frequency-domain and time-domain. Since time-domain identification methods have some attractive features compared to its counterpart, the time-domain identification methods have gained more and more attention in the past decades. Time-dependent state-space (TSS) representation and time-dependent autoregressive moving average (TARMA) representation are mainly two categories of time-domain identification methods.

Over the past decades many efforts have been undertaken to develop the TARMA representation based identification methods in a recursive manner [5-7]. Yet, most proposed recursive estimators are based on least-squares (LS) criterion due to its mathematical tractability, computational simplicity and optimality under Gaussian assumption. However, the performance of LS based identification methods deteriorates when the Gaussian assumption is not hold. Hence it is crucial to find a new criterion to expend the application range of the TARMA representation based methods.

The correntropy has been shown to obtain robust analysis and efficiently handle non-Gaussian noise in information theoretic learning (ITL) [8, 9]. Correntropy is widely used in many fields as a nonlinear and local similarity measure due to its simplicity and robustness.

In this paper, a novel robust estimator is established based on maximum correntropy criterion and kernelized TARMA model. The kernelized TARMA model is proposed by Ma [10], it represents time-varying parameters as a linear combination of kernel functions, by using "kernel trick" and sliding-window technique the computation complexity is fixed and only related to the window length. Moreover, by considering a ridge regression problem the proposed estimator is also capable of ill-posed problem. Finally, a recursive work flow of sliding-window exponentially weighted recursive maximum correntropy ridge regression kernelized TARMA (SWRMCRR-KTARMA) method is presented, by taking the assumption that time-varying system changes slowly.

The remainder of this paper is organized as follows: kernelized TARMA model and maximum correntropy criterion are introduced briefly in section 2. In section 3, the novel estimator is established, and the steps of identification and model structure selection is also discussed in this section. In section 4, a class of alpha stable distribution is introduced to model non-Gaussian impulsive noise, and the proposed approach is compared to the conventional LS based method which referred as exponentially weighted recursive pseudo-linear regression TARMA (EWRPLR-TARMA) method via a numerical case. At last, summary of the study is rendered in section 6.

2 Preliminaries

2.1 Kernelized TARMA model

The TARMA model with n_a, n_c designating respectively its autoregressive (AR) and moving average (MA) orders, is of the general form [11]

$$\boldsymbol{x}[t]+\sum_{i=1}^{n_a}\boldsymbol{A}_i[t]\boldsymbol{x}[t-i]=\boldsymbol{e}[t]+\sum_{i=1}^{n_c}\boldsymbol{C}_i[t]\boldsymbol{e}[t-i],\quad \boldsymbol{e}[t]\sim \mathrm{NID}\left(\boldsymbol{0},\boldsymbol{\Sigma}[t]\right) \tag{1}$$

with t designating normalized discrete time, $\boldsymbol{x}[t]$ the discrete-time non-stationary vibration signal modelled, $\boldsymbol{e}[t]$ an unobservable uncorrelated innovations sequence with zero mean and time-varying non-singular covariance matric $\boldsymbol{\Sigma}[t]$, and $\boldsymbol{A}_i[t],\boldsymbol{C}_i[t]$ the model's time-dependent AR and MA parameter matrices. $\mathrm{NID}(\cdot)$ stands for normally independently distributed random variables with indicated mean and covariance.

By using kernel transformation, the AR and MA parameter matrices can be expressed as

$$\boldsymbol{A}_i[t]\approx\begin{bmatrix}\boldsymbol{\omega}_{1,1}^{Ai}[t]^{\mathrm{T}}\boldsymbol{u}(t) & \cdots & \boldsymbol{\omega}_{1,k}^{Ai}[t]^{\mathrm{T}}\boldsymbol{u}(t)\\ \vdots & \ddots & \vdots\\ \boldsymbol{\omega}_{k,1}^{Ai}[t]^{\mathrm{T}}\boldsymbol{u}(t) & \cdots & \boldsymbol{\omega}_{k,k}^{Ai}[t]^{\mathrm{T}}\boldsymbol{u}(t)\end{bmatrix},\ \boldsymbol{C}_i[t]\approx\begin{bmatrix}\boldsymbol{\omega}_{1,1}^{Ci}[t]^{\mathrm{T}}\boldsymbol{u}(t) & \cdots & \boldsymbol{\omega}_{1,k}^{Ci}[t]^{\mathrm{T}}\boldsymbol{u}(t)\\ \vdots & \ddots & \vdots\\ \boldsymbol{\omega}_{k,1}^{Ci}[t]^{\mathrm{T}}\boldsymbol{u}(t) & \cdots & \boldsymbol{\omega}_{k,k}^{Ci}[t]^{\mathrm{T}}\boldsymbol{u}(t)\end{bmatrix} \tag{2}$$

The kernelized TARMA model is given by

$$\begin{aligned}
&\boldsymbol{x}[t]=-\sum_{i=1}^{n_a}\boldsymbol{A}_i[t]\boldsymbol{x}[t-i]+\sum_{i=1}^{n_c}\boldsymbol{C}_i[t]\boldsymbol{e}[t-i]+\boldsymbol{e}[t]\\
\Leftrightarrow\ &\boldsymbol{x}[t]=\boldsymbol{w}[t]^{\mathrm{T}}\boldsymbol{\varphi}[t]+\boldsymbol{e}[t]\\
\Leftrightarrow\ &\boldsymbol{x}[t]=\begin{bmatrix}\boldsymbol{\omega}_{1,1}^{A1}[t]^{\mathrm{T}} & \cdots & \boldsymbol{\omega}_{1,k}^{A1}[t]^{\mathrm{T}} & \cdots & \boldsymbol{\omega}_{1,1}^{Cn_c}[t]^{\mathrm{T}} & \cdots & \boldsymbol{\omega}_{1,k}^{Cn_c}[t]^{\mathrm{T}}\\ \vdots & \ddots & \vdots & \ddots & \vdots & \ddots & \vdots\\ \boldsymbol{\omega}_{k,1}^{A1}[t]^{\mathrm{T}} & \cdots & \boldsymbol{\omega}_{k,k}^{A1}[t]^{\mathrm{T}} & \cdots & \boldsymbol{\omega}_{k,1}^{Cn_c}[t]^{\mathrm{T}} & \cdots & \boldsymbol{\omega}_{k,k}^{Cn_c}[t]^{\mathrm{T}}\end{bmatrix}\begin{bmatrix}-\boldsymbol{x}[t-1]\otimes\boldsymbol{u}(t)\\ \vdots\\ \boldsymbol{e}[t-n_c]\otimes\boldsymbol{u}(t)\end{bmatrix}+\boldsymbol{e}[t]\\
\Leftrightarrow\ &\boldsymbol{x}[t]=\boldsymbol{\omega}[t]^{\mathrm{T}}\left(\boldsymbol{\varphi}[t]\otimes\boldsymbol{u}(t)\right)+\boldsymbol{e}[t]\\
\Leftrightarrow\ &\boldsymbol{x}[t]=\boldsymbol{\omega}[t]^{\mathrm{T}}\boldsymbol{\phi}[t]+\boldsymbol{e}[t]
\end{aligned} \tag{3}$$

where $\otimes$ is the Kronecker product, $\boldsymbol{w}[t]$ is the time-dependent parameter vector and $\boldsymbol{\varphi}[t]$ is the regression matrix, $\boldsymbol{\omega}[t]$ and $\boldsymbol{\phi}[t]$ are corresponding kernelized counterparts. $\boldsymbol{u}(t)$ is the transformed feature vector lying in the feature space, by using a Gaussian kernel the "kernel trick" can be expressed as follows

$$\boldsymbol{u}(t_i)^{\mathrm{T}}\boldsymbol{u}(t_j)=\kappa_k(t_i,t_j)=\exp\left(-\frac{\|t_i-t_j\|^2}{2\sigma_k^2}\right) \tag{4}$$

where σ_k designating the adjustable parameter.

The system's "frozen-time" characteristic matrix equation [12] is given by

$$\left|\boldsymbol{A}[\mathscr{B},t]\right|=\left|\boldsymbol{I}+\sum_{i=1}^{n_a}\boldsymbol{A}_i[t]\mathscr{B}^i\right|=0 \tag{5}$$

with $\mathscr{B}$ designating the backshift operator, $\mathscr{B}^i\boldsymbol{x}[t]=\boldsymbol{x}[t-i]$. Hence, the roots of the system can be derived from a general eigenvalue problem [13]

$$\left(\boldsymbol{D}[t]-\lambda_r[t]\boldsymbol{I}\right)\boldsymbol{V}_r[t]=\boldsymbol{0} \tag{6}$$

where $\lambda_r[t]$ and $\boldsymbol{V}_r[t]=\left[\lambda_r^{-n_a}\boldsymbol{L}_r,\ldots,\lambda_r^{-1}\boldsymbol{L}_r\right]^{\mathrm{T}}$ stand for r^{th} eigenvalue and eigenvector of $\boldsymbol{D}[t]$. The matrix $\boldsymbol{D}[t]$ is constructed from the AR parameter matrices as

$$\boldsymbol{D}[t]=\begin{bmatrix}\boldsymbol{0} & \boldsymbol{I} & \cdots & \boldsymbol{0}\\ \vdots & \vdots & \ddots & \vdots\\ \boldsymbol{0} & \boldsymbol{0} & \cdots & \boldsymbol{I}\\ -\boldsymbol{A}_{n_a}[t] & -\boldsymbol{A}_{n_a-1}[t] & \cdots & -\boldsymbol{A}_1[t]\end{bmatrix} \tag{7}$$

The "frozen-time" modal frequencies and damping ratios of the system can be computed by

$$f_r[t]=\frac{\left|\ln\lambda_r[t]\right|}{2\pi T_s},\ \zeta_r[t]=\frac{-\mathrm{Re}\left(\ln\lambda_r[t]\right)}{\left|\ln\lambda_r[t]\right|} \tag{8}$$

2.2 Maximum correntropy criterion

In general correntropy is local similarity measure between two arbitrary random variables of $X,Y\in\mathbb{R}$, with joint distribution function $F_{XY}(x,y)$, and is defined by [14]

$$V(X,Y)=E\left[\kappa_c(X,Y)\right]=\int\kappa_c(x,y)\,d\,F_{XY}(x,y) \tag{9}$$

where $\kappa(\cdot)$ is a kernel function that satisfies Mercer theory and $E(\cdot)$ denotes the expectation operator. In this paper, the shift-invariant Mercer kernel is the Gaussian kernel given by

$$\kappa_c(x,y)=G(e)=\exp\left(-\frac{e^2}{2\sigma_c^2}\right) \tag{10}$$

where $e=x-y$, and $\sigma_c>0$ stands for the kernel bandwidth.

Taking Taylor series expansion around $X-Y=0$, the correntropy can be expressed as

$$V(X,Y)=\sum_{n=0}^{\infty}\frac{(-1)^n}{2^n\sigma_c^{2n}n!}E\left[(X-Y)^{2n}\right] \tag{11}$$

In practice, however, the joint probability density function F_{XY} is unknown and only a limited number of data are available. Hence, the sample estimator of correntropy is estimated by

$$\hat{V}(X,Y)=\frac{1}{N}\sum_{i=1}^{N}G(e(i)) \tag{12}$$

For a ridge regression problem, with parameter weight vector $\boldsymbol{w}$, corresponding optimal problem based on the maximum correntropy criterion can be expressed as follows

$$\max_{\boldsymbol{w}} J_{MCC}=\max_{\boldsymbol{w}}\left[\sum_{i=1}^{N}E\left[\exp\left(-\frac{e^2(i)}{2\sigma_c^2}\right)\right]-\gamma\|\boldsymbol{w}\|^2\right] \tag{13}$$

3 Recursive maximum correntropy ridge regression kernelized TARMA approach

3.1 Ridge regression of kernelized TARMA model

The exponentially weighted mechanism is used here in order to put more emphasis on the recent data. Given the forgetting factor $0<\lambda\leq 1$ and the regularization parameter $\gamma\geq 0$, the weighted regularized maximum correntropy cost function is defined as

$$\max_{\boldsymbol{\omega}[t]}\left[\sum_{\tau=1}^{t}\lambda^{t-\tau}\kappa_c\left(\boldsymbol{x}[\tau]-\boldsymbol{\omega}[t]^{\mathrm{T}}\boldsymbol{\phi}[\tau]\right)-\frac{1}{2}\lambda^t\gamma\|\boldsymbol{\omega}[t]\|^2\right] \tag{14}$$

The solution to this optimal problem is given by

$$\boldsymbol{\omega}[t]=\left(\lambda^t\gamma\sigma_c^2\boldsymbol{I}+\tilde{\boldsymbol{\Psi}}[t]\boldsymbol{\Gamma}[t]\tilde{\boldsymbol{\Psi}}[t]^{\mathrm{T}}\right)^{-1}\tilde{\boldsymbol{\Psi}}[t]\boldsymbol{\Gamma}[t]\tilde{\boldsymbol{x}}[t] \tag{15}$$

with

$$\tilde{\boldsymbol{\Psi}}[t]\triangleq\left[\boldsymbol{\phi}[1],\boldsymbol{\phi}[2],\ldots,\boldsymbol{\phi}[t]\right] \tag{16}$$

$$\tilde{\boldsymbol{x}}[t]\triangleq\left[\boldsymbol{x}[1],\boldsymbol{x}[2],\ldots,\boldsymbol{x}[t]\right]^{\mathrm{T}} \tag{17}$$

$$\begin{aligned}\boldsymbol{\Gamma}[t]&\triangleq diag\left\{\lambda^{t-1}\exp\left(-\frac{\left\|\boldsymbol{x}[1]-\boldsymbol{\omega}[1]^{\mathrm{T}}\boldsymbol{\phi}[1]\right\|^2}{2\sigma_c^2}\right),\lambda^{t-2}\exp\left(-\frac{\left\|\boldsymbol{x}[2]-\boldsymbol{\omega}[2]^{\mathrm{T}}\boldsymbol{\phi}[2]\right\|^2}{2\sigma_c^2}\right),\ldots,\exp\left(-\frac{\left\|\boldsymbol{x}[t]-\boldsymbol{\omega}[t]^{\mathrm{T}}\boldsymbol{\phi}[t]\right\|^2}{2\sigma_c^2}\right)\right\}\\&\triangleq diag\left\{\lambda^{t-1}\exp\left(\frac{-1}{2\sigma_c^2}\boldsymbol{e}[1]^{\mathrm{T}}\boldsymbol{e}[1]\right),\lambda^{t-2}\exp\left(\frac{-1}{2\sigma_c^2}\boldsymbol{e}[2]^{\mathrm{T}}\boldsymbol{e}[2]\right),\ldots,\exp\left(\frac{-1}{2\sigma_c^2}\boldsymbol{e}[t]^{\mathrm{T}}\boldsymbol{e}[t]\right)\right\}\end{aligned} \tag{18}$$

where $diag(\cdot)$ is diagonal matrix operator, $\exp(\cdot)$ stands for exponential function with constant e, and $\boldsymbol{e}[t]\triangleq\boldsymbol{x}[t]-\boldsymbol{w}[t]^{\mathrm{T}}\boldsymbol{\varphi}[t]$.

By using the matrix lemma, Eq. (15) can be rewritten as follows

$$\boldsymbol{\omega}[t]=\tilde{\boldsymbol{\Psi}}[t]\left(\tilde{\boldsymbol{\Psi}}[t]^{\mathrm{T}}\tilde{\boldsymbol{\Psi}}[t]+\lambda^t\gamma\sigma_c^2\boldsymbol{\Gamma}[t]^{-1}\right)^{-1}\tilde{\boldsymbol{x}}[t] \tag{19}$$

Denote $\boldsymbol{Q}[t]=\tilde{\boldsymbol{\Psi}}[t]^{\mathrm{T}}\tilde{\boldsymbol{\Psi}}[t]+\lambda^t\gamma\sigma_c^2\boldsymbol{\Gamma}[t]^{-1}$ and $\boldsymbol{k}[t]=\tilde{\boldsymbol{\Psi}}[t-1]^{\mathrm{T}}\boldsymbol{\phi}[t]$, the following equation can be received

$$\boldsymbol{Q}[t]=\begin{bmatrix}\boldsymbol{Q}[t-1] & \boldsymbol{k}[t]\\ \boldsymbol{k}[t]^{\mathrm{T}} & \boldsymbol{\phi}[t]^{\mathrm{T}}\boldsymbol{\phi}[t]+\lambda^{t}\gamma\sigma_c^2 E[t]^{-1}\end{bmatrix} \tag{20}$$

where $E[t]$ □ $\exp\left(\frac{-1}{2\sigma_c^2}\boldsymbol{e}[t]^{\mathrm{T}}\boldsymbol{e}[t]\right)$, $\boldsymbol{\phi}[t]^{\mathrm{T}}\boldsymbol{\phi}[t]$ can be computed by using "kernel trick" as follows

$$\begin{aligned}\boldsymbol{\phi}[t]^{\mathrm{T}}\boldsymbol{\phi}[t]&=\left(\boldsymbol{\varphi}(t)\otimes\boldsymbol{u}(t)\right)^{\mathrm{T}}\left(\boldsymbol{\varphi}(t)\otimes\boldsymbol{u}(t)\right)\\&=\left(\boldsymbol{\varphi}(t)^{\mathrm{T}}\boldsymbol{\varphi}(t)\right)\kappa_k(t,t)\end{aligned} \tag{21}$$

where $\kappa_k\left(t_i,t_j\right)=\exp\left(-\frac{\left\|t_i-t_j\right\|^2}{2\sigma_k}\right)$.

The update rule for the matrix $\boldsymbol{Q}[t]^{-1}$ is

$$\boldsymbol{Q}[t]^{-1}=\begin{bmatrix}\boldsymbol{Q}[t-1]^{-1}+\boldsymbol{z}[t]\boldsymbol{z}[t]^{\mathrm{T}}r[t]^{-1} & -\boldsymbol{z}[t]r[t]^{-1}\\ -\boldsymbol{z}[t]^{\mathrm{T}}r[t]^{-1} & r[t]^{-1}\end{bmatrix} \tag{22}$$

with $\boldsymbol{z}[t]=\boldsymbol{Q}[t-1]^{-1}\boldsymbol{k}[t]$, $r[t]=\lambda^{t}\gamma\sigma_c^2E[t]^{-1}+\boldsymbol{\phi}[t]^{\mathrm{T}}\boldsymbol{\phi}[t]-\boldsymbol{z}[t]^{\mathrm{T}}\boldsymbol{k}[t]$

Considering Eq. (19) and Eq. (22), the kernelized parameter matrix $\boldsymbol{\omega}[t]$ can be obtained

$$\boldsymbol{\omega}[t]=\tilde{\boldsymbol{\Psi}}[t]\boldsymbol{Q}[t]^{-1}\tilde{\boldsymbol{x}}[t] \tag{23}$$

Finally, time-dependent AR and MA parameter matrices can be computed by

$$\begin{aligned}\boldsymbol{w}[t]^{\mathrm{T}}&=\left[\boldsymbol{A}_1[t],\ldots,\boldsymbol{A}_{n_a}[t],\boldsymbol{C}_1[t],\ldots,\boldsymbol{C}_{n_c}[t]\right]\\&=\boldsymbol{\omega}[t]^{\mathrm{T}}\left(\boldsymbol{I}_{k(n_a+n_c)}\otimes\boldsymbol{u}[t]\right)\\&=\left(\tilde{\boldsymbol{\Psi}}[t]\boldsymbol{Q}[t]^{-1}\tilde{\boldsymbol{x}}[t]\right)^{\mathrm{T}}\left(\boldsymbol{I}_{k(n_a+n_c)}\otimes\boldsymbol{u}[t]\right)\\&=\left(\boldsymbol{Q}[t]^{-1}\tilde{\boldsymbol{x}}[t]\right)^{\mathrm{T}}\begin{bmatrix}\boldsymbol{\varphi}[1]^{\mathrm{T}}\otimes\kappa_k(1,t)\\ \vdots\\ \boldsymbol{\varphi}[t]^{\mathrm{T}}\otimes\kappa_k(t,t)\end{bmatrix}\end{aligned} \tag{24}$$

This workflow is summarized in Table 1. However, the computational complexity of the proposed method is $O\left(t^2\right)$ at time step t due to the growing size $\boldsymbol{Q}[t]$, causing this method unable to use when t is a large number.

Initialization：

$\hat{\boldsymbol{w}}[0]^{\mathrm{T}}=\mathbf{0},\ \sigma_c,\ \sigma_k,\lambda,\gamma$

Computation $(t=1)$：

$$\hat{\boldsymbol{e}}[t|t-1]=\boldsymbol{x}[t]-\hat{\boldsymbol{x}}[t|t-1]=\boldsymbol{x}[t]-\hat{\boldsymbol{w}}[t-1]^{\mathrm{T}}\boldsymbol{\varphi}[t]$$

$$\boldsymbol{Q}[t]^{-1}=\left(\boldsymbol{\varphi}[t]^{\mathrm{T}}\boldsymbol{\varphi}[t]\kappa_k(t,t)+\lambda^t\gamma\sigma_c^2\boldsymbol{\Gamma}[t]^{-1}\right)^{-1}$$

$$\boldsymbol{w}[t]=\left(\boldsymbol{Q}[t]^{-1}\tilde{\boldsymbol{x}}[t]\right)^{\mathrm{T}}\left[\boldsymbol{\varphi}[t]^{\mathrm{T}}\otimes\kappa_k(t,t)\right]$$

Computation $(t>1)$：

$$\hat{\boldsymbol{e}}[t|t-1]=\boldsymbol{x}[t]-\hat{\boldsymbol{x}}[t|t-1]=\boldsymbol{x}[t]-\hat{\boldsymbol{w}}[t-1]^{\mathrm{T}}\boldsymbol{\varphi}[t]$$

$$E[t]=\exp\left(\frac{-1}{2\sigma_c^2}\hat{\boldsymbol{e}}[t|t-1]^{\mathrm{T}}\hat{\boldsymbol{e}}[t|t-1]\right)$$

$$\boldsymbol{k}[t]=\tilde{\boldsymbol{\Psi}}[t-1]^{\mathrm{T}}\boldsymbol{\phi}[t]=\begin{bmatrix}\boldsymbol{\phi}[1]^{\mathrm{T}}\boldsymbol{\phi}[t]\\ \vdots\\ \boldsymbol{\phi}[t-1]^{\mathrm{T}}\boldsymbol{\phi}[t]\end{bmatrix}=\begin{bmatrix}\boldsymbol{\varphi}[1]^{\mathrm{T}}\boldsymbol{\varphi}[t]\kappa_k(1,t)\\ \vdots\\ \boldsymbol{\varphi}[t-1]^{\mathrm{T}}\boldsymbol{\varphi}[t]\kappa_k(t-1,t)\end{bmatrix}$$

$$\boldsymbol{z}[t]=\boldsymbol{Q}[t-1]^{-1}\boldsymbol{k}[t]$$

$$r[t]=\lambda^t\gamma\sigma_c^2E[t]^{-1}+\boldsymbol{\varphi}[t]^{\mathrm{T}}\boldsymbol{\varphi}[t]\kappa_k(t,t)-\boldsymbol{z}[t]^{\mathrm{T}}\boldsymbol{k}[t]$$

$$\boldsymbol{Q}[t]^{-1}=\begin{bmatrix}\boldsymbol{Q}[t-1]^{-1}+\boldsymbol{z}[t]\boldsymbol{z}[t]^{\mathrm{T}}r[t]^{-1} & -\boldsymbol{z}[t]r[t]^{-1}\\ -\boldsymbol{z}[t]^{\mathrm{T}}r[t]^{-1} & r[t]^{-1}\end{bmatrix}$$

$$\hat{\boldsymbol{w}}[t]^{\mathrm{T}}=\left(\boldsymbol{Q}[t]^{-1}\tilde{\boldsymbol{x}}[t]\right)^{\mathrm{T}}\begin{bmatrix}\boldsymbol{\varphi}[1]^{\mathrm{T}}\otimes\kappa_k(1,t)\\ \vdots\\ \boldsymbol{\varphi}[t]^{\mathrm{T}}\otimes\kappa_k(t,t)\end{bmatrix}$$

TARMA model parameter estimation：

$$\left[\boldsymbol{A}_1[t],\ldots,\boldsymbol{A}_{n_a}[t],\boldsymbol{C}_1[t],\ldots,\boldsymbol{C}_{n_c}[t]\right]=\hat{\boldsymbol{w}}[t]^{\mathrm{T}}$$

Table 1: The pseudocode of RMCRR-KTARMA method

3.2 Sliding-window technique

In order to fixed the computational complexity, a sliding-window technique is adopted, allowing the proposed method can be operated in a recursive manner with low computational cost.

By using the sliding-window technique, the following quantities can be redefined

$$\begin{aligned}\vec{\boldsymbol{\Psi}}[t]&\triangleq\left[\boldsymbol{\varphi}[t-N+1],\boldsymbol{\varphi}[t-N+2],\ldots,\boldsymbol{\varphi}[t]\right]\\ \vec{\boldsymbol{x}}[t]&\triangleq\left[\boldsymbol{x}[t-N+1],\boldsymbol{x}[t-N+2],\ldots,\boldsymbol{x}[t]\right]^{\mathrm{T}}\\ \vec{\boldsymbol{\Gamma}}[t]&\triangleq diag\left\{\lambda^{N-1}E[t-N+1],\lambda^{N-2}E[t-N+2],\ldots,E[t]\right\}\end{aligned}\tag{25}$$

Corresponding cost function is

$$\max_{\boldsymbol{\omega}[t]}\left[\sum_{\tau=t-N+1}^{t}\lambda^N\kappa_c\left(\boldsymbol{x}[\tau]-\boldsymbol{\omega}[t]^{\mathrm{T}}\boldsymbol{\phi}[\tau]\right)-\frac{1}{2}\lambda^N\gamma\left\|\boldsymbol{\omega}[t]\right\|^2\right]\tag{26}$$

The solution to this problem is

$$\boldsymbol{\omega}[t]=\vec{\boldsymbol{\Psi}}[t]\left(\vec{\boldsymbol{\Psi}}[t]^{\mathrm{T}}\vec{\boldsymbol{\Psi}}[t]+\lambda^{N}\gamma{\sigma_c}^{2}\vec{\boldsymbol{\Gamma}}[t]^{-1}\right)^{-1}\vec{\boldsymbol{x}}[t] \tag{27}$$

Denote $\vec{\boldsymbol{Q}}[t]=\vec{\boldsymbol{\Psi}}[t]^{\mathrm{T}}\vec{\boldsymbol{\Psi}}[t]+\lambda^{N}\gamma\sigma_c^{2}\vec{\boldsymbol{\Gamma}}[t]^{-1}$ and $\vec{\boldsymbol{k}}[t]=\left[\boldsymbol{\phi}[t-N+1],\ldots,\boldsymbol{\phi}[t-1]\right]^{\mathrm{T}}\boldsymbol{\phi}[t]$, one can be obtained

$$\vec{\boldsymbol{Q}}[t]=\begin{bmatrix}\vec{\boldsymbol{Q}}^{*}[t-1] & \vec{\boldsymbol{k}}[t]\\ \vec{\boldsymbol{k}}[t]^{\mathrm{T}} & \boldsymbol{\phi}[t]^{\mathrm{T}}\boldsymbol{\phi}[t]+\lambda^{N}\gamma\sigma_c^{2}E[t]^{-1}\end{bmatrix} \tag{28}$$

where $\vec{\boldsymbol{Q}}^{*}[t-1]$ can be obtained by removing first row and column of $\vec{\boldsymbol{Q}}[t-1]$.

By using upsized matrix inversion formula, the update process of $\vec{\boldsymbol{Q}}[t]^{-1}$ is

$$\vec{\boldsymbol{Q}}[t]^{-1}=\begin{bmatrix}\vec{\boldsymbol{Q}}^{*}[t-1]^{-1}+\vec{\boldsymbol{z}}[t]\vec{\boldsymbol{z}}[t]^{\mathrm{T}}\vec{r}[t]^{-1} & -\vec{\boldsymbol{z}}[t]r[t]^{-1}\\ -\vec{\boldsymbol{z}}[t]^{\mathrm{T}}\vec{r}[t]^{-1} & \vec{r}[t]^{-1}\end{bmatrix} \tag{29}$$

with $\vec{\boldsymbol{z}}[t]=\vec{\boldsymbol{Q}}^{*}[t-1]^{-1}\vec{\boldsymbol{k}}[t]$ and $\vec{r}[t]=\lambda^{N}\gamma\sigma_c^{2}E[t]^{-1}+\boldsymbol{\phi}[t]^{\mathrm{T}}\boldsymbol{\phi}[t]-\vec{\boldsymbol{z}}[t]^{\mathrm{T}}\vec{\boldsymbol{k}}[t]$.

Define

$$\vec{\boldsymbol{Q}}[t-1]^{-1}=\begin{bmatrix}\vec{\boldsymbol{A}} & \vec{\boldsymbol{B}}\\ \vec{\boldsymbol{C}} & \vec{\boldsymbol{D}}\end{bmatrix} \tag{30}$$

By using downsized matrix inversion formula, the following equation can be obtained

$$\vec{\boldsymbol{Q}}^{*}[t-1]^{-1}=\vec{\boldsymbol{D}}-\vec{\boldsymbol{C}}\vec{\boldsymbol{A}}^{-1}\vec{\boldsymbol{B}} \tag{31}$$

Consider Eq. (31) and Eq. (27), the kernelized parameter matrix $\boldsymbol{\omega}[t]$ can be obtained

$$\boldsymbol{\omega}[t]=\vec{\boldsymbol{\Psi}}[t]\vec{\boldsymbol{Q}}[t]^{-1}\vec{\boldsymbol{x}}[t] \tag{32}$$

Finally, time-dependent AR and MA parameter matrices can be computed by

$$\begin{aligned}\boldsymbol{w}[t]^{\mathrm{T}}&=\left[\boldsymbol{A}_1[t],\ldots,\boldsymbol{A}_{n_a}[t],\boldsymbol{C}_1[t],\ldots,\boldsymbol{C}_{n_c}[t]\right]\\&=\boldsymbol{\omega}[t]^{\mathrm{T}}\left(\boldsymbol{I}_{k(n_a+n_c)}\otimes\boldsymbol{u}[t]\right)\\&=\left(\vec{\boldsymbol{\Psi}}[t]\vec{\boldsymbol{Q}}[t]^{-1}\vec{\boldsymbol{x}}[t]\right)^{\mathrm{T}}\left(\boldsymbol{I}_{k(n_a+n_c)}\otimes\boldsymbol{u}[t]\right)\\&=\left(\vec{\boldsymbol{Q}}[t]^{-1}\vec{\boldsymbol{x}}[t]\right)^{\mathrm{T}}\begin{bmatrix}\boldsymbol{\varphi}[t-N+1]^{\mathrm{T}}\otimes\boldsymbol{\kappa}_k(t-N+1,t)\\ \vdots\\ \boldsymbol{\varphi}[t]^{\mathrm{T}}\otimes\boldsymbol{\kappa}_k(t,t)\end{bmatrix}\end{aligned} \tag{33}$$

This workflow is summarized in Table 2.

Initialization：

$\hat{\boldsymbol{w}}[0]^{\mathrm{T}}=\mathbf{0},\ \sigma_c,\sigma_k,\lambda,\gamma,N$

Computation$(1\le t\le N)$：

Table.1

Computation$(t>N)$：

Downsizing：obtain $\vec{\boldsymbol{Q}}^{*}[t-1]$ by removing the first row and column of $\vec{\boldsymbol{Q}}[t-1]$.

Compute $\vec{\boldsymbol{Q}}^{*}[t-1]^{-1}$ according to the downsized matrix inversion formula.

$\hat{\boldsymbol{e}}[t|t-1]=\boldsymbol{x}[t]-\hat{\boldsymbol{w}}[t-1]^{\mathrm{T}}\boldsymbol{\varphi}[t]$

$$E[t]=\exp\left(\frac{-1}{2\sigma_c^2}\hat{\boldsymbol{e}}[t|t-1]^{\mathrm{T}}\hat{\boldsymbol{e}}[t|t-1]\right)$$

$$\vec{\boldsymbol{k}}[t]=\vec{\boldsymbol{\Psi}}[t-1]^{\mathrm{T}}\boldsymbol{\phi}[t]=\begin{bmatrix}\boldsymbol{\phi}[t-N+1]^{\mathrm{T}}\boldsymbol{\phi}[t]\\ \vdots\\ \boldsymbol{\phi}[t-1]^{\mathrm{T}}\boldsymbol{\phi}[t]\end{bmatrix}=\begin{bmatrix}\boldsymbol{\varphi}[t-N+1]^{\mathrm{T}}\boldsymbol{\varphi}[t]\kappa_k(t-N+1,t)\\ \vdots\\ \boldsymbol{\varphi}[t-1]^{\mathrm{T}}\boldsymbol{\varphi}[t]\kappa_k(t-1,t)\end{bmatrix}$$

$$\vec{\boldsymbol{z}}[t]=\vec{\boldsymbol{Q}}^{*}[t-1]^{-1}\vec{\boldsymbol{k}}[t]$$

$$\vec{r}[t]=\lambda^N\gamma\sigma_c^2E[t]^{-1}+\boldsymbol{\varphi}[t]^{\mathrm{T}}\boldsymbol{\varphi}[t]\kappa_k(t,t)-\vec{\boldsymbol{z}}[t]^{\mathrm{T}}\vec{\boldsymbol{k}}[t]$$

$$\vec{\boldsymbol{Q}}[t]^{-1}=\begin{bmatrix}\vec{\boldsymbol{Q}}^{*}[t-1]^{-1}+\vec{\boldsymbol{z}}[t]\vec{\boldsymbol{z}}[t]^{\mathrm{T}}\vec{r}[t]^{-1} & -\vec{\boldsymbol{z}}[t]\vec{r}[t]^{-1}\\ -\vec{\boldsymbol{z}}[t]^{\mathrm{T}}\vec{r}[t]^{-1} & \vec{r}[t]^{-1}\end{bmatrix}$$

$$\hat{\boldsymbol{w}}[t]=\left(\vec{\boldsymbol{Q}}[t]^{-1}\vec{\mathbf{x}}[t]\right)^{\mathrm{T}}\begin{bmatrix}\boldsymbol{\varphi}[t-N+1]^{\mathrm{T}}\otimes\kappa_k(t-N+1,t)\\ \vdots\\ \boldsymbol{\varphi}[t]^{\mathrm{T}}\otimes\kappa_k(t,t)\end{bmatrix}$$

TARMA model parameter estimation：

$$\left[\boldsymbol{A}_1[t],\ldots,\boldsymbol{A}_{n_a}[t],\boldsymbol{C}_1[t],\ldots,\boldsymbol{C}_{n_c}[t]\right]=\hat{\boldsymbol{w}}[t]^{\mathrm{T}}$$

Table 2: The pseudocode of SWRMCRR-KTARMA method

3.3 Model structure selection

The model structure parameters of SWRMCRR-KTARMA include kernel bandwidth σ_c and σ_k, forgetting factor λ, the sliding-window length N, the regularization parameter γ, and AR and MA orders n_a and n_c.

Modal structure selection is generally based upon trail-and-error or integer optimization schemes, and the "fitness" one is finally selected. The "fitness" function can be established based on many rules, in this paper a normalized residual sum of squares (RSS) criterion is chosen as the "fitness" function, which can be seen

$$RSS=\sum_{t=1}^{N}\hat{\boldsymbol{e}}[t]^{\mathrm{T}}\hat{\boldsymbol{e}}[t]/N \tag{34}$$

Model structure selection of SWRMCRR-KTARMA can be tackled via following three basic steps:

Step 1: Given initial values of σ_c, σ_k, λ, N and γ based on prior knowledge of model parameter variation.

Step 2: Select AR and MA orders based on the minimization of the normalized RSS:

(a) Given the integer search space with n_a=n_c, and the fitness AR order $\hat{n}_a$ is selected when the decrease of RSS values is quite subtle.

(b) Given the integer search space $[0, \hat{n}_a]$, and the best fit MA order $\hat{n}_c$ can be selected in the same way as that of AR order.

Step 3: Optimizing initial parameters based on the model orders obtained in Step 2.

This process can be done while the fitness or suitable one is found. A detailed optimization scheme is beyond the scope of the current paper, and in this paper the initial parameters will be selected based on prior knowledge or normalized RSS criterion.

Remark 1: The kernel bandwidth σ_k reflects the non-linear power of the proposed method, it should be selected based on different problems. The kernel bandwidth σ_c controls the robustness to impulsive noise of proposed method, it should be selected properly to avoid the "over robust" problem.

Remark 2: The selection of forgetting factor and sliding-window length is a coupled problem. Both of them affect the tracking ability of the method, and forgetting factor should be very close to one in case N is relatively small. In this paper, the forgetting factor $\lambda = 1$ is initially recommended and the selection of N is based on normalized RSS criterion.

Remark 3: The regularization parameter γ deals with overfitting problem, which controls the variance of estimated regression parameters, however it does this at the expense of adding bias to the estimate. The selection of γ is a compromise issue.

4 Numerical case

4.1 Description of the underlying time-varying system

The simple three degree-of-freedom viscously damped system [15] can be seen in Figure 1, and the time-varying stiffness is

$$k_i(t) = k_{i,0} + k_{i,1} \cdot \sin\left(2\pi t / P_{i,1}\right) + k_{i,2} \cdot \sin\left(2\pi t / P_{i,2}\right) \quad (i = 2,3) \tag{35}$$

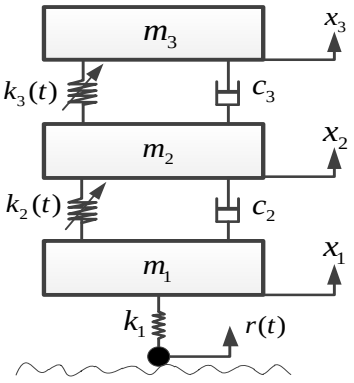


Figure 1: A 3DOF varying stiffness system

The parameters in Figure 1 is defined in Table 3, and the excitation is a stationary, Gaussian, zero-mean and white signal.

Parameters	Values
Mass (kg)	m_1=0.5, m_2=1.5, m_3=1.0
Damping (N·s·m^{-1})	c_2=0.5, c_3=0.3
Stiffness (N/m)	k_1=300, $k_{2,0}$=100, $k_{2,1}$=60, $k_{2,2}$=30, $k_{3,0}$=120, $k_{3,1}$=72, $k_{3,2}$=24
Period tuning factor	$P_{2,1}$=170, $P_{2,2}$=85, $P_{3,1}$=141.67, $P_{3,2}$=94.44

Table 3: Parameters of the underlying time-varying system

The theoretical reference values (baseline) of the modal parameters are obtained from "frozen-time" analysis of the time-varying system. The baseline modal characteristics are presented in Figure 2.

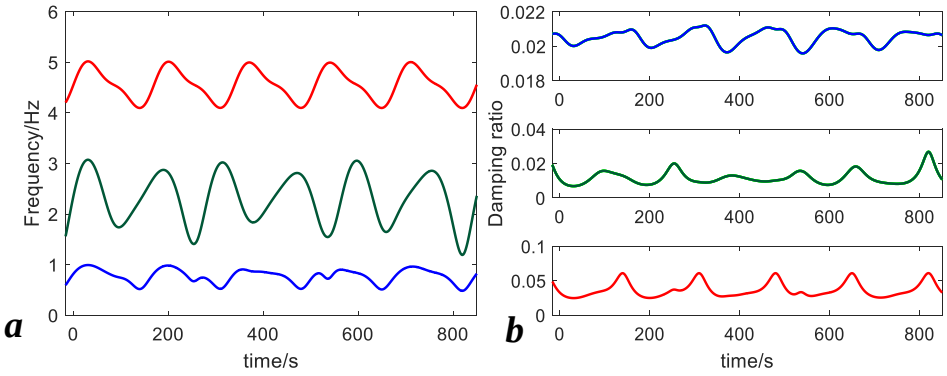


Figure 2: "Frozen-time" modal characteristics of the numerical time-varying system: (a) natural frequencies, and (b) damping ratios.

System's responses are reshaped via a detailed procedure can be seen in the reference [15].

4.2 Alpha-stable distribution for Non-Gaussian impulsive noise

In order to model the outliers/impulsive noise that exist in real test cases, a class of alpha-stable distribution is discussed in this section. There is no closed-form expression for the probability density function of alpha-stable distributions, but its characteristic function [16] is given

$$\Phi(t)=\exp\left\{j\mu t-\eta|t|^{\alpha}\left[1+j\beta\,\mathrm{sign}(t)\omega(t,\alpha)\right]\right\} \tag{36}$$

where

$$\omega(t,\alpha)=\begin{cases}\tan\dfrac{\alpha\pi}{2}, & \alpha\neq 1\\ \dfrac{2}{\pi}\log|t|, & \alpha\neq 1\end{cases}$$
$$\mathrm{sign}(t)=\begin{cases}1, & t>0\\ 0, & t=0\\ -1, & t<0\end{cases} \tag{37}$$

In order to compare the level of a desired signal to an impulsive noise, a mixture signal-to-noise ratio (MSNR) [17] is defined as

$$\mathrm{MSNR}_{\mathrm{dB}}=10\cdot\log_{10}\left(\frac{\sigma_{signal}^2}{\eta}\right) \tag{38}$$

where σ_{signal}^2 is the variance of the signal, and η is the dispersion parameter of the alpha-stable distribution. In this paper, a class of symmetric alpha-stable distribution ($\alpha=0.9,\beta=0,\mu=0$) is mainly considered.

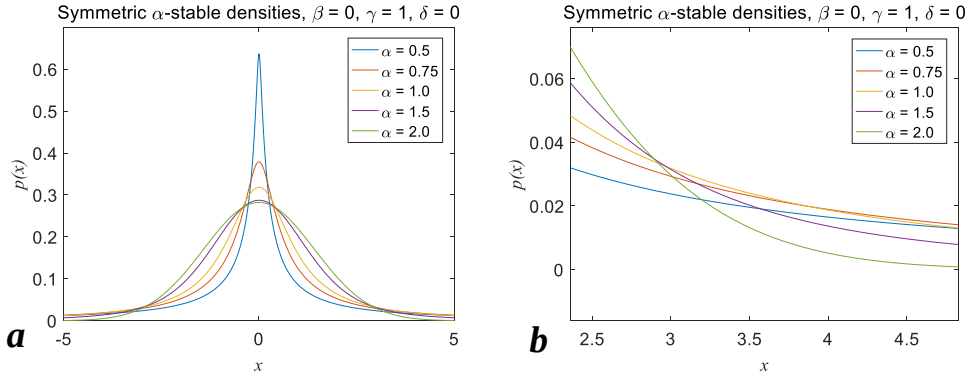


Figure 3: Probability density functions for alpha-stable distributions: (a) the overall shape of the PDFs, and (b) the tails of the PDFs.

4.3 Comparative results and discussions

In this section the proposed SWRMCRR-KTARMA method is employed to identify the numerical time-varying structure. Model order selection is achieved via the RSS criterion as shown in Figure 4, which suggest the fitness AR and MA order $n_a = 2, n_c = 2$. The forgetting factor $\lambda = 1$ is finally selected as the sliding-window length $N = 100$ is relatively small. The finally selected characteristics of SWRMCRR-KTARMA method and its LS counterpart EWRPLR-TARMA method are summarized in Table 4. Figure 5 illustrates the SWRMCRR-KTARMA and EWRPLR-TARMA based modal frequency estimates (with damping ratio $0 < \zeta_r[t] < 0.1$) from 30 Monte Carlo tests under Gaussian and non-Gaussian noise, along with their baseline counterparts.

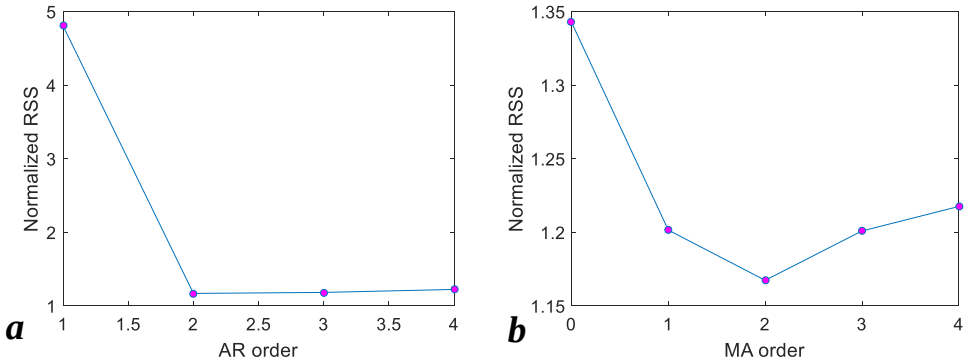


Figure 4: Model structure selection of SWRMCRR-KTARMA method: (a) AR order, and (b) MA order.

Identification method	Method characteristics	Identified model
EWRMC-TARMA	$\sigma_c = 1, \sigma_k = 10^4, N = 100, \lambda = 1, \gamma = 3\times10^{-3}$	KTARMA(2,2)
EWRPLR-TARMA	$\lambda = 0.991$	TARMA(2,2)

Table 4: Identification methods, their characteristics, and the identification models. (RMC denotes SWRMCRR-KTARMA method, RPLR denotes RPLR-TARMA method)

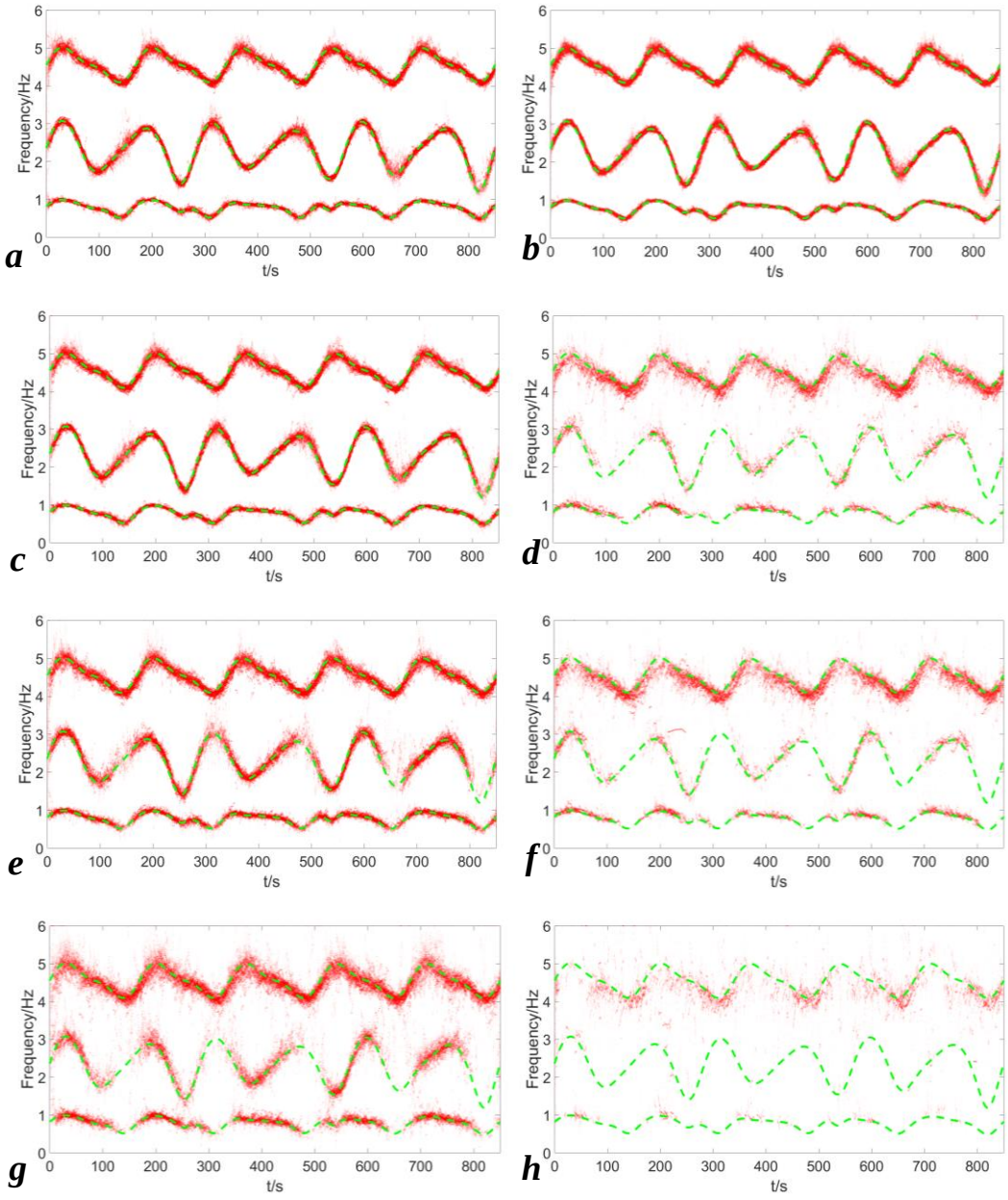


Figure 5: Modal frequencies estimated by SWRMCRR-KTARMA (left column) and EWRPLR-TARMA (right column) with Gaussian noise of SNR=20 dB and non-Gaussian impulsive noise of MSNR=30, 20 and 15 dB (from top bottom). (green lines: baseline values; red dots: modal frequency estimates of all 30 Monte Carlo runs)

In order to compare these methods by using natural frequency estimates, a mean absolute error (MAE) is introduced as

$$\mathrm{MAE}=\frac{1}{R}\sum_{i=1}^{R}\left(\frac{1}{N_e(i)}\sum_{t=1}^{N_e(i)}\left|f[t]-\hat{f}_i[t]\right|\right) \tag{39}$$

with $f[t]$ designating the baseline value of the modal frequency, $\hat{f}_i[t]$ its estimated value based on the i^{th} Monte Carlo run, $N_e(i)$ the effective number of estimation for the i^{th} Monte Carlo run. The MAE values and the average effective number of estimation obtained by each method under various added noise are summarized in Table 5 and Table 6.

As shown in Figure 5, the performance of proposed method is almost same as its LS counterpart under 20 dB Gaussian noise, and with MSNR decreasing, the performance of LS method becomes poorer, while the proposed method keeps a robust modal frequency estimation. A further validation can be seen in Table 5 and Table 6, which illustrate the similar estimation accuracy between proposed method and its counterpart under Gaussian noise, and a superior estimation accuracy and robustness are rendered under non-Gaussian noise.

Noise	Mode 1		Mode 2		Mode 3	
	RMC	RPLR	RMC	RPLR	RMC	RLPR
Gaussian SNR=20 dB	0.0353	0.0354	0.0707	0.0690	0.0743	0.0668
Non-Gaussian MSNR=30 dB	0.0376	0.0577	0.0770	0.2412	0.0758	0.2601
Non-Gaussian MSNR=20 dB	0.0443	0.0598	0.1101	0.2758	0.0994	0.2714
Non-Gaussian MSNR=15 dB	0.0676	0.1405	0.2033	0.9295	0.2090	0.6400

Table 5: The MAE values of modal frequency estimates under various added noise for all 30 Monte Carlo runs. (RMC denotes SWRMCRR-KTARMA method, RPLR denotes RPLR-TARMA method)

Noise	Mode 1		Mode 2		Mode 3	
	RMC	RPLR	RMC	RPLR	RMC	RLPR
Gaussian SNR=20 dB	7323	8025	9029	9299	9839	9996
Non-Gaussian MSNR=30 dB	7118	1243	8790	1141	9748	5327
Non-Gaussian MSNR=20 dB	5599	1223	6786	1042	9763	2293
Non-Gaussian MSNR=15 dB	3678	149	3513	194	9493	2091

Table 6: The average effective number of estimation under various noise for all 30 Monte Carlo runs. (RMC denotes SWRMCRR-KTARMA method, RPLR denotes RPLR-TARMA method)

5 Conclusion

In this work, A novel recursive robust estimator was proposed for output-only identification of time-varying structure. The proposed method was employed to identify a numerical time-varying system by using noise-corrupted response data, and compared with conventional least-squares criterion based method. The results indicate that the proposed method is able to track the dynamic of time-varying system under Gaussian noise environment and achieves similar performance with its LS counterpart. Moreover, it exhibits its advantages on superior estimation accuracy and robustness under the non-Gaussian impulsive noise.

References

[1] F. T. K. Au, R. J. Jiang and Y. K. Cheung, *Parameter identification of vehicles moving on continuous bridges*, Journal of Sound and Vibration, Vol. 269, No. 1, (2004), pp. 91-111.

[2] P. Verboven, B. Cauberghe, P. Guillaume, S. Vanlanduit and E. Parloo, *Modal parameter estimation and monitoring for on-line flight flutter analysis*, Mechanical Systems and Signal Processing, Vol. 18, No. 3, (2004), pp. 587-610.

[3] L. D. Avendaño-Valencia and S. D. Fassois, *Stationary and non-stationary random vibration modelling and analysis for an operating wind turbine*, Mechanical Systems and Signal Processing, Vol. 47, No. 1, (2014), pp. 263-285.

[4] L. Ljung, *System identification: theory for the user*, Prentice-Hall, Hemel Hempstead (1986).

[5] A. G. Poulimenos and S. D. Fassois, *Parametric time-domain methods for non-stationary random vibration modelling and analysis — A critical survey and comparison*, Mechanical Systems & Signal Processing, Vol. 20, No. 4, (2006), pp. 763-816.

[6] M. Niedzwiecki and T. Klaput, *Fast algorithms for identification of periodically varying systems*, IEEE Transactions on Signal Processing, Vol. 51, No. 12, (2003), pp. 3270-3279.

[7] X. Xie and R. Evans, *Discrete time stochastic adaptive control for time-varying systems*, IEEE Transactions on Automatic Control, Vol. 29, No. 7, (1984), pp. 638-640.

[8] P. Hao, S.-i. Kamata and Ieee, *Maximum correntropy criterion for discriminative dictionary learning*, *2013 20th IEEE International Conference on Image Processing*, Melbourne (2013), pp.4325-4329.

[9] W. Liu, P. P. Pokharel and J. C. Principe, *Correntropy: Properties and Applications in Non-Gaussian Signal Processing*, IEEE Transactions on Signal Processing, Vol. 55, No. 11, (2007), pp. 5286-5298.

[10] Z.-S. Ma, L. Liu, S.-D. Zhou, L. Yu, F. Naets, W. Heylen and W. Desmet, *Parametric output-only identification of time-varying structures using a kernel recursive extended least squares TARMA approach*, Mechanical Systems and Signal Processing, Vol. 98, (2018), pp. 684-701.

[11] M. D. Spiridonakos and S. D. Fassois, *Parametric identification of a time-varying structure based on vector vibration response measurements*, Mechanical Systems and Signal Processing, Vol. 23, No. 6, (2009), pp. 2029-2048.

[12] I. T. Jolliffe, *Introduction to multiple time series analysis*, Technometrics, Vol. 35, No. 1, (1993), pp. 88-89.

[13] W. Yang, L. Liu, S. D. Zhou and Z. S. *Ma, Moving Kriging shape function modeling of vector TARMA models for modal identification of linear time-varying structural systems*, Journal of Sound & Vibration, Vol. 354, (2015), pp. 254-277.

[14] B. Chen, X. Liu, H. Zhao and J. C. Principe, *Maximum correntropy Kalman filter*, Automatica, Vol. 76, (2017), pp. 70-77.

[15] A. G. Poulimenos and S. D. Fassois, *Parametric time-domain methods for non-stationary random vibration modelling and analysis - A critical survey and comparison*, Mechanical Systems and Signal Processing, Vol. 20, No. 4, (2006), pp. 763-816.

[16] P. G. Georgiou, P. Tsakalides and C. Kyriakakis, *Alpha-stable modeling of noise and robust time-delay estimation in the presence of impulsive noise*, IEEE Transactions on Multimedia, Vol. 1, No. 3, (1999), pp. 291-301.

[17] S. M. Nikias C L, *Signal processing with alpha-stable distribution and application*, John Wiley&Sons, New York (1995).

Identification of the modal parameters of systems with general damping.

N.Feng[1], E. Hahn[2], M.Yu[3]

[1]Shandong University, P.R. China

[2]School of Mechanical and Manufacturing Engineering
The University of New South Wales
Sydney NSW 2052, Australia
e-mail**: e.hahn@unsw.edu.au**

[3]Sun Yat-sen University, P.R. China

Abstract

The aim of this research is to model a system by an equivalent system which correctly reproduces the vibration behaviour of the original system over the frequency range of interest. This equivalent system is to be described by relevant modal parameters which are to be identified from motion measurements when the system is subjected to periodic force excitation at select excitation frequencies. It is assumed that the system can be represented by symmetric mass, damping and stiffness matrices. The damping matrix is not assumed to be diagonalisable. Earlier work was unable to satisfactorily identify a simple two degree of freedom system when the input data was accurate to only 2 digits. The identification involved numerical differentiation and it is here shown that such differentiation contributes minimally to computational error. Rather, this error is influenced by the number of input data sets. It is shown that significant improvement in identification accuracy is achieved when the number of input data sets is reduced to the minimum

1 Introduction

Correct modelling of a rotor bearing foundation system (RBFS) is an invaluable asset for the balancing and efficient running of turbomachinery but modelling of the foundation is still problematic [1-4]. A promising approach for such modelling uses motion measurements of the rotor and foundation at the bearing supports and at select points on the foundation model to identify relevant modal parameters for an equivalent foundation, i.e. one which, when substituted for the actual foundation, reproduces the vibration behaviour of the RBFS over the operating speed range of interest. If successful, such an identification technique would be applicable to support structures of existing turbomachinery.

In earlier work, an approach was developed which successfully identified, via numerical experiments, the modal parameters of an equivalent foundation for a relatively simple RBFS. This system consisted of an unbalanced rotor supported by two hydrodynamic bearings, the pedestals of which were fixed to a flexibly supported rigid foundation block; and used as input data the numerically generated motion of the foundation and forces transmitted to the foundation at the bearing supports [5]. However, these investigations assumed that the foundation damping matrix was diagonalisable using classical modal analysis. Ideally, one should remove such a restriction on the damping matrix and merely require the damping matrix to be symmetric. Such a generalisation significantly increases the difficulty of identifying the relevant modal parameters. Thus, when applied to a simple two degrees of freedom (DOF) lumped parameter system, satisfactory identification was unable to be achieved when the input measurement data was accurate to no more than 2 significant digits [6], presumably due to computational error. These earlier identification approaches involved the minimisation of functions of complex eigenvalues. The approaches

used measurement data sets pertaining to 24 excitation frequencies which spanned the excitation frequency range of interest and involved numerical differentiations. This paper investigates the possible contributions to computational error of the numerical differentiations and the number of utilised measurement data sets. The relevant theory is summarised and applied, via numerical experiments, to the same two DOF lumped parameter system as was used in ref. [6].

2 Notation

A $2n \times 2n$ modified system modal matrix with elements a_{jk}; $\mathbf{A}^T = \mathbf{\Phi}^{-1}$.

a_k real part of k^{th} eigenvalue: $a_k = -\xi_k \omega_k$.

b_k imaginary part of k^{th} eigenvalue: for k odd: $b_k = +\omega_k \sqrt{1-\xi_k^2}$; for k even: $b_k = -\omega_k \sqrt{1-\xi_k^2}$.

C $n \times n$ system damping matrix.

D $p \times p$ coefficient matrix in eqn (15).

f, F vector of applied forces as defined by eqn (6), $2n \times 1$ vector of complex amplitudes thereof.

g $n \times 1$ vector of applied forces.

K $n \times n$ system stiffness matrix.

$\mathbf{K}^*$ $2n \times 2n$ matrix defined by eqn (4).

k $2n \times 2n$ diagonal matrix defined by eqn (8).

k mode number; $k=1,2,...2n$.

M $n \times n$ system mass matrix.

$\mathbf{M}^*$ $2n \times 2n$ matrix defined by eqn (3).

m $2n \times 2n$ diagonal matrix defined by eqn (7) with diagonal elements m_k.

n number of system degrees of freedom.

p number of unknowns in eqn (13).

q, Q $n \times 1$ vector of displacements, $n \times 1$ vector of complex amplitudes thereof.

r number of excitation frequencies.

x, X $2n \times 1$ vector of velocities and displacements as defined by eqn (5), $2n \times 1$ vector of complex amplitudes thereof.

λ $2n \times 2n$ diagonal matrix of system eigenvalues with elements $\lambda_k = a_k + ib_k$, *rad/s*.

ξ_k damping ratio of the k^{th} mode.

η $2n \times 1$ vector of modal velocities and displacements.

Φ $2n \times 2n$ system modal matrix with elements ϕ_{jk}.

Ω excitation frequency, *rad/s*.

ω_k 'undamped natural frequency' of the k^{th} mode, *rad/s*.

3 Theory

For a general *n* DOF lumped parameter system subjected to periodic force excitation with frequency Ω, the equations of motion may be written as

$$\mathbf{M}\ddot{\mathbf{q}} + \mathbf{C}\dot{\mathbf{q}} + \mathbf{K}\mathbf{q} = \mathbf{g} \tag{1}$$

where $\mathbf{M}, \mathbf{C}, \mathbf{K}$ are symmetric mass, damping and stiffness matrices. Eqn (1) may be written in state space form as

$$\mathbf{M}^*\dot{\mathbf{x}} + \mathbf{K}^*\mathbf{x} = \mathbf{f} \tag{2}$$

where

$$\mathbf{M}^* = \begin{bmatrix} \mathbf{M} & \mathbf{0} \\ \mathbf{0} & -\mathbf{K} \end{bmatrix} \tag{3}$$

$$\mathbf{K}^* = \begin{bmatrix} \mathbf{C} & \mathbf{K} \\ \mathbf{K} & \mathbf{0} \end{bmatrix} \tag{4}$$

$$\mathbf{x} = \begin{bmatrix} \dot{\mathbf{q}} & \mathbf{q} \end{bmatrix}^T \tag{5}$$

$$\mathbf{f} = \begin{bmatrix} \mathbf{g} & \mathbf{0} \end{bmatrix}^T . \tag{6}$$

Since $\mathbf{M}^*$ and $\mathbf{K}^*$ are symmetric matrices, the homogenous equation set obtained when $\mathbf{f} = \mathbf{0}$ constitutes an eigenvalue problem [7]. Assuming the eigenvalues are distinct, in the absence of rigid body modes, these eigenvalues will occur as complex conjugate pairs ($\lambda_{2i-1} = \overline{\lambda}_{2i}, i = 1 \ldots n$). Also, the corresponding eigenvectors will be complex conjugates, so that $\boldsymbol{\phi}_{2i-1} = \overline{\boldsymbol{\phi}}_{2i}$, *i*=1,….*n*. Further, these eigenvectors are orthogonal with respect to the $\mathbf{M}^*$ and $\mathbf{K}^*$ matrices, so that [7]:

$$\boldsymbol{\Phi}^T\mathbf{M}^*\boldsymbol{\Phi} = \mathbf{m} \tag{7}$$

$$\boldsymbol{\Phi}^T\mathbf{K}^*\boldsymbol{\Phi} = \mathbf{k} \tag{8}$$

$$\mathbf{m}^{-1}\mathbf{k} = -\boldsymbol{\lambda} . \tag{9}$$

Assuming periodic response with fundamental frequency Ω, one can write eqn (2) as

$$i\Omega\mathbf{M}^*\mathbf{X} + \mathbf{K}^*\mathbf{X} = \mathbf{F} . \tag{10}$$

Premultiplication of eqn (10) by $\boldsymbol{\Phi}^T$ and letting $\mathbf{X} = \boldsymbol{\Phi}\boldsymbol{\eta}$ and $\mathbf{A}^T = \boldsymbol{\Phi}^{-1}$ gives

$$\left[i\Omega\mathbf{m} + \mathbf{k}\right]\boldsymbol{\eta} = \boldsymbol{\Phi}^T\mathbf{F} \tag{11}$$

or

$$\left[i\Omega\mathbf{I} - \boldsymbol{\lambda}\right]\mathbf{A}^T\mathbf{X} - \mathbf{m}^{-1}\boldsymbol{\Phi}^T\mathbf{F} = \mathbf{0} . \tag{12}$$

Eqn (12) yields *2n* identification equations ($k = 1 \ldots 2n$)

$$\left(i\Omega - \lambda_k\right)\sum_{j=1}^{2n} a_{jk}X_j - \sum_{j=1}^{2n}\phi_{jk}F_j / m_k = 0 . \tag{13}$$

For any odd (or even) *k*, one can write eqn (13) using the measurements of X_j and F_j corresponding to a particular excitation frequency Ω. Provided measurements are available for at least as many frequencies as unknowns in eqn (13), one can solve for the unknowns λ_k, a_{jk} and ϕ_{jk}/m_k from the resulting set of nonlinear homogeneous simultaneous equations. The procedure adopted is to first solve for λ_k. Having found λ_k, substitution into eqn (13) and setting any one of the resulting unknowns a_{jk} and ϕ_{jk}/m_k equal to unity enables the solution of the remaining unknowns. On repeating this for all the other odd (or even) *k's*, one obtains the matrix $\mathbf{A}$, which yields the modal matrix $\mathbf{\Phi}$ and enables the computation of $\mathbf{m}$. The system response using these identified modal parameters is then given by:

$$\mathbf{X} = \mathbf{\Phi}\left[i\Omega\mathbf{I} - \boldsymbol{\lambda}\right]^{-1}\mathbf{m}^{-1}\mathbf{\Phi}^T\mathbf{F}\,. \tag{14}$$

4 Solution for the eigenvalues

Two approaches for solving for the eigenvalues λ_k, termed the BISECTION-MIN and the BISECTION-SI approach respectively, were compared in ref. [6]. Both approaches used bisection [8] to find the zeros of a function of the complex variable λ_k; the former used a minimisation approach while the latter used a simple iteration formulation [6]. While the BISECTION-SI approach was found to provide slightly, if at all, better identification than the BISECTION-MIN approach, the resulting identifications were still felt to be deficient and could presumably be improved if computational error could be reduced. Attention in this paper is focussed on improving the BISECTION-MIN approach, which is here briefly outlined.

Thus, for any given λ_k, using the measurements of X_j and F_j corresponding to *r* ($r \geq p$) excitation frequencies $\Omega_s, s = 1 \ldots r$, eqn (13) yields a set of *r* linear homogeneous simultaneous equations in the *p* complex unknowns a_{jk} and ϕ_{jk}/m_k ($p \leq 4n$). Using least squares regression, one can reduce the number of these equations from *r* to *p* to obtain:

$$\mathbf{DY} = \mathbf{0} \tag{15}$$

where $\mathbf{D}$ is a $p \times p$ coefficient matrix with complex elements which depend on the selected λ_k; and $\mathbf{Y}$ is the $p \times 1$ vector of the unknowns. Eqn (15) has a nontrivial solution only if the determinant of the coefficient matrix $\mathbf{D}$ is zero; so one seeks those values of λ_k which achieve this. However, this determinant may have a minimum at this value of λ_k, in which case it may never equal zero due to computational errors. Hence, it is safer to seek those values of λ_k for which Δ, the square of the determinant of the coefficient matrix $\mathbf{D}$, has a minimum value. Thus, one seeks the value of λ_k for which the differential coefficient of Δ with respect to λ_k (i.e. its slope Δ^*) is zero. Assuming that $\Delta = u(a,b) + iv(a,b)$ is an analytic function of the complex variable λ_k, Δ^* is given by [9]:

$$\Delta^* = v' - iu' \qquad ' \tag{16}$$

where *u'* and *v'* are the partial differential coefficients of *u* and *v* with respect to *b*. Note that if Δ is an analytic function of the complex variable λ_k, Δ^* is also given by [9]:

$$\Delta^* = u` + iv` \tag{17}$$

where *u`* and *v`* are the partial differential coefficients of *u* and *v* with respect to *a*.

The BISECTION-MIN approach uses bisection to find the roots of Δ*. These minimising (as distinct from maximising) values of a and b are the sought after values of a_k and b_k.

Possible computational sources of error in evaluating λ_k include truncation errors in evaluating the differential coefficients numerically, as well as round of errors in evaluating the determinants. Both of these issues are considered in the numerical experiments described below.

5 Numerical experiments and discussion of results

All modal parameter identifications were for the simple 2 DOF system investigated in ref. [7] and already considered in ref. [6], using the same input data. The schematic of the system is shown in Figure 1.

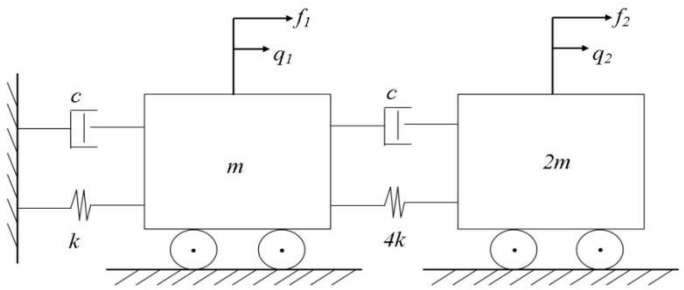


Figure 1**:** Schematic of 2 DOF system [7]. (*m*=1 *kg*, *c*=0.2 *N.s./m*, k =1*N/m*, $f_1 = sin\ \Omega t\ N$, f_2 =0)

Thus, for the given excitation force, the system frequency response amplitudes for the displacements q_1 and q_2 were calculated over the frequency range of from 0.05 to 3.5 rad/s in steps of 0.15 rad/s, giving 24 data sets in total. These computed amplitudes constituted the 'measurements'. These measurements were available to 15 digit accuracy whereupon they could be used to validate the identification softwares and provide the actual or correct modal parameters. Identification approach evaluations used 'measurements' rounded off to 2 digit accuracy as this was felt to better reflect attainable measurement accuracy in practice.

As noted in Section 4 above, the BISECTION-MIN approach assumed that the complex function Δ was analytic. If so, it should not matter whether eqn (16) or eqn (17) is used for its differential coefficient. This was checked and found to be the case, i.e. exactly the same eigenvalues were identified, regardless of which equation was used to evaluate the differential cofficient.

To date, the eigenvalue identifications used all 24 measurement data sets, and identified two natural frequencies at around 0.55 rad/s and 2.53rad/s. However, to evaluate the likelihood of error due to the numerical differentiations, it was decided to use only 5 measurement data sets, in order to avoid the need for least squares regression to obtain the 5x5 coefficient matrix **D**. And since f_2 =0 in the system being investigated, after dividing eqn (13) through by $(i\Omega - \lambda_k)$, it was quite simple to differentiate analytically the square of the determinant of the resulting coefficient matrix. The data sets selected were those corresponding to frequencies of 0.5rad/s, 0.65rad/s, 1.55rad/s, 2.45rad/s and 2.75 rad/s as these fell to either side of the already identified approximate natural frequencies and halfway between them. The resulting identified eigenvalues were the same, regardless of whether eqn (16) or eqn (17) was used for the numerical differentiation or whether the differentiation was analytical. It is concluded that the numerical differentiations inherent to the BISECTION-MIN approach do not introduce significant computation errors.

However, reduction in the number of utilised measurement data sets resulted in a significant improvement in the accuracy of the identified eigenvalues. These are shown in Table 1 where they are compared with actual values and with values previously obtained with the BISECTION-SI approach [6].

Eigenvalue	*Actual (Matlab)*	*BISECTION-MIN*	*BISECTION-SI*
$a_{1,2}$(15 digit)	-0.2225960260	-0.2225960260	-0.2225960260
$b_{1,2}$ (15 digit)	±2.578256744	±2.578256744	±2.578256744
$a_{3,4}$(15 digit)	-0.02740397403	-0.02740397403	-0.02740397403
$b_{3,4}$ (15 digit)	±0.5457949523	±0.5457949523	±0.5457949523
$a_{1,2}$(2 digit)	-0.22260	-0.22482	-0.17238
$b_{1,2}$ (2 digit)	±2.5783	±2.5800	±2.5797
$a_{3,4}$(2 digit)	-0.027404	-0.027027	-0.029075
$b_{3,4}$ (2 digit)	±0.54579	±0.54670	±0.54636

Table 1: Comparison of eigenvalues $\lambda_k = a_k + ib_k$ rad/s (15 digit and 2 digit data accuracy) using bisection software as applied to minimisation and simple iteration equation formulations.

The upper half of Table 1 compares the identified eigenvalues with the actual ones when using 'measurements' with 15 digit measurement accuracy. With such accuracy, one would expect near perfect identification of the eigenvalues. One can see that both the real parts and the imaginary parts of the eigenvalues were correctly identified to at least ten significant digits.

The lower half of Table 1 compares the identified eigenvalues with the actual ones when the 'measurements' were rounded off to two decimal digits. Results need only be given to five significant digits for this comparison. In all cases, there is less error in identifying the imaginary parts (the damped natural frequencies) than the real parts, which are indicative of the damping. Using the BISECTION-MIN approach, the maximum error in the real part identifications is no more than 1.4%; in the imaginary part identifications it is no more than 0.17%. The corresponding maximum error limits in the BISECTION-SI approach are 22.6% and 0.11% and the maximum error limits for the BISECTION-MIN approach when using 24 measurement data sets were even worse [6]. These relative identification superiorities have not been proven to hold under all circumstances and would differ with a different selection of measurement frequencies so that further research on the effect of measurement frequency selection is warranted. However, one can conclude that it is possible to significantly improve eigenvalue identification using the BISECTION-MIN approach by a judicious selection of measurement data sets.

Once the eigenvalues have been found, one can find for the *k'th* mode the remaining unknowns a_{jk} (j=1,…,4) and ϕ_{jk} / m_k by substituting the known eigenvalue λ_k into eqn (13) and setting any one of these unknowns equal to a constant. Here, it was convenient to set ϕ_{jk} / m_k equal to unity, resulting in five nonhomogeneous equations in four unknowns. Least squares regression could then be used to reduce this equation set to four equations in the four unknowns (in which case we still use data pertaining to all five excitation frequencies), or one is free, in theory, to discard any one of the equations to reduce the equation set to four equations in four unknowns (in which case we appear to use data pertaining to only four excitation frequencies) [10]. On repeating this for the other *k's*, one obtains the identified matrix $\mathbf{A}$, which yields the modal matrix $\mathbf{\Phi}$ **(**since by definition $\mathbf{A}^T = \mathbf{\Phi}^{-1}$ **)** and enables the computation of $\mathbf{m}$.

Actually, one should only need to perform the above computations for the odd or the even values of k since the modal vectors, and hence the columns of **A** are complex conjugates. However, because of truncation errors in the measurement data, discrepancies were found to occur when 2 digit data was used and one had to choose between the k=1 or k=2 results and also between the k=3 or k=4 results, not knowing which of the results were less erroneous. Here, one was aided by the results obtained when 15 digit data was used. In this case, not only were the computed columns of **A** exact complex conjugates, but all calculated values of a_{1k} (i.e. k=1,…4) equaled unity. Hence, those computed columns of **A** were selected in the 2 digit data computations which best agreed with this observed result.

Table 2 and Table 3 compare the actual nomalised modal matrix vectors with those identified using 2 digit data, as explained above, using either all 5 frequencies or only 4 frequencies in the computation of **A**. Only the first and third modal vectors are shown as the others are assumed to be complex conjugates. Also included are the normalised modal vectors obtained in earlier work [6] when 24 data sets (and all 24 frequencies) were used. There appears to be little difference in the identified modal vectors even though the eigenvalues used to calculate the previously obtained eigenvectors were significantly less accurate. Note that because of the normalisations, **m** is equal to the *4x4* identity matrix in all cases.

Φ_1 *(actual)*	Φ_1 *(24 frequencies)*	Φ_1 *(5 frequencies)*	Φ_1 *(4 frequencies)*
+.607+.036i	+.624 +.036i	+.658+.065i	+.666+.072i
-.258+.000i	-.284+.076i	-258+.035i	-.258-.010i
-.006-.235i	+.068-.219i	+.046-.278i	+.031-.258i
+.009+.099i	+.125+.138i	+.072+.073i	+.045+.069i

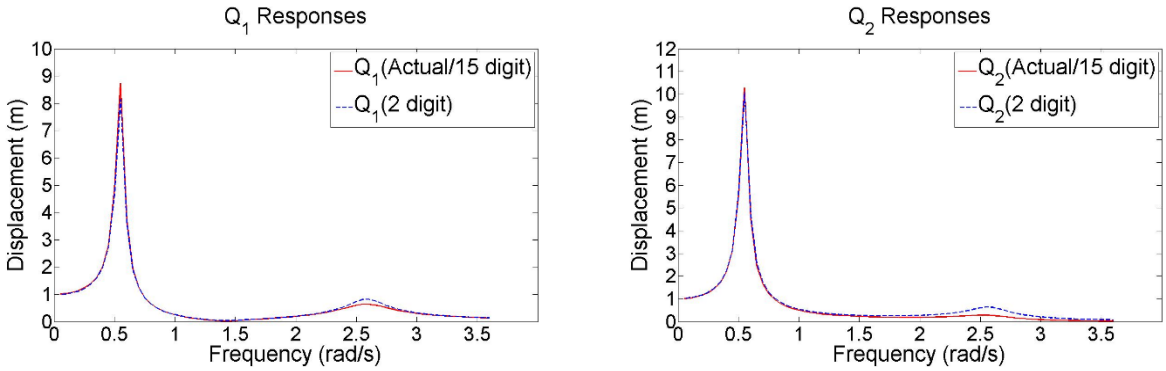
Table 2: Actual and identified normalised eigenvector elements corresponding to λ_1 (using 2 digit data for the 24, 5 or 4 frequencies).

Φ_3 *(actual)*	Φ_3 *(24 frequencies)*	Φ_3 *(5 frequencies)*	Φ_3 *(4 frequencies)*
+.365+.006i	+.338 -000i	+.313-.031i	+.309-.037i
+.429+.012i	+.501-.012i	+.528+.070i	+.534+.101i
-.023-.667i	-.056-.711i	-.003-.716i	+.027-.720i
-.017-.785i	-.072-.876i	+.044-.907i	+.087-.915i

Table 3: Actual and identified normalised eigenvector elements corresponding to λ_3 (using 2 digit data for 24, 5 or 4 frequencies).

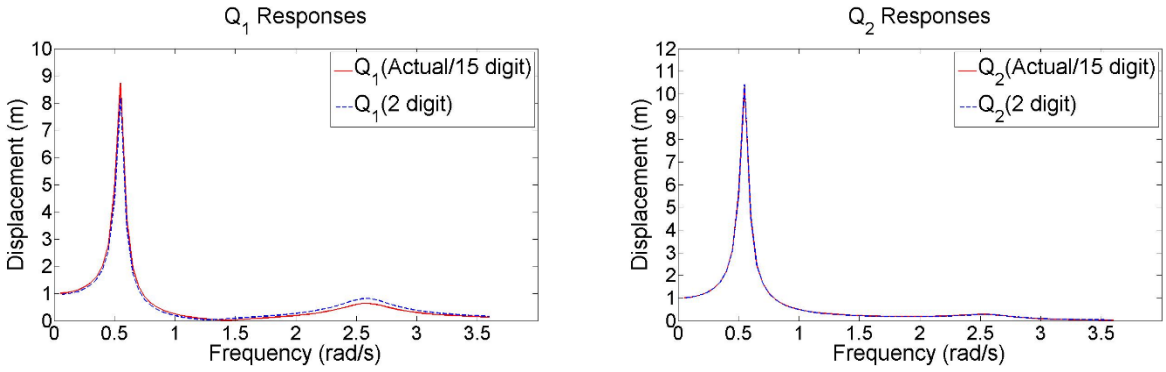
The above identified modal parameters constitue equivalent systems and one is now able to compute the system response predicted by these identified equivalent systems using eqn (14). Figure 2 compares the frequency response of the actual system with that predicted by the equivalent system based on the identification obtained in earlier work using the BISECTION-SI approach, which provided better identification than the BISECTION-MIN approach with 24 data sets [6]. Whereas the predicted frequency response using this identified system agrees perfectly with the actual response when measurement accuracy is to 15 digits, there are noticeable deviations in the vicinity of the natural frequencies when

measurement accuracy is to 2 digits, primarily due to the error in identifying the damping. Indeed, it is these deviations which motivated the present research. Figure 3 shows the same comparison except the equivalent system is now based on the identification obtained using the BISECTION-MIN approach with only 5 data sets (and the use of all five freqencies when identifying the columns of the **A** matrix). There is a significant improvement in the agreement between the actual response and the 2 digit data response in Figure 3 compared to that in Figure 2. Even though the agreement is not perfect, one can conclude that it is possible to significantly improve system identification using the BISECTION-MIN approach by a judicious selection of measurement data sets.



(a) Q_1 response (b) Q_2 response

Figure 2: Comparison of actual and identified frequency responses for Q_1 and Q_2 using 15 and 2 digit measurement accuracies. BISECTION-SI approach using 24 data sets [6].



(a) Q_1 response (b) Q_2 response

Figure 3: Comparison of actual and identified frequency responses for Q_1 and Q_2 using 15 and 2 digit measurement accuracies. BISECTION-MIN approach using 5 data sets.

6 Future work

Though the identification using the BISECTION-MIN approach with only 5 data sets has resulted in a significant improvement to that achieved to date, one can see from Figure 3 that there is room for improvement. There are also other indications that this identification approach still has potential shortcomings.

Thus, the eigenvalues should occur as complex conjugate pairs. This was not reflected in the results for the 2 digit measurement data where the first eigenvalue was found to be λ_1*= -0.22482+2.5800i rad/s* but the second eigenvalue was not calculated to be its complex conjugate as assumed in Table 1 and in subsequent computations; rather it was found to be λ_2*= -0.38849-1.7249i rad/s,* a result which was ignored at this stage.

Also, the 4 columns of the **A** matrix should occur as complex conjugate pairs. Again, this was not reflected in the results for the 2 digit measurement data. Table 4 shows the actual columns of the **A** matrix, with the first column corresponding to λ_1, the second column to λ_2 etc. Obviously $\boldsymbol{A_1}$ and $\boldsymbol{A_2}$ are not complex conjugates; nor are $\boldsymbol{A_3}$ and $\boldsymbol{A_4}$. Based on the knowledge that a_{1k} should equal unity (already noted above in Section 5), the accepted **A** matrix discarded the calculated first and third columns, using instead the complex conjugates of the second and fourth columns respectively. It is concluded that further accuracy investigations are warranted before application to higher order systems.

$\boldsymbol{A_1}$	$\boldsymbol{A_2}$	$\boldsymbol{A_3}$	$\boldsymbol{A_4}$
+1.12+.003i	+.947+.020i	+.796+.262i	+.969+.097i
-1.43+.218i	-.535-.148i	+3.34-1.07i	+2.45-.231i
+.159+1.89i	+.335-2.26i	+1.28+1.70i	+.442-.390i
-.044-1.33i	-.338+1.77i	-1.52-.165i	-.366-1.46i

Table 4: The **A** matrix using five 2 digit data sets and 5 frequency equations. In all cases, ϕ_{jk} / m_k = unity.

7 Summary of conclusions

Utilising force excitation and motion measurements, an identification approach, denoted as the BISECTION-MIN approach, has been developed for identifying the relevant modal parameters to form an equivalent system for an n DOF lumped parameter system with symmetric mass, damping and stiffness matrices, without the requirement for the damping matrix to be diagonalisable by classic modal analysis.

Numerical experiments show that one can use this approach to identify reasonably accurately the eigenvalues of a simple 2 DOF system even when the measurement data is only accurate to 2 significant digits. However, there can be significant error in the identified corresponding modal vectors.

Numerical experiments also show that the numerical differentiations inherent to this approach do not contribute significantly to computational errors.

It is possible to improve identification by a judicious selection of measurement data sets. Numerical experiments showed that there was a significant improvement in eigenvalue identification when the number of measurement data sets was reduced from tweny four to five.

If the measurement data is only correct to 2 significant digits, the error in the identified modal parameters noticeably affects the accuracy of response predictions when the actual system is replaced by the identified equivalent system.

Further accuracy investigations are warranted before application to higher order systems

References

[1] K.L. Cavalca, F. Cavalcante, E.P. Okabe, *An Investigation on the Influence of the Supporting Structure on the Dynamics of the Rotor System*, Mechanical Systems and Signal Processing, Vol.19, (2005), pp. 157-174.

[2] A.W. Lees, J.K. Sinha, M.I. Friswell, *Model-based identification of rotating machines*, Mechanical Systems and Signal Processing, Vol. 23, (2009), pp. 1884-1893.

[3] P. Pennacchi, N. Bachschmid, A. Vania, G. A. Zanetta, L. Gregori, *Use of modal representation for supporting structure in model-based fault identification of large rotating machinery: Part 1 – theoretical remarks*, Mechanical Systems and Signal Processing, Vol.20, No. 3, (2006), pp. 662-681.

[4] P. Pennacchi, N. Bachschmid, A. Vania, G. A. Zanetta, L. Gregori, *Use of modal representation for supporting structure in model-based fault identification of large rotating machinery: Part 2 – application to a real machine*, Mechanical Systems and Signal ProcessingVol.20, No. 3, (2006), pp. 682-701.

[5] M. Yu, N. Feng, E. Hahn, *On the identification of damped foundations in rotating machinery using modal parameters, Proceedings of the ISMA2016-USD2016 International Conference on Noise and Vibration Engineering, Leuven, Belgium, 2016 September 19-21*, Leuven (2016), pp. 989-998.

[6] M. Yu, N. Feng, E. Hahn, *Modal parameter based identification of systems with general damping, In: 9th Australasian Congress on Applied Mechanics (ACAM9)*, Engineers Australia, Sydney (2017), pp. 283-290.

[7] L. Meirovitch, *Computational methods in structural dynamics*, Sijthoff & Noordhoff, Rockville (1980).

[8] R. W. Hamming, *Numerical Methods for Scientists and Engineers*, Second edition, McGraw-Hill, New York (1973).

[9] E. Kreyszig, *Advanced Engineering Mathematics*, Eighth edition, John Wiley and Sons, U.S.A. (1999).

[10] A. Keane, S.A. Senior, editors, *Complementary Mathematics*, Science Press, Sydney (1959).

Automatic operational modal analysis using statistical modelling of pole locations

S. S. Christensen [1], **A. Brandt** [1]
[1] Department of Technology and Innovation University of Southern Denmark,
Campusvej 55, 5230, Odense M, Denmark
e-mail: **ssv@iti.sdu.dk**

Abstract
Modal parameter extraction can be a time-consuming task. There are many applications where operator interaction is undesirable, for example for structural health monitoring. This paper presents an algorithm for automated operational modal analysis (AOMA) that utilizes one of the strong features of the stabilization diagram, namely the feature that physical modes tend to stabilize on the frequency axis for increasing model order. By employing statistical probability analysis and introducing a decision rule, that is based on the Modal Assurance Criteria (MAC), all modes in a user selected frequency range are automatically added to the output data-set. The algorithm has been tested on four different data-sets, a laboratory plexiglass plate, a suspension bridge, a medium-rise building and a ship. The results suggest that, the combined use of statistical probability analysis and a MAC based decision rule, successfully estimate modal parameters in an automated manner.

1 Introduction

Modal parameters can be estimated from response data using a modal parameter estimation (MPE) algorithm [1]. Regardless of what MPE that is chosen there will be a number of operator driven decisions to be made. With present day technology, that allows for more and cheaper sensors as well as faster computers, it is sought to automate such decisions, as they are the bottle necks when it comes to estimating modal parameters. This must be done in a fast and consistent way.

Recently, many attempts to build an automated operational modal analysis (AOMA) algorithm involve the use of clustering algorithms [2, 3, 4, 5]. Among clustering algorithms, the K-Means Clustering and the Agglomerative Hierarchical Clustering, are methods used for OMA. They both work in a multidimensional space and look to find the optimal clusters in a data-set through iteration. The K-Means Clustering requires a predefined number of clusters, while the Agglomerative Hierarchical Clustering does not, but instead combines clusters one by one until it is terminated by a stopping rule, or to the point where only a single cluster remains. Due to the way that clustering algorithms work, there are a few challenges, namely how to formulate the multidimensional space. In its simple form it includes frequency and damping, but can be extended to also include information about mode shapes, RMS levels etc. Furthermore, the K-Means Clustering is dependent on a predefined number of clusters, while the Agglomerative Hierarchical Clustering requires a trigger level that terminates the algorithm before it adds too many clusters together.

Another attempt to develop an AOMA algorithm would include histogram analysis [6]. This approach fits a probability distribution (a histogram) to the stabilization diagram to aid in selecting a vertical column. The stabilization diagram, a plot showing the number of poles (model order) as a function of frequency, is a strong tool to locate physical poles, since they tend to stabilize on the frequency axis for increasing model order. In this paper, we investigate this idea, and extend it by adding a few decision rules, in an attempt to construct an AOMA algorithm that is robust.

Section 2 briefly uncovers the fundamental theory to MPE, alongside the methodology of the proposed AOMA algorithm. In section 3, we show how the proposed AOMA algorithm is performing on various data-sets, namely a laboratory plexiglass plate, a suspension bridge, a medium-rise building and a ship. The concluding remarks are found in Section 4.

2 Theory

A stochastic process $x(t)$ passing through a linear time-invariant system, the output $y(t)$, also a stochastic process, is only dependent on the impulse response function (time domain), see Equation 1.

$$y(t) = h(t) * x(t) \tag{1}$$

The $*$ denotes the convolution operator. Equation 1 can also be written as.

$$y(t) = \int_{-\infty}^{\infty} h(\tau)x(t-\tau)d\tau \tag{2}$$

Assuming wide-sense stationarity, the auto-correlation function, can be expressed as

$$R_{yy}(\tau) = \int_{-\infty}^{\infty}\int_{-\infty}^{\infty} R_{xx}(\tau+\rho_1-\rho_2)h(\rho_1)h(\rho_2)d\rho_1 d\rho_2 = R_{xx}(\tau) * h(\tau)h(-\tau) \tag{3}$$

while the cross-correlation functions becomes

$$R_{xy}(\tau) = \int_{-\infty}^{\infty} R_{xx}(\tau-\rho)h(\rho)d\rho = R_{xx}(\tau) * h(\tau) \tag{4}$$

$$R_{yy}(\tau) = \int_{-\infty}^{\infty} R_{xy}(\tau+\rho_1)h(\rho_1)d\rho_1 = R_{xy}(\tau) * h(-\tau) \tag{5}$$

Therefore, by knowing the correlation functions, we also know the impulse response functions of the system. The above could as well have been represented for the frequency domain. For more detail on the above, see [7].

For large structures like bridges, buildings, vessels etc., excitation by means of experimental equipment is not very practical, thus we do not know the input to the system. Therefore, by utilizing Equations 3-5, to extract the frequency response functions from correlation functions, the dynamic properties of the excitation force will be included in the total solution. For wide-sense stationary excitation, this is not an issue. However, the external forces on the structures mentioned in the start of this paragraph, are typically limited to vibrating machinery as well as traffic, wind and wave loads.

When talking MPE, there are two distinct categories, those operating directly in the time domain and those that extend to the frequency domain. Time domain identification extract information from the impulse response function, whilst frequency domain identification reaps information from frequency function.

In the following, the multi-reference Ibrahim Time Domain (MITD) method [8, 9] is used, although the AOMA algorithm, can be implemented for all MPE methods that can produce a stabilization diagram. The MITD method is very similar to the covariance driven SSI. MITD is based on building a Hankel matrix from the correlation functions, which then is solved by means of singular value decomposition in order to extract the states of the system. The size of the Hankel matrix is governed by the model order. It is typical to over-fit the model, thus yielding more poles, but also more spurious poles.

Typically a set of criteria, that governs whether a pole is physical or spurious, are set up. Such criteria can be related to restrictions or expectations to physical properties of the structure. As mentioned in the introduction, the stabilization diagram is a strong tool in separating physical poles from spurious ones.

A popular supplement to the stabilization diagram is the Modal Assurance Criteria given in Equation 6.

$$MAC_{rs} = \frac{\left|\{\psi\}_r^H \{\psi\}_s\right|^2}{\left(\{\psi\}_r^H \{\psi\}_r\right)\left(\{\psi\}_s^H \{\psi\}_s\right)} \tag{6}$$

where ^{H} is the Hermitian transpose (complex conjugate and transpose) and $\{\psi\}r$ and $\{\psi\}s$ are mode shapes originating from modes r and s. The MAC value can take any value between 0 and 1. For independent mode shapes $\{\psi\}_r \neq \{\psi\}_s$ and $MAC_{rs} = 0$, whereas for identical mode shapes $\{\psi\}_r = \{\psi\}_s$ and $MAC_{rs} = 1$.

2.1 Methodology

The proposed methodology is outlined in Figure 1.

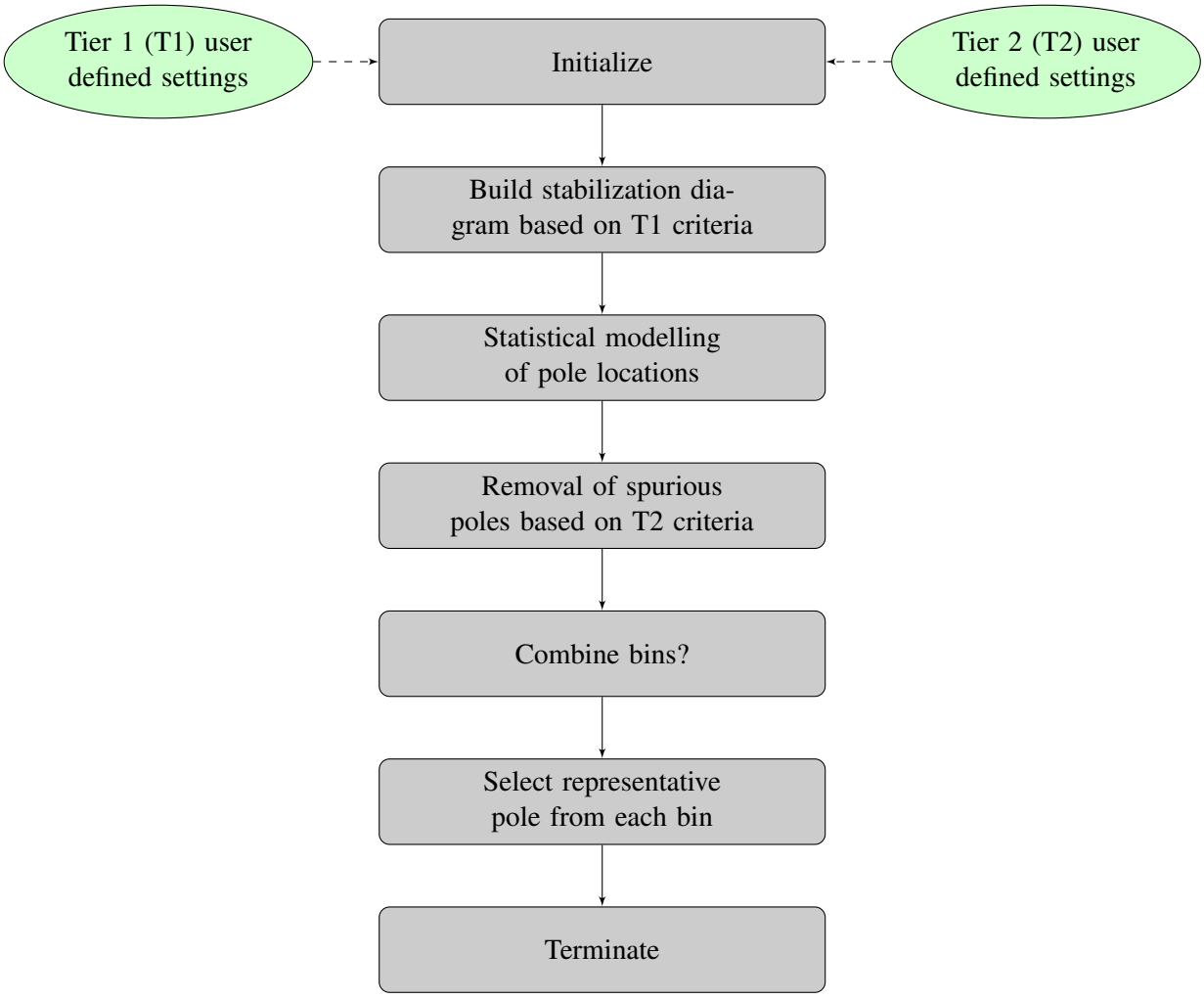


Figure 1: Flowchart of the proposed AOMA algorithm

A set of parameters must be defined before the AOMA algorithm can be initiated. These parameters are presented in Table 1, and are divided into two groups, i.e. Tier 1 and Tier 2. The former Tier is related to the MPE method chosen, which in this case involves assigning a model order and defining how much information that should be used of the correlation function [10, 11]. The latter Tier, on the other hand, is related to the application in question, and involves the statistical parameters that allow for the statistical modelling of the pole locations, and the steps leading to the selection of one representative pole for each mode shape found.

Parameter	Description	Suggested value
Tier 1		
NPoles	Number of poles (model order)	MPE dependent
NStart	First value in IR or CF	MPE dependent
NLines	Number of values in IR or CF	MPE dependent
Tier 2		
minFreq	Minimum frequency	Application dependent
maxFreq	Maximum frequency	Application dependent
NoBins	Number of bins	Application dependent
BinThreshold	Bin size threshold	Application dependent
MACThreshold	MAC value threshold	Application dependent
MinBinSize	Minimum bin size	Application dependent

Table 1: User defined settings

Depending on the application, some *a priori* sorting criteria can be applied to the pole sorting process. For instance, for under-damped systems, all physical poles always come in complex conjugate pairs, or for a suspension bridge, it is unlikely that the damping ratio for the first handful of modes shapes is high.

When the user defined settings are set up, the AOMA algorithm can start, and the stabilization diagram is built based on the Tier 1 user defined settings. A frequency bandwidth is the first parameter in the Tier 2 user defined settings, and dictates the frequency band of interest. The next step is to overlay the stabilization diagram by its probability distribution using the predefined resolution. In the following step, all bins below a certain threshold are discarded from further processing. By intuition, the mode shapes for each bin should have similar characteristics. By utilizing the MAC, a conformity check is made, and poles in each bin, that have poor MAC values in comparison to the majority of the poles in that bin, are removed. The AOMA algorithm is set to use a very high number of bins, and it is therefore possible that adjacent bins have similar MAC properties, if that is the case, they are combined into one bin. The combined bins must pass a check that ensure robustness, i.e. the size of the combined bins must contain a certain number of poles. The last step involves selecting one representative pole for each of the remaining bins. These poles are selected based on Equation 7.

$$\lambda_n = min\left(\left||\bar{\lambda_n}| - |\lambda_{n,i}|\right|\right) \tag{7}$$

where λ_n is the representative pole for bin n, $|\lambda_{n,i}|$ represents the absolute values for the poles in bin n having poles i, while $|\bar{\lambda_n}|$ denotes the average value for the absolute values for the poles in bin n.

3 Results and discussion

Since any measurement is finite, modal parameter estimates will always be erroneous. Good damping estimates require a long measurement duration. The data presented in this paper, can be considered to have sufficiently long measurements times. For more information on the data used, the reader is referred to the articles mentioned in each of the 4 subsections.

The Tier 1 and Tier 2 user defined settings, listed in Table 1, will to some degree have an influence on the estimates of the modal parameters for the proposed methodology for an AOMA algorithm. Variations in the Tier 1 user defined settings do not influence the results much, while altering the Tier 2 user settings has a larger impact. To show the integrity of the AOMA algorithm the same settings, except for the frequency band of interest, are used for all 4 data-sets. This paper is not a parameter study, but rather a demonstration, hence modifications to the Tier 1 and Tier 2 user defined settings will not be investigated further.

For all data-sets, no data were discarded, the correlation functions were produced using a block-size of 512 samples. The model order was chosen to 40 modes (or 80 poles), the first 5 lags were discarded and 100

samples in each correlation function were used. All frequency and damping estimates presented in this section are derived from MITD, that includes results from other papers.

3.1 Plexiglas Plate

The first data-set addresses a laboratory Plexiglas plate measuring 533 x 321 x 20 millimeters, whose response was recorded using 35 out-of-plane oriented uni-axial accelerometers in a double symmetric pattern. All sensors were mounted in the same plane (out-of-plane). The excitation was applied by gently tapping the tip of a pencil randomly around the plate during a measurement period of 5 minutes. This corresponds to approximately 42.500 cycles of the first natural frequency. For more details on the measurements, the reader is referred to [12].

In figure 2, two stabilization diagrams are shown. To the left, the stabilization diagram is overlaid by its probability distribution (step 3 in figure 1). The dashed line represents the bin threshold and the frequency interval of interest $100 - 900Hz$. To the right, MAC stable poles along with the automatically selected representative pole, are shown (step 6 in figure 1).

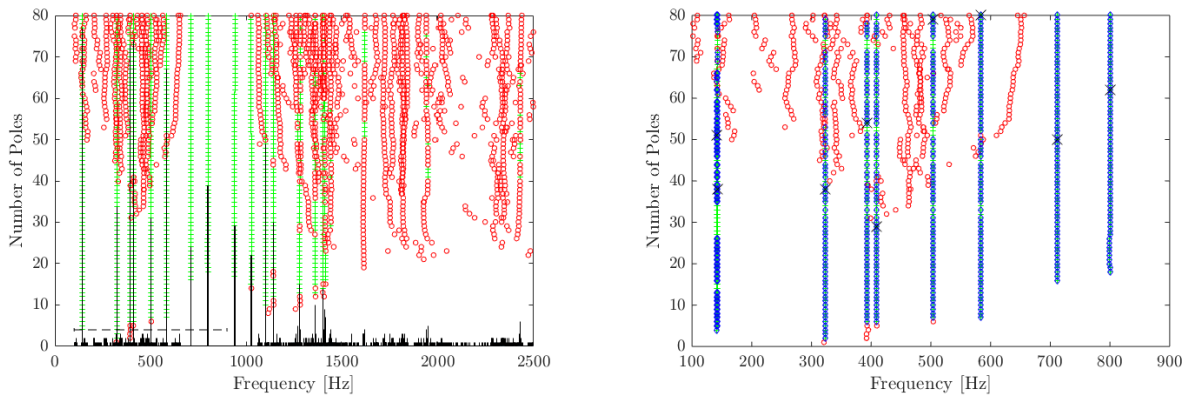


Figure 2: Stabilization diagrams of the modal parameter estimates for the laboratory Plexiglas Plate. Left: Stabilization diagram overlaid by its probability distribution (the dashed line represents the bin threshold and the frequency interval of interest). Right: Stabilization diagram indicating MAC stable poles and the automatically selected representative pole (zoomed into the frequency band of interest). Pole below bin threshold - Red circle ○. Pole above bin threshold - green plus +. Pole that is MAC stable - blue diamond ◇. Representative pole - black cross ×

Looking at the stabilization diagrams, it it clear to see that there is a large number of spurious poles in the frequency band of interest. Many of these spurious poles have one thing in common, being below the bin threshold, while all the remaining poles are above the bin threshold. This tendency accepts the fact that physical poles stabilize on the frequency axis for increasing model order, while spurious poles do not. In the subsequent step of the proposed algorithm the MAC value for each bin is utilized to detect and remove poles, i.e. poles in each bin that have poor MAC value relative to the majority of poles in that bin, are removed. One reason for this, is that it is likely that some spurious poles fall into bins of frequency stable poles. By checking the MAC value, such poles can easily be removed, as seen in the right stabilization diagram in Figure 2. In the final step one representative pole for each bin are picked, and the results are compared to a manual approach.

Automated		**Manual**	
Frequency, $[Hz]$	Damping, $[\%]$	Frequency, $[Hz]$	Damping, $[\%]$
141.928	3.08	141.904	3.24
142.577	3.10	142.585	3.06
323.177	2.66	323.261	2.67
393.044	2.61	393.045	2.54
408.771	2.52	408.798	2.45
503.724	2.44	503.774	2.41
583.667	2.45	583.571	2.38
712.006	2.41	711.322	2.41
799.829	2.19	798.754	2.27

Table 2: Comparison between the modal parameters found for the laboratory Plexiglas Plate, using the proposed automated procedure, and the manual approach according to [12]

This comparison is shown in Table 2. The AOMA algorithm successfully detects 9 modes, just like the manual approach. The frequency and damping estimates for both approaches are very similar. Furthermore, the AOMA algorithm manages to separate the first two closely spaced modes indicating that they are unique.

3.2 Little Belt Suspension Bridge

The second data-set addresses the Little-belt Suspension Bridge that has a main span of 600 meters, whose response was recorded using 30 horizontally oriented and 15 vertically oriented uni-axial geophones in a double symmetric pattern. All these sensors were mounted and in the same plane inside the closed box girder. The bridge was excited by a combination of wind and traffic loads during a measurement period of 60 minutes. This corresponds to approximately 560 cycles of the first natural frequency. For more details on the measurements, the reader is referred to [13].

In figure 3, two stabilization diagrams are shown. To the left, the stabilization diagram is overlaid by its probability distribution (step 3 in figure 1). The dashed line represents the bin threshold and the frequency interval of interest $0.05 - 0.9Hz$. To the right, MAC stable poles along with the automatically selected representative pole, are shown (step 6 in figure 1).

For these stabilization diagrams the frequency band of interest consists primarily of frequency stable poles, while at higher frequencies ($> 1.5Hz$), the stabilization diagrams are highly contaminated by spurious poles. The high number of spurious poles are related to the sampling frequency and the model order. For increasing model order, the number of poles (twice the model order), must be squeezed into a frequency interval, that is limited by a lower bound, DC ($0Hz$) and a higher bound, $f_s/2$, where f_s is the sampling frequency. The sampling frequency can be adjusted by down-sampling the original signal to an appropriate level. The model order must be selected accordingly. A compromise between choosing the right combination of model order and the sampling frequency is therefore necessary, for two reasons, to ensure that enough frequency stable poles are available, but also to keep the number of spurious poles to a minimum. In the stabilization diagram to the right in Figure 3, only a few poles were removed due to having poor MAC values relative to the majority of poles in their respective bin. The poles removed are concentrated around a model order of 18 (36 poles).

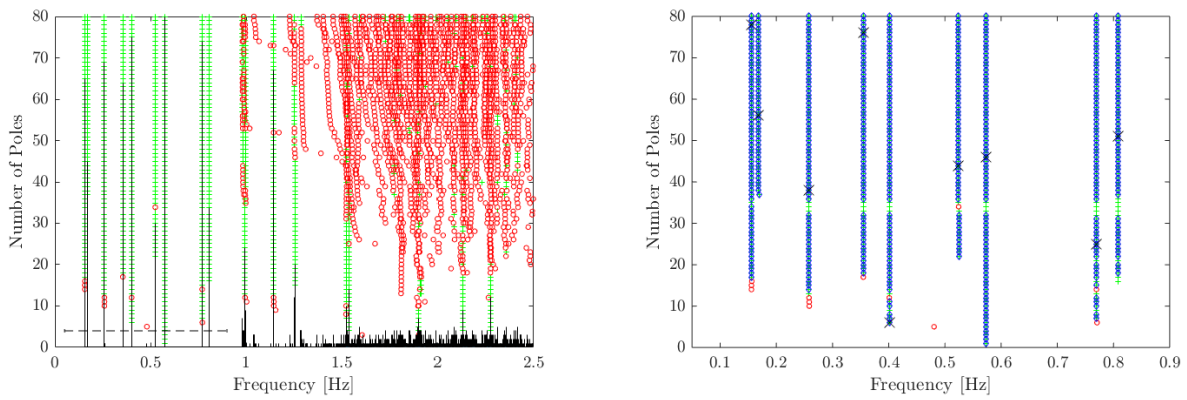


Figure 3: Stabilization diagrams of the modal parameter estimates for the Little Belt Suspension Bridge. Left: Stabilization diagram overlaid by its probability distribution (the dashed line represents the bin threshold and the frequency interval of interest). Right: Stabilization diagram indicating MAC stable poles and the automatically selected representative pole (zoomed into the frequency band of interest). Pole below bin threshold - Red circle ○. Pole above bin threshold - green plus +. Pole that is MAC stable - blue diamond ◇. Representative pole - black cross ×

Automated		**Manual**	
Frequency, $[Hz]$	Damping, $[\%]$	Frequency, $[Hz]$	Damping, $[\%]$
0.156	1.91	0.156	3.15
0.169	12.01	0.171	9.74
0.258	0.83	0.258	0.78
0.355	1.64	0.355	1.77
0.401	0.99	0.401	0.93
0.524	0.72	0.523	0.76
0.573	0.40	0.573	0.38
0.769	0.58	0.769	0.60
0.808	0.56	0.808	0.69

Table 3: Comparison between the modal parameters found for the Little Belt Suspension Bridge, using the proposed automated procedure, and the manual approach according to [13]

The AOMA algorithm successfully finds a total of 9 modes, which was also the case when using a manual approach, see [13]. The frequency estimates reported by the two approaches show resemblance. For the damping estimates found for the first two modes, the reported values using the AOMA algorithm are more distant from one another, in comparison to the damping estimates reported using the manual approach. In [13] it was found that by adjusting the number of lags used in the correlation function, the damping estimates for these two modes varied significantly. No particular pattern was detected, but a likely cause for this behavior is thought to be related to a close coupling of two modes, one mode with low damping and one mode with high damping. For the remaining 7 modes the damping estimates, for the two approaches, are within the boundary of acceptance.

3.3 Heritage Court Tower

The third data-set addresses the Heritage Court Tower located in downtown Vancouver, British Columbia in Canada. It is a medium-rise building measuring approximately 42.5 meters in height. The typical floor dimension is 25 x 31 meters, while the 3 lower levels measure 36 x 30 meters. The response was recorded

using 5 northerly oriented and 3 westerly oriented uni-axial accelerometers. The sensors were installed on the northern facade at 3 different levels. In the full study of the building, more sensors were available, but in this paper, only the data from setup 4 are used. The medium-rise building was primarily excited by wind loads during a measurement period of 10 minutes. This corresponds to approximately 725 cycles of the first natural frequency. For more details on the measurements, the reader is referred to [14].

In figure 4, two stabilization diagrams are shown. To the left, the stabilization diagram is overlaid by its probability distribution (step 3 in figure 1). The dashed line represents the bin threshold and the frequency interval of interest, $0.5 - 1.75Hz$. To the right, MAC stable poles along with the automatically selected representative pole, are shown (step 6 in figure 1).

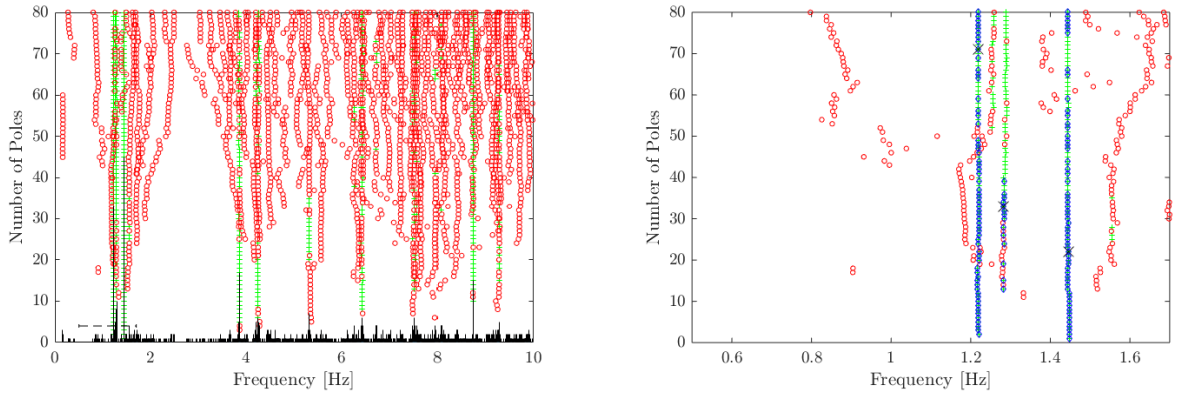


Figure 4: Stabilization diagrams of the modal parameter estimates for the Heritage Court Tower. Left: Stabilization diagram overlaid by its probability distribution (the dashed line represents the bin threshold and the frequency interval of interest). Right: Stabilization diagram indicating MAC stable poles and the automatically selected representative pole (zoomed into the frequency band of interest). Pole below bin threshold - Red circle ○. Pole above bin threshold - green plus +. Pole that is MAC stable - blue diamond ◇. Representative pole - black cross ×

In these stabilization diagrams, there are many spurious poles, both in the frequency band of interest and on either side of it. The AOMA algorithm manages the initial removal of spurious poles and the subsequent deselection of poles with poor MAC values. Finally one representative pole for each of the 3 modes within the frequency band of interest are selected. On the right-hand side stabilization diagram in Figure 4, it can be seen that there are many representative poles for the first and third mode, while for the second mode the number of representative poles are scarce. It is likely that this mode is weakly excited. However, the AOMA algorithm is still able to overcome this challenge.

Automated		**Manual**	
Frequency, $[Hz]$	Damping, $[\%]$	Frequency, $[Hz]$	Damping, $[\%]$
1.220	1.66	1.245	1.05
1.283	1.46	1.299	1.40
1.445	1.16	1.441	0.31

Table 4: Comparison between the modal parameters found for the Heritage Court Tower, using the proposed automated procedure, and the manual approach according to [14]

When comparing the results for the two procedures, namely the AOMA algorithm and the manual approach in [14], it is evident that the frequency estimates are agreeing well. However, for the damping estimates there are some discrepancies, especially for the third mode, which for the manual approach is reported at 0.31%,

whilst for the proposed AOMA algorithm it is 1.16%. The representative pole is selected based on Equation 7. For the 57 poles, the damping estimate is within 1.13% - 1.51%.

3.4 Ro-Lo Ship

The fourth data-set addresses a roll-on lift-off (Ro-Lo) ship with a total length of 210 meters and a width at main deck of 29.6 meters. The response was recorded using 22 horizontally oriented and 11 vertically oriented uni-axial accelerometers in a double symmetric pattern. All these sensors were mounted in the same plane at the main deck of the ship. Furthermore, the bow and stern were represented by 2 measurement points, each (2x2) measuring in all 3 directions (x,y,z). The ship was traveling at 18 knots in a calm sea state, hence it was primarily excited by the propeller loads as well as relative wave and wind loads during a measurement period of 90 minutes. This corresponds to approximately 4700 cycles of the first natural frequency. For more details on the measurements, the reader is referred to [15].

In figure 5, two stabilization diagrams are shown. To the left, the stabilization diagram is overlaid by its probability distribution (step 3 in figure 1). The dashed line represents the bin threshold and the frequency interval of interest, $0.5 - 4.0Hz$. To the right, MAC stable poles along with the automatically selected representative pole, are shown (step 6 in figure 1).

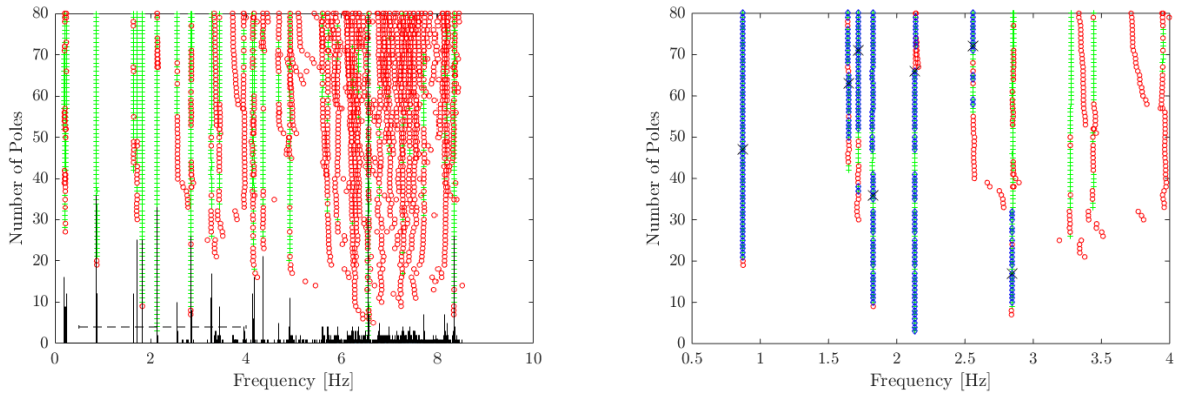


Figure 5: Stabilization diagrams of the modal parameter estimates for the Ro-Lo Ship. Left: Stabilization diagram overlaid by its probability distribution (the dashed line represents the bin threshold and the frequency interval of interest). Right: Stabilization diagram indicating MAC stable poles and the automatically selected representative pole (zoomed into the frequency band of interest). Pole below bin threshold - Red circle $\circ$. Pole above bin threshold - green plus $+$. Pole that is MAC stable - blue diamond $\diamond$. Representative pole - black cross $\times$

For the stabilization diagrams shown in Figure 5 the same tendency as for the Little Belt Suspension bridge is present, i.e. a large number of spurious poles are located at the higher frequencies ($> 5Hz\%$), also see Figure 3. In the frequency interval of interest there are a large sum of spurious poles. These are easily identified. Looking at the frequency interval in more detail, the first 5 modes are well represented by a sufficient number of poles. The 6th and 7th mode are represented, but with fewer poles. The automated algorithm cannot detect any modes between $3 - 4Hz$, though the experienced eye, can see an indication of up to 3 additional modes. The first column of poles appear to be frequency stable, but does not pass the MAC check, that ensures that only poles sharing the same MAC properties can qualify for any subsequent steps. This algorithm is looking for well represented mode shapes, and is not intended for separating mode shapes due to weakly excited modes, faulty equipment, missing sensors etc.

Automated		Manual	
Frequency, $[Hz]$	Damping, $[\%]$	Frequency, $[Hz]$	Damping, $[\%]$
0.871	1.78	0.871	1.62
1.647	0.27	N/A	N/A
1.718	1.09	1.723	1.36
1.825	0.88	1.823	0.94
2.135	1.13	2.137	1.07
2.558	1.60	2.538	1.09
2.846	0.93	2.856	1.62
N/A	N/A	3.273	0.14
N/A	N/A	3.425	1.73
N/A	N/A	3.956	1.92

Table 5: Comparison between the modal parameters found for the Ro-Lo Ship, using the proposed automated procedure, and the manual approach according to [15]

The AOMA algorithm detected 7 modes in the data-set, 6 of these modes were also reported by the manual approach, see Table 5. The manual approach were also able to detect the 3 higher order modes at $3.273Hz$, $3.425Hz$ and $3.956Hz$. The mode found at $1.647Hz$ is a harmonic and is also present in [15]. This algorithm is not designed to remove harmonics, but confirms that harmonics can be both frequency stable, and have similar MAC characteristics. For harmonic removal the reader is referred to [16]. Comparing the modes that were actually found, it is evident that the frequency estimates for the two procedures are similar. The damping estimates for the first 4 modes are complementing each other well, while for the last two modes, at $2.558Hz$ and $2.846Hz$, there are some discrepancies. The number of representative poles at these two modes are few. A possible explanation for the noticeable deviation in damping estimates could be that since a large number of non-representative poles was removed by the AOMA algorithm, a manual approach could just as well have selected one of such poles.

4 Conclusion

The proposed AOMA algorithm faced a number of challenges, in particular, closely spaced modes, weakly excited modes and harmonics. It could not distinguish harmonics from non-harmonic modes, but have overall shown to successfully identify well represented modes in an automated way, by using a combination of statistic moddeling of the pole locations, and a decision rule based on the MAC value of individual poles.

Acknowledgements

The work presented is supported by the INTERREG 5A Germany-Denmark program, with funding from the European Fund for Regional Development. Also a thanks to the great people involved in collecting and their willingness to share the data processed in this paper. This is a huge opportunity to develop tools that work on different applications in a robust way.

References

[1] R. J. Allemang, D. L. Brown, *A Unified Matrix Polynomial Approach to Model Identification*, Journal of Sound and Vibration, Vol. 211, No. 3, pp. 301-322.

[2] G. Zhang, J. Mab, Z. Chen, R. Wang, *Automated Eigensystem Realisation Algorithm for Operational Modal Analysis*, Journal of Sound and Vibration, Vol. 333, 2014, pp. 35503563.

[3] C. Devriendt, F. Magalhes, W. Weijtjens, G. De Sitter, . Cunha, P. Guillaume, *Structural Health Monitoring of Offshore Wind Turbines using Automated Operational Modal Analysis*, Structural Health Monitoring, Vol. 13(6), 2014, pp. 644659.

[4] R. Cardoso, A. Cury, F. Barbosa, *A Robust Methodology for Modal Parameters Estimation Applied to SHM*, Mechanical Systems and Signal Processing, Vol. 95, 2017, pp. 2441.

[5] E. Neu, F. Janser, A. A. Khatibi, A. C. Orifici, *Fully Automated Operational Modal Analysis using multi-stage clustering*, Mechanical Systems and Signal Processing, Vol.84, 2017, pp. 308323.

[6] M. Scionti, J. Lanslots, I. Goethals, A. Vecchio, H. Van der Auweraer, B. Peeters, B. De Moor, *Tools To Improve Detection of Structural Changes From In-Flight Flutter Data*, Proceedings of The 8th International Conference on Recent Advances in Structural Dynamics(IVSR), Southampton, UK, 2004 July.

[7] W. C. van Etten, *Introduction to Random Signals and Noise*, John Wiley & Sons, University of Twente, The Netherlands, 2005.

[8] S. R. Ibrahim, E. C. Mikulcik, *A Method for the Direct Identification of Vibration Parameters from the Free Response*, Shock and Vibration Bulletin, Vol. 47, 1977, pp. 183-198.

[9] K. Fukuzono, *Investigation of Multiple Reference Ibrahim Time Domain Modal Parameter Estimation Technique*, M.S. Thesis, Dept. of Mechanical and Industry Engineering, University of Cincinnati, 1986.

[10] M. Tarpo, P. Olsen, S. Amador, M. Juul, R. Brincker, *On Minimizing the Influence of the Noise Tail of Correlation Functions in Operational Modal Analysis*, Procedia Engineering, Vol. 199, 2017, pp. 1038-1043.

[11] E. Orlowitz, A. Brandt, S. Amador, M. Juul, R. Brincker, *Influence of Noise in Correlation Function Estimates for Operational Modal Analysis*, XXXVI International Modal Analysis Conference, 2018.

[12] E. Orlowitz, A. Brandt, *Comparison of Experimental and Operational Modal Analysis on a Laboratory Test Plate*, Measurement, Vol. 102, 2017, pp. 121-130.

[13] S. S. Christensen, M. S. Andersen, A. Brandt, *Dynamic Characterization of the Little Belt Suspension Bridge by Operational Modal Analysis*, Dynamics of Civil Structures, Vol. 2, 2017.

[14] R. Brincker, C. E. Ventura, *Introduction to Operational Modal Analysis*, John Wiley & Sons, Technical University of Denmark, Denmark, 2015.

[15] E. Orlowitz, A. Brandt, *Operational Modal Analysis for Dynamic Characterization of a Ro-Lo Ship*, Journal of Ship Research, Vol. 58, No. 4, December 2014, pp. 216-224.

[16] A. Brandt, *Comparison and Assessment of Methods to Treat Harmonics in Operational Modal Analysis*, International Conference on Structural Engineering Dynamics, Lagos, Portugal, 2015 June.

Variance computation of the Modal Assurance Criterion

S. Gres[1], **M. Döhler** [2], **P. Andersen**[3], **L. Mevel**[2]
[1] Aalborg University, Department of Civil and Structural Engineering,
Thomas Manns Vej 23, 9000 Aalborg, Denmark

[2] INRIA, University of Rennes, IFSTTAR/COSYS/SII, I4S
Campus de Beaulieu, 35042 Rennes, France

[3] Structural Vibration Solutions A/S,
NOVI Science Park, 9220 Aalborg, Denmark

Abstract
Modal validation is an integral part of any modal analysis scheme. Recent advances in efficient variance computation of modal parameter estimates from the output-only subspace-based identification algorithms made the computation of variance feasible for the modal parameters, such as natural frequencies, damping ratios and mode shapes. One of the other practical modal indicators is Modal Assurance Criterion (MAC), for which uncertainty computation scheme is missing. This paper builds on the previous results using the propagation of the measurement uncertainties to estimates of MAC. The sensitivity of the MAC with respect to output covariances is derived using a first order perturbations and the uncertainties are propagated using the Delta method. The influence of the underlying mode shape scaling on both the uncertainty of mode shapes and MAC is investigated. The results are presented in context of operational modal analysis (OMA) of a spring mass system.

1 Introduction

Noisy vibration measurements deployed for the modal identification call to appreciate the statistical uncertainties due to the unknown nature of the input, limited sample size and sensor noise that inherently affect the estimated parameters. A general framework to evaluate the variance of the modal parameters has been proposed first for the covariance driven subspace identification in [7]. As such that strategy involves propagation of the sample covariance through the sequence of system identification steps based on sensitivity analysis where the analytical sensitivities are derived using a first order perturbation. This was revised with an efficient implementation of the latter for the multi-order [4] and multi-setup [2] identification scenarios. The propagation of the sample covariance for the output-only data driven algorithms has been established through a link between the sensitivity of the covariance Hankel matrix to its data driven counterpart [6]. Consequently, this development has led the variance to become a practical modal information, amongst a few others, for industrial applications of the subspace-based system identification.

Once identified from the eigenstructure of the state transition matrix, natural frequencies, damping ratios and mode shapes are validated with simple metrics like variance or relative errors between the estimates from different model orders in a stabilization diagram. When it comes to the mode shapes some additional indicators are commonly used; one of them is MAC. MAC value is a real scalar bounded by zero and one, which depicts a degree of colinearity between two mode shape vectors [5]. In practice, it is a useful tool to assess the quality of conducted modal identification or cross correlate results between different modal tests, however, like estimates of the modal parameters, MAC is affected by the measurement uncertainties.

MAC can be deployed for the comparison of two mode shapes estimated from a single model order, between

different model orders, between two global model orders, between different data sets and lastly between the mode shape extracted from the finite element model and the mode shape estimated from the data collected from the corresponding structure. A strategy to propagate the mode shape covariance estimated from an arbitrary subspace identification algorithm to MAC estimated between different mode shapes is the subject of the present paper. Different mode shape normalization schemes are recalled in the next section. In Section 3 the analytical sensitivity of MAC is derived and Section 4 contains the results of the uncertainty quantification of the numerical simulations of a chain-like system both in the proposed and Monte Carlo frameworks.

2 Subspace system identification

Let model (1) represent a behavior of a d degree of freedom, viscously damped, linear time-invariant (LTI) structural system,

$$\begin{cases} M\ddot{u}(t) + D\dot{u}(t) + Ku(t) = v(t) \\ y(t) = C_a\ddot{u} + C_v\dot{u}(t) + C_d u(t) \end{cases} \tag{1}$$

where $y(t) \in \mathbb{R}^r$ is the output vector and $\dot{(\cdot)}$ expresses a derivative with respect to time t. Matrices K, M, D $\in \mathbb{R}^{d\times d}$ denote stiffness, mass and damping matrices respectively. Matrices C_a, C_v, $C_d \in \mathbb{R}^{r\times d}$ are selection matrices for accelerations, velocities and displacements where r is the number of sensors. Vectors $u(t)$, $v(t)$ $\in \mathbb{R}^d$ denote the continuous-time displacements and external forces respectively. Sampled with k discrete steps at rate $1/\tau$, System (1) can be represented with a discrete-time stochastic state-space model

$$\begin{cases} x_{k+1} = A_n x_k + w_k \\ y_k = C_n x_k + v_k \end{cases} \tag{2}$$

where $x_k \in \mathbb{R}^n$ are the states; $A_n \in \mathbb{R}^{n\times n}$, $C_n \in \mathbb{R}^{r\times n}$ are the state transition and observation matrices estimated for a model order n and vectors w_k with v_k denote the process and output noises respectively. The eigenfrequencies f_i, damping ratios ζ_i and mode shapes φ_i of the underlying mechanical system (1) are identified for $i = 1 \dots n$ from the i-th eigenvalue λ_i and eigenvector Φ_i of A_n such that

$$f_i = \frac{|\lambda_{ci}|}{2\pi},\ \zeta_i = \frac{-\Re(\lambda_{ci})}{|\lambda_{ci}|},\ \varphi_i = C_n\Phi_i \tag{3}$$

where the eigenvalue of the continuous system λ_{ci} is computed with $\mathrm{e}^{\lambda_{ci}\tau} = \lambda_i$. The $|(\cdot)|$ denotes modulus operator and $\Re(\cdot)$ and $\Im(\cdot)$ express real and imaginary parts of a complex variable. An example of a output-only data-driven identification algorithm, namely Stochastic Subspace Identification with Unweighted Principal Component, SSI-UPC, is given in the next paragraph.

2.1 SSI-UPC identification algorithm

The UPC algorithm is based on a projection of the 'future' data horizon $\mathcal{Y}^+$ onto the 'past' data horizon $\mathcal{Y}^-$, which associates the column space of the resulting projection matrix $\mathcal{H}$ with the column space of the extended observability matrix Γ whereas its rows space corresponds to the row space of the forward Kalman filter state sequence X. The projection can be written as

$$\mathcal{H} = \mathcal{Y}^+/\mathcal{Y}^- = \mathcal{Y}^+\mathcal{Y}^{-T}(\mathcal{Y}^-\mathcal{Y}^{-T})^{-1}\mathcal{Y}^- \tag{4}$$

where $\mathcal{H} \in \mathbb{R}^{(p+1)r\times N}$ with $N+p+q$ denoting the total number of samples such that parameters p, q are usually $p = q+1$. Matrices $\mathcal{Y}^+ \in \mathbb{R}^{(p+1)r\times N}$ and $\mathcal{Y}^- \in \mathbb{R}^{qr_0\times N}$ are defined such that

$$\mathcal{Y}^+ = \frac{1}{\sqrt{N}}\begin{bmatrix} y_{q+1} & y_{q+2} & \vdots & y_{N+q} \\ y_{q+2} & y_{q+3} & \vdots & y_{N+q+1} \\ \vdots & \vdots & \vdots & \vdots \\ y_{p+q+1} & y_{p+q+2} & \vdots & y_{p+q+N} \end{bmatrix},\ \mathcal{Y}^- = \frac{1}{\sqrt{N}}\begin{bmatrix} y_q^{r_0} & y_{q+1}^{r_0} & \vdots & y_{N+q-1}^{r_0} \\ y_{q-1}^{r_0} & y_q^{r_0} & \vdots & y_{N+q-2}^{r_0} \\ \vdots & \vdots & \vdots & \vdots \\ y_1^{r_0} & y_2^{r_0} & \vdots & y_N^{r_0} \end{bmatrix}$$

with r_0 labeling the reference channels. An efficient and numerically stable scheme to compute the Hankel matrix $\mathcal{H}$ has been proposed in [9] and [3]. Instead of the direct computation of the projection as in (4), it involves selecting an appropriate partition of the stacked and LQ decomposed $\mathcal{Y}^-$ and $\mathcal{Y}^+$ matrices.
Matrix $\mathcal{H}$ enjoys the factorization property into $\mathcal{H} \approx \Gamma_n X_n$ where $\Gamma_n \in \mathbb{R}^{(p+1)r\times n}$ and $X_n \in \mathbb{R}^{n\times N}$ are defined as

$$\Gamma_n = \begin{bmatrix} C_n \\ C_nA_n \\ \vdots \\ C_nA_n^p \end{bmatrix},\ X_n = \begin{bmatrix} G_n & A_nG_n & \dots & A_n^{q-1}G_n \end{bmatrix} \Sigma_{\mathcal{Y}^-}^{-1}\mathcal{Y}^- \tag{5}$$

where $G_n = \mathrm{E}(x_{k+1}y_k^T)$ expresses the cross covariance computed between the states at model order n and the outputs, and the matrix $\Sigma_{\mathcal{Y}^-} = \mathrm{E}((\mathcal{Y}^-\mathcal{Y}^{-T}))$ is the variance of $\mathcal{Y}^-$. In practice, only the estimates of the observability matrix $\hat{\Gamma}_n$ and the forward Kalman states $\hat{X}_n$ are computed. A well-known scheme to compute $\hat{\Gamma}_n$ and $\hat{X}_n$ is to balance the singular values of the estimate of the Hankel matrix, $\hat{\mathcal{H}}$, which SVD writes

$$\hat{\mathcal{H}} = \begin{bmatrix} U_1 & U_2 \end{bmatrix}\begin{bmatrix} D_1 & 0 \\ 0 & D_2 \end{bmatrix}\begin{bmatrix} V_1^T \\ V_2^T \end{bmatrix} \tag{6}$$

where $\hat{\Gamma}_n = U_1D_1^{1/2}$ and $\hat{X}_n = D_1^{1/2}V_1^T$. U_1 and V_1 are the left and right singular vectors corresponding to first n non-zero singular values D_1 and U_2 with V_2 are the left and right kernel of $\hat{\mathcal{H}}$ where $D_2 \to 0$. The estimate of the state transition matrix A_n for a single model order can be computed in a least-square sense from the shift invariance property of $\hat{\Gamma}_n$ such that $\hat{A}_n = \hat{\Gamma_n}_{\uparrow}^{\dagger}\hat{\Gamma}_{n\downarrow}$ and $\hat{C}_n$ is extracted directly from the first block rows of $\hat{\Gamma}_n$. An efficient multi-model order scheme for the computation of the system matrices was developed in [3]. The modal parameter estimation follows (3).

2.2 Mode shape normalization

The mode shape φ_i computed from (3) is called the unnormalized mode shape since its scaling is arbitrary and its components can be written as $\varphi_i = \begin{bmatrix}\varphi_{i,1}\ \varphi_{i,2}\ \dots\ \varphi_{i,r}\end{bmatrix}^T$. To make it comparable between different model orders, a normalization scheme is needed. Two well-known schemes are investigated, namely

1. One mode shape component is set to 1. This k-th component can e.g. be chosen as the component with the maximum amplitude ($k = \arg\max_j\{|\varphi_{i,j}|\}$), or any other selected entry of φ_i. The normalized mode shape can be written as
$$\tilde{\varphi}_i = \varphi_i/\varphi_{i,k}. \tag{7}$$
Note that the k-th component in this normalized mode shape has, by design, no uncertainty.

2. The mode shape is rotated such that the imaginary part of one component is 0 and the real part of this component is positive. This k-th component can be chosen as in case 1. Then the mode shape is rotated to the maximum angle of deflection. In addition, the norm of the mode shape is set to 1. Then, the normalized mode shape can be written as
$$\breve{\varphi}_i = \tilde{\varphi}_i/||\tilde{\varphi}_i||. \tag{8}$$

Note that the imaginary part of the k-th component in this normalized mode shape has, by design, no uncertainty.

Note that the MAC value, see (13), is independent of the chosen mode shape normalization, therefore its uncertainty should also be independent of the chosen normalization scheme. Both schemes are investigated in this paper for the analysis of the mode shape uncertainty.

3 Delta method for variance estimation

Assume $\hat{Y}$ to be a random matrix computed on N samples for which, as N goes to infinity, $\hat{Y}$ converges almost surely to θ and the Central Limit Theorem, CLT, holds $\sqrt{N}(\hat{Y}-\theta) \xrightarrow{\mathcal{L}} \mathcal{N}(0, \mathrm{cov}(\theta))$. This is e.g. the case for the output auto-covariance estimates computed from the measurements. Let $\mathrm{vec}(\cdot)$ denote vectorization operator and $\mathrm{vec}(X) = \mathrm{vec}(f(Y))$ be once differentiable in θ with a sensitivity matrix $\mathcal{J}_{X,Y} = \partial \mathrm{vec}(f(Y))/\partial \mathrm{vec}\,(Y)\Big|_{Y=\theta}$. The CLT formulated for $\hat{X}$ writes as

$$\sqrt{N}\left(\mathrm{vec}(\hat{X}) - \mathrm{vec}\,(f(\theta))\right) \xrightarrow{\mathcal{L}} \mathcal{N}(0, \mathcal{J}_{X,Y}\mathrm{cov}(\theta)\mathcal{J}_{X,Y}^T) \tag{9}$$

and the first order perturbation of X can be written as $\mathrm{vec}\,(\Delta X) = \mathcal{J}_{X,Y}\mathrm{vec}\,(\Delta Y)$. The covariance of the estimate $\hat{X}$ yields $\mathrm{cov}\left(\mathrm{vec}(\hat{X})\right) = \hat{\mathcal{J}}_{X,Y}\mathrm{cov}\left(\mathrm{vec}(\hat{Y})\right)\hat{\mathcal{J}}_{X,Y}^T$. In this way the covariance related to the output covariances in the Hankel matrix can be propagated to some function of it, in particular to the modal parameters and the MAC values. For the convenience of the notation the estimate symbol $(\hat{\cdot})$ is dropped in the next sections.

3.1 Variance of the mode shapes

The variance of the mode shapes is developed with respect to auto-covariance matrices of the measurements. The scheme in (10) follows the SSI-UPC algorithm developed in [1] and [6], here, for a single model order n. The first order perturbation of the mode shape $\Delta\varphi_i$ follows

$$\Delta\varphi_i = \mathcal{J}_{\varphi_i,(A_n,C_n)}\mathcal{J}_{(A_n,C_n),\Gamma_n}\mathcal{J}_{\Gamma_n,\mathcal{H}}\mathcal{J}_{\mathcal{H},\mathcal{R}}\mathrm{vec}(\Delta\mathcal{R}) \tag{10}$$

where $\mathcal{J}_{\varphi_i,(A_n,C_n)}$ is the sensitivity of the mode shape components with respect to the state transition and observation matrix computed at model order n, $\mathcal{J}_{(A_n,C_n),\Gamma}$ is the sensitivity of the state transition and observation matrix at model order n towards the observability matrix at order n, $\mathcal{J}_{\Gamma_n,\mathcal{H}}$ is the sensitivity of the observability matrix truncated at order n towards Hankel matrix and finally $\mathcal{J}_{\mathcal{H},\mathcal{R}}$ is the sensitivity of the Hankel matrix towards the auto-covariance matrices of the measurements. The auto-covariance matrices $\mathrm{vec}(\Delta\mathcal{R}) = \begin{bmatrix}\mathrm{vec}(\Delta\mathcal{R}_+)\\ \mathrm{vec}(\Delta\mathcal{R}_-)\end{bmatrix}$ where $\mathcal{R}_+$ and $\mathcal{R}_-$ are respectively the mean of the auto-covariance of each block of the past and future measurements. To easen the notation, the following perturbations can be written as

$$\Delta\varphi_i = \mathcal{J}_{\varphi_i,\mathcal{R}}\mathrm{vec}(\Delta\mathcal{R})$$

where $\mathcal{J}_{\varphi_i,\mathcal{R}} = \mathcal{J}_{\varphi_i,(A_n,C_n)}\mathcal{J}_{(A_n,C_n),\Gamma_n}\mathcal{J}_{\Gamma_n,\mathcal{H}}\mathcal{J}_{\mathcal{H},\mathcal{R}}$ is the chained sensitivity of the i-th mode shape towards the auto-covariance matrices of the measurements.

3.1.1 Uncertainty of normalized mode shape: normalization 1

To compute the variance of the normalized mode shape, the effect of the normalization must be accounted for. The first order perturbation of the first normalization scheme, which was developed in [7], writes as

$$\begin{aligned}\Delta\tilde{\varphi}_i &= \Delta\left(\frac{1}{\varphi_{i,k}}\right)\varphi_i + \frac{1}{\varphi_{i,k}}\Delta\varphi_i \\ &= -\frac{1}{\varphi_{i,k}^2}\Delta(\varphi_{i,k})\varphi_i + \frac{1}{\varphi_{i,k}}\Delta\varphi_i \\ &= \underbrace{\frac{1}{\varphi_{i,k}}\left(-\frac{1}{\varphi_{i,k}}\varphi_i e_k^T + I_r\right)}_{=\mathcal{J}_{\tilde{\varphi}_i,\varphi_i}}\Delta\varphi_i,\end{aligned}$$

using the fact that the (scalar) $\varphi_{i,k} = e_k^T\varphi_i$ where e_k is the k-th unit vector. The respective covariance of the real and imaginary mode shape part writes thus

$$\operatorname{cov}\left(\begin{bmatrix}\Re(\tilde{\varphi}_i)\\ \Im(\tilde{\varphi}_i)\end{bmatrix}\right) = \begin{bmatrix}\Re(\mathcal{J}_{\tilde{\varphi}_i,\varphi_i}\mathcal{J}_{\varphi_i,\mathcal{R}})\\ \Im(\mathcal{J}_{\tilde{\varphi}_i,\varphi_i}\mathcal{J}_{\varphi_i,\mathcal{R}})\end{bmatrix}\Sigma_{\mathcal{R}}\begin{bmatrix}\Re(\mathcal{J}_{\tilde{\varphi}_i,\varphi_i}\mathcal{J}_{\varphi_i,\mathcal{R}})\\ \Im(\mathcal{J}_{\tilde{\varphi}_i,\varphi_i}\mathcal{J}_{\varphi_i,\mathcal{R}})\end{bmatrix}^T. \tag{11}$$

where $\Sigma_{\mathcal{R}}$ can be easily estimated as a sample covariance on blocks of the data as in [1] and [6].

3.1.2 Uncertainty of normalized mode shape: normalization 2

Regarding the second normalization scheme depicted in (8), the first order perturbation of $\breve{\varphi}_i$ writes as

$$\begin{aligned}\Delta\breve{\varphi}_i &= \Delta\left(\frac{1}{||\tilde{\varphi}_i||}\right)\tilde{\varphi}_i + \frac{1}{||\tilde{\varphi}_i||}\Delta\tilde{\varphi}_i \\ &= -\frac{\tilde{\varphi}_i}{2||\tilde{\varphi}_i||^3}\Delta(||\tilde{\varphi}_i||^2) + \frac{1}{||\tilde{\varphi}_i||}\Delta\tilde{\varphi}_i \\ &= -\frac{\tilde{\varphi}_i}{||\tilde{\varphi}_i||^3}\Re(\tilde{\varphi}_i^H\Delta\tilde{\varphi}_i) + \frac{1}{||\tilde{\varphi}_i||}\Delta\tilde{\varphi}_i \\ &= \underbrace{\frac{1}{||\tilde{\varphi}_i||}\left(-\frac{\tilde{\varphi}_i}{||\tilde{\varphi}_i||^2}\Re(\tilde{\varphi}_i^H\mathcal{J}_{\tilde{\varphi}_i,\varphi_i}\mathcal{J}_{\varphi_i,\mathcal{R}}) + \mathcal{J}_{\tilde{\varphi}_i,\varphi_i}\mathcal{J}_{\varphi_i,\mathcal{R}}\right)}_{=\mathcal{J}_{\breve{\varphi}_i,\mathcal{R}}}\operatorname{vec}(\Delta\mathcal{R}),\end{aligned}$$

and thus for the covariance of the real and imaginary mode shape parts

$$\operatorname{cov}\left(\begin{bmatrix}\Re(\breve{\varphi}_i)\\ \Im(\breve{\varphi}_i)\end{bmatrix}\right) = \begin{bmatrix}\Re(\mathcal{J}_{\breve{\varphi}_i,\mathcal{R}})\\ \Im(\mathcal{J}_{\breve{\varphi}_i,\mathcal{R}})\end{bmatrix}\Sigma_{\mathcal{R}}\begin{bmatrix}\Re(\mathcal{J}_{\breve{\varphi}_i,\mathcal{R}})\\ \Im(\mathcal{J}_{\breve{\varphi}_i,\mathcal{R}})\end{bmatrix}^T. \tag{12}$$

3.2 Uncertainty of MAC

The computation of MAC between two complex valued mode shapes vectors φ and ψ estimated at model order n follows [5] and writes

$$\text{MAC} = \frac{|\varphi^H\psi|^2}{\varphi^H\varphi\psi^H\psi} = \frac{\varphi^H\psi\psi^H\varphi}{\varphi^H\varphi\psi^H\psi} \tag{13}$$

Two general cases for the MAC computation are distinguished namely, first when φ and ψ are estimates of a different mode shape, hereby denoted as cross-MAC, and second when $\varphi = \psi$ are the same mode shape estimate, denoted as auto-MAC. Note that auto-MAC yields

$$\text{MAC} = \frac{|\psi^H\psi|^2}{\psi^H\psi\psi^H\psi} = \frac{\psi^H\psi\psi^H\psi}{\psi^H\psi\psi^H\psi} = 1, \tag{14}$$

and has no uncertainty. To quantify the uncertainty of cross-MAC, the aim is to obtain the first order perturbation of (13) with respect to the real and the imaginary parts of the mode shape vectors, which writes as

$$\Delta\text{MAC} = \underbrace{\begin{bmatrix} \frac{\partial \text{MAC}}{\partial \Re(\varphi)} & \frac{\partial \text{MAC}}{\partial \Im(\varphi)} & \frac{\partial \text{MAC}}{\partial \Re(\psi)} & \frac{\partial \text{MAC}}{\partial \Im(\psi)} \end{bmatrix}}_{=\mathcal{J}_{\text{MAC},\varphi,\psi}} \begin{bmatrix} \Delta\Re(\varphi) \\ \Delta\Im(\varphi) \\ \Delta\Re(\psi) \\ \Delta\Im(\psi) \end{bmatrix} \tag{15}$$

where the covariance of the MAC can be expressed in terms of the covariance of the mode shapes and the analytical sensitivity $\mathcal{J}_{\text{MAC},\varphi,\psi}$. To derive $\mathcal{J}_{\text{MAC},\varphi,\psi}$, let us write the first order perturbation of (13) as

$$\Delta\text{MAC} = \frac{\Delta(\varphi^H\psi\psi^H\varphi)}{\varphi^H\varphi\psi^H\psi} - \frac{\varphi^H\psi\psi^H\varphi}{(\varphi^H\varphi\psi^H\psi)^2}\Delta(\varphi^H\varphi\psi^H\psi). \tag{16}$$

Since both the φ and ψ are column vectors the product $\varphi^H\psi$ is a complex scalar. Expressing the first term from (16) it holds

$$\Delta(\varphi^H\psi\psi^H\varphi) = \Delta(\varphi^H)\psi\psi^H\varphi + \varphi^H\Delta(\psi)\psi^H\varphi + \varphi^H\psi\Delta(\psi^H)\varphi + \varphi^H\psi\psi^H\Delta(\varphi). \tag{17}$$

The terms $\Delta(\varphi^H)\psi\psi^H\varphi$ and $\varphi^H\psi\psi^H\Delta(\varphi)$ are conjugates of each other, and so are $\varphi^H\Delta(\psi)\psi^H\varphi$ and $\varphi^H\psi\Delta(\psi^H)\varphi$. Thus, it follows

$$\Delta(\varphi^H\psi\psi^H\varphi) = 2\Re(\varphi^H\Delta(\psi)\psi^H\varphi) + 2\Re(\varphi^H\psi\psi^H\Delta(\varphi)) \tag{18}$$

$$= 2\Re(\psi^H\varphi\varphi^H\Delta\psi) + 2\Re(\varphi^H\psi\psi^H\Delta\varphi). \tag{19}$$

Finally, for every complex vectors y and x the real part of the inner product writes $\Re(y^Hx) = \Re((\Re(y) + \mathrm{i}\Im(y))^H(\Re(x) + \mathrm{i}\Im(x))) = \Re(y)^T\Re(x) + \Im(y)^T\Im(x)$, hence it holds

$$\Re(\psi^H\varphi\varphi^H\Delta\psi) = \begin{bmatrix} \Re(\varphi\varphi^H\psi)^T & \Im(\varphi\varphi^H\psi)^T \end{bmatrix} \begin{bmatrix} \Delta\Re(\psi) \\ \Delta\Im(\psi) \end{bmatrix} \tag{20}$$

and

$$\Re(\varphi^H\psi\psi^H\Delta\varphi) = \begin{bmatrix} \Re(\psi\psi^H\varphi)^T & \Im(\psi\psi^H\varphi)^T \end{bmatrix} \begin{bmatrix} \Delta\Re(\varphi) \\ \Delta\Im(\varphi) \end{bmatrix}. \tag{21}$$

The second term of (16) is derived with a scheme analogous to the one depicted in (17)-(21). After sorting the respective terms, the partial derivatives of the MAC with respect to the real and imaginary parts of the mode shapes are

$$\frac{\partial\text{MAC}}{\partial\Re(\varphi)} = \frac{2\Re(\psi\psi^H\varphi)^T}{\varphi^H\varphi\psi^H\psi} - \frac{\varphi^H\psi\psi^H\varphi\psi^H\psi}{(\varphi^H\varphi\psi^H\psi)^2}2\Re(\varphi)^T \tag{22}$$

$$\frac{\partial\text{MAC}}{\partial\Im(\varphi)} = \frac{2\Im(\psi\psi^H\varphi)^T}{\varphi^H\varphi\psi^H\psi} - \frac{\varphi^H\psi\psi^H\varphi\psi^H\psi}{(\varphi^H\varphi\psi^H\psi)^2}2\Im(\varphi)^T \tag{23}$$

and

$$\frac{\partial\text{MAC}}{\partial\Re(\psi)} = \frac{2\Re(\varphi\varphi^H\psi)^T}{\varphi^H\varphi\psi^H\psi} - \frac{\varphi^H\psi\psi^H\varphi\varphi^H\varphi}{(\varphi^H\varphi\psi^H\psi)^2}2\Re(\psi)^T \tag{24}$$

$$\frac{\partial\text{MAC}}{\partial\Im(\psi)} = \frac{2\Im(\varphi\varphi^H\psi)^T}{\varphi^H\varphi\psi^H\psi} - \frac{\varphi^H\psi\psi^H\varphi\varphi^H\varphi}{(\varphi^H\varphi\psi^H\psi)^2}2\Im(\psi)^T. \tag{25}$$

Combining (22)-(25) to the analytical sensitivity $\mathcal{J}_{\text{MAC},\varphi,\psi}$ after (15), the covariance of the MAC writes

$$\text{cov}\,(\text{MAC}) = \mathcal{J}_{\text{MAC},\varphi,\psi}\Sigma_{\varphi,\psi}\mathcal{J}_{\text{MAC},\varphi,\psi}^T.$$

4 Application

The presented scheme for the uncertainty computation is tested on a numerical simulation of a 6 degree of freedom (DOF) spring mass system in a Monte Carlo (MC) setup with 1000 simulations. The following application directly refers to the one in [6] that validated the variance estimation of natural frequencies and damping ratios in such a framework. In addition to the uncertainty quantification of MAC, this paper validates variance estimation for the mode shape computation. The chain-like system is excited with a white noise signal in all DOFs with sampling frequency of 50Hz for 2000 seconds and the responses are measured at 1, 2 and 5 DOF. Gaussian white noise with 5% of the standard deviation of the output is added to the response at each channel. The influence of the two underlying mode shape normalization cases, depicted in (7) and (8), on the variance computation is investigated.
Both the output-only data driven subspace-based system identification with the unweighted principal component (SSI-UPC) and the variance computation in the corresponding framework are set up with a single system order of 12, time lags of 15 and 200 blocks for the covariance computation of the data Hankel matrix. Six modes are tracked in each simulation. In both mode shape normalization cases the second component of the mode shape vector was selected for the normalization. The exact and calculated means of the real parts of the identified mode shapes with the respective Coefficients of Variation (CV) are depicted in Table 1 and Table 2.

DOF/Case		1	2	3	4	5	6
DOF_1	Exact	0.6834	0.8414	1.3228	-1.7442	-1.0222	-0.7374
	Mean MC	0.6826	0.8413	1.3226	-1.7428	-1.0220	-0.7380
	CV[%]	1.241	0.240	0.368	1.927	0.523	1.270
DOF_2	Exact	1	1	1	1	1	1
	Mean MC	1	1	1	1	1	1
	CV[%]	0	0	0	0	0	0
DOF_5	Exact	2.0962	-0.6158	0.2154	-2.5708	0.9707	-0.7207
	Mean MC	2.0957	-0.6157	0.2153	-2.5685	0.9710	-0.7204
	CV[%]	0.615	0.123	0.809	1.368	0.867	2.336

Table 1: Comparison of the exact and mean values with corresponding CV from Monte Carlo simulation of estimated mode shapes. Normalization scheme 1.

DOF/Case		1	2	3	4	5	6
DOF_1	Exact	0.2823	0.5824	0.7911	0.5344	0.5914	0.5134
	Mean MC	0.2819	0.5824	0.7910	0.5344	0.5915	0.5134
	CV[%]	1.040	0.159	0.120	0.977	0.389	1.429
DOF_2	Exact	0.4131	0.6922	0.5980	-0.3066	-0.5786	-0.6963
	Mean MC	0.4131	0.6922	0.5980	-0.3064	-0.5786	-0.6962
	CV[%]	0.2819	0.5824	0.7910	0.5344	0.5915	0.5134
DOF_5	Exact	0.8659	-0.4262	0.1288	0.7877	-0.5616	0.5018
	Mean MC	0.8659	-0.4262	0.1288	0.7870	-0.5614	0.5013
	CV[%]	0.144	0.116	0.661	0.797	0.605	1.995

Table 2: Comparison of exact and mean values with corresponding CV from Monte Carlo simulation of estimated mode shapes. Normalization scheme 2.

Both Table 1 and Table 2 reveal that calculated MC means are close to the exact values of the mode shapes, with the highest CV of 2.336% for mode 6. A comparison between the standard deviations of the mode shape components computed from the MC simulation, σ_{MC}, and the mean standard deviations from the perturbation theory (PT), σ_{PT} is depicted in Table 3 and Table 4.

DOF/Case		Standard deviation of $\Re(\phi)$ [$\cdot 10^{-2}$]						Standard deviation of $\Im(\phi)$ [$\cdot 10^{-2}$]					
		1	2	3	4	5	6	1	2	3	4	5	6
DOF_1	σ_{PT}	0.85	0.21	0.47	3.40	0.54	0.95	0.84	0.24	0.51	3.47	0.54	0.92
	σ_{MC}	0.84	0.20	0.46	3.52	0.53	0.97	0.80	0.23	0.51	3.50	0.54	0.91
DOF_2	σ_{PT}	0.00	0.00	0.00	0.00	0.00	0.00	0.00	0.00	0.00	0.00	0.00	0.00
	σ_{MC}	0.00	0.00	0.00	0.00	0.00	0.00	0.00	0.00	0.00	0.00	0.00	0.00
DOF_5	σ_{PT}	1.38	0.08	0.17	8.77	0.87	1.69	1.44	0.13	0.20	8.85	0.88	1.75
	σ_{MC}	1.27	0.07	0.17	8.97	0.88	1.67	1.32	0.12	0.19	9.01	0.86	1.79

Table 3: Standard deviations of real and imaginary part of the mode shapes from perturbation approach and Monte Carlo simulations. Normalization scheme 1.

DOF/Case		Standard deviation of $\Re(\phi)$ [$\cdot 10^{-2}$]						Standard deviation of $\Im(\phi)$ [$\cdot 10^{-2}$]					
		1	2	3	4	5	6	1	2	3	4	5	6
DOF_1	σ_{PT}	0.30	0.09	0.10	0.53	0.23	0.74	0.35	0.17	0.31	1.06	0.31	0.64
	σ_{MC}	0.30	0.09	0.10	0.55	0.23	0.73	0.33	0.17	0.30	1.06	0.32	0.65
DOF_2	σ_{PT}	0.22	0.06	0.14	0.81	0.22	0.29	0.00	0.00	0.00	0.00	0.00	0.00
	σ_{MC}	0.21	0.06	0.14	0.82	0.22	0.29	0.00	0.00	0.00	0.00	0.00	0.00
DOF_5	σ_{PT}	0.14	0.05	0.08	0.65	0.34	1.01	0.30	0.09	0.10	0.53	0.23	0.74
	σ_{MC}	0.13	0.05	0.08	0.66	0.34	0.99	0.30	0.09	0.10	0.53	0.23	0.74

Table 4: Standard deviations of real and imaginary part of the mode shapes from perturbation approach and Monte Carlo simulations. Normalization scheme 2.

Both Table 3 and Table 4 illustrate that the differences between the standard deviations obtained from the MC simulations and the mean standard deviations computed using perturbation theory (PT) are negligible. Higher standard deviations, on average, of all DOFs in Table 3 correspond to higher mean values of the mode shape components in Table 1. That results in a small differences between the CV of estimated DOFs which is illustrated, for the two normalization schemes, in Table 1 and Table 2 respectively.
Results presented so far were computed for a single sample size N, which, naturally, is the case when using such framework for uncertainty quantification in real-life applications. That, however, should hold for any sufficient data length. Analyzing results computed on different sample lengths provide arguments for deploying such framework and allow to draw some conclusions about the distribution properties of the estimated mode shapes. For that purpose introduce some variables that depend on standard deviations of $\Re(\phi)$ and $\Im(\phi)$ computed from the MC simulations such as

$$\begin{aligned}
&\sigma_{\Re(\phi_{r,i})_{\mathrm{MC}}} = \sqrt{\mathrm{var}\left(\Re(\phi_{r,i})\right)}, \quad \sigma_{\Im(\phi_{r,i})_{\mathrm{MC}}} = \sqrt{\mathrm{var}\left(\Im(\phi_{r,i})\right)}, \\
&\overline{\sigma}_{\Re(\phi)_{\mathrm{MC}}} = \sum_{r=1}^{3}\sum_{i=1}^{6} \sigma_{\Re(\phi_{r,i})_{\mathrm{MC}}}, \quad \overline{\sigma}_{\Im(\phi)_{\mathrm{MC}}} = \sum_{r=1}^{3}\sum_{i=1}^{6} \sigma_{\Im(\phi_{r,i})_{\mathrm{MC}}}, \\
&\alpha_{\Re(\phi)_{\mathrm{MC}}} = \overline{\sigma}_{\Re(\phi)_{\mathrm{MC}}}\sqrt{N}, \quad \alpha_{\Im(\phi)_{\mathrm{MC}}} = \overline{\sigma}_{\Im(\phi)_{\mathrm{MC}}}\sqrt{N}.
\end{aligned} \tag{26}$$

The $r = 1 \ldots 3$ denotes the number of measured DOF, $i = 1 \ldots 6$ denotes the number of identified modes and the $j = 1 \ldots MC$, where $MC = 1000$ and j denotes the j-th Monte Carlo simulation. Now, recall that proposed perturbation approach computes variance of the real and imaginary parts of the mode shape component, $\sigma_{\Re(\phi_{r,i})_{\mathrm{PT,j}}}$ and $\sigma_{\Im(\phi_{r,i})_{\mathrm{PT,j}}}$, for a single realization j, hence 1000 simulations enable to compute

the variance of $\sigma_{\Re(\phi_{r,i})_{\mathrm{PT}}}$ and $\sigma_{\Im(\phi_{r,i})_{\mathrm{PT}}}$ which, for the variables formulated in (26), writes

$$\overline{\sigma}_{\Re(\phi)_{\mathrm{PT}}} = \frac{1}{MC}\sum_{r=1}^{3}\sum_{i=1}^{6}\sum_{j=1}^{MC}\sigma_{\Re(\phi_{r,i})_{\mathrm{PT,j}}}, \quad \overline{\sigma}_{\Im(\phi)_{\mathrm{PT}}} = \frac{1}{MC}\sum_{r=1}^{3}\sum_{i=1}^{6}\sum_{j=1}^{MC}\sigma_{\Im(\phi_{r,i})_{\mathrm{PT,j}}}, \tag{27}$$

$$\sigma^{*}{}_{\Re(\phi)_{\mathrm{PT}}} = \sum_{r=1}^{3}\sum_{i=1}^{6}\sqrt{\mathrm{var}\left(\sigma_{\Re(\phi_{r,i})_{\mathrm{PT}}}\right)}, \quad \sigma^{*}{}_{\Im(\phi)_{\mathrm{PT}}} = \sum_{r=1}^{3}\sum_{i=1}^{6}\sqrt{\mathrm{var}\left(\sigma_{\Im(\phi_{r,i})_{\mathrm{PT}}}\right)},$$

$$\alpha_{\Re(\phi)_{\mathrm{PT}}} = \overline{\sigma}_{\Re(\phi)_{\mathrm{PT}}}\sqrt{N}, \quad \alpha_{\Im(\phi)_{\mathrm{PT}}} = \overline{\sigma}_{\Im(\phi)_{\mathrm{PT}}}\sqrt{N}.$$

Analysis of the variables in (26) and (27) computed on the data sets with different sample lengths is depicted on Figure 1.

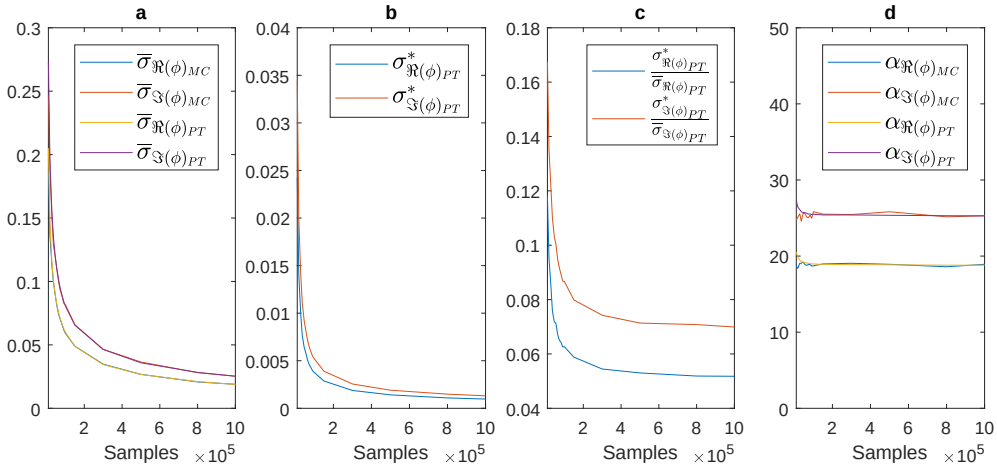


Figure 1: Sum of standard deviations of the mode shape components from Monte Carlo simulation and mean perturbation theory depending on number of samples (a). Standard deviation of the sum of standard deviations of the mode shape components from Monte Carlo simulation and mean perturbation theory (b). CV of the standard deviation of mode shape components from perturbation theory depending on number of samples (c). Sum of standard deviations of the mode shape components from Monte Carlo simulation and mean perturbation theory scaled with a square root of corresponding data length (d). Normalization 1.

Since mode shapes estimates are converging to their true value the $\overline{\sigma}_{\Re(\phi)_{\mathrm{MC}}}$, $\overline{\sigma}_{\Im(\phi)_{\mathrm{MC}}}$, $\overline{\sigma}_{\Re(\phi)_{\mathrm{PT}}}$ and $\overline{\sigma}_{\Im(\phi)_{\mathrm{PT}}}$ are converging to zero, which is illustrated in the 'a' part of Figure 1. The 'b' part shows that the errors in the perturbation approach converge to zero. The CVs $\sigma^{*}{}_{\Re(\phi)_{\mathrm{PT}}}/\overline{\sigma}_{\Re(\phi)_{\mathrm{PT}}}$ and $\sigma^{*}{}_{\Im(\phi)_{\mathrm{PT}}}/\overline{\sigma}_{\Im(\phi)_{\mathrm{PT}}}$ converge to a constant value of 5.5% and 7.5% respectively, see 'c' part of Figure 1, which illustrates that the relative error summed from all the mode shape components for selected model order n is very small. That also arguments for using the proposed framework while having just one measurement set. The 'd' part of Figure 1 illustrates that the pairs $\overline{\sigma}_{\Re(\phi)_{\mathrm{PT}}}$ and $\overline{\sigma}_{\Re(\phi)_{\mathrm{MC}}}$ with $\overline{\sigma}_{\Im(\phi)_{\mathrm{PT}}}$ and $\overline{\sigma}_{\Im(\phi)_{\mathrm{MC}}}$ converge with rate of order $\sqrt{N}$ to a similar constant, which also justifies estimating the variance of the mode shape components with the perturbation approach.

The MAC values computed between the mode shapes estimated at model order 6 from one arbitrary data set are depicted on Figure 2.

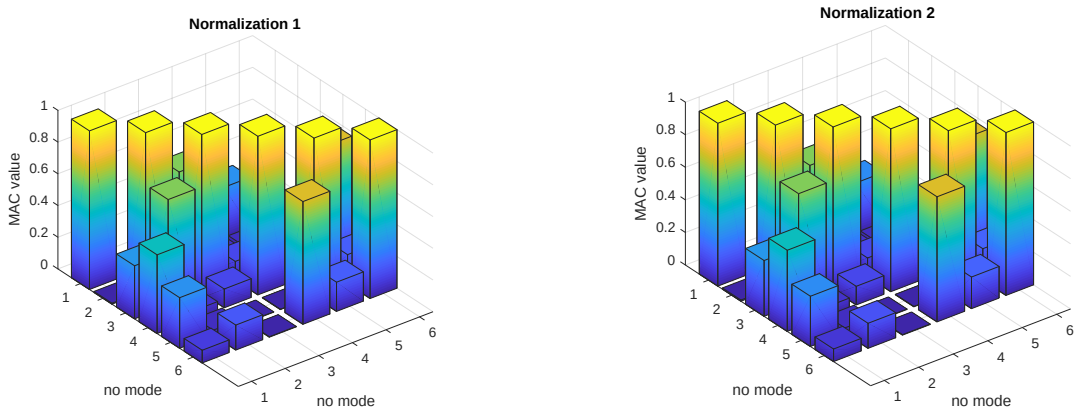


Figure 2: MAC values computed for one simulation. Normalization scheme 1 (left) and normalization scheme 2 (right).

As shown in (14) the diagonal of the MAC matrix plotted in Figure 2 is equal to one. The histograms of selected MAC values obtained from MC simulations with the corresponding standard deviations computed using the perturbation approach are depicted on Figure 3 and Figure 4 respectively.

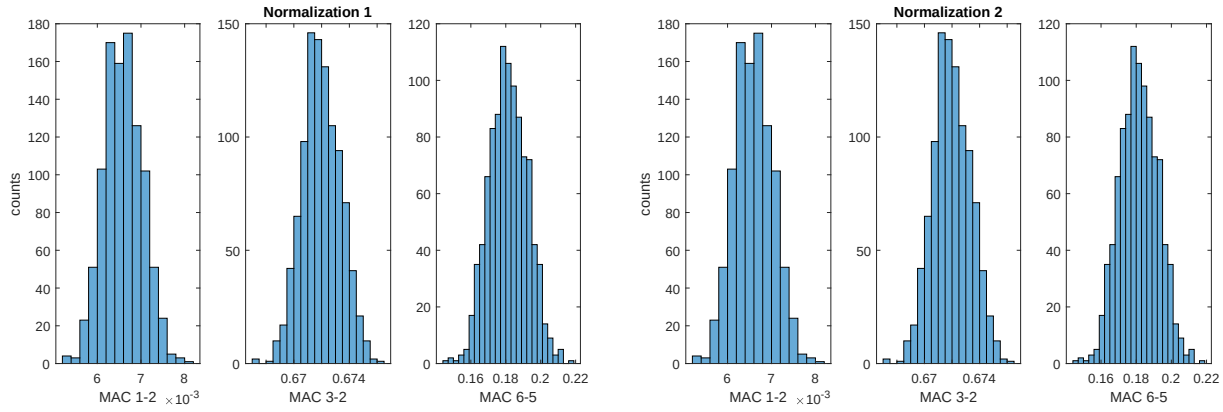


Figure 3: Selected histograms of MAC from Monte Carlo simulations.

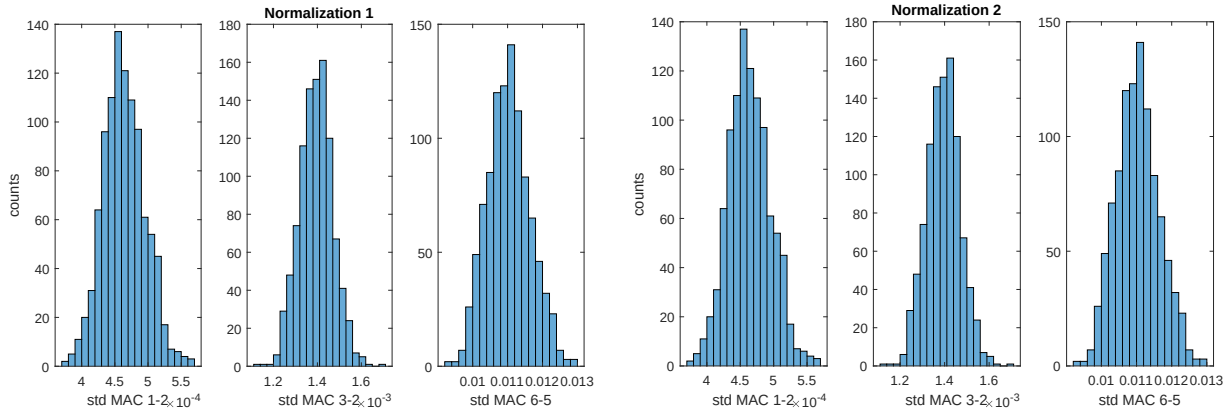


Figure 4: Selected histograms of standard deviations of MAC computed with perturbation approach.

The histograms illustrate the validity of Gaussian approximation of MAC stated by CLT in (9). In addi-

tion, the MAC values and the standard deviations of MAC for both normalization schemes are numerically identical, hence render its computation invariant towards the normalization of the mode shape. The standard deviations of the MAC obtained from the MC simulations and the mean standard deviations computed using the PT are presented in Table 5.

Standard deviation of MAC [$\cdot 10^{-2}$]													
Mode/Case		Normalization scheme 1						Normalization scheme 2					
		1	2	3	4	5	6	1	2	3	4	5	6
1	σ_{PT}	-	0.05	0.30	1.09	0.42	0.49	-	0.05	0.30	1.09	0.42	0.49
	σ_{MC}	-	0.04	0.28	1.11	0.42	0.49	-	0.04	0.28	1.11	0.42	0.49
2	σ_{PT}	0.05	-	0.14	0.14	0.10	0.59	0.05	-	0.14	0.14	0.10	0.59
	σ_{MC}	0.04	-	0.14	0.14	0.10	0.58	0.04	-	0.14	0.14	0.10	0.58
3	σ_{PT}	0.30	0.14	-	0.24	0.03	0.05	0.30	0.14	-	0.24	0.03	0.05
	σ_{MC}	0.28	0.14	-	0.23	0.03	0.05	0.28	0.14	-	0.23	0.03	0.05
4	σ_{PT}	1.09	0.14	0.24	-	0.13	1.06	1.09	0.14	0.24	-	0.13	1.06
	σ_{MC}	1.11	0.14	0.23	-	0.13	1.08	1.11	0.14	0.23	-	0.13	1.08
5	σ_{PT}	0.42	0.10	0.03	0.13	-	1.10	0.42	0.10	0.03	0.13	-	1.10
	σ_{MC}	0.42	0.10	0.03	0.13	-	1.09	0.42	0.10	0.03	0.13	-	1.09
6	σ_{PT}	0.49	0.59	0.05	1.06	1.10	-	0.49	0.59	0.05	1.06	1.10	-
	σ_{MC}	0.49	0.58	0.05	1.08	1.09	-	0.49	0.58	0.05	1.08	1.09	-

Table 5: Standard deviations of MAC values for both normalization schemes for perturbation approach and Monte Carlo simulations.

It can be observed that the differences between the standard deviations of MAC computed from MC simulations and the mean ones obtained from the perturbation approach are small.
The influence of data length on the standard deviations of MAC computed from MC simulations and the mean standard deviations obtained from the PT is illustrated in Figure 5.

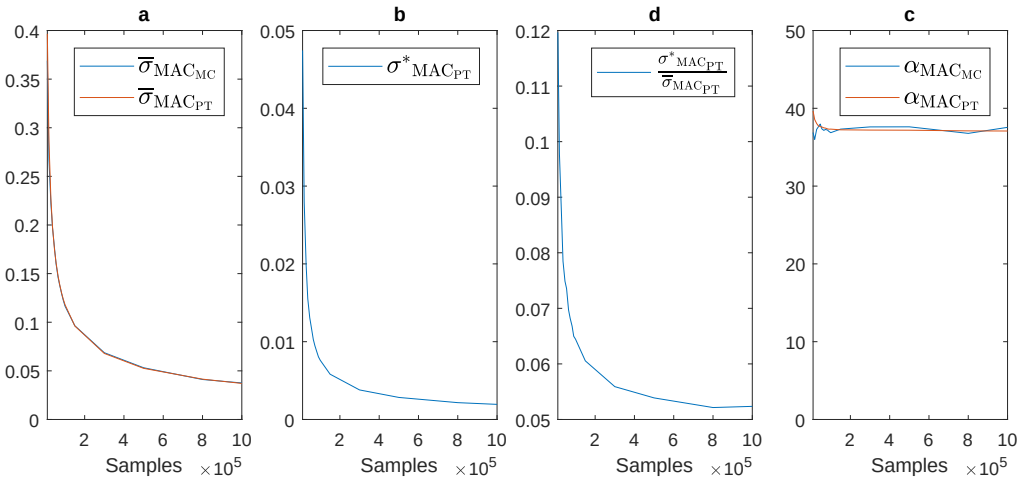


Figure 5: Sum of standard deviations of MAC from Monte Carlo simulation and mean perturbation theory depending on number of samples (a). Standard deviation of the sum of standard deviations of MAC from Monte Carlo simulation and mean perturbation theory (b). CV of the standard deviation of MAC from perturbation theory (c). Sum of standard deviations of MAC from Monte Carlo simulation and mean perturbation theory scaled with a square root of corresponding data length (d). Normalization 1.

The parameters used in this analysis follow a similar notation as in the case of mode shape uncertainties, see (26) and (27). The 'a' part of Figure 5 illustrates that the $\overline{\sigma}_{\mathrm{MAC_{MC}}}$ and $\overline{\sigma}_{\mathrm{MAC_{PT}}}$ are converging to zero. In addition, note that there is no visible difference between the results from MC simulations and

the mean ones obtained from PT. Second, the errors in the variance estimates of MAC computed with the perturbation approach, ${\sigma^*}_{\mathrm{MAC}_{\mathrm{PT}}}$, also converge to zero, which is presented in the 'b' part of Figure 5. The CV of the standard deviations of MAC, ${\sigma^*}_{\mathrm{MAC}_{\mathrm{PT}}}/\overline{\sigma}_{\mathrm{MAC}_{\mathrm{PT}}}$, computed using perturbation approach converge to a constant value of 5.2%, see 'c' part of Figure 5, which, like in the case of mode shape uncertainties, is small and arguments for using proposed framework while having just one measurement set. Lastly, the 'd' part of Figure 5 illustrates that both the $\overline{\sigma}_{\mathrm{MAC}_{\mathrm{MC}}}$ and $\overline{\sigma}_{\mathrm{MAC}_{\mathrm{PT}}}$ converges with rate $\sqrt{N}$ to a similar constant.

5 Conclusions

This paper presented an approach to quantify the statistical uncertainty of MAC computed between different mode shape vectors. Proposed method was verified against Monte Carlo simulations of a simple chain system where the resulting differences between two frameworks were negligible, as expected. Uncertainty quantification was found invariant towards the underlying schemes for mode shape normalization, as expected. Theoretical asymptotic properties of MAC were validated with simulations with increasing sample size. The future work will consists of real-life application of both the uncertainty quantification of mode shapes and MAC, through its implementation in the future release of the ARTEMIS MODAL PRO [8] software.

References

[1] M. Döhler, P. Andersen, and L. Mevel. Variance computation of modal parameter estimates from upc subspace identification. In *IOMAC - 7th International Operational Modal Analysis Conference*, Ingolstadt, Germany, 2017.

[2] M. Döhler, X.-B. Lam, and L. Mevel. Uncertainty quantification for modal parameters from stochastic subspace identification on multi-setup measurements. *Mechanical Systems and Signal Processing*, 36:562–581, 04 2013.

[3] M. Döhler and L. Mevel. Fast multi-order computation of system matrices in subspace-based system identification. *Control Engineering Practice*, 20(9):882 – 894, 2012.

[4] M. Döhler and L. Mevel. Efficient multi-order uncertainty computation for stochastic subspace identification. *Mechanical Systems and Signal Processing*, 38(2):346–366, 2013.

[5] R. J. Allemang. The modal assurance criterion (MAC): Twenty years of use and abuse. *Journal of Sound and Vibration*, 37, 01 2003.

[6] P. Mellinger, M. Döhler, and L. Mevel. Variance estimation of modal parameters from output-only and input/output subspace-based system identification. *Journal of Sound and Vibration*, 379(Supplement C):1 – 27, 2016.

[7] E. Reynders, R. Pintelon, and G. D. Roeck. Uncertainty bounds on modal parameters obtained from stochastic subspace identification. *Mechanical Systems and Signal Processing*, 22(4):948 – 969, 2008. Special Issue: Crack Effects in Rotordynamics.

[8] Structural-Vibration-Solutions-A/S. ARTEMIS MODAL PRO 6.0. In *http://svibs.com*, 2018.

[9] P. van Overschee and B. de Moor. *Subspace Identification for Linear Systems*. Springer, 1st edition, 1996.

Recent advances in swept sine controlled excitation and processing for Multi-Input Multi-Output FRFs estimation

U. Musella[1,2,3], **A. Longo**[3], **S. Vettori**[4], **S. Waimer**[1,2], **E. Di Lorenzo**[2], **B. Peeters**[2], **F. Marulo**[3], **P. Guillaume**[1]

[1] Vrije Universiteit Brussel, Department of Mechanical Engineering,
Pleinlaan 2, 1050, Ixelles, Belgium
e-mail: **umberto.musella.ext@siemens.com**

[2] Siemens Industry Software NV, Test Division,
Interleuvenlaan 68, 3001, Leuven, Belgium

[3] University of Naples "Federico II", Department of Industrial Engineering,
via Claudio 21, 80125, Napoli, Italy

[4] University of Rome "La Sapienza", Department of Civil and Industrial Engineering,
via Eudossiana 18, 00184, Rome, Italy

Abstract

MIMO swept sine excitation is nowadays largely used in environmental and modal testing of aerospace structures, being recognized as an optimal compromise between high quality FRFs and testing time. Due to the test levels that can be reached, monitoring the recordings of multiple transducers translates in the need of on-line controlling the signals, in order to keep them at a (safe) reference level. At the same time, FRFs obtained from MIMO sine tests can also be affected by the processing technique used to combine multiple sweeps. In this paper, a feed-forward control strategy for MIMO sine testing aiming to reduce the error between the responses and the references is presented. This approach moves towards a MIMO swept sine feedback control, with the capability of on-line modifying the model of the system obtained in a pre-test phase. Subsequently, with focus on Ground Vibration Testing, an advanced data processing technique is used to obtain an optimal modal model from the multiple sweeps.

1 Introduction

Nowadays Multiple-Input Multiple-Output (MIMO) sine sweep is one of the most popular excitation techniques for the modal testing of large aerospace structures. The success is related to the possibility of characterizing the dynamic response of the unit under test frequency-to-frequency, reaching high excitation levels and high quality FRFs, providing also preliminar information on potential non-linear behavior [1–4]. Some of these features were previously obtained running normal modes tests or combining normal modes with broadband or stepped sine excitations at the cost of extremely long testing times (normal modes and stepped sine) [5] or poor excitation levels (broadband random). For large aerospace structures, high-quality measurements are compulsory. Even if these tests are critical, they are scheduled in a period of extreme time pressure, with the full ready-to-use assembly that still needs to undergo additional testing stages, for example acoustic and thermal testing of large satellites [6]. Another application example is the Ground Vibration Testing (GVT) of large aircrafts, where the testing, required for flutter prediction analysis, is typically scheduled before the final painting and the maiden flight. With focus on GVT applications, recent studies addressed the problem that the FRFs and mode sets obtained with sine sweeps show a dependency on the FRFs estimation

method used to process the acquired data. For example, the necessity of MIMO sine testing to combine runs from multiple sweeps with different phases between the inputs in one data set, can require additional iterations (also involving broadband random data) to come up with a representative mode set. As a consequence, even if MIMO swept sine techniques proved to be an ideal compromise between high quality FRFs and testing time, it is acknowledged that there is still a significant amount of time that can be saved during the data analysis. As potential solution, for the specific case of fixed wing aircraft GVT, a data processing technique was proposed in the last years [7–9]: the Virtual Driving Point method (VDP). The VDP working principle consists in building a virtual single-input excitation from a single run (a single sweep) with multi-input excitation. Main advantage of this procedure is that each sweep can be performed individually and the measured data can be independently analyzed even in case of multi-input excitation.

From the practical perspective, an additional advantage of swept sine excitation is the possibility of using state-of-the-art feedforward control techniques to define reference levels for specific control channels, e.g. force transducers or accelerometers. This allows the *shaping* of the voltages driving the exciters, predicting the dynamic behaviour of the unit to be tested. This prediction relies on a system model obtained with a low-level pre-test random system identification. Due to potential non-linear behaviour that can be triggered at the (generally high) test levels reached during the actual sine sweeps, noise on the measurements and transient effects due to the sweeping itself (for instance beating phenomena [4], [10], [11]), the system can differ from the linear model estimated in the pre-test. The spectra of the control channels can therefore deviate from the reference and closed loop feedback control strategies are sought to compensate for these differences.

Different MIMO frequency domain algorithms can be used to control the multiple drives, as suggested by [12]. The work [13] additionally proposes an attractive approach that combines $\mathbb{CR}$-calculus, as described in [14–16], to traditional Gauss-Newton iterative algorithms, allowing to correct system identification errors during the convergence and therefore increase the convergence speed. The main challenges of MIMO swept sine controlled techniques are related to the on-line estimation of the responses (to be controlled) and the drives (to be updated) spectra from the continuously swept signals and the robustness of the developed closed-loop MIMO controller. For these reasons, a time domain implementation of the control strategy proposed in [13] is still under investigation. In the early development stage of the controller, in order to already tackle potential issues that can be encountered during an actual swept sine test, an innovative idea is to integrate the controller in a Virtual Shaker Testing environment [10], [11].

The purpose of this paper is to highlight recent research activities carried out to improve the current practice of MIMO swept sine testing for FRF estimation, with a specific focus on GVT. Specifically, in sec. 2 the limitation of state-of-the-art feedforward control is highlighted. The need for moving towards a feedback closed-loop control, and a potential control logic, to be developed in a Virtual Shaker Testing environment, are also covered in sec. 2. Sec. 3 provides an insight on the Virtual Driving Point technique as potential solution to process the acquired data during a MIMO swept sine testing for GVT allowing to overcome some of the limitations of processing data from different sweeps.

Since in this work most of the derivations are in the frequency domain, all the arrays are functions of the frequency f (in Hz), if not specified otherwise. Vectors are denoted by lower case bold letters, e.g. $\mathbf{a}$, and matrices by upper case bold letters, e.g. $\mathbf{A}$. An over-bar $\overline{\square}$ is used to indicate the complex conjugate operation and the Hermitian superscript $\square^H$ to indicate the complex conjugate transpose of a matrix, e.g. $\overline{\mathbf{a}}$ and $\mathbf{A}^H$. The dagger symbol $\square^\dagger$ is used to indicate the Moore-Penrose pseudo-inverse of a matrix, whereas the hat $\hat{\square}$ is used to emphasize the estimation of a quantity, e.g. $\hat{\mathbf{A}}$ is an estimate of the matrix $\mathbf{A}$. Time domain derivatives are indicated with dots $\dot{\square}$, for example $\dot{a}(t)$ and $\ddot{a}(t)$ are the first and second derivatives of the waveform $a(t)$, respectively.

2 Multi-Input Multi-Output swept sine controlled excitation

Fig. 1 is a schematic representation of a general MIMO vibration control test. A set of m voltages is sent to multiple exciters. Typically these signals (the so-called *drives*) drive m independent shakers or, possibly,

the multiple degrees of freedom of a multi-axis shaking table [17], [18]. The unit under test responses are recorded in ℓ control channels (the so-called *controls* or *pilots*).

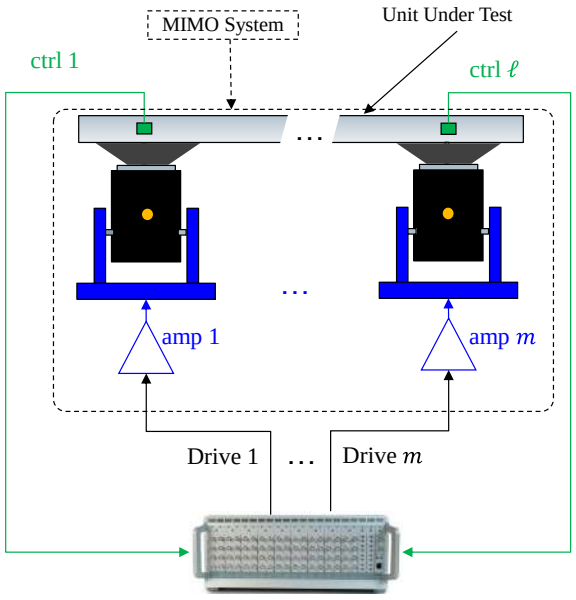


Figure 1: Schematic representation of a MIMO vibration control test.

During a MIMO test with swept sine excitation, the unit under test is excited with multiple swept sines over a user-defined frequency band. All the input signals are driven by the same instantaneous frequency.

The reasons to adopt a multi-input excitation for swept sine testing can be different, for example

- the need for testing heavy or slender structures that cannot be accommodated on a single shaker;
- the possibility of setting a defined phase between the responses to better characterize specific mode shapes.
- Multi-axis exciters can be used to perform a *true* single-axis test, by setting as reference very low response spectra in the off-axis directions.

In order to correctly calculate the FRFs, multiple averages with uncorrelated inputs are required. This is achieved by defining a number of sweeps equal or greater than the number of exciters, with different phase relations between the drives [2]. MIMO sine vibration *control* tests offer the additional attractive feature of guaranteeing that the response spectra of the control channels recordings match a specific reference level while sweeping with a specific sweep mode (linear or logarithmic) and sweep rate (in Hz/s or Octave/min).

The control target for a MIMO sine vibration control test is a set of ℓ control spectra, characterized by amplitude and phase (relative to the phase of the first control channel).

For each frequency, in case the full dynamic system is linear and time invariant, it is possible to write the Input-Output relation

$$\mathbf{y} = \mathbf{H}\mathbf{u} \tag{1}$$

where $\mathbf{y} \in \mathbb{C}^{\ell \times 1}$ and $\mathbf{u} \in \mathbb{C}^{m \times 1}$ are the spectra of the controls $\mathbf{y}(t) = \{y_1(t), \ldots, y_\ell(t)\}^T$ and the drives $\mathbf{u}(t) = \{u_1(t), \ldots, u_m(t)\}^T$, respectively and $\mathbf{H} \in \mathbb{C}^{\ell \times m}$ is the matrix of FRFs. For the sake of simplicity,

as most of the derivations are in the frequency domain, the terms drives,controls, responses and references are referred to the drives, controls, responses and reference spectra, respectively, if not specified differently.

In all the vibration control tests, a System Identification pre-test phase is always needed to estimate the system's FRFs. This is usually performed by running a low-level random test and using the so called H_1 estimator [19]

$$\hat{\mathbf{H}} = \hat{\mathbf{S}}_{\mathbf{yu}}\hat{\mathbf{S}}_{\mathbf{uu}}^{-1} \tag{2}$$

where $\hat{\mathbf{S}}_{\mathbf{yu}} \in \mathbb{C}^{\ell \times m}$ and $\hat{\mathbf{S}}_{\mathbf{uu}}^{-1} \in \mathbb{C}^{m \times m}$ are spectral density matrices estimated via Welch's averaged periodogram method [20] or other approaches.

Once the FRF is known, the system's *Mechanical Impedance Matrix* $\mathbf{Z}$ can be calculated. Generally an operation of pseudo-inversion is always needed because the number of controls can exceed the number of drives, in what is known in the MIMO control literature as *Rectangular Problem* [21].

2.1 Feedforward control

For each frequency line, independently, the control error

$$\mathbf{e} = \mathbf{r} - \mathbf{y} \tag{3}$$

needs to be reduced in the least square sense, in order for the responses to match the reference spectra. This means to find the optimal drives that minimize the cost function

$$J = \mathbf{e}^H\mathbf{e} = \mathbf{u}^H\mathbf{H}^H\mathbf{H}\mathbf{u} - \mathbf{u}^H\mathbf{H}^H\mathbf{r} - \mathbf{r}^H\mathbf{H}\mathbf{u} + \mathbf{r}^H\mathbf{r} \tag{4}$$

The drives that ideally reduce the error to zero are the ones that nullify the complex gradient

$$\mathbf{g} = \frac{\partial J}{\partial \mathbf{u}} = 2(\mathbf{H}^H\mathbf{H}\mathbf{u} - \mathbf{H}^H\mathbf{r}) \tag{5}$$

It is worth to notice that the derivative operation in eq. (5) should not be interpreted in the standard sense, as the real cost function of eq. (4) with respect to the (generally complex) drives fails the Cauchy-Riemann conditions (it is said to be *not analytic* in the space $\mathbb{C}^m$), as analyzed in details in [14] and [15]. Additionally [14], [15] and later [16], propose to tackle the problem considering a representation in *Conjugate Coordinates*. Alternatively, it is possible to consider as different independent variables the real and imaginary part of the drives ($\mathbf{u}_\mathrm{R}$ and $\mathbf{u}_\mathrm{I}$, respectively), so that $\frac{\partial J}{\partial \mathbf{u}} = \frac{\partial J}{\partial \mathbf{u}_\mathrm{R}} + \mathrm{i}\frac{\partial J}{\partial \mathbf{u}_\mathrm{I}}$, where i is the imaginary unit. Imposing that the complex gradient must nullify, the optimal drives are retrieved as

$$\mathbf{u}_{opt} = (\mathbf{H}^H\mathbf{H})^{-1}\mathbf{H}^H\mathbf{r} \tag{6}$$

In order to calculate the drives, as the real system plant is unknown, the best solution is to use information obtained from the system identification. To notice that the quantity $(\hat{\mathbf{H}}^H\hat{\mathbf{H}})^{-1}\hat{\mathbf{H}}^H$ is, for the general case of a rectangular problem, the pseudo-inverse of the FRF matrix according to Moore and Penrose $(\hat{\mathbf{H}}^H\hat{\mathbf{H}})^{-1}\hat{\mathbf{H}}^H = \hat{\mathbf{H}}^\dagger = \hat{\mathbf{Z}}$. Hence, an *estimate* of the optimal drives can be calculated as

$$\hat{\mathbf{u}}_{opt} = \hat{\mathbf{Z}}\mathbf{r} \tag{7}$$

With reference to the active control literature [12], the proposed approach, represented by the block scheme of figure 2, is a traditional feedforward control, also called *drives pre-shape* in environmental testing [10], [11].

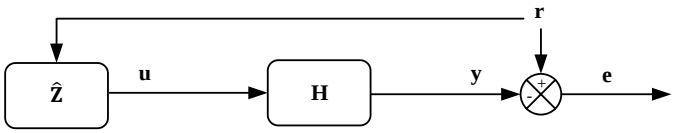


Figure 2: MIMO sine feedforward control, block scheme.

Harmonic Estimator The idea of an on-line frequency domain MIMO control for swept sine testing is closely dependent on the capability of on-line tracking the amplitude and phase of the response (to be corrected) and the drive (to be updated) waveforms, as shown in fig. 7. Among the different available solutions, an idea is the use of an Harmonic Estimator, as currently adopted, for example, in the Siemens Simcenter Testlab sine Control application [22] .

For a general sinusoidal waveform with fundamental natural frequency $2\pi\omega_f$

$$y(t) = |y(t)| \sin[\omega_f t + \phi(t)] = a_c \cos(\omega_f t) + a_s \sin(\omega_f t) \tag{8}$$

the amplitude and phase

$$|y(t)| = \sqrt{a_c^2 + a_s^2} \tag{9a}$$

$$\phi(t) = \text{atan}\left(\frac{a_c}{a_s}\right) \tag{9b}$$

can be calculated assuming that, within p periods, eq. (8) holds, and therefore the parameters a_c and a_s can be estimated in a least square sense using the acquired data (left-hand-side of eq. (8)).

For the on-line estimation during a continuous sine sweep, the frequency of the signals, and therefore the assumed argument $(\Phi(t) + \phi(t))$ of the sine wave in eq. (8), continuously varies with a specific sweep mode (linear or logarithmic), as reported in table 1.

Sweep mode	Frequency in Hz	Sine argument in rad
linear Up	$f(t) = f_{in} + \text{SR}_{\text{Hz/s}} t$	$\Phi(t) = 2\pi\left(f_{in} t + \frac{\text{SR}_{\text{Hz/s}}}{2} t^2\right)$
linear Down	$f(t) = f_{end} - \text{SR}_{\text{Hz/s}} t$	$\Phi(t) = 2\pi\left(f_{end} t - \frac{\text{SR}_{\text{Hz/s}}}{2} t^2\right)$
log. Up	$f_{log,up}(t) = f_{in}\, 2^{\text{SR}_{\text{Oct/min}} t/60}$	$\Phi(t) = 2\pi\left(\frac{60 f_{in}}{\text{SR}_{\text{Oct/min}} \log 2} 2^{\text{SR}_{\text{Oct/min}} t/60} - 1\right)$
log. Down	$f_{log,up}(t) = f_{end}\, 2^{-\text{SR}_{\text{Oct/min}} t/60}$	$\Phi(t) = 2\pi\left(-\frac{60 f_{end}}{\text{SR}_{\text{Oct/min}} \log 2} 2^{-\text{SR}_{\text{Oct/min}} t/60} - 1\right)$

Table 1: Different sweep modes and related sine arguments.

2.2 Development of the controller in a Virtual Shaker Testing environment

The MIMO sine feedforward control described in sec. 2.1 has been implemented in Matlab/Simulink. The amplitude and phase of the drives and responses are estimated on-line using a Matlab/Simulink implementation of the described on-line harmonic estimator. This solution moves towards a more advanced MIMO sine feedback controller to be implemented on a real-time platform for environmental testing and controlled acquisition purposes. The idea is to build a controller in a simulation environment that includes also a full

validated virtual model of the amplifiers and the vibration exciters. This approach allows already in the development stage to tackle potential issues that can be encountered during an actual test. It is therefore chosen, as excited system, a pair of virtual electro-mechanical lumped-parameters vibration exciters in twin configuration, result of the research [10] and [11] and represented in fig. 3. In the current work, no coupling structure is considered in the model, as highlighted by the dashed fill in fig. 3: the two shakers are therefore independently driven (but the approach considers a generally coupled system). The parameters used to model the shaker 1 are retrieved from the experimental test campaign performed to characterize a 6 kN shaker available at Siemens Industry Software N.V. HQ (Leuven, Belgium). Small differences, with respect to the parameters of the shaker 1, are introduced to obtain the parameters of the twin shaker 2.

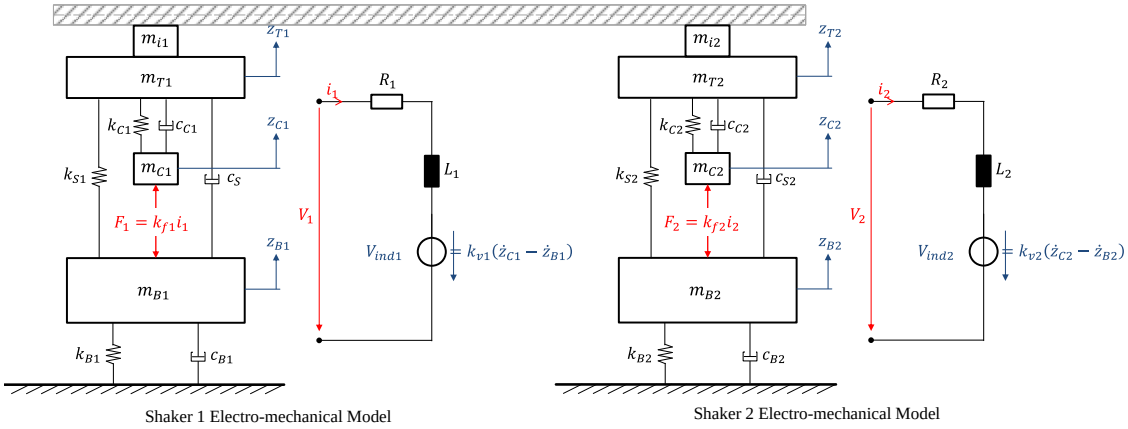


Figure 3: Schematic representation of the two lumped-parameters Virtual Shakers in twin configuration.

The selected control channels are the two virtual accelerometers located on the shaker heads (referring to fig. 3, the signals $\ddot{z}_{T1}$ and $\ddot{z}_{T2}$) whereas the drives are the voltages V_1 and V_2 sent to the the virtual amplifiers and powering the electrical parts of the shakers. The FRFs from the voltages to the control accelerations of the identified system are represented by the solid blue lines in fig. 4. The dashed red lines represent the FRFs of the system excited during the sine sweep: to introduce a system identification error, the lumped parameters slightly differ from the ones of the system excited during the identification (coil masses and lumped payloads m_i reduced of 1% for the shaker 1 and increased of the same amount for the shaker 2).

Fig. 5 shows the control results of the simulated MIMO swept sine control test (feedforward control). The figure shows some deviations of the control results in correspondence of the coil resonances. This is mainly due to the introduced system identification errors. This shows, as highlighted by eq. (7) and the block scheme in fig. 2 that the feedforward control approach strongly relies on the identified system and it is not able to react to any error, being mainly an open-loop control procedure. It is interesting to analyze the results from the dashed magenta curves in fig. 5, representing the control results with an ideally perfect system identification ($\hat{\mathbf{H}}$ and $\mathbf{H}$ are identical). Even in this case, due to the transient nature of the sweep, the system dynamic response is non-stationary and this causes the presence of a peak with side-lobes in the sweep direction [4], [11], [10]. It is worth to mention that, in order to predict this transient effect, a Virtual Shaker Testing approach that aims to simulate with high accuracy the full vibration test is the most complete solution. Fig. 6 shows a detail of the phenomenon varying the sweep rate. From the figure it can be seen that, increasing the sweep rate causes the main peak to increase, broaden and bend in the sweep direction.

The influence of these effects on FRF estimation with swept sine techiques has been extensively studied in literature [3] and [4]. Together with these phenomena, due to the transient nature of the excitation, non-linear behavior of the system, noise on the measurement and time variant effects, will unavoidably introduce

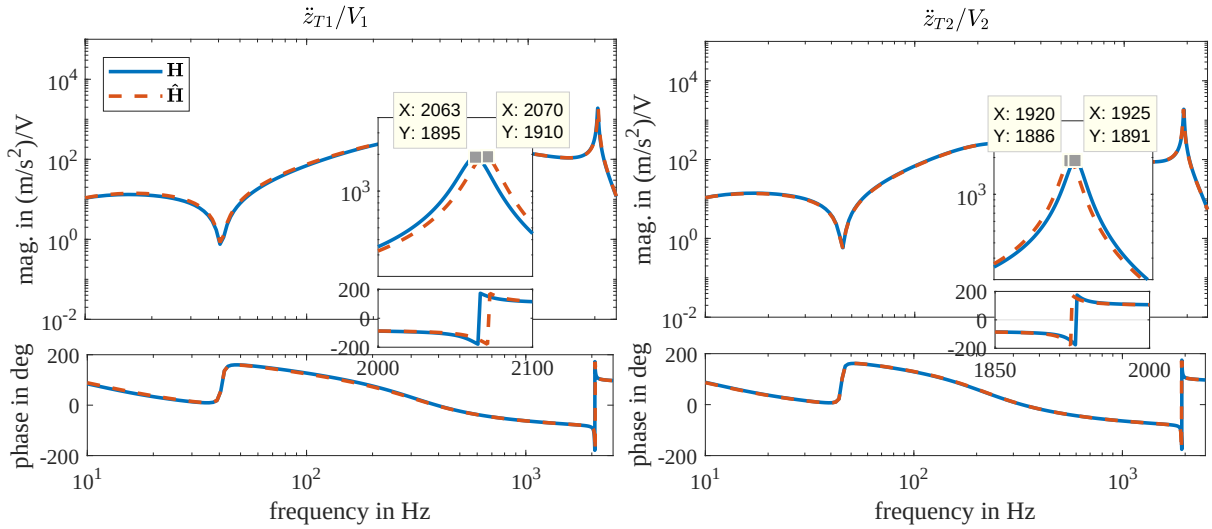


Figure 4: FRFs of the two Virtual Shakers in twin configuration (solid blue). The parameters of the shakers have been slightly modified during the runs to simulate system identification errors (dashed red line), as shown by the details across the (coil) resonances.

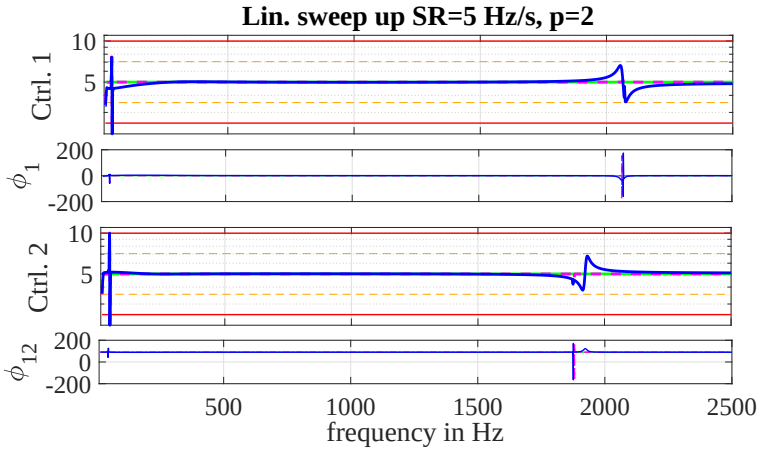


Figure 5: Control results for the MIMO sine sweep (feedforward) control simulations considering the ideal case of perfect system identification (dashed magenta) and the presence of system identification errors (solid blue). In solid green, dashed orange and solid red, are represented the reference, the alarm limits and the abort limits, respectively.

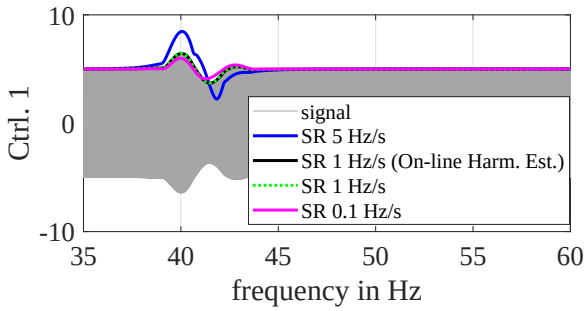


Figure 6: Beating phenomenon. Increasing the sweep rate causes the peak across the resonance to bend in the sweep direction with an increased magnitude and bandwidth.

system identification errors. The reference and the control spectra will generally differ, and an on-line feedback control is sought to keep the responses as close as possible to the desired (safe) levels.

2.3 Towards a MIMO sine feedback control

In order to compensate for the errors between the reference levels and the responses, an on-line feedback control for MIMO swept sine needs to be implemented. Fig. 7 shows a general block scheme for a feedback control in the frequency domain.

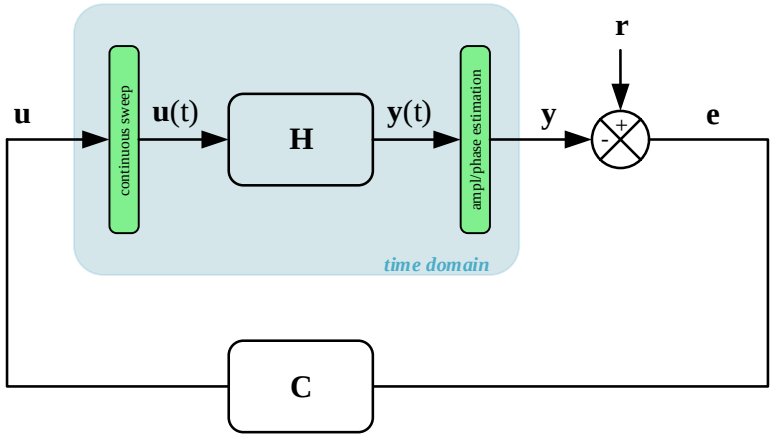


Figure 7: MIMO swept sine feedback control, block scheme. The green blocks highlight the necessary steps of generating a continuous sine sweep from the drives spectra (*continuous sweep* block) and estimating the response amplitude and phase from the time recordings (*ampl/phase estimation* block).

One of the techniques for MIMO swept sine control is proposed in the work [13]. This control method has the feature of updating, during the convergence, not only the drives, but also the mechanical impedance of the system, potentially allowing to rapidely compensate for non-linear behaviours. The idea of the controller is to update the drives combining the formulation proposed in [15] with Quasi-Newton methods, as attempted in [16] for MIMO Random testing. As a consequence of updating the Hessian matrix during the convergence, the estimated system (used for the first iteration) is also updated and eventually converges to the real system's FRFs (unknown during a real life test).

Fig. 8 shows the FRFs update capability of the feedback controller: the correction routine is started with no information from the pre-test system identification. For this extreme case, the routine assumes a general identity matrix as initial system, as shown by the dashed red curves of fig. 8. During the correction process, the FRF are then iteratively corrected (dashed magenta and green curve) until the real system FRFs (solid blue curves, unknown for the algorithm) are identified at the convergence.

An on-line implementation of this frequency domain technique is however very challenging and still in progress. The main difficulties come from the transient nature of the swept excitation associated with the MIMO control. Generally, as analyzed in detail in [12], the stability of the closed loop MIMO system is strongly influenced by the system's conditioning. To guarantee the Bounded-Input Bounded-Output (BIBO) stability, it is needed to optimally tune the step size of the correction algorithm. This tuning is based on the information obtained during the system identification and the hypothesis that the system is dominated by a single tonal component, which is not entirely respected during a continuous sweep.

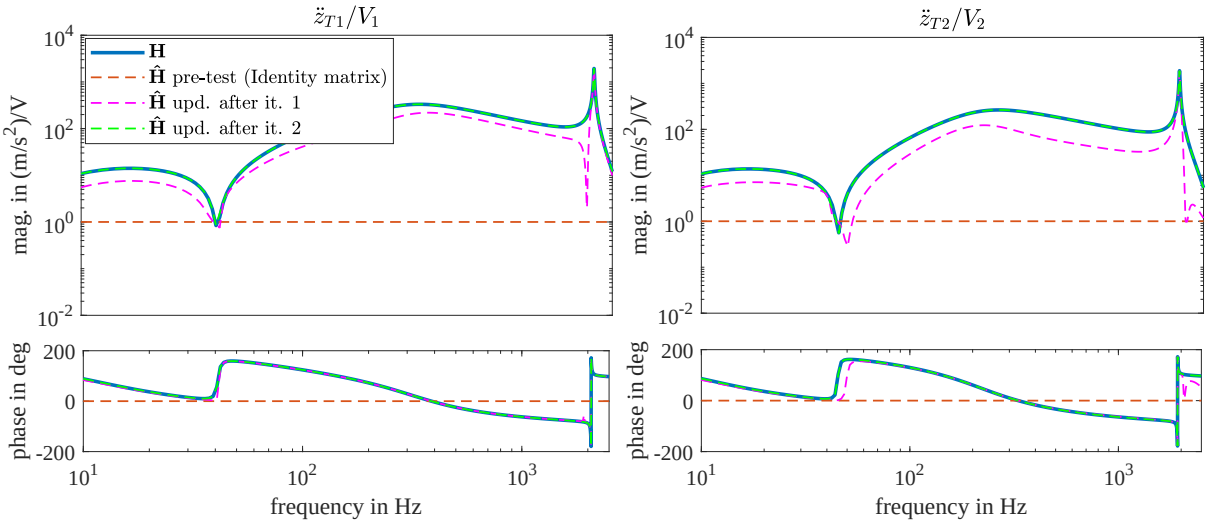


Figure 8: Impedance update during the drives correction (closed loop MIMO sine control). The algorithm is able to start without any information about the system (dashed red curves).

3 Beyond the Multi-Input Multi-Output classic processing for Ground Vibration Testing: the *Virtual Driving Point* method

With focus on GVT applications, recent studies addressed the problem that the FRFs and mode sets obtained during MIMO swept sine testing show a dependency on the estimation method [3]. For example, the necessity of MIMO sine testing to combine runs from multiple sweeps with different phases between the inputs in a single data set can require additional iterations (also combining broadband random data) to obtain a representative mode-set. The VDP method is a data processing technique for aircraft GVT, extensively discussed in [7] and [8]. The VDP working principle consists in building a virtual single-input excitation from a single sweep with multi-input excitation. With this procedure, each sweep can be performed individually and the measured data can be independently analyzed. The opportunity of analyzing several sweeps independently offers some clear advantages in terms of testing time, for example

- starting the modal identification before all the measurement runs have been completed;
- decreasing the needed number of sweeps to perform can be an important advantage in some specific cases, for example in case of multi-input excitation with a high number of shakers.

Also the analysis of the processed data becomes clearer and therefore faster, especially due to the independent evaluation of symmetric and anti-symmetric multi-input excitation from separated runs. This leads to clearer stabilization diagrams and mode shapes with respect to the traditional MIMO swept sine processing [3]. Another advantage of the VDP is the reduced impact of non-linearities on the obtained mode-set: since each run is processed individually, there is no influence of a non-linearity belonging to a symmetric sweep on the anti-symmetric one (and vice versa).

In this section, the inputs are the ℓ input forces, indicated with f, and the outputs are the N output accelerations distributed on the airframe, indicated with x. The acceleration-over-force FRF matrix between inputs and outputs is indicated with $\mathbf{G}$. It is worth to notice that from the perspective of the controlled swept acquisition, during a GVT, the forces are control channels and hence *outputs* for the controlled system $\mathbf{H}$ (force-over-voltage).

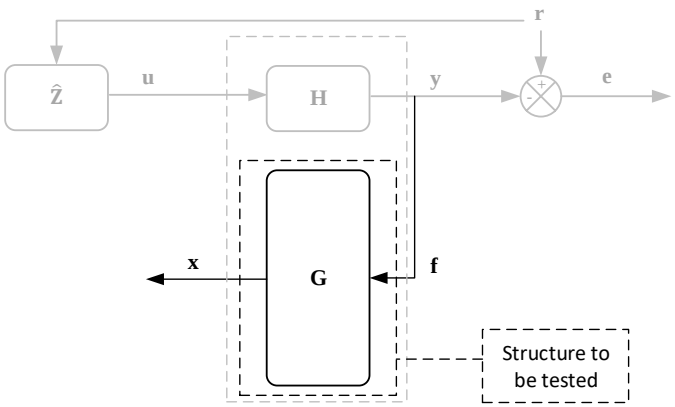


Figure 9: System FRF matrix, for the control input/output relation (in grey) and for the modal analysis, in black. To notice that the input forces to the system considered for the modal analysis ($\mathbf{G}$) are the outputs of the controlled system ($\mathbf{H}$).

3.1 Workflow

In this section the workflow of the VDP method is highlighted for the case of a two-input excitation with forces $f_1 = |f_1|e^{i\varphi_1}$ and $f_2 = |f_2|e^{i(\varphi_1+\varphi)}$. With reference to fig. 9, the tackled application is the one illustrated in fig. 10, where the inputs are the two shaker forces (control channels for the MIMO swept sine test) and the outputs the time recordings from accelerometers distributed on the airframe.



(a) (b)

Figure 10: GVT of an acrobatic electrical aircraft. (a) The voltages u_1 and u_2 from the data acquisition system drive two shakers collocated under the wings in order to control the forces of force cells as shown for the left-wing control channel f_2 in the detail (b) together with the driving-point channel x_i.

Two sequential sweeps are needed to obtain FRFs with standard methods. The input forces, control channels for the MIMO swept sine control are typically set in-phase and out-of-phase for the first and the second run, in order to excite consistently both the symmetric and anti-symmetric modes.

For each sweep, the workflow of the VDP method consists of two parts, first obtaining the Virtual Driving Point FRFs and then extracting the modal parameters , from the VDP FRFs. In the following, the procedure proposed in [7–9], to process the sweeps with the VDP is explained.

1. Time histories of the forces and of the accelerations measured during a single sweep performed by the

two shakers with a fixed relative phase between the forces applied to the system, need to be processed with a frequency spectra estimator to compute inputs and outputs frequency spectra. They are readily available, for example, as the harmonic estimation of the control responses.

2. For a single sweep, a *Virtual Force* f_v can be obtained considering

$$|f_v|^2 = |f_1|^2 + |f_2|^2 \tag{10}$$

$$f_v = \frac{|f_1| f_1 e^{-j\phi} + |f_2| f_2}{|f_v|} \tag{11}$$

3. The spectra of a *Virtual Channel* can be expressed as

$$x_v = \frac{|f_1| x_1 e^{-j\phi} + |f_2| x_2}{|f_v|} \tag{12}$$

The *Virtual Outputs* are obtained appending the virtual response x_v to the actual responses $\mathbf{x}$

$$\mathbf{x}_v = [\mathbf{x}\, x_v]^T = [x_1\, x_2\, ...\, x_N\, x_v]^T \tag{13}$$

4. The *Virtual* FRFs can be computed by dividing this new set of response spectra by the Virtual Force f_v as

$$\mathbf{G}_v = \mathbf{x}_v \frac{1}{f_v} \tag{14}$$

The *Virtual Driving Point* FRF is the last element of $\mathbf{G}_v$.

5. A state-of-the-art modal parameters estimator, such as Polymax [23], can be used to extract the modal parameters from the obtained FRFs. For GVT of small fixed wings aircrafts (where only two shakers are used to excite the airplane), the VDP method allows to analyze the data belonging to each sweep separately and independently. Two set of modal parameters are obtained, symmetric and anti-symmetric. In order to reconstruct a single and complete mode set for the system, the symmetric and anti-symmetric modes need to be gathered together.

6. The mode shapes contain an additional element related to the virtual response. This must be deleted because it represents a DOF that does not have a physical meaning and depends on the used scaling scheme. It could also influence the modal displacement values related to the other DOFs.

3.2 A simple example with a 3-DOF System

In this section the VDP method is applied to the lumped-mass system with three DOFs shown in fig. 11, allowing to understand its working principle and to compare the extracted modal parameters with the purely analytical ones, unavailable for real life experiments. The system is symmetric in terms of mass ($m = 0.05\,kg$), stiffness ($k = 10000\,N/m$) and damping ($c = 0.2\,Ns/m$). The damping model is proportional $\mathbf{C} = \alpha\mathbf{M} + \beta\mathbf{K}$ with $\alpha = 0$ and $\beta = 2 \cdot 10^{-5}\,s$.

Fig. 12 shows in the same plot the actual and the virtual driving point FRFs. The data has been obtained running a simulation with the MIMO sine sweep feedforward control discussed in sec. 2.1. Two sweeps are run by setting the forces F_1 and F_3 in phase (0 deg) and counter-phase (180 deg) in order to use traditional processing techniques for MIMO swept sine excitation and compare the results with the VDP calculations. The black and the green curves are the driving point FRFs (which are identical due to the uniformity of the

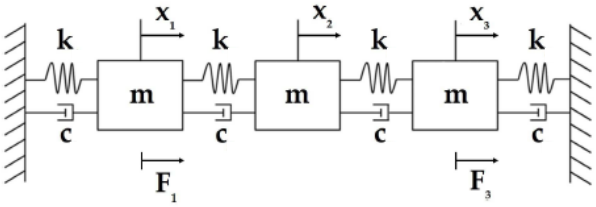


Figure 11: 3-DOFs model, $m = 0.05\,kg$, $k = 10000\,N/m$ and $c = 0.2\,Ns/m$.

system in terms of physical parameters). These two curves show the three peaks corresponding to the three modes. The red curve is the virtual driving point FRF obtained when applying the VDP method using data from the symmetric sweep: the peaks in the FRF are only two and they are related to the symmetric mode shapes (mass 1, 2, 3 in phase; mass 1 and 2 in phase, mass 3 out-of-phase). The blue curve is the virtual driving point FRF from the anti-symmetric sweep: the peak is only one and is related to the anti-symmetric mode shape (mass 1 and 2 in phase opposition).

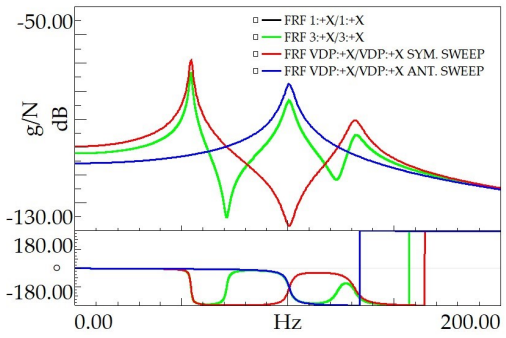


Figure 12: Driving point FRFs from the standard processing and FRFs Virtual Driving Points FRFs for the 3DOFs system. The green and the black curves are overlapped due to the uniformity of the physical parameters.

The symmetric and anti-symmetric FRFs are processed separately for the modal analysis step. Applying Polymax on the separated FRFs provides two different mode sets (symmetric and anti-symmetric modes) that need to be combined together.

Tab. 2 shows the comparison, in terms of natural frequencies, between the analytical values and the ones obtained by Polymax, (i) first processing the full data set with a standard technique and then (ii) merging the modes obtained processing the symmetric and anti-symmetric sweeps (from the VDP) separately. All the natural frequencies are identified with a negligible error.

Analytical	Standard processing	VDP
54.5	54.5	54.5
100.7	100.6	100.6
131.5	131.5	131.5

Table 2: Comparison of the natural frequencies obtained from the VDP, the standard processing and the analytical eigenvalues problem.

Also the mode shapes are exactly identified with the VDP, as shown in fig. 13 applying the Modal Assurance Criterion (MAC) between the VDP reconstructed mode set (Processing A) and the standard processing mode

set (Processing B).

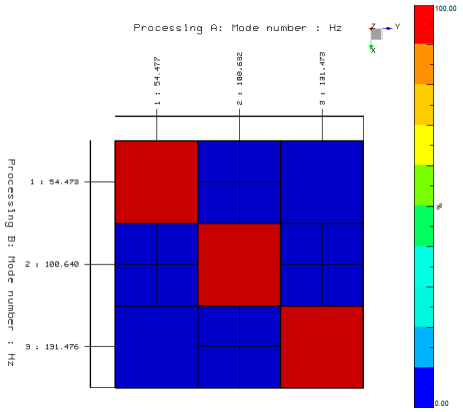


Figure 13: Modal Assurance Criterion between the modes obtained with the VDP (processing A) and with standard techniques (processing B).

Finally, the use of a lumped-parameter model allows the comparison with a theoretical formulation (resulting from the analytical solution of the eigenvalues problem) in terms of modal mass, stiffness and damping. The results are shown in table 3, obtained by processing the data with Polymax [23] and applying a Unity Modal Component scaling [1]. This provides an additional proof of the validity of the modal model obtained by processing the sweeps with the proposed Virtual Driving Point method.

Mode	Theoretical	Standard processing	VDP
1	0.1	0.1	0.099
2	0.1	0.1	0.1
3	0.1	0.1	0.099

(a) Modal mass in kg.

Mode	Theoretical	Standard processing	VDP
1	11715.73	11713.96	11685.11
2	40000	40000	40000
3	68284.27	71603.24	67746.82

(b) Modal stiffness in N/m.

Mode	Theoretical	Standard processing	VDP
1	0.23	0.23	0.23
2	0.8	0.8	0.8
3	1.36	1.43	1.35

(c) Modal damping in Ns/m.

Table 3: Comparison of the modal parameters. Mode sets obtained with the Polymax estimator and applying a Unity Modal Component scaling.

4 Conclusions

This paper proposes research directions to improve the current practice of estimating FRFs with Multi-Input Multi-Output (MIMO) swept sine controlled excitation, specifically targeting the testing of large aerospace

structures, e.g. Ground Vibration Testing (GVT) of fixed wing aircrafts. Regarding the need of keeping specific response levels to safe reference profiles, this paper underlines the limitations of a feedforward control approach and proposes the development of the MIMO controller in a Virtual Shaker Testing environment. In this way the full test set-up is considered (shakers, amplifiers and unit under test models) already in the control design phase, to assess potential transient issues that cannot be predicted otherwise. Regarding the control strategy, the idea is to move from a feedforward control to a feedback control technique with the attractive features of updating the identified FRFs during the sweeps. This capability is shown with the results obtained running the control routine for an extreme case with no information about the system identification (*blind* test).

For the specific case of GVT of fixed wing aircraft, this paper proposes to adopt the Virtual Driving Point (VDP) method to improve the processing that leads to the estimation of modal parameters from MIMO swept sine testing. The application of the VDP to a simple lumped parameters system shows that the modal model obtained from separate symmetric and anti-symmetric runs is consistent with the traditional processing and eventually with the theoretical solution. Processing the symmetric and the anti-symmetric sweeps independently and individually brings several advantages when performing GVT of fixed wings aircrafts, in terms of time required for the processing and quality of the obtained modal model.

Acknowledgements

The financial support of VLAIO is greatefully acknowledged (research grant ADVENT: ADvanced Vibration ENvironmental Testing).

References

[1] W. Heylen, S. Lammens, P. Sas, *Modal analysis theory and testing*, K.U. Leuven, Leuven (2016).

[2] S. Pauwels, J. Michel, M. Robijns, B. Peeters, J. Debille, *A new MIMO sine technique for accelerated, high quality FRF measurements*, in *Proc. Int. Conf. on Noise and Vibration Engineering*, Leuven (2006).

[3] S. Orlando, B. Peeters, G. Coppotelli, *Improved FRF estimators for MIMO sine sweep data*, in *Proc. Int. Conf. on Noise and Vibration Engineering*, Leuven (2008).

[4] G. Gloth, M. Synapius, *Analysis of swept-sine runs during modal identification*, Mechanical Systems and Signal Processing, Elsevier (2004) No. 18.

[5] B. Peeters, W. Hendricx, J. Debille, *Modern solutions for ground vibration testing of large aircrafts*, Sound and Vibration (2009), Vol. 43, No (1).

[6] P. Fortescue, G. Swinerd, J. Stark, *Spacecraft Systems Engineering*, 4th Edition, John Wiley&Sons (2011).

[7] U. Füllekrug, M. Boswald, D. Goge, Y. Govers, *Measurement of FRFs and modal identification in case of correlated multi-point excitation*, Shock and Vibration (2007), Vol. 15, No. 3.

[8] S. Giclais, P. Lubrina, C. Stephan, M. Boswald, Y. Govers, J. Ufer, N. Botargues, *New excitation signals for aircraft ground vibration testing*, in *Proc. of IFASD 2011*, Paris (2011).

[9] Y. Govers, M. Boswald, P. Lubrina, S. Giclais, C. Steohan, N. Botargues, *Airbus A350XWB ground vibration testing: efficient techniques for customer oriented on-site modal identification*, in *Proc. Int. Conf. on Noise and Vibration Engineering*, Leuven (2014).

[10] S. Waimer, E. Gentile, S. Manzato, B. Peeters, M. Wagner, P. Guillaume, *Modelling and experimental validation of a coupled electrodynamic shaker and test structure simulation model*, in: *Proc. Int. Conf. on Noise and Vibration Engineering*, Leuven (2016).

[11] S. Waimer, S. Manzato, B. Peeters, M. Wagner, P. Guillaume, *Modelling and simulation of a closed-loop electrodynamic shaker and test structure model for spacecraft vibration testing*, Advances in Aircraft and Spacecraft Science, No. 5, Techno Press (2018).

[12] S. Elliot, *Signal Processing for Active Control*, Academic Press, London (2001).

[13] M. Underwood, *Adaptive control method for multiexciter sine tests*, US Patent number 5299459 (1994).

[14] K. Kreutz-Deglado, The complex gradient operator and the $\mathbb{CR}$-calculus, Preprint, ArXiv (2009).

[15] L. Sorber, M. van Barel, L. de Lathauwer, *Unconstrained optimization of real functions in complex variables*, SIAM J. Optim., Vol. 879, Issue 22, No. 33, SIAM (2012).

[16] U. Musella, S. Manzato, B. Peeters, P. Guillaume, $\mathbb{CR}$*-calculus and adaptive array theory applied to MIMO random vibration control tests*, J. of Physics: CS, IOP Science (2016) Vol. 744, No. 1.

[17] U. Musella, L. Zanellati, M. Grottoli, F. Celiberti, B. Peeters, F. Marulo, P. Guillaume, *Driving a motion platform with a vibration control software for multi-axis environmental testing: challenges and solutions*, in *Proc. of the XXXVI IMAC*, Orlando (2018).

[18] U. Musella, G. D'Elia, A. Carrella, B. Peeters, E. Mucchi, F. Marulo, P. Guillaume, *A minimum drives automatic target definition procedure for multi-axis random control testing*, Mechanical Systems and Signal Processing, Elsevier (2018), No. 107.

[19] R. Pintelon, J. Schoukens *System Identification: a frequency domain approach*, John Wiley&Sons, Hoboken (2012).

[20] J. Bendat, A. G. Piersol, *Random data: analysis and measurement procedures*, Vol. 729, John Wiley &Sons, New York (2011).

[21] M. Underwood, *Multi-exciter testing applications, theory and practice*, in *Proc. of Institute of Environmental Sciences* (2002).

[22] Siemens Industry Software N.V., *LMS Test.Lab Environmental*, user manual (2016).

[23] B. Peeters, H. Van Der Auweraer, P. Guillaume and J. Leuridan, *The PolyMAX frequency-domain method: a new standard for modal parameters estimation?*, Shock and Vibration, Hindawi Limited (2004), Vol. 11, No. 3-4.

Automatic modal parameter selection using a statistical model and a Kalman filter

K. Soal [1,3]**, Y. Govers** [1]**, J. Bienert** [2]**, A. Bekker** [3]
[1] German Aerospace Center (DLR), Institute of Aeroelasticity
Bunsenstr. 10, 37073 Göttingen, Germany
e-mail: **keith.soal@dlr.de**

[2] Technische Hochschule Ingolstadt (THI), Department of Mechanical Engineering,
Esplanade 10, Ingolstadt, Germany

[3] Stellenbosch University, Department of Mechanical and Mechatronic Engineering,
Corner of Banghoek and Joubert Street, Stellenbosch, South Africa

Abstract
The automation of system identification is important for processing large amounts of data without expert user interaction. Automation is also important to maintain consistency in estimates, especially when investigating trends in data which could be masked by variations of mathematical parameters. This research presents a novel idea to obtain automatic modal parameter estimates based on a data driven statistical model and a Kalman filter. A key objective was to make observed data maximally informative. This lead to the development of a sliding predictive model using an optimized linear regression method to use system inputs which are not included in standard system identification. The method was first demonstrated on a numerical data set where it was found to improve system predictions. The method was then tested on full scale data from the German research vessel Polarstern during a voyage to the Arctic. The automatic Kalman estimates showed improved estimates using the combination of statistical model and modal parameters.

1 Introduction

System Identification provides a powerful tool for building mathematical models of dynamic systems. A system is an object on which different variables interact to produce observable signals. The models are aimed at linking these observations together into a pattern from which useful information can be extracted [1]. In mechanical engineering this framework has been successfully applied to structures, using vibration signals to extract modal parameters. These parameters can be used to build modal models which have applications in structural health monitoring, inverse force estimation and online flutter monitoring.

In order to achieve these outcomes the modal parameters must be accurately and automatically identified and tracked. This is not a trivial task when dealing with real structures with complex inputs, low excitation forces and noise. The first challenge involves dealing with unmeasurable input forces such as wind or wave loads, on large structures in actual operating conditions. Output only system identification or Operational Modal Analysis (OMA) was developed to identify modal parameters without knowledge of the input forces. This is achieved by making assumptions about the unmeasured forces which are modelled as stochastic white noise quantities. The drawback is that long records are often needed to fulfil these assumptions. This can result in a smearing of modal estimates across changing input parameters. The second challenge involves precessing the large amounts of data associated with the actual operation of a structure. Automation is important to

remove user interaction as well as to maintain consistency in the estimates when investigating trends in data, which could be masked by variations of mathematical parameters.

A key observation regarding the sensitivity of modal estimates to changing system inputs is that changes in physical parameters will cause detectable changes in the vibration properties [2]. These physical changes are propagated through the system properties (mass, damping and stiffness) as follows:

1. Environmental conditions - such as temperature, change Youngs modulus and consequently stiffness.
2. System configuration - through discrete mass changes due to cargo for example.
3. Boundary conditions - such as ice compared to open water effects damping and added mass differently.

A number of automation techniques have been investigated in literature. Most of the current techniques use information from the stabilisation diagram. These include clustering methods such as the Rule-based Intelligence [3], Consistent Mode Indicator [4], Fully Automatic Modal Parameter Selection (FAMPS) [5], Hierarchical Clustering [6] and Fuzzy Clustering [7]. These methods deal with the automatic modal parameter selection from one set of data. A different approach involves using current knowledge of the system to improve future identifications. Techniques include fuzzy C means clustering [8] and Least Squares Support Vector Machines (LSSVM) [9]. These techniques can be beneficial when large data sets are available.

This research presents an idea to both automate and improve the sensitivity of system identification and tracking by using a statistical model and a Kalman filter. A key objective was to make observed data maximally informative. This lead to the development of a sliding predictive model using an optimized linear regression method to use system inputs which are not included in the standard system identification. Since both the model prediction and the system identification estimates contain different uncertainties the Kalman filter is proposed as a method to combine both estimates in an optimal way.

2 Kalman Filter

The Kalman filter [10], is a predictor-corrector estimator that tries to obtain an optimal estimate of desired quantities from uncertain and noisy observations. It is based on a state space model of a system and real noisy measurements. The filter progresses iteratively with (1) a forward prediction of the system state in time (time update) followed by (2) a correction based on the predicted and measured system output (measurement update). The filter is optimal in the sense that if the noise is Gaussian, it minimizes the mean square error (error covariance) of the estimated parameters. The process is illustrated in Figure 1.

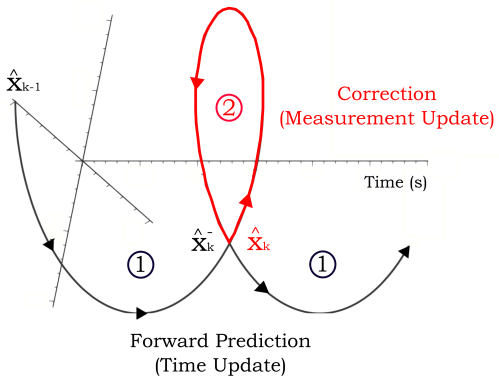


Figure 1: Kalman filter.

The Kalman filter is initiated with user defined parameters Q, R, P_{k-1} and $\hat{x}_{k-1}$. Q and R are the time invariant process and measurement noise covariances. The noise covariances are used to tune the model to

rely more on (trust) either the model or the measurements. The error covariance $P_{k-1} = E[e_{k-1}^{-} e_{k-1}^{-T}]$ is used as a minimization function by the Kalman gain K and can be initiated as any non zero value. The initial state estimate $\hat{x}_{k-1}$ can also be chosen arbitrarily and updated if faster convergence is required.

The iterative filter begins with a forward prediction of the state from $\hat{x}_{k-1}$ to $\hat{x}_k^-$ based on the model as shown in Equation 1. This is known as the priori or 'reason' estimate. The error covariance is also projected forward through the model to P_k^- in Equation 2. The measurement update then estimates the Kalman gain matrix K in Equation 3. The Kalman gain is used to blend the priori estimate with the residual $(y_k - H\hat{x}_k^-)$ to determine the posteriori or 'experience' state estimate $\hat{x}_k$ in Equation 4. The error covariance is then also updated based on the new Kalman gain in Equation 5. The filter then proceeds iteratively with forward predictions followed by measurement updates with optimal error covariance updates.

(1) Time update equations

$$\hat{x}_k^- = A\hat{x}_{k-1} \tag{1}$$

$$P_k^- = AP_{k-1}A^T + Q \tag{2}$$

(2) Measurement update equations

$$K_k = P_k^- H^T (HP_k^- H^T + R)^{-1} \tag{3}$$

$$\hat{x}_k = \hat{x}_k^- + K(y_k - H\hat{x}_k^-) \tag{4}$$

$$P_k = (I - K_k H)P_k^- \tag{5}$$

3 Idea

The idea is to automate modal parameter selection and reduce the uncertainty in the estimates using a statistical model and a Kalman filter. The model will be trained using environmental inputs and system identification outputs. In the current work on the polar research vessel Polarstern, the environmental inputs include water and air temperature - which effect the Youngs modulus and thus the stiffness, ship speed - which effects the draft and bow wave, which add mass, and wind velocity and wind direction. These will be used to build the state matrix A in Equation 1. The predictive model will be used by the Kalman filter to make forward predictions based on new environmental inputs and then combined in an optimal way with the system identification estimate at the future time step. The method is illustrated in Figure 2.

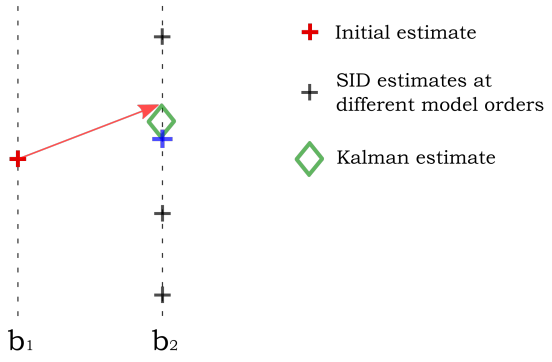
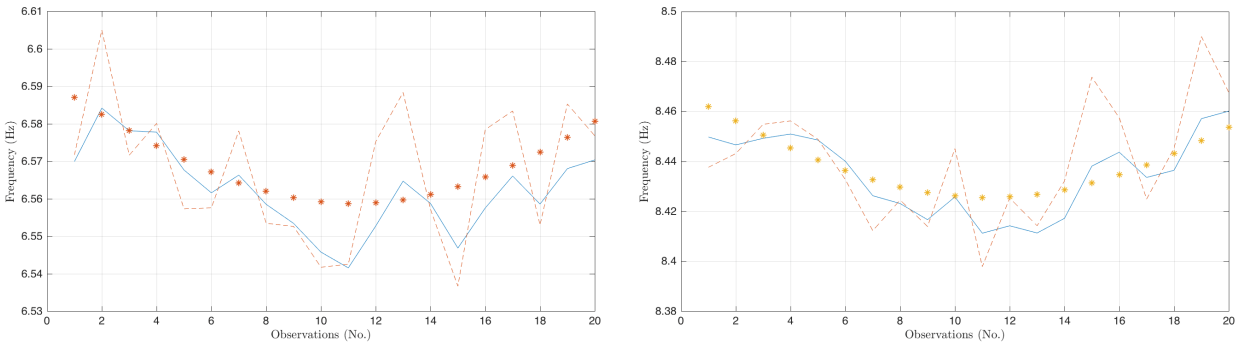


Figure 2: Model prediction and Kalman filter estimate. (SID - System Identification)

The statistical model prediction is made from time instance b_1 to time instance b_2 as shown by the red arrow. The prediction is then Kalman blended with the nearest stable pole in the stabilisation diagram, indicated by the blue plus symbol, to produce the Kalman estimate, indicated by the green diamond.

4 Numerical Simulation

The method is demonstrated numerically using a five Degree Of Freedom (DOF) system. A data set of 20 observations of each frequency is created and a normally distributed random error is added to each observation. A sinusoidal temperature variation is simulated through an approximate relationship between temperature, Youngs modulus and natural frequency. The measurement noise covariance R is calculated from the simulated data and the model noise covariance Q is tuned to trust the model slightly more than the measurements. The error covariance matrix P is updated in a loop in order to begin filtering with an optimal error covariance. The results of the simulation are presented for mode 3 and mode 4 in Figure 3a and 3b. The Kalman filter estimates are seen to be closer to the true values in general, and also show the sinusoidal trend in the temperature variation. The cumulative error is improved by 85 % for mode 3 and 89 % for mode 4.



(a) Mode 3.

(b) Mode 4.

Figure 3: Numerical simulation. $*$ True value $--\rightarrow$ True value + noise + temperature variation $\rightarrow$ Kalman filter estimate.

5 Polar Research Vessel and Arctic Expedition

Full scale measurements were performed on the German research icebreaker Polarstern, shown in Figure 4 and 5, during an expedition to the Arctic. The vessel is 118 m in length with a 25 m beam, 11 m draft and a displacement of 17 300 tonnes. Four diesel engines provide 14 000 kW of power through two shaft lines with variable pitch propellers. The vessel has a design speed of 15.5 knots, and can break through 1.5 m of ice at 5 knots and up to 3 m of ice by ramming.



Figure 4: Polarstern during a storm in open water. (AWI/F Mehrtens)



Figure 5: Polarstern in an Arctic ice field.

5.1 Measurement Setup

The Polarstern was instrumented with 23 accelerometers as shown in Figure 6. Measurements were conducted in the hull on deck F and the bridge on deck A. Accelerometers were orientated in the vertical direction along the ship length to measure normal bending and were placed on both port and starboard to measure torsion. Horizontal measurements were conducted to measure lateral bending and triaxial sensors were placed in the stern and bridge respectively.

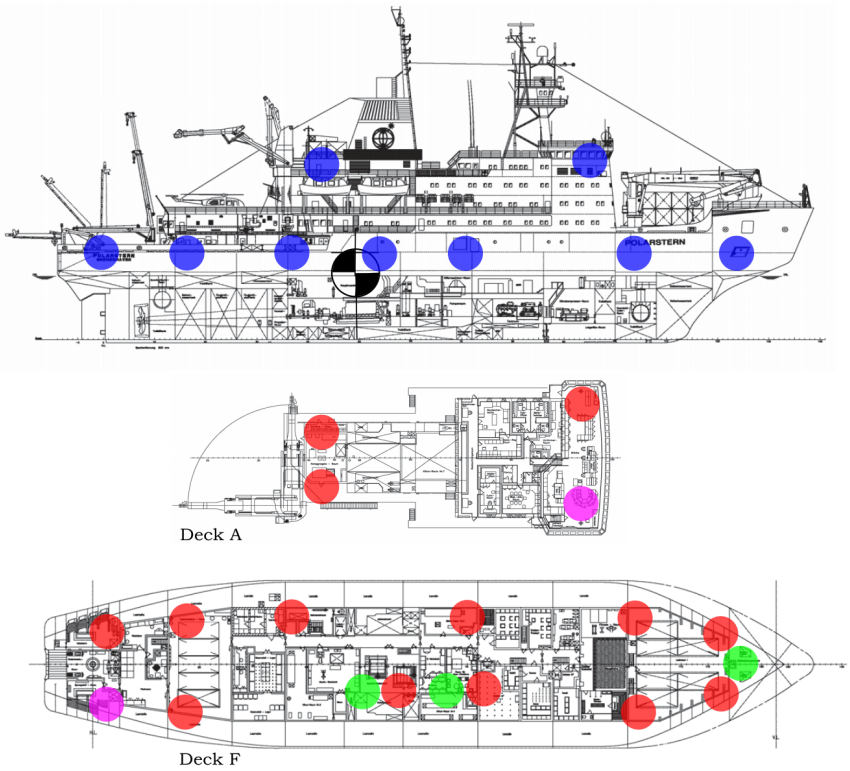


Figure 6: Measurement setup on the Polarstern: ● Accelerometer locations, ● Vertical (+Z) measurements, ● Transverse (+Y) measurements, ● Triaxial (+X, +Y, +Z) measurements

5.2 Field Measurements in the Arctic

Measurements were conducted during the PS100 research expedition to the Arctic in 2016. The cruise track of PS100 is shown in figure 7. The expedition started in Tromsø, Norway, on the 18th July heading north west into the Greenland sea and Fram strait, returning to Tromsø on 6th September after 51 days at sea. A wide variety of operational and environmental conditions were encountered during the voyage. Operational conditions included different cruising speeds, draft, trim and engine configurations. Different environmental conditions included swell heights, swell directions, swell periods, ice types, ice thickness's, air and water temperature variations and wind speeds and directions.

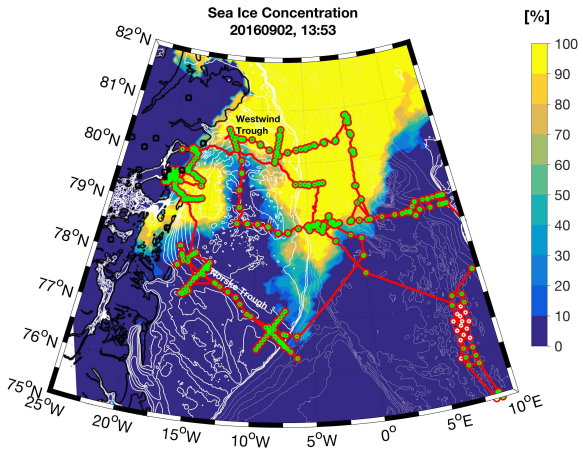


Figure 7: Cruise track of the PS100 expedition. (AWI/J Schaffer)

5.3 Open Data

The full scale data set from the PS100 expedition on the Polarstern to the Arctic is openly available at PANGAEA Data Archiving at https://doi.pangaea.de/10.1594/PANGAEA.882382. The data set contains raw acceleration time data in $.mat$ file format from 23 accelerometers. Environmental data from the data inventory system called Dship are also available. A metadata file contains information regarding measurement parameters and sensor locations. There are three main goals of making the data open source:

1. The results from this research can be tested, recreated and validated.
2. Opening the data to other researchers has the potential to be a force multiplier, bringing a diversity of ideas and solutions and providing additional human capital to drive innovation.
3. A variety of open source data sets will allow open and transparent benchmarking of state of the art algorithms.

6 Results

Stochastic Subspace Identification (SSI) was used to estimate the system parameters. SSI was performed on 20 minute data blocks with 75 % overlap. The 20 minute block was chosen to be long enough to include sufficient spectral information and over 3000 cycles of the lowest frequency, without over smearing the slower variations in environmental parameters.

6.1 Model Training

The first predictive model investigations where aimed at identifying case specific models. This was based on research by [11] who found that data driven bridge models showed clearer trends when split between increasing and decreasing temperature. Constant vessel speeds between 5 - 8 knots for over 100 minutes was defined as a test case. An algorithm was written which allowed a user to navigate through the data and interactively train the predictive model. The results of the modal parameter tacking from the constant speed training data using the pole weighted Modal Assurance Criteria (MACXP) are shown in Figure 8.

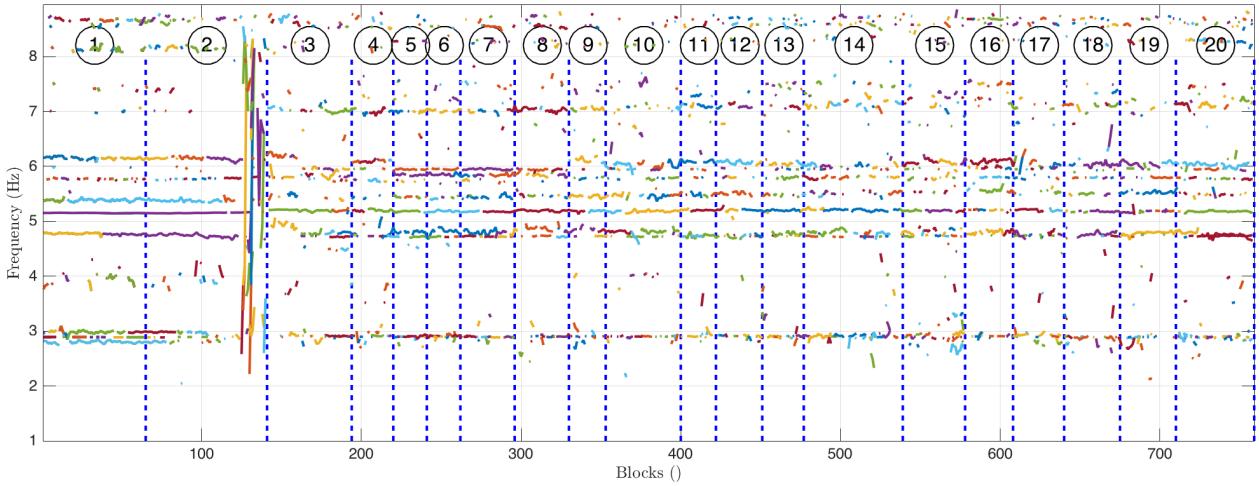


Figure 8: Constant speed modal parameter tracking.

It was observed that modes were not tracked in the same clusters or modal families throughout the data set, despite updating the eigenvectors at each identification. This can be seen by the colour variations in the dominant lines in Figure 8, which were identified as the global modes shown in Figure 9. These observations led to the development of a predictive sliding model, that would only use the most recent predictors which are appropriate for the current system parameters.

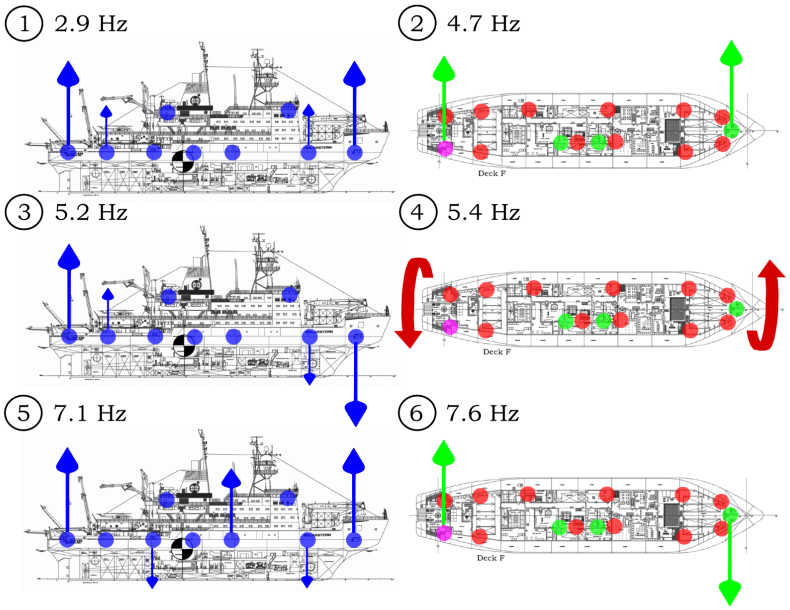


Figure 9: Polarstern mode shapes.

6.2 Predictive Sliding Model

The predictive sliding model was investigated on an alternating speed case containing 65 data blocks shown in Figure 10. A summary of the results is presented below. The interested reader is referred to [12] for further details.

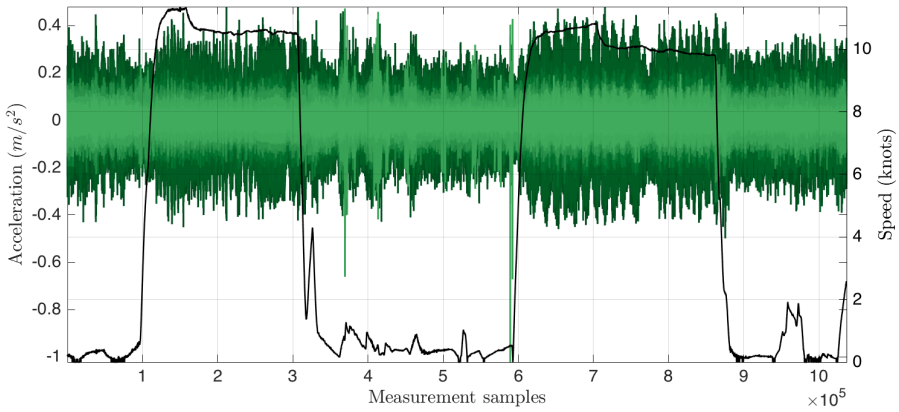
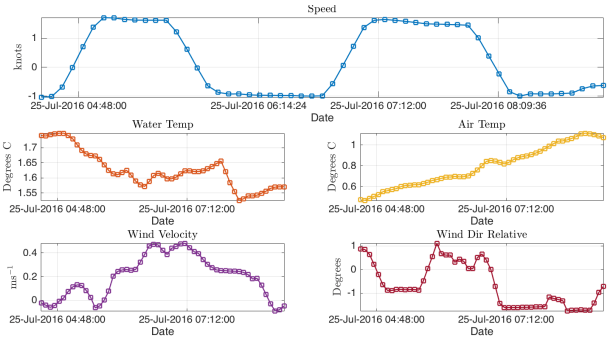
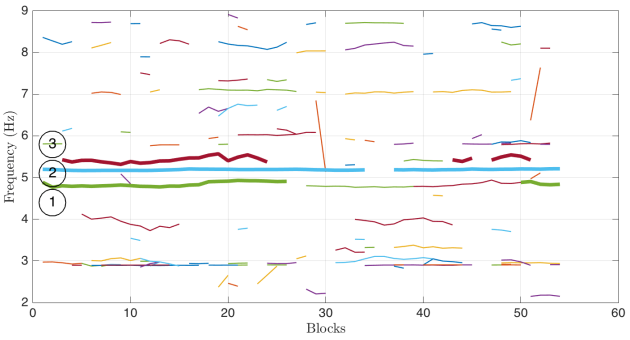


Figure 10: Acceleration time history and ship speed.

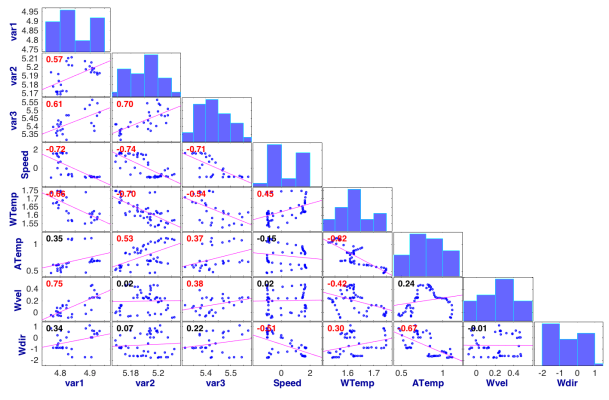
Figure 11 presents the predictive model work flow. The normalized predictor variables in Figure 11a show the alternating vessel speed, decreasing water temperature, increasing air temperature and varying wind conditions. The results of the modal tracking algorithm on the SSI estimates is shown in Figure 11b. Three modes are identified and flagged for prediction.



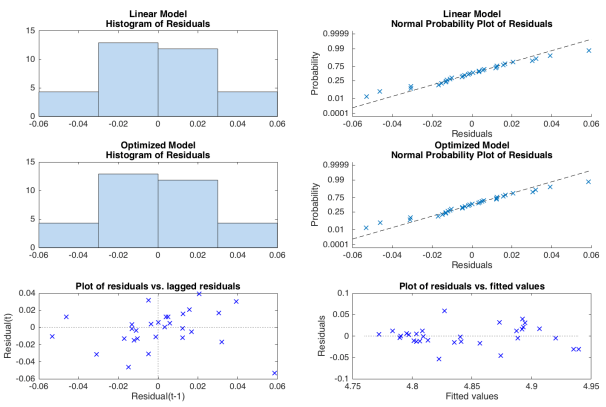
(a) Predictor variables.



(b) Modal tracking.



(c) Correlation.



(d) Residuals.

Figure 11: Predictive model work flow.

The correlation plot in Figure 11c show a number of dominant inter variable relationships. It is noted that R^2 values around 0.5 - 0.6 with p-value < 0.05 are considered significant due to the nature of complex real data. The residual plots in Figure 11d show only a slight improvement in the step optimization. A weak trend is visible in the lagged residuals which is expected to have a negative influence on the results.

The results of the prediction model and Kalman filter are shown in Figure 12. The first 20 blocks are used to train the predictive model. The blue circles show the SSI estimates, the red crosses show the model prediction of the training data and the dotted line shows the 95 % confidence bound. The model is seen to recreate the training data very accurately with a tight confidence bound.

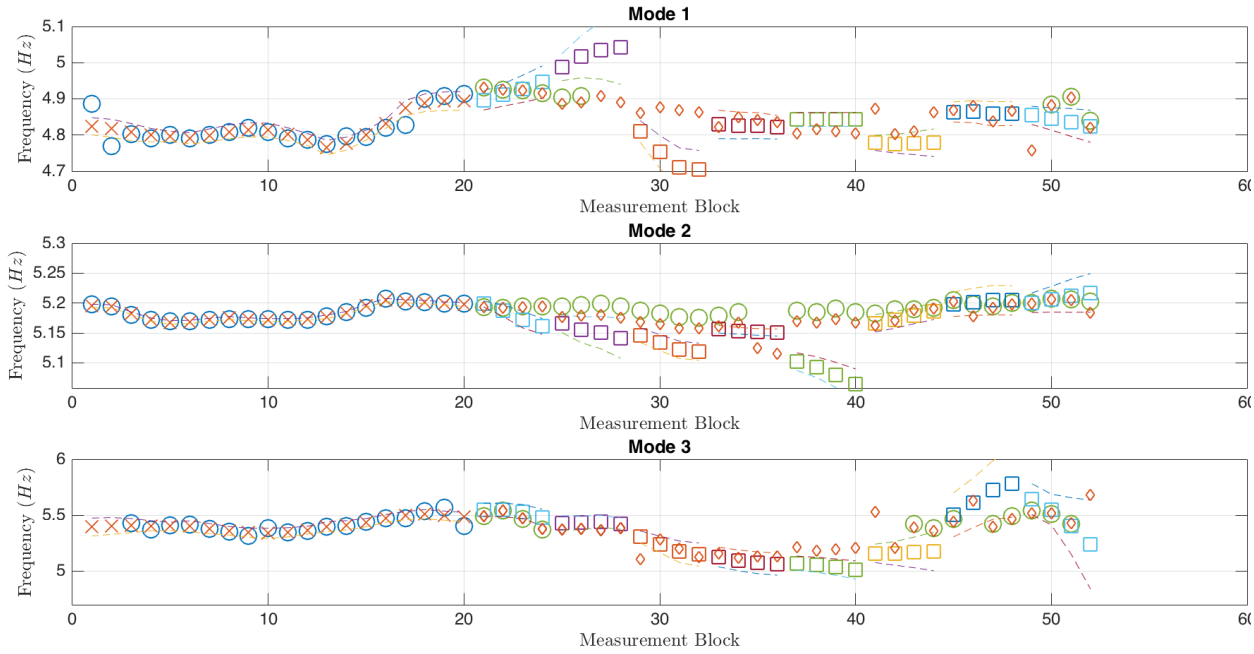


Figure 12: 4 block forward prediction. ◯ SSI training set × Training set prediction □ □ □ □ Statistical model prediction ◯ SSI estimates ◊ Kalman estimates

The 20 block predictive model is then used to make a 4 block forward prediction. The 4 blocks are then Kalman filtered and the 20 block training model window is slid forward by 4 blocks to now include the latest Kalman estimates. Each cluster of 4 block forward predictions is indicated by a different colour grouping of squares. These forward predictions show variability and at times lack continuity. Discontinuities are visible, most notably where there are no SSI estimates such as blocks 28 - 29 in mode 1. It can be seen that the Kalman estimates are however not highly effected by large model discontinuities. This is expected to be as a result of the Kalman filter optimization of the error covariance P for each 4 block cluster in a loop.

7 Conclusion

The use of a statistical model and a Kalman filter were investigated in order to automate system identification estimates as well as improve their sensitivity. The method was demonstrated numerically, where it was found to reduce the cumulative error by over 80 %. Model training on full scale data from the Polarstern led to the development of a sliding predictive model using an optimized linear regression method. The model was found to accurately re-create the training data set and was used to make predictions based on future system inputs. The Kalman filter estimates showed promising results as an optimal combination of the model prediction and the system identification estimates which both contain different uncertainties.

Acknowledgements

The authors gratefully acknowledge the National Research Foundation (NRF) of South Africa and the Alfred Wegener Institute (AWI) in Germany for funding which made this research possible.

References

[1] L. Ljung, *System Identification Theory for the User*. Englewood Cliffs, NJ, USA: Prentice Hall, 1987.

[2] C. Liu and J. T. DeWolf, "Effect of Temperature on Modal Variability of a Curved Concrete Bridge under Ambient Loads," *Journal of Structural Engineering*, vol. 133, no. 12, pp. 1742–1751, 2007.

[3] M. Scionti, J. Lanslots, I. Goethals, A. Vecchio, H. Van der Auweraer, B. Peeters, and B. De Moor, "Tools to Improve Detection of Structural Changes from In-Flight Flutter Data," *the VIII Int. Conf. on Recent Advances in Structural Dynamics*, 2003.

[4] R. S. Pappa, G. H. James, and D. C. Zimmerman, "Autonomous Modal Identification of the Space Shuttle Tail Rudder," *Journal of Spacecraft and Rockets*, vol. 35, no. 2, pp. 163–169, 1998.

[5] Y. Govers, *Parameter Identification of Structural Dynamic Models by Inverse Statistical Analysis*. PhD thesis, Deutsches Zentrum für Luft- und Raumfahrt (DLR), 2012.

[6] F. Magalhães, A. Cunha, and E. Caetano, "Online Automatic Identification of the Modal Parameters of a Long Span Arch Bridge," *Mechanical Systems and Signal Processing*, vol. 23, no. 2, pp. 316–329, 2009.

[7] P. Verboven, E. Parloo, P. Guillaume, and M. Van Overmeire, "Autonomous Structural Health Monitoring–Part I: Modal Parameter Estimation and Tracking," *Mechanical Systems and Signal Processing*, vol. 16, no. 4, pp. 637–657, 2002.

[8] E. Carden and M. Brownjohn, "Fuzzy Clustering of Stability Diagrams for Structural Health Monitoring," *Computer-Aided Civil and Infrastructure Engineering*, 2008.

[9] I. Goethals, B. Vanluyten, and B. De Moor, "Reliable Spurious Mode Rejection using Self Learning Algorithms," in *International Conference on Noise and Vibration Engineering (ISMA)*, (Leuven, Belgium), 2004.

[10] R. E. Kalman, "A New Approach to Linear Filtering and Prediction Problems," *Journal of Basic Engineering*, vol. 82, no. 1, 1960.

[11] I. Gonzales, M. Ülker-Kaustell, and R. Karoumi, "Seasonal Effects on the Stiffness Properties of a Ballasted Railway Bridge," *Engineering Structures*, vol. 57, pp. 63–72, 2013.

[12] K. Soal, *System Identification and Modal Tracking on Ship Structures*. PhD thesis, Stellenbosch University, 2018.

Identification and comparison of modal parameter in a structure during the vibration test using operational modal analysis

N. Costa[1], E. Camargo[2] , R. Pirk[2]
[1] Brüel & Kjær Brazil.
276, Laguna st, São Paulo, Brazil
e-mail: **naira.costa@bksv.com**

[2] Departamento de Ciência e Tecnologia Aeroespacial, Instituto de Aeronáutica e Espaço
Praça Eduardo Gomes, 50, 12.228-904, São José dos Campos, SP, Brazil

Abstract
During the development of a new aircraft, the Ground Vibration Test (GVT) is an essential test and this work presents the results of the modal analysis performed in a small and flexible structure simulating an aircraft. The objective was identified, compare and explore different methods – Experimental Modal Analysis and Operational Modal Analysis- in order to obtain the modal parameters of the structure. The reliability of an experimental and operational analysis was verified by modal assurance criterion calculations between the experimental data and validated by comparison and correlation with a finite element model.

1 Introduction

Ground Vibration testing is a very specialized and important test within the experimental modal analysis area (EMA). GVT is nearly performed shortly before first flight of an aircraft prototype and its represent, sometimes, a great pressure on manufacturer is high in order to keep the promised schedule for certification and delivery. This situation requires the constant improvements for this test. This paper discusses the GVT and show different techniques and methods in order to improve the test time and show that Operational techniques could be used, as an option to reduce the time schedule with satisfactory results.

The modal parameters of a structure are characterized by the modal shape, natural frequency and damping. When a structure is excited, the response results is a combination from vibrating modes acting simultaneously. Therefore, when analyzing this response it is possible to retrieve the modal parameters [2].

In the theoretical modal analysis, the systems can be represented by mathematical models, through auto-value and auto-vector problems, which can be described using analytical and numerical models. The finite element method [3] is widely diffused in several engineering sectors, with good results. On the other hand, experimental methods for the determination of modal parameters of structures could be divided in two main groups: Experimental Modal Analysis (EMA) and the Operational Modal Analysis (OMA).

During the GVT, the modal analysis technique is necessary to the knowledge of the dynamic behavior of the structure and used by the certification process. During the development phase, it is common to perform the complete modal analysis, where theoretical modal analysis techniques are adopted, as well as the experimental modal analysis are used to validate the update theoretical models. In EMA, the modal model of the dynamic system is obtained by the Frequency Response Functions (FRFs) results. A combination of excitation and response in different positions of the structure allows obtaining a set of FRFs, which provide the determination of the modal matrices (mass, stiffness and damping) and as a result the identification of the modal parameters of the structure [1]. On the other hand, using Modal Operational Analysis, the modal parameters are identified from the structure's own operating conditions, that is based only on the structural responses of the model [4].

This article presents the modal tests performed in a structure simulating a small and flexible aircraft structure. It is important to highlight that, in this initial investigation, a small-scale structure was used to characterize and compare numerical vs experimental results. These studies should be extended to a real aircraft structure in future works. In these tests, using the EMA and OMA techniques, two 200kN shakers were used for the structure excitation and sixty-four channels for the response measurements. Initially, EMA was adopted in order to identify the structural modes. In the second step, the structural parameters of the structure were identified, using OMA.

Finally, a correlation of the structural modal parameters of the structure obtained experimentally with those obtained by a numerical model using the Finite Element Method (FEM) was done.

2 Material and Methods

2.1 Experimental setup

The proposed experimental setup was carried out with 64 channels and 2 generators, divided into LAN XI® modules inside one frame (as shown in Figure 1) which monitor the signal from the sensors. Measurements were performed using 35 tri axial B&K accelerometers types 4535 and 4520 placed on the structure as shown in Figure 1. Also, two 200kN B&K shakers type 4825 was used in order to excite the structure with a sinusoidal and random signal. Data acquisition and analysis was performed using Labshop and BK Connect softwares both from B&K

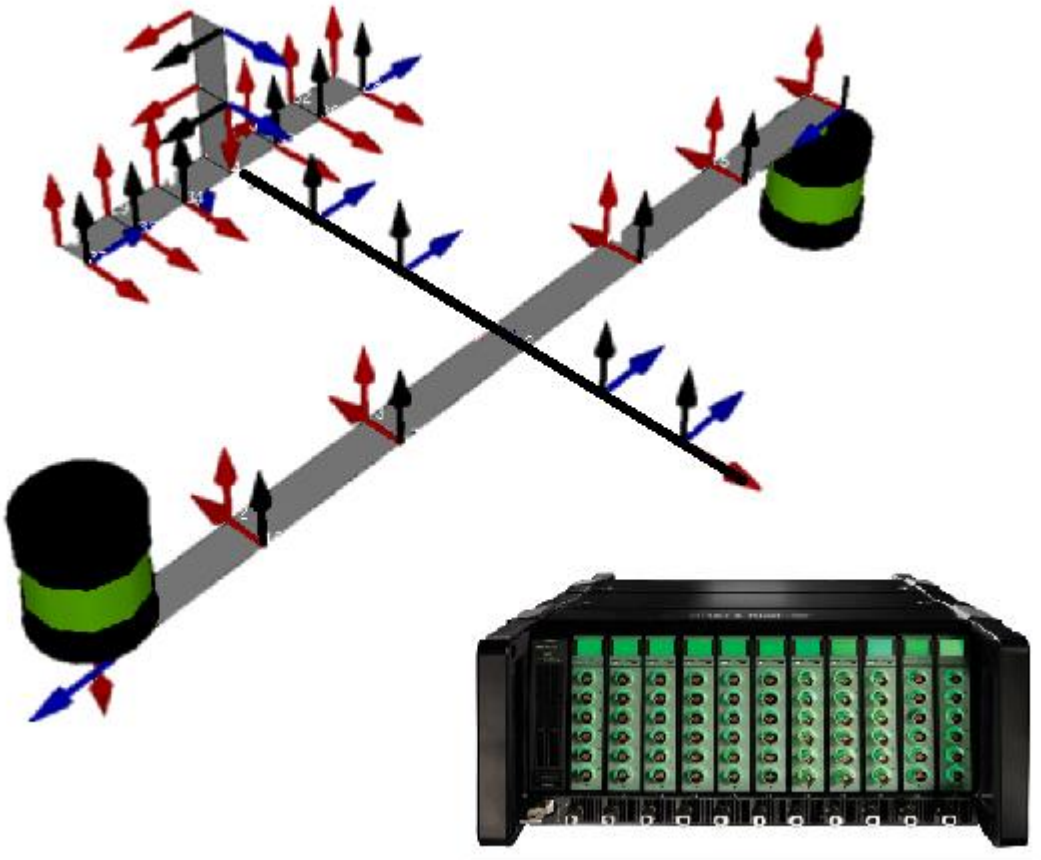


Figure 1: Experimental setup

The real structure is shown at Figure 2. Metal plates joined by rivets made the structure and divided into three sections: wing, main fuselage and tail set. For each section was installed a set of sensors so that could be realized independent measurements for each section. This approach allows, the modes be analyzed separately for each section, if necessary, facilitating the separation of the modes that can be coupled.



Figure 2: Real Experimental setup

For the numerical analysis, the Finite Element Method (FEM) was used. The validation of the numerical model was done through a comparison between EMA and OMA techniques, as described below.

2.2 Finite Element Model FEM

The finite element method is used as a numerical prediction technique for solving engineering problems, which consists of finding the distribution of one (or several) field variable (s) in a continuous domain, governed by an appropriate set of equations partial differential and boundary conditions. The FEM (see for example ZIENKIEWICZ [3] is based on two concepts:

• Transformation of the original problem into an equivalent integral formulation ("residual weighted" or variational);

• Approximation of the distributions of the field variables and the geometry of the continuous domain in terms of a set of form functions, which are locally defined within small sub-domains (finite elements) of the continuous domain.

By applying the element concept, the original problem for determining the distributions of field variables in a continuous domain is roughly transformed into a model of the field variables in some discrete (nodal) positions within each element. This transformation results in a set of algebraic equations for which numerical solution procedures are available.

The numerical model was constructed using the Ansys® software, in the free-free condition.. Figure 2 illustrates the geometry considered, as well as the finite element mesh generated for the structural analysis of the model of the aircraft structure.

.

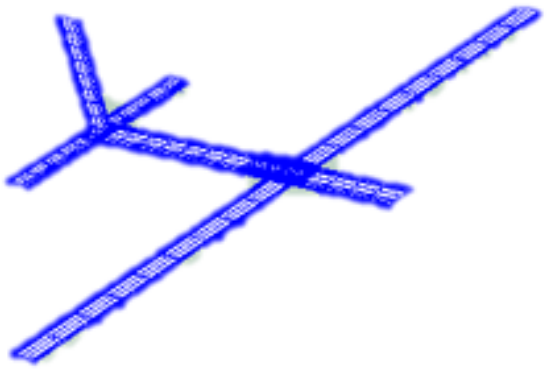


Figure 3: FEM Model

2.3 Test sequence

2.3.1 Experimental Modal Analysis

The Experimental Modal Analysis makes it possible to obtain the dynamic characteristics of the system from Frequency Response Functions (FRFs), defining a direct relation between the input (excitation) and the output (response) of the system [1]. In this way, these FRFs were used in a visual analysis to ensure that the source adopted, the 2 200kN shakers were able to excite the structural modes of the aircraft.

The FRF can be defined as the Laplace Transform of the impulse response function, [4]. In physical terms, the FRF represents the amplitude and the phase of the steady-state response of a system to a degree of freedom with viscous damping subjected to a unitary harmonic force and frequency ω.

For the definition of the resonance frequencies of the structure a swept sine signal was generated as shown in Figure 4.

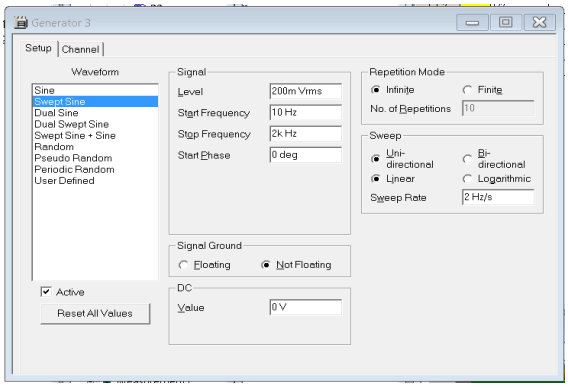


Figure 4: Sweep sine signal

From the sinusoidal sweep, with spectral components varying from 0 Hz to 200Hz, three FRF from driving points were obtained. Based on a simple visual analysis, the natural frequencies are clearly verified, as illustrate Figure 5.

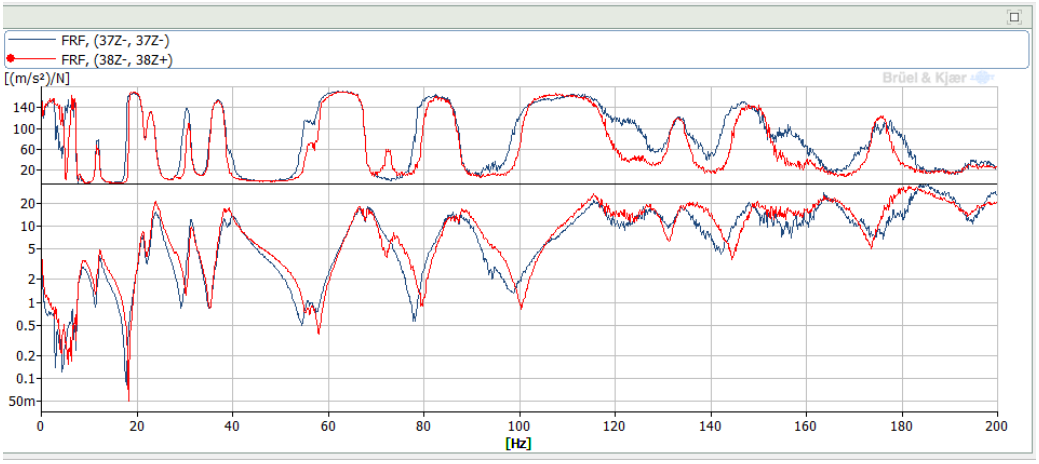


Figure 5: Sweepsine signal

2.3.2 Operational Modal Analysis

Operational Modal Analysis, also known as Modal Analysis based on responses alone, uses the operational excitation itself as input for measuring system response. [4]

The identification of modal parameters in the Operational Modal Analysis can be divided into two main groups: time domain analysis and frequency domain analysis. [8]

The main idea of OMA is to obtain physical information of the system from the functions of correlation and functions power spectral density, thus, the identification in the frequency domain extracts physical information from the system from the function of spectral density. While in the time domain the analyzes are performed dealing with a system with free response, in the frequency domain each mode has a small frequency band where the mode is dominant. Thus, in the frequency domain there is the advantage of natural modal decomposition, since it considers different frequency bands referring to the different modes of the system. For this study the frequency domain identification technique known as Advanced Frequency Domain Decomposition (EFDD) [9] was used.

The technique of Advanced Decomposition in Frequency Domain, EFDD, found in GADE et al [10] depends on the spectral decomposition of the measured response.

And is defined as:

$$G_{yy}(f) = H(f)G_{xx}(f)H^{*}(f) \tag{1}$$

Where Gyy (f), Gxx (f) and H (f) are the spectra of the measured response, unknown excitation and the Frequency Response Function (FRF), respectively.

Once confirmed that the chosen source of noise, two fans - in order to simulate a real operational condition, was able to excite the structure and to identify the structural modes, the fans was turn it on and the natural frequencies, modal forms and damping of the structure were obtained using the Operational Modal Analysis (OMA) technique, the results and the stabilization diagram are presented in item 3.2.

3 Results

The analysis of the results was divided into two parts: Analytical Results or FEM results and Experimental Results.

3.1 FEM Results

Using the Finite Element technique, the first three modes of flexion and the torsion mode of the structure were calculated from the Ansys software and their respective results are shown in Figure 6.

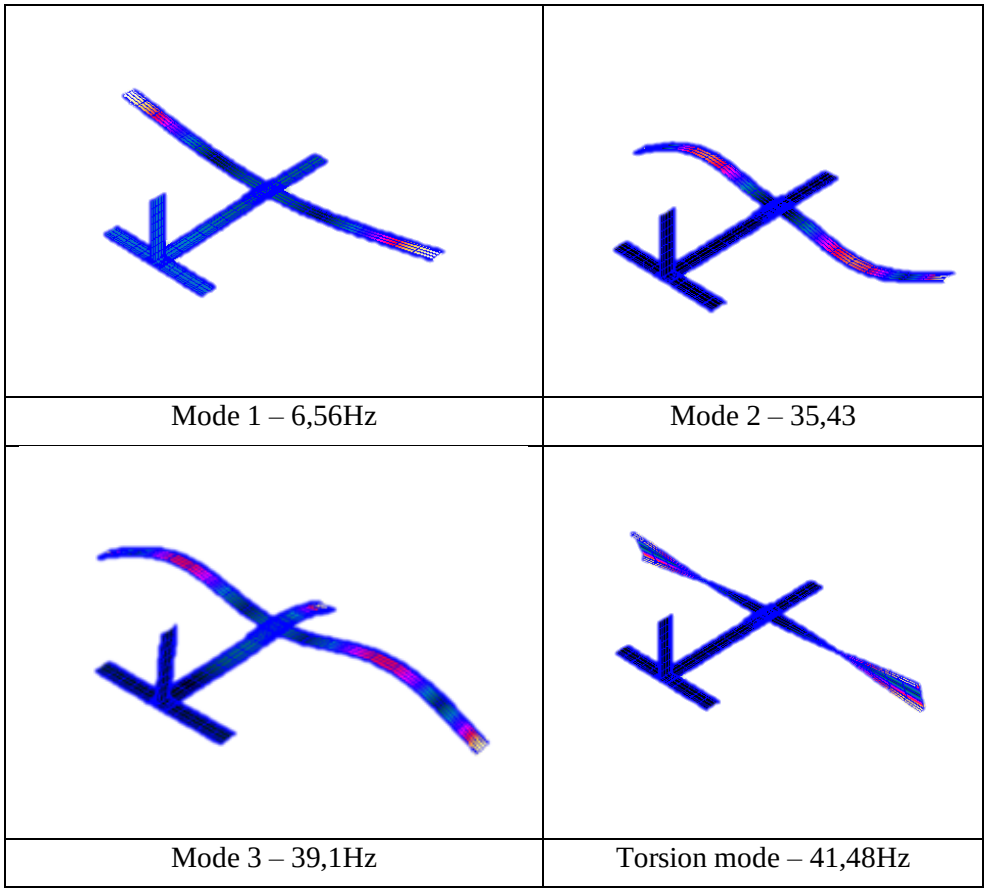


Figure 6: FEM Results

3.2 Experimental Results

3.2.1 Experimental Modal Results

The Experimental Modal Analysis technique, using the 2 shakers as an input reference (excitation), enabled the identification of the structural modes of the system. Figure 7 shows the stabilization diagram and the modes identified are show in Figure 9 with the modes shape.

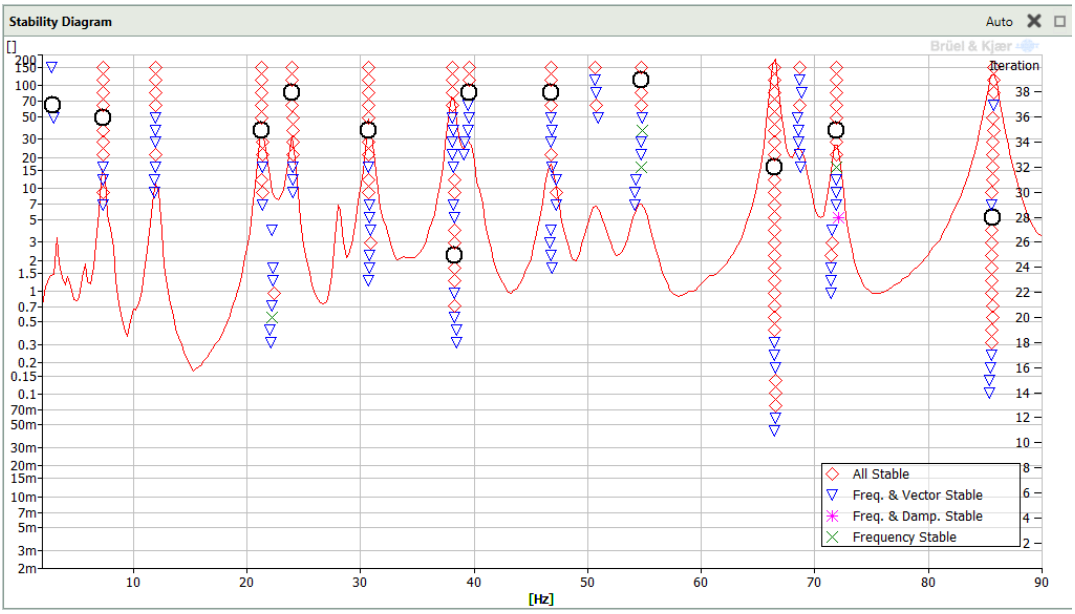
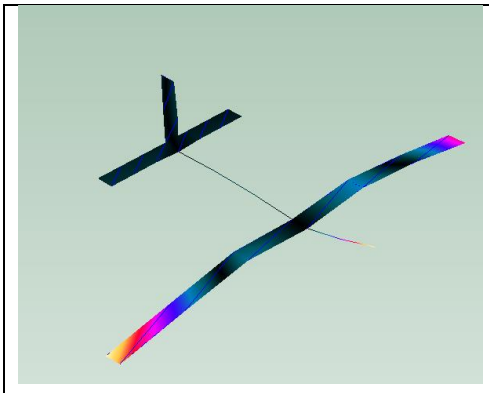
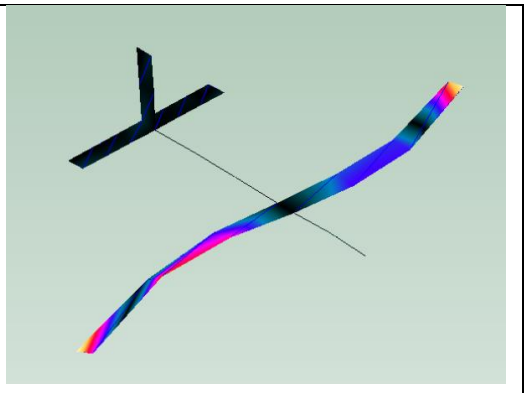


Figure 7: Stability Diagram

Figure 8 illustrate the AutoMAC from classical experimental measurements showing consistency during data acquisition and the results.

	7,345	30,739	38,288	46,766	66,422
7,345	1,000	0,090	0,246	0,065	0,016
30,739	0,090	1,000	0,027	0,013	0,049
38,288	0,246	0,027	1,000	0,040	0,017
46,766	0,065	0,013	0,040	1,000	0,037
66,422	0,016	0,049	0,017	0,037	1,000

Figure 8: Auto MAC

	
Mode 1 – 7,33Hz	Mode 2 – 30,73

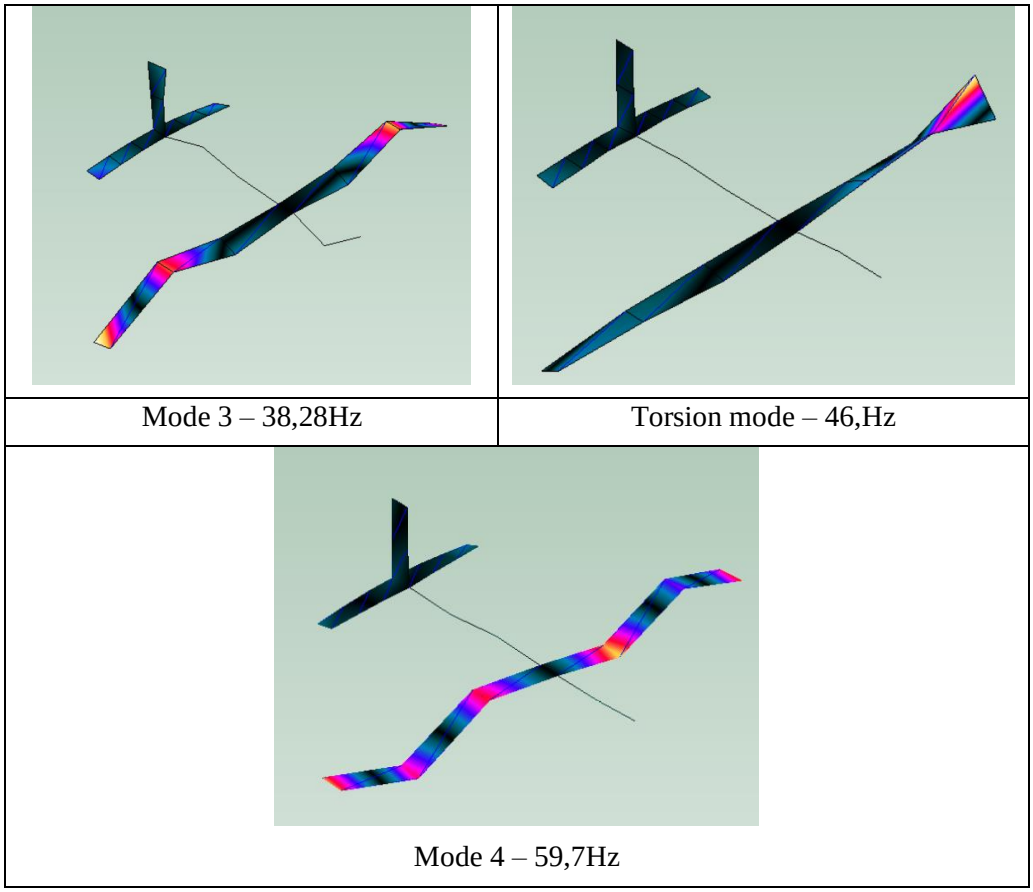


Figure 9: EMA Results

3.2.2 Operational Modal Results

Using the Operational Modal Analysis in the frequency domain (EFDD), [10] it was possible to identify the first four bending structural modes and the torsional mode of the structure (shown in Figure 2).

Figure 10 illustrates the stabilization diagram of Operational Modal Analysis, the blue circle illustrates that the mode found is stable

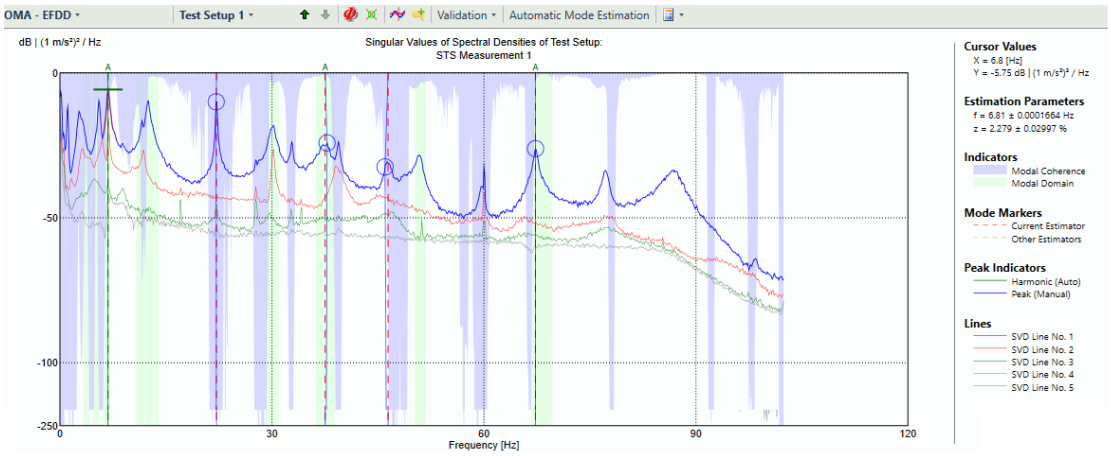
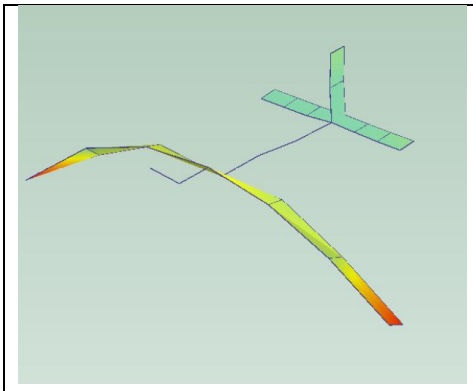


Figure 10: OMA Stabilization diagram

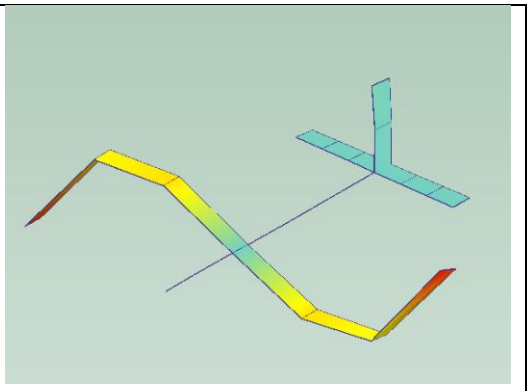
Figure 11 illustrate the AutoMAC from Operational experimental measurements showing consistency during data acquisition and the results. And, the modal shapes are illustrated in Figure 12.

	6,809	30,075	37,529	46,434	67,287
6,809	1,000	0,207	0,477	0,058	0,069
30,075	0,207	1,000	0,197	0,071	0,078
37,529	0,477	0,197	1,000	0,059	0,084
46,434	0,058	0,071	0,059	1,000	0,060
67,287	0,069	0,078	0,084	0,060	1,000

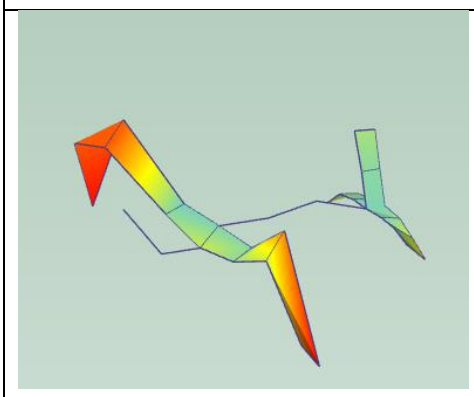
Figure 11: OMA Results



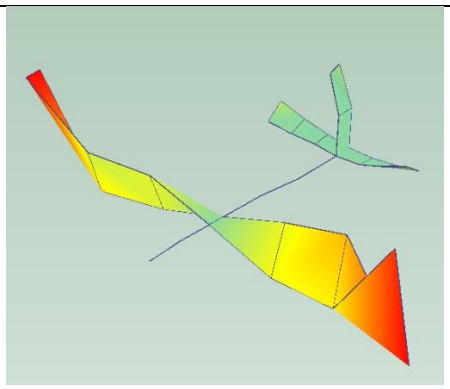
Mode 1 – 6,79Hz



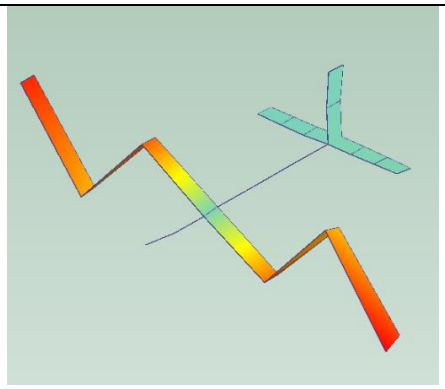
Mode 2 – 30,07Hz



Mode 3 – 37,5Hz



Torsion mode – 46,12Hz



Mode 4 – 67,2Hz

Figure 12: OMA Results

3.3 Results Comparison

Table 1 compares the results from FEM, Experimental Modal Analysis and Operacional Modal Analysis:

	Mode 1	Mode 2	Mode 3	Torsion Mode	Mode 4
FEM	6,56	35,43	39,1	41,48	-
EMA	7,35	30,73	38,28	46,76	66,42
OMA	6,80	30,07	37,52	46,43	67,28

Table 1: Results Comparison

From Table 1 it is possible to observe that the modes found in both the experimental model and the analytical model are of the same order of magnitude.

4 Conclusions

This work presented an experimental investigation on the behavior of the airplane structure, specially during the GVT test using different identification methods . In order to determine the vibratory behavior tests were carried out with the scale structure of the aircraft and the determination of its natural frequencies, modes of vibration and shape was done using the Experimental, Operational and Analytical Modal Analysis of the structure.

These type of analysis provide more flexibility and capabilities to address GVT requirements. The quality of results using OMA is also very convincing and had a fast and simple setup.

In general, the results obtained in all cases: Experimental Modal Analysis, Operational Modal Analysis and Finite Element Analysis proved to be quite effective, since the validation using MAC showed consistency of the modes found, and the comparison of the natural frequencies presented errors less than 3%.

Acknowledgements

The author would like to thank all partner involved in the DCTA vibration lab team.

References

[1] D. J Ewins. Modal Testing: Theory and Practice, Research Studies Press LTD. Second Edition, 2000.

[2] N. M. M. Maia, J. M. M. Silva, J. He, N. A. J. Lieven, R.M. Lin, G. W. Skingle, W.M., To and A. P. V Urgueira, Theoretical and Experimental Modal Analysis, Research Studies Press, Taunton, England, 468p.

[3] O. C. Zienkiewicz, The Finite Element Method - Vol. 1: Basic formulation and linear problems. McGraw-Hill, London, 1977.

[4] R. Brincker, P. Andersen, "Understanding Stochastic Subspace Identification" in Proc: 24th International Modal Analysis Conference (IMAC).St Louis (2006).

[5] H. Kuttruff. Acoustics: An Introduction. Spon Press, new ed edition,Dec. 2006.

[6] S. N. Y. Gerges; W. D. Fonseca and R. P. Dougherty. "State of the art beamforming software and hardware for applications (keynote lecture)". In 16th International Congress on Sound and Vibration - ICSV2009, Kraków, Poland, Jul. 2009.

[7] N. C. Costa. Estudo dos modos de vibração de estruturas aeronáuticas e espaciais utilizando a técnica de Análise Modal Operacional. MsC thesis, Instituto Tecnológico de Aeronáutica, São José dos Campos, Brazil, 2014.

[8] E. Camargo, N Jacobsen,. D. Strafacci, "Operational modal analysis on a modified helicopter". In Conference Proceedings of the Society for Experimental Mechanics Series, vol.1, p.265-273, 2011.

[9] S. Gade, N.Moller H. Herlufsen and H. Konstantin-Hasen, "Frequency Domain Techniques for Operational Modal Analysis", Proceedings of IOMAC Conference, Copenhagen, Denmark, 2005.

Output-only damping estimation of friction systems in ambient vibrations

T. Friis [1], **E.I. Katsanos** [1], **M. Tarpø** [2], **S. Amador** [1], **R. Brincker** [1]
[1] Technical University of Denmark, Department of Civil Engineering,
Brovej, Bygning 118, Kongens Lyngby, Denmark
e-mail: **tofri@byg.dtu.dk**

[2] Aarhus University, Department of Engineering,
Inge Lehmanns 10, 8000 Aarhus C, Denmark

Abstract
Working with dynamics in civil engineering applications, it is experienced that real structures have nonlinear damping. The nonlinearity of the damping can be induced by the hysteresis phenomenon, that occurs due to friction or softening geotechnical boundary conditions. Along these lines, this article focusses on assessing the performance of two output-only methods estimating the linear damping of a friction-induced nonlinearly damped system subjected to random vibrations. In particular, the method that employs auto regressive models and poly-reference, and the poly-reference Least Squares Complex Frequency method are included in the study. The methods are comparatively assessed by comparing their linear damping estimates of friction-induced nonlinear numerical simulations with theoretically derived estimates of equivalent linear damping. It is concluded that the output-only methods underestimate the damping when compared to theoretically derived equivalent linear damping for the present case of Coulomb-type friction-induced nonlinear damping.

1 Introduction

It is often experienced in modal analysis of civil engineering structures that they have nonlinear damping. The nonlinearity might have been introduced through the phenomenon of hysteresis, e.g., friction between sliding surfaces in joints, internal friction in materials or from nonlinear material behaviour like yielding. Additionally, the boundary conditions play an important role in civil engineering structures introducing uncertainty as it concerns the dynamic behavior of the structure. For example, there are plenty of cases in which the soil-foundation system experience softening stiffness that may also introduce nonlinear damping through the related hysteretic response. Moreover, the damping can in some cases even be time-varying due to the operational condition, e.g., aerodynamic damping of wind turbines, offshore structures in waves, bridges and bridge cables, high rise buildings and air planes [1, 2]. However, due to simplifications reasons and important mathematical advantages, linear systems are generally assumed when assessing the dynamic behaviour of mechanical systems or when dealing with design of civil engineering structures. Likewise, when identifying the dynamic behaviour of existing structures through the application of operational modal analysis (OMA), damping is assumed to be linear. The topic of this article is not to move towards identification of parameters of nonlinear damping models in operational conditions, but to assess the validity and accuracy of the OMA-based identification of the linear damping for structural systems that experience friction-induced nonlinear damping.

Similar investigations have already been conducted. Zhang et al. [3] investigated the effect of nonlinear stiffness and nonlinear viscous damping on OMA based identification. They concluded that these techniques can extract for nonlinear systems most underlying linear dynamic properties, the latter being related, though, with increased bias, i.e., mean error, and random error, i.e., variance error. Bajric et al [4] evaluated the OMA

damping estimates from simulated response of an aeroelastic model of an 8 MW offshore wind turbine and of an real 8 MW offshore wind turbine under nonoperating conditions. Based on the actual measurements, time-varying damping and natural frequency were detected while a relation between the natural frequency and the amplitude of the response was also established. Friis et al [5] investigated experimentally the performance of OMA methods when applied to friction coupled systems, which consisted of two platforms connected through a bridge loosely placed on top. Based on their findings they concluded that the applied methods were able to identify the underlying linear systems. However, these studies do not deal with the accuracy of OMA damping estimates when applied to friction-induced nonlinearly damped system. Thus, the research question that the present paper is answering is; how does the (best) linear approximation of the OMA based damping estimation fit with theoretical interpretations of equivalent linear damping (ELD) of Coulomb-type friction damped systems in random vibrations? In other words, does the OMA based damping estimation constitute the damping representative of a linear system that will have the same response level as the nonlinear one.

In order to satisfy the objective of the present paper, a numerical simulation study was carried out considering a frictionally damped steel prototype structure. Two different OMA methods were applied to the simulated nonlinear response and the pertinent damping estimates were compared with theoretical interpretations of ELD. The methods for estimating the ELD are based on different assumptions but all employing knowledge of the load, natural frequencies and the mass scaling of the systems, which makes them difficult to apply in practise compared to the OMA methods. Along these lines, this article provides a short description of the ELD and OMA methods and the numerical case study, and finally presents and discusses the findings of the present study.

2 Estimation of equivalent linear damping

For the present study of OMA-based damping estimation of friction systems in random vibrations, it is necessary to have a reference for the damping estimate in order to evaluate the accuracy and validity of the respective OMA estimates. For that purpose, three different methods are considered for estimating the equivalent linear damping. The methods and their inherited assumptions are published and described in Friis et al [6] and are therefore only briefly described in the following [1].

The present study is conducted on the basis of a simple structure, described numerically by a finite element model and, thus, it consists of multiple degrees-of-freedom (DOFs). The OMA-identified damping estimates is assessed with the use of the damping ratio, i.e., the ratio of critical damping, and naturally, also the equivalent linear damping will have to be formulated based on modal ratios of critical damping, $\zeta_{eq(j)}$. In the present case, the methods for ELD estimation are based on modal components by a modal decomposition of the response in the time domain by using the pseudo inverse of the mode shape matrix considering more degrees of freedom than the number of modes in order to avoid the issue of overfitting [7].

Regarding the first ELD estimation method used herein, the equivalent linear damping is estimated by balancing the intensity of the response with the integrated effect of the spectral density of the excitation, and hence referred to as the intensity balance method in the following. By assuming a stationary flat broad band excitation around the natural frequency of the mode, the equivalent linear damping can be estimated by:

$$\zeta_{eq(j)} = \pi \frac{S_{0(j)}}{2\sigma_{q_j}^2 \omega_j^3 m_j^2} \tag{1}$$

where m_j is the mass scaling of the system, i.e., modal mass, ω_j is the natural angular frequency, $S_{0(j)}$ is the flat (or average) spectral input at the natural frquency, $\sigma_{q_j}^2$ is the variance of the modal response and j is indicating the mode in question.

The second method, an alteration of a method by Iourtchenko and Dimentberg [8], is based on stochastic averaging of the response in terms of displacement and velocity, by introducing slowly varying amplitude

[1] A journal paper with the derivation of the methods is submitted to Elsevier

and phase, forcing in such a way, the energy to be constant over an oscillation amplitude. With the applied assumption of the method it is referred to as the stochastic averaging method in the following. More details about the stochastic averaging can be found elsewhere [9]. Through this method it is possible to establish the following relation for the equivalent linear damping ratio as described by Eq. (2). The resemblance to the first method in Eq. (1) is notable, however, the second method employs the Rayleigh distribution and the variance the amplitudes of the response, $\sigma^2_{Q_j}$, whereas the first method employs the variance of the entire response.

$$\zeta_{eq(j)} = \frac{\pi S_{0(j)}}{(4-\pi)\sigma^2_{Q_j}\omega_j^3 m_j^2} \tag{2}$$

The third method modifies the so-called energy-dissipation method by Liang and Feeny [10–12]), and is founded entirely on physics. This method is based on the energy relation of a system in the manner, that the energy of all conservative terms in the nonlinear equation of motion is calculated, and then the estimation of a system's damping is based on the amount of the dissipated energy:

$$W_d = W_e - W_i \tag{3}$$

where W_d is the dissipated energy, W_e is the external energy and W_i is the internal energy. Practically, the amount of dissipated energy is calculated similarly to Eq. (3) in modal components and subsequently, a linear modal damping model is fitted to estimate the equivalent linear damping. The method is referred to as the energy balance method in the following.

3 Output-only methods for estimation of linear damping

Two state-of-the-art OMA methods are utilised herein. Especially, the Auto Regressive - Poly-Reference method (AR-PR) is chosen to identify the modal characteristics of both the linear and the friction-induced nonlinear system, while similar identification is conducted mainly in the frequency domain by the use of the Poly-reference Least Squares Complex Frequency method (pLSCF). For the former case, the AR-PR method, the estimates of modal characteristics are conducted in time domain based on correlation functions, while for pLSCF method, the modal characteristics are estimated from half spectral density matrices, thus, also based on correlation functions. A detailed description of the aforementioned OMA methods is considered out of the scope of the current article, and hence, only a short overview is provided next along with relevant references.

3.1 Auto regressive models and poly-reference

The present method is one of the simplest methods within the engineering area of OMA and can be found described in detail in the literature, [7, 13–18]. The outline of the procedure is to compute auto regressive (AR) models in a poly-reference sense based on estimated correlation functions:

$$\mathbf{R}_y(\tau) = \mathbb{E}\left[\mathbf{y}(t)\mathbf{y}^T(t+\tau)\right] \tag{4}$$

where $\mathbb{E}$ is the expectation operator, $\mathbf{y}(t)$ is the response vector in time, t, and τ is the time lag. By interpreting the correlation functions as free decays, $\mathbf{Y}(n)$, and employing the AR models, the measured response can be expressed as:

$$\mathbf{Y}(n) - \mathbf{A}_1\mathbf{Y}(n-1) - \mathbf{A}_2\mathbf{Y}(n-2) - \ldots - \mathbf{A}_{na}\mathbf{Y}(n-na) = 0 \tag{5}$$

where $\mathbf{A} = [\mathbf{A}_{na}, \mathbf{A}_{na-1}, \ldots \mathbf{A}_1]$ is denoted the polynomial coefficient matrices of the AR models, $\mathbf{Y}(n) = [\mathbf{y}_1(n), \mathbf{y}_2(n), \ldots \mathbf{y}_{nc}(n)] \in \mathbb{R}^{nr \times nc \times np}$ is the free decays at sample n to the number of samples np with nr being the number of outputs and nc being the number of inputs.

In order to estimate the polynomial coefficient matrices in a poly-reference manner, two block Hankel matrices are formed and a least squared problem is solved. The modal characteristics are then estimated by forming the companion matrix of the polynomial coefficients and computing the eigenvalue decomposition. The main advantage of using the present method, other than its simplicity, is the possibility to exclude noisy time lags of the correlation function. For the present study, the first couple of lags, in accordance with [19], and the so-called noise tail are removed in an automated manner by the method described in detail in Tarpø et al [20]. Finally, the physical poles are also sorted from the mathematical ones in an automated manner by excluding poles with relatively unrealistic poles, i.e., modes with negative or high damping.

3.2 Poly-reference Least Squares Complex Frequency

The pLSCF method is a poly-reference generalised version of the Least Squares Complex Frequency method and is well described in the literature (see [21–24]). The main idea of the method is to model the relation between each response and all external excitations in the frequency domain by means of a right matrix-fraction description:

$$\hat{\mathbf{H}}_o(\omega) = \mathbf{N}_o(\omega)\mathbf{D}^{-1}(\omega) \tag{6}$$

where $\hat{\mathbf{H}}_o(\omega)$ is the estimated o-th row of the half spectral density matrix, $\mathbf{N}_o(\omega)$ is the o-th numerator row-vector polynomial, $\mathbf{D}(\omega)$ is the common denominator matrix polynomial and o is indicating the output number from 1 to nc.
Both the numerator row-vector polynomial and and the common denominator matrix polynomial are described in terms of the polynomial basis functions, $\Omega_j(\omega)$, and matrix coefficients, $\mathbf{B}_{oj}$ and $\mathbf{A}_j$:

$$\mathbf{N}_o(\omega) = \sum_{j=0}^{n} \Omega_j(\omega)\mathbf{B}_{oj}, \quad \mathbf{D}(\omega) = \sum_{j=0}^{n} \Omega_j(\omega)\mathbf{A}_j \tag{7}$$

where n is the considered model order.

The coefficients of Eq. (7), i.e., $\mathbf{B}_{oj}$ and $\mathbf{A}_j$, are estimated by either minimising a nonlinear least squared cost function or an approximated linear least squared problem. When the coefficients are estimated, it is possible to compute the poles and modal participation factors, and subsequently the mode shapes, by the eigenvalue decomposition of the companion matrix containing the obtained coefficients. With the estimation of the modal parameters stability diagram can be constructed by varying the model order of the of Eq. (7) in the classical sense. For the present study, the estimation method has been coupled with an agglomerative hierarchical clustering algorithm, running on the stable poles, to collect the physical poles in an automatic manner.

The main advantages of the pLSCF method is its efficiency and the very clear stabilisation diagrams. However, the pLSCF method has a tendency to introduce bias in the damping estimates when statistical errors and/or noise in the tail of the correlation functions are included in the computation of the half spectral matrix. This particular issue is dealt with in the classical sense of applying an exponential window to the correlation functions and subtracting the applied damping from the modal estimates. For more on increasing the accuracy of the estimates see El-Kafafy et al [25].

4 Numerical case study

A testbed, for employing the comparative assessment between the ELD and OMA-based damping estimates, was established by creating a finite element model of a simple T-shaped steel structure, see Fig. 1. This respective model was created by using three dimensional beam elements and the system equivalent reduction and expansion process, proposed by O'Callahan [26], was used to reduce the structural system of 156 (initial) degrees-of-freedom to 10 with 10 modes. Furthermore, two types of damping were considered: (i) linear

proportional damping and (ii) friction-induced nonlinear damping. The latter was introduced by including a Coulomb friction element to the top of the structure, being perpendicular to the horizontal top element and in parallel to the third DOF (see Fig. 1). With this particular installation of the friction element only the second mode of the first four modes was effected by the friction-induced nonlinear damping. Thus, the analysis and the consequent discussion of the results are exclusively focused on the second mode. Moreover, by creating the friction system in this particular manner, the amount of included fiction-induced nonlinear ramifications of the modal properties were reduced to a minimum. With a sufficiently high ratio of the intensity of the external excitation to the friction force, i.e., insuring the friction element is in the sliding regime for the vast majority of the response, no change of the linear natural frequencies and mode shapes was introduced, i.e., changes of the frequencies and mode shapes without consideration of the friction element. On the contrary, had the employed friction mechanism been of a type that includes a stiffness, e.g., elasto-plastic element (Jenkins element) or any kind of hysteresis-related element, a change in natural frequency would have occurred depending on the amplitude of the response. This particular friction stiffness effect is not included in the study described in the present article, thereby, purely the case of friction-induced nonlinear damping is investigated.

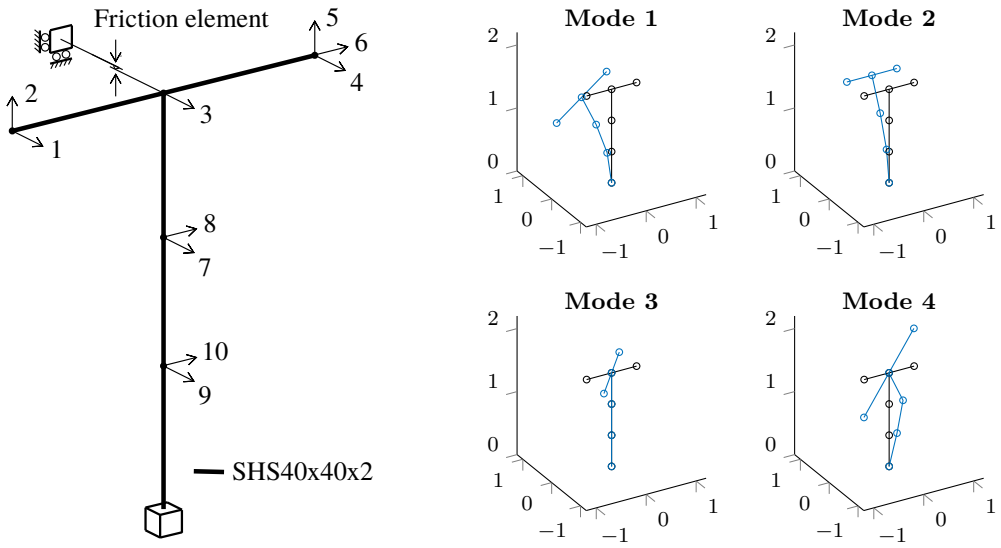


Figure 1: Sketch of the simulated T-shaped steel structure with numbering of DOFs and mode shapes of the first four modes.

To simulate the response of the friction-induced nonlinear structure, the system of second-order differential equations with the classical linear system with the inertia term, viscous damping term, stiffness term and load term is left unchanged. The nonlinear friction force is simply considered through an additional term, $\mathbf{B}\,\mathbf{f}_d(\mathbf{y}(t))$. Thus, the system of equations becomes:

$$\mathbf{M}\ddot{\mathbf{y}}(t) + \mathbf{C}\dot{\mathbf{y}}(t) + \mathbf{K}\mathbf{y}(t) + \mathbf{P}\mathbf{f}_d(\mathbf{y}(t)) = \mathbf{x}(t) \tag{8}$$

where, $\mathbf{M}$, $\mathbf{C}$ and $\mathbf{K}$ are the system matrices of the linear system, $\mathbf{P}$ is the damper placement matrix, $\mathbf{f}_d(\mathbf{y}(t))$ is the nonlinear force from the friction element and $\mathbf{x}(t)$ is the external excitation.

Nonlinear numerical simulations of the friction damped system is carried out by using the algorithm proposed by Lu et al [27]. The time-stepping method is employing the second-order differential equation (Eq. (8)) in a first order format, i.e., a state-space format. The state-space version of Eq. (8)) is subsequently formulated in discrete time format by assuming linear variation of the damper force and external force between time-steps. The nonlinear damping force is then treated by its iteration within each time-step. More details about the aforementioned simulation process can be found elsewhere [27].

In the present case study, the system was subjected to uncorrelated, normally distributed white noise in all 10 DOFs, enabling a comparative study of ELD estimates and OMA damping estimates through 500

Monte Carlo simulations. For each of the 500 simulations, a new excitation series was generated preserving though identical spectral level. Furthermore, for each of the 500 Monte Carlo simulations, both a numerical simulation with only linear damping and simulation with both friction-induced nonlinear damping and linear damping were carried out. For the two cases, referred to as the linear and nonlinear case in the following respectively, the total amount of damping was kept approximately at the same level. Table 1 lists the damping ratios adopted herein for the Monte Carlo simulations along with the vibration frequencies of the first four modes and the friction force.

An important parameter of the simulation study conducted herein is the length (i.e., duration) of the individual simulations that affects substantially the accuracy of the ELD-based damping estimates, the latter being the reference basis to compare with the OMA-identified damping ratios. Additionally, the current study is dealing with random generation of white noise excitation and the estimation of the equivalent linear damping for nonlinear systems subjected to random vibrations. Thus, a rather long simulation length is necessary before the intensity of the load and response is equal between the individual simulations. With these considerations in mind, it was found that an equivalent simulation length of approximately 15,000 periods of the two lowest modes (≈25min) was appropriate to be considered herein.

Mode	1	2	3	4
f_j [Hz]	10.10	10.39	27.58	57.54
ζ_j [%]	1.5	10 / 1.5	3.0	1.5
f_c [N]		0 / 2.5		

Table 1: Natural frequencies, damping ratios and friction force of the simulated structure. Where two values are listed: linear / nonlinear case.

5 Comparison and discussion of linear OMA damping estimates with theoretical equivalent linear damping

The main results of the study will be presented and discussed in this chapter focusing on the ELD and OMA-identified damping estimates of the second mode, the latter being affected by the friction. Especially, two cases are presented and associated with the investigation of: (i) linear damping considered at a level approximately identical to the damping of the nonlinear, friction-related system, (ii) friction-induced nonlinear damping with a relatively small addition of linear damping. By including the case related to the linear damping estimation, the effect of the relatively high damping on the estimation methods can be evaluated without consideration of the friction-induced nonlinearity. In this manner, it is possible to distinguish between the effects of inherited assumptions in the methods and the effects of the friction-induced nonlinear damping.

The first of the two following subsections (section 5.1) presents and discusses the ELD estimates of the two cases. The second subsection (section 5.2) is then presenting and discussing the OMA estimates of the two cases, with comparison to the ELD estimates in the nonlinear case. By including the ELD estimates, it enables the possibility to have a reference of what the OMA damping estimates should be in both cases and not only in the linear case. Thus, it is assumed that the ELD estimates are more accurate in the sense that they constitute the damping representative of a linear system that will have the same response level as the nonlinear one. A small study was conducted to make sure that this is actually the case. From the study, it was concluded that an equivalent linear system based on ELD estimates compared to one with OMA-based estimates is more representative of the nonlinear system. Especially, the response levels, i.e., variances, were identical for the linear system based on ELD estimates and the nonlinear one.

5.1 Equivalent linear damping (ELD) estimates

Fig. 2 shows plots of normalised probability distributions of the equivalent linear damping ratios of the second mode for the two cases using the three different methods; (left) purely linear damping, (right) friction-induced nonlinear damping with a relatively small addition of linear damping. All ELD and OMA-based damping estimations have been found to be normal distributed and are therefore plotted as such. Moreover, the mean values are indicated by vertical lines and circles in Fig. 2 and listed in Table 2 together with the coefficient of variation (CoV), i.e., the standard deviation divided by the mean value.

As can be seen in Fig. 2, the energy balance method has almost zero variance in the linear case with the line-like shape of the distribution. The latter is not valid for the nonlinear damping case, for which the damping ratio estimates were found to be scattered, however in smaller extent than the damping estimates of the intensity balance and stochastic averaging method respectively. These two methods result in higher dispersion for the damping ratios estimated for the nonlinear case compared to the linear one. For both the linear and the nonlinear case, it is also notable that two of the methods, i.e., the intensity balance and the energy balance method respectively, led to identical mean damping ratio estimates, and for the linear case their mean values are equal to the second mode-related input damping ratio considered for the simulations in the linear case. On the contrary, the mean of the ELD estimates of the method based on stochastic averaging in the linear case are underestimated compared to the input damping ratio of the simulations, while in the nonlinear case, the mean of the ELD estimates is higher compared to the other two methods. These observation are collaborated in Friis et al [6], where it is found that the assumption of constant energy over a cycle of oscillation is introducing bias for higher damping ratios. Along these lines, the superiority (i.e., higher accuracy), found to be associated with ELD estimates from the intensity balance and energy balance method respectively, led the authors to exclude the stochastic average method for the OMA estimates assessment that follows.

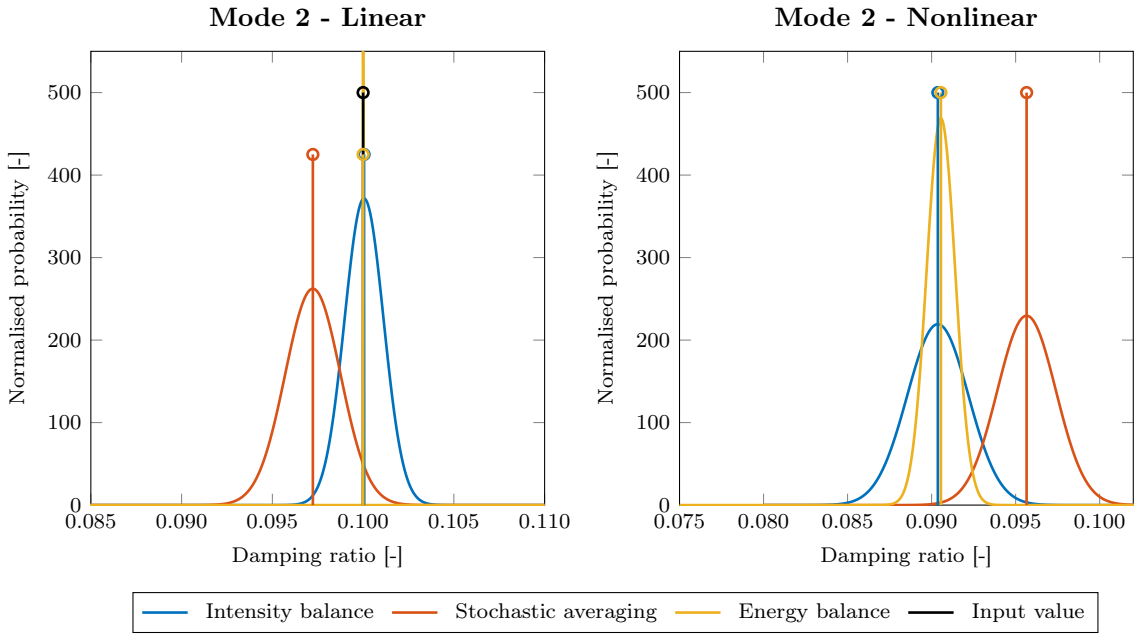


Figure 2: Equivalent linear damping estimates (normalised probability distributions) of mode 2 in the two cases; (left) purely linear damping, (right) friction-induced nonlinear damping with a small addition of linear damping.

5.2 Comparison and discussion of OMA estimates with ELD estimates

As for the ELD estimates, Fig. 3 shows plots of normalised probability distributions of the OMA-identified linear damping estimates related to the second mode while considering both the linear and the nonlinear case respectively. Regarding the former case, the mean of the OMA-identified estimates are calculated quite similar to the input value (i.e., the difference was found to be within the range of 0-2 ‰) indicating almost negligible bias for the OMA-identified estimates. Comparing the variance of the OMA-based damping ratios, the two methods, i.e., the pLSCF and the AR-PR, resulted in almost identical CoV's (Table 2). Likewise the linear case, the OMA methods applied also for the nonlinear case led to damping ratios with almost identical mean and variance (i.e., CoV) estimates, the latter, is though found higher compared to the linear case. Comparing the CoV's of the two ELD estimation methods, i.e., the methods based on intensity and energy balancing, the same quantifiable increase in variance is found from the linear case to the nonlinear. This observation might indicate a variation of the actual amount of damping between simulations in the nonlinear case, stemming from variation of the external excitation from simulation to simulation generating different responses, although almost with identical intensities, i.e., variances. When the responses are slightly different, the damping might also be slightly different when dealing with amplitude dependent damping. However, it is important to mention that the increase, and the similarity in the increase, might simply come from the fact that nonlinearity is introduced, and that the methods might be effected in the same manner.

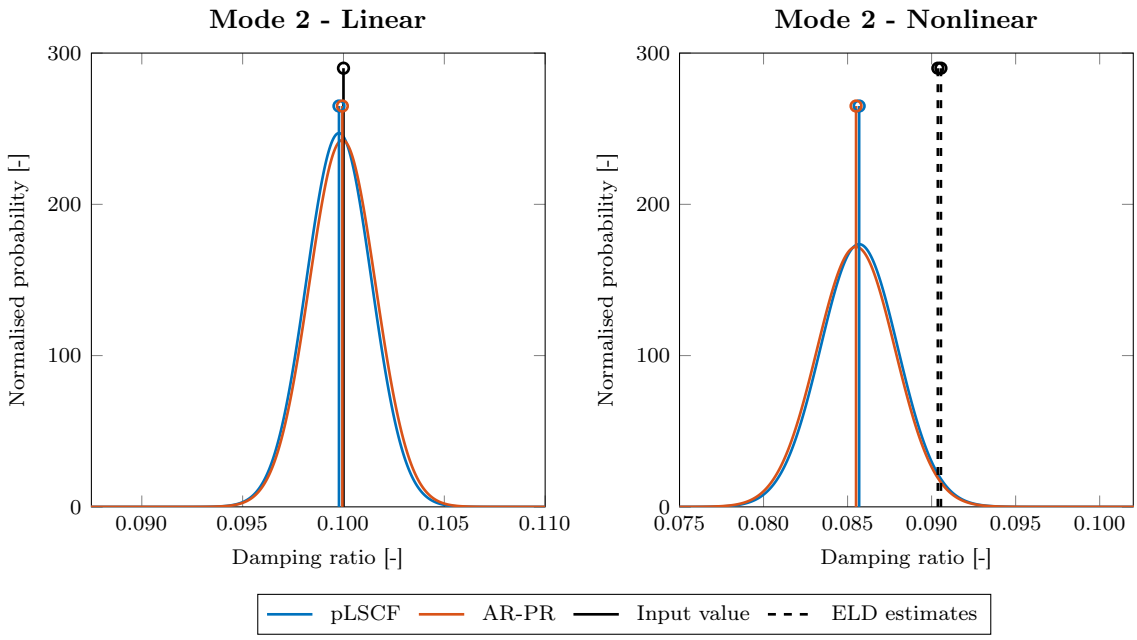


Figure 3: OMA damping estimates of mode 2 in the two cases; (left) purely linear damping, (right) friction-induced nonlinear damping with a small addition of linear damping. Including comparison with ELD estimates in the nonlinear case.

Finally, as can be seen in Table 3, the mean values of OMA-based damping estimates were calculated slightly lower (approximately 5-6%) than the ELD estimates. Such a difference indicates that the OMA methods underestimate the damping of the system with the friction-induced nonlinear damping.

Case	Assessment entity	Intensity balance	Stochastic averaging	Energy balance	pLSCF	AR-PR
Linear	$\bar{\zeta}_2$ [%]	**10.0**	9.72	**10.0**	**9.98**	**9.99**
	$CoV(\zeta_2)$ [%]	1.07	1.56	0.00	1.62	1.65
Nonlinear	$\bar{\zeta}_{eq(2)}$ [%]	**9.04**	9.57	**9.06**	**8.57**	**8.55**
	$CoV(\zeta_{eq(2)})$ [%]	2.01	1.82	0.940	2.68	2.71

Table 2: Mean values of equivalent linear damping and OMA linear damping estimates of mode 2 in the two cases; (i) purely linear damping, (ii) friction-induced nonlinear damping with a small addition of linear damping.

6 Conclusion

The purpose of this study was to assess the damping estimation performance of OMA-based methods on structural systems in random vibrations experiencing friction-induced nonlinear damping. A Coulomb-type friction mechanism, appropriately introduced at the top of a finite element model of a simple T-shaped prototype steel structure, ensured a numerical testbed for the investigation. Two OMA based methods were comparatively assessed in terms of their related damping estimation potential by comparing their linear damping estimates with theoretically derived estimates of equivalent linear damping. This assessment was based on 500 Monte Carlo friction-induced nonlinear numerical simulations and three different theoretically derived methods were employed for estimation of equivalent linear damping. The study mainly revealed the following.

(i) From an assessment of the theoretically derived estimates of equivalent linear damping estimates, two methods were found to give similar estimates and to be applicable as a reference for the OMA-based methods, in the particular case with damping ratios of approximately 9%.

(ii) From employment of the two OMA methods for estimation of linear damping of the T-shaped structure, both methods were found to provide almost identical results. Furthermore, the OMA-based estimates showed no bias when the OMA methods were applied to responses from linear simulations where the damping ratios are known in advance.

(iii) The two methods for estimation of equivalent linear damping that were found applicable for the comparative study and the two OMA methods showed higher dispersion in their respective estimates when employed to simulated responses of the structure with friction-induced nonlinear damping compared to the case of linear proportional damping.

(iv) Comparison between the equivalent linear damping estimations with the OMA-based ones revealed a difference of 5-6% indicating that the OMA methods underestimate the system's damping, when the latter is of the friction-induced nonlinear kind.

The underestimation of the damping by the OMA methods together with the effect of including a stiffness component in the friction-induced nonlinearity, which was not included in the present study, calls for additional research to fully comprehend the implications for OMA estimates when friction, and friction like phenomena as hysteresis, influence the dynamic response of a structure.

Acknowledgements

The authors acknowledge the funding received from Centre for Oil and Gas - DTU/Danish Hydrocarbon Research and Technology Centre (DHRTC).

References

[1] F. Chen, J. Liu, Y. Chen, *Flutter analysis of an airfoil with nonlinear damping using equivalent linearization*, Chinese Journal of Aeronautics 27 (1) (2014) 59–64.

[2] P. J. Murtagh, B. Basu, *Identification of equivalent modal damping for a wind turbine at standstill using Fourier and wavelet analysis*, Proceedings of the Institution of Mechanical Engineers, Part K: Journal of Multi-body Dynamics 221 (4) (2007) 577–589.

[3] E. Zhang, R. Pintelon, P. Guillaume, *Modal Identification Using OMA Techniques: Nonlinearity Effect*, Shock and Vibration (2015).

[4] A. Bajrić, J. Høgsberg, F. Rüdinger, *Evaluation of damping estimates by automated Operational Modal Analysis for offshore wind turbine tower vibrations*, Renewable Energy 116 (2018) 153 – 163.

[5] T. Friis, A. Orfanos, E. Katsanos, S. Amador, R. Brincker, *Effect of friction-induced nonlinearity on OMA-identified dynamic characteristics of offshore platform models*, Rotating Machinery, Vibro-Acoustics & Laser Vibrometry. Conference Proceedings of the Society for Experimental Mechanics Series 7 (15) (2018).

[6] T. Friis, E. Katsanos, S. Amador, R. Brincker, *Damping estimation of friction systems in random vibrations*, Nonlinear Dynamics Conference Proceedings of the Society for Experimental Mechanics Series 1 (14) (2018).

[7] R. Brincker, C. Ventura, Introduction to Operational Modal Analysis, Wiley, 2015.

[8] D. Iourtchenko, M. Dimentberg, *In-service identification of non-linear damping from measured random vibration*, Journal of Sound and Vibration 255 (3) (2002) 549 – 554.

[9] J. Roberts, P. Spanos, *Stochastic averaging: An approximate method of solving random vibration problems*, International Journal of Non-Linear Mechanics 21 (2) (1986) 111 – 134.

[10] J.-W. Liang, B. F. Feeny, *Balancing energy to estimate damping parameters in forced oscillators*, Journal of Sound and Vibration 295 (3) (2006) 988 – 998.

[11] J.-W. Liang, *Damping estimation via energy-dissipation method*, Journal of Sound Vibration 307 (2007) 349 – 364.

[12] B. F. Feeny, *Estimating damping parameters in multi-degree-of-freedom vibration systems by balancing energy*, Journal of Vibration and Acoustics, Transactions of the ASME 131 (4) (2009).

[13] H. Vold, J. Kundrat, G. T. Rocklin, R. Russell, *A Multi-Input Modal Estimation Algorithm for Mini-Computers*, SAE Technical Paper (1982).

[14] H. Vold, *The Numerical Implementation of a Multi-Input Modal Estimation Method for Mini-Computers*, Proceedings of 1st International Modal Analysis Conference (1982).

[15] L. Ljung, System identification: Theory for the user, Prentice-Hall, 1987.

[16] A. C. Harvey, Time series models, Philip Allan Publishers Ltd., 1981.

[17] S. M. Pandit, S. M. Wu, Time series and system analysis with applications, John Wiley & Sons, 1983.

[18] J. P. Norton, An introduction to identification, Academic Press, 1986.

[19] E. Orlowitz, A. Brandt, *Influence of Noise in Correlation Function Estimates for Operational Modal Analysis*, Proceedings of the 36th International Modal analysis conference, Society of Experimental Mechanics (2018).

[20] M. Tarpø, P. Olsen, S. Amador, M. Juul, R. Brincker, *On minimizing the influence of the noise tail of correlation functions in operational modal analysis*, Procedia Engineering 199 (2017) 1038–1043.

[21] P. Guillaume, P. Verboven, S. Vanlanduit, H. V. der Auweraer, B. Peeters, *A poly-reference implementation of the least-squares complex frequency domain-estimator*, In Proceedings of the 21st International Modal Analysis Conference (2003).

[22] B. Peeters, H. Van der Auweraer, P. Guillaume, J. Leuridan, *The PolyMAX frequency-domain method: a new standard for modal parameter estimation?*, Shock and Vibration 11 (3-4) (2004) 395–409.

[23] B. Peeters, H. Van der Auweraer, *PolyMAX: A revolution in operational modal analysis*, Proceedings of the 1st International Operational Modal Analysis Conference (2005).

[24] C. Rainieri, G. Fabbrocino, Operational Modal Analysis of Civil Engineering Structures, Springer, 2014.

[25] M. El-kafafy, T. De Troyer, B. Peeters, P. Guillaume, *Fast maximum-likelihood identification of modal parameters with uncertainty intervals: A modal model-based formulation*, Mechanical Systems and Signal Processing 37 (1-2) (2013) 422–439.

[26] J. O'Callahan, *System equivalent reduction and expansion process*, Proceedings of the 7th International Modal analysis conference, Society of Experimental Mechanics (1989) 29–37.

[27] L.-Y. Lu, L.-L. Chung, L.-Y. Wu, G.-L. Lin, *Dynamic analysis of structures with friction devices using discrete-time state-space formulation*, Computers & Structures 84 (15–16) (2006) 1049 – 1071.

Approaches to the remote mapping of vehicle noise sources in a reverberant environment

A. Papaioannou[1], S. Elliott[1], J. Cheer[1]
[1] Institute of Sound and Vibration Research
University Road, SO17 1BJ, Southampton, UK
e-mail: **A.Papaioannou@soton.ac.uk**

Abstract
In this paper, new methods for the remote acoustic source mapping of vehicle noise sources are considered. This work initially considers the effect of a wall reflection on conventional methods of processing the signals from a remote microphone array. The use of alternative array processing techniques to discriminate against the reflections are then considered and used, to produce a 'heatmap' of the array response as a noise source is moved around within the chamber. In a first step, an inverse impedance weighting strategy is considered, to distinguish the desired physical source location from the one created due to the reflections. In a second step, additional restrictions are also taken into account such as the ability of the microphone array to suppress the high levels for sources close to the microphones and an optimised weighting strategy is introduced and applied.

1 Introduction

The exterior sound emission of a vehicle is an increasingly important criterion for the homologation of road vehicles. The latest limit value of 74 dB(A) is already a major challenge for car manufacturers and an even lower limit of 68 dB(A) is in plan for the near future. Therefore, measurement of the drive-by noise of vehicles is important to ensure lower sound levels for people living close to roads. Until recently, it has been measured outdoors according to ISO – 362-1:2015, [1]. However, drive-by noise can now be estimated in a laboratory environment, with a stationary vehicle on a rolling road, [2], by processing and identifying the individual sources of noise on the vehicle and then synthesising the pressures that would be measured in a drive-by test, [3-4]. Within this method, the tire-road noise is separately energetically added to the powertrain noise and the final result is compared to the outdoor measurement, [5-6].

The indoor estimation of pass-by noise has advantages over outdoor measurements in terms of the repeatability and robustness of the measurements. However, the use of chambers with imperfectly anechoic walls can distort the results in certain frequency bands. With the aim of overcoming this limitation, new approaches to the mapping of the vehicle pass-by noise sources in a reverberant environment are developed in this paper, utilising optimal beamforming.

2 Formulation

As a first step, we may assume that a specific noise source on the vehicle can be represented by a compact monopole source radiating omnidirectionally. If a microphone is positioned a distance of r from the source, the pressure is, [7],

$$p_i(r) = Z_i(r)q = j\omega\rho_0 q\frac{e^{-jkr}}{4\pi r} \quad \text{(Pa)} \tag{1}$$

Where Z_i is the transfer impedance and q is the source strength.

Assuming an array of 41 microphones positioned on a line 7.5 m away from the source and a rigid wall 3 meters behind it, then the contributions due to the various reflections from the wall could be modelled as an image source, placed 13.5 meters away from the linear array, as shown in Figure 1.

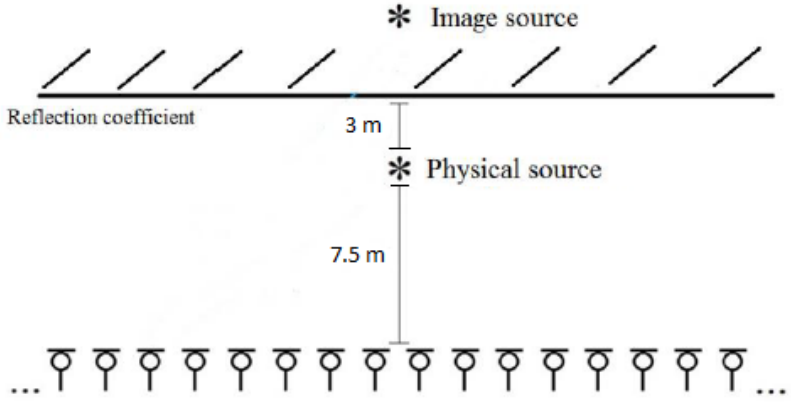


Figure 1: Environment of pass-by noise measurement with a rigid wall

The array output due to the source at each point is initially calculated by adding the contributions from each microphone together, so that

$$\mathrm{p(x)} = \frac{1}{41}\sum_{\mathrm{i=1}}^{41} \mathrm{p_i(x)} \quad \text{(Pa)} \tag{2}$$

This uniform weighting corresponds to that of a broadside array using a delay and sum beamformer with a far-field directivity pointing towards the source. The pressure can also be expressed in terms of the Sound Pressure Level (SPL), which is given as

$$\mathrm{SPL(x)} = 20\log_{10}\left(\frac{\mathrm{p_{rms}(x)}}{\mathrm{p_{ref}}}\right) \quad \text{(dB)} \tag{3}$$

So that SPL is independent of the phase of *p(x)* and hence the frequency. In this case, p_{ref} is chosen to be the array output pressure when the source is positioned at the physical source location in Figure 1. By moving the source around the room, a heatmap in terms of the sound pressure level at each point can be created, as shown in Figure 2. From this plot, it can be seen that the uniform linear array generates a high estimate of the SPL in the near field of the array.

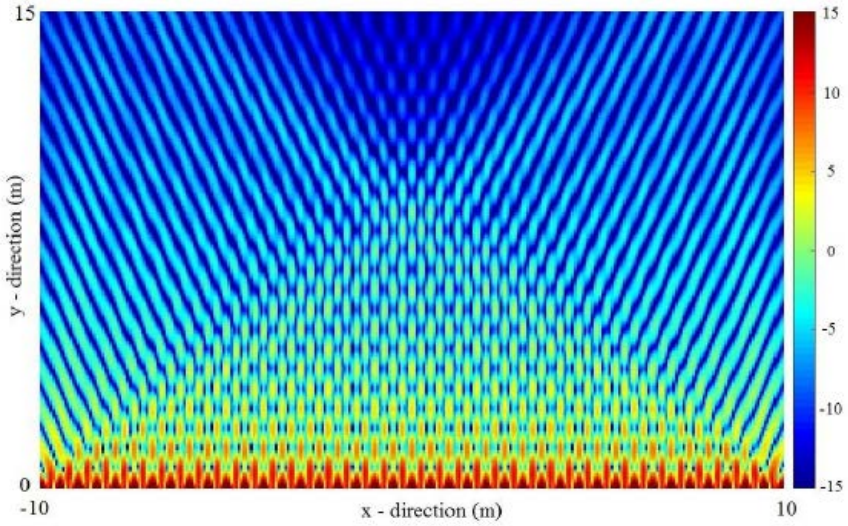


Figure 2: Heatmap of the sound pressure level due to a monopole source measured using a 41 – microphone array (1 kHz) and the uniform weighting method

To provide further insight into those results, Figure 3 shows the Sound Pressure Level estimated along the x = 0 axis, moving away from the array towards the physical source location at x = 7.5 m and the image source at 13.5 m for various working frequencies.

It can be seen that the response of the array to the image source is approximately 10 dB less than the one to the physical source, and hence the image source will significantly alter the estimate of the source strength. It is also shown in Figure 3 that the weighting strategy offers poor results at very low frequencies below around 100 Hz and only delivers 4 and 8 dB level difference between the physical and image source points at 50 and 100 Hz respectively. To overcome these limitations, the next step is to apply appropriate weighting to the microphones in order to achieve further discrimination against the image source strength and points close to the array.

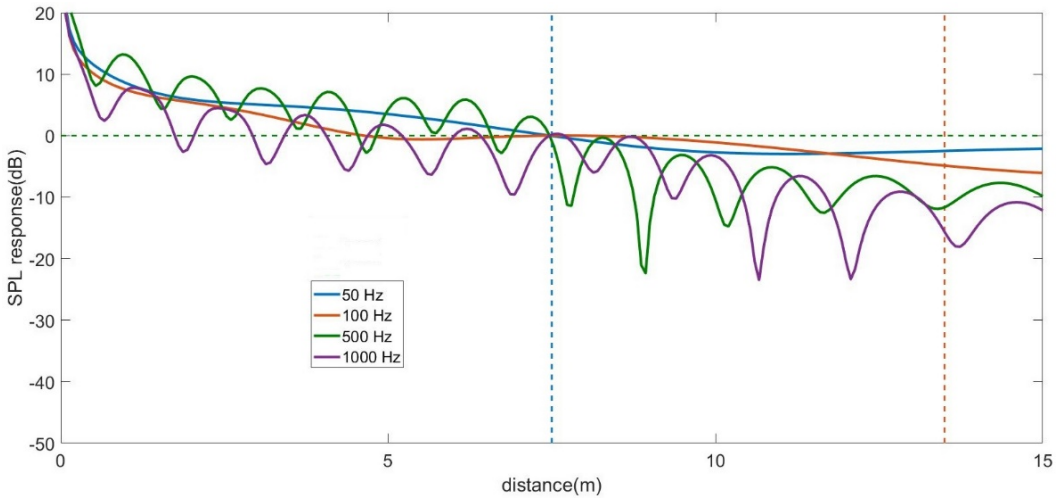


Figure 3. Sound pressure level at x = 0 m over distance in the y – direction using the uniform weighting for f = 50, 100, 500, 1000 Hz

3 Inverse impedance weighting synthesis

A simple method of weighting the microphones would be to use the inverse of the impedance measured when the source is placed at y = 7.5 m, x = 0 m. The heatmap is then constrained to deliver unity gain for the point where the physical source is placed. The weights are, thus, equal to

$$w_i = \frac{1}{Z_{i,y=7.5,x=0}} \tag{4}$$

Where $Z_{i,y=7.5,x=0}$ is the impedance between the i-th microphone and the physical source position. The overall output of the array is then equal to the sum of the weighted pressures

$$p(x) = \frac{1}{41}\sum_{i=1}^{41} w_i p_i(x) \quad \text{(Pa)} \tag{5}$$

Since all terms, $w_i p_i(x)$, in this symmetry are equal to unity when the source is at the reference position, x = 0, y = 7.5 m, this array processing strategy is similar to the one used in the far-field delay-and-sum approach. As a result, the heatmap in terms of the sound pressure level is transformed, as shown in Figure 5. From this plot, it can be seen that the physical source SPL is at 0 dB, as enforced, and the level elsewhere is significantly attenuated compared to the uniformally weighted array results in Figure 4. For reference, the amplitude and the phase of the array weights used to produce the heatmap in Figure 5 are shown in Figure 6(a), (b). From the plots, it can be seen that the inverse impedance weighting scheme results in array shading that compensates for the path length differences between the physical source and each of the array microphones.

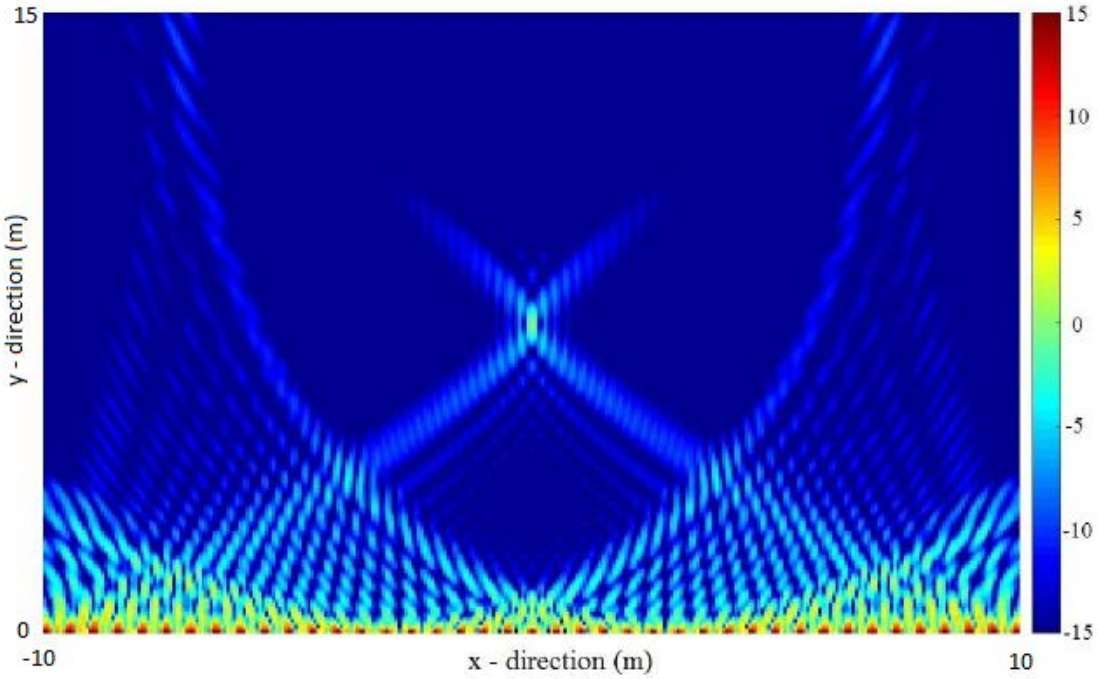


Figure 4. Heatmap in terms of the sound pressure level for a monopole source with a 41 – microphone array (1 kHz) using the inverse impedance weighting

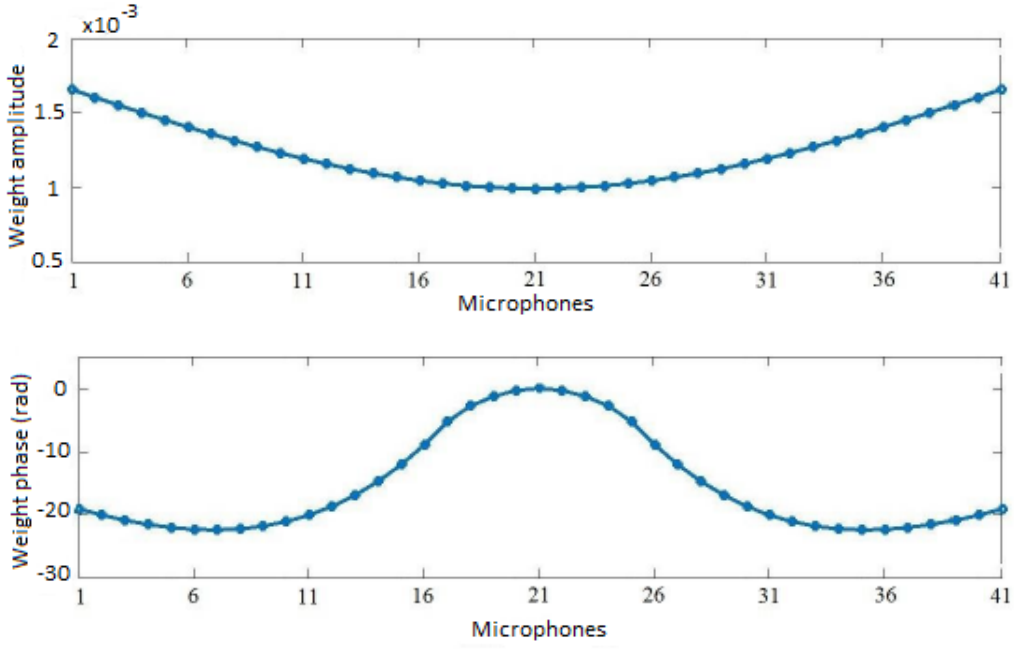


Figure 5(a), (b). Amplitude and phase of the inverse impedance weights

To provide a clear picture of the results presented in Figure 5, the sound pressure level is again plotted along y-axis at x = 0 m at four discrete frequencies. From these results, it can be seen that, at 1 kHz, the weighting provides a 23.5 dB level difference between the physical and the image source (assuming that there is no noise absorption provided by the rigid wall), while retaining the physical source level at unity gain. However, the level is very high (up to 30 dB) when the source is placed very close to the array. The method is also limited at low frequencies around 100 Hz and only delivers a level of difference of 3 and 9 dB between the physical and image source points at 50 and 100 Hz, as shown in Figure 6.

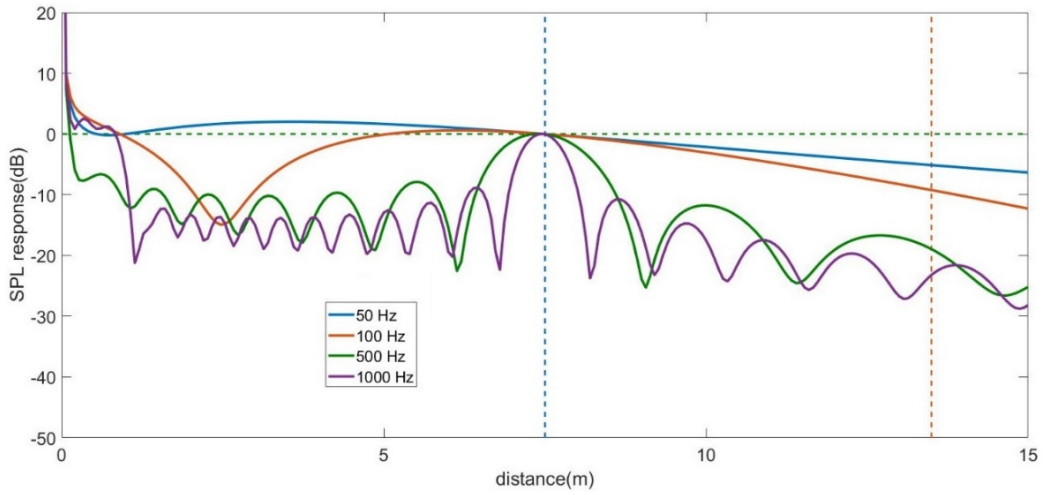


Figure 6. Sound pressure level at x = 0 m over distance in the y – direction using the inverse impedance weighting for f = 50, 100, 500, 1000 Hz

4 Optimised weighting synthesis

In an attempt to overcome the limitations highlighted on the inverse impedance weights, an alternative strategy that directly optimises the array weights will be presented in this section. In this case, the microphone array weights are specified by performing a linear optimisation of the weights w_i subject to three constraints:

- The weights provide unity gain for the physical source position i.e. $p_{y=7.5,x=0} = \frac{1}{41}\sum_{i=1}^{41} w_i p_i = 1$
- The weights provide zero gain for the image source position i.e. $p_{y=13.5,x=0} = \frac{1}{41}\sum_{i=1}^{41} w_i p_i = 0$
- The weights are kept to the minimum magnitude possible in order to discriminate against the positions close to the microphone array i.e. $min \sum_{i=1}^{41} |w_i|$

The weight calculation is split into two parallel optimisation problems in Matlab. The first one solves the least-squares curve fitting problem of the form $min \frac{1}{2}\left[\frac{1}{41}\sum_{i=1}^{41} w_i p_i - 1\right]_2^2$ subject to $\frac{1}{41}\sum_{i=1}^{41} w_i p_i = 0$. The second one adds the supplementary constraint $min \sum_{i=1}^{41} |w_i|$ by setting numerical bounds on each w_i. The function used utilises the method of the Lagrange multipliers which is a strategy for finding the local maxima and minima of a function subject to equality constraints [44]. The only prerequisite is that the used functions have continuous first partial derivatives as is the case in the considered problem..

To assess the performance of this weights optimisation process, the total pressure at each source point is again estimated using Equation 5, but with the calculated w_i. The heatmap in terms of the sound pressure level is shown in Figure 7 and the corresponding amplitude and phase of the optimised array weights are shown in Figure 10(a) and 10(b) respectively. It is interesting to see from both the amplitudes of the array weights and the heatmap in Figure 7 that this optimisation method effectively creates two separate arrays at either end of the microphone array, both focused on the physical source location. It can be seen from Figure 7 that this results in an effective triangular – type array behaviour.

To provide a consistent analysis of this array processing method, the sound pressure level is plotted along the y-axis at x = 0 m in Figure 9 with lines indicating the positions where the physical and image sources are located. At 1 kHz, it can be seen from Figure 9 that the weighting creates a 43.1 dB level difference between the physical and the image source (assuming there is no sound absorption by the rigid wall), while retaining the physical source level slightly lower than unity gain (-0.6 dB). As a result, the optimized weighting enhances the level difference between the two source points by about 20 dB compared to the inverse impedance weighting strategy. However, the optimized weighting also discriminates against the source points close to the microphone array reducing the level from 30 dB to -18 dB. In principal, there would be no signal for a source at the image location if the optimization problem

above was satisfied, but the finite level difference illustrates that the optimisation problem does not have a solution, particularly at low frequencies, as shown in Figure 9. In particular, it can be seen that the weighting strategy offers poor results in very low frequencies only delivering 4 to 8 dB level difference between the physical and image source points at 50 and 100 Hz.

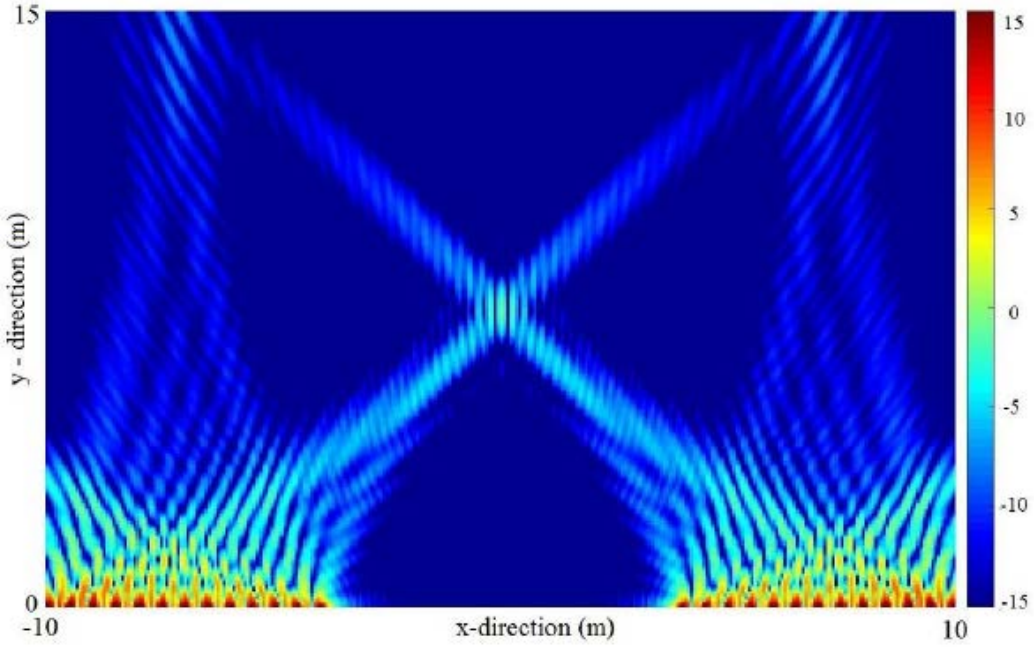


Figure 7. Heatmap in terms of the sound pressure level for a monopole source with a 41 – microphone array (1 kHz) using the optimised weighting

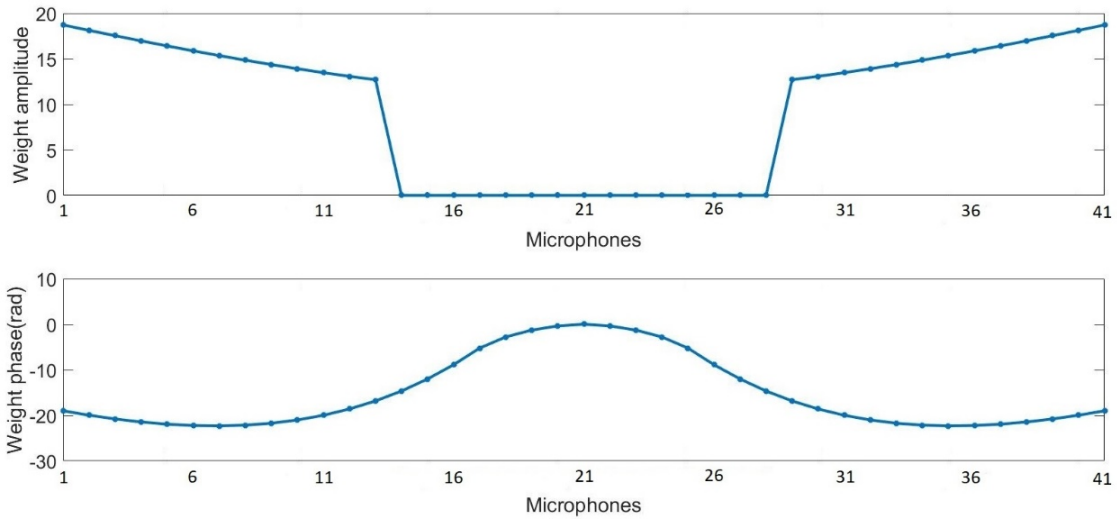


Figure 8(a), (b). Amplitude and phase of the optimised weights

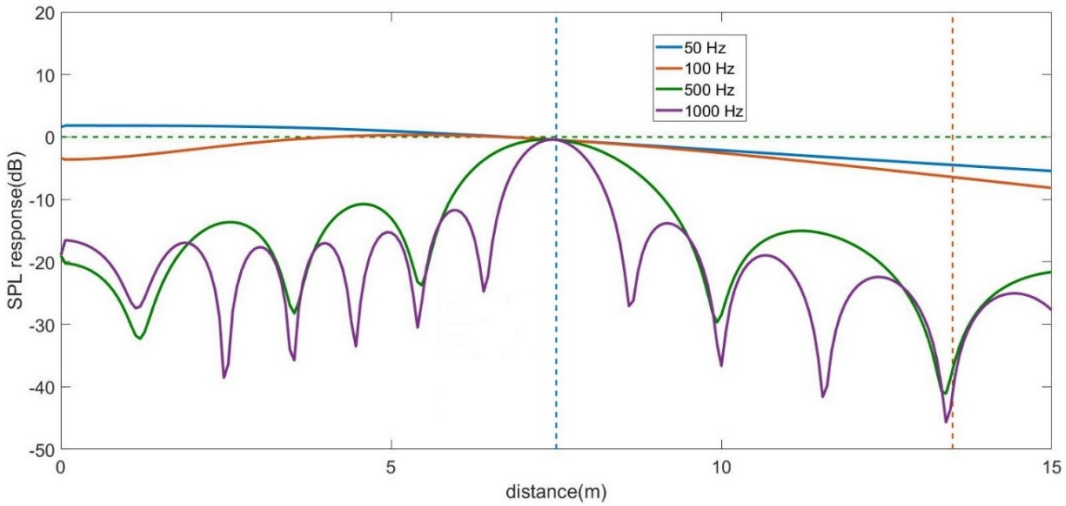


Figure 9. Sound pressure level at x = 0 m over distance in the y – direction using the optimised weighting for f = 50, 100, 500, 1000 Hz

To provide a clear comparison between the three considered array weighting methods, Figure 13 shows the difference between the physical and image source strengths for the three different weighting strategies, which correspond to the discrimination that the array provides against the image source. It should be noted that in contrast to the uniform array weighting, the inverse impedance and optimised weighting assume a known position for the image source, and so the results will be degraded if the position of the physical source with respect to the wall is not exactly where it is assumed to be in Figure 1. Nevertheless, at frequencies above 100 Hz, the inverse impedance method achieves a significant performance increase, with a 10 dB discrimination between 2 and 10 kHz, whilst the optimised weighting achieves a performance increase of about 25 dB over the same frequency range.

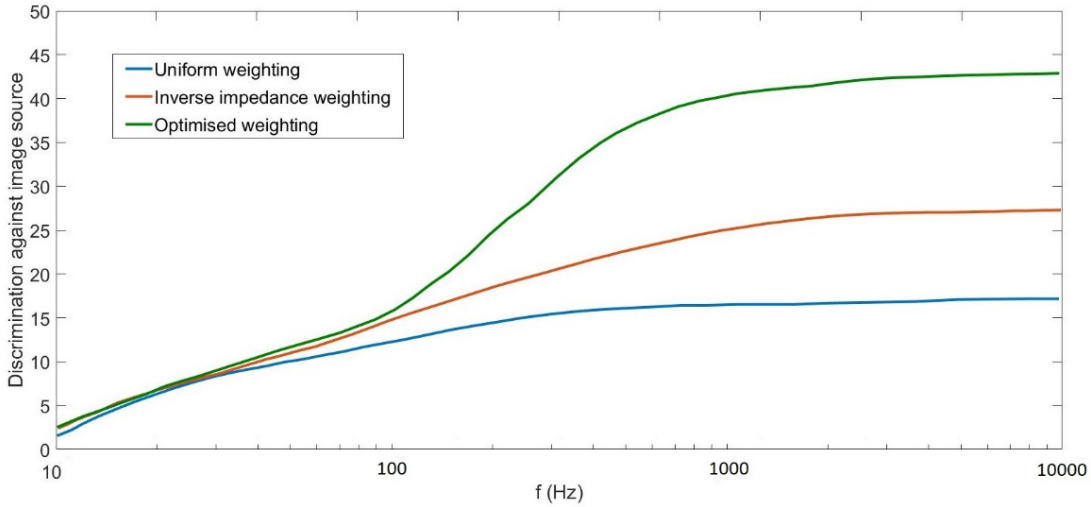


Figure 10: Difference between the level at the assumed image source and that at the physical source for the 3 different array weighting methods

5 Conclusions

In this paper, new approaches to the acoustic source identification for the synthesis of vehicle pass-by noise sources have been considered. The effect of a wall reflection on conventional methods of processing the signals from the far field microphone array has been examined and two alternative array processing

techniques to discriminate against the reflections are considered. A ‘heatmap’ of the array response as a noise source is moved around within the measurement chamber has then been produced, while two different weighting strategies are considered to distinguish the desired physical source location from the one created due to the reflections. Additional restrictions are also taken into account such as the ability of the microphone array to suppress the physically high sound pressure levels at the points close to the microphones, therefore, an optimised weighting strategy is introduced and applied.

Acknowledgements

The authors gratefully acknowledge the European Commission for its support of the Marie Sklodowska Curie program through the ETN PBNv2 project (GA 721615).

References

[1] *Measurement of noise emitted by accelerating road vehicles -- Engineering method -- Part 1: M and N categories* (ISO362-1:2015).

[2] *Measurement of noise emitted by accelerating road vehicles -- Engineering method -- Part 1: M and N categories* (ISO362-1:2016)

[3] A. Schuhmacher, Y. Shirahashi, M. Hirayama, Y. Ryu, *Indoor pass-by noise contribution analysis using source path contribution concept*, Proceedings of the 2012 International Conference on Modal Analysis Noise and Vibration Engineering (ISMA 2012), Leuven, pp. 3697-3709.

[4] U. Kim, M. Maunder, D. Mawdsley, P. Grant, *Simulation Method to meet new pass-by noise requirements*, Sound & Vibration/September 2015

[5] M. Kramer, P. Brandstatt, A. Ickinger, *Comparison of pass-by noise from real track and simulated measurement at the roller test bench*, Inter Noise 2016, Hamburg

[6] S. Guidati, R. Sottek, K. Genuit, *Simulated pass-by in small rooms using noise synthesis technology*, CFA/DAGA 2004, Strasbourg

[7] F. Fahy, D. Thompson, *Fundamentals of Sound and Vibration: Second Edition*, CRC Press, 2015

Model-based acoustic characterisation of muffler components and extrapolation to inhomogeneous thermal conditions

M. H. Alkmim[1], **J. Cuenca**[1], **L. de Ryck**[1], **P. Göransson**[2]
[1] Siemens Industry Software, Interleuvenlaan 68, B-3001 Leuven, Belgium
e-mail: **mansour.alkmim@siemens.com**

[2] Marcus Wallenberg Laboratory for Sound and Vibration Research, KTH Royal Institute of Technology, Teknikringen 8, SE-10044, Stockholm, Sweden

Abstract
A methodology for evaluating the acoustic behaviour of two-port inhomogeneous media in experimentally unavailable thermal conditions is proposed. The method consists of an inverse estimation of the geometrical and material properties of the object at room temperature followed by a forced thermal input. The properties of interest for the inverse estimation are the spatially-varying cross-section and/or bulk properties. The underlying model relies on a transfer matrix approach, allowing for a representation of spatially inhomogeneous objects as piece-wise equivalent homogeneous fluids, while ensuring continuity conditions between successive elements. A model of non-stationary thermal conduction is used as a first approximation, where an integral formulation accounts for the cumulative effect of multiple homogeneous elements. In order to evaluate the validity of the extrapolation, a validation against a fully numerical simulation is presented in two cases, namely a simple expansion chamber and a complex muffler.

1 Introduction

Mufflers or silencers are commonly used as noise reduction devices for gases transmitted through exhaust pipes. Understanding their properties and behaviour is essential in order to achieve better designs in terms of noise perception and weight reduction. The noise radiated from a muffler arises from three main mechanisms, namely the pulsated pressure waves from the periodic combustion process, the turbulent flow of exhaust gases and structural vibrations, partially caused by the other two sources [1].

A standard procedure to characterize mufflers as acoustic filters is to measure their transmission response from a known acoustic source. The impedance tube setup [2] is particularly attractive as it considers a plane wave approximation, reducing the problem to one spatial dimension. Such tests are well-controlled and repeatable in a limited frequency range; however, these do not represent the operational use of the tested system. Indeed, high-temperature flow of gases denser than air is common in car mufflers, for instance. As a consequence, a major limitation in current laboratory testing is that room temperature sound transmission loss measurements are not representative of most real systems.

Cases where high temperature gradients are encountered such as in automotive mufflers, propulsion and power generating systems benefit from the consideration of thermal effects in the design stage; despite the complexity and cost of such experimental setup. Since the works of Kapur et al. [3], Munjal and Prasad [4] and Peat [5], the study of analytical solutions for plane waves propagation with temperature gradient in straight ducts have been investigated. In most cases, the solutions are restricted to small temperature gradients, no mean

flow, small Mach number, among others. To close this gap, Sujith et al. [6, 7] proposed an analytical solution for the sound propagation in ducts under more general conditions by applying suitable transformations to the wave equation. Although the solution therein is valid only for small mean Mach number, the analytical expressions are developed by only considering linear and exponential temperature profiles. Subsequently, by using the analytical solution obtained previously, Sujith [8] derived the transfer matrix method with the axial mean temperature gradient effect included. Later, a correction of inconsistencies therein was proposed by Howard [9] in which a validation against a numerical solution was conducted. Although some progress was made for analytical solutions, its applications are still restricted to regular geometries and boundary conditions. Moreover, real mufflers can feature complex geometries where a simple linear temperature gradient is not enough to predict their behaviour.

As a first approximation, many mufflers can be conveniently described as series of duct components with different cross sections. By assuming plane waves propagating in a rigid-walled tube filled with an inviscid fluid, the so-called transfer matrix method (TMM) [1] conveniently relates the state variables – pressure and flow – from the filter inlet to its outlet. Moreover, the TMM parameters are not affected by connections to external elements downstream or upstream as long as these can be assumed linear [10]. This is advantageous to design mufflers as multiple expansion chambers where the elemental four-pole matrices can be multiplied sequentially to obtain an overall four-pole matrix for the whole system.

This paper addresses the difficulty of performing STL measurements in operational conditions by means of a model-based procedure relying on room temperature STL measurements. The proposed approach consists of an inverse estimation of the geometrical and material model parameters of a two-port inhomogeneous medium, followed by a simulation of its acoustic behaviour in experimentally unavailable thermal conditions. The model relies on the TMM, allowing for a piece-wise representation of spatial inhomogeneity and ensuring continuity conditions between successive elements. The cost function for the inverse estimation procedure is defined as a 2-norm distance between a measured sound transmission loss and its semi-analytical TMM counterpart. A complicating aspect is the fact that such an inverse estimation procedure is subjected to multiple local minima, in particular due to resonances. A recently proposed methodology [11] is used to overcome such local minima. A paper at this conference details its use in the case of muffler components [12].

The properties of interest for the inverse estimation are the spatially-varying cross-section and/or bulk properties of the medium (flow resistivity, porosity, tortuosity, ...), allowing to represent a variety of one-dimensional objects which can include perforated elements and rigid porous elements which can be modelled as equivalent-fluids. In this paper, however, efforts are concentrated in investigating the temperature extrapolation, hence, only examples considering air as a homogeneous medium are considered, the purpose of the inverse estimation being to identify the geometry of the muffler.

The extrapolation of the acoustical model from room temperature conditions to a forced thermal regime is performed under the assumption that the effects of temperature in the acoustic behaviour arise as a variation in the speed of sound. The temperature profiles can take into account different thermal conditions such as conduction, or a superposition of conduction and convection effects. Two application examples are provided, the goal being to evaluate the validity of the semi-analytical model with temperature extrapolation against a fully numerical simulation in cases including expansion chambers and mufflers.

2 Methodology

2.1 Transfer matrix method

The classical technique to relate the state variables from the inlet and outlet under plane wave assumption is the transfer matrix method (TMM). The TMM or four-pole representation is a convenient way of evaluating acoustical performance because only the four-pole parameters are needed in the analysis of a mufflers as it can readily provide a value for the normal Sound Transmission Loss (STL).

Adopting the notation showing in Figure 1, the transfer matrix formalism using a pressure-flow formulation is given by [1]

$$\begin{bmatrix} p_{\text{in}} \\ S_{\text{in}} v_{\text{in}} \end{bmatrix} = \mathbf{T} \begin{bmatrix} p_{\text{out}} \\ S_{\text{out}} v_{\text{out}} \end{bmatrix}, \tag{1}$$

where p_{in} and p_{out} are the acoustic pressure at the inlet and outlet respectively, v_{in} and v_{out} are the acoustic particle velocity at the inlet and outlet respectively and S_{in} and S_{out} are the cross-sectional area of the inlet (upstream) and outlet (downstream) pipe respectively.

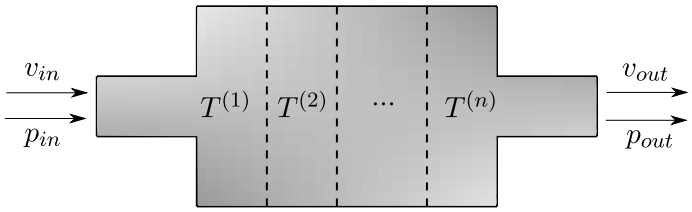


Figure 1: TMM of a multi-layered two-port component using pressure-flow formulation.

The transfer matrix of a multi-layered two-port component can be expressed as

$$\mathbf{T}(\omega) = \prod_{n=1}^{N} \mathbf{T}_n(\omega, \mathbf{x}_n), \tag{2}$$

where the properties of layer n are

$$\mathbf{x}_n = \{L_n, S_n, k_n, Z_n\}, \tag{3}$$

where L_n and S_n are the layer length and cross sectional area respectively. The homogeneous media properties are defined by its wave number k_n and its impedance Z_n. For the case of a homogeneous medium filled with air, both parameters are readily available and can be obtained by the expressions $Z_{air} = \rho_{air} c$ and $k_{air}(\omega) = \omega/c$ where c is the speed of sound and ω the angular frequency. Alternatively, an equivalent fluid model can be used to describe other mediums such as rigid porous and perforated plates. The Johnson-Champoux-Allard (JCA) [13, 14] is a well established phenomenological model that could be used in this case [12].

The transfer matrix of layer n is given by

$$\mathbf{T}_n(\omega, \mathbf{x}_n) = \begin{bmatrix} \cos(k_n L_n) & \dfrac{-Z_n}{iS_n} \sin(k_n L_n) \\ \dfrac{iS_n}{Z_n} \sin(k_n L_n) & \cos(k_n L_n) \end{bmatrix}. \tag{4}$$

The sound transmission loss of the multi-layer component can be obtained as [1]

$$\text{STL} = 20 \log_{10} \left(\frac{1}{2} \left| T_{11} + T_{12} \frac{S_{\text{out}}}{Z_{\text{out}}} + T_{21} \frac{Z_{\text{in}}}{S_{\text{in}}} + T_{22} \frac{Z_{\text{in}}}{Z_{\text{out}}} \frac{S_{\text{out}}}{S_{\text{in}}} \right| \right). \tag{5}$$

2.2 Inverse estimation methodology

The parameter search is formulated as a minimisation problem [15]

$$\min f_{\text{obj}}(\mathbf{x}) = \sum_m |\text{STL}(\mathbf{x}, \omega_m) - \text{STL}_0(\mathbf{x}_0, \omega_m)|^2, \tag{6}$$

where $\mathbf{x_0}$ are the true parameters (accessible by direct measurement only) and $\mathbf{x}$ are the model parameters, including design variables of all layers. $\text{STL}_0(\mathbf{x}_0, \omega_m)$ denotes the measured sound transmission loss (STL) at frequency ω_m and $\text{STL}(\mathbf{x}, \omega_m)$ denotes the STL predicted by the model at frequency ω_m.

The systems under consideration are finite and involve geometrical and material discontinuities, which induce a non-monotonous sound transmission loss with respect to frequency, for instance due to resonances. This results in the problem (6) exhibiting local minima, attributed to the similarity of the response or STL for different combinations of the design variables. The simplest example of this is the similarity of the STL of an expansion chamber whose length is allowed to take values having a common factor. The inverse estimation problem is then solved for $\mathbf{x}$ using a recently developed stepwise optimisation framework [11]. A companion paper at this conference [12] includes an illustration of the method for the inverse estimation of material and geometrical properties using a sound transmission loss measurement setup.

2.3 Heat conduction model and extrapolation

A simplified model is here used for simulating the thermal behaviour of the system when exposed to a constant temperature at the inlet. The model consists of thermal conduction [16] in a multi-layered system whose components consist of equivalent fluid media. The purpose of such a simplified model is to carry out the extrapolation procedure proposed in this paper by means of a analytical description. Although also tractable by analytical means in the case of simple geometries, heat convection and radiation are not considered.

As a hypothesis, the thermal diffusivity of the multi-layer system $\delta(x)$ is assumed to vary slowly in x. The heat equation can thus be written as

$$\frac{\partial \tau}{\partial t}(x,t) = \delta(x) \frac{\partial^2 \tau}{\partial x^2}(x,t), \tag{7}$$

where τ is the temperature, x is the distance along the system and t is time. An imposed temperature is considered at the inlet, as

$$\tau(x = 0, t) = \tau_{\text{in}}. \tag{8}$$

Furthermore, room temperature is assumed at rest and at infinity, which may be expressed as

$$\tau(x, t = 0) = \tau(\infty, t) = \tau_{\text{atm}}. \tag{9}$$

The solution is obtained via the Laplace domain, leading to the temperature profile of a continuously layered medium in the form

$$\tau(x,t) = \tau_{\text{atm}} + (\tau_{\text{in}} - \tau_{\text{atm}}) \operatorname{erfc}\left(\frac{1}{2\sqrt{t}} \int_0^x \frac{d\xi}{\sqrt{\delta(\xi)}} \right). \tag{10}$$

This expression thus defines the temperature profile as a function of the input temperature, ambient temperature and the thermal diffusivity profile. It is worth noting that for a system consisting of a finite number of homogeneous layers, the thermal diffusivity is piecewise constant and the integral reduces to a step function. The obtained temperature profile is then introduced in the speed of sound in air as

$$c(x) = \sqrt{\gamma R \tau(x)}, \tag{11}$$

where $\gamma = 1.4$ is the ratio of specific heats and $R = 287\,\text{J}\cdot\text{K}^{-1}\text{mol}^{-1}$ is the gas constant.

3 Numerical validation

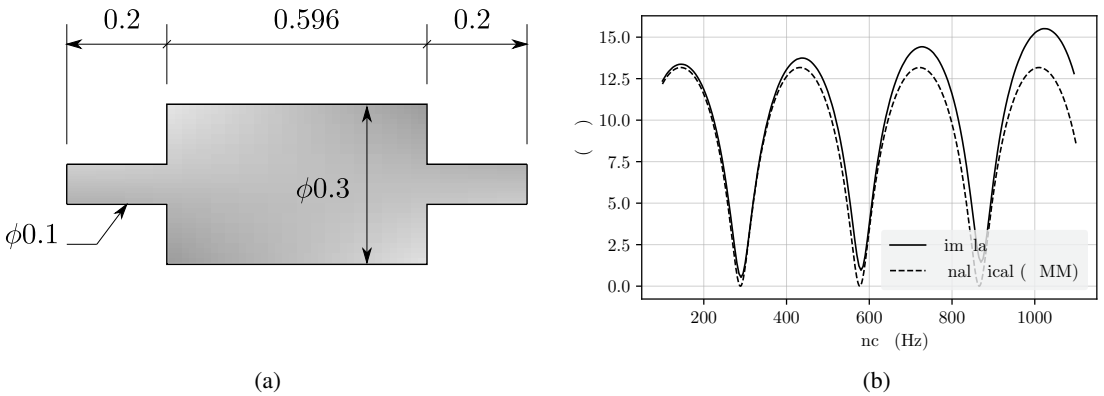
The aim of this section is to validate the thermal extrapolation technique against a fully numerical simulation in order to assess the quality of the inverse estimated model. Two cases are considered: (3.1) single expansion chamber and (3.2) complex muffler formed by multiple expansion chambers. The numerical simulation is performed using Simcenter 12.0 for meshing and thermal-flow simulation. With the obtained temperature field the sound speed can be calculated for each element. The acoustic finite element simulation is performed using LMS Virtual.lab 13.8. The simulation was performed considering the frequency range from 100 Hz to 1100 Hz with a 5 Hz step. The environmental conditions are conventional, with atmospheric pressure at 101351 MPa and ambient temperature at 293 K. The boundary conditions for the thermal-flow simulation considers a slow flow condition with inlet flow $v = 0.001$ m/s and external condition given by an imposed temperature of 573 K. The outlet flow has the same flow velocity. A mixing length turbulence model for thermal-flow solver is employed. The duct wall consider is Aluminium A356 with thickness of 2 mm and tetrahedral shape (TET4) with element size of 51.5 mm for the single expansion chamber and 25 mm for the complex muffler. For the acoustic meshing, the tetrahedral shape (TET4) with same element size of their respective thermal simulation are used for mapping convenience. Isotropic air is used as the material which contains the properties from Table 1.

Table 1: Air properties at ambient temperature

Mass Density	$\rho = 1.2041\ \mathrm{kg \cdot m^{-3}}$
Speed of Sound	$c = 343.21\ \mathrm{m \cdot s^{-1}}$
Thermal Conductivity	$\kappa = 0.023\ \mathrm{W \cdot mm^{-1} \cdot K^{-1}}$
Isobaric specific heat capacity	$c_p = 1.005\ \mathrm{kJ \cdot kg^{-1} \cdot K^{-1}}$

3.1 Single expansion chamber

The expansion chamber has the same dimensions as described in [17] and reproduced in Figure 2 (a). Figure 2(b) shows the simulated STL of the single expansion chamber and a STL calculate analytically using TMM at ambient temperature for reference.



(a) (b)

Figure 2: (a) Dimensions of expansion chamber in m and (b) STL of expansion chamber comparing a simulated result with analytical using TMM at ambient temperature.

It can be noted from Figure 2 that the simulated STL does not match the analytical STL. The discrepancy between the STL increases as the frequency increase. This occurs because the analytical model utilizes a one-dimensional propagation approximation (plane wave assumption) which does not account for attenuation

and it also does not capture higher order modes. This limitation of such a one-dimensional model is well known [1]. As a matter of fact, the three-dimensional effects play a role well below the cut-on frequency of the first higher order mode. Taking into account the limitations of the TMM, the inverse estimation approach only considers the values for the STL for frequencies up to 300 Hz. The obtained retrieved geometry of the expansion chamber can be seen in Table 2 and in Figure 3.

Table 2: Dimension of original and retrieved expansion chamber

	Diameter (m)	Length (m)
Original	0.300	0.596
Retrieved	0.304	0.591

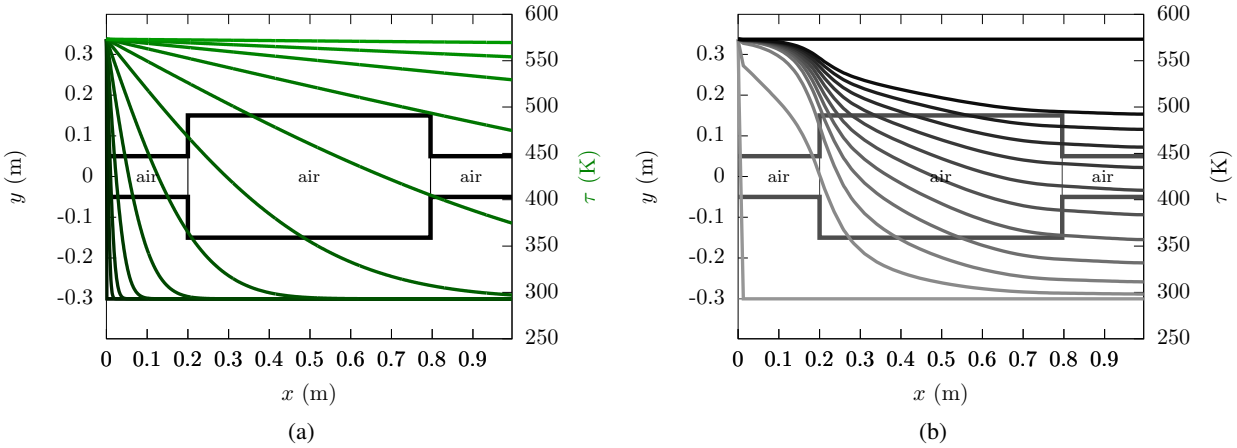


Figure 3: Retrieved geometry and the two transient temperature profiles considered: (a) from heat conduction model and (b) from duct centerline in the performed thermal-flow simulation.

The retrieved values show good agreement with the original dimension and it gives confidence to tackle the temperature extrapolation problem. The two temperature extrapolation scenarios are shown in Figure 3. The profiles from Figure 3 (a) are obtained from the heat conduction model from Section 2.3 and the profiles in Figure 3 (b) are extracted from the expansion chamber centerline in the performed thermal-flow simulation.

Although the initial conditions for the two temperature extrapolation scenarios are the same, a considerable difference in temperature profiles can be seen in Figure 3 where it is possible to observe the transient evolution of the temperature profiles along the system. In Figure 3(a) the first profiles show a very abrupt temperature change and gradually, as time increases, the outlet temperature increases and the profiles become almost linear. This behaviour is due to the simplified thermal model, which does not include the effect of different cross section areas. On the other hand, the simulated scenario from Figure 3(b) shows a less abrupt and a more gradual outlet temperature change between each profile, as it takes into account cross-section variations.

In this simple case with symmetrical geometry, the temperature profile can be easily obtained, which is not the case for complex geometries. For this reason, both the simulated temperature profiles and the heat conduction model temperature profiles are considered for the acoustic performance calculation that follows.

Figure 4 shows the comparison between semi-analytical and FEM-simulated STL considering the heat conduction model and the FEM temperature profiles. The selected profiles are as follows: (a) constant temperature $\tau = 293$ K, (b) - (e) intermediate profiles with boundary condition that can be referred at Table 3 and (f) at constant $\tau = 573$ K. A comparison between the profiles shows a difference in attenuation levels, mostly in the intermediate profiles. Besides, a shift in the STL frequency domain due to the temperature change can be clearly observed for the intermediate profiles in Figure 4 and less noticeable in Figure4. This

frequency shift has a relevant impact in the region of the first dip (or lobe). This phenomenon is critical as it can change the location of optimal sound transmission loss content, alter the muffler's performance and consequently, audio perception. The quantification of this frequency shift is shown in Figure 5 where, the difference between analytical (TMM) with heat conduction and FEM-simulated profiles is compared with the fully simulated STL. For the difference between analytical (TMM) with heat conduction profile and fully simulated STL (green curve), It can be seen a considerably increase in the shift as it approaches intermediate profiles having its maximum value for the profile 7. The large frequency shift in this case is expected because the comparison with the simulated profiles does not match perfectly. However, for small temperature gradients (profiles 9 to 12) the error is considerably small. For the difference between analytical (TMM) with simulated profile and fully simulated STL, the frequency shift is within the resolution of the frequency domain which is 5 Hz. This shows that the analytical model can yield good results compared to the FEM simulation, and the choice of thermal model has a significant impact in the acoustic behaviour. In cases where the temperature profiles are unavailable, the heat conduction model could be used for small temperature gradient.

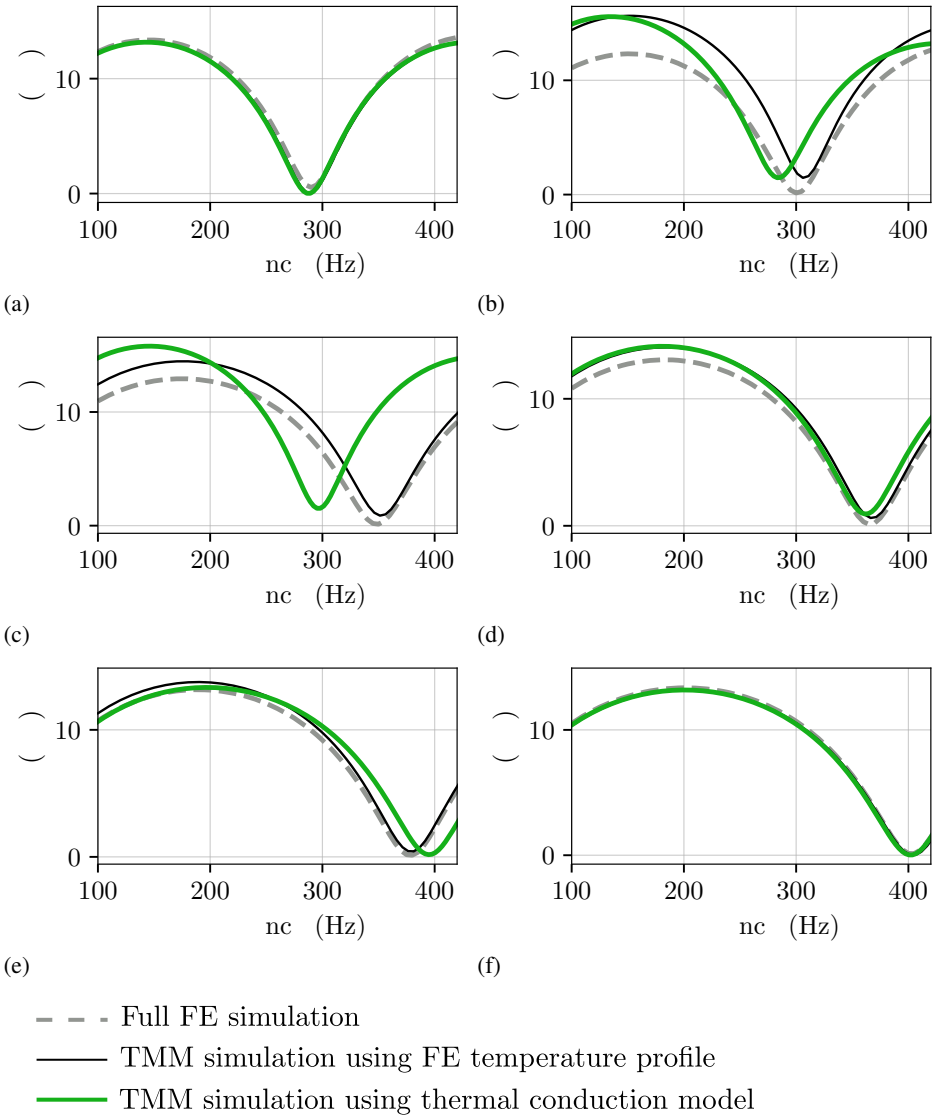


Figure 4: Comparison of single expansion chamber STL between the two methods, analytical (extrapolation) and FE simulation, for the heat conduction model and simulated temperature profiles where (a) is at constant $\tau = 273$ K, (b) - (e) are intermediate profiles (refer to Table 3) and (f) is at constant $\tau = 573$ K.

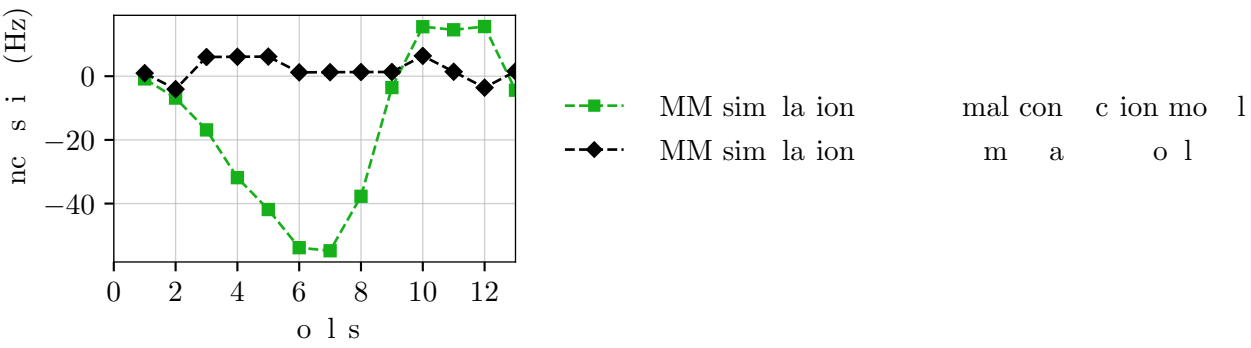


Figure 5: Frequency shift at the STL dip with respect to the full FE simulation considering the TMM simulation with thermal conduction model and with FE temperature profile.

Table 3: Boundary conditions for each profile ($\tau(0)$ - $\tau(L)$, where L is the total length of the system).

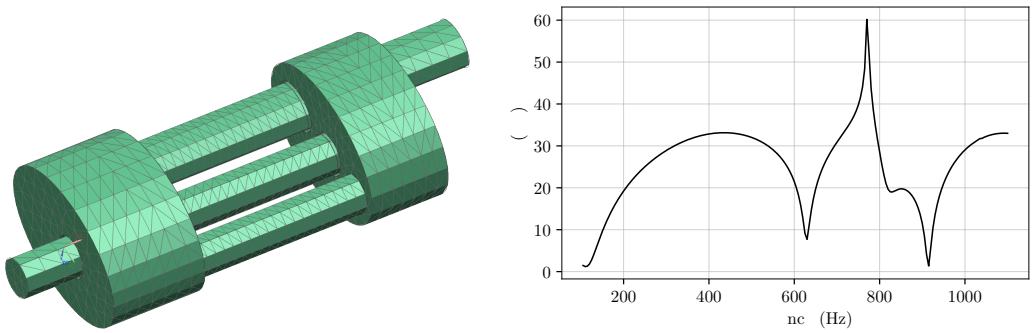
Profiles	**Fig 4.**	$\tau_{\text{conduction}}$ [K]	τ_{FEM} [K]
profile 1	(a)	293-293	293-293
profile 2	-	573-293	573-293
profile 3	(b)	573-293	573-300
profile 4	-	573-293	573-320
profile 5	-	573-293	573-335
profile 6	-	573-293	573-355
profile 7	(c)	573-293	573-380
profile 8	-	573-300	573-410
profile 9	(d)	573-375	573-440
profile 10	-	573-475	573-460
profile 11	(e)	573-530	573-475
profile 12	-	573-553	573-495
profile 13	(f)	573-573	573-573

3.2 Complex muffler

In this section, a similar analysis is made for a complex muffler geometry. The main objective here is to reconstruct a one-dimensional profile that behaves in an equivalent manner as the muffler with a complex geometry. Due to the non-uniqueness of the one-dimensional path connecting the inlet to the outlet, a simple heat conduction model temperature profile is considered as a first approximation. The complex muffler consists of three ducts with two intermediate expansion chambers, as shown in Figure 6 (a). Figure 6 (b) shows the simulated STL at ambient temperature. As it can be seen, a peak in amplitude occurs at around 760 Hz which represents a transversal mode. The region of main interest, however, is in the first lobe which occurs around 610 Hz.

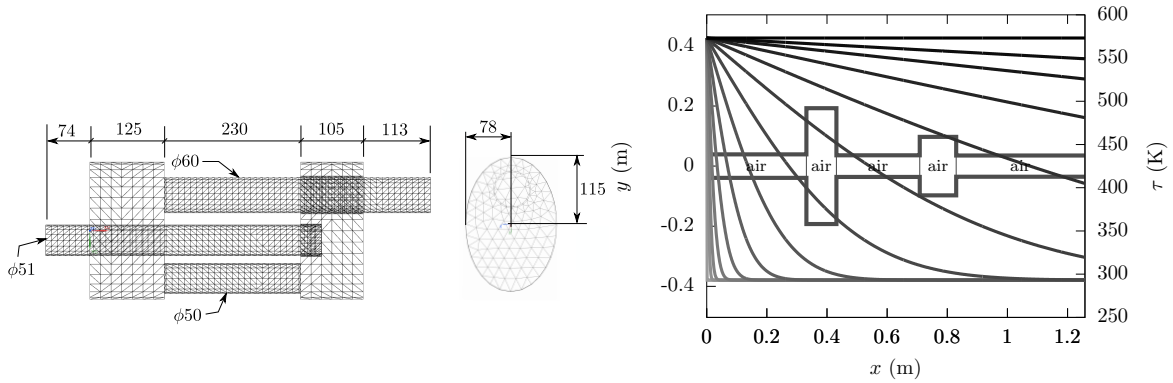
Based on this observation and to avoid second modes in the optimization scheme, only frequencies up until 700 Hz are considered in the inverse estimation. The inverse estimation retrieve an equivalent geometry as shown in Figure 7 with exact dimensions for each section described in Table 4. Although it is quite challenging to compare the original and retrieved geometry, the retrieved geometry does resemble the original muffler since both the complex muffler and the retrieved ones are basically a combination of multiple connections and expansions.

Figure 8 shows the comparison between analytical STL considering the same heat conduction model temperature profiles as previously and a fully simulated STL . The quantification of frequency shift of the dip



(a) (b)

Figure 6: (a) Simcenter 3D model of complex muffler and (b) simulated STL at ambient temperature.



(a) (b)

Figure 7: (a) 3D geometry of complex muffler (dimensions in mm) and (b) retrieved equivalent 1D geometry and imposed temperature profiles.

Table 4: Retrieved complex muffler dimensions for each section

Sections	1	2	3	4	5
Length (m)	0.2343	0.1000	0.1077	0.2773	0.2140
Radius (m)	0.0400	0.1146	0.0230	0.1056	0.0190

can be seen in Figure 9. As expected, there is barely a shift for the constant temperature. The shift error increases considerably as it approaches the intermediate profiles, it been the highest at profile 8. For very high gradient and very small gradient there is a relatively good match. However, the intermediate profiles result in a considerably frequency shift and are not very representative of the acoustic behaviour of the muffler. For this case, a simple heat conduction consideration is not enough to model the thermal behavior of a complex muffler and a more representative model is needed.

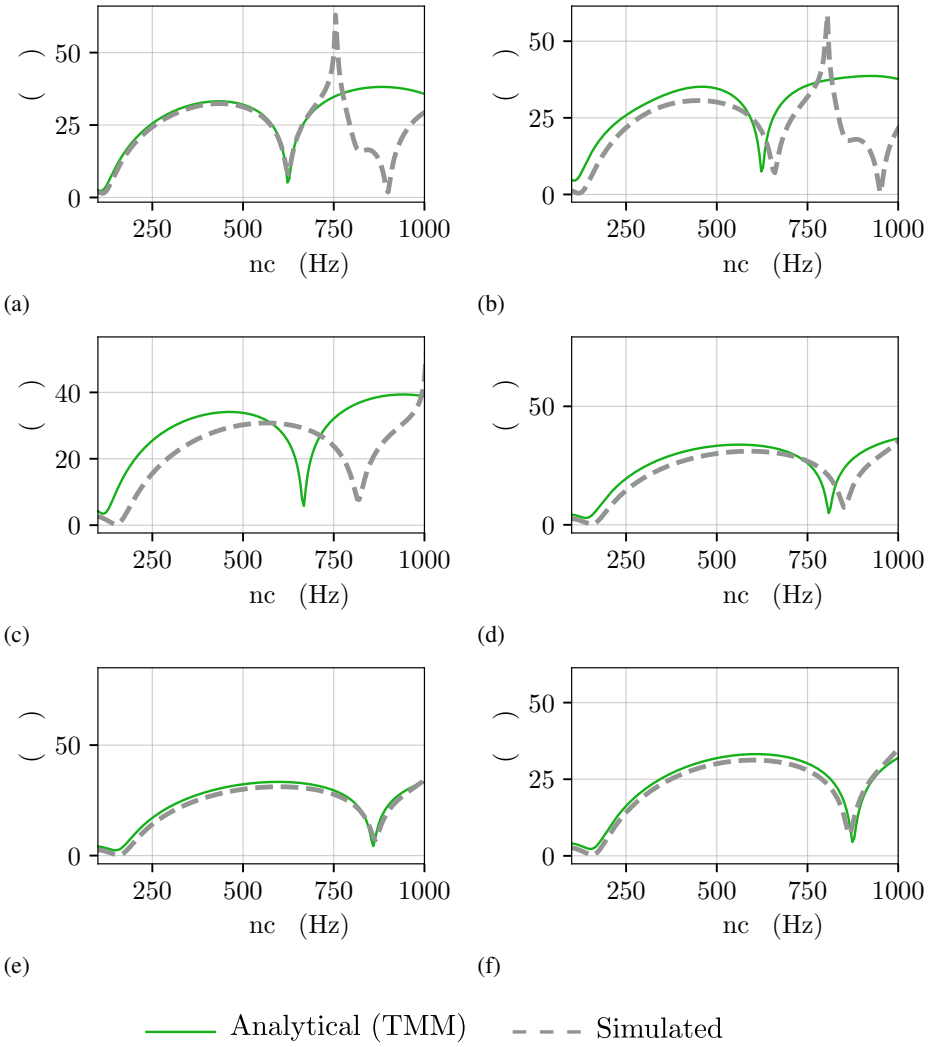


Figure 8: Comparison of the complex muffler STL between the two analytical model with heat conduction model temperature profiles and the fully simulated model where (a) is at constant $\tau = 273$ K, (b) - (e) are intermediate profiles (refer to Table 3) and (f) is at constant $\tau = 573$ K.

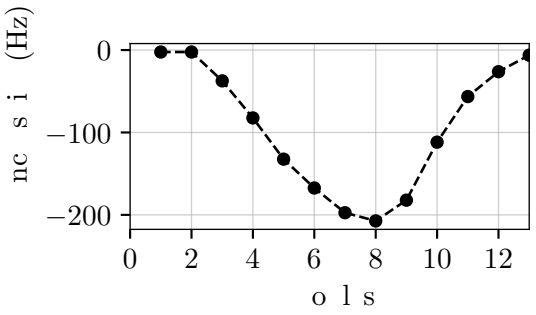


Figure 9: Frequency shift at the STL dip considering the difference between analytical (TMM) with heat conduction compared to the fully FEM simulated model.

4 Conclusion

This paper is concern with the acoustic characterization of mufflers to inhomogeneous thermal conditions. The STL is sensitive to thermal conditions; therefore standard room-temperature measurements are often not representative of operating conditions. Model extrapolation allows to simulate a laboratory object in operating thermal conditions, or to retrieve ISO-comparable tests from thermally-inhomogeneous measurements. Possible applications include experiment-based design of multi-layer media, for instance for performance optimisation in realistic conditions. Experimental and three-dimensional numerical validations are required in order to determine the range of validity of the extrapolation procedure. Further work would require a refined model of thermal processes in porous media.

From a classical or standard STL measurement in impedance tube, two extra steps are added in order to extrapolate the laboratory results to operational conditions unavailable for precise testing. The first step concerns the inverse estimation on the STL itself to retrieve an equivalent geometry for complex components. One advantage of the equivalent geometry is that it allows for a easy and fast way to extrapolate the model to new conditions and a feasible alternative to fully numerical simulations. The method could retrieve the original geometry successfully for the simple case of an expansion chamber. For the more complex muffler studied the equivalent geometry with axial symmetry included some of the relevant characteristics of the original object. The second step involves the temperature extrapolation as such. The latter was compared with finite elements numerical simulations and it showed promising results. Indeed, the main effect sought in the extrapolation is the frequency shifting of the acoustic filter response, like the resonances from the studied expansion chambers. This part is induced by the temperature effect on the sound speed. Nevertheless, the dependency on cross sections seems to play an important role in the thermal model, as seen in the finite element model, which requires further investigation for a more accurate (semi) analytical model. Finally, the attenuation or gain remains to be modeled within this extended but still simple physical model.

Acknowledgments

We gratefully acknowledge the European Commission for its support of the Marie Sklodowska Curie program through the H2020 ETN PBNv2 project (GA 721615). This article is also based upon work from COST Action DENORMS CA15125, supported by COST (European Cooperation in Science and Technology). Finally, the authors would like to thank Edgar Matas, Elvira Galiullina, Karim Hamiche, Korcan Kucukcoskun and Raphael Hallez for their help with the numerical modeling in Simcenter.

References

[1] M. L. Munjal. *Acoustics of Ducts and Mufflers With Application to Exhaust and Ventilation System Design*. John Wiley & Sons, May 1987. ISBN 978-0-471-84738-0.

[2] ASTM E2611-09. Standard test method for measurement of normal incidence sound transmission of acoustical materials based on the transfer matrix method. Technical report, ASTM International, West Conshohocken, PA, 2009.

[3] A. Kapur, A. Cummings, and P. Mungur. Sound propagation in a combustion can with axial temperature and density gradients. *Journal of Sound and Vibration*, 25(1):129–138, November 1972.

[4] M. L. Munjal and M. G. Prasad. On plane-wave propagation in a uniform pipe in the presence of a mean flow and a temperature gradient. *The Journal of the Acoustical Society of America*, 80(5):1501–1506, 1986.

[5] K.S. Peat. The transfer matrix of a uniform duct with a linear temperature gradient. *Journal of Sound and Vibration*, 123(1):43–53, May 1988.

[6] R.I. Sujith, G.A. Waldherr, and B.T. Zinn. An exact solution for one-dimensional acoustic fields in ducts with an axial temperature gradient. *Journal of Sound and Vibration*, 184(3):389–402, July 1995.

[7] B. Karthik, B. Manoj Kumar, and R. I. Sujith. Exact solutions to one-dimensional acoustic fields with temperature gradient and mean flow. *The Journal of the Acoustical Society of America*, 108(1):38–43, July 2000.

[8] R. I. Sujith. Transfer matrix of a uniform duct with an axial mean temperature gradient. *The Journal of the Acoustical Society of America*, 100(4):2540–2542, October 1996.

[9] Carl Q. Howard. The Corrected Expressions for the Four-Pole Transmission Matrix for a Duct with a Linear Temperature Gradient and an Exponential Temperature Profile. *Open Journal of Acoustics*, 03 (03):62–66, 2013.

[10] M.G. Prasad and M.J. Crocker. Studies of acoustical performance of a multi-cylinder engine exhaust muffler system. *Journal of Sound and Vibration*, 90(4):491–508, October 1983.

[11] Peter Göransson, Jacques Cuenca, and Timo Lähivaara. Parameter estimation in modelling frequency response of coupled systems using a stepwise approach. *Submitted*, 2018/4/20.

[12] Jacques Cuenca, Peter Göransson nad Laurent De Ryck, and Timo Lähivaara. Inverse parameter estimation in resonant, coupled fluid-structure interaction problems. In *ISMA/USD*, 2018/9/17-19.

[13] David Linton Johnson, Joel Koplik, and Roger Dashen. Theory of dynamic permeability and tortuosity in fluid-saturated porous media. *Journal of Fluid Mechanics*, 176(-1):379, March 1987.

[14] Yvan Champoux and Jean-F. Allard. Dynamic tortuosity and bulk modulus in air-saturated porous media. *Journal of Applied Physics*, 70(4):1975–1979, August 1991.

[15] Jacques Cuenca, Christophe Van der Kelen, and Peter Göransson. A general methodology for inverse estimation of the elastic and anelastic properties of anisotropic open-cell porous materials—with application to a melamine foam. *Journal of Applied Physics*, 115(8):084904, February 2014.

[16] L. Theodore. *Heat Transfer Applications for the Practicing Engineer*. John Wiley & Sons, 2011.

[17] Ling-Kuan Xuan, Jing-Feng Gong, Ping-Jian Ming, Guo-Yong Jin, and Wen-Ping Zhang. A time-domain finite volume approach for prediction of muffler transmission loss including thermal effects. *Proceedings of the Institution of Mechanical Engineers, Part C: Journal of Mechanical Engineering Science*, 228: 108–118, January 2014.

The design of a low-cost directional warning sound system for electric vehicles

N. Kournoutos [1], **J. Cheer** [1], **S.J. Elliott** [1]
[1] Institute of Sound and Vibration Research, University of Southampton,
University Rd, Southampton SO17 1BJ, UK
e-mail: **N.Kournoutos@soton.ac.uk**

Abstract
Electric vehicle warning sounds are now required by law in many countries due to safety concerns, but this additional noise source may increase unwanted noise pollution. Therefore, the design of an electric vehicle warning sound system that can produce a directional sound field has been investigated. This paper introduces two design suggestions for a system with comparable performance to the conventional loudspeaker array, but at a significantly lower manufacturing and maintenance cost, suitable for wider commercial adoption. The first method utilises a single loudspeaker attached to a length of perforated piping which acts as a directional acoustic radiator, which is analogous to the shotgun microphone. The second approach replaces the standard loudspeaker array with inertial actuators mounted to a vehicle body panel and these are driven to radiate a controlled directional sound field. A simulation based comparison between the suggested configurations and a conventional loudspeaker array of equivalent physical dimensions is presented.

1 Introduction

Within the past couple of decades, Electric Vehicles (EVs) and Hybrid-Electric Vehicles (HEVs) have increased their share of the passenger vehicle market, and given the desire and support of public and authorities alike for ecologically friendlier means of transportation, it is reasonable to assume that this presence is only going to grow stronger in the future. A wider integration of EVs in public and private transport should result in better living conditions for urban areas, with reduced air pollution due to lower carbon dioxide emissions, and reduced noise pollution, due to the quiet operation of electric motors [1].

Focussing on the subject of noise generated by vehicles, it has been studied and established that indeed EVs produce significantly less engine noise than Internal Combustion Engine (ICE) equipped vehicles. However, it is factors such as aerodynamics and the interaction of tyres with the road that dominate as noise sources for higher speeds, at which both types of vehicle produce similar noise levels [2]. Still, research results point out that for speeds below the 30 km/h limit, EVs are consistently quieter compared to typical ICEs [3].

A point of concern regarding this quiet operation of EVs is the lack of detectability it may provide for pedestrians, cyclists and other vulnerable road users. Researchers and institutions have investigated the extent to which this lack of audible cues poses a safety issue and whether it necessitates the use of external warning sounds for EVs. Though results do not unanimously reach a verdict [4], [5], and opposition to the adoption of warning sounds has been expressed [6], legislation for the mandatory use thereof has been coming into effect across different countries [7], [8]. For the purpose of rendering vehicles audibly detectable while avoiding excessive unwanted noise, surveys have been conducted to determine the characteristics of an effective warning sound. The guidelines for Acoustic Vehicle Alerting Systems (AVAS) first initiated by

the European Commission are being adopted globally and constitute a standard manufacturers of EVs are required to meet [9].

Apart from refining the content of the warning sound itself, an approach to ensure detectability while minimising the vehicle's overall contribution to noise is to generate a directional sound field. In-depth research on a directional warning sound system has been performed in the past through the European Commission project eVADER (electric Vehicle Alert for Detection and Emergency Response), which included investigation of methods to direct the sound field at specific targets identified as vulnerable road users [10], [11], [12]. The suggested solution uses an array of loudspeakers installed at the front bumper of the vehicle, which can achieve a high degree of selective beamforming. However, such a configuration requires a high cost of manufacture and maintenance due to its components, especially if intended for implementation in affordable passenger vehicles.

The aim of this paper is to investigate methods that are capable of producing directional sound fields, and that are suitable for integration as warning sound systems for EVs, while maintaining a lower cost than conventional loudspeaker arrays. Two approaches to designing such a system are investigated. The first concept is a low cost acoustic radiator consisting of a single loudspeaker attached to a perforated pipe, which generates the directivity of an end-fire array that would otherwise require multiple sound sources. The second approach utilises an array of structural actuators, lower in cost and potentially more robust than loudspeaker drivers, which force the vibration of a panel–possibly belonging to the body of the vehicle. By controlling this vibration, the system can be tuned to achieve a directional sound field with selective beamforming capabilities.

Section 2 introduces the principles of operation and the mathematical models used to simulate a conventional multiple loudspeaker array, the low-cost end-fire radiator and the structural array. In addition, the acoustic indicators used to evaluate each system are defined. Section 3 presents a comparative study of the three systems, detailing the parameters for which the simulations are run and showcasing their results.

2 Theory

2.1 Loudspeaker Array

The most straightforward way to achieve a high degree of directivity over a significant bandwidth is to use an array of multiple individual acoustic sources. As the primary concern of this paper regards only the potential directivity performance when it comes to the loudspeaker array, particular properties inherent in a loudspeaker driver are not investigated in this model. Assuming an output volume velocity U_n, where n denotes the index of the loudspeaker in the array, the total sound field radiated by N loudspeakers is equivalent to the linear superposition of the sound fields radiated by each one individually; thus, the total pressure at position r is given by

$$p\left(r\right) = \frac{j\rho_0\omega_0}{4\pi}\sum_{n=1}^{N} U_n \frac{e^{-jkr_n}}{r_n}, \tag{1}$$

where ρ_0 is the density of air, ω_0 is the angular frequency, k is the acoustic wavenumber and r_n is the distance from the n-th source to the pressure evaluation position. The complex values of the volume velocities U_n can be adjusted individually at each frequency in order to control the directivity of the system. The process for this optimisation is further elaborated in Section 2.4.

2.2 Low Cost End-Fire Acoustic Radiator

In 1991, Holland and Fahy developed a "Low-Cost End-Fire Acoustic Radiator"[13]. The design consisted of an array of holes drilled in a pipe to which a horn compression driver was attached. The resulting directivity

was shown to approach that of a multiple loudspeaker array in an end-fire configuration. The potential use of this directional sound source as an AVAS has also been investigated in [14] and [15]. Due to the simplicity of its components, the end-fire radiator may be rendered a less expensive, more robust alternative to a loudspeaker array as long as it can match its acoustic performance.

The principle of operation for the end-fire radiator is as follows: Considering a pipe where a number of holes have been drilled along its main axis, as in Figure 1, for any sound wave travelling down its length, each individual hole acts as a sound source that radiates to the external space. Given that the output from each hole is delayed due to the propagation of sound along the length of the pipe, these "sources" also display a delay between each other given by l/c_0, where l is the spacing between consecutive holes and c_0 the speed of sound in air.

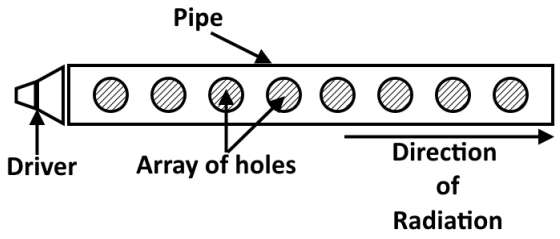


Figure 1: Example schematic, not to scale, for the end-fire radiator.

The end result is a configuration that radiates sound similarly to an end-fire array consisting of a number of sources equal to the number of holes drilled in the pipe. The directivity pattern, sensitivity and frequency range of operation of this array is primarily dependent on the physical parameters such as the size, spacing and number of the holes as well as the dimensions of the pipe itself.

Mathematical Model

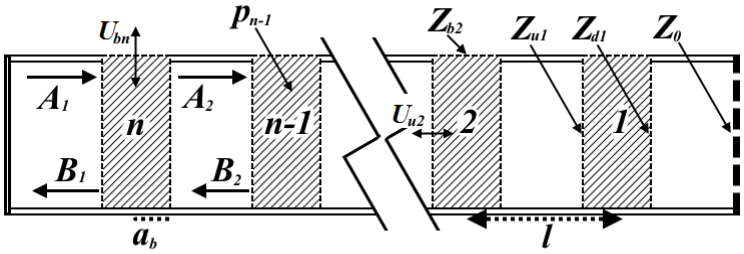


Figure 2: Schematic for the mathematical model of the end-fire radiator.

The mathematical model, which has been presented and analysed in [13] and [15], is constructed to estimate the sound field radiated by each hole and calculate the sound pressure levels in the far field. The system can be effectively modelled using acoustic transmission line theory, while approximating the fluid within the pipe as inviscid and ignoring any external coupling between holes. Figure 2 presents a schematic diagram of the end-fire radiator including the parameters considered in the mathematical model.

The impedance at the end of the pipe opposite to the source is taken as $Z_0 = \frac{\rho_0 c_0}{S}$, which corresponds to an anechoic termination, with S being the cross-sectional area of the pipe. The impedance transformation is

used to extract the impedance Z_{d1} downstream of the first hole, which is given as

$$Z_{d1} = \frac{\rho_0 c_0}{S} \left\{ \frac{Z_0 + j(\frac{\rho_0 c_0}{S} \tan(kl)}{\frac{\rho_0 c_0}{S} + iZ_0 \tan(kl)} \right\}. \tag{2}$$

It can be assumed that the acoustic pressure remains uniform in the area of the hole, given the small dimensions compared to the wavelength in question, and considering the continuity of volume velocity, the impedance upstream of the hole Z_{u1} is

$$Z_{u1} = \frac{1}{1/Z_{d1} + 1/Z_{b1}}. \tag{3}$$

In the specific case of the end-fire radiator, the impedance Z_{b1} corresponds to the value at the site of the respective hole. As the volume velocity through the hole will not generally be high enough to cause viscous flow, this radiation impedance can be approximated as

$$Z_b = \rho_0 c_0 \left[\frac{k^2}{4\pi} + j \frac{k\,(t + 1.5\alpha_b)}{\pi \alpha_b^2} \right], \tag{4}$$

where variables t and a_b refer to the thickness of the pipe and the diameter of each hole respectively. The value of Z_b is the same for all holes as they are identical in this system, although the sizes of the holes could be tuned to modify the response as investigated in [13], [15]. Using the value of Z_{u1} in place of Z_0 in equation (2), the downstream impedance from the second hole can be calculated, and subsequently all the respective impedances for each hole along the pipe.

In the region between the sound source and hole n, part of the plane wave of amplitude A_1 is reflected backwards with amplitude B_1, due to the impedance change caused by the hole as shown in Figure 2. The pressure p_n at the region of this hole is thus given as

$$p_n = A_1 + B_1 = 2A_1 \left(\frac{Z_{un}}{Z_{un} + \rho_0 c_0 / S} \right). \tag{5}$$

The acoustic pressure p_{n-1} at the location of each hole can then be expressed in terms of p_n, Z_{un-1}, Z_{dn} and the distance l between consecutive holes as

$$p_{n-1} = p_n \left\{ \frac{Z_{un-1} \left(\frac{\rho_0 c_0}{S} + Z_{dn} \right) [\cos(kl) - i \sin(kl)]}{Z_{dn} \left(\frac{\rho_0 c_0}{S} + Z_{un-1} \right)} \right\}. \tag{6}$$

Using equation (6), the acoustic pressure at every hole can be calculated using the known impedances. The total radiated pressure can then be calculated as in Section 2.1, using equation (1), with U_n replaced by the volume velocity through each hole of the pipe, which is given by

$$U_{bn} = \frac{p_n}{Z_{bn}}. \tag{7}$$

The mathematical model of the endfire radiator predicts a low frequency limit for its ability to achieve reasonable directivity, expressed though the relation

$$kL = 4\pi \tag{8}$$

where L is the distance between the first and last holes on the pipe. This means that the overall length of the array needs to be a least twice the wavelength of the lowest frequency.

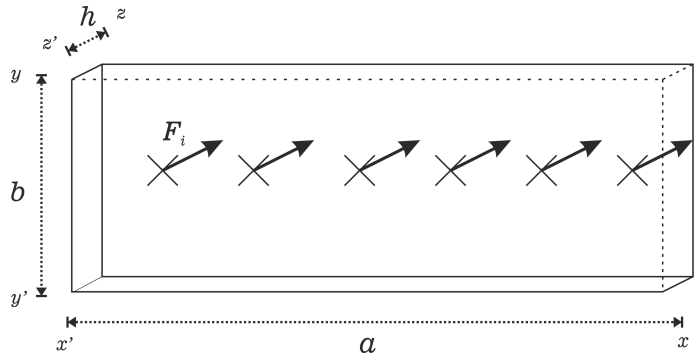


Figure 3: Schematic for the mathematical model of the structural array. A rectangular plate of thickness h is excited by a number of individual point forces F_i perpendicular to the plane defined by its sides a and b.

2.3 Structural Array

A typical dynamic loudspeaker, such as the ones used in [11] and considered when modelling the loudspeaker array in Section 2.1, utilises a voice coil to drive a diaphragm that, through its vibration, radiates the sound. This system, though capable of good performance and bandwidth, could be liable to failure when exposed to the environment when mounted on the exterior of a vehicle, and is relatively expensive to manufacture and maintain. Sound radiation could instead be achieved by an inertial actuator forcing a panel instead of a voice coil acting upon a diaphragm. This could potentially provide a lower cost with increased robustness, since the system would not rely on the relatively fragile diaphragms used in loudspeakers.

The proposed structural array would consist of a number of inertial actuators acting upon a panel which could form part of the vehicle's body to further minimise cost and better integrate the system. As with a loudspeaker array, the interference effects from vibrations caused by multiple actuators cause a directional radiated sound field. One of the key differences between the systems is that instead of multiple diaphragms being independent from each other, the vibration of the radiating panel at any one point is affected by the force applied by every actuator.

Mathematical Model

Figure 3 illustrates the geometry and approximations considered for the mathematical model of the structural array. The panel is taken as a thin rectangular plate with length a, height b and length h. The inertial actuators have been approximated by single point forces acting perpendicularly to the ab plane. In practice an actuator will have finite dimensions, however, since the actuators would be small compared to the size of the panel considered in this application, this is a reasonable approach considering the mathematical and computational simplicity that it offers.

The mathematical model for the structural array is based on the vibration of a rectangular thin plate which is simply supported along the edges, as presented in [16]. A separable solution of the transverse modal displacement for such a system is of the form

$$w_{mn}(x,y,t) = \sum_{m=1}^{\infty}\sum_{n=1}^{\infty} W_{mn} \sin k_m x \sin k_n y e^{j\omega t} \tag{9}$$

where W_{mn} is the modal amplitude and m, n are the modal indices for modes along the x and y axes respectively. For boundary conditions of zero transverse displacement along the edges, the wavenumber eigenvalues in each coordinate direction are

$$\begin{aligned} k_m &= m\pi/a, \qquad m = 1,2,3,... \\ k_n &= n\pi/b, \qquad n = 1,2,3,... \end{aligned} \tag{10}$$

and the discrete frequencies at which the system resonates are given by

$$\omega_{mn} = \left(\frac{EI}{\rho h}\right)^{1/2} \left[k_m^2 + k_n^2\right], \tag{11}$$

where E is Young's modulus of elasticity and ρ is the density of the plate, while I is the moment of inertia per unit width. For an input forcing function of a point force, $f(x,t) = F\delta(x - x_i)\delta(y - y_i)e^{j\omega t}$ located at $x_i,\ y_i$, the modal amplitudes are given by

$$W_{mn} = \frac{4F \sin k_m x_i \sin k_n y_i}{M(\omega^2 - \omega_{mn}^2)}, \tag{12}$$

where M is the mass of the plate.

The acoustic pressure in the far field, at a distance r from the defined centre point of the plate can be calculated using the Rayleigh integral in terms of the complex transverse velocities $\dot{w}(\boldsymbol{r}_S)$ at points $\boldsymbol{r}_S$ on the surface S, such that the pressure is given by

$$p\left(\boldsymbol{r}\right) = \int_S \frac{j\omega\rho_0 \dot{w}(\boldsymbol{r}_s)e^{-jkR}}{2\pi R} dS, \tag{13}$$

where $R = |\boldsymbol{r} - \boldsymbol{r}_s|$. The complex velocity $\dot{w}(\boldsymbol{r}_S)$ can be expressed as

$$\dot{w}(\boldsymbol{r}_S) = \dot{W}_{mn} \sin\left(\frac{m\pi x}{a}\right)\left(\frac{n\pi y}{b}\right) \qquad \{^{0\leq x\leq a}_{0\leq y\leq b}\}. \tag{14}$$

The total acoustic pressure at a point described by the coordinates (r, θ, ϕ) in the far field, radiated from the panel upon which a number of N point forces act at coordinates (x_i, y_i), is expressed upon evaluation of the integral in equation (13) as

$$p\left(r,\theta,\phi\right) = \sum_{m=1}^{\infty}\sum_{n=1}^{\infty} \frac{j\omega\rho_0 e^{-jkr}}{2\pi r} \frac{ab}{mn\pi^2} \left[\frac{(-1)^m e^{-j\alpha} - 1}{(\alpha/m\pi)^2 - 1}\right]\left[\frac{(-1)^n e^{-j\beta} - 1}{(\beta/n\pi)^2 - 1}\right] \sum_{i=1}^{N} \dot{W}_{mn}(i), \tag{15}$$

where $\alpha = ka\sin\theta\cos\phi$ and $\beta = kb\sin\theta\sin\phi$.

2.4 Array Optimisation and Performance Metrics

A method of quantifying a system's directivity performance is through the acoustic contrast between the average mean square pressure in a bright zone and the average mean square pressure in a dark zone. As defined in [17], the acoustic contrast at a given frequency is

$$AC = \frac{\boldsymbol{p}_B^H \boldsymbol{p}_B}{\boldsymbol{p}_D^H \boldsymbol{p}_D} = \frac{\boldsymbol{q}^H \boldsymbol{H}_B^H \boldsymbol{H}_B \boldsymbol{q}}{\boldsymbol{q}^H \boldsymbol{H}_D^H \boldsymbol{H}_D \boldsymbol{q}}, \tag{16}$$

where $\boldsymbol{q}$ is the vector containing the complex source strengths, $\boldsymbol{p}_B$, $\boldsymbol{p}_D$ are the vectors containing the amplitudes of the complex pressures in the bright and dark zones respectively, $\boldsymbol{H}_B$, $\boldsymbol{H}_D$ are the matrices of complex transfer responses between the sources and the measuring points in the bright and dark zones, while the superscript H indicates the Hermitian complex conjugate transpose.

Source Strength Optimisation

The definition of two distinct zones between which a contrast can be measured allows for the formulation of an optimisation problem. The value of acoustic contrast is maximised when $\boldsymbol{p}_B^H \boldsymbol{p}_B$ is maximised under the constraint that $\boldsymbol{p}_D^H \boldsymbol{p}_D$ remains constant at value d, resulting in the *Lagrangian*:

$$L = \boldsymbol{q}^H \boldsymbol{H}_B^H \boldsymbol{H}_B \boldsymbol{q} - \lambda(\boldsymbol{q}^H \boldsymbol{H}_D^H \boldsymbol{H}_D \boldsymbol{q} - d) \tag{17}$$

	Loudspeaker Array
No. of loudspeakers	6
Spacing between loudspeakers	14.3 cm
Array length	71.5 cm
	End-Fire Radiator
No. of holes	10
Hole radius	6 mm
Spacing between holes	8 cm
Effective array length	72 cm
Pipe length	80 cm
Pipe radius	2 cm
Pipe thickness	3 mm
	Structural Array
No. of actuators	6
Spacing between actuators	14.3 cm
No. of modes considered (x-direction)	12
No. of modes considered (y-direction)	8
Panel dimensions	1 m $\times$ 0.2 m $\times$ 3 mm
Panel density	2700 kg/m^3
Young's modulus	70 GPa
Poisson ratio	0.334
Frequency of first mode	192.25 Hz

Table 1: Set simulation parameters specific to each system.

with the positive and real Lagrange multiplier λ. By setting the complex differential of L with respect to $\boldsymbol{q}$ to zero, and under the assumption that $\boldsymbol{H}_D^H \boldsymbol{H}_D$ is invertible, yields the eigenvalue problem

$$\lambda \boldsymbol{q} = [\boldsymbol{H}_D^H \boldsymbol{H}_D]^{-1} \boldsymbol{H}_B^H \boldsymbol{H}_B \boldsymbol{q} = \boldsymbol{M} \boldsymbol{q}. \tag{18}$$

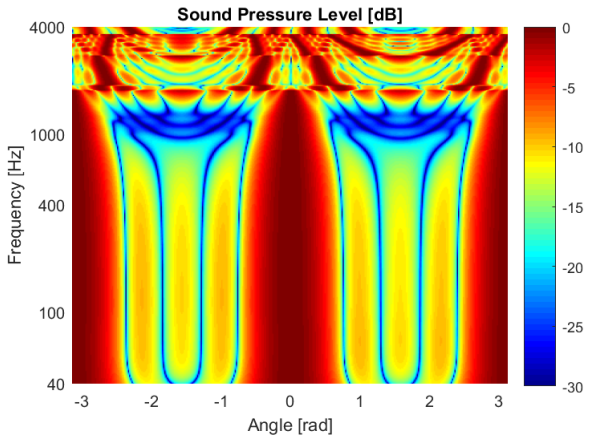
The source strength vector $\boldsymbol{q}$ that maximises the acoustic contrast is proportional to the eigenvector of the matrix $\boldsymbol{M}$ corresponding to its largest eigenvalue [17]. Therefore by adjusting the source strengths according to the values of said eigenvector, the overall radiated sound field will be characterised by the maximum possible acoustic contrast. In the cases of the loudspeaker array and the structural array, this would be the method of achieving the highest degree of directivity, by controlling each individual loudspeaker driver or actuator respectively.

3 Simulations

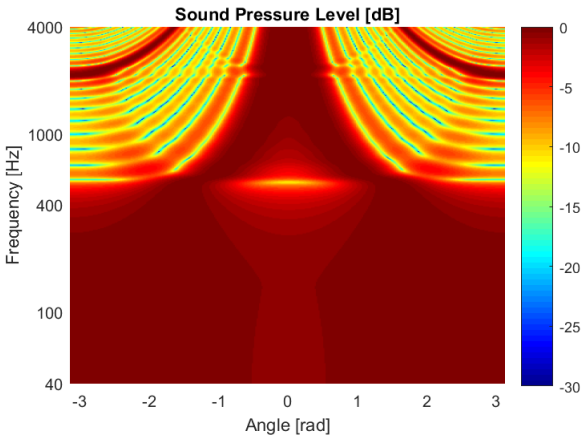
3.1 Simulation Parameters

The performance of the investigated systems has been evaluated through simulations using the mathematical models presented above. Vehicle warning sounds currently in use and in development are mostly limited to frequencies between 100 Hz and 3 kHz. An operating range from 40 Hz to 4 kHz is therefore deemed as suitable to include all potential components of a warning sound and provide a clear picture of each system's frequency response.

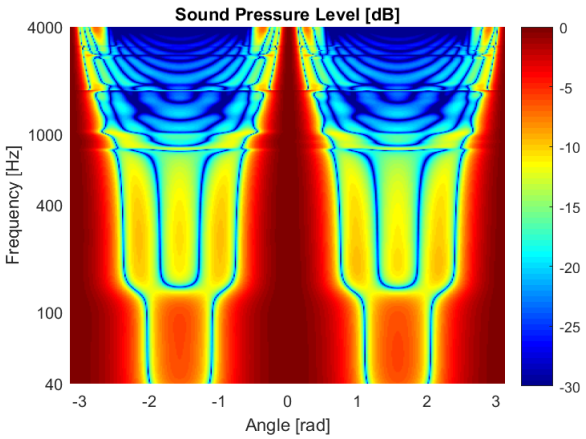
The complex acoustic pressure is estimated using equations (1) and (15) for a distance $r = 5\ m$ from the centre of each array and a θ angle coverage of 360^o, with the ϕ angle kept at 0^o, corresponding to the plane of movement for the vehicle. Calculations are performed for 360 measurement points evenly distributed along



(a) Loudspeaker Array



(b) End-Fire Radiator



(c) Structural Array

Figure 4: Normalised SPL frequency response as a function of the observation angle for a simulated six loudspeaker array, the end-fire radiator, and the structural array.

a 5 m radius circle sharing the centre of the array in question. A designated bright zone covering an angle $\theta_B = 60^o$ in the forward direction, and the dark zone defined by its explementary angle θ_D, are used to calculate the acoustic contrast and optimise the outputs of the loudspeaker and structural arrays to achieve the highest possible degree of directivity. Other general parameters which are common in all simulations are the density of air taken as $\rho_0 = 1.225\ kg/m^3$, and the speed of sound in air as $c_0 = 340.27\ m/s$.

Table 1 shows the parameters which are associated with each system. Six loudspeakers form the loudspeaker array, as with the array used for the system presented in [11]. Investigations of the effects that the physical characteristics have on the directivity performance have been carried out in [13] and [15]. The physical characteristics of the pipe are chosen to ensure the optimum compromise between operational bandwidth at the frequencies needed for warning sounds and implementation within the confines of a passenger vehicle. The structural array features six actuators, placed at intervals identical to the loudspeakers in the above case, to offer a more direct and substantial comparison between their performances. The panel, placed with its main plane facing the forward direction, has been given the dimensions of $1 \times 0.2 \times 0.003\ m$, a reasonable size to fit in a vehicle, and its material chosen has been chosen as aluminium.

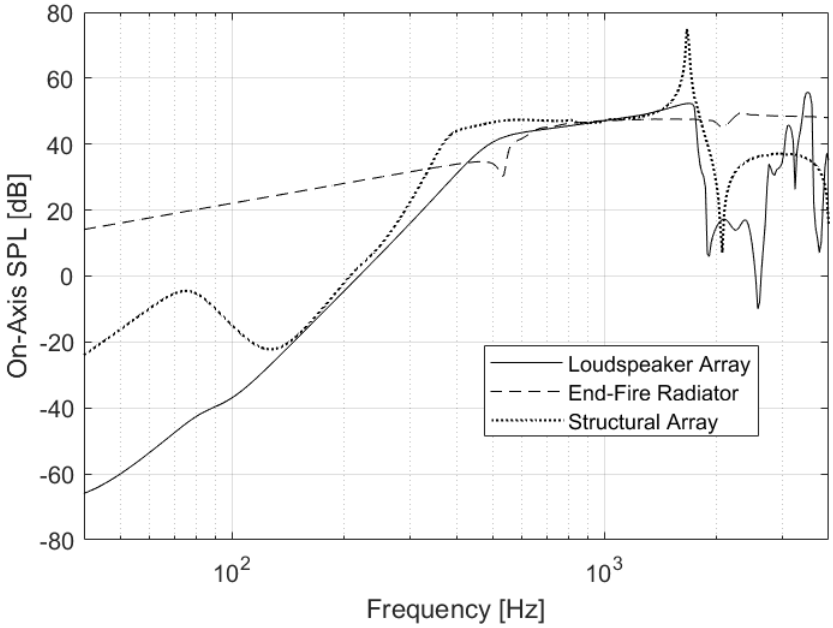


Figure 5: On-axis SPL frequency response for a six loudspeaker array, the end-fire radiator and the structural array.

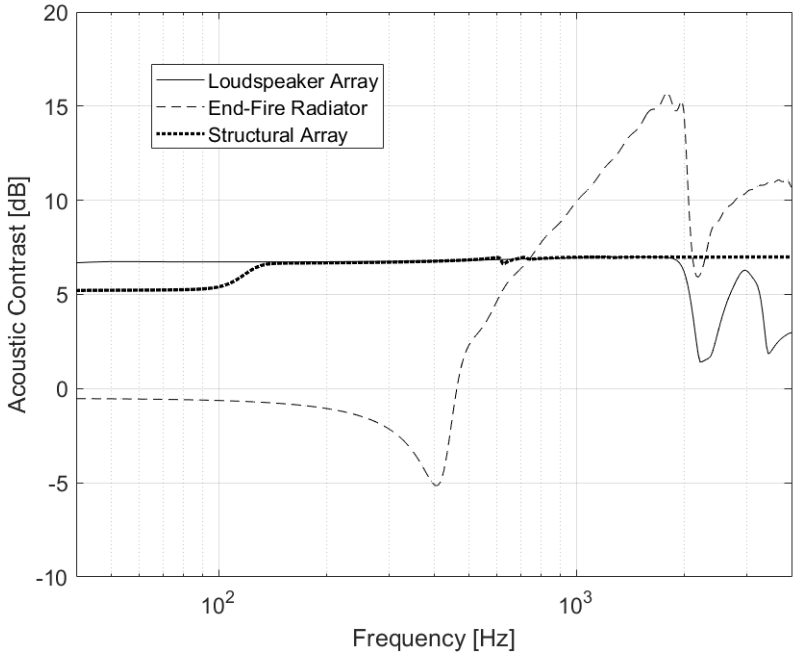


Figure 6: Acoustic contrast frequency response comparison between a six loudspeaker array, the end-fire radiator and the structural array.

3.2 Comparison of Results

Figure 4 shows the Sound Pressure Level (SPL) frequency response as a function of the observation angle for the three simulated systems. The values have been normalised to allow a more straightforward comparison of the systems' directivity. The zero degree angle corresponds in each case to the presumed forward direction; both the loudspeaker array and the structural array have been optimised to maximise their output within the aforementioned θ_B angle centred around this direction.

Given the parameters set in Table 1, the low frequency limit of the endfire radiator estimated according to equation 8 should be as high as 945 Hz. Still, an observable albeit reduced directivity remains for frequencies above 500 Hz. Its directivity performance improves as frequency increases until the 2 kHz mark, however beyond that side lobes of significant intensity appear. The loudspeaker array maintains its directivity across the entire spectrum investigated, although along with the increase in frequency, there is an overall increase in the output SPL in every direction. The structural array also displays a directional behaviour throughout the tested frequency range, while limiting the increase in SPL observed in the previous case.

The on-axis SPL frequency response for each configuration is shown in Figure 5. In this instance no normalisation has been performed, but for better comparison the gain has been adjusted so that the estimated SPL at 1kHz is equal for all three cases. The low frequency limit of the endfire radiator seen in Figure 4 is also visible here. In the case of the loudspeaker and structural arrays, the response across the investigated frequency range is characterised by a similar low frequency limit as well as dips and peaks at frequencies above 1.5 kHz, behaviour which is not evident when investigating the normalised output.

Acoustic Contrast

Figure 6 shows the acoustic contrast over frequency for all three systems. Although the end-fire radiator appears capable of achieving the highest contrast, its operational bandwidth is limited and its performance at frequencies below 1 kHz is rather poor. Both the loudspeaker and structural arrays show a flat response across the majority of the frequency range investigated, indicating a large operational bandwidth, although the maximum contrast achieved is significantly lower than that of the end-fire radiator. While the structural array displays a low frequency limit, presumably due to the dominance of the first mode of the plate, its performance at frequencies higher than 2 kHz surpasses that of the loudspeaker array.

4 Conclusions

This paper presents two directional sound system concepts for the implementation of warning systems in an electric vehicle, in the form of an end-fire radiator and a structural actuator array. Cost efficiency and durability given the application were taken into account for these designs. Analytical mathematical models were developed for both systems which allow for a parameter optimisation, given the restrictions imposed by their in-vehicle implementation, to produce directional sound fields across a frequency range suitable for warning sounds. The analytical models were used to perform a series of simulations to compare the performance of the systems to a conventional loudspeaker array. Simulation results indicate that all systems are capable of achieving high directivity, however in the case of the end-fire radiator the operational bandwidth is limited. The structural array displays a constant acoustic contrast over frequency and surpasses the performance of the loudspeaker array at the upper end of the investigated frequency range.

Acknowledgements

The authors gratefully acknowledge the European Commission for its support of the Marie Sklodowska Curie program through the ETN PBNv2 project (GA 721615).

References

[1] N. Campello-Vincente et al., *The Effect of Electric Vehicles on Urban Noise Maps*, Applied Acoustics, Vol. 116, No. 7/8, January 2017, pp. 59-64.

[2] N. Campillo-Davo, A. Rassili, *NVH Analysis Techniques for Design and Optimisation of Hybrid and Electric Vehicles*, Shaker Verlag Publications (2016).

[3] G. Marberg, *Noise from Electric Vehicles - A Literature Survey*, Compett (2013).

[4] M. Muirhead, L.K. Walter, *Analysis of STATS19 Data to Examine the Relationship Between the Rate of Vehicle Accidents Involving Pedestrians and Type Approval Noise Levels*, Transport Research Laboratory, July 2011.

[5] J. Wu, R. Austin, C.L. Chen, *Incidence Rates of Pedestrian and Bicyclist Crashes by Hybrid Electric Passenger Vehicles: An Update*, NHTSA, US Department of Transportation, October 2011.

[6] U. Sandberg, L. Goubert, P. Mioduszewski, *Are Vehicles Driven in Electric Mode So Quiet That They Need Acoustic Warning Signals?*, in M. Burgess, editor, *Proceedings of The 20th International Congress on Acoustics, Sydney, Australia, 2010 August 23-27*, Sydney (2010), pp. 1835-1845.

[7] National Highway Traffic Safety Administration (NHTSA), *Minimum Sound Requirements for Hybrid and Electric Vehicles - Final Rule*, US Department of Transportation, November 2016.

[8] Economic Commission for Europe of the United Nations (UNECE), *Regulation No 138 of the Economic Commission for Europe of the United Nations (UNECE) Uniform provisions concerning the approval of Quiet Road Transport Vehicles with regard to their reduced audibility [2017/71]*, January 2017.

[9] Japan Automobile Standards Internationalisation Centre (JASIC), *Guidelines for Measures Against Quietness Problem of Hybrid Vehicles*, Informal Group on Quiet Road Transport Vehicles, January 2010.

[10] F. Dubois, G. Baudet, J.C. Chamard, *EVADER: Electric Vehicle Alert for Detection and Emergency Response* , in *Proceedings of the Acoustics 2012 Nantes Conference, 2012 April 23-27*, Nantes (2012), pp.1051-1055.

[11] D. Quinn, J. Mitchell, P. Clark, *Development of a next-generation audible pedestrian alert system for EVs having minimal impact on environmental noise levels - project eVADER* , in *Proceedings of 43rd International Congress on Noise Control Engineering, Melbourne, Australia, 2014 November 16-19*, Melbourne (2014).

[12] E. Parizet, W. Ellermeier, R. Robart, *Auditory Warnings for Electric Vehicles: Detectability in Normal-Vision and Visually-Impaired Listeners*, Applied Acoustics, Vol. 86, December 2014 pp. 50-58.

[13] K.R. Holland, F.J. Fahy, *A Low-Cost End-Fire Acoustic Radiator*, Journal of the Audio Engineering Society, Vol. 39, No. 7/8, July/August 1991, pp. 540-550.

[14] J. Cheer, T. Birchall, P. Clark, J. Moran, S.J. Elliott, F.M. Fazi, *Design and implementation of a directive electric car warning sound*, Proceedings of the Institute of Acoustics, Vol. 35, Pt. 1 (2013).

[15] J. Carbajo, S.J. Elliott, J. Cheer, *Study of a low-cost end-fire array for use in electric vehicles*, in W. Kropp, editor, *Proceedings of The 2016 International Congress and Exhibition on Noise Control Engineering, Hamburg, Germany, 2016 August 21-24*, Hamburg (2016), pp. 4456-4466.

[16] C.R. Fuller, S.J. Elliott, P.A. Nelson, *Active Control of Vibration*, Academic Press, London (1996).

[17] S.J. Elliott, J. Cheer, *Regularisation and Robustness of Personal Audio Systems*, ISVR Technical Memorandum, No. 995, December 2011.

Tailoring Phononic-like topologies for controlling the structural-acoustic coupling in fluid-filled cylinders

Y. Vered[1], I. Bucher[1]
[1] Dynamics Laboratory, Mechanical Engineering, Technion
Technion City, Haifa 3200003, Israel
e-mail: **syoavv@campus.technion.ac.il**

Abstract
Periodic structures exhibit both pass and stop bands and can be utilized for passive control of structural-acoustic coupling in fluid-filled cylinders. Equations of motion of a complex unit cell geometry, incorporating structural-acoustic coupling, are derived by a finite element analysis. It is essential to model unit cells with many degrees of freedom to properly describe the local acoustic impedance. When the structure locale acoustic impedance resembles that of the fluid, the whole structure exhibits significant structural-acoustic coupling effects, and vice versa. By using the Floquet-Bloch theorem and the wave finite element method, the dispersion curves of fluid-filled waveguides can be numerically computed. The present study exploits the sparsity of fluid-filled waveguide model matrices to improve current numerical method. A new factor is presented to quantity the structural-acoustic coupling effect. Several examples which influence the structural-acoustic coupling effect at a desired frequencies range, are described.

1 Introduction

Fluid-filled acoustic waveguides are the basis for many non-destructive testing methods for material properties estimation. Most of these methods neglect the fluid-structure interaction (FSI) and therefore their model consists of a simple plane wave propagating mode with phase velocity equal to the intrinsic speed of sound of the fluid medium up to the cut-off frequency [1]. When the fluid specific acoustic impedance [2] differs from that of the elastic waveguide in several orders of magnitude this assumption stands. But when the impedances ratio is smaller, the FSI cannot be neglected anymore. When modelling fluid-filled waveguides which exhibit FSI the characteristic equation yields at least two propagating modes at all frequencies [3,4], all of them are non-planar. These facts lead to inaccuracies in the different non-destructive testing methods when studying the liquid as a wave propagation medium.

Periodic structures study is interconnected from early days to these of vibrations and acoustics, ever since Newton's sound propagation in air model and Rayleigh's study of continuous systems. Periodic structures are known to exhibit a frequency dependent behavior, most notably their dispersion curves consist of both pass and stop bands [5]. References [6,7] present an extended overview of the historical origin, and discussed both analytical and numerical methods for periodic structures. Since analytical methods can only analyze simple structures, therefore the need to use numerical computational methods has increased.

One common approach employs the transfer matrix method which has been widely used over the years, worthy of noting are the early works of Lin and McDaniel [8] and of Sen Gupta [9]. Zhong [10,11] exploited the mathematical properties of the transfer matrix to overcome some of the numerical problems. Mace et al [12] introduced the wave finite element (WFE) method which relies on the previous works mentioned and is capable of analyzing the dispersion curves and modal behavior of complex periodic structures. In recent years there has been considerable development in the study of infinite and finite-length waveguides with the use of the WFE, a few notable works are [13–18]. In [14] Mencik and Ichchou extended the WFE to be capable of analyzing fluid-filled elastic wave guides.

This work focused on the investigation of the coupling in a fluid filled periodic waveguides by using numerical methods, particularly WFE method. We aimed to develop a deeper comprehensive understanding of the FSI coupling nature, that will allow us to set design requirements in future work. To achieve this goal an improvement to the numerical conditioning of the formulation suggested by [14] is adopted. We propose using the participation factor (PF) [19] of each mode, a scalar property that describes the coupling of each propagating mode from energy flow perspectives. The suggested method is applied to several examples using PF to better understand the strength of the coupling as a function of frequency in different structures.

In this paper, the WFE is used to derive the dispersion curves and the PF of axisymmetric fluid-filled waveguides is presented to assess the coupling level. In the first part we exploit the structure of the coupled mass and stiffness matrices of the unit cell to introduce a different approach to the condensation of the inner element DOF. Then, the formulation of the Floquet's multiplier eigenvalue problem by two methods that enhance numerical stability. In the second part a comparison between the analytical and numerical solution of fluid-filled cylindrical tubes is established, followed by a case study of several periodic waveguides which either increase or decrease the coupling effects as a function of frequency. Several conclusions are drawn from the results and their implications are discussed.

2 Methodology (Wave finite element formulation of fluid-filled waveguide)

2.1 Finite element analysis of a unit cell

Consider a 3D fluid-filled waveguide composed of an infinite number of repetitive unit cells along its axis.

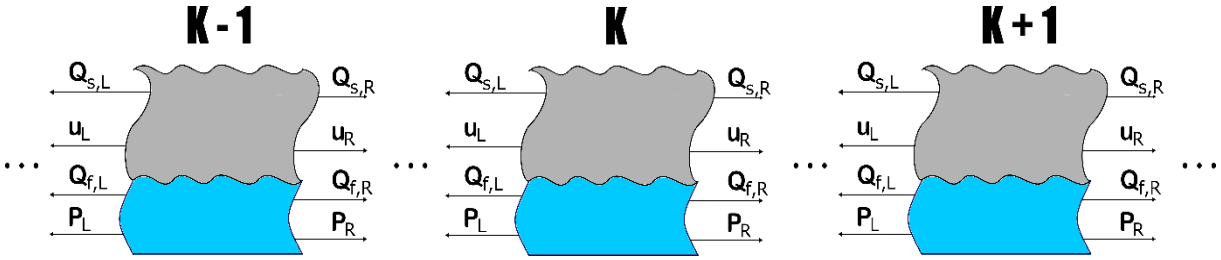


Figure 1: A schematic fluid-filled waveguide divided to repetitive unit cells. Blue area – liquid medium. Grey area – solid medium.

The fluid-filled unit cell was modeled using a commercial finite element software (Abaqus). The unit cell is meshed such that the left and right surfaces nodes match. Then the stiffness and mass matrices of the coupled model are exported to Matlab. The equation of motion of the fluid-filled unit cell can be written in the following manner [20]:

$$\begin{bmatrix} \mathbf{M}_s & \mathbf{0} \\ -\mathbf{S}_{fs} & \mathbf{M}_f \end{bmatrix} \begin{bmatrix} \ddot{\mathbf{u}} \\ \ddot{\mathbf{p}} \end{bmatrix} + \begin{bmatrix} \mathbf{K}_s & \mathbf{S}_{fs}^T \\ \mathbf{0} & \mathbf{K}_f \end{bmatrix} \begin{bmatrix} \mathbf{u} \\ \mathbf{p} \end{bmatrix} = \begin{bmatrix} \mathbf{Q}_s \\ \mathbf{Q}_f \end{bmatrix}. \tag{1}$$

Where subscripts s, f and fs stand for solid, fluid and solid-fluid accordingly. **M, K and** S are the mass, stiffness and coupling matrix accordingly. **u** is a vector representing the displacements degrees of freedom (DOF) of the solid, **p** vector represents the pressure DOF of the liquid, and **Q** stands for the generalized forces. Each sub-block can be partitioned to the left, right, and inner DOF similar to the general expression suggested by [21].

$$\left[\begin{array}{ccc:ccc} \mathbf{M}_{s,LL} & \mathbf{M}_{s,LR} & \mathbf{M}_{s,LI} & & & \\ \mathbf{M}_{s,RL} & \mathbf{M}_{s,RR} & \mathbf{M}_{s,RI} & & \mathbf{0} & \\ \mathbf{M}_{s,IL} & \mathbf{M}_{s,IR} & \mathbf{M}_{s,II} & & & \\ \hdashline -\mathbf{S}_{fs,LL} & -\mathbf{S}_{fs,LR} & -\mathbf{S}_{fs,LI} & \mathbf{M}_{f,LL} & \mathbf{M}_{f,LR} & \mathbf{M}_{f,LI} \\ -\mathbf{S}_{fs,RL} & -\mathbf{S}_{fs,RR} & -\mathbf{S}_{fs,RI} & \mathbf{M}_{f,RL} & \mathbf{M}_{f,RR} & \mathbf{M}_{f,RI} \\ -\mathbf{S}_{fs,IL} & -\mathbf{S}_{fs,IR} & -\mathbf{S}_{fs,II} & \mathbf{M}_{f,IL} & \mathbf{M}_{f,IR} & \mathbf{M}_{f,II} \end{array}\right]\left[\begin{array}{c} \ddot{\mathbf{u}}_L \\ \ddot{\mathbf{u}}_R \\ \ddot{\mathbf{u}}_I \\ \hdashline \ddot{\mathbf{p}}_L \\ \ddot{\mathbf{p}}_R \\ \ddot{\mathbf{p}}_I \end{array}\right] + \left[\begin{array}{ccc:ccc} \mathbf{K}_{s,LL} & \mathbf{K}_{s,LR} & \mathbf{K}_{s,LI} & \mathbf{S}_{fs,LL}^T & \mathbf{S}_{fs,RL}^T & \mathbf{S}_{fs,IL}^T \\ \mathbf{K}_{s,RL} & \mathbf{K}_{s,RR} & \mathbf{K}_{s,RI} & \mathbf{S}_{fs,LR}^T & \mathbf{S}_{fs,RR}^T & \mathbf{S}_{fs,IR}^T \\ \mathbf{K}_{s,IL} & \mathbf{K}_{s,IR} & \mathbf{K}_{s,II} & \mathbf{S}_{fs,LI}^T & \mathbf{S}_{fs,RI}^T & \mathbf{S}_{fs,II}^T \\ \hdashline & & & \mathbf{K}_{f,LL} & \mathbf{K}_{f,LR} & \mathbf{K}_{f,LI} \\ & \mathbf{0} & & \mathbf{K}_{f,RL} & \mathbf{K}_{f,RR} & \mathbf{K}_{f,RI} \\ & & & \mathbf{K}_{f,IL} & \mathbf{K}_{f,IR} & \mathbf{K}_{f,II} \end{array}\right]\left[\begin{array}{c} \mathbf{u}_L \\ \mathbf{u}_R \\ \mathbf{u}_I \\ \hdashline \mathbf{p}_L \\ \mathbf{p}_R \\ \mathbf{p}_I \end{array}\right] = \left[\begin{array}{c} \mathbf{Q}_{s,L} \\ \mathbf{Q}_{s,R} \\ 0 \\ \hdashline \mathbf{Q}_{f,L} \\ \mathbf{Q}_{f,R} \\ 0 \end{array}\right]. \tag{2}$$

Where subscripts L, R and I stand for left surface right surface and interior DOF, and the interior generalized forces are assumed to be equal zero. By rearranging the generalized DOF we can get the following form

$$\left[\begin{array}{c:c|c:c|c:c} \mathbf{M}_{s,LL} & \mathbf{0} & \mathbf{M}_{s,LR} & \mathbf{0} & \mathbf{M}_{s,LI} & \mathbf{0} \\ -\mathbf{S}_{fs,LL} & \mathbf{M}_{f,LL} & -\mathbf{S}_{fs,LR} & \mathbf{M}_{f,LR} & -\mathbf{S}_{fs,LI} & \mathbf{M}_{f,LI} \\ \hline \mathbf{M}_{s,RL} & \mathbf{0} & \mathbf{M}_{s,RR} & \mathbf{0} & \mathbf{M}_{s,RI} & \mathbf{0} \\ -\mathbf{S}_{fs,RL} & \mathbf{M}_{f,RL} & -\mathbf{S}_{fs,RR} & \mathbf{M}_{f,RR} & -\mathbf{S}_{fs,RI} & \mathbf{M}_{f,RI} \\ \hline \mathbf{M}_{s,IL} & \mathbf{0} & \mathbf{M}_{s,IR} & \mathbf{0} & \mathbf{M}_{s,II} & \mathbf{0} \\ -\mathbf{S}_{fs,IL} & \mathbf{M}_{f,IL} & -\mathbf{S}_{fs,IR} & \mathbf{M}_{f,IR} & -\mathbf{S}_{fs,II} & \mathbf{M}_{f,II} \end{array}\right]\left[\begin{array}{c} \ddot{\mathbf{u}}_L \\ \ddot{\mathbf{p}}_L \\ \hline \ddot{\mathbf{u}}_R \\ \ddot{\mathbf{p}}_R \\ \hline \ddot{\mathbf{u}}_I \\ \ddot{\mathbf{p}}_I \end{array}\right] + \left[\begin{array}{c:c|c:c|c:c} \mathbf{K}_{s,LL} & \mathbf{S}_{fs,LL}^T & \mathbf{K}_{s,LR} & \mathbf{S}_{fs,RL}^T & \mathbf{K}_{s,LI} & \mathbf{S}_{fs,IL}^T \\ \mathbf{0} & \mathbf{M}_{f,LL} & \mathbf{0} & \mathbf{K}_{f,LR} & \mathbf{0} & \mathbf{K}_{f,LI} \\ \hline \mathbf{K}_{s,RL} & \mathbf{S}_{fs,LR}^T & \mathbf{K}_{s,RR} & \mathbf{S}_{fs,RR}^T & \mathbf{K}_{s,RI} & \mathbf{S}_{fs,IR}^T \\ \mathbf{0} & \mathbf{K}_{f,RL} & \mathbf{0} & \mathbf{K}_{f,RR} & \mathbf{0} & \mathbf{K}_{f,RI} \\ \hline \mathbf{K}_{s,IL} & \mathbf{S}_{fs,LI}^T & \mathbf{K}_{s,IR} & \mathbf{S}_{fs,RI}^T & \mathbf{K}_{s,II} & \mathbf{S}_{fs,II}^T \\ \mathbf{0} & \mathbf{K}_{f,IL} & \mathbf{0} & \mathbf{K}_{f,IR} & \mathbf{0} & \mathbf{K}_{f,II} \end{array}\right]\left[\begin{array}{c} \mathbf{u}_L \\ \mathbf{p}_L \\ \hline \mathbf{u}_R \\ \mathbf{p}_R \\ \hline \mathbf{u}_I \\ \mathbf{p}_I \end{array}\right] = \left[\begin{array}{c} \mathbf{Q}_{s,L} \\ \mathbf{Q}_{f,L} \\ \hline \mathbf{Q}_{s,R} \\ \mathbf{Q}_{f,R} \\ \hline \mathbf{0} \\ \mathbf{0} \end{array}\right]. \tag{3}$$

And thus we get the standard form of partitioned single unit element as derived in [22]

$$\left[\begin{array}{c|c|c} \mathbf{M}_{fs,LL} & \mathbf{M}_{fs,LR} & \mathbf{M}_{fs,LI} \\ \hline \mathbf{M}_{fs,RL} & \mathbf{M}_{fs,RR} & \mathbf{M}_{fs,RI} \\ \hline \mathbf{M}_{fs,IL} & \mathbf{M}_{fs,IR} & \mathbf{M}_{fs,II} \end{array}\right]\left[\begin{array}{c} \ddot{\mathbf{q}}_L \\ \hline \ddot{\mathbf{q}}_R \\ \hline \ddot{\mathbf{q}}_I \end{array}\right] + \left[\begin{array}{c|c|c} \mathbf{K}_{fs,LL} & \mathbf{K}_{fs,LR} & \mathbf{K}_{fs,LI} \\ \hline \mathbf{K}_{fs,RL} & \mathbf{K}_{fs,RR} & \mathbf{K}_{fs,RI} \\ \hline \mathbf{K}_{fs,IL} & \mathbf{K}_{fs,IR} & \mathbf{K}_{fs,II} \end{array}\right]\left[\begin{array}{c} \mathbf{q}_L \\ \hline \mathbf{q}_R \\ \hline \mathbf{q}_I \end{array}\right] = \left[\begin{array}{c} \mathbf{Q}_{fs,L} \\ \hline \mathbf{Q}_{fs,R} \\ \hline \mathbf{0} \end{array}\right]. \tag{4}$$

Note that each mass submatrix $\mathbf{M}_{fs,XY}$ is built of 3 submatrices $\mathbf{M}_{s,XY}$, $\mathbf{M}_{f,XY}$ and $-\mathbf{S}_{fs,XY}$, Eq.(3), organized in a lower triangular form. Where both $\mathbf{M}_{s,XY}$ and $\mathbf{M}_{f,XY}$ are symmetric positive definite. Also each stiffness submatrix $\mathbf{K}_{fs,XY}$ is built of 3 submatrices $\mathbf{K}_{s,XY}$, $\mathbf{K}_{f,XY}$ and $\mathbf{S}_{fs,YX}^T$, Eq.(3), organized in an upper triangular form. Where both $\mathbf{K}_{s,XY}$ and $\mathbf{K}_{f,XY}$ are symmetric semi-positive definite, and in particular $\mathbf{K}_{s,II}$ and $\mathbf{K}_{f,II}$ are positive-definite.

Assuming harmonic excitation with angular frequency ω. The time derivative transforms to

$$\frac{d}{dt} \to i\omega, \tag{5}$$

substituting Eq.(5) in Eq.(4) yields

$$\left[\begin{array}{c|c|c} \tilde{\mathbf{D}}_{\mathrm{fs,LL}} & \tilde{\mathbf{D}}_{\mathrm{fs,LR}} & \tilde{\mathbf{D}}_{\mathrm{fs,LI}} \\ \hline \tilde{\mathbf{D}}_{\mathrm{fs,RL}} & \tilde{\mathbf{D}}_{\mathrm{fs,RR}} & \tilde{\mathbf{D}}_{\mathrm{fs,RI}} \\ \hline \tilde{\mathbf{D}}_{\mathrm{fs,IL}} & \tilde{\mathbf{D}}_{\mathrm{fs,IR}} & \tilde{\mathbf{D}}_{\mathrm{fs,II}} \end{array}\right]\left[\begin{array}{c} \mathbf{q}_{\mathrm{L}} \\ \hline \mathbf{q}_{\mathrm{R}} \\ \hline \mathbf{q}_{\mathrm{I}} \end{array}\right]=\left[\begin{array}{c} \mathbf{Q}_{\mathrm{fs,L}} \\ \hline \mathbf{Q}_{\mathrm{fs,R}} \\ \hline \mathbf{0} \end{array}\right],\ \tilde{\mathbf{D}}_{\mathrm{fs,XY}}=\mathbf{K}_{\mathrm{fs,XY}}-\omega^2\mathbf{M}_{\mathrm{fs,XY}}. \tag{6}$$

Where $\tilde{\mathbf{D}}_{\mathrm{fs,XY}}$ is the dynamic stiffness matrix. The inner DOF can be removed using dynamic condensation, such that Eq.(6) transform to

$$\mathbf{D}_{\mathrm{fs}}\mathbf{q}_{\mathrm{E}}=\mathbf{Q}_{\mathrm{fs,E}},\quad \mathbf{D}_{\mathrm{fs}}=\tilde{\mathbf{D}}_{\mathrm{fs,EE}}-\tilde{\mathbf{D}}_{\mathrm{fs,EI}}\tilde{\mathbf{D}}_{\mathrm{fs,II}}^{-1}\tilde{\mathbf{D}}_{\mathrm{fs,IE}}\ . \tag{7}$$

Where E stand for exterior, and

$$\tilde{\mathbf{D}}_{\mathrm{fs,EE}}=\left[\begin{array}{c|c} \tilde{\mathbf{D}}_{\mathrm{fs,LL}} & \tilde{\mathbf{D}}_{\mathrm{fs,LR}} \\ \hline \tilde{\mathbf{D}}_{\mathrm{fs,RL}} & \tilde{\mathbf{D}}_{\mathrm{fs,RR}} \end{array}\right],\quad \tilde{\mathbf{D}}_{\mathrm{fs,EI}}=\left[\begin{array}{c} \tilde{\mathbf{D}}_{\mathrm{fs,LI}} \\ \hline \tilde{\mathbf{D}}_{\mathrm{fs,RI}} \end{array}\right],\quad \tilde{\mathbf{D}}_{\mathrm{fs,IE}}=\left[\tilde{\mathbf{D}}_{\mathrm{fs,IL}}\ \middle|\ \tilde{\mathbf{D}}_{\mathrm{fs,IR}}\right],\quad \mathbf{q}_{\mathrm{E}}=\left[\begin{array}{c} \mathbf{q}_{\mathrm{L}} \\ \hline \mathbf{q}_{\mathrm{R}} \end{array}\right],\quad \mathbf{Q}_{\mathrm{fs,E}}=\left[\begin{array}{c} \mathbf{Q}_{\mathrm{fs,L}} \\ \hline \mathbf{Q}_{\mathrm{fs,R}} \end{array}\right]. \tag{8}$$

2.2 Condensed stiffness matrix formulation

Eq.(7) requires the inversion of $\tilde{\mathbf{D}}_{\mathrm{fs,II}}$ at each frequency of interest. In most cases the matrix $\tilde{\mathbf{D}}_{\mathrm{fs,II}}$ is an ill-conditioned matrix, and therefore a power series expansion is introduced for the derivation [16]

$$\mathbf{D}_{\mathrm{fs}}=\mathbf{D}_{\mathrm{fs},0}-\omega^2\mathbf{D}_{\mathrm{fs},1}-\omega^4\mathbf{D}_{\mathrm{fs},2}+O\left(\omega^6\right). \tag{9}$$

Here the matrix coefficients are given by:

$$\begin{aligned} \mathbf{D}_{\mathrm{fs},0}&=\mathbf{K}_{\mathrm{fs,EE}}-\mathbf{K}_{\mathrm{fs,EI}}\mathbf{K}_{\mathrm{fs,II}}^{-1}\mathbf{K}_{\mathrm{fs,IE}} \\ \mathbf{D}_{\mathrm{fs},1}&=\mathbf{M}_{\mathrm{fs,EE}}-\mathbf{K}_{\mathrm{fs,EI}}\mathbf{K}_{\mathrm{fs,II}}^{-1}\mathbf{M}_{\mathrm{fs,IE}}-\mathbf{M}_{\mathrm{fs,EI}}\mathbf{K}_{\mathrm{fs,II}}^{-1}\mathbf{K}_{\mathrm{fs,IE}}+\mathbf{K}_{\mathrm{fs,EI}}\mathbf{K}_{\mathrm{fs,II}}^{-1}\mathbf{M}_{\mathrm{fs,II}}\mathbf{K}_{\mathrm{fs,II}}^{-1}\mathbf{K}_{\mathrm{fs,IE}}\,. \\ \mathbf{D}_{\mathrm{fs},2}&=\mathbf{M}_{\mathrm{fs,EI}}\mathbf{K}_{\mathrm{fs,II}}^{-1}\mathbf{M}_{\mathrm{fs,IE}}+\mathbf{K}_{\mathrm{fs,EI}}\mathbf{K}_{\mathrm{fs,II}}^{-1}\mathbf{M}_{\mathrm{fs,II}}\mathbf{K}_{\mathrm{fs,II}}^{-1}\mathbf{M}_{\mathrm{fs,II}}\mathbf{K}_{\mathrm{fs,II}}^{-1}\mathbf{K}_{\mathrm{fs,IE}} \\ &\quad-\mathbf{M}_{\mathrm{fs,EI}}\mathbf{K}_{\mathrm{fs,II}}^{-1}\mathbf{M}_{\mathrm{fs,II}}\mathbf{K}_{\mathrm{fs,II}}^{-1}\mathbf{K}_{\mathrm{fs,IE}}-\mathbf{K}_{\mathrm{fs,EI}}\mathbf{K}_{\mathrm{fs,II}}^{-1}\mathbf{M}_{\mathrm{fs,II}}\mathbf{K}_{\mathrm{fs,II}}^{-1}\mathbf{M}_{\mathrm{fs,IE}} \end{aligned} \tag{10}$$

In order to compute Eq.(9) at each frequency, a single inversion of $\mathbf{K}_{\mathrm{fs,II}}$ is required. This matrix is almost always ill-conditioned because it represents both the elastic waveguide and the inner fluid stiffness which defers in orders of magnitude. To overcome this obstacle we exploit the upper triangular block form [23] leading to

$$\mathbf{K}_{\mathrm{sf,II}}^{-1}=\left[\begin{array}{c|c} \mathbf{K}_{\mathrm{s,II}}^{-1} & -\mathbf{K}_{\mathrm{s,II}}^{-1}\mathbf{S}_{\mathrm{fs,II}}^{T}\mathbf{K}_{\mathrm{f,II}}^{-1} \\ \hline \mathbf{0} & \mathbf{K}_{\mathrm{f,II}}^{-1} \end{array}\right]. \tag{11}$$

Eq.(11) involves the inversion of the two substructure matrices which can be done directly. If the matrices are ill-condition we can exploit their properties, mainly their sparsity and positive definite to use different factorization methods.

2.3 Transfer matrix formulation

The transfer matrix relates the generalized DOF and forces of the left exterior surface to that of the right exterior surface. The transfer matrix can be computed directly from the condensed stiffness matrix as

$$\mathbf{T}=\begin{bmatrix} -\mathbf{D}_{\mathrm{fs,LR}}^{-1}\mathbf{D}_{\mathrm{fs,LL}} & \mathbf{D}_{\mathrm{fs,LR}}^{-1} \\ -\mathbf{D}_{\mathrm{fs,RL}}+\mathbf{D}_{\mathrm{fs,RR}}\mathbf{D}_{\mathrm{fs,LR}}^{-1}\mathbf{D}_{\mathrm{fs,LL}} & -\mathbf{D}_{\mathrm{fs,RR}}\mathbf{D}_{\mathrm{fs,LR}}^{-1} \end{bmatrix}. \tag{12}$$

The derivation of the transfer matrix involves the inversion of the condensed dynamic stiffness matrix upper right block matrix, $\mathbf{D}_{\mathrm{fs,LR}}$, which again suffers from all of the numerical problems that were discussed earlier about the inversion of the inner dynamic stiffness matrix, $\tilde{\mathbf{D}}_{\mathrm{fs,II}}$. A new power series expansion is introduced:

$$\mathbf{D}_{\mathrm{fs,LR}}^{-1}=\mathbf{D}_{\mathrm{fs,LR},0}^{-1}+\omega^2\mathbf{D}_{\mathrm{fs,LR},1}^{-1}+\omega^4\mathbf{D}_{\mathrm{fs,LR},2}^{-1}+O\left(\omega^6\right). \tag{13}$$

Where the matrix coefficients are given by:

$$\begin{aligned} \mathbf{D}_{\mathrm{fs,LR},0}^{-1}&=\left(\mathbf{K}_{\mathrm{fs,LR}}-\mathbf{K}_{\mathrm{fs,LI}}\mathbf{K}_{\mathrm{fs,II}}^{-1}\mathbf{K}_{\mathrm{fs,IR}}\right)^{-1} \\ \mathbf{D}_{\mathrm{fs,LR},1}^{-1}&=-\mathbf{D}_{\mathrm{fs,LR},0}^{-1}\left(-\mathbf{M}_{\mathrm{fs,LR}}+\mathbf{M}_{\mathrm{fs,LI}}\mathbf{K}_{\mathrm{fs,II}}^{-1}\mathbf{K}_{\mathrm{fs,IR}}+\mathbf{K}_{\mathrm{fs,LI}}\mathbf{K}_{\mathrm{fs,II}}^{-1}\mathbf{M}_{\mathrm{fs,IR}}-\mathbf{K}_{\mathrm{fs,LI}}\tilde{\mathbf{D}}_{\mathrm{fs,II},1}^{-1}\mathbf{K}_{\mathrm{fs,IR}}\right)\mathbf{D}_{\mathrm{fs,LR},0}^{-1} \\ \mathbf{D}_{\mathrm{fs,LR},2}^{-1}&=\mathbf{D}_{\mathrm{fs,LR},1}^{-1}\mathbf{D}_{\mathrm{fs,LR},0}\mathbf{D}_{\mathrm{fs,LR},1}^{-1} \\ &+\mathbf{D}_{\mathrm{fs,LR},0}^{-1}\left(\mathbf{M}_{\mathrm{fs,LI}}\mathbf{K}_{\mathrm{fs,II}}^{-1}\mathbf{M}_{\mathrm{fs,IR}}-\mathbf{M}_{\mathrm{fs,LI}}\tilde{\mathbf{D}}_{\mathrm{fs,II},1}^{-1}\mathbf{K}_{\mathrm{fs,IR}}-\mathbf{K}_{\mathrm{fs,LI}}\tilde{\mathbf{D}}_{\mathrm{fs,II},1}^{-1}\mathbf{M}_{\mathrm{fs,IR}}+\mathbf{K}_{\mathrm{fs,LI}}\tilde{\mathbf{D}}_{\mathrm{fs,II},2}^{-1}\mathbf{K}_{\mathrm{fs,IR}}\right)\mathbf{D}_{\mathrm{fs,LR},0}^{-1} \end{aligned}, \tag{14}$$

where

$$\tilde{\mathbf{D}}_{\mathrm{fs,II},1}^{-1}=\mathbf{K}_{\mathrm{fs,II}}^{-1}\mathbf{M}_{\mathrm{fs,II}}\mathbf{K}_{\mathrm{fs,II}}^{-1},\quad \tilde{\mathbf{D}}_{\mathrm{fs,II},2}^{-1}=\mathbf{K}_{\mathrm{fs,II}}^{-1}\mathbf{M}_{\mathrm{fs,II}}\mathbf{K}_{\mathrm{fs,II}}^{-1}\mathbf{M}_{\mathrm{fs,II}}\mathbf{K}_{\mathrm{fs,II}}^{-1}. \tag{15}$$

The procedure of deriving the transfer matrix required us only one additional matrix inversion for the calculation of $\mathbf{D}_{\mathrm{fs,LR},0}^{-1}$. We again exploit the upper triangular block form of all the stiffness matrices which resolve in the following statement

$$\mathbf{D}_{\mathrm{fs,LR},0}^{-1}=\left(\mathbf{K}_{\mathrm{fs,LR}}-\mathbf{K}_{\mathrm{fs,LI}}\mathbf{K}_{\mathrm{fs,II}}^{-1}\mathbf{K}_{\mathrm{fs,IR}}\right)^{-1}=\left[\begin{array}{c|c} \hat{\mathbf{K}}_{\mathrm{s,LR}} & \hat{\mathbf{S}}_{\mathrm{fs,RL}}^{T} \\ \hline \mathbf{0} & \hat{\mathbf{K}}_{\mathrm{f,LR}} \end{array}\right]^{-1}=\left[\begin{array}{c|c} \hat{\mathbf{K}}_{\mathrm{s,LR}}^{-1} & -\hat{\mathbf{K}}_{\mathrm{s,LR}}^{-1}\hat{\mathbf{S}}_{\mathrm{fs,RL}}^{T}\hat{\mathbf{K}}_{\mathrm{f,LR}}^{-1} \\ \hline \mathbf{0} & \hat{\mathbf{K}}_{\mathrm{f,LR}}^{-1} \end{array}\right], \tag{16}$$

where

$$\begin{aligned} \hat{\mathbf{K}}_{\mathrm{s,LR}}&=\mathbf{K}_{\mathrm{s,LR}}-\mathbf{K}_{\mathrm{s,LI}}\mathbf{K}_{\mathrm{s,II}}^{-1}\mathbf{K}_{\mathrm{s,IR}} \\ \hat{\mathbf{K}}_{\mathrm{f,LR}}&=\mathbf{K}_{\mathrm{f,LR}}-\mathbf{K}_{\mathrm{f,LI}}\mathbf{K}_{\mathrm{f,II}}^{-1}\mathbf{K}_{\mathrm{f,IR}} \\ \hat{\mathbf{S}}_{\mathrm{fs,RL}}^{T}&=\mathbf{S}_{\mathrm{fs,RL}}^{T}+\mathbf{K}_{\mathrm{s,LI}}\mathbf{K}_{\mathrm{s,II}}^{-1}\mathbf{S}_{\mathrm{fs,II}}^{T}\mathbf{K}_{\mathrm{f,II}}^{-1}\mathbf{K}_{\mathrm{f,IR}}-\mathbf{K}_{\mathrm{s,LI}}\mathbf{K}_{\mathrm{s,II}}^{-1}\mathbf{S}_{\mathrm{fs,RI}}^{T}-\mathbf{S}_{\mathrm{fs,IL}}^{T}\mathbf{K}_{\mathrm{f,II}}^{-1}\mathbf{K}_{\mathrm{f,IR}} \end{aligned}. \tag{17}$$

By solving the following eigenvalue problem

$$\mathbf{T}\begin{bmatrix}\mathbf{q}_{\mathrm{L}}\\ \mathbf{Q}_{\mathrm{fs,L}}\end{bmatrix}=\lambda\begin{bmatrix}\mathbf{q}_{\mathrm{L}}\\ \mathbf{Q}_{\mathrm{fs,L}}\end{bmatrix},\qquad \lambda=e^{-ik\Delta}=e^{-i\mu}\ , \tag{18}$$

where λ is the Floquet multiplier, k is the modal wavenumber, Δ is the unit cell length, and μ is the dimensionless wavenumber. Both the propagating and evanescent modes of the waveguide are found.

2.4 Zhong's method

In many cases the matrices $\hat{\mathbf{K}}_{\mathrm{s,LR}}$, $\hat{\mathbf{K}}_{\mathrm{f,LR}}$ may be ill-conditioned, furthermore the eigenvalue problem arises by using the transfer matrix approach is numerically unstable [16]. Zhong and Williams [10] have derived a method of projecting the transfer matrix eigenvalue problem to a numerically stable generalized eigenvalue problem by using symplectic matrices. As part of their derivation it was assumed that the condensed dynamic stiffness matrix $\mathbf{D}_{\mathrm{fs,LR}}$ is symmetric which is not true for our current formulation. We wish to convert the condensed dynamic matrix into a symmetric representation by introducing the following auxiliary variable

$$\boldsymbol{\psi} = \frac{1}{\omega^2}\mathbf{p} \ . \tag{19}$$

It can be shown that substituting the transformation defined by Eq.(19) to the E.O.M of Eq.(6) yields a symmetric dynamic stiffness matrix. Since the condensed dynamic stiffness matrix formulation now contains only inversion addition and multiplication of symmetric matrices it follows that the condensed dynamic matrix must be also symmetric when using the auxiliary variable.

By using Zhong's method a numerically stable generalized eigenvalue problem is derived

$$\begin{bmatrix} \mathbf{D}_{\mathrm{LR}} - \mathbf{D}_{\mathrm{RL}} & -\left(\mathbf{D}_{\mathrm{LL}} + \mathbf{D}_{\mathrm{RR}}\right) \\ \mathbf{D}_{\mathrm{LL}} + \mathbf{D}_{\mathrm{RR}} & \mathbf{D}_{\mathrm{LR}} - \mathbf{D}_{\mathrm{RL}} \end{bmatrix} \mathbf{w} = \frac{1}{\lambda + \lambda^{-1}} \begin{bmatrix} \mathbf{0} & \mathbf{D}_{\mathrm{LR}} \\ -\mathbf{D}_{\mathrm{LR}} & \mathbf{0} \end{bmatrix} \mathbf{w}, \qquad \mathbf{w} = \begin{bmatrix} \mathbf{u}_{\mathrm{L}} \\ \boldsymbol{\psi}_{\mathrm{L}} \\ \frac{\mathbf{u}_{\mathrm{L}}}{\lambda} \\ \boldsymbol{\psi}_{\mathrm{L}} \end{bmatrix} . \tag{20}$$

This equation provides the Floquet multipliers and the projected eigenvectors. The projection of the eigenvectors of the desired modes back to the original coordinates also suffers from numerical difficulties, Waki et al [16] have shown how to find the original generalized coordinates avoiding these difficulties.

2.5 Participation factor by power consideration

The total modal power of each propagating mode in the waveguide is

$$P = -\frac{1}{2}\Re\left\{\mathbf{Q}^H\dot{\mathbf{q}}\right\} = \frac{1}{2}\Im\left\{\omega\mathbf{Q}^H\mathbf{q}\right\} . \tag{21}$$

Where $\bullet^H$ is the transpose conjugate operator and $\Re$, $\Im$ are the real and imagine parts of the complex scalar.

The power propagates either in the fluid medium or in the elastic medium. We now introduce the elastic participation factor (PF) which indicates the ratio of the power that flows through the elastic waveguides of each mode to the total power flowing through both waveguides

$$PF = \frac{P_{\mathrm{s}}}{P} = \frac{P_{\mathrm{s}}}{P_{\mathrm{s}} + P_{\mathrm{f}}} = \frac{\Im\left\{\mathbf{Q}_{\mathrm{s,L}}^H\mathbf{u}_{\mathrm{L}}\right\}}{\Im\left\{\mathbf{Q}_{\mathrm{s,L}}^H\mathbf{u}_{\mathrm{L}}\right\} + \Im\left\{\mathbf{Q}_{\mathrm{f,L}}^H\mathbf{p}_{\mathrm{L}}\right\}} \ . \tag{22}$$

In an ideal rigid wall waveguide the PF will be zero for all the propagating modes at all frequencies. In a more realistic case of a coupled waveguide each mode transfers energy both in the fluid and through the elastic envelope, the closer the PF of a mode is to one-half the mode couples the elastic and the fluid more strongly. Therefore, we can analyze how strongly the fluid-filled waveguide is coupled by examining the propagating modes PF at each frequency.

3 Numerical examples

In this Part five numerical examples are considered. In all of the examples we consider an axisymmetric waveguide, the fluid under consideration is water, the solid is steel, the fluid solid interaction surface is of circular shape with constant radius, the outer solid surface is also of circular shape with constant radius, and the unit cell length is constant. The materials properties and constant geometrical dimensions can be found in Table 1.

Property	Symbol	Dimension	Unit
Water density	ρ_F	1000	Kg/m^3
Water speed of sound	c_F	1500	m/s
Steel density	ρ_S	7800	Kg/m^3
Steel Young's modulus	E	$210 \cdot 10^9$	Pa
Steel Poisson's ratio	ν	0.3	
Inner radius	a	0.01	m
Outer radius	b	0.025	m
Unit cell length	Δ	0.01	m

Table 1: Materials properties and geometrical dimensions for numerical examples.

The first example is of a full cylindrical tube unit cell, Figure 2.A, for which there are analytical solution and its object is to demonstrate the method and to clarify the basics of the FSI coupling effects.

The second and third examples are of a thin square unit cell and X shaped unit cell accordingly, Figure 2.B and 2.C, for which no analytical solution exists and from which we further enrich our knowledge of the FSI coupling effects.

The last two examples are of special unit cells, Figure 2.D and 2.E, from which arise frequency bands that mimics our first example while other frequency bands mimic the propagations of sound in a free fluid medium, in which the fluid and the structure are decoupled. For each of the configuration a change in a single parameter was investigated.

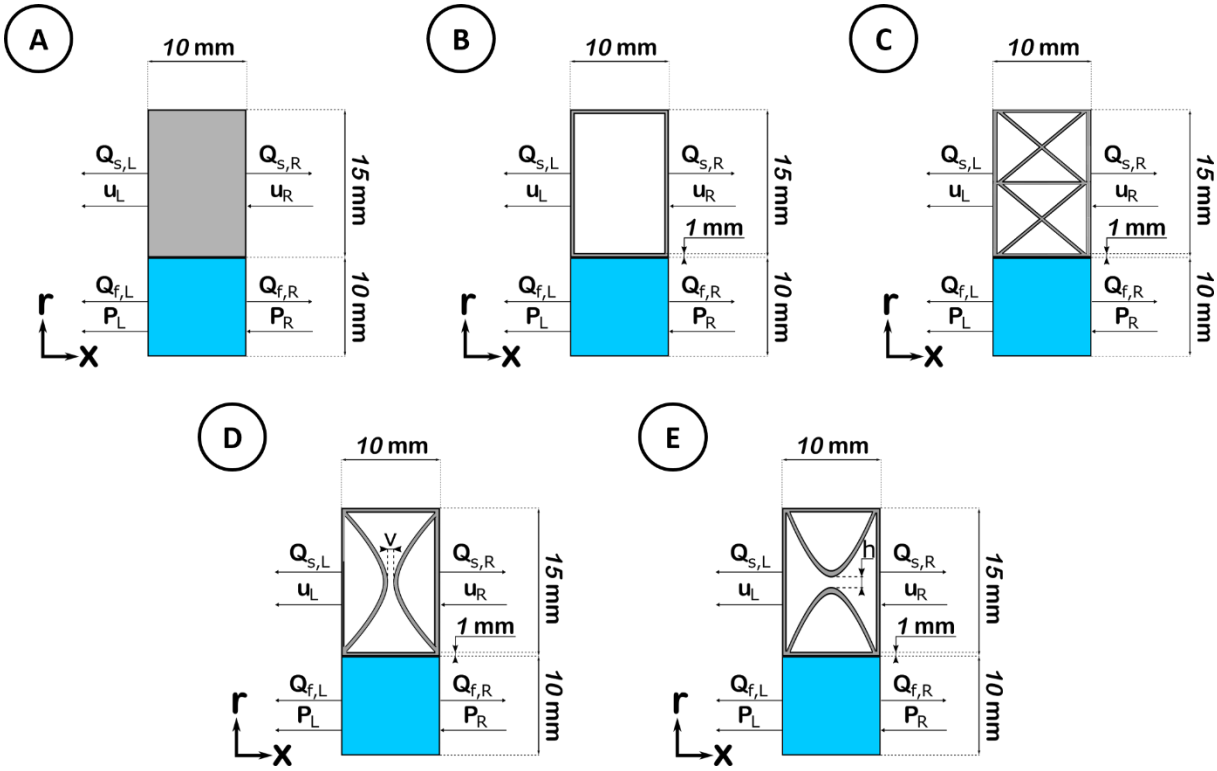


Figure 2: Different unit cell models used in numerical examples: A - a full circular tube, B - thin square unit cell, C - X design unit cell, D - V design unit cell, E - H design unit cell. Blue – water medium. Grey – steel medium.

3.1 Circular tube filled with water

In this section we consider a circular steel tube filled with water, the modal wavenumbers can be found analytically by assuming a normal mode solution in the longitudinal direction of the tube and solving the boundary problem of the radial and circumferential directions [3,4]. Figure 2.A shows the unit cell of the upper half of the axisymmetric tube. The analytical and numerical dispersion curves are presented in Figure 3, in which we can see an excellent agreement of the numerical method results to the analytical ones. It is important to emphasize that even in the simple geometry the complexity of solving the boundary problem to achieve the analytical modal wavenumber is non negligible, in fact it turns out that using the proposed WFE method is faster for the derivation of the dispersion curves.

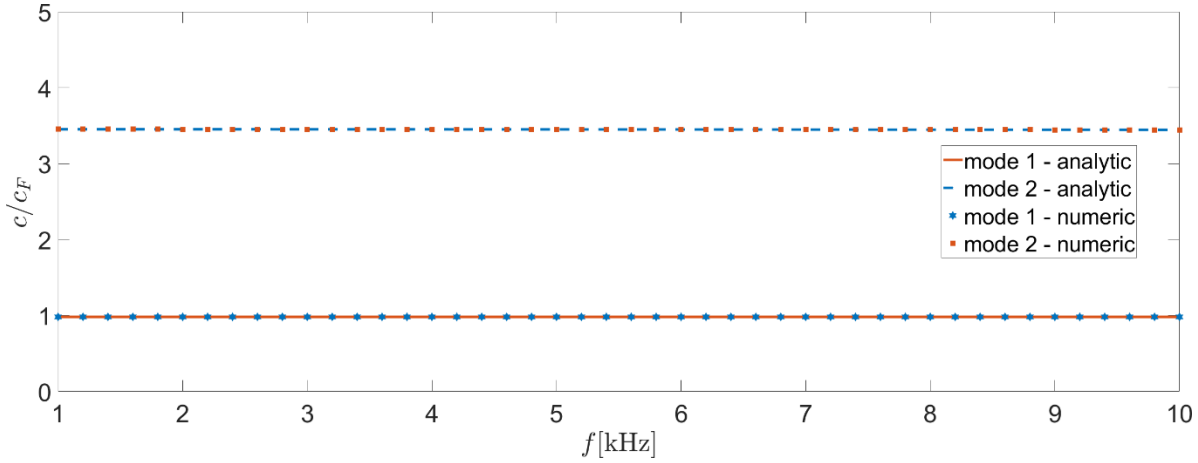


Figure 3: Analytical and numerical dispersion curves of a fluid-filled circular tube.

In a full cylindrical waveguide there are at least two propagating modes at all frequencies [4], the first mode phase velocity is a bit smaller than thus of intrinsic speed of sound of the medium $c_1 / c_F \approx 98\%$ and is almost constant for all frequencies. The second mode phase velocity is larger than the intrinsic speed of sound and its slope is close to constant at small frequencies.

Figure 4 shows the participation factor of each propagating mode we can note that the first mode propagates energy almost exclusively in the fluid domain while the second mode energy propagates both in the fluid and in the elastic domain, in the frequency range between 1-10 kHz the dispersion curves are close to constant and the PF are well separated.

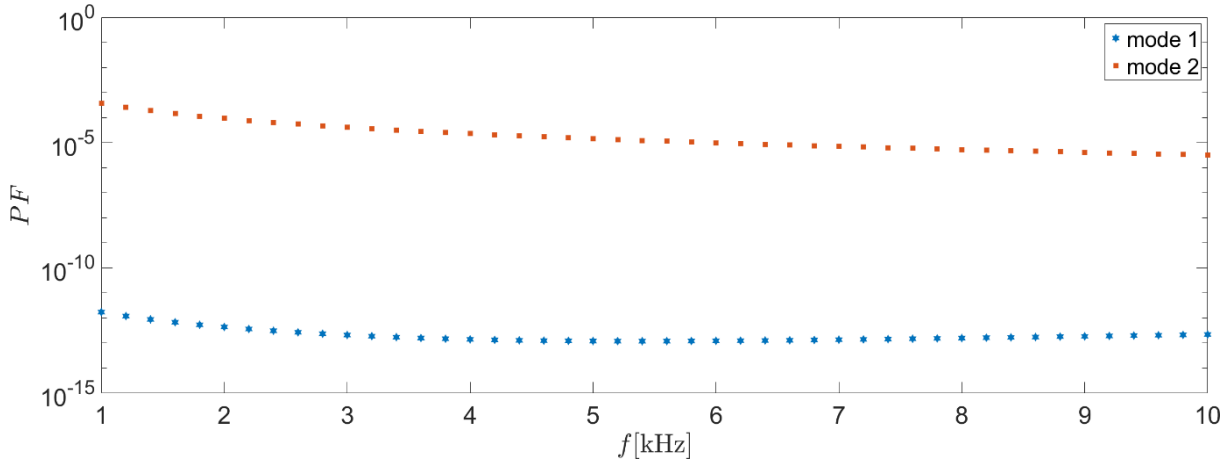


Figure 4: Circular tube participation factor.

3.2 Thin square and X unit cells

In this section we consider two possible configurations of the waveguide, the first (Figure 2.B) is a thin square shell that is supposed to reduce the radial stiffness of the structure and therefore will affect the radial impedance, the second (Figure 2.C) is a thin X shape shell which should maintain the low radial stiffness but increase the capability of the structure to endure radial pressure.

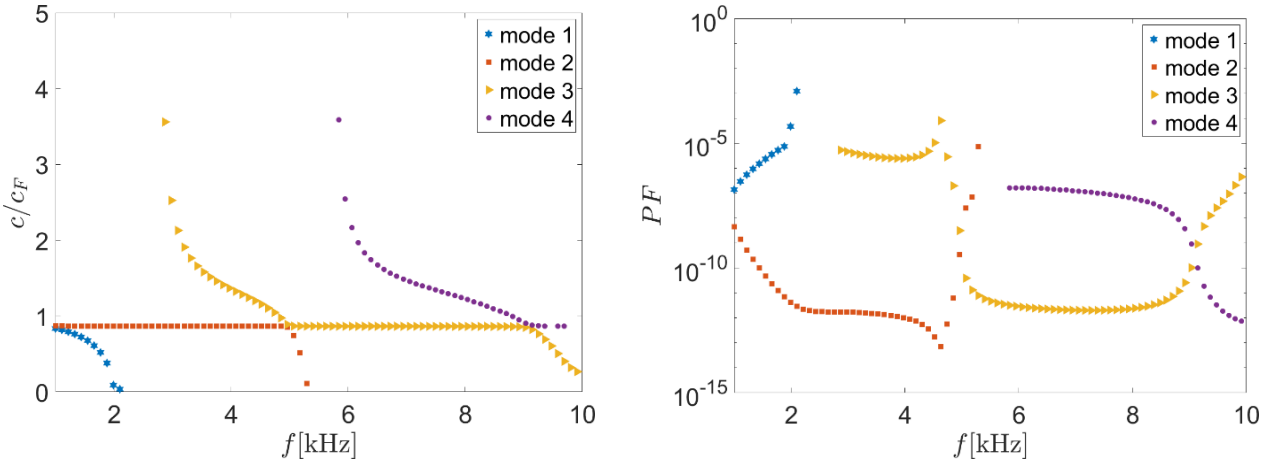


Figure 5: Left – thin square unit cell dispersion curves. Right – thin square unit cell participation factor.

Figure 5 shows that at low frequency range we have two propagating modes in the waveguides which have a similar phase velocity, the first mode's phase velocity decreases at higher frequencies until it reaches the stop band at 2.1 kHz, the PF of the two modes at low frequencies are also close but as we approach the stop band the PF of the second mode decrease while the PF of the first mode increase rapidly, which means that the power is concentrated in the fluid. In the stop band only the second mode propagate, its phase velocity

is smaller than thus of the intrinsic speed of sound $c_1 / c_F \approx 87\%$ and its power factor resembles that of the first mode of the circular tube. The first cut-off frequency is 2.87 kHz, the third propagating mode PF resembles that of the second mode of the circular tube while its phase velocity decrease rapidly. At frequency of 5 kHz the second and third modes switches roles, afterward the second mode decay and another stop band starts, until a second cut off frequency at 5.84 kHz. Then the two propagating modes behave as in the previous pass band.

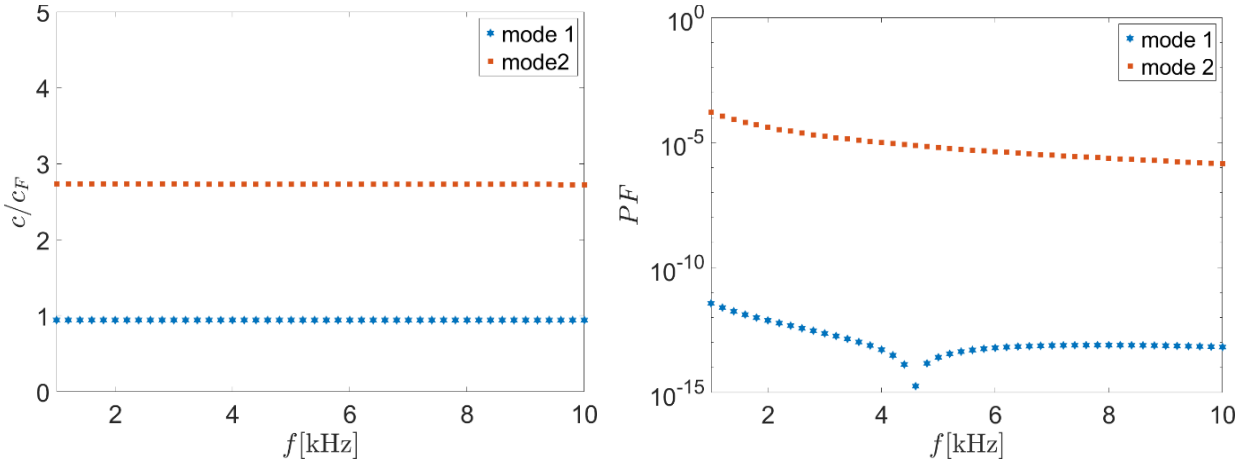


Figure 6: Left – X design unit cell dispersion curves. Right – X design unit cell participation factor.

Figure 6 shows that the X unit cell modes behave more similarly to thus of the circular tube, the first mode phase velocity is closer to thus of the intrinsic speed of sound of the medium $c_1 / c_F \approx 94\%$ then that of the square shell, the second mode phase velocity is smaller than that of the second mode of the circular tube, but its slope resembles that of the second mode of the circular tube. The PF of the x unit cell is similar to that of the circular tube, the main difference is the antiresonance of the first mode PF at 4.6 kHz, a further investigation of the structures dynamics is need in order to understand the physical meaning of these antiresonance and to use them in future design.

3.3 V and H unit cells

We wanted to design a section that will give us a clear stop band similar to this of the square shell while still having a large cut-off frequency and capability to withhold large pressures similar to the x section therefore we suggested two unit cells which resembled the thin square but added non isotropic stiffness by using bend leaf springs that has a minimal longitudinal distance of v in the V unit cell and minimal radial distance of h in the H unit cell as shown in Figure 2.D and 2.E**.**

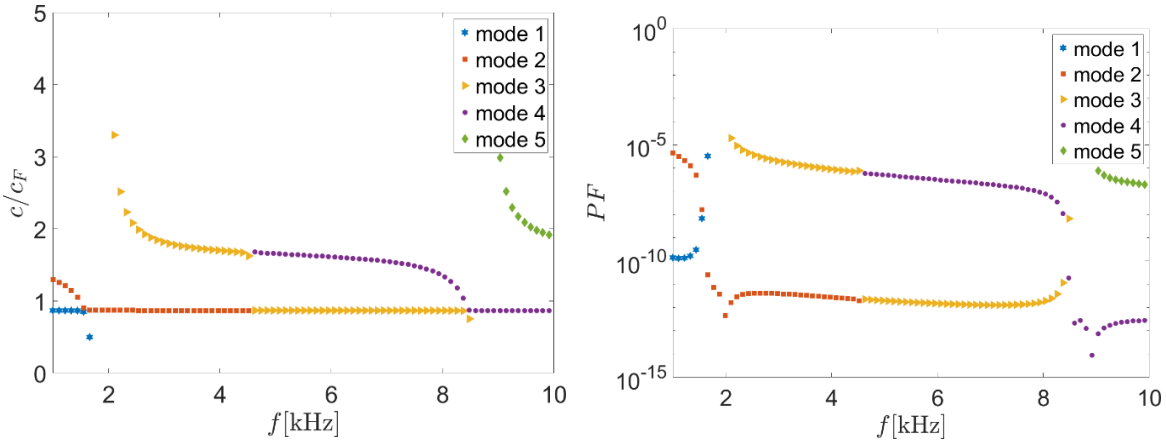


Figure 7: Left – V unit cell dispersion curves. Right – V unit cell participation factor. v = 1.5 mm.

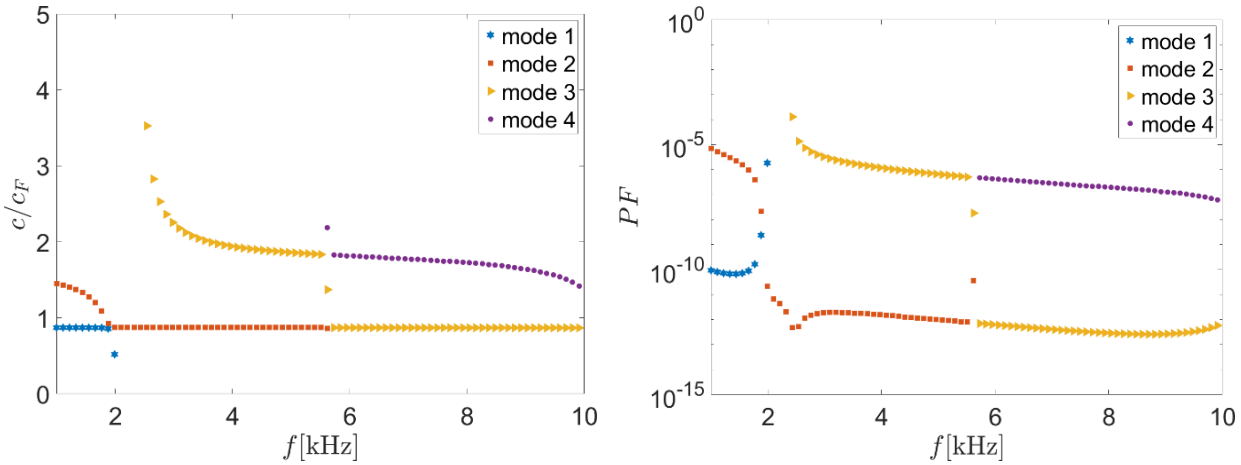


Figure 8: Left – H unit cell dispersion curves. Right – H unit cell participation factor. h = 1.5 mm.

Figure 7 shows that at low frequencies the V unit cell has similar behavior to that of the thin square the first and second modes propagate at close phase velocities, where the first mode phase velocity is again smaller than the intrinsic speed of sound $c_1 / c_F \approx 87\%$ .Around frequency of 1.5 kHz the first mode phase velocity decays rapidly and the second mode phase velocity takes its place, the same can be seen from the PF of the two modes. At a frequency of 1.69 kHz a stop bands start in which the second mode phase velocity has constant slope, but the PF has an antiresonance similar to the one observed at the X unit cell. The first cut off frequency is near 2 kHz, after the cut off frequency the third mode phase velocity has almost constant slope and the PF of the second and third modes in this frequencies range are well separated. At frequency of 4.5 kHz another cut off occur the second mode stops propagating, the third mode propagate takes its role and the fourth modes take the role of the third mode. The PF between at the second pass band resembles these of the full tube but the higher phase velocity differs significantly.

Figure 8 shows that the H unit cell behave almost the same as the V unit cell, but at a scaled frequency axis. To analyze the differences in the behavior between the V and H unit cells we define four zones of interest. The first is at low frequencies up to the first stop band, the second is the first stop band up to the first cut off, the third is from the first cut off up to the second cut off, and the fourth is from the second cut off up to the second stop band. Table 2 shows the lowest mode normalized phase velocity and the four zone frequencies width for different values of v and h.

	c_1 / c_f [%]	$\Delta f_{\text{zone I}}$ [kHz]	$\Delta f_{\text{zone II}}$ [kHz]	$\Delta f_{\text{zone III}}$ [kHz]	$\Delta f_{\text{zone IV}}$ [kHz]
v=1.5[mm]	87	1.69	0.37	2.49	3.98
v=2.5[mm]	87.1	1.56	0.37	2.26	3.71
h=1.5[mm]	86.7	2.03	0.48	3.14	5.35
h=2.5[mm]	87.1	2.02	0.48	3.13	5.34

Table 2: First mode phase velocity and the four zones frequencies range for different V and H unit cells.

We can see that the H unit cell zones have a larger frequency width, while having almost the same phase velocity for the first mode. This fact gives us the ability to mimic the desired behavior at a larger frequency range and can be taken into account at future designs depends on the desired behavior. Also, the change in the distance, either v or h, has not changed any property significantly when comparing to the same design.

4 Concluding remarks

The wave propagation model of fluid-filled waveguides is the basis of many non-destructive models. Analytic solution exists only for simple geometries and therefore numerical approaches are needed. Using periodic structure as the elastic envelope of the waveguide allow us to manipulate the dispersion curves at specific frequencies range. The need for a design parameter for fluid-filled waveguides is crucial for many engineering problem. The wave finite element method uses the finite element method to derive the dynamic model of a unit cell. Then the Floquet's multipliers, the propagating and the evanescent modes are found numerically from the condensed dynamic model that connect the surfaces at each end of the unit cell. The classical numeric approach for the condensation process suffers from ill-conditioning and therefore an improvement in the form of series expansion is proposed. The eigenproplem associated with the Floquet's multipliers also suffers from ill-conditioning since each multiplier comes in pairs of λ and λ^{-1}. By using auxiliary problem we symmetrize the non-symmetry dynamic model, then by using symplectic algebra a numerically stable projection of the eigenproblem is solved. A participation factor is suggested, which allow us to observe the prefer medium of energy flow for each propagating mode at various frequencies.

A simple example, of a water filled cylindrical tube, shows an excellent agreement of the suggested method to analytic solution. By investigating the participation factor of each mode the coupling behavior of the cylindrical tube is better understood. This is followed by several examples of complex geometries for which no analytic solution exist. The numerical examples shows that for the coupled problem a slow model always propagates at a phase velocity smaller than that of the fluid medium and a small participation factor. A second mode propagates in the pass band frequencies, at the start of each stop band the second mode replace roles with the first, slow mode, and the first mode decays. The participation factors of the different examples is also studied and at discreet frequencies antiresonance are observed for some of the examples. This anomalies may be connected to zeros or resonances of one of the subsystems of the coupled waveguide. A further investigation is needed in order to understand the cause for those antiresonances so we will be able to use them to achieve our design goal.

In summary, the wave finite element method suggested here can be used as the basis of analyzing and designing method of fluid-filled waveguides. The participation factor allows us to investigate the dynamic coupling from energy flow perspective. Therefore, the participation factor may be used as the basis of a geometrical optimization problem that will able us the designing of a tailored waveguide capable of exhibit strong of weak coupling at different frequencies as needed from its applications.

References

[1] U. Ingård, *On the Radiation of Sound into a Circular Tube, with an Application to Resonators*, The Journal of the Acoustical Society of America. 20 (1948) 665.

[2] A. Pierce, *Acoustics: an introduction to its physical principles and applications*, 1981.

[3] V.A. Del Grosso, *Analysis of Multimode Acoustic Propagation in Liquid Cylinders with Realistic Boundary Conditions- Application to Sound Speed and Absorption Measurements*, Acustica. 24 (1971) 299–311.

[4] L.D. Lafleur, F.D. Shields, *Low- frequency propagation modes in a liquid- filled elastic tube waveguide*, The Journal of the Acoustical Society of America. 97 (1995) 1435–1445.

[5] L. Brillouin, *Wave Propagation in Periodic Structures: Eletric Filters and Crystal Lattices*, 1946.

[6] D.J. Mead, *Wave propagation in continuous periodic structures: Research contributions from Southampton, 1964-1995*, Journal of Sound and Vibration. 190 (1996) 495–524.

[7] M.I. Hussein, M.J. Leamy, M. Ruzzene, *Dynamics of Phononic Materials and Structures: Historical Origins, Recent Progress, and Future Outlook*, Applied Mechanics Reviews. 66 (2014) 040802.

[8] Y.K. Lin, T.J. McDANIEL, *Dynamics of Beam-Type Periodic Structures*, Journal of Engineering for

Industry. (1969) 1133–1141.

[9] G. Sen Gupta, *Dynamics of Periodically Stiffened Structures Using a Wave Approach*, Southampton University, 1971.

[10] W.X. Zhong, F.W. Williams, *on the Direct Solution of Wave-Propagation for Repetitive Structures*, Journal of Sound and Vibration. 181 (1995) 485–501.

[11] W.X. Zhong, F.W. Williams, *Wave Problems for Repetitive Structures and Symplectic Mathematics*, Proceedings of the Institution of Mechanical Engineers, Part C: Journal of Mechanical Engineering Science. 206 (1992) 371–379.

[12] B.R. Mace, D. Duhamel, M.J. Brennan, L. Hinke, *Finite element prediction of wave motion in structural waveguides*, The Journal of the Acoustical Society of America. 117 (2005) 2835–2843.

[13] D. Duhamel, B.R. Mace, M.J. Brennan, *Finite element analysis of the vibrations of waveguides and periodic structures*, Journal of Sound and Vibration. 294 (2006) 205–220.

[14] J.M. Mencik, M.N. Ichchou, *Wave finite elements in guided elastodynamics with internal fluid*, International Journal of Solids and Structures. 44 (2007) 2148–2167.

[15] J.M. Mencik, M.N. Ichchou, *A substructuring technique for finite element wave propagation in multi-layered systems*, Computer Methods in Applied Mechanics and Engineering. 197 (2008) 505–523.

[16] Y. Waki, B.R. Mace, M.J. Brennan, *Numerical issues concerning the wave and finite element method for free and forced vibrations of waveguides*, Journal of Sound and Vibration. 327 (2009) 92–108.

[17] J.M. Renno, B.R. Mace, *On the forced response of waveguides using the wave and finite element method*, Journal of Sound and Vibration. 329 (2010) 5474–5488.

[18] J.M. Mencik, D. Duhamel, *A wave-based model reduction technique for the description of the dynamic behavior of periodic structures involving arbitrary-shaped substructures and large-sized finite element models*, Finite Elements in Analysis and Design. 101 (2015) 1–14.

[19] I. Bucher, R. Gabai, H. Plat, A. Dolev, E. Setter, *Experimental travelling waves identification in mechanical structures*, Mathematics and Mechanics of Solids. (2017).

[20] Simulia, *Abaqus 6.14 Theory Guide*, Providence, RI ., 2014.

[21] D.J. Mead, *Vibration response and wave propagation in periodic structures*, Journal of Engineering for Industry. 93 (1971) 783–792.

[22] D.J. Mead, *General theory of harmonic wave prop in linear periodic systems with multiple coupling*, Journal of Sound and Vibration. 27 (1973) 235–260.

[23] D. Bernstein, *Matrix mathematics: Theory, facts, and formulas with application to linear systems theory*, 2005.

Resonant metabarriers as seismic attenuators in granular media

R. Zaccherini[1], A. Palermo[2,3], S. Krödel[4], V. K. Dertimanis[1], A. Marzani[2], C. Daraio[3], E. N. Chatzi[1].
[1] ETH Zürich, Zürich, Switzerland, Department of Civil, Environmental and Geomatic Engineering
Stefano-Franscini-Platz 5, 8093 Zürich, Switzerland
e-mail: **zaccherini@ibk.baug.ethz.ch**

[2] University of Bologna, Bologna, Italy, Department of Civil, Chemical, Environmental and Materials Engineering - DICAM
Zamboni 33, 40126 Bologna, Italy

[3] California Institute of Technology, Division of Engineering and Applied Science
California Blvd 1200 E, MC 104-44, Pasadena, California 91125, USA

[4] ETH Zürich, Zürich, Switzerland, Department of Mechanical and Process Engineering
Leonhardstr. 21, 8092 Zürich, Switzerland

Abstract
Arrays of surface resonators forming so-called metabarriers are capable of converting seismic Rayleigh waves into less dangerous shear waves traveling in the bulk, attenuating the ground motion at the surface. However, this phenomenon pertains to resonant materials inserted in homogeneous media which feature properties rather different to those of natural soils. In this work, we experimentally investigate the ability of a resonant metabarrier embedded below the surface of an inhomogenous medium, i.e. a granular unconsolidated material, to attenuate the incoming surface waves. Although unable to diverge their propagation into the bulk, we find that surface resonators in granular media achieve attenuation of Rayleigh waves by up to 50 % around their resonant frequency. The findings can be used as a starting point for future real-scale implementations for seismic protection systems in stratified soils presenting an inhomogeneous stiffness profile at the seismic Rayleigh waves scale.

1 Introduction

Locally resonant metamaterials are artificial composites capable of affecting wave propagation at diverse wavelengths [1, 2, 3]. They typically comprise structured arrangements of repetitive elements whose size and spacing is smaller than the wavelengths they affect. As artificial materials, they exhibit properties that do not stem from the properties of the base materials, but instead from the particular geometry and arrangement of their units. In particular, it has been shown that resonant metamaterials are capable of blocking [4], absorbing [5], focusing [6, 7], or bending elastic waves [8]. A primary challenge lies in extending the potential of metamaterials to protect critical civil infrastructures from seismic waves, a task that naturally brings forth a question of scale. To date, proposed schemes explore designs of metastructures arranged around or underneath the foundations of critical infrastructures to open band gaps in the low frequency spectrum of seismic waves and thereby act as a “seismic shield”. Cylindrical resonators with four side holes [9], chain of mass-in-mass system consisting of cycloidal pendulum swinging in the opposite direction to the seismic oscillation [10] or arrays of iron spheres, each one connected to a bulk of concrete through six iron or rubber ligaments [11], form some of the metastructure designs proposed for attenuation of seismic waves in homogeneous media. In the context of surface waves

mitigation, a proof of applicability of such metamaterials has been offered by a forest, densely populated with trees [12], that can act like a “natural” resonant metamaterial for Rayleigh waves. In a forest, the surface wave bandgaps originate from the coupling between the vertical component of the incoming waves and the trees, which behave like vertical resonators. The same concept has been exploited to design a resonant metabarrier comprising meter-size resonant units embedded below the soil surface [13], capable of converting seismic Rayleigh waves into less harmful shear bulk waves. In detail, around the resonant frequency of the units, the Rayleigh wave energy diverges from the surface due to the classical "avoided crossing" behavior between Rayleigh-like solutions and local resonances [14]. This phenomenon can be broadened in frequency utilizing arrays of vertical oscillators with smoothly varying natural frequencies, exploiting a rainbow trapping (or metawedge) arrangement [15].

However, in most cases, seismic waves do not propagate through homogeneous media. In fact, soil is typically anisotropic and inhomogenous and exhibits a non-linear elastic behavior even at small level of strain [16]. To account for more realistic soil conditions, the homogeneous soil assumption may be replaced, at a first step, with an unconsolidated granular material. Granular media feature a stiffness profile (i.e. a shear G and bulk B elastic profile), that follows a power-law dependency with the compacting pressure $p = \rho g z$, where ρ designates the density, g the gravitational constant and z the depth. This assumption allows for the consideration of diverse aspects that are typical of soil dynamics, as the propagation of multi-modal dispersive surface waves [17]. Unlike the propagation in homogeneous media, where non-dispersive Rayleigh waves occur due to the coupling between pressure P and shear waves SV at the stress-free surface, in unconsolidated granular media multiple, dispersive surface waves arise as a result of the so-called "mirage" effect [18], i.e. the upward bending of the compressional and shear rays which couple in each point of the granular material. These surface acoustic waves, guided between the surface and deep stiffer layers [19], present a sagittal polarization and resemble the fundamental (non-dispersive) Rayleigh solutions for a strong pressure compaction of the granular packing [20], hence the term Rayleigh-like waves. Recent studies [19,21] have revealed the existence of an infinite number of these acoustic modes propagating within the surface granular layer with very low velocities.

Our previous study on the interaction of sagittal waves travelling in granular media and a metabarrier [22] disclosed that the conversion of surface waves into less harmful shear waves, observed in homogeneous media, is prevented by the stiffness gradient of the material. In more detail, when surface waves in granular materials encounter a resonant metabarrier, the fundamental first order mode strongly couples with the surface resonators which swing in phase with the granular medium channeling the energy to the surface. The dispersion curve of this hybrid mode is akin to the lower branch of a Rayleigh wave when interacting with surface resonators [13,15]. Conversely, no hybridization occurs between the higher order surface modes and the vertical oscillators and there is no dispersion branch akin to the upper repelling branch of Rayleigh waves when interacting with surface resonators [13,15].

The extent of mitigation offered by the metabarrier remains a topic that is open for exploration. To this end, we here extend our experimental investigation to characterize the surface wave attenuation offered by a small-scale resonant metabarrier in an unconsolidated granular medium. The metabarrier consists of a grid of sub-wavelength mechanical oscillators, employed in Ref. [22], embedded under the surface of the granular medium. Here, we first examine the interaction between Rayleigh-like waves and the surface resonators. Then, we estimate the overall wave mitigation induced by the metabarrier at the surface. In particular, we investigate the amount of the particle velocity attenuation produced by the small-scale metabarrier at different frequency values, close to the natural resonant frequency of the surface oscillators.

2 Laboratory setup and Measurements

The unconsolidated granular medium employed in the small-scale experiment consists of silica micro particles with a diameter of 150 μm and density 1600 kg/m^3. The material presents compressional and shear wave speeds defined through a power-law expression $V_{P,S} = \gamma_{P,S} \cdot (\rho g z) \cdot \alpha_{P,S}$ [19, 23] where g represents the gravity acceleration, ρ the material density and z the depth. We assume the same coefficients values obtained in [19] for the same material: $\gamma_P = 14.4$, $\gamma_S = 6.42$, $\alpha_P = 0.31$, $\alpha_S = 0.31$. Such parameters slightly deviate from those predicted by the Hertz-Mindlin theory due to the strong

contact disorders among granular particles caused by little imperfections of their sizes and shapes [20, 21, 24]. The material is poured inside a wooden box (2000x1500x1000 mm) up to 830 mm in height (see Fig. 1a), after a paperboard plate is inserted at the bottom to reduce the wave reflections from the crate base. We mix the medium and flatten the surface before each data recording to achieve a uniform compaction of the material. The same experimental setup has been used to study the interaction between surface resonators and guided surface acoustic modes [22].

The small-scale metabarrier comprises 102 vertical resonators (height 24 mm, diameter 20 mm) embedded under the surface of the granular medium in a triangular lattice arrangement (12 lines, with 8-9 resonators alternately per line) with a lattice constant a = 2.5 cm (see Fig. 1c). Such arrangement allows attaining the highest resonator density at given lattice constant and, accordingly, the greatest ground motion attenuation when embedded in a homogenous medium [13]. Each resonator is made up of a cylindrical steel mass (height 12 mm, diameter 12 mm) glued on top of a spring designed with a truss-like geometry. A rigid cylindrical shell encloses the internal structure of the resonator (Fig. 1b). Both the spring and the cylindrical casing are 3D-printed in Acrylonitrile Butadiene Styrene ($E = 2.5\,GPa,\ \nu = 0.3,\ \rho = 1400\,Kg/m^3$). Only the first vertical frequency is taken into account during the resonator design process. The vertical frequency of the resonators, which depends on the diameter, the length and the angle values of the truss elements, is set to 500 Hz. This value is experimentally calculated and verified by exciting the resonators by means of a piezo actuator. However, after inserting the resonators in the granular medium, we register a significant shift of the natural frequency to $f_r = 410\,Hz$, ascribable to the soft behavior of the granular material that acts as a further spring in series with the resonator truss-like spring.

The medium is mechanically excited by an 8-mm diameter metallic rod attached to an electromagnetic shaker and buried in the granular material with an angle of 20° from the normal to the free surface, 375 mm distance from the box edge. The shaker is driven by a waveform generator, which produces a Ricker waveform centered at 500 Hz, as the frequency of the resonators. We record the surface velocity field generated by the point source by means of a Laser-Doppler vibrometer mounted on a scanning stage moving in a two-dimensional plane parallel to the surface. A very thin layer of a powdered sand (150-250 μm-diameter Glasperlen) is spread at the surface in order to enhance the laser signal quality. At each measurement point, 32 signals are averaged by means of an oscilloscope in order to decrease the signal to noise ratio. The employed processes are controlled via a MATLAB interface.

We measure, by means of the vibrometer, the particle velocity at the surface along the 1000 mm-long middle line of the box with constant step of Δx=6 mm (line measurement) and over a 330x600 mm area with constant steps of Δx=8.5 mm (area measurement). To investigate the attenuation properties of the resonant metabarrier, identical measurements are performed with and without the resonators.

3 Underlying Physics

3.1 Interaction between a resonant metabarrier and guided surface acoustic modes in granular media

We recall the fundamentals of the dynamics of guided surface acoustic modes interacting with an array of vertical resonators. The reader may refer to Ref. [22] for a more exhaustive explanation of such interaction.

Guided surface acoustic modes (GSAMs) arise from the combination of compressional (P) and shear (SV) waves [20], bent and driven toward the surface by the depth-increasing stiffness profile of the granular medium. Recent experimental observations reveal the existence of an infinite number of these surface P-SV waves, characterized by very low propagation speeds due to the drop in granular packing rigidity near the free surface [21].

To predict the dispersive properties of surface P-SV waves travelling in the experimental setup, we model a portion of the granular medium with a Bloch wave–finite element (FE) approach. In particular, we develop a 2D model of the unit cell, a vertical stripe of the granular medium in plane-strain conditions

using COMSOL Multiphysics©. The Bloch form wave solution is obtained by applying periodic Bloch-Floquet boundary conditions (BCs) at sides of the unit cell. The properties of the material are defined by means of its density and its compressional and shear velocities. The unit cell has a height $h = 3m$ and a width $d = 0.012m$, which allows the wavenumber to reach the value $k_{max} = 260\,rad/m$. We impose free boundary conditions at the surface and clamped condition at the bottom. Moreover, we insert a Perfectly Matched Layer (PML) at the bottom region to avoid wave reflection. In accordance with the findings of recent studies on GSAMs traveling in unconsolidated granular media [19], an infinite number of surface modes arise from the dispersion relation. Fig. 2a shows the dispersion curves of the first five low-order GSAMs. It is worth pointing out that the order of these modes corresponds to the number of zeros in their vertical displacement profiles along the depth, including the one at $z \to \infty$, or the number of "phases" [19,22] (see fig. 2b).

Similarly, to evaluate the dispersive properties of surface waves while interacting with the metabarrier, we consider a 2D model of the unit cell consisting of a vertical stripe of the granular medium with a resonator modelled as a truss-mass point element (of mass $m_{eq} \cdot d = m_r \cdot A$ and frequency f_r, where m_r is the resonator mass and A is the surface area over which the resonator stress is considered distributed uniformly). Fig. 3a shows the dispersion curves of the first five low-order GSAMs when interacting with the resonant metabarrier and fig. 3b their displacement depth profiles. The dispersion curve of the first-order mode (P-SV_{1_m}) becomes completely flat around the natural frequency of the resonators (410 Hz) due to the hybridization occurring between the first-order P-SV_1 wave and the resonators (see Fig. 3a). This mode resembles the lower branch of a Rayleigh wave when coupling with the resonators [13,15]. The other GSAMs (P-SV_{2_m}, P-SV_{3_m}, P-SV_{4_m}, P-SV_{5_m}) are not hybridized but they undergo a so-called down-conversion mechanism at the antiresonance (460 Hz) [21]: their displacement depth profile loses one of its phases and is transformed into the profile of the previous-order mode (see Figs. 2b-3b). The absence of the repelling upper branch, typical of Rayleigh waves when interacting with surface resonators, confirms that GSAMs do not withstand the Rayleigh-to-shear conversion phenomenon observed in homogeneous media, here prevented by the gravity-induced stiffness gradient of the granular medium [22].

4 Results and Discussion

4.1 1D Seismograms and Dispersion Relations

The seismograms with (Fig. 4b) and without (Fig. 4a) the metabarrier computed from the line measurement illustrate the dispersive behavior of the granular medium. Although several acoustic modes occur, only two wavetrains dominate the seismogram without the resonators (Fig. 4a), carrying most of the energy: a quasi-compressional (P) wave and a packet of Rayleigh-like (P-SV) waves, traveling at lower velocities. In the seismogram with the resonators (Fig. 4b), the wavetrains previously identified appear together with new surface modes, direct and reflected, generated by the interaction between resonators and waves. The six vertical lines, located from 0.22 to 0.52 m, represent the oscillations of the resonators. Surface waves coming out from the metabarrier exhibit reduced amplitudes, whereas higher particle velocities occur in front of the resonant region (from 0.1 to 0.22 m from the source) due to the wavefield reflection. It is worth noting that the overall wave mitigation detected at further distances from the source depends not only on the interaction between resonators and waves, but also on the geometric spreading and material damping. Since these two phenomena affect our experimental data, and in order to rule out the portion of attenuation ascribable to the geometric spreading and the material damping, we will next compare the particle velocity spectra with and without the resonators at the same positions.

We compute the dispersion relations with (Fig. 5b) and without (Fig. 5a) the metabarrier from the linear Radon transform of the seismograms, restricting our analysis to the P-SV modes. The blue dotted curves in Figs. 5a-b represent the dispersion curves of the first two order surface waves obtained from the numerical models. The experimental dispersion relation without the metabarrier (Fig. 5a) displays the frequency content and the phase velocity of the first two order P-SV modes dominating the seismograms.

The first order P-SV_1 wave travels at 60-80 m/s, the second order P-SV_2 at 50 m/s. The numerical curves are in excellent agreement with the experimental ones. The experimental dispersion relation of P-SV waves travelling within the metabarrier confirms the hybridization between the first order P-SV_1 wave and the metabarrier resonance (Fig. 5b). The hybrid mode P-SV_{1_m} presents a close-zero phase velocity around the resonant frequency (410 Hz), which results from the energy confinement of the resonators. In fact, the P-SV_{1_m} carries most of the energy, thus saturating the spectrum, and, consequently, no trace of the second P-SV_{2_m} mode can be detected from the experimental data. Nonetheless, the numerical prediction (blue dotted lines in Fig. 5b) reveals the absence of the hybridization phenomenon between the second order surface mode and the metabarrier, as already explained in the "Underlying Physics" section.

4.2 Surface wave spectra

To get further insight into the amplitude reduction at the surface, we analyze the particle velocities computed from the line measurement with (Fig. 6b) and without (Fig. 6a) the resonators in the frequency domain, as a function of both the distance from the source and the frequency. The medium appears mainly excited in the frequency range 200-500 Hz (Fig. 6a). This is expected since the excitation signal used, the Ricker wavelet, is centered at 500 Hz and because the surface modes carrying more energy present a frequency content within that range [22]. Moving away from the source, the amplitude decreases due to geometric spreading and material damping. When analyzing the surface wave spectrum with the resonators (Fig. 6b), the particles located before the metabarrier, which is placed between 0.22-0.52 m from the source, show larger amplitudes, particularly for frequency values beyond 410 Hz, confirming the wave reflection previously observed in the seismogram (Fig. 4b). The six red vertical lines represent the oscillations of the resonators going in resonance. Conversely, the particles located behind the metabarrier, beyond 0.55 m from the source (Fig. 6b), present lower velocity amplitudes due to the interaction between resonators and surface waves. The largest attenuation occurs within the frequency range from 400 to 550 Hz, nearby the resonator resonant frequency 410 Hz. To this reason, we deepen our study to the experimental data within the frequency range 400-550 Hz, where we expect to measure the highest attenuation.

4.3 Surface area attenuation and Surface Attenuation along the symmetry axis of the sandbox

To quantify the wave attenuation at the surface, we analyze the frequency domain data recorded over the area (area measurement) with and without the resonators. In particular, for each position in the surface area, we evaluate the ratio ($V_{with}/V_{without}$) between the maxima of the particle velocity with (V_{with}) and without ($V_{without}$) the resonators computed between 400 and 550 Hz. Results, shown in Fig. 7, clearly highlight the wave mitigation produced by the metabarrier. The color intensity scale is set from 0 to 2 to better show the attenuation of the particle motion. A significant portion of energy is gathered on the resonators (round red dots) going in resonance: the Laser-Doppler vibrometer records amplitudes five times greater when passing on them. The red wavefront, located in front of the metabarrier, proves that a part of surface waves is reflected backward. As a whole, we measure a reduction of particle motion up to 50% (blue color) behind the metabarrier and by around 25% at sides (light-blue color).

To better highlight the dependence of the attenuation intensity on frequency, we display the particle velocities recorded along the symmetry axis of the sandbox at three different values of frequency: 425 Hz (Fig. 8a), 475 Hz (Fig. 8b) and 525 Hz (Fig. 8c), between 400 and 550 Hz, namely the frequency range of the detected attenuation zone. The velocity values are displayed as a function of the distance from the source with (red dots) and without (green dots) the resonators. The two grey dotted vertical lines mark the position of the metabarrier. At the front of the metabarrier (0.1-0.22 m from the source), the particle velocity when the resonators are embedded (red dots) exceeds the one (green dots) without the metabarrier. The amount of wave reflection does not change significantly in the three panels at different frequency values, suggesting that the reflection mechanism stems from the pure coupling between P-SV modes travelling respectively in the pristine granular material and in the granular material endowed with

vertical resonators. Conversely, the attenuation detected both within the metabarrier and behind it, is reduced for increasing frequency values beyond the resonator frequency 410 Hz. In particular, the velocity particle reduction produced by the metabarrier is higher at 425 Hz, the frequency value closest to the resonant frequency (410 Hz). This decrease in particle motion may be primarily attributed to the interaction between the surface modes and the resonators. In all the three panels, right after the end of the metabarrier (0.52 m from the source), we detect a slight increase of the particle velocity, which reveals that part of the surface waves is driven under the resonator array when encountering the resonant region, and eventually re-emerge at the surface.
We remark that the noticeable oscillations, present in all the three panels both with and without the resonators, are a characteristic of the surface modes travelling in a vertically heterogeneous medium [16].
To rigorously determine the amount of attenuation that the small-scale metabarrier is capable of producing, we evaluate the particle velocity reduction detected when the metabarrier is embedded below the soil surface at 425 Hz (see Fig. 8a) as follows:

$$Att(r) = 100 \cdot \frac{U(r) - U_{res}(r)}{U(r)} \tag{1}$$

where $U(r)$ and $U_{res}(r)$ represent the particle velocity without and with the resonators, respectively, and r is the distances from the source. The result is displayed in Fig. 8d: within the resonant region, we detect an attenuation up to 90 %, behind it up to 60 %, on average. The major attenuation perceived within the resonant region suggests the most effective location to place these metastructures is under the foundations of building.

5 Conclusions

We experimentally analyzed the attenuation produced in a small-scale experiment comprising a seismic metabarrier composed of 102 sub-wavelength resonators arranged under the surface of an unconsolidated granular material in a triangular lattice arrangement. Although the particular depth-increasing stiffness profile of the medium prevents the delocalization mechanism of surface waves observed in homogeneous media, a significant attenuation is detected, especially in the frequency range 400-550 Hz, around the natural frequency of the resonators. Such wave mitigation is induced by the hybridization mechanism involving surface waves and resonators. We find that the largest attenuation is obtained within the metabarrier, meaning that the best place to arrange the metastructure would be underneath the foundations of buildings. In order to enhance the performance of the metabarrier, the so-called rainbow-trapping mechanism [24] could be exploited by varying the frequency of each resonator line along the metastructure.
The findings are further valid in stratified soils featuring a power-law elastic profile at the seismic wave scale [25] and can be used as a starting point of metamaterial-inspired future actual-scale implementations for seismic protection systems.

6 Figures

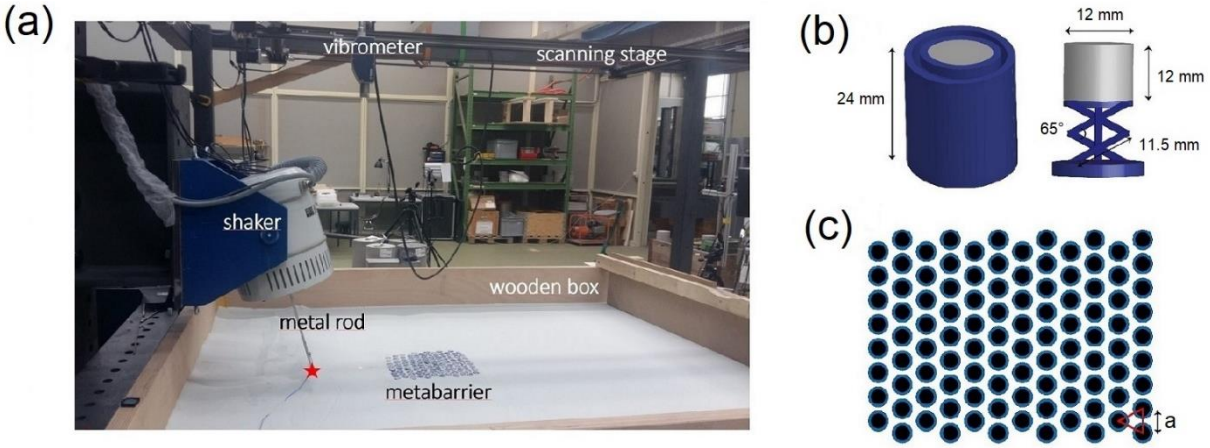


Figure 1: (a) Photo of the experimental setup used in the small-scaled experiment at the IBK structure laboratory at ETH Zurich. (b) Drawing of the 3D resonator model. (c) Sketch of the metabarrier arrangement.

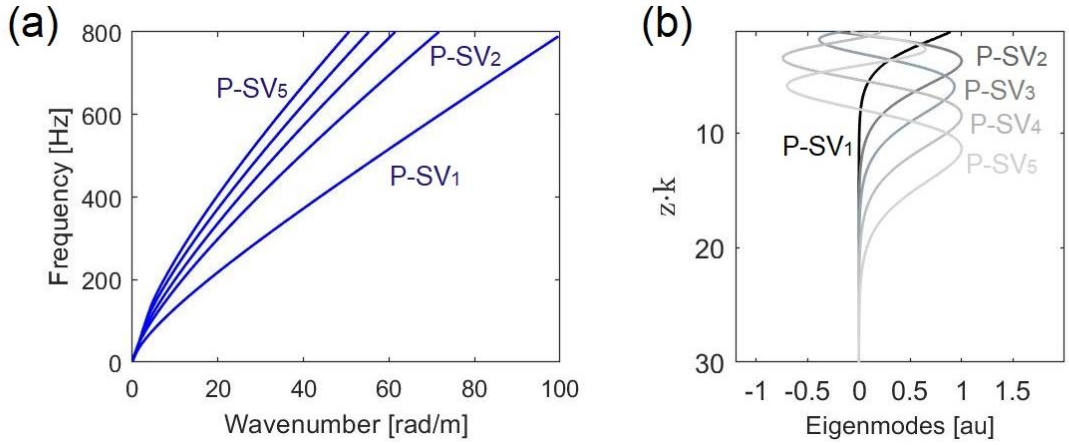


Figure 2: Numerical dispersion curves of the GSAMs traveling in the granular medium (a) and mode shapes at the antiresonance frequency (b). Data reproduced from [22], with permission from the publisher.

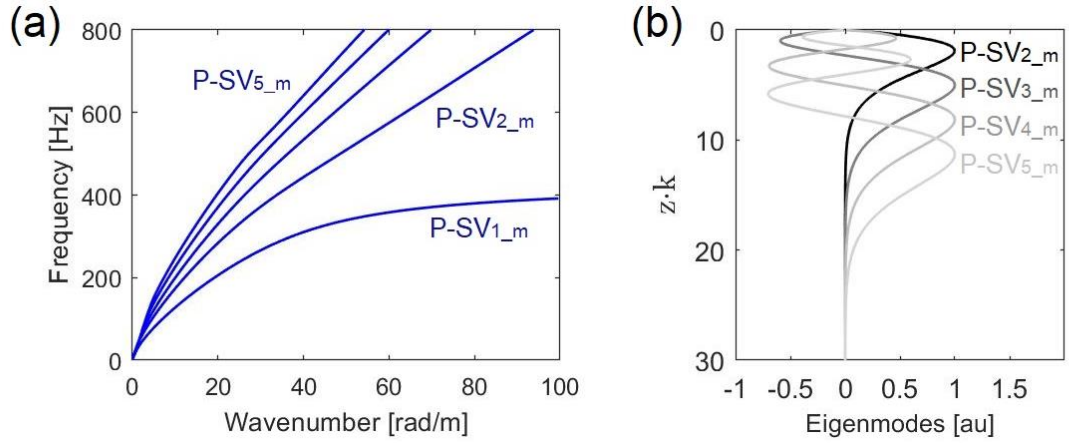


Figure 3: Numerical dispersion curves of the GSAMs traveling in the granular medium with the metabarrier (a) and mode shapes at the antiresonance frequency (b). Data reproduced from [22], with permission from the publisher.

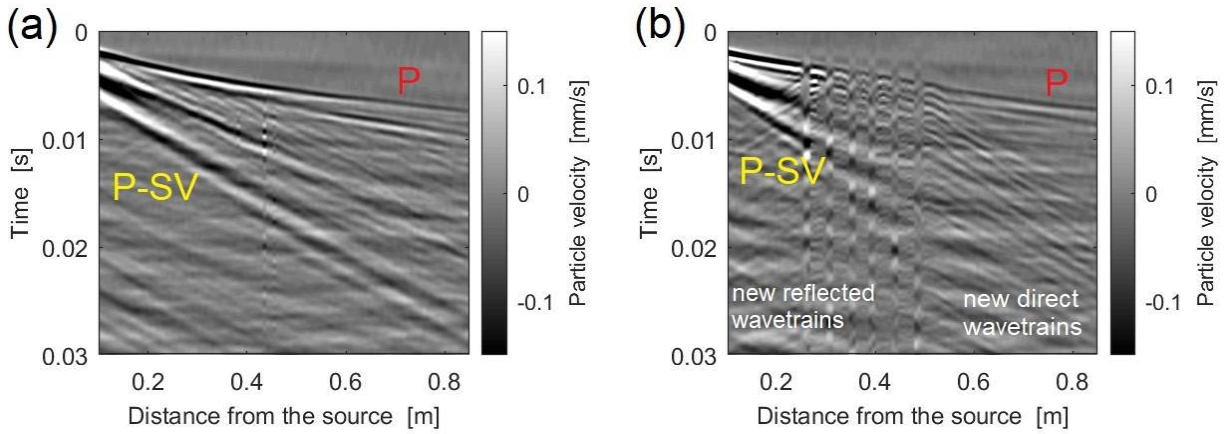


Figure 4: (a) Seismogram without the metabarrier. Data reproduced from [22], with permission from the publisher. (b) Seismogram with the metabarrier.

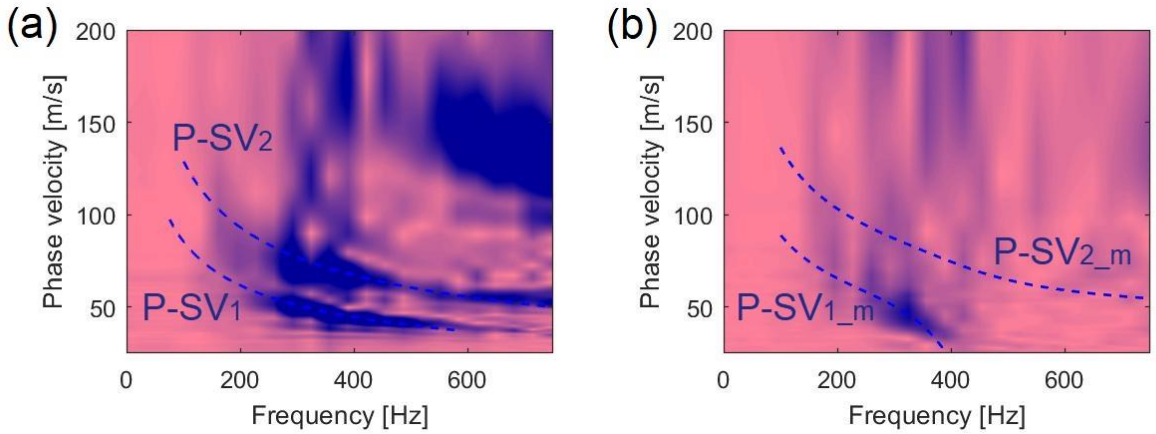


Figure 5: (a) Dispersion relation phase velocity – frequency without the metabarrier. Data reproduced from [22], with permission from the publisher. (b) Dispersion relation phase velocity – frequency with the metabarrier.

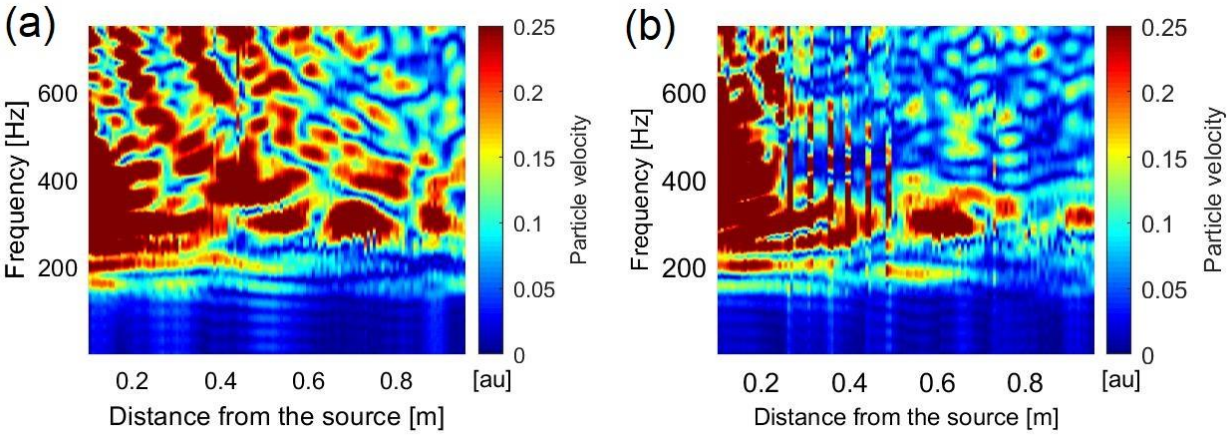


Figure 6: Surface wave spectrum with (b) and without (a) the metabarrier.

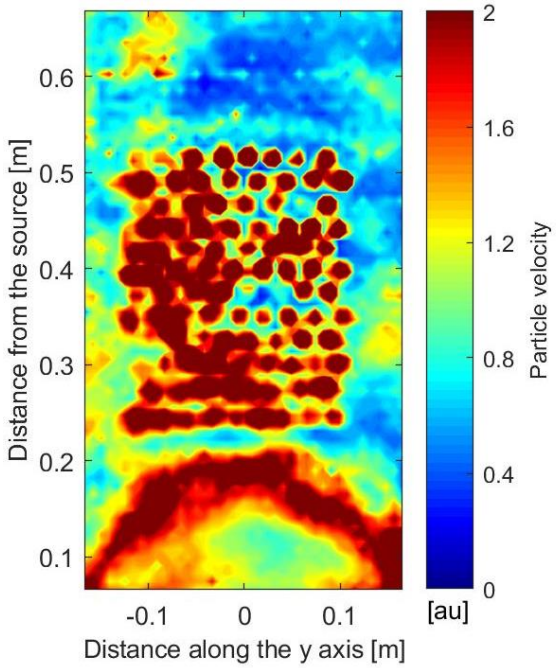


Figure 7: 2D Scan of the surface: ratio between the maximum values of particle velocities with (V_{with}) and without ($V_{without}$) the resonators computed between 400 and 550 Hz.

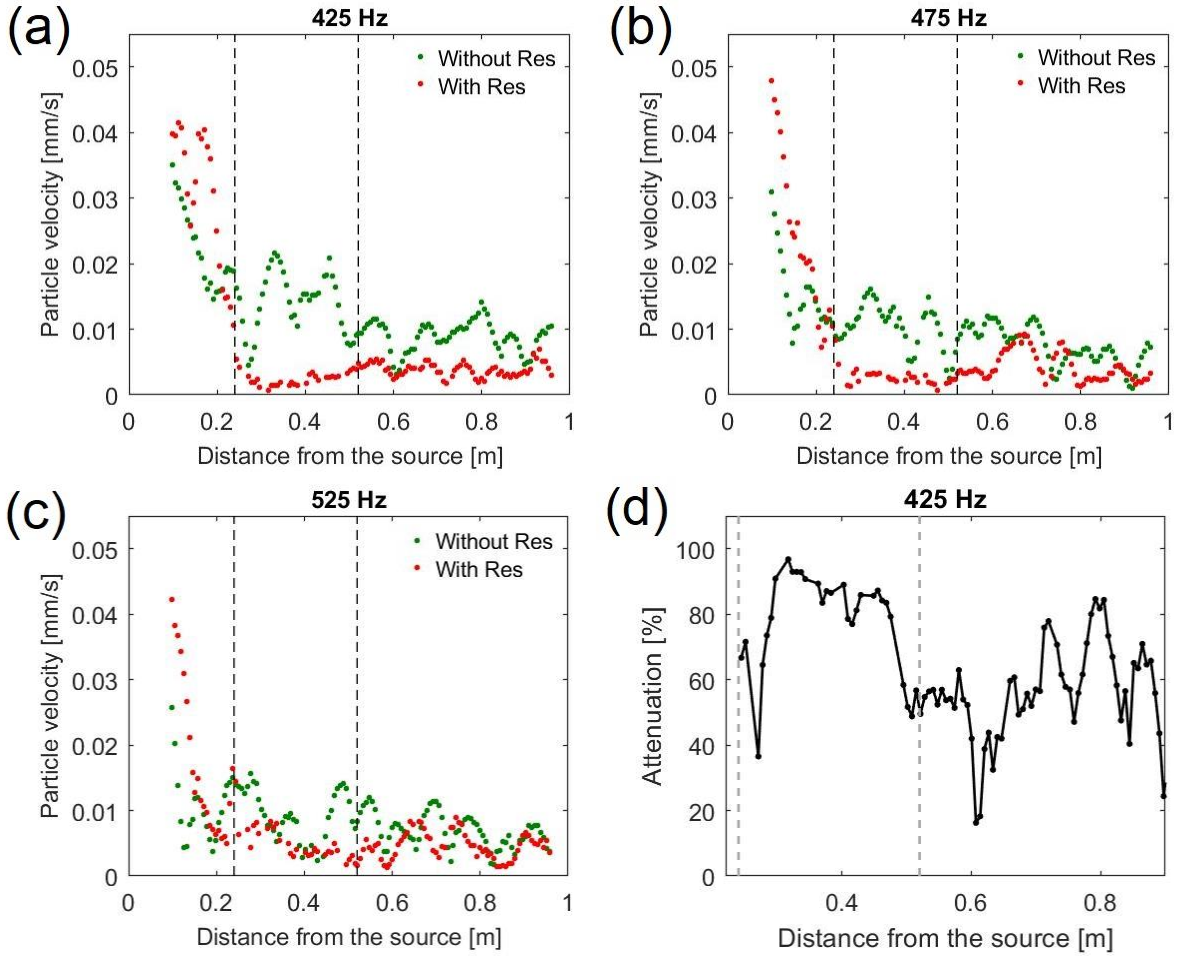


Figure 8: Regression of particle vertical velocity at surface as a function of the distance from the source at 425 Hz (a), 475 Hz (b), 525 Hz (c). (d) Particle velocity attenuation at 425 Hz.

References

[1] B. L. Davis, M. I. Hussein, *Nanophononic Metamaterial: Thermal Conductivity Reduction by Local Resonance*, Phys. Rev. Lett., Vol. 112, 055505 (2014).

[2] Y. Ding, Z. Liu, C. Qiu, J. Shi, *Metamaterial with Simultaneously Negative Bulk Modulus and Mass Density*, Phys. Rev. Lett., Vol. 99, 093904 (2007).

[3] A. Colombi, *Resonant metalenses for flexural waves in plates*, J. Acoust. Soc. Am., Vol. 140, EL423 (2016).

[4] Z. Liu, X. Zhang, Y. Mao, Y. Y. Zhu, Z. Yang, C. T. Chan, P. Sheng, *Locally resonant sonic materials*, Science, Vol. 289, 1734 (2000).

[5] N. I. Landy, S. Sajuyigbe, J. J. Mock, D. R. Smith, W. J. Padilla, *Perfect Metamaterial Absorber*, Phys. Rev. Lett., Vol. 100, 207402 (2008).

[6] J. B. Pendry, *Negative Refraction Makes a Perfect Lens*, Phys. Rev. Lett., Vol. 85, No. 18, (2000), pp. 3966-3969.

[7] M. Ambati, N. Fang, C. Sun, X. Zhang, *Surface resonant states and superlensing in acoustic metamaterials*, Phys. Rev., Vol. B75, 195447 (2007).

[8] J. B. Pendry, D. Schurig, D. R. Smith, *Controlling electromagnetic fields*, Science, Vol. 312, (2006), pp. 1780–1782.

[9] S. Kim, M. P. *Das, Seismic Waveguide of Metamaterials*, arXiv1202.1586v1 (2012).

[10] G. Finocchio, O. Casablanca, G. Ricciardi, U. Alibrandi, F. Garescì, M. Chiappini, B. Azzerboni, *Seismic metamaterials based on isochronous mechanical oscillators*, Appl. Phys. Lett., Vol. 104, 191903 (2014).

[11] Y. Achaoui, B. Ungureanu, S. Enoch, S. Brûlé, S. Guenneau, *Seismic waves damping with arrays of inertial resonators*, Extreme Mech. Lett., Vol. 8, pp. 30–37 (2016).

[12] A. Colombi, P. Roux, S. Guenneau, P. Gueguen, R. V. Craster, *Forests as a natural seismic metamaterial: Rayleigh wave bandgaps induced by local resonances*, Sci. Rep., Vol. 6, 19238 (2016).

[13] A. Palermo, S. Krödel, A. Marzani, C. Daraio, *Engineered metabarrier as shield from seismic surface waves*, Sci. Rep., Vol. 6, 39356 (2016).

[14] N. Boechler, J. K. Eliason, A. Kumar, A. A. Maznev, K. A. Nelson, N. Fang, *Interaction of a Contact Resonance of Microspheres with Surface Acoustic Waves*, Phys. Rev. Lett., Vol. 111, 036103 (2013).

[15] A. Colombi, D. Colquitt, P. Roux, S. Guenneau, R. V. Craster, *A seismic metamaterial: The resonant metawedge*, Sci. Rep., Vol. 6, 27717 (2016).

[16] R. I. Borja, *Plasticity*, Springer, 978-3-642-38547-6 (2013).

[17] S. Foti, C. G. Lai, G. J. Rix, C. Strobbia, *Surface Wave Methods for Near-Surface Site Characterization*, International Standard Book 13, 978-1-4822-6682-5 (2015).

[18] C. Liu, S. R. Nagel, *Sound in sand*. Phys. Rev. Lett., Vol. 68, 2301 (1992).

[19] V. Aleshin, V. Gusev, V. Tournat, *Acoustic modes propagating along the free surface of granular media*, Soc. Am., Vol. 121, 2600 (2007).

[20] X. Jacob, V. Aleshin, V. Tournat, P. Leclaire, W. Lauriks, V. E. Gusev, *Acoustic Probing of the Jamming Transition in an Unconsolidated Granular Medium*. Phys. Rev. Lett., Vol. 100, 158003 (2008).

[21] V. E. Gusev, *Acoustic Waves in an Elastic Channel near the Free Surface of Granular Media*, Phys. Rev. Lett., Vol. 96, 214301 (2006).

[22] A. Palermo, S. Krödel, K. H. Matlack, R. Zaccherini, V. K. Dertimanis, E. N. Chatzi, A. Marzani, C. Daraio, *Hybridization of guided surface acoustic modes in unconsolidated granular media by a resonant metasurfaces*, Phys. Rev. Appl., Vol. 9, 054026 (2018).

[23] L. Bodet, A. Dhemaied, R. Martin, R. Mourgues, F. Rejiba, V. Tournat, *Small-scale physical modeling of seismic-wave propagation using unconsolidated granular media*, Geophysics, Vol. 79, No. 6, (2014), pp. T323-T33.

[24] S. Krödel, N. Thoméa, and C. Daraio, *Wide band-gap seismic metastructures*, Extreme Mech. Lett. 4, 111 (2015).

[25] L. Y. Faust, *Seismic Velocity as a Function of Depth and Geologic Time*, Geophysics, Vol. 16, (1951), p. 192.

The influence of uncertainties in periodic structures for vibro-acoustic problems

J. Henneberg[1,2], **J. S. Gomez Nieto**[1], **K. Sepahvand**[1], **A. Gerlach**[2],
H. Cebulla[3], **S. Marburg**[1]
[1] Chair of Vibroacoustics of Vehicles and Machines, Technical University of Munich, Germany
e-mail: **johannes.henneberg@tum.de**

[2] Corporate Research and Advance Engineering, Robert Bosch GmbH, Germany

[3] Professorship for Textile Technologies, Technical University Chemnitz, Germany

Abstract
Periodic structures have recently received significant attention in the field of vibro-acoustics. Based on periodic resonant structures, stop band materials can be attained. The purpose is to generate structures with particular dynamic behavior in order to attenuate wave propagation within certain frequency ranges. To transfer the promising results achieved in science during the last years to a broad band of applications in industry, it is necessary to quantify the influence of uncertainties in periodic structures. In this study, the influence of geometrical and material uncertainties on periodic structures is investigated. Therefore, a finite element model of an epoxy plate with beam resonators is developed. The behavior of stop band material with uncertain input parameters is studied based on non-sampling stochastic methods. The results are used to show the necessity of taking uncertainties in periodic structures into account. The performed stochastic simulations are suitable to define manufacturing tolerances for the production of stop band material.

1 Introduction

Acoustic metamaterials received growing attention in recent years. Due to their possibility to gain acoustic properties which can not be found in nature, they are useful in applications with vibroacoustic issues. In particular, the possibility to attain structures with band gap behavior is used. In analogy to photonic crystals, a phononic crystal by locally resonant material is presented by [1]. High sound transmission loss can be achieved at certain frequencies with a three dimensional lattice of rubber coated lead spheres in epoxy. In the study [2], flexural waves in thin plates with spring-mass resonators are investigated. It is shown that wave propagation can be attenuated by locally attached spring-mass resonators. The sound transmission loss of similar structures have been considered in [3]. Replacing a single resonator in each unit cell with multiple smaller appropriately damped resonators can broaden the frequency band of increased sound transmission loss in a metamaterial-based plate significantly. The effect of periodic, tuned resonators with regard to vibroacoustics is investigated in the studies [4,5]. The stop band behavior of a sandwich plate with a stepped resonator has been explained in [6]. It has been shown that the sound transmission of the sandwich plate is significantly reduced within the stop band of the structure. The studies [7, 8] investigate the attenuation of structural vibrations in a duct by applying locally resonant metamaterials. It is shown that the combination of different resonator configuration in one structure can lead to combined stop bands if they are appropriate designed. Resonant stop band material is suitable to reduce mechanical cross-coupling in phased array transducers as shown in [9]. Another approach to realize acoustic metamaterial is using very thin membrane with adjustable concentrated masses, known as membrane-type acoustic metamaterials [10, 11]. Further

investigations on different aspects of acoustic metamaterial can be found in [12–18].

All in all, the results found in literature show that stop band materials based on periodic structures are a suitable solution for vibroacoustic applications. Nonetheless, real industrial applications of these structures are quite small. One reason for this is the missing evaluation of the influence of uncertainties. One of the few works addressing seismic metamaterials with the focus of robust-to-uncertainties optimal design is presented by [19]. The study [20] investigates the influence of point defects in a phononic crystal Timoshenko beam. In [21], the influence of point defects in periodic crystal thin plates is investigated. In all those studies, however, the impact of parameter uncertainty e.g. manufacturing tolerances has been ignored. An effective method to overcome such drawback is to use stochastic analysis, as introduced in this paper.

Uncertainty quantification in such material can be investigated using two techniques, i.e. sampling and non-sampling based methods. Monte Carlo simulation plays a major role in the former method in which large number of samples of uncertain parameters are required to realize the structure responses [22, 23]. Though even the method is straightforward to use, it suffers the lack of convergence for large uncertainty and ineffective in terms of computational time for large number of parameter realizations. The latter, in contrast, shows reasonable accuracy and computational efficiency for representation of parameter uncertainty. The method is based on a radically different approach, namely constructing the functional dependence expressed in terms of spectral decomposition with unknown coefficients and orthogonal polynomial basis [24–30]. Among various available non-sampling techniques, the generalized Polynomial Chaos (gPC) expansion method has received considerable attention, particularly for non–Gaussian random variables. The gPC is able to represent uncertainties in parameters as an expansion of orthogonal polynomials of standard random variables. Here, in this paper, this method is applied to adjust uncertain parameters in acoustic metamaterials. The results show that uncertainty in topology of resonators leads to a randomly distributed band gap. Based on this results, manufacturing tolerances of the periodic structure can be tolerated to attain a band gap within a certain frequency band.

This work is structured as follows: initially, we focus on theoretical background employed in this study. The finite element model is presented in section 3. The band gap behavior and the results of the uncertainty quantification are given in section 4. Finally, a conclusion is drawn.

2 Theoretical background

In the following section, the theoretical background for methods employed in this work are presented briefly. First, the generalized polynomial chaos expansion is presented for representation of uncertain parameters. Afterwards, the calculation of dispersion relations in periodic structures is described. Therefore, the Bloch theorem is applied. Structures with two dimensional periodicity are investigated.

2.1 Discretization of random parameters

Using finite element method to numerical simulation of periodic structures under uncertainty requires to discretize uncertain parameters. In this way, it is common to employ truncated expansions to discretize random input parameters and structure responses. The generalized Polynomial Chaos (gPC) expansion permits such a discretization. The idea is that a uncertain quantity of interest can be approximated by summation of polynomials with random independent variables having deterministic coefficients. The uncertainty produces a new dimension which is sought as a set of orthogonal functions. The classical gPC expansion employs Hermite polynomials with multidimensional random variables as a trial basis for the probability space to represent uncertainty. Using this approach, the random parameter $P(\xi)$ is approximated using truncated expansion as [25]

$$P(\xi) \approx \sum_{i=0}^{N} p_i \Psi_i(\xi)\,, \qquad \text{and} \qquad N = \frac{(n+k)!}{n!k!} - 1 \tag{1}$$

where p_i are deterministic unknown coefficient functions, k is the maximum order of the expansion, n denotes the random dimensionality and Ψ_i are a set of orthogonal polynomials in terms of the random variable ξ with the orthogonality relation of

$$\langle \Psi_i, \Psi_j \rangle = \mathrm{E}[\Psi_i, \Psi_j] = \mathrm{E}[\Psi_i^2]\delta_{ij} = h_i^2 \delta_{ij} \tag{2}$$

in which h_i is the norm of the polynomial. The unknown deterministic coefficients can be determined using Galerkin projection as

$$p_i = \frac{\langle P(\xi), \Psi_i(\xi) \rangle}{\langle \Psi_i(\xi)^2 \rangle}, \qquad i = 0, 1, 2, \ldots \tag{3}$$

where 5

$$\langle P(\xi), \Psi_i(\xi) \rangle = \mathrm{E}[P(\xi), \Psi_i(\xi)] = \int_\Omega P(\xi)\Psi_i(\xi) f(\xi) \mathrm{d}\xi \tag{4}$$

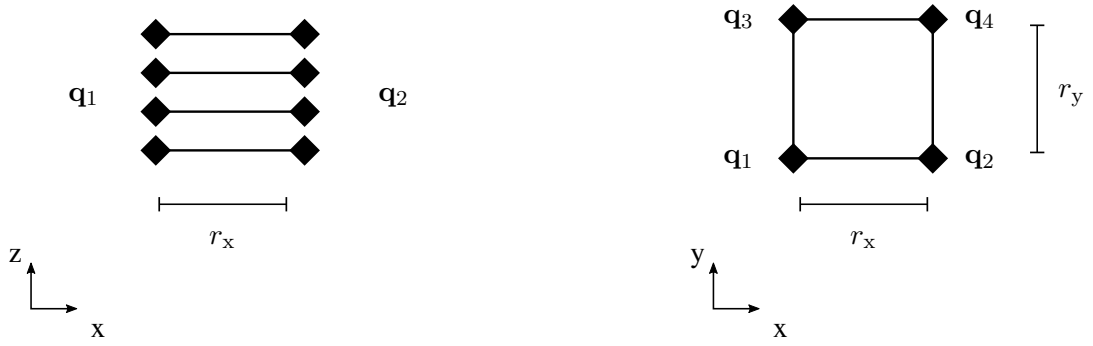
here, f is the probability density function (PDF) corresponding to the random variable ξ and Ω denotes the random domain. While the first few coefficients of parameters with small uncertainty range seem to be enough for accurate gPC representation, higher order expansion is used to accurate representation of parameters having large uncertainty. Details of numerical simulation using the gPC expansion are given in many works, cf. [25, 26, 28–31].

2.2 Dispersion in periodic infinite structures

Periodic structures can be characterized with its dispersion relations. Thus, the wave propagation in such structures is described. In order to obtain the dispersion relations, an approach employing the Bloch theorem is applied [32]. For this purpose, the structure is described by a unit cell (UC) representing the fundamental, repeated unit of the structure [33]. For time harmonic waves with angular frequency ω a response variable ψ can be expressed by

$$\psi = W e^{i(\omega t - k_\mathrm{x} r_\mathrm{x} - k_\mathrm{y} r_\mathrm{y})}, \tag{5}$$

with W describing the wave mode through the thickness of the structure.



(a) one-dimensional periodicity

(b) two-dimensional periodicity

Figure 1: Generalized displacements $\mathbf{q}$ in wave finite element method.

Accordingly, the generalized displacements $\mathbf{q} = [\mathbf{q}_1 \quad \mathbf{q}_2]^\mathrm{T}$ in an element with one dimensional periodicity, cf. Fig. 1 (a), are related to each other as [34]

$$\mathbf{q}_2 = \lambda_\mathrm{x} \mathbf{q}_1, \tag{6}$$

with

$$\lambda_{\mathrm{x}} = e^{-\mathrm{i}k_{\mathrm{x}} \cdot r_{\mathrm{x}}}, \tag{7}$$

where r_{x} and k_{x} represent the length of the periodic lattice and the wavenumber in the direction of periodicity, respectively. The generalized displacements can by described dependent on $\mathbf{q}_1$

$$\mathbf{q} = \Lambda_{\mathrm{R}} \mathbf{q}_1 \qquad \text{with} \qquad \Lambda_{\mathrm{R}} = \begin{bmatrix} \mathbf{I} & \lambda_{\mathrm{x}} \mathbf{I} \end{bmatrix}^{\mathrm{T}}. \tag{8}$$

The equation of motion in the absence of damping

$$\left[\mathbf{K} - \omega^2 \mathbf{M} \right] \mathbf{q} = \mathbf{f}, \tag{9}$$

can then be expressed as

$$\left[\mathbf{K} - \omega^2 \mathbf{M} \right] \Lambda_{\mathrm{R}} \mathbf{q}_1 = \mathbf{f}. \tag{10}$$

With the assumption of zero forces at the node $\mathbf{q}_1$

$$\Lambda_{\mathrm{L}} \mathbf{f} = 0 \qquad \text{with} \qquad \Lambda_{\mathrm{L}} = \begin{bmatrix} \mathbf{I} & \lambda_{\mathrm{x}}^{-1} \mathbf{I} \end{bmatrix} \tag{11}$$

the eigenvalue problem can be reduced to

$$\Lambda_{\mathrm{L}} \left[\mathbf{K} - \omega^2 \mathbf{M} \right] \Lambda_{\mathrm{R}} \mathbf{q}_1 = 0. \tag{12}$$

This eigenvalue problem can be solved for ω which is a function of the wavenumber k_{x}. The solutions for $\omega(k_{\mathrm{x}})$ characterize the free wave propagation in the periodic structure. This approach can be applied easily to two-dimensional periodicity, cf. Fig. 1 (b). Therefore, the vector with generalized displacements changes to

$$\mathbf{q} = \begin{bmatrix} \mathbf{q}_1 & \mathbf{q}_2 & \mathbf{q}_3 & \mathbf{q}_4 \end{bmatrix}^{\mathrm{T}}. \tag{13}$$

Consequentially, the reducing matrices are given by

$$\Lambda_{\mathrm{R}} = \begin{bmatrix} \mathbf{I} & \lambda_{\mathrm{x}} \mathbf{I} & \lambda_{\mathrm{y}} \mathbf{I} & \lambda_{\mathrm{x}} \lambda_{\mathrm{y}} \mathbf{I} \end{bmatrix}^{\mathrm{T}} \qquad \text{and} \qquad \Lambda_{\mathrm{L}} = \begin{bmatrix} \mathbf{I} & \lambda_{\mathrm{x}}^{-1} \mathbf{I} & \lambda_{\mathrm{y}}^{-1} \mathbf{I} & \lambda_{\mathrm{x}}^{-1} \lambda_{\mathrm{y}}^{-1} \mathbf{I} \end{bmatrix}, \tag{14}$$

with

$$\lambda_{\mathrm{x}} = e^{-\mathrm{i}k_{\mathrm{x}} \cdot r_{\mathrm{x}}} \qquad \text{and} \qquad \lambda_{\mathrm{y}} = e^{-\mathrm{i}k_{\mathrm{y}} \cdot r_{\mathrm{y}}}. \tag{15}$$

A detailed elaboration of the theory, known as wave finite element method, can be found in [34] and [35].

In two dimensional periodicity, $\omega(k_{\mathrm{x}}, k_{\mathrm{y}})$ is a function of the wavenumbers $k_{\mathrm{x}}, k_{\mathrm{y}}$. Thus, the eigenvalue problem has to be solved for any combination of the wavenumbers in order to obtain a dispersion surface. Due to the periodicity of the structure, only the first Brillouin zone (BZ) needs to be considered to identify band gaps [33]. In case of symmetric unit cells, the calculation of the band gap can be reduced to the contour of a part of the BZ, the so called irreducible Brillouin zone (IBZ). Thus, the computational effort to identity band gaps can be reduced.

3 Finite element model

The spectral discretization method explained in previous section allows us to investigate the impact of uncertainties in geometrical parameters of periodic structures on the stop band via a finite element model. Therefore, a unit cell representing the generic model is considered. By applying the Bloch theorem, this structure in assumed to be repeated infinitely in x and y direction, cf. Fig. 2. The UC consists of a plate like structure with an added beam resonator. The applied geometry is equal to the example presented in [36]. The simulations are carried out with commercial software Comsol Multiphysics [37]. The finite element model is meshed with hexagonal elements with quadratic formulation. In order to obtain a model with a small amount of degrees of freedom and little mesh dependency of the results, a mesh convergence study is carried

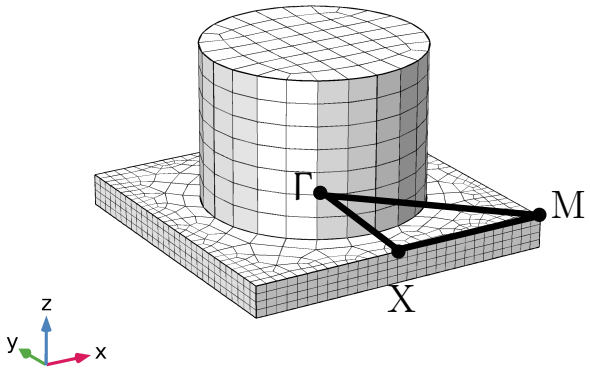


Figure 2: Finite element model used for the uncertainty quantification in periodic structures with contour of the irreducible Brillouin zone ΓXM

out. The guidelines given in [38] are applied. The error induced by the mesh can be denoted to less then than 2% error for the band gap when changing the element edge length to halve. An epoxy material with Young's modulus $E = 2500$ MPa, Poisson's ratio $\nu = 0.3$, and mass density $\rho = 1.14\frac{g}{cm^3}$ is considered. The material model is assumed to have linear elastic behavior in accordance to Hooke's law. As the unit cell is repeated infinitely, the analysis with uncertain inputs in this unit cell can be interpreted as analysis of different specimens wherein one specimen all periodic structures are identical. This may be useful, to identify the influence of manufacturing tolerances which are caused by processes repeated after producing one specimen. However, the changes due to the uncertainty have to be identical for each unit cell within the periodic structure.

The above mentioned FEM model is considered then as black-box to investigate the impact of parameter uncertainty on the band gap. To this end, the band gap is considered as random output approximated using the gPC expansion with unknown deterministic coefficients. The stochastic non-intrusive method is employed, cf. [39], where a set of collocation points are generated in the random domain. The FEM model is then executed for realizations of samples of band gap at each collocation point. Once the realizations are known, a least-square minimization procedure is used to calculate the unknown deterministic coefficients. This leads to a closed form for the band gap depending to uncertainty in the random input parameters. The results are presented in the following section.

4 Numerical results

The influence of uncertain input parameters on the band gap is investigated with parameters having a predefined probability density function. In this study, the uncertainty in parameters are assumed to be characterized by beta distributions owing the fact that the parameters are defined within positive range. The boundary values of uncertain input parameters and shape factors of the employed beta distributions, α and β, are given in Table 1.

Table 1: Range of input uncertain parameters with associated distribution shape factors Beta(α, β).

Uncertain parameter	boundary values	distribution factors
Plate thickness	$[0.9\ \text{mm}, 1.1\ \text{mm}]$	Beta$(4, 4)$
Resonator length	$[4.5\ \text{mm}, 5.5\ \text{mm}]$	Beta$(4, 4)$
Resonator radius	$[3.15\ \text{mm}, 3.85\ \text{mm}]$	Beta$(6, 6)$
Young's modulus	[2250 MPa, 2750 MPa]	Beta$(4, 4)$

In a first step, the deterministic solution of the unit cell model is calculated. Fig 3 shows the dispersion curves in a band diagram. The calculation along the contour of the IBZ is suitable due to the symmetry of the unit cell. Referring to the nomenclature of crystallography, for details see [40, 41], the unit cell of this study represents a p4mm lattice. In [42], the probability to obtain the full band gap on the contour of the IBZ is denoted to 99.46% for a p4mm lattice. In order to characterize the band gap behavior, the band gap center

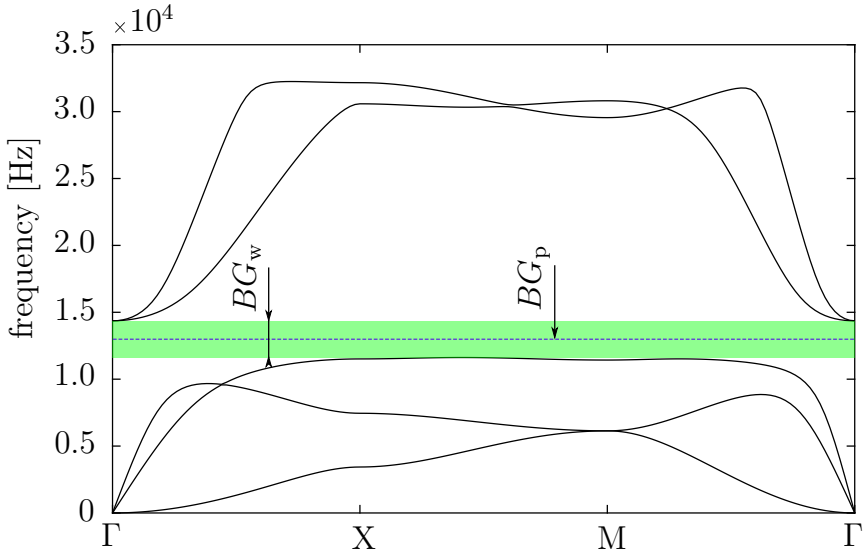


Figure 3: Bravais lattice with the contour of the irreducible Brillouin zone ΓXMΓ and the dispersion curves of the unit cell with highlighted band gap center position BG_p and band gap width BG_w.

position BG_p and the width of the band gap BG_w are analyzed as output values cf. Fig 3. The calculation is easily done by

$$BG_\text{p} = \frac{BG_\text{ub} + BG_\text{lb}}{2}, \tag{16}$$

with BG_lb and BG_ub being the lower and upper frequency boundary of the band gap, respectively. The band gap width BG_w is defined by

$$BG_\text{w} = BG_\text{ub} - BG_\text{lb}. \tag{17}$$

Caused by the beam resonator, the periodic structures has a resonant stop band. The band gap center position is obtained at $BG_\text{p} = 12988$ Hz and with a band gap width $BG_\text{w} = 2738$ Hz for the deterministic model. In a parameter study, the influence of different geometrical parameters to the band gap behavior of the structure is analyzed. Therefore, plate thickness, resonator length, resonator radius, and the Young's modulus are changed in a range from 90% to 110% with regard to the nominal values. The results are shown in Fig. 4. It can be seen that the band gap behavior is sensitive to geometrical changes of the investigated parameters.

However, the band gap width and band gap center position behave differently. The change of band gap center position is almost linear for all three parameter within the investigated ranges. The relation between plate thickness and resonator radius, and band gap center position are characterized by a positive gradient of nearly the same value. In contrary, resonator length and band gap center position are related by a negative gradient. Regarding the band gap width, a similar behavior is found for plate thickness and resonator radius. However, in this case the influence of changes of the resonator radius has higher impact then of the plate thickness. A particular relation is obtained for the sensitivity to changes of the resonator length. Especially when reducing the resonator length, the influence decreases. Furthermore, an extrema is obtained at a band gap width of 2790 Hz.

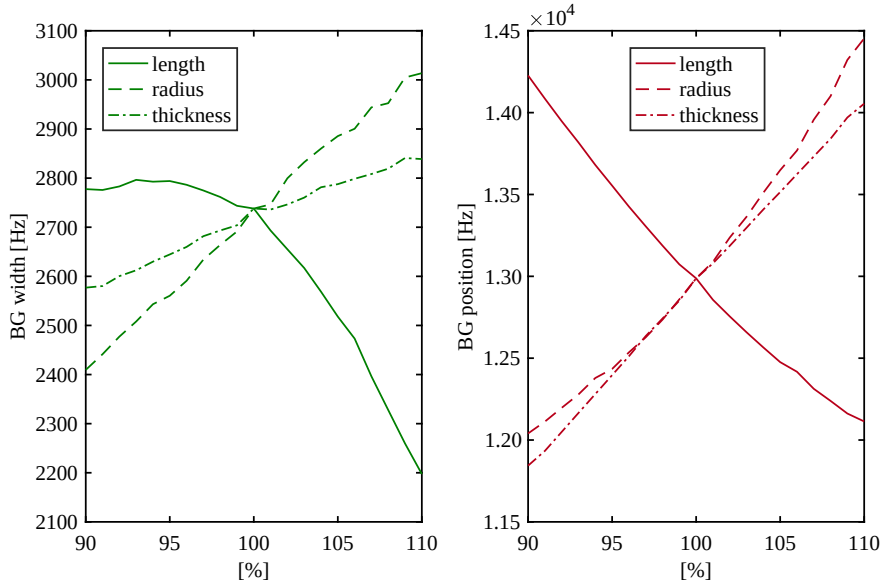
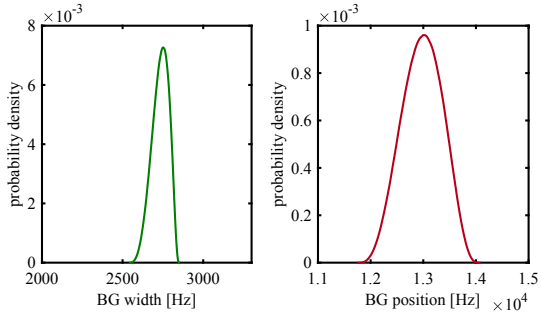
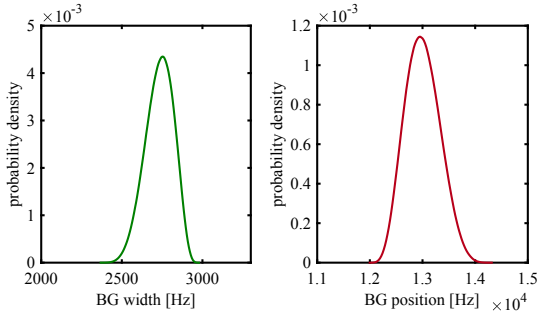


Figure 4: Parameter study to identify the influence of plate thickness, resonator radius, and resonator length to band gap center position and band gap width.

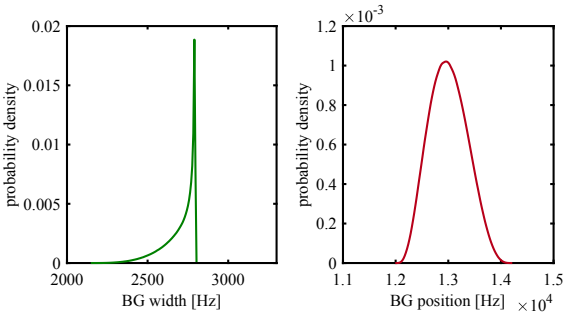
In Fig. **??**, the results for the uncertainty quantification in a unit cell are given. The belonging mean value and standard deviation are given in Table 2. The obtained PDFs for the band gap center position are similar for the three parameters considered as single uncertain inputs. This is due to the similar magnitude of the gradient obtained is the parameter study. Concerning the band gap width, the lower influence of the plate thickness compared to the resonator radius results in a lower standard deviation. As in case of the parameter study, a particular behavior is obtained in the PDF for the band width BG_w when the resonator length is considered as an uncertain input parameter. The accumulation at a band gap width of 2790 Hz is related to the extrema which is found in the parameter study. In a secondary investigation, a unit cell with two uncertain input parameters, resonator length and radius, is considered. The resulting PDFs show similar mean values for band gap center position and band gap width compared to the investigations with only one uncertain input parameter. However, taking two uncertain input parameters into account results in an increased standard deviation for both, band gap center position and band gap width. Furthermore, the PDFs show nearly symmetrical behavior.



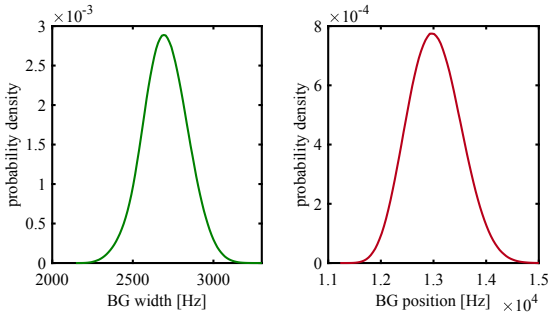
(a) Uncertain input: plate thickness



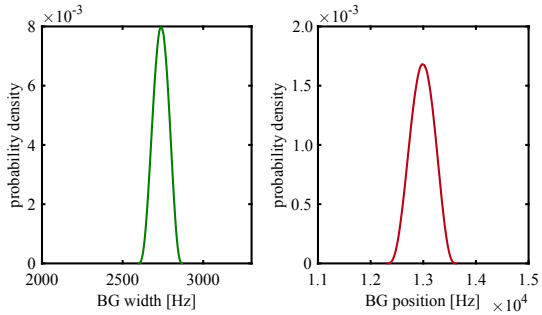
(b) Uncertain input: resonator radius



(c) Uncertain input: resonator length



(d) Uncertain input: radius and length of resonator



(e) Uncertain input: Young's modulus

Figure 5: Probability density functions of band gap width and band gap position for various uncertain inputs parameters in a unit cell.

As mentioned above, the unit cell is assumed to be repeated infinitely. Thus, the results can be interpreted as an uncertainty quantification in periodic structures where the uncertainty arises between different specimens but parameters of the periodic structure are equal within the one specimen. Taking this into account, a scenario where the thickness varies between each specimen seem most likely. Assuming a molding manufacturing processes, uncertainties are induced by the closing and opening process between every fabricated specimen. However, depending the manufacturing process also resonator length and resonator radius could be changed between each specimen. In such a case, the given model of a unit cell is suitable to quantify the influence of uncertainties to the band gap behavior.

Table 2: Mean value and standard deviation from uncertainty quantification in a unit cell. The values are given for the band gap position BG_{p} and the band gap width BG_{w}.

uncertain input		mean value [Hz]	standard deviation [Hz]
plate thickness	BG_{p}	12979	380
	BG_{w}	2733	52
resonator radius	BG_{p}	13001	329
	BG_{w}	2732	88
resonator length	BG_{p}	13000	359
	BG_{w}	2702	100
resonator length & radius	BG_{p}	13021	498
	BG_{w}	2700	139
Young's modulus	BG_{p}	12986	216
	BG_{w}	2738	46

5 Conclusion

The authors presented a study on uncertainty quantification in periodic structures. Fur this purpose, a generic model consisting of a plate like structure with an added beam resonator is investigated. Due to the resonant behavior of the periodic structure, a band gap is achieved where no free wave propagation possible. This band gap is characterized by the band gap center position and the band gap width. In stochastic analysis, the influence of uncertainties in the geometrical and material parameters is investigated. Thus, a spectral discretization method, namely the generalized polynomial chaos expansion, is employed to consider the uncertain parameters in stochastic finite element simulation. The authors conclude that applying the gPC expansion to a unit cell is suitable to quantify the influence of uncertainties which arise between different specimens. Based on the calculated PDFs and statistical moments, manufacturing tolerance for periodic structures can be defined in order to obtain a band gap behavior within certain requirements.

References

[1] Z. Liu, X. Zhang, Y. Mao, Y. Y. Zhu, Z. Yang, C. T. Chan, P. Sheng, Locally resonant sonic materials, Science 289 (5485) (2000) 1734–1736.

[2] Y. Xiao, J. Wen, X. Wen, Flexural wave band gaps in locally resonant thin plates with periodically attached spring-mass resonators, Journal of Physics D: Applied Physics 45 (19) (2012) 195401.

[3] Y. Xiao, J. Wen, X. Wen, Sound transmission loss of metamaterial-based thin plates with multiple subwavelength arrays of attached resonators, Journal of Sound and Vibration 331 (25) (2012) 5408 – 5423.

[4] C. C. Claeys, K. Vergote, P. Sas, W. Desmet, On the potential of tuned resonators to obtain low-frequency vibrational stop bands in periodic panels, Journal of Sound and Vibration 323 (2013) 1418–1436.

[5] C. C. Claeys, P. Sas, W. Desmet, On the acoustic radiation efficiency of local resonance based stop band materials, Journal of Sound and Vibration 333 (2014) 3203–3213.

[6] Y. Song, L. Feng, J. Wen, D. Yu, X. Wen, Reduction of the sound transmission of a periodic sandwich plate using the stop band concept, Composite Structures 128 (2015) 428 – 436.

[7] C. Claeys, N. G. R. de Melo Filho, L. V. Belle, E. Deckers, W. Desmet, Design and validation of metamaterials for multiple structural stop bands in waveguides, Extreme Mechanics Letters (2016) –.

[8] N. F. Melo, C. Claeys, E. Deckers, B. Pluymers, W. Desmet, Dynamic metamaterials for structural stopband creation, SAE Int. J. Passeng. Cars - Mech. Syst. 9 (2016) 1013–1019.

[9] J. Henneberg, A. Gerlach, H. Storck, H. Cebulla, S. Marburg, Reducing mechanical cross-coupling in phased array transducers using stop band material as backing, Journal of Sound and Vibration 424 (2018) 352 – 364.

[10] G. Ma, M. Yang, S. Xiao, Z. Yang, P. Sheng, Acoustic metasurface with hybrid resonances, Nat. Mater. 13 (9) (2014) 873–878.

[11] F. Langfeldt, J. Riecken, W. Gleine, O. von Estorff, A membrane-type acoustic metamaterial with adjustable acoustic properties, Journal of Sound and Vibration 373 (2016) 1 – 18.

[12] H. Peng, P. F. Pai, H. Deng, Acoustic multi-stopband metamaterial plates design for broadband elastic wave absorption and vibration suppression, International Journal of Mechanical Sciences 103 (2015) 104 – 114.

[13] M. Chen, D. Meng, H. Zhang, H. Jiang, Y. Wang, Resonance-coupling effect on broad band gap formation in locally resonant sonic metamaterials, Wave Motion 63 (2016) 111 – 119.

[14] B. Assouar, M. Oudich, X. Zhou, Acoustic metamaterials for sound mitigation, Comptes Rendus Physique 17 (5) (2016) 524 – 532, phononic crystals / Cristaux phononiques.

[15] H. Ruiz, C. Claeys, E. Deckers, W. Desmet, Numerical and experimental study of the effect of microslits on the normal absorption of structural metamaterials, Mechanical Systems and Signal Processing 70-71 (2016) 904 – 918.

[16] M. Lewińska, V. Kouznetsova, J. van Dommelen, A. Krushynska, M. Geers, The attenuation performance of locally resonant acoustic metamaterials based on generalised viscoelastic modelling, International Journal of Solids and Structures 126 (Supplement C) (2017) 163 – 174.

[17] Y. Wu, K. Yu, L. Yang, R. Zhao, X. Shi, K. Tian, Effect of thermal stresses on frequency band structures of elastic metamaterial plates, Journal of Sound and Vibration 413 (Supplement C) (2018) 101 – 119.

[18] A. Kruisová, M. Ševčík, H. Seiner, P. Sedlák, B. Román-Manso, P. Miranzo, M. Belmonte, M. Landa, Ultrasonic bandgaps in 3d-printed periodic ceramic microlattices, Ultrasonics 82 (2018) 91 – 100.

[19] P.-R. Wagner, V. K. Dertimanis, E. N. Chatzi, J. L. Beck, Robust-to-uncertainties optimal design of seismic metamaterials, Journal of Engineering Mechanics 144 (3) (2018) 04017181.

[20] K.-C. Chuang, Z.-Q. Zhang, H.-X. Wang, Experimental study on slow flexural waves around the defect modes in a phononic crystal beam using fiber bragg gratings, Physics Letters A 380 (47) (2016) 3963 – 3969.

[21] Z.-J. Yao, G.-L. Yu, Y.-S. Wang, Z.-F. Shi, Propagation of bending waves in phononic crystal thin plates with a point defect, International Journal of Solids and Structures 46 (13) (2009) 2571 – 2576.

[22] R. M. Orris, M. Petyt, Random response of periodic structures by a finite element technique, Journal of Sound and Vibration 43 (1) (1975) 1–8.

[23] J.-M. Mencik, D. Duhamel, A wave finite element-based approach for the modeling of periodic structures with local perturbations, Finite Elements in Analysis and Design 121 (2016) 40–51.

[24] R. G. Ghanem, P. D. Spanos, Stochastic finite elements: A spectral approach, Dover, Mineola, 1991.

[25] K. Sepahvand, S. Marburg, H.-J. Hardtke, Uncertainty quantification in stochastic systems using polynomial chaos expansion, International Journal of Applied Mechanics 2 (2) (2010) 305–353.

[26] K. Sepahvand, S. Marburg, Stochastic dynamic analysis of structures with spatially uncertain material parameters, International Journal of Structural Stability and Dynamics 14 (8) (2014) 1440029(15).

[27] K. Sepahvand, M. Scheffler, S. Marburg, Uncertainty quantification in natural frequencies and radiated acoustic power of composite plates: Analytical and experimental investigation, Applied Acoustics 87 (2015) 23–29.

[28] K. Sepahvand, S. Marburg, Random and stochastic structural acoustic analysis, in: S. A. Hambric, S. H. Sung, D. J. Nefske (Eds.), Engineering Vibroacoustic Analysis: Methods and Applications, John Wiley & Sons, New York, 2016, Ch. 10, pp. 305–338.

[29] K. Sepahvand, Spectral stochastic finite element vibration analysis of fiber-reinforced composites with random fiber orientation, Composite Structures 145 (2016) 119–128.

[30] K. Sepahvand, Stochastic finite element method for random harmonic analysis of composite plates with uncertain modal damping parameters, Journal of Sound and Vibration 400 (2017) 1–12.

[31] D. Xiu, G. E. Karniadakis, The wiener–askey polynomial chaos for stochastic differential equations, SIAM Journal on Scientific Computing 24 (2) (2002) 619–644.

[32] F. Bloch, Über die quantenmechanik der elektronen in kristallgittern, Zeitschrift für Physik 52 (7-8) (1929) 555–600.

[33] L. Brillouin, Wave Propagation in Periodic Structures: Electric Filters and Crystal Lattices, Dover Publications, 1953.

[34] B. R. Mace, E. Manconi, Modelling wave propagation in two-dimensional structures using finite element analysis, Journal of Sound and Vibration 318 (4) (2008) 884 – 902.

[35] R. Langley, A note on the force boundary conditions for two-dimensional periodic structures with corner freedoms, Journal of Sound and Vibration 167 (2) (1993) 377 – 381.

[36] M. Collet, M. Ouisse, M. Ruzzene, M. Ichchou, Floquet–bloch decomposition for the computation of dispersion of two-dimensional periodic, damped mechanical systems, International Journal of Solids and Structures 48 (20) (2011) 2837 – 2848.

[37] COMSOL Multiphysics Reference Manual, 5th Edition (2017).

[38] P. Langer, M. Maeder, C. Guist, M. Krause, S. Marburg, More than six elements per wavelength: The practical use of structural finite element models and their accuracy in comparison with experimental results, Journal of Computational Acoustics 25 (4) (2017) 1750025.

[39] K. Sepahvand, Spectral stochastic finite element vibration analysis of fiber-reinforced composites with random fiber orientation, Composite Structures 145 (2016) 119 – 128.

[40] C. Kittel, Introduction to solid state physics, Hoboken, NJ : J. Wiley, c2005., 2005.

[41] P. Radaelli, Symmetry in Crystallography: Understanding the International Tables, IUCr texts on crystallography, OUP Oxford, 2011.

[42] F. Maurin, C. Claeys, E. Deckers, W. Desmet, Probability that a band-gap extremum is located on the irreducible brillouin-zone contour for the 17 different plane crystallographic lattices, International Journal of Solids and Structures 135 (2018) 26 – 36.

Diffusion-based design of locally resonant sub-systems using a reduced wave finite element framework

C. Droz [1], **R. Boukadia** [1], **M. Ichchou** [2], **W. Desmet** [1]
[1] Noise and Vibration Research Group, PMA Division, KU Leuven, Belgium

[2] Vibroacoustics and Complex Media Research Group, LTDS, Ecole Centrale de Lyon, France

Abstract
This paper presents a diffusion formulation for the Wave Finite Element (WFE) Framework, applied to the design of micro-resonators for low-frequency vibration control. First, the information resulting from diffusion analysis is compared with the one provided by a direct application of Bloch theory, in the case of periodically distributed resonators. Main advantages of diffusion methods are that the spacing between the resonators can be modified without resuming unit-cell analysis and that scattering effects, inherently produced by the host structure, can be distinguished from the sole resonator's influence. Then, the method is combined with an existing wave-based state vector reduction scheme to further reduce the computational efforts. Formulation is introduced and applied to a rectangular host structure with 3D-modeled resonators bonded on its surface. Eventually, damping-related transmission, reflection and diffusion effects produced by the resonators are studied around their harmonic frequency.

1 Introduction

Locally resonant materials have been widely studied over the past years especially in transportation and aerospace industry, where vibroacoustic requirements are increasingly demanding. A broad range of low- or mid-frequency phenomena can occur in these structures, which can be exploited to enhance their dynamic or acoustic responses. Innovative lightweight meta-structures with incorporated vibration control systems can therefore be engineered to enhance broadband vibroacoustic performances. The concept of tuned mass damping (or harmonic oscillators) can be implemented at the material's scale to achieve vibration control, often using periodically distributed resonators [1, 2].

In periodic waveguides, we distinguish Bragg-type bandgaps from local resonance (LR) effects: the first is ruled by the ratio between the periodic unit-cell dimension and the wavelength of propagating waves. The second is produced by internal resonances and depends on the waveguide's unit-cell inner dynamics. In this case, resonators can be artificially distributed to produce LR bandgaps without altering the host structure. Bloch theory is often used in this case to design and tune the resonators so that certain modes can be suppressed from the overall structure in the selected bandwidth [3, 4]. It is evident that such LR can be obtained without requiring a periodic distribution pattern, as in vibration control strategies based on multiple tuned mass dampers (TMD). Therefore, the use of Bloch/unit-cell modeling methods has two weaknesses: 1) it is based on a perfect periodicity assumption and yields often undesired Bragg-type dispersion effects, and 2) the modeling and computational effort being related to the dimensions of the unit-cell, it increases with the spacing between resonators.

An alternative modelling strategy is proposed in this paper, based on the wave diffusion properties of the harmonic oscillator. In this context, 'diffusion' refers to an elastic wave's reflection, transmission, and absorption process, as well as its specular and diffuse scattering analogues. In the Wave Finite Element Framework, the diffusion coefficients were first used by Mencik and Ichchou [5] to establish the junction between

two waveguides. Applications were proposed for wave scattering analyses with angular incidence [6], pipes [7, 8], curved periodic waveguides (see Errico et al. [9, 10]) and to evaluate the scattering effects through a variety of waveguides' junctions [11]. Wave diffusion analyses were also used to perform damage inspection in composite panels [12]. Recent studies addressed the coupling between electro-mechanical waveguides (see Lousoan et al. [13]).

Yet, these methods have failed so far to address large-scaled realistic structures, mainly due to the ill-conditioned nature of the scattering problem. The above-mentioned can thus be limited to small-scaled waveguides, or neglect decaying or evanescent waves. In this work a well-conditioned formulation is proposed and combined with a reduced-order modeling strategy [14] to perform fast diffusion analyses in a 3D modeled resonator bonded on a host structure and investigate the reflected, transmitted and diffusely scattered waves produced around the resonance frequency.

2 Periodic locally resonant system design

2.1 Bloch-based design

Consider a waveguide consisting of a host structure with periodically distributed resonators bonded on its surface. Bloch-based design can be achieved by considering a periodic unit-cell whose length depends on the spacing d between resonators. Then, denoting $\mathbb{K}$, $\mathbb{C}$ and $\mathbb{M}$ the finite element stiffness, damping and mass matrices of the periodic waveguide's unit-cell, the wave dispersion characteristics can be computed by solving the inverse Bloch problem Eq.(1):

$$[\mathbb{K}(\Delta) + j\omega\mathbb{C}(\Delta) - \omega^2\mathbb{M}(\Delta)]\Phi = 0 \tag{1}$$

where Δ is the propagation constant matrix and Φ is the wave solution.

For frequency-dependent problems such as diffusion or forced response analyses, one can solve the Direct Bloch problem Eq.(2) instead:

$$[\mathbb{D}_{RL}(\omega)\Delta^{-1} + (\mathbb{D}_{RR}(\omega) + \mathbb{D}_{LL}(\omega)) + \mathbb{D}_{LR}(\omega)\Delta]\Phi = 0 \tag{2}$$

where the dynamic stiffness sub-matrix is denoted $\mathbb{D}_{ab}(\omega) = \mathbb{K} + j\omega\mathbb{C} - \omega^2\mathbb{M}$ with a and b stand for left or right sides. Dynamic condensation is usually performed on matrix $\mathbb{D}$, and Component Mode Synthesis is generally used to increase computation efficiency.

The resolution of Eq.(2) provides a set of eigenvalues and vectors (wave shapes) describing the free wave propagation characteristics in the infinite waveguide. The propagation constants $\Delta = \{\lambda_i\}$ relate the displacements between two consecutive unit-cells and can be used to distinguish positive, negative, propagating and evanescent waves. For positive-going waves, the bandgap phenomenon is associated with a reduction of the propagation constant's norm $|\lambda|$ between 1 (propagating) and 0 (evanescent). It should be reminded that this indicator does not reflects a local attenuation ratio, but is related to the unit-cell's scale. An equivalent spatial attenuation in dB per unit-length can be derived using the complex wavenumber $k = \Re(k) + j\Im(k)$ definition: $\lambda = \exp(-jkd)$, which provides a simple estimation of the classical spatial attenuation indicator α:

$$\alpha(dB/m) = 10\frac{\log_{10}\left(|\frac{u_{n+1}}{u_n}|^2\right)}{d} \tag{3}$$

The expression Eq.4 can be approximated into:

$$\alpha(dB/m) \approx 8.686 \times \Im(k) \tag{4}$$

The value of α can be chosen instead of $|\lambda|$ to evaluate the attenuation performances of the periodic waveguide. For Direct Bloch resolution, a wave matching algorithm is then used to track flexural wave's frequency dependent solutions inside the bandgap.

2.2 FE Modeling and materials

The host structure is a thin rectangular beam of dimensions 3 cm $\times$ 1.1 m. The resonators are made of a 3D printed polymer. Material and damping properties used in the FE model are described in Table 1. The influence of the resonator's damping properties will be further investigated in sec.4.3.

Part-Component	Density ρ	Young Modulus E	Shear mod. G	Loss factor η (%)
Host	2700	70×10^9	26.3×10^9	0.2
Resonator	1400	1.8×10^9	0.54×10^9	5
Mass	2700	70×10^9	26.3×10^9	0.2

Table 1: Material properties of the waveguide and resonator models.

A parametric model of the periodic unit-cell is shown in Fig. 1 and numerical applications are based on the dimensions of table 2. The length l_0 represents the spacing between the resonators. The resonator is centered on the waveguide unit-cell in the y-direction and can be placed arbitrarily along the x-direction as it remains periodic. The unit-cell is converged and meshed using linear elements and a total of 5500 DOFs.

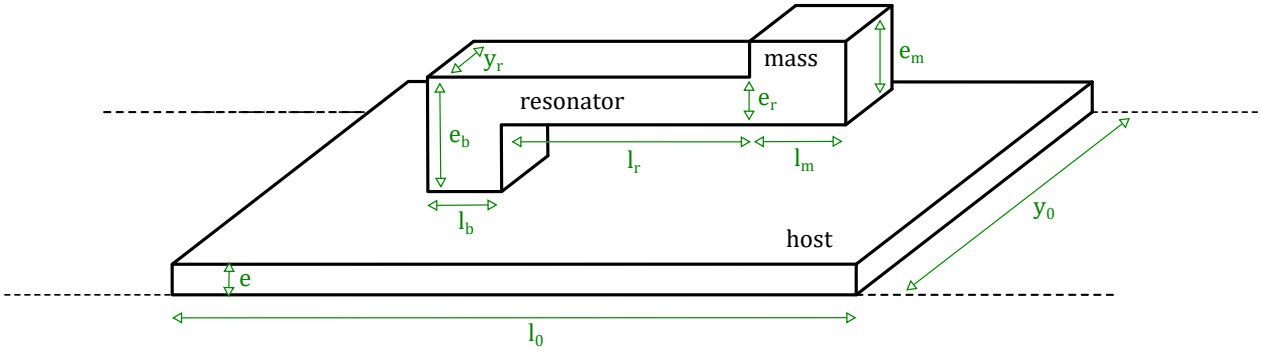


Figure 1: Description of the periodic unit-cell use for Bloch analyses.

Parameter	value (mm)	Parameter	value (mm)
l_0	55	e	2.5
y_0	30	y_r	15
l_b	10	e_b	9
l_r	30	e_r	3
l_m	10	h_m	13

Table 2: Geometric model of the tuned mass damper and periodic unit-cell description.

2.3 Interpretation of the band diagram

Dispersion diagram shown in Fig.2.a is computed using periodic Bloch model for the unit-cell described above. The first local resonance is identified at 339 Hz, corresponding to the bending mode of the tuned mass damper. Bandgap is observed for the transverse vertical (flexural) wave, while the shear, torsional and longitudinal waves are not affected by the resonator. The wave attenuation $\Im(k)$ is presented on the colormap while the propagation constant norm $|\lambda|$ is plotted in Fig. 2.b. Both indicating a drastic attenuation between 320 Hz and 360 Hz.

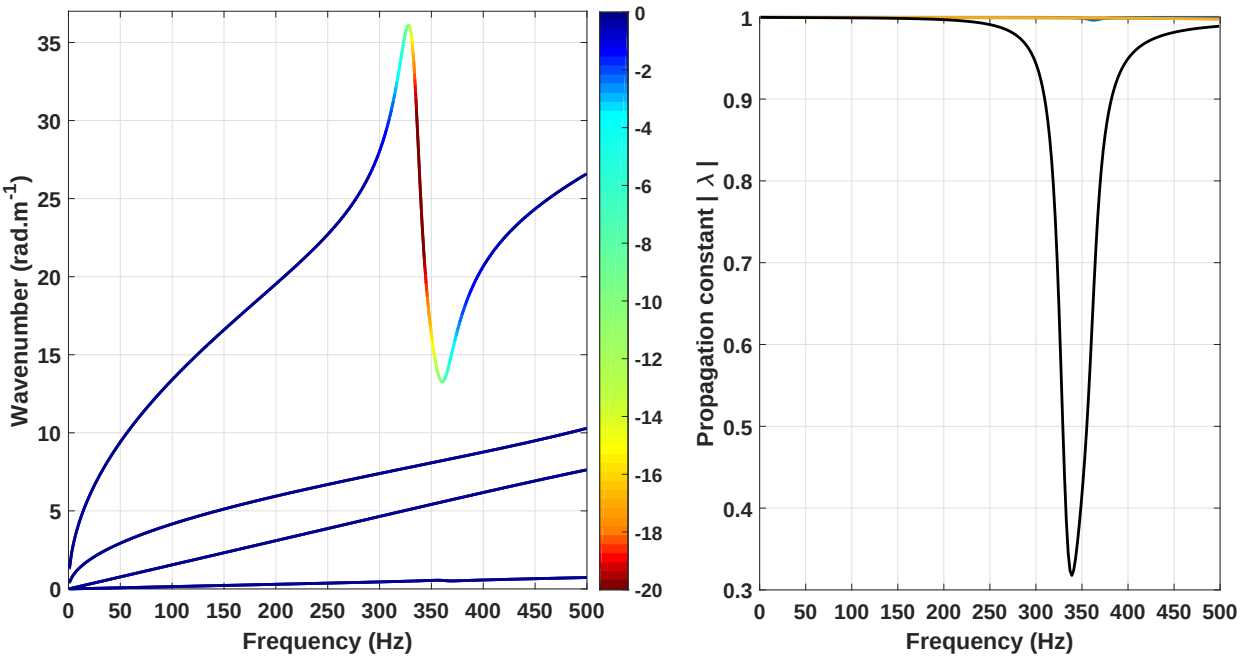


Figure 2: Dispersion diagram calculated using Bloch theory on periodic unit-cell model. (a) Wavenumber (real and imaginary). (b) Norm of the complex propagation constant.

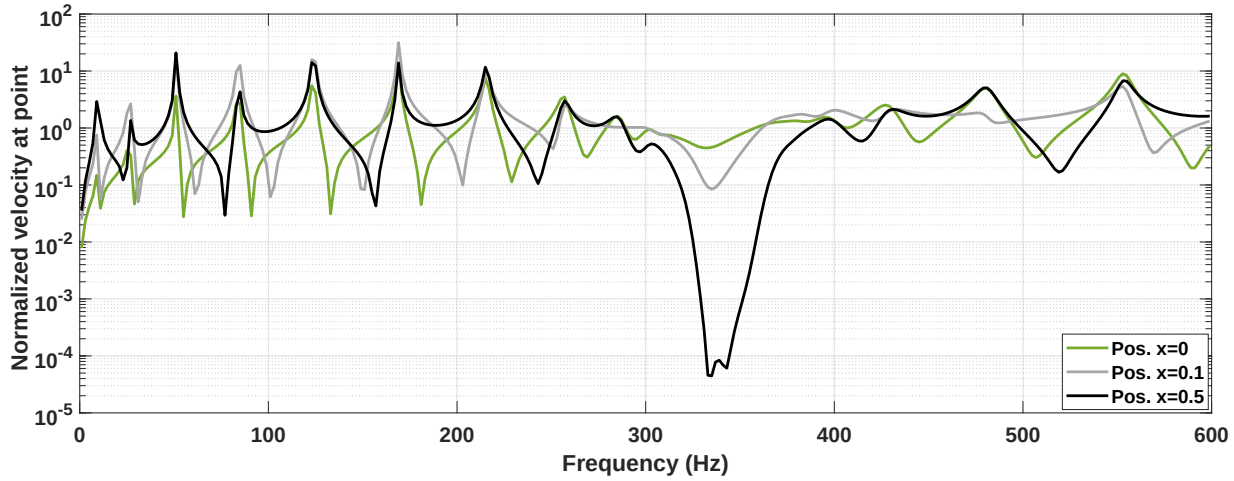


Figure 3: FRF of the free-clamped waveguide to point force excitation at the free end. Three positions from excitation point (0 cm, 10 cm, 50 cm).

The dispersion results are compared with the finite waveguide's dynamic response in Fig. 3. Clamped-free boundary conditions are considered and a point force excitation is applied at a free end. Normal velocities are plotted at three distances: 0 cm, 10 cm and 50 cm from the excitation point, corresponding to 0, 1 and 9 resonators, respectfully. Dynamic modes are clearly suppressed in the resonance bandwidth and strongly damped from 300 Hz to 400 Hz.

Far for the source excitation, the dynamic response exhibits a gap well predicted by the propagation constant, while in the near-field the presence of the resonators only suppresses the waveguide's modes. We can conclude from these results that the propagation constants provided by Bloch-based analyses are an efficient

way to design a network of periodically distributed tuned mass dampers. However, it is emphasized that the value of $|\lambda|$ only stands for the wave transmitted amplitude, but does not distinguishes internal dissipation, diffusion nor reflection, which produce different vibration attenuation.

3 Waveguide Diffusion Modeling

3.1 Concept

The proposed modeling strategy consists in replacing the locally resonant unit-cell by two semi-infinite waveguides connected using a small section of the waveguide supporting the resonator. Therefore, Bloch theory is no longer applied to the global unit-cell as above, but on the elementary waveguide's cross-section, involving only 312 DOFs. Wave solutions will be denoted (Λ, Ψ) for this base waveguide's solutions, instead of (Δ, Φ) for the global periodic unit-cell. The diffusion-based model is illustrated in Fig. 4.

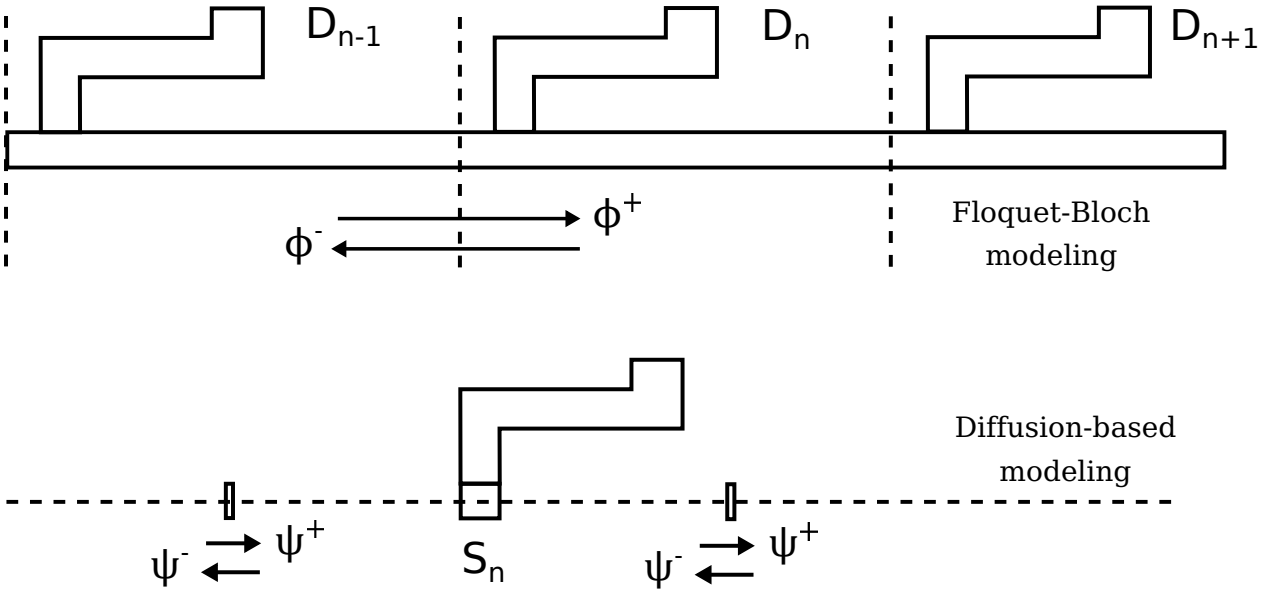


Figure 4: Concept of diffusion-based modeling.

3.2 Diffusion relations

Denoting $[\Psi^+, \Psi^-]$ the wave basis and $\mathbb{S}$ the condensed coupling element matrix, the local dynamic equilibrium can be rewritten using the state vectors expansion on the positive and negative-going wave amplitudes. Reorganizing the transmitted and reflected wave amplitudes and expressing in terms of the incident waves yields the following expression of the R and T coefficients:

$$\left\{ \begin{array}{c} R \\ T \end{array} \right\} = \left[\begin{array}{cc} A & B \\ C & D \end{array} \right]^{-1} \left\{ \begin{array}{c} \alpha \\ \beta \end{array} \right\} \tag{5}$$

where the matrix terms A, B, C and D are written:

$$A = \mathbb{D}_{RL}\Psi^{-}\Lambda + (\mathbb{D}_{RR} + \mathbb{S}_{LL})\Psi^{-} \tag{6}$$
$$B = \mathbb{S}_{LR}\Psi^{+} \tag{7}$$
$$C = \mathbb{S}_{RL}\Psi^{-} \tag{8}$$
$$D = (\mathbb{S}_{RR} + \mathbb{D}_{LL})\Psi^{+} + \mathbb{D}_{LR}\Psi^{+}\Lambda \tag{9}$$

The coefficients $\alpha_j = \mathbb{Q}_1(\lambda_j)\Psi_j^{+}$ and $\beta_j = \mathbb{Q}_2\Psi_j^{+}$ are the source terms associated with the incident wave of index j while $\mathbb{Q}_1$ and $\mathbb{Q}_2$ are the unit-cell dynamic projection matrices at the edges of the coupling element. Note that a modal synthesis can also be used to reduce the condensation effort on matrix $\mathbb{S}$. A major advantage however is that the wave basis remains unchanged and resonators' designs can be investigated without recomputing wave solutions.

3.3 Reduced formulation

Considering a wave projection basis Θ, built using the Wave Finite Element method, from a reduced subset of Bloch waves [14] (interested reader can also refer to Ref. [15, 16, 17, 18, 19] for further developments on reduced WFEM). Reduced dynamic stiffness matrix is therefore denoted $\tilde{\mathbb{D}}$ and $\tilde{\Psi} = \Theta^T\Psi$ is the reduced state vector, the spectral problem can be rewritten as:

$$[\Theta^T\mathbb{D}_{RL}(\omega)\Theta\tilde{\Lambda}^{-1} + \Theta^T(\mathbb{D}_{RR}(\omega) + \mathbb{D}_{LL}(\omega))\Theta + \Theta^T\mathbb{D}_{LR}(\omega)\Theta\tilde{\Lambda}]\tilde{\Psi} = 0 \tag{10}$$

The solutions of Eq.10 can be used to rewrite the diffusion equation (Eq.5) as:

$$\begin{bmatrix} \Theta^T & 0 \\ 0 & \Theta^T \end{bmatrix} \begin{bmatrix} A & B \\ C & D \end{bmatrix} \begin{Bmatrix} R \\ T \end{Bmatrix} = \begin{bmatrix} \Theta^T & 0 \\ 0 & \Theta^T \end{bmatrix} \begin{Bmatrix} \alpha \\ \beta \end{Bmatrix} \tag{11}$$

which results in the following reduced scattering and source coefficients:

$$\tilde{A} = \tilde{\mathbb{D}}_{RL}\tilde{\Psi}^{-}\tilde{\Lambda} + (\tilde{\mathbb{D}}_{RR} + \Theta^T\mathbb{S}_{LL}\Theta)\Psi^{-} \tag{12}$$
$$\tilde{B} = \Theta^T\mathbb{S}_{LR}\Theta\tilde{\Psi}^{+} \tag{13}$$
$$\tilde{C} = \Theta^T\mathbb{S}_{RL}\Theta\tilde{\Psi}^{-} \tag{14}$$
$$\tilde{D} = (\Theta^T\mathbb{S}_{RR}\Theta + \mathbb{D}_{LL})\tilde{\Psi}^{+} + \mathbb{D}_{LR}\tilde{\Psi}^{+}\tilde{\Lambda} \tag{15}$$

and

$$\tilde{\alpha} = \Theta^T\alpha\Theta \tag{16}$$
$$\tilde{\beta} = \Theta^T\beta\Theta \tag{17}$$

However, note that the coupling matrix is projected on the reduced wave basis: $\Theta^T\mathbb{S}_{ab}\Theta$. This operation may produce inaccuracies for evanescent wave diffusion properties, if the junction between the waveguide and the coupling part exhibit strong mismatch. This assumption is tested in the application example below.

4 Numerical validations

4.1 Validation of the ROM procedure

State vector projection on a reduced set of Bloch waves is highly effective to describe the propagation of free waves. However, the junction between the waveguide section and the coupling singularity may not be approximated correctly by the proposed state vector projection. Let us consider two coupling elements: model

(a) contains only the resonator with a small waveguide junction, while model (b) includes a large section of the waveguide whose dimension is the initial periodic unit-cell length. Model (b) is therefore expected to allow positive-going highly evanescent waves to decay along the coupling element, thus increasing the Bloch projection accuracy and the junction with the waveguide model.

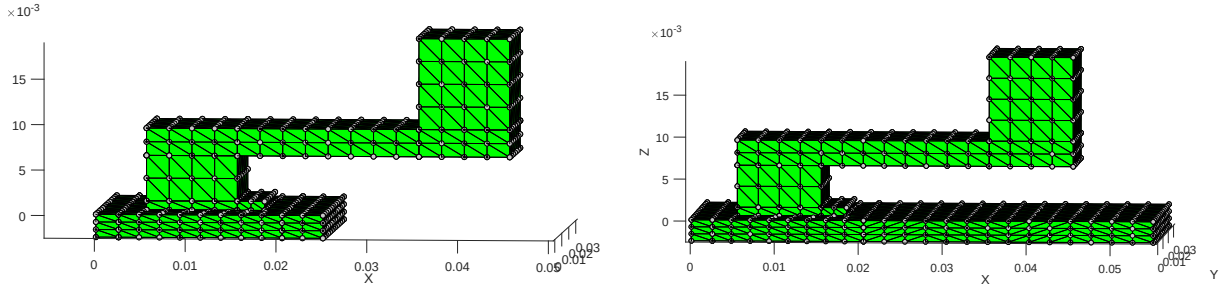


Figure 5: Two types of coupling element models. (a) Small coupling element and (b) Large coupling element (unit-cell standard length).

Diffusion coefficients are compared with the full solution. First we observe that dashed and continuous lines are close together. It means that the produced error is mainly due to the Component Mode Synthesis (CMS) reduction achieved on the coupling element. Inside the bandgap, the reduction scheme increases the initial CMS error. It can be explained since the internal resonance of the tuned mass damper produces near-field components (evanescent waves) that are not well described by the reduced wave basis. On the other hand, the short coupling (a) element appears less sensitive to the reduction than model (b), outside the bandgap. This can result from the fact that a higher number of modes are needed in model (b) to describe the inner dynamics of cell, compared with model (a).

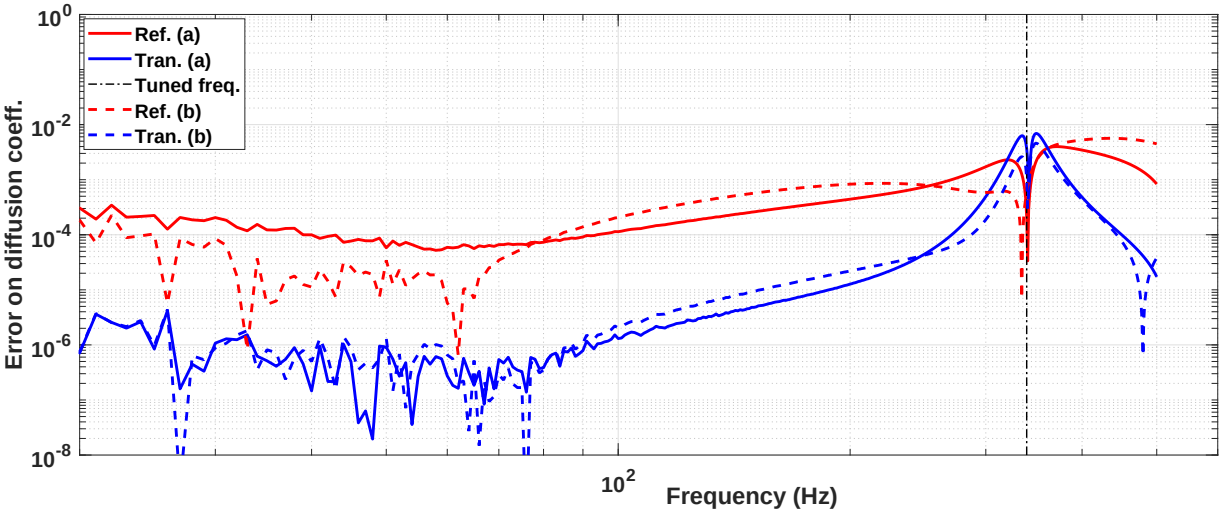


Figure 6: Error produced by the projection using different coupling element configurations.

It can be concluded that the projection of the coupling element on a reduced wave basis does not affect significantly the computed diffusion coefficients' accuracy in the considered example. In terms of CPU, the state vector reduction provides an overall reduction factor between 20× and 30×, depending on the requested accuracy.

4.2 Bloch vs. Diffusion information

The reflection and transmission coefficients are represented in Fig.7 for the model studied in Sec.2. Since the resonator is damped, dissipation occurs at resonance. Diffused wave coefficient is derived from energy balance and indicates the residual waves components:

- Transmission into propagating wavetypes (i.e. positive conversion)
- Transmission into evanescent waves (i.e. positive diffusion)
- Dissipation in the coupling element (i.e. absorption)
- Reflection into propagating wavetypes (i.e. negative conversion)
- Reflection into evanescent waves (i.e. negative diffusion)

In the context of the design of vibroacoustic metamaterials or locally resonant tuned mass dampers, the overall objective is to reduce (either by conversion or dissipation) the mechanical energy carried by the first-order flexural waves. In this regard, the residual component in Fig.7 contains both the specular (propagating) and diffuse (evanescent) scattering, as well as the wave absorption coefficient. It provides a good estimation of the resonator's performance.

The 'diffused' coefficient therefore corresponds to:

$$\{\text{diffused}\} = \{\text{positive diffusion}\} + \{\text{negative diffusion}\} + \{\text{absorption}\} \tag{18}$$

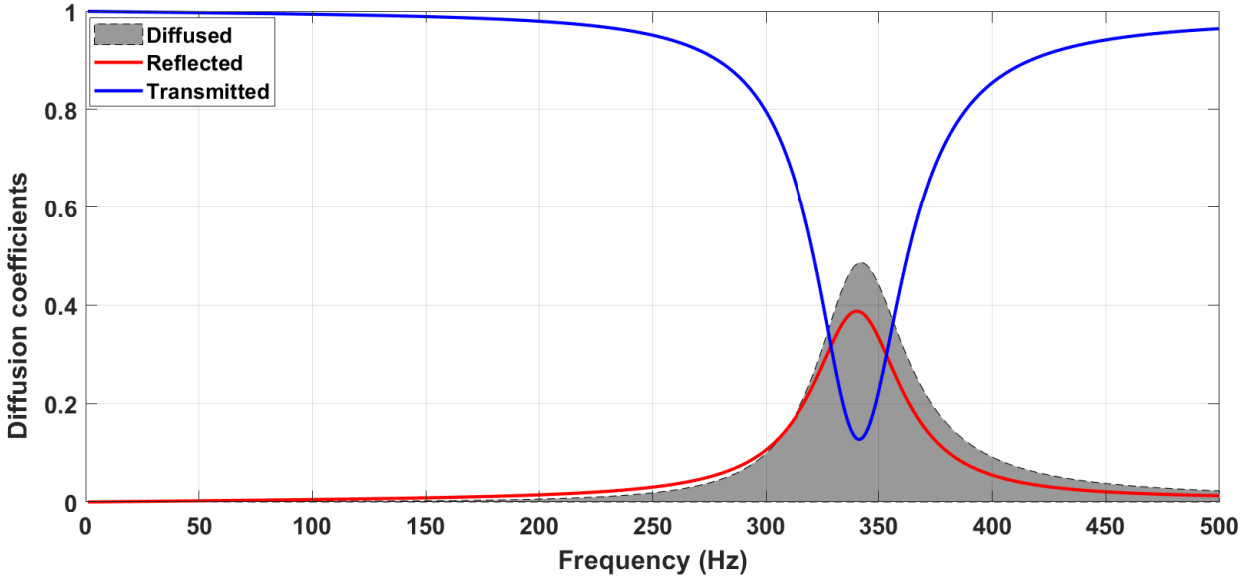


Figure 7: Diffused, reflected and transmitted waves through the resonator's coupling element.

As expected, the diffusion pic is located at the same frequency as the bandgap from Bloch analysis, and the transmission curve and propagation constants display similar patterns and are almost superposed. This time, an additional information is provided by the diffusion analysis: the Reflected and Diffused coefficients, where one can notice that the absorption is slightly higher than the reflection. In the following, the proposed diffusion model is used to investigate the influence of a resonator's design parameter on the absorption and reflection coefficients and on the overall dynamic response.

4.3 Vibration absorption performances and finite response

Additionally, for the selected waveguide, each new resonator can be analyzed without re-computing Bloch solutions, hence resulting in a considerable gains in terms of computational efforts (see Table 3). Indeed, the coupling element can be condensed (3 sec.) for the selected model, and diffusion analysis can be achieved in 7 sec. (0.2 sec. with the reduced wave basis) against 184 seconds for each design using the standard Bloch unit-cell analysis.

Modeling strategy	Unit-cell (Bloch)	Reduced diffusion
Added computation time per resonator's design (s)	**184**	**3.2**

Table 3: Computation times depending on the modelling choice and use of reduced WFEM formulation. All calculations are made with the same processor.

A parametric analysis is proposed in Fig.9 for the resonator's damping properties. The influence of the loss factor η on the distribution of transmitted and diffused waves is evaluated. Although the bandgap classically decreases in depth while its bandwidth increases with damping (see Reflection curve), the reflection is progressively replaced by the absorption starting from $\eta = 5\%$. Noteworthy, as the reflection decreases with damping, the absorption reaches a maximum then decreases, hence reducing the resonator's overall efficiency above $\eta \geq 10\%$. A compromise could therefore be reached for values of the damping, in order to achieve a low wave transmission while privileging absorption over reflection.

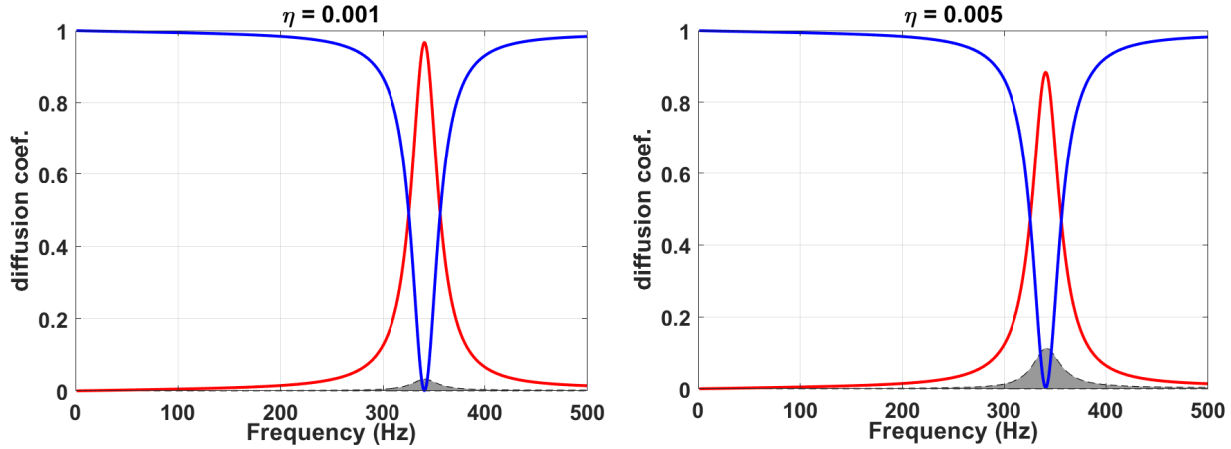


Figure 8: Influence of damping on the resonator's absorption and reflection coefficients.

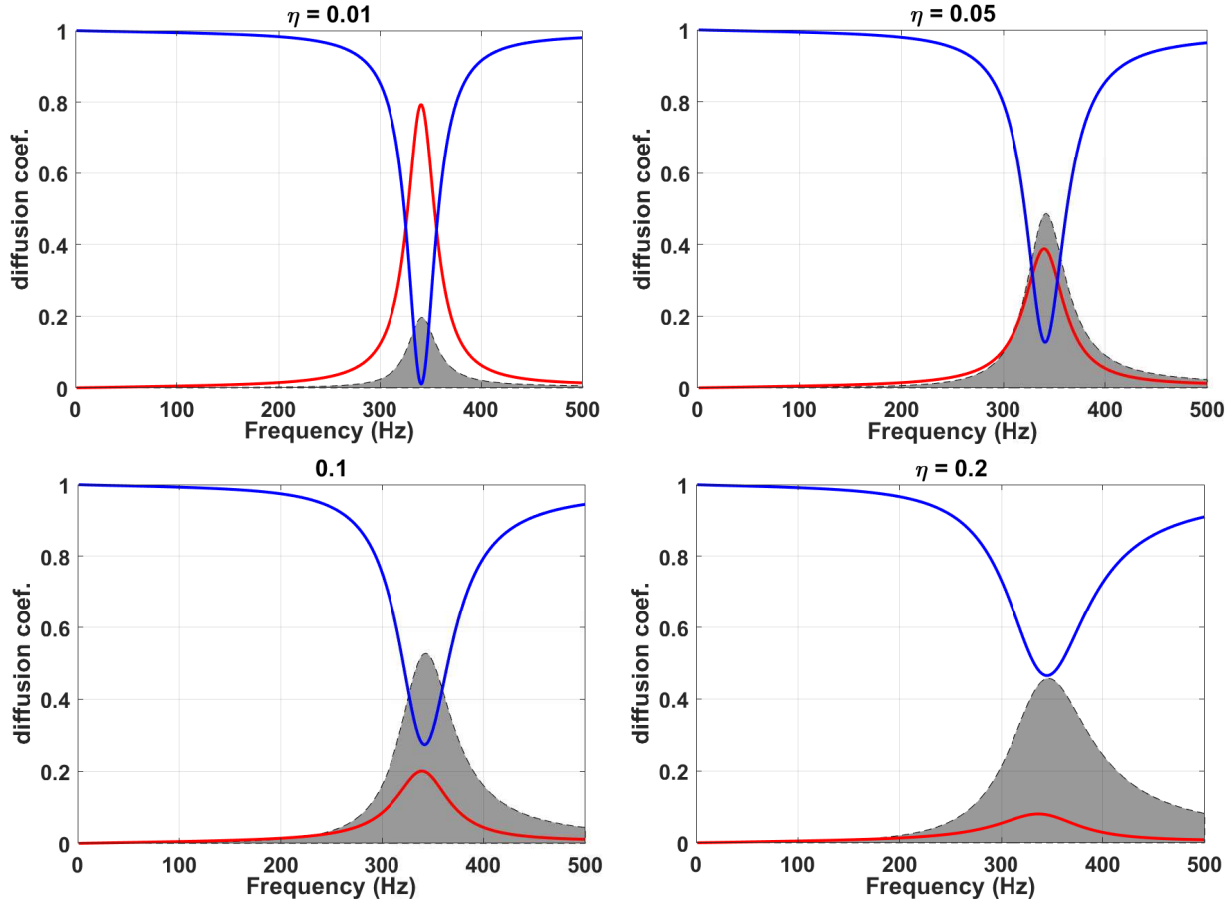


Figure 9: Influence of damping on the resonator's absoption and reflection coefficients.

The dynamic response for different damping values is shown in Fig.11. Note that an increased damping suppresses modes around the bandgap, thus it significantly increases the controlled bandwidth. Above these values damping becomes counter-productive within the bandgap region.

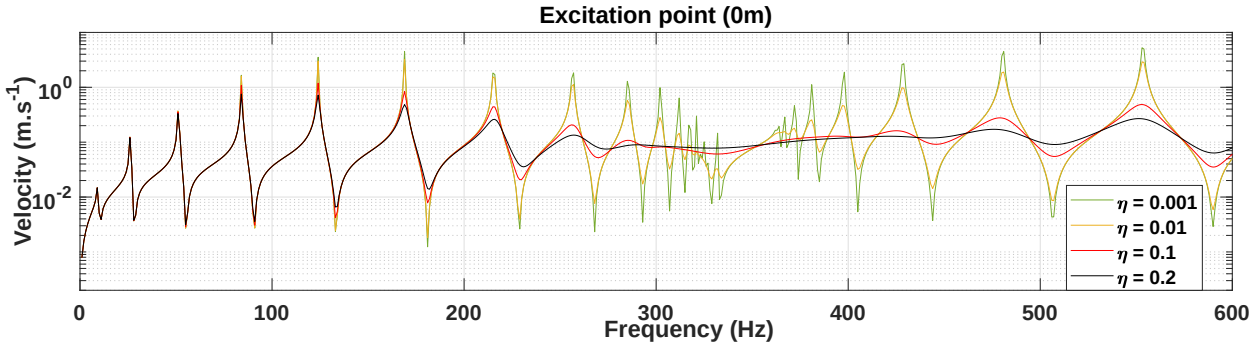


Figure 10: Influence of damping on the finite waveguide's dynamic response. Three posistions from excitation point (0 cm, 10 cm, 50 cm) and four values of the damping ($\eta = 0.001 - 0.2\%$)

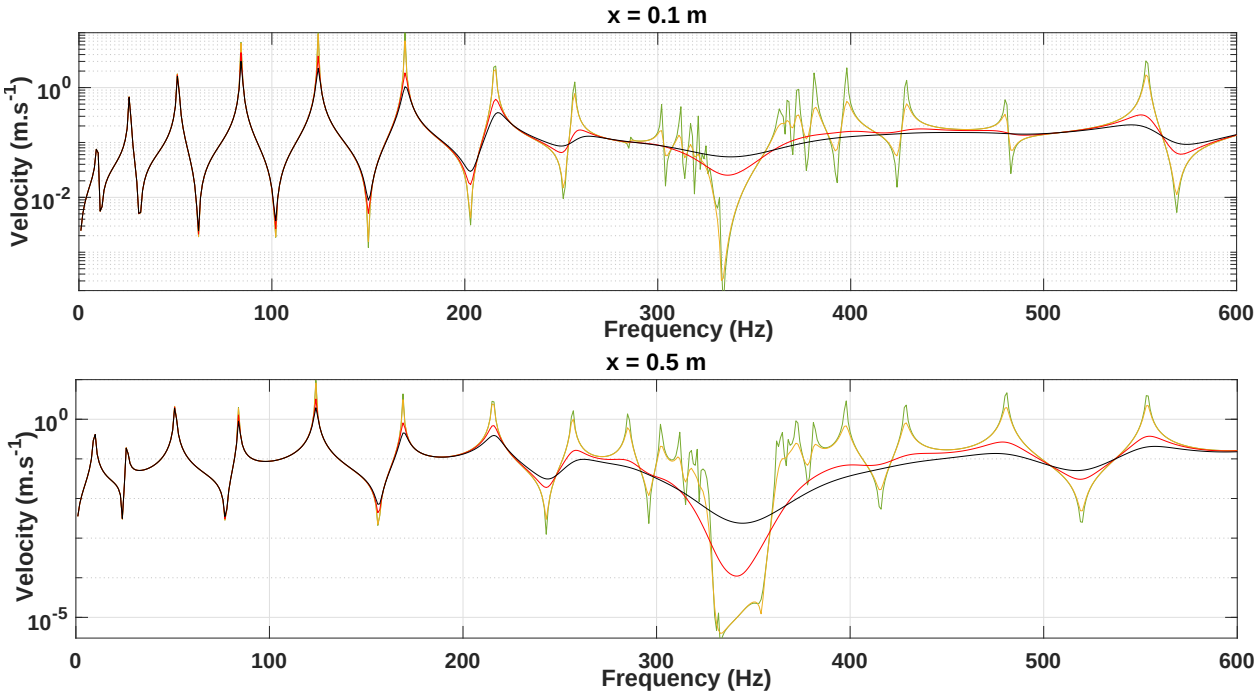


Figure 11: Influence of damping on the finite waveguide's dynamic response. Three posistions from excitation point (0 cm, 10 cm, 50 cm) and four values of the damping ($\eta = 0.001 - 0.2\%$)

5 Conclusions

In this paper an alternative diffusion-based methodology was used to study a locally resonant sub-structure and compared with Bloch diagram analyses. The method proved highly effective to predict wave reflection, transmission, and diffusion coefficients, including evanescent conversion and absorption. A reduced formulation based on Bloch wave expansion was proposed to reduce the computation effort so that the influence of resonators' damping properties could be investigated. It is emphasized that better damping models could be implemented, as the coupling dynamic stiffness matrix can involve viscoelastic materials or external loads. The proposed methodology provides additional information compared with Bloch analyses. It is hoped that the proposed method will prove efficient for the fast design optimization of Bragg or locally resonant metamaterials.

References

[1] Igusa, T., Xu, K. (1994). *Vibration control using multiple tuned mass dampers*. Journal of sound and vibration, 175(4), 491-503. (https://doi.org/10.1006/jsvi.1994.1341)

[2] Yamaguchi, H., Harnpornchai, N. (1993). *Fundamental characteristics of multiple tuned mass dampers for suppressing harmonically forced oscillations*. Earthquake engineering & structural dynamics, 22(1), 51-62. (https://doi.org/10.1002/eqe.4290220105)

[3] Xiao, Y., Wen, J., Wen, X. (2012). *Broadband locally resonant beams containing multiple periodic arrays of attached resonators*. Physics Letters A, 376(16), 1384-1390. (https://doi.org/10.1016/j.physleta.2012.02.059)

[4] Claeys, C., Deckers, E., Pluymers, B., Desmet, W. (2016). *A lightweight vibro-acoustic metamaterial demonstrator: Numerical and experimental investigation*. Mechanical Systems and Signal Processing, 70, 853-880. (https://doi.org/10.1016/j.ymssp.2015.08.029).

[5] Mencik, J. M., Ichchou, M. N. (2005). *Multi-mode propagation and diffusion in structures through finite elements*. European Journal of Mechanics-A/Solids, 24(5), 877-898. (https://doi.org/10.1016/j.euromechsol.2005.05.004)

[6] Mitrou, G., Ferguson, N., Renno, J. (2017). *Wave transmission through two-dimensional structures by the hybrid FE/WFE approach*. Journal of Sound and Vibration, 389, 484-501. (https://doi.org/10.1016/j.jsv.2016.09.032)

[7] Ben Souf, M.A., Kessentini, A., Bareille, O., Taktak, M., Ichchou, M. N., Haddar, M. (2017). *Acoustical scattering identification with local impedance through a spectral approach*. Comptes Rendus Mcanique, 345(5), 301-316. (https://doi.org/10.1016/j.crme.2017.03.006)

[8] Becht, P., Deckers, E., Claeys, C., Pluymers, B., Desmet, W. (2016). *Using the resonance behavior of finite pipes for defect detection based on the wave-scattering*. Proceedings of ISMA 2016 - International Conference on Noise and Vibration Engineering, 2014, p. 1147-1161. (http://past.isma-isaac.be/downloads/isma2016/papers/isma2016_0775.pdf)

[9] Errico, F., Ichchou, M., De Rosa, S., Bareille, O., Franco, F. (2018). *A WFE and hybrid FE/WFE technique for the forced response of stiffened cylinders*. Advances in Aircraft and Spacecraft Science, 5(1), 1-19. (https://doi.org/10.12989/aas.2018.5.1.001)

[10] Errico, F., Ichchou, M., De Rosa, S., Bareille, O., Franco, F. (2018). *The modelling of the flow-induced vibrations of periodic flat and axial-symmetric structures with a wave-based method*. Journal of Sound and Vibration, 424, 32-47. (https://doi.org/10.1016/j.jsv.2018.03.012)

[11] Gravenkamp, H. (2018). *Efficient simulation of elastic guided waves interacting with notches, adhesive joints, delaminations and inclined edges in plate structures*. Ultrasonics, 82, 101-113. (https://doi.org/10.1016/j.ultras.2017.07.019)

[12] Droz, C., Bareille, O., Laine, J.P., Ichchou, M. (2018). *Wave-based SHM of sandwich structures using cross-sectional waves*, Structural Control and Health Monitoring, vol. 25(2), e2085. (https://doi.org/10.1002/stc.2085)

[13] Lossouarn, B., Aucejo, M., De, J. F. (2018). *Electromechanical wave finite element method for interconnected piezoelectric waveguides*. Computers & Structures, 199, 46-56. (https://doi.org/10.1016/j.compstruc.2018.01.009).

[14] C. Droz, J. P. Lainé, M. Ichchou, G. Inquiété. (2014). *A reduced formulation for the free-wave propagation analysis in composite structures*, Composite Structures, vol. 113, p. 134-144. (https://doi.org/10.1016/j.compstruct.2014.03.017)

[15] C. Droz, M. Ichchou, J. P. Lainé. (2014). *Numerical prediction of dispersion characteristics for high-order waves in composite waveguides*, Proceedings of ISMA 2014 - International Conference on Noise and Vibration Engineering, 2014, p. 4203–4216. (http://past.isma-isaac.be/downloads/isma2014/papers/isma2014_0043.pdf)

[16] Zhou, C.W., Laine, J.P., Ichchou, M., Zine, A.M. (2015). *Wave finite element method based on reduced model for one-dimensional periodic structures*. International Journal of Applied Mechanics, 7(02), 1550018. (https://doi.org/10.1142/S1758825115500180)

[17] Droz, C., Zhou, C., Ichchou, M., Lainé , J. P. (2016). *A hybrid wave-mode formulation for the vibro-acoustic analysis of 2D periodic structures*, Journal of Sound and Vibration, Vol. 363, p. 285-302. (https://dx.doi.org/10.1016/j.jsv.2015.11.003)

[18] Fan, Y. , Zhou, C.W., Laine, J.P., Ichchou, M., Li, L. (2018). *Model reduction schemes for the wave and finite element method using the free modes of a unit cell*. Computers & Structures, 197, 42-57. (https://doi.org/10.1016/j.compstruc.2017.11.015)

[19] Boukadia, R., Droz, C., Ichchou, M., Desmet, W. (2018). *A Bloch wave reduction scheme for ultrafast band diagram and dynamic response computation in periodic structures*, Finite Elements in Analysis and Design, vol. 148, p.1-12. (https://doi.org/10.1016/j.finel.2018.05.007)

Broadband resonance suppressions using a resonant beam damper with embedded acoustic black hole features

Tong Zhou[1], Li Cheng[1]
[1] Department Mechanical Engineering, The Hong Kong Polytechnic University
e-mail: **li.cheng@polyu.edu.hk**

Abstract
This article presents a study of a novel vibration control device in the form of a resonant beam damper (RBD) with 'Acoustic Black Hole' (ABH) features. Both enriched dynamic characters of the ABH taper and enhanced system damping brought by ABH effects are exploited to develop this so-called ABH-featured RBD (ABH-RBD) for broadband vibration control. The numerical simulations and experimental measurements show that, without the tedious tuning process, the multiple resonant peaks of a primary structure can be suppressed effectively by the proposed ABH-RBD, except for some specific resonances. Three typical vibration control effects are found by a strategic parameter study: interaction dominated, damping enhancement and their combinations. Further analyses of these control mechanisms are carried out by contrastive studies with a uniform beam absorber. The influence of the attachment locations on the performance of ABH-RBD is also noticed and discussed.

1 Introduction

Add-on vibration reduction devices are commonly used to suppress structural vibrations [1]. A dynamic vibration absorber (DVA) is tuned for neutralizing vibratory energy through its interaction with the host structure [2]. Through a precise tuning of the DVA parameters, the vibration response of the primary structure can be significantly reduced at the tuning frequency owing to its strong interaction with the DVA. Damping helps extend the working frequency band of the DVA at the expenses of compromising the control performance at the tuning frequency [3]. To achieve the maximum vibration attenuation within the targeted frequency band, both the frequency and the damping of the absorber have to be meticulously tuned and optimized [4]. Various designs of DVAs have been attempted [5] such as the so-called resonant beam damper (RBD), shown in Figure 1(a), where the fundamental bending mode of a cantilever absorber is utilized to generate the interaction with the primary system [6, 7]. To broaden the working bandwidth around the targeted frequency, multi-layered beam-type neutralizers, composed of several stacked beams with slightly different lengths, were also proposed [8]. Multi-degree-of-freedom (DOF) DVAs have also been studied, whose parameters need to be tuned to each structural resonance so that multiple resonant peaks of the primary structure can be controlled in a wide frequency range [9, 10]. Alternatively, multiple 1-DOF DVAs have also been attempted on beams [11-13] or plates [14, 15], with each absorber dealing with a particular structural resonance. However, the tuning procedure of the entire absorber system in this case becomes quite complicated and tedious since the whole cluster of DVAs needs to be tuned simultaneously due to their mutual interactions [11, 15].

Another option is to use a waveguide absorber (WA) based on the waveguide phenomenon to draw the vibratory energy away from the primary system [1, 16]. A WA needs to be properly designed to provide sufficient energy dissipation to achieve multi-resonance attenuations. To ensure the maximum increase in the added loss factor to the primary system, the mechanical impedance of the WA and that of the primary structure at the attachment point should be matched to satisfy the impedance-matching condition [16]. Meanwhile, it is shown that both the attachment locations and the number of absorbers to be used are

important for generating sufficient control effects [17-19]. Efforts have also been made to reduce the dimension and the occupation space of the absorbers through various structural designs [20, 21].

Despite their widespread use, both DVAs and WAs pose problems for broadband vibration reductions in terms of design and implementations. For the former, the physical parameters of the DVA cluster need to be meticulously tuned, which is a quite tedious and complex process. In addition, structural or operational changes in the primary structure may jeopardize the effectiveness of the designed DVAs. For the latter, conventional structural elements can hardly provide the required energy dissipations unless multiple absorbers with large structural dimensions and massive damping materials are used.

To tackle these problems, this study presents a new add-on device by capitalizing on a combined DVA and WA principle through the exploitation of the unique features of the so-called 'Acoustic Black Hole' (ABH) phenomenon. The targeted outcome is a compact and light weighted vibration reduction device to achieve the broadband vibration suppressions without a complex tuning procedure. Meanwhile, it should be robust enough to accommodate structural and operational variations in the primary vibrating system.

Studies on ABH have been drawing an increasing attention in the vibration community during the last two decades. In the one-dimensional case, an ABH wedge (Figure 1(b)) is tailored to have a thickness variation according to a power function, $h(x) = \varepsilon x^m, m \geq 2$, in which x is the taper length coordinate. When flexural waves travel towards the tip of the taper, their phase and the group velocities gradually reduce and the wave amplitude increase progressively. If the thickness of the taper goes to zero, the bending waves will take an infinitely long time to travel inside the tapered area, resulting in zero wave reflections [22-28]. Owing to the high energy density within the tip region as a result of the wave compression and focalization, a small amount of damping materials turns out to be enough to create a significant damping increase in the entire taper.

In this paper, we discuss a resonant beam damper (RBD) configuration by embracing the ABH principle, referred to as 'ABH-RBD' (Figure 1(c)) for the suppressions of broadband resonant peaks of a host structure, exemplified by a beam. The configuration of ABH-RDB is first described, followed by a description of the simulation model and numerical analysis method. For illustration purposes, a beam is selected as a benchmark case. The vibration suppression capacity of the ABH-RDB is then demonstrated with control mechanisms revealed and verified by experiments

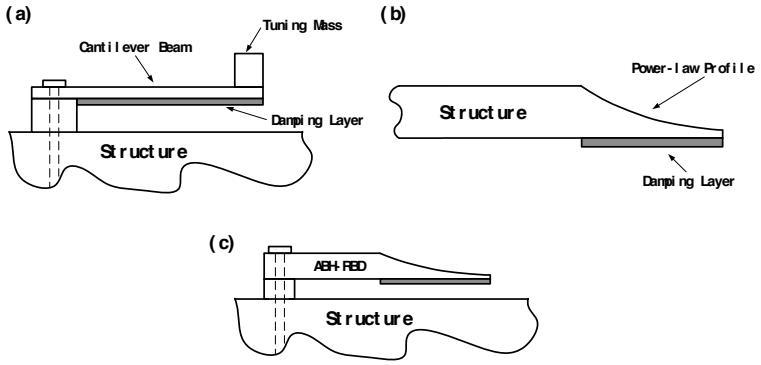


Figure 1: (a) Resonant Beam Damper, (b) ABH featured beam (c) ABH-RBD

2 Numerical model

As shown Figure 2, the configuration under investigation contains a primary host structure (a uniform beam) and an auxiliary ABH-RBD connected by a small connector. The length (denoted by L) and the thickness of the host uniform beam are 300mm and 8mm, respectively. The ABH-RBD can be further divided into two sub-sections: a tapered portion with an ABH thickness profile and a uniform portion. The uniform region of the ABH-RBD is $1/6 \cdot L$ long and 3mm thick. The tapered portion has the same length as the uniform portion and the thickness varies from 3mm to 0.1mm following a parabolic variation law ($h(x) = \varepsilon x^2 + h_0$, where ε is a constant). A viscoelastic damping layer with a constant thickness ($h_d = 1\text{mm}$) is

coated over the surface of the entire tapered region. The total weight and the total length of the ABH-RBD is 9.2% and 1/3 of that of the primary system, respectively. A small connector with a dimension of 8×1 mm is located at $60\% \cdot L$ from the left end of the host beam and mounted over the surface of the primary system. The width of all elements is set to be the same (20mm). The coating material on the ABH taper is a viscoelastic tape, 3M^{TM} F9473P [35], with a constant Young's modulus and loss factor η_d adopted in simultations. The rest of the system is set to be aluminum with material parameters tabulated in Table 1.

Finite element (FE) simulations were conducted using COMSOL^{TM}. A 2D FE model was built under the plane stress condition in the solid mechanics interface. The boundary conditions of the host beam were set to be clamped-clamped. The damping layer and the connector were meshed with quadrilateral elements whilst other parts being meshed using triangular elements. The small connector was set to be a rigid domain. A transverse point excitation was imposed at $20\% \cdot L$ of the host beam. Cross point responses were calculated at $83.3\% \cdot L$ of the host beam from the left end.

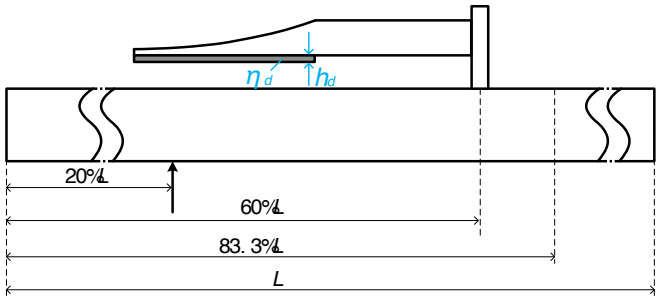


Figure 2: Schematics of the host beam with an ABH-RBD

	Aluminum	Damping Layer
Young's modulus	70 GPa	30 MPa
Density	2700 kg/m^3	980 kg/m^3
Poisson's ratio	0.3	0.499
Loss factor	0.1%	0.9

Table 1: Material parameters used in the simulation

3 Numerical results and discussions

3.1 Vibration reduction phenomena

Effects of the proposed ABH-RBD are first numerically demonstrated. It can be seen from Figure 3 that both the driving (Figure 3(a)) and cross (Figure 3(b)) point mobility curves of the primary host beam without the ABH-RBD show complex dynamics with multiple resonant peaks within a broad frequency range. With the deployment of the ABH-RBD, most of resonant peaks are suppressed substantially except for some specific resonances. Note this vibration reduction has been achieved without particular tuning of the ABH-RBD parameters. To further demonstrate the generic nature of the observed phenomena, the dimension of the primary beam used above is changed to a longer and thinner one, but with the same total weight as the previous one, thus exhibiting richer dynamic complexities (Figure 4). It can be seen that using the same ABH-featured device on this different beam also leads to a significant reduction in the structural vibration level over the entire frequency range. However, Figure 4 shows that no significant and systematic reductions can be obtained at the very low frequency range. This is understandable since systematic ABH effects can only be expected above a certain frequency when local modes within the ABH taper appear. Nevertheless, the proposed ABH-RBD is found to be effective for suppressing the vibrational responses of different host beams using the same ABH-RBD without a particular parameter tuning.

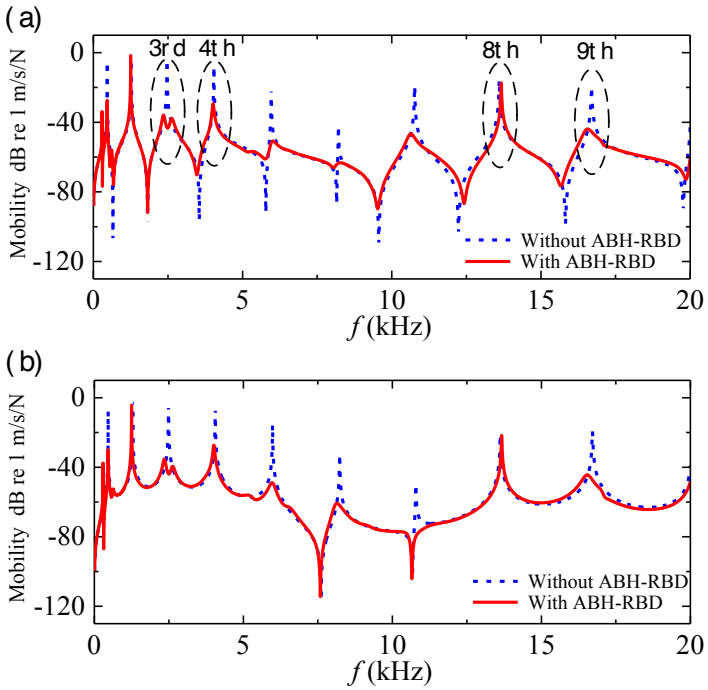


Figure 3: Comparisons of the (a) driving and (b) cross point mobility of the primary host beam with and without ABH-RBD

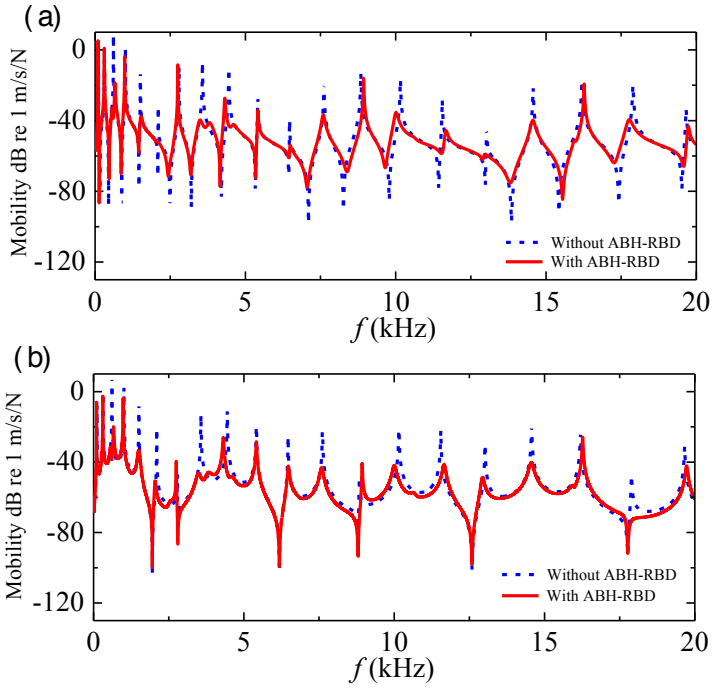


Figure 4: Comparisons of the (a) driving and (b) cross point mobility of the second host beam with and without ABH-RBD

3.2 Control Mechanisms

Analyses are conducted for some typical peaks using the driving point mobility curve in Figure 3(a). Some typical resonant peaks are labeled, regrouped and identified by dash circles in this figure. The first group is

exemplified by the 3rd resonant peak, marked in Figure 3(a). It can be seen that the ABH-RBD reduces its vibration amplitude by splitting the peak into two, similar to a conventional DVA. The 4th resonant peak represents another typical category for which the original resonance peak is reduced without being split. For the third category, i.e. the 9th one at a higher frequency, the original resonance peak seems to be smoothed, shifted without obvious splitting. Meanwhile, the ABH-RBD has little effects on some resonance peaks, exemplified by the 8th resonance frequency.

In order to explore the underlying physics, these different types of peak reductions are scrutinized. By strategically varying the properties of the ABH-RBD, the ABH-induced DVA effect (mainly due to the interaction) and WA effect (mainly due to the wave trapping and absorption) can be separated. Typical control effects are analyzed through investigating the driving point mobility of the combined vibratory system, first over the frequency band (2-5 kHz) containing the 3rd and 4th resonant peaks and then over the one (13-18 kHz) including the 8th and 9th peaks. The driving point mobility of the primary host beam without ABH-RBD is also provided as a reference.

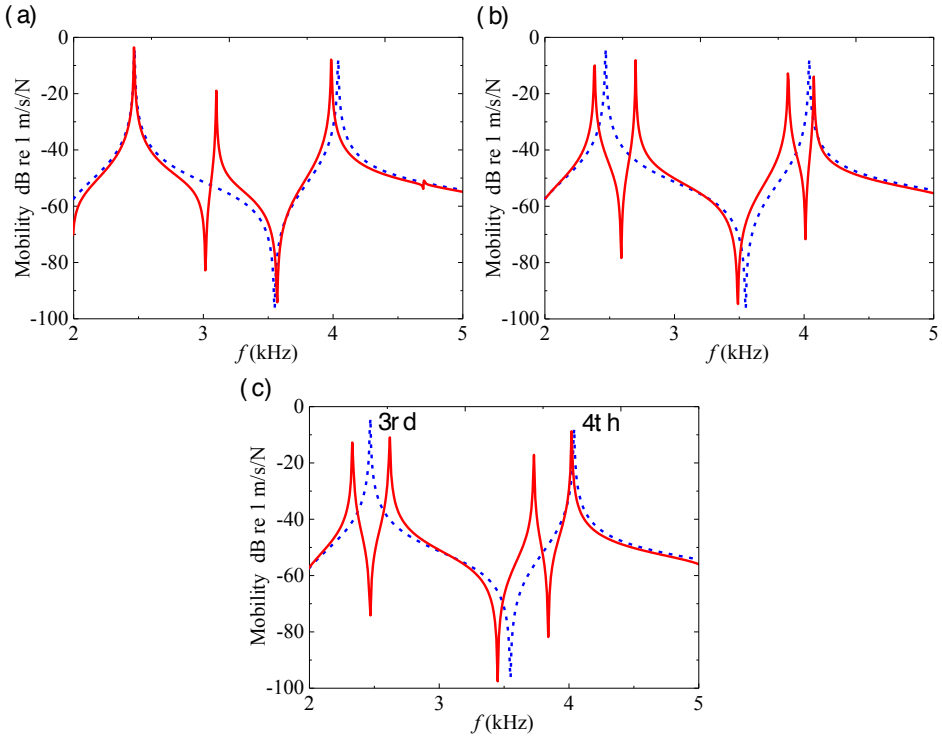


Figure 5: Driving point mobility of the combined vibratory system with undamped coating layers ($\eta_d = 0$) having 3 thicknesses: (a) $h_d = 0$mm, (b) $h_d = 0.5$mm and (c) $h_d = 1$mm (solid line '—'); driving point mobility of the primary host beam without ABH-RBD is set as a reference (dash line '---')

To single out the effect of structural interaction, the loss factor η_d (refer to Figure 2) of the coating materials over the tapered portion of the ABH-RBD is first set to zero to eliminate the energy dissipation effect. The dynamics of the ABH-RBD can then be varied by changing the thickness of the undamped coating layer (h_d in Figure 2). It can be seen from Figure 5 that with the increase of h_d, the additional peak caused by the ABH-RBD is gradually shifted to the low frequencies and approaches the 3rd resonant peak due to the mass loading effect. Reaching $h_d = 1$mm (same as the one adopted in Figure 3), the frequency matching condition is satisfied so that strong interactions between the ABH-RBD and the host beam take place around the 3rd original resonance. This is typical of a conventional DVA, resulted from the frequency matching between the DVA and the host structure as well as the strong coupling between both. This peak reduction can be categorized as "interaction-dominated". It is relevant to note that the undamped ABH-RBD system has little influence on the position of 4th resonance as $h_d = 1$mm.

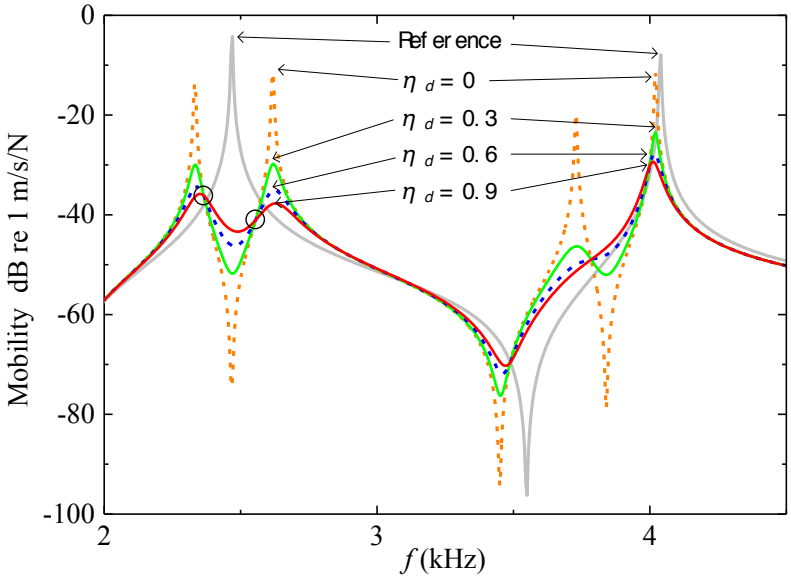


Figure 6: Driving point mobility of the combined vibratory system with absorbing coating layers with a constant thickness ($h_d = 1$mm) but different loss factors (η_d); the reference is the driving point mobility of the primary host beam without ABH-RBD

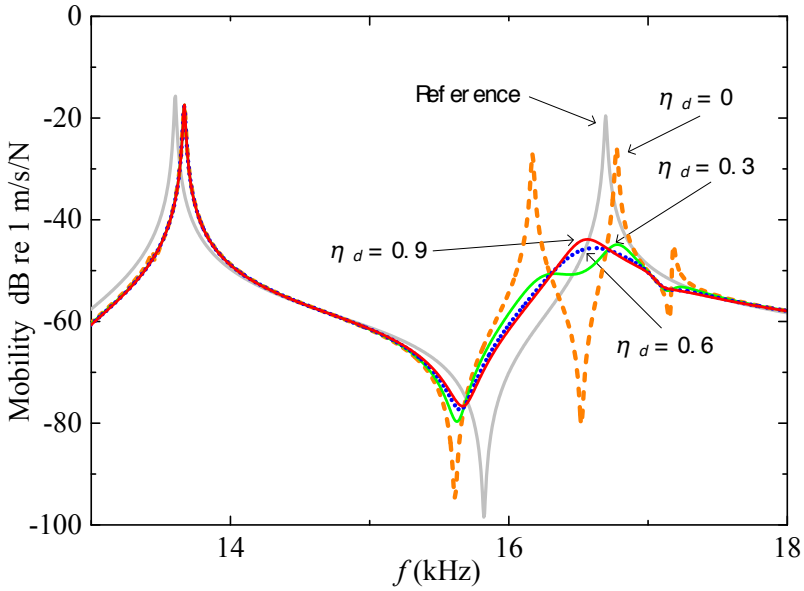


Figure 7: Driving point mobility of the combined vibratory system with absorbing coating layers with a constant thickness ($h_d = 1$mm) but different loss factors (η_d); the reference is the driving point mobility of the primary host beam without ABH-RBD

The damping of the coating layers is then taken into considerations in Figure 6. Keeping h_d = 1 mm, the loss factor of the damping layer (η_d) is varied. An increase in the material damping is expected to enhance the ABH effect [23] to generate more significant energy extractions and dissipations from the host structure. Focusing again on the 3rd and 4th peak frequency range in Figure 6(a), it can be seen that the 4th peak are gradually reduced when material damping increases, without splitting. This is the typical phenomenon generated by the damping enhancement in the overall system due to the waveguide absorber effect of the ABH-RDB. This peak reduction is therefore categorized as “damping-dominated”. It is also relevant to re-examine the changes of the 3rd peak (interaction-dominated) due to changes in the system damping. Typical of conventional DVAs, the response curves with different η_d intersect around two fixed points, well

documented as the fixed-point theory in the literature [1, 4]. Obviously, a lower damping would better promote structural interactions, producing more significant narrow-band vibration reductions. An increased damping, however, helps widen the reduction band at the expenses of sacrificing the reduction level. This is also consistent with previous analyses based on conventional DVAs [15].

Adopting the same methodology, changes in another typical peak (identified as the 9th peak in Figure 3(a)) are examined in Figure 7 through varying the loss factor (η_d) of the coating material. The peak splitting phenomenon can be seen when η_d is low, suggesting an interaction-dominated feature. When η_d increases, however, the overall system damping quickly increases, leading to an obvious smoothing of the peak due to the imposing damping effect. This happens despite of a relatively small amount of damping material used in the taper of the ABH-RBD. Higher damping level does not necessarily bring about better control performance, which is consistent with the fixed-point theory of conventional DVAs [4]. This type of peak reduction, which seems to occur more frequently in the higher frequency range, is categorized as a combination of the interaction- and damping-dominated phenomenon. In the higher frequency range, the broadband ABH absorption effects become more dominant, leading to the combined interaction- and damping-dominated vibration reduction.

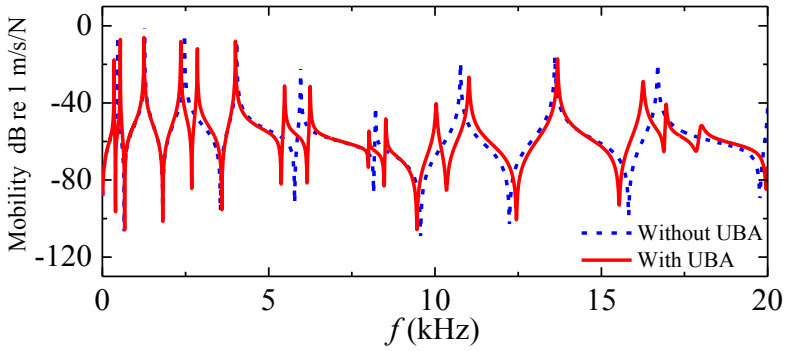


Figure 8: Comparisons of the driving point mobility of the initial host beam with and without the UBA

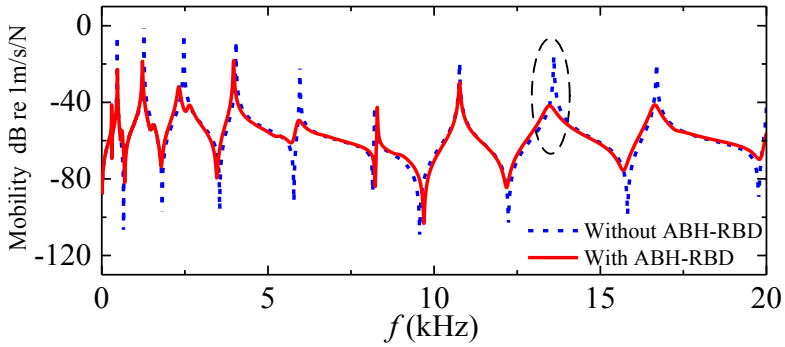


Figure 9: Driving point mobility of the combined vibratory system with and without an ABH-RBD attached at 80%·L of the primary host beam

To further confirm the superiority of the ABH-RBD, the uniform beam absorber (UBA) with the same total weight and thickness (the uniform portion) and the same damping treatment as the ABH-RBD is added to the primary beam at the same location as before (Figure 3). It can be seen from Figure 8 that, although the use of the UBA indeed changes the system dynamics, evidenced by the shift of some resonant peaks alongside the creations of new ones, these peak reductions, albeit noticeable at some frequencies, are marginal compared with Figure 3(a). This is due to the limited wave-trapping and energy dissipating capacity of the UBA. With the same amount of damping materials used in both cases, the inherent damping of the ABH-RBD well exceeds its uniform counterpart (UBA), due to the superior energy trapping capability of the ABH taper. Meanwhile, the ABH-RBD exhibits much richer dynamics in terms of the number of modes or natural frequencies. This would increase the chance of creating frequency matching to create

effective interactions between the ABH-RBD and the primary beam. Therefore, ABH-specific features are vital and essential for the generated broadband vibration control effects.

It is relevant to note that ABH-RBD seems to be ineffective for some resonance peaks such as the 8th resonant peak shown in Figure 3(a). Analyses show that this is due to the attachment location of the ABH-RBD on the primary beam, which, at this particular frequency, generates no energy transfer from the primary beam to the ABH-RBD. In the present case, by moving the attachment location of the ABH-RBD to another arbitrarily chosen point, say 80%·L, it can be seen that the 8th resonant peak (circled in Figure 9) can now be successfully suppressed. This also implies that multiple ABH-RBDs could be used to avoid this situation, and to increases the vibration reductions at the same time.

4 Experimental results

Experiments were conducted to provide a qualitative verification of the predicted broadband vibration suppression phenomena and the corresponding typical vibration control effects. An ABH-RBD, shown in Figure 10, was manufactured by the electro discharge machining (EDM) method. Its total length is 120mm with a width of 19mm. The tapered portion has the same length (60mm) as the uniform portion and the thickness varies from 3mm to 0.2mm according to the quadratic power-law function ($h(x) = \varepsilon x^2 + h_0$). The ABH-RBD was mounted to a host beam ($500 \times 5 \times 20\text{mm}$) through a cuboid connector ($5 \times 4 \times 19\text{mm}$) using a super glue. Both the host beam and the ABH-RBD were made of stainless steel. A multi-layered 3M^{TM} F9473PC adhesive tape with a total thickness of 2.08mm was coated over the surface of the tapered portion of the ABH-RBD. To further increase the energy dissipation capacities of the soft damping material, a liner made of polycoated Kraft is bounded on the outside surface of the damping tape. The added weight of the ABH-RBD is 10.2% that of the primary beam.

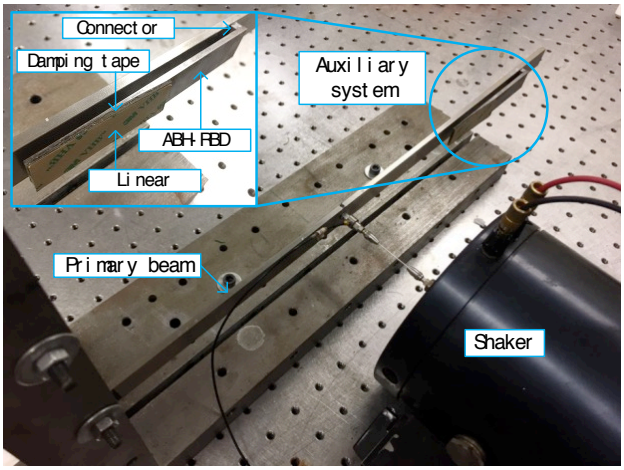


Figure 10: Experimental set-up

The primary beam was mounted on a rigid metallic frame with its other end free, mimicking clamped-free boundary conditions. The attachment position of the ABH-RBD was 10%·L from the free end of the host beam. A periodic chirp excitation was used to excite the primary structure at 60%·L from the free end using an electromagnetic shaker. The input force signal was measured by a force transducer (B&K 8203) and amplified by a charge amplifier (B&K 2635). A Polytec^{TM} laser scanning vibrometer (PSV 400) was used to measure the dynamic responses of the host beam. In addition to the driving point mobility, cross point mobility was also measured at 30%·L of the host beam from the free end.

The measured driving point mobility curves of the host beam with and without ABH-RBD and UBA are compared in Figure 11. It can be seen that, when the ABH-RBD is mounted, the resonant peaks of the primary system are effectively suppressed over the broad frequency range of interest, except for some particular frequencies, which is consistent with the general vibration reduction phenomena predicted by

numerical simulations. In particular, typical resonance peak variations, as analyzed above, can also be seen. For example, the interaction-dominated peak reduction with the split-up phenomenon can be clearly seen, as marked by the first circle in Figure 11(a), as well as some other peaks. Note that this happened without particular tuning of the ABH-RBD. Meanwhile, we do observe some peaks, i.e. the second circled peak, on which, the ABH-RBD seems to be in-effective, due to the attachment location. Most of peaks, however, are reduced around the original resonance frequency owing to either ABH-induced broadband damping enhancement, or the combined interaction and damping effect at higher frequencies. The ABH-RBD was then replaced by a uniform beam absorber (UBA) with the same total weight, the same thickness (uniform portion) and the same damping treatment. It can be seen from Figure 11 (b) that the dynamics of the primary host beam are affected, as evidenced by alterations on the mobility curves. Although the added damping allows some peak reductions at some particular frequencies, the overall reduction level, however, is relatively low as compared with that provided by the ABH-RBD.

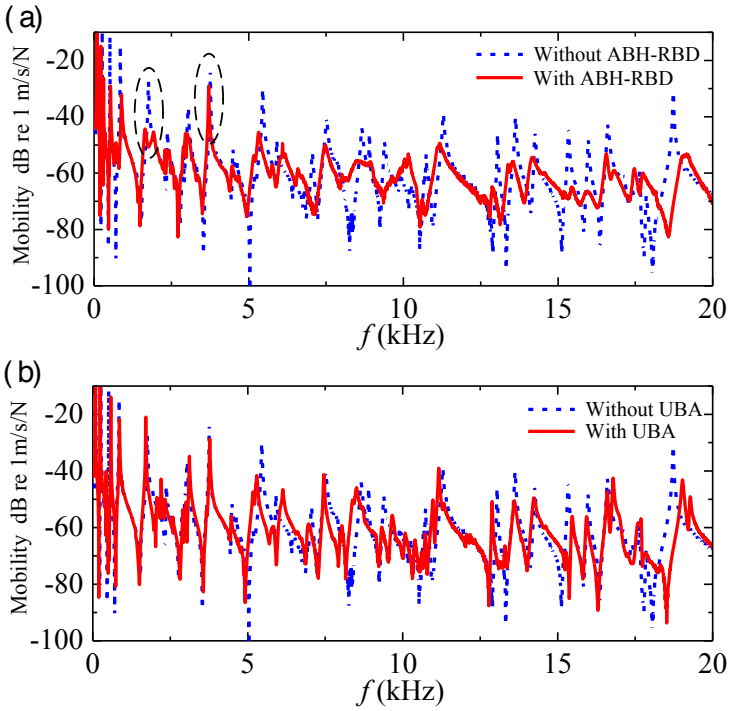


Figure 11: Comparisons of the measured driving point mobility of the primary host beam with and without (a) ABH-RBD and (b) UBA.

5 Conclusions

In this paper, we propose a new type of vibration control device for the broadband vibration suppressions of vibrating structures. By capitalizing on the Acoustic Black Hole (ABH) phenomena, the proposed ABH-featured Resonant Beam Damper (ABH-RBD) embraces the principles of both dynamic vibration absorbers and waveguide absorbers. With a relatively simple and easily achievable configuration, the ABH-featured add-on device does not require complex parameter tuning in the design process, showing certain robustness for accommodating structural variations in the primary structure.

Using a beam as a benchmark structure, the effectiveness of the proposed ABH-RBD, as well as the underlying mechanisms, are demonstrated through numerical simulations and confirmed through experimental measurements. It is shown that, the ABH-specific features of the device, in terms of its enriched dynamics and enhanced damping, maximizes the structural interaction as well as energy extraction and dissipation from the host structure. As a result, broadband vibration reductions can be achieved, by using the same ABH-RBD on different primary systems, provided the location of the attachment is properly

chosen. Analyses reveal three typical vibration reduction mechanisms. Interaction-dominated peak reduction is similar to conventional dynamic absorber. The rich dynamics of the ABH element increase the chance of creating better frequency matching with the primary structure, thus promoting more effective interactions. The damping-dominated peak reductions are due to the remarkable energy trapping capability of the ABH taper, despite the small amount of damping materials used. In the high frequency range, when the broadband ABH absorptions are more dominant, the enhanced damping is combined with the interaction effect, thus resulting in a significant vibration reduction, manifested by a smoothing and shifting of the resonance peaks of the primary structure.

Acknowledgements

The authors would like to acknowledge the Research Grant Council of the Hong Kong SAR (PolyU 152009/15E and PolyU 152026/14E) and National Science Foundation of China (No. 11532006) for financial support.

References

[1] D.J. Mead, *Passive vibration control*, John Wiley & Sons, New York, 1998.

[2] J.B. Hunt, *Dynamic vibration absorbers*, Mechanical Engineering Publications, London, 1979.

[3] D.J. Inman, *Engineering vibration*, Prentice Hall, New Jersey, 2001.

[4] J.P. Den Hartog, *Mechanical vibrations*, Courier Corporation, New York, 1956.

[5] B.G. Korenev, L.M. Reznikov, *Dynamic vibration absorbers: theory and technical applications*, John Wiley & Sons, New York, 1993.

[6] A.D. Nashif, D.I.G. Jones, J.P. Henderson, *Vibration damping*, John Wiley & Sons, New York, 1985.

[7] D.I.G. Jones, A.D. Nashif, H. Stargardter, *Vibrating beam dampers for reducing vibrations in gas turbine blades*, Journal of Engineering for Power 97 (1) (1975) 111-116.

[8] M. Brennan, *Characteristics of a wideband vibration neutralizer*, Noise Control Engineering Journal 45 (5) (1997) 201-207.

[9] L. Zuo, S.A. Nayfeh, *Minimax optimization of multi-degree-of-freedom tuned-mass dampers*, Journal of Sound and Vibration 272 (3) (2004) 893-908.

[10] H. Yamaguchi, *Vibrations of a beam with an absorber consisting of a viscoelastic beam and a spring-viscous damper*, Journal of Sound and Vibration 103 (3) (1985) 417-425.

[11] D. Manikanahally, M. Crocker, *Vibration absorbers for hysterically damped mass-loaded beams*, Journal of Vibration and Acoustics 113 (1) (1991) 116-122.

[12] J. Snowdon, *Vibration of cantilever beams to which dynamic absorbers are attached*, The Journal of the Acoustical Society of America 39 (5A) (1966) 878-886.

[13] D.A. Rade, V. Steffen, *Optimisation of dynamic vibration absorbers over a frequency band*, Mechanical Systems and Signal Processing, 14 (5) (2000) 679-690.

[14] R. Jacquot, *Suppression of random vibration in plates using vibration absorbers*, Journal of Sound and Vibration 248 (4) (2001) 585-596.

[15] C. Yang, D. Li, L. Cheng, *Dynamic vibration absorbers for vibration control within a frequency band*, Journal of Sound and Vibration 330 (8) (2011) 1582-1598.

[16] E.E. Ungar, L.G. Kurzweil, *Preliminary Evaluation of Waveguide Vibration Absorbers*, Bolt Beranek and Newman Inc. Cambridge Ma, 1984.

[17] G.G. Lee, *Analytical and experimental studies of beam waveguide absorbers for structural damping*, Naval Postgraduate School, Monterey, California, 1988.

[18] Y. Shin, S. Watson, K. Kim, *Passive vibration control scheme using circular viscoelastic waveguide absorbers*, Journal of pressure vessel technology 115 (3) (1993) 256-261.

[19] S.J. Watson, *Experimental studies of circular viscoelastic waveguide absorbers for passive structural damping*, Naval Postgraduate School, Monterey, California. 1989.

[20] C.M. Pray, S.A. Hambric, T.E. McDevitt, C.B. Burroughs, *Characterization of folded beam waveguide absorbers for damping of flexural vibrations in a thick plate*, Noise Control Engineering Journal 48 (6) (2000) 185-192.

[21] E.E. Ungar and L. Kurzweil, *Structural damping potential of waveguide absorbers*, Bolt Beranek and Newman Inc. Cambridge Ma,1984.

[22] M.A. Mironov, *Propagation of a flexural wave in a plate whose thickness decreases smoothly to zero in a finite interval*, Soviet Physics Acoustics 34 (3) (1988) 318-319.

[23] V.V. Krylov, F.J.B.S. Tilman, *Acoustic 'black holes' for flexural waves as effective vibration dampers*, Journal of Sound and Vibration 274 (3) (2004) 605-619.

[24] L. Tang, L. Cheng, H. Ji, J. Qiu, *Characterization of acoustic black hole effect using a one-dimensional fully-coupled and wavelet-decomposed semi-analytical model*, Journal of Sound and Vibration 374 (2016) 172-184.

[25] T. Zhou, L. Tang, H. Ji, J. Qiu, L. Cheng, *Dynamic and static properties of double-layered compound acoustic black hole structures*, International Journal of Applied Mechanics 9 (05) (2017) 1750074.

[26] L. Tang, L. Cheng, *Enhanced Acoustic Black Hole effect in beams with a modified thickness profile and extended platform*, Journal of Sound and Vibration 391 (2017) 116-126.

[27] L. Tang, L. Cheng, *Broadband locally resonant band gaps in periodic beam structures with embedded acoustic black holes*, Journal of Applied Physics 121 (19) (2017) 194901.

[28] L. Tang, L. Cheng, *Ultrawide band gaps in beams with double-leaf acoustic black hole indentations*, Journal of the Acoustical Society of America 142 (5) (2017) 2802-2807.

Metamaterial characterization for acoustic cloaking applications

A. Hanford [1], **P. Kerrian**[1], **B. Beck**[1], **D. Capone** [1]
[1] The Pennsylvania State University
State College, PA, United States of America
e-mail: **ald227@psu.edu**

Abstract
Acoustic metamaterials rely on sub-acoustic wavelength materials to achieve their unique material properties. An application of interest requires acoustic metamaterials that are homogeneous but anisotropic materials. Previous work has demonstrated at least three types of unit cells exhibit homogeneous anisotropic mass density and homogeneous isotropic bulk modulus. An analysis into the methods used to characterize the effective material parameters of different unit cells with water as the background fluid was performed. Nondestructive acoustic excitation techniques were used to extract the material parameters of different grades of foam to identify use in an acoustic metamaterial to determine if they exhibited the desired homogeneous anisotropic behavior. Different grades of foam glass exhibited varying degrees of anisotropic stiffness. The metamaterial unit cell behaved as expected, demonstrating anisotropic mass density and isotropic bulk modulus.

1 Introduction

Acoustic ground cloaks, which conceal an object on a rigid reflecting surface, utilize a linear coordinate transformation to map the flat surface to a void by compressing space into two cloaking regions consisting of a homogeneous anisotropic acoustic metafluid. Previous work has demonstrated that multiple material solid inclusion metamaterials are possible candidates for use in an acoustic ground cloak [1]. One of the primary challenges to building an anisoptic metamaterial unit cell is finding acceptable sub-scale materials with appropriate material properties. For a multiple material unit cell to be used for in water applications, metal foams are a possible solution. Figure 1 is an Ashby chart of metallic foams that relates density and Young's modulus [2]. The light blue circle indicates the region where a potential foam should be located for use in a dual material unit cell [3]. Clearly, there are very few potential foams that posses the desired material properties. The primary focus of this work is to determine if any candidate materials are acceptable for use in a dual inclusion metamaterial.

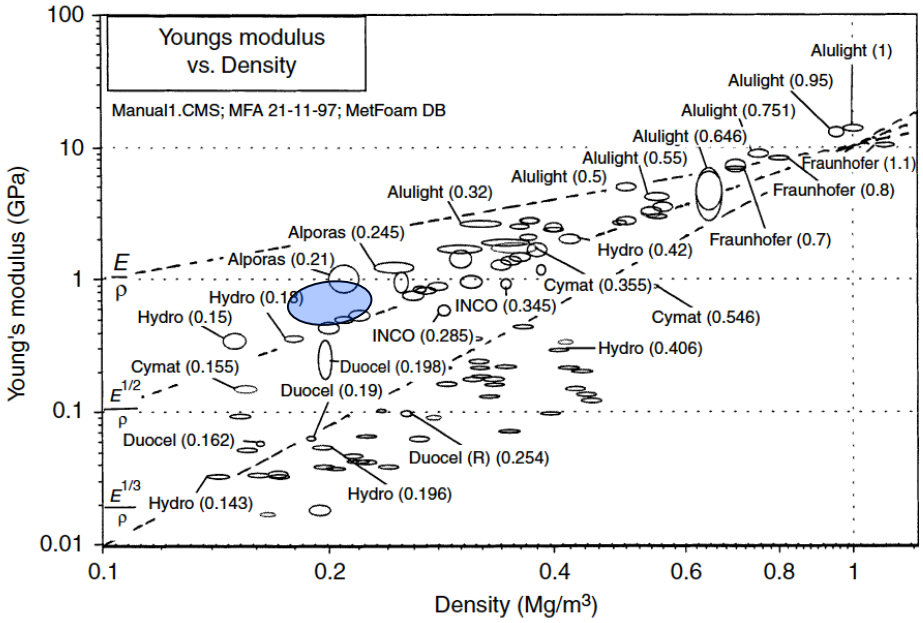


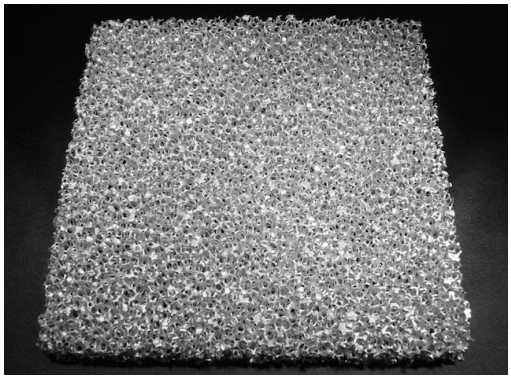
Figure 1: Example Ashby chart for metallic foams plotting Young's modulus vs density that were available in 1997. The blue circle indicates the region where a foam should fall with the desired parameters. Image taken and adapted from [2].

2 Candidate Materials

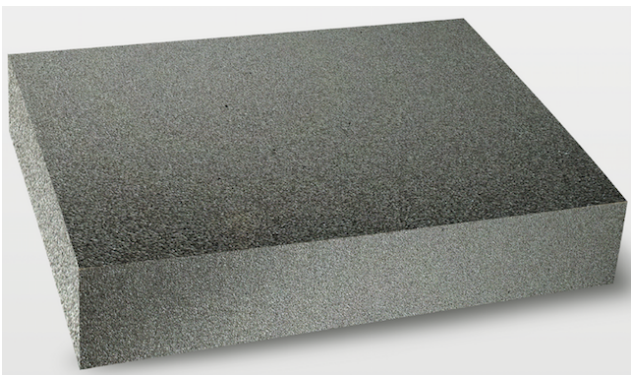
In order to create an anisotropic metamaterial that exhibits the desired material parameters for use in an acoustic ground cloak, a foam inclusion with a density of roughly 160 [kg/m^3] and a Young's modulus of roughly 500 [MPa] is required [3]. Previous authors have numerically simulated a metallic foam without actually supplying a specific material. Popa *et. al* [1] referenced a commercially available silicon carbide foam from ERG Duocel ® and an unidentified aluminum foam. After searching commercially available materials, two types of foam were identified as potential candidate materials. The first was an open cell aluminum foam from ERG Duocel ® [4], seen in Figure 2a, which comes in three different degrees of porosity. The manufacture reported values that range in density from 3% to 12% of fully dense aluminum and a Young's modulus of roughly 100 [MPa]. Secondly, a closed cell glass foam from Pittsburgh Corning [5], seen in Figure 2b, was found with densities ranging from 115 [kg/m^3] to 200 [kg/m^3] with a Young's modulus between 900 [MPa] and 2144 [MPa]. These foams match well for the density requirement, but deviate from the desired Young's Modulus. In order to be certain, different gauge samples of each type of foams were tested to verify the reported material parameters.

Before proceeding, it is worthwhile to discuss a basic assumption for material characterization tests that foam materials may not explicitly satisfy. The techniques utilized in this chapter require that the material being characterized is homogeneous and isotropic, which is completely valid for most solid materials. Foam materials have introduced an additional substance, commonly air or gas, into the native material. The resulting composite can either form an open cell metallic lattice structure, as seen for the aluminum foam in Figure 2a, or a closed cell foam with small gaseous inclusions, as seen for the glass foam in Figure 2b. The question of whether global isotropy is maintained can create uncertainty in any extracted material parameter values because waves may travel through the foams differently than a material that has a periodic continuous crystalline structure. Despite the incertitude of the validity of this assumption, traditional techniques for material characterization were tried first.

One of the more common techniques used to extract Young's modulus for a solid material is using an Instron machine [6]. Instron machines apply compressive and tensile loads at varying degrees of stress to the material samples. The strain, which describes the material deformation, is measured at various load stresses and the Young's modulus is extracted via Hooke's Law. Utilizing tensile and compressive load tests on foam materials often fail quickly because the foam materials are not as strong as traditional metals. Figure 3 contains pictures of the initial attempts to characterize a foam glass sample. Figure 3a shows the assembly for a tensile test, however, the component quickly



(a) ERG Duocel ® Aluminum Foam



(b) Pittsburgh Corning Glass Foam

Figure 2: Photos of the two types of foams tested. Photos from companies websites [4, 5].

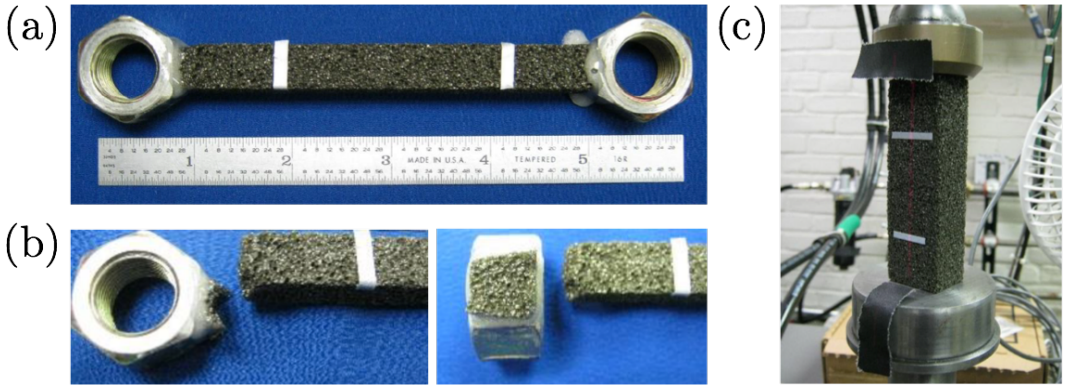


Figure 3: Photos of traditional Instron testing. (a) Glass foam sample in configuration for tensile load test which failed, as seen in (b), because of fracture at joints. (c) Configuration for compressive load test.

failed at small stress levels by breaking at the end joint as seen in Figure 3b. Figure 3c is the set-up for a compressive load test. Unlike the tensile test, the compressive load test was able to provide an estimate for Young's modulus, but the test failed because the brittle nature of the glass foam caused the sample to crumble at the ends. Additionally there was significant variability for samples of different sizes, creating additional uncertainty in the accuracy of the estimates.

Given the failure of the Instron methods, it was clear that an alternative testing method was needed. Because the ultimate environment in which these foam materials would be tested is underwater, a test method that would extract the desired material parameters underwater would be ideal. Two potential methods for underwater material characterization include a pulse tube test to extract impedance or a volumetric compression test to extract bulk modulus. The underwater equivalent of an impedance tube in air, a pulse tube determines the impedance of sample material from the complex reflection coefficient measured by a hydrophone in a water filled tube. For the volumetric compression test, a sample of the material is submerged in a sealed rigid walled container. A determined volume of water is injected into the container, resulting in an increase in the pressure within the chamber. The bulk modulus of the sample can be calculated from the change in pressure to the change in volume. Unfortunately, neither of these resources were available at the time of testing, so a different technique was utilized.

3 Theoretical Background

The technique that was selected for this dissertation leverages the fundamentals of acoustics and vibrations. When a solid bar is excited by an excitation force, the response will be a superposition of the natural modes of the system. Depending upon the excitation force, three classes of wave motion could potentially be excited. Longitudinal waves are compressional waves in which the disturbance travels parallel to the axis of the bar. Torsional waves exhibit a twist or angular rotation around the neutral axis of the bar. Flexural bending waves result in a transverse displacement with respect to the direction of wave propagation. Longitudinal and torsional waves are described by a traditional second order wave equation while flexural bending waves are described by a fourth order equation of motion. Any fundamentals of acoustic book contains the derivation of the equations of motion and natural frequencies for bars with free-free boundary conditions, and the reader is directed there for more information [7]. For longitudinal waves, the nth natural frequency of a free-free bar is given by

$$f_{Ln} = \frac{n}{2L}\sqrt{\frac{Y}{\rho}} \tag{1}$$

where n is the mode number, L is the length of the bar, Y is the Young's Modulus, and ρ is the density. For torsional waves, the nth natural frequency of a free-free bar is given by

$$f_{Tn} = \frac{n}{2L}\sqrt{\frac{12h^2\beta}{w^2+h^2}}\sqrt{\frac{Y}{2\rho(1+\nu)}} \tag{2}$$

where n is the mode number, L is the length of the bar, h and w are the height and width of the bar cross section, Y is the Young's modulus, ν is Poisson's ratio, ρ is the density and β is a constant dependent upon the ratio of w to h. For all the bars tested, h/w was equal to 1 so β was 0.141. Finally, utilizing Euler-Bernoulli beam theory, the nth natural frequency of a free-free bar for flexural bending was is

$$f_{Fn} = \frac{\pi\kappa}{8L^2}\sqrt{\frac{Y}{\rho}}(2n+1)^2 \tag{3}$$

where κ is the radius of gyration $\kappa = h/\sqrt{12}$, h is the height of the cross section, L is the length of the bar, Y is the Young's modulus, ρ is the density, and n is the mode number. For a sample of unknown material properties, density can easily be calculated from the weight of the sample divided by the volume. Therefore, knowing the density, the geometry of the sample and the first natural frequency, Young's modulus can be calculated from either the longitudinal or flexural bending modes. Poisson's ratio can then be calculated from the torsional natural frequency.

Given the dimensions of the beams selected, Timoshenko beam theory would provide a better estimate for the Young's modulus for the flexural bending modes because it accounts for the effects of shear deformation and rotary effects. However, Timoshenko beam theory requires an accurate knowledge of Poisson's ratio, which is unknown given the uncertainty of the behavior of the foam bars. As a result, slight discrepancies in the extracted values of Young's Modulus exist for those extracted for longitudinal and flexural bending modes. For the desired purpose of finding an acceptable foam material for use in a dual inclusion unit cell, the density of the foam material is of more importance to adjust the anisotropic density tensor components of the overall unit cell. Because the Young's modulus of the foam material only affects the effective bulk modulus of the unit cell, Euler Bernoulli beam theory is sufficient to ensure the foam materials exhibit a Young's modulus value within an acceptable range.

When an object experiences an excitation force, such as an impulsive force from an impact hammer, the structure will vibrate and the vibration will radiate an audible sound. The radiated sound can be captured with a microphone and the frequency content of the signal can be calculated from the autospectrum of the microphone signal. Depending upon the location of excitation, multiple types of vibrational modes will be excited, which will appear as peaks in the sound spectrum. Properly identifying which peaks in the received spectra correspond to the different types of modes is essential to accurately predict the material properties of the sample. Fortunately, the higher modes of longitudinal and torsional waves are related by integer multiples of the fundamentals while flexural bending modes are related by a $(2n+1)^2$ relation. For example, consider a steel bar with a length of 8.89 [cm] and a square cross section of 1.27 [cm] by 1.27 [cm]. Steel has a density of 7650 [kg/m^3], a Young's modulus of 195 [GPa] and a Poisson's ratio of 0.28. Figure 4 shows the frequency of each of the three mode types plotted as a function of mode number. Because there is a distinct separation in frequency between the fundamentals of each of the mode types, relating higher modes back to the fundamental is relatively straight forward. The difference in the slopes of the longitudinal and torsional waves is related to the additional terms in the natural frequency equation for the torsional wave, specifically the $2(1+\nu)$ which converts Young's modulus to shear modulus. Before applying this technique to foam materials where the response to an excitation is uncertain, a preliminary test was performed on an additive manufactured steel bar. This bar was selected to learn more about solid metal deposition's ability to print fully dense parts in an attempt to leverage additive manufacturing for other aspects of the project.

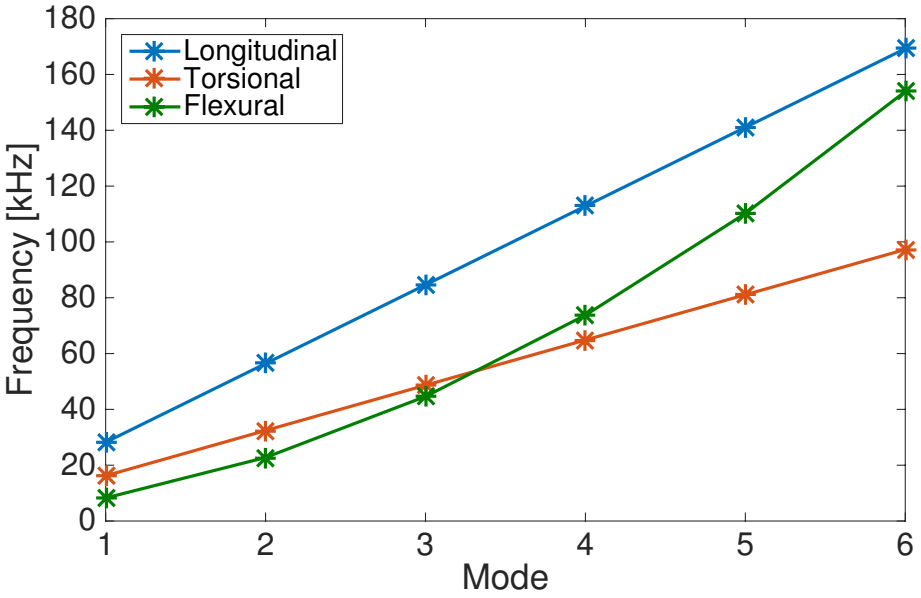


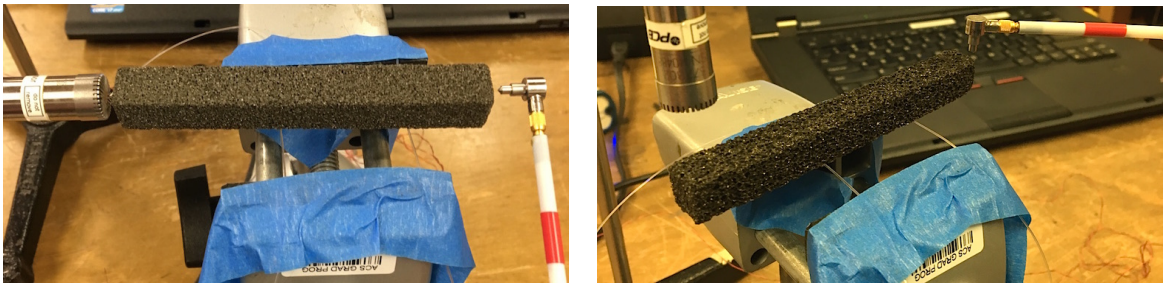
Figure 4: Plot of frequency vs mode number for longitudinal (blue), torsional (orange) and flexural (green) modes for a 1.27 [cm] x 1.27 [cm] x 8.89 [cm] steel bar.

4 Experimental Procedure

In order to quantify the response of the system, either the vibrations of the bar need to be measured with an accelerometer or the radiated sound recorded with a microphone. Traditional experimental modal analysis commonly uses an accelerometer mounted to the surface to measure the vibration. However, trying to test very light foam samples complicates the measurement procedure because an accelerometer weighs on the same order or more than the foam bar. Therefore, the boundary condition for the side with the accelerometer is no longer a free boundary condition and is now a mass loaded boundary condition. As a result, the equations for the natural frequency of free-free bar are no longer valid and more complicated equations would need to be derived in order to accurately extract the material parameters. The alternative approach is to utilize a microphone that is not attached to foam bar to measure the radiated sound. Because only the frequency of vibration is desired and not the relative amplitude of vibration, as would be required to determine mode shapes, using the microphone is a perfectly acceptable alternative to an accelerometer.

Figure 5 shows the experimental set-up for the two excitation locations designed to excite different classes of wave motion. The set up depicted in Figure 5a is intended to excite the longitudinal waves. The microphone is oriented parallel to the cross section of the beam while the impact hammer excites the opposite end of the bar. The second orientation is intended to excite torsional and flexural waves. As seen in Figure 5b, the impact hammer excites a corner on the top of the bar and the microphone is aligned with the opposite diagonal corner. Two thin pieces of fishing line are stretched across a small vice grip and the bar is rested on top of the strings in order to simulate a free free boundary condition. The fishing line is thin enough that it does not impede the vibration of the bar, and slightly moving the bar for each impact, so the strings are in contact at different points on bar for each average, negate any effect on the overall measurement.

The bar depicted in Figure 5 is one of the glass foam samples. All the samples tested were cut to have the same dimensions of a 1.27 [cm] by 1.27 [cm] cross section and a length of 8.89 [cm]. For the experiments, a National Instruments 4431 USB data acquisition system was used to acquire the signals from the PCB 086E80 impact hammer and the half inch PCB 378B02 microphone at a sample rate of 102.4 [kHz]. An in-house LabView code was used to record the data and calculate



(a) Longitudinal Excitation (b) Flexural Excitation

Figure 5: Experimental set up for two types of bar excitation: (a) logitudinal excitation and (b) flexural excitation. The bar is excited with a tap from an impact hammer and the radiated sound is measured with a microphone either aligned with the long axis (a) or with the opposite corner from the excitation (b).

the autospectrum of the microphone signal. Figure 6 shows the microphone autospectrum for the additive manufactured steel bar. Examining the peaks in the longitudinal excitation curve, the most prominent peak appears at a frequency around 27 [kHz] and corresponds to the first longitudinal mode. The two lower peaks in the spectrum at 7.3 [kHz] and 18.4 [kHz] correspond to first two flexural bending wave modes and roughly follow the $(2n+1)^2$ relation. Examining the flexural excitation curve, the biggest difference is the lack of the longitudinal peak which is expected because tapping on the top corner of the bar is less likely to excite a mode that travels along the long axis of the bar. The absence of the 27 [kHz] peak confirms its correspondence to the longitudinal mode. An additional peak appears in the spectrum at roughly 16 [kHz] and corresponds to the first torsional mode. A pair of peaks around 32 [kHz] are the second torsional mode and third flexural mode respectively. The relations between the peaks aligned well with what the fundamental theory suggested. Given the dimensions of the bar and the fundamental frequencies of the longitudinal and torsional modes, the Young's modulus and Poisson's ratio of the bar can be calculated. The density of the bar was measured to be 7653 [kg/m^3], 99.4% of the density of solid steel. The Young's modulus was calculated to be 179 [GPa] with a Poisson's ratio of 0.20; both slightly lower than traditional steel, but within a reasonable range.

5 Metal Foams Results

Having confirmed the ability of the measurement technique to accurately extract the material parameters of a solid steel sample, the first samples tested were the open cell ERG Duocel ® aluminum foams. Three samples of aluminum foam were obtained that had a different number of pores per inch (PPI): 10, 20 and 40. No specific material parameter data is available for foams with explicit PPI. Figure 7 shows the microphone autospectrum for longitudinal and flexural excitation

Table 1: ERG Aluminum Foam Material Parameter Results

Material	**Density**	**Young's Modulus**	
		Longitudinal	**Flexural**
	[kg/m^3]	[MPa]	[MPa]
ERG PPI 10	245	247	189
ERG PPI 20	230	268	160
ERG PPI 40	205	245	190

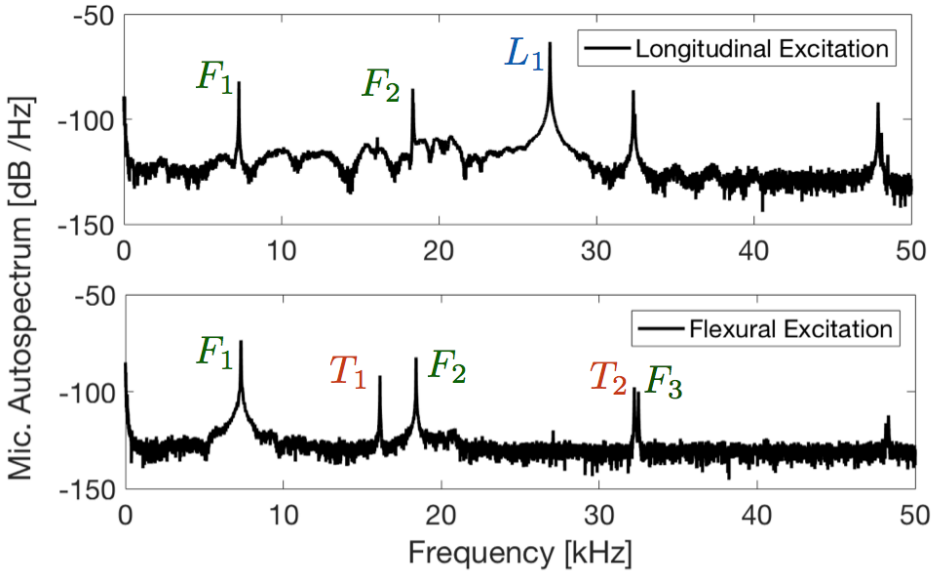
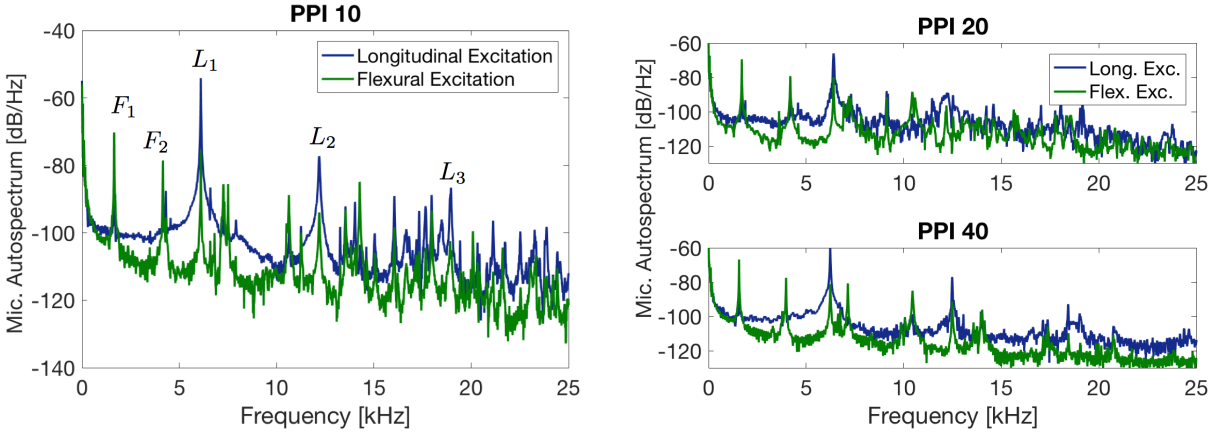


Figure 6: Microphone autospectrum for logitudinal and flexural excitaitons. The longitudinal, torsional and flexural modes are labeled. Notice the longitudinal is not present in the flexural excitation as expected.

of the three different foam grades. Integer multiple peaks are present for longitudinal excitation for each foam sample and the flexural peaks follow the expected relation. No torsional peaks could be identified for the aluminum foam bars. Table 1 contains the extracted material parameters for the metal foam bars. The discrepancy in the Young's modulus is attributed to Euler Bernoulli vs Timoshenko beam theory.

Ultimately, the aluminum foam was determined be an unacceptable material because the density and Young's modulus were too low, which would result in a smaller effective bulk modulus for the dual-inclusion unit cell. Additionally, the open cell nature of the foam posed problems for implementing in an underwater application. Any open cell metallic foam sample would need to be sealed with some type of wrap to trap the air in order to maintain the density. If water flooded the cavity, then the material would no longer be less dense the background fluid, negating the ultimate objective of having an anisotropic density tensor component less than the background fluid.



(a) ERG Duocel ® PPI 10

(b) ERG Duocel ® PPI 20 and 40

Figure 7: Microphone Autospectrum for ERG Duocel ® Foams.

6 Glass Foam Results

Unlike the open cell aluminum foam, the glass foam materials made by Pittsburgh Corning ® have significantly more attractive attributes including being closed cell, corrosion resistant, and impermeable to water. As a result, there is no need to seal the inclusions to maintain the density of the material. The original application for the glass foam is thermal insulation in both the building and industrial marketplaces. Five different grades of the foam glass were generously sent by the manufacturer: FOAMGLAS® ONE™, HLB 800, HLB 1200, HLB 1600 and HLB 2400. Figure 8a shows photos of two of the foam bars. In addition to different grades, samples of each grade were sent that were cut from different orthogonal directions from the original source block. Samples cut from the vertical plane are referred to as up - down, ↕, and samples cut from a horizontal direction are referred to as side - side, ↔. Figure 8b shows a diagram indicating the directions the samples were cut from the source block. Two bars were cut from each combination of foam grade and orientation for a total of 20 bars. The density of each bar was determined by measuring the specific bar dimensions and weighing the samples.

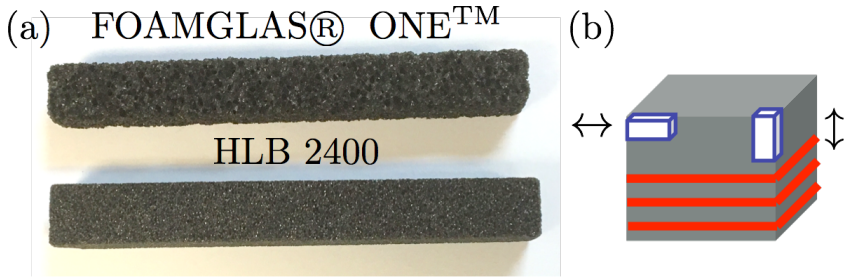
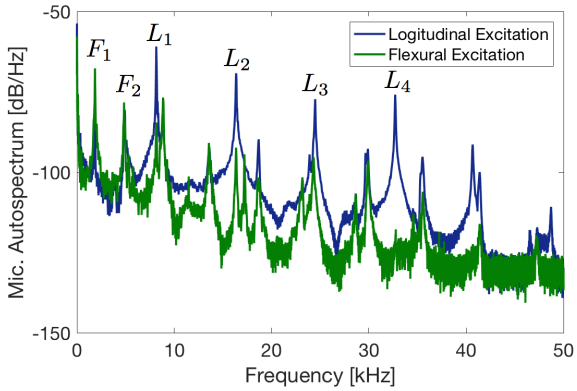
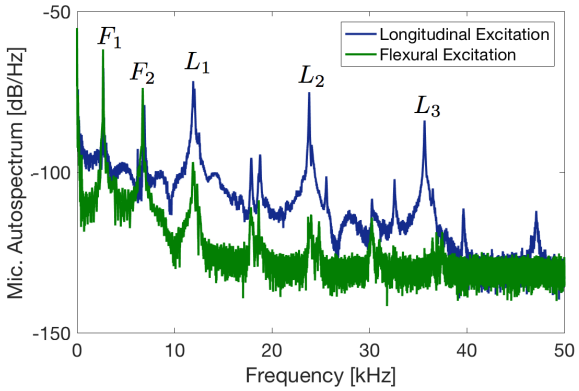


Figure 8: (a) Photos of the FOAMGLAS® ONE™ and HLB 2400 bars. (b) Diagram indicating the directions the samples were cut from the source block.

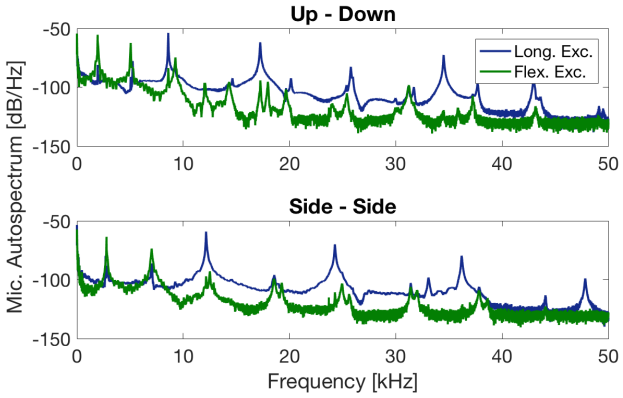
Figure 9 contains the microphone autospectrum for the longitudinal and flexural excitations for both directions of three grades of glass foam. Figures 9a and 9b show the labeled peaks for the up - down and side - side orientation of the FOAMGLAS® ONE™ sample. Each orientation displays the attributes expected for longitudinal and flexural waves. However, the torsional peaks do not appear prominently in the spectra as in the solid sample. Instead there are additional peaks in the spectrum that do not explicitly follow an integer relation that would indicate a specific mode type. The other interesting fact is that fundamental frequencies of both the longitudinal and flexural modes of the two orientations are not the same. For the up - down orientation, the fundamental frequency of the longitudinal mode is 8.2 [kHz], while for the side - side orientation it is 11.9 [kHz]. The discrepancy is too large to be accounted for in a small size difference in the length of the bar. Additionally, the densities for both orientations were the same which indicates that the Young's modulus of the two orientations are different. The same trend was seen for all grades of glass foam, as seen in Figures 9c and 9d for the HLB 800 and HLB 1200 foams respectively.



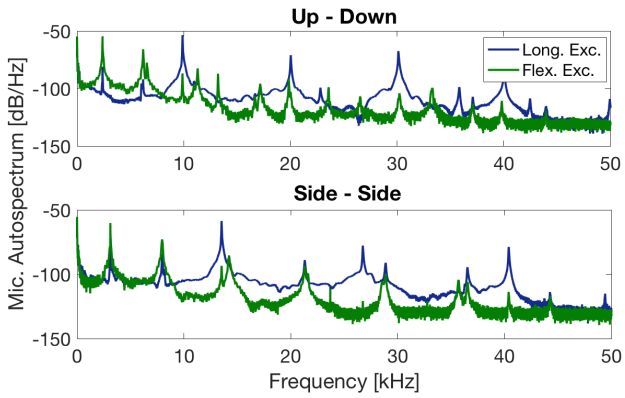
(a) FOAMGLAS® ONE™ Up - Down



(b) FOAMGLAS® ONE™ Side - Side



(c) HLB 800 Foam



(d) HLB 1200 Foam

Figure 9: Microphne autospectrum of three different grades of glass foam: (a) and (b) FOAMGLAS® ONE™, (c) HLB 800, and (d) HLB 1200. Longitudinal excitations are plotted in blue and flexural excitations are plotted in green.

Table 2 contains the measured density and Young's modulus calculated from both the longitudinal and flexural mode theory. No Poisson's ratio was calculated because it was not possible to determine which peaks corresponded to the torsional waves. Examining the values in the table it is clear that the side - side orientations clearly have a higher Young's modulus than the up - down orientation. Additionally, the Young's modulus for the flexural modes is slightly lower than the longitudinal, which is most likely attributed to the fact that the cross section of the bars were not significantly smaller than the length as required for Euler Bernoulli theory. Each value was calculated from an average of the extracted results from at least two individual foam bars.

Table 2: Measured Material Parameters of the Foam Glass

Material	**Orientation**	**Density**	**Young's Modulus**	
			Longitudinal	**Flexural**
		[kg/m^3]	[GPa]	[GPa]
FG ONE	↕	101	0.28	0.22
	↔	99	0.62	0.49
HLB 800	↕	110	0.34	0.25
	↔	110	0.71	0.59
HLB 1200	↕	146	0.60	0.52
	↔	145	1.12	0.94
HLB 1600	↕	150	0.48	0.41
	↔	150	1.25	1.08
HLB 2400	↕	168	0.78	0.65
	↔	168	0.65	0.57

The primary implications of the results in Table 2 is that the foam glass is inherently anisotropic. The mostly likely reason for the unexpected anisotropy is traced back to the manufacturing process of the glass foam. As with most closed cell foam materials, the native substance is heated to a molten form and then an substance is mixed in causing a reaction which produces tiny pockets of gas. As the foam cools to room temperature, gravity most likely pulls on the gas bubbles resulting in ellipsoidal gaseous inclusions rather than perfectly spherical bubbles, which produces the anisotropy. In order to investigate the anisotropy further, additional samples were cut for the HLB 800 and HLB 1600 grades from both provided orientations. The new samples were cut perpendicular, indicated as 90°, to the original samples, indicated as 0°. The supposition is that the side - side samples should have a significantly smaller difference than the up - down samples and the 90° sample for the up - down orientation should be similar to both side - side orientations.

Figure 10 depicts the results of the longitudinal excitation of the new and old samples of the HLB 1600 foam. As expected there is a slight deviation in the side - side samples and the 90° up - down samples is consistent with the side - side samples. The only outlier is the up - down 0° which supports the notion that gravity created ellipsoidal gaseous inclusions are producing the anisotropy. More broadly speaking, the glass foam is an orthotropic material because there are planes of isotropy, as indicated with the red lines in Figure 8b.

The effective material parameters of the dual inclusion unit cell are primarily determined from the material parameters of the foam inclusion. Specifically the density of the foam controls the y density tensor component and the Young's modulus of the foam controls effective bulk modulus. The objective of this work was to determine whether any of the foam glass materials were acceptable for use in a dual inclusion inclusion metamaterial. Despite the overall goal of creating an anisotropic mass density metamaterial, it is important to remember that material for the dual inclusion unit cell should be isotropic, which some grades of the glass foam clearly are not. Examining the material values in Table 2, the HLB 2400 glass foam has material parameters close to the desired range

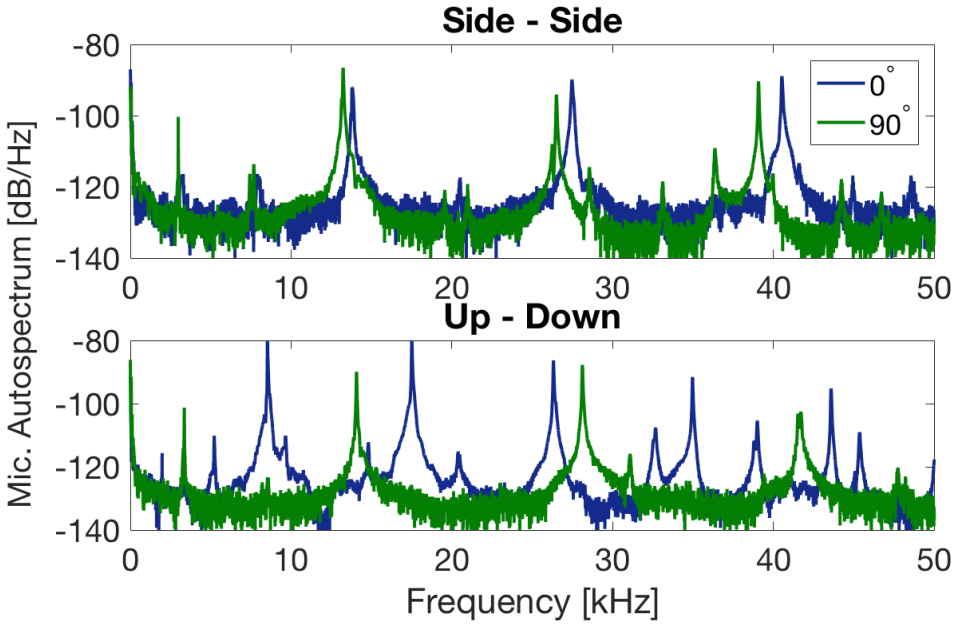


Figure 10: Microphone autospectrum for the HLB 1600 grade glass foam for logitudinal excitaitons of orthogonal samples cut from the side - side and up - down orientations.

and a significantly smaller range of anisotropy than the other foams as seen in Figure 11. Because of the separation in controlling the effective density and bulk modulus, and the overall goal of demonstrating underwater anisotropic density, it was determined that the deviations of the HLB 2400 grade glass foam were small enough that Young's modulus isotropy could be assumed. Thus, it was decided that the HLB 2400 grade glass foam was the best material available for use in a dual inclusion unit cell.

7 Conclusion

A traditional Instron tensile and compressive load test was unsuccessful at extracting the material parameters of certain foam materials. Instead an acoustic method was used to extract the Young's modulus from longitudinal and flexural modes. Despite the lack of a homogeneous isotropic periodic crystalline structure, foam materials behaved rather consistently with what the theory suggested. Between the open cell aluminum foam and the closed cell glass foam, it was decided that the highest gauge of glass foam was the best option for use in a dual inclusion unit cell. The Young's modulus of aluminum foam was too small for the desired application and the challenge of preserving the air volume posed significant challenges and could potentially create unintended negative effects. Even though the glass foam is inherently anisotropic, the HLB 2400 had a significantly lower degree of anisotropy than the other foams and the two components are close enough that the foam could be considered isotropic.

References

[1] B.-I. Popa, S. A. Cummer, *Homogeneous and compact acoustic ground cloaks*, Phys. Rev. B, Vol. 83, (2011), pp. 224304.

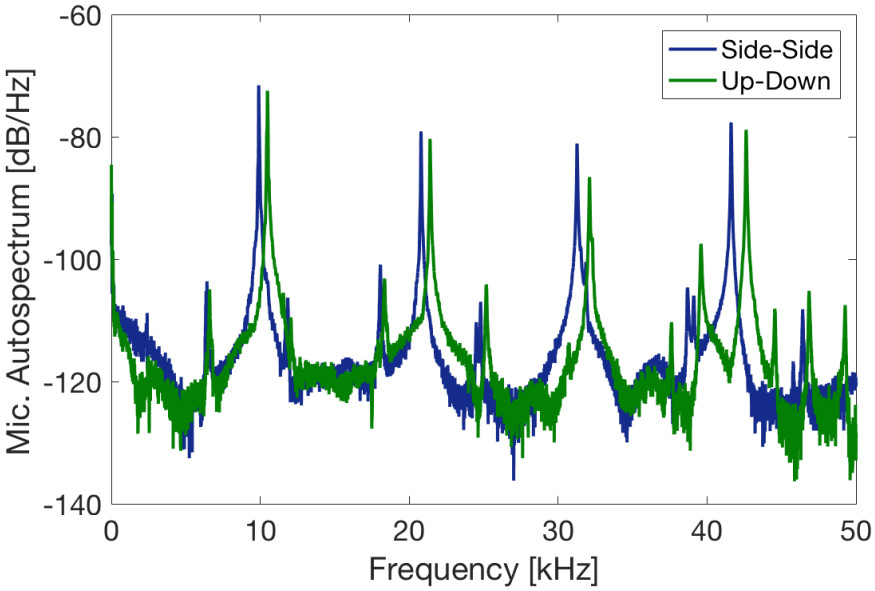


Figure 11: Microphone autospectrum for longidutinal excitation of the HLB 2400 grade glass foam. The degree of anisotropy is significantly smaller than for other grades of glass foam as seen in the peaks of the two orientations.

[2] M. F. Ashby, A. G. Evans, N. A. Fleck, L. J. Gibson, J. W. Hutchinson, H. N. G. Wadley, *Metal Foams: A Design Guide*, Butterworth-Heinemann Boston (2000).

[3] P. Kerrian, A. Hanford, *Experimental and numerical advancements in underwater solid inclusion metamaterials*, Journal of the Acoustical Society of America.

[4] *http://www.ergaerospace.com/material-applications-guide.html.*

[5] *http://www.industry.foamglas.com/en/industry/products /foamglas_hlb_insulation/.*

[6] *http://www.instron.us/en-us/testing-solutions.*

[7] L. E. Kinsler, A. R. Frey, A. B. Coppens, J. V. Sanders, *Fundamentals of acoustics*, Fundamentals of Acoustics, 4th Edition, by Lawrence E. Kinsler, Austin R. Frey, Alan B. Coppens, James V. Sanders, pp. 560. ISBN 0-471-84789-5. Wiley-VCH, December 1999., (1999), pp. 560.

Attenuation of the mass-spring-mass effect in the sound transmission loss of double panel partitions using vibro-acoustic resonant metamaterials

N. G. R. de Melo Filho[1,2], **L. Van Belle**[1,2], **C. Claeys**[1,2], **E. Deckers**[1,2], **W. Desmet**[1,2]
[1] KU Leuven, Department of Mechanical Engineering,
Celestijnenlaan 300, B-3001, Leuven, Belgium
e-mail: **noegeraldo.rochademelofilho@kuleuven.be**

[2] DMMS lab, Flanders Make

Abstract

Double panel partitions with a foam core suffer from a poor sound transmission loss at the mass-spring-mass resonance frequency. This paper investigates the use of vibro-acoustic resonant metamaterials as a solution to improve the acoustic insulation performance for this vibro-acoustic problem while adding only 8% of mass to the complete double panel. To design the metamaterial, unit cell analysis is applied to calculate dispersion curves and predict the stop band behaviour, while the sound transmission loss is predicted with Heckls model extended with the equivalent dynamic mass of the metamaterial. The dynamic mass is obtained from the dispersion curves analysis, which allows to take into account complex and realizable resonator geometries. The designed metamaterial double panel is realized and its experimentally measured insertion loss shows a strong improvement around the mass-spring-mass resonance of the original double panel. The predicted insulation performance agrees well with the measured performance, validating the proposed method.

1 Introduction

Double panel partitions with a foam core are widely used in building applications. Besides offering high thermal insulation, they are lightweight and offer a high sound transmission loss (STL). These kind of sandwich panels outperform the acoustic mass-law over a wide frequency range. However, due to their configuration a mass-spring-mass resonance is created at which the two panels resonate on the stiffness of the core material, resulting in a strongly reduced STL in that frequency range [1, 2]. Classical solutions to address this problem are mainly based on mass addition or increase the thickness of the core material. This results in a heavy and bulky structure, which conflicts with the current trend to lightweight design.

Resonant vibro-acoustic metamaterials are a potential novel lightweight solution, be it in a confined and tunable frequency region [3, 4, 5, 6, 7, 8]. They can be obtained by the addition of resonators to a host structure on a sub-wavelength scale. This leads to a Fano-type interference around the tuned frequency of the resonator, creating a stop band frequency region where free wave propagation is prohibited [9, 5]. It is known that resonant stop bands for flexural waves lead to an increased STL in their frequency range [10, 11, 12]. Since the mass-spring-mass resonance of a double panel partition is confined to a well-defined frequency range, resonant vibro-acoustic metamaterials are a potential solution [13, 14, 15, 16, 17].

In previous work, the authors applied the metamaterial solution to a double panel partition separated by an air gap to enhance the STL at the mass-air-mass resonance [17]. To predict the STL of such double panels, a combination of the Multiple Reflection Theory [18] and the equivalent dynamic metamaterial mass was proposed and validated. This paper extends this work to double panel sandwich partitions with foam core.

To predict the STL performance of a metamaterial double panel partition with a foam core, Heckl's model [2] is combined with the dynamic mass of a metamaterial [17, 19]. Heckl's model assumes a locally reacting core material, which means that no wave propagation is allowed in the core. This model is chosen because it shows a satisfactory average error below ± 5 dB between STL predictions and measurements [20]. It uses Kirchhoff's plate theory for two infinite panels coupled by the stiffness of a locally reacting material to derive the sound power for acoustic plane wave excitation incident at a certain angle [2]. By incorporating the dynamic mass of the metamaterial in Kirchhoff's plate theory of the treated panel, Heckl's model is extended to predict the STL enhancement due to the stop band effect. Since the equivalent dynamic mass of the metamaterial is calculated using the stop band limits obtained from dispersion curves analysis, which are obtained through finite element (FE) unit cell (UC) modeling [19], the proposed method can work with complex and realizable resonators geometries. Using this method, a metamaterial solution is designed to target the mass-spring-mass resonance of a double partition panel with locally reacting material core. The solution is realized and its acoustic insulation performance is experimentally evaluated. The experimental results validate the proposed method and demonstrate the potential of resonant metamaterials to tackle the mass-spring-mass resonance vibro-acoustic problem of double panels.

This paper is organized as follows. In Section 2 the double panel is defined. In Section 3 the metamaterial design is introduced. Section 4 introduces the extension of Heckl's model with the equivalent dynamic mass of a metamaterial and discusses the STL performance predictions. In Section 5 the experimental setup used to measure the sound insertion loss (IL) is explained and the locally reacting material properties and the measured IL of the double panel partitions are analyzed and compared to the numerical predictions. Finally, Section 6 summarizes the main findings of this work.

2 Problem definition

A commercially available double panel partition with an A2 (420×591 mm) acoustic wetted surface area is considered. The double panel partition is composed of 4 layers: a 3.3 mm particle board layer which composes the first panel, a 71.7 mm foam layer, assumed to be locally reacting, and a 15.6 mm plaster layer in combination with an 3.3 mm particle board layer forming the second panel (Fig. 1).

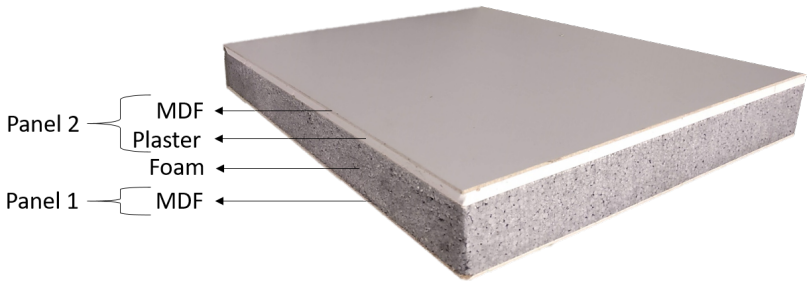


Figure 1: Double panel partition layers.

The material properties of the particle board and plaster are retrieved through weighing and model updating [21]. An experimental modal analysis is performed for each material on a 30×250 mm cantilever beam. The measured mode shapes and natural frequencies are used to update the numerical FE model of each cantilever beam composed of 300 linear shell elements. The average mismatch in natural frequencies up to 1100 Hz is 2% for the particle board beam and 0.5% for the plaster beam. The foam core material is assumed to be locally reacting. Its material properties are retrieved through weighing and curve fitting, where the Young's modulus and damping are acquired as detailed in Section 5.2. All retrieved material properties are listed in Table 1.

Table 1: Properties of the sandwich panel materials.

	Young's modulus (E)	Poisson's ratio(ν)	Density (ρ)	Thickness (h)	Damping (η)
Particle board	3533.58 MPa	0.13	765.5 kg/m^3	3.3 mm	/
Plaster	1968.56 MPa	0.2	791.9 kg/m^3	15.6 mm	/
Foam	5.4 MPa	/	16.83 kg/m^3	71.7 mm	8.7%

The mass-spring-mass resonance frequency f_{MKM} of the bare panel can be calculated as [2]:

$$f_{MKM} = \frac{1}{2\pi}\sqrt{s\left(\frac{1}{m_1'} + \frac{1}{m_2'}\right)} \tag{1}$$

for normal incidence, where $s = E_{foam}/h_{foam}$, with E_{foam} and h_{foam} the Young's modulus and thickness of the foam and m_1' and m_2' the masses per area of each panel (Fig. 1). This results in $f_{MKM} = 954$ Hz for the bare double panel partition in this study.

3 Metamaterial design

The metamaterial solution is tuned to create a stop band around the mass-spring-mass resonance frequency of the bare panel at 954 Hz. The resonators are added only to panel 1, since this is the panel with the lowest mass, which increases the metamaterial effectiveness [5]. The targeted wave types are the bending waves, since these are acoustically relevant. A mass addition of 50% w.r.t. the particle board panel is aimed for, which results in a total mass addition of 8% w.r.t. the complete structure.

Table 2: Poperties of the resonator material.

	E	ν	ρ	η
PMMA	4850 MPa	0.31	1188.38 kg/m^3	2.5%

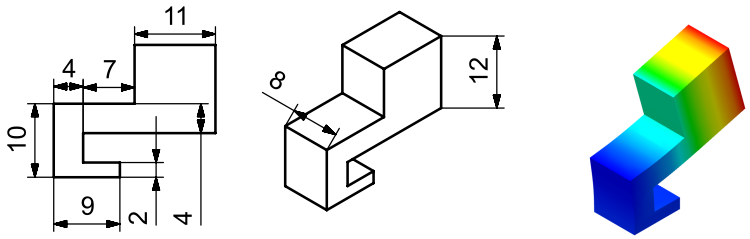
To create a stop band, the designed mode of the resonator needs to exert a non-zero net force on the host structure, the resonators need to be added on a sub-wavelength scale and the interaction between resonator and host structure need to be accounted for. The cantilever beam-like resonator has been proven to fulfil these conditions [22, 23]. The resonator dimensions are defined to comply with the targeted stop band frequency region, allowed mass addition, sub-wavelength spacing and interaction between resonator and host structure (Fig. 2). The resonators are laser cut from a 8 mm polymethyl methacrylate (PMMA) panel. The material properties of the PMMA are obtained from previous work [22] (Table 2). The resonators are added to the particle board host structure on a rectangular grid of 40×38 mm (Fig. 3). The metamaterial double panel realisation is then manufactured by adding the resonators to the bare double panel by means of adhesive bonding (Loctite® 406).

The stop band behaviour is analyzed using dispersion curves, which are calculated through FE based UC modeling, using Bloch-Floquet periodicity boundary conditions [24, 25]. The dispersion curves represent the free wave propagation in the infinite periodic structure consisting of the infinitely repeated single UC in two dimensions. In this paper, damping is not considered in the UC. Stop bands are identified as frequency zones where no free wave propagation is found in the dispersion curves along the irreducible Brillouin contour (IBC) [24].

Since the resonators are added only to the particle board panel, the wave propagation is only studied for that panel. The UC size corresponds to the 40×38 mm grid on which the resonators are added. Two UCs are modeled:

- A bare particle board UC, modeled with 158 linear shell elements, which serves as a benchmark,

- A metamaterial UC, modeled with 158 linear shell elements for the particle board host structure and 1028 linear solid elements for the resonator, which is used to define the SB limits.



(a) (b)

Figure 2: The designed resonator dimensions in mm (a) and its out-of-plane bending mode at 1160 Hz (b).

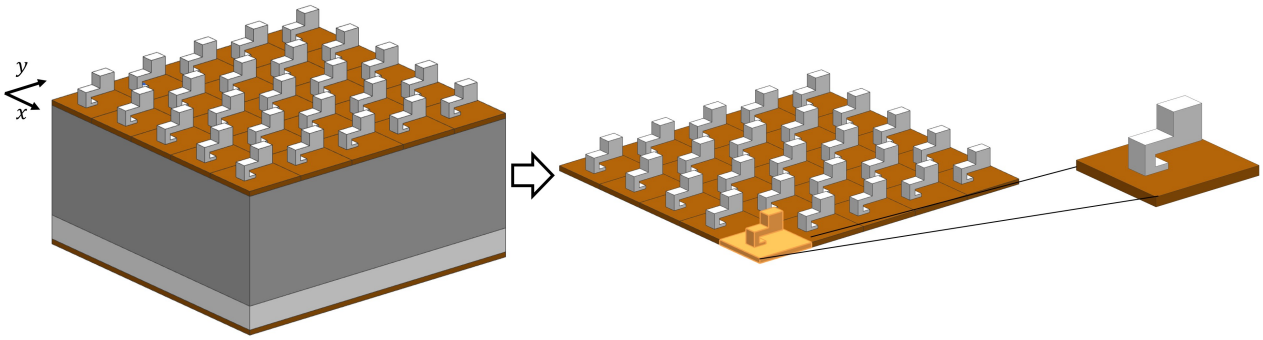
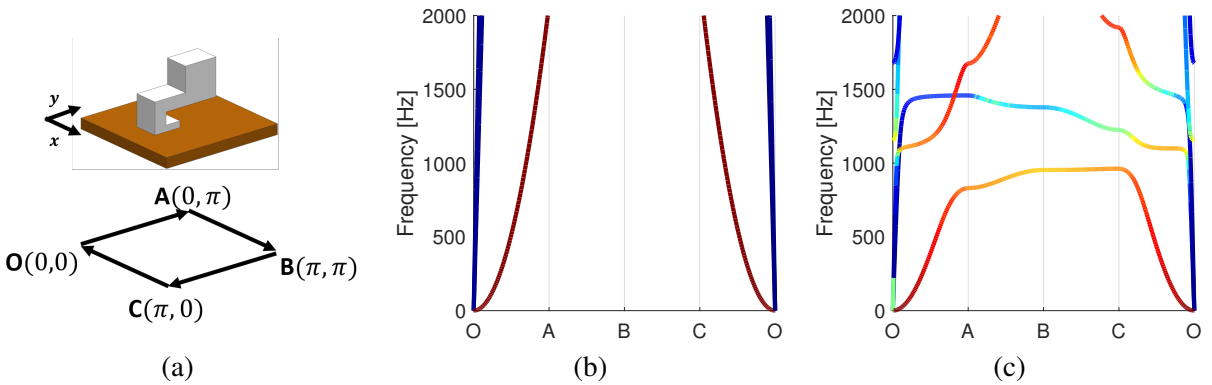


Figure 3: Complete metamaterial double panel (right), metamaterial plate considered in periodic structure analysis (center) and its representative UC of the upper panel (left).

The dispersion curves are calculated along the IBC, defined in Fig. 4a [26]. While no stop band is obtained for the bare host structure (Fig. 4b), a stop band for the bending waves is obtained between $962 - 1045$ Hz for the metamaterial UC (Fig. 4c).



(a) (b) (c)

Figure 4: Along the IBC (a) the dispersion curves of the metamaterial UC (c) show a stop band for the bending waves (red curves) as opposed to no stop band in the bare host structure (b).

4 Equivalent dynamic mass based STL

This section describes the proposed method to predict the STL of a metamaterial double panel partition with a locally reacting material core. First, Heckl's model is briefly described. Next, the dynamic mass of a metamaterial plate is calculated. Eventually, the proposed method is used to predict the STL of the bare and metamaterial double panel.

4.1 Heckl's model

A complete description of Heckl's model is given in [2]. Heckl's model is based on the coupling of the bending wave equations of two plates by a locally reacting material interlayer and uses the continuity of pressure to derive the sound power transmitted through the panel due to an acoustic plane wave excitation incident onto the panel at a certain angle. The sound power transmission coefficient τ can be defined as:

$$\tau_\theta = \left| \frac{1}{\left[1 - \omega^2 \frac{m_1'' + m_2''}{2s} + j\omega \frac{m_1'' + m_2''}{2Z} \left(1 - \frac{Z^2 + \omega^2 m_1'' m_2''}{s\left(m_1'' + m_2''\right)}\right)\right]} \right|^2, \tag{2}$$

with:

$$Z = \rho_0 c_0 / \cos\theta, \quad m_*'' = m_*'[1 - (k_0^4/k_{B_*}^4)\sin^4\theta], \quad k_{B_*}^4 = \omega^2 m_*'/B_*, \quad B_* = [E_*/(1-\nu_*^2)]h_*, \tag{3}$$

where ω is the angular frequency, $j^2 = -1$, k_0 is the wave number in air with density ρ_0 and speed of sound c_0, θ is the angle of acoustic plane wave incidence , m' is the mass per unit area and $* = 1, 2$ denotes the panel number. For the foam core, a complex stiffness $s = E_{foam}(1 + j\eta_{foam})/h_{foam}$ is considered to include the damping effect with η_{foam} the loss factor of the foam. Since the mass-spring-mass resonance frequency lies far below the coincidence frequency of both panels, the damping in the panels is neglected.

By integrating the transmission coefficient over the angles of incidence, the diffuse field transmission coefficient $\overline{\tau}$ is obtained using the Paris equation [1]:

$$\overline{\tau} = \frac{\int_0^{\theta_l} \tau_\theta \cos\theta \sin\theta d\theta}{\int_0^{\theta_l} \cos\theta \sin\theta d\theta}, \tag{4}$$

where $\theta_l = 90^o$ is the maximum angle of incidence used in this paper.

4.2 Equivalent dynamic metamaterial mass

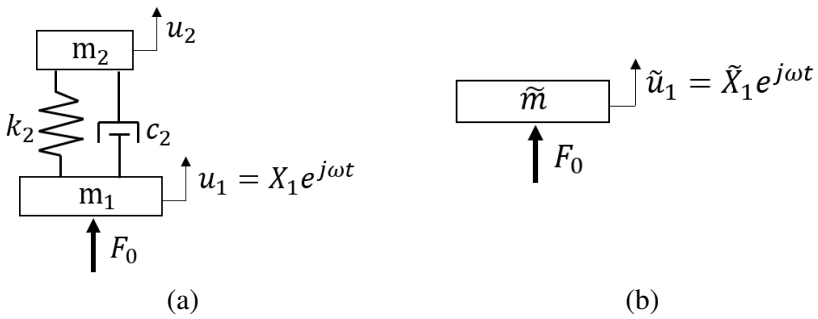
Heckl's model is based on the static mass of both panels. Consequently, it does not include the metamaterial stop band behaviour. To include this effect, the dynamic mass of the metamaterial panel will be incorporated.

The equivalent dynamic mass of the metamaterial plate is calculated by simplifying the defined UC to a 2 degree-of-freedom (DOF) system using the stop band limits acquired from dispersion curves analysis, as described in [19, 17]. Consider a 2 DOF system consisting of a host structure mass m_1, to which a mass-spring-damper resonator (m_2, k_2, c_2) is attached. This system, excited by a force F_0 at m_1, is now simplified to an equivalent 1 DOF system with dynamic mass $\tilde{m}$ (Fig. 5b) by imposing the equality of the displacements u_1 and $\tilde{u}_1$. Solving for the equivalent dynamic mass $\tilde{m}$ gives [27]:

$$\tilde{m} = \frac{F_0}{-\omega^2 X_1} = m_1 + m_2 \left[\frac{\frac{2j\zeta_2\omega}{\omega_2} + 1}{1 + \frac{2j\zeta_2\omega}{\omega_2} - \left(\frac{\omega}{\omega_2}\right)^2} \right]. \tag{5}$$

where $\zeta_2 = \frac{c_2}{2\sqrt{k_2 m_2}}$ is the modal damping ratio of the mass-spring-damper resonator (m_2, k_2, c_2) with natural frequency $\omega_2 = \sqrt{k_2/m_2}$.

For the undamped system with $\zeta_2 = 0$, $\tilde{m}$ can take negative values between frequency limits $\omega = \omega_2$ and ω_β, at which $\tilde{m} = 0$ [17]. This negative dynamic mass reflects an observability problem caused by considering only the first DOF of the 2 DOF system to derive $\tilde{m}$. The frequency region where $\tilde{m}$ is negative corresponds to the stop band frequency range [27, 28].



(a) (b)

Figure 5: The 2 DOF system (a) is replaced by a 1 DOF system (b) with equivalent dynamic mass $\tilde{m}$ [17].

To apply Eq. 5 to a realizable metamaterial solution, a simplification of the metamaterial solution to a 2 DOF system is required (Fig. 6). To this end, 4 variables need to be found: ζ_2, m_1, m_2 and ω_2. The damping ζ_2 is obtained from the material properties of the resonator (Table 2). By applying conservation of mass, m_1 can be obtained in function of m_2 as:

$$m_1 = m_{HS} + m_{Res} - m_2. \tag{6}$$

where m_{HS} and m_{Res} are the mass of the host structure UC and resonator respectively.

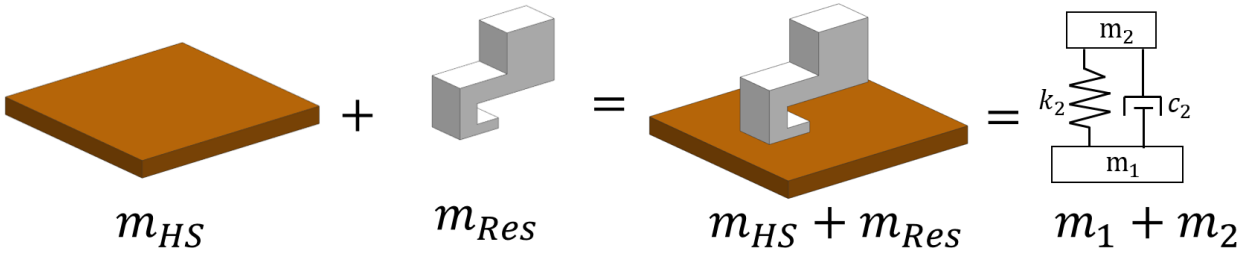


Figure 6: Masses of the metamaterial UC compared to the masses of the simplified 2 DOF system.

The two parameters m_2 and ω_2 are obtained through a comparison of the frequency limits of the negative dynamic mass obtained from the undamped form of Eq. (5) with the frequency limits of the bending wave stop band predicted using the dispersion curves along the IBC:

$$\begin{aligned} \omega_2 &= \omega_L, \\ \omega_\beta &= \omega_U, \end{aligned} \tag{7}$$

where ω_L and ω_U are respectively the lower and upper frequency limits of the predicted stop band. Furthermore, m_2 can be obtained by evaluating the undamped form of Eq. (5) at ω_U, since $\tilde{m}(\omega_U) = 0$. Eventually, the equivalent dynamic mass $\tilde{m}$ of the metamaterial is calculated as:

$$\tilde{m} = m_{HS} + m_{Res} + \frac{m_{HS} + m_{Res}}{1 - \frac{1}{1 - \left(\frac{\omega_U}{\omega_L}\right)^2}} \left[\frac{\frac{2j\zeta_2\omega}{\omega_L} + 1}{1 + \frac{2j\zeta_2\omega}{\omega_L} - \left(\frac{\omega}{\omega_L}\right)^2} - 1 \right]. \tag{8}$$

4.3 STL predictions

The STL is predicted for the bare and metamaterial case for both normal and diffuse incidence. For the bare structure, Heckl's model is applied with the parameters listed in Table 1. For the metamaterial double panel, Heckl's model is combined with the equivalent dynamic mass by replacing m_1' with the equivalent mass $\tilde{m}'$ per unit area. The parameters used to calculate $\tilde{m}'$ are listed in Table 3 .

Table 3: Parameters used to calculate the dynamic mass of the metamaterial panel.

m_{HS}	m_{Res}	ω_L	ω_U	ζ_2
3.8 g	2.0 g	962 Hz	1045 Hz	2.5 %

For both normal (Fig. 7) and diffuse incidence (Fig. 8), the bare panel shows an STL dip at f_{MKM}, followed by a an enhanced STL with increasing frequency. For the metamaterial double panel, the predicted STL shows a strong improvement in the frequency region around f_{MKM}. However, an STL decrease is predicted for this metamaterial double panel before and after the predicted stop band frequency region. This happens due to the creation of two new mass-spring-mass resonances in the metamaterial double panel at 748 Hz and 1118 Hz. These frequencies can be calculated by replacing m_1' with $\tilde{m}'$ in the dynamic mass equation (1) and filling in the originally predicted f_{MKM} in the frequency term of $\tilde{m}'$, resulting in two new mass-spring-mass resonances. In conclusion, the metamaterial solution shows potential to improve the STL around the original mass-spring-mass frequency range due to its tuned stop band effect, at the expense of two new mass-spring-mass resonances.

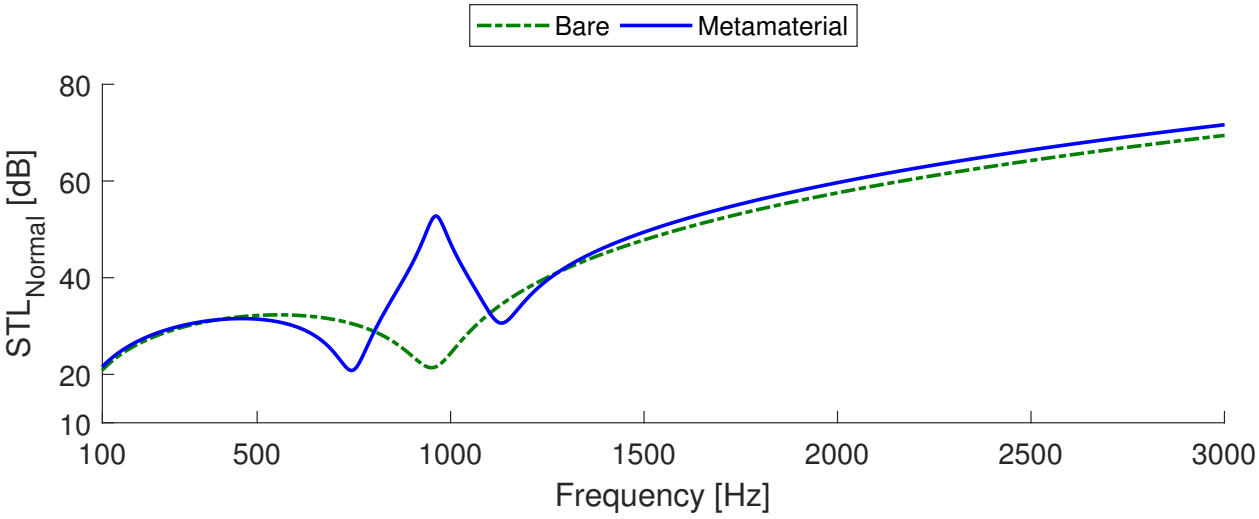


Figure 7: STL prediction for normal incidence for the bare and metamaterial double panel partitions. A strong improvement is obtained around the bare panel mass-spring-mass with the metamaterial double panel.

5 Experimental validation

This section describes the measurement setup and procedure, followed by a discussion of the IL measurement results for the double panel partition and the comparison with the corresponding STL prediction to update the foam material parameters. Eventually, the IL measurement results for the metamaterial double panel partition are discussed and compared with the corresponding STL predictions by means of the calculated IL improvement ΔIL.

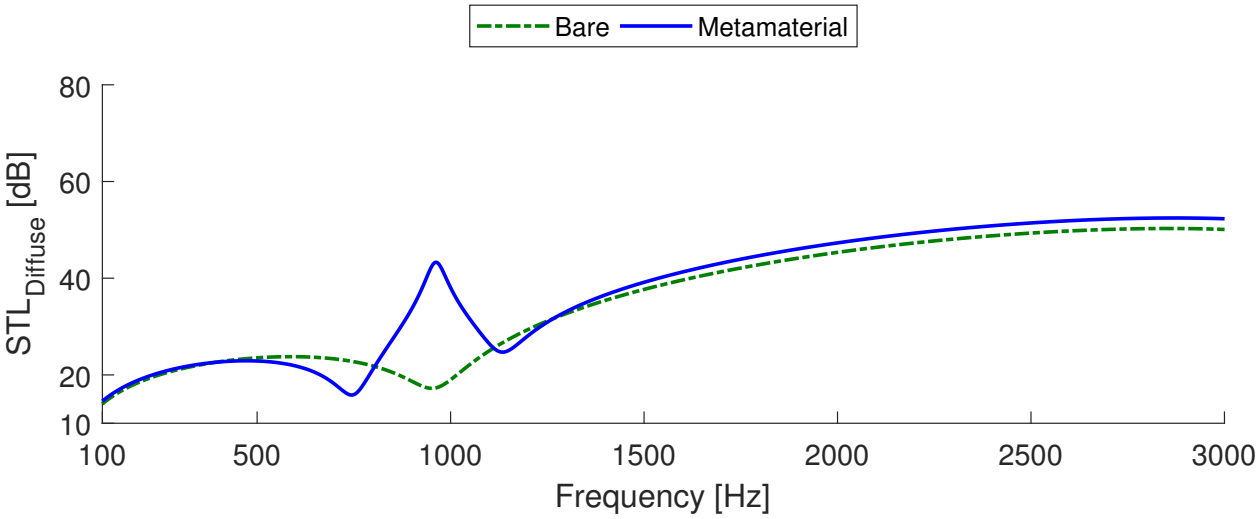


Figure 8: STL prediction for diffuse incidence for the bare and metamaterial double panel partitions. A strong improvement is obtained around the bare panel mass-spring-mass with the metamaterial double panel.

5.1 Test setup

The KU Leuven Soundbox is used to experimentally evaluate the acoustic insulation performance of the realized panels [29] (Fig. 9). It is composed of 5 reinforced concrete walls and a 35 mm thick aluminum front wall with A2 aperture, onto which the test specimen is clamped with a steel clamping frame using 52 bolts. Since STL measurements are difficult in such a setup, IL measurements are carried out. IL differs from STL, because it carries information from the testing environment [29]. The double panel partitions used in the tests have total dimensions of 860×640 mm, since part of this area is used to install the panels on the KU Leuven Soundbox (Fig. 10). While clamping the panels, care is taken not to compress the foam core due to excessive torque on the bolts. The panel composed of plaster and particle board is always facing towards the cavity.

The IL is obtained by measuring the sound power radiated through the open A2 aperture, W_{open}, and the sound power radiated through the A2 aperture closed by one of the panels, W_{closed}, due to a loudspeaker excitation inside the cavity. This allows the IL to be calculated as:

$$IL\,(f) = 10 \log_{10} \frac{W_{open}}{W_{closed}}. \tag{9}$$

The sound power is measured using a B&K sound intensity PP probe type 2681 with a spacer of 12 mm, which allows measurements from 125 Hz to 6300 Hz [30]. To highlight the metamaterial effect the IL difference ΔIL is also calculated as:

$$\Delta IL = IL_M - IL_B, \tag{10}$$

where IL_M is the IL of the metamaterial double panel, and IL_B is the IL of the bare double panel. To simplify the interpretation of the IL and ΔIL results, they are averaged in 12^{th} octave bands.

5.2 Bare panel results

For the update of the foam material parameters, the diffuse field STL prediction is compared to the measured IL. Diffuse STL predictions are used since the acoustic field inside the Soundbox around the mass-spring-mass resonance frequency region resembles a diffuse field rather than normal incidence. The Young's modulus of the foam is updated to match the frequency of the measured IL dip of the bare double panel with the predicted mass-spring-mass resonance STL dip. The damping in the foam mainly controls the STL amplitude



(a) (b)

Figure 9: IL measurements on the KU Leuven Soundbox are based on measurements of the sound power radiated through the open (a) and closed (b) aperture, excited by a loudspeaker on the inside (blue circle).



Figure 10: Metamaterial double panel clamped on the KU Leuven Soundbox with A2 aperture.

and slope around this dip [18]. Using a non-linear optimization algorithm in MATLAB R2018a®(*fminunc*), the damping is updated to fit the slope of the predicted diffuse field STL with the slope of the measured IL around the mass-spring-mass resonance frequency range, from 728 Hz to 1727 Hz. The fit is obtained by minimizing the standard deviation of the difference between predicted STL and measured IL in 12^{th} octave bands. The latter facilitates the update by smoothing out the structural modal behaviour of the panel and acoustic cavity modes in the measured IL.

The predicted normal and diffuse STL amplitudes are higher than the measured IL (Fig. 11). The modes of the panel and cavity influence the measured IL, causing a mismatch between measurement and prediction

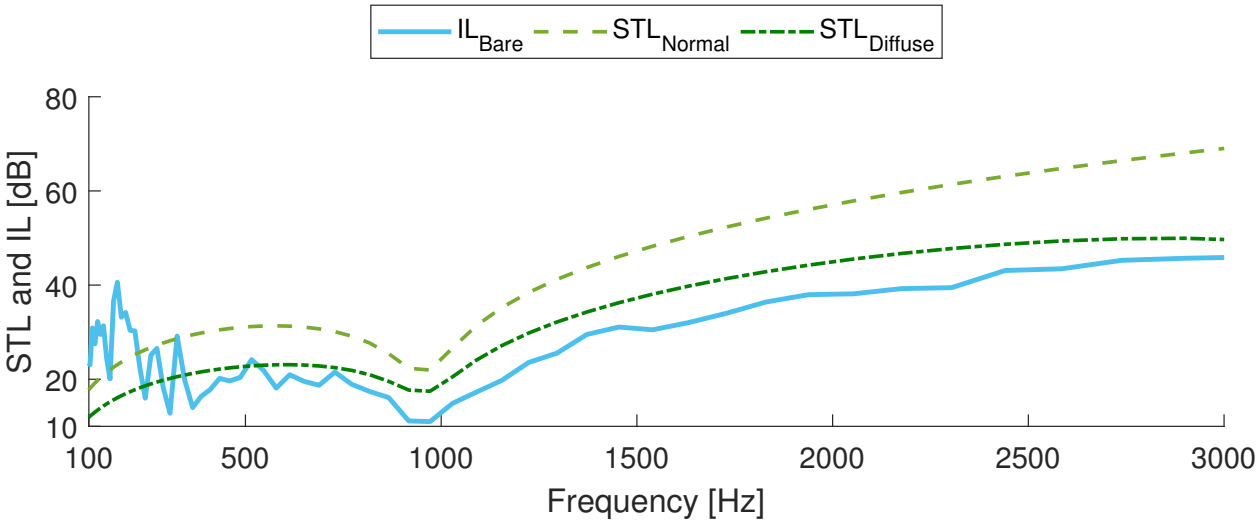


Figure 11: Measured IL for the bare double panel partition and comparison with the STL prediction for normal and diffuse incidence, averaged in 12^{th} octave bands.

for frequencies below 400 Hz due to the inherent difference between the IL and STL definition. For higher frequencies the average error between the diffuse field incidence STL prediction and the measured IL is 5 dB for frequencies above 400 Hz, which is in agreement with [20].

5.3 Metamaterial panel results

The metamaterial double panel strongly outperforms the bare double panel around the predicted stop band frequency region, while adding only 8% of mass (Fig. 12). Before the stop band, the metamaterial panel is outperformed by the bare panel due to its down-shifted mass-spring-mass resonance. After the stop band both panels have similar IL performance.

To reduce the influence of cavity modes and amplitude difference between predicted STL and measured IL, the ΔIL (Eq. 10) is calculated. A good agreement between predicted ΔSTL for diffuse field and measured ΔIL is found. The predicted ΔSTL for normal incidence overestimates the peak performance as well as the strength of the two mass-air-mass resonance dips. These results both validate the proposed STL prediction method as well as the potential of the metamaterial double panel solution. In addition, the R-value of both panels is calculated to obtain a single acoustic performance value [31]. For the metamaterial double panel an R-value of 22 dB is obtained, which outperforms the bare double panel for which the R-value is 21 dB.

6 Conclusion

Resonant metamaterials are applied to enhance the STL of a double panel partition with a foam core at its mass-spring-mass resonance frequency, where the untreated double panel suffers from a reduced STL. A commercially available double panel is used, with an particle board panel at one side and a combined particle board and plasterboard panel on the other side, sandwiching a locally reacting foam core. Resonators are designed and added to the particle board panel on one side to create a bending wave stop band in that panel around the mass-spring-mass resonance frequency of the bare double panel. A method to predict the STL of such metamaterial double panel is proposed and validated. The metamaterial double panel is realized and its acoustic insulation performance evaluated experimentally.

The realized structure validates the potential of resonant metamaterials to improve the STL in the frequency region around the mass-spring-mass resonance for double panel partitions with a locally reacting core material. A strong improvement in the measured IL is achieved due to the stop band effect, with a mass addition

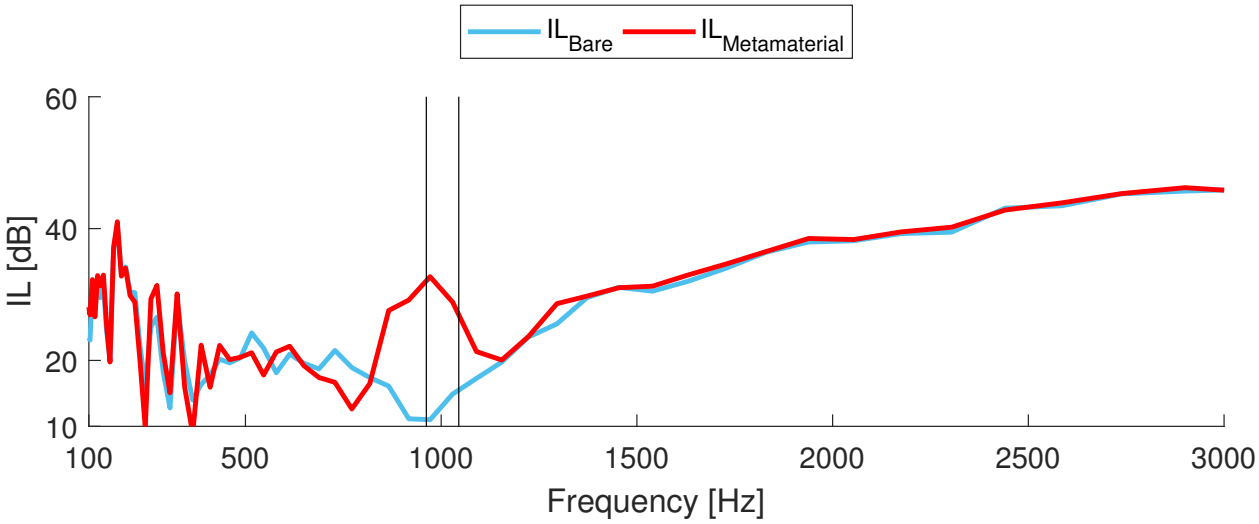


Figure 12: The realized metamaterial panel strongly outperforms the bare panel in the predicted stop band frequency region (black vertical lines).

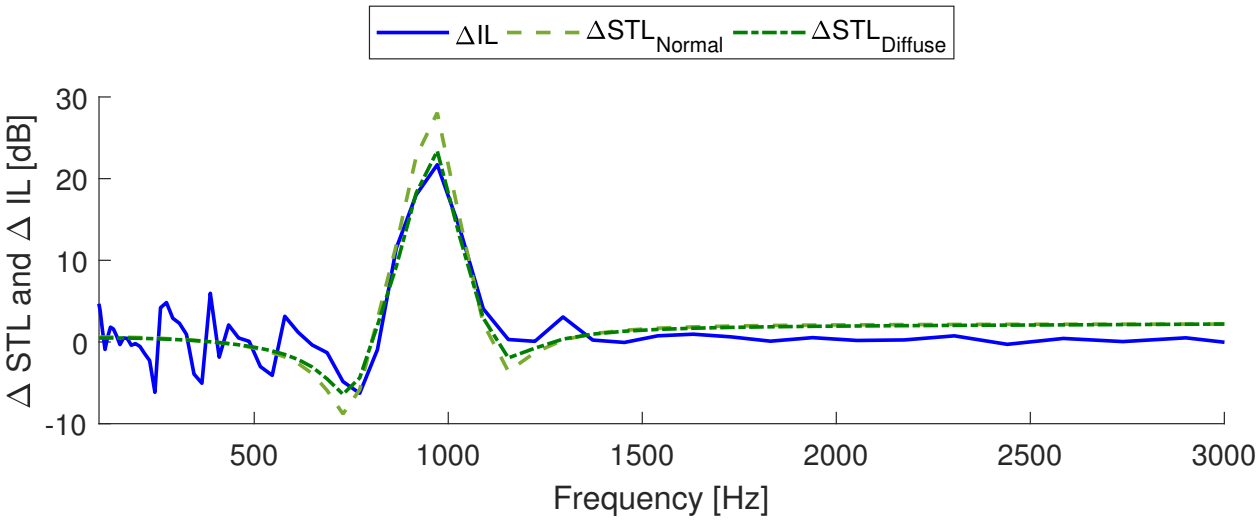


Figure 13: The predicted diffuse field ΔSTL accurately predicts the stop band effect on the acoustic insulation performance of the double panel, while the normal incidence ΔSTL leads to an overestimation.

to the bare double panel of only 8%. This improvement results in an increase of the single acoustic performance R-value of 1 dB. The good agreement between measurements and predictions also validates the accuracy of the proposed method to design and predict the metamaterial double wall performance based on the combination of Heckl's model with the equivalent dynamic mass of a metamaterial. Since the dynamic mass calculation relies on dispersion curves obtained from FE based UC modeling, this method allows fast and accurate predictions for realizable and complex resonator geometries.

Acknowledgments

The research of N. F. Melo is funded by a PhD Scholarship Sciences without Borders CNPq Brazil (201414/2014-7). The research of L. Van Belle is funded by a grant from the Research Foundation - Flanders (F.W.O.). Elke Deckers is a postdoctoral fellow of the Research Foundation - Flanders (F.W.O.). This research was partially supported by Flanders Make, the strategic research centre for the manufacturing industry.

References

[1] F. J. Fahy, *Sound and structural vibration: radiation, transmission and response*, Academic press (2012).

[2] M. Heckl, *The tenth sir richard fairey memorial lecture: Sound transmission in buildings*, Journal of Sound and Vibration, Vol. 77, No. 2, (1981), pp. 165–189.

[3] P. Sheng, X. Zhang, Z. Liu, C. Chan, *Locally resonant sonic materials*, Physica B: Condensed Matter, Vol. 338, No. 1, (2003), pp. 201–205.

[4] P. F. Pai, *Metamaterial-based broadband elastic wave absorber*, Journal of Intelligent Material Systems and Structures, Vol. 21, No. 5, (2010), pp. 517–528.

[5] C. Claeys, K. Vergote, P. Sas, W. Desmet, *On the potential of tuned resonators to obtain low-frequency vibrational stop bands in periodic panels*, Journal of Sound and Vibration, Vol. 332, No. 6, (2013), pp. 1418–1436.

[6] R. Zhu, X. Liu, G. Hu, C. Sun, G. Huang, *A chiral elastic metamaterial beam for broadband vibration suppression*, Journal of Sound and Vibration, Vol. 333, No. 10, (2014), pp. 2759–2773.

[7] T. Wang, M. Sheng, Z. Guo, Q. Qin, *Acoustic characteristics of damped metamaterial plate with parallel attached resonators*, Archives of Mechanics, Vol. 69, No. 1, (2017), pp. 29–52.

[8] N. G. Rocha de Melo Filho, L. Sangiuliano, C. Claeys, E. Deckers, W. Desmet, *Vibro-acoustic metamaterial for increased stl in acoustic resonance driven enviroments*, *Noise and vibration emerging methods - NOVEM*, Ibiza - Spain.

[9] C. Goffaux, J. Sánchez-Dehesa, A. Yeyati, P. Lambin, A. Khelif, J. Vasseur, B. Djafari-Rouhani, *Evidence of fano-like interference phenomena in locally resonant materials*, Physical Review Letters, Vol. 88, No. 22.

[10] C. C. Claeys, P. Sas, W. Desmet, *On the acoustic radiation efficiency of local resonance based stop band materials*, Journal of Sound and Vibration, Vol. 333, No. 14, (2014), pp. 3203–3213.

[11] Y. Xiao, J. Wen, X. Wen, *Sound transmission loss of metamaterial-based thin plates with multiple subwavelength arrays of attached resonators*, Journal of Sound and Vibration, Vol. 331, No. 25, (2012), pp. 5408–5423.

[12] L. Van Belle, E. Deckers, C. Claeys, W. Desmet, *Sound transmission loss of a locally resonant metamaterial using the hybrid wave based-finite element unit cell method*, *11th International Congress on Engineered Material Platforms for Novel Wave Phenomena-Metamaterials 2017*, Marseille, France, pp. 364–366.

[13] S. Hettler, *Vibroacoustic behaviour of sandwich structures with spatially distributed resonators*, Ph.D. thesis, Universitt Stuttgart (2013).

[14] M. Oudich, X. Zhou, M. B. Assouar, *General analytical approach for sound transmission loss analysis through a thick metamaterial plate*, Journal of Applied Physics, Vol. 116, No. 19, (2014), pp. 193509.

[15] A. Hall, E. Calius, G. Dodd, K. Chan, *Development of locally resonant structures for sonic barriers*, *Health Monitoring of Structural and Biological Systems 2013*, Vol. 8695, International Society for Optics and Photonics, Vol. 8695, 86953M.

[16] J. Li, S. Li, *Sound transmission through metamaterial-based double-panel structures with poroelastic cores*, Acta Acustica united with Acustica, Vol. 103, No. 5, (2017), pp. 869–884.

[17] N. G. Rocha de Melo Filho, L. Van Belle, C. Claeys, E. Deckers, W. Desmet, *Dynamic mass based sound transmission loss prediction of vibro-acoustic metamaterial double panels applied to the mass-air-mass resonance*, Journal of Sound and Vibration, submitted.

[18] K. Mulholland, H. Parbrook, A. Cummings, *The transmission loss of double panels*, Journal of Sound and Vibration, Vol. 6, No. 3, (1967), pp. 324–334.

[19] N. G. Rocha de Melo Filho, L. Van Belle, C. Claeys, E. Deckers, W. Desmet, *On the use of the dynamic mass of metamaterials to calculate the transmission loss based on the acoustic mass law*, *13th International Conference on Theoretical and Computational Acoustics*, Vienna.

[20] V. Hongisto, *Sound insulation of double panels-comparison of existing prediction models*, Acta acustica united with acustica, Vol. 92, No. 1, (2006), pp. 61–78.

[21] W. Heylen, S. Lemmens, P. Sas, *Modal analysis theory and testing*, KU Leuven, PMA division (2014).

[22] C. Claeys, N. G. R. de Melo Filho, L. Van Belle, E. Deckers, W. Desmet, *Design and validation of metamaterials for multiple structural stop bands in waveguides*, Extreme Mechanics Letters, Vol. 12, (2017), pp. 7–22.

[23] L. Van Belle, C. Claeys, E. Deckers, W. Desmet, *On the impact of damping on the dispersion curves of a locally resonant metamaterial: Modelling and experimental validation*, Journal of Sound and Vibration, Vol. 409, (2017), pp. 1–23.

[24] L. Brillouin, *Wave propagation in periodic structures*, McGraw-Hill Book Company, 2nd Ed. (1946).

[25] B. R. Mace, E. Manconi, *Modelling wave propagation in two-dimensional structures using finite element analysis*, Journal of Sound and Vibration, Vol. 318, No. 4, (2008), pp. 884–902.

[26] F. Maurin, C. Claeys, E. Deckers, W. Desmet, *Probability that a band-gap extremum is located on the irreducible brillouin-zone contour for the 17 different plane crystallographic lattices*, International Journal of Solids and Structures, Vol. 135, (2018), pp. 26–36.

[27] P. F. Pai, H. Peng, S. Jiang, *Acoustic metamaterial beams based on multi-frequency vibration absorbers*, International Journal of Mechanical Sciences, Vol. 79, (2014), pp. 195–205.

[28] C. Sugino, Y. Xia, S. Leadenham, M. Ruzzene, A. Erturk, *A general theory for bandgap estimation in locally resonant metastructures*, Journal of Sound and Vibration, Vol. 406, (2017), pp. 104–123.

[29] M. Vivolo, *Vibro-acoustic characterization of lightweight panels by using a small cabin*, Ph.D. thesis, PhD Thesis, Arenberg Doctoral School, University of Leuven (2013).

[30] B. . Kjaer, *Sound Intensity (br0476)*, DK-2850 Naerum, Denmark (1993).

[31] E. ISO, *717-1: 1996*, Acoustics-Rating of sound insulation in buildings and of building elements-Part, Vol. 1, (2006), pp. 717–1.

Design tool for realisable vibro-acoustic metamaterials based on their NVH performance

M. Clasing Villanueva [1,2], C. Claeys [1,2], N.G.R. de Melo Filho [1,2], E. Deckers [1,2], K. Geurts [3], I. Van de Weyenberg [3], P. Campestrini [3], B. Pluymers [1,2], W. Desmet [1,2]
[1] KU Leuven, Department of Mechanical Engineering,
Celestijnenlaan 300, B-3001, Leuven, Belgium
e-mail: **matias.clasingvillanueva@kuleuven.be**

[2] DMMS lab, Flanders Make

[3] Flanders Make, Oude Diestersebaan 133, 3920 Lommel, Belgium

Abstract
Vibro-acoustic metamaterials have shown to be an interesting candidate for improving the noise and vibration behaviour of lightweight systems. Recent studies have reported this new concept to significantly attenuate vibration or reduce acoustic transmission for targeted and tunable frequency ranges, referred to as stopbands. The resonant-based metamaterials can be applied to a wide range of designs and are producible by a variety of manufacturing process, making their design process a challenging and highly experience driven task. This paper discusses a design tool for metamaterials which evaluates their NVH performance for several combinations of designs and production processes. The proposed tool allows to obtain a metamaterial design based on its predicted NVH performance through the creation of solution spaces. These spaces are generated considering the main metamaterial performance indicators, such as stopband location and width, vibration attenuation and transmission loss.

1 Introduction

Increasing customer requirements and more restrictive regulations have driven the Noise and vibration Harshness (NVH) behaviour into a key design criterion of products and machines. Ecological trends, however, reduce the applicability of traditional (heavy) NVH solutions. In view of this challenging task of merging NVH and lightweight requirements, novel solutions are required.

Vibro-acoustic metamaterials have potential to be candidates for superior lightweight NVH insulation, be it at least in a specific target and tuneable frequency region, referred to as stopbands [1]. These stopbands result from resonant cells arranged on a subwavelength scale of the host structure on which they are embedded [2, 3, 4]. Previous papers from the authors explained the resonant based metamaterials working principles, listed their driven parameters [5] and showed, both numerically and experimentally, the potential for acoustic insulation [1, 6] and vibration reduction [7] in a low frequency zone. More recently, tools to predict transmission loss and vibration attenuation have been developed and validated based on the application of dynamic mass and the acoustic mass law [8, 9].

This article discusses the introduction of a design tool for these vibro-acoustic metamaterials and is structured as follows. Section 2 discusses the rationale of the metamaterial concept and describes the numerical prediction of the stopband behaviour, transmission loss and vibration reduction for a given design. Section 3 and 4 describe the rationale and the implementation of the design tool, respectively. The article ends with the main conclusions.

2 Resonant based metamaterials

Metamaterials with stopband behaviour can be obtained through a variety of materials and combinations. However, two conditions need to be met:

- Resonant cells have to be added to a host structure on a scale smaller than the structural wavelengths to be influenced [2],
- The net sum of the forces on the hosting structure contributed by a resonant system should be non-zero [10].

The type of eligible designs for these resonant additions heavily depend on the structure to which the resonant systems are added. Figure 1 shows a first example of a periodic metamaterial. The host structure is a rectangular core sandwich panel. The internal cavities of this periodic core sandwich panel allow inclusion of the resonant systems while the combination of excellent mechanical properties and low mass can be obtained. For the resonant structure, a design is chosen that resembles a mass-spring system: two thin legs are used to connect a heavy mass to a host structure (Figure 2). The connection legs will determine the stiffness while the thick part of the resonator will determine the mass of this resonant structure.

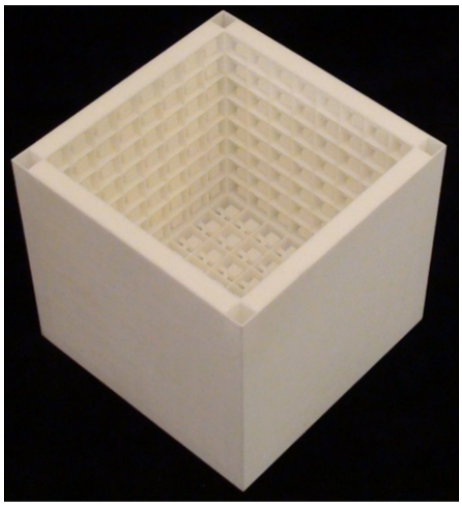


Figure 1: Picture of the acoustic demonstrator as shown via the following link **`https://youtu.be/tOch_GsGaXg`**

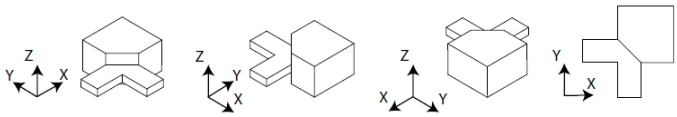


Figure 2: Type of resonant structure to be added in a periodic core to obtain stopband behaviour

A second design is shown in Figure 3. The resonant structures, or resonators, are made through laser cutting of a Plexiglass (PMMA) plate and are designed as cantilever beams with an end point mass, and supporting feet to glue the structures to a flat surface.

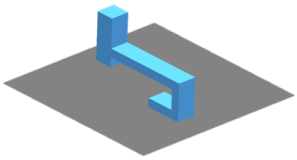


Figure 3: Resonant structure (blue) to be added to a flat surface (grey) to introduce stopband behaviour

To assess whether the addition of these resonant structures will introduce a stopband, the wave propagation needs to be investigated. From literature, it is known that wave propagation through infinite periodic structures can be investigated by means of unit cell modelling [11, 12]. Based on an undamped Finite Element (FE) model of the unit cell and the application of periodicity boundary conditions, dispersion curves for freely propagating waves in an infinite periodic structure can be derived. Frequency zones for which no solutions are found, correspond to frequency zones without free wave propagation and thus a stopband region. Thus, by building a FE model of the unit cell of a metamaterial, both the resonance frequency of the resonant structure and the dispersion curves can be calculated.

As an example of the effect of these stopbands, Figure 4 shows the vibration levels along different sections of a metamaterial duct (Figure 5), together with the numerically predicted stopband, for a duct that is excited at section 0. More details on the design and the measurements can be found in reference [7]. A picture of the duct itself is shown in Figure 5. The predicted stopband zone clearly corresponds to the zone of reduced vibrations.

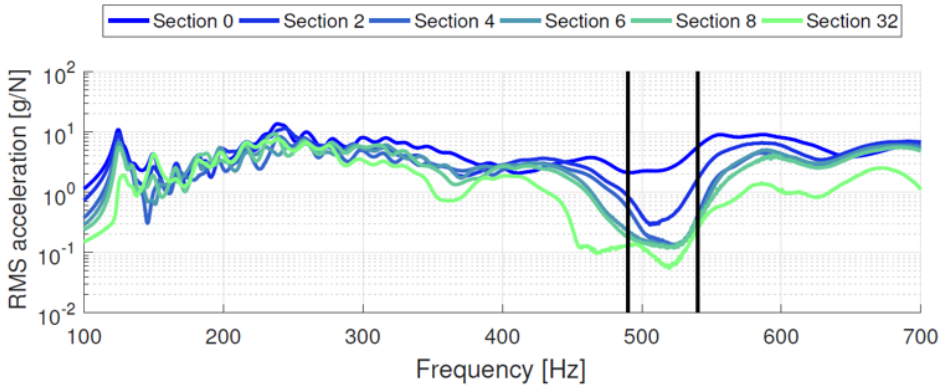


Figure 4: Vibration levels along the duct of Figure 5 with the inclusion of the resonant system design of Figure 3.

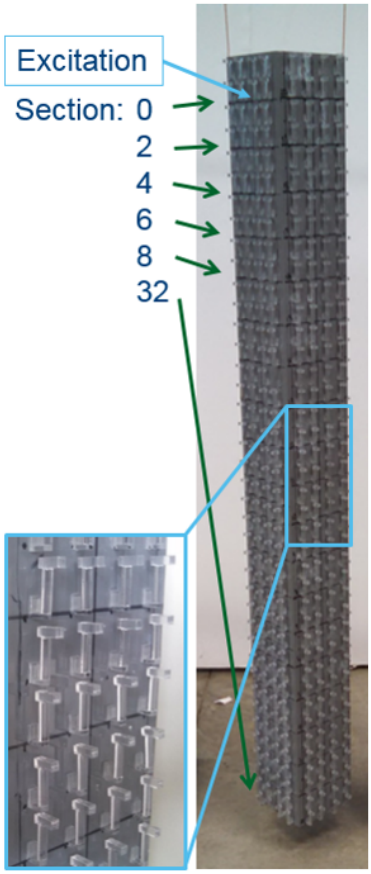


Figure 5: Picture of the PVC duct with added resonant systems of Figure 3 to induce stopband behaviour.

Figure 6 shows a third example of a metamaterial solution applied to a twin sheet thermoformed panel. In this case, the resonant system is created by milling slits in the thermoformed panel; the unit cell is shown in Figure 7. More details and experimental validation of this design, can be found in reference [9].

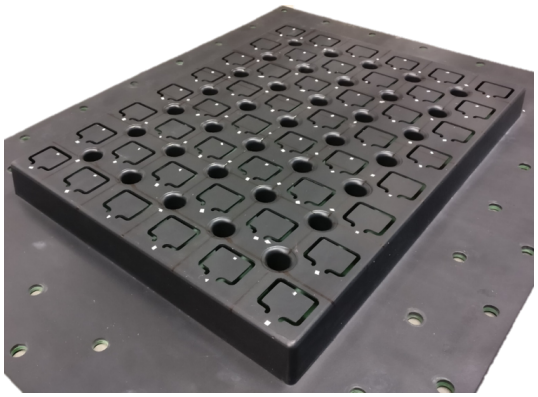


Figure 6: Thermoformed metamaterial twin sheet panel, produced by Vitalo.

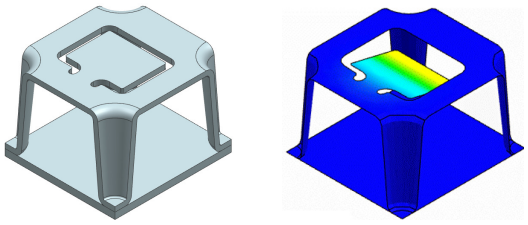


Figure 7: Thermoforming resonant structure made by the slits cuts in the structure

3 Design tool for vibro-acoustic metamaterials

The existing design process of metamaterials still corresponds to a non-trivial procedure, that requires a number of design iterations. The stopband frequencies and stopband width depend on design parameters such as material properties, geometric dimensions of the design, mass addition and resonator spacing. Furthermore, limitations regarding the possibilities of the production process and boundary conditions of the applications, e.g. allowable added weight and space, need to be taken into account. In the typically used design process the resulting metamaterial performance parameters are only obtained at the end of the process (Figure 8), resulting in an iteration over the design parameters until the required NVH performance is reached.

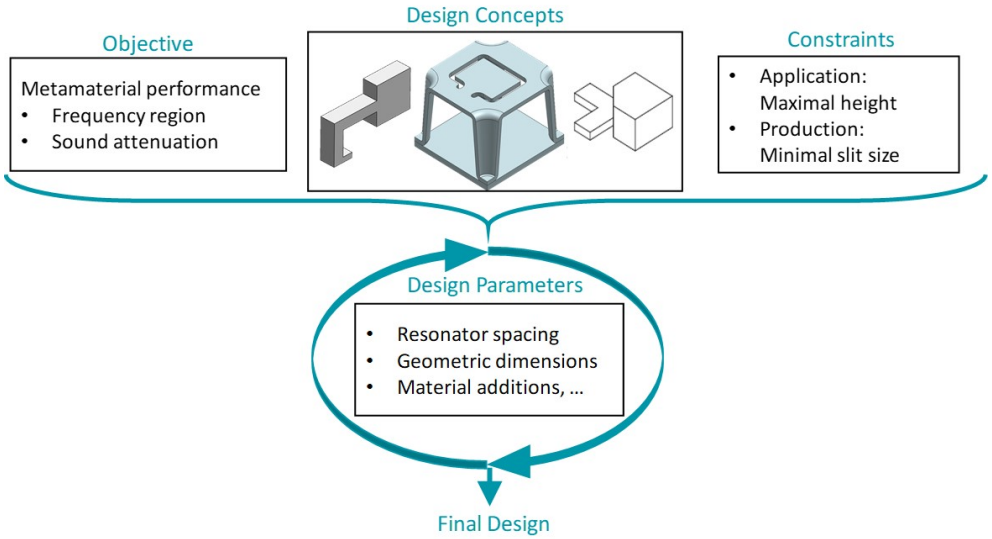


Figure 8: The typically used metamaterial design process flow

3.1 Design tool approach

The proposed approach focuses on the ability of evaluating the feasible metamaterial designs according to their expected NVH performance. Therefore, a tool is created which allows to compare different metamaterial designs, for a given design concept and under specific aplication dependent restrictions, and gives the best elegible design parameters for the required application.

This tool calculates, for all eligible designs, the metamaterial performance parameters such that the best suitable design can be selected. The designs can be evaluated based on the following criteria: frequency range, material, size limitations, type of metamaterial design concept. To ease comparison, the solutions are mapped onto solution spaces, which show, for a combination of criteria, the best performing designs.

Different solution spaces for the application can be defined according to customer requirements, such as the stopband width $[Hz]$, peak transmission loss $[dB]$, expected vibration attenuation per UC decay $[dB]$ and the target resonance frequency $[Hz]$, with adjustable constraints, such as the resonator mass $[kg]$ and volume $[m^3]$. A summary for the methodology of the proposed design tool is presented in Figure 9.

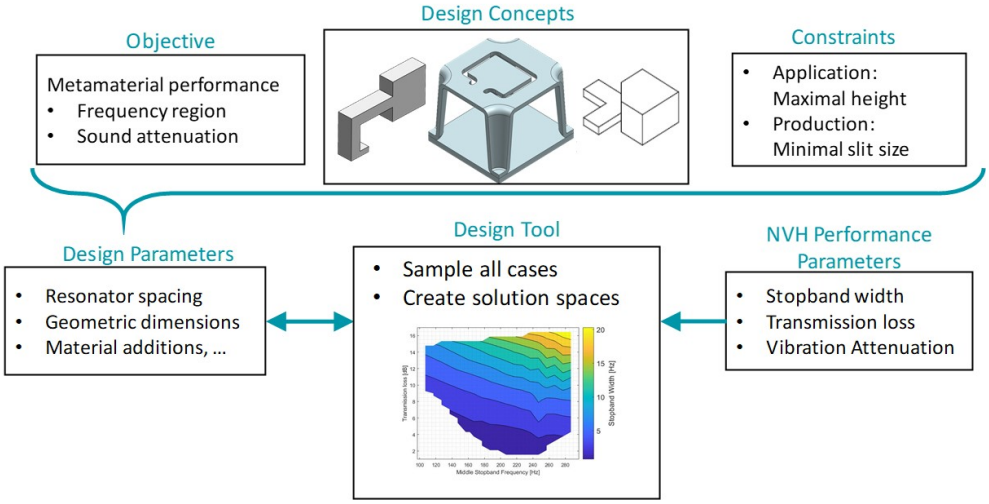


Figure 9: Schematic representation of the design tool approach

3.2 Implementation of the Design tool

The design tool allows to generate solution spaces for a chosen resonator design concept and allows to take into account limitations of the application. In this section, an example of the design tool is presented for the design concept shown in the Figure 10.

Starting from a chosen design concept, a parametric model is implemented for which the design parameters can be changed. In the example of this section, this design consists of a 2D cantilever resonator design extruded to obtain a 3D object. A sketch of the 2D design is shown on left side of Figure 10, and an isometric view is given at the right side. The design was parametrized according to the design parameters indicated in the Figure 10.

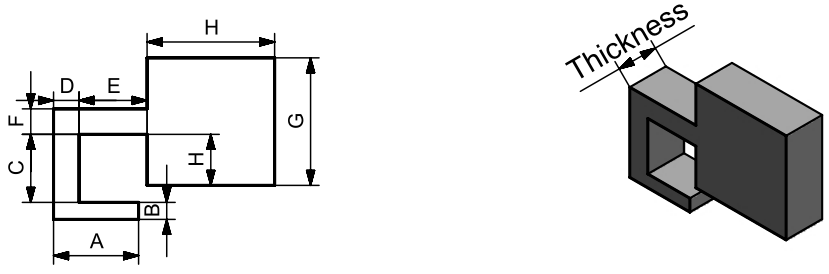
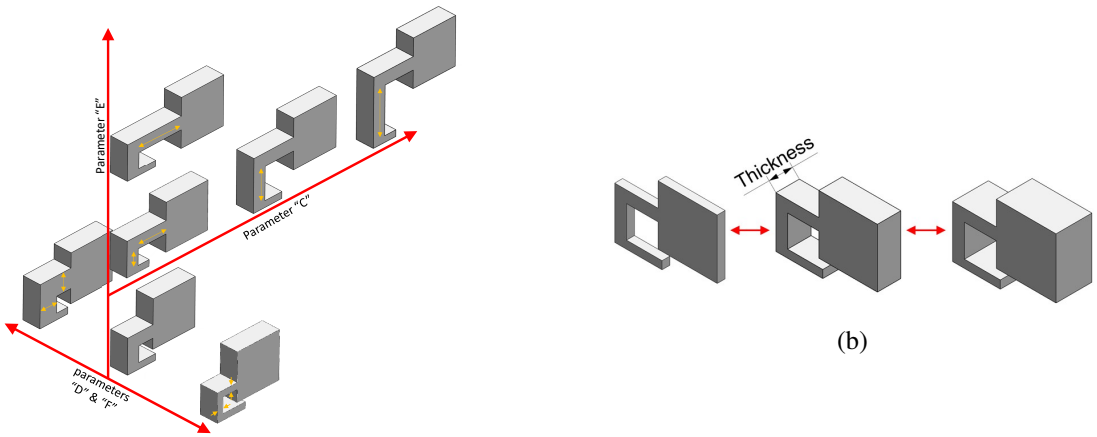


Figure 10: Dimension parameters related for the metamaterial design concept of the Figure 3.

A Monte Carlo simulation is performed from the parametrized model. Figure 11 shows the iteration process through the parameters listed as ”C”, ”D”, ”E”, ”F” and ”Thickness” on the Figure 10. The complete iteration process generates a data set containing the stopband frequencies, transmission loss and vibration reduction

for all eligible designs for the given concept. The tool then allows to sort the data such that at each point in the desired solution space the design with the highest selected performance parameter is shown.



(a) (b)

Figure 11: Schemes for the iteration process through the design parameters, (a) Beam parameters, (b) thickness

Depending on the customer constraints and application considerations the solution spaces will be different. In order to present an example of a solution space, Table 1 shows a set of customer constraints and design parameters. Figure 12 presents a solution space for the design concept of Figure 10, as a function of the peak transmission loss, the middle frequency of the stopband and the stopband width. This tool allows to evaluate the effect of setting certain constraints and to select the design concept obtaining the best performance.

Resonator material	Plexiglass
Target frequency $[Hz]$	$750 - 850$
Peak transmission loss $[dB]$	> 10

Table 1: Design and NVH parameters for the example of the application of the design tool.

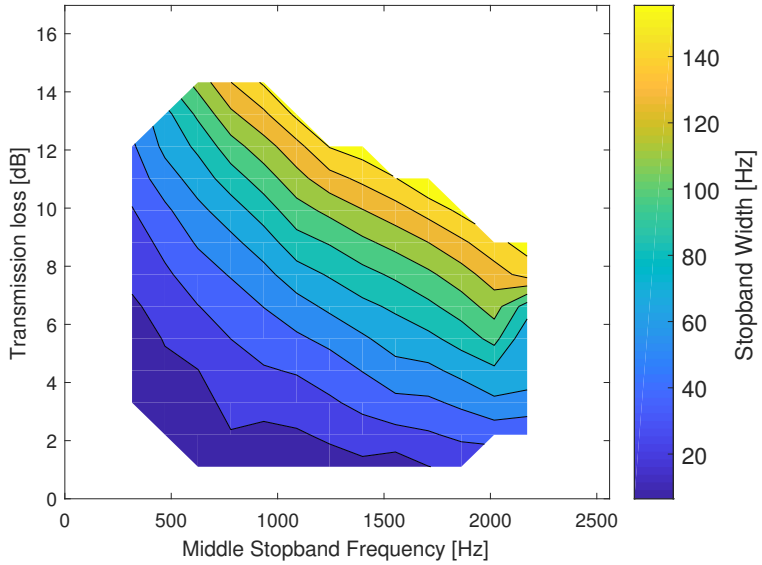
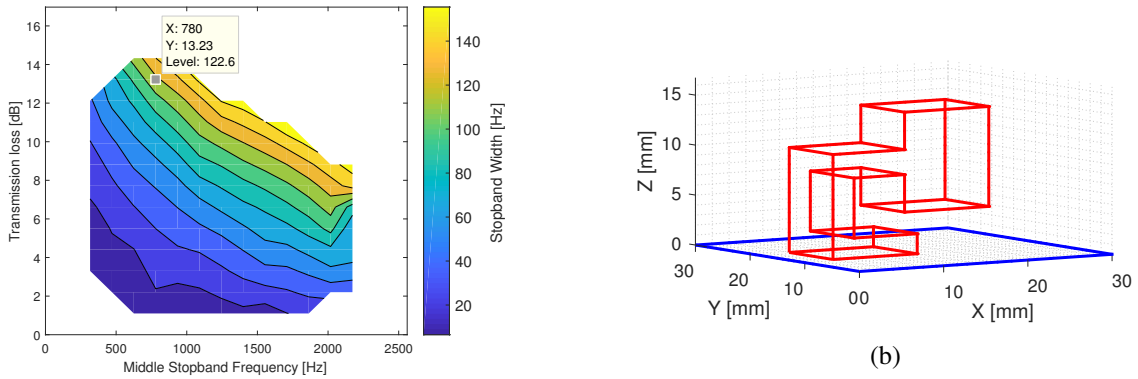


Figure 12: Example solution space obtained for target resonance frequency $[Hz]$, peak transmission loss $[dB]$, and stopband width $[Hz]$.

Considering the target frequency in Table 1, it is possible to select the desired outcome from the solution space (Figure 13a), for which then the resulting metamaterial design is shown (Figure 13b). Furthermore, the results for transmission loss considering a diffusive field and vibration attenuation can be obtained from the given selection [8] to review if the desired outcome is achieved; Figure 14 shows the results for both.



(a) (b)

Figure 13: (a) Selection of optimal resonator design from solution space, (b) resonator design selected from the solution space

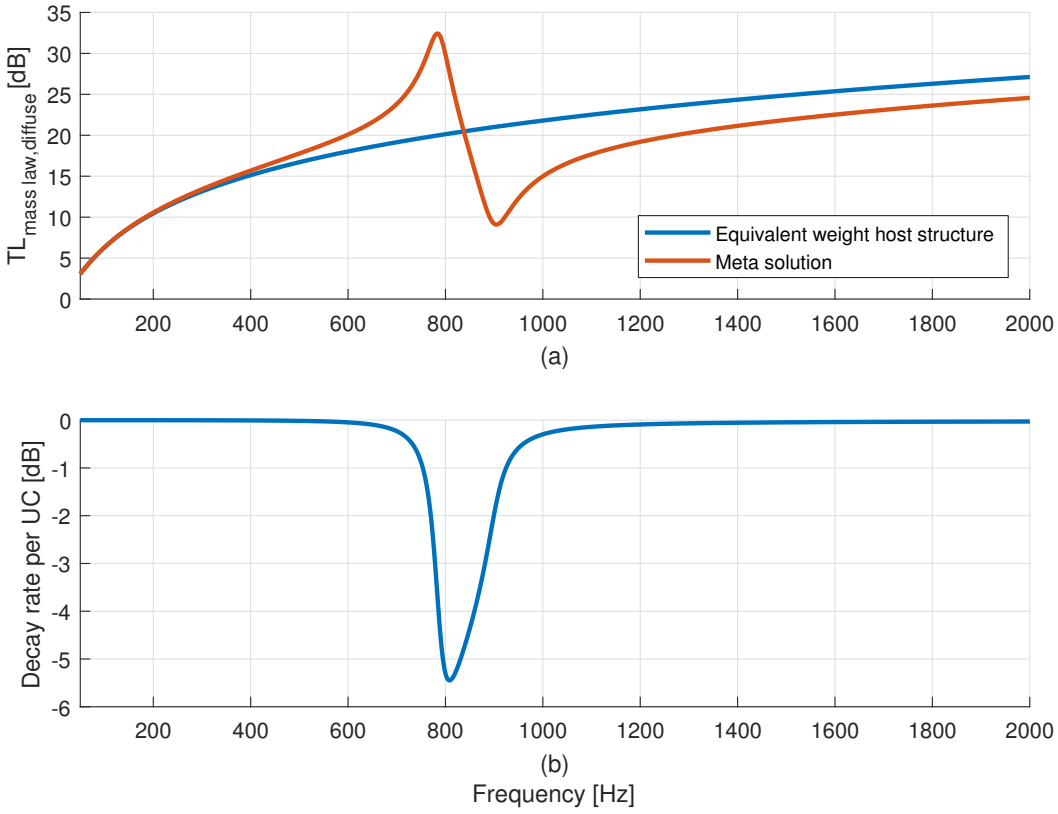


Figure 14: (a) Transmission loss for diffusive incidence acoustic field, (b) Structural vibration decay rate in propagation direction.

4 Conclusions

Vibro-acoustic metamaterials show a high potential as lightweight NVH insulation, be it at least in targeted frequency ranges, referred to as stopbands. The design of the metamaterial is, however, often experience-based and requires an iterative process. This paper discusses a design tool to facilitate the design of resonant metamaterials to improve NVH behaviour. The design tool is based on a parametrized model of a metamaterial concept and allows to visualize solution spaces, taking into account the application specific limitations. This allows the user to select the desired performance, and link it with a suitable design.

Acknowledgements

The authors gratefully acknowledge the KU Leuven Research Fund for their support through an IOF-Leverage project. This research is partially supported by Flanders Make, the Strategic Research Centre for the Manufacturing Industry. The research of M. Clasing Villanueva is funded by a PhD CONICyT Becas Chile scholarship. The research of N. F. Melo is funded by a PhD Scholarship Sciences without Borders CNPq Brazil (201414/ 2014-7). Elke Deckers is a postdoctoral fellow of the Research Foundation- Flanders (F.W.O.).

References

[1] C. Claeys, E. Deckers, B. Pluymers, W. Desmet, *A lightweight vibro-acoustic metamaterial demonstrator: Numerical and experimental investigation*, Mechanical Systems and Signal Processing, Vol. 70-71, (2016), pp. 853–880.

[2] J. Pendry, A. Holden, D. Robbins, W. Stewart, *Magnetism from conductors and enhanced nonlinear phenomena*, IEEE Transactions on Microwave Theory and Techniques, Vol. 47, No. 11, (1999), pp. 2075–2084.

[3] F. Lemoult, N. Kaina, M. Fink, G. Lerosey, *Wave propagation control at the deep subwavelength scale in metamaterials*, Nature Physics, Vol. 9, No. 1, (2012), pp. 55–60.

[4] C. Goffaux, J. Sánchez-Dehesa, A. L. Yeyati, P. Lambin, A. Khelif, J. O. Vasseur, B. Djafari-Rouhani, *Evidence of fano-like interference phenomena in locally resonant materials*, Physical Review Letters, Vol. 88, No. 22.

[5] C. C. Claeys, K. Vergote, P. Sas, W. Desmet, *On the potential of tuned resonators to obtain low-frequency vibrational stop bands in periodic panels*, Journal of Sound and Vibration, Vol. 332, No. 6, (2013), pp. 1418–1436.

[6] C. Claeys, E. Deckers, B. Pluymers, W. Desmet, *Enhanced lightweight nvh solution based on vibro-acoustic metamaterials*, ATZ Extra.

[7] C. Claeys, N. G. R. de Melo Filho, L. V. Belle, E. Deckers, W. Desmet, *Design and validation of metamaterials for multiple structural stop bands in waveguides*, Extreme Mechanics Letters, Vol. 12, (2017), pp. 7–22.

[8] N. G. Rocha de Melo Filho, L. Van Belle, C. Claeys, E. Deckers, W. Desmet, *On the use of the dynamic mass of metamaterials to calculate the transmission loss based on the acoustic mass law*, *13th International Conference on Theoretical and Computational Acoustics*, Vienna.

[9] N. G. Rocha de Melo Filho, L. Sangiuliano, C. Claeys, E. Deckers, W. Desmet, *Vibro-acoustic metamaterial for increased stl in acoustic resonance driven enviroments*, *Noise and vibration emerging methods - NOVEM*, Ibiza - Spain.

[10] G. Wang, X. Wen, J. Wen, L. Shao, Y. Liu, *Two-dimensional locally resonant phononic crystals with binary structures*, Physical Review Letters, Vol. 93, No. 15.

[11] L. Brillouin, *Wave propagation in periodic structures*, McGraw-Hill Book Company, 2nd Ed. (1946).

[12] R. Langley, *A note on the force boundary conditions for two-dimensional periodic structures with corner freedoms* (1993).

Long-range coupling of waveguides

F. Mezzani [1], **F. Coppo** [1], **A. Carcaterra**[1]
[1] Sapienza, University of Rome, Department of Mechanical and Aerospace Engineering,
via Eudossiana 18, 00184, Rome, Italy
e-mail: **federica.mezzani@uniroma1.it**

Abstract
Recently the authors proposed a model and related analysis on waves in long-range metamaterials. Nonlocal elasticity can be produced by several interacting forces acting between particles at long distance, as Coulomb or magnetic-static forces. The chance of introducing this long-distance forces has a disruptive effect in the elastic dynamics. In fact, classical elasticity is based only upon closest particles interaction in which short range-elastic forces act. A particular characteristic of these forces is that they can couple distant structures, as for example two elastic beams or rods, each made of an elastic support with embedded magnets. The interaction produces intra-forces and inter-forces that change the dynamics of the coupled structure. This paper investigates new phenomena that can be observed in such unusual systems, providing a theoretical framework, as well as numerical simulations.

1 Introduction

Metamaterials represent a rather new science, though extensively studied. The subject involves mainly acoustic and electromagnetic metamaterials, for which the atypical refraction index produces uncommon effects and opens to new technological developments, as the chance to achieve invisible cloaking [1] or holographic images [2].
The increasing enhancement of additive manufacturing and micro-nanotechnologies [3, 4], and the consequent complex microstructures these materials are composed by, support the achievement of particular dynamic behaviours, as unusual wave propagation [5] and exceptional dissipation features [6, 7, 8, 9], i.e. all those phenomena classical dynamic can desribe only by introducing unconventional mathematical models [10, 11, 12].
In this context, the present work analyses elastic metamaterials and unveils some remarkable effects, namely superluminal and hypersonic propagation, and negative group velocity, as a consequence of the introduction of long-range interactions. These new connections, additional to the conventional elastic ones, have the effect to modify the topology of the interactions and, thus, the dynamic response of the structure.
Long-range interactions have been investigated: in [13, 14, 15, 16, 17], Tarasov presents a mathematical model, in which nonlocal connections affect the static response of the structure. Zingales in [18, 19, 20, 21] discusses how the dynamic behaviour is influenced by this type of interactions, but only numerical solutions confirm his theory. The novelty introduced in our work is the chance to discuss the dynamic response in terms of analytical solutions. The proposed mathematical model is based on the nonlocal elasticity theory developed by Eringen, in which several types of long-range connections are investigated. However, even tough in his study is complete from a mathematical point of view, the effect related to wave propagation are discussed only in [22].
The present work not only analyses a specific type of long-range interaction, but also provides a thorough investigation of the different propagation phenomena, suggesting a map of the possible scenarios according to the intrinsic physical properties of the system. A similar analysis was conducted by [23] and [24], but it is applied to micro and nano scales only.

Here, the straightforward approach showed in [25] has been applied to the topic investigated in [26]. The analysed system is composed by two identical, continuous, unbounded waveguides (*twin system*), in which long-range interactions act in addition to the conventional elastic connections. A Gauss-like type of force is used to model these long-range interactions, and it mimics magnetic coupling. The advantages related to the application of this type of forces was already demonstrated: they accurately model natural forces and lead to analytical solution of the equation of motion, since their Fourier Transform has an analytical expression. A long-range interaction exists within one waveguide, but also in the case of the *twin system*. Indeed, with no external connection involved, it can be seen how the two identical rod-like structures are coupled with each other, thanks to the magnetic interaction only. The mathematical analysis anticipates the existence of unconventional propagating phenomena, which are confirmed by numerical simulations.

2 Long-range waves and integro-differential equations

In this section, the contribution of long-range forces is considered as additional to the conventional elastic one.
Let us examine first the interaction between two points, belonging to the same three-dimensional medium. If their initial configuration is at $\boldsymbol{x}$ and $\boldsymbol{\xi}$, their mutual force is:

$$\mathbf{F}\left(\boldsymbol{x}+\boldsymbol{u}(\boldsymbol{x},t),\boldsymbol{\xi}+\boldsymbol{u}(\boldsymbol{\xi},t)\right)=f(|\mathbf{r_s}|)\mathbf{r_s} \tag{1}$$

where

$$\mathbf{r_s}=\boldsymbol{x}-\boldsymbol{\xi}+\mathbf{u}(\boldsymbol{x},t)-\mathbf{u}(\boldsymbol{\xi},t) \tag{2}$$

and $\mathbf{u}(\boldsymbol{x},t)$ is the displacement in the elastic medium.

The interaction forces are modelled so to have the following properties: i) they guarantee the legitimacy of the action-reaction principle and ii) they decay with the distance, $\lim_{|\mathbf{r}|\to\infty} f(|\mathbf{r}|)\mathbf{r}=0$. These assumptions are conventional for many natural forces as gravitational force, molecular bond, magnetostatic and Coulomb.
Any formulation of the equation of motion, which considers the contribution of these forces, assumes a non-linear feature, since the ordinary concept of short-range interaction is left aside. If this interaction is extended from particle-particle to master-cluster or all-to-all and the particle distribution within the medium is assumed as infinitely dense, the long-range interaction appears as an integral contribution over the entire domain of the solid. The obtained equation of motion for a continuous, unbounded, three-dimensional elastic medium is:

$$\rho\,\mathbf{u}_{tt}(\boldsymbol{x},t)+E\,\mathbf{u}_{xx}(\boldsymbol{x},t)+\int_{\boldsymbol{\xi}\in\mathbb{R}^3} f_1(|\mathbf{r}|)\mathbf{r}\,dV=0 \tag{3}$$

The chance to achieve closed form solutions for the problem of equation (3) has been outlined in [25]. The authors propose a straightforward method to linearise the long-range force with respect to $\mathbf{u}(\boldsymbol{x},t)-\mathbf{u}(\boldsymbol{\xi},t)$, under the assumption of small deformations. Indeed, as long as the force is in the form $\boldsymbol{F}\left(\boldsymbol{r}\right)=f\left(|\boldsymbol{r}|\right)\boldsymbol{r}$, it can be linearised by using Taylor's expansion up to the first order, as:

$$f(|\mathbf{r}|)\mathbf{r}\sim(\boldsymbol{x}-\boldsymbol{\xi})\,f_0+\boldsymbol{h}_0\boldsymbol{\varepsilon}+f_0\boldsymbol{\varepsilon} \tag{4}$$

As shown in [25], the first term represents the static antisymmetric component, the other two are the dynamic components that rule the behaviour of the structure; the former is a second order tensor depending on the

gradient of the force with respect to the distance, the latter is related to the pre-stress exerted by the long-range forces.
The resulting equation of motion, for the dynamic component of the displacement only, is:

$$\rho \mathbf{w}_{tt} + E\mathbf{w}_{xx} + \bar{\boldsymbol{h}_0} \cdot \mathbf{w} - [\boldsymbol{h}_0 * \mathbf{w}] + \bar{f_0}\mathbf{w} - [f_0 * \mathbf{w}] = 0 \tag{5}$$

with clear notation of the symbols (see [25]). The variables are space-dependant.

3 Gauss-like force and one-dimensional approach

The one-dimensional counterpart of equation (5) is here considered, when the long-range interaction force is assumed to be of a Gauss-like type $f(r) = \mu e^{-\beta r^2}$. The parameter μ, which can be either positive or negative depending on whether the actions is attractive or repulsive, controls the intensity of the force. β rules the length of interaction. [25] enlightens the advantages of using such forces, as they accurately model natural forces', and guarantee the achievement of analytical solutions.

According to [25], equation (5) becomes:

$$\rho \frac{\partial^2 w}{\partial t^2} - E\frac{\partial^2 w}{\partial x^2} - g(x) * w(x) = 0 \tag{6}$$

This approach discloses closed form analytical solutions, able to unveil propagation properties and phenomena. Indeed, an analytical expression of the dispersion relationship is obtained:

$$\rho\omega^2 - Ek^2 + G(k) = 0 \tag{7}$$

with $G(k) = \mathcal{F}\{g(x)\} = \dfrac{\mu}{2\sqrt{2}\beta^{\frac{3}{2}}} k^2 e^{-\frac{k^2}{4\beta}}$, if

$$w(x,t) = \iint_{-\infty}^{+\infty} W(k,\omega) e^{j(kx-\omega t)} dk\, d\omega \tag{8}$$

which leads to:

$$\Omega = \pm\sqrt{1 - \chi e^{-\frac{K^2}{4}}} \tag{9}$$

The resulting propagating phenomena have been clearly exposed in [25].

4 Twin waves

Long-range forces are a useful tool to perform desired and unusual propagating behaviours within a structure. Furthermore, the same long-range characteristic opens new scenarios in the coupling between structures and the chance to remotely control some of them arise.
A coupled system, as in Figure 1, consisting of two identical waveguides, is considered. As long as the mutual distance between the two rod-like structures is smaller than the typical interaction length, the inter-body forces play a non-negligible role, which effects the equation of motion and the consequent dynamic behaviour of the overall structure: indeed, the motion of each particle is the result of the actions generated by both its belonging waveguide and the other one.

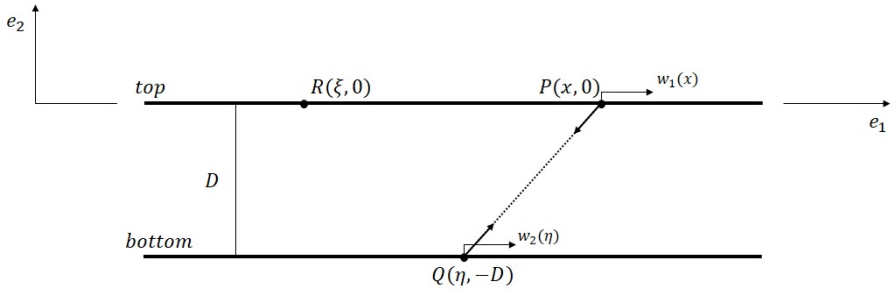


Figure 1: Twin waves model

For this model, it is assumed that i) the cross-interaction depends on the distance between the points $\boldsymbol{P}$ and $\boldsymbol{Q}$, $|\boldsymbol{r}| = \left[(x - \eta + \varepsilon_{d1})^2 + D^2\right]^{\frac{1}{2}}$, where $\varepsilon_{d1} = w_1(x) - w_2(\eta)$, and ii) the motion to be longitudinal only, which means the components on the x-axis are the non-neglected ones.
The long-range force, according to [25], is:

$$\boldsymbol{F}(\boldsymbol{r}) = f(|\boldsymbol{r}|)\,\boldsymbol{r} = f_0 \cdot (\boldsymbol{x} - \boldsymbol{\eta}) + \boldsymbol{h_0 \varepsilon_d} + f_0 \boldsymbol{\varepsilon_d} \tag{10}$$

if the action exerted by the bottom waveguide on the top one is considered, it becomes:

$$\boldsymbol{F}(\boldsymbol{r}) = \mu e^{-\beta |\boldsymbol{r_0}|^2} \begin{bmatrix} (x-\eta) - 2\beta (x-\eta)^2 [w_1(x) - w_2(\eta)] + [w_1(x) - w_2(\eta)] \\ D - 2\beta D (x - \eta) \end{bmatrix} \tag{11}$$

If the forces along the z-axis can be assumed overall balanced, only the x component remains.

$$F_x(x, \eta) = \mu e^{-\beta\left[(x-\eta)^2 + D^2\right]} (x - \eta) - \mu e^{-\beta\left[(x-\eta)^2 + D^2\right]} \left[1 - 2\beta (x - \eta)^2\right] \tag{12}$$

Only the third term produces a non-null result when the integral is applied and the expression of the long-range interaction due to the coupling is:

$$\int_{\eta \in \mathbb{R}} \mu e^{-\beta D^2} e^{-\beta (x-\eta)^2} \left[1 - 2\beta (x - \eta)^2\right] w_2(\eta)\, d\eta = -l(x) * w_2(x) \tag{13}$$

This represents the long-range contribution due to the bottom waveguide on the upper one.

Combining equation (6) and (13), equation (3), which represents the dynamics of the top waveguide, becomes:

$$\rho \frac{\partial^2 w_1(x,t)}{\partial t^2} - E \frac{\partial^2 w_1(x,t)}{\partial x^2} - g(x) * w_1(x) - l(x) * w_2(x) = 0 \tag{14}$$

Similarly, the equation of motion for the bottom waveguide is:

$$\rho \frac{\partial^2 w_2(x,t)}{\partial t^2} - E \frac{\partial^2 w_2(x,t)}{\partial x^2} - g(x) * w_2(x) - l(x) * w_1(x) = 0 \tag{15}$$

5 Insights into the dispersion relationship

If the displacement is assumed as in equation (8), analytic forms of the dispersion relationship can be obtained, with a structure analogous to equation (7).

For $w_1(x,t) = \varphi_1(x)e^{-j\omega t}$ and $w_2(x,t) = \varphi_2(x)e^{-j\omega t}$, the system of dispersion relationships related to the coupled structure is:

$$\begin{cases} -\rho_1\omega^2\Phi_1 + E_1k^2\Phi_1 - G_1\Phi_1 - L\Phi_2 = 0 \\ -\rho_2\omega^2\Phi_2 + E_2k^2\Phi_2 - G_2\Phi_2 - L\Phi_1 = 0 \end{cases} \tag{16}$$

It is convenient to discuss the problem in terms of the non-dimensional parameters $\Omega = \sqrt{\frac{\rho}{E\beta}}\omega$, $K = \frac{1}{\sqrt{\beta}}k$, $\Delta = D\sqrt{\beta}$ and $\chi = \frac{\mu}{2\sqrt{2}E\beta^{\frac{3}{2}}}$. In [25], it was already underlined the importance of the parameter χ, which measures the intensity of the long-range interactions, through their corresponding elastic modulus E^*, with respect to the conventional interactions, represented by the Young's modulus E.
Since the two waveguides are identical, it is reasonable to assume that the displacements in the two rods is a function of the same frequency and wavenumber. This means that the dispersion relationships (16) can be combined in one fourth-order equation, with two couples of solution, here reported:

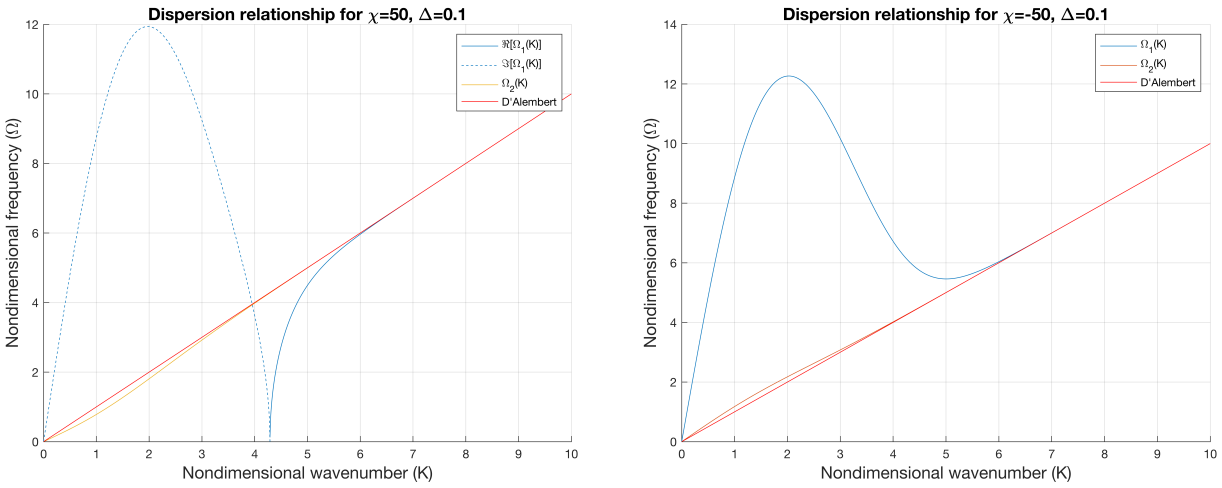
$$\begin{cases} \Omega_1 = \pm\sqrt{K^2 - \chi K^2 e^{-\Delta^2 - \frac{K^2}{4}} - \chi K^2 e^{-\frac{K^2}{4}}} \\ \Omega_2 = \pm\sqrt{K^2 - \chi K^2 e^{-\Delta^2 - \frac{K^2}{4}} + \chi K^2 e^{-\frac{K^2}{4}}} \end{cases} \tag{17}$$

6 Numerical simulations

In [25], it is shown as the parameter χ plays a key role in the dynamic of the one-dimensional waveguide system, conditioning phase and group velocity and, hence, the overall response. It is revealed the arising of new phenomena, as superluminal and hypersonic effects, wave stopping and negative group velocity.
We analyse the *twin-wave* system as extension of the one-dimensional case, aiming at unveiling further intrinsic properties of the long-range interactions and possibly new and various propagating phenomena.
Therefore, the dispersion relationships are examined as varying with respect to the parameter χ.
Figure 2 shows the trend of the nondimensional dispersion relationship for $\chi = -50$ and $\chi = 50$, with respect to the conventional D'Alembert waveguide. A unique curve, one for each solution of Ω, describes the behaviour of the entire system, since the two rods are identical and a single equation contains both the intra-body and the inter-body long-range interaction contributions. The mutual distance between the waveguides is set to $\Delta = 0.1$ and both the positive solutions of Ω are displayed.

For both values of χ, one solution, namely Ω_1, produces interesting effects. When the parameter χ is positive, a region of no propagation appears for low values of the nondimensional wavenumber K. Indeed, for such values of K, only complex values of Ω_1 are obtained. With no chance to damp the divergent contribution of the solution, the system is subdued to instability. A steep slope closes the unstable band and unveils a narrow wavenumber region in which the group velocity tends to infinite and superluminal propagation arises, before the system converges to the D'Alembert model. For negative values of χ, the curve has both a maximum and a minimum, at which the group velocity vanishes. This means that for positive χ the existence of a wave-stopping region is proved. Furthermore, while the positive slope implies conventional propagation, the negative slope reveals negative group velocity. On the other hand, the solution related to Ω_2 does not show remarkable effects. This is due to the destructive combination in the solution between the two long-range contributions, the one related to the intra-body interactions and the one given by the magnetic coupling, which causes the annihilation of the long-range effect.
A propagation map is presented in Figure 3. It shows different propagating scenarios, occurring at the varying of the parameter χ, accordingly with the effects discussed for the dispersion curves. Because of the aforementioned reason, the map is given for Ω_1 only.

Each line is an isofrequency contour. The instability region is surrounded by the superluminal propagation region; the negative group velocity is delimited by the conventional propagation regimes.



(a) Positive χ (b) Negative χ

Figure 2: Dispersion relationship

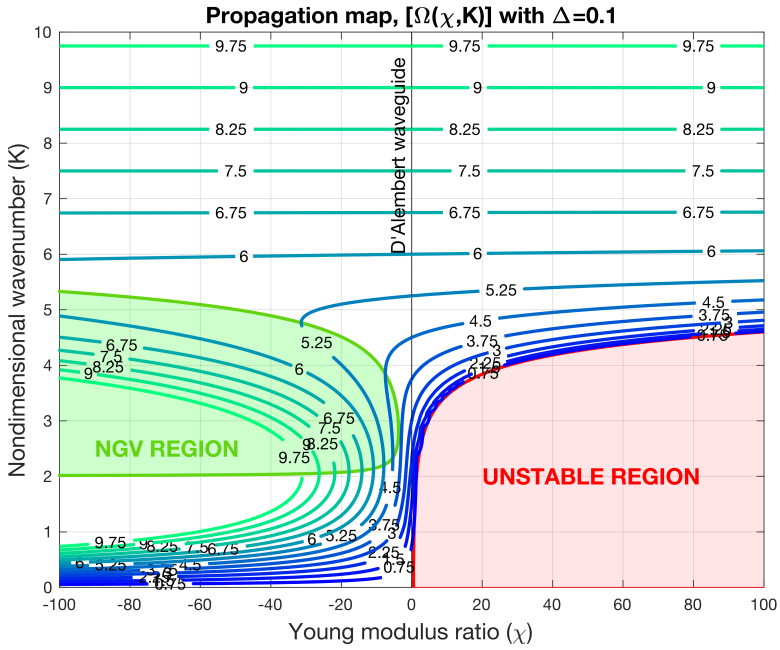


Figure 3: Propagation map

To conclude the investigation, space-time visualization are presented in Figure 4, in which the history line of the displacement in the both waveguides is displayed. According to Figure 2, at low wavenumbers (Figure 4), both phase and group velocity are positive. However, the increasing of the wavenumber induces a changing in the group velocity, which becomes negative and discordant, with respect to the phase velocity.

7 Conclusions

The work here presented shows the effects of long-range interactions on the dynamic of a system composed by two identical waveguides. These nonlocal interactions mimic a magnetic coupling and act additionally with respect to the elastic connections.

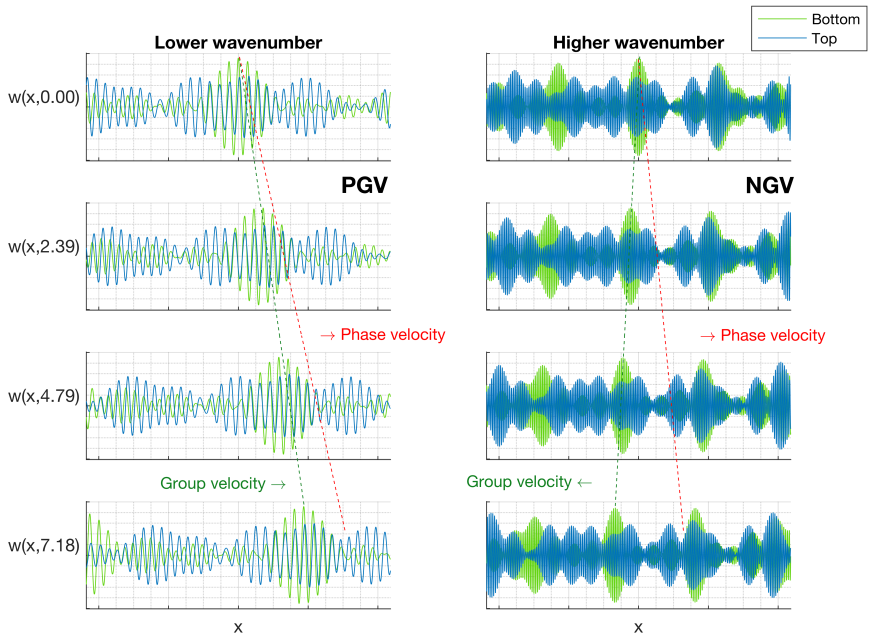


Figure 4: Space-time visualization

The mathematical approach is based on the one proposed in [25], in which a Gauss-like force is used to model the long-range interactions. Its properties have, indeed, the great advantage to produce closed form solutions for the dispersion relationship.
The analysis is discussed in terms of the nondimensional parameter χ, which provides an esteem of the strength of the long-range interactions, through their effective Young's modulus E^*, compared to the conventional ones, represented by E.
Interesting phenomena appear: instability region and superluminal propagation are characteristic effects associated to the dispersion relationship obtained for positive values of χ; wave-stopping and negative group velocity are instead related to negative χ. A propagating map summarises all the possible propagating scenarios. The space-time visualizations conclude and confirmed what previously observed.

References

[1] D. Schurig, J. J. Mock, B. J. Justice, S. A. Cummer, J. B. Pendry, A. F. Starr, and D. R. Smith, "Metamaterial electromagnetic cloak at microwave frequencies," *Science*, vol. 314, pp. 977–980, nov 2006.

[2] J. Hunt, J. Gollub, T. Driscoll, G. Lipworth, A. Mrozack, M. S. Reynolds, D. J. Brady, and D. R. Smith, "Metamaterial microwave holographic imaging system," *Journal of the Optical Society of America A*, vol. 31, p. 2109, sep 2014.

[3] T. A. Schaedler, A. J. Jacobsen, A. Torrents, A. E. Sorensen, J. Lian, J. R. Greer, L. Valdevit, and W. B. Carter, "Ultralight metallic microlattices," *Science*, vol. 334, pp. 962–965, nov 2011.

[4] J. Bauer, S. Hengsbach, I. Tesari, R. Schwaiger, and O. Kraft, "High-strength cellular ceramic composites with 3d microarchitecture," *Proceedings of the National Academy of Sciences*, vol. 111, pp. 2453–2458, feb 2014.

[5] A. Madeo, P. Neff, I.-D. Ghiba, and G. Rosi, "Reflection and transmission of elastic waves in non-local band-gap metamaterials: A comprehensive study via the relaxed micromorphic model," *Journal of the Mechanics and Physics of Solids*, vol. 95, pp. 441–479, oct 2016.

[6] N. Roveri, A. Carcaterra, and A. Akay, "Vibration absorption using non-dissipative complex attachments with impacts and parametric stiffness," *The Journal of the Acoustical Society of America*, vol. 126, pp. 2306–2314, nov 2009.

[7] A. Carcaterra, A. Akay, and I. M. Koç, "Near-irreversibility in a conservative linear structure with singularity points in its modal density," *The Journal of the Acoustical Society of America*, vol. 119, pp. 2141–2149, apr 2006.

[8] A. Carcaterra and A. Akay, "Fluctuation-dissipation and energy properties of a finite bath," *Physical Review E*, vol. 93, mar 2016.

[9] A. Carcaterra and A. Akay, "Dissipation in a finite-size bath," *Physical Review E*, vol. 84, jul 2011.

[10] A. Carcaterra, A. Akay, and C. Bernardini, "Trapping of vibration energy into a set of resonators: Theory and application to aerospace structures," *Mechanical Systems and Signal Processing*, vol. 26, pp. 1–14, jan 2012.

[11] A. Carcaterra, F. dell'Isola, R. Esposito, and M. Pulvirenti, "Macroscopic description of microscopically strongly inhomogenous systems: A mathematical basis for the synthesis of higher gradients metamaterials," *Archive for Rational Mechanics and Analysis*, vol. 218, pp. 1239–1262, may 2015.

[12] *Metamaterials: wave propagation control*, 2016.

[13] V. E. Tarasov and G. M. Zaslavsky, "Fractional dynamics of coupled oscillators with long-range interaction," *Chaos: An Interdisciplinary Journal of Nonlinear Science*, vol. 16, p. 023110, jun 2006.

[14] V. E. Tarasov, "Lattice model of fractional gradient and integral elasticity: Long-range interaction of grÃijnwald–letnikov–riesz type," *Mechanics of Materials*, vol. 70, pp. 106–114, mar 2014.

[15] V. E. Tarasov and G. M. Zaslavsky, "Fractional dynamics of systems with long-range interaction," *Communications in Nonlinear Science and Numerical Simulation*, vol. 11, pp. 885–898, dec 2006.

[16] V. E. Tarasov, "Lattice with long-range interaction of power-law type for fractional non-local elasticity," *International Journal of Solids and Structures*, vol. 51, pp. 2900–2907, aug 2014.

[17] V. E. Tarasov, "Continuous limit of discrete systems with long-range interaction," *Journal of Physics A: Mathematical and General*, vol. 39, pp. 14895–14910, nov 2006.

[18] M. Zingales, "Wave propagation in 1d elastic solids in presence of long-range central interactions," *Journal of Sound and Vibration*, vol. 330, pp. 3973–3989, aug 2011.

[19] M. D. Paola and M. Zingales, "Long-range cohesive interactions of non-local continuum faced by fractional calculus," *International Journal of Solids and Structures*, vol. 45, pp. 5642–5659, oct 2008.

[20] M. D. Paola, G. Failla, and M. Zingales, "Physically-based approach to the mechanics of strong nonlocal linear elasticity theory," *Journal of Elasticity*, vol. 97, pp. 103–130, aug 2009.

[21] M. D. Paola, A. Pirrotta, and M. Zingales, "Mechanically-based approach to non-local elasticity: Variational principles," *International Journal of Solids and Structures*, vol. 47, pp. 539–548, mar 2010.

[22] A. Eringen, "Linear theory of nonlocal elasticity and dispersion of plane waves," *International Journal of Engineering Science*, vol. 10, pp. 425–435, may 1972.

[23] N. Challamel, L. Rakotomanana, and L. L. Marrec, "A dispersive wave equation using nonlocal elasticity," *Comptes Rendus Mécanique*, vol. 337, pp. 591–595, aug 2009.

[24] D. D. Vescovo and I. Giorgio, "Dynamic problems for metamaterials: Review of existing models and ideas for further research," *International Journal of Engineering Science*, vol. 80, pp. 153–172, jul 2014.

[25] A. Carcaterra, F. Coppo, F. Mezzani, and S. Pensalfini, "Long-range retarded elastic metamaterials: wave-stopping, negative and hypersonic group velocity," *Physical Review X*, Under review.

[26] F. Mezzani, F. Coppo, S. Pensalfini, N. Roveri, and A. Carcaterra, "Twin-waves propagation phenomena in magnetically-coupled structures," *Procedia Engineering*, vol. 199, pp. 711–716, 2017.

Control of edge modes in finite vibro-acoustic resonant metamaterials

L. Sangiuliano [1,2], **E. Deckers** [1,2], **C. Claeys** [1,2]
[1] Department of Mechanical Engineering, KU Leuven, Belgium
e-mail: **luca.sangiuliano@kuleuven.be**

[2] DMMS lab, Flanders Make

Abstract
Metamaterials have shown great potential as lightweight and performant vibro-acoustic solutions. Made from conventional materials, metamaterials exhibit stop band behavior resulting from the dynamic interaction between a host structure and its resonant additions on a subwavelength scale. In these stop bands, metamaterials outperform common vibro-acoustic solutions, beating the mass law. Stop band behavior can be predicted in the design stage with unit cell modeling, assuming the metamaterial to be an infinite periodic structure. In any practical application, structures have a finite size and their dynamic behavior is influenced by the boundary conditions. This paper analyzes numerically and experimentally the interaction of a 1D finite sized metamaterial with different boundary conditions. The effect of the edge modes on the predicted stop band behavior is investigated. Two methods are proposed to reduce the influence of edge modes and to achieve the designed stop band behavior performance also in the finite metamaterial system.

1 Introduction

Combining lightweight design with compact dimensions and performant noise, vibrations and harshness treatments in a unique solution has driven the research in the vibro-acoustic field over the past decades. Among novel lightweight vibro-acoustic solutions, locally resonant metamaterials have shown their potential due to their superior noise and vibration insulation properties, be it at least in some targeted frequency ranges referred to as stop bands. Vibrational stop band behavior can be achieved by adding elastic resonant structures to an elastic host structure on a subwavelength scale [1]. Using the unit cell modeling approach [2, 3, 4], the stop bands are predicted by modeling the smallest representative portion of the infinite periodic structure, the unit cell (UC), and by applying periodic Bloch-Floquet boundary conditions [5, 6]. However, in any practical application structures are of finite size. The dynamic behavior of structures is influenced by their dimensions, defects in the lattice and by the boundary conditions. Therefore, the stop band predicted by the UC modeling for the infinite periodic metamaterial system may not be preserved in its finite counterpart and modes with local behavior can occur in the predicted stop band frequency region [7, 8, 9, 10, 11]. These modes can impair the designed stop band performance, by reducing the frequency range of the stop band and the attenuation of the vibrations inside. In other cases, these modes that develop also at the interface matrix-fluid can be exploited to enhance the sound transmission loss of a partition [12]. In order to design efficient metamaterial solutions for any industrial application, it is important on the one hand to assess to which extent a stop band, predicted in an infinite periodic system, is preserved in the finite counterpart and on the other hand to derive guidelines to control these modes.

This paper investigates the interaction of a 1D finite metamaterial beam with different boundary conditions. In particular, it analyses the influence of the edge modes in the finite metamaterial beam on the width of the predicted stop band. A numerical analysis and an experimental validation are presented. For the numerical

analysis, a Finite Element (FE) model describes both the UC of the infinite periodic metamaterial system and its finite counterpart. UC analysis and modal analysis are used to predict stop band behavior in the infinite and finite system, respectively. Numerical results show how edge modes reduce the predicted stop band width in the finite metamaterial system. Two methods are provided to preserve the width of the predicted stop band in the finite metamaterial system, which regard the tuned frequency and the position of the resonant structures in the finite lattice. These methods already showed to control the modes in the predicted stop band observed in phononic crystals [11], in acoustic coating with resonant additions [12] and in locally resonant structures [9], but they are not used to control the edge modes in resonant metamaterials. The numerical findings are experimentally validated with a metamaterial system which consists of an aluminum beam as host structure and beam-like resonators made from polymethyl methacrylate (PMMA) as resonant structures, as used in previous works [13, 14, 15]. A frequency response function (FRF) based comparison is used to correlate the experimental results to the numerical results.

This paper is organized as follows: after the introduction, section 2 describes the host structure, the resonant structures and the metamaterial system. Section 3 discusses stop band behavior in the infinite and finite metamaterial system, using numerical results from the UC analysis and the modal analysis. In section 4 two methods are proposed to eliminate edge modes from the predicted stop band frequency range: numerical and experimental results are presented. The paper ends with the conclusions by summing up the findings.

2 Problem definition

This section briefly describes the host structure and the resonant structures of the 1D metamaterial system. The UC of the metamaterial system is presented. The numerical results for the infinite system and the finite counterpart, obtained with the UC analysis and the modal analysis, respectively, are discussed.

2.1 Host structure

The host structure of the 1D metamaterial system consists of an aluminum beam of rectangular cross-section 30 x 2 mm and length 1080 mm. The combination of material and dimensions of the host structure is chosen to have a flexible system with pronounced modal behavior at the low-frequency range below 1000 Hz.
The material parameters of the host structure are obtained from a rectangular sample of dimensions 276 x 563 x 2 mm, cut out from the same panel from which the host structure is constructed. The density is retrieved through a weight measurement, while the Young's modulus, Poisson's ratio and structural damping are obtained based on the correlation between the mode shapes retrieved with a FE model and the experimentally measured mode shapes. The FE model is modeled in NX Nastran 12 with 9729 linear CQUAD4 shell elements [16] and free boundary conditions. The sample is tested for freely suspended boundary conditions and a roving hammer approach and one lightweight accelerometer, type PCB 352A24 and weight 0.8 g, are used. The retrieved material properties are reported in Table 1. The difference between the mode shapes numerically calculated and experimentally retrieved is less than 1%.

Young's Modulus	Poisson's ratio	Density	Structural damping
68.07 GPa	0.325	2690.2 kg/m^3	0.25%

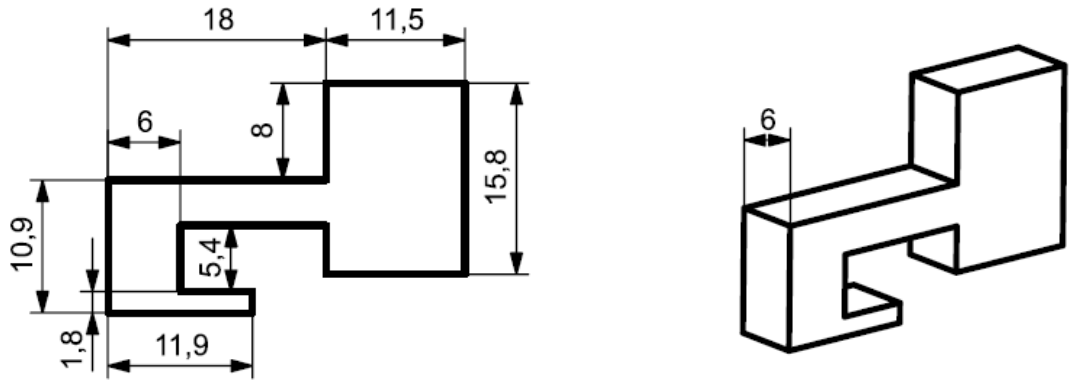
Table 1: Material parameters of the aluminum host structure.

2.2 Resonant structures

The resonance based stop band relies on Fano-like interference [17]. Therefore, stop band behavior is obtained when the resonant structures are added onto the host structure on a scale smaller than the structural

wavelength that propagates in the host structure at the tuned frequency of the resonators [18]. Moreover, the net sum of the forces of the resonant structure on the host structure should be non-zero [19]. To meet these two requirements, the resonator geometry has a similar design as the one used in previous works [13, 14, 15], which consists of a cantilever-like beam and an end point mass. The geometry is shown in Figure 1.

The resonant structures are made by laser cutting PMMA. The material properties of the PMMA are the



(a) (b)

Figure 1: Geometry of the resonant structures. (a) Side view. (b) ISO view. The dimensions are given in mm.

same as used in [13] and they are reported in Table 2. The method to retrieve the material parameters can be found in [13, 15]. The resonant structure is designed to have an out-of-plane mode at 800 Hz. An FE model of the resonant structure is used to predict the resonance frequency. The numerical model consists of 472 linear CHEXA8 solid elements [16] and clamped boundary conditions applied at the base of the resonant structure. As in previous works [13], the resonance frequency of the produced resonators is retrieved by attaching them on a shaker and measuring the velocity at the tip of their end point mass using a Scanning Laser Doppler Vibrometer (SLDV). A set of 35 resonators is measured of which a subset of 18 resonators is chosen. These resonators are chosen in order to have the Root Mean Square (RMS) average of their resonance frequencies of 800 Hz with a spread of $\pm$ 0.9%.

Young's Modulus	Poisson's ratio	Density	Structural damping
4.85 GPa	0.31	1188.4 kg/m^3	5%

Table 2: Material parameters of the PMMA resonant structures.

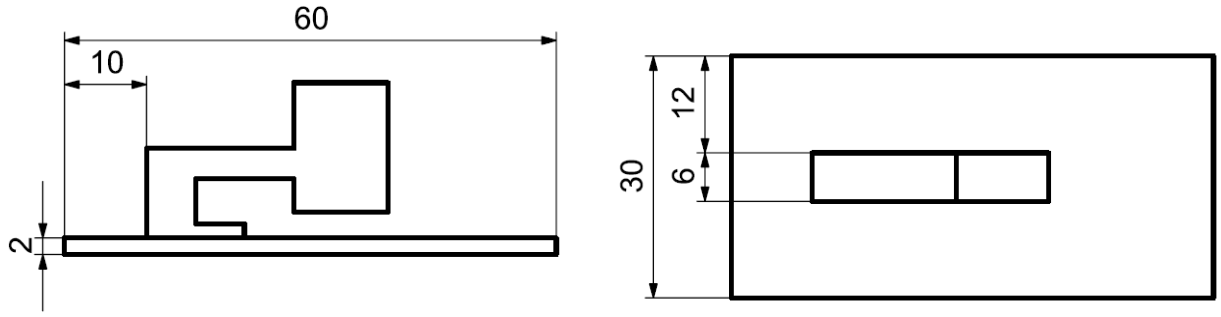
2.3 Metamaterial configuration

The resonant structure is added onto a UC of dimensions 60 x 30 mm, in order to be subwalength at 800 Hz and to achieve stop band behavior. The resonant structures are attached on the host structure with superglue as shown in Figure 2. Each resonant structure adds about 22% of mass to the UC.

The FE model of the metamaterial UC consists of 210 linear CQUAD4 shell elements for the host structure and 472 linear CHEXA8 solid elements for the resonant structure. The finite metamaterial beam consists of 18 UCs repeated along its longitudinal axis.

3 Stop band behavior in infinite and finite structure

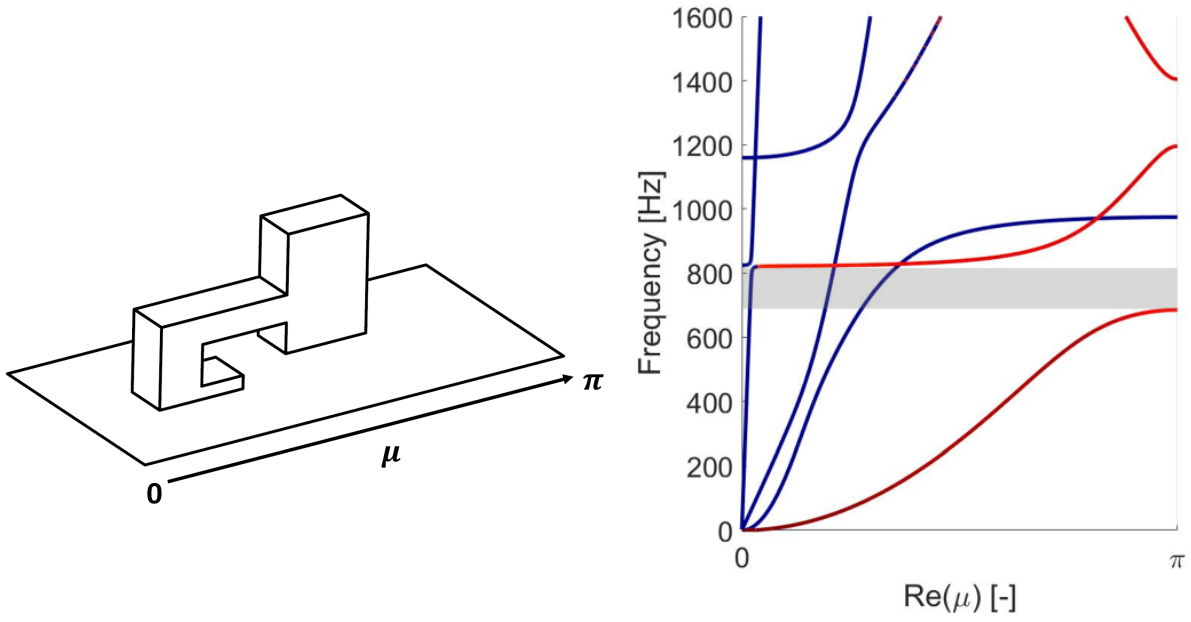
In this paper, stop band behavior in the infinite structure is predicted using UC modeling in combination with Bloch-Floquet periodic boundary conditions. An undamped FE approach is used to model the UC to describe



(a) (b)

Figure 2: Geometry of the UC assembly made by host structure and resonant structure. (a) Side view. (b) Top view. The dimensions are given in mm.

the wave propagation in 1D waveguide systems [4, 5, 6]. The wave propagation direction for the analyzed 1D waveguide is along the longitudinal axis of the beam, as sketched in Figure 3(a). The dispersion diagram in Figure 3(b) shows the results from the UC analysis. A distinction among the curves in the dispersion diagram is made based on percentage of the out-of-plane versus the in-plane motion of the host structure. The waves with an out-of-plane motion greater than 80% with respect to the in-plane motion are considered bending waves and they are indicated in red; all the curves in blue color indicate in-plane, longitudinal and torsional waves. A stop band for the bending waves opens up between 685 Hz and 815 Hz, as indicated by the gray shaded area in Figure 3.



(a) (b)

Figure 3: (a) Sketch of the UC with the resonant element in the reciprocal wave space. (b) Dispersion diagram for the analyzed UC. The horizontal axis represent the real value of propagation constant μ and the vertical axis represents the frequency. The gray shaded area indicates the stop band frequency range for the bending waves.

Stop band behavior in the finite metamaterial system is identified with modal analysis. The natural frequencies of the finite metamaterial system are calculated applying the following boundary conditions:

- simply supported (SS): fixed translations and free rotations. For SS boundary conditions, it is known

that the natural frequencies of the finite structure sample on the dispersion curves of the corresponding infinite periodic structure [20, 21, 22].

- clamped-free (CF): fixed translations and rotations at the left hand side and free translations and rotations at the right hand side. The orientation of the UC in the finite metamaterial system is in accordance with Figure 2. These boundary conditions are chosen because of their extreme kinematic characteristics among the other boundary conditions: no degrees of freedom (DOF) constrained for the free boundary conditions and all the DOF constrained for the clamped boundary conditions.

Figure 4(a) shows the natural frequency distributions for the finite metamaterial beam with SS and CF boundary conditions. For both the SS and CF boundary conditions the natural frequencies mainly lay in the pass band frequency range, with exception of few modes in the predicted stop band frequency range, the latter indicated by the red lines. In the SS case, these modes are torsional, therefore they are not affected by the stop band, which is designed to target the bending waves, as shown in Figure 3(b). In the CF case, besides the torsional modes, two bending modes occur in the predicted stop band. These modes develop from the edges, where they have the highest amplitude and they decay rapidly with the distance from the edge, as observed in Figure 4(b). For their mode shapes, a distinction is made between these two modes. The mode that develops from the clamped boundary conditions, thus named clamped edge mode, has an in-phase motion of the resonator with respect to the host structure. The mode that develops from the free boundaries, thus named free edge mode, has an out-of-phase motion. Because of the presence of the edge modes, the stop band width in the finite metamaterials system with CF boundary conditions is smaller than the one predicted by the UC analysis, whereas for the SS case, the stop band in the finite case coincides with the predicted one.

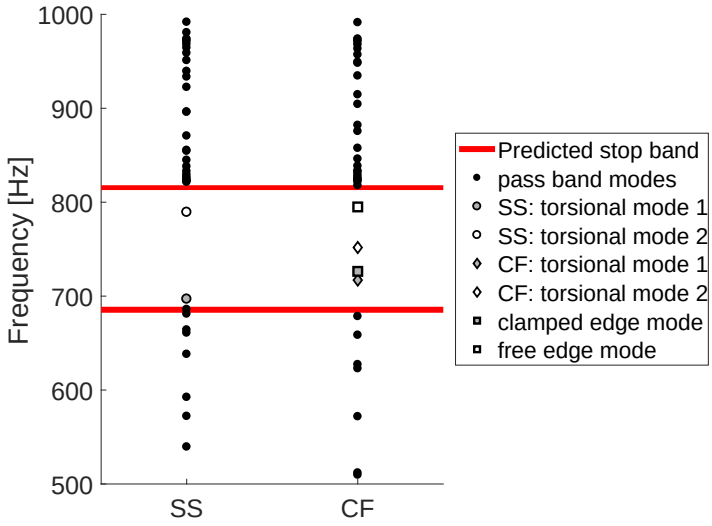
The bending modes of a SS beam can be described by using only the propagating solutions of the beam equation [23]. The undamped UC model indicates in which regions no freely propagating waves are found, and therefore the modes of SS beam will not lie in a stop band [24]. For all the other boundary conditions, the decaying waves together with the propagative waves are solution of the equation of motion of the beam. Therefore, due to the set of propagative and decaying waves that satisfies the CF boundary conditions, edge modes are present in the predicted stop band. This effect is described by other authors as lattice symmetry-breaking, which occurs when a discontinuity in the lattice due to defects [10] or free boundary conditions in phononic crystals [11] breaks the periodicity in the infinite periodic structure.

4 Elimination of edge modes from the predicted stop band

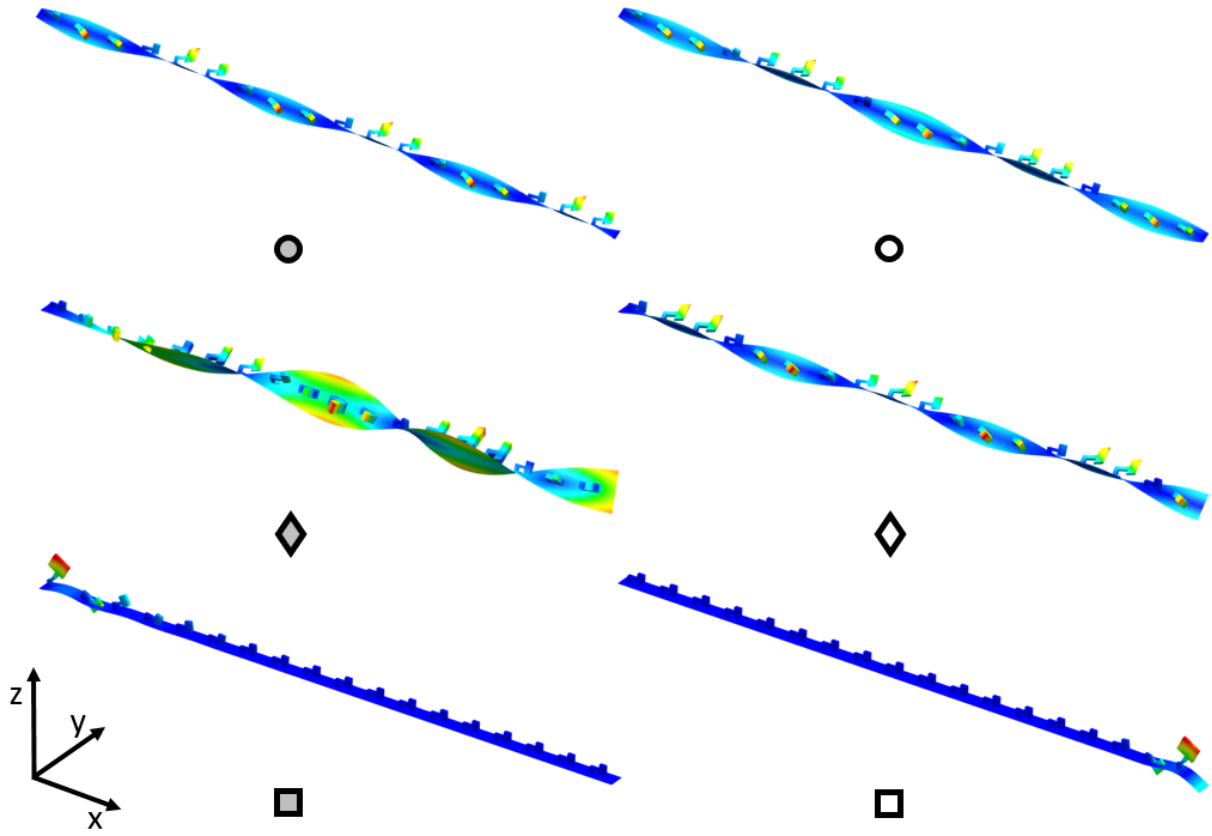
The results in section 3 shows that stop band behavior, predicted with the UC modeling, may be affected by the boundary conditions in the finite metamaterial system. Two methods are proposed in this section, in order to preserve the predicted stop band width and the attenuation of the vibration at its inside also in the finite metamaterial system.
In the first method the tuned frequency of the edge resonators is varied; in the second method the position of the resonators in the lattice is changed. Numerical results and experimental validations are presented.

4.1 Variation of the tuned frequency of the edge resonators

Edge modes are localized modes at the boundary of the finite metamaterial system, as observed in Figure 4(b) and described in section 3. These modes can be controlled by varying locally the mechanical properties of the finite metamaterial system, as proposed in [11, 12]. In this case study, the resonance frequency of the edge resonators is varied with the aim to eliminate the edge mode in the predicted stop band frequency range. This method may be used when there are constraints on the position of the resonant structures during the manufacturing process of the metamaterial system.



(a)



(b)

Figure 4: Numerical results from the modal analysis on the SS and CF metamaterial beam. (a) Natural frequency distribution for the finite metamaterial system with SS and CF boundary conditions (b) Mode shapes of the modes in the predicted stop band frequency range.

4.1.1 Numerical parameter investigation

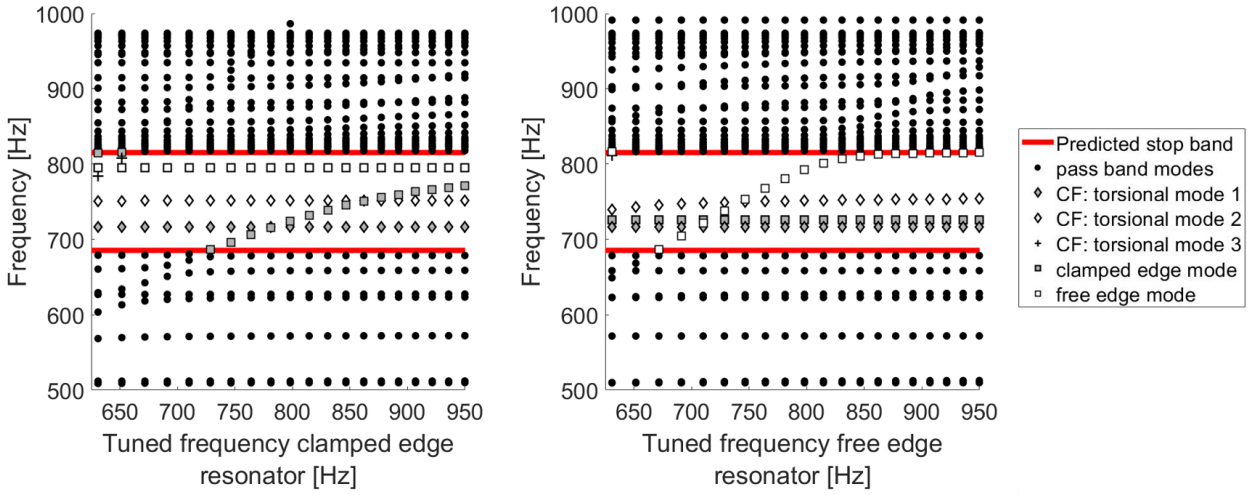
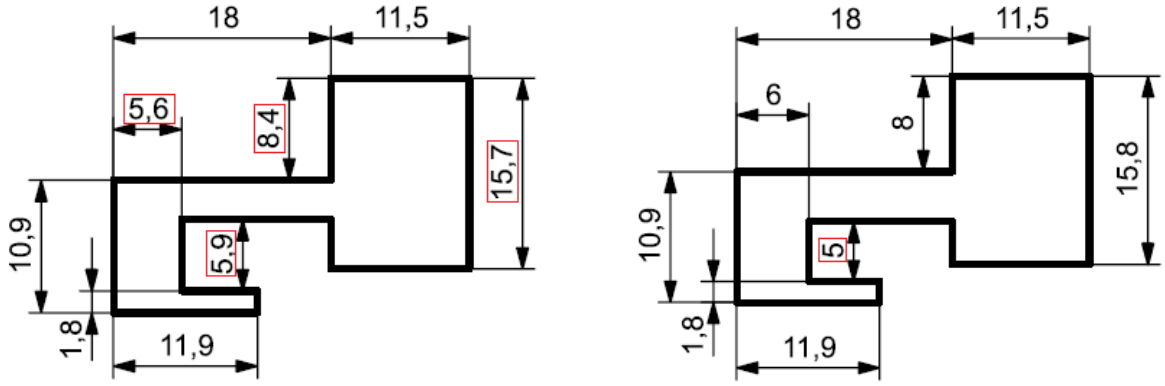


Figure 5: Natural frequency distribution of the CF metamaterial beam with different tuned frequency of the edge resonators. (Left) Variation of the tuned frequency for the clamped edge resonator only. (Right) Variation of the tuned frequency for the free edge resonator only.

A numerical parameter investigation is performed to determine the influence of the resonance frequencies of the resonators at the edge of the host structure on the edge modes of the entire system. In order to perform a fast parameter study, only the Young's Modulus of the resonators at the edge is varied, keeping the geometry of the resonators and the other material properties unchanged. In reality, geometry variation influences both the mass and the stiffness of the resonant structure. However, the approach used in the parameter investigation provides reliable results for small variations of the geometry that leads to a negligible mass variation with respect to the stiffness variation.
The Young's Modulus is varied between $3e9$ GPa and $7e9$ GPa with a step of $0.2e9$ GPa. A modal analysis is run for every configuration. In order to highlight the effect on the modal response of the metamaterial system in the stop band due to the variation of the tuned frequency of the edge resonators, the analysis is performed separately once for the clamped and once for free edge resonator, while keeping the Young's Modulus of the other constant as reported in Table 2. The results of the parameter investigations are shown in Figure 5.
By varying the frequency of the clamped edge resonator, the frequency at which the clamped edge mode occurs is strongly affected, while the other modes inside the stop band remain almost unaffected. The same behavior is observed for the free edge resonator. For the clamped edge resonator, a lower tuned frequency with respect the original one makes the clamped edge mode occur outside the predicted stop band frequency range, below its lower bound. It can also be observed that, when the tuned frequency is below 650 Hz, the clamped edge mode starts occurring again in the predicted stop band from its upper bound in combination with an additional torsional mode, which was not present in the original configuration.
For the free edge resonator, a higher tuned frequency as well as a lower tuned frequency with respect to the original one moves the free edge mode outside the predicted stop band frequency range. However, for low tuned frequencies, no modes are present in the stop band only for a narrow range of values of tuned frequencies, which goes from about 630 to 670 Hz. Therefore, for such low tuned frequencies a good precision in the production of the manufactured resonators and of the entire metamaterial system is required to avoid edge modes in the stop band. Below 630 Hz the free edge mode and an additional torsional mode appears again in the predicted stop band from its upper bound, as observed for the clamped edge resonator.

Based on the results of Figure 5, two new resonator designs are made with a small variation in the beam-like body of the original resonator design: the clamped edge resonator is designed to have a resonance frequency of 663 Hz and the free edge resonator of 913 Hz. The free edge resonator is chosen to be tuned to a higher

frequency rather than a low frequency in order to have a more robust design for the reasons stated in the previous paragraph. Figure 7 shows the natural frequencies distribution for the CF metamaterial system in original and optimized configuration, the latter is the configuration with the edge resonators from Figure 6. In the CF optimized configuration, the torsional modes remain unaffected by the variation of the tuned frequency of the edge resonators, as observed already in the Figure 5. The clamped edge mode is no longer present in the predicted stop band, while the free edge mode occurs right below the upper bound of the predicted stop band.



(a) (b)

Figure 6: (a) Dimensions of the clamped edge resonator. (b) Dimensions of the free edge resonator. The dimensions are given in mm. The dimensions changed with respect to the original design are indicated by the red box.

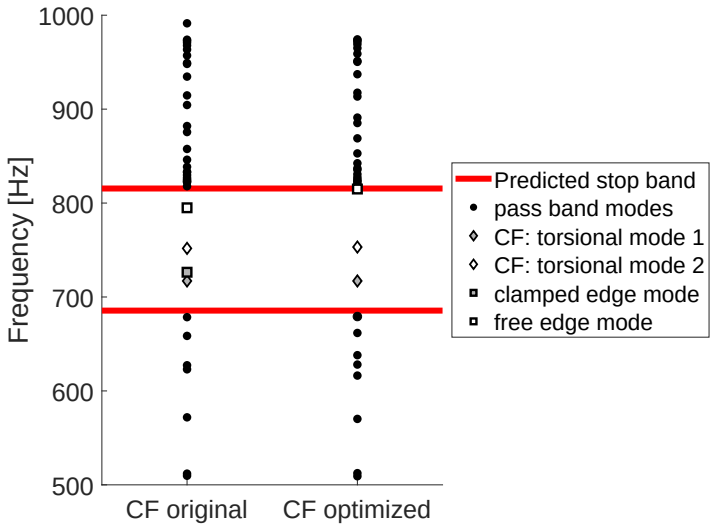


Figure 7: Natural frequency distribution for the CF metamaterial beam in original and optimized configuration.

4.1.2 Experimental setup

The manufactured metamaterial beam is clamped with a heavy clamp of about 15 kg to a rigid aluminum wall as shown in Figure 8. Impact test with hammer excitation is used to excite the metamaterial beam. The vibration response of the system is measured with a Polytec PSV-500 Scanning Laser Doppler Vibrometer

(SLDV). The response of the system is evaluated over 57 points in 19 sections of 3 points each, 1 at the center and 2 at the side of the section, which are located at the edge of each UC. The first section is located close to the clamped boundary, whereas the last section is located at the free boundary. In order to excite both the edge modes and the least the torsional modes in the metamaterial beam, two different excitation locations are chosen: the center point of the first section and the center point of the last section. The RMS value of the Frequency Response Function (FRF) velocity/force $RMS_{\frac{v}{F}}$ is calculated per frequency across the response points, as expressed by equation (1):

$$RMS_{\frac{v}{F}}(\omega) = \sqrt{\frac{1}{N}\sum_{i=1}^{N}\left|\frac{v_i}{F}(\omega)\right|^2}, \tag{1}$$

where ω is the frequency, $\frac{v_i}{F}(\omega)$ indicates the FRF velocity/force per response point and N is the number of response points.

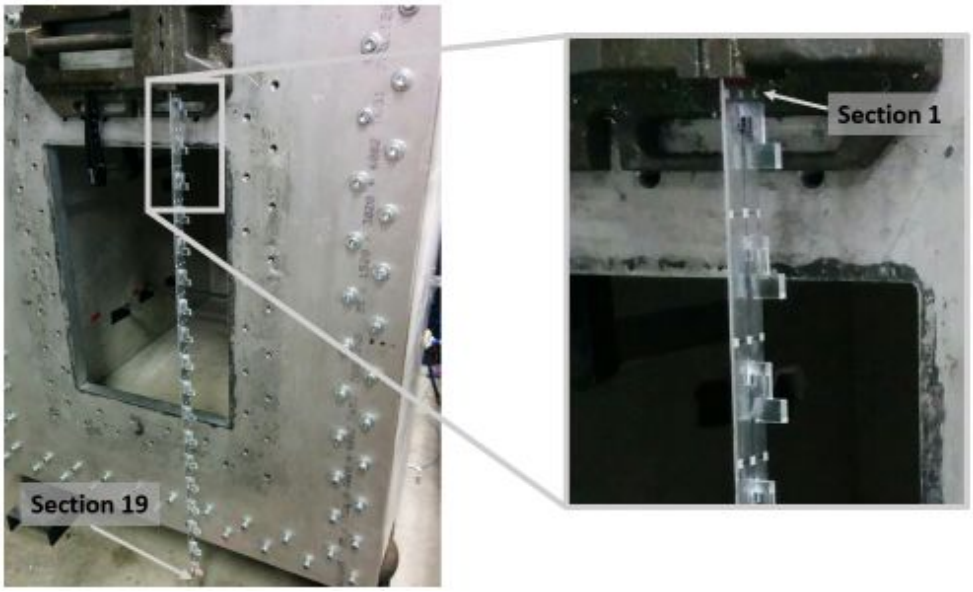


Figure 8: Experimental setup of the CF metamaterial beam. The first and the last measurement sections are indicated.

4.1.3 Experimental and numerical results

Two different configurations of the metamaterial system are tested: the original configuration with all the resonators tuned at the same tuned frequency and the optimized configuration with the new design of the edge resonators shown in Figure 6. The experimental FRFs are correlated with the numerical FRFs calculated in NX Nastran 12 using SOL108 direct frequency response analysis [16]. Figure 9 compares the experimental and numerical results for the original and optimized metamaterial configurations.

In the original metamaterial configuration, the pronounced peaks in the predicted stop band indicate the location of the edge modes and they are well captured by the numerical and experimental results. The small peaks at 717 Hz and 751 Hz are caused by the torsional modes, which are slightly excited during the test. For the excitation at the clamped edge (Figure 9(a)), the edge mode location measured is at higher frequency with respect to the one simulated. This shift can be attributed to the scatter in the resonance frequency of the manufactured resonator and to the accuracy in the position of the resonator from the edge, given that the edge modes are highly sensitive to both the variation of the tuned frequency, as shown in Figure 5, and the position

from the edge, as demonstrated in the following section 4.2. For the excitation at the free edge (Figure 9(b)), the free edge mode location measured is in good agreement with the one calculated numerically.

Comparing the original and the optimized configuration, one can observe that in the latter the peaks are moved from the predicted stop band and the range of attenuation coincides with the designed stop band width. The clamped edge mode shifts below the lower bound of the stop band, whereas the free edge mode moves right to the upper limit of the stop band, as predicted. After the upper bound of the stop band, the optimized configuration has a higher vibration response with respect to the original configuration, due to the redistribution of the modes in that frequency range.

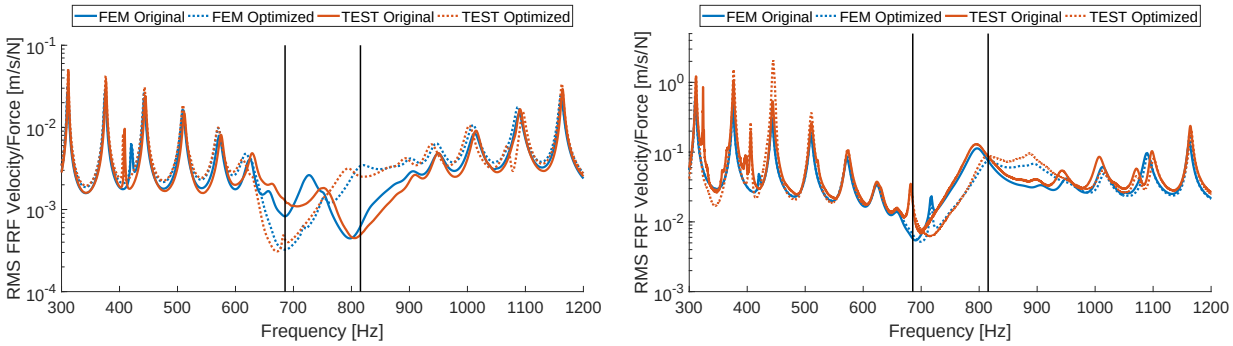


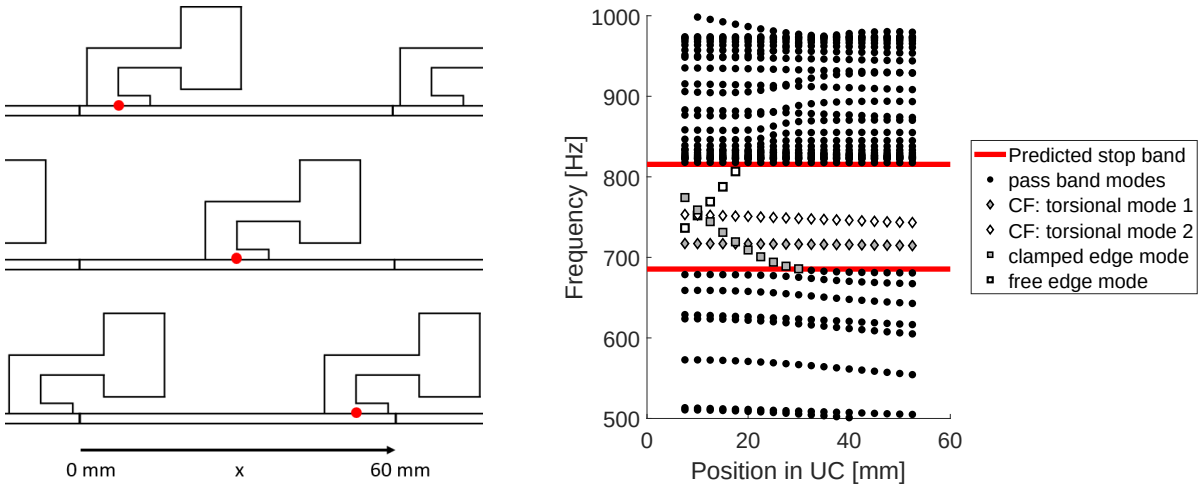
Figure 9: Comparison numerical and experimental FRF for the CF metamaterial beam in original and optimized configuration. (a) Excitation in section 1 at the clamped edge. (b) Excitation in section 19 at the free edge.

4.2 Variation of the position of the resonators in the finite metamaterial system

Section 4.1 demonstrates how the variation of the mechanical properties of the edge resonators can influence the edge modes. In this section, the position of the resonators in the UC in the finite metamaterial system is varied to eliminate the edge modes from the predicted stop band frequency range. In order to preserve the periodicity in the finite metamaterial system, all the resonant structures are moved along the axis of the beam in x direction according to Figure 10(a). On the one hand the stop band predicted by the UC analysis is not affected by moving the position of the resonant structure along the axis the beam, since it is calculated for an infinite periodic system, on the other hand the stop band for the finite metamaterial system may be strongly dependent from the position of the resonant additions, as also stated in [9, 11]. This method can be used when there are no constraints on the position of the resonant structure for the manufacturing process of the metamaterial system.

4.2.1 Numerical parameter investigation

The FE model of the finite metamaterial beam is used to study the sensitivity of the edge modes with respect to the position of the resonant structures in the UC. The results are shown in Figure 10(b). The same resonators of Figure 1 are moved in positive x-axis direction with a step of $2.5mm$. The position of the resonator in the UC is referred to the center of its base, indicated by the red dot in Figure 10(a). One can observe that both the clamped and the free edge modes do not occur anymore in the predicted stop band when the resonant structures are located far from the left edge of the UC. According to the chosen reference system, this results in a configuration with the edge resonators far from the clamped edge and close to the free edge.



(a) (b)

Figure 10: Numerical results for the variation of the position of the resonators in the UC. (a) Sketch of three different positions of the resonators in the UC. The red dot indicates the center of the base of the resonator. (b) Natural frequency distribution of the CF metamaterial beam with respect to the position of the resonator in the UC. The position of the resonator in the UC refers to the red dot in (a).

4.2.2 Experimental validation

The experimental validation of the numerical results are made for the metamaterial configuration with the resonant structure at the center of the UC. The center of the base of the resonator is moved from 16 mm from the edge, as in the previous configuration, to 30 mm from the edge. This configuration is chosen based on the results in Figure 10(b). The picture of the manufactured configuration is shown in Figure 11. The excitation and the response locations are the same used in section 4.1.



Figure 11: Manufactured CF metamaterial beam with resonant structures in the center of the UC.

4.2.3 Experimental and numerical results

As for the previous section, experimental tests and numerical analysis are carried out and compared in Figure 12. The original metamaterial configuration with the resonator at the side of the UC used in the section 4.1

is compared with the metamaterial configuration with the resonator in the center of the UC. The peaks in the predicted stop band are no longer present in the configuration with the resonator in the center of the UC. The clamped edge mode shifts to below the lower bound of the stop band and the free edge mode shifts to above the upper bound of the stop band, as predicted. Moreover, the vibration response after the stop band is lower than the optimized configuration presented in section 4.1, although both of the configurations have no edge modes in the predicted stop band frequency range. Therefore by choosing an optimal location of the resonant structures in the finite metamaterial system the stop band width designed is maintained and the attenuation outside the stop band may be also improved.

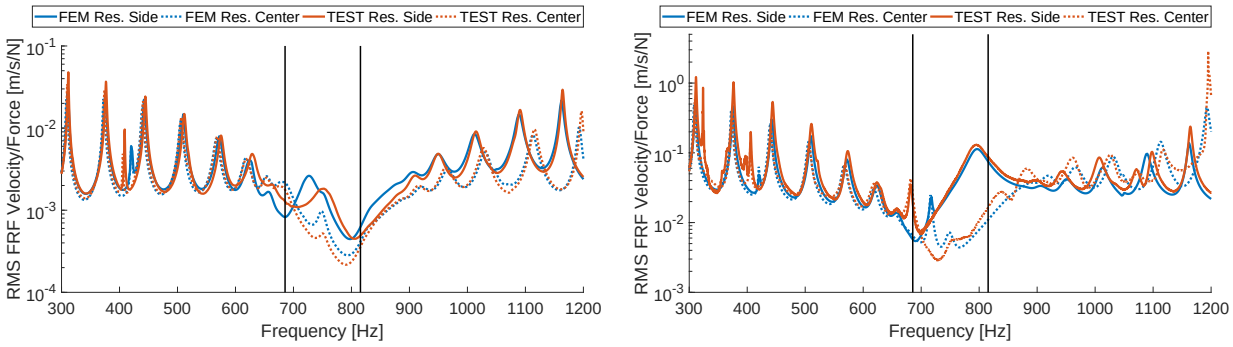


Figure 12: Comparison numerical and experimental FRF for the CF metamaterial beam with the resonators at the side and in the center of the UC. (a) Excitation in section 1 at the clamped edge. (b) Excitation in section 19 at the free edge.

5 Conclusions

This paper investigates the effect of boundary conditions on the stop band width in a finite 1D metamaterial beam. Edge modes in the finite metamaterial system show to reduce the stop band width predicted by the UC analysis. Two methods are proposed to preserve the stop band width for which was designed. The first method consists in varying the resonance frequency of the edge resonators and it may be adopted when there are manufacturing constraints on the position of the resonant structures. The second method consists in varying the position of the resonators in the lattice by retaining the periodicity and it may be used when there are no manufacturing constraints on the position of the resonant structures.

For both methods, a numerical parameter analysis studies the sensitivity of the edge modes with respect to the resonance frequency of the edge resonators and their position in the lattice. Both methods demonstrate to be effective for the elimination of the edge modes from the predicted stop band frequency range. Moreover, an optimal position of the resonators in the lattice provides also an improved attenuation outside the stop band with respect to the configuration with the edge resonators tuned at different resonance frequencies. Experimental results are carried out on the manufactured metamaterial beam. The experimental results are in good correlation with the numerical results and confirm the numerical findings.

Acknowledgements

The Research Fund KU Leuven is gratefully acknowledged for its support. This research was also partially supported by Flanders Make, the Strategic Research Centre for the manufacturing industry. The research of E. Deckers is funded by a grant from the Research Foundation - Flanders (FWO).

References

[1] Z. Liu, X. Zhang, Y. Mao, Y. Zhu, Z. Yang, C. T. Chan, P. Sheng, *Locally resonant sonic materials*, Science, Vol. 289, No. 5485, (2000), pp. 1734–1736.

[2] L. Brillouin, *Wave propagation in periodic structures: electric filters and crystal lattices*, Courier Corporation (2003).

[3] D. Mead, *Wave propagation in continuous periodic structures: research contributions from southampton, 1964–1995*, Journal of sound and vibration, Vol. 190, No. 3, (1996), pp. 495–524.

[4] B. R. Mace, D. Duhamel, M. J. Brennan, L. Hinke, *Finite element prediction of wave motion in structural waveguides*, The Journal of the Acoustical Society of America, Vol. 117, No. 5, (2005), pp. 2835–2843.

[5] B. R. Mace, E. Manconi, *Modelling wave propagation in two-dimensional structures using finite element analysis*, Journal of Sound and Vibration, Vol. 318, No. 4-5, (2008), pp. 884–902.

[6] A. Diaz, A. Haddow, L. Ma, *Design of band-gap grid structures*, Structural and Multidisciplinary Optimization, Vol. 29, No. 6, (2005), pp. 418–431.

[7] A. Hvatov, S. Sorokin, *Free vibrations of finite periodic structures in pass-and stop-bands of the counterpart infinite waveguides*, Journal of Sound and Vibration, Vol. 347, (2015), pp. 200–217.

[8] K. Billon, M. Ouisse, M. Collet, E. Sadoulet-Reboul, *Design of smart metamaterials for vibration control: extension of bloch approach to handle finite system boundary conditions*, *Health Monitoring of Structural and Biological Systems XII*, Vol. 10600, International Society for Optics and Photonics, Vol. 10600, 106001J.

[9] Y. Xiao, J. Wen, G. Wang, X. Wen, *Theoretical and experimental study of locally resonant and bragg band gaps in flexural beams carrying periodic arrays of beam-like resonators*, Journal of Vibration and Acoustics, Vol. 135, No. 4, (2013), pp. 041006.

[10] R. K. Pal, M. Ruzzene, *Edge waves in plates with resonators: an elastic analogue of the quantum valley hall effect*, New Journal of Physics, Vol. 19, No. 2, (2017), pp. 025001.

[11] B. L. Davis, A. S. Tomchek, E. A. Flores, L. Liu, M. I. Hussein, *Analysis of periodicity termination in phononic crystals*, *ASME 2011 International Mechanical Engineering Congress and Exposition*, American Society of Mechanical Engineers, 973–977.

[12] P. Méresse, C. Audoly, C. Croënne, A.-C. Hladky-Hennion, *Acoustic coatings for maritime systems applications using resonant phenomena*, Comptes Rendus Mecanique, Vol. 343, No. 12, (2015), pp. 645–655.

[13] C. Claeys, N. G. R. de Melo Filho, L. Van Belle, E. Deckers, W. Desmet, *Design and validation of metamaterials for multiple structural stop bands in waveguides*, Extreme Mechanics Letters, Vol. 12, (2017), pp. 7–22.

[14] A. Nateghi, L. Sangiuliano, C. Claeys, E. Deckers, B. Pluymers, W. Desmet, *Vibration attenuation in pipes: design and experimental validation of a resonant metamaterial solution*, *6th ECCOMAS Thematic Conference on Computational Methods in Structural Dynamics and Earthquake Engineering*, 17379–17379.

[15] L. Sangiuliano, C. Claeys, E. Deckers, B. Pluymers, W. Desmet, *Force isolation by locally resonant metamaterials to reduce nvh*, *SAE Technical Paper*, 01-1544, SAE International.

[16] Siemens, *NX Nastran 12, Quick Reference Guide*, Siemens PLM Software Inc. (2017).

[17] C. Goffaux, J. Sánchez-Dehesa, A. L. Yeyati, P. Lambin, A. Khelif, J. Vasseur, B. Djafari-Rouhani, *Evidence of fano-like interference phenomena in locally resonant materials*, Physical review letters, Vol. 88, No. 22, (2002), pp. 225502.

[18] C. C. Claeys, K. Vergote, P. Sas, W. Desmet, *On the potential of tuned resonators to obtain low-frequency vibrational stop bands in periodic panels*, Journal of Sound and Vibration, Vol. 332, No. 6, (2013), pp. 1418–1436.

[19] G. Wang, X. Wen, J. Wen, L. Shao, Y. Liu, *Two-dimensional locally resonant phononic crystals with binary structures*, Physical review letters, Vol. 93, No. 15, (2004), pp. 154302.

[20] G. S. Gupta, *Natural flexural waves and the normal modes of periodically-supported beams and plates*, Journal of Sound and Vibration, Vol. 13, No. 1, (1970), pp. 89–101.

[21] D. Mead, S. Parthan, *Free wave propagation in two-dimensional periodic plates*, Journal of Sound and Vibration, Vol. 64, No. 3, (1979), pp. 325–348.

[22] C. C. Claeys, P. Sas, W. Desmet, *On the acoustic radiation efficiency of local resonance based stop band materials*, Journal of Sound and Vibration, Vol. 333, No. 14, (2014), pp. 3203–3213.

[23] L. Cremer, M. Heckl, *Structure-borne sound: structural vibrations and sound radiation at audio frequencies*, Springer Science & Business Media (2013).

[24] D. J. Mead, *Free wave propagation in periodically supported, infinite beams*, Journal of Sound and Vibration, Vol. 11, No. 2, (1970), pp. 181–197.

Formation mechanisms of vibration bandgaps based on block diagrams of wave transmission

S. Tomita[1], S. Nakano[1], R. Omote[1]
[1] Toyota Central R&D Labs., Inc.
41-1, Yokomichi, Nagakute, Aichi 480-1192, Japan
e-mail: **stomita@.tytlabs.co.jp**

Abstract

Structural design, with respect to lightweighting, is required to reduce the environmental burden. However, typical lightweighting requirements conflict with the noise and vibration (NV) performance. To satisfy both a combination of lightweighting and NV performance, vibro-acoustic metamaterials are being investigated as innovative alternatives. These metamaterials have wave filtering characteristics, referred to as bandgaps, which are caused by structural periodicities. To apply vibro-acoustic metamaterials for engineering applications, it is important to adequately address the finite periodic structures.

This paper presents an analytical model of wave transmission to determine the bandgaps of finite periodic structures. To understand the formation mechanism of these band gaps, we employ a one-dimensional waveguide for modelling, and show block diagrams of elastic wave propagation inside periodic structures. Finally, the finite periodic structures are optimized to minimize the transmission ratio of elastic waves.

1 Introduction

Structural design, with respect to lightweighting, is required to reduce environmental burden. However, typical lightweighting requirements conflict with the noise and vibration (NV) performance. It is a challenging task to satisfy the combination of lightweighting and the NV performance. To effectively address this trade-off problem, vibro-acoustic metamaterials have been investigated as an innovative lightweighting approach. These metamaterials have elastic wave filtering characteristics referred to as bandgaps, which are formed by structural periodicities. By applying the metamaterials for vibration transfer path, it is possible to reduce sound radiation using less additional mass.

Mathematical analysis methods to obtain the bandgaps of periodic structures are well-established. For example, it was reported that the bandgaps could be obtained from a unit cell by assuming a periodic boundary condition and Bloch's theorem [1]. Based on this method, the effects of the structural periodicities on the formation of the bandgaps were investigated [2]. In addition, Claeys et al. investigated changes of the bandgaps caused by the distribution of local resonators in a unit cell [3]. In this way, the formation mechanism of the bandgaps was researched in detail. However, these studies assume periodic boundary conditions. Thus, they are only appropriate for structures with finite and exact periodicities.

On the other hand, it is important to consider finite periodic structures to apply vibro-acoustic metamaterials to engineering products. Furthermore, it is known that varying the structural parameters of unit cells improves NV performance. For example, Reichl et al. demonstrated that the vibration response of one-dimensional (1D) metamaterials with heterogeneously distributed local resonators could be reduced relative to those with homogeneously distributed local resonators using H_2 norm related to the area under the frequency response function of a lumped mass model [4]. Furthermore, Ba'ba'a et al. noted that the bandgaps of finite lumped metamaterials are related to the poles of the transfer function [5]. These studies indicate that it is important to consider varying the structural parameters of unit cells for optimization of bandgaps.

This paper presents an analytical model of wave transmission to obtain bandgaps of finite periodic structures with unit cells of varying structural parameters. To understand the formation mechanism of bandgaps, we adopt 1D waveguides for construction of the analytical model and provide block diagrams of elastic wave propagation inside the periodic structures. Furthermore, we optimize the distribution of the structural parameters to extend the frequency ranges of bandgaps based on the present model.

In Section 2 of this paper, the analytical model of wave transmission is presented, and the model is expressed as a block diagram. In Section 3, the model is verified by comparing the wave filtering characteristics to the dispersion curve obtained using a method based on Bloch's theorem. In Section 4, the parameters of the present model are optimized to minimize the transmission ratio. Finally, the conclusions of this paper are highlighted in Section 5.

2 Modelling elastic wave propagation in 1D structure

This section outlines the analytical model used to obtain the bandgaps of finite periodic structures. Furthermore, the model is expressed as a block diagram to better understand the formation mechanism of the bandgaps.

2.1 Block diagram model

Firstly, the transmission matrix of an element is formulated as shown in Figure 1.

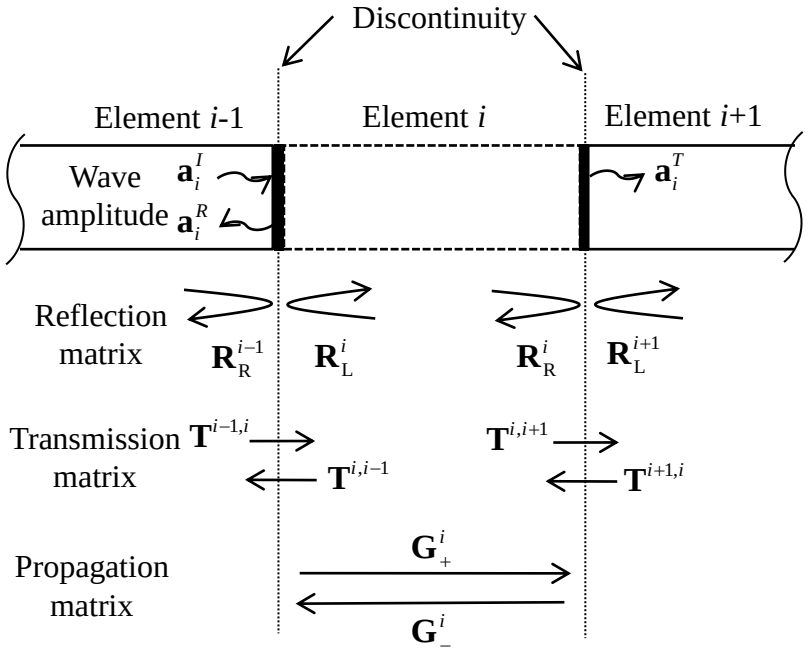


Figure 1: Definition of transmission, reflection and propagation matrices

The relationship between the incident and reflected waves at the left discontinuity of the element is expressed as follows:

$$\mathbf{a}_i^R = \mathbf{R}_{\mathrm{D}}^i \mathbf{a}_i^I , \tag{1}$$

where $\mathbf{a}_i^R, \mathbf{a}_i^I$ are vectors of amplitudes of the reflected and incident waves, $\mathbf{R}_{\mathrm{D}}^i$ is the reflection matrix as expressed in Equation (2).

$$\mathbf{R}_{\mathrm{D}}^i = \mathbf{R}_{\mathrm{R}}^i + \mathbf{T}^{i+1,i}\left(\mathbf{I} - \mathbf{G}_{-}^i \mathbf{R}_{\mathrm{R}}^i \mathbf{G}_{+}^i \mathbf{R}_{\mathrm{L}}^i\right)^{-1} \mathbf{G}_{-}^i \mathbf{R}_{\mathrm{R}}^i \mathbf{G}_{+}^i \mathbf{T}^{i-1,i}. \tag{2}$$

In addition, a block diagram of wave reflection is expressed as shown in Figure 2.

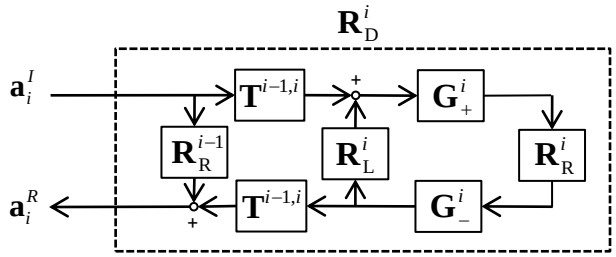


Figure 2: Block diagram of wave reflection (one element)

Next, the relationship between the incident and transmitted waves at the element is expressed as follows:

$$\mathbf{a}_i^T = \mathbf{T}_{\mathrm{E}}^i \mathbf{a}_i^I, \tag{3}$$

where $\mathbf{a}_i^T$ is a vector of amplitude of the transmitted wave, $\mathbf{T}_{\mathrm{E}}^i$ is a transmission matrix as expressed in Equation (4).

$$\mathbf{T}_{\mathrm{E}}^i = \mathbf{T}^{i,i+1}\left(\mathbf{I} - \mathbf{G}_{+}^i \mathbf{R}_{\mathrm{L}}^i \mathbf{G}_{-}^i \mathbf{R}_{\mathrm{R}}^i\right)^{-1} \mathbf{G}_{+}^i \mathbf{T}^{i-1,i}. \tag{4}$$

In addition, a block diagram of wave reflection shown in Figure 3.

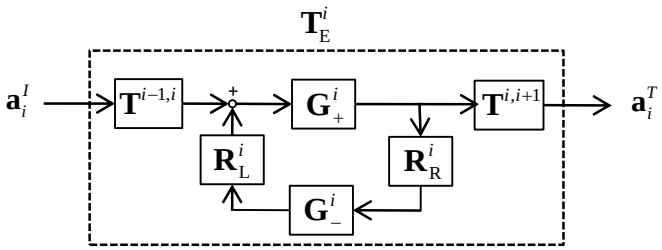


Figure 3: Block diagram of wave transmission (one element)

Based on the above formulation, wave transmission of the periodic structure (Figure 4) is defined.

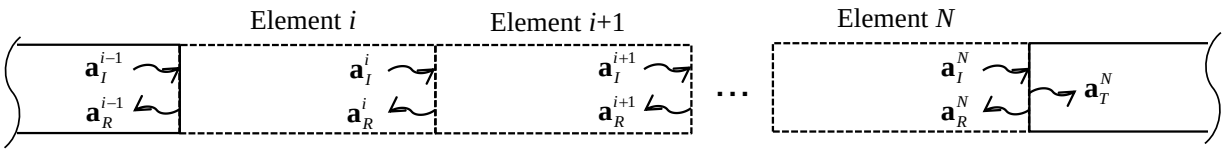


Figure 4: Block diagram of wave transmission (N elements)

Reflection at the left discontinuity of *i*-th element is expressed as follows:

$$\mathbf{a}_i^R = \mathbf{R}_{\mathrm{D}}^i \mathbf{a}_i^I , \tag{5}$$

where $\mathbf{R}_{\mathrm{D}}^i$ is a reflection matrix shown in Equation (6).

$$\mathbf{R}_{\mathrm{D}}^i = \mathbf{R}_{\mathrm{R}}^i + \mathbf{T}^{i+1,i}\left(\mathbf{I} - \mathbf{G}_-^i \mathbf{R}_{\mathrm{D}}^{i+1} \mathbf{G}_+^i \mathbf{R}_{\mathrm{L}}^i\right)^{-1} \mathbf{G}_-^i \mathbf{R}_{\mathrm{D}}^{i+1} \mathbf{G}_+^i \mathbf{T}^{i-1,i} . \tag{6}$$

A block diagram of the reflection is shown in Figure 5(a). The reflection matrices $\mathbf{R}_{\mathrm{D}}^i$ ($i = i+1, \ldots, N$) are nested functions. Using these reflection matrices, transmission from the *i*-th to the *N*-th element can be expressed as follows:

$$\mathbf{a}_N^T = \mathbf{T}^{iN} \mathbf{a}_i^I , \tag{7}$$

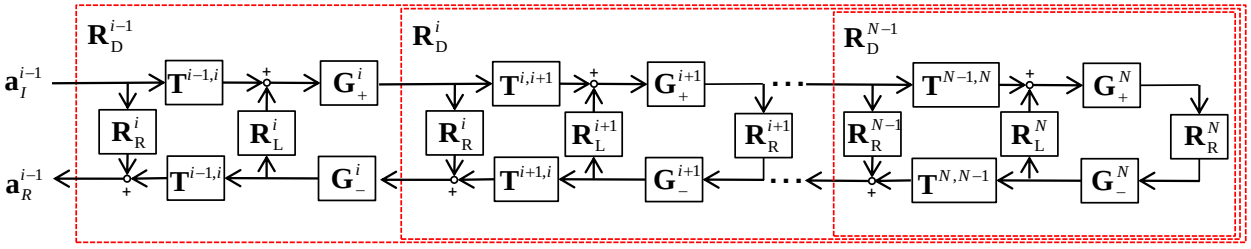
where $\mathbf{T}^{iN}$ is a transmission matrix as expressed in Equation (8).

$$\mathbf{T}^{iN} = \mathbf{T}^N \prod_{i}^{N-1} (\mathbf{I} - \mathbf{G}_+^i \mathbf{R}_{\mathrm{L}}^i \mathbf{G}_-^i \mathbf{R}_{\mathrm{D}}^{i+1})^{-1} \mathbf{G}_+^i \mathbf{T}^{i-1,i} . \tag{8}$$

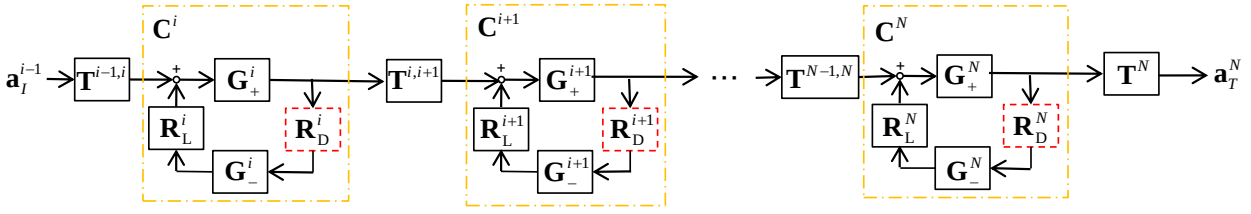
A block diagram of the wave transmission is shown in Figure 5 (b). If $(\mathbf{I} - \mathbf{G}_-^i \mathbf{R}_L^i \mathbf{G}_+^i \mathbf{R}_D^{i+1})^{-1} \mathbf{G}_+^i$ is replaced as expressed in Equation (9), the block diagram can be simplified as shown in Figure 5 (c).

$$\mathbf{C}^i = (\mathbf{I} - \mathbf{G}_+^i \mathbf{R}_{\mathrm{L}}^i \mathbf{G}_-^i \mathbf{R}_{\mathrm{D}}^{i+1})^{-1} \mathbf{G}_+^i . \tag{9}$$

As shown above, wave transmission of the periodic structures can be expressed by a repetition of **T** (the transmission matrices of each discontinuity) and **C** (the matrices of wave loop in each element).



(a) Block diagram of wave reflection



(b) Block diagram of wave transmission



(c) A simplified block diagram of wave transmission

Figure 5: Block diagrams of transmission and reflection of the periodic structures

2.2 Transmission, reflection and propagating matrices

The transmission, reflection and propagating matrices are defined using analytical solutions of flexural waves based on Euler-Bernoulli beam theory [6]. The generalized displacement and internal force vectors **w** and **f** are defined as follows:

$$\mathbf{w} = \begin{bmatrix} v & \theta \end{bmatrix}^T, \ \mathbf{f} = \begin{bmatrix} m & f \end{bmatrix}^T, \tag{10}$$

where, v , θ, m and f are the displacement, slope, moment and force, respectively. The relationship between these vectors is defined as follows:

$$\begin{Bmatrix} \mathbf{w} \\ \mathbf{f} \end{Bmatrix} = \begin{bmatrix} \boldsymbol{\Psi}^+ & \boldsymbol{\Psi}^- \\ \boldsymbol{\Phi}^+ & \boldsymbol{\Phi}^- \end{bmatrix} \begin{Bmatrix} \mathbf{a}^+ \\ \mathbf{a}^- \end{Bmatrix}, \tag{11}$$

where **a** is the wave amplitude vector, $\boldsymbol{\Psi}$ represents the displacement matrices as expressed in Equation (12), and $\boldsymbol{\Phi}$ represents the internal force matrices as expressed in Equation (13). The subscripts + and – indicate the positive and negative deflection of wave propagation, respectively.

$$\boldsymbol{\Psi}^+ = \begin{bmatrix} 1 & 1 \\ -jk_b & -k_b \end{bmatrix}, \ \boldsymbol{\Psi}^- = \begin{bmatrix} 1 & 1 \\ jk_\mathrm{b} & k_\mathrm{b} \end{bmatrix}, \tag{12}$$

$$\boldsymbol{\Phi}^+ = \begin{bmatrix} -jk_b^3 & k_b^3 \\ -k_b^2 & k_b^2 \end{bmatrix}, \ \boldsymbol{\Phi}^- = \begin{bmatrix} jk_b^3 & -k_b^3 \\ -k_b^2 & k_b^2 \end{bmatrix}, \tag{13}$$

where k_b is wave number of the flexural wave as expressed in Equation (14).

$$k_\mathrm{b} = \sqrt[4]{\frac{\rho A}{EI}\omega^2}, \tag{14}$$

where ω is frequency, E is Young's modulus, A is the cross-sectional area, and ρ is the mass density. The propagating matrix can be expressed using the wave number, as follows.

$$\mathbf{G}^\pm = \begin{bmatrix} e^{-jk_b l} & 0 \\ 0 & e^{-k_b l} \end{bmatrix}, \tag{15}$$

where l represents the length of the beam element. The displacement continuity and force equilibrium conditions are expressed as follows:

$$\mathbf{w}_\mathrm{A} = \mathbf{w}_\mathrm{B}, \tag{16}$$

$$\mathbf{f}_\mathrm{A} = \mathbf{f}_\mathrm{B}. \tag{17}$$

The reflection and transmission at a discontinuity of the beam shown in Figure 6 are defined as follows:

$$\mathbf{a}_\mathrm{A}^- = \mathbf{R}\mathbf{a}_\mathrm{A}^+, \ \mathbf{a}_\mathrm{B}^+ = \mathbf{T}\mathbf{a}_\mathrm{A}^+. \tag{18}$$

Substituting Equation (11) into Equation (16) and (17), the reflection and transmission matrices **R**, and **T** can be given by Equation (19) and (20).

$$\mathbf{R} = -\left[-\boldsymbol{\Phi}_\mathrm{B}^+(\boldsymbol{\Psi}_\mathrm{B}^+)^{-1}\boldsymbol{\Psi}_\mathrm{A}^- + \boldsymbol{\Phi}_\mathrm{A}^-\right]^{-1}\left[-\boldsymbol{\Phi}_\mathrm{B}^+(\boldsymbol{\Psi}_\mathrm{B}^+)^{-1}\boldsymbol{\Psi}_\mathrm{A}^+ + \boldsymbol{\Phi}_\mathrm{A}^-\right], \tag{19}$$

$$\mathbf{T} = -\left[\boldsymbol{\Phi}_{\mathrm{A}}^{-}(\boldsymbol{\Psi}_{\mathrm{A}}^{-})^{-1}\boldsymbol{\Psi}_{\mathrm{B}}^{+} - \boldsymbol{\Phi}_{\mathrm{B}}^{+}\right]^{-1}\left[\boldsymbol{\Phi}_{\mathrm{A}}^{-}(\boldsymbol{\Psi}_{\mathrm{A}}^{-})^{-1}\boldsymbol{\Psi}_{\mathrm{A}}^{+} - \boldsymbol{\Phi}_{\mathrm{A}}^{-}\right]. \tag{20}$$

As previously seen, the reflection, transmission, and propagating matrices are defined to compute the analytical model, as expressed in Equation (8).

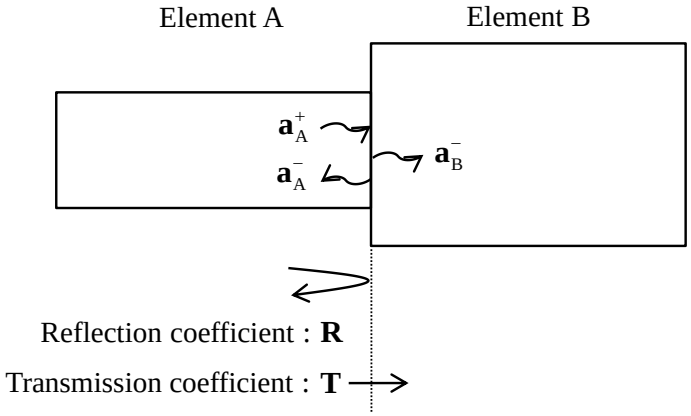


Figure 6: Discontinuity of Euler-Bernoulli beam

3 Formation of bandgaps

3.1 Periodic structure

The transmission ratio of a periodic structure is computed using the commercial software MATLAB R2017b (Mathworks, Inc). The periodic structure has a periodicity of the cross-section area as shown in Figure 7 and Table 1. The computed transmission ratio of the flexural wave is shown in Figure 8. The transmission ratio near 1500 Hz decreases in association with an increase of the number of unit cells.

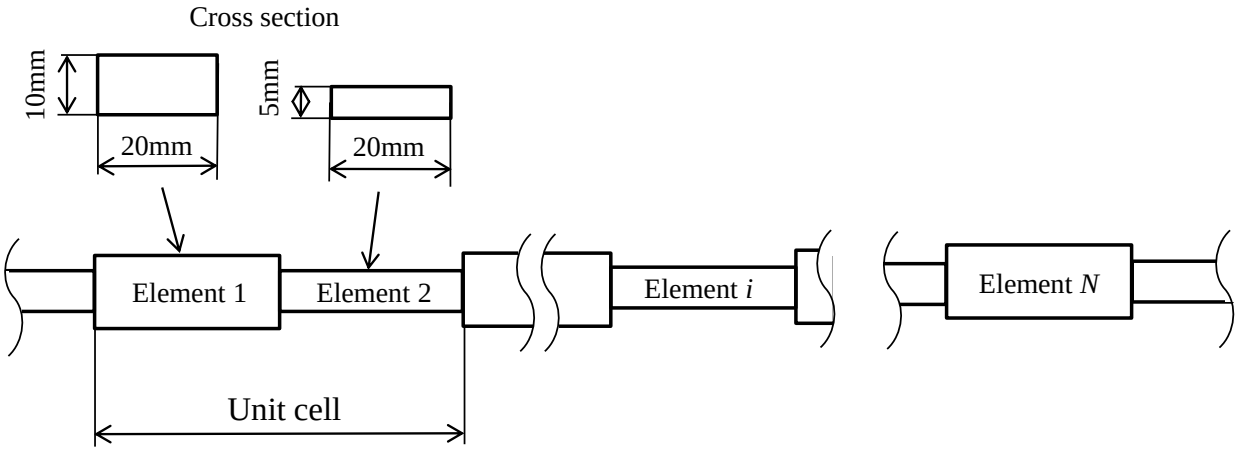


Figure 7: Example of periodic structure

Table 1: Parameters of periodic structure

Element	Young's modulus[GPa]	Density [kg/m^3]	Length [m]	Area [m^2]	Second moment of area [m^4]
i : odd	210	7.8×10^3	0.05	1.0×10^{-4}	2.08×10^{-10}
i : even				2.0×10^{-4}	1.67×10^{-9}

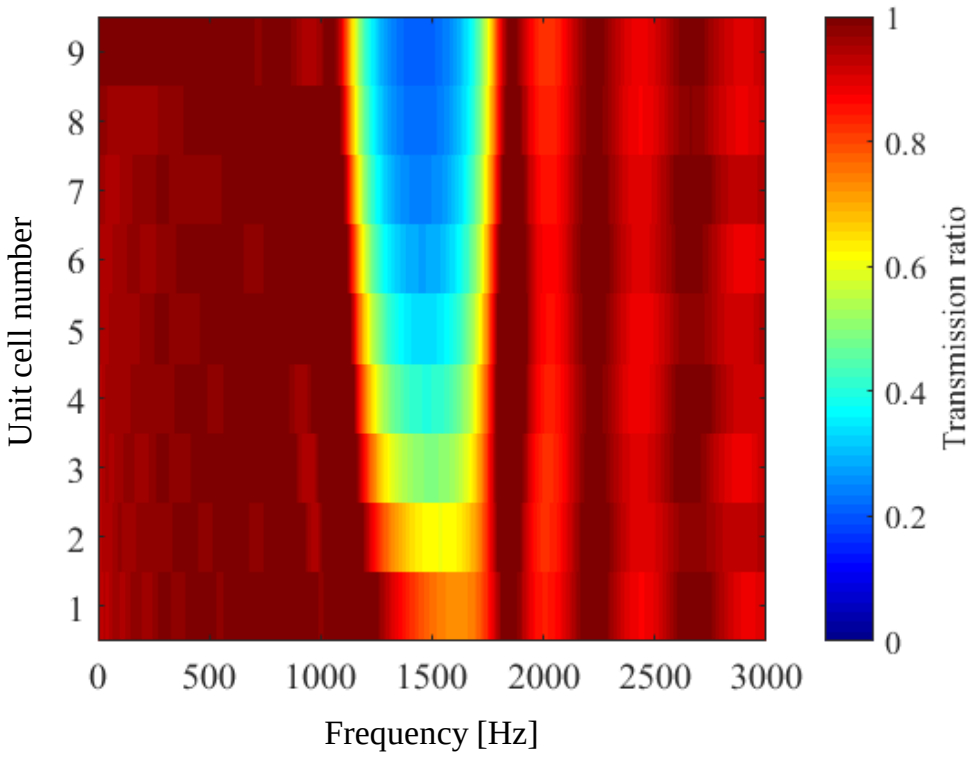
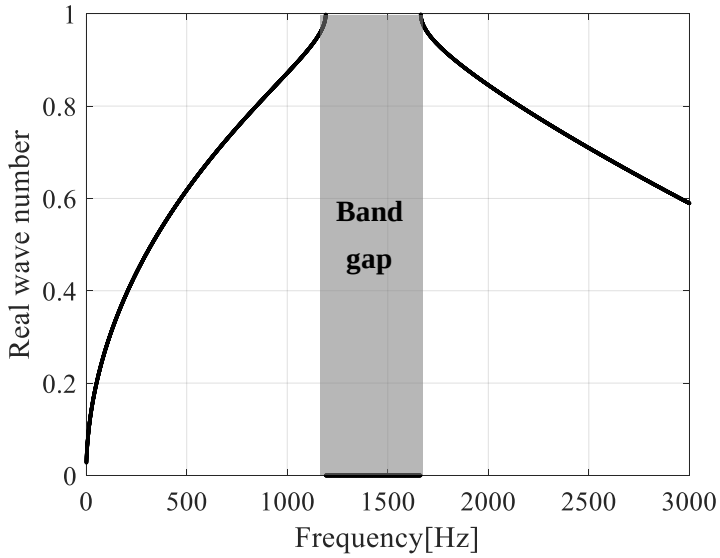


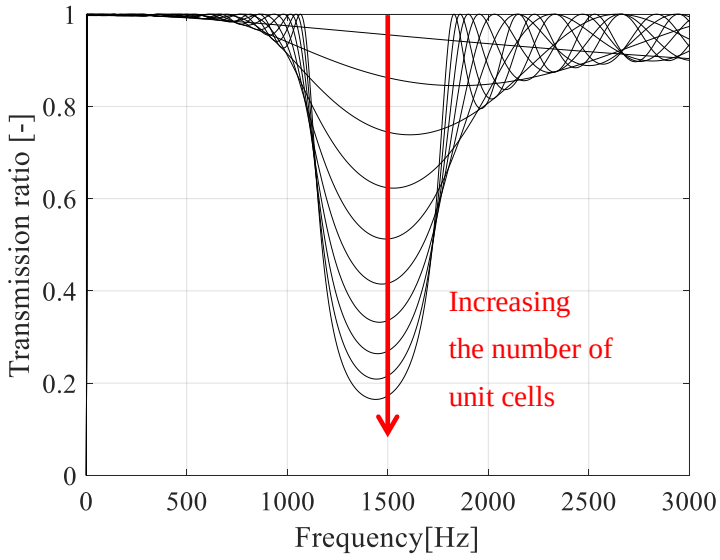
Figure 8: Formation of bandgap

3.2 Verification of wave propagation modelling

To verify the analytical model, the transmission ratio is compared to a dispersion curve obtained using a method based on Bloch's theorem. Figure 9 (a) shows the dispersion curve obtained by this method. The dispersion curve gives a bandgap near 1500 Hz. Figure 9 (b) shows the transmission ratio of the flexural wave computed by the presented analytical model. The frequency range with the reduced transmission ratio is in agreement with the bandgap frequency. Thus, it is verified that our formulation gives the appropriate transmission ratio of the periodic structures.



(a) Dispersion curve



(b) Change of transmission ratio by increasing the number of unit cells

Figure 9: Formation of bandgap

4 Optimization of wave transmission

Next, an optimization of the periodic structure is demonstrated to investigate the effects of varying the structural parameters of the unit cells over the frequency range of the bandgaps.

4.1 Optimization problem

The problem of minimizing the wave transmission ratio in a frequency range of interest is defined. The design parameters γ are the element lengths L_i ($i = 1 \sim N$) as follows:

$$\boldsymbol{\gamma} = \{L_1, L_2, \mathrm{L}\ L_i, \mathrm{L}\ L_N\}. \tag{21}$$

Parameters other than the element lengths are constrained. The evaluation function is a summation of the transmission ratio of the flexural wave propagation in the frequency range ($f_i \in [f_{\min}, f_{\max}]$), as follows:

$$\boldsymbol{\gamma}^{*} = \min\left[\varepsilon(\boldsymbol{\gamma})\right], \tag{22}$$

$$\varepsilon(\boldsymbol{\gamma}) = \sum_i T(f_i), \tag{23}$$

where T is transmission ratio of the flexural wave propagation. The total volume of finite periodic structures remains constant, i.e.,

$$\sum_{i=1,3,5,\ldots} L_i = const., \quad \sum_{i=2,4,6,\ldots} L_i = const. \tag{24}$$

Furthermore, the element lengths L_i is constricted as follows.

$$L_i \in [L_{\min}, L_{\max}]. \tag{25}$$

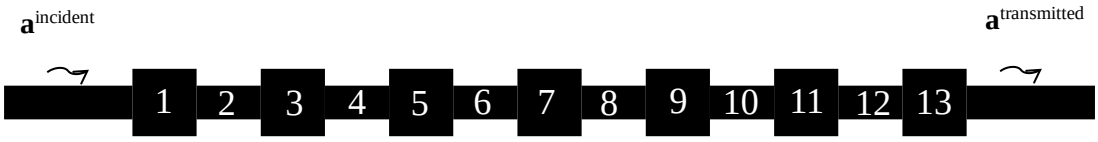
In this paper, this problem is solved using the parameters shown in Table 2 and the initial condition is defined by the parameters as shown in Table 1. Optimization is performed using a constrained non-linear interior point algorithm referred to as fmincon in MATLAB.

Table 2: Parameters for optimization

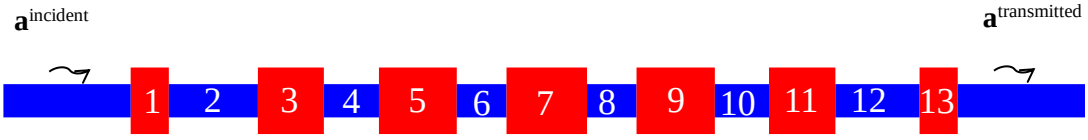
N	$f_{\min}$[Hz]	$f_{\max}$[Hz]	$L_{\min}$[mm]	$L_{\max}$ [mm]
13	1000	2000	30	70

4.2 Example of optimized periodic structure

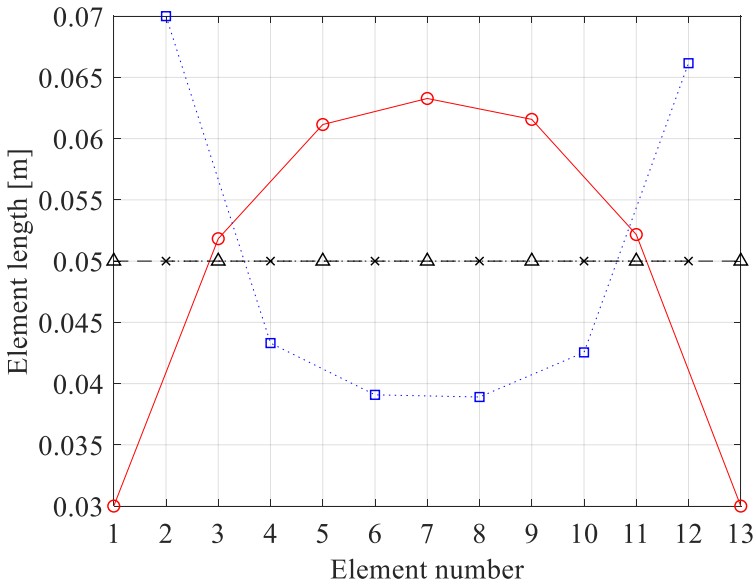
Figure 10 (a) and (b) show the initial and optimized structures, respectively. In addition, the lengths of the beam elements are plotted in Figure 10 (c). As a result of the optimization, the lengths of the beam elements are distributed heterogeneously, and the summation of the transmission ratio in the frequency range of interest is reduced. This result indicates the possibility that varying the structural parameters of the unit cells can extend the frequency range of the bandgaps.



(a) Initial structure



(b) Optimized structure



(b) Element length of initial and optimized structures

Figure 10: Initial and optimized structures

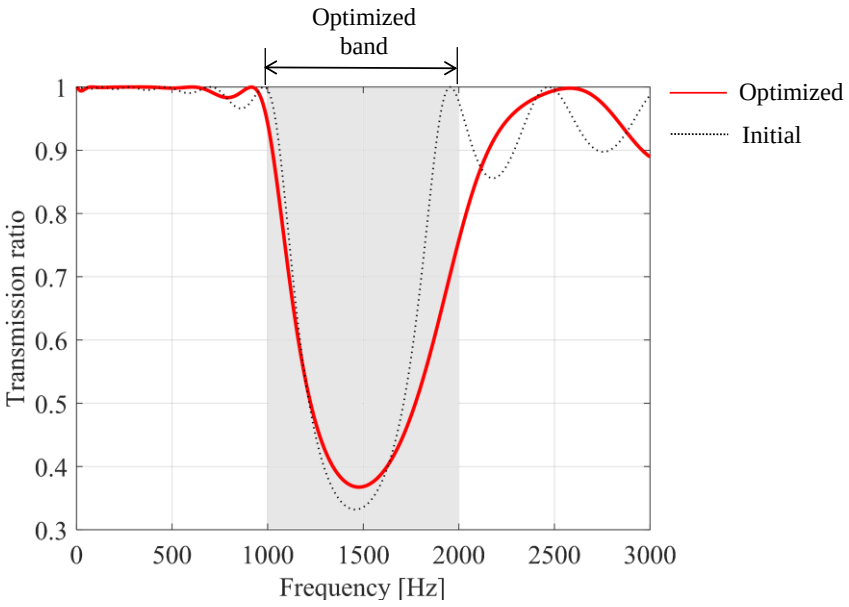


Figure 11: Wave transmission ratios of initial and optimized structures

5 Conclusion

In this paper, we present an analytical model to obtain the bandgaps of finite periodic structures. To understand the formation of these bandgaps, the analytical model is expressed as a block diagram. The diagram shows that the transmission ratio can be expressed by repetition of the transmission matrices of the discontinuities and the matrices of the wave loop in the elements.

Furthermore, the finite periodic structure is optimized to minimize the wave transmission ratio in the frequency range of interest. The result of the optimization indicates the possibility that varying the structural parameters of the unit cells can extend the frequency range of the bandgaps.

References

[1] D. Mead, *Wave propagation in continuous periodic structures: Research contributions from Southampton, 1964–1995*, Journal of Sound and Vibration, Vol. 190, (1996), pp. 495-524.

[2] Y. Xiao, J. Wen, D. Yu, X. Wen, *Flexural wave propagation in beams with periodically attached vibration absorbers: Band-gap behavior and band formation mechanisms*, Journal of Sound and Vibration, Vol. 332 (2013), pp. 867-893.

[3] C. Claeys, N.G.R. de Melo Filho, L. Van Belle, E. Deckers, W. Desmet, *Design and validation of metamaterials for multiple structural stop bands in waveguides*, Extreme Mechanics Letters, Vol. 12 (2017) , pp. 7-22.

[4] K.K. Reichl, D.J. Inman, *Lumped mass model of a 1D metastructure for vibration suppression with no additional mass*, Journal of Sound and Vibration, Vol. 403 (2017), pp. 75-89.

[5] H. Al Ba'ba'a, M. Nouh, T. Singh, *Pole distribution in finite phononic crystals: Understanding Bragg-effects through closed-form system dynamics*, The Journal of the Acoustical Society of America, Vol. 142 (2017), pp. 1399-1412.

[6] S.-K. Lee, B. Mace, M. Brennan, *Wave propagation, reflection and transmission in non-uniform one-dimensional waveguides*, Journal of Sound and Vibration, Vol. 304 (2007), pp. 31-49.

Influence of damping on the sound insulation of infinite and finite locally resonant metamaterial plates

L. Van Belle [1,2], **C. Claeys** [1,2], **E. Deckers** [1,2], **W. Desmet** [1,2]
[1] KU Leuven, Department of Mechanical Engineering,
Celestijnenlaan 300 B, B-3001, Heverlee, Belgium
e-mail: **lucas.vanbelle@kuleuven.be**

[2] DMMS lab, Flanders Make

Abstract

This paper discusses the impact of damping in the resonator and host structure on the sound transmission loss of a vibro-acoustic locally resonant metamaterial plate. The uncoupled vibro-acoustic behaviour is assessed by comparing the dispersion curves for bending wave propagation to the trace propagation constant for plane wave propagation in the surrounding acoustic medium. Next, the sound transmission loss of the vibro-acoustically coupled infinite periodic structure is calculated using the hybrid Wave Based - Finite Element unit cell method. To obtain numerically less expensive sound transmission loss approximations, a dispersion curve based equivalent infinite plate approach is also applied. The results for infinite structures are compared to their finite structure counterparts using the Finite Element Method. Damping, in particular in the resonator, is found to have an important impact on the sound transmission loss of locally resonant metamaterials plates. This underlines the necessity to include damping in the sound insulation performance predictions.

1 Introduction

Vibro-acoustic locally resonant metamaterials (LRMs) have recently emerged as a possible novel lightweight and compact solution for vibration and noise reduction. These materials exhibit resonance based stop bands (SBs) for structural wave propagation, which can be obtained by adding or embedding resontors to or in a flexible host structure on a sub-wavelength scale [1, 2, 3, 4]. Regular lightweight materials exhibit worse noise, vibration and harshness (NVH) behaviour due to their increased stiffness over mass ratio. The SB behaviour of LRMs enables superior vibration and noise reduction in targeted and tunable frequency ranges. More specifically, resonance based SBs for the acoustically relevant out-of-plane bending waves can generate a frequency zone of increased sound transmission loss (STL), outperforming the acoustic mass-law. This has been investigated for LRM plates [5, 6, 7, 8, 9, 10, 11, 12], double-walls [13], solids [14, 15] and honeycomb panel based acoustic enclosures [16].

The resonance based SB mechanism of these LRMs makes them suitable for NVH problems in confined frequency bands, especially in the hard-to-address low frequency region. However, their narrowband nature limits the applicability of LRMs for broadband NVH improvements [17]. Damping has been shown to have an important impact on the vibration attenuation performance of LRMs, broadening the frequency range of attenuation, at the expense of peak attenuation performance [3, 4, 18, 19, 20, 21, 22]. For LRM designs with resonators added to or embedded in a flexible host structure, damping in the resonators mainly affects the vibration attenuation in the frequency range in and around the SB, while damping in the host structure mainly affects the frequency range outside the SB [18]. While the STL of such vibro-acoustic metamaterials has been investigated, only Wang et al. [8] briefly discuss the impact of damping, stating that damping in the resonators smooths the STL peaks and dips.

Since practical LRM realizations currently often include materials with intrinsic damping, this paper investigates the influence of damping in the resonator and host structure of an LRM plate on the STL performance to enable better vibro-acoustic performance predictions and identify possible beneficial damping effects. Similar to [5, 23], a plate-type LRM with bending wave SB behaviour is considered, consisting of a flexible plate host structure with sub-wavelength, periodically attached resonators. Such a configuration is relevant for a variety of applications, like structural panels in vehicles, aircraft, acoustic enclosures for machines and lightweight partitions in building acoustics. To gain insight in the damping influenced STL enhancements, the STL predictions for infinite periodic structures are related to damped dispersion curves for the wave propagation in the infinite periodic LRM structure. Furthermore, since current literature is often limited to infinite periodic structure representations for STL calculations of LRM plates, their predictive value is verified by comparing with the finite LRM plate performance.

This paper is organized as follows. Section 2 describes the general problem setting for the STL of an LRM plate and gives a brief overview of the analysis methods used for dispersion curve calculations of infinite periodic structures and for STL calculations of infinite and finite LRM plates. In Section 3 the LRM design is introduced and the influence of damping on the STL is investigated for an infinite periodic LRM plate, related to the damped dispersion curves and compared to the STL of the finite LRM plate counterpart. Section 4 summarizes the main conclusions.

2 Methodology

2.1 Problem description

The considered LRM consists of an (in)finite flat plate host structure with periodically attached resonators with spatial period L_x and L_y in the xy-plane (Fig. 1a), although periodicity is not strictly required for resonance based SB behaviour [16, 24]. The LRM plate is coupled to two semi-infinite acoustic domains above and below. The structure is excited from one side by an incident acoustic plane wave of amplitude A and wave vector $\mathbf{k_a} = (k_{ax}, k_{ay}, k_{az}) = -k_a(\sin\theta\cos\psi, \sin\theta\sin\psi, \cos\theta)$ with elevation and azimuth angles θ and ψ as defined in Fig. 1a. The acoustic wavenumber is given by $k_a = \omega/c_a$ in the acoustic medium with soundspeed c_a and density ρ_a, while time harmonic behaviour with $e^{j\omega t}$ dependence is considered with $j^2 = -1$, angular frequency ω and time t. By exploiting periodicity, the infinite periodic structure can be represented by a single vibro-acoustic UC (Fig. 1b) and application of the Bloch-Floquet theorem [25].

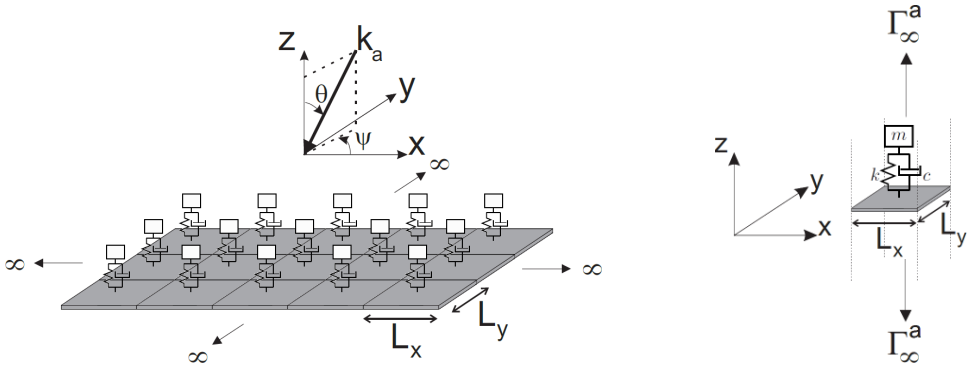


Figure 1: The sound transmission problem for an infinite periodic LRM plate, consisting of a flat plate with periodically attached mass-spring-damper resonators (a) and the corresponding vibro-acoustic UC (b).

2.2 Dispersion curve calculation

The SB behaviour of the LRM plate is predicted using dispersion curves, describing the structural wave propagation through the infinite periodic LRM plate. The infinite periodic structure is represented by the $L_x \times L_y$ sized structural LRM UC (Fig. 1b), which is modeled using the Finite Element Method (FEM). This results in the following time harmonic equations of motion:

$$\mathbf{D}(\omega)\mathbf{q} = \mathbf{f}, \tag{1}$$

with generalized displacements and forces $\mathbf{q}$ and $\mathbf{f}$ and the frequency dependent dynamic stiffness matrix $\mathbf{D}(\omega)$. Application of Bloch-Floquet periodicity boundary conditions, relating the generalized displacements and forces on either side of the UC by means of the propagation constants $\mu_x = k_x L_x$ and $\mu_y = k_y L_y$, to Eq. (1) results in a general dispersion eigenvalue problem (EVP) in ω and (μ_x, μ_y) [25]:

$$\mathbf{A}(\omega, \mu_x, \mu_y)\mathbf{q}^{(red)} = \mathbf{0}, \tag{2}$$

with $\mathbf{q}^{(red)}$ a reduced set of generalized displacements and $\mathbf{A}$ a matrix depending on the frequency and propagation constants. In this work, the dispersion curves are solved for the undamped UC along the irreducible Brillouin contour (IBC) using the $\omega(\mu)$ approach, by imposing real (μ_x, μ_y) and solving the dispersion EVP to real ω [4]. This allows identifying an SB as a frequency range in which no freely propagating wave solutions are found for the targeted wave type(s). To gain insight in the solutions inside the SB and to include the effect of damping, the $\mu(\omega)$ approach as presented by the authors in [18] is followed. This approach solves the dispersion EVP to generally complex μ for given real ω and in-plane propagation directions ψ for which the ratio $\mu_x/\mu_y = \tan(\psi)L_y/L_x$ is real and rational [25].

By including the acoustic trace propagation constant $\mu_a = \sqrt{(k_{ax}L_x)^2 + (k_{ay}L_y)^2}$ in the dispersion curves of the LRM plate, the uncoupled vibro-acoustic performance can be assessed [5, 7, 9, 23]. Frequency zones of efficient acoustic radiation are found as bending wave solutions for which $\sqrt{\mu_a^2 - \mathrm{Re}(\mu)^2}$ is real. Coincidence frequencies are found when bending wave solutions intersect with the acoustic trace propagation constant. The critical coincidence frequency f_c occurs for grazing incidence ($\theta = 90°$), when $\mu_a = \mathrm{Re}(\mu)$.

2.3 Infinite plate STL

To quantify the STL of the infinite periodic LRM plate and to account for the vibro-acoustic interaction, the hybrid Wave Based - Finite Element (WB-FE) UC method is applied [12]. The infinite periodic system is again represented by a single, now vibro-acoustic UC (Fig. 1b). The structural part of the UC is described using the same FE UC model as before and is coupled to two semi-unbounded periodic acoustic WB domains, above and below the structure. The upper acoustic domain is excited by an acoustic plane wave as described in Section 2.1. The steady-state pressure fields in the semi-unbounded, periodic WB domains are approximated by a weighted sum of periodic wave functions that fulfil the governing acoustic Helmholtz equation and satisfy both the Sommerfeld radiation condition and Bloch-Floquet periodicity boundary conditions. The FE and WB subdomains are coupled using a direct hybrid WB-FE coupling strategy and the resulting system of equations is solved for the nodal degrees of freedom in the FE domain and the wave function contributions in the WB domains.

The resulting WB wave function contributions for a given incident plane wave with angles θ and ψ are used to calculate the oblique sound power transmission coefficient $\tau_{\theta,\psi}$ and the $\mathrm{STL}_{\theta,\psi} = -10\log_{10}(|\tau_{\theta,\psi}|)$. The diffuse sound power transmission coefficient can be obtained from the $\tau_{\theta,\psi}$ as follows [5, 28]:

$$\tau_d = \frac{\int_0^{2\pi}\int_0^{\theta_l} \tau_{\theta,\psi}\sin(\theta)\cos(\theta)d\theta d\psi}{\int_0^{2\pi}\int_0^{\theta_l} \sin(\theta)\cos(\theta)d\theta d\psi}, \tag{3}$$

with the limiting angle chosen as $\theta_l = 78°$ in this work, also referred to as field incidence [28, 29, 30, 31].

Since the hybrid WB-FE UC method can become computationally expensive for large UC models, the impact of damping on the STL of the LRM plate can be approximated by post-processing the dispersion curves obtained with the $\mu(\omega)$ approach. Besides offering a fast STL approximation, this also allows linking the damped dispersion curves to quantitative STL predictions. Since the resonators are added on a sub-wavelength scale, an equivalent medium representation is introduced to obtain an analytical STL approximation of the equivalent infinite plate [5, 6, 13, 26]. Consider, for generality, the corrected bending wave dispersion relation $k_C(\omega)$ of a thick, isotropic, homogeneous infinite plate of thickness h [32]:

$$k_C^4 - \omega^2 k_C^2 \left[\frac{\rho}{\kappa G} + \frac{\rho}{E}\right] - \frac{12\omega^2\rho(1-\nu^2)}{Eh^2} + \frac{\omega^4\rho^2}{\kappa G E} = 0 \tag{4}$$

with bending wavenumber k_C, density ρ, complex Young's modulus $E = E_0(1+j\eta)$ with Young's modulus E_0 and η the structural damping loss factor, shear modulus $G = E/(2(1+\nu))$, Poisson coefficient ν, and $\kappa = 5/(6-\nu)$ the shear correction coefficient [27]. Considering the in-plane propagation direction ψ, k_C in Eq. (4) can be replaced by the bending wave dispersion solution $k_b(\omega, \psi)$ obtained with the $\mu(\omega)$ approach in the first Brillouin zone. This allows Eq. (4) to be reformulated in terms of the density ρ, which results in the following equivalent dynamic mass density ρ_{eq}:

$$\rho_{eq} = \frac{\omega^2 k_b^2(E+\kappa G) + \frac{12\omega^2\kappa G(1-\nu^2)}{h^2} - \sqrt{[-\omega^2 k_b^2(E+\kappa G) - \frac{12\omega^2\kappa G(1-\nu^2)}{h^2}]^2 - 4\omega^4 k_b^4 \kappa G E}}{2\omega^4}, \tag{5}$$

for given ω and ψ. Next, the surface impedance of the equivalent infinite plate subjected to an acoustic plane wave incident at elevation angle θ can be written in terms of this ρ_{eq} [32, 28]:

$$Z_{eq,\theta,\psi} = j\omega\rho_{eq}h\left(\frac{1 - \frac{k_a^2\sin^2(\theta)Eh^2}{12\rho_{eq}\omega^2(1-\nu^2)} + \frac{h^2}{12}\left[k_a^2\sin^2(\theta)(1+\frac{E}{\kappa G}) - \frac{\omega^2\rho_{eq}}{\kappa G}\right]}{1 + \frac{h^2}{12}\left[k_a^2\sin^2(\theta)(\frac{E}{\kappa G}) - \frac{\omega^2\rho_{eq}}{\kappa G}\right]}\right), \tag{6}$$

which give rise to following oblique sound power transmission coefficient [33]:

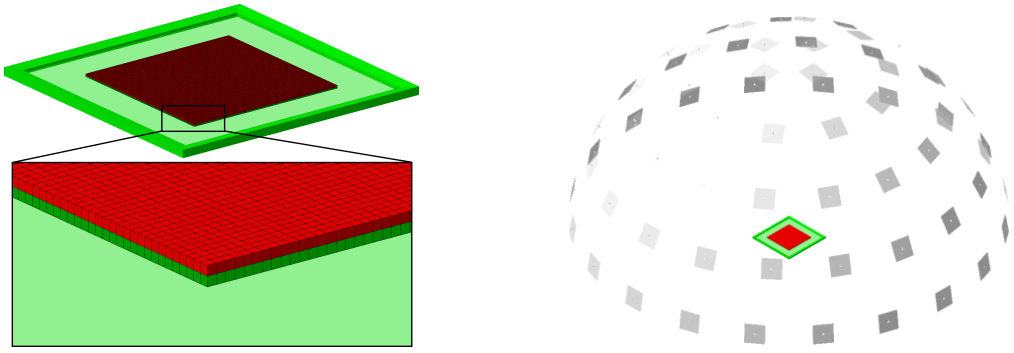
$$\tau_{eq,\theta,\psi} = \frac{1}{\left|1 + \frac{Z_{eq,\theta,\psi}\cos\theta}{2\rho_a c_a}\right|^2}, \tag{7}$$

from which the STL is obtained.

2.4 Finite plate STL

For practically realizable LRM plates, finite structure dimensions have to be considered. In this work, the STL of a finite LRM plate with simply supported boundary conditions is analyzed. For these boundary conditions, the structural modes have been shown to sample on the dispersion surface of the corresponding infinite periodic structure [23]. Apart from the non-resonant sound transmission, also resonant sound transmission occurs for the finite plate due to the structural modes. While non-resonant sound transmission is under mass control, resonant sound transmission is under damping control [32, 33].

The finite plate STL is calculated using a vibro-acoustic FE model of an $n \times m$ UCs sized plate, strongly coupled to two semi-unbounded acoustic FE domains on either side and separated by a symmetry plane (Fig. 2a) using the software *Virtual.Lab 13.6*. The semi-unbounded acoustic domains are modeled using one layer of 3D acoustic FE elements and Automatically Matched Layer boundary conditions to approximate the Sommerfeld radiation condition. The LRM plate is excited by a set of distributed plane waves on the incident side, representing an acoustic diffuse field (Fig. 2b), from which the diffuse STL is obtained [34, 35].



(a) (b)

Figure 2: Finite plate FEM-AML model with upper (red mesh) and lower (green mesh) acoustic halfspace separated by a symmetry plane (light green rectangle) (a) and distributed plane wave excitation (b).

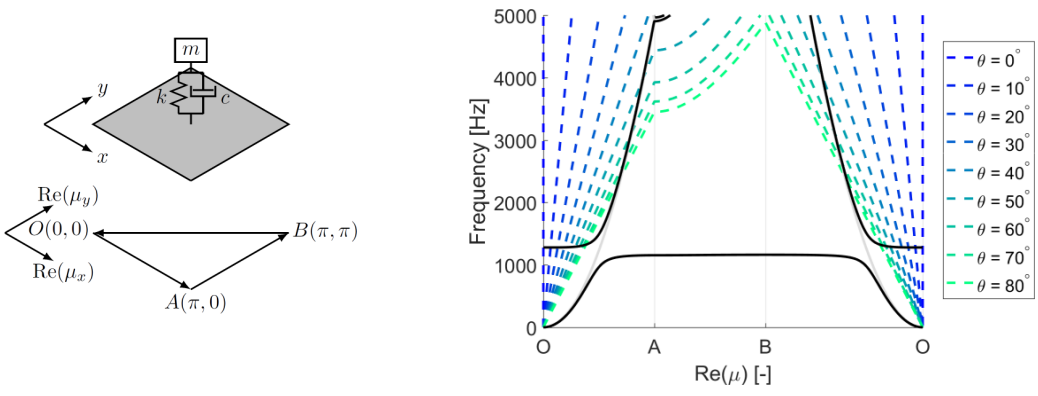
3 Application

3.1 Description metamaterial

The LRM plate consists of a 5 mm thick steel plate host structure ($E_0 = 210$ GPa, $\rho = 7800$ kg/m^3, $\nu = 0.3$, $f_c = 2343$ Hz), with mass-spring-damper resonators added with 0.05×0.05 m periodicity. The resonators are tuned with their natural frequency to 1171 Hz, target the out-of-plane plate response and add 20% mass relative to the host structure [23]. Structural damping with loss factor η is considered in the host structure, while damping in the resonators is introduced by means of viscous damping c, with damping ratio ξ. The LRM UC and the corresponding IBC convention are shown in Fig. 3a. The FE model of the UC consists of 100 quadratic quadrilateral shell elements.

3.2 Dispersion curves

The dispersion curves obtained with the $\omega(\mu)$ approach along the IBC for the undamped bare and LRM UC in the frequency range of interest up to 5000 Hz are presented in Fig. 3b. Only the acoustically relevant out-of-plane bending waves are presented and the acoustic trace propagation constant is added for different incidence angles θ.

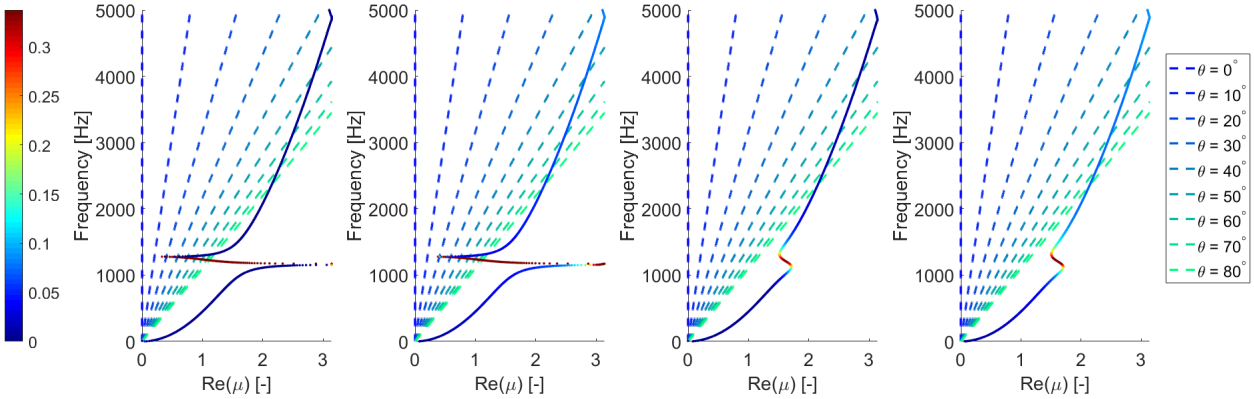


(a) (b)

Figure 3: LRM UC and IBC definition (a), bending wave dispersion curves (solid lines) and acoustic trace propagation constant for incidence angles θ (dashed lines) for the bare (—) and LRM (—) plate (b).

An SB is obtained for the bending waves between $1162 - 1279$ Hz. Since coincidence frequencies are found at the intersections between the bending wave solutions and the acoustic trace propagation constant, the tuning of the SB below the original critical coincidence frequency leads to an additional coincidence zone after the SB, because of the cut-on repeated bending wave mode as shown in [23].

Since previous $\omega(\mu)$ approach does not provide insight in the wave propagation inside the SB frequency range and does not account for damping effects, dispersion curves are calculated using the $\mu(\omega)$ approach. A single in-plane propagation direction is chosen, $\psi = 0°$, corresponding to the OA direction in the IBC of Fig. 3. Complex μ dispersion curves are calculated for frequencies $f = 1 - 1 - 5000$ Hz, focussing on the bending waves, while the effect of damping in host structure and resonator is assessed by varying η and ξ between 0 and 0.1 (Fig. 4).



(a) (b) (c) (d)

Figure 4: $\mu(\omega)$ dispersion curves along $\psi = 0$ for $\eta = 0, \xi = 0$ (a), $\eta = 0.1, \xi = 0$ (b), $\eta = 0, \xi = 0.1$ (c) and $\eta = 0.1, \xi = 0.1$ (d), coloured according to $|\mathrm{Im}(\mu)|$, with acoustic trace propagation constant for incidence angles θ.

For the undamped UC, the $\mu(\omega)$ approach finds the same freely propagating wave solutions as the $\omega(\mu)$ approach (Fig. 4a). Inside the SB, complex μ solutions are now found, corresponding to spatially decaying bending waves. These strongly attenuated solutions inside the SB also intersect with the acoustic trace propagation constant. As discussed in [18], damping in the host structure mainly affects the solutions outside the SB, increasing the wave attenuation (Fig. 4b). The coincidence intersections away from the SB now occur with damped bending waves. Damping in the resonator mainly affects the frequency range in and around the SB, broadening the frequency range of wave attenuation, but reducing the wave attenuation inside the SB (Fig. 4c). The closing of the dispersion curves by means of a complex μ loop causes the intersections with the acoustic trace propagation constant in the coincidence zone after the SB to disappear. The coincidence intersections away from the SB are less affected, since the attenuation increase outside and further away from the SB is limited. Damping in both constituents combines these effects (Fig. 4d).

The influence on acoustic radiation is further illustrated by evaluating the difference between $\mathrm{Re}(\mu)$ for the bending wave solution and the acoustic trace propagation constant for grazing incidence ($\theta = 90°$) (Fig. 5) [23]. The propagative solutions in the shaded region ($\mathrm{Re}(\mu) - \mu_a < 0$) lead to efficient acoustic radiation. For the LRM without damping and with damping in the host structure only, a clear zone of efficient acoustic radiation is predicted after the SB (Figs. 5a and 5b). Introducing damping in the resonator shows potential to alleviate this introduced zone of efficient acoustic radiation (Figs. 5c and 5d). The analysis of the dispersion curves obtained with either the $\mu(\omega)$ or $\omega(\mu)$ approach, however, does not yield quantitative STL predictions.

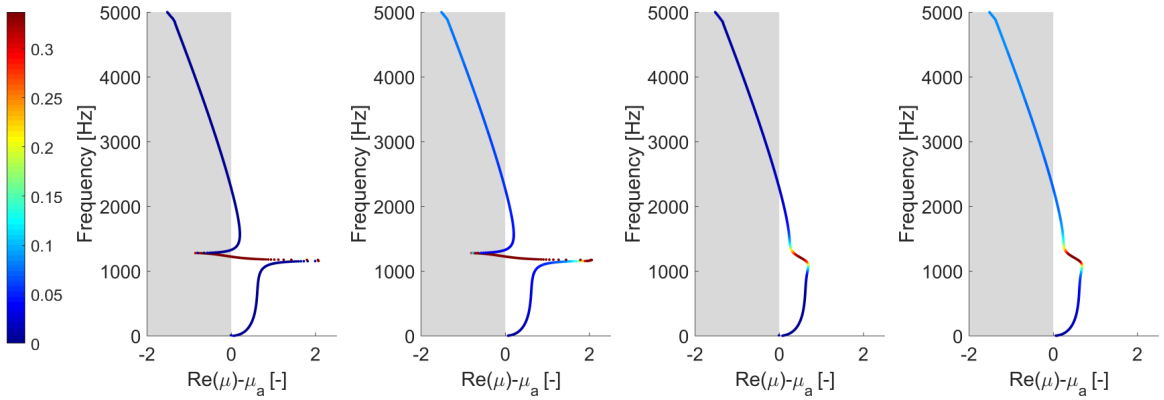


Figure 5: Difference $\mathrm{Re}(\mu) - \mu_a$, for $\eta = 0, \xi = 0$ (a), $\eta = 0.1, \xi = 0$ (b), $\eta = 0, \xi = 0.1$ (c) and $\eta = 0.1, \xi = 0.1$ (d), coloured according to $|\mathrm{Im}(\mu)|$, with the zone of efficient acoustic radiation in gray.

3.3 Infinite plate STL

The STL of the infinite periodic LRM plate is calculated using the WB-FE UC approach [12]. The same in-plane propagation direction $\psi = 0°$ is used and the elevation angle θ of the incident acoustic plane wave is varied. The same FE discretization is used for the structural UC, while for the WB domain a truncation factor $N_p = 2$ for the wave functions is applied. The effect of damping in host structure and resonator on the STL is again assessed by varying η and ξ between 0 and 0.1. The oblique incidence STL is calculated for frequencies $f = 1 - 1 - 5000$ Hz (Fig. 6).

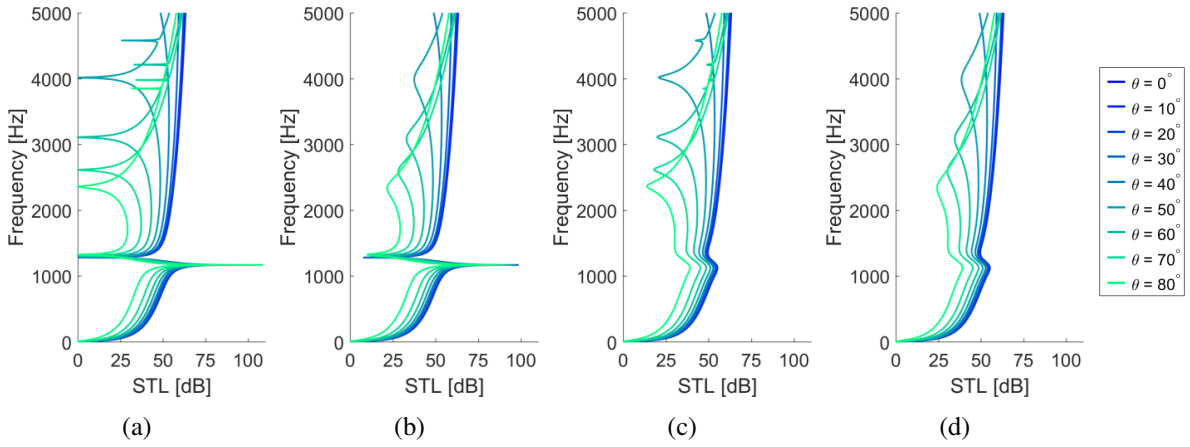


Figure 6: STL for $\eta = 0, \xi = 0$ (a), $\eta = 0.1, \xi = 0$ (b), $\eta = 0, \xi = 0.1$ (c) and $\eta = 0.1, \xi = 0.1$ (d), for incidence angles θ, along $\psi = 0$, calculated using the hybrid WB-FE UC method.

For the undamped UC, a strongly increased STL is obtained inside the SB zone, around the tuned resonator frequency (Fig. 6a). The STL peak occurs where the distance between the bending wave solution and the acoustic trace propagation constants becomes large (Fig. 4a). The STL peak is followed by a strong STL dip, related to the introduced coincidence zone after the SB. For different θ, the STL peak occurs at the same frequency, while the STL dip frequency depends on the intersection of the repeated bending wave solution and acoustic trace propagation constant for the corresponding θ. The intersections with the spatially decaying bending waves inside the SB do not lead to additional STL dips. After $f_c = 2343$ Hz, outspoken STL dips are caused by oblique coincidence with the regular bending wave solutions. Around 4000 Hz

and higher, narrow STL dips are found, related to subsidiary coincidence [5, 36, 37]. This is caused by the periodicity of the wave solutions in the infinite periodic structure, resulting in the intersection of the acoustic trace propagation constant and the subsidiary periodic Bloch wave (Fig. 7).

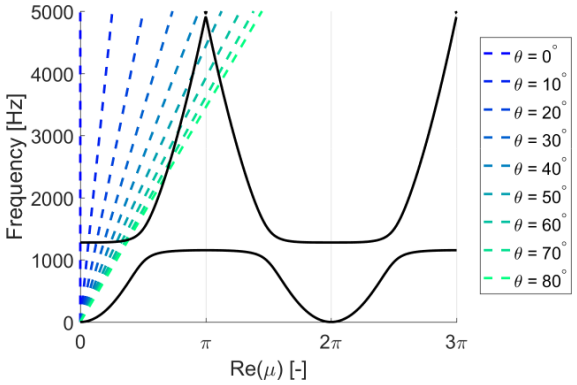
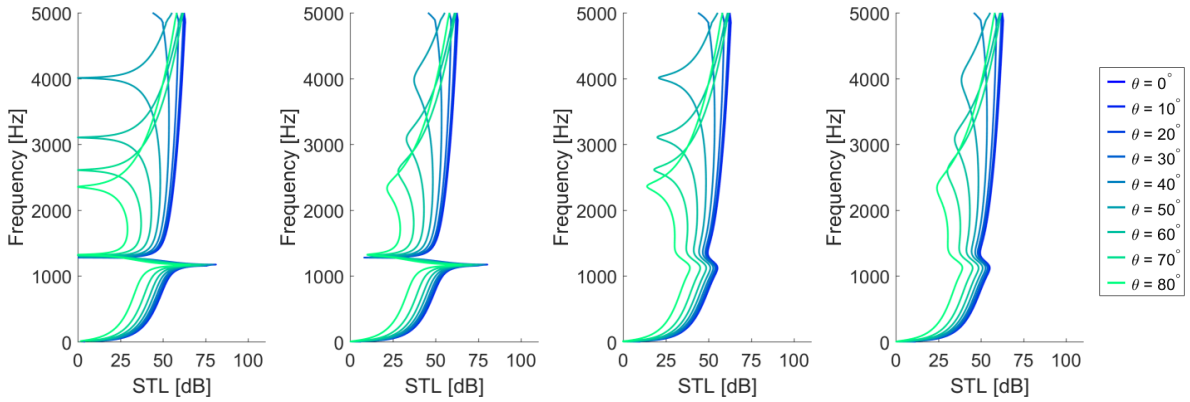


Figure 7: Subsidiary coincidence found as intersection between the acoustic trace propagation constant for incidence angles θ (dashed lines) and higher order Bloch modes in the infinite periodic LRM plate (solid lines), shown for the $\psi = 0°$ propagation direction.

Damping in the host structure leads to a limited reduction of the STL peak in the SB (Fig. 6b), as expected from the limited influence on the dispersion curves in that frequency range. The introduced coincidence dips after the SB show a minor STL increase compared to the undamped LRM plate. Outside the SB, the STL at the regular coincidence dips strongly increases as the coincidence intersections of the acoustic trace propagation constant now occur with strongly attenuated bending waves, resulting in the expected damping effect at coincidence [32, 33]. Similarly, the subsidiary coincidence STL dips are damped out. Damping in the resonator causes the influenced frequency regions to switch (Fig. 6c). The STL in and around the SB is strongly influenced, improving the STL in the introduced coincidence zone after the SB, but also reducing the STL peak inside the SB. Due to the lower attenuation of the bending waves away from the SB, the STL improvement at the regular coincidence dips is less outspoken as compared to damping in the host structure, while damped subsidiary coincidence STL dips can still be observed. As for the damped dispersion curves, damping in both constituents combines these mainly complementary effects on the STL (Fig. 6d).

To verify if quantitative STL predictions can be obtained from the $\mu(\omega)$ dispersion curves, without the need to calculate the STL of the fully coupled infinite periodic structure, the equivalent infinite plate approach is applied to the earlier calculated bending wave dispersion curves (Fig. 8).



(a) (b) (c) (d)

Figure 8: STL for $\eta = 0, \xi = 0$ (a), $\eta = 0.1, \xi = 0$ (b), $\eta = 0, \xi = 0.1$ (c) and $\eta = 0.1, \xi = 0.1$ (d) for incidence angles θ, along $\psi = 0$, calculated using the equivalent infinite plate approach.

Good agreement is obtained with the STL predictions of the hybrid WB-FE UC method, especially for the LRM plate with damping. Fluid loading effects, omitted in the equivalent infinite plate approach, are of limited influence due to the high density plate and low density acoustic medium. Some discrepancies are still present:

- The periodicity of the wave solutions causes aliasing of the dispersion curves at the edge of the first Brillouin zone at $f_{\lambda/2} = 4934$ Hz, limiting the valid frequency range. Above this frequency, however, resonance based SBs are not guaranteed since the sub-wavelength criterion is violated [3].
- The STL peak is underestimated for the LRM without damping (Fig. 8a) and with damping in the host structure only (Fig. 8a). This is caused by the periodicity of the wave solutions, resulting in a bifurcation of the $\mu(\omega)$ dispersion solutions inside the SB at the boundaries of the Brillouin zones [18], limiting the maximum value of μ. For sufficient resonator damping, this is alleviated as the closing of the dispersion curves causes the wave solutions to not longer attain the edges of the Brillouin zones.
- The subsidiary coincidence effect is not accounted for, since only the solution inside the first Brillouin zone is used. This does not affect the vibro-acoustic performance prediction around the SB zone.

While the introduced equivalent plate approach results in an approximation of the STL for the considered LRM plate, the method allows for fast vibro-acoustic performance predictions for damped LRM structures in the sub-wavelength frequency range. Since the method uses $\mu(\omega)$ dispersion curves, more complex resonator designs can also be considered than is the case for pure analytical equivalent medium methods.

3.4 Finite plate STL

To account for finite size effects and to verify the infinite periodic structure STL predictions, the STL of a simply supported 0.6×0.6 m LRM plate is considered, consisting of 12×12 UCs. The LRM plate is modeled with 5184 linear quadrilateral shell elements, with 12×12 attached mass-spring-damper resonators. Each of the acoustic domains is discretized with 5184 linear hexahedral solid elements. Both FE meshes are valid up to at least 5000 Hz. The LRM plate is excited using a set of 67 acoustic plane waves, distributed on a hemisphere with radius 4.243 m and with amplitudes generated in order to represent a diffuse field excitation with amplitude 1 Pa [34, 35]. The STL is calculated for the undamped LRM plate, as well as for the damped LRM plate with $\eta = 0, 0.01, 0.1$ and $\xi = 0, 0.01, 0.1$, in the frequency range $5 - 5 - 5000$ Hz (Fig. 9).

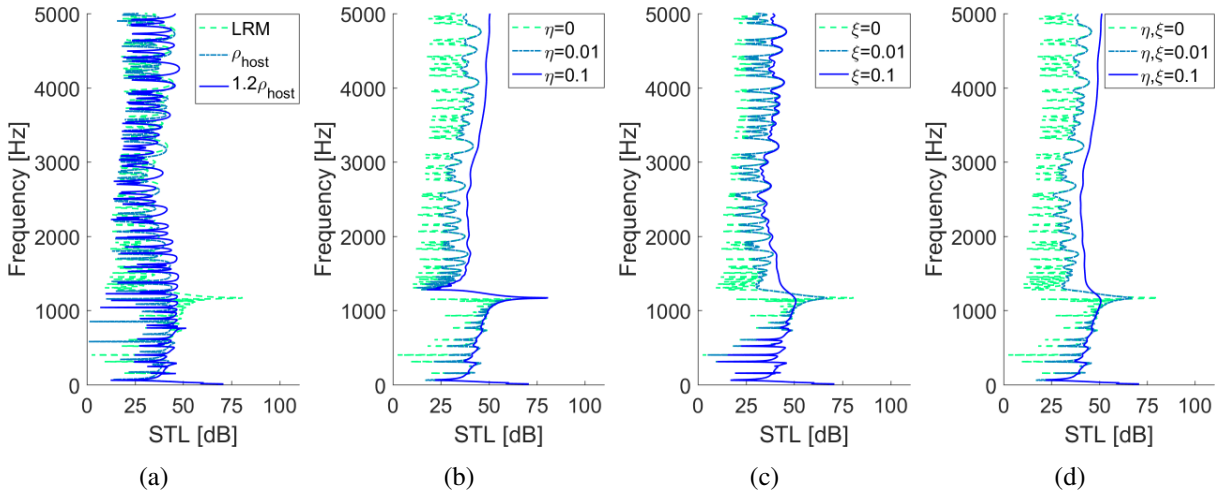


Figure 9: Finite plate diffuse STL, calculated using FEM–AML, for the undamped LRM (a) and for the LRM with damping in host structure (b), resonator (c) and both host structure and resonator (d).

The undamped LRM plate clearly shows the STL peak-dip behaviour related to the bending wave SB (Fig. 9a). Inside the SB, no structural modes are present and the transmission is non-resonant, whereas the modes outside the SB cause resonant STL dips. The high modal density right before and after the SB is related to the highly dispersive bending wave mode before and after the SB observed in the dispersion curves [23]. Further away from the SB, the STL tends to the STL of a bare plate with mass density $1.2\rho_{host}$ and $\rho_{host} = 7800$ kg/m^3 respectively before and after the SB. This is caused by the in-phase and anti-phase motion between host structure and resonator respectively before and after the SB. Damping in the host structure leaves the STL peak-dip largely unaffected (Fig. 9b). Outside the SB, the increased wave attenuation results in strongly damped resonant STL dips. Damping in the resonator strongly affects the STL in and around the SB, enhancing the STL dip after the SB, but reducing the peak STL inside the SB (Fig. 9c). The closing of the dispersion curves around the SB (Fig. 5c) causes the bending wave solutions to move away from the zone of efficient acoustic radiation, while it also results in freely propagating modes before and after the SB to disappear in a broadening frequency range around the SB. Together with the broadening zone of attenuation around the SB, the resonant STL dips before and after the SB are strongly improved. Damping in both constituents again combines these complementary effects (Fig. 9d).

To assess the representativeness of the STL predictions of the infinite periodic LRM plate for its finite plate performance, the infinite and finite plate diffuse STL are compared for the damped LRM plate with $\eta = 0.1$, $\xi = 0.1$ and $\eta, \xi = 0.1$ (Fig. 10). For the diffuse STL calculation with the hybrid WB-FE UC method, $\theta_l = 78°$ and $d\theta = 0.1°$ are used in Eq. (3). Good agreement is obtained in and around, as well as outside the SB. Inside the SB, no structural modes are present and the STL corresponds to the non-resonant sound transmission found for the infinite periodic structure. The structural modes outside the SB cause the finite plate STL to fluctuate around the non-resonant STL predictions for the infinite LRM plate. The damping influenced coincidence region at higher frequencies also shows good agreement. Some discrepancies are still present, since the set of plane waves used in the finite and infinite plate STL calculations differs. In the low frequency range, the dimensional effects related to stiffness and size of the finite partition result in the infinite plate STL underestimating the finite plate performance [30, 38]. In general, the predicted impact of damping on the STL of the infinite periodic LRM plate corresponds well to its finite size counterpart, especially in and around the targeted SB frequency range.

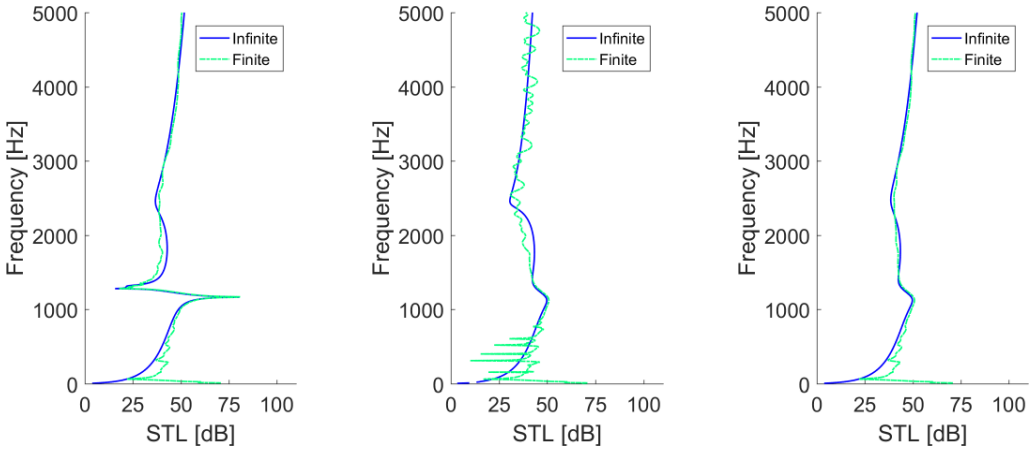


Figure 10: Comparison of diffuse STL using hybrid WB-FE UC for the infinite (—) and FEM-AML for the finite (- -) LRM plate for $\eta = 0.1, \xi = 0$ (a), $\eta = 0, \xi = 0.1$ (b) and $\eta = 0.1, \xi = 0.1$ (c).

4 Conclusion

The influence of damping on the STL of a vibro-acoustic LRM plate is investigated. Both undamped and damped dispersion curves are analyzed and compared to the acoustic trace propagation constant to identify zones of efficient radiation. Mainly damping in the resonator affects the SB zone and shows potential to enhance the zone of efficient radiation after the SB. To obtain quantitative STL predictions, the hybrid WB-FE UC method is applied to calculate the STL of the infinite periodic LRM plate for plane wave excitation. Damping in the host structure mainly affects the frequency range outside the SB, enhancing the regular coincidence zone. Damping in the resonator strongly affects the SB region, enhancing the coincidence zone after the SB at the expense of reduced peak STL in the SB, with a more limited STL improvement further away from the SB. To enable fast STL approximations and to obtain quantitative STL predictions from available damped dispersion curves, an equivalent infinite plate approach is applied, showing good agreement with the hybrid WB-FE UC method in the sub-wavelength frequency range and in presence of damping. Eventually, the finite LRM plate performance is assessed to account for resonant sound transmission effects and to compare with the infinite LRM plate STL predictions. Good agreement is found, especially in the SB frequency range where no modes are present and hence non-resonant sound transmission occurs. This underlines the importance of accounting for damping to obtain accurate LRM plate STL performance predictions and demonstrates the value of damped UC based calculations for vibro-acoustic performance predictions.

Acknowledgements

The research of L. Van Belle and E. Deckers is funded by grants of the Research Foundation - Flanders (F.W.O.). The Research Fund KU Leuven is gratefully acknowledged for its support. This work is partially supported by Flanders Make, the strategic research centre for the manufacturing industry.

References

[1] L. Brillouin. *Wave propagation in periodic structures*. McGraw-Hill Book Company, 2nd edition, 1946.

[2] C. Goffaux, J. Sánchez-Dehesa, A. L. Yeyati, P. Lambin, A. Khelif, J. O. Vasseur, and B. Djafari-Rouhani. Evidence of Fano-like interference phenomena in locally resonant materials. *Physical Review Letters*, 88(22), May 2002.

[3] C. Claeys, K. Vergote, P. Sas, and W. Desmet. On the potential of tuned resonators to obtain low-frequency vibrational stop bands in periodic panels. *Journal of Sound and Vibration*, 332(6):1418–1436, Mar 2013.

[4] M. I. Hussein, M. J. Leamy, and M. Ruzzene. Dynamics of phononic materials and structures: Historical origins, recent progress, and future outlook. *Applied Mechanics Reviews*, 66(4):040802, May 2014.

[5] Y. Xiao, J. Wen, and X. Wen. Sound transmission loss of metamaterial-based thin plates with multiple subwavelength arrays of attached resonators. *Journal of Sound and Vibration*, 331(25):5408–5423, Dec 2012.

[6] P. Li, S. Yao, X. Zhou, G. Huang, and G. Hu. Effective medium theory of thin-plate acoustic metamaterials. *The Journal of the Acoustical Society of America*, 135(4):1844–1852, Apr 2014.

[7] Y. Song, L. Feng, J. Wen, D. Yu, and X. Wen. Reduction of the sound transmission of a periodic sandwich plate using the stop band concept. *Composite Structures*, Feb 2015.

[8] T. Wang, M. Sheng, and Q. Qin. Sound transmission loss through metamaterial plate with lateral local resonators in the presence of external mean flow. *The Journal of the Acoustical Society of America*, 141(2):1161–1169, Feb 2017.

[9] M. Oudich, X. Zhou, and M. B. Assouar. General analytical approach for sound transmission loss analysis through a thick metamaterial plate. *Journal of Applied Physics*, 116(19):193509, Nov 2014.

[10] B. Assouar, M. Oudich, and X. Zhou. Sound insulation and energy harvesting based on acoustic metamaterial plate. In Tribikram Kundu, editor, *Health Monitoring of Structural and Biological Systems 2015*. SPIE-Intl Soc Optical Eng, Mar 2015.

[11] B. Assouar, M. Oudich, and X. Zhou. Acoustic metamaterials for sound mitigation. *Comptes Rendus Physique*, 17(5):524–532, May 2016.

[12] E. Deckers, S. Jonckheere, L. Van Belle, C. Claeys, and W. Desmet. Prediction of transmission, reflection and absorption coefficients of periodic structures using a hybrid wave based - finite element unit cell method. *Journal of Computational Physics*, 356:282–302, Mar 2018.

[13] J. Li and S. Li. Sound transmission through metamaterial-based double-panel structures with poroelastic cores. *Acta Acustica united with Acustica*, 103(5):869–884, 2017.

[14] X. Liu, Z.and Zhang, Y. Mao, Y. Y. Zhu, Z. Yang, C. T. Chan, and P. Sheng. Locally resonant sonic materials. *Science*, 289(5485):1734–1736, 2000.

[15] K.M. Ho, Z. Yang, X.X. Zhang, and P. Sheng. Measurements of sound transmission through panels of locally resonant materials between impedance tubes. *Applied Acoustics*, 66(7):751–765, 2005.

[16] C. Claeys, E. Deckers, B. Pluymers, and W. Desmet. A lightweight vibro-acoustic metamaterial demonstrator: Numerical and experimental investigation. *Mechanical Systems and Signal Processing*, 70-71:853–880, Mar 2016.

[17] Wu, Y., Yang, M., and Sheng, P. Perspective: Acoustic metamaterials in transition. *Journal of Applied Physics*, 123(9), 090901, 2018.

[18] L. Van Belle, C. Claeys, E. Deckers, and W. Desmet. On the impact of damping on the dispersion curves of a locally resonant metamaterial: Modelling and experimental validation. *Journal of Sound and Vibration*, 409:1–23, 2017.

[19] A.O. Krushynska, V.G. Kouznetsova, and M.G.D. Geers. Visco-elastic effects on wave dispersion in three-phase acoustic metamaterials. *Journal of the Mechanics and Physics of Solids*, 96:29–47, 2016.

[20] M.A. Lewińska, V.G. Kouznetsova, J.A.W. van Dommelen, A.O. Krushynska, and M.G.D. Geers. The attenuation performance of locally resonant acoustic metamaterials based on generalised viscoelastic modelling. *International Journal of Solids and Structures*, 2017.

[21] H. Peng, P. Frank Pai, and H. Deng. Acoustic multi-stopband metamaterial plates design for broadband elastic wave absorption and vibration suppression. *International Journal of Mechanical Sciences*, 103:104–114, Nov 2015.

[22] Y. Sun, S. Li, and Z. Jiao. Acoustic response of multi-stopband local resonance plate. *Modern Physics Letters B*, 31(31):1750295, 2017.

[23] C. Claeys, P. Sas, and W. Desmet. On the acoustic radiation efficiency of local resonance based stop band materials. *Journal of Sound and Vibration*, 333(14):3203–3213, Jul 2014.

[24] A.O. Krushynska, V.G. Kouznetsova, and M.G.D. Geers. Towards optimal design of locally resonant acoustic metamaterials. *Journal of the Mechanics and Physics of Solids*, 71:179–196, Nov 2014.

[25] B. R. Mace and E. Manconi. Modelling wave propagation in two-dimensional structures using finite element analysis. *Journal of Sound and Vibration*, 318(4-5):884–902, Dec 2008.

[26] Y. Wu, Y. Lai, and Z.-Q. Zhang. Effective medium theory for elastic metamaterials in two dimensions. *Physical Review B*, 76(20):205313, 2007.

[27] N.G. Stephen. Mindlin plate theory: best shear coefficient and higher spectra validity. *Journal of Sound and Vibration*, 202(4):539–553, 1997.

[28] F. J. Fahy. *Sound and structural vibration: radiation, transmission and response*. Academic press, 2012.

[29] V. Hongisto. Sound insulation of double panels-comparison of existing prediction models. *Acta acustica united with acustica*, 92(1):61–78, 2006.

[30] A. Pellicier and N. Trompette. A review of analytical methods, based on the wave approach, to compute partitions transmission loss. *Applied Acoustics*, 68(10):1192–1212, 2007.

[31] K.A. Mulholland, H.D. Parbrook, and A. Cummings. The transmission loss of double panels. *Journal of Sound and Vibration*, 6(3):324–334, 1967.

[32] L. Cremer, M. Heckl, and B.A.T. Petersson. *Structure-borne sound: structural vibrations and sound radiation at audio frequencies*. Springer, 2005.

[33] C. Hopkins. *Sound insulation*. Routledge, 2012.

[34] K. De Langhe, C. Moser, R. Boeykens, and K. Kucukcoskun. Sound transmission loss predictions of aircraft panels: an update on recent technology evolutions. In *INTER-NOISE and NOISE-CON Congress and Conference Proceedings*, volume 253, pages 3354–3365. Institute of Noise Control Engineering, 2016.

[35] K. Vansant. Latest developments in solving large simulation models in view of pass-by noise. AIA-DAGA, 2013.

[36] D. J. Mead. Free wave propagation in periodically supported, infinite beams. *Journal of Sound and Vibration*, 11(2):181–197, 1970.

[37] W. Maysenhölder. Sound transmission through periodically inhomogeneous anisotropic thin plates: Generalizations of Cremer's thin plate theory. *Acta Acustica united with Acustica*, 84(4):668–680, 1998.

[38] M. Villot, C. Guigou, and L. Gagliardini. Predicting the acoustical radiation of finite size multi-layered structures by applying spatial windowing on infinite structures. *Journal of sound and vibration*, 245(3):433–455, 2001.

Revisited impedance tube for standard and metamaterial testing

L. A. Nascimento[1], G. K. Rodrigues[1], L.P.R. de Oliveira[1]
[1] São Carlos School of Engineering, University of São Paulo
Av. Trabalhador Sancarlense 400, 13566-590, São Carlos – SP, Brazil
e-mail: **leopro@sc.usp.br**

Abstract
Many engineering structures can be classified as waveguides. The Kundt´s tube is one of the most well known system of this kind, both for didactic or laboratory tests purposes. Both absorption and transmission-loss can be assessed with such devices by following international standards, which require the acoustic field to prescribe plane waves, with bandwidth limited by the tube diameter. Above this frequency limit, plane waves may still occur, but the presence of radial and azimuthal modes prevent straightforward standardized analysis. However, this system is still representative of other slender engineering structures, such as exhaust pipes, HAVC systems, ventilation units, etc. for mid and high-frequencies. Hence, the classical impedance tube exercise is revisited in this work, incorporating extra microphones, which allow the visualization and identification of non-planar modes. Standard porous absorption materials are tested, to validity the exercise, that should also be useful for mid- and high-frequency testing of smart metamaterials.

1 Introduction

There are consolidated methods in vibroacoustics, for the evaluation of reflection and acoustic absorption coefficients in materials. Among these methods, the impedance tube method, or Kundt´s tube, consists of propagating waves in a rigid wall tube from one end, while the material under test is at the other end. Seybert and Ross [1] inaugurated the estimate of acoustic property of normal incidence from two measurements along the tube, taking into account the wave fronts that propagated in opposite directions. Years later, Chung and Blaser [2,3] advanced in the description of the instrumentation and calibration necessary to realize an estimate of acoustic properties based on the transfer function method. The widely accepted international standards ASTM E1050 [4] and ISO 10534-2 [5] are based upon these contributions.

The transfer function method requires simple instrumentation, but it has a number of practical and theoretical limitations, which restrict its range of operation to a short band, in relation to the audible range. From a practical point of view, questions of uncertainty [6], location of microphones [7], calibration [8], among others, have been studied. In recent decades, the academic community has been struggling to give greater consistency and coverage to the impedance tube, which is still relevant to these days [9,10]. Regarding the theoretical basis, there is an important limitation in the frequency range, under which sound wave propagate in the direction of the tube main axis (plane waves). The diameter of the tube, and hence the are of the sample material under test, are limited by the wavelength of the azimuthal waves, which violate the basic hypothesis of plane propagation and, hence, the useful frequency range of the experimental apparatus.

The objective of this work is to show that it is possible to use an acoustic instrumentation system, similar to the method of transfer function in the impedance tube, that is able to identify the absorption of samples in frequency bands higher than the azimuthal modes. By identifying the frequencies in which non-planar propagations occur, it is possible to devise strategies to expand the useful range of the impedance tube, as already suggested by Kimura et al. [11].

The methods of using the impedance tube, described in the literature and international standards, are based on the fact that below a certain frequency the sound propagates in the waveguide as flat wave fronts. Both

international standards point to the higher cutoff frequency of the tube being related to the wavelength corresponding to the tube inner radios, i.e.,

$$f_{ISO} \approx f_{ASTM} < \frac{0,58 \cdot c_0}{d} \tag{1}$$

where c_0 is the local speed of sound and d is the inner tube diameter.

Taking the expression for the steady state sound propagation in cylindrical coordinates (2), as demonstrated by Munjal [12], it is possible to conclude that there exists a region in which the eigenvalues *m* and *n* are null. This greatly simplifies the propagation function, according to the derivation in Eqs. (2) to (4):

$$p(x,r,\theta) = \sum_{m=-\infty}^{\infty} \sum_{n=0}^{\infty} \left(p_{m,n}^{+} e^{-ik_{m,n}^{+} x} + p_{m,n}^{-} e^{+ik_{m,n}^{-} x} \right) f_{m,n}(r) e^{im\theta} \tag{2}$$

$$p(x,r,\theta) = \left(p_{0,0}^{+} e^{-ik^{+} x} + p_{0,0}^{-} e^{+ik^{-} x} \right) f_{0,0}(r) \tag{3}$$

$$p(x,r,\theta) = p(x) = P^{+} e^{-ikx} + P^{-} e^{+ikx} \tag{4}$$

This approach is key for mathematical demonstrations of the transfer function method, which imposes, however, the basic hypothesis that *m* and *n* are null. This means that the sound pressure should be approximately constant in any cross section of the tube, which is true for plane waves. The graphical representation of the influence of these eigenvalues on propagation modes are illustrated in Figure 1, while the expressions [13] relating ω_{mn} and *k* to the tube inner radios *R* and the n[th] non-negative root of the Bessel function first derivative of order *m*, a_{mn}, are:

$$k_n = \frac{\omega}{c_0} \sqrt{1 - \left(\frac{\alpha_{mn}}{R} \frac{c_0}{\omega} \right)^2} \tag{5}$$

$$\omega_{mn} = \frac{c_0}{R} \sqrt{k_n^{\,2} + \alpha_{mn}^{\,2}} \tag{6}$$

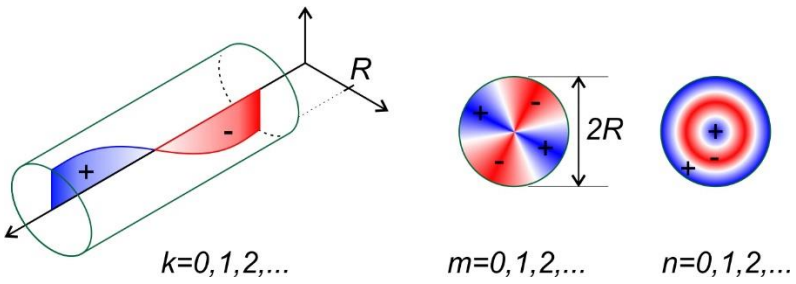


Figure 1: Wave propagation modes in cylindrical coordinates

Considering the boundary conditions for longitudinal propagation (rigid termination) and for radial propagation (rigid wall), it is possible to estimate with a certain accuracy, the frequencies of some normal and radial modes. In the case of the longitudinal modes ($k > 0$), the natural frequencies can be obtained via Eq.(7), while for the radial modes ($n > 0$), the frequencies can be estimated by via Eq. (8). However, for the azimuthal modes, these boundary conditions are not well defined in this problem.

$$\text{sen}\left(k_n\right) = 0 \tag{7}$$

$$\text{J}'\left(\alpha_{mn}\right) = 0 \tag{8}$$

For a tube of 1 m in length and 73.6 mm in internal diameter, the standard points out that normal propagation should be considered up to about 2700 Hz. At the same time, Eq.(8) shows that the first radial mode happens at about 5435 Hz. Therefore, one can conclude that, between these two frequencies, longitudinal modes coexist with azimuthal ones and, if able to be considered, would double the useful range of the impedance tube. The strategy proposed here for identifying these azimuthal modes is to sum up the complex pressure values observed by microphones placed in the same cross section and observe the behavior of this sum along this frequency range. If the result of the superposition return a magnitude higher than that of each original signal, there is constructive interference and, therefore, signals are in phase. The opposite is true in the presence of azimuthal modes, to whom destructive interference is expected. In these cases, the resulting sum should render a smaller magnitude and the conclusion that there must be an azimuth nodal line between these two microphones, as suggested in Fig.1 for $m > 0$.

To illustrate this strategy, two distinct generic points of the same section of the tube are taken, both at the same distance from the center of the tube, *i.e.*, at the same longitudinal and radial coordinates. In light of the equations developed for the transfer function method, Equation (2) is simplified for this case, resulting in:

$$p_1(\omega,\theta_1) = P(x,r,\omega)e^{im\theta_1} \tag{9}$$

$$p_2(\omega,\theta_2) = P(x,r,\omega)e^{im\theta_2} \tag{10}$$

In case both microphones are in phase, $\theta_1 = \theta_2 = \theta$, the sum results in $p_1 = p_2 = 2P$ with $P > p1$ and $P > p_2$. If there is a phase difference $\Delta\theta$ between the mics, the sum $p_1 = p_2 = 2Pe^{im\theta}$, which is only smaller than each component if $\pi/2m < \Delta\theta < 3\pi/2m$. For the first azimuthal modes ($m = 1$) that is indeed the case and one can state that there will be a nodal plane (or even an odd number of nodal planes) between those two microphone positions, since:

$$\left|p_1(\omega,\theta_1) + p_2(\omega,\theta_2)\right| < \left|p_1(\omega,\theta_1)\right| + \left|p_2(\omega,\theta_2)\right| \tag{11}$$

In this work, the signals of nine microphones were taken along an impedance tube and a code was generated in MATLAB® that compared these signals according to the statement in Eq.(11), indicating where there are first-order nodal lines between the microphones. The arrangement of the microphones and overall setup are detailed in the next section.

2 The test bench

To perform the experiments, an impedance tube, test piston and a loudspeaker box have been built out of low cost, thick walled, construction tubing, namely, polypropylene random copolymer (PPR) pipes and fittings. The connections used in the hydraulic installations were adapted to the instrumentation required for the tests, as is the example of the microphone mounts, machined from aluminum and glued to the PPR fittings. The main tube is 1m long, 90mm external diameter and 73.6mm internal diameter. To complete the assembly, a full range flat response loudspeaker (FRS 8-8) and 9 condenser microphones (GRAS 40PH) have been used, in arrangements of 3 mics per section in 3 equidistant sections on the tube (Fig.2).

The impedance tube, also known as Kundt´s tube is an experimental apparatus used for a variety of purposes, including sound velocity estimation and acoustic impedance tests on materials and metamaterials. In this method, a speaker is installed at one end of the tube and a specific termination at the other end. The tube is instrumented in different ways in order to estimate properties of the termination, the medium or other variables associated with sound propagation.

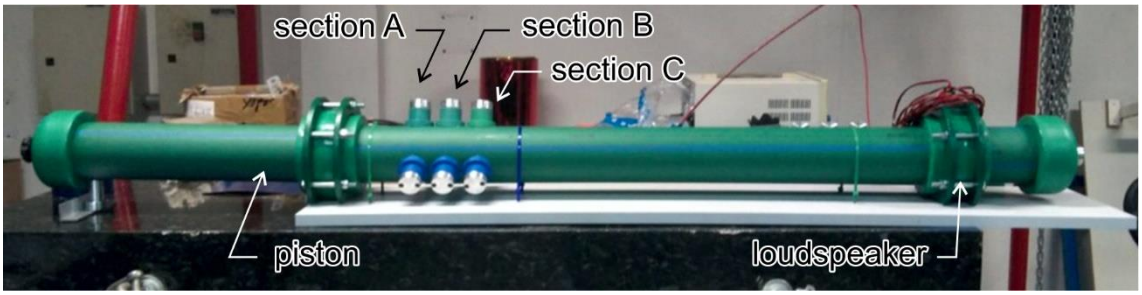
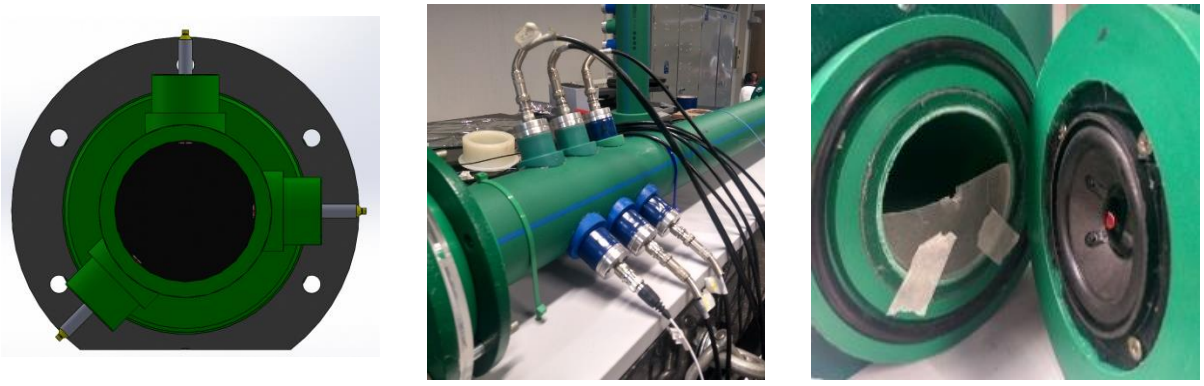


Figure 2: Picture of the complete tube assembly

Impedance tube instrumentation methods, according to technical standards, require only two microphones installed in different axial coordinates of the tube. In this work, however, an expanded method of instrumentation is proposed, aiming to achieve two objectives: (i) to increase the reliability of measurement for each section of the tube in the plane propagation regime and (ii) to relate different pressure values to points from same section in order to identify the azimuthal modes.

Figures 3(a) and 3(b) show views of this expanded instrumentation. The 9 microphones of the model were installed, divided into 3 sections spaced 50mm apart, the first section being 750mm from the source and the last one 150mm from a rigid nylon termination. In each section, the microphones are disposed asymmetrically, as shown in Fig. 3(a). This arrangement does not particularly facilitate the visualization, or even the excitation of any specific azimuthal mode; on the contrary, as seen in Eq.(2), due to the axisymmetric nature of the tube/loudspeaker assembly, azimuthal modes would not be well excited. In order to allow their assessment, a half circle slab is added near the speaker to act as a deflector (Fig.3c). As for the radial modes, those are above the frequency range of interest in this work.



(a) (b) (c)

Figure 3: Instrumentation details (a) schematic view of one section, (b) detailed photo of micfophone inserts and (c) speaker section with optional deflector.

Finally, the microphones were connected to a LMS Scadas Mobile data acquisition system from Siemens Industry Software. This system also generated the signal sent to the loudspeaker in the tube, after being amplified. In addition, for all tests, the microphones received the calibrations as suggested by ISO and ASTM standards. All tests were performed at a frequency range of 0 to 4000 Hz, with a resolution of 0.1953 Hz.

3 Results and discussion

In order to evaluate the consistency of the experimental apparatus in relation to the theory described and expected, relationship curves were plotted for each section, taking the microphones two by two. Then, an

experimental modal analysis was performed with the pressure values of the microphones as outputs, using the LMS Scadas data acquisition system running Test.Lab. Then, the pressure amplitude summing curves were plotted, two by two per section, in order to identify non-normal modes above the cutoff frequency for the given diameter. Finally, the frequencies identified by the modal analysis were used as reference to evaluate the frequencies of non-normal modes identified in the amplitude curves summed.

A final hypothesis, considered in this work, is that the loudspeaker installed at the end of the tube does not favor the appearance of non-normal modes, since the displacement of its membrane mainly occurs in the axial direction of the tube. To circumvent this problem, an obstacle was added at this end, which would unbalance the flat sound emission of the loudspeaker, favoring the appearance of non-normal modes in the tube. The optional obstacle can be seen in Fig.3(b). In addition, all tests were performed using the rigid tube termination, consisting of a nylon piston, fitted to the tube by means of o-rings.

3.1 Plane-wave propagation

The curves of Fig.4 are the transmissibility taken from each pair of microphone in section A (the closest to the test specimen). It is expected that, for frequency values below about 2700 Hz, the microphone curves have the same sound pressure amplitude (flat waves). In fact, it is observed that, for frequencies below 2719 Hz, the amplitude ratios between the pairs of microphones are very close to 1. Above this, there is no behavior pattern in these curves. For the frequencies below the cutoff, the ratios between the amplitudes of the microphones have a maximum difference of 1% between them, except in 3 regions of instability, as can be seen in Fig. 4, due to resonances of the system in these frequencies. Thus, even with the imbalance in the sound emission caused by the shield, it is still possible to identify the region of flat propagation for frequencies below the cut, as predicted by the bibliography. Based on this, it is inferred that the experimental apparatus is consistent for the next trials.

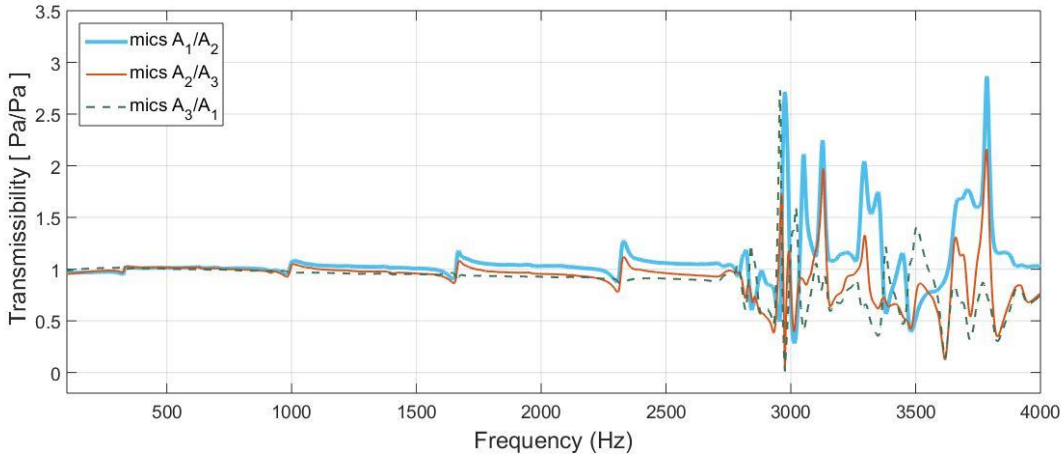


Figure 4: Pressure transmissibility functions for pairs of microphoes

3.2 Acoustic modal analysis

In order to identify these azimuthal modes, an experimental modal analysis was performed using the LMS Scadas Mobile acquisition system and the Test.Lab software from Siemens Industry Software. In this process, the electrical signal sent to the speaker terminals was adopted as reference while considering as output the pressure values measured in each of the 9 microphones installed in the structure. On each of these curves, a polynomial curve is adjusted in order to estimate the modal parameters of the system. Finally, based on the estimated modal parameters, it is possible to indicate some vibration modes of the system, which should show the flat or azimuthal characteristic of each one. This analysis can be done either by

observing the relative phase between each response point (acoustic pressure) or graphically, plotting said modes. Here, a license is given to assign a spatial direction to a scalar quantity (acoustic pressure), which, however, can assist intuitively in the visualization of modes.

By means of this method, 32 acoustic modes were identified in a frequency range of 100 to 4000 Hz. Of these 32 modes, the first 18 correspond to the plane propagation modes, the 18th mode corresponding to the frequency of 2780 Hz. In these first 18 identified modes, all three microphones of the same section have similar amplitude and phase, while there are differences of amplitude and phase between microphones of different sections, according to longitudinal propagation modes.

The last 14 modes identified are mostly non-normal azimuthal modes. However, there are normal modes that may be of interest for analyzing the samples in the tube in this frequency range. As mentioned before, azimuthal modes will present differences of amplitude and phase in at least two of the three microphones in the same section. To illustrate these modes, generic examples of non-normal modes are taken for a tube of cylindrical section, as in Fig. 5. In this case, mics 1 and 2 would register pressure values that are 180º (or π rd) appart. Assuming that the observed pressure values are a continuous function of space and time, this condition guarantees that there must be an odd number of nodal planes between this pair of microphones.

Table 1 shows the frequency values for the first 14 modes above the first cutoff frequency. Each mode is related to the phase of the pressure function considering only its real part, approximated to 0 or π, since only real modes are considered. Finally, as observed in Section 1, it is worth mentioning that the radial modes for the cylindrical structure with the given internal diameter start to emerge from approximately 5400 Hz. This ensures that the indicated non-normal modes are essentially azimuthal. In addition, the proposed instrumentation does not allow the identification of radial modes, since there are only pressure points taken close to the diameter of the tube.

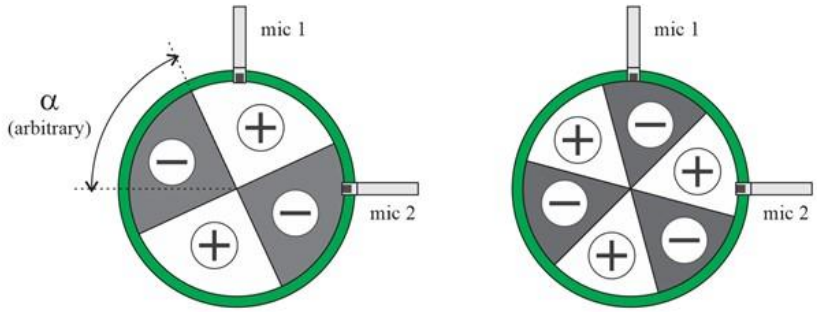


Figure 5: Visualization of azimuthal modes of different orders associated with the position of the microphones in an impedance tube section

3.3 Graphical interpretation

Now, we try to identify the same non-normal modes identified in the previous section, based only on the observation of the pressure data acquired by the microphones during the test. As described in section 1, it is hypothesized that when the simple sum of the pressure amplitudes between two microphones of the same section results in a smaller value than each plot, there is a phase difference between these pressure functions, which indicates the existence of an odd number of nodal lines between the measurement points and possibly an azimuthal mode.

Based on this, a code in MATLAB® was written with the purpose of comparing all curves and identifying those points, or regions in frequency, where there is destructive sum. The algorithm generates curves that are null when the sum of the amplitudes is greater than at least one of the plots and ‘1’ in destructive sum frequencies. The curves shown in Figures 6, 7 and 8, show the three paired comparison in each of the sections, A, B and C, respectively.

Table 1: Relative phase angle between microphones for modes above the 1st cutoff frequency (* are longitudinal modes)

	Section A Mic #			Section B Mic #			Section C Mic #		
# Modo – Frequência (Hz)	**1**	**2**	**3**	**1**	**2**	**3**	**1**	**2**	**3**
19 – 2821,3 Hz	0	0	π	0	0	π	0	0	π
20 – 2829,1 Hz	0	0	π	0	0	π	0	0	π
21 – 2870,9 Hz	0	0	π	π	0	π	π	0	π
22 – 2980,8 Hz	0	π	π	0	π	π	π	π	0
23 – 3057,8 Hz	0	π	π	0	0	0	π	0	π
24 – 3071,9 Hz	0	0	π	0	0	0	0	π	0
25 – 3137,7 Hz	0	π	π	0	π	π	π	π	π
26 – 3190,7 Hz	0	0	0	0	π	π	0	π	π
***27** – 3268,5 Hz	0	0	0	0	0	0	0	0	0
28 – 3366,2 Hz	0	π	0	0	π	π	π	0	0
***29** – 3448,7 Hz	0	0	0	0	0	0	0	0	0
30 – 3589,5 Hz	0	π	π	π	0	π	0	π	0
31 – 3654,1 Hz	0	π	0	π	0	π	0	π	0
32 – 3803,2 Hz	0	0	0	π	0	0	0	0	0

By comparing the modal approach to the destructive phase analyses performed by the proposed algorithm (Table 2), one can conclude that the algorithm shows a number of false positives. In all, considering the other sections, the method developed identifies 10 of the 14 non-normal modes indicated by the modal analysis. However, it is possible to verify clear patterns among some of the values, especially those slightly above the cutoff frequency for flat waves, where the first azimuthal modes occur. Table 2 highlights the proximity of some close values obtained by the two methods.

3.4 Metamaterial testing

3.4.1 Unit cell conceptual design and preliminary tests

The proposed approach for a metamaterial testing, under this framework, looks towards a unit cell fabricated using the Fused Deposition Method (FDM). This manufacture technique grows in popularity for its capability of creating somehow complex geometries at a reasonable cost. In addition, piezo disks are combined, in an attempt to try and improve the performance of the metamaterial.

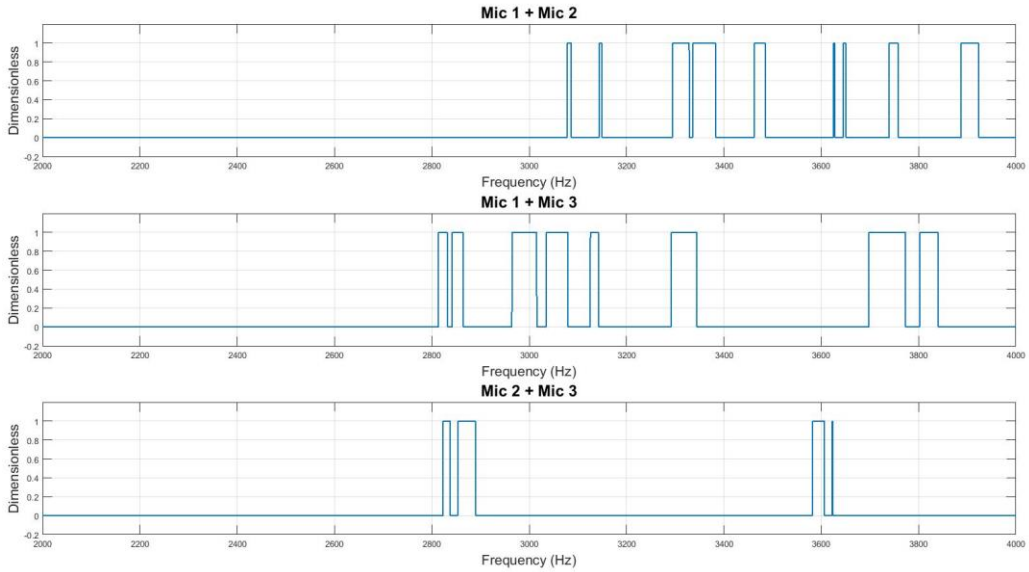


Figure 6: Visualization of modes for the microphones in section A

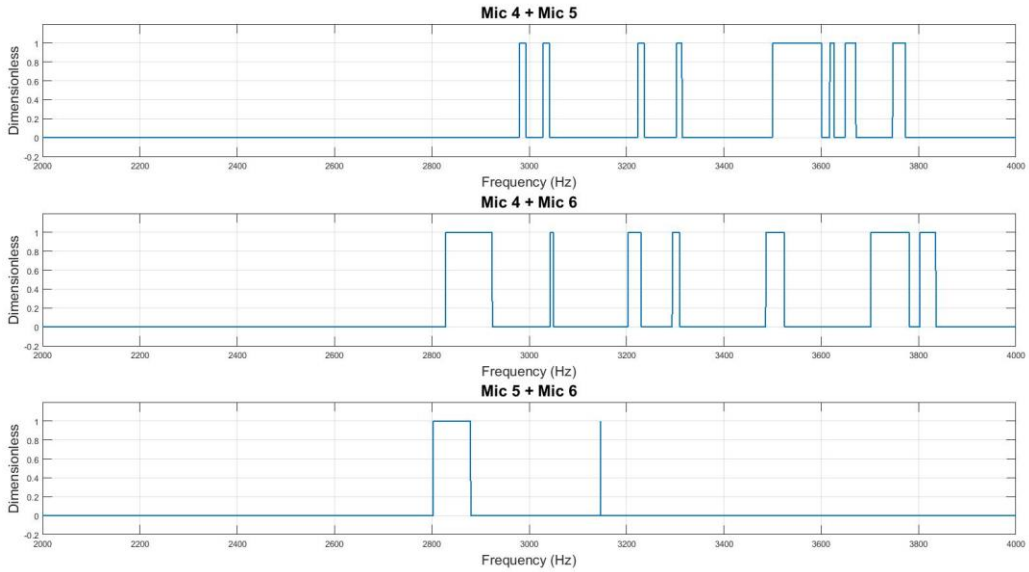


Figure 7: Visualization of modes for the microphones in section B

As known from the literature, the parts created by FDM exhibit anisotropic behavior. However, it is reasonable to assume a planar isotropy, in the direction of the deposition planes, as no preferential directions are observed there [14]. This can be verified in Fig. 9, which shows the filament deposition patterns; the beams labeld as 'Vx' and 'V+' have the infill structure deposited accordingly. The beams compared in this study differ only on the internal fiber direction, as described in Tab. 3, where b is the width, L the total length, L_u the cantilever free length, t the thickness, m the total beam mass and α the angle of the infill (see also Fig. 10). The plane isotropy assumption can also be verified in Fig. 10, which shows the base excitation FRFs obtained from the bare beams (before applying the piezos). As dynamic flexional load is applied, no major deviation is observed between the structures on the frequency response, for both Vx and V+ beams.

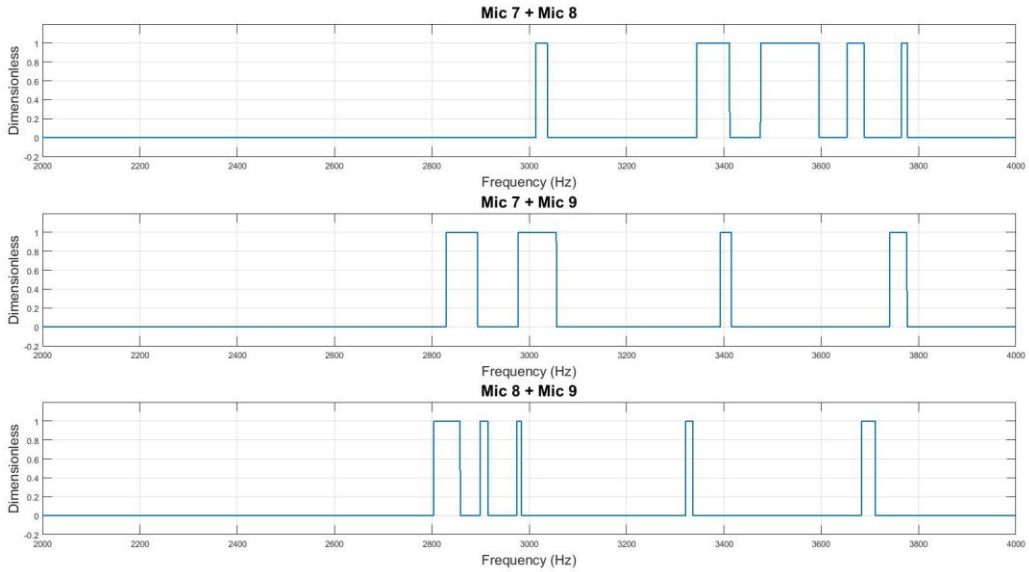


Figure 8: Visualization of modes for the microphones in section C

Table 2: Frequencies estimated by summation and modal analysis methods

Mic. 1 + Mic. 2 Freq. (Hz)		Mic. 1 + Mic. 3 Freq. (Hz)		Mic. 2 + Mic. 3 Freq. (Hz)	
Sum	**Modal**	**Sum**	**Modal**	**Sum**	**Modal**
2793			2821	2795	2821
2963	2990	2841	2829	2830	2829
3085	3058	2891	2871	2876	2871
3144	3138	2989	2981	2974	3071
3310		3061	3058		3366
3373	3366		3072	3595	
3481		3138	3138		3654
3745		3312			
3915		3729	3590		
		3819			

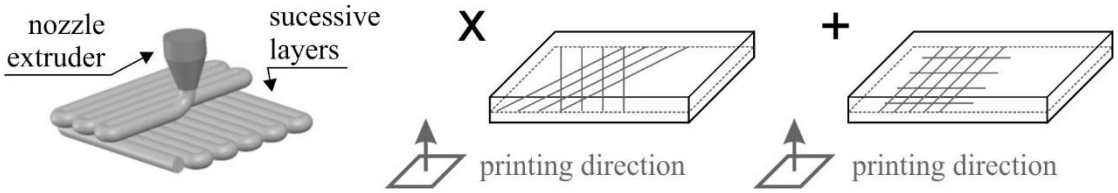


Figure 9: FDM process and structure labeling (after [14])

Table 3: Frequencies estimated by summation and modal analysis methods

beam	*b* [mm]	*L* [mm]	L_u [mm]	*t* [mm]	*m* [g]	α [º]
Vx	30	180	127	5	26	+/- 45 º
V+	30	180	127	5	22	90 º /0 º

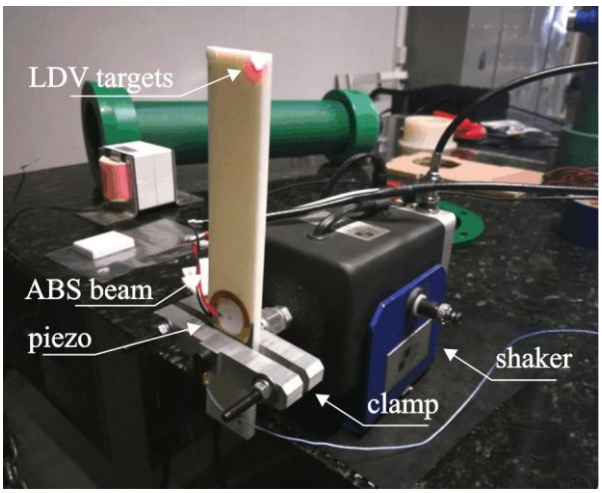


Figure 10: FDM process and structure labeling (after [14])

As the piezo disks are attached to the beams, an increase on the stiffness is expected. Also, due to the electromechanical coupling, some passive circuitry (see Tab. 4) is connected in order to evaluate the coupling strength. As observed in Fig. 12, in comparison with the results in Fig. 11, an increase on stiffness is more dominant over the mass contribution, and no relevant mechanical attenuation is achieved, using either a resistive or a shunt circuitry, indicating a rather weak electro-mechanical coupling between the ABS beam and the piezoelectric disk.

The electric response (Fig 13) presents a zero for the shunt circuit at the expected frequency, *i.e.* the shunt resonance (near 60 Hz). One would expect to observe this effect as an attenuation on the mechanical response as well but, due to the weak coupling, a rather small disturbance is seen instead (*c.f.* Fig 12) and no significant attenuation is achieved.

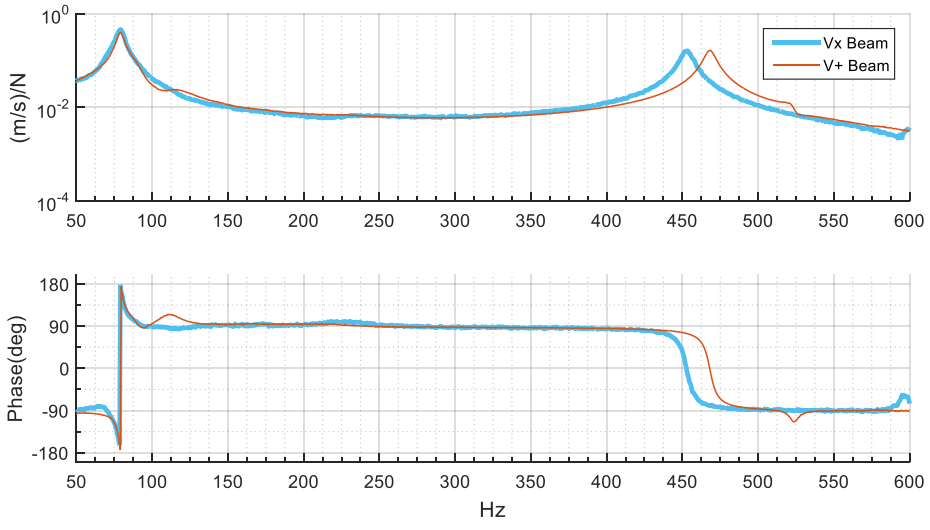


Figure 11: Bare beams tip mobility functions

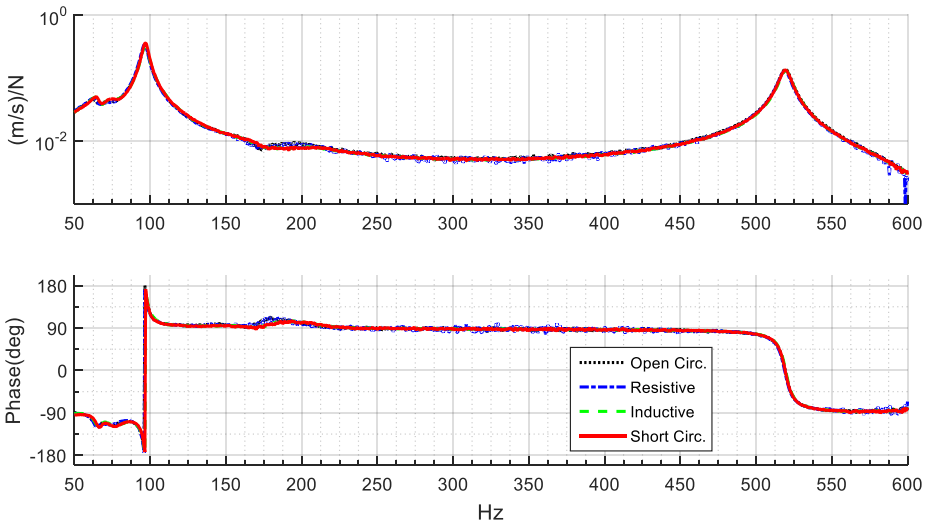


Figure 12: Smart beam tip mobility functions for different circuits

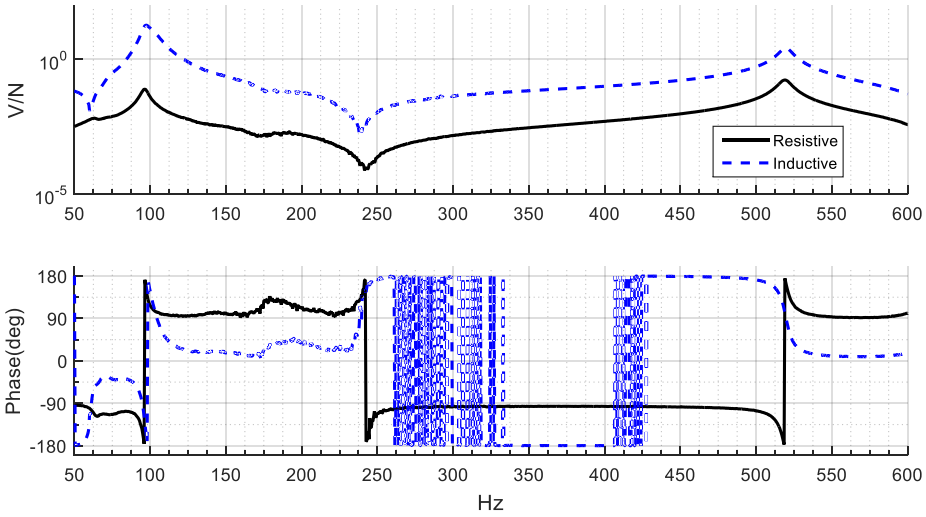


Figure 13: Smart beam electro-mechanical frequency response function for different ciucuits

3.4.2 Future work

The research presented in this paper is ongoing. The tests presented in section 3.4.1 are being used to validate models (both 3D FEM and state-space representations [15]) of the electromechanical system. Eventually a beam-like resonator will be used as suggested in Fig. 14, subject to plane wave excitation. The full unit cell concept models include (optional) polymeric membranes and/or porous materials. As the former aims at increasing the vibro-acoustic coupling, the latter should provide extra passive damping or, in other words, have its absorption properties enhanced by the resonant structure. The use of piezoelectric elements on the cell design will depend on the achieved coupling: (i) while with enough coupling one could envisage actively active control schemes [16], (ii) rather low coupling could still provide means for energy harvesting or condition monitoring [17, 18], as preliminary tests have shown a significant electric potential for the shunt circuit experiment.

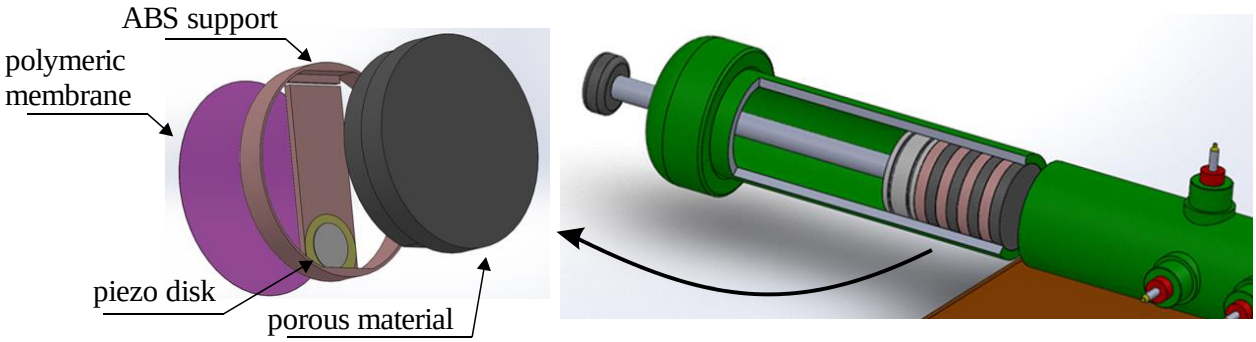


Figure 14: Conceptual unit cell design and periodic arrangement for testing on a waveguide

Finally, it should be mentioned that the use of membranes would render this solution infeasible for waveguides that are supposed to allow mass flow to go across the unit cells (such are HAVC of exhaust systems) but could still be used as modified Helmholtz resonators for that matter. There are at least other two uses of such unit cells, which consider the arrangement of the membranes parallel to the flux or arrays of cells mounted on panels for room acoustics.

4 Conclusions

Although it is possible to identify the frequency bands where the first azimuthal modes occur in the impedance tube, the sum method still proved to be inaccurate. In all, it was possible to identify 10 of the 14 modal frequencies indicated by the experimental modal analysis. Therefore, it was not possible to identify exactly for which frequency values certain azimuthal modes are excited.

Furthermore, it is necessary to understand more in depth how the relationship between the modes of longitudinal and azimuthal propagation occurs in this frequency range. Furthermore, it is necessary to understand how the influence of higher modes in this range occurs, in both upper and lower normal modes.

The impedance tube instrumentation also influences the results. The higher the frequency, the longer the wavelengths approximate the dimensions of the instruments and artifacts used in the construction, creating more complex phenomena in the tube, which are not contemplated by this model. Other effects such as the influence of the boundary layer on the pressure measured by the microphones in the tube should also be studied.

Finally, the use of such devices for metamaterial testing poses difficulties as cells designed for higher frequencies may not be tested using standard methods. This paper discussed means for addressing this issue and highlighted ongoing research towards that end.

Acknowledgements

The authors acknowledge the financial assistance of the Brazilian National Council for Scientific and Technological Development - CNPq (grant number 307369/2013-7) and the scholarships awarded to the first and second authors by CAPES Foundation and CNPq, respectively.

References

[1] Seybert, A.F.; Ross, D.F. *Experimental determination of acoustic properties using a two-microphone random-excitation technique*. The Journal of the Acoustical Society of America, v. 61, n. 5, p. 1362–1370, (1977).

[2] Chung, J.Y.; Blaser, D.A. *Transfer function method of measuring in-duct acoustic properties I.* Theory. The Journal of the Acoustical Society of America, v. 68, n. 3, p. 907–913, set. (1980a).

[3] Chung, J.Y.; Blaser, D.A. *Transfer function method of measuring in-duct acoustic properties II*. Experiment. The Journal of the Acoustical Society of America, v. 68, n. 3, p. 914–921, set. (1980b).

[4] ASTM E1050, *Standard Test Method for Impedance and Absorption of Acoustical Materials Using a Tube, Two Microphones and a Digital Frequency Analysis System*

[5] ISO 10534-2:1998, Acoustics - *Determination of sound absorption coefficient and impedance in impedance tubes - Part 2: Transfer-function method.*

[6] Bodén, H.; Åbom, M. *Influence of errors on the two-microphone method for measuring acoustic properties in ducts*. The Journal of the Acoustical Society of America, v. 79, n. 2, p. 541–549, (1986).

[7] Katz, B.F.G. *Method to resolve microphone and sample location errors in the two-microphone duct measurement method*. The Journal of the Acoustical Society of America, v. 108, n. 5, p. 2231–2237, (2000).

[8] Boonen, R.; Sas, P.; Desmet, W.; Lauriks, W.; Vermeir, G. *Calibration of the two microphone transfer function method with hard wall impedance measurements at different reference sections*. Mechanical Systems and Signal Processing, v. 23, n. 5, p. 1662–1671, (2009).

[9] Pelletier, W.; Holt, G.; Wanjura, J. *Simplified Three-Microphone Acoustic Test Method*. Instruments, v.1, n.1, p.4, 28 (2017).

[10] Arunkmar, B.; Jeyanthi, S. *Design and Analysis of Impedance Tube for Sound Absorption Measurement*. ARPN Journal of Engineering and Applied Sciences, v. 12, n. 5, (2017).

[11] Kimura, M.; Kunio, J.; Schuhmacher, A.; Ryu, Y. *A new high-frequency impedance tube for measuring sound absorption coefficient and sound transmission loss*. In: *Internoise 2014*, Melbourne, (2014).

[12] Munjal, M.L. *Acoustics of ducts and mufflers with application to exhaust and ventilation system design*.Wiley, New York, (1987).

[13] Rienstra, S.W.; Hirschberg, A. *An Introduction to Acoustics*. Dover Publications, Eindhoven: (2004).

[14] Lovo, J.F.P.; Fortulan, C.A.; da Silva, M.M. *Optimal deposition orientation in fused deposition modeling for maximizing the strength of three-dimensional printed truss-like structures*, Proceedings of the Institution of Mechanical Engineers, Part B: Journal of Engineering Manufacture 095440541877460. doi: 10.1177/0954405418774603, (2018).

[15] de Oliveira, L.P.R.; Varoto, P.S., Sas, P.; Desmet, W. *A state-space modeling approach for active structural acoustic control*, Shock and Vibration, v.16 (6): 607-621 (2009)

[16] Mosquera-Sanchez, J.A.; de Oliveira, L.P.R. *A multi-harmonic amplitude and relative-phase controller for active sound quality control*, Mechanical Systems and Signal Processing, v.45(2): 542-562, (2014).

[17] Trindade, M.A.; Pagani, C.C., Jr.; Oliveira, L.P.R. *Semi-modal active vibration control of plates using discrete piezoelectric modal filters*, Journal of Sound and Vibration, v.351: 17-28 (2015).

[18] da Silva, M.M.; Venter, G.S.; Varoto, P.S; Coelho, R.T. *Experimental results on chatter reduction in turning through embedded piezoelectric material and passive shunt circuits*, Mechatronics, v.29: 78-85 (2015).

Small-world based interactions in elastic metamaterials

N.Roveri [1], **S.Pensalfini** [1], **A.Carcaterra** [1]
[1] Sapienza University of Rome, Department of Mechanical Engineering,
Via Eudossiana 18, 00184, Rome, Italy
e-mail: **nicola.roveri@uniroma1.it**

Abstract
The problem of wave propagation control in one-dimensional systems, characterized by long-range interactions, has been the main topic of several publications in recent years. The introduction of magnetostatic or electrostatic forces modify the conventional connectivity based on the short-range interaction, classically studied in structural mechanics. The present paper provides a new definition of long-range force, based on the concept of small-world network. The small-world model, born in the field of social networks, is herein suitably applied to a regular lattice by the introduction of additional, randomly selected, elastic connections between different points, which modify the waves propagation within the structure. It is shown that the modified system exhibits a much higher propagation speed, one of the remarkable characteristic of the newly defined metamaterial or in general multi-$DOFs$ system.

1 Statement of the problem

Metamaterial science is gaining a wide interest in the scientific community [1; 2; 3; 4]. In recent papers [5; 6; 7] the authors investigated some particular features of long-range metamaterials [1]. The presented physical context considers particles interacting not only by closest neighbor forces, but also through long-distance actions [8]. For a specific choice of the function that describes the long-range force, unexpected results have been obtained, in terms of dispersion curve, phase velocity and group velocity [6]. Wave-stopping effects and supersonic regions of propagation have been identified and explored by the authors. Another topic the authors are concerned with is the swarms synchronization by long-range interactions in vehicular traffic, which is under publication. The synergy between this two topics is investigated in this work. The authors want to improve the energy exchange performances within a mechanical structure, by the means of long range connections, through a simple typology and topology of the connections.
So far, the studies carried on by the authors on metamaterials have been focused on the wave propagation in a $1D$ waveguide characterized by an interaction "all with all": each DOF is connected with all the others. It is easy to understand that such topology for the connections is rather complex to be realized in practice. The aim here is to reproduce long range effects replacing the "all with all" connections with a few random connections between non-consecutive resonators, i.e the long range connections, which are already elastically connected to the closest neighbors, as inspired by the small-world theory.

Small-world models have been initially studied in the field of social networks [9], [12], after the first experiments, the small-world theory have been generalized and studied as a branch of the theory of graphs [13]. One of the results underlined by these studies is that modifying a graph characterized by a strongly regular lattice, substituting few randomly-selected connections with long-range (again randomly-selected) connections, the information travel along the graph with a significantly higher velocity, without altering the local characteristics of the model itself. The application to dynamic systems has shown results that are related to a high propagation speed and to a strong synchronization [14], [15], [16], [17],[18]. In the following it is shown that, applying the Small-World theory to a mechanical structure, introducing a few random long-range

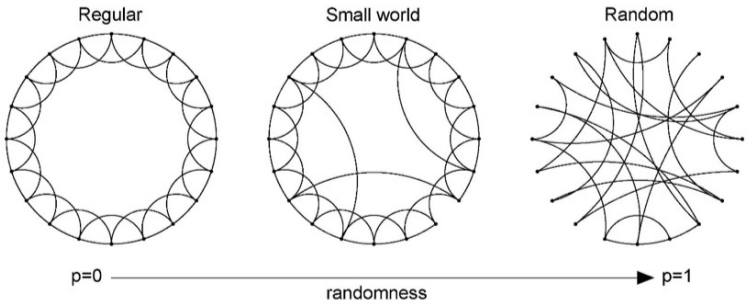


Figure 1: Example of Small world model.

interactions between the degrees of freedom, it produces a strong and quick diffusion of energy along the entire structure.

2 Brief introduction to the small-world theory

The term small-world has been used by Stanley Milgram in his work on social networks [9]. In the paper the Author introduces the small-world problem analyzing the intermediate acquaintance chain that connects two randomly chosen people in the world. The experiment that Milgram carried out lead to assert that, taken randomly two people in the US, these are separated by a chain of relationships involving six acquaintance links: for this reason, his study is often called six degrees of separation. Although the problem has been initially studied in the field of social networks, later it has been reconsidered in several other scientific fields approaching a strict definition of a small world model, still studied as a branch of the theory of graphs. This model [13] provides a robust mathematical basis to the Milgram experiment, besides the mathematical foundation, in this article, an innovative significant concept is introduced. In the ordinary theory of graph, the connection topology is assumed to be either completely regular or completely random. In [13], the authors fill the gap, considering regular networks rewired to introduce some amount of disorder. They showed these structures exhibit small characteristic path lengths, like random graphs, but with a modest addition or random connections. The dynamic of such small-world is shown to be characterized by high propagation speed, a key effect in the present paper. Technically, Watts and Strogatz consider a network made of vertices and unoriented links, initially characterized by a strongly regular pattern (in our case the short-range interactions between resonators) that is randomly modified until a completely random pattern is obtained. The process is pictorially described in Figure 1. In Figure 1, p is the probability that in the network one of the initial regular connection has been changed to connect distant vertices (in our case, the chance of including connections between distant $DOFs$). This probability can be increased from $p = 0$, representing the regular connection architecture, up to $p = 1$, the case of a completely random graph. The effects of this progressive modification, is studied using two parameters:

- $C(p)$: Cluster coefficient, it quantifies the amount of local interaction, among local groups of close by nodes. To define the clustering coefficient, suppose that a vertex v has k_v neighbors: at most $\frac{k_v(k_v-1)}{2}$ edges can exist between them and this happens when every neighbor of v is connected to every other neighbor of v. Let C_v denote the fraction of these allowable edges that actually exist and define C as the average of C_v over all v. In our case $C(p)$ is a measure of the closest neighbors interaction in the waveguide;

- $L(p)$: Characteristic length of the paths, is the characteristic separation that is present between two nodes of the graph, however they are chosen. L is the number of edges in the shortest path between two vertices, averaged over all pairs of vertices.This parameter provides an indirect measure of the

collective behavior of the network, that in our case is related to the synchronization effects of the $DOFs$.

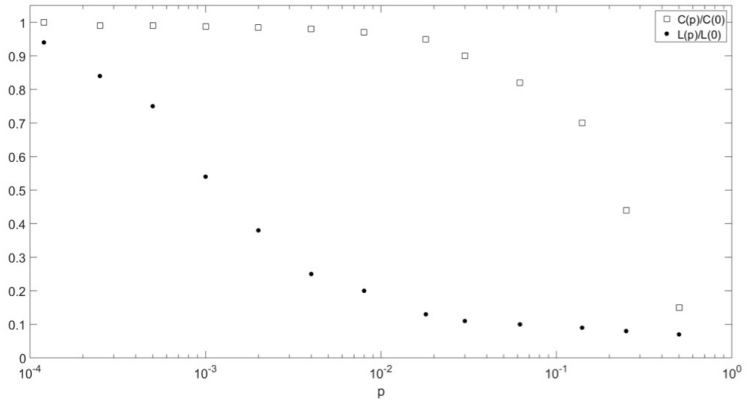


Figure 2: Path length $L(p)$ and clustering coefficient $C(p)$ for the family of randomly connected graph of Figure 1.

Figure 2 shows how the global feature $L(p)$ is very sensitive to p, while the local feature $C(p)$ is insensitive to p variations, at least in the region of small p. A remarkable characteristic for this study, is that the collective behavior of a network can be activated by an insemination of a moderate perturbation of random connections, permitting the local information to travel much faster than possible in regular local connectivity architectures. The intriguing result of the small-world theory is represented by the fact that this activation is possible using a moderate number of random long-range connectivity, meaning the perturbation to be introduced with respect to the standard model is low-cost and technically feasible by a small number of hyper-connected nodes. An additional added value of this control strategy is related to the random nature of the extra connectivity. Since the driving parameter to activate the collective response is $L(p)$, controlled by p, it means if the connections are individually altered but leaving $p = constant$, the level of collective behavior remains constant. This clarifies that in a connected swarm, we have the chance of modifying the connectivity architecture still preserving its capability to quickly spread the energy among the entire structure. The basic idea of this paper is that these effects can be used in the development of new connectivity architectures to be used among mechanical structures, as it will be shown in the next sections.

3 Analytical model for a 1D long-range waveguide

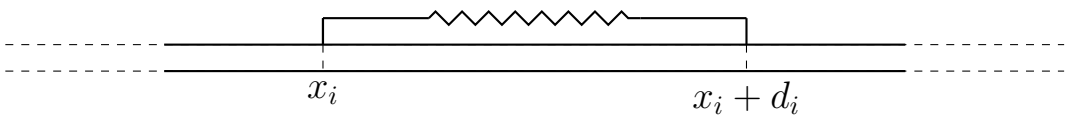


Figure 3: Rod with purely elastic long-range connections.

The system represented in Figure 3 is an infinite and continuous rod that can be considered a $1D$ waveguide characterized by elastic long-range interactions. In this case a rod of steel with $\rho = 7500\ \frac{Kg}{m^3}$, $E = 220\ GPa$, and section $S = 10^{-4}\ m^2$ is considered. As previously stated, the authors are interested in analyzing systems with long-range, randomly determined, elastic interactions; indeed the length of the springs and the position along the rod are randomly defined.

The equation of motion, with obvious meaning of the symbols, for the described system is:

$$\rho\frac{\partial u^2}{\partial t^2} - E\frac{\partial u^2}{\partial x^2} + \gamma\sum_i \{[(u(x) - u(x+d_i))\,\delta(x-x_i)] + [(u(x) - u(x-d_i))\,\delta(x-\tilde{x_i})]\} = 0 \qquad (1)$$

where $\tilde{x_i} = (x_i + d_i)$, u is the longitudinal displacement and γ is the elastic constant of the long-range connections. The summation term takes into account the elastic long-range connections and $i = 1, 2, .., n$ is the index for the randomly connected resonators and di is their distance.
The aim of this work is to evidence a faster propagation in the previously introduced system, in respect to the classical elastic one, without injecting external energy: a passive method to control the wave and energy velocity transmission to all the resonators of a $1D$ waveguide is here indeed investigated with the introduction of long range connections. To obtain the dispersion relation, the Fourier Transform in time and space is performed:

$$-\rho\omega^2\hat{\hat{u}} + Ek^2\hat{\hat{u}} + \gamma\sum_i \left\{\left[\left(\hat{\hat{u}} - \hat{\hat{u}}e^{id_ik}\right) * e^{-ix_ik}\right] + \left[\left(\hat{\hat{u}} - \hat{\hat{u}}e^{-id_ik}\right) * e^{-i\tilde{x_i}k}\right]\right\} = 0 \qquad (2)$$

where $\hat{\hat{u}}$ is the transformed displacement, in time and space domains. In previous papers [5; 6; 7] a closed form solution for the dispersion curve has been obtained for specific choices of the long-range force. Unfortunately, in this case, an analytical solution for equation (1) is not easily obtainable, this prevents to obtain an analytical expression for the dispersion curve and the phase velocity. This problem is overcame using a numerical approach, performing simulations over an equivalent discrete system, to evaluate the time needed to spread the energy among the structure.

3.1 Discrete equation of motion for a 1D waveguide

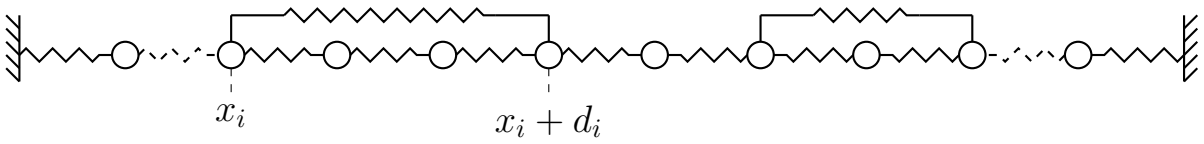


Figure 4: Discrete waveguide with purely elastic long-range connections.

A discrete version of the equation (1) is here considered: a waveguide composed by $N = 100$ degrees of freedom with equal masses and connected with equal springs (Figure 4). Introducing the vector $x(t) = [w(x_1,t), w(x_2,t), ...w(x_N,t)]^T$, where $x_i = i\varepsilon$ (ε is the discretization step along the waveguide and is equal to $0.1\ m$, that is five times shorter then the shortest wavelength), $\mathbf{M}$ is the mass diagonal matrix, $\mathbf{K}$ is the stiffness tridiagonal matrix and $\mathbf{K_{lr}}$ is the long-range stiffness matrix with sparse symmetric but not diagonal structure. The stiffness of the springs and the mass of the particles are obtained from the physical parameters of the continuous rod presented above and are equal to $k = \frac{E}{SL} = 2200000\ [\frac{N}{m}]$, with $L = \varepsilon N$, $m = 0.075\ [Kg]$ and $k_{lr} = k$. The other fundamental parameter in this study is the density of the connections $p = \frac{n}{N}$, where n is the number of long-range connections. In matrix form the equation of motion becomes:

$$\mathbf{M}\ddot{\boldsymbol{x}} + \mathbf{K}\boldsymbol{x} + \mathbf{K_{lr}}\boldsymbol{x} = 0 \qquad (3)$$

$$\mathbf{K} = \begin{pmatrix} 2k & -k & 0 & \cdots & 0 \\ -k & 2k & -k & \cdots & 0 \\ 0 & -k & 2k & -k & 0 \\ \vdots & \vdots & \ddots & \ddots & \vdots \\ 0 & 0 & \cdots & -k & 2k \end{pmatrix} \qquad \mathbf{K_{lr}} = \begin{pmatrix} 0 & 0 & 0 & \cdots & 0 & 0 \\ 0 & k_{2,2} & \cdots & -k_{2,10} & \cdots & 0 \\ 0 & \vdots & \ddots & 0 & 0 & 0 \\ \vdots & k_{10,2} & \vdots & k_{10,10} & \ddots & \vdots \\ 0 & \vdots & \vdots & \vdots & \ddots & \vdots \\ 0 & 0 & \cdots & 0 & 0 & 0 \end{pmatrix}$$

where $\mathbf{K}$ is the conventional elastic stiffness matrix, while $\mathbf{K_{lr}}$, which shows here, for explicatory purpose, the long range connection between the DOF 2 and 10 only, accounts for the long range terms only.
First of all the modal analysis is performed and the eigenvalues and the natural frequencies of the two systems are evaluated, to understand how the long-range elastic interactions affect the modal properties of the system. Figure 5 shows the comparison between the eigenvalues of the elastic and the long-range waveguide for $p = 6\%$.

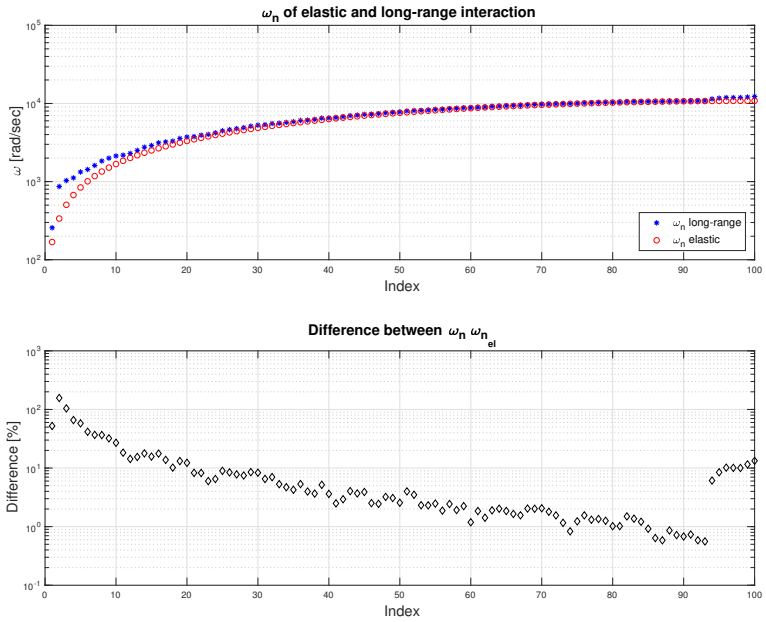


Figure 5: Starting form the figure on top, natural frequencies of the elastic and long-range waveguides and relative difference between two frequencies, plotted versus the mode index.

It can be seen in Figure 5 how the first and the last natural frequencies are deeply influenced by the presence of the long-range connections, which produces a stiffening of the structure at low and high frequencies, leaving the majority of the natural frequency roughly unchanged. Figure **??** shows the eigenvalues and the modal energies of the structure: both the symmetric and asymmetric modes are activated. The stems accounts for the modal energy of the long-range structure: there is a selection in the propagating mode shapes, empowering some at the expenses of others, in particular the 43rd mode is the most energetic.

Each random realization gives to the modified system a different topology of connections. In order to evaluate the statistical validity of the properties highlighted in Figure 5 and Figure **??**, an ensemble of 100 trials are considered for the density value of 6%. Figure 7 represents the eigenvalues for 100 different configuration connections with $p = 6\%$: the modal parameters are slightly affected by random realizations, however the considerations draw for Figure 5 still hold for each sample of the population and for the mean (over the samples) eigenfrequency $\bar{\lambda}$ curve. The same statistical study has been performed on the modal energy (lower plot in Figure 8). In this figure it is evident a shifting of energy in the higher modes for some configurations and the already examined distribution for the modes in the middle.

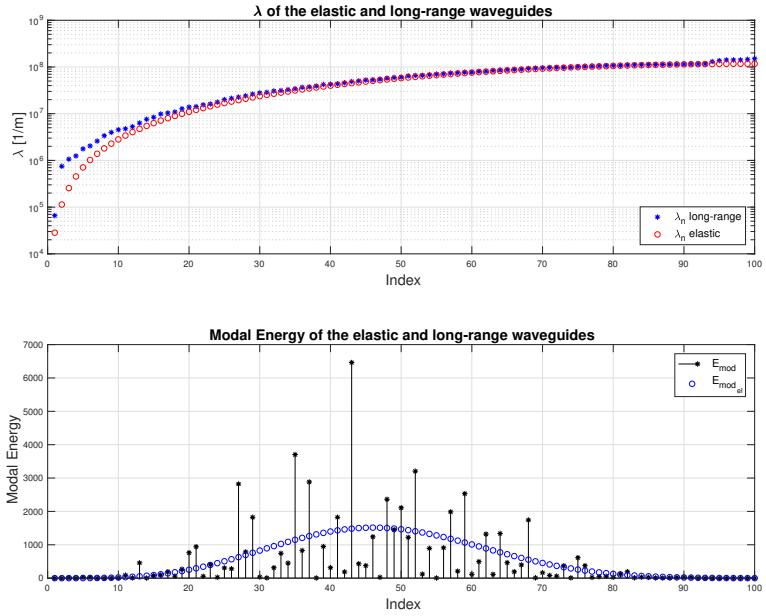


Figure 6: Starting from the figure on top, eigenvalues of the elastic and long-range waveguides and the modal energy of the system.

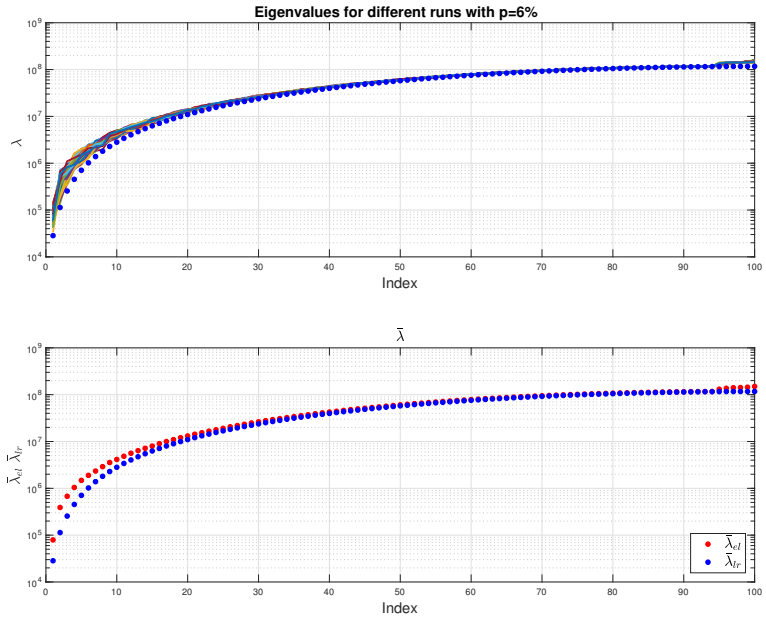


Figure 7: Starting form the figure on top, 100 curves of eigenvalues for $p = 6\%$, the average and the standard deviation of the eigenvalues, plotted versus the mode index.

The procedure is repeated, with p that ranges within the interval $[1, 15]\%$ with a step of size 1%, once p is fixed, 100 randomly connected models are considered, then p is increased and the analysis is repeated: results are shown in Figure 9. As far as the density of connection increases, the structure becomes more and more stiff at low and high frequencies. The same study on the modal energies is represented in Figure 10 and as observed in Figure **??** the most energetic modes of the average modal energy are between 40 and 50. The blue dots are the modal energies of the elastic structure, each color of the stem is the average modal energy for 100 trials for a given p. Increasing the p, the modal energy increases, especially for the higher modes.

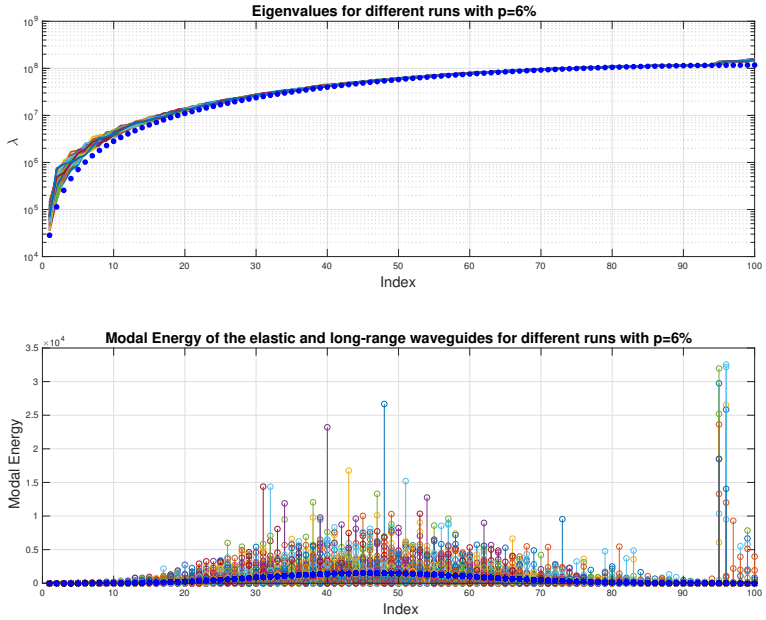


Figure 8: Starting form the figure on top, 100 curves of eigenvalues for $p = 6\%$ and the corresponding modal energy for each run, plotted versus the mode index.

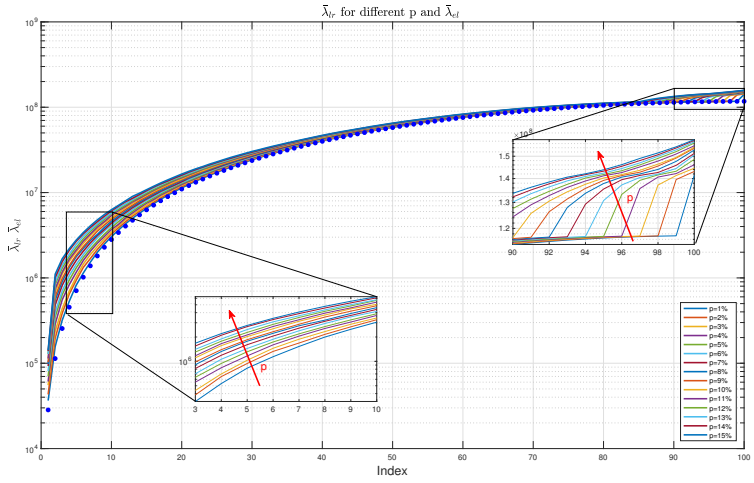


Figure 9: Each curve is the average of 100 runs at the same p, for $p = 1 - 15\%$.

4 Numerical simulations and discussions

In the present section the equation of motion of the standard ($\mathbf{K_{lr}} = 0$) and of the modified models ($\mathbf{K_{lr}} \neq 0$) in equation 3 are numerically evaluated with ®MATLAB, (ODE45 function). The system is excited by an initial non-zero displacement, imposed to the first two $DOFs$ of the waveguide, $x_1 = 0.05\ m$ and $x_2 = 0.02\ m$ respectively; moreover the study begin setting $p = 6\%$ and the number of $DOFs$ is $N = 100$.

Figure 11 shows that the energy sharing process is much faster in the modified structure. In fact at the time τ_2 the energy is spread almost to each DOF in the long-range waveguide, as shown in detail in Figure 12, while remains confined below the $30th\ DOFs$ in the elastic structure.

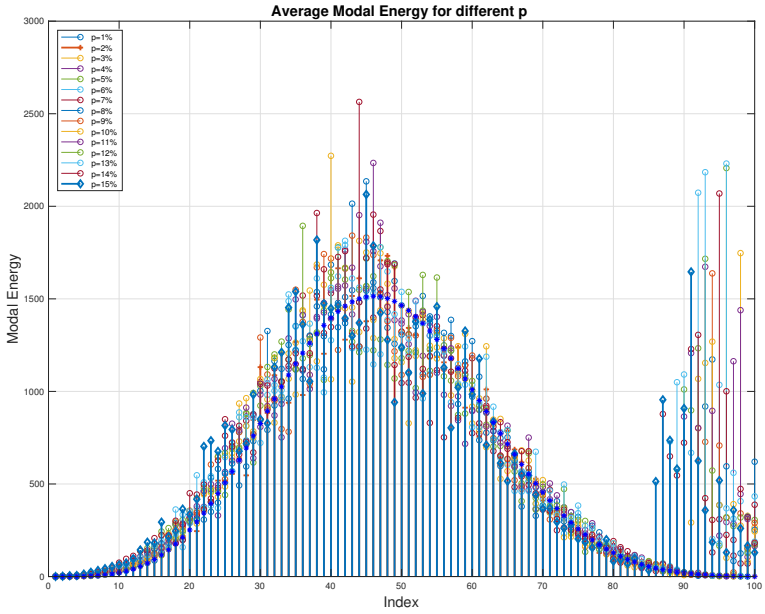


Figure 10: Each curve is the average of 100 runs at the same p, for $p = 1 - 15\%$, $p = 1\%$ and $p = 15\%$ are respectively marked with a $+$ and a $\diamondsuit$.

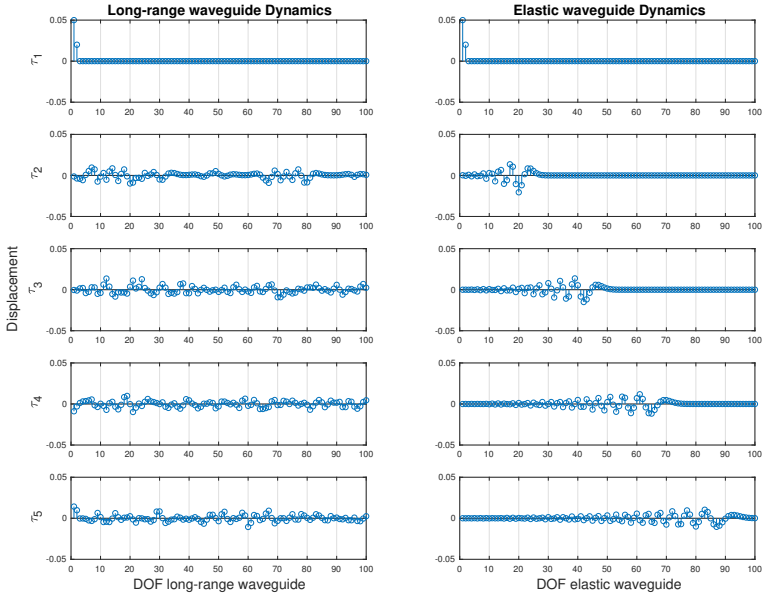


Figure 11: Starting from the subplot on top the waveguides dynamics at five different instants of time. Left: long-range waveguide; Right: elastic waveguide.

In Figure 12 the second and third subplots show the effect of the long range connections, which, almost instantaneously, propagate the local excitation far away from the original point of injection, i.e. to the 73rd resonator. Figure 11 and 12 show indeed, the benefit of a few, additional, random connections, means that the topology not necessarily must be a priori known, pledging the transmission of the information with no effort related to the design of the multi-$DOFs$ system. On the other hand the randomness of the connections does not allow an exact prevision of the time response of the system at any given time instant.

To appreciate the energy transmission along the waveguides, the average in time of the mechanical energy of each oscillator are here introduced:

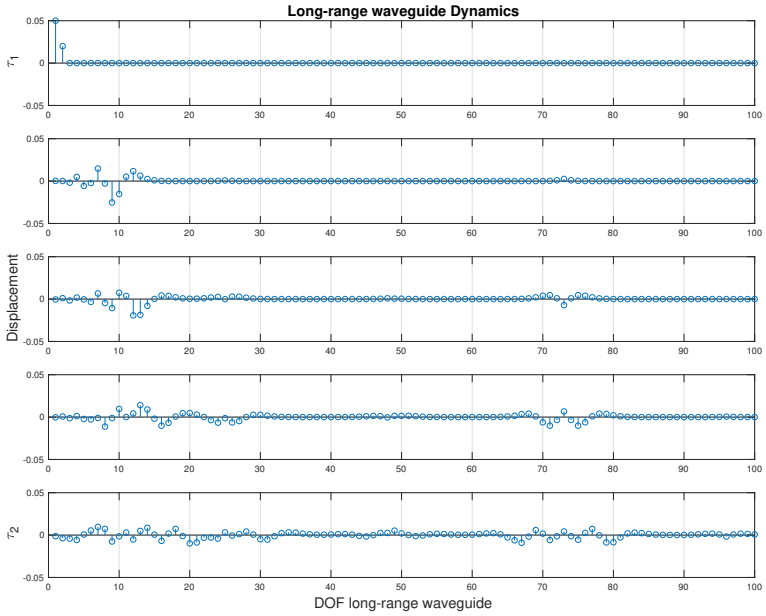


Figure 12: The long-range waveguide dynamics at five different instants of time between τ_1 and τ_2.

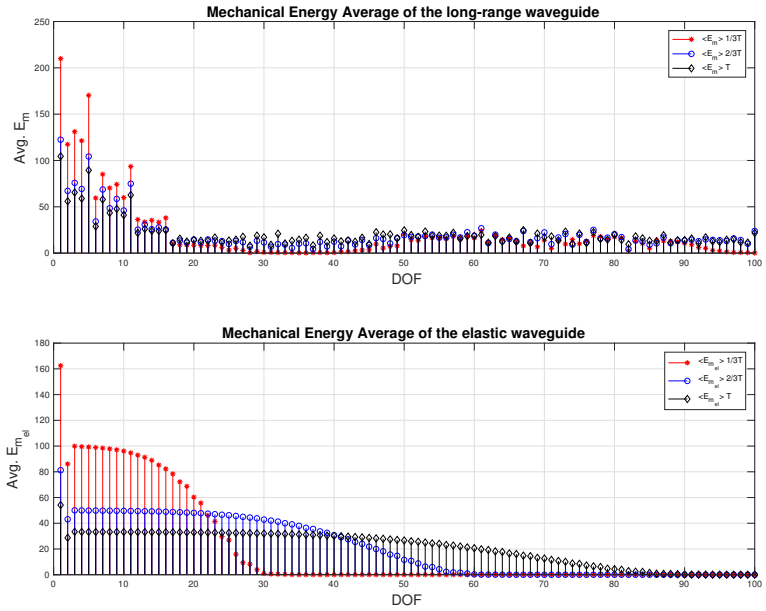


Figure 13: Average of the mechanical energy for each DOF of the long-range and the elastic waveguide at three different time.

$$E_{DOF_n}(j) \approx \frac{\sum_0^{t_j} m_n \dot{x}_n^2}{j} \qquad n = 1, ..., N$$

$$\mathbf{E_{DOF}}(j) = \begin{pmatrix} E_{DOF_1}(j) \\ \vdots \\ E_{DOF_n}(j) \\ \vdots \\ E_{DOF_N}(j) \end{pmatrix} \tag{4}$$

where E_{DOF_n} is the average energy of the $n-th$ DOF at the $j-th$ time, namely the average mechanical energy of each DOF is considered roughly equal to two times the kinetic energy of each oscillator (equation 4). In Figure 13 $\mathbf{E_{DOF}}$ is plotted at three different instants. It is easy to appreciate how fast is the redistribution of the energy through all the $DOFs$ in the long-range structure compared to the standard case.

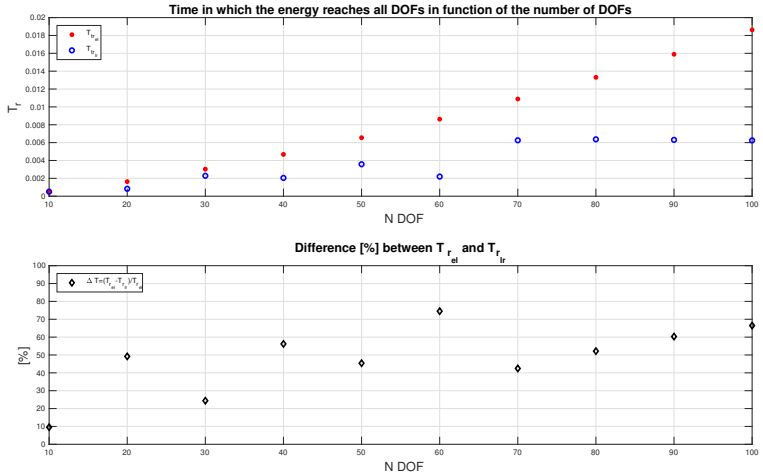


Figure 14: Starting from the subplot on top the time T_r in which the energy spreads to each DOF of the waveguide both for the elastic and the long-range waveguides for different numbers of $DOFs$ is shown. Below the % Difference between the time of the elastic waveguide $T_{r_{el}}$ and the long-range one $T_{r_{lr}}$ for different numbers of $DOFs$ is plotted.

For the standard elastic waveguide, it is possible to empirically evaluate the phase velocity taking into account the reflection time and the length of the waveguide. Introducing the reflection time, which is the instant when the initial excitation, applied to one side of the structure, has reached all resonators.
For the long-range system, an alternative definition of a characteristic time is needed, since the initial excitation does not progressively propagate to contiguous resonator only, but it gets (randomly) scattered over the entire structure. For example, if the connection is between one of the first $DOFs$ with one of the last, the response of the last resonator (which would determines the reflection time for the standard case) may occur before that central $DOFs$ have been reached. To our extent, an interesting parameter is the time after that all $DOFs$ have been reached by the initial excitation. To determine this time, E_r (the r stands for reflection time) is introduced and defined as a tenth of the energy equipartition value, E_0/N where E_0 is the energy initially injected within the structure (equation 5). In the dynamics of the system, at least for one time step, each DOF has a content of energy greater or equal to E_r. The time of interest T_r, in particular $T_{r_{lr}}$ for the long-range waveguide and $T_{r_{el}}$ for the elastic one, is the time in which all resonators have been through the energy threshold E_r.

$$E_r = \frac{E_0}{N}\frac{1}{10} \tag{5}$$

The results of the numerical simulations are shown in Figure 14 : T_r is plotted for different structures with

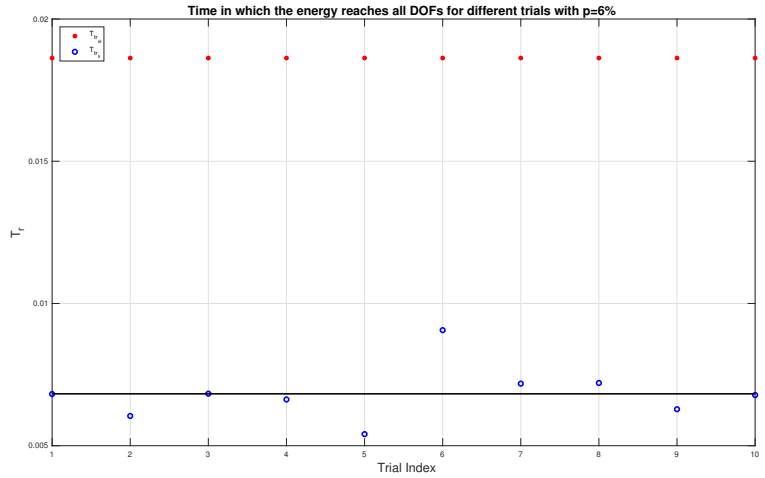


Figure 15: Time in which the energy spreads along the waveguide: the long-range one $(T_{r_{lr}})$ and the time for the standard model that is here represented just as a reference for 10 different trials with $p = 6\%$ and 100 $DOFs$.

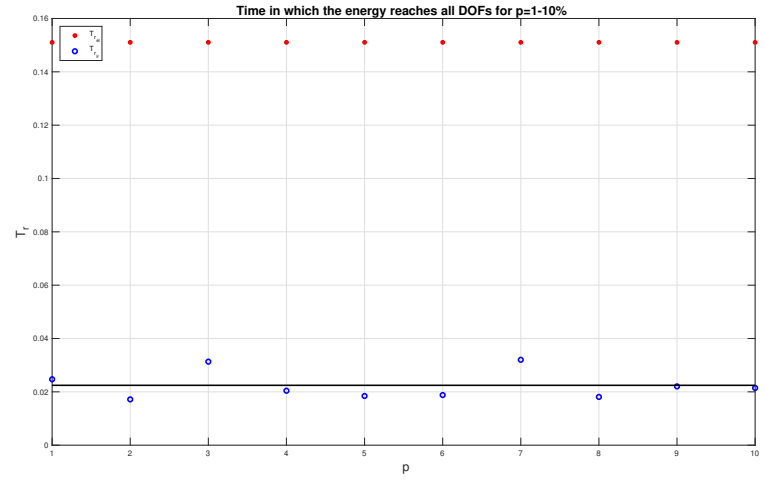


Figure 16: Time in which the energy spreads along the waveguide both for the elastic $(T_{r_{el}})$ and the long-range one $(T_{r_{lr}})$ for $p = 1 - 10\%$ and 100 $DOFs$.

different $DOFs$ number, both for the long-range and elastic waveguide. In the elastic waveguide the time increases linearly as expected [19]. In the lower subplot the difference in percentage between the two waveguides is presented. For the long-range structure $T_{r_{lr}}$ increases more slowly with respect to the elastic system and the time difference between the two waveguides increases with the increasing number of $DOFs$. The difference for N=100 is of the order of 70%.
In order to test the statistical validity of the previous findings, in Figure 15 is presented T_r for different realizations of random connections, for $p = 6\%$ and 100 $DOFs$. The system shows a sensitivity of the investigated time to different realization of random connections, even though the time in the long-range waveguide is always much lower then the one of the elastic system, i.e. roughly 60% lower irrespectively of the realization. Another interesting result is shown in Figure 16, where the investigated time is evaluated in function of the density of connections, bounded within $[1, 10]\%$, for $N = 100$. For p that varies between $1\%$and 10%, there

is not a significant change in the time of energy transmission, which is roughly 90% smaller that the time of the elastic waveguide. It should be pointed out that Figure 16 shows just one explicatory example, among the population of different random structures characterized by the same density of connections: however several trials have been performed without an evidence of significant different results.

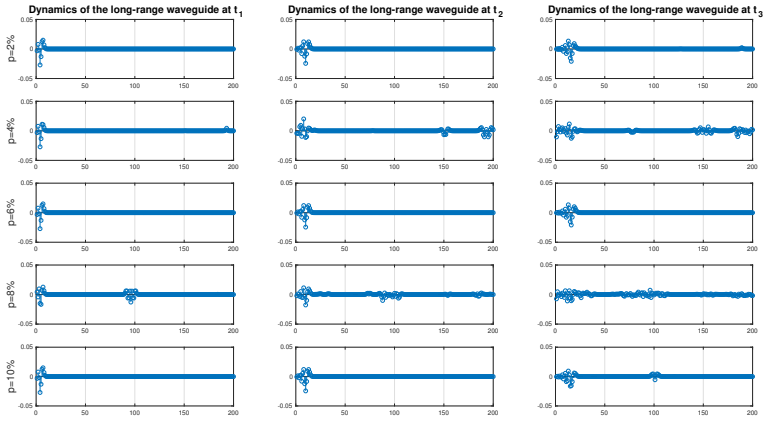


Figure 17: The waveguides dynamics at three different instants of time (column), for five different $\%$ of connections (row).

The small sensitivity to the density of connections is shown also in Figure 17, which represents three different times of the dynamic evolution for five different values of p. The scattering of energy seems indeed more effective for the examples with 4 and 8% than the ones with 6 and 10%.
In conclusions, a qualitative comparison between T_r plotted in Figure 16 and the path length $L(p)$ in Figure 2 is here drawn. T_r provides indeed information on how fast the energy is spread all over the entire elastic structure, which can be related to the path length introduced for the small world model, which tells the shortest path between any two nodes of the graph. While in Figure 2 $L(p)$ has a significant drop for low values of p, meaning that in these cases the random connections are too few to radically change the way the information is shared within the graph, our modified structure exhibits a T_r that is radically different form the original elastic structure, even for p as low as 1%. In other words, with the parameters adopted here, especially with $N = 100$, the simulations do not capture the transition between a regular behavior to a *collective* one, in function of p, but they capture the *collective* behavior only in Figure 16, in analogy with the final constant trend of $L(p)$ in Figure 2 for $p > 0.01$. A possible explanation for that may rely on the limited number of $DOFs$ adopted in our simulations, i.e. at most 100 due to the computation time, which prevent us to perform experiments with $p < 1\%$ (0.1), i.e. at least 1 long range connection has to take place over 100 $DOFs$. As a future research activity, the number of $DOFs$ will be significantly increased, in order to better investigate the, potential, transition between a regular to a collective behavior in our modified elastic structure.

5 Conclusions

The problem of wave propagation control in one-dimensional systems characterized by long-range interactions has been here analyzed. In particular, taking the advantage of concepts originally introduced in the small-world networks, the paper has shown that the addition of a few random long-range interactions between the degrees of freedom of a standard waveguide produces a strong and quick diffusion of energy along the whole structures.
The modified system shows indeed a relevant reduction in term of transmission time greater then 70%, with only 2% of long-range density of connections.
Due to limitations set by the computation time, these early numerical experiments have been performed with

a limited number of $DOFs$, at most 100. As a future research activity, the number of $DOFs$ will be significantly increased, in order to better investigate the, potential, transition between a regular to a collective behavior in our modified elastic structure, which characterize the original small world model investigated by Watts and Strogatz [13].
In this field, the literature has been mainly focused on the capillary control of the state of each DOF, to obtain a target dynamic for the entire structure, in this respect this paper proposes a new prospective, showing that a substantial modification of the propagation speed can be achieved if a few random, long range connections, are considered. The results obtained in this work for a simple one-dimensional waveguide are going to be generalized to different structure, indeed the application of this method in the field of swarm of drones and connected mobility it is one of the research topic in the actual and future work of the authors.

References

[1] A. Carcaterra, F. dell'Isola et al. *Macroscopic description of microscopically strongly inhomogenous systems: A mathematical basis for the synthesis of higher gradients metamaterials* Archive for Rational Mechanics and Analysis, vol. 218 (3), 2015, pp. 1239-1262.

[2] Gerasimov, R. A., Eremeyev et al. *Computer simulation of the mechanical properties of metamaterials*. In Journal of Physics: Conference Series (Vol. 738, No. 1, p. 012100), 2016. IOP Publishing.

[3] F. dell'Isola, et al. *Against the Fragmentation of Knowledge: The Power of Multidisciplinary Research for the Design of Metamaterials* Advanced Methods of Continuum Mechanics for Materials and Structures. Springer Singapore, 2016. 523-545.

[4] Madeo, Angela, et al. *Wave propagation in relaxed micromorphic continua: modelling metamaterials with frequency band-gaps*. arXiv preprint arXiv:1309.1722 (2013).

[5] A. Carcaterra, F. Coppo, F. Mezzani, S. Pensalfini. *Metamaterials: wave propagation control*. Conference Paper. ISMA 2016 Proceedings, KU Leuven, 2016

[6] A. Carcaterra, F. Coppo, F. Mezzani, S. Pensalfini. *Long-range retarded elastic metamaterials: wave-stopping, negative and hypersonic group velocity*. Physical Review,Under review

[7] F. Mezzani, F. Coppo, S. Pensalfini, N. Roveri, A. Carcaterra. *Twin-waves propagation phenomena in magnetically-coupled structures*. Conference Paper. Proceedings of EURODYN 2017.

[8] V. E. Tarasov, G. Zaslavsky. *Fractional dynamics of systems with long-range interaction*, Communication in nonlinear science and numerical simulation 11 (2006) 885-898

[9] S. Milgram, *The Small-World Problem*, Psychology Today, vol. 1, no. 1, pp. 61-67, 1967.

[10] M. Gerla, E.-K. Lee, G. Pau and U. Lee, *Internet of Vehicles: From Intelligent Grid to Autonomous Cars and Vehicular Clouds*, 2014.

[11] H. Ozaki, *Reaction and anticipation in the car-following behaviour.*, in Transportation and Traffic Theory. Proceedings of the 12th International Symposium on the Theory of Trafic Flow and Transportation, New York, eds C. F. Daganzo, 1993, pp. 349-362.

[12] A. Barrat, M. Barthlemy and A. Vespignani, *Dynamical processes on complex networks*, Cambridge University Press, 2008.

[13] D. J. Watts and S. H. Strogatz, *Collective dynamics of ?small-world? networks*, Nature magazine, vol. 393, pp. 440-442, 1998.

[14] M. Dorigo, M. Birattari, S. Garnier, H. Hamann, M. Montes de Oca, C. Solnon and T. Sttzle, *Swarm Intelligence*, in 9th International Conference, ANTS, Brussels, Belgium,, September 10-12, 2014.

[15] E. Schll, S. H. Klapp and P. Hvel, *Control of Self-Organizing Nonlinear Systems*, Springer, 2016.

[16] T. Gross and H. Sayama, *Adaptive Networks: Theory, Models and Applications*, Springer Science & Business Media, 2009.

[17] E. Bonabeau, M. Dorigo and G. Theraulaz, *Swarm Intelligence: From Natural to Artificial Systems*, OUP USA, 1999.

[18] A. Arenas, A. Diaz-Guilera, J. Kurths, Y. Moreno and C. Zhou, *Synchronization in complex network*, Physics Reports, vol. 469, no. Issue 3, pp. 93-153, 2008.

[19] N.Roveri, A. Carcaterra,A. Akay, *Energy equipartition and frequency distribution in complex attachments.* ,The Journal of the Acoustical Society of America, 2009, 126.1: 122-128.

Dynamic FEM simulation of wheel-rail rolling contact with friction in an Eulerian frame - Application to curve squeal

V.-V. Lai [1,2], **O. Chiello** [2], **J.-F. Brunel** [1], **P. Dufrénoy** [1]
[1] Univ. Lille, CNRS, Centrale Lille, FRE 2016 - LaMcube -
Laboratoire de Mécanique Multiphysique Multiéchelle, F-59000, Lille, France

[2] Univ Lyon, IFSTTAR, CEREMA, UMRAE, F-69675, Lyon, France
e-mail: **van-vuong.lai@polytech-lille.fr**

Abstract
The aim of this paper is to develop a full Finite Element (FE) computational method for the dynamics of wheel/rail frictional rolling contact systems in order to calculate reference solutions for curve squeal. The proposed method is characterized by the use of a fine FE discretization of the contact surface in an Eulerian frame, non-smooth frictional contact laws and model reduction techniques. An application to the wheel/rail frictional rolling contact is presented in both quasi-static and dynamic cases. The validation of the approach in quasi-static conditions is carried out by comparison with CONTACT software. Stability and transient results show that the technique is able to simulate friction-induced vibrations at high frequencies.

1 Introduction

There is always rolling contact forces transferred within a finite area of contact between the rolling wheels and the rail of a railway system. These forces are generated by wheel load or by friction due to wheel motion on the rail. Even if friction mechanisms are rather weak, they may be an important source of vibration and noise.

As an example, in the case of a tight radius curve (radius lower than 200m), squeal can be generated due to the lateral slip of the wheel on the head of the rail. This noise is characterized by high sound pressure levels (130 dB at 0.9m from the wheel) at pure medium and high frequencies. The mechanism causing the instability is however still controversial. A negative slope of the friction coefficient depending on sliding velocity is introduced in some models as a source of the instability whereas squeal can also occur in the case of constant friction due to mode coupling instability in other models.

There are actually several wheel/rail rolling contact models with some simplifications. Equivalent point-contact models are based on analytic formulas or heuristic laws of frictional rolling contact [1, 2]. They give good results in slightly non linear dynamic cases close to pure rolling [3]. However, in the cases of large slips and high-frequency dynamics, surface contact models with discretization of the contact zone are more adapted. They need a discretization of the contact zone. The variational theory of Kalker [2] which is used in Pieringer's model [4] performs some simplifications as the semi-analytical computation of the local contact flexibilities or influence functions (Boussinesq and Cerruti elastic half-space assumptions, contact/friction decoupling). In the case of friction-induced vibrations in curves characterized by large slips, high frequency dynamics and very fast evolutions in the contact zone, the impact of these simplifications is unknown.

Finite element wheel/rail frictional rolling contact models use commercial softwares [5, 6] but the calculation is generally performed in a Lagrangian reference frame, which greatly limits its performance and is not adapted to high frequency dynamics.

The aim of the paper is to propose a full finite Element method for modeling friction induced vibration of the wheel-rail contact in curves. The wheel-rail contact is simulated by surface contact models with a discretization of the contact zone and non-smooth frictional contact laws. To reduce computational costs, simulations are performed in a Eulerian reference frame and modal reduction strategies are used. Instabilities are analyzed through two types of analysis: stability analysis to predict unstable modes assuming a full steady steading in the contact zone, and a transient analysis which allows to introduce non linearities and to determine the amplitude of vibrations. Reduction base including free-interface modes and static attachment modes is used to reduce computing duration. The proposed approach is applied for contact between the rail and the wheel during curving.

2 Finite Element (FE) formulation in the time-domain

2.1 Contact problem in the Eulerian frame

A wheel/rail rolling contact is considered, as shown in Fig. 1. The $z-$axis is chosen to coincide with the common normal to the two surfaces in contact, the longitudinal $x-$axis corresponds to the rolling direction and the $y-$axis refers to the lateral direction. The wheel rolling speed is V in a direction parallel to $x-$axis . In case of curving, wheel relative lateral velocities ΔV_y and longitudinal velocities ΔV_x have to be considered. The wheel may also have a relative angular velocity $\Delta\omega_z$ around their common normal (or spin).

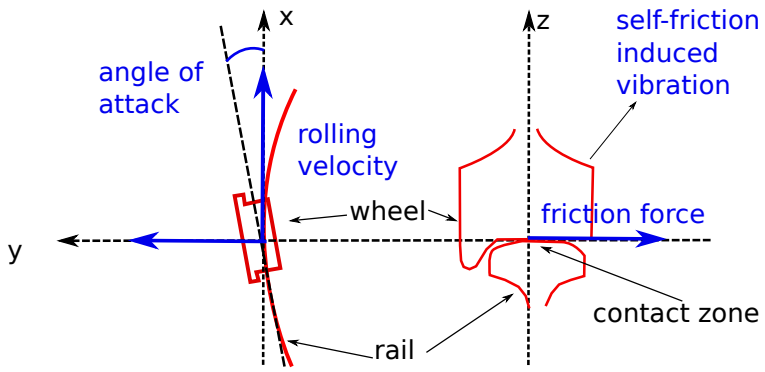


Figure 1: Coordinate system, kinetic variables and applied forces

According to [7], in the Eulerian frame which moves with the point of contact, the relative sliding instantaneous velocities (or creep velocities) between the wheel and the rail at a fixed point of the potential contact interface are given by:

$$\begin{aligned}\dot{s}_x &= v_x^W - v_x^R = \Delta V_x - \Delta\omega_z y + V(\frac{\partial u_x^W}{\partial x} - \frac{\partial u_x^R}{\partial x}) + (\dot{u}_x^W - \dot{u}_x^R)\\ \dot{s}_y &= v_y^W - v_y^R = \Delta V_y + \Delta\omega_z x + V(\frac{\partial u_y^W}{\partial x} - \frac{\partial u_y^R}{\partial x}) + (\dot{u}_y^W - \dot{u}_y^R)\end{aligned} \tag{1}$$

where R, W denote respectively the rail and the wheel. $\mathbf{u}(x, y, z, t)$ and $\mathbf{v}(x, y, z, t)$ denote respectively the displacement and velocity fields of the structure in the Eulerian frame and the notation $\dot{u} = \frac{\partial u}{\partial t}$ refers to the time partial derivative. The terms involving $V\frac{\partial u}{\partial x}$ represent the deformation contributions due to rolling in the Eulerian frame whereas the terms involving $\dot{u}$ simply represent the dynamic contributions.

2.2 Contact laws

To deal with unilateral contact on the interface, a non-regularized Signorini law is chosen:

$$\begin{aligned} \Delta u_n - g &\leq 0 \\ r_n &\leq 0 \\ (\Delta u_n - g) r_n &= 0 \end{aligned} \tag{2}$$

where $\Delta u_n = u_n^W - u_n^R$ is the normal relative displacement on the potential contact interface, r_n is the normal contact stress and g is the initial gap. This law simply conveys that (i) there is no interpenetration between the two bodies, (ii) the interface only undergoes compression and (iii) it respects the condition of complementarity. A equivalent semi-regularized form of the law uses the projection on the negative real set (cf. for instance [8]):

$$r_n = \text{Proj}_{\mathbb{R}^-}\left(r_n - \rho_n \Delta u_n\right) \qquad \forall \rho_n > 0 \tag{3}$$

where $\text{Proj}_{\mathbb{R}^-}(x) = \min(x, 0)$ and ρ_n is a positive real number called normal augmentation parameter.

To deal with frictional contact, a non-regularized Coulomb law with a constant friction coefficient μ is used:

$$\begin{aligned} \|\mathbf{r}_t\| &\leq -\mu r_n \\ \|\mathbf{r}_t\| = -\mu r_n &\Rightarrow \exists \lambda > 0,\ \dot{\mathbf{s}}_\mathbf{t} = -\lambda \mathbf{r}_t \\ \|\mathbf{r}_t\| < -\mu r_n &\Rightarrow \dot{\mathbf{s}}_\mathbf{t} = 0 \end{aligned} \tag{4}$$

where $\dot{\mathbf{s}}_\mathbf{t}$ is the vectorial creep velocity with components $\dot{s}_x$ and $\dot{s}_y$ defined in equation (1) and $\mathbf{r}_t$ is the tangential stress due to friction. This law states that the frictional reaction cannot be greater than a limit $-\mu r_n$. If the limit is reached, the material particle slides and has a direction opposed to the direction of the reaction (slip state). In other cases, the relative velocity is null (stick state).

A equivalent semi-regularized form of the law uses the projection on the Coulomb cone (cf. for instance [8]):

$$\mathbf{r}_t = Proj_{\mathcal{C}}\left(\mathbf{r}_t - \rho_t \dot{\mathbf{s}}_\mathbf{t}\right) \qquad \forall \rho_t > 0 \tag{5}$$

where $Proj_{\mathcal{C}}(\mathbf{x}) = \min(\frac{\mu |r_n|}{\|\mathbf{x}\|}, 1)\mathbf{x}$ and ρ_t is a positive real number called tangential augmentation parameter.

2.3 Dynamics equations and FE discretization

Convective terms in the equations of motion induced by the Eulerian frame are only significant in the case where the rotational speed is in the order of magnitude of the eigenfrequencies ([9]). In the following application, the effects of the convective terms are neglected because the wheel rotational speed is assumed to be low in comparison to the wheel/rail eigenfrequencies.

The displacement field $\mathbf{u}$ must verify the equations of continuum mechanics [10] together with the local formulations of contact equations Eqs. (3) and (5). In order to introduce FE approximations, the principle of virtual power is used for the system dynamics and the contact laws are written in weak forms [11]:

$$\begin{gathered} \text{Find } \mathbf{u} \in \mathcal{U} \text{ and } \mathbf{r} \text{ such as } \forall \mathbf{u}^* \in \mathcal{U}^o \text{ and } \forall \mathbf{r}^* \\ \int_\Omega \rho \mathbf{u}^*.\ddot{\mathbf{u}} d\Omega + \int_\Omega \epsilon(\mathbf{u}^*) : \sigma(\mathbf{u}) d\Omega = \int_\Omega \mathbf{u}^*.\mathbf{f}_s d\Omega + \int_{\partial\Omega_F} \mathbf{u}^*.\mathbf{f}_d ds + \int_{S_c} \mathbf{u}^*.\mathbf{r} ds \\ \int_{S_c} r_n^* r_n ds = \int_{S_c} r_n^* \text{Proj}_{\mathbb{R}^-}\left(r_n - \rho_n \Delta u_n\right) ds \\ \int_{S_c} \mathbf{r}_t^* \mathbf{r}_t ds = \int_{S_c} \mathbf{r}_t^* \text{Proj}_C\left(\mathbf{r}_t - \rho_t \dot{\mathbf{s}}_\mathbf{t}\right) ds \end{gathered} \tag{6}$$

where Ω is the whole structure. $\mathbf{f_s}$ and $\mathbf{f_d}$ are respectively a volume load in Ω and a surface load on a surface $\delta\Omega_F$.$\epsilon(\mathbf{u})$ and $\sigma(\mathbf{u})$ stand respectively for the symmetric gradient and the stress tensor corresponding to any displacement field $\mathbf{u}$, the notation $\ddot{\mathbf{u}} = \frac{\partial^2 \mathbf{u}}{\partial t^2}$ refers to the double time partial derivative, $\mathcal{U} = \{\mathbf{u} | \mathbf{u} = \mathbf{u}_d \text{ on } \partial\Omega_u\}$ and $\mathcal{U}^0 = \{\mathbf{u} | \mathbf{u} = \mathbf{0} \text{ on } \partial\Omega_u\}$. $\delta\Omega_u$ is the part of the boundary of the domain Ω where a displacement $\mathbf{u_d}$ is prescribed on. S_c is the potential contact zone.

By using appropriate shape interpolation functions for unknown and test displacement and reaction fields $(\mathbf{u}, \mathbf{r}, \mathbf{u}^*, \mathbf{r}^*)$, finite element discretization of Eq. (6) directly gives:

$$\begin{aligned} \mathbf{M\ddot{U}} + \mathbf{C\dot{U}} + \mathbf{KU} &= \mathbf{F} + \mathbf{P_n}^T\mathbf{R_n} + \mathbf{P_t}^T\mathbf{R_t} \\ \mathbf{R_n} &= \int_{S_c} \mathbf{N_n}^T \text{Proj}_{\mathbb{R}^-}(\mathbf{N_n}(\mathbf{H_n^{-1}R_n} - \rho_n(\mathbf{P_nU} - \mathbf{G}))ds \\ \mathbf{R_t} &= \int_{S_c} \mathbf{N_t}^T \text{Proj}_{\mathcal{C}}(\mathbf{N_t}(\mathbf{H_t^{-1}R_t} - \rho_t\dot{\mathbf{S}}_\mathbf{t}(\mathbf{P_tU}, \mathbf{P_t\dot{U}})))ds \end{aligned} \tag{7}$$

where $\mathbf{U}$, $\mathbf{R_n}$ and $\mathbf{R_t}$ denote respectively the vectors of nodal displacements, equivalent normal reactions and equivalent friction forces, $\mathbf{M}, \mathbf{C}, \mathbf{K}$ are respectively the mass, damping and stiffness matrices of the structure without contact, $\mathbf{G}$ is the vector of nodal initial gaps and $\mathbf{N_n}, \mathbf{N_t}$ are the shape function vectors on the contact interface. In addition, $\mathbf{P_n}, \mathbf{P_n}$ are matrices allowing to pass the contact reactions from the local relative frame to the global frame whereas $\mathbf{H_n} = \int_{S_c} \mathbf{N_n}^T\mathbf{N_n}ds$ and $\mathbf{H_t} = \int_{S_c} \mathbf{N_t}^T\mathbf{N_t}ds$ are transformation matrices from nodal to equivalent forces. Finally, $\dot{\mathbf{S}}_\mathbf{t}(\mathbf{P_tU}, \mathbf{P_t\dot{U}})$ denotes the vector of nodal creep velocities which can be determined linearly from local displacement and velocity vectors, taking into account quasi-static creep velocities (cf. Eq. (1)).

3 Reduction strategies

The principle is to search an approximated solution $\mathbf{U} = \mathbf{Bq_r}$ of the problem spanned by a reduced basis $\mathbf{B}$ which leads to a reduced dynamics equation:

$$\mathbf{M_r\ddot{q}_r} + \mathbf{C_r\dot{q}_r} + \mathbf{K_rq_r} = \mathbf{B}^T(\mathbf{F} + \mathbf{P_n}^T\mathbf{R_n} + \mathbf{P_t}^T\mathbf{R_t}) \tag{8}$$

where $\mathbf{M_r}, \mathbf{C_r}, \mathbf{K_r} = \mathbf{B}^T(\mathbf{M_r}, \mathbf{C_r}, \mathbf{K_r})\mathbf{B}$ and the size of the system is reduced to the number of modes in basis $\mathbf{B}$.

In this paper, the proposed basis B includes free-interface normal modes of the structure and static attachment modes $\mathbf{B} = [\Phi \quad \Phi_s]$. Matrix Φ contains the real solutions of the free and undamped system:

$$(\mathbf{K} - \omega^2\mathbf{M})\mathbf{U} = \mathbf{0} \tag{9}$$

whereas Φ_s make the base statically complete by adding static solutions to unitary forces (normal and tangential) on the contact interface:

$$\mathbf{K}\Phi_s = \mathbf{P_c}^T \tag{10}$$

A stronger approximation consists in neglecting the dynamic terms in the reduced equations corresponding to attachment modes. However, bases Φ and Φ_s are not orthogonal which is a necessary condition in order to separate the contributions of normal modes and attachments modes. This can be fixed by using residual attachment modes defined by:

$$\tilde{\Phi}_s = \Phi_s - \Phi(\Phi^T\mathbf{K}\Phi)^{-1}\Phi^T\mathbf{P_c}^T \tag{11}$$

These modes are the static displacement responses to unit contact reactions after the elimination of the contribution of normal modes. It can be easily verified that $\tilde{\Phi}_s^T\mathbf{K}\Phi = \mathbf{0}$.

The use of basis $\mathbf{B} = [\Phi \quad \tilde{\Phi}_s]$ in Eq. (8) together with the elimination of the dynamic terms relating to attachments modes gives:

$$\begin{aligned} \Phi^T\mathbf{M}\Phi\ddot{\mathbf{q}} + \Phi^T\mathbf{C}\Phi\dot{\mathbf{q}} + \Phi^T\mathbf{K}\Phi\mathbf{q} &= \Phi^T(\mathbf{F} + \mathbf{P_n}^T\mathbf{R_n} + \mathbf{P_t}^T\mathbf{R_t}) \\ \tilde{\Phi}_s^T\mathbf{K}\tilde{\Phi}_s\mathbf{q_s} &= \tilde{\Phi}_s^T(\mathbf{F} + \mathbf{P_n}^T\mathbf{R_n} + \mathbf{P_t}^T\mathbf{R_t}) \end{aligned} \tag{12}$$

where $\mathbf{q}$ and $\mathbf{q_s}$ are the generalized coordinate vectors corresponding respectively to normal modes and residual attachment modes such that $\mathbf{U} = \Phi\mathbf{q} + \tilde{\Phi}_s\mathbf{q_s}$. A total decoupling between the generalized equations corresponding to free-interface normal modes and residual static attachment modes is obtained.

In addition, noticing that:

$$\begin{aligned} \tilde{\Phi}_s^T\mathbf{K}\tilde{\Phi}_s\mathbf{q_s} &= (\Phi_s^T - \mathbf{P_c}\Phi(\Phi^T\mathbf{K}\Phi)^{-1}\Phi^T)\mathbf{K}(\Phi_s - \Phi(\Phi^T\mathbf{K}\Phi)^{-1}\Phi^T\mathbf{P_c}^T)\mathbf{q_s} \\ &= (\mathbf{P_c}\Phi_s - \mathbf{P_c}\Phi(\Phi^T\mathbf{K}\Phi)^{-1}\Phi^T\mathbf{P_c}^T)\mathbf{q_s} \\ &= \mathbf{P_c}\tilde{\Phi}_s\mathbf{q_s} \\ &= \mathbf{P_c}(\mathbf{U} - \Phi\mathbf{q}) \end{aligned} \tag{13}$$

and including the above expression in Eq. (8) gives:

$$\begin{aligned} \Phi^T\mathbf{M}\Phi\ddot{\mathbf{q}} + \Phi^T\mathbf{C}\Phi\dot{\mathbf{q}} + \Phi^T\mathbf{K}\Phi\mathbf{q} &= \Phi^T(\mathbf{F} + \mathbf{P_n}^T\mathbf{R_n} + \mathbf{P_t}^T\mathbf{R_t}) \\ \mathbf{P_c}\mathbf{U} &= \tilde{\Phi}_s^T(\mathbf{F} + \mathbf{P_n}^T\mathbf{R_n} + \mathbf{P_t}^T\mathbf{R_t}) + \mathbf{P_c}\Phi\mathbf{q} \end{aligned} \tag{14}$$

It must be emphasized that, with this formulation, contact displacements $\mathbf{P_c}\mathbf{U}$ can be directly calculated from expanded forces and normal modes coordinates.

This reduction strategy consists in solving the global dynamics using free-interface normal modes and adding a local static residual flexibility controlled by matrix $\tilde{\Phi}_s^T$ in the expression of the contact displacements. This method gets very close to models such Pieringer's one [4] combining modal dynamics and static local resolutions of the kind of CONTACT software. However, in the proposed method, the local flexibility is calculated numerically by finite elements instead of using semi-analytical influence functions derived from Boussinesq's approximations. In addition, it takes into account the static normal/tangential coupling in the contact zone.

4 Stability analysis

The aim of the stability analysis is to address the mechanism of curve squeal due to frictional contact through the determination of the evolution of small perturbations around the steady sliding equilibrium.

4.1 Quasi-static equilibrium

The quasi-static or steady sliding equilibrium is first obtained by neglecting the dynamic terms in Eqs. (1) and (7):

$$\begin{aligned} \mathbf{K}\mathbf{U^e} &= \mathbf{F} + \mathbf{P_n^T}\mathbf{R_n^e} + \mathbf{P_t^T}\mathbf{R_t^e} \\ \mathbf{R_n^e} &= \int_{S_c} \mathbf{N_n^T}\mathrm{Proj}_{\mathbb{R}^-}(\mathbf{N_n}(\mathbf{H_n^{-1}}\mathbf{R_n^e} - \rho_n(\mathbf{P_n}\mathbf{U^e} - \mathbf{G})))ds \\ \mathbf{R_t^e} &= \int_{S_c} \mathbf{N_t^T}\mathrm{Proj}_{\mathcal{C}}(\mathbf{N_t}(\mathbf{H_t^{-1}}\mathbf{R_t} - \rho_t\dot{\mathbf{S}}_\mathbf{t}^\mathbf{e})ds \end{aligned} \tag{15}$$

where $\dot{\mathbf{S}}_\mathbf{t}^\mathbf{e} = \dot{\mathbf{S}}_\mathbf{t}(\mathbf{P_t}\mathbf{U^e}, \mathbf{0})$ is the vector of nodal quasi-static creepage velocities.

Assuming that some solutions of Eq. (15) exist and can be calculated, it notably provides the status of the nodes on the contact interface as a function of the equivalent normal reactions r_n^e and friction forces $\mathbf{r}_t^e$. The facing nodes are in contact if $r_n^e < 0$. These contact nodes are then sliding if $\|\mathbf{r}_t^e\| = -\mu r_n^e$ and sticking if $\|\mathbf{r_t^e}\| < -\mu r_n^e$.

4.2 Complex Eigenvalue Analysis (CEA) in case of full steady sliding

Stability analysis is only carried out in the case of full steady sliding (no sticking region) and maintained contact configuration: it is thus assumed that for each node in contact at equilibrium, bilateral contact and sliding Coulomb friction laws apply. In order to perform the stability analysis, these laws have to be linearized. On effective contact region, the linearized forms of Eqs. (3) and (5) with the above assumptions can be written (cf. for instance [12]):

$$\begin{aligned} \Delta u_n &= 0 \\ \mathbf{r}_t &= -\mu r_n \mathbf{t} - c_b \dot{u}_b \mathbf{b} \end{aligned} \tag{16}$$

where $c_b = -\mu r_n^e / \|\dot{\mathbf{s}}_t^e\|$ is a damping term due to the linearisation of the sliding direction of the friction force and $\mathbf{b}$ is the tangential direction orthogonal to $\mathbf{t}$.

Searching a discrete solution of the form $\mathbf{U^e} + \tilde{\mathbf{U}} \exp(\lambda t)$ where $\tilde{\mathbf{U}}$ stands for the complex displacement vector corresponding to small harmonic perturbations around the equilibrium, the linearized form of equation (7) leads to a constrained non symmetric eigenvalues problem:

$$\begin{aligned} (\lambda^2 \mathbf{M} + \lambda(\mathbf{C} + \mathbf{C_b}) + \mathbf{K})\tilde{\mathbf{U}} &= (\tilde{\mathbf{P}}_\mathbf{n}^T + \mu \tilde{\mathbf{P}}_\mathbf{t}^T)\tilde{\mathbf{R}}_\mathbf{n} \\ \tilde{\mathbf{P}}_\mathbf{n}\tilde{\mathbf{U}} &= 0 \end{aligned} \tag{17}$$

where $\mathbf{C_b}$ is the damping matrix provided by the linearisation of the sliding direction of friction force [12, 14, 13] and $\tilde{\mathbf{P}}_\mathbf{n}, \tilde{\mathbf{P}}_\mathbf{t}$ are new projections matrices such that $\tilde{\mathbf{P}}_\mathbf{n}$ is the restriction of $\mathbf{P_n}$ on nodes in the effective contact region at equilibrium whereas $\tilde{\mathbf{P}}_\mathbf{t}$ is the restriction of $\mathbf{P_t}$ on components in direction $\mathbf{t}$ on nodes in the effective contact region. In stable cases, modes corresponding to eigenvalues with negative real part are stable. In this case, the perturbations corresponding to these modes vanish and no vibration occur. On the other hand, modes corresponding to eigenvalues with positive real part are unstable. Some perturbations corresponding to these modes tend to diverge which can lead to self-sustained vibrations. The divergence rate of a mode is notably defined as $\mathrm{Re}(\lambda)/\mathrm{Im}(\lambda)$ where $(\mathrm{Re}(\lambda), \mathrm{Im}(\lambda))$ are respectively the real and imaginary parts (pulsation) of the mode. This rate corresponds to a negative damping rate.

4.3 Reduced CEA formulations

Solving such a large non-symmetric eigenvalue problem needs model reduction. The approximation consisting in neglecting the dynamic part of the attachments modes is also tested for the stability analysis. The same technique used in section 3 is applied. The reduction is first performed with basis $\mathbf{B} = [\Phi \quad \tilde{\Phi}_s]$ composed of free-interface component modes Φ and static attachment residual modes $\tilde{\Phi}_s$ defined on effective contact region. The dynamic effects corresponding the residual attachment modes are then neglected leading to the following constrained eigenvalue problem:

$$\begin{aligned} (\lambda^2 \Phi^T \mathbf{M}\Phi + \lambda \Phi^T(\mathbf{C} + \mathbf{C_b})\Phi + \Phi^T \mathbf{K}\Phi)\tilde{\mathbf{q}} &= \Phi^T(\tilde{\mathbf{P}}_\mathbf{n}^T + \mu \tilde{\mathbf{P}}_\mathbf{t}^T)\tilde{\mathbf{R}}_\mathbf{n} \\ \tilde{\mathbf{P}}_\mathbf{n}\tilde{\mathbf{U}} &= \tilde{\Phi}_s^T(\tilde{\mathbf{P}}_\mathbf{n}^T + \mu \tilde{\mathbf{P}}_\mathbf{t}^T)\tilde{\mathbf{R}}_\mathbf{n} + \tilde{\mathbf{P}}_\mathbf{n}\Phi\tilde{\mathbf{q}} \\ \tilde{\mathbf{P}}_\mathbf{n}\tilde{\mathbf{U}} &= \mathbf{0} \end{aligned} \tag{18}$$

where $\tilde{\mathbf{q}}$ is the generalized vector corresponding to free-interface normal modes.

From the two last lines of Eq. (18), normal reactions $\tilde{\mathbf{R}}_\mathbf{n}$ can be expressed as a function of the generalized vector $\tilde{\mathbf{q}}$:

$$\tilde{\mathbf{R}}_\mathbf{n} = -\mathbf{I}_n \tilde{\Phi}_s^T (\tilde{\mathbf{P}}_\mathbf{n}^T + \mu \tilde{\mathbf{P}}_\mathbf{t}^T))^{-1} \tilde{\mathbf{P}}_\mathbf{n} \Phi \tilde{\mathbf{q}} \tag{19}$$

where $\mathbf{I}_n$ is the boolean localization matrix such that $\tilde{\mathbf{P}}_\mathbf{n} = \mathbf{I}_n \tilde{\mathbf{P}}_\mathbf{c}$ Finally, using the above expression in the reduced eigenvalue problem gives:

$$(\lambda^2 \Phi^T \mathbf{M}\Phi + \lambda \Phi^T(\mathbf{C} + \mathbf{C_b})\Phi + \Phi^T(\mathbf{K} + \mathbf{K_c})\Phi)\tilde{\mathbf{q}} = \mathbf{0} \tag{20}$$

where $\mathbf{K_c}$ is a non-symmetric stiffness matrix taking account the effect of the local residual flexibility of the structure due to normal and friction forces:

$$\mathbf{K_c} = (\tilde{\mathbf{P}}_\mathbf{n}^T + \mu\tilde{\mathbf{P}}_\mathbf{t}^T)(\mathbf{I}_n\tilde{\Phi}_s^T(\tilde{\mathbf{P}}_\mathbf{n}^T + \mu\tilde{\mathbf{P}}_\mathbf{t}^T))^{-1}\tilde{\mathbf{P}}_\mathbf{n} \tag{21}$$

This reduction strategy consists in solving the global dynamics using free-interface normal modes and adding a local static residual stiffness controlled by matrix $\mathbf{K_c}$. This matrix plays the same role than 2-DOF Hertzian stiffness/Coulomb friction relations in the case on equivalent point contact models but is calculated by finite elements.

5 Numerical methods for non linear simulations

For the computation of the quasi-static solution (Eq. (15)) and dynamics solutions at each time step (Eq. (7)), an iterative fixed point algorithm on equivalent contact reactions and friction forces is used with a stop criterion based on forces convergence [14]. This algorithm is appropriate to the formulation of the frictional contact laws as non linear projections. The main advantage of the fixed point algorithm is that the integrator matrix remains constant at each iteration. In the simulations presented in this paper, the augmented parameters ρ_n, ρ_t are chosen as the smallest eigenvalue of the integrator matrix condensed on the contact degrees of freedom [15].

For the computation of the transient solution, the chosen time integration method is a modified θ-method. This is a first-order scheme developed by Jean [8] and appropriate to unilateral contact dynamics. It notably allows to compute quasi-inelastic shocks. The detail of the scheme with an application to friction-induced vibrations can be found for instance in Loyer's work [14].

6 Results

In this section, an application of the methodology presented in the previous sections is proposed for the case of rolling contact of a wheel and a rail with lateral creepages. The model is first described. Secondly, the model is validated in quasi-static conditions with CONTACT software. A stability analysis is then carried out. Transient calculations are finally performed with reduction and results are discussed.

6.1 Description of the model

The material behavior is assumed to be linearly elastic, isotropic and undergoing small deformations. The material data of the wheel and the rail are listed in Tab. 1.

Data	Wheel	rail
Young's modulus (GPa)	206.9	205
Poisson's ratio	0.288	0.3
Density (kg/m^3)	7800	7800

Table 1: Material data of the wheel and the rail

A vertical displacement u_{z0} is applied at the hub of the wheel. For the discretization by finite elements, compatible meshes on the interface are considered: facing nodes of the wheel and the rail in potential contact have identical tangential coordinates x and y. The potential contact area is meshed with elements of length 1 mm as shown in Fig. 2.

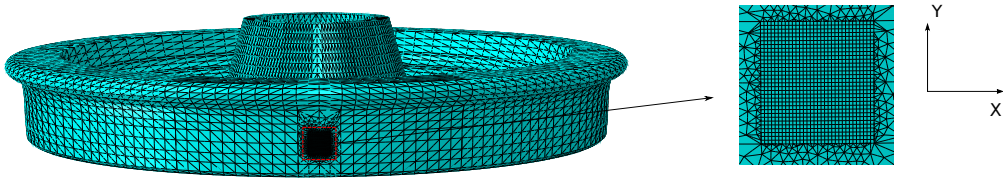
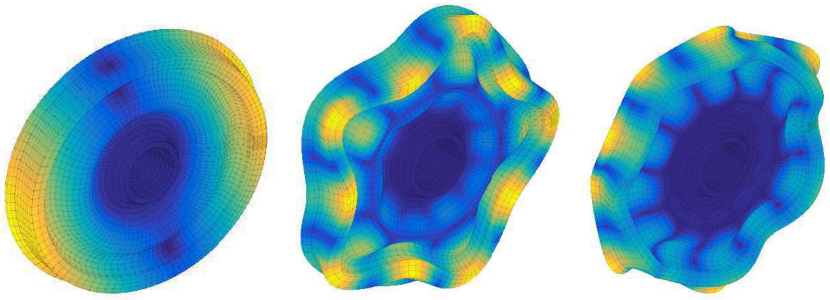


Figure 2: FE model of the wheel with fine mesh on the contact zone

6.1.1 Wheel dynamics

The dynamic behavior of the wheel is assumed to be linear and lightly damped so that a real modal basis can be used. This basis is presumed to be known in the frequency range of interest. A mode is characterized by its natural circular frequency ω_i, its vertical and lateral modal amplitudes at the contact point Φ_z and Φ_y (assumed to be normalized with respect to mass) and its structural damping factor Ξ.

The 100 first natural frequencies and corresponding free-interface modes have been calculated up to 8000 Hz. Three kinds of mode may be distinguished: the radial modes (r,m,n), the axial modes (a,m,n) and the circumferential modes (c,m,n) where n is the number of nodal diameters and m is the number of nodal circles. This classification is necessary to obtain a convergence of eigenvalues depending on the model mesh.



(a) (b) (c)

Figure 3: a: Mode axial of 136.4 Hz ($m = 0, n = 1$), b:Mode radial of 3281 Hz ($m = 1, n = 5$) et c: Mode axial of 3417 Hz ($m = 0, n = 6$)

Chosen modal damping factors η depend on the nodal diameters [3]:

$$\begin{cases} \eta = 10^{-3} & \text{if} \quad n = 0 \\ \eta = 10^{-2} & \text{if} \quad n = 1 \\ \eta = 10^{-4} & \text{if} \quad n \geq 2 \end{cases} \tag{22}$$

6.1.2 Rail dynamics

The rail model consists of one periodically supported rail of type UIC60 provided by ESI-Group (Fig. 4). This rail has 48m length. The space between sleepers is 60cm. However the dynamic of sleepers and ballast is neglected because of its low frequency domain.

The rail hysteresis damping is $\eta = 0.02$. The rail ends with an anechoic termination of 6 meters composed of 5 lengths $L = (0.6, 0.6, 0.6, 1.2, 3.0)$m which are associated variable structural damping $\eta = 0.1 \rightarrow 1$ to avoid the reflection of waves. Pads that connect the rail and the sleepers are modeled by springs $(Kx = Ky = 36e6, Kz = 180e6)$N/m. The pad hysteresis damping is $\eta = 1$.

The dynamic response obtained by FEM is compared with the dynamic response obtained with the analytical model as Timoshenko beam [16]. The vertical mobilities at the center point between two sleepers and on

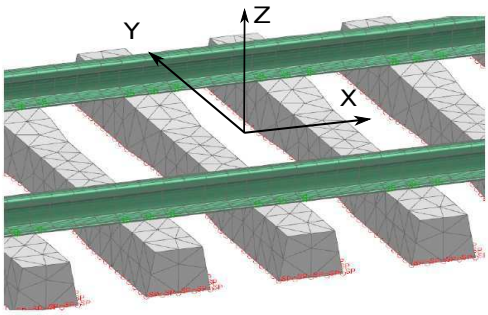


Figure 4: Rail model

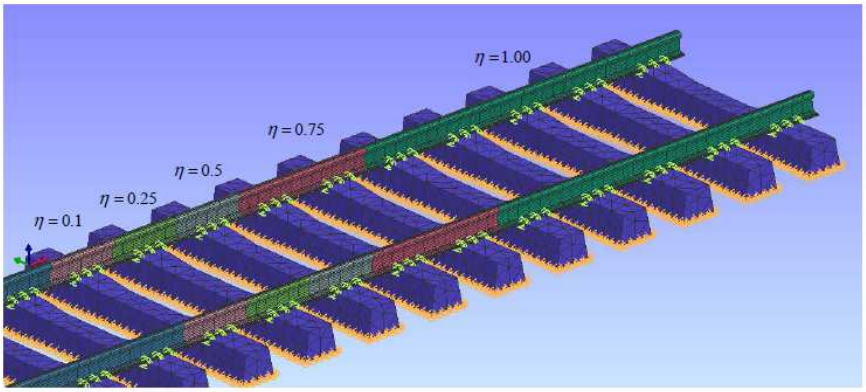
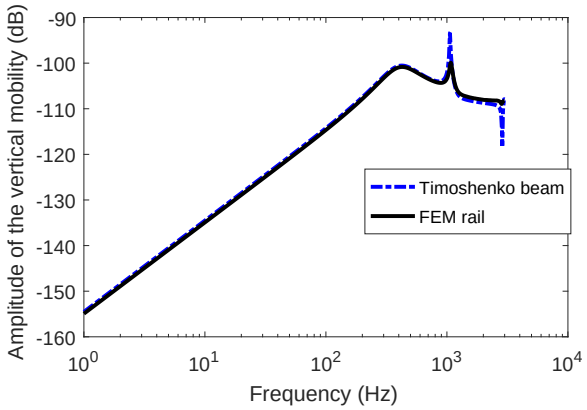
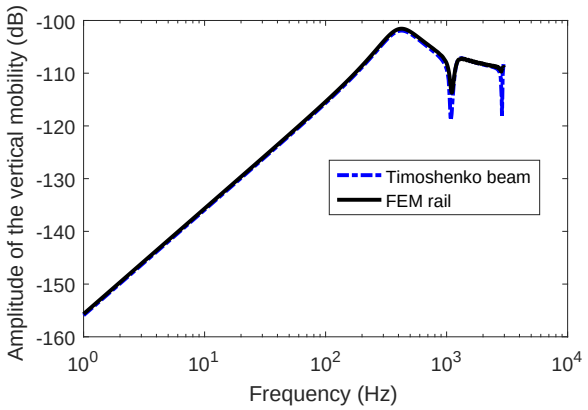


Figure 5: Rail anechoic termination

a sleeper are represented in Fig. 6. The frequencies of the peaks are close. However the amplitudes are different at the peak that associates to the distance between two sleepers. This difference results from the uniform distribution of the springs that connect the rail and the sleepers. In the Timoshenko beam, there is only a spring that connects the rail and the sleepers.



(a) between two sleepers



(b) on a sleeper

Figure 6: Vertical mobility

6.2 Quasi-static results

In this section the wheel/rail quasi-static rolling contact with lateral creepage is considered. The rolling is performed in the $-x$ direction with $V = 10$ m/s. An vertical displacement $u_{z0} = 0.35$ mm is applied leading

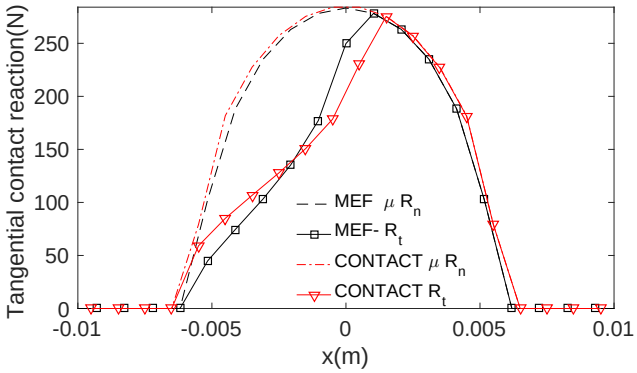


Figure 7: Quasi-static frictional stresses on a line $y = 0$ for $\Delta V_y/V = 0.2\%$ and $\mu = 0.3$

to a resultant vertical contact force of about 66 kN. A friction coefficient $\mu = 0.3$ is considered. Longitudinal and spin creepages are set to zero ($\Delta V_x = \Delta\omega_z = 0$).

For an imposed lateral creepage $\Delta V_y/V = 0.2\%$, the longitudinal distributions of the normal contact reactions and frictional reaction on the center line of the contact zone ($y = 0$) are presented in Fig. 7. As expected, a stick zone occurs at the leading edge of the contact and a slip zone occurs at the trailing edge of the contact. The comparison of the results obtained with the proposed full FE method and the results provided by CONTACT software shows a good agreement in the slip zone and some differences for the tangential stresses in the stick zone.

6.3 Stability results

Stability analysis is carried out in case of full sliding using a higher creepage $\Delta V_y/V = 1\%$. In order to solve the non symmetric eigenvalue problem, the reduction strategy presented in section 4.3 (contact static approximation) is performed. 4 unstable modes whose real parts are positive are obtained. The frequency of these unstable complex modes are 334, 918, 1670 and 3417 Hz respectively. These frequencies obtained get close to those observed experimentally. Figs. 9 to 12 show the unstable modes shape. There are 3 axial wheel modes of (2,3,4) nodal diameters and one wheel mode (a,1,6). The obtained frequencies get close to those observed experimentally.

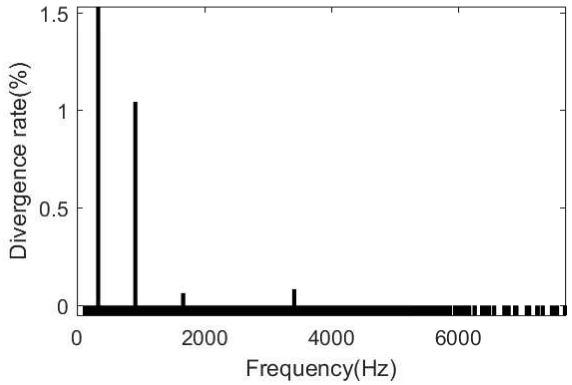
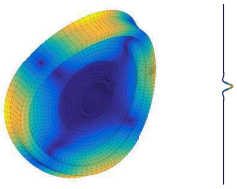
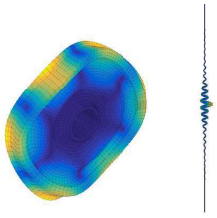


Figure 8: Divergence rate of the complex modes



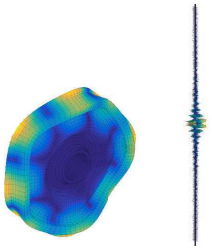
(a) Wheel (b) Rail

Figure 9: Unstable mode shape 1 (334 Hz)



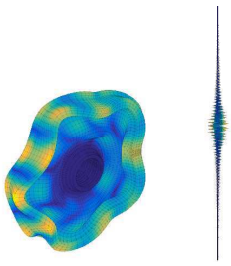
(a) Wheel (b) Rail

Figure 10: Unstable mode shape 2 (918 Hz)



(a) Wheel (b) Rail

Figure 11: Unstable mode shape 3 (1670 Hz)



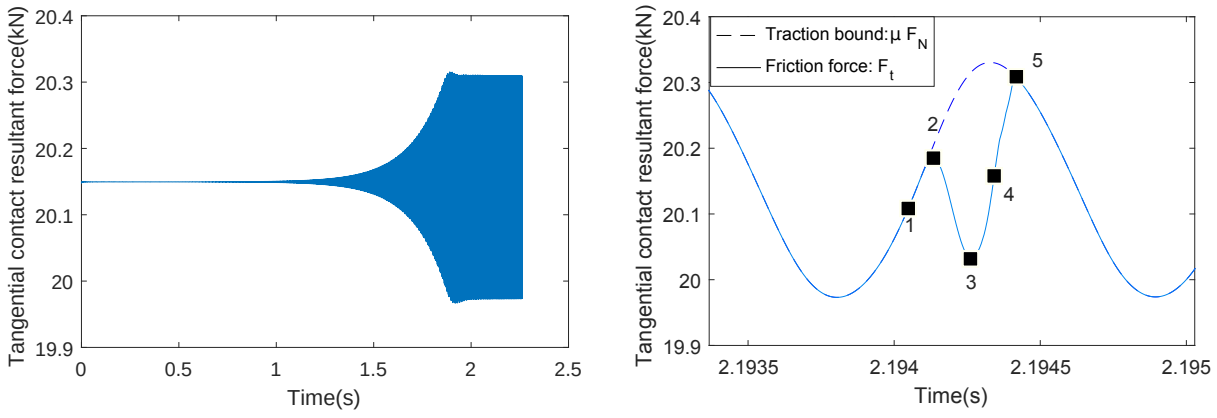
(a) Wheel (b) Rail

Figure 12: Unstable mode shape 4 (3417 Hz)

6.4 Transient results

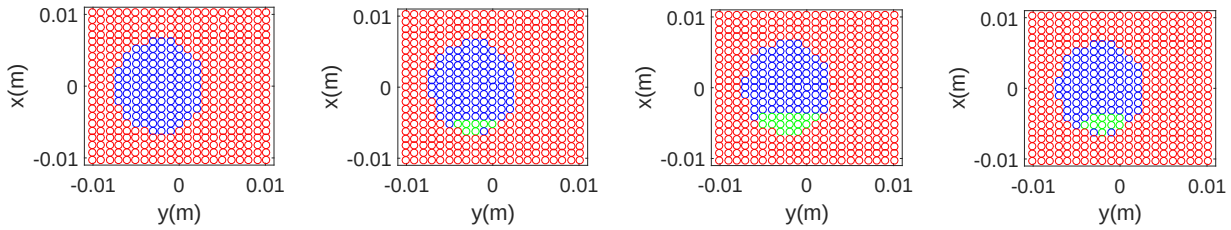
Transient results corresponding to the unstable case founded in the previous section are determined using a numerical time integration from given initial conditions. In all the following results, the integration starts from the equilibrium i.e. the initial displacements are the displacements obtained from the quasi-static solution and the initial velocities are null. The parameters $V_x = 10$ m/s, $\mu = 0.3$ and $\Delta V_y/V = 1\%$ are used. The time step for the integration is $\Delta t = 1\mu$s.

Fig. 13a show the time series of the lateral contact resultant forces F_t. The tangential resultant force increases until a pronounced stick/slip oscillation builds up as shown in Fig. 13b. When the tangential contact resultant force is smaller than the traction bound μF_n, a transient stick zone appears at the leading edge of the effective contact region as shown in Fig. 14.



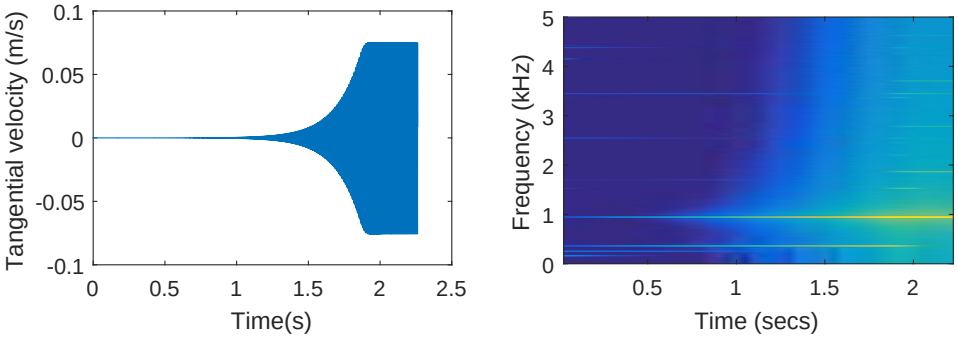
(a) Temporal evolution (b) Zoom on time series

Figure 13: Tangential contact resultant force. The status of the contact points at the time steps marked with Arabic numerals is represented Fig. 14



(a) 1&5 (b) 2 (c) 3 (d) 4

Figure 14: Status of nodes in the potential contact zone: no contact zone (red), slip zone (blue) and stick zone (green)



(a) Temporal evolution (b) Spectrogram (time-frequency)

Figure 15: Tangent velocity of a point outside the contact zone

The time series of the lateral velocity of a point outside the contact zone is presented in the Figure 15a. The spectrogram in Fig. 15b allows to observe which frequencies are present in the solution and when they appear. At the beginning, there are two major frequencies: 334 and 919 Hz which get very close to the natural frequencies of to the two first unstable modes provided by stability analysis. In the stationary step where nonlinear events happen, the dominant frequency is $f_0 = 919$ Hz and its harmonic frequencies $f_k = kf_0$ appear.

7 Conclusion

In this paper, a method is presented for the modeling and analysis of the high-frequency friction-induced instabilities of wheel/rail frictional rolling contact in time and frequency domains. A full finite element formulation around the stationary position in an Eulerian reference frame is derived with a fine discretization of the contact surface combined with unilateral and Coulomb friction laws with constant friction coefficient. Both stability analysis and transient calculation are performed not only to determine unstable modes and frequencies but also to determine the amplitude and the full spectrum of vibrations.

In order to reduce the computational effort, a reduction strategy is proposed for both domains. The technique consists in simply adding a residual static contact flexibility to the free-interface normal modes when solving the frictional contact equations (contact static approximation).

The method is tested in the case of wheel/rail frictional rolling contact. The obtained results are first compared to analytical results and Kalkers theory in the quasi-static case. Application to narrow curves configuration shows that self-excited vibrations of the wheel / rail curve contact could occur due to mode coupling instability (with constant friction coefficient). The results of transient dynamics exhibit are consistent with the stability analysis and exhibit the corresponding localized stick/slip oscillations in the contact zone.

Acknowledgements

This work was carried out within the CERVIFER project backed by the ADEME organization and the Haut-de-France region. It was also supported by the LabEx CeLyA of University of Lyon, operated by the French National Research Agency (ANR-10-LABX-0060/ANR-11-IDEX-0007). The authors gratefully acknowledge the support of these institutions.

References

[1] J. Ayasse, H. Chollet, *4 Wheel–Rail Contact*, Handbook of railway vehicle dynamics, CRC Press (2006), pp. 85.

[2] J.-J. Kalker, *Wheel-rail rolling contact theory*, Wear, Elsevier (1991), pp. 243-261.

[3] D. Thompson, *Railway noise and vibration: mechanisms, modelling and means of control*, W Elsevier (2008).

[4] A. Pieringer, *A numerical investigation of curve squeal in the case of constant wheel/rail friction*, Journal of Sound and Vibration, Elsevier (2014), pp. 4295-4313.

[5] J. Dahlberg, B. Alfredsson, *Transient rolling of cylindrical contacts with constant and linearly increasing applied slip*, Wear, Elsevier (2009), pp. 316-326.

[6] M. Toumi, H. Chollet, H. Yin, *Finite element analysis of the frictional wheel-rail rolling contact using explicit and implicit methods*, Wear, Elsevier (1991), pp. 243-261.

[7] K.-L. Johnson, *Contact mechanics*, Cambridge university press (1987).

[8] M. Jean, *The non-smooth contact dynamics method*, Computer methods in applied mechanics and engineering, Elsevier (1999), pp. 235-257.

[9] P. Chambrette, L. Jezequel, *Stability of a beam rubbed against a rotating disc*, European journal of mechanics. A. Solids, Elsevier (1992), pp. 107-138.

[10] M. Raous, S. Barbarin, D. Vol, *Numerical characterization and computation of dynamic instabilities for frictional contact problems*, Friction and Instabilities, Springer (2002), pp. 233-291.

[11] A.-D. Kudawoo, *Problèmes industriels de grande dimension en mécanique numérique du contact: performance, fiabilité et robustesse*, Université de Provence-Aix-Marseille I (2012).

[12] D. Brizard, O. Chiello, J.-J. Sinou, X. Lorang, *Performances of some reduced bases for the stability analysis of a disc/pads system in sliding contact*, Journal of Sound and Vibration, Elsevier (2011), pp. 703-720.

[13] X. Lorang, F. Foy-Margiocchi, Q.-S. Nguyen, P.-E. Gautier, *TGV disc brake squeal*, Journal of Sound and Vibration, Elsevier (2006), pp. 735-746.

[14] A. Loyer, J.-J. Sinou, O. Chiello, X. Lorang, *Study of nonlinear behaviors and modal reductions for friction destabilized systems. Application to an elastic layer*, Journal of Sound and Vibration, Elsevier (2012), pp. 1011-1041.

[15] H.-B. Khenous, J. Pommier, Y. Renard, *Hybrid discretization of the Signorini problem with Coulomb friction. Theoretical aspects and comparison of some numerical solvers*, Applied Numerical Mathematics, Elsevier (2006), pp. 163-192.

[16] J.-F. Hamet, *Railway noise: use of the Timoshenko model in rail vibration studies*, Acta Acustica united with Acustica, S. Hirzel Verlag (1999), pp. 54-62.

[17] B. Ding, G. Squicciarini, D.-J.T hompson, *Effects of rail dynamics and friction characteristics on curve squeal*, Journal of Physics: Conference Series, IOP Publishing (2016), pp. 012146.

Apodization and phase methods applied to the seismic detection of underground objects

E. Rustighi [1], **Q. Leclère** [2], **J.M. Muggleton** [1]
[1] University of Southampton, Institute of Sound and Vibration Research
Highfield campus, Southampton, UK
e-mail: **erustigh@soton.ac.uk**

[2] INSA-Lyon, Laboratoire Vibrations Acoustique
25b av Jean Capelle, 69621 Villeurbanne Cedex, France

Abstract
This paper presents the use of signal processing techniques such as apodization and phase based methods with the aim of improving the quality of images created from the seismic data array. These signal processing techniques, which are commonly used for non-destructive testing and biomedical ultrasonic arrays, are implemented. Apodization techniques used are Dual Apodization, Dual Apodization with Cross-Correlation, Complex Dual Apodization and Spatially Variant Apodization. The phase methods used are Phase Coherence Factor, Sign Coherence Factor, Coherence Factor Map, Instantaneous Phase Image and Instantaneous Phase Weight. The paper presents a comparison between the different techniques based on simulated data. The use of such techniques results in an improvement in the seismic images with no extra cost or modification of the experimental technique.

1 Introduction

The vast majority of the utility infrastructures are buried and any programmed or emergency maintenance involve excavations which are likely to disrupt the traffic. A recent UK study estimated that streetworks cost the UK 7bn annually. Controlled trials carried out by UK Water Industry Research have shown that, even when sophisticated detection techniques are employed, detection rates are often poor and, as a result, far more excavations are carried out than would otherwise be necessary for maintenance and repair. In response to this, a large multi-centre programme, Mapping the Underworld [1]–[3], is being undertaken in the UK, dating back to 2004, to research a range of technologies that could be combined into a single device to accurately locate buried pipes and cables. The University of Southampton has been the lead in developing novel vibro-acoustic techniques [4]. One of the developed techniques is based on the generation of directional shear waves and the detection and analysis of the subsequent reflections at the ground surface. Cross-correlation functions between the measured ground velocities and a reference ground velocity measurement adjacent to the excitation are used to generate a cross-sectional image of the ground using a time domain stacking approach [5]. The conventional technique uses the Total Focusing Method (TFM), whereby the array signals are focused on the range and bearing of each pixel in turn and summed, for every source/receiver combination [6]. Preliminary results on this technique have previously shown the possibility of detecting both plastic and metal water pipes and air-filled metal pipes. However, to date, no signal processing improvement has been proposed.

Ultrasonic phased array systems have been largely used in the past in the field of medical diagnostic [7] and in the nondestructive evaluation of metal strcutures [8]. Many different types of signal processing techniques have been proposed in the past. The aim of this paper is to extend the use of such techniques to the de-

tection of buried objects. Although the array configuration is the same in medical, mechanical and seismic applications the problems differ in the frequency range of application, material dispersion and wave types. In fact the seismic application deals with frequencies of the order of 500 Hz, significantly much below the ultrasound region usually adopted in medical and mechanical applications. Also, for the detection of shallow objects the dispersivity of the soil can be neglected. Most distinctively, transducers applied to the soil will generate three types of waves, i.e. compressional, shear and Rayleigh waves. The fact that the algorithms for seismic detection have to cope with three waves travelling at different speeds make this application unique. In this paper signal processing techniques, such as dual apodization and phase based methods, are applied to the seismic detection of a shallow buried object for the first time.

The following section describes the numerical computation of the simulated signal. The next section describes the conventional scanning methodology [5]. The next two sections describe the application of dual apodization and phase based methods respectively. Finally, before conclusions are drawn, a comparison between the two families of techniques is presented.

2 Numerical Data generation

Numerical data is used in this paper since it allows benchmarking of the different algorithms in an ideal case where the location of the target is known. The use of numerical data also permits testing of the different algorithms against the presence of high noise and/or strong surface waves.

The data has been generated numerically using a wave-propagation model, as presented in a simpler form in [5]. It is assumed that a transmitter (shaker) placed on the surface of soil generates body and surface waves which propagate and scatter against a point reflector (buried object). A linear equally-spaced array of receivers (geophones) is used to gather soil velocity due to the wave propagation. Figure 1 shows the location of transmitter, receiver and reflector in the half-space (x, z) and it indicates their coordinates. The transmitted signal is generated in the frequency domain, subjected to delay and frequency-dependent attenuation to simulate propagation, then transformed back into the time domain to obtain time-histories of the velocities at each sensor location. A band limited white noise signal is used as source signal. The bandwidth is chosen from 50 to 1000 Hz, being a realistic bandwidth for shallow seismic exploration [5].

It is assumed that the source generates compressional, shear and Rayleigh waves. Compressional and shear waves are recorded by the sensors after reflecting off the target. Rayleigh waves are assumed to travel only on the free surface and are recorded during direct propagation. The propagation of shear waves along the surface has been included in part of the simulation to simulate the excitation of strong surface waves.

The law of propagation, or transfer function $H_{rt}(\omega)$, is applied independently to each wave. It expresses the changes in magnitude and phase of the transmitted signal due to time of flight, hysteretic damping, and geometrical attenuation:

$$H_{rt}(\omega) = A\mathrm{e}^{-\eta_D \omega \frac{d_{rt}}{c}} \left(\frac{d_{rt}}{d_{\mathrm{ref}}}\right)^n \mathrm{e}^{-\mathrm{i}\omega \frac{d_{rt}}{c}}, \tag{1}$$

where A is an amplitude contribution factor, η_D is the loss factor associated to the wave, d_{rt} is the distance covered by the wave between transmitter t and receiver r, c is the wave speed, d_{ref} is a reference distance and n is the geometric power attenuation constant. The first factor of the equation express the dissipation, the second one the geometrical spreading and the third represents the linear change of phase with distance. Table 1 gives the parameters used in the simulations.

To create the full simulated time histories, two propagation paths are considered between each sensor transmitter combination: a direct path along the surface, and a reflected path via the target. The distance covered by surface waves is

$$d_{rt} = |x_t - x_r|, \tag{2}$$

while the distance covered by scattered waves is

$$d_{rt} = \sqrt{(x_P - x_t)^2 + (z_P)^2} + \sqrt{(x_P - x_s)^2 + (z_P)^2}. \tag{3}$$

To obtain the time domain signals at each geophone the numerical transfer functions are inverse Fourier Transformed. After inverse Fourier transforming the individual signals, white noise has been added to them and the signals have been summed together. In particular, two different levels of noise will be used. A small (20 dB SNR) and a large noise (10 dB SNR) will be used to compare the different algorithms. A sampling frequency $f_s = 5000$ Hz has been used for all the numerical simulations. A perfect point reflector at a depth of 0.7 m and centred with respect to the array has been considered. The sensor array used in the simulations has an aperture of 6 m including 7 sensors 1 m apart from each other. The transmitter is placed consecutively at the same location of each sensor (overlapped configuration). The simulations provide the time domain signals for each combination of transmitter-receiver as in a real experiment.

The data of the simulation has also to be pre-processed, in order to get time-of-flight information from the broadband signals. For each receiver-transmitter pair the cross power spectral density, $C_{rt}(\omega)$, between the transmitted signal and the received one is calculated averaging over 10 windowed chunks (Hanning window). The cross correlation is then obtained using the generalised cross-correlation (GCC) [9], [10]

$$s_{rt}(t) = \frac{1}{2\pi}\int_{-\infty}^{\infty} \Psi(\omega) C_{rt}(\omega) \mathrm{e}^{\mathrm{i}\omega t} \mathrm{d}\omega. \tag{4}$$

In this paper the Scott GCC has been used which implies

$$\Psi(\omega) = \frac{\gamma_{rt}(\omega)}{|C_{rt}(\omega)|} \tag{5}$$

where $\gamma_{rt}^2(\omega)$ is the coherence between the received and transmitted signal.

From each signal $s_{rt}(t)$ it is then possible to calculate the Hilbert transform $\hat{s}_{rt}(t) = \mathscr{H}[s_{rt}(t)]$ [11]. From each signal the analytic signal $S_{rt}(t)$ is then given as:

$$S_{rt}(t) = s_{rt}(t) + \mathrm{i}\hat{s}_{rt}(t). \tag{6}$$

The magnitude and phase of S_{rt} give the instantaneous amplitude (or envelope) and the instantaneous phase respectively of the signal $s_{rt}(t)$. Hence the instantaneous amplitude $A_{rt}(x, z)$ can be expressed as

$$A_{rt}(t) = \sqrt{s_{rt}^2(t) + \hat{s}_{rt}^2(t)}, \tag{7}$$

while the instantaneous phase $\varphi(t)$ is given by

$$\varphi(t) = \arctan \frac{\hat{s}_{rt}(t)}{s_{rt}(t)}. \tag{8}$$

The limitations of this model are that non-unity reflection coefficient and wave conversion at the target or at the surface are not considered. Also all the signals are summed together without taking into account the actual vectorial components. Finally, the ground is considered homogeneous. In reality the structure of soil is subject to both anomalous heterogeneity, for example caused by objects other than the desired target, and more ordered heterogeneity caused by particular soil structures. Despite these limitations, this model can be used effectively to compare different signal processing techniques.

3 The conventional stacking methodology

The method previously used for the imaging of the section underneath the array of geophones is based on the Total Focusing Method (TFM) [5], [6]. According to this method the beam is focused at every point in the target region. The TFM post-processing algorithm proceeds by first discretising the target region, (x, z) plane, into a grid of pixels. The signals from all the elements in the array are then summed to synthesise a focus at every point in the grid. Although this focusing method requires a high computation time, the

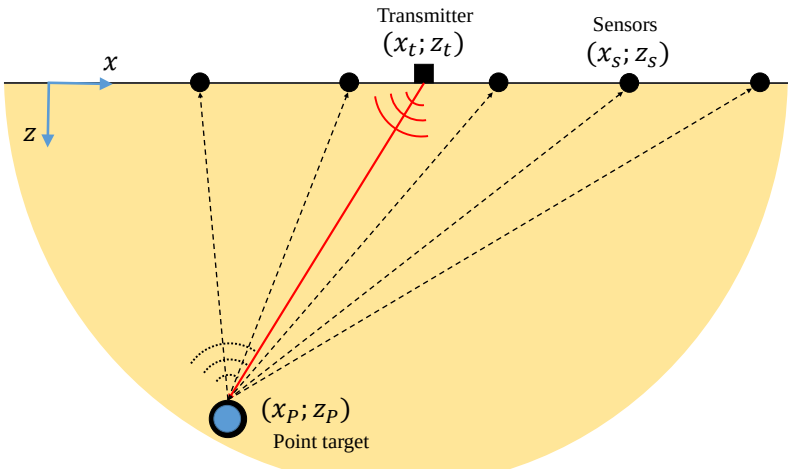


Figure 1: Schematic showing the distribution of geophones and source with respect to the target in the cross-sectional area (x, z) of the semi-infinite space

Parameters		Shear wave	Rayleigh wave	Compressional wave
Wavespeed	c	90 ms^{-1}	85.3 ms^{-1}	298.5 ms^{-1}
Amplitude contribution	A	1	0.2	0.2
Damping	η_D	0.005	0.005	0.005
Reference distance	d_{ref}	0.1 m	0.1 m	0.1 m
Geometric spreading coefficient	n	1	1	1

Table 1: Simulation parameters

focusing is carried out for each possible shakergeophone location pair and therefore it uses the maximum amount of information available for each point.

Although different signals can be chosen, in the uniform TFM presented here the instantaneous amplitude $A_{rt}(t)$, given by Equation 7, is used to obtain the intensity of the image, $I(x, z)$ at any point in the scan, with the following formula:

$$I_{\mathrm{TFM}}(x, z) = \frac{1}{M^2} \sum_{r=1}^{M} \sum_{t=1}^{M} A_{rt}(\tau_{rt}(x, z)) \tag{9}$$

where $\tau_{rt}(x, z)$ the time of flight between receiver, r, and transmitter, t, when the array is focused at position (x, z) in the plane:

$$\tau_{rt}(x, z) = \frac{\sqrt{(x - x_t)^2 + (z)^2} + \sqrt{(x - x_r)^2 + (z)^2}}{c}. \tag{10}$$

It has also been decided for each excitation to remove the nearest sensors from the stacking, so to reduce the effect of strong surface waves, as usually done in experimental practice.

The first row of Figures 2 and 12 gives the results for uniform TFM as a reference. For each technique four images are provided. The first column shows the results in the case of small surface wave (only Rayleigh wave) and small background noise (20 dB SNR). The second column presents the results in the case of small surface wave (only Rayleigh wave) and large background noise (10 dB SNR). The third column refers to strong surface wave contribution (Rayleigh and shear waves) and small background noise added (20 dB SNR). Finally the last column presents the results in the case of strong surface wave contribution and large noise.

4 Apodization techniques

In conventional TFM the lateral resolution is limited by the main lobe width, which in turn depends on the aperture size relative to the wavelength [12]. The contrast resolution is limited by the sidelobe levels. For example, the resolution of a uniform array is related to the aperture L of the array with the formula

$$\Delta\phi_{3\mathrm{dB}} \approx \frac{\lambda}{L}. \tag{11}$$

The aperture of the array is $6\ \mathrm{m}$ hence the beamwidth goes from 17.2 degrees to 0.86 degrees from 50 to 1000 Hz. Moreover, for 'thinned array', for which $d > \lambda/2$, grating lobes appear as well. Since in the simulation $d = 1\ \mathrm{m}$ and $c = 90\ \mathrm{ms}^{-1}$ grating lobes appear for $f > 45\ \mathrm{Hz}$.

Apodization is a term borrowed from optics which indicates techniques which aim at decreasing the main lobe width of the beamformer while keeping down side lobes. Weighting or shaping a finite aperture is the most conventional linear form of apodization and the one used in this paper. In particular only apodization in the receiving array will be considered. In this case, the apodized TFM takes the following form

$$I_{\mathrm{APO}}(x,z) = \frac{1}{M^2}\sum_{r=1}^{M}\sum_{t=1}^{M} w_r A_{rt}(\tau_{rt}(x,z)) \tag{12}$$

where w_r are apodization coefficients. The value of the coefficient depend on the type of apodization. For uniform apodization $w_{rt} = 1$ and for Hanning apodization $w_r = \frac{1}{2}\left(1 - \cos\left(\frac{2\pi r}{M}\right)\right)$.

The uniform apodization is related to narrower main lobe width and higher side lobes levels. The Blackman apodization is associated with low side lobes levels, but the high main lobe width results in a large defect representation. The triangular one results in intermediate values between all compared cases [13]. However, a compromise between resolution and contrast has to be reached. The dual Apodization technique, introduced in the next subsection, tries to reach this compromise. All the results of the different dual apodization techniques compared in this paper are given in Figure 2.

4.1 Dual Apodization (DA)

The Dual Apodization technique (DA) [14], [15] is a nonlinear procedure that, by computing two versions of the scanning image, each having a different apodization window, provides an image with good mainlobe resolution and low sidelobes. For example, as implemented in this paper, one image can be obtained using uniform weighting, and a second one using a Hanning window.

Implementing the uniform apodization produce images having a point spread function with a sharp main beam-width but high sidelobe levels, while implementing the Hanning apodization produces images having a point spread function with low sidelobe levels at the cost of a wider main beam [15].

At each spatial location, the minimum value from the pair of images is selected, assuming that a reflector should be present in all images:

$$I_{\mathrm{DA}}(x,z) = \min\left(I^{I}_{\mathrm{APO}}(x,z), I^{II}_{\mathrm{APO}}(x,z)\right) \tag{13}$$

4.2 Dual Apodization with Cross-Correlation (DAX)

Seo and Yen have proposed a particular type of dual apodization called dual apodization with cross-correlation (DAX) improving the signal to noise ratio [16]. The suggested approach aims at distinguishing the mainlobe dominated signals from the clutter dominated signals by using two different apodization functions I^{I}_{APO} and I^{II}_{APO}. It is assumed that these two apodization functions give similar mainlobe signals and very different clutter patterns. Hence, the degree of similarity can be quantified using normalized cross-correlation between

the two images. In particular, the normalised cross-correlation (NCC) is performed along the z direction and the normalized cross-correlation coefficient ρ is calculated as:

$$\rho(x,z) = \frac{\sum_z I^I_{\mathrm{APO}}(x,z) I^{II}_{\mathrm{APO}}(x,z)}{\sqrt{\sum_z \left[I^I_{\mathrm{APO}}(x,z)\right]^2}\sqrt{\sum_z \left[I^{II}_{\mathrm{APO}}(x,z)\right]^2}} \tag{14}$$

this gives a target-dependent pixel-by-pixel weighting matrix, which passes mainlobe dominated signals and attenuates clutter dominated signals. The final image is then obtained with an operation similar to DA:

$$I_{\mathrm{DAX}}(x,z) = \rho(x,z) \min\left(I^I_{\mathrm{APO}}(x,z), I^{II}_{\mathrm{APO}}(x,z)\right) \tag{15}$$

4.3 Complex DA (CDA)

In the complex DA (CDA) the analytic signal, $S_{rt}(t)$, is used in Equation (12) instead of the instantaneous amplitude $A_{rt}(t)$ [14]. This allows preservation of the original phase of the image which in this case is complex. Two versions of the image, one using uniform weighting, I^I_{APO}, and the other using Hanning weighting, I^{II}_{APO}, are then calculated. At each spatial location, if the real and imaginary components of the two images have opposite sign, zero is selected; otherwise the value which has the smaller absolute value of the two is selected. Eventually the absolute of the image is kept as final scanned image:

$$I_{\mathrm{CDA}} = \sqrt{I^2_{real} + I^2_{imag}}, \tag{16}$$

where

$$I_{real} = \begin{cases} 0, & \text{if} \quad \mathbb{R}\mathrm{e}\left(I^I_{\mathrm{APO}}\right)\mathbb{R}\mathrm{e}\left(I^{II}_{\mathrm{APO}}\right) \leq 0 \\ \min\left(|\,\mathbb{R}\mathrm{e}\left(I^I_{\mathrm{APO}}\right)|, |\,\mathbb{R}\mathrm{e}\left(I^{II}_{\mathrm{APO}}\right)|\right), & \text{if} \quad \mathbb{R}\mathrm{e}\left(I^I_{\mathrm{APO}}\right)\mathbb{R}\mathrm{e}\left(I^{II}_{\mathrm{APO}}\right) > 0 \end{cases} \tag{17}$$

and

$$I_{imag} = \begin{cases} 0, & \text{if} \quad \mathbb{I}\mathrm{m}\left(I^I_{\mathrm{APO}}\right)\mathbb{I}\mathrm{m}\left(I^{II}_{\mathrm{APO}}\right) \leq 0 \\ \min\left(|\,\mathbb{I}\mathrm{m}\left(I^I_{\mathrm{APO}}\right)|, |\,\mathbb{I}\mathrm{m}\left(I^{II}_{\mathrm{APO}}\right)|\right), & \text{if} \quad \mathbb{I}\mathrm{m}\left(I^I_{\mathrm{APO}}\right)\mathbb{I}\mathrm{m}\left(I^{II}_{\mathrm{APO}}\right) > 0 \end{cases} \tag{18}$$

CDA is especially powerful because the sidelobes for the point spread functions of the uniform and Hanning windows are opposite in sign and the result of CDA for a scene consisting of a single bright point would simply be the mainlobe of the sinc function [14]. CDA provides significantly lower sidelobes than DA for the one-dimesional case but is not as effective for two-dimensional images where the point spread function changes sign only along the cardinal directions.

4.4 Phase DA (PDA)

A new type of dual apodization is proposed here and it has been named Phase DA (PDA) because the discriminant between the two images is based on the phase of the image. The justification for this is similar to the justification for the phase based methods discussed in the next section. In the PDA the analytic signal $S_{rt}(t)$ is used instead of the instantaneous amplitude $A_{rt}(t)$ in Equation (12). From the two images, I^I_{APO} and I^{II}_{APO}, the minimum is taken only at location where the phase difference is less than $\pi/2$, otherwise the pixel value is set to zero

$$I_{\mathrm{PDA}} = \begin{cases} 0, & \text{if} \quad \angle\left(\frac{I^I_{\mathrm{APO}}}{I^{II}_{\mathrm{APO}}}\right) > \frac{\pi}{2} \\ \min\left(|I^I_{\mathrm{APO}}|, |I^{II}_{\mathrm{APO}}|\right), & \text{if} \quad \angle\left(\frac{I^I_{\mathrm{APO}}}{I^{II}_{\mathrm{APO}}}\right) \leq \frac{\pi}{2} \end{cases} \tag{19}$$

4.5 Spatially Variant Apodization

Stankwitz *et al* developed a spatially variant nonlinear apodization (SVA) technique, which uses the lateral phase differences between Hanning and uniformly apodized data to distinguish between mainlobe and clutter signals [14]. This is accomplished by taking advantage of the properties of raised-cosine weighting functions and finding the optimal apodization function on a pixel-by-pixel basis [14]. The method implemented here is the version where the real and imaginary part of the analytic signal are treated separately and the two dimensions, (x, z), are treated simultaneously although in an uncoupled minimisation.

In order to implement SVA the following steps have been taken:

1. Compute a reference image using the real signals:

$$I_{(0,0)}(x,z) = \frac{1}{M^2}\sum_{r=1}^{M}\sum_{t=1}^{M} s_{rt}(\tau_{rt}(x,z)); \tag{20}$$

2. Compute three more images $I_{(w_m,w_n)}(x,z)$ for $(w_m, w_n) = (0, 1/2)$, $(1/2, 0)$, and $(1/2, 1/2)$:

$$I_{(w_m,w_n)}(x,z) = I_{(0,0)}(x,z) + (w_n P + Q_m)w_m + w_n Q_n \tag{21}$$

   where

$$\begin{aligned} Q_m &= I_{(0,0)}(m-1,n) + I_{(0,0)}(m+1,n), \\ Q_n &= I_{(0,0)}(m,n-1) + I_{(0,0)}(m,n+1), \\ P &= I_{(0,0)}(m-1,n-1) + I_{(0,0)}(m+1,n+1) + \\ &\quad + I_{(0,0)}(m-1,n+1) + I_{(0,0)}(m+1,n-1) \end{aligned}$$

   where m and n are the pixel index in the x and z directions respectively;

3. If any of the three $I_{(w_m,w_n)}(x,z)$ has sign opposite to that of the original image, $I_{(0,0)}(x,z)$, then set $I^{\mathbb{R}}_{\mathrm{SVA}}(x,z) = 0$ otherwise, select the minimum magnitude:

$$I^{\mathbb{R}}_{\mathrm{SVA}} = \begin{cases} 0, & \text{if } I_{(0,0)}, I_{(0,1/2)}, I_{(1/2,0)}, \\ & I_{(1/2,1/2)} \text{ have opposite sign} \\ \min\left(|I_{(0,0)}|, |I_{(0,1/2)}|, |I_{(1/2,0)}|, |I_{(1/2,1/2)}|\right), & \text{if } I_{(0,0)}, I_{(0,1/2)}, I_{(1/2,0)}, \\ & I_{(1/2,1/2)} \text{ have same sign} \end{cases}; \tag{22}$$

4. Repeat the previous steps for the imaginary component of the signal $\hat{s}_{rt}(t)$;

5. Final image is $I_{\mathrm{SVA}}(x,z) = \sqrt{[I^{\mathbb{R}}_{\mathrm{SVA}}(x,z)]^2 + [I^{\mathbb{I}}_{\mathrm{SVA}}(x,z)]^2}$.

SVA allows each pixel in an image to receive its own frequency domain aperture amplitude weighting function from a continuum of possible weighting functions [14]. Stankwitz *et al* claim that SVA effectively eliminates finite-aperture induced sidelobes from uniformly weighted data while retaining nearly all of the good mainlobe resolution and clutter texture of the non apodized image.

5 Phase based methods

Phase based methods make use of the instantaneous phase of the analytical signals. The use of the phase is justified by the fact that the phase is much more resilient to noise than the amplitude [17]. Such methods rely on the phase to confirm the presence of target. These methods are based on the phase distribution in

the aperture data using dispersion measurements such as standard deviation or variance and aim at improve SNR. If a target is present, the phase in that particular location will be coherent within all images (receiver-transmitter couple), while, if there is no target/reflector, the phase will be random. The same argument can be done for the point spread function of the array: the phase dispersion is low at the main lobe, increases slightly at the side lobes but it is very high at grating lobes.

Here 5 methods are presented, considered to be representative and sufficiently different from each other. The results are shown in Figure 3. In all these results no apodization has been applied to the signal. Obviously is possible to combine all the methods in all possible combinations or present many more variants of the phase method.

5.1 Phase Coherence Factor (PCF)

The Phase Coherence Factor (PCF) proposes a change in the total fusing method where the sum is weighted by a function $\Gamma(x,z)$:

$$I_{\mathrm{TFM}}(x,z) = \frac{\Gamma(x,z)}{M^2}\sum_{r=1}^{M}\sum_{t=1}^{M}\sqrt{s_{rt}^2(\tau_{rt}(x,z)) + \hat{s}_{rt}^2(\tau_{rt}(x,z))}. \tag{23}$$

The weigthing function $\Gamma(x,z)$, also called PCF itself, is defined as:

$$\Gamma_{\mathrm{PCF}}(x,z) = \max\left[0, 1 - \frac{\gamma}{\sigma_0}\sigma(\varphi\tau_{rt}(x,z))\right] \tag{24}$$

where $\sigma(\varphi\tau_{rt}(x,z))$ is the standard deviation of the instantaneous phase calculated at the focusing point, γ is a sensitivity parameter and σ_0 is the total standard deviation. In the calculation of the standard deviation some care should be taken in considering the effect of wrapping [18]. The proposed weighting factor yields values in the range 0 to 1 as a function of the phase dispersion of the aperture data set. Also in the presented results the value of γ has been set equal to σ_0.

Without focusing errors, all phases are equal, $\sigma = 0$, and $\Gamma_{\mathrm{PCF}} = 1$. Out of the main lobe, the aperture data phases are different, the standard deviation increases, and the Γ_{PCF} decreases. Higher σ values provide increased suppression for out-of-focus signals.

5.2 Sign Coherence Factor (SCF)

The Sign Coherence Factor (SCF) can be seen as a particular case of PCF where the instantaneous phase is quantised to 0 or π [18]. Signals are considered fully coherent if their phases fall in one of these two values with $\pm\pi/2$ accuracy, which is the same as saying that all the aperture data have the same polarity.

From the signals is possible to calculate the polarity signal of the aperture data $b_{rt}(t)$ as

$$b_{rt}(t) = \begin{cases} -1, & \text{if} \quad s_{rt}(t) < 0 \\ +1, & \text{if} \quad s_{rt}(t) \geq 0 \end{cases} \tag{25}$$

Using the sign polarity signal of the aperture data the standard deviation of the quantised phase can be calculated by [18]:

$$\sigma^2(x,z) = 1 - \left[\frac{1}{M^2}\sum_{e=1}^{M}\sum_{r=1}^{M} b_{rt}(\tau_{rt}(x,z))\right]^2 \tag{26}$$

and the weight Γ_{SCF} for Equation (23) is obtained by

$$\Gamma_{\mathrm{SCF}}(x,z) = 1 - \sigma \tag{27}$$

Γ_{SCF} measures the coincidence in algebraic sign of the received signals. Signals are defined as fully coherent if all of them have the same polarity hence $\sigma = 0$ and $\Gamma_{\mathrm{SC}}(x,z) = 1$. The image is then obtained by using Γ_{SCF} in Equation (23).

5.3 Coherence Factor Map (CFM)

Martínez-Graullera *et al* introduced an alternative phase coherence descriptor based on the Fourier analysis of the phase distribution [19]. The introduced Coherence Factor Map (CFM) again gives a weight to be used in Equation (23):

$$\Gamma_{\mathrm{CFM}}(x,z) = \frac{1}{M^2}\sqrt{\left[\sum_{r=1}^{M}\sum_{t=1}^{M}\frac{s_{rt}(\tau_{rt}(x,z))}{A_{rt}(\tau_{rt}(x,z))}\right]^2 + \left[\sum_{r=1}^{M}\sum_{t=1}^{M}\frac{\hat{s}_{rt}(\tau_{rt}(x,z))}{A_{rt}(\tau_{rt}(x,z))}\right]^2} \tag{28}$$

Intuitively by dividing the in-phase and in-quadrature signals by the instantaneous amplitude only phase information is kept.

5.4 Instantaneous Phase Image (IPI) and Instantaneous Phase Weight (IPW)

Prado *et al* [13], [20] proposed a new phase-dispersion weighting for the final image but at the same time build the images using the instantaneous phase or the envelope of the instantaneous phase. The total focusing equation is modified so to use the instantaneous phase $\varphi_{rt}(t)$ as defined in Equation (8) directly in the focusing equation. In particular, the results shown in this paper are based on the envelope of the instantaneous phase:

$$I_{\varphi}(x,z) = \frac{1}{M^2}\sqrt{\left[\sum_{r=1}^{M}\sum_{t=1}^{M}\varphi_{rt}(\tau_{rt}(x,z))\right]^2 + \left[\sum_{r=1}^{M}\sum_{t=1}^{M}\hat{\varphi}_{er}(\tau_{er}(x,z))\right]^2} \tag{29}$$

where $\hat{\varphi}_{er}(t)$ is the Hilbert transform of $\varphi_{er}(t)$.

The weighting proposed is based on a statistical analysis of the instantaneous phase image $I_{\varphi}(x,z)$. First a threshold ε has been introduced so that it is decided if the calculated $I_{\varphi}(x,z)$ is due to random or coherent summation. The proposed threshold value depends only on the number of signals used in beamforming [13], [20]

$$\varepsilon \triangleq \frac{1}{\sqrt{\log_{10} M^2}} \tag{30}$$

From the statistical analysis of the IP image, a threshold level is defined in terms of the number of signals used for imaging. This threshold is applied to the IP image, resulting in a two-level image which gives a statistical indication of whether the pixels of a region in the image are related to a reflector or noise/artifacts. Because the proposed method uses only the instantaneous phase of the signals, it is less sensitive to attenuation than conventional DAS amplitude images. [20]

The instantaneous phase image (IPI) method is based on the threshold value ε to obtain a polarised image as

$$I_{\mathrm{IPI}}(x,z) = \begin{cases} 1, & \text{if} \quad |I_{\varphi}(x,z)| \geq \varepsilon \\ 0, & \text{if} \quad |I_{\varphi}(x,z)| < \varepsilon \end{cases} \tag{31}$$

The other option is to evaluate the probability error (or false indication) of a reflector

$$P_E(x,z) = \frac{\sigma(x,z)}{M^2}\log_{10}(M^2) \tag{32}$$

where $\sigma(x,z)$ is the standard deviation of $I_{\varphi}(x,z)$. Hence a weigthing is defined as

$$\Gamma_{\mathrm{PWF}}(x,z) = \begin{cases} 1, & \text{if} \quad |I_{\varphi}(x,z)| \geq \varepsilon \\ P_E(x,z), & \text{if} \quad v_{er}(t)|I_{\varphi}(x,z)| < \varepsilon \end{cases} \tag{33}$$

and the final image is given by $\Gamma_{\mathrm{PWF}}(x,z)I_{\varphi}(x,z)$.

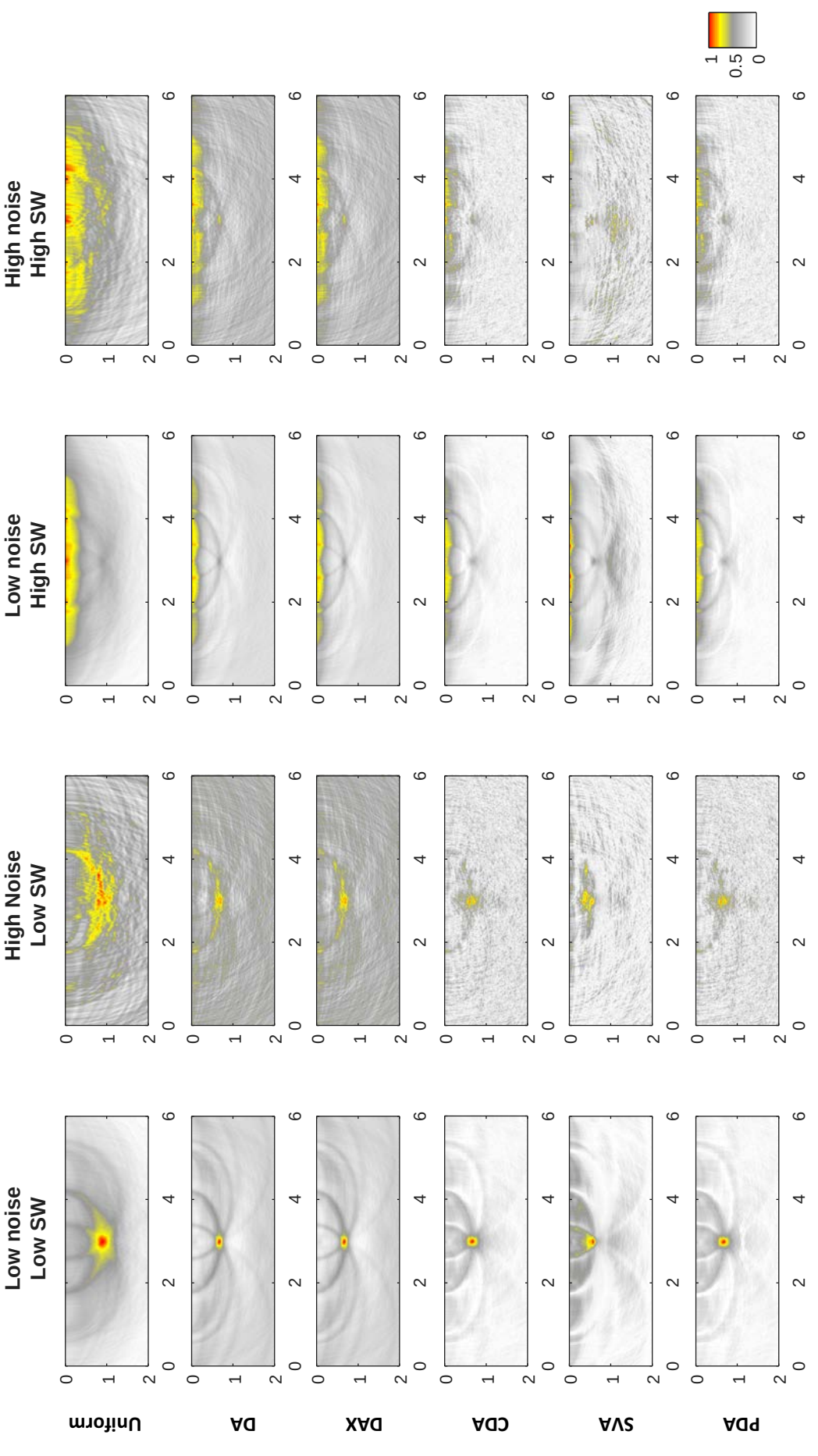


Figure 2: Dual apodization techniques in comparison to uniform TFM. First column: small surface wave (only Rayleigh wave) and small white noise (20 dB SNR). Second column: small surface wave and large white noise (10 dB SNR). Third column: strong surface wave (Rayleigh and shear waves) and small noise. Fourth column: strong surface wave and large noise.

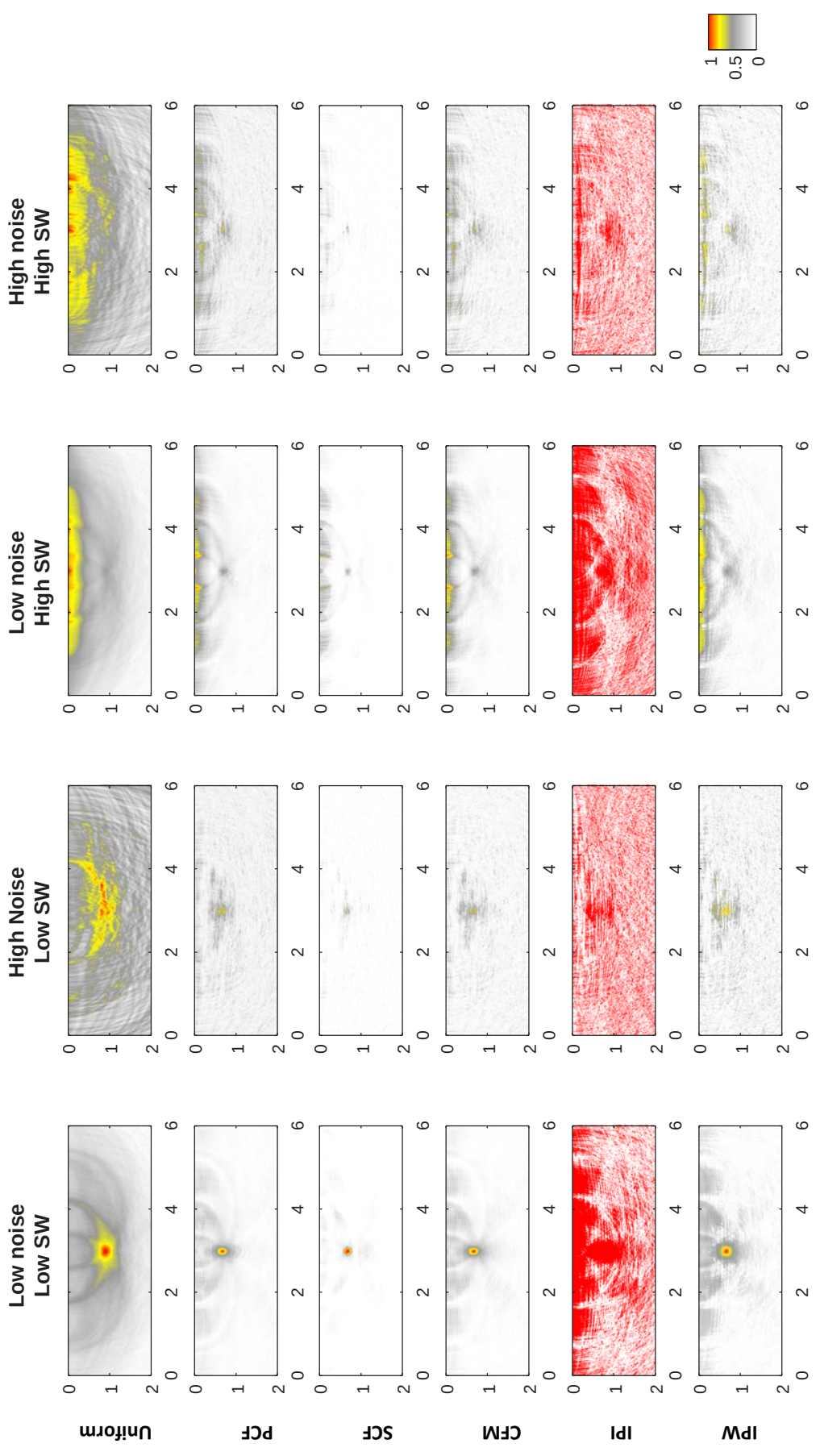


Figure 3: Instantaneous phase techniques in comparison to uniform TFM. First column: small surface wave (only Rayleigh wave) and small white noise (20 dB SNR). Second column: small surface wave and large white noise (10 dB SNR). Third column: strong surface wave (Rayleigh and shear waves) and small noise. Fourth column: strong surface wave and large noise.

6 Comparison

Two performance indices have been used to compare the images obtained with all the different techniques. A commonly used nondimensional index, is the Array Performance Indicator (API), which is defined as the area, $A_{6_{\mathrm{dB}}}$, within which the image is greater than 6 dB down from its maximum value, normalised to the square of the wavelength [6]. Since in this application we are using a broadband signal is not possible to define a wavelength for the normalisation and it has been decided to use the directly $A_{6_{\mathrm{dB}}}$ as an index.

The second index has been devised exploiting the fact that the location of the reflector is known. The Pinpoint Factor, γ_{PF}, is the ratio between the value of the image where the target is and the rms of the full image

$$\gamma_{\mathrm{PF}} = \frac{I(x_P, z_P)}{\mathrm{rms}[I(x, y)]}. \tag{34}$$

Figure 2 shows the scanned images for all DA techniques while Figure 4 shows the $A_{6_{\mathrm{dB}}}$ and Pinpoint Factor for all the DA techniques. All the DA techniques show a better resolution and are able to exactly pinpoint the location of the reflector in presence of low noise. In the presence of high noise all technique still show the reflector but DA and DAX show a high level background, i.e. a lower contrast. In the case of large surface wave high levels are present at shallow depths. However a trained operator could still be able to locate the target. In the case of large noise and surface wave CDA and PDA seem to perform the better removing a lot of scattering. The usefulness of the techniques is clear, as the removal of scatter potentially reduces the number of false positives. All the DA techniques show a lower $A_{6_{\mathrm{dB}}}$ than the uniform apodization with SVA performing better across the range. With respect to Pinpoint Factor CDA and PDA are performing better across the range while SVA seems to perform quite badly in the pinpoint accuracy.

Figure 3 shows the scanned images for all DA techniques while Figure 5 shows the performance indices for all the phase based methods. All phase methods are extremely accurate in pinpointing the reflector in case of low noise, apart from IPI which shows too much scatter (note that the image is binary). In the presence of high noise the methods still manage to see the reflector but giving a lower value. This is a good feature of the method since they do not loose resolution with noise and still manage to pinpoint the reflector although with lower contrast. Also the background scatter is kept low. In the case of large surface wave the shallow depth image is not very high and the images still keep some ability to locate the reflector. In the case of large noise and large surface wave the IPI seems to perform better and with less scatter. Looking just at the performance indices SCF seems to perform better than all the other techniques because of the very low scatter in the images. The second best is the IPW.

7 Conclusions

In this paper the potential benefits of dual apodization and phase based techniques for the detection of buried object have been studied. The scan images obtained from the different techniques have been compared using simulated data. Two performance indices have been proposed. The main advantages of using such techniques are a reduced scatter in the images. Especially phase methods are extremely accurate in pinpointing the reflector. The best performing DA technique is the CDA and the best performing phase technique is the SCF. It is clear that the production of this images can greatly enhance the location of buried objects. Future work should look at the effect that extended object, reflection phase change and wave conversion have on the detection. Also experimental data should be used for a more realistic comparison.

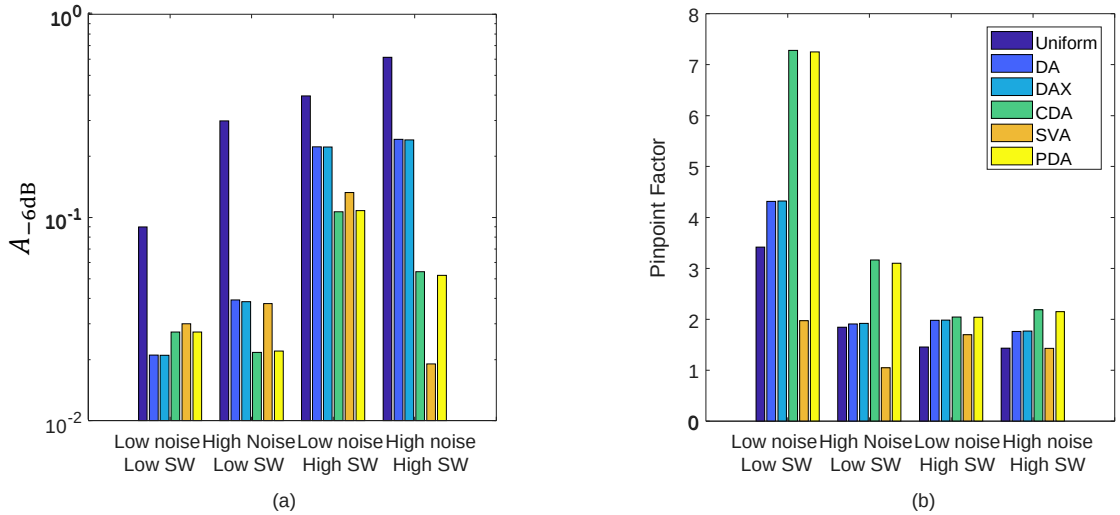


Figure 4: Performance indices for the DA techniques: (a) $A_{6_{\mathrm{dB}}}$; (b) Pinpoint factor.

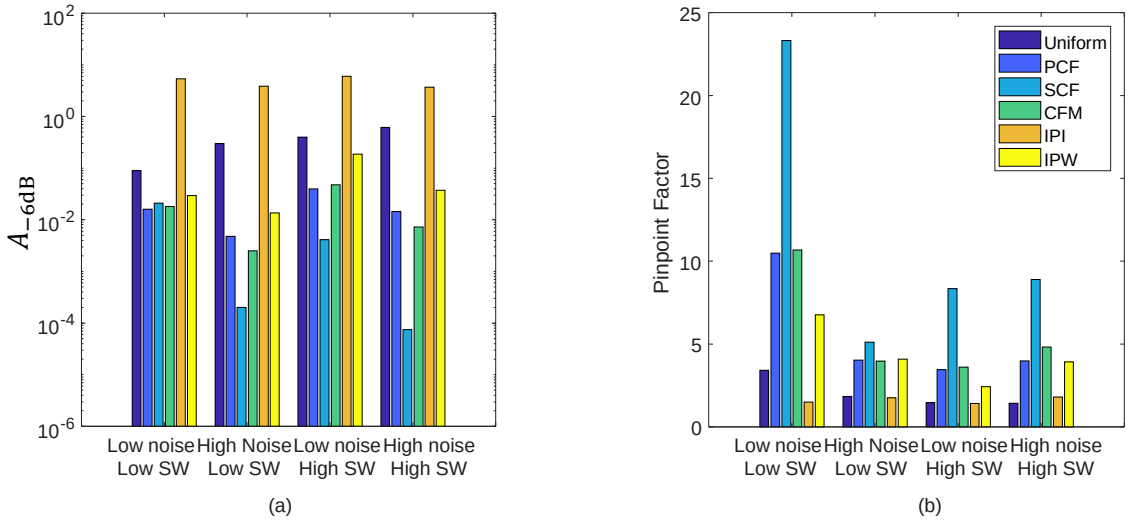


Figure 5: Performance indices for the phase based techniques: (a) $A_{6_{\mathrm{dB}}}$; (b) Pinpoint factor.

References

[1] C. Rogers, C. Overton, A. Cohn, S. Pennock, C. Jenks, J. Muggleton, E. Rustighi, P. Atkins, K. Foo, J. Cross, *et al.*, "Mapping the underworld", 2012.

[2] C. D. F. Rogers, "Assessing the Underworld 2014; remote sensing to support smart and liveable cities", in *2015 8th International Workshop on Advanced Ground Penetrating Radar (IWAGPR)*, 2015, pp. 1–4. DOI: 10.1109/IWAGPR.2015.7292634.

[3] Q. Dou, L. Wei, D. R. Magee, P. R. Atkins, D. N. Chapman, G. Curioni, K. F. Goddard, F. Hayati, H. Jenks, N. Metje, J. Muggleton, S. R. Pennock, E. Rustighi, S. G. Swingler, C. D. F. Rogers, and A. G. Cohn, "3D buried utility location using a marching-cross-section algorithm for multi-sensor data fusion", *Sensors*, vol. 16, no. 11, p. 1827, 2016, ISSN: 1424-8220. DOI: 10.3390/s16111827. [Online]. Available: http://www.mdpi.com/1424-8220/16/11/1827.

[4] J. M. Muggleton and E. Rustighi, "'Mapping the Underworld': Recent developments in vibro-acoustic techniques to locate buried infrastructure", *Géotechnique Letters*, vol. 3, no. July-September, pp. 137–141, Aug. 2013, DOI: 10.1680/geolett.13.00032.

[5] B. Papandreou, M. J. Brennan, and E. Rustighi, "On the detection of objects buried at a shallow depth using seismic wave reflections", *The Journal of the Acoustical Society of America*, vol. 129, no. 3, pp. 1366–1374, 2011.

[6] C. Holmes, B. W. Drinkwater, and P. D. Wilcox, "Post-processing of the full matrix of ultrasonic transmit–receive array data for non-destructive evaluation", *NDT & e International*, vol. 38, no. 8, pp. 701–711, 2005.

[7] B. A. Angelsen, H. Torp, S. Holm, K. Kristoffersen, and T. Whittingham, "Which transducer array is best?", *European Journal of Ultrasound*, vol. 2, no. 2, pp. 151–164, 1995.

[8] C. Fan, M. Caleap, M. Pan, and B. W. Drinkwater, "A comparison between ultrasonic array beamforming and super resolution imaging algorithms for non-destructive evaluation", *Ultrasonics*, vol. 54, no. 7, pp. 1842–1850, 2014.

[9] C. Knapp and G. Carter, "The generalized correlation method for estimation of time delay", *IEEE Transactions on Acoustics, Speech, and Signal Processing*, vol. 24, no. 4, pp. 320–327, 1976.

[10] Y. Gao, M. Brennan, and P. Joseph, "A comparison of time delay estimators for the detection of leak noise signals in plastic water distribution pipes", *Journal of sound and vibration*, vol. 292, no. 3-5, pp. 552–570, 2006.

[11] K. Shin and J. Hammond, *Fundamentals of signal processing for sound and vibration engineers*. John Wiley & Sons, 2008.

[12] J. A. Jensen, S. I. Nikolov, K. L. Gammelmark, and M. H. Pedersen, "Synthetic aperture ultrasound imaging", *Ultrasonics*, vol. 44, e5–e15, 2006, Proceedings of Ultrasonics International (UI05) and World Congress on Ultrasonics (WCU), ISSN: 0041-624X. DOI: https://doi.org/10.1016/j.ultras.2006.07.017. [Online]. Available: http://www.sciencedirect.com/science/article/pii/S0041624X06003374.

[13] V. T. Prado, "Ultrasonic non-destructive testing of plate-like structures using piezoelectric array transducers", 2014.

[14] H. C. Stankwitz, R. J. Dallaire, and J. R. Fienup, "Nonlinear apodization for sidelobe control in sar imagery", *IEEE Transactions on Aerospace and Electronic Systems*, vol. 31, no. 1, pp. 267–279, 1995.

[15] H. Wang, *System and method for adaptive beamformer apodization*, US Patent 6,436,044, Aug. 2002.

[16] C. H. Seo and J. T. Yen, "Sidelobe suppression in ultrasound imaging using dual apodization with cross-correlation", *IEEE Transactions on Ultrasonics, Ferroelectrics, and Frequency Control*, vol. 55, no. 10, pp. 2198–2210, Oct. 2008, ISSN: 0885-3010. DOI: 10.1109/TUFFC.919.

[17] J. Muggleton, M. Brennan, and Y. Gao, "Determining the location of buried plastic water pipes from measurements of ground surface vibration", *Journal of Applied Geophysics*, vol. 75, no. 1, pp. 54–61, 2011.

[18] J. Camacho, M. Parrilla, and C. Fritsch, "Phase coherence imaging", *IEEE transactions on ultrasonics, ferroelectrics, and frequency control*, vol. 56, no. 5, 2009.

[19] O. Martínez-Graullera, D. Romero-Laorden, C. J. Martín-Arguedas, A. Ibañez, and L. G. Ullate, "A new beamforming process based on the phase dispersion analysis", in *AIP Conference Proceedings*, AIP, vol. 1433, 2012, pp. 185–188.

[20] V. Prado, R. Higuti, C. Kitano, and O. Martinez-Graullera, "Instantaneous phase threshold for reflector detection in ultrasonic images", *IEEE transactions on ultrasonics, ferroelectrics, and frequency control*, vol. 61, no. 7, pp. 1204–1215, 2014.

Optimization of flow restrictor diameter in high speed railway vehicle suspensions

C. Ramiro [1], **P. Pintado** [1], **A.L. Morales** [1], **A.J. Nieto** [1], **J.M. Chicharro** [1]
[1] University of Castilla-La Mancha, Department of Mechanical Engineering,
Avenida Camilo José Cela, Ciudad Real, Spain
e-mail: **carmen.ramiro@uclm.es**

Abstract
High speed railway vehicle secondary suspensions are often composed of an air spring connected to a fixed volume reservoir via a flow restrictor. This work describes the pneumatic suspension models that the authors have developed to predict passenger comfort indexes. These models are used to determine optimum restrictor diameters for different railroad types and different vehicle speeds. Rail vertical profiles are generated as samples of ergodic random processes of given spectral density. Different rail quality levels can be attained by modifying parameters in a spectral density "template" expression. These samples are functions of distance (along the track) and can, therefore, be traversed at any speed. The numerical integration of the dynamic model excited by a given rail vertical profile allows us to determine comfort indexes according to EN 12299 standard. The numerical analysis just outlined is conducted for several rail quality levels, several vehicle speeds, and several restrictor diameters. Optimum diameters are obtained for any quality-speed combination.

1 Introduction

Railroad vehicle secondary suspensions are often pneumatic systems like the one shown in Figure 1. The air spring is often in series with an emergency rubber spring that would become the main compliant element, should the air pressure drop in emergency situations. Some configurations for high speed passenger railroad vehicles also include a primary suspension composed of a metallic spring and a viscous damper as shown in Figure 1.

The behaviour of the pneumatic and rubber components of the suspension need to be modelled in order to determine passenger accelerations when traversing a railroad of given profile. Thermodynamic models have been proposed to describe air spring – restrictor – reservoir systems [6, 3, 9, 5, 17, 18, 12], but there are two key ingredients of these models that are often provided without experimental support. Namely, the polytropic indexes for the air in the air spring and the reservoir, as well as the flow behaviour through the restrictor. The authors have experimentally characterised these two aspects of thermodynamic models ([16]). The main findings of this work will be abridged, for completeness, in Section 2. Likewise, the work to characterize and model the rubber spring will be succinctly presented in Section 3.

These models, along with the capability to numerically synthesise rail profiles of given power spectral density (PSD), allow us to simulate the behaviour of the suspension for different restrictor diameters, different rail quality levels, and different speeds. The simulated suspended mass accelerations can be filtered according to ([20]) to determine comfort levels. Maps of comfort level versus speed and PSD (as specified by some of the parameters on which it depends) for several restrictor diameters serve as an optimising tool to determine the most appropriate diameter for a given speed-PSD combination.

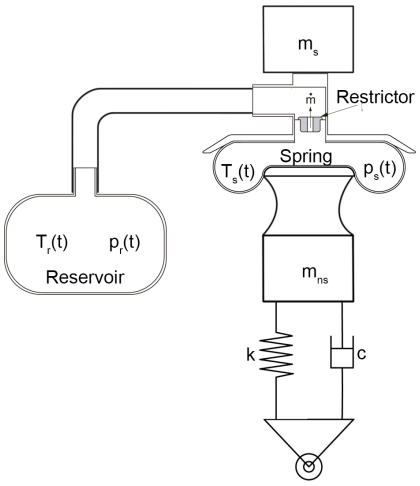


Figure 1: Suspension configuration schematics

2 Pneumatic system

The main findings of [16] will be presented in this section. In order to simplify the characterization of the pneumatic system, pressure and temperature in the entire volume of the air spring are considered uniform at any time. Likewise, pressure and temperature in the reservoir are also assumed uniform. Air behaviour is considered ideal and the fluid flow through the orifice is described as an experimentally fit functional relation between mass flow rate and pressure difference. The ideal gas relations are written as

$$\frac{p_s}{\rho_s} = R_g T_s \qquad \frac{p_r}{\rho_r} = R_g T_r \tag{1}$$

where R_g is the gas constant for air, p is pressure, ρ density, and T is temperature (subscript s refers to spring, and r to reservoir). If polytropic indexes could be defined and found for the air in the spring (n_s) and the air in the reservoir (n_r), then

$$\frac{p_s}{\rho_s^{n_s}} = c_s \qquad \frac{p_r}{\rho_r^{n_r}} = c_r \tag{2}$$

where c_s and c_r are constants determined from the initial conditions. Since the gas leaving the spring has to reach the reservoir, continuity reads

$$-\frac{d}{dt}(\rho_s V_s) = \frac{d}{dt}(\rho_r V_r) \tag{3}$$

where V_s and V_r are the spring and reservoir volumes, respectively, though only the latter is constant. Mass flow rate is a function of pressure drop that can be written as

$$\frac{d}{dt}(\rho_r V_r) = f(p_s - p_r) \tag{4}$$

where the function $f(p_s - p_r)$ describes the restrictor and must be experimentally obtained.

Spring force is

$$F = (p_s - p_a) A_s \tag{5}$$

where p_a is the atmospheric pressure;

The system of seven algebraic–differential equations in seven unknowns may be numerically integrated for any excitation input $x(t)$, given initial conditions $p_s(t=0)$, $T_s(t=0)$, $p_r(t=0)$, $T_r(t=0)$, and provided that $V_s(x, p_s)$, $A_s(x, p_s)$, $f(p_s - p_r)$, n_s, n_r, p_a are known functions and parameters.

A specific pneumatic system was tested in the laboratory to determine all functions and parameters mentioned in the previous paragraph. Figure 2 shows the air spring placed in a 100 kN capacity 80 mm stroke universal testing machine (MTS model 810 fitted with a load cell model 20F-03). Temperature, pressure, force and displacement are recorded during any single test.



Figure 2: Experimental setup

Four of the six raw signals measured for a very low frequency case (0.01 Hz, 20 mm restrictor diameter, and 6 mm displacement amplitude) are shown as an example in Figure 3. In this example, temperature amplitudes in the reservoir are larger than one degree Celsius, and about half a degree in the air spring. Therefore, the isothermal assumption, which has been adopted for low frequency in many previous works, does not seem accurate in this case.

Density, in both the air spring and the reservoir, may be computed as a function of time from the pressure and temperature measurements ($\rho_s = p_s/(R_g T_s)$, $\rho_r = p_r/(R_g T_r)$). Figure 4 shows the calculated density (in the reservoir) obtained from the pressure and filtered temperature signals. Now that instantaneous pressure and density are available, one may try to infer a functional relation between the two (if it exists).

Polytropic indexes may be obtained from $\ln p$ versus $\ln \rho$ plots. Figure 5 shows some constant amplitude loops as an example. The slope of the curve is the polytropic index.

Figure 6a shows the cloud of values for n_s, obtained as the $\ln p_s$–$\ln \rho_s$ slope described in the previous paragraph, for several test conditions and as a function of frequency. Each data point in the plot is obtained for a given displacement amplitude and a certain restrictor diameter, but several amplitudes (from 2 to 6 mm) and diameters (from 5 to 20 mm) are blended in Figure 6a. The plot proves that the influence of these parameters (amplitude and diameter) may be neglected, since the relative standard deviation (c_v) is less than 2.9% for any frequency.

The experimental results show that the polytropic index in the reservoir (Fig. 6b) is approximately 1.2 for the lowest frequency tested, and drops quickly becoming isothermal ($n_r \approx 1$) for frequencies above 0.1 Hz. The polytropic index in the spring is slightly smaller (than n_r) for low frequencies and, although it drops at a lower rate, it also becomes isothermal for frequencies above 0.3 Hz.

Another aspect of air spring – reservoir systems that needs to be characterized is the flow through the orifice or, more specifically, the relation between pressure difference and air mass flow rate.

The experimental setup lends itself to determine mass flow rate ($\dot{m}$) from the temperature and pressure measurements. Figure 7 shows root mean square (rms) mass flow rate as a function of rms pressure difference (Δp) for four different orifice diameters (d =5, 10, 14, and 20 mm). The experimental results (circle data

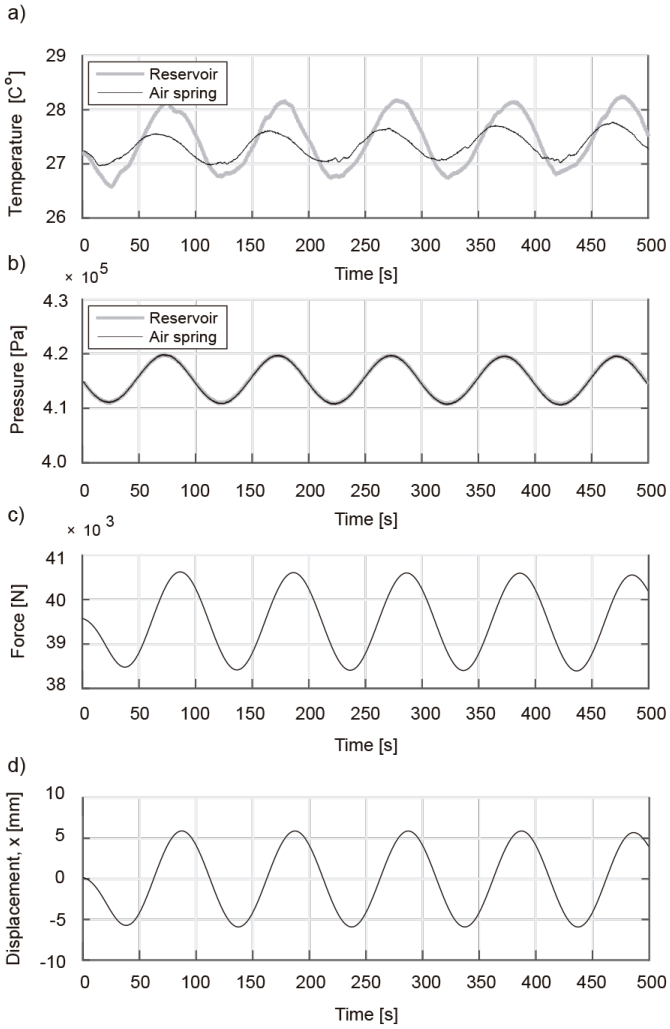


Figure 3: Example of recorded signals (20 mm orifice, 6 mm amplitude, 0.01 Hz)

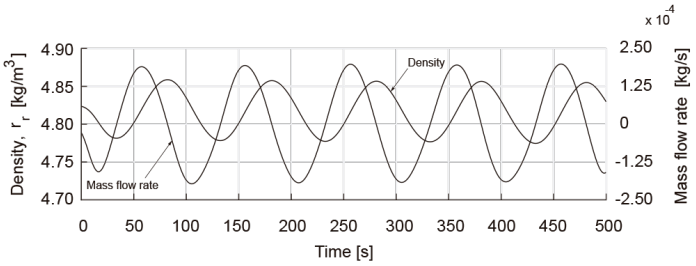


Figure 4: Reservoir density ($\rho_r = p_r/(R_g T_r)$) and mass flow ($\dot{m} = \dot{\rho}_r V_r$) for 20 mm orifice, 6 mm amplitude, 0.01 Hz.

points in the figure) hint at a functional relation of the type $\dot{m} = A d^b \Delta p^c$, where parameters A, b and c are to be determined to minimize error. Returned values of exponent b were not far from 2 while exponent c was close to 0.5 ($b = 1.80$, $c = 0.56$, rmse$= 5\ 10^{-4}$ kg/s). This comes as a surprise since it may be taken as an inkling that the complex (conceivably) compressible flow through the orifice can nonetheless be described

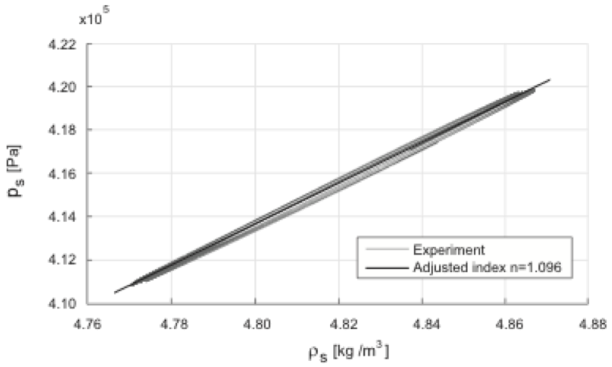


Figure 5: Air spring pressure vs density (logarithmic scale, 20 mm orifice, 6 mm amplitude, 0.01 Hz).

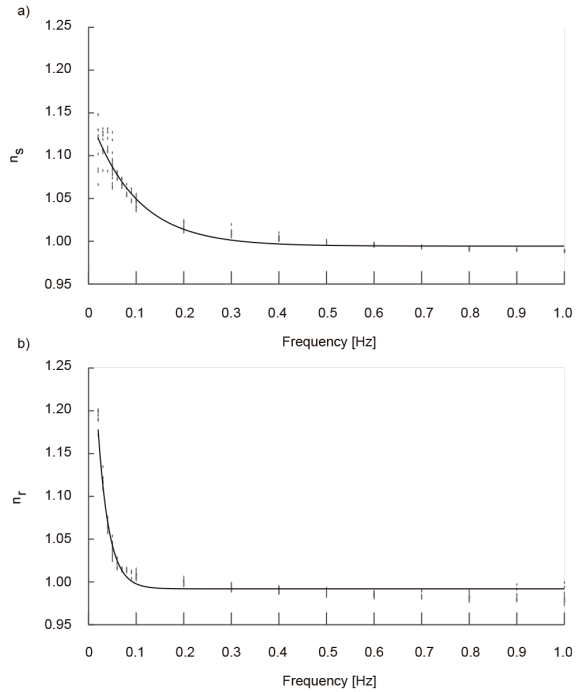


Figure 6: Air spring (a) and reservoir (b) polytropic indexes as a function of frequency.

by a simple incompressible–flow local head loss. In fact, by imposing a relation of the type

$$\dot{m} = \pi d^2 \left(\frac{\rho \Delta p}{8k} \right)^{1/2} \tag{6}$$

one may obtain the local head loss coefficient k using an average density.

Figure 7 shows the experimental data along with the outcome of Eq. 6 for each diameter using $k = 0.677$ and an average density (the mean of the reservoir density time averages for all tests corresponding to the diameter in question). These functions approximate experimental data quite accurately (rmse$= 6.9\,10^{-4}$ kg/s, $R^2 = 0.9994$) except for the case of the 20 mm diameter restrictor. Accuracy may be improved using a diameter–specific head loss as shown in Figure 7.

This mass flow description, along with the experimentally determined polytropic indexes and air spring volume as a function of displacement and pressure, allow us to integrate the system of Equations 1– 5 for

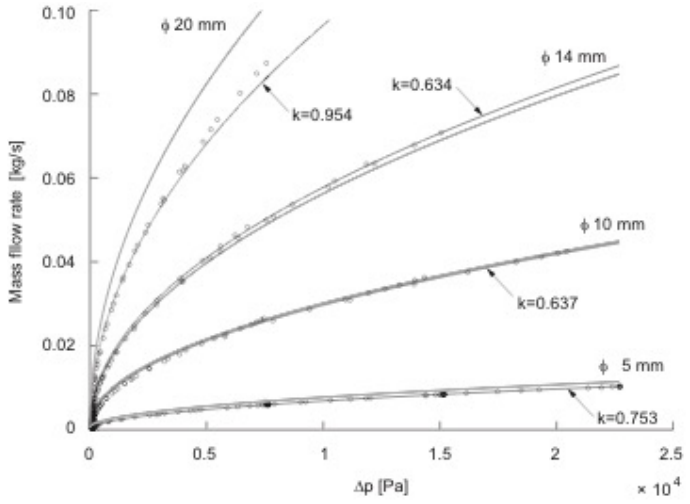


Figure 7: Root mean square (rms) mass flow rate as a function of rms pressure drop.

any given displacement input. It is also possible to include Equations 1– 5 as part of the global system of equations that describes the behaviour of the system shown in Figure 1.

3 Safety spring behaviour

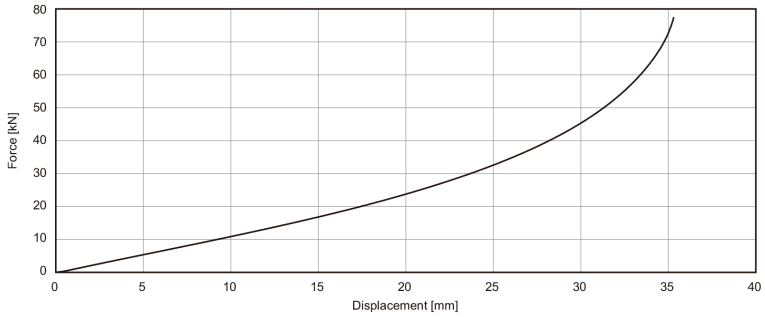


Figure 8: Rubber spring nonlinear elastic behaviour

The rubber block between the unsuspended mass and the air spring in Figure 1 serves, as mentioned in the introduction, as an emergency spring which becomes the main compliant element should the air pressure drop. The mechanical behaviour of rubber is not easily modelled. The main findings of [15] will be presented in this section. Figure 8 shows the elastic force–displacement curve. The test was conducted "backwards" by progressively allowing the spring to stretch from a highly compressed stable initial state. The entire test took 10 hours. The waiting allowed for all viscous or frictional effects to be removed from the measurements, including the very slow stress relaxation.

Figure 9 shows low frequency ($f = 0.01$ Hz) force–displacement cycles for harmonic displacement of several amplitudes and the same mean. The elastic curve is superimposed on this plot to visualise the significance of the added effects. The plot shows that the apparent stiffness increases as the amplitude decreases, suggesting the presence of internal friction. Viscous effects are, for the most part, removed from the response

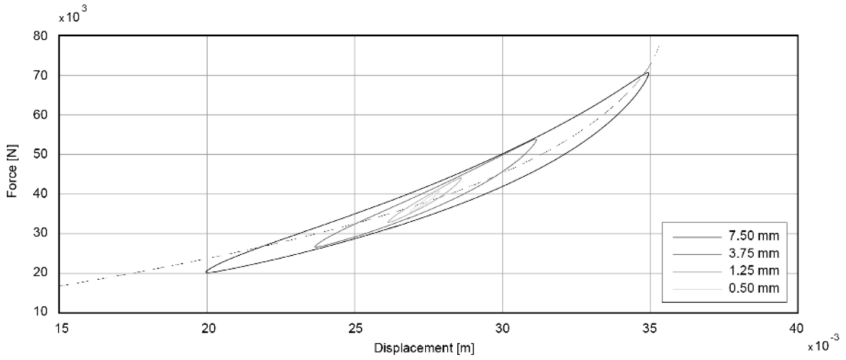


Figure 9: Low frequency ($f = 0.01$ Hz) force–displacement cycles for harmonic displacement of amplitudes $A = 0.50, 1.25, 3.75, 7.50$ mm and mean value $x_m = 27.35$ mm.

since the frequency is very low. These effects were added performing medium frequency and medium amplitude tests.

The spring behaviour described and quantified above may be replicated to satisfactory accuracy with the model in Figure 10, which is composed of three branches: a non–linear elastic branch the force–displacement curve of which should fit, as closely as possible, the behavior shown in Figure 8; a soft friction branch to reproduce the dissipation and softening with amplitude shown in Figure 9; and finally, a viscous branch to incorporate the stiffening with frequency (with a mild increase in dissipation).

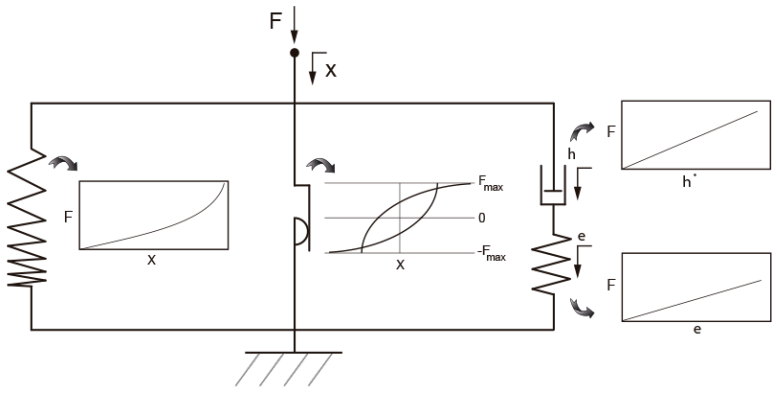


Figure 10: Proposed model for rubber spring behaviour

As proven in [15], the model predicts force–displacement behaviour for harmonic inputs of any given amplitude and frequency. It may therefore be incorporated in the general suspension model of Figure 1 to simulate its behaviour when travelling at a given speed on a specific rail profile.

4 Rail profile

Railroad vertical irregularities can be measured and decomposed in its spatial frequency content. Some expressions have been proposed to describe the spectral density of vertical irregularities. For example, the following expression can be found in [13]:

$$S_v(\Omega) = \frac{A_v \cdot \Omega_c^2}{(\Omega^2 + \Omega_r^2)(\Omega^2 + \Omega_c^2)} \tag{7}$$

where S_v is vertical displacement spectral density, Ω is spatial frequency (rad/m), A_v a coefficient that may be modified to represent different levels of irregularities (or rail quality), and Ω_c and Ω_r are cutoff spatial frequencies ($\Omega_c = 0.8246$ rad/m, $\Omega_r = 0.0206$ rad/m). Figure 11 shows $S_v(\Omega)$ for six different values of A_v that cover a wide range of rail qualities. These are the values of A_v to be used in the simulations to be presented in the next section.

Random profile samples with a given spectral density may be synthesized with a random phase procedure. One such sample is shown in Figure 12 as a function of distance along the track (s). Profiles are converted to time signals when the train speed is selected ($t = s/v$). Any of these time records is the input displacement signal for the equations that model the suspension as described in previous sections. The output is the suspended mass acceleration. Suspended mass acceleration records may be filtered according to [20] in order to take into account the variable influence on comfort of the different frequencies of which the acceleration signal is composed. Reference [20] also defines a comfort index that can be used to compare designs, configurations and conditions.

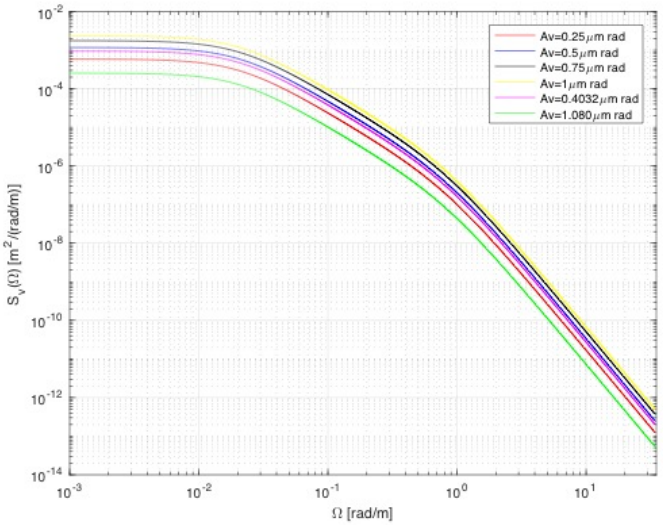


Figure 11: Rail irregularity Power Spectral Density

5 Comfort indexes

The procedure outlined in the previous sections has been implemented to determine comfort indexes for different restrictor diameters, different train speeds, and several rail quality levels (as represented by parameter A_v). A pictorial representation of the process is depicted in Figure 12. Figure 13 shows comfort indexes as a function of speed for three different diameters. Each of the three plots of the figure corresponds to a given A_v value ($A_v = 0.25\,\mu$m rad, Fig. 13a, $A_v = 0.75\,\mu$m rad, Fig. 13b, $A_v = 1\,\mu$m rad, Fig. 13c). It

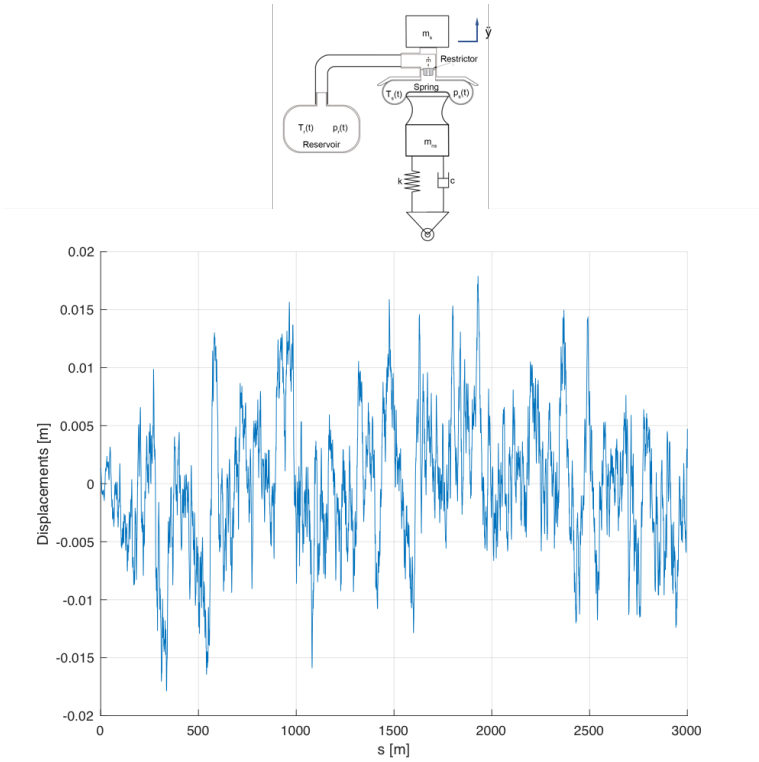


Figure 12: Rail irregularity sample

comes as no surprise that comfort worsens (comfort index increases) as velocity grows and as parameter A_v becomes larger. Nevertheless, it is worth noticing that the curves for different diameters cross each other at speeds that depend on rail quality. This result suggests that comfort may benefit from designs with adjustable restrictor diameters, so that the optimum could be chosen depending on speed and rail quality. Focusing, for example, on a rail quality for which $A_v = 1\ \mu$m rad (Fig. 13c) we infer that a diameter of 15 mm should be used for speeds below 250 km/h, but a larger diameter (20 mm) should be used for higher speeds. Figure 14 rearranges the data showing comfort indexes as a function of A_v for three different diameters. Each of the three plots of the figure corresponds to a given speed ($v = 140$ km/h, Fig. 14a, $v = 240$ km/h, Fig. 14b, $v = 300$ km/h, Fig. 14c). For example, when travelling at 140 km/h (Fig. 14a), a 10 mm diameter should be used for high quality rail profiles (A_v below 0.6 μm), but a larger diameter should be used when the rail profile worsens.

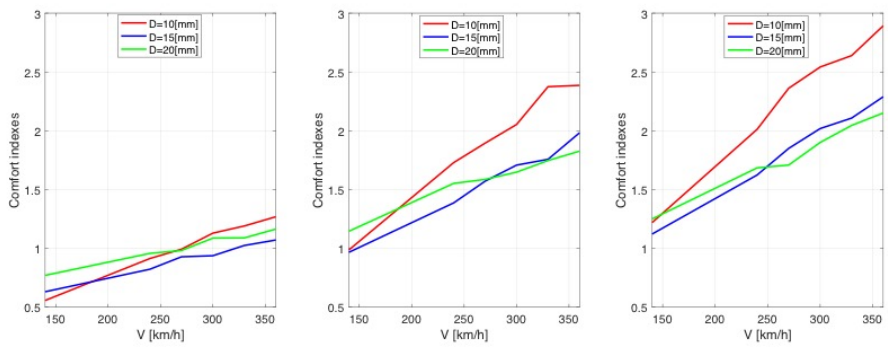


Figure 13: Comfort indexes versus speed, (a) $A_v = 0.25\ \mu$m rad, (b) $A_v = 0.75\ \mu$m rad, (c) $A_v = 1\ \mu$m rad

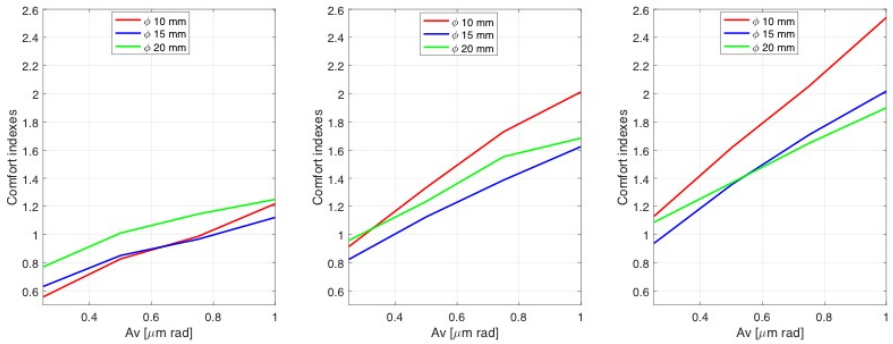


Figure 14: Comfort indexes versus A_v, (a) $v = 140$ km/h, (b) $v = 240$ km/h, (c) $v = 300$ km/h

Figura 15 shows comfort indexes as a function of parameter A_v and speed. A decision map can be obtained from this figure to determine the most appropriate diameter for each speed–A_v combination.

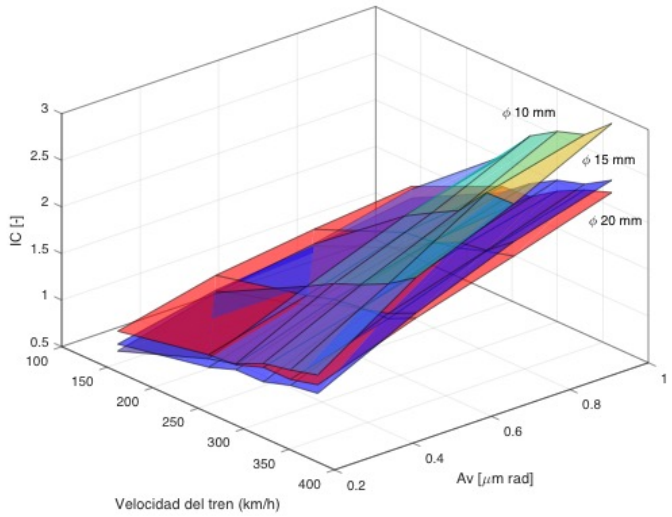


Figure 15: Comfort indexes versus A_v and speed

6 Conclusions

The thermodynamic behaviour of pneumatic systems cannot be ignored when simulating the performance of passenger rail vehicle suspensions. Contrary to what has traditionally been accepted, experimentally measured polytropic indexes for the air spring and the reservoir tend to isotropic when frequency grows. Since usual suspension configurations include a rubber emergency spring, the complicated behaviour of rubber needs to be incorporated in suspension models as well. Comfort indexes have been obtained by simulating the suspension model traversing a given road profile at a given speed. Results show that comfort may be improved by devising an adaptive suspension to use different restrictor diameters depending on speed and rail quality.

7 Acknowledgements

The authors are grateful for the support received from National Project TRA–2014–53552–R entitled "Mejora del confort del transporte ferroviario de alta velocidad mediante suspensiones neumaticas adaptativas y amortiguadores magnetoreologicos" financed by the MINECO (España) and from Regional Project PEII–2014–034–P entitled "Analisis y diseño de elementos neumaticos activos para el control de vibraciones" financed by the Junta de Comunidades de Castilla – La Mancha. They would also like to show their gratitude to "Patentes Talgo" railway vehicle manufacturer for their comments and suggestions as well as for providing suspension components for the tests.

References

[1] A. Alonso, N. Gil-Negrete,J. Nieto, et al. *Development of a rubber component model suitable for being implemented in railway dynamic simulation programs*, Journal of Sound and Vibration, Vol. 332, (2013), pp. 3032-3048.

[2] A. Alonso , J.G. Giménez, J. Nieto, J. Vinolas, *Air suspension characterisation and effectiveness of a variable area orifice*, Vehicle System Dynamics, Vol. 180, No. 4, (2010), pp. 271-286.

[3] BI. Bachrach, E.Rivin, , *Analysis of a damped pneumatic spring*, Journal of Sound and Vibration, Vol. 86, No. 2, 1983), pp. 191-197.

[4] M. Berg, *A non-linear rubber spring model for rail vehicle dynamics analysis*, Vehicle System Dynamics, Vol. 30(3-4), (1998), pp. 197-212.

[5] S. Bruni, J. Vinolas, M. Berg, O. Polach, S. Stichel, *Modelling of suspension components in a rail vehicle dynamics context*, Vehicle System Dynamics, Vol. 49, No. 7, (2011), pp. 1021-1072.

[6] C. Erin, B. Wilson, *An improved model of a pneumatic vibration isolator: theory and experiment*, Journal of Sound and Vibration, Vol. 218(1), (1998), pp. 81-101.

[7] W.P. Fletcher, A.N. Gent, *Non-linearity in the dynamic properties of vulcanized rubber compounds*, Transactions of the Institution of Rubber Industry 29 (1953), pp. 226-280.

[8] A. Homeyer, C. Maßmann, *Moderne verfahren zur auslegung von luftfedersystemen*, ZEV+DET Glas. Ann., Vol. 122, No. 9-10, Academic Press (1988), pp. 549-554.

[9] L. Mazzola, M. Berg, *Secondary suspension of railway vehicles-air spring modelling: Performance and critical issues*, Proc IMechE Part F: J Rail and Rapid Transit, Vol. 228, No. 3, (2014), pp. 225-241.

[10] Miguel de Priego J.C, *Optimización de suspensiones neumaticas de vehiculos ferroviarios.*, Universidad Politecnica de Madrid, Madrid, Spain (2004).

[11] A.J. Nieto, A.L. Morales, A. González, J.M. Chicharro, P. Pintado, *An analytical model of pneumatic suspensions based on an experimental characterization*, Journal of Sound and Vibration, Vol. 313 , No. 1-2, (2008), pp. 290-307.

[12] N. Oda, K. Nishioka, S. Nishimura, *The damping of the orifice in the air spring*, Osaka Sumitomo Metal Industries, LTD paper (1971).

[13] ORE Question B176, *Bogies with steered or steering wheelsets*, Report N^{o} 1: Specifications and preliminary studies, Vol (2): Specification for a bogie with improved curving characteristics, Ultrech, (1989).

[14] A.R. Payne, R.E. Wittaker, , *Low strain dynamic properties of filled rubbers*, Rubber Chemistry and Technology, Vol. 44(2), (1971), pp.440-478.

[15] P. Pintado, C. Ramiro,M. Berg, A.L. Morales, A.J. Nieto, J.M. Chicharro, J.C. Miguel de Priego, E. García, *On the mechanical behavior of rubber springs for high speed rail vehicles*, Journal of Vibration and Control, DOI: 10.177/1077546317732206.

[16] P. Pintado, C. Ramiro,A.L. Morales, A.J. Nieto, J.M. Chicharro, *The dynamic behavior of pneumatic vibration isolators*, Journal of Vibration and Control, DOI: 10.177/1077546317730243.

[17] G. Quaglia, M. Sorli, *Air suspension dimensionless analysis and design procedure*, Vehicle System Dynamics, Vol.35, No. 6, (2001), pp. 443-475.

[18] K. Toyofuku, C. Yamada, T. Kagawa, T. Fujita, *Study on dynamic characteristic analysis of air spring with auxiliary chamber*, J SAE Review, Vol. 20, No. 4, Academic Press (1999), pp. 349-355.

[19] UIC CODE 518 OR, *Testing and acceptance of railway vehicles from the point of view of dynamic behaviour, safety track fatigue and running behaviour*, International Union of Railways, (1999).

[20] UNE-EN 12299, *Aplicaciones ferroviarias. Comodidad de viaje para los viajeros. Medición y evaluación*, AENOR, (2000).

Modelling of the track supports with elements over elastic foundation together with dynamic internal degrees of freedom

B. Blanco [1,2,3], **L. Kari** [3], **N. Gil-Negrete** [1,2], **A. Alonso** [2,4]
[1] Ceit, Donostia / San Sebastián, Spain
e-mail: **bblanco@ceit.es**

[2] Universidad de Navarra, Tecnun, Donostia / San Sebastián, Spain

[3] KTH Royal Institute of Technology, Stockholm, Sweden

[4] CAF I+D, Beasain, Guipúzcoa, Spain

Abstract
Formulation of the Timoshenko elements is improved with the use of internal degrees of freedom (iDOF) representing the local displacements, leading to a new finite element approach specially devoted to the numeric analysis of the track dynamics. The dynamic formulation of the local displacement is proved to correct the frequency content of the track model. Regarding time domain studies, this approach avoids the displacement underestimation and shear discontinuity between elements, which are sources of inaccuracies and irregular behaviour. Those rail sections located above the supports are modelled with Timoshenko element over elastic foundation (TEEF), and the rest with conventional Timoshenko elements (TIM4). By using TEEF prompt disruption of the contact force at support surpassing is avoided, and the frequency response of the track around the 'pinned-pinned' frequency is corrected. Moreover the TEEF formulation is extended in order to account for the sleeper pitch rotation, and evaluation of its influence over the track dynamics is performed.

1 Introduction

At railway vehicle operation the contact between rail and wheel originates forces with a marked dynamic behaviour. This dynamic behaviour is normally attributed to irregularities at the contact profiles and varying track stiffness. The latter is known as parametric excitation. Accurate evaluation of the contact forces is of utmost importance for the study of railway track and vehicle dynamics. The former has a main role in the assessment and prediction of rail corrugation [1], ballast settlement [2] and wheel-rail noise [3]. Because of it, track modelling is a key point in the development of prediction tools, and since several decades ago up to nowadays it has been the subject of numerous investigations.

In the review presented in Ref. [4], the track models are divided in two groups, depending on whether they are devoted to the analysis in frequency or time domains. Normally, time domain simulations are preferable to be performed with numeric or semi-analytic models, while frequency analysis can be computed efficiently with analytic models. Numeric models based on finite elements techniques has been extensively used for the analysis of non-linearities [5, 6, 7], distributed track supports [8, 9], transitions [10], ground vibration [11], impact response [12] and sleeper voids [13]. In general terms, numeric models permit studying a wide range of situations, but in some cases an elevated computational cost could make them unsuitable.

In this work, a numeric methodology is presented in order to improve the description of some track components at a reduced computational cost. The main components of the track that the model should describe are rails, pads, sleepers and ballast. Depending on the frequency range of interest and the model goal, the level of detail in the modelling of each component will vary. Usage of 3D finite elements on the representation of sleepers and ballast involves a high computational cost, therefore it is restricted to studies focused on the ground vibration [10], non-linear ballast behaviour [7] and coupling of the rails through the sleepers [14]. This paper is focused on the accurate modelling of rail and pads, which have been separately studied by the current authors in previous work. The dynamics of ballast and sleepers are represented with simplified models. Ballast is taken as a massless system and its flexibility and dissipative properties are introduced with Kelvin-Voigt elements. This assumption implies a lack of accuracy at low frequencies, but it has a negligible effect on the medium-high frequency range. On the other hand, sleepers are modelled as rigid masses, which, in spite of being a widely used simplification, neglects the existence of bending modes around 450 and 750 Hz, thus more research into this topic would be necessary in order to justify this simplification.

Regarding rail modelling, most time domain models use beam elements based on Euler-Bernoulli and Timoshenko theories. The former is accurate in the rail modelling below 500 Hz, while the latter extends its validity up to 1.5 kHz by accounting for shear deformation and rotational inertia. Beyond that limit, Timoshenko theory starts to lose accuracy, since it does not consider resonances involving section deformation, although many track phenomena can be still analysed with enough precision. Nevertheless, Timoshenko validity can be extended by implementing torsional and warping motions [15] or modelling the rail section with several beams [16]. Finally, modelling with 3D elements encompasses a wide range of frequencies [17], but the computational cost increases significantly. For all these reasons, Timoshenko beam remains as a common choice at the rail modelling.

The performance of conventional Timoshenko elements with four DOF and cubic shape functions [18] presents some drawbacks. These are due to underestimation of the local deformation [19] and shear discontinuities at the element nodes. Some studies have dealt with this problem, by using TIM7 elements [20] together with moving DOF [21], modifying the contact stiffness [22] and implementing local displacement of the element [23]. In Ref. [23] the local displacement of conventional Timoshenko elements is formulated with two approaches, one static and another dynamic, both based on the analytic solution of a clamped-ends Timoshenko beam loaded by a point force. The dynamic approach is proved to correct the hindrances of TIM4 elements and the frequency content of the track at a lower number of DOF modelling the rail.

The accurate modelling of the rail-pads is also addressed in this work. Most track models using beam theories represent rail-pads with a vertical Kelvin-Voigt interaction between the rail and the sleeper, i.e. neglecting the fact that the rail is not supported at a concentrated point but over a certain length. It involves misdirection of the frequency response around the 'pinned-pinned' frequency, and in time domain, it leads to a prompt disruption of the contact force each time a support is surpassed. The correction of the frequency response is tackled by some models with rotational stiffness and damping constraining rail bending at the support positions [24, 25]. However, rotational interaction does not achieve a total correction of the frequency domain response, and it has a null impact on the contact force disruption at time domain response. Both inaccuracies can be removed with a distributed model of support [8, 9]. In Ref. [8] several elements are used to model the rail length over the support, while in Ref. [9] it is modelled by using one element derived from the Timoshenko beam equation over elastic foundation.

The proposed methodology joins the work presented in Refs. [9, 23]. In Ref. [23] the total displacement is seen as the superposition of two systems, which are denoted as global and local. Here the global system corresponds to that presented in Ref. [9], and it is enhanced with the implementation of the local displacements for TEEF and TIM4 element. Instead of addressing the local displacement as a system superposition, here it is directly introduced as internal element DOF. This is an analogous development to the previously proposed, but its implementation is more compact and generic. Moreover, in Ref. [24] the sleeper rotation along its longitudinal axis (sleeper pitch motion) is accounted for, but no further assessment of its influence is performed. Here the TEEF formulation is extended in order to account for that motion, and the impact on the track dynamics is studied. The paper is divided as follow: the second section makes some comments of

the general features of the model. The third section extends the TEEF formulation to account for the sleeper pitch motion. The fourth section establishes the formulation of the iDOF. Fifth and sixth sections study the frequency and time domain results of the model, respectively. And finally, conclusions are commented in seventh section.

2 Description of the track model

The global system is associated to the common FE modelling, and it contains those DOF representing vertical displacement and bending rotation of the rail, as well as the motion of sleepers. In this paper, those DOF are denoted as external since they might define the displacement field of several elements. On the other hand, local system accounts for the displacements inside the finite element, which are out of the accuracy range of the global system. It is represented by DOF whose motion only contribute directly to the displacement field of the elements in which they are implemented, and therefore they are denoted as iDOF.

The global system used in this work is directly taken from Ref. [9]. The modelling of the global system is presented schematically in Fig. 1 (a), in which TEEF elements are used at the support positions and TIM4 elements between supports. In Ref. [9] the description of the local displacement is performed with a static approach. In this work, the dynamic behaviour of the local system is accounted for by using the methodology proposed in Ref. [23] for the TIM4 element, and extending it for the TEEF. The dynamic approach is based on a modal superposition of the vibration modes corresponding to a clamped-ends Timoshenko beam, which should also introduce the viscoelastic foundation for the TEEF, as it shown by Fig. 1 (b). In order to account for the total flexibility of the local system an infinite number of vibration modes would be necessary. Apart from increasing the number of iDOF, a high number of vibration modes would force to reduce the time-step length to an unacceptable size. This problem is circumvented by applying the mode acceleration method [26] in an analytical way, resulting in a residual flexibility, $F_{\mathrm{res}} = K_{\mathrm{res}}^{-1}$. The parameters of the track are taken from Ref. [24], which are gathered in Tab. 1.

Table 1: Parameters for the track (Ref. [24]). UIC60 rail type.

Young's modulus (GPa)	E	210	Shear modulus (GPa)	G	80.8
Cross-sectional area (cm^2)	A	76.9	Mass density (kg/m)	ρ	60.3
Shear coefficient	κ	0.4	Inertia moment (cm^4)	I	3055
Pad stiffness (MN/m)	K_{p}	350	Pad damping (kNs/m)	C_{p}	48
Ballast stiffness (MN/m)	K_{b}	70	Ballast damping (kNs/m)	C_{b}	47
Sleeper spacing (m)	l	0.6	Sleeper mass (kg)	M_{s}	160
Wheel mass (kg)	M_{w}	550	Contact coeff. (GN/m$^{3/2}$)	K_{c}	118.6
Support length (m)	L_{s}	0.16	Sleeper rotational inertia (kgm^2)	I_{s}	1.586

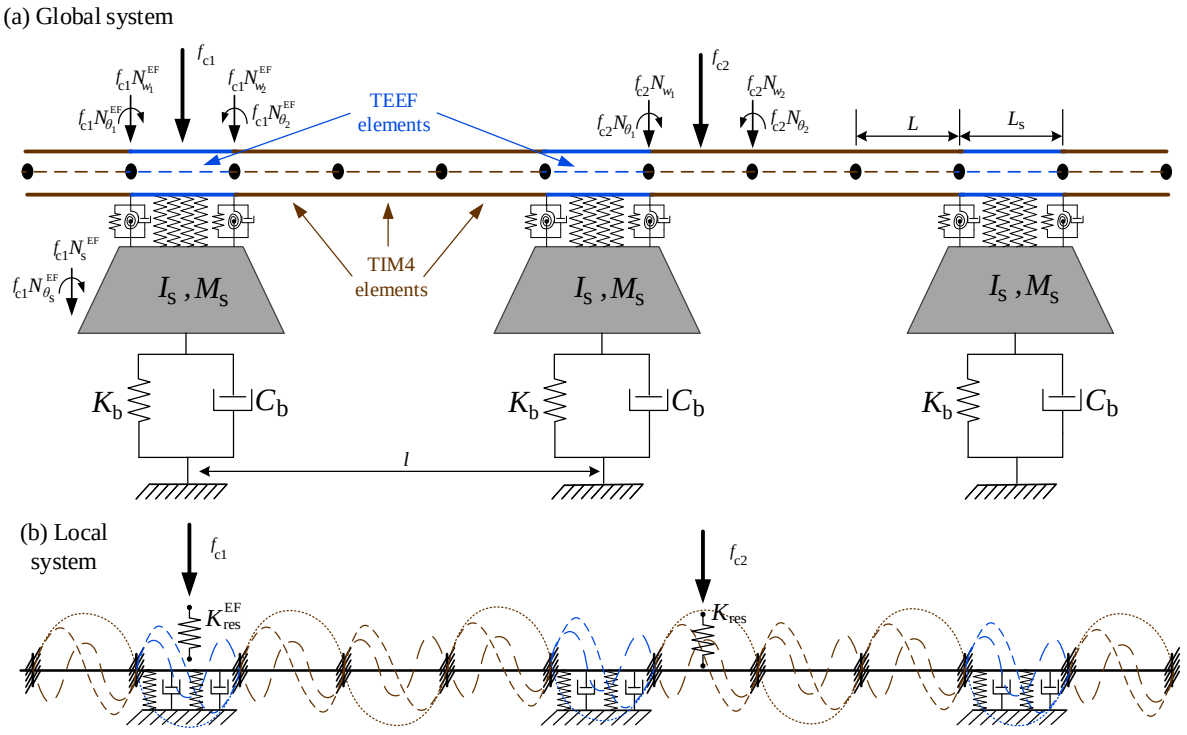


Figure 1: Track modelling using global (a) and local (b) systems. The rail sections above the supports use TEEF and the rest are represented with TIM4 elements.

3 Shape functions of the element DOF

3.1 External DOF

The shape functions associated to the external DOF (eDOF) of TIM4 and TEEF are the static solutions of the corresponding equilibrium equations. For the TIM4 element the shape functions read

$$N_{w_1}(x) = \frac{1}{1+\Phi}\left[1 - 3\left(\frac{x}{L}\right)^2 + 2\left(\frac{x}{L}\right)^3 + \Phi\left(1 - \frac{x}{L}\right)\right], \tag{1}$$

$$N_{\theta_1}(x) = \frac{x}{1+\Phi}\left[1 - 2\frac{x}{L} + \left(\frac{x}{L}\right)^2 + \frac{\Phi}{2}\left(1 - \frac{x}{L}\right)\right], \tag{2}$$

$$N_{w_2}(x) = \frac{1}{1+\Phi}\left[3\left(\frac{x}{L}\right)^2 - 2\left(\frac{x}{L}\right)^3 + \Phi\frac{x}{L}\right], \tag{3}$$

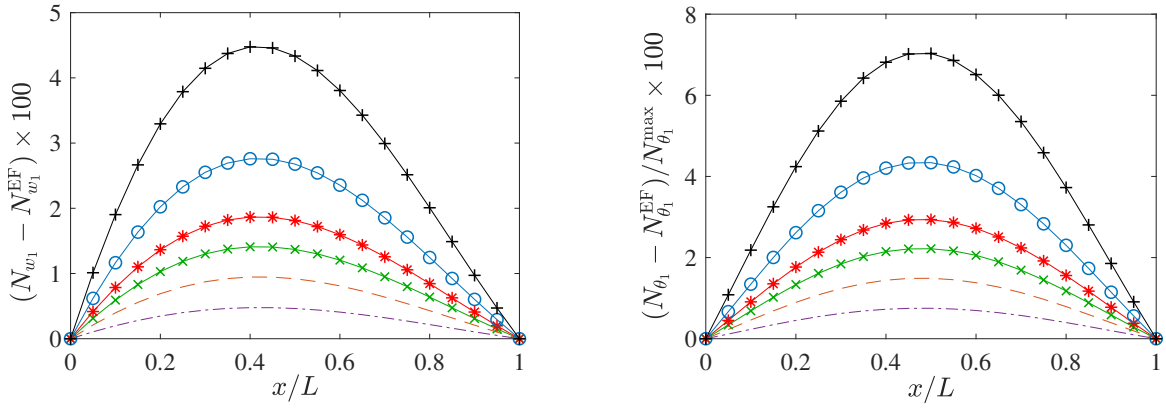
$$N_{\theta_2}(x) = \frac{x}{1+\Phi}\left[\left(\frac{x}{L}\right)^2 - \frac{x}{L} - \frac{\Phi}{2}\left(1 - \frac{x}{L}\right)\right], \tag{4}$$

where x is the spatial coordinate, L is the element length and $\Phi = 12EI/GA\kappa L^2$. The derivation can be found in Ref. [18], as well as the elementary mass and stiffness matrices. The shape functions of the TIM4 are gathered in $\mathbf{N}_{\mathrm{TM}}$. On the other hand, shape functions of the TEEF are derived following the procedure presented in Ref. [9], in which the differential equation to solve is

$$w^{\mathrm{IV}} - \frac{k_{\mathrm{d}}}{\kappa AG}w^{\mathrm{II}} + \frac{k_{\mathrm{d}}}{EI}w = \frac{q_{\mathrm{s}}}{EI}, \tag{5}$$

where roman numerals denote the spatial derivative, and q_{s} is the distributed shear load due to the sleeper movement. The shape functions of the TEEF, $\mathbf{N}_{\mathrm{EF}}$, are obtained by imposing unitary displacement at the

DOF of interest and vanishing value at the rest. $\mathbf{N}_{\mathrm{EF}}$ accounts for the potential energy absorbed by the elastic foundation, therefore it results in a lower deformation along the element than $\mathbf{N}_{\mathrm{TM}}$, for a same force or displacement applied at a nodal position. The difference between $\mathbf{N}_{\mathrm{EF}}$ and $\mathbf{N}_{\mathrm{TM}}$ is shown in Fig. 2. As the distributed pad stiffness increases the difference becomes larger.



(a) Difference between $N_{w_1}^{\mathrm{EF}}$ and N_{w_1}.

(b) Difference between $N_{\theta_1}^{\mathrm{EF}}$ and N_{θ_1}.

Figure 2: Difference between shape functions of the TEEF with respects to those from TIM4 for different distributed stiffness. The element length is 0.5 m. Distributed stiffness: (--) 0.1 $\mathrm{GN/m^2}$, (−−) 0.2 $\mathrm{GN/m^2}$, (-×-) 0.3 $\mathrm{GN/m^2}$, (-∗-) 0.4 $\mathrm{GN/m^2}$, (-o-) 0.6 $\mathrm{GN/m^2}$, (-+-) 1 $\mathrm{GN/m^2}$. Parameters from the UIC60 rail. [9]

In the TEEF formulation the vertical and pitch motions of the sleeper cause deformation of the rail section as it is schematically shown in Fig. 3. In Ref. [9] the sleeper is assumed to be infinitely rigid to the pitch motion, and only the vertical motion is accounted for by defining $q_{\mathrm{s}} = k_{\mathrm{d}} w_{\mathrm{s}}$. Here the sleeper pitch, θ_{s}, is introduced through its inertia, I_{s}, and the distributed shear load,

$$q_{\mathrm{s}} = k_{\mathrm{d}} w_{\mathrm{s}} + k_{\mathrm{d}} \left(x - L_{\mathrm{s}}/2\right) \sin\theta_{\mathrm{s}} \approx k_{\mathrm{d}} w_{\mathrm{s}} + k_{\mathrm{d}} \left(x - L_{\mathrm{s}}/2\right) \theta_{\mathrm{s}}. \tag{6}$$

The shape functions for both sleeper motions are obtained substituting Eq. (6) into Eq. (5), imposing unitary displacement at the study sleeper DOF, and vanishing values at the rest. The shape functions for the sleeper movement are displayed in Fig. 4. The vertical and pitch motions of the sleeper will be the fifth and sixth DOF of the TEEF, respectively. The interaction of the sleeper with the rail through the elastic foundation is noticeable for the case of the vertical motion, on the contrary, the shape function of the sleeper pitch motion shows an negligible coupling between sleeper pitch and rail displacement. Although these results affect only the formulation of the TEEF, they point out an overall low influence of the sleeper pitch motion.

3.2 Internal DOF

The formulation of the iDOF is based on the vibration modes of a clamped-ends Timoshenko beam, which are used as shape functions. Following, the mathematical development is presented accounting for the presence of a viscoelastic foundation. The derivation is analogous to that presented in Ref. [23] whether k_{d} and c_{d} are assumed vanishing. The dynamic equilibrium of the section reads

$$\kappa AG\left(\frac{\partial\theta(x,t)}{\partial x} - \frac{\partial^2 w(x,t)}{\partial x^2}\right) + \rho A \frac{\partial^2 w(x,t)}{\partial t^2} = -k_{\mathrm{d}} w(x,t) - c_{\mathrm{d}} \dot{w}(x,t), \tag{7}$$

$$EI\frac{\partial^2\theta(x,t)}{\partial x^2} + \kappa AG\left(\frac{\partial w(x,t)}{\partial x} - \theta(x,t)\right) - I\rho\frac{\partial^2\theta(x,t)}{\partial t^2} = 0. \tag{8}$$

Assuming a modal solution in the form

$$w(x,t) = W(x)\mathrm{e}^{st} \quad ; \quad \theta(x,t) = \Theta(x)\mathrm{e}^{st}, \tag{9}$$

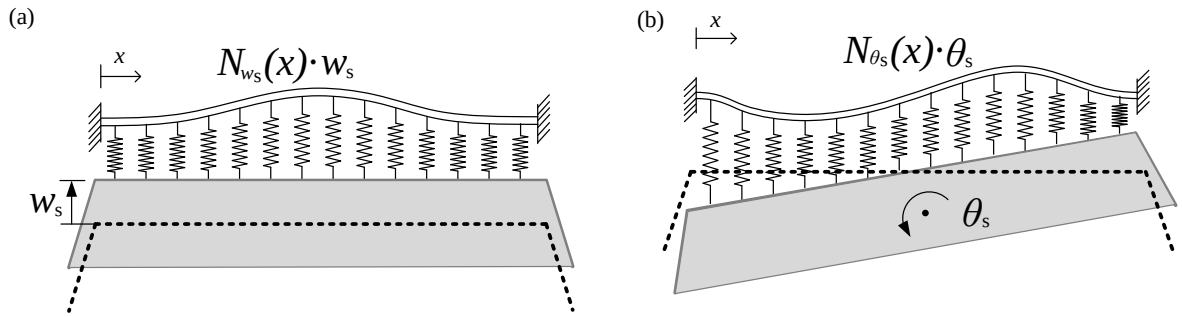


Figure 3: Qualitative representation of the interaction between the rail and sleeper through the elastic foundation for vertical (a) and pitch (b) motions.

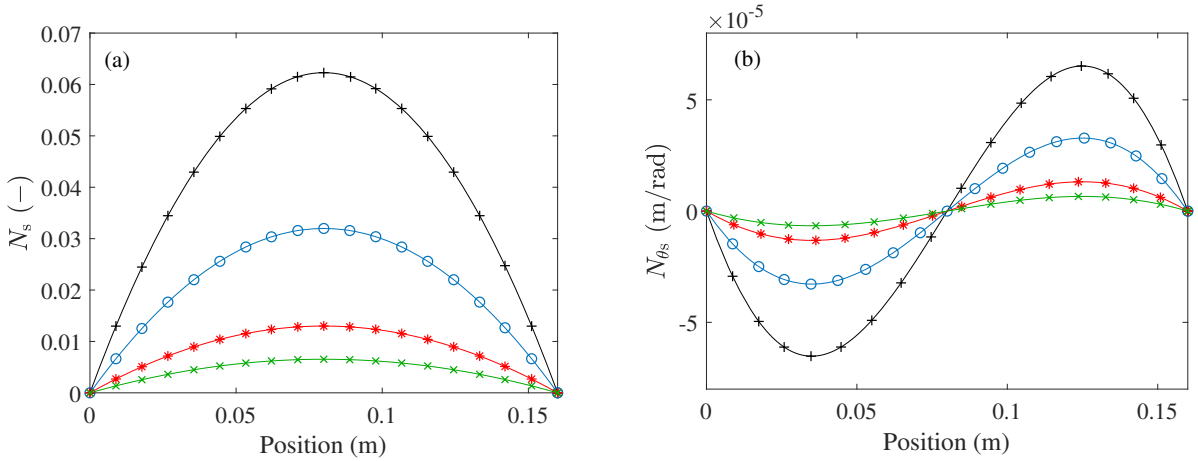


Figure 4: Shape functions of the vertical (a) and pitch (b) motions of the sleeper for several values of the distributed pad stiffness. Distributed stiffness: (-×-) 0.5 GN/m^2, (-*-) 1.0 GN/m^2, (-o-) 2.5 GN/m^2, (-+-) 5.0 GN/m^2. Parameters from the UIC60 rail.

the differential equations (7) and (8) become

$$\kappa AG\left(\Theta^{\mathrm{I}} - W^{\mathrm{II}}\right) + \left(\rho A s^2 + k_{\mathrm{d}} + c_{\mathrm{d}} s\right) W = 0, \tag{10}$$

$$EI\Theta^{\mathrm{II}} + \kappa AG\left(W^{\mathrm{I}} - \Theta\right) - I\rho\Theta s^2 = 0, \tag{11}$$

which is a coupled system of differential equations. It can be merged as

$$W^{\mathrm{IV}} - \left[\frac{s^2\rho}{E}\left(\frac{E}{\kappa G} + 1\right) + \frac{k_{\mathrm{d}} + c_{\mathrm{d}} s}{\kappa AG}\right] W^{\mathrm{II}} + \left[\frac{s^2\rho}{E}\left(\frac{s^2\rho}{kG} + \frac{A}{I} + \frac{k_{\mathrm{d}} + c_{\mathrm{d}} s}{\kappa AG}\right) + \frac{k_{\mathrm{d}} + c_{\mathrm{d}} s}{EI}\right] W = 0. \tag{12}$$

In turn, the bending rotation can be expressed in terms of the vertical displacement as

$$\Theta = \frac{EI}{\kappa AG + I\rho s^2}\left[W^{\mathrm{I}}\left(\frac{\kappa AG}{EI} - \frac{\rho A s^2 + k_{\mathrm{d}} + c_{\mathrm{d}} s}{\kappa AG}\right) + W^{\mathrm{III}}\right] = D_1\left(D_2 W^{\mathrm{I}} + W^{\mathrm{III}}\right). \tag{13}$$

The Eq. (12) has an homogeneous solution formed by four exponential terms,

$$W = P_1 \mathrm{e}^{\lambda_1 x} + P_2 \mathrm{e}^{-\lambda_1 x} + P_3 \mathrm{e}^{\lambda_2 x} + P_4 \mathrm{e}^{-\lambda_2 x}, \tag{14}$$

where λ_i are the characteristics roots of the differential equation (12). The coefficients P_i are obtained by imposing the clamped-ends boundary conditions, $W = \Theta = 0$, at $x = 0$ and $x = L$, which lead to

$$\begin{bmatrix} 1 & 1 & 1 & 1 \\ \mathrm{e}^{\lambda_1 L} & \mathrm{e}^{-\lambda_1 L} & \mathrm{e}^{\lambda_2 L} & \mathrm{e}^{-\lambda_2 L} \\ C_1 & -C_1 & C_2 & -C_2 \\ C_1 \mathrm{e}^{\lambda_1 L} & -C_1 \mathrm{e}^{-\lambda_1 L} & C_2 \mathrm{e}^{\lambda_2 L} & -C_2 \mathrm{e}^{-\lambda_2 L} \end{bmatrix} \begin{bmatrix} P_1 \\ P_2 \\ P_3 \\ P_4 \end{bmatrix} = \mathbf{\Lambda P} = \mathbf{0}, \tag{15}$$

where $C_1 = \left(\lambda_1^3 + D_2\lambda_1\right) D_1$ and $C_2 = \left(\lambda_2^3 + D_2\lambda_2\right) D_1$. Those values of s that make $\det(\mathbf{\Lambda}) = 0$, are the natural frequencies of the vibration modes.

For the local modes of the TEEF, the presence of viscous forces at the equation leads to complex values of the natural frequencies, $s = \beta + \mathrm{i}\alpha$. The value of s is rearranged to express it in terms of an absolute natural frequency, $\omega = |s|$, and a damping coefficient, $\zeta = \left(1 - \beta^2/\omega^2\right)^{1/2}$. The Tab. 2 gathers the natural frequencies and damping coefficients of the first five local vibration modes, for several stiffness of the foundation and a constant value of the distributed viscous damping. The vibration modes are distinguished by means of the number of periods composing the modal shape, and the dominant type of strain involved in their motion. The data shows that distributed foundation has a low impact on the highest modes, in fact only the first vibration mode varies significantly. An extreme case is the mode involving dominant bending strain, which has a null sensitivity to the foundation presence. In spite of the small differences between vibration modes of TIM4 element and TEEF, for the shake of coherence the proper vibration modes are used at the formulation of iDOF. Since the damping is kept constant, the value of ζ does not show noticeable changes.

Table 2: Natural frequencies (kHz) of the vibration modes for several distributed pad stiffness. Element length 16 cm and parameter from UIC60 rail. $c_\mathrm{d} = 300$ kNs/m.

period/element length		$k_\mathrm{d} = 0$ $K_\mathrm{p} = 0$	$k_\mathrm{d} = 1\,\mathrm{GN/m^2}$ $K_\mathrm{p} = 160\,\mathrm{MN/m}$	$k_\mathrm{d} = 2.5\,\mathrm{GN/m^2}$ $K_\mathrm{p} = 400\,\mathrm{MN/m}$	$k_\mathrm{d} = 5\,\mathrm{GN/m^2}$ $K_\mathrm{p} = 800\,\mathrm{MN/m}$
Half period (shear)	ω (kHz)	6.279	6.312	6.362	6.444
	ζ	0.063	0.063	0.062	0.061
1 period (shear)	ω (kHz)	12.408	12.424	12.448	12.488
	ζ	0.031	0.031	0.030	0.030
1 period (bending)	ω (kHz)	17.111	17.111	17.112	17.113
	ζ	0.001	0.001	0.001	0.001
3/2 period (shear)	ω (kHz)	18.894	18.905	18.922	18.950
	ζ	0.021	0.021	0.021	0.021
2 period (shear)	ω (kHz)	25.283	25.291	25.303	25.324
	ζ	0.016	0.016	0.016	0.016

Once the frequencies of the vibration modes are obtained, the coefficients P_i defining the modal shape are derived from Eq. (15). Since $\mathbf{\Lambda P} = \mathbf{0}$ is an indeterminate system, one of the terms in $\mathbf{P}$ should be assumed in order to calculate the rest. In this way non-normalized expressions of W and Θ are derived. Usually, normalization is achieved by imposing a unitary value of the modal mass. In this case, the presence of distributed damping leads to complex modal shapes which make difficult their accurate normalization. Since one of the component is much larger than the other, the largest one is taken as real and the normalization is done with respect to it.

4 Formulation of the Timoshenko element with internal DOF

Once the static shape functions of the eDOF and the vibration local modes have been obtained, they are gathered as the elementary shape functions in $\mathbf{N}^{(\mathrm{e})} = \left[\mathbf{N}^{\mathrm{ext}} \;\; \mathbf{N}^{\mathrm{int}}\right]$, where the superscripts 'ext' and 'int' refer to external and internal DOF, respectively. The stiffness and mass matrices are defined as

$$\mathbf{K}^{(\mathrm{e})} = \int_L \mathbf{B}_{\mathrm{b}}^{\mathrm{T}} EI \mathbf{B}_{\mathrm{b}} \mathrm{d}x + \int_L \mathbf{B}_{\mathrm{sh}}^{\mathrm{T}} GA\kappa \mathbf{B}_{\mathrm{sh}} \mathrm{d}x + k_{\mathrm{d}} \int_L {\mathbf{N}^{(\mathrm{e})}}^{\mathrm{T}} \mathbf{N}^{(\mathrm{e})} \mathrm{d}x, \tag{16}$$

$$\mathbf{M}^{(\mathrm{e})} = \rho A \int_L {\mathbf{N}^{(\mathrm{e})}}^{\mathrm{T}} \mathbf{N}^{(\mathrm{e})} \mathrm{d}x + \rho I \int_L {\mathbf{N}_{\mathrm{b}}^{(\mathrm{e})}}^{\mathrm{T}} \mathbf{N}_{\mathrm{b}}^{(\mathrm{e})} \mathrm{d}x, \tag{17}$$

where $\mathbf{N}_{\mathrm{b}}$ is the bending rotation interpolation vector, $\mathbf{B}_{\mathrm{b}}$ and $\mathbf{B}_{\mathrm{sh}}$ are the vectors which transform nodal displacements into bending and shear strains, respectively. For a certain i-th DOF the generic expressions of the previous vectors are

$$N_{\mathrm{b}i} = \frac{EI}{\kappa AG + I\rho\omega^2} \left[N_i^{(\mathrm{e})\mathrm{I}} \left(\frac{\kappa AG}{EI} - \frac{\rho A\omega^2 + k_{\mathrm{d}} + c_{\mathrm{d}}\omega}{\kappa AG} \right) + N_i^{(\mathrm{e})\mathrm{III}} \right], \tag{18}$$

$$B_{\mathrm{b}i} = \frac{\mathrm{d}N_{\mathrm{b}i}^{(\mathrm{e})}}{\mathrm{d}x}, \tag{19}$$

$$B_{\mathrm{sh}i} = \frac{\mathrm{d}N_i^{(\mathrm{e})}}{\mathrm{d}x} - N_{\mathrm{b}i}^{(\mathrm{e})}. \tag{20}$$

Since the shape functions of the eDOF are derived statically, $\omega = 0 \;\; \forall \;\; i \in \mathrm{ext}$. In a similar way, if the matrices are derived for the elements without elastic foundation, TIM4, k_{d} is set at 0. For the case of the stiffness matrix it becomes

$$\mathbf{K}^{(\mathrm{e})} = \begin{bmatrix} \mathbf{K}^{\mathrm{ext}} & \mathbf{K}^{\mathrm{cross}} \\ \mathbf{K}^{\mathrm{cross}} & \mathbf{K}^{\mathrm{int}} \end{bmatrix} = \begin{bmatrix} \mathbf{K}^{\mathrm{ext}} & \mathbf{0} \\ \mathbf{0} & \mathrm{diag}\left(\boldsymbol{\omega}^2\right) \end{bmatrix}. \tag{21}$$

The resulting $\mathbf{K}^{(\mathrm{e})}$ shows that external and internal DOF are uncoupled statically, which is obvious since global system reaches exact solutions for static loads acting at the external nodes. The terms associated to the internal nodes representing the local system become a diagonal matrix due to the orthogonality between vibration modes and, because of normalization of the modal masses, each term equals the squared natural frequency of the associated vibration mode. The mass matrix results in

$$\mathbf{M}^{(\mathrm{e})} = \begin{bmatrix} \mathbf{M}^{\mathrm{ext}} & \mathbf{M}^{\mathrm{cross}} \\ \mathbf{M}^{\mathrm{cross}} & \mathbf{M}^{\mathrm{int}} \end{bmatrix} = \begin{bmatrix} \mathbf{M}^{\mathrm{ext}} & \mathbf{M}^{\mathrm{cross}} \\ \mathbf{M}^{\mathrm{cross}} & \mathbf{I} \end{bmatrix}. \tag{22}$$

In this case there is a coupling between the external and internal DOF, meaning that dynamic loads at external nodal positions cause response of the iDOF. The normalization of the vibration modes leads to the identity matrix, $\mathbf{I}$, at the iDOF representing the local system. In this modelling the damping is provided by ballast, pads, and also, a certain level of modal damping, $\boldsymbol{\zeta}$, is associated to the iDOF. Therefore, regarding the beam elementary matrices, the one corresponding to damping is defined as

$$\mathbf{C}^{(\mathrm{e})} = c_{\mathrm{d}} \int_L {\mathbf{N}^{(\mathrm{e})}}^{\mathrm{T}} \mathbf{N}^{(\mathrm{e})} \mathrm{d}x + \mathrm{diag}\left(2\boldsymbol{\zeta} \circ \boldsymbol{\omega}\right), \tag{23}$$

where c_{d} is the distributed damping due to the pad, which becomes vanishing at TIM4 elements.

5 Frequency-domain validation of the model

After defining the elementary matrices, the track system matrices are assembled for mass, $\mathbf{M}$, damping, $\mathbf{C}$, and stiffness, $\mathbf{K}$, which are used to obtain the track frequency response as

$$\mathbf{H}(\omega) = \left(-\omega^2\mathbf{M} + \mathrm{i}\omega\mathbf{C} + \mathbf{K}\right)^{-1}. \tag{24}$$

The Fig. 5 shows the impact of using iDOF on the track response. The track is modelled with 101 bays to ensure an accurate prediction of the amplitude at the 'pinned-pinned' frequency. Each bay is modelled with 1 TIM4 element for the bay and 1 TEEF for each support. Regarding the iDOF, TEEF includes one DOF associated to a vibration mode at 6351.8 Hz with a damping coefficient of 0.063. On the other hand, TIM4 element includes 3 iDOF with the highest vibration mode occurring at 6620.4 Hz. No internal damping has been implemented at TIM4 element iDOF. This configuration of iDOF corrects predictions of the response according to Timoshenko theory up to about 6 kHz, coinciding with the value of the highest vibration modes of the iDOF. As compared with the proposed formulation, using only eDOF leads to a general stiffening of the model unless the number of elements is increased. Deviation between both approaches becomes noticeable above around 200 Hz in Fig. 5, with the most significant inaccuracies around the 'pinned-pinned' frequency.

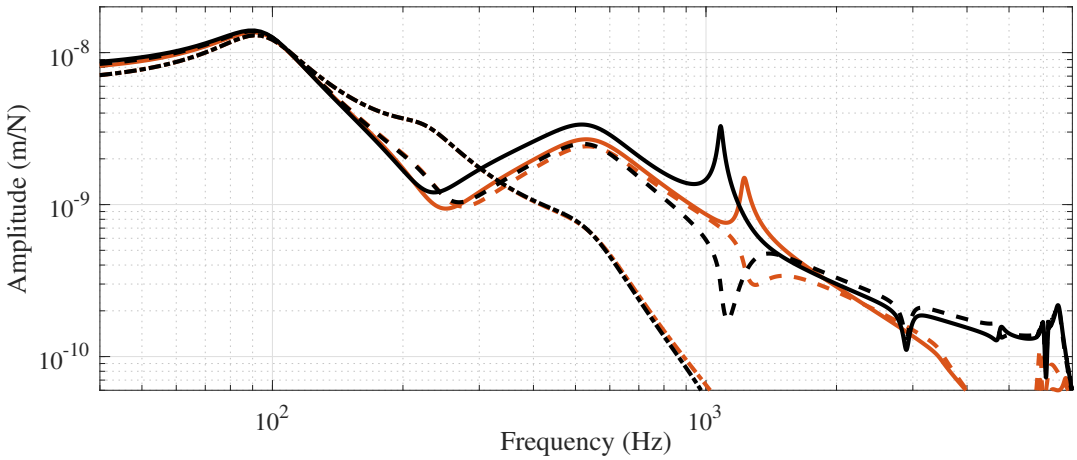


Figure 5: Frequency response of the track with only eDOF (orange) and introducing iDOF (black). The rail response for mid-span (—) and above sleeper (– –) excitations are plotted, as well as the sleeper response (– · –). Track modelled with 101 bays. 1 TEFF and 1 TIM4 element at each bay.

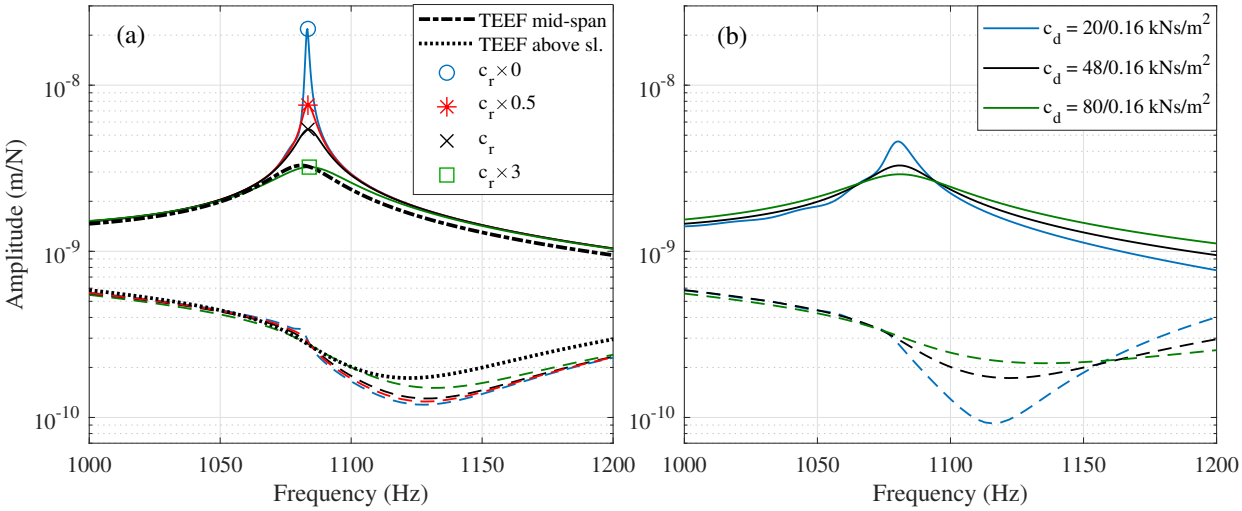


Figure 6: Impact of the damping values on the frequency response of the track model around the 'pinned-pinned', depending on the support modelling. (a) Influence of the damping value at the rotational interaction for concentrated model of support. (b) Influence of several distributed pad damping values for the TEEF.

The response around the 'pinned-pinned' frequency resembles that of a very poorly damped resonance.

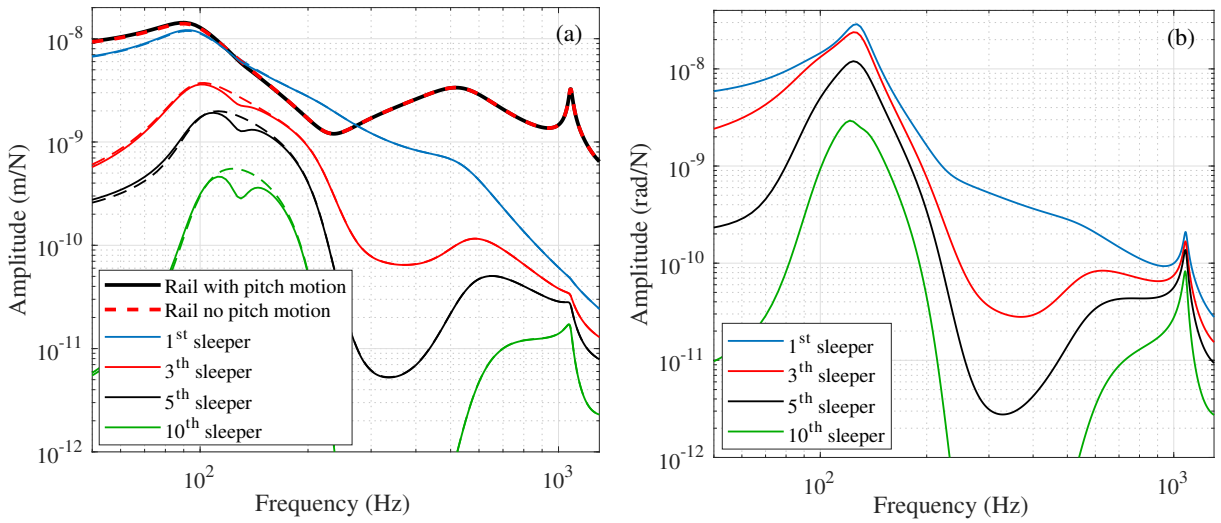


Figure 7: Influence of TEEF formulation including the sleeper pitch motion at the track response. Rail excitation at the mid position between supports. (a) Vertical response of the rail and sleepers with pitch and vertical motions (solid line) and with only vertical motion (dashed line). (b) Rotation of the sleeper.

Conventional modelling of support with only vertical Kelvin-Voigt elements tends to exaggerate it. The rectification based on including also rotational Kelvin-Voigt elements acts at the response through the rotational damping, while the associated stiffness has a negligible influence. Fig. 6 (a) shows the impact of the rotational damping at the response amplitude around the 'pinned-pinned' frequency. The value $c_\mathrm{r} = C_\mathrm{p} L_\mathrm{s}^2/12$ is obtained from integration of the distributed damping over the support length, and it is used in Ref. [24]. Taking the solution of TEEF with $C_\mathrm{p} = 48\,\mathrm{kNs/m^2}$ as reference, c_r should be 3 times higher to obtain the correct value of the 'pinned-pinned' resonance, however that increment is not still enough to correct the underestimation of the anti-resonance amplitude. This fact has a significant importance since the anti-resonance determines in a large extend the amplitude of the contact force, which means that concentrated interaction support modelling results in overestimation of the contact forces around the 'pinned-pinned' frequency. In this simulations internal damping is not introduced at the TIM4 iDOF, which could be another way to correct in some level the response.

The resonance amplitude estimated by the TEEF has a less marked dependency on the pad damping, as it is shown in Fig. 6 (b). It leads to the conclusion that 'pinned-pinned' resonance is geometrically restricted by the TEEF, which partially constrains the formation of that mode. On the contrary, rotational damping reduces the amplitude of a pure 'pinned-pinned' resonance, whose shape is not significantly affected by rotational stiffness. In relative terms, the damping introduced through TEEF equally affects the amplitudes of both resonance and anti-resonance, while the rotational damping has a lower influence at the anti-resonance amplitude.

Fig. 7 (a) and (b) show results for the track model considering the sleeper rotational inertia. The impact on the track dynamics at medium-high frequency range is negligible as compared with the model assuming no pitch motion, and it has a noticeable influence over sleeper responses only around 100 Hz. In Fig. 7 (a) the vertical displacements of several sleeper are displayed, where the rotation of the sleeper creates a small anti-resonance at 130 Hz. In Fig. 7 (b) is observed that the anti-resonance at the vertical sleeper motion, is caused by a resonance at the pitch motion. At the 'pinned-pinned' frequency, the rotation of the sleeper is amplified but the response at the rail remains the same. In general terms, the effect of the sleeper rotation is almost imperceptible at the contact position, and it arises only at a certain distance from the excitation. Therefore, it only could affect the coupling between wheelsets, but even so the impact on the response does not seem to be enough to involve significant differences.

6 Time-domain response

The procedure of the time domain simulations is similar to that followed in Refs. [9, 23]. Direct numerical integration of the equation of motion is based on the Newmark method. The convergence is reached with an iterative Newton-Raphson scheme. The contact force between wheel and rail is established with a non-linear Hertzian spring

$$f_{\mathrm{c}} = \begin{cases} K_{\mathrm{c}}\delta^{3/2} + C_{\mathrm{c}}\dot{\delta} & \delta > 0 \\ 0 & \delta \leq 0 \end{cases}, \tag{25}$$

where δ is the interpenetration between wheel and rail surfaces, K_{c} is the Hertzian coefficient and C_{c} is the contact damping that is assumed vanishing in this case. If the Eq. (25) is developed as in Ref. [23] the definition of a contact element is reached, which couples wheel and rail and makes possible the resolution of the equation of motion. The simulations were performed using four elements per bay, with one of them being a TEEF whether distributed support is implemented. 61 bays are used to model the track. Five bays use iDOF, two at each side of the central one. Each element of those bays use three iDOF.

The time domain simulations are performed with the parameters from Tab. 1, assuming that both wheel and rail are perfectly smooth and the excitation is only parametric. The wheel is subjected to its own weight and a constant external load of 100 kN. Fig. 8 (a) and (b) display the contact force response for two speeds, 24 and 36 m/s. The latter speed makes the sleeper passing frequency, V/l, matches with the first wheel-track resonance around 60 Hz, (in Fig. 5 first resonance occurs at 90 Hz but the wheel mass shifts it to a lower frequency) leading to a higher amplitude of the response. Using conventional Timoshenko elements with only eDOF results in completely unrealistic response, which can be corrected in a large extend by representing the local displacement of the element with a purely static approach, as in Ref. [9]. However, the discontinuity of shear at the element boundary causes a still noticeable discontinuity, which is only removed with the implementation of iDOF and residual flexibility.

The track response of the model with only TIM4 elements, thus concentrated supports, together with iDOF is also shown in Fig. 8. In spite of iDOF reduce to a negligible level the discontinuities at the element boundaries, the concentrated supports induce the prompt disruption of the solution at their positions. That unrealistic solution is corrected by using TEEF with iDOF, in which only a slight change of slope is noticeable at the contact forces, when the wheel surpasses the nodes of the TEEF. The resulting response is smoothed and close to be sinusoidal, in accordance with the excitation type and the structure nature.

7 Conclusions

Internal DOF are proved to extend the validity range of the Timoshenko element up to any required frequency. The methodology was previously stated to enhance the performance of conventional Timoshenko elements, but here it is further developed for the Timoshenko element over elastic foundation (TEEF), which is used to model the rail dynamics at the support positions. Moreover, the methodology is exposed in a compact way with the definition of internal and external DOF. This study has also addressed the impact of pad damping at the response around the 'pinned-pinned' frequency. For concentrated support modelling, the rotational damping should be overestimated by a factor of 3 in order to match the amplitude of the resonance with that obtained from TEEF, and even so, the anti-resonance is not totally corrected. It points out that TEEF formulation not only damps the 'pinned-pinned' mode but it also constrains its propagation. Besides, the work deals with the sleeper pitch motion concluding that it has a negligible impact on the rail dynamics, and only response of sleepers far from excitation are slightly affected. Finally, the performance of the methodology is tested for time domain simulations, showing that track modelling based on TEEF with iDOF is able to smooth the contact force response at the support positions, likewise it makes negligible the discontinuity at the element boundaries by addressing the shear continuity problem.

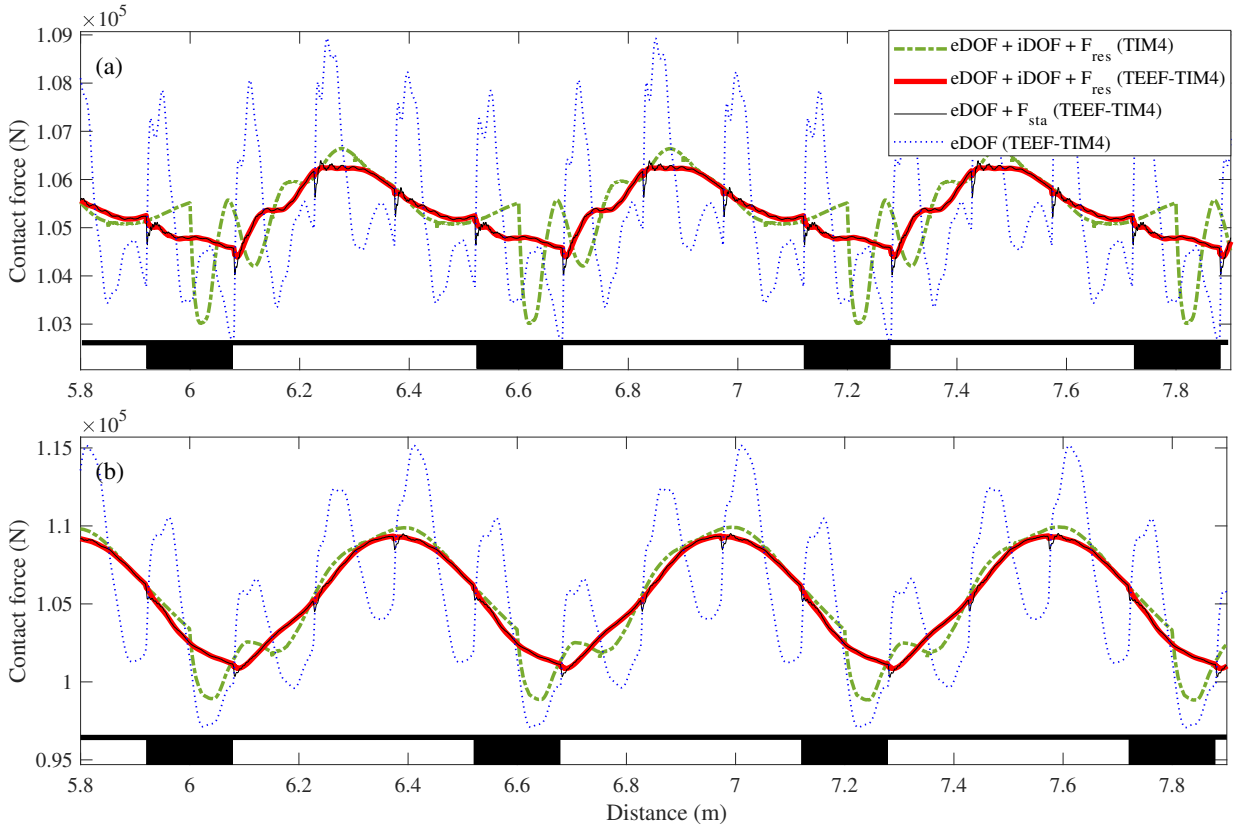


Figure 8: Time domain response of the contact force for smooth surfaces. Speed: 24 (a) and 36 m/s (b). Support positions are denoted with ■.

Acknowledgements

The authors acknowledge the support provided by Project TRA2013-45596 (Ministerio de Economía y Competitividad) and the professor Stefano Bruni from the Politecnico di Milano, whose interest and comments on previous studies have inspired part of this work.

References

[1] S.L. Grassie, *Rail corrugation: characteristics, causes, and treatments*, Proc. Inst. Mech. Eng. F J. Rail Rapid Transit, Vol. 223, No. 6 (2009), pp. 609-625.

[2] T. Abadi, L. Le Pen, A. Zervos, W. Powrie, *A Review and Evaluation of Ballast Settlement Models using Results from the Southampton Railway Testing Facility (SRTF)*, Procedia Eng., Vol. 143 (2016), pp. 999-1006.

[3] D.J. Thompson, *Railway Noise and Vibration: Mechanisms, Modelling and Means of Control*, Elsevier Science (2009).

[4] K.L. Knothe, S.L. Grassie, *Modelling of railway track and vehicle/track interaction at high frequencies*, Veh. Syst. Dyn., Vol. 22 (2007), pp. 209-262.

[5] S.G. Koroma, M.F.M Hussein, J.S. Owen, *The effects of preload and nonlinearity on the vibration of railway tracks under harmonic load*, J. Low Freq. Noise Vib. Act. Control, Vol. 34, No. 3 (2015), pp. 289-306.

[6] S. Bruni, A. Collina, *Modelling the viscoelastic behaviour of elastomeric components: An application to the simulation of train-track interaction*, Veh. Syst. Dyn., Vol. 34, No. 4 (2000), pp. 283-301.

[7] A. Paixão , J.N. Varandas, E. Fortunato, R. Calçada, *Non-Linear behaviour of geomaterials in railway tracks under different loading conditions*, Procedia Eng., Vol. 143 (2016), pp. 1128-1135.

[8] R. Ferrara, G. Leonardi, F. Jourdan, *A contact-area model for rail-pads connections in 2-D simulations: sensitivity analysis of train-induced vibrations*, Veh. Syst. Dyn., Vol. 51, No. 9 (2013), pp. 1342-1362.

[9] B. Blanco, A. Alonso, L. Kari, N. Gil-Negrete, J. G. Giménez, *Distributed support modelling for vertical track dynamic analysis*, Veh. Syst. Dyn., Vol. 56, No. 4 (2017), pp. 529-552.

[10] M. Shahraki, C. Warnakulasooriya, K.J. Witt, *Numerical study of transition zone between ballasted and ballastless railway track*, Transp. Geotech., Vol. 3 (2015), pp. 58-67.

[11] A. El Kacimi, P.K. Woodward, O. Laghrouche, G. Medero, *Time domain 3D finite element modelling of train-induced vibration at high speed*, Comput. Struct., Vol. 118 (2013), pp. 66-73.

[12] I. Grossoni, S. Iwnicki, Y. Bezin, C. Gong, *Dynamics of a vehicle-track coupling system at a rail joint*, Proc. Inst. Mech. Eng. F J. Rail Rapid Transit, Vol. 229, No. 4 (2015), pp. 364-374.

[13] A. Lundqvist, T. Dahlberg, *Load impact on railway track due to unsupported sleepers*, Proc. Inst. Mech. Eng. F J. Rail Rapid Transit, Vol. 21 (2005), pp. 67-77.

[14] M. Oregui, Z. Li, R. Dollevoet, *An investigation into the vertical dynamics of tracks with monoblock sleepers with a 3D finite-element model*, Proc. Inst. Mech. Eng. F J. Rail Rapid Transit, Vol. 230, No. (2016), pp. 891-908.

[15] D. Kostovasilis, D.J. Thompson, M.F.M. Hussein, *A semi-analytical beam model for the vibration of railway tracks*, J. Sound Vib., Vol. 393 (2017), pp. 321-337.

[16] T.X. Wu, D.J. Thompson, *A double Timoshenko beam model for vertical vibration analysis of railway track at high frequencies*, J. Sound Vib., Vol. 224, No. 2 (1999), pp. 329-348.

[17] J. Martínez-Casas, J. Giner-Navarro, L. Baeza. F.D. Denia, *Improved railway wheelset-track interaction model in the high-frequency domain* J. Comput. Appl. Math, Vol. 309, (2017), pp. 642-653.

[18] J.S. Przemieniecki, *Theory of Matrix Structural Analysis*, McGraw-Hill, New York (1968).

[19] J.C.O. Nielsen, A. Igeland, *Vertical dynamic interaction between train and track influence of wheel and track imperfections*, J. Sound Vib., Vol. 187 (1995), pp. 825-839.

[20] R.E. Nickel G.A. Secor, *Convergence of consistently derived Timoshenko beam finite elements*, Int. J. Numer. Methods Eng., Vol. 5 (1972), pp. 243-253.

[21] K. Koro, k. Abe, M. Ishida, T. Suzuki, *Timoshenko beam finite element for vehicle-track vibration analysis and its application to jointed railway track*, Proc. Inst. Mech. Eng. F J. Rail Rapid Transit, Vol. 218, No. 2 (2004), pp. 159-172.

[22] S.C. Yang, *Enhancement of the finite-element method for the analysis of vertical train-track interactions*, Proc. Inst. Mech. Eng. F J. Rail Rapid Transit, Vol223, No. 6, (2009), pp. 609-220.

[23] B. Blanco, A. ALonso, N. Gil-Negrete, L. Kari, J.G. Giménez, *Implementation of Timoshenko element local deflection for vertical track modelling*, Under review in Vehicle System Dynamics (2018).

[24] T. Mazilu, *Green's functions for analysis of dynamic response of wheel/rail to vertical excitation*, J. Sound Vib., Vol. 306 (2007), pp. 31-58.

[25] X. Jin, C. Xinbiao, W. Zefeng, Z. Zhongrong, *Effect of sleeper pitch on rail corrugation at a tangent track in vehicle hunting*, Wear, Vol. 265 (2008), pp. 1163-1175.

[26] J.M. Dickens J.M. Nakagawa, M.J. Wittbrodt, *A critique of mode acceleration and modal truncation augmentation methods for modal response analysis*, Comput Struct, Vol. 62, No. 6 (1997), pp. 985-998.

Enabling the optimisation of the primary suspension with passive components for an industrial railway vehicle model

T. Lewis [1], **Y. Li** [1], **J. Jiang** [1], **S. Neild** [1], **G. Tucker** [2], **S. Iwnicki** [2], **R. Goodall** [2], **M. Smith** [3]
[1] Department of Mechanical Engineering, University of Bristol,
Queen's Building, University Walk, Bristol, BS8 1TR, UK
e-mail: **tl1485@bristol.ac.uk**

[2] Institute of Railway Research, University of Huddersfield,
Queensgate, Huddersfield, HD1 3DH, UK

[3] Department of Engineering, University of Cambridge,
Trumpington Street, Cambridge, CB2 1PZ, UK

Abstract
The use of inerters in the lateral suspension of railway vehicles has been proven, in recent studies using lumped mass models, to provide benefits to both track wear and passenger comfort. Validation of these enhancements using an industry standard simulation tool is essential if the railway industry is going to adopt this new piece of technology. The problems associated with this, however, come in the form of large numerical matrices, slow inversion times, and the inability to perform systematic investigations of candidate vibration absorber configurations. This paper proposes a Location Matrix method of simulation which enables the optimisation of interchangeable suspension networks within large dynamic systems. This method, which requires only the base M, C and K matrices, is validated on a simple system, and it is found that for railway vehicles, optimisations on semi-linearised models can be performed. Nonlinearities arising from the varying contact patch normal force mean that further research is needed before a full analysis can take place.

1 Introduction

Passive suspensions can be characterised using networks comprising springs, dampers and inerters, which, via the mechanical to electrical force-current analogy, relate respectively to inductors, resistors and capacitors. An inerter [1] is a two-terminal mechanical suspension element which generates a force proportional to the relative acceleration between its terminals. First introduced into Formula 1 under the pseudonym *J-Damper* [2], the inerter enables mechanical networks to simulate any passive response. Research into their vibration suppression benefits is rich, and comes in the fields of road vehicles [3–5], buildings [6–8] and optical tables [9], amongst others. Conventional passive railway vehicle suspensions make use of springs and dampers to suppress unwanted vibrations. Active methods of suppressing railway vehicle vibration have been successfully studied in [10–12]; however problems relating to measurement error, fault tolerances, actuator malfunction and torque requirements are increasingly making passive control with the addition of inerters more appealing. The implementation of inerters in railway vehicle suspension systems has been investigated, in previous numerical studies using lumped mass models [13–15], and they have been found to be beneficial in terms of improving ride comfort and curving performance.

Research into the use of inerters using the modelling software, VAMPIRE® , is ongoing [16] with the aim of reinforcing the findings reported using lumped mass models. VAMPIRE® is a widely used industry stan-

dard simulation tool, which provides the means to model railway vehicles more realistically and in greater detail. Simply adding an inerter in parallel to an existing suspension does not necessarily provide the desired benefits. To fully investigate the benefits of inerter-based suspension networks it is necessary to first explore all, or as many as possible spring/damper/inerter networks and identify the optimum network with an optimum set of element parameters. This is difficult to achieve in VAMPIRE® as the simulations would be computationally intensive and the software does not lend itself to the systematic investigation of a wide range of absorber configurations. The matrices defining the Equations of Motion (EOMs) of the system can be exported from VAMPIRE® ; however, for a full vehicle model they are large, and it can be difficult to identify the physical meaning of every matrix entry such that they can be modified to accommodate different device dynamics during an optimisation procedure. This problem is compounded if additional degrees of freedom are present in the suspension. To this end, this paper establishes an approach named the Location Matrix method, with the aim of enabling the optimisation of primary suspension vibration suppression devices with any number of internal states, using exported numerical matrices from VAMPIRE® .

The method proposed in this paper provides the user with a time domain analysis simulation tool within which Laplace admittance functions of suspension networks of any complexity can be varied accordingly. It is applicable to any dynamic system and eliminates SIMULINK® errors occurring as a result of algebraic loops when the inerter is modelled in parallel due to its acceleration dependence. It reduces the simulation time considerably when the number of Degrees of Freedom (DOFs) is large, due to the increased complexity of matrix inversions, and importantly can be used on systems where only the numerical rather than algebraic mass, stiffness and damping matrices of the base system without the vibration suppression device are known. The structure of this paper is as follows: Section 2 introduces the generalised Location Matrix method in detail, whilst Section 3 validates it using a simple MATLAB® model. Section 4 discusses the extent to which it can be applied to railway vehicles, and overall conclusions are drawn in Section 5.

2 The Location Matrix Method of Dynamic System Modelling

The following is a derivation of the method conceived to transform the EOM of a generalised n-DOF dynamic system, which includes an optimisable suspension network $Y(s)$, from Laplace to state-space form. Consider the following Laplace EOM:

$$s^2 M_0 \tilde{\underline{x}} + sC_0 \tilde{\underline{x}} + K_0 \tilde{\underline{x}} + sY(s) L_m \tilde{\underline{x}} = B\tilde{\underline{u}}. \tag{1}$$

where M_0 is the mass matrix, $Y(s)$ is the admittance function of the suspension network under investigation, L_m is the Location Matrix which identifies coupling locations and coefficients corresponding to the addition to the model of the $Y(s)$ suspension network, while C_0 and K_0 are respectively the damping and stiffness matrices for the rest of the system. $\underline{x}$ is the state matrix, $\underline{u}$ is the input matrix, with inputs denoted by B, s is the Laplace variable, $\tilde{\underline{x}}$ is the Laplace transform of $\underline{x}$ and $\tilde{\underline{u}}$ the Laplace transform of $\underline{u}$.

If the term $sY(s)L_m\tilde{\underline{x}}$ is ignored, Equation 1 describes the base model without the inclusion of the suspension network, $Y(s)$. If there are m identical copies of the $Y(s)$ suspension network in various locations within the model, the symmetric Location Matrix, L_m, can be written in the form VV^T where $V \in \mathbb{R}^{\mathrm{n}\times\mathrm{m}}$. The i^{th} column of V, where $i = 1 \ldots m$, identifies the parameters and coupling positions which are required to correctly alter the EOMs of the overall system when the i^{th} $Y(s)$ suspension network is included in the model. It hence follows that:

$$sV_i^T \tilde{\underline{x}} = \Delta v_i \tag{2}$$

where Δv_i is the relative change in velocity between the DOFs associated with the i^{th} device. The force to

acceleration transfer function of the $Y(s)$ suspension network can be written as,

$$Y'(s) = \frac{Y(s)}{s} = \frac{F_i}{\Delta a_i}, \tag{3}$$

where F_i is the force exerted on the i^{th} device and Δa_i is the associated relative change in acceleration at the i^{th} device. $Y'(s)$ must be positive-real [17]; I.E $|\alpha - \phi| \leq 1$ where α and ϕ denote respectively the highest powers of s on the numerator and denominator of $Y'(s)$.

$$Y'(s) = \frac{\beta_0 s^p + \beta_1 s^{p-1} + \cdots + \beta_{p-1} s + \beta_p}{s^p + \alpha_1 s^{p-1} + \cdots + \alpha_{p-1} s + \alpha_p}. \tag{4}$$

The following equations show the result of the transformation of the now positive semi-definite function $Y'(s)$ into state-space form, using one example of the non-unique canonical decomposition technique.

$$Y'(s) = c_1(sI - A_1)^{-1} b_1 + d_1 \tag{5}$$

$$A_1 = \begin{bmatrix} 0 & 1 & 0 & \dots & 0 \\ 0 & 0 & 1 & \dots & 0 \\ \vdots & \vdots & \vdots & \ddots & \vdots \\ 0 & 0 & 0 & \dots & 1 \\ -\alpha_p & -\alpha_{p-1} & -\alpha_{p-2} & \dots & -\alpha_1 \end{bmatrix} \tag{6}$$

$$b_1 = \begin{bmatrix} 0_{p\times 1} \\ 1 \end{bmatrix} \tag{7}$$

$$c_1 = \begin{bmatrix} (\beta_p - \alpha_p\beta) & (\beta_{p-1} - \alpha_{p-1}\beta) & \dots & (\beta_2 - \alpha_2\beta) & (\beta_1 - \alpha_1\beta) \end{bmatrix} \tag{8}$$

$$d_1 = \beta_0 \tag{9}$$

It is possible to obtain L_m for large industrial systems using reverse engineering and analysing a range of MCK matrices with differing suspension parameters. However, it is extremely difficult to interpret these matrices and decompose L_m into the VV^T format, due to lack of algebraic information, the large numbers of DOFs and hence a very complicated and varied set of couplings for each $Y(s)$ network. It has been found that the decomposition of L_m is not unique and there exists more solutions in the form of UU^T. Equating VV^T and a discovered UU^T, it can be shown that $V = UQ$ where $Q = U^T V^{-T}$, $QQ^T = I$, and hence $V_i^T = Q^T U_i^T$. Substituting $V = UQ$ into Equation 2,

$$sQ^T U_i^T \underline{\tilde{x}} = \Delta v_i \tag{10}$$

and multiplying by Q^{-T},

$$sU_i^T \underline{\tilde{x}} = \Delta v_{fi} \tag{11}$$

a fictitious set of states is introduced, denoted by the subscript f. The following equations show how the now fictitious forces (F_{fi}) and accelerations (a_{fi}) relate to the physical system:

$$F_{fi} = QF_i \tag{12}$$

$$Y'(s) = \frac{F_i}{\Delta a_i} = \frac{F_{fi}}{\Delta a_{fi}} \tag{13}$$

The derivation of the state-space simulation method begins with $L_m = UU^T$ and hence adjoins fictitious states w_f, with the use of fictitious accelerations a_f. If the input to $Y'(s)$ for the i^{th} fictitious suspension network location is the change in relative fictitious accelerations of various system DOFs, ${U_i}^T \underline{x} s^2$, then r copies of the state Y' can be adjoined as follows, where $F_{{Y'}_{fi}}$ are the fictitious $Y'(s)$ suspension forces at the i^{th} fictitious suspension network location,

$$\underline{\dot{w}}_{f1} = A_1 \underline{w}_{f1} + b_1 {U_1}^T \underline{\tilde{x}} s^2, \tag{14}$$

$$F_{{Y'}_{f1}} = c_1 \underline{w}_{f1} + d_1 {U_1}^T \underline{\tilde{x}} s^2, \tag{15}$$

to

$$\underline{\dot{w}}_{fr} = A_1 \underline{w}_{fr} + b_1 {U_r}^T \underline{\tilde{x}} s^2, \tag{16}$$

$$F_{{Y'}_{fr}} = c_1 \underline{w}_{fr} + d_1 {U_r}^T \underline{\tilde{x}} s^2. \tag{17}$$

Let $\underline{z}$ be the forces provided by $Y(s)$:

$$\underline{z} = Y'(s) L_m \underline{\tilde{x}} s^2 = UY'(s)U^T \underline{\tilde{x}} s^2 = (U_1 Y'(s) {U_1}^T + U_2 Y'(s) {U_2}^T + ... + U_r Y'(s) {U_r}^T) \underline{\tilde{x}} s^2. \tag{18}$$

$Y'(s) {U_i}^T \underline{\tilde{x}} s^2$ describes the i^{th} set of fictitious $Y'(s)$ forces as defined in Equation 17. Therefore, making suitable substitutions, Equation 18 can be written as,

$$\underline{z} = U_1(c_1 \underline{w}_{f1} + d_1 {U_1}^T \underline{\tilde{x}} s^2) + U_2(c_1 \underline{w}_{f2} + d_1 {U_2}^T \underline{\tilde{x}} s^2).... + U_r(c_1 \underline{w}_{fr} + d_1 {U_r}^T \underline{\tilde{x}} s^2). \tag{19}$$

Equation 1 can now be modified to include $\underline{z}$, defining the suspension forces provided by the $Y(s)$ device,

$$M_0 \underline{\tilde{x}} s^2 + C_0 \underline{\tilde{x}} s + K_0 \underline{\tilde{x}} + \underline{z} = B \underline{\tilde{u}}. \tag{20}$$

Multiplying by s, substituting in Equation 19 for $\underline{z}$, and hence introducing the $Y'(s)$ states $\underline{\dot{w}}_{f1}, \ldots, \underline{\dot{w}}_{fr}$,

$$M_0 \underline{\tilde{x}} s^3 + C_0 \underline{\tilde{x}} s^2 + K_0 \underline{\tilde{x}} s + \sum_{i=1}^{r} U_i (c_1 \underline{\dot{w}}_{fi} + d_1 U_i^T \underline{\tilde{x}} s^3) = B \underline{\tilde{u}} s, \tag{21}$$

Substituting for $\underline{\dot{w}}_{fi}$ using Equation 16, a new system EOM can be formed:

$$M_0\tilde{\underline{x}}s^3 \;+\; C_0\tilde{\underline{x}}s^2 \;+\; K_0\tilde{\underline{x}}s \;+\; \sum_{i=1}^{r} U_i(c_1(A_1\underline{w}_{fi} \;+\; b_1{U_i}^T\tilde{\underline{x}}s^2) \;+\; d_1U_i^T\tilde{\underline{x}}s^3) \quad = \quad B\tilde{\underline{u}}s. \tag{22}$$

Grouping powers of s, and performing the reverse substitutions:

$$M_0' = M_0 + \sum_{i=1}^{r} U_i d_1 U_i^T, \tag{23}$$

$$C_0' = C_0 + \sum_{i=1}^{r} U_i c_1 b_1 U_i^T, \tag{24}$$

a generalised and simplified EOM can be formed:

$$M_0'\tilde{\underline{x}}s^3 + C_0'\tilde{\underline{x}}s^2 + K_0\tilde{\underline{x}}s + \sum_{i=1}^{r} U_i(c_1A_1\dot{\underline{w}}_{fi}) = B\tilde{\underline{u}}s. \tag{25}$$

The entire system can now be written in the time domain, in state-space form, with the fictitious states $\underline{w}_{fi}$ adjoined as follows:

$$\frac{d}{dt}\begin{bmatrix} \ddot{\underline{x}} \\ \dot{\underline{x}} \\ \underline{x} \\ \underline{w}_{fi} \\ \vdots \\ \underline{w}_{fr} \end{bmatrix} = A_{ss}\begin{bmatrix} \ddot{\underline{x}} \\ \dot{\underline{x}} \\ \underline{x} \\ \underline{w}_{fi} \\ \vdots \\ \underline{w}_{fr} \end{bmatrix} + B_{ss}\dot{\underline{u}} \tag{26}$$

$$A_{ss} = \begin{bmatrix} -{M_0'}^{-1}C_0' & -{M_0'}^{-1}K_0 & 0 & -{M_0'}^{-1}U_1c_1A_1 & \dots & -{M_0'}^{-1}U_rc_1A_1 \\ I & 0 & 0 & 0 & \dots & 0 \\ 0 & I & 0 & 0 & \dots & 0 \\ b_1{U_1}^T & 0 & 0 & A_1 & \dots & 0 \\ \vdots & \vdots & \vdots & \vdots & \ddots & 0 \\ b_1{U_r}^T & 0 & 0 & 0 & 0 & A_1 \end{bmatrix} \tag{27}$$

$$B_{ss} = \begin{bmatrix} {M_0'}^{-1}B \\ 0_{(2n+r)\times 1} \end{bmatrix} \tag{28}$$

A more visually understandable realisation of Equation 26 is described below, where the deletion of the state $\underline{x}$ results in the deletion of the third row and column of A_{ss}, forming A_{ss}', (a similar manipulation to B_{ss} occurs) and Equation 26 is integrated with respect to time.

$$\dot{X} = {A_{ss}}'X + {B_{ss}}'\underline{u} \tag{29}$$

$$X = \begin{bmatrix} \dot{\underline{x}} & \underline{x} & \int \underline{w}_{fi} & \dots & \int \underline{w}_{fr} \end{bmatrix}' \tag{30}$$

$$A_{ss}{}' = \begin{bmatrix} -M_0'^{-1}C_0' & -M_0'^{-1}K_0 & -M_0'^{-1}U_1c_1A_1 & \dots & -M_0'^{-1}U_rc_1A_1 \\ I & 0 & 0 & \dots & 0 \\ b_1{U_1}^T & 0 & A_1 & \dots & 0 \\ \vdots & \vdots & \vdots & \ddots & 0 \\ b_1{U_r}^T & 0 & 0 & 0 & A_1 \end{bmatrix} \tag{31}$$

$$B_{ss}{}' = \begin{bmatrix} M_0'^{-1}B \\ 0_{(n+r)\times 1} \end{bmatrix} \tag{32}$$

3 Validation of the Location Matrix Method Using a Low-Order Model in MATLAB®

Before testing this method on an industrial railway vehicle model, it is necessary to validate it using a simpler system. The system chosen is a standard two-mass oscillator, shown in Figure 1, and contains a direct $Y(s)$ connection between the two masses. Figure 2 shows the six candidate $Y(s)$ networks, and Table 1 denotes the values of all the parameters used. The initial validation uses the true Location Matrix,

$$L_m = \begin{bmatrix} 1 & -1 \\ -1 & 1 \end{bmatrix} \tag{33}$$

and compares the responses of mass 1 to input forces F_{s1} and F_{s2} on masses 1 and 2 respectively, using the L1 version of $Y(s)$, calculated three ways:

- **Tfsys A**. The standard formation of the Laplace EOMs, incorporating $Y(s)$ into the system matrix manually.
- **Tfsys Lm**. A slight variation of Tfsys A in which a Location Matrix is used in conjunction with the base mass, damping and stiffness matrices of the system.
- **YsLm SS**. The fully automated Location Matrix method, using the L_m decomposition, laid out in Section 2.

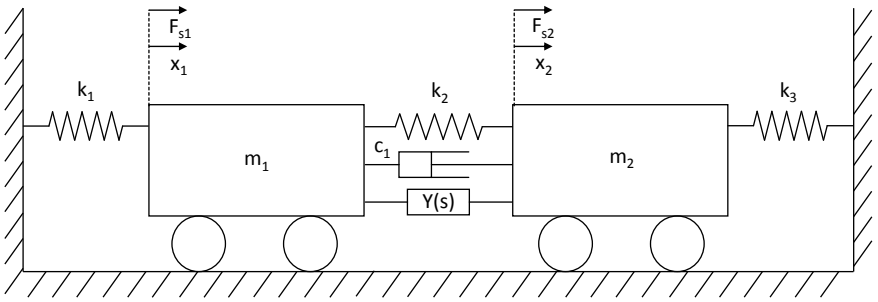


Figure 1: The two-mass oscillator used to test the Location Matrix theory in MATLAB®

The forces F_{s1} and F_{s2} can be either harmonic or step in nature, as detailed in Figure 3.

Parameter	Value	Unit
m_1	1250	kg
m_2	3000	kg
k_1	8×10^5	N/m
k_2	9×10^5	N/m
k_3	6.8×10^5	N/m
c_1	6.3×10^4	Ns/m
k_y	2.55×10^5	N/m
k_s	2.99×10^5	N/m
c_s	5.20×10^4	Ns/m
b_s	6.67×10^3	kg
b_{s2}	4×10^3	kg

Table 1: The values of the masses and components of Figure 1, along with the fixed values of the $Y(s)$ network components from Figure 2

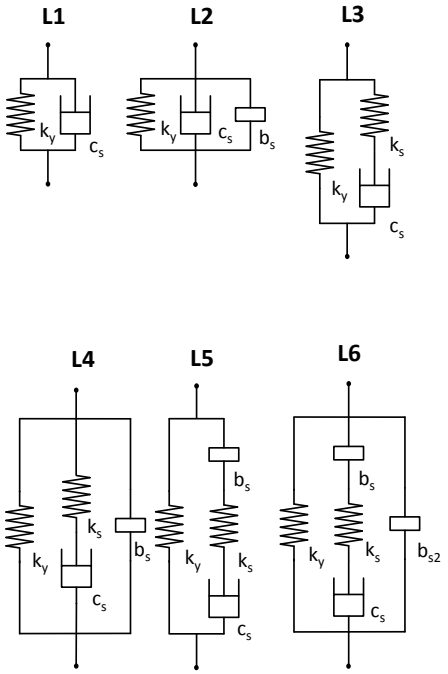
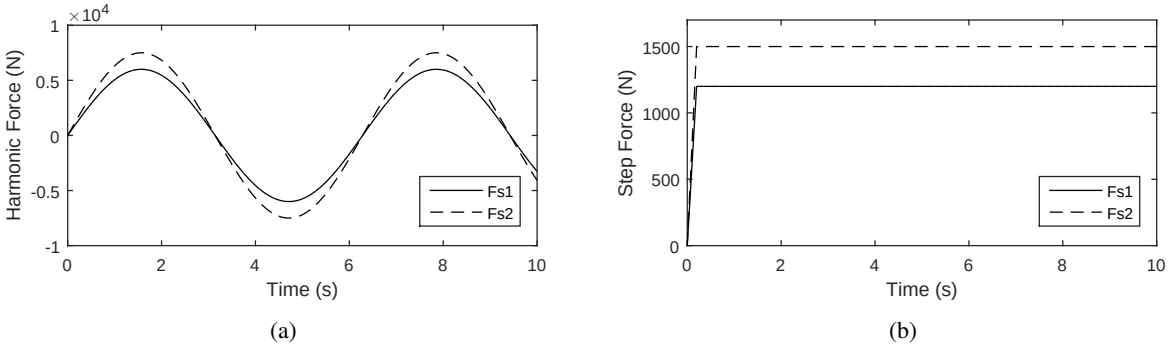
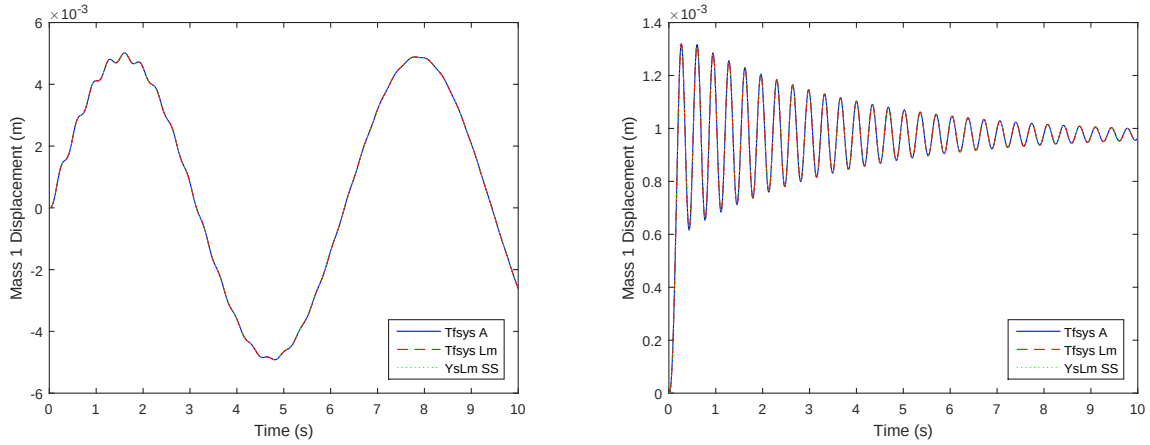


Figure 2: The $Y(s)$ networks



(a) (b)

Figure 3: The input forces at mass 1 (F_{s1}) and mass 2 (F_{s2}), for the harmonic and step input cases.



(a) (b)

Figure 4: A comparison between the three methods of simulating the simple dynamic system, with the original location matrix, in response to the harmonic input (a), and the step input (b) at mass 1, using an L1 $Y(s)$ layout

Figure 4 shows the matching responses using the three methods described above, and therefore confidence can be gained in the Location Matrix method analysis technique. The next step in the validation procedure is to test a number of different Location Matrices and different $Y(s)$ layouts. Firstly, returning to the notation used in Section 2, two different V matrices are arbitrarily defined as:

$$V_1 = \begin{bmatrix} 1 \\ -1 \end{bmatrix} \tag{34}$$

$$V_2 = \begin{bmatrix} 1 & 1 & 5 \\ -1 & -34.6 & 0 \end{bmatrix} \tag{35}$$

These The fact that V_2 has no physical meaning in conjunction with Figure 1 is not important as it is the theoretical method that is being tested here. These two V matrices correspond to test cases 1 and 2. The two corresponding Location Matrices can be formed using VV^T to ensure their symmetricity, and hence two decompositions into UU^T can be performed, each in two ways:

- Single Value Decomposition (SVD). This produces a diagonal matrix s, and unitary matrices U_s and V_s, such that $U_s V_s$ = I and $U_s \kappa V_s = L_{mi}$. It follows that $U = U_s\sqrt{\kappa}$.
- Eigenvalue Decomposition. This decomposition results in $L_{mi} = U_e \Sigma U_e' = (U_e\sqrt{\Sigma})(\sqrt{\Sigma}U_e')$, where U_e is a matrix of the system's eigenvectors and the diagonal matrix Σ contains the system's eigenvalues. This is very similar to the SVD, and the resulting U matrix is defined as $U = U_e\sqrt{\Sigma}$.

This is simulating the situation where the V matrices cannot be intuited from the system as it is too complicated and has a large number of DOFs.

Table 2 shows the difference in the Euclidian Norm of the UU^T Location Matrix for each of the decomposition techniques ($\Delta_{Lm_{svd}}$ and $\Delta_{Lm_{eig}}$ for SVD and Eignenvalue Decomposition respectively), for each test case, and the original VV^T Location Matrix. The minute differences assert the fact that both decomposition techniques yield the same results. The Eigenvalue decomposition will be used for the rest of the analysis in this paper as it is slightly more simplistic in nature. The equations:

	$\Delta_{Lm_{svd}}$	$\Delta_{Lm_{eig}}$
Test 1	8.04×10^{-16}	0
Test 2	5.86×10^{-14}	7.11×10^{-15}

Table 2: Discrepancies between the norm of the Location Matrices formed by VV^T and UU^T. Δ_{Lm} relates to the type of decomposition technique, and the test number relates to the test cases shown in Equations 34 - 35

$$U_{2_{svd}} = \begin{bmatrix} -0.9922 & 5.1005 \\ 34.6141 & 0.1462 \end{bmatrix}, \tag{36}$$

$$U_{2_{eig}} = \begin{bmatrix} -5.1005 & -0.9922 \\ -0.1462 & 34.6141 \end{bmatrix}, \tag{37}$$

$$L_{m2_{svd}} \approx L_{m2_{eig}} = \begin{bmatrix} 0.0270 & -0.0336 \\ -0.0336 & 1.1982 \end{bmatrix}, \tag{38}$$

show the U matrices for Test, now introducing the fictitious states, and the identical nature of the resulting Location Matrix. Simulation of the two-mass system, with identical inputs, is then performed using the Location Matrix method, with the original inputs, for each U decomposition case, and a variety of $Y(s)$ cases. The resulting identical responses for every $Y(s)$ and decomposition case further consolidates the validity of the Location Matrix method, and eliminates the problems arising with simulating parallel inerter based systems in SIMULINK® due to the presence of algebraic loops. Figure 5 shows the results for Test 2.

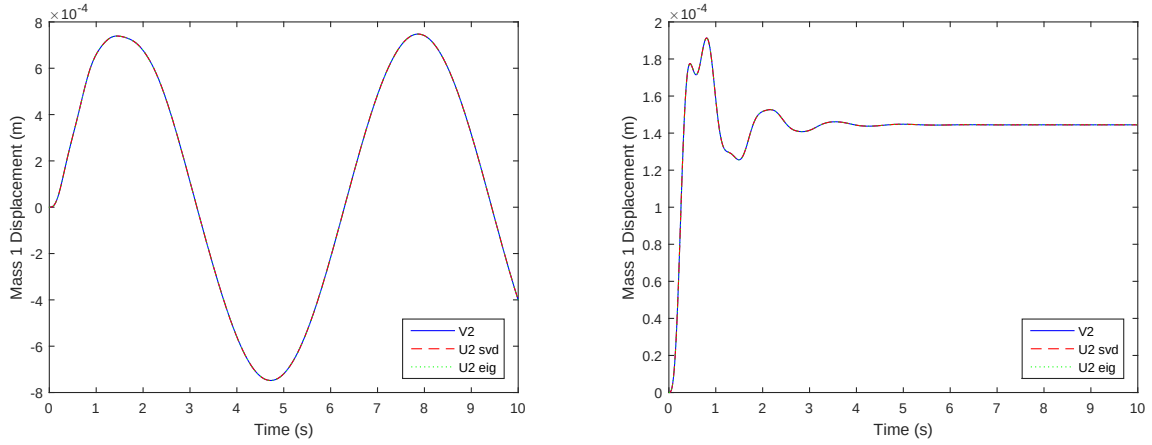


Figure 5: A comparison between the three Location Matrix methods for test case 2 (see Equations 35 - 37) of simulating the simple dynamic system in response to the harmonic input (a), and the step input (b) at mass 1, using an L6 $Y(s)$ layout

4 Application to Railway Vehicle Suspension Optimisation

The Location Matrix method detailed in Section 2 has been used alongside VAMPIRE® to simulate a four-axle railway vehicle [18] with the aim of optimising its lateral suspension and improving its curving performance and passenger comfort. Passenger comfort is quantified by the RMS lateral carbody acceleration when the vehicle is subject to a 5km stretch of lateral track disturbance, taken from a real track. However, to

firstly validate the method on this large railway vehicle model, a simpler input of lateral forcing at the front wheelset in used.

Applying Equation 1 to the railway vehicle, M_0, C_0 and K_0 are respectively the mass, damping and stiffness matrices exported from VAMPIRE® for the hypothetical base model with no primary lateral suspension at all, which amongst other things contain information regarding the wheel-rail contact patch forces. The primary lateral suspension elements are therefore included in the $Y(s)$ part of Equation 1. B includes wheel-rail contact force information when the input $\underline{u}$ matrix consists of real track disturbance data, and is simply unity when $\underline{u}$ is a forcing input. For the forcing input case, $\underline{u}$ is a positive lateral force onj the centre of mass of the front wheelset for the 1st second, an equal and opposite force for the 6th second, and zero at all other times.

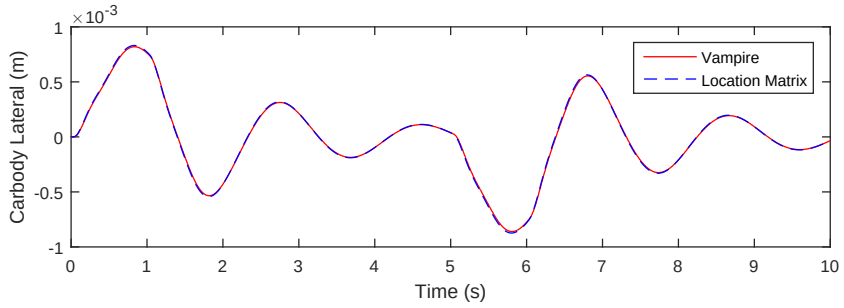


Figure 6: A comparison between the VAMPIRE® and Location Matrix method of simulation, showing the carbody lateral movement with a lateral forcing input of 10kN

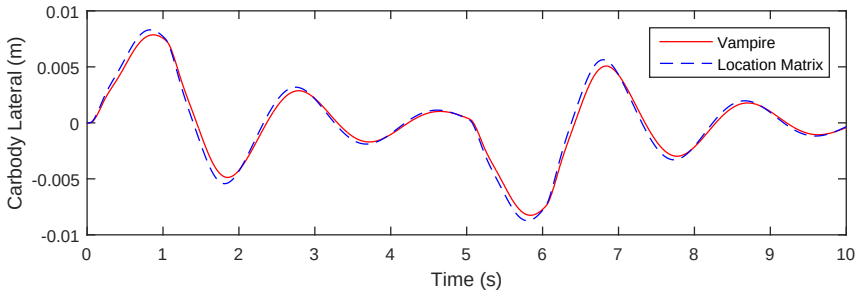


Figure 7: A comparison between the VAMPIRE® and Location Matrix method of simulation, showing the carbody lateral movement with a lateral forcing input of 100kN

Figures 6 and 7 show how the VAMPIRE® and Location Matrix simulations compare for lateral step force magnitudes of respectively 10kN and 100kN, specifically focussing on the carbody's lateral motion, and using an L1 bush layout with default parameter values. It is clear that a closer match occurs at the lower forcing input, and at the higher forcing input the Location Matrix method predicts slightly higher amplitudes of oscillation. It should be noted that at a lateral force of 10kN, many different $Y(s)$ suspension layouts with and without inerters have been tested with the Location Matrix method and the comparisons with VAMPIRE® are correct to a very high degree of accuracy. The transient analysis within VAMPIRE® has been linearised to the extent that there is there is no friction saturation at the contact patch, meaning that a linear contact model is used, however it is impossible to linearise the M_0, C_0 and K_0 matrices completely as the normal force of the vehicle on the track (perpendicular to the wheel's profile) is not distributed equally or consistently when the vehicle is displaced or exhibits hunting motion, resulting in the creep force parameters within the system matrix (Equation 27) varying during the simulation. This cannot be accounted for using the Location Matrix method in its current form as values within the base exported matrices cannot vary, and therefore the time varying normal force is the key factor changing the exported matrices from VAMPIRE® .

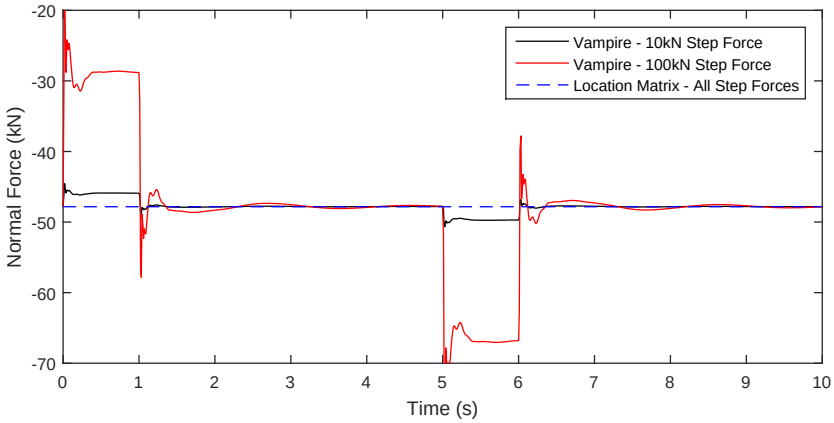


Figure 8: Showing how the normal force at the front left wheel-rail contact patch of the four axle railway vehicle changes during the lateral wheelset 1 step input simulation. Note the vertical (z) direction is defined as positive downwards

Figure 8 demonstrates the extent to which the normal force at the front right wheel contact patch varies during the simulation. When the lateral track displacement is used as the input, and when the stability of the vehicle is assessed using a standard stability track (where the vehicle is excited and then the oscillations are left to die away) comparisons between the VAMPIRE® and Location Matrix methods of calculation yield different results in terms of respectively the RMS lateral acceleration of the carbody, and the steady state displacement of the wheelset.

Although one cannot be certain that the time varying normal force is the only phenomenon which results in a change in the overall system matrix, it can be concluded that although the Location Matrix method can be used to provide preliminary optimisations for a lateral suspension device on a constant normal force and linear contact four axle railway vehicle model, further investigations are required for a full nonlinear analysis. This will most likely come in the form of incorporating VAMPIRE® directly into the MATLAB® optimisation program.

5 Conclusions

This paper has presented and validated a method for simulating and optimising dynamic systems by which interchangeable suspension elements can be incorporated at certain locations via their admittance functions in the Laplace Domain, whilst the base mass, stiffness and damping matrices are used unchanged. This Laplace to state-space Location Matrix method has the potential to allow large scale dynamic systems exported from industrial software to be analysed and chosen suspension networks with admittance functions $Y(s)$ to be optimised for a range of cost functions. The method has been validated using a simple MATLAB® model, and for a range of inerter and non-inerter based suspension networks. When applied to four-axle railway vehicles, a much higher order model, the system responses to small to medium forcing inputs are correct. However, as the inputs and resulting displacements become higher, the system becomes more and more nonlinear, hence changes in base stiffness and damping matrices become significant and can no longer be ignored, therefore the Location Matrix method becomes less effective at simulating responses. This method has potential to produce preliminary optimisations for linearised railway vehicle models and is beneficial to the modelling of any system which includes interchangeable inerter based suspension networks due to its ease of application and the elimination of algebraic loops within SIMULINK® . However, future optimisations of inerter based industrial railway vehicle suspension systems which include all system nonlinearities need to be investigated.

Acknowledgments

The authors would like to thank the EPSRC (Grant References: EP/M507994/1 and EP/P013546/1) and the Royal Society (Grant Reference: IE151194) for funding this research.

References

[1] M. Smith, "Synthesis of mechanical networks: The inerter," *IEEE Transactions on Automatic Control*, vol. 47(10), pp. 1648–1662, 2002.

[2] M. Z. Q. Chen, C. Papageorgiou, F. Scheibe, F.-C. Wang, and M. C. Smith, "The missing mechanical circuit element," *IEEE Circuits and Sytems Magazine*, 2009.

[3] F. Scheibe and M. Smith, "Analytical solutions for optimal ride comfort and tyre grip for passive vehicle suspensions," *Vehicle System Dynamics*, vol. 47(10), pp. 1229–1252, 2009.

[4] S. Evangelou, D. J. N. Limebeer, R. S. Sharp, and M. C. Smith, "An h infinity loop-shaping approach to steering control for high-performance motorcycles," *Lecture Notes in Control and Information Sciences*, vol. 329, pp. 257–275, 2006.

[5] J. Z. Jiang, M. Smith, and N. E. Houghton, "Experimental testing and modelling of a mechanical steering compensator," *International Symposium on Communications, Control and Signal Processing*, pp. 249–254, 2008.

[6] I. F. Lazar, S. A. Neild, and D. J. Wagg, "Using an inerter-based device for structural vibration suppression," *Earthquake Engineering Structural Dynamics*, vol. 43, pp. 1129–1147, 2014.

[7] F.-C. Wang, C.-W. Chen, M.-K. Liao, and M.-F. Hong, "Performance analyses of building suspension control with inerters," *46th IEEE Conference on Decision and Control*, 2007.

[8] S. Y. Zhang, J. Z. Jiang, and S. Neild, "Optimal configurations for a linear vibration suppression device in a multi-storey building," *Structural Control and Health Monitoring*, vol. 24, no. 3, pp. e1887–n/a, 2017. e1887 STC-16-0018.R2.

[9] Y.-C. Chen, S.-Y. Wu, and F.-C. Wang, "Vibration control of a three-leg optical table by mechatronic inerter networks," *SICE Annual Conference 2014*, 2014.

[10] R. Goodall and T. X. Mei, "Mechatronic strategies for controlling railway wheelsets with independently rotating wheels," in *2001 IEEWASME International Conference on Advanced Intelligent Mechatronics Proceedings 6-12 July 2001 Como, Italy*, pp. 225–230, 2001.

[11] T. X. Mei and R. M. Goodall, "Practical strategies for controlling railway wheelsets with independently rotating wheels," *Journal of Dynamic Systems, Measurement, and Control*, vol. 125, pp. 354–360, 203.

[12] T. X. Mei and R. M. Goodall, "Robust control for independently rotating wheelsets on a railway vehicle using practical sensors," *IEEE Transactions on Control Systems Technology*, vol. 9(4), pp. 599–607, 2001.

[13] J. Jiang, T. Mei, and M. Smith, "Curving performance for railway vehicles with advanced passive suspensions," in *23rd International Symposium on Dynamics of Vehicle on Road and Tracks, IAVSD*, 2013.

[14] J. Z. Jiang, A. Z. Matamoros-Sanchez, A. Zolotas, R. M. Goodall, and M. C. Smith, "Passive suspensions for ride quality improvement of two-axle railway vehicles," *IMECHE: Journal of Rail and Rapid Transit*, vol. 229(3), pp. 315–329, 2015.

[15] T. Lewis, J. Jiang, S. Neild, C. Gong, and S. Iwnicki, "Improving ride comfort and trackwear of two-axle railway vehicles using inerter-based lateral suspension layouts," in *Noise and Vibration Emerging Methods, NOVEM*, 2018.

[16] Y. Zhao, G. Tucker, R. Goodall, S. Iwnicki, J. Jiang, and M. Smith, "Developing an inerter model using multibody dynamics software," in *25th International Symposium on Dynamics of Vehicle on Road and Tracks, IAVSD*, 2017.

[17] F. F. Kuo, *Network Analysis and Synthesis*. John Wiley and Sons, 2nd ed., 1962.

[18] RSSB, "Bogiepassenger 39t 15yaw vehicle model, https://www.rssb.co.uk/research-development-and-innovation/research-reports-catalogue/pb009847, accessed 23/10/2017."

An investigation on the influence of pantograph friction on its interaction with a catenary using co-simulations

P. Zdziebko[1], A. Martowicz[1], T. Uhl[1]
[1] AGH University of Science and Technology, Department of Robotics and Mechatronics
Al. A. Mickiewicza 30, 30-059 Krakow, Poland
e-mail: **zdziebko@agh.edu.pl**

Abstract
The paper discusses an important phenomenon in a railway pantograph mechanism, i.e. contribution of friction in its overall performance. A pantograph must fulfill many conditions to be allowed for operation, one of them is that friction force has to be kept within the specific tolerances. There is yet another requirement to improve contact quality between pantograph contact strip and catenary. To improve the quality of contact it is desirable to reduce the values of standard deviation and peak-to-peak value of the contact force. The paper presents the results of numerical investigation on the influence of pantograph on its interaction with a catenary. The analysis was carried out employing the multi-domain co-simulation approach previously developed by the authors. The results are presented for various run speeds. The study has proven the existence of a significant impact of the friction phenomenon on the pantograph interaction with overhead contact lines.

1 Introduction

A railway pantograph is a mechanism, which takes part in electric power delivery to a train or electrified multiple unit (EMU) in electrified railways. A pantograph strip is in mechanical contact with a contact wire of an overhead contact lines system (called also *catenary*). Basic components of the pantograph-catenary system are presented in Figure 1.

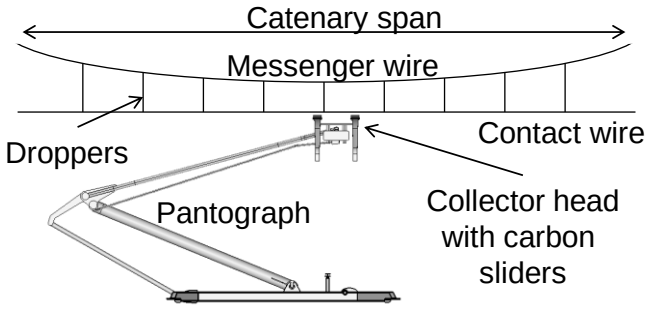


Figure 1: Pantograph-catenary system

Proper dynamic interaction between pantograph and catenary is crucial for adequate performance of this system. It is desirable to keep pantograph slider and catenary contact wire in continuous contact. During a high speed run, the contact force identified between sliders and contact wire (marked as CF hereunder) fluctuates as it was already reported in many papers [1-4]. An exemplary course of CF is presented in Figure 2, considering a 600 m long run and magnification for the two central spans are depicted accordingly.

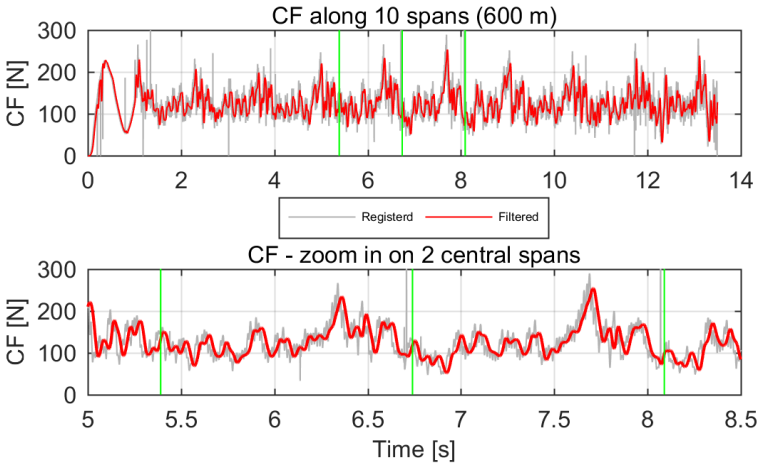


Figure 2: Exemplary course of the CF Pantograph

The fluctuations that are exhibited by CF are undesirable, because local minimal values in the CF course may lead to detachments of a pantograph slider from a contact wire. On the other hand, high peaks may cause an increased wear of both sliders and contact wire. Contact losses are unfavorable because they cause arcing phenomenon between pantograph carbon slider and copper contact wire. This condition leads to temperature increase in the pantograph-catenary interface area – even up to 1200 °C. Such high temperature field may cause destruction of the material in that interface through the ablation phenomenon [5]. The arcing is also a source of voltage and electromagnetic disturbances.

The pantograph mechanism has a number of revolute joints in its structure. The pantograph which is described in this paper is the 160 ECT model produced by EC Engineering company. Figure 3 depicts kinematic pairs in that mechanism. Linear arrows mean suspension of the pantograph slider, whereas circular arrows depict revolute joints with the rotation degree of freedom along the Y direction. The *Nominal torque* is the torque between pantograph frame and lower arm exerted by the pneumatic actuator. This torque is responsible for opening the pantograph mechanism and provide static uplift force exerted by the slider on the contact wire of the catenary.

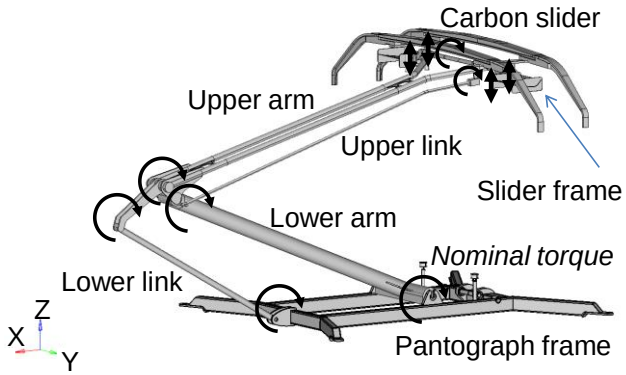


Figure 3: 160ECT pantograph mechanism

The presence of friction in kinematic pairs is inevitable. In this paper, the authors investigate the influence of friction on the quality of pantograph-catenary contact. The standard deviation (STD) and the peak-to-peak value (Peak-Peak) of CF are utilized as the quality indicators of the pantograph-catenary dynamic interaction. It is favorable to keep the values of these parameters as small as possible to provide

smooth contact between the system components, therefore a number of numerical simulations were carried out to study the influence of friction on the pantograph-catenary dynamic interaction.

2 Case study

From the data provided by the pantograph manufacturer (not allowed to be published here), it was observed that the values of friction forces for particular pieces of pantographs can vary, even though they are within the certification ranges. Therefore, the authors decided to investigate the influence of pantograph friction forces on the quality of the dynamic interaction with a catenary employing numerical simulations.

Various train run speeds are analyzed in the range of 110 – 200 km/h, with increment of 5 km/h (19 cases). It is well known that aerodynamic forces acting on the pantograph components are crucial for general pantograph-catenary dynamic interaction, because they influence the actual slider uplift force. Therefore, for a particular run speed, appropriate forces acting of the pantograph components are also considered in the simulations. Moreover, each piece of a pantograph has to be certified and, among the others, the friction force in the pantograph mechanism has to be evaluated separately. A single piece of a pantograph was tested using dedicated test stand and the difference between pantograph uplift forces was identified, when going both upward and downward. This value is also known as the double friction force (DFF), and has to be kept within the specific limits declared by the European Standard [6]. The DFF is directly related to the friction in the kinematic pairs in the mechanism. Therefore, the friction coefficient in the pantograph numerical model was identified adequately to produce the same DFF as the measured value in the test stand. The results of numerical model validation are presented in Figure 4.

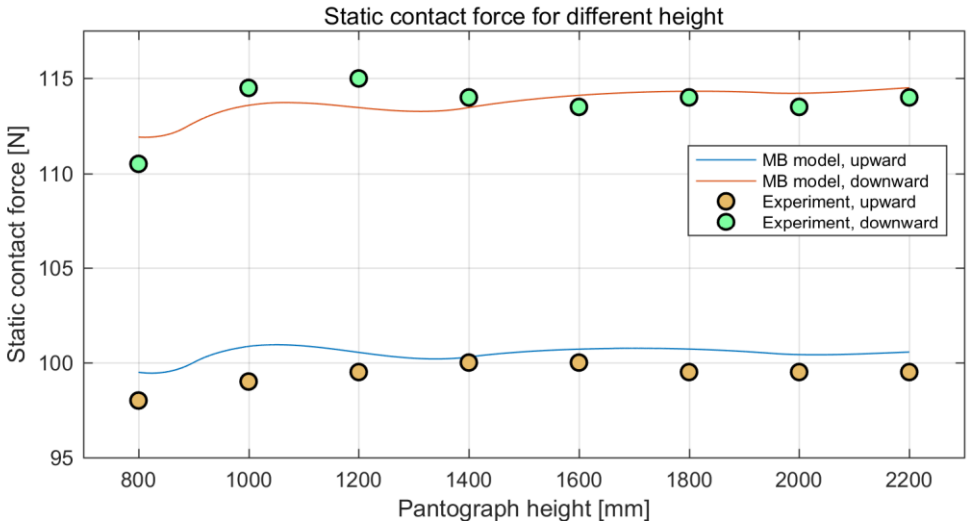


Figure 4: Uplift force variation caused by friction

When the nominal friction coefficient in kinematic pairs was identified, 10 deviations from that value were taken into consideration (within the range of ±25% with respect to the nominal value with an increment of 5%). It was assumed that the friction force deviations may originate from the assembly quality, materials' properties and other uncertainties. In total, 19 various speeds and 11 values of friction coefficients were studied, producing 209 cases to be computed. Each simulation takes about 45 minutes using a standard computer workstation.

3 Multi-domain co-simulation setup

The investigation presented in this paper was conducted employing the multi-domain co-simulation algorithm for pantograph-catenary dynamic simulation. This computational environment was recently presented by the authors [2]. The procedure includes the most important phenomena which are necessary for a reliable pantograph-catenary simulation. The catenary is modeled with the Finite Element Method (FEM) which allows to determine the initial static equilibrium of a catenary under gravity and tensioning forces in contact and messenger wires and to consider nonlinearities in its structure (nonlinear properties of droppers, relatively large displacements and the contact with the pantograph slider). Realistic Multibody (MB) pantograph-rail vehicle model allows to take into account a vibration field caused by the track irregularities. Moreover, electromagnetic and aerodynamic forces acting on the pantograph components as well as friction in kinematic pairs are also considered in the simulation setup. More details on these contributing partial models can be found in the papers recently published by the authors [2-4, 7]. The diagram of the dynamic simulation of pantograph-catenary interaction is presented in Figure 5.

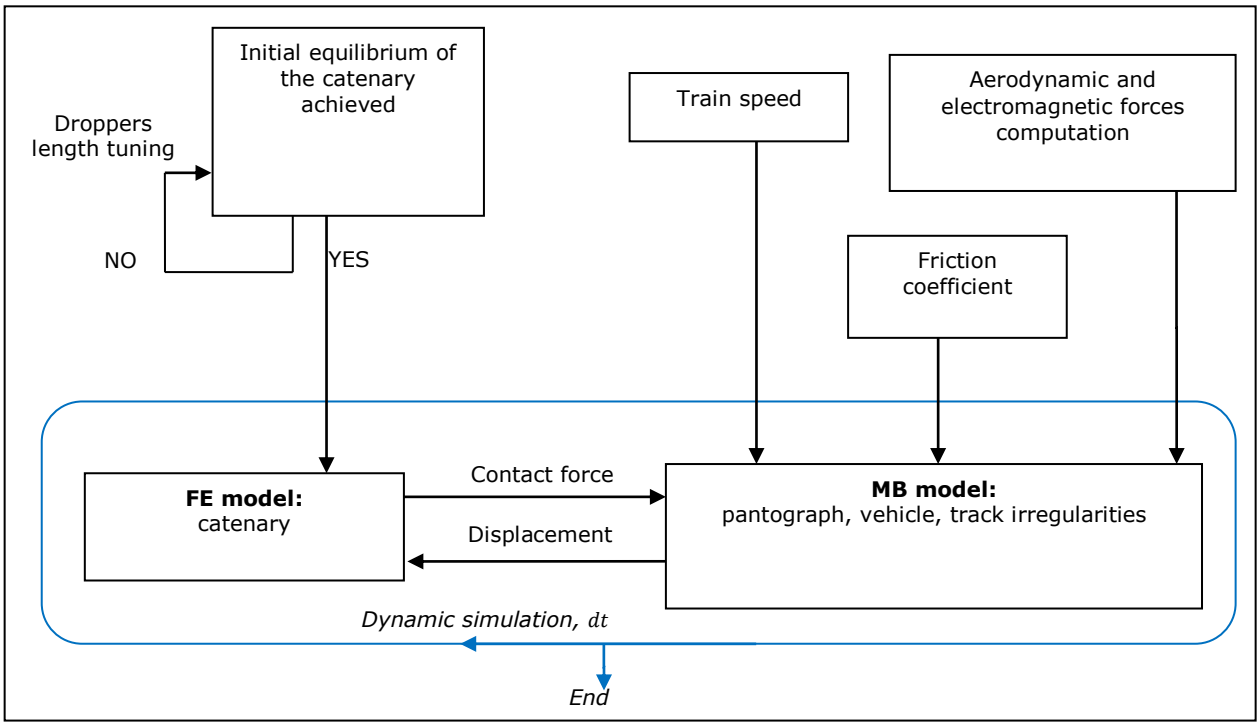


Figure 5: Co-simulation algorithm utilized in the analysis

The main procedure of the algorithm can be summarized as follows:

- The catenary model is built employing the FEM. Iterative static simulations are then run to determine proper lengths of droppers, that allow to have proper pre-sag in the middle of a single catenary span considering gravity and tensioning forces in the catenary wires.
- In parallel, aerodynamic forces acting on the pantograph are computed employing the Fluid Structure Interaction (FSI) approach. As a result, drag, cross and lift forces acting on the pantograph components are calculated. Electromagnetic forces are also computed considering adopted power supply scenario and employing the Biot-Savart law.
- Subsequently, the pantograph-rail vehicle MB model is created and the forces described in the previous step are passed into the MB model. The pantograph-rail vehicle model also includes track profiles designed according to the adopted Power Spectral Density function.

- When the FE catenary and the MB pantograph-rail vehicle models are created, the dynamic simulation is initiated. The MB code is run first and an actual pantograph slider position is transferred into the FEM code. Then, the dynamic step of the FEM catenary model is computed and the resulting contact force is passed back into the MB code. The MB code is computed again considering the actual contact force received from the FEM code and the new position resulting from chosen run speed. This procedure is repeated in the loop to cover the entire simulation period *t* with given time step *dt*.
- As a result, the CF course is computed. Then the statistical analysis is performed after filtration using the low-pass filter with cut-off frequency 20 Hz and after limiting the CF course to the two central spans according to the European Norm 50318 [8].

4 Aerodynamics

The aerodynamic forces acting on the pantograph components are crucial for proper total uplift force computation, especially at high speed runs. They were computed employing the FSI model and the following air flow speeds were investigated: 120, 140, 160 and 180 km/h. The numerical model was validated based on the experimental data and the results from FSI analysis are considered to be correct. More details on the FSI model validation can be found in the authors previous works [2-3, 7]. An exemplary results from the FSI simulation are presented in Figure 6, where the velocity magnitude in the train run direction is presented for the air flow at the speed of 160 km/h.

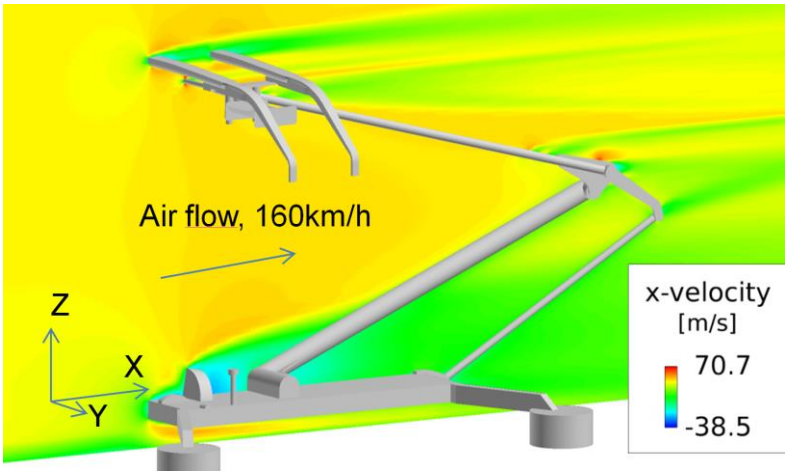


Figure 6: FSI analysis results (velocity magnitude in the train run direction)

Aerodynamic forces computation for a single air flow speed, using the proposed numerical model is time-consuming. It takes about 15 hours utilizing a workstation. Therefore, it is assumed that the aerodynamic forces for all other run speeds are approximated applying the last-square fitting method with second order polynomial. The results of the forces fitting are presented in Figure 7. It can be observed that it is possible to get an acceptable fitting of the approximating curve to the experimental data, thanks to which the force values for intermediate flow speeds can be easily obtained.

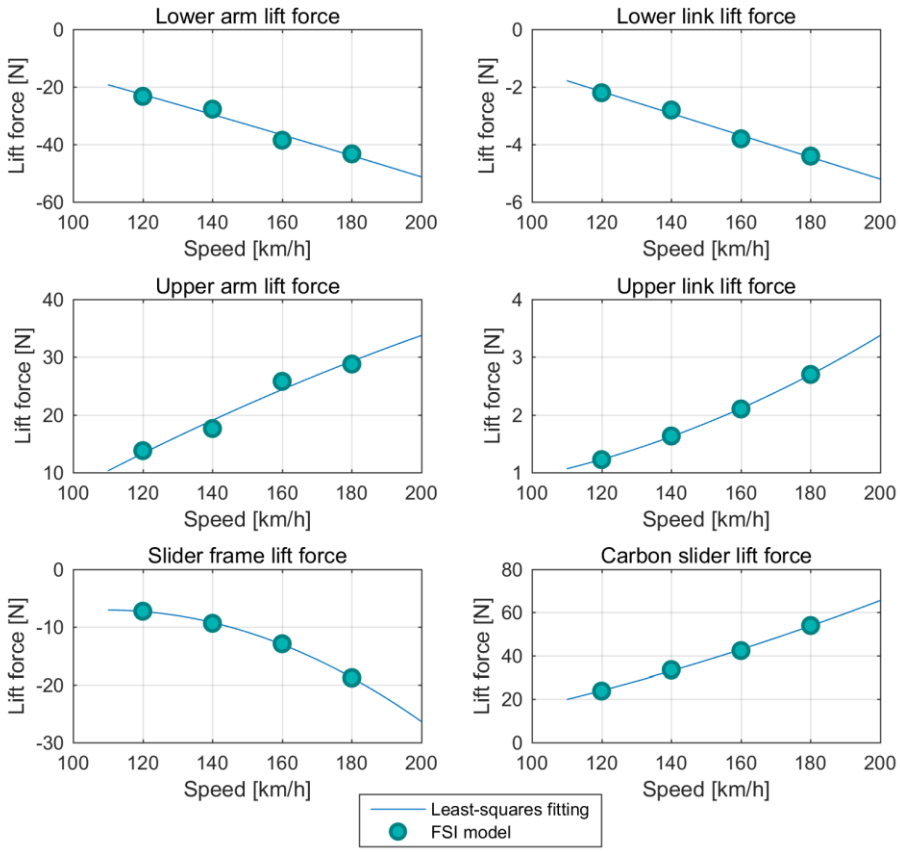


Figure 7: Results of aerodynamic lift forces fitting for pantograph components

5 Electromagnetic force

In normal operational conditions, high current flows through the catenary wires to meet the power demand of a train. According to the electromagnetic induction rule, magnetic field is generated around a conductor with current. The pantograph slider (which also conducts electricity) is located in that magnetic field, therefore the generated electromagnetic force is acting on it. The multi-domain co-simulation algorithm utilized in this paper takes into consideration the above-mentioned electromagnetic force. The sub-model for electromagnetic force computation was previously introduced by the authors in recent paper [2], but main assumptions of the carried out calculations are also presented below for clarity of the reported study. A general scheme of the utilized pantograph-catenary system is presented in Figure 8. The polyline $|DEFG|$ corresponds to the catenary contact wire whereas the section $|AB|$ represents the pantograph's contact strip.

In the adopted energy supply case, we assume two rail vehicles travelling one after the other, and they are powered from a single traction substation (3 kV system). Both of the trains have the same power demand of 10.5 MW. The following data regarding the electric currents has been taken in the calculations:

$$\begin{gathered} i_{TRAIN1} = i_{TRAIN2} = 3500 \text{ A} \\ i_{TRAIN1+2} = 7000 \text{ A} \\ i_{PANTO_AC} = \frac{i_{TRAIN1}}{2}[A] \\ i_{PANTO_BC} = \frac{i_{TRAIN1}}{2}[A] \end{gathered} \tag{1}$$

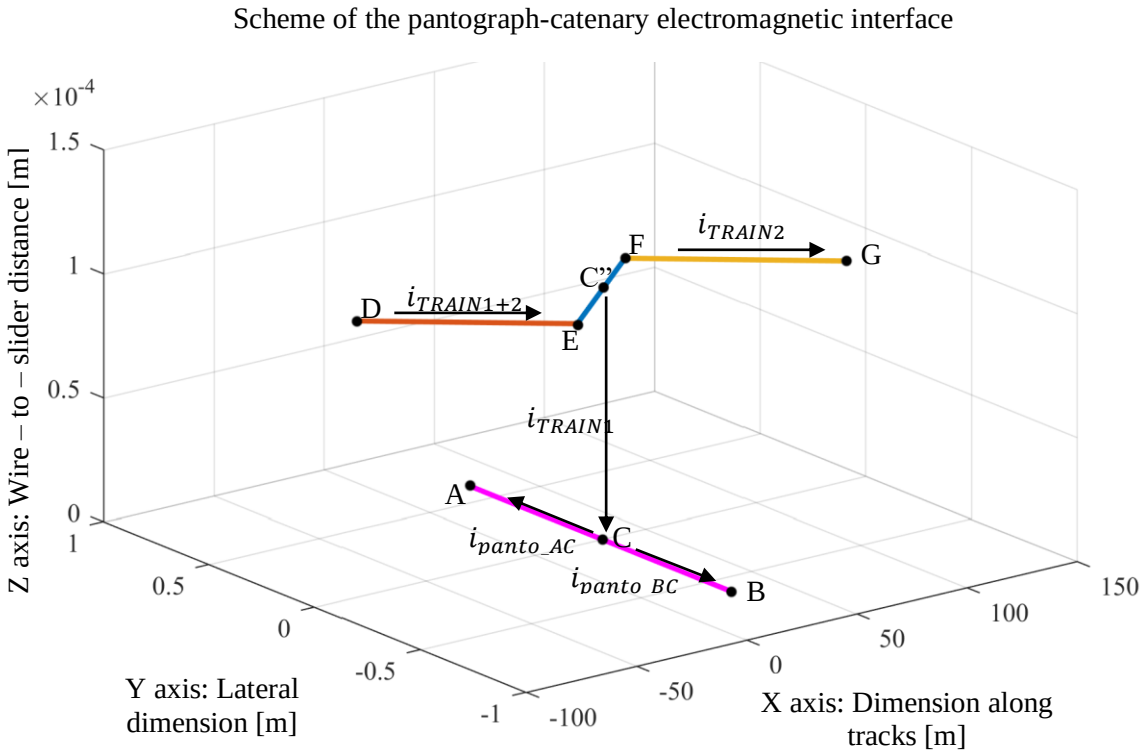


Figure 8: The pantograph-catenary electromagnetic interface

The distance between pantograph slider contact strip and catenary contact wire is considered to be $\overline{|CC"|} = 0.1\ mm$. The length of each catenary span equals 60 m, which means that three sections are taken into consideration, the catenary lateral stagger is ±0.2 m, while the length of the contact strip $\overline{|AB|} = 1.2m$. The magnetic induction is computed at finite number of points on the contact strip (which is divided into 12000 segments) using the Biot-Savart's law. The total magnetic induction at a particular point is calculated as a sum of magnetic induction contributions from all analyzed wires exhibiting the assumed current flow ($\overline{|DE|}, \overline{|EC"|}, \overline{|C"F|}, \overline{|FG|}$. So, for example if we consider the point B (Figure 8) at the slider, the total magnetic induction is as follows

$$\overrightarrow{B_{Total_at_B}} = \overrightarrow{B_{DE_at_B}} + \overrightarrow{B_{EC"_at_B}} + \overrightarrow{B_{C"F_at_B}} + \overrightarrow{B_{FG_at_B}} \tag{2}$$

and the individual magnetic induction contributions are calculated according to the formula shown for an example section $\overline{|EC"|}$

$$\overrightarrow{B_{EC"_at_B}} = \frac{\mu_0 \mu}{4\pi} \int \frac{i_{TRAIN1+2}\, \vec{ds} \times \vec{r}}{r^3} \tag{3}$$

where:

$\overrightarrow{B_{EC"_at_B"}} - Magnetic\ field\ originating\ from\ wire\ |EC"|\ at\ point\ B$

$\mu_0, \mu - permeability\ of\ vacuum\ and\ relative\ permeability\ of\ air, respectively$

$\vec{ds} - \ \ wire\ element\ length\ in\ the\ direction\ of\ current\ flow$

$\vec{r} - \ vector\ measured\ from\ the\ wire\ element\ to\ the\ point\ at\ which\ the\ field\ is\ computed$

After the magnetic induction calculations, the electromagnetic force acting on the pantograph slider is computed separately for its all parts. Based on that the total force is calculated by summing. For the analyzed scenario, the following components of electromagnetic force were computed

$$F_{TOTAL_X} = 31.6N,\ F_{TOTAL_Y} = 0N,\ F_{TOTAL_Z} = -0.013N \tag{4}$$

Although the highest component is acting in the direction of pantograph travel, the static uplift force of the pantograph is influenced by the electromagnetic force due to the mechanical properties of the pantograph's kinematic chain, i.e. the interactions existing between its elements. The MB pantograph model was utilized to investigate the uplift force with and without electromagnetic force. The results are presented in Figure 9.

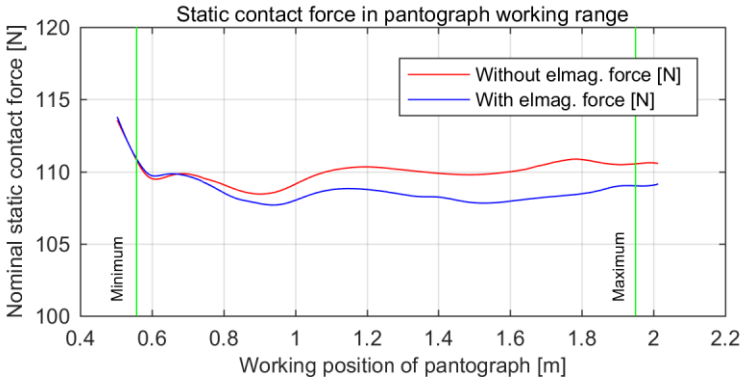


Figure 9: Uplift force with and without electromagnetic force

It can be observed, that the highest influence of the contact force is registered when the pantograph is working in the operational height of 1.5 – 1.8 m. In this range, the electromagnetic force causes a change of the nominal uplift force up to 2 N.

6 Results

At first, the analysis was performed for a single run speed 160 km/h. The nominal case (the friction change at the 0% level) takes into account the friction experimentally identified for the tested pantograph. Ten deviations from the nominal case were investigated, i.e. friction change by -25%, -20%, -15%, -10%, -5%, 5%, 10%, 15%, 20%, 25%, accordingly. It is assumed, that the friction deviations may result from an assembly or manufacturing uncertainties. The results are presented in Figure 10. The STD of CF was chosen as a reliable quality indicator of the mechanical contact in the pantograph-catenary interface.

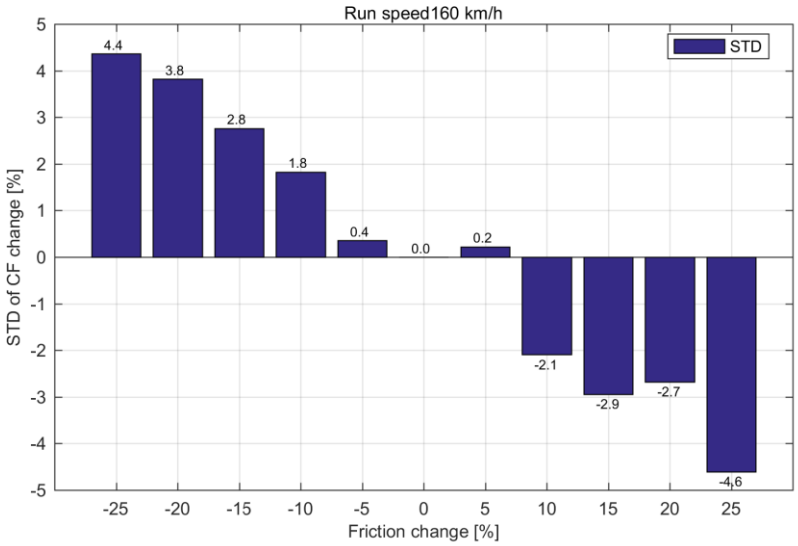


Figure 10: An influence of friction in pantograph joints on the STD of CF at run speed 160 km/h

Considering the outcomes of the simulations, it can be concluded, that the friction variation has a non-negligible impact on the STD of the CF for run speed 160 km/h, especially at the highest friction change taken into account, i.e. at the +/-25% level. Small friction changes (i.e. within the -5% up to 5% change range) almost do not affect the STD of CF. The friction decrease in the range (-25% – -10%) causes a deterioration of the interaction between the pantograph strip and contact line (the STD of CF increases by 4.4%). The friction increase has a positive influence on the contact quality, because more energy is dissipated in the entire system, and the STD of CF can be decreased by 4.6% comparing to the nominal case.

Then, the scope of the analysis was extended to address various run speeds, in the range 110 – 200 km/h specifically. An influence of the friction in the pantograph mechanism is expressed in the paper as the change of the STD of CF with reference to the nominal case, i.e. characterizing the nominal friction ratio for a particular run speed. The results are presented in Figure 11.

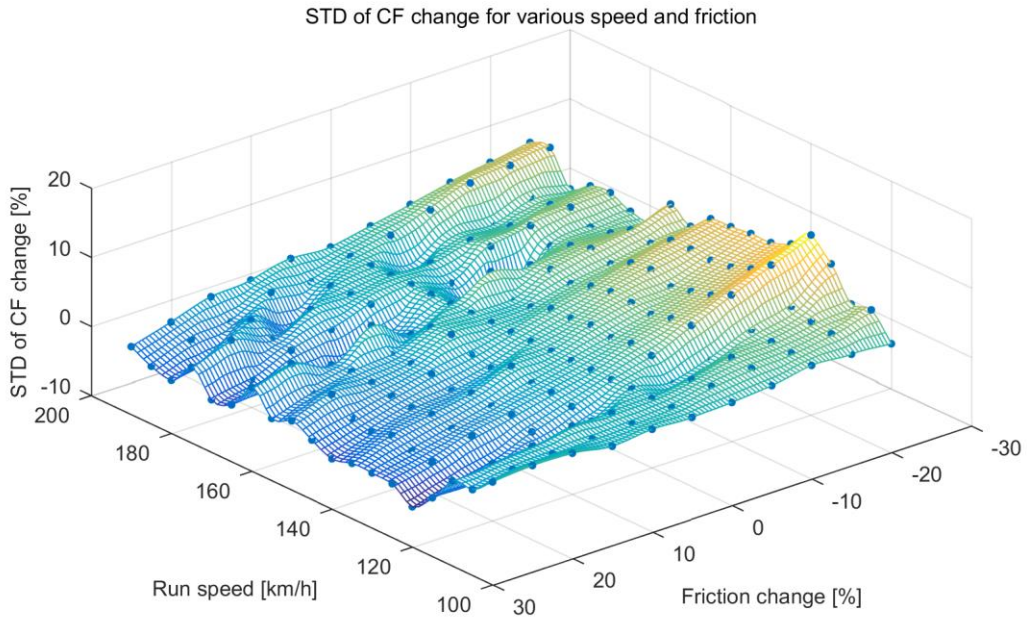


Figure 11: An influence of friction in pantograph joints on the STD of CF for various run speeds

It can be observed that for almost all of the analyzed cases, the STD of CF increases when the friction is reduced and the STD decreases while friction increases. Intensity of this phenomenon depends on a particular run speed, but it is visible at most for the case of 130 km/h. Similar monotonicity is observed for other run speeds, and this can be caused by the fact that more energy is dissipated in the case when friction in pantograph mechanism in increased. In the range of 170 – 190 km/h this trend is disturbed and some local minima and maxima appear. It is also visible in Figure 12, where the results of STD of CF (already shown in Figure 11) are presented with different perspective.

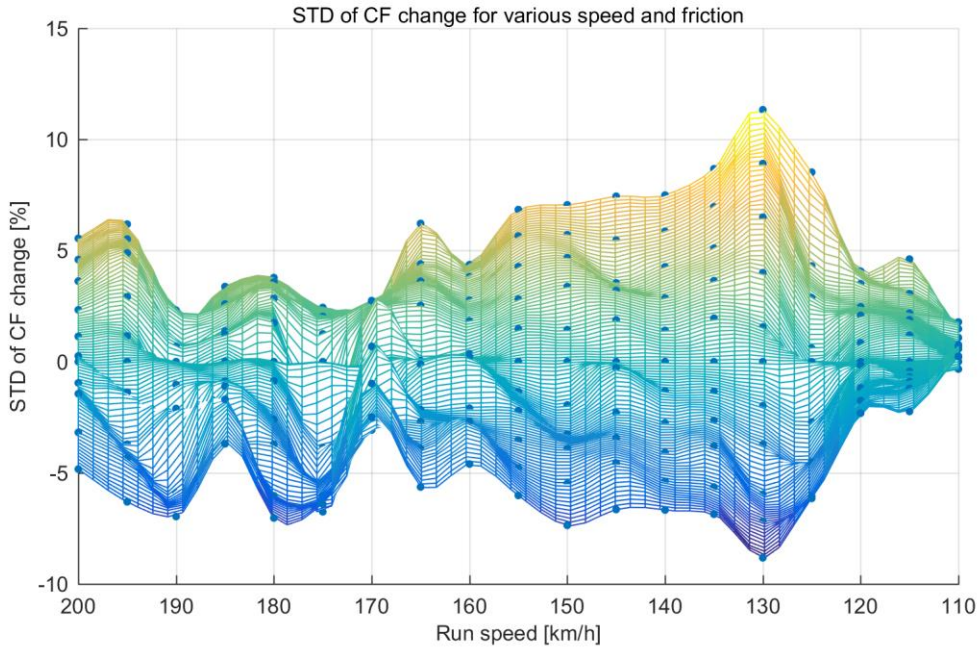


Figure 12: An influence of friction in pantograph joints on the STD of CF for various run speeds, second view highlighting disturbed monotonicity of the relationships between friction, run speeds and STD of CF

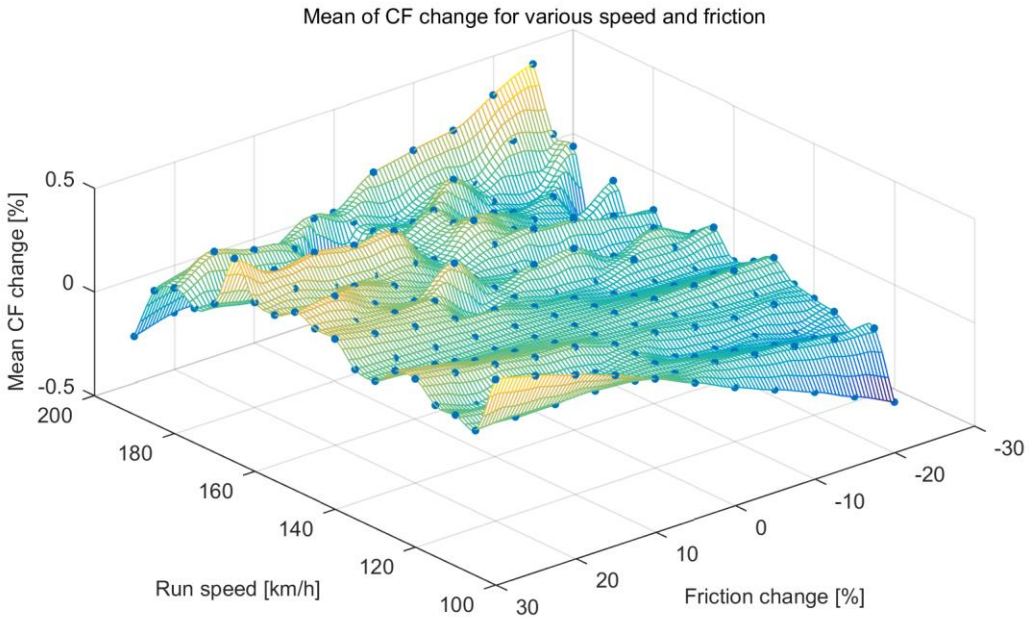


Figure 13: An influence of friction in pantograph joints on the mean CF for various run speeds

The values of the mean CF for various run speeds and friction forces are presented in Figure 13. Slightly different nature of the changes has been registered for the mean value of the CF comparing to the STD of CF. It can be noticed that these changes are not that significant as in case of the STD of CF. Monotonicity was also identified for the most extreme run speeds that were analyzed, i.e. 110 and 200 km/h. For the case of 110 km/h the mean CF increases with the increase of the friction in the pantograph structure. For the case of 200 km/h, in turn, the studied characteristics decreases while increasing friction. Between the above mentioned extreme speeds, character of volatility of the mean value

of CF cannot be clearly defined. However, the mean CF varies within the range of +/-1% of its nominal value for the investigated input parameter domain. Hence, it might be concluded that the mean value of the CF is not significantly affected by the friction change in the discussed domain.

7 Conclusions

Based on the obtained results of the co-simulation algorithm the following final remarks were drawn to summarize the paper:

1. The multi-domain co-simulation approach can be successfully utilized to simulate the entire pantograph-catenary system. The co-simulation method considering the interactions between FEM catenary model and Multibody pantograph-rail vehicle model was performed. The adopted approach concerns the most important phenomena which are present in the system, i.e. nonlinearity of catenary droppers, wave propagation and reflections in a catenary structure and real kinematic chain of a three dimensional pantograph Multibody model. Moreover, aerodynamic, electromagnetic and friction forces acting on the pantograph components are considered.

2. The friction coefficient for the pantograph joints was identified and effectively implemented in the numerical model. 10 deviations from the nominal friction coefficient were investigated within the range of ±25% of the nominal friction, to study the influence of the friction deviation on the pantograph-catenary contact quality for various run speeds in the range 110 – 200 km/h.

3. The study has shown, that the STD of the CF increases while decreasing the friction coefficient in the pantograph components and the mentioned property decreases when the friction coefficient increases. This behavior is observed for run speeds in the range 110 - 170 km/h and 190 – 200 km/h. In the range of run speeds 170 – 190 km/h some disturbances of this monotonicity are observed. This is probably caused by resonances of the catenary structure. – but this supposition has to be investigated more deeply in the future. The mean value of the CF is not significantly affected by the friction coefficient in the analyzed cases - the identified influence is less than 1% for the most extreme cases.

Acknowledgments

The research has been partially supported by EU within the program H2020-EU.1.3.1. - Fostering new skills by means of excellent initial training of researchers, project ID: 764547 titled: Dynamic virtualisation: modelling performance of engineering structures. The work was also partially supported by the AGH Grant no. 15.11.130.627 and carried out employing the infrastructure of the Centre of Energy AGH (Czarnowiejska 36, 30-054 Kraków, Poland). The authors would like to thank the EC Engineering company for providing pantograph data.

References

[1] M. Aboshi, and K. Manabe, *Analyses of Contact Force Fluctuation between Catenary and Pantograph.* Quarterly Report of RTRI, Vol. 41, No. 4, 2000, pp. 182-187.

[2] P. Zdziebko, A. Martowicz, T. Uhl, *An investigation into multi-domain simulation for a pantograph - catenary system*, ITM Web of Conferences, Vol. 15, (2017).

[3] P. Zdziebko, A. Martowicz, T. Uhl, *Contact force control for a high speed pantograph using co-simulations*, in J. Awrejcewicz, M. Kaźmierczak, J. Mrozowski, P. Olejnik, editors, *Vibration, Control and Stability of Dynamical Systems*, Department of Automation, Biomechanics and Mechatronics, Łódź (2017), pp. 587-598.

[4] P. Zdziebko, T. Uhl, *Finite element analysis of pantograph-catenary dynamic interaction.* Archives of Transport, Vol. 39, No. 3, (2016), pp. 77-85.

[5] G. Zhu, G. Gao, G. Wu, Z. Gu, J. Wu, J. Hao, *Modeling pantograph–catenary arcing.* Proceedings of the Institution of Mechanical Engineers, Part F: Journal of Rail and Rapid Transit, Vol. 230, No. 7, (2016), pp. 1687-1697.

[6] European Standard EN 50367, *Railway applications. Current collection systems. Technical criteria for the interaction between pantograph and overhead line* (2012).

[7] P. Zdziebko, A. Martowicz, T. Uhl, *Influence of the mechanical properties of pantograph structural parts on its interaction with a catenary*, in J. Awrejcewicz, editor, *Dynamical Systems in Applications*, Springer (2018) (accepted).

[8] European Standard EN 50318, *Railway applications. Current collection systems. Validation of simulation of the dynamic interaction between pantograph and overhead contact line*, (2002).

Sensitivity of dynamic responses of railway prestressed concrete sleepers with under sleeper pads to impact energy

C. Ngamkhanong[1,2], K. Goto[2,3] , S. Kaewunruen[1,2]
[1]Department of Civil Engineering, School of Engineering, University of Birmingham, Birmingham B152TT, United Kingdom
e-mail: **cxn649@student.bham.ac.uk**

[2]Birmingham Centre for Railway Research and Education, School of Engineering, University of Birmingham, Birmingham B152TT, United Kingdom

[3]Railway Dynamics Division, Railway Technical Research Institute, Japan

Abstract
In railway track, under sleeper pads (USPs) have recently been adopted as a resilient component placed underneath the concrete sleepers to moderate track stiffness. By the insertion, USPs are generally used to improve railway track resilience in special locations such as turnouts, bridge ends, viaducts, track transitions etc. However, railway tracks usually face high-intensity impact loading due to any imperfection of either wheel or rail. This paper presents a nonlinear 3D finite element model of prestressed concrete sleepers with under sleeper pads in to order to study the effect of USPs under high impact loading. This study has confirmed field studies that the sleepers with USPs tend to have lesser flexures, contact force and impact energy. However, this study reveals that the sleeper with USPs could be amplified by the large amplitude impact energy. These behaviours imply that the applications of USPs should be very careful since the USPs could trade off the desired benefits by aggravating dynamic behaviour of sleepers with under sleeper pads.

1 Introduction

Railway sleepers are a major structural component in ballasted railway tracks. The main functions of sleepers are to transfer train axle loads from the rails onto the underlying ballast bed and supporting system, and to secure rail gauge for safe passages of trains and rolling stocks. It has been noted that railway sleepers are safety-critical components [1, 2]. Generally, there are two groups of track components: superstructure and substructure. Superstructure components consist of rail, fastening system, sleeper and ballast, they sometimes include rail pad, under sleeper pad, and ballast mat. Substructure counterparts comprise subballast, formation, geotextiles and foundation [3, 4]. Under sleeper pads (USP) are resilient pads installed underneath the sleepers as an attachment to provide additional track resiliency between the sleepers and ballast. The typical cross section of the ballasted railway track with under sleeper pad is shown in figure 1. USP is often used in ballasted tracks with concrete sleepers. USP can also be applied in various operational environments such as conventional main lines, urban or high speed lines or light rail and metro lines. Nowadays, USP has been developed and used widely and heavily in central Europe such as in Austria, Czech Republic and Germany. Additionally, several counties have carried out pilot trials such as in Sweden, Australia, and China. USP is made of polyurethane elastomer with a foam structure including encapsulated air voids. USP is classified by the bedding modulus as very soft, soft, medium stiff and stiff USP [5-10]. Different types of USP can be used at different locations and for different purposes, as described in table 1.

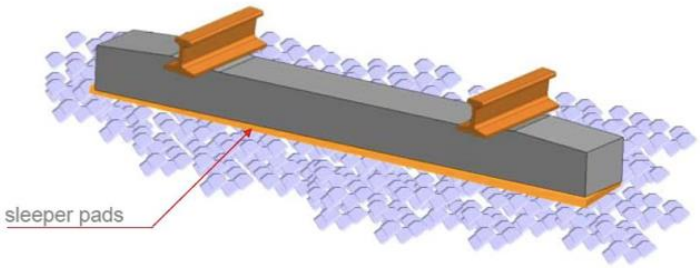


Figure 1: Typical ballasted railway track and its components with USP [1]

Table 1: USP applications and characterisations [11]

Fields of application of USP	USP			
	Very soft	Soft	Medium stiff	Stiff
	$C_{stat} \leq 0.10$	$0.10 < C_{stat} \leq 0.15$	$0.15 < C_{stat} \leq 0.25$	$0.25 < C_{stat} \leq 0.35$
Improve track quality (reduce ballast breakage and track/turnout pressure)			■	■
Transition zones			■	■
On existing structures with reduced ballast thickness			■	■
Reduction of long-pitch low-rail corrugation in tight curves			■	■
Reduction of ground-borne vibration		■	■	

The main objectives for using USP are to moderate track stiffness; to reduce ground borne vibrations; and to reduce ballast breakage [12-16]. USPs could reduce track stiffness in special areas such as turnout systems (switches and crossings) or bridge transitions. The vibration of sleepers could also be isolated by the USP so that the ballast and formation are uncoupled from the wheel/rail interaction, reducing the ground vibrations affecting surrounding areas and structures. The reduced ballast damage is accomplished by a reduction of contact pressure, and thus wears, in the sleeper/ballast interface. A more uniform load distribution is achieved by the use of USP, resulting in the reduction of the contact pressure and the smaller variations of support stiffness along the track. It was also noted that USP can lead to higher railway track economic values and to have substantial wider social benefits [17-20].

An application of USPs in Australia was initially trailed back in 1980s on open plain tracks. The outcome showed little improvement at the time whilst the delamination and degradation of the USP material were the key negative issues found in the field [21-28]. In recent years, the performance of the USPs has been improved through the outcomes from the test results in central Europe and in Austria, which show a promising quality and durability of USPs. Despite the benefits of USP have been presented [29], contradict outcome has been reported by Trafikverkets (Swedish Transport Administration). After several years of field inspections and observations, Trafikverkets reported that there has been no or very little influence of USPs on ballast size reduction and contamination resulting in track quality [30]. This could be a reason why the utilisation of USPs is not significant globally. Moreover, The USP has different effects on lateral track resistance. It cannot be confirmed whether positive or negative effects will occur at this stage. However, USP can lead to excessive sleeper vibration, resulting in ballast dilation or ballast spreading. Generally, railway track experience impact load, which is a shock load applied in short duration [2, 31]. The use of USPs for attenuating impact load and excessive vibration has been studied in the fields at specific locations

such as dipped rails/welds, glue insulated joint etc [32-38]. However, the numerical studies into such the behaviour have been limited and not investigated.

The dynamic responses of railway concrete sleepers with under sleeper pads to high-intensity impact loading conditions are presented in this study. A three-dimensional finite element model has been established that can simulate and predict the responses of reinforced and prestressed concrete members. A three-dimensional nonlinear finite element model of a full-scale railway prestressed concrete sleeper for static analysis was firstly developed using the general-purpose finite element analysis package, ANSYS [39-41]. The static finite element model has been validated by the static full-scale experiment [41]. The experimental details were based on the European Standard [42]. The calibrated finite element model has been extended to include ballast support and in situ boundary conditions [43]. The extended model was linked to LS-Dyna for impact analysis. The impact analysis has been validated against the drop impact tests [44-46]. The initial velocities of drop mass corresponding to actual train load were applied to the rail. These can generate different impact energies. This study will focus on the sensitivity of impact energy to the dynamic responses of prestressed concrete sleepers with stiff USP. The dynamic responses including von mis stress, maximum displacements and accelerations of concrete sleepers with and without USP are highlighted.

2 Finite Element Modelling

Firstly, the general-purpose finite element analysis package, ANSYS was used to develop and model a three-dimensional finite element model of a full-scale railway prestressed concrete sleeper for static analysis. Concrete was modelled using SOLID65 solid elements where each node has three degree of freedom (trainslation in x,y and z). The modulus of elasticity of concrete (f'c) was estimated based on AS3600 [47] using the compressive strengths of 80 MPa. As for prestressing wire, LINK8 truss element was taken into account to withstand the initial strain attributed to prestressing forces, by assuming perfect bond between these elements and concrete. It should be note that this truss element cannot resist neither bending moments nor shear forces. Since bond slip is hardly observed under failure modes [48-50], the perfect bond between pre-stressing wires and concrete was assumed. The dynamic materials properties associated with strain rate of concrete and prestressing wires can be calculated. The 0.2% proof stress is 1,700 MPa and the ultimate stress is 1,930 MPa. The static and dynamic elasticity of moduli of pre-stressing wire are 190,000 MPa.

The extended finite element model was calibrated using vibration data [41, 49]. The updated finite element model was then transferred to LS-Dyna [45, 46], as shown in figure 2. The simulation results were achieved by assigning the initial velocity to the drop mass to generate an impact event, similarly to the actual drop tests. There are two cases considered in this study, 1.94m/s and 4.34 m/s. It is noted that these velocities are equivalent to the 600kg falling mass with the drop height of 0.2m and 1m, respectively. It is found that the finite element model is fairly sufficient for use in predicting impact responses of the prestressed concrete sleepers. The trends of peak acceleration responses are quite close to each other, although there is certain phase difference.

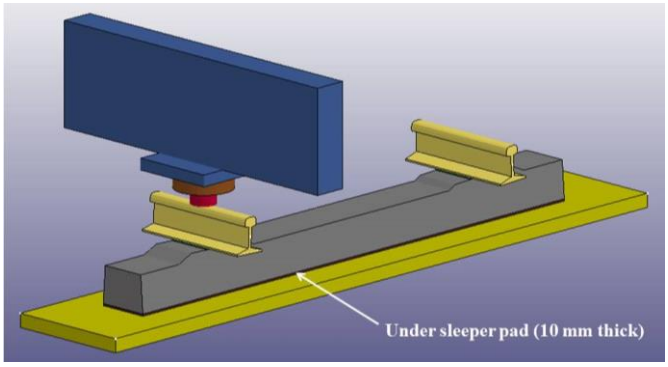


Figure 2: Finite element model of sleeper with under sleeper pad

3 Results and discussions

In this study, the stiff USP, which has the elastic modulus of 550MPa, is used. In this analysis, the initial velocities of 0.74m/s, 1.94m/s, 3.14m/s, 4.34m/s and 5.45m/s of drop mass are considered. Time histories of wheel-rail contact force are presented in figure 3. It is clearly seen that wheel-rail forces reduce significantly when using USP. It is interesting that pulse duration increases when USP is used because the support is softer. Thus, the support play a role on impact response as the impact magnitude decreases as the track stiffness, whilst, pulse duration is inversely proportional to the stiffness [50]. It should be note that the pulse durations are in the range of 3-4 ms. It is clearly seen that the use of USP can significantly reduce wheel/rail contact force by about 10%. The impact energy input is then calculated. It should be noted that the impulse is the area under the impact load history or the integral of force over the time. The different initial velocities of drop mass generate different impact energy. The impact energies of applied force to sleepers with and without USP are presented in table 2. It should be noted that even contact forces significantly reduce when using USP, the impact energies slightly decrease since pulse durations increase.

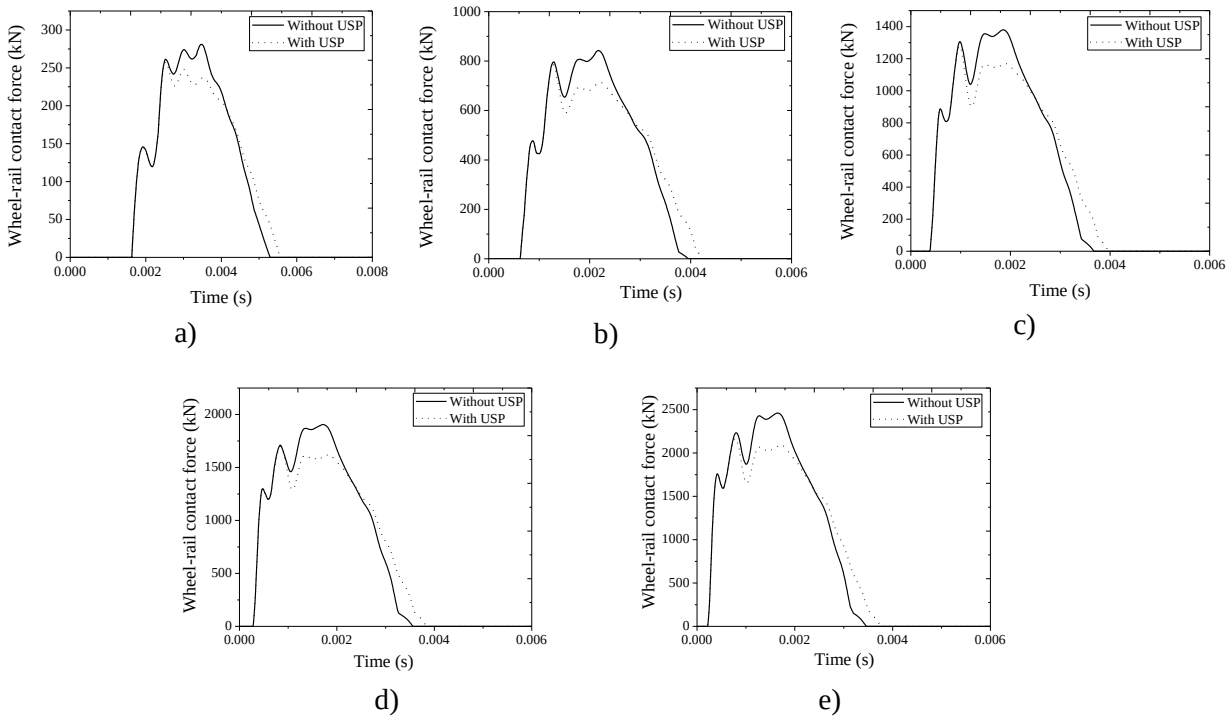


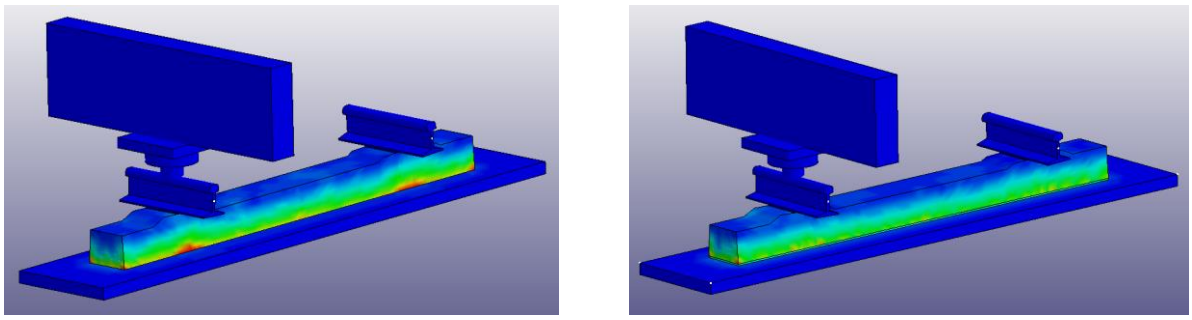
Figure 3: Wheel-rail contact force subjected to impact loads with the initial velocities of a) 0.74m/s b) 1.94m/s c) 3.14m/s d) 4.34m/s e) 5.54m/s

Table 2: Contact force and impact energy

Case	Initial velocity (m/s)	Contact force (kN)		Impact energy (kNs)	
		Without USP	With USP	Without USP	With USP
A	0.74	288	258	647	639
B	1.94	843	785	1766	1755
C	3.14	1380	1279	2888	2866
D	4.34	1905	1699	4001	3974
E	5.54	2461	2171	5121	5066

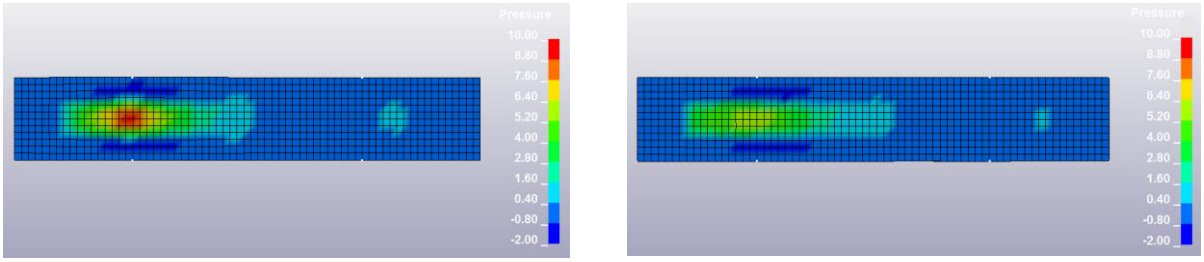
Figure 4 shows the comparison of von mises stress contour between sleepers without and with USP before applying load. It is seen that the dynamic stress concentration on the concrete sleeper is less than that with

USP especially at rail seat. Figure 5 illustrates the distribution of contact pressure on ballast under impact load case E. It is clearly seen that USP can significantly reduce the contact pressure especially at rail seat. This illustrates that USP can redistribute the impact load actions better along the concrete sleeper.



a) b)

Figure 4: Von-mises stress contour of sleeper a) without USP b) with USP



a) b)

Figure 5: Contact pressure distribution on ballast a) without USP b) with USP under impact load

Figure 6 presents the effects of stiff USP on the dynamic responses of the concrete sleepers subjected to impact loads. Even though it is noticeable that the use of USP can obviously decrease the contact force and impact energy stress, von-mises stresses, displacements and accelerations of sleeper at both rail seat and mid-span slightly increase when using USP. USP has negative effect on sleeper maximum displacements at both rail seat and mid-span. It is interesting that about 30-40% increase of displacement at rail seat in all velocities are observed. This is because there is a reduction of concrete sleeper stiffness due to the adaptation of USP. This is confirmed by the previous field measurement conducted that the rise of sleeper vibration was observed when USP were taken into account. Although the impact force and impact energy reduce when using USP, the sleeper displacement slightly decreases. This is because the use of USP affects the overall track characteristics by reducing track stiffness and making track softer. This has more influence than impact force which leads to increase the sleeper displacement. The acceleration vibrations are also presented in term of insertion gain. Figure 7 demonstrates the insertion loss in concrete sleepers due to USP. It is clearly seen that USP can increase vibrations of concrete sleepers at both rail seat and mid-span. Thus, USPs tend to have large acceleration amplitude vibrations, especially when excited by a high-frequency impact force.

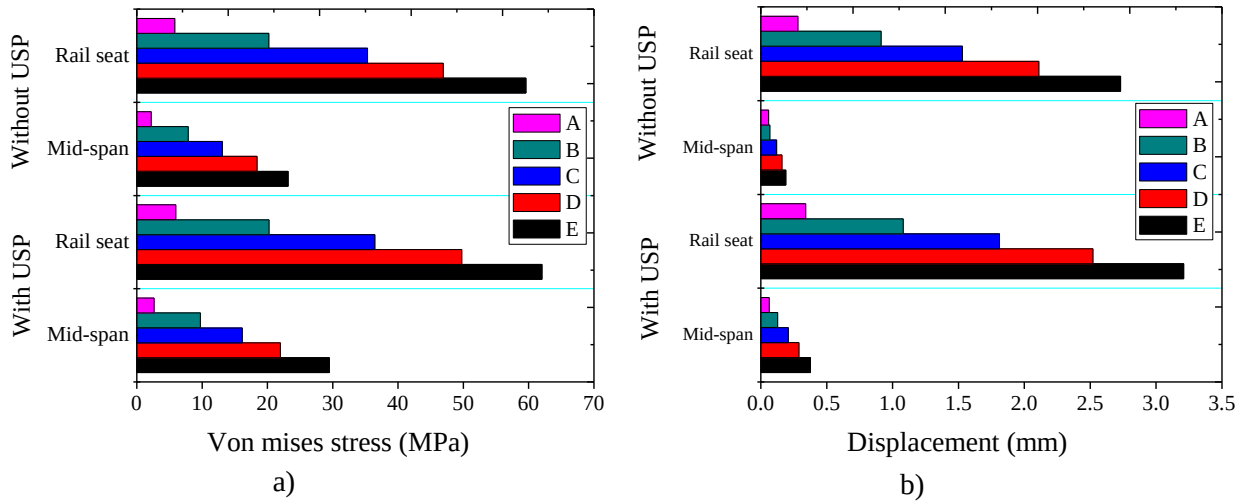


Figure 6: Effects of USP on the maximum dynamic responses of railway concrete sleeper subjected to impact loads

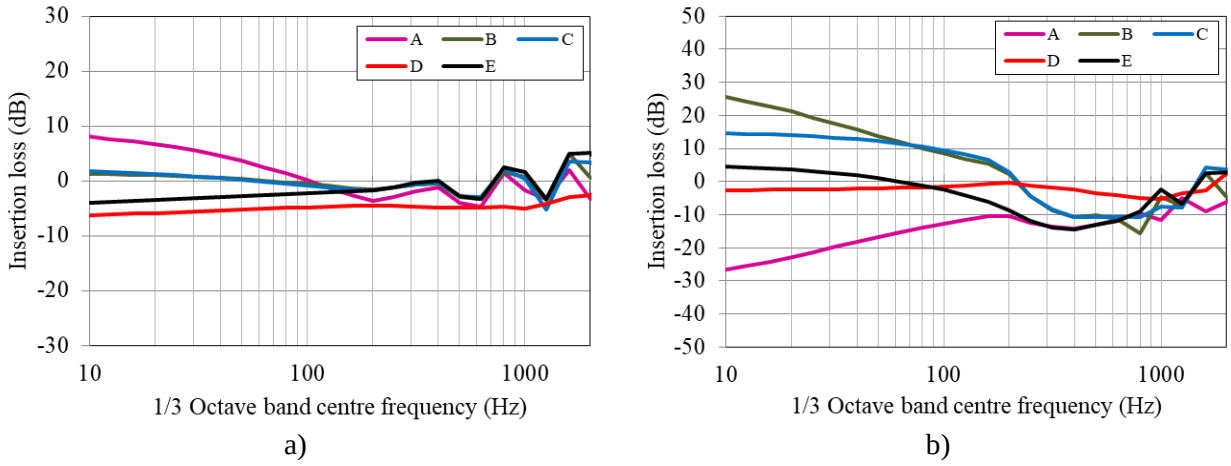


Figure 7: Insertion loss due to USP at a) rail seat b) mid-span

4 Conclusions

The emphasis of this study is placed on the effects of under sleeper pads on the dynamic responses of railway concrete sleeper subjected to high intensity impact loading. Finite element models of sleeper with USP have been conducted and analyzed using LS-DYNA. The initial velocities of drop mass are applied as an impact load. The models have been validated against the experimental results. The velocities applied to the mass corresponds to the drop mass of 600kg with the variations of height. The results show that the USPs will decrease stiffness of sleepers, then significantly reduce contact forces by about 10-30%. However, only the slight reductions of impact energy are observed in all cases. This is because the pulse duration may increase when using USPs which can increase the impact energy even the contact forces reduce. Although the studies have found that the sleepers with USPs tend to have lesser flexures, contact forces, this numerical study and previous field data also confirm that a railway track with USPs could experience a large displacement and acceleration amplitude vibrations, especially when excited by a high-frequency impact force. It can be concluded that the use of USPs should be very careful since the USPs may have a trade-off impact that could aggravate dynamic behaviour of sleepers with under sleeper pads.

Acknowledgements

The authors would also like to thank British Department for Transport (DfT) for Transport – Technology Research Innovations Grant Scheme, Project No. RCS15/0233; and the BRIDGE Grant (provided by University of Birmingham and the University of Illinois at Urbana Champaign). The second author gratefully acknowledges the Japan Society for the Promotion of Science (JSPS) for his JSPS Invitation Research Fellowship (Long-term), Grant No L15701, at Track Dynamics Laboratory, Railway Technical Research Institute and at Concrete Laboratory, the University of Tokyo, Tokyo, Japan. The authors are sincerely grateful to the European Commission for the financial sponsorship of the H2020-RISE Project No. 691135 "RISEN: Rail Infrastructure Systems Engineering Network", which enables a global research network that tackles the grand challenge of railway infrastructure resilience and advanced sensing in extreme environments (www.risen2rail.eu) [51].

References

[1] S. Kaewunruen, A.M. Remennikov, *Non-destructive testing (NDT): A tool for dynamic health monitoring of railway track structures*, Materials Australia, Vol. 39, No. 6, (2006).

[2] A.M. Remennikov, S. Kaewunruen, *A review on loading conditions for railway track structures due to train and track vertical interaction*, Structural Control and Health Monitoring, Vol. 15, (2008), pp. 207-234.

[3] B. Indraratna, C. Rujikiatkamjorn, W. Salim, *Advanced Rail Geotechnology – Ballasted Track*, CRC Press, London, UK (2011).

[4] C. Ngamkhanong, S. Kaewunruen, C. Baniotopoulos, *A review on modelling and monitoring of railway ballast*, Structural Monitoring and Maintenance, vol. 4, (2017), pp. 195-220.

[5] A. Johansson, J.C.O. Nielsen, R. Bolmsvik, A. Karlström, *Under sleeper pads – influence on dynamic train-track interaction*, Wear, Vol. 265, (2008), pp. 1479–687.

[6] International Union of Railway, *USP Report, Under sleeper pads*, Project no. I/05/U/440, Summarising report, (2009).

[7] International Union of Railway, *USP recommendations, Under Sleeper Pads, Recommendations for Use*, UIC-Leaflet, Draft Document, (2013).

[8] R. Schilder, *USP-under sleeper pads, Applications and benefits of elastic elements in ballasted tracks*, UIC project no. I/05/U/440, Paris 17 (2006)

[9] J. Jenkins, S. Stephenson, G. Clayton, G. Morland, D.L. Lyon, *Incidences des paramètres caracteristiques de la voie et des vehicules sur les efforts dynamics verticaux qui se développent entre rail et roue*, Rail International, Vol. 3, No. 10, 1974, pp. 682-702.

[10] S. Lakuši, M. Ahac, I. Haladin, *Experimental investigation of railway track with under sleeper pad*, 10th Slovenian road and transportation congress, Portoroz˘, Slovenija (2010).

[11] International Union of Railway, *UIC Leaflet 917 Guidelines for under sleeper pad*, Paris, France, 2015.

[12] T. Dahlberg, *Railway track stiffness variations-consequences and countermeasures*, Int. J. Civ. Eng., Vol. 8, No. 1, 2010, pp. 1–12.

[13] P. Schneider, R. Bolmsvik, J.C.O. Nielsen, *In situ performance of a ballasted railway track with under sleeper pads*, J. Rail Rapid Transit,Vol. 225, No. 3, 2011, pp. 299-309.

[14] W. Stahl, *Improvement of ballasted tracks using sleeper pads – investigations and experiences in Germany*, Munich University of Technology (2004).

[15] F. Müller-Boruttau, U. Kleinert , *Betonschwellen mit elastischer Sohle*, ETR, Vol. 50, No. 3, (2001).

[16] V.L. Marine, M.J.M.M. Steenburgen, I.Y. Sheets, *Combating RCF on switch points by tuning elastic track properties*, Wear, Vol. 271, No. 1, (2009), pp. 158-167.

[17] S. Setsobhonkul, S. Kaewunruen, J.M. Sussman, *Lifecycle Assessments of Railway Bridge Transitions Exposed to Extreme Climate Eventsm*, Front. Built Environ., vol. 3, 2017.

[18] C. Nhamkhanong, A.T. Nascimento, S. Kaewunruen, *Economics of track resilience*, World Multidisciplinary Civil Engineering-Architecture-Urban Planning Symposium, IOP Conference

Series: Material Science and Engineering, 2018 (accepted).
[19] A. Ortega, S. Blainey, J. Preston, *Installation of under sleeper pads on ballasted railway tracks: An economic analysis of their potential implementation*, Proc IMechE, Part F: J Rail and Rapid Transit, (2017).
[20] M.H. Bin Osman, S. Kaewunruen, *Uncertainty Propagation Assessment in Railway-Track Degradation Model Using Bayes Linear Theory*, Journal of Transportation Engineering, Part A: Systems, Vol. 144, No. 7, (2018).
[21] S. Kaewunruen, A. Aikawa, A.M. Remennikov, *Vibration attenuation at rail joints through under sleeper pads*, Procedia Engineering, Vol. 189, (2017), pp. 193-198.
[22] S. Kaewunruen, J.M. Sussman, H.H. Einstein, *Strategic framework to achieve carbon-efficient construction and maintenance of railway infrastructure systems*, Frontiers in Environmental Sciences, Vol. 3, No, 6, (2015).
[23] S. Nimbalkar, B. Indraratna, S.K. Dash, D. Christie, *Improved performance of railway ballast under impact loads using shock mats*, ASCE Journal of Geotechnical & Geoenvironmental Engineering, Vol. 138, No. 3, (2012), pp. 281-294.
[24] S. Kaewunruen, A.M. Remennikov, *Under sleeper pads: field investigation of their role in detrimental impact mitigation*, Proceedings of the 13th International Railway Engineering Conference, Edinburgh, UK, 2015 June 30 - July 1.
[25] P. Schneider, R. Bolmsvik, J.C.O. Nielsen, *In-situ performance of a ballasted railway track with under sleeper pads*, Journal of Rail and Rapid Transit, Vol. 225, No. 3, (2011), 299-309.
[26] UIC: International Union of Railway, *UIC Leaflet: Guideline for Under Sleeper Pads*, Paris, France (2014).
[27] M.V. Tuler, S. Kaewunruen, *Life cycle analysis of mitigation methodologies for railway rolling noise and groundbourne vibration*, Journal of Environmental Management, Vol. 191, (2017), pp. 75-82.
[28] R. Tavares de Freitas, S. Kaewunruen, *Life cycle cost evaluation of noise and vibration control methods at urban railway turnouts*, Environments, Vol. 3, No. 4, (2016), pp. 34.
[29] R. Schilder, *USP (under sleeper pads) – a contribution to save money in track maintenance*, in AusRAIL PLUS (Sydney: AusRAIL PLUS), (2013).
[30] B. Larsen, *Under Sleeper Pads on the Ofoten Line*, Proceedings of the 19th Nordic Seminar on Railway Technology, Luleå, Sweden (2016).
[31] C. Ngamkhanong, S. Kaewunruen, B.J.A. Costa, *State-of-the-Art Review of Railway Track Resilience Monitoring*, *Infrastructures*, Vol. 3, (2018).
[32] A. Paixão, J.N. Varandas, E. Fortunato, R. Calçada, *Numerical simulations to improve the use of under sleeper pads at transition zones to railway bridges*, Engineering Structures, Vol. 164, (2018), pp.169-182.
[33] H. Li, G.R. McDowell, *Discrete element modelling of under sleeper pads using a box test*, Granular Matter, Vol.20, No. 2, (2018), pp. 2-26.
[34] L. Le Pen, G. Watson, A. Hudson, W. Powrie, *Behaviour of under sleeper pads at switches and crossings–Field measurements,* Proceedings of the Institution of Mechanical Engineers, Part F: Journal of Rail and Rapid Transit, Vol. 232, No. 4, (2018), pp. 1049-1063.
[35] S. Kaewunruen, *Discussion of "Mitigation of Ground Vibration Generated by High-Speed Trains on Saturated Poroelastic Ground with Under-Sleeper Pads"*, ASCE Journal of Transportation Engineering, Vol. 141, No. 1, (2015).
[36] J. Mottahed, J.A. Zakeri, S. Mohammadzadeh, *Field and numerical investigation of the effect of under-sleeper pads on the dynamic behavior of railway bridges*, Proc IMechE, Part F: J Rail and Rapid Transit, in press, (2017).
[37] J.A. Zakeri, M. Esmaeili, H. Heydari-Noghabi, *A field investigation into the effect of under sleeper pads on the reduction of railway-induced ground-borne vibrations*, Proc IMechE, Part F: J Rail and Rapid Transit, Vol. 230, (2016), pp. 999–1005.
[38] S. Kaewunruen, T. Ishida, A.M. Remennikov, *Dynamic Performance of Concrete Turnout Bearers and Sleepers in Railway Switches and Crossings*, Advances in Civil Engineering Materials, (2018) doi.org/10.1520/ACEM20170103. ISSN 2379-1357.
[39] S. Kaewunruen, A.M. Remennikov, *Effect of a large asymmetrical wheel burden on flexural response and failure of railway concrete sleepers in track systems*, Engineering Failure Analysis, Vol. 15,

No. 8, (2008), pp. 1065-1075.
[40] S. Kaewunruen, A.M. Remennikov, *Experimental simulation of the railway ballast by resilient materials and its verification by modal testing*, Experimental Techniques, Vol. 32, No. 4, (2008), pp. 29-35.
[41] S. Kaewunruen, A.M. Remennikov, *Nonlinear finite element modeling of railway prestressed concrete sleeper*, *Proceedings of the 10th East Asia-Pacific Conference on Structural Engineering and Construction, EASEC*, Vol. 4, (2006), pp. 323-328.
[42] S. Kaewunruen, and A.M. Remennikov, *Experimental and numerical studies of railway prestressed concrete sleepers under static and impact loads*, Civil Computing, Vol. 3, (2007), pp. 25-28.
[43] E.K. Gamage, S. Kaewunruen, A.M. Remennikov, T. Ishida, *Toughness of Railroad Concrete Crossties with Holes and Web Openings*. Infrastructures, Vol. 2, No. 3, (2017).
[44] E.K. Gamage, S. Kaewunruen, A.M. Remennikov, T. Ishida, *Reply to Giannakos, K. Comment on: Toughness of Railroad Concrete Crossties with Holes and Web Openings*. Infrastructures, Vol 2, No. 5, (2017).
[45] British Standards Institute (BSI), *European Standard BS EN13230 Railway applications*. Track. Concrete sleepers and bearers, London UK, (2016).
[46] S. Kaewunruen, A.M. Remennikov, *Low-velocity impact analysis of prestressed concrete sleepers*. *Concrete Institute of Australia's 23rd Biennial Conference 07, October 18-20, Adelaide, Australia,* (2007).
[47] S. Kaewunruen, A.M. Remennikov, "Impact responses of prestressing tendons in railway concrete sleepers in high speed rail environment*s." Proceedings of the 5th Computational Methods in Structural Dynamics and Earthquake Engineering, May 25-27, Crete Island, Greece,* (2015).
[48] S. Kaewunruen, A.M. Remennikov, S. Minoura, *Dynamic responses of railway ultra-high-strength concrete sleepers under extreme impact loading*. *Proceedings of the 6th Computational Methods in Structural Dynamics and Earthquake Engineering, June 15-17, Rhodes Island, Greece,* (2017).
[49] Standards Australia, *Design of concrete structures*, Australian Standard: AS3600-2001, (2001).
[50] Z. Cai, *Modelling of rail track dynamics and wheel/rail interaction*, PhD Thesis, Department of Civil Engineering, Queen's University, Ontario, Canada (1992).
[51] S. Kaewunruen, M.J. Sussman, M Akira, *Grand Challenges in Transportation and Transit Systems*. Frontiers in Built Environment, Vol. 2, (2016).

Enhancing the dynamic performance of a pantograph-catenary system via inerter-based damping technology

M. Zhu[1], S. Y. Zhang[1], J. Z. Jiang[1], J. Macdonald[1], S. Neild[1]
[1] Faculty of Engineering, University of Bristol
Queen's Building, University Walk, Bristol, BS8 1TR, UK.
e-mail: **ming.zhu@bristol.ac.uk**

Abstract
A key aim in designing pantograph-catenary (P-C) systems is to maintain an optimal contact force between the pantograph and catenary cables, which guarantees the power transmission efficiency while minimising wear and damage of the contacting elements. However, with increased operation velocity, undesirable vibrations between the pantograph and the catenary can result in poorer power transmission and load damage. To allow faster travel, advanced vibration suppression techniques for P-C system are needed. Here we consider enhancing the performance by adopting inerter-based damping technologies. A typical time-varying lumped model of a P-C system is considered in this work. Optimal suspension configurations show that up to a 25% reduction in contact force variance can be achieved comparing with a traditional passive system.

1 Introduction

The pantograph-catenary system is the most feasible way to power high-speed trains at present. An uplift mechanism keeps the pantograph current collectors or the panhead in contact with the contact wire. A good contact performance between the pantograph and catenary is the most significant factor for maintaining a stable power supply. The dynamics of the pantograph-catenary system play a crucial role in the current collection quality. As the train's speed increases, the vibrations of the pantograph-catenary system become stronger, which deteriorates the power transmission and accelerates the wear of the contact components [1]. To balance the power transmission behaviour and mechanical wear, a novel pantograph design is needed.

The inerter [2, 3] opens up new possibilities for passive control of mechanical systems. The inerter is a mechanical device with two terminals having the property that the generated force is proportional to the relative acceleration between its terminals. Applications of the inerter to control of motorcycle steering instabilities [4], vehicle suspension [5, 6], buildings [7, 8], railway vehicle suspension [9, 10] and landing gears [11,12] have been identified. The results have shown that the performance of the systems can be significantly improved with the use of inerters. The inerter has been successfully deployed in Formula 1 racing since 2005, under the name of J-damper.

Different mathematical models and simulation methods have been introduced to quantitatively study pantograph-catenary interaction. In these works, the finite element method (FEM) is usually applied to model the catenary system. Andrea et al. [13] built a FEM model of the catenary which applied a procedure based on the penalty method to simulate the contact between wire and collector. Cho et al. [14] proposed both the formulation of a nonlinear dropper and the proper implementation of a time-integration method for the FEM of pantograph–overhead contact line dynamics. A modelling method based on the analytical expressions of nonlinear cable and truss elements was proposed by Yang et al. in [15]. Athough the FEM is accurate, the model is complicated and time-consuming. Hence some simpler catenary models are also proposed. For example, Wu et al. [16] modeled the catenary system as a time-varying stiffness with a single-degree-of-freedom model of the pantograph.

This paper is structured as follows. In Section 2, the simplified catenary model with lumped time-varying parameters and a two-degree-of-freedom pantograph model are presented. In Section 3, candidate absorber layouts and the optimization procedure are proposed and discussed. The optimisation results and the corresponding time domain responses are shown in section 4. In Section 5, the conclusion is drawn.

2 Modelling of the pantograph-catenary system

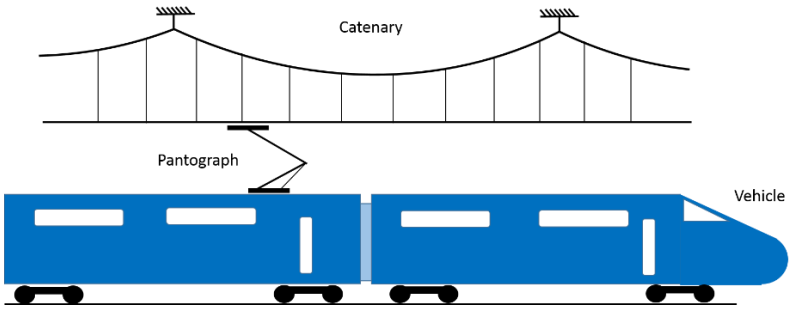


Figure 1: Schematic of pantograph-catenary system.

The pantograph-catenary system shown in Figure 1 is a complicated system which consists of two longitudinal wires connected by some droppers together with a pantograph. A mathematical model of the complete overhead suspension system and the catenary is difficult to define because it is a distributed system. Some FEM models of catenary system have been established, but these models are usually complicated and time-consuming to simulate. Simplified models with lumped time-varying parameters have been shown to be sufficiently accurate for control and design purposes [17]. Here we consider the model from reference [18] in Figure 2, which models the dynamics of the catenary and a two-degree-of-freedom pantograph. The system parameters are shown in Table 1 where m_c, k_c, c_c are the equivalent mechanical parameters of the catenary system, presenting periodic behaviour along each span. Fourier series expressions of equivalent parameters of catenary system including the first, second and third harmonics are applied using [18]

$$\begin{aligned} m_c(t) &= m_{c0} + \sum_{i=1}^{3} m_{ci} \cos\left(\frac{2i\pi}{L} X(t)\right) \\ c_c(t) &= c_{c0} + \sum_{i=1}^{3} c_{ci} \cos\left(\frac{2i\pi}{L} X(t)\right) \\ k_c(t) &= k_{c0} + \sum_{i=1}^{3} k_{ci} \cos\left(\frac{2i\pi}{L} X(t)\right) \end{aligned} \quad , \tag{1}$$

where $X(t)$ is the horizontal distance of the pantograph from a reference tower. The values of m_{ci}, c_{ci} and k_{ci} are given in Table 1. In Figure 2, k_1 and c_1 represent the contact stiffness and damping between panhead and catenary. The remaining parameters care for the two-degree of freedom system modelling the pantograph. During normal operation, the pantograph is always in contact with the catenary, which implies that $x_1 \equiv x_c$ and the contact force $F_c = k_1(x_2 - x_1) + c_1(\dot{x}_2 - \dot{x}_1)$ is nonnegative, where x_c, x_1, x_2 are the displacements of catenary, contact surface and upper frame. It has been checked that this condition always hold in our investigation presented here.

The pantograph is modelled as a two-degree-of-freedom system shown in Figure 2. A linear system can approximate the pantograph dynamics in the vicinity of the working configuration. In the default model, only a damper, represented by c_3, is installed in primary suspension system. For default model, the suspension force F_d in Figure 2 can be presented as

$$F_d = -c_3 \dot{x}_3, \tag{2}$$

where $\dot{x}_3$ is the velocity of lower frame.

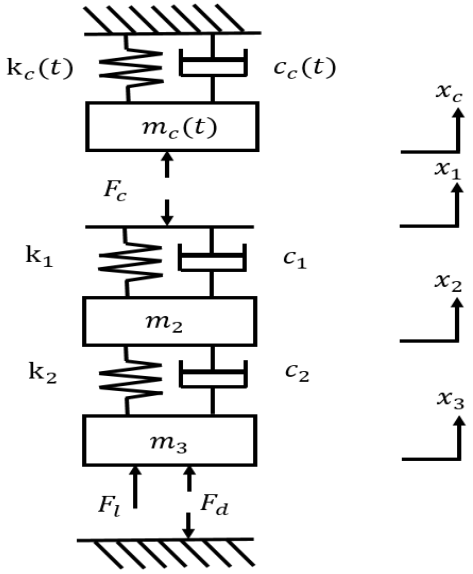


Figure 2: The lumped model of pantograph-catenary system with time-varying parameters.

Parameters	Notation	Value
Lower frame parameters	m_3	9.5 kg
	c_3	5000 Ns/m
Upper frame parameters	m_2	7.6 kg
	c_2	20 Ns/m
	k_2	3421 N/m
Head parameters	c_1	5000 Ns/m
	k_1	10^5 N
Catenary mass parameters	m_{c0}	195 kg
	m_{c1}	100 kg
	m_{c2}	20 kg
	m_{c3}	5 kg
Catenary damping parameters	c_{c0}	240 Ns/m
	c_{c1}	240 Ns/m
	c_{c2}	50 Ns/m
	c_{c3}	12 Ns/m
Catenary stiffness parameters	k_{c0}	7000 N/m
	k_{c1}	3360 N/m
	k_{c2}	650 N/m
	k_{c3}	160 N/m
Span length	L	65.52 m
Uplift force	F_l	100 N

Table 1. Model parameters.

If aerodynamic forces are ignored, the motion of the whole system is governed by

$$\begin{aligned} m_c(t)\ddot{x}_1 &= -k_c(t)x_1 - c_c(t)\dot{x}_1 + k_1(x_2 - x_1) + c_1(\dot{x}_2 - \dot{x}_1) \\ m_2\ddot{x}_2 &= -k_1(x_2 - x_1) - c_1(\dot{x}_2 - \dot{x}_1) + k_2(x_3 - x_2) + c_2(\dot{x}_3 - \dot{x}_2), \\ m_3\ddot{x}_3 &= -k_2(x_3 - x_2) - c_2(\dot{x}_3 - \dot{x}_2) + F_d + F_l \end{aligned} \tag{3}$$

where F_l is the uplift force which is set to be 100 N in this work, same as the value used in [19].

3 Candidate layouts and optimization procedure

Our aim is to redesign primary suspension system between lower frame and base to achieve a better performance of pantograph-catenary system in the range of operation speed. Three candidate layouts (S2, S3, S4 in Figure 3) including 3 elements (one spring, one damper and one inerter) are considered in this paper. The S1 in Figure 3 is the default structure which used in traditional pantograph.

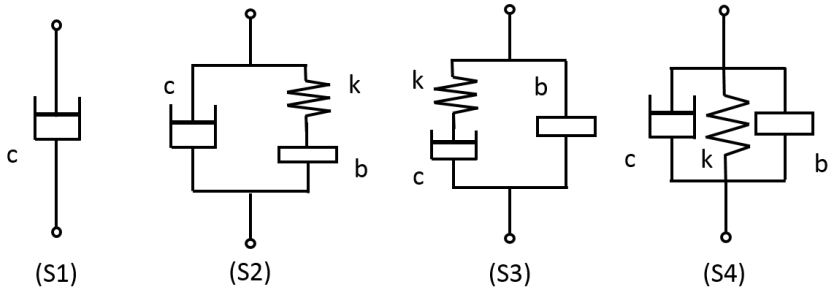


Figure 3: Candidate suspension device layouts.

The transfer functions of proposed candidate layouts are represented by $Y(s) = \frac{F(s)}{V(s)}$, where $F(s)$ and $V(s)$ are the force at the terminals and the relative velocity across the terminals in the Laplace domain. The suspension force F_d can be expressed by

$$F_d = -\mathrm{sY(s)}\tilde{x}_3, \tag{4}$$

where $\tilde{x}_3$ is the displacement of lower frame in the Laplace domain.

A key aim in designing pantograph systems is to maintain an optimal contact force between the pantograph and catenary cables. This force balances the need for satisfactory power transmission and minimum wear and damage of the contacting elements, which is apparent for high-speed trains. The root-mean-square of difference between contact force $F_c(v,t)$ and uplift F_l are calculated to evaluate this performance of the pantograph-catenary system. The performance index function $\delta(v)$ can be definite as

$$\delta(v) = rms(F_c(v,t) - F_l), v \in [20\mathrm{m/s}, 100\mathrm{m/s}]. \tag{5}$$

The cost function in this work is the value of $\delta(v)$ at nominal operation speed v_{op}

$$J = \delta|_{v=v_{op}}. \tag{6}$$

In order to make sure the performances of proposed layouts are not worse than the default one at all speed values considered, a constraint on performance index function is applied,

$$D_\delta(v) = \delta(v)|_{default} - \delta(v)|_{Si} \geq 0, i \in \{1,2,3,4\}, v \in [20\mathrm{m/s}, 100\mathrm{m/s}], \tag{7}$$

where Si represent the candidate layouts.

Apart from this, the maximum pantograph vertical displacement is related to the operation safety of pantograph-catenary system. According to BS EN50367:2012 (Technical criteria for the interaction between pantograph and overhead line), maximum pantograph vertical amplitude should not be bigger than 80 mm, which means vertical displacement of panhead is also a crucial index to be considered. The maximum panhead displacement $d_{max}(v)$ can be calculated as

$$d_{max}(v) = max(d(v,t)), v \in [20\mathrm{m/s}, 100\mathrm{m/s}], \tag{8}$$

where $d(v,t)$ is the time history of the panhead displacement with the operation speed v.

An additional constraint on the maximum panhead displacement is also applied, in the optimisation, which can be definite as

$$D_{\max}(v) = d_{max}(v)|_{default} - d_{max}(v)|_{Si} \geq 0, i \in \{1,2,3,4\}, v \in [20\text{m/s}, 100\text{m/s}]. \quad (9)$$

In the simulation, the nominal operation speed is selected as $v_{op} = 75$ m/s in this work. The 'patternsearch' and 'fminsearch' in MATLAB are used for optimization.

4 Optimization results and discussion

The optimal results with corresponding optimum parameter values for the four layouts are shown in Table 2.

No.	Structure parameters			Performance	
	b (kg)	c (Ns/m)	k (N/m)	J (N)	d_{max} (mm)
default	/	5000	/	55(-)	44
S1	/	5000	/	55(0%)	44
S2	3.16	2061	154	42(23%)	37
S3	0.03	2211	32715	41(25%)	39
S4	10.00	2126	301	42(23%)	37

Table 2: The optimization results and the optimum parameter values.

From Table 2, the optimal value of S1 is the same as the default one where $c_3 = 5000$ Ns/m. In order to explain this phenomenon, a sensitivity analysis of S1 is carried out. Take $c_3 = 2000$ Ns/m as an example. The constraints values of $D_\delta(v)$ and $D_{\max}(v)$ are calculated as

$$D_\delta(v) = \delta(v)|_{default,c_3=5000} - \delta(v)|_{S1,c_3=2000}, \quad (10)$$

$$D_{\max}(v) = d_{max}(v)|_{default,c_3=5000} - d_{max}(v)|_{S1,c_3=2000}. \quad (11)$$

From Figure 4(a), D_δ is bigger than 0 in the whole speed sector, which satisfies the constraint on performance index function. From Figure 4(b), $D_{\max}$ is smaller than 0 between 0 m/s to about 35 m/s and between about 45 m/s to 60 m/s, which means the constraint on maximum panhead displacement is not satisfied when $c_3 = 2000$ Ns/m.

For the parameter c_3 varying from 0 to 10000 Ns/m, the contours of D_δ and $D_{\max}$ can be gained on the c_3-velocity plane as shown in Figure 5. Figure 5(a) is the contours of D_δ on the c_3-velocity plane. The colourful region means $D_\delta > 0$, which satisfies the constraint of performance index function. If we cut through the solid red in Figure 5(a), the cross section is shown as Figure 4(a). Figure 5(b) is the contours of $D_{\max}$ on the c_3- velocity plane. The colourful region means $D_{\max}$ is bigger than zero which satisfies the constraint of the maximum panhead displacement. Similarly, the Figure 4(b) is also the cross section if we cut through the solid red in Figure 5(b).

From Figure 5(a), when we decrease the value of c_3, the constraint on performance index function can be satisfied in the whole range of operation speed. From Figure 5(b), larger value of c_3 can satisfy the constraint on the maximum panhead displacement at low speed (between about 0 to 35 m/s) while smaller value of c_3 can satisfies the constraint on the maximum panhead displacement at high speed (between about 70 to 100 m/s). Above all, if structure S1 is applied in the primary suspension, we can't find a better value of c_3 to achieve better performance while satisfying the two constraints at the same time.

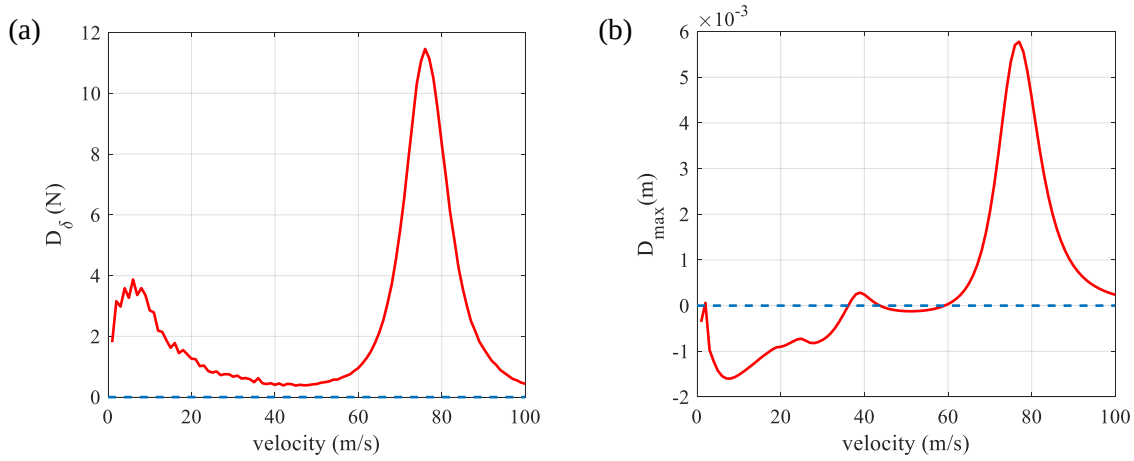


Figure 4: (a) Difference of performance index function $\delta(v)$ in velocity domain between $c_3 = 5000$ Ns/m and 2000 Ns/m; (b) Difference of maximum panhead displacement in velocity domain between $c_3 = 5000$ Ns/m and 2000 Ns/m.

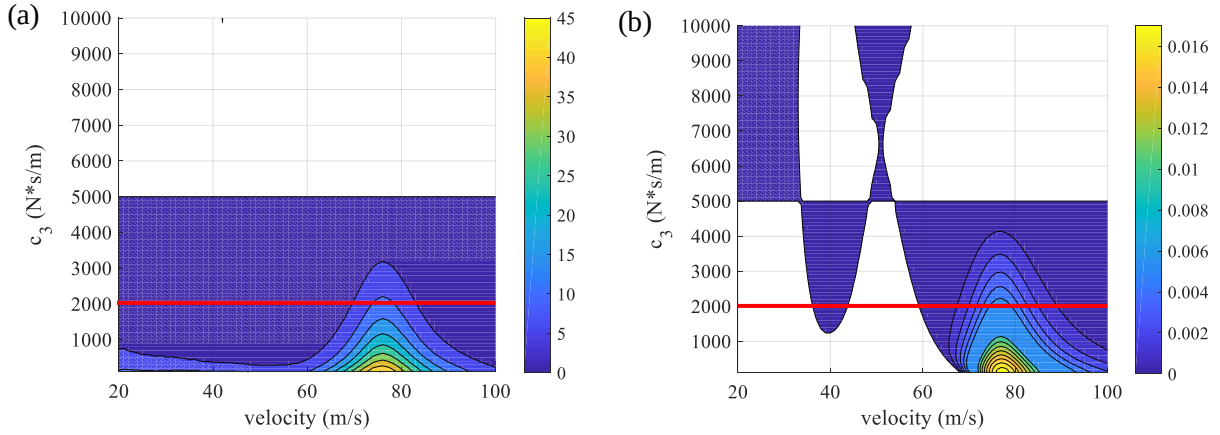


Figure 5: (a) The contours of D_δ, (b) The contours of D_{max}.

It can be also seen from Table 2, the proposed three inerter-based structures (S2, S3, S4) can provide significant performance improvement, with up to 25%. The corresponding results are shown in Figure 6. Figure 6(a) suggests that all the proposed configurations (S2, S3, S4) satisfy the two constraints. According to Table 2, the S3 gain the largest improvement (25%) in the proposed cost function *J* while its maximum panhead displacement is higher than that of S2 and S4. The performance of S2 and S4, both with 23% improvement, are very similar to each other.

It can be seen that the maximum panhead displacement of S2 and S4 (37 mm) is smaller than that of S3 (39 mm), which shows better performance on operation safety.

The responses in time domain are also analyzed to validate the optimization results. The responses in time-domain of the whole system are harmonic because the whole system is harmonic parametric self-excited system. The responses at operation speed of 75 m/s (between 28 s and 30 s) are shown on Figure 7. From Figure 7(a), the contact forces oscillate around 100 N. The variance of contact forces of inerter-based configurations S2, S3, S4 are significantly smaller than S1, which is consistent with the result shown on Table 2. It can be seen from Figure 7(b), the maximum panhead displacements of inert-based configurations are also smaller than default one, which verify the maximum panhead displacement constraint. It also can be noted that the maximum panhead displacement of S3 is larger than S2 and S4 in time domain as is obtained in Figure 6.

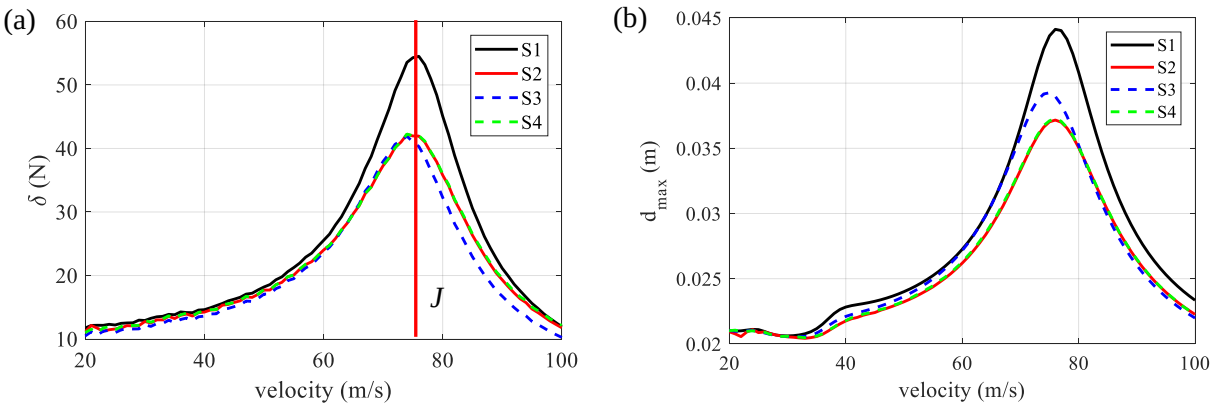


Figure 6: The $\delta(v)$ and $d_{max}(v)$ of different candidate layouts with velocity from 20 m/s to 100 m/s.

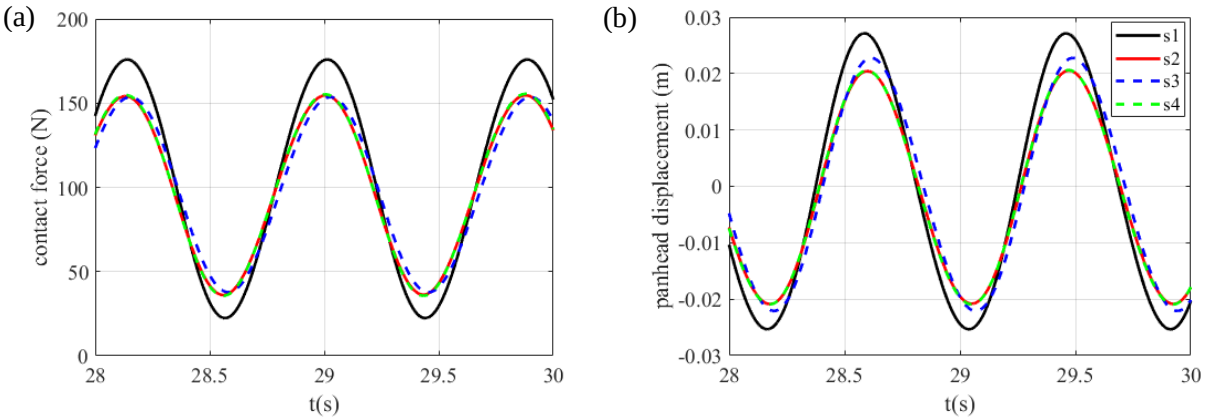


Figure 7: Response in time domain: (a) contact forces of S1, S2, S3, S4 in time domain; (b) Panhead displacement of S1, S2, S3, S4 in time domain.

5 Conclusion

The inerter-based vibration suppression technology is applied in pantograph-catenary system in this paper. Three different candidate layouts consisting of one inerter, one damper and one spring are discussed. It has been shown that the inerter-based devices can significantly improve the performance in contact force and reduce the maximum panhead displacement at the same time, which can't be achieved by the traditional primary absorber. Inerter-based device shows huge application prospects to increase the reliability and reduce the maintenance cost of pantograph-catenary system by effectively suppressing the vibration.

6 Acknowledgements

The authors would like to acknowledge the support of the EPSRC, the University of Bristol and the China Scholarship Council. Ming Zhu is supported by the joint scholarship of University of Bristol and the China Scholarship Council; Sara Ying Zhang, Jason Zheng Jiang are supported by the EPSRC grant EP/P013546/1 and Royal Society IE151194; Simon Neild is supported by EPSRC fellowship EP/K005375/1.

Reference

[1] Poetsch, G., EVANS, J., Meisinger, R., Kortüm, W., Baldauf, W., Veitl, A., & Wallaschek, J. (1997). *Pantograph/catenary dynamics and control*. Vehicle system dynamics, 28(2-3), 159-195.

[2] Smith, M. C. (2002). *Synthesis of mechanical networks: The inerter*. IEEE Transactions on automatic control, 47(10), 1648-1662.

[3] Firestone, F. A. (1933). *A new analogy between mechanical and electrical systems*. The Journal of the Acoustical Society of America, 4(3), 249-267.

[4] Evangelou, S., Limebeer, D. J., Sharp, R. S., & Smith, M. C. (2006). *Control of motorcycle steering instabilities*. IEEE control systems, 26(5), 78-88.

[5] Papageorgiou, C., & Smith, M. C. (2006). *Positive real synthesis using matrix inequalities for mechanical networks: application to vehicle suspension*. IEEE Transactions on Control Systems Technology, 14(3), 423-435.

[6] Smith, M. C., & Wang, F. C. (2004). *Performance benefits in passive vehicle suspensions employing inerters.* Vehicle system dynamics, 42(4), 235-257.

[7] Zhang, S. Y., Jiang, J. Z., & Neild, S. (2017). *Optimal configurations for a linear vibration suppression device in a multi-storey building*. Structural Control and Health Monitoring, 24(3).

[8] Lazar, I. F., Neild, S. A., & Wagg, D. J. (2014). *Using an inerter-based device for structural vibration suppression*. Earthquake Engineering & Structural Dynamics, 43(8), 1129-1147.

[9] Wang, F. C., & Liao, M. K. (2010). *The lateral stability of train suspension systems employing inerters*. Vehicle System Dynamics, 48(5), 619-643.

[10] Jiang, J. Z., Matamoros-Sanchez, A. Z., Goodall, R. M., & Smith, M. C. (2012). *Passive suspensions incorporating inerters for railway vehicles*. Vehicle System Dynamics, 50(sup1), 263-276.

[11] Li, Y., Howcroft, C., Neild, S. A., & Jiang, J. Z. (2017). *Using continuation analysis to identify shimmy-suppression devices for an aircraft main landing gear*. Journal of Sound and Vibration, *408*, 234-251.

[12] Li, Y., Jiang, J. Z., Neild, S. A., & Wang, H. (2017). *Optimal Inerter-Based Shock–Strut Configurations for Landing-Gear Touchdown Performance*. Journal of Aircraft, 1-9.

[13] Collina, A., & Bruni, S. (2002). *Numerical simulation of pantograph-overhead equipment interaction*. Vehicle System Dynamics, 38(4), 261-291.

[14] Cho, Y. H. (2008). *Numerical simulation of the dynamic responses of railway overhead contact lines to a moving pantograph, considering a nonlinear dropper*. Journal of sound and vibration, 315(3), 433-454.

[15] Song, Y., Liu, Z., Wang, H., Lu, X., & Zhang, J. (2015). *Nonlinear modelling of high-speed catenary based on analytical expressions of cable and truss elements*. Vehicle System Dynamics, 53(10), 1455-1479.

[16] Wu, T. X., & Brennan, M. J. (1998). *Basic analytical study of pantograph-catenary system dynamics*. Vehicle System Dynamics, 30(6), 443-456.

[17] Allotta, B., Papi, R., Pugi, L., Toni, P., & Violi, A. G. (2001, July). *Experimental campaign on a servo-actuated pantograph*. In Advanced Intelligent Mechatronics, 2001. Proceedings. 2001 IEEE/ASME International Conference on (Vol. 1, pp. 237-242). IEEE.

[18] Pisano, A., & Usai, E. (2008). *Contact force regulation in wire-actuated pantographs via variable structure control and frequency-domain techniques*. International Journal of Control, 81(11), 1747-1762.

[19] Balestrino, A., Bruno, O., Landi, A., & Sani, L. (2000). *Innovative solutions for overhead catenary-pantograph system: wire actuated control and observed contact force*. Vehicle System Dynamics, 33(2), 69-89.

Mitigation of friction-induced vibrations in braking systems: prediction of the mitigation limit

B. Bergeot [1], **S. Bellizzi** [2], **S. Berger** [1]
[1] INSA CVL, Univ. Orléans, Univ. Tours, LaMé EA 7494,
F-41034, 3 Rue de la Chocolaterie, CS 23410, 41034 Blois Cedex, France
e-mail: **baptiste.bergeot@insa-cvl.fr**

[2] Aix Marseille Univ, CNRS, Centrale Marseille, LMA UMR 7031, Marseille, France

Abstract
In this paper, we investigate a problem of passive mitigation of friction-induced vibrations due to mode coupling instability in breaking systems. For this purpose, the well-known Hultèn's model is coupled to one Nonlinear Energy Sinks (NES). In previous work by the authors [1], an asymptotic analysis has been performed on the system allowing to explain the steady-state response regimes observed in the numerical simulations and predict some of them. However, because of the appearance of a three-dimensional critical manifold, the prediction of the mitigation limit (i.e. the friction coefficient value which separates harmful situations from harmless situations) has been not performed. This present work completes this previous study using a general dynamics reduction method allowing to obtain one dimensional critical manifolds. The mitigation limit is therefore predicted and compared, for validation purposes, to numerical integration of the system.

1 Introduction

The squealing noise is due to dry friction in braking systems. It does not affect the quality of breaking but it is the source of significant noise nuisance. This phenomenon also called mode-coupling instability corresponds to a dynamic instability. It can be explained by the appearance of self-sustained oscillations - Limit Cycle Oscillation (LCO) - induced by dry friction and due to the coalescence of modes in self-excited systems.

Research is always active to understand the generation of a disc brake squeal and to predict and reduce it. Recent papers are for example based on non conventional analysis techniques such as probabilistic approach incorparing incertainty in the parameters of the model to predict instabilities [2, 3] or statistical approach from data obtained from different pad designs [4].

A more traditionally framework is considered here to investigate the problem of passive mitigation of friction-induced vibrations due to mode coupling instability in breaking systems. The well-known two degrees of freedom Hultèn's model is used as simplified analytic model to gain insight the mechanisms controlling brake squeal generation. This model is sufficient to investigate the mode-coupling instability ([5, 6, 7, 2]). This model is one of the models discussed in the review paper [8].

In the previous work by the authors [1], the mitigation squeaking noise was considered using the concept of Targeted Energy Transfer (TET)[9]. TET is a passive control method which consists in coupling an essentially nonlinear attachment also named Nonlinear Energy Sink (NES) to the primary system. The NES involves a mass, an essential cubic restoring force and a linear damping force. The addition of a NES drastically modifies the dynamic of the whole system giving access to complicate (nonlinear) dynamics

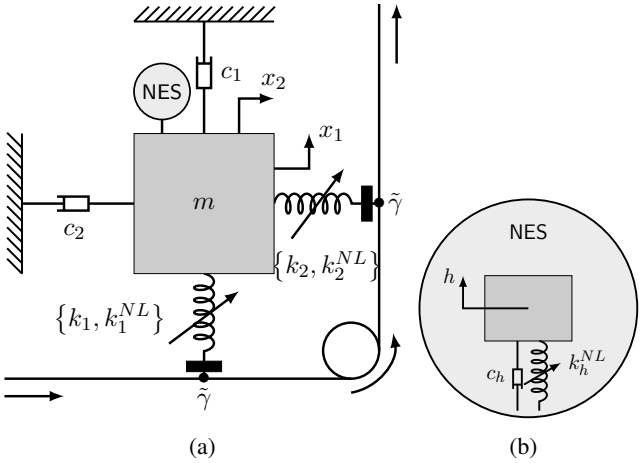


Figure 1: (a) Mechanical system with NES. (b) Zoom on the NES.

fostering the energy transfer from the primary system to the NES[10]. This phenomenon is called energy pumping.

Using the well-known Hultèn's model coupled to two ungrounded NESs, Bergeot et al. [1] showed that the use of NES appears to be an interesting way to control mode-coupling instability in braking systems. To analyze the steady-state response regimes, the system is partitioned in slow-fast dynamics using complexification-averaging approach due to the presence a small dimensionless parameter related to the mass of the NES. The slow-fast nature of the system allowed us to use multiple scale approach to analyze it. In particular, the shape of the Critical Manifold of the slow-flow and the associated stability properties provide an analytical tool to explain the existence of three regimes: periodic response regimes, strongly modulated responses regimes and no mitigation regimes that appear when the trivial solution is unstable. A complete suppression regimes is also observed.

The procedure gives access to the boundary values of the friction coefficient corresponding to the transition from complete suppression regime to periodic response regimes and from periodic response regimes to strongly modulated responses are predicted analytically. However the prediction of the boundary value between strongly modulated responses and no mitigation responses is not performed, this highlights that global structure of possible response regimes can not be deduced from local stability analysis of a slow flow subsystem with dimension larger than one. The prediction of this boundary value could be important in the context of engineering applications and this is the object of this present work.

The aim of the present work is i) to show that mode-coupling instability in braking systems can be mitigated with only one NES and ii) to provide an analytic prediction of the boundary value between strongly modulated responses and no mitigation responses.

The paper is organized as follows. In Sect. 2, the system under study including the Hultèn's model (the primary system) coupled to one ungrounded NES is presented and a reduction of the dynamics on the unstable mode of the primary system is performed. In Sect. 3 the reduced system is first analyzed following the Geometric Singular Perturbation Theory writting first the reduced system as a slow-flow system using a complexification-averaging method. Next the prediction of the mitigation limit is introduced and discussed when the friction parameter is used as a bifurcation parameter. Finally, analytical prediction proposed in Sect. 3 are compared to direct numerical simulations of the whole system.

2 System under study

2.1 Mechanical model

The system considered here is shown Fig. 1. It is composed by the simple 2 degrees-of-freedom (DOFs) self-excited system proposed by Hultèn [11] (the primary system) coupled to one NES with mass m_h, damping coefficient c_h and cubic stiffness coefficient k_h^{NL} (and without linear stiffness) attached on the system in an ungrounded configuration.

We focus on the analysis on the capacity of the NES attachments to suppress or mitigate vibrations when the primary system is unstable.

The system is decribed by the follwing equations:

$$\ddot{x}_1 + \epsilon\eta_1\dot{x}_1 + x_1 - \epsilon\gamma x_2 + \epsilon\varphi_1 x_1^3 + \epsilon\mu(\dot{x}_1 - \dot{h}_1) + \epsilon\alpha\left(x_1 - h_1\right)^3 = 0 \tag{1a}$$

$$\ddot{x}_2 + \epsilon\eta_2\dot{x}_2 + (1 - 2\epsilon a)x_2 + \epsilon\gamma x_1 + \epsilon\varphi_2 x_2^3 = 0 \tag{1b}$$

$$\epsilon\ddot{h} + \epsilon\mu(\dot{h} - \dot{x}) + \epsilon\alpha\left(h - x_1\right)^3 = 0 \tag{1c}$$

where x_1 and x_2 (respectively h) are the displacements of the primary mass (respectively of the NES mass).

As shwon in [1], Eq. (1) results from a scaling of time ($t = \omega_1\tilde{t}$ with $\omega_1^2 = k_1/m$) and a scaling of the parameters with respect to the mass ratio $\epsilon = m_h/m$ assuming $0 < \epsilon << 1$ where coefficients η_1, η_2, φ_1, φ_2, γ, μ, α, a are adopted to be of order unity. The coefficients η_1 and η_2 characterize the damping terms (c_1, c_2) of the Hulten model, φ_1 and φ_2 are the associated cubic stiffness coefficients (k_1^{NL}, k_2^{NL}) whereas γ is the friction coefficient. The parameters μ and α characterize the damping coefficient (c_h)and the cubic stiffness coefficient (k_h^{NL}) of the NES. Finally, the coefficient a is defined as $\sqrt{k_2/k_1} = 1 - \epsilon a$.

2.2 Reduction of the dynamics

To simplify asymptotic analysis in next section, it is convenient to introduce new coordinates as

$$u_1 = x_1 + \epsilon\, h \qquad u_2 = x_2 \qquad v = x_1 - h, \tag{2a}$$

giving reciprocally,

$$x_1 = \frac{u_1 + \epsilon\, v}{1 + \epsilon} \qquad x_2 = u_2 \qquad h = \frac{u_1 - v}{1 + \epsilon}. \tag{3a}$$

Using Eqs. (3), Eq. (1) is transformed into the following form

$$\ddot{u}_1 + \epsilon\eta_1\dot{u}_1 + u_1 - \epsilon\gamma u_2 + \epsilon(\varphi_1 u_1^3 - u_1 + v) = 0 \tag{4a}$$

$$\ddot{u}_2 + \epsilon\eta_2\dot{u}_2 + (1 - 2\epsilon a)u_2 + \epsilon\gamma u_1 + \epsilon\varphi_2 u_2^3 = 0 \tag{4b}$$

$$\ddot{v} + (1 + \epsilon)\mu\dot{v} + \epsilon v + (1 + \epsilon)\alpha v^3 + \epsilon\eta_1\dot{u}_1 + (1 - \epsilon)u_1 - \epsilon\gamma u_2 + \epsilon\varphi_1 u_1^3 = 0, \tag{4c}$$

where a first-order Taylor series around $\epsilon = 0$ has been performed.

The reduction of the dynamics is performed on the first two equations of Eqs. (4) (the primary system) using the biorthogonal transformation (see for example [12]).

Let $\mathbf{u} = (u_1, u_2, \dot{u}_1, \dot{u}_2)^t$ (the " ^{t} " is the usual notation for transpose operator), Eqs. (4a) and (4b) can be written as a system of first order differential equations (state-space form)

$$\dot{\mathbf{u}} = \mathbf{A}\mathbf{u} + \epsilon\mathbf{f}\left(\mathbf{u}, v\right), \tag{5}$$

where the matrix $\mathbf{A}$ is defined by

$$\mathbf{A} = \begin{bmatrix} 0 & 0 & 1 & 0 \\ 0 & 0 & 0 & 1 \\ -1 & \gamma\epsilon & -\epsilon\eta_1 & 0 \\ -\gamma\epsilon & -1+2a\epsilon & 0 & -\epsilon\eta_2 \end{bmatrix} \tag{6}$$

and the vector function $\mathbf{f}$ is easily deduced from Eqs. (4a) and (4b). It is important to note that the matrix $\mathbf{A}$ also characterizes the linear part of the primary system written on its state-space form.

The following eigenvalue problems:

$$\mathbf{A}\mathbf{r} = \lambda\mathbf{r} \quad \text{and} \quad \mathbf{A}^t\mathbf{l} = \lambda\mathbf{l}, \tag{7}$$

where $\mathbf{A}^t$ denotes the transpose of $\mathbf{A}$, are solved giving:

- two pairs of complex conjugates eigenvalues: λ_1 and λ_1^*, and λ_2 and λ_2^* (the " * " is the usual notation for the complex conjugate),
- two pairs of complex conjugates eigenvectors of $\mathbf{A}$: $\mathbf{r}_1$ and $\mathbf{r}_1^*$, and $\mathbf{r}_2$ and $\mathbf{r}_2^*$, called *right eigenvectors* of $\mathbf{A}$,
- two pairs of complex conjugates eigenvectors of $\mathbf{A}^t$: $\mathbf{l}_1$ and $\mathbf{l}_1^*$, and $\mathbf{l}_2$ and $\mathbf{l}_2^*$, called *left eigenvectors* of $\mathbf{A}$.

The right and left eigenvectors satisfy the biorthogonality properties i.e $\mathbf{L}^t\mathbf{R}$ and $\mathbf{L}^t\mathbf{A}\mathbf{R}$ are diagonal matrices where $\mathbf{R} = [\mathbf{r}_1\ \mathbf{r}_1^*\ \mathbf{r}_2\ \mathbf{r}_2^*]$ and $\mathbf{L} = [\mathbf{l}_1\ \mathbf{l}_1^*\ \mathbf{l}_2\ \mathbf{l}_2^*]$. It is convenient to normalize the two sets of eigenvectors $\mathbf{r}_i$ and $\mathbf{l}_i$ in order to obtain

$$\mathbf{L}^t\mathbf{R} = \mathbf{I} \quad \text{giving} \quad \mathbf{L}^t\mathbf{A}\mathbf{R} = \mathbf{D} \tag{8}$$

where $\mathbf{I}$ is the identity matrix and $\mathbf{D} = \mathrm{diag}(\lambda_1, \lambda_1^*, \lambda_2, \lambda_2^*)$.

Performing now the change of variables

$$\mathbf{u} = \mathbf{R}\mathbf{q} \ \text{ or equivalently } \ \mathbf{q} = \mathbf{L}^t\mathbf{u}, \tag{9}$$

Eq. (5) becomes

$$\dot{\mathbf{q}} = \mathbf{D}\mathbf{q} + \epsilon\mathbf{L}^t\mathbf{f}\left(\mathbf{R}\mathbf{u}, v\right). \tag{10}$$

Eqs. (10) and (4c), which are equivalent to Eqs. (4), define the Full Non-Averaged System (FNAS).

From now we assume that only one pair of eigenvalues of the perturbed system, here denoted without lost of generality (λ_1, λ_1^*), may have positive real part whereas the second pair (λ_2, λ_2^*) always has negative real part. Hence, and because the coupling terms are of the order of magnitude of ϵ, after some exponentially decaying transients the components q_2, q_2^* become small, i.e. $q_2 \sim q_2^* \sim O(\epsilon)$. Therefore, all terms related to q_2, q_2^* can be omitted from further consideration and Eq. (10) becomes

$$\dot{q}_1 = \lambda_1 q_1 + \epsilon\mathbf{l_1}\mathbf{f}\left(\mathbf{r}_{11}q_1 + \mathbf{r}_{11}^*q_1^*, v\right) \tag{11}$$

where $\mathbf{r}_{11}$ denotes the first component of the vector $\mathbf{r}_1$.

Eqs. (11) and (4c) define the reduced equations of motion. Note that the previous reduction is valid during transient when the amplitudes are relatively small and therefore must be questioned when large amplitudes of oscillation are reached.

2.3 About the order of magnitude of the eigenvalues and eigenvectors

Looking at Eq. (6), the matrix $\mathbf{A}$ appears as a perturbed matrix $\mathbf{A} = \mathbf{A}_0 + \epsilon\mathbf{A}_1$ where the matrix $\mathbf{A}_1$ results from the damping and friction forces. The perturbed system (5) is a circulatory system [1] while the unperturbed system, defined by $\mathbf{A}_0$ is not. It can be shown that $\mathbf{A}$ is regularly perturbed with respect to its eigenvalues. Indeed, the determinant $\det(\mathbf{A})$ do not contain singular terms. Therefore, the matrix $\mathbf{D}$ can be written as follow $\mathbf{D} = \mathbf{D}_0 + \epsilon\mathbf{D}_1$, where $\mathbf{D}_0 = \mathrm{diag}(j, -j, j, -j)$ (from now, $j^2 = -1$) is a diagonal matrix with the eigenvalues of $\mathbf{A}_0$ on its diagonal and $\mathbf{D}_1 \sim O(1)$. On the contrary, the perturbed system is no regularly perturbed with respect to its eigenvectors, i.e. the eigenvectors of $\mathbf{A}$ do not tend toward the eigenvectors of $\mathbf{A_0}$ when $\epsilon \to 0$. Consequently, as the most restrictive assumption for further analysis, we assume that left and right eigenvectors are of order 1 (i.e. $\mathbf{R}, \mathbf{L} \sim O(1)$), even if they can contain terms of order ϵ.

Taking into account previous remarks, the eigenvalue λ_1 is written as follows

$$\lambda_1 = j + \epsilon\left(\rho_u + j\nu_u\right) = \epsilon\rho_u + j\left(1 + \epsilon\nu_u\right), \tag{12}$$

where $1 + \epsilon\nu_u$ is the frequency for which the observed steady-state responses are assumed to oscillate and the real part is of order ϵ (i.e. $\rho_u \sim O(1)$). Therefore, Eq. (11) becomes

$$\dot{q}_1 = jq_1 + \epsilon\left(\rho_u + j\nu_u\right)q_1 + \epsilon\mathbf{l_1}\mathbf{f}\left(\mathbf{r}_{11}q_1 + \mathbf{r}_{11}^*q_1^*, v\right). \tag{13}$$

Finally grouping Eqs. (13) and (4c), the reduced equations of motion take the following form

$$\begin{aligned}\dot{q}_1 - jq_1 - \epsilon\left(\rho_u + j\nu_u\right)q_1 - \epsilon\mathbf{l}_{31}\left(\varphi_1(\mathbf{r}_{11}q_1 + \mathbf{r}_{11}^*q_1^*)^3 - \left(\mathbf{r}_{11}q_1 + \mathbf{r}_{11}^*q_1^*\right)\right) + \\ \epsilon\mathbf{l}_{41}\varphi_2(\mathbf{r}_{21}q_1 + \mathbf{r}_{21}^*q_1^*)^3 + \epsilon\mathbf{l}_{31}v = 0 \qquad (14a)\\ \ddot{v} + (1+\epsilon)\mu\dot{v} + \epsilon v + (1+\epsilon)\alpha v^3 + \epsilon\eta_1(\mathbf{r}_{31}q_1 + \mathbf{r}_{31}^*q_1^*) + (1-\epsilon)(\mathbf{r}_{11}q_1 + \mathbf{r}_{11}^*q_1^*) - \\ \epsilon\gamma(\mathbf{r}_{21}q_1 + \mathbf{r}_{21}^*q_1^*) + \epsilon\varphi_1(\mathbf{r}_{11}q_1 + \mathbf{r}_{11}^*q_1^*)^3 = 0, \qquad (14b)\end{aligned}$$

where $\mathbf{r}_{ij}$ (respectively $\mathbf{l}_{ij}$) denotes the i-th component of the vector $\mathbf{r}_j$ (respectively $\mathbf{l}_j$). Note that Eqs. (14) characterize one unknown complex variable q_1 and one unknown real variable v. Eqs. (14) define the Reduced Non-Averaged System (RNAS).

3 Asymptotic analysis of the reduced system

3.1 The slow-flow

In this section, RNAS (14) is analyzed following the *Geometric Singular Perturbation Theory* (GSPT) ([13, 14]) writing first the system as a slow-flow system.

The following change of variables is first applied to complexify the variable v as

$$\psi = \dot{v} + jv \tag{15a}$$

and the complex variables q_1, and ψ are next replaced by

$$q_1 = \phi e^{jt} \tag{16a}$$

$$\psi = \xi e^{jt}, \tag{16b}$$

where ϕ and ξ are the complex slow modulated amplitude of the fast component e^{jt}.

[1] A circulatory mechanical system has a non-symmetric stiffness matrix due for example to friction or follower forces.

After some algebraic manipulations followed by an averaging over one period $T = 2\pi$ of the resulting equations, Eqs. (14) reduce to

$$\dot{\phi} = \epsilon \left(\left(\rho_u - j\nu_u + \mathbf{l}_{31}\mathbf{r}_{11}\right)\phi - 3\left(\mathbf{l}_{31}|\mathbf{r}_{11}|^2\mathbf{r}_{11}\varphi_1 + \mathbf{l}_{41}|\mathbf{r}_{21}|^2\mathbf{r}_{21}\varphi_2\right)|\phi|^2\phi + \frac{j\mathbf{l}_{31}}{2}\xi \right) \tag{17a}$$

$$\begin{aligned}\dot{\xi} = &-\mathbf{r}_{11}\phi - \frac{1}{2}(\mu + j\omega_u)\xi + \frac{3j\alpha}{8}|\xi|^2\xi \\ &+ \epsilon\left(\left(\mathbf{r}_{11} + \gamma\mathbf{r}_{21} - \eta_1\mathbf{r}_{31}\right)\phi - \frac{1}{2}(\mu - j)\xi - 3|\mathbf{r}_{11}|^2\mathbf{r}_{11}\varphi_1|\phi|^2\phi + \frac{3j\alpha}{8}|\xi|^2\xi \right).\end{aligned} \tag{17b}$$

where $|.|$ denotes the modulus of a complex number.

For the future analysis, it is convenient to rewrite Eqs. (17) considering real variables. To achieve this, polar coordinates are introduced as

$$\phi = se^{j\theta_\phi} \tag{18a}$$

$$\xi = re^{j\theta_\xi}, \tag{18b}$$

where s and θ_ϕ (respectivily r and θ_ξ) characterized the modulus and the argument of ϕ (respectivaly ξ). Substituting Eq. (18b) into Eq. (17) and separting in real and imaginary part, Eq. (17) reduce to

$$\dot{s} = \epsilon f(s, r, \delta) \tag{19a}$$

$$\dot{r} = g_1(s, r, \delta, \epsilon) \tag{19b}$$

$$\dot{\delta} = g_2(s, r, \delta, \epsilon), \tag{19c}$$

where $\delta = \theta_\phi - \theta_\xi$. The expressions of the functions f, g_1 and g_2 are given Appendix A.

Eqs. (19) appear to have the slow-fast form where s is the slow variable whereas r and δ are the fast variables. Eqs. (19) can be reformulated by switching from the *fast* time scale t to the *slow* time scale $\tau = \epsilon t$ giving

$$s' = f\left(s, r, \delta\right) \tag{20a}$$

$$\epsilon\, r' = g_1\left(s, r, \delta, \epsilon\right) \tag{20b}$$

$$\epsilon\, \delta' = g_2\left(s, r, \delta, \epsilon\right), \tag{20c}$$

where $' = \frac{d}{d\tau}$. Solutions of slow-fast system (19) or (20) can exhibit slow and fast epochs characterized by slow and fast motions. This will be considered in the following Section in the framework of the GSPT.

3.2 The Critical Manifold and its stability

Stating $\epsilon = 0$, Eqs. (19) and (20) reduce, respectively, to:

$$\dot{s} = 0 \tag{21a}$$

$$\dot{r} = g_1(s, r, \delta, 0) \tag{21b}$$

$$\dot{\delta} = g_2(s, r, \delta, 0), \tag{21c}$$

the *fast subsystem* which is a family of dynamical systems for the fast variables ξ and

$$s' = f\left(s, r, \delta\right) \tag{22a}$$

$$0 = g_1\left(s, r, \delta, 0\right) \tag{22b}$$

$$0 = g_2\left(s, r, \delta, 0\right), \tag{22c}$$

the *slow subsystem* which is a system of Differential Algebraic Equations (DAE). The goal of the GSPT is to characterize the dynamic of the initial system (19) or (20) using the fast and slow subsystems (21) or (22).

Considering the slow subsystem, the nonlinear equations (22b) and (22c) define the so-called *Critical Manifold* S as [14]

$$S := \left\{ (s, r, \delta) \in R^3 \;\middle|\; g_1(s, r, \delta, 0) = 0 \text{ and } g_2(s, r, \delta, 0) = 0 \right\}. \tag{23}$$

Looking at Eqs. (42) and (43), the nonlinear equations takes the form

$$g_1(s, r, \delta, 0) = -\frac{\mu}{2} r - (\mathbf{r}_{11}^R \cos(\delta) - \mathbf{r}_{11}^I \sin(\delta)) s = 0 \tag{24a}$$

$$g_2(s, r, \delta, 0) = \frac{3\alpha}{8} r^2 - \frac{\omega_u}{2} - (\mathbf{r}_{11}^R \sin(\delta) + \mathbf{r}_{11}^I \cos(\delta)) \frac{s}{r} = 0. \tag{24b}$$

Combining Eqs. (24a) and (24b) leads to the modulus equation

$$s^2 \left(\mathbf{r}_{11}^{R^2} + \mathbf{r}_{11}^{I^2} \right) = H(r), \tag{25}$$

where

$$H(r) = H_1^2(r) + H_2(r)^2 \qquad \text{with} \qquad H_1(r) = -\frac{\mu}{2} r \qquad \text{and} \qquad H_2(r) = \left(\frac{3\alpha}{8} r^2 - \frac{1}{2} \right) r, \tag{26}$$

and to the characterization of the argument δ as

$$\cos(\delta) = \frac{r \left(3r^2 \alpha \mathbf{r}_{11}^R + 4\mu \mathbf{r}_{11}^I - 4\mathbf{r}_{11}^R \right)}{8s \left(\mathbf{r}_{11}^{R^2} + \mathbf{r}_{11}^{I^2} \right)} \qquad \text{and} \qquad \sin(\delta) = \frac{r \left(3r^2 \alpha \mathbf{r}_{11}^R - 4\mu \mathbf{r}_{11}^R - 4\mathbf{r}_{11}^I \right)}{8s \left(\mathbf{r}_{11}^{R^2} + \mathbf{r}_{11}^{I^2} \right)}. \tag{27}$$

Hence the Critical Manifold S appears to be a curve in the (s, r)-plane.

Stability analysis of the SIM is now carry out considering the fast subsystem (21). It can be shown that the Jacobian matrix reads as

$$\begin{bmatrix} \dfrac{dH_1(r)}{dr} & -H_2(r) \\ \dfrac{1}{r} \dfrac{dH_2(r)}{dr} & \dfrac{H_1(r)}{r} \end{bmatrix}, \tag{28}$$

and using the Routh-Hurwitz criterium we can deduce that a fixed point of Eq. (21) is stable if $H'(r) > 0$ and unstable if $H'(r) < 0$. Hence the subset of S satisfying $H'(r) > 0$ defines the attractive zone for the fast dynamics whereas the subset of S satisfying $H'(r) > 0$ define the repulsive zone.

Exploiting the polynomial properties of H, it can be shown that the local extrema of H (i.e $H'(r) = 0$) occur at

$$r^M = \frac{2}{3\sqrt{\alpha}} \sqrt{2 - \sqrt{1 - 3\mu^2}} \qquad \text{and} \qquad r^m = \frac{2}{3\sqrt{\alpha}} \sqrt{2 + \sqrt{1 - 3\mu^2}}, \tag{29}$$

if the following relation holds

$$\mu < \frac{1}{\sqrt{3}}, \tag{30}$$

and in this case $r^M < r^m$.

When condition (30) is satisfied, the two points (s^m, r^m) and (s^M, r^M) where the two scalars s^M and s^m are defined by $s^m = \sqrt{\frac{H(r^m)}{\mathbf{r}_{11}^{R^2} + \mathbf{r}_{11}^{I^2}}}$ and $s^M = \sqrt{\frac{H(r^M)}{\mathbf{r}_{11}^{R^2} + \mathbf{r}_{11}^{I^2}}}$ characterize the bounds where S ceases to be attractive connecting stable and unstable (repulsive) parts of S. These two points are called *fold points*. A typical CM is depicted Fig. 2 where the green points correspond to the fold points. The two scalars r^d and r^u (see the red points on Fig. 2), which will be used later, are defined by $H_n(r_n^m) = H_n(r_n^d)$ and $H_n(r_n^M) = H_n(r_n^u)$ giving

$$r_n^d = \frac{2\sqrt{2}}{3\sqrt{\alpha}} \sqrt{1 - \sqrt{1 - 3\mu^2}} \qquad \text{and} \qquad r_n^u = \frac{2\sqrt{2}}{3\sqrt{\alpha}} \sqrt{1 + \sqrt{1 - 3\mu^2}}. \tag{31a}$$

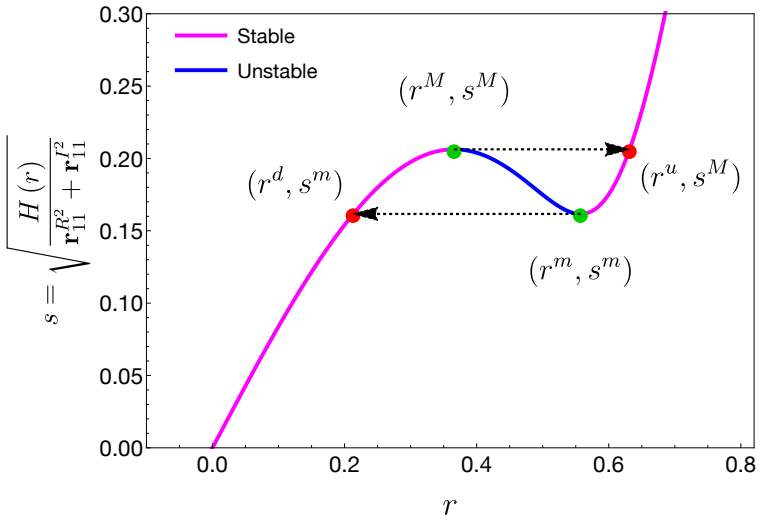


Figure 2: Typical *Critical Manifold* (CM). Set of parameters (40) is used with $\mu = 0.35$.

3.3 Fixed points and folded singularities of the slow flow

The dynamic of the slow subsystem (22) is now characterized in S.

Substituting Eq. (25) into Eq. (22a) results in

$$\left(\sqrt{\frac{H(r)}{\mathbf{r}_{11}^{R2} + \mathbf{r}_{11}^{I2}}}\right)' = f\left(\sqrt{\frac{H(r)}{\mathbf{r}_{11}^{R2} + \mathbf{r}_{11}^{I2}}}, r, \delta\right) \tag{32}$$

Next using Eq. (22b), Eq. (32) reduces to

$$\frac{dH(r)}{dr} r' = f_r(r), \tag{33}$$

where the expression of f_r is given Appendix B.

A (regular) fixed points of Eq. (33) is defined as the roots of the following nonlinear equations in presence of constraint

$$f_r(r) = 0 \quad \text{with} \quad \frac{dH(r)}{dr} \neq 0. \tag{34}$$

Assuming $\epsilon \ll 1$, a fixed point of Eq. (33) is an ϵ-approximation of a fixed point of Eq. (19) which characterizes a periodic solution of Eq. (14). As usual, stability of the fixed points are found looking for the sign of $\frac{d}{dr}\left(\frac{f_r(r)}{H'(r)}\right)$.

A singular fixed points of Eq. (33) is defined as the roots of the following nonlinear equations

$$f_r(r) = 0 \quad \text{and} \quad \frac{dH(r)}{dr} = 0. \tag{35}$$

Assuming condition (30), singular fixed points can exists among the fold points defined Eq. (29).

3.4 Prediction of the mitigation limit

Four main types of response regimes may be observed when a NES is attached on an unstable system: complete suppression of the instability, mitigation through Periodic Response (PR), mitigation through Strongly

Modulated Response (SMR) or no mitigation. These four types of responses have been observed and analyzed in the case of a Van de Pol oscillator coupled to one NES [15]. They have been also observed by Bergeot et al. [1] studying mitigation of a mode-coupling instability in breaking systems using two NESs. In the present study we classify these regimes into two categories depending on the fact that the NES acts or not and therefore separating harmless situations from harmful situations:

1. **Harmless situation:** the NES acts resulting to the following regimes
   (a) *Complete suppression.* The trivial fixed point of the slow-flow is reached. In this case, due to the additional damping, the NES attachment stabilizes the system, i.e. the trivial fixed point, common to both the non-averaged system and the slow-flow, becomes stable.
   (b) *Mitigation through Periodic Response.* A nontrivial stable fixed point of the slow-flow is reached. In this case, the steady-state of the non-averaged system response regime is a periodic regime, i.e. LCOs with an amplitude smaller than amplitude of the LCOs undergone by the primary system.
   (c) *Mitigation through Strongly Modulated Response.* In this case, the steady-state response regime is a quasiperiodic regime which exhibits a "fast" component and a "slow" component corresponding to the envelope of the signal. The term "Strongly modulated response" has been introduced in [16] for the study of a harmonically forced linear system coupled to a NES. SMR for the non-averaged system corresponds to relaxation oscillation of the slow-flow. To ensure the existence of SMRs, condition (30) must be respected.
2. **Harmful situation:** the NES does not act resulting to
   (a) *No mitigation.* The NES is not able to mitigate the instability and the non-averaged system saturates on a LCO which has an amplitude close to that of the case without NES. Regarding the slow-flow, it reaches a stable fixed point with large amplitude.

The nature of the steady-state regime depends on two things about the slow-flow. Firstly, it depends on the initial conditions to know where the slow dynamics leads the trajectory on S. Secondly, it depends on the fixed points (position and stability) which orientates the dynamics on S at the slow time scale. Here, for convenience and in accordance with real word situations, we consider a set of initial conditions $\{s(0), r(0)\}^t$ as a small perturbation of the trivial solution $\mathbf{0}$.

Considering the two situations described above and the previous comments, the **mitigation limit** with respect to the friction parameter γ (the chosen bifurcation parameter in this work) is introduced in the following definition. The definition can be adapted to other parameters.

Definition 3.1 *Considering a set of initial conditions (for the slow-flow) $\{s(0), r(0)\}^t$ as a small perturbation of the trivial solution $\mathbf{0}$, the **mitigation limit** of the friction parameter γ is defined as the value of γ , denoted γ_{ml}, which separates harmful situations from harmless situations.*

The definition 3.1 is based only on the nature of the steady-state regimes when 1:1 resonance occurs. This may be questioned regarding the amplitudes of these regimes but it is admitted in this study.

The method to predict the steady-state regimes, and consequently the mitigation limit, is now presented. As a result of the reduction method presented in Sect. 2.2, the slow-flow (17) is equivalent to that of a 1 DOF primary system coupled to one NES. This allows to predict easily the nature of the steady-state regimes. In keeping with [15], conditions to ensure that the system undergoes a harmless situation are stated below assuming that the NES respects condition (30).

Result 3.1 *The conditions to obtain **harmless situations** are split in two cases:*

Case a. *We assume that the slow-flow has a stable fixed point $\{s_s^*, r_s^*\}$ (trivial or nontrivial) on the first attractive part of the critical manifold S. In this case, the system is in a* ***harmless situation*** *if*

$$r_s^* < r^M. \tag{36}$$

In this case harmless situation corresponds to Complete suppression for the trivial fixed point or Mitigation through Periodic Response for the nontrivial fixed points.
If (36) *is not respected one must pass to Case b.*

Case b. *We assume that the system has at least one nontrivial unstable fixed points on a stable part of the critical manifold S; denoted $\{s_u^*, r_u^*\}$. In this case, the system is in an* ***harmless situation*** *if*

$$r_u^* < r^u. \tag{37}$$

In this case harmless situation corresponds to Mitigation through Periodic Response or Mitigation through Strongly Modulated Response.

Conversely, the system is in an ***harmful situation*** *if the system is nether in Case a, nor in Case b.*

We give now a quantitative definition of the *mitigation limit* γ_{ml} of the system.

Result 3.2 *Let γ_{lim}, the value of the parameter γ after which the slow-flow has no more nontrivial unstable fixed points and γ^s the value of the parameter γ such that*

$$r_u^* = r^u, \tag{38}$$

where r^u is defined by Eq. (31)*.*

The theoretical prediction of the mitigation limit, denoted γ_{ml}^{th}, is defined as follows

$$\gamma_{ml}^{th} = \begin{cases} \gamma^s, & \text{if } \gamma^s < \gamma_{lim} \quad (39a) \\ \gamma_{lim}, & \text{if } \gamma^s > \gamma_{lim}. \quad (39b) \end{cases}$$

4 Numerical illustrations of the steady-state response regimes

The purpose of this section is to illustrate some steady-state response regimes by means of direct numerical integration of the FNAS (10), the RNAS (14) and the slow-flow (17). To achieve this, the following set of parameters is used

$$\eta_1 = 0.4,\ \eta_1 = 1,\ \varphi_1 = 8,\ \varphi_2 = 2,\ \epsilon = 0.01,\ \alpha = 4 \tag{40}$$

with $\mu = 0.35$ and for three de different values of γ: 1.5, 1.67 and 2 leading respectively to *Mitigation through Periodic Response*, Mitigation through Strongly Modulated Response and *No mitigation* of the LCO (see Fig 3). As expected the RNAS is a good approximation of the FNAS during transient and it is valid during steady-state regime only when the latter has a relatively small amplitude, as it is here for *Mitigation through Periodic Response*. On the other hand, the slow-flow appears to be alway a good approximation of the RNAS.

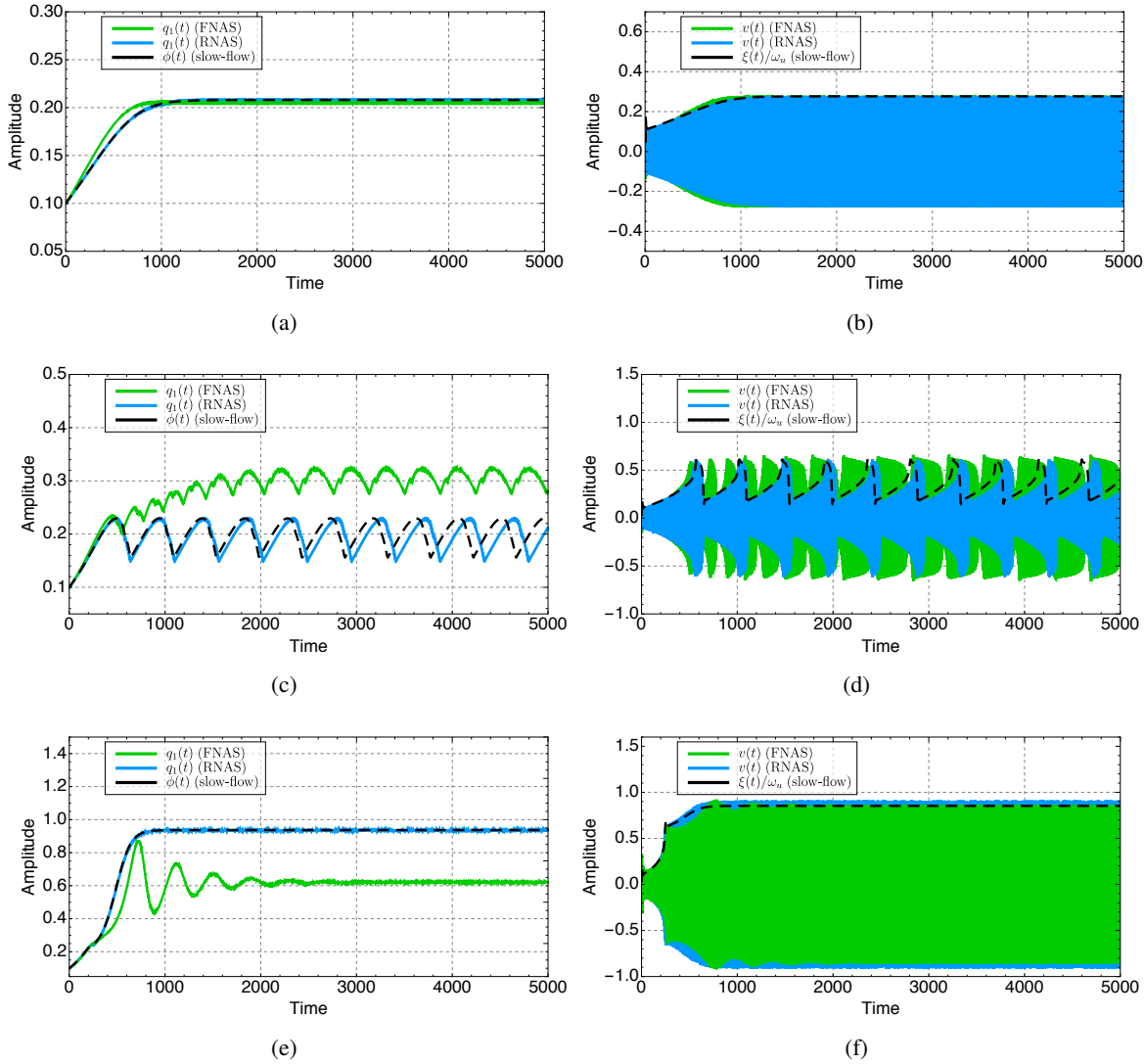


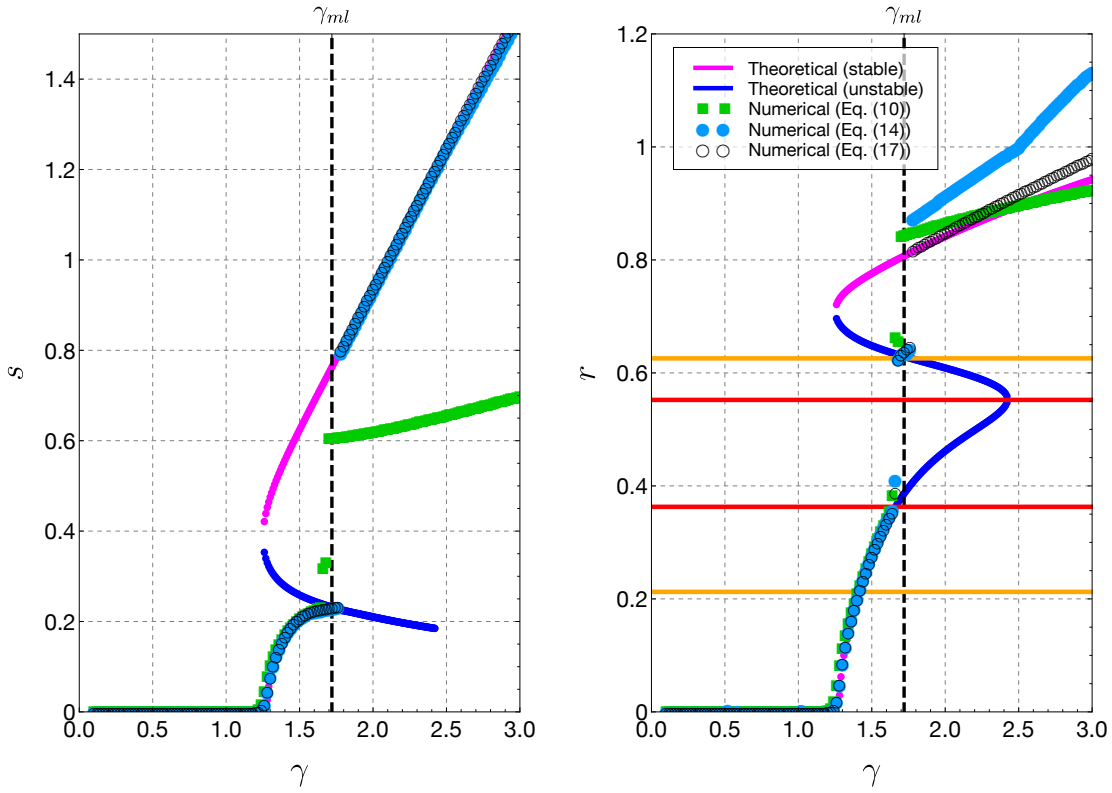
Figure 3: Direct numerical integration of the FNAS (10), the RNAS (14) and of the slow-flow (17). Set of parameters (40) is used with $\mu = 0.35$. (a) and (b) $\gamma = 1.5$; (c) and (d) $\gamma = 1.67$; (e) and (f) $\gamma = 2$.

5 Comparison of theoretical results with numerical simulations

In this section, analytical predictions proposed in Results 3.1 and 3.2 are compared to direct numerical integration of the system.

The comparison between the theoretical bifurcation diagram, obtained from Eq. (34) and the maximum steady-state amplitudes obtained from numerical simulations of the Full Non-Averaged System (FNAS) (10), the Reduced Non-Averaged System (RNAS) (14) and of the slow-flow (17b) using the set of parameters (40) is presented in Figs. 4 and 5 for different values of the NES parameter μ. The graphs of the maximum steady-state amplitude give a numerical estimation of the mitigation limit as the value of γ for which the last jump of the amplitude is observed.

In Fig 4, where $\mu = 0.35$, the amplitude jump appears at $\gamma \approx 1.67$ for the FNAS and at $\gamma \approx 1.74$ for both the RNAS and the slow-flow (see the last jump of the amplitude of the variable s Fig 4(a) and r Fig 4(b). Hence the reduction of the dynamic causes here a slight increase in the value of the mitigation limit. However, the slow-flow, can predict the mitigation limit observed with the RNAS. Previous values must be compared to the theoretical prediction $\gamma_{ml}^{th} \approx 1.72$ which is given, for $\mu = 0.35$, by Eq. (39a). Here γ_s is obtained solving Eq. (38) graphically in Fig. 4(b) as the intersection of the branch of the larger unstable fixed points (dark



(a) (b)

Figure 4: Comparison between theoretical bifurcation diagram (magenta dots for stable fixed points and blue dots for unstable fixed points) and maximum steady-state amplitudes obtained from numerical simulations of the Eq. (10) (green filled squares), Eq. (14) (blue filled circles) and Eq. (17) (black empty circles). Bifurcation diagram and maximum steady-state amplitudes are plotted for the variables (a) s and (b) r. In the latter, red horizontal lines correspond to r^M and r^m (with $r^M < r^m$) and orange horizontal lines correspond to r^u and r^d (with $r^d < r^u$). Set of parameters (40) is used with $\mu = 0.35$.

blue curve) and r^u (upper orange horizontal line). Therefore, a good agreement between prediction and direct numerical simulations is observed. Moreover, we can state here the same conclusion about amplitudes as in Sect. 4, with, in addition, a significant difference observed between the amplitude of the slow-flow and that of the RNAS after the jump. This can be due to the fact that the assumption of 1:1 resonance capture is not respected anymore. Indeed, an FFT performed on the signals shows the appearance of additional harmonics in the steady-state response regimes of the RNAS. Note that these harmonics are not present in the steady-state response regimes of the FNAS. However, all these differences do not affect the good prediction of the mitigation limit.

In Fig 5, only graphs with respect to the variable r are presented with $\mu \approx 0.4$, 0.45 and 0.57. One can see that the last amplitude jump appears at $\gamma \approx 1.85$, 1.94 and 1.9 for both the RNAS and the slow-flow and they are well predicted by the theoretical values ($\gamma_{ml}^{th} \approx 1.87$, 1.98 and 1.95 respectively[2]). These results allows to validate the asymptotic study presented in Sect. 3.

However, the comparison between the mitigation limits observed on the graph of the maximum steady-state amplitudes of the FNAS (the amplitude jump appears at $\gamma = 1.67$, 1.65 and 1.63) and the theoretical prediction highlights the limits of the dynamics reduction method presented in Sect. 2.2. Indeed, the theoretical values overestimate now the mitigation limit observed with FNAS when μ increases. The overestimation of

[2]When $\mu = 0.4$ and 0.45, the theoretical prediction γ_{ml}^{th} is given by Eq. (39a) whereas it is given by Eq. (39b) for $\mu = 0.57$. Like γ_s, the value of γ_{lim} is determined graphically.

the mitigation is due to a bad estimation of amplitudes before the jump (see Fig. 5), even if the amplitudes are small. The causes of these discrepancies are not yet known, this will be subject of future work.

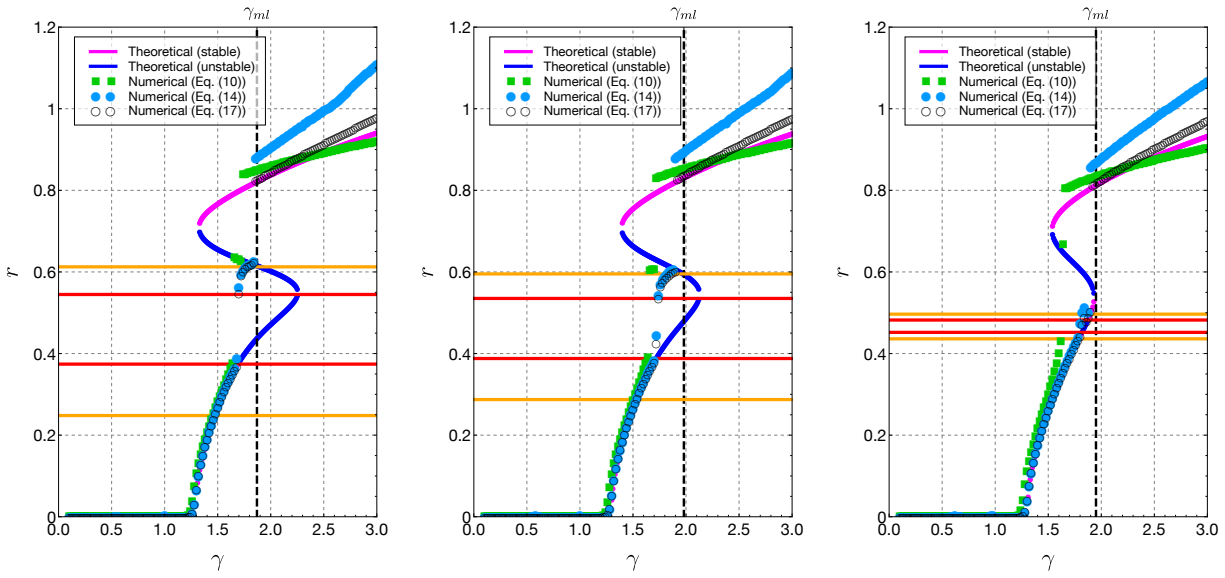


Figure 5: Same caption as for Fig. 4(b) with $\mu = 0.4$, 0.45 and 0.57.

6 Conclusion

We studied the capacity of Nonlinear Energy Sinks (NES) to mitigate vibrations due to mode-coupling instability in braking systems. As an extension of a previous work [1], we used here a general dynamics reduction method allowing to obtain a one dimensional critical manifolds and consequently to predict all the steady-state response regimes observed using direct numerical integration of the equations of motion. In particular, the mitigation limit, defined as the value of the friction coefficient which separates harmful situations from harmless situations, has been predicted. The comparison with numerical simulation allows to validate the used asymptotic analysis but highlights the limits of the dynamic reduction method. Indeed, overestimations of the mitigation limit are observed for large value of NES damping parameter. The causes of these discrepancies are not yet known and will be subject of future work.

A Slow-fast system

The function f, g_1 and g_2 characterizing the slow-fow system (19) are given here after.

$$\begin{aligned} f(s,r,\delta) \;=\; & \frac{1}{2}\Big(2s\rho_u - r\cos(\delta)\mathbf{l}_{31}^I + r\sin(\delta)\mathbf{l}_{31}^R - 2s\mathbf{l}_{31}^I\mathbf{r}_{11}^I + 2s\mathbf{l}_{31}^R\mathbf{r}_{11}^R \\ & -6s^3\mathbf{l}_{31}^I\mathbf{r}_{11}^{I^2}\mathbf{r}_{12}^I\varphi_1 + 12s^3\mathbf{r}_{11}^I\mathbf{r}_{12}^I\mathbf{l}_{31}^R\mathbf{r}_{11}^R\varphi_1 + 6s^3\mathbf{l}_{31}^I\mathbf{r}_{12}^I\mathbf{r}_{11}^{R^2}\varphi_1 \\ & +6s^3\mathbf{r}_{11}^{I^2}\mathbf{l}_{31}^R\mathbf{r}_{12}^R\varphi_1 + 12s^3\mathbf{l}_{31}^I\mathbf{r}_{11}^I\mathbf{r}_{11}^{R^2}\mathbf{r}_{12}^R\varphi_1 - 6s^3\mathbf{l}_{31}^R\mathbf{r}_{11}^R\mathbf{r}_{12}^R\varphi_1 \\ & -6s^3\mathbf{l}_{41}^I\mathbf{r}_{21}^{I^2}\mathbf{r}_{22}^I\varphi_2 + 12s^3\mathbf{r}_{21}^I\mathbf{r}_{22}^I\mathbf{l}_{41}^R\mathbf{r}_{21}^R\varphi_2\omega_u + 6s^3\mathbf{l}_{41}^I\mathbf{r}_{22}^I\mathbf{r}_{21}^{R^2}\varphi_2\omega_u \\ & +6s^3\mathbf{r}_{21}^{I^2}\mathbf{l}_{41}^R\mathbf{r}_{22}^R\varphi_2\omega_u + 12s^3\mathbf{l}_{41}^I\mathbf{r}_{21}^I\mathbf{r}_{21}^R\mathbf{r}_{22}^R\varphi_2\omega_u \\ & -6s^3\mathbf{l}_{41}^R\mathbf{r}_{21}^{R^2}\mathbf{r}_{22}^R\varphi_2\omega_u\Big) \end{aligned} \tag{41}$$

$$
\begin{aligned}
g_1(s,r,\delta,\epsilon) \quad &= -\frac{r\mu}{2} + s\sin(\delta)\mathbf{r}_{11}^{I} - s\cos(\delta)\mathbf{r}_{11}^{R} + \epsilon\left(-\frac{r\mu}{2} - s\sin(\delta)\mathbf{r}_{11}^{I} - s\gamma\sin(\delta)\mathbf{r}_{21}^{I}\right.\\
&+s\eta_1\sin(\delta)\mathbf{r}_{31}^{I} - s\eta_1\cos(\delta)\mathbf{r}_{31}^{R} + s\cos(\delta)\mathbf{r}_{11}^{R} + s\gamma\cos(\delta)\mathbf{r}_{21}^{R}\\
&-3s^3\sin(\delta)\mathbf{r}_{11}^{I^2}\mathbf{r}_{12}^{I}\varphi_1 + 6s^3\cos(\delta)\mathbf{r}_{11}^{I}\mathbf{r}_{12}^{I}\mathbf{r}_{11}^{R}\varphi_1 + 3s^3\sin(\delta)\mathbf{r}_{12}^{I}\mathbf{r}_{11}^{R^2}\varphi_1\\
&\left.+3s^3\cos(\delta)\mathbf{r}_{11}^{I^2}\mathbf{r}_{12}^{R}\varphi_1 + 6s^3\sin(\delta)\mathbf{r}_{11}^{I}\mathbf{r}_{11}^{R}\mathbf{r}_{12}^{R}\varphi_1 - 3s^3\cos(\delta)\mathbf{r}_{11}^{R^2}\mathbf{r}_{12}^{R}\varphi_1\right) \qquad (42)
\end{aligned}
$$

$$
\begin{aligned}
g_2(s,r,\delta,\epsilon) \quad &= \quad \frac{-3r^3\alpha + 8s\cos(\delta)\mathbf{r}_{11}^{I} + 8s\sin(\delta)\mathbf{r}_{11}^{R} + 4r}{8r}\\
&+\epsilon\left(\frac{1}{2s}\left(2s\nu_u + r\sin(\delta)\mathbf{l}_{31}^{I} + r\cos(\delta)\mathbf{l}_{31}^{R} + 2s\mathbf{r}_{11}^{I}\mathbf{l}_{31}^{R} + 2s\mathbf{l}_{31}^{I}\mathbf{r}_{11}^{R}\right.\right.\\
&+6s^3\mathbf{r}_{11}^{I^2}\mathbf{r}_{12}^{I}\mathbf{l}_{31}^{R}\varphi_1 + 12s^3\mathbf{l}_{31}^{I}\mathbf{r}_{11}^{I}\mathbf{r}_{12}^{I}\mathbf{r}_{11}^{R}\varphi_1 - 6s^3\mathbf{r}_{12}^{I}\mathbf{l}_{31}^{R}\mathbf{r}_{11}^{R^2}\varphi_1\\
&+6s^3\mathbf{l}_{31}^{I}\mathbf{r}_{11}^{I^2}\mathbf{r}_{12}^{R}\varphi_1 - 12s^3\mathbf{r}_{11}^{I}\mathbf{l}_{31}^{R}\mathbf{r}_{11}^{R}\mathbf{r}_{12}^{R}\varphi_1 - 6s^3\mathbf{l}_{31}^{I}\mathbf{r}_{11}^{R^2}\mathbf{r}_{12}^{R}\varphi_1\\
&+6s^3\mathbf{r}_{21}^{I^2}\mathbf{r}_{22}^{I}\mathbf{l}_{41}^{R}\varphi_2 + 12s^3\mathbf{l}_{41}^{I}\mathbf{r}_{21}^{I}\mathbf{r}_{22}^{I}\mathbf{r}_{21}^{R}\varphi_2 - 6s^3\mathbf{r}_{22}^{I}\mathbf{l}_{41}^{R}\mathbf{r}_{21}^{R^2}\varphi_2\\
&\left.+6s^3\mathbf{l}_{41}^{I}\mathbf{r}_{21}^{I^2}\mathbf{r}_{22}^{R}\varphi_2 - 12s^3\mathbf{r}_{21}^{I}\mathbf{l}_{41}^{R}\mathbf{r}_{21}^{R}\mathbf{r}_{22}^{R}\varphi_2 - 6s^3\mathbf{l}_{41}^{I}\mathbf{r}_{21}^{R^2}\mathbf{r}_{22}^{R}\varphi_2\right)\\
&+\frac{1}{8r}\left(-3r^3\alpha - 4r - 8s\cos(\delta)\mathbf{r}_{11}^{I} - 8s\gamma\cos(\delta)\mathbf{r}_{21}^{I} + 8s\eta_1\cos(\delta)\mathbf{r}_{31}^{I}\right.\\
&-8s\sin(\delta)\mathbf{r}_{11}^{R} - 8s\gamma\sin(\delta)\mathbf{r}_{21}^{R} + 8s\eta_1\sin(\delta)\mathbf{r}_{31}^{R} - 24s^3\cos(\delta)\mathbf{r}_{11}^{I^2}\mathbf{r}_{12}^{I}\varphi_1\\
&-48s^3\sin(\delta)\mathbf{r}_{11}^{I}\mathbf{r}_{12}^{I}\mathbf{r}_{11}^{R}\varphi_1 + 24s^3\cos(\delta)\mathbf{r}_{12}^{I}\mathbf{r}_{11}^{R^2}\varphi_1 - 24s^3\sin(\delta)\mathbf{r}_{11}^{I^2}\mathbf{r}_{12}^{R}\varphi_1\\
&\left.\left.+48s^3\cos(\delta)\mathbf{r}_{11}^{I}\mathbf{r}_{11}^{R}\mathbf{r}_{12}^{R}\varphi_1 + 24s^3\sin(\delta)\mathbf{r}_{11}^{R^2}\mathbf{r}_{12}^{R}\varphi_1\right)\right) \qquad (43)
\end{aligned}
$$

B Slow subsystem

The function f_r characterizing Eq. (33) is given here after.

$$
\begin{aligned}
f_r(r) \quad &= \quad \frac{r^2}{8\left(\mathbf{r}_{11}^{I^2} + \mathbf{r}_{11}^{R^2}\right)}\left\{-4\left(\mu^2 + 4\left(\frac{3r^2\alpha}{8} - \frac{1}{2}\right)^2\right)\right.\\
&\left[\left(\mathbf{r}_{11}^{I^2} + \mathbf{r}_{11}^{R^2}\right)\left(-\rho_u + \mathbf{l}_{31}^{R}\left(-\mathbf{r}_{11}^{R} - \frac{3}{4}r^2\mathbf{r}_{12}^{R}\varphi_1\left(\mu^2 + 4\left(\frac{3r^2\alpha}{8} - \frac{1}{2}\right)^2\right)\right)\right)\right.\\
&+\mathbf{l}_{31}^{I}\left(\mathbf{r}_{11}^{I}\left(\mathbf{r}_{11}^{I^2} + \mathbf{r}_{11}^{R^2}\right) + \frac{3}{4}r^2\left(\mathbf{r}_{12}^{I}\left(\mathbf{r}_{11}^{I^2} - \mathbf{r}_{11}^{R^2}\right) - 2\mathbf{r}_{11}^{I}\mathbf{r}_{11}^{R}\mathbf{r}_{12}^{R}\right)\varphi_1\left(\mu^2 + 4\left(\frac{3r^2\alpha}{8} - \frac{1}{2}\right)^2\right)\right)\\
&-\frac{3}{2}r^2\mathbf{r}_{11}^{I}\mathbf{r}_{12}^{I}\mathbf{l}_{31}^{R}\mathbf{r}_{11}^{R}\varphi_1\left(\mu^2 + 4\left(\frac{3r^2\alpha}{8} - \frac{1}{2}\right)^2\right) + \frac{3}{4}r^2\left(\mathbf{l}_{41}^{I}\left(\mathbf{r}_{22}^{I}\left(\mathbf{r}_{21}^{I^2} - \mathbf{r}_{21}^{R^2}\right) - 2\mathbf{r}_{21}^{I}\mathbf{r}_{21}^{R}\mathbf{r}_{22}^{R}\right)\right.\\
&\left.\left.+\mathbf{l}_{41}^{R}\left(-2\mathbf{r}_{21}^{I}\mathbf{r}_{22}^{I}\mathbf{r}_{21}^{R} + \left(-\mathbf{r}_{21}^{I^2} + \mathbf{r}_{21}^{R^2}\right)\mathbf{r}_{22}^{R}\right)\right)\varphi_2\left(\mu^2 + 4\left(\frac{3r^2\alpha}{8} - \frac{1}{2}\right)^2\right)\right]\\
&-\left(\mathbf{r}_{11}^{I^2} + \mathbf{r}_{11}^{R^2}\right)\\
&\left.\left[\mathbf{l}_{31}^{I}\left(-4\mu\mathbf{r}_{11}^{R} + \mathbf{r}_{11}^{I}\left(3r^2\alpha - 4\right)\right) + \mathbf{l}_{31}^{R}\left(-4\mu\mathbf{r}_{11}^{I} + \mathbf{r}_{11}^{R}\left(-3r^2\alpha + 4^4\right)\right)\right]\right\} \qquad (44)
\end{aligned}
$$

References

[1] B Bergeot, S Berger, and S Bellizzi. Mode coupling instability mitigation in friction systems by means of nonlinear energy sinks : numerical highlighting and local stability analysis. *Journal of Vibration and Control*, 2017.

[2] L. Nechak, S. Berger, and E. Aubry. Non-intrusive generalized polynomial chaos for the robust stability analysis of uncertain nonlinear dynamic friction systems. *Journal of Sound and Vibration*, 332(5):1204–1215, 2013.

[3] L. Nechak and J. J. Sinou. Hybrid surrogate model for the prediction of uncertain friction-induced instabilities. *Journal of Sound and Vibration*, 396:122–143, 2017.

[4] Oberst S and J.C.S Lai. Statistical analysis of brake squeal noise. *Journal of Sound and Vibration*, 330:2978–2994, 2011.

[5] A.F. D'Souza and A.H. Dweib. Self-excited vibrations induced by dry friction, part 2: Stability and limit-cycle analysis. *Journal of Sound and Vibration*, 137(2):177–190, 1990.

[6] M Eriksson and S Jacobson. Friction behaviour and squeal generation of disc brakes at low speeds. *Proceedings of the Institution of Mechanical Engineers, Part D: Journal of Automobile Engineering*, 215(12):1245–1256, 2001.

[7] N Hoffmann and L Gaul. Effects of damping on mode-coupling instability in friction induced oscillations. *{ZAMM} - Journal of Applied Mathematics and Mechanics / Zeitschrift für Angewandte Mathematik und Mechanik*, 83(8):524–534, 2003.

[8] N.M. Kinkaid, O.M. O'Reilly, and P. Papadopoulos. Automotive disc brake squeal. *Journal of Sound and Vibration*, 267:105–166, 2003.

[9] A.F. Vakakis and O.V. Gendelman. Energy pumping in nonlinear mechanical oscillators: Part II - Resonance capture. *Journal of Applied Mechanics*, 68:42–48, 2001.

[10] A. F. Vakakis, O. V. Gendelman, L. A. Bergman, D. M. McFarland, G. Kerschen, and Y. S. Lee. *Nonlinear Targeted Energy Transfer in Mechanical and Structural Systems*. Springer-Verlag, Berlin, New York, 2008.

[11] J. Hultén. Friction phenomena related to drum brake squeal instabilities. In *ASME Design Engineering Technical Conferences, Sacramento, CA*, 1997.

[12] L. Meirovitch. *Fundamentals of Vibrations*, chapter 7. McGraw-Hill, 2001.

[13] N Fenichel. Geometric singular perturbation theory for ordinary differential equations. *Journal of Differential Equations*, 98:53–98, 1979.

[14] C.K.R.T. Jones. Geometric singular perturbation theory. In Russell Johnson, editor, *Dynamical Systems*, volume 1609 of *Lecture Notes in Mathematics*, pages 44–118. Springer Berlin Heidelberg, 1995.

[15] O. V. Gendelman and T. Bar. Bifurcations of self-excitation regimes in a Van der Pol oscillator with a nonlinear energy sink. *Physica D*, 239(3-4):220–229, February 2010.

[16] Y. Starosvetsky and O. V. Gendelman. Strongly modulated response in forced 2dof oscillatory system with essential mass and potential asymmetry. *Physica D*, 237(13):1719–1733, August 2008.

Structural modification of tool holder geometry as a chatter avoidance method

T. Gibbons [1], **E. Ozturk** [2], **L. Xu** [3], **N. Sims** [1]
[1] Dynamics Research Group (DRG), Department of Mechanical Engineering, University of Sheffield, Sheffield, UK e-mail: **t.gibbons@sheffield.ac.uk**

[2] Advanced Manufacturing Research Centre with Boeing, University of Sheffield, Sheffield, UK

[3] The Boeing Company

Abstract
Chatter is a self-excited vibration that occurs during cutting operations such as milling, which leads to undesirable consequences such as poor surface finish and increased tool wear. The traditional approach to avoiding chatter involves experimentally determining the tool tip frequency response function (FRF) of the machine with each tool holder in place, a very time-consuming procedure. This paper proposes a new structural modification (SM) method for the optimisation of tool holder geometry. Firstly, a direct frequency domain SM method is presented, which allows the user to select an optimum tool holder geometry without any knowledge of the interface properties. Secondly, an inverse SM method is presented, which allows the user to optimise the tool holder geometry using a single experimental model and a single numerical model, again with no knowledge of the interface properties. Both the direct and inverse methods are then demonstrated using experimental data.

1 Introduction

Milling operations involve moving a rotating tool with multiple teeth relative to a workpiece in order to remove material. As each tooth impacts the workpiece relative motion between the two structures can occur, causing a wave to be imprinted onto the surface of the workpiece. As the following tooth passes, the wavy surface is removed and replaced by another. If these waves are out of phase, the instantaneous thickness of the chip being removed will grow exponentially, causing the unstable excitation of the tool commonly known as chatter.

Chatter vibrations can lead to unacceptable surface finish, increased tool wear, and amplified noise levels. Since the onset of chatter can be parametrised by the spindle speed (Ω) and depth of cut b (as shown in Fig. 1), manufacturers are often forced to reduce speeds and depths in an attempt to avoid chatter. Ultimately leading to a reduction in production rates and increase in production costs.

Another common method to avoid the onset of chatter is to optimise the structural dynamics of the milling machine in an attempt to optimise the stability threshold seen in Fig. 1. This stability diagram can be calculated from the point frequency response function (FRF) at the tool tip and it can be shown that the locations of the peaks (Ω^l_{best}) are directly proportional to the natural frequency of the cutting tool.

$$\Omega^l_{best} = \frac{\omega_n}{2\pi(l+1)N_t} \tag{1}$$

where ω_n is the natural frequency of the tool in rad/s, $l \in 0, 1, 2, ...$ is the mode number, and N_t is the number of teeth on the tool. Therefore, the location (or spindle speed) of the stable peaks can be optimised via the natural frequency of the tool. This is commonly achieved by selecting an optimal tool length and/or

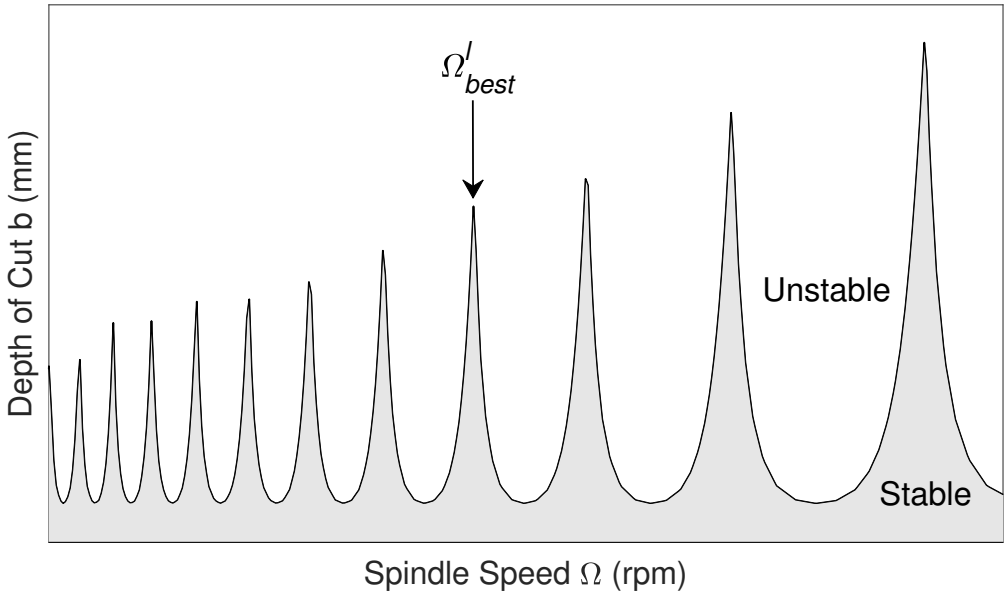


Figure 1: Example stability lobe diagram showing the stability threshold in the spindle speed vs. depth of cut plane

tool holder geometry. A clear disadvantage of this method is the need to experientially determine the natural frequency of each available tool length and tool holder geometry.

In order to reduce the experimental cost of selecting an optimum set-up, Schmitz et al. developed the receptance coupling substructure analysis (RCSA) method [1]. This allowed the user to predict the tool tip frequency response function (FRF) and therefore the stability of any tool/tool holder combination, using only a single experimental model. Using a dynamic substructuring method, the user can subtract the base tool/tool holder from the experimental model before adding that of another tool/tool holder combination. However this requires numerical models of both tools and tool holders. Therefore when using RCSA to select an optimum set-up from a large range, a large database of numerical models is required.

The accuracy of the RCSA method is highly dependent on knowledge of the interface properties between tool and tool holder and tool holder and spindle. Interface stiffness and damping must be included in the (de)coupling process in order to achieve reliable results. Several methods have been presented for the calculation of these values [2], and most involve updating the interface properties of a numerical model to match experimental data. However, this requires a high level of expertise in numerical modelling as well as capturing the experimental data the user is trying to avoid.

The structural modification method presented in this paper has two clear advantages over the RCSA method. Firstly, the stability of any tool holder geometry can be predicted using a single experimental model without any knowledge of the interface dynamics. Secondly, an inverse method is developed which allows for simple optimisation of tool holder geometry without having to construct numerical models of each available tool holder. The method suffers a single disadvantage when compared to RCSA in that only the tool holder diameter can be optimised. However, it will be demonstrated that the tool holder diameter alone can have a significant effect on the dynamics at the tool tip and therefore the stability of the milling operation.

2 Theory

Structural modification, as presented by Mottershead and Ram [3], involves the combination of two (or more) dynamic models to predict the dynamic properties of more complex structures. Consider models A and B, with l and m degrees of freedom (DOFs) respectively, which are to be combined at p locations to form model

C. At a particular frequency, it is given that:

$$\boldsymbol{Y}_A = [\mathbf{H}_A]_{l\times l}\boldsymbol{F}_A \qquad \boldsymbol{Y}_B = [\mathbf{H}_B]_{m\times m}\boldsymbol{F}_B \qquad \boldsymbol{Y}_C = [\mathbf{H}_C]_{n\times n}\boldsymbol{F}_C \tag{2}$$

where $\boldsymbol{Y}$ is the harmonic displacement vector, $\boldsymbol{F}$ is the harmonic force vector, $\mathbf{H}$ is the frequency response function matrix containing receptances H_{ij}, describing the displacement at DOF i due to forcing at DOF j, and $n = l + m - p$.

By applying compatibility ($\boldsymbol{X}_C$=$\boldsymbol{X}_A$+$\boldsymbol{X}_B$) and equilibrium ($\boldsymbol{F}_C$=$\boldsymbol{F}_A$+$\boldsymbol{F}_B$) conditions at the p connection nodes; it is given that:

$$\mathbf{H}_C^{-1} = \mathbf{H}_A^{-1} + \mathbf{H}_B^{-1} \tag{3}$$

This formulation is inconvenient for numerical application as it involves multiple matrix inversions, however it may be rewritten as:

$$\begin{aligned}\mathbf{H}_C^{-1} &= \mathbf{H}_A^{-1}[\mathbf{I} + \mathbf{H}_A\mathbf{H}_B^{-1}]\\ \mathbf{H}_C &= [\mathbf{I} + \mathbf{H}_A\mathbf{H}_B^{-1}]^{-1}\mathbf{H}_A\end{aligned} \tag{4}$$

This forms the basis of most frequency domain dynamic substructuring methods, including RCSA. For instance, model A could be an experimental model of the spindle and model B a numerical model of a tool/tool holder combination. Then C would allow the user to predict the dynamics of the machine with the new tool holder. The need to include interface properties comes from the fact that two beam-like structures are coupled end-to-end i.e. models A and B only have one common DOF. The requirement to include interface dynamics can be removed by seeking to modify the existing tool holder rather than replace it with another. In this case, A could be an experimental model of some base tool holder, and B a numerical model of some local modification (i.e an increase in diameter) to that tool holder.

2.1 The direct method

Since model B is a local modification, further simplifications can be made using the method by Özgüven [4]. Both models may be partitioned into sub-matrices, separating DOFs that are involved with the modification and those that are not.

$$\mathbf{H}_A = \begin{bmatrix}\mathbf{H}_{AOO} & \mathbf{H}_{AOI}\\ \mathbf{H}_{AIO} & \mathbf{H}_{AII}\end{bmatrix} \qquad [\mathbf{H}_B]^{-1} = \begin{bmatrix}\mathbf{0} & \mathbf{0}\\ \mathbf{0} & \mathbf{B}_{II}\end{bmatrix} \tag{5}$$

where the subscript *O* denotes the DOFs not involved with the modification and *I* denotes the DOFs that are modified. This partitioned matrix form reduces the number and size of the operation to one matrix inversion of an $m \times m$ matrix. The global model is then given by:

$$\begin{aligned}\mathbf{H}_{CII} &= [\mathbf{I} + \mathbf{H}_{AII}\mathbf{B}_{II}]^{-1}\mathbf{H}_{AII}\\ \mathbf{H}_{COI}^{\mathrm{T}} &= \mathbf{H}_{CIO} = \mathbf{H}_{AOI}[\mathbf{I} - \mathbf{B}_{II}\mathbf{H}_{CII}]\\ \mathbf{H}_{COO} &= \mathbf{H}_{AOO} - \mathbf{H}_{AOI}\mathbf{B}_{II}\mathbf{H}_{CIO}\end{aligned} \tag{6}$$

This allows the user to predict the effect of any local modification $\mathbf{B}$. However, in order optimise the modification, numerical models for each and every modification must be constructed. The optimisation process can be simplified by using the inverse structural modification method.

2.2 The inverse method

If we are to only partially construct the modification matrix in Eq. (4), leaving it as a function of some unknown geometric modification parameter (for instance tool holder diameter) α i.e. $\mathbf{B} = \mathbf{B}(\alpha)$, then the inverse problem may also be solved.

$$\mathbf{H}_C = \frac{\mathrm{adj}(\mathbf{I} + \mathbf{H}_A\mathbf{B}(\alpha))\mathbf{H}_A}{\det(\mathbf{I} + \mathbf{H}_A\mathbf{B}(\alpha))} = \frac{\det(\mathbf{I} + \mathbf{H}_A\mathbf{B}(\alpha))[\mathbf{I} + \mathbf{H}_A\mathbf{B}(\alpha)]^{-1}\mathbf{H}_A}{\det(\mathbf{I} + \mathbf{H}_A\mathbf{B}(\alpha))} \tag{7}$$

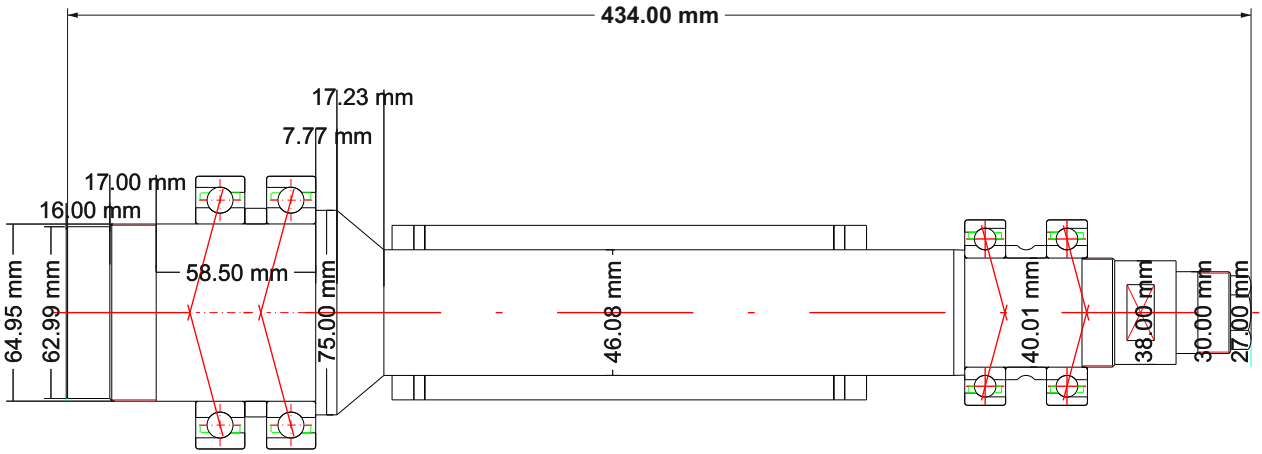


Figure 2: Diagram showing the dimensions and bearing locations of the experimental spindle rig

The antiresonance of the ij^{th} receptance is then given by $[\text{adj}(\mathbf{I}+\mathbf{H}_A\mathbf{B}(\alpha))\mathbf{H}_A]_{ij} = 0$, whilst its natural frequencies are given by $\det(\mathbf{I}+\mathbf{H}_A\mathbf{B}(\alpha)) = 0$. For simple modifications these equations may have algebraic solutions for the modification parameter α; however, for more complex modifications a numerical solution may be necessary.

It is possible to make further simplifications to Mottershead's [3] method by applying the same matrix partitions as with the direct method (Eq. (5)); by doing so the size of the matrix operations are reduced and the likelihood of an algebraic solution increased. Eq. (7) can then be written as:

$$\begin{aligned}
\mathbf{H}_{CII} &= \frac{\text{adj}(\mathbf{I}+\mathbf{H}_{AII}\mathbf{B}_{II}(\alpha))\mathbf{H}_{AII}}{\det(\mathbf{I}+\mathbf{H}_{AII}\mathbf{B}_{II}(\alpha))} \\
\mathbf{H}_{COI}^{\mathrm{T}} = \mathbf{H}_{CIO} &= \frac{\det(\mathbf{I}+\mathbf{H}_{AII}\mathbf{B}_{II}(\alpha))\mathbf{H}_{AOI}[\mathbf{I}-\mathbf{B}_{II}(\alpha)\mathbf{H}_{CII}]}{\det(\mathbf{I}+\mathbf{H}_{AII}\mathbf{B}_{II}(\alpha))} \\
\mathbf{H}_{COO} &= \frac{\det(\mathbf{I}+\mathbf{H}_{AII}\mathbf{B}_{II}(\alpha))[\mathbf{H}_{AOO}-\mathbf{H}_{AOI}\mathbf{B}_{II}(\alpha)\mathbf{H}_{CIO}]}{\det(\mathbf{I}+\mathbf{H}_{AII}\mathbf{B}_{II}(\alpha))}
\end{aligned} \tag{8}$$

This formulation allows for the natural frequencies of the global structure to be repositioned using only the measured receptances at the modification DOFs I by setting $\det(\mathbf{I}+\mathbf{H}_{AII}\mathbf{B}_{II}(\alpha)) = 0$.

3 Experiment

The structural modification theory is now validated on a spindle rig. The spindle rig consists of a HSKA63 milling spindle, bearings and bearing housing, similar to any five axis milling machine, but is suspended on a smaller simpler structure. Validation on a spindle rig has several advantages over validation on a milling machine. Firstly, because of the simpler supporting structure, many of the low frequency modes associated with the machine are removed; therefore, concentration can be given to the dominant bending modes of the tool, tool holder, and spindle. Secondly, the spindle rig can be tested in cold conditions, meaning nonlinearities such as thermal softening of the bearings [5] are removed, thus making the data more repeatable. A schematic diagram of the spindle rig's geometry is shown in Fig. 2.

In order to investigate SM for chatter avoidance in high speed milling, two tool holders of different geometries were chosen. A cylindrical untapered holder of length 0.134 m and diameter 0.024 m; and a tapered tool

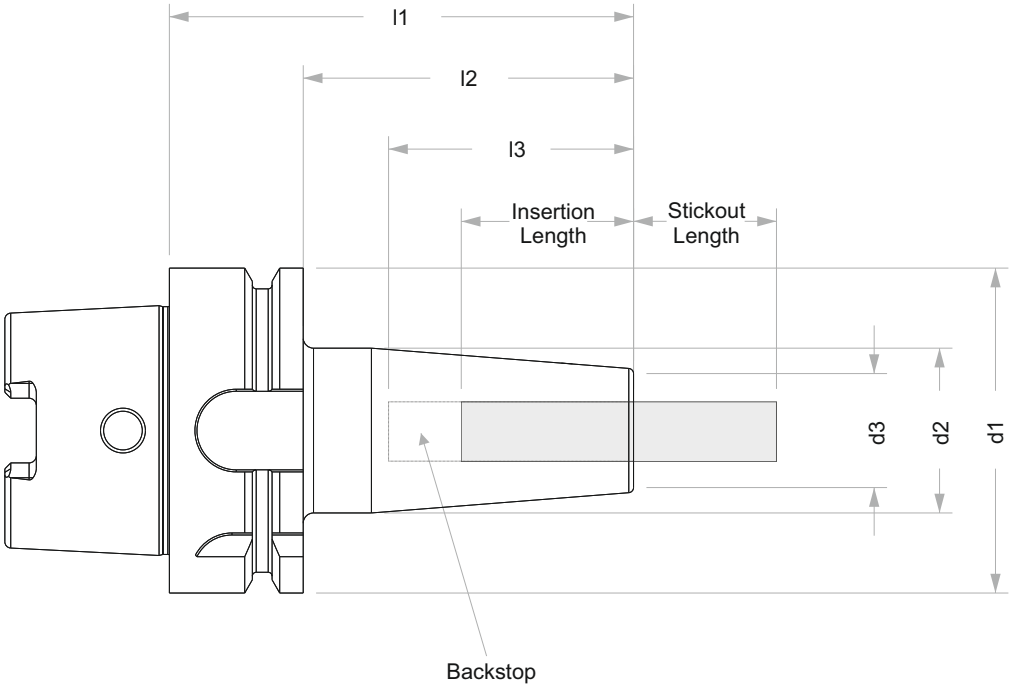


Figure 3: Diagram showing the dimensions for both the unmodified and modified holders

holder of length 0.134 m and diameter ranging between 0.024 m and 0.034m. These holders will be referred to as the unmodified and modified holders, respectively. Both holders had a HSKA63 spindle interface. The geometries of both holders are summarised in Fig. 3 and Table. 1. It is important to note that the geometries of the tool holders differ only in the base diameter d2, as this is this parameter that will be modified.

A two fluted end mill of total length 0.083 m was inserted into both holders with a stickout length of 0.037 m. Then, each of the tool holders were clamped into the spindle, and their tool tip frequency response functions measured, these results are compared in Fig. 4. It can be seen that the simpler structure of the spindle rig results in a single dominant bending mode in both cases, and the larger base diameter gives rise to a mode with a significantly lower amplitude and higher natural frequency.

3.1 Methodology

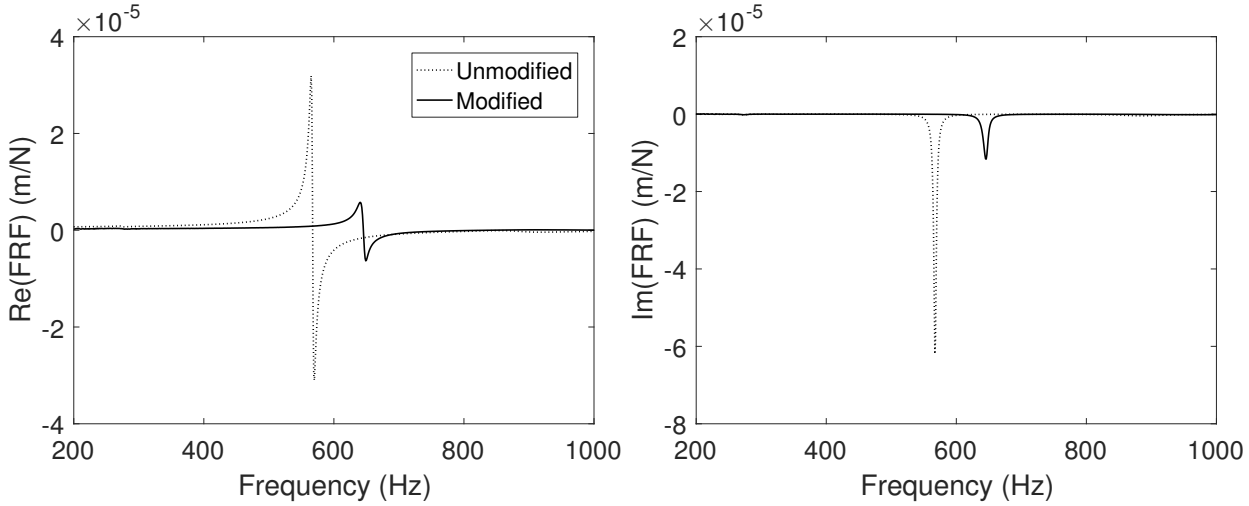
This section describes how each of the models (A and B), defined in section 2 and shown in Fig. 5 are constructed in order to apply higher rank SM theory to to optimise the tool holder geometry.

3.1.1 Model B

It is convenient to begin the methodology by discussing model B, or the modification model, which is a numerical model that describes the difference in diameter between the unmodified and modified holders. The geometry is a circular tube of length 0.134 m with an inner diameter of 0.024 m. The outer diameter varies between 0.024 m and 0.034 m, as shown in Fig. 3. A numerical model was constructed with the

	l1(mm)	**l2**(mm)	**l3**	**d1**(mm)	**d2**(mm)	**d3**(mm)
Unmodified	160	134	47	64	**24**	24
Modified	160	134	47	64	**34**	24

Table 1: Dimensions of the modified and unmodified tool holders



(a) Real (b) Imaginary

Figure 4: Real (a) and Imaginary (b) frequency response function plots comparing the tool tip dynamics of the unmodified ($\cdots$) and modified (—) holders on the spindle rig

geometrical properties shown, and standard steel material properties (density $\rho = 7750$ kg m^{-3}, Young's Modulus $E = 200$ GPa).

It is important to keep the dimensions of model B as low as possible for two reasons. Firstly, each node in the numerical model must also occur in the experimental model A, and experimental data inherently contains error. But also, if the inverse SM method is to be used, by keeping the number of nodes to a minimum, it is more likely that a solution can be found.

Whilst minimising the dimensions of model B has its advantages, it also carries with it some disadvantages. The number of modes included in a numerical model equals the size of the elemental matrices (stiffness **K** and mass **M**), i.e. a numerical model with a 2×2 stiffness matrix only accounts for the first two modes of the structure. Hence, when model B is minimised it becomes a truncated model and does not account for the out of range modes.

However, in order to minimise the experimental cost of the method, it was decided that the geometry of model B would be modelled using only two beam elements, one for the tapered section of the holder and one for the untapered section. The first beam lies between nodes n_2 and n_3 and the second between nodes n_3 and n_4 and each beam has two DOFs, translation y and rotation θ, as shown in Fig. 5. Therefore the dimensions of the element matrices are 6×6.

Beam one is a tapered Timoshenko tube, constructed from the beam element matrices given in [6], it has an inner diameter of 0.024 m, an outer diameter between 0.024 m and 0.034 m, and a length of 0.064 m. Whilst the second beam is an untapered Timoshenko tube, constructed from the standard Timoshenko beam element matrices [7], with an inner diameter of 0.024 m, an outer diameter of 0.034 m, and a length of 0.07 m. Timoshenko beam elements were used over Euler-Bernoulli beam elements, since it has already been shown that they describe the dynamics of tool holders with greater accuracy [8].

The global mass and stiffness matrices for model B were then assembled using the direct stiffness method, which applies compatibility and equilibrium conditions in a similar manner to SM. The global mass and stiffness matrices are then given by

$$\mathbf{M} = \begin{bmatrix} \left[\mathbf{M}_{22}\right]_{2\times2} & \left[\mathbf{M}_{23}\right]_{2\times2} & \mathbf{0} \\ \left[\mathbf{M}_{32}\right]_{2\times2} & \left[\mathbf{M}_{33}\right]_{2\times2} & \left[\mathbf{M}_{34}\right]_{2\times2} \\ \mathbf{0} & \left[\mathbf{M}_{43}\right]_{2\times2} & \left[\mathbf{M}_{44}\right]_{2\times2} \end{bmatrix} \tag{9}$$

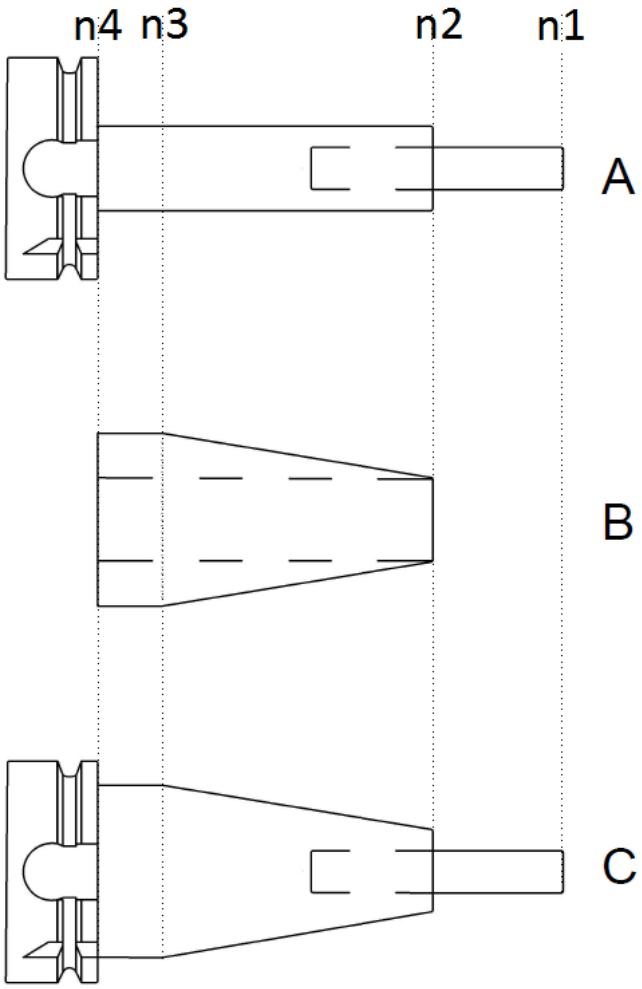


Figure 5: Diagram detailing the location of the nodes included in models A B C

and

$$\mathbf{K} = \begin{bmatrix} [\mathbf{K}_{22}]_{2\times2} & [\mathbf{K}_{23}]_{2\times2} & \mathbf{0} \\ [\mathbf{K}_{32}]_{2\times2} & [\mathbf{K}_{33}]_{2\times2} & [\mathbf{K}_{34}]_{2\times2} \\ \mathbf{0} & [\mathbf{K}_{43}]_{2\times2} & [\mathbf{K}_{44}]_{2\times2} \end{bmatrix} \tag{10}$$

$$\tag{11}$$

respectively, where the subscripts ij refer to the nodes $n2$-$n4$, and

$$[K_{ij}]_{2\times2} = \begin{bmatrix} K_{y_i y_j} & K_{y_i \theta_j} \\ K_{\theta_i y_j} & K_{\theta_i \theta_j} \end{bmatrix} \tag{12}$$

Then finally, for a particular frequency ω model B is given by:

$$\mathbf{B}_{II} = \mathbf{K} - \omega^2 \mathbf{M} \tag{13}$$

3.1.2 Model A

To construct model A, the experimental translational mode shapes ϕ_r were measured using standard impact test equipment. An impulse hammer was used to excite the system at the base of the holder, and the response

was measured at eighteen equally spaced locations between the tool tip and the base of the holder. The tip of the holder was chosen as the excitation location because the tool tip was found to be too flexible for a steel tipped hammer. To the eighteen measured frequency response functions H_{ij}, where $i \in \{1, 2, ..., 18\}$ and $j = 5$, curves were fitted between 0 Hz and 5000 Hz and a modal model extracted .

In total eight modes (ϕ_r) were extracted with natural frequencies between 273 Hz and 4045 Hz. Then to each of the eight modes a polynomial of order three was fitted in the least-squares sense. A least squares curve fit finds the optimum fit to the measured mode shapes by minimising the sum of the squared residuals, where a residual is defined as the difference between the measured value and the fitted value. Each of the eight polynomials were then differentiated to get the rotational mode shapes $\phi_r^{(1)}$ [9]. Then for each of the four nodes n_1 to n_4 shown in Fig. 5, the translational and rotational FRFs (H_{ij}, N_{ij}, L_{ij}, P_{ij}) were constructed such that:

$$H_{ij}(\omega) = \frac{Y_i(\omega)}{F_j(\omega)} = \sum_{r=1}^{N} \frac{\phi_r(x_i)\phi_r(x_j)}{\lambda_r^2 - \omega^2} \qquad N_{ij}(\omega) = \frac{\Theta_i(\omega)}{F_j(\omega)} = \sum_{r=1}^{N} \frac{\phi_r^{(1)}(x_i)\phi_r(x_j)}{\lambda_r^2 - \omega^2}$$
$$L_{ij}(\omega) = \frac{Y_i(\omega)}{M_j(\omega)} = \sum_{r=1}^{N} \frac{\phi_r(x_i)\phi_r^{(1)}(x_j)}{\lambda_r^2 - \omega^2} \qquad P_{ij}(\omega) = \frac{\Theta_i(\omega)}{M_j(\omega)} = \sum_{r=1}^{N} \frac{\phi_r^{(1)}(x_i)\phi_r^{(1)}(x_j)}{\lambda_r^2 - \omega^2} \tag{14}$$

where Y_i is the displacement at DOF i, F_j is the force at DOF j, Θ_i is the rotation at DOF i, M_j is the moment at DOF j, $\phi_r(x_i)$ is the rth translational mode shape at DOF i, $\phi_r^{(1)}(x_i)$ is the rotational mode shape at DOF i, and λ_r is the rth eigenvalue.

The accuracy of this method depends largely on the number of data points included in the polynomial fitting. Increasing the number of data points was found to increase the accuracy of the rotational mode shapes, whilst decreasing the efficiency of the method. It was found that using eighteen data points continuously produced accurate results for all modes, although it was not always necessary.

Although some of the translational FRFs (H_{ij}) were measured directly, the regenerated curves were used so as not to include noise in the SM equations. Small errors, such as noise, in the input can lead to large errors in the output because of the matrix inversions. Whilst curve fitting also causes small errors, it was found that better results could be obtained using the smooth regenerated FRFs.

Model A was then constructed, for a particular frequency ω, as follows:

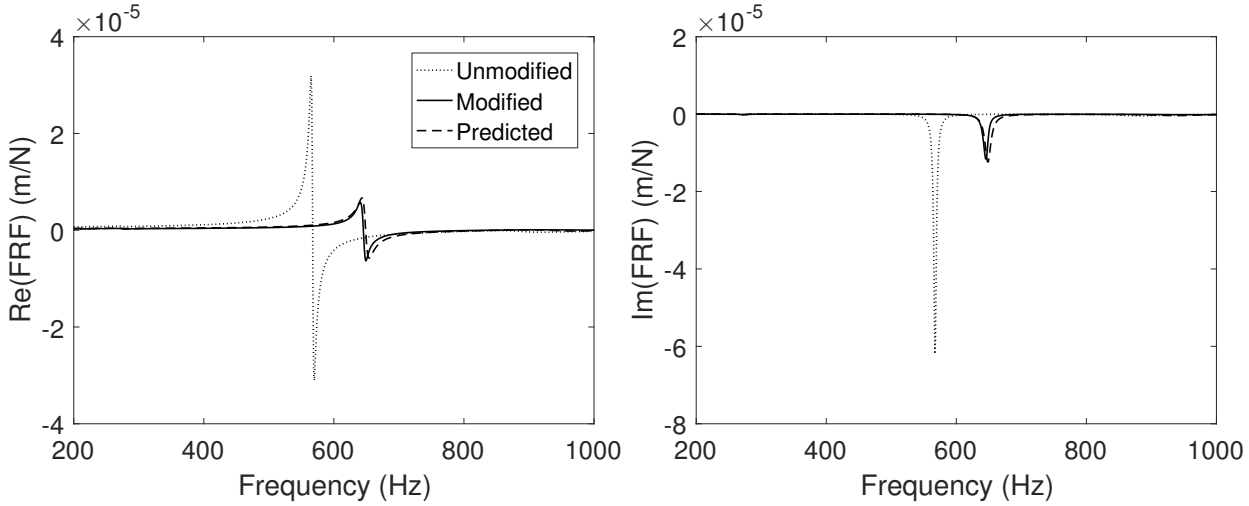
$$\begin{aligned}\mathbf{H}_A &= \begin{bmatrix} [\mathbf{H}_{AOO}]_{2\times2} & [\mathbf{H}_{AOI}]_{2\times6} \\ [\mathbf{H}_{AIO}]_{6\times2} & [\mathbf{H}_{AII}]_{6\times6} \end{bmatrix} \\ &= \left[\begin{array}{c|ccc} \left[\mathbf{G}_{11}\right]_{2\times2} & \left[\mathbf{G}_{12}\right]_{2\times2} & \left[\mathbf{G}_{13}\right]_{2\times2} & \left[\mathbf{G}_{14}\right]_{2\times2} \\ \hline \left[\mathbf{G}_{21}\right]_{2\times2} & \left[\mathbf{G}_{22}\right]_{2\times2} & \left[\mathbf{G}_{23}\right]_{2\times2} & \left[\mathbf{G}_{24}\right]_{2\times2} \\ \left[\mathbf{G}_{31}\right]_{2\times2} & \left[\mathbf{G}_{32}\right]_{2\times2} & \left[\mathbf{G}_{33}\right]_{2\times2} & \left[\mathbf{G}_{34}\right]_{2\times2} \\ \left[\mathbf{G}_{41}\right]_{2\times2} & \left[\mathbf{G}_{42}\right]_{2\times2} & \left[\mathbf{G}_{43}\right]_{2\times2} & \left[\mathbf{G}_{44}\right]_{2\times2} \end{array}\right] \end{aligned} \tag{15}$$

where the subscripts 1-4 refer to the nodes n_1-n_4, and

$$\left[\mathbf{G}_{ij}\right]_{2\times2} = \begin{bmatrix} H_{ij}(\omega) & N_{ij}(\omega)) \\ L_{ij}(\omega) & P_{ij}(\omega) \end{bmatrix} \tag{16}$$

3.2 Direct structural modification

Using the models constructed in section. 3.1, the direct SM method was carried out by applying Eq. (6) over a frequency range of 1 Hz to 5000 Hz with a 1 Hz increment. The resultant matrix (for each frequency) $\mathbf{H}_{CII}$ contains the four FRFs (H_{11},N_{11},L_{11},P_{11}), from which the translational FRF H_{11} was extracted. The predicted result is presented in Fig. 6 alongside its experimental counterpart and that of the unmodified



(a) Real (b) Imaginary

Figure 6: Real (a) and Imaginary (b) frequency response function plots comparing the experimental tool tip dynamics of the unmodified ($\cdots$) and modified holders (—), with the predicted result (- -) from the spindle rig

holder. It should be noted that the experimental tool tip FRF from the modified holder was constructed from the measured mode shapes, since the excitation was applied at the base of the holder and not the tool tip.

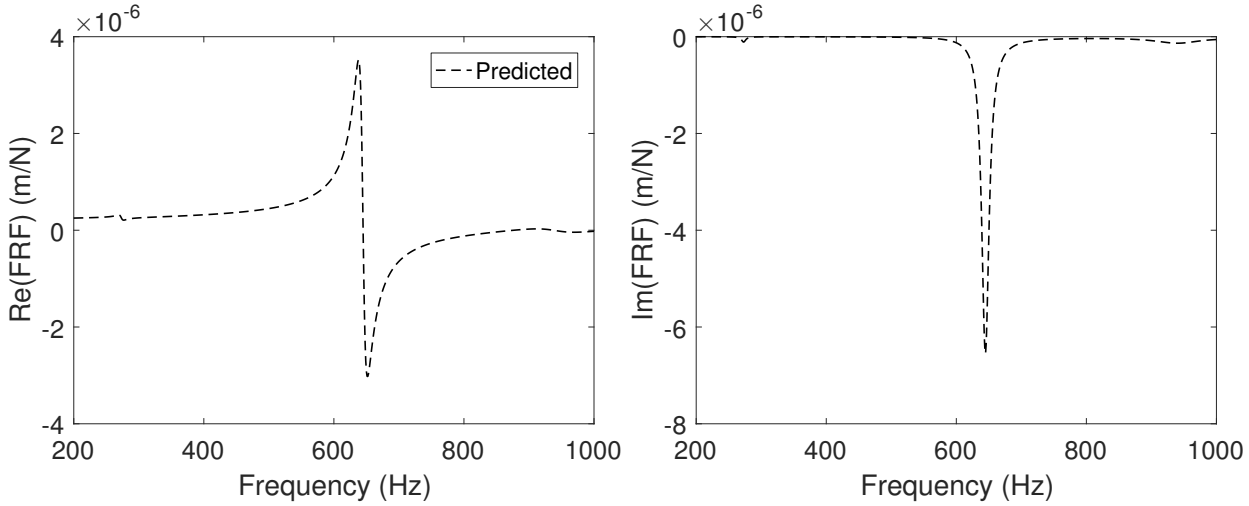
It can be seen that the predicted result shows a very high correlation with the experimental data. The single mode occurs at 646 Hz, within 1% of the measured mode at 649 Hz, whilst the predicted amplitude (of the imaginary part) is within 7% of the measured value. It is clear that the direct SM of tool holder geometry has a clear advantage over RCSA, in that these results have been obtained without including any unknown interface properties. Hence, using this method it is possible to choose the optimum holder for a given operation without having to take any further measurements such as contact stiffness or damping. However, optimisation using the direct method, as well as RCSA, still require numerical models of each and every possible modification. The inverse SM method is now applied to the same problem in order to resolve this issue.

3.3 Inverse structural modification

To apply inverse SM, model A was constructed using the same methodology as in section 3.1.2. Then, the same beam elements as before were used to construct model B; however, a symbolic variable $d2$ was used for the outer diameter of the beams instead of inputting an actual value. Therefore, the tapered beam has an inner diameter of 0.024 m and an outer diameter ranging between 0.024 m and $d2$, and the untapered beam has an inner diameter of 0.024 m and an outer diameter of $d2$. In doing so, model B becomes a symbolic matrix and a function of $d2$.

Since the natural frequency of the modified holder occurs at 646 Hz, inverse SM was used to seek a value of $d2$ which would result in a mode at 646 Hz, therefore $w_{seek} = 2\pi(646)$ rad/s. Referring back to section 2, Eq. (8), the natural frequencies of the modified model C are given by

$$\det(\mathbf{I} + \mathbf{H}_{AII}\mathbf{B}_{II}(d2)) = 0 \tag{17}$$



(a) Real (b) Imaginary

Figure 7: Real (a) and Imaginary (b) frequency response function plots showing the predicted result (...) from the direct SM method on the spindle rig with a base diameter d2=0.042 m

To solve this, the matrix $\mathbf{H}_{AII}$ is given by

$$\mathbf{H}_{AII} = \begin{bmatrix} \left[\mathbf{G}_{22}(\omega_{seek})\right]_{2\times2} & \left[\mathbf{G}_{23}(\omega_{seek})\right]_{2\times2} & \left[\mathbf{G}_{24}(\omega_{seek})\right]_{2\times2} \\ \left[\mathbf{G}_{32}(\omega_{seek})\right]_{2\times2} & \left[\mathbf{G}_{33}(\omega_{seek})\right]_{2\times2} & \left[\mathbf{G}_{34}(\omega_{seek})\right]_{2\times2} \\ \left[\mathbf{G}_{42}(\omega_{seek})\right]_{2\times2} & \left[\mathbf{G}_{43}(\omega_{seek})\right]_{2\times2} & \left[\mathbf{G}_{44}(\omega_{seek})\right]_{2\times2} \end{bmatrix} \tag{18}$$

and model B is given by

$$\mathbf{B}_{II}(d2) = \mathbf{K}(d2) - \omega_{seek}^2 \mathbf{M}(d2) \tag{19}$$

Then, evaluating Eq. (17) results in a polynomial in $d2$ of order 36, with complex coefficients. Since $d2$ is real, the real and imaginary parts of the polynomial are set to zero and solved individually. The polynomials are too large to solve analytically, however using MATLAB's vpasolve function, a numerical solution was found, giving 36 possible diameters. However, some of these solutions can be instantly disregarded, firstly all negative solutions were removed, and then solutions outside of the possible range for $d2$ were also discounted. Since the base diameter $d2$ cannot exceed the flange diameter $d1$, it has an allowable range of $0.024 < d2 < 0.064$ m. This resulted in two possible solutions, 0.033 m and 0.042 m. It is already known that a diameter of 0.034 m results in a mode at 646 Hz, hence the first solution is correct to within 1 mm.

The validity of the second solution was verified by carrying out the direct SM method covered in section 3.2. This time a base diameter of 0.042 m was used in model B. The results are shown in Fig. 7. It can be seen that, as predicted, a mode occurs at 646 Hz when the tool holder has a diameter of 0.042 m.

Therefore, using a single experimental model and a single (partially constructed) numerical model, it is possible to predict a tool holder geometry that will shift the dominant natural frequency of the tool to any frequency ω_{seek}. By substituting ω_{seek} into Eq. 1, it is therefore possible to predict an optimum tool holder geometry that will shift the peaks in the stability threshold to any value by solving a single equation.

4 Conclusion

Optimising the geometry of a tool holder in order to avoid the onset of chatter can be an experimentally expensive operation, and traditionally requires the manufacturer to construct experimental models of the machine with each tool holder in place. In order to streamline this process the RCSA can be used, which

requires only a single experimental model alongside numerical models of each and every tool holder. However, the RCSA method also requires knowledge of the interface dynamics between the tool and tool holder and between the tool holder and spindle - a problem that has prevented the method from significant industrial application.

This paper has presented a new structural modification method for the optimisation of tool holder geometry. Firstly, it was demonstrated that the direct SM method can be used to select an optimum tool holder geometry from the available range whilst removing the requirement to include the interface dynamics. Secondly, it was shown using the inverse SM method, that the peaks in the stability lobe diagram can be shifted to an optimum spindle speed using a single experimental model and a single numerical model with no knowledge of the interface properties.

Acknowledgements

This work was co-funded through the EPSRC Industrial Doctorate Centre in Machining Science (EP/I01800X/1) and by The Boeing Company.

References

[1] T. L. Schmitz and G. S. Duncan, "Three-component receptance coupling substructure analysis for tool point dynamics prediction," *Journal of Manufacturing Science and Engineering*, vol. 127, no. 4, pp. 781–790, 2005.

[2] T. L. Schmitz, K. Powell, D. Won, G. S. Duncan, W. G. Sawyer, and J. C. Ziegert, "Shrink fit tool holder connection stiffness/damping modeling for frequency response prediction in milling," *International Journal of Machine Tools and Manufacture*, vol. 47, no. 9, pp. 1368 – 1380, 2007.

[3] J. E. Mottershead and Y. M. Ram, "Inverse eigenvalue problems in vibration absorption: passive modification and active control," *Mechanical systems and signal processing*, vol. 20, no. 1, pp. 5–44, 2006.

[4] H. N. Özgüven, "Structural modifications using frequency response functions," *Mechanical Systems and Signal Processing*, vol. 4, no. 1, pp. 53–63, 1990.

[5] A. Delgado, E. Ozturk, and N. Sims, "Analysis of non-linear machine tool dynamic behavior," *Procedia Engineering*, vol. 63, pp. 761 – 770, 2013.

[6] C. To, "A linearly tapered beam finite element incorporating shear deformation and rotary inertia for vibration analysis," *Journal of Sound and Vibration*, vol. 78, no. 4, pp. 475 – 484, 1981.

[7] D. Thomas, J. Wilson, and R. Wilson, "Timoshenko beam finite elements," *Journal of Sound and Vibration*, vol. 31, no. 3, pp. 315–330, 1973.

[8] A. Ertürk, H. Özgüven, and E. Budak, "Analytical modeling of spindle–tool dynamics on machine tools using timoshenko beam model and receptance coupling for the prediction of tool point frf," *International Journal of Machine Tools and Manufacture*, vol. 46, no. 15, pp. 1901–1912, 2006.

[9] T. Gibbons, E. Öztürk, and N. Sims, "Rotational degree-of-freedom synthesis: An optimised finite difference method for non-exact data," *Journal of Sound and Vibration*, vol. 412, pp. 207 – 221, 2018.

Bifurcations and limit cycles due to self-excitation in non-linear systems with joint friction: Phenomena and approximation schemes

J. Kappauf [1], **H. Hetzler** [1]
[1] University of Kassel, Department of Mechanical Engineering, Engineering Dynamics Group
Mönchebergstraße 7, 34125, Kassel, Germany
[1] e-mail: **kappauf@uni-kassel.de**

Abstract
In this contribution calculation methods for approximating periodic limit cycles of self-excited dynamical systems with frictional damping are discussed. Particularly in industrial application, e.g. the analysis of brake squeal recently, the so-called *Energy-Balance* has attracted a lot of interest [11] and will be compared to classical methods like *Averaging* and the *Harmonic Balance* method, which are commonly used for direct approximation of limit cycles. Focussing on the effect of joint damping, a short overview on modelling of joint friction is given. In the second part two methods, the *Harmonic Balance* and *Energy Balance* method, for non-linear analysis of dynamical systems are discussed and the bifurcation behaviour for two minimal models taken from literature [5, 6] is studied.

1 Introduction

For smooth non-linear systems the investigation of stability and bifurcations leading to limit cycle oscillations has a long tradition [10]. In particular, HOPF-Bifurcations of steady states leading to periodic limit cycles are a common phenomenon in non-linear dynamical systems, especially for the further discussed self-excited systems. In technical applications e.g. the analysis of brake noise, these occurrence of self-excited vibrations has to be determined, to assess and avoid NVH effects during operation.
For providing stability of fixed points for particular operation conditions in terms of LYAPUNOV for different initial conditions mostly the *Complex Eigenvalue Analysis* (CEA) is applied. However, this is not sufficient in general when dealing with non-linearities, e.g. joints or contacts, because they can cause further solution branches, where vibrations can occur [7]. Moreover, contact implies nun-smooth forces and linearisation is no longer applicable.

In literature, in terms of NVH referring to brake systems the destabilisation of the steady state is often related to the following mechanisms [5]:

- negative friction gradient
- flutter instability / mode coupling

In the first case, self-excited oscillations could occur when the velocity gradient of the friction coefficient μ is negative in some operating conditions. Measurements of friction coefficients e.g. for brake pad applications show this common phenomenon very clearly [4]. The occurrence of this negative gradient can lead to self-excitation, if the structure exhibits not enough viscous or structural damping. this mechanism is usually associated with *groan* or *muh* noise.

Dealing with *mode coupling* respectively *flutter instability*, the circulatorical forces in the equations of motion excite the system. Within this contribution a two degree of freedom model is investigated in [8] and shows the effect of mode coupling clearly. Depending on the friction coefficient $\mu = \text{const}$ the stability of the steady state configuration changes.

As a standard approach in industrial applications, the onset of self-excitation is assessed based on an CEA [10]. When considering non-smooth non-linearities e.g. joints and contacts, suitable methods for the stability analysis of the non-linear system are still required.

For the analysis of bifurcation phenomena dissipation is usually modelled as non-linear but essentially smooth viscous damping. In the following a short review on joint friction models is given, before the chosen non-linear approximation methods for periodic self-excited oscillations are discussed. After a subsequent presentation of two well-known minimal models for NVH analysis of brake systems the results of the bifurcation analysis are shown. The contribution closes with a short summary and an outlook.

2 Joints in mechanical systems

In real engineering applications, dissipation is a well-known but not sufficiently understood phenomenon. While *damping* is usually modelled as non-linear but smooth viscous or structural damping, one of the main sources of dissipation is frictional damping, which is an essentially non-smooth mechanism. Machinery usually consists of many assembled components, where dissipation or excitation of the friction in the joints are highly relevant when analysing the dynamical behaviour of the system.
An example of a frictional contact of two jointed components is shown in Fig. 1, where $\mathbf{F}_\mathrm{N}$ denotes the normal force of the contact, μ is the friction coefficient and $\mathbf{F}_\mathrm{T}$ the friction force.

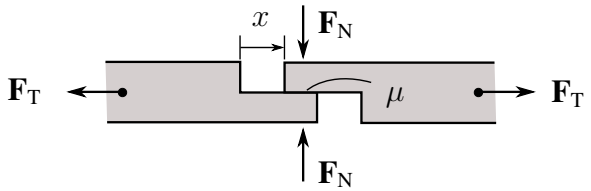


Figure 1: Example for frictional contact of two jointed components [6]

Starting with LEONARDO DA VINCI to AMONTONS and COULOMB, the phenomenon of frictional damping has interested scientists for centuries. During this research process, different friction force models were established, which are often separated into three groups: *quasi-static*, *dynamic* and *hysteretic* friction models [1].

When dealing with *quasi-static friction* models, the friction force $\mathbf{F}_\mathrm{T}$ is a function with respect to the relative velocity $||\vec{v}_\mathrm{rel}||$ of the contact surfaces. In the simplest case it is a constant function, which corresponds with the COULOMB friction model. For some materials, the dissipation is independent from the relative velocity [1], while there are other investigations, e.g. from STRIBECK, which show a velocity-dependent friction behaviour.

When using quasi-static friction models like the classical COULOMB model, dynamical effects of the contact region can not be modelled. Therefore, some *dynamic friction models* were established, e.g. the DAHL-, LUGRE- and the so-called LEUVEN model [1]. Here, the dynamic behaviour of $\mathbf{F}_\mathrm{T}$ is given by differential equations with respect to the state variables of the system and possibly auxiliary variables to capture the internal dynamics of the frictional contact.

The present paper focusses on the dynamic behaviour of systems with COULOMB friction elements.

3 Approximation Methods

The equations of motion for autonomous mechanical systems under the influence of joint friction read

$$\dot{\mathbf{z}} = \mathbf{f}(\mathbf{z};\nu), \quad \mathbf{z} = [\mathbf{q}, \dot{\mathbf{q}}]^\top \in \mathbb{R}^{2N_d \times 1}, \quad \nu \in \mathbb{R} \tag{1}$$

where the state space vector $\mathbf{z}$ contains the state variables (for mechanical systems position $\mathbf{q}$ and velocity $\dot{\mathbf{q}}$) and the scalar parameter ν controls stability and bifurcation. In general, analytical solutions are not available, hence numerical calculation schemes are needed for the direct approximation of periodic solutions of the self-excited system. Therefore, suitable methods were established and two of them will be shortly described in this paragraph: a *Harmonic Balance* scheme and the *Energy Balance* method. In the following, these methods will be compared to results of the *Averaging* method [5, 6].

3.1 Harmonic Balance

Approximating limit cycles of self-excited mechanical systems is a well known procedure [2, 9, 13]. One of the most common methods is the *Harmonic Balance Method* (HBM). Since periodic solutions are sought for, a truncated FOURIER series

$$\mathbf{z}_{\text{HB}}(t) = \hat{\mathbf{z}}_{\text{c},0} + \sum_{k=1}^{H} \hat{\mathbf{z}}_{\text{c},k} \cos(k\omega t) + \hat{\mathbf{z}}_{\text{s},k} \sin(k\omega t) \tag{2}$$

is chosen as ansatz to describe periodic solutions. Here, H is the number of ansatz functions, ω the base frequency and $\hat{\mathbf{z}}_{\text{c},k}$, $\hat{\mathbf{z}}_{\text{s},k}$ are the FOURIER coefficients with respect to the harmonic to order k. Substituting eq. (2) into the equations of motion in state space formulation (1), the FOURIER approximation can not fulfil them exactly due to truncation and a residuum

$$\mathcal{R}(\mathbf{z}_{\text{HB}};\nu) = \dot{\mathbf{z}}_{\text{HB}} - \mathbf{f}(\mathbf{z}_{\text{HB}};\nu) \tag{3}$$

can be introduced. To obtain equations for calculating the $N_d(2H+1)+1$ unknowns, the coefficients and frequency of the truncated FOURIER series, one can choose different procedures. Some authors prefer substituting $\mathbf{z}_{\text{HB}}$ in $\mathbf{f}$ and balance the harmonic terms up to H^{th} order, if $\mathbf{f}$ is differentiable [2]. Especially for both strong or non-smooth nonlinearities, e.g. joints or nonlinear potenial forces, this procedure is not efficient, as $\mathbf{f}$ is not differentiable in this case.

Hence, a more general way is based on a GALERKIN projection, which demands that the error w.r.t. the function space of the ansatz functions vanishes. Therefore, the residuum, eq. (3), is projected on the ansatz functions of the FOURIER series

$$\int_0^T (\dot{\mathbf{z}}_{\text{HB}} - \mathbf{f}(\mathbf{z}_{\text{HB}};\nu)) \cos(k\omega t) \mathrm{d}t = 0, \quad k = 0, 1, 2, ..., H, \tag{4a}$$

$$\int_0^T (\dot{\mathbf{z}}_{\text{HB}} - \mathbf{f}(\mathbf{z}_{\text{HB}};\nu)) \sin(k\omega t) \mathrm{d}t = 0, \quad k = 1, 2, ..., H, \tag{4b}$$

which leads to $N_d(2H+1)$ equations, where T provides uniqueness of the desired solution. Compared to several alternative conditions, the *integral phase condition* [12] proofed very good numerical robustness. It selects that solution $\mathbf{u}(t)$ near $\tilde{\mathbf{z}}(t)$, which can be a first approximation of the periodic solution $\mathbf{z}(t)$, so that the functional

$$D(\sigma) = \int_0^T ||\mathbf{u}(t+\sigma) - \tilde{\mathbf{z}}(t)||^2 \mathrm{d}t \tag{5}$$

is minimized, where t represents time and σ the phase shift. To obtain the extremal value of the functional, one has to set its derivation with respect to σ

$$\frac{\partial D}{\partial \sigma} = 2 \int_0^T \Big([\mathbf{u}(t+\sigma) - \tilde{\mathbf{z}}(t)]^\top \dot{\mathbf{u}}(t+\sigma) \Big) \, \mathrm{d}t \tag{6}$$

to zero [3]. Identifying $\mathbf{u}(t+\sigma) = \mathbf{z}_{\text{HB}}(t)$ the phase condition reads

$$\int_0^T \Big([\mathbf{z}_{\text{HB}}(t) - \tilde{\mathbf{z}}(t)]^\top \mathbf{f}(\mathbf{z}_{\text{HB}}; \mu) \Big) \, \mathrm{d}t = 0. \tag{7}$$

This algebraic equation system eqs. (4),(7) can be solved by NEWTON-RAPHSON iteration.

However, eq. (7) is a condition for extrema, thus one has to apply a sufficient condition for minima. Partial integration of eq. (7), according to [13], and differentiation with respect to σ yields

$$\frac{\partial^2 D}{\partial \sigma^2} = - \int_0^T \tilde{\mathbf{z}}(t)^\top \ddot{\mathbf{z}}_{\text{HB}}(t) \mathrm{d}t > 0 \tag{8}$$

for the sufficient minimum condition of the functional D, which has to be fulfilled. Otherwise a phase shift $\sigma_{\text{corr}} = \pi$ is added and the calculation is restarted.

To make the calculation of eq. (4) numerically more efficient than solving them by use of numerical integration, a so-called *Alternating Frequency Time* (AFT) method is applied. Following [9] the FOURIER ansatz (2) is transformed into complex notation and

$$\mathbf{z}_{\text{HB}}(t) = \mathrm{Re}\left\{ \sum_{k=0}^{H} \hat{\mathbf{Z}}_k \mathrm{e}^{\mathrm{i}k\omega t} \right\}, \quad \hat{\mathbf{Z}}_k = \hat{\mathbf{z}}_{\mathrm{c},k} - \mathrm{i}\hat{\mathbf{z}}_{\mathrm{s},k} \in \mathbb{C}^{2N_d \times 1}, \tag{9}$$

is obtained, where $\hat{\mathbf{z}}_{\mathrm{s},0} = \mathbf{0}$. Transforming the projection in eq. (4) by multiplying eq. (4b) with the imaginary unit i and subtracting that product from eq. (4a) yields the GALERKIN projection in complex notation, which reads

$$\mathcal{R}_k = \int_0^T \left(\dot{\mathbf{z}}_{\text{HB}} - \mathbf{f}(\mathbf{z}_{\text{HB}}; \nu) \right) \mathrm{e}^{-\mathrm{i}k\omega t} \mathrm{d}t = 0, \quad k = 0, 1, 2, ..., H, \tag{10}$$

where $\mathrm{Re}(\mathcal{R}_k)$ equates eq. (4a) for $k \geq 0$, respectively $\mathrm{Im}(\mathcal{R}_k)$ equates eq. (4b) for $k \geq 1$. Introducing a dimensionless time scale $\omega t = \tau$ and multiplying eq. (10) with $\frac{1}{\pi}$ yields the FOURIER coefficients

$$\tilde{\mathcal{R}}_k = \begin{cases} 2\tilde{\mathcal{R}}_0 & \\ \tilde{\mathcal{R}}_k & k \geq 1 \end{cases} = \frac{1}{\pi} \int_0^{2\pi} \left(\omega \mathbf{z}'_{\text{HB}} - \mathbf{f}(\mathbf{z}_{\text{HB}}; \nu) \right) \mathrm{e}^{-\mathrm{i}k\tau} \mathrm{d}\tau, \tag{11}$$

see [9]. Hence, within this notation the FOURIER spectrum of the residuum is approximated and evaluated using the *Fast Fourier Transformation* (FFT) in MATLAB. This solution procedure can schematically be written as

$$\{\tilde{\mathcal{R}}_k\} = \mathrm{FFT}[\mathcal{R}(\mathbf{z}_{\text{HB}}; \nu)], \tag{12}$$

which implies changing from time into the frequency domain and where $\{\mathcal{R}_k\}$ denotes the coefficients of the residuum [9]. Here, the approximative solution $\mathbf{z}_{\text{HB}}$ is constructed by using the FOURIER coefficients $\hat{\mathbf{Z}}_k$ and the base frequency ω, see eq. (9).

Hence, before substituting the approximation into eq. (3), there is an alternation from frequency to time domain respectively a *inverse* FFT. For mechanical systems, further optimizations exist for this procedure, e.g. only using coefficients of the displacement $\mathbf{q}_{\text{HB}}(t)$ as unknown and provide the derivations $\dot{\mathbf{q}}_{\text{HB}}(t)$ and $\ddot{\mathbf{q}}_{\text{HB}}(t)$ analytically for the FOURIER ansatz.

To this end, HBM is a possible method for calculating periodic solutions in dynamical systems, where only periodicity of the solution is demanded and increasing the truncation number H can improve accuracy of the approximation.

3.2 Energy Balance

One problem of the HBM for large scaled dynamical systems, e.g. finite element models of a brake system, is finding initial conditions for the high number of unknowns in the algebraic system, especially for a higher truncation number H. To avoid this and to reduce calculation effort, a so-called *Energy Balance* method has been established [11].

Before presenting the calculation procedure, some general remarks on energy in dynamical systems should be made. The derivation with respect to time t of the total energy of an autonomous dynamical system is given by

$$\frac{\mathrm{d}}{\mathrm{d}t}\left(E_{\text{kin}} + E_{\text{pot}}\right) = \dot{\mathbf{q}}^{\top}\mathbf{Q}^{\text{D}}, \tag{13}$$

where E_{kin} denotes the kinetic and E_{pot} the potential energy, while $\dot{\mathbf{q}}^{\top}\mathbf{Q}^{\text{D}}$ is the projection of non-conservative, generalised forces $\mathbf{Q}^{\text{D}}$ on the generalised velocity vector $\dot{\mathbf{q}}$. In this autonomous case, the rate of change of the total energy only depends on $\dot{\mathbf{q}}^{\top}\mathbf{Q}^{\text{D}}$. Balancing the energy flux of the system over a period T for a solution $\mathbf{q}(t)$ leads to

$$\Delta E_{\text{kin}} + \Delta E_{\text{pot}} = \int_0^T \dot{\mathbf{q}}^{\top}\mathbf{Q}^{\text{D}}. \tag{14}$$

To obtain periodic solutions, the deviation of the total energy over its period T must be zero to ensure the excitation and dissipation rate being equal over one period.

After crossing the HOPF bifurcation point of the dynamical system, periodic limit cycles can occur. For generating an ansatz for periodic solutions, information from the eigenvalues λ_i and eigenvectors $\hat{\mathbf{z}}_i$ of the linear subsystem of eq. (1) is used, where the linearisation is done with respect to one of the rest positions of the non-linear system.
The main assumption of the discussed method demands that the shape of the emerging limit cycle is assumed to be equal to the mode shape of the unstable eigenvector $\hat{\mathbf{q}}_{\text{u}}$ of the linear subsystem, where for the corresponding eigenvalue $\mathrm{Re}(\lambda_{\text{u}}) > 0$ holds. In this formulation of the *Energy Balance*, only the generalised displacement components $\hat{\mathbf{q}}_{\text{u}}$ are used. Moreover, the base frequency of the periodic solution is required to be the imaginary part of the unstable eigenvalue λ_{u}, respectively $\omega_{\text{u}} = \mathrm{Im}(\lambda_{\text{u}})$.

Within this assumptions, the approximative solution is given by

$$\mathbf{q}_{\text{EB}}(t) = A_{\text{EB}}\left(\mathrm{Re}(\hat{\mathbf{q}}_{\text{u}})\cos(\omega_{\text{u}}t) - \mathrm{Im}(\hat{\mathbf{q}}_{\text{u}})\sin(\omega_{\text{u}}t)\right) \tag{15}$$

where A_{EB} is a scaling parameter. Substituting this approximation (15) into eq. (14) and setting the deviation of the total energy to zero yields one equation

$$\mathcal{R}_{\text{EB}} = \int_0^{T_{\text{u}}} \dot{\mathbf{q}}_{\text{EB}}^{\top}\mathbf{Q}^{\text{D}}(\mathbf{q}_{\text{EB}}, \dot{\mathbf{q}}_{\text{EB}}) = 0 \tag{16}$$

for calculating the scaling parameter A_{EB}, where $T_{\text{u}} = \frac{2\pi}{\omega_{\text{u}}}$. Making use of the unstable modes of the linear subsystem decreases the computational effort while these requirements limit the space of possible solutions compared to the HBM.

4 Minimal models

For having a closer look at the presented methods, some minimal models will be discussed, which were taken from literature [5, 6]. Focussing on the topic of NVH and brake squeal, two well known models were chosen to picture the self-excited effects of negative friction gradient and mode coupling. In the following paragraph bifurcation behaviour of the mechanical systems under the influence of COULOMBs joint friction as well as accuracy of the chosen numerical methods is discussed.

4.1 1DoF Oscillator with Coulomb friction

The first model is a one degree of freedom oscillator with friction between lower surface/belt and non-smooth COULOMB friction, see Fig. 2. For $D < 0$, the system is self-excited by a negative friction gradient, as it was discussed in the introduction. The equation of motion reads

$$m\ddot{x} + d\dot{x} + kx + k_3x^3 \in \mu F \,\mathrm{Sign}(v_0 - \dot{x}) + R\,\mathrm{Sign}(\dot{x}), \tag{17}$$

where m denotes mass, d viscous damping, $\mu = \mu(v_0 - \dot{x})$ the velocity depending friction coefficient, F contact force, k linear and k_3 non-linear stiffness coefficient, v_0 the velocity of the belt and R COULOMBs friction force in the joint. Here, the set-valued sign-function has been used to account for sticking and sliding:

$$\mathrm{Sign}(\dot{x}) = \begin{cases} \mathrm{sign}(\dot{x}), & |\dot{x}| > 0 \\ [-1, 1], & |\dot{x}| = 0 \end{cases} \tag{18}$$

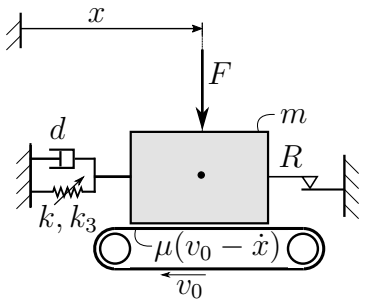


Figure 2: One degree of freedom friction oscillator with COULOMB friction joint model [5]

Expressing the sliding friction coefficient μ between mass and belt as a truncated TAYLOR series leads to [5]

$$\mu(v_0 - \dot{x}) \approx \mu_0 - \mu_1\dot{x} - \mu_3\dot{x}^3. \tag{19}$$

When $v_0 \gg \dot{x}$, the contact will always be sliding, hence the equations of motion read

$$m\ddot{x} + (d + \mu_1 F)\dot{x} + kx - \mu_0 F \in -k_3x^3 - \mu_3 F\dot{x}^3 + R\,\mathrm{Sign}(\dot{x}). \tag{20}$$

Introducing the dimensionless quantities

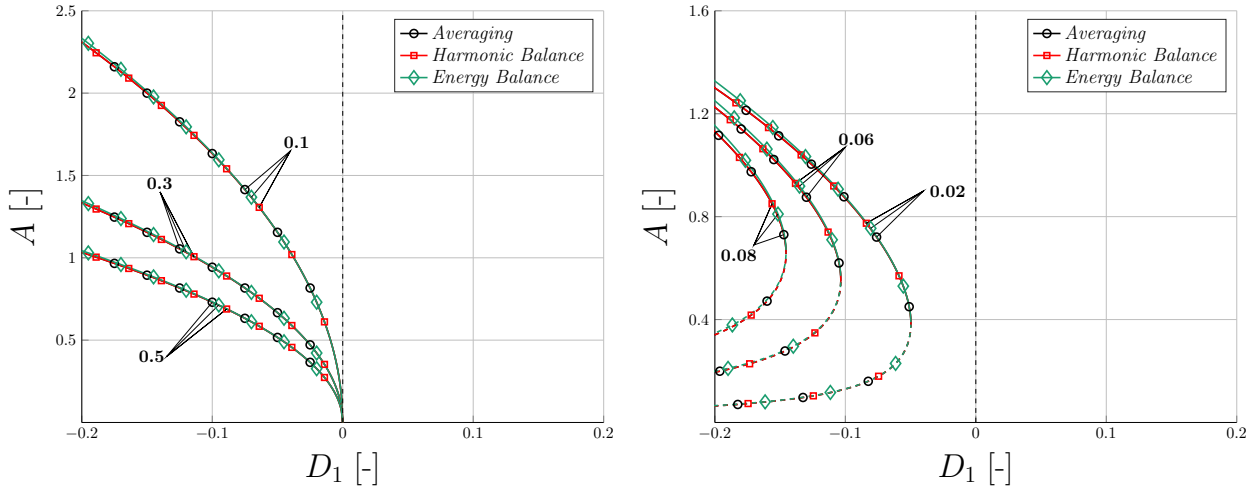
$$q = \frac{(x - x_0)}{L}, \omega_0 = \sqrt{\frac{k}{m}}, \tau = \omega_0 t, D_1 = \frac{d + \mu_1 F}{2\omega_0 m}, D_3 = \frac{\omega_0 \mu_3 F}{m}, \kappa = \frac{k_3}{k}, \rho = \frac{R}{kL}$$

leads to the dimensionless equations of motion

$$q'' + 2D_1q' + q \in -\kappa q^3 - D_3q'^3 + \rho\,\mathrm{Sign}(q') \tag{21}$$

where q is the displacement related to the rest position x_0 of the system. Applying the methods presented in chapter 3, the bifurcation behaviour of eq. (21) is studied for different parameter configurations of D_3 and ρ with respect to the bifurcation parameter D_1 and at first $\kappa = 0$ holds.

While the results of the *Harmonic Balance* and *Energy Balance* method were computed with MATLAB, the results from *Averaging* were taken from literature [5]. The results show good agreement near the HOPF bifurcation point at $D_1 = 0$ for the smooth system, see Fig. 3a. Obviously for non-smooth COULOMB friction, the solution of *Energy Balance* deviates slightly from the other methods solution when leaving the environment of the HOPF bifurcation.



(a) Amplitude A of stationary periodic solutions of different approximation methods for various values of D_3

(b) Amplitude A of stationary periodic solutions of different approximation methods for various values of ρ and $D_3 = 0.3$

Figure 3: Amplitudes of stationary periodic solutions depending on the damping D_1 for different values D_3 and COULOMB friction force ρ, while $\kappa = 0$ holds.

Furthermore the effect of non-linear potential forces on the *Energy Balance* method is studied. In the following COULOMBs dimensionless friction force ρ is not considered to avoid superposition of these two impacts. Introducing the kinetic and potential energy of eq. (21)

$$E_{\text{kin}} = \frac{1}{2} q'^2 \text{ and } E_{\text{pot}} = \frac{1}{2} q^2 + \frac{\kappa}{2} q^2 \tag{22}$$

and applying them to the energy balance in eq. (14) leads to

$$\underbrace{\frac{1}{2}\left(q'_{\text{EB}}(T_{\text{u}})^2 - q'_{\text{EB}}(0)^2\right)}_{=0} + \underbrace{\frac{1}{2}\left(q_{\text{EB}}(T_{\text{u}})^2 - q_{\text{EB}}(0)^2\right)}_{=0} + \underbrace{\frac{\kappa}{4}\left(q_{\text{EB}}(T_{\text{u}})^4 - q_{\text{EB}}(0)^4\right)}_{=0} = \int_0^{T_{\text{u}}} -2D_1 q'^2_{\text{EB}} - D_3 q'^4_{\text{EB}} \, \mathrm{d}\tau, \tag{23}$$

while $q_{\text{EB}}(t)$ denotes the periodic approximation of the limit cycle with period T_{u}. Hence, the *Energy Balance* method is unable to include effects of non-linear conservative forces, see eq. (23). Upcoming effects on the base frequency ω_{u} of the solution cannot be considered. Progressive stiffness characteristics lead to relations between amplitude and frequency as a analysis with HBM of the DUFFING oscillator showed, for instance [13].

4.2 2DoF Oscillator with Coulomb friction

Taking into account the structural coupling of the systems state variables, a linear spring c_3 generates the energetic exchange of the degrees of freedom, see Fig. 4. The dimensionless equations of motion for the minimal model are given by

$$\begin{bmatrix} 1 & 0 \\ 0 & 1 \end{bmatrix} \begin{Bmatrix} q''_1 \\ q''_2 \end{Bmatrix} + \begin{bmatrix} 2D_1 & 0 \\ 0 & 2D_1 \end{bmatrix} \begin{Bmatrix} q'_1 \\ q'_2 \end{Bmatrix} + \begin{bmatrix} 1+p & -\kappa+\mu \\ -\kappa & 1-p \end{bmatrix} \begin{Bmatrix} q_1 \\ q_2 \end{Bmatrix} \in - \begin{Bmatrix} \rho_1 \operatorname{Sign}(q'_1) \\ \rho_2 \operatorname{Sign}(q'_2) \end{Bmatrix}, \tag{24}$$

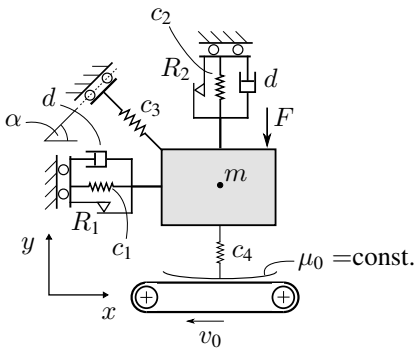


Figure 4: Two degree of freedom oscillator with COULOMB friction force R_i and belt [6]

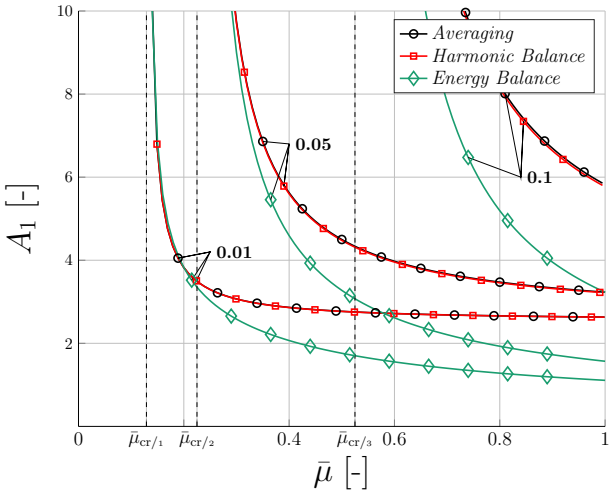
with dimensionless quantities

$$k = \frac{1}{2}(k_1 + k_2 + k_3 + k_4),\ \kappa = \frac{k_3 \sin(\alpha)\cos(\alpha)}{k},\ \rho_i = \frac{R_i}{kL}$$
$$\Delta k = \frac{1}{2}(k_1 - (k_2 + k_4) + k_3(\sin^2(\alpha) - \cos^2(\alpha))),\ D_1 = \frac{d}{2\omega_0^2 m}$$
$$\omega_0 = \sqrt{\frac{k}{m}},\ \tau = \omega_0 t,\ p = \frac{\Delta k}{k},\ \bar{\mu} = \mu_0 \frac{c_4}{c},\ q_1 = \frac{x - x_0}{L},\ q_2 = \frac{y - y_0}{L}$$

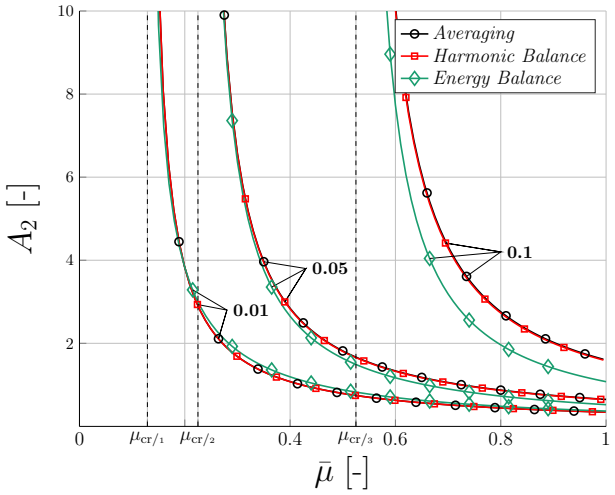
taken from [6]. With respect to the friction coefficient $\bar{\mu}$, bifurcation behaviour can be analysed by using the presented methods for predicting periodic limit cycles. First, the stability of the steady state configuration for the linear subsystem of eq. (24) can be analysed. Further calculations yield the critical value of $\bar{\mu}$ with

$$\bar{\mu}_{\mathrm{cr}} = \frac{4D_1^2 + \kappa^2 + p^2}{\kappa}, \tag{25}$$

for more detail see [6]. For the comparison of the calculation methods, the influence of dissipation in self-excited system is of high interest. Therefore, variations in D_1 and ρ_i were done and compared to results from the *Averaging* method, which were taken from [6].



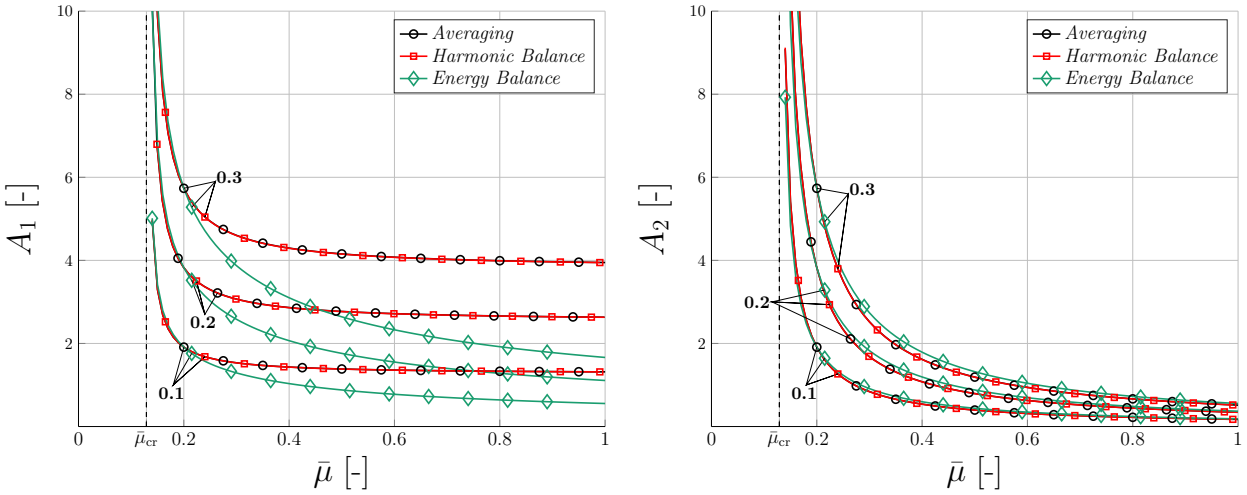
(a) Amplitude A_1 of stationary periodic solutions of different approximation methods for various values of D_1



(b) Amplitude A_2 of stationary periodic solutions of different approximation methods for various values of D_1

Figure 5: Amplitudes of stationary periodic solutions depending on the bifurcation parameter $\bar{\mu}$ for different damping values D_1 with COULOMB friction force ($p = 0.05, \kappa = 0.1, \rho_i = 0.2$).

The results from variation of both viscous damping (Fig. 5) and frictional damping (Fig. 6) show the *Energy Balance* over-predicted the damping level of the occurring limit cycle massively when increasing the bifurcation parameter $\mu > \mu_{\text{cr}}$. Especially for the amplitude A_1, a loss of accuracy is determined for $\mu \gg \mu_{\text{cr}}$.



(a) Amplitude A_1 of stationary periodic solutions of different approximation methods for various values of ρ_i

(b) Amplitude A_2 of stationary periodic solutions of different approximation methods for various values of ρ_i

Figure 6: Amplitudes of stationary periodic solutions depending on the bifurcation parameter $\bar{\mu}$ for different COULOMB friction force values ρ_i ($D_1 = 0.01, p = 0.05, \kappa = 0.1$).

Obviously the *Energy Balance* is unable to deal with COULOMB joint friction for configurations off the HOPF point in an accurate way; the amplitudes are significantly stronger damped compared to the *Harmonic Balance* and *Averaging* method.
Moreover, the shape of the limit cycle is already given, see eq. (15). When non-linearities especially in anisotropic cases dominate the dynamic behaviour of the system, this method will lead to inaccurate approximation because the balance of energy yields a rather an average damping and excitation value over one period T_{u}. Here, the single scaling parameter A_{EB} cannot account for amplitude ratio and phase shift of the amplitudes. Nevertheless, good approximation near the bifurcation point may be obtained.

5 Conclusion and Outlook

Within this contribution the effect of non-smooth damping on the bifurcation behaviour for different approximation schemes for periodic solutions of two minimal models were discussed. Besides viscous damping, strong influence of frictional damping in joints on the emerging limit cycles was shown for the two presented oscillators. Compared to results of the *Averaging* method taken from literature [5, 6], *Energy Balance* leads to good agreement near the bifurcation point at $\bar{\mu}_{\text{cr.}}$. Moreover, *Energy Balance* is not able to consider non-linear potential forces and no parameter is given for increasing accuracy, e.g. the truncation order H for *Harmonic Balance*.
Apart from $\bar{\mu} = \bar{\mu}_{\text{cr.}}$ the approximation becomes more inaccurate compared to the well-known *Averaging* and *Harmonic Balance* method. Hence, *Energy Balance* merely reflects an average dissipation and excitation balance over one period of the frequency ω_{u}, which seems to be not valid distant to the HOPF bifurcation point. Here, the non-linearities dominate, the scaling parameter A_{EB} cannot enhance amplitude ratio and phase shift of the amplitudes which is already specified by the eigenvectors of the linear subsystem, which are chosen as ansatz functions

In future studies, the effectiveness of other methods for calculating periodic solutions, e.g. *Asymptotic Nu-*

meric Method [2], will be investigated and applied, combined with the already implemented methods, to more complex dynamical systems. Here, different joint friction models, e.g. JENKINS or MASING elements should be used and their regularisations should be studied. In addition, the implementation of suitable path tracking schemes is intended, combined with using homotopy methods for finding isolated solution branches.

References

[1] S. Bograd, P. Reuss, A. Schmidt, L. Gaul, M. Mayer, *Modeling the dynamics of mechanical joints*, Journal of Mechanical Systems and Signal Processing, Vol. 25 (2011), pp. 2801-2826.

[2] B. Cochelin, C. Vergez, *A high order purely frequency-based harmonic balance formulation for continuation of periodic solutions*, Journal of Sound and Vibration, Vol. 324 (2009), pp. 243-262.

[3] E. Doedel, *AUTO: A Program for the Automatic Bifurcation Analysis of Autonomous Systems*, Congressus Numerantium, Vol. 30 (1981), pp. 265-284.

[4] M. Eriksson *Friction and contact phenomena of disc brakes related to squeal*, Acta Universitatis Upsaliensis, (2000).

[5] H. Hetzler, *On the effect of nonsmooth Coulomb friction on Hopf bifurcations in a 1-DoF oscillator with self-excitation due to negative damping*, Nonlinear Dynamics, Vol. 69 (2012), pp. 601-614.

[6] H. Hetzler, *Bifurcations in autonomous mechanical systems under the influence of joint damping*, Journal of Sound and Vibration, Vol. 333 (2014), pp. 5953-5969.

[7] D. Hochlenert, U. Von Wagner *How Do Non-linearities Influence Brake Squeal?*, SAE International, Technical Paper 2011-01-2365 (2011).

[8] N. Hoffmann, L. Gaul *Effects of damping on mode-coupling instabilityin friction induced oscillations*, Zeitschrift für angewandte Mathematik und Mechnaik, Vol. 83 (2003), pp. 524-534.

[9] M. Krack, J. Gross, *The harmonic balance method and its application to nonlinear vibrations-Introduction and current state of the art*, Institute of Aircraft Propulsion Systems, University of Stuttgart (2018).

[10] S. Kruse, M. Tiedemann, B. Zeumer, P. Reuss, H. Hetzler, N. Hoffmann *The influence of joints on friction induced vibration in brake squeal*, Journal of Sound and Vibration, Vol. 340 (2015), pp. 239-252.

[11] R. Lemaire, Thierry Pasquet, Chassis Brakes International *A Novel Approach for the Estimation of Amplitude of Brake Systems' Unstable Modes*, Symposium Contribution, EuroBrake (2015).

[12] B. Marx, W. Vogt, *Dynamische Systeme - Theorie und Numerik*, Spektrum, Akademischer Verlag (2011).

[13] A.H. Nayfeh., & D.T. Mook *Nonlinear oscillations*, John Wiley & Sons (2008).

Flutter testing using ambient excitation

J.E. Cooper[1]
[1] University of Bristol, Department of Aerospace Engineering
University Walk, Bristol, BS81TR, UK
e-mail: **j.e.cooper@bristol.ac.uk**

Abstract
This paper reviews the importance of flight flutter testing in the certification of aircraft and, in particular, the need for accurate prediction of modal parameters during the test campaign to enable good estimation of the flutter boundaries. The use of ambient modal analysis techniques are considered as a means to enable flutter testing when excitation devices are not available, or are not used between flight test points. A number of different analysis methods are considered, and it is shown that better modal parameter estimates and flutter predictions are obtained when minimum order realization methods (e.g. the ERA/DC method) are used, particularly when the unmeasured excitation is coloured, or when the frequency range of the excitation is limited.

1 Introduction

The airworthiness regulations (e.g. EASA and FAA) require that all prototype aircraft are demonstrated to be free from flutter and this goal is achieved via flight flutter testing which is a key part of the certification process [1]. A key to the entire process is the accurate estimation of modal parameters from the flight flutter tests which usually make use of acceleration responses to some form of excitation, often using the aircraft control surfaces.

In fields such as Civil Engineering, it is often the case that the response to unmeasured ambient excitation due to the wind or traffic is used to determine the modal parameters (natural frequencies, damping ratios and mode shapes) of structures such as bridges [30], chimneys or tall buildings. Such methods have occasionally been used for flight flutter testing but relatively infrequently, probably due to the narrow frequency range that is excited by turbulence. There has been recent interest in the use of such methods for flight flutter testing.

After overviewing aeroelasticity and flight flutter testing, this paper reviews the use of ambient modal parameter estimation methods as a means to identify natural frequencies, damping ratios and mode shapes, and to predict the flutter speed. The type of algorithm used is explored in relation to being able to accurately identify the correct number of modes and to reduce the effect of coloured noise on the modal parameter estimates.

2 Aeroelasticity

Aeroelasticity [1-4] is the science that concerns the interaction of flexible bodies and aerodynamic flows, and in particular, the relationship between the aerodynamic, elastic and inertia forces which is often defined using the well-known Collar's aeroelastic triangle [2] shown in figure 1. These interactions are of importance for fixed wing aircraft in two key areas:

(a) static aeroelasticity, where the deformation of the aircraft influences the wing lift distribution and resulting drag, can lead to the statically unstable condition of divergence, and usually reduces the effectiveness of the control surfaces.

(b) dynamic aeroelasticity, which includes the critical phenomenon of flutter which is a violent unstable oscillation which can result in structural failure due to the structure extracting energy from the air stream. Other dynamic effects include the nonlinear phenomena of buffet, Limit Cycle Oscillations and the interaction of the Flight Control System often referred to as Aeroservoelasticity

A further related area is that of the static and dynamic loads [1] that result from flight manoeuvres, ground manoeuvres and gust/turbulence encounters. Many 1000s of load cases are considered to define the critical design loads over the aircraft structure which define the sizing of all the structure and hence the overall weight. Aircraft designers aim to produce aircraft which are of minimum weight but are able to withstand all of the predicted loads throughout the aircraft's lifetime, and also ensure that instabilities such as flutter do not occur.

3 Flight Flutter Testing

Uncertainties in the aeroelastic model used for flutter calculations mean that calculated flutter speeds will almost certainly be inaccurate to some extent, especially in the transonic region. It is therefore a requirement of the certification process to validate the flutter behaviour and demonstrate freedom from aeroelastic instability over the flight envelope in a flight flutter test (FFT) [5]. Such an approach whereby numerical models are validated, and updated where necessary, using experimental test data is used throughout the certification process [1] e.g. Ground Vibration Testing (FE model) and Wind Tunnel Testing (steady aerodynamics model).

On the basis of calculations, a nominal flight envelope is cleared to permit a first flight to take place. Thereafter, the flight programme takes place before every other flight test at each flight envelope point because of the safety critical nature of flutter. The basic flutter clearance philosophy seeks to gradually extend the flight envelope by assessing the flutter stability of the aircraft at progressively increasing speed and Mach number, for instance using the test points shown in Figure 2.

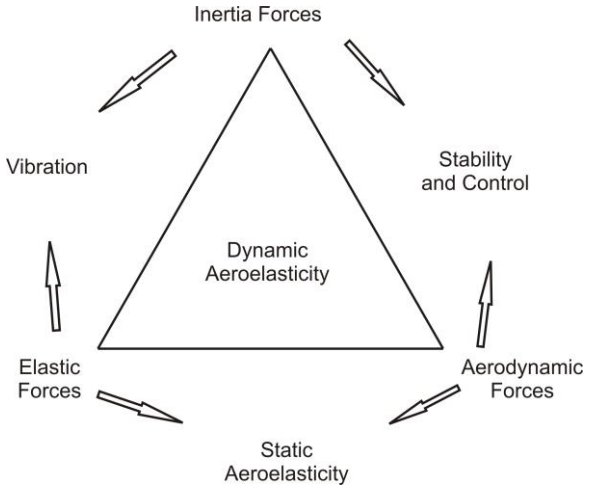


Figure 1. Collar's Aeroelastic Triangle

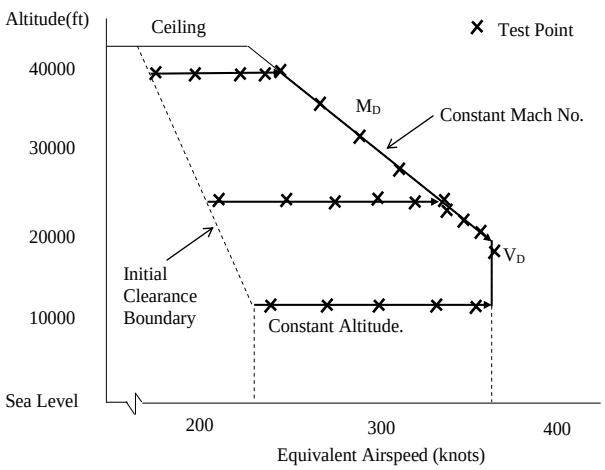


Figure 2. Flight Flutter Test Envelope

It is normal to assess the flutter stability by identifying the natural frequency and damping of the complex /damped modes of the aircraft at each test point. The allowable flight envelope is expanded from an

initially agreed boundary by examining the results along lines of increasing airspeeds at constant altitude and lines of constant Mach number, as indicated in Figure 2.

The usual procedure at each test point is:
(a) to excite vibration of the aircraft over the frequency range of interest and to measure its response,
(b) to curve-fit the excitation and response signals in the time or frequency domain and so to identify the model parameters [13] and
(c) to determine whether it is safe to proceed to the next test point

A variety of excitation devices can be used, namely (a) control surface movements via stick/pedal input or explosive charges, (b) control surface movement via a signal from the Flight Control System, (c) movement of aerodynamic vane fitted to aircraft flying surface or engine/store or (d) inertia exciter mounted in the fuselage. The aircraft response is measured using typically around 20-100 accelerometers, far fewer than for a GVT. The most common excitation signals are pulse (via stick/pedal or explosive charge) and chirp (a fast frequency sweep applied as a signal to the control surface, vane or inertia exciter). Where excitation devices are available on both sides of the aircraft, then excitation may be applied in or out of phase in order to exploit symmetry/antisymmetry; doing this will simplify the analyses and provide results with more confidence.

Sometimes the response of the aircraft to natural turbulence is used [24,30], the subject of this paper, but such an approach is not usually recommended because the excitation is not 'white' and not guaranteed to excite adequately all the modes of interest), and the difficulty of maintain a steady flight condition for suitable amount of time.

The damping values may be compared to results from previous test points and the damping trends for each mode extrapolated to allow progression to the next test point (i.e. by defining a permitted increment in speed or Mach number). Other techniques such as the flutter margin method [10,11,15], the Jury stability criterion [19] or others [17,18] can be used to estimate the flutter speed based upon the measured test data. The test process is complete when the extrapolated damping values are still positive at a margin (typically 15 %) above the design dive speed for each Mach number.

4 Modal Parameter Estimation from Ambient Test Data

There has been much work, particularly in the testing of Civil Engineering structures, devoted to identifying the modal parameters of a structure when it is subject to random ambient excitation [25, 27 – 29], sometimes termed operational modal analysis. A wide range of techniques have been proposed, primarily based in the time domain [30]. A great deal of insight can be deduced by considering the problem in terms of the data correlations used for the analysis [8,9,12]. Furthermore, the understanding that the correlation plot versus lag value gives exactly the same curve as that of the Impulse Response Function, and this has led to application of a number of methods for ambient response analysis.

There has been some work in the aerospace field exploring such methodologies for wind tunnel and flight flutter testing. Of note is the work by Matsuzaki and co-workers on the prediction of flutter boundaries [16,19,20] however there have been numerous other studies of this important problem [21-24].

4.1 Mathematical Modelling

In the time domain, it is well known that the response at time instant j, y_j, of a m degree of freedom (dof) to an unknown input ε_j can be written as an autoregression such that

$$y_j + a_1 y_{j-1} + a_2 y_{j-2} + \cdots + a_{2m} y_{j-2m} = \varepsilon_j \tag{0.1}$$

and this equation can be extended to include moving average terms so

$$y_j + a_1 y_{j-1} + a_2 y_{j-2} + \cdots + a_{2m} y_{j-2m} = b_0 \varepsilon_j + b_1 \varepsilon_{j-1} + b_2 \varepsilon_{j-2} + \cdots + b_{2n} \varepsilon_{j-2n} \tag{0.2}$$

Pre-multiplying equation (1) by y_{j-k} and taking expectations leads to an expression including auto and cross correlation terms such that

$$\begin{aligned} &R_{yy}(k) + a_1 R_{yy}(k-1) + a_2 R_{yy}(k-2) + \cdots + a_{2m} R_{yy}(k-2m) \\ &= b_0 R_{y\varepsilon}(k) + b_1 R_{y\varepsilon}(k-1) + b_2 R_{y\varepsilon}(k-2) + \cdots + b_{2n} R_{y\varepsilon}(k-2n) \end{aligned} \tag{0.3}$$

where the correlation terms are estimated from N data points by

$$R_{y\varepsilon}(k) = \frac{1}{N} \sum_{j=1}^{N} y_j \varepsilon_{j+k} \tag{0.4}$$

The formulation of equation (1) is exactly the same as that used for the modelling of impulse response functions (i.e. as a summation of exponentially damped sinusoids) and is the underlying mathematical formulation for a wide range of well-known techniques [12] for both impulse response testing and also ambient modal analysis (such as Least Squares Complex Exponential, Polyreference, ERA, etc.) It can be shown that the direct Least Squares solution of equation 1 for N points (N > 2m) results in a set of simultaneous equations in terms of autocorrelations such that

$$\begin{bmatrix} R_{yy}(0) & R_{yy}(1) & \cdots & R_{yy}(2m-1) \\ R_{yy}(1) & R_{yy}(0) & & R_{yy}(2m-2) \\ \vdots & & & \vdots \\ R_{yy}(2m-1) & & \cdots & R_{yy}(0) \end{bmatrix} \begin{bmatrix} -a_1 \\ -a_2 \\ \vdots \\ -a_{2m} \end{bmatrix} = \begin{bmatrix} R_{yy}(1) \\ R_{yy}(2) \\ \vdots \\ R_{yy}(2m) \end{bmatrix} \tag{0.5}$$

and thus for a system excited by an unknown random input, one can simply compute the autocorrelations, solve the simultaneous equations in (1.5) and then calculate the frequencies and damping ratios from the roots of the characteristic equation with a_j as the coefficients. The size of the above set of simultaneous linear equations depends solely upon the size of the number of modes that are included in the model.

Such an approach has difficulties and errors are likely to occur in the computations as

i. the assumption of a white excitation is unlikely in the real world.
ii. the exact number of modes are usually unknown

and consequently, a range of different methodologies have to be used to eliminate the bias

i. overspecify the mathematical model order – an approach frequently used in the modal testing world as the system modes tend to stabilize to correct values however, there is then the need to eliminate spurious modes. Often “stability plots” are used for this purpose.
ii. employ a more sophisticated noise model, for instance using the Moving Average terms in equation (2) however, for the ambient excitation problem this requires a two-stage process to be used in order to identify the coefficients of the noise terms.

iii. solve the equations using only correlation terms that are not likely to be corrupted by the coloured noise inputs e.g. shift the correlation terms by some constant value p, depending upon the amount of "colour" on the input signal so that

$$\begin{bmatrix} R_{yy}(p) & R_{yy}(p+1) & \cdots & R_{yy}(p+2m-1) \\ R_{yy}(p+1) & R_{yy}(p) & & R_{yy}(p+2m-2) \\ \vdots & & & \vdots \\ R_{yy}(p+2m-1) & & \cdots & R_{yy}(p) \end{bmatrix} \begin{bmatrix} -a_1 \\ -a_2 \\ \vdots \\ -a_{2m} \end{bmatrix} = \begin{bmatrix} R_{yy}(p+1) \\ R_{yy}(p+2) \\ \vdots \\ R_{yy}(p+2m) \end{bmatrix} \tag{0.6}$$

A further point to note is that the above formulations can be readily extended to include simultaneous measurements at different points on the structure, so that mode shapes can be identified as well. The AR and ARMA models now become vectorized [25] and the correlation terms include cross-correlations with different points on the structure.

The Eigensystem Realisation Algorithm using Data Correlations (ERA/DC) [7] is an extension of the ERA method developed originally for the analysis of impulse response functions; however, as it is based on fitting correlation terms it readily becomes useful for ambient response data sets [30]. The formulation enables the ability to increase the model order as in point i. above but also to produce a minimum order realization which reduces the amount of results that need to be considered. Similarly, point iii. can also be tackled through the selection of the correlation terms that are used. There have been applications of ERA or similar methods to the analysis of measured correlations, but this reduces the capabilities that can be achieved using the full ERA/DC method [26,27].

The underlying mathematical model is based upon the discrete state space equations which are given, in the usual notation as

$$x_{i+1} = Ax_i + Bu_i \qquad y_i = Cx_i + Du_i \tag{0.7}$$

which relate the output y_i to input u_i via the system states x_i For an impulse response, the state-space equations can be written in terms of the Markov equations

$$y_{k+1} = CA^k B \tag{0.8}$$

The formulation follows by defining a Hankel matrix such that

$$H_j = \begin{bmatrix} y_j & y_{j+1} & \cdots & y_{j+\eta} \\ y_{j+1} & y_{j+2} & \cdots & y_{j+\eta+1} \\ \vdots & \vdots & & \vdots \\ y_{j+\xi} & y_{j+\xi+1} & \cdots & y_{j+\xi+\eta+1} \end{bmatrix} \tag{0.9}$$

and then block correlation matrices

$$U_j = \begin{bmatrix} R_j & R_{j+1} & \cdots & R_{j+\eta} \\ R_{j+1} & R_{j+2} & \cdots & R_{j+\eta+1} \\ \vdots & \vdots & & \vdots \\ R_{j+\xi} & R_{j+\xi+1} & \cdots & R_{j+\xi+\eta+1} \end{bmatrix} \quad and \quad U_{j+1} = \begin{bmatrix} R_{j+1} & R_{j+2} & \cdots & R_{j+\eta+1} \\ R_{j+2} & R_{j+3} & \cdots & R_{j+\eta+2} \\ \vdots & \vdots & & \vdots \\ R_{j+\xi+1} & R_{j+\xi+2} & \cdots & R_{j+\xi+\eta+2} \end{bmatrix} \tag{0.10}$$

where $R_j = H_j H_0^T$

and then the Singular Value Decomposition (SVD) of the first block matrix is performed so that

$$U_j = PDQ^T \tag{0.11}$$

where D is a diagonal matrix of descending non-negative singular values.

After some manipulation it can be shown that the state-space system matrix A can be found as

$$A = D^{-\frac{1}{2}} P^T U_{j+1} Q D^{-\frac{1}{2}} \tag{0.12}$$

and the eigenvalues of this matrix lead directly to the system frequencies and damping ratios. The size of the matrices determined from the SVD can be varied depending upon the number of singular values that are kept. For data sets such as those occurring in flight flutter tests, it is usual to vary the number of singular values considered and to use techniques such as "stability plots" in order to distinguish the system modes from the mathematical "spurious poles" where much user interaction is required to find the system modes – for the plots shown in this work the user is interested in looking for poles that don't change much in terms of varying natural frequency and damping ratios.

A further method of distinguishing between the system and spurious pole is to analyze the data in the opposite direction to the decaying system that is measured [6]. Such an approach simply means that the damping ratio of the system modes changes sign; however, interestingly it can be shown that most of the spurious poles become unstable and can easily be eliminated from the stability plots [13].

5 Test Results

5.1 Simulated 4 DOF Rectangular wing

The first system used to illustrate the use of the methods is a simple unswept cantilever rectangular wing modelled using two bending and two torsion modes [1] shown in fig 1. Figure 2 shows the frequency and damping behavior over the speed range up to 80 m/s. It can be seen that flutter occurs at 77m/s and consists of a classical binary flutter involving the first bending and torsion modes. Random noise sequences with a uniform frequency content across the frequency range of interest was generated and applied to the wing of a range of different speeds in the form of a uniform vertical gust field.

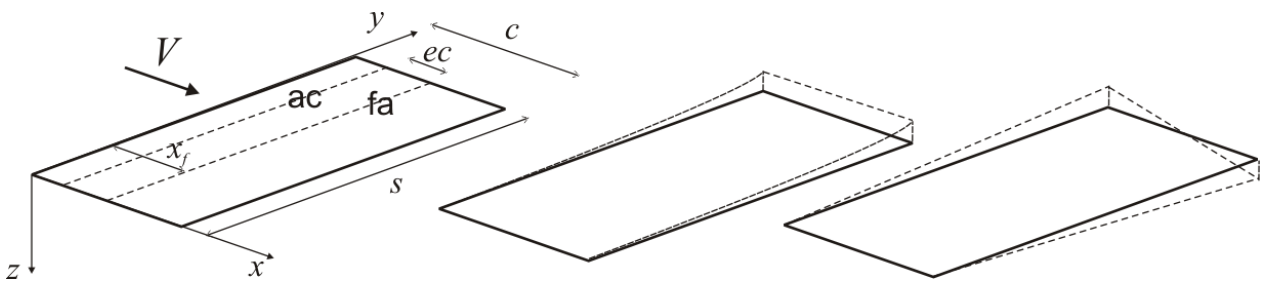


Figure 1. Simulated Rectangular Wing Model

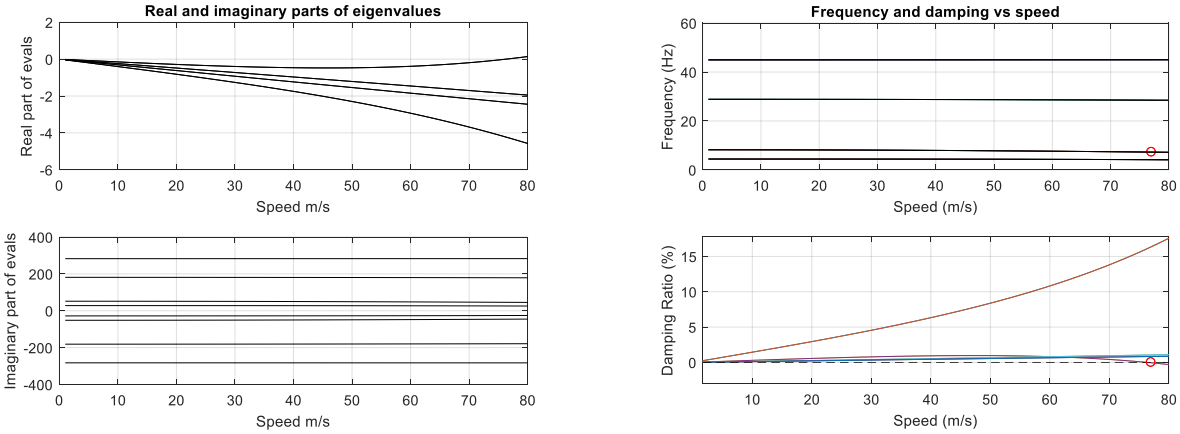


Figure 2. Eigenvalue Frequency and Damping Trends vs Speed.

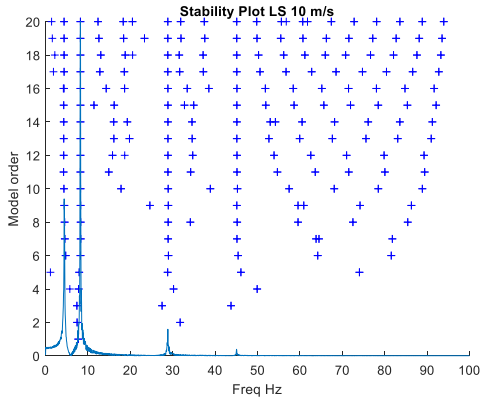


Figure 3a. 10 m/s Stability Plot. LS.

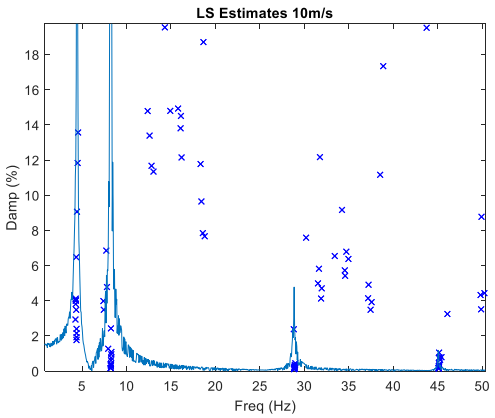


Figure 3b. 10 m/s Freqs vs Dampings. LS.

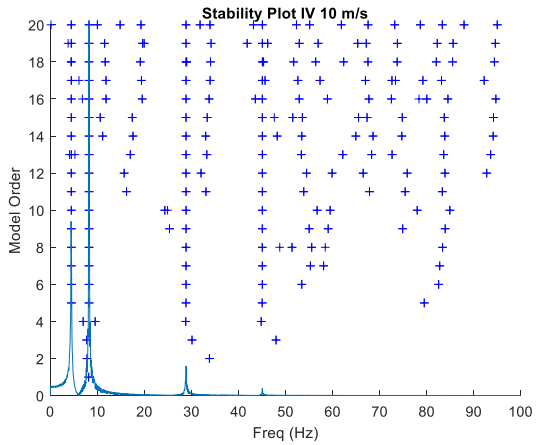


Figure 4a. 10 m/s Stability Plot. IV.

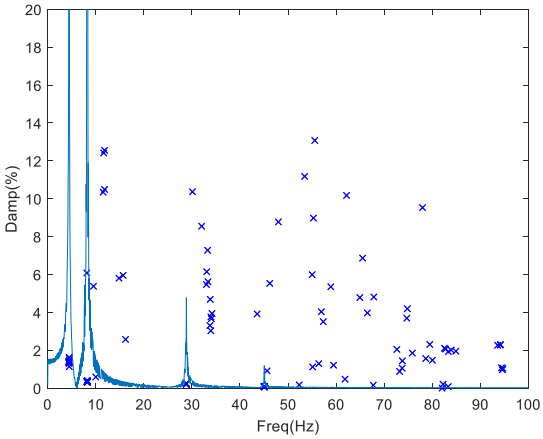


Figure 4b. 10 m/s Freqs vs Dampings. IV.

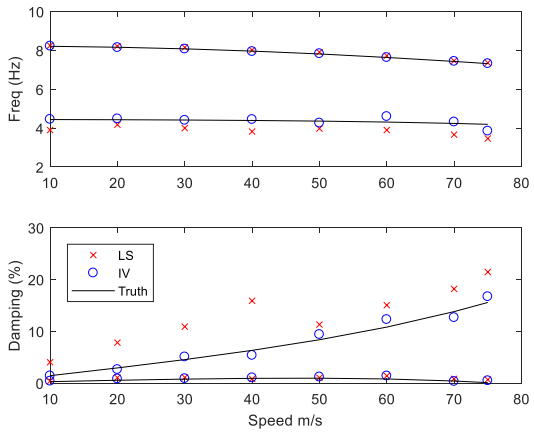


Figure 5. Frequency and damping estimated trends and true values.

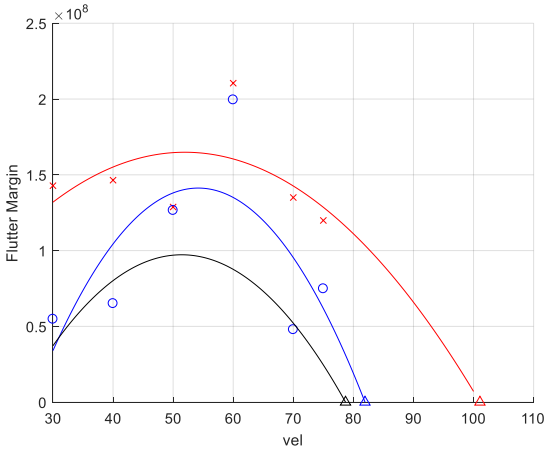


Figure 6. Flutter Margin Predictions Using Estimated Frequency and Dampings

Figures 3 and 4 show the frequency and damping estimates obtained using the Least Squares (LS) and Instrumental Variables (IV) methods, the latter being obtained by shifting all of the correlation terms that were used, as in equation (6). Both stability plots, for increasing model order, and also frequency vs damping plots for all results are shown. In both cases it is clear that an increased model order produces stabilized estimates of the system modes; however, there is a need to distinguish the spurious modes. The results obtained using the IV method converged quicker and there is much less scatter on the system poles.

Figure 5 shows the frequency and damping trends that are achieved using the stabilized values for both approaches, and these are compared to the true values. The estimates obtained using the IV approach are much closer to the true values than the LS method. Predictions for the lower frequency mode (1st bending) with the higher damping values are worse than the 1st torsion mode which is the one that couples with the bending mode to flutter at 77 m/s. Figure 6 shows the comparative Flutter Margin trends for the different approaches. The errors in the frequency and damping estimates result in flutter speed predictions that are greater than the true values, particularly for the LS technique.

5.2 Wind Tunnel Model Test

The second set of test data considered was from a real experimental test campaign generated by Dr Daniella Raveh and team [32] which consisted of ambient responses for a range of different wind speeds from 4 different accelerometers. The data was analyzed using a range of methods to determine the frequency and damping trends, including PSD and the ERA/DC method.

Figure 7 shows sample time histories from the four accelerometers and Figure 8 typical averaged power spectra. These spectra were analyzed using the simple half power approach to produce the frequency and damping trends illustrated in figure 9. The modes that make up the flutter mechanism are depicted in red and blue; the damping value of the bending mode (in red) cannot be found when the system approaches flutter as the peak reduces and widens, becoming merged into the more dominant mode with the reduced flutter. Note also that over 30 m/s there is another mode that suddenly appears with a very low damping; this was suspected to be a vibration occurring elsewhere in the experimental set-up and was not considered to be part of the flutter mechanism

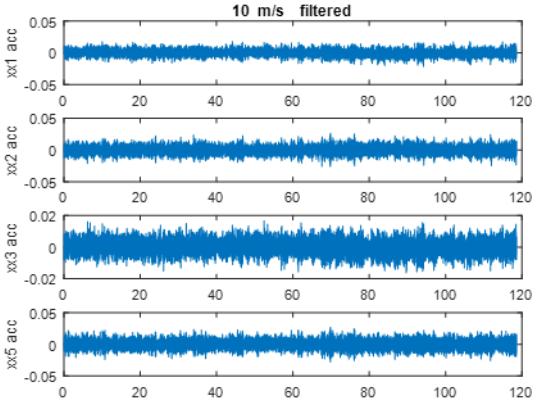


Figure 7. Ambient Response Time Histories

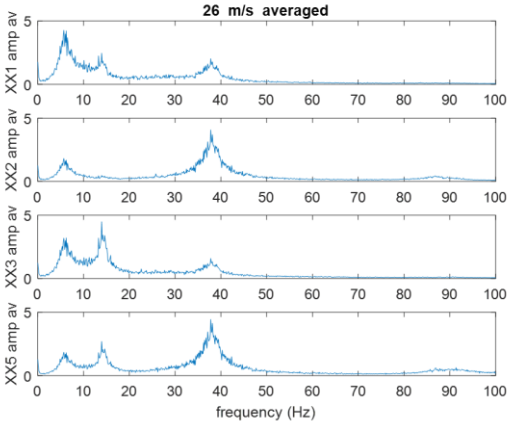


Figure 8. Sample Power Spectra from All Accelerometers

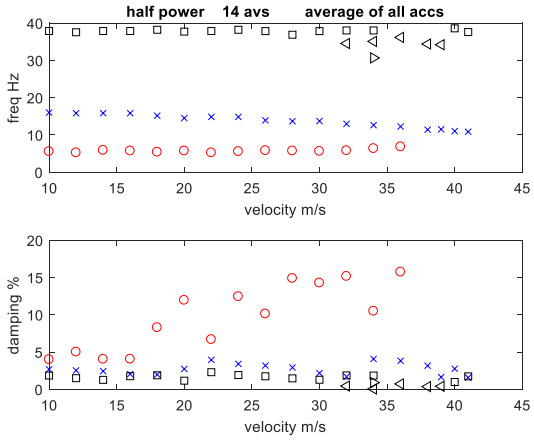


Figure 9. Freq and Damping Trends. PSD.

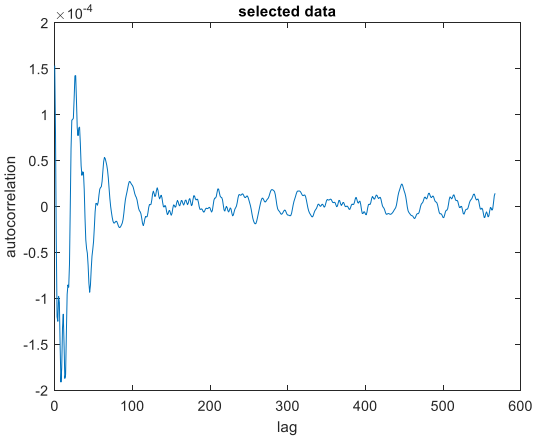
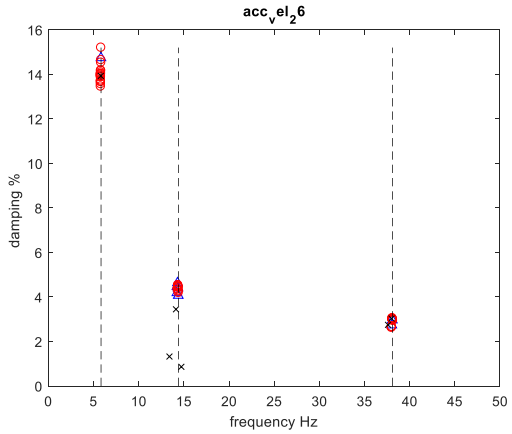


Figure 10. Correlation Function



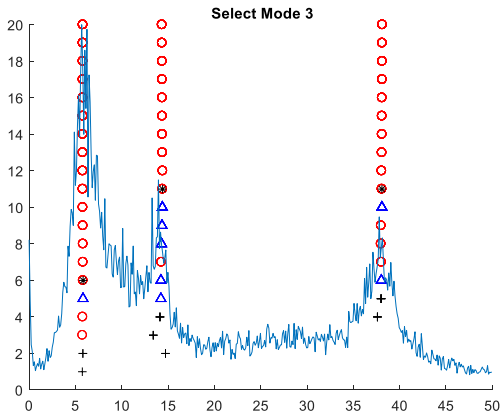


Figure 11. Typical Stability and Freq vs Damping Plots

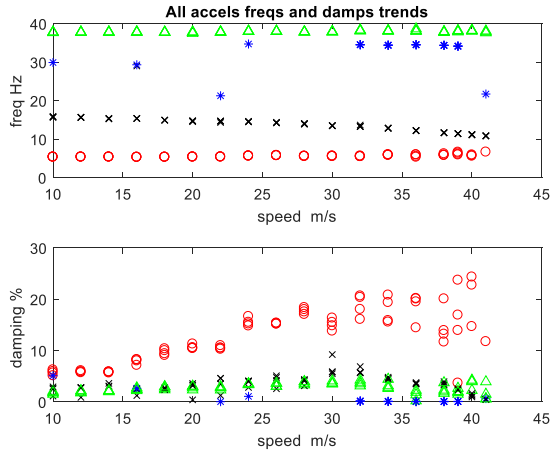


Figure 12. Freq and Damping Trends for all Accelerometers

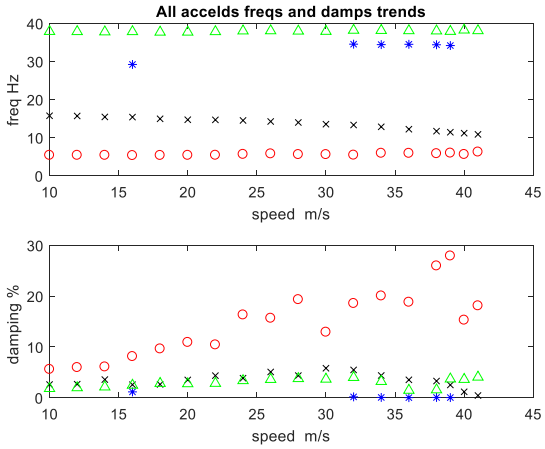


Figure 13. Freq and Damping Trends for Combined Analysis

Figure 10 shows a typical correlation function that can be generated from the ambient response which is of a format that can be analyzed by a range of different time domain system identification methods. The correlations close to a zero-lag value are more likely to be corrupted with noise, so it is best to ignore some of the these before performing the curve-fit. Here, the analysis was performed using the ERA/DC method, ignoring those correlation values that are likely to be biased and using a larger amount of overspecification (60 modes). Figure 11 shows typical analysis results where the model order is that taken for the minimum order realization. It can be seen that the stability plots are very well behaved and easy to interpret.

Figures 12 and 13 show the frequency and damping trends for each of the individual accelerometer analyses and for a combined analysis (achieved by formulating the Hankel data matrices to include inputs from all of the accelerometers) respectively. The characteristic binary flutter behavior is clearly seen for the lowest two modes, indicating that flutter occurs just above 41m/s. The lightly damped mode can be seen above 30 m/s but as indicated above, this appeared to be an unrelated phenomenon.

6 Conclusions

A number of approaches for computing the natural frequencies and damping ratios from the ambient response of aeroelastic systems have been discussed and demonstrated using a 4 degree of freedom simulated system and a wind tunnel wing model. It has been shown that it is feasible to produce accurate estimates of the modal parameters, but that care must be taken to eliminate biased estimates, in this case through the use of an overspecified mathematical model which in turn leads to the need to distinguish system from spurious modes.

Acknowledgements

The author is extremely grateful to Dr Daniella E. Raveh from Technion, Israel, for supplying the wind tunnel test data that is used in part of this work.

References

[1] Wright JR and Cooper JE, *Introduction to Aircraft Aeroelasticity and Loads*. John Wiley, 2nd edition, 2015.

[2] Collar, A. R., *The First Fifty Years of Aeroelasticity*, Aerospace, vol. 5, no. 2, pp. 12–20, 1978

[3] Garrick, I. E. and Reed W. H., *Historical Development of Aircraft Flutter*, Journal of Aircraft, vol. 18, pp. 897–912, Nov. 1981

[4] Livne E., *Future of Airplane Aeroe*lasticity, Journal of Aircraft, Vol. 40, No. 6 (2003), pp. 1066-1092.

[5] M.W. Kehoe, A Historical Overview of Flight Flutter Testing, NASA Tech Memo 4720 1995.

[6] J.E. Cooper, *The Use of Backwards Models for Modal Parameter Identification* Mechanical Systems and Signal Processing, v6 n3 1992, pp217 - 228.

[7] J-N Juang, J.E. Cooper & J.R. Wright *An Eigensystem Realisation Algorithm using Data Correlations (ERA/DC) for Modal Parameter Identification,* Control - Theory and Advanced Technology, v4 n1 1988, pp 5-14.

[8] M.J.Desforges, J.E.Cooper & J.R.Wright *Spectral and Modal Parameter Estimation from Output Only Measurements* Mechanical Systems and Signal Processing. v9 n2 1995, pp 169-186.

[9] J.E. Cooper, M.J.Desforges & J.R.Wright *Modal Parameter Identification using an Unknown Coloured Random Input* Mechanical Systems and Signal Processing v9 n6 1995, pp 685-695.

[10] G. Dimitriadis & J.E. Cooper, *Flutter Prediction from Flight Flutter Test Data* AIAA J.Aircraft v38 n2 2001 pp 355 - 367

[11] G Dimitriadis and JE Cooper, *Comment on Flutter Prediction from Flight Flutter Test* Data J Aircraft v43 n3 2006 pp 862-863.

[12] J.E. Cooper, *Comparison of Some Time Domain System Identification Techniques using Approximate Data Correlations,* International Journal of Analytical and Experimental Modal Analysis v4 April 1989, pp 51-57.

[13] J.E. Cooper *Parameter Estimation Techniques for Flight Flutter Testing* AGARD-SMP Specialists meeting on Advanced Aeroservoelastic Testing and Data Analysis, May 1995.

[14] Abbasi AA & Cooper JE, *Statistical Evaluation of Flutter Boundaries from Flight Flutter Test Data* Aeronautical Journal v113 n1139 pp41 – 51 2009.

[15] Zimmerman, N. H., and Weissenburger, J. T., *Prediction of Flutter Onset Speed Based on Flight Testing at Subcritical Speeds*, Journal of Aircraft, Vol. 1, No. 4, 1964, pp. 190–202.

[16] Matsuzaki, Y., and Ando, Y., *Estimation of Flutter Boundary from Random Responses Due to Turbulence at Subcritical Speeds*, Journal of Aircraft, Vol. 18, No. 10, 1981, pp. 862–868.

[17] Nissim, E., and Gilyard, G. B., *Method for Experimental Determination of Flutter Speed by Parameter Identification*, NASA TR-2923, June 1989.

[18] Cooper, J. E., Emmett, P. R., Wright, J. R., and Schofield, M. J., *Envelope Function: A Tool for Analyzing Flutter Data, Journal of Aircraft*, Vol. 30, No. 5, 1993, pp. 785–790.

[19] Torii, H., and Matsuzaki, Y., *Flutter Margin Evaluation for Discrete Time Systems*, Journal of Aircraft, Vol. 38, No. 1, 2001, pp. 42–47.

[20] Torii, H., and Matsuzaki, Y., *Flutter Boundary Prediction Based on Nonstationary Data Measurement*, Journal of Aircraft, Vol. 34, No. 3, 1997, pp. 427–432.

[21] Peeters, B., De Troyer, T., Guillaume, P., and Van der Auweraer, H., *In-Flight Modal Analysis—A Comparison Between Sweep and Turbulence Excitation*, International Conference on Noise and Vibration Engineering, Dept. of Mechanical Engineering, Katholieke Universiteit Leuven, Leuven, Belgium, Sept. 2006, pp. 1627–1641.

[22] Zeng, J., and Kukreja, S. L., *Flutter Prediction for Flight/Wind-Tunnel Flutter Test Under Atmospheric Turbulence Excitation*, Journal of Aircraft, Vol. 50, No. 6, 2013, pp. 1696–1709

[23] Nahom, T., Kogan, T., Iovnovich, M., and Raveh, D. E., *Evaluation of an ARMA Flutter Boundary Prediction Method Based on Discrete-Time Structural Responses to Turbulence Excitation in Flight-Tests*, 56th Israel Annual Conference on Aerospace Sciences, Faculty of Aerospace Engineering Paper WeL2T4-03, Technion, Israel, March 2016.

[24] Iovnovich M, NahomT, Presman M, Avsaid, D, Braier T and Raveh D E¶ *Assessment of Advanced Flutter Flight-Test Techniques and Flutter Boundary Prediction Methods* To appear in the Journal of Aircraft.

[25] CS Huang, *Modal Identification of Structures using ARMAV Model for Ambient Vibration Measurement*. Proceedings 12th WCEE 2000

[26] Dar-Yun Chiang and Chang-Sheng Lin *Identification of modal parameters from ambient vibration data using eigensystem realization algorithm with correlation technique*. Journal of Mechanical Science and Technology 24 (12) (2010) 2377~2382

[27] Dar-Yun Chiang, Chang-Sheng Lin, and Fang-He Su, *Identification of Modal Parameters from Ambient Vibration Data by Modified Eigensystem Realization Algorithm* Journal of Aeronautics, Astronautics and Aviation, Series A, Vol.42, No.2 pp.079 - 086 (2010)

[28] Juan Martin Caicedo, Shirley J. Dyke and Erik A. Johnson. *Natural Excitation Technique and Eigensystem Realization Algorithm for Phase I of the IASC-ASCE Benchmark Problem: Simulated Data* J. Eng. Mech., 2004, 130(1): 49-60

[29] J.M.W. Brownjohn, F. Magalhaes, E. Caetano, A.Cunhab, *Ambient vibration re-testing and operational modal analysis of the Humber Bridge* , Engineering Structures 32 (2010) 2003_2018

[30] B. Peeters and G. De Roeck *Stochastic System Identification for Operational Modal Analysis*: Journal of Dynamic Systems, Measurement, and Control 2001, Vol. 123 pp 659 – 667

[31] M.J.Desforges & J.E. Cooper , *Detecting Changes in Modal Parameters Using Ambient Response Data* DAMAS Conference 1997.

[32] Daniella E. Raveh, Michael Iovnovich, and Tzlil Nahom. *Wind-Tunnel Study of the ARMA Flutter Prediction Method*, 2018 AIAA/ASCE/AHS/ASC Structures, Structural Dynamics, and Materials Conference, AIAA SciTech Forum, (AIAA 2018-0702)

Developing and analysing an electromechanical model of a bio-inspired flapping wing mini UAV

M. Park[1], A. Abolfathi[1*], J. D. Biggs[2], Y. Ventikos[1]
[1] University College London, Department of Mechanical Engineering
Roberts Engineering Building, Torrington Place, London, UK WC1E 7JE
[*] e-mail: **a.abolfathi@ucl.ac.uk**

[2] Politecnico di Milano, Department of Aerospace Science & Technology
Via La Masa 34, 20156 Milano, Italy

Abstract
The purpose of this paper is to describe and analyse an electromechanical model of a mini flapping wing mechanism for the purpose of system optimisation. The system comprises of a small DC motor connected to a voltage source, a gearbox and a slider crank that drives two wings. The DC gearmotor is modelled considering its both mechanical and electrical components. An equivalent viscous damper is considered to model the mechanical losses of the gearmotor. The crank mechanism is assumed massless and the inertia of the wings only considered in the model. The aerodynamic drag and lift are modelled using an equivalent viscous damping model as an energy sink. The parameters of the system are estimated using published experimental data and manufacturer datasheets for the corresponding DC gearmotor. The energy efficiency as the ratio of aerodynamic power to the input electrical power of the system and also the aerodynamic power are used as two measures to evaluate the system performance.

1 Introduction

Flying insects have evolved over millions of years and have become very successful species [1]. They are optimised flying machines which are outperforming any man-made air vehicles. In recent years, there have been several attempts to mimic the flapping wing mechanism of insects and to develop mini and micro Flapping Wing Unmanned Aerial vehicles (FWUAVs) [2,3]. It is suggested that the insect flight mechanism is a resonant oscillator that can exchange the kinetic and strain energy during a flapping cycle which allows most of the muscle energy being converted to the aerodynamic forces [4]. Similarly, any flapping wing mini aerial vehicle should be optimised in order to minimise the energy losses in the system and produce the highest possible lift. This can be achieved by adding an elastic energy storage element to the system and tuning the resonance frequency of the flapping system to match with the flapping frequency e.g. [5–10].

Madangopal et al. [6] designed a flapping wings mechanism using a four-bar mechanism. They attached a linear spring to the wings to mimic the energy storage mechanism of insect thorax. They investigated the energy consumption of the mechanism. Khan and Agrawal [8] provided a model of a four-bar flapping mechanism to which wings were attached using a rotational spring. Mechanical losses were assumed of viscous damping type and inertia of linkages and motor were included in their model. Khan and Agrawal [11] suggested an increase in the inertia of the motor to smooth the torque requirement of the flapping mechanism. Baek et al. [12] introduced an electromechanical model of flapping wing mechanism by assuming a single degree of freedom linear oscillator with viscous damping that modelled the flapping wing. They studied the nondimensional equations for different values of damping ratio and considered two cases of constant speed and constant current. They concluded that the battery and motor resistance have a considerable effect on the efficiency of the system. Lau et al. [13] manufactured two flapping wings mechanism of slider-crank type. One of them included an elastic storage mechanism and they showed that

the mechanism with elastic element outperforms the conventional slider-crank mechanism in term of energy consumption.

In this paper, an electromechanical model of mini FWUAV powered by rotary DC motor is developed. This makes it possible to include effects of the electrical motor on the dynamics of the flying machine and to obtain the optimum parameters for the system. The main difference between the current study and the previous studies is the inclusion of the frictional losses in the hinges. This provides a platform to more accurately capture the dynamics of the system and enables accurate energy analysis.

2 Electro-Mechanical model

The rotary motion of a DC motor can be converted to the flapping motion of the wings through a crank and slider mechanism. A schematic view of such mechanism is shown in Figure 1 (a). The movement of the slider is confined to the vertical axis as shown in Figure 1 (b).

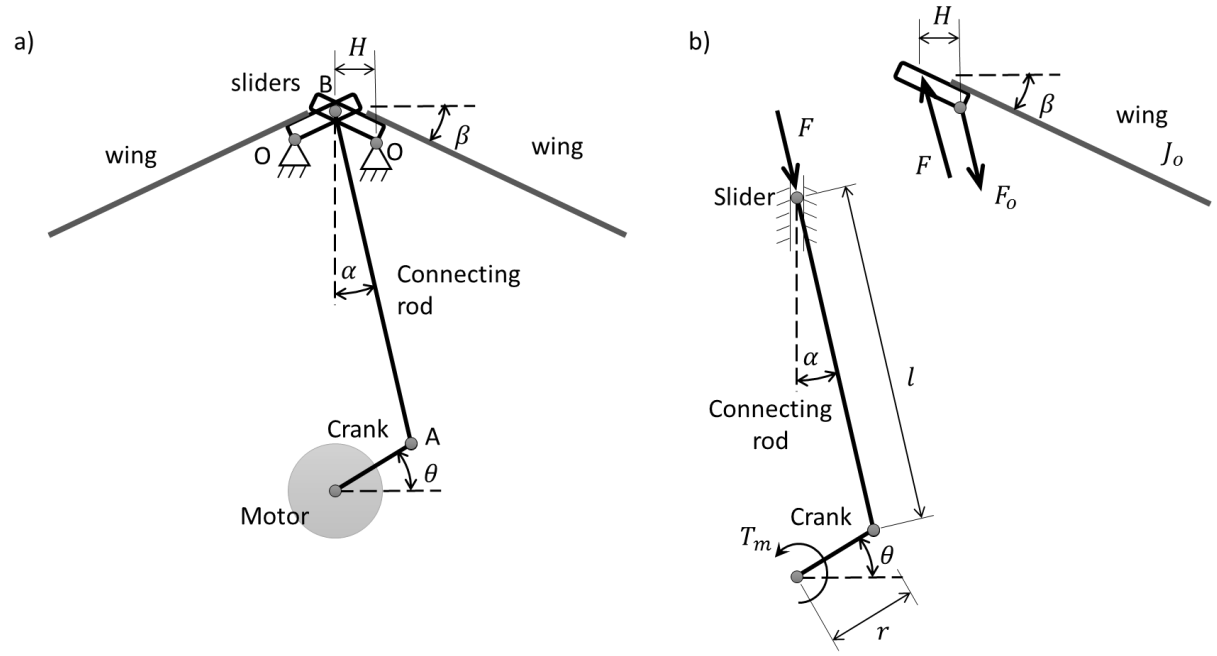


Figure 1: a) the schematic view of a flapping mechanism for a microdrone; b) Free body diagram of the wing and the crank and connecting rod, demonstrating the dimensions and the slider path of motion.

Assuming massless cranks and considering a viscous damping model to account for aerodynamic forces the equation of motion for the wings can be obtained as,

$$J_0\ddot{\beta} + c_a\dot{\beta} = FH(\sin\alpha\tan\beta + \cos\alpha) \tag{1}$$

where J_O is the combined moment of inertia of the wings about the hinge O, c_a is the equivalent aerodynamic damping coefficient. The counter clockwise direction and internal forces in tension are considered as positive directions. Geometrical parameters are defined in Figure 1. Angles α and β can be determined in terms of rotation of the crank θ. The equation of motion for the crank can be used to obtain the reaction force F in term of motor torque T_m,

$$T_m - T_f = Fr(\sin\theta\sin\alpha + \cos\theta\cos\alpha) \tag{2}$$

where T_f is the torque due to frictions in the hinges which accounts for mechanical losses in the flapping mechanism. The friction torque can be obtained by evaluating the reaction force,

$$T_f = F\mu r_e \tag{3}$$

where μ is the coefficient of friction and r_e is the effective radius. This formulation allows estimation of μr_e using experimental data which is described in the next section.

Coreless DC motors are commercially available at sizes that are suitable for mini air vehicles. The equivalent circuit of such a motor is shown in Figure 2 where R is the coil resistance, L is its inductance, e_{EMF} is the back electromotive force, T_1 is the coil torque, J_m is motor inertia, ω_1 is the motor speed, b_m is mechanical loss coefficient of the motor. Gear ratio is $1{:}n$, J_g is gear inertia, b_g is the gear loss coefficient, T_2 is gear torque and ω_2 is gear speed which is equal to $\dot{\theta}$.

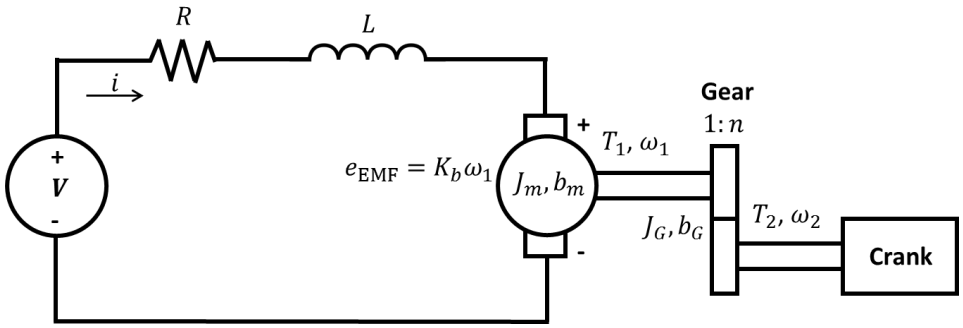


Figure 2: DC motor equivalent circuit.

The governing equations of the DC gearmotor can be obtained as,

$$V = L\frac{di}{dt} + Ri + e_{\text{Emb}} \tag{4}$$

$$T_2 - T_m = (J_G + n^2 J_m)\frac{d\omega_2}{dt} + (b_G + n^2 b_m)\omega_2 \tag{5}$$

$$T_1 = K_b i \tag{6}$$

$$T_1\omega_1 = T_2\omega_2 \tag{7}$$

$$e_{\text{EMF}} = K_b\omega_1 \tag{8}$$

As the mechanical losses of the gearmotor are estimated from the measurement provided by the manufacturer of the DC gearmotor, the mechanical losses of the gear and motor are substituted with an equivalent loss coefficient $b = b_G + n^2 b_m$. Equations (1) to (8) can be used to model the flapping drone in Matlab Simulink. The input to the model is the electrical voltage and the response of the system can be obtained. The model can be used to optimise the system as described in section 4.

3 Parameter estimation

Lau et al. [13] reported the experimental results on a flapping wing crank slider mechanism which are used to obtain the parameter for the simulations of this study. Their system incorporated a DC gearmotor (Precision Microdrive 206–102) for which the performance curves are produced by the manufacturer [14].

Using the manufacturer data, the parameters of the gearmotor are obtained which enabled to replicate the measured performance curves with an error of less than 5%. The estimated parameters for the gearmotor are given in Table 1.

Parameter	value
R	9.5 ohm
L	29×10^{-3} H
K_b	0.01 Nm/A
J	1.77×10^{-10} kgm^2
J_G	1×10^{-10} kgm^2
b	5×10^{-6} Ns
n	25

Table 1: Estimated parameters of DC gearmotor

The average power required to operate the flapping wing mechanism in different conditions is reported in reference [13]. The mechanical power of the system was measured running the flapping wings mechanism normally in the air, in a vacuum and when the wings were removed. This allowed a power analysis in absence of any elastic element by evaluating the total instantaneous power as the sum of inertia, aerodynamic and mechanical losses,

$$P_{\text{mech}} = P_{\text{aero}} + P_{\text{inertia}} + P_{\text{losses}} \tag{9}$$

where P_{mech} is the gearmotor output power, P_{aero} is the aerodynamic power, P_{inertia} is the inertia power required to accelerate and deaccelerate the masses of the system and P_{losses} are the mechanical losses in the system. The inertia power is of apparent power type and its average over a cycle is zero and does not contribute to the total power consumption of the system. However, it needs to be considered in the motor selection. It also increases the mechanical losses in the system due to an increase in reaction force hence the friction in joints. The average mechanical power can be obtained using the following equation,

$$\bar{P}_{\text{mech}} = \frac{1}{T}\int_T T_m \dot{\theta}\, dt \tag{10}$$

where T is the period. Similarly, the average aerodynamic power and the average mechanical losses power can be obtained,

$$\bar{P}_{\text{aero}} = \frac{1}{T}\int_T c_a \dot{\beta}^2 dt \tag{11}$$

$$\bar{P}_{\text{losses}} = \frac{1}{T}\int_T F\mu r_e \dot{\theta}\, dt. \tag{12}$$

An initial estimate for friction losses parameter μr_e can be obtained by assuming a constant rotational speed ($\dot{\theta} = 2\pi f$ where f is flapping frequency) and evaluating an average reaction force and comparing it with the measurement result of the mechanical power when the wings were removed in reference [13]. Similarly, the values for damping term c_a is obtained by evaluating the difference between the measured power of the system running in the air and running in the vacuum. The initial value can be obtained by assuming the increased mechanical losses is negligible and the difference can be approximated as the aerodynamic power given by equation (11). The estimations are updated through an iterative process taking into account the effect of increased losses to match the simulation results with the measurements. The dimensions of the flapping wing system and the estimated parameters are given in Table 2. The simulation results and measurements for the mechanical power and the total input electrical power are compared in Figure 3. The simulation can model the real system with a good accuracy.

Parameter	value
r	5 mm
l	20 mm

H	6 mm
J_o	7.205×10^{-8} kgm^2
c_a	1.8×10^{-5} Ns
μr_e	1.3×10^{-3} m

Table 2: Flapping wing mechanisms parameters values. r, l, H and J_o are adopted from reference [13] and c_a and μr_e are estimates.

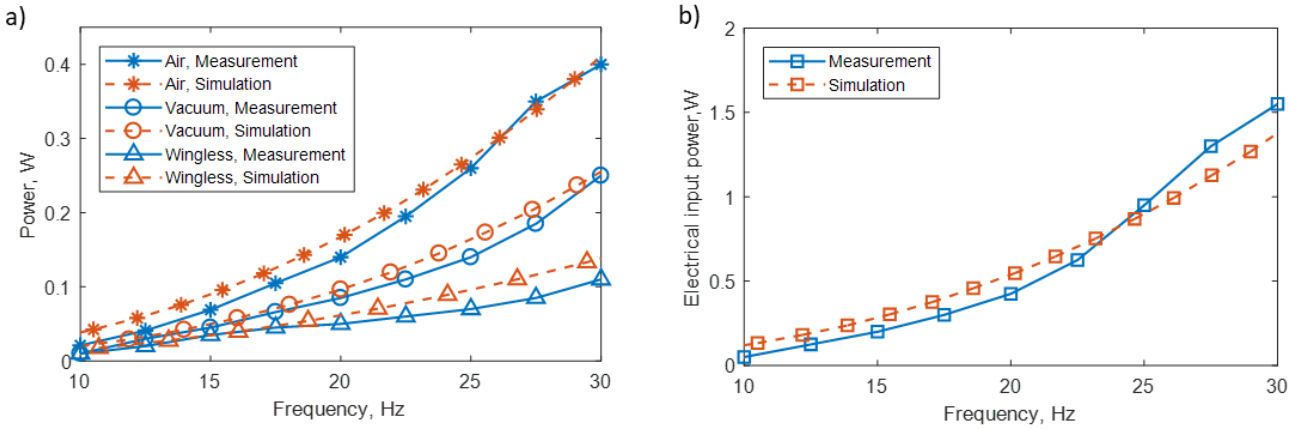


Figure 3: Mechanical power and input electrical power as a function of flapping frequency; solid lines: measurement result reproduced after [13], dashed lines: simulation results. a) Mechanical power of the flapping mechanism operating in the air, in a vacuum and when wings are removed. b) Input electrical power when the system operates in air.

4 Optimisation

Parameters of the system can be optimised using the model developed in this paper. The two important measures of performance for a flying machine are the energy efficiency and the aerodynamic power. The energy efficiency is defined as the ratio of aerodynamics power to the input electrical power here. The power dissipated through the viscous damper c_a can be considered as a measure of aerodynamic lift. The crank length is considered here first. The minimum size for the moving parts are dictated by manufacturability and crank length of 5 mm was used in the model of this study. It should be noted that the crank and the connecting rod are assumed massless and the effect of its increased mass and inertia is not considered here. The flapping angle is kept constant to compare just the effect of the length of cranthe k on the performance of the system. The efficiency and aerodynamic power are plotted in Figure 4 for three different input voltages as a function of the crank length.

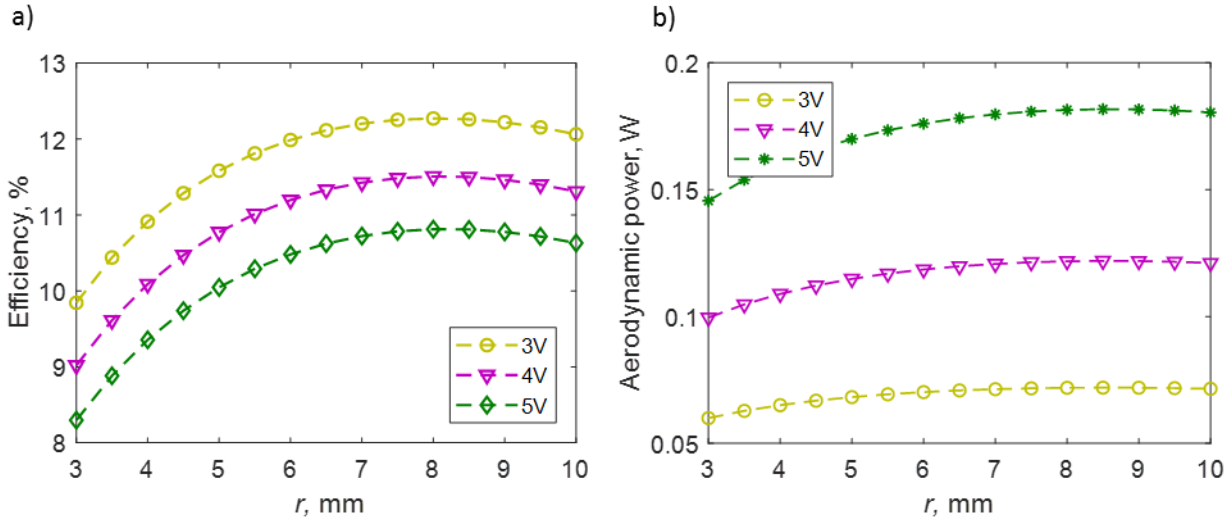


Figure 4: The efficiency and the aerodynamic power as a function of crank length for three different input voltages. a) Efficiency, b) aerodynamic power.

The efficiency and aerodynamic power increase with increasing the crank length initially and the maximum can be achieved for a length of 8 mm in this case. For lengths larger than 7 mm the aerodynamic power is almost constant. The highest efficiency can be achieved with an input voltage of 3 V. However, the aerodynamic power for this voltage is lower than the other two as expected. The higher efficiency for an input voltage of 3V is a result of the motor design which is tuned to operate at this voltage. The effect of changing the length of the connecting rod l on the system performance is shown in Figure 5. Increasing the length l cause a sharp increase in the efficiency for smaller lengths but the increase become smaller for larger lengths than 15 mm. Thus, a length of about 15 mm is a good compromise between the efficiency and the weight of the flying drone. The aerodynamic power is less sensitive to the changes in the connecting rod length after initan ial rapid increase for small lengths.

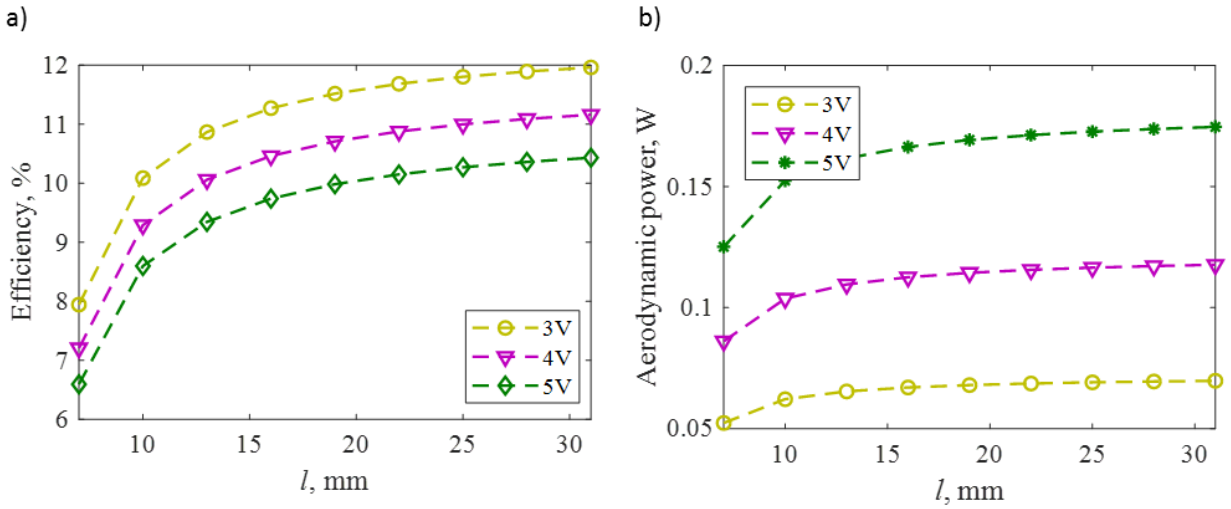


Figure 5: The efficiency and the aerodynamic power as a function of the length of the connecting rod l for three different voltages. a) Efficiency, b) aerodynamic power.

The size of the wings is very important for any flying machine as it is the interface between the mechanical power and the aerodynamic lift. It is important to know if the size that is chosen for a specific design is the optimum choice. The relation between the wing size and the lift is complex. Here, only a very simple viscous damper is used to model the aerodynamic lift. However, it is still possible to

investigate how changes in the wing size can affect the performance of the system. For the sake of simplicity, it is assumed that the inertia of the wings J_o and the aerodynamic viscous damping coefficient c_a are linearly related. A ratio α is defined between the new values and nominal values for the wing inertia and the aerodynamic damping coefficient,

$$\alpha = \frac{c_a}{(c_a)_{\text{nominal}}} = \frac{J_o}{(J_o)_{nominal}}. \tag{13}$$

The nominal values for c_a and J_o are given in Table 2. The efficiency and the aerodynamic power as a function of α are shown in Figure 6. By increasing α, the aerodynamic power increases as expected, however, the increased loads cause a decrease in the frequency of the flapping and changes in aerodynamic power become negligible for α greater than 0.7. Thus, a value of α about 0.9 which corresponds to maximum efficiency provides the optimum working condition.

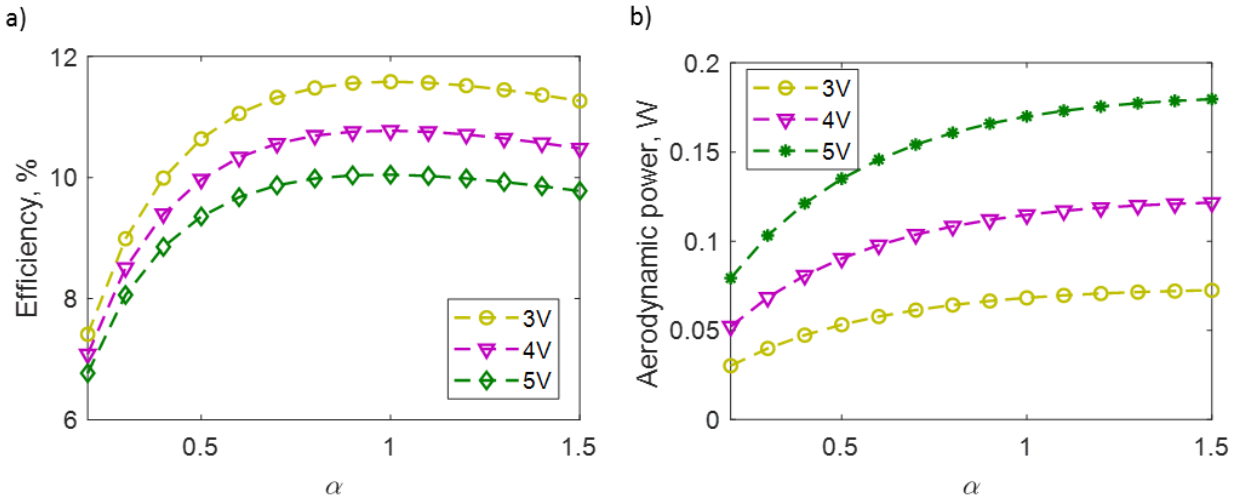


Figure 6: The efficiency and the aerodynamic power as a function of α for three different input voltages. a) Efficiency, b) aerodynamic power.

5 Conclusions

A mathematical model of a flapping wing mechanism is provided in this paper. The model includes two main parts, the electromechanical model of the DC gearmotor and the mechanical model of the flapping mechanism. A crank slider mechanism is used to convert the rotational motion to the flapping motion of the wings. The model includes the effect of friction which allows justifying the increase in losses due to inertia and aerodynamic forces. The parameters of the system are estimated using the published data and it is shown that the model can predict the experimental results with a good accuracy. The system efficiency and aerodynamic power are used as two measures of performance. The effects of the crank and connecting rod lengths on the performance of the system are investigated and optimum lengths are suggested. A linear relation between the inertia of the wing and the aerodynamic damping coefficient is assumed and the effect of changing the wing parameters on the performance is studied. A smaller size wing can slightly outperform the nominal size wing in term of the efficiency.

References

[1] C.P. Ellington, *The novel aerodynamics of insect flight: applications to micro-air vehicles*, Journal of Experimental Biology 202 (1999) pp. 3439-3448.

[2] D. Floreano, R.J. Wood, *Science, technology and the future of small autonomous drones*, Nature. 521 (2015) pp. 460–466. doi:10.1038/nature14542.

[3] G. Cai, J. Dias, L. Seneviratne, *A Survey of Small-Scale Unmanned Aerial Vehicles: Recent Advances and Future Development Trends*, Unmanned Systems, 02 (2014) pp. 175–199. doi:10.1142/S2301385014300017.

[4] C.H. Greenewalt, *The Wings of Insects and Birds as Mechanical Oscillators*, Proceedings of the American Philosophical Society, 104 (1960) 605–611. doi:10.2307/985536.

[5] G. Fischer, A.G. Cox, M.A. Gogola, M.K. Gordon, N.O. Lobontiu, D.J. Monopoli, E. Garcia, M. Goldfarb, *Elastodynamic locomotion in mesoscale robotic insects, in: Y. Bar-Cohen (Ed.), Smart Struct, in Proceedings Volume 3669, Smart Structures and Materials 1999: Electroactive Polymer Actuators and Devices*, Newport Beach, CA, United States, 1999, pp. 362–368. doi:10.1117/12.349694.

[6] R. Madangopal, Z.A. Khan, S.K. Agrawal, *Biologically Inspired Design Of Small Flapping Wing Air Vehicles Using Four-Bar Mechanisms And Quasi-steady Aerodynamics*, Journal of Mechanical Design, 127 (2005) 809. doi:10.1115/1.1899690.

[7] A. Cox, D. Monopoli, D. Cveticanin, M. Goldfarb, E. Garcia, *The Development of Elastodynamic Components for Piezoelectrically Actuated Flapping Micro-Air Vehicles*, Journal of Intelligent Material Systems and Structures 13 (2002) 611–615. doi:10.1106/104538902032463.

[8] Z.A. Khan, S.K. Agrawal, *Design of flapping mechanisms based on transverse bending phenomena in insects, in Proceedings 2006 IEEE International Conference on Robotics and Automation, Automn* 2006, ICRA 2006., IEEE, n.d.: pp. 2323–2328. doi:10.1109/ROBOT.2006.1642049.

[9] S. Avadhanula, R.J. Wood, D. Campolo, R.S. Fearing, *Dynamically tuned design of the MFI thorax, in Proceedings 2002 IEEE International Conference on Robotics and Automation (Cat. No.02CH37292)*, 20002 11-15 May, Washington, DC, USA (2002) pp. 52–59. doi:10.1109/ROBOT.2002.1013338.

[10] E. Steltz, S. Avadhanula, R.S. *Fearing, High lift force with 275 Hz wing beat in MFI, in IEEE/RSJ International Conference on Intelligent Robots and Systems* 2007 29 Oct.-2 Nov., San Diego, CA, USA (2007), pp. 3987–3992. doi:10.1109/IROS.2007.4399068.

[11] Z.A. Khan, S.K. Agrawal., *Design and Optimization of a Biologically Inspired Flapping Mechanism for Flapping Wing Micro Air Vehicles, in: Proceedings 2007 IEEE International Conference on Robotics and Automation*, 2007 10-14 April, Roma, Italy, (2007), pp. 373–378. doi:10.1109/ROBOT.2007.363815.

[12] S.S. Baek, K.Y. Ma, R.S. Fearing, *Efficient resonant drive of flapping-wing robots, Efficient resonant drive of flapping-wing robots*, 2009 10-15 October, St. Louis, MO, USA, (2009), pp. 2854–2860. doi:10.1109/IROS.2009.5354725.

[13] G.-K. Lau, Y.-W. Chin, J.T.-W. Goh, R.J. Wood, *Dipteran-Insect-Inspired Thoracic Mechanism With Nonlinear Stiffness to Save Inertial Power of Flapping-Wing Flight*, IEEE Transactions on Robotics. 30 (2014), pp. 1187–1197. doi:10.1109/TRO.2014.2333112.

[14] DC Gearmotor | Precision Microdrives, https://www.precisionmicrodrives.com/product-catalogue/dc-gearmotor (accessed June 22, 2018).

Dynamic behavior and vibration analysis of tensegrity - membrane structures

P. Kurka [1], **V. Paiva** [1], **L. Teixeira** [1], **J. Izuka** [2], **P. Gonzalez** [1]
[1] UNICAMP, Department of Mechanical Engineering,
Mendeleyev street, 200, Campinas - SP, Brazil
e-mail: **kurka@fem.unicamp.br**

[2] UNICAMP-Limera, Faculty of Applied Sciences,
Pedro Zaccaria street, 1300, Limeira - SP, Brazil

Abstract
The present work aims to develop a reliable kinematic and dynamic model of a Tensegrity Membrane structure. The modeling of the dynamic system is preceded by the determination of the static configuration. This configuration depends on the pre-tensioning of the cables and membrane. The dynamics of the structure are represented by its eigen-modes and natural frequencies. The stiffness depends on the materials properties and on the pre-tension, which is calculated in the force density method and considered in the modal analysis. Numerical results of the kinematics and the vibration of the structure are presented. The adaptive force density method is used to in order to achieve the relation between the pretension of the structure's elements. Static analysis is performed in order to incorporate the pretensions into the structure's elements. Comparisons of the natural frequencies are made between tensegrities with and without membrane.

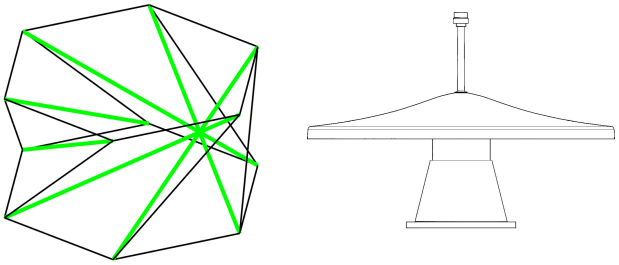
1 Introduction

Tensegrity structures have many applications in civil, mechanical, robotic, biomechanical and aerospace areas. The main advantage of this type of structure is its geometric adaptability. Tensegrity structures are formated by rigid bodies (bars) and cables, which are always in compression and tension, respectively. If the initial configuration of the tensegrity is in compression, when applying a force in a certain point of the structure, then it will open and will create a new equilibrium stable structure, capable of supporting this load.

The numerical model of tensegrity systems is of great interest in the stiffness controllers design, mainly because this kind of structure presents a nonlinear behavior. Motro [1] showed a linear model that gives a good approximation of the nonlinear behavior of simple structures. Bel Hadj Ali [2] proposed a tensegrity structure model to obtain the modal characteristics in order to develop a vibration control strategy. In his work, Bel Hadj Ali reduced the structural response to acceptable levels at minimum control cost. Sultan [3] used the Lagrange's method to model a four-bar tensegrity-membrane system and determined a set of differential-algebraic equations to active control design. Other parameter to consider is the opening mechanism. In the literature, there are several proposals as Pellegrino [4], who suggested to vary the bars or cables size. Arsenault [5] replaced tendons by springs and added actuators that change the bars length. Zhang e Ohsaki [6] used the force density algorithm to find the shape of the tensegrity given the pre-stresses in the cables, responsible for the expansion of the structure. Moored [7], Bel Hadj Ali [8] and Schenk [9] applied the energy method to determine analytically the actuator force necessary for opening system.

Some applications in the spatial area of tensegrity-membrane structures are radar antennas [11], membrane reflectors [12] [13], the support structure of optical membranes [14] and solar sails [15].

The tensegrity structure considered in the present work contains 6 bars, forming two hexagonal bases (Figure 1(a)). The distance between them, i.e. the height of the structure, changes during the movement, but the two bases remain parallel to each other all time. The movement is driven by the cables connecting the bases, which will be referred as vertical cables. The lengths of this cables change in the same rate so the bases remain parallel.



(a) *6 bars.* (b) *Reflector Antenna.*

Figure 1: Tensegrity and Reflector Antenna structures.

This system could be applied on a satellite antenna, for example, as a deployable stand for the reflector, replacing the cone and also part of the the structures below the reflector surface (Figure 1(b)).

The contribution of the present work is to propose a methodology to model the openning mechanism and to represent the vibration characteristics of a tensegrity structure with six bars and a membrane. The method for solving the kinematics of the opening mechanism was validated experimentally with a four bars tensegrity structure [16], [17]. A vibration analysis of the model was done through finite element method and the results were compared with a commercial software.

This paper is organized as follows. Section 2 shows the static model that describes the tensegrity structure geometry and the opening mechanism. Section 3 presents the dynamics characteristics, which are obtained through the finite element method. Section 4 describes the necessary conditions of the twist angle and the velocity of the inclined cables to open the tensegrity structure. Section 5 presents the simulations results of the tensegrity structure with and without membrane element and opening mechanism developed in the softwares Ansys® and Matlab®. Section 6 discusses the results obtained and draws the relevant conclusions.

2 Static model

A tensegrity structure with 6 bars, which goal is to be the stand of a reflector antenna, is modeled geometrically through nodal analysis. The methodology is described in the section 2.1. Opening mechanism is studied and described in the section 2.2.

2.1 Tensegrity structure configuration

The geometry of the tensegrity structure, as shown [22], is defined by nodes, connectivity matrices and members. The nodes are the extremity of the bars and tendons. The members are the bars and tendons itself. The 3D expression of the nodes is shown by (Eq 1):

$$\mathbf{n_l} \in \Re^3 \tag{1}$$

The nodes are organized in the matrix $\mathbf{N}$, where the coordinates of each node are contained in the vectors $\mathbf{x}$, $\mathbf{y}$, and $\mathbf{z}$ as follows:

$$\mathbf{N} = \begin{Bmatrix} \mathbf{n_1} \\ \vdots \\ \mathbf{n_n} \end{Bmatrix} = \begin{bmatrix} \mathbf{x} & \mathbf{y} & \mathbf{z} \end{bmatrix} \tag{2}$$

The members ($\mathbf{m}_k$) are the result of the difference between nodes interconnected. It can be written as:

$$\mathbf{m}_k = \mathbf{n}_{ik} - \mathbf{n}_{jk} \tag{3}$$

where the terms $\mathbf{n}_{ik}$ and $\mathbf{n}_{jk}$ are, respectively, the i^{th} and j^{th} nodes that are related to the k^{th} member.

The members are organized in the matrix $\mathbf{M}$. The corresponding member lengths in each direction are defined by the vectors $\mathbf{u}$, $\mathbf{v}$ and $\mathbf{w}$ as follows:

$$\mathbf{M} = \begin{Bmatrix} \mathbf{m}_1 \\ \vdots \\ \mathbf{m}_m \end{Bmatrix} = \begin{bmatrix} \mathbf{u} & \mathbf{v} & \mathbf{w} \end{bmatrix} \tag{4}$$

The matrices $\mathbf{M}$ and $\mathbf{N}$ are related by the connectivity matrix $\mathbf{C}$:

$$\mathbf{C}.\mathbf{N} = \mathbf{M} \tag{5}$$

With the definitions presented above, one can start with the structure's force analysis.

The equilibrium equation can be written in function of the nodal coordinates. To do this, it must enter the force density (q) concept. Which it is the ratio between the traction or compression forces and the length of the members. That relation is shown in the equation 6 to an arbitrary member k:

$$q_k = \frac{s_k}{l_k} \tag{6}$$

So, it is possible to obtain the force density matrix $(\mathbf{E})$:

$$\mathbf{E} = \mathbf{C}^T\mathbf{Q}\mathbf{C} \tag{7}$$

where,

$$\mathbf{Q} = diag(\mathbf{q}) \tag{8}$$

The $diag(\mathbf{vec})$ is a diagonal matrix with the terms of the vector $\mathbf{vec}$.The equilibrium equation in nodes coordinates function. For structures without fixations, there are:

$$\begin{cases} \mathbf{E}.\mathbf{x} = \mathbf{0} \\ \mathbf{E}.\mathbf{y} = \mathbf{0} \\ \mathbf{E}.\mathbf{z} = \mathbf{0} \end{cases} \tag{9}$$

The equation 9 is not linear due to the fact that the force densities are in function of the members length, that are dependent of the nodes positions. However, it can be linearized, predetermining the values of the force densities.

2.1.1 Form-finding method

The problem in working with tensegrity structures lies in finding the structure's equilibrium form. Some researchers as [25] used analytical approaches and [26] used nonlinear methods to solve this problem. The method used in the present study uses the force density concept and the methodology explained in [19], which will be explained below.

2.1.2 Force Density Method

Schek presents in one of his works the definition of force density where it's pointed the leverage of determining the final structure's configuration by the solution of a linear system [23]. However, the method has disadvantages of having few restrictions on the final shape of the structure, although some methods to restrain the final form exist. This disadvantage is due to the fact that the inputs of the model are only the force densities and the fixed nodes of the structure.

2.1.3 Condition of non-degeneracy

To obtain structures with n_d dimensions, the matrix $\mathbf{E}_{nxn}$ must have the following condition:

$$rank(\mathbf{E}_{nxn}) = n - h' \tag{10}$$

where,

$$h' = n_d + 1 \tag{11}$$

Choosing force density values that makes $\mathbf{E}$ have the required rank value is one of the difficulties of this process of determining the form of tensegrity structures. In [24], three types of processes are listed. The first process would be the intuitive method, whose application would be for systems that have few members. Another process would be the analytical method, where the matrix is analyzed in a symbolic way, and it is possible to arrive at the relations between force densities in which the desired results can be obtained.

There is also the iterative method, where the values of q_k are evaluated step by step until the desired rank is obtained for the matrix $\mathbf{E}$. This method will be described in the next topic.

2.1.4 Iterative method

In [18] and [19], is proposed a iterative method in order to obtain the desired rank of $\mathbf{E}$.

First, initial values for the vector $\mathbf{q}^i$ is chosen. From this vector, $\mathbf{E}$ is obtained by using Equations 7 and 8. Then, through Equation 12, the eigenvectors and eigenvalues of $\mathbf{E}$ are obtained.

$$\mathbf{E} = \Phi^T \Lambda \Phi \tag{12}$$

For the rank of E to have the value shown in Equation 10, there must be a number of h' (Equation 11) zeros between the eigenvalues of the matrix Λ. Therefore, in the iterative method, we analyze the values of the diagonal matrix Λ and observe if the number of zeros is equal to h'. If it is not, there's two possibilities. The first case would be the number of zeros being smaller than h'. For this case, simply substitute those smaller values to zero in order to reach the required number of zeros. The second case would be that the number of zeros are larger than h'.

For this work, only case 1 is addressed. Therefore, giving continuity to the iterative method, a new value of Λ by replacing the h' smaller values with zero. This new Λ will be denoted as $\overline{\Lambda}$. With this new matrix, $\overline{\mathbf{E}}$ is calculated through Equation 12.

Using $\overline{\mathbf{E}}$, one can get $\overline{\mathbf{q}}$, which are the updated values of force densities, with the Equation 13. The formulation of this equation is detailed in [19].

$$\overline{\mathbf{q}} = (\mathbf{R}^T\mathbf{R})^{-1}\mathbf{R}^T\mathbf{g} \tag{13}$$

With $\overline{\mathbf{q}}$ and the Equation 7, $\mathbf{E}^{i+1}$ is obtained, which is the updated force density matrix. Then, using Equation 12, we get a new value of Λ, which will be denoted by Λ^{i+1}. If this eigenvalue matrix does not yet have the required number of zeros, the iterative process is repeated until this condition is reached.

Also, through this method, some restrictions can be introduced to the configuration of the structure that the method can find.

One of these constraints is that of force density, in which a relation can be established between the force densities of each member by writing them by means of the following equation:

$$\mathbf{Fq} = \mathbf{0} \tag{14}$$

Where we establish the relations between the force density vector components $\mathbf{q}$ through the matrix $\mathbf{F}$.

Further, the heights of the nodes of the tensegrity structure can be determined by Equation 15 as shown in [19].

$$\mathbf{C}^T diag(\mathbf{Cz})\mathbf{q} = \mathbf{0} \tag{15}$$

These height restrictions and force densities can be written as the following linear equation system:

$$\begin{pmatrix} \mathbf{F} \\ \mathbf{C}^T diag(\mathbf{Cz}) \end{pmatrix} \mathbf{q} = \mathbf{Gq} = \mathbf{0} \tag{16}$$

The solution of this system is given by:

$$\mathbf{q} = \phi(\mathbf{R}\phi)^{-1}\mathbf{g} \tag{17}$$

where ϕ is the null space of $\mathbf{G}$.

Finally, to consider these constraints in the iterative method, to find $\overline{\mathbf{q}}$ it's used Equation 17 instead of Equation 13.

After finding the value of the force density vector, one must calculate the final form of the structure. Thus, the homogeneous Equation 18 must be solved, in order to find the nodal coordinates $\mathbf{X}$.

$$\mathbf{HX} = \mathbf{0} \tag{18}$$

where,

$$\mathbf{H} = \begin{bmatrix} \mathbf{E} & \mathbf{O}_n & \mathbf{O}_n \\ \mathbf{O}_n & \mathbf{E} & \mathbf{O}_n \\ \mathbf{E} & \mathbf{O}_n & \mathbf{E} \end{bmatrix} \tag{19}$$

$$\mathbf{X} = \begin{Bmatrix} \mathbf{x} \\ \mathbf{y} \\ \mathbf{z} \end{Bmatrix} \tag{20}$$

As shown in [18], the solution for the Equation 18 is given by:

$$\mathbf{X} = \mathbf{A}\overline{\mathbf{A}}^{-1}\overline{\mathbf{X}} \tag{21}$$

where $\mathbf{A}$ is the null space of $\mathbf{H}$ and $\overline{\mathbf{A}}$ is the corresponding components in $\mathbf{A}$ of related to the independent set of nodal coordinates $\overline{\mathbf{X}}$.

The form-finding procedure is summarized in Figure 2.

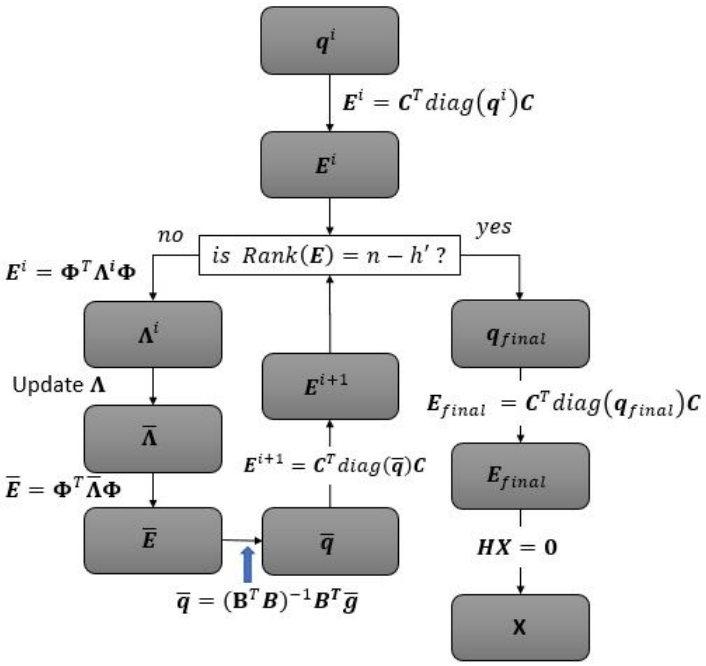


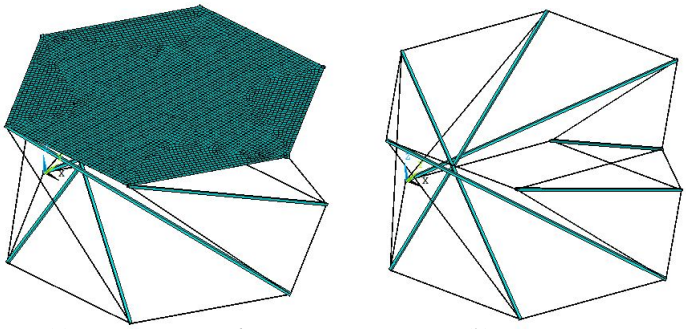
Figure 2: Flowchart showing the iterative process to find force density vector values.

2.1.5 Finding the shape of a Tensegrity-Membrane structure

In [20], the shape of a tensegrity-membrane structure is found by minimizing the potential energy of the system. However, the same procedure used for tensegrities without membranes can be applied in this case, such as the iterative method described in section 2.1.4. This can be achieved by replacing the membrane with tendons that develop the same function in the model. Therefore, after finding the tractions in each tendon and the nodes forces, the finite element method can be used to calculate the membrane displacements necessary to exert the same equilibrium forces in the resultant system. Thus, the necessary behavior of the membrane is determined so it performs the same function of the tendons used to calculate the equilibrium configuration. Then, the membrane to be used in the final model of the system can be defined. When the deployed configuration is obtained, one starts to the development of its dynamic model.

2.2 Opening mechanism

As the lower base is fixed (equation 22), the shape of the tensegrity is determined by the positions of the nodes in the upper base (figure4). These can be given in function of the height h, twist angle φ and side l of



(a) *Tensegrity-Membrane*. (b) *Tensegrity*.

Figure 3: Tensegrity and Tensegrity-Membrane structures.

the hexagon (equation 23).

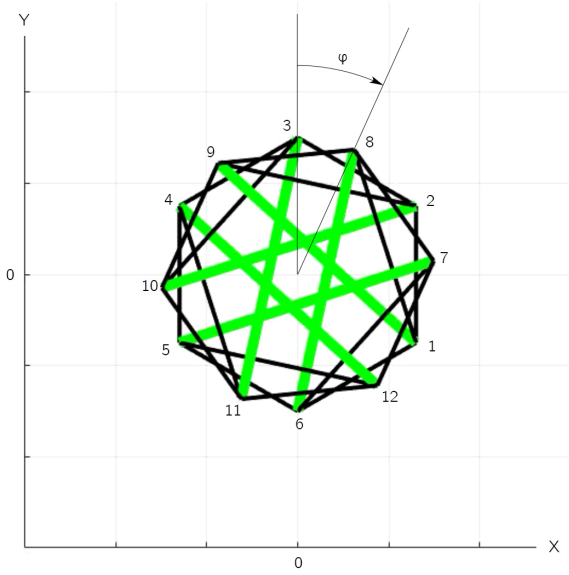


Figure 4: Top view.

$$N_{lw} = l \begin{bmatrix} \frac{\sqrt{3}}{2} & \frac{\sqrt{3}}{2} & 0 & -\frac{\sqrt{3}}{2} & -\frac{\sqrt{3}}{2} & 0 \\ -0.5 & 0.5 & 1 & 0.5 & -0.5 & -1 \\ 0 & 0 & 0 & 0 & 0 & 0 \end{bmatrix} \tag{22}$$

$$N_{up} = l \begin{bmatrix} cos(\frac{\pi}{6} - \varphi) & sin(\varphi) & -cos(\varphi + \frac{\pi}{6}) & -cos(\frac{\pi}{6} - \varphi) & -sin(\varphi) & cos(\varphi + \frac{\pi}{6}) \\ sin(\frac{\pi}{6} - \varphi) & cos(\varphi) & sin(\varphi + \frac{\pi}{6}) & -sin(\frac{\pi}{6} - \varphi) & -cos(\varphi) & -sin(\varphi + \frac{\pi}{6}) \\ \frac{h}{l} & \frac{h}{l} & \frac{h}{l} & \frac{h}{l} & \frac{h}{l} & \frac{h}{l} \end{bmatrix} \tag{23}$$

$$N = \begin{bmatrix} N_{lw} & N_{up} \end{bmatrix} \tag{24}$$

The distance between nodes 1 and 9 is equal to the length of a strut b. Then, the height h can be expressed in function of b, l and φ (equation 25). Analogously, the vertical cable v separates nodes 1 and 8 and can be given in function of the height (equation 26).

$$h = \sqrt{b^2 - \left(-lcos\left(\varphi + \frac{\pi}{6}\right) - l\frac{\sqrt{3}}{2}\right)^2 - \left(lsin\left(\varphi + \frac{\pi}{6}\right) + \frac{l}{2}\right)^2} \tag{25}$$

$$v = \sqrt{h^2 + \left(lsin(\varphi) - l\frac{\sqrt{3}}{2}\right)^2 + \left(lcos(\varphi) - \frac{l}{2}\right)^2} \tag{26}$$

3 Modal analysis

The dynamic characteristic of the tensegrity structure are determined numerically thought a Finite elements model. A bar element with stiffness in axial direction is used in the structure bars and cables. The membranes is represented by the Shell element.

3.1 Bar element

The displacement solution of the bar element can be approximated by:

$$u_{axial} = \omega_1 u_{axial_1} + \omega_2 u_{axial_2} \tag{27}$$

where ω_1 and ω_2 are shape functions. This shape functions can be written as:

$$\omega_1 = \frac{L - x}{L}, \tag{28}$$

and

$$\omega_2 = \frac{x}{L}, \tag{29}$$

where, x is the position on the element and L is its length.

This shape functions can be organized in the displacement interpolation matrix ($\mathbf{H}$) as:

$$\mathbf{H} = \begin{Bmatrix} \omega_1 \\ \omega_2 \end{Bmatrix} \tag{30}$$

The stiffness matrix of an element, as shown in [21], is given by Equation 31

$$\overline{\mathbf{k}}_e = \int_V \mathbf{B}^T \mathbf{C} \mathbf{B} dV \tag{31}$$

where $\mathbf{B}$ is the strain-displacement matrix, $\mathbf{C}$ is the material matrix and V is the element volume. For the bar element, $\mathbf{C} = E$ and $V = AdL$. The $\mathbf{B}$ matrix is calculated as $\frac{\partial \mathbf{H}}{\partial x}$. Thus, using the terms presented above and using Equation 31, the stiffness matrix for the element is calculated.

The mass matrix for the bar element is obtained using the Equation 32.

where ρ is the bar element density.

$$\mathbf{M}_e = \int_V \rho \mathbf{H}^T \mathbf{H} dV \tag{32}$$

In local coordinates, the bar element is written as:

$$\mathbf{r}_e^T = \begin{bmatrix} u_{axial_1} & u_{axial_2} \end{bmatrix} \tag{33}$$

The vector $\mathbf{r}_e$ in local coordinates can be transformed into globals coordinates $\mathbf{R}_e$ through the following expression:

$$\mathbf{R}_e = \mathbf{T}^T \mathbf{r}_e, \tag{34}$$

where $\mathbf{T}$ is the transformation matrix with angles formed between the local and global coordinates. The stiffness matrix is described as:

$$\mathbf{K}_e = \mathbf{T}^T \overline{\mathbf{k}}_e \mathbf{r}_e, \tag{35}$$

In order to take into account the pretensions applied in the cables and the bars of the structure, the geometric stiffness matrix ($\mathbf{K}_G$) presented in [19], which is given by:

$$\mathbf{K}_G = \mathbf{I} \otimes \mathbf{E} \tag{36}$$

where $\mathbf{I}$ is the identity matrix and $\mathbf{E}$ is the equilibrium matrix.

3.2 Shell element

The Shell element used in this paper is presented in [21]. It's used an eight node element and it's considered isotropic material for the material matrix ($\mathbf{C}$) and a plane stress state.

The dynamic model will be obtained through a finite element mesh built over the geometry defined by the static model. From this dynamic model, one can calculate the natural frequencies and modes of the structure.

4 Kinematic model

A tensegrity prism which bases have n sides is stable when the twist angle reaches the value given in equation 37, in that case, the height is maximum and v is minimum. If we try to shorten the vertical cables more than this minimum, the structure becomes more tensioned instead of moving up or down. In this model, the twist angle goes from 0 to $\pi/$, taking v from maximum to minimum and h from zero to maximum.

$$\varphi_s = \frac{\pi}{2} - \frac{\pi}{n} \tag{37}$$

The only variable we truly control is v, so we can assign a velocity/acceleration to v to calculate time. Now, the positions of the nodes are determined for each instant of time.

5 Simulations

We used the following parameters in this simulation: hexagon side $l = 0.3m$, bar length $b = 0.6m$ and twist angle φ going from 0 to $\pi/3rad$, leading h to vary from 0 to $0.3m$ (Figure 5) and the vertical cable from 0.52 to $0.42m$ (Figure 6(a)).

A small pull of 20% in the vertical cable caused this model to reach its maximum height. This high sensitivity of the height to the vertical cable, if properly managed, may become an advantage instead of a problem for the designer, therefore it has been highlighted.

The relationship between h and v depends only on geometry, not being affected by materials properties or time. We may assume a velocity of $0.01m/s$ for this (approximately) $0.1m$ reduction of the inclined cable,

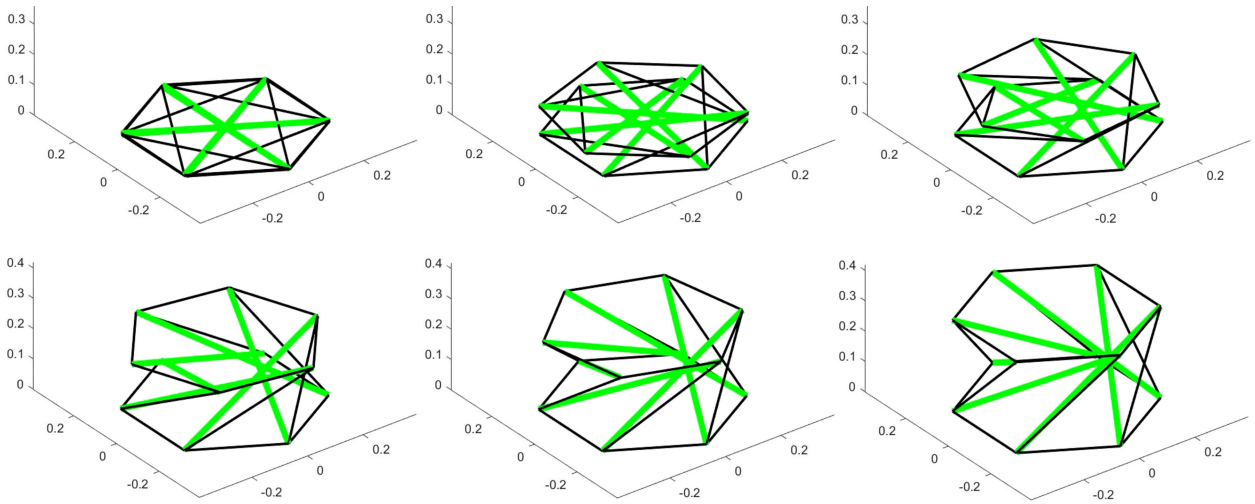
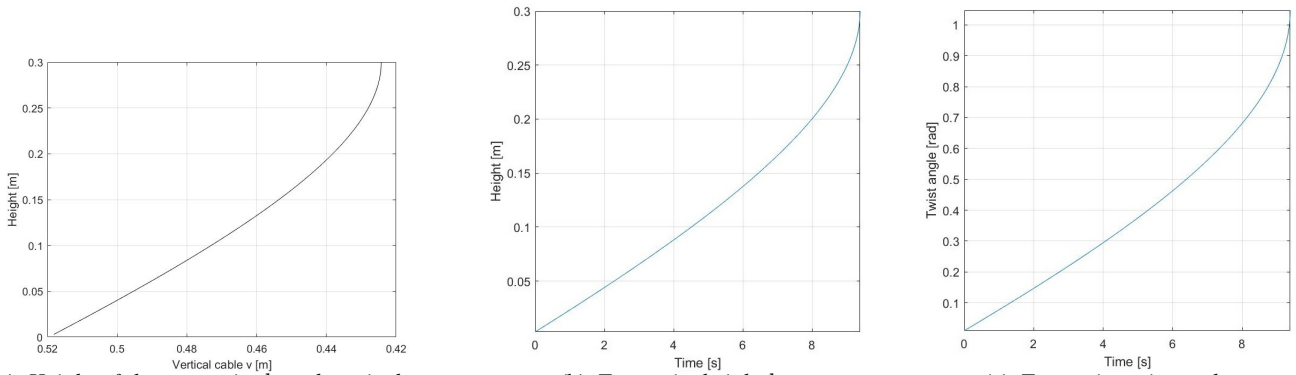


Figure 5: Tensegrity expansion.



(a) *Height of the tensegrity h and vertical cable pulling v.*

(b) *Tensegrity height h.*

(c) *Tensegrity twist angle φ.*

Figure 6: Tensegrity kinematic results.

leading to a reasonable time of around $10s$ for the expansion process. Height and twist angle are expected to increase with time and the graphs confirm it (Figure 6(c)).

As v was forced to decrease linearly over time and the relationship between h and v is known, h's curve in time had to be similar, except increasing instead of decreasing. The same applies to the behavior of the vertical cable v.

5.1 Tensegrity structure with and without membrane

5.1.1 Finding the shape of the tensegrity structure

The method presented in Sections 2.1.2 - 2.1.4 was implemented with the help of Matlab® software. The four nodes chosen as input data for the method can be seen in the Table 1.

Position	x (mm)	y (mm)	z (mm)
Node 1	459	-265	0
Node 2	459	265	0
Node 3	0	530	0
Node 4	459	-265	300

Table 1: Positions of predetermined nodes

The initial force densities used in the routine in Matlab® is shown in Table 2.

	Base Tendons	Top Tendons	Vertical Tendons	Vertical Bars
Force Density [N/m]	1.0	1.0	2.0	-2.0

Table 2: Initial force densities

Also, the restriction was used that the members of each portion of the structure (Top, base and vertical members) had equal force densities between them. Finally, the height of the frame was restricted to 300 mm.

The configuration obtained after 262 iterations is the same presented in Figure 1(a) and the values of the nodes were the same shown in Eq 23, but with $l = 306mm$, $h = 300mm$ and $\varphi = 60^o$. The application of this method reached the goal of achieving the configuration of the structures proposed and finding the pretension values presented in the structure. Also, it makes possible the subsequent modal analysis of the pretensioned structure. It is perceived by the results that the height restriction was met and that there were some variations in the predetermined nodes.

The force densities, and the final tensile and compression forces, are shown in Table 3. Then, in order to the configuration of the structure to be met, its pre-stresses must obey the same proportion of the forces presented in Table 3.

	Force density [N/m]	Member lengths [mm]	Member forces [N]
Base Tendons	1.2624	306.0	0.3863
Top Tendons	1.2624	306.0	0.3863
Vertical Tendons	1.2624	428.5	0.5410
Vertical bars	-1.2624	609.0	-0.7688

Table 3: Pretensions present in the final configuration of the structure.

5.1.2 Modal analysis of the structure

Modal analysis was performed using bar elements for the bars and tendons, and shell elements for the membrane. Also, the pre-tension of the structure was considered during the simulations.

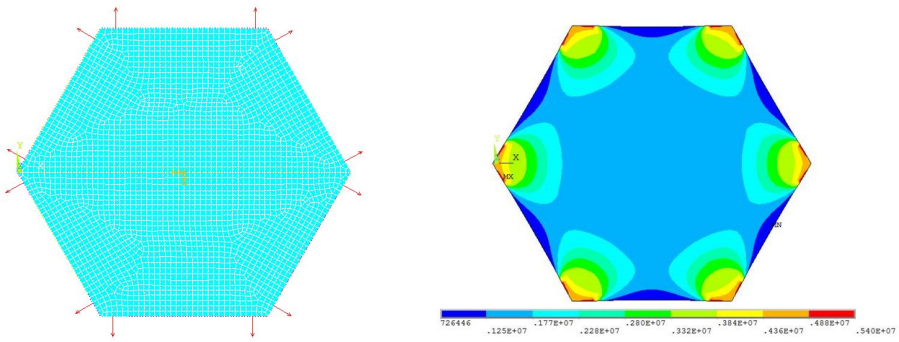
The simulated structure is composed of 1 mm diameter nylon lines, 5 mm square steel bars and a thin membrane of $51\mu m$. The properties of the materials used are shown in the Table 4.

	Young's Module [GPa]	**Poisson** [-]	**Density** [kg/m^3]
Nylon tendons	2.000	0.30	1130
Steel bars	200.000	0.30	7800
Membrane	0.165	0.34	1400

Table 4: Properties of the materials used in the simulation

For tensegrity structures, the addition of pretension in their longiline elements is simple. So, in considering efforts in only one direction, one can only insert a stress directly to the elements.

However, for the membrane, a static structural simulation is performed in which a restriction is applied to the center of the membrane and pressure forces are applied at its ends. These constraints and force application can be seen in Figure 7(a). The force applied to the membrane is equivalent to the force due to the pre-tension that occurs at the node where the ends of the membrane are connected.



(a) Boundary conditions. (b) Stress Map.

Figure 7: Boundary conditions for the membrane simulation and its stress map

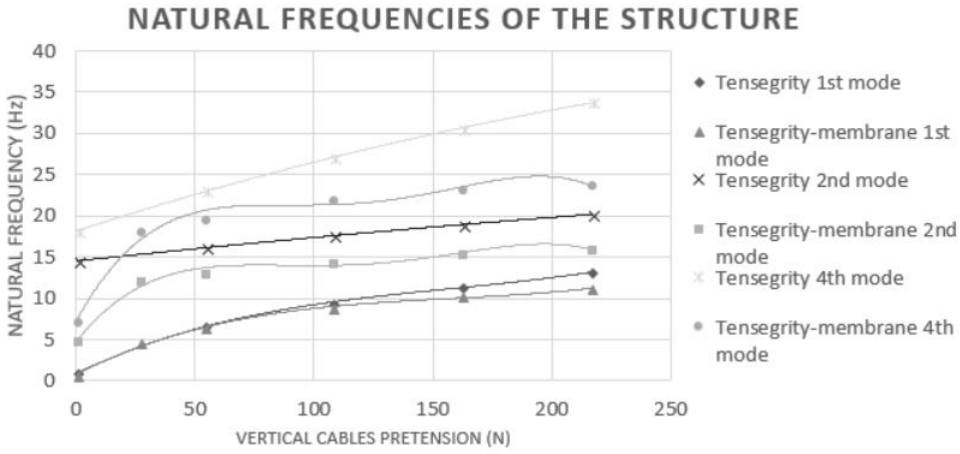
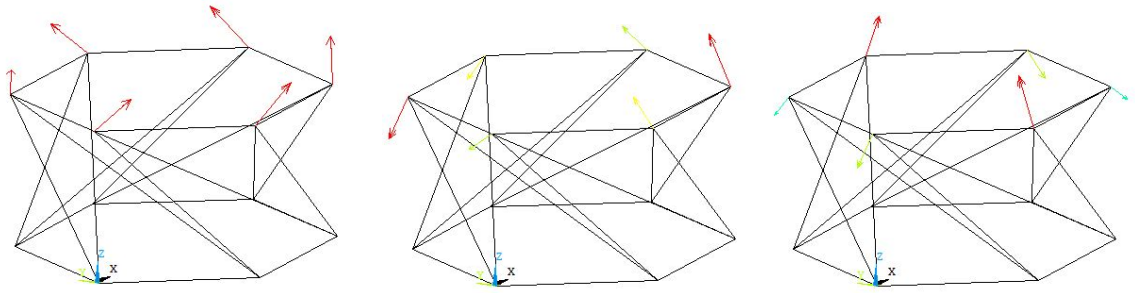


Figure 8: Behavior of the natural frequencies of vibration in relation to the tension in the vertical tendons.

Once the stress map shown in Figure 7(b), is entered, the map is inserted into the simulation of the complete structure, shown in Figure 3(a).

For the finite element analysis, it was used one truss element for each bar and tendon. For the membrane, it was used shell elements with size of approximately $7mm$. Also, the structure is fixed at the six nodes located at the lower base of the tensegrity.

First, the behavior of the first vibrating mode for membrane and non-membrane structures was evaluated. The behavior of the natural frequency of the first mode of vibration in relation to the pretension applied in the vertical tendons can be seen in Figure 8.



(a) 1st mode - Tensegrity without membrane.

(b) 2nd mode - Tensegrity without membrane.

(c) 4th mode - Tensegrity without membrane.

Figure 9: Vibration mode of the tensegrity structure without membrane

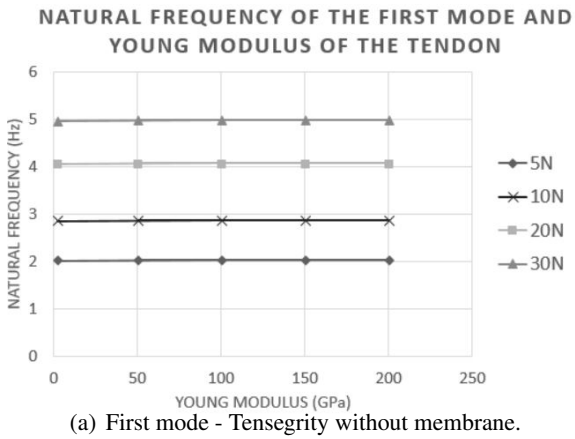
It can be seen from the Figure 8 that the natural frequency of the first mode increases for greater pretension on the structures. Also, the frequencies of this mode is similar for the structure with and without membrane. However, the behavior of the natural frequencies between both structures are different for the second and fourth mode when pretension iss is near to zero. This behavior is due to the mode of vibration of the membrane. For low pretensions, the second and fourth mode of the membrane are lower than the modes of the tendon and rod structure, shown in Fig 9. Thus, this modes is influenced only by the membrane. But, for higher pretensions, the second and fourth modes become a couple of the modes of the structure and membrane. At this higher pretension, the behavior is approximately linear but still always lower than the tensegrity structure without membrane.

The influence of the material type of the structure on its dynamic behavior was investigated. Simulations with modulus of elasticity between $2Gpa$ and $200GPa$ were performed. Observing the Figure 10(a), it will be appreciated that, for the first vibration mode (Fig 9(b)), the modulus of elasticity of the material has little influence. For this case, the pre-tension applied has a predominant influence.

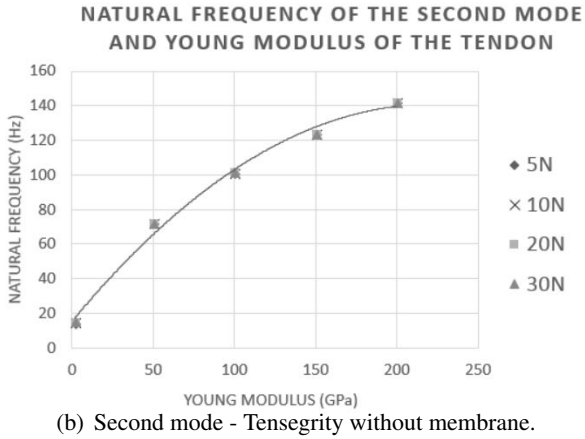
However, the second mode (Fig 9(b)) is strongly influenced by the elasticity modulus of the tendon. However, it has little influence of the applied pretension, as can be observed in Figure 10(b). The explanation would be that while in the first mode of vibration there is little deformation of the tendons and bars, in the second mode this is predominant.

6 Discussions of the results and conclusions

The mechanical behavior of a tensegrity and a tensegrity-membrane are studied in this paper. A tensegrity with 6 bar accomplished to a membrane is proposed to substitute a satellite reflector antenna. The deployment requirement is analyzed though the opening mechanism. Using a 0.6m bar, the total height of the tensegrity varies from 0.0m to 0.3m. This amplitude was achieved by pulling the cable in 0.1m. This hight sensitivity of the height to the vertical cable can bring saves regarding cable volume/mass and energy of the pulling motor.The adaptive force density method is used to achieve a tensegrity configuration similar to that studied in the kinematics section. Also, with this method, is possible to obtain the pretension presented in the



(a) First mode - Tensegrity without membrane.



(b) Second mode - Tensegrity without membrane.

Figure 10: First and second vibration mode vs. young modulus and vs. pre-tensioning of the vertical tendons

structure. This result was found after 262 iterations and makes possible the modal analysis of the structure through the finite element method (FEM). Static analyses are made in order to incorporate the pretension into the FEM model. Thereon, modal analysis is performed to analyze the vibration behavior of the structure. For lower pretensions, the behavior of the second and fourth modes of the tensegrity-membrane structure is different from that presented by tensegrity structures composed only by tendons and bars. This behavior takes place due to the low natural frequency presented by the membrane with low pretension. So, for the lower pretensions, the natural frequency of the membrane is lower than that of the tendon and bar of the structure. For higher pretensions, the modes of the membrane and the tensegrity are coupled. Also, it's noted that, the young modulus of the tendon, for this structure, only affects the affects the second mode. The first mode is mainly influenced by the pretension, while the second, is mainly influenced by the young modulus. This behavior could present design advantages.

References

[1] R. Motro, S. Najari, P. Jouanna, *Tensegrity systems. From design to realization*, *Proceedings of the First International conference on Lightweight structures in architecture*, Sydney, 1986.

[2] N. Bel Hadj Ali, I. Smith I, *Dynamic behavior and vibration control of a tensegrity structure*, International journal of solids and structures, Vol. 47, No. 1285-1296, 2010, pp 1-12.

[3] S. Yang, C. Sultan, *Tensegrity systems. Active Control of Four-Bar Tensegrity-Membrane Systems*, Dynamic Systems and Control Conference, San Antonio, DSCC2014-5886, 2014, pp 1-9.

[4] S. Pelegrino, *Deployable Structures*, 1st edition, Springer, 2001.

[5] M. Arsenault, C. Gosselin, *Kinematic and static analysis of a 3-PUPS spatial tensegrity mechanism*, Mechanism and machine theory, Vol. 44, No. 162-279, 2009, pp 1-18.

[6] J. Zhang, M. Ohsaki, *Tensegrity structures form, stability, and symmetry*, 1st edition, Springer, 2015.

[7] K. Moored, H. Bart-Smith H, *Investigation of clustered actuation in tensegrity structures*, International journal of solids and structures, Vol. 46, No. 3272-3281, 2009, pp 1-10.

[8] N. Bel Hadj Ali, L. Rhode-Barbarigos, I. Smith, *Analysis of clustered tensegrity structures using a modified dynamic relaxation algorithm*, International journal of solids and structures, Vol. 48, No. 637-647, 2011 pp 1-11.

[9] M. Schenk *Theory and design of statically balanced tensegrity mechanisms*, MSc. dissertation, Delft university of technology, 2006.

[10] D. Cadogan, J. Lin, M. Grahne, *The development of inflatable space radar reflectarrays*, 40th Structures, Structural Dynamics, and Materials Conference and Exhibit, 1999.

[11] M. Leipold, H. Runge, C. Sickinger, *Large SAR membrane antennas with lightweight deployable booms*, 28th ESA Antenna Workshop on Space Antenna Systems and Technologies, ESA/ESTEC, 2005.

[12] K. Berger, L. Horta, B. Taleghani, *Static Testing of an Inflatable/Rigidizable Hexapod Structure*, 45th AIAA/ASME/ASCE/AHS/ASC Structures, Structural Dynamics & Materials Conference, 2004.

[13] S. Pellegrino, *Deployable membrane reflectors*, *Proceedings 2nd World Engineering Congress*, 2002.

[14] N. Footdale, W. Murphey, E. Peterson, *Design and Testing of Self-Deploying Membrane Optic Support Structure Using Rollable Composite Tape Springs*, 54th AIAA/ASME/ASCE/AHS/ASC Structures, Structural Dynamics, and Materials Conference, 2013.

[15] G. Greschik, M. Mikulas, *Design Study of a Square Solar Sail Architecture*, Journal of Spacecraft and Rockets, 2002

[16] V. Paiva, P. Kurka, J. Izuka, *Kinematics and dynamics of a tensegrity structure in expansion*, 31st Congress of the International Council of the Aeronautical Sciences, 2018.

[17] L. Teixeira, J. Izuka, P. Kurka, *A Numerical and experimental analysis of the dynamics of a tensegrity-membrane structure*, 31st Congress of the International Council of the Aeronautical Sciences, 2018.

[18] J. Y. Zhang, M. Ohsaki, *Tensegry Structures: Form, Stability and Symmetry*, Springer, 2015.

[19] J.Y. Zhang, M. Ohsaki, *Adaptive force density method for form-finding problem of tensegrity structures*, International Journal of Solids and Structures, (2006).

[20] S. Yang, C. Sultan, *Modeling of tensegrity-membrane systems*, International Journal of Solids and Structures, vol. 82, (2016), pp. 125-143.

[21] K. J. Bathe, *Finite Element Procedures*, Prentice-Hall, 1996.

[22] R. E. Skelton, M. de Oliveira, *Tensegrity Systems*, Springer US, 2009.

[23] H. J. Schek, *The force density method for form finding and computation of general networks*, Computer Methods in Applied Mechanics and Engineering, (1974), pp-115-132.

[24] N. Vassart, R. Motro, *Multiparametered Formfinding Method: Application to Tensegrity Systems*, International Journal of Solids and Structures, (1999), pp.125-143.

[25] Reg. Connelly and M. Terrell, *Globally rigid Symmetric Tensegrities*, Structural Topology, 1995

[26] S. Pellegrino, *Mechanics of kinematically indeterminate structures*, Phd Thesis, Cambridge University, 1986

Contactless manipulation of silicon wafers using acoustic levitation

I. Bucher* R. Gabai, R. Shaham and S. Davis
Dynamics Laboratory, Mechanical Engineering, Technion
Technion City, Haifa 3200003, Israel
*e-mail: **bucher@technion.com**

Abstract

Described in this paper is a system capable of controlling the position of silicon wafers with no mechanical contact by means of an ultrasonically controlled layer of air. The system exploits several high-frequency annular actuators to produce standing and traveling waves that affect the air layer underneath the wafer. By controlling the pressure and the flow with ultrasonic vibrations, the wafer can be held at a fixed elevation or to be moved to a given a *x,y* position or a desired rotation angle, θ. The ultrasonic vibration amplitude affects, the vertical *z*-axis' elevation which can also be precisely controlled.

The paper briefly describes the dynamics of the individual annular vibrating elements, the sensing systems and finally shown is a laboratory demonstrator with full control of an acoustically levitated silicon wafer.

1 Introduction

Silicon wafers are employed in electronic chip production, and are very sensitive to particle contamination. During the inspection process, these wafers need to be manipulated and positioned at a suitable configuration and orientation. The latter is carried out by sub-micrometer accurate positioning devices that are affected by friction and vibration that are efficiently transferred through optimized waveguides. In such embodiments, the wafer is mechanically held by manipulators that transfer contaminating particles. Presented in this paper is a stage capable of manipulating the position and rotation of silicon wafers with no mechanical contact, with near zero friction forces and a precisely controlled levitation gap. To produce the forces and torques required for controlling the *x,y,z* and rotation-θ of a wafer, near-field acoustic levitation is employed [1–3]. After several years of research and optimization, the number of required actuators has been reduced to 3 identical annular actuators that are controlled to produce ultrasonic bending vibration [4,5]. These actuators, are capable of producing any sort of standing or directional traveling waves that induce forces due to elevated pressure or tangential torques due to viscous forces of the air caused by the traveling waves of vibration forcing tangential air flow [3,4]. The present paper introduces a conceptual laboratory implementation of a completely contactless stage based on near-field acoustic levitation. For such a stage to work, concurrent engineering design of all aspects – vibration and modal decomposition, mechanics, actuation, sensing, electronics, and closed-loop control, is crucial. Some aspects of these disciplines and their role in this endeavor is described herein.

In order to produce near field acoustic levitation, sufficiently large ultrasonic vibrating must be generated affecting a narrow film of gas contained between two flat surfaces. The one-dimensionless parameter controlling the air layer's pressure is the squeeze number [1,6,7], defined as:

$$\sigma = \frac{12\mu\omega r_0^2}{p_a h_0^2}. \tag{1}$$

The squeeze number, σ (typically $20\cdots100$), depends on the vibration frequency-ω (~30KHz), a typical dimension of the contained area-r_0 (~100mm), air viscosity-μ (1.8253e-5 Pa·sec), the ambient pressure -

p_a (1e5 Pa) and finally the average squeeze film height or air-gap - h_0 (3-100 μm). The thin layer of air entrapped between the wafer and the ultrasonically vibrating elements remains confined to this region due to the viscosity of the air that becomes important at these frequencies. The squeeze film experiences an elevated average pressure due to compressibility of the air and as a secondary effect of the rapid oscillations of the underlying structure [1]. This average pressure (~1e3-1e4 Pa), although considered as a second order effect, is able to levitate the wafer or any flat object placed above it at a fixed elevation. It was demonstrated that it is possible to control the levitation gap by changing the vibrations amplitude of the lower surface [6,8]. Tangential force can be generated by introducing traveling waves in the ultrasonic excitation device [9,10] these create lateral pressure gradient within the squeeze film producing shear forces on the levitated wafer that cause parallel motion. These forces, although small, can move the wafer in the direction of the ultrasonic waves as motional friction introduced by air viscosity is negligible.

Stages based on the near field acoustic levitation principal in a single axis are presented at [21], [22]. A wafer transportation system (in one dimension), based on near-field acoustics is described in [23]. The acoustic levitation principle does not require any contact with the wafer for both holding and propulsion. However, it cannot be utilized in vacuum chambers.

Stages for wafer handling often require high performance with fast response, positioning error within the micrometer range and better, high noise attenuation and robustness to uncertainties. Many works deal with stage control tasks, such as [11][12][13]. In this work the H_∞ control design method was chosen for its robustness properties and control on the performances. This method allows shaping the MIMO system control loop by shaping the frequency domain models [14].

The present paper describes a proof of concept work with relatively inexpensive sensors with low accuracy. Still, the validity of the physical model and the mechatronics model are representative for more precise sensing and positioning. The paper is structured as follows: First, the concept, stage composition, and its principle of operation are described. Then, a dynamic model for the actuator and stage system is shown. A brief description of the system model and control loop follows. Finally, a typical response in closed loop as validation of the experimental system is provided.

2 Traveling waves based, acoustic levitation motor (ALM)

The key element of the wafer aligner is an annular structure, as shown in figure 1. The actuator is designed to operate at a single designated frequency. At the basis of each ‘leg’ resides a commercial bolted Langevin actuator tuned to 28KHz. A stepped horn mechanical amplifier is connected to the actuator with a small diameter segment to allow bending (see figure 1) and therefore traveling wave deformations can take place. Owing to its cyclic symmetry, the annulus has pairs of modes with the same number of nodal diameters, e.g. there are 2 eigenvectors per frequency, such as shown in figure 1. These mode shapes have interlacing nodal lines [15], and any pair has the same natural frequency. As a result, 2 mode shapes can be combined to form a traveling wave deformation [4]. Clearly, this is the case for perfectly axisymmetric structures, [15], and under certain conditions can be exhibited in cyclically symmetric structures having the same natural frequency for the so called sine and cosine mode pair [16]. A complete structural optimization procedure was carried out on the annular system to support traveling wave vibrations at resonance.

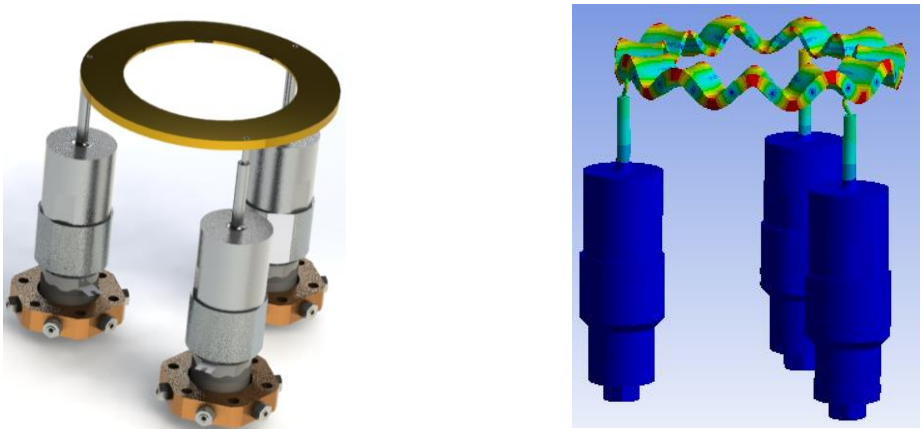


Figure 1. Left: Single acoustic levitation motor (ALM) (out of 3) driven by 3 piezoelectric transducers. Right: Instantaneous vibration amplitude at 28KHz when driven at the 11 nodal diameter mode (Finite element model [17])

Consider a dynamically deforming annulus, as shown in figure 2, the annulus experiences bending deformations that are a combination of 2 modes with $\kappa = 11$ nodal diameters.

$$w(\theta,t) = \eta_c(t)\phi_c(\theta) + \eta_s(t)\phi_s(\theta) = \eta_c(t)\cos\kappa\theta + \eta_s(t)\sin\kappa\theta \tag{2}$$

where $\eta_c(t) = A_c\cos\omega t + A_s\sin\omega t,\ \eta_s(t) = B_c\cos\omega t + B_s\sin\omega t$.

The annulus is optimized to have radially uniform vibration amplitudes as shown in [5]. Since both modes, $\phi_c(\theta), \phi_s(\theta)$ have the same natural frequency [4] both operate in resonance, simultaneously. Furthermore, one can dictate desired modal coordinate values via the corresponding generalized forces [5] as a function of the forces at each of the 3 Langevin piezo driven actuators (see figure 1):

$$\begin{bmatrix} Q_c \\ Q_s \end{bmatrix} = \sqrt{\frac{2}{3}} \begin{bmatrix} 1 & -\frac{1}{2} & -\frac{1}{2} \\ 0 & \sqrt{\frac{3}{2}} & \sqrt{\frac{3}{2}} \end{bmatrix} \begin{pmatrix} f_1(t) \\ f_2(t) \\ f_3(t) \end{pmatrix} \triangleq \mathbf{Tf},\ \ \mathbf{T} \in \mathbb{R}^{3\times 3}, \mathbf{f} \in \mathbb{R}^{3\times 1}. \tag{3}$$

Where $f_1(t), f_2(t), f_3(t)$ are the forces generated by the 3 actuators in figure 1 and Q_c, Q_s are the generalized, modal forces affecting the two modes $\eta_c(t), \eta_s(t)$.

The deformed state and the instantaneous pressure within the squeeze-film is shown in Fig.2.

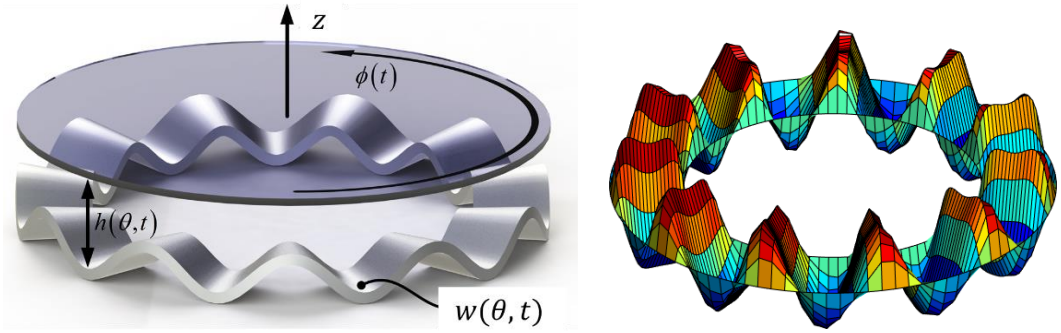


Figure 2. Left: A disk held by the elevated pressure in the narrow air-gap, $h(\theta,t)$. Right: Instantaneous pressure in the squeezed film within the narrow air gap. Note that positive pressure peaks are larger than negative ones. The pressure was computed by numerically solving the nonlinear Reynold equation (see [2])

The shear stresses exerted on the acoustically levitated object at low speeds, are (see [9]):

$$\tau_{z\theta} = \mu \frac{\partial v_\theta}{\partial z}\bigg|_{z=h} = r\frac{h}{2}\frac{\partial p}{\partial \theta} + \mu r\dot{u}_\theta + \frac{\rho h\ddot{u}_\theta}{3} \approx r\frac{h}{2}\frac{\partial p}{\partial \theta} \tag{4}$$

where μ, p are the air's viscosity and pressure while $h, \theta, v_\theta, u_\theta$ are the air-gap (see figure 2), the circumferencial coordiante, the air tangential velocity at the wafer interface and the angular displacement of the wafer. Assuming that pressure is nearly radially uniform, the extrted torque is [9]:

$$Torque \approx \iint \tau_{z\theta} dA = \int_0^{2\pi}\int_{r_{in}}^{r_{out}} \frac{hr}{2}\frac{\partial p}{\partial \theta} dr d\theta \approx \frac{\left(r_{out} - r_{in}\right)^2}{4}\int h dp \,. \tag{5}$$

Since both $h = h(\theta, t)$ and $p = p(\theta, t)$ are periodic in θ, a non-zero average torque develops when h and p are not in phase and the area entrapped in the close curve obtained by plotting *h* vs *p* is not zero. This is indeed the case here due to viscosity where the pressure lags the air gap when traveling waves vibration of the annulus are present. The system in figure 2 was simulated by releasing the wafer from an initial air gap and waiting for stabilization of the air gap [6]. Plotting *h* vs *p* illustrates the dynamic change in gap and torque.

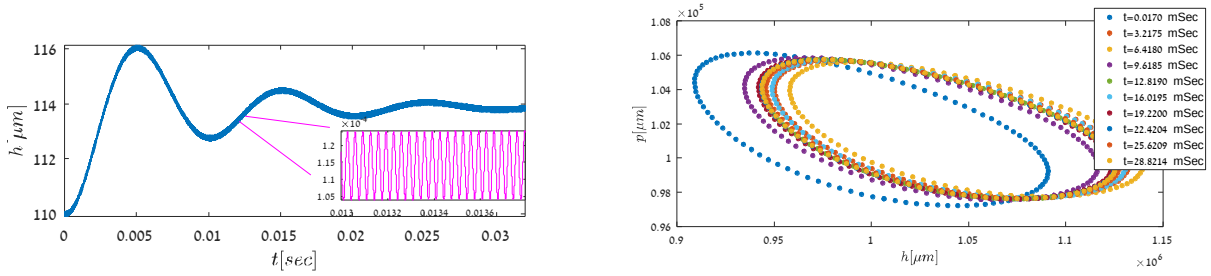


Figure 3. Left: Transient average air gap between wafer and annulus. Right: Pressure $p(\theta, t_0)$ vs air gap $h(\theta, t_0)$ along the annulus for several time instances (until steady state). Showing that the enclosed area i.e. Torque is non-zero.

2.1 Controlling the modal coordinate of the annulus

The modal coordinates vector, $\boldsymbol{\eta}$, can be retrieved from 3 point sensors using (3) (see [5]), via:

$$\boldsymbol{\eta} = \mathbf{T}\mathbf{s},\ \boldsymbol{\eta} \triangleq \begin{pmatrix}\eta_c & \eta_s & \eta_0\end{pmatrix}^T,\ \mathbf{s} \triangleq \begin{pmatrix}s_1 & s_2 & s_3\end{pmatrix}^T \tag{6}$$

where s_1, s_2, s_3 are the displacements measured on the ring where the 3 actuators are connected (see figure 1) and η_c, η_s, η_0 are the cosine, sine modal coordinates and the uniform *z* motion.

It can be shown (see [4,5]) that by setting the relative phases between the actuators, according to:

$$f_1(t) = A\cos(\omega t),\quad f_2(t) = A\cos(\omega t + \varphi_2),\quad f_3(t) = A\cos(\omega t + \varphi_3) \tag{7}$$

the vibration pattern according to (2) can be set to any combination of positive or negative on going traveling waves, or standing waves. Specifically, the proportions of standing to traveling waves (*SWR*, see [18]) or its inverse (Traveling waves ratio, *TWR*, see [5]) can be controlled by setting only the relative phases. Assuming all actuators are identical (having the same magnitude), and by modifying the phases (φ_2, φ_3), a map of the *TWR* can be produced at a certain operating frequency. A simulated map for $\kappa = 11$ is shown in figure 3. The map is symmetric along a line from $\varphi_2 = 0, \varphi_3 = 0$ to $\varphi_2 = 2\pi, \varphi_3 = 2\pi$. Along this line, *TWR* is unity. This means that the annulus is vibrating in a standing wave. Below this line, the wave propagates in a clockwise direction and above it to the opposite direction.

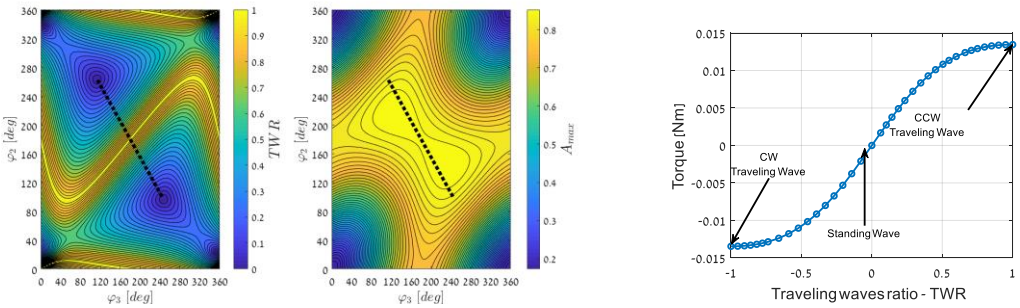


Figure 4. Left: Traveling wave ratio (*TWR*) on the annulus as a function of the relative phases. Middle: vibration amplitude as a function of the excitation phase differences. Right: Computed torque according to (5) as a function of the *TWR*.

Examination of figure 4 leads to adopting an operation strategy. Choosing $u \in [-1,1]$ as the control parameter, the selected path maintaining a nearly constant amplitude is given by:

$$\varphi_2(u) = \pi/3 \cdot u + \pi, \quad \varphi_3(u) = -\pi/3 \cdot u + \pi. \tag{8}$$

Choosing $u = \pm 1$ sets the excitation phases for a pure traveling wave in either clockwise or counter-clockwise direction, whereas setting $u = 0$ provides the conditions for a pure standing wave.

The annulus was tested in the laboratory by applying 3 phased sinusoidal forces according to (7) and (8) in an open loop manner, where the rotation was measured by a magnetic shaft encoder. The experimental system and the effect of modifying the relative phases can be seen in figure 5.

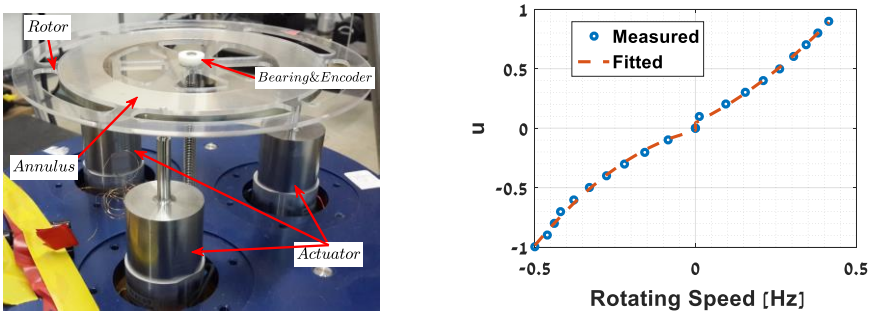


Figure 5. Left: Experimental system consisting of an aluminum annulus, 3 ultrasonic actuators and a levitated (transparent) object. The levitated object is help radially by a loose Teflon bearing, free to move in the z-direction. **Right**: Measured (circles) rotation speed as a function of the phase control parameter and fitted model (Dashed). The discontinuity near *u*=0 is due to the static friction in the Teflon bearing.

3 Complete acoustic levitation, a realization of a wafer aligner

Having established the ability to control the rotational torque or tangential forces by controlling the ultrasonic vibration in an annulus, it has been suggested to employ 3 annuli in an arrangement as shown in figure 6. The configuration shown can control the levitation height by changing the ultrasonic vibration amplitudes of the annuli (as in [8]) and to produce a combination of forces, by individual control of the TWR in each ALM affecting the *x*,*y*,θ degrees of freedom.

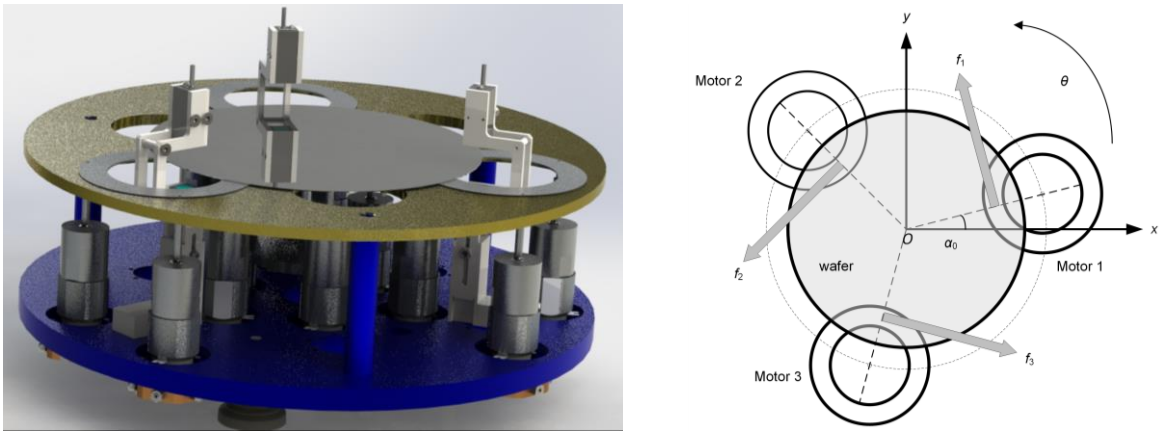


Figure 6. Left: Cad model showing a silicon wafer acoustically levitated by 3 acoustic levitation motors (ALM). Right: Top view showing the tangential forces exerted on the wafer by the 3 ALMs.

The three ALMs are located on a circular perimeter having a radius R around the origin O and equally spaced by $2\pi/3$ from each other. The *x-y* axes are not aligned with any of the ALMs but rotated with an angle α_0. Forces are generated within the area the wafer covered on each annulus. Since this area is symmetric, it is reasonable to assume that the forces are tangential to the annuli, as illustrated in figure 6. The individual forces act in a tangential direction represented by unit vectors $\hat{\mathbf{d}}_j$. The force applied by the j[th] ALM (j=1,2,3) is $\mathbf{f}_j = \hat{\mathbf{d}}_j p_j(t)$ where $p_j(t)$ is related to the TWR (see figure 4 for a single ALM) and to changes in the overlapping area of the annulus and the wafer. As a result, the forces acting on the wafer are:

$$f_x(t) = \sum_{j=1}^{3}\left(\hat{\mathbf{d}}_j \cdot \hat{\mathbf{e}}_x\right) p_j(t), \quad f_y(t) = \sum_{j=1}^{3}\left(\hat{\mathbf{d}}_j \cdot \hat{\mathbf{e}}_y\right) p_j(t), \quad Torque(t) = \sum_{j=1}^{3}\left(\mathbf{r}_j \times \hat{\mathbf{d}}_j\right) p_j(t) \tag{9}$$

where $\hat{\mathbf{e}}_x, \hat{\mathbf{e}}_y$ are unit vectors in the global x and y directions and $\mathbf{r}_j$ are vectors to where $\mathbf{f}_j$ act. By introducing 3 generalized degrees of freedom, $\mathbf{q} = \begin{bmatrix} x & y & \theta \end{bmatrix}^T$, the equations of motion become:

$$\mathbf{M}\ddot{\mathbf{q}} + \mathbf{C}\dot{\mathbf{q}} = \mathbf{f}, \quad \mathbf{f} \triangleq \begin{pmatrix} f_x(t) & f_y(t) & Torque(t) \end{pmatrix}^T. \tag{10}$$

These equations describe the in-plane equations of motion for a levitated wafer, having mass m and rotation moment of inertia J, whereas $\mathbf{M} = \mathrm{diag}(m, m, J)$ is the matrix of inertia, and $\mathbf{C} = \mathrm{diag}\left(c_x, c_y, c_\theta\right)$ is the damping matrix. Since the dynamics are slow, a linear damping model with coefficients c_x, c_y, c_θ is being used. It is worth nothing that the acoustically levitated wafer resides on an air-film with no n-plane stiffness. Also, the force vector exhibits nonlinear dependency on the overlap area of the wafer and the annuli and thus on the generalized degrees of freedom. This dependency introduces coupling between all degrees of freedom that is handled by the MIMO controller discussed later. The measurement of the wafer position and configuration is briefly discussed below.

3.1 Sensing for closed loop operation

In order to achieve continuous acoustic levitation, it is important to provide sufficient ultrasonic vibrations of the annuli. These are exposed to variable loads and excitation signals. Due to physical coupling of the ALMs and the wafer, the natural frequencies each ALM exhibit a slow drift. To ensure continuous operation, an Autoresonance (AR) algorithm (see [4,19]) using digital (FPGA) processors operated at 10MHz sampling frequency is employed. Each annulus is digitally controlled employing an optical sensor (Keyence LK-H008) to measure directly the annuli vibrations feeding the 3 AR circuits, as illustrated in figure 7.

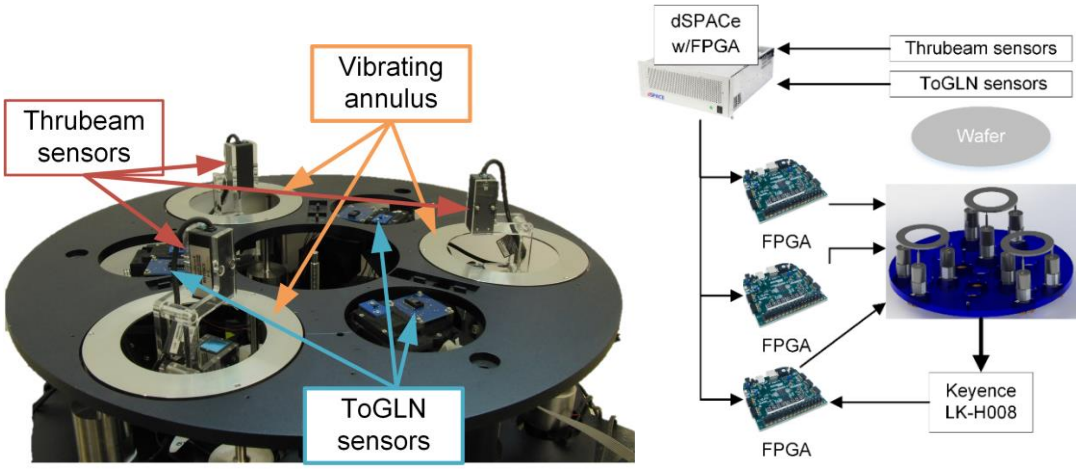


Figure 7. Left: Photograph of the laboratory system, showing Thrubeam laser sensors sensing the edge of the wafer, ToGLN dark-laser mouse sensors measuring the wafer's incremental motion thus providing information about its rotation. Right: Block diagram of the control hardware. Showing 3 FPGA controlling the 3ALMs and the overall DSP (dSpace) controller, employing another FPGA (Xlinx) controller.

4 Closed-loop Control design

The model described in (10) is a MIMO system with three outputs - the wafer's *x,y* position and rotation, θ and three inputs – the force commands affecting $p_j(t)$ in (9). Indeed the magnitude and sign of $p_j(t)$ is determined by the 3 FPGA controllers (see figure 7) that modify the TWR of each annulus according to the control algorithm. By defining a transformation $\mathbf{U}$, that transforms the ALMs forces, $p_j(t)$ to generalized forces, $\mathbf{f}$ through a transformation matrix $\mathbf{f}(t)=\mathbf{U}\mathbf{p}(t)$. The transformation $\mathbf{U}$ is nearly constant for small motions around an equilibrium condition. This transformation depends on various geometry related parameters, scaling, on amplifier gains and sensor sensitivities and it can be estimated from an in-situ experiment as was done in practice. The importance of this transformation is its use in decoupling the actuation vector, via

$$\mathbf{p}(t)=\mathbf{U}^{-1}\mathbf{f}(t). \tag{11}$$

Applying the decoupling transformation, three independent SISO systems are obtained. Applying the Laplace transformation to (10), the transfer function of the diagonal model is from $\mathbf{f}$ to $\mathbf{q}$ - $\mathbf{P}_0$ is obtained and easily transformed back to the physical model - $\mathbf{P}$:

$$\mathbf{P}_0=\mathrm{diag}\left(\frac{1}{ms^2+c_x s},\frac{1}{ms^2+c_y s},\frac{1}{Js^2+c_\theta s}\right).\quad \mathbf{P}=\mathbf{P}_0\cdot\mathbf{U}^{-1} \tag{12}$$

This decomposition of $\mathbf{P}$ allows designing three independent controllers, C_x, C_y, C_θ, each for every degree of freedom. Define the uncoupled system controller $\mathbf{C}_0=\mathrm{diag}\left(C_x,C_y,C_\theta\right)$.

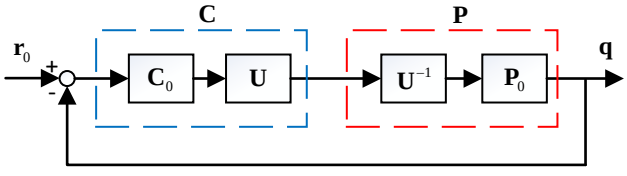


Figure 8. Closed loop decoupling and re-coupling. Note that the red line contains the physical model and the controller of the decoupled model is within the blue dashed line.

The configuration of the closed loop position control for the levitated wafer and a block diagram of the closed-loop control, based on the uncoupled plant is shown in figure 8.

A robust controller was designed using loop-shaping methodology. Designing a robust controller requires weighting the plant input and output for the robustness regions. Here, the uncoupled controller was used as the plant input weighting function. Since the dynamics of the wafer is slow, the measured position of the wafer was filtered to reduce the bandwidth of the controller. This low-pass filter is the plant output weighting function. Sample performance and the layout of the decoupled controller and the coupling transformation are shown in figure 9.

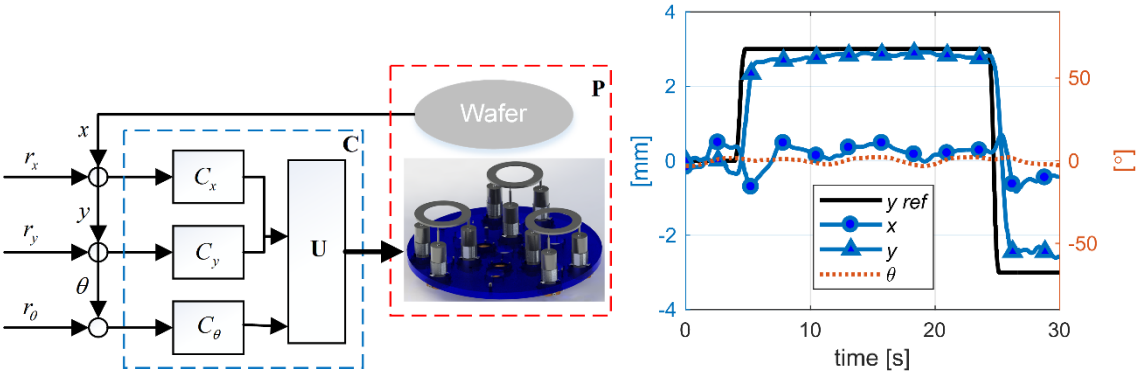


Figure 9. Left: Closed loop decoupling and re-coupling at the actuator (ALM) level. Right: Response in the y direction to a step command in the control. Note the decoupling with rotation and *x* motion.

The performance of the experimental system and the control are best viewed in a video summary shown in the reference link in [20].

5 Summary and conclusions

Presented is an ultrasonic stage able to manipulate a silicon wafer using controlled vibration in 3 annuli. In order to achieve the goals of this system, tight modal control of each of the rings is required and combination of vibration to form traveling and standing waves. The research is interdisciplinary and vibration, auto resonance control, as well as mechatronics, control theory, sensing and model estimation all play an important role in building a successful demonstrator. The key issues are related to accurate modeling and design of vibrations in a structure having cyclic symmetry.

Acknowledgements

The first author would like to thank Prof. E. Balmes (SDTools™) for his hospitality help and in the finite element modeling of the piezo-ceramic actuators and the ultrasonic transducers presented here during a sabbatical spent at in Arts et Métiers ParisTech.

References

[1] W.E. Langlois, Isothermal squeeze films, Q. Appl. Math. 20 (1962) 131–150.

[2] A. Minikes, I. Bucher, S. Haber, Levitation force induced by pressure radiation in gas squeeze films, J. Acoust. Soc. Am. 116 (2004). doi:10.1121/1.1760110.

[3] A. Minikes, R. Gabay, I. Bucher, M. Feldman, On the sensing and tuning of progressive structural vibration waves, IEEE Trans. Ultrason. Ferroelectr. Freq. Control. 52 (2005). doi:10.1109/TUFFC.2005.1516029.

[4] S. Davis, R. Gabai, I. Bucher, Realization of an Automatic, Contactless, Acoustic Levitation Motor via Degenerate Mode Excitation and Autoresonance, Sensors Actuators A Phys. (2018).

[5] R. Gabai, D. Ilssar, R. Shaham, N. Cohen, I. Bucher, A rotational traveling wave based levitation device – Modelling, design, and control, Sensors Actuators, A Phys. 255 (2017). doi:10.1016/j.sna.2016.12.016.

[6] A. Minikes, I. Bucher, Coupled dynamics of a squeeze-film levitated mass and a vibrating piezoelectric disc: Numerical analysis and experimental study, J. Sound Vib. 263 (2003). doi:10.1016/S0022-460X(02)01121-5.

[7] A. Minikes, I. Bucher, G. Avivi, Damping of a micro-resonator torsion mirror in rarefied gas ambient, J. Micromechanics Microengineering. 15 (2005). doi:10.1088/0960-1317/15/9/019.

[8] D. Ilssar, I. Bucher, H. Flashner, Modeling and closed loop control of near-field acoustically levitated objects, Mech. Syst. Signal Process. 85 (2017). doi:10.1016/j.ymssp.2016.08.011.

[9] A. Minikes, I. Bucher, Noncontacting lateral transportation using gas squeeze film generated by flexural traveling waves - Numerical analysis, J. Acoust. Soc. Am. 113 (2003). doi:10.1121/1.1564014.

[10] I. Bucher, D. Ilssar, R. Gabai, N. Cohen, R. Shaham, S. Davis, Controlled acoustic levitation - Physical model and real-time digital implementation, in: IEEE/ASME Int. Conf. Adv. Intell. Mechatronics, AIM, 2016. doi:10.1109/AIM.2016.7576809.

[11] M. Van de Wal, G. Van Baars, F. Sperling, O. Bosgra, Multivariable Hx/μ feedback control design for high-precision wafer stage motion, Control Eng. Pract. 10 (2002) 739–755. doi:10.1016/S0967-0661(01)00166-6.

[12] G. Avivi, I. Bucher, A method for reducing the inaccuracy of harmonic ratios in the dynamics of a multiple-degrees-of-freedom MEMS scanning mirror, J. Micromechanics Microengineering. 18 (2008). doi:10.1088/0960-1317/18/2/025028.

[13] Y. Xie, Y. Tan, R. Dong, Nonlinear modeling and decoupling control of XY micropositioning stages with piezoelectric actuators, IEEE/ASME Trans. Mechatronics. 18 (2013) 821–832. doi:10.1109/TMECH.2012.2187794.

[14] F. Wang, X. Zhao, D. Zhang, Z. Ma, X. Jing, Robust and precision control for a directly-driven XY table, Proc. Inst. Mech. Eng. Part C J. Mech. Eng. Sci. 225 (2011) 1107–1120. doi:10.1177/2041298310392832.

[15] S.A. Tobias, R.N. Arnold, The influence of dynamical imperfection on the vibration of rotating disks, Proc. Inst. Mech. Eng. 171 (1957) 669–690.

[16] M. Kim, J. Moon, J.A. Wickert, Spatial modulation of repeated vibration modes in rotationally periodic structures, J. Vib. Acoust. 122 (2000) 62–68.

[17] I. Bucher, D. Ilssar, N. Cohen, Near-field acoustic levitation and non-contacting translation with traveling waves, in: XIX Symp. VISHNO, June 17-19, Vib. Shock Noise, Aix en Provence, France, 2014.

[18] I. Bucher, R. Gabai, H. Plat, A. Dolev, E. Setter, Experimental travelling waves identification in mechanical structures, Math. Mech. Solids. (2017). doi:10.1177/1081286517732825.

[19] S. Davis, I. Bucher, Automatic vibration mode selection and excitation; combining modal filtering with autoresonance, Mech. Syst. Signal Process. 101 (2018) 140–155. doi:10.1016/j.ymssp.2017.08.009.

[20] I. Bucher, Dynamics Laboratory, acoustic levitation aligner, (2018). https://www.youtube.com/watch?v=WJjtHhg_DVU.

Squeal measurement with 3D scanning laser doppler vibrometer: handling of the time varying system behavior and analysis improvement using FEM expansion

G. Martin[1], E. Balmes[1,2], G. Vermot des Roches[1], T. Chancelier[3]
[1] SDTools, 44 Rue Vergniaud, 75013 Paris, France
e-mail: **martin@sdtools.com**

[2] ENSAM, PIMM, 151 Bld de l'Hopital, 75013 Paris, France

[3] Chassis Brakes International, Drancy, France

Abstract
In the presence of squeal, Operational Deflection Shapes (ODS) are classically performed to analyze behavior. A simple numeric example is used to show that two real shapes should dominate the response. This justifies an ad-hoc procedure to extract main shapes from the real brake time measurements. The presence of two shapes is confirmed despite variations with wheel position and reproducibility tests. To obtain a high spatial density measurement, 3D Scanning Laser Doppler Vibrometer is interesting but leads to iterative measurements on a time-varying system. An algorithm to merge sequential measurement and extract main shapes is detailed. Even with a high-density 3D SLDV measurement, shapes characterizing the squeal event are still only known on accessible surfaces. Minimum Dynamic Residual Expansion (MDRE) is thus finally used to estimate motion on a full FE mesh which eases interpretation and highlights areas where the test and the model contain errors.

1 Introduction

Squeal being an undesired condition, its appearance is never predicted by initial design models, when they exist, and experiments are needed to understand the exact conditions of occurrence. Two major techniques are classically used to perform vibration measurements on brake systems: accelerometer measurements and 3D Scanning Laser Doppler Vibrometer measurement. The specificities of each measurement techniques are reminded in Table 1.

Table 1: Characteristics of accelerometer and 3D-SLDV measurements

	Accelerometer	3D-SLDV
Synchronous measurement	Yes	No
Setup time	Long	Acceptable
Wireframe density	Low	High
Without contact	No	Yes
Rotating parts	No	Yes
Hidden parts	Yes	No

The 3D-SLDV is interesting because the setup time is reasonable, it is without contact, and it can offer a high number of measured points. However, only visible parts can be measured. Some accelerometers can be used to add missing information but this still does not include tight areas or junctions. The main disadvantage of the 3D-SLDV to measure a squeal phenomenon is that measurements are sequential. This is a problem because as will be highlighted in section 3, brake squeal is a time varying phenomenon.

The first objective of this study was to propose an experimental strategy to extract shapes that characterize the limit cycle associated with a squeal occurrence. To propose and adequate strategy it is first necessary to have prior knowledge of the expected properties. Section 2 uses a simple numerical model [1] to illustrate that the shapes associated with squeal instabilities are expected to be dominated by the combination of two real modes with contributions that may be quite sensitive to changes.

Knowing that a limit cycle is expected to be composed of a time varying combination of fixed shapes, Section 3 exploits time-frequency analyses of experimental measurements to demonstrate that indeed two real shapes dominate the response and have variations that are coherent with the changes due wheel position. A reproducibility test further demonstrates that, while different experiments can lead to notable frequency shifts, the shapes underlying the limit cycle are fairly constant. This first analysis is performed using test on the drum brake test bench shown in figure 1 left.



Figure 1 : Experimental setups. Left drum-brake used for section 3.
Right : disk-brake used for sections 4-5.

Because of the low spatial density, the accelerometer measurements can be difficult to exploit. The second objective of this paper is thus to present the strategy developed to extract principal shapes from 3D-SLDV measurements. The algorithm is described in Section 4 and applied on the brake shown in figure 1 right.

Finally, despite a quite high spatial resolution of the laser measurement, many parts are not accessible to the measurement. As a result, using mode shape expansion techniques to estimate the full FE response from measurements appears as a necessity to provide understanding of inconsistencies between model and test and thus pave the way for the proposition of modifications. The Minimum Dynamic Residual (MDRE) method [2] is applied in Section 5 to illustrate the potential uses. It is shown that expanded shapes give better understanding of the brake motion and that distribution of the residual energy after expansion gives insight on modeling errors.

2 Expected shapes in a squeal event: a simple example

To motivate the procedure used to analyze shapes during a squeal event, a simple numeric example is detailed here. As motivated in [1], the complex mode shapes come from the linearization of the model around a chosen state (pressure, velocity…). The linearized model provides a system of the form

$$[M]\{\ddot{q}(t)\} + [C]\{\dot{q}(t)\} + [K_s + K_u]\{q(t)\} = \{f_{ext}(t)\} \qquad (1)$$

where $q, \dot{q}$ et $\ddot{q}$ are displacements, velocities and acceleration, M, C, K are respectively the mass, damping and stiffness matrices supposed constant. The stiffness matrix can be decomposed in a symmetric part K_s, coming from the elastic properties of each components and the linearization of the normal contact loads and a non-symmetric part K_u linked to the fluctuation of the tangential loads induced by the fluctuation of

the normal loads. It is classical to project the system in the real mode basis $[\Phi]$, found by solving the system with $[C] = 0$ and $K_u = 0$ (which is equivalent to consider a friction coefficient $\mu = 0$). Projected in this basis, the complex modes are solution of

$$\left(\begin{bmatrix} \omega_j^2 & \\ & \end{bmatrix} + [\Phi^T K_u \Phi] + \lambda_j [\Phi^T C \Phi] + \lambda_j^2 [I]\right)\{\psi_{jR}\} = 0 \qquad (2)$$

with restitution on the full set of Degrees Of Freedom (DOFs) computed using $\{\psi_j\} = [\Phi]\{\psi_{jR}\}$.

The simplified brake shown in Figure 2 is used as an illustration. The disc (blue) and the backplate (yellow) are made of steel and the friction (green) is made of an orthotropic softer material, about 5GPa with an additional Rayleigh damping (see the introduction of [1] for details). The model is clamped at 4 locations at the interface between the backplate and the friction (similar to the one circled in the figure).

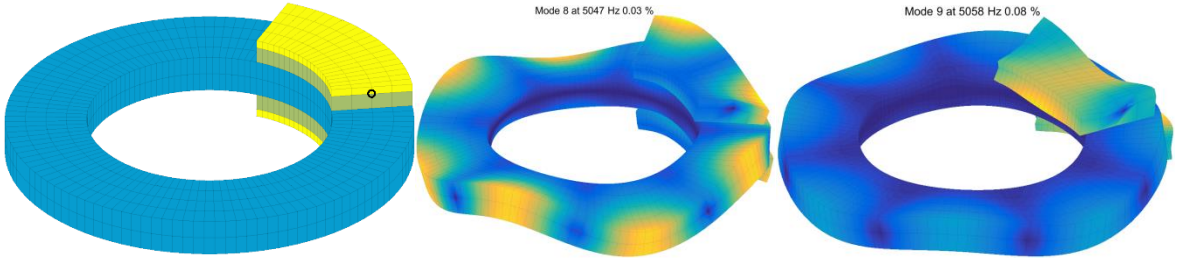


Figure 2 : Simple brake model geometry (left) and real mode shapes #8 and #9. (right)

This model has an unstable (negative damping) complex mode at 5050Hz which corresponds to the interaction between the two real modes #8, with a mostly out-of-plane deformation, and #9 with mostly a deformation of the pads sliding on the disc.

To confirm that the complex mode shape mainly comes from the interaction between the two real shapes, the friction coefficient is swept from 0 to 0.2 (not a physical value but still relevant for the interpretation). The left of Figure 3 shows that the complex modes #8 and #9 are stable at first (as indicated by the red dots). Then with the increase of the friction coefficient, mode #8 becomes unstable, while the damping of mode #9 increases.

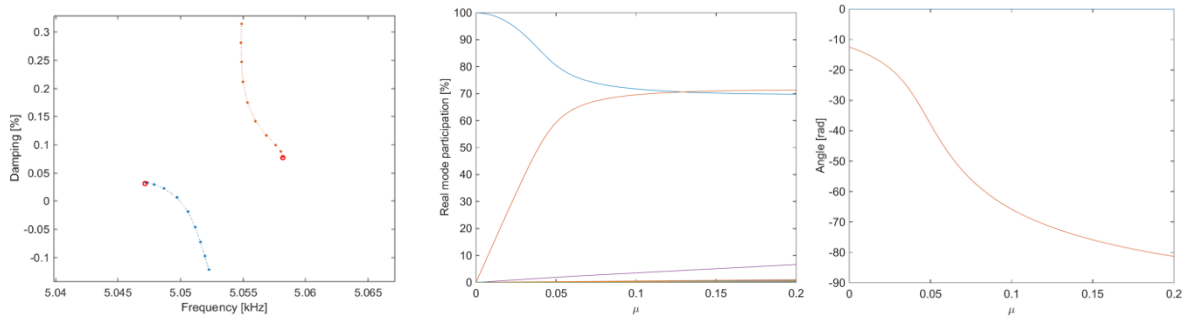


Figure 3 : Evolution of complex modes with the friction coefficient: roots (left), real mode participation to the complex mode #8 (middle) and phase between real modes #8 and #9 (right)

From (2), it is possible to look at the evolution of the real mode participation (ψ_{jR}) of each modal DOF with the normalization $\|\psi_R\| = 1$. Figure 3 center thus shows the participation of the real modes to complex mode #8, which become unstable, evolves from 100% of real mode #8 (blue line) to 70% of real mode #9 (red line) and 70% of real mode #8. Figure 3 illustrates the significant evolution of the phase relation between contributions of real modes #8 and #9 to complex mode #8.

To evaluate the pertinence to use only two real modes to interpret the unstable modes, equation (2) is reduced on the 2 real mode shapes #8 and 9, leading (with the assumption of modal damping) to

$$\left(\begin{bmatrix}1 & 0\\ 0 & 1\end{bmatrix}\lambda_j^2+\begin{bmatrix}2\zeta_8\omega_8 & 0\\ 0 & 2\zeta_9\omega_9\end{bmatrix}\lambda_j+\begin{bmatrix}\omega_8^2 & 0\\ 0 & \omega_9^2\end{bmatrix}+\begin{bmatrix}k'_{11} & k'_{12}\\ k'_{21} & k'_{22}\end{bmatrix}\right)\{\psi_{jR}\}=0 \qquad (3)$$

The comparison between the system reduced on the two real modes on the one hand and on all real modes on the other hand is provided by Figure 4. The accuracy of frequencies is not as good with only two shapes, but the coupling still occurs and the damping computation is almost unchanged.

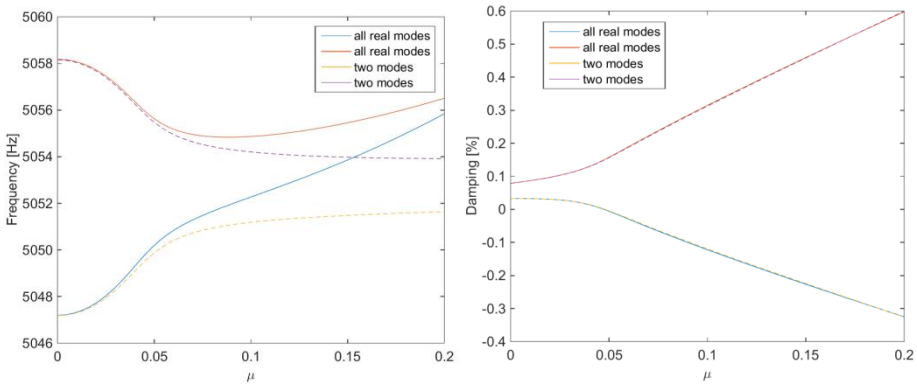


Figure 4 : Complex modes frequency (left) and damping (right) for variable friction coefficient. Reduction on two real modes (dashed lines) and on all real modes (full lines).

The common practice in presence of coupled modes is to try separating the frequencies. Doing so on the two shape reduced model, by moving away their frequencies with the same percentage (modifying k_1, k_2, c_1, c_2 but not the non-symmetric stiffness part), results in the evolution of the complex frequencies and damping shown in Figure 5. As mode #9 damping decreases, mode #9 one increases until it is no longer unstable. The dot lines represent the values of the frequencies $f_8\, f_9$ and dampings $\zeta_8\, \zeta_9$. When the frequencies are moved away, the influence of the coupling stiffness decreases, and the mode parameters converge toward the ones without coupling at all.

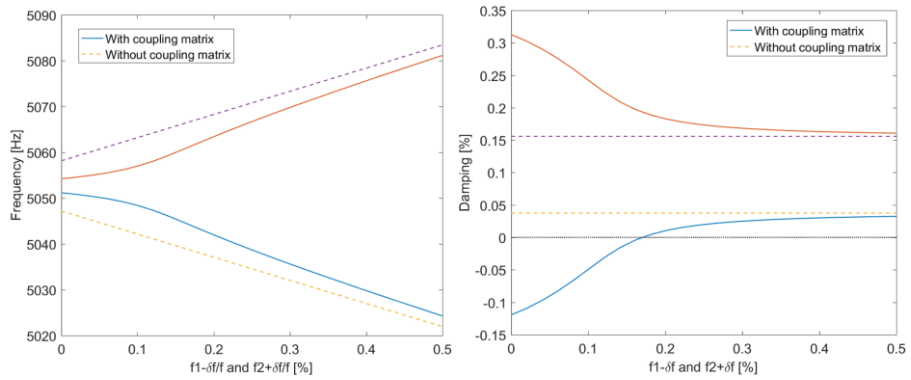


Figure 5 : Complex mode frequency and damping for varying frequency shift of real modes #8 and #9

3 Time frequency analysis

With the objective of extracting the characteristics of a limit cycle, it is first necessary choose a strategy to extract shape information. The test case used for illustration is the drum brake of figure 1 left. The measurement is performed using 38 accelerometers measured simultaneously. The measurement geometry was built [2] from the numerical mode shapes, using the MSeq algorithm [3], to distinguish the modes in a frequency band around 900Hz. In the picture, the drum was removed to see the internal instrumentation. For this brake, a low frequency squeal occurrence (about 900Hz) has been found on vehicle and needed to be reproduced on bench for further analysis.

To analyze the evolution of the squeal with time, the Gabor transform is used to decompose the signal in the time-frequency domain. It consists in a Short Time Fourier Transform where at each time step, the signal is convolved with a Gaussian window whose standard deviation $\sqrt{\Delta t^2}$ is used to choose the compromise between time and frequency resolution, fixed by the Heisenberg-Gabor equality $\sqrt{\Delta t^2}\sqrt{\Delta f^2} = \frac{1}{4\pi}$.

The Gabor transform is applied to the measurement on an arbitrary sensor with a very good frequency resolution $\sqrt{\Delta f^2} = 0.5Hz$ which induces a quite poor time resolution $\sqrt{\Delta t^2} = 0.1592s$. This is acceptable because the squeal behavior evolution with time is slow. Figure 6 left shows that during the squeal, the frequency shifts between 906Hz and 913Hz. Three time slices on the right of the figure also highlight the amplitude evolution of the main resonance. A smaller peak of amplitude, constant in frequency at 900Hz, is present for each measurement and is due to an harmonic of the power supply of the bench (50Hz). It is interesting to note that this choice is notably different from earlier practice which used much shorter buffers in favor of a better time resolution.

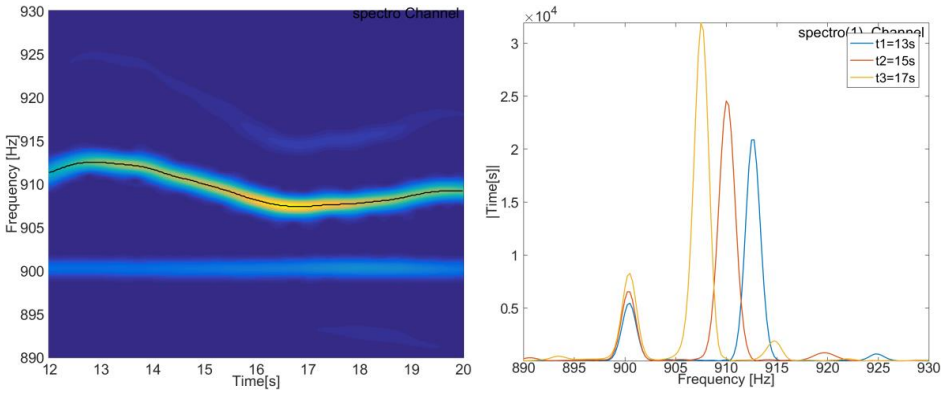


Figure 6 : Gabor transform of a squeal measurement (left), time slices (right)

To evaluate in detail the evolution of the behavior, at each instant t, the frequency where the amplitude is maximum $f_{max}(t)$ is found, and the corresponding shape $\{y(f_{max}(t), t)\}$ is extracted. All these shapes are concatenated and real plus imaginary parts are decomposed with the Singular Value Decomposition providing sorted real shapes $\{U_j\}$

$$[F] = [\Re(\cdots y(f_{max}(t), t)\cdots)\ \Im(\cdots y(f_{max}(t), t)\cdots)]_{NS\times 2NT} = \sum_j \{U_j\}\sigma_j\{V_j\}^T \qquad (4)$$

with NS the number of sensors and NT the number of time steps.

The family $[\cdots y(f_{max}(t), t)\cdots]$ can then be decomposed on these real shapes, leading to

$$[\cdots y(f_{max}(t), t)\cdots] \approx \sum_j \{U_j\}_{NS\times 1}\{a_j(t)\}_{1\times NT} \qquad (5)$$

with $a_j(t) = \sigma_j \times (v_j(t) + iv_j(t + NT))$.

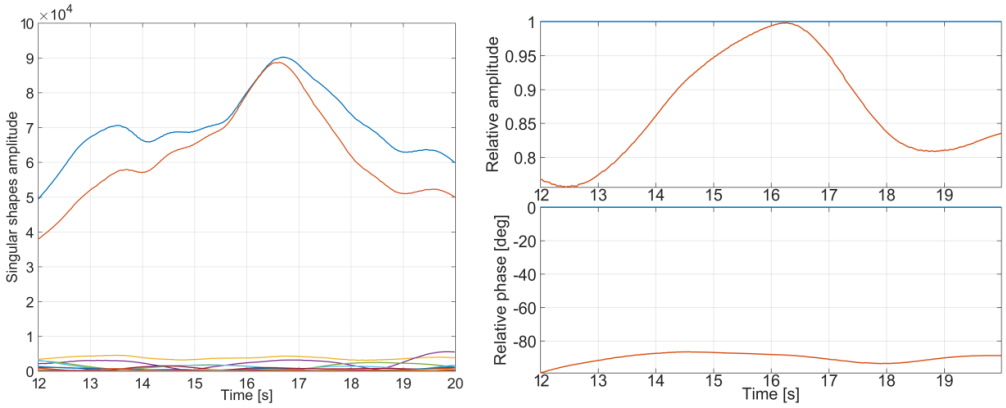


Figure 7 : Time evolution of the main real shapes $|a_j(t)|$ (left) and relative evolution between the two main shapes $a_2(t)/a_1(t)$.

Figure 7 left shows the time evolution of $|a_j(t)|$ and it is clear that the limit cycle shape has only two significant amplitudes and is thus well represented the by two main real shapes $[U_1 U_2]$. The relative evolution between the two main shapes $a_2(t)/a_1(t)$ is analyzed on the right and show an amplitude ratio in the range 0.75-1 and a low phase evolution between -85° and -100°. Thus the limit cycle, despite the evolution of the complex shape, stays in the same subspace in an analogous way than the numerical result illustrated in section 2.

It is also important to evaluate reproducibility. For this purpose, a second squeal event has been measured a day after the first measurement, leading to potential evolution of parameters such as pressure map, relative component placement or temperature. The time-frequency evolution of this second measurement and for the same sensor is shown on Figure 8. A quite important frequency shift is also found from 917Hz to 925Hz and is in average more than 10Hz higher than the first one.

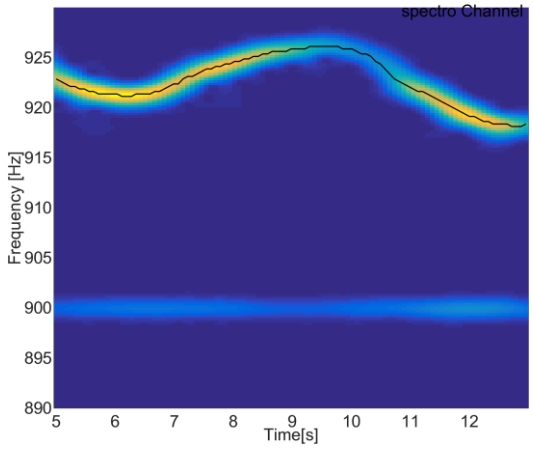


Figure 8 : Gabor transform of the second squeal measurement.

The family containing the two measurement, normalized to have the same weight

$$[y(t)] = \left[\frac{[\cdots y_1(f_{max}(t),t)\cdots]}{\|\cdots y_1(f_{max}(t),t)\cdots\|} \; \frac{[\cdots y_2(f_{max}(t),t)\cdots]}{\|\cdots y_2(f_{max}(t),t)\cdots\|}\right] \qquad (6)$$

is used and decomposed as in (4) and (5). The evolutions of the amplitudes $|a_{j,1}(t)|$ and $|a_{j,2}(t)|$, related to the common main real shapes shown in Figure 9. The predominance of the two main real shapes is a bit less clear than when the first measurement was decomposed alone (see Figure 7 left), but still there.

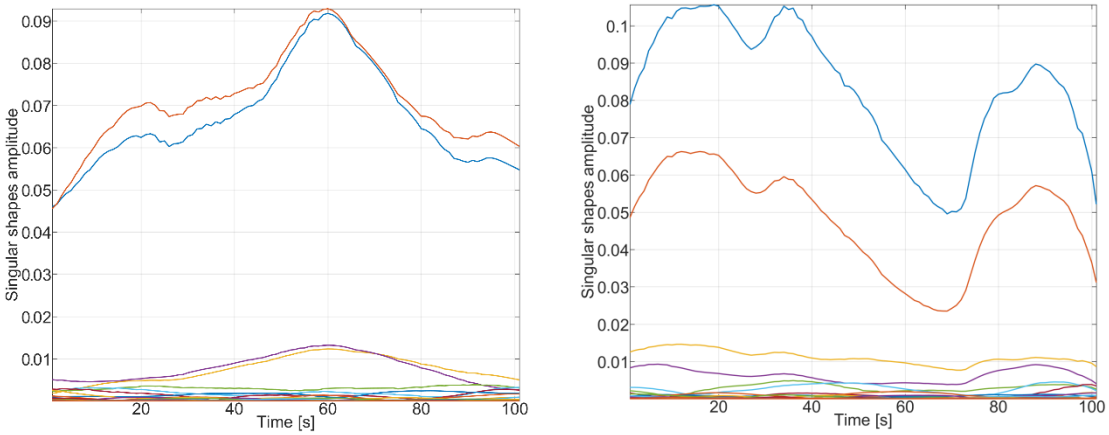


Figure 9 : Time evolution of the common main real shape amplitudes for the first measurement $|a_{j,1}(t)|$ (left) and the second measurement $|a_{j,2}(t)|$ (right).

4 Extraction of principal shapes from laser measurements

Tests limited to accelerometers have a very limited resolution. 3D-SLDV measurements allow a higher spatial density but lead to sequential measurements. The objective of this section is thus to introduce a methodology for shape extraction in this context. The test case is the disk brake of figure 1 right. The measurements have been performed using the Polytec Scanning Laser Doppler Vibrometer PSV500 using the test geometry visible in Figure 11. This system presents a squeal occurrence at about 4250Hz. To extract the two main shapes from the sequential measurements, three reference monoaxial accelerometers have been disposed on the structure as reference: one on the caliper, one on the anchor bracket and one on the arm.

In order to aggregate the sequential measurements, the hypothesis used is that a subspace of response shapes of dimension two remains constant during the squeal.

For each point i of the wireframe presented in the introduction, a time measurement is performed (0,1s) containing three measured signals Xi, Yi, Zi at the scanned point and reference accelerometers

$$\begin{bmatrix} x^i(t) \\ y^i(t) \\ z^i(t) \\ \vdots \\ a_{Ref}(t) \end{bmatrix}_{i\in[1,N_{laser}]} \tag{7}$$

For each laser position i, the two main real shapes $[\Phi_1^i \Phi_2^i]$ are extracted using the SVD (4). To concatenate each measured point, two main shapes at the references $[\phi_1 \phi_2]_{|ref}$ are needed. These are obtained using again an SVD on the restriction at reference accelerometers of all the previously extracted main shapes

$$[\Phi_1^1 \Phi_2^1 \dots \Phi_1^i \Phi_2^i \dots \Phi_1^N \Phi_2^N]_{|ref} = \sum_j \{\phi_j\}_{|ref} \sigma_j \{V_j\}^T \tag{8}$$

Finally, for each measured point i, the objective is to find the best linear combination $[\lambda^i]$ of $[\Phi_1^i \Phi_2^i]$, that minimizes the Euclidian distance with the target shape at references $[\phi_1 \phi_2]_{|ref}$

$$\left[\lambda^i\right]=\left[\Phi_1^i \Phi_2^i\right]^+_{|ref}\left[\phi_1 \phi_2\right]_{|ref} \quad (9)$$

and the concatenation for each point of

$$\left[\tilde{\phi}_1^i \tilde{\phi}_2^i\right] =\left[\Phi_1^i \Phi_2^i\right]\left[\lambda^i\right] \quad (10)$$

forms the two main shapes.

This procedure has been applied to the 3D-SLDV measurement of the brake disc presented in introduction. Around 4250Hz, the two main shapes shown in Figure 10 have been extracted.

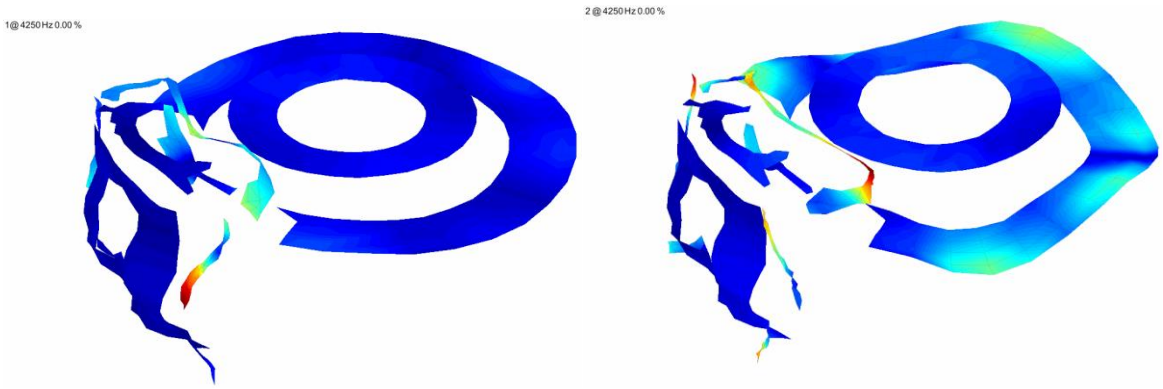


Figure 10 : Visualization of the two main shapes extracted from all the sequential time measurement with the proposed method

The first shape shows mainly a deformation of the bracket. The second shape shows another deformation of the bracket with a deformation of the disc.

5 Expanding the results to full FEM size

Despite the high spatial resolution of the 3D-SLDV measurement, information such as hidden parts or interfaces between components are missing. Using a FEM to perform expansion is useful for two main reasons: it evaluates the deformations at all FEM DOFs which helps in analyzing the shapes and depending on the used algorithm, it can highlight areas where the FEM is doubtful which orients model updating procedures.

As illustrated in Figure 11, the test wireframe has been constructed in two parts: one in the direct view to measure the disc, a part of the caliper and a part of the anchor bracket and one through the mirror to measure the remaining parts of the caliper and the anchor bracket. The experimental wireframe geometry is overlaid with the FEM and clearly illustrates the missing areas.

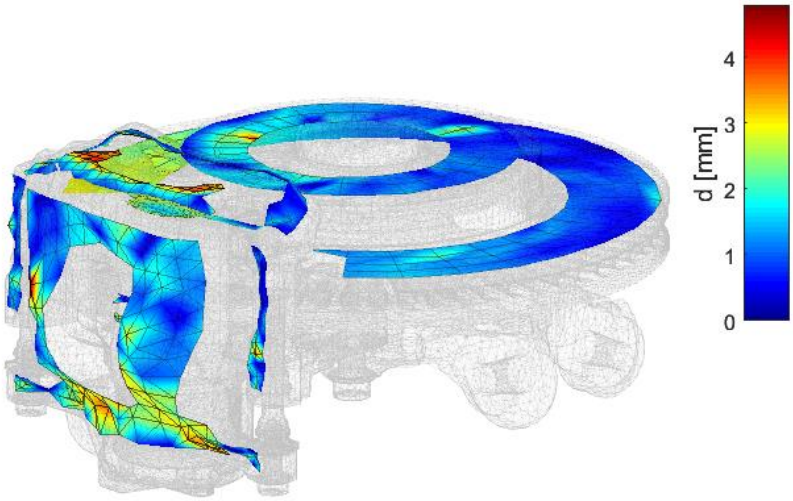


Figure 11 : Measurement wireframe on top of the FEM

The two shapes obtained from the exploitation of the limit cycle measurements are used to perform expansion with a FEM. The MDRE [4] algorithm is used, which consists in finding the shape $\{\hat{\phi}\}$ that minimizes the weighted sum of two energies: ϵ_{Mod} linked to the residual force $Z(\omega)\{\hat{\phi}\} = \{R_L(\omega)\}$ (not zero because the model is not exact) and ϵ_{Test} linked to the measurement error (the error between the measured shape and the observation at sensors of $\{\hat{\phi}\}$). The cost function is then written

$$\mathrm{J} = \epsilon_{\mathrm{Mod}} + \gamma\epsilon_{\mathrm{Test}} \tag{11}$$

with γ the weighting between the two errors. *In more* details, to measure the residual force, the static displacement which it engenders *is* computed *as*

$$\{R_D(\omega)\} = [K]^{-1}\{R_L(\omega)\} = [K]^{-1}\, Z(\omega)\{\hat{\phi}\} \tag{12}$$

and the deformation energy linked to this residual displacement is the error of model

$$\epsilon_{Mod} = \{R_D(\omega)\}^H [K]\{R_D(\omega)\} \tag{13}$$

To express the measurement error, the expanded shape is observed at sensors using the observation matrix $[c]$ and compared with the measured shape using the classical Euclidian norm

$$\epsilon_{Test} = \left([c]\{\hat{\phi}\} - \{y_{Test}\}\right)^T \left([c]\{\hat{\phi}\} - \{y_{Test}\}\right) \tag{14}$$

From these two errors, the cost function can be put in a matrix form (see [4] and [2]) and thus the expanded mode shape can be found directly for each value of γ.

Nevertheless, full resolution of MDRE is generally not accessible [5], so that the reduction proposed in [2] is a major contribution. The FEM is reduced on a basis combining the response to unit loads at sensors, for the result to be at least as good as the static expansion, and the free modes of the structure (considering the friction coefficient equals to zero), for the expansion to be exact if the model matches perfectly the measurements. This family of shapes is orthonormalized with respect to mass and stiffness matrices, leading to the basis

$$[T] = \left[[\Phi]_{NM} [\Phi^{\perp}]\right] \tag{15}$$

with $[\Phi]_{NM}$ the free mode shapes and $[\Phi^{\perp}]$ the part of the response to unit loads at sensors that is orthogonal to the free modes (this part will be called later enrichment).

Furthermore, this model reduction can be useful if the expansion is used in combination with an updating procedure, to speed up the parametrized studies. It also permits a quick evaluation of the MDRE result with several values of the parameter γ which allows more or less measurement error.

Rather than absolute measurement and model errors, relative errors are introduced to ease interpretation of the role of parameter γ. The relative measurement error is defined by

$$\epsilon_{Test}^{R} = \frac{\sqrt{\epsilon_{Test}}}{\|y_{Test}\|} \tag{16}$$

and the relative model error by

$$\epsilon_{Mod}^{R} = \frac{\epsilon_{Mod}}{\{\hat{\phi}\}^{T}[K]\{\hat{\phi}\}} \tag{17}$$

Because of the chosen reduction basis, the DOFs q_R can be decomposed in those linked to the free modes q_M and those linked to the enrichment $q_{M^\perp}$. In this basis, the stiffness matrix is diagonal with first the mode pulsations ω_M^2 and then the pseudo-pulsations $\omega_{M^\perp}^2$. From this property, the model error can be decomposed in the part linked to the free modes and the part linked to the enrichment

$$\epsilon_{Mod} = \{R_D\}_{|M}{}^{T} \begin{bmatrix} \ddots & & \\ & \omega_{\mathrm{M}}^2 & \\ & & \ddots \end{bmatrix} \{R_D\}_{|M} + \{R_D\}_{|\mathrm{M}^\perp}{}^{T} \begin{bmatrix} \ddots & & \\ & \omega_{\mathrm{M}^\perp}^2 & \\ & & \ddots \end{bmatrix} \{R_D\}_{|\mathrm{M}^\perp} \tag{18}$$

Several expansions with an increasing γ from 1 to 1e10 have been performed on the disc brake test case. The evolution of the relative measurement and model errors is shown in Figure 12.

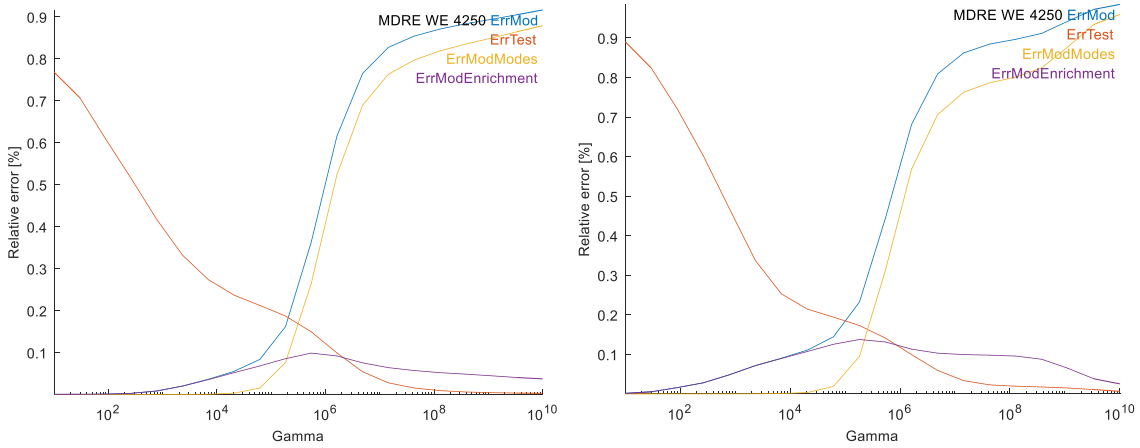


Figure 12 : Evolution of relative model and measurement error with γ. Left: first main shape, right: second.

For a very low value of $\gamma = 1$, the relative model error is really low but the expanded shape does not match the measurements. When increasing the value of γ, the measurement error decreases with at first an incresing model error linked to the enrichment (up to $\gamma = 10e5$). Then, the measurement error continues to decrease but with a strong increase of the model error linked to the free modes: to represent the measurement well, the free modes are used but do not satisfy well the mechanical equilibrium of the model. The free mode subspace seems thus relevant but does not have the good frequency distribution.

Choosing an intermediate γ (5e+05), the expanded mode shapes are show in Figure 13.The first one is dominated by the deformation of the right column and the right side of the caliper. The second shape is mostly a deformation of the whole caliper and again the right column. The analysis of the squeal behavior

with the expanded shapes is simpler than with only the deformations at sensors. It can help providing modification propositions to impact the phenomenon.

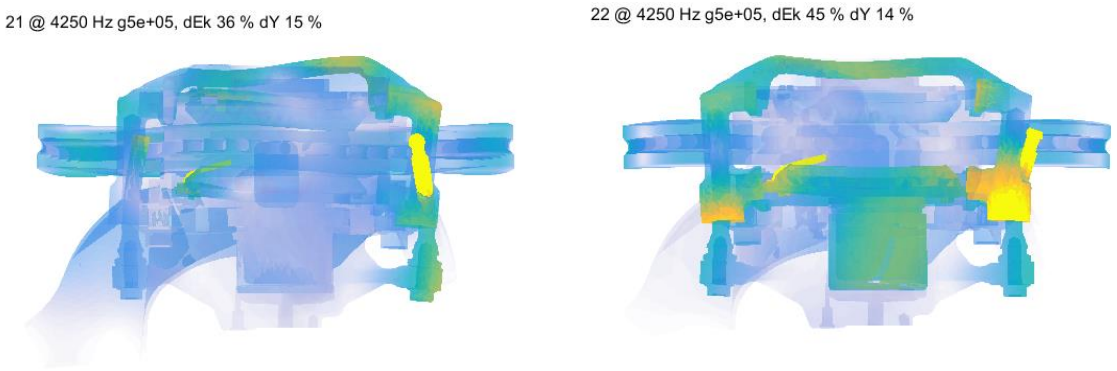


Figure 13 : Expansion result for the two extracted experimental shapes form the limit cycle measurements.

The expansion can also be used to analyze the model quality. Indeed, the energy distribution coming from the residual forces shows areas of the model where the mechanical equilibrium is poor. This residual energy can be split in two: the residual energy related to the free mode shapes, and the residual energy related to the enrichment shapes.

Figure 14 shows that the residual energy related to the enrichment shapes is mostly a concentration of energy near the sensor locations



Figure 14 : Model error on the enrichment shapes

Figure 15 shows residual energy distribution on the free mode shapes. This energy is more global with nevertheless several concentration areas: in the sliding contact between the pad and the disc (A), at each contact between the pad and the caliper (B) and between the columns and the caliper (C). Using these residual energy maps helps defining a relevant parametrization of the model to perform model updating if needed.

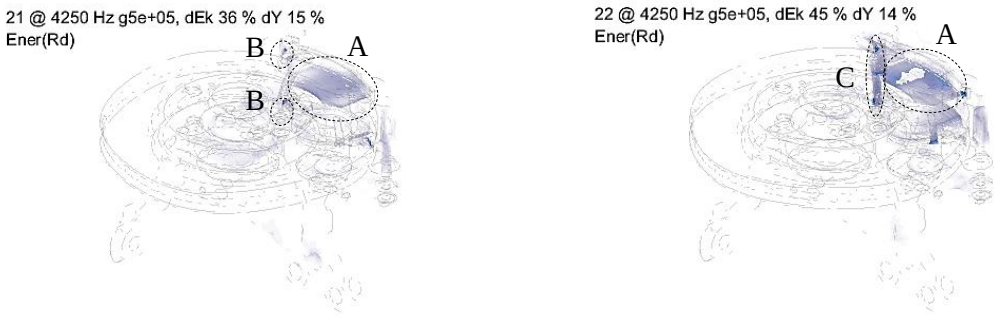


Figure 15 : Model error on the free mode shapes

6 Conclusion

This study showed that the interpretation of the squeal behavior as an interaction between two real shapes makes sense, not only numerically but also experimentally. The reproducibility of the phenomenon, despite frequency shifts, is good when the subspace is compared instead of the complex shapes directly: the limit cycle lies in a two-dimensional subspace with a slow variation of relative amplitude and phase. The time/frequency analysis strategy retained is very simple and more advanced techniques such as the Hilbert transform could be considered [6]. Tracking of modes during the cycle and before the squeal instability would be a useful complement to the test performed here. It would correspond to force appropriation and could be coupled to auto-resonance techniques [7].

The two-dimensional subspace is sufficiently stable to allow a piecewise reconstruction combining reference sensors and 3D-SLDV measurements. This leads to field measurements of squeal shapes, but still only measures accessible surfaces and thus fail to give indications about the behavior of junctions.

Finally, the expansion of the two shapes extracted from the limit cycle measurements provides a fully detailed estimation of the test shapes. The proposed reduction methodology enables practical studies on industrial models and the results can be interpreted in terms of shapes of interest and possibly as a basis to localize errors to be used in model updating analysis. Combining expansion and updating is a clear perspective of this work.

References

[1] G. Vermot Des Roches, “Frequency and time simulation of squeal instabilities. Application to the design of industrial automotive brakes,” Ph.D. thesis, Ecole Centrale Paris, CIFRE SDTools, 2011.

[2] G. Martin, “Méthodes de corrélation calcul/essai pour l’analyse du crissement,” Ph.D. thesis, CIFRE SDTools, Arts et Metiers ParisTech, Paris, 2017.

[3] E. Balmes and others, “Orthogonal Maximum Sequence Sensor Placements Algorithms for modal tests, expansion and visibility,” *IMAC*, vol. 145, p. 146, 2005.

[4] E. Balmes, “Review and Evaluation of Shape Expansion Methods,” *IMAC*, pp. 555–561, 2000.

[5] N. Nifa, “Solveurs performants pour l’optimisation sous contraintes en identification de paramètres,” Ph.D. thesis, Université Paris-Saclay, 2017.

[6] M. Feldman, *Hilbert Transform Applications in Mechanical Vibration: Feldman/Hilbert Transform Applications in Mechanical Vibration*. Chichester, UK: John Wiley & Sons, Ltd, 2011.
[7] S. Davis and I. Bucher, "Automatic vibration mode selection and excitation; combining modal filtering with autoresonance," *Mech. Syst. Signal Process.*, vol. 101, pp. 140–155, Feb. 2018.

A periodic $\mathcal{H}_2$ state feedback controller for a rotor-blade system

J. F. Camino[1] **and I. F. Santos**[2]
[1] University of Campinas
School of Mechanical Engineering
13083-860, Campinas, SP, Brazil
e-mail: **camino@fem.unicamp.br**

[2] Technical University of Denmark
Department of Mechanical Engineering
DK-2800, Kgs. Lyngby, Denmark

Abstract
Many engineering applications have as their main component rotor-blade systems whose dynamics can be represented by a linear time-varying model. Since rotor-blade systems exhibit periodic dynamics, standard linear time-invariant analysis and synthesis techniques cannot be directly used and are not able to guarantee closed-loop stability and performance. Although there exist many results for periodic systems, the design of controllers for such systems is, in general, a difficult task. Its practical application is challenging, from the computational and experimental aspects. This paper presents the application of a periodic $\mathcal{H}_2$ control problem in a rotor-blade system in order to attenuate the tip vibration. The proposed control design is based on a periodic Riccati differential equation (PRDE). The Floquet-Lyapunov theory is used to represent the dynamics in an adequate coordinate system, so that the PRDE can be efficiently solved. A robustness analysis is also perfomed. Numerical experiments show the effectiveness of the proposed approach.

1 Introduction

Linear time-varying (LTV) differential equations are widely used to model natural phenomena, engineering systems, and many other situations. For instance, time-varying models have been used to describe the dynamic behavior of an idealized human operator in [35, 48] and to estimate the stiffness of human elbow joint during cyclic voluntary movement in [6]. In the field of economics, the dynamics of the yield curve and key macroeconomic variables can be modeled through linear time-varying models [7]. In the rendezvous problem for satellites in elliptic orbits [40], the relative motion of a deputy satellite with respect to the chief satellite can be described by a time-varying linearized equation of motion.

In a trajectory tracking problem for mechanical systems [36], it is common to use a generator to provide an off-line open-loop optimal trajectory, basically composed of an ideal system state and control input, which satisfies the nonlinear system dynamics and ensures that the system output follows a given reference. Then, considering that the design objective is to keep the actual plant state near its ideal value, under small perturbations, a linear time-varying model can be used for control design [4]. In [44], an LTV model has been used in the steps to obtain a flatness-based open-loop control law. A sequence of linear time-varying approximations is used in [2, 16] to solve a nonlinear optimal control problem.

Periodic systems are a particular class of LTV systems that appear frequently in engineering applications, since machinery with rotating parts is found in many mechanical systems, such as vehicles, airplanes, ships

and wind-turbines, among others [20, 37]. Active control of rotor-blade systems has been an attractive approach to improve performance, suppress vibrations, and prolong machinery lifetime [23, 32, 46]. However, due to the periodic time-varying nature of the problem, applications of classical LTI analysis and synthesis techniques are not suitable.

One of the most important results available to analyze periodic systems is known as Floquet-Lyapunov decomposition. It provides a coordinate change that reduces a homogeneous periodic system to a linear time-invariant system. This decomposition was used in [24] to analyze helicopter rotor dynamics, in [47] to design a periodic state feedback controller for a mistuned bladed disk, and in [41] to design a periodic observer-based controller for mechanical systems. It was shown in [15] that the vibration of rotor-blade systems can be attenuated using control forces acting on the hub. The presence of parametric vibration effects due to vibration coupling between rotor and blades was analyzed in [14]. A periodic LQR controller was proposed in [28] with guaranteed performance and closed-loop stability, and a discrete-time periodic $\mathcal{H}_2$ controller was proposed in [10] for vibration reduction using actively twisted blades.

The $\mathcal{H}_2$ norm has been extensively used to quantify system performance as an objective function for a large class of optimal control problems [39, 45]. The $\mathcal{H}_2$ control problem consists of stabilizing the closed-loop system while minimizing its $\mathcal{H}_2$ norm, from the disturbance input to the performance output [13, 39, 45]. The notion of the $\mathcal{H}_2$ norm and synthesis conditions for the $\mathcal{H}_2$ state feedback control problem for continuous-time periodic systems are found in [17, 18]. Algorithms to solve the underlying set of periodic time-varying Lyapunov and Riccati equations [1, 8, 9], which frequently appear in control and systems theory, have been extensively investigated in the last decades [19, 26, 30, 31].

In this paper, an $\mathcal{H}_2$ state feedback controller is designed to attenuate the tip vibration of a rotor-blade system. The periodic time-varying control design is formulated in terms of a matrix Riccati differential equation. Although the design guarantees stability and performance, an analysis of the robustness of the $\mathcal{H}_2$ controller with respect to stability is also provided.

2 Control design

This section presents the proposed periodic $\mathcal{H}_2$ optimal control design, used to improve the performance and robustness of the rotor-blade system.

To access the best achievable performance, it is assumed henceforth that all the states are available for feedback and, thus, the controller is a full state feedback gain. In case not all states are available for feedback, a periodic observer can be designed, since the separation principle still holds [4, 50], with possible decrease in performance and robustness [5, 21].

Consider the following linear time-varying system

$$\begin{aligned} \dot{x}(t) &= A(t)x(t) + B_u(t)u(t) + B_w(t)w(t) \\ z(t) &= C_z(t)x(t) + D_{zu}(t)u(t) + D_{zw}(t)w(t) \end{aligned} \tag{1}$$

where all the matrices have compatible dimensions, are continuous functions of time, and bounded. Then, the closed-loop system using the state feedback law

$$u(t) = K(t)x(t)$$

is given by

$$\begin{aligned} \dot{x}(t) &= A_{cl}(t)x(t) + B_{cl}(t)w(t) \\ z(t) &= C_{cl}(t)x(t) + D_{cl}(t)w(t) \end{aligned} \tag{2}$$

with

$$A_{cl}(t) = A(t) + B_u(t)K(t), \quad B_{cl}(t) = B_w(t), \quad C_{cl}(t) = C_z(t) + D_{zu}(t)K(t), \quad D_{cl}(t) = D_{zw}(t)$$

Before presenting the control design, some well-known results are introduced in the next section. For a detailed exposition, see the comprehensive sources [8, 11, 52] and references therein.

2.1 Preliminary facts

Consider the following linear time-varying system H given by

$$H := \begin{cases} \dot{x}(t) = A(t)x(t) + B(t)v(t) \\ y(t) = C(t)x(t) + D(t)v(t) \end{cases} \tag{3}$$

where all the matrices have compatible dimensions, are continuous functions of time, and bounded. The vectors $y(t)$ and $v(t)$ are the output and the input signals, respectively.

A convenient notion of stabilizability and detectability is given in the next definition [38].

Definition 1. *System* (3) *is said to be stabilizable if there exists a bounded matrix function $K(t)$ such that $\dot{x}(t) = (A(t) - B(t)K(t))x(t)$ is exponentially stable. System* (3) *is said to be detectable, if there exists a bounded matrix function $L(t)$ such that $\dot{x}(t) = (A(t) - L(t)C(t))x(t)$ is exponentially stable.*

The next Lemma 2 provides a classical version of the Lyapunov stability theorem for continuous-time linear time-varying systems [38], which was first proved for the discrete-time case in [3]. A version for periodic systems can be found in [8].

Lemma 2. *Assume the pair $(A(t), B(t))$ is stabilizable and the pair $(A(t), C(t))$ is detectable. Then, either of the following statements is a sufficient condition for system* (3) *to be exponentially stable:*

1. *There exists a bounded nonnegative definite matrix solution $L_c(t)$ of the equation*

$$\dot{L}_c(t) = L_c(t)A'(t) + A(t)L_c(t) + B(t)B'(t)$$

2. *There exists a bounded nonnegative definite matrix solution $L_o(t)$ of the equation*

$$-\dot{L}_o(t) = A'(t)L_o(t) + L_o(t)A(t) + C'(t)C(t)$$

In system theory, mainly in optimal control problems [29, 49], the Riccati equation plays an important role [1, 9, 33]. The next Lemma 3 states the conditions for the solution of the Riccati differential equation to be unique and stabilizing [38].

Lemma 3. *Assume the pair $(A(t), B(t))$ is stabilizable and the pair $(A(t), C(t))$ is detectable. Then, there exists a unique bounded solution $X(t) \geq 0$ of the following Riccati equation*

$$0 = \dot{X}(t) + A'(t)X(t) + X(t)A(t) - X(t)B(t)B'(t)X(t) + C'(t)C(t)$$

Furthermore, the system $\dot{x}(t) = (A(t) - B(t)B'(t)X(t))x(t)$ is exponentially stable.

The next Lemma 4 provides another important result, called Floquet-Lyapunov decomposition [11, 22, 52], which can be used to transform the homogeneous T-periodic system

$$\dot{x}(t) = A(t)x(t), \qquad A(t+T) = A(t) \tag{4}$$

into a linear time-invariant system.

Lemma 4. *Consider the T-periodic linear system* (4)*. Let the associated transition matrix be denoted by $\Phi_A(t, t_0)$. Define a matrix function $P(t)$ and a constant matrix W via the equations*

$$P(t) = e^{Wt}\Phi_A(0, t) \qquad \textit{and} \qquad e^{WT} = \Phi_A(T, 0) \tag{5}$$

Then, the transition matrix $\Phi_A(t, t_0)$ can be written as

$$\Phi_A(t, t_0) = P^{-1}(t)e^{W(t-t_0)}P(t_0)$$

Moreover, system (4) *is reducible in the sense of Lyapunov and its origin $x = 0$ is an exponentially stable equilibrium if, and only if, W is Hurwitz.*

From this previous result, it becomes clear that the class of linear periodic systems is reducible in the sense of Lyapunov [22]. Furthermore, the change of variable $\eta(t) = P(t)x(t)$ transforms (4) into the linear time-invariant system

$$\dot{\eta}(t) = W\eta(t) \tag{6}$$

To see this fact, observe that the system dynamics in the η-coordinate is given by

$$\dot{\eta} = \hat{A}(t)\eta(t)$$

with

$$\hat{A}(t) = P(t)A(t)P^{-1}(t) + \dot{P}(t)P^{-1}(t)$$

whose transition matrix can be shown to be

$$\Phi_{\hat{A}}(t, t_0) = P(t)\Phi_A(t, t_0)P^{-1}(t_0) = e^{W(t-t_0)}$$

which is exactly the transition matrix of system (6).

The monodromy matrix Ψ_A, which is usually defined as the transition matrix computed over one period, i.e. $\Psi_A = \Phi_A(T, 0)$, is a crucial element for the stability analysis of periodic systems. The characteristic roots of $e^{WT} = \Psi_A$ are called the *multipliers associated with* $A(t)$ and the characteristic roots of W are called *characteristic exponents*. As a direct consequence of Lemma 4, the stability of (4) is characterized by the location of these roots.

Using the Floquet-Lyapunov transformation above, the periodic system (3) becomes

$$\begin{aligned} \dot{\eta}(t) &= \hat{A}\eta(t) + \hat{B}(t)v(t) \\ y(t) &= \hat{C}(t)\eta(t) + \hat{D}(t)v(t) \end{aligned} \tag{7}$$

with

$$\hat{A} = W, \qquad \hat{B}(t) = P(t)B(t), \qquad \hat{C}(t) = C(t)P^{-1}(t), \qquad \hat{D}(t) = D(t)$$

Notice that the system matrix $A(t)$ is transformed into a constant matrix W. However, all the other matrices still remain time-varying. In this new coordinate, it is possible to apply an extra similarity transformation to convert W, for instance, to a real block diagonal form.

A procedure for computing the Floquet-Lyapunov transformation using Chebyshev polynomials is presented in [42]. Another procedure that uses a Fourier series expansion to transform a periodic system into an LTI system in the modal form is provided in [51] and applied in [15]. Modal analysis techniques for linear time-varying systems can be found in [12, 27, 34].

2.2 Periodic state feedback $\mathcal{H}_2$ synthesis

The $\mathcal{H}_2$ norm for linear time-invariant (LTI) systems can be computed from the controllability or the observability gramians [43, 53]. The computation of these norms is readily performed by solving the corresponding algebraic Lyapunov equation. For linear time-varying (LTV) systems, there exist distinct characterizations of the $\mathcal{H}_2$ norm, which are straightforward extensions of the LTI case, but, in general, they are not equivalent [45]. As shown in the next Lemma 5, the $\mathcal{H}_2$ norm for a T-periodic system can be defined in a similar way as the LTI case, using the controllability and the observability gramians [17].

Lemma 5. *Consider system H given by* (3) *with $D(t) = 0$. Assume the T-periodic system matrix $A(t)$ is exponentially stable. Let the controllability gramian $L_c(t)$ and the observability gramian $L_o(t)$ be bounded solutions of the following equations*

$$\begin{aligned} \dot{L}_c(t) &= L_c(t)A'(t) + A(t)L_c(t) + B(t)B'(t) \\ -\dot{L}_o(t) &= A'(t)L_o(t) + L_o(t)A(t) + C'(t)C(t) \end{aligned}$$

Then, the $\mathcal{H}_2$ norm of (3) *is given by*

$$\|H\|_2^2 = \frac{1}{T}\int_0^T \mathrm{Tr}\left[C(\tau)L_c(\tau)C'(\tau)\right]\mathrm{d}\tau = \frac{1}{T}\int_0^T \mathrm{Tr}\left[B'(\tau)L_o(\tau)B(\tau)\right]\mathrm{d}\tau$$

The proposed $\mathcal{H}_2$ optimal control problem consists in finding a state feedback gain $K(t)$ such that the $\mathcal{H}_2$ norm of the closed-loop system is minimized. The next Lemma 6 provides, as shown in [18], a Riccati differential equation that characterizes the solution of the $\mathcal{H}_2$ state feedback control problem for system (1), with $D_{zw}(t) = 0$.

Lemma 6. *Consider system* (1) *with $D_{zw}(t) = 0$. Assume that $(A(t),\ B_u(t))$ is stabilizable, $D_{zu}(t)$ is injective for each t, and that the periodic system $(A(t), B_u(t), C_z(t), D_{zu}(t))$ does not have invariant zeros in the unit circle. Then, the optimal solution of the $\mathcal{H}_2$ problem is*

$$K(t) = -R^{-1}(t)\left(B_u'(t)X(t) + D_{zu}'(t)C_z(t)\right)$$

where $R(t) = D_{zu}'(t)D_{zu}(t)$, and $X(t)$ is the stabilizing positive semidefinite solution of the periodic Riccati differential equation

$$\begin{aligned}\dot{X}(t) + A'(t)X(t) + X(t)A(t) + C_z'(t)C_z(t)\\ - \left(X(t)B_u(t) + C_z'(t)D_{zu}(t)\right)R^{-1}(t)\left(B_u'(t)X(t) + D_{zu}'(t)C_z(t)\right) = 0\end{aligned}$$

There exist appropriate techniques that can be used to solve the periodic Riccati differential equation above [19, 26, 30, 31].

2.3 Robustness analysis

It is interesting to verify how robust the stability of the closed-loop system is, using the proposed periodic $\mathcal{H}_2$ state feedback controller, when the system model is uncertain. For this analysis, different approaches can be used.

The necessary and sufficient conditions for asymptotic stability of continuous-time linear time-varying systems and, in particular, for periodic systems presented in [25], are explored. These conditions provide a function $\bar{\rho}(t)$ that bounds all the system trajectories, for a prescribed set of initial conditions, as stated in the next Lemma 7 from [25].

Lemma 7. *For a given $\rho_0 > 0$, let $\bar{\rho}(t) = \rho_0\lambda_{\max}^{1/2}(X(t,t_0))$, where $X(t,t_0)$ is the solution of the following Lyapunov differential equation*

$$\frac{\partial}{\partial t}X(t,t_0) = A(t)X(t,t_0) + X(t,t_0)A'(t), \quad X(t_0,t_0) = I$$

and let

$$\rho_T = \max_{t\in[t_1,t_1+T]} \bar{\rho}(t), \quad t_1 \geq t_0$$

Then, the T-periodic system (4) *is asymptotically stable if, and only if,*

$$\rho_T < \infty \quad \textit{and} \quad \bar{\rho}(t_1+T) < \bar{\rho}(t_1), \quad \forall t_1 \geq t_0$$

Moreover, there always exists an initial condition $x_0 \in \Omega_0$, with $\Omega_0 = \{x \mid x'x \leq \rho_0^2,\ \rho_0 > 0\}$, such that the associated trajectory reaches the bound $\bar{\rho}(t)$, in the sense that $x'(t)x(t) = \bar{\rho}^2(t)$.

It is also possible to analyze the region of stability of the closed-loop system, using the computed $\mathcal{H}_2$ controller, as a function of the system's uncertainties. For this test, the stability is verified by computing the multipliers associated with the closed-loop systems, obtained by the feedback connection of each uncertain open-loop model with the $\mathcal{H}_2$ controller.

3 Rotor-blade dynamics

The two-dimensional rotor-blade system shown in Figure 1 consists of a rotor with four flexible blades, rotating in a suspended hub, with angular velocity Ω. The hub motion is described in the inertial (x, y)-coordinate system. The angular position of blade 1 is given by $\theta(t)$. A detailed derivation of the model is found in [14, 15].

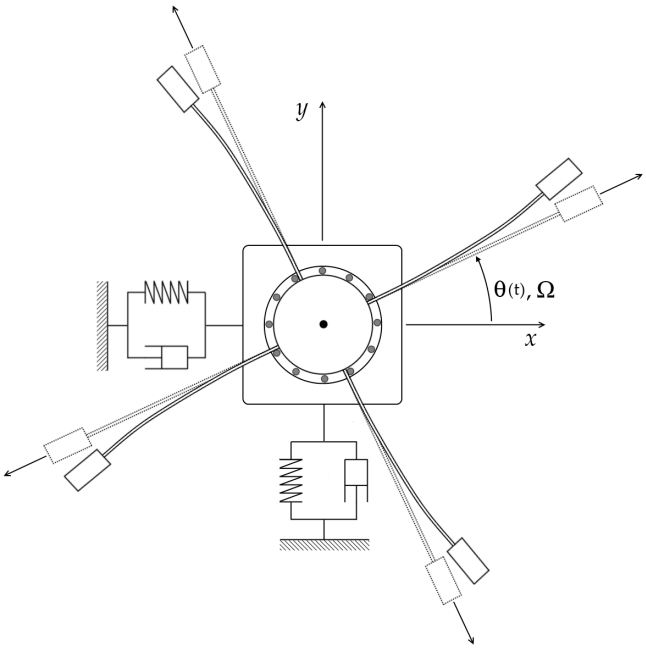


Figure 1: Two-dimensional model of the rotor-blade system.

Considering that the system rotates at the constant angular velocity $\Omega = 300$ rpm, the equation of motion is given by

$$M(t)\ddot{q}(t) + D(t)\dot{q}(t) + S(t)q(t) = Q_u u(t) + p(t) + w(t) \tag{8}$$

where $M(t)$ is the mass matrix, $D(t)$ is the damping matrix, $S(t)$ is the stiffness matrix, Q_u is the input matrix, $u(t)$ is the control input force, $p(t)$ is the periodic force due to the unbalance, and $w(t)$ is the exogenous disturbance acting on the system.

The system matrices, with period $T = 2\pi/\Omega = 0.2$ seconds, are given by

$$M(t) = \begin{bmatrix} 10.99 & 0 & -0.135S_0 & -0.135S_1 & -0.135S_2 & -0.135S_3 \\ 0 & 9.09 & 0.135C_0 & 0.135C_1 & 0.135C_2 & 0.135C_3 \\ -0.135S_0 & 0.135C_0 & 0.161 & 0 & 0 & 0 \\ -0.135S_1 & 0.135C_1 & 0 & 0.161 & 0 & 0 \\ -0.135S_2 & 0.135C_2 & 0 & 0 & 0.161 & 0 \\ -0.135S_3 & 0.135C_3 & 0 & 0 & 0 & 0.161 \end{bmatrix}$$

$$D(t) = \begin{bmatrix} 1.200 & 0 & -0.270\omega C_0 & -0.270\omega C_1 & -0.270\omega C_2 & -0.270\omega C_3 \\ 0 & 1.500 & -0.270\omega S_0 & -0.270\omega S_1 & -0.270\omega S_2 & -0.270\omega S_3 \\ 0 & 0 & 0.800 & 0 & 0 & 0 \\ 0 & 0 & 0 & 0.800 & 0 & 0 \\ 0 & 0 & 0 & 0 & 0.800 & 0 \\ 0 & 0 & 0 & 0 & 0 & 0.800 \end{bmatrix}$$

$$S(t) = \begin{bmatrix} 6.6\times10^4 & 0 & 0.135\omega^2 S_0 & 0.135\omega^2 S_1 & 0.135\omega^2 S_2 & 0.135\omega^2 S_3 \\ 0 & 7.7\times10^4 & -0.135\omega^2 C_0 & -0.135\omega^2 C_1 & -0.135\omega^2 C_2 & -0.135\omega^2 C_3 \\ 0 & 0 & \hat{S}_0 & 0 & 0 & 0 \\ 0 & 0 & 0 & \hat{S}_1 & 0 & 0 \\ 0 & 0 & 0 & 0 & \hat{S}_2 & 0 \\ 0 & 0 & 0 & 0 & 0 & \hat{S}_3 \end{bmatrix}$$

$$Q_u = \begin{bmatrix} 1 & 0 & 0 & 0 & 0 & 0 \\ 0 & 1 & 0 & 0 & 0 & 0 \\ 0 & 0 & 0.299 & 0 & 0 & 0 \\ 0 & 0 & 0 & 0.299 & 0 & 0 \\ 0 & 0 & 0 & 0 & 0.299 & 0 \\ 0 & 0 & 0 & 0 & 0 & 0.299 \end{bmatrix}$$

where $S_k = \sin(\omega t + \pi k/2)$, $C_k = \cos(\omega t + \pi k/2)$ and $\hat{S}_k = 1961 + 0.102\omega^2 - 16.85 S_k$, with $\omega = 2\pi/T = 10\pi$ rad/s, and $k = 0, 1, 2, 3$.

The matrices $M(t)$, $D(t)$, $S(t)$, and Q_u above are obtained from the system matrices given in the appendix of [14] after removing the second bending mode of the blades, i.e., after removing the 4th, 6th, 8th, 10th lines and columns.

By defining the state space vector $x(t) = \begin{bmatrix} q'(t) & \dot{q}'(t) \end{bmatrix}'$, equation (8) can be written in following the state space form

$$\dot{x}(t) = A(t)x(t) + B_u(t)u(t) + B_w(t)w(t) + f(t) \tag{9}$$

where

$$A(t) = \begin{bmatrix} 0 & I \\ -M^{-1}(t)S(t) & -M^{-1}(t)D(t) \end{bmatrix},$$

$$B_u(t) = \begin{bmatrix} 0 \\ M^{-1}(t)Q_u \end{bmatrix}, \quad B_w(t) = \begin{bmatrix} 0 \\ M^{-1}(t) \end{bmatrix}, \quad f(t) = \begin{bmatrix} 0 \\ M^{-1}(t) \end{bmatrix} p(t)$$

The displacement vector q has six generalized coordinates that account for the hub motion, in the (x, y)-directions, and the tip deflection of each one of the four blades. Thus, the system has 6 degrees of freedom and the state x has 12 entries.

The mechanical system has six actuators that can independently control all six degrees of freedom. Two actuators are located in the hub, providing forces in the (x, y)-directions, and the other four are located in each one of the blades.

As observed in [14], the force $p(t)$, due to unbalances, is usually known or well estimated when the system rotates at constant speed. Thus, it is possible to cancel out this effect, as performed in [28], using the following feedforward control law

$$u_f(t) = -\left(B_u'(t)B_u(t)\right)^{-1} B_u'(t)f(t)$$

The next section presents the numerical results in which the unbalance is neglected, since it is assumed that a preliminary feedforward control law can always be applied to cancel its effect.

4 Numerical results

For the numerical simulations, the matrices $A(t)$, $B_u(t)$, and $B_w(t)$ are provided in Section 3 and the matrices $C_z(t)$, $D_{zu}(t)$, and $D_{zw}(t)$ are given by

$$C_z(t) = 10\begin{bmatrix} N \\ 0_{6,12} \end{bmatrix}, \quad N = \text{blkdiag}(0_2, I_4, 0_2, I_4), \quad D_{zu}(t) = \sqrt{0.1}\begin{bmatrix} 0_{12,6} \\ I_6 \end{bmatrix}, \quad D_{zw}(t) = 0$$

where $0_{n,m}$ and $I_{n,m}$ are the zero and the identity matrices of size $n \times m$, respectively, and the operation $\text{blkdiag}(X_1, \ldots, X_n)$ denotes the block diagonal matrix concatenation of its arguments.

Using Lemma 4, a Floquet-Lyapunov decomposition can be computed to represent system (1) in a new coordinate $\eta(t)$, as shown in (7), so that the system dynamic matrix $A(t)$ is transformed into a constant matrix W. In the first step of this process, the monodromy matrix $\Phi_A(T, 0)$, generated by the open-loop matrix $A(t)$, is computed and, subsequently, matrix W and the matrix function $P(t)$ are determined using (5). Afterwards, a similarity transformation is used to represent W in a block diagonal form. The obtained matrix W is given by $W = \text{blkdiag}(W_1, \ldots, W_6)$, with

$$W_1 = \begin{bmatrix} -0.5253 & 0.6891 \\ -0.6891 & -0.5253 \end{bmatrix}, \quad W_2 = \begin{bmatrix} -0.5605 & 12.8302 \\ -12.8302 & -0.5605 \end{bmatrix}, \quad W_3 = \begin{bmatrix} -2.5467 & 9.2207 \\ -9.2207 & -2.5467 \end{bmatrix}$$

$$W_4 = \begin{bmatrix} -1.6028 & 11.8287 \\ -11.8287 & -1.6028 \end{bmatrix}, \quad W_5 = \begin{bmatrix} -2.4885 & 12.5150 \\ -12.5150 & -2.4885 \end{bmatrix}, \quad W_6 = \begin{bmatrix} -2.4885 & 12.5148 \\ -12.5148 & -2.4885 \end{bmatrix}$$

The eigenvalues of W are given by: $-0.5253 \pm \text{j}0.6891$, $-0.5605 \pm \text{j}12.8302$, $-1.6028 \pm \text{j}11.8287$, $-2.4885 \pm \text{j}12.5150$, $-2.4885 \pm \text{j}12.5148$, and $-2.5467 \pm \text{j}9.2207$. Thus, the open-loop system is asymptotically stable, although lightly damped mainly due to the eigenvalues near the imaginary axis.

Using Lemma 6, the periodic $\mathcal{H}_2$ state feedback controller is designed by solving the associated periodic Riccati differential equation. The $\mathcal{H}_2$ norm of the open-loop system, computed using Lemma 5, is 39.5693. On the other hand, the $\mathcal{H}_2$ norm of the closed-loop system is 15.5883, which corresponds to a decrease of approximately 60%.

A time domain simulation is performed using a Gaussian white noise input $w(t)$ with zero mean and covariance matrix equals to $100I$. The system is assumed to be at rest with initial condition $x_0 = x(0) = 0$. Figure 2 and Figure 3 show, respectively, the hub position in the x-direction and the blade 1 tip deflection, for the open-loop (dashed black line) and the closed-loop (solid red line) systems. The other blades have similar behavior as blade 1.

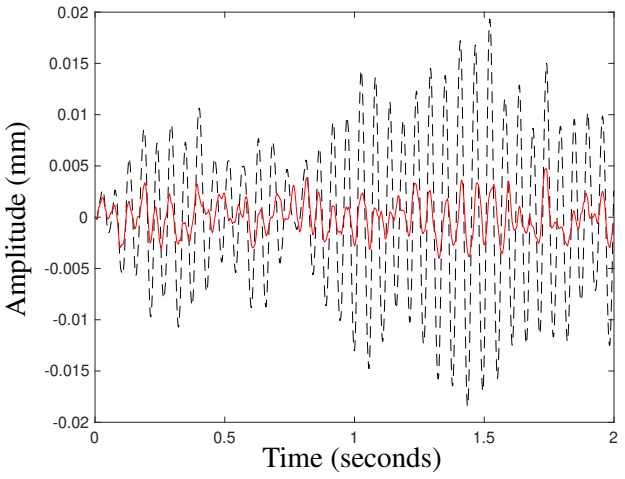


Figure 2: Blade 1 tip deflection.

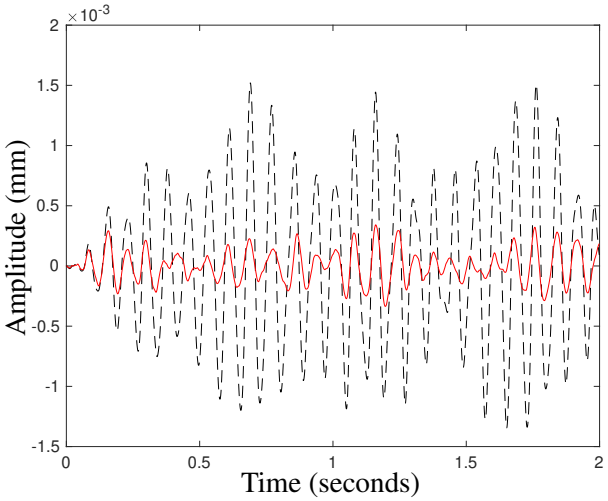


Figure 3: Hub position in the x-direction.

The next Figure 4 shows the curve given by function $\bar{\rho}(t)$ (solid black line) from Lemma 7, proposed in [25], and the 2-norm of the solution $x(t)$ (dotted red line) of the closed-loop system, for a set of 100 randomly generated initial conditions satisfying $x_0' x_0 = \rho_0^2 = 1$. As it can be observed from this figure, the function $\bar{\rho}(t)$ bounds $\|x(t)\|_2 = (x'(t)x(t))^{1/2}$ for all system trajectories and, clearly, there must exist an initial condition x_0 such that the boundary $x'(t)x(t) = \bar{\rho}^2(t)$ is reached.

To verify how robust the closed-loop stability is under parameter variation, it is assumed that the mass matrix $M(t)$ varies in the range $\alpha M(t)$, for $\alpha \in [10^{-3}, 70]$, and the damping matrix $D(t)$ varies in the range $\beta D(s)$,

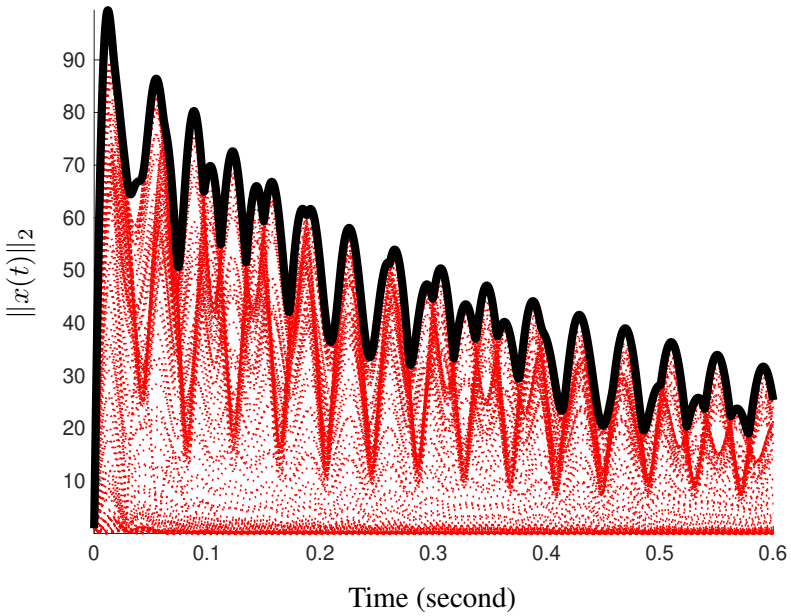


Figure 4: Function $\bar{\rho}(t)$ (solid black line) and $\|x(t)\|_2$ (dotted red line) for a set of 100 randomly generated initial conditions such that $x_0' x_0 = 1$.

for $\beta \in [0, 15]$. Since $M(t)$ needs to be invertible, the lower bound for α was chosen as 10^{-3}. The upper bounds for α and β were arbitrarily chosen. For a mesh of points in the $\alpha\beta$-region, the maximum absolute value γ of the 12 multipliers associated with each closed-loop system is computed.

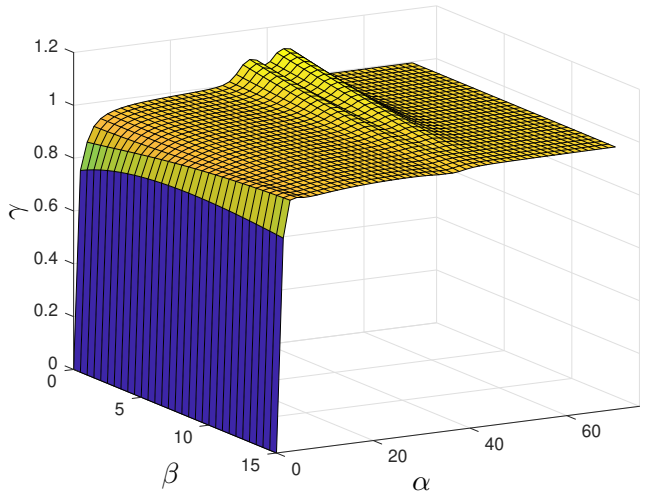


Figure 5: Stability surface defined by α, β and γ.

Figure 5 shows the plot of the parametric surface defined by α, β and γ. The closed-loop system is asymptotically stable if, and only if, $\gamma < 1$. Notice that for small values of α, which correspond to a mass matrix whose periodic entries have small amplitude, stability is guaranteed for any β. However, the system becomes unstable in the region where γ exceeds unity, which occurs in the vicinity of $\alpha = 40$ for a set of values of β. This fact is illustrated in Figure 6, which is a zoom of Figure 5, and in Figure 7, which shows the view of the $\alpha\beta$-plane for $\gamma \leq 1$. In Figure 7, the stable region is represented by the yellow mesh, and the unstable region otherwise.

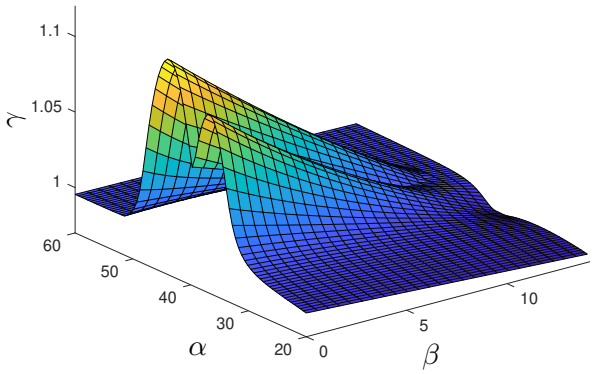


Figure 6: Zoom of the stability surface.

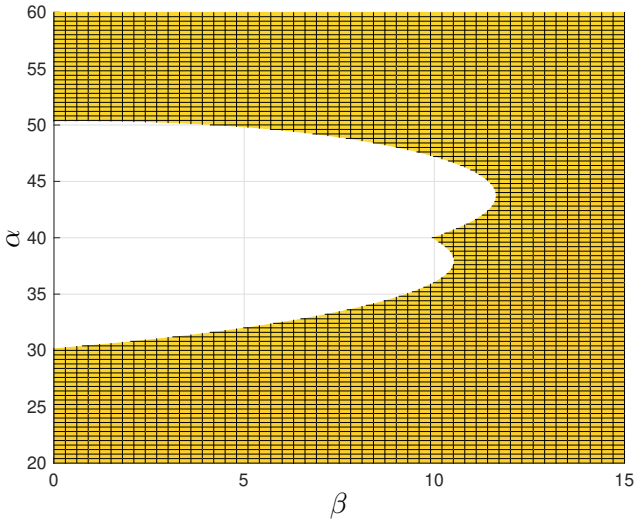


Figure 7: View of the $\alpha\beta$-plane for $\gamma \leq 1$.

5 Conclusion

In this paper, a periodic $\mathcal{H}_2$ state feedback controller was designed to attenuate the tip vibration of a two-dimensional rotor-blade system. The periodic dynamics of this system has 6 degrees of freedom: two related to the hub motion and one for each blade transverse deflection. The system is fully actuated. The unbalanced was neglected, since its effect can be canceled by a feedforward control law.

A Floquet-Lyapunov decomposition was applied to the system such that the system matrix $A(t)$ is reduced to a constant matrix W. A similarity transformation is also used to represent W in a block diagonal form with the characteristic exponent on the diagonal. Afterwards, the $\mathcal{H}_2$ state feedback controller is computed from the solution of a periodic Riccati differential equation.

The $\mathcal{H}_2$ norm of the open- and closed-loop systems are computed from the solution of a periodic Lyapunov differencial equation. It was readily verified that the periodic controller was capable of reducing significantly the vibration of the tip deflection, as was expected. The reduction measured in terms of the two-norm of closed-loop system was approximately 60%. However, different choice for the output matrices C_z and D_{zu} would lead to different performance and attenuation level.

An analysis of the robustness of the $\mathcal{H}_2$ controller was performed a posteriori. An envelop that bounds all the system trajectories, for a prescribed set of initial conditions, was computed. It was assumed that the mass matrix and the damping matrices were uncertain matrices inside a given region of uncertainty, and the stability of the closed-loop system for each uncertain model was analyzed. It was readily verified that the $\mathcal{H}_2$ controller is robust for most of the uncertain models, but there are some combinations of mass and stiffness matrices for which the closed-loop system will be unstable.

Acknowledgments

This work is supported by the funding agencies CAPES, CNPq, and FAPESP Grant Number 17/18629-3.

References

[1] H. Abou-Kandil, G. Freiling, V. Ionescu, and G. Jank. *Matrix Riccati Equations in Control and Systems Theory*. Birkhäuser, Basel, Switzerland, 2003.

[2] Z. Aganovic and Z. Gajic. The successive approximation procedure for finite-time optimal control of bilinear systems. *IEEE Transactions on Automatic Control*, 39(9):1932–1935, Sept. 1994.

[3] B. D. O. Anderson and J. B. Moore. Detectability and stabilizability of time-varying discrete-time linear systems. *SIAM Journal on Control and Optimization*, 19(1):20–32, Jan. 1981.

[4] M. Athans. The role and use of the stochastic linear-quadratic-Gaussian problem in control system design. *IEEE Transactions on Automatic Control*, 16(6):529–552, 1971.

[5] M. Athans. A tutorial on the LQG/LTR method. In *American Control Conference*, pages 1289–1296, Athens, Greece, June 1986.

[6] D. J. Bennett, J. M. Hollerbach, Y. Xu, and I. W. Hunter. Time-varying stiffness of human elbow joint during cyclic voluntary movement. *Experimental Brain Research*, 88:433–442, 1992.

[7] F. Bianchi, H. Mumtaz, and P. Surico. The great moderation of the term structure of UK interest rates. *Journal of Monetary Economics*, 56(6):856–871, 2009.

[8] S. Bittanti, P. Colaneri, and G. D. Nicolao. The periodic Riccati equation. In Bittanti et al. [9], pages 127–162.

[9] S. Bittanti, A. J. Laub, and J. C. Willems, editors. *The Riccati Equation*. Springer-Verlag, New York, USA, 1991.

[10] C. Brillante, M. Morandini, and P. Mantegazza. Periodic controllers for vibration reduction using actively twisted blades. *The Aeronautical Journal*, 120(1233):1763–1784, Nov. 2016.

[11] R. W. Brockett. *Finite Dimensional Linear Systems*. John Wiley & Sons, New York, USA, 1970.

[12] I. Bucher and D. J. Ewins. Modal analysis and testing of rotating structures. *Philosophical Transactions of The Royal Society of London*, 359:61–96, Jan. 2001.

[13] B. M. Chen and A. Saberi. Necessary and sufficient conditions under which an H_2 optimal control problem has a unique solution. *International Journal of Control*, 58(2):337–348, 1993.

[14] R. H. Christensen. *Active Vibration Control of Rotor-Blade Systems, Theory and Experiment*. PhD thesis, Dept. of Mechanical Engineering, Technical University of Denmark, Kgs. Lyngby, Denmark, 2004.

[15] R. H. Christensen and I. F. Santos. Design of active controlled rotor-blade systems based on time-variant modal analysis. *Journal of Sound and Vibration*, 280(3):863–882, 2005.

[16] T. Çimen and S. P. Banks. Nonlinear optimal tracking control with application to super-tankers for autopilot design. *Automatica*, 40:1845–1863, 2004.

[17] P. Colaneri. Continuous-time periodic systems in H_2 and H_∞. Part I: Theoretical aspects. *Kybernetika*, 36(2): 211–242, 2000.

[18] P. Colaneri. Continuous-time periodic systems in H_2 and H_∞. Part II: State feedback problems. *Kybernetika*, 36 (3):329–350, 2000.

[19] L. Dieci. Numerical integration of the differential Riccati equation and some related issues. *SIAM J. Numer. Anal.*, 29:781–815, 1992.

[20] A. D. Dimarogonas, S. A. Paipetis, and T. G. Chondros. *Analytical Methods in Rotor Dynamics*. Elsevier, New York, USA, 1983.

[21] J. C. Doyle. Guaranteed margins for LQG regulators. *IEEE Transactions on Automatic Control*, 23(4):756–757, 1987.

[22] N. P. Erugin, editor. *Linear Systems of Ordinary Differential Equations, with Periodic and Quasi-Periodic Coefficients*, volume 28 of *Mathematics in Science and Engineering*. Academic Press, 1966.

[23] R. Firoozian and R. Stanway. Active vibration control of turbomachinery: A numerical investigation of modal controllers. *Mechanical Systems and Signal Processing*, 2(3):243–264, 1988.

[24] P. P. Friedmann. Numerical methods for determining the stability and response of periodic systems with applications to helicopter rotor dynamics and aeroelasticity. *Computers & Mathematics with Applications*, 12(1): 131–148, Jan. 1986.

[25] G. Garcia, P. L. D. Peres, and S. Tarbouriech. Necessary and sufficient numerical conditions for asymptotic stability of linear time-varying systems. In *Proceedings of the 47th IEEE Conference on Decision and Control*, pages 5146–5151, Cancun, Mexico, Dec. 2008.

[26] J. J. Hench, C. S. Kenney, and A. J. Laub. Methods for the numerical integration of Hamiltonian systems. *Circuits, Systems, and Signal Processing*, 13(6):695–732, 1994.

[27] H. Irretier. Mathematical foundations of experimental modal analysis in rotor dynamics. *Mechanical Systems and Signal Processing*, 13(2):183–191, 1999.

[28] C. S. Jakobsen, J. F. Camino, and I. F. Santos. Rotor-blade vibration control using a periodic LQR controller. In *Proceedings of the 2013 SBAI/DINCON*, pages 1–07, Fortaleza, CE, Brazil, Oct. 2013.

[29] R. E. Kalman. Contribution to the theory of optimal control. In *Bol. Soc. Mat. Mexicana*, volume 5, pages 102–119, 1960.

[30] H. Kano and T. Nishimura. Periodic solutions of matrix Riccati equations with detectability and stabilizability. *International Journal of Control*, 29(3):471–487, 1979.

[31] C. S. Kenney and R. B. Lepnik. Numerical integration of the differential matrix Riccati equation. *IEEE Transactions on Automatic Control*, 30(10):962–970, Oct. 1985.

[32] Y. A. Khulief. Vibration suppression in rotating beams using active modal control. *Journal of Sound and Vibration*, 242(4):681–699, 2001.

[33] P. Lancaster and L. Rodman. *Algebraic Riccati Equations*. Oxford University Press, New York, USA, 1995.

[34] K. Liu. Extension of modal analysis to linear time-varying systems. *Schock and Vibration*, 226(1):149–167, 1999.

[35] D. T. McRuer and E. S. Krendel. Dynamic response of human operators. Technical report, WADC-TR-56-524, Oct. 1957.

[36] M. J. V. Nieuwstadt and R. M. Murray. Real-time trajectory generation for differentially flat systems. *International Journal of Robust and Nonlinear Control*, 8:995–1020, 1998.

[37] J. S. Rao. *Rotor Dynamics*. John Wiley & Sons, New York, USA, 1983.

[38] R. Ravi, A. M. Pascoal, and P. P. Khargonekar. Normalized coprime factorizations and the graph metric for linear time-varying systems. In *Proceedings of the 29th IEEE Conference on Decision and Control*, pages 1241–1246, Honolulu. Hawaii, Dec. 1990.

[39] M. Rotea. The generalized H_2 control problem. *Automatica*, 29(2):373–385, Mar. 1993.

[40] R. E. Sherrill, A. J. Sinclair, S. C. Sinha, and T. A. Lovell. Lyapunov-Floquet control of satellite relative motion in elliptic orbits. *IEEE Transactions on Aerospace and Electronic Systems*, 51(4):2800–2810, Oct. 2015.

[41] S. C. Sinha and P. Joseph. Control of general dynamic systems with periodically varying parameters via Liapunov-Floquet transformation. *ASME Journal of Dynamic Systems, Measurement, and Control*, 116(4):650–658, 1994.

[42] S. C. Sinha and D. H. Wu. An efficient computational scheme for the analysis of periodic systems. *Schock and Vibration*, 151(1):91–117, 1991.

[43] R. E. Skelton, T. Iwasaki, and K. M. Grigoriadis. *A Unified Algebraic Approach to Linear Control Design*. Taylor & Francis, Inc., Bristol, USA, 1998.

[44] M. Staudecker, K. Schlacher, and R. Hansl. Passivity based control and time optimal trajectory planning of a single mast stacker crane. In *Proceedings of the 17th IFAC World Congress*, pages 875–880, Seoul, korea, July 2008.

[45] A. A. Stoorvogel. The robust $\mathcal{H}_2$ control problem: A worst-case design. *IEEE Transactions on Automatic Control*, 38(9):1358–1370, 1993.

[46] G. Szász and G. T. Flowers. Vibration suppression in bladed-disk assemblies with deliberate mistuning via magnetic bearings. *Journal of Vibration Control*, 6(6):903–921, 2000.

[47] G. Szász and G. T. Flowers. Time periodic control of a bladed disk assembly using shaft based actuation. *ASME Journal of Vibration and Acoustics*, 123(3):395–398, 2001.

[48] W. W. Wierwille. A theory for optimal deterministic characterization of time-varying human operator dynamics. *IEEE Transactions on Human Factors in Electronics*, 6(1):53–61, Sept. 1965.

[49] J. C. Willems. Least squares stationary optimal control and the algebraic Riccati equation. *IEEE Transactions on Automatic Control*, 16(6):621–634, Dec. 1971.

[50] J. C. Willems and S. K. Mitter. Controllability, observability, pole allocation, and state reconstruction. *IEEE Transactions on Automatic Control*, 16(6):582–595, 1971.

[51] J. Xu and R. Gasch. Modale behandlung linearer periodisch zeitvarianter bewegungsgleichungen. *Archive of Applied Mechanics*, 65(3):178–193, 1995.

[52] V. A. Yakubovich and V. M. Starzhinskii. *Linear differential equations with periodic coefficients*, volume 1–2. John Wiley & Sons, New York, USA, 1975.

[53] K. Zhou, J. C. Doyle, and K. Glover. *Robust and Optimal Control*. Prentice-Hall, Upper Saddle River, USA, 1996.

Model-based analysis of the dynamic behaviour of the wing drive line of a robotic hummingbird

S. Timmermans [1], **D. Vandepitte** [1]
[1] KU Leuven, Department of Mechanical Engineering,
Celestijnenlaan 300 B, B-3001, Heverlee, Belgium
e-mail: **siemen.timmermans@kuleuven.be**

Abstract

This paper proposes a method to investigate the influence of the drive line parameters on the performance of a flapping wing nano air vehicle. A model-based approach is developed to complement the experimental approach used in traditional flapping wing research. An adapted 1 degree of freedom mass spring damper model is used. The flapping wing aerodynamics are incorporated using quasi-steady theory. The model is validated for different load cases with experiments on a dedicated experimental set-up. A model for the drive line with an adapted wing load moving in a single degree of freedom is selected. This model is used to analyse the dynamics of the drive line. The optimal operation frequency is shown to be the natural frequency of the system. The advantage of using a resonance-supported system is proven. The model can be used to optimise efficiency by means of a sensitivity analysis of the drive line parameters. The potential of the method is demonstrated by optimising the gear ratio and the spring stiffness.

1 Introduction

A growing interest in nano air vehicles (NAVs) is seen lately both from scientific and from industrial side since they give specific advantages in certain environments. NAVs are defined in this paper as unmanned air vehicles with a total wing span around 15cm or smaller. Their small size allows flight indoors or in confined spaces which offers possibilities their bigger counterparts cannot offer. Despite their small size, these nanorobots are often equipped with sensors or a camera which allows measurements in inaccessible or poisonous areas. Practical usage in different situations imposes specific requirements on the nanorobot. The main requirements are small size, high payload capacity, long flight duration, high agility and autonomous operation[1].

Existing nano air vehicles are divided into categories based on their mechanism to generate thrust forces and forces to control the nanorobot[2]. A flapping wing nano air vehicle (FWNAV) is a special type of nanorobot developed to comply with the requirements mentioned above. This class of nanorobots copies the wing motion of some small birds and insects[3]. The wings move in a horizontal stroke plane at high frequencies to produce both the thrust force and the force to control the attitude and stability of the nanorobot. Forces produced in nature exceed the values calculated with classical aerodynamics[4]. The objective is to benefit from the mechanisms observed in nature to have the same high force generation[5, 6]. Prototypes with different sizes are being developed. The smallest FWNAVs copy insects and bumblebees like the Harvard Robobee[7, 8]. Bigger concepts are based on hummingbirds like the Aerovironment Nano Hummingbird[9] and the Purdue robotic hummingbird[10].

A dedicated drive line system needs to be developed to generate the high frequency wing motion for FW-NAVs. The drive line is subjected to high aerodynamic and inertial forces from the wing. Different drive line configurations are available.

- A first system uses a crank shaft mechanism to transfer a rotational motor motion to the high frequency back and forth flapping motion[11, 12]. The motor works continuously around its optimal point of operation. The load on the motor is however very non-linear and extra hardware is necessary to control the nanorobot stability. This system was developed for a first FWNAV prototype at the KU Leuven[13].
- Another configuration uses a direct transmission from the motor to the wing motion and the motor is driven with an alternating current[10, 14, 15]. This system reduces the complexity of the drive line and therefore the robustness of the system increases. Control can be exerted by actively adapting the motor current[16]. This system can easily be combined with a spring to support the motion. The system is currently used in the reference prototype.
- A third configuration uses a piezoelectric actuator[17]. This is often chosen for very small designs.

As the drive line is an essential part of the FWNAV, it strongly affects the final performance of the nanorobot. Careful selection and design of the drive line are important to optimise flight time, payload capacity and stability of the FWNAV. Parameters setting can be done in a purely experimental way but many time consuming and costly experiments are necessary to accomplish an optimisation. A model-based approach is often preferred to optimise the drive line of flapping wing nanorobots[10, 12, 15, 18, 19, 20, 21]. A mathematical model for the drive line provides more insight in the physical phenomena at the basis of flapping wing flight. This approach is chosen in this paper and it reveals the parameters that have a large influence on the efficient operation of the nanorobot. The model can be used in an optimisation approach or in a design tool to identify optimal values for both system and operational parameters of the drive line.

An experimental set-up is developed simultaneously for parameter identification and validation purposes. A hummingbird size set-up is chosen in this work because this size allows to easily adjust the drive line parameters in the experimental set-up.

Section 2.1 describes the physical drive line system, together with the different loads that are applied and the test set-up used in this work. Section 2.2 explains the mathematical model and the parameter identification procedure. Section 3.1 discusses the model simulation results and section 3.2 shows the advantage of the model-based approach to do a dynamic analysis of the drive line operational and system parameters.

2 Materials and methods

2.1 Flapping wing drive line

2.1.1 Wing kinematics

In order to generate the necessary forces to keep the flapping wing nanorobot in the air, the small wings have to make a very fast reciprocating motion. When looking at the wing motion of insects and small birds, two main motion components are identified: a horizontal motion where the wing glides through the air, called the wing stroke motion, and a rotation of the wing around an axis in the wing in order to obtain an optimum inclination angle relative to the local air stream, called the wing pitch motion. When mimicking small birds and insects, the two main wing motions are copied mechanically (shown in figure 1).

The wing stroke motion (indicated in figure 1 on the left) is the main component in flapping wing nanorobots. It is often assumed to be sinusoidal ([15, 21]) and can be characterised by an amplitude ϕ_{max} and a frequency *f*. The amplitude of the motion is a value between $0°$ and $90°$. The maximum amplitude is physically limited by system design. The frequency is a design parameter of the system. The useful frequency range for flapping is taken to be in the interval from 16Hz to 26Hz. This range is based on the physical characteristics of the wings that are used in the reference prototype and most experiments are done in this range.

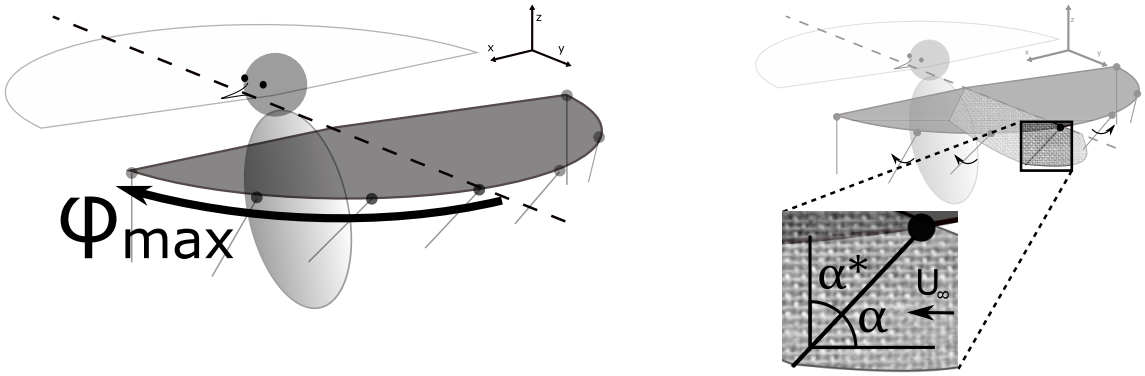


Figure 1: Illustration of the wing motion in flapping wing nanorobots. Left figure shows the wing stroke motion. Right figure shows the wing pitch motion.

The wing pitch motion (indicated in the right figure with small arrows) is not actuated in most flapping wing nanorobots. The wing is free to rotate as a result of the aerodynamic forces acting on the wing and inertial forces of the wing on the one hand and restoring forces from an elastic element on the other hand. The value of the wing pitch angle during the major portion of the wing stroke cycle is an important design parameter. A stopper element imposes this maximum wing pitch angle, further called the inclination angle α (see right in figure).

2.1.2 Oscillating drive system

The wing stroke motion is actively driven in this work using a direct drive system. A spring is added to the system to support the motion and to store elastic energy. Figure 2 shows a general scheme of a direct drive system.

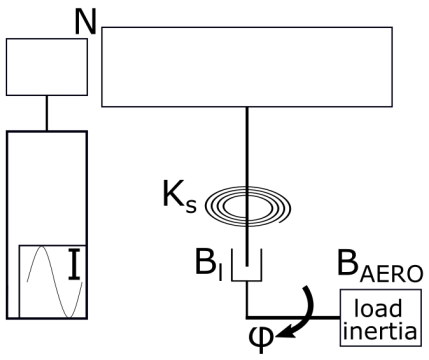


Figure 2: Adapted mass spring damper model for the drive line of flapping wing nanorobots.

The drive line is modelled as a discrete mass spring damper system. The system is driven by a sinusoidal current through a DC motor providing the input torque. The main contribution to the total system inertia comes from an oscillating load that is fixed at the end of the drive line (load specified in section 2.1.3). A gear transmission drives the load. A spring supports the oscillating motion. The main contribution to the damping comes from the aerodynamic drag on the load and from friction in the system. The output of the system is the amplitude of the load oscillations.

The wing pitch motion is not actuated in the set-up.

2.1.3 Oscillating load

Three types of loads are attached to the oscillating drive line system in this work: inertia beams (load 1 in figure 3), wings moving with two active degrees of freedom (load 2 in figure 3) and wings with one active degree of freedom and one non-active (load 3 in figure 3). The difference between the latter two load types originates in the way the wings are attached to the oscillating drive line (discussed in the last paragraph of this section).

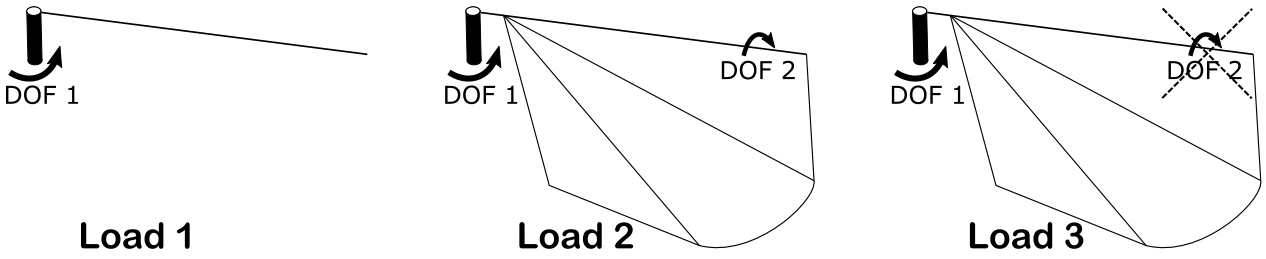


Figure 3: Different load configurations used in this work.

The inertia beams are a bundle of tubular bars that are mounted at the end of the wing drive line. Their rotational moment of inertia is chosen in order to be able to conduct experiments in the frequency range which is specified. The different bundles differ in length and thus in rotational moment of inertia. They have negligible aerodynamic resistance. The specifications of the inertia beams are given in table 1. J is the rotational moment of inertia of the inertia beams and L is the length of the inertia beam. The calculated natural frequency f_0 of the beams in the reference set-up is also added.

Inertia 1	L = 80mm	J = 2.82e-07	$f_0 = 21.24$Hz
Inertia 2	L = 75mm	J = 2.37e-07	$f_0 = 22.16$Hz
Inertia 3	L = 68mm	J = 2.03e-07	$f_0 = 22.95$Hz

Table 1: Inertia beam properties.

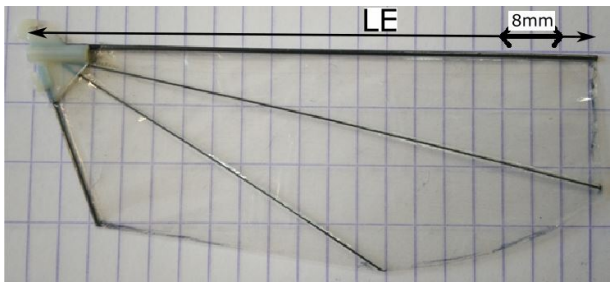


Figure 4: Wing shape and location of wing veins (example wing 1).

Every wing has the same shape (figure 4). Wing variants differ only in size and stiffness. A wing is made of carbon fibre composite beams that are connected at the base of the wing, called the wing root. The structure is both light and stiff. The membrane that runs over the beams is Mylar. Wing parameters are given in table 2 and the wing size is characterised by the length of its leading edge (LE). Wings with the annotation stiff are fabricated with stiff carbon beams. The other wings are more flexible with different diameter beams. The calculated natural frequency f_0 of the wings in the reference set-up is added. The higher natural frequency for wing 1 (marked with star) is the result of a reduced wing weight because of a change in the fabrication procedure of the wing.

For the third load type, the wing inclination angle is fixed at a value of $90°$. This fixes one degree of freedom of the flapping wing system. The wing only generates aerodynamic drag and no vertical thrust force is generated as a result of the $90°$ inclination angle.

Wing 1	LE = 73.5mm	J = 2.33e-07	-	$f_0 = 22.25$Hz*
Wing 2	LE = 68.4mm	J = 2.95e-07	-	$f_0 = 21.00$Hz
Wing 3	LE = 63.3mm	J = 2.87e-07	-	$f_0 = 21.14$Hz
Wing 4	LE = 63.3mm	J = 3.64e-07	Stiff	$f_0 = 19.81$Hz
Wing 5	LE = 60.0mm	J = 3.40e-07	Stiff	$f_0 = 20.21$Hz

Table 2: Wing properties.

2.1.4 Experimental set-up

A set-up is used to identify model parameters and to validate model results. The set-up uses an exact copy of the mechanical wing drive line system of the flapping wing reference prototype. Conclusions drawn with the modelling approach can therefore be extrapolated without adaptation. The drive line in the set-up with drive electronics, sensors and measurement electronics is presented in figure 5.

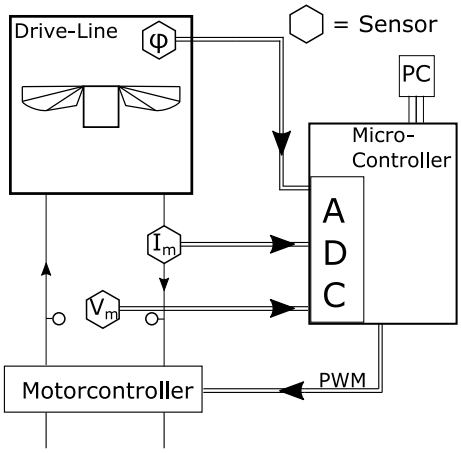


Figure 5: Set-up with location of sensors, drive electronics and microcontroller.

The set-up is controlled with an NRF52 microcontroller and sensors are read with the same microcontroller. The Nordic development board is used. This allows quick adaptation of the sensor configuration and easy programming of the actuation electronics. The motor is driven with the PmodHB3 low current bridge module. A PWM signal is used to control the motor current. The current is measured instantaneously with a hall effect AC current sensor, type L18P003S05. The range of the sensor is $\pm$3A and an analog output voltage is directly read by the analog to digital converter (ADC) on the microcontroller. With a resolution of 14 bits for the ADC, this gives a theoretical accuracy that is smaller than 1μA. The current is measured in a series configuration with the motor, immediately in front of the motor terminals. The current measurement results are validated using another current sensor (type ACS712). The voltage is measured instantaneously over the motor terminals. This is done directly with the ADC inputs of the microcontroller. Results are validated with a scope. The stroke angle is measured instantaneously with a hall-based rotary magnetic position sensor, type AS5600. An analog output voltage is applied directly to the 14-bit ADC of the microcontroller which gives a high accuracy. A small circular diametric magnet is mounted on the stroke axis. Results are validated using a slow motion camera. Time is measured instantaneously with the micro-controller 16MHz clock and synchronised with the different measurements. This allows easy data processing. The flapping frequency is calculated from the measured time and validated using a stroboscope.

2.2 Dynamic modelling approach

2.2.1 Mathematical model formulation

The mathematical model used in this paper is state of the art in the literature[20]. The expression for a mass spring damper system is combined with the DC motor equation. The gear transmission is added and the terms are rearranged into the expression for an adapted mass spring damper system (1). The motor equation is used to calculate the voltage over the terminals (2).

$$J_s\ddot{\phi} + B_l\dot{\phi} + B_{AERO}|\dot{\phi}|\dot{\phi} + K_s\phi = Ki \tag{1}$$

$$V_m = Ri + K_eN\dot{\phi} \tag{2}$$

J_s is the total inertia of the system calculated as $J_s = J_L + J_G + N^2J_m$ with J_L the load inertia, J_G the gear inertia, J_m the motor inertia and N the gear ratio. B_l is the total linearised damping to be identified in the section on parameter identification (section 2.2.2). B_{AERO} is the aerodynamic damping calculated with the theory of quasi-steady aerodynamics as $B_{AERO} = 0.5R^4\bar{c}r_3^3\bar{C}_D(\alpha)$ where the drag coefficient is identified in the section on parameter identification. K_s is the spring stiffness. K is the projected torque constant. R is the motor resistance. K_e is the back-EMF constant. Expression 1 describes the change of the stroke angle as a function of time. The complete derivation of the mathematical expression can be found in the paper of Zhang et al.[20].

Three assumptions are applicable when using this model formulation.

- The stroke dynamics dominate the flapping wing motion and the inclination angle dynamics have a negligible influence on the stroke dynamics. The mean inclination angle is usually only taken into account when calculating the aerodynamic drag. The influence of this assumption is studied by adapting the drive line system in order to effectively reduce the number of degrees of freedom to one in certain experiments (see section 2.1.3, use load type 3).
- Quasi-steady theory can be used to describe the drag coefficient. The unsteady phenomena that occur in flapping flight are not captured with this expression. This work tries to cope with this limitation by identifying the drag coefficient using an experimental approach (see section 2.2.2).
- The stroke angle varies in a sinusoidal way. Fitting of the experimentally measured data with a sine function shows the motion is indeed sinusoidal (see figure 6). This conclusion is consistent in all experiments.

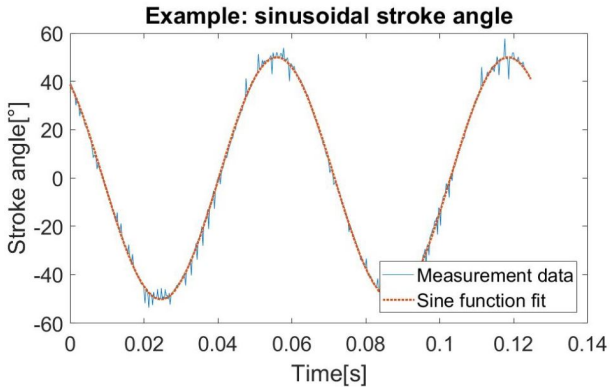


Figure 6: Validation of the sinusoidal stroke angle assumption.

The mathematical expression is solved using matlab Simulink. Experimental inputs are measured and extracted from the data. These inputs are then fitted with a sine function and used by Simulink.

2.2.2 Parameter identification

The numerical values for the model parameters are needed in order to do the simulations. The quality of the model simulations depend on the accuracy of the parameters that are used. Two types of parameters are used in the model: parameters that can be calculated from the respective datasheets and analytical expressions on the one hand and parameters for which no easy calculation procedure exists on the other hand. For this last type of parameters, an identification procedure is followed.

The motor is a 2.6g and 7mm brushless DC motor. Different versions of this motor are tested in a simplified test set-up and the parameters of the datasheet are validated. No further updating is required. The motor used in the experiments has a terminal resistance of 1.4Ω, a torque constant of 0.81Nmm/A and a rotor inertia of 0.5gcm^2. The gear transmission is custom made for the set-up. The gear ratio can be varied in the test set-up if necessary. The springs are tested over the entire operation region for linearity and accuracy of the spring constant. The value of the datasheet can be used without further updating. The aerodynamic damping is calculated using a quasi-steady aerodynamic model. The main parameter that remains unknown in the expression is the drag coefficient. This parameter has to be identified using the procedure below. Also the total linear damping and the total inertia of the system are experimentally identified.

This paragraph describes the procedure to identify the missing parameters. One frequency sweep experiment with constant current amplitude input is sufficient. Constant current amplitude means a constant torque is applied to the drive line. The drive line is actuated for 5 seconds at every frequency in the frequency range. Five seconds are necessary to eliminate the effects of possible transients. The natural frequency can then be defined easily from the experiment data and the total inertia can be calculated. The same constant input is applied to the mathematical model. An estimated value is used as starting point for the parameters that still have to be identified. The damping coefficient is updated, both the total linear damping and via the drag coefficient, to make the simulations match the experimental data and this way the last parameters are identified.

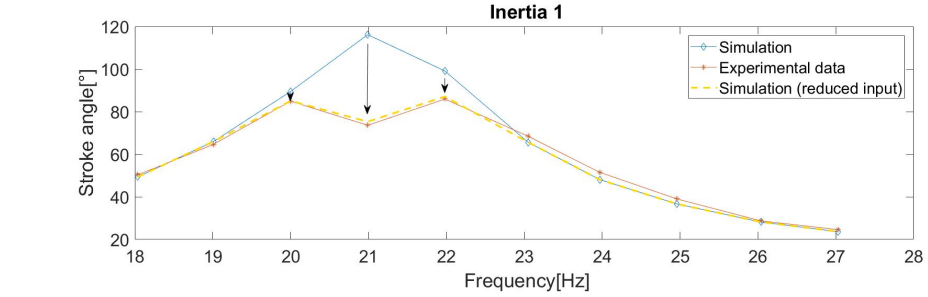
3 Results

3.1 Model verification

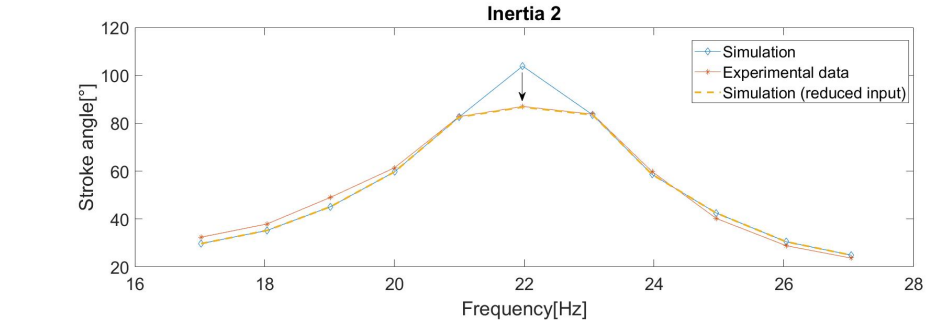
The three types of loads are applied to the experimental set-up and the same frequency sweep experiment is done as described in section 2.2.2. The results of experiments and simulations are compared in the next sections for the different load types.

3.1.1 Load 1: inertia beam

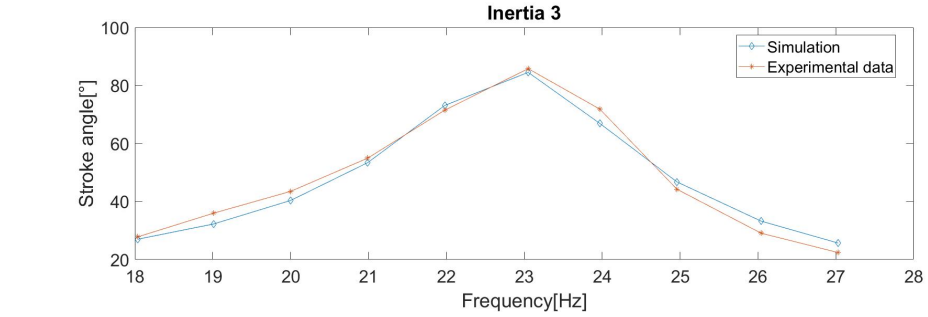
The model parameter identification (section 2.2.2) is done once for each inertia. The comparison between the experimental frequency sweep and the inertia beam model simulations is shown in figure 7. The model accurately predicts the stroke angle in the entire frequency range. The accuracy of the results is similar for the different inertia beams. A peak in amplitude is identified in the plots on the frequency matching the calculated natural frequency of table 1. The small linear frictional damping present in the drive line and the absence of aerodynamic damping cause an articulated peak in the figures. In figures 7a) and 7b), the amplitude of the input current had to be artificially reduced in order not to damage the set-up. To have a good comparison, also the simulated input current was reduced. In reality, the peak amplitude of the frequency sweep will be even more pronounced which is indicated on the figures by doing the simulation without reducing the input current.



a)



b)



c)

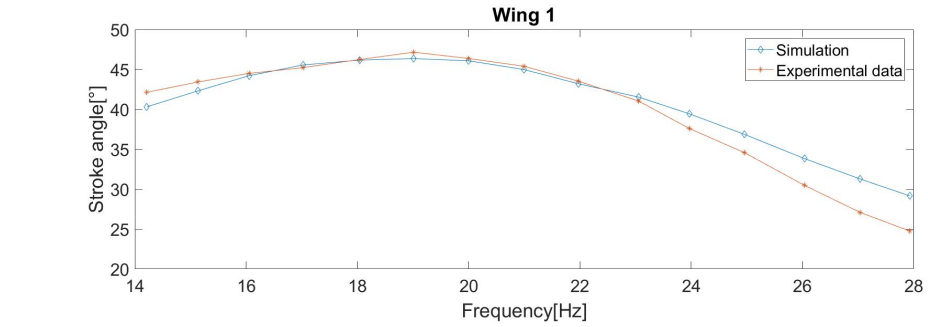
Figure 7: Constant input frequency sweep, comparison between simulations and experimental data for load type 1 (inertia beams).

3.1.2 Load 2: wing moving with two active degrees of freedom

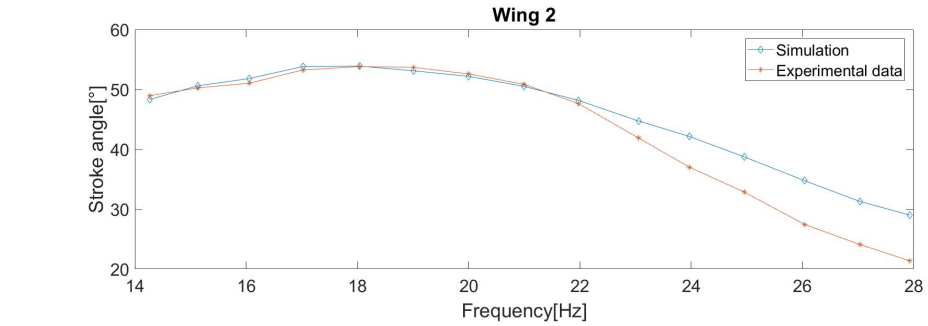
The goal in this section is to obtain a model for a wing that is free to move in its two degrees of freedom, generating vertical thrust forces. Wing 1, wing 2 and wing 3 are used in this section. The wing configuration is the result of an experimental optimisation process and flexibility is present in the wing. The model parameter identification (section 2.2.2) is done once for each wing. The comparison between the experimental frequency sweep and the resulting model simulations is shown in figure 8. The model is able to predict the stroke angle in the frequency range close to the peak frequency. A peak amplitude is identified at a frequency that is higher than the calculated natural frequency (table 2). The peak is less pronounced in these figures compared to the previous figures. This is explained by the large amount of aerodynamic damping caused by the flapping wing.

3.1.3 Load 3: wing moving with 1 active degree of freedom

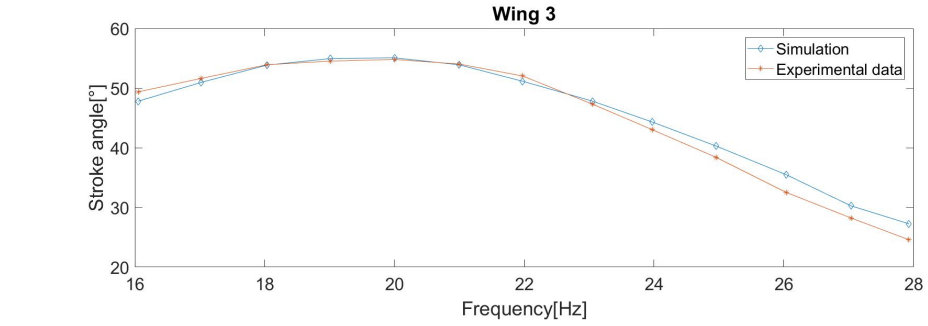
A model for load 3 is developed in this paragraph. Wing 4 and 5 are used and their angle of attack is fixed. The model parameter identification (section 2.2.2) is done once for each wing. The comparison between the experimental frequency sweep and the resulting model simulations is given in figure 9. The model predicts



a)



b)



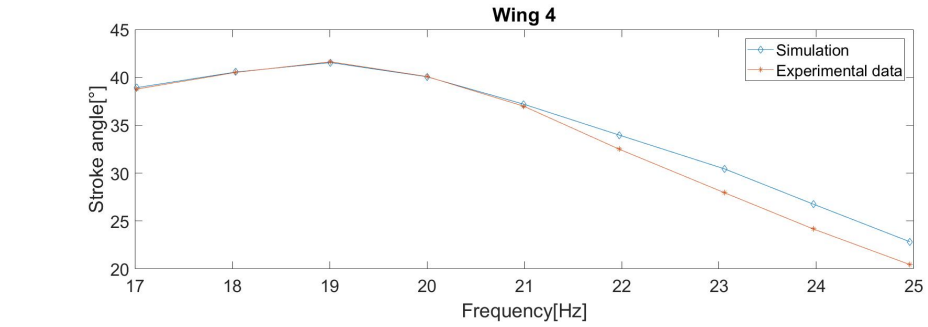
c)

Figure 8: Constant input frequency sweep, comparison between simulations and experimental data for load type 2 (2 DOF wings).

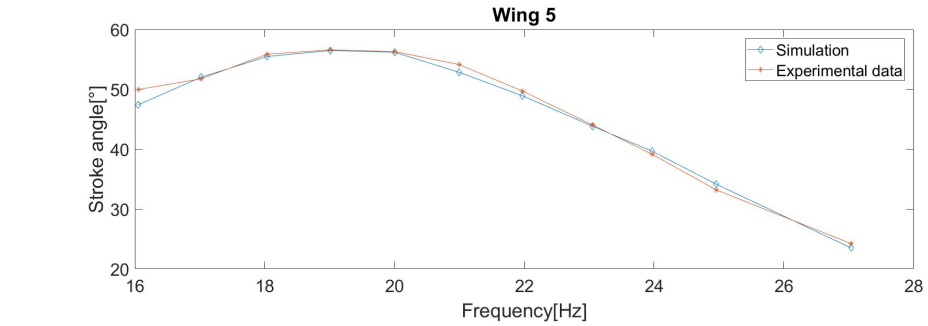
the stroke angle well in the entire frequency range. The accuracy of the results is similar for both wings and comparable to the accuracy obtained with the inertia beams. A peak amplitude is again identified at a frequency that is higher than the calculated natural frequency (table 2). The aerodynamic damping is maximal in this load type because the wing inclination is fixed at $90°$ which maximises the generated drag force.

3.1.4 Result discussion

The best model accuracy is obtained for the first load type (figure 7). The model predicts the stroke angle in the entire frequency range. Only small differences in absolute value are observed between the model simulations and the experimental data. The biggest differences between the plots of simulated data and experimental data are observed for load type 2 with two degrees of freedom (wings 1, 2 and 3, figure 8). The numerical error made by the simulations compared to the experiments is reduced when using the model for load type 3 which has a single degree of freedom (wing 4 and 5, figure 9). The observed numerical errors can be explained by looking back at the assumptions made in section 2.2.1. None of the assumptions apply to the case with the first load type. This explains the accuracy of the fit and small differences are mainly caused



a)



b)

Figure 9: Constant input frequency sweep, comparison between simulations and experimental data for load type 3 (1 DOF wings).

by experiment variability and measurement imperfections. Besides a larger absolute error in the second load type, the error also increases for a bigger wing. This indicates that an important source of modelling errors is in the one degree of freedom approximation used in the model. Also the influence of the increasing flexibility with increasing wing size can play a role in these errors. A second observation for this load type is that the numerical error increases when the frequency of operation increases above the peak amplitude frequency. This indicates that the assumption of quasi-steady aerodynamics becomes an important source of modelling errors in this frequency range. The contribution of the wing pitch motion to the generated forces relative to the wing stroke motion increases at increasing frequency (and resulting low stroke amplitude). The forces generated during the wing pitch motion are not taken into account with the quasi-steady approximation so the error becomes large in this regime. The principal sources of modelling errors are eliminated (second degree of freedom blocked, reduced flexibility of the wing and absence of wing pitch motion) when using the third load type which explains the increased accuracy.

Based on the accuracy considerations, it seems that the model for the first load type is preferred for further analysis. An oscillating inertia beam serves no practical use in flapping wing nanorobots as the aerodynamic forces produced by the inertia beam are negligible but the model can be used to do a sensitivity analysis of the drive line parameters. The relative influence of the parameters on the performance helps optimising the drive line design. Conclusions drawn with this model about absolute power consumption or efficiency of the flapping wing nanorobot are meaningless in the absence of aerodynamic damping. The drive line model can be seen as a validation tool for the rest of the modelling approach because the drive line remains unchanged for the different load types. The model for the regular flapping wing can be used to do a sensitivity analysis of the model parameters, to optimise the drive line system and in a design tool for flapping wing robots. The model describes the set-up used in the reference prototype so conclusions about power consumption or efficiency are meaningful. Quantitative results are only valid in a small range around the normal point of operation because of the decreasing accuracy. The results further away from this point can be used but they have to be interpreted more qualitatively. To overcome this issue, it makes sense to do the analysis with the third load type. Aerodynamic effects are present in this case, in contrast to the first load case, which increases

the reliability of the results. A sensitivity analysis can be done with this model focusing on the optimisation of the drive line system.

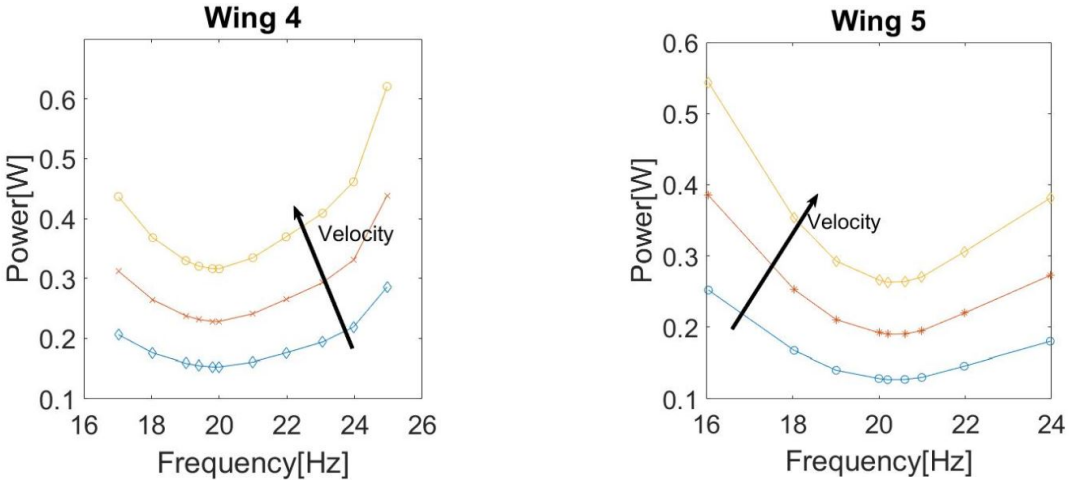
3.2 Dynamic analysis drive line

The dynamic analysis of the drive line is done using the model of section 3.1.3 (load type 3). A good trade-off between accuracy of the fit and usefulness of the conclusions is obtained and results can be translated easily to a flapping wing nanorobot prototype.

3.2.1 Operational frequency

Two frequencies are generally considered when doing a dynamic analysis of an oscillating drive line: the peak frequency and the natural frequency. The peak frequency is the frequency that maximises the amplitude of the stroke angle and is already mentioned in section 3.1. The natural frequency is calculated as the ratio of the total inertia over the spring stiffness and is a system characteristic (calculated in table 1 and 2). The peak frequency is lower than the natural frequency in strongly damped systems as can be seen on figure 8 and figure 9. It is important to decide at which frequency the system needs to be tuned to minimise energy consumption.

Zhang et al.[21] demonstrate that the force generated by the wing depends strongly on the amplitude of the velocity of the wing aerodynamic centre. In order to compare the energy consumption for different flapping frequencies in an objective way, the amplitude of the velocity of the wing needs to be constant for the entire frequency range that is tested. The optimal operation frequency for a chosen wing configuration can be identified by studying the electrical input power need for a chosen value of the wing velocity. Figure 10a) shows the input power for curves of the same velocity for wing 4. Figure 10b) shows the input power for curves of the same velocity for wing 5. The required input power is always minimum at the respective natural frequency. The same conclusion was obtained from experimental data (not shown).



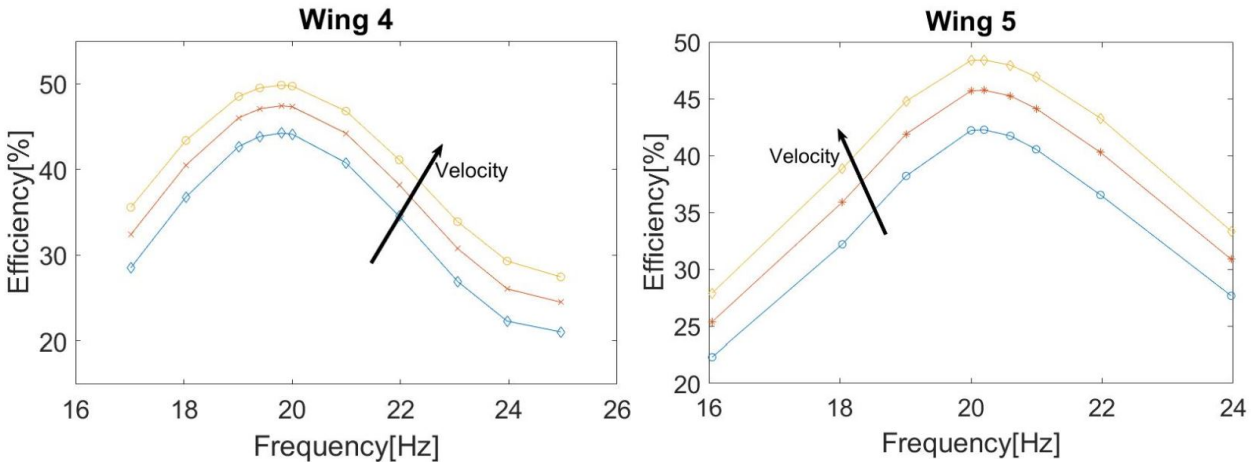
a) b)

Figure 10: Input power as a function of frequency and wing velocity.

3.2.2 Efficiency

When doing an optimisation of the drive line parameters for a particular wing, an indicator of efficiency is used for comparison. Efficiency of flapping wing nanorobots is defined as the ratio of the useful power from

the generated force of the wings over the input power at the motor terminals. The useful power generated by the wings is calculated as the total aerodynamic torque times the wing angular velocity. The input power is calculated using the motor equation (expression 2). Plotting this parameter for the same velocities as above leads to the same conclusion.



a) b)

Figure 11: Efficiency as a function of frequency and wing velocity.

3.2.3 Torque considerations

The validated model is used to demonstrate the advantage of adding a spring to the drive system for a system driven at its natural frequency. The total torque provided by the motor is consumed in the system by different physical mechanisms. The different torque contributions are shown for wing 4 at its natural frequency.

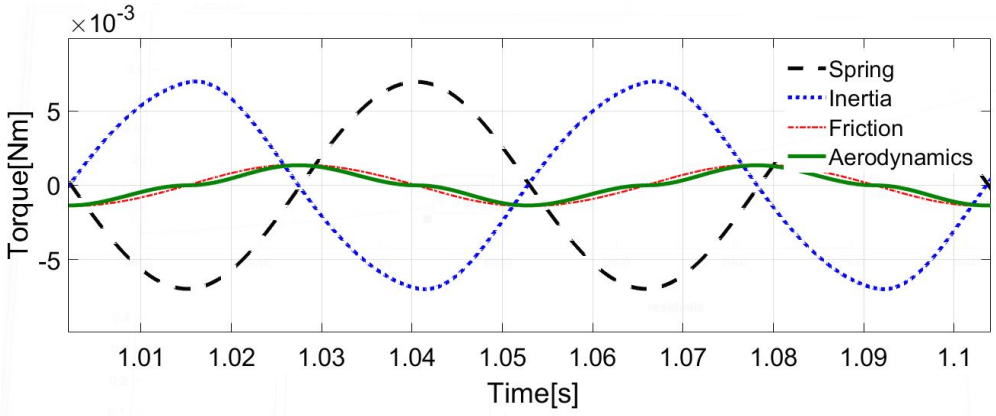


Figure 12: The different torque contributions in a flapping wing system.

For the wing used in the simulation, the inertial torque is substantially higher than the damping torque. Adding a spring to the system and tuning the system to the natural frequency cancels out the inertial torque. This clearly indicates the advantage of using a resonance-supported system. The advantage fades out when flapping at an off-resonance frequency, which explains the results shown on the power and efficiency plots in the previous sections. Careful tuning of the flapping frequency is necessary.

3.2.4 Sensitivity analysis

Sensitivity analysis is a useful method in a general optimisation approach to study the parameters in the drive line. It identifies the parameters with the largest influence on the performance which helps to make better design decisions. The drive line model is a powerful tool for sensitivity analysis. The validated model simulates the drive line behaviour without the need for extensive experimental testing. An optimisation of the efficiency is the objective in this work. The approach is demonstrated for the gear ratio and the spring stiffness. A similar approach can be followed for every parameter to achieve a detailed analysis of the entire drive line. An influence of the wing velocity on the efficiency is seen in figure 11. The different simulations are executed for the same wing velocity amplitude to eliminate this effect.

The first analysis studies the gear ratio N and the other parameters are kept constant. These parameters add an extra constraint on the optimisation of the system and it is not possible to draw conclusions about a general optimum. It is however possible to study the relative influence of a parameter in the given system. A change of the gear ratio affects the apparent rotational inertia of the motor. The natural frequency changes accordingly and the efficiency has to be studied when flapping at the adapted natural frequency to have a meaningful comparison between the different configurations. The result is shown in figure 13. Only discrete steps in the gear ratio are feasible because of the physical constraints of the system.

A final conclusion can only be drawn if the motor is able to handle the torque required with this gear ratio, which is indeed verified here. A gear ratio close to 13 is therefore recommended as a significant efficiency gain can be obtained, on the condition that other parameters remain unchanged. If the precise setting of the gear ratio would be infeasible because of physical constraints of the system, a gear ratio in the range of 10 to 15 is still acceptable without detrimental effects on the efficiency.

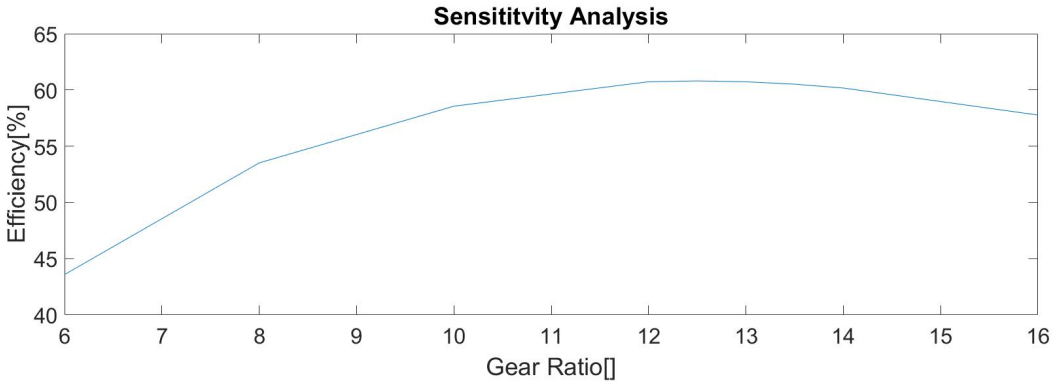


Figure 13: Sensitivity of the drive line efficiency to the gear ratio.

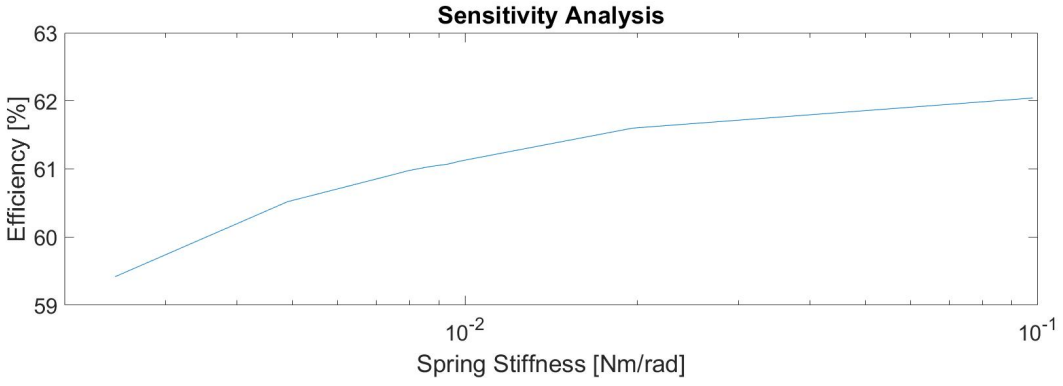


Figure 14: Sensitivity of the drive line efficiency to the spring stiffness.

A similar approach is followed to study the influence of spring stiffness on efficiency. Again the oscillating wing is simulated at its adapted natural frequency and the wing velocity is kept constant between the different experiments in a series. Figure 14 summarises the results in a wide frequency range.

Comparison of the absolute values of the two figures shows that the gear ratio has more effect than the spring stiffness. This is an interesting conclusion when designing flapping wing drive lines.

4 Conclusion

This paper describes a method to study the drive line of a flapping wing nano air vehicle based on a mathematical model. The model is used for the development and optimisation of the flapping wing drive line. The physical drive line is described using the expression for an adapted mass spring damper system. The expression incorporates the load attached to the drive line. The motor is taken into account using the DC motor equation. Several load types are studied in this work: inertia beams, wings allowed to move in one degree of freedom and wings allowed to move in the usual two degrees of freedom characteristic to flapping wing nanorobots. The drive line behaviour is simulated using the model for the different load cases and experimentally validated. Afterwards the model is used to study the drive line dynamics and in an optimisation approach.

Despite some numerical differences between simulation results and experiments, the model for the real wing can be used for optimisation purposes and as a design tool on the condition that simulations are done close to the nominal working point. The model for a one degree of freedom wing allows to draw conclusions in a much broader working domain and to transfer these conclusions to the actual nanorobot drive line.

The model is used to confirm that the most efficient operational frequency is the natural frequency of the drive line system. The advantages of a spring supported system when flapping at the natural frequency are shown by means of a study of the torques present in the drive line. An optimisation approach based on a sensitivity analysis is proposed, maximising the efficiency of the system. This is demonstrated for two system parameters, showing the potential of a model-based approach for optimisation purposes.

Acknowledgements

The authors gratefully acknowledge the financial support of FWO-Vlaanderen (project G0B55.13).

References

[1] Wilkins, P., “Insect-like Flapping, the propulsion of micro air vehicles,” *Annex of PhD Dissertation: Some Unsteady Aerodynamics Relevant to Insect-inspired Flapping-wing Micro Air Vehicles*, 2008, pp. 391–403.

[2] Petricca, L., Ohlckers, P., and Grinde, C., “Micro- and nano-air vehicles: State of the art,” *International Journal of Aerospace Engineering*, Vol. 2011, 2011.

[3] Hedrick, T. L., Tobalske, B. W., Ros, I. G., Warrick, D. R., and Biewener, a. a., “Morphological and kinematic basis of the hummingbird flight stroke: scaling of flight muscle transmission ratio,” *Proceedings of the Royal Society B: Biological Sciences*, Vol. 279, No. 1735, 2012, pp. 1986–1992.

[4] Ellington, C. P., van den Berg, C., Willmott, A. P., Thomas, A. L. R., Willmott, P., and Thomas, A. L. R., “Leading edge vortices in insect flight,” *Nature*, Vol. 384, 1996, pp. 626–630.

[5] Weis-fogh, T., “Energetics of hovering flight in hummingbirds and in drosophila,” *Journal of Experimental Biology*, 1972, pp. 79–104.

[6] Madangopal, R., Khan, Z. A., and Agrawal, S. K., "Biologically Inspired Design Of Small Flapping Wing Air Vehicles Using Four-Bar Mechanisms And Quasi-steady Aerodynamics," *Journal of Mechanical Design*, Vol. 127, 2005, pp. 809–816.

[7] Teoh, Z. E., Fuller, S. B., Chirarattananon, P., Prez-Arancibia, N. O., Greenberg, J. D., and Wood, R. J., "A hovering flapping-wing microrobot with altitude control and passive upright stability," *IEEE International Conference on Intelligent Robots and Systems*, 2012, pp. 3209–3216.

[8] Wood, R., "The First Takeoff of a Biologically Inspired At-Scale Robotic Insect," *IEEE Transactions on Robotics*, Vol. 24, No. 2, 2008, pp. 341–347.

[9] Keenon, M., Klingebiel, K., Won, H., and Andriukov, A., "Development of the nano hummingbird: A tailless flapping wing micro air vehicle," *Proc. 50th AIAA Aerosp. Sci. Meeting Including New Horizons Forum Aerosp. Expo., Aerosp. Sci. Meetings*, 2012.

[10] Zhang, J., Cheng, B., Roll, J. A., Deng, X., Yao, B., and Member, S., "Direct Drive of Flapping Wings under Resonance with Instantaneous Wing Trajectory Control," *IEEE International Conference on Robotics and Automation (ICRA)*, 2013, pp. 4029–4034.

[11] Baek, S. S., Ma, K. Y., and Fearing, R. S., "Efficient resonant drive of flapping-wing robots," *2009 IEEE/RSJ International Conference on Intelligent Robots and Systems, IROS 2009*, 2009, pp. 2854–2860.

[12] Arabagi, V., Hines, L., and Sitti, M., "A simulation and design tool for a passive rotation flapping wing mechanism," *IEEE/ASME Transactions on Mechatronics*, Vol. 18, No. 2, 2013, pp. 787–798.

[13] Leys, F., Reynaerts, D., and Vandepitte, D., "Outperforming hummingbirds' load-lifting capability with a lightweight hummingbird-like flapping-wing mechanism." *Biology open*, Vol. 213, No. 5, 2016, pp. 725–734.

[14] Campolo, D., Azhar, M., Lau, G. K., and Sitti, M., "Can DC motors directly drive flapping wings at high frequency and large wing strokes?" *IEEE/ASME Transactions on Mechatronics*, Vol. 19, No. 1, 2014, pp. 109–120.

[15] Azhar, M., Campolo, D., Lau, G.-k., Hines, L., and Sitti, M., "Flapping Wings via Direct-Driving by DC Motors," *2013 IEEE International Conference on Robotics and Automation (ICRA)*, 2013, pp. 1397–1402.

[16] Timmermans, S., Leys, F., and Vandepitte, D., "Model-based Evaluation of Control Roll, Pitch, Yaw moments for a Robotic Hummingbird," *Journal of Guidance, Control, and Dynamics*, Vol. 40, No. 11, 2017, pp. 2933–2939.

[17] Jafferis, N. T., Graule, M. A., and Wood, R. J., "Non-linear resonance modeling and system design improvements for underactuated flapping-wing vehicles," *IEEE International Conference on Robotics and Automation (ICRA)*, 2016, pp. 3234–3241.

[18] Campolo, D., "Motor selection via impedance-matching for driving nonlinearly damped, resonant loads," *Mechatronics*, Vol. 20, No. 5, 2010, pp. 566 – 573.

[19] Hines, L., Campolo, D., and Sitti, M., "Liftoff of a motor-driven, flapping-wing microaerial vehicle capable of resonance," *IEEE Transactions on Robotics*, Vol. 30, No. 1, 2014, pp. 220–232.

[20] Zhang, J., Cheng, B., and Deng, X., "Instantaneous wing kinematics tracking and force control of a high-frequency flapping wing insect MAV," *Journal of Micro-Bio Robotics*, 2016, pp. 67–84.

[21] Zhang, J. and Deng, X., "Resonance Principle for the Design of Flapping Wing Micro Air Vehicles," *IEEE Transactions on Robotics*, Vol. 33, No. 1, 2017, pp. 183–197.

Focussing flexural waves for accretion removal from a beam

T.P. Waters[1], P. Harris[1], H. Mulchandani[1], I. Stothers[2]
[1] Institute of Sound and Vibration Research, University of Southampton, Southampton, UK.
e-mail: **tpw@isvr.soton.ac.uk**

[2] Ultra Electronics Precision Control Systems, St. Johns Innovation Park, Cowley Road, Cambridge, UK.

Abstract
Ice accretes onto structures such as aircraft wings and wind turbine blades during operation and must be removed cost effectively. In this paper, a low energy approach is proposed whereby flexural waves are focussed to create a shock response at a target point where the bond shear strength between the accretion and substrate is exceeded. Focussing is achieved through a chirp excitation waveform which compensates for wave dispersion. An experiment was performed on a long aluminium beam driven by a small electrodynamic shaker. Dispersion is seen to compress the chirp waveform in time as it propagates towards a chosen focal point, close to which the peak acceleration is maximum. An ice substitute (plaster), was accreted onto the beam and the input gain increased until the accretion debonded. Electrical energy consumption by the shaker was measured. This transient approach to accretion removal provides alternative amplification to resonance of the structure or actuator, and the focal point can be moved at will in real time.

1 Introduction

There are many examples of beam or plate-like structures that must be kept free from dirt, such as windows, or other accreted material including blockages in pipes, fouling of ship hulls and ice on cables and aircraft lifting surfaces. This paper is motivated particularly by the latter, where previous attempts have been made to remove ice from wing leading edges using high level shock or vibration response.

Shock induced ice removal was first proposed by Goldschmidt in 1937 [1] which led to a number of patents in the intervening decades for 'electro-impulsive' de-icing systems [2]. Such devices discharge large pulses of current through coils in close proximity to the surface. This momentarily induces Eddy currents in the metallic structure generating a large electromagnetic repulsive force, sufficient to dislodge ice. Potential drawbacks of the technology reported in the literature include structural fatigue, limited range of the actuators and electromagnetic interference with avionic systems [3]. Electro-expulsive de-icing works on a similar principle whereby current is passed through parallel conductors to generate an impulsive repelling force to deform a wing boot or erosion shield. A few such systems are now in operation for limited applications, e.g. on the horizontal stabilizer of corporate jets.

Vibration induced ice removal has not proceeded as far up the Technology Readiness Level (TRL) scale, despite concerted efforts over some decades. Most recent activity has explored the deployment of piezoelectric actuators to induce large vibration fields. Venna et al., for example, used a single piezoelectric actuator to successfully remove ice patches from a wing leading edge structure by exciting low frequency structural resonances [4],[5]. However, de-icing times were of the order of several minutes suggesting that heating of the actuator may have been a factor. Struggl et al. adopted a similar approach but with multiple piezoelectric actuators to remove ice accreted onto a wing section in an icing wind tunnel, although few details are provided [6]. Endres et al. conducted similar tests and compared the performance of their low frequency vibration based system with an electro-expulsive system, concluding that the performances of both depended on the environmental conditions such as temperature, ice thickness and position [7]. An alternative to exciting structural resonances is to drive the piezoelectric actuator at its (typically ultrasonic)

resonance frequency, as first proposed by Adachi et al [8]. They observed that frost accumulation on a plate could be suppressed ('anti-icing') by attaching a Langevin type ultrasonic actuator and driving it at resonance. Most subsequent work in this field has been conducted by researchers at Pennsylvania State University (PSU) who have concentrated their efforts on de-icing rotorcraft wings. Ramanathan et al. proposed the excitation of guided shear horizontal (SH) waves using piezoelectric plate actuators in their d15 mode to generate large shear stresses at the ice interface. Whilst found to be viable in theory, instantaneous debonding was not achieved in practice and, where de-icing did occur, heating of the actuator was deemed to have played a significant part. Palacios et al. considered SH waves for anti-icing of a plate [9]. They measured the static shear strength of ice to aluminium in the presence of ultrasonic excitation; significant reductions in shear strength were observed. Water was prevented from freezing on the plate at high voltages (>450V) but, again, thermal effects were reportedly significant. Zhu et al. compared a similar ultrasonic technique to a thermal de-icing system using the same electrical power [10]. Ultrasonic vibration successfully removed the ice after about 90s whereas the thermal system did not. The temperature of the piezoelectric actuator was not significantly elevated in this case and so removal of the ice was attributable largely to vibrational effects. In his review paper of 2014, Palacios summarises various de-icing experimental campaigns at PSU, highlights actuator bonding as a critical issue, and alludes to the potential benefits of transient as opposed to harmonic excitation.

Kalkowski et al. [11] deployed a single piezoelectric plate actuator on a long anechoically terminated beam and instantaneously debonded an ice substitute (plaster) using incident waves alone. Whilst practically more convenient to experiment on, the use of an ice substitute also precluded thermal effects. The electrical power requirements to remove the accretion were predicted reasonably accurately using a Semi Analytical Finite Element (SAFE) model of the actuator coupled to the beam.

Driving piezoelectric actuators harmonically at their resonance frequency can be problematic, as reported in [12]. Heating of the actuator causes shifts in the resonance frequency, and large stresses in the actuator itself can cause it to crack or debond from the structure. In this paper, an alternative approach is sought whereby mechanical amplification is obtained by means other than resonance of the actuator or structure.

Guided waves in beam and plate-like structures can be categorised as either dispersive or non-dispersive. Dispersive waves travel with different group velocities at different frequencies such that a broadband pulse-like disturbance will tend to spread out as it propagates along the waveguide. Conversely, if one chooses a dispersed input disturbance appropriately such that low frequencies are 'given a headstart' over high frequencies, then a large impulsive response can be obtained if all frequencies are focussed to arrive at a specified point at the same instant. In principle, the required excitation waveform can be determined by time reversal acoustics [14], as demonstrated on a beam by Francoeur et al. [15]. However, there are a number of practical difficulties to overcome in implementing time reversal, particularly in relation to the required arrays of sensors and actuators.

In this paper, an analytically derived excitation waveform is adopted that achieves a similar focussing effect. Unlike time reversal mirrors, no sensor array is required and a single actuator is sufficient. Prior knowledge of the dispersion relation is required, hence the technique is restricted in its current form to uniform plate-like and beam-like structures, the latter being the focus of this paper. Section 2 outlines the formulation of the chirp waveform for excitation of a beam, based on the derivation detailed in [16],[17], and presents example waveforms. Section 3 describes an experimental rig comprising a uniform beam excited by an electrodynamic actuator and provides experimental validation of the dispersion curve for flexural waves. In section 4, the actuator is driven with a chirp waveform to focus waves at a target point and the peak acceleration is plotted as a function of distance along the beam. In section 5, the technique is implemented at high excitation levels to remove an ice substitute positioned on the beam at the designated focal point. Conclusions are drawn in section 6.

2 The chirp waveform

A chirp signal $f(t)$ of duration T has the general form

$$f(t)=\begin{cases} F\sin\phi(t) & 0\le t\le T \\ 0 & t>T \end{cases} \tag{1}$$

where F is a constant, ϕ is the instantaneous phase, and the instantaneous circular frequency ω is given by

$$\omega(t)=\frac{\mathrm{d}\phi(t)}{\mathrm{d}t} \tag{2}$$

An expression is sought for $\omega(t)$ given prior knowledge of the wave dispersion relation such that all frequency components arrive synchronously at some focal point a distance x_f from the force at x=0. The velocity of a wave packet centred at frequency ω, is given by its group velocity,

$$c_g=\left(\frac{\mathrm{d}\left(\mathrm{Re}\{k\}\right)}{\mathrm{d}\omega}\right)^{-1} \tag{3}$$

where k is the wavenumber. At low frequencies, where the wavelength is much larger than the thickness, flexural waves in a beam are adequately described by Euler-Bernoulli theory. The wavenumber for propagating waves is real, if damping is neglected, and given by [18]

$$k=a\omega^{\frac{1}{2}} \tag{4}$$

where

$$a=\left(\frac{\rho A}{EI}\right)^{\frac{1}{4}} \tag{5}$$

In Eq. (5), E, ρ and ν are the Young's modulus, density and Poisson ratio, and A, I and h are the cross section area, second moment of area and thickness respectively. Substituting for k from Eq. (4) into Eq. (3) gives the group velocity as

$$c_g=\frac{2}{a}\omega^{\frac{1}{2}} \tag{6}$$

The time of flight (TOF) to the focal point,

$$TOF(\omega)=\frac{x_f}{c_g(\omega)} \tag{7}$$

decreases with frequency and so the instantaneous frequency of the chirp excitation must increase monotonically with time in order that lower frequencies are given a 'head start'. Denote the start frequency of the chirp by $\omega_0=\omega(0)$. Then, in order for any frequency ω to arrive at $x=x_f$ at the same instant as frequency ω_0, its launch must be delayed until time

$$t=TOF(\omega_0)-TOF(\omega)=x_f\left(\frac{1}{c_g(\omega_0)}-\frac{1}{c_g(\omega)}\right) \tag{8}$$

Substituting for the group velocity from Eq. (6),

$$t=\frac{a}{2x_f}\left(\omega_o^{-\frac{1}{2}}-\omega^{-\frac{1}{2}}\right) \tag{9}$$

Rearranging for ω gives

$$\omega(t) = \frac{1}{b_2 t^2 + b_1 t + b_0} \tag{10}$$

where $$b_2 = \frac{4}{a^2 x_f^2} \qquad b_1 = -\frac{4}{a x_f}\omega_0^{-\frac{1}{2}} \qquad b_0 = \omega_0^{-1} \tag{11}$$

The instantaneous phase is obtained by integrating the instantaneous frequency which gives

$$\phi(t) = 2\left(\frac{1}{b_1} - \frac{1}{2b_2 t + b_1}\right) \tag{12}$$

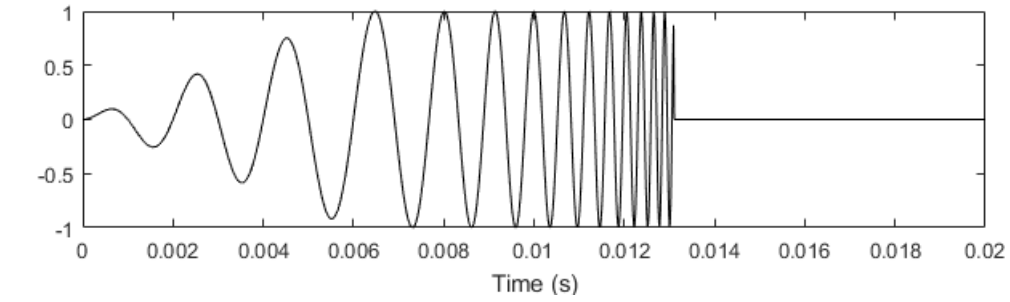
In practice, it can be beneficial to precede the chirp by a linear ramp of duration *n* cycles to reduce unwanted transients in the response, i.e.

$$f(t) = \begin{cases} \dfrac{t}{T_r} F \sin \omega_0 t & 0 \le t \le T_r \\ F \sin \phi(t) & T_r \le t \le T_r + T \\ 0 & t > T_r + T \end{cases} \tag{13}$$

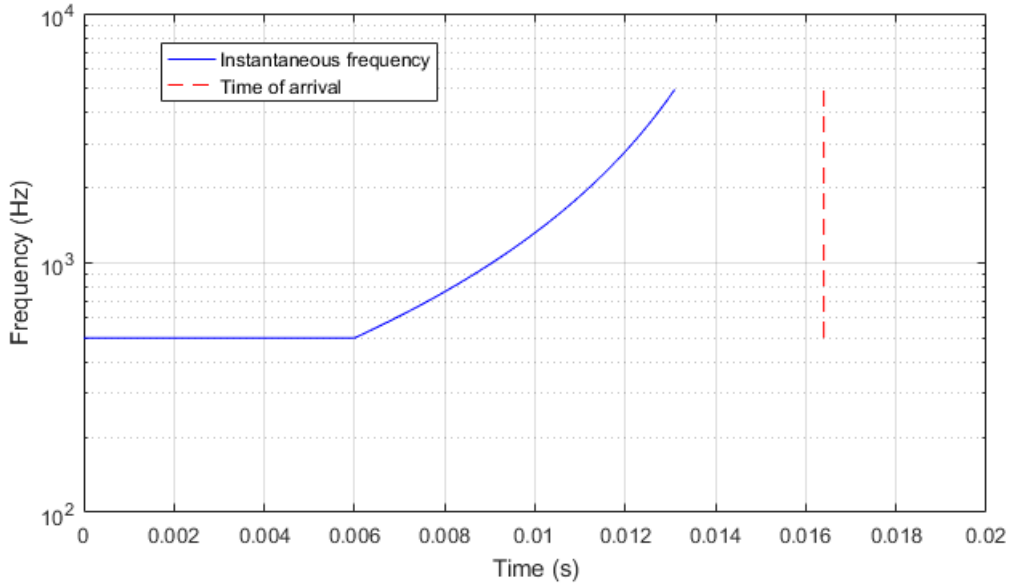
where $T_r = \dfrac{2\pi n}{\omega_0}$ is the duration of the ramp.

Figure 1(a) shows an example of a chirp waveform of bandwidth 500 Hz to 5 kHz preceded by a ramp of three cycles duration at 500Hz. The instantaneous frequency is shown in Figure 1(b) from which the time of flight to the focal point at 2.5 m can be seen to vary between about 10.5 ms at 500 Hz and 3.3 ms at 5 kHz. The difference in these times of flight determines the duration of the chirp and hence the input power. Therefore the peak response can be expected to increase with distance of the focal point from the source in the absence of attenuation [16].

Note that, whilst the various frequency components share a common arrival time shown by the dashed line in Figure 1(b), they do not necessarily all do so at a wave crest. Consequently, the peak response may not be at a maximum at the intended focal point.



(a)



(b)

Figure 1: Chirp excitation signal. (a) waveform, and (b) instantaneous frequency as a function of time.

3 Experimental set-up

A vibration experiment was conducted using the chirp waveform presented in section 2, firstly at low levels of excitation as a proof of concept and as further validation of the model presented in [16]. An aluminium beam, shown schematically in Figure 2, was suspended at several points along its 5m length. Its ends were buried in dry 'silver' sand of tapering depth to approximate anechoic terminations, giving a working section of about 3.5 m. The beam has a solid rectangular cross section of width 19.05 mm ($\frac{3}{4}$ inch) and thickness 3.175 mm ($\frac{1}{8}$ inch). The beam was excited using an electrodynamic shaker (Data Physics V4) powered by a power amplifier (Data Physics PA300E). The shaker was attached to the centreline of the beam, at about 0.5 m from the entrance to one of the sand boxes, via a short stinger. The responses at remote positions on the beam were measured using a roving miniature accelerometer (PCB 352C22). The terminal voltage across the shaker coil was measured for the purpose of normalising responses. Transient measurements were acquired using a Picoscope 3203D virtual scope and an arbitrary waveform generator; transfer function measurements for system identification purposes were conducted using a Data Physics Quattro spectrum analyser.

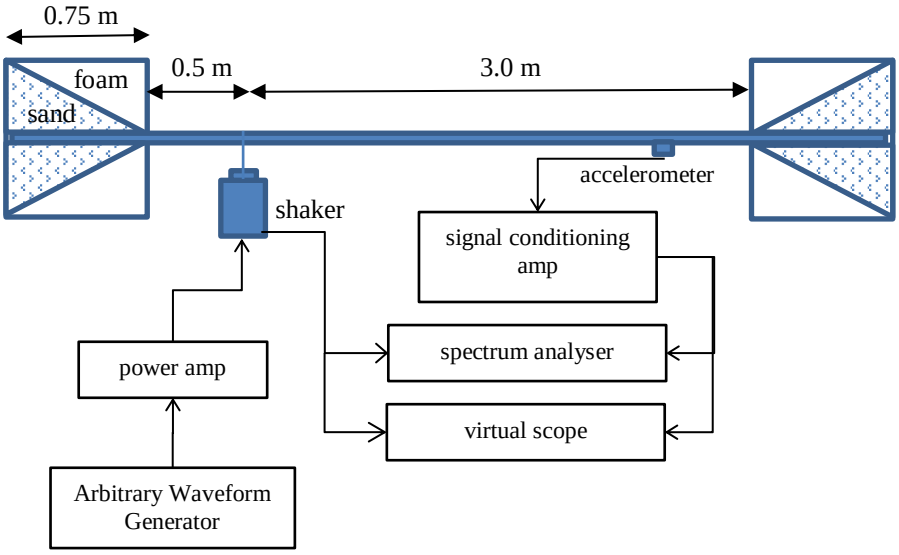


Figure 2: Schematic of experimental rig.

The dispersion curve for flexural waves along the beam was measured in the standard way using three transfer accelerances $H_1(\omega)$ to $H_3(\omega)$ that were equally spaced in the far field of the shaker and sand boxes [19]. An estimate of the wavenumber *k* is given by

$$\cos k\Delta = \tfrac{1}{2}\left(\frac{H_1(\omega)}{H_2(\omega)} + \frac{H_3(\omega)}{H_2(\omega)}\right) \tag{14}$$

where Δ is the sensor spacing, chosen to be 0.03 m. Figure 3 shows the measured dispersion curve overlaid with that expected from Euler-Bernoulli theory when nominal cross section dimensions and material properties (Young's modulus of 68 GPa and density of 2700 kgm^{-3}) are assumed. Notwithstanding modulations due to beam resonances, these parameter values give good agreement and were subsequently used in Eq. (5) to compute the chirp excitation waveform.

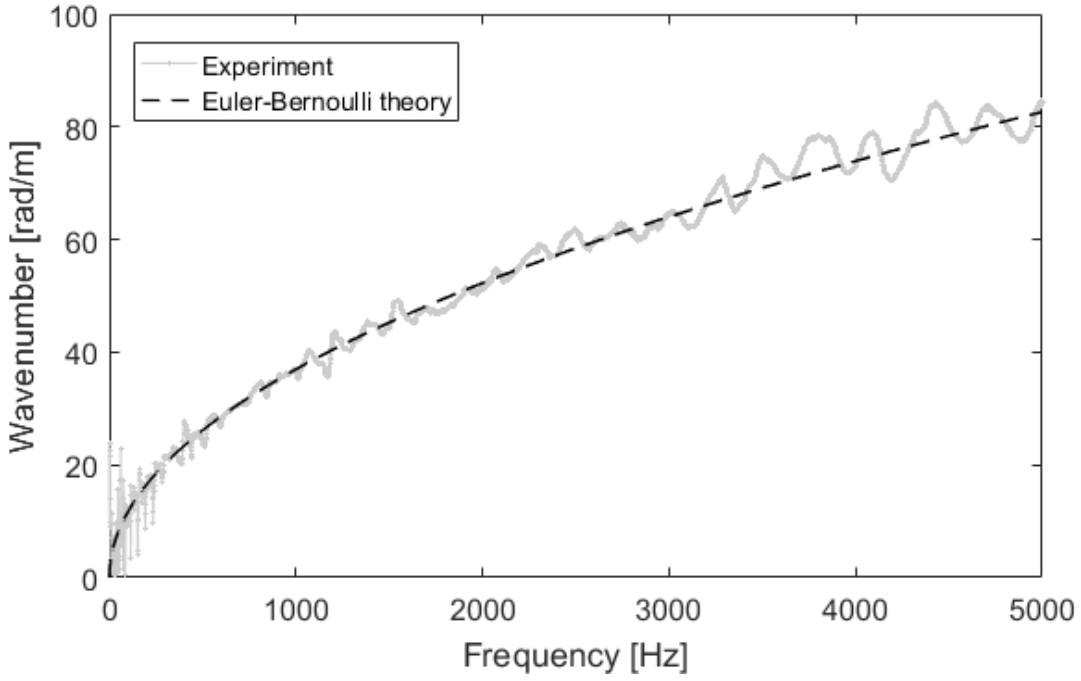


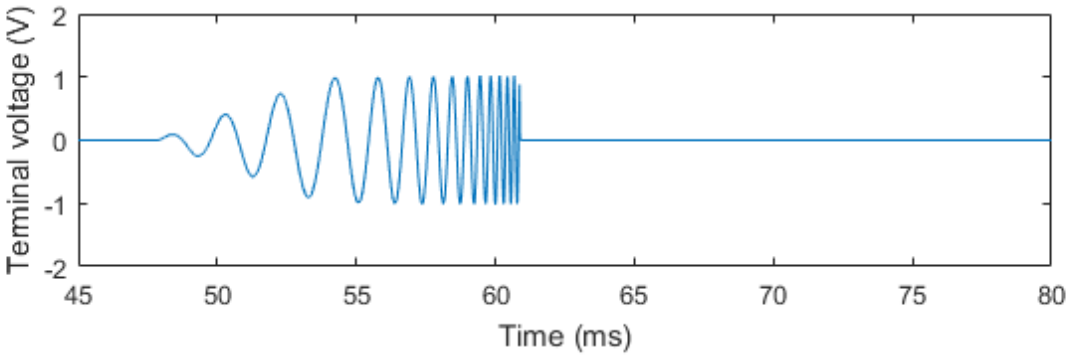
Figure 3: Measured and theoretical dispersion relations for flexural waves in an aluminium beam.

4 Wave focussing results

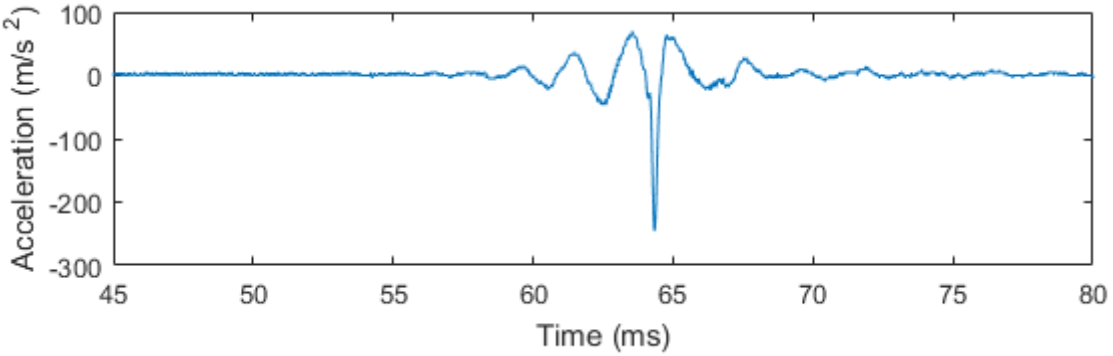
A chirp excitation was implemented, using Eq. (11) to (13), intent on producing a peak response at a nominal distance of 2.50 m from the shaker. The chirp was preceded by three cycles at the start frequency, ramped linearly in amplitude, to reduce unwanted transients from the onset of the chirp. The bandwidth selected for the chirp was from 500 Hz to 5 kHz, as illustrated in section 2, since (i) simulations suggest that a decade is sufficient for the chirp technique to be effective [16]; (ii) the impedance of the shaker is reasonably flat prior to the onset of inductance controlled behaviour; (iii) the beam is reasonably anechoic, although this is a convenience rather than a requirement; and (iv) this frequency range excluded the primary resonance of the shaker at about 100Hz, which would otherwise cause prohibitively large travel of the shaker armature when subsequently driven at high amplitudes.

The Picoscope data acquisition system was used to acquire the shaker terminal voltage and the accelerometer signal for each of ten or more chirp events and compute the mean of the maxima and minima for both channels. The accelerometer was moved along a 2.7 m length of the beam in increments of 20 mm in the vicinity of the focal point and 40mm elsewhere. At each position the largest positive and negative accelerations were noted from the response waveform together with the peak input voltage.

Figure 4 shows the time histories of the input voltage and acceleration response at a position close to the focal point. Setting aside the initial three cycles prior to the frequency sweep, it is apparent that the waveform has been compressed significantly in time due to wave dispersion in transit to the receiver position.



(a)



(b)

Figure 4: Measured time histories due to chirp excitation. (a) shaker terminal voltage, and (b) accelerometer response at 2.56 m from shaker.

Figure 5 shows the maximum and minimum accelerations normalised by peak voltage as a function of distance along the beam. Within 0.2 m of the shaker contributions from evanescent waves are evident, immediately beyond which the peak acceleration is reasonably independent of position. In this region the high frequencies, which are launched towards the end of the chirp waveform, lag behind the initially launched low frequencies, such that interference effects are limited. The response here is consistent with the peak-hold response due to a slow sine sweep excitation over the same bandwidth as the chirp. In the vicinity of the nominal focal point there is a maximum at 2.43 m, and an equally large minimum at 2.56 m. These extrema are about 2.4 times larger than the peak response in the nearfield and about 3.4 times larger than that just outside the nearfield. At the intended focal point of 2.50 m, indicated by the red markers, the positive and negative acceleration peaks are about equal in magnitude and neither is large. This discrepancy in the true location of the focal point arises because, whilst all frequency components are arranged to arrive simultaneously at 2.5 m, they are not necessarily at a wave crest when they do so. The peak stress (and velocity), however, *do* generally occur close to the intended focal point, and this is discussed further in [16]. Several smaller and broader maxima and minima are apparent.

Also shown in Figure 5 are the corresponding predictions from an electromechanical model of the shaker coupled to the beam. The model is the same as that reported in detail in [16] except that the point mass at the driving point has been reduced to 3g to represent the stinger alone since there is no force gauge in this experimental set-up. The results are in very close agreement, with some minor discrepancy in the peak at 2.7 m. This is close to the entrance of one of the sand boxes which may have given rise to a non-negligible nearfield.

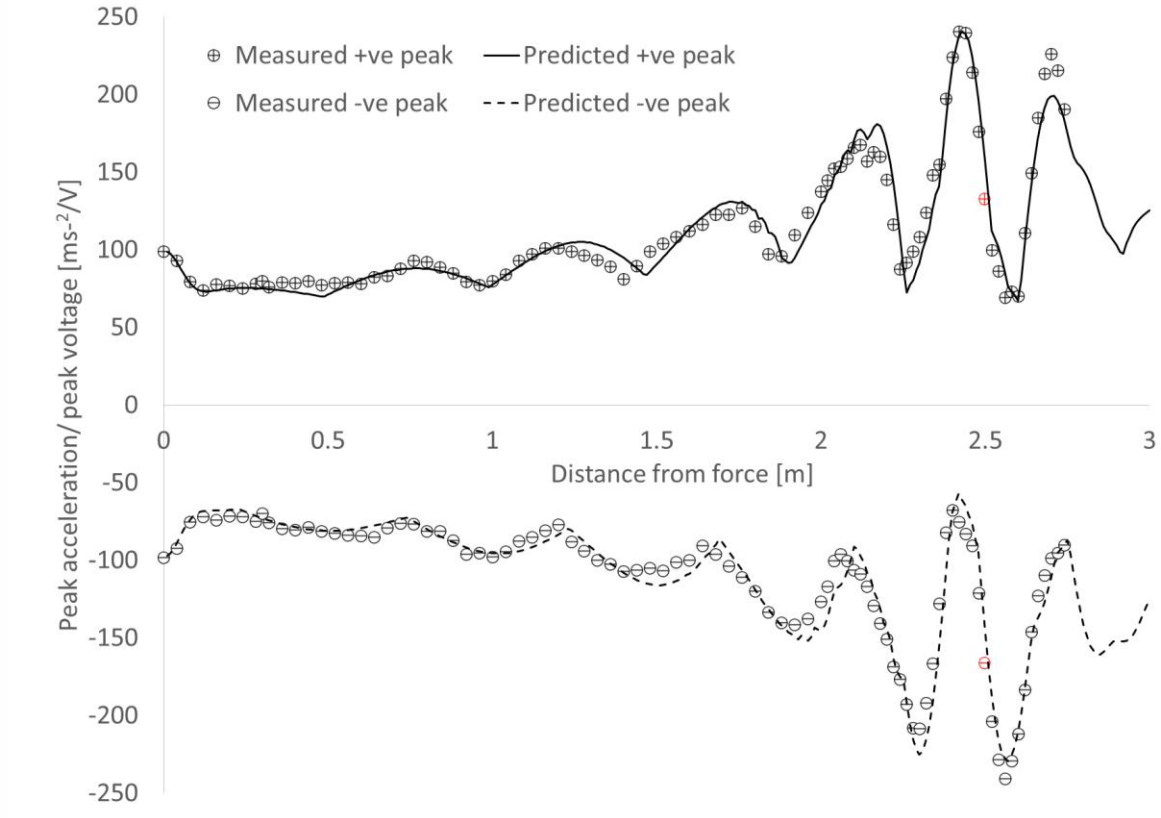


Figure 5: Peak acceleration per volt as a function of distance along beam from shaker. The red markers correspond to the intended focal point at 2.5 m.

5 Accretion removal results

The adhesion strength of ice accreted onto a substrate varies considerably depending on many factors such as the type of ice, temperature and the surface roughness of the substrate. Chu et al. summarised the outcomes of numerous experimental studies [20]. Typical values cited include 0.12MPa for rime ice, 0.41MPa for glaze ice and 1.5MPa for refrigerated ice. Due to the practical challenges of experimenting with ice an ice substitute was used in this study. Gypsum finishing plaster is reported to have a shear strength of about 0.3MPa, and its Young's modulus (3 GPa) and density (1000 kg/m^3) are not too dissimilar from ice [11]. It is therefore a convenient and cost effective alternative to hiring icing chambers and tunnels for proof of concept feasibility studies of this nature.

A single plaster specimen at a time was prepared on the beam, at the known focal point. The specimens extended across the full width of the beam (19mm) and were approximately 30-40 mm long, and of similar thickness to the beam (2-3mm). Each specimen was left to cure for a day or longer prior to conducting a decretion measurement. Plaster from the same batch was used to create a corresponding simple shear lap specimen, shown in Figure 6, by which the shear strength of each batch of plaster could be estimated statically. The aluminium substrates for the lap tests were short lengths cut from an identical beam to that used for dynamic testing. All aluminium surfaces were cleaned of oil and grease prior to plastering with a minimum of abrasion.

Decretion measurements from the long beam using transient excitation proceeded as follows. A focal point of 2.5m was chosen and the chirp waveform was generated as reported in section 2. Whilst this was shown in section 3 to result in acceleration maxima at 2.43 m and 2.56 m, the validated model predicts that the shear stress due to flexural waves does occur at the intended focal point of 2.5 m. Several chirp events were triggered manually at a particular amplifier gain, and then repeated at increasing levels of gain until the plaster 'pinged' off the beam. For these measurements, the Data Physics power amplifier was replaced with a LDS PA500 to facilitate larger electrical inputs. For each measurement, the shaker voltage and current were acquired from which the electrical power consumption over the duration of the chirp was inferred.



(a) (b) (c)

Figure 6: Simple lap shear test arrangement. (a) Schematic, (b) image of specimen, and (c) image of specimen under load.

Figure 7 shows consecutive images taken from a movie of accreted plaster being removed from the beam by means of chirp excitation. Table 1 lists the electrical input required for each of five samples together with the estimated static strength of each batch of plaster. The average power and total energy per chirp are plotted against static strength in Figure 8. There is significant variability in the electrical power required which is partially correlated to variability in the plaster batches due to factors such as water content and curing time. Other sources of variability include surface treatments of substrates and, in the case of dynamic tests, dimensions of the plaster samples. The results suggest an average power of the order of 0.1kW to remove an accretion of interfacial area 6-8 cm^2. This far exceeds typical power requirements for electro-thermal melting of ice (~4W/cm^2) quoted in reference [12]. However, the energy consumption is extremely low on account of the chirp duration being milliseconds in duration as compared to tens of seconds.



(a) (b)

(c) (d)

Figure 7: Frozen frames at the moment of accretion removal.

	Static tests	Dynamic 'chirp' tests		
Sample	Estimated shear strength (kPa)	Peak instantaneous power (W)	Average power (W)	Energy (J)
1	288	1150	253	3.31
2	125	534	122	1.60
3	368	651	152	1.99
4	199	883	202	2.65
5	103	530	122	1.60

Table 1: Summary of static and dynamic testing of plaster samples. The static strength values correspond to the largest incremented static load prior to failure of the specimen. The dynamic results correspond to the amplifier gain at which removal of the plaster sample occurred.

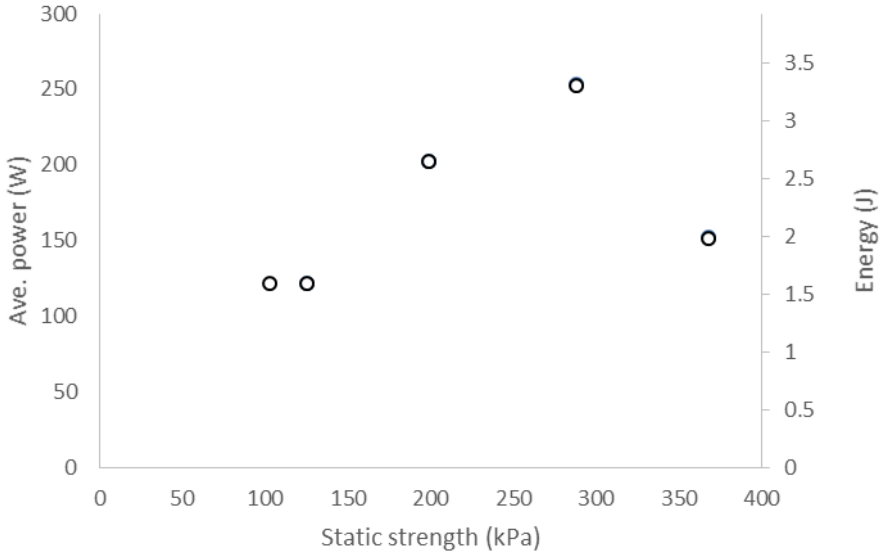


Figure 8: Electrical power and energy required for a single chirp excitation to debond plaster from beam as a function of estimated static strength.

6 Conclusions

A method has been implemented experimentally to focus flexural waves in a uniform beam using a single electrodynamic actuator. Prior knowledge of the dispersion relation is assumed in order to formulate a chirp excitation waveform that ensures that all constituent frequencies arrive synchronously at a designated position. The measured acceleration waveform is pulse-like at specific positions close to but either side of the intended focal point and up to 3.5 times larger than expected in the far field under similar broadband excitation. Measured results are in close agreement with an electromechanical model of the system. The model predicts that a similar peak in shear stress occurs, at the intended focal point, which is useful for the purpose of removing accreted material from the beam.

Small patches of plaster, with similar shear bond strength as rime ice, were accreted onto the beam at the focal point. The shaker was driven with a high amplitude chirp waveform to generate a sufficiently large peak shear stress at the location of the accretion for it to debond from the beam. The average electrical power required to invoke delamination varied from 120-250W over the five samples tested which compares unfavourably with electro-thermal de-icing requirements reported in the literature. However, delamination is almost instantaneous thereby requiring very little energy by comparison. The potential of the technique for practical applications of accretion removal is dependent on generalisation of the technique to more realistic and complex geometries.

Acknowledgements

The authors are grateful to the National Aerospace Technology Exploitation Programme (NATEP) in the UK for its financial support under grant FAC046.

References

[1] R. Goldschmidt. *Improvements in and relating to de-icing equipment, for example for aircraft*, GB patent number GB505433A (1937).

[2] Z. Goraj, *An overview of the deicing and anti-icing technologies with prospects for the future, 24th International Congress of the Aeronautical Sciences*, Yokohama, Japan (2004)

[3] G.N Labeas, I.D. Diamantakos, M.M. Sunaric, *Simulation of electroimpulse de-icing process of aircraft wings*, Journal of Aircraft, Vol. 43, No. 6, (2006), pp. 1876-1885.

[4] S. Venna, Y-J. Lin, G. Botura, *Piezoelectric transducer actuated leading edge de-icing with simultaneous shear and impulse forces*, Journal of Aircraft, Vol. 44, No. 2, AIAA (2007), pp. 509-515.

[5] S. Venna, Y-J. Lin, *Mechatronic development of self-actuating in-flight de-icing structures*, IEEE/ASME Transactions on Mechatronics, Vol. 11, No. 5, (2006) pp. 585-592.

[6] S. Struggl, J. Korak, C. Feyrer, *A basic approach for wing leading deicing by smart structures, Proceedings of SPIE, Sensors and Smart Structures Technologies for Civil, Mechanical, and Aerospace Systems*, Vol. 7981, San Diego (2011).

[7] M. Endres, H. Sommerwerk, C. Mendig, M. Sinapius, P. Horst, *Experimental study of two mechanical de-icing systems applied on a wing section tested in an icing tunnel*, CEAS Aeronautical Journal, Vol. 8, Issue 3, (2016), pp. 429-439.

[8] K. Adachi, K. Saiki, H. Sato, *Supression of frosting on a metal surface using ultrasonic vibrations, Proceedings of the IEEE Ultrasonics Symposium*, Place (1998), pp. 759-762.

[9] J.L. Palacios, H. Gao, E.C. Smith, J.L. Rose, *Ultrasonic shear wave anti-icing system for helicopter rotor blades, Proceedings of the American Helicopter Society 62nd Annual Society*, Phoenix USA (2006).

[10] Y. Zhu, J.L. Palacios, J.L. Rose, E.C. Smith, *De-icing of multi-layer composite plates using ultrasonic guided waves, 49th AIAA Structures, Structural Dynamics and Materials Conference*, Schaumburg, USA (2008).

[11] M. Kalkowski, T.P. Waters, E. Rustighi, *Delamination of surface accretions with structural waves: piezo-actuation and power requirements*, Journal of Intelligent Materials Systems and Structures, Vol. 28, Issue 11, SAGE (2017), pp. 1454-1471.

[12] J. Palacios, *A review of ultrasonic vibration for de-icing of aircraft, International Conference on Vibration and Vibro-acoustics*, China (2014).

[13] S. Ramanathan, V.V. Varadan, V.K. Varadan, *Deicing of helicopter blades using piezoelectric actuators, Proc. SPIE 3990, Smart Structures and Materials: Smart Electronics and MEMS, Newport Beach USA* (2000).

[14] M. Fink, *Time reversed acoustics*, Physics Today, Vol. 50, No. 3, (1997), pp. 34-40.

[15] D. Francoeur, A. Berry, *Time reversal of flexural waves in a beam at audible frequency*, Journal of the Acoustical Society of America, Vol. 124, No. 2, (2008), pp. 1006-1017.

[16] T.P. Waters, *A chirp excitation for focussing flexural waves*, Journal of Sound and Vibration (in press).

[17] O. Kwon, *Measurement of the wavenumber dispersion relationship in a resonant dispersive structure by signal shaping*, MSc dissertation, ISVR, University of Southampton (1995).

[18] K.F. Graff, *Wave motion in elastic solids*, Dover Publications (1975).

[19] B. Zhang, T.P. Waters, B.R. Mace, *Identifying joints from measured reflection coefficients in beam-like structures with application to a pipe support*, Mechanical Systems and Signal Processing, Vol. 24, No. 3 (2010), pp. 784-795.

[20] M.C. Chu, R.J. Scavuzzo, *Adhesive shear strength of impact ice*, AIAA Journal, Vol. 29, No. 11, AIAA (1991), pp. 1921-1926.

Non-stationary random vibration modeling and analysis: kernel versus adaptable Functional Series TAR methods

C.N. Kapsalas [1], **S.D. Fassois** [1], **J.S. Sakellariou** [1]
[1] Stochastic Mechanical Systems & Automation (SMSA) Laboratory,
University of Patras, Department of Mechanical Engineering & Aeronautics, 265 04 Patras, Greece
e-mail: **fassois@mech.upatras.gr**

Abstract
Functional Series Time-dependent AutoRegressive, FS-TAR, modeling constitutes a powerful tool for the effective representation and analysis of zero-mean non-stationary random vibration. Yet, a main difficulty pertains to the need for determining the specific functional subspaces upon which the model parameters and innovations variance are to be projected. This study focuses on kernel based versions of the models, aiming at alleviating this problem while also allowing for infinite dimensional functional subspaces. This leads to improved modeling flexibility at the expense of reduced model parsimony. A batch estimation method is presented, and is subsequently successfully assessed via its application to the modeling and analysis of a non-stationary random vibration signal measured on an operating fan. Critical comparisons with an alternative, Adaptable FS-TAR, method and certain simpler approaches are also made.

1 Introduction

The modeling and model-based analysis of non-stationary random vibration is an important and a challenging problem that has been receiving increased attention in recent years [1, 2, 3]. The available methods are broadly classified as non-parametric or parametric, with the former being based upon non-parametric representations of the vibration energy as functions of time and frequency (time-frequency distributions) and having received most of the attention. On the other hand, parametric methods are also of interest, offering various potential advantages, such as representation parsimony and accuracy.

In this study Gaussian zero-mean random vibration signals are considered, with non-stationary expressed in terms of a continuously varying with time second order moment, that is AutoCovariance Function (ACF), also implying a Power Spectral Density (PSD) dependent upon time. For such signals parametric methods are mostly based on time-dependent representations, such as Time-dependent Autoregressive Moving Average (TARMA) models [1]. A TARMA(n_a, n_c) model, with n_a, n_c designating its AR and MA orders, respectively, is of the form:

$$x[t] + \sum_{i=1}^{n_a} a_i[t] \cdot x[t-i] = e[t] + \sum_{i=1}^{n_c} c_i[t] \cdot e[t-i] \qquad e[t] \sim NID(0, \sigma_e^2[t]) \tag{1}$$

with $t = 1, \ldots, N$ designating normalized (by the sampling period) discrete time, $x[t]$ the non-stationary signal modelled, $e[t]$ an unobservable innovations (uncorrelated) signal with zero mean and Time-Varying (TV) variance $\sigma_e^2[t]$, and $a_i[t], c_i[t]$ the model's TV AR and MA parameters, respectively. NID$(\cdot, \cdot)$ stands for normally independently distributed with the indicated mean and variance. In this study the special AutoRegressive (AR) form of the model in which n_c, and thus all MA parameters are zero, is considered.

TAR (and TARMA) models may be classified according to any constraints explicitly imposed on the evolution of their parameters, that is the AR parameters and the innovations variance. They may thus be of

unstructured parameter evolution (no explicit constraints), stochastic parameter evolution (stochastic constraints), and deterministic parameter evolution (deterministic constraints) [1]. Among these, the last class, is appropriate for modeling non-stationary random vibration in the usual case where the underlying structural dynamics undergo smooth deterministic transitions, and have received significant attention. The usual form for such models is that of Functional Series Time-dependent AutoRegressive or AutoRegressive Moving Average (FS-TAR or FS-TARMA) representations, which are TAR/TARMA models with parameters and innovations variance projected upon functional subspaces, each consisting of a commonly finite number of basis functions of time; see next section and references such as [1, 4, 5, 6, 7, 8].

Yet, FS-TARMA modeling is often challenging, mainly due to the need for properly specifying the model structure, that is selecting the model order and the functional subspaces. This is conventionally accomplished via trial and error procedures using candidate model orders and basis functions along with structure selection criteria, such as the Bayesian Information Criterion (BIC) [1]. Somewhat more systematic procedures are based on genetic algorithms, backward regression [1], forward regression [9] or complex optimization schemes characterized by significant computational complexity [10]. The subclass of Adaptable FS-TARMA (AFS-TARMA) models [10] (see [11] for a related approach) has been specifically developed for overcoming this difficulty, and offers a promising approach. Yet, following the selection of a specific functional family, model estimation involves (even in the pure AR case) the optimization of non-quadratic (although, markedly, low dimensionality) problem.

The present study explores the possibility of an alternative approach, possibly alleviating the aforementioned problems, via the use of kernel FS-TAR models. In this context, following the selection of a specific functional family (in the form of a kernel function) there is no need to explicitly select specific basis functions. In fact the functional subspaces, for either the AR parameters or the innovations variance, may even be infinite dimensional [12, pp.35-36], offering the possibility of improved flexibility (arbitrary deterministic time evolutions may be accurately captured) at the price of reduced parsimony (the AR parameters and innovations variance are pointwise, that is for each time instant, specified). Kernel-TAR models may be thus thought of as a combined parametric / non-parametric representations; that is parametric in terms of the dynamics (TAR part) but non-parametric in terms of the parameter evolution. In this sense they may be – although not precisely – related to unstructured parameter evolution models, such as the Recursive AR (RAR) models [1]; for this reason a comparison with Recursive Least Squares TAR (RLS-TAR) modeling is also considered in subsection 4.2. Kernel FS-TARMA models are considered in a recent work within a time-recursive estimation context [13], while the estimation of related kernel TV models in the frequency domain is considered in [14] and of related general Linear Parameter Varying (LPV) models in [15].

The *goals* of this study are: (a) The presentation of batch method for the estimation of kernel FS-TAR models (including the AR parameters and innovations variance) based on a given data record $x[1], x[2], \ldots, x[N]$. (b) The assessment of the method via its application for the modeling and analysis of a non-stationary random vibration signal measured on a operating fan, and, (c) a critical comparison of the kernel FS-TAR method to its Adaptable FS-TAR (AFS-TAR) counterpart, as well as to the non-parametric spectrogram and the Recursive Least Squares TAR (RLS-TAR) method. The comparisons involve estimation, model parsimony versus modeling flexibility, achievable prediction accuracy, achievable spectral accuracy and resolution, and ease of use aspects.

The paper is organized as follows: Functional Series TAR (FS-TAR) models and their parametrizations are presented in section 2. The estimation of kernel FS-TAR models is addressed in section 3. The assessment of the method and comparisons to alternatives is, via an application case study, presented in section 4, while concluding remarks are summarized in section 5.

2 Functional Series TAR (FS-TAR) models and their parametrizations

FS-TAR models. Functional Series TAR models are of the form of Equation (1), with their TV parameters and innovations variance expanded upon appropriate, finite or infinite dimensional, functional subspaces

defined by proper sets of orthogonal functions:

$$\mathcal{F}_{\text{AR}} := \left\{G_{a(1)}[t], ..., G_{a(p_a)}[t]\right\} \qquad \mathcal{F}_{\sigma_e^2[t]} := \left\{G_{s(1)}[t], ..., G_{s(p_s)}[t]\right\} \tag{2}$$

with $\mathcal{F}$ designating functional subspace spanned by the specified *basis functions*, p_a, p_s the AR and innovations variance subspace dimensionalities. The TV AR parameters and the innovations variance are then expressed as:

$$a_i[t] := \sum_{j=1}^{p_a} a_{i,j} \cdot G_{a(j)}[t] \qquad \sigma_e^2[t] := \sum_{j=1}^{p_s} s_j \cdot G_{s(j)}[t] \tag{3}$$

with $a_{i,j}$ and s_j designating the corresponding *coefficients of projection*. Collecting the coefficients of projection into the vectors[1]:

$$\boldsymbol{a}_i := [a_{i,1} \dots a_{i,p_a}]_{p_a \times 1}^T \quad (i = 1, \dots, n_a) \qquad \boldsymbol{s} := [s_1 \dots s_{p_s}]_{p_s \times 1}^T \tag{4}$$

and the respective basis functions into the vectors:

$$\boldsymbol{g}_a[t] := \left[G_{a(1)}[t] \dots G_{a(p_a)}[t]\right]^T \qquad \boldsymbol{g}_s[t] := \left[G_{s(1)}[t] \dots G_{s(p_s)}[t]\right]^T \tag{5}$$

the TV model parameters (3) may be also expressed as:

$$a_i[t] = \boldsymbol{a}_i^T \cdot \boldsymbol{g}_a[t] \qquad \sigma_e^2[t] = \boldsymbol{s}^T \cdot \boldsymbol{g}_s[t] \tag{6}$$

and the FS-TAR model as:

$$x[t] + \sum_{i=1}^{n_a} \left(\boldsymbol{a}_i^T \cdot \boldsymbol{g}_a[t]\right) \cdot x[t-i] = e[t] \qquad e[t] \sim NID(0, \boldsymbol{s}^T \cdot \boldsymbol{g}_s[t]) \tag{7}$$

Note that common functional subspaces are considered in the sequel, so that $\boldsymbol{g}_a[t] \equiv \boldsymbol{g}_s[t] \equiv \boldsymbol{g}[t]$. In the considered AR case, the innovations $e[t]$ depends linearly on the AR coefficient of projection vectors $\boldsymbol{a}_i$, so that for *finite* parametrizations (finite p_a) and *pre-selected* AR order (n_a) and AR functional subspace (basis functions), Prediction Error (PE) estimation leads to a classical, Linear Least Squares (LLS) estimator. Following this, the innovations signal may be estimated and its variance coefficient of projection vector $\boldsymbol{s}$ may be obtained via a number of techniques [5].

The main issues with FS-TAR modeling pertain to properly specifying the model structure, that is selecting the model order and the functional subspace(s). As already indicated, this is conventionally accomplished via trial and error procedures using candidate model orders and basis functions along with structure selection criteria, such as the BIC [1], while more systematic procedures based on genetic algorithms, backward regression [1], or forward regression [9] principles have been also suggested.

Adaptable FS-TAR (AFS-TAR) models. This subclass of FS-TAR models, introduced in [10], aims at alleviating the functional subspace (basis functions) selection problem. The idea consists of using specific families of functions (such as decaying trigonometric functions or B-splines), with their members being directly parametrized in terms of a parameter vector $\boldsymbol{\delta} = [\boldsymbol{\delta}_a^T \; \boldsymbol{\delta}_s^T]^T$, so that for a *selected family and subspace dimensionalities* p_a, p_s, $\boldsymbol{\delta}$ (and thus the specific functions required) are *estimated* based on the available signal samples. The TV AR parameters and innovations variance are thus expressed as explicit functions of $\boldsymbol{\delta}_a$, $\boldsymbol{\delta}_s$:

$$a_i[t] = \sum_{j=1}^{p_a} a_{i,j} \cdot G_{b_a(j)}[t, \boldsymbol{\delta}_a] \qquad \sigma_e^2[t] = \sum_{j=1}^{p_s} s_j \cdot G_{b_s(j)}[t, \boldsymbol{\delta}_s] \tag{8}$$

AFS-TAR model estimation is accomplished via a Separable Nonlinear Least Squares (SNLS) type procedure that achieves simultaneous estimation of the basis functions and the coefficients of projection through

[1] Bold face lower/upper case characters designate column vector/matrix quantities, respectively. Transposition is designated by ^{T}.

a reduced dimensionality, constrained, non-quadratic optimization problem tackled via Particle Swarm Optimization (PSO) and gradient-type refinement. Details are provided in [10].

Kernel FS-TAR models. In kernel FS-TAR models the TV AR parameters and innovations variance are projected upon *potentially infinite dimensional* functional subspaces ($p_a, p_s \to \infty$) from a *pre-selected functional family*, without the need to explicitly specify the selected functions. As a consequence, the AR parameters and the innovations variance are arithmetically determined at each time instant. Evidently, the potentially infinite functional subspace dimensionality and the alleviation of the need to specify the basis functions constitute the main advantages of this subclass, which offers improved modeling flexibility at the price of reduced parsimony.

3 Estimation of kernel FS-TAR models

AR parameter estimation. The estimation problem is evidently ill-posed in the case $p_a \to \infty$, hence a regularization term involving the l_2 norm of the coefficient of projection vectors $\boldsymbol{a}_i$ is added to the standard Ordinary Least Squares cost function, thus leading to a Kernel-based Regularized Least Squares (KReLS) type cost function [16, 17]:

$$J_a := \frac{1}{2}\sum_{i=1}^{n_a} \boldsymbol{a}_i^T \boldsymbol{a}_i + \frac{\gamma}{2}\sum_{t=1}^{N} \Bigg(\underbrace{x[t] + \sum_{i=1}^{n_a} \boldsymbol{a}_i^T \cdot \boldsymbol{g}[t] \cdot x[t-i]}_{e[t]} \Bigg)^2 \tag{9}$$

with the estimator then being:

$$\{\widehat{\boldsymbol{a}}_1, \dots \widehat{\boldsymbol{a}}_{n_a}\} := \underset{\boldsymbol{a}_1 \dots \boldsymbol{a}_{n_a}}{\arg\min}\, J_a \tag{10}$$

In the above cost function γ (> 0) represents the user-tuned *regularization parameter*. The cost function is equivalent to that used within the context of Least Squares Support Vector Machines (LS-SVM) [18], and the solution procedure, below, mainly follows that of [15] which refers to general Linear Parameter Varying (LPV) models; also see [14] for related TV model estimation in the frequency domain.

Differentiating the cost function J_a with respect to each $\boldsymbol{a}_i$ leads to:

$$\boldsymbol{a}_i = -\sum_{t=1}^{N} w[t] \cdot \boldsymbol{g}[t] \cdot x[t-i] \tag{11a}$$

$$\text{with:} \qquad w[t] := \gamma \cdot \underbrace{\left(x[t] + \sum_{i=1}^{n_a} \boldsymbol{a}_i^T \cdot \boldsymbol{g}[t] \cdot x[t-i] \right)}_{e[t]} = \gamma \cdot e[t] \tag{11b}$$

with the rightmost part of the above obtained via the model expression (7).

Substituting Equation (11a) into the TV AR parameter expression of Equation (6) leads to:

$$a_i[t] = \sum_{\tau=1}^{N} w[\tau] \cdot x[\tau - i] \cdot \underbrace{\boldsymbol{g}_a^T[\tau] \cdot \boldsymbol{g}_a[t]}_{K[\tau,t]} = \sum_{\tau=1}^{N} w[\tau] \cdot x[\tau - i] \cdot K[\tau, t] \tag{12a}$$

$$\text{with:} \qquad K(\tau, t) := \boldsymbol{g}^T[\tau] \cdot \boldsymbol{g}[t] \tag{12b}$$

designating a symmetric ($K(\tau, t) = K(t, \tau)$) and positive semi-definite *kernel function* satisfying the Mercer conditions [12, pp. 37-39].

Evidently, from the latter of Equations (12a), and for pre-selected kernel functions[2], the TV AR parameters may be fully specified iff the sequence $w[t]$ $(t = 1, 2, \ldots, N)$ is obtained. Towards this end, using Equation (12a) and the latter of Equations (11b), the FS-TAR model of Equation (7) may be written as:

$$x[t] = \sum_{\tau=1}^{N} \Bigg(\underbrace{\sum_{i=1}^{n_a} x[\tau - i] \cdot K[\tau, t] \cdot x[t - i]}_{O(t,\tau)} \Bigg) w[\tau] + \gamma^{-1} \cdot w[t] \tag{13}$$

in which $x[t - i] \equiv 0$ for $t \leq i$. Writing the above expression for $t = 1, 2, \ldots, N$ leads to the following set of linear equations:

$$\boldsymbol{x} = (\boldsymbol{O} + \gamma^{-1} \boldsymbol{I}_N) \boldsymbol{w} \tag{14}$$

where the (t, τ) element of matrix $\boldsymbol{O}$ is defined as $O(t, \tau) := \sum_{i=1}^{n_a} x[\tau - i] \cdot K[\tau, t] \cdot x[t - i]$, $\boldsymbol{I}_N$ the $N \times N$ unity matrix, and:

$$\boldsymbol{x} := [x[1] \ldots x[N]]^T_{N \times 1} \qquad\qquad \boldsymbol{w} := [w[1] \ldots w[N]]^T_{N \times 1}$$

This may be solved, in a unique way, in terms of the unknown $w[t]$'s:

$$\widehat{\boldsymbol{w}} = (\boldsymbol{O} + \gamma^{-1} \boldsymbol{I_N})^{-1} \boldsymbol{x} \tag{15}$$

and the TV AR parameters are obtained via Equation (12a).

Remark. The estimation problem associated with the cost function of Equation (9) may be shown to be equivalent to that of Maximum A Posterior (MAP) estimation with the regularization term corresponding to a prior condition on the parameters following a zero-mean Gaussian distribution. The regularization parameter γ essentially defines a trade-off between bias-variance for the estimated parameters, while the kernel matrix is closely related to the parameter covariance matrix. Further details in [17], [18, pp. 12-13, 122-144], and references therein.

TV innovations variance estimation. The innovations variance $\sigma_e^2[t]$ is estimated in a similar fashion, using its Instantaneous Variance (IV) estimates [5]. The cost function in this case is:

$$J_{\sigma_e^2} := \frac{1}{2} \boldsymbol{s}^T \boldsymbol{s} + \frac{\gamma}{2} \sum_{t=1}^{N} \Bigg(e^2[t] - \underbrace{\boldsymbol{s}^T \cdot \boldsymbol{g}[t]}_{\sigma_e^2[t]} \Bigg)^2 \tag{16}$$

with the $\boldsymbol{s}$ estimator being:

$$\widehat{\boldsymbol{s}} := \arg\min_{\boldsymbol{s}} J_{\sigma_e^2} \tag{17}$$

Differentiating the cost function with respect to $\boldsymbol{s}$ yields:

$$\boldsymbol{s} = \sum_{t=1}^{N} w[t] \cdot \boldsymbol{g}[t] \tag{18a}$$

$$\text{with:} \qquad w[t] := \gamma \cdot \Bigg(e^2[t] - \overbrace{\boldsymbol{s}^T \cdot \boldsymbol{g}[t]}^{\sigma_e^2[t]} \Bigg) \quad \Longrightarrow \quad e^2[t] = \boldsymbol{s}^T \cdot \boldsymbol{g}[t] + \gamma^{-1} \cdot w[t] \tag{18b}$$

Substituting (18a) into the latter of Equations (6) leads to:

$$\sigma_e^2[t] = \sum_{\tau=1}^{N} w[\tau] \cdot \underbrace{\boldsymbol{g}^T[\tau] \cdot \boldsymbol{g}[t]}_{K[\tau,t]} = \sum_{\tau=1}^{N} w[\tau] \cdot K[\tau, t] \tag{19}$$

[2]The specification of a single kernel function allowing for the direct computation of the inner product without designating the functional basis $\boldsymbol{g}[t]$ constitutes the so called *kernel trick* [18, pp. 36-39], [15].

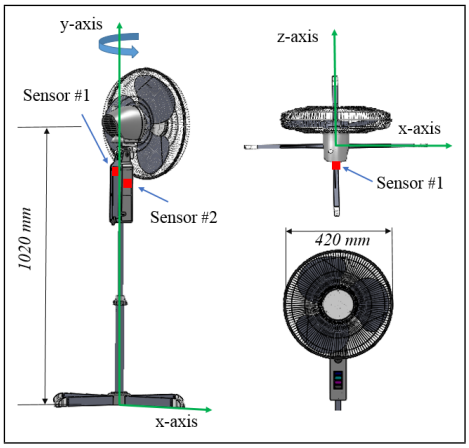


Figure 1: Schematic diagram of the fan and the sensors.

where, as before, $K(\tau,t) := \boldsymbol{g}^T[\tau]\cdot\boldsymbol{g}[t]$. Evidently, for pre-selected kernel functions, the TV innovations variance may be specified iff the sequence $w[t]$ $(t=1,2,\ldots,N)$ is obtained. Towards this end, substituting Equation (18a) into the latter of Equations (18b), leads to:

$$e^2[t] = \sum_{\tau=1}^{N}\Big(\underbrace{\boldsymbol{g}^T[\tau]\cdot\boldsymbol{g}[t]}_{K[\tau,t]}\Big)w[\tau] + \gamma^{-1}\cdot w[t] = \sum_{\tau=1}^{N}K[\tau,t]\cdot w[\tau] + \gamma^{-1}\cdot w[t] \tag{20}$$

Writing the above expression for $t=1,2,\ldots,N$ leads to the following set of linear equations:

$$\boldsymbol{e}^2 = (\boldsymbol{K} + \gamma^{-1}\boldsymbol{I}_N)\boldsymbol{w} \tag{21}$$

with $\boldsymbol{K}$ designating the $N\times N$ matrix with (τ,t)-th element $K(\tau,t)$ and:

$$\boldsymbol{e}^2 := [e^2[1]\ldots e^2[N]]^T_{N\times 1} \qquad\qquad \boldsymbol{w} := [w[1]\ldots w[N]]^T_{N\times 1}$$

This may be solved, in a unique way, in terms of the unknown $w[t]$'s:

$$\widehat{\boldsymbol{w}} = (\boldsymbol{K} + \gamma^{-1}\boldsymbol{I_N})^{-1}\boldsymbol{e}^2 \tag{22}$$

and the TV innovations variance obtained from Equation (19).

4 Application case study: random vibration modeling and analysis for an operating fan

In this section an application case study pertaining to the modeling and analysis of the non-stationary random vibration measured on the poll of an operating fan is undertaken. FS-TAR modeling using both kernel and adaptable models is presented, along with comparisons with simple non-parametric (spectrogram) and unstructured parameter evolution (Recursive Least Squares TAR, RLS-TAR) modeling (see [1] and references therein).

Second order moment non-stationarity (the first order moment being zero) is due to a low frequency yaw motion and high frequency blade rotation (this is however not evident as it is beyond the studied frequency bandwidth).

Acquisition	Data acquisition system: NI c-DAQ 9184 Sensor type: piezoelectric accelerometer (PCB 352C22, sensitivity 10.28 mV/g) Initial sampling frequency: 1 651.6 (Hz) Signal length: 98 998 samples (59.94 s)
Pre-processing	Chebyshev II lowpass filtering (filter order 8, cutoff frequency 58.985 Hz) Re-sampling frequency: 117.97 (Hz) Signal length used for modeling: 7 000 samples

Table 1: Signal acquisition and pre-processing.

4.1 The experimental set-up and the non-stationary random vibration

A schematic diagram of the fan, indicating the two sensor locations on the poll, is presented in Figure 1. Vibration signals are obtained via PCB 352C22 accelerometers, with the presently employed signal obtained from Sensor #1 (along the z-axis). Signal acquisition is active for 59.94 s. The signal is initially sampled at a relatively high frequency (1 651.6 Hz), low-pass filtered and re-sampled at 117.97 Hz, followed by sample mean removal and scaling to the [-1,1] range. Further details on the equipment used and signal pre-processing are provided in Table 1. An $N = 7000$ sample long portion of the signal, depicted in Figure 2, is used for modeling and analysis.

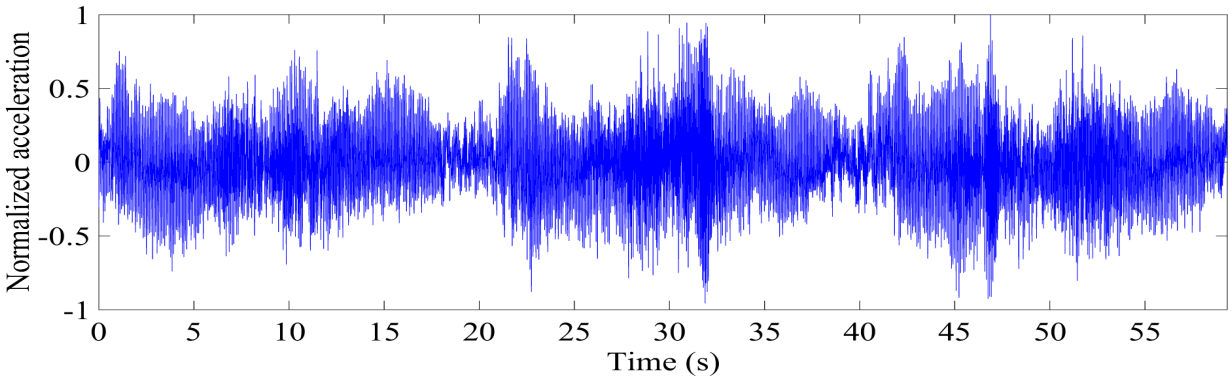


Figure 2: The normalized, $N = 7000$ sample-long, non-stationary random vibration signal modeled.

4.2 Preliminary modeling and analysis: spectrogram and RLS-TAR methods

Preliminary, non-parametric and parametric, modeling and analysis is based on the spectrogram and Recursive Least Squares TAR (RLS-TAR) modeling, respectively [1].

The Spectrogram. The signal's Short Term Fourier Transform (STFT) based spectrogram (256 sample long Hamming window, 51 sample advance - see Table 2) is depicted in Figure 3(a). The spectrogram reveals at least six main frequency modes between 0.1 - 3 Hz, 11 - 13 Hz, 15 - 20 Hz, 24 - 26 Hz, 28 - 40 Hz, and 48 - 51 Hz.

Recursive Least Squares TAR (RLS-TAR) modeling. These are unstructured parameter evolution TAR models estimated using a properly selected forgetting factor λ which controls the parameter evolution 'smoothness'. A forward, backward and final forward pass over the signal is implemented in order to alleviate the effects of the initial conditions, with the final results being those of the last pass [1].

Various model orders and forgetting factors are examined, with a model order $n_a = 21$ estimated with a forgetting factor $\lambda = 0.990$ selected as best. The initial covariance matrix is set equal to $\boldsymbol{P}[0] = \alpha \cdot \boldsymbol{I}$, with

Model	Model Structure & Estimation Details	RSS/SSS† (%)
Spectrogram	MATLAB spectrogram function 256 sample-long Hamming window 205-sample long overlap (51-sample long advance)	-
RLS-TAR(21)	forward-backward-forward runs Forgetting factor: $\lambda = 0.990$ Initial covariance: $\boldsymbol{P}[0] = 10^4 \boldsymbol{I}$	5.38
kernel FS-TAR(21)	kernel: Radial Basis Functions AR parameters: $\sigma = 150$, $\gamma = 10^4$ AR parameters: Condition number‡ 3.55×10^6 Innovations variance: $\sigma = 150$, $\gamma = 10^{-1}$ Innovations variance: Condition number‡ 38.51	2.81
AFS-TAR(21)$_{[7,7]}$	Basis functions: $G_{b_a(1)}[t] = 1$, $G_{b_a(2k)}[t] = \sin[k\delta t]$, $G_{b_a(2k+1)}[t] = \cos[k\delta t]$ $(k = 1, 2, 3)$ Estimated $\delta = 0.0050$ (rad) (AR parameters) Estimated $\delta = 0.0049$ (rad) (innovations variance) Optimization: MATLAB lsqnonlin function (TolFun = 10^{-4}, TolX = 10^{-4})	5.44
†Residual Sum of Squares over Series Sum of Squares ‡Condition number of the inverted matrix		

Table 2: Method details, selected models, and their prediction performance.

$\alpha = 10^4$, while the innovations TV variance is estimated using a $M = 250$ sample long moving window over the estimated innovations (model residuals) $\widehat{e}[t]$, that is:

$$\widehat{\sigma}_e^2[t] = \frac{1}{2M+1} \sum_{\tau=t-M}^{t+M} \widehat{e}^2[\tau]$$

The achieved Residual Sum of Squares over the Series Sum of Squares is 5.38% (also see Table 2).

The RLS-TAR(21) model based frozen TV PSD estimate is depicted in Figure 3(b). This is in gross overall agreement with the spectrogram, but provides increased accuracy and resolution, and clarifies details of the vibration modes within the 15-20 Hz frequency range.

4.3 Kernel FS-TAR modeling and analysis

The AR order is maintained at $n_a = 21$, while a Radial Basis Function (RBF) kernel [14]:

$$K[\tau, t] := exp\left(-\frac{(\tau - t)^2}{2\sigma^2}\right)$$

with implicitly defined basis functions of the form:

$$G_k[t] = \frac{t^k}{\sqrt{k!}} exp\left(-\frac{t^2}{2\sigma^2}\right)$$

is employed. It is noted that the user-selected parameter σ controls the 'smoothness' of the estimated TV parameters (a role analogous to that of λ in the RLS-TARMA method). The regularization parameter γ is also user selected; the higher it is the higher the emphasis on the second (RSS) part of the J cost function

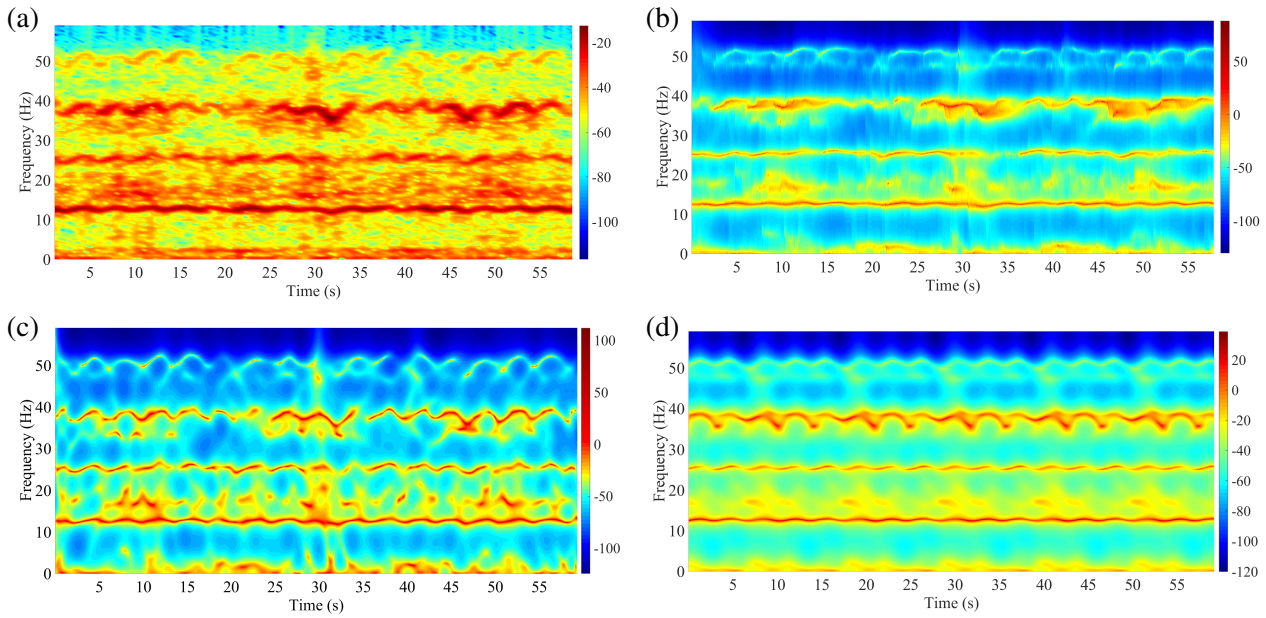


Figure 3: Time-frequency analysis of the non-stationary vibration: (a) spectrogram, (b) RLS-TAR(21) model based frozen PSD, (c) kernel TAR(21) model based frozen PSD, and (d) AFS-TAR$(21)_{[7,7]}$ model based frozen PSD.

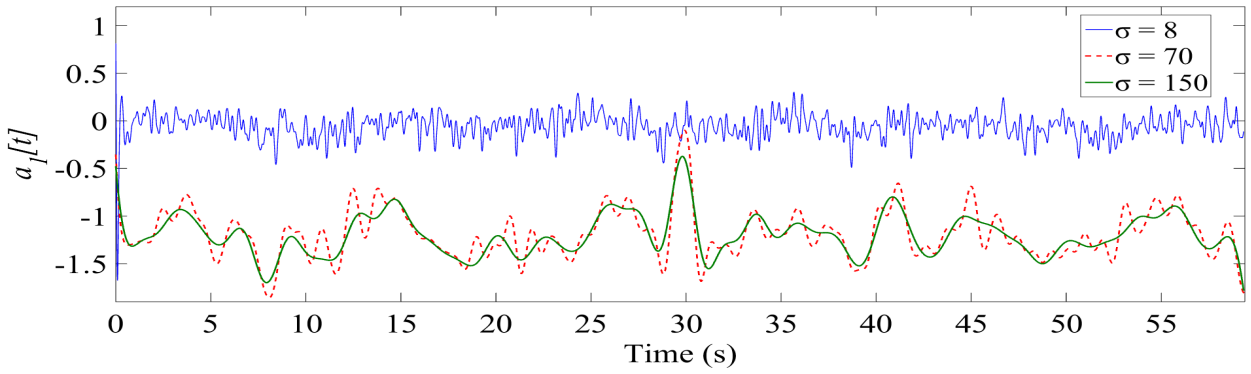


Figure 4: Kernel TAR(21) model: effect of three values of σ on an estimated parameter trajectory.

(9). Of course, both σ and γ may be treated as hyper-parameters and estimated via approaches such as maximization of the marginal likelihood or k-fold cross-validation [19, 17]. The effect of three distinct values of σ on a selected TV parameter is depicted in Figure 4. The values finally selected are $\sigma = 150$ both for AR parameter and innovations variance estimation, and $\gamma = 10^4$, $\gamma = 10^{-1}$ for AR parameter and innovations variance estimation, respectively. The estimated model is successfully validated based on residual (estimated innovations) whiteness [1]. The Residual Sum of Squares over the Series Sum of Squares achieved is significantly reduced (compared to the RLS-TAR case) at 2.81% (estimation details are provided in Table 2).

The kernel FS-TAR(21) model based frozen TV PSD is depicted in Figure 3(c). It is in good agreement with the spectrogram and its previously obtained RLS-TAR(21) model based counterpart. Yet, it exhibits further improvements in accuracy and resolution.

4.4 Adaptable FS-TAR modeling and analysis

Adaptable FS-TAR modeling is presently employing trigonometric basis functions of the form:

$$G_{(2k)}[t,\delta] = \sin[k\,\delta\,t], \qquad G_{(2k+1)}[t,\delta] = \cos[k\,\delta\,t] \qquad k = 0,1,2,3,\ldots$$

(obviously $k = 0$ leads to $G_{(1)}[t] = 1$) with the fundamental frequency corresponding to δ being:

$$\omega = \delta/T \qquad \text{(rad/s)}$$

with T designating the sampling period. This selection is motivated by the very nature of the problem (periodic yaw motion). Note that δ is presently allowed to assume distinct values for the TV AR parameters and the TV innovations variance.

Estimation is based on Separable Non-Linear Least Squares (S-NLS), as presented in [10], while the AR order is, like before, maintained at $n_a = 21$. Different possible numbers of basis functions are considered, separately for the AR parameters and the innovations variance, with 7 (corresponding to $k = 0,1,2,3$) selected based on criteria such as the RSS/SSS and the Bayesian Information Criterion (BIC) (AR parameter case).

The obtained values of δ are as follows:

$$\text{AR parameters: } \delta_a = 0.0050\,\text{(rad)} \iff \omega_a = 0.590\,\text{(rad/s)} \iff f_a = 0.094\,\text{(Hz)}$$

$$\text{Innovations variance: } \delta_s = 0.0049\,\text{(rad)} \iff \omega_s = 0.578\,\text{(rad/s)} \iff f_s = 0.092\,\text{(Hz)}$$

with the minor difference attributed to estimation error. The estimated model is successfully validated based on residual (estimated innovations) whiteness [1]. The achieved Residual Sum of Squares over the Series Sum of Squares is at 5.44%, which is slightly higher than that of the previous cases (further details are provided in Table 2).

The AFS-TAR$(21)_{[7,7]}$ model based frozen TV PSD estimate is depicted in Figure 3(d). It is in good gross agreement with its previous counterparts, while exhibiting a clearly cyclostationary (periodic) behavior as a direct consequence of the selected trigonometric family of basis functions.

4.5 Discussion

(a) *General comment.* The non-parametric spectrogram is generally useful for providing initial, though rough, insight into the TV PSD and the underlying dynamics. The RLS-TAR method provides significantly improved detail and information, while the kernel FS-TAR and AFS-TAR methods provide further improvements. The focus of the comments below is on the latter two methods.

(b) *Estimation.* Estimation is somewhat simpler for kernel FS-TAR models compared to their AFS-TAR counterparts, mainly because it is solely based on *linear* operations, and thus also offers a *unique* solution. Yet, the selection of the kernel function and mainly that of γ and σ may be important, and requires trial and error procedures. On the other hand, AFS-TAR estimation also requires caution in selecting a proper functional family and the subspace dimensionality. Moreover, estimation is partly non-linear, hence additional care needs to be exercised for proper initialization and for avoiding potential local extrema [10]. Model validation is a useful tool for detecting such cases.

(c) *Model parsimony versus modeling flexibility.* AFS-TAR models employ finite dimensional subspaces (presently $p = 7$), and thus offer parsimony and best information compression (a total of $n_a p_a + p_s = 154$ parameters fully specify the present model). Yet, the penalty for this parsimony may be reduced modeling flexibility in cases of complex time dependency of the dynamics, when finite dimensional subspaces may lack flexibility. On the other hand, kernel FS-TAR need a high number of parameters, as each AR parameter and the innovations variance need to be specified at each time instant. Yet, this (with the use of potentially high dimensional subspaces) may offer improved modeling flexibility.

(d) *Achievable prediction accuracy.* In this study prediction accuracy, quantified in terms of the RSS/SSS, has been best for the kernel FS-TAR model (at 2.81%), while that of the AFS-TAR model has been higher (at 5.44%), and close to that of its RLS-TAR counterpart (5.38%). It is conjectured that this is due to the reduced modeling flexibility of the AFS-TAR model, as the trigonometric basis functions limit its ability to capture non-periodic dynamics that may be present in the signal.

(e) *Achievable spectral accuracy and resolution.* In terms of 'frozen' TV spectral analysis, the kernel FS-TAR and AFS-TAR modeling achieve similar results, and clear improvements over their spectrogram and RLS-TARMA counterparts. They both capture the main cyclic component in spectral evolution, which is characterized by a frequency very close to that estimated by the AFS-TAR model ($f_a = 0.094$ Hz), which is related to the yaw motion of the fan. Furthermore, the kernel FS-TAR based TV PSD seems to offer an edge over its AFS-TAR counterpart, with somewhat improved resolution and flexibility in representing any kind of spectral evolution, that is also any non-cyclic components that may be present. It also seems to provide somewhat crisper views, with 'deeper' valleys and 'higher' ridges in the $15 - 21$ Hz and $33 - 36$ Hz frequency ranges.

5 Concluding remarks

This study has focused on a kernel Functional Series Time-dependent AR (kernel FS-TAR) method for the modeling and analysis of zero mean non-stationary random vibration signals. In contrast to previously available FS-TAR methods, the functional subspaces for the TV AR parameters and innovations variance need not be explicitly determined, while they may also be infinite dimensional. This offers improved flexibility and obvious advantages to the broad class of FS-TARMA models, but, at the same time, leads to non-parsimonious representations. Estimation is based on linear techniques, warranting uniqueness, but the problem dimensionality is high. The selection of the regularization parameter (trading estimation bias with variance) and any parameters related to the kernel functions is important and often done based on trial and error.

The kernel FS-TAR method has been employed for the modeling and analysis of the non-stationary random vibration signal obtained on an operating fan, and its performance has been contrasted to that of the Adaptable FS-TAR (AFS-TAR) method, while comparisons with the spectrogram and the Recursive Least Squares TAR (RLS-TAR) method have been also made. The results of this application case study have confirmed the high performance characteristics of the two FS-TAR methods, which are in quite good agreement and capture the mostly periodic nature (due to the periodic yaw motion) of spectral evolution. Yet, the kernel FS-TAR method exhibits an edge in terms of achievable prediction accuracy and TV PSD analysis. It is evident that they both constitute valuable tools for non-stationary random vibration modeling and analysis warranting further work and assessments.

References

[1] A.G. Poulimenos, S.D. Fassois, *Parametric time-domain methods for non-stationary random vibration modelling and analysis–a critical survey and comparison*, Mechanical Systems and Signal Processing, Vol. 20, No. 4 (2006), pp. 763–816.

[2] L.D. Avendao-Valencia, S.D. Fassois S.D, *Parametric non-stationary random vibration modeling and its application to Structural Health Monitoring*, in Encyclopedia of Earthquake Engineering, edited by M. Beer, E. Patelli, I. Kougioumtzoglou, I. Siu-Kui Au, Springer-Verlag (2014), pp. 1-18, 2014.

[3] L.D. Avendao-Valencia, S.D. Fassois, *Stationary and non-stationary random vibration modeling and analysis for an operating wind turbine*, Mechanical Systems and Signal Processing, Vol. 47(1-2), (2014), pp. 263-285, 2014.

[4] M.D. Spiridonakos, S.D. Fassois, *FS-TARMA models for non-stationary vibration analysis: an overview and comparison*, *Proceedings of the 15th IFAC Symposium on System Identification, Saint-Malo, France, 2009 July 6-8, (2009).*

[5] M.D. Spiridonakos, S.D. Fassois, *Non-stationary random vibration modeling and identification via Functional Series Time-Dependent ARMA models: a critical survey*, Mechanical Systems and Signal Processing, Vol. 47, No. 1-2 (2014), pp. 175–224.

[6] M.D. Spiridonakos, A.G. Poulimenos, S.D. Fassois, *Output-only identification and dynamic analysis of time-varying mechanical structures under random excitation: a comparative assessment of parametric methods*, Journal of Sound and Vibration, Vol. 329, (2010), pp. 768-785.

[7] A.G. Poulimenos, S.D. Fassois, *Output-only stochastic identification of a time-varying laboratory structure via Functional Series TARMA models*, Mechanical Systems and Signal Processing, Vol. 23, (2009), pp. 1180-1204.

[8] M.D. Spriridonakos, S.D. Fassois, *Parametric identification of a time-varying structure based on vector vibration response measurements*, Mechanical Systems and Signal Processing, Vol. 23, (2009), pp. 2029-2048.

[9] Y. Li, H.L. Wei, S. Billings, P. Sarrigiannis, *Time-varying model identification for time-frequency feature extraction from EEG data*, Journal of Neuroscience Methods, Vol. 196, No. 1 (2011), pp. 151–158.

[10] M.D. Spiridonakos, S.D. Fassois, *Adaptable Functional Series TARMA models for non-stationary signal representation and their application to mechanical random vibration modeling*, Signal Processing, Vol. 96(A) (2014), pp. 63–79.

[11] W. Yang, L. Liu, S. Zhou, Z. Ma *Moving kriging shape function modeling of vector TARMA models for modal identification of linear time-varying structural systems*, Journal of Sound and Vibration, Vol. 354, (2015), pp. 254–277.

[12] B. Shölkopf, A. Smola, *Learning with kernels*, MIT Press (2002).

[13] Z. Ma, L. Liu, S. Zhou, L. Yu, F. Naets, W. Heylen, W. Desmet, *Parametric output-only identification of time-varying structures using a kernel recursive extended least squares TARMA approach*, Mechanical Systems and Signal Processing, Vol. 98, (2018) pp. 684–701.

[14] J. Lataire, D. Piga, R. Tóth, *Frequency-domain least-squares support vector machines to deal with correlated errors when identifying linear time-varying systems*, IFAC Proceedings Volumes, Vol. 47, No. 3, (2014) pp. 10024–10029.

[15] R. Tóth, V. Laurain, W-X. Zheng, K. Poolla, *Model structure learning: A support vector machine approach for LPV linear-regression models*, *Proceedings of the 50th IEEE Conference on Decision and Control and European Control Conference (CDC-ECC), Orlando, USA, 2011 December 12-15, (2011).*

[16] J. Hainmueller, C. Hazlett, *Kernel regularized least squares: reducing misspecification bias with a flexible and interpretable machine learning approach*, Political Analysis, Vol. 22, (2014), pp. 143–168.

[17] G. Pilonetto, F. Dinuzzo, T. Chen, G. De Nikolao, L. Ljung, *Kernel methods in system identification, machine learning and function estimation: a survey*, Automatica, Vol. 50 (2014), pp. 657–682.

[18] J.A. Suykens, T. Van Gestel, J. De Brabanter, B. De Moor, J. Vandewalle, *Least Squares Support Vector Machines*, World Scientific (2002).

[19] T. Chen, L. Ljung, *Implementation of algorithms for tuning parameters in regularized least squares problems in system identification*, Automatica, Vol. 49, No. 7, (2013), pp. 2213–2220.

Numerical and experimental modal analysis of structures under gyroscopic influence in ALE formulation

T. Weidauer [1], **K. Willner** [1]
[1] FAU Erlangen-Nürnberg, Chair of Applied Mechanics,
Egerlandstrasse 5, 91058, Erlangen, Germany
e-mail: **tim.weidauer@fau.de**

Abstract
A test set-up for the modal analysis of gyroscopic, rotationally symmetric systems is presented. It employs laser Doppler vibrometry along with automatic impulse excitation installed on a rotary table and is applied to a glass structure rotating about its figure axis. The effects of gyroscopic influences on the modal behaviour such as the split of eigenfrequencies and the treatment of complex eigenmodes as travelling waves are deduced analytically and shown experimentally. Finally numerical computations using the Arbitrary-Lagrangian-Eulerian (ALE) finite element formulation separating the rigid body rotation from the mesh deformation are conducted. With the combination of analytical, experimental and numerical analysis a broad overview of modal characteristics of gyroscopic systems is given.

1 Introduction

The oscillatory behaviour of rotating structures is of interest in many applications, e.g. disc brakes, turbines or gyroscopes. The latter are frequently used devices in the fields of navigation or stabilization as sensors for measuring rotation and its rate. The accompanying gyroscopic effects introduce several phenomena into a system's dynamics, which this paper aims to give an overview of. Section 2 starts with the mathematical background towards the modal characteristics of a vibrating structure under rotation. It is followed by several sections discussing a representative example in the form of a rotating wine glass. While section 3.1 starts with some analytical investigations, section 3.2 and 3.3 present experimental and numerical results.

2 Dynamics of gyroscopic systems

This section gives a brief discussion of how the dynamics of a system are affected when it is subject to a rotational motion with angular velocity Ω. In the course of this, a short comparison between a standard non-gyroscopic and a gyroscopic system is conducted. The focus lies on the modal characteristics, such as eigenvectors and eigenfrequencies. For further details, references are given throughout the chapter supplemented by [1], [2] or [3].

In the field of structural dynamics the equations of motion for linear systems are classically written in second order matrix form

$$\boldsymbol{M}\ddot{\boldsymbol{y}} + \boldsymbol{K}\boldsymbol{y} = \boldsymbol{f}(t) \quad \leftrightarrow \quad \boldsymbol{M}\ddot{\boldsymbol{y}} + \boldsymbol{G}\dot{\boldsymbol{y}} + \boldsymbol{K}\boldsymbol{y} = \boldsymbol{f}(t) \tag{1}$$

for n degrees of freedom (DoFs) $\boldsymbol{y} \in \mathbb{R}^n$ with mass matrix $\boldsymbol{M} = \boldsymbol{M}^\mathsf{T}$, stiffness matrix $\boldsymbol{K} = \boldsymbol{K}^\mathsf{T}$ and external forcing function $\boldsymbol{f}(t)$. The left equation describes an undamped, non-gyroscopic system with $\Omega = 0$, while the right equation introduces gyroscopic effects with the gyroscopic matrix $\boldsymbol{G}(\Omega) = -\boldsymbol{G}(\Omega)^\mathsf{T}$. In the

following, it is assumed that either version of (1) describes the same *rotationally symmetric* system with equations of motion of dimension $n = 2$. With the exponential ansatz

$$\boldsymbol{y} = \tilde{\boldsymbol{y}}\, e^{\lambda t} \tag{2}$$

one finds the quadratic eigenvalue problem

$$\left[\boldsymbol{M}\lambda^2 + \boldsymbol{K}\right]\tilde{\boldsymbol{y}} = \boldsymbol{0} \quad \leftrightarrow \quad \left[\boldsymbol{M}\lambda^2 + \boldsymbol{G}\lambda + \boldsymbol{K}\right]\tilde{\boldsymbol{y}} = \boldsymbol{0}. \tag{3}$$

Substitution with $u := \lambda^2$ for retrieval of a linear form yields

$$\left[\boldsymbol{M}u + \boldsymbol{K}\right]\tilde{\boldsymbol{y}} = \boldsymbol{0} \quad \leftrightarrow \quad \left[\boldsymbol{M}u + \boldsymbol{G}\sqrt{u} + \boldsymbol{K}\right]\tilde{\boldsymbol{y}} = \boldsymbol{0}. \tag{4}$$

As a system of $n = 2$ DoFs is considered, one finds the characteristic equation as a second-order polynomial in u by building the determinant of (4) with the two solutions $u_{1,2}$. Both of them yield a pair of conjugated complex purely imaginary eigenvalues

$$\{\lambda_1, \bar{\lambda}_1\} = \pm\sqrt{u_1} \quad \text{and} \quad \{\lambda_2, \bar{\lambda}_2\} = \pm\sqrt{u_2}, \tag{5}$$

leading to the eigenfrequencies $\omega_j = |\Im\{\lambda_j\}|$. The appearance as conjugated pairs can be expected from several viewpoints:

1. It is known that quadratic eigenproblems for $\boldsymbol{M}$-$\boldsymbol{K}$ or $\boldsymbol{M}$-$\boldsymbol{G}$-$\boldsymbol{K}$ systems yield eigenvalues symmetric with respect to the real axis in the GAUSSian plane. In the first case with $\boldsymbol{G} = \boldsymbol{0}$, they also lie symmetrically to the imaginary axis, [4].

2. As a real solution $\boldsymbol{y} \in \mathbb{R}^n$ has to be found for (1) and ansatz (2) for itself is complex for a vibratory system, its conjugated complex equivalent has to be an admissible solution too for truncation of the imaginary parts via superposition.

3. As will be shown later, the complex eigenvectors $\tilde{\boldsymbol{y}}$ of a rotating system can be regarded as waves travelling on the symmetric structure. Their travelling velocity is determined by $\Im\{\lambda\}$, while their travelling direction $\mathrm{sgn}(\Im\{\lambda\})$ is generally unconstrained. I.e. they can wander in either direction, leading to conjugate complex eigenvalues $\pm\lambda$, [5].

When the system is not rotating, one finds double modes due to its symmetry, i.e. degenerate (but still orthogonal) eigenmodes $\tilde{\boldsymbol{y}}$ belonging to the same (double) eigenvalue λ. From a mathematical point of view this fact can be explained by employing group theory. Symmetric modes with wave number $\tilde{n} \geq 1$ span *two-dimensional* subspaces and thus have to exist as double modes with the same eigenvalue λ, [6]. These specific symmetry properties in the dynamics no longer pertain under rotation with $\Omega > 0$ as they are broken by the Coriolis forces acting on the structure. These gyroscopic non-inertial forces perturb the degeneracy by splitting the double eigenvalue λ in two distinct (but closely neighbouring) parts λ_1 and λ_2 and rendering the double eigenmodes $\tilde{\boldsymbol{y}}$ complex, [7]. Thus in the gyroscopic state one finds closely split eigenfrequencies $\omega_2 > \omega_1$ and complex eigenmodes $\tilde{\boldsymbol{y}}_1$ and $\tilde{\boldsymbol{y}}_2$ differing in the phases of their components. This frequency split introduces beating into the system's oscillatory response, which is discussed in the next section 2.1. The details of the actual frequency split will be addressed in 2.2.

2.1 Beating phenomena in gyroscopic systems

In the free oscillations of rotating systems, typically beating can be observed. Its emergence is outlined in the following for the homogeneous solution $\boldsymbol{y}(t)$ to the linear systems in (1). For both kinds, $\boldsymbol{y}(t)$ is obtained from superposition of the eigensolutions associated with λ_j with $j = 1, 2$ out of ansatz (2) via

$$\boldsymbol{y}(t) = \underbrace{\tilde{\boldsymbol{y}}_1 e^{\lambda_1 t} + \tilde{\boldsymbol{y}}_2 e^{\lambda_2 t}}_{\text{compl. part}} + \underbrace{\bar{\tilde{\boldsymbol{y}}}_1 e^{\bar{\lambda}_1 t} + \bar{\tilde{\boldsymbol{y}}}_2 e^{\bar{\lambda}_2 t}}_{\text{conj. compl. part}} \tag{6}$$

$$= \underbrace{\tilde{\boldsymbol{y}}_1 e^{\lambda_1 t} + \bar{\tilde{\boldsymbol{y}}}_1 e^{\bar{\lambda}_1 t}}_{\text{eigensolution } \boldsymbol{p}_1} + \underbrace{\tilde{\boldsymbol{y}}_2 e^{\lambda_2 t} + \bar{\tilde{\boldsymbol{y}}}_2 e^{\bar{\lambda}_2 t}}_{\text{eigensolution } \boldsymbol{p}_2} \tag{7}$$

$$= \underbrace{\tilde{\boldsymbol{y}}_1 e^{\lambda_1 t}}_{\text{wave } \boldsymbol{w}_1} + \underbrace{\bar{\tilde{\boldsymbol{y}}}_2 e^{-\lambda_2 t}}_{\text{wave } \boldsymbol{w}_2} + \underbrace{\bar{\tilde{\boldsymbol{y}}}_1 e^{-\lambda_1 t}}_{\text{conj. } \bar{\boldsymbol{w}}_1} + \underbrace{\tilde{\boldsymbol{y}}_2 e^{\lambda_2 t}}_{\text{conj. } \bar{\boldsymbol{w}}_2}. \tag{8}$$

Equations (6) to (8), with $\bar{(\bullet)}$ denoting conjugate complex quantities, are permutations of the same sum relying on different interpretations of how the single terms interact:

- classical superposition of a *complex* part with its *conjugate complex* equivalent in (6)
- superposition of two *real* eigensolutions $\boldsymbol{p}_1$ and $\boldsymbol{p}_2$ in (7)
- superposition of two waves $\boldsymbol{w}_1$ and $\boldsymbol{w}_2$ travelling counter-directional with λ_1 and $-\lambda_2$ $(= \bar{\lambda}_2)$ on the structure together with their conjugate complex representations in (8).

These three equivalent forms can be summarized component-wise to a phasor

$$y^{(k)}(t) = 2\, Y_{(k)}(t)\, \cos\left(\Phi^{(k)}(t)\right) \tag{9}$$

for each DoF k similar as shown in [8]. For this step the *constant* modal phases

$$\tilde{\varphi}_j^{(k)} = \arctan\left(\frac{\Im\{\tilde{y}_j^{(k)}\}}{\Re\{\tilde{y}_j^{(k)}\}}\right) \tag{10}$$

have to be extracted component-wise from the complex eigenvectors

$$\tilde{\boldsymbol{y}}_j = \sum_k^n |\tilde{y}_j^{(k)}|\, e^{i\tilde{\varphi}_j^{(k)}}\, \boldsymbol{e}_k \tag{11}$$

with the unity basis vectors $\boldsymbol{e}_k$. Combination with the angles $\omega_j t$ of the complex pointers $e^{\lambda_j t} = e^{i\omega_j t}$ in (6) to (8) yields *time-dependent* phases

$$\phi_j^{(k)}(t) = \tilde{\varphi}_j^{(k)} + \omega_j t \tag{12}$$

for each DoF k in the sum terms. For the overall system's answer $\boldsymbol{y}(t)$ this results in a *time-dependent* envelope

$$Y_{(k)}(t) = \sqrt{|\tilde{y}_1^{(k)}|^2 + |\tilde{y}_2^{(k)}|^2 + 2\,|\tilde{y}_1^{(k)}| \cdot |\tilde{y}_2^{(k)}| \cos\left(\Delta\phi^{(k)}(t)\right)} \tag{13}$$

with

$$\Delta\phi^{(k)}(t) = \phi_2^{(k)}(t) - \phi_1^{(k)}(t) \tag{14}$$

$$= (\omega_2 - \omega_1)t + (\tilde{\varphi}_2^{(k)} - \tilde{\varphi}_1^{(k)}) \tag{15}$$

$$= \Delta\omega t \; + \; \Delta\tilde{\varphi}^{(k)} \tag{16}$$

involving the *beating frequency*

$$\Delta\omega = \omega_2 - \omega_1 > 0\,. \tag{17}$$

Investigating the roots of the envelope $Y_{(k)}(t)$ in (13) gives the conditions for the existence of nodes of the vibrational pattern. One finds that these nodes are neither stationary nor fixed on the structure. In fact, they are travelling on the geometry and define a rotating motion of the oscillations on the body. For mathematical details, the reader is referred to [8]. In addition to the envelope also the equally *time-dependent* phase

$$\Phi^{(k)}(t) \;=\; \arctan\left(\frac{|\tilde{y}_1^{(k)}|\sin\left(\phi_1^{(k)}(t)\right) + |\tilde{y}_2^{(k)}|\sin\left(\phi_2^{(k)}(t)\right)}{|\tilde{y}_1^{(k)}|\cos\left(\phi_1^{(k)}(t)\right) + |\tilde{y}_2^{(k)}|\cos\left(\phi_2^{(k)}(t)\right)}\right) \tag{18}$$

of the overall system answer $\boldsymbol{y}(t)$ is derived. After lengthy operations it can be rewritten as

$$\Phi^{(k)}(t) \;=\; \phi_{\mathrm{m}}^{(k)}(t) \,+\, \arctan\left(\frac{|\tilde{y}_2^{(k)}| - |\tilde{y}_1^{(k)}|}{|\tilde{y}_2^{(k)}| + |\tilde{y}_1^{(k)}|}\,\tan\left(\frac{\Delta\phi^{(k)}(t)}{2}\right)\right) \tag{19}$$

with

$$\begin{aligned}\phi_{\mathrm{m}}^{(k)}(t) &= {}^1\!/_2\big(\phi_1^{(k)}(t) + \phi_2^{(k)}(t)\big)\\ &= {}^1\!/_2(\omega_2+\omega_1)t + {}^1\!/_2(\tilde{\varphi}_2^{(k)} + \tilde{\varphi}_1^{(k)})\\ &= \omega_{\mathrm{m}}t \,+\, \tilde{\varphi}_{\mathrm{m}}^{(k)}.\end{aligned} \tag{20}$$

including the *middle frequency*

$$\omega_{\mathrm{m}} = {}^1\!/_2(\omega_1 + \omega_2). \tag{21}$$

Together with $\Delta\omega$ it builds the set of characteristic parameters of a beating oscillation. For the case of $\tilde{y}_1^{(k)} = \tilde{y}_2^{(k)} = \tilde{y}^{(k)}$ the overall solution $\boldsymbol{y}(t)$ corresponds DoF-wise to the well-known form

$$y^{(k)}(t) = 2\,\tilde{y}^{(k)}\cos\big(\underbrace{\frac{\omega_1-\omega_2}{2}}_{\Delta\omega/2}t\big)\cos\big(\underbrace{\frac{\omega_1+\omega_2}{2}}_{\omega_{\mathrm{m}}}t\big), \tag{22}$$

describing an oscillation with ω_{m} while its amplitude is modulated with frequency $\Delta\omega/2$.

Equations (6) to (22) can be simplified noticeably for the non-gyroscopic case due to the intact double eigenvalue $\lambda_1 = \lambda_2 = \lambda$ with its now *real* eigenvectors $\tilde{\boldsymbol{y}} = \bar{\tilde{\boldsymbol{y}}}$. The steps are not shown here, but with straight-forward operations one arrives at a solution $\boldsymbol{y}(t)$ without any modulation as one would expect. No beating is present and the oscillations occur with $\omega_{\mathrm{m}} = \omega$. Both the envelope (13) and the phase of the solution (18) lose their time-dependence, while the latter also adopts the same constant phase value for all DoFs. This stands in agreement with the standard case of undamped, non-gyroscopic systems, whose eigensolutions from double eigenvalues originate as *standing* waves from the superposition of *forward* and *backward travelling* waves with the *same* velocity ω from eigenvalue $\pm\lambda$. The envelope of this standing wave deflates to an oscillating and otherwise fixed and time-invariant pattern on the body with frequency ω.

2.2 Eigenfrequency split due to gyroscopic forces

Earlier the split of degenerate eigenvalues λ and their double frequencies ω was mentioned. This split is directly dependent on the rotational velocity Ω and can be computed from the gyroscopic eigenproblem

$$(\lambda^2\boldsymbol{M} + \lambda\boldsymbol{G}(\Omega) + \boldsymbol{K})\,\tilde{\boldsymbol{y}} = \boldsymbol{0}, \tag{23}$$

given in a *non-rotating* inertial frame. Pre-multiplication with $\tilde{\boldsymbol{y}}^{\mathsf{H}}$, where $(\bullet)^{\mathsf{H}}$ denotes the conjugate transpose, yields

$$\lambda^2 \tilde{\boldsymbol{y}}^{\mathsf{H}} \boldsymbol{M} \tilde{\boldsymbol{y}} + \lambda \tilde{\boldsymbol{y}}^{\mathsf{H}} \boldsymbol{G} \tilde{\boldsymbol{y}} + \tilde{\boldsymbol{y}}^{\mathsf{H}} \boldsymbol{K} \tilde{\boldsymbol{y}} = \boldsymbol{0}. \tag{24}$$

With the projections of the system's matrices $\boldsymbol{M}$ and $\boldsymbol{K}$ in the modal subspace

$$\tilde{M} = \tilde{\boldsymbol{y}}^{\mathsf{H}} \boldsymbol{M} \tilde{\boldsymbol{y}} \quad \in \mathbb{R}^{1\times 1}, \tag{25}$$

$$\tilde{K} = \tilde{\boldsymbol{y}}^{\mathsf{H}} \boldsymbol{K} \tilde{\boldsymbol{y}} \quad \in \mathbb{R}^{1\times 1} \tag{26}$$

the Rayleigh-Quotient is formulated as

$$\omega^2 = \frac{\tilde{K}}{\tilde{M}}\,. \tag{27}$$

Furthermore, one defines the purely imaginary projection of the gyroscopic matrix $\boldsymbol{G}(\Omega) =: \Omega \hat{\boldsymbol{G}}$ as

$$\tilde{G}^* = \tilde{\boldsymbol{y}}^{\mathsf{H}} \hat{\boldsymbol{G}} \tilde{\boldsymbol{y}} \quad \in \mathbb{C}^{1\times 1} \tag{28}$$

and solves with $\tilde{G} := |\Im\{\tilde{G}^*\}|$ and $\lambda = i\omega$ equation (24) for the eigenfrequency ω as per

$$\omega_{1,2} = \omega_\Omega \mp \frac{\Delta\omega}{2} \tag{29}$$

with

$$\omega_\Omega = \sqrt{\left(\Omega \frac{\tilde{G}}{2\tilde{M}}\right)^2 + \omega^2} \qquad \text{and} \qquad \Delta\omega = \Omega \frac{\tilde{G}}{\tilde{M}}\,. \tag{30}$$

Equation (29) is based on the fact, that the root term in (30) depends on the employed eigenvector $\tilde{\boldsymbol{y}}$ in (23) and (24), but gives constant base values ω_Ω for the two eigenvectors of a double mode. Meanwhile (28) changes its sign inside of a double mode, thus increasing or decreasing ω_Ω via $\Delta\omega$ by a constant value.

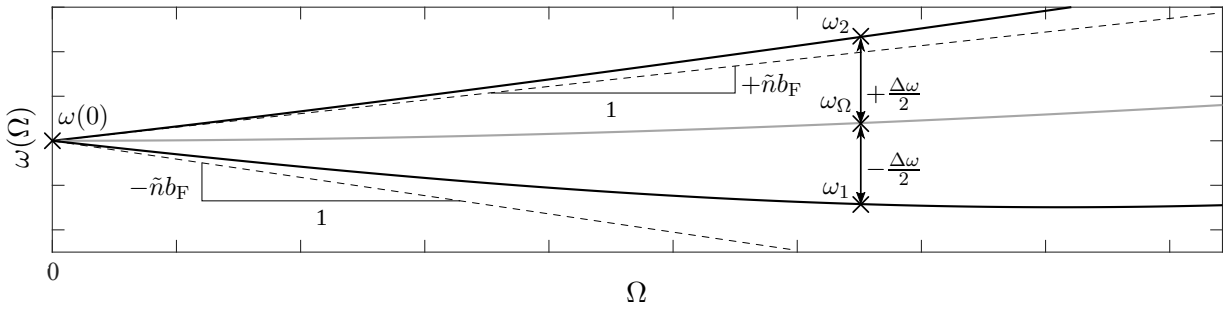


Figure 1: Dependence of the eigenfrequency ω on the rotational velocity Ω.

Figure 1 shows the frequency split together with the non-linear growth of the base value ω_Ω due to the stiffening influence of the rotation on the system. The actual split of $\omega(0)$ into $\omega_{1,2}$ via $\Delta\omega$ happens linearly in Ω and symmetrically to the respective base value. Thus, in the regime of small rotational velocities the approximation

$$\omega_{1,2} \approx \omega \mp \frac{\Delta\omega}{2} = \omega \mp \tilde{n}\,(b_\mathrm{F} + 1)\,\Omega \tag{31}$$

of the split values $\omega_{1,2}$ is admissible, when the increase in ω_Ω is negligible. This approach yields the straight dashed lines in Figure 1 departing in $\omega(0)$ from each other. The slope of these diverging lines is determined by the sensitivity of the structure's eigenfrequency towards gyroscopic influences. It is denoted here with the product $\pm\tilde{n}(b_\mathrm{F}+1)$ of the modes wave number $\tilde{n}$ and the so-called *Bryan's Factor* b_F – a vital quantity in the development and design of gyroscopes. Both terms are introduced in detail in the next section by means of a rotating wine glass as application example.

3 Application example – a rotating wine glass

The investigation of the dynamic behaviour of rotating bodies and their accompanying phenomena on the modal characteristics emerged with [9]. G. H. Bryan established the virtue of Coriolis forces on a rotating ring and axisymmetric shells based on his studies of a spinning wine glass. A similar glass is considered here as example and investigated in the following analytically, experimentally and numerically.

3.1 Analytical investigations

Bryan made the observation that when a vibrating structure is subject to rotation, the vibrational pattern precesses *with respect to the structure* at rate ν_Ω proportional to the structure's own rotational velocity Ω. For an outside observer, the point P_v of the vibration pattern with velocity ν_0 rotates less than the material point P_m it coincided with at the beginning. A visualization of this effect similar to [10] is given in Figure 2.

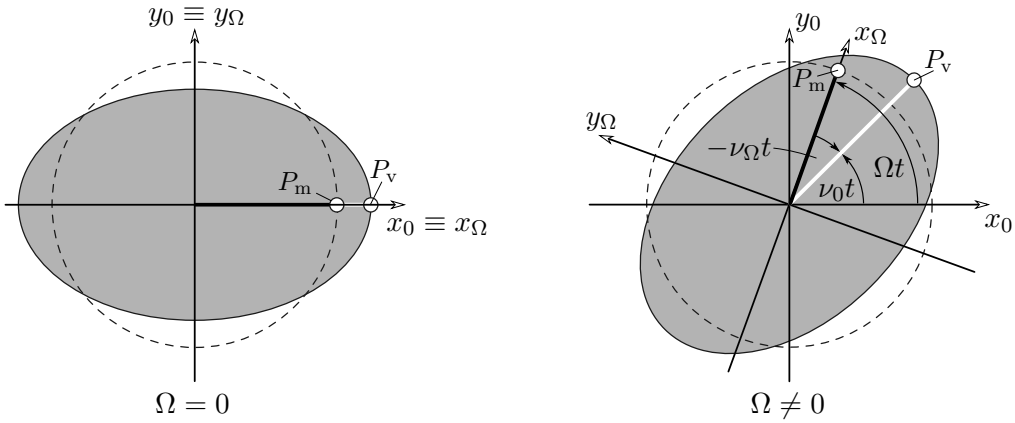


Figure 2: Visualization of Bryan's Factor b_F, cf. [10].

The three rotational rates are linked via $\nu_0 = \nu_\Omega + \Omega$ and the *Bryan's Factor* b_F following

$$b_\mathrm{F} = \frac{v_0}{\Omega} - 1 = \frac{\nu_\Omega}{\Omega}, \tag{32}$$

see [9] or [11]. The author of [5] derives a general formula for the special case of an axisymmetric shell on a rotating base, which corresponds closely to the presented experiment in section 3.2. He deduces

$$\nu_\Omega = -\frac{2\Omega}{\tilde{n}^2 + 1} \qquad \text{and} \qquad \nu_0 = \Omega\,\frac{\tilde{n}^2 - 1}{\tilde{n}^2 + 1} \tag{33}$$

for the rates of precession ν_Ω and ν_0 of the vibrational pattern for a co-rotating and an outside observer. Here $\tilde{n}$ stands again for the azimuthal wave number characterizing the cyclic symmetric modes of an axisymmetric structure. Therefore, one can derive

$$b_\mathrm{F} = -\frac{2}{\tilde{n}^2 + 1} \tag{34}$$

and use this relationship in the assessment of the experimental and numerical results' quality in section 3.2 and 3.3. Table 1 gives the analytical results for wave numbers $\tilde{n} = 2 \ldots 7$ for comparison. Picking mode with wave number $\tilde{n} = 2$ as an example, the vibrational pattern travels from a *co-rotating* observer's perspective $\{x_\Omega, y_\Omega\}$ with $\nu_\Omega = -0.4\,\Omega < 0$, i.e. *counter-directional* to the sense of Ω, or from the perspective $\{x_0, y_0\}$ of an *outside* observer *co-rotational* at a rate of $\nu_0 = 0.6\,\Omega$. This lagging effect of the vibrational pattern can be linked to the frequency split in equation (29) and (31) with the substitution

$$\Delta\omega = 2\,(b_\mathrm{F} + 1)\,\tilde{n}\Omega \tag{35}$$

yielding the alternative forms

$$b_{\mathrm{F}} = \frac{\Delta\omega}{2\tilde{n}\Omega} - 1 = \frac{\tilde{G}}{2\tilde{n}\tilde{M}} - 1 = \mathsf{const.}, \tag{36}$$

with all quantities computed in the *inertial* frame $\{x_0, y_0\}$[1]. It can be seen that b_{F}, determining the extent of the frequency split as a proportionality constant, is based on the scalar projections $\tilde{G}$ and $\tilde{M}$ of the transformed gyroscopic eigenproblem (24). They are functions of the moments of inertia of the system about its rotational axis and its two lateral axes, i.e. depend on the geometric shape of the body. The system's stiffness properties, which are accounted for in $\tilde{K}$, are of no importance for this matter and only influence the eigenfrequency base value ω_Ω by means of the Rayleigh-Quotient ω^2 in (27). As mentioned before, the Bryan's Factor b_{F} scales the slope of the departing straight lines in the $\omega(\Omega)$-Plot in Figure 1, representing the sensitivity of the eigenvalues and frequencies with respect to the rotational velocity Ω. In the course of this, it correlates closely with the beating frequency $\Delta\omega$ in (17) in section 2.1.

$\tilde{n}$	2	3	4	5	6	7
b_{F}	-0.40	-0.20	-0.12	-0.08	-0.05	-0.04

Table 1: Analytical Bryan's Factors b_{F} for $\tilde{n} = 2 \dots 7$ from (34).

Regarding this matter, many others such as [11] can be mentioned, where the authors derive a linear theory for discussing this effect in a rotating annular disc. [12] gives an overview over several approaches for wave superposition in rotating discs and how imperfections influence their vibrations. In [13] equations (33) are expanded to accelerated rotatory motion and explained in the context of solid-state wave gyroscopes.

3.2 Experimental investigations

In the following, the experimental investigations are described. The section at hand presumes the reader is familiar with the basics of experimental modal analysis and its terminology. For details on the general approach and the mathematical background [14] is recommended. The results throughout this section are given in Hz, i.e. the relation $\omega = 2\pi f$ holds for transformation.

3.2.1 Test set-up

The test set-up consists of a rotary table *RK3E VL* by manufacturer *Shimpo*, on which the glass is mounted by clamps. Its spinning speed can be adjusted smoothly with a pedal and is capped around $250.52\,\mathrm{min}^{-1} \approx 4.24\,\mathrm{Hz}$. The actual angular velocity at the time is measured with the help of a Hall sensor registering magnets passing by on the circumference of the table's spinning disc. Additionally, an elastic stop was fixated on the rotary table, which brushes against an outside, stationary plate equipped with an acceleration sensor. Its signal serves as clock pulse, separating single revolutions from each other. The glass itself is covered with a white coating of around $20\,\mu\mathrm{m}$ thickness, which was required for performing the 3D digitalization of the geometry. A photograph of the whole test rig is depicted in Figure 3.

3.2.2 Test procedure

For the modal analysis the structure is excited at distinct points $j = 1, 2 \dots 100$ in radial direction employing an automatic modal hammer, which executes and records the impacts on the structure. The time history of

[1] See [7] for the approach with a *rotating* frame of reference.

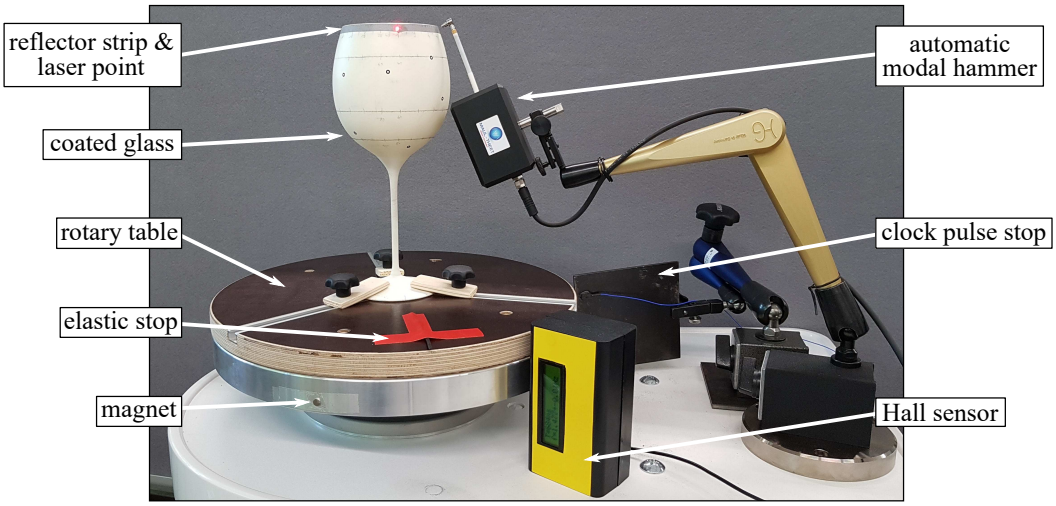


Figure 3: Test rig in the laboratory.

the ensuing velocity oscillations in $\mathrm{mm\,s^{-1}}$ is measured by means of a laser Doppler vibrometer focussed on the spatially fixed point $i = 1$ on a reflector strip applied around the glass rim, see Figure 4. Hence, a roaming excitation procedure is performed, recording the transmission behaviour in form of the frequency response functions $H_{ij} = H_{1j}$ (FRFs) for the evaluation of the structure's modal characteristics.

The 100 measurement nodes are divided in four rows on the glass, where the first one contains 40 excitation locations. The numbering is done in top-view counter-clockwise direction. Row two to four were given a coarser resolution with only 20 measurement points each as section 3.2.5 will show that the modes of interest possess most of their details near the rim.

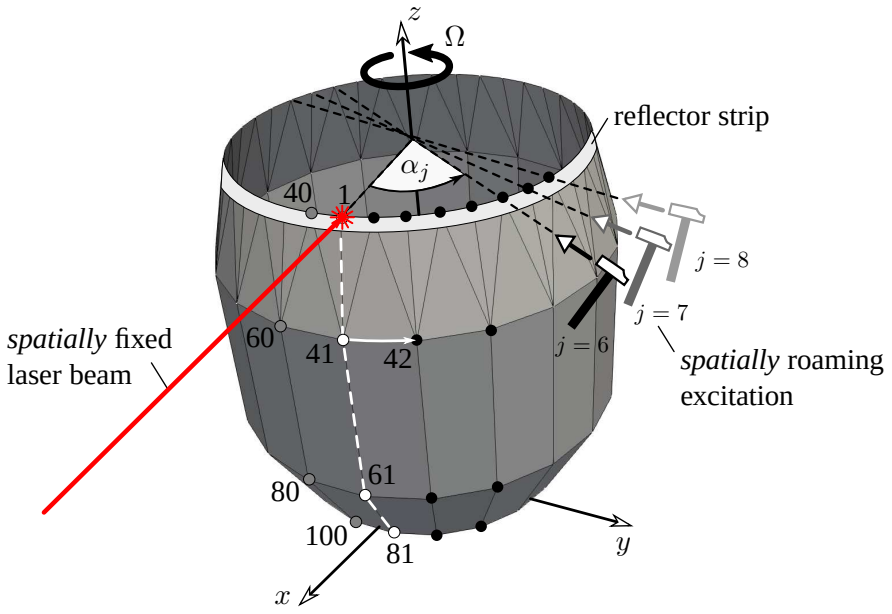


Figure 4: Test set-up with measurement points $j = 1 \ldots 100$ and node $j = 1$ as response node.

With the depicted experimental set-up two kinds of modal analyses were performed:

- Analysis A) with $\Omega = 0$
  As a first step, the glass was examined while still-standing. This conforms to a standard modal analysis with roaming excitation measuring all hundred FRFs H_{1j}. In this scenario, the material and the spatial (inertial) perspective coincide at all times. The results are discussed briefly in sections 3.2.4 and 3.2.5.

- Analysis B) with $\Omega > 0$
  In the second experimental phase, the modal analysis was performed under rotation, requiring a more sophisticated testing procedure illustrated in Figure 4:

  – At first, laser and hammer are aligned for the still-standing glass with *material* points $i = 1$ and j, building a *spatially* fixed set-up with angle α_j for measuring the transmissibility H_{1j}.
  – Subsequently, the glass is accelerated to the desired constant angular velocity Ω and with triggering the hammer the recording is started. At this stage, the measurement locations i and j are still aligned in space, but no longer bound to distinct material points on the glass. I.e. the hammer hits the targeted *spatial* point, but a random *material* point of the glass. At the same time, the laser measures the radial oscillations of its targeted *spatial* response point while the oscillating *material* points of the reflector strip travel below the beam throughout the whole recording phase.
  – For the next excitation point $j + 1$ the glass is stopped and its point $i = 1$ aligned again with the laser. In this configuration, the hammer is now adjusted to its new spatial location $j+1$, the glass is accelerated again and the next measurement $H_{1j+1}$is recorded. The results of this test series are shown and discussed in sections 3.2.4 and 3.2.5.

3.2.3 Challenges in the test set-up

The described set-up poses several challenges for the data acquisition, especially for Analysis B) when $\Omega > 0$. Some of them are discussed in the following:

To begin with, the glass possesses imperfections and is mounted on the test rig by hand, i.e. deviations in shape and position from an ideal rotatory symmetric and fully centred structure ensue. Efforts were made to minimize and quantify these influences with the help of the 3D digitalization. Additionally, the velocity signals of the laser vibrometer were integrated in the frequency domain and evaluated back in time as displacements curves for single revolutions of the glass. Eventually, the misalignment could be minimized, but not fully removed for the test rig, which leads to amplification of Ω and its harmonics $k\Omega$ with $k = 1, 2, \ldots$ in the spectrum. A post-processing of the signals via cepstral analysis, [15], might be of interest here for further investigations.

Furthermore, as the reflector strip is constantly moving below the laser point, noise enters the response signal dependent on how fast the structure rotates. This dependence on Ω can be seen in Figure 5(a). It was supposed that the introduced noise was of random nature, thus the problem was addressed with an H_1 estimator for the response signal by averaging *several* measurements for acquiring a *single* FRF H_{1j}. To a certain extent, this approach was successful and the noise could be reduced. Figure 5(b) shows how the spectrum and thus the signal's quality improve, the more averages are considered up to $n_{\mathrm{avg}} = 30$. For example, the (split) eigenfrequency peaks of the mode with $\tilde{n} = 6$ at around $4822\,\mathrm{Hz}$ cannot be identified from the measurement of a single FRF, but only becomes visible, when the averaging method is employed. However, it can be argued that the noise is still too dominant in the higher frequency regimes, leading to errors in these areas.

Finally, one has to be aware that with the presented set-up only radial oscillations of the glass's goblet are detectable, i.e. tangential deformation can not be identified. This becomes apparent, when evaluating the low frequency regime where bending modes orthogonal to the radial laser direction are present. Sections 3.2.4 and 3.2.5 discuss this point briefly while focussing on the other results of the modal analysis. In particular the eigenfrequencies and their corresponding modes were of interest, whereas damping coefficients were neglected.

3.2.4 Experimental results I – Eigenfrequencies and Bryan's Factor

The eigenfrequencies were measured for values of $\Omega = 0$ and full speed $\Omega = 254.4\,\mathrm{min}^{-1} \approx 4.24\,\mathrm{Hz}$. Table 2 shows the measurements, where the frequency split becomes immediately apparent. The values were

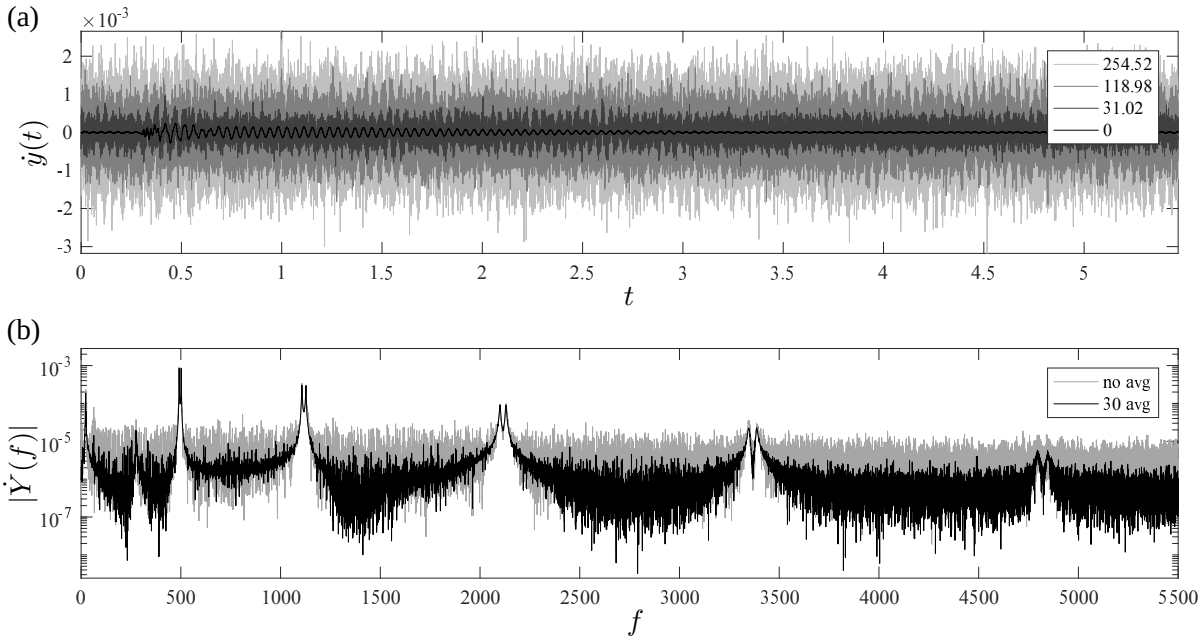


Figure 5: Noise dependence on rotational velocity Ω in min^{-1}:
(a) Time domain in s with various rotational velocities, no excitation.
(b) Frequency domain in Hz with and without averaging.

rounded mildly to integer format for a clearer representation, showing the evolution of f over the mode wave number $\tilde{n}$ and Ω. It can be seen that in the tested regime the presumption of a symmetric frequency split in equation (31) was justified.

$\tilde{n}$	2	3	4	5	6	7
$\Omega = 0\,\mathrm{Hz}$	497	1117	2115	3367	4822	6416
$\Omega = 4.24\,\mathrm{Hz}$	492 502	1107 1127	2100 2130	3347* 3387*	4797* 4847*	6386* 6446*
$f(4.24) - f(0)$	-5 +5	-10 +10	-15 +15	-20* +20*	-25* +25*	-30* +30*

Table 2: Measured eigenfrequencies $f(\Omega)$ in Hz, '*'-values not clearly identifiable due to noise.

Figure 6 shows a representative plot of the recorded time histories. One can see the slowly varying envelope based on the beating phenomena due to the frequency split. As a pre-trigger was used before the recording phase, one can also see the underlying noise level, owing to the movement of the reflector strip before the actual oscillations are initiated.

Additionally to the values given in Table 2, two more eigenfrequencies were perceptible in the low frequency regimes around $23\,\mathrm{Hz}$ and $275\,\mathrm{Hz}$. They are less prominent in the spectra, but by comparison with the numerical results of section 3.3 they could be identified as the first and second beam-like bending modes of the glass. As no measurement points were placed on the glass's shaft they emerge only as distorted rigid body motions of the glass's goblet in the experiment, where the first one would correspond to $\tilde{n} = 1$.

Figure 7 shows cut-outs of Campbell plots of $f(\Omega)$ for the modes with wave numbers $\tilde{n} = 3$ and $\tilde{n} = 4$. For these diagrams, the time histories $\dot{y}(t)$ of the excited glass were recorded for 25 different rotational speeds Ω from $0\,\mathrm{Hz}$ to $4.24\,\mathrm{Hz}$. As expected a single frequency $f = f_1 = f_2$ can be found for $\Omega = 0$, which splits

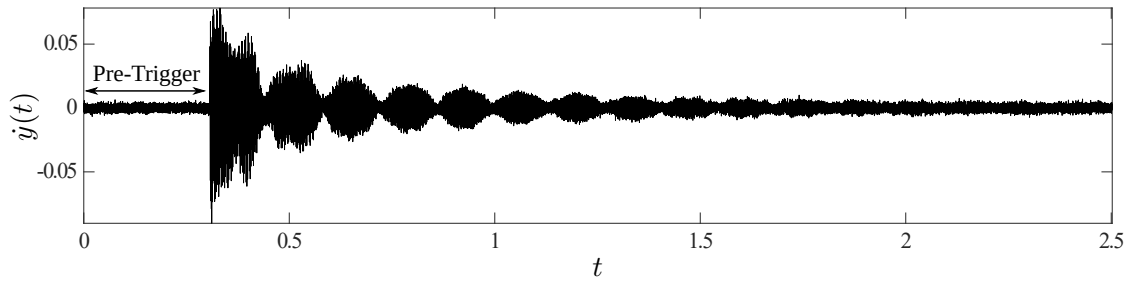


Figure 6: Exemplary time history in s with beating envelope under $\Omega \approx 3\,\mathrm{Hz}$.

up the further Ω increases. Again it is obvious that for these low rotational speeds the split happens linearly and symmetrically to $\omega_\Omega \approx \omega$ respectively $f_\Omega \approx f$.

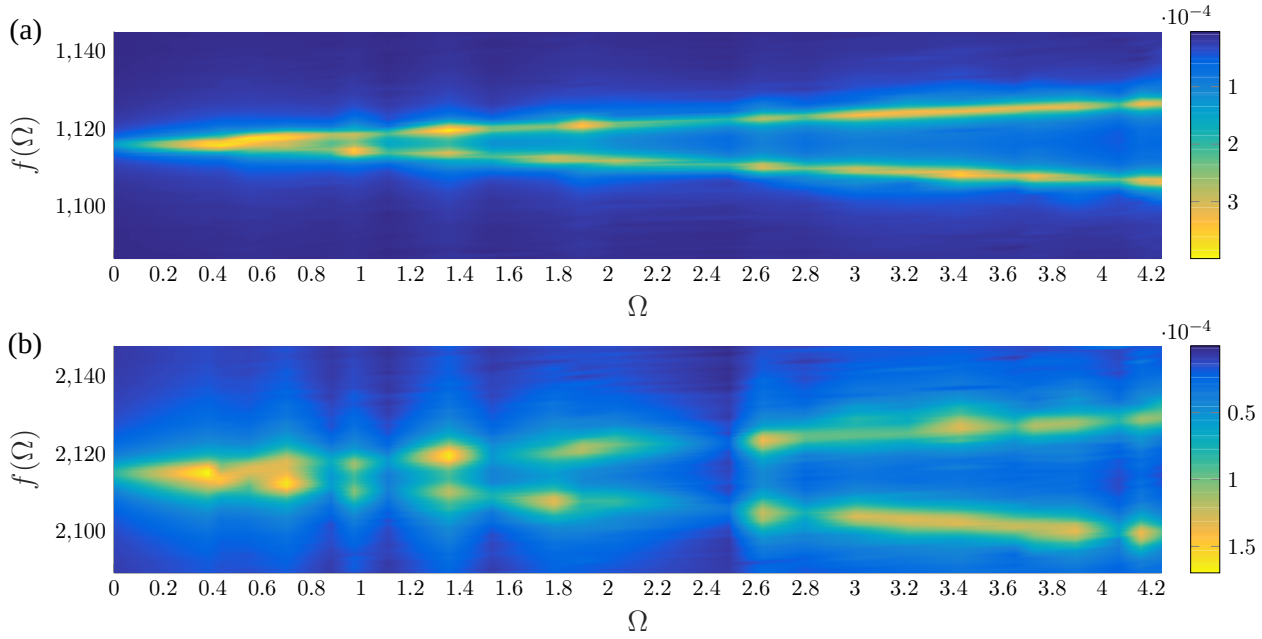


Figure 7: Evolution of $f(\Omega)$ in Hz for mode with (a) $\tilde{n} = 3$ and (b) $\tilde{n} = 4$.

Additionally, the Bryan's Factor b_F can be computed for each mode according to equation (36) and compared with the analytical results of Table 1. Table 3 shows the close agreement of the analytical solution with the experimental values for wave numbers $\tilde{n} = 2, 3, 4$. As in the higher frequency regime the noise becomes more dominant, errors start to grow and the close agreement is lost.

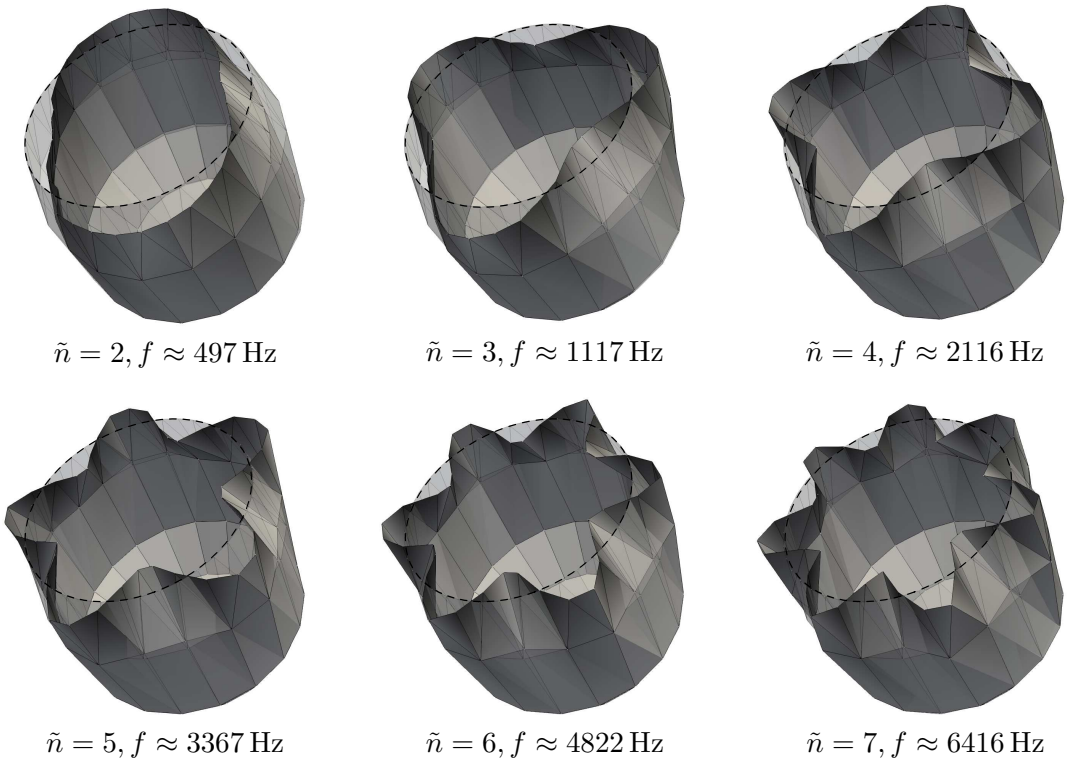
$\tilde{n}$	2	3	4	5	6	7
$b_{\mathrm{F,exp}}$	-0.41	-0.21	-0.12	-0.06*	-0.02*	+0.01*
$b_{\mathrm{F,an}}$	-0.40	-0.20	-0.12	-0.08	-0.05	-0.04

Table 3: Experimental and analytical Bryan's Factors by (34), '*'-values not clearly identifiable due to noise.

3.2.5 Experimental results II – Eigenmodes and travelling waves

Together with the eigenfrequencies, also the eigenmodes were identified. Beginning with the still-standing case, the real-valued results are shown in Figure 8. As mentioned earlier, the glass shows most of its details

of its modes near the rim, which exhibits deformation according to wave number $\tilde{n}$ over its circumference. The chosen density of 40 measurement points on the rim suffices to represent the mode shapes adequately up to $\tilde{n} = 4$. For higher wave numbers, the measurement mesh shows gradually to be too coarse, despite the general shape of the modes still being recognizable.



$\tilde{n} = 2, f \approx 497\,\mathrm{Hz}$ $\tilde{n} = 3, f \approx 1117\,\mathrm{Hz}$ $\tilde{n} = 4, f \approx 2116\,\mathrm{Hz}$

$\tilde{n} = 5, f \approx 3367\,\mathrm{Hz}$ $\tilde{n} = 6, f \approx 4822\,\mathrm{Hz}$ $\tilde{n} = 7, f \approx 6416\,\mathrm{Hz}$

Figure 8: Measured mode shapes and eigenfrequencies for $\tilde{n} = 2 \ldots 7$ for the still-standing glass.

For the rotating case, the general outline of the ascertained mode shapes does not change noticeably, but the modes are complex now. I.e. the depicted shapes in Figure 8 would only resemble the real or imaginary part of the whole complex mode at full speed $\Omega = 4.24\,\mathrm{Hz}$. For illustration of the overall complexity of the modes, Figure 9 shows a plot of the phases of the radial DoFs for $\tilde{n} = 2$. One can see, the phase changing twice in agreement with $\tilde{n} = 2$ from $-\pi$ to $+\pi$ over the glass's circumference.

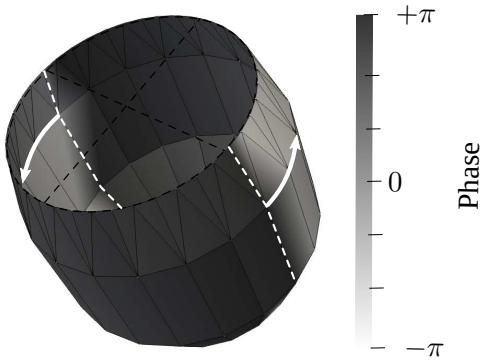


Figure 9: Phase change in radial DoFs of the complex mode with $\tilde{n} = 2$.

Figure 10 shows different states

$$\tilde{\boldsymbol{y}}_j(\tau) = \sum_k^n |\tilde{y}_j^{(k)}|\, e^{i(\tilde{\varphi}_j^{(k)} + \omega_1 \tau)}\, \boldsymbol{e}_k \tag{37}$$

of the real part of mode $\tilde{n} = 3$ over pseudo-time τ where the deformational pattern (white) travels on the glass structure while the actual measurement locations (black) vibrate but do not rotate.

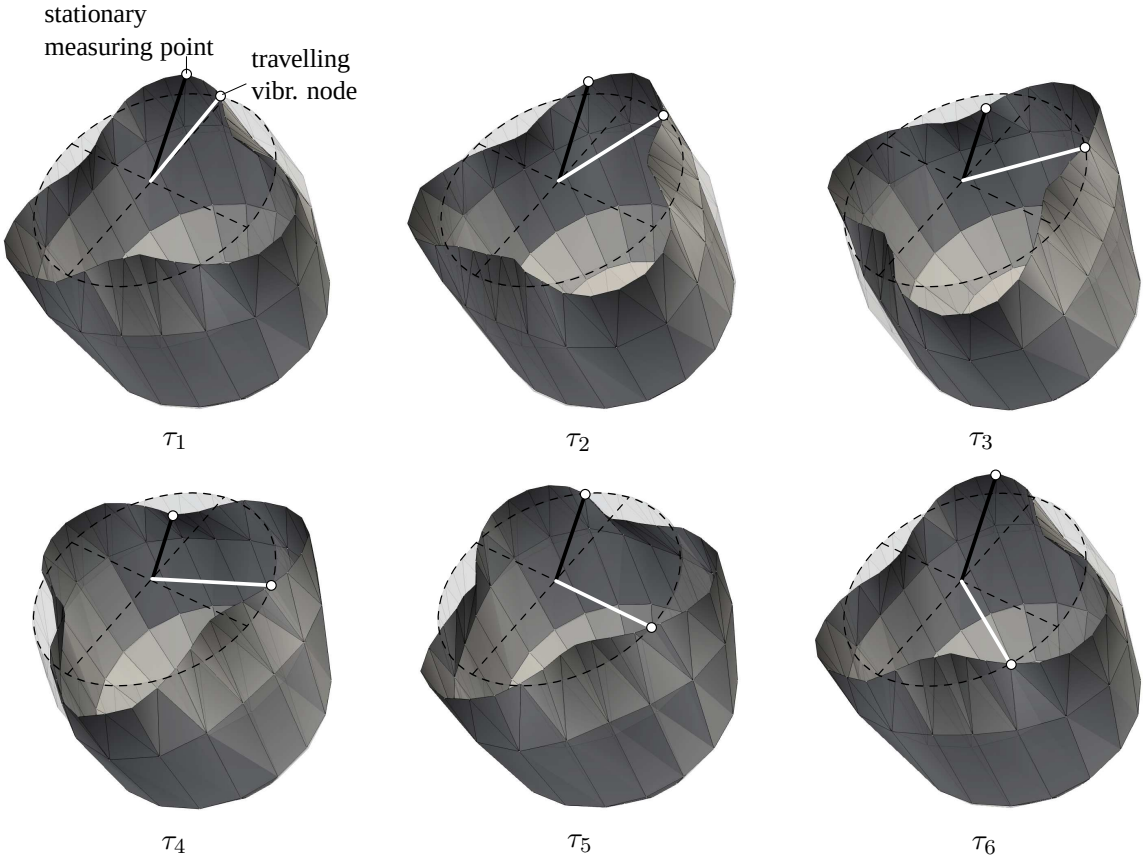


Figure 10: Sequence of the real part of mode with $\tilde{n} = 3$ at pseudo-times $\tau_l, l = 1 \ldots 6$.

3.3 Numerical investigations

After the experimental investigations were carried out, numerical simulations employing the finite element method were conducted. Hereby an *Arbitrary-Lagrangian-Eulerian* formulation was used for integrating the gyroscopic effects into the model, which stems from the field of rolling contact. It separates the rotational movement as rigid body rotation from the actual deformation of a body by means of separated Eulerian and Lagrangian viewpoints. This allows the finite element mesh to stand still and only account for deformation without any rotational movement. In a way, this approach is quite similar to the outlined procedure of Analysis B) in section 3.2.2. The details of the formulation can be found in [16] or [17].

In Figure 11 finite element meshes of the wine glass can be seen – one for the whole glass and one solely for the goblet. They consist of $28\,447$ and 2961 quadratic hexahedral elements containing $119\,544$ and $48\,036$ DoFs. The geometry was derived from a 3D mapping of the glass with an *ATOS 3D* scanner, which was imported as mesh. The glass model possesses the parameters

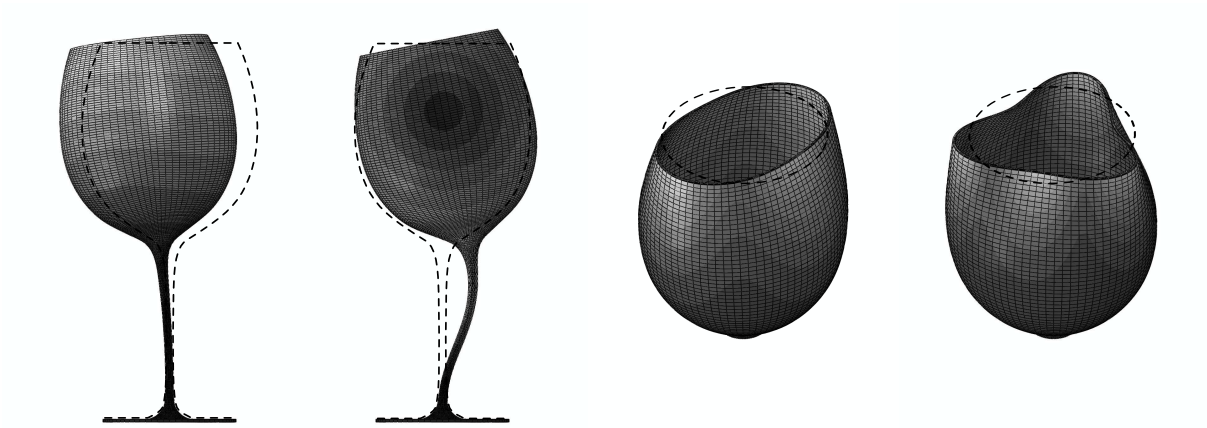
$$\varrho = 2.7\,\mathrm{kg/m^3},\ E = 63\,000\,\mathrm{MPa},\ \nu = 0.275 \tag{38}$$

and is clamped at its foot. In this configuration an angular velocity of $\Omega = 4.24\,\mathrm{Hz}$ is applied. Table 4 shows the results for the eigenfrequencies with and without rotation together with the error $\varepsilon_{f,\mathrm{exp}}$ towards the experimental values. It can be seen that for this moderate rotational velocity the split happens again quite symmetrically to its unsplit base value. Additionally, the numerical Bryan's Factors b_F are given, showing close agreement with the analytical solution in (34).

$\tilde{n}$	2	3	4	5	6	7
$\Omega = 0\,\mathrm{Hz}$	507	1107	2108	3367	4833	6437
$\varepsilon_{f,\mathrm{exp}}$	$+2.01\,\%$	$-0.90\,\%$	$-0.33\,\%$	$0\,\%$	$+0.23\,\%$	$+0.33\,\%$
$\Omega = 4.24\,\mathrm{Hz}$	501.4 511.8	1097.1 1117.5	2093.15 2123.2	3347.9 3387.2	4809.6 4857.8	6409.30 6466.4
$f(4.24) - f(0)$	-5.6 +4.8	-9.9 +10.5	-14.9 +15.2	-19.1 +20.2	-23.4 +24.8	-27.7 +29.4
$b_{\mathrm{F,num}}$	-0.39	-0.20	-0.11	-0.07	-0.05	-0.04
$b_{\mathrm{F,an}}$	-0.40	-0.20	-0.12	-0.08	-0.05	-0.04

Table 4: Numerically computed eigenfrequencies $f(\Omega)$ in Hz and Bryan's Factors.

A selection of the computed modes is depicted in Figure 11. Besides the double modes of the glass's goblet, the first two bending modes of the glass as a whole could be identified numerically, where the experimental test set-up was not able of capturing them correctly. These results conclude the investigations of the glass.



$f \approx 22\,\mathrm{Hz}$ $f \approx 256\,\mathrm{Hz}$ $f \approx 507\,\mathrm{Hz}$ $f \approx 1107\,\mathrm{Hz}$

Figure 11: Selection of numerically computed modes and eigenfrequencies for the still-standing glass.

4 Summary and conclusion

Gyroscopic forces may influence the modal behaviour of rotating structures significantly, depending on the present angular velocity. Under consideration of rotationally symmetric systems, the mathematical background for these influences was provided and applied to an example in form of a wine glass. A test set-up was presented and discussed together with its challenges and the obtained measurement results. Finally, numerical computations employing an ALE finite element algorithm were conducted and agreement between theory, experimental observations and numerical results could be achieved. With these three perspectives a broad overview of structural dynamics in the presence of gyroscopic forces was presented.

Acknowledgements

The authors thank the graduate students Albanik Islami and Christine Hanowski for conducting parts of the measurements shown in this paper. They also thank the Institute of Manufacturing Technology (LFT) of the FAU Erlangen-Nürnberg for the 3D digitalization of the glass structure.

References

[1] G. Genta, *Dynamics of rotating systems*, Mechanical Engineering Series, Springer, New York, 2005.

[2] R. Gasch, K. Knothe, R. Liebich, *Strukturdynamik: Diskrete Systeme und Kontinua*, Springer, 2012.

[3] T. Weidauer, K. Willner, *Reduced Order Modelling for Non-Linear Rotating Systems in ALE Formulation with Contact*, in *Nonlinear Dynamics, Volume 1, Proceedings of the 36th IMAC*, Orlando, FL, US, 2018.

[4] M. Geradin, D.J. Rixen, *Mechanical Vibrations: Theory and Application to Structural Dynamics*, in *Wiley*, 2015.

[5] N.E. Egarmin, *Precession of vibrational standing waves of a rotating axisymmetric shell*, in *Mechanics of Solids*, Vol. 1, pp. 142-148, 1986.

[6] R. Perrin, T. Charnley, *Group theory and the bell*, Journal of Sound and Vibration, Vol. 31, No. 4, pp. 411-418, 1973.

[7] E. Yilmaz, D. Bindel, *Effects of imperfections on solid-wave gyroscope dynamics*, in *IEEE SENSORS 2013 - Proceedings*, pp. 1-4, 2013.

[8] H. Fleischer, *Spinning Modes*, in F.A. Emmerling, A.H. Heinen, editor, *Forschungs- und Seminarberichte aus dem Gebiet Technische Mechanik und Flächentragwerke*, 1/94, UniBw München, 1994.

[9] G. H. Bryan, *On the beats in the vibrations of a revolving cylinder or bell*, in *Proceedings of the Cambridge Philosophical Society*, Vol. 7, pp. 101-111, 1890.

[10] E. Yilmaz, D. Bindel, *Temperature Sensitivity and Shape Optimization of Solid-State Wave Gyroscopes*, in *IEEE Sensors Journal*, Vol. 16, No. 16, pp. 6213-6221, 2016.

[11] S. V. Joubert, M. Y. Shatalov, T.H. Fay, *Rotating structures and Bryan's effect*, American Journal of Physics, Vol. 77, pp. 520-525, 2009.

[12] S. A. Tobias, R. N. Arnold, *The Influence of Dynamical Imperfection on the Vibration of Rotating Disks*, in *Proceedings of The Institution of Mechanical Engineers 1847-1982*, Vol. 171, pp. 669-690, 1957.

[13] V. Zhuravlev, *Theoretical foundations of solid-state wave gyroscopes*, in *Mechanics of Solids*, Vol. 28, pp. 3-15, 1993.

[14] D.J. Ewins, *Modal testing: theory, practice and application*, 2nd edition, in *Mechanical engineering research studies: Engineering dynamics series*, Research Studies Press, Hertfordshire, England, 2000.

[15] R. B. Randall, *A history of cepstrum analysis and its application to mechanical problems*, Mechanical Systems and Signal Processing, Vol. 97, pp. 3-19, 2017.

[16] U. Nackenhorst, *The ALE-formulation of bodies in rolling contact: Theoretical foundations and finite element approach*, Computer Methods in Applied Mechanics and Engineering, Vol. 193, No. 39, pp. 4299-4322, 2004.

[17] U. Nackenhorst, *Rollkontaktdynamik, Numerische Analyse der Dynamik rollender Körper mit der Finite-Elemente Methode*, Habilitation, IfM, Universität der Bundeswehr Hamburg, 2000.

Electromagnetic vibration analysis of main transformer for railway

K. Fukui[1], T. Noda[1]
[1] Mitsubishi Electric Corporation
8-1-1, Tsukaguchi-honmachi, Amagasaki, Hyogo, 661-8661, Japan
e-mail: **Fukui.Kenji@ct.MitsubishiElectric.co.jp**

Abstract
The purpose of this study is to construct a numerical analysis technique for reducing electromagnetic vibration of the main transformer for railway use with front loading. Reduction of vibration and noise is required since vibration and noise of railroad equipment affects ride quality. The transformer targeted in this study is a shell-type, and the coil group which is the vibration source is tightened in the coil axis direction by the tank. Then, vibration test of only coil group was carried out, a relation between tightening force in the axial direction of the coil group and natural frequency was grasped and a numerical analysis model was constructed. In addition, a coil group model of arbitrary tightening distribution was constructed based on the compression test result of the spacer between coils. It was confirmed that the actual measurement of electromagnetic vibration and the analysis result show good agreement.

1 Introduction

Transformers for electric railway vehicles are devices that transform the voltage of electricity obtained from overhead lines in order to supply power to the main circuits for driving the vehicles and auxiliary circuits such as those for air conditioning and lighting. Since the main transformer is installed in the limited space of the upper part of the vehicle and under the floor, coordination between vehicle-body structural factors (structure, dimensions, mass, etc.) is important. Moreover, as types of transformers, “core-type” and “shell-type” are available; however, to achieve coordination with the body structure, the transformer used for the railways vehicles is the shell type. In recent years, demands for ride comfort in regard to railway vehicles have been increasing year by year, so measures to reduce vibration and noise are required. Under those circumstances, it is becoming more important to consider vibration and noise in the design process.

Vibration and noise of a transformer are roughly divided into two categories. One is “excitation” vibration and noise due to the magnetostrictive phenomenon generated by excitation of the transformer’s core. The other is “energization” vibration and noise caused by the electromagnetic force generated by energization of the coil. The former, namely, excitation vibration and noise, is conspicuous when the railway vehicle is stopped; that is, as a fundamental frequency, its dominant frequency is twice the operating frequency of the transformer, and it contains harmonic components. The latter, namely, energization vibration and noise, is conspicuous when the vehicle is running under power and regenerating (so the load on the transformer is high) and operating at low speed (so the noise during running is small), and its dominant frequency is twice the operating frequency of the transformer.

Excitation vibration and noise was lowered by the development of iron-core material composed of 6.5% silicon steel (with small magnetostriction) and a combination of directional silicon-steel plate and step wrapping [1-7]. Regarding energizing vibration and noise, while observation results (such as noise variation due to tightening pressure of the coil) and studies on electromagnetic force have been published, a method for lowering noise has not been developed yet [8-9].

In this research, which aimed to devise a method for reducing energizing vibration and noise, a numerical-analysis model of a transformer for railway vehicles was constructed. Concerning conventional core-type transformers, examples of studying a modeling method of a coil and its coil tightening force, investigating the vibration propagation path from the coil to the tank of the transformer, and calculating the noise radiated from the tank have been reported [10-11]. As for shell-type transformers, unlike core-type transformers, it is difficult to model a non-uniform tightening force. Therefore, in this research, first, to grasp the vibration characteristics when the coil is tightened with uniform tightening force at the beginning and, next, to define different tightening forces at the site, stress-strain characteristics were acquired. After that, a numerical analysis model with a uniform tightening force of the coil was constructed. Then, a modeling method of non-uniform tightening force was studied, and models of iron core, tank, and oil were added to the coil model. Finally, actual measurements and analysis results concerning vibration during actual operation were compared, and the validity of the investigated modeling method was demonstrated.

2 Structure of shell-type transformer for railway rolling stock

In this study, a shell-type transformer for railway vehicles—installed under the vehicle floor—was focused on. The tank of a shell-type transformer is structured to fit to its contents (i.e., a “form fit” structure), and the coil and iron core of the transformer are housed inside the transformer tank, which is filled with oil for insulation and cooling. The iron core is a laminated electromagnetic steel plate, which is fastened and fixed in the tank in the direction of lamination of the steel plate. As for the coil, numerous coils are laminated, and in the same manner as the iron core, the coil is fixed in the tank by tightening it in the direction of coil lamination. Part of the coil is a surrounded by the iron core (“iron-core part” hereafter), and a part of it is not surrounded by the iron core. The part that is tightened by the tank is the part not enclosed by the iron core (“tightened part” hereafter). Consequently, the fastening forces in the coil-lamination direction in regard to the tightened part and the iron-core part are different. Spacers are inserted between the coils to ensure insulation and oil-flow paths. Each coil is formed by winding an insulated-coated wire in the radial direction, and the coil-tightening direction, axial direction of the coil, and coil-lamination direction are all the same.

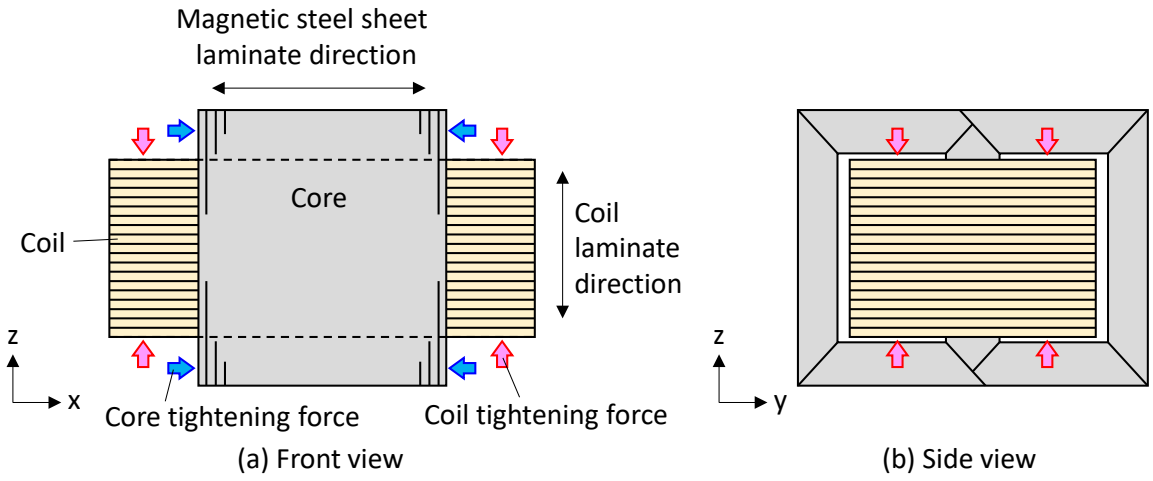


Fig. 2-1: Lamination direction of coil group and iron core as well as tightening force

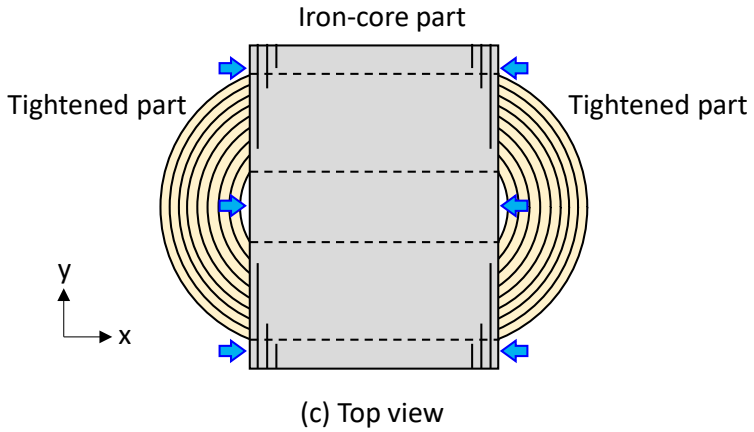


Fig. 2-1: Lamination direction of coil group and iron core as well as tightening force

3 Experimental

3.1 Experimental mode analysis of coil

To construct a numerical-analysis model of the laminated structure of the coil and spacers, experimental mode analysis (i.e., an experiment) targeting the coil only was used. The object of the analysis was only the coil, and for the purpose of tightening, a threaded rod penetrating two iron holding plates on both sides of the coil was made up. A spring (with a known spring constant) was set at one end of the threaded rod, and the tightening force was adjusted by controlling the displacement of the spring (by tightening the threaded rod). Although, in the case of an actual unit, the tightening forces in the tightened part and in the iron-core part differ, to build a numerical analysis model by a method reported in a previous study [1], it was assumed that the tightening force of the coil was uniform throughout the model. Moreover, to determine the influence of the tightening force on vibration characteristics, the experiment was carried out with the tightening force set as four conditions. Responses of the outer surface of the coil and the holding plates on both sides of the coil when an impact hammer was vibrated perpendicularly to the coil-tightening direction and the core-tightening direction were measured with a triaxial acceleration sensor, and a transfer function was obtained.

As for the results of the experimental mode analysis, the tightening force was confirmed to transition between four modes: torsion, shear, bending, and expansion. Natural frequencies of the mode in which the transition was confirmed [Hz] are listed in Table 3.1-1. A positive correlation between the tightening force and the natural frequency of the mode in which the transition occurs was confirmed. If there is no mass change due to the tightening force, and if the dimensional change is sufficiently small, the change in natural frequency is taken as being due to the change in the stiffness of the coil. Since the coil is a laminate of a conductor and a spacer, and the spacer is made of wood, it is considered that the spacer greatly contributes to the change in the coil stiffness by tightening.

Mode	Tightening force [MPa]			
	0.5	1.0	2.0	3.0
Torsion	44.4	45.9	50.7	55.8
Shear	70.4	64.4	72.2	77.9
Bending	165.8	174.5	191.8	201.6
Expansion	258.9	271.7	279.5	284.2

Table 3.1-1: Natural frequency of modes at which transition was confirmed [Hz]

3.2 Compression test on spacer

Regarding the part tightened by the tank (tightened part) and the part surrounded by the iron core (iron-core part), to define the spring constant of the spacer at an arbitrary tightening force, the load-displacement characteristic of the spacer was obtained by compression test. A general material is used for the conductor of the coil, and it has high rigidity compared with that of the spacer, and in consideration that the spacer has a significant influence on the vibration of the entire coil, the spacer itself was subjected to a compression test. To attain the same state as a real unit, an oil-impregnated spacer was tested. The stress-strain characteristics of the spacer obtained from the compression test are shown in Fig. 3.2-1. According to this figure, although the stress-strain characteristics are nonlinear overall, when the stress exceeds 0.5 MPa, they are almost linear.

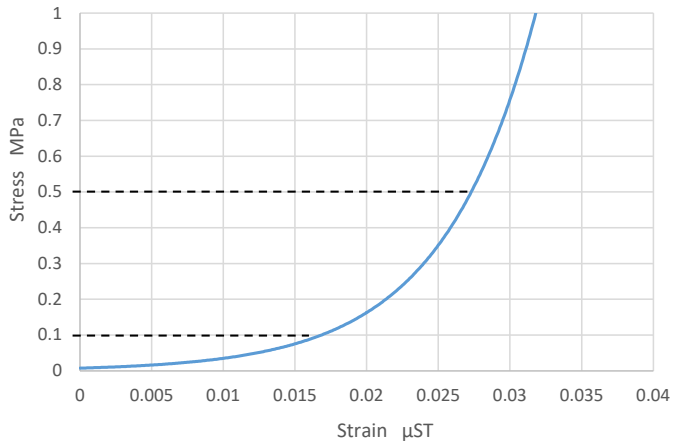


Fig. 3.2-1: Stress-strain relationship (obtained by compression test) for the spacer

4 Numerical analysis

4.1 Modelling

First, the coil only was subjected to the experimental mode analysis. Since the coil has a flat-plate structure, it was modeled as a shell element. The coil has a structure in which the conducting wire is wound in the radial direction; therefore, it is considered that its in-plane behavior and bending behaviour differ, and its different material properties are defined by its in-plane and bending behavior. The spacers between the coils were modeled with spring elements. The spring constant in the tightening direction defined the equivalent spring constant obtained from the compression-test results and the dimensions of the spacer. The spring constant in the direction orthogonal to the tightening direction was set to a value one-tenth of that in the fastening direction as the initial value. In addition, the test jig was modeled with shell and bar elements, and the material property of the jig was defined as the value for the material of the jig. Since the longitudinal modulus of elasticity of the shell element modeling the coil and the spring constant in the direction perpendicular to the tightening direction of the spring modeling the spacer are not well-grounded, they were fitted to the modes obtained by the experimental mode analysis.

Natural frequencies obtained by the experimental tests and numerical analysis (after adjustment) are plotted in Figure 4.1-1, the corresponding MAC(Modal Assurance Criterion) values are listed in Table 4.1-1, and typical vibration modes obtained by the experimental test and numerical analysis (at tightening force of 3.0 MPa) are shown (as representative examples) in Fig. 4.1-2. The relative error of the natural

frequency is about ± 5% or less, and the MAC values obtained by the experimental test and numerical analysis agree well fairly well to very well. As a result of the fitting, the rigidity in the coil plane decreased to about 15%. This result is thought to be due to the fact that even though the conductor is not integrated in the radial direction, it is modeled as one in the created numerical-analysis model. Also, at a tightening force in the range of 0.5 to 3.0 MPa, the spring constant in the tightening direction of the spacer was constant regardless of the tightening force. As shown in Fig. 3.2-1, it is also fairly linear at 0.5 MPa or greater. The spring constant in the direction perpendicular to the tightening direction of the spacer becomes linear with increasing tightening force; it is thus concluded that the change of the natural frequency due to the change of the fastening force can be expressed as the change of the spring constant in the in-plane direction of the spacer.

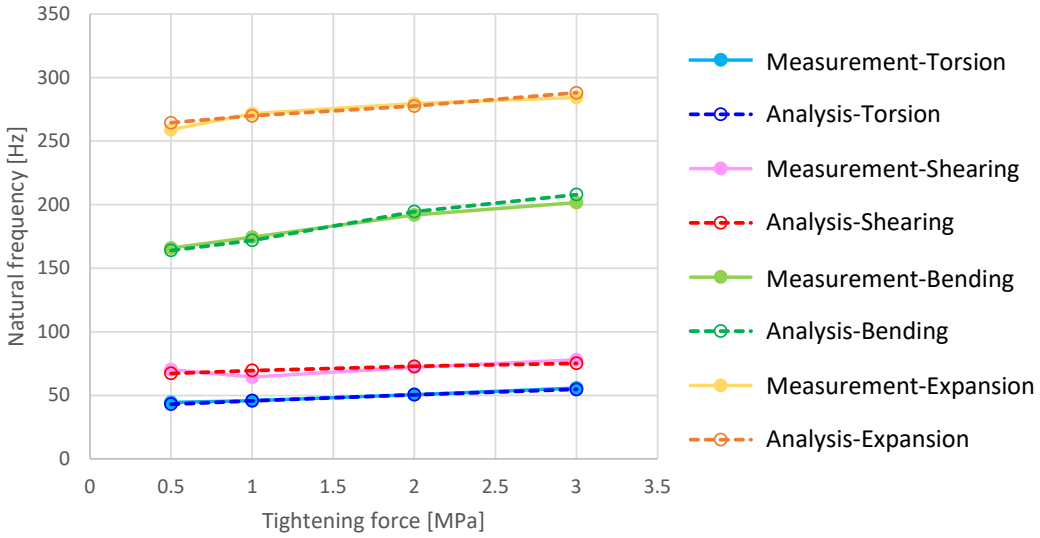


Fig. 4.1-1: Natural frequency determined by experimental test and numerical analysis

Tightening force (MPa)	Mode			
	Torsion	Shear	Bending	Expansion
0.5	0.33	0.40	0.43	0.59
1	0.40	0.44	0.77	0.68
2	0.47	0.44	0.92	0.77
3	0.45	0.56	0.91	0.78

Table 4.1-1: MAC values obtained by experimental tests and analytical model

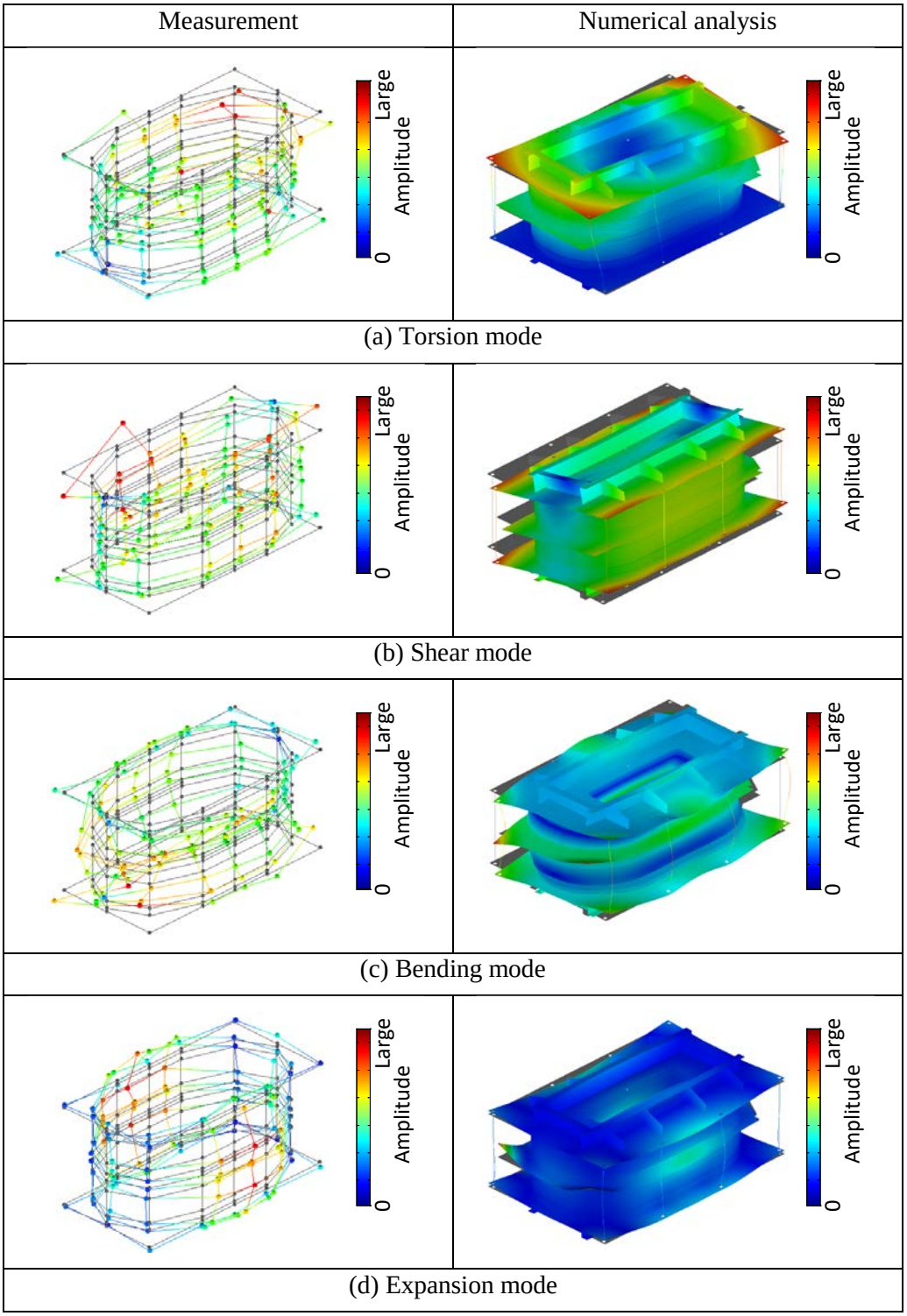
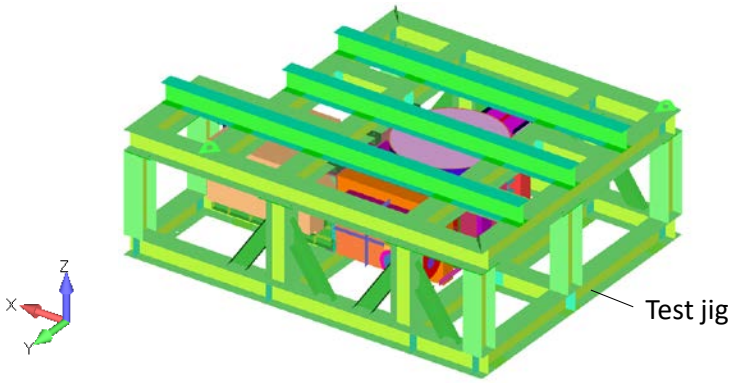


Fig. 4.1-2: Natural-vibration modes determined by test and analysis (tightening force: 3.0 MPa)

4.2 Definition of tightening force

As stated in Section 4.1, the coil was modeled in the case that the tightening force was uniform; however, the tightening force of the coil in a real unit differs in regard to the tightened section and the iron-core section. In this section, different tightening forces are modeled by varying the spring constant of the spacer. The tightening force of the part tightened by the tank in an actual unit is within the range of that set as the tightening condition in the experimental mode analysis, and since the spring constant in the tightening direction is constant, and the spring constant in the direction perpendicular to the tightening direction is proportional to the tightening-surface pressure, the spring constant of the spacer at any tightening force can be calculated. Since the part surrounded by the iron core is not tightened, the tightening force in a real unit is roughly 0 MPa. Although the spring constant of the tightened part could be estimated from the test results for the tightening-force range of 0.5 to 3.0 MPa, it is not possible to calculate the spring constant of the spacer for tightening force less than 0.5 MPa. Accordingly, the stress-strain characteristic of the spacer obtained as described in Section 3.2 and the spring constant in the direction orthogonal to the tightening direction are estimated under the assumption they are equal even if the ratio of the spring constant in the direction perpendicular to the tightening direction and the tightening direction for tightening force of 0.5 MPa is less than 0.5 MPa. The spring constant in the tightening direction at an arbitrary tightening force is obtained from Fig. 3.2-1, and it is used as the spring constant in the tightening direction. Spring constant is obtained by using a similarity ratio from an arbitrary tightening force in the direction perpendicular to the fastening direction, the spring constant in the tightening direction when tightening force is 0.5 MPa, and spring constant in the direction perpendicular to the tightening direction of the numerical-analysis model with tightening force of 0.5 MPa.

Since the Young's modulus at tightening force of 0 MPa cannot be calculated from the relation between strain and stress for the spacer (shown in Fig. 3.2-1), it is assumed that the tightening force on the iron-core part is 0.1 MPa. The iron core, tank, oil, and test jig are added to the numerical-analysis model of the coil (modeling non-uniform tightening force). The tank was regarded as a plate material, the iron core, oil, and test jig used were modelled as shell elements, volume elements, and shell elements, respectively, by using Nastran’s added-mass method (MFLUID). The tank and the test jig were made of steel, for which standard physical-property values were used. Standard values were also used for oil density. As for the modulus of longitudinal elasticity of the iron core in the in-plane direction of the electromagnetic steel sheet, the catalog value for electromagnetic steel plate was used, and the value used for the electromagnetic-steel-plate lamination direction was about 1/1000th of that for the in-plane direction [12-13]. Equivalent density was used for density. Contact elements were used for connecting the coil and the tank as well as the iron core and the tank. As for the transformer and the test jig, bolt-fastened parts were connected with rigid elements. The degree of freedom of the test jig was constrained by the parts bolt fastened to the floor surface. The appearance of the established numerical-analysis model is shown in Fig. 4.2-1.



(a) Overall view of model

Fig. 4.2-1: External view of numerical-analysis model

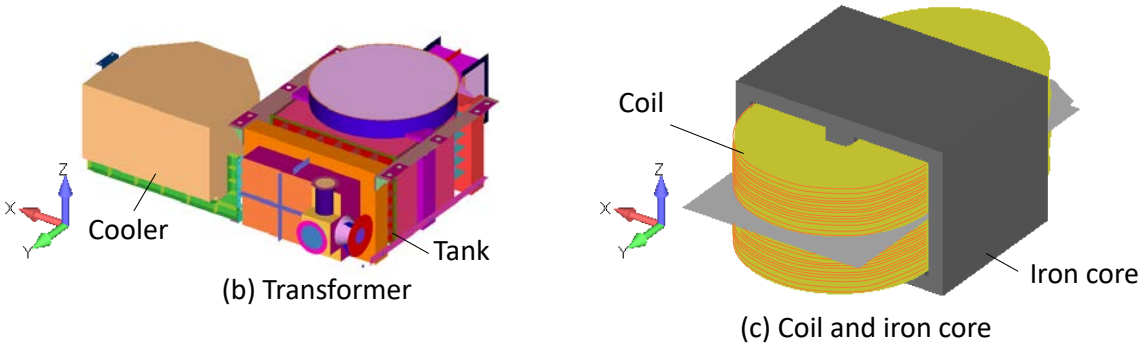


Fig. 4.2-1: External view of numerical-analysis model

4.3 Electromagnetic force

To calculate the response of the transformer during operation, the electromagnetic force generated by the coil was calculated. The electromagnetic force generated by the coil is obtained from the outer product of current flowing in the coil and magnetic flux density due to the magnetic field formed in the coil, and it can be calculated by calculating the magnetic flux density (by using magnetic-field-analysis software or the like) from the current and coil shape. For the current value, the value described in the design document was used, the frequency of the current was taken as 60 Hz, the frequency of the electromagnetic force was taken as 120 Hz, and the method used for analyzing the magnetic field was nonlinear-static-magnetic-field analysis. The result of integrating the electromagnetic forces for each coil at the instant of maximum current is shown in Fig. 4.3-1. The coil numbers shown in the figure represent each coil, and the total number of coils went up to coil #26. According to the figure, the electromagnetic force in the coil-tightening direction is predominant compared to those in the in-plane directions of the coil. Moreover, the electromagnetic force in the tightening direction was reversed in sign between coils #1 to #13 and coils #14 to #26. This trend implies that the coil is a plane object, with coils #13 and #14 as the boundary at which the direction of current flow becomes opposite. The obtained electromagnetic force is defined as that for the coil part of the numerical-analysis model, and frequency response of the transformer is analyzed.

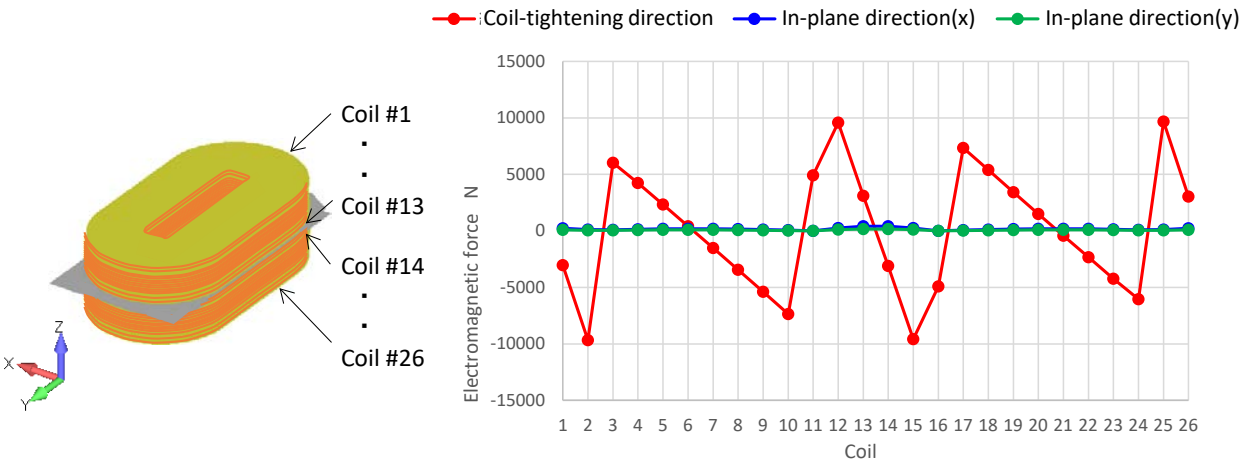


Fig. 4.3-1: Electromagnetic forces at the moment of maximum coil current

4.4 Discussions

The vibration of the tank during actual operation was compared in terms of actual measurements and the results of the numerical analysis. The evaluation direction was taken as the direction normal to the outer wall of the tank (in Fig. 4.4-1, evaluation points 1, 2, and 3 represent the z-, y-, and x-directions, respectively), and the frequency of the current was taken as 120 Hz. The results corresponding to the evaluation points shown in Fig. 4.4-1 are plotted in Fig. 4.4-2. According to the plot, the absolute values of the analysis results are 2 to 6 dB lower than those for a real unit. The reason that the absolute values of the analysis results are smaller than the measurements of an actual unit is given as follows: Although there is an error between the MAC values determined by the experimental test and by the numerical analysis, and a path traveling through the structure and a path traveling through the fluid represent the propagation paths from the coil to the tank, in this calculation, the path through which the fluid travels was not considered; that is, only of the path traveling through the structure was evaluated. Accordingly, the error in the electromagnetic force can be considered as the reason. Although there is an error between the absolute values, the mutual relationships between the measurements and the analysis results for each evaluation point are consistent. Moreover, when the electromagnetic force is defined as all directions (case 1), only in the in-plane x-direction (case 2), in the in-plane y-direction of the coil (case 3), and only in the coil-tightening direction (case 4), the relative error was less than ± 1 dB only in cases 1 and 4. This result is explained by the fact that the electromagnetic force is predominant in the coil-tightening direction (as shown in Fig. 4.3-1). For the electromagnetic force input into the numerical analysis, that in the coil-tightening direction only is thus considered sufficient.

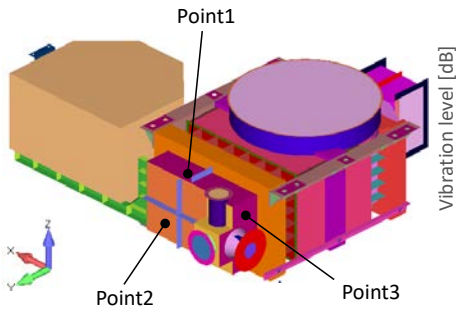


Fig. 4.4-1: Evaluation points

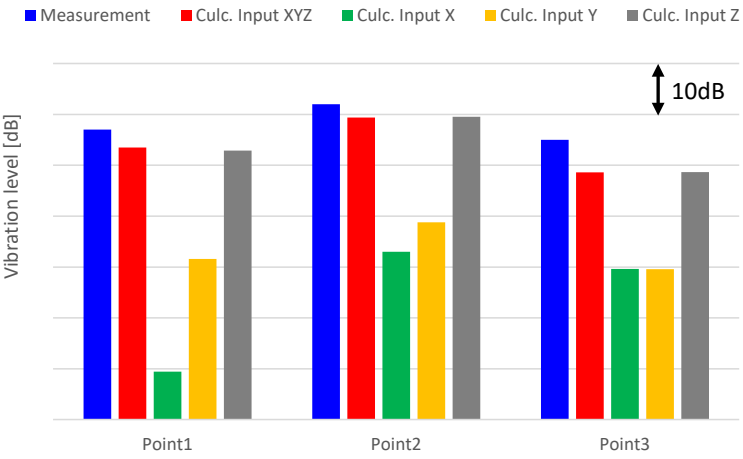


Fig. 4.4-2: Evaluation results

5 Summary

To devise a method for reducing energizing vibration and noise in a transformer, a numerical-analysis model of a transformer—in which the tightening force of the coil is not uniform—was constructed. Vibration measured during actual operation was compared with results of numerical analysis, and the effectiveness of the constructed model was verified. The results of this study are summarized as follows.

(1) Vibration during actual operation would be predicted by the model of the transformer, which defines electromagnetic force in the coil (modeling non-uniform tightening force), with relative error of -6 to -2 dB. Although there is an error in the absolute values, the mutual relationship between the actual-unit

measurements and analysis results for each evaluation point is consistent. The reason that the calculation results are smaller than the measurements of an actual unit is considered as follows: Although there is an error between the MAC values determined by the experimental test and by the numerical analysis, and a path traveling through the structure and a path traveling through the fluid represent the propagation paths from the coil to the tank, in this calculation, the path along which the fluid travels was not considered; that is, only of the path traveling through the structure was evaluated. Accordingly, the error in the electromagnetic force can be considered as the reason.

(2) Electromagnetic force is dominant in coil-axis direction, the calculation results for the case that the electromagnetic force was defined in all directions and the case it was defined in the coil-axis direction only had error of 1 dB or less. It is concluded from this finding that the electromagnetic force only in the coil-axis direction is sufficient as input into the established numerical-analysis model.

(3) The longitudinal elastic modulus of the spacer between the coils was almost completely non-linear when the tightening force was 0.5 MPa or less, but it was approximately linear at 0.5 MPa or more.

(4) The natural frequency of the coil in torsion, shearing, bending, and expansion modes when the tightening force was taken as uniform over the entire surface was found to have a positive correlation with the tightening force in the range of 0.5 to 3.0 MPa. It was also found that a spring orthogonal to the tightening direction acting as the spring constant of the spacer can express the change of the natural frequency due to the change of the tightening force of the coil as a linear change of the spring constant.

References

[1] Ninomiya H., Tanaka Y., Hiura A., Takada Y., “Magnetortriction and applications of 6.5% Si steel sheet” J.Appl.Phys. Vol.69, No.8 Pt2B (1991), pp.5358-5360.

[2] Yamashita S., Suga Y., Okamoto M., “Magnetism noise characteristies of a 6.5% silicon steel sheet.” The Annual Meeting record I.E.E. Japan, Vol.1991, No.14 (1991), pp.14-11.

[3] Kurosawa M., Namura N., Yamada S., “Electrical Steel. Grain Oriented Electrical Steel Sheet for Low-Noise Transformer Core, "27-35 New RGH".” KAWASAKI STEEL GIHO Vol.29, No.3 (1997), pp.174-176.

[4] Mogi H., Mizokami M., Akisue O., Kubota T., “Transformer Noise Characteristics with Vibration-damping Grain-oriented Silicon Steel”, MAG, Vol.29, No.3 (2002), pp.86-91

[5] Ishida M., Okabe S., Sato K., “Analysis of Noise Emitted from Three-Phase Stacked Transformer Model Core”, KAWASAKI STEEL GIHO Vol.29, No.3 (1997), pp.164-168.

[6] Oda Y., Okubo T., Takata M., “Recent Development of Non-Oriented Electrical Steel in JFE Steel”, JFE GIHO No.36 (2015), pp.6-11.

[7] Takamiya T., Hanazawa K., Suzuki T., “Recent Development of Grain-Oriented Electrical Steel in JFE Steel.”, JFE GIHO No.36 (2015), pp.1-5.

[8] IMECHEFSKE C. K., “Correlation power transformer tank vibration characteristics to winding looseness”, Insight, Vol.37 (1995), pp.599-604.

[9] Hori Y., Hiraishi K., “The Axial Direction Vibration of the Transformer Coil”, Association of Electric Quadrivium Meeting, (1969), pp.734-735.

[10] Itoh S., Murakami H., Tsujiuchi N., “Transient Vibration Response of Transformer Coils under External Short Circuit (Nonlinear Vibration Analysis of a Fluid-Structure Interacted Problem)”, Transactions of the Japan Society of Mechanical Engineers, Series C,Vol.60, No.570 (1994), pp.394-398

[11] Yoshida K., Hoshino T., Murase S., Murakami H., Miyashita T., “Electromagnetic noise design of a transformer”, Transactions of the Japan Society of Mechanical Engineers, Series C,Vol.78, No.789 (2012), pp.215-226

[12] Mizuno S., Noda S., Min Z., Akimoto K., Abe S., Yamada S., “Natural Vibration Characteristic of Transformer Iron Core” Dynamics & Design Conference 2012 (2012), pp.501-1-501-6.

[13] Fukui K., Yokomaku T., “Fundamental study on vibration characteristics of the transformer core”, Dynamics & Design Conference 2015 (2015), pp.543-1-543-11.

Load and deflection estimation of a fast catamaran towing-tank model via reduced order modeling and optimal natural observer

F. Saltari [1,2]**, D. Dessi** [1]**, E. Faiella** [1]**, F. Mastroddi** [2]
[1] Marine Technology Research Institute,
Via di Vallerano 139, 00128, Rome, Italy

[2] Sapienza University of Rome, Department of Mechanical and Aerospace engineering,
Via Eudossiana 18, 00184, Rome, Italy
e-mail: **francesco.saltari@uniroma1.it**

Abstract
This paper presents a reliable methodology that allows using large (in time) but sparse (in space) data from sensors to get a full picture of the dynamic response of a scaled model catamaran structure. Increasing the amount of information relative to the structural behavior is critical for some applications like structural health monitoring and condition-based maintenance. Loads and elastic deflections are estimated by combining the information obtained from the measured structural data with a finite element model of the system given that some statistical properties of the estimated outputs are preliminary known. Craig-Bampton method is used to achieve a reduced-order model since it is particularly suited to describe the modal response along with the estimation of the concentrated forces. A natural second-order observer is then defined to provide an optimal estimation of forces and elastic deflections. The validation of this technique is pursued by comparing estimated and known values of the response and a sensitivity analysis of the accuracy is considered as well.

1 Introduction

The development of structural monitoring systems on-board vehicles aims to achieve a full-picture of the vehicle response under operating conditions. The gathered information are indeed useful for improving design or for implementing structural health monitoring (SHM) strategies. In this paper, we deal with filling the gap between the information made available from sensors and those necessary to carry out some tasks like those indicated above. Following this path, we intend to transform point-wise measurements into a continuous spatial representation of the monitored structure plus some additional information which are not directly available. In particular, target of this estimation will be the structural deflections and the ambient loads of an elastically scaled model of a fast catamaran tested in the towing-tank. The physical model is an elastic segmented model made up by a backspline scaling the ship bending flexibility, and a hull divided into several segments, which in turn are attached to the backspline.

Transforming discrete measurements into a continuous representation needs some additional information about the system to avoid arbitrary hypotheses about its behavior; for this reason, a mathematical representation of the system in terms of a finite-element model will provide the link between the sensor measurements. Although the number of degrees of freedom (DoFs) of a FE model is highly influenced by the discretization, the number of DoFs of a sufficiently refined model is still too high for the present case, in which the critical nodes are the sensors. This well-known issue can be solved by reducing the problem size. Modal truncation techniques over finite-element analysis is usually the way to obtain a computationally cost-effective model.

However, the modal truncation is not a reliable and efficient tool when the structure is subjected to impulsive phenomena, such as slam impacts, requiring a very a large number of vibration modes to get an approximated reconstruction of the external forces and the global structural behavior. Craig-Bampton technique is an alternative method which reduces the DoFs of the structural model in a more efficient way for the present scope. The main feature of this approach is the capability to keep unchanged the information in some physical points (master DoFs) within the set of the reduced DoFs. Moreover, the behavior of the system in the frequency range of concern can be recovered by employing additional DoFs that have the physical meaning of vibration modes [1]. These features allows for estimating the elastic deformations even when external forces are concentrated in space and time. These characteristics make the present technique also useful for system sub-structuring. In the framework of virtual sensing, this sub-structuring method has been used to evaluate loads and deflections by employing accelerometers at interface locations [2]. Once a numerical model suitable for the sensor setup is available, the successive question is relative to choose the correct approach to estimate the continuous structural displacements by using a limited number of measurements. For this purpose the most popular and used tool is Kalman filter that is a recursive filter that employs a numerical model and noisy data for state estimation. The estimate is performed by obtaining a gain matrix that, given the statistical characteristics of process and measurement noise, provides the most likely value of the state over time [3, 4]. However, the Kalman filter seems not suitable for this purpose since it intrinsically requires the external forces as input or, at least, that their statistical distribution is Gaussian. However, this hypothesis is too restrictive since the hydrodynamic forces are described by narrow-band spectra in usual conditions [5]. More recent approaches, still frame-able in the field of optimal estimators, such as the augmented Kalman filter [7, 8] and the joint input-state estimator [9, 10], aim to solve this issue by estimating the external input within the filter loop. However, all the mentioned methods are not natural for a second-order mechanical system [11, 12], namely they do not ensure the kinematic relationship present within the problem. Consider the following single input-single output linear dynamic system recast in first order form:

$$\begin{aligned} \begin{Bmatrix} \dot{p} \\ \dot{v} \end{Bmatrix} &= \begin{bmatrix} 0 & 1 \\ -k/m & -d/m \end{bmatrix} \begin{Bmatrix} p \\ v \end{Bmatrix} + \begin{bmatrix} 0 \\ 1/m \end{bmatrix} u + w \\ y &= c_p p + c_v v + d_u u + v \end{aligned} \tag{1}$$

where p is the displacement, v the velocity, u the input, w the process noise, m, d, k, respectively, the mass, the damping and the stiffness, y the output, v the process noise and c_p, c_v and d_u, respectively, the coefficients that express the output though p, v and u. The state estimation equation associated to the dynamics in Eq. (1) is generally expressed as follows:

$$\begin{Bmatrix} \dot{\hat{p}} \\ \dot{\hat{v}} \end{Bmatrix} = \begin{bmatrix} 0 & 1 \\ -k/m & -d/m \end{bmatrix} \begin{Bmatrix} \hat{p} \\ \hat{v} \end{Bmatrix} + \begin{bmatrix} 0 \\ 1/m \end{bmatrix} u + \begin{bmatrix} l_p \\ l_v \end{bmatrix} (y - c_p \hat{p} - c_v \hat{v} - d_u u) \tag{2}$$

where $\hat{p}$ and $\hat{v}$ are the estimates of p and v. The optimal estimators, such as those introduced above, provide a gain matrix $[l_p\, l_v]^\mathsf{T}$ such that the desired relationship $\dot{\hat{p}} = \hat{v}$ is lost unless $l_p = 0$ (never possible [12]) or the residue $y - c_p \hat{p} - c_v \hat{v} - d_u u \to 0$. The last case is only possible when the external loads are known and the modeling uncertainties are negligible. Consequently, in this work the authors employ a natural second-order observer following an approach similar to [14, 16]. However, this observer has in its formulation free-parameters that have to be decided to enhance its accuracy. For this purpose, an optimization process is carried out to minimize the state-error and the measurement post-fit residual, recovering in this way the modeling errors that negatively affect the response estimation. From one side, the minimization of state error covariance is the same process within the Kalman filtering. However, the optimization process allows us to consider an external force spectral density making this process more consistent with the physics of the problem. From the other side, the minimization of covariance associated to post-fit residual tends to reduce the measurement residue as well as to consider data gathered in a previous learning phase. The paper is organized as follows: in Sec. (2) the experimental case study object of the paper is presented, whilst the theoretical background is provided in Sec. (3). Finally, Sec. (4) reporting the main results ends the paper before the concluding remarks.

2 The experimental case study

2.1 Physical model description

The experimental model of the catamaran being the object of the analysis is a model built with the elastic backbone approach, whose goal is to decouple the structural and hydrodynamic functions of the structure. This technique involves the construction of a structural frame that scales the elastic behavior of the full-scale model [5] and a segmented hull, where the segments - rigidly connected to the backbone beams - transmit hydrodynamic force and moments. Moreover, the experimental model includes a segmented wetdeck connected to the truss to transmit the loads generated by slamming impacts. The model is illustrated in Figure 1 where it is possible to observe the catamaran below carriage with its metallic backbone and segments. The main rigid-body characteristics of the model are listed in Table 1.



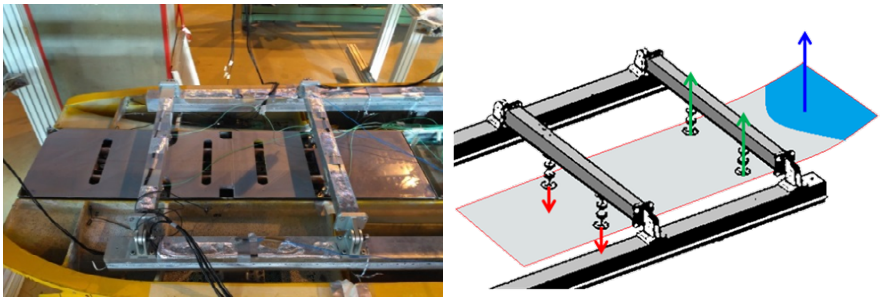
Figure 1: Experimental model under the carriage.

The backbone truss is made of aluminum and includes several structural components: two longitudinal beams, two transverse beams, a central beam in the symmetry plane, and two hinged beams near the bow to support the wetdeck as shown in Figure 2. The truss is connected to the segments by using stiff vertical

Table 1: Main model parameters.

Variable	value
Mass	206.8 Kg
Length Overall	3.96 m
CoG	1.628 m
Pitch radius	1.143 m

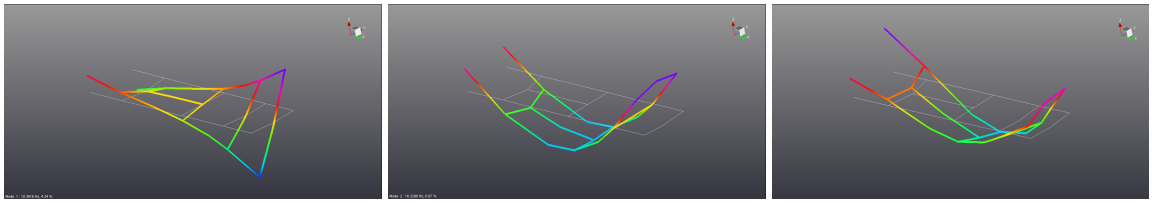
elements called legs. The role of the hull segments is to transfer concentrated hydrodynamic force to the elastic backbone via the legs. Each demi-hull is divided into four segments as shown in Figure 1. In order to ensure a certain stiffness and lightness, the segments are made with fiberglass laminate with a stiffening core material. The gaps between adjacent segments is made water-tight by using thin rubber straps. On the other hand, the wetdeck is made up by different materials such as fiberglass, wood and PLA in order to make it robust enough and, in turn, it is segmented in two parts, with length of 1/3 and 2/3 length overall, respectively for the forward and the backward part. The forward part, where all the slamming phenomena occur, is connected to the two hinged beams. A great number of structural lab tests have been carried out on the model, such as static and vibration tests, that has been used to enhance the numerical model. These tests were carried out hand in hand with the construction of the model, involving different configurations and parts of the catamaran. The results related with vibration tests of the final configuration are presented. For a deeper insight, please refer to [6]. The experimental first six elastic mode shapes of the free-free structure with the corresponding natural frequencies and damping ratios are shown in Figure 3. The free-free conditions have been reproduced by hanging the present model by means of 8 soft springs in order to keep the frequencies



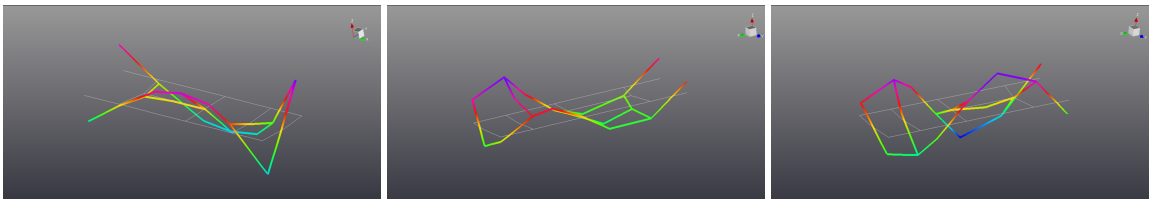
(a) Wetdeck view (b) Working principle of wetdeck balance

Figure 2: Wetdeck arrangement.

of the rigid-body modes with frequency lower than 2.0 Hz [5]. Finally, natural frequencies and modes have been computed by means of Polymax. Further wet vibration tests have been carried out showing a general decrease of the natural frequencies. Table 2 shows natural frequencies and damping of modes that can refer to those shown in Figure 3



(a) $f_1 = 10.36$ Hz, $\zeta_1 = 0.042$ (b) $f_2 = 16.33$ Hz, $\zeta_2 = 0.007$ (c) $f_3 = 23.65$ Hz, $\zeta_3 = 0.019$



(d) $f_4 = 29.33$ Hz, $\zeta_4 = 0.015$ (e) $f_5 = 46.36$ Hz, $\zeta_5 = 0.008$ (f) $f_6 = 55.41$ Hz, $\zeta_6 = 0.01$

Figure 3: Natural modes from dry vibration tests.

Table 2: Wet vibration tests: natural frequencies and damping.

mode	1	2	3	4	5	6
$f_n[Hz]$	8.63	12.02	15.45	23.19	35.51	38.69
ζ_n	0.022	0.004	0.006	0.017	0.013	0.011

Eventually, the experimental campaign, that main results are provided in Sec. (4), has been performed at the CNR-INSEAN towing-tank basin Emilio Castagneto in Rome, that is a 220 m long, 9 m wide and 3.5 m deep linear basin equipped with wavemaker system, able to generate regular waves and irregular sea according to different kind of spectra. The monitoring of the elastic deflections and the hydrodynamic loads is applied to a scaled physical naval model tested in towing tank with on board acquired data. Some details about the towing system and the sensor layout follows. However, deeper insights about design and model assessments can be found in [5].

The model was towed by an eight-drive wheels carriage moving on a railroad guide. The complex towing system was such that it would only allow for heave and pitch modes by means of a barycentric hinge connected to vertically oriented linear bearing and a fork-type device at the stern.

Heterogeneous data related to strains, rigid-body motion and internal forces have been used. This vast amount of data has been recorded by means of a manifold of synchronized DEWE-43 modules. In particular, the sensor used for this analysis consists of 36 HBM strain gages spread to cover the whole backbone (Figure 4), and Rodymm Krypton optical system to measure all six rigid-body DOFs.

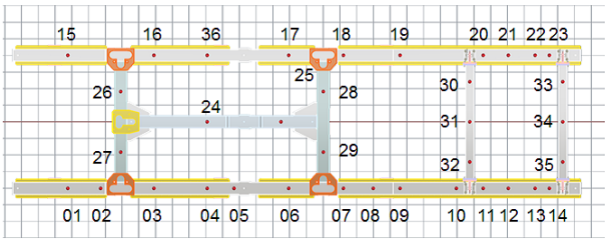
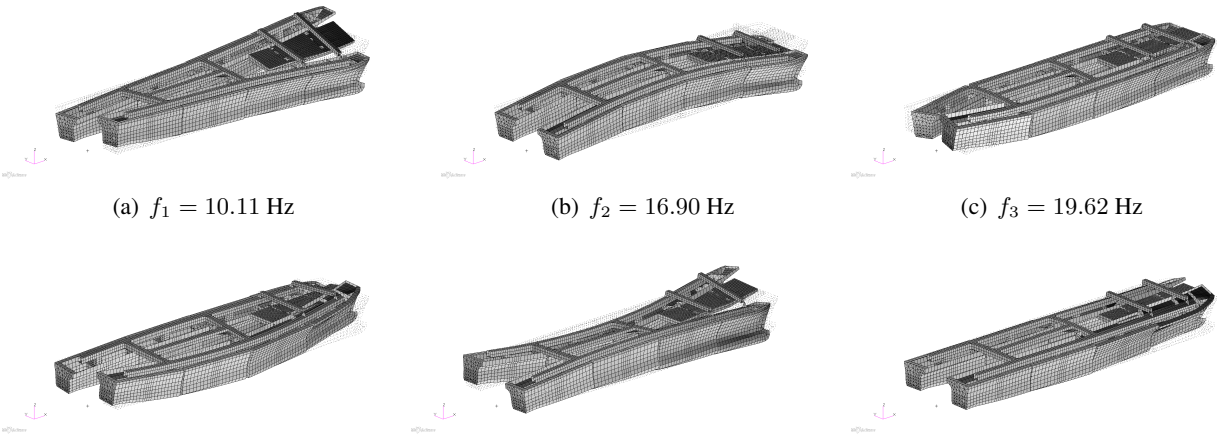


Figure 4: Strain gages layout.

2.2 Numerical model description

The physical model introduced in Sec. (2) has been modeled by means of a detailed FE model. The development of present FE model has been particularly challenging since the mass properties are highly influenced by sensor layout and hull mass distribution. In order to obtain a numerical model as close to the experimental one as possible, a model updating has been carried out in a cascade way by updating the structural components step by step during the model assembly stage. Hence, first the properties of backbone has been update by experimental vibration tests of the bare metallic frame up to a frequency of 120 Hz and then, an equivalent model of wetdeck has been generated in order to model its stiffness and mass. Finally, a final updating is performed considering the whole structure in order to reach a good matching between the experimental dry modes and the first two numerical vibration modes. The FE natural modes and frequencies are shown in Figure 5. Notice that the first two modes and frequencies are very close to the experimental ones. Moreover it is possible to notice some vibration modes not identified in the experimental tests, such as the modes of the symmetric torsion of forward part of the trusses with frequency 27.71 Hz. Finally a proportional damping matrix has been assumed by taking into account the experimental damping ratios.



(a) $f_1 = 10.11$ Hz (b) $f_2 = 16.90$ Hz (c) $f_3 = 19.62$ Hz

(d) $f_4 = 19.75$ Hz (e) $f_5 = 20.15$ Hz (f) $f_6 = 27.71$ Hz

Figure 5: Natural modes from dry numerical modal analysis.

3 Theoretical background

The estimation of elastic deflections is performed by combining two techniques: the Craig-Bampton reduction and an optimal observer. The Craig-Bampton technique allows us to reduce the problem size and can be carried out within the FE framework. The successive and most challenging step is to design a natural observer, based on a finite set of measurements, which is "optimal" in giving back a trustworthy representation of our physical system.

3.1 Sensor datasets

To clarify how the data is processed, two main group of variables are defined:

- **Active measurements** y_a. This is the input processed by the presented method to build the approximation model. These data are provided by sensors constituting the permanent sensor array upon which the expert monitoring system will be permanently based.
- **Virtual measurements**. This is the new information that is obtained from the output, directly or through simple models.

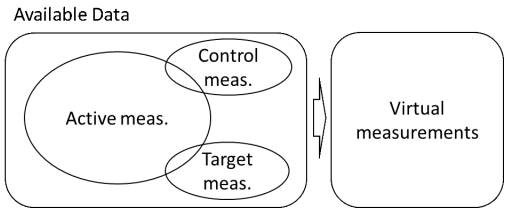


Figure 6: Classification of sensor datasets.

Since it is our aim to validate the present method against the **available measurements**, a more comprehensive classification of the information is used in the present paper:

- **Active measurements** y_a, as seen above.
- **Target measurements** y_t. It includes the data upon which the procedure internally tries to minimize its errors, or conversely to refine its capability to predict the correct values.
- **Control measurements** y_c. These are available measurements used to check the final performances but which do not drive the optimization procedure.

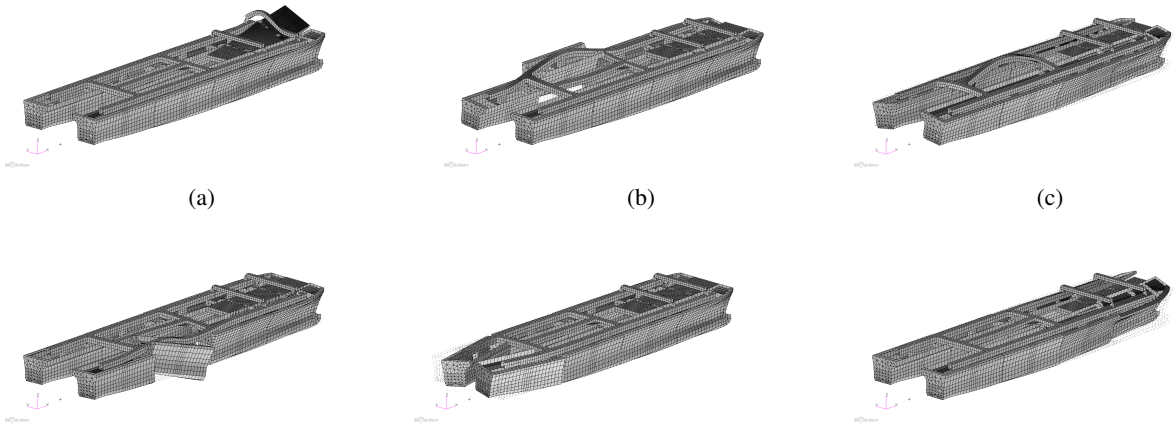
The introduction of the AI set corresponds to performing the so-called "learning phase" when the system is installed on-board our vehicle or in the monitored structure; the Target Measurements are obtained by means of an additional array of sensors that after the "learning phase" is removed. The reason for which the Target Meas. are not included in the Active Measurements set is because the design of the optimal observer would change if more input variables are fed to the system after completion of the "learning phase". These concepts are further explained in the diagram above. The Target and the Control Measurements are distinct sets because we are specifically interested in evaluating the performances in points which did not take part to the optimization process. On the other hand, the Control Measurements may include all the input variables (Active Meas. Set), but is more indicating if at least some control variables are not fed as input to the system, since we trivially expect that good predictions are obtained in the Active data (even if the system is not strictly an interpolator).

3.2 Craig-Bampton Method

The Craig-Bampton method [1] is a technique that allows for reduction of the number of degrees of freedom u of a structural problem if the dynamic response is limited to a certain frequency range. This method differs from the modal truncation by the capability to include physical displacements in the set of generalized coordinates; this provides a set of reduced DoFs on which the decomposition depends, which are called *master* and hereafter denoted by $\mathsf{u_M}$. Besides the master DoFs, an additional set of modal DoFs η is considered to complete structural dynamics behavior in the interest frequency range. By taking into account this reduction technique, the physical DoFs u can be expressed by superimposition as:

$$\mathsf{u} = \begin{Bmatrix} \mathsf{u_M} \\ \mathsf{u_S} \end{Bmatrix} = \begin{Bmatrix} \mathsf{u_M} \\ \mathsf{S u_M} + \mathsf{Z_S}\eta \end{Bmatrix} = \begin{bmatrix} \mathsf{I} & \mathsf{0} \\ \mathsf{S} & \mathsf{Z_S} \end{bmatrix} \begin{Bmatrix} \mathsf{u_M} \\ \eta \end{Bmatrix} = \mathsf{R_{cb}} \begin{Bmatrix} \mathsf{u_M} \\ \eta \end{Bmatrix} \tag{3}$$

where $\mathsf{R_{cb}}$ is the Craig-Bampton transformation matrix. The dynamics of the slave DoFs $\mathsf{u_S}$ depends on the *master* DoFs by means of the *boundary modes* S obtained by a static condensation, as well as the dynamics associated to the *fixed-boundary modes* $\mathsf{Z_S}$. For the present case study (see Sec. (2)) an amount of 23 master



(a) (b) (c)

(d) (e) (f)

Figure 7: Craig-Bampton modes: examples of *boundary modes* (a,b,c,d) and *fixed-boundary modes*(e,f)

DoFs has been considered, that are chosen by selecting:

- the vertical displacements and rotations about the transversal axis in each connection point between segments and backbone (8 points with DoFs 3 and 5);
- the vertical displacements in each connection point between the forward part of the wetdeck and relative bars (4 points with DoF 3);
- the vertical and lateral displacements as well as the rotation about the vertical axis of the hinge point of the CoG (1 point with DoFs 2,3 and 6).

These DoFs are introduced in order to have the minimum number of variables able to describe in a complete fashion the concentrated forces exchanged between the segmented hull and the backbone as well as the constraint force exchanged with the seakeeping bar. Then, a user dependent number of fixed-boundary modes is considered in order to have also a displacement space complete enough for the interest frequency range. Thus, the transformation matrix in Eq. (3) allows to get a reduced order system whose dynamic behavior is described by the following mass and stiffness matrices:

$$\begin{aligned} \mathsf{M_{cb}} &= \begin{bmatrix} \mathsf{M_{MM}} + \mathsf{S^T M_{SS} S} & \mathsf{S^T M_{SS} Z_S} \\ \mathsf{Z_S^T M_{SS} S} & \mathsf{I} \end{bmatrix} \\ \mathsf{K_{cb}} &= \begin{bmatrix} \mathsf{K_{MM}} + \mathsf{K_{MS} S} & \mathsf{0} \\ \mathsf{0} & \Omega_\mathsf{S} \end{bmatrix} \end{aligned}$$

According with the sensor datasets definition of Sec. (3.1), the second order linear dynamic system can be expressed as follows:

$$M_{cb}\ddot{q} + D_{cb}\dot{q} + K_{cb}q = f + w \tag{4}$$

$$y_a = C^a_{cb}q + v_a \tag{5}$$

$$y_t = C^t_{cb}q + v_t \tag{6}$$

$$y_c = C^c_{cb}q + v_c \tag{7}$$

where $q^T = \{u_M^T \ \eta^T\}$ is the vector of the reduced generalized coordinates, D_{cb} is the structural damping matrix expressed by means of Craig-Bampton modes, f is the vector of the hydrodynamic forces, w is the process noise, v_a, v_t and v_c are the measurement noises and C^a_{cb}, C^t_{cb} and C^c_{cb} are the output matrix respectively associated to active, target and control measurements.

3.3 Natural second-order observer

The estimate of loads and elastic deflections needs for a further and more important step. In this work, the optimal observer that has been used resumes and expands the characteristics of the one proposed in [12], making it suitable to estimate the external forces and the elastic deflections of the scaled model of catamaran. Additional elements with respect to [12], are *i)* the use of a non-symmetric observer; *ii)* the introduction of two objective functions to be optimized, one -classic- which aims to the minimization of the state error and the other-one that aims to minimize the residues at the points defined as Target Meas. in Sec. (3.1) ; *iii)* the use of a-priori estimate of the statistics associated with external forces (as in this case the power spectral density) to improve the estimation of the dynamics that are actually excited.

The state equations of the unknown input linear second order observer of Eq. (4) can be generally expressed as follows:

$$M_{cb}\ddot{\hat{q}} + D_{cb}\dot{\hat{q}} + K_{cb}\hat{q} = L(y_a - C^a_{cb}\hat{q}) \tag{8}$$

where the symbol $\hat{\bullet}$ refers to each estimated quantity and L is the observer gain. By defining the state error $e = q - \hat{q}$, the Eqs. (4,8) provide the error dynamics as

$$M_{cb}\ddot{e} + D_{cb}\dot{e} + K_{cb}e + LC^a_{cb}e = f + w + Lv \tag{9}$$

The Fourier transform of Eq. 9 yields

$$[-\omega^2 M_{cb} + i\omega D_{cb} + K_{cb} + LC^a_{cb}]\,\tilde{e}(\omega) = \tilde{f}(\omega) + \tilde{w}(\omega) + L\tilde{v}(\omega) \tag{10}$$

where the symbol $\tilde{\bullet}$ is used to represent the Fourier transform. By defining

$$H_O(\omega) = [-\omega^2 M_{cb} + i\omega D_{cb} + K_{cb} + LC^a_{cb}]^{-1} \tag{11}$$

Eq. 10 provides the frequency response of the state error as

$$\tilde{e} = H_O(\omega)(\tilde{f} + \tilde{w} + L\tilde{v}) \tag{12}$$

If the statistical features of the forcing terms and process and measurement noise are stochastic, known and uncorrelated each other, by means of Eq. (12), the system response to stochastic inputs is obtained as follows

$$\Phi_{ee}(\omega) = H^*_O(\omega)(\Phi_{ff}(\omega) + \Phi_{ww}(\omega) - L\Phi_{vv}(\omega)L^T)H^T_O(\omega) \tag{13}$$

where $\Phi_{\bullet\bullet}$ indicates the power spectral densities. On the other hand, it is possible to define also the post-fit measurement residual by means of Eq. 7:

$$\tilde{z} = \tilde{y}_t - \tilde{\hat{y}}_t = [I - C^t_{cb}H_O(\omega)L]\tilde{y}_t \tag{14}$$

This relationship is however influenced by the noise present in $\mathsf{t_t}$ and from non-optimal estimation of state. In a similar way of Eq. 13, the power spectral density of the post-fit measurement residual can be processed using the data gathered in the learning phase:

$$\Phi_{\mathsf{zz}}(\omega) = \left[\mathsf{I} - \mathsf{C}^{\mathsf{t}}_{\mathsf{cb}}\mathsf{H}_O(\omega)\mathsf{L}\right]^* \Phi_{\mathsf{y_t y_t}}(\omega) \left[\mathsf{I} - \mathsf{C}^{\mathsf{t}}_{\mathsf{cb}}\mathsf{H}_O(\omega)\mathsf{L}\right]^{\mathsf{T}} \tag{15}$$

Finaly, Eqs. (13,15) yield the covariances of the state error and post-fit residual

$$\begin{aligned} \mathsf{P} &= \int_{-\infty}^{+\infty} \Phi_{\mathsf{ee}}(\omega) d\omega \\ \mathsf{S} &= \int_{-\infty}^{+\infty} \Phi_{\mathsf{zz}}(\omega) d\omega \end{aligned} \tag{16}$$

Note that these two quantities depend on the gain matrix L. The aim is to assess and minimize the covariances of Eq. (16) by find the optimal free parameters that make up the matrix L. This optimization process will be discussed in Sec. (3.4).

3.4 Optimization Process

3.4.1 Objectives

Generally speaking, an optimal estimator is obtain when the gain matrix is computed to minimize the trace of P, that represents the norm 1 of the variance of the errors on the state. This is the same operation generally operated in Kalman filtering, considering, however, only the displacements in the state vector. Though the external forces are not directly measured, the knowledge of their power spectral densities, along with the characterization of the process and measurement noises, allows us to compute the observer to get the most likely estimation of the state (see Eq.13). In case of low measurement noise, a high gain observer is always obtained. However, in the presence of noise in the output data, the observer should be able to penalize the estimation of the dynamics that have a noise higher then the useful signal. On the other hand, minimizing $tr(\mathsf{S})$ means designing an observer that makes the post-fit residues converge to zero. This information must be managed carefully since it does not ensure the convergence of displacements throughout the structure and, generally, it may be conditioned by measurement noise. However, the minimization of $tr(\mathsf{S})$ could be very helpful in the case some measurements are available only in an early learning stage since the resulting observer addresses the estimation to converge also in that points that are no longer directly monitored. The natural second-order observer proposed in this work is synthesized by minimizing $tr(\mathsf{P})$ as well as $tr(\mathsf{S})$.

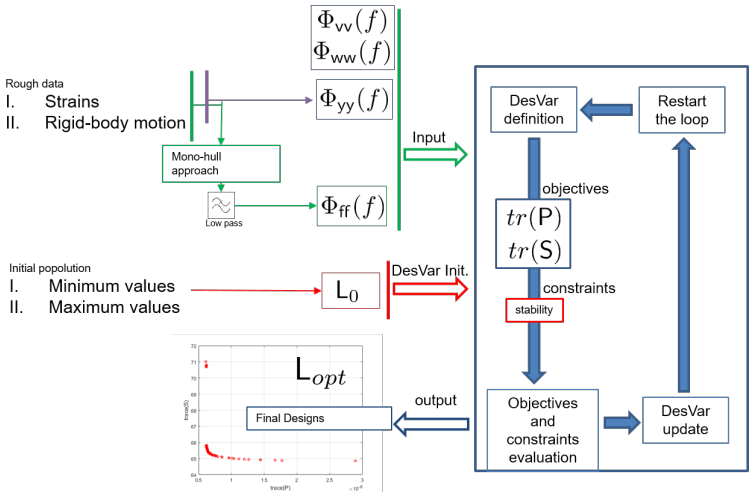


Figure 8: Optimization process loop.

3.4.2 Inputs

The optimization process starts by providing the spectral densities matrices of the forces and response. Both the spectral densities have been estimated by considering the record outputs during the towing tank campaign and recast in order to estimate the structural behavior of the model in an effective way. The external forces spectral densities are obtained by estimating the forces in a least-squares sense. To this end, the transfer function has been considered that concerns only the Master DoFs of the system made symmetrical with respect to the xz plane:

$$\tilde{\hat{\mathsf{f}}} = \left[-\omega^2 \hat{\mathsf{M}} + \hat{\mathsf{K}}\right]^{-1} \hat{\mathsf{C}}^{\dagger}\, \tilde{\mathsf{y}} \tag{17}$$

where $\hat{\mathsf{M}}$ and $\hat{\mathsf{K}}$ are the mass and stiffness matrices of the statically condensed system with xz plane symmetry constraints. This approach allows to get a rough frequency representation of the external forces, that, subsequently are filtered in order to take into account only the wave loading in the hulls regions (low-pass filtering sufficiently below the first natural frequency < 7 Hz) and the slamming phenomena on the wetdeck (below the first wetdeck natural frequency < 40 Hz). The uncertainties related the reconstruction of the external forces are introduced into the user-defined process noise along with other structural uncertainties. On the other hand, the spectral densities of the outputs ($\Phi_{\mathsf{yy}}(f)$) are obtained by considering the rough data without any filtering process.

3.4.3 Design variables

The estimate of optimal gain matrix represents a multi-objective optimization problem, where the set of design variable is made up by all the elements of L. [12] suggests how to decompose the observer in order to consider just a limited number of design variables for the optimization process,

$$\mathsf{L} = \mathsf{C}_{\mathsf{cb}}^{a\,\mathsf{T}} \mathsf{G} \tag{18}$$

where the diagonal elements of G (whose number is the same of active sensors) could be enough to obtain an optimal observer. This shape allows also to preserve the symmetry of the problem. This observer is such that a weight for each sensor is assigned by means of the diagonal elements of G. However, this approach may be too restrictive to achieve a good optimum since relies only to a weight assigned to each sensor. Although, it is still possible to perform the optimization with all the elements of the gain matrix L (though the likelihood to find a global optimum is low due to high number of design variables involved), the authors propose an alternative observer decomposition:

$$\mathsf{L} = \mathsf{Z}_{\mathsf{cb}}^{-\mathsf{T}} \mathsf{W} \mathsf{C}_{\mathsf{cb}}^{a\,\mathsf{T}} \mathsf{G} \tag{19}$$

where Z_{cb} is the eigenvector matrix that diagonalizes M_{cb} and K_{cb}, whereas W is a matrix that weighs the normal modes according to how these modes are supposed to be influenced by external forces and their own dynamics. Therefore, in this work, only the diagonal elements of W and G are used to synthesize the best observer with the minimum number of variables.

3.5 Quality indicators

In order to quantify the error that is committed by using the present approach, the authors refer to two different functions called *Time Response Assurance Criterium* (TRAC) and *Frequency Response Assurance Criterium* (FRAC) introduced in [17] and defined as follows:

$$TRAC(t) = \frac{\| \hat{\mathsf{y}}_{\mathsf{c}}(t)^{\mathsf{T}} \mathsf{y}_{\mathsf{c}}(t) \|^2}{(\hat{\mathsf{y}}_{\mathsf{c}}(t)^{\mathsf{T}} \hat{\mathsf{y}}_{\mathsf{c}}(t))(\mathsf{y}_{\mathsf{c}}(t)^{\mathsf{T}} \mathsf{y}_{\mathsf{c}}(t))} \tag{20}$$

$$FRAC(f) = \frac{\| \tilde{\hat{\mathsf{y}}}_{\mathsf{c}}(f)^{\mathsf{H}} \tilde{\mathsf{y}}_{\mathsf{c}}(f) \|^2}{(\tilde{\hat{\mathsf{y}}}_{\mathsf{c}}(f)^{\mathsf{H}} \tilde{\hat{\mathsf{y}}}_{\mathsf{c}}(f))(\tilde{\mathsf{y}}_{\mathsf{c}}(f)^{\mathsf{H}} \tilde{\mathsf{y}}_{\mathsf{c}}(f))} \tag{21}$$

The functions above represent, respectively, the similarity of the estimate time and frequency response of the control sensor array with the measured ones. The values are between 0 and 1, hence these functions are good candidates for being considered quality indicators. The average of the values over time $\overline{TRAC}$ and frequency $\overline{FRAC}$ in the interest range are assumed as indicators for the quality of the estimation as a function of the number and distribution of sensors.

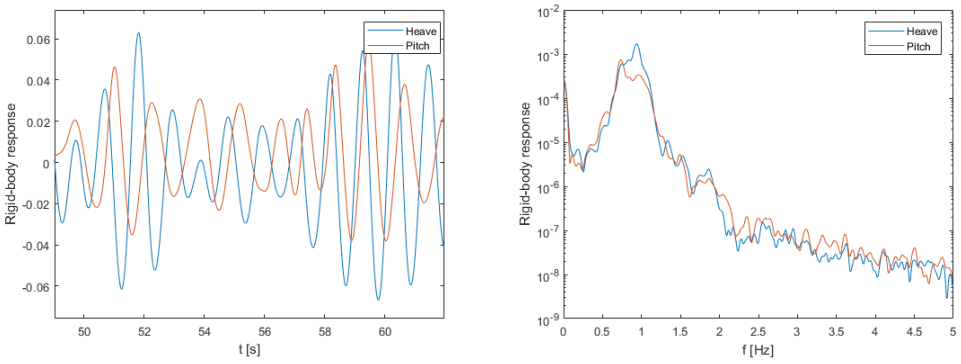
4 Results

The method presented in Sec. (3) has been applied on the experimental data collected during the experimental campaign in the towing-tank with the scaled model described in Sec. (2). The results shown here concern in particular a run in irregular (stochastic) sea following a JONSWAP spectrum, which is a general law describing the distribution of energy between the waves of different period and phase into which the wave elevation can be decomposed. The test condition of the considered run is reported in Table 3 in terms of speed, significant wave height and period:

Table 3: Sea condition of the considered run in irregular sea.

Speed	1.779 m/s
wave height	0.1053 m
Period	0.798 s

The considered run has been chosen since several wetdeck slamming events occurred and consequently the dynamic response of the catamaran exhibits all the hydroelastic features that make this problem worth to be investigated. Moreover, the presence of impulsive loading yields a broad-band excitation of the natural modes and provides consequently a challenging test-case for the present method. Figure 9 shows the rigid-body motion response by means of the time domain recorded data (a) and their spectral density (b) in the rigid-body modes frequency range. Concerning the structural behavior, the strain gage responses are shown in Figure 10 considering the sum of the spectral densities of all the strain gages.



(a) Time responses (b) Power spectral densities

Figure 9: Time and frequency responses of Heave and Pitch.

4.1 Estimation of forces and elastic deflections

In this section the response of the catamaran in terms of forces and elastic deflections is analyzed and discussed for the sea condition listed in Table 3. Here, the sets of Active, Target and Control measurements coincide, so that all the sensors are used for state updating, gain matrix evaluation and estimation of elastic displacements quality indicators. Otherwise, remind that the estimation of forces is contaminated by process

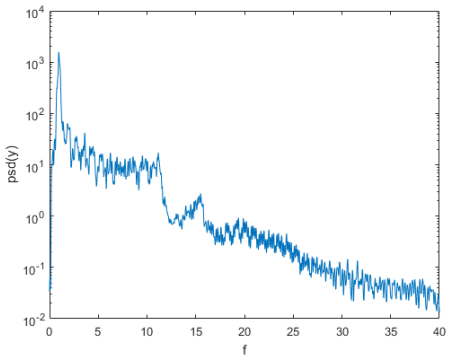
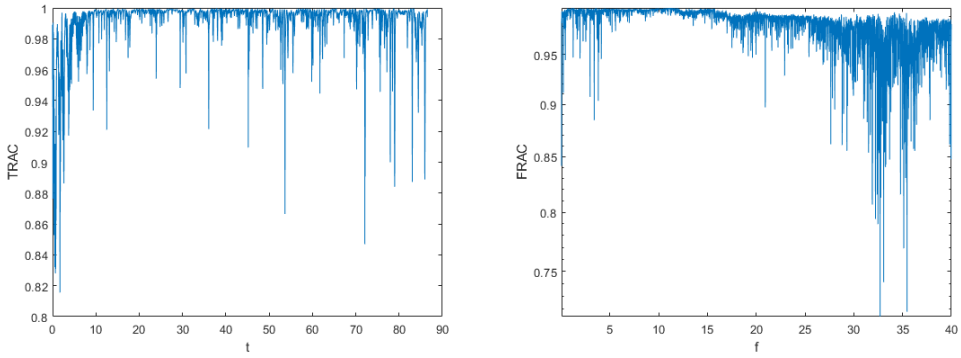


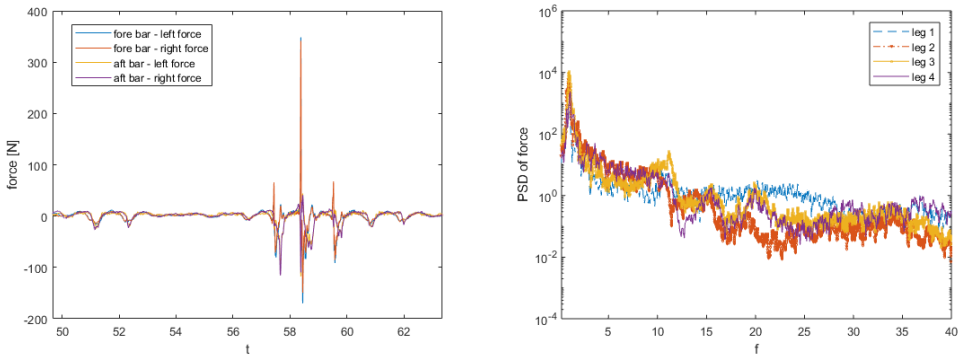
Figure 10: Sum of power spectral densities of strain outputs.



(a) Time response assurance criterion (b) Frequency response assurance criterion

Figure 11: Time and frequency response assurance criterion of strain outputs.

noise as shown in Eq. (4). The strain gages response in Figure 10 shows two clearly resonant peaks about 12 Hz and 16 Hz. The observer is then computed according to the method proposed in Sec. (3) and its capability to give the right estimation of the sought variables is assessed by means of TRAC and FRAC (see Sec. (3.5)) in Figure 11 considering all the available sensors. One of the most interesting results concerning this run is the prediction of the forces in the wetdeck region, whose time response estimation is shown in Figure 12a. The results show a clear symmetry of the hydrodynamic forces under the wetdeck. The responses of the concentrated forces acting on each segment of the right demihull are shown in Figure 12b, where the leg number connecting the segments to the backbone is sorted in ascending order from bow to stern.



(a) Time histories of concentrated forces on wetdeck region

(b) Frequency response of concentrated forces acting on the leg connecting the segments to the right backbone beam

Figure 12: Concentrated forces over the structure.

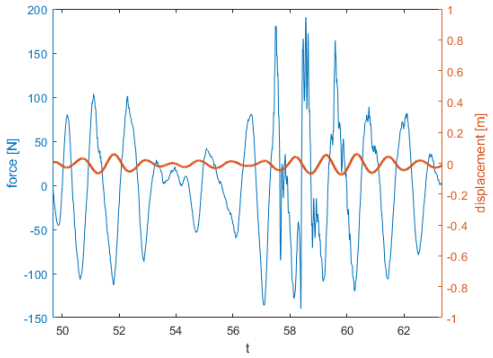
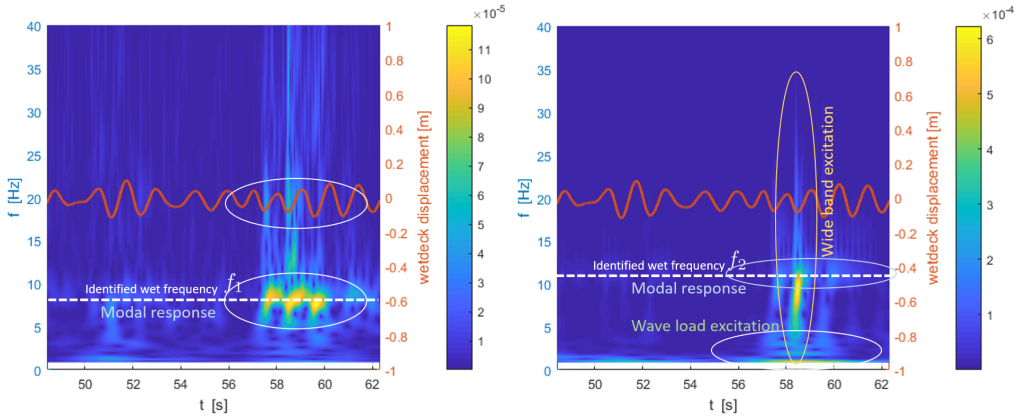


Figure 13: Time response of the force on the second segment of the right hull starting from the bow.

The time response of the force on the second segment of the right demihull is shown in Figure 13 compared with the vertical displacement of the point in which the forces are exchanged. Further interesting result concern the time-frequency domain response of the deflection field projected on the vibration modes. In Figure 14 are shown the response of first two vibration modes by means of wavelet transform. Figure 14a shows the response of the split mode. It can be noticed that the main contribution swings from 7 Hz and 9 Hz, that is nearly the value that came out from the vibration tests carried out with the wet configuration (see Sec. 2.1). This particular behavior is due to an unsteady distribution of the added (hydrodynamic) mass caused by heave and pitch motion. The vertical two-node bending mode, instead, presents evident wide-band instant responses due to the impacts in the wetdeck region.



(a) First mode (b) Second mode

Figure 14: Vibration modes wavelet spectrum. The red line represent the vertical displacement of wetdeck center in time domain.

After the slamming, the wavelet spectrum shows an halo at about 12 Hz that points out the associated modal response. It is worth to notice that these two effects are superimposed to the wave load response at very low frequency.

4.2 Sensitivity analysis as a function of measurement sets

According with classification of the the measurement set in Sec. (3), a sensitivity analysis on the number of the considered strain gages is carried out. In order to simplify the description of the current analysis, the available measurements are divided into 4 groups by considering the strain gages layout in Figure 4:

g_1 : 1-36

g_2 : 1,3,5,7,9,12

g_3 : 16,18,22

g_4 : 14,25-29,30,32,34

The sensitivity analysis is then carried out by considering six cases according to the classification in Sec. 3.1, as reported in Table 4.

Table 4: Set classification with the values of average FRAC and TRAC for each subset case.

subset	Case 1	Case 2	Case 3	Case 4	Case 5	Case 6
Active	g_1	$g_1 \cap g_2$	$g_1 \cap (g_2 \cup g_3)$	$g_1 \cap (g_2 \cup g_3 \cup g_4)$	$g_1 \cap (g_2 \cup g_3)$	$g_1 \cap (g_2 \cup g_3 \cup g_4)$
Target	g_1	g_1	g_1	g_1	$g_1 \cap g_2$	$g_1 \cap (g_2 \cup g_3)$
Control	g_1	g_1	g_1	g_1	g_1	g_1
$\overline{TRAC}$	0.9922	0.9875	0.9833	0.9203	0.9861	0.8348
$\overline{FRAC}$	0.9809	0.9661	0.9290	0.8460	0.9458	0.8180

For each case of considered subset for Active, Target and Control meas., the values of $\overline{TRAC}$ and $\overline{FRAC}$ has been computed and reported in the same Table 4.

Table 4 indicates that the higher the number of sensors used the better is the estimation. However, it shows that also reducing drastically the number of sensor (as in Case 4 and Case 6) the average values of FRAC and TRAC still remain acceptable. However, it is shown that, despite having the same number of active sensors, Case 4 provide a better estimation than Case 6 since all non active sensors are considered as target and used in the observer design stage.

5 Concluding remarks

In this paper a numerical technique aimed to extend the capabilities of a monitoring system has been presented using as test case a scaled model of a catamaran equipped with several sensors. In this way, the elastic deflection field has been reconstructed and unknown measurements like the estimation of the hydrodynamic loads acting on the segments have been obtained. This tool is the first step toward a robust methodology to support structural health monitoring and predictive maintenance strategies. To match the nature of the present problem, the involved methodology includes the use of an optimal second order observer that has been synthesized by minimizing the state error and the measurement residual covariances given some hypotheses about the frequency content of the hydrodynamic loads. Moreover, since the technique requires a mathematical model providing the physical relationship between the experimental measurements, a reduced order (FE) model based on Craig-Bampton technique has been exploited. The effectiveness of the proposed method has been assessed by means of two quality estimators in the time and frequency domains, along with a sensitivity analysis of the accuracy of the estimations with respect to the number of sensor involved, that is, the amount of information in input. The force and the elastic deflections have been estimated with reference to a test carried out in the towing-tank for an irregular sea condition which makes the catamaran experience severe impacts at the wetdeck. The results, and in particular the estimation of the unknown hydrodynamic load, show a response in agreement with the expected impulsive behavior typical of the slamming phenomena.

ACKNOWLEDGMENTS

The experimental campaign upon which this work is based was supported by the U. S. Office of Naval Research (ONR) under NICOP agreement under the guidance of program officer Paul Hess.

References

[1] Bampton, M.C.C., Craig, R.R. Jr., *Coupling of substructures for dynamic analyses*. AIAA Journal, Vol. 6, No. 7 (1968), pp. 1313-1319.

[2] Kullaa, J., *Virtual sensing of structural vibrations using dynamic substructuring*. Mechanical Systems and Signal Processing, Vol. 79, (2016), pp. 203-224.

[3] Kalman, R.E., Bucy, R.S., *New results in linear filtering and prediction theory*. J. Basic Engineering Transactions on ASME, Series D 83 (3), pp 95 – 108.

[4] Hwang, J., Kareemb, A., Kim, W., *Estimation of modal loads using structural response*. Journal of Sound and Vibration, Vol. 326, (2009), pp. 522–539.

[5] Dessi, D., Faiella, E., Geiser, J., Alley, E., Dukes, J., *Design, assessment and testing of a fast catamaran for FSI investigation*. 31st Symposium on Naval Hydrodynamics Monterey, California, 11-16 September 2016.

[6] Dessi, D., Faiella, E., Geiser, J., Alley, E., Dukes, J., *Design and structural testing of a physical model for wetdeck slamming analysis*. Progress in the Analysis and Design of Marine Structures: Proceedings of the 6th International Conference on Marine Structures, Lisbon, 2017.

[7] Lourens, E., Reynders, E., De Roeck, G., Degrande, G., Lombaert, G., *An augmented Kalman filter for force identification in structural dynamics*. Mechanical Systems and Signal Processing, Vol. 27, (2012), pp. 446–460.

[8] Naets, F., Cuadrado, J., Desmet, W., *Stable force identification in structural dynamics using Kalman filtering and dummy-measurements*. Mechanical Systems and Signal Processing, Vols. 50–51, (2015), pp. 235-248.

[9] Lourens, E., Papadimitriou, C., Gillijns, S., Reynders, E., De Roeck, G., Lombaert, G., *Joint input-response estimation for structural systems based on reduced-order models and vibration data from a limited number of sensors*. Mechanical Systems and Signal Processing, Vol. 29, (2012), pp. 310-327.

[10] Maes, K., Smyth, A.W., De Roeck, G., Lombaert, G., *Joint input-state estimation in structural dynamics*. Mechanical Systems and Signal Processing, Vols. 70-71, (2016), pp. 445-466.

[11] Balas, M.J., *Do all linear flexible structures have convergent second-order observer?*. . Proceedings of the American Control Conference, Philadelphia, Pennsylvania, June 1998

[12] Hernandez, E.M., *A natural observer for optimal state estimation in second order linear structural systems*. Mechanical Systems and Signal Processing, Vol. 25, (2011), pp. 2938-2947.

[13] Demetriou, M.A., *Natural second-order observers for second-order distributed parameter systems*. Systems & Control Letters, Vol. 51, (2004), pp. 225-234.

[14] Demetriou, M.A., *Natural second-order observers for second-order distributed parameter systems*. Systems & Control Letters, Vol. 51, (2004), pp. 225-234.

[15] Belvin, W.K., *Second-Order State Estimation Experiments Using Acceleration Measurements*. Journal of guidance, control, and dynamics, Vol. 17, No. 1, (1994)

[16] Hernandez, E.M., *Optimal model-based state estimation in mechanical and structural systems*. Struct. Control Health Monit., Vol. 20, (2013), pp. 532–543

[17] Iliopoulos, A.N., Weijtjens, W., Van Hemelrijck, D., Devriendt, C., *Prediction of dynamic strains on a monopile offshore wind turbine using virtual sensor*. J. Phys.: Conf. Ser., Vol. 628, (2015), conf. 1

Characterization of reaction wheel micro-vibrations

W. De Munter[1], T. Delabie[1], D. Vandepitte[1]
[1] KU Leuven, Department Mechanical Engineering
Celestijnenlaan 300 B, B-3001, Heverlee, Belgium
e-mail: **wim.demunter@kuleuven.be**

Abstract
Reaction wheels are considered to be the largest contributors of vibrations on board a spacecraft. In order to estimate the effect on the pointing stability, the reaction wheel micro-vibrations have to be characterized first. In this paper, the micro-vibrations of two of the reaction wheels designed and developed at the KU Leuven, are modelled and tested. The micro-vibration model allows to predict the resonance modes of the reaction wheel assembly and the imbalances. These characteristics can then be verified by a dedicated micro-vibration test. The results of the micro-vibration tests showed that one of the wheels has a significant misalignment and a loose part in the assembly, while the other wheel showed the expected first harmonic to have the largest amplitude due to imbalances. The resonance modes were difficult to identify in the applied wheel speed range; therefore some additional tests are planned to increase the accuracy of the measurements.

1 Introduction

The majority of space missions today require a high pointing performance to obtain high-quality data from space. High-resolution Earth observation images, precise astronomical measurements or high-data rates by inter-satellite laser communications are a few examples that can be achieved with a high pointing precision and stability. The pointing stability is determined by the ability of the spacecraft to attenuate the different types of disturbances that are acting on the spacecraft. Low-frequency disturbances generally originate external to the spacecraft, resulting from sources such as aerodynamic drag, solar pressure, gravity gradient and magnetic gradient. High disturbances, on the other hand, generally originate from internal sources such as heat pumps or rotating wheels [1].

The low-frequency (external) disturbances (< 1Hz) can easily be corrected for by the Attitude Determination & Control System (ADCS). This spacecraft subsystem determines the orientation – also referred to as attitude – by means of a set of sensors and calculates the necessary action to be executed by a set of actuators, in order to maneuver the satellite to the desired attitude and stabilize it in this final orientation. The high-frequency (internal) disturbances (> 1Hz) cannot be eliminated by the ADCS itself, since the ADCS bandwidth is usually equal or less than 1 Hz. Other strategies therefore exist to reduce the effect on the pointing error of these high-frequency disturbances or 'jitter', such as a fine-steering mirror in the optical path of the payload and passive or active vibration isolation [1].

The largest contributors to the mechanical jitter onboard a spacecraft are considered to be the reaction wheels [2]. Reaction wheels are the prime actuators of the ADCS and primarily consist of a flywheel (a rotating mass) which is typically supported by a pair of ball bearings and driven by a brushless DC motor. The operating principle of a reaction wheel (or a momentum wheel) on a spacecraft is based on the conservation of momentum. By maintaining the flywheel at a rotational speed, a wheel provides momentum to the spacecraft. By varying the flywheel rotational speed, a reaction torque is generated. This reaction torque provides maneuvering or pointing capability to a spacecraft [3].

Although reaction wheels deliver high accuracy and agile pointing, these devices generate vibrations which are referred to as 'micro-vibration' because the resulting vibration on the satellite level is generally small, in the range of micro-g. These micro-vibrations are a combination of static and dynamic imbalances, motor disturbances, bearing irregularities or control errors (such as cogging and torque ripple) [4]. Taking into account that the pointing error is proportional to the root sum square of all disturbance amplitudes [5], it is of great importance to get a priori knowledge of the micro-vibrations of the reaction wheels to accurately predict the influence on the (optical) payload instruments and to take appropriate actions.

During the past 5 years, an entire ADCS with in-house made reaction wheels for CubeSats has been developed at the Department of Mechanical Engineering of the KU Leuven. CubeSats are small satellites that exists of one or more standardized units. One unit (1U) has dimensions of 10 x 10 x 10cm with a mass of about 1kg. Combining these units results in several derivatives such as (2U)- and (3U)- CubeSats. Compared to traditional satellites, this standardized type of spacecraft typically have shorter development cycles, smaller development teams, and, consequently, lower cost, both for the development and for the launch of the satellites. This low-cost access to space allowed universities and research institutes across the world to join the rapidly growing space community, while (inter)national space agencies recognized the potential of small spacecraft for (risk-taking) deep-space missions and technology demonstration missions. Today, however, small spacecraft are no longer seen as solely educational projects or technology demonstrators. Smallsats are making their way in almost every area of space: communication, remote sensing, science, and exploration.

In the remainder of the paper a study about the KU Leuven reaction wheel micro-vibrations will be discussed. In section 2, the current and future KU Leuven reaction wheel designs are explained. In section 3, a micro-vibration model of the KU Leuven reaction wheel will be presented together with some first estimates about the structural eigenmodes. In section 4, the micro-vibration tests are explained and the results are being analyzed and discussed. Finally, in section 5, the main results are summarized and the next steps to further improve the micro-vibration tests are considered.

2 KU Leuven reaction wheel design

In this section, the current and future KU Leuven reaction wheel designs are discussed. Driving factors for the current design were simplicity and affordability, which resulted in a sub-optimal reaction wheel performance. Secondly, the new or future design will be discussed to highlight the main adaptions with respect to the current design.

2.1 Current design

In this section the KU Leuven reaction wheel design is briefly presented. This design has outer dimensions of 40x40x28mm and a mass of 80g [6]. Its performance is characterized by the available motor torque of 0.5mNm and the theoretical maximal rotation speed of 10 000rpm. A cutout drawing of the KU Leuven reaction wheel is illustrated in Figure 1.

The total design exists of a brushless DC motor, a compact Oldham coupling, the rotor or flywheel, two radial bearings, and an upper and lower housing.

A **brushless DC motor** is used because of its high reliability and efficiency. The motor we use is the Faulhaber 1509T006, which has a flat design and delivers a torque up to 0.5mNm. The vacuum compatible version with an extended temperature range of -40 to 85C, was used to make the motor resilient to the space environment.

The motor is connected to the rotor by means of a **compact Oldham coupling**. This type of coupling is composed of three parts: one attached to the motor axis, one incorporated in the rotor design, and a middle

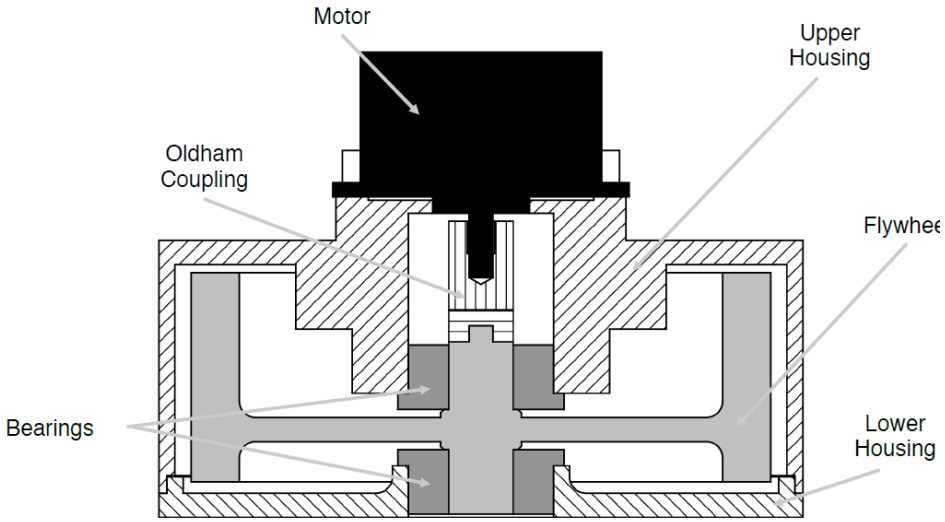


Figure 1: Cutout of the current reaction wheel design

part in between. This latter part is made of bronze for its excellent gliding properties and has two grooves that are perpendicular to each other and that mate with the other two coupling components.

The **rotor or flywheel** is optimized to have a high momentum for a low weight. It is precision machined out of stainless steel. Although a spoken rotor design would reduce the mass slightly, we opted for a full flange motor because it reduces the inherent imbalance and is produced more easily.

The rotor is supported by **two deep-groove ball bearings**. These bearings were preferred since they possess low friction torque thanks to their low contact surface, and are compact. For the bearing lubrication, special precautions must be taken due to the vacuum environment the reaction wheels will operate in. A vacuum-compatible grease was selected, with the downside of higher resulting friction. A flanged design was chosen to reduce the space needed for integration, because it adds stiffness compared to a snap ring fixture and because it facilitates the manufacturing of the reaction wheel housing.

Alternative bearing designs were also considered in [7]. Fluid and/or gas bearings are typically characterized by a high lifetime and low vibrations, but were ruled out due to the need for a pressurized lubricant or gas, which is not preferred in spacecraft. Magnetic bearings, on the other hand, are extremely complex and power demanding.

Finally, the **upper and lower housing** support the entire structure. The motor and bearings are mounted respectively on and in this structure and it interfaces with the structure of the satellite.

Three sets of 3 reaction wheels were already manufactured and assembled according to this design. Two reaction wheels of the total of 9 were used for the micro-vibrations tests as discussed in section 4.

2.2 Future design

The downside of using COTS components for the design of the reaction wheel is the dependency on existing products, which make it difficult to fully optimize the reaction wheel performance. The main disadvantages of the current design are the sub-optimal torque-speed characteristic of the Faulhaber brushless DC motor together with the necessary (Oldham) coupling, and the radial bearings which cannot support axial loads.

Therefore the KU Leuven is working on a new design based on the out-runner principle, as shown in Figure 2. In this design, the Faulhaber motor on top of the housing is replaced by a stator with carefully placed windings, while the flywheel, foreseen with magnets, is acting as the rotor. This avoids the coupling with respect to the current design. Furthermore, the motor torque-speed characteristic can be optimized over the desired speed range.

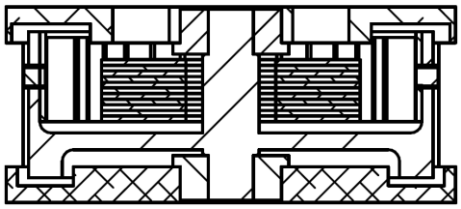


Figure 2: Cutout of the new reaction wheel design

Finally, angular bearings are considered instead of the previous chosen deep-groove ball bearings in order to reduce the micro-vibrations. This change is important especially for sensitive science missions on small spacecraft.

This outrunner reaction wheel is still under development and consequently no reaction wheels were already manufactured according to this new design.

3 KU Leuven reaction wheel micro-vibration model

The micro-vibration model of the KU Leuven reaction wheel introduced in this section is a combination of a structural dynamic model (theoretical model) and a disturbance model (empirical model). The proposed micro-vibration model is built based on the theoretic of rotor dynamics [8] and the models from [2] and [3]. For this model the following assumptions were made:

- The flywheel is assumed to be a rigid body within the frequency region of interest
- Gravity is not included (it does not affect the structural modes of the system)
- The micro-vibration model does not necessarily represent all structural modes of the complete reaction wheel assembly; the modes related to internal constructions, e.g. the coupling, are not taken into account

3.1 Structural dynamic model

For the structural dynamic model, the flywheel or rotor is modelled as a rigid disk supported by two radial bearings which are modelled each as a spring-damper system connected to the ground, as illustrated in Figure 3.

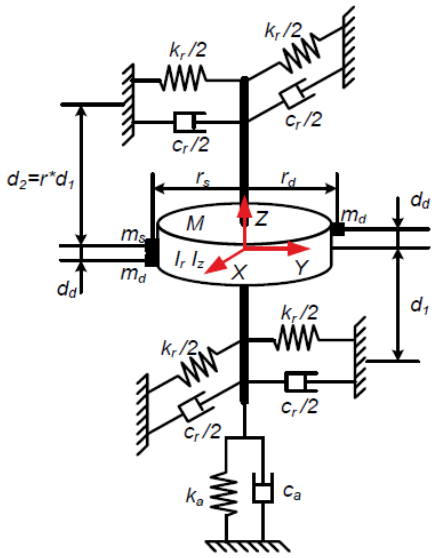


Figure 3: Illustration of the structural dynamic model [3]

The equations of motion can be derived using the Lagrange method for 5 degrees of freedom $q = \{x, y, z, \theta, \phi\}$, since the sixth degree (rotation about the z-axis) represents the motor torque and is not considered in the micro-vibration model. With m the mass of the rotor, I_r and I_z the moment of inertia for the radial and axial direction respectively, k_r and k_a the bearing stiffness in the radial and axial direction respectively, c_r and c_a the bearing damping coefficients in the radial and axial direction respectively, d_1 and d_2 the distances between the rotor's center of mass and the lower and upper bearing respectively, and the relative position $r = d_2/d_1$ of the rotor disk between the two bearings, and assuming that the rocking motions θ and ϕ have a small amplitude, these equations of motion can be further linearized to form the compact matrix Equation 1. The entire derivation of this equation can be found in [8].

$$\mathbf{M}\ddot{q} + \mathbf{C}(\Omega)\dot{q} + \mathbf{K}q = 0 \tag{1}$$

with,

$$q = \begin{Bmatrix} x \\ y \\ z \\ \theta \\ \phi \end{Bmatrix}, \qquad \mathbf{M} = \begin{bmatrix} m & 0 & 0 & 0 & 0 \\ 0 & m & 0 & 0 & 0 \\ 0 & 0 & m & 0 & 0 \\ 0 & 0 & 0 & I_r & 0 \\ 0 & 0 & 0 & 0 & I_r \end{bmatrix}$$

$$\mathbf{C}(\Omega) = \begin{bmatrix} c_r & 0 & 0 & 0 & \frac{1}{2}c_r d_1(1-r) \\ 0 & c_r & 0 & \frac{1}{2}c_r d_1(1-r) & 0 \\ 0 & 0 & c_a & 0 & 0 \\ 0 & 0 & \frac{1}{2}c_r d_1(1-r) & \frac{1}{2}c_r d_1^2(1+r^2) & -\Omega I_z \\ \frac{1}{2}c_r d_1(1-r) & 0 & 0 & \Omega I_z & \frac{1}{2}c_r d_1^2(1+r^2) \end{bmatrix}$$

$$\mathbf{K} = \begin{bmatrix} k_r & 0 & 0 & 0 & \frac{1}{2}k_r d_1(1-r) \\ 0 & k_r & 0 & \frac{1}{2}k_r d_1(1-r) & 0 \\ 0 & 0 & k_a & 0 & 0 \\ 0 & 0 & \frac{1}{2}k_r d_1(1-r) & \frac{1}{2}k_r d_1^2(1+r^2) & 0 \\ \frac{1}{2}k_r d_1(1-r) & 0 & 0 & 0 & \frac{1}{2}k_r d_1^2(1+r^2) \end{bmatrix}$$

With this proposed structural dynamic model, it is already possible to predict the resonant frequencies as a function of rotor speeds Ω when neglecting the damping of the system (i.e. $c_r = c_a = 0$). The frequency of the axial mode can directly be calculated by Equation (1). The frequencies of the translational and rotational mode can be calculated by numerically solving Equation (2), which is obtained by re-writing Equation (1) with the help of the complex coordinate method. It has 4 real roots, two of which are positive.

$$\omega^4 - \left(\frac{\Omega I_z}{I_r}\right)\omega^3 - \left(\frac{k_r}{m} + \frac{(1+r)^2 k_r d_1^2}{2I_r}\right)\omega^2 + \left(\frac{\Omega k_r I_z}{m I_r}\right)\omega + \left(\frac{(1+r)^2 k_r^2 d_1^2}{4 m I_r}\right) = 0 \tag{2}$$

A Campbell diagram is then the most common way to illustrate these resonant frequencies. In Figure 4 the Campbell diagram with the predicted resonance frequencies of the KU Leuven reaction wheel is illustrated for which the parameters from Table 2 were used. From this figure, an axial mode of around 1365Hz, a rocking mode of 311Hz, and a translational mode of 687Hz are expected at standstill and are summarized in Table 1.

Mode	Calculated frequency
Radial	1365
Axial	687
Rocking	311

Table 1: Calculated/predicted eigenfrequencies at standstill ($\omega = 0$rpm) of the KU Leuven reaction wheel

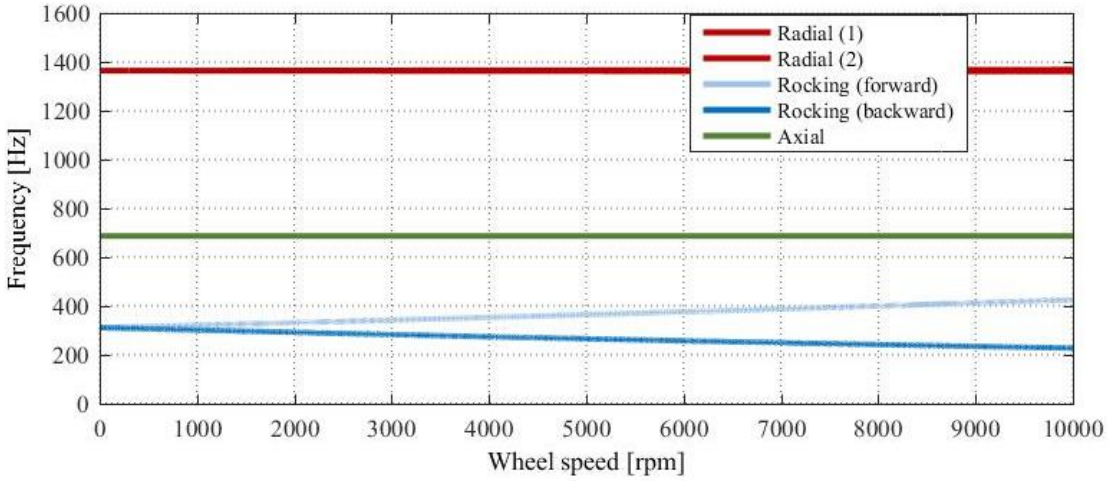


Figure 4: Campbell diagram with the calculated resonance modes of the KU Leuven reaction wheel assembly

The influence of the wheel speed on the rocking mode is clearly visible. The two diverging frequencies are called the forward and backward whirl. For the frequencies at 1365Hz this divergence is less pronounced, considering them as one (radial) translational mode.

Parameter	Value	Obtained from
I_z [kg m²]	$9.594 \cdot 10^{-12}$	CAD model
I_r [kg m²]	$7.778 \cdot 10^{-12}$	CAD model
m [kg]	$40.82 \cdot 10^{-3}$	CAD model
d_1 [m]	$5.75 \cdot 10^{-3}$	Technical drawing
d_2 [m]	$0.75 \cdot 10^{-3}$	Technical drawing
r [-]	0.13	Calculation ($= d_2/d_1$)
k_r [N/m]	$2.9 \cdot 10^{6}$	Estimation [11]
k_a [N/m]	$0.76 \cdot 10^{6}$	Estimation [11]

Table 2: Parameters used for the micro-vibration model of the KU Leuven reaction wheel

The resonance frequencies of the reaction wheel assembly should also be visible in the resulting waterfall plots from the micro-vibration tests. The predicted/calculated values from table can therefore be used as a reference value to easier distinguish them from the unavoidable noise in the test results.

3.2 Disturbance model

In the previous section, a structural dynamic model was proposed and the resonance frequencies were predicted by means of this model. In this model, however, the right-hand side of the equation was considered to be zero. In reality, micro-vibrations are induced by the reaction wheel assembly which can be categorized into fundamental sub and/or higher harmonic disturbances. The fundamental harmonic disturbances are considered to be the most significant micro-vibration source and are caused by the static

and dynamic imbalances of the flywheel. The sub/higher harmonic disturbances are caused by irregularities in the reaction wheel assembly, such as bearing imperfections.

The static unbalance U_s can be expressed in two ways: (1) by means of an additional small mass m_s at a distance r_s from the rotor's center of mass as illustrated Figure 3, or (2) by means of the total mass of the rotor m which experience a certain eccentricity ε due to limited manufacturing capabilities. Equation (3) formulates both expressions. The static imbalance is typically given in g-mm.

$$U_s = m_s r_s = m\varepsilon \tag{3}$$

In the same way, the dynamic imbalance U_d can be expressed in two ways: (1) by means of two additional small masses m_d on a distance r_d from the rotor's center of mass and an axial distance d_d in between them as illustrated in Figure 3, or (2) by means of the total axial inertia of the rotor I_z which experience a certain angular error χ due to limited manufacturing capabilities. Equation (4) formulates both expressions. The dynamic imbalance is typically given in g-mm².

$$U_d = 2m_d r_d d_d = I_z \chi \tag{4}$$

Since all components of the KU Leuven reaction wheels were manufactured with certain tolerances, the worst case can be calculated for both imbalances (assuming the tolerances were met during manufacturing). In Table 3 the worst case imbalance were calculated according to the tolerances of the design.

Imbalance	Maximum error	Maximum imbalance
Static	$\varepsilon = 40\mu$m	$U_s = 1.6$g-mm
Dynamic	$\chi = 6.2$mrad	$U_d = 59$g-mm²

Table 3: The maximum predicted imbalances according to the KU Leuven reaction wheel design tolerances

The excitation of both imbalances can now be added to Equation (1) to obtain the full micro-vibration model. In addition to the imbalance disturbances at the fundamental harmonic ($h = 1$), the disturbances due to irregularities in the reaction wheel assembly are also added at other harmonics ($h \neq 1$).

$$\mathbf{M}\ddot{q} + \mathbf{C}(\Omega)\dot{q} + \mathbf{K}q = U_{im}(\Omega t) + U_{irr}(h\Omega t) \tag{5}$$

with,

$$U_{im}(\Omega t) = \begin{Bmatrix} -U_s\Omega^2 \sin(\Omega t) \\ U_s\Omega^2 \cos(\Omega t) \\ 0 \\ U_d\Omega^2 \cos(\Omega t) \\ U_d\Omega^2 \sin(\Omega t) \end{Bmatrix}, \qquad U_{irr}(h\Omega t) = \begin{Bmatrix} -\sum_i^{n_f} U_i^f \Omega^2 \sin\left(h_i^f \Omega t + \beta_i^f\right) \\ \sum_i^{n_f} U_i^f \Omega^2 \cos\left(h_i^f \Omega t + \beta_i^f\right) \\ 0 \\ \sum_i^{n_t} U_i^t \Omega^2 \cos\left(h_i^t \Omega t + \beta_i^t\right) \\ \sum_i^{n_t} U_i^t \Omega^2 \sin\left(h_i^t \Omega t + \beta_i^t\right) \end{Bmatrix}$$

where U_i are the harmonic amplitudes of ith harmonic, h_i is the ith harmonic number, and β_i is a random phase angle.

The left-hand side of Equation (5) should be similar for reaction wheels made according to the same design, while the right-hand side is unique for each reaction wheel, since this part of the equation depends on the actual eccentricity and bearing irregularities.

4 Micro-vibration testing

The aim of the micro-vibration tests are two-fold: (1) to validate the micro-vibration model as described in the previous section (in order to be able to accurately define the effect on the pointing system of a spacecraft structure), and (2) to evaluate the quality of the manufacturing and assembly of the KU Leuven reaction wheels. This can be done based on the so-called waterfall plots, which can be created from the micro-vibration test data.

In this section, first the test setup will be described, next the test procedure that is applied and the processing of the data, and finally the test results are analyzed and discussed.

4.1 Test setup

4.1.1 Data acquisition

The total test setup is illustrated in Figure 5. One of the KU Leuven reaction wheels was mounted on a measuring cell via an aluminum reaction wheel mounting plate. The measuring cell itself was rigidly mounted on an air table.

For the measuring cell, the Kistler Dynamometer, type 9119AA1, was chosen. This dynamometer consists of four 3-component piezo-electric force sensors mounted under high preload between a cover plate and two lateral base plates. The force sensor current signals were further converted into a proportional voltage signal by the Kistler multichannel charge amplifier, type 5070A. The 6 amplified signals (3 forces and 3 torques) of the amplifier were finally sampled by a LMS acquisition system at a rate of 3200Hz. A 10N/V and a 1Nm/V setting was applied for the three forces and three torques respectively.

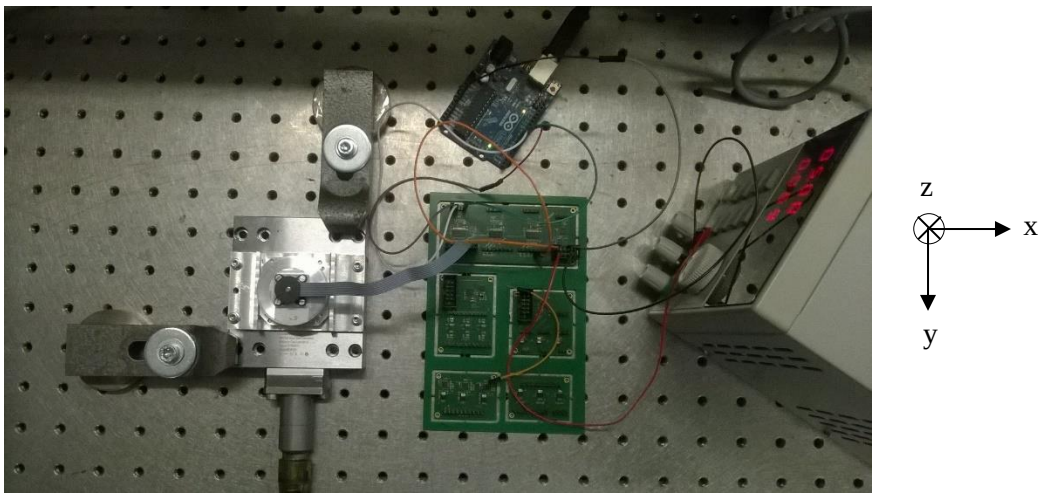


Figure 5: Illustration of the micro-vibration test setup

4.1.2 Frequency range of the test setup

It is important to only measure the reaction wheel vibrations. Therefore, the Kistler dynamometer was rigidly mounted on a Newport RS2000 air table to isolate the dynamometer from ambient seismic

vibrations (< 10Hz). Furthermore, the first resonance of the test setup itself was measured to be around 2000 Hz, using an impact hammer while measuring the forces of the dynamometer. The force/force (dynamometer/hammer) transmissibility curve of these impact measurements is illustrated in Figure 6 for the three directions (according to the axes as illustrated in Figure 5). From these data, the characterization of the wheels was thus limited to be within the range of 10 and <2000Hz.

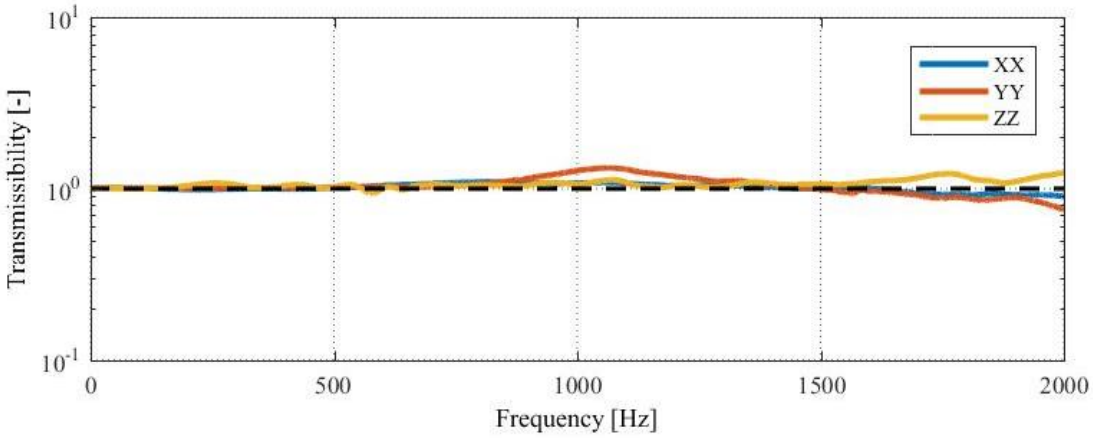


Figure 6: The measured transmissibility (force-to-force) of the impact test to determine the characterization frequency range

4.2 Test procedure

Two of the KU Leuven reaction wheels were used for the micro-vibration tests. Through the remainder of this paper, these reaction wheels will be defined as RW1 and RW2. Although both wheels have the same design, they were made by two different manufacturers.

In order to acquire the desired waterfall plots, the forces and torques need to be measured over the entire wheel speed range. Since the micro-vibration model, as proposed in Section 3, is only valid for steady-state conditions, the wheel speed should be constant over the measuring period at each wheel speed.

Two different approaches are usually applied to get these data with steady-state conditions: (1) by taking measurements at each wheel speed separately (with an increase in wheel speed between two consecutive measurements), or (2) by performing a spin-down of the reaction wheel where the time history of the measurement data can be subdivided into quasi steady-state time slices. For the latter option, it is assumed that the friction torque in the reaction wheel is very low, such that the wheel speed slowly decreases over time, and the wheel speed can be considered as steady-state over each time slice. Since the tested KU Leuven reaction wheels have relatively large friction torque, the first option has been chosen for obtaining the time history.

The wheel speed was increased from 0rpm to 2000rpm in steps of 50rpm for each wheel. After each 30s, the wheel speed was commanded to increase, resulting in a total measuring time of 1230s or 21.5min, as illustrated in Figure 7 for RW1.

The KU Leuven reaction wheels are driven by means of a PWM-signal and an encoder gives back the real wheel speed. The wheel speeds were controlled by a simple PID controller based on the rate feedbacks. A power supply provided the necessary supply voltage to the motors of the reaction wheels.

Since the wheel speed control and the vibration measurements were not commanded from one platform, these two data sets (wheel speed measurements and vibration measurements) are inherently not synchronized. The synchronization is discussed in the next section.

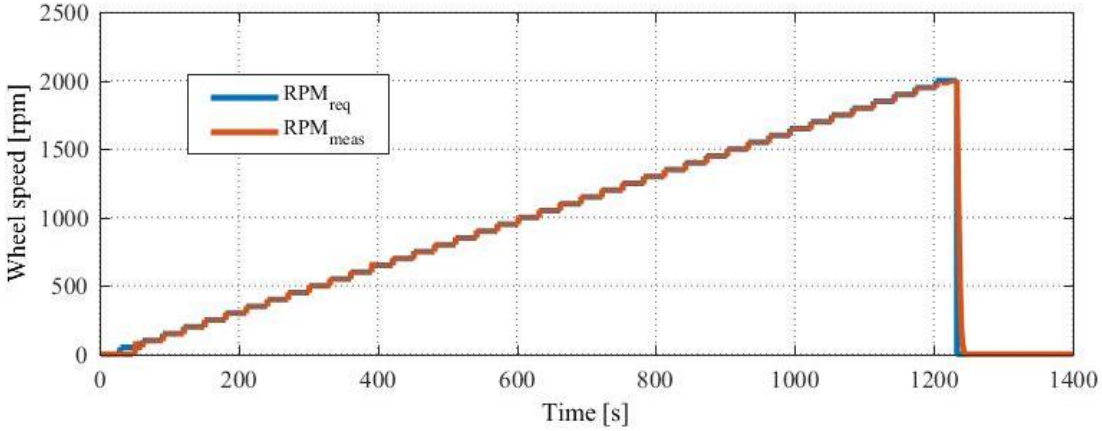


Figure 7: The wheel speed profile of RW1 during the entire micro-vibration test (blue: required wheel speed, red: measured wheel speed)

4.3 Test data processing

The obtained dynamometer data were loaded into Matlab and processed first. The processing steps are illustrated in Figure 8.

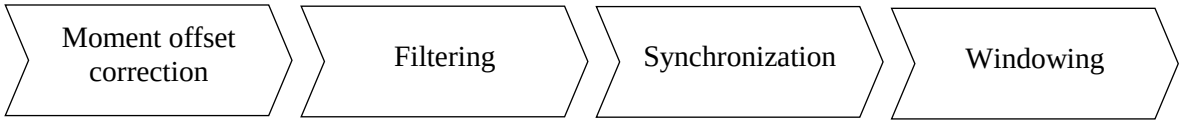


Figure 8: Illustration of the processing steps in Matlab

First, the measured moments M_m^{DF} in the dynamometer frame were compensated for the offset between the reaction wheel center and the reference frame of the dynamometer according to Equation (6), with F_m^{DF} the measured forces and v^{DF} the offset vector from the origin of the dynamometer to the center of the reaction wheel, both in the dynamometer frame (DF).

$$M = M_m^{DF} - v^{DF} \times F_m^{DF} \tag{6}$$

Next, a 7th order Butterworth filter was applied on the data with a cutoff frequency of 1500Hz. Subsequently, the speed and vibration data were visually synchronized. Since the wheel speed was increased each 30s, a small increase in amplitude should be identified in the vibration data for each axis, which is illustrated in Figure 9.

Finally, a Hanning window was applied on a small time period of 10s at each wheel speed while executing the Fast Fourier Transformation (fft) to transform the time data to the frequency domain.

In each time period of 30s, the wheel speed increases relatively fast to the required wheel speed (< 5s). Taking into account a time period of about 10s to ensure the dynamic behavior of the system has damped out, and a safety margin of 5s synchronization uncertainty, the Hanning window was applied over the data from each 15th to 25th second at each wheel speed. This is clearly visualized in Figure 10.

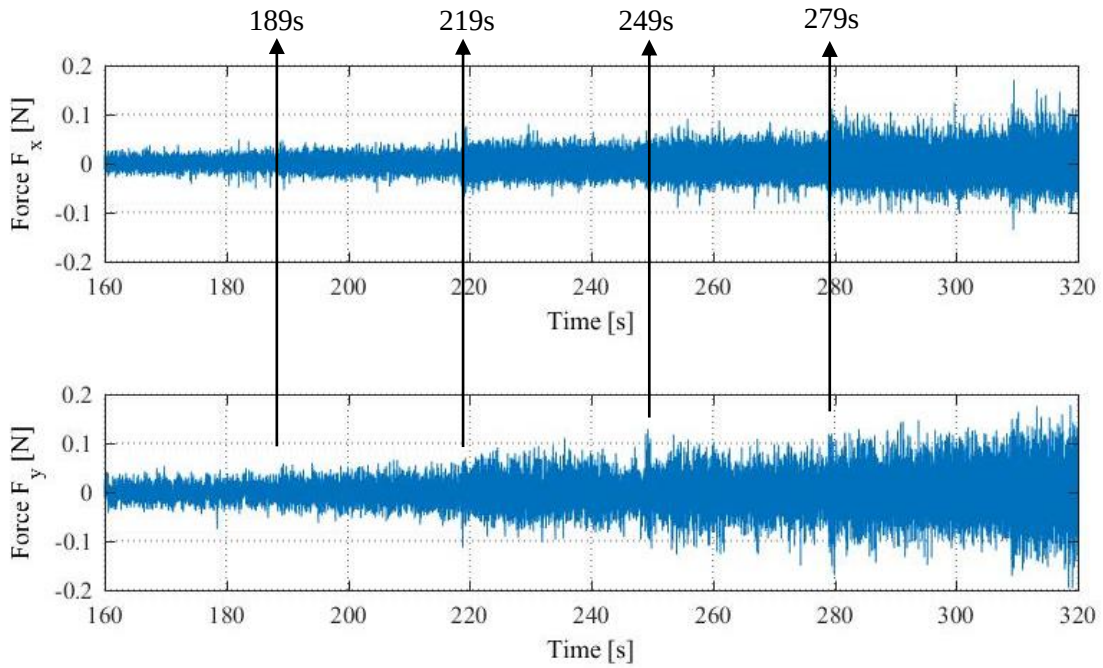


Figure 9: Illustration of the visual synchronization procedure; an increase in amplitude is identified for both force signals of RW1 at the same time with a 30s time interval in between

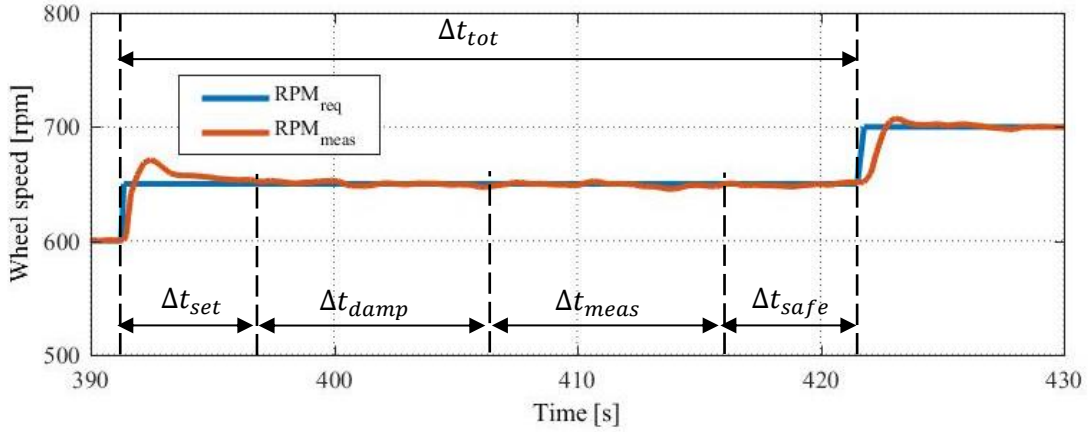


Figure 10: Illustration of the time periods per wheel speed on a detail of Figure 7 for RW1, with $\Delta t_{tot} =$ 30s the total time period per required wheel speed, $\Delta t_{set} <$ 5s the settling time, $\Delta t_{damp} =$ 10s the time to damp out the dynamics of the system, $\Delta t_{meas} =$ 10s the actual time period used to calculate the spectrum, and $\Delta t_{safe} =$ 5s the safety margin on the synchronization uncertainty.

4.4 Test results

By grouping the calculated spectra of each wheel speed together, the waterfall plots can be generated for each signal. The amplitude density spectra (ASD) for RW1 and RW2 are shown in Figure 11 and Figure 12.

For both wheels, some general conclusions can be made first. As expected, the spectra for the x- and y-forces and moments are almost the same. Furthermore, the z- moment is negligible compared to the other two moments, since this is the driven torque of the motor.

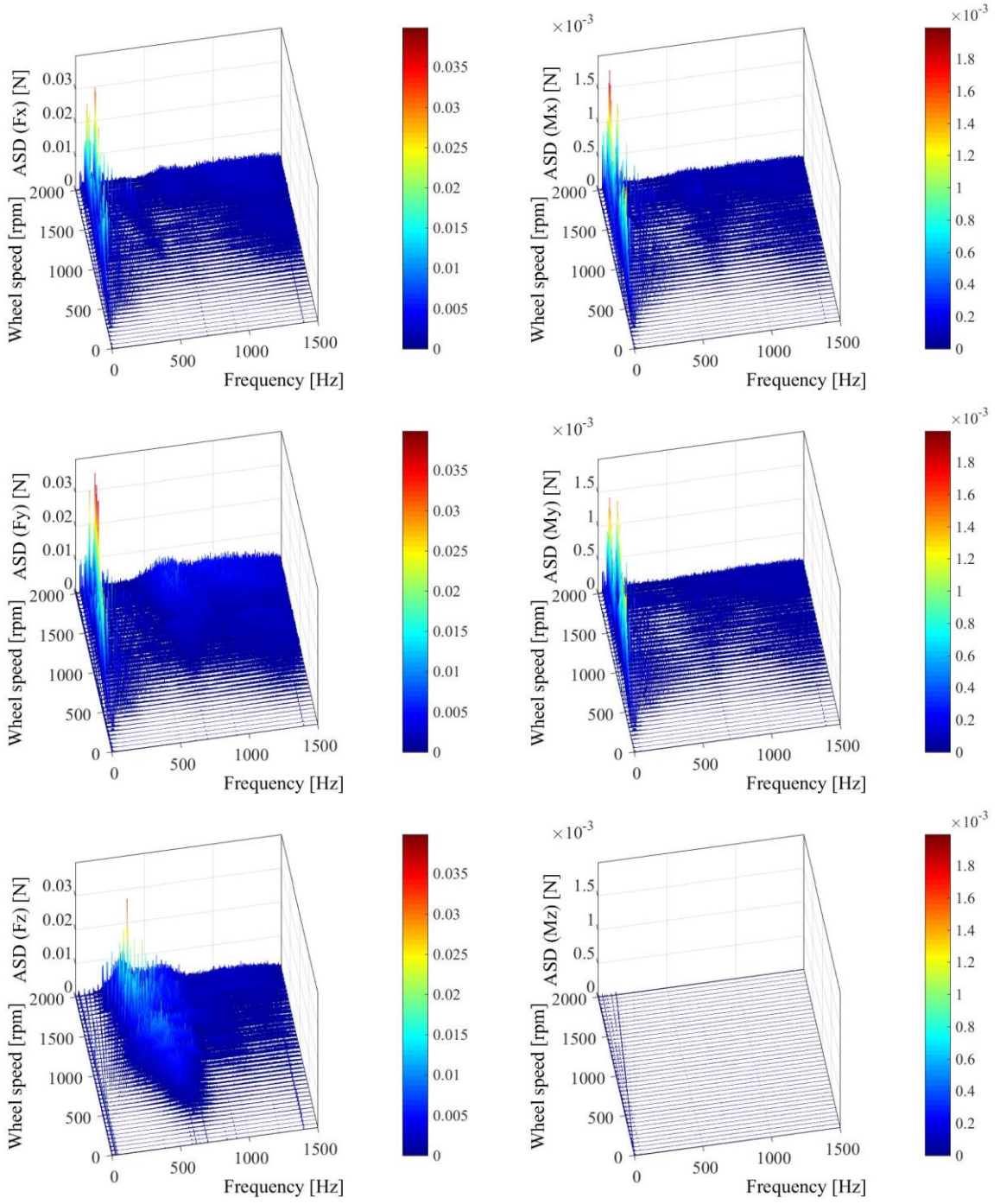


Figure 11: Amplitude Density Spectra (ASD) for RW1

Specifically for RW1, the ASD waterfall plots from Figure 11 are difficult to interpret. In the range of 500 to 1500Hz (above about 800rpm), broadband noise can be seen. This can be credited to a loose part that was shaking. During assembly of the bearings in the reaction wheel housings, it was noticed that the intentional tight fit couldn't be attained due to the fact that the tolerances were not met by the manufacturer. Furthermore, the second harmonic is the largest peak value, and not the first harmonic as expected, which means that the bearings experience some misalignment with respect to each other. The large forces in the z-axis supports this hypothesis, according to [10].

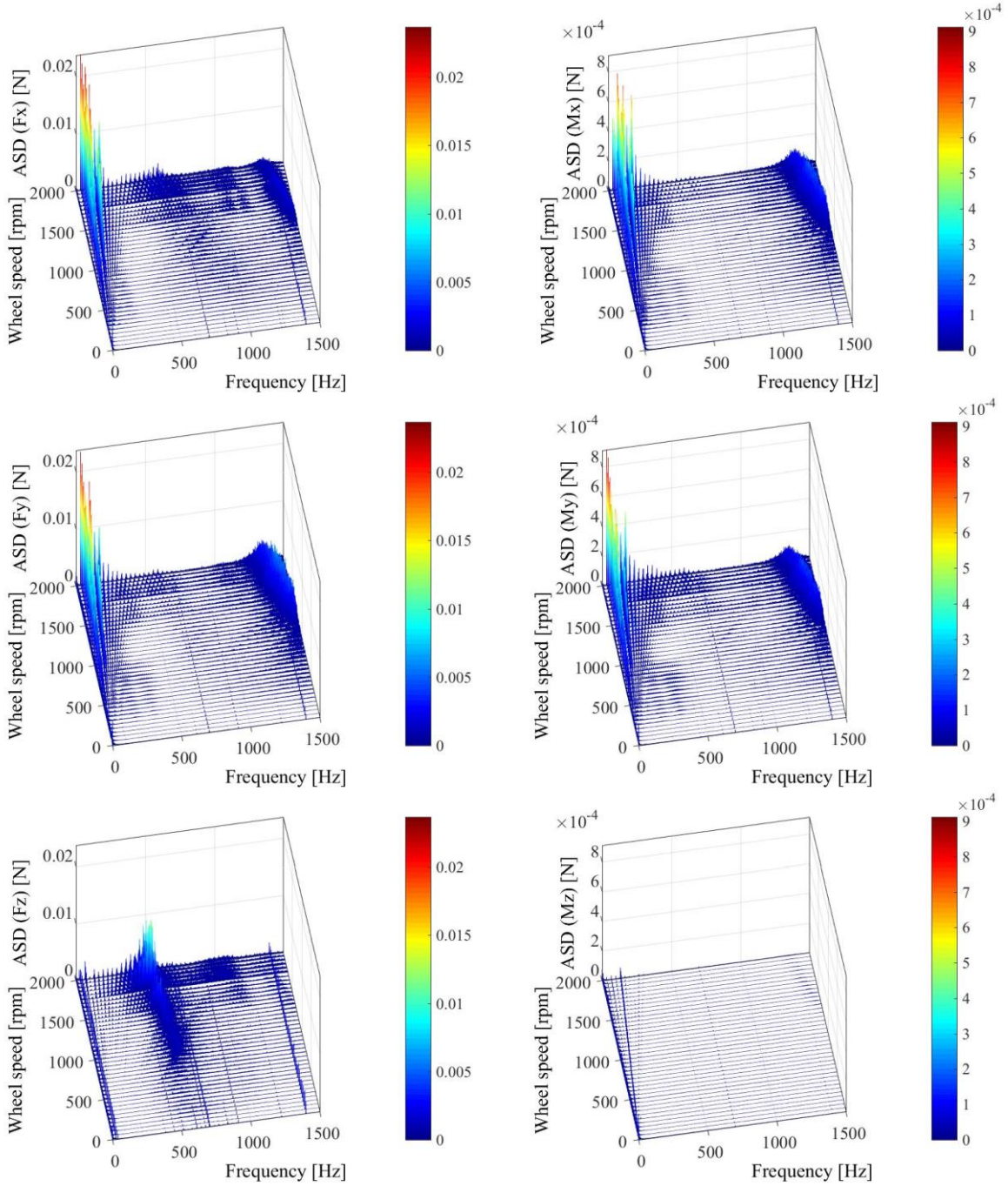


Figure 12: Amplitude Density Spectra (ASD) for RW2

Better results (i.e. as expected) are obtained for RW2, as can be seen in Figure 12. For this reaction wheel, made by a different manufacturer, the first harmonic is the largest peak value, originating from the unavoidable imbalance. Furthermore, a strong amplification is seen around 650Hz, mainly in the Fz-signal. Comparing to the results of the micro-vibration model of section 3.1, this amplification could correspond to the axial mode, which was calculated to be around 687Hz. Also some amplifications are seen in the higher frequency regions around 1300 – 1500Hz. It seems to be the back whirl of the rocking mode, which does not correspond to the predicted values of the micro-vibration model.

Based on the measured amplitudes of the forces and moments at the first harmonic, the static and dynamic imbalances can be calculated according to Equation (5), respectively. At the highest wheel speed (2000

rpm), the highest signal-to-noise is obtained for this calculation. The results for RW2 are listed in Table 4 together with the maximum predicted imbalances of Table 3. The measured imbalances are 3 times smaller than the maximum predicted imbalances and are in the magnitude range of comparable CubeSat reaction wheels commercially available [6].

Imbalance	Maximum imbalance	Measured imbalance
Static	$U_s = 1.6$g-mm	$U_s = 0.5$g-mm
Dynamic	$U_d = 59$g-mm²	$U_d = 20$g-mm²

Table 4: Measured imbalances based on the force and moment amplitudes at the first harmonic.

5 Conclusion

In this paper, the need to accurately characterize the reaction wheel behavior is explained first where after the KU Leuven reaction wheel design was given. A micro-vibration model, which was a combination of a theoretical structural dynamic model and an empirical disturbance model, was proposed to predict the resonance modes and the imbalances of the KU Leuven reaction wheels. Finally, the performed micro-vibration tests were discussed and the results were analyzed.

5.1 Future considerations

Since the generated waterfall plots from these first micro-vibration tests were difficult to interpret, such that the predictions of the micro-vibration model could not be verified, more tests are planned. Some considerations are already summarized here in order to increase the quality of the measurement data:

- If possible, the wheel speed should be controlled from the same software platform (e.g. LMS) to avoid the synchronization problem
- If possible, the wheel speed limit should be increased from 2000rpm to at least 4000rpm or higher. At higher speeds, the resonance amplifications are more pronounced and the signal-to-noise ratio will increase.
- If possible, longer time periods (> 30s) can be taken at each wheel speed, e.g. 60s. This of course doubles the total measurement time, but allows to make more than one spectrum and to average these spectra.

Acknowledgements

Strategic Basic (SB) PhD fellow at Research Foundation – Flanders (FWO).

References

[1] J. Vandersteen, *Observation and Estimation for spac*e, PhD thesis, KU Leuven, Belgium (2012).

[2] R. A. Masterson, *Development and Validation of Reaction Wheel Disturbances Models: Empirical Model, Journal of Sounds and Vibration*, Vol. 249, pp. 5757-598 (2002).

[3] P. Le, *Micro-disturbances in reaction wheels*, PhD thesis, TU Eindhoven, The Netherlands (2017).

[4] D. Kim, *Micro-vibration model and parameter estimation method of a reaction wheel assembly*, Journal of Sound and Vibration, Vol. 333, No. 4 (2012).

[5] M. J. Sidi, *Spacecraft Dynamics and Control*, Cambridge University Press (1997).

[6] T. Delabie, R. Boonen, D. Vandepitte, *Building, Testing and Analyzing Robust and Accurate CubeSat Reaction Wheels*, in *Proceedings of The 10th International ESA Conference on Guidance, Navigation & Control Systems, Salzburg, Austria, 2017 May 29 – June 2*, Salzburg (2017).

[7] J. Goyvaerts, *Design and Implementation of a low-cost Attitude Determination and Control System for CubeSats*, MSc thesis, Dept. Mech. Eng., KU Leuven, Belgium (2011).

[8] G. Genta, *Dynamics of rotating systems*, Springer – Mech. Eng. Series (2005).

[9] J. Shields, et al., Characterization of CubeSat Reaction Wheel Assemblies, in Journal of Small Satellites, Vol. 6, No. 1, Deepak Publishing (2017), pp. 565-580.

[10] W. Heylen, S. Lammens, P. Sas, *Modal Analysis Theory and Testing*, Katholieke Universiteit Leuven, Departement Werktuigkunde, Leuven (1997).

[11] E. P. Gargiulo Jr, *A simple way to estimate bearing stiffness*, article in Machine Design (1980).

Simulation and experimental validation of gas-engine blade dynamics during milling

S. Nikolaev [1], **I. Kiselev** [2], **V. Kuts** [2], **S. Voronov** [2]
[1] Skolkovo Institute of Science and Technology, Center for Design, Manufacturing and Materials,
Nobel str, 3, Moscow, Russia
e-mail: **s.nikolaev@skoltech.ru**

[2] Bauman Moscow State Technical University, Department of Applied Mechanics,
2-nd Baumanskaya str., 5, Moscow, Russia

Abstract
This paper is dedicated to the simulation of turbine blade milling dynamics taking into account stock and machine tool dynamic properties for accurate prediction of unsafe milling modes. Its important to note that blade eigenfrequencies and damping ratios which largely determine system dynamics vary during machining due to material removal. The special methodology is proposed to identify blade modal parameters and update its finite-element model. Damping-frequency dependencies were built for each mode shape with least-squares fitting and used for precise milling dynamics simulation in special 3DCUT software. The proposed methodology is tested on a case of rational milling modes analysis for the gas-engine blade. The results of milling simulation are in a good agreement with experimental results, therefore proposed methodology can be extended to other parts such as bladed disks, engine stators, flexible body parts.

1 Introduction

Basic researches in the field of modal parameters identification in time- and frequency-domain are related to such scientists as D. Bishop, Richardson M., Allemang R., Brown D., Rixen D., Peeters B., Ewins D., Sas P., Heylen W., et al. One of the main problems in the experimental modal analysis is correct damping identification. P. Van Overschee and B. De Moor have developed the Stochastic Subspace Identification in order to overcome this problem, especially for testing in operational conditions. The model updating methods have been developed by Huang X., Friswell M., Motterhead J., Dascotte E., and others [1]. Researches, devoted to the numerical modeling of milling dynamics also have to be mentioned and include research papers by Altintas Y., Stepan G., Insperger T., Gouskov ., Voronov ., Kiselev I., Tlusty J., Budak E., et al. This paper follows the researches of Kiselev, Voronov, Gouskov, and others where it was shown [2, 3] that the complex model of 5-axis milling process includes the system of nonlinear differential equations of second order with variable coefficients. One and maybe the most important problem of milling process simulation for proper milling mode selection is a need for part and tool dynamic properties identification. These models are usually built with the finite-element method and always contain some uncertainties, caused by unknown properties of part clamping and also by some scatter in the geometry of part blank. It's worth noting that dynamic properties of the blade change over time due to material removal. Further sections contain experiments description, milling dynamics simulation and milling modes evaluation and selection.

The main aim of this paper is to investigate the influence of part dynamic properties and especially of damping on the milling process stability. The experiments and simulations were made for the part, similar to gas-engine compressor blade, but made from the aluminum alloy (D16T). The part was made using DMG Ultrasonic 10 CNC machine, with 3 stages: rough, semi-finishing and finishing machining (fig. 1) using

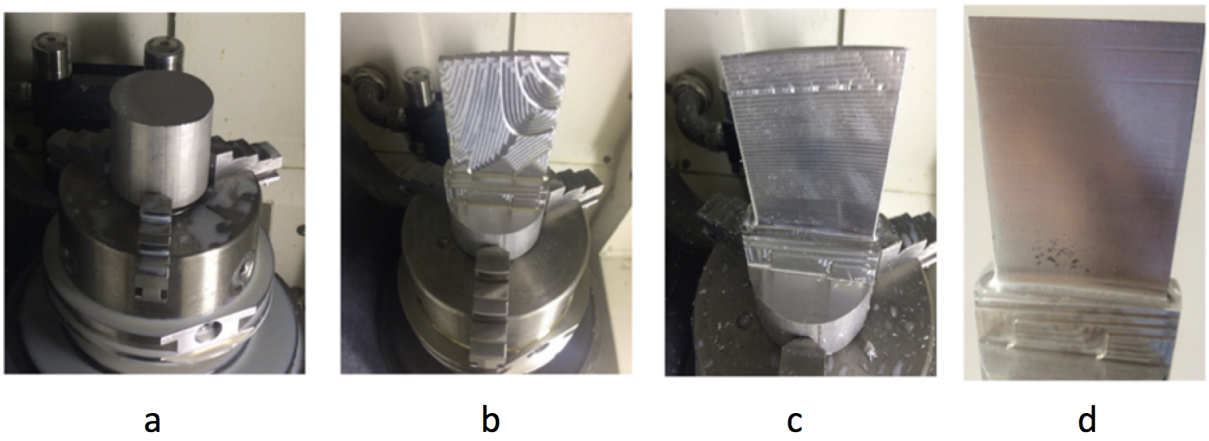


Figure 1: Stages of blade milling

helical tool path. 2-teeth conical ball mill was used for finishing machining which is of highest interest since the vibrations during this stage define the turbine blade surface quality. Finishing stage was performed with feed rate equal to 450 mm/min and machining allowance 100 μ m.

2 Dynamic properties identification

2.1 Modal testing

The main task for the testing is to analyze the part modal parameters evolution during finishing stage of machining. Special procedure was developed to solve this problem. The multiple impact tests were done during the machining with cutter being taken away from the part. Analog-digital converter National Instruments 4431, impact hammer BruelKjaer 8206, laser vibrometer Polytec PDV 100 and house code to collect and analyze data in LabView and Matlab was used to perform parameters identification. Time-domain stochastic subspace identification is used for each impact test. The method was chosen because of the improved accuracy in conditions of small damping and robustness in presence of noise [9]. The two lowest eigenfrequencies define the process dynamics for investigated blade, so the results have been obtained for them. 10 impact test have been done during the finishing stage of blade milling and the the dependencies of two lowest eigenfrequencies on the tool path were built. The frequencies evolve during machining as shown on the (fig. 2).

The damping ratios also are being changed during the process as it's shown on the fig. 2. The regression curves have been built for each damping ratio, showing its dependence on the eigenfrequency value. Least-square method has been implemented in order to build the damping-frequency curves:

$$\zeta(f) = p_1.(f/f_{ref})^n + p_2.(f/f_{ref})^{n-1} + .. + p_n.(f/f_{ref}) + p_{n+1} \quad (1)$$

where n - polynomial order, f - frequency, f_{ref} - reference frequency (mean value on the investigated frequency range, p_i, $i \in [1..n+1]$- polynomial parameters.

These regression curves are used in special software 3DCUT for milling dynamics simulation and milling modes selection.

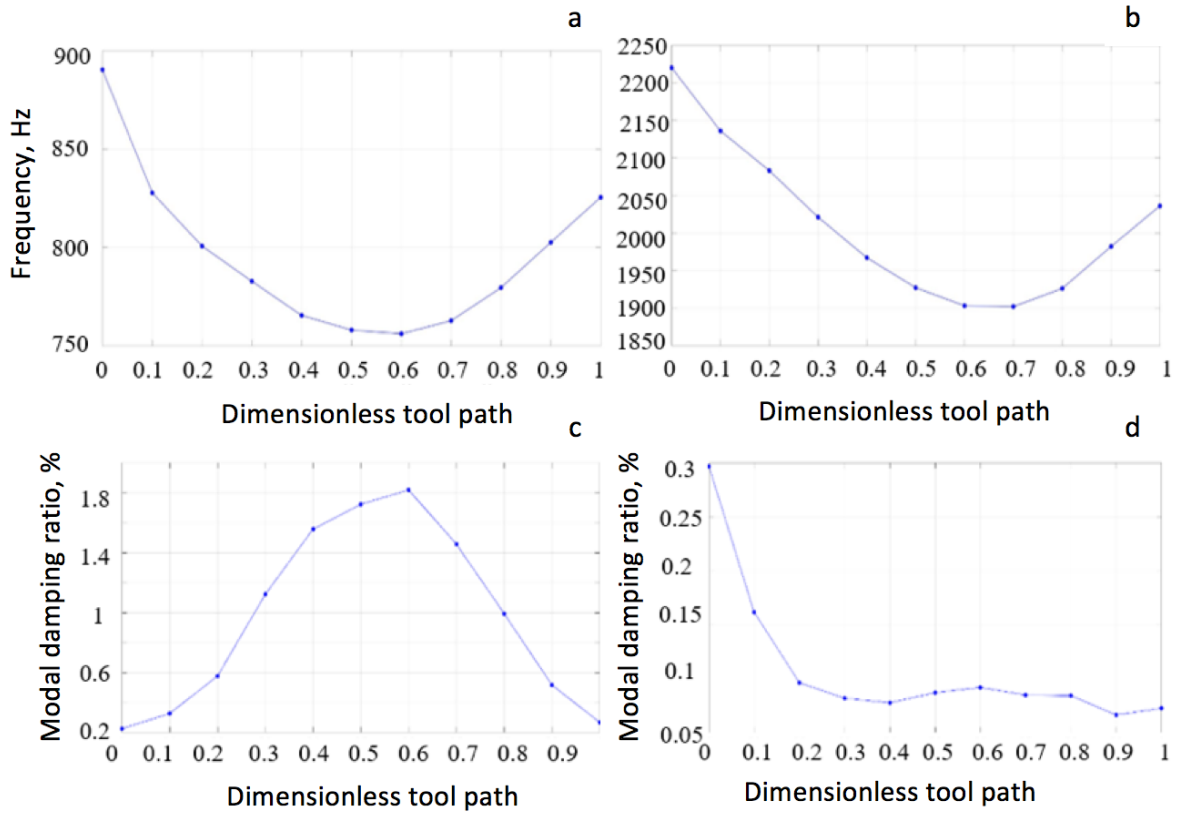


Figure 2: Blade eigenfrequencies (a, b) and damping (c, d) evolution curves for two lowest modeshapes

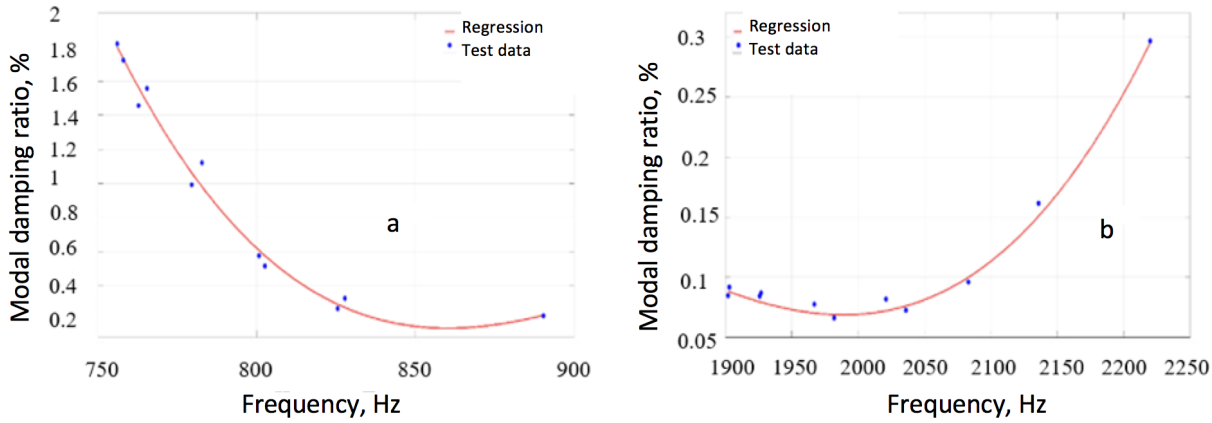


Figure 3: Damping ratios evolution

2.2 Model updating

The eigenfrequencies, obtained from modal testing and those obtained from finite-element analysis always differ. The main reason is in uncertainties in joints properties as well as errors in blade blank geometry. The model updating procedure is performed using the house-made code in this research.

The updating is done by solving an optimization task of frequencies error minimization by varying the elastic properties of the FE model in each finite element in some range. Following [4] the elastic properties could be defined:

$$\mathbf{P}_i = \mathbf{P}_{i-1} + \mathbf{S}^{+}(\mathbf{f}_i - \mathbf{f}^{exp}) \tag{2}$$

where $\mathbf{P}_i, \mathbf{P}_{i-1}$ - parameters vectors on the current and previous iterations of updating procedure, $\mathbf{f}_i$, $\mathbf{f}^{exp}$ - vectors of test and FEM eigenfreguencies, $\mathbf{S}^{+}$ - pseudo-inverse sensitivity matrix

The sensitivity coefficients - components of matrix $\mathbf{S}$ could be found analytically, finding the derivative of the eigenfrequencies by elastic properties in particular finite elements [5]:

$$s_i^e = (\omega_i^2)/(m_i E_e)(\mathbf{q}_i^e)^T \mathbf{K}^e \mathbf{q}_i^e \tag{3}$$

where s_i^e sensitivity coefficient of element e corresponding to modeshape i, ω_i - eigenfrequency, m_i - modal mass of modeshape i, $\mathbf{q}_i^e$ eigenvector, corresponding to element e degrees of freedom, $\mathbf{K}^e$- element stifness matrix, E_e - current value of elasticity module in the element.

Finite element model of the blade is built using 10-node tetrahedral elements and consists of 150 000 nodes. The two lowest modeshapes, which define the blade dynamics during milling are the first bending and first torsion modes. The eigenvalue solution is performed using subspace iteration method in 3DCUT software.

The error in determining the eigenfrequencies is 2.8% and 4.4% for the first and second frequencies, respectively. The errors in determining the eigenfrequencies for the considered part are quiet small and occur mainly due to errors in modeling the geometry of the blank surface, and inaccuracies in specifying the properties of the material. As it can be seen from the graph (fig. 4, the errors change during the process and decrease toward the end of the machining. Despite the fact that in the considered problem the calculated eigenfrequencies differ not so much from experimental values, it is worth noting that in real conditions the blade blank is clamped in the rig and the contact stiffness of this fastening has a greater influence on the eigenfrequencies of the blade, and could be up to 15 %.

The elastic modulus values in each finite element are chosen as updating parameters. The maximum change in the modulus of elasticity $\Delta E_{max} = 30\%$, the maximum change in the modulus of elasticity in one iteration $\Delta E_{max_{iteration}=5\%}$, the parameter space is divided into 10 clusters. A value of convergence criteria, upon which the updating stops was chosen on the level of 0.2%. The errors in natural frequencies decreased to 0.2% and 0.18%, respectively. Therefore, the updating procedure allows to adjust the blank model and minimize the influence of blank geometry uncertainty for accurate dynamics simulation.

There is an opportunity to take into account the material removal during milling by adaptive re-meshing in 3DCUT software. 20 frames of remeshing are done for the investigated part. These frames are spread along the tool path during finishing stage of milling. Eigenfrequencies evolution taking into account material removal before and after model updating are built (fig. 4).

The updated finite-element model and damping regression curves are used for milling dynamics simulation using special geometry algorithm [6] in 3DCUT software (fig. 5).

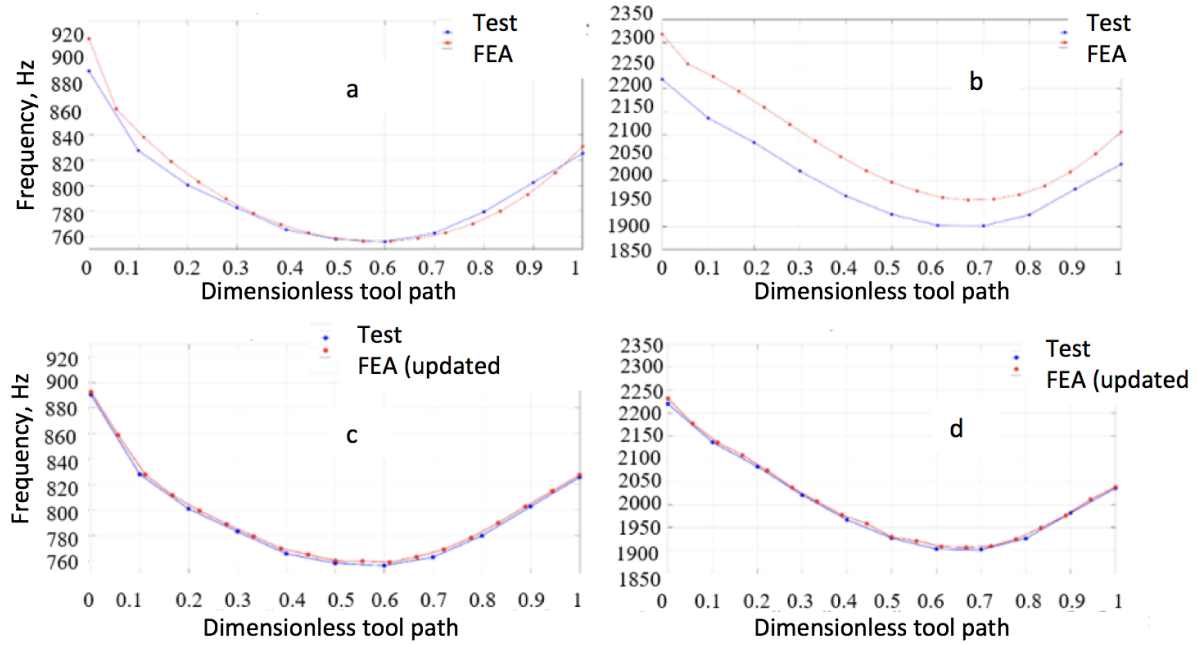


Figure 4: Two lowest eigenfrequencies evolution curves before (a, b) and after model updating (c, d)

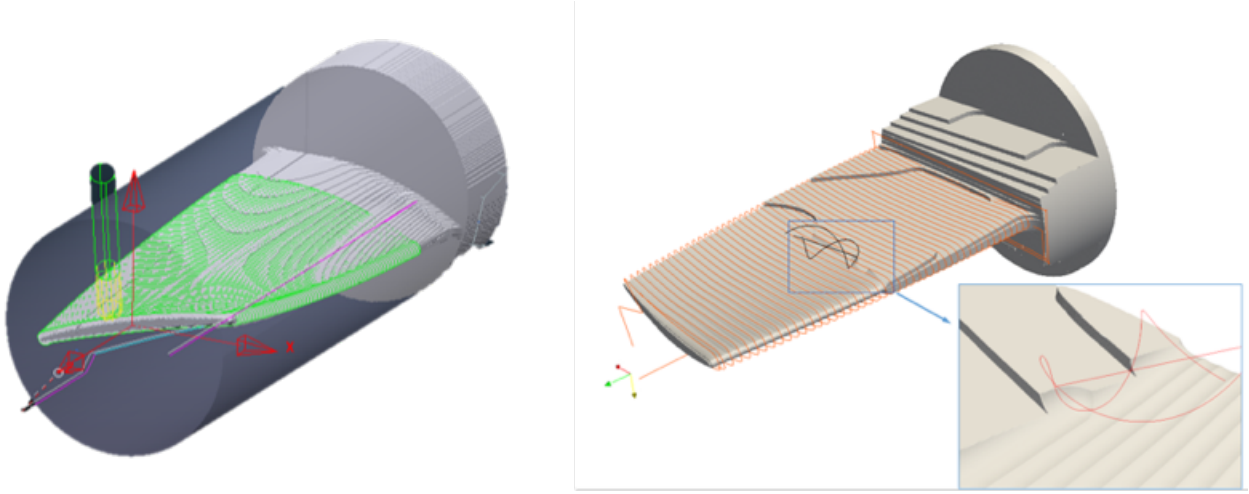


Figure 5: Milling simulation in 3DCUT software

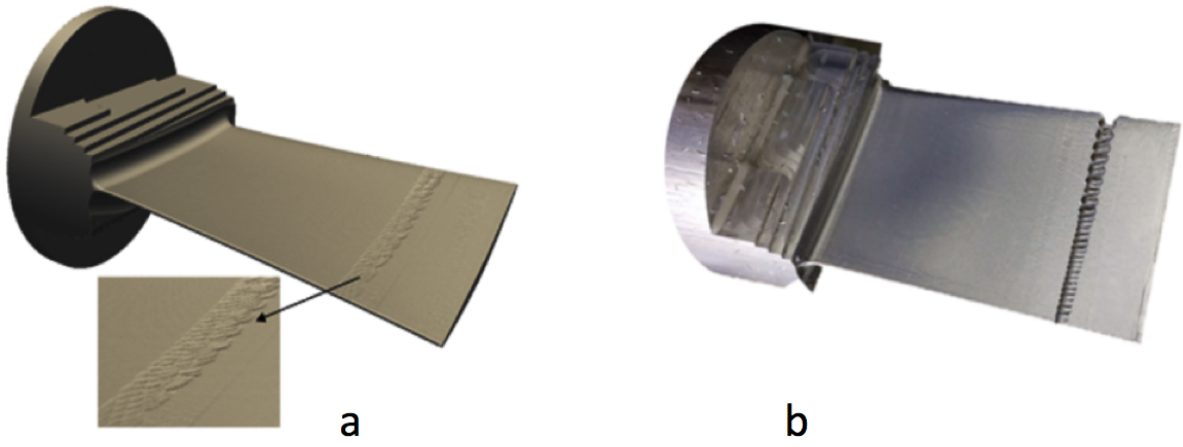


Figure 6: The blade surface obtained with simulation in 3DCUT (a), and the result of milling (b) with constant velocity of tool rotation.

3 Machining simulation

So-called ”chatter”, or self-excited vibrations in the tool-part system cause significant cutting forces increasing. ”Chatter” occurs on the frequency, which is close to one of the part or tool eigenfrequencies. The special algorithm is used to detect the ”chatter” in the vibrational signal obtained from simulation. The algorithm is based on the singular spectral analysis [7] in combination with demodulation and filtration. The ratio between maximum amplitude on the frequency, non-fold to the tooth-pass frequency and the maximum amplitude on the tooth-passing frequency are considered as a dimensionless indicator of ”chatter” occurrence in the system. The approbation of the proposed algorithm is done on several test objects [8], analyzing both experimental and simulation results.

The new way of multivariate simulation results interpretation is proposed - the milling map, which automates the process of optimal milling mode selection. Optimal milling modes guarantee that there will be no ”chatter marks” on the blade surface. It is shown on the fig. 6 that the final surface contains unacceptable ”chatter” marks after the machining on the certain tool rotational velocity.

To overcome these problems the multivariate process simulation was performed with tool velocity as a parameter. The milling maps have been built using updated finite-element model and damping regression curves (fig. 8). Blue markers on the map show the stable milling modes, the red ones correspond to developed ”chatter”. Yellow markers are for the transient modes, where chatter begins to emerge. There are corresponding plots for two representative modes shown on the (fig. 8). As it can be seen from the graphs, the amplitude of the vibrations for ”chatter” mode is an order of magnitude larger than for a stable cutting process.

The optimal milling mode with variable tool velocity was chosen using the provided milling map (shown with the green curve) and also the high-quality surface of the blade was obtained (fig. 7).

4 Conclusions

The results of blade modal analysis make it possible to conclude that it is necessary to take into account the change in the damping coefficients and the blank eigenfrequencies during machining in order to obtain reliable dynamics simulation results for selection rational milling modes.

Application of the developed methods of model identification in combination with milling dynamics simulation software makes it possible to solve the problem of selecting rational milling modes for thin-walled

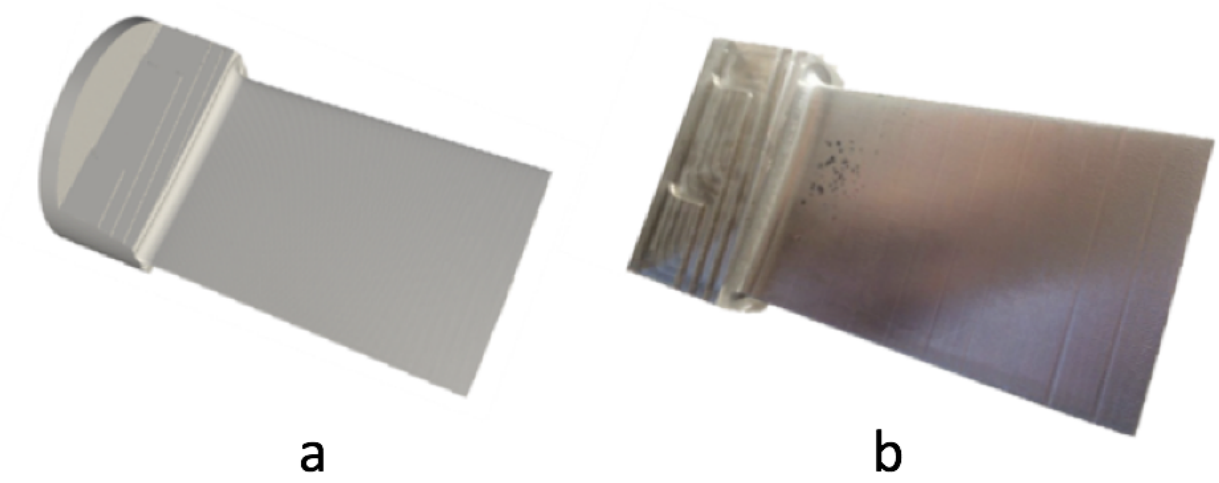


Figure 7: The blade surface after milling on the optimal machining mode. a - simulation, b - experiment

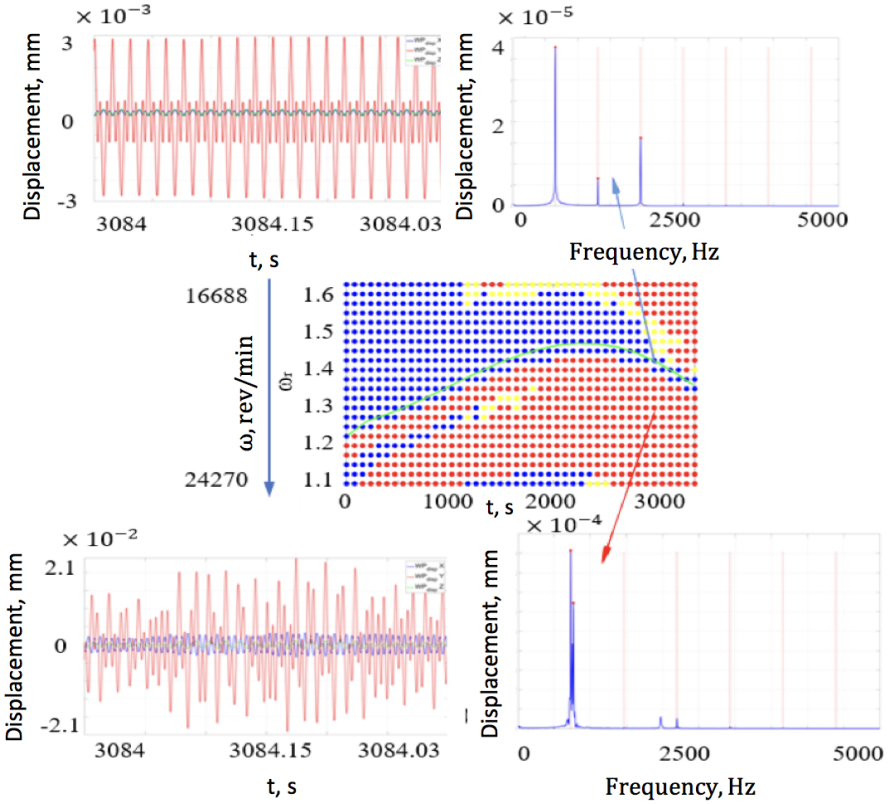


Figure 8: The milling map for considered blade

curved parts with increased requirements for surface quality.

References

[1] E. Dascotte *Model updating for structural dynamics: past, present and future outlook*, International Seminar on Modal Analysis, Leuven, Belgium. 2011. P. 145-169.

[2] S. Voronov, A. Gouskov, *Dynamic Models Generalization of Manufacturing Systems with Single-Point Cutting Considering Equations of New Surface Formation*, Proceedings of 2nd Workshop on Nonlinear Dynamics and Control of Mechanical Processing. Budapest (Hungary). 2001. P. 1-10.

[3] H. Paris, G. Peigne, R. Mayer *Surface shape prediction in high-speed milling*, International Journal of Machine Tools and Manufacture. 2004. V. 44/15. P. 15671576.

[4] M. Friswell, J. Mottershead, *Finite element updating in structural dynamics*, Dordrecht: Kluwer Academic Press, 1999. 292 p.

[5] X. Huang, Y. Xie *Evolutionary Topology Optimization of Continuum Structures: Methods and Applications*, New Jersey: John Wiley and Sons, 2010. 240 p.

[6] S. Voronov, I. Kiselev, *Dynamics of flexible detail milling* Proceedings of the Institution of Mechanical Engineers, Part K: Journal of Multi-body Dynamics. 2011. V225. 4. P. 299-309.

[7] J. Elsner, A. Tsonis, *Singular spectrum analysis: a new tool in time series analysis*, Berlin: Springer Science Business Media, 2013. 169 p.

[8] V.Kuts, S.Nikolaev. I.Kiselev, *Application of Combined Technique for chatter prediction in 5-axis milling*, Lecture Notes in Mechanical Engineering, Springer International Publishing AG, 2018

[9] P. Van Overschee, B. De Moor, *Subspace identification for linear systems: Theory Implementation Applications*, Berlin: Springer Science Business Media, 2012. 268 p.

Pneumatic single hit test rig for analysis of the stress wave profile of non-uniform impacting rods

J. Burgert [1], **C. Moilanen** [2] ,**W. Seemann** [1], **J. Montonen, J. Miettinen** [3], **P. Saarenrinne** [2]
[1] KIT Karlsruhe, Institute of Engineering Mechanics,
Kaiserstrasse 10, 76131 Karlsruhe, Germany
e-mail: **jens.burgert@kit.edu**

[2] TUT Tampere, Department of Mechanical Engineering and Industrial Systems,
Korkeakoulunkatu 10, FI-33720 Tampere, Finland

[3] TUT Tampere, Department of Materials Science,
Korkeakoulunkatu 10, FI-33720 Tampere, Finland

Abstract
Impacting rods are used in various devices in practical life but also for scientific experiments such as the split Hopkinson pressure bar. In order to validate numerical results of the stress wave with respect to the influence of the piston geometry, a pneumatic single hit test rig is set-up. After the hit of the impacting piston onto the rod a stress wave is propagating both into the piston and the rod. The resulting stress wave in the rod is measured in close proximity to the impact zone by using two different measurement techniques. The first method is based on digital image correlation. Since the distortion of the rod is very small, the displacements have to be detected very precisely to yield good results. More reliable results can be achieved by the second method: measuring the distortion with the well-known strain gauges.
In this contribution the set-up of the test rig is presented and measurement results are shown. Finally, the measurement results are compared with numerical results which yield good agreement.

1 Introduction

Impacting rods are used in many technical applications and in experimental devices. The most important experimental set-up is the split Hopkinson bar apparatus which consists of two rods, with a specimen to be investigated in between. One of the rods is hit by a third rod which leads to a rectangular pulse that propagates towards the specimen at which the wave is partly reflected and transmitted. These waves are detected by strain gauges located in the middle of the rods. This enables to determine the constitutive law of the specimen at high strain rates.
As an example of a technical application the percussion drilling process can be mentioned. The drilling process is initiated by high frequency hits of a piston onto the drilling rod. After each hit, a stress wave propagates both into the piston and the rod. It is difficult to predict the stress wave shape that finally arrives at the rock since it is influenced by many factors, such as friction, material properties and geometry variation of the impacting partners and the non-linear rock drill-bit interaction.
In 1959, Fischer [1] first examined the collision of fundamental forms and compared the analytical, geographical and numerical methods with measurement results which have been obtained using strain gauges. Lundberg *et al.* [2] have theoretically determined the optimal wave with respect to efficiency in percussive drilling depending on the duration of the stress pulse. For a given finite duration, the optimal shape is exponential whereas the optimal wave shape for short duration is almost rectangular. A numerical model based

on finite element method to improve the penetration depth per hit has been presented in [3]. A similar model has been used to model the split Hopkinson bar apparatus in [4].
Kaiwen *et al.* [5] have discussed different measurement techniques for the split Hopkinson bar (i.e. X-ray micro computed tomography, laser gap gauge and digital image correlation) and revealed that the digital image correlation technique is a promising way to obtain high resolution full-field strain information in high strain rate tests. This measurement technique has also been sucessfully applied for wood that has been tested with the split Hopkinson pressure bar in [6].

The objective of this work is to apply the digital image correlation technique to stress the influence of the geometries of the impacting partners on the wave shape. The results are compared with the results yielded by applying the conventional strain gauge measurement technique. The experimental set-up and the two measurement techniques are described in Section 2. Another aim of this work is to validate a numerical model, which is presented in detail in [7]. The main idea of the numerical model is given in Section 3. In Section 4 the results are presented followed by the conclusion in Section 5.

2 Experimental set-up

The schematic sketch of the experimental set-up, which contains a gun that accelerates the piston, is depicted in Figure 1. The velocity of the piston can be adjusted by varying the pressure in the pressure chamber. After

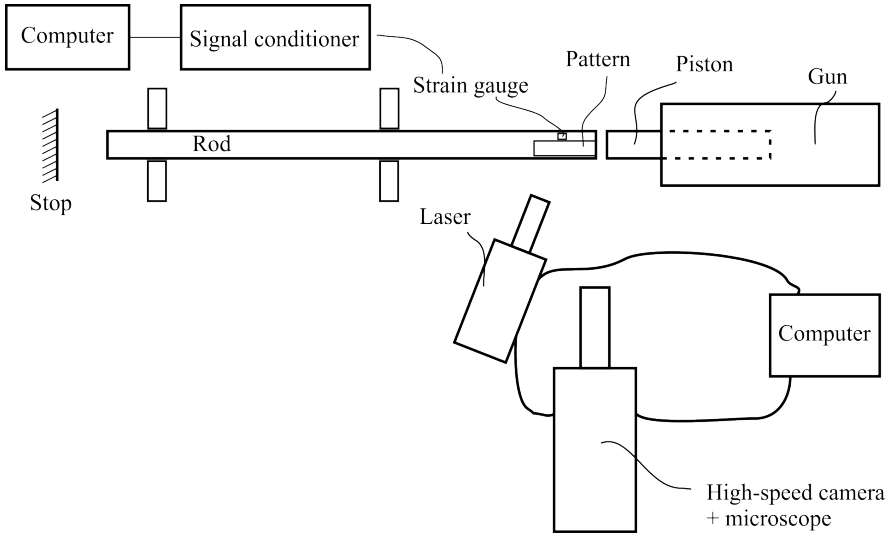


Figure 1: Schematic sketch of the experimental set-up

the impact, pressure waves propagate both into the piston and the rod. The strain at the beginning of the rod is detected by using two different measurement methods.
The first method is an image-based approach with a high-speed camera that takes pictures of a special pattern at a very high frequency. By evaluating the pattern the displacement field can be determined which enables to calculate the strain field subsequently.
The second method uses the well-known strain gauges to determine the strain at one position. The rod is supported freely at its left end and can move axially until it reaches the stop.

2.1 Gun

In Figure 2, the schematic sketch of the gun is shown. Due to the incoming air into the pressure chamber, the bushing tries to move to the right. However, the motion is prevented by the balls that are located on the trigger. The bushing is not able to move to the right until the balls vanish. By pushing the trigger, the trigger moves to the left whereby the balls drop down on the lower outer diameter of the trigger. Thus, the pressure chamber opens and the pressurized air flows towards the piston which leads to its acceleration.
The velocity of the piston can be adjusted by varying the pressure within the pressure chamber. However, a direct regulation of the impact velocity is not possible.

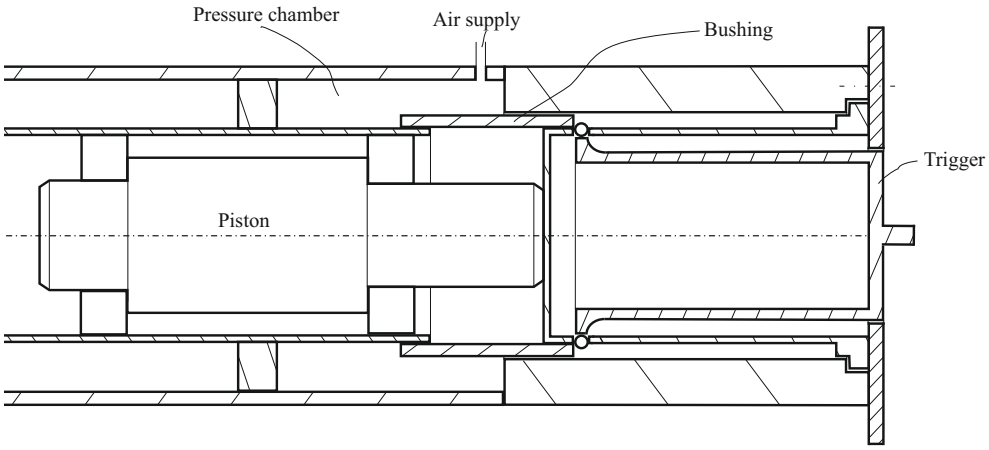


Figure 2: Schematic sketch of the gun

2.2 Image correlation measurement

Image based measurement systems, such as the image correlation method, provide significant benefits with respect to the conventional measuring method of using strain gauges. The main advantage is that an entire strain field can be measured with only one experiment. It is also possible to measure the strain at several positions with strain gauges, but most measurement systems are restricted in the amount of channels they can process. In addition, the image correlation method is contact-free so that materials with no access for strain gauges can be examined.
Observing the motion of the material with a high-speed camera enables to get an insight of what happens in the material at a certain time. Therefore, the interpretation of the measured phenomena can be explained and visualized.
For the image correlation technique pictures at very high frame rates have to be taken by a high-speed camera. At high frame rates, an external illumination is needed. Therefore, a laser triggered by a high-speed camera sends laser pules shortly before the pictures are taken. Without the laser illumination, the pictures taken would be completely black.
For further evaluation, the pictures are sent to the computer and examined applying the DaVis 8.4 FlowMaster software of the company LaVision.
The software subdivides the frames into so called interrogation windows of size $n \times n$ as shown in Figure 3. In order to determine the displacement field, the cyclic correlation between the interrogation windows is calculated with [8]

$$C(dx, dy) = \sum_{x=0,y=0}^{x<n,y<n} I_1(x, y) I_k(x + dx, y + dy), \; -\frac{n}{2} < dx, dy < \frac{n}{2}. \tag{1}$$

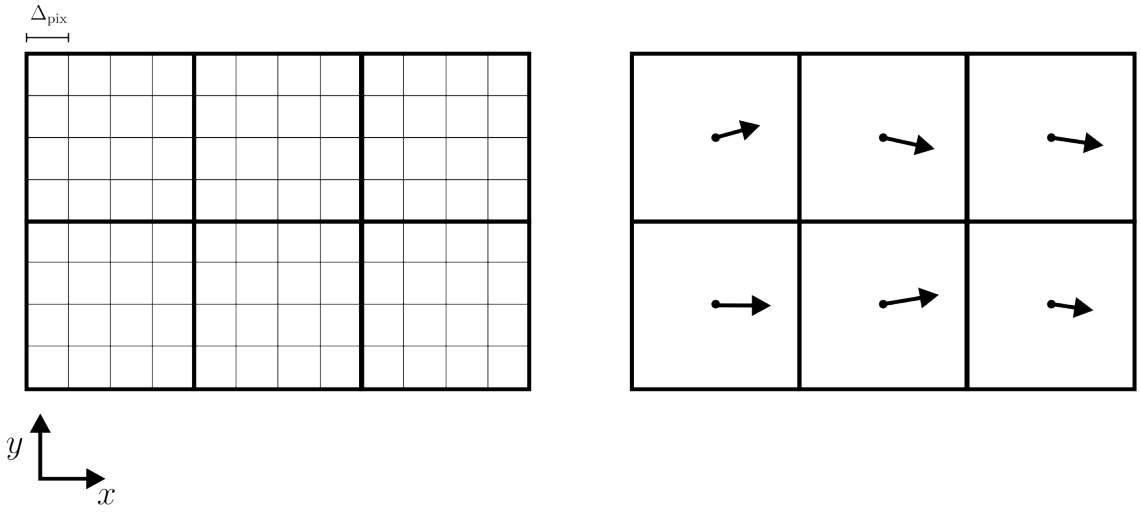


Figure 3: Frame subdivided into interrogation windows (left) and the corresponding displacement field after the evaluation (right)

I_1, I_k express the intensity values of one interrogation window of the first and kth frame respectively. The correlation function $C(dx, dy)$ describes the correlation strength at the cyclic integer shift (dx, dy). It is well-known, that the correlation function $C(dx, dy)$ can also be calculated in the frequency space by determining the two dimensional FFT of both I_1 and I_k and multiplying them complex conjugated. Subsequently, the inverse FFT of the product is calculated which yields the correlation function $C(dx, dy)$. This way is much faster compared to the direct evaluation of equation 1.
The correlation function $C(dx, dy)$ enables only to detect displacements with pixel accuracy. The accuracy can be improved by a three-point estimator that fits a Gaussian bell in each direction using the correlation peak $C(i, j)$ at pixel shift i, j and its direct neighbors $C(i-1, j), C(i+1, j)$ in $x-$direction and $C(i, j-1), C(i, j+1)$ in $y-$direction [9, 10]. The sharper the correlation peaks are, the better the method works. The used pattern is specially designed to get sharp peaks with low noise.
On the right hand side of Figure 3 an example of the corresponding vector field is presented. For every interrogation window a displacement vector is determined. Subsequently, the strains in $x-$direction

$$\varepsilon_{xx} = \frac{\partial u_x}{\partial x} \tag{2}$$

are calculated by applying central differences

$$\varepsilon_{xx} = \frac{u_{i+1,x} - u_{i-1,x}}{2n\Delta_{\text{pix}}}, \tag{3}$$

where $u_{i\pm1,x}$ describes the displacement in x-direction at interrogation window $i \pm 1$, n corresponds to the number of pixels in one direction of the interrogation window and Δ_{pix} represents the width of one pixel. To reduce noise, the displacements are averaged in $y-$direction. Since linear elastic material behavior is assumed, the stress in $x-$direction can be calculated with Hooke's law

$$\sigma_{xx} = E\varepsilon_{xx}, \tag{4}$$

and Young's modulus E.

Applying image based measurement systems to detect the wave shape of a propagating stress wave faces two major challenges. The first challenge is to realize a reasonable resolution for the wave shape which is

demanding due to the very fast wave propagation speed. Therefore, the frame rate of the high-speed camera has to be extremely high. The main properties of the used high-speed camera are depicted in table 1.

Name	Photron FASTCAM SA5
Frame rate	7000 fps at maximum resolution 1024×1024 pixels 232500 fps at resolution 192×104 pixels
Bit depth	12 bit
Pixel size	$20\,\mu\mathrm{m}$

Table 1: Main properties of the high-speed camera

It can be seen that the maximum resolution decreases with increasing frame rate. The resolution of the wave shape can be improved by taking materials with low wave propagation speed.
The second challenge is the main difficulty in using high-speed cameras for the calculation of wave shapes: The displacement field detection has to be very accurate in order to get reliable solutions for the strain calculation. This can be explained by the fact that for the strain calculation, not the absolute values of the displacements is important but the difference between them. The key determinants to improve the accuracy of the strain calculation can be derived by examining the central difference formula. According to the DaVis software manual, an accuracy up to $0.05\ \Delta_{\mathrm{pix}}$ for the displacement detection can be achieved. If it is assumed that the displacement at interrogation window $i-1$ can be determined exactly, the strain calculates as follows

$$\varepsilon_{\mathrm{cal}} = \frac{u_{i+1,x} + 0.05\Delta_{\mathrm{pix}} - u_{i-1,x}}{2n\Delta_{\mathrm{pix}}} = \underbrace{\frac{u_{i+1,x} - u_{i-1,x}}{2n\Delta_{\mathrm{pix}}}}_{\varepsilon_{xx}} + \underbrace{\frac{0.025}{n}}_{\varepsilon_{\mathrm{err}}}. \tag{5}$$

Since the accuracy of the displacement determination also depends on Δ_{pix}, the error is independent of the pixel width Δ_{pix}.
Based on equation 5 three possibilities to improve the measurements can be derived. The first possibility is obviously to increase the interrogation window (larger n). However, due to the high frame rate the resolution is already very low. This implies that the number of evaluation points will be decreased. Moreover, to achieve good results for the central finite difference calculation of the strain, the spatial distance $2n\Delta_{\mathrm{pix}}$ between the evaluated interrogation windows has to be small. Therefore, it can be concluded that Δ_{pix} has to decrease which leads in turn to the fact that only a very small part of the rod can be covered. The second possibility is to improve the accuracy of the measurement, which can be achieved by using a microscope. The last possibility is to lower the error sensitivity. For steel, the occurring strains are very low. Thus, small errors in the determination of the strain already have significant impact on the result. It has to be considered that for the calculation of the strain linear elastic material behavior is assumed. As a consequence, the actual strains should not exceed the yield limit.

2.3 Strain gauge measurements

The strain gauge that has been implemented is placed in the region of the pattern so that the results of the strain gauge can be compared with the results that are obtained with the image correlation method. The characteristics of the strain gauge are shown in table 2.

Name	Kyowa KFG-2-120-C1-11L5M2R
Gauge factor	2
Gauge length	2 mm
Gauge resistance	$120.4 \pm 0.4\,\Omega$

Table 2: Characteristics of the strain gauge

The measurement device that hast been used is called Siemens LMS Scadas Mobile equipped with DSP module SCM-VB8-II with maximum frame rate of $200\,\mathrm{kHz}$.

2.4 Piston and rod

The restrictions of the measurement devices in terms of maximum frame rate motivate to consider other materials than steel for the rod. The distance the wave propagates between two samplings is calculated by

$$\Delta l = c\Delta t = \frac{c}{f}. \tag{6}$$

For steel ($c_{\mathrm{steel}} \approx 5000\,\mathrm{ms}^{-1}$) and frame rate $f = 200\,\mathrm{kHz}$ the travel distance of the wave Δl equals $2.5\,\mathrm{cm}$. A better spatial resolution can be achieved by considering materials with lower wave propagation speed. Moreover, to get reliable results with the image correlation method, it is advantageous that the material exhibits high strain at the yield limit. Therefore, for the rod of length $305.5\,\mathrm{cm}$ and constant diameter $41\,\mathrm{mm}$ POM-material with the following material properties

Name	POM-C
Density	$1410\,\mathrm{kgm}^{-3}$
Young's modulus	$2800\,\mathrm{MPa}$
Tensile strength	$66\,\mathrm{MPa}$
Compression strength	$72\,\mathrm{MPa}$

Table 3: Material properties of the rod material

has been chosen. Since the strain in the piston has not been detected, the wave propagation speed of the piston does not have to be considered. Therefore, the piston is made of hardened steel. The dimensions of the piston can be seen in Figure 4.

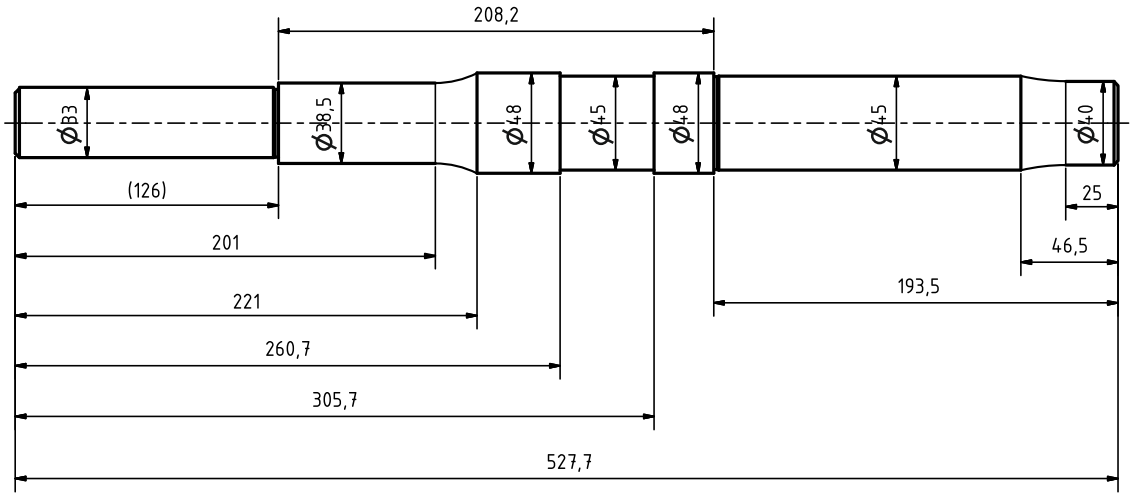


Figure 4: Dimensions of the piston

3 Simulation model

Analytical solutions for the wave propagation in rods with non-uniform geometries only exist for very few (i.e. exponentially varying) cross sections [11]. Therefore, numerical methods have to be applied for arbitrary geometries.
The dynamics of the rod ($i = 1$) and piston ($i = 2$) can mathematically be described by the partial differential equation for the displacement $u_i(x, t)$

$$\frac{\partial}{\partial x}\left[E_i(x)A_i(x)\frac{\partial u_i}{\partial x}\right] = \rho_i(x)A_i(x)\frac{\partial^2 u_i}{\partial t^2}, \quad i = 1, 2 \tag{7}$$

in which E is the Young's modulus, ρ describes the mass density and the area of cross section is denoted by A. This equation simplifies for constant material properties and constant cross sections to the well-known 1D wave equation [12]

$$\frac{\partial^2 u_i}{\partial t^2} - c_{0,i}^2\frac{\partial^2 u_i}{\partial x^2} = 0, \quad c_{0,i} = \sqrt{\frac{E_i}{\rho_i}}, \quad i = 1, 2 \tag{8}$$

with wave propagation speed c_0. This equation can analytically be solved by the d'Alembert solution

$$u_i(x, t) = f_i(x - c_{0,i}\,t) + g_i(x + c_{0,i}\,t), \quad i = 1, 2 \tag{9}$$

where f and g are arbitrary functions.
The main idea of the numerical approach is to approximate the geometry of both piston and rod by piecewise constant cross sections so that equation 9 can be applied to constant cross sections. At the impact zone between piston and rod and at each change of cross section transition conditions have to be formulated which can be derived by claiming force and displacement equilibrium

$$u_1(\hat{x}, t) = u_2(\hat{x}, t), \tag{10}$$

$$E_1(\hat{x})A_1(\hat{x})\frac{\partial u_1}{\partial x}(\hat{x}, t) = E_2(\hat{x})A_2(\hat{x})\frac{\partial u_2}{\partial x}(\hat{x}, t) \tag{11}$$

with $x = \hat{x}$ being the spatial coordinate of the impact zone or of a change of cross section. It is important to stress that the condition force and displacement equilibrium at the impact zone only holds if the transmitted force is a compressional force. Otherwise, piston and rod will separate. By taking a large number of constant cross section elements a good approximation of the geometries can be achieved.

4 Results

In Figure 5 the results for both measurement methods and for the simulation are depicted. All results are evaluated on one position on the rod at $6\,\mathrm{cm}$ distance from the impact zone. It can be seen that a sudden change in stress occurs due to the impact. The agreement of the image correlation method with the strain gauge result is very good immediately after the impact. However, the stress curve of the image correlation method decreases rapidly until no measurement is possible anymore. The reason for this is that the rod is moving axially after the hit and the camera is taking pictures from the same position all the time. In Section 2.2 it has already been discussed that in order to get reliable results, the number of pixels and the pixel size has to be very low. This in turn leads to the mentioned problem that the pattern moves out of the picture.

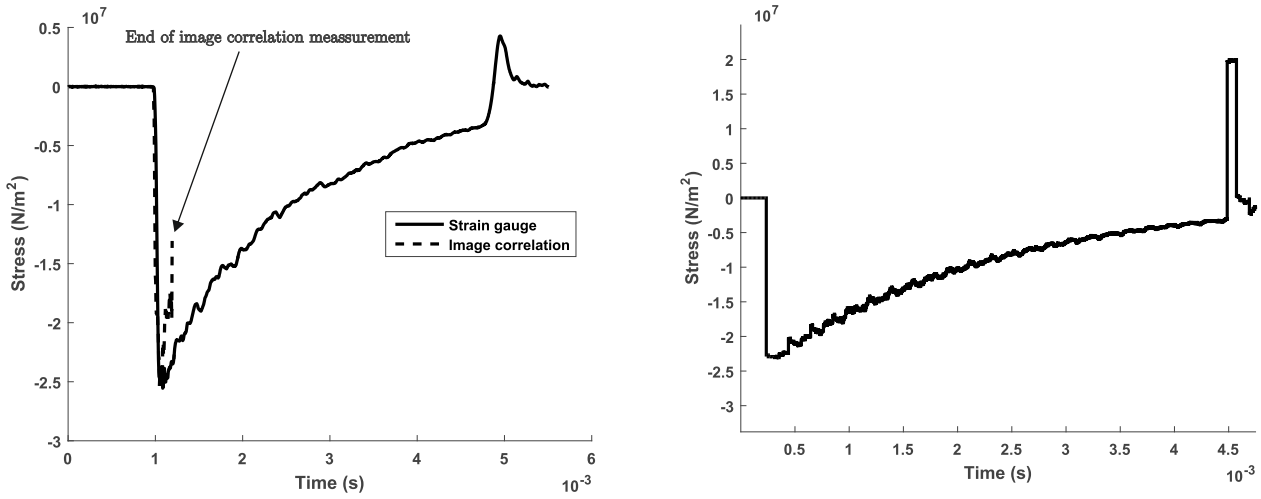


Figure 5: Comparison of image correlation method with strain gauge measurement (left) and simulation result (right)

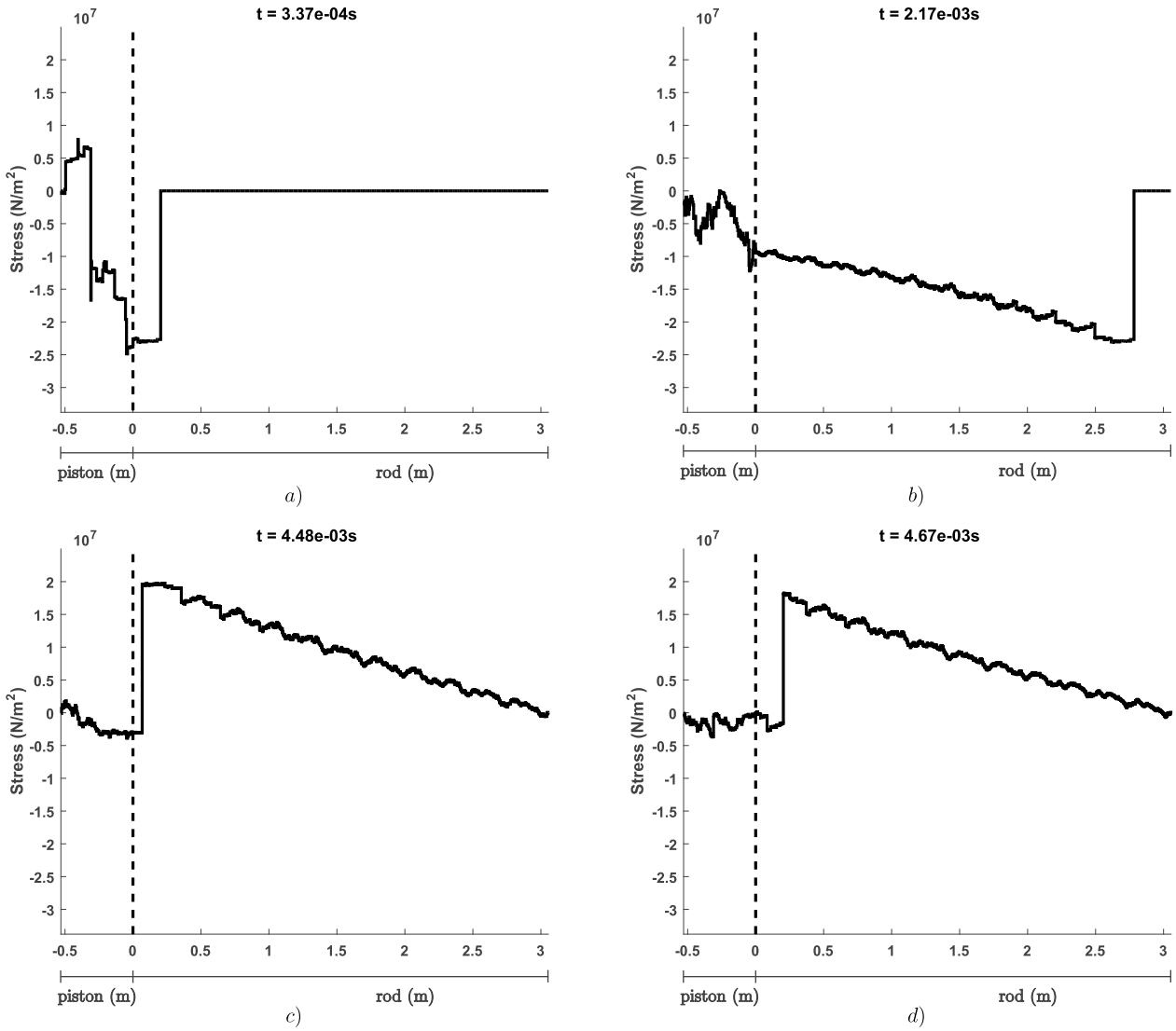


Figure 6: Numerical simulation of the stress at piston (to the left of dashed line) and rod (to the right of dashed line) $a)$ shortly after the impact, $b)$ before the stress wave reaches the end of the rod, $c)$ shortly before reflected wave reaches impact zone and $d)$ after the separation

After the impact, the stress continuously decreases until it changes suddenly to a tensile stress peak. This phenomenon can be explained by interpreting the simulation results shown in Figure 6, where the stress at every spatial position of the piston and rod is depicted at different times.
The dashed line displays the transition between piston and rod. In Figure 6a) the situation shortly after the impact is depicted. The stress wave front already propagates approximately $0.2\,\mathrm{m}$ into the rod. At the same time, the wave front that propagates into the piston is already reflected at its free end on the left because the wave propagation speed of steel is ≈ 3.5 times higher than the wave propagation speed of POM. The material points of the rod right of the wave front are at rest and have not been influenced by the impact yet. The wave front of the rod continues propagating until it almost reaches its free end in Figure 6b). At its free end, the stress wave is reflected and returns in form of a tensile stress wave towards the transition zone. Just before the tensile stress wave reaches the impact zone, it reaches the evaluation point by which the tensile stress peak both in the simulation and for the strain gauge measurement can be explained (Figure 6c)). Since a tensile force cannot be transmitted at the impact zone, piston and rod separate and move independently as soon as the tensile stress wave arrives at the transition. This leads to the change of the transition conditions from force and displacement equilibrium to the boundary condition of free ends for piston and rod. At the resulting free end, the tensile stress wave is reflected again (Figure 6d)). The time duration of the stress peak in the simulation corresponds to the time between the arrival of the tensile stress wave until the arrival of the reflected stress wave.
The height of the tensile stress peak in the simulation is considerably higher than the one detected using strain gauges. A possible explanation for the difference is the fact that material damping is not considered in the simulation model. Apart from the differences in amplitude of the peaks, the qualitative behavior of the stress shape can be described adequately.
At this point, it is advantageous to verify the presumptions with pictures taken with the high-speed camera.

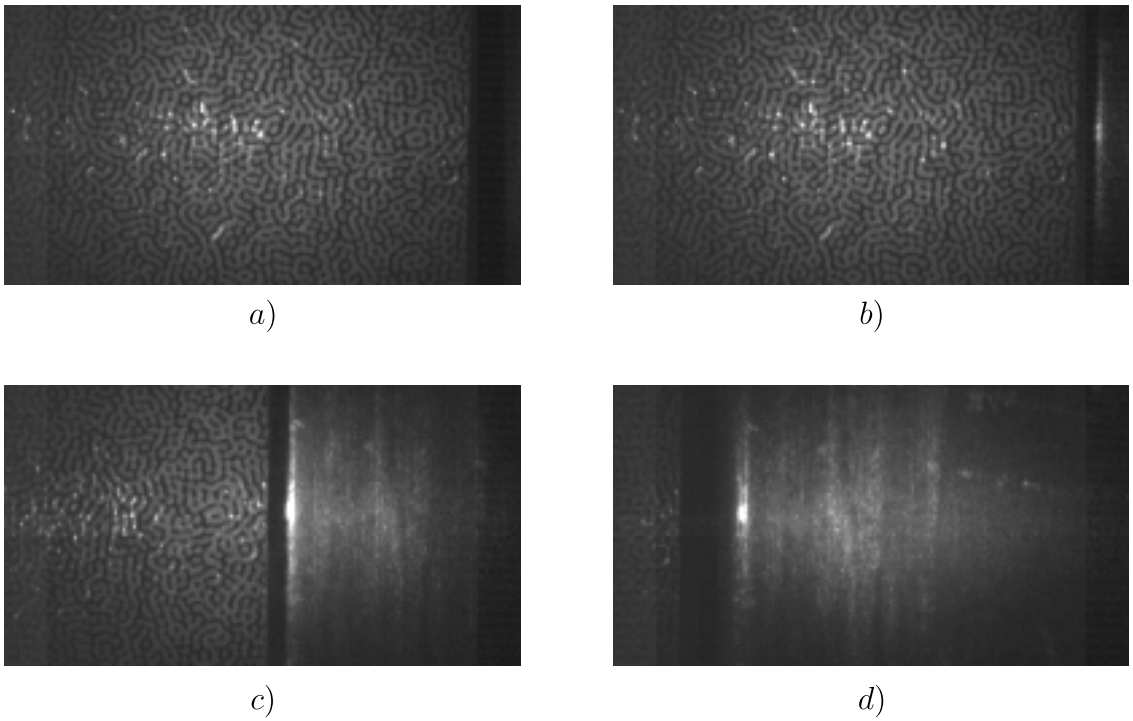


Figure 7: Sequence of camera pictures from a) rod is at rest and waiting for the piston over b) the hit and c) movement together until d) the separation

A sequence of camera pictures from the rod being at rest until rod and piston are separated is presented in Figure 7. By comparing the time between the hit and the separation both in Figure 7 and Figure 5 it can be confirmed that piston and rod separate as soon as the reflected tensile stress wave arrives at the impact zone.

Moreover, the high-speed camera can be used to detect the impact velocity of the piston. The dependency of different impact velocities on the wave shape is depicted in Figure 8.

The measurement results confirm the expectations: The higher the impact velocity the higher is the stress

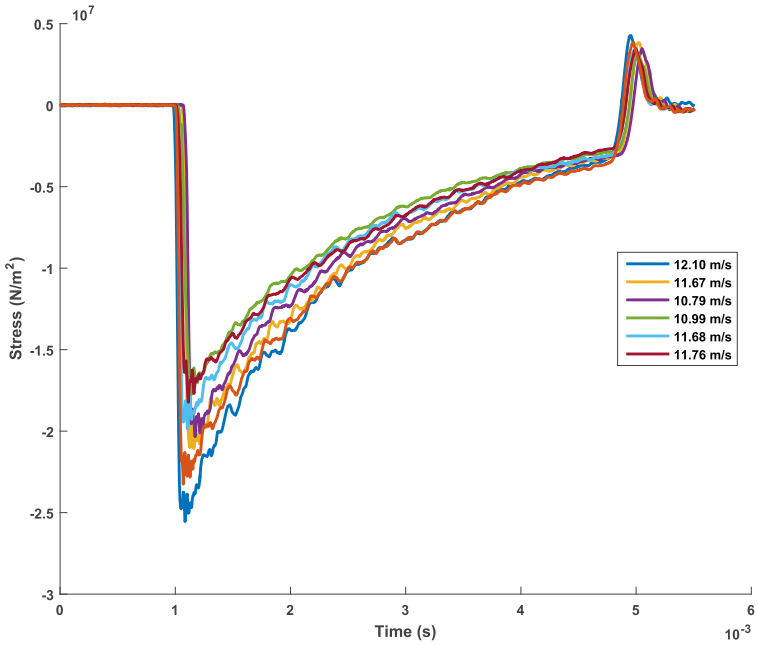


Figure 8: Strain gauge measurement at different piston velocities

peak immediately after the impact. The duration between impact and separation is independent of the impact velocity since it is only dependent on the material properties of the rod. Moreover, the measurement results show that the results are repeatable.

5 Conclusion

In this paper two different measurement methods for the evaluation of stress wave shapes have been investigated and compared with simulation results. The simulation results yield qualitatively very good accordance with the strain gauge measurement results. However, the image correlation method only yields reliable results at the beginning of the impact. The reason is that the image correlation method cannot measure the strain directly but has to measure the displacements first. The strain of most materials at the yield limit is very low. Therefore, in order to get reliable results, the displacements have to be detected very precisely. If higher strains are of interest the image correlation can still be applied. Although the image correlation method could not detect the desired stress wave shape, the combination of strain gauges together with a high-speed camera turns out to be very useful. On the one hand the high-speed camera can be used to determine the piston velocity just before the impact and on the other hand the overall movement of the impacting partners can be observed. This leads to a better understanding of the system and can be used to verify some phenomena.

The qualitative behavior of the stress wave shape can be predicted very well by the simulation model. Therefore it can be concluded that one-dimensional theories yield good results for such impact problems. Further improvements of the numerical model will be to include material damping. Moreover, the influence of the geometries of the impacting partners will be examined.

References

[1] H.C. Fischer, *On longitudinal impact I- Fundamental cases of one-dimensional elastic impact, theories and experiments*, Journal of Applied Scientific Research, Vol. 8, No. 1, 1959, pp. 105-139.

[2] B. Lundberg, P. Collet, *Optimal wave with respect to efficiency in percussive drilling with integral drill steel*, International Journal of Impact Engineering, Vol. 37, No. 8, Elsevier (2010), pp. 901-906.

[3] J. Montonen, E. Keskinen, M. Cotsaftis, J. Miettinen, W. Seemann, *Dynamics of Single-Hit Pneumatic Test Drill for Pulse-Shaping Analysis of Impacting Waves*, *Proceedings in ASME International Mechanical Engineering Congress and Exposition, San Diego, California USA, 2013 November 15-21.*

[4] E. Keskinen, T. Vuoristo, V. Kuokkala, M. Martikainen, *Numerical analysis of Hopkinson split bar apparatus*, *Proceedings of SEM Annual Conference and Exposition on Experimental and Applied Mechanics, Portland, Oregon US, 2005 June 7-9.*

[5] X. Kaiwen, Y. Wei, *Dynamic rock tests using split Hopkinson (Kolsky) bar system, A review*, Journal of Rock Mechanics and Geotechnical Engineering, Vol. 7, No. 1, CSRME (2015), pp. 27-59.

[6] C. Moilanen, P. Saarenrinne, B. Engberg, T. Bjrkqvist, *Image-based stress and strainmeasurement of wood in the split-Hopkinson pressure bar*, Measurment Science and Technology, Vol. 26.

[7] J. Burgert, W. Seemann, F. Hartenbach, *Optimization of the piston geometry to generate a desired stress wave shape*, *Proceedings of the 88th Annual Meeting of the International Association of Applied Mathematics and Mechanics, Weimar, Germany, 2017 December*, pp. 675-676.

[8] O. Ronneberger, M. Raffel, J. Komenhans, *Advanced Evaluation Algorithms for Standard and Dual Plane Particle Image Velocimetry*, *Proceedings of the 9th International Symposium on Applications of Laser Techniques to Fluid Mechanics, Lisbon, Portugal, 1998 Juli 13-16.*

[9] C. E. Willert, M. Gharib, *Digital Particle Image Velocimetry*, Journal of Experiments in Fluids, Vol. 10, No. 4, Springer (1991), pp. 181-193.

[10] J. Westerweel, *Fundamentals of digital particle image velocimetry*, Journal of Measurement Science and Technology, Vol. 8, No.12, 1997, pp. 1379-1392.

[11] S. Guo, S. Yang, *Wave motions in non-uniform one-dimensional waveguides*, Journal of Vibration and Control, Vol. 18, No. 1, SAGE (2011), pp. 92-100.

[12] P. Hagedorn, A. DasGupta, *Vibrations and Waves in Continuous Mechanical Systems*, WILEY (2007).

Simulation and digital twin for mechatronic product design

H. Van der Auweraer[1,3], S. Donders[1], D. Hartmann[2], W. Desmet[3,4]
1 Siemens Industry Software NV, Interleuvenlaan 68, B-3001 Leuven, Belgium
e-mail: **herman.vanderauweraer@siemens.com**

2 Siemens Corporate Technology, Otto-Hahn-Ring 6, 81739 Munich, Germany

3 University of Leuven – KU Leuven, Department of Mechanical Engineering, Division PMA, Celestijnenlaan 300, B-3001 Heverlee, Belgium

4 DMMS core lab, Flanders Make

Abstract
The use of digital twins and simulation models to construct, evaluate and validate designs has become an intrinsic part of every product creation process. The use in production, operation and service has been increasing in the last years, for example model predictive control or simulation-based assist systems. The challenges – and opportunities – however are multifold. Interoperability of models, model transformation and co-simulation are key to realize system level simulation. Computing performance alone cannot address the requirements posed by ever more complex systems and applications like massive design space exploration or interactive simulation, expressing the need for disruptive solver solutions. But also modeling technology needs to be extended. Integrating the digital twin with data measured on the physical assets, reusing all previously established engineering knowledge, allows new applications such as virtual sensing, model based control and hybrid system modeling including hardware, software and numerical components.

1 Introduction

The digital twin is the virtual copy of a real asset. It integrates all data, models (engineering, data-based, simulation), and otherwise structured information of a product, plant, infrastructure system, or production process. The data can be generated during design, engineering, manufacturing, commissioning, operation, or service. Integrating all information is key to leverage existing and create new business opportunities. Depending on the application under investigation, the digital twin may represent a product, a production system or a production or construction process. In all cases however, the objective is to have a digital representation suited to the purpose in terms of level of detail, completeness, accuracy, and execution speed. The digital twin can be used in product design, simulation, monitoring, optimization and servicing and is an important concept in the industrial Internet of Things.

Simulation is then the execution of a model of a real world system to study its behavior, evaluate an architecture or parameter space with the goal to optimize design, production, operation, and service. Examples are 3D CAE models with attached physics, models of logical behavior and effect based (1D) models of the system, test-based models, and system simulation models as a mixture of all.

Digital twins are created in the same design and modeling environment that designers and engineers use in the various stages of product development. The key element with a digital twin is that the model acts as a unique reference which is retained throughout all stages of the product's lifecycle, including but not limited to the functional description, concept evaluation, performance optimization, variant tracking and inspection and maintenance. Typically, a digital twin will be a “living” entity, being extended, completed and updated throughout the asset’s lifecycle, further enriched with data obtained during the physical asset’s operation.

The concept of the digital twin requires three elements [11]: the physical product in real space, its digital twin in virtual space and the information that links the two.

Sensors connected to the physical product can collect data and send it back to the digital twin, and their interaction can help optimize the product's performance. For example, sensors might detect when a car's engine oil needs changing, and the car's digital twin will have an overlay image indicating the new information, which can appear on the owner's smartphone or the manufacturer's product lifecycle management (PLM) system.

The present paper will focus on the simulation digital twin used in the product creation, verification and validation stages. More encompassing descriptions, including the broader framework of production and production systems can be found e.g. in [24]. What is key to the digital twin is that it constitutes an essential part of the industrial Digitalization strategy and that its realization depends heavily on advanced software tools and processes, including multiphysics simulation, experimental verification and data management. Interoperability of methods and data originating from heterogeneous sources and applications is hence a key challenge to be addressed.

Several factors have now converged to bring the concept of the digital twin to the forefront as a disruptive trend [34], with a boost of engineering news bandwidth since 2017 [38][39][40][41][50][54]. In fact, Gartner [34] predicts that by 2021, half of the large industrial companies will use digital twins, resulting in those organizations gaining a 10% improvement in effectiveness.

The outline of this paper is as follows. Section 2 provides the state of the art of the digital twin. Section 3 provides the Siemens vision on the digital twin throughout the product lifecycle. Section 4 reviews enabling technologies: simulation and test models, model order reduction (MOR) schemes and co-simulation, etc. Section 5 provides case studies of the digital twin in action. The paper is concluded in Section 6.

2 State of the art of the digital twin

The concept of digital twins is not new. For more than 30 years, product and process engineering teams have used 3D renderings of computer-aided design models, asset models and process simulations.

NASA was the first to work with pairing technology – the precursor to today's digital twin – already from the early days of space exploration onwards [30][41]. The challenge has been to operate, maintain or repair systems when you aren't within physical proximity to them; after all, the systems would travel beyond the ability to see them or to monitor them physically. When disaster struck Apollo 13 in 1970, it was the innovation of mirrored systems still on earth that allowed engineers and astronauts to determine how they could rescue the mission. Today, NASA uses digital twins to develop new recommendations, roadmaps, and next-generation vehicles and aircraft [4][11][22]. The term digital twin was first defined by Dr. Michael Grieves at the University of Michigan around 2003 in a University of Michigan Executive Course on Product Lifecycle Management (PLM), as referenced in his book in 2011 [8]. In his 2014 white paper [11], he outlined the concept of a digital twin as a virtual representation of what has been manufactured. He promoted the idea of comparing a digital twin to its engineering design to better understand what was produced versus what was designed, tightening the loop between design and execution.

The Air Force Research Laboratory linked the digital twin to the operational phase of the aircraft lifetime. According to their 2011 vision [5], when the physical aircraft is delivered, a digital twin of the aircraft – specific to that tail number, including deviations from the nominal design – will be delivered as well. The digital twin will be flown virtually through the same flight profiles as recorded for the actual aircraft by its on-board structural health monitoring (SHM) system. The model will be updated/calibrated/validated w.r.t. sensor readings recorded by the SHM system. When damage is found, it will be added to the Digital Twin, such that it continually reflects the current state of the aircraft. Also, "prognostics" for the airframe will be possible by flying the digital twin through possible future missions. Main outcome is in the area of fleet management: the digital twin model will be used to determine when & where structural damage is likely to occur, and when to perform maintenance. In this line of thought, Tuegel et al. [7] propose a process that utilizes an ultrahigh fidelity model of individual aircraft by tail number, a Digital Twin, to integrate computation of structural deflections and temperatures in response to flight conditions, with resulting local damage and material state evolution.

The concept of digital thread (the use of digital tools and representations for design, evaluation, and life cycle management) was introduced in [14] in 2013. A digital thread describes and defines a component in a reusable digital format [48]. This refers to a digital twin comprised of advanced modelling and simulation tools that link materials, design, processing and manufacturing. This is claimed to be a future game-changer that provides the agility and tailorability needed for rapid development and deployment, while also reducing risks. According to [19], the future aircraft lifecycle management will be predictive, integrated, individualized and preventive, thanks to the digital thread / digital twin technology. The importance of the digital thread is underlined in the NASA Vision 2040 on materials modelling [48]. It is stated that the connection of this structural paradigm viewpoint with that of the design of materials paradigm, with all its potential impact, is still lacking and will require more work. It is also stated that companies that have established a digital thread and accompanying digital culture are reporting high payoff in terms of efficiency increases and cost savings; however, to date progress has occurred on either the material or structures side of the house with only limited connection between the two.

The different waves of simulation in system development, announcing the digital twin era, were introduced by Boschert and Rosen in 2016 [24]. As shown in a Siemens graphic in Figure 1, simulation is evolving from a troubleshooting tool to adding customer value in the form of digital twins. In the digital twin era, simulation is a core functionality of systems by means of seamless assistance along the entire lifecycle, e.g. supporting operation and service with direct linkage to operational data. Boschert and Rosen focus on the use of the digital twin in the design and engineering phase, as well as the operation and service phase.

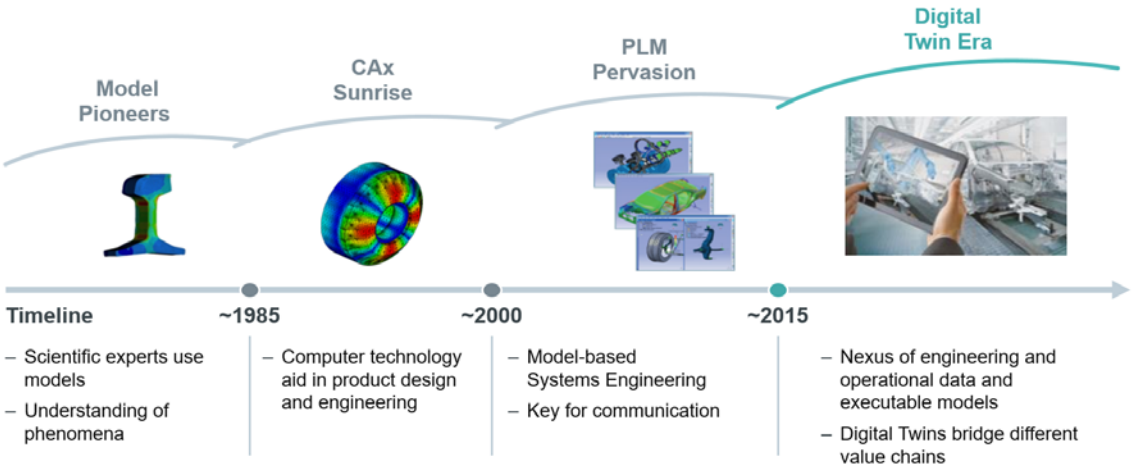


Figure 1: Simulation is evolving from a troubleshooting tool to adding customer value through digital twins.

With recent developments that have resulted in higher availability and affordability of sensors, data acquisition and computer networks, the ground is fertile for implementing high-tech methodologies to modernize today's industry [20]. This has resulted in ever more sensors and networked machines, continuously generating high volume data which is known as Big Data [12]. Cyber-Physical Systems (CPS) can be further developed for managing Big Data and leveraging the interconnectivity of machines. Networked machines will be able to perform more efficiently, collaboratively and resiliently [12]. This trend is transforming manufacturing industry to the next generation, namely Industry 4.0 [23]. This represents the combination of Cyber-Physical Systems, the Internet of Things, and the Internet of Systems. In short, it is the idea of smart factories in which machines are augmented with web connectivity and connected to a system that can visualize the entire production chain and make decisions on its own. The digital twin can become instrumental in its capability to model a range of identically manufactured products, and accompany each of them in their lifecycle, subject to the same loads and conditions in a virtual environment, and predicting their state throughout the product lifetime.

Many software vendors are now marketing the digital twin or similar concepts. A good overview of the technology status is given in the Gartner eBook [50] and the NAFEMS Benchmark magazine of April 2018, see [51][52][53] and especially [54].

3 Digital twin throughout the product lifecycle

At the Siemens PLM Software 11th annual analyst conference in Boston, Sept 5-8 2017, Siemens PLM Software described its approach to the digital twin as creating a holistic, actionable set of digital twins that encompass all aspects of the product lifecycle, spanning product, production and performance [35][36][39]. There are in fact at least three lifecycle stages that require a digital twin, each of which needs to be created and connected to the others. These include the:

- Digital Product Twin – used during product development;
- Digital Production Twin – used during manufacturing engineering and production operations;
- Digital Performance Twin – used for product simulation and during the utilization of the product.



Figure 2: The three phases for the digital twin are called “Ideation”, “Realization” and “Utilization” [35].

The digital twin understands and models the entire value chain process and helps to create a digital thread across the product and process lifecycle. To get maximum value and productivity an enterprise that creates complex products or processes can benefit from an actionable, holistic digital twin concept. An actionable, holistic digital twin is a living model fed by analytics and exercises by math-based simulations. These are multi-function simulations involving mechanics, electronics and embedded software that are combined to create a predictive engineering analytics function that inform companies how to improve their product data and process design, production and maintenance approaches. This provides business value well beyond the predictive maintenance use cases common in digital twin discussions today [41].

Of course depending on the specific domain, e.g. the construction industry, connotations of the digital twin are much broader than the perspective covered in this paper. For the sake of brevity, in this paper the focus is on the product centric point of view.

4 Enabling technologies

4.1 Simulation and test models

PLM vendors currently offer a wide range of tools to enable efficient virtual and model-based design of industrial products. These tools span a wide range of complexity and applicability, depending on the stage of the design where they are deployed. In practice a dichotomy between two key approaches is observed:

- System simulation tools (i.e. based on analytical models and functional relations, also referred to as 1D simulation tools) are used to simulate complete systems or sub-systems and are predominantly used in the conceptual design phase. The individual components of a system are simplified via integral or global methods aimed at rendering only their main characteristics, emphasis being put on describing their interaction with the numerous other components in the studied system. At their core are lumped parameter system models formulated as Ordinary Differential Equations (ODE) or

Differential Algebraic Equations (DAE). The simulated time ranges from fractions of a second up to minutes. The related CPU time ranges from some hundred times real-time, down to real-time. Real time applications require very simple descriptions of components and thus rely on empirical or phenomenological models. As a result, a priori predictivity (i.e. the ability to predict the system behavior without a priori experimental evidence) is low. While originally mainly used in the concept phase, such 1D system simulation models are increasingly forming the core of the integrated Multiphysics system description in complex mechatronic systems.

- Geometry-based 3D simulation tools are used for detailed component design and are the traditional performance validation (and optimization) complement of CAD (Computer Aided Design) based product descriptions. They are applied to single components, or small sub-systems of few components. They aim at accurately predicting the detailed phenomena determining their behavior by resolving the related fundamental equations. They are mainly used in the detailed design and engineering phase, for acquiring a detailed understanding of the interactions of complex phenomena and for optimizing proposals resulting from the concept phase. One can distinguish
    - Multi-body simulation (MBS) method: here, the structure is composed of various rigid or elastic bodies. Connections between the bodies can be modelled with kinematic constraints (such as joints) or force elements. A system-level calculation then yields the forces and displacements that can be analyzed or can serve as input to FE calculations e.g. for NVH.
    - Finite Element (FE) method: the full domain is discretized into finite elements, that are approximated with simple or more complex shape functions. Calculating the mechanical response of the assembled system then yields the system-level prediction. FE is used for detailed 3D prediction of structural vibrations, noise, acoustics, electromagnetic excitation.
    - Boundary Element (BE) method: here, the boundaries of the domain are discretized and modelled with simple or more complex shape functions. A calculation of the mechanical response of the assembled system then yields the system-level prediction. It is used for detailed 3D predictions e.g. of acoustics and electromagnetic radiation.
    - Computational Fluid Dynamics (CFD) method: the branch of fluid mechanics methods using numerical analysis and data structures to analyze problems involving fluid flows. Computers are used to perform the calculations required to simulate the interaction of liquids and gases with surfaces defined by boundary conditions.

  3D simulations are typically built up by leveraging the availability of detailed geometrical description of the domain to be simulated (CAD files). The simulated time ranges from fractions of milliseconds up to multiple seconds. The related CPU time is significant, around 10^4 times the real time, down to real-time (multi-body simulation models that can run in the loop with high fidelity as compared to 1D models). The accent of 3D simulation is on high predictability in order to characterize a component or sub-system. The 3D simulations are mostly used in the detailed engineering phase, for optimizing and validating detailed component models up to system simulation models. Even though these tools enable high-fidelity results, they are often much too computationally expensive for full system level evaluation in a fast design process. 1D models offer the potential to perform fast simulation and real-time performance for XiL applications, but they lack the parameter traceability to design variables to be useful in a general design process.

Hybrid Test-CAE modelling approaches are possible from the refinement engineering stage onwards, with the availability of first test prototypes [33]. One example is the creation of hybrid models in which a 3D model of a newly designed component is combined with an experimentally identified model of an already existing component (prototype). Especially in case of re-using complex components with nonlinear behavior in a future design, such hybrid modelling approaches can be very interesting. In this phase, also the correlation and updating user scenario is relevant, for instance by improving a Finite Element Model (FEM) based on Experimental Modal Analysis (EMA) results from a vibration test. Moreover, the reduced EMA model can also have a value to be used directly in a state estimation environment, representing part of the realistic physics of the system in a concise representation.

4.2 Building blocks to respond to current industrial challenges

The digital twin vision extends the need of advanced building blocks to respond to today's industrial challenges. This is supported by a double exponential growth of capability in simulation technology. On the one hand, computational hardware is developing exponentially according to Moore's law [1]. On the other hand, efficiency of simulation algorithms is subject to exponential growth as well [2].

Model order reduction (MOR, see e.g. [2][3]) is a key technology for digital twins. A wide range of different MOR technologies have been developed for specific fields, e.g. MOR methods for multi-body systems have been reviewed and developed in [13]; MOR schemes that are fit for purpose for flexible multi-body systems have been worked out in [6][16][57]. Dedicated MOR schemes for FEM-based vibro-acoustics systems have been developed in [45]. By splitting computations in an off-line and an on-line phase, computational effort is shifted to an off-line phase allowing interactive simulation during the on-line phase. However, not only does this imply a speed-up of calculations, but due to their reduced information set, reduced order models protect intellectual property efficiently. While from the mesh of full 3D simulations geometries can be recovered, this is not the case for reduced order models. In particular since the output generally focuses on the quantity of interest, i.e. a temperature at a single location rather than a complete temperature field. In addition, reduced order models can be efficiently containerized using available standards such as the functional mock up interface (FMI, [10]) thus increasing usability.

Another key technology is to be able to combine different modelling approaches in a single calculation. To couple the models, different approaches exist. One may embed state equations with a description of the plant system (e.g. MBS or 1-D model) into these of the control (or vice versa) to enable the use of one solver, or adopt a true co-simulation approach where each system part runs its own solver [29].

State estimation is a time domain approach to predict the true values of states of a model, given a set of measurements – see overviews in [25][33][37]. Two main method families exist: the Kalman filter and the Moving Horizon estimator (MHE). The basic idea is to use a weighted sum of both the measurements and model predictions to make an overall optimal prediction of the true value of the states. These states can be internal states to the physical system, or augmented states (states that are added to the system equation, and that can represent inputs/parameters that are unknown or cannot be measured directly). Virtual sensors can be introduced via numerical calculations on top of internal system states, or as augmented states. The choice of weights is often inspired by the measurement noise level and model accuracy. This way, the model is continuously synchronized with measurement data, and can be used for analysis and control.

Of course these particular modelling, simulation and optimization technology building blocks are only a subset of the technologies relevant for digital twins. Many more building blocks contribute to digital twins, e.g. Internet of Things (IoT) in the case of digital twins for embedded software design applications [46][55].

5 Case studies

In this Section, a number of digital twin case studies is shortly described along with targeted application areas across the product lifetime (Ideation, Realization and/or Utilization).

5.1 Electric motor thermal virtual sensor

Digital twins condense the engineering knowledge of products and complex systems into digital models. In particular, simulation models allowing predicting the expected behavior in the future are highly valuable assets. In particular, leveraging advances in model order reduction, allows to use corresponding models in an online fashion, parallel to the operation. From a parallel simulation corresponding with the real system, physical values can be deduced that are not accessible by sensors. This opens up new operation paradigms.

For example, consider the efficient thermal control of an electric motor. Electrical motors are subject to thermal derating requiring temperature control [63]. Large-scale electric drives are exposed to high levels

of stress due to induction heating on start-up. Frequent starts without a sufficient interval for cooling can result in motors overheating. However, measuring the temperature of the actual rotors turning at high speed within the motor is close to impossible. Thus, controls are often based on very conservative heuristics.

In principle, corresponding temperatures can be calculated by means of 3D thermal simulations in a sufficiently accurate manner. In the case of the electric motors considered, linear convection-diffusion models are used. Corresponding 3D models are typically available from the detailed engineering phase in product design. However, they are computationally too demanding to be used during operation. Using model order reduction, corresponding models for background simulation can be realized – in this paper, Krylov methods are adopted. Being highly efficient to evaluate, they allow not only to be extended by uncertainty quantification methods, but they also enable continuous calibration using available sensors on the stator side. Thus, by means of continuously-calibrated background simulation models, temperatures not accessible to sensors can be virtually measured, see Figure 3.

Using for instance augmented reality devices, the user can at any time virtually look inside the motor to observe temperature distribution, see Figure 4. This allows the cooling times required for electric motors to be significantly reduced, ultimately enhancing the plant availability. Enriched with methods for uncertainty quantification, confidence intervals can be provided for the rotor temperature (ref. Figure 3) allowing to go close to operational limits and thus increasing availability. Such an optimized process that can prevent motor overheating and reduces the downtimes required during the cool-off phase, which can save up to €210,000 per hour depending on the use case and corresponding industry [62].

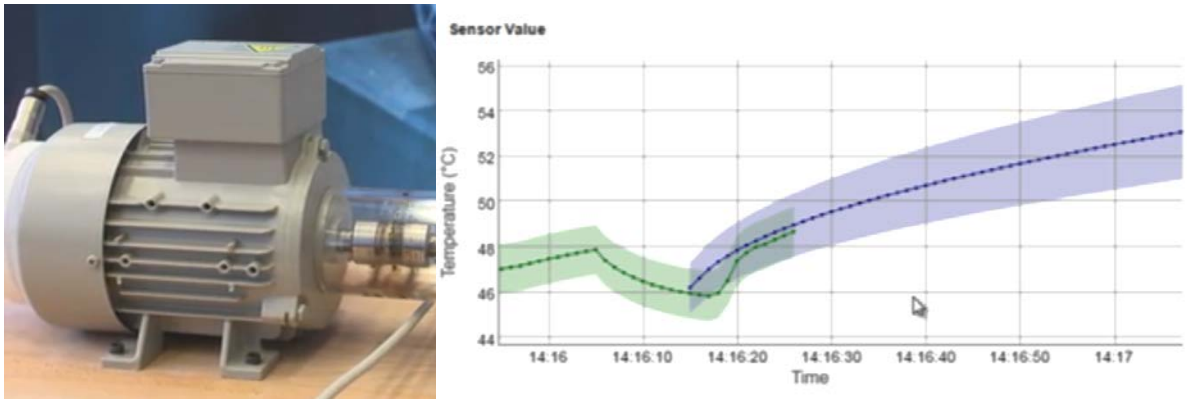


Figure 3: Proof of concept along a small motor – operation parallel digital twins enabled by model order reduction combined with online calibration and uncertainty quantification allows monitoring unmeasurable temperatures on the rotor (in green) and predicting future scenarios of the same temperature (in blue) [63].

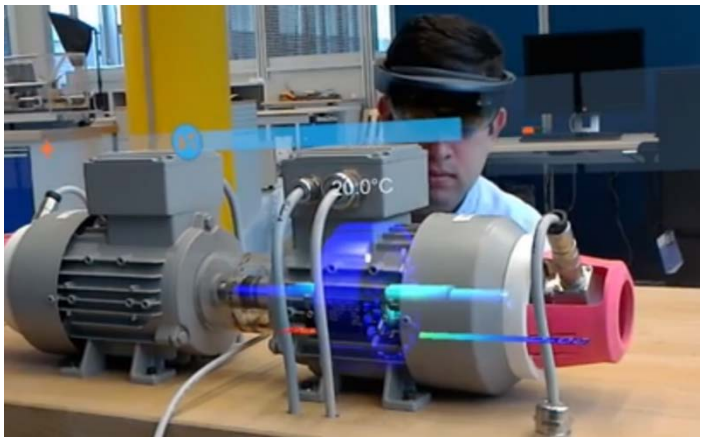


Figure 4: Combined with novel human-computer interaction devices, new operation paradigms are possible, e.g. online 3D visualization of temperature fields inside the motor / on the rotor during operation [62].

5.2 Case study on manufacturing: milling with robots

As addressed before, the core concept of digital twins is to leverage digital models of the products in various scenarios. In doing so, digital twins need to interact with their environment as the real products. Very often this is realized by setting boundary conditions or initial conditions appropriately, e.g. in the case of the electric motor as presented in Section 5.1. However, these interactions could be of a much more complex nature, requiring also sophisticated digital models of the environment itself. When it comes to manufacturing processes, these interactions can be extremely complex, requiring highly sophisticated models.

A typical use case of a manufacturing process is milling. During milling very high process forces occur, requiring extremely stiff structures to prevent any quality issues due to deflection of the machine tool. Because of their flexibility, large working space and low costs, robots could be an attractive alternative. However, as compared to machine tools, robots are extremely soft structures, such that the process forces lead to large deflections of the robot head and therefore to quality issues. Although digital twins of the mechanical robot behavior in terms of mechanical models are available to very high levels of accuracy [32], detailed force models at sufficient accuracy and speed are not available to compensate for the forces efficiently also for large working pieces.

Providing appropriate models of the process itself allows closing the control loop and compensating for the forces. In doing so, digital twins of the machine tool combined with digital twins of the subtractive manufacturing process allow compensating for mechanical limitations of the machine. As shown in Figure 5, the error can be reduced by over 90% as compared to uncompensated approaches. This opens up new options for introducing robots in machining. For example, loading robots of machine tools could perform roughening operations while the machine tool is finishing the parts. A multitude of other machining applications could benefit from this combination of digital twins and complex environment models [61].

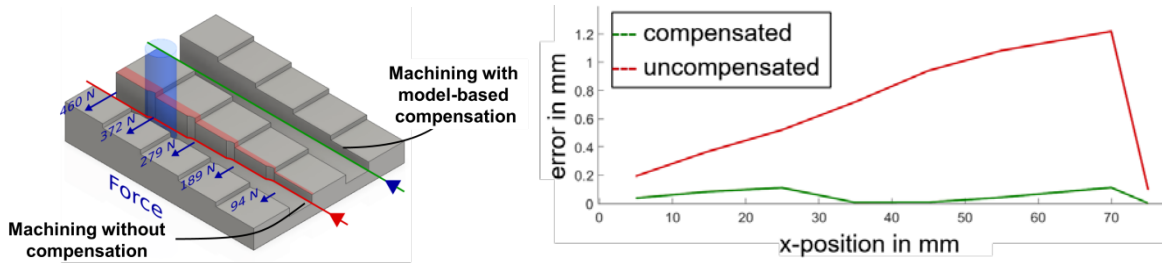


Figure 5: the digital twin allows reducing manufacturing errors of machining aluminum with robots by more than 90%, thus opening up new application fields for robots.

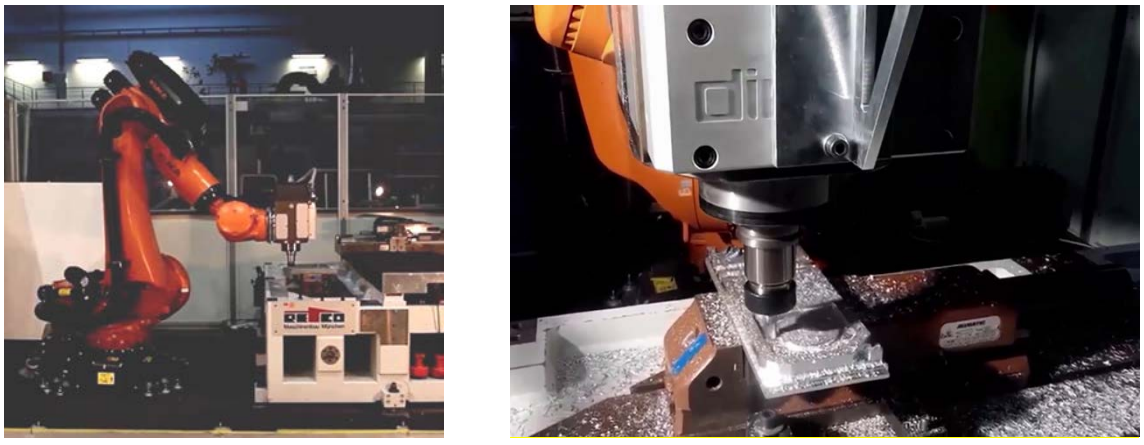


Figure 6: Robot machining aluminum with industrial quality and a digital twin based control combining a digital twin of the robot with a simulation model of the manufacturing process [61].

5.3 Electric aircraft (eAircraft) enabled by the digital twin

The aircraft business has significantly evolved in recent years with many new entrants adopting to the same standard design configuration that has been in use since 1954. Furthermore, a myriad of new concepts are being introduced. Innovation goes bottom up, from small to large, with unmanned air vehicles (UAV) becoming manned again, and new concepts being introduced for urban and regional transport and logistics purposes. Most of the new concepts include electric motors, since that enables new architecture solutions and design concepts, and since this is seen as the only viable path to reaching the "Flight Path 2050" goals of 75% CO_2 emission reduction per passenger km [9]. Often the new concept is achieved with a hybrid electric solution, as the power density of kerosene is still much higher than of state of the use batteries. In fact, it is believed that for the next 20-30 years to come, kerosene will be an important carrier for energy for long flights, but by separating the energy generation from the thrust generation, and combining electric motors with traditional propulsion, you can burn much less fuel for the same flight mission with hybrid-electric propulsion unit [43]. With the new design concepts, you can get the peak power from the battery, and the turbine does not have to be sized for post-V1 single engine take-off, so it can become smaller, more efficient and downsized. Electric propulsion will allow to build new concepts that have distributed propulsion systems. This will lead to new structural, systems and propulsion architectures, for which new industrial solutions as additive manufacturing and generative design will play important role.

One crucial element for an eAircraft is a high energy density and power densification. Siemens AG is a world leader in electric drives for this purpose. For instance, the Siemens eAircraft SP260D achieves a record level of 5.2 kW/kg engine (a record, and factor 5 more as compared to electric engines in trains and cars that achieve about 1 kW/kg). The second crucial element is to take benefit from digital twin technology throughout the product lifecycle [31], as shown in Figure 7. For designing such complex highly integrated products, a close link in the development process is needed between electromagnetics, electronics, structural performance, thermal properties and software and systems. For the eAircraft, this has been provided by the wide prediction range of the Simcenter portfolio [58][59]. To illustrate the benefits: starting from the knowledge base of the existing SP 260 engine, the new SP 200D engine with a significantly changed design was achieved in just 9 months and 19 days by adopting digital twin technology, achieving a 50% increase in the achieved torque to mass ratio.

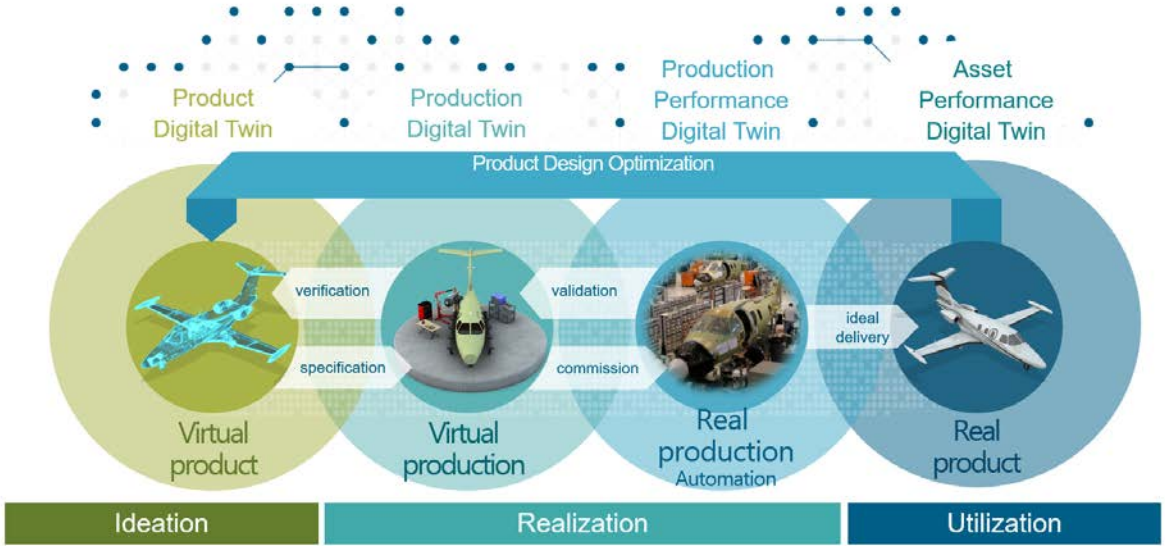


Figure 7: Siemens eAircraft, supported by the digital twin throughout the product lifecycle.

5.4 Additive manufacturing

Recently, Additive Manufacturing is coming up as a disruptive technology, providing a very wide range of design freedom and unique product properties as compared to the traditional design approach [42]. The technology is highly compatible to the digital twin technology in the realization phase, as one prints something very close to what one has already modelled. A virtual correction step of the modelled structure is however required to create the actual digital twin.

More specifically, in case of metal parts produced through selective laser melting, due to the highly dynamic nature of the melting and solidification process, high amount of thermal stress is accumulated in the produced part. The accumulated thermal stresses lead to deformations which could lead to manufacturing problems (e.g. re-coater crashing). To counter such thermal deformations, so-called support structures are used to anchor the printed object to the build plate during the build-up of the structure and to limit the deformations. However, these support structures are removed in a post-processing step after the printing and due to the internal thermal stresses, the part deforms compared to the structure that still had the supports. One can virtually perform a distortion analysis in Simcenter 3D [58], and compensate the structure to be printed for the expected distortion. This way, one can achieve a digital twin model that closely resembles the eventually printed structure and the original CAD design. In Figure 8 and Figure 9, this process is illustrated for a blade structure. The digital twin can be used to virtually analyze the effect of defects due to the additive manufacturing process.



Figure 8: Siemens' additively manufactured example of a gas turbine blade.

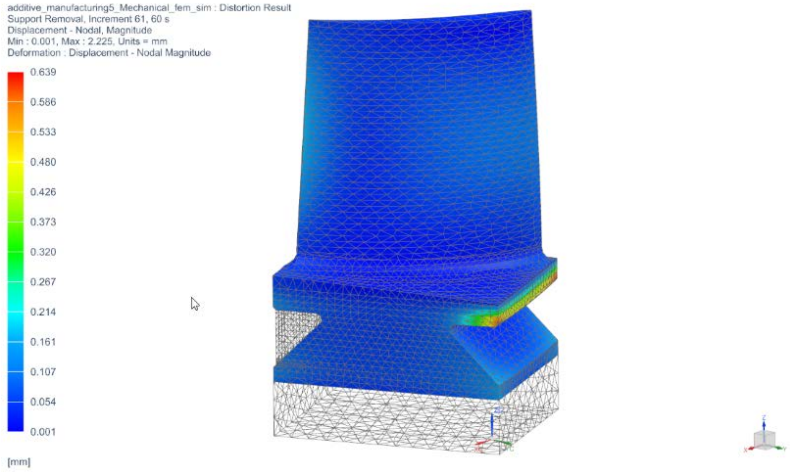


Figure 9: Distortion analysis w.r.t. the effect of removal of support structure (on the right side, a displacement is shown). Simcenter 3D [58] enables compensating the predicted structure w.r.t. expected distortion, hence allows printing it without a distortion.

5.5 Composites manufacturing simulation

Composites manufacturing simulation technology [56] has emerged in CAE products as Simcenter 3D [58] to enhance the level of realism of lightweight composites product models. With a draping simulation, one can predict the actual fiber orientation, which has a significant influence on the product dynamics and fatigue performance. Infusion modelling helps predicting the flow front and allows to find the optimal process conditions in order to avoid dry spots and reduce the void content, which adversely affect the product strength properties. A curing simulation helps predicting the effect of the thermo-mechanical curing process on the material and product properties [27]. All these technologies add to the realism of the product performance prediction, hence to the digital twin performance in the ideation phase. It is believed that still basic research has to be done into multi-scale materials modelling and process simulation on a nano-scale, to be able to fully understand the composite product performance [48]. For the B-pillar application case

shown in Figure 10, the ideation phase digital twin can enable optimizing the NVH behavior and strength of the B-pillar, and also determine the performance in case of a crash analysis (side impact of the vehicle).

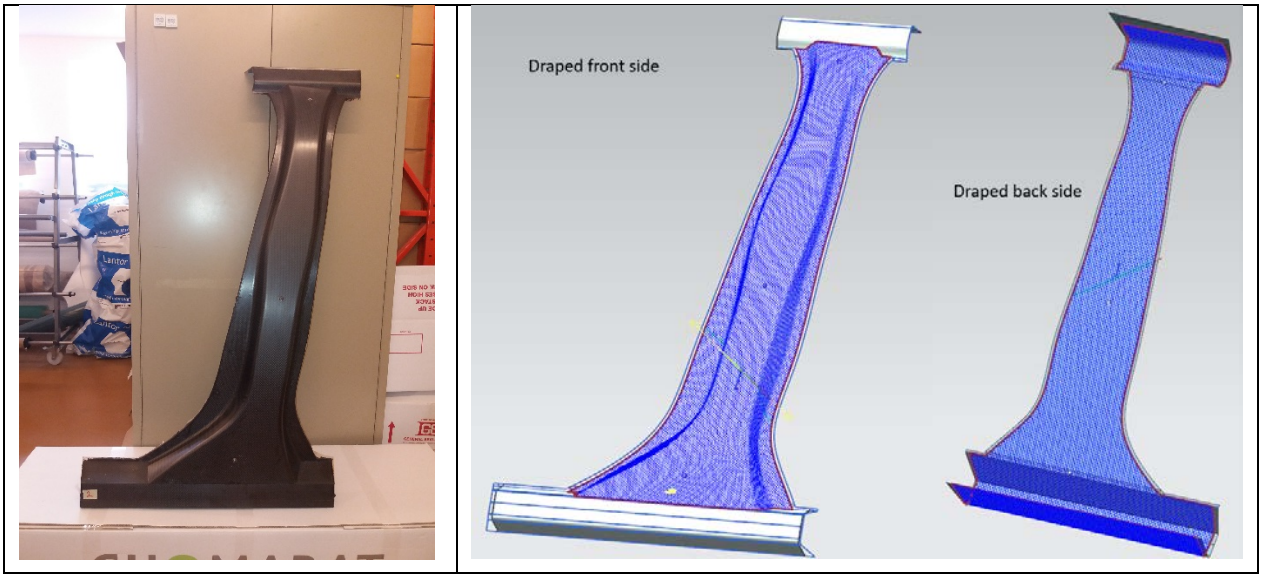


Figure 10: Manufactured B-pillar (left); Draped B-pillar that is used to obtain the fiber orientations (right).

The same technologies also add to the digital twin power in the realization phase, by predicting the performance of the product 'as manufactured'. For the realization phase, one also needs to establish a digital twin of the composites manufacturing device, as to enable the optimization of the manufacturing process parameters based on a digital twin of the manufacturing device.

5.6 Rear twist beam suspension

A digital twin in both the ideation and utilization phases can be instrumental to get insight in quantities that are hard to measure (such as the wheel forces in multiple directions simultaneously) or impossible to directly measure (such as the stress/strain distribution on a complex component). This rationale is pursued in the next application case – the virtual sensing analysis of a rear twist beam suspension [17][33][60].

The model adopted is a linear Finite Element (FE) model reduced thanks to a model reduction technique which includes the first 10 eigenmodes of the free-free structure and residual attachment modes computed at the connection points, to improve computational performance [33]. Due to its particular shape a twist beam suspension has the desirable property of being more compliant in the vertical direction of motion in order to improve ride. On the other hand it has a more stiff behavior in the plane parallel to the road so to improve handling. Most of the times it is interesting for the engineer to have a knowledge of the wheel force in the vertical as well as in the in-plane direction. For this reason this case addresses multiple force estimation: three forces will be estimated at the application point shown in Figure 11.

It was shown by means of virtual exercises in [28] that an optimal sensor placement strategy can be very beneficial in achieving a reliable force estimation by using a very limited set of well-chosen and well-positioned sensors. An optimal sensor placement strategy had been designed in [28]. The strategy relies on several steps, e.g. training of the model, screening of the sensors based on distance metrics and a final selection criteria based on the Popov-Belevitch-Hautus (PBH) observability criteria.

A full experimental validation is available in [60] by investigating the twist beam suspension in a clamped configuration and excited at one tyre (see Figure 12). An example of what can be achieved in force and torque estimation is shown in Figure 13, comparing the results with the quantities measured through the load cell.

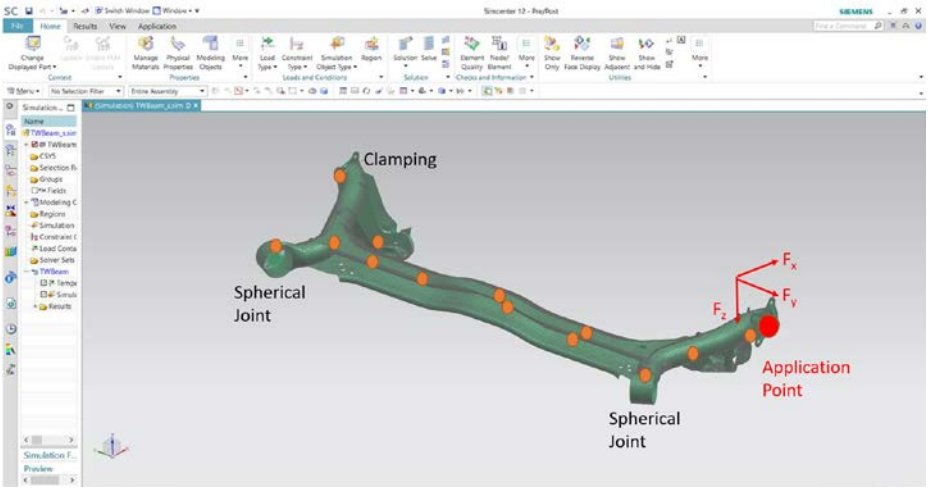


Figure 11: Finite Element model of the twist beam rear suspension.

As explained in [28][33], the stiff in-plane forces estimated with noisy data are not correctly captured. That is observed in the estimation of Load Y in Figure 13. The system is ill-conditioned and ill-posed, and the optimal sensor placement can only mitigate this effect improving the results but not overcome it. Still this is very valuable information as one can opt to select a smaller subset of sensors that are optimally placed, to yield results with accuracy close to the much larger subset of sensors randomly distributed. Indeed 12 sensors are selected in [49] for obtaining the good estimation proposed in Figure 13. The strain field identification is also proposed in [49] in a coupled force and state estimation. No appreciable improvement is obtained for the strain estimation through an optimal selection because of the latter is optimal in view of loads estimation. Figure 14 shows the strain field measurements that can be achieved for this case. An example of what can be achieved in the force measurements is shown in Figure 15.

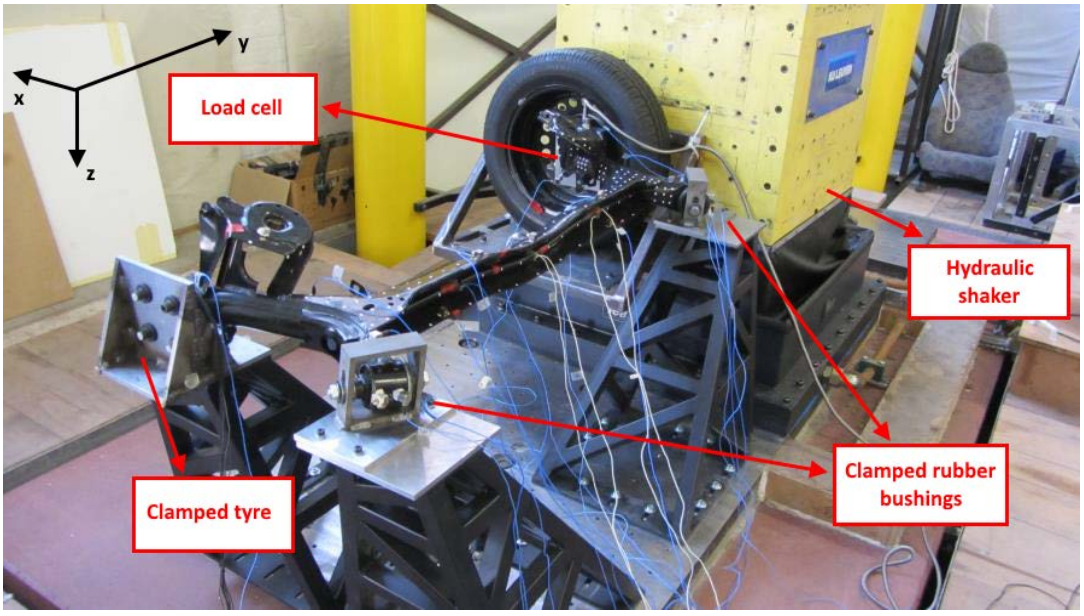


Figure 12: Twist beam suspension, clamped configuration: clamped bushings, one clamped tyre, excitation given by a 6DoFs hydraulic shaker at the other tyre.

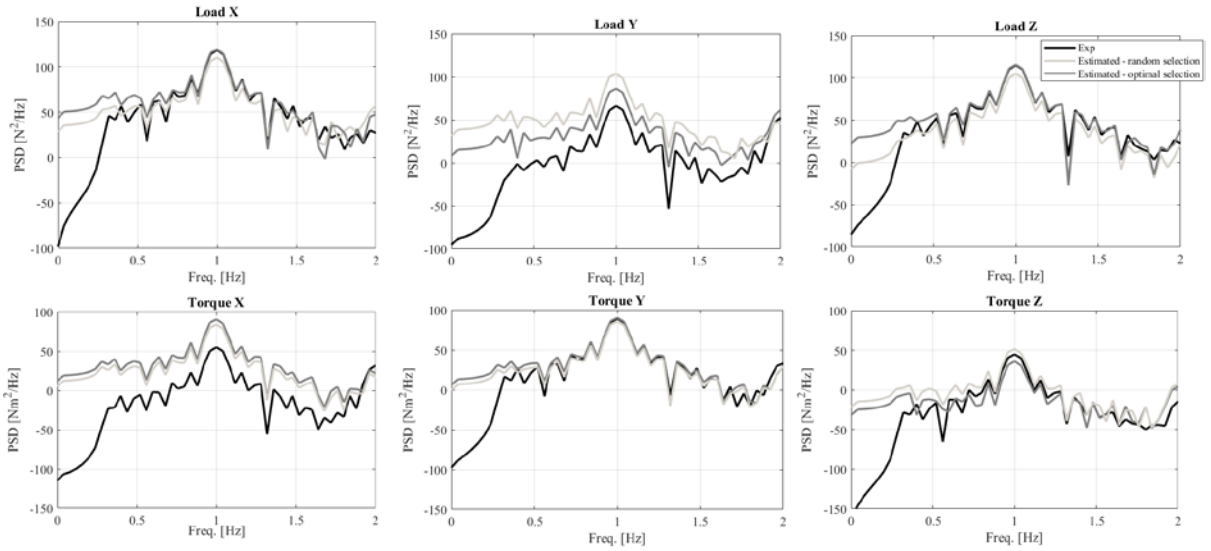


Figure 13: Frequency content of the force and torque estimation (excitation 1Hz). Comparison between optimal selection and random selection.

Secondly, one can use computer vision techniques to show the stress (displacement) field of the virtual twist beam projected on the camera images of the test setup [17]. This is shown in Figure 16 for the displacement field.

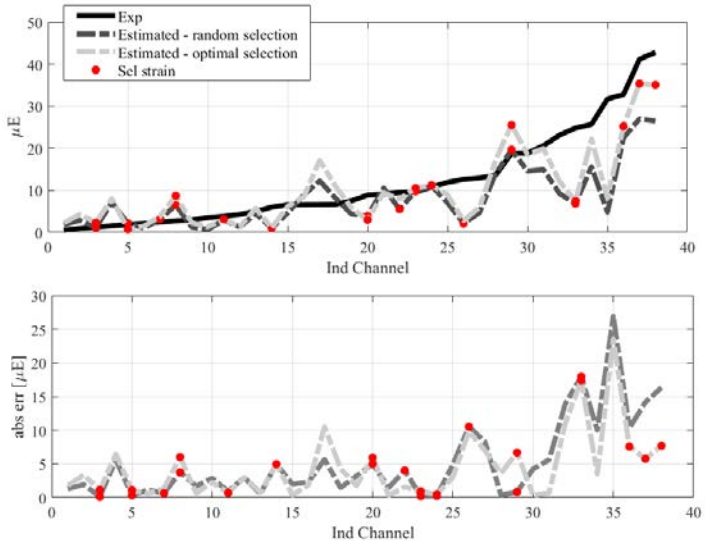


Figure 14: Strain field estimation. Comparison between the absolute values of the estimated strains through random selection and optimal selection. Excitation 1Hz.

The digital twin of the twist beam is an accurate representation of the real structure, but sufficiently reduced to run at the core of a state estimation scheme to measure quantities that are hard to measure directly, such as wheel forces in multiple directions, and the strain [60]. It can also be used to extract additional information out of measurements, e.g. showing the displacement field live on the camera images extracted from the test setup [17], as shown in Figure 16.

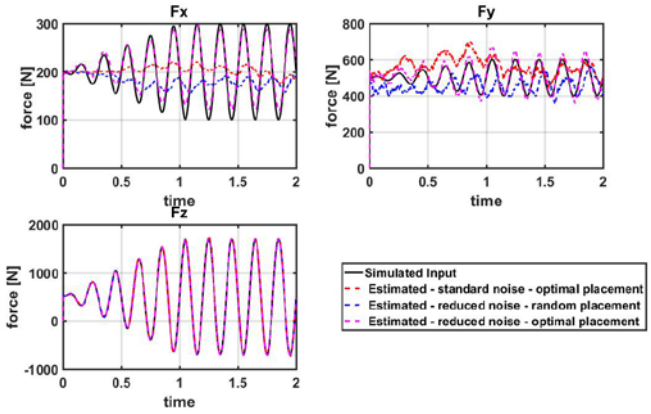


Figure 15: Force estimation comparison (standard vs. Reduced noise levels in the sensors; random vs. optimal placement). The optimal placement saves a lot of sensor positions, while generating a similar accuracy as random.

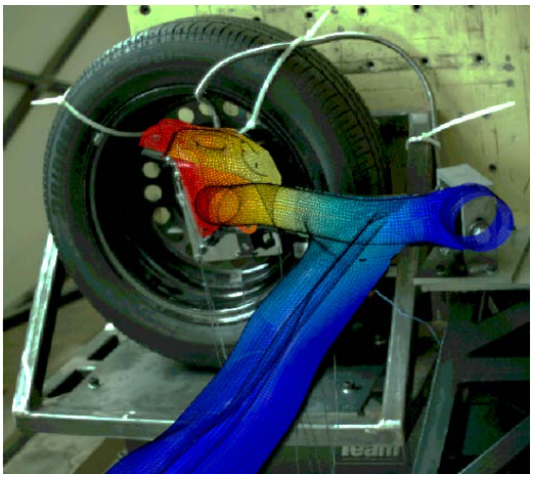


Figure 16: Using computer vision techniques to show the displacement field of the virtual twist beam projected on the camera images of the test setup [17].

5.7 Electro-mechanical drivetrain (part of a weaving loom)

This case is an electro-mechanical drivetrain, which is part of a weaving loom. The main driver in weaving loom development is towards increasing the operational velocities to maximize the production rate while ensuring a durable solution (i.e. guaranteed lifetime and predictable maintenance). Such a machine has several interacting subsystems which require a small synchronization error to ensure that weaving process is not disturbed. Closely linked to the synchronization error and lifetime is the energy consumption in the machine which often require conflicting design changes. To ensure that next generation designs can be further pushed in terms of these criteria, it is invaluable that the machine behavior is investigated during the lifetime or even prototyping phase to gain understanding how the actual operational conditions differ from the assumptions made during the virtual prototyping. That's where the digital twin comes into play.

The model used during virtual prototyping is now repurposed as a digital twin, which acts as a specific representation on one particular machine within the full fleet. The digital twin represents the system in its true operation conditions and runs in parallel with the real machine to provide information on all variables that are impossible or impractically to measure. The variables of interest for mechanical systems are amongst others the transmission errors, the internal and external forces and energy loss sources at component level. This process is carried out using a virtual sensing approach as described in Figure 17.

The first step is that a limited set of sensors is installed on the machine, the model predicts these measurements and updates the model accordingly. Once the model complies with reality up to a certain extent, any variable can be derived which is presented as a 'virtual sensor'. The technical challenges are present on both the modeling, estimation and instrumentation front (for a detailed overview, see [37]). For the modeling, it involves tailoring the model complexity to the available measurement set (or devising a measurement strategy based on a particular model). With respect to the estimators, it is the concurrent estimation of both external loads, unknown parameters and the states which is the core research problem. The estimation of external loads requires embedding all relevant information in a mathematical formulation to ensure a well-defined mathematical problem [47][49]. With respect to the instrumentation it is important to include the sensor deficiencies and characteristics as their input or lack of it has a significant influence on the overall performance.

The targeted result is that all this information can be fed back to the design phase ("Ideation") as it allows the manufacturer to size its components based on the real loading conditions and perform virtual prototyping on a model that has a more accurate quantified representation of reality.

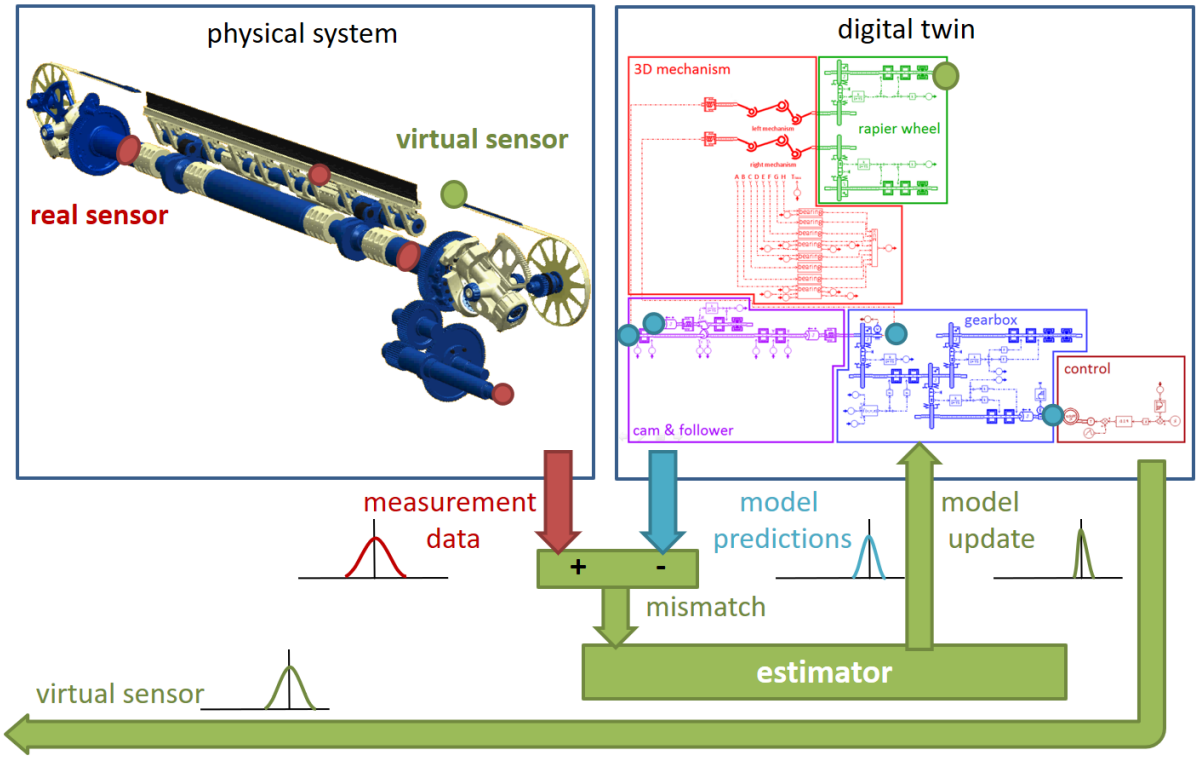


Figure 17: a weaving loom and its digital twin adopted in a virtual sensing approach. Note that the CAD representation (left) has been distorted in order not to reveal the real dimensions.

6 Conclusions and future work

The digital twin concept sits at the center of digitalization, linking all models and data related to products, their production, and their operational performance and providing them to designers, engineers, operators and service technicians across vertical domains.

A digital twin for products is typically created using the Systems Driven Product Development (SDPD) methodology, which drives the creation of intelligent system models. Technologies like generative and probabilistic design, system simulation and model transformation are the basis for these intelligent models. Key enablers for SDPD include comprehensive, semantic digital thread data models as well as a complete set of integrated tools, which include Multiphysics 1D and 3D simulation, CFD and Test-based models and multi-attribute optimization. These tools enable to create model-based system representations and digital twins of the product. These digital twins are able to comprehend the impact of design changes on the product as well as the production system and provide engineers, operators and service technicians with essential information to optimize the use and performance of a product and prevent system outages. Technically, this is realized by combining virtual models and real-life data, thus creating “hybrid models” of physical assets keeping the digital twin in sync with the real world. Several examples in various industrial sectors and covering a variety of design challenges have been presented in this paper.

At an increasing speed, new opportunities to leverage the digital twin in all phases of product creation, manufacturing and operation lifecycle stages are emerging. This also implies a continuous demand for novel modeling, simulation and test data integration capabilities to answer these demands. Already at an early design stage, digital twins paired with fast simulation technology for fluid dynamics, electromagnetics or acoustics can shorten design cycles from several weeks down to just one day. This goes up to real-time models, enabling transparent interchange of physical and digital twin parts and enabling human in the loop interaction. All these aspects raise the need to develop new solutions that leverage ever-increasing CPU power, while at the same time reducing mathematical complexity and abstracting models for field use. The ultimate goal is that simulation algorithms can be computed in real time so that they can run in parallel to

the physical process, providing the user with enhanced decision support on optimal usage by means of augmented reality and virtual sensing. By realizing these opportunities, the digital twin finally reaches all life cycle phases, and it closes the feedback loop back to the design of a new generation of better, even more user-centered products. Adopting a machine learning approach to guide the users, generate innovative designs and merge modeling with ubiquitous data from the Internet of Things, further breakthroughs are explored and will enable the further innovation of product design, production and operation.

Acknowledgements

This paper was prepared in the frame of the Siemens Company Core Technology (CCT) "*Simulation and Digital Twin*". The Research Fund KU Leuven is kindly acknowledged for its support. Especially for the use cases, we own gratitude and acknowledgements to a range of funded R&D projects and colleagues:

- For the electric motor virtual sensor use case, we gratefully acknowledge Birgit Obst, Matthias Herz and Utz Wever from Siemens AG, Corporate Technology.
- For the case study on manufacturing, we gratefully acknowledge Florian Schnös and Michael Zäh from the Technical University of Munich as well as Birgit Obst and Utz Wever from Siemens AG, Corporate Technology.
- For the case study on eAircraft, we acknowledge the Siemens eAircraft program and Thierry Olbrechts.
- For the case study on additive manufacturing, we gratefully acknowledge Hunor Erdelyi, Michele Garibaldi, Tom van Eekelen and Etienne Lemaire. We kindly acknowledge the DG06 Walloon project "Développement d'un démonstrateur industriel dédié à l'additive manufacturing" (ANYSHAPE4.0, 2016-2020).
- For the composites manufacturing simulation case, we kindly acknowledge Kristof Vanclooster, Luca Spina, Jim Gilbert, Frederic Pascon and Cédric Lequesne. We acknowledge VLAIO (Flemish government agency Flanders Innovation & Entrepreneurship) for funding the FlandersMake project "Virtual design platform for sheet material products" (VIDESPRO, 2015-2018). We thank Noesis Solutions and University of Calabria (through the thesis of Luca Spina) for the collaboration. We moreover acknowledge the European Commission for funding the FP7-2013-NMP-ICT-FoF R&D project "Enabling Next Generation COmposite Manufacturing by In-Situ Structural Evaluation and Process Adjustment" (ECOMISE, 2013-2016), and we gratefully acknowledge the SKYWIN Walloon project "Technologies Avancées pour Pièces Complexes et Intégrées" (TECCOMA), part of Plan Marshall SKYWIN (2015-2019).
- For the case study on the twist beam, we gratefully acknowledge Roberta Cumbo, Tommaso Tamarozzi, Francesco Cosco and Frank Naets. VLAIO is kindly acknowledged for funding the project "EfficieNt DURability testing ANd vehiCle usage Evaluation" (ENDURANCE, 2017-2019). The research of T. Tamarozzi is funded by the VLAIO Innovation Mandate 160343, "Virtual Mates". The EC is gratefully acknowledged for funding the EC Marie Curie IAPP project 285808 "Innovative Concept Modelling Techniques for Multi-Attribute Optimization of Active Vehicles" (INTERACTIVE, 2011-2015), in which Francesco Cosco performed a secondment from GeG to KU Leuven. The research of Frank Naets is funded by a grant from the Research Foundation – Flanders (FWO). This research was also partially supported by Flanders Make, the strategic research centre for the manufacturing industry.
- For the electro-mechanical drivetrain (part of a weaving loom) case, we gratefully acknowledge Jan Croes. This research was kindly supported by the EC through the project "Energy Software Tools for Sustainable Machine Design" (ESTOMAD, 2010-2012) and by VLAIO through the FlandersMake SBO project "Model based Force Measurements" (MoForM, 2016-2020).

References

[1] R. Schaller, "*Moore's law: past, present and future*", IEEE spectrum 34 (6), 52-59, 1997.

[2] A. Antoulas, "*Approximation of large-scale dynamical systems*", SIAM, 2005.

[3] W. Schilders, H. Van der Vorst, J. Rommes, "*Model order reduction: theory, research aspects and applications*", Springer, 2008.

[4] B. Piascik, J. Vickers, D. Lowry, S. Scotti, J. Stewart, A. Calomino, "*Materials, Structures, Mechanical Systems, and Manufacturing Roadmap*", NASA, Technology Area 12, November 2010.

[5] P.A. Kobryn, E.J. Tuegel, "C*ondition-based Maintenance Plus Structural Integrity (CBM+SI) & the Airframe Digital Twin*", The Air Force Research Laboratory, March 2011.

[6] G. Heirman, W. Desmet (sup.), P. Sas (sup.), "*Model Reduction Techniques to Improve the Efficiency of Flexible Multibody Simulations*", PhD thesis, KU Leuven, May 2011.

[7] E.J. Tuegel, A.R. Ingraffea, T.G. Eason, S.M. Spottswood, "*Reengineering Aircraft Structural Life Prediction Using a Digital Twin*", International Journal of Aerospace Engineering, Vol. 2011, No. 154798, 2011.

[8] M. Grieves, "*Virtually Perfect: Driving Innovative and Lean Products through Product Lifecycle Management*", Space Coast Press, Cocoa Beach, Florida, November 18, 2011.

[9] European Commission, "*Flightpath 2050, Europe's Vision for Aviation*", 2011.

[10] T. Blochwitz et al., "*The functional mockup interface for tool independent exchange of simulation models*", Proceedings of the 8th International Modelica Conference; March 20th - 22nd, Technical University Dresden, Germany, pp. 105-114, 2011.

[11] E.H. Glaessgen, D.S. Stargel "*The Digital Twin Paradigm for Future NASA and U.S. Air Force Vehicles*", Proc. 53rd Structures, Structural Dynamics and Materials Conference – Special Session on the Digital Twin, AIAA, Honolulu, Hawaii, USA, 2012.

[12] J. Lee, E. Lapira, B. Bagheri, H. Kao, "*Recent advances and trends in predictive manufacturing systems in big data environment*", Manufacturing Letters, pp. 38-41, 2013.

[13] Naets, F., Desmet, W. (sup.), Vandepitte, D. (sup.), "*Development of System-level Model Reduction Techniques for Flexible Multibody Simulation*", PhD thesis, KU Leuven, May 2013.

[14] United States Air Force, "*Global Horizons*", AF/ST TR 13-01, June 21, 2013.

[15] M. Grieves, "*Digital Twin: Manufacturing Excellence through Virtual Factory Replication*", white paper, 2014.

[16] T. Tamarozzi, "*Efficient Numerical Simulation Strategies for Flexible Multibody Systems with Variable Topology*", PhD thesis, KU Leuven, February 2014.

[17] F. Cosco, F. Naets, W. Desmet, "*Use of concept modelling for online input force estimation*", Proc. International Conference on Noise and Vibration Engineering (ISMA2014), Leuven, Belgium, September 15-17, 2014.

[18] H. Niu, N. Arrigoni, L. Broglia, "*MBSE Approach for the investigation and the development of a new Excavator*", Presentation at SAE 2014 Commercial Vehicle Engineering Congress, Oct 2014.

[19] P.A. Kobryn, "MBE & the Aircraft Digital Thread", NIST MBE Summit, December 17, 2014.

[20] J. Lee, B. Bagheri, H.-A. Kao, "*A Cyber-Physical Systems architecture for Industry 4.0-based manufacturing systems*", Manufacturing Letters, Vol. 3, pp. 18-23, January 2015.

[21] R. Rosen G. von Wichert, G. Lo, K. Bettenhausen, "*About the importance of autonomy and digital twins for the future of manufacturing*", In: Proceedings of the 15th IFAC symposium on information control problems in manufacturing, Ottawa, Canada, May 11-13, 2015.

[22] NASA, *NASA Technology Roadmaps, "TA 11: Modeling, Simulation, Information Technology, and Processing"*, July 2015.

[23] B. Marr, "*Why Everyone Must Get Ready For The 4th Industrial Revolution*", Forbes, April 2016.

[24] S. Boschert, R. Rosen, "*digital twin– The Simulation Aspect*", In: Hehenberger P., Bradley D. (eds) Mechatronic Futures. Springer, Cham, 2016.

[25] H. Van der Auweraer, S. Gillijns, S. Donders, J. Croes, F. Naets, W. Desmet, "*State Estimation: A Model-Based Approach to Extend Test Data Exploitation*", in Special Topics in Structural Dynamics, Volume 6, Conference Proceedings of the Society for Experimental Mechanics Series, D. Di Miao et al. (eds.), The Society of Experimental Mechanics, 2016.
[26] U. Rüde et al., "*Research and education in computational science and engineering*", arXiv preprint arXiv:1610.02608, 2016.
[27] F. Pascon, T. van Eekelen, C. Brauner, M. Bach, "*An integrated virtual tool chain for the simulation of thermoset composite manufacturing processes*", SAMPE Europe Conference 2016, Liege (Belgium), September 13-15, 2016.
[28] T. Tamarozzi, E. Risaliti, W. Rottiers, K. Janssens, W. Desmet, "*Noise, ill-conditioning and sensor placement analysis for force estimation through virtual sensing*", Proc. Intl. Conference on Noise and Vibration Engineering (ISMA2016), Leuven, Belgium, September 19-21, 2016.
[29] C. Gomes, C. Thule, D. Broman, P.G. Larsen, H. Vangheluwe, "*Co-simulation: State of the Art*", Cornell University Library, arXiv:1702.00686v1, February 2017.
[30] B. Marr, "*What Is Digital Twin Technology - And Why Is It So Important?*", Forbes, March 2017.
[31] Siemens PLM Software, "*eAircraft - shaping the future of aviation*", June 2017, **https://www.youtube.com/watch?v=pGnqc883JHg**.
[32] F. Cugnon, M. Ghassempouri, M. Armendia, "*Machine tools mechatronic analysis in the scope of EU Twin-Control project*", NAFEMS World Congress, Stockholm, Sweden, June 11-14, 2017
[33] H. Van der Auweraer, T. Tamarozzi, E. Risaliti, M. Sarrazin, J. Croes, B. Forrier, F. Naets, W. Desmet: "*Virtual sensing based on design engineering simulation models*", Proc. ICEDyn2017, Ericeira, Portugal, July 3-5, 2017.
[34] K. Panetta, "*Top Trends in the Gartner Hype Cycle for Emerging Technologies 2017*", Gartner, August 15, 2017.
[35] J. Bohman, J. Leuridan, M. O'Brien, "*Ideation*", Siemens PLM Software Annual Industry Analyst Conference, Boston, USA, Sept. 5-8, 2017.
[36] Z. Feuer, D. Hoz, R. Wolf, "*Driving the Digital Enterprise & Realizing the Digital Twin*", Siemens PLM Software Annual Industry Analyst Conference, Boston, USA, Sept. 5-8, 2017.
[37] J. Croes, W. Desmet (sup.), F. Cosco (cosup.), "*Virtual Sensing in Mechatronic Systems – State Estimation using System Level Models*", PhD thesis, KU Leuven, 241 pp., September 2017.
[38] C. Pettey, "*Prepare for the Impact of Digital Twins*", Gartner, September 18, 2017.
[39] CIMdata, "*Realizing the digital twin– Siemens PLM Software Analyst Conference 2017*", October 3, 2017.
[40] K. Panetta, "*Gartner Top 10 Strategic Technology Trends for 2018*", Gartner, October 3, 2017.
[41] CIMdata, "*Siemens PLM Software: the Actionable, Holistic Digital Twin*", October 11, 2017.
[42] H. Erdelyi, A. Remouchamps, S. Donders, L. Farkas, C. Liefooghe, T. Craeghs, W. Van Paepegem, "*Lattice structure design for additive manufacturing based on topology optimization*", Proc. NAFEMS Seminar "Simulation Driven Engineering", Neuendettelsau, Germany, Nov. 20-21, 2017.
[43] F. Anton, "*Siemens eAircraft*", Hannover Messe, 2017.
[44] D. Hartmann, "*The changing Role of Simulation – From Mathematics to Digital Twins*", Seminar "Future and Emerging Mathematical Technologies in Europe", Leiden, The Netherlands, December 13, 2017.
[45] A. van de Walle, W. Desmet (sup.), "*The Power of Model Order Reduction in Vibroacoustics and its Applications in Model-based Sensing*", PhD thesis, KU Leuven, January 2018.
[46] V.B. Singh, T. Benoit, V. Braibant, "*Breaking down silos with contract based design for industrial software development: illustrated through an aerospace case study*", Proc. 9th ERTS, European congress on Embedded Real Time Software and Systems, Toulouse, France, Jan 31-Feb 2, 2018.
[47] M. Kirchner, J. Croes F. Cosco W. Desmet, "*Exploiting input sparsity for joint state/input moving horizon estimation*", Mechanical Systems and Signal Processing, 101, MSSP16-220, 237-253, 2018.
[48] X. Liu, D. Furrer, J. Kosters, J. Holmes, "*Vision 2040: A Roadmap for Integrated, Multiscale*

Modeling and Simulation of Materials and Systems", NASA/CR 2018-219771, 2018.
[49] B. Forrier, "*Virtual torque sensing: A model-based approach for indirect measurement of dynamic operational loads on mechatronic powertrains*", PhD thesis, KU Leuven, April 2018.
[50] CIMdata, "*Digital Twins – Changing the Way We Engineer, Validate, Market, and Operate our Products*", eBook, April 2018.
[51] F. Halvorsen, "*Simulation – The Brains behind Digital Twins*", In NAFEMS Benchmark, Apr. 2018.
[52] F. Chinesta, E. Abisset-Chavanne, J.-L. Duval, "*When Data Joins Physics – More than a "digital Twin" – A new paradigm for simulation-based engineering*" , In NAFEMS Benchmark, April 2018.
[53] M. Halpern, "*What Few People Discuss About Digital Twins*", In NAFEMS Benchmark, Apr. 2018.
[54] D. Wagg, "*The Digital Twin for Engineering Applications*", In NAFEMS Benchmark, April 2018.
[55] V.B. Singh, "*Digital Twin and Embedded Software*", Siemens Simcenter Community blogpost, April 24, 2018.
[56] K. Vanclooster, L. Spina, S. Donders, R. Lombardi, R. D'Ippolito, L. Farkas, D. Mundo, "*Linking Manufacturing Simulation with Functional Performance Engineering for Composites Applications*", Proc. ISMA 2018, Leuven, Belgium, September 17-19, 2018.
[57] F. Naets, T. Tamarozzi, W. Rottiers, S. Donders, H. Van der Auweraer, W. Desmet, "*Model order reduction for nonlinear dynamics engineering applications*", Proc. ISMA 2018, Leuven, Belgium, September 17-19, 2018.
[58] Siemens PLM Software, "*Simcenter 3D*", Version 12, 2018.
[59] Siemens PLM Software, "*Simcenter Amesim*", Version 16.1, 2018.
[60] R. Cumbo, T. Tamarozzi, K. Janssens, W. Desmet, "*Kalman-based load identification and full field estimation analysis on industrial test cases*", Submitted to Mechanical Systems and Signal Processing, 2018.
[61] Siemens, "*Loading Robots with a Will to Mill*", Pictures of the Future, The Future of Manufacturing, 2018.
[62] Siemens, "*Virtual Sensor opens a World of Efficiency for Large Motors*", Pictures of the Future, Simulation and Virtual Reality, 2018.
[63] D. Hartmann, M. Herz, U. Wever, "*Model Order Reduction, a Key Technology for Digital Twins*", in Reduced-Order Modeling (ROM) for Simulation and Optimization, Springer 2018.

On the dynamic stiffness of air springs at medium-high frequencies

N. Gil-Negrete [1,2]**, F.J. Nieto** [1,2], **A. Pradera-Mallabiabarrena** [1], **J. Gonzalez-Prada** [1]
[1] Tecnun, Dep. of Mechanics and Materials, University of Navarra. San Sebastian, Spain
e-mail: **ngilnegrete@ceit.es**

[2] Ceit-IK4 Technology Center, Division of Transport and Energy. San Sebastián, Spain

Abstract
Vertical static and dynamic stiffness of a commercial air spring is investigated. Experimental measurements of the dynamic stiffness of the air spring are conducted first in an Instron hydraulic testing machine, up to 400Hz, with and without auxiliary air reservoir. Experiments allow concluding that structural vibrations modes might exist in the structure-borne vibration transmission frequency range, whose frequency and amplitude depend on the pressure and excitation amplitude. Furthermore, a FEM model developed in ABAQUS and validated by comparison to measurements, allows establishing that construction parameters influence the dynamic behavior of the air spring. More precisely the angle at which fibers are disposed has the highest influence in the natural frequency of the first vibration mode.

1 Introduction

Many engineering applications require the use of elastic, resilient, bushings or mounts to decouple the vibration from a source to a receiving structure. In order to improve isolation, air springs, instead of full rubber mounts, have been adopted in industry and vehicles.

Air-springs as suspension elements are more and more employed in the suspension system of vehicles. Their soft stiffness, combined with the weight of the car body, lead to low vertical mode of the vehicle that works as a low pass filter that minimises the transmission of vibrations at higher frequencies. Thus, it is widely accepted as an excellent solution to improve passengers' comfort, being adopted, for example, as secondary suspension elements of railway vehicles [1-2].

An air-spring is composed of an elastic chamber, usually manufactured of rubber to which reinforcing fibres are added, and filled with air at different working pressures. The elastic chamber is connected to an auxiliary air reservoir through a pipe, enabling the possibility of controlling the pressure into the air-spring in order to maintain the height of the vehicle constant [3].

The vertical static and dynamic behaviour of an air-spring for different applications (railway vehicles, cars, machinery) at low frequencies (usually up to 20Hz) has been extensively studied (see, for example, references [2-6]). Alonso et al. [2] even propose a solution to optimise the behaviour of air springs used as secondary suspension system in railway vehicles and improve the comfort of passengers. In absence of air reservoir, it has been experimentally stated that the vertical dynamic stiffness of the air-spring is almost constant at a particular pressure. When the air-spring is connected to the auxiliary air reservoir the dynamic stiffness shows a peak that could be interpreted as the natural frequency due to the air blocked within the connecting pipe.

Nevertheless, the dynamic behaviour of air-springs at the highest frequencies has not been studied thoroughly. As any other finite structure, air springs are subjected to resonance frequencies that can increase the transmissibility of this suspension element. In the case of railway vehicles, for example, the wheel-rail contact is an important source of vibrations and noise, transmitted to the car body through suspension elements. Structure borne transmission vibration occurs in a frequency range up to 300Hz

approximately [1]. In case the resonance frequencies of the air spring lie in this range of frequencies a significant reduction in the isolation might occur.

Concerning modelling in the 0-20Hz frequency range, different models have been proposed and studied in literature, with different complexity levels [2-5, 7]. They are usually classified into equivalent mechanical models and thermodynamic models. Typical equivalent mechanical models include the Nishimura model, Simpack model, Vampire model, Berg model; typical thermodynamic models implement a mathematical description of the transformations taking place in the thermodynamic state of the air filling the bellow, the auxiliary reservoir and the connecting pipe. Thermodynamic models are based on the physical properties of the system [4]. Mechanical models on the other hand, such as vampire, simpack or Nishimura models, consist of a number of springs, dashpots and masses; some of the values of the parameters can be derived from the physical quantities of the air-spring, reservoir and pipe system [2-4]. When there is not a direct connection or difficulties are encountered, experimentation has also been widely used (when possible) to obtain model parameters [3, 9].

Mazzola and Berg [4] compare the performance of six air spring models with respect to vertical dynamics in the 0-20Hz frequency range. Alonso et al. [2] also include an interesting review of some analytical models. Some other authors propose their own analytical models, i.e. Nieto et al [5] and Chang et al [8].

Although many of this popular analytical models address the influence of geometry of the elastic chamber (volume and effective area of the bellow), the influence of the number and disposal of reinforcing fibres in these physical parameters (and, thus, in the lateral or vertical stiffness of the air-spring) cannot evaluated. The application of nonlinear Finite Element Analysis (FEA) can overcome this limitation of parameter calculation formulae and allows investigating the impact of fibre angle, fibre cross sectional area and spacing in the static stiffness [10-12]. Till now, FEM models of air-springs have only been applied to evaluate the static vertical stiffness, ignoring the influence of constructive details in the dynamic behaviour and natural frequencies of the air-spring.

The present research is focused in experimentally studying the dynamic behaviour of a small air-spring in the 0-400Hz frequency range, both with and without an auxiliary air reservoir and connecting pipe. Furthermore, a FEM model of the air spring is proposed, that enables establishing which are the most influencing parameters in the vertical stiffness and resonant frequencies of the air spring. The model could be used to optimize the internal structure of the air-spring when seeking for a particular behaviour of the suspension element in the 0-400Hz. Furthermore, parameters for analytical models could be extracted from the simulations.

2 Experimental characterization of a commercial air spring in the medium-high frequency range

A typical air spring for machinery and tool applications was selected; due to its size it could be tested in a high stroke frequency machine (see Figure 1). It is a single-bellows air-spring, of 145mm of diameter and working height of 90mm. It is made of natural rubber, reinforced with two layers of nylon fibers. The air spring could be connected to an auxiliary air reservoir, as shown in Figure 2.

The static and dynamic stiffness were measured in a commercial hydraulic Instron testing machine, MHF25l, equipped with a LVDT of ±25mm and calibrated force sensor of ±20kN. Previous to static and dynamic tests the inner pressure in the air-spring was increased to 2, 4 and 6 bars and the force exerted by the air-spring was measured. The static tests were conducted in displacement control at a test speed of 0.2 mm/s, low enough in order to ignore viscous effects of rubber and effects associated to the flow of air between the air-spring and the reservoir. Applied displacement was of ±5mm.

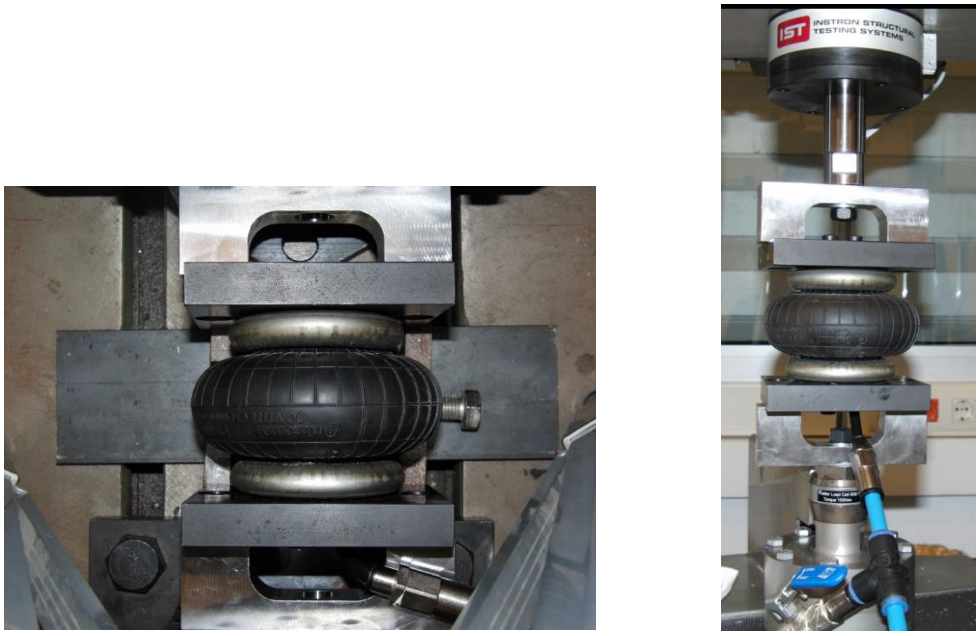


Figure 1: Selected air spring at ambient pressure, mounted in the Instron MHF25 testing machine

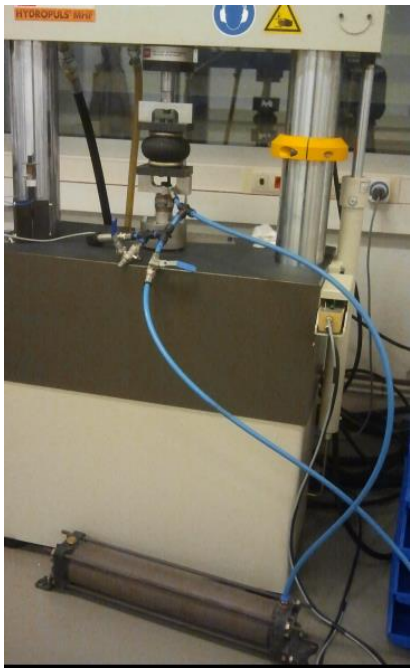


Figure 2: Air-spring and auxiliary air reservoir

Results of quasi-static tests are shown in Figure 3. The force exerted in the air spring at a nominal working height of 90mm when different pressures are considered are in good agreement with the data sheet provided by the manufacturer (see Figure 4). The air spring reaction force might be expressed as:

$$F = p\, A_{eff}$$

Where p is the internal pressure and A_{eff} is known as the effective area of the air spring. The vertical air spring stiffness corresponds to the change in force when a vertical displacement is applied and it is attributed to two phenomena: internal volume (pressure) variation due to the compression of the air spring and variation in the effective area that the pressure is acting on. Mathematically [8]:

$$K = \frac{dF}{dz} = A_{eff}\frac{dp}{dz} + p\frac{dA_{eff}}{dz} = -nA_{eff}\frac{p}{V}\frac{dV}{dz} + p\frac{dA_{eff}}{dz}$$

Considering that the characteristics of the air in the bellow, given that the air mass is maintained constant, are expressed as:

$$pV^n = constant$$

The static stiffness of the air spring is calculated as the slope of the load/displacement loops in Figure 3 and it is pressure dependent, changing from 51 N/mm at 2bar to 127 N/mm at 6bar (see Table 2).

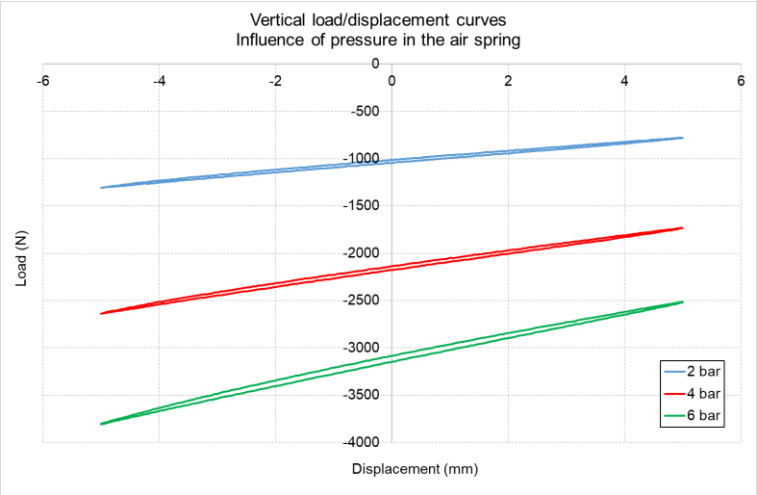


Figure 3: Measured static load/displacement curves

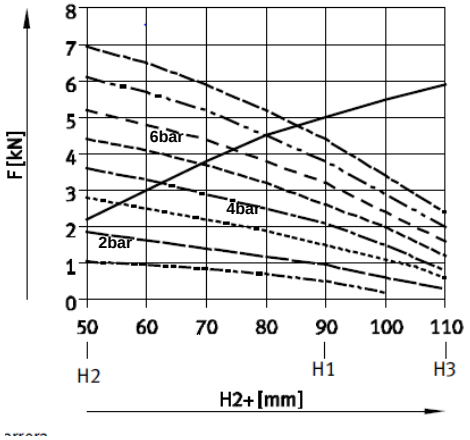


Figure 4: Data sheet from manufacturer – forces at different pressure levels [13]

The dynamic stiffness was measured up to 400Hz by means of stepped sine tests at different amplitudes and pressures, with and without the auxiliary air reservoir. Results in Figure 5, Figure 6 and Figure 7 allow concluding:

- The first resonance at the lowest frequency, 15Hz, corresponds to the natural frequency of the air blocked within the connecting pipe [2]. It disappears when the air reservoir is eliminated from the system
- The stiffness of the system with auxiliary air reservoir converges to the one without it after the lowest resonance [2]
- As test frequency is increased, the stiffness magnitude increases its value by 10 due to the appearance of a new peak (Figure 5)
- Results in Figure 6 show that stiffening of the air spring occurs regardless the pressure in the bellows, even at ambient pressure, confirming that it is due to a structural mode. It was further confirmed by a slow motion video recorded at the resonant frequency, in which it was seen that it belongs to the first vertical mode of the structure
- Higher pressure in the bellow leads to higher natural frequency and higher dynamic stiffness of the air spring (Figure 6)
- The resonant frequency and the amplitude of the dynamic stiffness are also dependent on the amplitude of the excitation, leading to a non-linear behaviour (Figure 7)

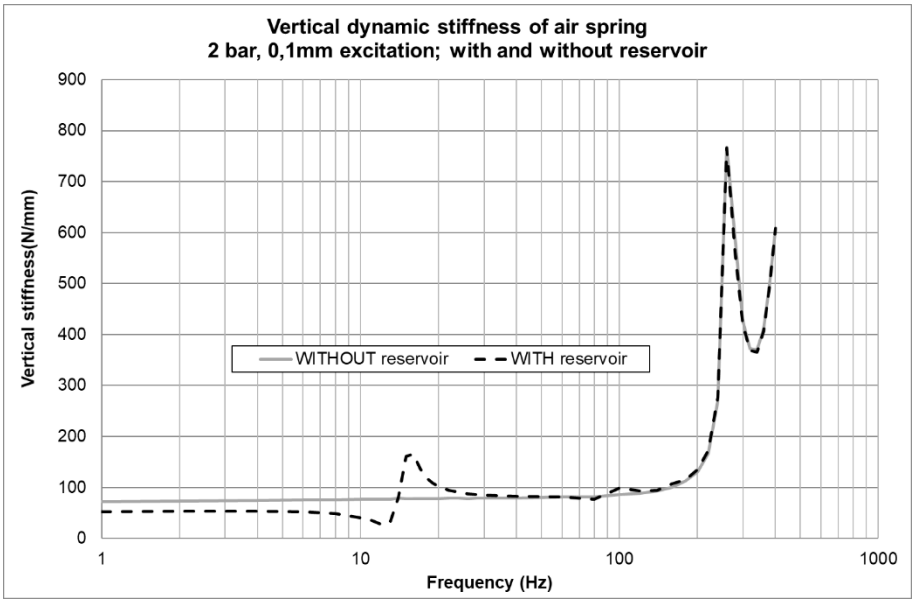


Figure 5: Dynamic vertical stiffness of air spring, with and without air reservoir

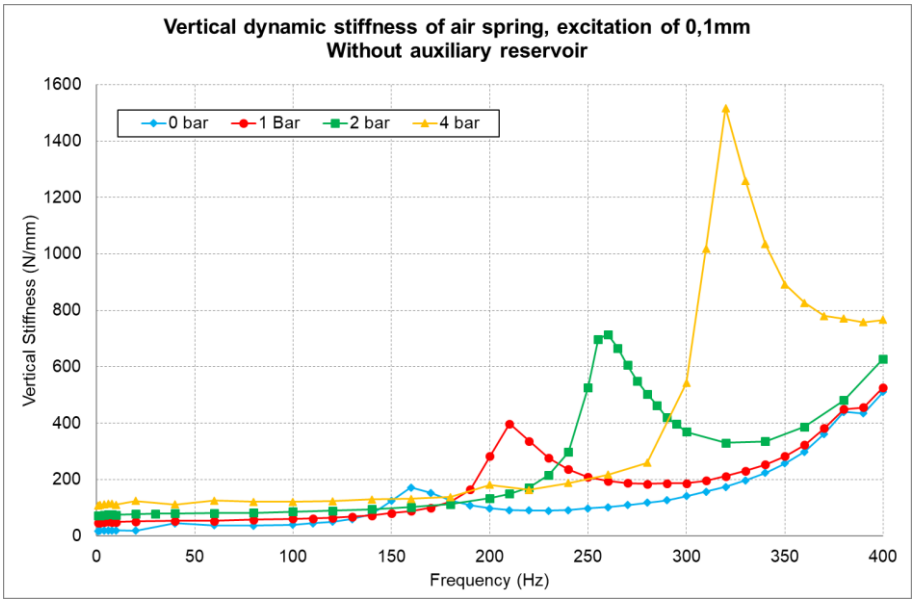


Figure 6: Dynamic vertical stiffness of air spring at different pressures

The most important conclusion of this experimental research is that structural modes of the air spring might be found in the structure borne vibration transmission frequency range, thus reducing isolation provided by these elements. The natural frequency of the air spring and the magnitude of the dynamic stiffness are highly dependent on the working pressure of the air spring.

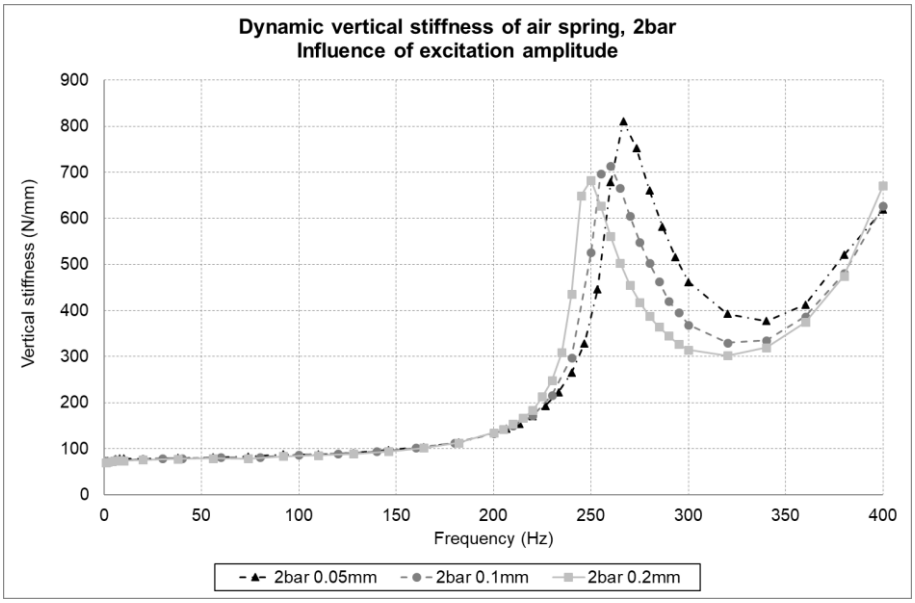


Figure 7: Influence of excitation amplitude in the vertical dynamic stiffness of air spring at 2bar

3 FEM model of the air spring

The elastic chamber or bellows of an air spring is a relatively complex structure, consisting of rubber reinforced by uniaxial fibers. FEM arises as a suitable tool to evaluate the influence that construction elements of the air spring have in the static stiffness and resonant frequencies of the air spring. In order to develop an accurate model some information was collected from the manufacturer (see Figure 8) and finally the air spring was cut to get some data on the real geometry (height, thickness, diameter, etc) and size and disposal of the fibers.

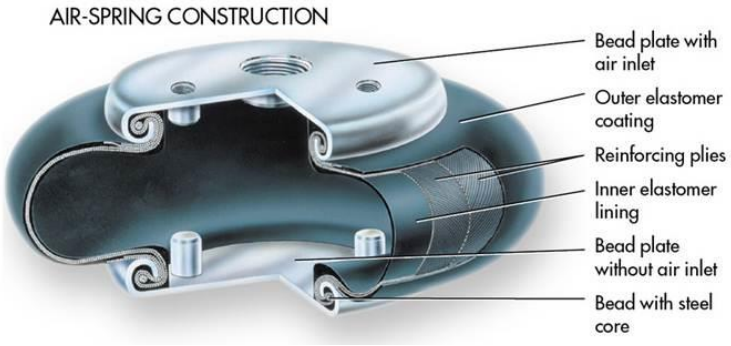


Figure 8. Inner structure of the bellow, provided by manufacturer [13]

It was discovered that there were two layers of nylon fibers, with a diameter of approximately 0,5mm per fiber. Fiber spacing was difficult to determine and it was assumed to be 1mm. The fibers were disposed at an angle of 60º an -60º at each layer (corresponding 0º to the circumferential arrangement). Natural rubber was supposed to be of Shore A 50 hardness. No other information was available from manufacturer or direct observation of the air-spring.

The FEM model of the air-spring was built in ABAQUS, making use of the rebar element option to deal with reinforced structures available in the software [14]. Rebars are used within ABAQUS to define layers of uniaxial reinforcement in membranes, shell, surface or solid elements. Shell elements were selected in the case of the air-spring, the bellows thickness being much smaller than the surface. Two upper and lower

plates were also considered and introduced in the model as rigid plates compared to the bellow (Figure 9). The air inside the cavity was not discretized; the coupling between the air inside a cavity and the structure was modelled through hydrostatic fluid modelling capabilities of ABAQUS [14, 15]. The model was composed of 6791 S4-type elements.

As for material properties, rubber material shows non-linear elasticity that could be represented by hyperelastic models available in commercial finite element codes [16]. Material dependent constants in phenomenological strain energy functions should be fitted from experiments conducted in uniaxial and shear deformation modes in material specimens. Nevertheless, the absence of available material samples made it impossible to conduct a thorough characterization of the elastic properties of rubber. An elastic behavior was therefore assumed, that could be valid at low deformations, adopting a value of 2MPa for the Young's modulus, which approximately corresponds to a rubber of Shore A 50 hardness [17]. Rubber was assumed to be incompressible and, thus, a Poisson coefficient of 0,495 was adopted. Regarding the nylon of the fibers, a Young's modulus of 3100MPa and a density of 1140 kg/m^3 were considered, according to literature.

The air reservoir was not taken into account in the model developed in ABAQUS and, thus, only static stiffness and dynamic calculations without reservoir could be conducted. Three different steps were defined:

1. A static step to increase the inner pressure of the air spring to the desired working value. The upper and lower metallic plates were encastred in the working position and the pressure in the reference point of the cavity was increased up to 2, 4 and 6 bars.
2. In the working position and the desired pressure, a natural frequency extraction was conducted to obtain the resonance frequencies and mode shapes of the air spring.
3. Finally, the upper metallic plate was displaced vertically in order to calculate the static stiffness of the air spring.

Figure 9, middle and right, show the undeformed and deformed shape of the air-spring respectively, for an inner pressure of 4 bars.

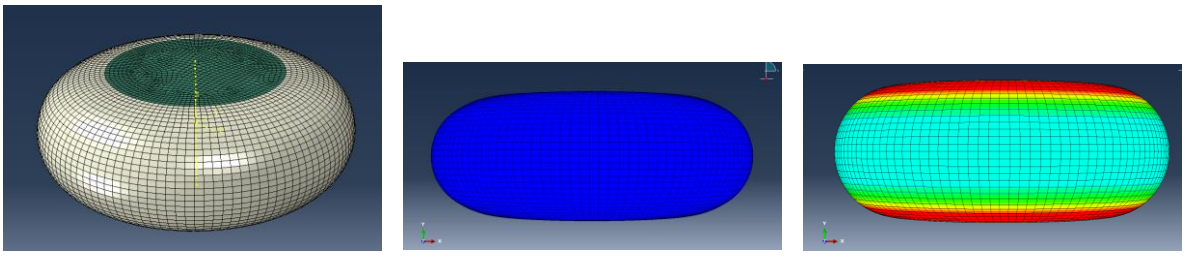


Figure 9. FEM model off the air-spring. Left: green surface corresponds to metal plates and white surface is the elastic bellow; Middle: undeformed shape; Right: deformed shape under 4bar inner pressure

Simulation results are compared to experimental ones in order to validate the FEM model developed. Static force-displacement curves are compared in Figure 10 and Figure 11, for internal pressures of 2 and 4bar. Results corresponding to 6bar are not shown, but they follow a similar pattern. Simulations predict satisfactorily the static stiffness of the air spring in vertical direction. According to Table 1 and Table 2 the force exerted by the air spring for different inner pressures is predicted with errors below 5%. Higher differences, about 10%, are observed in the pressure dependent static stiffness.

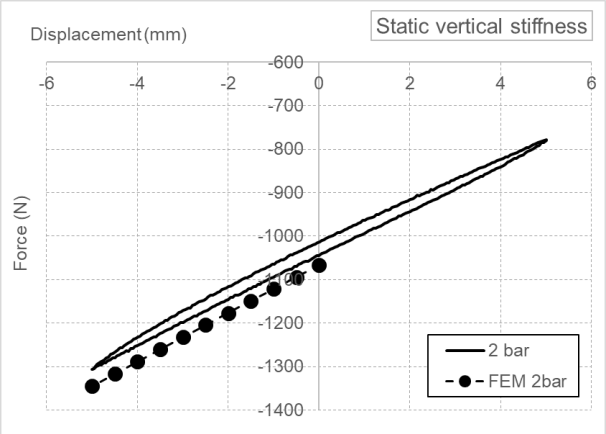


Figure 10: Experiments vs. simulation, 2 bar

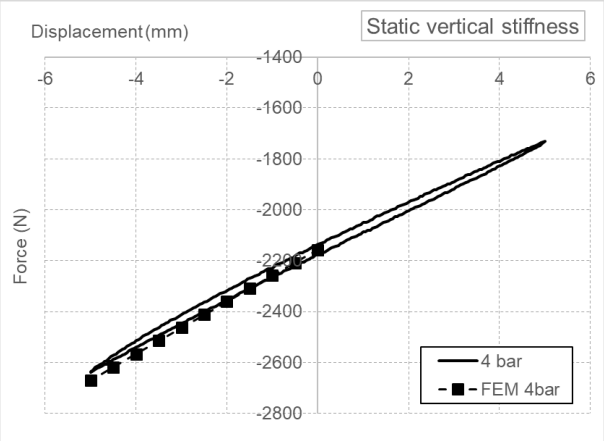


Figure 11: Experiments vs. simulation, 4 bar

Pressure (bar)	*Force (N) at pressure*	*FEM (N)*	*% error*
2	1045	1067	2.1%
4	2177	2157	0.9%
6	3146	3273	4.0%

Table 1: Force after applying inner pressure

Pressure (bar)	*Static stifness (N/mm)*	*FEM (N/mm)*	*% error*
2	51.3	55.6	8.4%
4	88.7	98.7	11.3%
6	127.3	140.5	10.4%

Table 2: Static stiffness (N/mm)

Concerning natural frequencies of the air-spring, values at 2bar and 4bar could only be compared, in a frequency range up to 400Hz where only one vibration mode is appreciated. The natural frequency is better predicted at the highest pressure, being the errors below 10% in both cases. The first vibration mode calculated corresponds to the first vertical vibration mode, as illustrated in Figure 12.

Pressure (bar)	*Natural frequency 1st mode (Hz)*	*FEM (Hz)*	*% error*
2	250	225.67	9.7%
4	320	306.87	4.1%

Table 3: Natural frequency of the first structural mode of the air spring

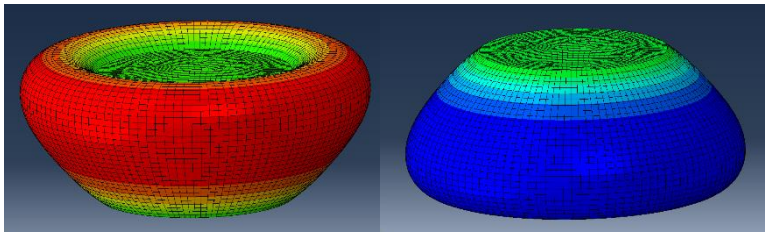


Figure 12: Mode shape 1

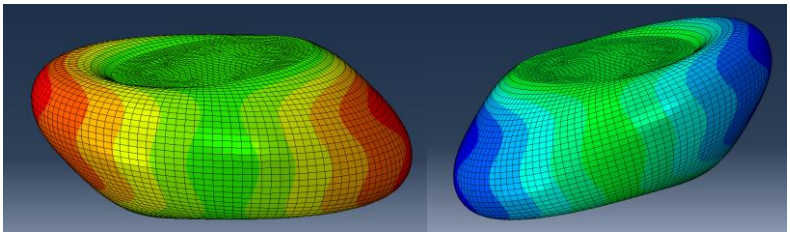


Figure 13: Mode shape 2 of the air spring

Considering the approximations adopted in the geometry and the lack of data for an accurate definition of the rubber and nylon materials, it is concluded that the model satisfactorily predicts the behavior of an air spring without auxiliary air reservoir. The FEM model might also be used to obtain physical quantities related to analytical models of air-springs without having to perform experiments, as shown in Figure 14, where the vertical displacement has been extended to 20mm. The effective area increases with applied deformation while the volume of the air spring decreases.

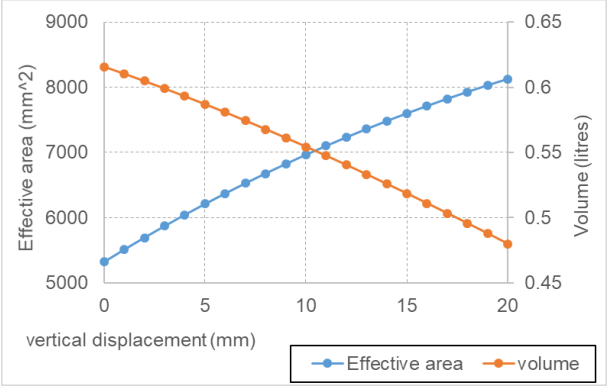


Figure 14. Calculation of effective area and volume of the air spring

4 Design parameter sensitivity analysis

Finally, the FEM model developed in section 3 has been used to evaluate the impact of several constructive parameters in the static stiffness and natural frequency values of the air spring. Parameters considered are: orientation angle of fibers, fiber spacing and diameter of the cross-sectional area of the fibers.

The most influencing parameter is the orientation of the fibers in the air spring. According to Figure 15 differences might be expected specially when the orientation angle is changed between 30º and 70º. Table 4 shows that significant differences might appear in static stiffness and also in the natural frequency of the 1st mode of vibration, which could reduce its value to around 100Hz at 20º, well below the 300Hz estimated at 60º.

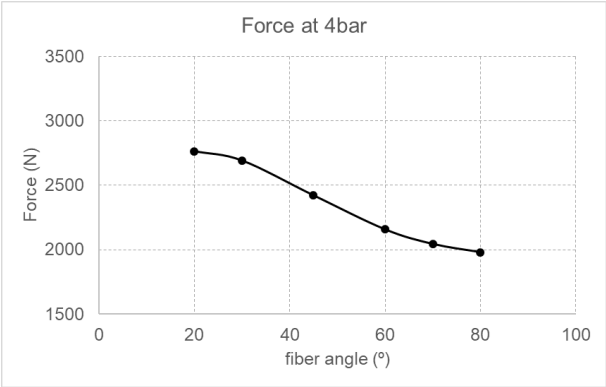


Figure 15: Force exerted by the air spring when internal pressure is set to 4bar. Influence of angle

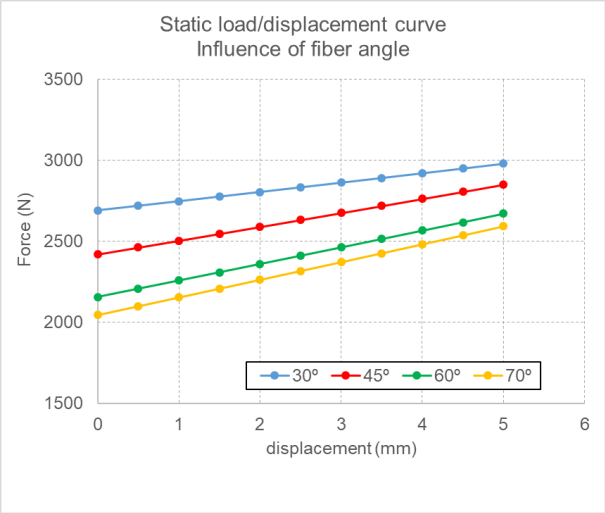


Figure 16: Load/displacement curves for different fiber angles

Fiber angle (º)	*Force (N) at 4 bar*	*Static stiffness (N/mm)*	*Natural frequency 1st mode (Hz)*	*Natural frequency 2nd mode (Hz)*
20	2763.44		95.204	338.47
30	2691.07	57.8	156.07	383.92
45	2420.81	85.9	251.86	407.14
60	2157.36	102.7	306.87	392.03
70	2044.96	109.6	327.43	369.55
80	1980.85		338.72	347.79

Table 4. Evolution of air-spring characteristics with the angle of fibers

On the other hand, the spacing of fibers in the layers does not seem to influence much the results of static stiffness, at least in the range considered here, between 0.5 – 1.5mm, see Figure 17. According to Table 5 the first natural frequency remains unaffected by the changes in the spacing of the fibers; it is the second vibration mode the one that changes the value in a higher degree due to the fiber spacing.

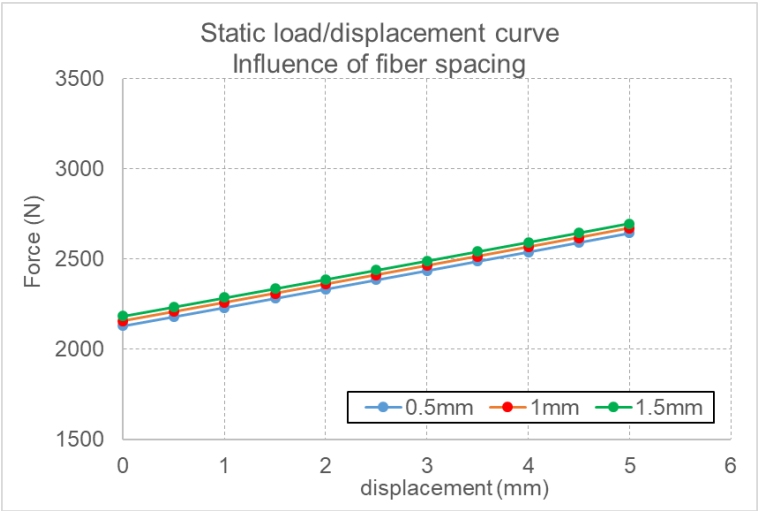


Figure 17: Load/displacement curves for different fiber spacing values

Fiber spacing (mm)	*Natural frequency 1st mode*	*Natural frequency 2nd mode*
0.5	296.57	437.07
1	306.87	392.03
1.5	308.9	369.95

Table 5: Evolution of air-spring natural frequencies with the fiber spacing in the layers

Finally, the influence of the size of the cross sectional area of the fibers could be evaluated. Diameter of the fibers have been changed between 0,3mm and 0,7mm. An increase in the cross-sectional area seems to increase the force exerted by the air spring when it is subjected to 4bar internal pressure (Figure 18); it might have to do with a small reduction in the effective area of the air spring. Nevertheless, the range of values should be expanded in order to extract more definite conclusions. Once again the natural frequency of the first vibration mode remains practically unaffected by the changes in the fiber diameter in the range of values considered here; it is the second mode the one that changes the value of the resonant frequency when the cross-sectional area is modified.

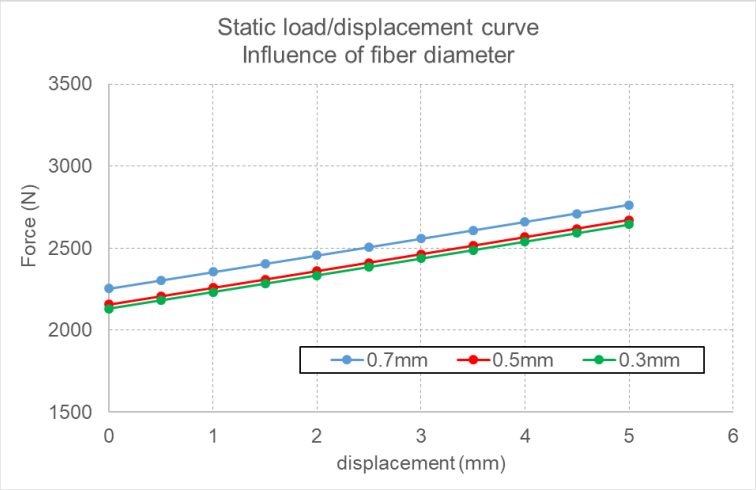


Figure 18: Load/displacement curves for different fiber diameters

fiber diameter (mm)	*Natural frequency 1st mode (Hz)*	*Natural frequency 2nd mode (Hz)*
0.3	306.71	342.03
0.5	306.87	392.03
0.7	296.96	435.82

Table 6: Evolution of air-spring natural frequencies with the fiber diameter

5 Conclusions

Experimental measurements have been conducted in a commercial air-spring in vertical direction, connected to an air reservoir and disconnected from it.

Both the force exerted by the air spring and the static stiffness have found to be pressure dependent.

From dynamic measurements without the auxiliary air reservoir, the existence of natural frequencies below 400Hz of the air spring has been confirmed, being the frequency value and the amplitude of the stiffness dependent on the pressure and amplitude of excitation, resulting in a non-linear behaviour. When the air reservoir is connected, it is confirmed that the further increase in the stiffness appreciated at the highest frequencies has a structural origin.

The stiffness of the air spring is not maintained constant in the whole frequency range. The structural mode of the air spring might increase in an order of magnitude the dynamic stiffness of the air spring in the structure-borne vibration transmission frequency range, with the risk of reducing the isolation provided by the suspension element.

A FEM model of the air spring has been developed in ABAQUS, making use of the Rebar facilities implemented in the commercial code for reinforcing elements. Despite assumptions adopted when creating the model for the material behaviour of rubber and nylon, and for some structural elements of the air spring such as the diameter or spacing of fibers, the model satisfactorily reproduces the observed behaviour of the tested air spring. Errors in predicted static stiffness and values of resonant frequencies are below 10%.

The FEM model allows studying the influence of the different parameters in the response of the air spring and, thus, it is oriented to provide hints to designers in order to achieve desired static and dynamic behaviour. It has been stated that the angle at which reinforcing fibres are disposed has the greatest influence both in the static and dynamic stiffness of the air spring. The influence is higher in the 30º-70º range, being 0º the circumferential arrangement of the fibers. Natural frequencies at 100Hz might be found for the smaller angles considered.

Other parameters, such as spacing of fibers or diameter of the cross-sectional area of the fibers, have been found to have less influence in the results. The natural frequency of the first vibration mode in vertical direction remains practically unaffected by the changes in these parameters. Nevertheless, the research should be completed with more simulations, extending the range of variation of the parameters.

Acknowledgements

The authors acknowledge the Basque Government for the funding provided within the project VIRRAIL "Investigación en modelos y herramientas de simulación para vehículos ferroviarios" (ELKARTEK research program) to conduct part of the work presented here.

References

[1] A. Sañudo, *Development of a new methodology for the analysis of structure-borne vibration in railway vehicles*, PhD Thesis, University of Navarra, San Sebastián (2014)

[2] A. Alonso, J.G. Giménez, J. Nieto, J. Vinolas, *Air suspension characterisation and effectiveness of a variable area orifice*, Vehicle System Dynamics, vol. 48 (Supplement) (2010), pp. 271-286

[3] M. Presthus, *Derivation of air spring model parameters for train simulation*, MSc Thesis, Lulea University of Technology (2002)

[4] L. Mazzola, M. Berg, *Secondary suspension of railway vehicles-air spring modelling: Performance and critical issues*, Journal of Rail and Rapid Transit, vol. 228, No. 3 (2014) pp. 225-241

[5] A.J. Nieto, A.L. Morales, A. González, J.M. Chicharro, P. Pintado, *An analytical model of pneumatic suspensions based on an experimental characterization*, Journal of Sound and Vibration, vol. 313 (2008), pp. 290-307

[6] L. Bregant, M. Spagnol, R. Moras, *Dynamic Characterization of air spring for AVC applications, Proceedings of the ISMA 2010 Conference, Leuven, 2010, 20-22 September*, Leuven (Belgium) (2010), pp. 1717- 1724

[7] X. Li, Y. He, W. Liu, Y. Wei, *Rsearch on the vertical stiffness of a rolling lobe air spring*, Journal of Rail and Rapid Transit (2015)

[8] F. Chang, Z-H. Lu, *Dynamic model of an air spring and integration into a vehicle dynamnics model*, Proceedings of the Institution of Mechanical Engineers, part D: Journal of Automobile Engineering, vol. 222 (2008), pp. 1813-1825

[9] S. Bruni, J. Vinolas, M. Berg, *Modelling of suspension components in a rail vehicle dynamics context*, Vehicle System Dynamics, vol. 49, Nº 7 (2011), pp. 1021-1072

[10] H. Li, K. Guo, S. Chen, W. Wang, F. Cong, *Design of Stiffness for Air Spring Based on ABAQUS*, Mathematical problems in Engineering, vol. 2013, article ID 528218 (2013), 5 pages

[11] Shi Wenko, Jiang Wang, Huang Ying, Yao Weimin, *Finite Element Analysis of an Air Spring Concerning Initial Pressure and Parameters of Cord Fabric Layer*, *2009 Second Asia-Pacific Comference on Computational Intelligence and Industrial Applications* (2009), pp. 496-499

[12] Yang Weimin, Chen Can-hui, Chen Ya-ling, Ren Yan-sha, *Finite element analysis of an air spring for automobile suspension*, Journal of Beijing University of Chemical Technology, vol. 31, No. 3 (2004), pp. 105-109 (in english)

[13] FESTO, *Cilindros de fuelle*. Characteristics of commercial air-springs provided by manufacturer

[14] Abaqus 2018, *Simulia User Assistance 2018*

[15] N. Gil-Negrete, J. Vinolas, A. Rivas, *On the prediction of the dynamic stiffness of hydrobushings, Proceedings of the ISMA 2004 Conference, Leuven, 20-22 September*, Leuven (Belgium) (2004), pp. 3427-3437

[16] N. Gil-Negrete, *On the modelling and dynamic stiffness prediction of rubber isolators*, PhD Thesis, University of Navarra, San Sebastián (2004)

[17] ISO 48, *Rubber, vulcanized or thermoplastic – Determination of hardness (hardness between 10 IRHD and 100 IRHD)* (2010)

Dynamic optimization of an electro-spindle for robotic machining

A. Mora[1], G. Bianchi[2], M. Leonesio[2]
[1] SUPSI University of Applied Science of Southern Switzerland – DTI
via Cantonale 2c, 6928, Manno, Switzerland

[2] CNR; Institute of Intelligent Industrial Technologies and Systems for Advanced Manufacturing
via Alfonso Corti 12, 20133, Milano, Italy
e-mail: **giacomo.bianchi@itia.cnr.it**

Abstract
A methodology is proposed to optimize an electro-spindle for robotic machining applications. In addition to the common maximization of the material removal capability, other requirements are specific for the robotic application: minimization of the weight and estimation of the cutting force on the tool by a special embedded sensor. A parametric dynamic model of the spindle is built, integrating reduced order finite element models of the main structural elements (housing, rotating shaft, preload piston and tools), taking into account the boundary conditions provided by the robot end-effector. A damping solution based on elastomeric dampers is considered. The dynamic performance are evaluated by computing objective functions that take into account critical speeds, imbalance vibrations, regenerative chatter stability and forced vibrations for two reference milling operations. Additionally, the embedded sensor requires to assure a sufficient shaft displacement at sensor locations, to get the desired resolution in cutting force estimation.

1 Introduction

Industrial robots are more and more exploited to perform metal cutting operations like milling and deburring. A growing application requires trimming, drilling or milling of composites for the aerospace or automotive industries [1], where positioning accuracy in order of 0.1 mm is appropriate. The main advantages are agility, because of the high number of controlled axes, reduced cost, compared to a CNC machine tool with comparable workspace, and process intelligence, because of the adoption of adaptive and model-based control strategies able to cope with unknown workpiece variations, e.g. while deburring casted parts. The major drawbacks are robot poor static accuracy and high dynamic compliance, as well as lower resonance frequencies, compared to traditional CNC machine tools [2]. Vibration phenomena may affect, as in machine tools, the quality of machined parts and the tools and spindle useful life. These vibrations occur at specific machining conditions depending on robot [3] and spindle dynamic properties [4]. In particular, spindle dynamics plays a paramount role due to the high cutting velocities typical of robotic machining. additionally, control strategies that can mitigate vibration and accuracy issues often require sensing the actual cutting force. In fact, a force feedback can be used to adapt the feed or the trajectory to the actual material to be removed from the workpiece or, more rarely, to estimate and compensate robot structural deformation, caused by its low static stiffness [5].

On these premises, the goal of this work is to present a methodology to design an optimal electro-spindle taking into account the specific requirements of robotic machining (basically concerned with high power/weight ratio and high cutting dynamic stability), and integrating a high-dynamic force sensor for process monitoring purpose.

Vibrations can be classified into forced and self-excited vibrations [6]. Forced vibrations are due to nominal force variability in interrupted cutting, typical of milling: significant vibrations occur when harmonics of the cutting forces coincide with a natural frequency of the machining system. Forced vibrations are predicted computing the cutting forces and knowing the dynamic compliance of the machining system. Additionally, self-excited vibrations, can occur, mainly ascribed to regenerative chatter: relative vibrations between the active cutting edge and the workpiece generate a surface waviness that will modify the actual chip thickness of the subsequent cutting edge, when it will be engaged on the same position [8]. In this case, the process stability limit is a function of the spindle speed, as depicted by the "Stability Lobes Diagram" (SLD), that takes into account system dynamic response and process parameters.

Spindle optimization aimed at avoiding such vibration phenomena is a well-known problem. Based on the above-mentioned theory, different typologies of objective functions could be defined. In practice, two different features must be combined: the level of detail and constraint in cutting operations definition (e.g., the spindle speed can be fixed or free in a range) and the approach used to manage the multi-objective nature of the optimization (e.g., weighted summation, minmax approach, pareto set, etc.). Dealing with regenerative chatter, Abele et al. in [9] use spindle simulation models for design optimization. The optimization can be aimed at achieving maximum dynamic stiffness at all speeds, for general operations, or to reach maximum axial depth of cut at the specified speed, with a designated cutter, for a specific operation (i.e. to get the working point inside a stability pocket of the SLD). The same approach is followed by Altintas in [10] for the optimization of bearing spacing to obtain either maximum dynamic stiffness or maximum chatter-free depth of cut for multiple flute cutters. The same work presents a non-linear FE model of the spindle that includes bearing preload, gyroscopic and centrifugal speed effects. In Albertelli et al. [11], the objective function to be maximized is a weighted summation of the critical depths of cut associated to a set of reference milling operation. The greater and lower tooth passing frequency associated to the targeted milling operations defines the frequency range of dynamic compliance that affects the interested performance: while the superior bound takes origin by process damping phenomenon [12], the inferior bound is usually set considering the effect of the position of the first stability lobe, but a rigorous criterion is not provided. Tackling vibration problem in a more general way, Zhang et al. in [13] observe that, normally, cutting parameters optimization aims at improving final surface quality and maximizing Material Removal Rate (MRR), while the stable depth of cut is treated as a constraint, together with technological limitations on cutting velocity. In this perspective, also force vibrations become of paramount importance.

While spindle design usually relies on classical parameters like bearings spacing and topology, shaft and housing material and sizing, the adoption of particular damping devices like squeeze film dampers or elastomer rings at bearings support could provide new design possibilities and enhance the dynamic performance of the spindle. Elastomer rings, in particular, have demonstrated to be effective in reducing vibrations of rotating machinery [14], while accurate and relatively simple models are available to evaluate their effect in design phase. For instance, Bonfitto et al. [15], using a biaxial excitation and displacement sensors, extracted the response of the elastomer thanks to Genetic Algorithm optimization. The results show a good agreement between the elastomer model, exploited in a FE model of a pump shaft, and the experimental measurements.

As mentioned before, cutting force measurement for monitoring and control is another essential feature in a spindle for robot milling. Zäh and Rösch [16] developed a compensation of static deflection due to cutting forces by a model-based fuzzy controller: this approach uses a force dynamometer at the workpiece to measure process-forces and an acceleration sensor at the spindle to detect chatter. Another approach for online compensation uses a spindle holder with integrated force sensors to measure cutting forces and calculate the resulting deviation [17]. Thus, the complexity using additional sensors is removed. Anyway, all these solutions are usually rather expensive or do not guarantee the necessary bandwidth to analysis dynamic cutting forces in high speed cutting operations.

In this paper, a methodology is presented for the design of a new spindle for robot milling operations that takes into account all the aforementioned issues by means of a holistic modelling approach. In fact, together with the usual design parameters like bearings spacing, house and shaft stiffness and inertia, elastomeric bearing supports are modelled and optimized.

Cutting force are estimated measuring shaft deflection by inductive displacement sensors. To assure the prescribed measurement resolution, a proper constraint on minimum induced displacement at sensor location is considered. Thus, the proposed design methodology allows the spindle to exploit profitably both an the embedded high-dynamics cutting force sensor that enables the adoption of monitoring and adaptive control strategies.

The paper is structured as follows. Firstly, the system under study is explained. Secondly, the proposed modelling and optimization approach is developed. Here, the model used for the optimization is illustrated. Then, the results of Multi-Objective optimization on the reference case are shown, with a detailed analysis of the main solution clusters. Finally, conclusions are presented.

2 Electro-spindle for robotic machining

The envisaged application scenario is to perform machining operations in a small workshop or design department by a medium sized robot. The spindle must satisfy constraints on weight, limited by the maximum payload of the robot, and on the housing outer diameter, to assure adequate dexterity in approaching complex work pieces. The target machining tasks are deburring and light milling: in both cases, to limit cutting forces, High-Speed Cutting (HSC) is adopted. To avoid selecting an optimal design linked to a single case, two different milling operations/tools have been considered. A key element in spindle design is bearing disposition (see following figure): a common solution for high-speed electro-spindles is composed by two fixed bearings in tandem in front (B1 and B2) and two floating bearings in tandem on the rear (B3, B4). In traditional spindle solutions, the axial preload is applied by a set of helical spring acting on the seat of the rear bearing unit, which can move along the spindle axis thanks to a ball bushing bearing between the Housing and the Rear Bushing support. To allow force control schemes, shaft-housing displacement in X and Y directions is measured by inductive eddy current sensors. The cutting force is then evaluated through static & dynamic calibration. One inductive sensor is placed near the spindle nose along the shaft axis Z in order to measure the axial displacement of the shaft due thermal expansion and speed-dependent ball bearings kinematics.

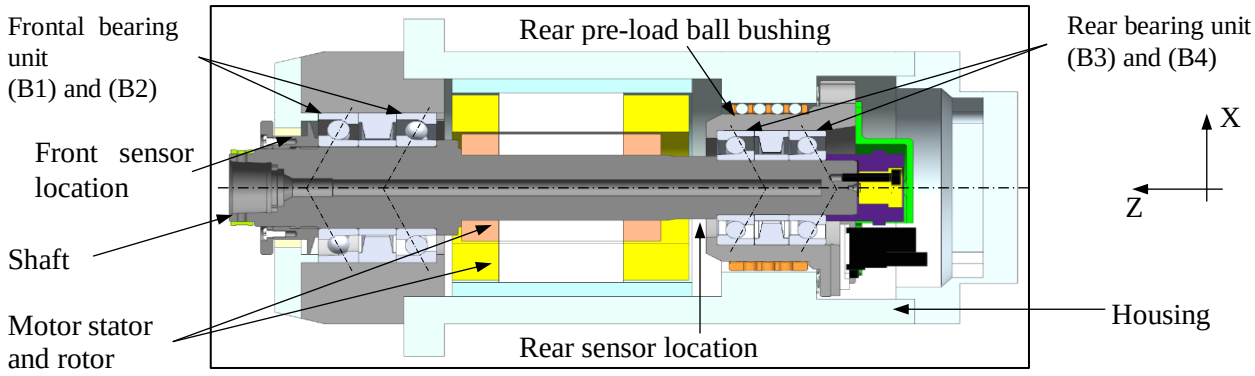


Figure 1: Electrospindle main components (tool and tool-holder not shown)

3 Methodology

3.1 Structure model

As described also by Abele et al. in [9], the spindle is modelled using a finite element method (FEM) for all main components: shaft, housing, the bushing used as seat for the rear bearing unit, tool and tool holder. For some components (e.g. motor stator and rotor, water cooling system) where a detailed representation would be uselessly complex, an equivalent homogeneous material, characterized in past experimental campaigns [18], is adopted. Due to the nonlinearity of the bearing caused by the Hertzian contact and the speed dependency, a linearization is performed applying to the spindle the axial preload and linearizing the bearing stiffness at four different spindle speeds. The tool is connected to a manual tool-holder HSK25C that is fixed to the shaft through a lumped linear bending compliance.

In order to automatize the spindle analysis and reduce the optimization computational time, the FE models of the spindle components are simplified, applying the Craig Bampton reduction techniques [20], and exported to the MATLAB environment. In this way, most of the thousands of DOFs of the original meshes are represented as dependent DOFs, while few tenths DOFs are preserved as independent DOFs, to represent boundary connections (e.g. bearing connections, tool tip etc) and internal dynamics of each component. The obtained modal stiffness matrix $[\widetilde{K}_i]$, modal mass matrix $[\widetilde{M}_i]$ and mode shape matrix $[\Phi_i]$, for each $i-th$ component, is processed to add a uniform modal damping (relative damping 3%) and then modelled in MATLAB Simulink environment as standard ABCD elements. Structural components are connected by compliant connector elements representing respectively the ball bearing, the HSK tool-holder and the damped bearing supports, obtaining the overall spindle dynamic model, from the interaction of the various components.

To analyse the spindle dynamics is important to properly represent its boundary conditions, i.e. the dynamic stiffness of the supporting structure, that, for the examined case, is the end-effector of a medium size anthropomorphic robot. A modal analysis on a similar robot [3] has shown that robot's most significant structural resonances are located at low frequencies (e.g. 10-40Hz), while spindle dynamics and cutting process are at much higher frequencies (i.e. higher than 250 Hz). For this reason, in the frequency range of interest, the constraint realized by the robot can be represented as a small inertia connected to the spindle housing, modelled then in free-free conditions.

As the dynamic behaviour of the spindle depends on its speed, because bearing's stiffness decreases at high speed (while gyroscopic effects are negligible for the examined shaft and maximum speed), computing the stability lobe diagram referring to the dynamic compliance at null velocity can produce significant approximations. The spindle speed operational range has been therefore divided in 3 sections: the spindle is linearized at each speed, computing the corresponding dynamic compliance at the tool tip. For each FRF the SLD is computed only in the surrounding speed range. After that, all portions of the stability lobe diagram are joined together to obtain an approximated overall SLD. As shown in the following figure, spindle dynamics is clearly speed-dependent for the smaller tool (diameter 6), while, for the bigger tool (diameter 12), the stability limit is basically due to the resonance at 780 Hz, that is marginally affected by the speed: the SLDs computed at the different speeds are therefore very similar. Hence, for the optimization, only the diagram at the highest speed allowed by the tool (30'000 RPM) is used, for the bigger tool.

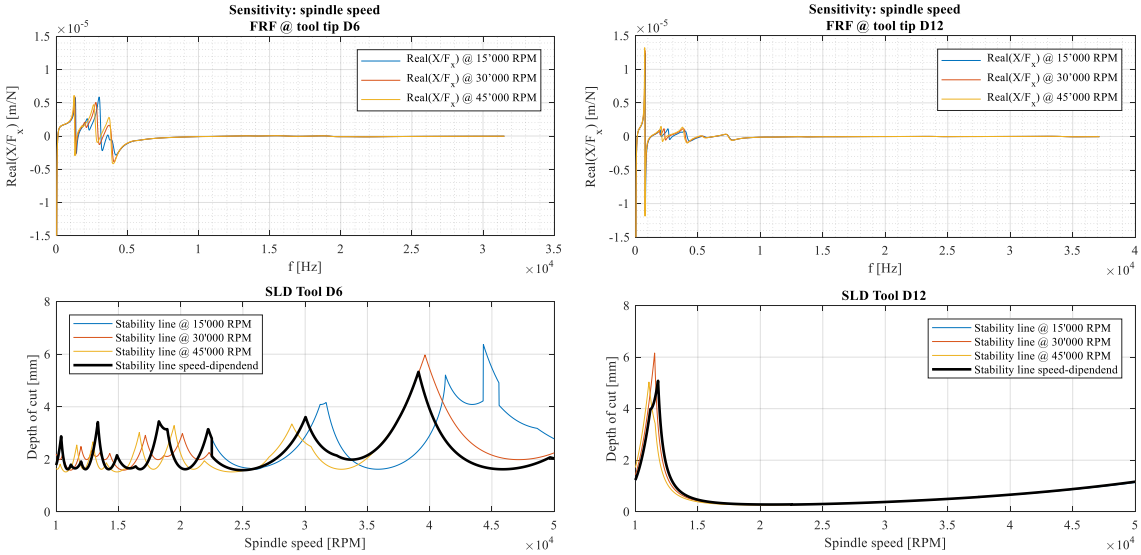


Figure 2: Dynamic compliance at the tool tip for three rotation speeds and corresponding SLD diagrams, for the two examined tools (diameters 6 and 12mm).

3.2 Dampers models

To alleviate both forced vibration and chatter instabilities, modal damping must be increased, to reduce peak dynamic compliance. For this reason, two suspension systems are designed, between the housing and the front bearing unit and the rear bearing unit, in order to provide the optimal elastic and damping reaction force.

In order to limit the spindle complexity and cost, a damping solution based on elastomeric materials has been investigated. Damping in elastomeric materials (e.g. rubber) is characterized by an elastic component (storage modulus) and a damping component (loss modulus). For each elastomer, the ratio between the two quantities is defined by the Loss Factor $\eta(f)$, which is frequency-dependent. Usually the maximum Loss Factor value is near 1, producing a dynamic compliance with a phase delay of approximately 45° (i.e. the stored elastic energy and the maximum dissipated energy have comparable magnitudes).

In the below graph are depicted two dynamic stiffness of elastomers (commercial name E-A-R Isodamp [19]).

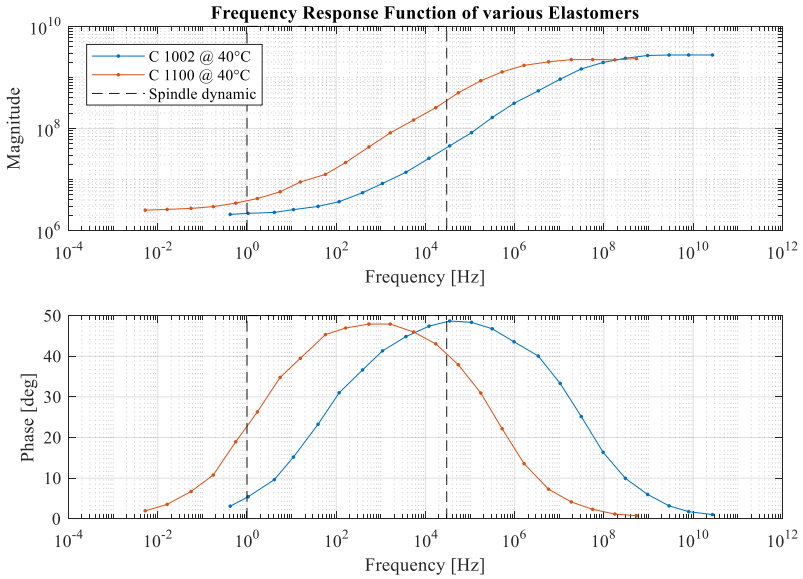


Figure 3: Dynamic stiffness of EAR C1002 and C1100 elastomeric materials

3.3 Optimization problem

The Multi-Objective optimization is set up with Objective Functions (OF) referable to three main performances categories:

1) **Forced vibrations**: in the frequency range excited by the milling process, the displacement response at the tool tip has to be minimized for each of the two tools considered. The OF analysed are the highest resonance peak in this frequency range and the RMS value of the dynamic compliance.
2) **Chatter instability**: the stable depth of cut in respect to regenerative instability is a crucial parameter of machining operations. For this reason, the depth of cut stable at all speeds, $b_{\lim}$, is considered as performance to be maximized. In addition, to appreciate the presence of wide stability pockets in the useful spindle speed range, the average value of the stability boundary b_{med} is calculated. Notice that in this way, assuming the width of cut to be constant, we are indirectly maximizing the Material Removal Rate (MRR), since $MRR^{\max} = b_{\lim} \cdot a_e \cdot \left(f_z \cdot z \cdot n \right)$, where a_e is the width of cut, f_z is the feed per tooth, z is the flutes number and n the spindle speed.
3) **Vibration due to rotor imbalance**: at high speed, imbalance can excite synchronous vibrations. Even if the spindle shaft is balanced by the manufacturer, additional imbalance can occur due to the tool and the accuracy of the HSK coupling. The spectrum of displacement at the tool tip is evaluated adopting a specific grade of precision of equilibrature G , in the spindle speed range. The related performance indices are the RMS and maximum value of the displacement spectrum at tool tip, which are to be minimized.

To guarantee safety, reliability and performance of the spindle, constraints have to be satisfied:

- Considering the high-speed application, bending instability due to the critical speeds must be considered. Two alternative acceptable conditions are considered: in the first one, the first bending spindle resonance frequency is larger than 1.5 times the maximum spindle speed. In the second case, if the first bending resonance frequency is smaller than 0.5 the maximum spindle speed, than the second bending resonance frequency must be larger than the maximum spindle speed. The second condition is often used in small, high speed, spindles, where it is quite difficult to satisfy the first constraint. During run-up and run-down, the spindle has to go quickly through the first resonance.
- To assure the requested resolution in cutting force estimation, the shaft radial displacement, where the sensor is located, under the radial force corresponding to the desired force resolution (F_{res}) must be larger than the inductive sensor resolution.

The following Design Variables (DV) are considered for spindle optimization:

- Frontal and rear shaft supports: the visco-elastic suspension, with an elastomeric film, is placed between the bearing casing and the spindle housing, as described in chapter 3.2. Design Variable of for the suspension consist of in a gain that multiplies the dynamic stiffness of the elastomer: by a physical point of view, the gain is the "quantity" of material in the suspension. In this way, the elastic and damping characteristic will increase proportionally according to the Loss Factor curve of the selected material.
- Shaft and housing proprieties (i.e. stiffness and inertia). Those components are represented, during optimization, as reduced order inertia and stiffness matrices. It is therefore impossible to operate structural modifications using geometrical DVs. Nevertheless, in order to give preliminary overall indications to the designer, DVs are defined to modulate, by a unique scalar multiplier, the inertia and stiffens matrices of the shaft and the housing. Those actions correspond to the adoption of a different "virtual material", with modulated density and Young modulus. For the shaft, the modal damping in kept constant, while, for the housing, also the modal viscous damping is considered as an independent DV, to investigate the possible adoption of damping solutions in the fixed structure.
- Frontal bearing disposition. As described in chapter **Fout! Verwijzingsbron niet gevonden.**, the frontal bearing unit is composed by two bearings in tandem with a spacer (disposition D1). To modify the frontal tilting stiffness of the shaft, the bearing can be attached side-by-side toward the spindle nose (D2) or toward the motor side (D3).

Considering the high number of DVs (11), the strong non-linearity of the Objective and Constraint functions and the presence of some integer DVs, such as the bearing disposition, a Genetic Algorithm (GA) approach was adopted [22]. The Multi-Objective optimization identifies the dominant individuals that describe the Pareto front.

3.4 Analysis target frequency range

An important decision, in setting up the optimization and modelling approach, is the definition of the proper frequency range of analysis. It must allow a correct evaluation of the selected Objective Functions and Constraints.

The frequency range to analyse machining dynamical performance is derived from the considered minimum and maximum tooth passing frequencies (TPF).

Firstly, let the lower bound of the relevant frequency range be identified. In SLD, the lobes corresponding to a single resonance frequency can be numbered with respect to the number of entire oscillation cycles that occur between subsequent teeth passes, whose periodicity depends on tooth passing frequency. The "1-st lobe" corresponds to one oscillation cycle, i.e. to a TPF that is close to the chatter frequency, the 2-nd lobe corresponds to a TPF that is near half of chatter frequency, and so on for the 3-rd, 4-th …, n-th lobe.

Beyond 1-st lobe, stability limit increases indefinitely, giving, at high speeds, no practical limitation to the cutting process. Therefore, for a given TPF, the dynamic behaviour of the system at frequencies sufficiently lower than the TPF is irrelevant. This is the reason why, for high speed milling, machine structural dynamics (typically significant at low frequencies) is less important than local spindle and tool dynamics, usually characterized by higher resonances frequencies. Note that a high TPF does not imply necessarily a high cutting speed, but only a high spindle speed: high spindle speeds are required to get an adequate cutting velocity with small tool diameters.

It is well known that the critical depth of cut is inversely proportional to the minimum of the real-part of the dynamic compliance [8]. Adopting a modal decomposition and assuming that significant resonances are spaced, the analysis can be tackled considering a single resonance (i.e. dynamical system with a single DoF) for each direction defining the milling plane, denoted respectively as X and Y. Then, a threshold can be defined as the ratio between the real part minimum and the negative residual value of the dynamic compliance at higher frequencies: this ratio defines how much the stable depth increases moving away from the frequency associated to the worst situation.

Let a one DoF dynamical system be considered with mass *m*, undamped natural frequency ω_n and relative damping ξ. The real part of the dynamic compliance is:

$$G_R(\omega) := \Re\left(G(\omega)\right) = -\frac{\frac{1}{m}\left(\omega^2 - \omega_n^2\right)}{\left(\omega^2 - \omega_n^2\right)^2 + 4\xi^2\omega^2\omega_n^2} \tag{1}$$

It can be demonstrated that:

$$\min_{\omega}(G_R) = -\frac{1/m}{4\omega_n^2\xi(1+\xi)} \tag{2}$$

Now, we can identify a frequency ω_{th}, beyond the resonance, where the real part of the dynamic compliance becomes negligible, namely, smaller than a given fraction, denoted by "α", of the absolute minimum. Frequency ω_{th} is the limit value of the following minimization problem:

$$\begin{aligned} & G_R(\omega) > \alpha \min_{\omega}\left(G_R(\omega)\right), \text{ with } \omega \in R^+ \quad \Rightarrow \quad G_R(\omega) > -\frac{1/m}{4\omega_n^2\xi(\xi+1)}\alpha \quad \Rightarrow \\ & \Rightarrow \omega > \omega_{th} = \frac{\sqrt{\alpha\left(-2\alpha\xi^2 + 2\xi^2 + 2\sqrt{\alpha^2\xi^4 - 2\alpha\xi^4 - \alpha^2\xi^2 - 2\alpha\xi^3 + \xi^4 + 2\xi^3 + \xi^2} + \alpha + 2\xi\right)}}{\alpha}\omega_n \end{aligned} \tag{3}$$

The given expression is used to identify the minimum resonance frequency that has to be considered, in order to neglect components in the real part of the dynamic compliance smaller than the maximum allowed error $\alpha \cdot \min_{\omega}\left(G_R(\omega)\right)$ in the analysed frequency range. The lowest resonance frequency to be taken into account, ω_{inf}, produces the maximum error at the lower limit of the frequency interval used to compute the SLD, i.e. $\omega_n = \omega_{\text{inf}}$: the first lobe associated to this resonance must be uninfluential according to condition (3) at the minimum spindle speed Ω_{min}. Considering the limiting case, knowing the analytical relationship between spindle velocity Ω_{min}, chatter frequency ω_{th} and resonance frequency ω_{inf}, according to 0-order approach and 1 DoF system, for the 1st lobe, the following equation can be written:

$$\Omega_{\text{min}} = \frac{\omega_{th}}{N\left(1 - \frac{\arctan\left(\frac{\omega_{th}{}^2 - \omega_{\text{inf}}^2}{2\xi\omega_{th}\omega_{\text{inf}}}\right)}{\pi}\right)} \tag{4}$$

where N is the number of the tool teeth. Substituting ω_{th} expression into equation (4) and solving w.r.t. ω_{inf} , it yields:

$$\omega_{\text{inf}} = L(\xi, \alpha, N) \cdot \Omega_{\text{min}} \tag{5}$$

where L is a rather long function depending on the number of teeth, the relative damping and the error factor *α.* For instance, function L is depicted in the figure below, for N=4.

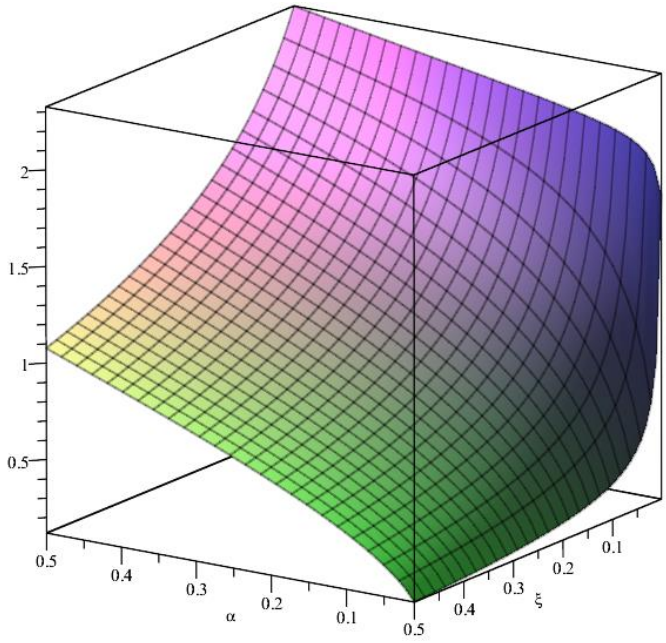


Figure 4. Function L for a tool with four cutters (N=4).

The described function is used, for a given tool and structure, to compute the lowest resonance frequency of interest.

The upper frequency limit is set assuming that, considering high order lobes (i.e. going toward the lower rotational speeds), process damping becomes important, increasing the stable depth of cut up to values that usually do not limit anymore the machining process. Typically, while computing the SLD, a maximum lobe order of 20 is considered [12]:

$$f_{SLD}^{\max} = 20 \cdot TPF^{\max} \tag{6}$$

where $f_{SLD}^{\max}$ is the maximum frequency and $TPF^{\max}$ the maximum tooth passing frequency.

4 Results

In our case the anthropomorphous robot used has an arm length about 1.5 m and a payload 16 kg. The limitis on spindle housing diameter and the overall mass are taken from a commercial electrospindle; respectively ø100 mm and $10-12kg$. The motor power is fixed at 6 kW adopting the same value of a similar commercial spindle, used for HSC machining, with a toolholder HSK25C. The small tool adopted is ø6x65 while the big one is ø12x105. They use the same cutting speed range $V_C = 400-1000\ {}^{m}\!/_{\min}$, assuming machining of Aluminium 6061, with a radial depth of cut $a_e = D/10$ and a feed per tooth $a_z = 0.05\ {}^{mm}\!/_{tooth}$.

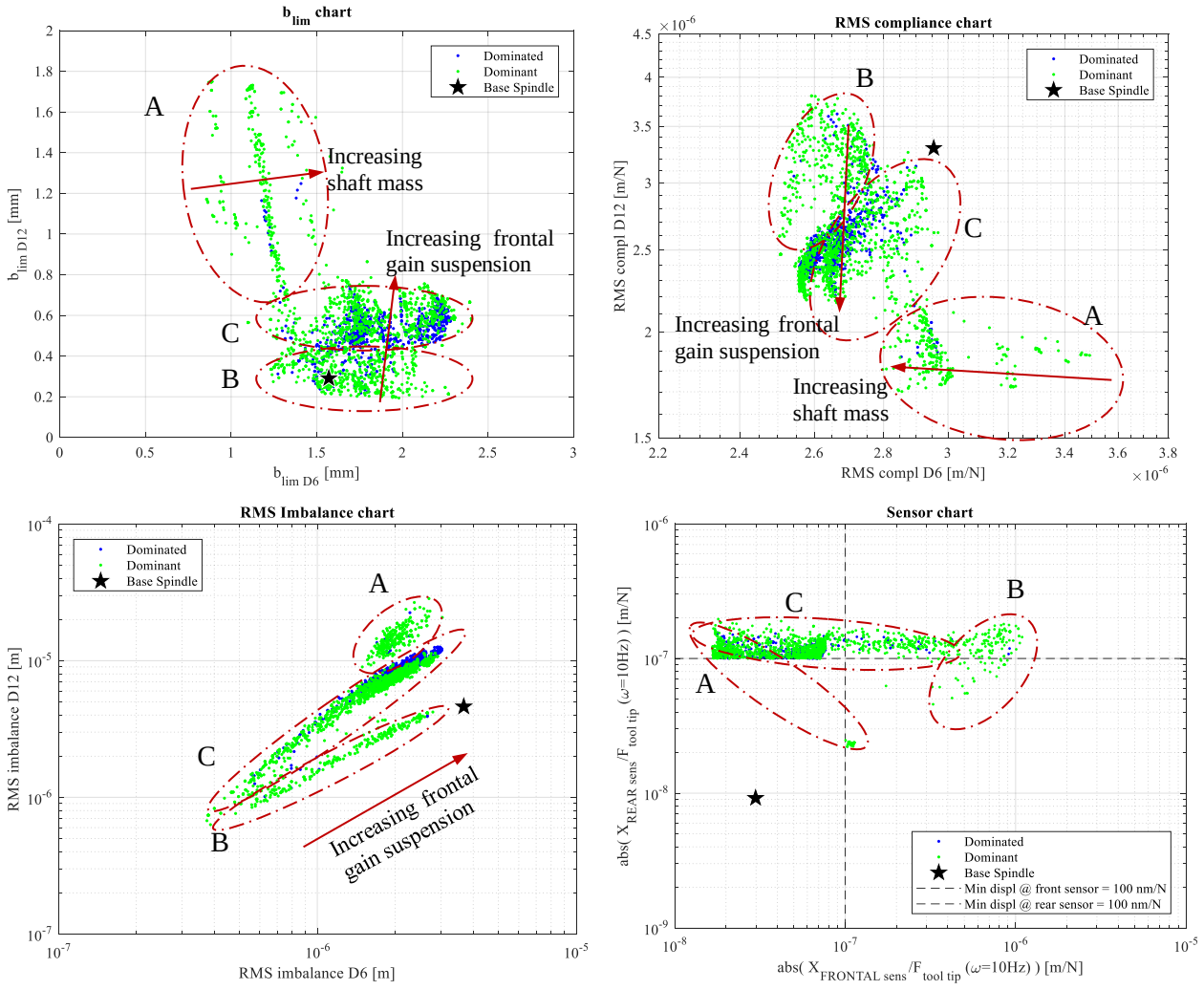
The effect of Housing's damping has been evaluate computing a quadratic Response Surface on the Dominant population (several thousand spindle configurations) for the OF $b_{\lim}$. The ANOVA shown a limited significance (p-value > 0.05), therefore the Housing's modal damping has been fixed to $\tilde{\xi} = 3\%$ in the following analyses.

4.1 Multi-objective solutions

The cloud of dominant solutions provided by the GA is represented, in the following figures, for different sections of the (DV, OF) hyperspace in order to identify clusters of similar solutions and trade-off between different OFs. The chosen planes are:

- b_{lim} for the two tools (to be maximized)
- RMS value of the dynamic compliance at the tool tip in the frequency range of the cutting forces (to be minimized)
- RMS value of the spectrum of the displacement at tool tip, caused by the 1 per turn rotational imbalance of the shaft, adopting a pessimistic grade of balancing precision of $G = 6.3 \, {}^{mm}/_{s}$ (to be minimized)
- Static displacement measured by the frontal and rear inductive sensor under a unitary radial force applied at tool tip (it must be bigger than sensor's resolution, equal to $100 \;\; nm$)
- The two DVs that represent the gain applied to the elastomeric curve. The curve is normalized in order to have the same static stiffness of the commercial spindle (very stiff and without damping) with a unitary gain.

In the following graphs are also depicted the results of the reference commercial spindle, with a comparable size (by the "Base Spindle" black star). The cloud of dominant points has been manually classified in three sets, across the different plots.



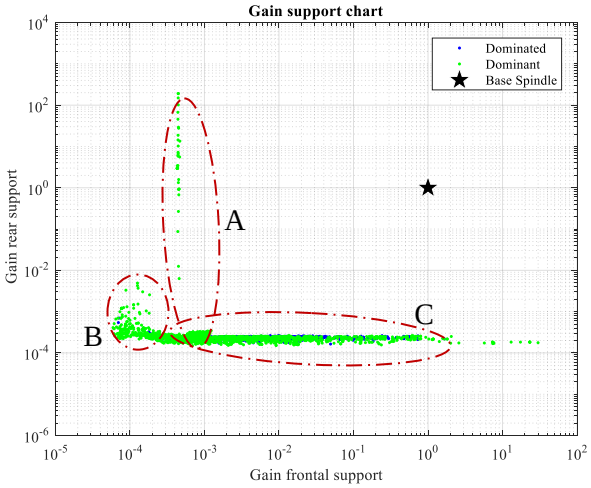


Figure 5: Pareto front for various spindle Performances and Design Variable

The three clusters are:

- Cluster A: is characterized by the "standard" bearing arrangement, where the frontal bearings are spaced (D1). The shaft is 15% stiffer and 15% lighter than the standard solution. Both front and rear suspensions are very selective (about $10^{-3}, 2 \cdot 10^{-4}$). Large improvement of the cutting performance as well as forced vibrations for the big tool (D 12 mm): 5 times the standard depth of cut. Increase of imbalance vibrations. Cutting performances of the smaller tool are more or less the same of the commercial spindle, but big improvements are noticed in imbalance vibrations. Housing's stiffness has to be increased by $+15\%$, keeping the same mass.
- Cluster B: is characterized by attached bearing configuration where B1 moves towards B2 (D3). This bearing configuration leads to a reduction of the frontal tilting stiffness. In this way, vibrations introduced by the cutting forces generate larger displacement at the rear suspension. The shaft is stiffer ($+30\% \ldots +45\%$) in comparison to the Base Spindle, but the shaft mass is basically unchanged ($-15\% \ldots +15\%$). The elastomeric suspension is quite soft both in frontal and rear side. For this reason, the inductive sensor can measure correctly in both locations. Chatter response, as well as forced vibrations, are increased only for tool D6, while for tool D12 are about the same as the commercial spindle. Appreciable improvements are noticed in the imbalance response for both tools.
- Cluster C: is characterized by attached bearings configuration where B1 moves towards B2 (D1). The elastomeric suspension must be finely tuned in the rear support while in the front support it can assume a wide range of gains. For this reason, the inductive sensor can measure always in the rear location and, for some configurations, also in the front one. Cutting performance, as well as forced vibrations, are increased for both tools. Appreciable improvements are noticed in the imbalance chart for both tools. The shaft is stiffer (about 45%) and lighter ($-30\% \ldots -15\%$) in comparison to the Base Spindle. The housing's stiffness can be reduced till $-30\% \ldots -15\%$ keeping approximatively the same mass.

4.2 Detailed analysis of sample solutions

After a global view on the trade-off between the DV and OF, let consider in this chapter, two sample solutions in detail, to better appreciate the differences between clusters A and C, reassumed in the following table:

Spindle Model	Front. Bearing config.	$K_{housing}$	$M_{housing}$	K_{shaft}	M_{shaft}	Gain of suspension frontal (rear)	$b_{lim\ D6}$ ($b_{lim\ D12}$)	RMS compliance Tool D6 (Tool D12)
EU	**-**	**-**	**-**	**-**	**-**	**-**	**mm**	**m/N**
Commercial	**Spaced**	**1**	**1**	**1**	**1**	**1 (1)**	**1.57 (0.30)**	**2.95 e-6 (3.30 e-6)**
Cluster A solution	**Attached to motor side**	**1**	**1**	**1.15**	**0.85**	**7e-4 (3e-4)**	**1.15 (1.5)**	**3 e-6 (1.8 e-6)**
Cluster C solution	**Attached to motor side**	**1**	**1.15**	**1.30**	**0.85**	**5.4e-2 (2e-4)**	**2.20 (0.85)**	**2.58 e-6 (2.21 e-6)**

Table 1: Sample solutions in cluster A and C, in comparison to the reference spindle

4.2.1 Sample solution for Cluster A

The dynamic compliance at tool tip and the SLD for this solution are depicted below.

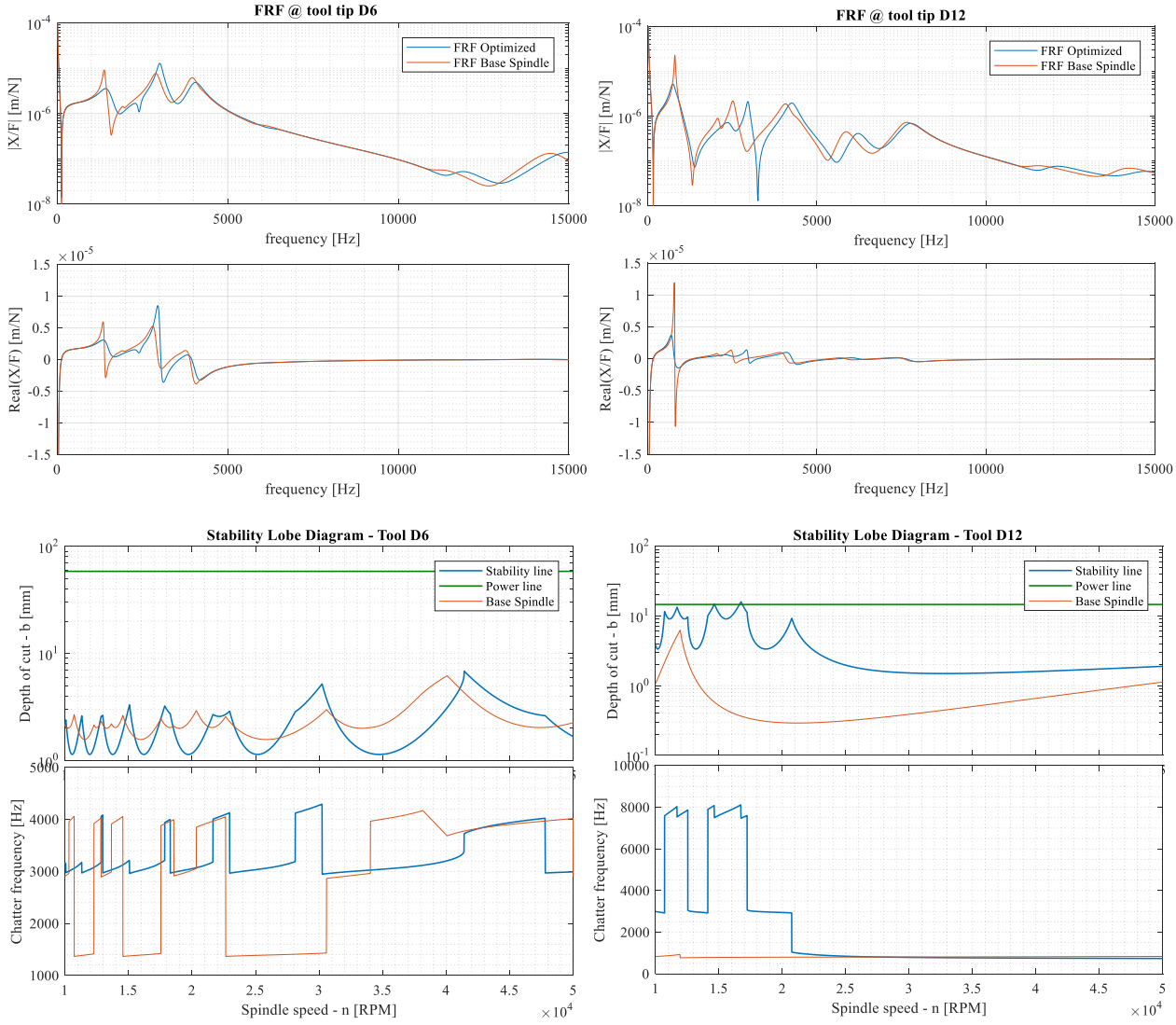


Figure 6: FRF at tool tip and SLD for tool ø6 and ø12, cluster A sample solution

In the SLD, the “power line”, indicates the depth of cut that requires the maximum available motor power.

For A cluster, strong improvements are noticed in the performances of tool D12, also confirmed by the Real part of the compliance. This is mainly due to the increased damping of the main resonances, visible in the dynamic compliance. Thanks to this strong improvement, the motor power can be better exploited and heavier machining is now possible. For tool D6, the first resonance is no more a limiting factor and the second resonance, at 3000 Hz, becomes the new constraint.

4.2.2 Sample solution for cluster C

The dynamic compliance at the tool tip and the SLD for this solution are depicted below.

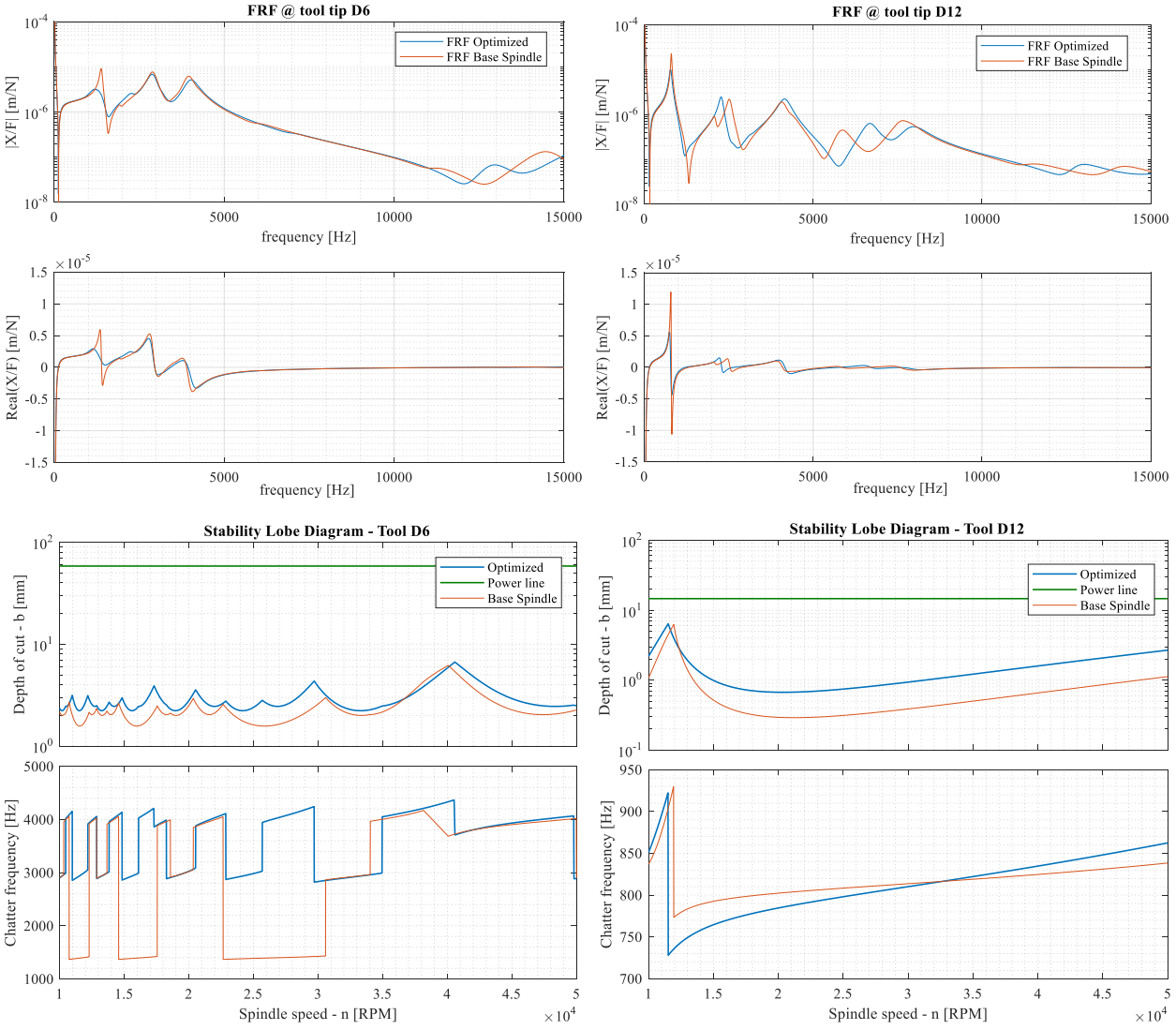


Figure 7: FRF at tool tip and SLD for tool ø6 and ø12, cluster C

Cluster C is characterized by the improvement for both tools: the first resonance of tool D6 is no more a limiting factor and for this reason, the lobe train associated to this resonance disappears in favour of the second and third resonance. For tool D12, the first resonance continues to be the constraint for the cutting process but since the height of the min(real(X/F)) became smaller, the stability line moves up.

5 Conclusions and further developments

A comprehensive Multi-Objective optimization approach has been proposed to design a spindle for robotic machining, taking into account both forced vibrations, machining instability, imbalance and critical speed. The analysis of the obtained Pareto Front allows the classification of different solution clusters. Generally, the obtained design shows a low static stiffness and an improved damping of the key resonance frequencies, bringing a significant improvement of cutting performance.

Further investigations will evaluate the possibility of realizing the prescribed stiffer and lighter spindle shaft, by a composite solution, with an hollow shafr in carbon fiber.

The next step of the study will be the experimental evaluation of the elastomeric damper performances. The validated model will be used to design the spindle, following the indications of the performed optimization, in collaboration with a spindle manufacturer. Finally, the prototype spindle will be tested, analysing the dynamic, the machining performances and the performance of the cutting force measurement system.

Acknowledgements

This work has been developed in the framework of the project Robotic Machining, a Bilateral cooperation project between CNR / Institute for Industrial Technologies and Automation and RFBR / Moscow State University of Technology "STANKIN" (msut "STANKIN"), from 2015 to 2017, with the technical collaboration of the spindle builder Capellini SRL.

References

[1] Denkena, B., Bergmann, B., & Lepper, T. (2017). *Design and optimization of a machining robot.* Procedia Manufacturing, 14, 89–96. https://doi.org/10.1016/j.promfg.2017.11.010

[2] Iglesias I., Sebastiàn M.A., Ares J.E., *Overview of the state of robotic machining: Current situation and future potential*. Procedia Engineering, Vol 132, 2015, Pag 911-917.

[3] M. Leonesio, E. Villagrossi, M. Beschi, A. Marini, G. Bianchi, N. Pedrocchi, L.M. Tosatti, V. Grechishnikov, Y. Ilyukhin, A. Isaev, Vibration Analysis of Robotic Milling Tasks, Procedia CIRP. 67 (2018) 262–267. doi:10.1016/j.procir.2017.12.210.

[4] Y. Chen, F. Dong, *Robot machining: recent development and future research issues*, Int. J. Adv. Manuf. Technol. 66 (2013) 1489–1497. doi:10.1007/s00170-012-4433-4.

[5] C. Lehmann, M. Halbauer, D. Euhus, D. Overbeck, *Milling with industrial robots: Strategies to reduce and compensate process force induced accuracy influences*, Proc. 2012 IEEE 17th Int. Conf. Emerg. Technol. Fact. Autom. (ETFA 2012). (2012) 1–4. doi:10.1109/ETFA.2012.6489741.

[6] Quintana G., *Chatter in machining process: A review.* International Journal of Machine Tools & Manufacture, Vol. 51, (2011), page 363-376.

[7] Altintas Y. *Manufacturing automation: metal cutting mechanics, machine tool vibrations, and CNC design.* 2nd edition. New York: Cambridge University Press; 2012.

[8] Altintas Y. and Budak, E., *Analytical prediction of stability lobes in milling*, Annals of the CIRP, Vol 44, (1995), page 357-362

[9] Abele E., Altintas Y., Brecher C., *Machine tool spindle units.* CIRP Annals – Manufacturing Technology, Vol 59, 2010, page 781-802.

[10] Altintas Y., Cao Y., *Virtual Design and Optimization of Machine Tool Spindles.* CIRP Annals, Vol 54, pages 379-382 .

[11] Albertelli P., Facciotti G., Leonesio M., Bianchi G., Monno M., *Model-Based Design of Electro-Spindles for High Performance Machining*, CIRP ICME '10 - 7th CIRP International Conference on Intelligent Computation in Manufacturing Engineering, 23-25 June, Capri, Italy.

[12] Cau N., Leonesio M., Zanotti E., Parenti P., Bianchi G. (2009), *Integrated Machine Tool Design*. In: 2nd International Researchers Symposium on INNOVATIVE PRODUCTION MACHINES AND SYSTEMS (IPROMS 2009). 22 - 24 July 2009, Ischia, Italy. ISBN: 978-88-95028-38-5.

[13] Zhang X., Zhu L., Zhang D., Ding H., Xiong Y., *Numerical robust optimization of spindle speed for milling process with uncertainties*. International Journal of Machine Tools and Manufacture. Vol 61, Oct 2012, pages 9-19

[14] Liebich R., Scholz A, Wieschalla M., *Rotors supported by elastomer-ring-dampers – Experimental and numerical investigations.* 10th International Conference on Vibrations in Rotating Machinery, Dec 2012

[15] Bonfitto A., Tonoli A, Amati N., *Viscoelastic Dampers for rotors: Modelling and Validation at component and System Level*, Applied Science, Vol 7, No 11, 2017

[16] M. F. Zaeh and O. Roesch, "*Improvement of the machining accuracy of milling robots*" Prod. Eng. Res. Devel., vol. 8, no. 6, pp. 737–744, 2014.

[17] B. Denkena and T. Lepper, "*Enabling an Industrial Robot for Metal Cutting Operations*" Procedia CIRP, vol. 35, pp. 79–84, 2015

[18] P. Albertelli; G. Bianchi; M. Monno. *Motor Spindle Modelling and Experimental Characterization*. 2017 10th CIRP International Workshop on Modelling of Machining Operations.

[19] EAR *Standard parts catalog and Engineering Design Guide*, www.earsc.com

[20] Craig R.R., Bampton M.C.C, *Coupling of Substructures for Dynamic Analysis*, AIAA Journal, Vol 6, No 7, July 1968, page 1313-1319

[21] Della Pietra L. Adiletta G., *The Squeeze Film Dampers Over Four Decades of Investigations. Part I: Characteristics and Operating*. The Shock and Vibrations Digest, Vol 34, pages 97-126. March 2002.

[22] MATLAB, *Gloabal Optimization Toolbox User's Guide*. Version 3.4.2, March 2017

Experimental and numerical mode shape tracing from components to whole motorbike chassis

E. Bonisoli[1], D. Lisitano[1], L. Dimauro[1]
[1] Politecnico di Torino, Department of Mechanical and Aerospace Engineering
Corso Duca degli Abruzzi, 24 - 10129 Torino, Italy
e-mail: **elvio.bonisoli@polito.it**

Abstract
This paper aims to analyse the most influent component mode shapes on the dynamic properties of a whole motorbike frame. Experimental and numerical modal analyses have been carried out on chassis, swingarm, engine, wheel and different subsystems of increasing complexity. The component global modes shapes are traced from component to assembly with both Modal Assurance Criterion. The most influent mode shapes of each component are highlighted and their effects on the global motorbike dynamics are discussed. The component to assembly method results to be a preliminary tool to have an objective evaluation of the most important modes of components on which possible improvements can be suggested.

Keywords: motorbike dynamics, Experimental Modal Analysis, Numerical Modal Analysis.

1 Introduction

The study of the dynamic behaviour of a motorbike has some fundamental differences with respect to the much more studied automobile dynamics. Motorcycles are inherently unstable and they move in three dimensions, instead an automobile largely moves in two dimensions. Hence, the primary target of a motorbike design is to avoid that its instability occurs during normal functionality. Relevant effects on the motorbike dynamics take place when motorbikes are cornering at large roll angles because the motion of the tyres is no longer in plane with the suspension system. During this phase, the main components, like chassis and swingarm, significantly affect the global dynamic response of the system. In these circumstances also the joints that connect the several components, as the rear shock absorber, play a fundamental role, since their stiffness strongly influence motorbike stability and also durability and integrity of tyres. Currently, the dynamic performance of a motorbike chassis is evaluated only through on road tests necessary to have bikers' feedbacks.

In the last decades, many authors developed mathematical models with rigid bodies to simulate the dynamic behaviour of motorcycles. Flexible elements to simulate the frame are implemented in [1]. In particular, the wheel has a predominant effect on the global dynamics. The multibody approach is used in [2] where a rigid multibody model of the motorbike is developed and simulations results under sudden braking and impacts with curbs were compared to the experimental ones, in order to characterise the intrinsically unstable behaviour of the motorcycle. Moreover, flexible body models were assumed for the rear swingarm and for the body, comparing the results with the rigid body model. Using the same manoeuvres, also the dynamic response of the rear shock absorber and vibration response and drivability of the motorbike were studied.

Lake et al. [3] propose an historical overview on motorcycle dynamics highlighting that its behaviour is described by three physically significant modes at low frequency. They are related respectively to: motorcycle instability (capsize), global side-to-side motion of the entire vehicle (weave) and rotation of the front frame relative to the main frame (wobble). The impact of the chassis flexibility on fundamental

modes is also presented; the material properties of chassis and swingarm influence the fundamental modes.

The frame is usually an important part of any two wheeler and it should be strong enough to support loads, twist, vibrations and other stresses acting on the vehicle. It is like a skeleton upon which parts like gearbox and engine are mounted. Therefore, the chassis should not buckle on uneven road surfaces. A numerical modal analysis was performed on two models of two-wheeler chassis [4-5], trying to reduce undesired vibrations and obtain a satisfying weight reduction improving material, while in [6] Dixit et al. performed a numerical modal analysis on a rear swingarm, trying to understand and to model its structural dynamics. The numerical results, calculated under different load variations, were used as basic for an optimisation process of the component through hardening treatment, in order to increase the strength and to improve the suspension arm life.

The numerical model has been updated and its correlation with the experimental results is quite good. The main aim of this paper is to trace the whole motorbike dynamics, moving from component to assembly. The method is applied both numerically and experimentally to compare the results.

The paper is organised as follow: in §2 the experimental and numerical analysis on component and assemblies are presented, with relative comparisons. In §3 the component mode shapes are traced from component to assembly; the influence of the components is discussed. Finally, some considerations regarding the most influent modes and their impact on motorbike performance are presented.

2 Experimental and numerical modal analysis

The motorbike, object of this research activity, is developed and produced by Mahindra Moto3 Racing Team for the World Championship of 2017. Only the main structural components were studied: chassis (Fig. 1, a), swingarm (Fig. 1, c), engine (Fig. 1, b) and rear wheel (Fig. 1, d). Two subsystems (Fig. 1, e and f) and the complete assembly (Fig. 1, g) are also analysed in order to describe the whole motorcycle dynamics moving from component to assembly. The interaction with the tyre and pavement is neglected.

The chassis and the swingarm are two boxes structures in aluminum alloy, made up of several parts connected through welding points. The internal cavities are used for electronic cables and lubricant oil. The wheel is made of magnesium and aluminum alloy, manufactured by multi-directional forging in order to ensure an extremely lightweight component with improved mechanical properties. The wheel includes the transmission pinion and the rear brake disk. It presents seven spokes with curved shape geometry.

The engine is produced in foundry aluminum. In the first subsystem, chassis with engine, the engine sits inside the chassis and it is connected to the frame using three steel pins. The wheel is connected to the rear swingarm using another pin in order to perform the second subsystem. Finally, the connection of the whole assembly is realised by a pivot bolt linking chassis, swingarm and a leverage connected with the rear shock-absorber.

2.1 Experimental modal analysis

The experimental modal analysis (EMA) is carried out on the actual motorbike frame and all the components are shown in Fig. 1. The engine was considered only as an added rigid mass, thus any EMA was carried out only on it alone. Roving hammer experimental modal analysis was performed on components, sub-assemblies and full assembly in free-free conditions. The structure response is measured using two mono-axial and two tri-axial accelerometers connected to a Siemens SCADAS mobile. LMS Test.Lab software is used for modal data acquisition and analysis.

The excitation points for each configuration are selected in according with MoGeSeC criterion [7] to obtain a good compromise between geometry representation and expected motorbike modal behaviour. The number of excited DoFs and the number of identified modes in each configuration are reported in Table 1. The identification of component modal properties results quite clean: as expected the components

are very low damped, the mode shapes are almost completely orthogonal and the synthetised FRFs are in very good agreement with the experimental ones. The same considerations are also confirmed in the two sub-assemblies and in the full assembly, with an increasing value of damping ratio due to the increasing number of contacts, even if the system continues to be almost linear.

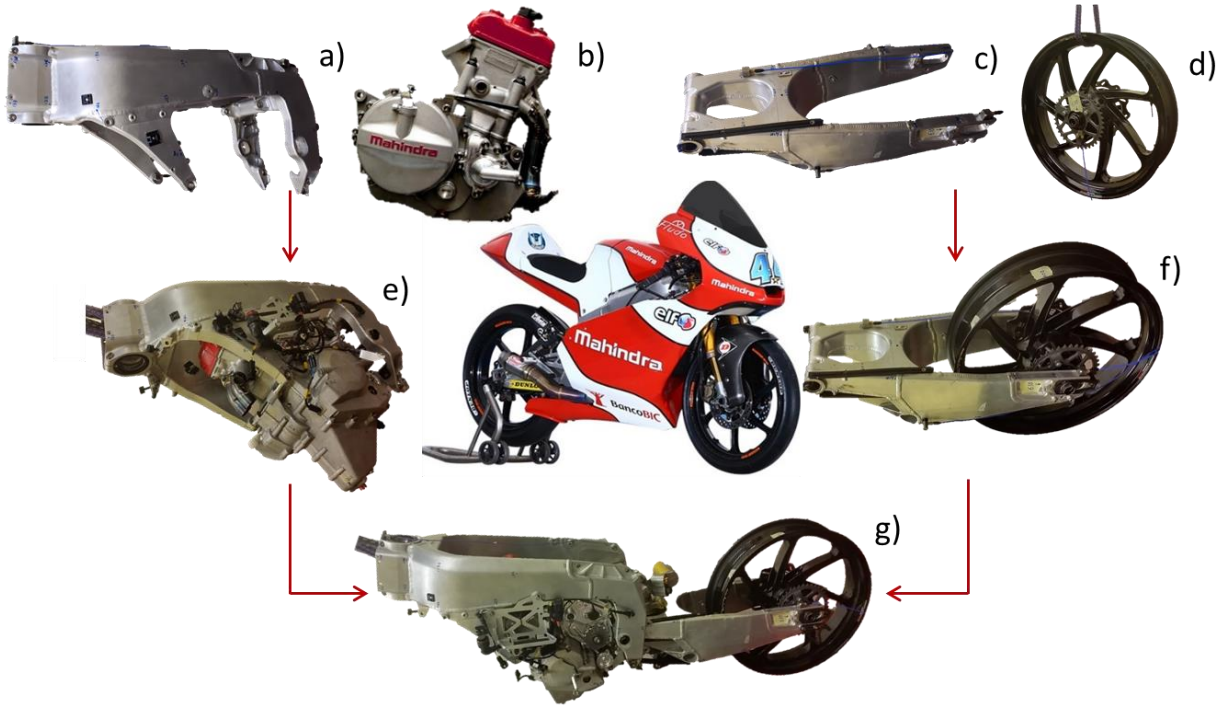


Figure 1: Components (a, b, c, d), sub-assemblies (e, f) and full motorbike assembly (g)

Configuration	DoFs	# of identified resonances	Frequency range
chassis	90	20	0÷1000
swingarm	60	16	0÷1500
wheel	22	14	0÷1000
chassis – engine	106	14	0÷1000
swingarm – wheel	77	20	0÷1000
chassis – engine – swingarm – wheel	164	37	0÷1000

Table 1: EMA excited nodes and modal shapes

2.2 Numerical modal analysis

The CAD model reproduces all the components including steel pins, leverage and shock absorber used to assembly the motorbike frame. Each component is made of several part welded together, modelled as bonded contact between flexible bodies in the finite element model. In the first sub-assembly four pins are used to connect the engine to three points on the chassis. The engine is considered as a rigid body, therefore rigid connections are used to model its contacts with the chassis. One steel pin and the relative blocking plates link the rear wheel to the swingarm. Finally, the connection between the two sub-assemblies is obtained using the leverage system between chassis and swingarm, including the rear shock absorber and a steel hollowed pivot between chassis and swingarm. The rear shock absorber translation is blocked, as in the experimental analysis. The numerical models are shown in Fig. 2. Each of the

experimental configurations is also numerically analysed, using Ansys software. In the finite element analysis (FEA), the geometries are discretised using tetrahedral solid mesh. Real modal analysis is performed, therefore no damping effect is considered. The size of each model and the number of computed mode shapes are reported in Table 2.

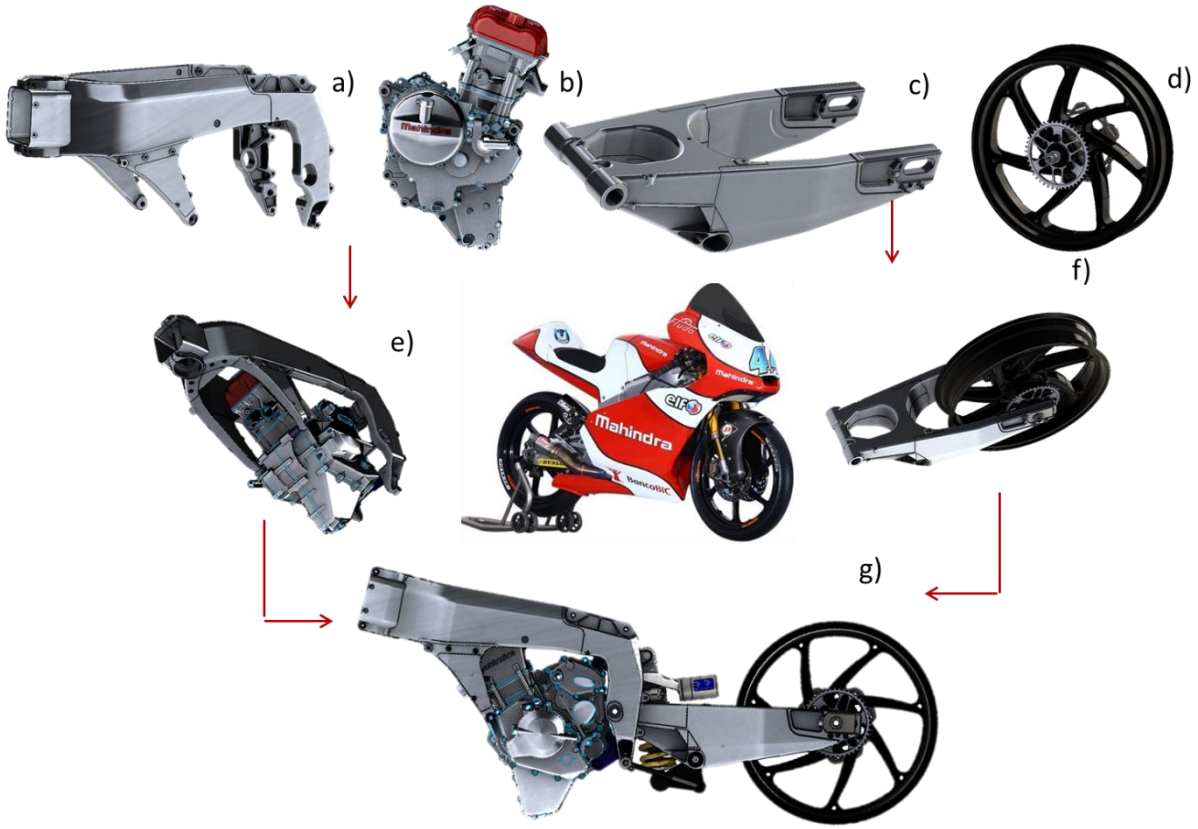


Figure 2: Components (a, b, c, d), sub-assemblies (e, f) and full motorbike assembly (g)

Configuration	DoFs	# of identified resonances	Frequency range
chassis	2218338	27	0÷1350
swingarm	721176	14	0÷1600
wheel	1979784	34	0÷1600
chassis – engine	1471554	14	0÷1000
swingarm – wheel	2684886	34	0÷1250
chassis – engine – swingarm – wheel	3503976	26	0÷750

Table 2: FEA excited nodes and modal shapes

2.3 EMA – FEA comparison

The modal properties obtained from experimental tests and numerical analysis for each component are compared through the well-known Modal Assurance Criterion (MAC) Eq. (1) [8]. It is defined as the normalised scalar product between two modes j, and k. Hence it results equal to 100% if two modes are identical, while it reaches 0% if they are orthogonal:

$$MAC_{j,k} = \frac{\left[\boldsymbol{\varphi}_j^T \boldsymbol{\varphi}_k\right]^2}{\left[\boldsymbol{\varphi}_j^T \boldsymbol{\varphi}_j\right]\left[\boldsymbol{\varphi}_k^T \boldsymbol{\varphi}_k\right]} \tag{1}$$

Material densities were updated to have a comparable weight between the real component and the model. The Young modulus of each component is tuned using Eq. (2), to have comparable natural frequencies in experimental and numerical analysis [9]:

$$\Delta E = E(\varepsilon^2 - 1) \text{ and } \varepsilon = \sum_{r=1}^{n}\left[\frac{\omega_{exp,r}}{\omega_r}\right]^2 \Big/ \sum_{r=1}^{n}\frac{\omega_{exp,r}}{\omega_r} \tag{2}$$

where the not dimensional parameter ε is evaluated with respect to unitary values, according to a minimization of the sum of *r* natural frequencies ω_r of the coupled EMA vs. FEA mode shapes in a least mean square sense.

The resulting density and Young modulus of each component are reasonably close to the material literature values for all the components. Weight, Young modulus and density of each component are shown in Table 3.

Component	Weight [kg]	Young modulus *E* [GPa]	Density [kg/m^3]
chassis	5.132	69.43	3064
swingarm	3.715	64.62	2815
wheel	2.203	19.05	1159

Table 3: Material properties of components

The MAC matrices between experimental and numerical results of the three components are reported in Fig. 3. The systems modes are spaced with respect to the corresponding natural frequencies: if the EMA and FEA analyses are perfectly aligned, the iso-frequency is a straight 45° inclined line (black dashed lines in Fig. 3).

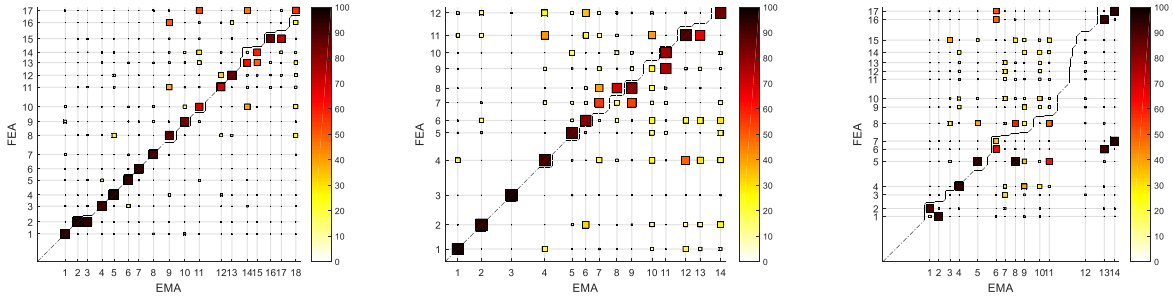


Figure 3: EMA – FEA MAC matrices: chassis (left), swingarm (middle), wheel (right)

The modal analysis of the chassis model is in very good agreement with the experimental results (Fig. 3, left), the first 18 experimental mode shapes are very well reproduced by the FEM model both in shapes and natural frequency. The mean MAC value on all the mode shape is 82.30%. Also the swingarm model gives quite robust results (Fig. 3, middle): the first 6 mode shapes are in very good agreement, with a mean MAC value of 85.32%. At higher frequency the MAC value is slightly lower, but however the mean MAC value results 85.11%. The wheel model is even aligned (Fig. 3, right). Indeed, also for this component six global mode shapes are very well replicated by the model either as mode shapes and as natural frequencies. More complex or localised modes are not very well aligned due to the low number of point tested in the experimental campaign.

The two sub-assemblies and the full assembly, called motorbike later, are also compared with the relative FEM models, as shown in Fig. 4.

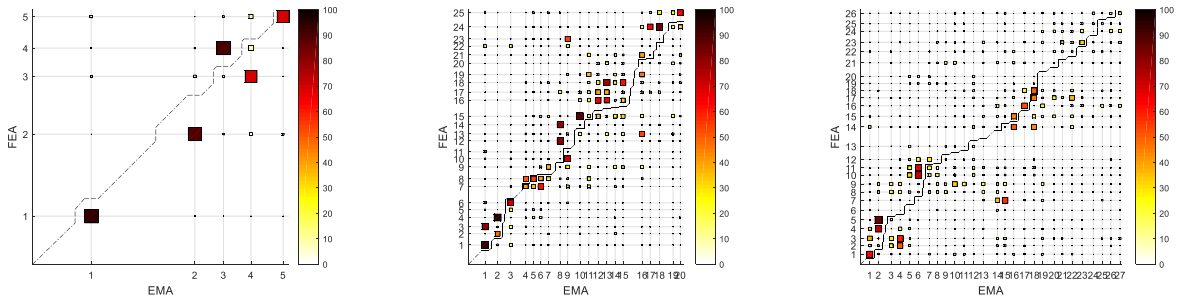


Figure 4: EMA – FEA MAC matrices:
chassis and engine (left), swingarm and wheel (middle), motorbike (right)

The model of the chassis with the engine includes also four steel pins, linking the two components. The unique updating parameters are the material properties of these pins, because chassis was already updated and the engine is considered as a rigid body. The natural frequency of some chassis modes decreases, due to the added mass, while for others it increases, due to the added stiffness. The first five modes are quite aligned both in shapes and natural frequencies with a high value of correlation. The 3rd and 4th mode shapes, quite close in frequency, are switched between EMA and FEA.

The model of the swingarm with the wheel includes the already updated components, and the hollowed steel rod with two aluminum plates to block the wheel. Only the stiffness of the hollowed rod can be updated. The MAC is quite diagonal; the modes at lower frequencies are better described. The numerical model presents many modes in the same frequency range, due to couples of modes of the wheel that are not always well identified in the experimental results.

The complete model is obtained assembling the two sub-assemblies with the pivot, leverage and rear shock absorber. The MAC is enough orthogonal; all the correlated couples of EMA and FEA mode shapes are really closed to the iso-frequency line, therefore also the corresponding natural frequencies are close.

The numerical model seems to be quite accurate and robust to describe the analysed system vibrational dynamics.

3 Mode shape tracing

The main aim of this work is to trace the components mode shapes in the sub-assembly and full assembly of the motorbike frame, to understand which of the component mode shapes are influent in the complete motorbike assembly. The target can be achieved comparing the mode shapes of the sub-assemblies and components. The MAC from component to assembly gives detection of the component mode shapes still visible in the assembly. The detection of the component mode shapes in the assembly is performed using Modal Assurance Criterion, Eq. (1). The mode shapes of each component are compared with the relative sub-assembly, and the two sub-assemblies are compared with respect to the motorbike.

Five comparisons are performed: 1) chassis / chassis and engine; 2) swingarm / swingarm and wheel; 3) wheel / swingarm and wheel; 4) chassis with engine / motorbike; 5) swingarm with wheel / motorbike. The analysis is performed using both experimental and numerical data.

In Table 4 the chassis modes are traced in the chassis with engine sub-assembly and finally in the complete assembly. Four chassis modes are followed in the three systems in both experimental and numerical modal analysis: the vertical bending of the chassis, the global torsion of the chassis and two horizontal bending in phase and out of phase.

Three swingarm modes are traced up to the complete motorbike: the swingarm horizontal bending in phase and out of phase and the torsion. Also the wheel modes are traced up to the full assembly; four modes are followed: the first bending with respect to the rotation axis, the first global wheel bending, a drum mode and a bell mode. The torsion of both chassis and swingarm are shown in Tables 4-5.

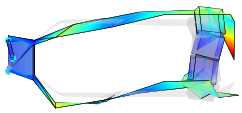
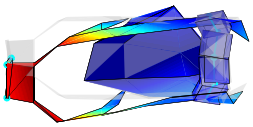
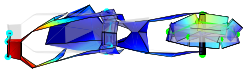
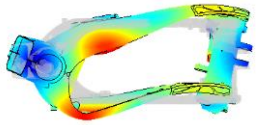
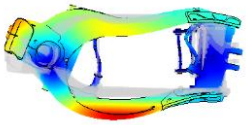
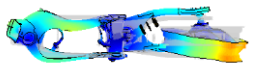
Chassis	Chassis+engine	Motorbike	MAC	Description
			4-1: 8.10% 1-4: 96.92%	Torsion
4) 309.1 Hz	1) 177.5 Hz	4) 177.6 Hz		
			3-3: 32.04% 3-15: 47.07%	
3) 303.4 Hz	3) 485.5 Hz	15) 480.5 Hz		

Table 4: Mode shape tracing chassis

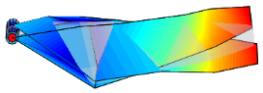
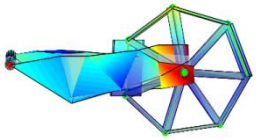
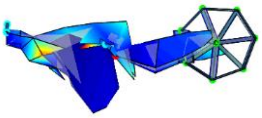
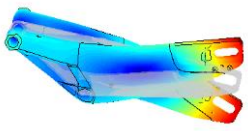
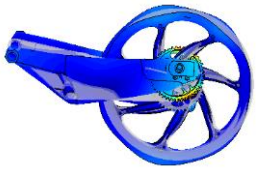
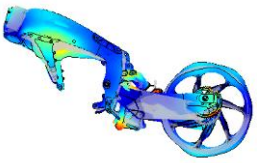
Swingarm	Swingarm+wheel	Motorbike	MAC	Description
			3-10: 76.80% 10-23: 38.76%	Torsion
3) 494.8 Hz	10) 607.4 Hz	23) 650.7 Hz		
			3-16: 76.80% 16-22: 76.49%	
3) 495.5 Hz	16) 634.9 Hz	22) 634.4 Hz		

Table 5: Mode shape tracing swingarm

The torsion of the chassis is highlighted in both the sub-assembly and in the final assembly. This confirms what is presented in [10]; this mode is quite exited during high speed curves [11-12]. The torsion of the swingarm is traced in the relative sub-assembly and quite well also in the final motorbike assembly. This mode shape is very excited when coming into corners. Hence the composition of both the torsional modes is quite important for the stiffness of the motorbike during cornering. The four wheel modes founded in the two-wheel vehicle are quite influent also in the global motorbike behaviour in the interested working frequency range. The first two modes are structural modes excited during curves, the others are bell modes very important for the vibration comfort, but especially for tyre performance during races, because their vibrations are directly transferred to the bikers through the frame. In this context also the chassis flexibility takes a fundamental role in vibration reduction for a major comfort and drivability sensation.

Conclusions

The modal behaviour of a racing complete motorbike, manufactured by Mahindra racing team, has been investigated from an experimental and numerical point of view, to understand the role of each component of the global motorbike dynamics. A very good agreement between component models and relative

experimental outcomes is obtained. The different subsystems are tuned through the updating of the elastic properties of the joints between the different components to improve the model robustness.

The single component modes evolution is traced, increasing subsystems complexity up to the full motorbike. Chassis, swingarm and rear wheel of the motorbike are assumed as the primary components. Modal assurance criterion is used to follow the primary components mode shapes in the structure up to the whole motorbike chassis. The bending and twisting swingarm mode shapes result to be traceable increasing the number of system components.

Acknowledgements

The authors would like to thank Mahindra Moto Racing for the material provided and for the opportunity to involve the authors in this interesting work regarding motorcycle dynamics. Grateful thanks to Prof. Lorenzo Peroni, supervisor of Politecnico di Torino Racing Team called 2Wheels, and to Eng. Rosario Di Corte for their support and interaction with Mahindra Racing Team.

References

[1] S.M. Olivieri, M. Calì, L. Catalano, *Dynamics of motorcycle using flexible elements, International Design Conference*, Dubrovnik, Croatia, (2002), pp. 1227-1236.

[2] G., Ferretti, B. Scaglioni, A. Rossi, *Multibody model of a motorbike with a flexible swingarm*, *Proceedings of 10th International Modelica Conference*, Lund, Sweden, (2014), pp. 273-282.

[3] K. Lake, R. Thomas, O. Williams, *The influence of compliant chassis components on motorcycle dynamics: an historical overview and the potential future impact of carbon fibre*, International Journal of Vehicle Mechanics and Mobility, Vol. 50, No. 7, (2012), pp. 1043-1052.

[4] B.B. Harshal, *Study of experimental modal analysis on two wheeler frame*, International Journal of Engineering, Science & Research Technology, Vol. 4, No. 7, (2015), pp. 2518-2520.

[5] S. Hiremath, N. Kumar, G. Nagareddy, L. Rathod, *Modal analysis of two wheeler chassis*, International Journal of Engineering, Science & Research Technology, Vol. 5, No. 7, (2016), pp. 68-73.

[6] V.S. Dixit, M.R. Nukulwar, S.T. Shinde, S.S. Pimpale, *Vibration response and optimization of swing arm through hardening*, International Journal of Current Engineering and Technology, Vol. 6, No 2, (2016), pp. 562-567.

[7] E. Bonisoli, C. Delprete, C. Rosso, *Proposal of a modal-geometrical-based master nodes selection criterion in modal analysis*, Mechanical Systems and Signal Processing, Vol. 23, (2008), pp. 606-620.

[8] R.J. Allemang, D.L. Brown, *A correlation coefficient for modal vector analysis*, *Proceedings of IMAC*, (1982), pp. 110-116.

[9] E. Bonisoli, C. Rosso, C. Delprete, F. Stratta, *Inverse eigensensitivity approach in model updating of avionic components*, *Proceedings of 30th IMAC*, Jacksonville, Florida, USA, (2012), pp. 149-165.

[10] M. Bocciolone, F Cheli, M. Pezzola, R. Viganò, *Static and dynamic properties of a motorcycle frame: experimental and numerical approach*, *WIT Transactions on Modelling and Simulations*, Vol. 41, (2005), pp. 517-526.

[11] V. Cossalter, A. Doria, M. Massaro, L. Taraborrelli, *Experimental and numerical investigation on the motorcycle front frame flexibility and its effect on stability*, Mechanical Systems and Signal Processing, Vol. 60-61, (2015), pp. 452-471.

[12] V. Cossalter, *Motorcycle dynamics*, Lulu, Morrisville, North Carolina, USA, (2006).

Accurate product model development for the simulation of the dynamic behaviour of deep drawn components

F. Greco [1,2], **E. Deckers** [1,2,*], **J. Stroobants** [3], **S. Van Poppel** [3], **F. Maurin** [1,2], **W. Desmet** [1,2]
[1] KU Leuven, Department of Mechanical Engineering,
Celestijnenlaan 300 B, B-3001, Heverlee, Belgium
[*] Corresponding author. E-mail address: **elke.deckers@kuleuven.be**

[2] DMMS-D core lab, Flanders Make, Belgium

[3] CoDesignS core lab, Flanders Make vzw,
Oude Diestersebaan 133, B-3920 Lommel, Belgium

Abstract
The intrinsic variability of the deep drawing process and the local variations of the stiffness of the manufactured components, due to plastic hardening and residuals stresses, give rise to nominally identical components with different dynamic properties. This work considers two simulation frameworks for an accurate product model development: the first one is based on a purely numerical approach while the second one consists in a reverse engineering framework, where the product model is computed starting from laser scan measurements on the manufactured component; this procedure can be realized either by (i) a triangular surface reconstruction that forms the starting point to obtain a finite element mesh or by (ii) fitting a smooth B-spline surface on the point cloud data that can be used directly for the analysis employing the paradigm of isogeometric analysis (IGA). In this context, it is also shown how a model updating procedure of the stiffness can be easily implemented using IGA, to further improve the accuracy of the product model.

1 Introduction

Deep drawing is a manufacturing process widely used in, among others, automotive industry to create nearly finished products at high volume rates, starting from a blank sheet material [1]. Because of the large deformations involved in the process, predicting the exact shape of the manufactured component is a quite challenging task but still important for the correct evaluation of its performance. The two main factors that drive the shape change of the manufactured component and its relative variability, with respect to the nominal CAD design, are the thinning/thickening phenomenon and the residual stresses. The former correspond to a change of the thickness with respect to the initial values of the blank, while residual stresses have a non-zero resultant in terms of bending moment and, therefore, they cause a shape change often referred to as the spring-back [2, 3] effect. In addition, the dynamic stiffness of the component is also altered because of their presence [4, 5].

Based on these considerations, it is evident that an accurate product model is necessary for the performance analysis of a deep drawn component, especially in the context of dynamic vibrational and vibro-acoustic simulations. In fact, the dynamic behaviour of a product can vary significantly because of small geometrical details, with this phenomenon becoming particularly relevant in the mid-to high frequency range, where structural wavelengths are smaller than the characteristic dimensions of the product [6, 7]. Although the numerical simulation of deep drawing has been widely treated in the literature [8, 9], predicting the vibro-

acoustic behaviour of the final component is a research direction that has been only recently initiated [10, 11, 12]. In two recent works [13, 14], the authors of this paper considered the development of an accurate product model using respectively the classical finite element method (FEM) and the recently introduced paradigm of isogeometric analysis (IGA) [15, 16].

The most convenient approach for the product model development is a purely numerical framework, where in a first step the forming process is simulated and then a product model with the correct thickness distribution, mapped from the forming simulation results, is created [13]. However, even if the forming process is accurately simulated, the results cannot take into account the intrinsic variability involved in the deep drawing process and, therefore, a geometrical error will be present in the model.

To improve the results, the product model can be reconstructed starting from surface measurements on the actual manufactured component. In particular, a point cloud can be gathered using a laser scanning system [17, 18] and, after processing the data, either an FEM [13] or an IGA model [14] can be created. These product models, reconstructed from the real geometry, provide a more accurate framework for the numerical vibro-acoustic simulations but some error is still present since the stiffness of the numerical model does not (locally) match that of the component. The original value of the Young's modulus of the blank should be characterized, however can still change locally because of plastic straining [19, 20]. And, in addition, the residual stresses are also altering the dynamic stiffness of the product. Therefore, for a higher level of accuracy, model updating becomes necessary [21].

This work reviews the procedure of the FEM and IGA models creation, as described in [13] and [14], for the specific case of a DP600 steel cup, and then considers a model updating procedure of the material stiffness implemented in the framework of IGA. In fact, in this context IGA is a particularly convenient tool because the same basis functions are used to describe both the geometry and the solution field and, therefore, an optimization procedure can be realized by directly updating the geometrical and material parameters, without resorting to the expensive procedure of mesh generation. Thanks to this property, IGA has been shown already to provide excellent results when applied e.g. to structural shape optimization [22, 23]. In a similar fashion, IGA is used in this work to employ a parametric description of the Young's modulus and to directly update it throughout the optimization procedure.

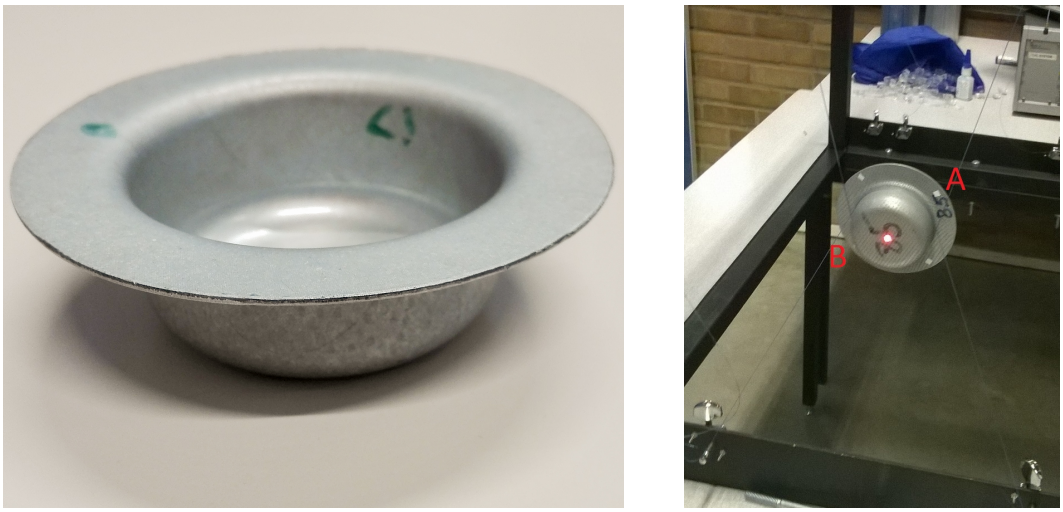
The outline of the paper is the following: in Section 2 the studied component is briefly described. Section 3 considers the development of a product model with the purely numerical approach, while Section 4 considers the development of a product model based on surface measurements. The model updating procedure proposed in this work is then presented in Section 5 and concluding remarks follow.

2 The case study

A DP600 [24] steel cup is considered in this work and is depicted in Fig. 1a. The cup is produced from a circular blank with a diameter of 100 mm and a nominal thickness of 0.97 mm, while applying a blank-holder force of 45 kN and a drawing depth of 24 mm. These parameters are chosen in a way to avoid rupture and defects such as tearing, earing, wrinkling and necking[1]. The final weight of the cup is approximately 60 g.

In order to assess the validity of the numerical product models, the dynamic behaviour of the component is tested experimentally. In particular, according to Fig. 1b, it is opted to mimic free-free boundary conditions. This is obtained by fixing the cup with two thin nylon strings. The structural displacement of the cup is measured using a *Polytec PSV-500 Scanning Vibrometer*. This laser scanning vibrometer is preferred to accelerometers to avoid the addition of mass that may change the dynamic behaviour of this light-weight component. The cup is excited with a hammer with impedance head type *PCB 086C03*.

Referring to Fig. 1b, where the reflecting labels used for the measurements are visible, the cup is hammered in point A and the frequency response function (FRF), measured in point B, is considered in this work and is used to validate the numerical models. The first nine natural frequencies are also extracted from the FRF measurement and used for validation.



(a) (b)

Figure 1: The studied component (a) and the set-up of its experimental testing (b).

3 Development of a product model through a forming simulation

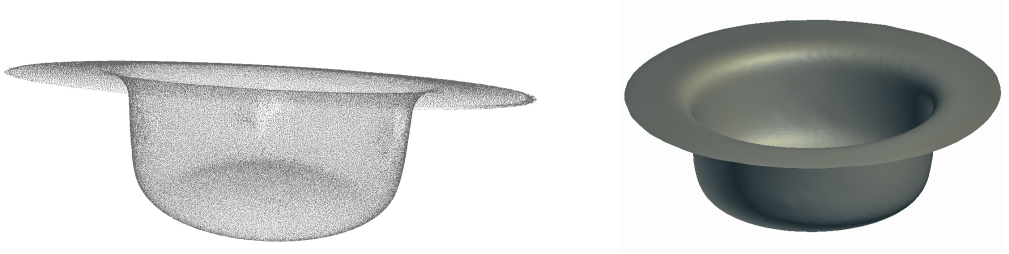
In order to obtain a first and less expensive evaluation of the performance of a component, an accurate process simulation can be the starting point for the creation of a product model, which is then used for the numerical analysis. In this work the dynamic behaviour of the product is considered. For the case study described in the previous section, the creation of a product model is obtained in [13] starting from a forming simulation with the commercial code Autoform and the Incremental module, which uses shell elements with an implicit time integration scheme [1]. The material behaviour is described through the following properties:

- for the hardening curve, the Ludwik law [25] is chosen and the strain hardening exponent, the yield strength and the ultimate tensile strength have to be specified;
- for the yield surface, the Hill criterion [26] is chosen and the normal anisotropy coefficients have to be specified;
- for the forming limit curve (FLD), the Arcelor V9 model [27] is chosen.

The mechanical characteristics of the material, to be used in the above laws, are determined by tensile tests. A proper choice of the friction coefficient is also crucial for the accurate simulation of the process and in [13] its value is found by comparing the results of the FEM simulation with strain and thickness measurements and points on the forming limit diagram, coming from the manufactured component.

Starting from the output of the forming simulation in Autoform, a product model is generated for the dynamic analysis. To this end, the Autoform results are exported in the STEP format and a quad-dominant mesh is generated using the Altair HyperWorks tools SimLab and HyperMesh [28]. The thickness distribution predicted by the forming simulation is also mapped on this mesh using The ResultsMapper tool.

The FEM product model is compared to the experimental results discussed in Section 2 by considering the first 9 natural frequencies of the component and the FRF in point B. The natural frequencies predicted with the FEM model and their error with respect to the measurements are reported in Table 1. The error is in the order of a few percent. Also the FRF results, reported in Fig. 2, confirm that the numerical model is able to provide a first approximate prediction of the dynamic behaviour of the component.



(a) (b)

Figure 3: The initial point cloud (a) and the reconstructed triangular surface with Laplacian smoothing (b).

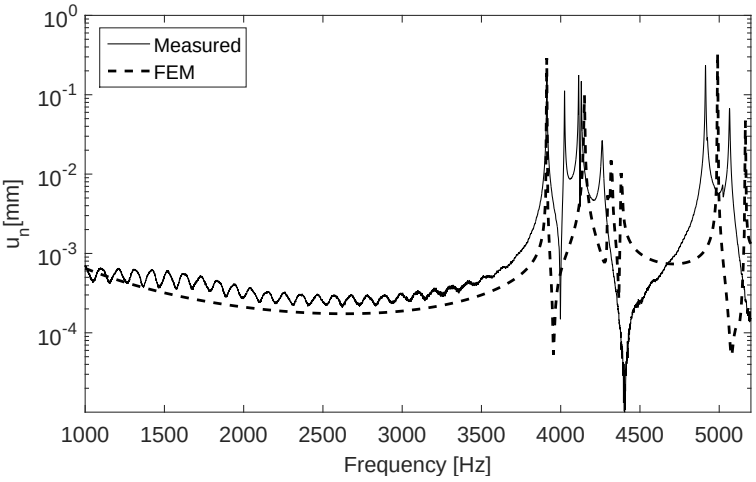


Figure 2: A comparison between the FRF measured in point B and its FEM prediction.

Freq	Err %
3912	-0.03
4150	3.14
4299	4.51
4321	4.64
4385	2.89
4991	1.57
5165	4.86
5266	4.86
5355	5.73

Table 1: The first nine natural frequenciesof the component predicted with the FEM model and their error with respect to the measurements.

4 Development of a product model through surface scanning

4.1 Point data acquisition and processing

In order to build a more accurate product model, the exact geometry of a component can be considered by reconstructing it from surface measurements. To this end, coordinate measuring machines (CMMs) are a useful tool to gather a point cloud from the surface of a component that is later processed to obtain a finite element model. In this work, a *Coord3 MC16 CMM*, equipped with the *Nikon Metrology* laser line scanner *LC60Dx* is considered, which gives an accuracy on the acquisition of a single point in the order of $25\mu m$.

Given the fact that the cup is a thin component, the numerical simulations can be performed using the shell framework, which is computationally much more efficient that a three-dimensional finite element analysis. Therefore, a finite element model corresponding to the mid-surface of the component needs to be reconstructed starting from the point data. For this purpose, the open source processing tool meshlab [29] is used. The initial point cloud coming form the scanner is divided in two parts, corresponding to the inner and to the outer surface of the cup. For each of them a triangular surface is reconstructed using the ball-pivoting algorithm [30]. Eventual holes or missing parts that are present in the point cloud can also be closed with meshlab. The initial point cloud and the reconstructed surface are shown in Fig. 3.

Because of the measurements noise, the reconstructed surfaces present irregularities that can be reduced using surface smoothing [31]. Different smoothing methodologies are considered in [13] but here, for the sake of brevity, we report only the results obtained with standard Laplacian smoothing (Fig. 3b). Once the inner and outer surfaces are constructed, the mid-surface of the component can be obtained using the

Hausdorff distance [32] of the inner points from the outer surface and their normals. In particular, for each point $\boldsymbol{x}$ on the inner surface, with unit normal $\boldsymbol{n}$ and thickness t, the corresponding point $\boldsymbol{x}'$ on the mid-surface is computed as

$$\boldsymbol{x}' = \boldsymbol{x} + \frac{t}{2}\boldsymbol{n}. \tag{1}$$

This gives a new point cloud, where the ball-pivoting algorithm and a further smoothing step are applied, such that a final smooth description of the mid-surface is obtained.

4.2 FEM simulation

The mid-surface triangulation, with the relative thickness descriptions, can be directly used as an FEM mesh within the shell framework by associating to each node the corresponding thickness. This approach is followed in [13] but we note that it is also possible to generate a new mesh with less degrees of freedom. The results of the dynamic simulation for the FRF and for the natural frequencies are reported in Fig. 4 and Table 2 respectively, where some improvement can be observed with respect to the previous case of a purely numerical approach. In particular, the predicted FRF is able to correctly reproduce the dynamic behaviour of the component in the low-frequency region, while a peak shift is still present towards high frequencies.

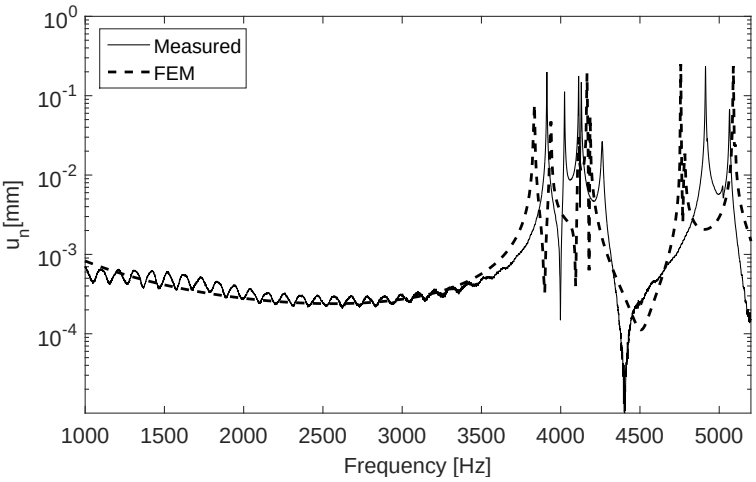


Figure 4: A comparison between the FRF measured in point B and its FEM prediction.

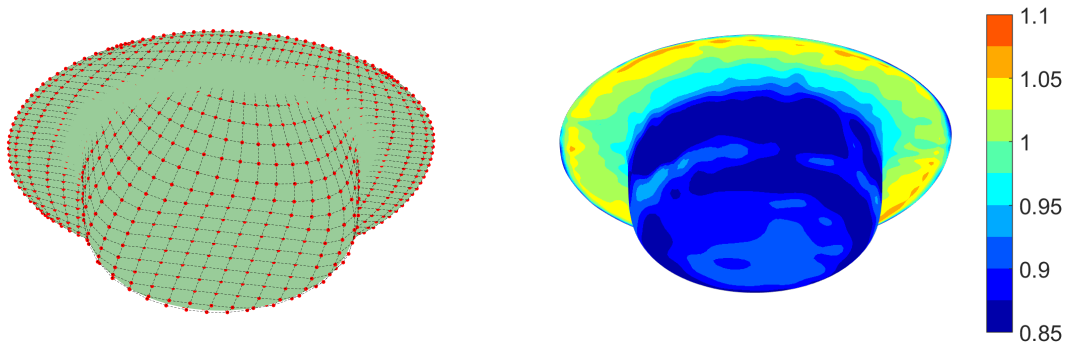
Freq	Err %
3832	-2.06
3936	-2.19
4111	-0.05
4167	0.90
4184	-1.83
4757	-3.19
4780	-2.95
5088	1.32
5100	0.70

Table 2: The first nine natural frequenciesof the component predicted with the FEM model and their error with respect to the measurements.

4.3 IGA framework

IGA is a recent, innovative numerical methodology and as compared to FEM offers the possibility to use the same basis functions, i.e. B-splines or NURBS (non-uniform rational B-splines) for both the CAD geometry description and the numerical analysis [15], avoiding the need for a (sometimes) expensive meshing step. For this reason, in the context of reverse engineering, IGA appears particularly suited for the reconstruction of a smooth surface model that can be directly used for the simulation of the dynamic behaviour of a component [14]. In fact, point cloud fitting with parametric curves and surfaces is a well-known methodology because of the high-order and tailor-able smoothness of splines functions [33, 34]. By combining the reconstruction properties of B-splines with the advantages introduced by IGA in the numerical analysis a reverse engineering framework, particularly useful for deep drawn components, is obtained [14].

As for the traditional FEM, the numerical IGA model is also based on a shell approach with the advantage that, because of the higher inter-element continuity of IGA basis-functions, a rotation-free Kirchhoff-Love formulation can be used [35]. Therefore, an IGA model of the mid-surface of the component is necessary. In principle, both the inner and the outer surface could be fitted with a parametric surface and the mid-surface



(a) (b)

Figure 5: IGA model of the cup; (a) the B-spline parametric description of the mid-surface, with the control points highlighted by circles; (b) the reconstructed thickness distribution.

could be obtained by comparing the two resulting surfaces. However, the process of defining such a mid-surface is not straightforward and, in addition, possible fitting errors of the two surfaces could be amplified. For this reason, a more efficient approach is to process the point data in the same way of the classical FEM approach, described in Section 3, and then to fit only one parametric surface directly to the point cloud that describes the mid-surface.

For the cup considered in this work, a B-spline surface, described by a 32×32 grid of control points, is fitted to the mid-surface and depicted in Fig. 5a. Another advantage of the IGA framework is that also the thickness of the component can be described in a smooth, parametric way using the same B-spline functions used to fit the geometry, as shown in Fig. 5b. This thickness distribution is then included in the analysis by considering the exact thickness value in each Gauss point during the matrix assembly procedure.

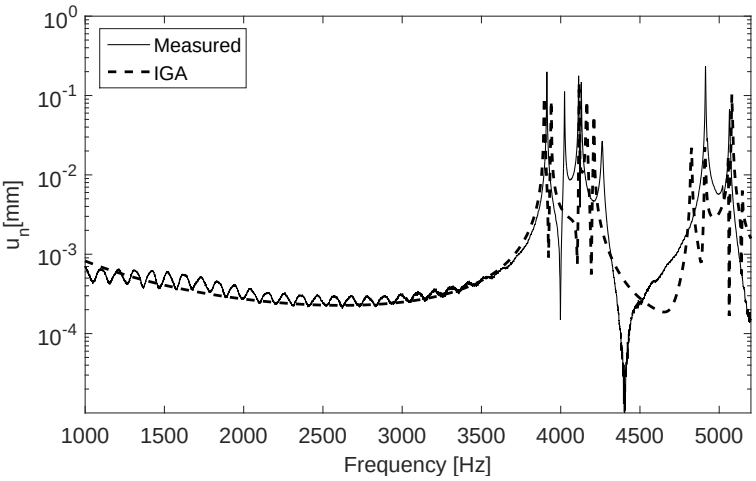


Figure 6: A comparison between the FRF measured in point B and its IGA prediction.

Freq	Err %
3898	-0.39
3939	-2.12
4116	0.08
4164	0.82
4208	-1.26
4824	-1.83
4911	-0.30
5060	0.77
5081	0.32

Table 3: The first nine natural frequenciesof the component predicted with the IGA model and their error with respect to the measurements.

The IGA numerical prediction for the FRF and for the natural frequencies are reported in Table 3 and Fig. 6 respectively. The results present the same level of accuracy of those obtained with the FEM in Section 3 but, remarkably, IGA requires a smaller number of degrees of freedom for the surface description.

5 Model stiffness updating

Observing the results discussed in the previous sections it can be noted that an accurate description of the geometry improves the prediction of the dynamic behaviour of the component, as compared to results ob-

tained with the purely numerical framework of Section 3. The results are sufficiently accurate, especially in the low-frequency region. However, when moving towards higher frequencies, an FRF mismatch due mainly to a frequency shift is observed (Fig. 6).

As the exact geometry is used for the simulation, the first consideration is that a possible source of inaccuracy for the prediction of the natural frequencies and the subsequent frequency shift in the high frequency region is due to the uncertainty on the Young's modulus E and on the density ρ of the steel. For the component considered in this work, the density has been calculated with an estimated standard deviation of 0.5% by measuring the weight of 20 components of a batch. As far as the Young's modulus is concerned, the value indicated by the steel supplier is used in the numerical simulations. However, different values of E can be found in the literature for the DP600 steel [13] which suggests a significant uncertainty on its value.

What is even more relevant, for the application considered in this study, is that the value of E can change locally because of plastic straining phenomena [19, 20]. And in addition, as mentioned in the introduction, the residual stresses can also locally alter the dynamic stiffness of the component. Therefore, as an innovative contribution of this work, a stiffness updating procedure is proposed, which relies on the possibility to use a parametric description of the young modulus E in the IGA framework. In fact, in a similar fashion as done for the thickness, the value of E can be expressed parametrically through the B-spline functions and can be evaluated for each Gauss point during the assembly of the stiffness matrix. An optimization procedure is then proposed to retrieve a proper distribution of E that reproduces the real dynamic behaviour.

In particular, given a parametric surface $S(\xi, \eta)$, described through the B-spline basis functions N_k $(k = 1, \dots, N)$ and the control points $\mathbf{P}_k$:

$$S(\xi, \eta) = \sum_{k=1}^{N} N_k(\xi, \eta)\mathbf{P}_k, \tag{2}$$

a parametric distribution of the Young's modulus $e(\xi, \eta)$ is also considered:

$$e(\xi, \eta) = \sum_{k=1}^{N} N_k(\xi, \eta)\mathbf{E}_k, \tag{3}$$

where the control variables are describing the (unknown) Young's modulus distribution. The optimization problem is therefore stated as follows:

$$\begin{aligned} \text{find} \quad & \mathbf{E}_1, \dots, \mathbf{E}_N \\ \text{minimizing} \quad & \varepsilon = \varepsilon_{int} + \alpha\varepsilon_{\omega} \\ \text{subject to} \quad & \mathbf{E}_{min} \leq \mathbf{E}_k \leq \mathbf{E}_{max} \quad k = 1, \dots, N, \end{aligned} \tag{4}$$

where $\mathbf{E}_{min}$ and $\mathbf{E}_{max}$ are respectively the lower and upper bounds of E that are set at $\pm 5\%$ of its nominal value, while ε indicates the error between numerical and experimental predictions to be minimized and is defined as a Pareto combination of an integral error ε_{int} and an error on the frequencies ε_{ω}. The former is defined as

$$\varepsilon_{int} = \int_{\omega_1}^{\omega_2} |\log \|u_n\| - \log \|u_e\||d\omega, \tag{5}$$

where $\|u_n\|$ and $\|u_e\|$ are the modules of the (complex) FEM and experimental displacements respectively, while ω_1 and ω_2 define the frequency range considered, in this case from 2000 to 5000 Hz. Since the FRF values vary over several orders of magnitude, their logarithm is considered in the evaluation of the integral. The frequency error ε_{ω} is defined as

$$\varepsilon_{\omega} = \sum_{k=1}^{n_f} (\omega_k^{(n)} - \omega_k^{(e)})^2, \tag{6}$$

where $\omega_k^{(n)}$ and $\omega_k^{(e)}$ are the k-th numerical and experimental frequencies respectively, for k going from 1 to 9 in the case considered in this study. The Pareto parameter α is chosen such that ε_{int} and ε_ω are in the same order of magnitude.

The aforementioned optimization problem is solved using a matlab implementation based on genetic algorithms [36]. In fact, FRFs residuals are known to cause serious discontinuities in the topology of the objective functions and, although some strategies are possible to still use gradient based methods [37], genetic algorithms are preferred in this work for their simplicity.

The optimization is run for the $32 \times 32 = 1024$ control variables using a population of 1000 individuals and 200 generations. The natural frequencies and the FRF predicted with the resulting model are reported in Table 4 and Fig. 7 respectively, where it can ne observed how a significant imporvement is obtained in the accuracy of the model. An even better agreement with measurements can be expected by considering a larger population and properly tuning the genetic algorithm parameters or considering other optimization methodologies can be the topic of future research.

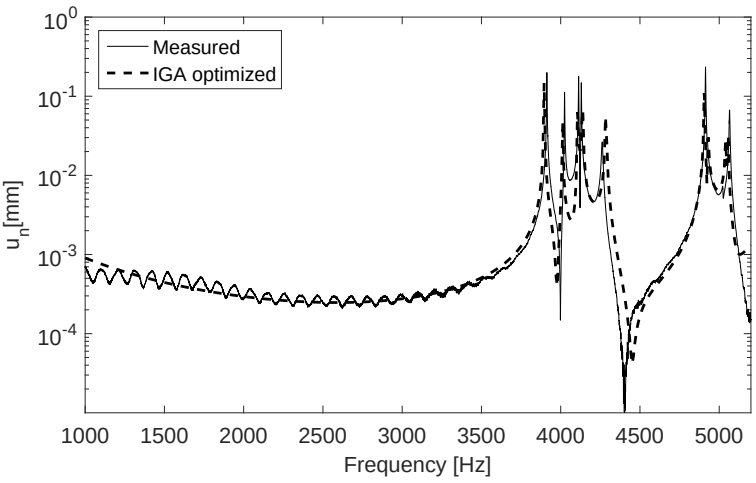


Figure 7: A comparison between the FRF measured in point B and the IGA prediction with the optimized model.

Freq	Err %
3896	-0.42
4012	-0.31
4108	-0.13
4136	0.16
4285	0.55
4907	-0.14
4926	0.02
5044	0.45
5055	-0.20

Table 4: The first nine natural frequenciesof the component predicted with the IGA optimized model and their error with respect to the measurements.

The resulting Young's modulus distribution is shown if Fig. 8. Although it is difficult to individuate a general trend, the figure suggests that the stiffness of the component increases in the curved zones on the flange, while it decreases on the bottom. From a numerical point of view, the new Young's modulus distribution allows a correct representation of the dynamic behaviour of the component. However, assessing the correctness of this distribution (i.e. whether it matches the one of the physical component only in the numerical analysis or also in reality) and relating it to the effects of the forming process can also be the topic of future research.

6 Concluding remarks

This work considered the development of an accurate product model for the simulation of the dynamic behaviour of deep drawn components. It was shown how a purely numerical framework, based on an FEM simulation of a forming process, is already an efficient and relatively easy to apply methodology. To improve the results, a more accurate geometrical model can be obtained starting from surface measurements on the component. In this context, IGA showed some advantages with respect to the traditional FEM approach. Finally, in order to improve the correlation with measurements, an updating procedure has been proposed, based on an optimization framework where the Young's modulus is parametrically described in the context of IGA and updated through an optimization procedure. This allows one to locally reproduce the stiffness of the formed component and, therefore, a further improvement in the accuracy of the numerical model is obtained.

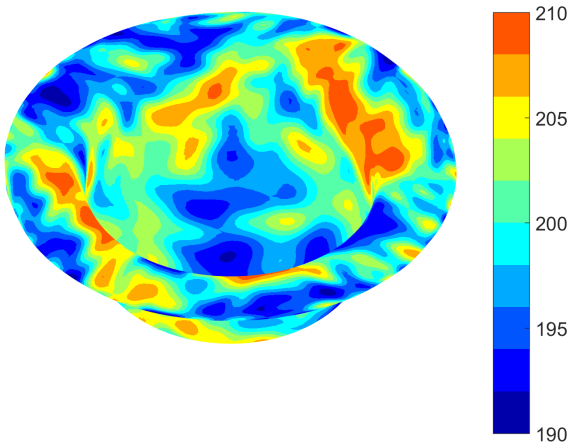


Figure 8: The Young's modulus distribution resulting from the optimization.

Acknowledgements

The Research Fund KU Leuven is gratefully acknowledged for its support. This research is supported by Flanders Make, the strategic research centre for the manufacturing industry, and is part of 'Virtual Design Platform for Sheet Material Products' (VIDESPRO icon). E. Deckers is a postdoctoral fellow of the Research Foundation - Flanders (F.W.O.). The research of F. Maurin if funded by an Experienced Researcher grant within the European ANTARES Project, under the FP7 Marie Curie Programme (GA606817).

References

[1] M. Colgan and J. Monaghan, "Deep drawing process: analysis and experiment," *Journal of Materials Processing Technology*, vol. 132, pp. 35–41, jan 2003.

[2] D. P. Koistinen and N.-M. Wang, eds., *Mechanics of Sheet Metal Forming*. Boston, MA: Springer US, 1979.

[3] T. Gnaeupel-Herold, T. Foecke, H. J. Prask, and R. J. Fields, "An investigation of springback stresses in AISI-1010 deep drawn cups," *Materials Science and Engineering: A*, vol. 399, no. 1, pp. 26–32, 2005.

[4] A. C. Bezerra, L. C. Vieira, D. A. Rade, and A. Scotti, "On the influence of welding residual stresses on the dynamic behavior of structures," *Shock and Vibration*, vol. 15, pp. 447–458, 2008.

[5] M. X. Shi, B. Liu, Z. Q. Zhang, Y. W. Zhang, and H. J. Gao, "Direct influence of residual stress on the bending stiffness of cantilever beams," *Proceedings of the Royal Society A: Mathematical, Physical and Engineering Sciences*, vol. 468, no. 2145, pp. 2595–2613, 2012.

[6] E. Hills, B. Mace, and N. Ferguson, "Acoustic response variability in automotive vehicles," *Journal of Sound and Vibration*, vol. 321, pp. 286–304, 2009.

[7] M. Kompella and R. Bernhard, "Measurement of the statistical variation of structural-acoustic characteristics of automotive vehicles," in *Proceedings of the SAE Noise and vibration Conference (Warrendale, USA)*, 1993.

[8] A. Mamalis, D. Manolakos, and A. Baldoukas, "Simulation of sheet metal forming using explicit finite-element techniques: effect of material and forming characteristics: Part 1. Deep-drawing of cylindrical cups," *Journal of Materials Processing Technology*, vol. 72, no. 1, pp. 48–60, 1997.

[9] L. Menezes and C. Teodosiu, "Three-dimensional numerical simulation of the deep-drawing process using solid finite elements," *Journal of Materials Processing Technology*, vol. 97, no. 1, pp. 100–106, 2000.

[10] V. M. S. Sathya Dev, S. Angadi, and S. Roy, "Forming and Modal Analysis of Sheet Metal Oil Pan," *SAE Technical Paper*, 2002.

[11] R. Echempati and A. Fox, "Integrated metal forming and vibration analysis of sheet metal parts," *Engineering with Computers*, vol. 29, no. 3, pp. 307–318, 2012.

[12] V. K. Balla, L. Coox, E. Deckers, F. Greco, B. Pluymers, and W. Desmet, "A study of vibro-acoustic property variation of components manufactured through deep drawing process," *Applied Acoustics*.

[13] F. Greco, E. Deckers, J. Stroobants, S. Van Poppel, K. Linck, and W. Desmet, "Finite element simulation of the dynamic behaviour of deep drawn components with accurate thickness description," *Finite Elements in Analysis and Design*, vol. 138, pp. 12–20, 2018.

[14] F. Greco, L. Coox, F. Maurin, V. K. Balla, E. Deckers, and W. Desmet, "Reverse engineering of deep drawn components with an isogeometric framework," *Computers and Structures*, vol. 201, pp. 15–25, 2018.

[15] T. J. R. Hughes, J. A. Cottrell, and Y. Bazilevs, "Isogeometric analysis: CAD, finite elements, NURBS, exact geometry and mesh refinement," *Computer methods in applied mechanics and engineering*, vol. 194, no. 39, pp. 4135–4195, 2005.

[16] J. A. Cottrell, T. J. R. Hughes, and Y. Bazilevs, *Isogeometric analysis: toward integration of CAD and FEA*. John Wiley & Sons, 2009.

[17] S. Son, H. Park, and K. H. Lee, "Automated laser scanning system for reverse engineering and inspection," *International Journal of Machine Tools and Manufacture*, vol. 42, no. 8, pp. 889–897, 2002.

[18] K. Lee, H. Park, and S. Son, "A Framework for Laser Scan Planning of Freeform Surfaces," *The International Journal of Advanced Manufacturing Technology*, vol. 17, pp. 171–180, jan 2001.

[19] F. Morestin and M. Boivin, "On the necessity of taking into account the variation in the young modulus with plastic strain in elastic-plastic software," *Nuclear Engineering and Design*, vol. 162, no. 1, pp. 107–116, 1996.

[20] K. Yamaguchi, H. Adachi, and N. Takakura, "Effects of plastic strain and strain path on youngs modulus of sheet metals," *Metals and Materials*, vol. 4, no. 3, pp. 420–425.

[21] V. Arora, "Comparative study of finite element model updating methods," *Journal of Vibration and Control*, vol. 17, no. 13, pp. 2023–2039, 2011.

[22] W. A. Wall, M. A. Frenzel, and C. Cyron, "Isogeometric structural shape optimization," *Computer methods in applied mechanics and engineering*, vol. 197, no. 33, pp. 2976–2988, 2008.

[23] J. Kiendl, R. Schmidt, R. Wüchner, and K. U. Bletzinger, "Isogeometric shape optimization of shells using semi-analytical sensitivity analysis and sensitivity weighting," *Computer Methods in Applied Mechanics and Engineering*, vol. 274, pp. 148–167, 2014.

[24] M. Mihalikova, M. Nemet, and V. Girman, "DP600 steel research of dynamic testing," *Metalurgija*, vol. 54, no. 1, pp. 211–213, 2015.

[25] P. Ludwik, "Elemente der Technologischen Mechanik," 1909.

[26] R. Hill, *The mathematical theory of plasticity*. Clarendon Press, 1998.

[27] F. Cayssials and X. Lemoine, "Predictive model of FLC (Arcelor model) upgraded to UHSS Steels," *24th IDDRG Conference, Besançon*, 2005.

[28] "HyperWorks Starter Manual," 2011.

[29] P. Cignoni, M. Callieri, M. Corsini, M. Dellepiane, F. Ganovelli, and G. Ranzuglia, "MeshLab: an Open-Source Mesh Processing Tool," *Eurographics Italian Chapter Conference*, vol. 2008, pp. 129–136, 2008.

[30] F. Bernardini, J. Mittleman, and H. Rushmeier, "The ball-pivoting algorithm for surface reconstruction," *IEEE Transactions on Visualization and Computer Graphics*, vol. 5, no. 4, pp. 349–359, 1999.

[31] A. Belyaev and Y. Ohtake, "A Comparison of Mesh Smoothing Methods," *Israel-Korea Bi-national conference on geometric modeling and computer graphics*, pp. 1–5, 2003.

[32] P. Cignoni, C. Rocchini, and R. Scopigno, "Metro: Measuring Error on Simplfied Surfaces," *Compututer Graphics Forum*, vol. 17, no. 2, pp. 167–174, 1998.

[33] L. Piegl and W. Tiller, *The NURBS Book*. Monographs in Visual Communications, Berlin, Heidelberg: Springer Berlin Heidelberg, 1995.

[34] P. Dierckx, *Curve and Surface Fitting with Splines*. 1993.

[35] J. Kiendl, K. U. Bletzinger, J. Linhard, and R. Wüchner, "Isogeometric shell analysis with Kirchhoff-Love elements," *Computer Methods in Applied Mechanics and Engineering*, vol. 198, no. 49-52, pp. 3902–3914, 2009.

[36] A. Chipperfield, "The MATLAB Genetic Algorithm Toolbox," *IEE Colloquium on Applied Control Techniques Using MATLAB*, vol. 1995, pp. 10–10, 1995.

[37] R. Pascual and M. Razeto, "A Robust FRF-based technique for Model Updating," in *Proceedings of ISMA2002*, vol. 3, pp. 1037–1046, 2002.

Transmission of vibrations between towed and towing agricultural machines

J. Brunetti [1], **W. D'Ambrogio** [1], **A. Fregolent** [2a], **G. Lacerra** [2]
[1] Università dell'Aquila, Dipartimento di Ingegneria Industriale e dell'Informazione e di Economia,
Via G. Gronchi 18, I-67100, L'Aquila (AQ), Italy

[2] Università di Roma La Sapienza, Dipartimento di Ingegneria Meccanica e Aerospaziale,
Via Eudossiana, 18, I-00184, Roma, Italy
[a] e-mail: **annalisa.fregolent@uniroma1.it**

Abstract
In the research framework of acoustic and vibration problems, the vibrations produced by the agricultural machinery have a relevant position, because the vibrations due to the soil irregularity and to the operation of the machinery are transmitted to the seat of the tractor's operator, inducing comfort and safety problems, that are of interest of the National Institute for Insurance against Accidents at Work (INAIL). The objective of this work is to investigate the effect of machinery on the vibrations transmitted to the tractor's operator introducing a simplified model of an agricultural machine, considering not only the DoFs (degrees-of-freedom) relative to the tractor but also the ones relative to the machinery. Moreover, a model of the three point linkage between the tractor and the machinery and a model of the hitch for trailed machinery are proposed. The dynamic substructuring is exploited to couple the model of the tractor with the machinery through the linkage system and the transmissibility of an excitation force from the source to the operator's seat is investigated.

1 Introduction

In the research framework of acoustic and vibration problems, the vibrations produced by the agricultural machinery have a relevant position, assuming indeed a double role: firstly, the vibrations due to the soil irregularity and to the operation of the machinery are transmitted to the seat of the tractor's operator [1], inducing comfort and safety problems [2, 3]; secondly, they are always combined with annoying sound emission [4], encountering the limitations imposed by the international and national regulations. The control of noise and vibration on the operator is of interest of the National Institute for Insurance against Accidents at Work (INAIL). Despite the study of the tractor dynamics and the induced vibrations have been deeply investigated in the literature [5], relatively few works deal with the influence of the agricultural machinery in the transmission of vibration.

The objective of this work is to investigate the effect of mounted, semi-mounted and trailed machinery on the vibrations transmitted to the tractor's operator introducing a simplified model of an agricultural machine, considering not only the DoFs (degrees-of-freedom) relative to the tractor but also the ones relative to the machinery.

Moreover, a model of the three points linkage between the tractor and the machinery and a model of the hitch for trailed machinery are proposed. The dynamic substructuring [6] is exploited to couple the model of the tractor with the machinery through the linkage system. The linkage systems are modeled by finite elements methods and reduced by the Craig-Bampton method [7]. The reduced order models are used to perform a frequency based coupling of the substructures [8].

Eventually, the transmissibility of an excitation force from the source to the operator's seat is investigated, focusing on the influence of the linkage in the vibration transmission.

2 Theoretical background

The dynamic characterization of complex mechanical systems can be performed using the dynamic substructuring methods. The main advantage of these techniques is the possibility to investigate the effect of local modification on the dynamic behavior of a complex system. Moreover these techniques allow to use different types of models to represent each component substructure (i.e. lumped parameters models, FE models, experimental modal models).

2.1 Dynamic substructuring

Let us consider a structural system consisting of n coupled subsystems. The equation of motion of a linear time-invariant subsystem r may be written as:

$$[M]^{(r)}\{\ddot{u}(t)\}^{(r)} + [C]^{(r)}\{\dot{u}(t)\}^{(r)} + [K]^{(r)}\{u(t)\}^{(r)} = \{f(t)\}^{(r)} + \{g(t)\}^{(r)} \tag{1}$$

where:

$[M]^{(r)}$, $[C]^{(r)}$, $[K]^{(r)}$ are the mass, damping and stiffness matrices of subsystem r;
$\{u(t)\}^{(r)}$ is the vector of displacements of subsystem r;
$\{f(t)\}^{(r)}$ is the vector of external forces on subsystem r;
$\{g(t)\}^{(r)}$ is the vector of connecting forces with other subsystems (internal constraint forces).

The equation of motion of the n subsystems to be coupled can be written in a block diagonal format as:

$$[M]\{\ddot{u}(t)\} + [C]\{\dot{u}(t)\} + [K]\{u(t)\} = \{f(t)\} + \{g(t)\} \tag{2}$$

with

$$[M] = \begin{bmatrix} [M]^{(1)} & & \\ & \ddots & \\ & & [M]^{(n)} \end{bmatrix}, \quad [C] = \begin{bmatrix} [C]^{(1)} & & \\ & \ddots & \\ & & [C]^{(n)} \end{bmatrix}, \quad [K] = \begin{bmatrix} [K]^{(1)} & & \\ & \ddots & \\ & & [K]^{(n)} \end{bmatrix} \tag{3}$$

$$\{u(t)\} = \begin{Bmatrix} \{u(t)\}^{(1)} \\ \vdots \\ \{u(t)\}^{(n)} \end{Bmatrix}, \quad \{f(t)\} = \begin{Bmatrix} \{f(t)\}^{(1)} \\ \vdots \\ \{f(t)\}^{(n)} \end{Bmatrix}, \quad \{g(t)\} = \begin{Bmatrix} \{g(t)\}^{(1)} \\ \vdots \\ \{g(t)\}^{(n)} \end{Bmatrix} \tag{4}$$

The compatibility condition implies that any pair of matching DoFs at time t, i.e. DoF l on subsystem r and DoF m on subsystem s must have the same displacement, that is $u_l^{(r)}(t) - u_m^{(s)}(t) = 0$.

This condition can be generally expressed as:

$$[B]\{u(t)\} = \{0\} \tag{5}$$

where each row of $[B]$ corresponds to a pair of matching DoFs. Note that $[B]$ is, in most cases, a signed Boolean matrix and it can be written by distinguishing the contribution of the different subsystems:

$$[B] = \begin{bmatrix} [B]^{(1)} & \cdots & [B]^{(n)} \end{bmatrix}$$

The equilibrium condition for internal constraint forces, arising from the compatibility conditions, implies that the sum of connecting forces at a pair of matching DoFs must be zero, i.e. $g_l^{(r)}(t) + g_m^{(s)}(t) = 0$: this holds for any pair of matching DoFs at time t. Furthermore, if DoF k on subsystem q is not a connecting DoF at time t, it must be $g_k^{(q)}(t) = 0$: this holds for any non-connecting DoF at time t.

Overall, the above conditions can be expressed as:

$$[L]^T \{g(t)\} = \{0\} \tag{6}$$

where the matrix $[L]$ is a Boolean localization matrix. Note that the number of rows of $[L]^T$ is equal to the number of non-interface DoFs plus the number of pairs of equilibrium interface DoFs.

Eqs. (2-6) can be put together to get the three field formulation, i.e the total system describing the coupling among any number of substructures:

$$\begin{cases} [M]\{\ddot{u}(t)\} + [C]\{\dot{u}(t)\} + [K]\{u(t)\} = \{f(t)\} + \{g(t)\} \\ [B]\{u(t)\} = \{0\} \\ [L]^T \{g(t)\} = \{0\} \end{cases} \tag{7}$$

The coupling problem solved using either primal or dual assembly. In the primal assembly, a unique set of interface DoFs is defined and the interface forces are eliminated by automatically satisfying the interface equilibrium. This is obtained by stating that:

$$\{u(t)\} = [L]\{q(t)\} \tag{8}$$

where $\{q\}$ is the unique set of DoFs, including also non-interface DoFs. Since Eq. (8) states that the DoFs of all subsystems are obtained from the unique set $\{q\}$, the compatibility condition holds for any set $\{q\}$, i.e.

$$[B]\{u(t)\} = [B][L]\{q(t)\} = \{0\} \qquad \forall \{q\} \tag{9}$$

Hence, $[L]$ represents the nullspace of $[B]$:

$$[L] = \text{null}([B]) \tag{10}$$

Since the compatibility condition in Eq. (7) is satisfied by the choice of the unique set $\{q\}$, the system of equations is:

$$\begin{cases} [M][L]\{\ddot{q}(t)\} + [C][L]\{\dot{q}(t)\} + [K][L]\{q(t)\} = \{f(t)\} + \{g(t)\} \\ [L]^T \{g(t)\} = \{0\} \end{cases} \tag{11}$$

Pre-multiplying the dynamic equilibrium equation by $[L]^T$ and noting that $[L]^T\{g(t)\} = \{0\}$, the assembled system reduces to:

$$[L]^T[M][L]\{\ddot{q}(t)\} + [L]^T[C][L]\{\dot{q}(t)\} + [L]^T[K][L]\{q(t)\} = [L]^T\{f(t)\} \tag{12}$$

i.e.

$$[\tilde{M}]\{\ddot{q}(t)\} + [\tilde{C}]\{\dot{q}(t)\} + [\tilde{K}]\{q(t)\} = \{\tilde{f}(t)\} \tag{13}$$

Equation (13) can be written in the frequency domain by letting $\{\tilde{f}(t)\} = \{\tilde{F}(\omega)\}\, e^{j\omega t}$ and $\{q(t)\} = \{Q(\omega)\}\, e^{j\omega t}$:

$$\left[-\omega^2[\tilde{M}] + j\omega[\tilde{C}] + [\tilde{K}]\right]\{Q(\omega)\} = \{\tilde{F}(\omega)\} \tag{14}$$

Hence,

$$\{Q(\omega)\} = \left[-\omega^2[\tilde{M}] + j\omega[\tilde{C}] + [\tilde{K}]\right]^{-1}\{\tilde{F}(\omega)\} = [H(j\omega)]\{\tilde{F}(\omega)\} \tag{15}$$

where

$$[H(j\omega)] = \left[-\omega^2[\tilde{M}] + j\omega[\tilde{C}] + [\tilde{K}]\right]^{-1} \tag{16}$$

is the desired receptance matrix of the assembled system.

2.2 Modal reduction, the Craig-Bampton method

With this technique, the number of DoFs of each substructure (r) can be reduced by retaining the physical DoFs connecting substructure (r) with other substructures.

The full set of DoFs $\{u^{(r)}\}$ of a substructure r is partitioned as:

$$\left\{u^{(r)}\right\} = \begin{Bmatrix}\{u\}_b \\ \{u\}_i\end{Bmatrix} \tag{17}$$

i.e. boundary (subscript b) and interior (subscript i) DoFs, where the superscript (r) is dropped for the sake of simplicity. Boundary degrees of freedom are those connecting the r^{th} substructure to the other substructures.

According to [7], the displacements field is expressed as a linear combination of static deformation modes $[\Phi_c]$

$$[\Phi_c] = \begin{bmatrix}[I]_b \\ [\Phi_c]_i\end{bmatrix} \tag{18}$$

and of a truncated set of m ($m \ll i$) fixed interface modes $[\Phi]$:

$$[\Phi] = \begin{bmatrix}[0]_b \\ [\Phi]_i\end{bmatrix} \tag{19}$$

Therefore,

$$\{u\}^{(r)} = \begin{Bmatrix}\{u\}_b \\ \{u\}_i\end{Bmatrix} = \begin{bmatrix}[I]_b & [0]_b \\ [\Phi_c]_i & [\Phi]_i\end{bmatrix}\begin{Bmatrix}\{u\}_b \\ \{q\}_m\end{Bmatrix} = [\Gamma]^{(r)}\{q\}^{(r)} \tag{20}$$

where $\{q\}_m$ is the set of modal coordinates, $[\Gamma]^{(r)}$ is the transformation matrix and $\{q\}^{(r)}$ is the reduced set of generalized coordinates.

Substituting Equation (20) in Equation (1) and premultiplying all the terms by $[\Gamma]^{(r)^T}$ one obtains:

$$[\hat{M}]^{(r)}\{\ddot{q}(t)\}^{(r)} + [\hat{C}]^{(r)}\{\dot{q}(t)\}^{(r)} + [\hat{K}]^{(r)}\{q(t)\}^{(r)} = \{\hat{f}(t)\}^{(r)} + \{\hat{g}(t)\}^{(r)} \tag{21}$$

where

$$[\hat{M}]^{(r)} = [\Gamma]^{(r)^T}[M]^{(r)}[\Gamma]^{(r)} \qquad \{\hat{f}(t)\}^{(r)} = [\Gamma]^{(r)^T}\{f(t)\}^{(r)} \tag{22}$$

and so on for other matrices and vectors.

2.3 Transmissibility

In general, the transmissibility is the nondimensional ratio between forces or displacements at different DoFs of a vibrating system. It is a very useful concept since it allows to understand how vibrations are amplified or attenuated in a complex system.

The definition of the transmissibility for a multi DoFs system is not trivial. We use the displacement transmissibility $T_{ij}^d = x_i/x_j$ (with $f_i = 0$, no constraint acting on DoF i) and the force transmissibility $T_{ij}^f = F_i/F_j$ (with $x_i = 0$, the DoF i is blocked and F_i represents the constraint reaction).

3 Models

The system under investigation is composed by an agricultural tractor linked to one machinery. In this section the models of the component substructures are presented: the agricultural tractor, the linkage system (three points linkage or hitch) and the machinery.

3.1 Lumped parameter model of the agricultural tractor

The tractor is represented as a lumped parameter model in the longitudinal plane, shown in Figure 1. The model is composed of two lumped masses m_1 and m_3 representing respectively the seat with the operator and the front axle, and of a rigid body representing the tractor frame that is characterized by a mass m_2 and a moment of inertia I_2. The operator's seat is connected to the frame by the spring k_1 and the damper c_1. The frame is connected directly to the rear axle and the rear wheels are characterized by a stiffness k_2 and damping c_2. The front axle m_3 is connected to the frame by a suspension with stiffness k_3 and damping c_3 and the front wheels are characterized by a stiffness k_4 and damping c_4.

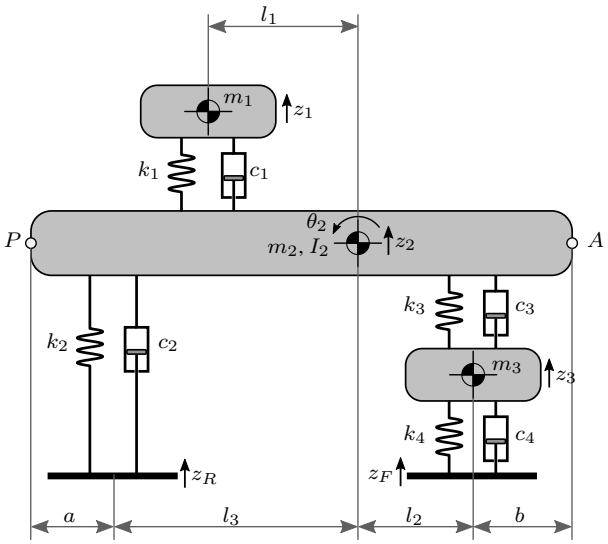


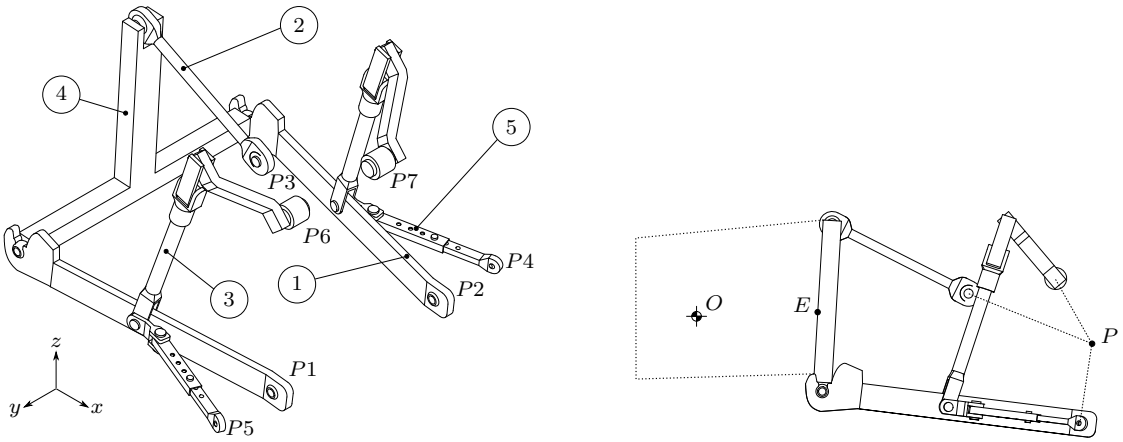
Figure 1: Lumped parameter model of an agricultural tractor.

The displacements of the two masses in the vertical direction z_1 and z_3 are considered. For the tractor frame, the displacement z_2 in vertical direction and the rotation θ_2 around the CoG are considered. Moreover, the displacement of the contact points of the front and rear wheels with the ground are taken into account by

the DoFs z_F and z_R respectively. The points A and P in Figure 1 represent the connection points with the linkage systems.

3.2 Reduced order model of the rear mounted three points linkage

The rear mounted three point linkage is the connecting substructure between the tractor and the rear mounted machinery. It is shown in Figure 2(a) where, according to the international standard ISO 730, the two lower links ①, the upper link ② and the lift rods ③ are highlighted. In the represented system, the implement ④ and the two struts ⑤ are also shown. The implement represents the connection to the machinery, while the points $P1$ to $P7$ are the link points with the tractor.



(a) Rear mounted three point linkage.

(b) Boundary nodes of the reduced order model of the rear mounted three point linkage with a mounted machinery.

Figure 2: Rear mounted three points linkage.

A finite element model of the linkage is developed to investigate its dynamic behavior. The model is subsequently reduced for the sake of dynamic substructuring using the Craig Bampton method. The boundary nodes of the Craig-Bampton reduction are shown in Figure 2(b) where P is the connecting point to the tractor, E and O are respectively the connecting point and the CoG of the rear mounted machinery.

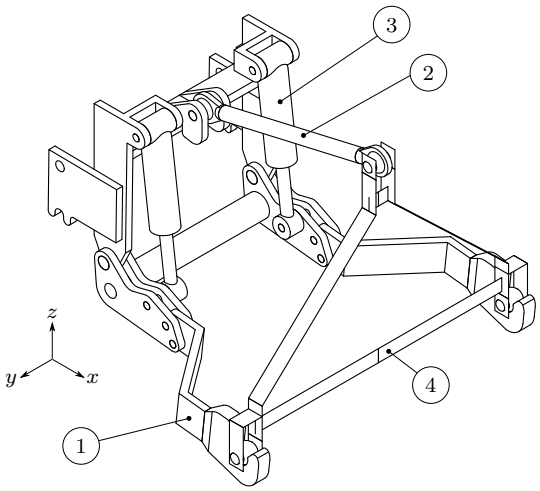
3.3 Reduced order model of the front three points linkage

The front mounted three point linkage is the connecting substructure between the tractor and the front mounted machinery. It is shown in Figure 3(a) where, according to the international standard ISO 8759, the same element ①-④ as in the rear mounted three points linkage are highlighted.

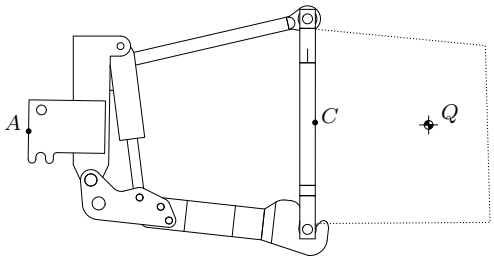
Also in this case, the finite element model of the linkage is developed to investigate its dynamic behavior. The model is subsequently reduced for the sake of dynamic substructuring using the Craig Bampton method. The boundary nodes of the Craig-Bampton reduction are shown in Figure 3(b) where A is the connecting point to the tractor, C and Q are respectively the connecting point and the CoG of the front mounted machinery.

3.4 Reduced order model of the hitch and of the trailed machine frame

The hitch is a mechanical connection between the tractor and the trailed machinery. Figure 4(a) shows the coupling device used in the attachment of non-balanced trailers to agricultural towing vehicles.

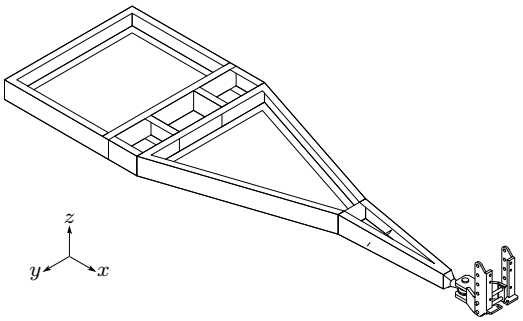


(a) Front mounted three point linkage.

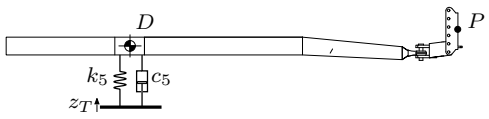


(b) Boundary nodes of the reduced order model of the front mounted three point linkage with a mounted machinery.

Figure 3: Front mounted three points linkage.



(a) Hitch with the frame of the trailed machinery.



(b) Boundary nodes of the reduced order model of the hitch with the frame of the trailed machinery.

Figure 4: Hitch connection with a trailed machinery.

The boundary nodes of the Craig-Bampton reduction are shown in Figure 4(b) where P is the connecting point to the tractor frame, D is the trace of the axle of the towed machinery, k_5 and c_5 are respectively the stiffness and the damping of the wheels. The vertical displacement of the contact point of the wheels with the ground is taken into account by the DoF z_T.

4 Results

The aim of the present work is the study of the vibration transmission from the agricultural machinery to the operator seat trough the different linkage systems. The models presented in the previous section are used: (a) to investigate the dynamic behavior of the component substructures using the transmissibility, and (b) to highlight, using the substructuring approach, how the coupling between the agricultural tractor and the machinery modifies the dynamics.

The numerical parameters and the geometrical dimensions of the tractor model are shown in Table 1. Moreover, for the trailed machinery model, the adopted parameters are $k_5 = 2e5$ N/m and $c_5 = 2347$ Ns/m.

Parameter	Value	
$\{m_1 \quad m_2 \quad m_3\}$	$\{88 \quad 7655 \quad 900\}$	kg
I_2	15938	kg m^2
$\{k_1 \quad k_2 \quad k_3 \quad k_4\}$	$\{16 \quad 894 \quad 640 \quad 748\}$	kN/m
$\{l_1 \quad l_2 \quad l_3\}$	$\{0.28 \quad 1.68 \quad 1.16\}$	m
$\{a \quad b\}$	$\{0.25 \quad 0.25\}$	m

Table 1: Parameters of the tractor.

4.1 Transmissibility analysis of the agricultural tractor

To characterize the dynamic behavior of the agricultural tractor, the displacement transmissibility from the wheels to the tractor frame and to the seat are evaluated and shown in Figure 5. The results show that the displacement excitation applied on the two wheels is amplified for some frequency range by the dynamics of the tractor. In particular, for the seat, at the frequency of about 2 Hz, the amplification of the rear wheel displacement is higher than the amplification of the front wheel, this is probably due to the presence of the suspension on the front axle. The opposite occurs at around 1.5 Hz where the front axle suspension seems to increase the transmissibility.

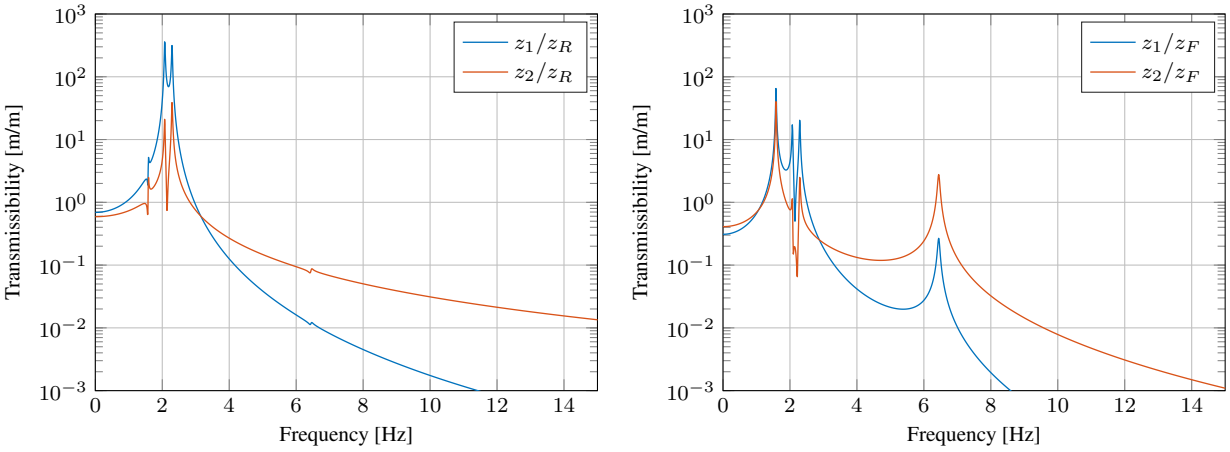


Figure 5: Displacement transmissibilities between the rear z_R and the front z_F wheel of the tractor and the CoG of the tractor frame z_2 and the seat z_1

4.2 Transmissibility of the linkage systems

To investigate how the excitation on the machinery is transmitted to the tractor trough the linkage system, the force transmissibility is evaluated. For the three points linkage, it is defined between the machinery and the connection to the tractor frame, while for the hitch the transmissibility is defined between the axle of the towed machinery and the connection to the tractor frame.

Figure 6 shows the transmissibility between the force excitation in either horizontal or vertical direction at the CoG of rear mounted machinery O and the linking points $P1 - P7$ of the rear three point linkage system. Due to the symmetry of the system with respect to the longitudinal plane, only the transmissibility of the points $P1$, $P2$, $P4$ and $P6$ are represented. The results show that, both the horizontal and the vertical excitations are amplified for frequencies higher than 30 Hz, but for the range of interest of the operator safety (i.e lower than 10 Hz) only the excitation in vertical direction is amplified.

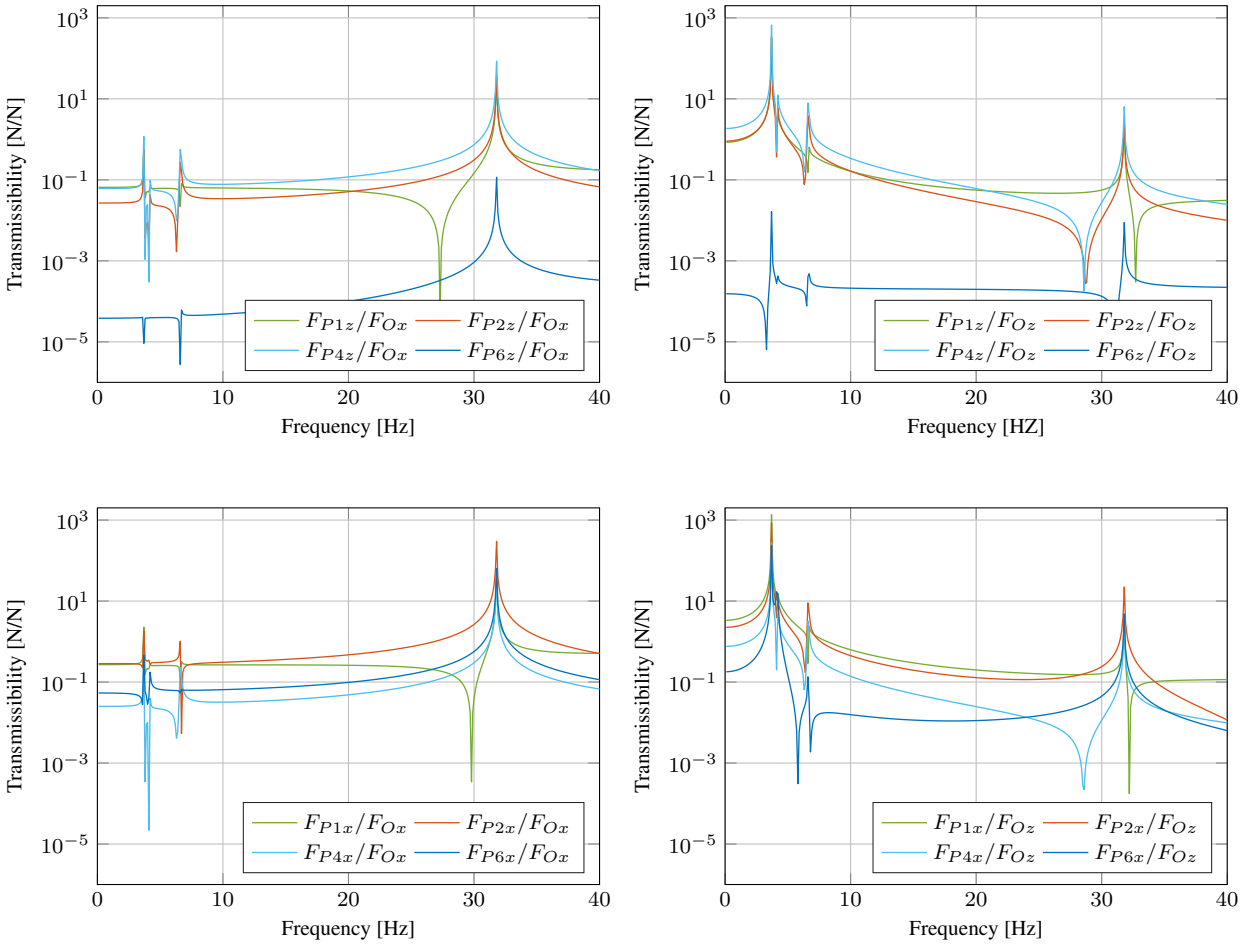


Figure 6: Force trasmissibilities between the CoG of the mounted machine O and: a) the link points of the rear three points linkage $P1$, $P2$; b) the joints of the struts $P4$; c) the joints of the lift rods $P6$

Figure 7 shows the transmissibility between the force excitation in either horizontal or vertical direction at the point C on the implement of the front mounted machinery, and the connecting point A of the front three point linkage system. The results show that the force excitation in the vertical direction is amplified in both horizontal and vertical directions at the connection point with the tractor, while the horizontal excitation is amplified only in vertical direction.

Figure 8 shows the transmissibility between the force excitation in either horizontal or vertical direction at the point D on the axle of the rear trailed machinery, and the connecting point P of the hitch. The results show that the force excitation in the vertical direction is amplified in both horizontal and vertical directions

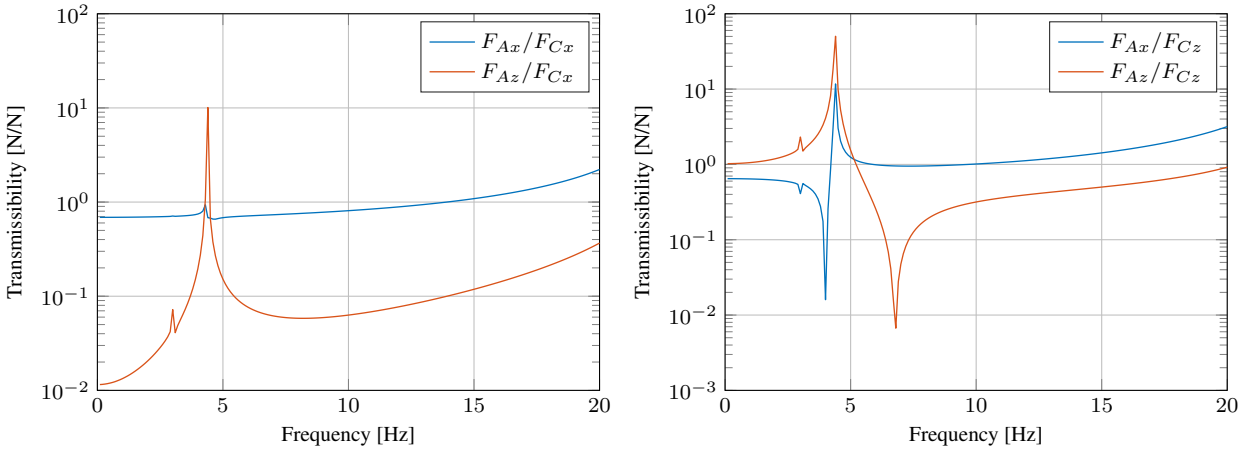


Figure 7: Force transmissibilities between the point C on the implement of the front mounted machine and the point A on the tractor.

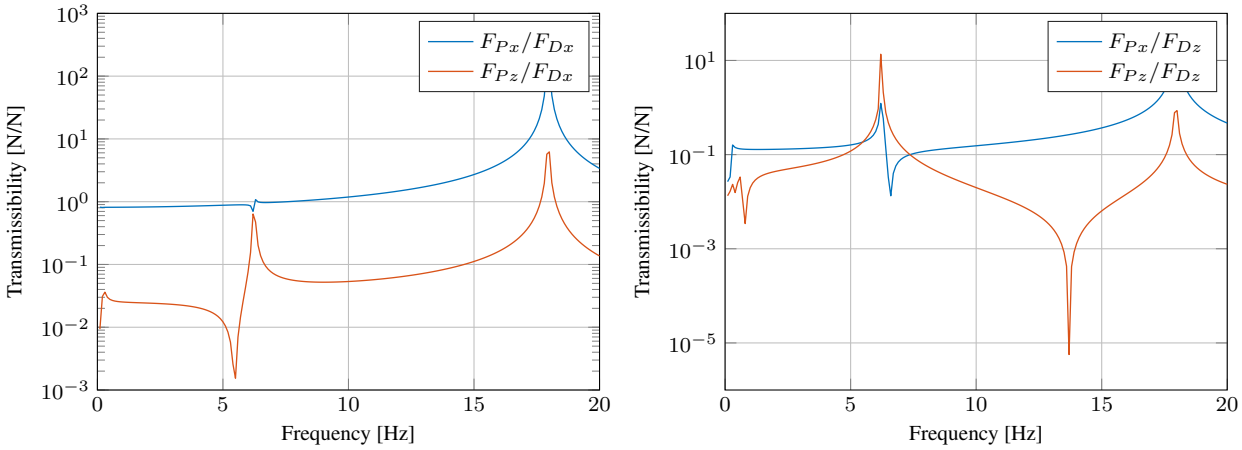


Figure 8: Force transmissibilities between the axle D of the trailed machine and the point P on the tractor.

at the connection point with the tractor, while the horizontal excitation is generally attenuated in the vertical direction but it is transmitted without attenuation in the horizontal direction, with a significant amplification above 15 Hz.

4.3 Substructuring analysis of the tractor and machinery set

The models of the front and rear three points linkages are reduced using the Craig Bampton technique with 10 fixed interface modes.

Figure 9 shows the results of the coupling between the tractor and the mounted machinery trough the rear three points linkage. The inertance FRFs between either the vertical or rotational DoF of the point O of the machinery and Dofs z_1 or z_2 on the tractor are shown. The results highlight the presence of 5 modes below 10 Hz: some of these resonances were observed in the transmissibilities of the component substructures.

Figure 10 shows the results of the coupling between the tractor and the mounted machinery trough the front three points linkage. The inertance FRFs between either the vertical or rotational DoF of the point Q of the machinery and Dofs z_1 or z_2 on the tractor are shown. The results highlight the presence of 5 modes below 10 Hz: some of these resonances were observed in the transmissibilities of the component substructures.

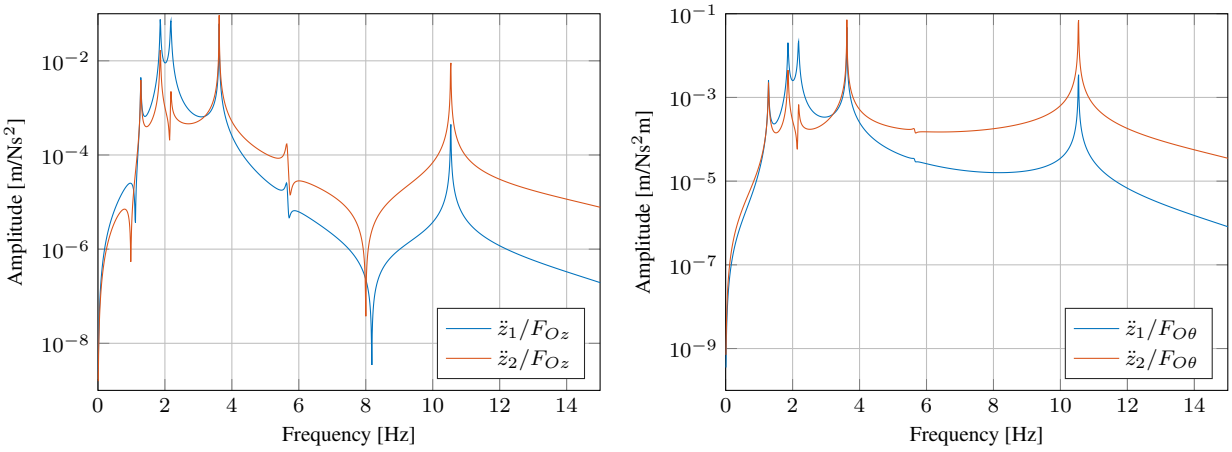


Figure 9: FRFs of the coupled system composed by the agricultural tractor with a mounted machine on the rear three points linkage.

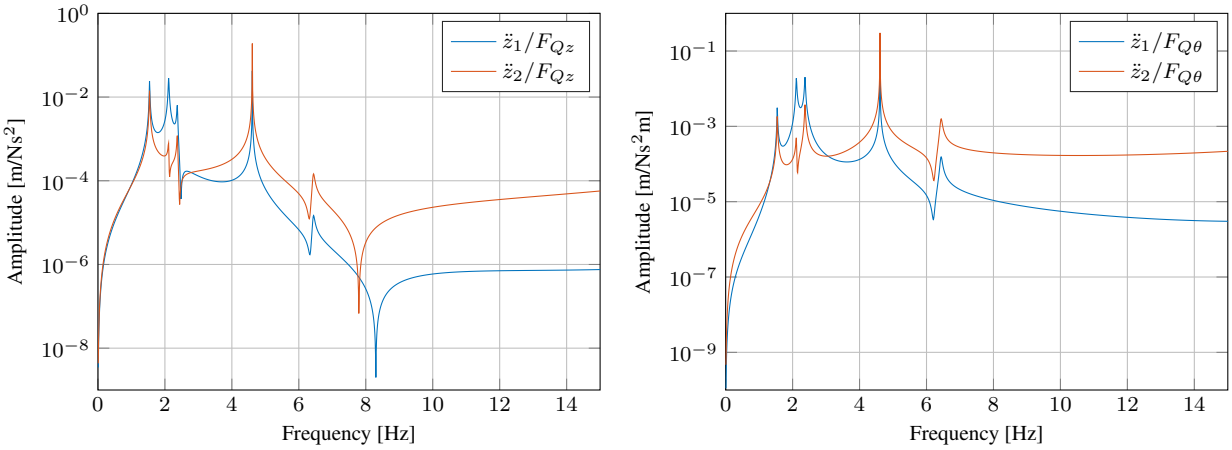


Figure 10: FRFs of the coupled system composed by the agricultural tractor with a mounted machine on the front three points linkage.

Conclusions

In this paper, the vibration transmission from the agricultural machinery to the operator seat trough different linkage systems is studied. In particular, the effect of mounted and trailed machinery on the vibrations transmitted to the tractor's operator is investigated by introducing a simplified model of an agricultural machine that considers not only the DoFs relative to the tractor but also the ones relative to the machinery. Moreover, different linkage systems between the tractor and the machinery are modeled: rear and front three points linkages and hitch.

Dynamic substructuring is exploited to couple the model of the tractor with the machinery through the linkage system. To highlight how the coupling between the agricultural tractor and the machinery modifies the dynamics, the FE models of the linkage systems are reduced by the Craig-Bampton method and used to perform a frequency based coupling of the substructures.

To characterize the dynamic behavior of the component substructures, the transmissibility of an excitation from the source to the operator's seat is investigated. Results highlight the influence of the linkage in the vibration transmission.

Aknowledgments

This research was developed in the frame of the Project No.BRIC-ID26 funded by INAIL (National Institute for Insurance against Accidents at Work and Occupational Diseases).

The authors acknowledge also Fabio Picca and Emanuele Savone for the contribution to this work given during their master thesis and in the subsequent cooperation.

References

[1] R. Stayner, *Whole-body Vibration and Shock: A Literature Review: Extension of a Study of Overtravel and Seat Suspensions*, University of Southampton, Institute of Sound and Vibration Research, 2001.

[2] H. C. Boshuizen, P. M. Bongers, C. T. Hulshof, *Self-reported back pain in tractor drivers exposed to whole-body vibration*, International archives of occupational and environmental health, Vol. 62, No. 2, 1990, pp. 109–115.

[3] M. Bovenzi, A. Betta, *Low-back disorders in agricultural tractor drivers exposed to whole-body vibration and postural stress*, Applied ergonomics, Vol. 25, No. 4, 1994, pp. 231–241.

[4] J. Depczynski, R. C. Franklin, K. Challinor, W. Williams, L. Fragar, *Farm noise emissions during common agricultural activities*, Journal of agricultural safety and health, Vol. 11, No. 3, 2005, pp. 325–334.

[5] P. Servadio, N. P. Belfiore, *Influence of tyres characteristics and travelling speed on ride vibrations of a modern medium powered tractor part i: Analysis of the driving seat vibration*, Agricultural Engineering International: CIGR Journal, Vol. 15, No. 4, 2013, pp. 119–131.

[6] D. de Klerk, D. J. Rixen, S. Voormeeren, *General framework for dynamic substructuring: history, review and classification of techniques*, AIAA journal, Vol. 46, No. 5, 2008, pp. 1169–1181.

[7] R. Craig, M. Bampton, *Coupling of substructures for dynamic analyses*, AIAA journal, Vol. 6, No. 7, 1968, pp. 1313–1319.

[8] J. Brunetti, A. Culla, W. D'Ambrogio, A. Fregolent, *Selection of interface dofs in hub-blade(s) coupling of ampair wind turbine test bed*, in *Topics in Experimental Dynamic Substructuring - Proceedings of the 31st IMAC, A Conference on Structural Dynamics, 2013*, volume 2, 2014.

Modal analysis tools at V2i: improved pre- and post-processing with modified p-LSCF algorithm

S.Hoffait[1], S. Moschini[1], J.Ligot[1], D. Simon[1]
[1] V2i s.a.
LIEGE Science Park, Avenue du Pré-Aily 25, 4031, Liège, Belgium
e-mail: **s.hoffait@v2i.be**

Abstract

In the industrial environment, modal analysis activities are often reduced to the identification task. However, a complete procedure is mandatory to guarantee the accuracy of the results and to allow an easy dissemination of the results. In this framework, V2i is developing a toolbox using a combination of internally developed tools and commercial software and hardware.

The current work describes the different tools developed by V2i including: an optimal sensor placement, the sketch of the measurement mesh using a portable measuring arm, the actual measurements, the identification based on a modified version of the p-LSCF method and a visualization tool using reduction and expansion techniques.

The toolbox application is presented on a simple test case to demonstrate the achieved improvement in terms of outcome maximization of the modal analysis process.

1 Introduction

When speaking with customers, a modal analysis often comes down to the measurement and identification phases. These two parts of the process cannot be considered as stand - alone if the goal is to reach the best possible accuracy of the results. Ad hoc pre and post operations are essential to achieve the highest quality of the analysis outcome. The available commercial solutions provide several methods and tools to complement the pure data acquisition stage but frequently a tailored solution is required to respond to the client's specific needs. Therefore, additional tools can be implemented in conjunction with the commercial solutions.

The complete toolbox proposed by V2i includes:

- An optimal sensor placement tool. Starting from the numerical modal analysis results, the tool determines the set of sensor locations which returns the highest possible linear independency of the target mode shapes. The candidate sensor positions are restrained by the definition of the accessible surfaces. The implemented method also gives information on the target modes observability considering both the accessible and optimized set of sensors locations.
- The sketch of the measurement mesh on the investigated object using a portable measuring arm. The arm enables the precise knowledge of the sensors position and orientation which in turns reduces the error on the correlation indicators.
- The measurements performed thanks to commercial software and hardware suitable for both hammer and shaker excitations. These measurements are then imported into the V2i toolbox via the universal file format.
- An identification software based on a modified version of the Poly-reference Least-Square Complex Frequency method (p-LSCF). Compared to the method described in the literature [2], the assessment of the damping ratio is modified.

- Mode shapes visualization using reduction and expansion techniques, allowing an easier understanding of the modal deformation. Two methods have been implemented: an expansion using the SEREP method restrained on the skin faces and a projection based on the modal deformations at nodes paired with the experimental points.

Figure 1 shows the complete process implemented to perform a modal analysis. The use of some tools is restrained by the availability or not of numerical results.

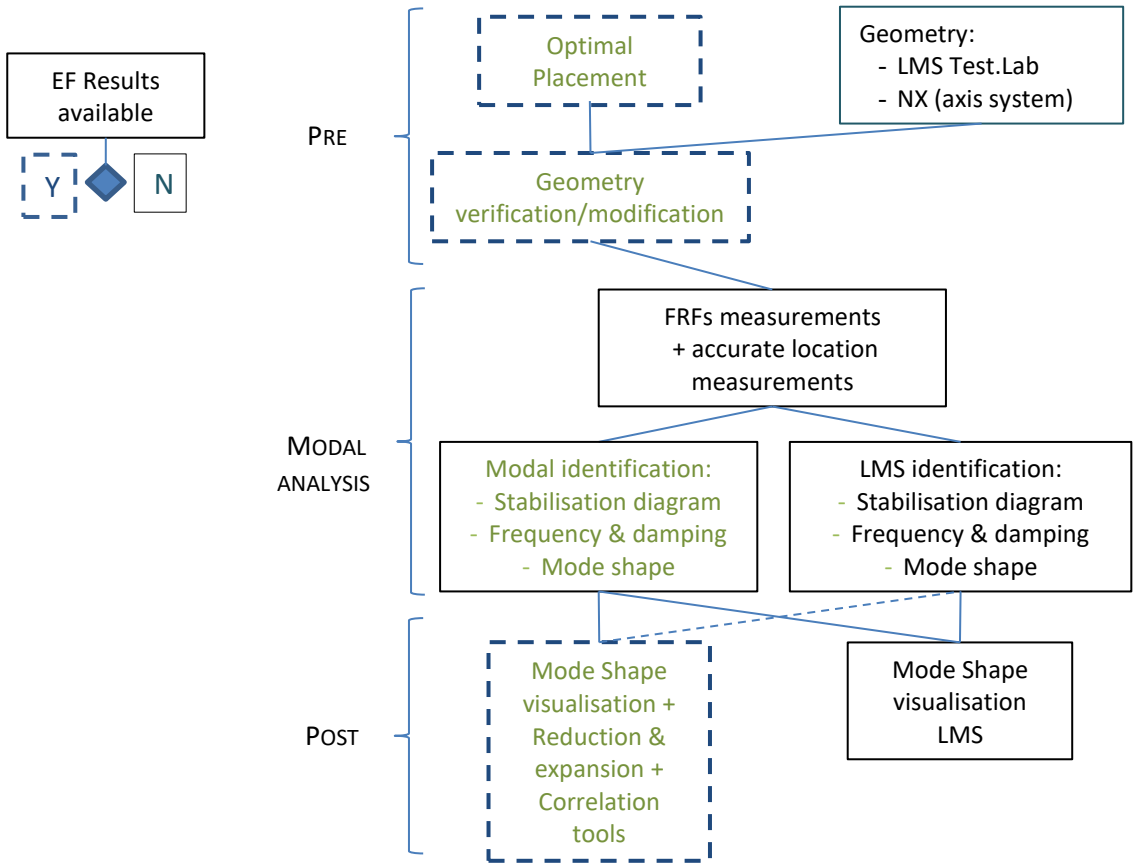


Figure 1: Modal analysis process diagram

2 The V2i toolbox for modal analysis

The current section aims to provide additional details regarding the theoretical backgrounds of three important blocks of the developed toolbox: the optimal placement, the identification algorithm and the visualization tools.

2.1 Optimal Sensor Placement

Modal analysis campaigns in industrial application often come down to a compromise among the reliability of the results, the available number of sensors and the time spent for the collection of experimental data. An intermediate preprocessing step has been foreseen to optimize beforehand the number and the location of sensors in order to exploit at best the resources allocated for the experimental stage.

2.1.1 Placement algorithm

The procedure is based on the methodology developed by Kammer [1] and it takes as input the modes computed from the finite element model of the structure and the maximum number of sensor to include in the modal analysis. The sensor placement process starts from a large set of candidate sensor locations from which the optimal sensor configuration will be selected. The procedure iteratively analyses the different sensor configurations targeting the one which ensures the highest linear independence of the selected modes and contemporarily maximizes the amount of information available in the sensor data. The methodology is implemented for monoaxial sensors even if triaxial accelerometers are typically used in modal analysis campaigns. An extension to triaxial sensors is found [3] but it resulted to be too cumbersome in terms of computational cost and it has therefore been discarded.

From a mathematical point of view, the optimal sensor placement problem is cast in the form of a state estimation problem and the output equation assumes a static Fisher model

$$z_s = \Phi_s q + v \tag{1}$$

in which z_s is the response at the sensor location for the sensor set *s*, Φ_s is the matrix containing the target mode shape partitioned to the sensor set *s*, q is the target modal response and v is a random noise characterized by zero mean and covariance matrix Q.

Applying an unbiased efficient estimator, the estimate error covariance matrix is

$$X = E[(q - \hat{q})(q - \hat{q})^T] = [\Phi_s^T Q^{-1} \Phi_s]^{-1} = F^{-1} \tag{2}$$

where F is the Fisher matrix information. Under the realistic hypothesis of sensors being affected by uncorrelated noise having similar noise statistics, the noise has no impact on the optimal placement strategy. Therefore, the methodology proposed by Kammer can be applied also in the more general case where no a priori noise statistic information is available.

The best estimation of the target modal response will be obtained by the sensor set which maximizes the Fisher matrix information in a suitable norm. In particular, the sensor set will be chosen in such a way that the determinant of the matrix F is maximized and consequently F will be full rank.

The contribution of each sensor location to the rank of the information matrix is computed starting from the eigenvectors Ψ and the eigenvalues λ of F and it corresponds to the diagonal of the following matrix

$$H = \Phi_s \Psi \lambda^{-1} \Psi^T \Phi_s^T \tag{3}$$

The algorithm computes the matrix E at each step and its diagonal elements are sorted in descending order. The sensor location which corresponds to the lowest ranked element is eliminated from the pool of available sensor locations. The optimized sensor set is obtained once the initial set of possible sensor locations is iteratively reduced to the desired number of sensors for the modal analysis.

2.1.2 Guided placement and mode observability check

The algorithm described in the previous section will return the sensor location set which maximizes the target modal response considering each finite element model node as possible location.

In several cases it is not possible to access all the area of the investigated structure either for safety reason or due to lack of space for the placement of a given sensor. The limited accessibility of a structure has a major influence on the detectability of local modes and the eventual unobservability could not be fully captured from the standard AutoMAC computation. As the placement methodology aims to maximize the strength of the target modal response in the sensor data, the inclusion of unobservable modes may lead to a suboptimal sensor set which tries to capture a mode which presents quasi-zero mode shape for the totality or the great majority of the candidate sensor locations.

The analysis of the diagonal terms of the inverse of the Fisher information matrix of Equation (2) computed at the first iterative step of the algorithm helps in the identification of the unobservable modes without

requiring any additional processing step. In particular, the diagonal term correspondent to an unobservable mode will be significantly higher than the one correspondent to an observable mode.

The algorithm can be therefore guided towards a meaningful optimal placement not only by limiting the initial set of locations to the effectively accessible ones but also by eliminating the modes which would be by default impossible to capture correctly. Moreover, in order to keep the computational time below acceptable limits, all the degrees of freedom for which the sum of the modal amplitude is lower than a defined threshold are removed in the first step.

A second improvement has been achieved by considering the size of the sensors. The placement does not may identify as optimal 2 nodes which could eventually be measured by a single sensor. In this case, in a post analysis stage, only the location which gives the highest contribution to the determinant of F is retained leaving the possibility for an eventual additional sensor to be placed on the structure.

A third improvement is achieved by weighting the modes according to their modal mass to privilege the sensor placement which enhances the identification of the most significative structural modes.

The methodology will be applied to a meaningful test case whose results are reported in Section 3. As anticipated in Section 2.1.1, the placement algorithm considers each degree of freedom as measured separately. The flow diagram related to the Optimal placement block is shown in Figure 2

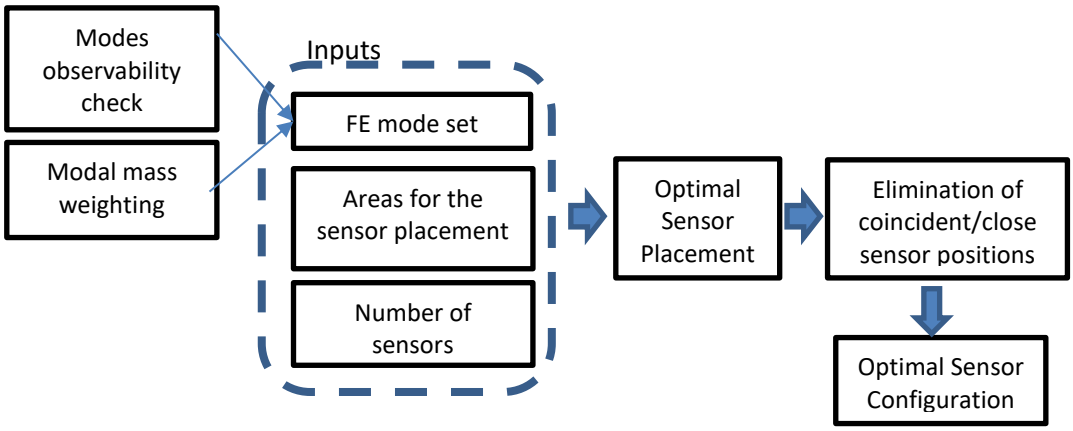


Figure 2: Optimal placement block flow diagram

2.2 Modal Analysis – Measurement and Identification

The propaedeutic step of section 2.1 aims to enhance the quality of the outcome of the modal analysis campaign central phases: the measurements and the identification. The Siemens LMS software and acquisition hardware are used to measure the Frequency Responses Functions (FRFs). If a high spatial resolution is expected or a high accuracy correlation is requested, precise geometrical measurements of the accelerometer locations or of the laser measurement points can be performed thanks to a portable measuring arm (Figure 3). The information about the orientation of the sensor is retrieved by taking a measurement point for each face of the accelerometer. The geometry of the measurement mesh can then be updated according to the new available information before the actual start of the measuring campaign which will allow to collect a suitable amount of data. The measured FRFs will then be transferred to the identification algorithm in order to extract the modal characteristics of the analyzed structure.

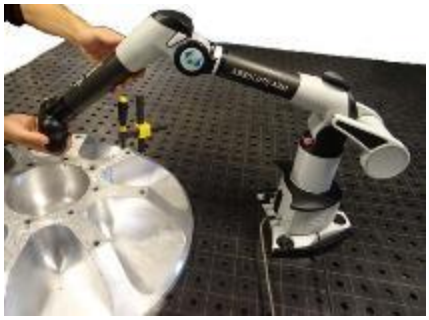


Figure 3: Romer Absolute Portable arm [4]

2.2.1 The V2i identification algorithm

The Poly-Reference Least-Square Complex Frequency (p-LSCF - [2]) identification method available in commercial solution is known to deliver clear stabilization diagram in which the stochastic poles (also known as the mathematical poles) are separated from the physical poles. It is shown in literature that this interesting property is achieved thanks to an appropriate choice of the constraint in the solving of the least-square problem. The same study demonstrates also that, in case of low signal to noise ratio, the damping ratio assessment is underestimated [5]. This situation can occur when the damping level is high and when the noise on the measurement is not as good as desired. Different solutions have been proposed to improve the damping estimation such the Frequency-domain maximum likelihood estimation [6]. However, these kind of identification methods are iterative and more time consuming, therefore not suitable in many industrial cases.

A new solution is developed at V2i to tackle the damping underestimation and to improve the pole identification by solving two least-square problems: one for each of the two opposite choices of constraint. The stabilization diagram is built according to the p-LSCF method, allowing to obtain a clear diagram, but the frequencies and the damping ratios are computed with the second resolution on the paired poles. To the authors' knowledge, the proposed method is not yet described in the literature. A future paper will describe more deeply the developed methodology.

In order to assess the improvement achieved, the method is tested on a simple test case. A clamped beam numerical model is built and the FRFs are computed at 10 equally spaced points considering an excitation applied at the beam tip. The damping ratio is imposed to be equal to 1 percent for each mode. Artificial uncorrelated noise (uniformly distributed random value between a certain percentage of the maximal value of the real- and the imaginary part of the FRF) is added to the real- and the imaginary parts of the FRFs independently (Figure 4).

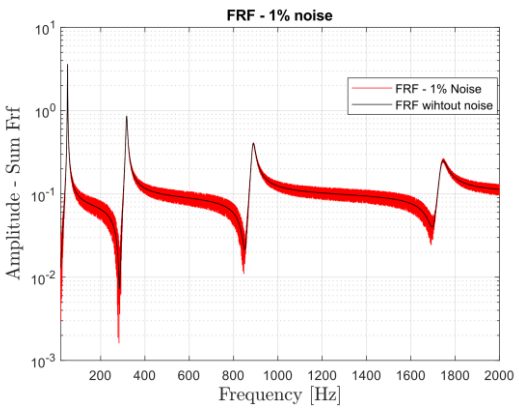


Figure 4: Simulated FRFs with and without noise

Three different modal identification methods (p-LSCF, LSCE and proposed modified p-LSCF) are used to assess the sensitivity with respect to the noise level on the accuracy of the pole estimation.

The main conclusions derived from the comparison of the three methodologies are:

- Clear stabilisation diagrams are generated by the p-LSCF (Polymax) and the proposed methods;
- The LSCE method stabilization diagram is polluted by mathematical poles therefore, the pole selection becomes difficult especially for the higher orders;
- The poles are well separated thus the error on the frequencies estimation is low for the three methods;
- The damping ratio is underestimated for the p-LSCF method and overestimated for the two other methods. The influence of making the stochastic poles unstable in the p-LSFE method is higher than in the case where the mathematical poles are stable (proposed method and LSCE). The relative error is lower when the proposed method or the LSCE method are applied.

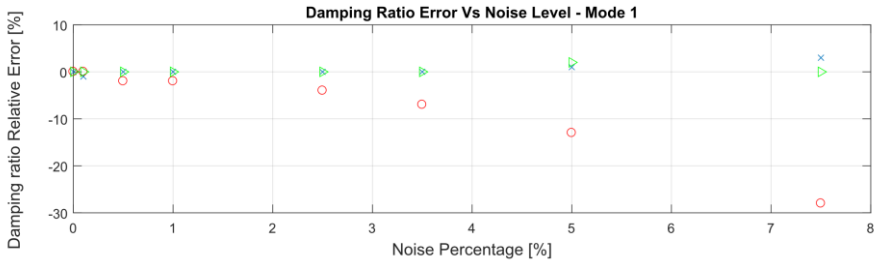


Figure 5: Damping ratios relative error for different level of added noise – Mode 1: red circle - p-LSCF, green triangle - LSCE and blue cross - modified p-LSCF

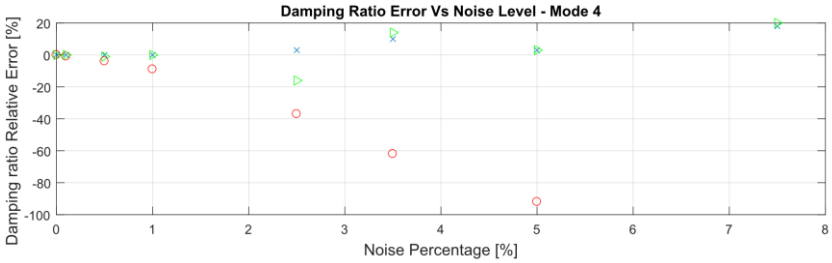


Figure 6: Damping ration relative error for different level of added noise – Mode 4: red circle - p-LSCF, green triangle - LSCE and blue cross - modified p-LSCF

Figure 7 compares the poles identified for the two considered constraints. For the classical p-LSCF method, the mathematical poles are separated to the physical poles (real part of opposite sign). For the second type of constraint (link to the sense of rotation on the unitary circle), all the poles are of same sign. The difference on the radius estimation (frequency) is relatively low. The error on the real part pole estimation is higher for the classical p-LSCF method, which induces a higher error on the damping ratio estimation. Therefore, the proposed methodology is capable of performing a more accurate poles identification with a minimum incidence on the total identification computational cost.

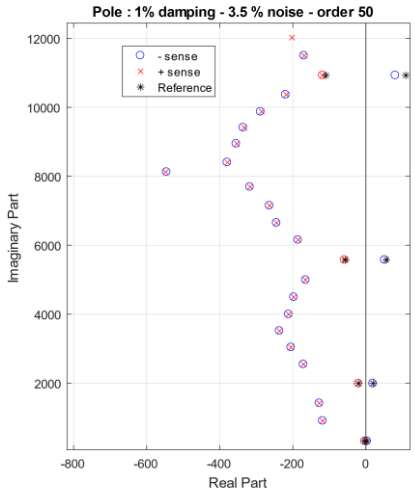


Figure 7: Influence on the mathematical pole stability

2.3 Expansion and reduction techniques for visualization and correlation

Natural frequencies and damping ratios are an important part of the modal identification of a structure but the mode shapes are often the ultimate goal of a modal analysis campaign. In the proposed toolbox, the mode shapes are computed using the LSFD algorithm [7]. For most of the cases, only a few measurement points are available, making the classical wireframe visualization difficult to interpret and understand for a non-expert public. Moreover, tools to easily perform the correlation between the experimental data and the numerical models are in general not directly available in commercial software (even if the actual trend shows that will be available in the future).

An in-house software tool has been developed to fulfill these needs and improve the modal analysis results sharing.

Two kinds of tools are available to ease the interpretation of the experimental mode shapes and to perform correlation with the numerical mode shapes:

1) The reduction of the finite element model on the experimental point set is automatically performed by searching the closest finite element nodes to each of the measurement points. The searching base for the nodes set is reduced to the skin nodes. A final visual check of the paired node/point is performed to avoid possible mistakes.
2) The expansion of the experimental results on the finite element modal basis is implemented. Due to the difficulty to import the mass and stiffness matrices from the numerical model, the SEREP method [8] is considered which is based on only the modal basis information. The user can choose to take into account all the finite element nodes or only the nodes of the skin. The reduction to the skin nodes does not affect the accuracy of the method. The expansion allows in most of the case to ease the interpretation of the mode shape and to communicate more efficiently with the customer the results of the analyses.

The correlation (MAC computation) can be calculated on the reduced data or on the expanded data.

3 Results

3.1 Test case description

The test object considered for the validation of the proposed methodology is a pyramidal structure which can be used as tooling for shaker based vibration tests. The tooling purpose makes of the outmost importance the accurate determination of its modal behavior to guarantee a correct interpretation of the vibration tests.

The structure is made of Aluminum and it weights approximately 220 kg.

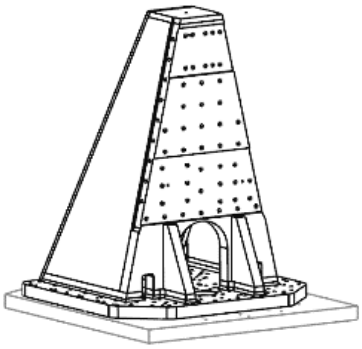


Figure 8: Geometry of the considered structure

An updated finite element model has been implemented in a commercial software to extract the modes shapes of the structure considering it clamped to the shaker table. Among the mode set computed between 50 and 2000 Hz, 7 modes have been identified as crucial for the modal analysis. Two modes are shown in Figure 9.

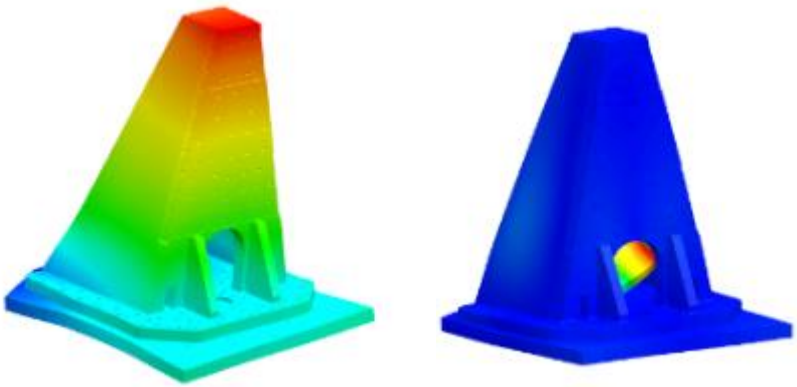


Figure 9: Example of a global and a local mode

3.2 Optimal Placement

A set of 20 sensors is placed using the optimal placement algorithm in order to ensure the best possible detection of the modes of interest. The placement areas are limited to the accessible areas of the structure: the external surfaces, the top, the upper surface of the base and part of the internal wall.

The algorithm returns the points indicated in red in Figure 10.

The zoom of Figure 11 draws the attention to the limitation of the original methodology highlighted in section 2.1.2. As the algorithm considers the full point set as possible location, it can identify two optimal location which would fall under the same sensor area. In such a situation, the proposed modified algorithm

preserves only the position which guarantees global higher linear independence of the target mode set. The final sensor number is then reduced to 7 which correspond to the MAC of Figure 13

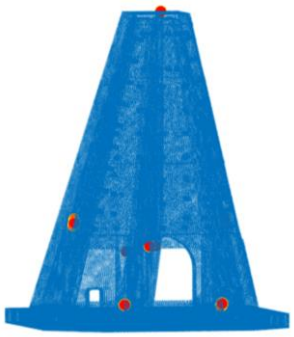


Figure 10: Optimal placement

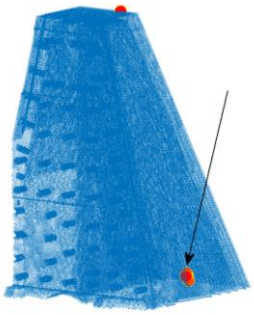


Figure 11: Detail of the optimal placement: coincident accelerometers

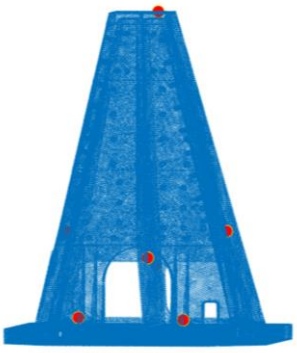


Figure 12: Proposed set

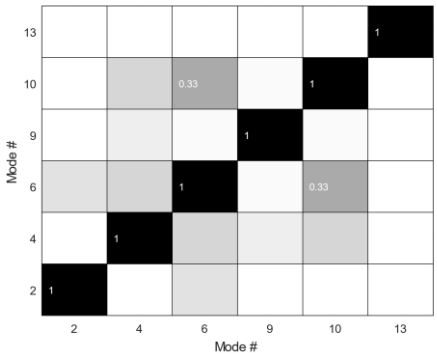


Figure 13: AutoMAC correspondent to the proposed sensor set

In order to highlight the potentiality of the applied methodology a sensor set of equal size (7 sensors) has been manually chosen identifying the maxima of the considered mode set. The positioning is shown in Figure 14 and the corresponding AutoMAC is shown in Figure 15. The two sets share some common points but comparing the AutoMAC of Figure 13 and Figure 15 it is clear the advantage deriving form the optimal placement algorithm especially when it comes to the correlation among modes which are closely spaced in frequency.

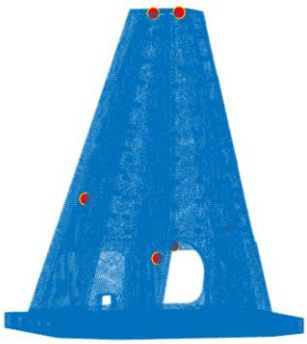


Figure 14: Manually chosen set of 7 sensors

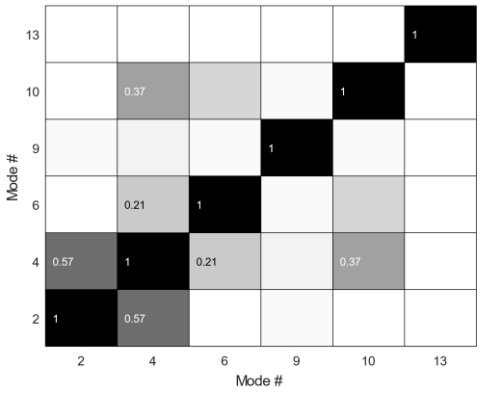


Figure 15: AutoMAC correspondent to a manual chosen set of 7 sensors.

One of the most relevant challenges of the modal analysis in the industrial environment is to find an efficient way to represent the obtained results. It is evident from Figure 12 that a representation of mode shapes based on only the selected point would not allow to visually capture the envelope of the mode shapes. Therefore 12 sensor locations have been added to the optimal set, bringing the total number of measurement points to 19. The extended sensor set eliminates the correlation between mode 5 and mode 10. Conversely, the attempt to correctly capture mode 2 results in a sensor set which provides a worse AutoMAC for the modes 2 and 4 given the high similarity of their mode shapes.

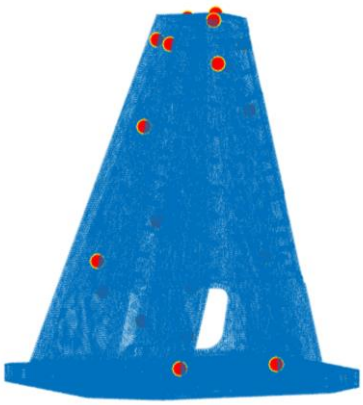


Figure 16: Extended point set

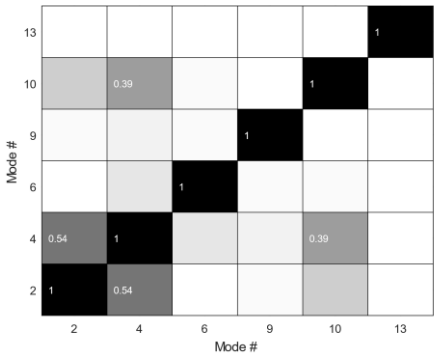


Figure 17: AutoMAC correspondent to the extended point set

3.3 Modal identification

Measurements of the FRFs are performed thanks to LMS Test.Lab software. The specimen is excited by an impact hammer on a point located on the top part of the tooling while the response is measured at the points determined as being optimal.

The measured FRFs are injected as input in the modal identification algorithm. Interface tools have been developed to allow the transfer of data between commercial software and the in-house identification tools using the universal file format.

In this paper, the results obtained with the proposed modified version of the p-LSCF is compared to the results coming from the use of the Polymax and the LSCE algorithm available in commercial software.

Table 1 compares the results (frequencies and damping ratio) identified with the three different algorithms. Figure 18 to Figure 20 show the stabilization diagrams obtained for the three methods (the modified p-LSCF is built with V2i software and the two others with LMS Test.Lab). The poles which are not clearly stabilized are not considered. These correspond for most of them to mode not well excited (orthogonal to the excitation). A MIMO analysis will be needed to identify properly these poles.

The following conclusions can be drawn:

- There are no significant differences in the identified frequencies;
- The damping ratio determined with the modified p-LSCF and the LSCE algorithm are similar but are higher than the ones determined with Polymax. The available data do not allow to judge which is the most correct estimation, anyway the considered testcase proves that a special attention has to be taken when dealing with highly damped modes (or with low signal to noise ratio).
- The stabilization diagrams for the two versions of the p-LSCF give clear stabilization diagram with the non-physical poles eliminated. The LSCE diagram is really complicated to interpret. Due to noise level and the considered frequency bandwidth, a high order is needed to stabilize on all the modes.

Frequency [Hz]			
#	Modified-PLSCF	Polymax	LSCE
1	130	129.75	130.25
2	287.25	291.25	/
3	400	399.75	397.5
4	543.75	539.5	/
5	628.25	628.25	628.25
6	750.5	751.75	/
7	813.75	814.25	813.5
8	833.25	833	833.25

Damping ratio [%]			
#	Modified-PLSCF	Polymax	LSCE
1	3.5	2.9	3.5
2	2.9	0.43	/
3	2.2	2.00	2.2
4	4.1	1.68	/
5	0.28	0.26	0.29
6	1.71	1.96	/
7	2.26	1.62	2.2
8	0.62	0.59	0.61

Table 1: Comparison of identified frequencies and damping ratio for: a) modified p-LSCF – b) Polymax – c) LSCE

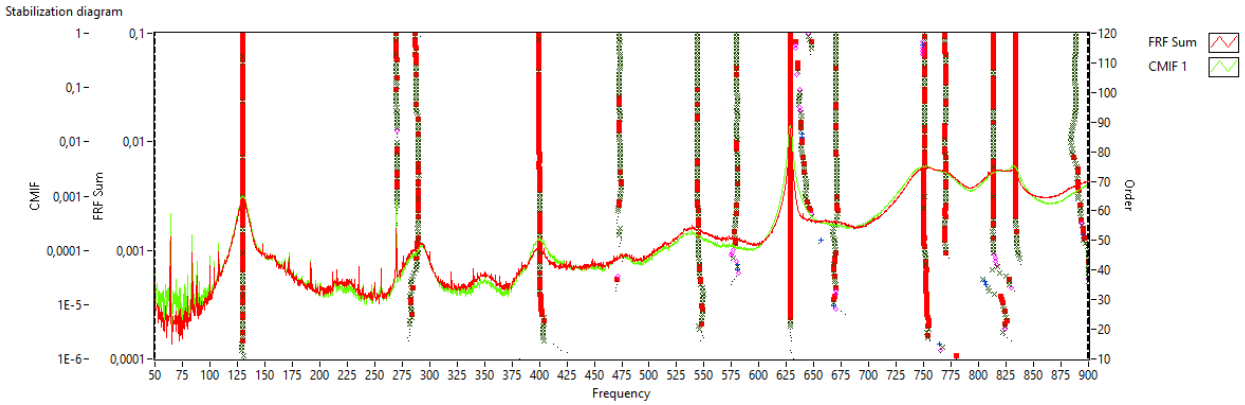


Figure 18: Modified p-LSCF stabilization diagram (

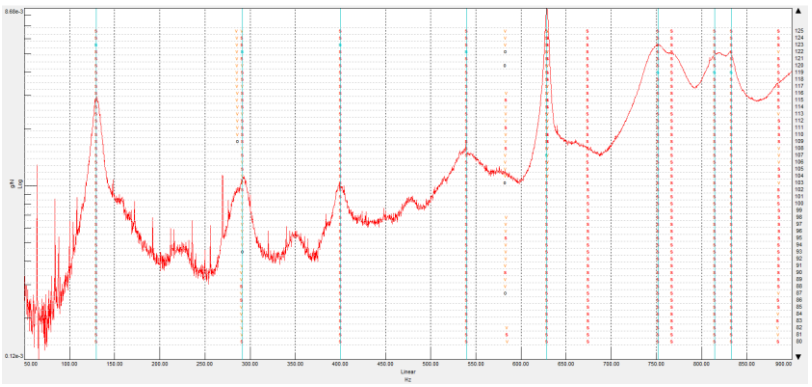


Figure 19: Polymax stabilization diagram

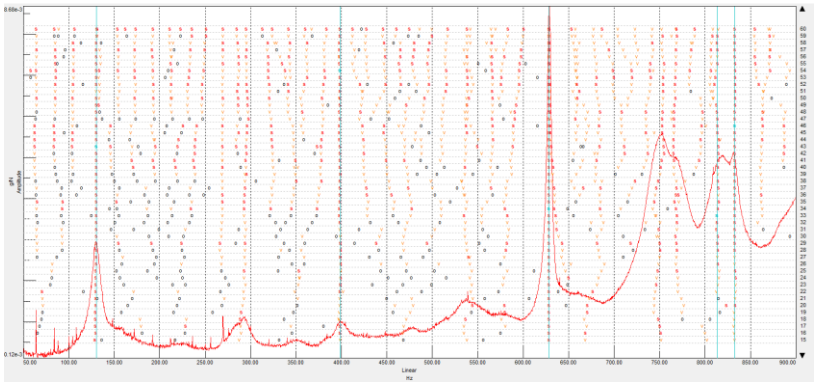


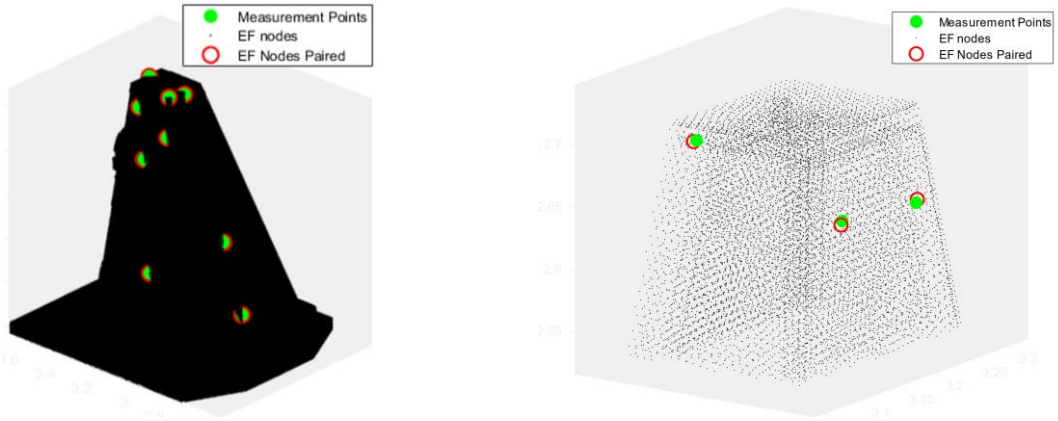
Figure 20: LSCE stabilization diagram

From these poles, the mode shapes are computed using the LSCF algorithm.

The test case shows that the modification of the p-LSCF algorithm allows keeping a clear stabilization diagram characteristic with an improvement in the damping ratio assessment in case of low signal-to-noise ratios.

3.4 Correlation – reduction/expansion

The developed toolbox allows to perform the numerical -experimental correlation and therefore to improve the efficiency of the result dissemination. First, the reduction is made, i.e. the experimental measurement points are paired with the finite element nodes. Visualization tools allows checking the accuracy of the association operation (Figure 21). If needed, manual definition of the pairing experimental/numerical points can be performed.



(a) *(b)*

Figure 21: Pairing operation – reduction: (a) all paired points and (b) detailed view on top points

After the reduction step, the Modal Assurance Criterion matrix can be computed. For this particular application, the analysis of the MAC shows that some modes are not well correlated. In particular, for the modes #4 and #6, this can be explained with a poor excitation in the maximum effective mass direction. As final check, the toolbox allows the visual comparison of the mode shapes on the reduced or on the expanded modes shapes for the experimental and the numerical results.

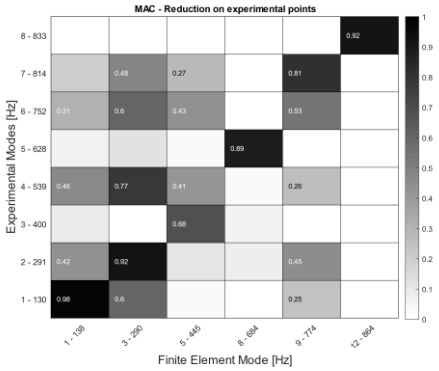
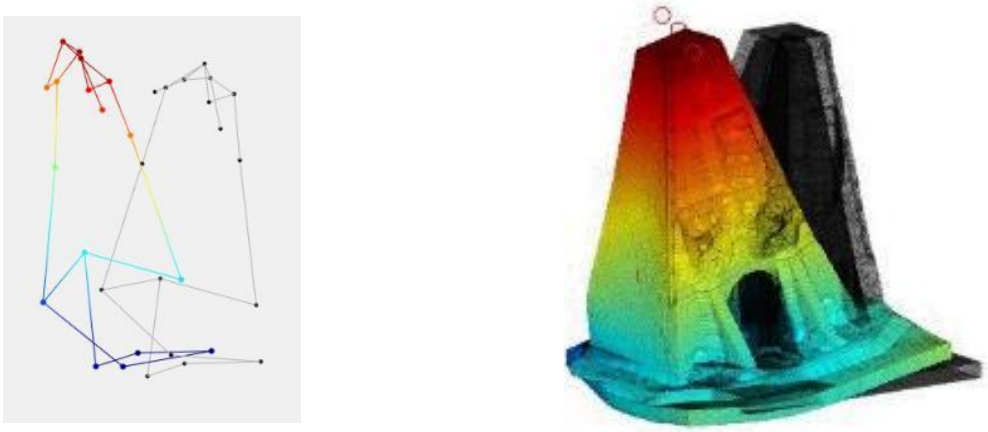


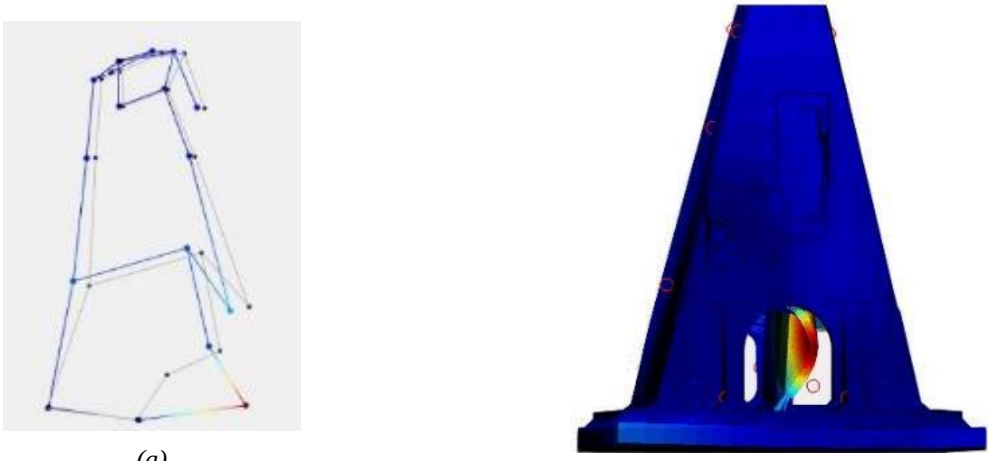
Figure 22: Modal Assurance Criterion – Reduction

As shown in Figure 23 and Figure 24, the expansion of the experimental results on the numeric mode shape basis makes easier the understanding of how and where is located the deformation of each considered mode. The dissemination of the result is more efficient. Such results of the expansion are only possible if a) the numerical model is well correlated or b) a sufficient number of modes is introduced in the modal basis.



(a) *(b)*

Figure 23: Mode shape #1 – global mode: (a) measured and (b) expansion



(a) *(b)*

Figure 24: Mode shape #5 – local mode: (a) measured and (b) expansion

4 Conclusions

A complete toolbox is presented in order to enhance in the reachable quality of the modal analysis results, including an improvement of standard methodologies.

A traditional optimal sensor placement approach has been revised to make the algorithm more suitable to industrial frameworks allowing to predefine the placement areas and the sensor size. A prefilter of the mode base based on the effective mode observability has been also implemented to ensure the optimality of the selected sensor set.

The core element of modal analysis, the identification algorithm, has been ameliorated: a modified version of the well-known p-LSCF identification methods is proposed to merge in a single algorithm the advantages of a clear stabilization diagram and a diminished pollution of the unstable poles on the stable ones.

As final step, reduction and expansion techniques are implemented to allow the computation of numerical/experimental correlation and to improve the ease of results dissemination along with their transferability.

In a further work, the toolbox will be enriched with customizable additional identification method and indicators. From an experimental point of view, the plan is to add an automatic measurement process using a 6-axis robotic arm driven by the CAD model.

Acknowledgements

Part of the present work is carried out in the framework of the "AERO+" project funded by Wallonia DG06 under contract N°7445.

References

[1] D. Kammer and L. Yao, "Enhancement of on-orbit modal identification of large space structures through sensor placement," *Journal of Sound and Vibration,* vol. 171, no. 1, pp. 119-139, 1994.

[2] B. Peeters, H. Van der Auweraer, P. Guillaume and J. Leuridan, "The PolyMAX frequency-domain method: a new standard for modal parameter estimation?," *Shock and Vibration* , vol. 11, pp. 395-409, 2004.

[3] D. C. Kammer and M. L. Tinker, "Optimal placement of triaxial accelerometers for modal vibration tests," *Mechanical Systems and Signal Processing,* vol. 18, no. 1, pp. 29-41, 2004.

[4] "ROMER Absolute Arm," HEXAGON Manufacturing Intelligence. [Online].

[5] B. Cauberghe, P. Guillaume, P. Verboven, S. Vanlanduit and E. Parloo, "On the influence of the parameter constraint on the stability of the poles and the discrimination capabilities of the stabilisation diagrams," *Mechanical Systems and Signal Processing,* vol. 19, pp. 989-1014, 2005.

[6] P. Guillaume, P. Verboven and S. Vanlanduit, "Frequency-domain maximum likelihood identification of modal parameters with confidence intervals," in *Proceeding of the 23rd International Seminar of Modal Analysis* , Leuven (Belgium), September 1998.

[7] J. Busturia and J. Giminez, "Multi-excitation Multi-response Non-linear Least Squares Algorithm," in *Proceeding of ISMA 10*, Leven, Belgium, 1985.

[8] J. O'Callahan, P. Avitabile and P. Riemer, "System Equivalent Reduction Expansion Process (SEREP)," in *Proceeding of the Seventh International Modal Analysis Conference* , Las Vegas, Nevada, 1989.

Towards an application of an active tendon in rotorcraft: A numerical and experimental study of coupled bending-torsion vibration of a beam-tendon system

V. Ondra[1], **R. Dibble** [1], **B. Titurus**[1]
[1] University of Bristol, Department of Engineering,
Queen's Building, University Walk, Bristol, BS8 1TR, United Kingdom
e-mail: **vaclav.ondra@bristol.ac.uk**

Abstract

This paper presents a numerical and experimental study of coupled bending-torsion vibration of a beam loaded by a tendon-induced axial force. The rotating beam-tendon system is described using a set of partial differential equations and free vibration analysis is performed. The model is validated against a bench-top experiment which features a reinforced open-section cantilever beam subjected to tendon loading. A satisfactory agreement between the numerical and experimental results is obtained and it is shown that the tendon not only reduces the natural frequencies of the beam, but also introduces frequency loci veering. The validated model is then used to perform a case study on the Bo105 helicopter to present some benefits of incorporating a tendon in a rotorcraft blade, making a first step towards an active tendon concept. This concept should eventually allow rotorcraft to operate with a variable rotor speed, thereby increasing their performance and efficiency.

1 Introduction

In recent decades there has been a growing interest in many fields of technology, including civil, mechanical and aerospace engineering, in active and adaptive control of structures [1]. A far-reaching motivation of this study is to develop a new concept for rotorcraft blade control, whereby an active tensile member (hereafter referred to as a tendon) would be used as a means of adaptively manipulating a rotor's dynamic properties. Once this control mechanism has been perfected, it should also help to reduce air pollution and noise emission, decrease a fuel burn and increase the overall performance of rotorcraft. These benefits would be achieved by allowing rotorcraft to operate at a wider range of rotor speeds as opposed to the current state-of-the-art designs where the rotor speed is almost constant in order to avoid potentially harmful resonances of the blades [2]. This concept was already introduced in [3–5], but many of its aspects have not yet been fully addressed and experimentally validated.

Tendons or other means of applying compressive axial loading have already been used in a number of applications, often as actuators or a means of vibration control. A comprehensive review of active cable and tendon control can be found in [1, 6]. From a number of studies that utilised tendons, a few used a similar configuration to the present one, i.e. a beam-like structure loaded by a tendon. For example, in [7, 8] a tendon was used for vibration control of a simple cantilever beam. It was found that vibration energy of the beam in a prescribed frequency range can be removed by applying and releasing the tension in a specific manner, thereby effectively suppressing the vibration of the beam. These studies mainly focused on the control aspects of the problem, but the modelling of the dynamic response was also performed using the Euler-Bernoulli beam theory and the presence of the tendon was accounted for by an axial force. The same approach of modelling a beam-cable system was also employed in [9] with the difference that the tendon was

made of a shape-memory alloy. It was shown therein that in addition to the vibration suppression by means of an active control, a significant amount of damping can be introduced to the system by the tendon. In the previous studies, simple beam models with an axial force were considered, partly because the dynamics of such axially-loaded beams has been well understood [10]. In contrast, the use of cable that is mounted inside a helicopter tail boom for response suppression was numerically and experimentally investigated in [11]. Unlike in the previous studies, the system was modelled using the finite element method. It was shown that the cable can be tuned as a active vibration absorber which not only positions an antiresonance at the excitation frequency for a critical location on the primary structure, but also shifts the natural frequencies of the system. The interaction between the primary structure and the cable in terms of eigenvalue curve veering was also observed.

The present paper deals with the dynamic analysis of the beam-tendon system which is an idealisation of the active tendon concept whose development motivates this study. The present paper extends [3] by considering the bending-torsion coupling of the primary beam and using a more sophisticated model of the tendon. To the best knowledge of the authors, the same means of modelling has not yet been reported in literature. The paper is organised as follows: in section 2 the mathematical model of the beam-tendon system and the numerical approach used to obtain the modal properties are introduced. Then, the experimental set-up is described in section 3 and the computed results are compared to the experimental ones. In section 4 it is briefly shown how the presence of the tendon modifies the rotor properties of the Bo105 helicopter. Lastly, the discussion and future challenges are given in section 5.

2 Modelling approach

The system under consideration is a rotating straight cantilever beam with a cross-section which has one axis of symmetry (therefore featuring bending-torsion coupling) and is axially loaded by a tendon. The tendon is attached to the beam's tip, passes through its whole body (parallel to the neutral axis) and is fixed at the same location as the beam. The tendon can be placed in any location on the axis of symmetry of the cross-section. A tip mass which serves as a tendon attachment point is located at the free end of the beam (see the experimental set-up in Fig. 1 for detail).

The beam is modelled by means of the Houbolt-Brooks equations [12] which were modified to include the effect of the tendon-induced axial force while the tendon is modelled using the wave equations [13] augmented by the effects of centrifugal forces. The blade and tendon are coupled via the boundary conditions at the tip (free end). At the root, both are fixed so their displacements are equal to zero. At the tip, the displacement of both are identical and the tendon-induced axial force contributes to the shear and moment conditions of the blade. Since the tendon is free to vibrate inside the blade, no other connectivity conditions were enforced.

A set of partial differential equations (PDEs) describing the blade with the tendon can be written as (the terms that are not included in the original Houbolt-Brook equations [12] are underlined and the pre-twist $\beta(x)$ is equal to zero)

$$\left(EI_1 w'' - Te_A\phi + \underline{Pe_P\phi}\right)'' - \left(Tw' - \underline{Pw'} + \Omega^2 mxe\phi\right)' + m(\ddot{w} + e\ddot{\phi}) = 0, \tag{1a}$$

$$\left(EI_2 v''\right)'' - \left(Tv' - \underline{Pv'}\right)' + m(\ddot{v} - \Omega^2 v) = 0, \tag{1b}$$

$$\begin{aligned}\left(\left[-GJ - Tk_A^2 + \underline{Pk_A^2}\right]\phi'\right)' - (Te_A - \underline{Pe_P})w'' + \underline{P(e-e_P)\beta_y\phi''} \\ + \Omega^2 m\left(xew' + \left[k_{m2}^2 - k_{m1}^2\right]\phi\right) + m(k_m^2\ddot{\phi} + e\ddot{w}) = 0,\end{aligned} \tag{1c}$$

$$Pw_{\mathrm{t}}'' - \left(T_{\mathrm{t}} w_{\mathrm{t}}'\right)' - m_{\mathrm{t}}\ddot{w}_{\mathrm{t}} = 0, \tag{1d}$$

$$Pv_{\mathrm{t}}'' - \left(T_{\mathrm{t}} v_{\mathrm{t}}'\right)' - m_{\mathrm{t}}\left(\ddot{v}_{\mathrm{t}} - \Omega^2 v_{\mathrm{t}}\right) = 0, \tag{1e}$$

where $\dot{(\bullet)}$ and $(\bullet)'$ are time and spatial partial derivatives, respectively, $w(t,x), v(t,x)$ are, respectively, flapping (out-of-plane of rotation) and lead-lag (in-plane of rotation) bending displacements of the beam, $\phi(t,x)$ is a torsional displacement, x is the independent spatial variable measured along initial position of the elastic axis ($0 \leq x \leq R$), R is the length of the beam, t is time, EI_1 and EI_2 are the flapping and lead-lag rigidity, respectively, GJ is the torsional rigidity, e_A is the distance between tensile and elastic axes, e is the distance between mass and elastic axes, Ω is the angular velocity of rotation, m is the mass of the beam per unit length, k_A is the polar radius of gyration of cross-sectional area, k_{m1} and k_{m2} are the polar radii of gyration, k_m is the polar radius of gyration of cross-sectional mass about elastic axis, β_y is a cross-sectional parameter, $w_\mathrm{t}(t,x), v_\mathrm{t}(t,x)$ are flapping and lead-lag transversal displacements of the tendon, respectively, P is the applied tension (always positive) of the tendon, m_t is the mass of the tendon per unit length, and e_P determines the position of the tendon. If $e_P = 0$ the tendon coincides with the elastic axis whereas for $e_P = e$ with the mass axis. The centrifugal forces acting on the beam and the tendon are given by

$$T = \Omega^2 \int_x^R m\hat{x}\,\mathrm{d}\hat{x}, \qquad T_\mathrm{t} = \Omega^2 \int_x^R m_\mathrm{t}\hat{x}\,\mathrm{d}\hat{x}, \tag{2}$$

Equations (1a)-(1c) are the modified Houbolt-Brooks equations which include the tendon-induced axial force P. Since these equations are based on the Euler-Bernoulli theory, which neglects the transverse shear deformation, rotary inertia effects and warping, an infinitely rigid planar cross-section that remains planar and normal to the elastic axis after the deformation is assumed [14]. Equations (1d) and (1e) are the wave equations describing the motion of the tendon under the assumption that its cross-sectional area remains unchanged during deformation (the Poisson's effect is not included) [13].

The PDEs are accompanied by an appropriate set of boundary conditions (BCs) which ensure the coupling between the tendon and the beam at the tip. The boundary conditions at the fixed end (for $x = 0$) are

$$v = w = \phi = v' = w' = w_\mathrm{t} = v_\mathrm{t} = 0, \tag{3}$$

and at the free end (for $x = R$)

$$Q = 0 = (GJ - \underline{P(e - e_P)\beta_y - Pk_A^2})\phi', \tag{4a}$$

$$M_y = 0 = EI_1 w'', \tag{4b}$$

$$M_z = 0 = EI_2 v'' + \underline{Pe_P}, \tag{4c}$$

$$V_z = 0 = -M_y' + m_\mathrm{tip}\ddot{w} - \underline{Pw'} + \Omega^2 mex\phi + \underline{Pw_\mathrm{t}'}, \tag{4d}$$

$$V_y = 0 = -M_z' + m_\mathrm{tip}\ddot{v} - \underline{Pv'} + \Omega^2 mex + \underline{Pv_\mathrm{t}'}, \tag{4e}$$

$$w_\mathrm{t} = w + e_P\phi, \tag{4f}$$

$$v_\mathrm{t} = v + e_P, \tag{4g}$$

where m_tip is the mass located at the tip. Equation (3) prescribes zero displacements and slopes of the blade, and zero displacements of the tendon at the fixed end. Equations (4a)-(4c) prescribe zero torque and moments (including the moments induced by the tendon) at the tip of the blade. The blade is coupled with the tendon through the shear boundary conditions (Eqs. (4d) and (4e)), and the displacement equality at the tip enforced by Eqs. (4f) and (4g). The tip mass, characterised by m_tip, also contributes to the shear boundary conditions at the tip.

It should be noted that while the rotating beam-tendon system has not yet been studied in literature, a beam featuring the bending-torsion coupling loaded by an axial force placed in an arbitrary position of the cross-section has been previously considered. In particular, in [15,16] a system of equations describing such beam, albeit without inertial forces ($m = 0$), was used to analyse its structural stability. The same set of equations, augmented by the inertial forces ($m \neq 0$), was also used in [17] to investigate the response to deterministic

and random excitation. The PDEs introduced in Eqs. (1a)-(1c) reduce to the equations used in [17] when the centrifugal force T is removed, and to the equations used in [15, 16] for $m = 0$.

In order to evaluate the modal properties (natural frequencies and mode shapes) of the beam-tendon system, an assumption of the normal mode is used. A solution of any given dependent variable is expressed as the multiplication of the time-invariant mode shape and the time-varying harmonic function of the constant frequency in the following form

$$\begin{gathered} w(t,x) = W(x)\mathrm{e}^{\mathrm{i}\omega t}, \quad v(t,x) = V(x)\mathrm{e}^{\mathrm{i}\omega t}, \quad \phi(t,x) = \phi(x)\mathrm{e}^{\mathrm{i}\omega t}, \\ w_{\mathrm{t}}(t,x) = W_{\mathrm{t}}(x)\mathrm{e}^{\mathrm{i}\omega t}, \quad v_{\mathrm{t}}(t,x) = V_{\mathrm{t}}(x)\mathrm{e}^{\mathrm{i}\omega t}. \end{gathered} \tag{5}$$

Substituting the normal mode forms into Eqs. (1) and (4) allows one to eliminate time and rewrite the PDEs into a system of first order ordinary differential equations (ODEs) that, together with the BCs, define a boundary value problem. This boundary value problem can then be solved by a Matlab bvp4c solver [18] for unknown natural frequencies ω and corresponding mode shapes $W(x)$, $V(x)$, $\phi(x)$, $W_{\mathrm{t}}(x)$ and $V_{\mathrm{t}}(x)$. This solver is very versatile since it uses a collocation method but may suffer from a decreased numerical performance if an appropriate starting guess is not provided.

3 Experimental validation

In this section, the theoretical model is validated using a bench-top experiment. A similar experiment has been already presented in [3], where the pure bending of an Euler-Bernoulli beam loaded by a tendon has been considered.

3.1 Experimental set-up description

The picture of the bench-top experiment can be seen in Fig. 1. The beam (whose properties are detailed in section 3.2) is rigidly clamped at one and free at the other end. The tendon is attached to the tip mass mounted at the free end of the beam, and passes freely inside the beam towards the clamp where its flexural motion is constrained. The tendon then continues through the clamp and pulley and is attached to a hanging platform. The tension of the tendon, and hence the axial load applied to the beam, is controlled by the amount of mass placed on the platform. The tendon can be attached in several discrete positions along the cross-sectional axis. Two notable positions, i.e. the mass and elastic axis, that are further discussed in this paper are marked in the inset in Fig. 1. The applied tension and the placement of the tendon will be shown to have an influence on the dynamic response of the system.

The beam is excited using a modal shaker to obtain frequency response functions (FRFs). A shaker was preferred to a modal hammer because of the repeatability that is required due to a large number of measurements needed to validate the theoretical model for a wide range of loading cases. Moreover, it was also observed in [3] that few tendon-dominated modes can be excited using a modal hammer. The shaker was controlled via a modular control and data acquisition (DAQ) system. Random excitation, which linearises possible weak non-linearities, such as the friction between the tendon attachment and the tip mass, was used to excite the frequency range between 5 and 400 Hz. The response data were collected from the tip using two small uni-directional accelerometers placed perpendicularly to each other. A higher number of accelerometers was not used because it was found that their combined mass had a significant disturbing influence on the modal properties of the beam. The laser displayed in Fig. 1 was not used in this study.

The response data and the input force were used to estimate the FRFs using the H_v-estimator [19] for the all considered load cases. The load was varied using the weight plates in one kilogram increments from 1 kg to 44 kg. The natural frequencies (damping and mode shapes are not discussed in this paper) were estimated using the least-square complex frequency (LSCF) estimator [20].

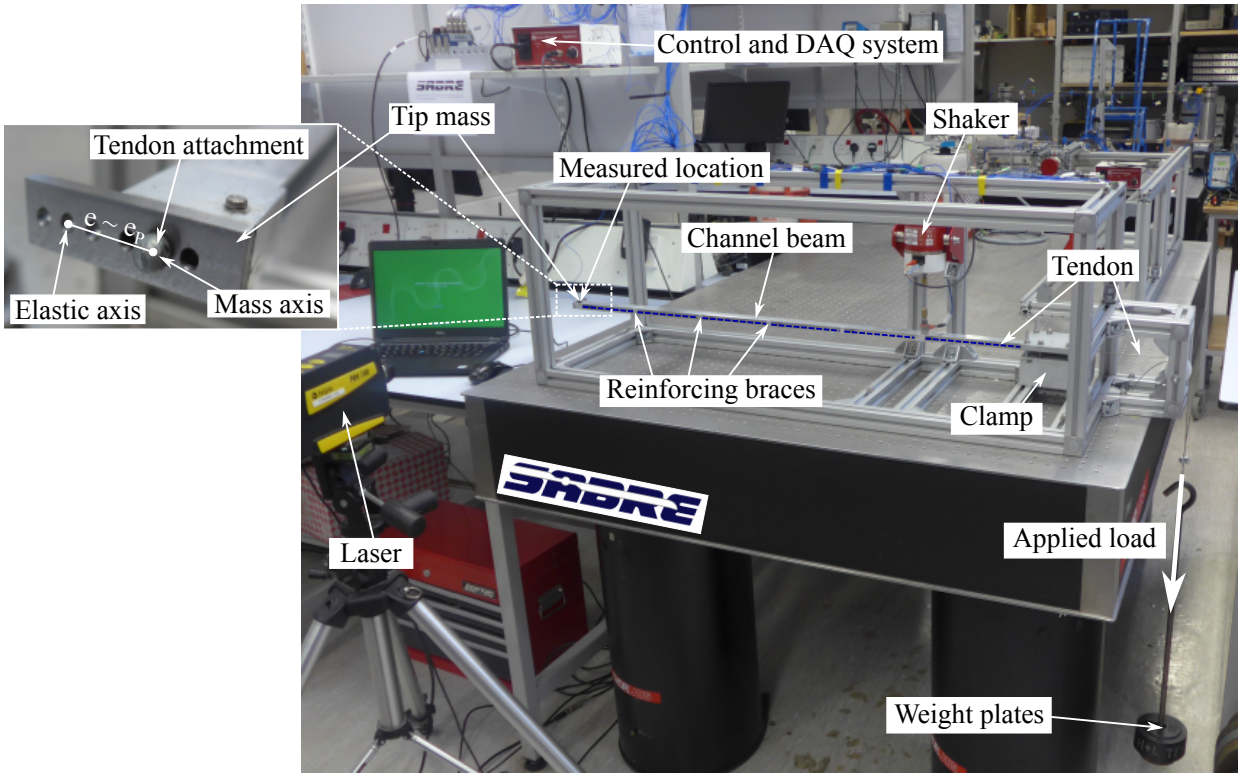


Figure 1: Experimental set-up. The cantilever beam subjected to the tendon-induced axial force generated by the applied load is excited by a shaker to obtain the frequency response functions for the estimation of modal properties which are then used to validate the theoretical model.

3.2 Nominal channel beam and tendon properties

A beam with the channel cross-section, which was reinforced by several braces (see Fig. 1), was used to validate the theoretical model. The selection of this beam was a compromise based on the following criteria which were proposed to ensure that the effect of the tendon is observable while the beam is a representative idealisation of a rotorcraft blade:

- *Bending-torsion coupling* - most modern rotocraft blades exhibit a certain amount of bending-torsion coupling. This coupling is introduced due to their design and the use of composite material. In the present study, the beam was made of aluminium, so the coupling was introduced through the choice of the cross-sectional geometry.
- *The number of modes* - the number and character of the vibration modes (flapping, lead-lag, torsional or coupled) should be similar to a typical rotorcraft blade. For the Bo105 helicopter studied in section 4 there are 10 modes between 5 Hz and 450 Hz. The experimental beam was designed in such a way that it has similar number and character of modes in a comparable frequency range. This was achieved by the choice of the material (aluminium) and geometry of the beam.
- *The effect of the tendon* - The tendon should produce observable effects in the investigated loading range. In particular, the reduction of the natural frequency for the first two modes should be at least 5 % of their nominal values. In order to achieve such reduction, the rigidity of the beam was lowered by using a thin-walled profile.
- *Boundary conditions* - a typical hingeless rotorcraft blade is fixed at the root and free at the other end. In addition, a tip mass is often used to improve the overall performance, vibration and acoustics of helicopters [21]. Therefore, a cantilever beam with a tip mass (which acts as an attachment point for the tendon) was used.

- *Euler-Bernoulli theory* - The theoretical model was derived based on the Euler-Bernoulli theory which neglects the transverse shear deformation, rotary inertia effects and sectional warping. Therefore, the experimental beam should be in line with the idealisation used. However, due to the previous requirements (open, thin-walled profile needed to emphasise the tendon effects and bending-torsion coupling), the assumptions of the Euler-Bernoulli theory would be violated. Therefore, it was attempted to reinforce the beam with several braces to minimise the influence of the neglected effects.

The nominal properties of the beam seen in Fig. 1 are $R = 1\,\mathrm{m}$, $A = 9.47 \times 10^{-5}\,\mathrm{m}^2$, $EI_1 = 169.30\,\mathrm{N\,m}^2$, $EI_2 = 354.26\,\mathrm{N\,m}^2$, $GJ = 2.42\,\mathrm{N\,m}^2$ and $e = 0.0191\,\mathrm{m}$. The beam was weighted and the mass was found to be $m = 0.2478\,\mathrm{kg\,m}^{-1}$. Likewise, the mass of the tip is $m_{tip} = 0.0269\,\mathrm{kg}$. Other parameters can be computed from the above parameters in a standard manner as outlined in [12, 22]. The tendon is made of a steel wire with $m_\mathrm{t} = 0.0125\,\mathrm{kg\,m}^{-1}$.

3.3 Validation of the theoretical model without the tendon

Before including the tendon into the experiment, the model of the beam with and without the tip mass was validated. The purpose of this step was to obtain the underlying model of the beam, which is defined using Eqs. (1a)-(1c) without the axial force P, as accurately as possible so that the effect of the tendon can be studied separately.

Firstly, the beam without the tip mass is considered. The comparison of the experimental and computed nominal natural frequencies can be found in Fig. 2. It can be seen in Fig. 2(c) that the relative error of almost all modes is greater than 5 % with the greatest error over 15 % for 3rd lead-lag (3L-L) mode. Therefore, it was

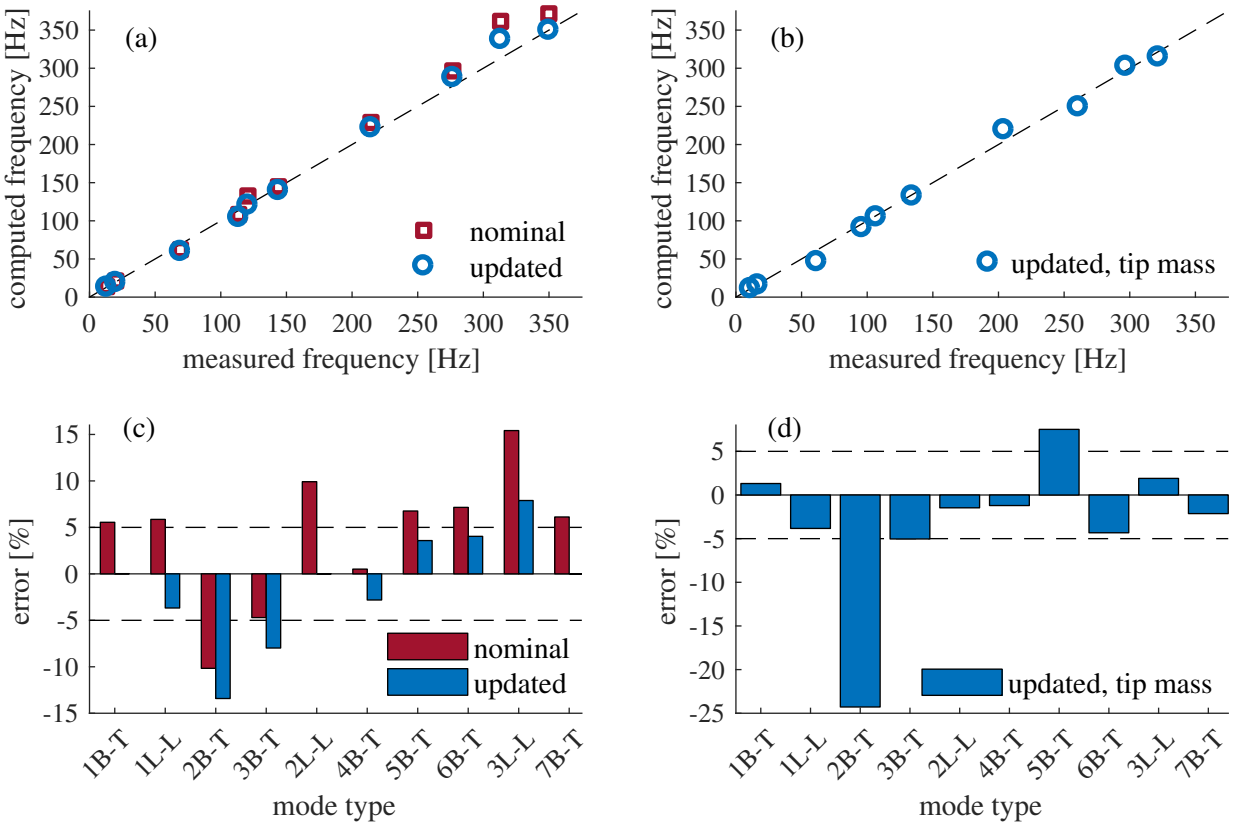


Figure 2: Comparison of experimental and computed natural frequencies without the tendon: (a) no tip mass, (b) with tip mass, (c) error for no tip mass, and (d) error with the tip mass. xB-T means the x$^{\mathrm{th}}$ mode dominated by the bending-torsion motion, whereas xL-L is the x$^{\mathrm{th}}$ lead-lag mode.

decided to update selected model parameters such that the difference between the two sets of frequencies is minimised. The updating was performed using a single-objective multi-variable optimisation using a genetic algorithm [23], whereby the objective function was defined by the error between the measured and computed natural frequencies. EI_1, EI_2 and GJ were selected for the optimisation since the natural frequencies are the most sensitive to these three parameters and their uncertainty.

The optimised bending and torsional rigidities, EI_1, EI_2 and GJ, were 89.11 %, 82.79 % and 95.54 % of their nominal values, respectively. The resulting natural frequencies and their comparison with the experimental values can be seen again in Fig. 2(a) and (c). Although the nominal parameters have not been dramatically changed, the overall character of the error between the measured and updated frequencies is very different. The error of almost all modes has decreased under the 5 % threshold. Unfortunately, the error of the 3rd and 4th mode has increased while the error of the 9th mode (3L-L) decreased but remained higher than 5 %. It is believed that if more parameters were used for the optimisation the resulting error would be lowered. However, more parameters have not been used to avoid creating an artificial model matching the limited set of experimental results. Moreover, it is also possible that the model used cannot accurately represent the experimental beam due to the Euler-Bernoulli theory assumptions violation. This assertion will be supported in section 3.4 where it is shown that the error is intrinsic to the model of the beam without the tendon and therefore has negligible effects on the model with the tendon.

Having the parameters of the model for the beam without the tip mass updated, these parameters were used to compute the natural frequencies of the model with the tip mass. The experimental and computed results are again compared in Fig. 2(b) and (d). No additional updating was performed because the tip mass could be easily measured. As expected, the magnitude of all natural frequencies reduced when the tip mass was added. When compared to the experiment, it can be seen that the error of some modes even decreased. Unfortunately, the error of the 3rd mode increased significantly, approaching 25 % and the error of 7th mode (5B-T) has also exceeded 5 %. The errors of all other modes are lower than 5 % which is herein considered as an acceptable error which can be explained by the violations of the Euler-Bernoulli theory assumptions used in the theoretical model.

3.4 Validation of the theoretical model with the tendon

The Campbell diagram, which shows the dependence of the natural frequencies on the applied load, is obtained for the case when the tendon coincides with the mass axis can be seen in Fig. 3. Two sets of frequency loci can be distinguished in both the numerical and experimental data. There are ten beam-dominated modes present which decrease very slowly with the increasing load (this effect is better seen in Fig. 5). It can also be noticed that for very low applied load, these frequency loci are very close to those obtained for the beam without the tendon. The other modes, which increase rapidly with the added masses, are the tendon-dominated modes. Experimentally, seven of such modes were captured. However, there would be many more for very low loading. Such modes have not been sufficiently excited in the experiment and even numerically, they were not obtained. The inability of the solution method to find the higher modes for low loading seems to be caused by the need to provide extremely accurate starting guess. Unfortunately, due to a very large number of modes it is very difficult to find such a starting guess that would lead to all the modes. The beam-dominated and tendon-dominated modes interact with each other through mode veering. The number of veering regions is very high for the higher frequency regions and lower loading due to the large number of the tendon-dominated modes in that region. A selected veering region is shown in Fig. 6 and discussed in more detail in section 3.6.

Overall, the agreement between the experiment and theoretical results is deemed to be satisfactory. In particular, the rapidly increasing tendon-dominated modes match the measured values very well. The computed and experimentally measured beam-dominated modes exhibit the same trends with systematic discrepancies manifested as frequency offsets. In order to explain the offsets and to emphasize the effect of the tendon, four loading configurations are studied in Fig. 4 (for applied load equal to 1, 15, 30 and 44 kg).

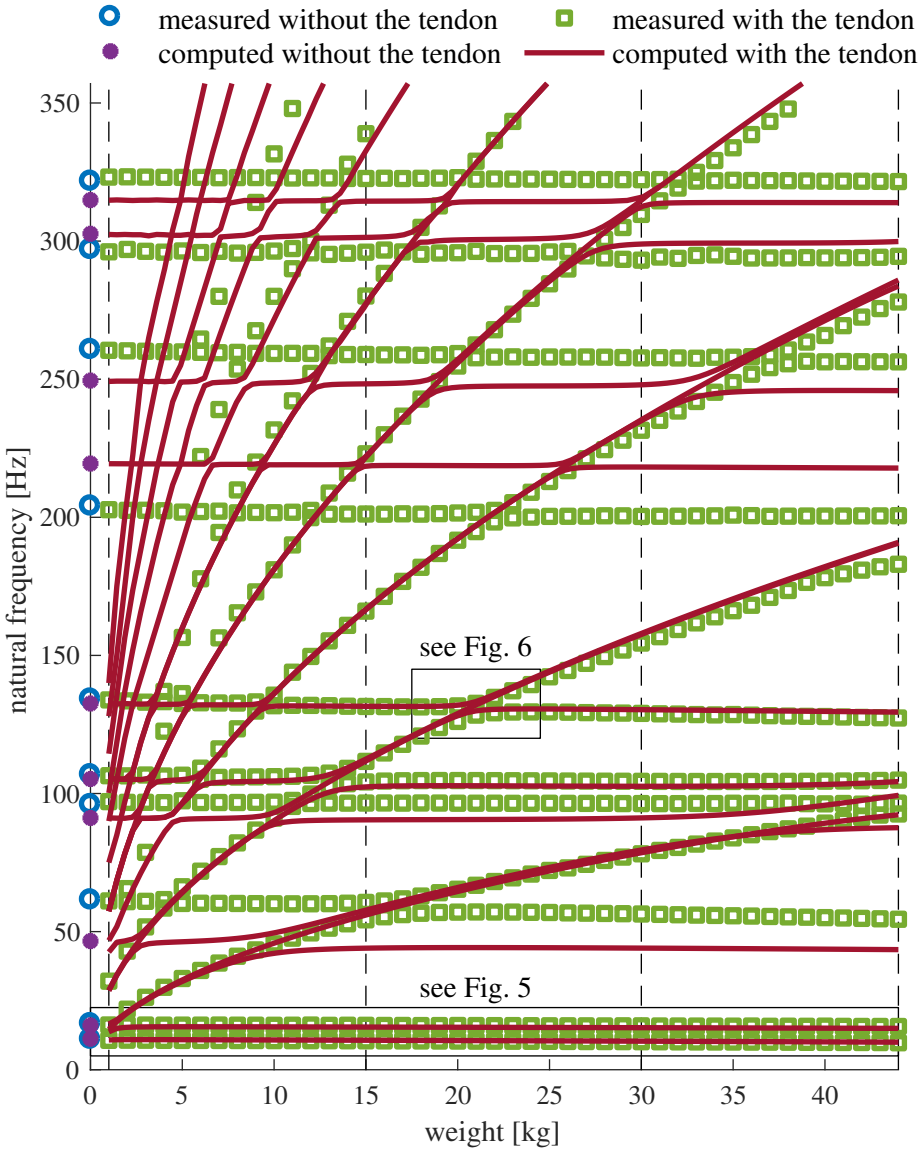


Figure 3: Comparison of the computed and measured Campbell diagrams. Rapidly increasing natural frequencies belong to the tendon-dominated modes while almost constant frequency loci belong to the beam-dominated modes.

The reduction of the natural frequency caused by the tendon is shown in Fig. 4(a). It can be seen that for almost all captured modes, the frequency decreases with the increased applied load. In addition, the reduction is much higher for the first mode (over 10 %) than for the rest of the modes. Some of the values for the first three modes could not have been obtained (n/a in Fig. 4) because of the presence of veering in the Campbell diagram (see Fig. 5 for detail of the first mode). While the reduction of the natural frequency depends on the applied load, the errors between the experimental and computed values stay almost constant with increasing load as evidenced by Fig. 4(b). A small variance of these errors can be explained by the standard experimental errors.The error for the beam with the tip mass but without the tendon (from Fig. 2(d)) is shown Fig. 4(b) in blue in order to demonstrate that the error for different loads cases is not only constant, but also comparable to the error for the beam without the tendon. Since the error is invariant with the applied load while the anticipated reduction of the natural frequency is observed, it can be concluded that the effect of the tendon was captured correctly by the model. This also supports the previous assertion that the error in Fig. 2(d) and the offset in the frequency loci in Fig. 3 is caused solely by the errors associated with the modelling of the beam using the Euler-Bernoulli theory.

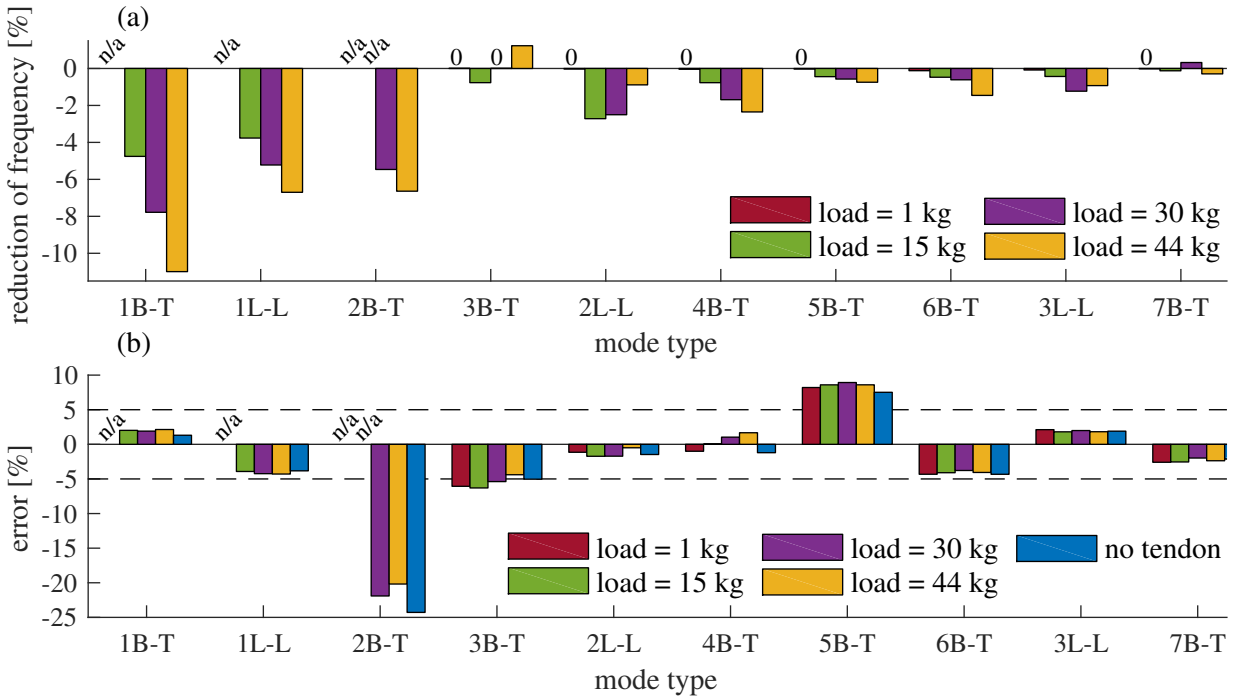


Figure 4: The effect of the tendon for the four loading configurations: (a) reduction of the natural frequency and (b) error between the measured and computed frequencies. The missing values could not be obtained due to the presence of veering.

3.5 The effect of the position of the tendon

All the results presented so far were obtained for the case where the tendon coincides with the mass axis of the beam, as depicted in the inset of Fig. 1. Figure 5 compares the previous results with the results obtained, both computationally and experimentally, for the tendon placed in the elastic axis. It can be seen that the position of the tendon has an influence on the natural frequencies of the beam-dominated modes. The computed results correspond to the experimental values qualitatively quite well although there are quantitative differences. These differences, however, correspond to the error that is intrinsic to the model of the beam as discussed in section 3.4. The results indicate that the higher reduction of the frequency can be achieved by placing the tendon in the mass axis. This is in line with the conclusions of stability analysis made in [15, 16] that the critical load is at its maximum when the axial force coincides with the elastic axis.

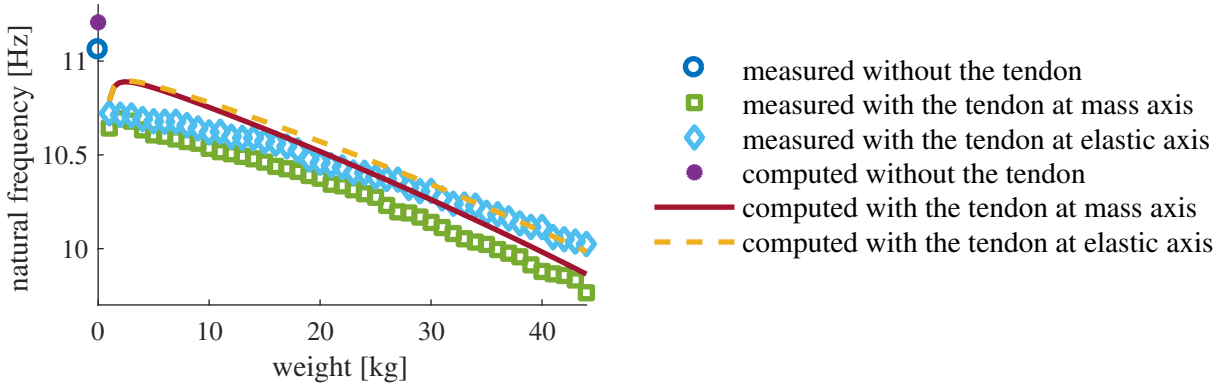


Figure 5: Comparison of experimental and computed natural frequencies of the first flapping mode with the tendon placed in either mass or elastic axis

Although it is reasonable to expect that the measured frequencies produce smooth trends with increasing loads, some small deviations can be observed in Fig. 5. These deviations are very small (not exceeding 0.1 Hz) and can be explained by the presence of the standard experimental errors. It is believed that these small deviations caused a variance of the error shown in Fig. 4(b) which would be otherwise constant. Furthermore, Fig. 5 also shows why some of the values in Fig. 4 were not evaluated. Specifically, for the load equal to 1 kg it would be meaningless to compare the computed and measured frequencies, because the computed values are influenced by veering caused by the tendon modes that have not been excited in the experiment.

3.6 The veering in the beam-tendon system

In Fig. 3 a number of veering regions can be seen, one of which is enlarged in Fig. 6. The computed modes are also added to illustrate the veering. Typical signs of veering can be observed - two modes converge, but then suddenly diverge and continue on the trajectory of the other mode while swapping all their properties including the damping ratio and mode shapes. It can be seen that the mode shape in inset 1a became the mode shape in inset 3c which is located at the different frequency locus. Similarly, the mode shape in 3a swapped with that in 1c. The frequency curve which passes through the veering regions unchanged is associated with the motion of the tendon in the lead-lag direction. Since this motion is not coupled to bending-torsion vibration of the beam, it is not influenced by the veering as also evidenced by the mode shapes in insets 2a-2c. A similar phenomenon was also observed in [11] for a symmetric cable where it raised concerns with regards to the application of the tuned vibration absorber developed therein. The veering is a frequent and important phenomenon occurring in the studied beam-tendon system as seen in Fig. 3 and will be therefore studied closely in the future.

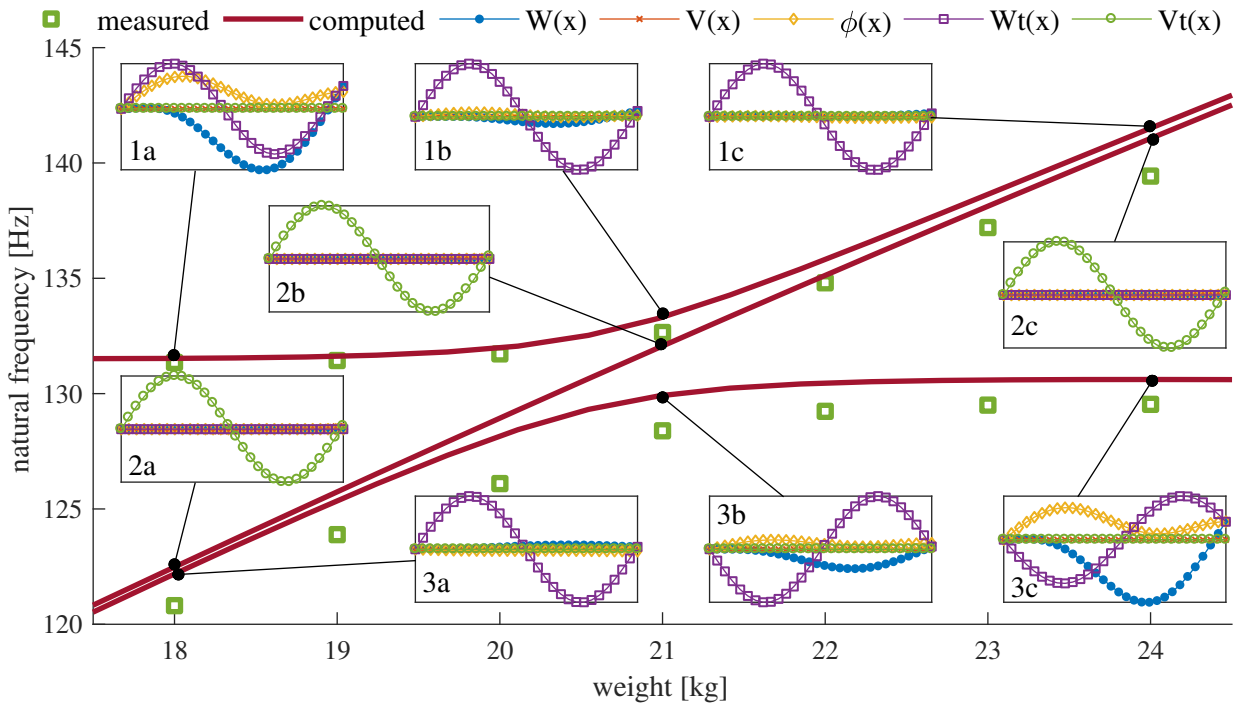


Figure 6: Veering in the beam-tendon system. The mode shapes displayed have been obtained numerically.

4 A helicopter case study

This section describes an application of the tendon as a means of manipulating the dynamic properties of a helicopter rotor blade, highlighting its benefits and potential as well as future challenges that will have to be addressed.

4.1 Selected helicopter and rotor description

The selected helicopter is the Bo105, currently produced by Airbus Helicopters. The Bo105 is a light, widely used, multi-purpose helicopter deployed in medical services, police, search and rescue, and military missions. This helicopter was selected as its rotor blade structural and airfoil aerodynamic data are well defined, and because this helicopter is used a reference aircraft in SABRE project [5].

The Bo105 features a four-bladed hingeless main rotor and a two-bladed teetering tail rotor. The main rotor blade is used in this study since it is more suitable for the application of the proposed control mechanism. The equivalent uniform structural properties of each Bo105 blade are $R = 4.912\,\mathrm{m}$, $EI_1 = 10\,000\,\mathrm{N\,m^2}$, $EI_2 = 170\,000\,\mathrm{N\,m^2}$, $GJ = 4850\,\mathrm{N\,m^2}$, $m = 5.5\,\mathrm{kg\,m^{-1}}$, $k_{m1} = 0.090\,\mathrm{m}$, $k_{m2} = 0.0648\,\mathrm{m}$, $e = -0.01\,\mathrm{m}$, $e_A = 0\,\mathrm{m}$, $k_A = 0.041\,\mathrm{m}$ and $m_{\mathrm{tip}} = 0\,\mathrm{kg}$. Since the blades have initial linear pre-twist characterised by $\beta(x) = -0.022x + 0.0663\,\mathrm{rad}$, this pre-twist was also considered in Eq. (1) in the same way as in [12]. The Bo105 helicopter operates with the reference (nominal) rotor speed $\Omega_{\mathrm{ref}} = 44.4\,\mathrm{rad\,s^{-1}}$. For the purpose of this study, a nylon rope with $m_{\mathrm{t}} = 0.0887\,\mathrm{kg\,m^{-1}}$ is used as a tendon and the reference tendon tension was chosen to be $P_{\mathrm{ref}} = 5250\,\mathrm{N}$.

4.2 Selected results for the helicopter case study

The comparison of the baseline and modified frequency diagrams can be seen in Fig. 7(a). The blue solid frequency loci represent the response of the baseline rotor with nominal parameters where the first ten modes are considered, and the rotor speed is varied between 0 and 1.2 of the reference rotor speed Ω_{ref}. It might appear that the dynamic behaviour of the rotor has been significantly changed by the tendon since many new modes and veering regions, especially at higher frequencies, have emerged (red dashed lines). However, after a close examination of the frequency diagram and related mode shapes (not shown), it can be found that all new loci are related to modes that are dominated by the motion of the tendon and do not therefore have a significant influence on the blade's dynamics. However, the tendon does influence the blade-dominated modes by reducing their frequency and by creating a number of veering regions. The former is at the moment seen as the key effect of the tendon that can be utilised to control the dynamic behaviour of the rotor.

It can be noticed in Fig. 7(a) that there is a major difference between the behaviour of the blade- and tendon-dominated modes. While the blade-dominated modes increase with the increasing rotor speed due to the centrifugal effects, the tendon-dominated modes decrease. This is caused by the fact that the tendon, which is modelled as a taut string, loses its tension due to the applied centrifugal force which leads to the rapid decrease of its natural frequencies. The preceding observation indicates that should the tendon have a desired effect, i.e. to influence the dynamic behaviour of the blade-dominated modes by shifting their frequencies, the applied tension must be higher than the centrifugal force at that rotor speed. To meet this requirement, the tendon tension must be actively controlled based on the variations in the rotor speed and other flying conditions. Otherwise, the tendon-induced axial load could cause stability issues at the low rotor speeds while having little effect at the operational ones. Such situation is depicted in Fig. 7(a) as well - while the reduction of the first blade-dominated mode at the reference rotor speed is relatively minor, the same tendon tension led to a complete disappearance of the first mode at the low rotor speed. The first mode emerges at 0.1 of the reference rotor speed. Such behaviour can potentially lead to the loss of stability and is therefore one of the reasons why the active control of the tendon tension may be of paramount importance in the future.

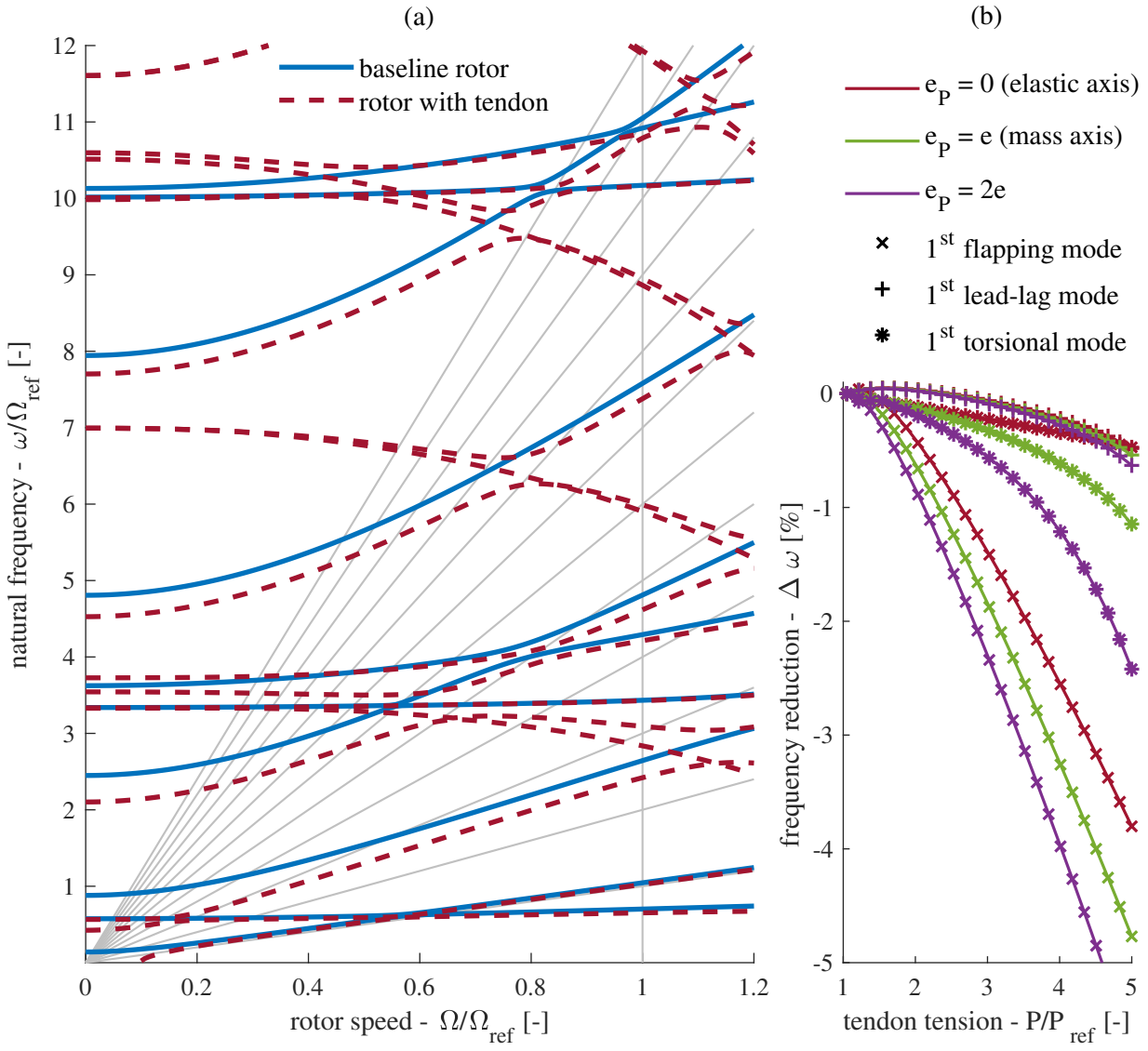


Figure 7: A case study of the Bo105 helicopter rotor blade with the tendon: (a) the comparison of the baseline and modified frequency diagrams and (b) the relative frequency reduction at reference rotor speed evaluated for three different positions of the tendon within the blade and a range of tendon tensions

The dependence of the relative frequency reduction on the applied tension and the position of the tendon in the blade is shown in Fig. 7(b). Three different tendon positions have been considered - the tendon coincides either with the elastic axis, mass axis or further behind the mass axis. It is seen that by increasing the applied tension, the frequency reduction is increased as well. However, similar to the experiment this reduction is not the same for all modes. For example, the frequency of the first flapping mode was reduced more than the lead-lag one, which is in line with the experimental observation in Fig. 4. The position of the tendon also has a considerable effect. In particular, the torsion-dominated mode is significantly influenced. While the frequency of this mode reduces linearity in the investigated range of tension when the tendon coincides with the elastic axis, the reduction is approximately quadratic when the tendon lies elsewhere. Moreover, it seems that increasing the offset of the tendon from the elastic axis leads to a more substantial reduction of the natural frequency of the torsional mode. Therefore, to achieve the optimal performance of the active tendon in the future, not only the tendon tension must be controlled, but also the position of the tendon in the airfoil must be considered.

5 Discussion

In previous sections, the theoretical model of the rotating beam-tendon system has been introduced, its experimental validation has been conducted and a case study on the Bo105 helicopter has been presented. In this section, the main findings, assumptions and limitations are discussed, and directions for the future work are outlined.

The validation of the theoretical model given by Eq. (1) was conducted in section 3 using the natural frequencies. The validation was performed on the beam exhibiting the bending-torsion coupling which was meant to be a representative idealisation of a helicopter blade. In order to select the beam, a number of criteria, summarised in section 3.2, have been used. Unfortunately, while attempting to design the beam which would sufficiently demonstrate the tendon-induced effects, the assumptions of the Euler-Bernoulli theory were violated by selecting the thin-walled, open-section channel beam. Consequently, a good match was obtained only for the tendon-dominated modes, while, despite having the correct trends, the natural frequencies of the beam-dominated modes were offset from the measured ones. However, it was demonstrated using Fig. 2(d) and Fig. 4(b) that the offsets are the same for all loading configurations. Therefore, they are not caused by the tendon and merely originate from the violation of the Euler-Bernoulli assumptions. It can be therefore assumed that if the beam was modelled with a better accuracy, the overall agreement between the experimental and computational results would be improved.

It was found, both numerically and experimentally, that the tendon introduces two effects to the beam-tendon system. Firstly, it reduces the natural frequency of the beam-dominated modes and, secondly, it creates a number of veering regions. Both of these findings were also obtained in [3, 11], but the former was not observed in other studies [7–9] where only the latter effect was captured while modelling the tendon as an axial force. It was also observed that the position of the tendon inside the beam has an influence on the quantitative and qualitative reduction in the frequencies. In particular, the torsional modes seem to exhibit qualitative changes with the varying position of the tendon as shown in Fig. 7(b). However, reliable experimental results for the varying position of the tendon were unfortunately obtained for only the first mode, and, since no experimental results are available in literature, a general conclusion about the effect of the tendon position cannot yet be formulated. In particular, the effect of the position of the tendon on the torsional modes should be experimentally verified.

A number of assumptions have been considered to obtain the PDEs in Eq. (1) that describe the beam-tendon system. Most importantly, the Euler-Bernoulli theory was used. In order to facilitate this theory, the transverse shear deformation, rotary inertia effects and the sectional warping were neglected [14]. It is believed that the violation of these assumptions in the experimental set-up led to an inaccurate match with the experimental data despite an attempt to reinforce the experimental beam by the braces. The Euler-Bernoulli theory was used in this study to provide the first insights into the possibilities and challenges associated with the tendon. However, for the future development of the concept, especially with regards to its application in rotorcraft, a more general theory will have to be used. Although a large number of refined beam theories is available in literature [14], the composite beam theory appears to be the most general and widely accepted [24]. The use of the composite beam theory would be also preferable since the rotorcraft blades are usually made of composite materials, and the theory is able to capture all required effects, including warping and large deformation. The tendon was modelled as a taut string where it was assumed that its diameter remains constant [13]. Since a light-weighted tendon that would be suitable for the final application in rotorcraft will be most likely very compliant, its model will have to be adjusted. However, modelling the Poisson's effect in the wave equations renders the PDEs non-linear [13] and therefore unsuitable for the design studies. Similarly, any non-linearities (caused for example by joints, friction or large deformations) are currently not included in the analysis or experiment since their existence and importance are unknown.

The PDEs describing the beam-tendon system have been solved using a Matlab bvp4c solver [18] to obtain the modal properties. This solver is known to be very versatile, but requires a good starting guess to find all solutions in the frequency range of interest. In particular, it is very difficult to obtain the symmetric modes at the same natural frequency. The presence of the symmetric or almost-symmetric modes is, however, inherent

to the system so, in order to make the solution approach more robust, a method that does not require a starting guess should be used in further studies. Recently, a differential quadrature method (DQM) [25] has gained some popularity in structural dynamics, so its use will be considered for the present problem as well.

In section 4, a case study of the Bo105 helicopter was presented. From the results, it can be concluded that (i) the tendon can provide a means of reducing the natural frequencies of the blade-dominated modes, (ii) the control of the tension must be used to avoid not only potentially harmful resonances but also stability issues related to the tendon, (iii) the tendon position in the airfoil should be considered as a design variable and (iv) the veering caused by the varying tension and rotor speed should be further explored. Although the obtained results are encouraging, much work, such as a thorough consideration of aerodynamic stability issues, needs to be conducted before the concept can be commissioned. Nevertheless, the results of the case study highlighted the potential of the active tendon to provide a means of control required to adaptively avoid the harmful resonances at different operational conditions. This, possibly in conjunction with other morphing concepts [5], should enable rotocraft to operate over a wider range of rotor conditions, thereby increasing their efficiency and decreasing their fuel burn, air pollution and noise emission in the future.

6 Conclusion

This paper presented a numerical and experimental study of the coupled bending-torsion vibration of the tendon-loaded beam. The beam-tendon system was modelled using a set of partial differential equations and the free vibration analysis was performed using the collocation method. A test rig consisting of an open-section cantilever beam and the tendon that provides the axial load was used to experimentally validate the theoretical model. A satisfactory agreement between the numerical and experimental results was obtained and it was shown that the tendon not only reduces the natural frequencies of the beam, but also introduces frequency loci veering. Since the study was motivated by the future application of an active tendon in rotorcraft, the numerical model was augmented by considering the centrifugal effects and a case study performed on the Bo105 helicopter showed that the active tendon concept has potential to influence the rotor blade dynamic properties.

Acknowledgements

V. Ondra and B. Titurus would like to acknowledge the financial support of the European Community's Horizon 2020 Program provided through the project "Shape Adaptive Blades for Rotorcraft Efficiency (SABRE)", Grant Agreement 723491, and R. Dibble would like to thank The UK Vertical Lift Network and ESPRC for their support and funding.

References

[1] S. Korkmaz, *A review of active structural control: challenges for engineering informatics*, Computers and Structures, Vol. 89, No. 23-24 (2011), pp. 2113-2132.

[2] G.A. Misté, E. Benini, *Variable-speed rotor helicopters: performance comparison between continuously variable and fixed-ratio transmissions*, Journal of Aircraft, Vol. 53, No. 5 (2016), pp. 1189-1200.

[3] R.P. Dibble, B. Titurus, *Helicopter rotor blade modal tuning using internal preloads*, *Proceedings of International Seminar on Modal Analysis*, (2016).

[4] R.P. Dibble, B.K.S. Woods, B. Titurus, *Static aeroelastic response of a rotor blade under internal axial loading*, *Proceedings of European Rotorcraft Forum*, (2017).

[5] J. Rauleder, B.G. van der Wall, A. Abdelmoula, D. Komp, S. Kumar, V. Ondra, B. Titurus, B.K.S. Woods, *Aerodynamic rerformance of morphing blades and rotor systems*, *Proceedings of AHS International 74th Annual Forum & Technology Display*, (2018).

[6] A. Preumont, *Vibration Control of Active Structures: An Introduction*, Springer Netherlands (2012).

[7] S. Nudehi, R. Mukherjee, S.W. Shaw, *Active vibration control of a flexible beam using a buckling-type end force*, Journal of Dynamic Systems, Measurement, and Control, Vol. 128, No. 2 (2006).

[8] J. Issa, R. Mukherjee, S.W. Shaw, *Vibration suppression in structures using cable actuators*, Journal of Vibration and Acoustics, Vol. 132, No. 3 (2010).

[9] P. Thomson, G.J. Balas, P.H. Leo, *The use of shape memory alloys for passive structural damping*, Smart Materials and Structures, Vol. 4, No. 1 (1995).

[10] L.N. Virgin, *Vibration of Axially-Loaded Structures*, Cambridge University Press (2007).

[11] J.L. du Bois, N.A.J. Lieven, S. Adhikari, *A tensioned cable as an adaptive tuned vibration absorber for response suppression in rotorcraft*, *Proceedings of International Conference on Noise and Vibration Engineering*, (2012).

[12] J.C. Houbolt, G.W. Brooks, *Differential equations of motion for combined flapwise bending, chordwise bending, and torsion of twisted nonuniform rotor blades*, NACA Technical Note 3905 (1957).

[13] A.H. Nayfeh, P.F. Pai, *Linear and Nonlinear Structural Mechanics*, Wiley (2008).

[14] M. Rafiee, F. Nitzsche, M. Labrosse, *Dynamics, vibration and control of rotating composite beams and blades: A critical review*, Thin-Walled Structures, Vol. 119 (2017), pp. 795-819.

[15] V.Z. Vlasov, *Thin-walled Elastic Beams*, The Israel Program for Scientific Translations Ltd (1961).

[16] Z.P. Bazant, L. Cedolin, *Stability of Structures: Elastic, Inelastic, Fracture and Damage Theories*, World Scientific (2010).

[17] S.H.R. Eslimy-Isfahany, J.R. Banerjee, *Dynamic response of an axially loaded bending-torsion coupled beam*, Journal of Aircraft, Vol. 33, No. 3 (1996), pp. 601-607.

[18] J. Kierzenka, L.F. Shampine, *A BVP solver based on residual control and the Matlab PSE*, ACM Transactions on Mathematical Software, Vol. 27, No. 3 (2001), pp. 299-316.

[19] J.S. Bendat, A.G. Piersol, *Random Data: Analysis and Measurement Procedures*, John Wiley & Sons, Inc. (2000).

[20] B. Peeters, H. Van Der Auweraer, P. Guillaume, J. Leuridan, *The PolyMAX frequency-domain method: a new standard for modal parameter estimation?*, Shock and Vibration, Vol. 11 (2004), pp. 395-409.

[21] A. Brocklehurst, G.N. Barakos, *A review of helicopter rotor blade tip shapes*, Progress in Aerospace Sciences, Vol. 56 (2013), pp. 35-74.

[22] D.H. Hodges, E.H. Dowell, *Nonlinear equations of motion for the elastic bending and torsion of twisted nonuniform rotor blades*, NASA Technical Note D-7818 (1974).

[23] J.S. Arora, *Introduction to Optimum Design*, Academic Press (2011).

[24] D.H. Hodges, *Nonlinear Composite Beam Theory*, American Institute of Aeronautics and Astronautics (2006).

[25] C.W. Bert, M. Malik, *Differential quadrature method in computational mechanics: A review*, Applied Mechanics Reviews, Vol. 49, No. 1 (1996), pp. 1-28.

Dynamics and control of adaptive airbags for UAV impact protection

Z. Wolejsza[1], J. Holnicki-Szulc[1], C. Graczykowski[1], K. Hinc[2], R. Faraj[1]
T. Kowalski[2], G. Mikulowski[1], K. Kazmierczak[1], R. Wiszowaty[1], P. Pawlowski[1]
[1] Institute of Fundamental Technological Research Polish Academy of Sciences, Department of Intelligent Technologies, ul. A.Pawińskiego 5b 02-106, Warsaw, Poland
e-mail: **zwol@ippt.pan.pl**

[2] Adaptronica sp. z o.o., ul. Szpitalna 32, 05-092 Łomianki, Poland

Abstract
Small drones with total mass of a few kilograms are becoming more and more popular in many applications increasing the probability of occurrence of emergency situations caused by an equipment failure or a human error. In case of a fall from a high altitude very often it is possible to use parachute rescue systems, which however require relatively long time for deployment and development of braking forces. The touchdown velocity may be large enough to exceed limit accelerations for UAV equipment. The paper presents the concept of deployable airbag systems, in particular with adaptive flow control, which provides a possible solution to the above-mentioned problems. The paper discusses the overall control and adaptation strategy. Simplified methods for mathematical modeling are proposed and formulated for an example on a cylindrical airbag. The conceptual part is concluded with the presentation of the methodology of experimental verification and results of initial tests of the integrated airbag system.

1 Introduction

Small drones with a total mass of a few kilograms are becoming more and more popular in many applications including aerial surveillance and monitoring, filming, laser scanning etc. The popularity of this type of UAV's applications increases the probability of occurrence of emergency situations caused by an equipment failure or a human error. Drones very often operate over densely populated urban areas, therefore it becomes crucial to protect people or objects on the ground. The second objective is the minimisation of shock loads transferred to a fragile and expensive electronic equipment on board of a UAV (e.g. cameras and lenses, lidars).

In case of a fall from a high altitude (approx. above 10-15m) very often it is possible to use parachute rescue systems, which however require relatively long time for deployment and development of braking forces. The vertical velocity close to the touchdown is in this case large enough to excess limit accelerations for UAV equipment, which very often can be estimated as approx. 20g.

These drawbacks can be avoided by application of deployable airbag systems, in particular with adaptive flow control. The problems of dynamics and control for adaptive impact and shock absorption (including the application of inflatable structures pneumatic systems) are research topics for more than 15 years at the Department of Intelligent Technologies of IPPT PAN [1]. The concept is based in general on the application of semi-active or real-time control over mechanical characteristics of a shock absorbing structure in order to provide the optimal level of resistance forces minimizing dangerous accelerations levels.

1.1 Systems of Adaptive Impact Absorption

One of the first adaptive impact absorbing systems were active hydraulic aircraft landing gears developed in the 1970s in NASA Langley Research Center. In these devices, the damping force generated by the absorber was controlled by changes of pressure of the applied fluid. However, such technology required large amount of the energy submitted to the system and had caused technical problems related to ensuring large flow rates and pressure ranges. The above shortcomings were eliminated by applying landing gears based on servo-valves, where the control was performed in a semi-active way.

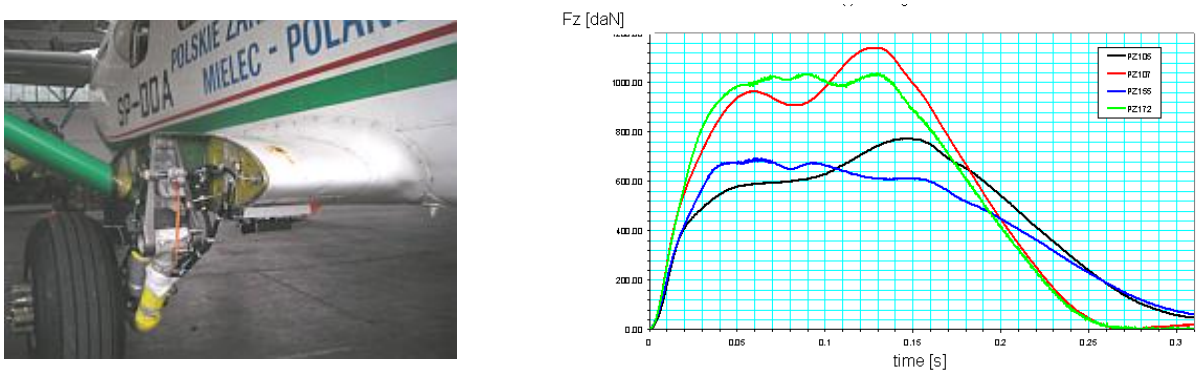


Figure 1: Adaptive aircraft lading gear (FP7 project ADLAND - flight tests, experimental results)

The system of the adaptive impact absorption was successfully implemented for a semi-active aircraft landing gear within the FP6 research project ADLAND [2], [3]. Introduction of the intelligent materials in the design of the adaptive absorbers allowed for substantial shortening of the system response time and it enabled real-time control of the damping force generated by the absorber. Within the project two alternative solutions were tested: the magneto-rheological valve based on the application of the magneto-rheological fluid and the magnetic head and the valve based on piezoelectric actuator controlling flow of the standard hydraulic fluid.

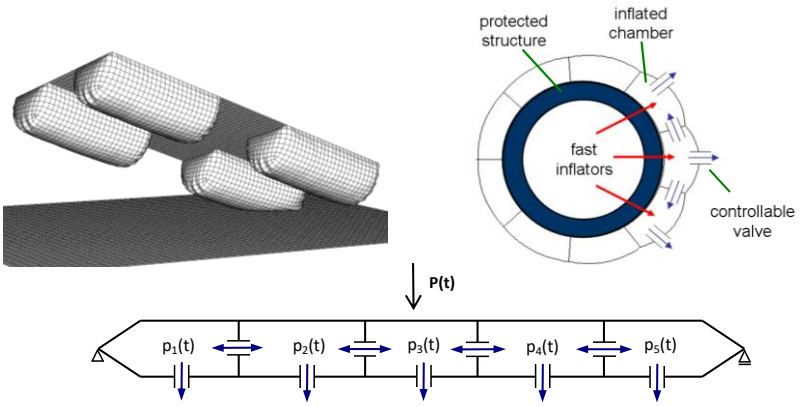


Figure 2: Adaptive Inflatable Structures: a) emergency flow control-based airbags, b) inflatable fenders, c) adaptive inflatable barrier

The airbag system for UAVs proposed and presented in this paper belongs to a wider class of Adaptive Inflatable Structures. The concept is based on application of compressed gas and controlling its pressure as an effective methodology allowing for adaptation of energy absorbing structures (e.g. airbags, fenders, barriers - Fig.2) to actual impact loading [4]. Adaptive Inflatable Structures contain sealed chambers filled with compressed gas and equipped with controllable inflators and discharge valves. Pressure adjustment relies on appropriate initial inflation of particular chambers and control of the gas flow between the chambers and outside the structure during the process of deformation. Appropriate change of the actual

value of pressure in different parts of the structure enables adaptation to dynamic loading of various energy, amplitude and location.

The real-time controlled fully pneumatic adaptive landing gear for small UAV was developed and described in [6]. The introduction of the controlled flow of the gas between the chambers allowed to dissipate the impact energy within the first compression stroke and to mitigate oscillatory movement after 0,25 s. The control procedure introduction decreased the maximum deceleration level of the drop-weight from 12 m/s^2 to 8 m/s^2.

The piezoelectric valves provide very fast response of the system, however with limited the flow rate of the gas. One of the proposed solution to this problem is application of flow-driven high performance valves. Two different devices (membrane valve and a bistable valve) with different working principles are presented in [7], which provide effective, semi-active three stage control sequence “close-open-close”. In the case of membrane valve the rapid destruction of clamping elements results in different deformation modes of two membranes forming the valve, caused by the gas flow. The operating principle is depicted for three stages of operation in Fig.3.

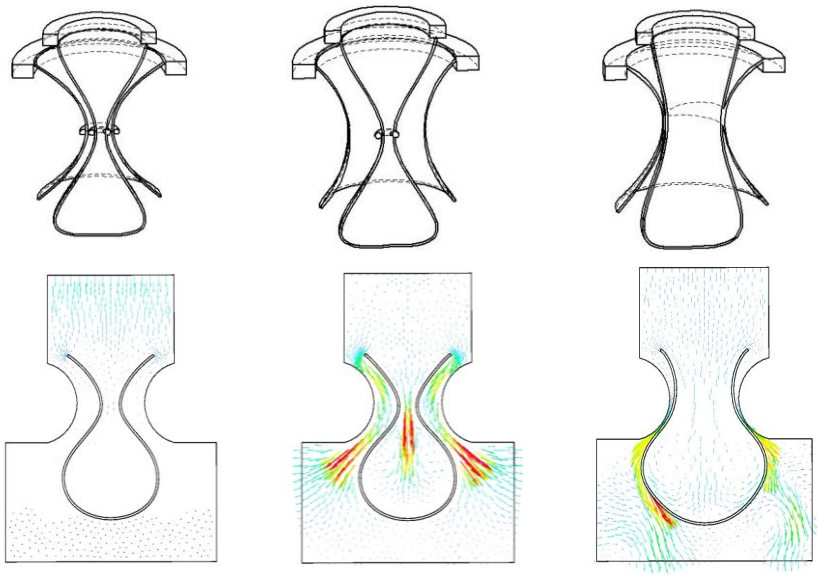


Figure 3: The cross-section of the membrane valve and simulation of the gas flow during subsequent stages of valve operation.

2 Adaptation technique for AD-BAG system

The emergency landing system should be developed as a module which is entirely independent from the autopilot and other onboard subsystems of the UAV lest the accident can result from their failure. In order to provide efficient and reliable operation of the AD-BAG system the influence of following problems and challenges has to be reduced:

- instant detection of the UAV’s failure,
- stabilization of the UAV’s spatial orientation,
- fast inflation of the emergency airbag,
- possibly precise prediction of the impact conditions,
- proper gas release to avoid ‘stiff contact’ or ‘rebound’.

Detection of the UAV's failure can be implemented using inertial sensors and should result in turning off the engines so as stabilization of spatial orientation can be obtained in passive way. The prediction of loading conditions resulting from the contact with the ground or on-ground obstacle [8] can be can implemented in a number of pretty different ways e.g., based on the measurements of AGL (altitude above ground level). The AGL can be measured once and then the impact conditions can be estimated. Nevertheless, such measurement requires the use of radar altimeter or LIDAR, etc., what results in quite complex and expensive solution. On the other hand, the AGL can be estimated using inertial, barometric sensors and GPS. Unfortunately, for reliability of such solution the terrain map should be available for online use of developed system. Other alternatives relates to the velocity estimation techniques. The measurements of velocity relative to the ground and in result the emergency system should update predicted impact condition and sequentially re-adapt in real-time until the contact with obstacle is detected and finally calculated scenario is implemented.

The impact absorption of the system protected by airbags includes gas compression and then its release to ensure dissipation of impact energy. In order to provide more efficient impact mitigation than in case of passive solutions, the airbag should be closed at the beginning of the process so that gas is only compressed. After fast increase of internal pressure the gas release should be activated and finally the release opening should be closed. In case of different impact conditions the moment of gas release and size of airbag opening should be selected carefully. The significant challenge is very short time period between each control action (time periods at the level of single milliseconds). To minimize probability of errors during adaptation to impact conditions, the system characteristics should be adjusted by single control action, similarly as in case of adaptable pneumatic shock-absorber presented in [9]. The more efficient and more robust but simultaneously more complex solutions involve online control of the internal pressure or deceleration of the UAV [10] as well as additional kinematic feedbacks [11].

The general scheme of emergency system operation is shown in Fig. 4. The generic sequence of actions performed by the system is valid for all of impact prediction techniques discussed above.

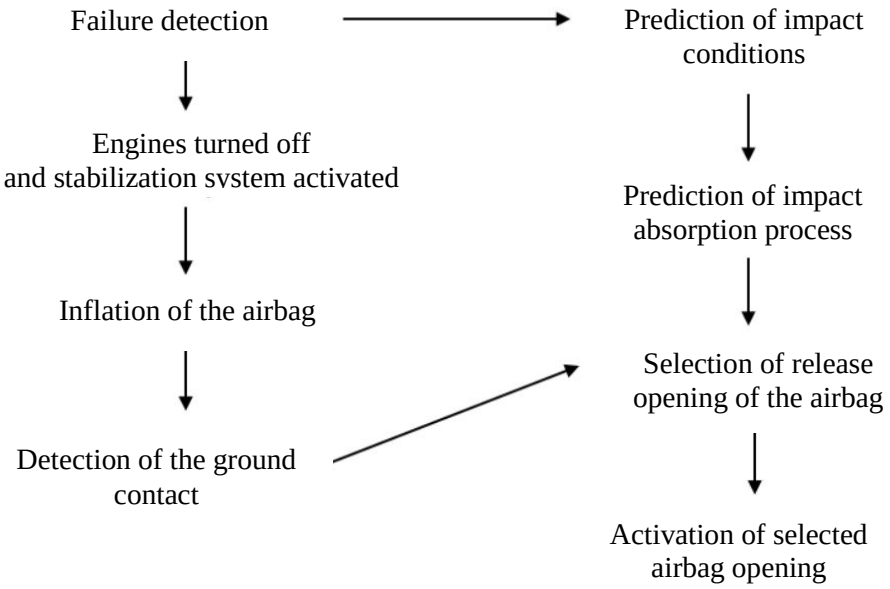


Figure 4: The general scheme of emergency system operation

3 Mathematical models of the process of emergency landing with adaptive airbag

In this section, we consider falling object with attached adaptive airbag made of thin fabric and equipped with a controllable valve, which enables the outflow of gas to the environment. The object approaches the ground with certain initial velocity. When impact with the ground occurs the airbag is compressed and considerably deformed, which causes an increase of internal pressure of the gas. Simultaneously pressure is reduced by leakage of gas through the airbag fabric and its controlled outflow through the valve. The objective of the adaptive airbag is to dissipate the entire impact energy and to optimally mitigate the impact process by reduction of generated forces and corresponding deceleration of the impacting object.

In order to simplify the modeling process, it is assumed that airbag inflation and its full deployment is accomplished before contact with the ground. Therefore, the process of airbag inflation and the case of impact with airbag being not fully deployed is not considered. Moreover, it is assumed that impact velocity is relatively low and it does not cause significant wave propagation effects in a given volume of gas. Accordingly, the thermodynamic processes arising in the system are modelled with the use of Uniform Pressure Method (UPM), which assumes that gas pressure, temperature, and density are uniformly distributed in the entire airbag. The UPM method utilizes the balance of mass and energy of the gas, the equation of gas state as well as the definitions of gas leakage and outflow, which are expressed either as ordinary differential or algebraic equations. In the considered problem, the UPM-based modelling is conceded as a sufficiently precise tool for the preliminary simulation of the response of adaptive airbag.

In general, two approaches to the modelling of the process of emergency landing with adaptive airbag can be proposed:

- Extended Uniform Pressure Method (E-UPM), in which the falling object is modeled as one degree-of-freedom system, its movement is described by single equation of motion, the thermodynamic processes arising in the gas are modeled with the use of UPM, while deformability of the airbag is taken into account by introducing additional terms and coefficients into the governing equations;
- the combination of Finite Element Method and Uniform Pressure Method (FEM-UPM), in which the falling object and the airbag are modeled by classical approaches of continuum mechanics, their motion and deformation are described by partial differential equations and solved by FEM, the thermodynamic processes arising in gas are modeled with the use of UPM and, moreover, appropriate coupling conditions between gas and airbag fabric are applied.

The main advantage of the E-UPM approach is elimination of complex simulation of airbag deformation occurring during landing, which requires precise modelling of airbag fabric and time-dependent conditions of contact with the ground. Instead, the simplified approach effectively utilises the analogy between the response of compressed adaptive airbag and the response of compressed single-chamber pneumatic cylinder equipped with controllable valve. The additional physical phenomena which have to be considered during modelling of the adaptive airbag are the following:

- the area of contact between the airbag and the ground significantly changes during the process (in typical impact scenario it rises);
- the volume of the airbag changes nonlinearly in terms of airbag compression;
- when airbag fabric is not completely air-tight then additional outflow of gas and reduction of pressure are caused by fabric leakage;

- when airbag fabric is characterized by non-negligible bending stiffness its deformation during airbag compression causes generation of additional reaction forces.

The E-UPM approach effectively utilizes analytical description of airbag deformation in terms of actual airbag compression and, in case of highly extensible fabric, in terms of internal pressure. The assumption of extensible fabric significantly simplifies the analysis. For given initial shape of the airbag the fundamental geometrical relations can be used to express actual area of contact with the ground A_C and actual volume V in terms of actual stroke of the airbag s and to obtain functions $A_C(s)$ and $V(s)$. Alternatively, the above dependencies can be obtained from the numerical simulation conducted by using FEM-UPM approach or from the experiment. As a result, the contact force between the airbag and the ground can be expressed as a function of its actual stroke and internal pressure of gas: $F_C(s,p) = A_C(s)\left(p - p_{ext}\right)$.

In addition, the possible structural forces arising as a result of deformation of fabric of considerable bending stiffness are introduced into the E-UPM model by additional visco-elastic forces $F_A(s,\dot{s})$, which enter the equation of motion of the landing object. Eventually, the influence of gas leakage through the airbag fabric is taken into account by introducing the additional terms in the equations governing balance of mass of gas inside the airbag and thermodynamic balance of gas energy.

3.1 The example of cylindrical airbag

The illustrative example of landing with the use of horizontally located cylindrical airbag made of inextensible material is presented in Fig. 5. The process consists of the stage before contact with the ground (A), the stage of gradual compression of the lower part of the airbag (B), and the stage of uniform compression of the entire airbag (C). The second and third stage differ by the relation between the area of contact with the ground A_C and the area when pressure of gas acts directly on the horizontal falling object A_p.

Determination of actual airbag shape effectively utilizes the assumption of weightless fabric, which allows to conclude that the lateral parts of airbag cross-section remain circular. Therefore, the analysis for the second stage of the process includes four unknowns: horizontal coordinate of the point of contact with the ground, the coordinates of the point being the centre of the circle defining lateral parts of airbag cross-section and radius of this circle. In turn, four governing equations include: the equations of circle for both points of contact, the condition that airbag is tangent to the ground at the point of contact and condition of constant length of the airbag perimeter. During the third stage of the process the analysis is significantly simplified due to the fact that the point of contact of the airbag with the ground and with the falling object have the same horizontal coordinate. The detailed derivation of the shape of airbag surface is left to the reader.

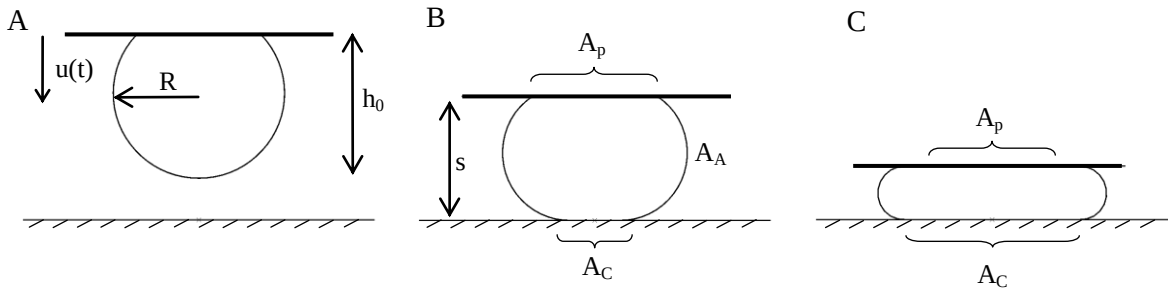


Figure 5: Three stages of the process of landing with adaptive airbag

Next, the area of contact with the ground $A_C(s)$, the lateral area of the airbag $A_A(s)$ and volume of airbag $V(s)$ can be found by calculating appropriate integrals over airbag surface. Let us note that assumption of

weightless airbag fabric allows to determine total force acting on the horizontal falling object, which in both the second and the third stage of the process equals to the contact force between the airbag and the ground $F_C(s,p) = A_C(s)(p - p_{ext})$. The proof is fundamental and it is also left to the reader.

Eventually, the proposed analytical model of airbag-assisted emergency landing consists of three ordinary differential equations which describe motion of the falling mass, balance of mass of the gas and thermodynamic balance of gas energy. Two latter equations take into account definition of gas outflow through the valve q_v (which depends on actual area of the valve A_v) and definition of outflow caused by fabric leakage. The system of equations is complemented by equation of gas state and proper initial conditions. The complete model of emergency landing takes the form:

$$M\frac{d^2u}{dt^2} - Mg + A_C(s)(p - p_{ext}) + F_{\mathrm{A}}(s,\dot{s}) = 0 \tag{1}$$

$$\frac{dm}{dt} = -q_V(p,T,p_{ext},A_V) - CA_A(s)\sqrt{\frac{2(p-p_A)p}{RT}} \tag{2}$$

$$\left[q_V(p,T,p_{ext},A_V) + CA_A(s)\sqrt{\frac{2(p-p_A)p}{RT}}\right]c_{\mathrm{p}}\mathrm{T} + \frac{d(mc_{\mathrm{V}}\mathrm{T})}{dt} + p\frac{dV}{dt} = 0 \tag{3}$$

$$f(p,V,m,T) = 0 \tag{4}$$

$$\text{IC:}\quad u(0) = 0, \dot{u}(0) = v_0, p(0) = p_0, m(0) = m_0 \tag{5}$$

The above system of equations can be solved with the use of arbitrary numerical method. The verification of the E-UPM model against more precise FEM-UPM model was conducted for problem of compression of cylindrical airbag discussed in the above example. The comparison conducted for kinematic, static and thermodynamic quantities had revealed satisfactory correspondence of both applied methods [12]-[13].

The proposed E-UPM approach is based exclusively on physical principles and geometrical considerations and, moreover, does not require linearization or neglecting of the selected terms. Therefore, it is expected to be more precise than known from the literature analytical models based on alternate stiffness and damping terms, which model response of the airbag in approximate way. The proposed model seems to be sufficient for basic assessment of the effectiveness of emergency landing systems based on adaptive airbags.

4 Experimental verification

The integrated ADBAG airbag and control systems have been verified experimentally in a laboratory conditions. The objective of the experiments is to demonstrate operability of the system in an emergency situation and ability to protect a falling object against a ground impact.

4.1 Configuration of the stand

The testing setup has been configured to conduct drop tests of the assembled AD-BAG mockup. The available drop heights are up to 25 m performed on a guided truck. The testing object is a mockup of 1.5 kg weight, protected by an airbag of 50 dm3 volume. The airbag is automatically activated and filled with a compressed gas during the test. Synchronized measurements are configured to acquire the following magnitudes: interface force under the airbag, kinematics of the falling object: displacement, velocity, acceleration via digital image analysis method.

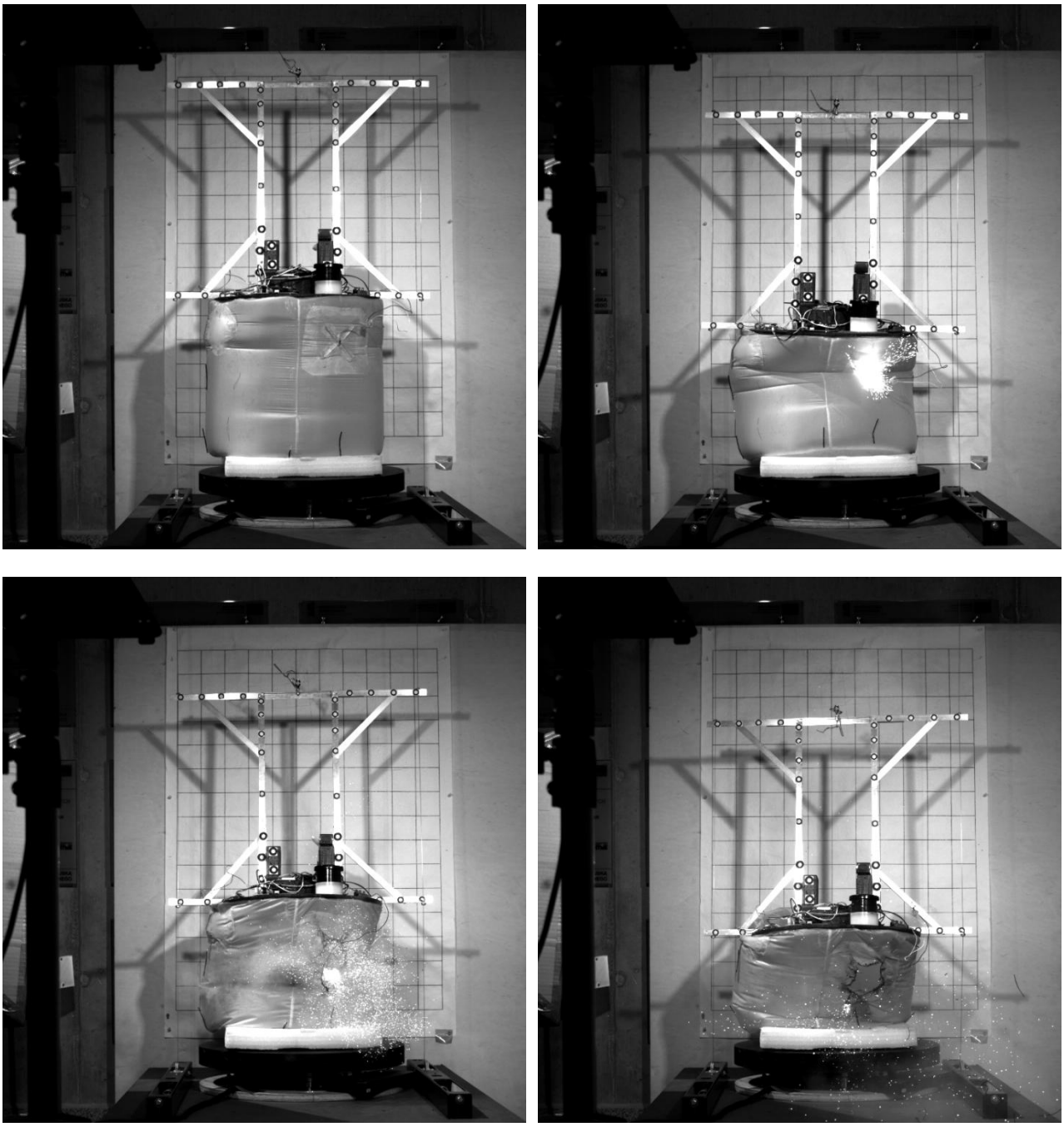


Figure 6: A sequence of the airbag initialization and operation

The interface force is measured with a measuring plate based on three piezoelectric sensors with measuring range 10 kN. The data acquisition is performed with a SCADAS Mobile system and the image recording is conducted with a Phantom 611 fast digital camera. The data acquisition procedure is synchronised with a digital signal provided by a dedicated controller based on a FPGA processor.

4.2 Testing procedure

The first step is lifting the object to a predefined height e.g. 5 m. Afterwards, the drop is conducted and the electronic unit is activated, which is programmed to carry out the following steps:

1. recognition of a free fall phenomenon which equates an emergency situation;
2. activation of the airbag and pressurizing it with air;
3. recognition of a touchdown moment,
4. initialization of adaptive system of the air release in order to match the airbag response and the actual the impact energy.

4.3 Tests results

An exemplary sequence of the airbag operation is depicted in Fig. 6. The upper left photo represents a state of the airbag after contact with the touchdown surface but before initialization of the release valve. The following photos (upper right and lower left) depict the process of the valve opening. The photo placed in the lower right corner shows the outflow valve completely open.

As a whole, the system operability is demonstrated and the ability of the system to adapt to the recognized impact condition is available.

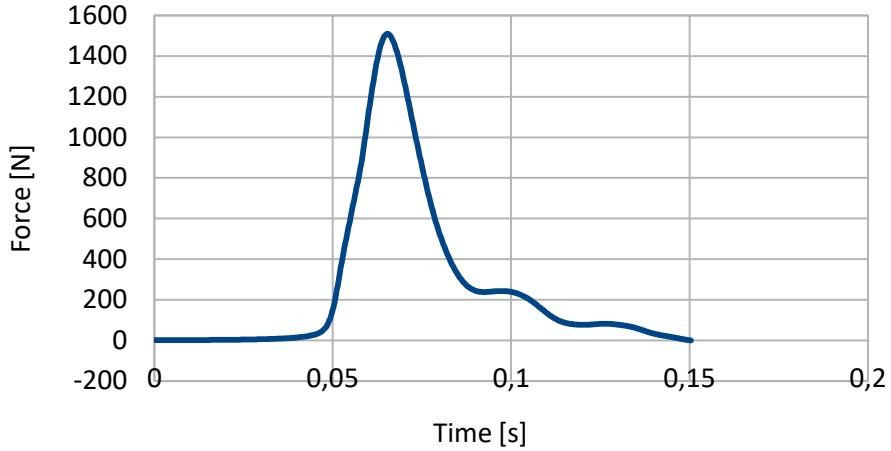


Figure 7: Interface force of the airbag in time domain

A time history of the force measured on the interface between the airbag textile and the touchdown surface is ploted in Fig. 7. The maximum force recorded during tests does not exceed 1,5 kN. The second force peak at time instant 0,1 s represents the influence of the adaptive valve in the airbag. The conducted investigation confirmed functionality of the system and its readiness for the following development phase – tuning the control parameters.

Acknowledgments

The article was prepared with the support of the project: "Adaptive airbags for unmanned aerial vehicles emergency landing (ADBAG)" co-financed from the European Regional Development Fund within the Operational Programme Smart Growth 2014-2020, Measure 1.2. Sectoral R&D Programs. Contract No .: POIR.01.02.00-00-0083 / 16. The period of the project implementation: 01.01.2017-30.06.2019.

References

[1] J. Holnicki-Szulc, C. Graczykowski, G. Mikulowski, A. Mroz, P. Pawlowski, R. Wiszowaty, Adaptive impact absorption - the concept and potential applications, International Journal of Protective Structures, Vol. 6, Issue: 2 (2015), pp. 357-377.

[2] G. Mikulowski, P. Pawlowski, Z. Wolejsza, Adaptive landing gear (in polish: Podwozie lotnicze z adaptacyjnym systemem absorpcji energii), Journal of Aeronautica Integra, vol. 2, no. 1, (2007)

[3] G. Mikulowski, R. LeLetty, Advanced Landing Gears for Improved Impact Absorption, in proceedings of 11th International Conference on New Actuators/5th International Exhibition on Smart Actuators and Drive Systems, Bremen, Germany, (2008), June 27-30.

[4] C. Graczykowski, J. Holnicki-Szulc, Crashworthiness of inflatable thin-walled structures for impact absorption, Mathematical Problems in Engineering, Vol. 2015, (2015), pp. 830471-1-22

[5] Graczykowski, J. Holnicki-Szulc, Protecting offshore wind turbines against ship impacts by means of Adaptive inflatable Structures, Shock and Vibration, Vol. 16, No. 4, (2009), pp. 335-353

[6] G. Mikulowski, R. Wiszowaty, Pneumatic Adaptive Absorber: Mathematical Modelling with Experimental Verification, Mathematical Problems In Engineering, Article No. 7074206 (2016)

[7] P.Pawłowski, M. Ostrowski, C. Graczykowski, High performance valves for adaptive inflatable structures with flow driven control, Smart2013, 6th Eccomas Thematic Conference On Smart Structures And Materials, 2013-09-03/09-06, Torino (IT), (2013),pp.1-10

[8] K. Sekuła, C. Graczykowski, J. Holnicki-Szulc, On-line impact load identification, Shock and Vibration, Vol. 20, No. 1, (2013), pp. 123-141

[9] Faraj, C. Graczykowski, Adaptable Pneumatic Shock Absorber, Journal of Vibration and Control, in review, (2018)

[10] C. Graczykowski, R. Faraj, Development of control systems for fluid-based adaptive impact absorbers, Mechanical Systems and Signal Processing, in review, (2018)

[11] R. Faraj, C. Graczykowski, Hybrid Prediction Control for self-adaptive fluid-based shock absorbers, Journal of Sound and Vibration, in review, (2018)

[12] C. Graczykowski, Mathematical models and numerical methods for the simulation of adaptive inflatable structures for impact absorption, Computers and Structures, Vol. 174, (2016), pp. 3-20

[13] C. Graczykowski, Inflatable Structures for Adaptive Impact Absorption, Ph.D. Thesis, IPPT PAN (2011)

Structural intensity on irregular shells

F. Pires [1,2,*], **S. Vanlanduit** [2,3], **J.J.J. Dirckx** [1]
[1] University of Antwerp, Department of Physics,
Groenenborgerlaan 171, 2020 Antwerp, Belgium
e-mail: **felipe.pires@uantwerpen.be**

[2] Vrije Universiteit Brussel, Department of Mechanical Engineering,
Pleinlaan 2, 1050 Brussel, Belgium

[3] University of Antwerp, Department of Electromechanical Engineering,
Groenenborgerlaan 171, 2020 Antwerp, Belgium

Abstract
The topic of structural intensity analysis has been mainly focused on assessing the energy taking place on plate-like structures. This work presents a method which allows the same assessment on shells with arbitrary shape. By invoking the Kirchhoff-Love postulates, the current method enables the assessment of power transfer taking place on the shell's mid-surface from data available at one of the sample's outer surface. The mentioned data are the displacement vector components represented by the standard unit vectors of the Euclidian space and the spatial coordinates describing the studied shell. By including the assumption that the sample can be represented as an assembly of plates, the experimental displacement data are projected on a mesh, whose shape resemble the original analyzed shell. With this approach, the displacement fields could be properly differentiated along a predefined local coordinate system, leading to the necessary inputs for the structural intensity assessment.

1 Introduction

The Structural Intensity (SI) analysis is an useful approach that allows the assessment of energy transmission on general structures. The computation of this term is widely documented in literature in the case of real plate-like structures by invoking the Kirchhoff plate theory [1]. For such samples, if this assumption is taken into account, the spatial derivatives of the out-of-plane displacements and a priori knowledge of its material properties are sufficient inputs to compute the SI vector fields [2, 3]. However, if such an analysis is done on real irregular shells, the displacement fields in all orthonormal directions and the data describing the sample's shape are required. Besides, it becomes less troublesome to process and differentiate the displacement fields in a set of curvilinear coordinates of the analyzed shell [4, 5].

Due to these extra inputs, which were absent in the case of plates, a more elaborate data processing was developed and is presented in this work. Here, not just the Kirchhoff-Love postulates are used to formulate the terms present in the SI vector fields, but it is also assumed that the analyzed sample can be treated as a Finite-Element-Method model and whose elements are planar.

The measuring technique that was used to record both the experimental shape and displacement data from a shell was the Digital Image Correlation (DIC) [6] technique and the related results were exported as a dense point cloud. The interpolation of the measured results were then projected on a customized mesh on the basis of a global least-squares minimization via Finite-Element (FE) shape functions [7]. After this projection, the data could be differentiated along a predefined set of local coordinates and the assessment of the SI was made

possible.

The proposed method was able to compute a SI vector field that was consistent and expected from the analyzed shell, since the dominant energy transmission paths strongly converged to the region where a damper was installed. These preliminary results suggested that, by invoking the Kirchhoff plate theory and by approximating the analyzed sample to an assembly of plates, the SI can be assessed for any irregular and thin shell.

2 Theory

2.1 Structural intensity

The final objective of this work is to compute the energy transmission that takes place on irregular shells by processing experimental data. To formulate the equations from which this quantity can be assessed, proper assumptions and approximations that describe the behavior of the analyzed sample need to be invoked. By assuming that the shell behaves in accordance with the Kirchhoff-Love postulates [1] and that the scalars components of the time-averaged SI vector field are aligned with a set of curvilinear coordinates $\mathbf{e}_1$ and $\mathbf{e}_2$ [4], it follows that

$$\mathbf{I} = I_1\mathbf{e}_1 + I_2\mathbf{e}_2, \tag{1}$$

where

$$I_1 = -(\pi f)\mathfrak{Im}\{Q_1u_3^* + M_{11}a_1^* + M_{12}a_2^* + N_{11}u_1^* + N_{12}u_2^*\}, \tag{2}$$

$$I_2 = -(\pi f)\mathfrak{Im}\{Q_2u_3^* + M_{21}a_1^* + M_{22}a_2^* + N_{21}u_1^* + N_{22}u_2^*\}. \tag{3}$$

The subscripts "1" and "2" indicate that the related field is pointing at the direction $\mathbf{e}_1$ and $\mathbf{e}_2$, respectively; the subscript "3" indicates that the field's direction is normal to the shell's surface; the scalars u represent the displacements of the mid-surface; a, the rotations about the normals; Q_1 and Q_2 are the components of the shear force, M_{11}, M_{22} and M_{12} are the components of the bending moment; and N_{11}, N_{22} and N_{12} are the ones from the membrane force.

It must be noted that the SI is defined on the mid-surface from a analyzed shell. Moreover, the terms related to the generalized forces (Q_i, M_{ij}, N_{ij}) are estimated via the strains; which, in turn, can be represented as functions of the terms u and a, if proper assumptions and approximations are used to represent the shell's behavior.

2.2 Kirchhoff-Love plate model

2.2.1 General theory of thin shells

This section presents the simplifications that were used to derive the generalized forces, which are required for the SI assessment. In the current work, not just the Kirchhoff-Love postulates are assumed to describe the shell's behavior, but that the studied shell can be approximated to a Kirchhoff-Love plate model [8], i.e., to an assembly of planar plates. By using this approach, the displacement and strain components acquire relatively simpler forms and vary linearly as functions of the shell's thickness. With these statements, it holds that

$$\mathbf{u}^{h/2} = \mathbf{u} + \frac{h}{2}\mathbf{a}, \tag{4}$$

$$\mathbf{u}^{h/2} = \{u_1^{h/2} \quad u_2^{h/2} \quad u_3^{h/2}\}^T, \quad \mathbf{u} = \{u_1 \quad u_2 \quad u_3\}^T, \quad \mathbf{a} = \{a_1 \quad a_2 \quad 0\}^T, \tag{5}$$

where h is the thickness value of the shell and $\mathbf{u}^{h/2}$ is the displacement on the shell's outer-surface. Moreover, the linearlized Green-Lagrange strain on the outer-surface $\boldsymbol{\varepsilon}^{h/2}$ can be formulated as a function of 2 strain components and is recast as

$$\boldsymbol{\varepsilon}^{h/2} = \boldsymbol{\gamma} + \frac{h}{2}\boldsymbol{\chi}, \tag{6}$$

$$\boldsymbol{\varepsilon}^{h/2} = \{\varepsilon_{11}^{h/2} \quad \varepsilon_{22}^{h/2} \quad \varepsilon_{12}^{h/2}\}^T, \quad \boldsymbol{\gamma} = \{\gamma_{11} \quad \gamma_{22} \quad \gamma_{12}\}^T, \quad \boldsymbol{\chi} = \{\chi_{11} \quad \chi_{22} \quad \chi_{12}\}^T, \tag{7}$$

where $\boldsymbol{\gamma}$ is the membrane strain and $\boldsymbol{\chi}$ is the bending strain. In turn, the terms $\boldsymbol{\varepsilon}^{h/2}$ and $\boldsymbol{\chi}$ can be recast as functions of the displacement's and rotation's spatial derivatives:

$$\varepsilon_{ij}^{h/2} = \frac{1}{2}(u_{i,j}^{h/2} + u_{j,i}^{h/2}), \quad \chi_{ij} = \frac{1}{2}(a_{i,j} + a_{j,i}), \quad \text{for} \quad i,j = \{1,2\}, \tag{8}$$

where the subscripts "$,i$" and "$,j$" indicate the spatial derivatives of the referred terms along the directions "i" and "j", respectively.

2.2.2 Generalized forces

By defining the bending and membrane strains and with a knowledge about the sample's stiffness matrix $\mathbf{D}$, the bending moment $\mathbf{M}$ and membrane force $\mathbf{N}$ of the shell's elements are defined as

$$\mathbf{M} = \frac{h^3}{12}\mathbf{D}\boldsymbol{\chi}, \quad \mathbf{N} = h\mathbf{D}\boldsymbol{\gamma}, \tag{9}$$

$$\mathbf{M} = \{M_{11} \quad M_{22} \quad M_{12}\}^T, \quad \mathbf{N} = \{N_{11} \quad N_{22} \quad N_{12}\}^T, \tag{10}$$

Since the shell is represented as a Kirchhoff-Love plate model, the shear force $\mathbf{Q}$ is retrieved by deriving the equilibrium conditions of a differential element [5]. Hence,

$$\mathbf{Q} = \{Q_1 \quad Q_2\}^T = \{M_{11,1} + M_{12,2} \quad M_{22,2} + M_{12,1}\}^T, \tag{11}$$

being the subscript ",1" and ",2" an indication that the term M_{ij} is differentiatied along the directions "1" and "2", respectively. The terms' components of the shear force $\mathbf{Q}$ are made explicit by differentiating the bending moment $\mathbf{M}$ in Eq. (9):

$$M_{ii,i} = \frac{h^3}{12}\frac{E}{1-\nu^2}(\chi_{ii,i} + \nu\chi_{jj,i}), \quad M_{ij,i} = \frac{h^3}{12}\frac{E}{1+\nu}\chi_{ij,i}, \quad \text{for} \quad i,j = \{1,2\}. \tag{12}$$

In turn, the derivatives of the bending strain scalar components shown in Eq. (12) are accessible by differentiating χ_{ij} in Eq. (8):

$$\chi_{ij,i} = \frac{1}{2}(a_{i,ij} + a_{j,ii}), \quad \text{for} \quad i,j = \{1,2\}. \tag{13}$$

From the Eqs. (8, 13), it can be noted that 1$^{\text{st}}$ order derivatives of the term $\mathbf{u}^{h/2}$ and 2$^{\text{nd}}$ order derivatives of $\mathbf{a}$ are required to assess all components of the SI equations [Eqs. (1, 2, 3)]. As it will be clear in Section 2.4, the chosen approach to differentiate these data ($\mathbf{u}^{h/2}$ and $\mathbf{a}$) is accomplished by considering these vectors as local degrees of freedom (DoF) of a mesh with planar elements.

However, the aim of this work is to assess the SI on the basis of experimental data, which is usually not represented on the basis of a local coordinate system ($\mathbf{e}_1$, $\mathbf{e}_2$, $\mathbf{e}_3$) (as it is the case of $\mathbf{u}^{h/2}$ and $\mathbf{a}$), but rather to a predefined Cartesian one ($\mathbf{e}_x$, $\mathbf{e}_y$, $\mathbf{e}_z$). Moreover, the point cloud with which the experimental data is initially represented may not be equal in number or position with respect to the nodes of a mesh that should contain the local DoFs. The next Sections are used to explain the following necessary steps to solve these issues: project the experimental data to the nodes of a mesh, transform the coordinate system with which the data is represented and data differentiation.

2.3 Projection of experimental displacements & assessment of rotations

If the assembly of planar plates is treated as a Finite-Element mesh, the data on its nodes can store the generalized DoFs $\tilde{\boldsymbol{\psi}}$ and shape functions N. Therefore,

$$\hat{\boldsymbol{\psi}}(\mathbf{x}) = \sum_{b=1}^{c} N_b(\mathbf{x}) \cdot \tilde{\boldsymbol{\psi}}_b, \tag{14}$$

where c is the total number of nodes in an element, b is the node numbering, $\mathbf{x}$ represents the spatial coordinates within that very element and $\hat{\boldsymbol{\psi}}$ is the generalized term within the element. The strategy used to project experimental data on a mesh was through the global least-squares minimization via shape functions [7]. The minimization problem can be formulated as

$$\min \sum_{a=1}^{d} \left| \hat{\boldsymbol{\psi}}(\mathbf{x}_a) - \boldsymbol{\psi}(\mathbf{x}_a) \right|^2, \tag{15}$$

where $\boldsymbol{\psi}$ represents an experimental and general term and d is the total number of measurement points. By substituting Eq.(14) into Eq.(15) and by considering the terms Ψ, $\tilde{\Psi}$ and $\boldsymbol{\Phi}$ as assembled matrices of the terms ψ, $\tilde{\psi}$ and $\boldsymbol{\phi}$, respectively; it follows that

$$\tilde{\Psi} = \left[\left[\boldsymbol{\Phi}^T \boldsymbol{\Phi} \right]^{-1} \boldsymbol{\Phi}^T \right] \Psi. \tag{16}$$

In the current work, the experimental data that is extracted from a real sample is the displacement of an outer-surface and which is defined here as $\mathbf{U}_{exp}^{h/2}$. If the term Ψ in Eq.(16) is substituted by $\mathbf{U}_{exp}^{h/2}$, one acquires,

$$\tilde{\mathbf{U}}^{h/2} = \left[\left[\boldsymbol{\Phi}^T \boldsymbol{\Phi} \right]^{-1} \boldsymbol{\Phi}^T \right] \mathbf{U}_{exp}^{h/2}, \tag{17}$$

where $\tilde{\mathbf{U}}^{h/2}$ is a vector stored on the nodes of the mesh and which is represented in the Cartesian coordinate system. The other 3 DoFs are the rotations related to $\tilde{\mathbf{A}}$, which can be assessed by subtracting the normals of the mesh under its deformed configuration (denoted here as $\mathbf{n}_{def}$) with the original normals of the mesh in its reference configuration, i.e., $\mathbf{e}_3$. Therefore, the global DoFs related to the rotation $\tilde{\mathbf{A}}$ is assessed by

$$\tilde{\mathbf{A}} = \mathbf{n}_{def} - \mathbf{e}_3. \tag{18}$$

2.4 Transformation of coordinate systems & spatial derivatives

After acquiring all DoFs for the nodes of the mesh, one can transform the terms $\tilde{\mathbf{U}}^{h/2}$ and $\tilde{\mathbf{A}}$ from the global basis ($\mathbf{e}_x$, $\mathbf{e}_y$, $\mathbf{e}_z$) to the local one ($\mathbf{e}_1$, $\mathbf{e}_2$, $\mathbf{e}_3$), so the terms $\tilde{\mathbf{u}}^{h/2}$ and $\tilde{\mathbf{a}}$ are present. By deciding that triangular elements would be the constituents of the mesh and by knowing that 2$^{\text{nd}}$ order derivatives are required for the current application [Eq. (13)], at least 6-noded triangular elements with quadratic shape functions are required. Therefore, by adding this information into Eq. (14) and by substituting $\tilde{\boldsymbol{\psi}}$ for either $\tilde{\mathbf{u}}^{h/2}$ or $\tilde{\mathbf{a}}$, it follows that

$$\hat{\mathbf{u}}^{h/2}(\mathbf{x}) = \sum_{b=1}^{6} N_b(\mathbf{x}) \cdot \tilde{\mathbf{u}}_b^{h/2}, \quad \hat{\mathbf{a}}(\mathbf{x}) = \sum_{b=1}^{6} N_b(\mathbf{x}) \cdot \tilde{\mathbf{a}}_b. \tag{19}$$

It was also decided to analyze the local displacement, rotation and their spatial derivatives in the barycentric coordinates of each element. By denoting that $\bar{N}$ is a shape function at these specific coordinates within each element, it holds that

$$\mathbf{u}^{h/2} = \sum_{b=1}^{6} \bar{N}_b \cdot \tilde{\mathbf{u}}_b^{h/2}, \quad \mathbf{a} = \sum_{b=1}^{6} \bar{N}_b \cdot \tilde{\mathbf{a}}_b, \tag{20}$$

where $\mathbf{u}^{h/2}$ and $\mathbf{a}$ are the displacement and rotation terms at the elements' barycenters. Since the shape functions are quadratic, 1st and 2nd order derivatives of $\mathbf{u}^{h/2}$ and $\mathbf{a}$ can also be assessed by differentiating the shape functions. Hence, the terms $\mathbf{u}^{h/2}_{,i}$, $\mathbf{a}_{,i}$ and $\mathbf{a}_{,ij}$ can also be computed. At this point, the terms $\mathbf{u}^{h/2}$, $\mathbf{a}$, $\mathbf{u}^{h/2}_{,i}$, $\mathbf{a}_{,i}$ and $\mathbf{a}_{,ij}$ should be available and one has all necessary terms to assess the strains [Eq. (8)], generalized forces [Eq. (9, 11-13)] and the SI vector fields [Eqs. (1, 2, 3)] on the mesh.

3 Materials

It has been decided to perform the measurements on a circular membrane made out of silicon, whose thickness and diameter were 1mm and 12cm, respectively (Figure 1). Its Young's modulus was estimated to be 8MPa and the Poisson's coefficient was assumed to be 0,3.

A loudspeaker was chosen to excite the membrane from one of its sides with single-sine pressure waves. To ensure that most of the energy was being delivered to the sample, the space between the loudspeaker and the membrane was isolated by a chamber. The device that would absorb the injected power was a long strip of a viscous polymer. One extreme end of this damper was fixed to the center of the membrane, while the other end was fixed near the loudspeaker. By choosing this configuration, it was possible to carefully pull the polymer strip from inside the chamber up to the point where the membrane would show a curved-conical shape. After manipulating the membrane's shape with the viscous polymer and installing the loudspeaker, a fine speckle pattern was drawn on the outer-surface of the shell, so a correlation between deformed and undeformed configurations could be computed via the DIC technique.

The recording of the images were done by 2 high-speed cameras, which were installed in front of the membrane and the DIC correlation was carried out by the Istra4D software. After preparing the set-up, the membrane was excited with an harmonic pressure of 70 Hz by the loudspeaker and the captured images were correlated and exported. At the end of this process, a point cloud consisting of the displacement at the outer-surface ($\mathbf{U}^{h/2}_{exp}$) and its spatial coordinates ($\mathbf{x}$) were available.

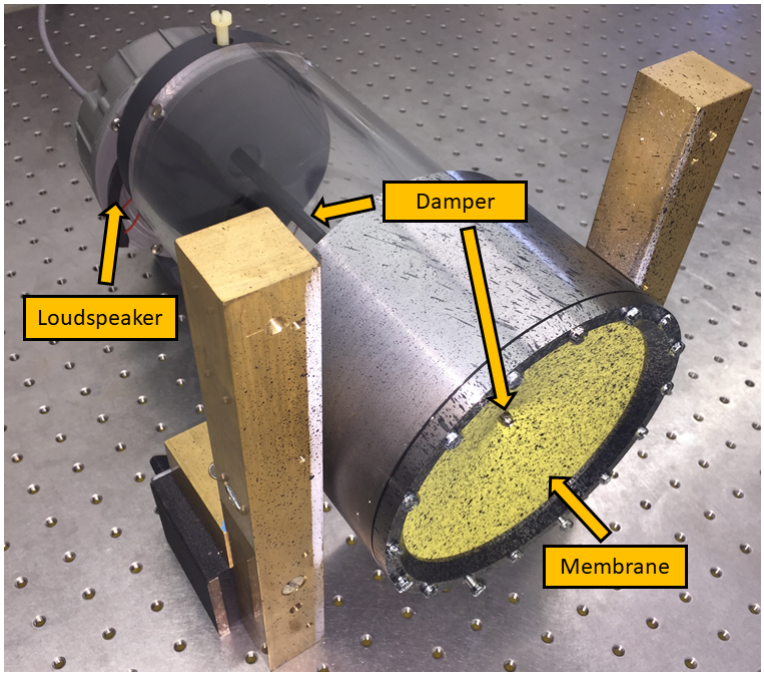


Figure 1: Set-up

4 Methods

4.1 Projection and computation of the mesh's global degrees of freedom

After preparing the set-up described in Section 3, a densely populated point cloud containing both the displacement $\mathbf{U}_{exp}^{h/2}$ and its corresponding spatial coordinates $\mathbf{x}$ are correlated from the sample's outer-surface. Since the information regarding the sample's shape can be acquired from that point cloud, a quadratic mesh that resembles the membrane's outer-surface can be customized. As pointed out in Section 2.4, 6-noded triangular elements were chosen to be the constituents of this mesh.

Afterwards, Eq.(17) is used to project the displacement $\mathbf{U}_{exp}^{h/2}$ at the nodes of the mesh, so the term $\tilde{\mathbf{U}}^{h/2}$ is made available and from which the global rotation $\tilde{\mathbf{A}}$ is retrieved on the basis of Eq.(18). At the end of this process, every node of the mesh should contain 6 DoFs (3 scalar components of the global displacement $\tilde{\mathbf{U}}^{h/2}$ and 3 of the global rotation $\tilde{\mathbf{A}}$).

4.2 Transformation of coordinate systems

The components of the SI vector fields shown in Eq.(1, 2, 3) are defined on the basis a local triad of unit vectors ($\mathbf{e}_1$, $\mathbf{e}_2$, $\mathbf{e}_3$). Therefore, the terms $\tilde{\mathbf{U}}^{h/2}$ and $\tilde{\mathbf{A}}$, which are defined in a predefined Cartesian coordinate system, need to be reoriented to a local basis. It has been decided that the tangent directions $\mathbf{e}_1$ and $\mathbf{e}_2$ would point at the same direction as the principal curvatures of the mesh. These tangent directions were computed via a multi-scale curvature estimation method [9] and $\mathbf{e}_3$ was defined to be the always perpendicular to the elements' surfaces.

After defining the local basis of unit vectors, the scalar components of the global DoFs ($\tilde{\mathbf{U}}^{h/2}$ and $\tilde{\mathbf{A}}$) can be represented by the triad ($\mathbf{e}_1$, $\mathbf{e}_2$, $\mathbf{e}_3$). After changing the coordinate system, the local representation from the global DoFs are at hand, i.e., the terms $\tilde{\mathbf{u}}^{h/2}$ and $\tilde{\mathbf{a}}$.

4.3 Data differentiation & strain estimation

Since the terms $\tilde{\mathbf{u}}^{h/2}$ and $\tilde{\mathbf{a}}$ are available, Eq.(20) can be used to compute the values related to the displacements and rotations at the barycentric coordinates of the elements, i.e., the terms $\mathbf{u}^{h/2}$ and $\mathbf{a}$. By differentiating the quadratic shape functions of these very equations, the spatial derivatives from both terms are also accessible. As shown in Eq.(8), 1^{st} order derivatives of $\mathbf{u}$ and $\mathbf{a}$ are necessary to compute the strains $\boldsymbol{\varepsilon}^{h/2}$ and $\boldsymbol{\chi}$.

Moreover, it was evident from the shear force formulation in Eqs.(11, 12, 13) that 2^{st} order derivatives of $\mathbf{a}$ are also necessary. Since it was established that quadratic shape functions would be used to build the mesh, all these terms can be assessed and the following terms should be available: $\mathbf{u}^{h/2}$, $\mathbf{u}_{,i}^{h/2}$, $\mathbf{a}$, $\mathbf{a}_{,i}$ and $\mathbf{a}_{,ij}$. The fields obtained by differentiating the shape functions are all present in the right-hand side of Eqs.(8, 13) and the terms $\boldsymbol{\varepsilon}^{h/2}$, $\boldsymbol{\chi}$ and $\boldsymbol{\chi}_{,i}$ can all be assessed.

4.4 Mid-surface data, generalized forces & structural intensity assessment

The last step consists in assessing the displacement and strain of the sample's mid-surface, i.e, the terms $\mathbf{u}$ and $\boldsymbol{\gamma}$. By analyzing Eqs.(4, 6), one can see that the mentioned terms are the only unknowns and that the other terms are available at the barycentric coordinate of the mesh's elements. Hence, by substituting the terms $\mathbf{u}^{h/2}$, $\mathbf{a}$, $\boldsymbol{\varepsilon}^{h/2}$ and $\boldsymbol{\chi}$ in Eqs.(4, 6) and by having a priori knowledge of the sample's thickness h, the terms $\mathbf{u}$ and $\boldsymbol{\gamma}$ can be recovered.

At this point, all necessary terms that are required to compute the generalized forces $\mathbf{Q}$, $\mathbf{M}$ and $\mathbf{N}$ are at hand, which are accessible by using Eqs.(9, 11, 12, 13). After acquiring the latter terms, one can finally compute the SI vector fields via the Eqs.(1, 2, 3).

5 Results

The shape and displacement measurements have been performed on the circular membrane under an excitation frequency of 70 Hz. After correlating the images' that were captured by the high-speed cameras', a point cloud containing both data of interest were exported from the Istra4D software. Approximately 25.000 points have been correlated during this procedure and the terms $\mathbf{U}_{exp}^{h/2}$ and $\mathbf{x}$ were exported.

Afterwards, a quadratic mesh containing 3.964 nodes and 1.906 triangular elements was developed. Its shape overlapped with the spatial coordinates $\mathbf{x}$ and the experimental displacement data $\mathbf{U}_{exp}^{h/2}$ was projected on that mesh by using Eq.(17). After this step, the global DoFs related to $\tilde{\mathbf{A}}$ was computed by using Eq.(18). Figure 2 presents the 6 DoFs that were projected and computed on the quadratic mesh at t=0s.

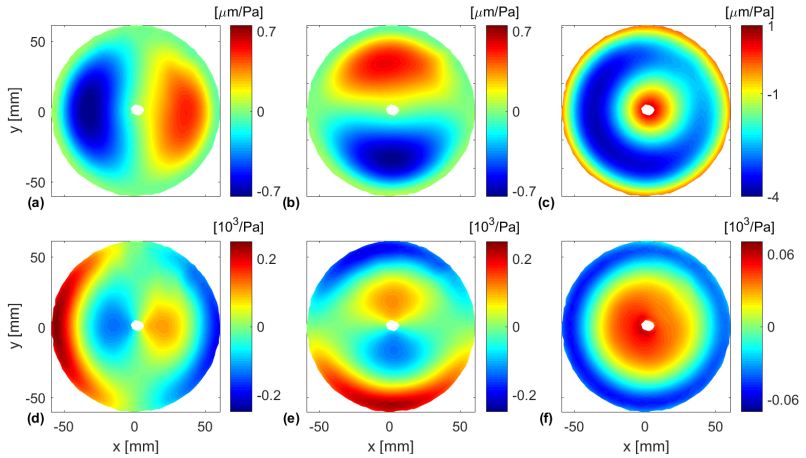


Figure 2: Representation of the global 6 DoFs on the customized mesh: 3 scalar displacements components at the sample's outer-surface ($\tilde{\mathbf{U}}^{h/2}$) (1$^{\text{st}}$ row) and 3 global rotations ($\tilde{\mathbf{A}}$) (2$^{\text{nd}}$ row) at t=0s. The scalar components are defined in the directions $\mathbf{e}_x$ [(a), (d)], $\mathbf{e}_y$ [(b), (e)] and $\mathbf{e}_z$ [(c), (f)].

Since the data has been successfully projected, one needs to define the tangent directions in which the spatial derivatives will be carried out. As explained in the Section 4.2, the principal curvature directions of the mesh were used for this purpose. Figure 3 presents these directions, which correspond to the local coordinates $\mathbf{e}_1$ [Figure 3 (a)] and $\mathbf{e}_2$ [Figure 3 (b)]. To complete the triad of unit orthonormal vectors, the normal coordinate $\mathbf{e}_3$ was also computed and defined to be alligned with the normal direction of the shell.

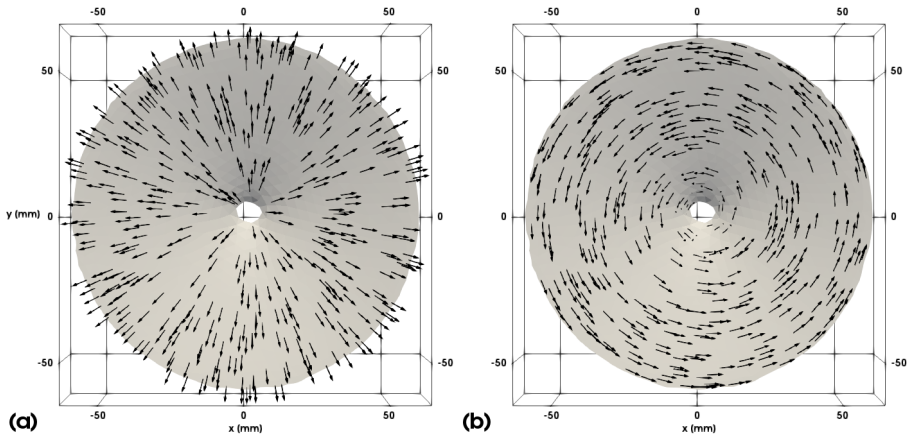


Figure 3: Direction of the tangent local coordinates $\mathbf{e}_1$ and $\mathbf{e}_2$

After defining the triad ($\mathbf{e}_1$, $\mathbf{e}_2$, $\mathbf{e}_3$), it was possible to transform the global DoFs $\tilde{\mathbf{U}}^{h/2}$ and $\tilde{\mathbf{A}}$ to their representation in the newly defined basis and the terms $\tilde{\mathbf{u}}^{h/2}$ and $\tilde{\mathbf{a}}$ were assessed. With these latter terms at hand, one can compute these very fields and the necessary spatial derivatives in both tangent coordinates $\mathbf{e}_1$ and $\mathbf{e}_2$ in the elements' barycenter [Eq.(20)]. By performing the calculations, the terms $\mathbf{u}^{h/2}$; $\mathbf{a}$; $\mathbf{u}^{h/2}_{,i}$; $\mathbf{a}_{,i}$ and $\mathbf{a}_{,ij}$ are made available. Since the necessary differentiations have been carried out, the strains and related derivatives $\boldsymbol{\varepsilon}^{h/2}$, $\boldsymbol{\chi}$ and $\boldsymbol{\chi}_{,i}$ could be also computed with Eqs.(8, 13).

The remaining step consists in assessing the displacement $\mathbf{u}$ and membrane strain $\boldsymbol{\gamma}$ from the shell's mid-surface. As explained in Section 4.4, these terms can be estimated, since they are the only unknowns in Eqs.(4, 6) at this point. At the end of this process, all terms that are necessary for the assessment of the SI are available, i.e., $\mathbf{u}$, $\mathbf{a}$, $\boldsymbol{\gamma}$, $\boldsymbol{\chi}$ and $\boldsymbol{\chi}_{,i}$. Figure 4 presents some of these terms at the direction $\mathbf{e}_1$ to show the quality of the processed data [terms of Eqs.(4, 6)].

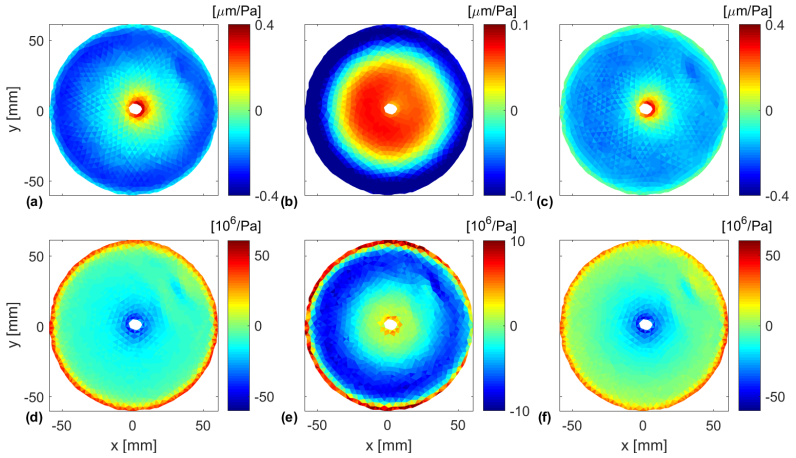


Figure 4: The first row presents the terms $u_1^{h/2}$ (a), $\frac{h}{2}a_1$ (b) and u_1 (c) [terms of Eq.(4)], while the second one, the strains $\varepsilon_{11}^{h/2}$ (d), $\frac{h}{2}\chi_{11}$ (e) and γ_{11} (f) [terms of Eq.(6)].

The last step consists on estimating the generalized forces $\mathbf{Q}$, $\mathbf{M}$ and $\mathbf{N}$ by using the terms related to the strains ($\boldsymbol{\gamma}$, $\boldsymbol{\chi}$ and $\boldsymbol{\chi}_{,i}$) in combination with the sample's material properties through Eqs.(9, 11, 12, 13). By acquiring these remaining terms, Eqs.(1, 2, 3) are used to visualize the SI on the analyzed sample. The processed energy transmission paths can be seen in Figure 5.

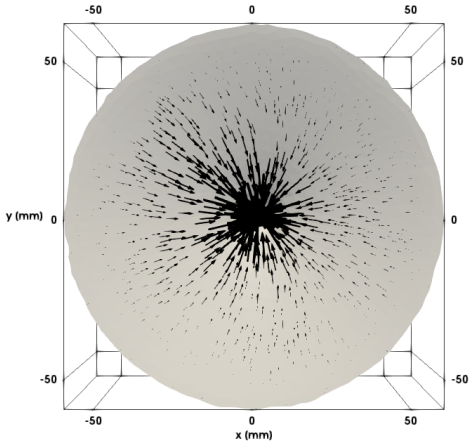


Figure 5: Estimated structural intensity of the circular membrane at 70 Hz

6 Discussion

The approach to project experimental data on a customized FE mesh showed to be useful when differentiations along the local coordinates need to be computed. This is confirmed by analyzing the quality of the spatial derivatives shown in the second row of Figure 4. Moreover, by comparing the displacement and strain at the outer-surface [Figures 4 (a,d)] with the ones related to the mid-surface [Figures 4 (c,f)], it can be noted that the bending strain play a big role in the sample's dynamic behavior.

Lastly and most importantly, the proposed method could estimated an energy transmission, which was expected from the built set-up. It can be seen in Figure 5 that the SI vector fields strongly converge to the region where the viscous damper was installed, i.e., at the center of the circular membrane. Due to these preliminary results, it is suggested that the method described in Section 4 is suitable to assess the SI on thin and irregular shells.

Acknowledgements

Financial support for this work was supplied by the Research Foundation of Flanders (FWO), (grant No. G049414N)

References

[1] C. J. Miguel, and D. Feit, *Sound, structures, and their interaction*, MIT press Cambridge, MA, USA (1986).

[2] F. Semperlotti, S.C. Conlon, *Structural damage identification in plates via nonlinear structural intensity maps*, the journal of acoustical society of america, (2010), 127, pp. EL48-53.

[3] N.B. Roozen, J.L. Guyader, C. Glorieux, *Measurement-based determination of the irrotational part of the structural intensity by means of test functional series expansion*, Journal of sound and vibration, (2015), 356, pp. 168–180.

[4] L. Gavric, G. Pavic, *A finite element method for computation of structural intensity by the normal mode approach*, Journal of sound and vibration, (1993), 164, pp. 29-43.

[5] E. Ventsel, and T. Krauthammer, *Thin plates and shells: theory: analysis, and applications*, CRC press (2001).

[6] H. Schreier, J.-J. Orteu, M. A. Sutton, *Image correlation for shape, motion and deformation measurements*, Springer US (2009).

[7] S. Avril, F. Pierron, *General framework for the identifcation of constitutive parameters from full-field measurements in linear elasticity*, International Journal of Solids and Structures, (2007), 44, pp. 14-15.

[8] D. Chapelle, and K.-J. Bathe, *The finite element analysis of shells-fundamentals*, Springer Science & Business Media (2010).

[9] D. Panozzo, E. Puppo, and L. Rocca, *Efficient multiscale curvature and crease estimation*, *Proceedings of Computer Graphics, Computer Vision and Mathematics, Brno, Czech Republic*, Brno (2010), (1)6.

A multi-level uncertainty integration strategy for forward model-driven SHM

P. Gardner[1], **C. Lord**[1] **R. J. Barthorpe**[1]
[1] University of Sheffield, Department of Mechanical Engineering,
Mappin Street, Sheffield, UK, S1 3JD
e-mail: **pagardner1@sheffield.ac.uk**

Abstract
Conducting full-system testing can be costly and infeasible in many structural health monitoring (SHM) applications. In addition, many SHM methodologies require data from all likely damage scenarios in order to produce robust classifications. Forward model-driven SHM is an approach in which validated numerical models simulate full-system outputs under different damage scenarios, which are subsequently used as training data for machine learning methods, improving the problem of a lack of available data. Here a framework is proposed in which uncertainties characterised at a sub-system level, using sub-system experimental data, are integrated into full-system predictions. The proposed methodology for multi-level uncertainty integration seeks to propagate sub-system parameter uncertainties whilst inferring any model discrepancies at each level. This paper demonstrates the effectiveness of multi-level uncertainty integration for forward model-driven SHM on a numerical case study.

1 Introduction

Forward model-driven structural health monitoring (SHM) is the process by which computational models, (referred to as *simulators*) are utilised in a forward manner in order to generate damage features of a real world structure. Subsequently, the simulated damage features are used as training data for pattern recognition or machine learning techniques and decision bounds identified [1]. These approaches are useful as they seek to resolve problems with the lack of available damage state data common to most SHM applications. As a result, any forward model-driven strategy should not require damage state data at a full-system level (unless available) in order to resolve issues associated with data-driven approaches. As a consequence forward model-driven methods must employ a strategy that provides confidence in a full-system prediction without traditional validation at the full-system level. This provides the motivation for developing a multi-level uncertainty integration strategy.

Multi-level uncertainty integration is a process whereby a structure is divided into levels, where at the top is the full-system and below are potentially multiple levels of sub-systems, each with a number of simulators. For each sub-system it is expected that damage state data can be obtained, therefore allowing the simulators at this level to be calibrated and validated. The approach allows these sub-system models to feed into each other up until the full-system level. The key assumption is that uncertainty quantification can be adequately performed and understood at multiple sub-system levels and that all damage mechanisms of interest can be understood at a sub-system level.

This paper seeks to adapt a subfunction discrepancy approach used in health economics in order to gain confidence in whether to finance drug treatments [2]. The main idea is that model discrepancies, due to missing physics, approximations or assumptions, can be captured at each sub-system simulator and validated. These discrepancies are propagated through to the full-system level with each simulators' parameter uncertainties providing improved confidence in the full-system predictions and correcting simulator inadequacies.

The outline of this paper is as follows. Section 2 outlines the general approach to multi-level uncertainty integration and the importance of quantifying model discrepancy. A numerical case study is presented in Section 3 demonstrating the application of the multi-level uncertainty integration strategy. Finally, Section 4 states conclusions and further work.

2 Multi-Level Uncertainty Integration Strategy

Forward model-driven SHM relies on the ability to generate validated simulators of full-systems for various damage mechanisms of interest. A complication is that observational data for each of these damage states are not obtainable at a full-system level. This creates a problem in validating and gaining confidence in full-system simulators under damage, when observational data are often not available, motivating the development of a multi-level uncertainty integration strategy for forward model-driven SHM.

A multi-level uncertainty integration strategy uses a combination of validated sub-system simulators at various levels e.g. at material, component or sub-assembly level, in order to capture behaviours of the full-system, for which observational data cannot be obtained, with the aim of producing the required outputs under these behaviours. In an SHM context, the desired full-system outputs are damage sensitive features and the behaviours are generally the changes of these features under damage types of interest (although additional environmental changes may be included). Consequently, the method divides a full-system structure into a number sub-system simulators that meet certain requirements. Firstly, there must be an output that can be measured experimentally and used to validate the sub-system simulator for the required inputs $\boldsymbol{x}^{sub} \in \boldsymbol{x}^{full}$ (where the superscripts sub and $full$ indicate the sub-system and full-system levels). Secondly, it is imperative that the functional relationship contains a set of parameters $\boldsymbol{\theta}^{sub} \in \boldsymbol{\theta}^{full}$ and inputs $\boldsymbol{x}^{sub} \in \boldsymbol{x}^{full}$ that are included in or affect the full-system simulator. Accordingly, experimental data at each sub-system can be used to validate and make inferences about their respective simulator. Uncertainty quantification for each sub-system may be employed to quantify parameter, model discrepancy and observational uncertainties [3], leading to confidence in the sub-system simulator. These inferences can be propagated through to the next level of the strategy. A key assumption of a multi-level uncertainty integration strategy is that the physics controlling changes at a full-system level can be captured at multiple sub-system levels, in addition to corrections for model discrepancies and quantification of uncertainties. Once propagated to a full-system level, this results in a complete understanding of the full-system uncertainties and should reduce model form errors or missing physics to a negligible level for the desired output quantity.

The approach outlined in this paper adapts a subfunction discrepancy technique [2] in order to integrate uncertainties from sub to full-system level. The method in this paper relies on the use of each sub-system simulator being defined as a statistical model of the form presented in Eq. (1).

$$\boldsymbol{z}(\boldsymbol{x}) = \boldsymbol{y}(\boldsymbol{x}) + e = \eta(\boldsymbol{x}, \boldsymbol{\theta}) + \delta(\boldsymbol{x}) + e \tag{1}$$

Where $\boldsymbol{z}(\boldsymbol{x})$ and $\boldsymbol{y}(\boldsymbol{x})$ are observational and bias corrected simulator outputs given the inputs $\boldsymbol{x}$ respectively. The bias corrected simulator output is equal to the sum of the simulator $\eta(\boldsymbol{x}, \boldsymbol{\theta})$ and the model discrepancy $\delta(\boldsymbol{x})$, where $\boldsymbol{\theta}$ are parameters of the simulator. The observations are assumed to be uncertain reflected in the addition of e.

The subfunction method for the simplest case - one level, one sub-system simulator and one full-system simulator, where all the parameters are contained within the sub-system simulator - can be defined mathematically as in Eqs. (2) and (3).

$$\boldsymbol{y}^{sub}(\boldsymbol{x}) = \eta^{sub}(\boldsymbol{x}, \boldsymbol{\theta}) + \delta^{sub}(\boldsymbol{x}) \tag{2}$$

$$\boldsymbol{z}^{full} = \boldsymbol{y}^{full}(\boldsymbol{x}) + e^{full} = \eta^{full}(\boldsymbol{y}^{sub}(\boldsymbol{x}), \boldsymbol{\theta}) + e^{full} \tag{3}$$

In this case, by performing inferences and validating the sub-system level simulator using Eq. (2), confidence can be made in the outputs of the full-system model under the input $\boldsymbol{x}$. It is assumed in this example that model discrepancy is found only at the sub-system level. This means that the model discrepancy at a full-system is only dependent on that of the sub-system. It is noted that it is possible to add model discrepancy at a full-system level (Eq. (3)); this maybe useful for correcting non-input dependant model form errors.

Model discrepancy - the mismatch between simulator and observational data - can be formulated as several options. In Eq. (1) the model discrepancy is described as having a functional form, implying that the simulator does not include all physics and may have assumptions or approximations that affect the functional output. Considering a model discrepancy of this form is important for robust statistical inferences to be made [4]. In this paper a Gaussian Process (GP) regression model is utilised for inferring the functional form of the model discrepancy. GPs provide a Bayesian framework for inferring the functional mapping between inputs and outputs via a non-parametric formulation. Here a GP is used in order to map the simulator and observational data residuals. Accordingly, it is assumed that the residuals for different inputs are modelled as jointly Gaussian distribution. In order to preserve conciseness of this paper, the reader is referred to [5, 6] for more information on GPs.

3 Case Study

A numerical case study is presented as a demonstration of the multi-level uncertainty integration strategy from Section 2. The full-system is a linear four degree of freedom shear structure where each of the four masses is supported by a bolted beam Fig. 1a. The objective is to calculate the distributions of the four natural frequencies $\boldsymbol{\omega}_n = \{\omega_1, \omega_2, \omega_3, \omega_4\}$, as two damage types are introduced to the structure - an open crack of length l_{cr} at the midpoint of any of the four beams, and a reduction in the non-dimensionalised clamping force f, at any of the four bolted joints. For simplicity both damage types are assumed to only affect the stiffness K of the full-system and in a quasi-static manner where $K = (K_b \times K_j)/(K_b + K_j)$. Accordingly, the functional mapping of the full-system is defined as $X^{full} \rightarrow \boldsymbol{y}^{full}$ where $\boldsymbol{y}^{full} = \boldsymbol{\omega}_n$, $X^{full} = \{\boldsymbol{l_{cr}}, \boldsymbol{f}\}$ and the mapping depends on parameters $\boldsymbol{\theta}^{full}$. In addition, parameter distributions in this case study are fixed for both simulator and 'true' behaviours, stated in Table 1 (meaning that calibration is not pursued). The parameter distributions have been chosen so that a range of distributions are represented. Throughout the case study uncertainty propagation is performed via a Monte-Carlo approach using 500 draws from the parameter distributions in simulated cases. For experimental tests 50 repeats are performed, each repeat is an independent draw for the parameter distributions.

The first stage of a multi-level uncertainty integration strategy is to divide the full-system into corresponding sub-systems, for which there must be measurable outputs and either parameters or outputs that affect the full-system. This study divides the four degree of freedom shear structure by one level at which there are two sub-systems - the beam and bolted joint - presented in Fig. 1. The reason for this is that static deflection tests can be performed for an increase in damage in each sub-system, and subsequently, stiffness values can be determined from the experimental tests. Additionally, both sub-systems inform of the full-system response as each can be used to quantify the stiffness reduction under their respective damage type. The sub-systems can be defined as follows. For the beam sub-system (simulator one, level one): $\eta^{sub}_{1,1} : \boldsymbol{x}^{sub}_{1,1} \rightarrow \boldsymbol{y}^{sub}_{1,1}$ where $\boldsymbol{x}^{sub}_{1,1} = \boldsymbol{l}_{cr}$, and $\boldsymbol{y}^{sub}_{1,1} = \boldsymbol{K}_b$ the beam tip stiffness. For the joint sub-system (simulator two, level one): $\eta^{sub}_{2,1} : \boldsymbol{x}^{sub}_{2,1} \rightarrow \boldsymbol{y}^{sub}_{2,1}$ where $\boldsymbol{x}^{sub}_{2,1} = \boldsymbol{f}$, and $\boldsymbol{y}^{sub}_{2,1} = \boldsymbol{K}_j$ the joint stiffness. A full-system simulator is then formed as $\eta^{full} : \boldsymbol{x}^{full} \rightarrow \boldsymbol{y}^{full}$ for the inputs $X^{full} = \{\boldsymbol{n}_{cr}, \boldsymbol{n}_f, \boldsymbol{y}^{sub}_{1,1}(\boldsymbol{x}^{sub}_{1,1}), \boldsymbol{y}^{sub}_{2,1}(\boldsymbol{x}^{sub}_{2,1})\}$ and outputs $\boldsymbol{y}^{full} = \boldsymbol{\omega}_n$. The following subsections describe how each system is constructed with details on the simulator and numerical experimental data.

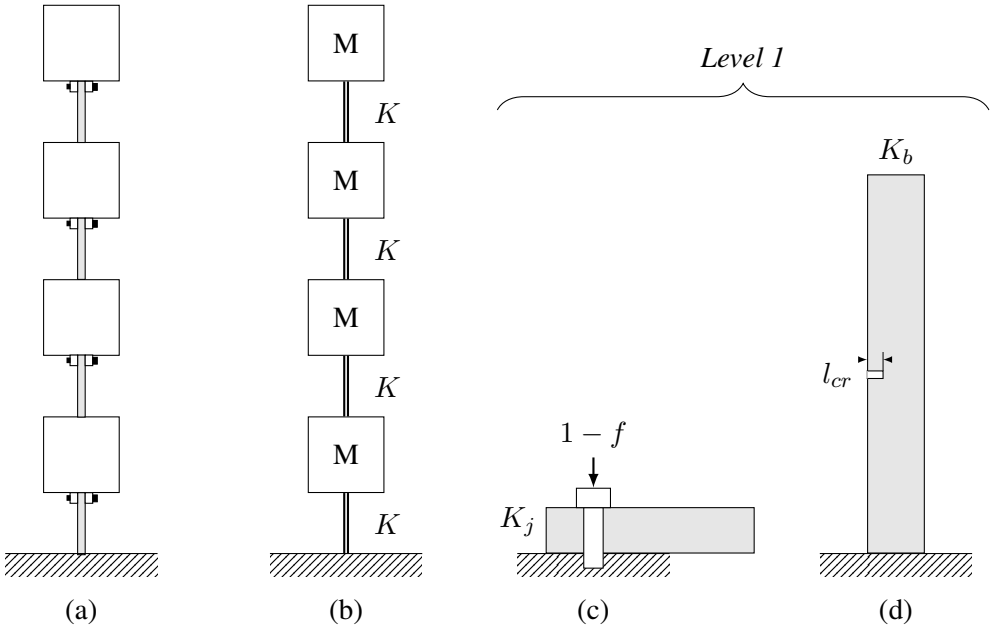


Figure 1: Schematics of the four degree of freedom shear structure; where (a) is the 'true' full-system with beams bolted to the underside of each plate, (b) is the full-system simulator where M is the mass of the blocks and K is the stiffness (a combination of the bolt and beam stiffness in series), (c) is the bolted joint sub-system for a reduction in the non-dimensionalised clamping force f, and (d) is the cantilever beam sub-system with a crack of length $\boldsymbol{l}_{cr}$.

3.1 Beam Sub-system

The four stiffness values K from the full-system are affected by the tip stiffness of a cantilever beam K_b. In this case study any of the four beams can be damaged by a midpoint crack x_{cr}, of increasing crack length l_{cr}, as depicted in Fig. 1d. In order to illustrate the fact that 'All models are wrong but some are useful' [7] - due to missing physics and/or approximations - the 'true' behaviour and the simulator are derived from different numerical models in the literature. The 'true' behaviour for the change in stiffness from an open crack is

Parameter		Value	System	'True'	Simulator
Beam length	l_b	$175mm$	$sub_{1,1}$, $full$	✓	✓
Beam width	w_b	$25mm$	$sub_{1,1}$, $full$	✓	✓
Beam thickness	t_b	$5mm$	$sub_{1,1}$, $full$	✓	✓
Plate length	l_p	$300mm$	$full$	✓	✓
Plate width	w_p	$250mm$	$full$	✓	✓
Plate thickness	t_p	$25mm$	$full$	✓	✓
Elastic Modulus	E	$\mathcal{N}\left(71, 0.5^2\right) GPa$	$sub_{1,1}$, $full$	✓	✓
Density	ρ	$\mathcal{N}\left(2700, 100^2\right) kg/m^3$	$full$	✓	✓
Beam length crack location	x_{cr}	$87.5mm$	$sub_{1,1}$	✓	✓
Crack model parameter	α	0.667	$sub_{1,1}$	✓	
Initial joint stiffness	K_{ji}	$\mathcal{W}ei\left(50005, 100\right) N/m$	$sub_{1,2}$, $full$	✓	✓
Rate of joint stiffness change	κ	$\mathcal{U}\left(4.9, 5.1\right)$	$sub_{1,2}$	✓	
Joint stiffness magnitude at $f=1$	p	$\mathcal{U}\left(1.99, 2.01\right)$	$sub_{1,2}$	✓	✓
Linear joint model gradient	β	$\mathcal{U}\left(-1.72, -1.68\right)$	$sub_{1,2}$		✓

Table 1: Parameters of the four degree of freedom shear structure. The 'true' and simulator columns refer to which numerical models the parameters are used in.

formulated using the numerical model defined by Christides and Barr [8] in Eq. (4). A bilinear stiffness model, by Sinha et al [9], forms the simulator, presented in Eq. (5). Both stiffness models are solved using the Euler-Bernoulli bending beam equation in Eq. (6) via numerical integration, where the beam stiffness is calculated via $K_b = -F/y_{tip}$ (y_{tip}[1] is the tip deflection). This means that both the 'true' behaviour and simulator for the beam sub-system map $\boldsymbol{l}_{cr} \rightarrow \boldsymbol{K}_b$. The simulator for this sub-system is the first simulator at level one - denoted $\eta^{sub}_{1,1}$.

$$EI(x) = \frac{EI_0}{1 + C\exp(-2\alpha|x - x_{cr}|/t_b)} \tag{4}$$

$$EI(x) = \begin{cases} EI_0 & \text{if } x \leq x_{cr,1} \text{ or } x \geq x_{cr,2} \\ EI_0 - E(I_0 - I_c)\frac{x - x_{cr,1}}{x_{cr} - x_{cr,1}} & \text{if } x_{cr,1} \leq x \leq x_{cr} \\ EI_0 - E(I_0 - I_c)\frac{x_{cr,2} - x}{x_{cr,2} - x_{cr}} & \text{if } x_{cr} \leq x \leq x_{cr,2} \end{cases} \tag{5}$$

$$\frac{\partial^2 y}{\partial x^2} = -\frac{M(x)}{EI(x)} \tag{6}$$

Where E is the elastic modulus, x is the distance along the length of the beam and M the bending moment. The second moment of areas $I_0 = (w_b t_b^3)/12$ and $I_0 = w_b(t_b - l_{cr})^3/12$ contribute to the constant $C = (I_0 - I_c)/Ic$, where w_t and t_b are the beam width and thickness respectively. The parameter α is set according to experimental work performed by Christides and Barr [8]. In the bilinear model positions beside the crack are calculated by $x_{cr,1} = x_{cr} - l_{eff}$ and $x_{cr,2} = x_{cr} + l_{eff}$ where the effective length of the stiffness reduction of the crack is $l_{eff} = 1.5t_b$, as defined by Sinha et al. [9].

The experiment for this sub-system is a static deflection test, due to the quasi-static assumptions in Eqs. (4) and (5). The beam was forced from $\boldsymbol{F} = \{100, 150, ..., 500\}N$ for each crack length $\boldsymbol{l}_c = \{0, 0.1, ..., 0.9\} \times t_b mm$ and the tip deflection $\boldsymbol{y}_{tip}$ measured (numerically using Eqs. (4) and (6)) with observational uncertainty distributed $\mathcal{N}\left(0, 1^2\right) mm$ $(= e^{sub}_{1,1})$. The experimental beam stiffness at the tip, was subsequently estimated via the gradient from least squares linear regression between the force and tip deflection.

The statistical equation in the form of Eq. (1) can be formulated as in Eq. (7).

$$\boldsymbol{z}^{sub}_{1,1}(\boldsymbol{x}^{sub}_{1,1}) = \eta^{sub}_{1,1}(\boldsymbol{x}^{sub}_{1,1}, \boldsymbol{\theta}^{sub}_{1,1}) + \delta^{sub}_{1,1}(\boldsymbol{x}^{sub}_{1,1}) + e^{sub}_{1,1} \tag{7}$$

Where $\boldsymbol{z}^{sub}_{1,1}(\boldsymbol{x}^{sub}_{1,1}) = \boldsymbol{K}^{exp}_b(\boldsymbol{l}_{cr})$ (the experimental beam tip stiffness), $\boldsymbol{x}^{sub}_{1,1} = \boldsymbol{l}_{cr}$. The bilinear numerical model forms the simulator $\eta^{sub}_{1,1}(\boldsymbol{x}^{sub}_{1,1}, \boldsymbol{\theta}^{sub}_{1,1})$, where $\boldsymbol{\theta}^{sub}_{1,1} = \{l_b, w_b, t_b, E, x_{cr}\}$ and the output is $\boldsymbol{y}^{sub}_{1,1}(\boldsymbol{x}^{sub}_{1,1}) = \boldsymbol{K}_b(\boldsymbol{l}_{cr})$. Both the observational uncertainty $e^{sub}_{1,1}$ and model discrepancy $\delta^{sub}_{1,1}(\boldsymbol{x}^{sub}_{1,1})$ are assumed unknown. Consequently, a GP regression model is utilised to infer both the model discrepancy and observational noise, regressing from crack lengths $\boldsymbol{l}_{cr}$ to the residual stiffness $\Delta\boldsymbol{K}_b = \boldsymbol{K}^{exp}_b - \boldsymbol{K}^{mode}_b$ where $mode$ indicates the simulator output at the modal values of the parameter distributions. Initially a leave-one-out validation process was used, where the 50 samples for each crack length were omitted periodically in training. However very little changes in the functional form were witnessed, leading to the full experimental data set being used in training. The bias corrected beam tip stiffness is compared to the simulator output and the experimental results in Fig. 2. This demonstrates the ability of a GP regression model to capture the functional form of the discrepancy whilst estimating a homoscedastic observational uncertainty (the results may be improved with a hetroscedastic observational uncertainty model in the GP regression model [10], this is left as an area for further research). The normalised mean squared error (NMSE) between the bias corrected and experimental data means are 0.097. showing good agreement.

[1]The notation y here indicates the deflection and not an output.

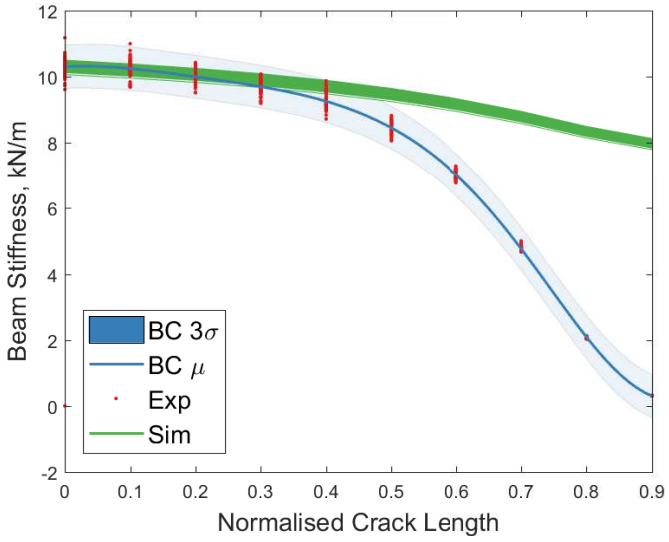


Figure 2: Comparison bias corrected (BC), experimental (exp) and simulator (sim) beam tip stiffness $\boldsymbol{K}_b$ for different crack lengths $\boldsymbol{l}_{cr}$.

3.2 Bolted Joint Sub-system

The bolted joint stiffness $\boldsymbol{K}_j$ at any of the four locations in the full-system can be damaged via a reduction in the clamping force, parametrised by a non-dimensional clamping force $\boldsymbol{f}$, presented in Fig. 1c. The 'true' behaviour and simulator output of $\boldsymbol{K}_j$, for a reduction in $\boldsymbol{f}$, are modelled numerically as shown in Eqs. (8) and (9) respectively; where Eq. (8) is a quasi-static bolt loosening model defined by Todd et al. [11, 12] and Eq. (9) is a linear fit of that numerical model. Consequently, the bolted joint sub-system maps $\boldsymbol{f} \rightarrow \boldsymbol{K}_j$. The simulator for this sub-system is the second simulator at level one - denoted $\eta^{sub}_{1,2}$.

$$K_j(f) = K_{ji} \times \tanh\left(\kappa(1-f)\right)\left(p + (1-p)\tanh\left(\kappa\frac{f}{1-f}\right)\right) \tag{8}$$

$$K_j(f) = K_{ji} \times (\beta f + p) \tag{9}$$

Where K_{ij} is the initial stiffness of the bolted joint, κ adjusts the rate of stiffness change, p adjusts the stiffness function magnitude at $f = 1$ and β is the gradient of the linear model. It is noted that the stiffness function is maximum at $f = 1$ and minimum and $f = 0$ to correspond with a reduction in force, meaning that the outputs for $\boldsymbol{f}$ are reversed.

The experiment for this sub-system is also static deflection test, due to the quasi-static assumptions in Eqs. (8) and (9). The beam was forced from $\boldsymbol{F} = \{100, 150, ..., 500\}N$ for each reduction in non-dimensionalised clamping force $\boldsymbol{f} = \{1, 0.9, ..., 0.1\}$ and the tip deflection measured (using Hooke's law $F = -K_j y$) with observational uncertainty distributed $\mathcal{N}\left(0, 1^2\right) mm$ $(= e^{sub}_{2,1})$. Again the experimental joint stiffness is estimated from the gradient of a least squares linear regression model.

The statistical equation in the form of Eq. (1) can be formulated as in Eq. (10).

$$\boldsymbol{z}^{sub}_{2,1}(\boldsymbol{x}^{sub}_{2,1}) = \eta^{sub}_{2,1}(\boldsymbol{x}^{sub}_{2,1}, \boldsymbol{\theta}^{sub}_{2,1}) + \delta^{sub}_{2,1}(\boldsymbol{x}^{sub}_{2,1}) + e^{sub}_{2,1} \tag{10}$$

Where $\boldsymbol{z}^{sub}_{2,1}(\boldsymbol{x}^{sub}_{2,1}) = \boldsymbol{K}^{exp}_j(\boldsymbol{f})$ (the experimental joint stiffness), $\boldsymbol{x}^{sub}_{2,1} = \boldsymbol{f}$. The simulator $\eta^{s}ub_{2,1}(\boldsymbol{x}^{sub}_{2,1}, \boldsymbol{\theta}^{sub}_{2,1})$, is linear numerical model (Eq. (8)) where $\boldsymbol{\theta}^{sub}_{2,1} = \{p, \beta, K_{ji}\}$ and the output is $\boldsymbol{y}^{sub}_{2,1}(\boldsymbol{x}^{sub}_{2,1}) = \boldsymbol{K}_j(\boldsymbol{f})$. Using a GP regression model, both the observational uncertainty $e^{sub}_{2,1}$ and model discrepancy $\delta^{sub}_{2,1}(\boldsymbol{x}^{sub}_{2,1})$ are

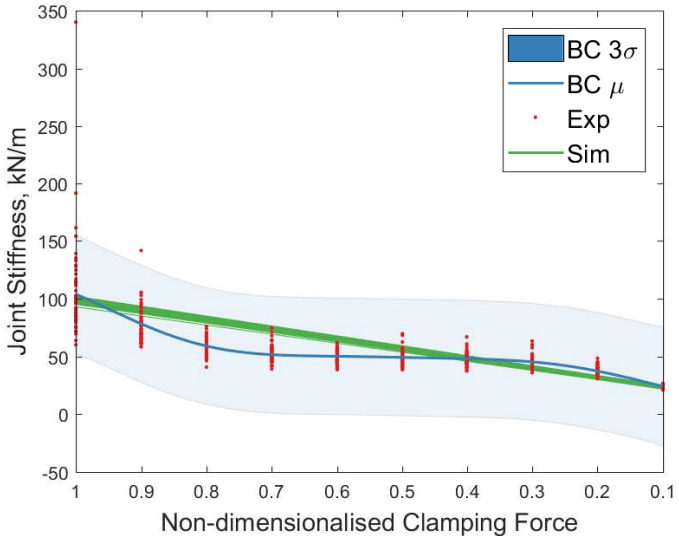


Figure 3: Comparison of bias corrected (BC), experimental (exp) and simulator (sim) joint stiffness $\boldsymbol{K}_j$ for a reduction in non-dimensionalised clamping force $\boldsymbol{f}$ - it is noted that the axis is reversed as [11, 12].

inferred in the same manner to the beam sub-system, regressing between $\boldsymbol{f}$ and $\Delta\boldsymbol{K}_j = \boldsymbol{K}_j^{exp} - \boldsymbol{K}_j^{mode}$. Similarly to the beam sub-system an initial leave-one-out validation process was employed, and due to relatively small changes in the functional form the full experimental data set was used in training. Fig. 3 shows a comparison for the bias corrected, simulator and experimental joint stiffness for a reduction in clamping force. As with the beam-subsystem, the bias corrected joint stiffness captures the functional form of the model discrepancy, which is not captured by the simulator. Homoscedastic assumptions in the GP regression model again mean that a homoscedastic observational uncertainty is inferred. The NMSE between the bias corrected and experimental data means are 0.001 showing excellent agreement.

3.3 Full-System Integration

The full-system is an undamped linear spring-mass system (Fig. 1b) where the spring stiffnesses K, are composed of the beam tip stiffness and bolt stiffness in series $K = (K_b \times K_j)/(K_b + K_j)$. The four degree of freedom system can be solved via an eigenvalue problem for the natural frequencies of the system. For this case study the 'true' and simulator numerical models are equivalent with the only difference being the input values for the beam tip and joint stiffnesses under damage. This means that there is no model discrepancy at the full-system level resulting in Eq. (11); due to the assumption that all the model discrepancy due to damage can be captured at a sub-system level. The percentage difference of natural frequency $\Delta\boldsymbol{\omega}_n$ is used as a damage feature in this case study, as it is a more damage sensitive feature compared to natural frequency [13].

$$\boldsymbol{z}^{full}(X^{full}) = \eta^{full}(X^{full}, \boldsymbol{\theta}^{full}) + e^{full} \tag{11}$$

Where $\boldsymbol{z}^{full}(X^{full}) = \Delta\boldsymbol{\omega}_n(X^{full})$, the percentage differences of the experimental four natural frequencies under damage. There are several inputs to the full-system $X^{full} = \{\boldsymbol{n}_{cr}, \boldsymbol{n}_f, \boldsymbol{y}_{1,1}^{sub}(\boldsymbol{x}_{1,1}^{sub}), \boldsymbol{y}_{2,1}^{sub}(\boldsymbol{x}_{2,1}^{sub})\}$ where $\boldsymbol{n}_{cr}$ and $\boldsymbol{n}_f$ indicate the floor in which the damage occurs, for the crack and loosened bolt respectively. As $\boldsymbol{n}_{cr}$ and $\boldsymbol{n}_f$ are only position inputs for this simple system it is assumed there no input dependent model discrepancy term is required. The other inputs are $\boldsymbol{y}_{1,1}^{sub}(\boldsymbol{x}_{1,1}^{sub}) = \boldsymbol{K}_b(\boldsymbol{l}_{cr})$, - the beam tip stiffness under a midpoint crack - $\boldsymbol{y}_{2,1}^{sub}(\boldsymbol{x}_{2,1}^{sub}) = \boldsymbol{K}_j(\boldsymbol{f})$, - the joint stiffness from a reduction in clamping force (dependent on their sub-system model discrepancy). The full-system simulator $\eta^{full}(X^{full}, \boldsymbol{\theta}^{full})$ also depends on the

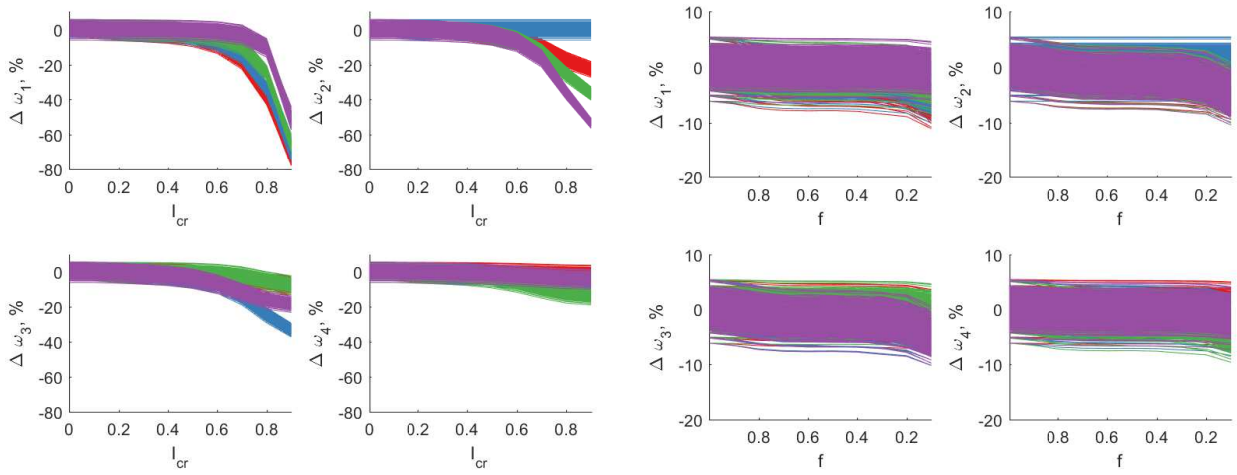


Figure 4: Bias corrected outputs - the percentage difference of the four natural frequencies $\Delta\boldsymbol{\omega}_n$ - for damage at different floors of the full-system $\boldsymbol{n}_{cr} = \boldsymbol{n}_f = \{1, 2, 3, 4\}$ (red, blue, green, purple); where (a) is an increase in crack length at the midpoint $\boldsymbol{l}_{cr}$ and (b) is a reduction in the non-dimensionalised clamping force $\boldsymbol{f}$. For (b) it is noted that the x-axis is reversed as [11, 12].

parameter set $\boldsymbol{\theta}^{full} = \{l_b, w_b, t_b, l_p, w_p, t_p, E, \rho, K_{ij}\}$. The numerical nature of this case study allows the comparison of both 'true' and simulator outputs, $\Delta\boldsymbol{\omega}_n$, under these damage types.

500 Monte Carlo realisations, drawn from the outputs of level one and the full system parameters, were generated in order to compare the bias corrected, simulator and 'true' full-system outputs. Figure 4 presents the bias corrected $\Delta\boldsymbol{\omega}_n$ under increasing crack length and for a reduction in clamping force. As expected, the increase in crack length has a greater effect on the natural frequencies of the system compared to a reduction in clamping force (reflected in the stiffness reductions in Figs. 2 and 3). The first natural frequency is the most affected by an increase in crack length, with a comparable reductions in the first, second and third natural frequencies for a reduction in clamping force. Figure 5 demonstrates an example comparison of the output distributions for $\Delta\omega_1$, where both damage types are located at the first floor and the only damage type is an increase in crack length. A visual comparison shows that for the first four damage states $\boldsymbol{l}_{cr} = \{0, 0.1, 0.2, 0.4\} \times t_b$, the distributions are very similar, after which the simulator fails to capture the correct distribution forms, whereas the bias corrected simulator maintains a good fit.

Hypothesis testing using the Kolmogorov-Smirnoff two sample test were performed at each damage scenario, for each natural frequency, totalling to 6400 combinations. A significance level, the upper bound of the probability of type 1 errors, was $\alpha_H = 0.01$. The percentage of null hypotheses H_0, that were not rejected, for both the bias corrected and simulator outputs at a full-system level, when compared to the 'true' outputs, were 97.4% and 30.7%. This demonstrates that the proposed uncertainty integration strategy outperforms an approach that does not consider model discrepancy, providing a significant improvement. In order to illustrate this further Fig. 6 presents a comparison between the uncertainty integration strategy and the original simulator for the first natural frequency; this was the worst performance of the uncertainty integration strategy. It can be seen that the performance of the uncertainty integration strategy is the same for all locations at 90% (in other natural frequencies there are differences at different locations). The original simulator however, performs best when damage is located at the highest floors, at 57%. This is because as damage is located at a lower floor it will have a greater affect on the first natural frequency of the system (as it is the first bending mode). Damage due to a crack located at the lower floors also affects the first natural frequency more than damage at the joint. This is expected from Figs. 2 and 3; both indicate the original simulator fails to capture the stiffness reduction for a crack to a greater extent than the due to a loosened bolt. The NMSEs for all 6400 combinations for both the original simulator and uncertainty integration strategy were 104 and

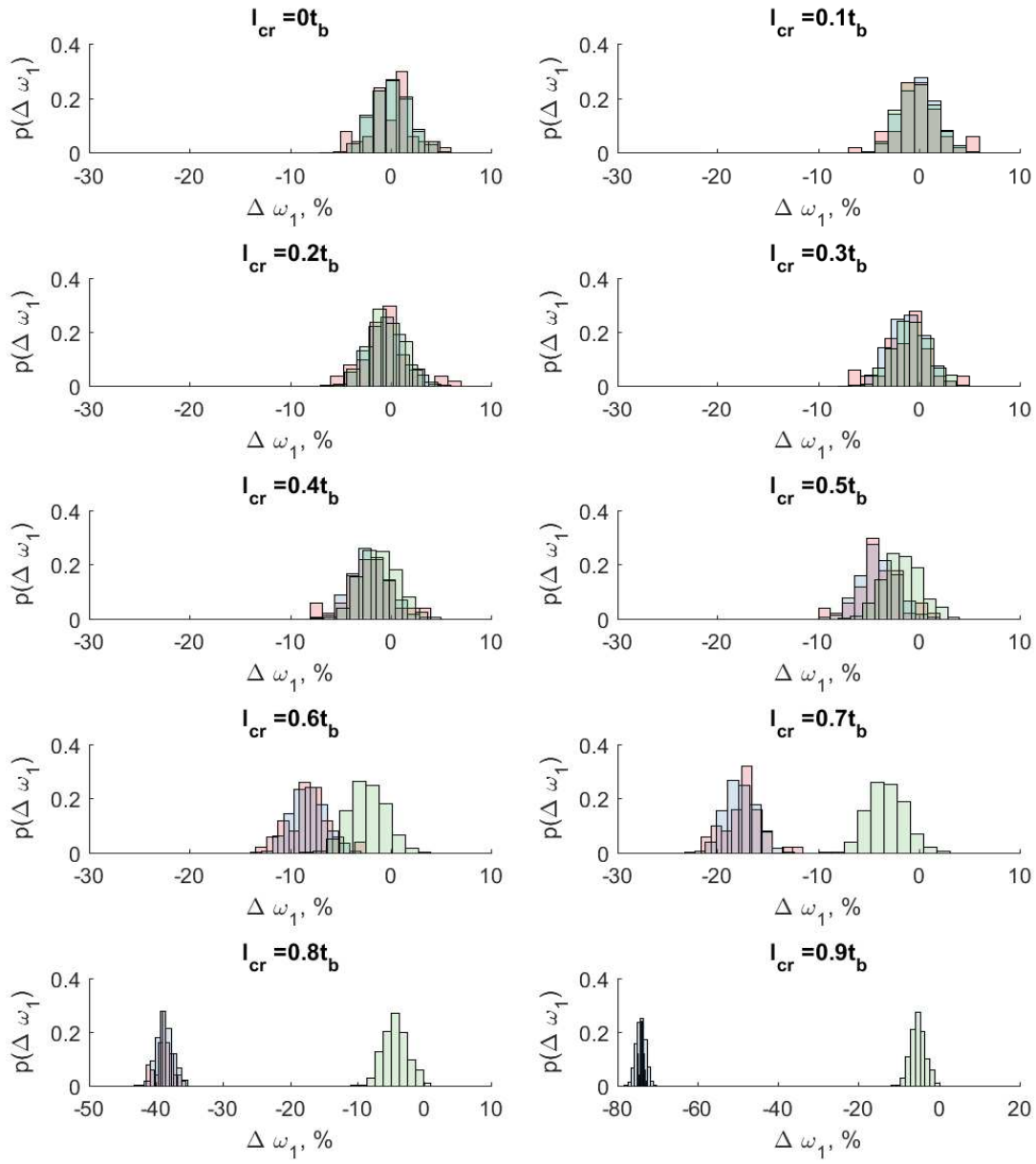


Figure 5: A comparison of $\Delta\boldsymbol{\omega}_1$ for increasing crack lengths at the midpoint of floor one; original simulator (green), uncertainty integration strategy (blue) and 'true' (red) outputs. It is noted that the axis limits are different for $\boldsymbol{l}_{cr} = \{0.8, 0.9\} \times t_b$ due to the large decrease in natural frequency.

0.005 respectively. This highlights the inability to capture the mean trend in the original simulator and the excellent agreement in the mean outputs for the uncertainty integration strategy and 'true' full-system.

In order to analyse these results further Fig. 7, a comparison of hypothesis test outcomes from all combinations of damage located at floor one, for the first natural frequency, are presented. This is chosen as the original simulator performs worse at this location, aiding the diagnoses of the difference in performance. The null hypothesis is rejected for all clamping force reductions when the crack length is at 90% of the beam

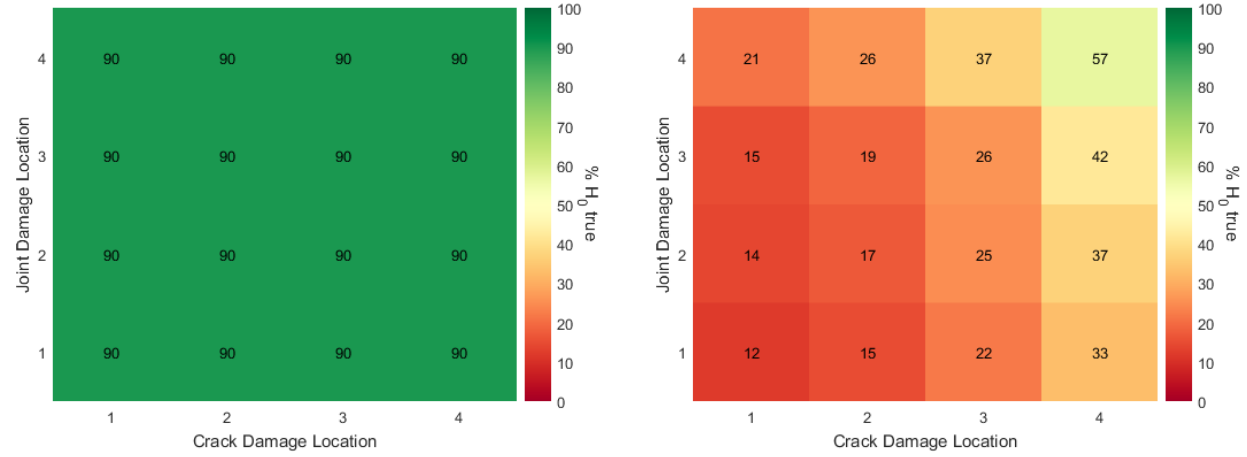


Figure 6: The percentage of null hypotheses H_0, that are not rejected for the first natural frequency; where (a) is the uncertainty integration strategy and (b) the original simulator.

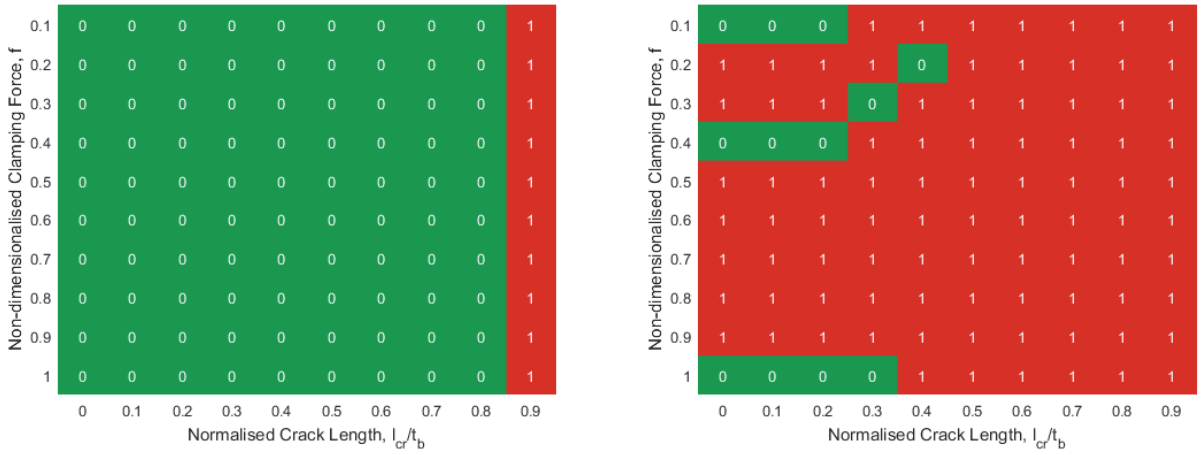


Figure 7: Kolmogorov-Smirnoff two sample hypothesis test results for the first natural frequency where both damage types are located at floor one; where (a) is the uncertainty integration strategy and (b) the original simulator.

thickness, for the uncertainty integration strategy. This indicates that the beam tip stiffness for this crack length has not accurately been captured, and should be an area of model improvement at the sub-system level. On the other hand, the original simulator fails to capture the majority of damage scenarios. It performs best when the crack length is small (under 30% of the beam thickness) and when the reduction in clamping force results in the linear model overlapping the hyperbolic tangent model (Fig. 3). Consequently, the failure to adequately capture the model form at a sub-system level will result in poor full-system performance and as all physics can never be fully captured in any model, a mechanism for quantifying the functional form and uncertainty due to model discrepancy is paramount.

To illustrate reasons for the results in Fig. 7, Fig. 5 presents a comparison of the output distributions from the 'true', original simulator and uncertainty integration strategy. The distributions are of $\Delta\boldsymbol{\omega}_1$ when both damage types are located at floor one, where $f = 1$, and crack length is increased. Figure 5 shows that for $\boldsymbol{l}_{cr} = 0, 0.1, 0.2, 0.3 \times t_b$ all three distributions are overlaid with little difference in the probability mass. As the crack length increases further, a shift in the output mean of the original simulator occurs in Fig. 7, leading

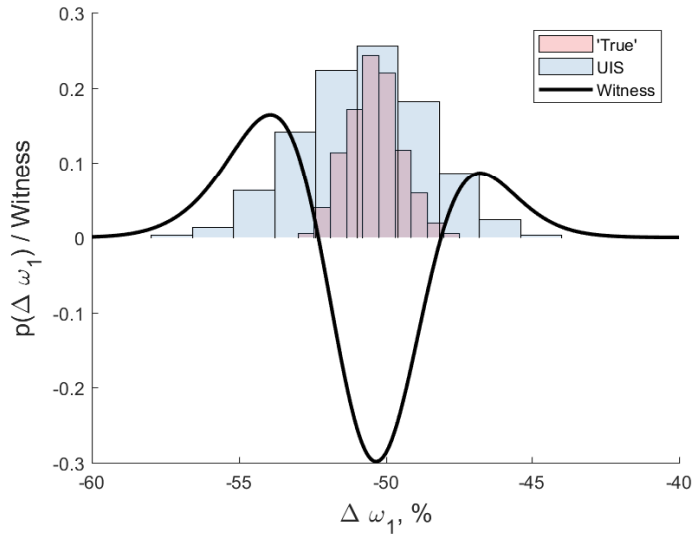


Figure 8: A comparison of the histograms and witness function of $\Delta\boldsymbol{\omega}_1$ for $l_{cr} = 0.9 \times t_b$ at floor one. UIS is the uncertainty integration strategy histogram and witness the witness function.

to a rejection in the null hypothesis. The uncertainty integration strategy provides a good fit with the 'true' full-system until $l_{cr} = 0.9 \times t_b$, where the true system has a greater variance - the percentage difference of the mean and variance at this damage extent are 0.01% and 4.69%. These differences are highlighted in Fig. 8, where the witness function, the difference between two kernel mappings of the samples [14, 15], is presented. The witness function was generated using a Gaussian kernel where the scale parameter σ, was set using a median heuristic. The witness function provides a visual illustration the offset in mean and smaller variance.

4 Conclusion

A multi-level uncertainty integration strategy based on a subfunction discrepancy approach has been demonstrated. The strategy seeks to divide a structure into different levels and sub-systems where validation of damage mechanisms is achievable. At each of these sub-systems model discrepancies are inferred in order to improve the predictive capability of the simulator. Finally, the sub-system model discrepancies and parameter uncertainties are propagated through to the full-system level providing confidence in predictions at a full-system level.

A numerical case study has been presented demonstrating the technique on a simple four degree of freedom shear structure. The objective of this study was to predict damage sensitive features - percentage differences of natural frequencies - when two types of damage were introduced to the structure, namely a midpoint crack of increasing length and a reduction in clamping force at the joint, for various positions in the structure. The full-system was divided into one level where there were two sub-systems, a beam sub-system and joint sub-system. At each of these sub-systems experimental data was generated from the 'true' process with the addition of observational uncertainty, and model discrepancies inferred between simulator outputs and the experimental data. The uncertainties and model discrepancies were propagated to the full-system level where, due to the numerical nature of the case study, a comparison was made with the 'true' outputs. Hypothesis testing was performed on the output distributions for the 6400 combinations of inputs. This demonstrated that the multi-level uncertainty strategy had improved the predictive performance from 30.7% to 97.4% of not rejecting the null hypotheses. In terms of mean predictions the strategy improved NMSEs from 104 to 0.005. The enhanced predictive capability clearly indicates the benefits of this approach for the case study.

Further research should be conducted into applying the methodology to a real world case study and for different types of simulator and model fidelities. The approach should also be applied with different divisions of a structure in order to quantify the differences in outputs due to the initial set up of the technique. Additionally, demonstration of the process with calibration included is left as further work. Finally, the inclusion of hetroscedastic Gaussian processes to better capture the model discrepancies from hetroscedastic experimental data should be pursued.

References

[1] P Gardner, C Lord, and R. J. Barthorpe. A Probabilistic Framework for Forward Model-Driven SHM. In *European Workshop on Structural Health Monitoring (EWHSM)*, pages 1–13, 2018.

[2] M. Strong, J. E. Oakley, and J. Chilcott. Managing Structural Uncertainty in Health Economic Decision Models. *Journal of the Royal Statistical Society: Series C (Applied Statistics)*, 61(1):25–45, 2012.

[3] M. C. Kennedy and A. O'Hagan. Bayesian calibration of computer models. *Journal of the Royal Statistical Society: Series B (Statistical Methodology)*, 63(3):425–464, 2001.

[4] J Brynjarsdóttir and A O'Hagan. Learning about physical parameters: the importance of model discrepancy. *Inverse Problems*, 30(11):114007, 2014.

[5] A O'Hagan and J. F. C. Kingman. Curve Fitting and Optimal Design for Prediction. *Journal of the Royal Statistical Society. Series B (Methodological)*, 40(1):1–42, 1978.

[6] C. E. Rasmussen and C. K. I. Williams. *Gaussian processes for machine learning.*, volume 14. 2004.

[7] G. E. P. Box and N. R. Draper. *Empirical Model-Building and Response Surfaces*. 1987.

[8] S. Christides and A. D. S. Barr. One-dimensional theory of cracked Bernoulli-Euler beams. *International Journal of Mechanical Sciences*, 26(11-12):639–648, 1984.

[9] J. K. Sinha, M. I. Friswell, and S Edwards. Simplified Models for the Location of Cracks in Beam Structures Using Measured Vibration Data. *Journal of Sound and Vibration*, 251(1):13–38, 2002.

[10] M Lazaro-Gredilla and M Titsias. Variational Heteroscedastic Gaussian Process Regression. *Proceedings of International Conference on Machine Learning (ICML 2011), Bellevue, Washington, USA*, page 8, 2011.

[11] M. D. Todd, J. M. Nichols, C. J. Nichols, and L. N. Virgin. An assessment of modal property effectiveness in detecting bolted joint degradation: Theory and experiment. *Journal of Sound and Vibration*, 275(3-5):1113–1126, 2004.

[12] J. M. Nichols and K. D. Murphy. *Modeling and Estimation of Structural Damage*. John Wiley & Sons, Ltd, Chichester, UK, feb 2016.

[13] P Gardner, R. J. Barthorpe, and C Lord. The Development of a Damage Model for the use in Machine Learning Driven SHM and Comparison with Conventional SHM Methods. In *Proceedings of ISMA2016 International Conference on Noise and Vibration Engineering*, pages 3333–3346, 2016.

[14] A Gretton. A Kernel Two-Sample Test. *Journal of Machine Learning Research*, 13:723–773, 2012.

[15] P Gardner, C Lord, and R. J. Barthorpe. An Evaluation of Validation Metrics for Probablistic Model Outputs. In *Proceedings of the ASME 2018 Verification and Validation Symposium*, 2018.

Railway suspension fault detection under variable operating conditions via random vibration signals and the stochastic Functional Model based method

T-C. Aravanis [1], **J. Sakellariou** [1], **S. Fassois** [1]
[1] Stochastic Mechanical Systems & Automation (SMSA) Laboratory,
University of Patras, Department of Mechanical Engineering & Aeronautics, 265 04 Patras, Greece
e-mail: **fassois@mech.upatras.gr**

Abstract
The problem of fault detection in railway vehicle suspension systems via random vibration signals under varying operating conditions, presently payload, is considered. The focus is on exploring the performance limits for small, incipient, faults, while maintaining low false alarm rates despite significant variations in the payload. The study is based on a recently introduced Functional Model (FM) method for robust fault detection and Monte Carlo simulations. Comparisons with an alternative state-of-the-art Principal Component Analysis based method are also made. The results indicate that the FM method, based on just two car body sensors and a narrow (0-40 Hz) frequency bandwidth, achieves very high to excellent detection performance for primary and certain secondary suspension faults, yet inadequate for certain small magnitude (5% to 20% reduction in suspension element properties) faults in the secondary suspension. The detection performance is significantly degraded when the PCA based method is employed.

1 Introduction

Railway vehicle safety is of paramount importance, with subsystems such as the suspension, wheels, and rail being of critical importance. This has led to significant research efforts over the past several years [1]-[13]. A significant part of work has focused on vibration based methods [10]-[13] which are attractive due to a number of advantages, including the wide availability of sensors and related equipment and their global nature; the latter referring to the capability of the methods to detect faults that are relatively 'remote' to the sensor location [14]. This characteristic is particularly important as it implies that fault detection on a vehicle may be potentially based on a low number of vibration sensors; a highly desirable feature leading to monitoring / diagnosis system simplicity and low installation and maintenance costs.

Vibration based fault detection in railway vehicle suspension has been considered via various methods within two main categories: Model-based and the data-based [2]. Methods of the first category utilize physics-based models and are mainly employed when the relationship between the excitation and response signals, obtained from the vehicle, is known, with detection often achieved via evaluation and monitoring of a sensitive to fault residual sequence [3]. 'Typical' methods within this category employ the Kalman Filter (KF) [4] - within a linear framework - or the Extended Kalman Filter (EKF) [5] - within a nonlinear framework. The obtained results indicate high effective, although in practice building highly accurate physics-based suspension models may be difficult and certain parameters may be unavailable. Furthermore, the accuracy of such methods may depend on various additional factors, including state vector initialization and EKF convergence [10].

Data-based methods are also useful, as no physic based models are required. These utilize random vibration response signals acquired on the vehicle, with the basic principle being that any fault will affect the vehicle dynamics and this may be detected on the measured response signals. The key thus is on the proper analysis

of the measured signals and the extraction and monitoring of signal 'features' that are sensitive to faults [2]. This processing may include time-domain (such as Principal Component Analysis, PCA, Canonical Variate Analysis, CVA) [6]), frequency-domain [7], time-frequency [8] or correlation analysis (cross correlation of two signals at different locations on the vehicle) [9].

Methods from both categories have been developed and tested via simulations with faults corresponding to 20% or higher reduction in the properties (such as stiffness or damping) of selected suspension elements mainly without considering uncertainty factors, such as a varying payload.

Yet, from a practical viewpoint, the introduction of an effective monitoring / diagnosis system is subject to two main requirements: (a) high detection performance for small, incipient, faults, and (b) robustness to varying operating conditions. The latter are due to a number of factors, including payload (number of carried passengers or luggage), travel speed, rail quality and so on. Meeting these requirements is a major challenge, especially as the two seem contradictory because increasing the detection sensitivity generally leads to reduced robustness. Essentially, this means that the monitoring / diagnosis system design has to be based on a proper trade off between a high 'detection rate' and a low 'false alarm rate'.

Although these issues have not yet been seriously dealt with within the context of fault detection for railway suspension systems, it is important to mention that the issue of robustness to varying operating and environmental conditions has received significant attention within the broader context of Structural Health Monitoring (SHM). The available methods may be classified in a number of categories. In a first category, the effects of varying conditions on the healthy dynamics may be explicitly modeled, and thus accounted for when fault detection is performed [15]; yet this presumes that the varying operating and environmental conditions are measurable. In a second category, the effects of varying operating and environmental conditions on the healthy dynamics are fully modeled using proper stochastic representations, such as Random Coefficient (RC) stochastic models [16] or Multiple Model (MM) representations [17, 18], so that discrepancies from these may be associated with the presence of fault or damage [17, 19]; this presumes the availability of a high number of signals/experiments for proper model construction. In a third category, the effects of varying operating and environmental conditions on the healthy dynamics are attempted to be removed using techniques such as Principal Component Analysis (PCA) on proper feature spaces, thus resulting in a 'reduced' representations of the part of the healthy dynamics which are not significantly affected by the varying conditions, but may be affected by the presence of faults [20]; this risks reducing the fault detection performance, while a high number of signals/experiments for constructing the 'reduced' representation is typically required.

The *goal* of the present study is the exploration of the potential for *simultaneous* satisfaction of the two main requirements via an innovative Functional Model (FM) based method recently introduced by the authors and co-workers [21]. More specifically the paper aims at exploring, through the FM based method, the following objectives:

(a) Potential achievement of high detection rate for small, incipient, faults.

(b) Potential achievement of low false alarm rate despite significant changes in the vehicle operating conditions, presently varying payload (number of carried passengers or luggage).

(c) Potential achievement of the above with a minimal number of sensors (only two are considered) and a very limited measurement bandwidth ($0 - 40\ Hz$). The importance of the first constraint is obvious, while that of the second relates to practical operation of the monitoring / diagnosis system under normal operating conditions with the excitation being provided by the rail within a limited frequency bandwidth.

The study is based on the conjecture that the Functional Model (FM) method for robust fault detection is in a position to potentially meet the above objectives as it is, by construction, capable of distinguishing the effects of varying operating conditions from those of faults, while operating with a low number of sensors, and achieving high detection sensitivity. This is due to the fact that high quality, data based, parametric stochastic models describing only the partial dynamics (hence operating with a low number of sensors) are

used, with the model parameters selected as the fault sensitive features; these are indeed known to have high sensitivity to incipient faults [22, 23].

The Functional Model based method for robust fault detection belongs to the wider family of FM based methods, introduced over the past several years mainly for fault/damage localization and magnitude estimation; the reader is referred to [14, 24, 25] and references therein. Its formulation for robust fault detection is nevertheless new, as it was first presented in [21] in a context similar to that of the present paper, with certain preliminary (demonstration) results presented, and subsequently on a damage detection problem for a composite beam in [26]. The present study constitutes a follow up of [21], going into more depth on the method and its interpretation, as well as on the particular application problem on which further issues and fault scenarios are considered, and the performance limits are explicitly explored. In addition, an interesting comparison with a PCA based method is presently made.

The rest of the paper is organized as follows: The railway suspension robust fault detection problem, along with the model, the faults and the experiments, are presented in Section 2. The Functional Model based method for robust fault detection is presented in Section 3, and the fault detection results, along with the comparison with the PCA based method, are presented in Section 4. Concluding remarks are finally summarized in Section 5.

2 The railway suspension robust fault detection problem

2.1 The railway vehicle suspension model

The railway suspension model employed is depicted in Figure 1. It consists of the car body, two bogie frames, four wheelsets, and the primary and secondary suspensions. It is a 9 degrees-of-freedom model that includes the following variables: bounce z, pitch ϕ, and roll θ for the car body and the two bogies (leading and trailing) describing the vertical dynamic behavior of the vehicle. The car body is connected to the two bogies, located at its front and rear ends, through secondary suspensions, while each bogie is connected to two wheelsets (modeled as massless point followers) through primary suspensions. The car and the bogies are modeled as rigid bodies. The primary and secondary suspensions are modeled by linear springs and viscous dampers with stiffness and damping constants K_p, C_p (primary suspension) and K_s, C_s (secondary suspension).

The vehicle is assumed to travel on a straight track at constant speed, with symmetrical loading of the two rails, and no wheel lift. Displacements in the lateral direction are assumed negligible. The model is excited by the track irregularity, which acts on subsequent wheelsets with specific time delays related to the vehicle traveling speed (further details in [21]). Vertical vibration acceleration responses are measured at points $Y1$ and $Y2$ (blue solid circles in Figure 1).

2.2 The faults and the variable operating conditions

Four *fault scenarios* are considered for the suspension elements shown in red in Figure 1:

- The *first fault scenario* corresponds to stiffness reduction (of various values) in the primary suspension's stiffness (right rail, first wheelset; K_{p_1}).
- The *second fault scenario* corresponds to stiffness reduction (of various values) in the secondary suspension's leading airspring K_{s_l} (right rail).
- The *third fault scenario* corresponds to damping reduction (of various values) in the primary suspension's damping coefficient (right rail, first wheelset; C_{p_1}).

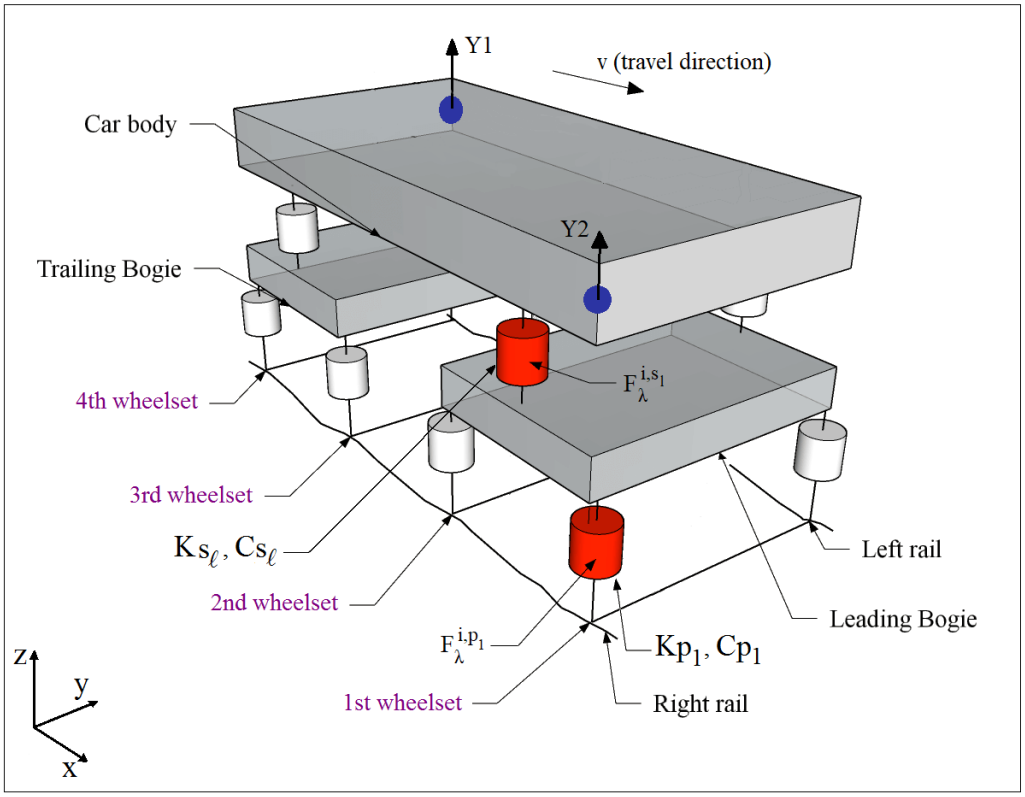


Figure 1: The railway vehicle suspension model employed. The blue solid circles represent accelerometer positions, while the suspension elements subject to fault are indicated in red.

- The *fourth fault scenario* corresponds to damping reduction (of various values) in the secondary suspension's leading airspring C_{s_l} (right rail).

The first two scenarios physically correspond to coil spring softening due to wear and/or aging of the coils and to loss of air (softening) from the secondary air chamber (airsping) due to a malfunction or due to changes in the environmental temperature that may lead to airspring softening or stiffening (air expansion at high temperatures). The last two, corresponding to damping characteristics, are related to damper degradation because of oil leakage due to wear on their seals or loosening of their mounting on the vehicle.

Faults within each scenario are designated as F_λ^{e,p_1}, F_λ^{e,s_l}, F_λ^{d,p_1}, and F_λ^{d,s_l}, respectively. In all cases λ designates fault magnitude (reduction percentage from the nominal value), with the magnitudes considered being $\lambda = [5, 10, 20, 30]\%$. It is noted that the first two magnitudes are quite small compared to those used in the literature, with the objective being the exploration of their detectability under varying payload. A summary of the fault scenarios is provided in Table 1.

As already mentioned, the variable operating condition refers to the payload, that is car body mass increase, due to passengers and/or luggage. Values of $k \in [0, 10]\%$, corresponding to $[0 - 3\ 280.4]\ kg$, are presently considered. Payload increase is assumed to be non-measurable under normal operation, that is when the diagnostic system is functioning (inspection phase). Yet, it is assumed that controlled experiments with measurable payloads may be performed once, during the method's baseline (training) phase.

2.3 The Monte Carlo experiments and the vibration signals

Vertical vibration acceleration responses are obtained at points $Y1$ and $Y2$ (Figure 1) using track irregularity displacement presently approximated by zero-mean Gaussian white noise. The employed travel speed is 70 km/h.

Fault Mode	Description
F_{λ}^{e,p_1}	Primary suspension, first wheelset, right rail coil spring stiffness reduction
F_{λ}^{e,s_l}	Secondary suspension, leading bogie, right rail airspring stiffness reduction
F_{λ}^{d,p_1}	Primary suspension, first wheelset, right rail damping coefficient reduction
F_{λ}^{d,s_l}	Secondary suspension, leading bogie, right rail damping coefficient reduction

Table 1: The considered fault scenarios (λ designates the fault magnitude, that is percentage of the reduction).

Simulation is based on MATLAB's `lsim` function at a high initial sample rate of f_s^{init} =3 200 Hz, subsequent low-pass filtering to 40 Hz through a Chebyshev II digital filter of order 12 and re-sampling at $f_s = 80\ Hz$. The final signals have frequency bandwidth in the $0 - 40\ Hz$ range; also see Table 2. Prior to processing, each signal is sample mean corrected and normalized to unit sample variance (division by its own sample standard deviation).

Monte Carlo simulation experiments are performed with the healthy system under 11 operating conditions (payload increase $k \in [0, 10]\%$ with a step of 1%) in the baseline (training) phase of the method. Also, with the healthy and faulty system under each fault scenario and magnitude ($\lambda = [5, 10, 20, 30]\%$ reduction) and 21 operating conditions (payload increase $k \in [0, 10]\%$ with a step of 0.5%) in the normal operation (inspection) phase of the method; notice that 10 of these conditions are not included in the baseline phase. Further details and the total number of experiments performed in each phase are provided in Table 2. As is evident, fault detection performance is to be based on thousands of experiments (test cases) in the inspection phase of the method.

Baseline (learning) phase		
Healthy System	1 experiment per payload Payload increase $k \in [0, 10]\%$ with a step of 1%	Total no. of experiments 11
Inspection (diagnosis) phase		
Healthy System (H)	50 experiments per payload Payload increase $k \in [0, 10]\%$ with a step of 0.5%	Total no. of experiments 1 050
Faulty System (F_{λ}^{i,p_1}, F_{λ}^{i,s_l})	50 experiments per payload under each λ Fault magnitude: $\lambda = 5, 10, 20, 30\%$ Payload increase $k \in [0, 10]\%$ with a step of 0.5%	Total no. of experiments per fault scenario: 4 200 (1 050 experiments per λ)
Signal bandwidth $0 - 40\ Hz$; sampling frequency f_s = 80 Hz; signal length N = 8 000 samples (112 s)		

Table 2: Details on the Monte Carlo experiments (baseline and inspection phases).

2.4 Effects of the faults and the variable operating conditions on the estimated dynamics

As vibration based methods rely on detecting the effects of faults on the considered dynamics, these are of obvious importance on potential fault detectability. In the present case, due to the impracticality of measuring the track irregularity, the dynamics considered are limited to the Transmittance Function (TF) [18] between points $Y1$ and $Y2$, that is the relationship between the vibration signals at the two measurement points ($Y2$ taken as input and $Y1$ as output; see Figure 1). Indicative Transmittance Function non-parametric estimates[1], are presented in Figure 2 for 'small' ($\lambda = 5\%$) and 'large' magnitude ($\lambda = 30\%$) faults, under varying operating conditions ($k = 0 - 10\%$ payload increase) for each case.

The results indicate that the effects of the 'small' magnitude faults on the dynamics are rather limited, but more pronounced for their 'large' magnitude counterparts, for instance in the [4-7] Hz and [21-24] Hz ranges. Based on these observations the detection of 'small' faults is expected particularly challenging.

[1]Obtained by the Welch method [27, pp. 186-187]; Hamming windowing, segment length of 1 024 samples, 95% overlap, frequency resolution $\delta f = 0.07\ Hz$, MATLAB function `tfestimate.m`.

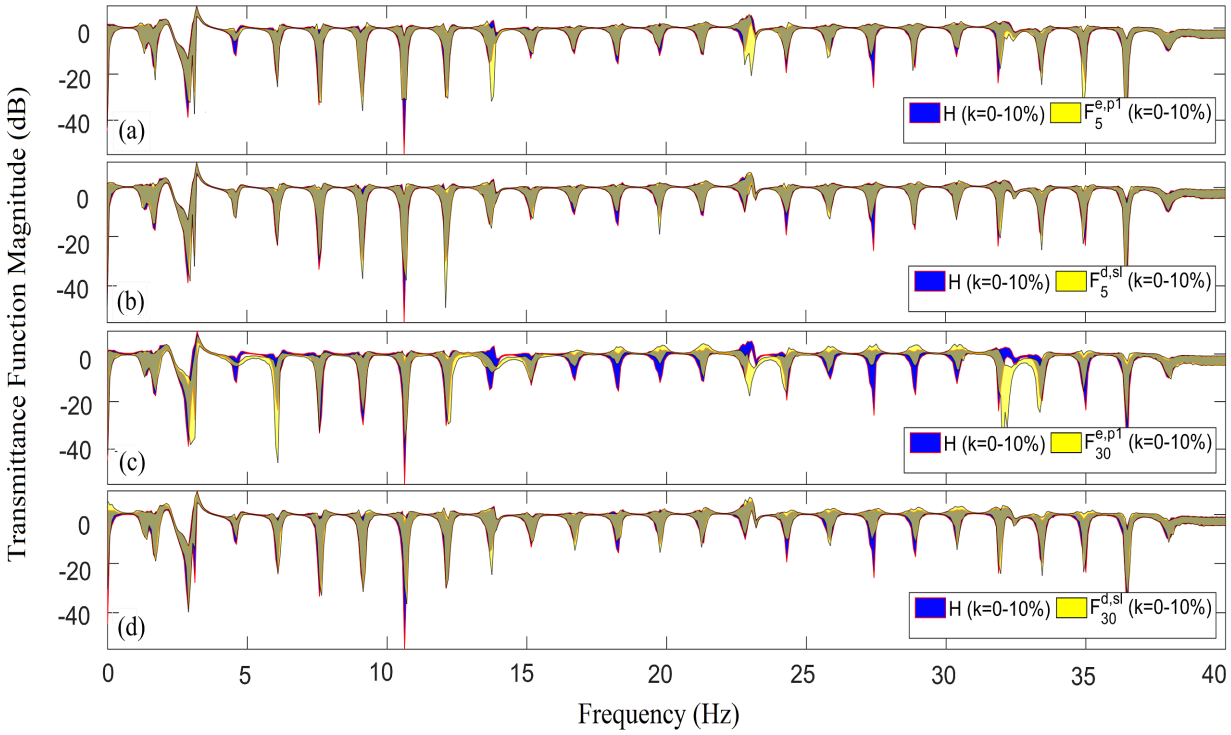


Figure 2: Effects of 'small' ($\lambda = 5\%$) and 'large' magnitude ($\lambda = 30\%$) fault on the dynamics: Transmittance Function magnitude (points $Y2$, $Y1$) for healthy and faulty dynamics under varying operating conditions: (a) Primary stiffness K_{p_1} fault ($\lambda = 5\%$), (b) secondary damping C_{s_l} fault ($\lambda = 5\%$), (c) Primary stiffness K_{p_1} fault ($\lambda = 30\%$), (d) secondary damping C_{s_l} fault ($\lambda = 30\%$). (10 excitation-response pair signals per payload for payload values $k = 0 - 10\%$ with a step of 0.5%; 210 curves per system health state.)

3 The stochastic Functional Model based method for robust fault detection

3.1 The concept

As already mentioned, since the rail induced excitations are not practically measurable, the method is solely based on random vibration acceleration response signals; presently just the responses at points $Y1$ and $Y2$ are considered in order to satisfy the objective of a low number of sensors. Of course, this severely limits the dynamics on which the method is to operate, rendering the problem more challenging[2].

The method's main idea is based on representing the considered (partial) dynamics under any operating condition in a proper 'feature' space, within which the healthy system state should, under all possible operating conditions (payloads), be represented via a certain subspace, referred to as the '*healthy subspace*'. Parametric representations of the dynamics, in the form of stochastic data-based AutoRegressive models with eXogenous (ARX) are selected, with the 'features' chosen to be the model's AR/X parameters; this selection being motivated by their high sensitivity to faults. The 'healthy subspace' is constructed in the *baseline (training) phase* of the method, using controlled experiments with the healthy system, in which the operating conditions (payload) are measurable. This is accomplished via an ARX type Functional Model (FM), which is capable of representing the healthy dynamics under any operating conditions. This model's parameters are functions of a number of *independent* scalar *scheduling variables*, each one representing a certain aspect

[2]It is clear that the use of additional sensors would include additional dynamics and facilitate fault detection.

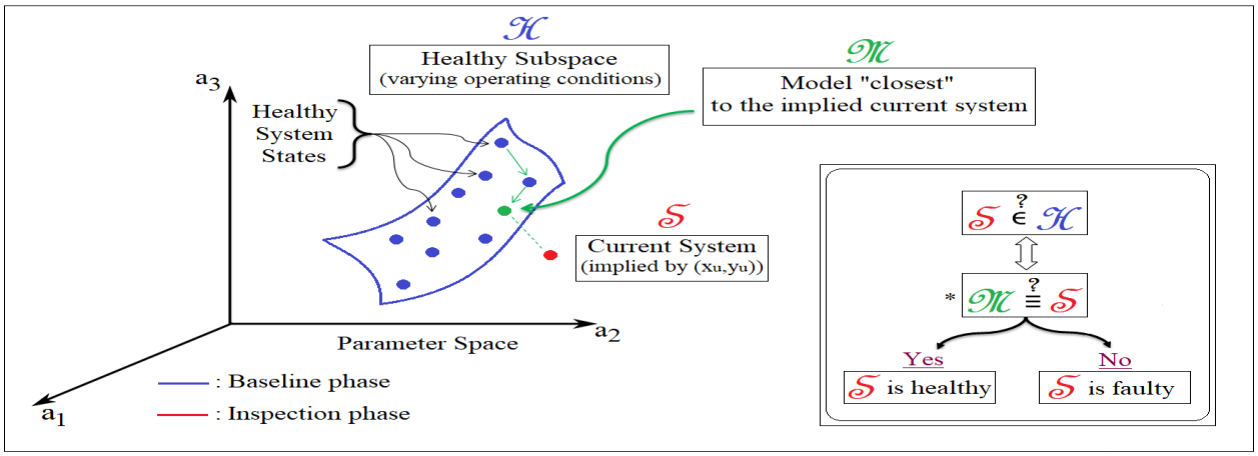


Figure 3: Schematic representation of the concept of the Functional Model based method for robust fault detection.

of the operating conditions; in the present study only the payload is varying, hence a single scheduling variable suffices. The model's functional parameters then define the 'healthy subspace' in the feature space, of dimensionality equal to the number of scheduling variables (that is independent variability sources); being unity in the present case.

In the method's normal operation (*inspection phase*), when the system is under an unknown health state and any (unknown) operating condition, a fresh vibration response signal pair is obtained (say x_u, y_u), based on which fault detection is to be achieved. Detection is to be *conceptually* based on whether or not the point representing the current system dynamics in the feature space resides or not in the 'healthy subspace'. In the affirmative case the current system is to be declared as healthy, else as faulty. Mathematically examining this 'residence' condition may be a bit tricky due to unavoidable estimation errors incurring in both the baseline and inspection phases (that is both the 'healthy subspace' and the current point). A convenient approach for examining it, and making a decision, is based on determining a specific conventional ARX model within the 'healthy subspace' that 'best' corresponds to the current dynamics, and then examining its validity. If valid, this model constitutes an appropriate representation of the current dynamics, implying that the current system is healthy; otherwise there is no appropriate representation of the current dynamics residing within the 'healthy subspace', implying that the current system is faulty. A simple schematic representation of this concept is provided in Figure 3 using a simplified 3D feature space consisting of three model parameters (a_1, a_2, a_3).

An important advantage of the method is that measurement of the operating condition variable(s) (presently the payload) is *not* required during inspection. Yet, it presupposes a deterministic cause-and-effect relationship between the variable operating condition variable(s) and the system dynamics. The number of independent variability sources (thus the 'healthy subspace' dimensionality) may be determined based on physical understanding or via data analysis.

3.2 The methodology

(a) The baseline (learning) phase

The Functional Model employed to represent the healthy (partial) dynamics under any operating condition is a Functionally Pooled AutoRegressive model with eXogenous excitation (FP-ARX) model of orders n_a, n_b [28]:

$$y_k[t] + \sum_{i=1}^{n_a} a_i(k) \cdot y_k[t-i] = \sum_{i=0}^{n_b} b_i(k) \cdot x_k[t-i] + e_k[t] \tag{1a}$$

$$e_k[t] \sim \text{NID}\big(0, \sigma_e^2(k)\big) \quad e_{k_1}[t], e_{k_2}[t] : \text{potentially correlated at time } t, \text{for any values of } k_1, k_2 \tag{1b}$$

$$a_i(k) := \sum_{j=1}^{p} a_{i,j} \cdot G_j(k), \qquad b_i(k) := \sum_{j=1}^{p} b_{i,j} \cdot G_j(k) \tag{1c}$$

with k designating the operating condition (scheduling) variable (presently the payload)[3], $x_k[t], y_k[t]$ the excitation and response signals (presently the two response signals), respectively, under operating condition k, and $e_k[t]$ the corresponding innovations signal assumed to be zero-mean and white (serially uncorrelated) with variance $\sigma_e^2(k)$ and uncorrelated with $x_k[t]$. Notice that the signals may be cross-correlated with their counterparts corresponding to different operating conditions (different k's). $t = 1, 2, 3, \ldots$ designates normalized (by the sampling period) discrete time, $a_i(k)$, $b_i(k)$ the $i-th$ AR and X parameter, respectively, while NID stands for Normally Independently Distributed.

As indicated by Eq. (1c), the AR and X parameters are modeled as explicit functions of k by using a p-dimensional functional subspace spanned by the (mutually independent) functions $G_1(k), G_2(k), \ldots, G_p(k)$ (*functional basis*). The constants $a_{i,j}$ and $b_{i,j}$ designate the AR and X coefficients of projection, respectively. The model of Eq. (1a) is referred to as an FP-ARX model of orders n_a, n_b and functional subspace dimensionality p, designated as FP-ARX$(n_a, n_b)_p$ model.

Such an FP-ARX$(n_a, n_b)_p$ model may be identified based on M excitation-response signal pairs, $(x_k[t],\ y_k[t])$ $k \in \{k_1, \ldots, k_M\}$, corresponding to sample values $k = k_1, k_2, \ldots, k_M$, of the operating condition variable k, with each signal being N samples long. Estimation of the AR/X projection coefficients and the innovations variance may be achieved via various methods, including Ordinary Least Squares, Weighted Least Squares, and Maximum Likelihood [28]. The model orders and the subspace functional basis may be selected via a proper version of the Bayesian Information Criterion (BIC); details are provided in [28].

(b) The inspection (diagnosis) phase

Fault detection is achieved based on a current (fresh) signal pair $(x_u[t], y_u[t])$ corresponding to *non-measurable* operating conditions (unknown value of k). Towards this end the 'consistency' of the current signal pair with the FP-ARX model needs to be examined, which is equivalent to examining whether or not the current point in the feature space 'resides' within the 'healthy subspace'. As previously explained, this is achieved by determining a specific conventional ARX model within the 'healthy subspace' that 'best' corresponds to the current dynamics (as expressed by the corresponding signals), and then examining its validity.

Thus, given the current signal pair $(x_u[t], y_u[t])$, a conventional ARX model is estimated *from within* the 'healthy subspace', that is from within the previously obtained FP-ARX model. This is achieved by estimating the value of the scheduling variable k as follows[4]:

$$\widehat{k} = \arg\min_{k} \sum_{t=1}^{N} e^2[t, k] \tag{2}$$

where $e[t, k]$ is the FP-ARX model residual sequence corresponding to the current signal pair and $\arg\min$ designating minimizing argument. Due to the non-quadratic dependence of the cost function on k, estimation is based on non-linear optimization, with golden search with parabolic interpolation [29] presently employed. The estimator $\widehat{k}$ may be shown [14] to be asymptotically Gaussian distributed, with mean equal to its true counterpart and variance coinciding with that of the Cramer-Rao lower bound, that is $\widehat{k} \sim \mathcal{N}(k, \sigma_{\hat{k}}^2)$.

The ARX model within the 'healthy subspace' is that obtained from the FP-ARX model of Eq. (1a) for the obtained estimate of k. Its innovations variance may be then estimated as:

$$\widehat{\sigma}_e^2(\widehat{k}) = \frac{1}{N} \sum_{t=1}^{N} e^2[t, \widehat{k}] \tag{3}$$

[3]Generalization to the multivariate case is conceptually straightforward [14].

[4]Estimators/estimates are designated by a hat.

Table 3: Baseline phase: ARX and FP-ARX model estimation details.

Estimated model	SPP	BIC	RSS/SSS (%)	Condition number of inverted matrix
ARX$(130, 129)$	61.70	-5.60	0.16	1.07×10^9
FP-ARX$(130, 129)_{p=2}$	169.20	-58.64	0.26	1.20×10^9

ARX Estimation method: Ordinary Least Squares (OLS; MATLAB function `arx.m`)
SPP: Signal samples Per estimated Parameter

FP-ARX estimation method: Ordinary Least Squares
Number of experiments (signal records) $M = 11$
Payload range k: $[0, 10]\%$ with step of 1%
The functional subspace is spanned by shifted Chebyshev Type II polynomials obeying the recurrence relation:
$a_{1n}G_{n+1}(x) = (a_{2n} + a_{3n}x)G_n(x) - a_{4n}G_{n-1}(x)$ with $G_0(x) = 0$, $G_1(x) = 1$
$x := k/k_{max} \in [0, 1] \subset \Re$; $a_{1n} = a_{4n} = 1$, $a_{2n} = -2$, $a_{3n} = 4$.
Functional subspace dimensionality: 2; Functions $G_1(x) = 1$, $G_2(x) = 4x - 2$
No. of projection coefficients: 520

Model validity is then examined via formal examination of the estimated innovations (residual) series uncorrelatedness (whiteness) hypothesis, presently accomplished via the Portmanteau Test [30]. Towards this end the Q statistic (below) follows chi-square (χ^2) distribution with r degrees of freedom under the null (H_o) hypothesis of a valid model[5], that is [30]:

$$Q := N(N+2) \cdot \sum_{\tau=1}^{r} (N-\tau)^{-1} \widehat{\rho}^2[\tau] \ \sim \ \chi^2(r) \tag{4}$$

in which N designates the residual series signal length (in number of samples), $\widehat{\rho}^2[\tau]$ the estimated (sample) normalized autocorrelation at lag τ, and r the (user selected) maximum lag considered. The null hypothesis is then accepted, at a (user selected) risk level α (probability of rejecting H_o even though it is correct) as follows:

$$\begin{array}{rcl} Q < \chi^2_{1-\alpha}(r) & \Longrightarrow & \text{Healthy system} \\ \text{Else} & \Longrightarrow & \text{Faulty system} \end{array} \tag{5}$$

with $\chi^2_{1-\alpha}(r)$ designating the chi-square distribution's $(1-\alpha)$ critical point.

4 Robust fault detection results and assessment

(a) Baseline (learning) phase

A random vibration pair of signals obtained from points $Y1$ and $Y2$ under nominal payload ($k = 0\%$) and the healthy system is first employed for obtaining a conventional ARX model based on standard procedures [27, pp. 203-205] (Matlab function: `arx.m`). This leads to an ARX(130,129) model characterized by zero time delay, that is $b_0 \neq 0$ in the exogenous (X) polynomial. This basic structure is then maintained in the FP-ARX modeling procedure [28] which is based on $M = 11$ distinct vibration signal pairs, each corresponding to different payloads ($k \in [0 - 10]\%$ with an increment of $\delta k = 1\%$ are used)[6]. Various functional subspace dimensionalities are considered, and the procedure leads to the selection of an FP-ARX(130,129) model with functional subspace consisting of the first $p = 2$ shifted Chebyshev type II polynomials [31, p. 782], that is an FP-ARX$(130,129)_2$ model. Estimation details are provided in Table 3.

[5] In which case the estimated innovations (residual) series $e[t, \widehat{k}]$ is uncorrelated (white).
[6] Note that $\delta k = 1\%$ corresponds to payload (mass) increase of $328.04\ kg$.

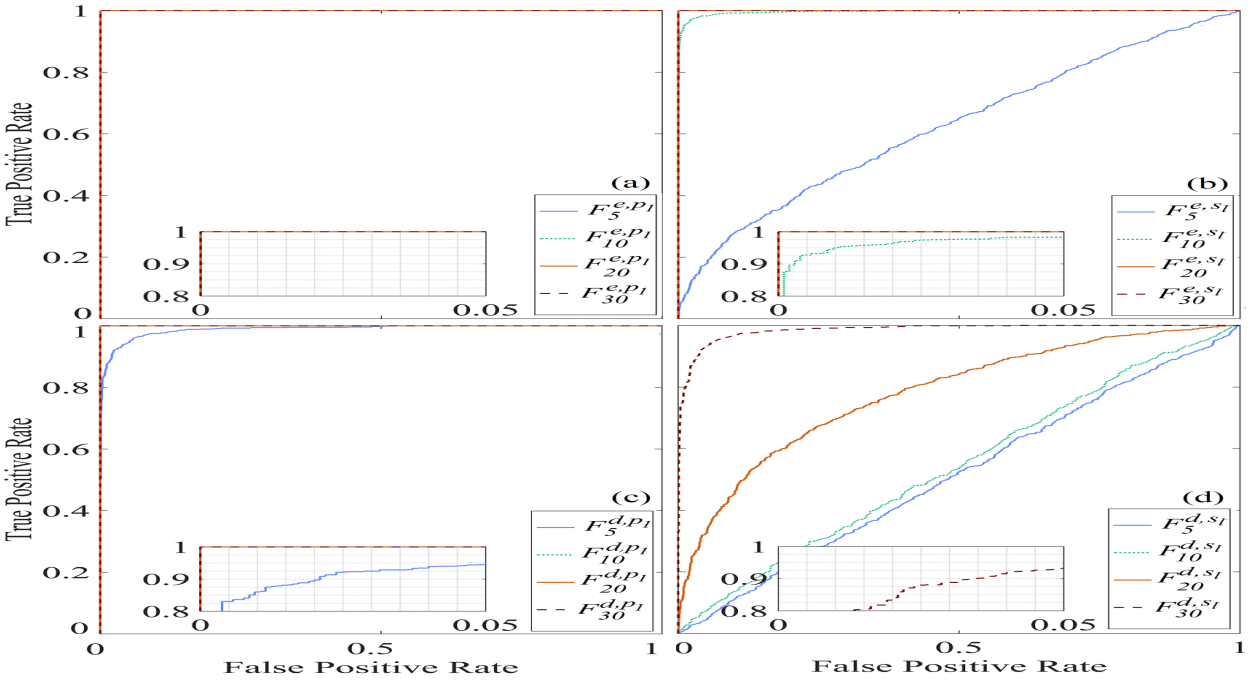


Figure 4: FM method fault detection performance: ROC curves for (a) primary stiffness faults of various magnitudes F^{e,p_1}, (b) secondary stiffness faults of various magnitudes F^{e,s_l}, (c) primary damper faults of various magnitudes F^{d,p_1}, (d) secondary damper faults of various magnitudes F^{d,s_l}. (1 050 healthy and 1 050 fault test cases per fault scenario.)

(b) Inspection (diagnosis) phase

Fault detection results for all four fault scenarios are subsequently presented for 5 250 test cases (experiments), 1 050 corresponding to the healthy system and 4 200 to its faulty counterpart (1 050 per fault scenario); details in Table 2. It should be noted that these experiments are all different from those used in the baseline phase, while the number of normalized ACF samples used in Q is selected equal to $r = 25$. The results are presented in terms of ROC curves[7].

Fault scenario F^{e,p_1}_{λ} *(stiffness reduction in the primary suspension)* – see Figure 4(a). Perfect ROC curves which include the (0,1) point implying excellent detection performance with no false alarms or missed faults.

Fault scenario F^{e,s_l}_{λ} *(stiffness reduction in the secondary suspension)* – see Figure 4(b). Perfect ROC curves for the two largest fault magnitudes ($\lambda = 20, 30\%$) implying excellent detection performance with no false alarms or missed faults. Quite good ROC curve for the $\lambda = 10\%$ magnitude, yet not for the smallest $\lambda = 5\%$ magnitude for which the ROC curve is inadequate. This reveals the sensitivity limits of the method, suggesting that faults as small as 5% stiffness reduction are not detectable.

Fault scenario F^{d,p_1}_{λ} *(damping reduction in the primary suspension)* – see Figure 4(c). Perfect ROC curves for the three largest fault magnitudes ($\lambda = 10, 20, 30\%$) implying excellent detection performance with no false alarms or missed faults. Yet, the ROC curve is not ideal, although still adequate, for the smallest $\lambda = 5\%$ magnitude.

Fault scenario F^{d,s_l}_{λ} *(damping reduction in the secondary suspension)* – see Figure 4(d). A probably adequate ROC curve only for the largest fault magnitude ($\lambda = 30\%$). Yet, inadequate ROC curves for the smaller $\lambda = 5, 10, 20\%$ magnitudes.

In summary, faults in the primary suspension are generally detectable even for magnitudes as small as $\lambda = 5\%$ reduction, while faults in the secondary suspension are not always detectable for magnitudes of $\lambda = 20\%$

[7] A Receiver Operating Characteristic, ROC, curve [32, pp. 34-35] represents the true positive rate, that is percentage of correct fault detections, versus the false positive rate, that is percentage of false alarms, for varying detection threshold.

reduction or less. In all cases, the detectability of faults associated with stiffness reduction is better than that of faults associated with damping reduction.

4.1 Comparison with an alternative method

An interesting comparison with an alternative method which is based on Principal Component Analysis (PCA), that is the U-PCA-ARX method [17], is now undertaken.

This method employs the centered PCA for defining an $n-$dimensional orthogonal coordinate system on which a random (due to estimation error) healthy ARX parameter vector may be projected, with the projections forming a set of mutually uncorrelated random variables. This is achieved by performing a PCA decomposition of the sample covariance matrix of the estimated (in the baseline phase) ARX parameter vectors. The decomposition provides the eigenvalues (in decreasing order) and the corresponding eigenvectors, with the latter defining the aforementioned transformed $n-$dimensional orthogonal coordinate system (principal coordinates). Fault detection is based on the ARX parameter vector projections into a subspace of the transformed coordinate system defined by q (properly selected, $q < n$) eigenvectors corresponding to the q 'smallest' eigenvalues. Parameter vector projections into this subspace are characterized by relatively 'low' variability in the healthy state, thus expected to exhibit discrepancies mainly under the presence of fault; thus leading to 'robust' fault detection.

(a) Baseline (learning) phase

The 11 pairs of vibration response signals of the baseline phase of the FM based method are presently used too for the estimation of corresponding ARX(130,129) models, $m_{o,i}$ $(i = 1, \ldots, 11)$, and their corresponding parameter vectors $\boldsymbol{a}_o = [\boldsymbol{a}_{o,1}, \ldots, \boldsymbol{a}_{o,11}]$ are sample mean corrected, with each element in the vector being normalized by its own sample standard deviation. The sample covariance matrix $\boldsymbol{P} = \frac{1}{p}\boldsymbol{a}_o^T\boldsymbol{a}_o$ (^{T} designating matrix transposition) is then computed and decomposed via $\boldsymbol{P} = \boldsymbol{U}\boldsymbol{S}^2\boldsymbol{U}$ into the diagonal matrix $\boldsymbol{S}^2$ that includes the (positive) eigenvalues of $\boldsymbol{P}$ (squared singular values, arranged in decreasing order), and the matrix $\boldsymbol{U}$ that is a real unitary matrix containing the eigenvectors of $\boldsymbol{P}$. The first h columns (principal components) of the eigenvectors matrix $\boldsymbol{U}$ – corresponding to the largest eigenvalues that explain a certain fraction $\gamma(\%)$ of the total parameter vector variability – are associated to the variable operating conditions acting on the healthy system, and the remaining q principal components being potentially affected by faults.

A 10×10 sample covariance matrix, corresponding to the first 5 AR and first 5 X parameters is constructed, and as it is a-priori known that only one uncertainty source (payload) affects the system, only the first component is rejected ($h = 1$), which may be shown to correspond to $\gamma = 83.3\%$.

(b) Inspection (diagnosis) phase

Using a fresh pair of vibration response signals from the current (unknown health state) system, a new ARX model m_u (characterized by parameter vector $\boldsymbol{a}_u$) is obtained. Following the aforementioned procedure, fault detection is based on an Euclidean norm pseudo-statistic, with fault being detected whenever this exceeds a certain threshold (details in [17]).

Fault detection results are presented in Figure 5, for the same test cases and a fashion similar to that of the previous method (ROC curves).

For *fault scenario* F_λ^{e,p_1} *(stiffness reduction in the primary suspension)* adequate performance, although somewhat inferior to that of the FM based method, is observed for the three largest fault magnitudes, which nevertheless becomes drastically inferior for the smallest fault magnitude ($\lambda = 5\%$).

For *fault scenario* F_λ^{e,s_l} *(stiffness reduction in the secondary suspension)* the detection performance is absolutely poor for all fault magnitudes.

For *fault scenario* F_λ^{d,p_1} *(damping reduction in the primary suspension)* the detection performance is problematic even for the largest magnitude fault ($\lambda = 30\%$), and absolutely poor for the two smallest fault magnitudes ($\lambda = 5, 10\%$).

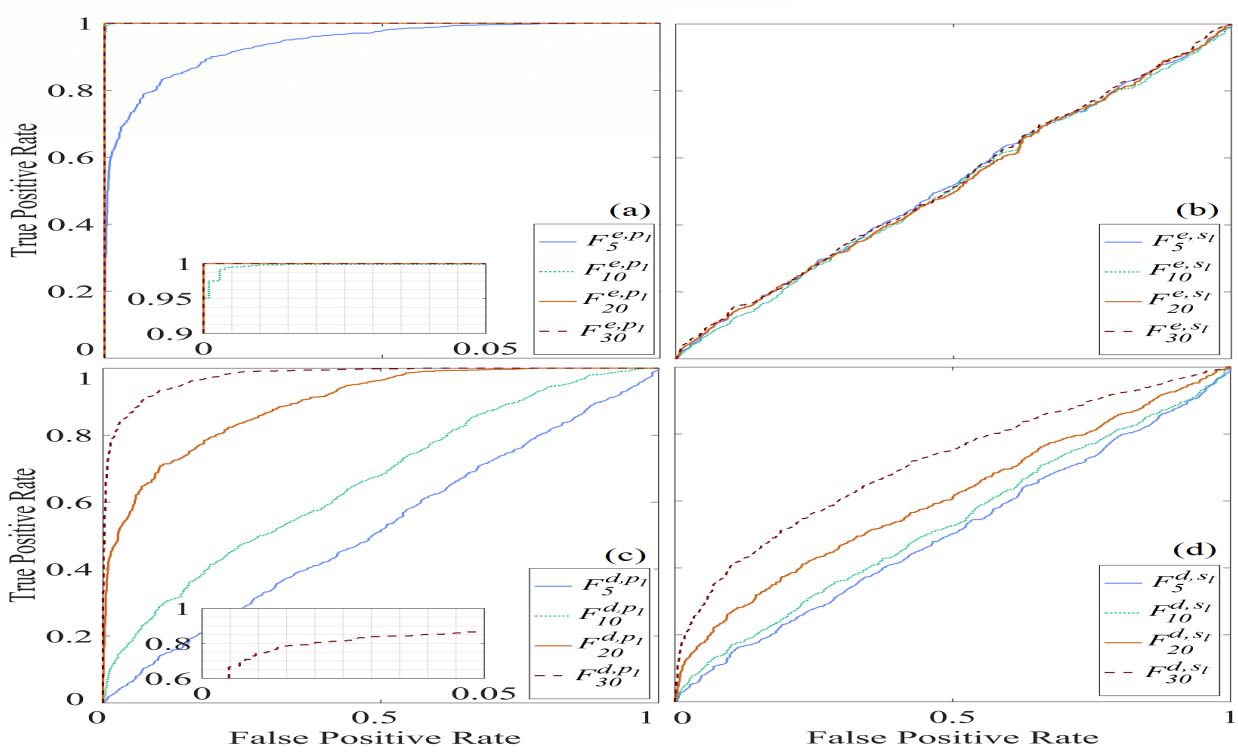


Figure 5: U-PCA-ARX fault detection method performance: ROC curves for (a) primary stiffness faults of various magnitudes F^{e,p_1}, (b) secondary stiffness faults of various magnitudes F^{e,s_l}, (c) primary damper faults of various magnitudes F^{d,p_1}, (d) secondary damper faults of various magnitudes F^{d,s_l}. (1 050 healthy and 1 050 fault test cases per fault scenario; 10×10 covariance matrix; 1 rejected component corresponding to $\gamma = 83.3\%$.)

For *fault scenario* F_{λ}^{d,s_l} *(damping reduction in the secondary suspension)* the detection performance is absolutely poor for all fault magnitudes.

In summary, the results obtained indicate performance characteristics clearly inferior to those of the FM based method, while also confirming that faults in the secondary suspension are harder to detect (compared to those in the primary suspension), and faults associated with damping reduction (in either the primary or secondary suspension) are harder to detect than faults associated with stiffness reduction.

5 Concluding remarks

The problem of fault detection in railway suspension systems under variable operating conditions (variable payload) via measurement of random vibration signals was considered via a novel Functional Model (FM) based method. The emphasis of the work was on exploring the limits of high detection performance for relatively small, incipient, faults, while, at the same time, keeping the false alarm rate low despite the variable operating conditions (robustness) due to varying payload. Moreover the diagnosis operation ought to be based on only few sensors and a very limited frequency bandwidth.

The potential fulfillment of these objectives was examined through Monte Carlo simulations, while comparisons with an alternative, PCA-based, fault detection method were also made.

The main conclusions drawn may be summarized as follows:

(a) Very high to excellent detection performance is possible mainly for spring elements (stiffness reduction), but also for damping elements, in the primary suspension for faults of magnitudes as low as 5%

reduction in the nominal values.

(a) Very high to excellent detection performance is possible for spring elements (stiffness reduction of at least 10%) in the secondary suspension. Detection performance is significantly degraded, varying from adequate (for fault magnitudes of 30%) to inadequate/poor (for fault magnitudes of 20% or smaller) for damping element faults in the secondary suspension.

(a) The detection performance is significantly degraded when an alternative PCA-based method is employed.

(a) It is important to underline that these performance characteristics were achieved based on only two vibration response sensors (accelerometers) placed on the car body, and signals limited to the $0 - 40Hz$ range.

Acknowledgements

This research was supported by Grant (56990000) from the Research Committee of the University of Patras via the 'K. Karatheodori' program.

References

[1] R. Gutiérrez-Carvajal, G.R. Betancur, L.F. Castañeda, G. Zajac *A fractional Fourier transform-based method to detect impacts between the bogie and the car body of a railway vehicle: a data-driven approach*, Journal of Rail and Rapid Transit, Vol. 232, No. 1, (2016), pp. 288-296.

[2] C. Li, S. Luo, C. Cole, M. Spiryagin, *An overview: modern techniques for railway vehicle on-board health monitoring systems*, Vehicle System Dynamics: International Journal of Vehicle Mechanics and Mobility Vol. 55, No. 7, (2017), pp. 1045-1070.

[3] H. Mori, H. Tsunashima, *Condition monitoring of railway vehicle suspension using multiple model approach*, Journal of Mechanical Systems for Transportation and Logistics, Vol. 3, No. 1, (2010), pp. 243-258.

[4] M. Jesussek, K. Ellermann, *Fault detection and isolation for a full scale railway vehicle suspension with multiple Extended Kalman Filter*, Vehicle System Dynamics: International Journal of Vehicle Mechanics and Mobility, Vol. 52, No. 12, (2014), pp. 1695-1715.

[5] M. Jesussek, K. Ellermann, *Fault detection and isolation for a nonlinear railway vehicle suspension with a hybrid Extended Kalman Filter*, Vehicle System Dynamics: International Journal of Vehicle Mechanics and Mobility, Vol. 51, No. 10, (2013), pp. 1489-1501.

[6] X. Wei, L. Jia, H. Liu, *A comparative study on fault detection methods of rail vehicle suspension systems based on acceleration measurements*, Vehicle System Dynamics: International Journal of Vehicle Mechanics and Mobility, Vol. 51, No. 5, (2013), pp. 700-720.

[7] Wei X, Jia L, Guo K, S. Wu, *On fault isolation for rail vehicle suspension systems*. Vehicle System Dynamics: International Journal of Vehicle Mechanics and Mobility, Vol. 52, No. 6, (2014), pp. 847-873.

[8] S. Azadi, A. Soltani, *Fault detection of vehicle suspension system using wavelet analysis*. Vehicle System Dynamics: International Journal of Vehicle Mechanics and Mobility, Vol. 47, No. 4, (2009), pp. 403-418.

[9] T.X. Mei, X.J. Ding, *Condition monitoring of rail vehicle suspensions based on changes in system dynamic interactions*, Vehicle System Dynamics: International Journal of Vehicle Mechanics and Mobility, Vol. 47, No. 9, (2009), pp. 1167-1181.

[10] J.S. Sakellariou, K.A. Petsounis, S.D. Fassois, *Vibration based fault diagnosis for railway vehicle suspensions via a Functional Model Based Method: a feasibility study*, Journal of Mechanical Science and Technology, Vol. 29, No. 2, (2015), pp. 471-484.

[11] L. Gasparetto, S. Alfi, S. Bruni, *Data-driven condition-based monitoring of high-speed railway bogies*, International Journal of Rail Transportation, Vol. 1, No. 1-2, (2013), pp. 42-56.

[12] A. Kowalska-Koczwara, F. Pachla, P. Stecz, K. Stypuła, T. Tatara, J. Lejk, M. Sokołowski *Vibration-based damage identification and condition monitoring of metro trains: Warsaw Metro case study*, Shock and Vibration, Vol. 2018, Article ID 8475684, 14 pages.

[13] X.Y. Liu, S. Alfi, S. Bruni, *An efficient recursive Least Square-based condition monitoring approach for a rail vehicle suspension system*, Vehicle System Dynamics: International Journal of Vehicle Mechanics and Mobility, Vol. 54, No. 6, (2016), pp. 814-830.

[14] C.S. Sakaris, J.S. Sakellariou, S.D. Fassois, *A time series Generalized Functional Model Based method for vibration-based damage precise localization in structures consisting of 1D, 2D and 3D elements*, Mechanical Systems and Signal Processing, Vol. 74, (2016), pp. 199-213.

[15] J. D. Hios and S. D. Fassois, *A Global Statistical model based approach for vibration response-only damage detection under various temperatures: a proof-of-concept study*, Mechanical Systems and Signal Processing, 2014, Vol. 49, No. 1-2, pp. 77-94.

[16] E. Figueiredo, L. Radu, K. Worden, C. R. Farrar, *A Bayesian approach based on a Markov–Chain Monte Carlo method for damage detection under unknown sources of variability*, Engineering Structures, Vol. 80, (2014), pp. 1-10.

[17] K.J. Vamvoudakis-Stefanou, J.S. Sakellariou, S.D. Fassois, *Vibration-based damage detection for a population of nominally identical structures: unsupervised Multiple Model (MM) statistical time series type methods*, Mechanical Systems and Signal Processing, Vol. 111, (2018), pp. 149-171.

[18] A.G. Poulimenos, J.S. Sakellariou, *A transmittance-based methodology for damage detection under uncertainty: an application to a set of composite beams with manufacturing variability subject to impact damage and varying operating conditions*, Structural Health Monitoring, (online 2018), in press.

[19] K.J. Vamvoudakis-Stefanou, J.S. Sakellariou, S.D. Fassois, *Random Coefficient model based damage detection for a population of nominally identical structures: An exploratory study*, in *Proceedings of the International Conference on Noise and Vibration Engineering (ISMA2016), Leuven, Belgium, 2016*.

[20] A. Gomez Gonzalez, S.D. Fassois, *A Supervised vibration-based statistical methodology for damage detection under varying environmental conditions & its laboratory assessment with a scale wind turbine blade, Journal of Sound and Vibration*, Vol. 366, (2016), pp. 484-500.

[21] T.-C.I. Aravanis, J.S. Sakellariou, S.D. Fassois, *Vibration based fault detection under variable non-measurable operating conditions via a stochastic Functional Model method and application to railway vehicle suspensions*, in *Proceedings of the Surveillance 9 International Conference, Fes, Morocco, 2017*.

[22] K.J. Vamvoudakis–Stefanou, J.S. Sakellariou, S.D. Fassois, *Random vibration response-only damage detection for a set of composite beams*, in *Proceedings of the International Conference on Noise and Vibration Engineering (ISMA2016), Leuven, Belgium, 2016*.

[23] F.P. Kopsaftopoulos, S.D. Fassois, *Scalar and vector time series methods for vibration based damage diagnosis in a scale aircraft skeleton structure*, Journal of Theoretical and Applied Mechanics, Vol. 49 No. 3, (2011), pp. 727-756.

[24] C.S. Sakaris, J.S. Sakellariou, S.D. Fassois, *Random-vibration-based damage detection and precise localization on a lab-scale aircraft stabilizer structure via the Generalized Functional Model Based Method*, Structural Health Monitoring, Vol. 16, No. 5, (2017), pp. 594-610.

[25] J.S. Sakellariou and S.D. Fassois, *Vibration based fault detection and identification in an aircraft skeleton structure via a stochastic Functional Model Based Method*, Mechanical Systems and Signal Processing, Vol. 22, (2008), pp. 557-573.

[26] T.-C.I. Aravanis, S. Kolovos, J.S. Sakellariou, S.D. Fassois, *Vibration-based damage detection for a composite beam under environmental and operational variability via a stochastic Functional Model Based Method*, in *Proceedings of the 5th International Conference of Engineering Against Failure (ICEAF V), Chios, Greece, 2018*.

[27] L. Ljung, *System Identification: Theory for the User*, 2nd Edition, Prentice-Hall (1999).

[28] J.S. Sakellariou, S.D. Fassois, *Functionally Pooled models for the global identification of stochastic systems under different pseudo-static operating conditions*, Mechanical Systems and Signal Processing, Vol. 72-73, (2016), pp. 785-807.

[29] G.E. Forsythe, M.A. Malcom, C.B. Moler, *Computer Methods for Mathematical Computations*, Prentice-Hall (1976).

[30] S.D. Fassois, J.S. Sakellariou, *Statistical Time Series Methods for SHM*, in Encyclopedia of Structural Health Monitoring, Boller, C., Chang, F. and Fujino, Y. (eds.), John Wiley and Sons Ltd, Chichester, UK, pp. 443-472, 2009.

[31] M. Abramowitz, I.A. Stegun, *Handbook of Mathematical Functions*, Dover (1970).

[32] R. Duda, P. Hart, D. Stork, *Pattern Classification*, 2nd Edition, Wiley (2000).

On the use of pseudo-damage to represent damage to structures in population-based Structural Health Monitoring

S. Walker[1], **C. Lord**[1], **N. Dervilis**[1], **E. Papatheou**[2] and **K. Worden**[1]
[1] Dynamics Research Group, Department of Mechanical Engineering,
University of Sheffield, Sheffield, UK
e-mail: **s.r.walker@sheffield.ac.uk**

[2] College of Engineering, Mathematics and Physical Sciences,
University of Exeter, North Park Road, Exeter, UK

Abstract
Population-based Structural Health Monitoring (SHM) presents opportunities to monitor populations of structures without prior knowledge of all damage states on individual structures. A critical stage in this process is identifying common features within a population of nominally similar structures. To address this challenge, an experimental study of a small population of similar test structures was carried out, with the aim of identifying how common features across the population differ between structures. The structures used were half sections of aircraft tailplanes, and each one was tested initially in an undamaged state, and then in pseudo-damaged states, where damage was replicated by the addition of small masses. Finally, one of the structure was subjected to real damage of varying severity in order to serve as a benchmark for the whole population.

1 Introduction

Conventional data-based Structural Health Monitoring (SHM) involves the gathering of data related to a structure in normal and damaged states, and by using feature extraction and classification, a map between measured features and the two states can be generated. This will be more important when type, location and severity are to be accurately identified. Consequently, this technique requires the operator to have knowledge of the structure being monitored in both normal and abnormal, or undamaged and damaged, states. In some cases this constraint is not limiting, since structures which are numerous and inexpensive can relatively easily be tested in an undamaged state, then again under the effect of some artificial damage, to give the necessary information. However, in the case of more expensive structures, deliberately damaging a structure to gain knowledge of the damaged state is not acceptable. In the case of a population of structures, for example a farm of wind turbines, further difficulties are introduced if the monitoring of individual structures is required. Individual structures in such a situation might be expected to show similar undamaged conditions, but it could be imagined that two wind turbines within an array could show significant variation in damaged states. For both these reasons, a method of SHM which does not require data from a damaged structure would be beneficial.

Population-based Structural Health Monitoring is an idea based on the concept of 'syndromic surveillance' originating in the field of healthcare informatics. Its application to SHM was first presented in 2008 [1] and subsequently discussed in [2] and [3]. Applied to SHM, the principals of this approach offer the opportunity to monitor populations of structures without requiring prior knowledge of the damaged states of all structures.

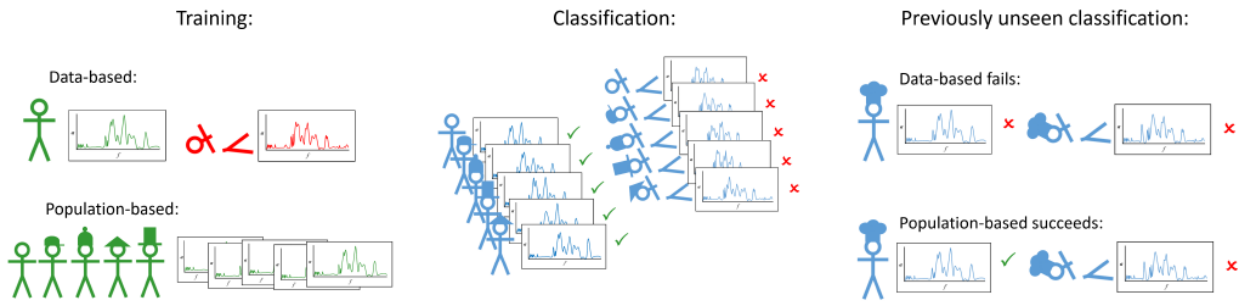


Figure 1: Data-based and Population-based Structural Health Monitoring

In the population-based SHM concept, data are gathered for a number of normal cases of similar structures within a population, allowing a single feature extraction and classification process to determine common indicators of damage, and to produce a single map. When presented with a previously unseen case which is similar to the cases making up the population, the strength of the normal population data allows the new case to be classified as normal (if it shares common features with the population), or abnormal if it does not.

The difference between data-based SHM and the population-based SHM concept is illustrated in Figure 1

The identification of similarities and common features between structures is one of the challenges in the development of this method. The purpose of this paper is to explore the variability of common damage sensitive features, such as natural frequencies and mode shapes, in a small population of similar structures under different types of 'damage' including a case of real damage to be used for comparison. Described here is the recording of data for such a population of structures, and the use of an affordable method of generating damaged data. This method, known as 'pseudo-damage', may allow damaged state data to be generated without the need to damage a structure, through the addition of small localised masses to simulate the effect of stiffness reduction as caused by damage. In order to test the variability of the structures and the suitability of the added masses, structures were tested in undamaged, pseudo-damaged, and damaged states.

The layout of this paper is as follows: the following section describes the test structures and all the experimental procedure in detail, including all types of damage applied. The third section describes the results of the modal analysis and the comparison of the cases examined. Finally, the paper is rounded off by a discussion followed by a short conclusions section.

2 Test Structures and Experiments

The structures studied in this work are sections of aircraft tailplane. These structures have a number of features which make them a suitable subject for this study: In comparison to many structures, aircraft structures are subject to stringent regulation and low manufacturing tolerances, meaning that the variation between structures should be minimal. Secondly, given the ultimate application of this work to wind turbine blades, the use of structures of a similar size and shape allowed the method to be developed at a suitable scale. More importantly, the tailplanes are real structures (not laboratory made-to-test specimens), and their testing can be considered an important step towards an actual implementation of SHM into real aircraft.

Tailplanes from Piper PA-28 'Cherokee' and PA-28 'Arrow' aircraft were used, both with NACA0012 profile and a chord of 0.76m. After removal from the aircraft, the rounded tips and elevators (elevators are the control surfaces to the rear of the tailplane) were removed, and each was cut in half to give two single tailplanes. The single Cherokee and Arrow tailplanes are designated *C* and *A* from hereon. Both tailplanes measure 0.61m from the leading edge tip to the trailing edge of the main tailplane. In the type C tailplane case, each structure was 1.81m in length with a fixed elevator section of 0.45m. Type A structures were 1.37m in length with a narrow edge section of 0.01m. Two type C and two type A tailplanes were used during this work.

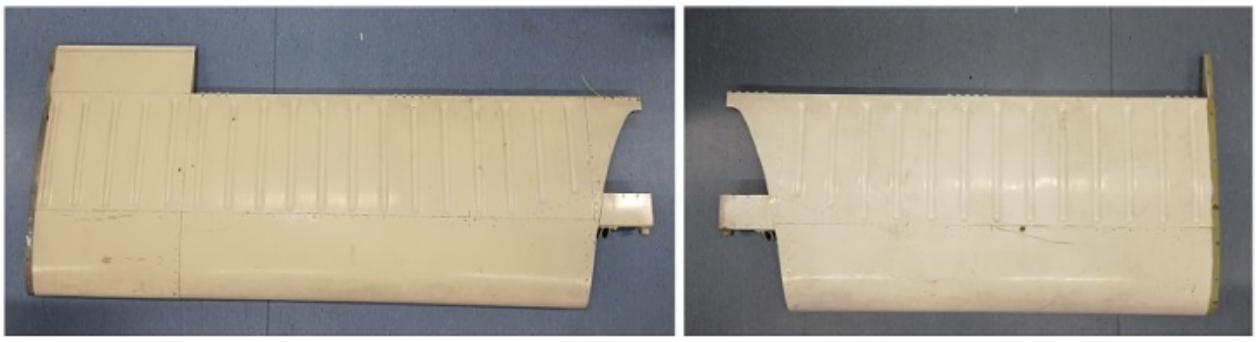


Figure 2: Examples of type C (l) and type A (r) tailplane structures

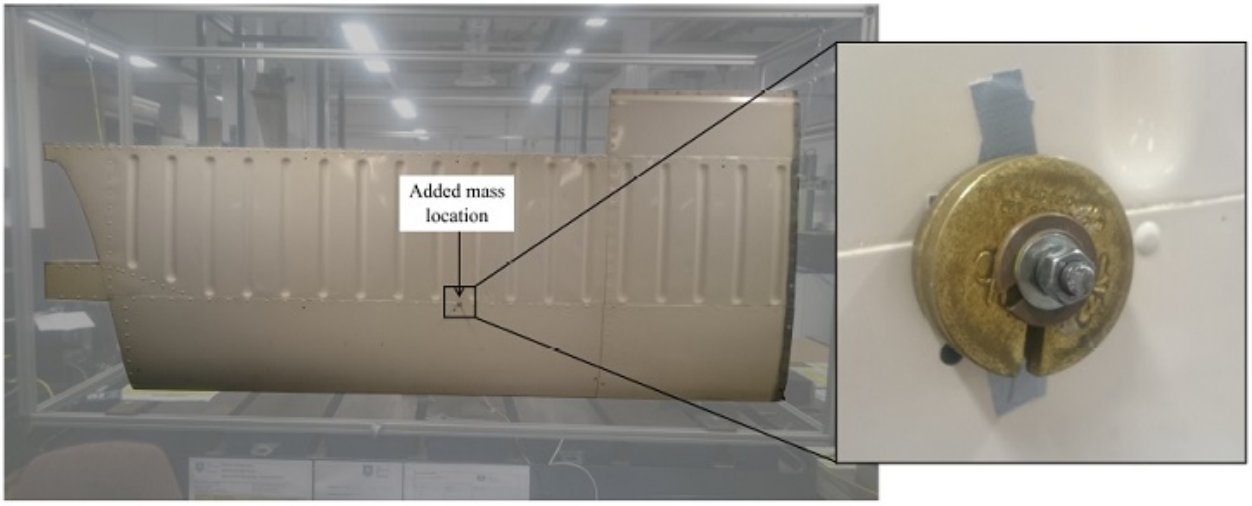


Figure 3: Location of the pseudo-damage added mass

Type C structures had masses of 6.735kg and 6.696kg (0.58% variation), and type A structures had masses of 4.848kg and 4.762kg (1.76% variation). Examples are shown in Figure 2.

2.1 Pseudo-damage

During this study, damage was simulated in two ways: By removing sections from the structure, and by adding mass to the structure, which can be thought of as pseudo-damage. Damage to a structure, in the form of a crack for example, will generally result in a local reduction in stiffness. For a very simple single degree of freedom system, stiffness k is related to mass m and natural frequency ω by:

$$\omega = \sqrt{k/m}$$

From this equation, it can be blithely extrapolated that the stiffness reduction caused by damage could be replicated by increasing mass, thus giving the same ω result. This method has been investigated previously in [4], and more thoroughly in [5] and [6]. It was also applied during the previous study on the same structures [2]. In order to allow comparison with these results, the same added mass location and mass were used in the new study. A mass of 104g was added to a point on the upper surface, above the main spanwise structural member, 808mm from the outer edge of the structure. The mass was made up of laboratory weights secured to a bolt, the head of which was glued to the structure. The nut, bolt and locking washer used were included in the total mass. The location of the mass on the structure and the mass itself are illustrated in Figure 3. A second added mass of half the mass of the original was also used. The first (108g) mass is subsequently referred to as added mass 2, with the second (54g) mass referred to as added mass 1.

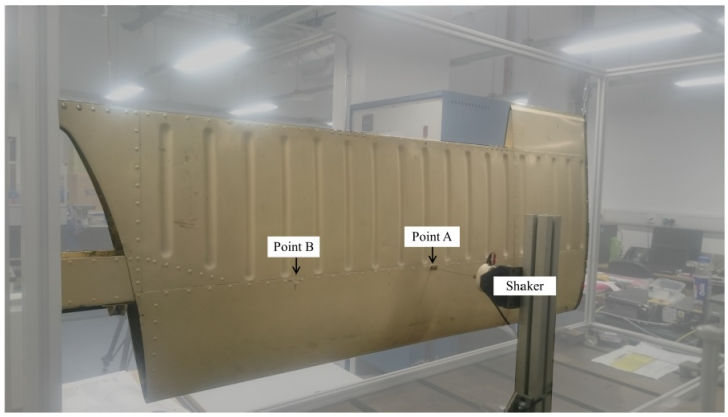


Figure 4: Rear view of mounted tailplane structure and shaker connection points A and B

2.2 Experiments

2.2.1 Experimental Rig

An aluminium frame mounted on a rigid table was used to hold the tailplane structures during tests. Tailplane structures were mounted vertically with the leading edge below the trailing edge. Structures were freely suspended using soft springs to approximate free-free boundary conditions. The mounting point closest to the original (i.e. before cutting the tailplane in two) centre of the tailplane was located on one of the elevator hinges, 112mm from the original centre and 156mm forward of the extreme of the trailing edge, as shown in Figure 4. The other spring was mounted on the end of the tailplane structure, at 200mm forward of the extreme trailing edge.

2.2.2 Excitation

Tailplane structures were excited using a Gearing & Watson electromagnetic shaker. The shaker was firmly fixed to the solid base of the table used to support the tailplane hanging frame, and the shaker body was thus assumed to be rigidly fixed. An electrodynamic shaker was used to excite the structure via a flexible drive rod. During testing, the structures were excited on the rear surface and deflection measured on the front surface. Both the top and bottom surfaces of each tailplane were used as the excitation surface and the measurement surface. In all cases, the excitation point was at the same location relative to the tailplane tip. This point was located 242mm in the x direction from the leading edge, and in the y direction 840mm from the tailplane tip. This point was named point A. A second point (point B) was also used during initial testing, as will be described later. Point B was located at the same distance from the leading edge as point A, but at 1290mm from the tailplane tip. The shaker installation position is shown in Figure 4.

The excitation signal used to drive the shaker was generated by the Scanning Laser Doppler Vibrometer (SLDV) control system. White noise excitation was used over a frequency range of 0-1kHz.

2.2.3 Frequency Response Measurement

The response of the structures was recorded using a Scanning Laser Doppler Vibrometer (SLDV). Laser vibrometry has a number of advantages over more conventional measurement using accelerometers, chief among which are the ability to measure the response of the entire surface of the structure during a single test, and the avoidance of any modification of the response due to the added mass of the measurement devices - it is essentially a non-contact measurement. The SLDV equipment used in this case was a tripod-mounted Polytec PSV-400 scanning head, controlled by a Polytec OFV-5000 controller, JSV-500 junction box, and DMS computer. The equipment has an optimal stand-off distance and was therefore located 2.343m from

the structure. In order to ensure the selection of the optimal measurement range, three ranges were tested, namely 1mm/s/V, 2mm/s/V and 5mm/s/V. Over multiple tests, a range of 2mm/s/V was found to yield the lowest number of overrange point responses (typically a few percent of overrange points on a single run, and zero overrange points for a five-run mean), so was subsequently used for final testing. 6400 spectral lines were recorded at each measurement point over the 0-1000Hz frequency range. This resulted in a resolution of 156.25mHz. Complex averaging over five samples was carried out using the SLDV software.

2.2.4 Measurement Points

Measurement points were set using a grid within the SLDV operating software. A range of point numbers and layouts were tested, and it was decided to employ a square grid system since this resulted in greater point density in the more geometrically complex areas of the structure (e.g. the area around the original tailplane centre). Additional points were added around the edge of the structure to give the resulting post-processed images the same shape as the structures. Following a sensitivity study, a point density of 25 was used in both C and A tailplane structures, yielding 442 points for type C structures, and 294 points for type A structures. These settings resulted in a total scan time of around 5 hours for the type C tailplane.

2.2.5 Repeatability Tests

Tests were repeated to highlight any aspects of the experimental setup which may affect the repeatability of the results:

Hanging and boundary conditions

Using structure C1, a full test over excitation range 0-1000Hz was repeated twice. Between tests, the shaker was detached from the structure, and the drive rod detached from the shaker. The structure was removed from the hanging frame, then re-hung and the shaker reconnected. Good correlation was shown between the two FRF results, suggesting that there was no bias caused by the hanging method or support structure.

Excitation Location

Structure C1 was tested with two different shaker installation positions, as illustrated in Figure 4. When subjected to the same 0-1000Hz white noise signal applied at each of the two points, the resulting frequency response functions were found not to differ significantly. Shaker location A was subsequently used for all testing. The reason for this selection is that it is possible that when using location B, the distance between the shaker mounting location and the centre of mass of the structure could restrict the structure should it wish to rotate about the z axis. Since location A is closer to the centre of the structure, the likelihood of this effect is reduced. However, no evidence of this effect was observed in either data set.

Drive Rod Length

Structure C1 was tested using two shaker drive rod lengths. In addition to the initial drive rod length of 183mm, a second drive rod length of 127mm was also used to ascertain whether the length of drive rod had an effect on the resulting FRFs. Results from drive rod A and B tests suggests that the choice is fairly arbitrary, but following the advice in the literature [7], in which it is noted that an overly long drive rod can lead to the introduction of additional resonances to the structure, the shorter of the two, drive rod length B (127mm) was subsequently used for all further testing.

Reference Measurement

In order to isolate the movement of the structure, a reference signal describing the excitation supplied to the structure is required. In this case, excitation was generated by the SLDV built-in signal generator. This signal was taken directly as the reference signal for SLDV tests.

2.3 Modal Analysis

Each test resulted in 'n' FRFs, where 'n' is the number of points for each structure (442 points in the Type C case and 294 points in the Type A case). For the undamaged and pseudo-damaged cases, six full tests were carried out for each structure, made up of no added mass, added mass 1 and added mass 2 for both the front and back of each test structure. The resulting FRFs were exported from the Polytec software as a universal file and the LMS PolyMAX package was used to extract modal frequencies. Having confirmed the location of stable modes using this package, the frequencies of the modes were extracted and MATLAB was used for further analysis. The Modal Assurance Criterion (MAC)was calculated in MATLAB.

2.4 Damage

In order to understand the effectiveness of pseudo-damage as a method for representing real damage, it was necessary to test a structure with real damage. To this end, one of the tailplanes was sacrificed to generate true damage data. Damage was incrementally added to a type C structure, centred at the same location at which pseudo-damage was installed (on the upper surface, above the main spanwise structural member, 808mm from the outer edge of the structure). A total of 17 damage cases were studied, with each of increasing severity. Damage was implemented by the removal of rivets between the lower section (leading edge), upper section and main structural member of the tailplane, and subsequently by the removal of material from the upper and lower sections. Details of each damage case and the subsequent change in structure mass are described in Table 1 and cases D1 to D13 are illustrated in Figure 5

Damage case	Description	Removed Mass (g)
undamaged	-	0 (Total mass 6.696 kg)
D1	1 rivet removed	0.1
D2	2 rivets removed	0.2
D3	linear cut (38mm) between rivet holes	0.3
D4	38mm x 4mm section removed from lower (leading edge) panel	0.6
D5	further 38mm x 12mm section removed from lower panel	1.5
D6	38mm x 12mm section removed from upper panel	2.1
D7	further 38mm x 24mm section removed from lower panel	3.3
D8	further 38mm x 24mm section removed from upper panel	4.0
D9	2 further rivets removed	4.2
D10	hole enlarged to 96mm x 96mm (upper and lower)	24.2
D11	hole enlarged to 144mm x 96mm (upper and lower)	36.0
D12	hole enlarged to 144mm x 144mm (upper and lower)	50.3
D13	hole enlarged to 192mm x 144mm (upper and lower)	66.9
D14	hole enlarged to 192mm x 192mm (upper and lower)	85.8
D15	2 further rivets removed	86.0
D16	hole enlarged to 216mm x 192mm (upper and lower)	96.7
D17	hole enlarged to 216mm x 216mm (upper and lower)	107.4

Table 1: Details of incremental damage to structure C2

3 Results

3.1 Undamaged case results

After experimental analysis as described in previous sections, structures were compared to study the variation between types of structures, individuals of the same type, and between the top and bottom surfaces of the

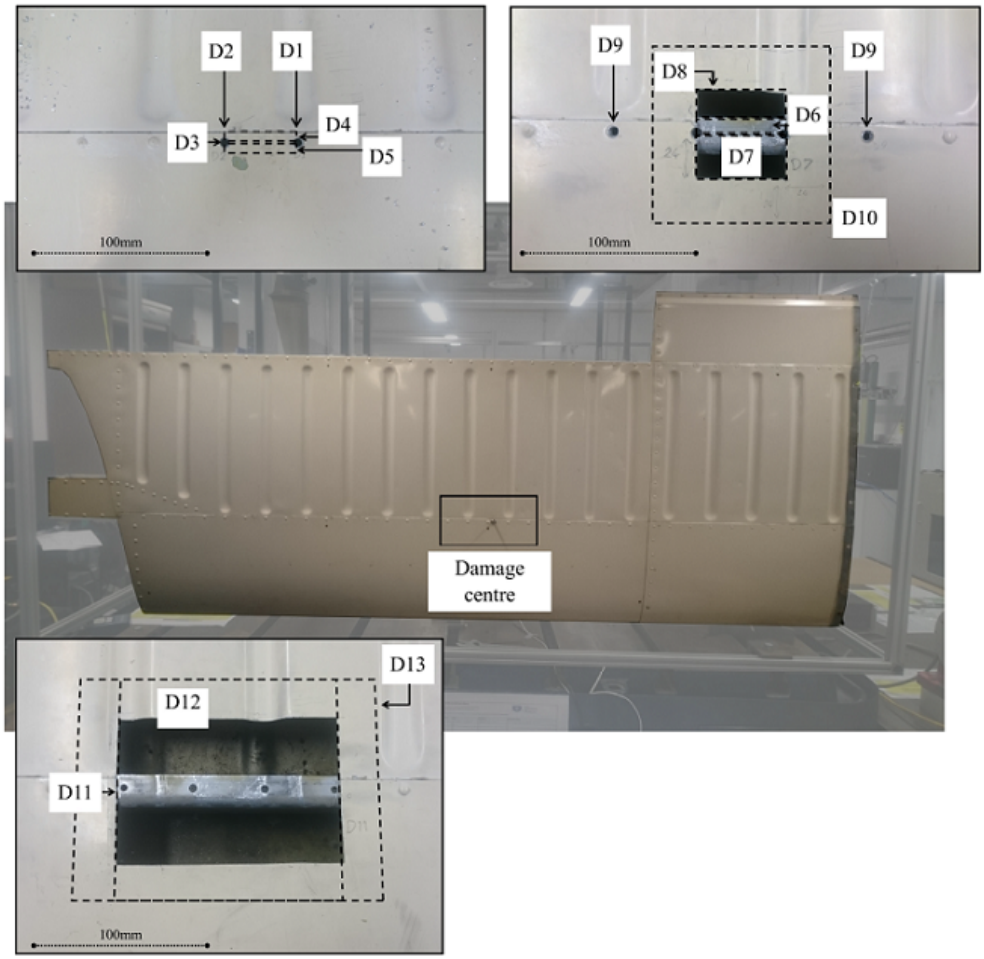


Figure 5: Photograph of damaged structure showing cases D1 to D13

structures.

Comparison of types

Due to differences in their size, mass and internal structure, significant variation in vibration response would be expected between the two types of structures (type A and type C, as described previously). Average FRFs for structures A2 and C2 are shown together in Figure 6(a), which confirm this.

Comparision of Top and Bottom

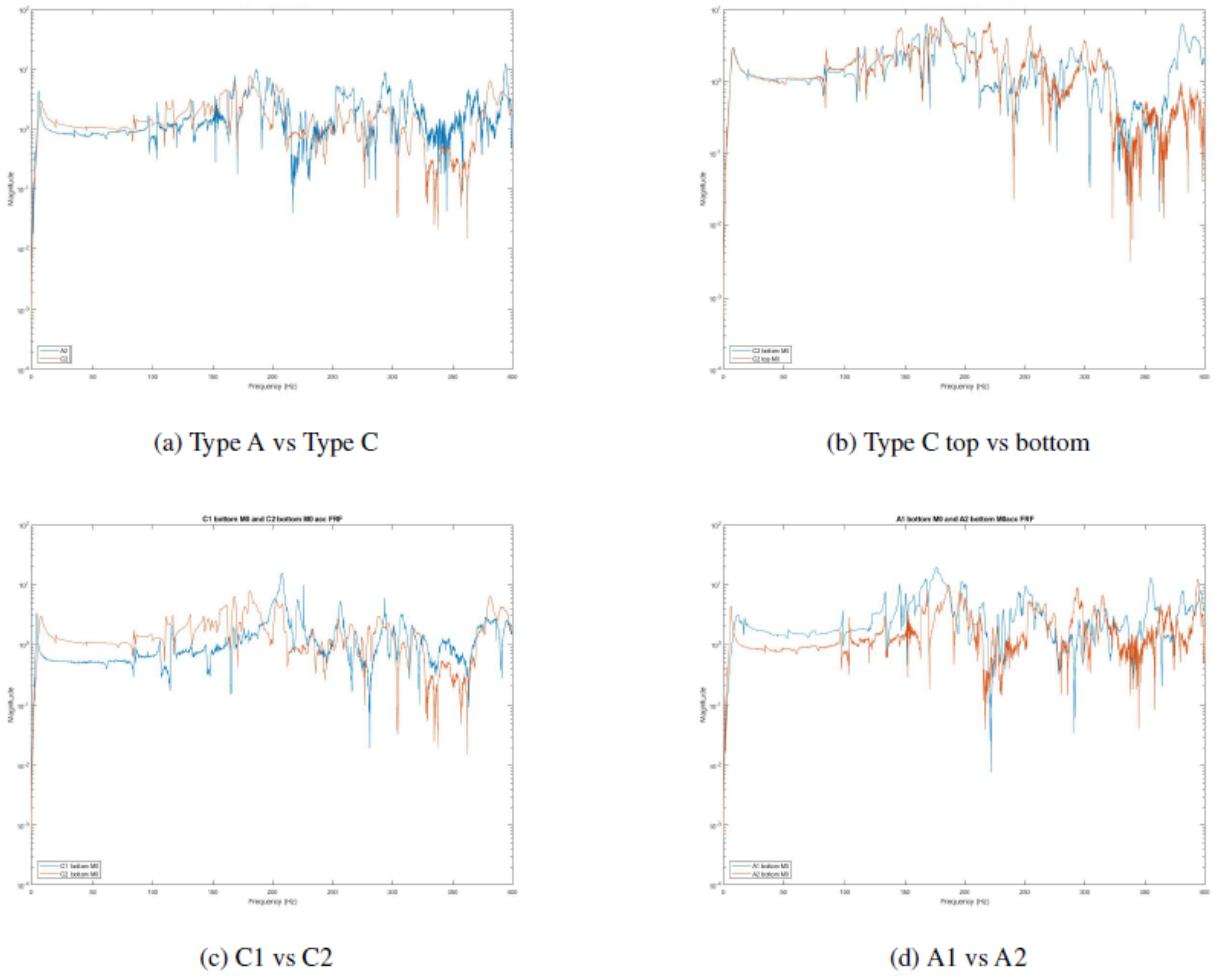
Structures were tested with excitation firstly applied to the original upward surface, then with excitation applied to the original bottom surface. FRF results for structure C1 with excitation applied to the top and bottom surfaces are given in 6(b).

Comparison of structures of the same type

Comparisons of similar structures are expected to show much less variation than intra-type comparisons. The variation between these structures is the fundamental focus of this work, since it is this variation which ultimately specifies the range of normal case variation in the population. FRF comparisons between structures C1 and C2 and A1 and A2 respectively are shown in Figure 6(c) and (d).

3.2 Pseudo-damage case results

Each structure was tested without additional mass, and with two added mass pseudo-damage cases. These were labelled M0, M1 and M2 respectively. M1 represents an added mass of 54g, and M2 an added mass of



(a) Type A vs Type C

(b) Type C top vs bottom

(c) C1 vs C2

(d) A1 vs A2

Figure 6: Comparison of undamaged case structures

108g. Two example FRFs illustrating the effect of M1 and M2 relative to the M0 case are given below, one for a type A structure and one for a type C structure.

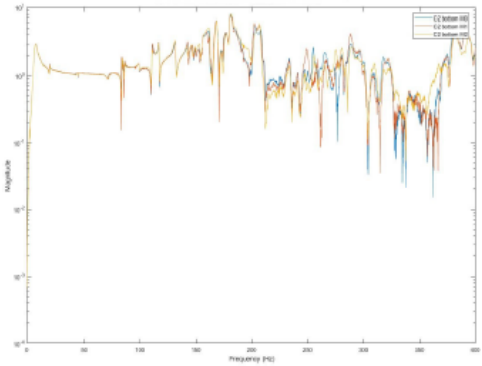
The MAC was also used to compare the similarity of modal results between the undamaged (M0) and M1, and M0 and M2 cases. These results are given alongside FRF comparison in Figure 8.

3.3 Damaged case results

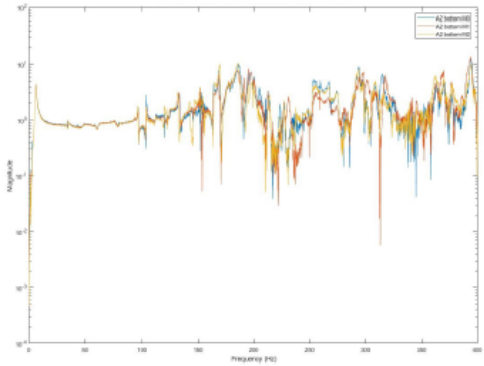
For clarity, only cases D1, D12 and D17 are illustrated in Figure 9. D1 represents the most minor damage case simulated, with the removal of one rivet from the structure. Case D12 is a hole of size 144mm x 144mm at the structure centre and a mass reduction of 50.3g. Case D17 is a hole of size 216mm x 216mm at the centre of the structure, with a mass removal of 107.4g. These two cases are significant for this work as the masses of removed material are closest to the pseudo-damage added masses in cases M1 and M2.

4 Discussion

The aim of this work was to assess the variability of common damage-sensitive features across a small population of similar, and real, structures with the ultimate purpose of providing a roadmap to a more comprehensive population-based SHM. Damage had to be introduced to all the structures, but since destructive



(a) Type C structure without and with M1 and M2 added mass pseudo-damage



(b) Type A structure without and with M1 and M2 added mass pseudo-damage

Figure 7: Comparison of FRFs for structures C2 and A2 bottom with no added mass (M0), 54g (M1) and 108g (M2)

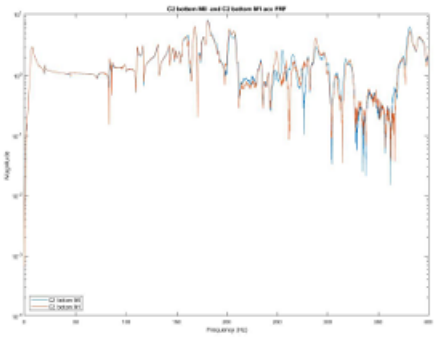
means create irreversible scenarios, and can also be unaffordable, pseudo-damage in the form of added mass was used throughout, except for one structure where a series of more realistic types of damage was applied.

The 'real' damage included rivet removal and the progressive cut of sections from the structure. This allowed for a chance to assess the suitability of added masses as a form of damage introduction - especially in the case of a population-based scheme. The MAC showed that the modal similarity between the undamaged structure and a structure with 54g added mass is greater than the similarity between the undamaged structure and one with 50.3g removed (Figure 10). The same trend is shown by comparing the M2 case (108g added mass) to the D17 case (107.4g removed) as illustrated in Figure 11, where greater MAC values are seen in the undamaged vs damaged case than in the undamaged vs pseudo-damaged case.

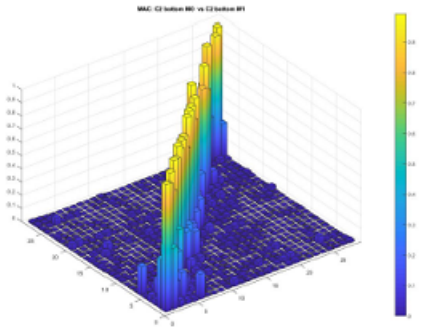
These data imply that it is challenging to attempt to directly relate the severity of the pseudo-damage with that of real damage. In the case here, this is mainly because the severe damage scenarios altered the stiffness as well as the mass of the structure, whereas the pseudo-damage was largely a mass effect.

To test this theory, the M2 108g added mass pseudo-damage case was compared to the full population of damaged case results, working from D17 to D1. MAC similarity was found to increase for all cases until D6, which was the damage case most closely approximated by the M2 pseudo-damage case. In this case, only 2.1g of material was removed. MAC values of over 0.5 are still only seen in the first five (i.e. three rigid body modes and flexible body modes one and two - see Table 2), which may suggest that for some cases the pseudo-damage method may require careful thought and consideration in its application if it is considered to be a suitable alternative to real damage tests. It is also worth noting the large difference in required additional mass to simulate the removal of a small mass. One may think that if the addition of 108g is required to simulate a damage case with a material removal of 2g, simulating a damage case with, for example, an order of magnitude greater material removal will require the addition of a perhaps unfeasible amount of pseudo-damage material. However, such an argument should be carefully considered, as equating the removal of mass in order to simulate severity cases of damage is clearly challenging, and may depend on material properties as well.

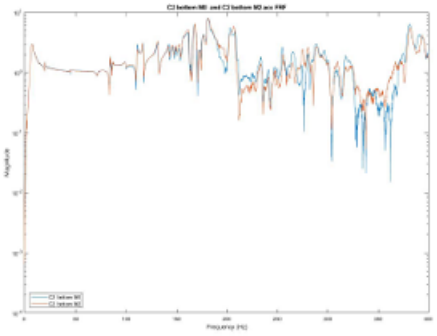
The MAC comparison of the M2 and D6 cases is shown in Figure 13.



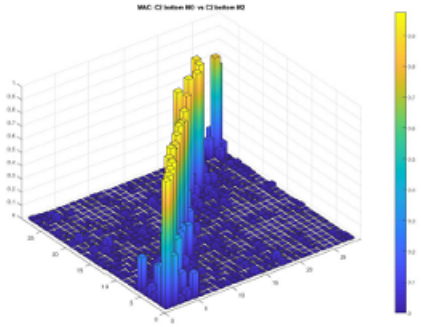
(a) MAC: Type C M0 vs M1



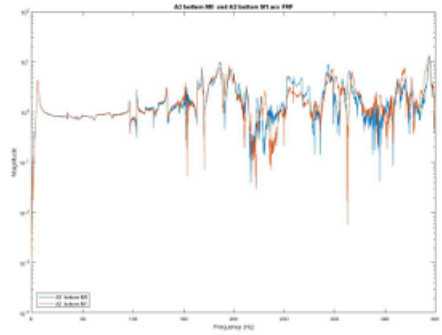
(b) FRF: Type C M0 vs M1



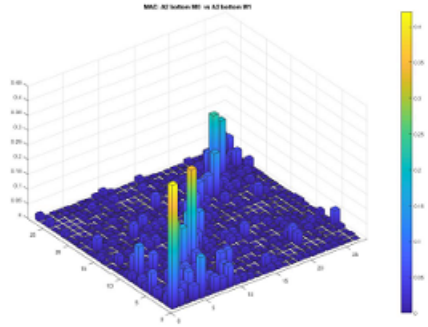
(c) MAC: Type C M0 vs M2



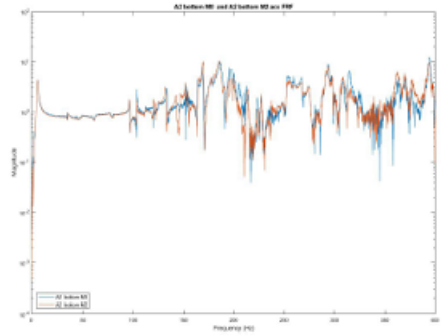
(d) FRF: Type C M0 vs M2



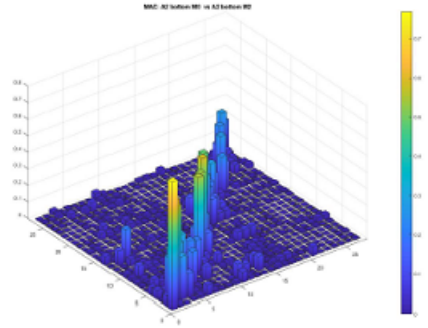
(e) MAC: Type A M0 vs M1



(f) FRF: Type A M0 vs M1



(g) MAC: Type A M0 vs M2



(h) FRF: Type A M0 vs M2

Figure 8: FRF and MAC comparison of pseudo-damaged case structures

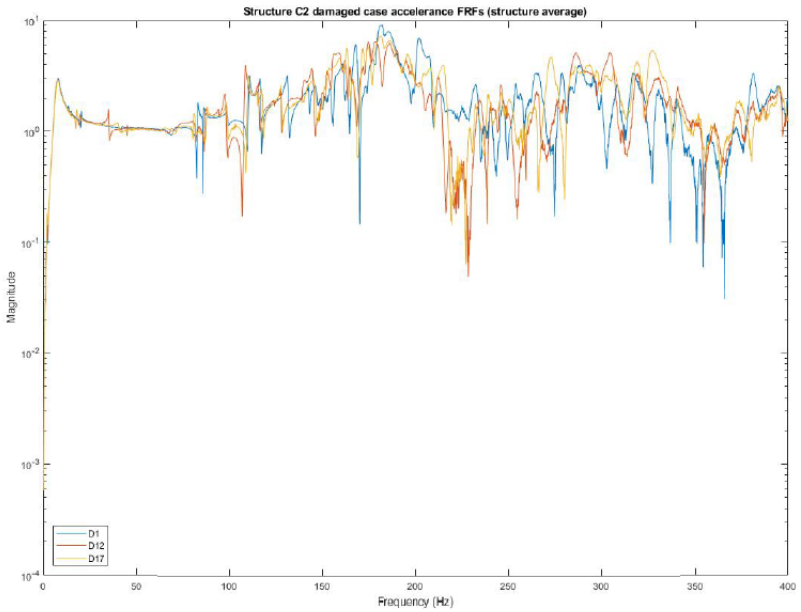
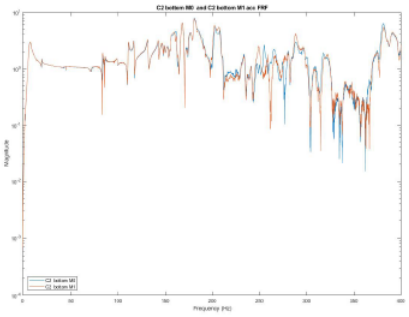


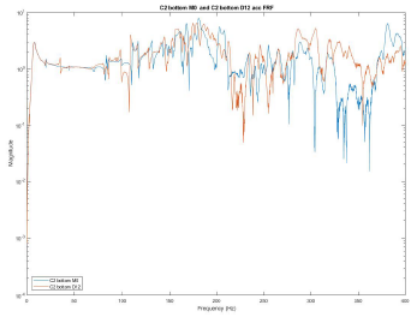
Figure 9: FRFs for structure C2 bottom in D1, D12 and D17 cases

Mode	MAC value
1	0.9746
2	0.9342
3	0.9194
4	0.9033
5	0.7994
6	0.4856
7	0.0078
8	0.0128
9	0.1189
10	0.2568

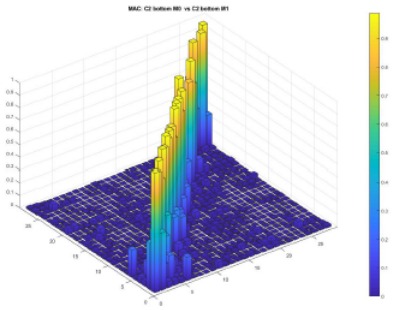
Table 2: MAC values for first 10 modes: C2 bottom M2 vs C2 bottom D6 cases. This was the structure which was subjected to 'real' damage.



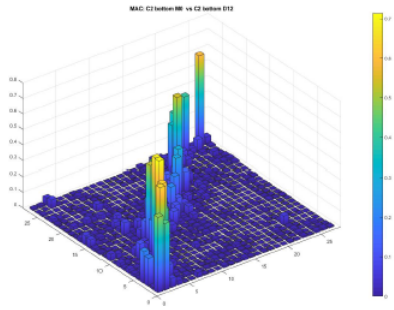
(a) FRF: Type C M0 vs M1



(b) FRF: Type C M0 vs D12

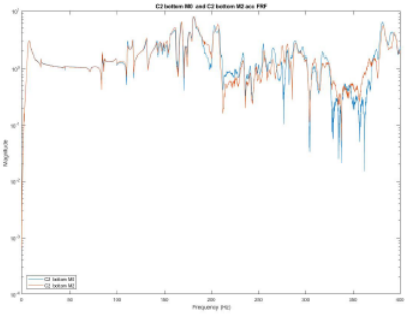


(c) MAC: Type C M0 vs M1

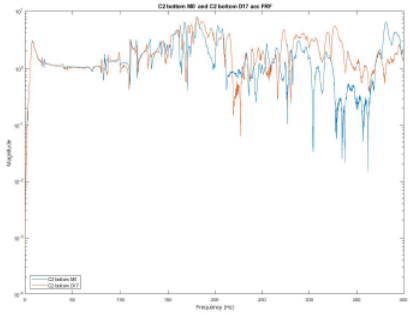


(d) MAC: Type C M0 vs D12

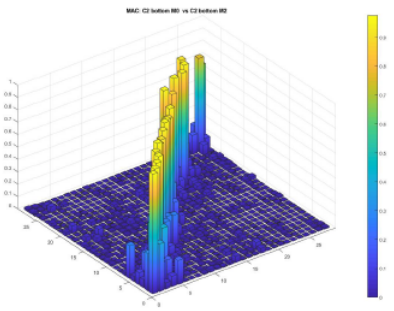
Figure 10: FRF and MAC comparison of undamaged vs pseudo-damaged and undamaged vs damaged case structures



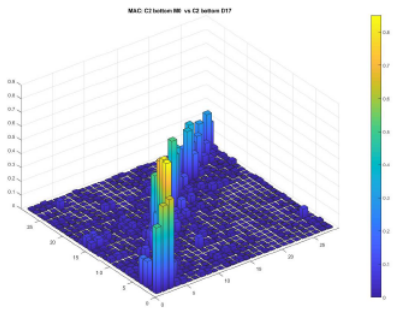
(a) FRF: Type C M0 vs M2



(b) FRF: Type C M0 vs D17

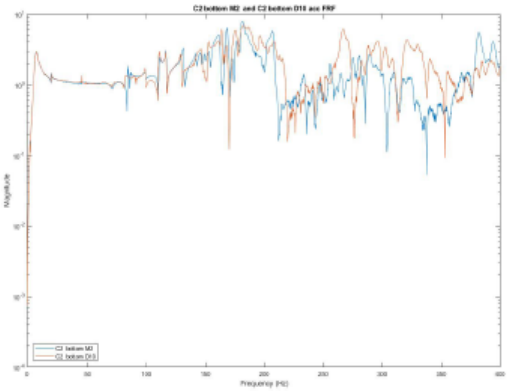


(c) MAC: Type C M0 vs M2

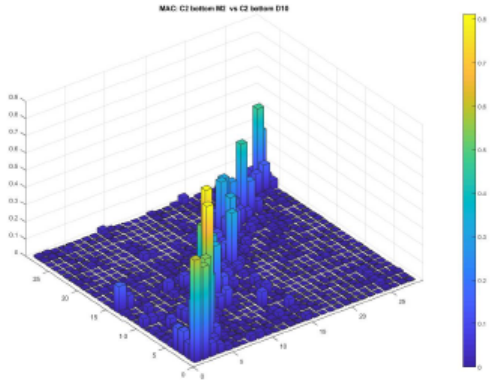


(d) MAC: Type C M0 vs D17

Figure 11: FRF and MAC comparison of undamaged vs pseudo-damaged and undamaged vs damaged case structures

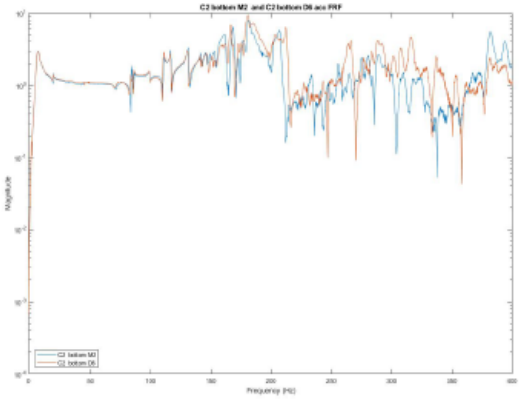


(a) FRF: Type C M2 vs D10

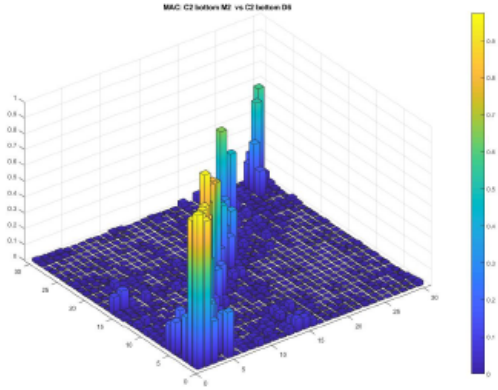


(b) MAC: Type C M2 vs D10

Figure 12: FRF and MAC comparison of pseudo-damaged (M2) and damaged (D10) case structures



(a) FRF: Type C M2 vs D6



(b) MAC: Type C M2 vs D6

Figure 13: FRF and MAC comparison of pseudo-damaged (M2) and damaged (D6) case structures

5 Conclusions

The aim of this work was to assess the variability of damage sensitive features in a small population of similar structures when subjected to different types of damage. The suitability of pseudo-damage in the form of added mass as a method of generating damaged structure data, was also briefly explored. Results of the tests described herein suggest that adding a point mass to a structure can simulate the stiffness reduction caused by damage, but only to a certain degree. The addition of 108g mass, for example, did not lead to a significant change in the location of modal frequencies, especially in lower frequency range, whereas the reduction of stiffness by the addition of even a small amount of real damage had a much greater effect on the frequency response of a structure. To replicate the effect of significant damage to a structure through the use of pseudo-damage may be challenging since the mass required would be large, and this implies that added masses should be carefully considered when damage severity is the main goal of the study.

Ultimately, this study can serve as a collection of data from a real structure under damaged states – and not just pseudo-damage cases – to be used as a reference for future studies. A numerical model of the tailplanes is currently under development, and the damaged structure will be crucial in its validation.

References

[1] S. Deering, G. Manson, K. Worden, D. W. Allen, C. R. Farrar, J. S. Lombardo *Syndromic Surveillance as a paradigm for SHM data fusion*, in *Proceedings of the 4th European Workshop on Structural Health Monitoring, Crakow, Poland, July 4-6*, (2008), pp. 998-1014.

[2] E. Papatheou, T. Rahman, R. Barthorpe, J. Park, K. Worden *An experimental investigation of feature complexity and diversity in nominally similar test structures*

[3] E Papatheou, N Dervilis, AE Maguire, I Antoniadou, K Worden *A performance monitoring approach for the novel Lillgrund offshore wind farm*, IEEE Transactions on Industrial Electronics, Vol 62, No 10, (2010), pp. 6636-6644

[4] L.Y. Cheung, K. Worden, J.A. Rongong *Damage detection in an aircraft component mode, Proceedings of the 19th International Modal Analysis* IMAC Conference: Kissimmee, Florida, Vol. XIX, (2001), pp. 1234–1241.

[5] E. Papatheou, G. Manson, R. J. Barthorpe, K. Worden *The use of pseudo-faults for novelty detection in SHM*, Journal of Sound and Vibration, Vol. 329, No. 12, Academic Press (2010), pp. 2349-2366.

[6] E. Papatheou, G. Manson, R. J. Barthorpe, K. Worden, *The use of pseudo-faults for damage location in SHM: An experimental investigation on a Piper Tomahawk aircraft wing*, Journal of Sound and Vibration, Vol. 333, No. 3, Academic Press (2012), pp. 971-990.

[7] D.J. Ewins, *Modal testing: theory, practice and application*, John Wiley & Sons, 2nd edition (2000).

Connecting nonlinearities: damage precursors detection and control methodology

E. Habtour [1,2,3], **T. Dragman**[2], **T. Masmeije**[2], **D. Di Maio**[2], **R. Haynes** [2], **A. Homborg**[1], **T. Tinga**[1,2]

[1] The Netherlands Defence Academy, Life Cycle Mangement, Den Helder, The Netherlands

[2] Univeristy of Twente, Applied Mechanics, Enschede, The Netherlands

[3] US Army Research Laboratory, Aberdeen Proving Ground, MD, USA
e-mail: **e.m.habtour@utwente.nl**

Abstract

Fatigue damage precursors identification and control procedure is developed for nonlinear aero-structures and dynamic systems exposed to realistic vibratory conditions. The identification is achieved by connecting nonlinearities between macro- and micro-states, and including those connection in the equations of motion; i.e. the interplay between the local nonlinearities (or materials micro-plasticity) and the global nonlinearities (nonlinear dynamic parameters). Exploiting the nonlinear connections is key in linking the health of a system to its control algorithms, which can manipulate the structural dynamic responses in order to slow the progression of fatigue. This approach allows for continual re-estimation of the dynamics of the macro-states due to degradations in the properties of the micro-states at unhealthy locations by identifying precursors to damage prior to crack formation. Capturing and controlling the interplay between the local and global nonlinearities appear to hold promise in extending the service-life of high-value systems.

1 Introduction

Current prognostics health management (PHM), structural health monitoring (SHM), and condition based maintenance (CBM) methods are capable of executing health assessment for high-value military and commercial aerospace platforms, vehicular systems, and infrastructures. However, there are intrinsic and extrinsic factors that limit the accuracy of measured and calculated parameters provided by PHMs/SHMs/CBMs. Some of the intrinsic factors are due to the complexity and diversity of health monitoring and management hardware required for collecting and processing data [1], and due to unavoidable design assumptions and correction factors embedded in the software [2]. On the other hand, the extrinsic factors tend to be application specific. For example, in aerospace platforms, these factors consist of variability in flight conditions, structural geometries, and type of materials [1]-[6]. The intrinsic and extrinsic factors can be mitigated but cannot be eliminated, thus, providing accurate identification and assessment of fatigued components can be extremely challenging. In military aviation, scheduled maintenance inspections are still required in order to reduce uncertainties in health measurements or estimates, which can be expensive and time consuming.

It is important to point out that the intrinsic and extrinsic factors have coupling effects, which often instigate or augment various nonlinearities at the system, subsystem, component, and materials levels. In many high-value systems, current state of the art in PHMs/SHMs/CBMs is based on linear or reduced models to assess the health of systems that are highly nonlinear [2]. In this paper, we focus on simulating the relevant nonlinearities that may ameliorate some of these intrinsic-extrinsic coupling effects, where the extrinsic factor is realistic vibration, and the intrinsic factor is nonlinearities in the outputs signal. Aero-structures are often exposed to high amplitude vibrations, which introduce additional and enhance existing nonlinearities

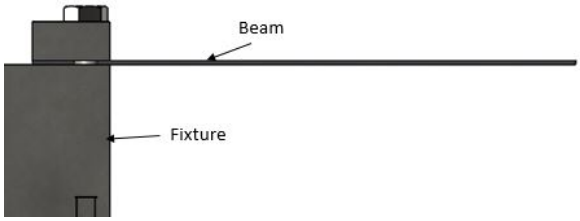


Figure 1: Cantilever beam setup for modeling

in aircraft [3, 6]. Indeed, light wight and flexible aero-structures such as helicopter blades, and aircraft wings are often exposed to fast and high amplitude motions [4, 5], which are the most encountered nonlinearity in aerospace applications. Consequently, the effective structural stiffness is modified based on the variation in periodic deflective motions, which can be exploited to detect fatigue [7]. Cole et al. have shown that nonlinear vibration is a practical method for simulating realistic flight dynamics and have been able to monitor changes in global nonlinear stiffness to assess fatigue severity [8]. Cole et al. have observed that the global nonlinear stiffness parameters were sensitive to fatigue damage precursors at the micro-state level, and proposed exploiting the nonlinear stiffness as an indicator for detecting changes in the materials mechanical properties prior to crack initiation. They defined damage precursor (DP) as any observable degradation of the material microstructural morphology and resulting changes in the physical properties prior to any detectable fatigue crack [8].

In this paper, we simulated the interplay between the micro-state nonlinearity, namely materials microplasticity, and the macro-state nonlinear stiffness to estimate changes in the global dynamic response of a beam-like structure. An aerospace alloy aluminum 7075-T6 was selected for this study. The simulation was accomplished analytically, where the material and geometric nonlinearities were contained in the equation of motion. The micro-states properties were obtained from the nano-indentation results performed by Haynes et al. for Al 7075 beams fatigued up to 25%, 50%, and 75% their fatigue-life [7]. The Harmonic-Balance method (HBM) was utilized to approximate a solution for the nonlinear differential model, and to provide a frequency response equation with the relevant nonlinear parameters. The main advantage of deriving a frequency response equation is to provide fast updates of the structural health-state, which may potentially allow for aligning PHM/SHM/CBM, and for integrating the health-state into flight control laws. The idea basic was demonstrated analytically by showing drifts in the structural dynamic response due to the development of damage precursors. Identifying changes in the nonlinear parameters is far more useful for a control system than locating and measure the size of a crack. Based on updates into the linear and nonlinear stiffness matrices, adaptive control algorithms could potentially ensure optimal operations below high stress regimes.

2 Approach

The equation of motion is, perhaps, one of the primary links between controls and structural dynamics theories. Thus, our approach consisted of : (i) connecting and amplifying nonlinearities to study the possibility of extracting health indicators sensitive enough to early fatigue build; (ii) demonstrating the concept analytically using thin aluminum 7075-T6 beam-like structures exposed to high amplitude harmonic excitations; and (iii) updating the effective structural stiffness in the equation of motion. The beam was modeled as a cantilever-beam attached to a rigid fixture as shown in Figure 1. The Young elastic modulus, E, and density, ρ, for aluminum 7075 are $71.7GPa$, and $2810kg/m^3$, respectively. The beam length, L, is $127mm$, and its cross-section area is $50 \times 1mm^2$.

2.1 Macro-State

In linear systems, Hooke′s law is adequate for approximating the displacement in structures exhibiting linear elastic deformation due to external loads in the form of restoring forces proportional to structural displacement, x. For thin and light weight structures, two common assumptions are applied when analyzing their structural dynamics: (i) these structures can endure reversible kinematic deformations before their inherent stress-strain characteristics show significant departure from the linear regime [8, 10]; and (ii) they also encounter kinematic nonlinearities before reaching the materials inherent plasticity [11]. In fact, the kinematic nonlinearity is manifested as a dynamic hardening or softening response, where the restoring force is proportional to the cubic structural displacement, x^3 [8]. In this case, the total restoring force is expressed in terms of the linear and nonlinear structural stiffness coefficients, k_1 and k_3, respectively, as:

$$F_r(x) = k_{eq}x \tag{1}$$

where, the equivalent structural stiffness is:

$$k_{eq} = k_1 + \alpha k_3 x^2 \tag{2}$$

Dynamicists use α, which is a dynamic hardening-softening factor, to describe or correct for potential nonlinearity in restoring forces. When α is positive, k_3 assists the linear restoring force, k_1x, in making the structure stiffer and resistive to applied loads. Subsequently, the maximum dynamic response amplitude occurs at a forcing frequency, ω, higher than the structure's fundamental frequency, ω_n [12]. This type of response is called dynamic hardening, which is analogous to stiffening in solid mechanics and materials since. The nonlinearity associated with k_3 is due to the potential energy stored in periodic bending. A negative α, on the other hand, opposes the linear restoring force. The oscillatory behavior of the structure may appear dynamically softer with a drop in its natural frequency [4]. This phenomenon is called dynamic softening. Dynamicists attribute the hardening−softening behavior to the kinematics of the structure and rarely to structural fatigue. For completeness, we mention another cubic nonlinearity associated with the beam inertia, m_i, which tends to oppose the restoring forces.

In this study, the global nonlinear equation of motion for the aluminum structure was derived from nonlinear Euler-Bernoulli beam theory [13]. The model includes both inertial and stiffness nonlinearities. For fatigued structures, the dynamic performance was estimated by updating the equivalent stiffness k_{eq} based on the evolution in the materials stiffness at the micro-state. For simplicity, we only focused the beam first flexural mode. Thus, the beam was exposed to simulated base sine-sweep excitation at an amplitude $1g$ near the beam's natural frequency for the following fatigue-life levels: 0% (pristine condition), 25%, 50%, and 75%.

2.2 Micro-State

Changes in the micro-state stiffness values were obtained from nano-indentation measurements in a separate study for the same fatigue-life levels [7], as shown in Figure 2. The measurements were conducted near the beam root, $0mm \rightarrow 1mm$ (Figure 2), where high stress concentrations occurred. The point $0mm$ is approximately at the beam-fixed boundary. Figure 2 shows the relevant changes in E for fatigue-life levels 25%, 50%, and 75%, where results are normalized by the average modulus of an un-fatigued Al 7075-T6 specimen. The indentation measurements show that the material experienced softening at 25% of fatigue-life followed by hardening and softening at 50% and 75% of life, respectively (Figure 2). Explanation of the material microscopic behavior after to various fatigue cycles is detailed in [7].

3 Modeling Development

The model assumes that the slender cantilever beam is an isotropic structure with uniform cross-sectional area, A, length, L, and volumetric density ρ. The beam is clamped to a rigid fixture, which can be excited

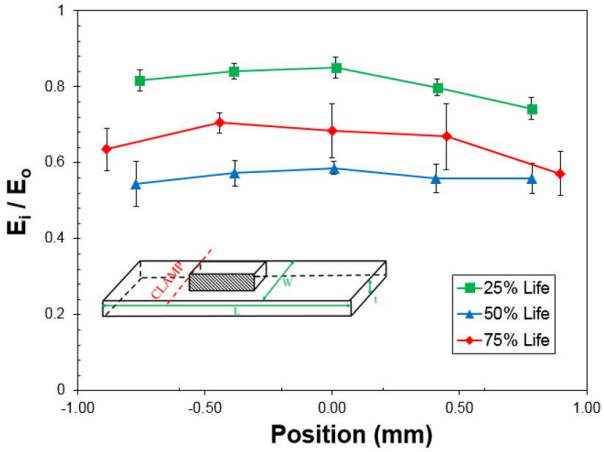


Figure 2: Changes in the elastic modulus obtained from nano-indentation measurements near beam root after various vibration fatigue cycles [7]

periodically in the transverse direction, as Shown in Figure 1. Since the study focuses on the beam first flexural mode, it is reasonable to assume that the transverse vibration is purely planar as long as the cross-section geometry are symmetric with respect to the beams centerline [13]. Stretch of the neutral axis of the beam can be neglected by applying the inextensibility assumption. Subsequently, effects due to warping and shear deformations are ignored. Therefore, nonlinear Euler-Bernoulli beam theory is applicable for modeling the transverse motion of the structure under investigation.

3.1 Nondimensional Time Domain

Including the nonlinear inertial and restoring forces into the equation of motion yields the following nonlinear differential equation [8]:

$$m\ddot{x} + c\dot{x} + m_i(x^2\ddot{x} + x\dot{x}^2) + k_1x + \alpha k_3x^3 = -mY_o sin(\omega t) \tag{3}$$

The over-dots denote derivatives with respect to time, t. The combined distributive mass and rotational inertia of the structure is m. The beam tip relative displacement, and the steady state base motion are x, and Y_o, respectively. The coefficient c is the system viscous damping, which causes an exponential dissipation of the systems natural dynamics over time. Rayleigh-Ritz procedure is applied to equation 3 to remove the spatial dependence. Further simplification is performed by redefining the temporal ordinary differential equation as function of a nondimensional time, τ, where, t, is transformed into a dimensionless variable based on the system's inverse natural frequency:

$$\tau = \omega_n t \tag{4}$$

The final dimensionless nonlinear differential equation normalized by the natural frequency and mass of the system is:

$$\ddot{\eta} + 2\zeta\dot{\eta} + m_n(\eta^2\ddot{\eta} + \eta\dot{\eta}^2) + \eta + k_n\eta^3 = -Y sin(\Omega\tau) \tag{5}$$

The dimensionless variables are:

$$\eta = \frac{x}{L}, \quad \Omega = \frac{\omega}{\omega_n}, \quad 2\zeta = \frac{c}{m\omega_n}, \quad m_n = \frac{m_i}{m}L^2, \quad k_n = \alpha\frac{k_3}{k_1}L^2 \tag{6}$$

3.2 Frequency Domain

To avoid expensive time-marching numerical techniques for solving the equation of motion, the Harmonic Balance Method (HBM) is utilized to provide direct steady-state periodic solution of the nonlinear differential equation [14]. HBM is a common methods for approximating periodic solutions for oscillatory systems

in many applications if transient is not present [9]. However, Nyfeh described the HBM as an analytical approach that is equivalent to performing a stepped-sine or slow sine-sweep testing [12]. In general, periodic solutions can be estimated using truncated Fourier series, where coefficients are determined by constructing series that satisfy the deferential equations [14]. Clearly, the accuracy of these solutions can be improved by increasing the number of terms obtained from Fourier series into trial solutions. In practice, however, reasonable accuracy of the solutions can be achieved by using limited number of terms in Fourier series. For the nonlinear system in this paper, an approximated periodic solution can be expressed with the following terms:

$$\eta = A\cos\phi + B\sin\phi \tag{7}$$

where, $\phi = \Omega\tau$. In addition η, the dimensionless velocity, acceleration, and cubic components will also have their own truncated terms. The forcing function is also assumed to be periodic, $Y = \Omega^2 Y_o \cos\phi$. Assembling the contribution of every variable into equation 5 produces four harmonics: $\cos\phi$, $\sin\phi$, $\cos 3\phi$, and $\sin 3\phi$, which are matched (or balanced). Splitting $\cos\phi$, and $\sin\phi$, harmonics, and neglecting higher ones yield the following:

$$H_c := -A\Omega^2 + 2\zeta B\Omega - \frac{3}{2}m_n AB^2\Omega^2 + A + \frac{3}{4}k_n\Big(A^3 + AB^2\Big) + \Omega^2 Y_o = 0 \tag{8}$$

$$H_s := -B\Omega^2 - 2\zeta A\Omega - \frac{3}{2}m_n A^2 B\Omega^2 + B + \frac{3}{4}k_n\Big(B^3 + A^2 B\Big) = 0 \tag{9}$$

H_c, and H_s are the $\cos\phi$, and $\sin\phi$ components, respectively. The autoperiodic force response amplitudes A, and B are unknowns, which can be obtained by varying the angular frequency Ω. To this end, Newton-Raphson method is utilized to numerically calculate A, and B for each Ω [15]. A frequency response approximation that resembles an FRF (frequency-response-function) can be achieved by performing polar transformation in equations 8 and 9. With additional algebraic manipulations, the system motion can be expressed in the following familiar frequency domain form:

$$\frac{X^2}{Y_o^2} = \frac{1}{\Big(\Omega_{1,2}^2 - k_{eq} + 2\mu\Big)^2 - 4\mu(\mu - k_{eq})} \tag{10}$$

where, X is a byproduct of the polar transformation procedure, which contains both A and B. The effective damping has a nonlinear inertial contribution:

$$\mu = \frac{2\zeta}{2 + m_n X^2} \tag{11}$$

The effective or equivalent stiffness is:

$$k_{eq} = 1 + \frac{3}{4}k_n X^2 \tag{12}$$

4 Results

Prior to numerically solving equations 8 and 9, a static deflection experiment was performed for three cantilever beams. Tip displacement measurements were obtained for each static load applied incrementally to the beam tip. The force-displacement results are shown in Figure 3. The tip displacement values in Figure 3 are normalized by the beam total free length. It can be concluded that Al 7075-T6 structures experience hardening behavior for high displacement. The k_1 and $k3$ values were estimated using a cubic polynomial curve fitting procedure, which was performed in Matlab (Figure 3). The experimental results show that the beam linear and nonlinear stiffness coefficients were approximately 10% higher than the theoretical values.

As mentioned above, Newton-Raphson method was applied to calculate the beam tip displacement amplitude due to 1g harmonic base excitation. The established convergence error for 0% fatigue-life was $\leq 10^{-10}$,

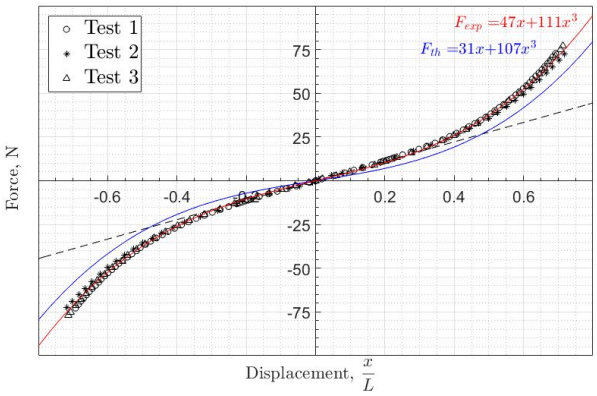


Figure 3: Restoring force due to nonlinear tip deflections of cantilever beams

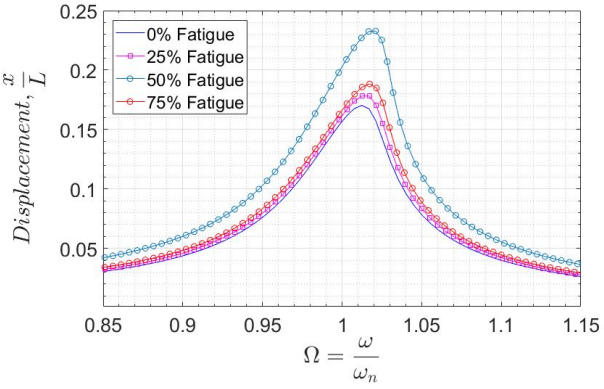


Figure 4: Beam tip maximum amplitudes due to 1g base harmonic excitation at fatigue-life levels: 0%, 25%, 50%, and 75%

which was set to be the accuracy criterion for all fatigue cases as well. The estimated changes in E obtained from the nano-indentation results were used to update the macro-state stiffness values in the beam spatial region $0mm \rightarrow 1mm$ for the following cases: 25%, 50%, and 75% fatigue-life. The dynamic maximum beam tip displacement provided in Figure 4 is normalized by the beam length, L, and plotted as a function of Ω.

As expected, the beam compliance increased when the number of fatigue cycles was increased. Compliance is defined as an increase in the beam tip deflection due to fatigue accumulation without an increase in the input force. Interestingly, the maximum compliance occurred at 50% of fatigue-life level. The beam appeared to experience softening-stiffing-softening behavior at 25%, 50%, and 75% fatigue levels, respectively. The softening-stiffing-softening behavior is illustrated in Figure 5, which shows the changes in the equivalent stiffness, keq, due to fatigue build up near the beam root. While this is a known behavior for aluminum 6061 subject to medium strain-rate fatigue conditions [16], it is possible, however uncertain, that Al 7075-T6 may have similar reaction to medium strain-rate vibration fatigue. Further studies will be required to gain insights into the mechanics of the softening-stiffing-softening behavior.

5 Conclusion

The structural dynamic behavior of Al 7075-T6 beam-like structures exposed to high harmonic base excitation was examined to gain insights into the influence of the nonlinear parameters in equation of motion on the

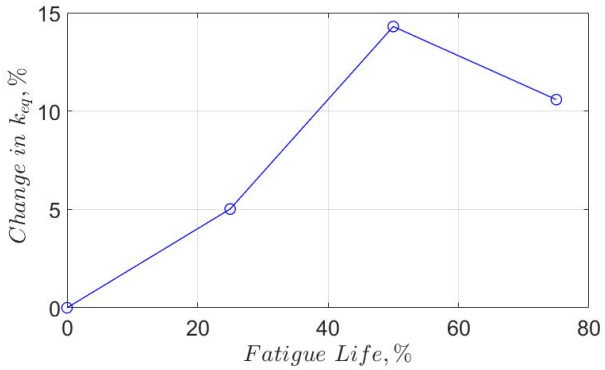


Figure 5: Change in k_{eq} due to 25%, 50%, and 75% fatigue

global dynamic performance. The Harmonic Balance method was utilized to produce a frequency-response equation, and a macro-state equivalent stiffness parameter based on updates in micro-state nonlinearities were acquired from the nonlinear dynamic analysis. The model was utilized to modify the parametric identification scheme based on changes in the materials health-state due to the development of damage precursors. The frequency-response equation is ideal for controls algorithms, thus, the evolution in the materials properties can be identified and controlled by adjusting the macro-states inputs. The parametric study revealed that the nonlinear stiffness coefficient is an important parameter for estimating and controlling the dynamic of aerospace structures. In general, nonlinear parameters are sensitive to damage precursors, thus, changes in those parameters must be included in calculating restoring forces instead of using a dynamic hardening-softening factor for control, which is not adequate. Estimating and controlling the health state of critical components in high-value system will continue to be challenging, but can be improved. Future research will focus on integrating PHM/SHM/CBM into basic adaptive control-system to study whether an integrated approach could ameliorate the effect of extrinsic factors such as aeroelastic instability, vibration fatigue, and thermal and solar loads.

References

[1] Tinga, T., R. Loendersloot, *Aligning PHM, SHM and CBM by understanding the physical system failure behaviour*, European Conference on the Prognostics and Health Management Society, Jul 8-10, 2014.

[2] Habtour, E., D. Cole, C. Kube, A. Svensken, M. Robeson, A. Dasgupta, *Damage Precursor Index (DPI) Methodology for Aviation Structures*, 8th European Workshop on Structural Health Monitoring Jul 3-7, 2016.

[3] Noel, P., G. Kerschen, *Nonlinear system identification in structural dynamics: 10 more years of progress*, Mechanical Systems and Signal Processing, Vol. 83 (2017), pp. 2-35.

[4] A. Carrella, D.J. Ewins, *Identifying and Quantifying Structural Nonlinearities in Engineering Applications from Measured Frequency Response Functions*, Mechanical Systems and Signal Processing, Vol. 25 (2011), pp. 1011-1027.

[5] Londono, J.M. , S.A. Neild, and J.E. Cooper, *Identification of backbone curves of nonlinear systems from resonance decay responses*, Journal of Sound and Vibration, Vol. 348 (2015), pp. 224-238.

[6] Holford, K. M. , M. J. Eaton, J. J. Hensman, R. Pullin, S. L. Evans, N. Dervilis, K. Worden, *A new methodology for automating acoustic emission detection of metallic fatigue fractures in highly demanding aerospace environments: An overview*, Progress in Aerospace Sciences, Vol. 90 (2017), pp. 111.

[7] Haynes,R.A., E. Habtour, T. C. Henry, D. P. Cole, V. Weiss, A. Kontsos, B. Wisner, *Damage Precursor Indicator for Aluminum 7075-T6 Based on Nonlinear Dynamics*, Nonlinear Dynamics, Vol. 1 Springer, Cham, (2019), pp. 303-313.

[8] Cole, D.P., E.M. Habtour, T. Sano, S.J. Fudger, S.M. Grendahl, A. Dasgupta, *Local Mechanical Behavior of Steel Exposed to Nonlinear Harmonic Oscillation*, Experimental Mechanics, 2017.

[9] Hill,T. L., S. A. Neild, D. J. Wagg, *Comparing the direct normal form method with harmonic balance and the method of multiple scales*, Procedia Engineering, Vol. 199 (2017), pp. 869-874.

[10] Yan, Z., H. E. Taha, T. Tan, *Nonlinear characteristics of an autoparametric vibration system*, Journal of Sound and Vibration, Vol. 390 (2017), pp. 1-22.

[11] Esmailzadeh, E., N. Jalili, *Parametric response of cantilever Timoshenko beams with tip mass under harmonic support motion*, International Journal of Non-Linear Mechanics, Vol. 33.5 (1998), pp. 765-781.

[12] Nayfeh, A. H. *Introduction to Perturbation Techniques*, New York: Wiley, 1981.

[13] Habtour, E., D.P. Cole, S.C. Stanton, R. Sridharan, A. Dasgupta, *Damage precursor detection for structures subjected to rotational base vibration*, International Journal of Non-Linear Mechanics, Vol. 82 (2016): pp. 49-58.

[14] Jordan, D. W., P. Smith,*Nonlinear ordinary differential equations: an introduction to dynamical systems*, Vol. 2. Oxford University Press, USA, 1999.

[15] Strang, G., *Computational science and engineering*, Vol. 791. Wellesley-Cambridge Press, 2007.

[16] Dowling, N. E., *Mechanical behavior of materials: engineering methods for deformation, fracture, and fatigue*, Pearson, 2012.

Modal strain identification using sub-microstrain fiber-optic Bragg grating data for damage detection of prestressed concrete structures

D. Anastasopoulos[1], **G. De Roeck**[1] **and E. P.B. Reynders**[1]
[1]KU Leuven, Department of Civil Engineering,
Kasteelpark Arenberg 40, 3001, Leuven, Belgium
e-mail: **dimitrios.anastasopoulos@kuleuven.be**

Abstract

Vibration-based damage identification can constitute a successful approach for Structural Health Monitoring (SHM) of civil structures. Modal characteristics depend on the stiffness of the structure, so monitoring their evolution over time allows, in principle, to identify structural damage. Modal strains are more sensitive to local damage than natural frequencies and mode shapes, but the monitoring of these quantities is challenging due to the very small strain levels occurring during ambient, or operational excitation. Two techniques are developed for obtaining sub-microstrain measurements from fiber-optic Bragg gratings with high accuracy and precision. The ability of the modal strains to identify structural damage is explored on prestressed concrete beams subjected to progressive damage tests (PDT). Changes of the amplitude and the curvature of the modal strains are observed from an early damaged state, indicating the presence of damage even when the cracks introduced during the PDT are nearly closed due to the prestressing force, when the applied load is removed. The results indicate that a robust SHM methodology based on modal strains can be developed.

1 Introduction

As many civil structures, such as bridges, dams and tunnels are approaching or even exceeding their original design life, the development of reliable structural health monitoring (SHM) techniques that provide information about the structure's condition becomes necessary [1]. Vibration-based structural health monitoring, usually abbreviated as VBSHM or VBM, is a non-destructive condition assessment method, based on the identification of changes in the dynamic characteristics of a structure, which are directly related to damage [2]. The main challenge for VBSHM is to identify dynamic characteristics that are as sensitive as possible to structural damage and at the same time as insensitive as possible to measurement noise, loading, and environmental factors such as temperature. Dynamic characteristics which are used very often in VBSHM are natural frequencies. However, natural frequencies are influenced by environmental factors, such as temperature, and that influence can be high enough to completely mask the presence of even severe damage, necessitating data normalization [3, 4]. Furthermore, natural frequencies are global structural characteristics and therefore they can not assess the location of damage while their sensitivity to certain types of damage can be low [5]. A promising alternative can be the monitoring of dynamic characteristics obtained from dynamic strain measurements, such as modal strains and modal curvatures which are more sensitive to local damage than modal displacements, offering in this way a higher accuracy in damage detection and localization [6, 7]. However, the accurate determination of modal strains is challenging given the very small (sub-microstrain) dynamic strain levels that are encountered in civil structures under ambient excitation. Ease of implementation and cost-effectiveness are important additional concerns [2].

The introduction of fiber-optic sensor (FOS) systems opened up new possibilities for strain-based SHM in

general, and VBSHM in particular [8]. In the past years, fiber-optic sensors such as interferometric FOS [9] that are based on the principle of low-coherence interferometry, have been successfully used in operational modal analysis for SHM [6]. High accuracy in dynamic strain measurements has been achieved with interferometric FOS [6]. However, interferometric FOS do not offer the benefit of measuring in a dense grid, since a limited amount of sensors can be continuously monitored from a single acquisition unit while their multiplexing capability is also limited [9]. Fiber Bragg Grating (FBG) sensors [10] share important advantages with other fiber optic sensors, such as electro-magnetic immunity, long-term stability, and resistance in harsh environments, but additionally they are easy to multiplex (i.e., many different sensors with different operating wavelengths can be inscribed into the same glass fiber) and they have a relatively low cost. Thanks to the multiplexing option, structures can be monitored with a large number of sensors and in a dense grid. FBGs are being used for real-time monitoring of railway infrastructure, wind turbines and bridges. The Tsing Ma Bridge in Hong Kong is an example of a structure on which FBGs are used for SHM purposes. There, the dynamic strains that are imposed on the bridge by the traffic are measured with a limited number of sensors; the corresponding strain amplitudes though are much larger than on most other structures (tens of microstrains) [11].

However, measuring the very small dynamic strains that occur in civil structures during ambient or operational excitation with high accuracy and precision and in a dense grid remains a very important challenge. Two methods have been recently proposed. The first method consists of replacing the standard wavelength shift detection algorithm in a commercial broadband FBG interrogator with a more advanced optical signal processing algorithm, such that sub-microstrain accuracy can be achieved with FBG sensing [12]. The second method is employing an FBG interrogator with a tunable laser source instead of a broadband one [13]. The tunable laser source scans each FBG sensor individually with a wavelength sweep. This offers a high wavelength resolution and therefore a high accuracy of the measured strain amplitudes. However, the sweep also introduces delays between the different FBG sensors. These delays are not compensated for in the first instance, instead a modal analysis is performed directly on the acquired data using an accurate parametric system identification technique. The strain mode shapes that are obtained in this way are complex due to the time delays introduced during the acquisition, and this complexity is then exploited for synchronization with a novel technique, the accuracy of which was already investigated in a different context [14]. Then, potential damage is identified by repetitively identifying strain mode shapes and monitoring the changes over time.

The method is presented through application in a progressive damage test (PDT) on a complex, prestressed fiber-reinforced concrete “roof” beam [15] and on a prestressed concrete beam of rectangular cross-section [16]. The beams are monitored with chains of multiplexed FBG sensors and conventional uniaxial accelerometers. They are dynamically excited with impulse hammer impacts at low force amplitudes, resulting in dynamic strains of sub-microstrain amplitude. Dynamic tests are performed at the end of each loading cycle and the data are used for strain-based modal analysis. The obtained dynamic characteristics of the various damage stages are then compared and shifts in their values are related to the presence and location of structural damage. Next to a direct comparison of the strain mode shapes, the top-to-bottom strain ratio and the shift of the neutral axis are also introduced as damage-sensitive features.

2 Strain acquisition

When dynamic strains are measured with FBGs, the ability to determine the Bragg wavelength shift with adequate accuracy and precision is essential. The aim of this research is to measure dynamic strains at the sub-microstrain scale which occur during ambient or operational excitation of civil structures, such as bridges, with high accuracy and precision for dynamic system identification and damage localization. For this purpose, two measurement techniques that make use of standard FBG strain sensors have been developed. In the first technique, which is described also in [12], a novel correlation algorithm, the Fast Phase Correlation algorithm (FPC) [17] is applied to obtain sub-microstrain accuracy and precision in wavelength-shift detection from a relatively low accuracy acquisition system with an absolute wavelength accuracy of

$\pm$30 pm, the FBGS FBG-SCAN 700. The main advantage of the SCAN 700 system is that it measures simultaneously all the sensors in the wavelength bandwidth. In the second technique [13], an acquisition system of relatively high absolute wavelength accuracy of $\pm$1 pm, the FAZ-Technologies FAZT-I4, is used. The FAZT-I4 uses a built-in peak detection algorithm for the identification of the Bragg wavelength shift while it does not simultaneously scan the various FBG sensors but instead makes a high-speed sweep scan of about 0.1 pm/ns along the wavelength bandwidth, achieving in this way high wavelength resolution. However, due to the sweep, a delay is introduced in the measurements which leads to a phase shift between the FBGs. A novel offline synchronization technique that is described in [14] is used to synchronize the FBGs. The technique makes use of the identified modal strains to calculate the time delay between the various FBGs and consequently corrects the modal strains.

2.1 FPC and FBGS FBG-SCAN 700

In the current section, the principles of the FPC peak-shift algorithm, which is used to increase the spectral resolution of the FBGS interrogator from 30 pm (hardware resolution) to 1 pm or 0.8 $\mu\epsilon$, is discussed. The FPC algorithm determines the wavelength shift $(\Delta\lambda)$ from the phase shift between the undisturbed or reference FBG spectrum $(R(\lambda))$ and the perturbed spectrum $(R'(\lambda) = R(\lambda + \Delta\lambda))$. One of the advantages of the FPC is that it takes into account the shape of the spectrum instead of only tracking the peak-shifts like the conventional algorithms, increasing in that way its accuracy and precision. Furthermore, it is less sensitive both to the peak-locking effect and to noise than conventional peak-shift detecting algorithms like the Maximum Detecting Algorithm or MDA [17]. The value of $\Delta\lambda$ is computed by means of the following equation:

$$\Delta\lambda = \underset{2\leqslant k\leqslant M}{\text{median}} \left(\left(\angle\Re'(k) - \angle\Re(k) \right) \frac{Nk\delta\lambda}{2\pi} \right) \tag{1}$$

where $\Re(k)$ and $\Re'(k)$ are the Fourier transforms of $R(\lambda)$ and $R'(\lambda) = R(\lambda + \Delta\lambda)$, respectively, k is the generic Fourier spectral line, M is the maximum number of Fourier spectral lines considered in the analysis, the symbol $\angle$ indicates the phase of the complex number and N is the number of samples used for each spectrum. The number of samples N depends on the wavelength scanning range $\lambda_{max} - \lambda_{min}$ and the wavelength resolution $\delta\lambda$ of the acquisition system:

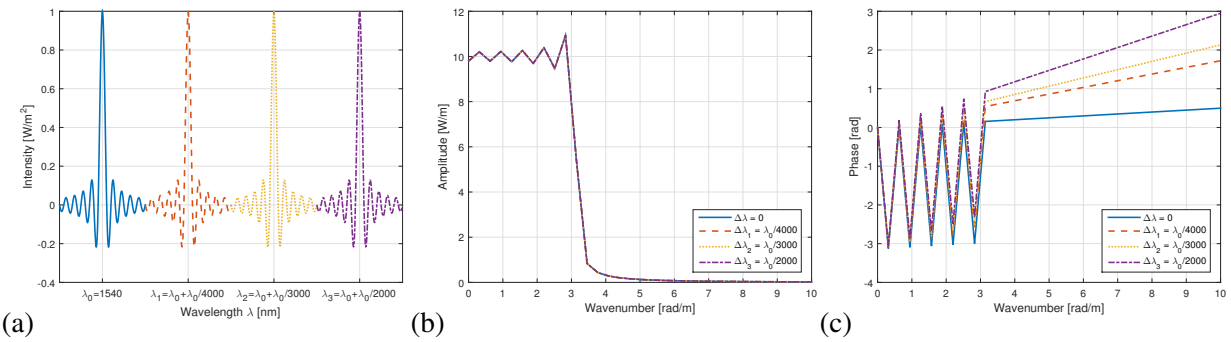
$$N = \frac{\lambda_{max} - \lambda_{min}}{\delta\lambda} \tag{2}$$

It must be noted that one normally chooses $M = N$. However, the value of M can be much lower than N without considerably affecting the performance of the algorithm, since only a few frequency lines of R and R' contain energy. Such an energy distribution is due to the shape of both spectra R and R', which can be approximated by $sinc$ functions [17] (figure 1a). For the purposes of the present research, $M = 9$ was considered as a good trade-off between execution speed and algorithm accuracy and precision.

The working principle of the FPC algorithm lays on the Fourier Transform property of a signal, that a wavelength shift creates only a phase shift of it while it does not change its amplitude. To demonstrate this Fourier property, a $sinc$ function is considered (figure 1(a)) as the shape of the spectrum, with a wavelength of λ_0=1540 nm. Wavelength shifts of $\Delta\lambda_1$=λ_0/4000 nm, $\Delta\lambda_2$=λ_0/3000 nm and $\Delta\lambda_3$=λ_0/2000 nm are applied to the signal, following the Fourier Transform property:

$$\mathcal{F}\left\{g(\lambda - \Delta\lambda)\right\} = e^{-i2\pi f\Delta\lambda} G(f) \tag{3}$$

where $g(\lambda)$ is the function representing the shape of the spectrum and $\Delta\lambda$ the wavelength shift. In figure 1, the amplitude and the phase of the $sinc$ signal are plotted, for four different wavelength shifts. It can be seen that the wavelength shifts do not alter the amplitude of the signal (all four amplitude graphs coincide in figure 1b) while they create phase shifts (figure 1c), which are used by the FPC algorithm in order to determine the wavelength shift according to equation 1.



(a) (b) (c)

Figure 1: (a) Shape of a $sinc$ function, (b) amplitude and (c) phase of the $sinc$ function: before the implementation of a wavelength shift (solid line) at λ_0=1540 nm and for three wavelength shifts equal to $\Delta\lambda_1=\lambda_0/4000$ nm (dashed line), $\Delta\lambda_2=\lambda_0/3000$ nm (dotted line) and $\Delta\lambda_3=\lambda_0/2000$ nm (dash-dotted line).

2.2 Synchronization and FAZ Technologies FAZT-I4

In the second method, an interrogator that offers high accuracy and precision for the purposes of this research is used, the FAZ Technology FAZT-I4. The absolute wavelength accuracy of the FAZT-I4 is better than $\pm$1 pm, giving significantly higher accuracy than the FBG-SCAN 700, whose absolute wavelength accuracy is about $\pm$30 pm. Therefore, the implementation of an optic algorithm for enhancing the modal strain identification is not required here. However, the I4 does not acquire the data from all FBG sensors simultaneously but instead makes a high speed linear sweep scan ($\approx$0.1 pm/ns) across its wavelength range, introducing a delay in the measurements (figure 2). This results in a phase shift between the sensors, which is important mainly for the high frequency modes (>250 Hz) although insignificant for the low frequency modes (0-20 Hz) that are mainly excited by ambient excitation in civil engineering structures. By applying the offline synchronization method that is described here [13, 14], the delay can be calculated and the strain mode shapes can be corrected. The technique makes use of the identified modal strains to calculate the time delay between the various FBGs and consequently corrects the modal strains. The technique assumes linear dynamic behavior of the structure and proportional damping of the structural modes.

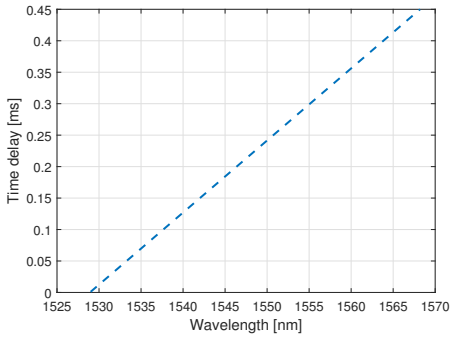


Figure 2: Nominal time delay-wavelength relationship due to the high-rate sweep of the FAZT-I4 ($\approx$0.1 pm/ns) as provided by the manufacturer.

The time delay δt^* can be estimated more accurately than in figure 2 by minimization of the objective function $f(\delta t)$ (equation 4) that gives the average difference between the mean phases (MP) of the complex modal strains, $\Phi_{\mathrm{com},m}$, and the reference modal strain, $\Phi_{\mathrm{ref},m}$, over all modes (n_{m}). The complex modal strains are defined here as the modal strains that need to be corrected (the modal strains obtained from the FBG sensors that are interrogated with a time delay due to the linear sweep) with respect to the reference modal strain (the modal strain obtained from the FBG sensor which is interrogated first).

$$\delta t^* = \mathrm{argmin} f(\delta t) = \mathrm{argmin} \frac{1}{n_{\mathrm{m}}} \sum_{m=1}^{n_{\mathrm{m}}} |\mathrm{MP}(\Phi_{\mathrm{com},m} e^{\lambda_{m1}\delta t}) - \mathrm{MP}(\Phi_{\mathrm{ref},m})| \tag{4}$$

The rescaling of the complex modal strains is obtained by multiplying them by a factor A_m (equation 5) which is defined as:

$$A_m = e^{\lambda_{m1}\delta t^*} \tag{5}$$

where $\lambda_{m1} = -\omega_m\xi_m + i\omega_m\sqrt{1-\xi_m^2}$ is the pole correspond to the natural frequency ω_m and modal damping ratio ξ_m of mode m.

2.3 Validation of the methods

Both methods are evaluated through an experimental modal analysis of a steel I-beam of type IPE 100 of the European Standard Universal I-Beams. The beam has a length of 3.0 m and steel rectangular plates are welded at its ends with dimensions 200x200x10 mm. The beam is suspended with flexible springs from fixed locations to approximate dynamic free-free boundary conditions (figure 3). The beam is excited with a shaker at low force amplitudes and its response is monitored with two chains of multiplexed FBG sensors directly glued along its flanges and conventional uniaxial accelerometers. The accelerometers measure the vertical acceleration of the beam (z-direction in figure 4) while the FBGs measure the longitudinal (horizontal) dynamic strains of the beam (x-direction in figure 4). Several dynamic tests were conducted and the average root mean square (RMS) strain value for all FBG sensors varies from 2 $\mu\epsilon$, for the test with the highest excitation amplitude, to 0.2 $\mu\epsilon$ for the test with the lowest excitation amplitude.

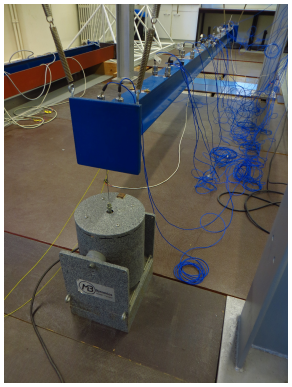
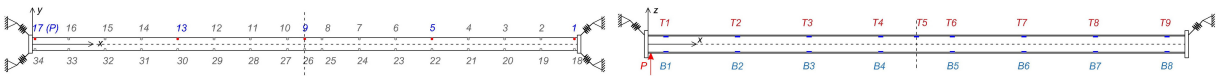


Figure 3: The experimental setup of the IPE 100 beam



(a) (b)

Figure 4: (a) Top beam view and the accelerometer setup and (b) front beam view and the FBG sensor setup

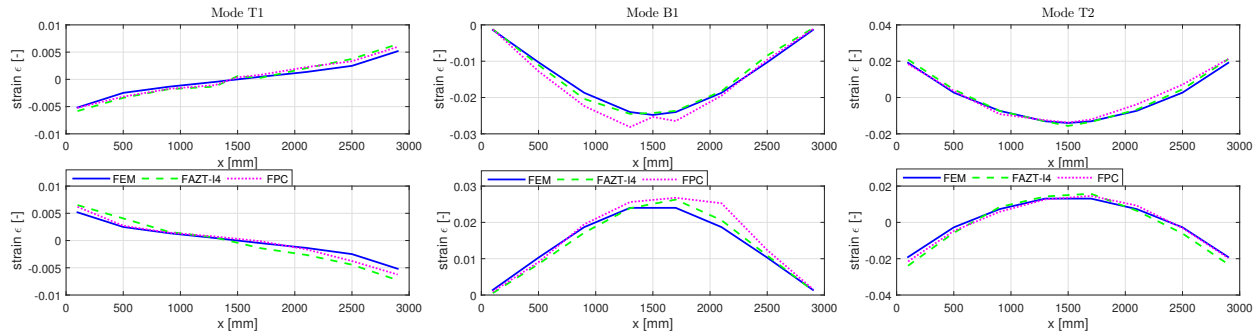
The modal analysis of the beam is performed using both acceleration and strain data. The system identification is conducted with MACEC [18]. The data-driven Combined deterministic-stochastic Subspace Identification (CSI-data) [19] algorithm is used, where both the input force and the measured beam response (accelerations and strains) are used for the identification. In the following, the results of the test with the lowest excitation amplitude are presented to demonstrate the high identification accuracy from low-excitation amplitude tests. As expected, high identification accuracy is obtained as well from the other tests with the higher excitation amplitude.

Six bending and torsion modes are identified in the frequency bandwidth of interest (0-250 Hz). All modes are selected from stabilization diagrams and their natural frequency values for both methods are summarized in table 1. The natural frequencies of a validated FEM that was built in ANSYS are also provided for comparison [12]. The differences in the natural frequencies between the two methods is attributed to the different temperature conditions between the two days that the validations experiments for the two methods have been conducted, which slightly influenced the modal characteristics of the beam.

Method	Mode T1	Mode B1	Mode T2	Mode T3	Mode B2	Mode T4
f_{FEM} [Hz]	31.17	61.14	72.76	129.74	173.63	204.40
f_{FAZT} [Hz]	32.61	61.28	72.13	130.71	175.04	203.35
f_{FPC} [Hz]	30.86	60.52	70.98	127.51	173.27	203.49

Table 1: Natural frequencies of the beam modes as identified with CSI-data algorithm for the two methods. The natural frequencies of the validated FEM are also given. With 'T' are denoted the torsion and with 'B' the in-plane bending modes.

In figure 5, the mass-normalized strain mode shapes of modes T1, B1 and T2 as identified from the FAZT-I4 after offline synchronization, and from FBG-SCAN 700 after applying the FPC algorithm are compared. The mass-normalized strain mode shape amplitude is well identified from both FAZT-I4 and the FPC algorithm for the presented modes. The same accuracy is observed for the other modes and thus they are not presented. As it can be observed in figure 5, the amplitude inconsistencies of both techniques with the validated FEM are quite small. Furthermore, the modal assurance criterion (MAC) is applied in comparison of the strain mode shapes. The strain mode shapes of the validated FEM are used as the reference strain mode shapes. The strain mode shapes are well identified as indicated from the MAC values that are larger than 0.98 for both cases. Therefore, the strain modes shapes that are identified from both methods can be used with confidence for damage identification purposes, as it will be shown in the following section.



(a) (b) (c)

Figure 5: Mass-normalized strain mode shapes. The top subplots correspond to the top flange fiber and the bottom to the bottom flange fiber. The continuous blue line corresponds to the FEM, the dashed green to the FAZT-I4 and the pink dotted to the FPC identified strain mode shapes.

3 Damage identification

The purpose of this research is to utilize strain mode shapes for damage identification and localization, as they are expected to be much more sensitive to local damage than natural frequencies and displacement mode shapes. The second method that makes use of the FAZT-I4 interrogator combined with the offline synchronization technique is used in the following case studies.

3.1 Prestressed concrete "Roof" beam (PCRB)

An I-shaped, pre-stressed concrete "roof" beam with two openings in its web serves as test structure (figure 6). The length of the beam is 6.0 m and its height varies linearly between its ends and its center from 0.75-0.90 m. Low relaxation strands with a nominal diameter of 12.5 mm are used for prestressing: 7 at the bottom and 1 at the top of the beam. The strands are given an initial stress of σ_{p0} = 1488 MPa (100% of $\sigma_{p0,max}$). The beam is supported on a steel table through two supports at 1.0 m from the ends. The static

boundary conditions approximate these of a simply supported beam. This is not the case for the dynamic behavior as an interaction between the beam and the steel table is expected because the steel table and the connecting supports can not be considered as infinitely stiff with respect to the concrete beam.

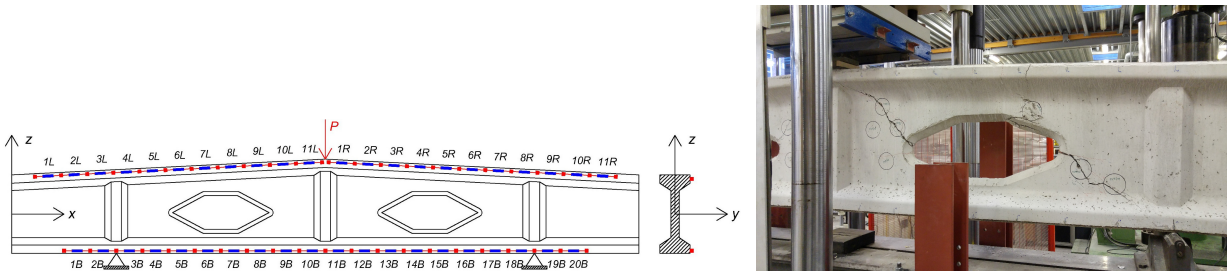


(a) (b)

Figure 6: The experimental setup of the modal test. (a) Side view of the experimental setup. (b) One of the connections for the FBG sensors.

3.1.1 Progressive damage test

The beam is subjected to a 3-point progressive damage test. The quasi-static load is applied at the middle of the beam (figure 7a). Eleven loading cycles were performed. In each cycle, the maximum load was increased by 50 kN with respect to the previous cycle. The beam failed in shear around the openings of the web (figure 7b) during the eleventh loading cycle for a load of 592 kN.



(a) (b)

Figure 7: The setup of the three FBG chains. The quasi-static force P for the PDT is applied in the direction of the red arrow. (b) The failure pattern of the beam.

3.1.2 Dynamic tests

The dynamic excitation of the beam is performed with hammer impacts in the vertical (z-axis in figure 7a) and the lateral (y-axis, out of plane in figure 7a) direction. The tests are performed at the beginning of each loading cycle, when the applied quasi-static load is zero. The response of the beam to the induced excitation is recorded with three chains of multiplexed Fiber-optic Bragg Grating (FBG) strain sensors; two at the top flange and one at the bottom flange (figure 7a) of the beam. The chains are attached on the side of the top and the bottom flange of the beam along its longitudinal direction through a clamping system, to measure axial dynamic strains, as shown in figures 6 and 7. The fiber is firmly fixed at discrete connections (figure 6b) to ensure the proper transfer of strains from the beam to the sensors; the distance between two consecutive connections is 25 cm and one sensor exists between them, measuring the average strain or macro-strain over this distance. The fibers are pretensioned to ensure that they would remain in tension due to the applied force during the PDT. Thermal insulation is also provided around the fibers to ensure that temperature fluctuations in the laboratory would not affect the measurements (figure 6). The strain acquisition system is the FAZT-I4 interrogator. The sampling frequency is 1000 Hz.

3.1.3 Modal Analysis

The modal analysis is performed using the dynamic strain data. The system identification is conducted with MACEC [18], using the covariance-driven Stochastic Subspace Identification (SSI-cov) [20] algorithm where only the measured response (strains) is used for the identification. The SSI-cov algorithm provides also the 95% confidence intervals (CI = $[-2\sigma, 2\sigma]$ for quantifying the uncertainty of the identified dynamic characteristics [21]. During data processing, the static or DC offset is removed from all measured signals. Furthermore, a fourth-order Butterworth filter with a high-pass frequency of 4 Hz is applied to all channels to remove the influence of the small temperature fluctuations on the strain measurements during the PDT.

3.1.4 Natural frequencies

Eleven bending, lateral and torsion modes are identified in the frequency range (0-400) Hz. Their natural frequency values for the undamaged beam are summarized in table 2. High identification accuracy for the natural frequency values is obtained since the 95% confidence interval (CI$_f$=$[-2\sigma_f, 2\sigma_f]$), as derived from the SSI-cov identification [21] is narrow. The natural frequencies of a validated finite element model (FEM) that is built in ANSYS are also provided for comparison.

When the experimentally identified and the numerically obtained natural frequencies are compared, a good match is observed for the lateral bending modes L1 and L2, the torsion modes T3 and T4, and the in-plane bending modes B2 and B3. On the contrary, for the remaining modes, a significant difference in the natural frequency values is observed. This is attributed to the interaction of the "roof" beam with the supporting beam, which is not taken into account by the FEM. In order to investigate which modes are influenced by the "roof" beam - supporting beam interaction, the modal assurance criterion (MAC) is applied. The MAC values for the first two lateral modes L1 and L2 and the last two in-plane bending modes B2 and B3 are approximating unity (> 0.98), indicating a high consistency between the calculated and the experimentally obtained modes. Therefore, for these modes, the assumption of free-free boundary condition applies and the system "roof" beam-supporting beam is decoupled. Hence, it is expected that any potential changes on the dynamic characteristics of these modes will originate from the damage that is induced to the "roof" beam and not from the interaction with the supporting steel beam.

The evolution of the natural frequencies and their 95% confidence intervals throughout the PDT is shown in figure 8 for the decoupled bending modes B2 and B3. A similar trend is observed for the decoupled lateral modes L1 and L2 and thus they are not presented. For the damage-sensitive modes, a constant reduction of their natural frequency values is observed, which is correlated with the increased level of damage of the beam. The percentile reduction of the natural frequency values varies from 4% to 9% for the different modes, depending on the degree that each mode is influenced by the damage.

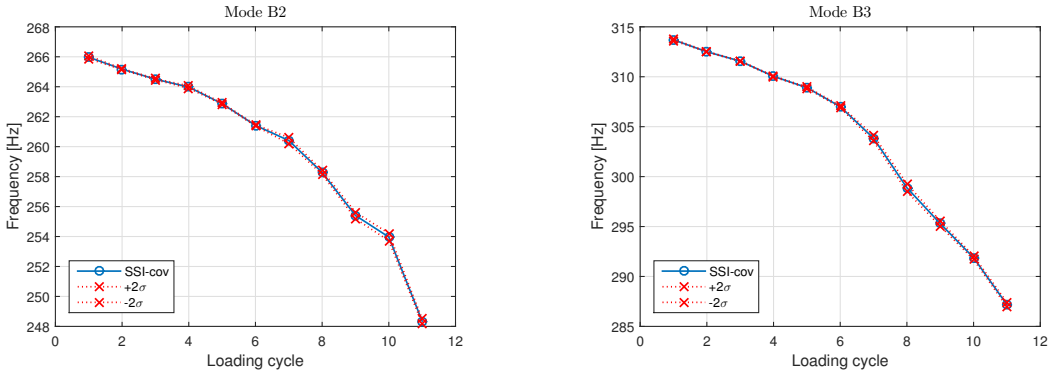


Figure 8: Evolution of the natural frequencies as identified from the FBG strain data (solid lines) and their 95% confidence intervals (CI$_f$=$[-2\sigma_f, 2\sigma_f]$) (dotted lines) for modes B2 and B3.

Method	Mode L1	Mode T1	Mode L2	Mode T2	Mode B1	Mode L3
EMA	27.20	35.50	75.30	93.00	127.50	131.00
FEM	27.40	55.40	77.15	108.70	115.40	141.90
Method	Mode T3	Mode L4	Mode T4	Mode B2	Mode B3	
EMA	178.00	216.60	244.80	265.90	313.70	
FEM	177.80	234.50	247.70	264.40	314.40	

Table 2: Natural frequency values of the undamaged beam. The vertical bending modes are denoted with 'B', the lateral bending modes with 'L' and the torsional modes with 'T'. EMA stands for experimental modal analysis and FEM for finite element model.

3.1.5 Strain mode shapes

The identified strain mode shapes of the beam are given in figure 9 for the decoupled modes (L1, L2, B2 and B3). A least-squares fit is applied for the determination of the scale factor c that links the strain mode shapes of the various cycles with the strain mode shapes of the first loading cycle. The least-squares fit is calculated to the modal strain values at the ends of the fibers i.e., the zones outside of the static supports. Since these zones are not stressed due to the static loading, their values are not expected to change due to the damage. To demonstrate the evolution of the modal strain shapes due to the damage, combined graphs of the modal strain shapes that were identified in each loading cycle are presented.

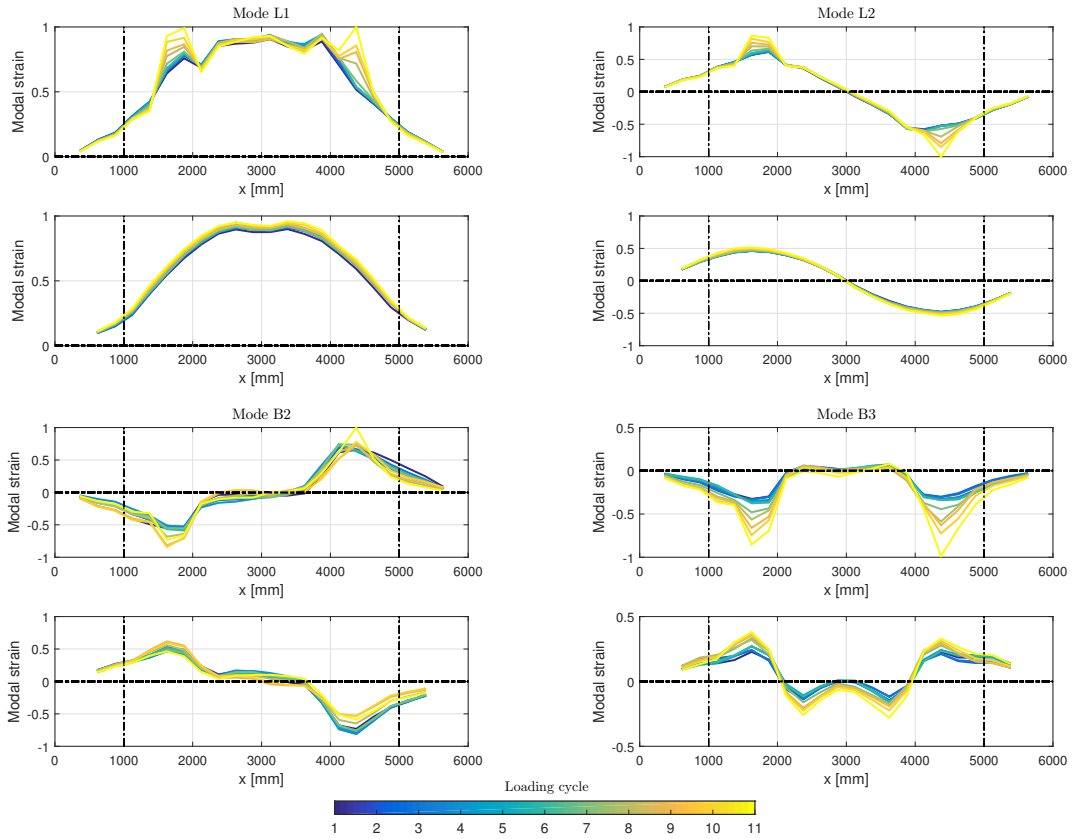


Figure 9: Evolution of the damage-sensitive strain mode shapes as identified from SSI-cov, for the 11 loading cycles. The top subplots correspond to the top flange fibers of the beam while the bottom subplots to the bottom flange fiber. The dash-dotted lines indicate the location of the supports.

Significant amplitude and curvature changes are observed in the vicinity of the damaged area (around the openings of the web), as it can be seen from the strain mode shapes in figure 9. The increase in curvature and

amplitude is directly related to the decrease of stiffness at certain locations of the beam (around 1500 mm and 4500 mm) where shear cracks were observed during the experiment (figure 7b). The evolution of the strain mode shapes during the different loading cycles is prominent. The larger amplitude values correspond to the last loading cycle, before the failure of the beam. The strain mode shapes appear to be more sensitive to damage at the top flange, which is in agreement with the observations during the experiment where most of the cracks were formed at the top of the beam. However, the strain mode shape of the third bending mode (mode B3 - figure 9) is influenced both at the top and the bottom of the beam from the damage, allowing in this way to identify also damage of moderate severity at the bottom flange of the beam.

Finally, a quantity for damage detection and localization is introduced: the top-to-bottom strain ratio (TBSR), which is defined as:

$$TBSR(x) = |\epsilon_{top}(x)| \setminus |\epsilon_{bottom}(x)| \tag{6}$$

where $|\epsilon_{top}(x)|$ is the absolute value of the longitudinal modal strain at the top of the beam, $|\epsilon_{bottom}(x)|$ is the absolute value of the longitudinal modal strain at the bottom of the beam, and x denotes, as before, the longitudinal coordinate. The TBSR is computed for the well-identified strain mode shapes of the in plane bending modes, B2 and B3. At the locations that the modal strains are approximating zero, mainly in the zone between 2700-3300 mm, the criterion is not applied since the division by very small quantities can yield inaccurate results. As can be clearly seen in figure 10, where the evolution of the TBSR values along the beam for modes B2 and B3 throughout the PDT are given, the influence of the damage is significant. A clear increase or decrease of the TBSR at the locations where the damaged was mainly observed during the PDT, indicates its high sensitivity as a damage indicator. These changes appear already from the second loading cycle and become really apparent after the sixth loading cycle. The largest changes are observed at the zones around 1500 mm and 4500 mm, where the most severe cracks were observed during the PDT. There, the TBSR values have an increase of up to 114% between the undamaged beam and the damaged beam of the last loading cycle. Therefore, the TBSR is considered as a high sensitivity measure of the level of damage.

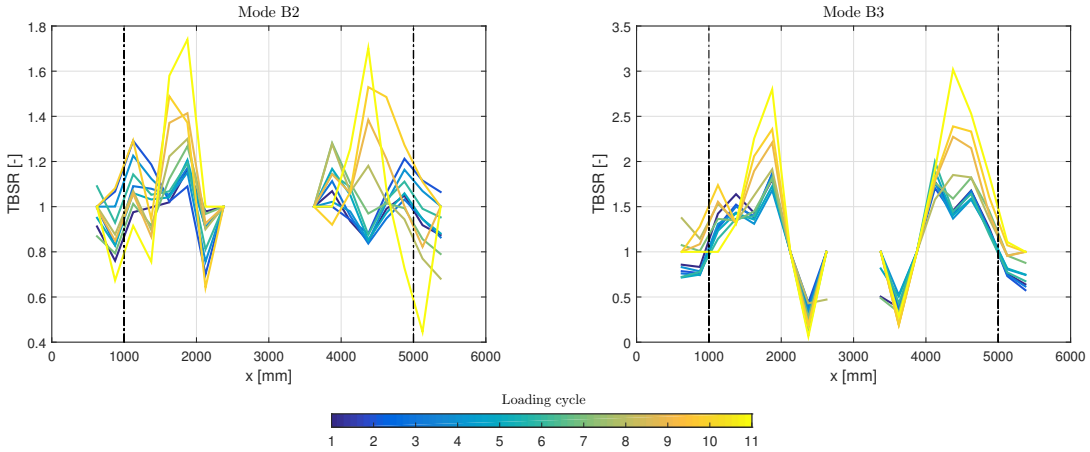


Figure 10: TBSR values between the undamaged beam strain mode shapes and the strain mode shapes of the various damage levels. The black dashed lines indicate the location of the supports.

3.2 Prestressed concrete beam (PCB)

A prestressed concrete beam of rectangular cross section (240x200 mm) serves as the test structure (figure 11). The length of the beam is 5.0 m. Low relaxation strands with a nominal diameter of 12.5 mm are used for prestressing: 3 at the bottom and 2 at the top of the beam. The strands are given an initial stress of σ_{p0} = 744 MPa (50% of $\sigma_{p0,max}$). High-strength concrete is used, of the class C70/85. The beam rests on two steel rollers at 0.4 m from the ends. Therefore, the static boundary conditions correspond to these of a simply supported beam.

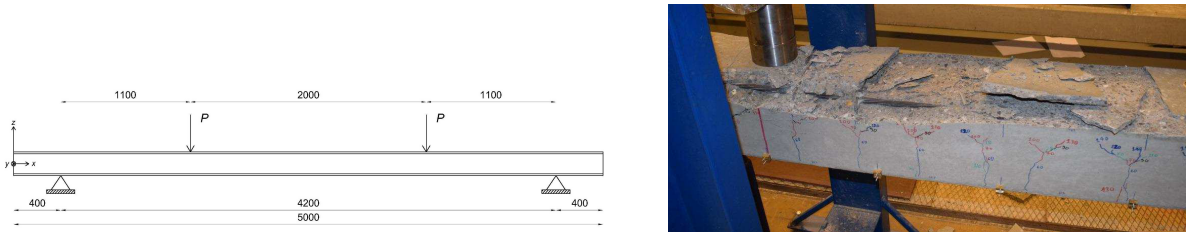


(a) (b)

Figure 11: (a) The experimental setup of the modal test and the PDT and (b) One of the tires used for approximating free-free dynamic boundary conditions.

3.2.1 Progressive damage test

The beam is subjected to a four-point bending PDT. The quasi-static loads are applied at two locations which are symmetric with respect to the midspan of the beam, using two hydraulic jacks (figure 12). The same load is applied from both hydraulic jacks, creating a zone of constant bending moment between them. Twelve loading cycles of increasing load were performed, where the load step is 20 kN for the first 3 cycles and 10 kN from the fourth cycle on. The first cracks on the beam formed during the third loading cycle for a load of about 55 kN. The beam failed during the 12^{th} loading cycle for a load of 142 kN from crushing of the concrete at the zone of the highest compressive stresses (between the points of the load application).



(a) (b)

Figure 12: (a) The four-point PDT. The quasi-static force P is applied in the direction of the arrows (dimensions in mm) and (b) the failure pattern of the beam. The bending cracks are also visible.

3.2.2 Dynamic tests

The dynamic tests are conducted after the end of each loading cycle. The response of the beam to the induced dynamic excitation is recorded with four chains of FBG strain sensors from FBGS, attached at the four edges of the beam as shown in figure 13. The same clamping system that was described in the PCRB section is used for PCB. The distance between two consecutive clamps is 25 cm and one FBG exists between them. The beam is dynamically excited in the vertical and the lateral direction with 15 impulse impacts (continuous measurement). The dynamic boundary conditions approximate those of a free-free vibrating beam. This is achieved with the use of inflated tires, as shown in figure 11b. After the end of each loading cycle, the beam is lifted from its supports by inflating the tires underneath it, so there is no contact with the static supports and the dynamic tests are conducted in free-free boundary conditions. After the end of the 8^{th} loading cycle (110 kN), the FBG chains are detached from the beam to avoid damaging them during the further loading and failure of the beam. Three accelerometers are attached on the beam to follow the evolution of the natural frequencies. Hence, the strain mode shapes are available for 9 load steps (for the undamaged beam and for the first 8 loading cycles), while the natural frequencies are available for 12 load steps (until failure).

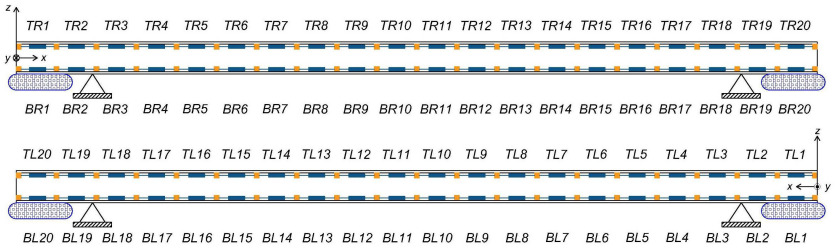


Figure 13: The setup of the four FBG chains (side beam view).

3.2.3 Modal analysis

Dynamic strain data obtained from the FBG sensors are used for the modal analysis. The average measured RMS strain values among all FBGs for hammer impact tests is $\approx 0.1\mu\epsilon$. The system identification is performed with the SSI-cov technique [20, 21]. The static or DC offset is removed from all measured signals. Furthermore, a fourth-order Butterworth filter with a high-pass frequency of 4 Hz is applied to all channels to remove the influence of the small temperature fluctuations on the strain measurements during the PDT.

3.2.4 Natural frequencies

Eight modes are identified in the frequency bandwidth (0-400) Hz. The identified natural frequencies for the undamaged beam are presented in table 3. High identification accuracy for the natural frequency values is obtained since the 95% confidence interval (CI$_f$=$[-2\sigma_f, 2\sigma_f]$), as derived from the SSI-cov identification [21] is narrow. The evolution of the natural frequencies and their 95% confidence intervals up to the 8^{th} loading cycle of the PDT when the FBG chains were removed is shown in figure 14 for the modes B1 and B2. A similar trend is observed for the other modes and thus they are not presented. A constant reduction of the natural frequency values is observed, which is correlated with the increased level of damage of the beam. The percentile reduction of the natural frequency values at this damage state varies from 2% to 4% for the different modes, depending on the degree that each mode is influenced by the damage. When the natural frequencies obtained from the acceleremoters are considered, the reduction of natural frequencies varies from 7% to 13.5% right before the failure of the beam.

Mode	Mode B1	Mode L1	Mode B2	Mode L2	Mode B3	Mode L3	Mode B4	Mode L4
f_{ssi} [Hz]	37.11	45.91	98.66	117.86	190.58	228.47	312.20	366.97

Table 3: Natural frequency values of the undamaged beam. The vertical bending modes are denoted with 'B' and the lateral bending modes with 'L'. EMA stands for experimental modal analysis.

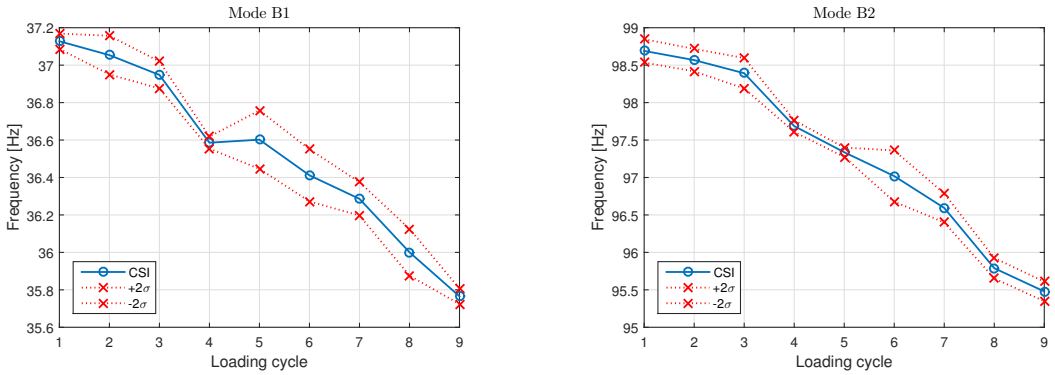


Figure 14: Evolution of the natural frequencies as identified from the FBG strain data (solid lines) and their 95% confidence intervals (CI$_f$=$[-2\sigma_f, 2\sigma_f]$) (dotted lines) for modes B1 and B2.

3.2.5 Strain mode shapes

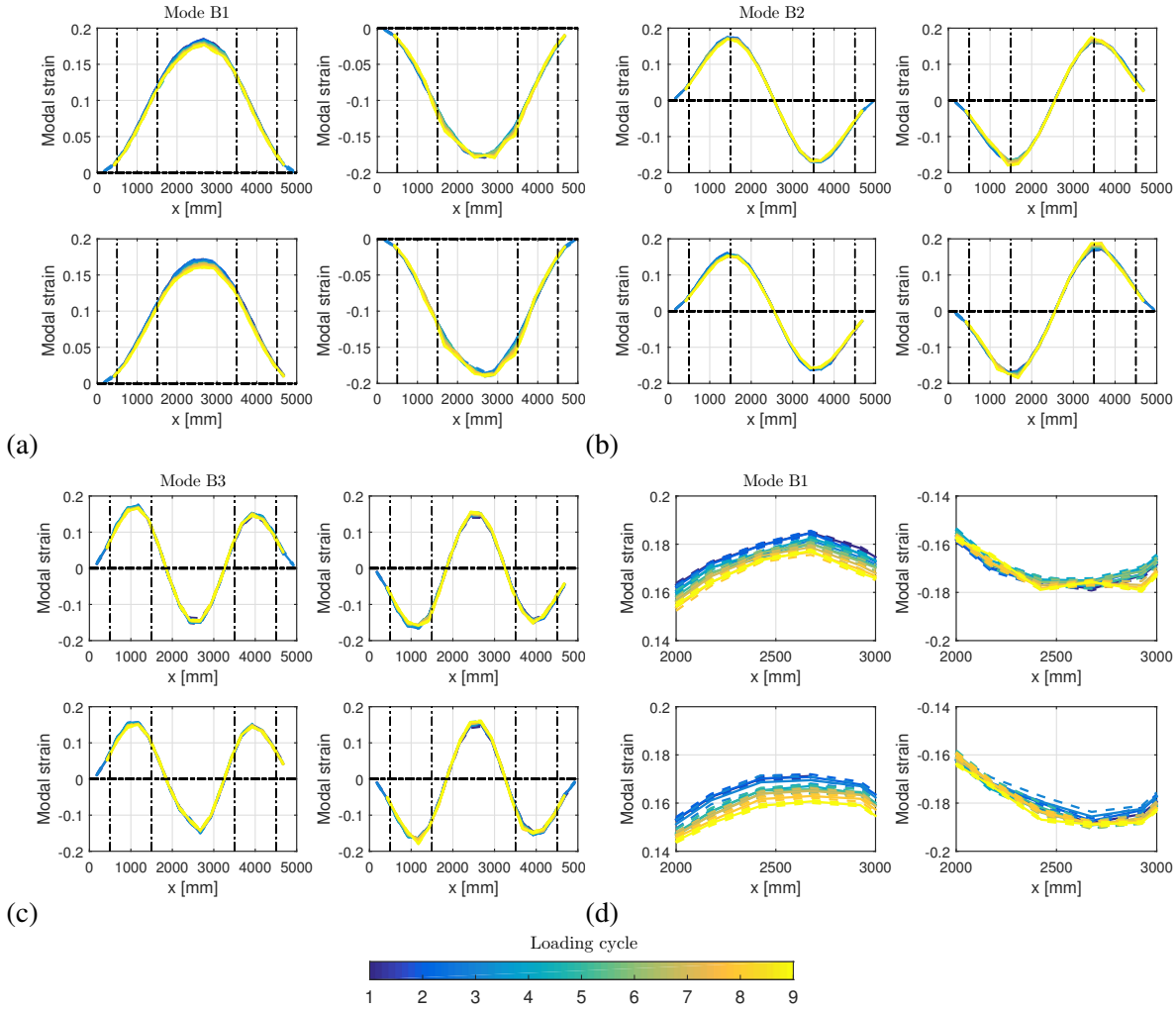


Figure 15: (a), (b) and (c), evolution of the in-plane strain mode shapes B1, B2 and B3, for the first 8 loading cycles, (d), detail of the zone 2000-3000 mm for mode B1. The first step corresponds to the undamaged beam. The top subplots correspond to the top fibers and the bottom to the bottom fibers. The left subplots correspond to the side of the beam with positive y-coordinates while the right subplots to the side of the beam with negative y-coordinates. The dash-dotted lines indicate the location of the supports and the location of the load application.

In this section, the influence of the increasing damage throughout the PDT on the strain mode shapes is investigated. Combined graphs are given, where the identified strain mode shapes in each loading cycle are plotted on top of each other. A normalization scheme [22] is applied that allows for a consistent re-scaling of the strain modes shapes and their 95% confidence interval ($\text{CI}_\epsilon = [-2\sigma_\epsilon, 2\sigma_\epsilon]$) so they can be directly compared within the different loading cycles. The in-plane bending strain mode shapes of modes B1, B2 and B3 with their CI_ϵ are shown in figures 15a-c. In figure 15d, the zone between the points that the loads are applied (2000-3000 mm) for mode B1 is presented in detail. Strain amplitude changes are observed in the vicinity of the damaged area (between the points of the load application) for all modes, as can be seen from the strain mode shapes in figures 15a-c and in detail in figure 15d. The CI_ϵ is quite narrow for all modes throughout the PDT indicating high identification accuracy and most important that the changes that are observed on the strain mode shapes are because of the increasing level of damage in the beam. The evolution of the strain mode shapes during the different loading cycles is prominent and follows the evolution of the cracks, even though the cracks are nearly closed after the static unloading of the beam due to the prestressing

force. The highest modal strain amplitude values at the location of the damage correspond to the damaged state after the end of the 8^{th} loading cycle at 110 kN (77% of the failure load at 142 kN), when the FBG chains were detached to avoid damaging them. More specifically, the amplitude of the bottom strain mode shapes is increasing with the increasing level of damage at the vicinity of the damaged zone (e.g. figure 15d-right column subplots) and the changes are more prominent at the locations of the cracks. On the contrary, the amplitude of the top strain mode shapes is decreasing in a uniform pattern at the vicinity of the damaged zone (e.g. figure 15d-left column subplots). This increase/decrease of the strain amplitude for the bottom/top strain mode shapes represents the shift of the neutral axis of the beam due to the increasing level of damage. Changes in the amplitude of the strain mode shapes are already identified after the end of the 3^{rd} loading cycle at 60 kN, when the beam reached its crack load, indicating early stage damage identification.

The height of the neutral axis (y_N) of the bending modes for the equivalent Euler-Bernoulli beam can be quantified with the use of the identified modal strains and is defined as:

$$y_N(x) = [\epsilon_{\text{bot}}(x)(H - 2d)]/[\epsilon_{\text{bot}}(x)\epsilon_{\text{top}}(x)] - H/2 \tag{7}$$

where $\epsilon_{\text{top}}(x)$ is the longitudinal modal strain at the top of the beam, $\epsilon_{\text{bot}}(x)$ is the longitudinal modal strain at the bottom of the beam, x denotes the longitudinal coordinate, H is the height of the beam and d is the distance between the longitudinal axis of the FBG chain and the top/bottom of the beam. The location of the beam where $y_N(x) = 0$, is defined in figure 13 and coincides with $H/2$. The $y_N(x)$ is calculated for the first three in-plane bending modes (B1, B2 and B3) and is shown if figure 16. At the locations where the modal strains are approximating zero, (figure 15), the $y_N(x)$ is not calculated since the division by very small quantities can yield inaccurate results. The changes in the $y_N(x)$ are significant and follow the increase of the damage in the beam. The first changes already appear after the beam exceeded its crack load at about 55 kN (during the 3^{rd} loading cycle at 60 kN).

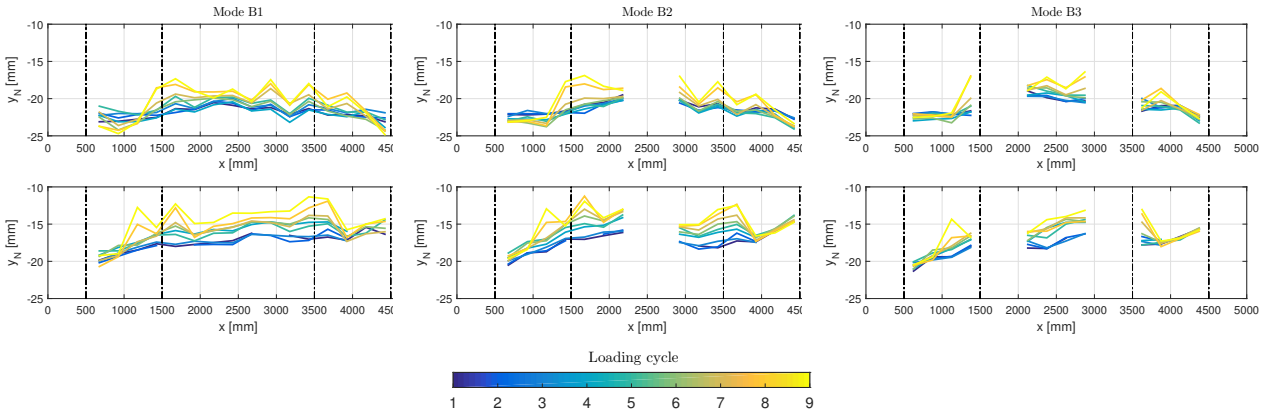


Figure 16: Evolution of the neutral axis height $y_N(x)$. The first step corresponds to the undamaged beam. The top subplots correspond to the $y_N(x)$ as obtained from the FBG chains on the side of the beam with positive y-coordinates while the bottom subplots to the $y_N(x)$ as obtained from the FBG chains on the side of the beam with negative y-coordinates. The dash-dotted lines indicate the location of the supports and the location of the load application.

4 Conclusion

In this article, a new method was presented for VBSHM by means of quasi-distributed longitudinal macro-strain FBG sensing. First, two methods for accurate dynamic strain measurements were presented. Both methods were implemented and validated in an experimental modal analysis of a steel I-beam. The dynamic strains that were measured on the beam had very low RMS strain values of the sub-microstrain level (≈0.2

$\mu\epsilon$), similar to the ones occurring on real structures during ambient or operational excitation. The dynamic characteristics obtained from the dynamic strains measured with the two methods, i.e. natural frequencies and strain mode shapes, were identified with high accuracy and precision, proving the capabilities of the proposed methods.

Second, since the accurate modal strain identification was deemed successful with the two methods, they were further implemented for damage identification and localization on prestressed concrete beams, subjected to progressive damage tests. The damage that was induced into the PCRB and the PCB by the PDT caused important changes in their natural frequencies and strain mode shapes identified from the FBG data in a relatively early stage. This confirms that strain mode shapes are very sensitive to local damage. The sensitivity becomes even larger when the ratio between the modal strain amplitudes at the top and the bottom of the beam (termed TBSR or top-to-bottom strain ratio in this article) is taken for the PCRB or the when the height of the neutral axis ($y_N(x)$) is calculated from the modal strains, where a consistent shift of the axis is observed throughout the PDT for the different damage levels for PCB.

Acknowledgements

The research presented in this article has been performed within the framework of the project G099014N "Robust vibration-based damage identification with a novel high-accuracy strain measurement system", funded by the Research Foundation Flanders (FWO), Belgium. The financial support of FWO is gratefully acknowledged.

References

[1] C.R. Farrar, K. Worden, *Structural Health Monitoring: A Machine Learning Perspective*, John Willey & Sons, (2013).

[2] J. Brownjohn, A. De Stefano, Y.L. Xu, H. Wenzel, A. Aktan, *Vibration-based monitoring of civil infrastructure: challenges and successes*, J. Civ. Struct. Health Monit., Vol. 1, No. 3-4 (2011), pp. 79–95.

[3] E. Reynders, G. Wursten, G. De Roeck, *Output-only structural health monitoring in changing environmental conditions by means of nonlinear system identification*, Struct. Health Monit., Vol. 13, No. 1, (2014), pp. 82–93.

[4] B. Peeters, G. De Roeck, *One-year monitoring of the Z24-bridge: environmental effects versus damage events*, Earthquake Engineering and Structural Dynamics, Vol. 30, No. 2 (2001), pp.149–171.

[5] A. Deraemaeker, E. Reynders, G. De Roeck G, J. Kullaa, *Vibration based Structural Health Monitoring using output-only measurements under changing environment*, Mech. Syst. Signal Pr., Vol. 22, No. 1, (2008), pp. 34–56.

[6] E. Reynders, G. De Roeck, P. Bakir, C. Sauvage, *Damage identification on the Tilff bridge by vibration monitoring using optical fibre strain sensors*, ASCE J. Eng. Mech., Vol. 133, No. 2, (2007), pp. 185–193.

[7] A.P. Adewuyi, Z.S. Wu, N.H.M.K. Serker, *Assessment of vibration-based damage identification methods using displacement and distributed strain measurements*, Struct. Health Monit., Vol. 8, No. 6, (2009), pp. 443–461.

[8] B. Glišić, D. Inaudi, *Fibre optic methods for structural health monitoring*, John Wiley & Sons, (2007).

[9] B.H. Lee, Y.H. Kim, K.S. Park, J.B. Eom, M.J Kim, B.S. Rho, H.Y. Choi, *Interferometric Fiber Optic Sensors*, Sensors, Vol. 12, No. 3, (2012), pp. 2467–2486.

[10] G. Meltz, W.W. Morey, W.H. Glenn, *Formation of Bragg gratings in optical fibers by a transverse holographic method*, Opt. Lett., Vol. 14, No. 15, (1989), pp. 823–825.

[11] T.H.T. Chan, L. Yu, H.Y. Tam, Y.Q. Ni, S.Y. Liu, W.H. Chung, L.K. Cheng, *Fiber bragg grating sensors for structural health monitoring of Tsing Ma bridge: background and experimental observation*, Eng. Struct., Vol. 28, No. 5, (2006), pp. 648–659.

[12] D. Anastasopoulos, P. Moretti, T. Geernaert, B. De Pauw, U. Nawrot, G. De Roeck, F. Berghmans, E. Reynders, *Identification of modal strains using sub-microstrain FBG data and a novel wavelength-shift detection algorithm*, Mech. Syst. Signal Pr., Vol. 86A, (2017), pp. 58–74.

[13] D. Anastasopoulos, K. Maes, G. De Roeck, E.Reynders, *A comparison of two data acquisition techniques for modal strain identification from sub-microstrain fbg data*, In *Proceedings of The International Conference on Experimental Vibration Analysis for Civil Engineering Structures EVACES 2017, San Diego, CA, USA, 2017 July 12-14*, San Diego (2017).

[14] K. Maes, E. Reynders, A. Rezayat, G. De Roeck, G. Lombaert, *Offline synchronization of data acquisition systems using system identification*, J. Sound Vib., Vol. 381, (2016), pp. 264–272.

[15] D. Anastasopoulos, M. De Smedt, L. Vandewalle, G. De Roeck, E. Reynders, *Damage identification using modal strains identified from operational fiber-optic bragg grating data*, Struct. Health Monit., (2018), Available online, DOI: 10.1177/1475921717744480

[16] D. Anastasopoulos, G. De Roeck, E. Reynders, *Damage identification on a prestressed concrete beam using modal strains identified from FBG data*, In *Proceedings of The 16$^{\text{th}}$ European Conference on Earthquake Engineering 16ECEE, Thessaloniki, Greece, 2018 June 18-21*, Thessaloniki (2018).

[17] A. Lamberti, S. Vanlanduit, B. De Pauw, F. Berghmans, *A novel fast phase correlation algorithm for peak wavelength detection of fiber Bragg grating sensors*, Opt. Express, Vol. 22, (2014), pp. 7099–7112

[18] E. Reynders, M. Schevenels, G. De Roeck, *MACEC 3.3: a Matlab toolbox for experimental and operational modal analysis.* Report BWM-2014-06, KU Leuven, Dept. Civil Engineering, Leuven (2014).

[19] E. Reynders, G. De Roeck, *Reference-based combined deterministic-stochastic subspace identification for experimental and operational modal analysis*, Mech. Syst. Signal Pr., Vol. 22, No. 3, (2008), pp. 617–637.

[20] B. Peeters, G. De Roeck, *Reference-based stochastic subspace identification for output-only modal analysis*, Mech. Syst. Signal Pr., Vol. 13, No. 6, (1999), pp. 855–878.

[21] E. Reynders, R. Pintelon, G De Roeck, *Uncertainty bounds on modal parameters obtained from Stochastic Subspace Identification*, Mech. Syst. Signal Pr., Vol. 22, No. 4, (2008), pp. 948–969.

[22] E. Reynders, K. Maes, G. Lombaert, G. De Roeck, *Uncertainty quantification in operational modal analysis with stochastic subspace identification: Validation and applications*, Mech. Syst. Signal Pr., Vol. 66–67, (2016), pp. 13–30.

Relations between the quality of identified modal parameters and measured data obtained by structural monitoring

S. Marwitz [1], **V. Zabel** [1]
[1] Bauhaus-Universität Weimar, Institute of Structural Mechanics,
Marienstraße 15, 99423, Weimar, Germany
E-mail: **simon.jakob.marwitz@uni-weimar.de**

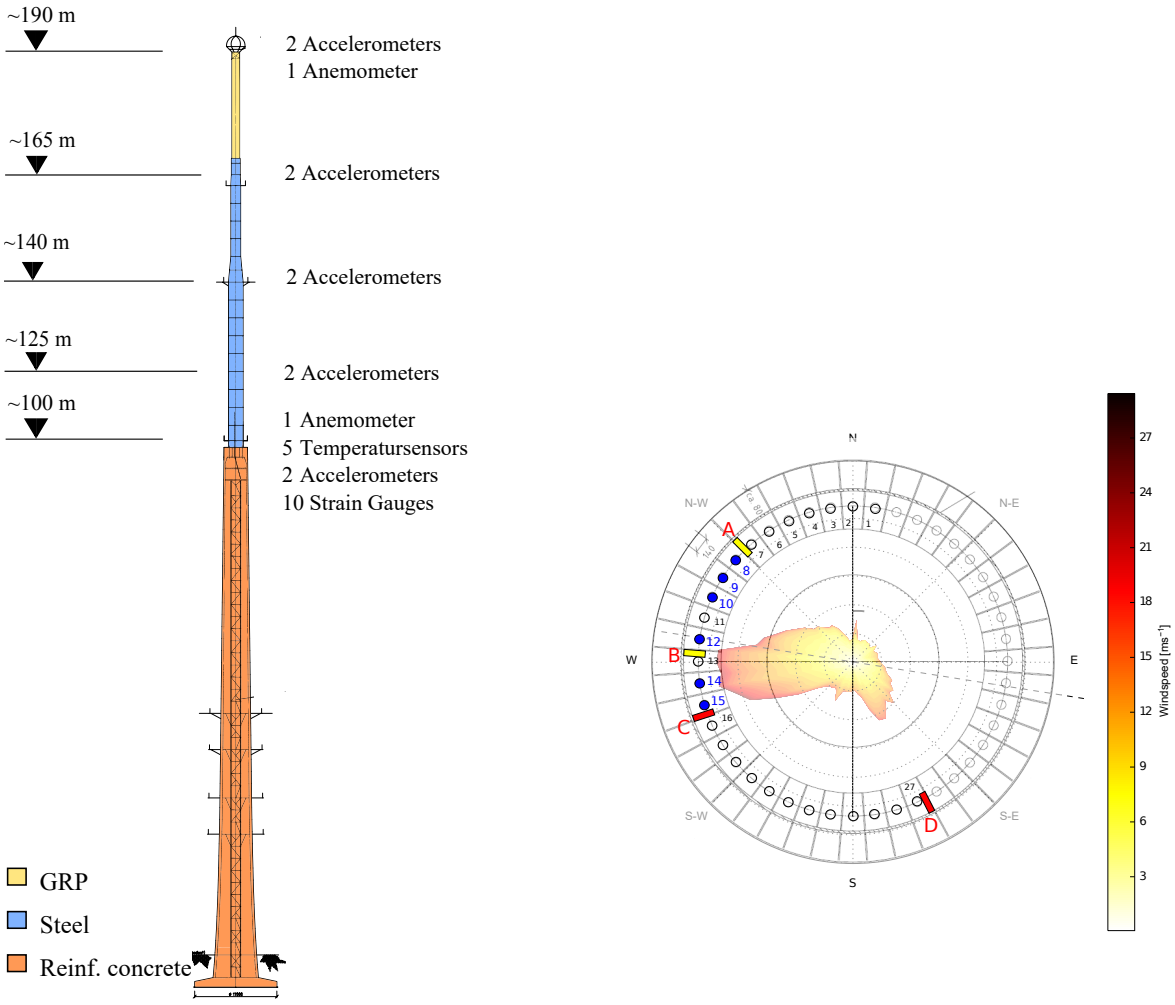
Abstract
In structural monitoring a structure's response to loads and environmental influences is continuously observed to reduce the uncertainties in the assessment of the actual structural condition, justify an extension of service life or to detect possible damage. In this study, a monitoring system using accelerometers and fibre bragg gratings was installed on a telecommunication tower with a rotationally-symmetric cross-section.
The quality of measured time histories is varying and affecting subsequent analyzes. Two approaches were used to estimate data quality. Modal parameters were estimated by an automated operational modal analysis. Relations were observed between the quality of the measured data and of the modal parameters as well as between the modal parameters and environmental conditions. The paired mode shapes (due to the symmetry) where shown to be spatially orthogonal. Results indicate, that monitoring the modal parameters of slender civil structures can be achieved, when the quality of acquired data reaches an acceptable minimum.

1 Introduction

Many civil structures, such as bridges or towers built in the 1960s and 1970s, will reach the end of their planned service life in the coming years. Furthermore, due to the development of design codes and further guidelines, it is often no longer possible to comply with these standards. However, in many cases continued use is reasonable or necessary and therefore an alternative assessment of the remaining bearing capacity and/or serviceability must be achieved. In these cases, structural monitoring offers an economic option for estimating certain structural parameters and measuring local stresses. The global dynamic properties as well as the intensity and frequency spectrum of loads are of particular interest for structures subject to dynamic loads such as bridges and masts/towers.

In this study, a monitoring system consisting of acceleration, strain and temperature sensors as well as anemometers was installed on a telecommunication tower. Traditional seismic accelerometers were used to capture the global vibration behavior. Local strains were acquired using Fibre Bragg Grating (FBG) sensors, which are not affected by electromagnetic radiation due to transmission operations. The use of FBGs for structural monitoring has been tested many times [1], but the recorded measurement data has been rarely used for Operational Modal Analysis (OMA) [e. g. [2, 3]. Structural monitoring and automated OMA using accelerometers, in contrast, is a well studied field (see e.g. [4, 5, 6]).

In the presented study, strain and acceleration measurement data was used to independently identify modal parameters and their standard deviations by means of OMA. These uncertainties were then related to different estimates of data quality and compared with each other. Restrictions, advantages and disadvantages are identified and recommendations for similar structural monitoring tasks are given.



(a) Structure of the telecommunication tower and positions of sensors along the height

(b) Positioning of the FBG strain gauges in the steel cylinder in the transition piece above the concrete cylinder. A-D: rosettes on walls, 8-15: uni-directional strain gauges on the bolts

Figure 1

2 Description of the Monitoringsystem

Telecommunication Tower As part of the monitoring task, a telecommunication tower, built in the 1970s, with a height of approximately 200 m was instrumented. It is a cantilever structure with a tapered, rotationally symmetric cross-section consisting of three parts: a prestressed concrete cylinder at the bottom, followed by a steel shaft and a glass-fibre reinforced plastics (GRP) cylinder on the top (Fig. 1a). Due to its exposed position and construction type, the tower is mainly excited by dynamic wind loads. Additionally, a tuned mass damper has been installed at the tower's tip, consisting of a steel/concrete ring with a mass of about 1000 kg, hanging on short pendulum rods and connected to friction spring dampers.

By means of a structural monitoring system the dynamic behavior of the tower and its relations to the environmental conditions should be investigated.

Measurement Devices The monitoring system was gradually extended over the course of three years. Sensor locations were chosen, based on preliminary short-term measurements and a numerical modal analysis

of a finite element model of the tower. In a first step three pairs of accelerometers (sensitivities: 10 V/g and 1 V/g), measuring horizontal vibrations, were placed about halfway up, at the tower's top and on the TMD, also at the top. Temperature sensors (Pt100) and anemometers at both locations were installed to record environmental influences.

In order to improve the system identification results and to achieve a higher spatial resolution of the mode shapes, another three pairs of acceleration sensors were installed along the upper half of the tower about a year later (Fig. 1a).

All analog signals from the sensores were digitized at distributed stations that connected to a controller at the ground. Using fibre-optic connections, the electromagnetic perturbations due to the transmission operations was substantially reduced, but could not be completely avoided. The dynamic amplitudes that were reached with the accelerometers during three years of operations were $\pm\ 0.95\,\mathrm{m\,s^{-2}}$ (RMS: $0.51\,\mathrm{m\,s^{-2}}$) and are well within the limits of all devices involved.

In the last expansion stage, several strain sensors were installed to identify local mechanical loads at the transition piece between the prestressed concrete shaft and the steel cylinder. In order to eliminate electromagnetic interference, fibre-optic strain gauges, i.e. fibre bragg gratings (FBG) were used. Four points on the wall of the steel cylinder were instrumented with customized FBG strain rosettes (see Fig. 1b. The majority of the measuring points were placed at locations were strains were expected to be highest due to the main wind directions. The rosettes were fixated on textile carrier mats glued to the walls. Strainless fibres are used for temperature compensation.

The used interrogator has 4 multiplexed channels which are operating in the wavelength range 1510 - 1590 nm. Due to the measuring principle, the application of an analogue anti-aliasing filter is not possible. However, the very low dynamic amplitudes of max. +- 45 $\mu\mathrm{m\,m^{-1}}$ (RMS: 12 $\mu\mathrm{m\,m^{-1}}$) show frequency components mainly concentrated at the lower natural frequencies in the range of up to 1.3 Hz.

Data Acquisition and Storage The two measurement systems (acceleration/environment and strains) were run independently at a sampling rate of $100\,\mathrm{Hz}$ and $20\,\mathrm{Hz}$, respectively. A coarse time synchronisation was achieved using the control PC to which both devices are connected. No exact time synchronisation was s, but considered to be possible (see e.g. [7]). Both devices were continuously acquiring data and storing slices of 1 hour in a binary format.

The data was transferred to a central server and processed further, daily. Processing included: unpacking, inspection for erroneous signals, inclusion of file statistics into a database, generation of time history plots and spectral plots and generation of daily email reports. A database of file statistics is needed in order to cut arbitrary slices of signals from the continuously recorded data, and thus allows to retrieve synchronized data from both measurement systems. Additionally, a constantly updated database allows to rapidly generate graphs of the long term evolution of the measured quantities.

Duration of Analyzed Data Sections As continuous measurements are available, the duration of the analyzed sections of the data could be chosen freely. With shorter sections, it is expected to observe better the changes of modal parameters due to changing loading conditions, i.e. wind characteristics are usually given as 10-minute means, whereas increasingly less cycles of oscillation would be included in the analysis, which affects the system identification results. Using longer sections improves the system identification but also smoothes out much of the short term environmental variance. The choice of a proper duration is therefore considered a bias-variance-dilemma. In this study, the whole data set was analyzed multiple times using sections of 10, 30, 60 and 120 minutes. Based on subjective evaluation, using 30-minute sections, a good trade off between bias of the identification results and capturing significant environmental variance can be achieved for the purpose of this study.

Signal Processing For each 30-minute slice of data, statistical characteristics such as minimum, maximum, variance, RMS and kurtosis were calculated, first. Subsequently, channels with measurement range overload or failures were marked as faulty in each data set and then only error-free data sets were further processed. A double (forward/reverse) band pass filter (Butterworth, 4th order) with cut-off frequencies (0.1 ... 5 Hz) was applied to these signals and the sampling rate was reduced to 10 Hz.

Data Quality Assessment The definition of the quality of measured data always depends on the field of application. A general approach is given in the Guide to the Expression of Uncertainty in Measurement [8]. However, the primary procedure makes use of repeated measurements, which can not be carried out in ambient vibration testing. In an alternative procedure, the characteristics of the full measurement chain are to be modeled using data sheets and other sources. This can not account for unknown sources of noise and interference that are strongly present in the monitoring system described in this study.

Alternatively, other commonly used criteria to judge on the quality of measured vibration data include the signal-to-noise ratio (SNR) of statistical evaluations of the signals. The estimation of the SNR in the input-output case can be done for example using coherence-based methodes (see e.g. [9]). However, considering the output-only case little information is available. Brincker and Ventura [10] give a rule-of-thumb that makes use of the singular-value spectrum, where "the noise level is indicated by the first singular value that becomes flat [...]". The signal level is then defined to be the peak value of the first singular value and thus the SNR can be defined. However, an extensive parametric study using synthetic data showed relations between derived SNR value versus the real SNR value which most likely resembles a sigmoid function.

For the purpose of this study, the ratio of singular values is used as a criterion to estimate data quality. Another criterion for data quality is the kurtosis of the signals, which is also adopted in this study. In ambient vibration testing the kurtosis is used to check the assumption, that the structural response measurements are normally distributed noise processes.

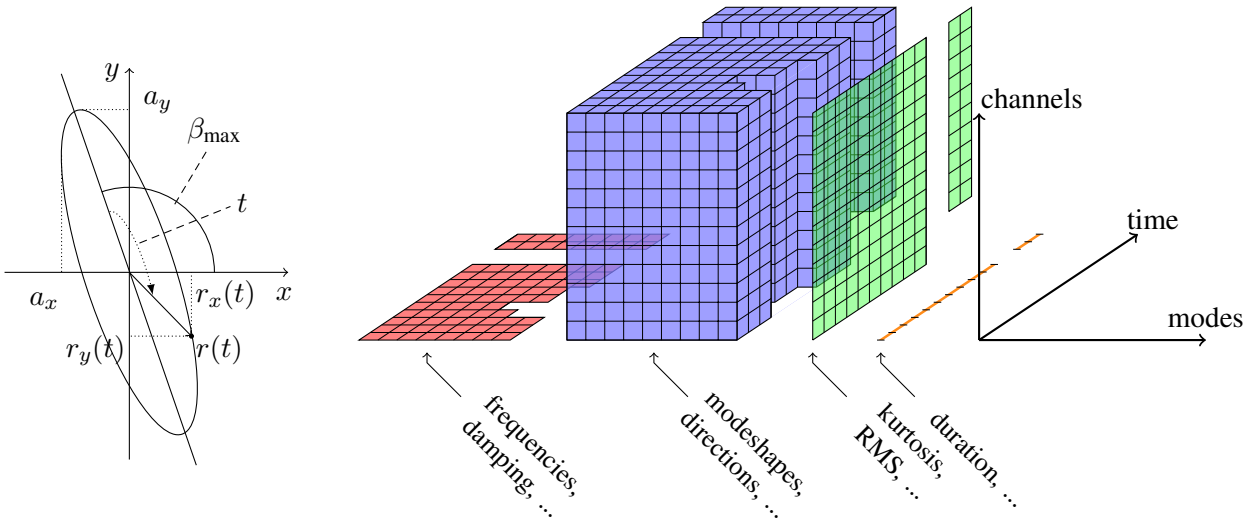
3 Operational Modal Analysis

The identification of modal parameters, i.e. natural frequencies, damping values and mode shapes, using structural response measurements only, is the aim of Operational Modal Analysis (OMA) (see e.g. [11]). Several parametric and non-parametric methods, operating in the frequency or time domain exist for this purpose. In this study, a parametric time domain method, the reference-based, data-driven Stochastic Subspace Identification (SSI) [12] was used. It identifies a linear state space model from the measured signals, from which the modal parameters can be determined. Two extensions to this method were employed: the estimation of the modal contributions of each identified mode to the measured signal using a Kalman filter [13] and the estimation of uncertainty bounds, i.e. variances, of the modal parameters using the first-order sensitivity of the modal parameter estimates to perturbations of the measured signal [14].

Selection of Analysis Parameters For all parametric methods of OMA, some analysis parameters may influence the identification process and the quality of the modal parameters to be identified (see e.g. [15]) and must be defined in advance. In the case of the SSI method these are: the dimension of the block-Hankel matrix, which is assembled from the measured data, and the model order of the identified state space system.

There are only few recommendations for choosing the number of block lines. In [16] the ratio of sampling rate (f_s) and lowest natural frequency (f_0): $p = {}^{f_s}/_{2f_0}$ is suggested. In the presented study, this value was determined empirically by maximizing the modal contributions for different excitation situations (weak, moderate and strong wind).

When using the acceleration measurement data, the best results are obtained at low wind speeds and a number of block lines of $p = 20 \ldots 25$. Strong wind identification results in lower modal contributions in



(a) Determination of the main direction of the mode shapes

(b) Example of multidimensional, sparse arrays of results along three (named) dimensions (borrowed from Python xarray documentation)

Figure 2

any configuration. The pair of sensors at approx. 100 m was selected as reference sensors, based on the mode shapes of a finite element model.

The diagonally arranged FBG of the strain rosettes were used as reference sensors for the strain measurement data. The highest modal contributions were achieved in moderate to strong winds using $p = 18 \ldots 23$. No reliable identification was possible in any configuration at low wind speeds, due to operating at the lower threshold of the strain measurement device.

The analysis of strain and acceleration data was carried out separately using the "number of block-lines" $p = 23$ and the "maximum model order" $n_{\max} = 200$.

Quality Assessment of Modal Parameters In the presented study, quality of modal parameters, is defined as low standard deviations or coefficient of variations. A method to estimate the uncertainties of modal parameters was developed by [17]. From multiple blocks of vibration data, the uncertainties can be computed and propagated through the applied OMA algorithm by utilizing first-order perturbations. This method was applied to SSI in [14] and optimized for efficient multi-order computations in [18]. The actual implementation in the Python programming language follows [18, 19].

As a dimensionless measure of quality, the coefficients of variation was computed from the variances and the mean values of the natural frequencies and the damping values. They show a linear relationship and therefore, to simplify further analyzes, the coefficient of variation of the identified natural frequencies was used as an estimate for the quality of modal parameters.

The number of blocks, used to compute the standard deviations of the modal results in each section, were chosen such that the 95% confidence intervals of the respective mean values, would fall within one standard deviation of the true value. A value of 30 blocks per section, or a block-length of 1 minute, respectively, was chosen, following the well known equations (see e.g. [9]).

Main Directions of Identified Mode shapes The SSI algorithms are generally capable of separating closely-spaced modes. In some cases, however, this separation can not be fully achieved. It can be observed, that the identified mode shapes of closely-spaced modes are often mapped as a complex combination of the two mode shapes, dominated by one of the two mode shapes.

This phenomenon can be represented graphically (Fig. 2a) by plotting the modal displacements of a measuring point, i.e. the components of the mode shape in two measuring directions at this point, over one period in the plane of motion. The result is an ellipse with amplitudes a_x, a_y and corresponding phase angles φ_x, φ_y in the x and y directions.

The main direction of this ellipse can be determined from the equation of the length of the directional vector

$$r(t) = \sqrt{r_x(t)^2 + r_y(t)^2} \quad \text{with} \quad r_{x,y}(t) = a_{x,y}\cos(\varphi_{x,y} + t)$$

and setting its first derivative w.r.t. time to zero. From $\dot{r}(t) = 0$ follows the time instance, where the position vector reaches maximum length i.e. the semi-major axis, and its angle, which is considered the main direction of the ellipse.

$$t_{\max} = -\frac{1}{2}\arctan\frac{a_x^2\sin(2\varphi_x) + a_y^2\sin(2\varphi_y)}{a_x^2\cos(2\varphi_x) + a_y^2\cos(2\varphi_y)}, \qquad \beta_{\max} = \arctan\frac{r_y(t_{\max})}{r_x(t_{\max})}$$

Depending on how well the two closely spaced modes are separated from each other by the OMA algorithm, the shape of the ellipse varies. As an indicator of the degree of separation, the ratio of the radii of the semi-major and semi-minor axis' can be selected.

This procedure analyzes only the identified mode shapes, which ideally occur as orthogonal pairs. The actual movements of the tower are always a combination of several modes and are not the subject of these analyses.

Automated Stabilization and Tracking When using parametric OMA methods, so-called mathematical solutions, are also identified in addition to solutions with a physical meaning. The distinction between spurious and physical modes is usually done manually using a stabilization diagram, where stable poles appear repeatedly at increasing model orders, while spurious poles are randomly distributed. For continuous structural monitoring an automated selection is necessary. In the presented study a three-stage cluster algorithm, developed in [20] and significantly improved in [21], was used for this purpose. The three stages are: clearing of physical and spurious poles, grouping of similar poles into several clusters and removal of small clusters.

However, not all modes are always sufficiently excited and therefore identified. The tracking of single modes over time becomes especially challenging when closely-spaced modes are present, as in this study. Additionally, due to mode splitting [22] the algorithm may identify the "real" modes at lower model orders and split modes at higher model orders. Since all modal parameters vary due to environmental influences, no similarity measure can be used for tracking the evolution of single modes. Literature suggests to use hard-validation criteria to sort out complex modes, which is also not applicable in cases of closely-spaced modes, as the identified mode shapes always lie in a subspace that is spanned by the two corresponding mode shapes of a pair of modes [10]. For the purpose of this study, where necessary, coarse frequency binning was applied and then only the results were exactly two modes were identified for a mode-pair were used further.

Storage and Organization of Results All quantities that result from the automated OMA are multidimensional. The dimensions are: time, measurement channels or measuring points and vibration modes. Most quantities fill only one or two of these dimensions, though. Additionally, the results are sparse in all of these dimensions, which means, in any dimension data points may be missing. For example: in dimension time, data may be missing due to downtimes of the monitoring system; in dimension channels, data may be missing due to failures of sensors or addition of new sensors; and most importantly in dimension modes: some modes may not always be excited sufficiently and thus can not be identified and are therefore missing (for examples see Figure 2b).

Efficient post-processing of the results, however, requires carefully aligned and consistent data sets and efficient routines to interactively explore the (multidimensional, sparse) data. This may include generation

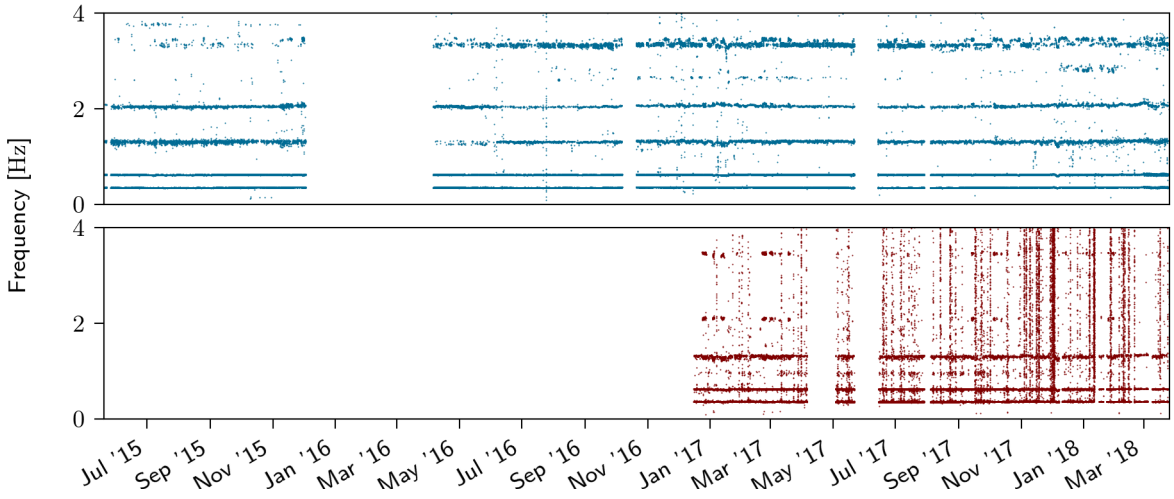


Figure 3: All identified natural frequencies over time. Top: from acceleration time series; Bottom: from strain time series

of different diagrams (histograms, scatter plots), evaluation of statistics (correlation coefficients, regressions) or the filtering of the data sets with respect to different result quantities.

The Python xarray package (`https://xarray.pydata.org`) fulfills these requirements and was chosen for this study. It uses the Unidata Common Data Model for self-describing scientific data and is based on well proven packages from the SciPy stack. Its usage proved to be very useful for post-processing the data sets, while the gradual assembly of the final data sets turned out to be more difficult than expected.

4 Results and Discussion

Using the methods described, the modal parameters as well as the estimates of data quality were determined from 18,145 (strain data) and 43,296 (acceleration data) data sets. Mean and variance estimates were also computed for a similar number of data sets containing environmental data. It should be mentioned, that the wind data had to be transformed from polar (wind direction and speed) to Cartesian coordinates (wind speeds in two directions), were an orthogonal least squares approach could be used to determine the mean wind directions.

Due to the large amount of data points in the diagrams, instead of the usual scatter plots two-dimensional histograms with a high number of bins in both directions were generated. Therefore they appear similar to a scatter plot, but outliers are not exaggerated by the visual perception of a dense scatter plot.

Relations of Modal Parameters with Environment Figure 3 shows all identified natural frequencies over time, both from the acceleration time series and from the strain time series. In the frequency range of consideration, the telecommunication tower has 5 natural frequencies, each of them occurring as a pair at closely spaced natural frequencies. Only three of these pairs of natural frequencies could be reliably identified from the strain time series, as the vibration amplitudes of the strains decrease with increasing frequency. Significant relationships can be recognized between natural frequencies and temperature (Fig. 4) as well as damping values and wind speed (Fig. 5). A temperature-dependency in structural stiffness is assumed to be the main reason for the change in natural frequencies with temperature. Several factors are conceivable for the observed increase of the damping values with increasing wind speeds: Increased aerodynamic damping, stronger activation of internal friction e.g. in structural connections or activation of the tuned mass damper with increasing levels of vibration.

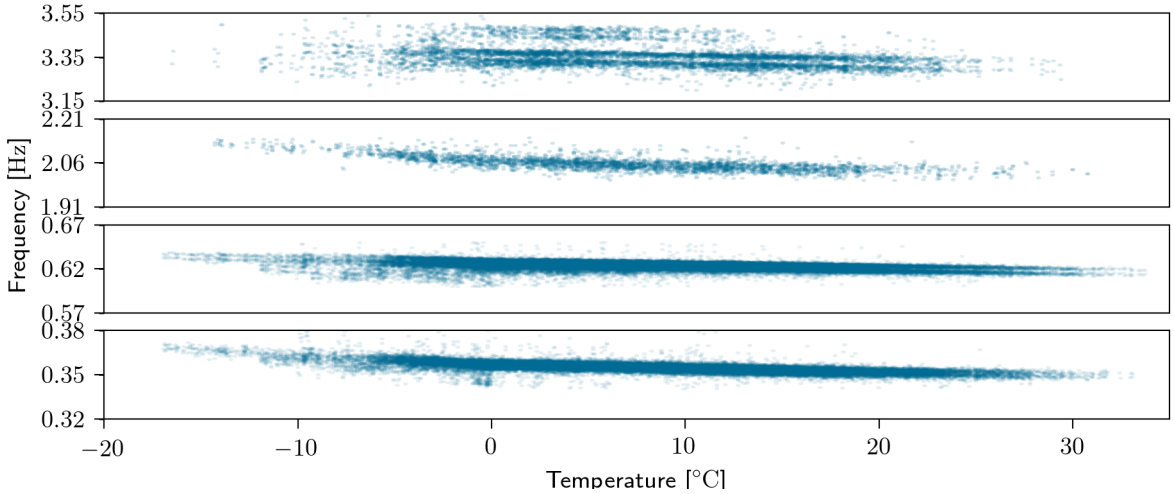


Figure 4: Natural frequencies related to ambient temperature for modepairs 1,2,4 and 5 (bottom to top). (Spearmans rank correlation coefficients: -0.73, -0.44, -0.72, -0.37)

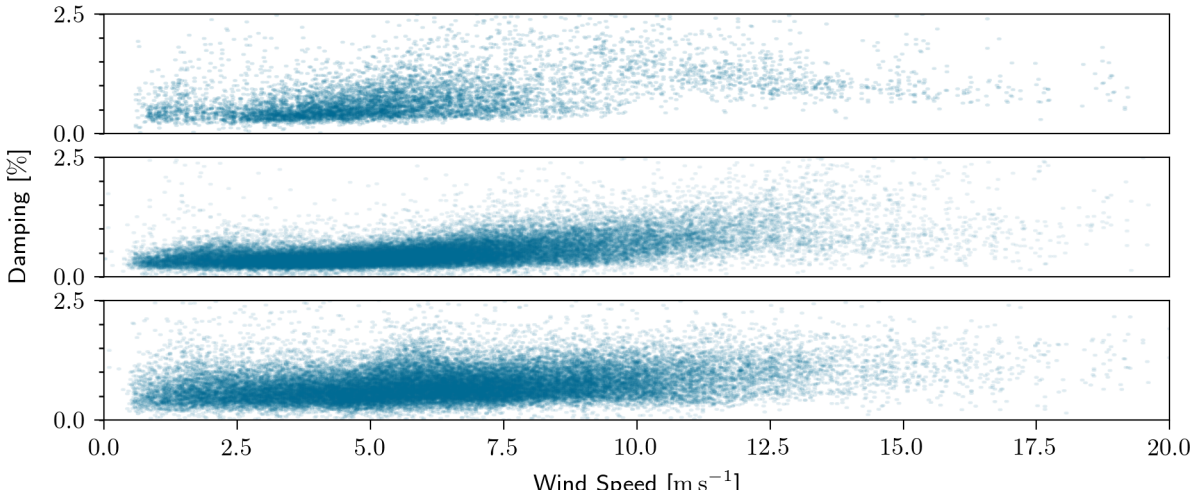


Figure 5: Damping ratios related to mean wind speed for modepairs 1,2 and 3 (bottom to top) (Spearmans rank correlation coefficients: 0.31, 0.55, 0.55)

Using the procedure outlined in section 3 to determine the orientation of the identified mode shapes, the relationships between wind directions and mode shape directions shown in Figure 6 could be identified. From the sideways plots of the marginal distributions, a main vibration direction can be clearly recognized, especially for the first two pairs of modes. The measuring point at the transition area between reinforced concrete and steel was selected as an example, but similar relations can be observed for the other measuring points and the main directions are almost equal at all points. Thus, the identified directions do not just arise from the OMA algorithm but have a physical origin. Additionally, they are only slightly influenced by changing wind directions. This means that even small imperfections of the rotational symmetry are sufficient to determine two main directions of vibration in contrast to a perfect numerical model, where the orientation is usually random.

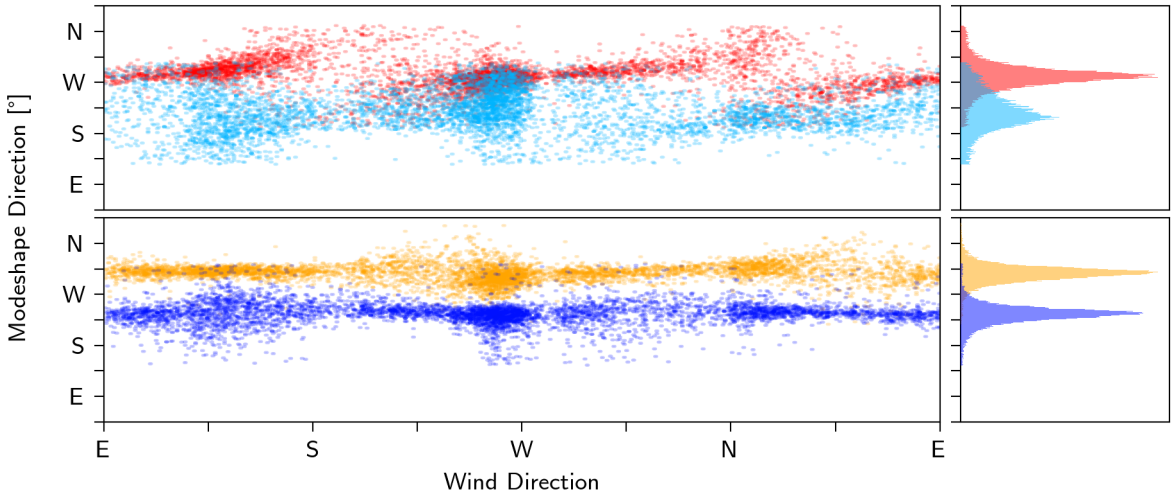


Figure 6: Main directions of the identified mode shapes related to wind directions. Top: first modepair, bottom: second modepair; right: histograms of the respective dataset

Relations of the Quality of Modal Parameters with Data Quality A quick inspection of randomly selected time series and also of the identified modal parameters reveals, that the quality of the acceleration measurements seems to be significantly higher than that of the strain measurements. As mentioned in section 3, the strain acquisition system was mostly operating at the lower resolution threshold of the device and therefore the time series a relatively high degree of noise. The lower graph of Figure 7 illustrates this observation: with decreasing vibration levels, identification results are scattered all along the frequency range. Additionally, higher natural frequencies can only be identified at higher vibration levels. The results from the acceleration time series (top graph), however, do not show such behavior, due to the vibration levels being well within the operating levels of sensors and acquisition devices.

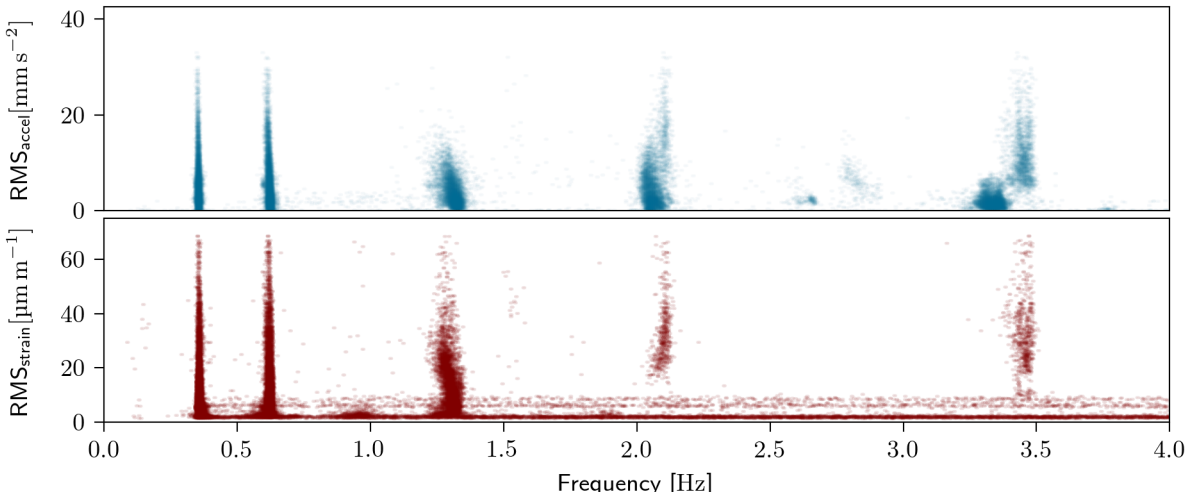


Figure 7: Identified natural frequencies over mean RMS of the time series. Top: from accelerations; bottom: from strains.

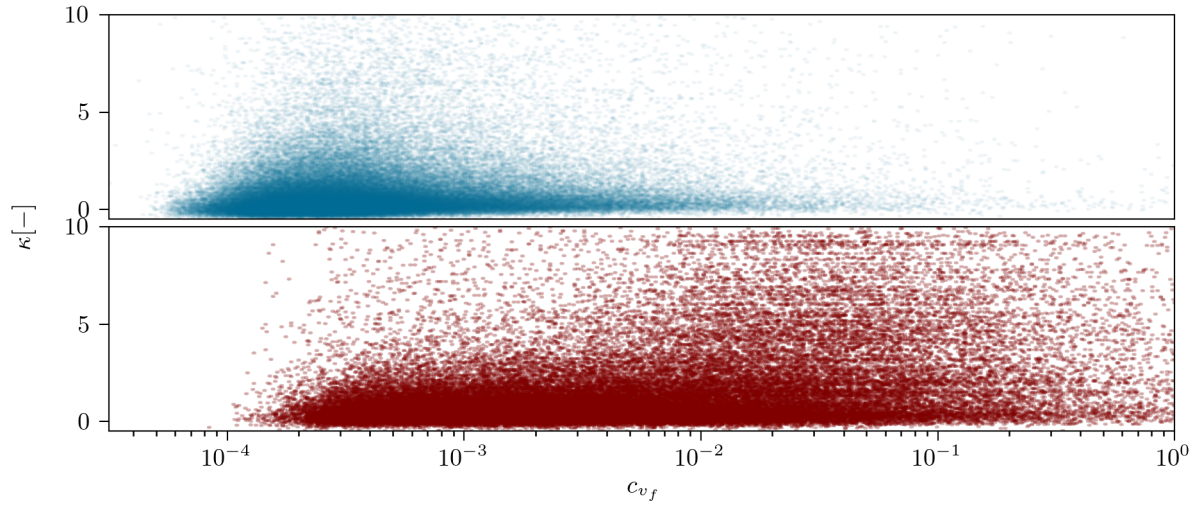


Figure 8: Coefficient of variation of the identified natural frequencies c_{v_f} related to kurtosis κ of the respective time series. Top: acceleration, bottom: strains. (Spearmans rank correlation coefficients 0.17, 0.37)

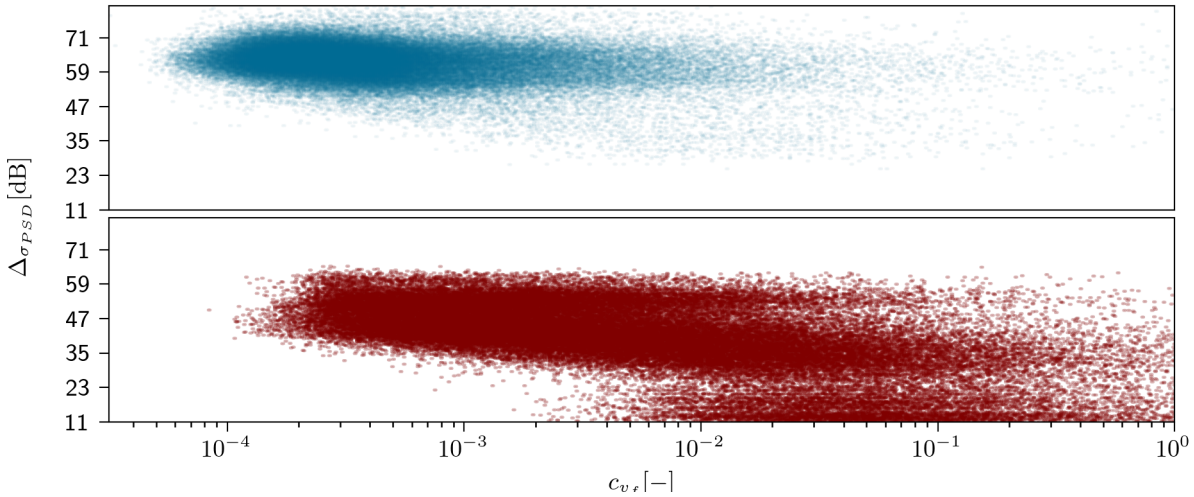


Figure 9: Coefficient of variation of the identified natural frequencies c_{v_f} related to the difference of two singular values of the singular value spectrum $\Delta_{\sigma PSD}$. Top: acceleration, bottom: strains. (Spearmans rank correlation coefficients -0.18, -0.6)

Figures 8 and 9 confirm the observations that the quality of the strain signals is significantly lower than that of the acceleration signals. Here, the coefficient of variation of the natural frequencies is related to the two measures of data quality, as defined in the previous section. From the bottom graph (strain) in Figure 8, it can be observed, that with increasing kurtosis the coefficient of variation increases, too. However, in the top part of the figure (acceleration) no such behavior can be observed.

A similar observation can be found by comparing the two graphs in Figure 9. Here, the coefficient of variation of the natural frequencies seems to increase with decreasing difference of the singular values of the singular value spectrum. Again, this observation is most clear in the bottom graph which corresponds to the "lower quality" strain measurements and only slightly visible when "high quality" acceleration signals (top graph) were used.

In conclusion, strain and acceleration measurements are of different quality. The two applied measures of data quality do not reflect this difference, though. However, when the signal-to-noise ratio of the measured data is low its effect on the quality of a modal identification can be quantified by either of these measures.

5 Conclusions

In this contribution it has been reported about a monitoring system that acquires vibratory accelerations in several levels as well as local strains on a rotationally symmetric telecommunication tower. Over the period of three years, both acceleration and strains as well as the environmental conditions temperature and wind were recorded. Using automated operational modal analysis, the modal parameters were determined from the acceleration and strain measurement data.

A comparison shows a good correspondence of the natural frequencies and damping values determined from both measured variables. As expected, the results determined from the strains scatter more strongly, especially at low vibration amplitudes.

The identified modal parameters were related to the environmental conditions. It was observed, that the natural frequencies have a slight tendency to decrease with increasing temperature, that the modal damping ratios increase with increasing wind speeds and that the main directions of the identified mode shapes are relatively constant, regardless of changing wind directions.

The acceleration sensors deliver high-quality measurement data at both low and high vibration amplitudes, given that their sensitivity is sufficient. The measurement data of the fiber optic strain sensors is of lower quality and can only be used for operational modal analysis when vibration levels exceed a certain level. Two different estimates of data quality can be related to the quality of the modal identification if the measured data is dominated by noise, as in the case of the strain measurements. For the quantification of uncertainties in these relations, a suitable methodology has been presented.

In this respect, strain-based output-only modal analysis is an alternative way of determining modal parameters if existing strain measurement technology is to be used or no accelerometers can be installed. In addition to life cycle analysis and estimation of local component stresses and strains, the strain measurement data can also be used to determine global structural parameters. Nevertheless, lower uncertainties are generally to be expected for the identification of modal parameters from measured accelerations, assuming suitable sensors. This is especially true for higher frequencies.

With regard to the analysis, the following observations emerge: The Stochastic Subspace Identification method in conjunction with an automatic stabilization algorithm is very well suited for identifying modal parameters from both high quality acceleration signals and lower quality strain signals. The method delivers reliable results even in the presence of closely spaced modes.

Acknowledgments

This research was partly funded by the German Research Foundation DFG under the Research Training Group 1462 ”Evaluation of Coupled Numerical and Experimental Partial Models in Structural Engineering”. Computational resources were used at the Digital Bauhaus Lab of the Bauhaus-Universität Weimar. Parts of the applied measurement equipment were purchased with the support of the European Funds for Regional Development (EFRE). The authors gratefully acknowledge the financial support.

References

[1] X. W. Ye, Y. H. Su, and J. P. Han. “Structural Health Monitoring of Civil Infrastructure Using Optical Fiber Sensing Technology: A Comprehensive Review”. In: *The Scientific World Journal* 2014 (2014), pp. 1–11.

[2] Tyler J Arsenault et al. “Development of a FBG based distributed strain sensor system for wind turbine structural health monitoring”. In: *Smart Materials and Structures* 22.7 (2013), p. 075027.

[3] Dimitrios Anastasopoulos et al. “Damage identification using modal strains identified from operational fiber-optic Bragg grating data”. In: *Structural Health Monitoring: An International Journal* (Dec. 2017).

[4] James Mark William Brownjohn et al. “Real-time performance monitoring of tuned mass damper system for a 183m reinforced concrete chimney”. In: *Journal of Wind Engineering and Industrial Aerodynamics* 98.3 (2010), pp. 169–179.

[5] Filippo Ubertini, Carmelo Gentile, and Annibale Luigi Materazzi. “Automated modal identification in operational conditions and its application to bridges”. In: *Engineering Structures* 46 (2013), pp. 264–278.

[6] Gustavo Oliveira et al. “Continuous dynamic monitoring of an onshore wind turbine”. In: *Engineering Structures* 164 (June 2018), pp. 22–39.

[7] K. Maes et al. “Offline synchronization of data acquisition systems using system identification”. In: *Journal of Sound and Vibration* 381 (2016), pp. 264–272.

[8] International Organization for Standardization (ISO). *Guide to the Expression of Uncertainty in Measurement*. Tech. rep. Geneva: ISO, 2008.

[9] Julius S. Bendat and Allan G. Piersol. *Random Data*. John Wiley & Sons, Inc., Jan. 2010.

[10] R. Brincker and C. Ventura. *Introduction to Operational Modal Analysis*. Wiley, 2015.

[11] Carlo Rainieri and Giovanni Fabbrocino. *Operational Modal Analysis of Civil Engineering Structures - An Introduction and Guide for Applications*. Berlin, Heidelberg: Springer, 2014.

[12] Bart Peeters and Guido de Roeck. “Reference-Based Stochastic-Subspace Identification for Output-Only Modal Analysis”. In: *Mechanical Systems and Signal Processing* (1999).

[13] F Javier Cara et al. “Modal contribution and state space order selection in operational modal analysis”. In: *Mechanical Systems and Signal Processing* 38.2 (2013), pp. 276–298.

[14] Edwin Reynders, Rik Pintelon, and Guido De Roeck. “Uncertainty bounds on modal parameters obtained from stochastic subspace identification”. In: *Mechanical Systems and Signal Processing* 22.4 (2008), pp. 948–969.

[15] Volkmar Zabel, Filipe Magalhães, and Christian Bucher. “The Influence of Parameter Choice in Operational Modal Analysis - a Case Study”. In: *Proceedings of the IMAC XXXIV: a Conference and Exposition on Structural Dynamics*. 2016.

[16] Edwin Reynders and Guido de Roeck. “Reference-Based combined deterministic-stochastic subspace identification for experimental and operational modal analysis”. In: *Mechanical Systems and Signal Processing* 22 (2008), pp. 617–637.

[17] R. Pintelon, P. Guillaume, and Joannes Schoukens. “Uncertainty calculation in (operational) modal analysis”. In: *Mechanical systems and signal processing* 21.6 (2007), pp. 2359–2373.

[18] Michael Döhler and Laurent Mevel. “Efficient multi-order uncertainty computation for stochastic subspace identification”. In: *Mechanical Systems and Signal Processing* 38.2 (2013), pp. 346–366.

[19] Michael Döhler, Palle Andersen, and Laurent Mevel. “Variance computation of modal parameter estimates from UPC subspace identification”. In: *IOMAC - 7th International Operational Modal Analysis Conference*. Ingolstadt, Germany, May 2017.

[20] Edwin Reynders, Jeroen Houbrechts, and Guido De Roeck. “Fully automated (operational) modal analysis”. In: *Mechanical Systems and Signal Processing* 29 (2012), pp. 228–250.

[21] Eugen Neu et al. “Fully Automated Operational Modal Analysis using multi-stage clustering”. In: *Mechanical Systems and Signal Processing* 84 (2017), pp. 308–323.

[22] Carlo Rainieri and Giovanni Fabbrocino. “Influence of model order and number of block rows on accuracy and precision of modal parameter estimates in stochastic subspace identification”. In: *International Journal of Lifecycle Performance Engineering 10* 1.4 (2014), pp. 317–334.

Robust damage detection using Bayesian virtual sensing with noise reduction and environmental effect elimination capabilities

J. Kullaa[1]
[1] Metropolia University of Applied Sciences, Department of Automotive and Mechanical Engineering
P.O. Box 4071, 00079 Metropolia, Finland
e-mail: **jyrki.kullaa@metropolia.fi**

Abstract

Structural health monitoring is based on output-only vibration measurements. In order to get an early warning of structural failure, the signal-to-noise ratio of the measurement data should be high. This can be achieved by Bayesian virtual sensors that are proved to be more accurate than the actual measurements. Virtual sensor data then replace the actual measurements in subsequent steps of damage detection. Environmental or operational influences can be removed by acquiring training data under different conditions and utilizing the correlation between the virtual sensors. The measurement of the underlying variables is not necessary. An extreme value statistics (EVS) control chart for the first principal component scores of the residuals is plotted for damage detection. Numerical simulations were performed for a structure subject to unknown random excitation and various environmental effects. Virtual sensors outperformed the raw measurements in damage detection, making early warning more plausible.

1 Introduction

Important structures can be equipped with a monitoring system sensing vibrations at several positions of the structure and detecting changes in the dynamic behaviour. The changes in the dynamic characteristics can be detected from extracted features, such as natural frequencies or mode shapes, or directly from the measured time histories. Some challenges still exist that must be solved to make the monitoring system reliable (sensitivity to small changes and minimum number of false alarms):

- Measurement error. The desired level of damage to be detected is relatively small, which means that the measured data must be accurate,
- Environmental or operational influences are often stronger than those of damage, which can make damage detection difficult,
- Response data are only available. The excitation cannot be measured or controlled. The data analysis method must be therefore insensitive to vibration amplitudes,
- Feature extraction must be automatic due to a vast amount of data,
- In model-based SHM, an accurate finite element model is needed, which may be expensive and challenging to build,
- The number of sensors should be large with simultaneous sampling of all channels.

The large number of sensors increases the hardware and maintenance costs (e.g. sensors, cables, data acquisition, data storage, assembly, and repair). Wireless sensor networks (WSN) are a possible solution with a large number of low-cost sensor nodes and automatic reconfiguration. Time synchronization in a WSN is an issue, because simultaneous sampling is required. Also, low-cost sensors may be less accurate than the more traditional high-quality sensors.

Environmental or operational variability affects the dynamic behaviour of the structure. Many experimental studies have demonstrated the environmental effects on the dynamic characteristics of large civil engineering structures. The main underlying variable is temperature [1–6], but also the influences of the water level in the dam [7], humidity on a wooden structure [8], traffic [9, 10], and wind [11] have been identified.

Because the underlying environmental or operational variables are not all known and their effects on the data are often complex, it may be difficult to build a model that predicts the variability in the data. Alternatively, the effects of environment can be removed using the vibration data alone by applying multivariate statistics, provided the data dimensionality is high enough to make the measurements redundant. Many techniques have emerged to take environmental or operational effects into account without measuring the underlying variables [8, 12–26]. The same approach can be used either in the time-domain or in the feature-domain.

This paper concentrates on data analysis for damage detection and localization and addresses several of the abovementioned issues. The data analysis is made in the time domain, so that no feature extraction is needed. Response is only measured, and data-based SHM and damage detection is employed. Training data are needed from the undamaged structure under different environmental and operational conditions. Environmental or operational quantities are treated as latent variables; they are not measured. Utilizing the correlation between the variables in the training data, those underlying influences can be eliminated. It is assumed that the sensor network is redundant, so that each sensor reading can be estimated using the covariance model. The residuals (the difference between the measured and estimated variables) are used in damage detection.

A novel feature is noise reduction in order to increase the detection performance. If the measurement error is large, small damage may remain undetected. Therefore, a high signal-to-noise ratio (SNR) is important to get an early warning. This can be achieved e.g. by using high-quality sensors or by applying virtual sensing (VS) techniques to a redundant sensor network. Empirical virtual sensing is traditionally used for sensor validation and sensor fault identification [27–39]. Assuming the sensor network is redundant, it is possible to estimate the signal of a single sensor using the remaining sensors in the network. In the present study, all sensors in the network are used to reconstruct the sensor under investigation, including the sensor's own signal. Bayes' rule gives an optimal weighting to all sensors resulting in virtual sensors with accuracy always higher than that of the physical hardware. Virtual sensing uses the same idea as in the removal of environmental or operational influences from the data discussed above. However, VS is applied independently to each measurement. Once processed, the data still include the prevailing dynamics and environmental or operational influences, as well as the effects of damage. Measurement error is only reduced. The measurement data are replaced with the virtual sensor data in the damage detection algorithm.

The paper is organized as follows. Bayesian virtual sensors are derived in Section 2. Damage detection under varying environmental or operational conditions is outlined in Section 3. Detection and localization of an open crack in a bridge girder is studied in Section 4 using a numerical finite element model to generate vibration measurements under different environmental and operational effects. Concluding remarks are given in Section 5.

2 Bayesian virtual sensing

Virtual sensing (VS) gives an estimate of a quantity of interest using the available measurements. Empirical VS is a data-based approach, estimating a physical sensor using hardware redundancy. The sensor might become faulty, and using historical data from the functioning sensor network, the sensor reading can be reconstructed. Analytical VS utilizes a mathematical model together with measurements to estimate a quantity of interest. For example, full-field data can be estimated using a limited number of sensors.

This study applies empirical virtual sensing to noisy measurements to estimate virtual sensors with less noise. Bayesian analysis is employed to a sensor network, and it is shown that the posterior is more accurate than the actual hardware.

Consider a sensor network measuring p simultaneously sampled variables $\mathbf{y} = \mathbf{y}(t)$ at time instant t. Each measurement $\mathbf{y}$ includes independent measurement error $\mathbf{w} = \mathbf{w}(t)$:

$$\mathbf{y} = \mathbf{x}_m + \mathbf{w} \tag{1}$$

where $\mathbf{x}_m = \mathbf{x}_m(t)$ are the true values of the measured degrees of freedom. The objective is to find a less noisy estimate for the true values $\mathbf{x}_m$ utilizing the noisy measurements $\mathbf{y}$ from the sensor network.

2.1 Bayes' rule

From Bayes' rule,

$$p(\mathbf{x}_m \mid \mathbf{y}) = \frac{p(\mathbf{y} \mid \mathbf{x}_m)\, p(\mathbf{x}_m)}{p(\mathbf{y})} \tag{2}$$

This, however, cannot be evaluated, because the distributions are not available. To proceed, only a subset of the physical sensors is estimated by partitioning each observation into observed variables $\mathbf{v}$ and estimated variables $\mathbf{u}$ (typically a single sensor u). The partitioned variables are

$$\mathbf{y} = \begin{Bmatrix} \mathbf{y}_u \\ \mathbf{y}_v \end{Bmatrix},\ \mathbf{x}_m = \begin{Bmatrix} \mathbf{x}_{m,u} \\ \mathbf{x}_{m,v} \end{Bmatrix},\ \mathbf{w} = \begin{Bmatrix} \mathbf{w}_u \\ \mathbf{w}_v \end{Bmatrix} \tag{3}$$

Measurement error $\mathbf{w}$ is assumed to be zero mean, independent of $\mathbf{x}_m$, with a known covariance matrix

$$\boldsymbol{\Sigma}_w = E(\mathbf{w}\mathbf{w}^T) = \begin{bmatrix} \boldsymbol{\Sigma}_{w,uu} & \boldsymbol{\Sigma}_{w,uv} \\ \boldsymbol{\Sigma}_{w,vu} & \boldsymbol{\Sigma}_{w,vv} \end{bmatrix} \tag{4}$$

where $E(\cdot)$ denotes the expectation operator. After partitioning, all distributions are conditioned with $\mathbf{y}_v$. Bayes' rule becomes

$$\begin{aligned} p(\mathbf{x}_{m,u} \mid \mathbf{y}) &= p(\mathbf{x}_{m,u} \mid \mathbf{y}_u, \mathbf{y}_v) \\ &= \frac{p(\mathbf{y}_u \mid \mathbf{x}_{m,u}, \mathbf{y}_v)\, p(\mathbf{x}_{m,u} \mid \mathbf{y}_v)}{p(\mathbf{y}_u \mid \mathbf{y}_v)} \\ &= \frac{p(\mathbf{y}_u \mid \mathbf{x}_{m,u})\, p(\mathbf{x}_{m,u} \mid \mathbf{y}_v)}{p(\mathbf{y}_u \mid \mathbf{y}_v)} \end{aligned} \tag{5}$$

The distributions in (5) can be evaluated as shown in the following.

2.2 Likelihood

Assuming Gaussian noise $\mathbf{w}$, the likelihood is obtained using Equation 1:

$$\begin{aligned} p(\mathbf{y}_u \mid \mathbf{x}_{m,u}) &= N(\mathbf{y}_u \mid \mathbf{x}_{m,u}, \boldsymbol{\Sigma}_{w,uu}) \\ &\propto \exp\left[-\frac{1}{2} (\mathbf{y}_u - \mathbf{x}_{m,u})^T \boldsymbol{\Sigma}_{w,uu}^{-1} (\mathbf{y}_u - \mathbf{x}_{m,u}) \right] \end{aligned} \tag{6}$$

2.3 Evidence

For simplicity but without loss of generality, assume zero-mean variables $\mathbf{y}$. The partitioned data covariance matrix $\mathbf{\Sigma}_y$ is

$$\mathbf{\Sigma}_y = E(\mathbf{y}\mathbf{y}^T) = \begin{bmatrix} \mathbf{\Sigma}_{y,uu} & \mathbf{\Sigma}_{y,uv} \\ \mathbf{\Sigma}_{y,vu} & \mathbf{\Sigma}_{y,vv} \end{bmatrix} \tag{7}$$

The precision matrix $\mathbf{\Gamma}_y$ is defined as the inverse of the covariance matrix $\mathbf{\Sigma}_y$ and is also written in partitioned form:

$$\mathbf{\Gamma}_y = \mathbf{\Sigma}_y^{-1} = \begin{bmatrix} \mathbf{\Gamma}_{y,uu} & \mathbf{\Gamma}_{y,uv} \\ \mathbf{\Gamma}_{y,vu} & \mathbf{\Gamma}_{y,vv} \end{bmatrix} \tag{8}$$

A linear minimum mean square error (LMMSE) estimate for $\mathbf{y}_u \mid \mathbf{y}_v$ is obtained by minimizing the mean-square error (MSE) and can be computed either using the covariance or precision matrix [38, 40]. If each sensor signal is estimated in turn, the formulas based on the precision matrix result in a more efficient algorithm [38]. The expected value of the estimated variable is:

$$\hat{\mathbf{y}}_u = E(\mathbf{y}_u \mid \mathbf{y}_v) = -\mathbf{\Gamma}_{y,uu}^{-1}\mathbf{\Gamma}_{y,uv}\mathbf{y}_v = \mathbf{K}\mathbf{y}_v \tag{9}$$

where $\mathbf{K} = -\mathbf{\Gamma}_{y,uu}^{-1}\mathbf{\Gamma}_{y,uv}$, and the error covariance MSE is

$$\mathrm{cov}(\mathbf{y}_u \mid \mathbf{y}_v) = \mathbf{\Gamma}_{y,uu}^{-1} \tag{10}$$

Notice that the covariance is the error compared to the noisy measurement, not to the noiseless (true) value.

The evidence $p(\mathbf{y}_u \mid \mathbf{y}_v)$ is also Gaussian with the mean and covariance from Equations 9 and 10, respectively:

$$\begin{aligned} p(\mathbf{y}_u \mid \mathbf{y}_v) &= N(\mathbf{y}_u \mid \mathbf{K}\mathbf{y}_v, \mathbf{\Gamma}_{y,uu}^{-1}) \\ &\propto \exp\left[-\frac{1}{2}(\mathbf{y}_u - \mathbf{K}\mathbf{y}_v)^T \mathbf{\Gamma}_{y,uu}(\mathbf{y}_u - \mathbf{K}\mathbf{y}_v)\right] \end{aligned} \tag{11}$$

The evidence is merely a normalizing factor, independent of $\mathbf{x}_{m,u}$. However, evidence will be utilized in damage detection to remove the environmental or operational effects, which will be discussed in Section 3.

2.4 Prior

The prior distribution $p(\mathbf{x}_{m,u} \mid \mathbf{y}_v)$ is obtained from the measurement model (1) by partitioning and conditioning, and applying the rule that the sum of two Gaussian variables is also a Gaussian variable. The prior mean is

$$\begin{aligned} E(\mathbf{x}_{m,u} \mid \mathbf{y}_v) &= E(\mathbf{y}_u \mid \mathbf{y}_v) - E(\mathbf{w}_u) \\ &= E(\mathbf{y}_u \mid \mathbf{y}_v) = \mathbf{K}\mathbf{y}_v \end{aligned} \tag{12}$$

and the prior covariance is obtained from

$$\mathrm{cov}(\mathbf{y}_u \mid \mathbf{y}_v) = \mathrm{cov}(\mathbf{x}_{m,u} \mid \mathbf{y}_v) + \mathbf{\Sigma}_{w,uu} \tag{13}$$

from which and (10),

$$\begin{aligned}\boldsymbol{\Sigma}_{\text{prior},uu} &= \text{cov}(\mathbf{x}_{m,u} \mid \mathbf{y}_v) \\ &= \text{cov}(\mathbf{y}_u \mid \mathbf{y}_v) - \boldsymbol{\Sigma}_{w,uu} = \boldsymbol{\Gamma}_{y,uu}^{-1} - \boldsymbol{\Sigma}_{w,uu}\end{aligned} \tag{14}$$

The prior distribution is also Gaussian:

$$\begin{aligned}p(\mathbf{x}_{m,u} \mid \mathbf{y}_v) &= N(\mathbf{x}_{m,u} \mid \mathbf{K}\mathbf{y}_v, \boldsymbol{\Sigma}_{\text{prior},uu}) \\ &\propto \exp\left[-\frac{1}{2}(\mathbf{x}_{m,u} - \mathbf{K}\mathbf{y}_v)^T \boldsymbol{\Sigma}_{\text{prior},uu}^{-1}(\mathbf{x}_{m,u} - \mathbf{K}\mathbf{y}_v)\right]\end{aligned} \tag{15}$$

Notice that the prior is not subjective. It is the distribution of the exact quantity, estimated without using the corresponding sensor signal.

2.5 Posterior

The posterior distribution (5) is obtained by some manipulation, resulting in

$$\begin{aligned}p(\mathbf{x}_{m,u} \mid \mathbf{y}) &= c_1 p(\mathbf{y}_u \mid \mathbf{x}_m) p(\mathbf{x}_{m,u} \mid \mathbf{y}_v) \\ &= c_2 \exp\left[-\frac{1}{2}(\mathbf{y}_u - \mathbf{x}_{m,u})^T \boldsymbol{\Sigma}_{w,uu}^{-1}(\mathbf{y}_u - \mathbf{x}_{m,u}) - \frac{1}{2}(\mathbf{x}_{m,u} - \mathbf{K}\mathbf{y}_v)^T \boldsymbol{\Sigma}_{\text{prior},uu}^{-1}(\mathbf{x}_{m,u} - \mathbf{K}\mathbf{y}_v)\right] \\ &= c_3 \exp\left[-\frac{1}{2}(\mathbf{x}_{m,u} - \hat{\mathbf{x}}_{m,u})^T \boldsymbol{\Sigma}_{\text{post},uu}^{-1}(\mathbf{x}_{m,u} - \hat{\mathbf{x}}_{m,u})\right]\end{aligned} \tag{16}$$

where c_1, c_2, and c_3 are constants and the posterior covariance $\boldsymbol{\Sigma}_{\text{post},uu}$ is

$$\boldsymbol{\Sigma}_{\text{post},uu} = \text{cov}(\mathbf{x}_{m,u} \mid \mathbf{y}) = (\boldsymbol{\Sigma}_{w,uu}^{-1} + \boldsymbol{\Sigma}_{\text{prior},uu}^{-1})^{-1} \tag{17}$$

and the posterior mean is

$$\hat{\mathbf{x}}_{m,u} = E(\mathbf{x}_{m,u} \mid \mathbf{y}) = \boldsymbol{\Sigma}_{\text{post},uu}(\boldsymbol{\Sigma}_{w,uu}^{-1}\mathbf{y}_u + \boldsymbol{\Sigma}_{\text{prior},uu}^{-1}\mathbf{K}\mathbf{y}_v) \tag{18}$$

Notice that the MSE of the posterior (17) is always less than that of the measurement error, $\boldsymbol{\Sigma}_{w,uu}$. Therefore, the posterior mean is more accurate than the actual measurement.

Equation 18 can also be written in the following form.

$$\hat{\mathbf{x}}_{m,u} = \left[\boldsymbol{\Sigma}_{\text{post},uu}\boldsymbol{\Sigma}_{w,uu}^{-1} \quad \boldsymbol{\Sigma}_{\text{post},uu}\boldsymbol{\Sigma}_{\text{prior},u}^{-1}\mathbf{K}\right]\begin{Bmatrix}\mathbf{y}_u \\ \mathbf{y}_v\end{Bmatrix} = \mathbf{a}_u^T\mathbf{y} \tag{19}$$

where $\mathbf{a}_u^T$ is

$$\mathbf{a}_u^T = \left[\boldsymbol{\Sigma}_{\text{post},uu}\boldsymbol{\Sigma}_{w,uu}^{-1} \quad \boldsymbol{\Sigma}_{\text{post},uu}\boldsymbol{\Sigma}_{\text{prior},uu}^{-1}\mathbf{K}\right] \tag{20}$$

Equation 19 shows that the posterior mean is a weighted sum of the measurements of all sensors in the network.

Generally, the predicted DOFs **u** may include several variables. In the sequel, **u** is one-dimensional including one sensor only. For each sensor *u*, a corresponding row vector $\mathbf{a}_u^T$ is computed. All these vectors can be assembled in a coefficient matrix **A** to estimate all virtual sensors simultaneously:

$$\hat{\mathbf{x}}_m = \mathbf{A}\mathbf{y} \tag{21}$$

where each row *u* of matrix **A** represents the corresponding sensor.

A diagonal covariance matrix is assumed with variances (17) in the corresponding row *u*.

2.6 Application of virtual sensing

Bayesian virtual sensing is applied to each measurement separately. Each measurement is assumed to be acquired under constant environmental or operational condition, so that the dynamic characteristics remain the same during the whole measurement period. Because the measurement period is typically of the order of a few seconds or minutes, this assumption is often valid. Therefore, the differences between measurements due to environmental or operational variability or damage remain in the data. The noise is only reduced.

Virtual sensors are then used in subsequent damage detection using virtual sensing again but in a different way as shown in the following.

3 Damage detection under different environmental or operational conditions

Virtual sensors are used in damage detection as if they were physical hardware. The measurement data are replaced with the virtual sensor data ($\mathbf{y} \leftarrow \hat{\mathbf{x}}_m$) (21). The damage detection algorithm used in this paper is briefly outlined. Each sensor in turn is estimated using the remaining sensors in the network. The residuals for each sensor are then generated:

$$\boldsymbol{\varepsilon}_u = \mathbf{y}_u - \hat{\mathbf{y}}_u \tag{22}$$

where $\mathbf{y}_u$ is a vector of virtual sensor data (Equation 18 or 19) and $\hat{\mathbf{y}}_u$ is the evidence mean (9), identified using training data (virtual sensors) from the undamaged structure. The training data consist of several measurements in order to take different environmental or operational conditions into account. Specifically, the data covariance matrix (7) is estimated using all training data. The environmental or operational influences can be eliminated using correlation between the features [24]. Once damage occurs, the correlation structure does not fit the experimental data producing a larger residual, which will then trigger an alarm.

All residuals are standardized according to the training data. All samples, training and test data, are subjected to principal component analysis (PCA). The first principal component (PC) is retained in order to find the direction with the largest change in the data space, which is supposed to indicate damage. If the first PC scores of the residuals are not normally distributed and the distribution is unknown, a generalized extreme value distribution can be used regardless of the data distribution [41]. The scores are divided into subgroups (of size n = 100) and the subgroup minima and maxima are recorded. Extreme value distributions are identified for both the subgroup minima and maxima of the in-control samples (training data). The control limits are computed to these distributions by choosing the probability of exceedance (here 0.001). The extreme values are plotted on a control chart [42] to see if the test samples exceed the control limits thus indicating damage.

The increased sensitivity to damage when using Bayesian virtual sensing can be explained by Equation 22. If no noise reduction is applied, $\mathbf{y}_u$ is the actual noisy measurement from which a less noisy estimate $\hat{\mathbf{y}}_u$ is subtracted. The noise of the original data thus remains in the residual. On the other hand, when applying Bayesian virtual sensing, $\mathbf{y}_u$ will have less noise than the actual measurement, and subtracting $\hat{\mathbf{y}}_u$ will result in a less noisy residual, which in beneficial to damage detection.

4 Numerical example

Numerical simulations were performed using a finite element model of a stiffened bridge deck (Figure 1). The structure was a 30 m long and 11 m wide. It had four longitudinal and three lateral stiffeners. Four-node discrete Kirchhoff quadrilateral shell elements were used with a diagonal mass matrix. The deck was

made of concrete with Young's modulus of E = 40 GPa (at temperature T = 0°C), Poisson ratio of ν = 0.15, density of ρ = 2500 kg/m^3, and thickness of 250 mm. The stiffeners were made of steel (E = 207 GPa, ν = 0.30, ρ = 7850 kg/m^3). The longitudinal stiffeners had a web with a thickness of t = 16 mm and a height of h = 1.4 m. The bottom flange had a thickness of t = 50 mm and a width of b = 700 mm. The lateral stiffeners were 1.4 m high and 30 mm thick.

The end nodes of the bottom flanges were simply supported. Longitudinal displacements were fixed only at one end of the bridge. The corners of the deck were supported in lateral and vertical directions.

Temperature had an effect on the concrete deck. It was assumed that the temperature along the width was constant, and along the length it was linearly varying. The ends of the bridge were at random temperatures between –20°C and +40°C. The relationship between the temperature and the Young's modulus was stepwise linear as shown in Figure 2. There is thus infinite number of possible distributions of Young's modulus in the bridge deck. Notice that temperature or Young's modulus were not measured, but they were considered latent variables.

Two independent random loads were applied at nodes 774 and 872 in vertical direction (green squares in Figure 1). Both excitation signals were low-pass filtered below 8.33 Hz. The standard deviation of either load was random between 30 N and 200 N. The excitation was not measured.

The response was computed with modal superposition using the first seven modes. The analysis period was 2 s with a sampling frequency of 2 ms. One measurement period then included 1001 samples from each sensor.

Vertical accelerations were measured at 28 points shown in Figure 1. Same amount of noise was added to the signals, so that the mean signal-to-noise ratio was approximately SNR = 48 dB. The standard deviation of the noise was $\sigma_w = 3 \cdot 10^{-6}$ m/s^2, which was assumed to be known. Using the physically measured 28 accelerations, the empirical Bayesian virtual sensors were estimated.

50 measurements were made from the undamaged structure under random environmental conditions. Damage was a crack that was simulated by removing contact at certain nodes. Damage location is plotted in red in Figure 1. Three different crack configurations were modelled with an increasing severity by removing contact at one, two, or three nodes, respectively. The nodes are shown in the detailed plot in Figure 1 showing the order in which the nodes were separated. Each damage scenario was monitored with three measurements under random environmental and operational conditions. As a result, the last nine measurements were from a damaged structure. Notice that the modelled crack was in the web and in the weld between the web and the flange, making damage detection quite challenging, because the flanges remained intact.

The first seven natural modes of the undamaged structure under nominal environmental conditions are shown in Figure 3. Figure 4 shows the first seven natural frequencies in each 59 measurements. The variability due to environmental variation is clearly seen. Visually, there are no clear changes in natural frequencies due to damage. The red circles show an additional natural frequency due to damage corresponding to the lateral flapping of the web at the crack.

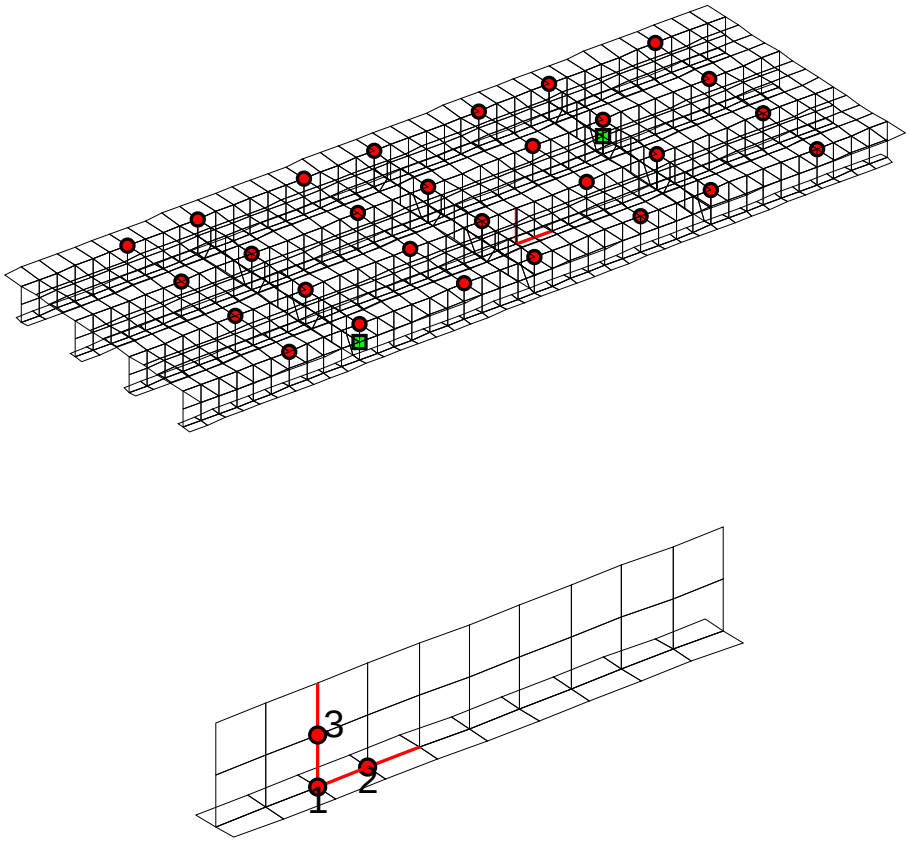


Figure 1: Top: Finite element model representing the real structure. The initial 28 sensor positions are shown as red circles and the two excitation points as green squares. Damage is shown with red lines. Bottom: A detail of the girder with damage. The crack is shown with red lines and the numbers indicate the order in which the connecting nodes separated to form an increasing crack size. The flange remained intact.

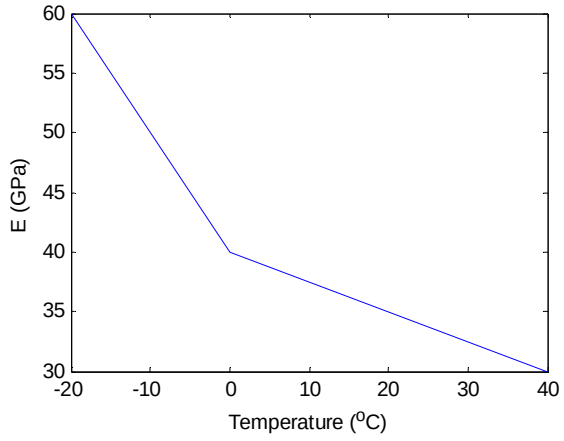


Figure 2: The effect of temperature on the Young's modulus of the concrete.

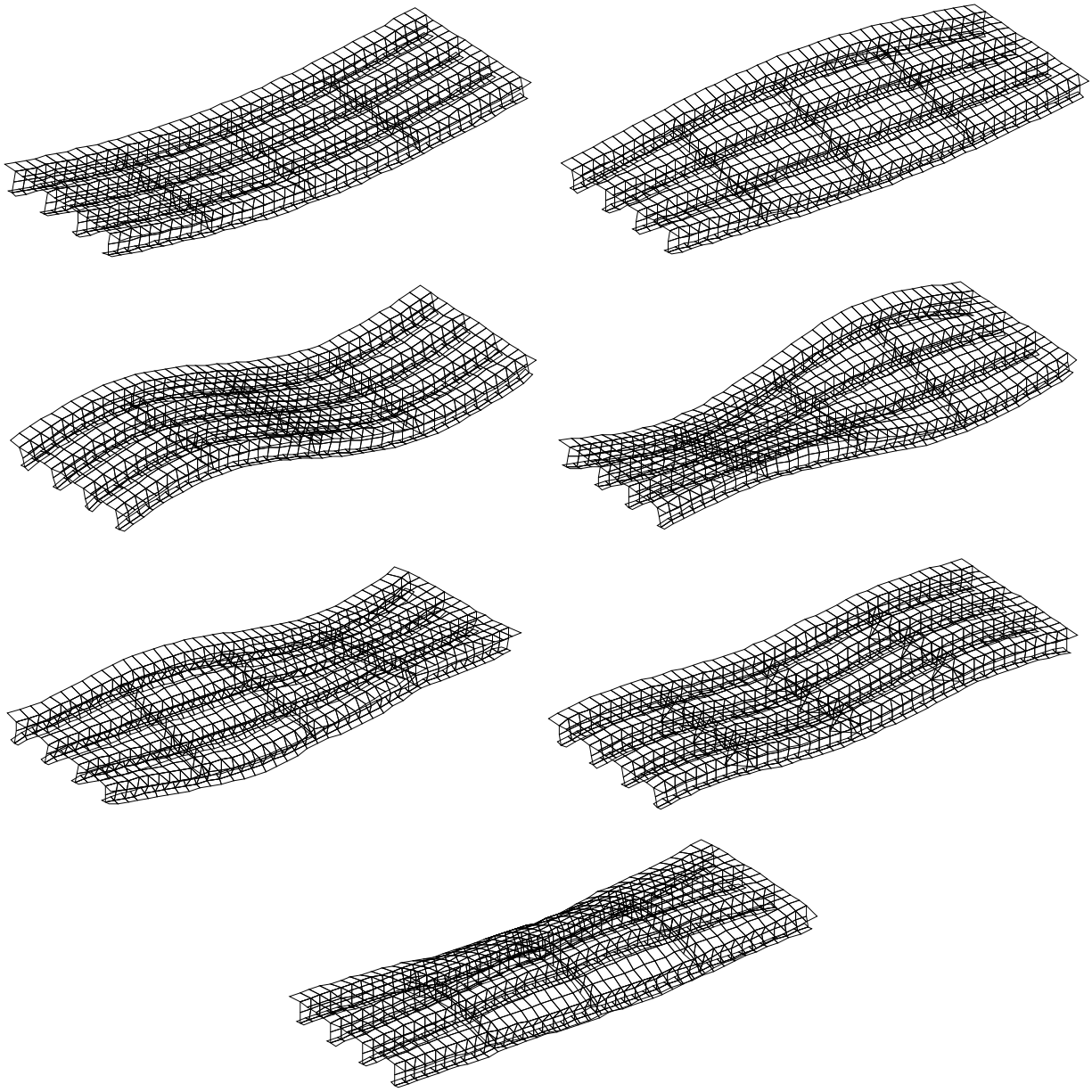


Figure 3: The first seven natural modes of the undamaged structure (T = 0°C).

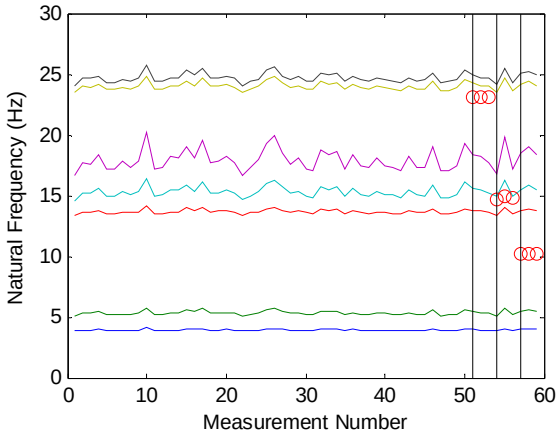


Figure 4: The first natural frequencies indicating the influences of the environmental variables. The data before the leftmost vertical line were from the undamaged structure, and the vertical lines indicate the three damage levels with an increasing severity. The red circles are additional natural frequencies due to damage.

The training data were the first 40 measurements. They were also used to design the control charts. Test data were the last 19 measurements, from which the last nine were from the damaged structure. The first principal component scores of the residuals (Equation 22) were plotted on the extreme value statistics (EVS) control chart using subgroups of size 100 [43].

Damage localization was based on the maximum discrepancy between the measurement and the estimate. The closest sensor from the damage was identified having the maximum average discrepancy.

The objective was not to create a very detailed finite element model. Instead, the purpose was to investigate the performance of Bayesian virtual sensors to damage detection compared to corresponding physical hardware. For the modelled damage, the noise level was deliberately chosen so that the comparison could be easily made. In addition, the selected noise level would give an indication of the possible crack size that can be detected with actual hardware. An open crack was modelled instead of a breathing crack, because it was shown in an earlier study that a breathing crack may be much easier to detect than an open crack due to resulting non-linear effects [44].

Figure 5 shows a detail of the acceleration of sensor 10. Three curves are shown: the noiseless data (blue), the actual noisy measurement (black), and the Bayesian virtual sensor (red). A larger noise level was used to make visual comparison possible. For the actual noise level, the standard deviation of the noise in all sensors is plotted in Figure 6 both for the hardware (red) and Bayesian virtual sensor (blue). It can be seen that the Bayesian virtual sensor was more accurate than the actual hardware. The standard deviation of the noise was decreased to one third on average. This noise reduction property was utilized in damage detection as shown next.

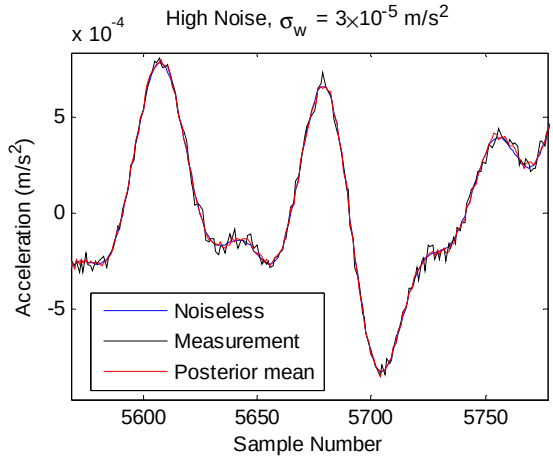


Figure 5: Time history of sensor 10. Blue: true (noiseless) data. Black: actual noisy measurement. Red: Bayesian virtual sensor. A larger measurement error was used to enable visual comparison.

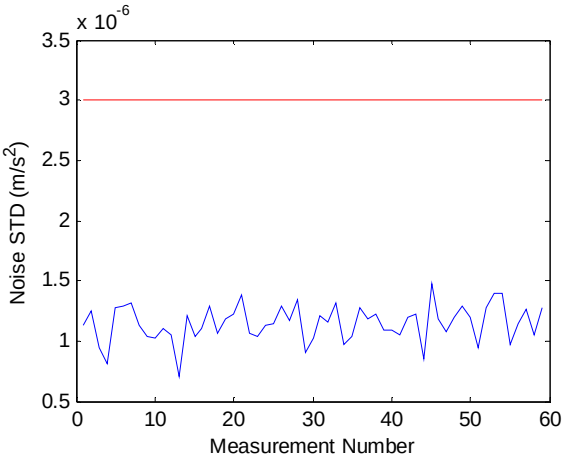


Figure 6: Standard deviation of noise in the actual sensor 10 (red) in each measurement, and the noise of the Bayesian estimate (blue).

EVS control charts for damage detection are shown in Figure 7. The left chart was plotted using the actual measurements indicating no damage, whereas the chart in the right that was plotted using the virtual sensors was able to detect damage levels 2 and 3. It should be noted that the measurement error (noise) was small indicating that high-quality sensors may be required to detect damage of this type and size. Nevertheless, with Bayesian virtual sensors it is possible to detect damage earlier than if using the physical hardware.

Damage was localized to sensor 10 (Figure 8) that was the next sensor to the right from the actual damage location and above the same girder. The closest sensor from the crack was sensor 11, which also showed a high residual. It was located above the intersection of the longitudinal and lateral stiffeners.

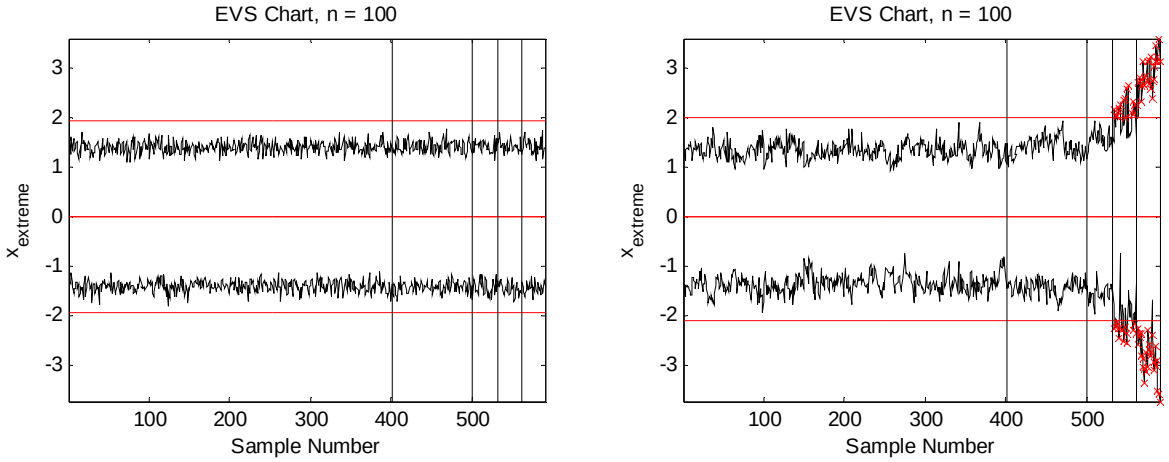


Figure 7: EVS control chart using actual measurements (left) and Bayesian virtual sensors (right). The data before the leftmost vertical line were used as training data, and the other vertical lines indicate the three damage levels with an increasing severity.

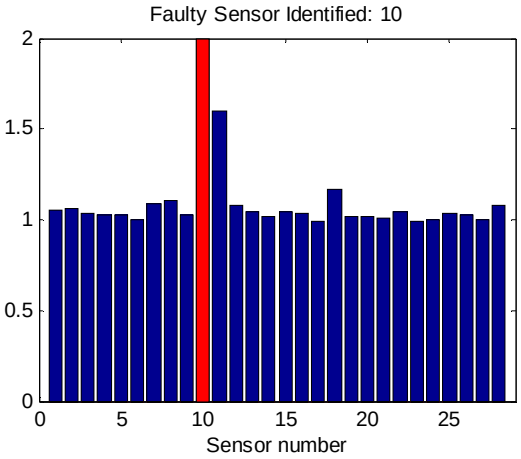


Figure 8: Damage localization

5 Conclusion

Bayesian virtual sensing was introduced and used in damage detection. With Bayesian VS it is possible to decrease the measurement error, making an early warning more achievable. Bayesian virtual sensing was applied to each measurement individually, so that the dynamics and environmental or operational influences remained, but noise was only decreased. The resulted virtual sensor data then replaced the actual measurements in damage detection.

Data analysis for damage detection was made in the time domain without a feature extraction process, without knowing the excitation or the environmental or operational variables, and without a mathematical model of the structure. Environmental and operational effects were eliminated using the correlation between the virtual sensors. Training data were used to build a correlation model of the undamaged structure under different environmental or operational conditions. The training data were used to estimate one sensor in turn using the remaining virtual sensors in the network. The virtual sensor data and the estimates were subtracted to generate the residuals. Principal component analysis was applied to the residuals, and the first principal component scores were used to design the extreme value statistics control chart for damage detection with appropriate control limits. Damage was localized to the closest sensor having the largest average residual.

The noise level used in the experiment was quite low, and the results indicated that high-quality sensors may be required to detect the introduced damage. Another study could be made by increasing the crack size gradually to find the smallest detectable crack size. In addition, other crack locations or damage scenarios could be studied.

The measurement error can be further decreased by increasing the number of sensors. The noise reduction rate, however, is not linear but would rapidly decrease as with any averaging process (for example, the standard error of the mean is proportional to $N^{-1/2}$, where N is the size of the sample).

The sensor network had 28 accelerometers, which were placed in a 4×7 grid. Optimal sensor placement for damage detection was left for future studies.

Acknowledgements

This research has been supported by Metropolia University of Applied Sciences.

References

[1] M.A. Wahab, G. De Roeck, *Effect of temperature on dynamic system parameters of a highway bridge*, Structural Engineering International, No. 4 (1997), pp. 266–270.

[2] C.R. Farrar, S.W. Doebling, P.J. Cornwell, E.G. Straser, *Variability of modal parameters measured on the Alamosa Canyon Bridge*, Proceedings of IMAC-XV: A Conference on Structural Dynamics, Orlando, Florida (1997), pp. 257–263.

[3] S. Alampalli, *Influence of in-service environment on modal parameters*, Proceedings of the 16th International Modal Analysis Conference, Santa Barbara, California (1998), pp. 111–116.

[4] P. Cornwell, C.R. Farrar, S.W. Doebling, H. Sohn, *Structural testing series: Part 4. Environmental variability of modal properties*, Experimental Techniques, Vol. 23, No. 6 (1999), pp. 45–48.

[5] B. Peeters, G. De Roeck, *One year monitoring of the Z24 Bridge: Environmental influences versus damage effects*, Proceedings of IMAC-XVIII: A Conference on Structural Dynamics, San Antonio, Texas, February 7–10, 2000, pp. 1570–1576.

[6] R.G. Rohrmann, M. Baessler, S. Said, W. Schmid, W.F. Ruecker, *Structural causes of temperature affected modal data of civil structures obtained by long time monitoring*, Proceedings of IMAC-XVIII: A Conference on Structural Dynamics, San Antonio, Texas, February 7–10, 2000, pp. 1–7.

[7] G.R. Darbre, J. Proulx, *The need for system identification techniques using ambient vibration data recorded on large dams*, Proceedings of the International Conference on Structural System Identification, Kassel, Germany, September 5–7, 2001, pp. 205– 213.

[8] J. Kullaa, *Elimination of environmental influences from damage-sensitive features in a structural health monitoring system*, Proceedings of the First European Workshop on Structural Health Monitoring, Paris, France, July 10–12, 2002, DEStech (2002), pp. 742–749.

[9] Á. Cunha, E. Caetano, C. Moutinho, F. Magalhães, *Continuous dynamic monitoring of bridges: Different perspectives of application*, Advanced Materials Research, Vol. 745, Trans Tech Publications (2013), pp. 89-99.

[10] G. Comanducci, F. Magalhães, F. Ubertini, Á. Cunha, *On vibration-based damage detection by multivariate statistical techniques: Application to a long-span arch bridge*, Structural Health Monitoring, Vol. 15, No. 5, Sage Publications (2016), pp. 505-524.

[11] W.-H. Hu, S. Thöns, R. G. Rohrmann, S. Said, W. Rücker, Vibration-based structural health monitoring of a wind turbine system. Part II: Environmental/operational effects on dynamic properties, Engineering Structures, Vol. 89, Elsevier (2015), pp. 273-290.

[12] G. Manson, *Identifying damage sensitive, environment insensitive features for damage detection*, Proceedings of the Third International Conference on Identification in Engineering Systems, Swansea, 2002, pp. 187–197.

[13] J. Kullaa, *Is temperature measurement essential in structural health monitoring?*, Proceedings of the 4th International Workshop on Structural Health Monitoring, Stanford, CA, September 15–17, 2003, DEStech (2003), pp. 717–724.

[14] H. Sohn, K. Worden, C.R. Farrar, *Statistical damage classification under changing environmental and operational conditions*, Journal of Intelligent Materials Systems and Structures, Vol. 13, No. 9 (2003), pp. 561–574.

[15] J. Kullaa, *Latent variable models to eliminate the environmental effects in structural health monitoring*, Proceedings of the Third European Conference on Structural Control, Volume II, Vienna, Austria, July 12–15, 2004, pp. S5-55–58.

[16] S. Vanlanduit, E. Parloo, B. Cauberghe, P. Guillaume, P. Verboven, *A robust singular value decomposition for damage detection under changing operational conditions and structural uncertainties*, Journal of Sound and Vibration, Vol. 284 (2005), pp. 1033–1050.

[17] A.-M. Yan, G. Kerschen, P. De Boe, J.-C. Golinval, *Structural damage diagnosis under varying environmental conditions—Part I: A linear analysis*, Mechanical Systems and Signal Processing, Vol. 19 (2005), pp. 847–864.

[18] A.-M. Yan, G. Kerschen, P. De Boe, J.-C. Golinval, *Structural damage diagnosis under varying environmental conditions—Part II: local PCA for non-linear cases*, Mechanical Systems and Signal Processing, Vol. 19 (2005), pp. 865–880.

[19] J. Kullaa, *Removing non-linear environmental influences from structural features*, Proceedings of the third European Workshop on Structural Health Monitoring, Granada, Spain, July 5–7, 2006, DEStech (2006), pp. 635–642.

[20] A.-M. Yan, J.-C. Golinval, *Null subspace-based damage detection of structures using vibration measurements*, Mechanical Systems and Signal Processing, Vol. 20 (2006), pp. 611–626.

[21] M. Basseville, F. Bourquin, L. Mevel, H. Nasser, F. Treyssède, *Merging sensor data from multiple temperature scenarios for vibration-based monitoring of civil structures*, Proceedings of the third European Workshop on Structural Health Monitoring, Granada, Spain, July 5–7, 2006, DEStech (2006), pp. 759–506.

[22] V. Lämsä, & J. Kullaa, *Nonlinear factor analysis in structural health monitoring to remove environmental effects*, Proceedings of the 6th International Workshop on Structural Health Monitoring, Stanford, CA, September 11–13, 2007, DEStech (2007), pp. 1092–1099.

[23] D. Gorinevsky, S.-J. Kim, S. Boyd, G. Gordon, S. Beard, F.-K. Chang, *Optimal estimation of accumulating damage trend from series of SHM images*, Proceedings of the 6th International Workshop on Structural Health Monitoring, Stanford, CA, September 11–13, 2007, DEStech (2007), pp. 1340–1346.

[24] J. Kullaa, *Eliminating environmental or operational influences in structural health monitoring using the missing data analysis*, Journal of Intelligent Material Systems and Structures, Vol. 20, No. 11 (2009), pp. 1381–1390.

[25] E.J. Cross, K. Worden, Q. Chen, *Cointegration: a novel approach for the removal of environmental trends in structural health monitoring data*, Proceedings of the Royal Society A 467 (2011), pp. 2712–2732.

[26] J. Kullaa, *Structural health monitoring under nonlinear environmental or operational influences*, Shock and Vibration (2014).

[27] A. Ray, R. Luck, *An introduction to sensor signal validation in redundant measurement systems*, IEEE Control System Magazine, Vol. 11 (1991), pp. 44–49.

[28] R. Dunia, S.J. Qin, T.F. Edgar, T.J. McAvoy, *Identification of faulty sensors using principal component analysis*, AiChe Journal, Vol. 42 (1996), pp. 2797–2812.

[29] R. Dunia, S.J. Qin, *Joint diagnosis of process and sensor faults using principal component analysis*, Control Engineering Practice, Vol. 6 (1998), pp. 457–469.

[30] M.I. Friswell, D.J. Inman, *Sensor validation of smart structures*, Journal of Intelligent Material Systems and Structures, Vol. 10 (1999), pp. 973–982.

[31] M. Abdelghani, M.I. Friswell, Sensor validation for structural systems with additive sensor faults, Structural Health Monitoring, Vol. 3 (2004), pp. 265–275.

[32] G. Kerschen, P. De Boe, J.-C. Golinval, K. Worden, *Sensor validation using principal component analysis*, Smart Materials and Structures, Vol. 14 (2005), pp. 36–42.

[33] J. Kullaa, *Sensor fault identification and correction in structural health monitoring*, Proceedings of ISMA2006, International Conference on Noise and Vibration Engineering, Leuven, Belgium, September 18–20, 2006, pp. 873–884.

[34] J. Kullaa, *Sensor fault identification and correction in vibration-based multichannel structural health monitoring*, Proceedings of the 6th International Workshop on Structural Health Monitoring, Stanford, CA, September 11–13, 2007, DEStech (2007), pp. 606–613.

[35] M. Abdelghani, M.I. Friswell, Sensor validation for structural systems with multiplicative sensor faults, Mechanical Systems and Signal Processing, Vol. 21 (2007), pp. 270–279.

[36] M.R. Hernandez-Garcia, S.F. Masri, 2008. Multivariate statistical analysis for detection and identification of faulty sensors using latent variable methods, Advances in Science and Technology, Vol. 56 (2008), pp. 501–507.

[37] J. Kullaa, *Three models for sensor validation*, Proceedings of the 7th International Workshop on Structural Health Monitoring, Stanford, CA, September 9–11, 2009, DEStech (2009), pp. 529–536.

[38] J. Kullaa, *Sensor validation using minimum mean square error estimation*, Mechanical Systems and Signal Processing, Vol. 24 (2010), pp. 1444–1457.

[39] J. Kullaa, *Detection, identification, and quantification of sensor fault in a sensor network*, Mechanical Systems and Signal Processing, Vol. 40 (2013), pp. 208–221.

[40] C.M. Bishop, *Pattern recognition and machine learning*, Springer (2006).

[41] K. Worden, D. Allen, H. Sohn, C.R. Farrar, *Damage detection in mechanical structures using extreme value statistics*, SPIE Proceedings, Vol. 4693, 9th Annual International Symposium on Smart Structures and Materials, San Diego, CA, 2002, pp. 289–299.

[42] D.C. Montgomery, *Introduction to statistical quality control*, 3rd edition, New York, Wiley (1997).

[43] J. Kullaa, F. Magalhães, Á. Cunha, *Structural health monitoring and damage detection of an arch bridge using a minimum mean square error estimator*, Life-Cycle of Engineering Systems: Emphasis on Sustainable Civil Infrastructure. Proceedings of the Fifth International Symposium on Life-Cycle Civil Engineering (IALCCE 2016). Delft, The Netherlands, 16–19 October 2016, Taylor & Francis (2016), pp. 777–784.

[44] J. Kullaa, M. Miettinen, *Fatigue crack modelling for damage detection*, Proceedings of the 8th European Workshop on Structural Health Monitoring, Bilbao, Spain, July 5–8, 2016.

Application of $\mathcal{H}^\infty$ estimation and oblique projections for experimental damage identification by SP2E

M. Vollmering[1], **A. Lenzen**[1]
[1] Structural Dynamics, Leipzig University of Applied Sciences,
Karl-Liebknecht-Straße 132, 04277 Leipzig
e-mail: **Armin.Lenzen@htwk-leipzig.de**

Abstract
In this contribution experimental damage localization of mechanical systems based on $\mathcal{H}^\infty$ estimation, an introduced difference process and state projection estimation error (SP2E) is studied. Because real structural excitations are presumed to be unknown, a general input is applied therein, which allows synchronization and normalization. Furthermore, state projections are introduced to enhance damage identification. Based on these theoretical results, SP2E is experimentally used to localize stiffness degradations and mass alterations in a laboratory set-up. Here, the usage of projection techniques for damage identification was proven. By analysing several different structural alteration positions and extents, an experimental sensitivity study has been conducted, which confirmed the applicability of SP2E for damage localization.

1 Introduction

In view of the life-cycle of buildings, one must consider different phases, namely design, construction, operation and demolition. The costs during maintenance are very important in view of the total building costs. To reduce maintenance costs, structural state identification and health monitoring is important, which is based on information about the structure by measuring and observing.

One can get dynamic structural responses as a consequence of deterministic excitations (e.g. impulses, sweeps). Because these test loads may be too cost-intensive or not applicable at all for large-scale structures, one should use ambient excitations instead. These stochastic loads (e.g. wind, traffic, waves) are not measurable, which makes more elaborate identification techniques necessary. Therefore, the stochastic subspace identification (SSI) technique allows to parametrize state space parameter and a measured power spectrum. Nevertheless, the application of those state space parameters for structural alteration identification may be a challenge. Several techniques have been defined for that, for instance methods based on numerically-derived mode shapes, curvatures, experimental flexibilities, and so on. Unfortunately, these (most often theoretically only described) methods may be inadequate for large-scale structures, like bridges, wind energy plants, and so forth.

In this contribution a new damage identification technique is presented and explained. It is named state projection estimation error (SP2E).[1–3] A very important element is the usage of $\mathcal{H}^\infty$ estimation theory. This method is an advantageous approach to deal with unknown structural excitations. Briefly summarizing the method, an $\mathcal{H}^\infty$ estimator is determined for both the reference and the potentially damaged structural state based on SSI results. Those estimators are then used to determine an (estimation error) difference process, whose average process power is a well-suited parameter to identify structural alterations. The average process power of the difference process can then advantageously be determined by using the solution of a Lyapunov equation.

To improve the structural alteration identification, the introduced difference process is further developed, essentially to reduce noise. For that, oblique projections of system states are introduced, which leads to method SP2E. This technique is based (from an algorithmic perspective) on structural measurements only, and a mechanical-analytical model (e.g. finite element model (FEM)) is not necessary.

Method SP2E has been verified in laboratory experiments. Here, some experimental results are shown and discussed based on a structural steel cantilever arm with 2.45m length. To get structural responses with eight uniaxial accelerometers, an ambient excitation was simulated by acoustic noise. Most importantly, the structure was subsequently altered by applying masses and reducing the stiffness by saw cuts.

By applying SP2E, the authors show that a mass increase of 0.5% of the structural total mass was detectable and locatable at different positions. In addition to that, saw cuts were locatable too. These studies were expanded for different alteration scenarios and repeated in over 100 experiments. All results were reproducible and indicated the correct alteration location, which confirms the experimental applicability of SP2E.

Nomenclature

Systems

T_{yu}	Transfer system $T_{yu} : y \leftarrow u$
$\left[\begin{array}{c\|c} A & B \\ \hline C & D \end{array}\right]$	Linear time-invariant state space
	$T_{yu}(\sigma) = C\big(\sigma I - A\big)^{-1}B + D$
	$\sigma x(\sigma) = Ax(\sigma) + Bu(\sigma)$
	$y(\sigma) = Cx(\sigma) + Du(\sigma),\ \sigma = (s, z)$

Matrices

0	Zero matrix
Λ, X	Eigenvalues and -vectors
Π	Solution of Lyapunov equation
A	System matrix
C	Observer matrix
I	Identity matrix
K_p	Gain matrix
L	User defined matrix
M	Covariance of w and v: Q, R_v, S
M_x	Measurement position x
N	Control matrix
P	Solution of Riccati equations
P_V	Projector onto $\mathcal{V}$
R_x	Covariance of x
S_x	Spectral density of x
U, V	Basis of spaces $\mathcal{U}$ and $\mathcal{V}$
Y, Z	Coupling matrices

Operations

$\|\times\|_{\mathcal{H}^2}$	Two-norm
$\|\times\|_{\mathcal{H}^\infty}$	Infinity-norm
$E\{\times\}$	Expectation
$\langle \times, \times \rangle$	Gramian matrix
$\times^T$	Transpose
$\times^*$	Conjugate transpose
$\times^{-1}$	Inverse
$\hat{\times}$	Estimate

Spaces

$\mathbb{C}$	Complex numbers
$\mathbb{N}$	Non-negative natural numbers
$\mathbb{R}$	Real numbers
$\mathcal{H}$, $\mathcal{K}$	Hilbert/Krein space
$\mathcal{U}$, $\mathcal{V}$	Complementary Subspaces
$\mathcal{W}$	Vector space

Scalar Quantities

γ	Upper bound
ω, θ	Angular frequency
j	Imaginary number
k, l	Discrete time-step
N	Number of samples
n	Number of states, system order
p	Number of measurement positions

Vectors

$\bar{P}$	Average power
d	Difference process
e	Estimation error
w, v	Process, measurement noise
x	State vector
y	Structural response

2 Damage localization: State projection estimation error (SP2E)

2.1 Outline

In this section the identification of a mechanical structure and its application for damage identification based on estimation theory is discussed. Because structural health monitoring systems must be able to distinguish between an undamaged and a damaged structural state, the indexes are chosen accordingly as 1)*reference* and 2)*potentially damaged* structural state. The subsequent theoretical development is summarized in table 1.

	Theoretical Issue	Objective
1.	The mechanical structure is measured (e.g. accelerations) during operation in two structural states by y_1 and y_2.[4]	In order to identify structural damage, a system shall be found to represent the measurement of each structural state.
2.	Experiments and thus an excitation is necessary to measure y_1 and y_2. Therefore, ambient excitations are superior to deterministic ones.[5]	Stochastic subspace identification (SSI) is an appropriate tool to determine the required systems based on measurements y only. If SSI is used, an FE-model is unnecessary
3.	The state space systems (following SSI) $T_{yn,1}(A_1, C_1)$ and $T_{yn,2}(A_2, C_2)$ of equation (1) cannot be compared (e.g. difference), because of unknown input processes w and v.	A normalization basis must be found to make both systems comparable, which the innovation form (e.g. equation (2)) allows. That is the common approach to represent the measurement at a mechanical structure.[6]
4.	To determine systems $T_{ye,1}(A_1, K_{p,1}, C_1)$ and $T_{ye,2}(A_2, K_{p,2}, C_2)$ following Kalman filtering theory and SSI concepts, a Riccati equation must be solved. Unfortunately, the equation may be unsolvable due to numerical problems.[7–9]	A major problem is positivity, hence the requirement for a positive definite spectrum $S_y(e^{j\theta})$.[7] To circumvent that, straightforward noise presumptions $Q = I$, $R = I$ and $S = 0$ can be used. Because this leads to a positive-definite input Gramian, a Riccati solution is guaranteed,[10] presuming a (Schur) stable A.
5.	The innovation form follows the Kalman filter, which is susceptible to noise uncertainties. Hence, $Q = I$, $R = I$ and $S = 0$ may lead to large estimation errors.[11,12]	A robust estimator must be determined. Here, the $\mathcal{H}^\infty$ theory allows to cope with noise uncertainties.[13]
6.	By using $\mathcal{H}^\infty$ theory, process e in equation (2) is not uniform. Furthermore, e is a general estimation error process, not an innovation process.[13]	The state space systems $T_{ye,1}$ and $T_{ye,2}$ based on $\mathcal{H}^\infty$ theory are inverted, which allows to apply a normalization basis in equation (6).

Table 1: Overview of the Theoretical Development

2.2 System identification and estimation theory

Stochastic subspace identification is a widespread technique, which is briefly discussed only below. The authors refer to standard literature, like Van Overschee and De Moor[14] and Katayama.[15] Very importantly, stochastic subspace identification is seen here as a technique to parametrize a state space system, rather then a tool which identifies modal data only.[6,16] Following that a very important result of stochastic subspace

identification is state space system $T_{yn}(A, C)$:

$$\begin{bmatrix} x_{k+1} \\ y_k \end{bmatrix} = \begin{bmatrix} A & I & 0 \\ C & 0 & I \end{bmatrix} \begin{bmatrix} x_k \\ w_k \\ v_k \end{bmatrix}, \quad T_{yn} = \left[\begin{array}{c|cc} A & I & 0 \\ \hline C & 0 & I \end{array}\right], \quad n_k = \begin{bmatrix} w_k \\ v_k \end{bmatrix} . \tag{1}$$

State space system $T_{yn}(A, C)$ represents the measurement of a mechanical structure and is parametrized by system identification techniques on the basis of measurement y (step 2 in table 1). Basically, the covariance based and the data driven approaches can be used for that. The identified system parameters then are $A \in \mathbb{C}^{n \times n}$ and $C \in \mathbb{C}^{p \times n}$. Here, n is the number of states and p the number of measured signals, thus $x \in \mathbb{C}^n$ and $y \in \mathbb{R}^p$. Modelled by process noise $w \in \mathbb{C}^n$, the mechanical system is excited by wind, traffic, waves, and so on. Nevertheless, measurement noise $v \in \mathbb{R}^p$ (e.g. static noise, quantizing noise) must be considered and both noise disturbances w and v are modelled as white noise processes.[10,15] This truly is inaccurate for real-life disturbances, but is used very commonly for an approximation.

The reference and the potentially altered structural states are defined by indexes 1 and 2. Two systems $T_{yn,1}(A_1, C_1)$ and $T_{yn,2}(A_2, C_2)$ follow and can be compared as the axiom II of Worden et al.[4] suggests. Unfortunately, a direct comparison (e.g. a difference) of both systems is rather useless, because signal disturbance processes w and v are unknown. Hence, both state space systems $T_{yn,1}$ and $T_{yn,2}$ are normalized differently (step 3 in table 1). Here, estimation theory leads to an alternative, for instance the Kalman filter in system identification.

Based on an identified system T_{yn}, various authors like Van Overschee and De Moor,[14] Katayama,[15] and so on discuss the determination of a Kalman filter in innovation form (state space system), which represents the measurement at a mechanical structure:[6]

$$\begin{bmatrix} \hat{x}_{k+1} \\ y_k \end{bmatrix} = \begin{bmatrix} A & K_p \\ C & I \end{bmatrix} \begin{bmatrix} \hat{x}_k \\ e_k \end{bmatrix}, \quad T_{ye} = \left[\begin{array}{c|c} A & K_p \\ \hline C & I \end{array}\right] . \tag{2}$$

To numerically compute a state space system following the innovation form of a Kalman filter (which leads to equation (2)), a discrete-time algebraic Riccati equation (step 4 in table 1) must be solved on the basis of a theoretical input Gramian according to Kailath et al.:[10]

$$M(\Pi_x) = E\left\{ \begin{bmatrix} w_k \\ v_k \end{bmatrix} \begin{bmatrix} w_k \\ v_k \end{bmatrix}^* \right\} = \begin{bmatrix} Q & S \\ S^* & R_v \end{bmatrix} = \begin{bmatrix} \Pi_x - A\Pi_x A^* & N - A\Pi_x C^* \\ N^* - C\Pi_x A^* & R_y(0) - C\Pi_x C^* \end{bmatrix} . \tag{3}$$

This Gramian does not describe real physical disturbances, because noise processes w and v are unknown. Hence, second order statistical parameters Q, R_v and S follow a pure theoretical description and states x may have no physical meaning here.

As has been discussed before, estimator equation (2) is determinable by solving a Riccati equation. To be solvable, several criteria (stability, observability, controllability and positivity) must be maintained in the frame of stochastic subspace identification.[7–9] Although stabilization methods (e.g.[7]) have been defined, a useful solution may be questionable for a physical interpretation. Hence, a rather straightforward choice $Q = I$, $R_v = I$ and $S = 0$ is undertaken, which is problematic in the frame of Kalman filtering, because this theory requires exact noise presumptions. The consequences of imprecise noise parameters on Kalman filtering have been repeatedly discussed, for instance by Simon[11] and Mangoubi[12] (step 5 in table 1).

Thus, noise uncertainties must be considered for the derivation of equation (2). That is possible by $\mathcal{H}^\infty$ theory, but not through Kalman filtering. The robust estimator approach can be explained with the help

of a general weighting matrix L, which allows to define a theoretical signal $z_k = Lx_k$. By estimating this signal (e.g. by $\hat{z}_k = L\hat{x}_k$), the central criterion of $\mathcal{H}^\infty$ estimation is defined by applying $\tilde{z}_k = z_k - \hat{z}_k$:

$$\lim_{N\to\infty} \frac{\sum_{k=0}^{N-1} \|\tilde{z}_k\|_2^2}{\sum_{k=0}^{N-1} \left(\|w_k\|_2^2 + \|v_k\|_2^2 \right)} < \gamma^2 \,. \tag{4}$$

This equation analyzes the worst-case scenario of noise disturbances w and v with regard to the weighted estimation error $\tilde{z}$. Centrally, that allows to take noise uncertainties into account. For clarity the initial state has been omitted above. Because a theoretical solution to the above estimation problem can be given for some special cases only, a suboptimal problem is introduced instead by defining an upper bound γ.[13]

Estimator (and thus Kalman filter too) are denoted by $T_{ye}(A, K_p, C)$. Central concept is the estimate of state, which follows the estimation error process $e \in \mathbb{R}^p$ and the gain $K_p \in \mathbb{C}^{n\times p}$. This approach is interesting here, because it allows recursive signal determination, in opposite to the former state space system $T_{yn}(A, C)$.

Most importantly, the numerical solvability is guaranteed and noise uncertainties have been taken into account by using $\mathcal{H}^\infty$ estimation. Although the numerical solution to Krein space based $\mathcal{H}^\infty$ estimation[13] is very similar to the Kalman filtering solution, process e is not an innovation process. However, Kalman filtering is recovered as γ tends to ∞. Here, the authors refer to Simon,[11] Hassibi et al.,[13] Mangoubi,[12] and so forth.

2.3 Synchronization and Normalization

In view of the above discussion, two state space systems $T_{ye,1}$ and $T_{ye,2}$ following $\mathcal{H}^\infty$ theory are present, which represent the measurement at a mechanical system in reference and potentially altered structural state. Consequentially, in *reference state* (calibration of monitoring system) measurement y_1 has been measured to identify $T_{yn,1}$ and $T_{ye,1}$. In opposite to that $T_{yn,2}$ and $T_{ye,2}$ are determined in a *potentially damaged state* of the mechanical system following y_2.

Unfortunately, a direct comparison of both state space systems $T_{ye,1}$ and $T_{ye,2}$ (e.g. as a difference) is useless, because driving estimation error processes e_1 and e_2 are not uniformly standardized (step 6 in table 1). To allow that, both processes should be standard inputs, like a white noise process in the stochastic case.

While the estimation error processes are unknown at first, measurement processes are present. Hence, the above problem can be circumvented by inverting the state space systems. Fortunately, the inversion follows a simple reordering of equation (2) in accordance to estimation theory as

$$\begin{bmatrix} \hat{x}_{k+1} \\ e_k \end{bmatrix} = \begin{bmatrix} A_p & K_p \\ -C & I \end{bmatrix} \begin{bmatrix} \hat{x}_k \\ y_k \end{bmatrix}, \quad T_{ey} = \left[\begin{array}{c|c} A_p & K_p \\ \hline -C & I \end{array}\right], \quad A_p = A - K_pC \,. \tag{5}$$

As can be seen here, both inverse state space systems $T_{ey,1}(A_{p,1}, K_{p,1}, C_1)$ and $T_{ey,2}(A_{p,2}, K_{p,2}, C_2)$ can be defined to have the same measurement process input.

Index 3 is introduced, which is a theoretical structural state. Now, the important idea is to use the same measurement process y_3 for both inverse systems $T_{ey,1}$ and $T_{ey,2}$, which synchronizes and normalizes the outcome, in this case estimation error processes e_1 and e_2. By applying process y_3 to both systems $T_{ey,1}$ and $T_{ey,2}$, synchronization and normalization of both processes e_1 and e_2 is achieved. This allows to introduce a difference process

$$d_k = e_{1,k} - e_{2,k} = \left(y_{3,k} - \hat{y}_{1,k}\right) - \left(y_{3,k} - \hat{y}_{2,k}\right) = -\hat{y}_{1,k} + \hat{y}_{2,k} \,. \tag{6}$$

Again the advantage of using $\mathcal{H}^\infty$ estimation can be seen here. Besides the consideration of noise uncertainties (which are unknown for bridges, offshore wind energy plants, airplanes, etc.), the general measurement process y_3 might differ from original signals y_1 and y_2. In summary both arguments emphasize the consideration of noise and model uncertainties, and $\mathcal{H}^\infty$ estimator are thus an appropriate choice.

2.4 Analysis of the Difference Process and Determination of Average Process Power

The defined difference process of equation (6) can directly be applied to determine d, which can be analysed based on the average process power. Henceforth, the difference process d shall be represented by a state space system, because a deeper understanding of that process and an advantageous numerical solution then follows subsequently.

In order to define a state space formulation of d, equation (6) is rewritten as an observer equation:

$$d_k = -\hat{y}_{1,k} + \hat{y}_{2,k} = -C_1\hat{x}_{1,k} + C_2\hat{x}_{2,k} = \begin{bmatrix} -C_1 & C_2 \end{bmatrix} \begin{bmatrix} \hat{x}_{1,k} \\ \hat{x}_{2,k} \end{bmatrix} . \tag{7}$$

To revise above, a theoretical measurement process y_3 is uniformly applied to the inverse systems $T_{ey,1}$ and $T_{ey,2}$. That allows to determine a control equation, which leads to the state space system:

$$\begin{bmatrix} \hat{x}_{1,k+1} \\ \hat{x}_{2,k+1} \\ d_k \end{bmatrix} = \begin{bmatrix} A_{p,1} & 0 & K_{p,1} \\ 0 & A_{p,2} & K_{p,2} \\ -C_1 & C_2 & 0 \end{bmatrix} \begin{bmatrix} \hat{x}_{1,k} \\ \hat{x}_{2,k} \\ y_{3,k} \end{bmatrix}, \quad T_{dy} = T_{ey,1} - T_{ey,2} = \left[\begin{array}{cc|c} A_{p,1} & 0 & K_{p,1} \\ 0 & A_{p,2} & K_{p,2} \\ \hline -C_1 & C_2 & 0 \end{array}\right] . \tag{8}$$

Based on that, it is very advantageous to determine a system, which maps standard input processes (white noise) w and v to the difference process d, as will be argued in the following. This system is referred to as T_{dn} for which different model approaches are possible.

To derive a state space system T_{dn}, the general input process y_3 is described here by system $T_{yn,3}(A_3, C_3)$ in accordance to equation (1). By applying system $T_{yn,3}(A_3, C_3)$, a state space representation is chosen:

$$\begin{bmatrix} \hat{x}_{1,k+1} \\ \hat{x}_{2,k+1} \\ x_{3,k+1} \\ d_k \end{bmatrix} = \begin{bmatrix} A_{p,1} & 0 & K_{p,1}C_3 & 0 & K_{p,1} \\ 0 & A_{p,2} & K_{p,2}C_3 & 0 & K_{p,2} \\ 0 & 0 & A_3 & I & 0 \\ -C_1 & C_2 & 0 & 0 & 0 \end{bmatrix} \begin{bmatrix} \hat{x}_{1,k} \\ \hat{x}_{2,k} \\ x_{3,k} \\ w_k \\ v_k \end{bmatrix} \tag{9a}$$

$$T_{dn} = T_{dy}T_{yn,3} = \left[\begin{array}{ccc|cc} A_{p,1} & 0 & K_{p,1}C_3 & 0 & K_{p,1} \\ 0 & A_{p,2} & K_{p,2}C_3 & 0 & K_{p,2} \\ 0 & 0 & A_3 & I & 0 \\ \hline -C_1 & C_2 & 0 & 0 & 0 \end{array}\right] . \tag{9b}$$

Because unknown noise disturbances w and v are modelled as white noise processes and state space system T_{dn} maps those to d, its system parameters may be advantageously applied to compute $R_d(0)$ by solving a Lyapunov equation:

$$\Pi_d = A_\Omega \Pi_d A_\Omega^* + B_\Omega M_3 B_\Omega^* . \tag{10}$$

Therein M_3 has been used, which is a presumed input Gramian matrix of disturbance processes according to equation (3). This leads to a numerical advantageous determination of $R_d(0)$:

$$R_d(0) = E\{d_k\, d_k^*\} = \begin{bmatrix} -C_1 & C_2 & 0 \end{bmatrix} \begin{bmatrix} \Pi_{11} & \Pi_{12} & \Pi_{13} \\ \Pi_{21} & \Pi_{22} & \Pi_{23} \\ \Pi_{31} & \Pi_{32} & \Pi_{33} \end{bmatrix} \begin{bmatrix} -C_1^* \\ C_2^* \\ 0 \end{bmatrix} . \tag{11}$$

The principal diagonal of $R_d(0)$ is referred to as $\bar{P}_d \in \mathbb{R}^p$, whose elements are the average process power of d at each measurement position. An analysis for that can be applied for damage identification.

2.5 Complementary Subspaces and Oblique Projections

While the average process power $R_d(0)$ of equation (11) can directly be applied to identify structural damage, it is enhanced in this section by projection techniques to suppress noise. The important idea is to exploit the structure of state space system T_{dn} in equation (9): Because d follows y_3, respectively $T_{yn,3}(A_3, C_3)$, the important frequency content of the difference process must be accordingly.

To apply this concept, complementary subspaces of T_{dn} are analysed in view of fundamental subspaces first. Then oblique projections are elaborated afterwards. This allows to split d in two elementary parts, which has some serious implications for damage identification. Finally, table 2 gives a summary of the new method state projection estimation error.

Basically, y_3 is a test signal which is applied to T_{dy} in equation (8), and can be understood as an approach for synchronization and normalization, as was pointed out in section 2.3. The response d must be in accordance to input y_3. Hence, a derivation which takes advantage of this concept is subsequently described. Therefore, an eigenvalue decomposition is applied:

$$\begin{bmatrix} A_{p,1} & 0 & K_{p,1}C_3 \\ 0 & A_{p,2} & K_{p,2}C_3 \\ 0 & 0 & A_3 \end{bmatrix} = X\Lambda X^{-1} = \sum_{i=1}^{3} X_i \Lambda_i \bar{X}_i, \quad X = \begin{bmatrix} X_1 & X_2 & X_3 \end{bmatrix} = \begin{bmatrix} X_{11} & 0 & X_{13} \\ 0 & X_{22} & X_{23} \\ 0 & 0 & X_{33} \end{bmatrix} . \tag{12}$$

A reasonable form of matrix X has been chosen here. Then, the inverse of X follows the Schur complement:

$$X^{-1} = \begin{bmatrix} \bar{X}_1 \\ \bar{X}_2 \\ \bar{X}_3 \end{bmatrix} = \begin{bmatrix} X_{11}^{-1} & 0 & -X_{11}^{-1}Y \\ 0 & X_{22}^{-1} & -X_{22}^{-1}Z \\ 0 & 0 & X_{33}^{-1} \end{bmatrix}, \qquad Y = X_{13}X_{33}^{-1}, \quad Z = X_{23}X_{33}^{-1} . \tag{13}$$

The found form of X and X^{-1} is bounded to very important constraints. Those can be found by applying the eigenvalue decomposition:

$$YA_3 = A_{p,1}Y + K_{p,1}C_3, \qquad ZA_3 = A_{p,2}Z + K_{p,2}C_3 . \tag{14}$$

Following the former equation, parameters Y and Z are easy determinable for special cases of $T_{yn,3}(A_3, C_3)$, which is observable by applying the defined closed-loop matrix A_p of equation (5) here:

$$T_{yn,3}(A_3, C_3) = \begin{cases} T_{yn,1}(A_1, C_1) \;\longrightarrow\; Y = I \\ T_{yn,2}(A_2, C_2) \;\longrightarrow\; Z = I \end{cases} . \tag{15}$$

Thus, an appropriate choice for $T_{yn,3}$ is the potentially damaged state $T_{yn,2}$, because signals y_2 are measurable at the moment of analysis. This leads to $y_3 \rightarrow y_2$ and can be applied in equation (8), which may allow a real-time damage identification. However, real-time applications are beyond the scope of this contribution.

Oblique projections are now defined based on determined properties. Therefore, complementary subspaces $\mathcal{U}$ and $\mathcal{V}$ are defined by

$$\mathcal{W} = \mathcal{U} \oplus \mathcal{V}, \mathcal{U} \cap \mathcal{V} = 0, \qquad \mathcal{U} = \text{span}(X_1, X_2),\ \mathcal{V} = \text{span}(X_3) . \tag{16}$$

In general, oblique projectors are defined by U and V, whose columns are a basis for $\mathcal{U}$ and $\mathcal{V}$ respectively, as Meyer[17] points out:

$$P_U = \left[\ U \ \middle|\ 0\ \right] \begin{bmatrix} U & V \end{bmatrix}^{-1}, \qquad P_V = I - P_U = \left[\ 0 \ \middle|\ V\ \right] \begin{bmatrix} U & V \end{bmatrix}^{-1} . \tag{17}$$

Here, P_U is a projector onto $\mathcal{U}$ along $\mathcal{V}$, while the complementary one P_V projects onto $\mathcal{V}$ along $\mathcal{U}$. Then, by applying subspaces

$$\left[\begin{array}{c|c} U & V \end{array}\right] = X = \left[\begin{array}{cc|c} X_1 & X_2 & X_3 \end{array}\right], \qquad \begin{bmatrix} U & V \end{bmatrix}^{-1} = X^{-1}, \tag{18}$$

projectors are derived following equation (17):

$$P_U = X_1\bar{X}_1 + X_2\bar{X}_2 = \begin{bmatrix} I & 0 & -Y \\ 0 & I & -Z \\ 0 & 0 & 0 \end{bmatrix}, \quad P_V = X_3\bar{X}_3 = \begin{bmatrix} 0 & 0 & Y \\ 0 & 0 & Z \\ 0 & 0 & I \end{bmatrix}. \tag{19}$$

2.6 State Projections

The determined projectors P_U and P_V are applied here to study essential elements:

$$x_{U,k} = P_U x_{\Omega,k} = \begin{bmatrix} I & 0 & -Y \\ 0 & I & -Z \\ 0 & 0 & 0 \end{bmatrix} \begin{bmatrix} \hat{x}_{1,k} \\ \hat{x}_{2,k} \\ x_{3,k} \end{bmatrix} = \begin{bmatrix} \hat{x}_{1,k} - Yx_{3,k} \\ \hat{x}_{2,k} - Zx_{3,k} \\ 0 \end{bmatrix} = \begin{bmatrix} \tilde{x}_{1,k} \\ \tilde{x}_{2,k} \\ 0 \end{bmatrix} \tag{20}$$

$$x_{V,k} = P_V x_{\Omega,k} = \begin{bmatrix} 0 & 0 & Y \\ 0 & 0 & Z \\ 0 & 0 & I \end{bmatrix} \begin{bmatrix} \hat{x}_{1,k} \\ \hat{x}_{2,k} \\ x_{3,k} \end{bmatrix} = \begin{bmatrix} Y \\ Z \\ I \end{bmatrix} x_{3,k}. \tag{21}$$

Because $T_{yn,1}$, $T_{yn,2}$ and $T_{yn,3}$ may have different model orders, parameters Y and Z are fundamental to determine state differences $\tilde{x}_1$ and $\tilde{x}_2$. These state differences essentially are noise, which is especially plausible for special cases $Y = I$ or $Z = I$ following equation (15).

Both processes x_U and x_V are central elements of system T_{dn}:

$$P_U x_{\Omega,k+1} = \begin{bmatrix} \tilde{x}_{1,k+1} \\ \tilde{x}_{2,k+1} \\ 0 \end{bmatrix} = \begin{bmatrix} A_{p,1} & 0 & -A_{p,1}Y \\ 0 & A_{p,2} & -A_{p,2}Z \\ 0 & 0 & 0 \end{bmatrix} \begin{bmatrix} \hat{x}_{1,k} \\ \hat{x}_{2,k} \\ x_{3,k} \end{bmatrix} + \begin{bmatrix} -Y & K_{p,1} \\ -Z & K_{p,2} \\ 0 & 0 \end{bmatrix} \begin{bmatrix} w_k \\ v_k \end{bmatrix} \tag{22}$$

$$P_V x_{\Omega,k+1} = \begin{bmatrix} Yx_{3,k+1} \\ Zx_{3,k+1} \\ x_{3,k+1} \end{bmatrix} = \begin{bmatrix} 0 & 0 & YA_3 \\ 0 & 0 & ZA_3 \\ 0 & 0 & A_3 \end{bmatrix} \begin{bmatrix} \hat{x}_{1,k} \\ \hat{x}_{2,k} \\ x_{3,k} \end{bmatrix} + \begin{bmatrix} Y & 0 \\ Z & 0 \\ I & 0 \end{bmatrix} \begin{bmatrix} w_k \\ v_k \end{bmatrix}. \tag{23}$$

Continuing, central elements of d are derived:

$$d_{U,k} = C_\Omega x_{U,k} = \begin{bmatrix} -C_1 & C_2 & 0 \end{bmatrix} \begin{bmatrix} \tilde{x}_{1,k} \\ \tilde{x}_{2,k} \\ 0 \end{bmatrix} = -C_1\tilde{x}_{1,k} + C_2\tilde{x}_{2,k} \tag{24}$$

$$d_{V,k} = C_\Omega x_{V,k} = \begin{bmatrix} -C_1 & C_2 & 0 \end{bmatrix} \begin{bmatrix} Y \\ Z \\ I \end{bmatrix} x_{3,k} = \big(-C_1Y + C_2Z\big)x_{3,k} = C_T x_{3,k}. \tag{25}$$

Process d_U can be interpreted as noise, because it follows x_U. On the other side d_V may describe structural damage and is determined by the observer matrix C_T and states x_3. Here, important key ideas of SP2E are observable: 1)The output is described by a difference of observer matrices C_1 and C_2 with regard to model order differences and appropriate column spaces, which is taken into account with Y and Z. 2)The difference process d is the response to a test signal y_3, which itself is described by x_3. It therefore is reasonable to use matrix C_T and states x_3 only to determine structural damage.

The identification of structural damage is conducted by analysing the average process power $R_d(0)$ (see section 2.4). To enhance this result, projection techniques have been applied, which led to process d_V in equation (25). Again, the average process power shall be applied by

$$R_{d,V}(0) = E\{d_{V,k}\, d_{V,k}^*\} = \begin{bmatrix} -C_1 & C_2 & 0 \end{bmatrix} \begin{bmatrix} Y \\ Z \\ I \end{bmatrix} \Pi_{33} \begin{bmatrix} Y^* & Z^* & I \end{bmatrix} \begin{bmatrix} -C_1^* \\ C_2^* \\ 0 \end{bmatrix} \tag{26a}$$

$$= \begin{bmatrix} -C_1 & C_2 \end{bmatrix} \begin{bmatrix} Y \\ Z \end{bmatrix} \Pi_{33} \begin{bmatrix} Y^* & Z^* \end{bmatrix} \begin{bmatrix} -C_1^* \\ C_2^* \end{bmatrix} . \tag{26b}$$

By comparing equations (11) and (26), central differences are apparent: In opposite to the determination of $R_d(0)$, the choice of matrix Π_{33} is relevant here. Unfortunately, because noise disturbances w and v are unknown, parameters (Q, R_v, S) and thus Π_{33} are unknown too (see equation (3)). However, by allowing $x_{2,k} \to \hat{x}_{2,k}$, and thus covariance matrix $\Pi_{33} \to \Pi_{22}$, a straightforward approach is chosen. This leads to $R_{d,V}(0)$, whose principal diagonal (denoted by $\bar{P}_{d,V}$) must be analysed to identify structural damage:

$$R_{d,V}(0) = \begin{bmatrix} -C_1 & C_2 \end{bmatrix} \begin{bmatrix} Y \\ I \end{bmatrix} \Pi_{22} \begin{bmatrix} Y^* & I \end{bmatrix} \begin{bmatrix} -C_1^* \\ C_2^* \end{bmatrix} = C_T \Pi_{22} C_T^* . \tag{27}$$

A damage identification algorithm based on SP2E with a focus on oblique projections is given in table 2.

	SP2E Step	Equations
1.	Identify (T_{yn}, T_{ye}) based on y for structural states 1 and 2.	(1), (2)
2.	Define the input y_3 (e.g. by $T_{yn,2}$) and reorder estimator parameters $(A_1, K_{p,1}, C_1)$ and $(A_2, K_{p,2}, C_2)$.	(9)
3.	Compute parameters (Y, Z) according to defined projectors.	(19)
4.	Solve Lyapunov equation (10) for $\Pi_{33} = 0$.	(10)
5.	Analyse the average process power $\bar{P}_{d,V}$.	(27)

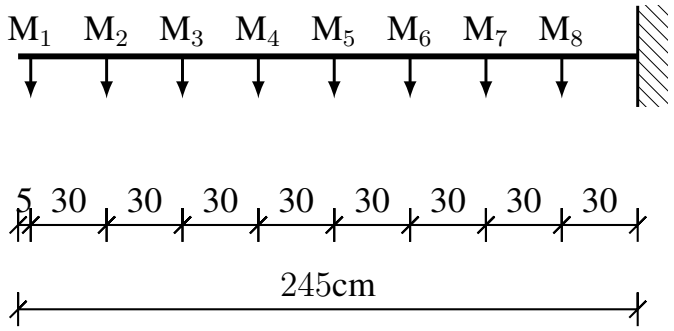
Table 2: Summary of Method SP2E

3 Experimental sensitivity studies to verify SP2E

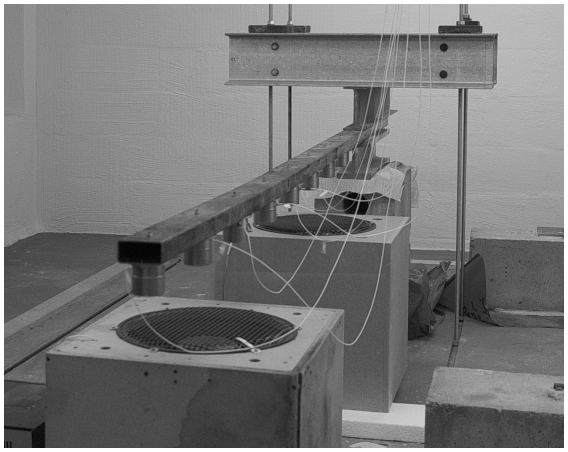
3.1 Description of laboratory experiments

To verify method SP2E, laboratory experiments have been studied at Leipzig University of Applied Sciences. Therein a steel rectangular hollow section $80 \times 40 \times 2.9$mm was built as a cantilever arm with measurement positions $\mathrm{M}_1 \ldots \mathrm{M}_8$ ($p = 8$, see figure 1a). This bending beam was excited by ambient vibrations, which were generated as acoustic noise given by two loudspeakers. The structural responses have been measured for 30min by eight equally spaced (30cm), uniaxial, piezoelectric accelerometers.

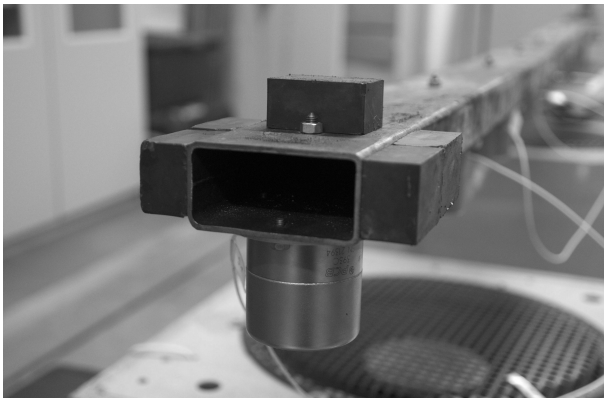
Experimental sensitivity studies have been conducted and published:[2,3] Four series of measurements, corresponding to four positions of mass alterations, were analysed. The structural alteration positions M_1, M_3, M_5 and M_7 were chosen. In each measurement series over 18 experiments have been carried out, in which additional structural masses 100g, 200g, 400g, 600g, 1000g and 1600g have been separately applied to the laboratory structure (see figure 1c). Each experiment was repeated to proof reproducibility. Even an additional mass of 100g (approximately 0.5% of the total structural mass) was localized.[2] In the following some experimental results are shown and discussed.



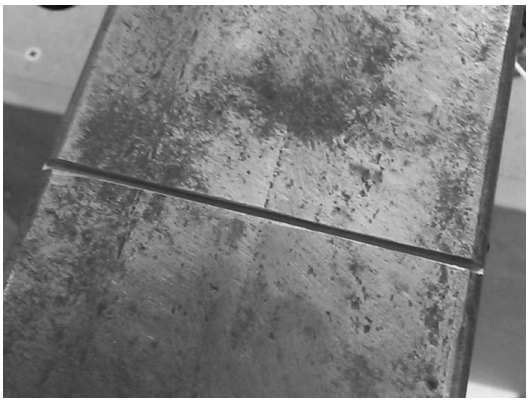
(a) Mechanical System: Cantilever Arm



(b) Laboratory Structure



(c) Mass Alteration of 1kg at M_1



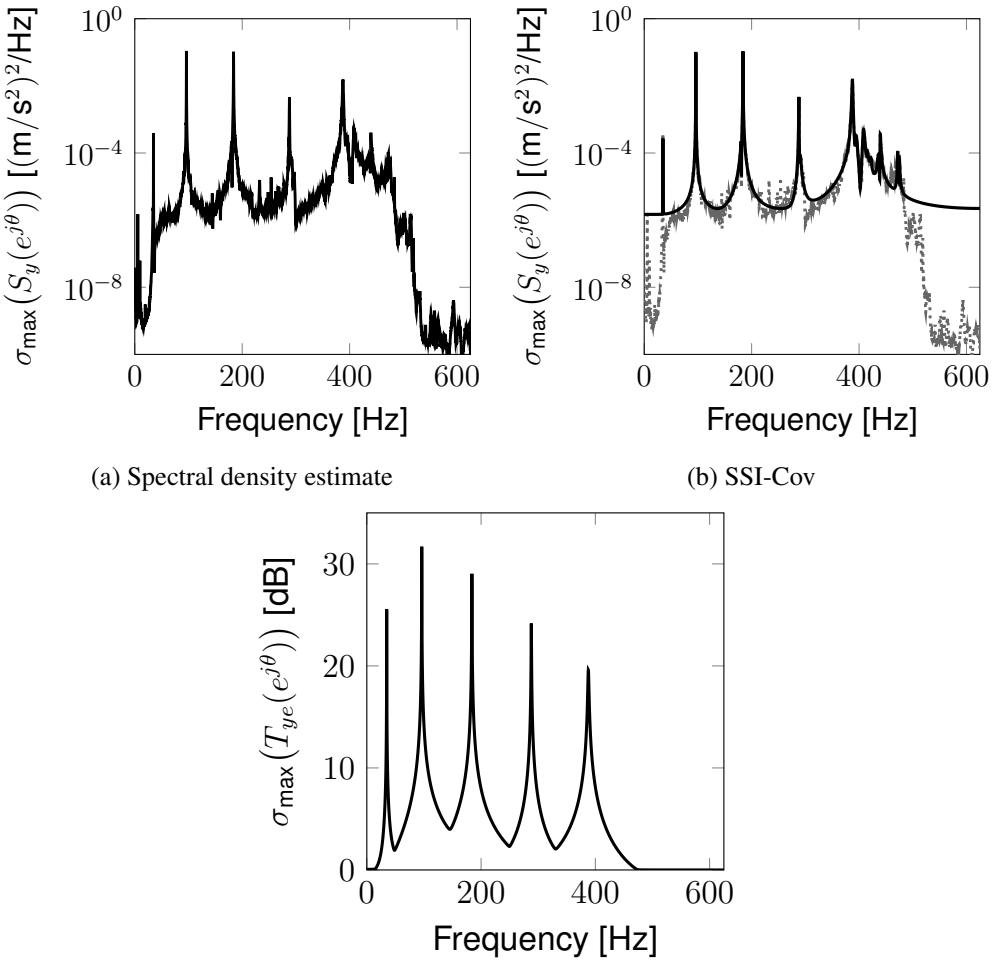
(d) Stiffness Degradation by 2.5mm Saw Cut (Material Thickness 2.9mm)

Figure 1: Laboratory Set-Up and Two Examples of Applied Structural Changes

3.2 Signal processing, system identification and $\mathcal{H}^\infty$ estimation

The identification of the structure was uniformly based on power spectral density estimates following Welch[18] with 270 averages (50% overlap). After computing covariance matrix functions $R_y(l)$ by inverse Fourier transform of an averaged periodogram (figure 2a), a system T_{yn} of the measurement at the mechanical structure was computed by covariance based stochastic subspace identification (SSI-Cov), which uses a singular value decomposition (figure 2b). Here, a constant number of block rows and columns 2^8 has been chosen. For rank determination a stabilization diagram was used.

Because of identified noise processes, model reduction was necessary, which led to a constant model order $n = 10$. Finally, state space systems $T_{ye,1}$ and $T_{ye,2}$ based on $\mathcal{H}^\infty$ theory and the 'filtering signals in additive noise' ($L = C, \gamma = 1$) were parametrized (figure 2c).



(a) Spectral density estimate

(b) SSI-Cov

(c) $\mathcal{H}^\infty$ estimator

Figure 2: Identification process of the reference state

3.3 Localization: $\sim 0.5\%$ of total structural mass

At first method SP2E was verified. This was done by applying SP2E to two different measurements of the same structural state: Here one can see an average process power of $\bar{P}_{d,V} \approx 10^{-9}(\mathrm{m/s^2})^2$. This value is plausible, because d shall be nearly zero, if no damage occurred. Overstepping this value indicates structural alterations (threshold-value).

Now in a first configuration an additional mass of 100g was applied at M_1, which is an additional mass of approximately 0.5%, considering a total mass of 19.4kg. This leads to frequency shifts of $\approx 0.5\%$. Standard modal techniques like MAC and CoMAC barely indicate structural damage here.

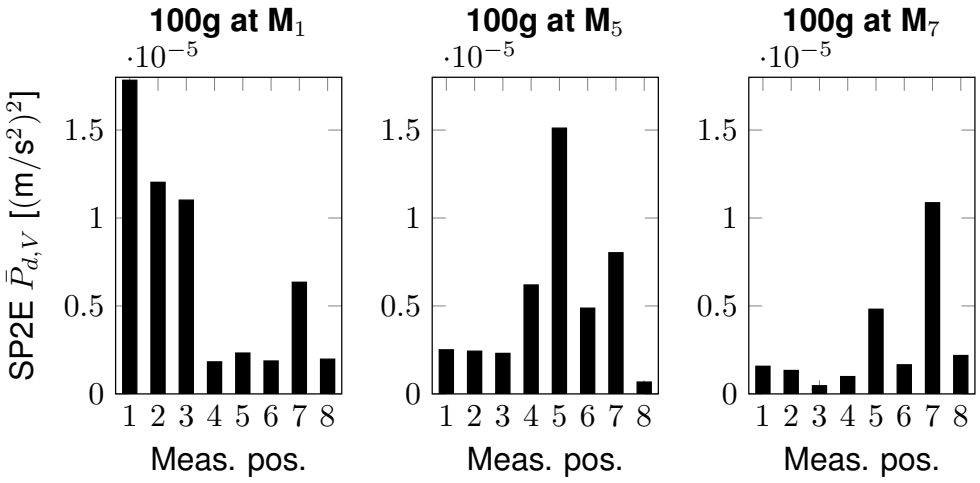


Figure 3: Localization of 0.5% total structural mass

The resulting $\bar{P}_{d,V}$ for the M_1 case is shown in the left of figure 3. Here, the average process power is larger than $10^{-5}(m/s^2)^2$ and measurement position M_1, the position of mass alteration, shows the greatest deviation. Afterwards an additional mass of 100g was successively applied at M_5 and M_7. Here, again the resulting $\bar{P}_{d,V}$ is larger then the threshold-value and has its greatest deviation where the mass has been applied. Thus, small structural alterations are locatable.

3.4 Localization: Alterations between measurement positions

While mass alterations have been applied at measurement positions in section 3.3, here magnets were employed between acceleration sensors. The results are shown in figure 4.

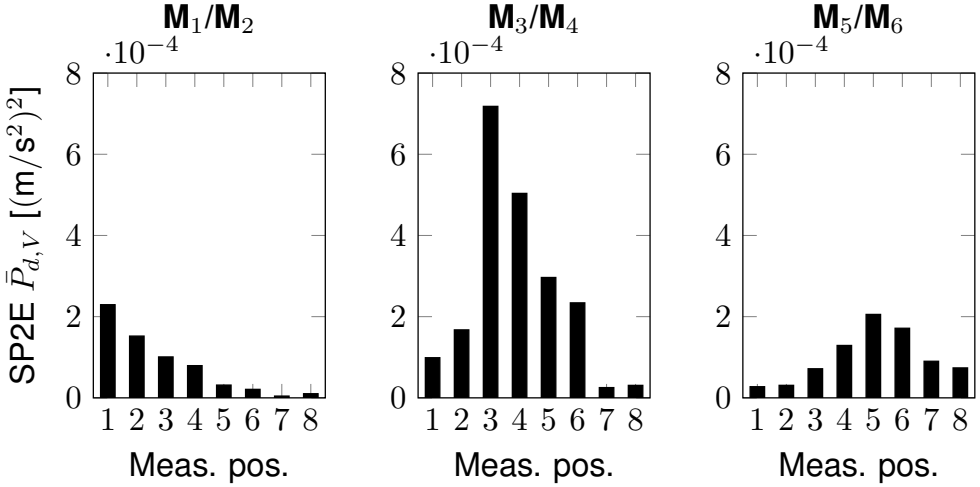


Figure 4: Localization of alterations between measurement positions

An additional mass of 1kg was applied in between measurement positions in three separate experimental configurations. In every case $\bar{P}_{d,V}$ is far larger than the reference value. Furthermore, always those two elements in $\bar{P}_{d,V}$ rise most, where additional mass has been applied. Thus, the localization in between measurement positions is experimentally observed.

3.5 Localization: Stiffness degradations

Rather then identifying mass alterations, structural health monitoring systems must be able to detect and localize stiffness degradations. Hence, the stiffness of the laboratory structure has been reduced by successively deepening a saw cut between M_5 and M_6. The damage identification results by SP2E are shown in figure 5.

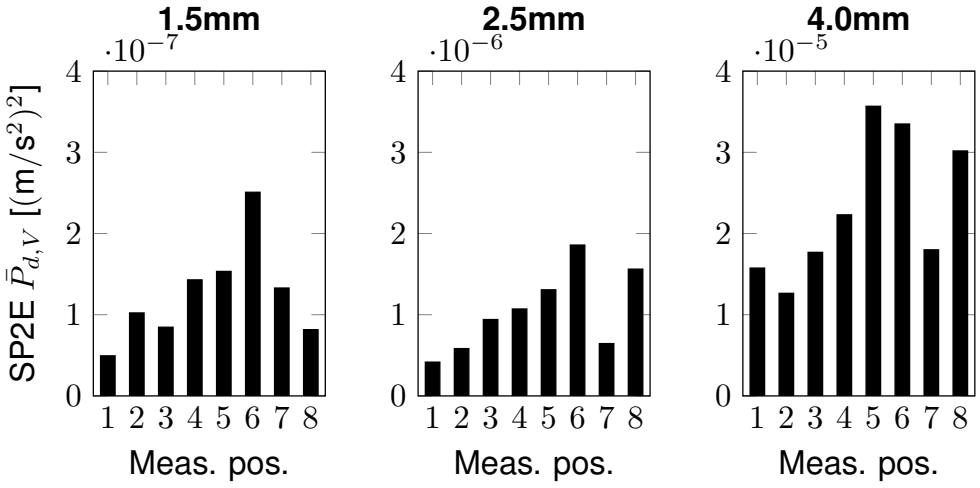


Figure 5: Localization of saw cuts (depth 1.5, 2.5 and 4mm) between M_5/M_6 (material thickness 2.9mm)

A saw cut has been applied. By increasing the experimentally induced damage, the result of SP2E (the average process power $\bar{P}_{d,V}$) constantly rises above the threshold-value. Furthermore, measurement positions M_5 and M_6 always are the largest, which indicates the correct damage position. In result, stiffness reductions are experimentally locatable by SP2E.

3.6 Experimental sensitivity study

Method SP2E has been experimentally analysed by conducting sensitivity studies.[2,3] In these studies additional structural mass was applied at the laboratory structure of figure 1b in separate configurations at M_1, M_3, M_5 and M_7. For each position a sequential increased additional mass of 100g, 200g, 400g, 600g, 1000g and 1600g was applied. By applying SP2E, the localization of experimentally added structural mass was successful.

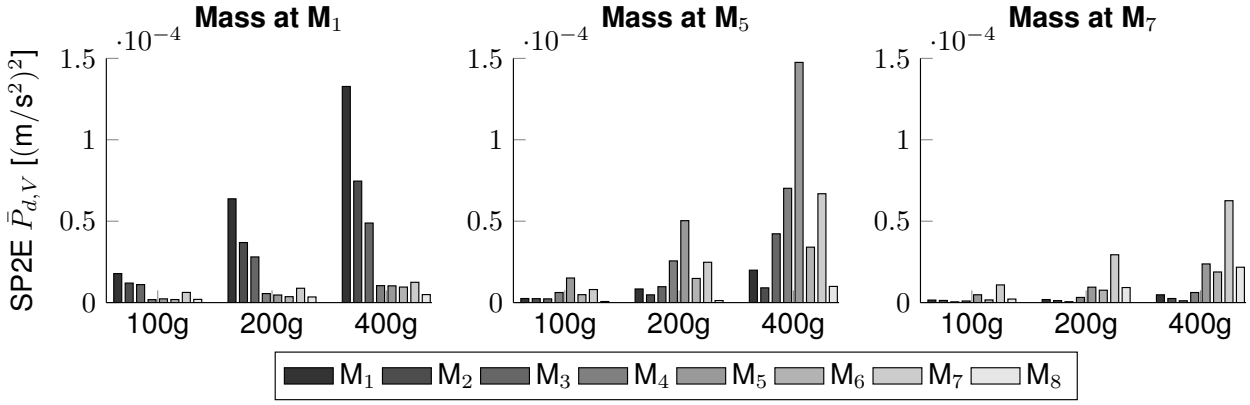


Figure 6: Excerpt of sensitivity study

By analysing the excerpt of sensitivity study in figure 6, the connection between increased values in average power $\bar{P}_{d,V}$ and the position of mass alteration becomes evident. Furthermore $\bar{P}_{d,V}$ increases as heavier additional mass is applied. In addition to that, reproducibility has been controlled by repeating the experiments. Hence, method SP2E is comprehensively verified.

4 Conclusions

This contribution covers the damage identification problem based on $\mathcal{H}^\infty$ estimation and state projection estimation error (SP2E). For that, a state space system is repeatedly parametrized with the help of output only identification and Krein space based $\mathcal{H}^\infty$ estimation to represent a measurement at a mechanical structure. Here, the average process power of the defined difference process must be analysed to identify structural damage. Because real structural excitations are unknown, an input is introduced, which allowed synchronization and normalization. This approach led to the introduction of a state space representation of the difference process and the definition of state projections for damage identification enhancement. By analysing laboratory experiments, experimental localization of induced stiffness degradations and applied masses by SP2E have been confirmed. Furthermore, the experimental results emphasize the advantage of applying projection techniques. Theory and verification of SP2E have been reviewed and published.[1–3] To be applicable at large-scale structures, the influence of environmental and operational conditions (e.g. temperature) must be compensated in future developments.

Acknowledgements

This research has been financed by 'Deutsche Forschungsgemeinschaft' (German Research Foundation, grant number LE 1107/4-1). The authors acknowledge gratefully the granted support.

References

[1] A. Lenzen and M. Vollmering. A new technique for damage localisation using estimates in krein spaces. *Proceedings of the 6th International Operational Modal Analysis Conference*, 2015.

[2] A. Lenzen and M. Vollmering. An output only damage identification method based on $\mathcal{H}_\infty$ theory and state projection estimation error (SP2E). *Structural Control and Health Monitoring*, 24(11), 2017.

[3] A. Lenzen and M. Vollmering. On experimental damage localization by SP2E: Application of $\mathcal{H}^\infty$ estimation and oblique projections. *Mechanical Systems and Signal Processing*, 104:648–662, 2018.

[4] K. Worden, C.R. Farrar, G. Manson, and G. Park. The fundamental axioms of structural health monitoring. In *Proceedings of the Royal Society of London A: Mathematical, Physical and Engineering Sciences*, volume 463, pages 1639–1664. The Royal Society, 2007.

[5] A. Cunha, E. Caetano, F. Magalhães, and C. Moutinho. Recent perspectives in dynamic testing and monitoring of bridges. *Structural Control and Health Monitoring*, 20(6):853–877, 2013.

[6] Edwin Reynders. System identification methods for (operational) modal analysis: review and comparison. *Archives of Computational Methods in Engineering*, 19(1):51–124, 2012.

[7] R.J. Vaccaro and T. Vukina. A solution to the positivity problem in the state-space approach to modeling vector-valued time series. *Journal of Economic Dynamics and Control*, 17(3):401–421, 1993.

[8] J. Mari. Modifications of rational transfer matrices to achieve positive realness. *Signal Processing*, 80(4):615–635, 2000.

[9] H. Akçay. Frequency domain subspace-based identification of discrete-time singular power spectra. *Signal Processing*, 92(9):2075–2081, 2012.

[10] T. Kailath, A.H. Sayed, and B. Hassibi. *Linear Estimation*. Prentice Hall, 2000.

[11] D. Simon. *Optimal State Estimation: Kalman, H_∞, and Nonlinear Approaches*. Wiley, 2006.

[12] R.S. Mangoubi. *Robust Estimation and Failure Detection: A Concise Treatment*. Advances in Industrial Control. Springer London, 2012.

[13] B. Hassibi, A.H. Sayed, and T. Kailath. *Indefinite-Quadratic Estimation and Control: A Unified Approach to H^2 and H^∞ Theories*. SIAM Studies in Applied Mathematics. Society for Industrial and Applied Mathematics, 1999.

[14] P. Van Overschee and B. De Moor. *Subspace Identification for Linear Systems: Theory, Implementation, Applications*. Kluwer Academic Publishers, 1996.

[15] T. Katayama. *Subspace Methods for System Identification*. Communications and Control Engineering. Springer, 2005.

[16] B. Peeters and G. De Roeck. Stochastic system identification for operational modal analysis: a review. *Journal of Dynamic Systems, Measurement, and Control*, 123(4):659–667, 2001.

[17] C.D. Meyer. *Matrix Analysis and Applied Linear Algebra*. Society for Industrial and Applied Mathematics (SIAM), 2000.

[18] P.D. Welch. The use of fast fourier transform for the estimation of power spectra: A method based on time averaging over short, modified periodograms. *IEEE Transactions on audio and electroacoustics*, 15(2):70–73, 1967.

A wave-based optimization strategy of curved joints for improved defect detection in coupled waveguides

V. Denis [1], **J.-M. Mencik** [1]
[1] INSA Centre Val de Loire, Université d'Orléans, Université de Tours, Laboratoire de Mécanique Gabriel Lamé, 3 Rue de la Chocolaterie, 41034 Blois, France
e-mail: **vivien.denis@insa-cvl.fr**

Abstract

This paper addresses a wave-based non-destructive testing technique for the detection of defects in assemblies of waveguides connected to curved joints. To achieve this goal, the wave finite element (WFE) method is used. It provides an efficient numerical means to compute waves in periodic structures (waveguides), and compute the reflection and transmission coefficients of these waves around defects and curved joints. The so-called scattering matrices of the defects and the joints can be formulated from a finite element modeling. The measured reflection coefficients due to defects are tightly connected to the characteristics of the curved joints. As it turns out, their characteristics can be tuned in an appropriate way to improve the magnitude of the reflected signals. An optimization procedure for the design of curved joints, using the WFE framework, is therefore proposed. Numerical experiments are carried out by considering two 2D waveguides — i.e., one healthy/perfect waveguide and a second one containing a defect — connected to a curved joint which is parametrized with respect to its curvature radius and its curvature angle.

1 Introduction

There is an increasing interest in non-destructive testing (NDT) of mechanical and civil engineering structures. These can be deteriorated by vibrations or corrosion hence resulting in small defects which affect their structural integrity. For straight waveguides such as beams or pipes, waves travel a long distance and can be highly sensitive to defects. A common NDT method is to identify and localize defects from the analysis of the reflected and transmitted signals when guided waves are generated at one or several excitation points [1]. However, engineering structures usually involve assemblies of straight waveguides and curved joints. Because of their reflection and transmission properties, curved joints may greatly impact or impede the identification of defects when they are placed between the defects and the excitation/observation points.

It is therefore crucial to study the impact of curved joints on the measurement of the reflected waves induced by the defects. There exist various works on this topic. Demma et al. [2] have analyzed the reflection/transmission coefficients for the waves in two straight waveguides which are connected to a curved waveguide (bend). It was found that the transmission coefficients strongly depend on the geometry of the bend. Also, the wave mode conversion which occurs due to the bend has been reported. Sanderson et al. [3] have used a finite element (FE) model to compute the reflection coefficients of waves, from a defect through a curved joint; it has been shown that a curved joint leads to an underestimation of the severity of the defect, because of the decrease of the echo amplitude through the joint. The authors have however proposed a strategy to reverse the distortion of the signal induced by the joint, to therefore obtain a good characterization of the defect. Verma et al. [4] have analyzed curved joints with different angles and radii of curvature using a time-domain FE model. Modification of the wave velocity of the transmitted waves, across the joints, has been observed along with the phenomena of wave energy loss. The authors have highlighted the dependency of the transmission coefficients on the curvature angle of the joints, and have reported the

effect of constructive or destructive mode interferences. Ni et al. [5] have investigated the influence of joints of different shapes in the detection of different types of defect in pipes. They have noticed that the detection sensitivity is influenced by the localization of the defects and the shapes of the joints.

Most of the numerical works on this topic make use of FE models and rely on a time domain approach to assess the reflection and transmission of waves from defects along waveguides. One advantage of this approach is that it is merely a numerical analogy of a practical problem. The shortcoming is that the related computational cost is very high, however, because of the space-time discretization. An alternative frequency approach is used in this paper. In this framework, the wave finite element (WFE) method is considered [6, 7]. It provides an efficient numerical means to compute waves in periodic structures, like straight waveguides, and compute the reflection and transmission coefficients of these waves at coupling elements like defects or curved joints. Mencik and Ichchou [8] have expressed the scattering matrix of a coupling element using the WFE formalism. In [9], the scattering matrix of a coupling element representing a part of a waveguide with a defect, modeled using the FE method, has been computed via the WFE method. Schaal et al. [10] and Bischoff et al. [11] have proposed a hybrid WFE / Boundary Element Method for modeling defect areas in waveguides. Finally, Mencik [12] and Silva et al. [13] have proposed reduced models of joints/junctions by using a component mode synthesis technique.

In this work, a WFE-based optimization strategy of curved joints is proposed to improve the detection of defects in assemblies of waveguides. Indeed, curved joints can be manufactured in such a way that they can improve the transmission of waves, from the defect to the measurement point. To the knowledge of the authors, this problem hasn't been tackled so far. The rest of the paper is organized as follows. In Section 2, the WFE method is presented. The strategy used to compute the waves traveling in straight waveguides is presented. In Section 3, the strategy used to compute the scattering matrix of coupling elements, including curved joints and parts of waveguides with defects, is proposed. Also, the optimization strategy to design curved joints is proposed with a view to improving the detection of defects. Numerical experiments are brought in Section 4. These concern one healthy waveguide and one waveguide containing a defect, connected together through a curved joint. The effect of the parameters of the curved joint on the measured reflected signal in the healthy waveguide is investigated.

2 WFE method

2.1 Substructure modeling

The WFE method focuses on the description of waves in one-dimensional periodic structures, i.e., structures made up of identical substructures — i.e., with a same length d — which are assembled to each other along a certain straight direction x (see Figure 1). Beam-like structures with straight cross-sections are particular cases of periodic structures which are usually referred to as waveguides. The strategy to determine the wave properties of periodic structures is explained hereafter.

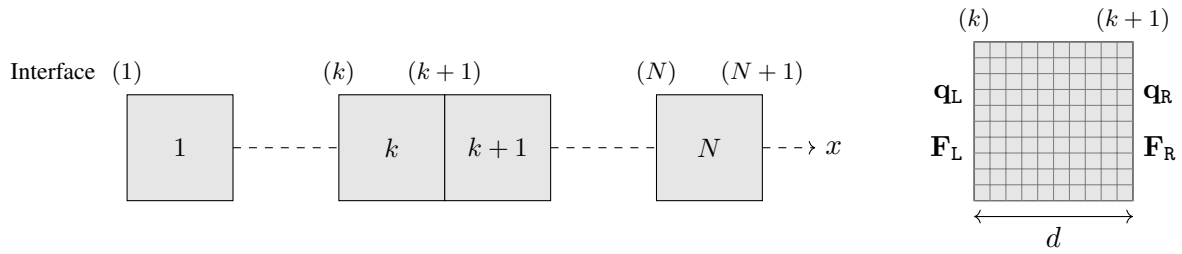


FIGURE 1 – Schematic of a periodic structure.

Within the framework of the WFE method, a FE model of a substructure is considered (see Figure 1). Here,

the left and right boundaries of the substructure are supposed to be meshed in the same way with the same number n of degrees of freedom (DOFs). Let us denote by $\mathbf{M}$, $\mathbf{K}$ and η the mass matrix, stiffness matrix and loss factor (damping effects) of the substructure, respectively. Also, let us denote by $\mathbf{D}$ the dynamic stiffness matrix (DSM) of the substructure, defined by :

$$\mathbf{D} = -\omega^2\mathbf{M} + (1 + \mathtt{i}\eta)\mathbf{K}, \tag{1}$$

where ω is the angular frequency. As it turns out, the dynamic equilibrium equation of the substructure can be expressed in the frequency domain as follows :

$$\mathbf{D}\mathbf{q} = \mathbf{F}, \tag{2}$$

where $\mathbf{q}$ and $\mathbf{F}$ are displacement and force vectors, respectively. These vectors can be partitioned into boundary (B) DOFs — i.e., those on the left and right boundaries — and internal/remaining (I) DOFs. This yields :

$$\begin{bmatrix} \mathbf{D}_{\mathtt{BB}} & \mathbf{D}_{\mathtt{BI}} \\ \mathbf{D}_{\mathtt{IB}} & \mathbf{D}_{\mathtt{II}} \end{bmatrix} \begin{bmatrix} \mathbf{q}_{\mathtt{B}} \\ \mathbf{q}_{\mathtt{I}} \end{bmatrix} = \begin{bmatrix} \mathbf{F}_{\mathtt{B}} \\ \mathbf{F}_{\mathtt{I}} \end{bmatrix} = \begin{bmatrix} \mathbf{F}_{\mathtt{B}} \\ \mathbf{0} \end{bmatrix}, \tag{3}$$

where the internal DOFs are assumed to be free from excitation sources.

The second step behind the WFE method is to condense the DSM of the substructure on the boundary DOFs. Hence, the dynamic equilibrium equation of the substructure gives

$$\mathbf{D}^*\mathbf{q}_{\mathtt{B}} = \mathbf{F}_{\mathtt{B}}, \tag{4}$$

where $\mathbf{D}^*$ is the condensed DSM, expressed by :

$$\mathbf{D}^* = \mathbf{D}_{\mathtt{BB}} - \mathbf{D}_{\mathtt{BI}}\mathbf{D}_{\mathtt{II}}^{-1}\mathbf{D}_{\mathtt{IB}}. \tag{5}$$

2.2 Wave propagation

Let us denote by $\mathbf{q}_{\mathtt{L}}$ and $\mathbf{q}_{\mathtt{R}}$ (resp. $\mathbf{F}_{\mathtt{L}}$ and $\mathbf{F}_{\mathtt{R}}$) the $n \times 1$ displacement (resp. force) vectors at the left ($\mathtt{L}$) and right ($\mathtt{R}$) boundaries of the substructure (respectively), and let us rewrite Eq. (4) as follows :

$$\begin{bmatrix} \mathbf{D}^*_{\mathtt{LL}} & \mathbf{D}^*_{\mathtt{LR}} \\ \mathbf{D}^*_{\mathtt{RL}} & \mathbf{D}^*_{\mathtt{RR}} \end{bmatrix} \begin{bmatrix} \mathbf{q}_{\mathtt{L}} \\ \mathbf{q}_{\mathtt{R}} \end{bmatrix} = \begin{bmatrix} \mathbf{F}_{\mathtt{L}} \\ \mathbf{F}_{\mathtt{R}} \end{bmatrix}, \tag{6}$$

where $\mathbf{D}^*_{\mathtt{LL}}$, $\mathbf{D}^*_{\mathtt{LR}}$, $\mathbf{D}^*_{\mathtt{RL}}$ and $\mathbf{D}^*_{\mathtt{RR}}$ are square matrices of size $n \times n$. Let us introduce the $2n \times 2n$ transfer matrix $\mathbf{S}$ of the substructure, expressed by [6, 8] :

$$\mathbf{S} = \begin{bmatrix} -\mathbf{D}^{*-1}_{\mathtt{LR}}\mathbf{D}^*_{\mathtt{LL}} & -\mathbf{D}^{*-1}_{\mathtt{LR}} \\ \mathbf{D}^*_{\mathtt{RL}} - \mathbf{D}^*_{\mathtt{RR}}\mathbf{D}^{*-1}_{\mathtt{LR}}\mathbf{D}^*_{\mathtt{LL}} & -\mathbf{D}^*_{\mathtt{RR}}\mathbf{D}^{*-1}_{\mathtt{LR}} \end{bmatrix}. \tag{7}$$

The transfer matrix links the displacement/force vectors between the right and left boundaries of the substructure, as follows :

$$\begin{bmatrix} \mathbf{q}_{\mathtt{R}} \\ \mathbf{F}_{\mathtt{R}} \end{bmatrix} = \mathbf{S} \begin{bmatrix} \mathbf{q}_{\mathtt{L}} \\ -\mathbf{F}_{\mathtt{L}} \end{bmatrix}. \tag{8}$$

In fact, it can be easily proven that the transfer matrix links the displacement/force vectors between two consecutive substructures. For instance, consider one substructure enclosed between two interfaces $(k-1)$ and (k) and a subsequent substructure enclosed between interfaces (k) and $(k+1)$. Hence, it can be shown that

$$\begin{bmatrix} \mathbf{q}^{(k)}_{\mathtt{L}} \\ -\mathbf{F}^{(k)}_{\mathtt{L}} \end{bmatrix} = \mathbf{S} \begin{bmatrix} \mathbf{q}^{(k-1)}_{\mathtt{L}} \\ -\mathbf{F}^{(k-1)}_{\mathtt{L}} \end{bmatrix} \qquad \text{and} \qquad \begin{bmatrix} \mathbf{q}^{(k+1)}_{\mathtt{R}} \\ \mathbf{F}^{(k+1)}_{\mathtt{R}} \end{bmatrix} = \mathbf{S} \begin{bmatrix} \mathbf{q}^{(k)}_{\mathtt{R}} \\ \mathbf{F}^{(k)}_{\mathtt{R}} \end{bmatrix}, \tag{9}$$

where the conventions $\mathbf{q}_{\mathtt{R}}^{(k)}$ and $\mathbf{q}_{\mathtt{L}}^{(k)}$ (resp. $\mathbf{F}_{\mathtt{R}}^{(k)}$ and $\mathbf{F}_{\mathtt{L}}^{(k)}$) are used to denote the displacement (resp. force) vector on the right boundary of the first substructure and the left boundary of the second substructure, respectively, with the property that $\mathbf{q}_{\mathtt{R}}^{(k)} = \mathbf{q}_{\mathtt{L}}^{(k)}$ and $\mathbf{F}_{\mathtt{R}}^{(k)} = -\mathbf{F}_{\mathtt{L}}^{(k)}$ (action-reaction law). By considering the power of the matrix $\mathbf{S}$, e.g., $\mathbf{S}^u$ where u is an integer, this yields the transfer matrix of an assembly of u substructures, which links the displacement/force vectors between two substructure interfaces (k) and $(k+u)$.

The computation of the eigenvalues and eigenvectors of the transfer matrix $\mathbf{S}$ yields the wave modes of the periodic structure. This can be done using efficient eigensolvers e.g. like the $\mathbf{S}+\mathbf{S}^{-1}$ transformation technique [14]. The eigenvalues are denoted by μ_j which refer to the wave parameters, with the property that $\mu_j = \exp(-\mathrm{i}\beta_j d)$ where β_j have the meaning of wave numbers. Also, the eigenvectors are denoted by $\boldsymbol{\phi}_j$ and refer to the wave shapes. They are given by $\boldsymbol{\phi}_j = [\boldsymbol{\phi}_{\mathtt{q}j}^T \; \boldsymbol{\phi}_{\mathtt{F}j}^T]^T$ where $\boldsymbol{\phi}_{\mathtt{q}j}$ and $\boldsymbol{\phi}_{\mathtt{F}j}$ are $n \times 1$ vectors of displacement components and force components, respectively.

Note that the transfer matrix $\mathbf{S}$ is symplectic [8], which means that the eigenvalues occur in pairs $(\mu_j, 1/\mu_j)$. As a result, there exist n eigenvalues μ_j defined so that $|\mu_j| < 1$ and which correspond to right-going wave modes, and n eigenvalues $\mu_j^\star$ defined so that $\mu_j^\star = 1/\mu_j$ — i.e., $|\mu_j^\star| > 1$ — and which correspond to left-going wave modes. The wave shapes can be partitioned accordingly into n right-going wave modes $\boldsymbol{\phi}_j$, and n left-going wave modes $\boldsymbol{\phi}_j^\star$.

3 Scattering matrix

The wave modes appear to be useful for expressing the displacement and force vectors of periodic structures. Consider for instance a periodic structure composed of N substructures. Hence, the following wave mode expansions can be considered to express the displacement and force vectors at a substructure interface (k) $(k = 1, ..., N+1)$ [7] :

$$\mathbf{q}_{\mathtt{L}}^{(k)} = \mathbf{q}_{\mathtt{R}}^{(k)} = \boldsymbol{\Phi}_{\mathtt{q}} \boldsymbol{\mu}^{k-1} \mathbf{Q} + \boldsymbol{\Phi}_{\mathtt{q}}^\star \boldsymbol{\mu}^{N+1-k} \mathbf{Q}^\star, \tag{10}$$

$$-\mathbf{F}_{\mathtt{L}}^{(k)} = \mathbf{F}_{\mathtt{R}}^{(k)} = \boldsymbol{\Phi}_{\mathtt{F}} \boldsymbol{\mu}^{k-1} \mathbf{Q} + \boldsymbol{\Phi}_{\mathtt{F}}^\star \boldsymbol{\mu}^{N+1-k} \mathbf{Q}^\star, \tag{11}$$

where $\boldsymbol{\Phi}_{\mathtt{q}} = [\boldsymbol{\phi}_{\mathtt{q}1} ... \boldsymbol{\phi}_{\mathtt{q}n}]$, $\boldsymbol{\Phi}_{\mathtt{q}}^\star = [\boldsymbol{\phi}_{\mathtt{q}1}^\star ... \boldsymbol{\phi}_{\mathtt{q}n}^\star]$, $\boldsymbol{\Phi}_{\mathtt{F}} = [\boldsymbol{\phi}_{\mathtt{F}1} ... \boldsymbol{\phi}_{\mathtt{F}n}]$ and $\boldsymbol{\Phi}_{\mathtt{F}}^\star = [\boldsymbol{\phi}_{\mathtt{F}1}^\star ... \boldsymbol{\phi}_{\mathtt{F}n}^\star]$ are square $n \times n$ matrices; also $\boldsymbol{\mu} = \mathtt{diag}\{\mu_j\}_{j=1,...,n}$ is the $n \times n$ diagonal matrix of eigenvalues μ_j which are associated to the right-going wave modes; finally, $\mathbf{Q}$ and $\mathbf{Q}^\star$ are $n \times 1$ vectors of wave amplitudes, for the right-going wave modes at the left end of the structure and the left-going wave modes at the right end of the structure, respectively.

By considering the wave mode expansions (10) and (11), the reflection and transmission coefficients of waves, for different waveguides connected to a coupling element, can be determined. The strategy consists in expressing the so-called scattering matrix of the coupling element using the wave mode shapes of the waveguides (cf. [8, 12]). The strategy is briefly recalled hereafter for the sake of clarity.

Consider first the case of a coupling element which represents a part of a waveguide containing a defect — e.g., a notch, a loss of rigidity,... — as shown in Figure 2(a). The whole waveguide can be partitioned into two homogeneous waveguides 1 and 2, which are connected to the coupling element. The wave modes of both waveguides 1 and 2 are similar. However, their numbers of substructures — say, N_1 and N_2 — are different. The dynamic equilibrium equation of the coupling element can be written as follows :

$$\mathbf{D}^{\mathtt{d}*} \, \mathbf{q}^{\mathtt{d}}\big|_\Gamma = \mathbf{F}^{\mathtt{d}}\big|_\Gamma \,, \tag{12}$$

where $\mathbf{D}^{\mathtt{d}*}$ is the condensed DSM of the coupling element; $\Gamma = \Gamma_1 \cup \Gamma_2$ is the coupling interface between the coupling element and the waveguides 1 and 2; $\mathbf{q}^{\mathtt{d}}\big|_\Gamma$ and $\mathbf{F}^{\mathtt{d}}\big|_\Gamma$ are the restrictions of the displacement and force vectors of the coupling element to the interface DOFs. Note that the computation of the condensed DSM $\mathbf{D}^{\mathtt{d}*}$ can be easily achieved by considering the Craig-Bampton method, as explained in [12]. In this framework, the displacement of the internal DOFs of the coupling element are expressed in terms of static modes and a reduced set of fixed interface modes.

Assume that the FE meshes of the waveguides and the coupling element are compatible across the coupling interface Γ. Hence, the coupling conditions yield

$$\mathbf{q}^{\mathtt{d}}\big|_{\Gamma} = \mathbf{q}|_{\Gamma} \quad \text{and} \quad \mathbf{F}^{\mathtt{d}}\big|_{\Gamma} = -\,\mathbf{F}|_{\Gamma}\,, \tag{13}$$

where $\mathbf{q}|_{\Gamma} = [(\mathbf{q}_1|_{\Gamma_1})^T(\mathbf{q}_2|_{\Gamma_2})^T]^T$ and $\mathbf{F}|_{\Gamma} = [(\mathbf{F}_1|_{\Gamma_1})^T(\mathbf{F}_2|_{\Gamma_2})^T]^T$ are the restrictions of the displacement and force vectors of the waveguides to the interface DOFs. Hence, Eq. (12) gives :

$$-\,\mathbf{D}^{\mathtt{d}*}\begin{bmatrix}\mathbf{q}_1|_{\Gamma_1}\\ \mathbf{q}_2|_{\Gamma_2}\end{bmatrix} = \begin{bmatrix}\mathbf{F}_1|_{\Gamma_1}\\ \mathbf{F}_2|_{\Gamma_2}\end{bmatrix}. \tag{14}$$

Let us express the displacement vectors $\mathbf{q}_1|_{\Gamma_1}$ and $\mathbf{q}_2|_{\Gamma_2}$, and the force vectors $\mathbf{F}_1|_{\Gamma_1}$ and $\mathbf{F}_2|_{\Gamma_2}$, in terms of wave shapes, see Eqs. (10-11). This yields :

$$\mathbf{q}_1|_{\Gamma_1} = \mathcal{L}_1^{\mathtt{d}}\left(\mathbf{\Phi}_{\mathtt{q}}\boldsymbol{\mu}^{N_1}\mathbf{Q}_1 + \mathbf{\Phi}_{\mathtt{q}}^{\star}\mathbf{Q}_1^{\star}\right) \tag{15}$$

$$\mathbf{q}_2|_{\Gamma_2} = \mathcal{L}_2^{\mathtt{d}}\left(\mathbf{\Phi}_{\mathtt{q}}\mathbf{Q}_2 + \mathbf{\Phi}_{\mathtt{q}}^{\star}\boldsymbol{\mu}^{N_2}\mathbf{Q}_2^{\star}\right) \tag{16}$$

$$\mathbf{F}_1|_{\Gamma_1} = \mathcal{L}_1^{\mathtt{d}}\left(\mathbf{\Phi}_{\mathtt{F}}\mathbf{Q}_1\boldsymbol{\mu}^{N_1} + \mathbf{\Phi}_{\mathtt{F}}^{\star}\mathbf{Q}_1^{\star}\right) \tag{17}$$

$$-\,\mathbf{F}_2|_{\Gamma_2} = \mathcal{L}_2^{\mathtt{d}}\left(\mathbf{\Phi}_{\mathtt{F}}\mathbf{Q}_2 + \mathbf{\Phi}_{\mathtt{F}}^{\star}\boldsymbol{\mu}^{N_2}\mathbf{Q}_2^{\star}\right) \tag{18}$$

where $\mathcal{L}_1^{\mathtt{d}}$ and $\mathcal{L}_2^{\mathtt{d}}$ are direction cosine matrices which project the local coordinate frame of the waveguides onto the coordinate frame of the coupling element. Introducing Eqs. (15–18) in Eq. (14) yields :

$$\begin{aligned}-\,\mathbf{D}^{\mathtt{d}*}&\left(\begin{bmatrix}\mathcal{L}_1^{\mathtt{d}}\mathbf{\Phi}_{\mathtt{q}}^{\star} & \mathbf{0}\\ \mathbf{0} & \mathcal{L}_2^{\mathtt{d}}\mathbf{\Phi}_{\mathtt{q}}\end{bmatrix}\begin{bmatrix}\mathbf{Q}_1^{\star}\\ \mathbf{Q}_2\end{bmatrix} + \begin{bmatrix}\mathcal{L}_1^{\mathtt{d}}\mathbf{\Phi}_{\mathtt{q}} & \mathbf{0}\\ \mathbf{0} & \mathcal{L}_2^{\mathtt{d}}\mathbf{\Phi}_{\mathtt{q}}^{\star}\end{bmatrix}\begin{bmatrix}\boldsymbol{\mu}^{N_1}\mathbf{Q}_1\\ \boldsymbol{\mu}^{N_2}\mathbf{Q}_2^{\star}\end{bmatrix}\right)\\ &= \left(\begin{bmatrix}\mathcal{L}_1^{\mathtt{d}}\mathbf{\Phi}_{\mathtt{F}}^{\star} & \mathbf{0}\\ \mathbf{0} & -\mathcal{L}_2^{\mathtt{d}}\mathbf{\Phi}_{\mathtt{F}}\end{bmatrix}\begin{bmatrix}\mathbf{Q}_1^{\star}\\ \mathbf{Q}_2\end{bmatrix} + \begin{bmatrix}\mathcal{L}_1^{\mathtt{d}}\mathbf{\Phi}_{\mathtt{F}} & \mathbf{0}\\ \mathbf{0} & -\mathcal{L}_2^{\mathtt{d}}\mathbf{\Phi}_{\mathtt{F}}^{\star}\end{bmatrix}\begin{bmatrix}\boldsymbol{\mu}^{N_1}\mathbf{Q}_1\\ \boldsymbol{\mu}^{N_2}\mathbf{Q}_2^{\star}\end{bmatrix}\right).\end{aligned} \tag{19}$$

Eq. (19) leads to

$$\begin{bmatrix}\mathbf{Q}_1^{\star}\\ \mathbf{Q}_2\end{bmatrix} = \mathbb{C}^{\mathtt{d}}\begin{bmatrix}\boldsymbol{\mu}_1^{N_1}\mathbf{Q}_1\\ \boldsymbol{\mu}_2^{N_2}\mathbf{Q}_2^{\star}\end{bmatrix}, \tag{20}$$

where $\mathbb{C}^{\mathtt{d}}$ is the scattering matrix of the defect, expressed by

$$\begin{aligned}\mathbb{C}^{\mathtt{d}} &= \begin{bmatrix}\mathbb{C}_{11}^{\mathtt{d}} & \mathbb{C}_{12}^{\mathtt{d}}\\ \mathbb{C}_{21}^{\mathtt{d}} & \mathbb{C}_{22}^{\mathtt{d}}\end{bmatrix} \\ &= -\left(\begin{bmatrix}\mathcal{L}_1^{\mathtt{d}}\mathbf{\Phi}_{\mathtt{F}}^{\star} & \mathbf{0}\\ \mathbf{0} & -\mathcal{L}_2^{\mathtt{d}}\mathbf{\Phi}_{\mathtt{F}}\end{bmatrix} + \mathbf{D}^{\mathtt{d}*}\begin{bmatrix}\mathcal{L}_1^{\mathtt{d}}\mathbf{\Phi}_{\mathtt{q}}^{\star} & \mathbf{0}\\ \mathbf{0} & \mathcal{L}_2^{\mathtt{d}}\mathbf{\Phi}_{\mathtt{q}}\end{bmatrix}\right)^{-1}\left(\begin{bmatrix}\mathcal{L}_1^{\mathtt{d}}\mathbf{\Phi}_{\mathtt{F}} & \mathbf{0}\\ \mathbf{0} & -\mathcal{L}_2^{\mathtt{d}}\mathbf{\Phi}_{\mathtt{F}}^{\star}\end{bmatrix} + \mathbf{D}^{\mathtt{d}*}\begin{bmatrix}\mathcal{L}_1^{\mathtt{d}}\mathbf{\Phi}_{\mathtt{q}} & \mathbf{0}\\ \mathbf{0} & \mathcal{L}_2^{\mathtt{d}}\mathbf{\Phi}_{\mathtt{q}}^{\star}\end{bmatrix}\right).\end{aligned} \tag{21}$$

In Eq. (20), $\mathbf{Q}_1^{\star}$ and $\mathbf{Q}_2$ are to be understood as the amplitudes of the reflected waves, in waveguides 1 and 2 respectively. Also, $\boldsymbol{\mu}_1^{N_1}\mathbf{Q}_1$ and $\boldsymbol{\mu}_2^{N_2}\mathbf{Q}_2^{\star}$ are the amplitudes of the incident waves, i.e., at the coupling interfaces between the waveguides and the defect. It should be emphasized that the components of the matrix term $\mathbb{C}_{11}^{\mathtt{d}}$ in Eq. (21) are the reflection coefficients for the waves traveling in waveguide 1. They do not depend on the excitation conditions which are applied at the other end of the waveguide (see Figure 2). Analyzing the reflection coefficients contained in the matrix $\mathbb{C}_{11}^{\mathtt{d}}$ is the key idea behind the identification and localization of defects in waveguides [11].

Consider now the case where a curved joint connects a first waveguide — namely, waveguide 1 — with a second one which contains a defect as shown in Figure 2(b). In this case, the analysis of the reflected waves in waveguide 1 involves considering the scattering matrices of the joint and the defects, as well as the coupling effects between those two coupling elements. The question which is raised here is whether the parameters of the joint can be tuned in such a way that the signature of the waves emanating from the defect can be maximized in waveguide 1, i.e., where sensors could be placed. Such an analysis can be undertaken as follows.



FIGURE 2 – (a) one waveguide with a defect ; (b) assembly involving one healthy waveguide, one waveguide with a defect, and one joint.

The system displayed in Figure 2(b) can be partitioned into three waveguides 1, 2 and 3, where waveguides 1 and 2 are coupled to the joint, and where waveguides 2 and 3 are coupled to the defect. The scattering matrix of the joint — namely, $\mathbb{C}^{\mathtt{j}}$ — can be expressed in the same way as (21) and involves the condensed DSM of the joint, say $\mathbf{D}^{\mathtt{j}*}$ (instead of $\mathbf{D}^{\mathtt{d}*}$). This yields

$$\begin{bmatrix} \mathbf{Q}_1^\star \\ \mathbf{Q}_2 \end{bmatrix} = \mathbb{C}^{\mathtt{j}} \begin{bmatrix} \boldsymbol{\mu}^{N_1}\mathbf{Q}_1 \\ \boldsymbol{\mu}^{N_2}\mathbf{Q}_2^\star \end{bmatrix} = \begin{bmatrix} \mathbb{C}^{\mathtt{j}}_{11} & \mathbb{C}^{\mathtt{j}}_{12} \\ \mathbb{C}^{\mathtt{j}}_{21} & \mathbb{C}^{\mathtt{j}}_{22} \end{bmatrix} \begin{bmatrix} \boldsymbol{\mu}^{N_1}\mathbf{Q}_1 \\ \boldsymbol{\mu}^{N_2}\mathbf{Q}_2^\star \end{bmatrix}, \tag{22}$$

where $\mathbf{Q}_1^\star$ and $\mathbf{Q}_2$ are the amplitudes of the reflected waves in waveguides 1 and 2 (respectively), and $\boldsymbol{\mu}_1^{N_1}\mathbf{Q}_1$ and $\boldsymbol{\mu}_2^{N_2}\mathbf{Q}_2^\star$ are the corresponding amplitudes of the incident waves. As for the defect, one has :

$$\begin{bmatrix} \mathbf{Q}_2^\star \\ \mathbf{Q}_3 \end{bmatrix} = \mathbb{C}^{\mathtt{d}} \begin{bmatrix} \boldsymbol{\mu}^{N_2}\mathbf{Q}_2 \\ \boldsymbol{\mu}^{N_3}\mathbf{Q}_3^\star \end{bmatrix} = \begin{bmatrix} \mathbb{C}^{\mathtt{d}}_{22} & \mathbb{C}^{\mathtt{d}}_{23} \\ \mathbb{C}^{\mathtt{d}}_{32} & \mathbb{C}^{\mathtt{d}}_{33} \end{bmatrix} \begin{bmatrix} \boldsymbol{\mu}^{N_2}\mathbf{Q}_2 \\ \boldsymbol{\mu}^{N_3}\mathbf{Q}_3^\star \end{bmatrix}, \tag{23}$$

where $\mathbf{Q}_2^\star$ and $\mathbf{Q}_3$ are the amplitudes of the reflected waves in waveguides 2 and 3 (respectively), and $\boldsymbol{\mu}_2^{N_2}\mathbf{Q}_2$ and $\boldsymbol{\mu}_3^{N_3}\mathbf{Q}_3^\star$ are the corresponding amplitudes of the incident waves. Let us define the scattering matrix of the system joint-waveguide 2-defect — namely, $\mathbb{C}^{\mathtt{jd}}$ — as follows :

$$\begin{bmatrix} \mathbf{Q}_1^\star \\ \mathbf{Q}_3 \end{bmatrix} = \mathbb{C}^{\mathtt{jd}} \begin{bmatrix} \boldsymbol{\mu}^{N_1}\mathbf{Q}_1 \\ \boldsymbol{\mu}^{N_3}\mathbf{Q}_3^\star \end{bmatrix} = \begin{bmatrix} \mathbb{C}^{\mathtt{jd}}_{11} & \mathbb{C}^{\mathtt{jd}}_{13} \\ \mathbb{C}^{\mathtt{jd}}_{31} & \mathbb{C}^{\mathtt{jd}}_{33} \end{bmatrix} \begin{bmatrix} \boldsymbol{\mu}^{N_1}\mathbf{Q}_1 \\ \boldsymbol{\mu}^{N_3}\mathbf{Q}_3^\star \end{bmatrix}. \tag{24}$$

The derivation of the scattering matrix $\mathbb{C}^{\mathtt{jd}}$ involves considering Eqs. (22) and (23). This yields :

$$\begin{bmatrix} \mathbf{Q}_1^\star \\ \mathbf{Q}_3 \\ \mathbf{Q}_2^\star \\ \mathbf{Q}_2 \end{bmatrix} = \begin{bmatrix} \mathbb{C}^{\mathtt{j}}_{11} & \mathbf{0} & \mathbb{C}^{\mathtt{j}}_{12} & \mathbf{0} \\ \mathbf{0} & \mathbb{C}^{\mathtt{d}}_{33} & \mathbf{0} & \mathbb{C}^{\mathtt{d}}_{32} \\ \mathbf{0} & \mathbb{C}^{\mathtt{d}}_{23} & \mathbf{0} & \mathbb{C}^{\mathtt{d}}_{22} \\ \mathbb{C}^{\mathtt{j}}_{21} & \mathbf{0} & \mathbb{C}^{\mathtt{j}}_{22} & \mathbf{0} \end{bmatrix} \begin{bmatrix} \boldsymbol{\mu}^{N_1}\mathbf{Q}_1 \\ \boldsymbol{\mu}^{N_3}\mathbf{Q}_3^\star \\ \boldsymbol{\mu}^{N_2}\mathbf{Q}_2^\star \\ \boldsymbol{\mu}^{N_2}\mathbf{Q}_2 \end{bmatrix}. \tag{25}$$

From the last two rows of the matrix equation (25), one obtains :

$$\begin{bmatrix} \mathbf{I} & -\mathbb{C}^{\mathtt{d}}_{22}\boldsymbol{\mu}^{N_2} \\ -\mathbb{C}^{\mathtt{j}}_{22}\boldsymbol{\mu}^{N_2} & \mathbf{I} \end{bmatrix} \begin{bmatrix} \mathbf{Q}_2^\star \\ \mathbf{Q}_2 \end{bmatrix} = \begin{bmatrix} \mathbf{0} & \mathbb{C}^{\mathtt{d}}_{23} \\ \mathbb{C}^{\mathtt{j}}_{21} & \mathbf{0} \end{bmatrix} \begin{bmatrix} \boldsymbol{\mu}^{N_1}\mathbf{Q}_1 \\ \boldsymbol{\mu}^{N_3}\mathbf{Q}_3^\star \end{bmatrix}, \tag{26}$$

that is

$$\begin{bmatrix} \mathbf{Q}_2^\star \\ \mathbf{Q}_2 \end{bmatrix} = \begin{bmatrix} \mathbf{I} & -\mathbb{C}^{\mathtt{d}}_{22}\boldsymbol{\mu}^{N_2} \\ -\mathbb{C}^{\mathtt{j}}_{22}\boldsymbol{\mu}^{N_2} & \mathbf{I} \end{bmatrix}^{-1} \begin{bmatrix} \mathbf{0} & \mathbb{C}^{\mathtt{d}}_{23} \\ \mathbb{C}^{\mathtt{j}}_{21} & \mathbf{0} \end{bmatrix} \begin{bmatrix} \boldsymbol{\mu}^{N_1}\mathbf{Q}_1 \\ \boldsymbol{\mu}^{N_3}\mathbf{Q}_3^\star \end{bmatrix}. \tag{27}$$

From the first two rows of the matrix equation (25), one obtains :

$$\begin{bmatrix} \mathbf{Q}_1^\star \\ \mathbf{Q}_3 \end{bmatrix} = \begin{bmatrix} \mathbb{C}^{\mathtt{j}}_{11} & \mathbf{0} \\ \mathbf{0} & \mathbb{C}^{\mathtt{d}}_{33} \end{bmatrix} \begin{bmatrix} \boldsymbol{\mu}^{N_1}\mathbf{Q}_1 \\ \boldsymbol{\mu}^{N_3}\mathbf{Q}_3^\star \end{bmatrix} + \begin{bmatrix} \mathbb{C}^{\mathtt{j}}_{12}\boldsymbol{\mu}^{N_2} & \mathbf{0} \\ \mathbf{0} & \mathbb{C}^{\mathtt{d}}_{32}\boldsymbol{\mu}^{N_2} \end{bmatrix} \begin{bmatrix} \mathbf{Q}_2^\star \\ \mathbf{Q}_2 \end{bmatrix}. \tag{28}$$

By considering Eq. (27), this yields

$$\begin{bmatrix}\mathbf{Q}_1^\star\\ \mathbf{Q}_3\end{bmatrix} = \left(\begin{bmatrix}\mathbb{C}_{11}^{\mathtt{j}} & \mathbf{0}\\ \mathbf{0} & \mathbb{C}_{33}^{\mathtt{d}}\end{bmatrix} + \begin{bmatrix}\mathbb{C}_{12}^{\mathtt{j}}\boldsymbol{\mu}^{N_2} & \mathbf{0}\\ \mathbf{0} & \mathbb{C}_{32}^{\mathtt{d}}\boldsymbol{\mu}^{N_2}\end{bmatrix}\begin{bmatrix}\mathbf{I} & -\mathbb{C}_{22}^{\mathtt{d}}\boldsymbol{\mu}^{N_2}\\ -\mathbb{C}_{22}^{\mathtt{j}}\boldsymbol{\mu}^{N_2} & \mathbf{I}\end{bmatrix}^{-1}\begin{bmatrix}\mathbf{0} & \mathbb{C}_{23}^{\mathtt{d}}\\ \mathbb{C}_{21}^{\mathtt{j}} & \mathbf{0}\end{bmatrix}\right)\begin{bmatrix}\boldsymbol{\mu}^{N_1}\mathbf{Q}_1\\ \boldsymbol{\mu}^{N_3}\mathbf{Q}_3^\star\end{bmatrix}. \tag{29}$$

Hence, the scattering matrix of the system joint-waveguide 2-defect can be expressed as follows :

$$\begin{bmatrix}\mathbb{C}_{11}^{\mathtt{jd}} & \mathbb{C}_{13}^{\mathtt{jd}}\\ \mathbb{C}_{31}^{\mathtt{jd}} & \mathbb{C}_{33}^{\mathtt{jd}}\end{bmatrix} = \begin{bmatrix}\mathbb{C}_{11}^{\mathtt{j}} & \mathbf{0}\\ \mathbf{0} & \mathbb{C}_{33}^{\mathtt{d}}\end{bmatrix} + \begin{bmatrix}\mathbb{C}_{12}^{\mathtt{j}}\boldsymbol{\mu}^{N_2} & \mathbf{0}\\ \mathbf{0} & \mathbb{C}_{32}^{\mathtt{d}}\boldsymbol{\mu}^{N_2}\end{bmatrix}\begin{bmatrix}\mathbf{I} & -\mathbb{C}_{22}^{\mathtt{d}}\boldsymbol{\mu}^{N_2}\\ -\mathbb{C}_{22}^{\mathtt{j}}\boldsymbol{\mu}^{N_2} & \mathbf{I}\end{bmatrix}^{-1}\begin{bmatrix}\mathbf{0} & \mathbb{C}_{23}^{\mathtt{d}}\\ \mathbb{C}_{21}^{\mathtt{j}} & \mathbf{0}\end{bmatrix}. \tag{30}$$

which allows to identify the matrix term $\mathbb{C}_{11}^{\mathtt{jd}}$ as :

$$\mathbb{C}_{11}^{\mathtt{jd}} = \mathbb{C}_{11}^{\mathtt{j}} + \mathbb{C}_{12}^{\mathtt{j}}\boldsymbol{\mu}_2^{N_2}\mathbb{C}_{22}^{\mathtt{d}}\boldsymbol{\mu}_2^{N_2}(\mathbf{I} - \mathbb{C}_{22}^{\mathtt{j}}\boldsymbol{\mu}_2^{N_2}\mathbb{C}_{22}^{\mathtt{d}}\boldsymbol{\mu}_2^{N_2})^{-1}\mathbb{C}_{21}^{\mathtt{j}}. \tag{31}$$

To derive Eq. (31), the analytical expression of the inverse of the 2×2 block matrix in the right hand side of Eq. (30) has been considered. In Eq. (31), $\mathbb{C}_{11}^{\mathtt{jd}}$ is the matrix of the apparent reflection coefficients, i.e., those observed in waveguide 1 when an incident wave is considered. As for the right hand side term of Eq. (31), the first matrix term $\mathbb{C}_{11}^{\mathtt{j}}$ contains the reflection coefficients which result from the joint disregarding the influence of the defect. The second matrix term is given by

$$\mathbb{R}^{\mathtt{d}} = \mathbb{C}_{12}^{\mathtt{j}}\boldsymbol{\mu}_2^{N_2}\mathbb{C}_{22}^{\mathtt{d}}\boldsymbol{\mu}_2^{N_2}(\mathbf{I} - \mathbb{C}_{22}^{\mathtt{j}}\boldsymbol{\mu}_2^{N_2}\mathbb{C}_{22}^{\mathtt{d}}\boldsymbol{\mu}_2^{N_2})^{-1}\mathbb{C}_{21}^{\mathtt{j}}, \tag{32}$$

which contains the reflection coefficients of the defect as observed through the joint. By tuning the parameters of the joint in an adequate way, it becomes possible to maximize the components of the matrix $\mathbb{R}^{\mathtt{d}}$, and therefore, to maximize the signature of the defect from measured data in waveguide 1. The following paragraph describes the strategy used for this matter.

Let us denote by $\mathbf{x}$ a set of joint parameters, i.e., some of its geometrical parameters (curvature radius, angle,...) and/or material parameters (Young's modulus, mass density,...). A measure of the matrix $\mathbb{R}^{\mathtt{d}}$, for a given set $\mathbf{x}$, can be proposed as follows :

$$g(\mathbf{x}) = \max_{f\in[f_{\min}-f_{\max}]} \|\mathbb{R}^{\mathtt{d}}\|_{\max}, \tag{33}$$

where $g(\mathbf{x})$ is the so-called cost function, which gives back the maximum value of the $\max$-norm of $\mathbb{R}^{\mathtt{d}}$ on a frequency range $[f_{\min} - f_{\max}]$, where the $\max$-norm of $\mathbb{R}^{\mathtt{d}}$ is given by $\|\mathbb{R}^{\mathtt{d}}\|_{\max} = \max_{ij} |\mathbb{R}_{ij}^{\mathtt{d}}|$. Hence, the determination of the optimal set $\mathbf{x}^{\mathtt{opt}}$ of the joint parameters can be obtained by solving the following optimization problem :

$$\mathbf{x}^{\mathtt{opt}} = \underset{\mathbf{x}}{\operatorname{argmax}}\, g(\mathbf{x}), \tag{34}$$

which yields the highest coupling coefficient among those of the reflection matrix $\mathbb{R}^{\mathtt{d}}$, on a particular frequency range. Practically, a genetic algorithm (here, the `ga()` MATLAB function in the Global optimization toolbox) can be used for finding the global optimum $\mathbf{x}^{\mathtt{opt}}$. In this paper, only two parameters will be considered, i.e., the internal curvature radius R_{int} and the curvature angle θ of the joint.

4 Numerical results

The proposed approach is applied to a simple case, which concerns three beam-like structures — namely, waveguides 1, 2 and 3 — with a curved joint and a defect as shown in Figure 3. The waveguides, the curved joint and the coupling element embedding the defect are meshed with four nodes plane stress finite elements. The geometrical and material properties of the waveguides are listed in Table 1. The defect is modeled by means of a local variation of the Young's modulus, i.e., $E^{\mathtt{d}} = E(1-\gamma)$, representing a crack of dimensions $x^{\mathtt{d}} \times y^{\mathtt{d}}$ (see Figure 3). The joint represents a curved beam with an angle of θ and an internal radius of

curvature of R_{int}, surrounded by two straight parts of small lengths $l_{\mathtt{a}}^{\mathtt{j}}$ and $l_{\mathtt{b}}^{\mathtt{j}}$. Note that the case $\theta = 0$ yields a straight beam (no curvature) of length $l_{\mathtt{a}}^{\mathtt{j}} + l_{\mathtt{b}}^{\mathtt{j}}$. Also, the lengths of waveguides 1, 2 and 3 are denoted as l_1, l_2 and l_3, respectively (see Table 2).

As for the waveguides, the substructures have a length $d = 5 \times 10^{-3}$ m, are meshed with $N_t = 20$ elements and do not contain internal DOFs (see Figure 3). This yields $n = 42$ DOFs on the left/right boundaries. Also, $N_s = 80$ elements are used to mesh the joint along the circumferential direction, while $N_d = 20$ elements are used to mesh the coupling element (defect) along the longitudinal direction. As mentioned in Section 3, the Craig-Bampton procedure is used to model the joint and the coupling element. In this case, 100 fixed interface modes are retained for both the joint and the coupling element ; this reduced set of fixed interface modes is sufficient for obtaining an accurate estimation of the condensed DSMs $\mathbf{D}^{\mathtt{d}*}$ and $\mathbf{D}^{\mathtt{j}*}$.

E	ρ	ν	η	h	b
210 GPa	7800 kg.m^{-3}	0.3	1×10^{-3}	0.1 m	0.05 m

TABLE 1 – Parameters of the waveguide.

R	θ	$l_{\mathtt{a}}^{\mathtt{j}}$	$l_{\mathtt{b}}^{\mathtt{j}}$	$l^{\mathtt{d}}$	l_1	l_2	l_3	$x^{\mathtt{d}}$	$y^{\mathtt{d}}$
[0.01 ... 0.4] m	[0 ... π] rad	0.1 m	0.1 m	0.05 m	0.4 m	0.2 m	0.15 m	0.01 m	0.02 m

TABLE 2 – Geometrical parameters of the joint and the defect.

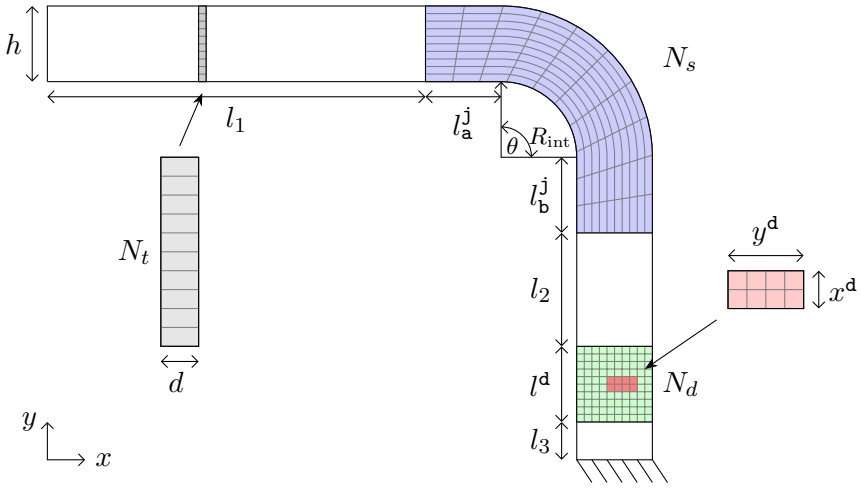


FIGURE 3 – Schematic of an assembly involving three healthy waveguides, one joint and one defect. (Gray shaded area) substructures ; (Blue shaded area) curved junction ; (Green shaded area) coupling element with the defect ; (small red shaded area) defect area.

The wave modes of the waveguides are computed with the WFE method (see Section 2.2). The dispersion curves — i.e., the frequency evolution of the real part of the wave numbers — for several propagating, evanescent and complex wave modes are displayed on a frequency band of $[10 - 40000]$ Hz as shown in Figure 4(a). Especially, the flexural mode (blue curve), the longitudinal mode (red curve) and the shearing mode (yellow curve) are shown. Two complex wave modes are also shown. The related mode shapes (displacement components) at 40000 Hz are displayed as shown in Figure 4(b).

4.1 Defect in a straight waveguide

Let us start with the simple case where the angle of the joint is $\theta = 0$, which means a straight waveguide. Figure 5 shows the apparent reflection coefficients (defect observed through the joint) in waveguide 1 for

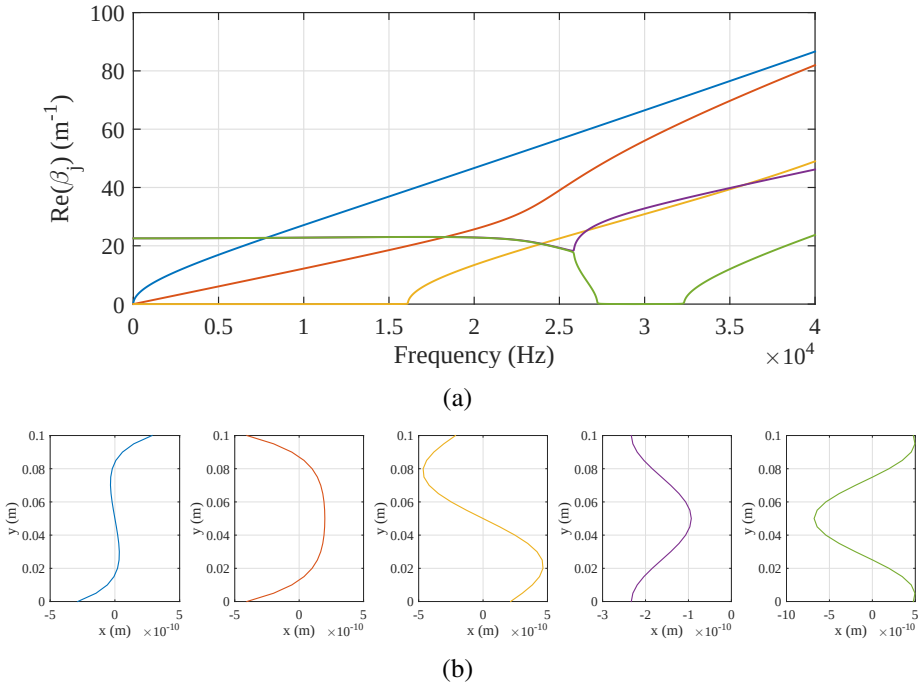


FIGURE 4 – (a) Dispersion curves and (b) mode shapes at 40 kHz for the first five wave modes.

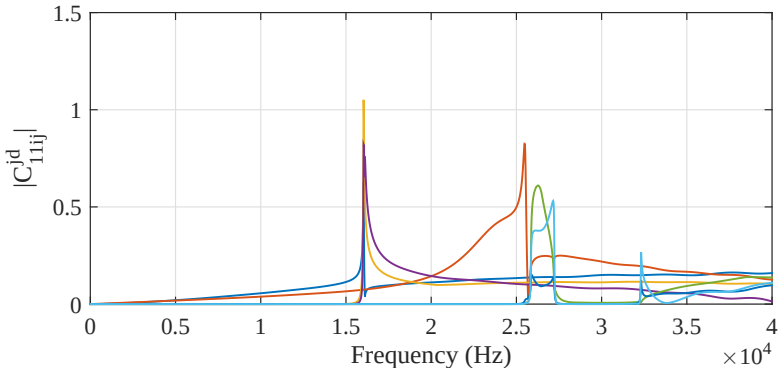
two types of defects A and B. Type A is an internal defect placed at the center of the coupling element, while Type B represents an external defect placed on the extrados of the waveguide. Two severity coefficients are also considered for modeling the defect, i.e., $\gamma = 0.9$ (Types A1 and B1) and $\gamma = 0.5$ (Types A2 and B2) in $E^{\mathtt{d}} = E(1-\gamma)$.

The moduli of the apparent reflection coefficients — i.e., the components of the matrix $\mathbb{C}_{11}^{\mathtt{jd}}$ — due to the defect A1 are plotted in Figure 5(a) for some wave modes. These involve the flexural, longitudinal and shearing modes, as well as the two complex modes 1 and 2 shown in Figures 4(a-b). It is seen that the defect can be detected by different waves, for different frequencies. Also, mode conversion occurs, i.e., the fact that a certain wave mode yields a reflected mode of different nature. Choosing the best wave for detecting and identifying the defect can be done by considering the max-norm of $\mathbb{C}_{11}^{\mathtt{jd}}$.

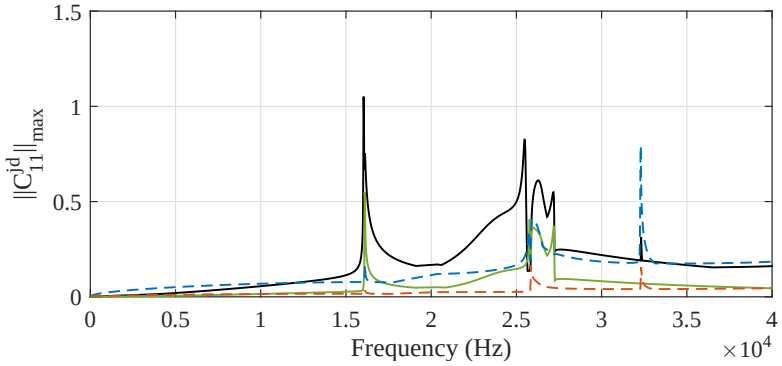
The frequency evolution of the max-norm $\|\mathbb{C}_{11}^{\mathtt{jd}}\|_{\max}$ is displayed in Figure 5(b) for the defects A1, A2, B1 and B2. The wave mode conversion phenomena involved for these different defects are not explicitly shown in this case due to the consideration of the max-norm, although revealed by the local peaks of the curves. It is shown in Figure 5(b) that the variation of $\|\mathbb{C}_{11}^{\mathtt{jd}}\|_{\max}$ depends on the kind of defect considered, and that the best waves for detecting the defects A1 and A2 are not necessarily those for detecting the defects B1 and B2. This is mostly linked to the way the wave mode shapes interfere with the shapes of the defects. For instance, the best choice for detecting the defect B1 is to consider the reflection from the longitudinal mode to the complex mode 2 at 3.2 kHz, while for defect A1, it is preferable to consider the reflection from the flexural mode to the shearing mode at 1.6 kHz.

4.2 Effect of the curved joint

The frequency evolution of the max-norm $\|\mathbb{C}_{11}^{\mathtt{jd}}\|_{\max}$, which results from a curved joint with an angle of $\theta = 3\pi/4$ and a radius of curvature of $R_{\text{int}} = 0.1$ m, is shown in Figure 6 for the defect A1. Compared to the case $\theta = 0$ (straight joint), it can be observed that $\|\mathbb{C}_{11}^{\mathtt{jd}}\|_{\max}$ admits different variations. The contributions of the joint and the defect can be highlighted by considering the max-norm of the matrices $\mathbb{C}_{11}^{\mathtt{j}}$ and $\mathbb{R}^{\mathtt{d}}$, see



(a)



(b)

FIGURE 5 – (a) Moduli of the apparent reflection coefficients for defect A1 in a straight waveguide : flexural $\rightarrow$ flexural (blue), longitudinal $\rightarrow$ longitudinal, (red) flexural $\rightarrow$ shearing (yellow), shearing $\rightarrow$ shearing (purple), complex mode 2 $\rightarrow$ complex mode 1 (green), longitudinal $\rightarrow$ complex mode 2 (blue), complex mode 2 $\rightarrow$ complex mode 2 (light blue) . (b) Max-norm $\mathbb{C}^{\mathtt{jd}}_{11}$ for defects A1 (black), A2 (green), B1 (dashed blue) and B2 (dashed red).

Eq. (31). Here, the contribution of the joint (dashed red curve) is clearly superior to that of the defect (green curve) especially at low frequencies. Peaks of large magnitude occur around 2.6 kHz and 2.8 kHz, which are however mostly due to the joint. The influence of the defect on the measured reflected signal follows from the analysis of the indicator $\|\mathbb{R}^{\mathtt{d}}\|_{\max}$. Its value is nevertheless influenced by the parameters of the joint.

4.3 Optimization of the joint parameters

A further insight about the effect of the joint parameters can be proposed for the defect A1. The maps of the cost functions $g(R_{\text{int}}, \theta)$ for $f \in [15-17]$ kHz and $f \in [25-28]$ kHz are shown in Figures 7(a) and 7(c). The general trend is that the magnitudes of the reflection coefficients increase as the angle of the joint decreases. Notice however that the variations of the cost functions are complex and that several local maxima occur, meaning high reflection coefficients. Besides, an absolute maximum can be observed at a non-zero angle ($R_{\text{int}} = 0.01$ m, $\theta = 0.34$ rad) as shown in Figure 7(a). What is meant by Figures 7(a) and 7(c) is that, if one constrains one parameter (e.g., an angle θ not equal to 0 or π), there exists one optimal choice for the second one which is not trivial (i.e., R_{int} not equal to 0 or 0.4 m). Figures 7(b) and 7(d) allows a better interpretation of these results as it shows which waves are involved in the computation of the cost function $g(R_{\text{int}}, \theta)$. For the sake of clarity, the flexural, longitudinal, shearing, and the complex modes (1 and 2) are denoted by 1, 2, 3, 4 and 5. For instance, $g(R_{\text{int}}, \theta) = \max_{f\in[f_{\min}-f_{\max}]} \|\mathbb{R}^{\mathtt{d}}\|_{\max} = \max_{f\in[f_{\min}-f_{\max}]} |\mathbb{R}^{\mathtt{d}}_{23}|_{\max}$ means that the coupling between the longitudinal mode and the shearing mode is mostly involved in the detection of

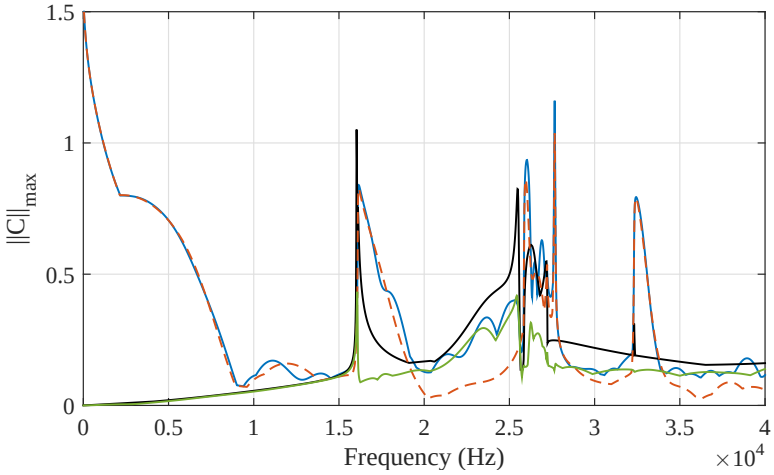


FIGURE 6 – Max-norm of the scattering matrix for defect A1 : $\|\mathbb{C}_{11}^{\mathtt{jd}}\|_{\max}$ for a straight joint (black), $\|\mathbb{C}_{11}^{\mathtt{jd}}\|_{\max}$ for a curved joint (blue), $\|\mathbb{C}_{11}^{\mathtt{j}}\|_{\max}$ for for a curved joint (dashed red), $\|\mathbb{R}^{\mathtt{d}}\|_{\max}$ for a curved joint (green).

the defect. Hence, regarding Figure 7(b), it is shown for instance that, for small angles, the coupling (3→3) yields the maximum reflection coefficient; the absolute maximum is obtained for the coupling (2→3); for higher angles, the coupling (1→1) is the most pertinent. Regarding Figure 7(d), the best reflection coefficient is almost always due to the coupling (2→2); other couplings are also relevant, e.g., (5→4) and (3→1).

To fix ideas, consider the case where the curvature angle of the joint is imposed, and that the best curvature radius for detecting a given defect is sought. Several simulations are performed as shown in Figure 8. For instance, for the defect A1 and an angle of $\theta = \pi/2$, the best curvature radius is found to be 0.146 m, which is due to the mode coupling (1→1). Note that, contrary to intuition, increasing the curvature radius in this case does not yield a better result. For $\theta = \pi/4$, it is observed that the best curvature radius is either 0.104 m or 0.400 m (absolute maximum). Physical constraints may restrain the choice of the appropriate radius in this case. As for the defect B1 when $\theta = \pi/2$, it appears that the best choice is R_{int} = 0.037 m.

5 Conclusion

A wave-based strategy has been proposed to identify defects in assemblies made up of straight waveguides and curved joints. Specifically, the influence of the parameters of the joints on the detection of the defects has been analyzed. To address this issue, the WFE method has been applied to compute waves in waveguides and the scattering matrices of the joints and defects. A whole scattering matrix which incorporates a joint and a defect has been formulated. It provides an efficient means to analyze the influence of the joint on the measured reflected signals induced by the defect. An optimization strategy has been proposed to select the joint parameters in an adequate way to magnify the reflected signals. Numerical experiments have been carried out concerning one healthy waveguide and one waveguide containing a defect, connected together through a curved joint. For a given type of defect and for a fixed curvature angle of the joint, it has become possible to find an optimal, non-trivial, value of the curvature radius of the joint. Results have shown that mode conversion phenomena are sometimes involved in the wave reflection mechanisms. The complexity of the wave interactions is however well handled by the WFE method. Further works may concern more complex waveguides (straight or stiffened pipes, fluid-filled) and joints with more complex topology and several tunable parameters.

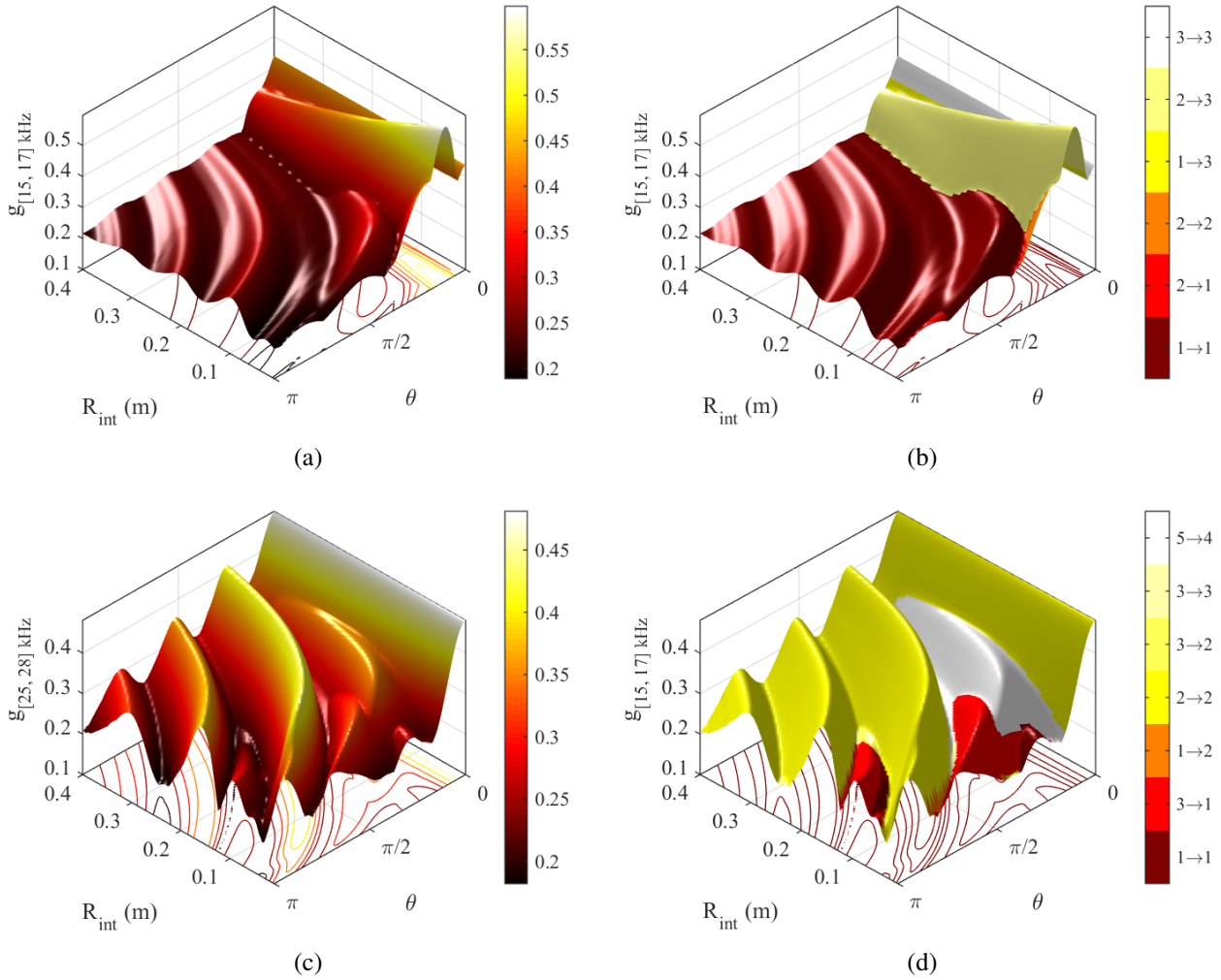


FIGURE 7 – (a,c) Map (θ, R_{int}, g) for defect A1 on range (a) [15, 17] kHz and (c) [25, 28] kHz. (b,d) Mode couplings involved in g on range (b) [15, 17] kHz and (d) [25, 28] kHz.

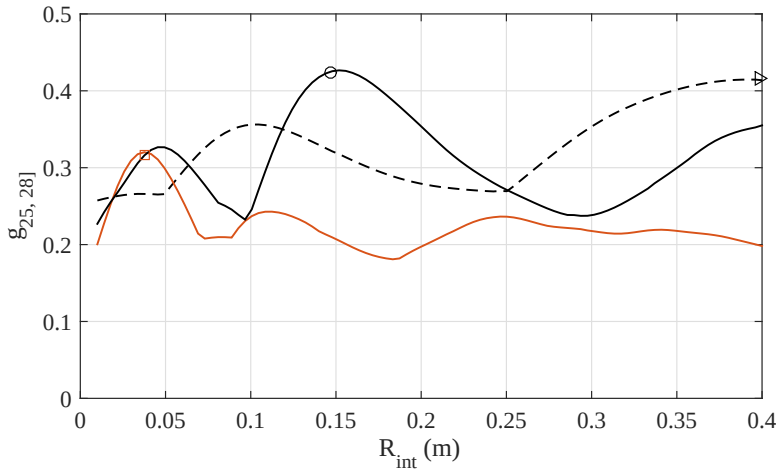


FIGURE 8 – Variation of the cost function $g(R_{\text{int}}, \theta)$ (on the frequency range [25-28] kHz) with R_{int} when $\theta = \pi/2$ (full black line) and $\theta = \pi/4$ (dashed black line) for defect A1, and when $\theta = \pi/2$ for defect B1 (full red line). Optimal values are indicated with a black circle, a black triangle and a red square.

Références

[1] Joseph L. Rose, A Baseline and Vision of Ultrasonic Guided Wave Inspection Potential, Journal of Pressure Vessel Technology 124 (3) (2002) 273.

[2] A. Demma, P. Cawley, M. Lowe, B. Pavlakovic, The Effect of Bends on the Propagation of Guided Waves in Pipes, Journal of Pressure Vessel Technology 127 (2005) 328.

[3] R. Sanderson, D. A. Hutchins, D. R. Billson, P. Mudge, The investigation of guided wave propagation around a pipe bend using an analytical modeling approach, J. Acoust. Soc. Am. 133 (3) (2013) 1404–1414.

[4] B. Verma, T. K. Mishra, K. Balasubramaniam, P. Rajagopal, Interaction of low-frequency axisymmetric ultrasonic guided waves with bends in pipes of arbitrary bend angle and general bend radius, Ultrasonics 54 (3) (2014) 801–808.

[5] J. Ni, S. Zhou, P. Zhang, Y. Li, Effect of Pipe Bend Configuration on Guided Waves-Based Defects Detection: An Experimental Study, Journal of Pressure Vessel Technology 138 (2015) 021203.

[6] W. X. Zhong, F. W. Williams, on the Direct Solution of Wave-Propagation for Repetitive Structures, Journal of Sound and Vibration 181 (3) (1995) 485–501.

[7] J.-M. Mencik, New advances in the forced response computation of periodic structures using the wave finite element (WFE) method, Computational Mechanics 54 (3) (2014) 789–801.

[8] J.-M. Mencik, M. N. Ichchou, Multi-mode propagation and diffusion in structures through finite elements, European Journal of Mechanics, A/Solids 24 (5) (2005) 877–898.

[9] M. N. Ichchou, J.-M. Mencik, W. Zhou, Wave finite elements for low and mid-frequency description of coupled structures with damage, Computer Methods in Applied Mechanics and Engineering 198 (15-16) (2009) 1311–1326.

[10] C. Schaal, S. Bischoff, L. Gaul, Damage detection in multi-wire cables using guided ultrasonic waves, Structural Health Monitoring : An International Journal 15 (3) (2016) 279–288.

[11] S. Bischoff, C. Schaal, L. Gaul, Efficient wave scattering analysis for damaged cylindrical waveguides, Journal of Sound and Vibration 333 (18) (2014) 4203–4213.

[12] J.-M. Mencik, Model reduction and perturbation analysis of wave finite element formulations for computing the forced response of coupled elastic systems involving junctions with uncertain eigenfrequencies, Computer Methods in Applied Mechanics and Engineering 200 (45-46) (2011) 3051–3065.

[13] P. B. Silva, J.-M. Mencik, J. R. F. Arruda, Wave finite element-based superelements for forced response analysis of coupled systems via dynamic substructuring, International Journal for Numerical Methods in Engineering 107 (6) (2015) 453–476.

[14] J.-M. Mencik, D. Duhamel, A wave-based model reduction technique for the description of the dynamic behavior of periodic structures involving arbitrary-shaped substructures and large-sized finite element models, Finite Elements in Analysis and Design 101 (2015) 1–14.

Vibration integrity assessment on LNG process pipework using a combined experimental and analytical approach

G. Wally[1], C. McIlwraith[1], M. Hutchinson[1]
[1] Wood PLC, Vibration, Dynamics and Noise
St. Vincent Street 319, G2 5LP, Glasgow, United Kingdom
e-mail: **gernot.wally@woodgroup.com**

Abstract
Vibration induced fatigue is a common root cause of failures for process piping. Failures can cause harm to human life and the environment and have severe cost implications. Experimental vibration integrity assessments of piping are typically carried out by utilising vibration and dynamic strain measurements in order to quantify the existing integrity threat. This case study shows an alternative assessment approach for process piping at a LNG processing facility (where direct dynamic strain assessment was not possible), in particular how to use experimental vibration data in combination with numerical analysis to predict the dynamic stresses in critical piping areas. This method uses vibration time trend data and frequency based ODS analysis to define numerical analysis boundary conditions. It also shows how the experimental and numerical data can be used to create a localized vibration criterion for the piping, ensuring that local non-expert operators can accurately assess the vibration severity without using specialized strain equipment.

1 Introduction

Concerns were raised by site personnel regarding vibration on main propane process pipework (Figure 1) at an Liquefied Natural Gas (LNG) processing facility. A fatigue failure would have not only caused a major safety problem but also a shut-down of the whole processing facility for an extended period of time. Therefore, a vibration integrity assessment had to be carried out in order to quantify the fatigue threat and to establish a safe operating envelope for a future planned increase in production (~20% increase in flowrates).



Figure 1: Process pipework under investigation (Inlet line to propane cooler)

These types of assessments are very common and normally consist of in-service vibration measurements in combination with dynamic strain measurements. The vibration behavior of the piping under investigation

was of random transient nature (Figure 2) which normally requires a data acquisition system which can collect data simultaneously at multiple points in all 3 translational directions.

After analysis of the vibration data and extraction of the vibration shapes a strain measurement is typically carried out in order to assess the critical dynamic stresses in-situ. For the assessment described in this case study, only a handheld 4-channel data analyzer was available and the recording of dynamic strain data was not possible due to access restrictions, and low process temperature (pipework ices up immediately after cladding is removed, offline strain gauging was not possible as process could not be shut down) of the piping. Therefore, a combination of an experimental assessment with a subsequent numerical analysis was required for the integrity assessment.

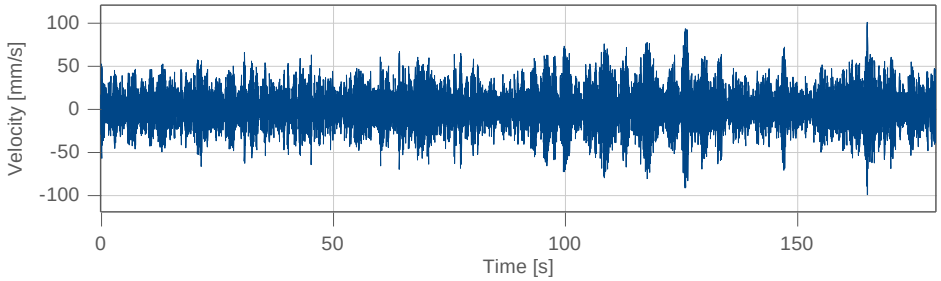


Figure 2: Time history vibration data (crest factor = 4.49; kurtosis = 3.29)

2 Experimental vibration assessment

2.1 Background

A common approach for experimental vibration assessment in the Oil and Gas industry is described in the Energy Institute (EI) Guideline for the Avoidance of Vibration Induced Fatigue Failures in Process Pipework [1]. This document provides guidance on the execution of vibration assessments and a vibration acceptance criterion (based on research published in [2]) for process pipework. Although other engineering bodies use their own guidelines ([3] [4]), in general the criterion curves are similar.

2.2 Methodology

When using the EI Guideline acceptance criterion for the pipework under investigation, it was apparent that the likelihood for a vibration induced integrity problem was very high (vibration in excess of the Danger criterion curve) and a more thorough investigation was required (Figure 3).

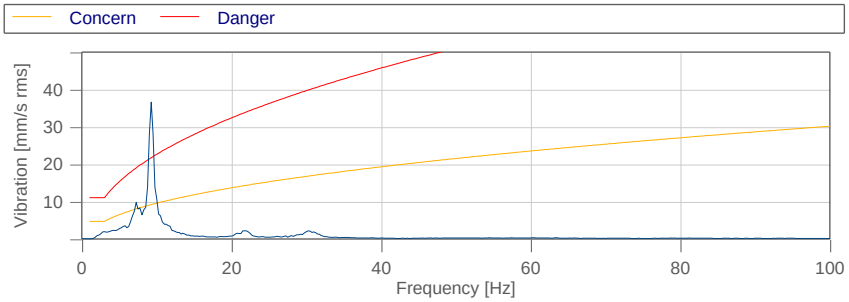


Figure 3: Vibration data vs. EI Guideline based Criterion [1]

The typical first step after a problem is found (i.e. vibration exceeds criteria curves) is the completion of an operational deflection shape (ODS) analysis in order to identify the vibration shapes and the locations where dynamic stresses may be elevated. There are two ways of performing an ODS analysis: Time based and Frequency based. The most common is the frequency based ODS analysis which uses vibration data captured with a handheld/low channel count FFT Analyzer at a stationary reference node and at multiple roving response nodes. This data is then used to create an ODS Force Response Function (FRF) which combines the magnitude of each roving node Auto Spectrum with the phase between the roving and the reference nodes of each Cross Spectrum.

$$ODSFRF(jw) = G_{xx}(cos\varphi + j * cos\varphi) \quad (1)$$

with

$$\varphi\,(w) = \text{atan}\frac{Im(G_{xy})}{Re(G_{xy})} \quad (2)$$

G_{xx} describes the Auto Spectrum of the roving node and G_{xy} describes the Cross Spectrum of the reference / response node. As described in [5]and [6] this approach is primarily only applicable for steady state vibration which for the pipework under investigation is not the case.

For a non-steady state (transient) vibration assessment, a time based ODS is more suitable however this requires a high-channel count (ideally more than 16 channels) data acquisition system which was not available for this assessment.

In order to capture a representative snapshot of the vibration response utilizing a low channel count (four channels) FFT analyzer, a series of time history data recordings (3-5 minutes) with the same physical setup as for frequency based ODS measurements (one stationary reference node and multiple roving response nodes) (Figure 4) was carried out. The longer time history recordings allowed for the full transient behavior of the piping vibration response to be captured.

This type of time history assessment will take longer for the collection of the data than the typical frequency ODS variant but this is tolerable if the process operating regime (i.e. flowrates and flow composition) for the piping is relatively stable for the duration of the assessment period.

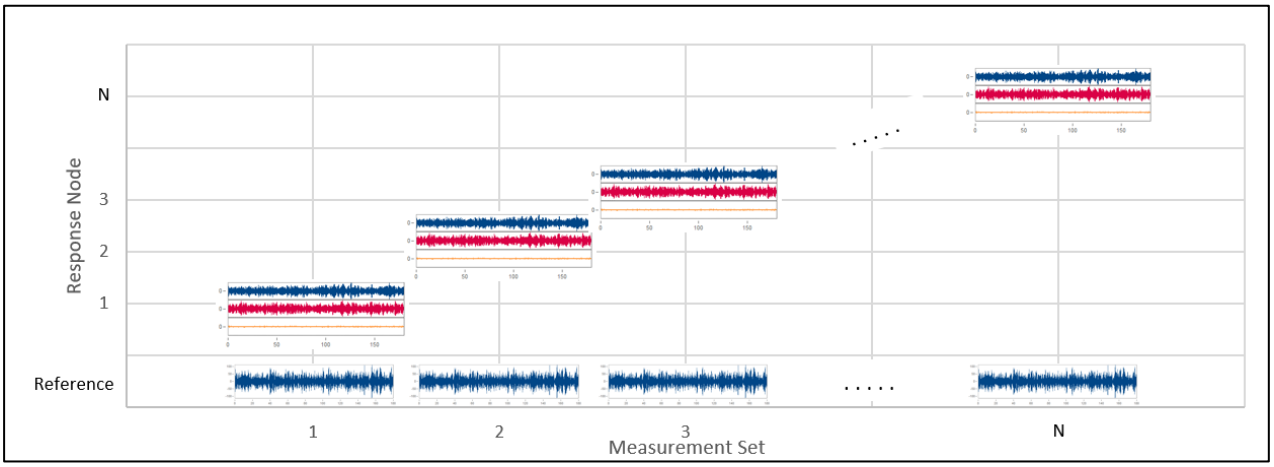


Figure 4: Schematic of data recording for “offline” frequency based ODS analysis

The advantage of using this approach is that it allows for modification and optimization of all relevant signal processing parameters during the post processing for optimum results. During traditional ODS assessments the parameters of influence are typically set in the analyzer and include settings such as number of lines, windowing function, type of averaging and number of averages. However, with time history data capture these settings are not only variable but the method also allows for data clean up and exclusion of spurious

sections which would not be possible during a data recording for the traditional frequency based ODS (where the stored data is already post processed in the analyzer) . As shown in Figure 5, even a slight change in analysis parameters can have a significant influence on the resulting FFT spectrum. Not only the magnitude can be affected but also certain frequency components (see ~7 Hz range in Figure 5) can be altered to a point where they are completely eliminated. This could result in the ODS wrongly animating the associated location which could subsequently lead to selecting the wrong points for a follow up measurement or using incorrect vibration shapes for the numerical analysis.

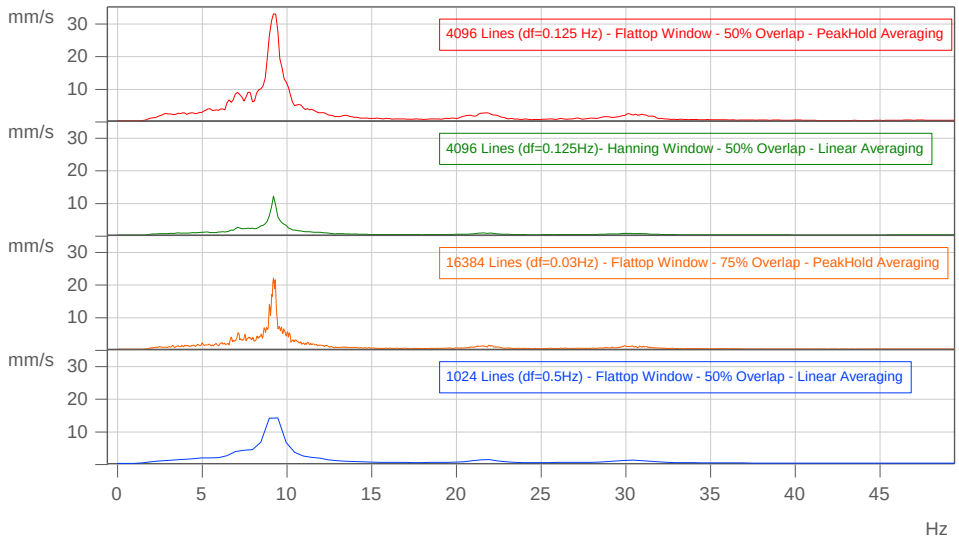


Figure 5: FFT spectrum of the same signal with varying analysis parameters

2.3 Results

A parametric study was carried out in order to find the ideal set of analysis parameters for the given data (df = 0.25 Hz; FlatTop; 50% Overlap; PeakHold Averaging), the data was then converted into ODS FRFs using the approach shown in equation (1).

The ODS FRFs were uploaded into a 3rd party software package for animation and vibration shape extraction. As in Figure 6, the pipework under investigation had dominant vibration modes at 5.25 Hz, 7.25 Hz and 9.25 Hz. The associated high stress locations with these vibration shapes would be on the elbow upstream of the propane cooler and the elbow upstream of the tee connection (as highlighted by the dotted circles in Figure 6).

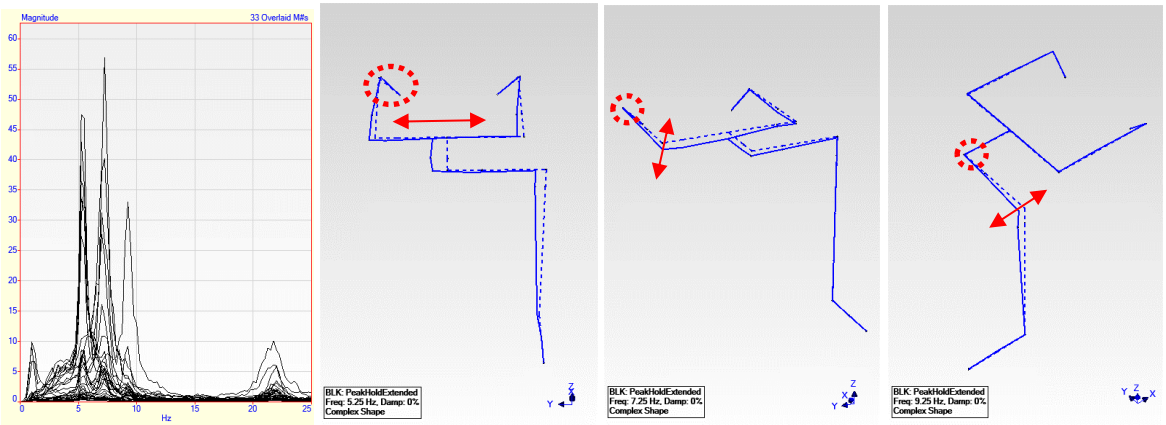


Figure 6: FFT plot showing 3 dominant frequencies and the associated ODS shapes

The next step in a typical vibration integrity assessment would be the installation of strain gauges at the identified high stress locations and monitoring of the dynamic stresses during representative operating conditions [1]. This strain data would not only be used to quantify the vibration induced integrity threat (as per [7] [8]) but also to create a site/location specific vibration criterion. When recording dynamic stress and vibration simultaneously a representative transfer function between two points can be created which can allow site personnel to use non-specialist equipment to give an indication of the dynamic stress levels (Figure 7).

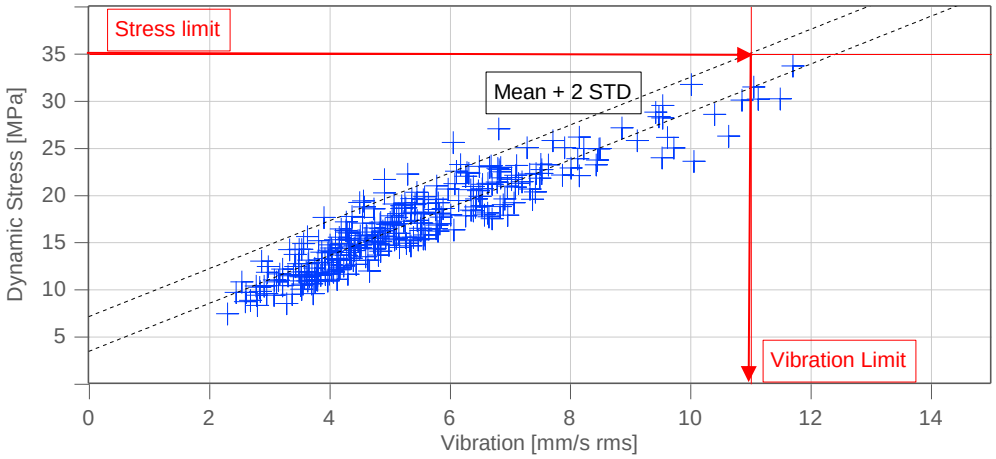


Figure 7: Example of stress vibration analysis to create customized vibration criterion

Due to operational restrictions and the associated temperature of the pipework a detailed dynamic stress assessment was not feasible and therefore a numerical analysis was the only practical method to quantify the dynamic stress levels.

3 Numerical Analysis

The first step of the analysis is the determination of the boundary conditions and the definition of the analysis method. In this particular case the excitation source is slugging flow (gas with a small fraction of congregated liquid) which drives the natural frequencies of the pipework (i.e. the slugs impact the pipe wall at every change in flow direction). An example of a typical forcing function for this type of excitation is shown in Figure 8, which shows a dominant characteristic peak in the force spectrum, which often occurs at relatively low frequencies (<10Hz), depending on void fraction.

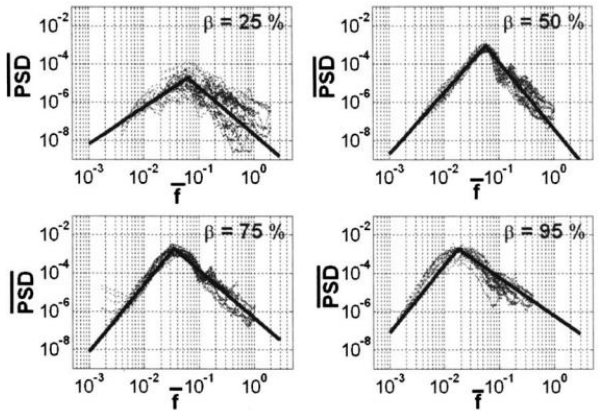


Figure 8: Examples of forcing power spectral densities created by multiphase flow / slugging (note frequency and amplitude axes are normalized) [9]

In order to determine accurate boundary conditions, the ODS shapes can be used to help tune the predicted vibration response and the natural frequencies in the frequency range of interest.

Mode	Measured	Calculated
1	**5.25 Hz**	**5.69 Hz**
2	**7.25 Hz**	**7.65 Hz**
3	**9.25 Hz**	**9.19 Hz**

Table 1: Natural frequency comparison

As shown in Table 1 and Figure 9, the selected boundary conditions result in a good agreement with the measurement data. The minor difference between the measured and simulated natural frequencies of the first two modes can be explained by the fact that the external cladding and insulation of the pipework (which would add mass and decrease natural frequency) was not included in the Finite Element Analysis (FEA) model.

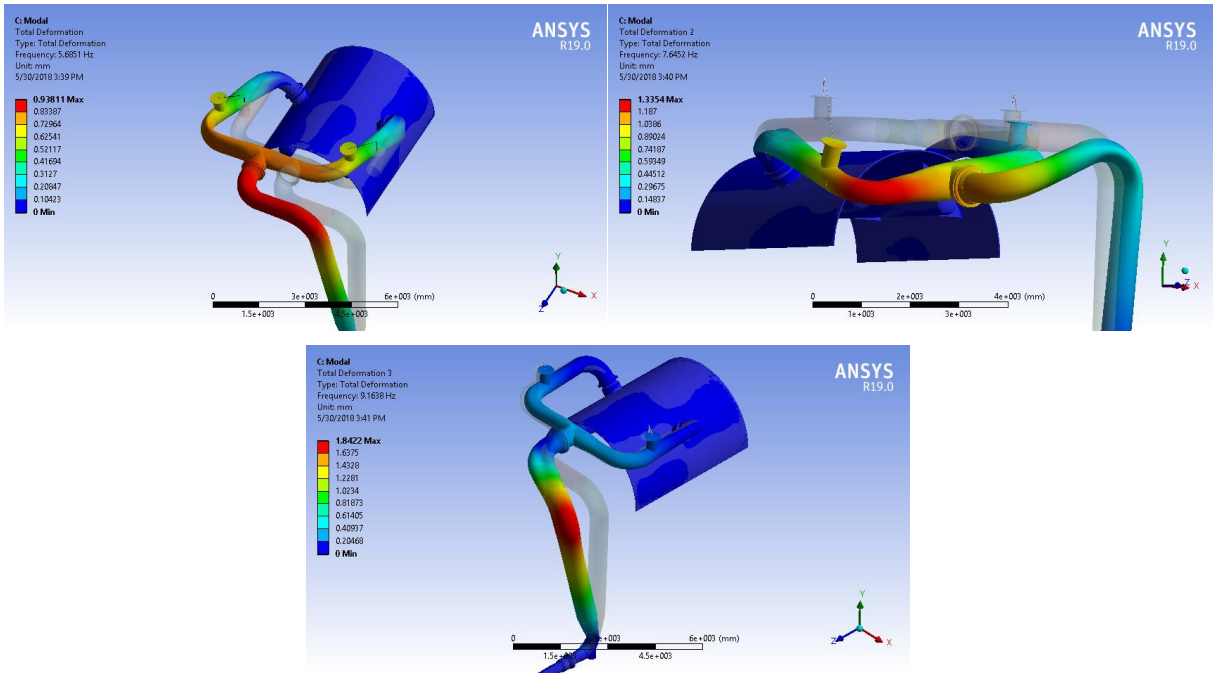


Figure 9: Mode shapes of first 3 natural frequencies

In order to find a suitable forcing profile a sensitivity study was performed to determine the ideal locations, directions and function for the application of the forces. The best results were obtained with forces applied at the main bends/flow direction changes which also coincide with the in-situ vibration excitation profile.

In order to replicate the exact excitation forces the scaling value for each directional component needs to be applied. This scaling value can be obtained analytically (if forcing function and input parameters are known), or experimentally by matching the overall vibration profile and the vibration response at critical locations. As shown in Figure 10, the agreement between measured and calculated vibration response is acceptable (typically within 1 Hz for frequency and 5% for magnitude) with only one of lower response directions overestimating the vibration levels. In general, minor overestimation of vibration levels is tolerable as it will typically lead to conservative stress estimates and therefore a higher safety margin.

After defining the forcing function and verifying the calculated response matches the measured response it is a relatively straight forward process to carry out a detailed integrity assessment. The numerical model normally provides all information required to determine the critical dynamic stresses and the associated

fatigue threat / life. For low to mid frequency pipework vibration the typical fatigue failure will occur on welded connections. Therefore, care needs to be taken regarding the mesh size of the numerical model and the applied stress extrapolation method around the welds so that the correct/applicable stress values can be obtained and compared to the appropriate limits.

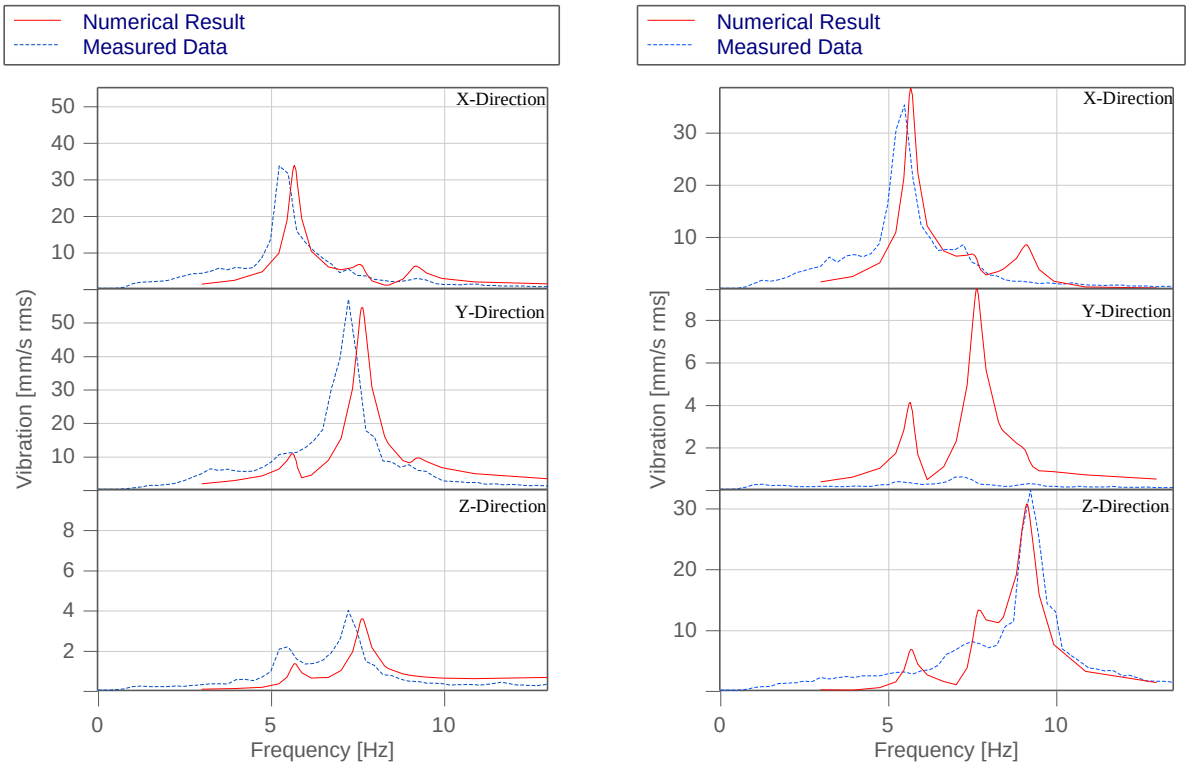


Figure 10: Comparison between calculated response and measured response at two key locations; (a) elbow upstream of cooler (high response for modes 1 and 2); (b) elbow at top of vertical pipe section (high response for modes 1 and 3)

In order to reduce conservatism, a commonly used methodology for the stress assessment of large structures is the hot-spot extrapolation method which includes the stress concentrations factors (SCFs) due to structural discontinuities and weld geometry (other typical assessment methods are: nominal stress and notch stress methods). The hot spot stress assessment has normally prescriptive rules for mesh size and quality [7][8]. However, all critical welds in this particular case are butt welds which from a stress extrapolation point is relatively insensitive to mesh size and type [10] and stress values can be taken directly from the numerical model (Figure 11).

Given the consequence of failure and the general uncertainty of numerical analysis, a conservative approach needs to be taken in order to factor in all contributing components at each critical location. There are sophisticated and well proven ways to achieve this (frequency-based fatigue assessment: [11] [12]). As a conservative screening approach, a simple node-wise summation of the stress amplitudes will provide a good indication for existing integrity issues.

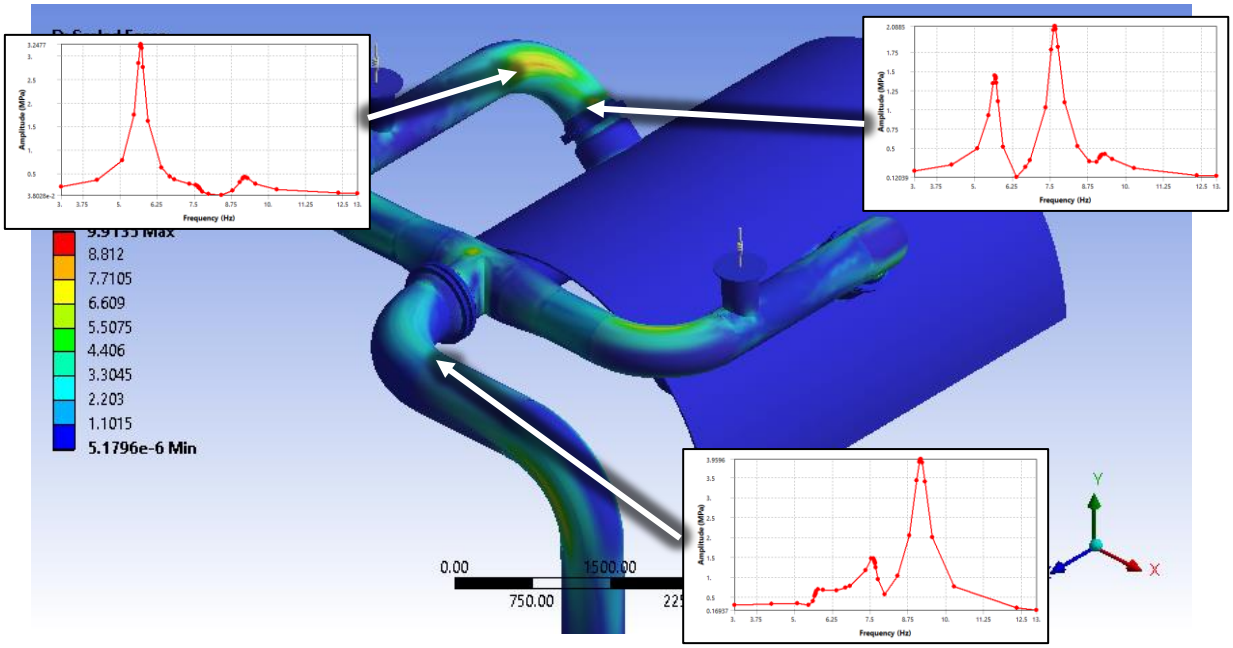


Figure 11: Overall stress plot and frequency stress response plots at critical locations

In this case the analysis showed that the overall dynamic stresses (Figure 11) for the recorded vibration levels were acceptable and no vibration induced integrity threat exists.

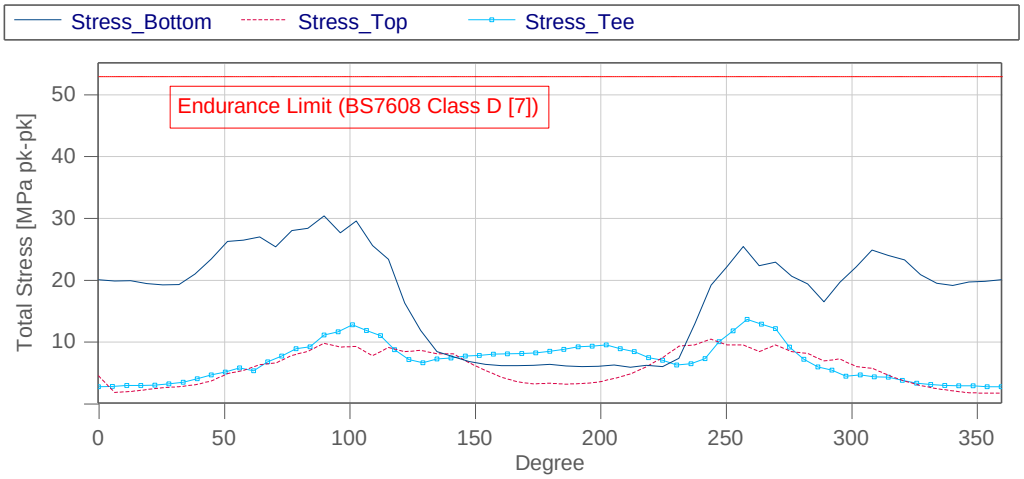
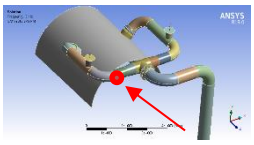


Figure 12: Total stresses around pipe circumference at critical locations

Based on the assumption that the overall dynamic response of the pipework does not change, the planned increase in flowrates (~20%) should also not cause an integrity issue as the increase of the dynamic forces and consequently the dynamic stresses will be ~44% (scaled by kinetic energy which is equivalent to flow velocity^2). With this increase the stresses will be still below the weld endurance limit including a reasonably safety margin.

In order to provide a measurable indicator for site personnel the measured vibration velocities in combination with the numerical stress results can be extrapolated to provide a safe operating window. In this specific case the critical vibration values measured at the reference location can be up to the values shown in Table 2 before the dynamic stresses are considered to be unacceptable. One important assumption for this approach is that the weld is of good quality and no factors which would decrease the endurance limit of the weld such as misalignment or surface impurities are present [7].



Direction	Overall Vibration limit
X	**45 mm/s rms**
Y	**75 mm/s rms**
Z	**6 mm/s rms**

Table 2: Overall vibration limits measured at the reference location (Flattop Window; df = 0.125 Hz; 50 % overlap; peak hold averaging)

4 Conclusion and Outlook

It has been shown how to carry out a frequency based ODS analysis on a transient problem using a low channel count data recorder and a series of time history data. It was also shown how the post processing settings can influence the quality of the ODS analysis and which general points need to be considered when applying the recorded data to numerical models for further detailed assessment. It was briefly described how dynamic stress and vibration data can be used to create customized vibration criteria for a specific problem area.

A potential improvement area for the assessment would be the inclusion of a detailed stress assessment. This would not only provide more data to calibrate the numerical model but also to create a more specific vibration criteria as a more detailed transfer function between stress and vibration could be created.

References

[1] Energy Institute, "Guidelines for the Avoidance of Vibration Induced Fatigue Failure in Process Pipework, 2nd Edition", 2008.

[2] J. Wachel and C. L. Bates, "Escape piping vibrations while designing" in *Hydrocarbon Processing*, 1976.

[3] VDI, "VDI 3842 - Schwingung in Rohrleitungssytemen", VDI, Duesseldorf, 2015.

[4] A. P. Institute, "API 579 - Fitness-for Service", API, Washington, D.C, 2007.

[5] M. Richardson, "Is it a mode shape or an operating deflection shape", *Sound & Vibration Magazine* , no. 30th Anniversary, March 1997.

[6] B. Schwarz and M. Richardson, "Introduction to Operational Deflection Shapes," in *CSI Reliability Week*, Orlando, 1999.

[7] British Standard Institution, "BS7608:2014 Guide to fatigue design and assessment of steel products", 2014.

[8] British Standard Institute, "PD5500 - Specification for unfired fusion welded pressure vessels", BSI, 2018.

[9] J.-L. Riverin and M. J. Pettigrew, "Vibration Excitation Forces Due to Two-Phase Flow in Piping Elements", *Journal of Pressure Vessel Technology*, vol. 129, pp. 7-13, 2007.

[10] B. Schmied, "Spannungskonzepte im Vergleich", in *Deutscher Verband für Schweißen und verwandte Verfahren e. V. - Ausschuss für Technik Sitzung Q1.1*, 2010.

[11] A. Halfpenny, "A frequency domain approach for fatigue life estimation from Finite Element Analysis", in *International Conference on Damage Assessment of Structures* , Dublin, 1999.

[12] M. Mrˇsnik, J. Slaviˇ and M. Bolteˇzar, "Frequency-domain methods for a vibration-fatigue-life estimation - Application to real data", *International Journal of Fatigue*, vol. 47, pp. 8-17, 2013.

Virtual Distortion Method based optimal sensor placement for damage identification

B. Blachowski [1], **A. Swiercz** [1], **L. Jankowski** [1]
[1] Institute of Fundamental Technological Research, Polish Academy of Sciences
Pawinskiego 5b, 02-106 Warsaw, Poland
e-mail: **bblach@ippt.pan.pl**

Abstract
The paper presents a novel method for sensor placement optimized towards effective identification of structural damages. The derivation of the method is based on the concept of virtual distortions together with information provided by a set of strain gauges. Then, a gradient oriented optimization is applied to identify sensor locations, which are the most sensitive to potential damage scenarios. Steepest descent method is utilized to determine the optimal values of the objective function. Additionally, dependence of the method on the applied excitation signal is discussed. Finally, effectiveness of the proposed methodology is demonstrated on an example of optimal search for sensor placement on a 6-bay planar truss structure.

1 Introduction

A successful implementation of any Structural Health Monitoring system relies on efficient placement of measurement sensors [5]. Optimal sensor placement is a topic of intensive research since eighties or even seventies of the last century. Because the exact solution of the optimal sensor placement problem requires large computational effort involving discrete optimization, a variety of different approximate methods have been proposed since that time.

One of the first attempts to solve the optimal sensor placement (OSP) problem for structural parameters identification was the work by Shah and Udwadia [16]. In their paper they first introduced a matrix representing sensitivity of measured output with respect to the parameters being identified. Then, using this matrix they applied algorithm dedicated to minimization of a certain norm of the covariance matrix of the estimate error. Motivated by the computational efficiency of their approach they proposed the trace of the covariance matrix as this norm.

Another milestone in the OSP methodology was an article published by Kammer [10]. He introduced a Fisher information matrix obtained from a set of selected mode shapes and suggested that minimization of the determinant of this matrix provides a good approximation for the optimal sensor placement. One has to mention that the iterative procedure described by Kammer was extremely efficient and the approximate solution of the OSP problem using this method could be obtained within a limited number of iterations. As a result, the method currently known as Effective Independence (EfI) became very popular among researchers and structural engineers.

A further development of the OSP methodology and in particular an application of information theory into this area was proposed by Papadimitriou [14]. He introduced the concept of information entropy and applied a genetic algorithm to solve a complex OSP problem for structures with dozens of degrees of freedom (DOFs).

At the end of this short literature review of the methods for OSP it is also worth to mention an interesting overview paper by Barthorpe and Worden [2] and a book by Xu and He [24] in which simultaneous placement

of different kind of sensors has been solved with aid of the Kalman filter technique. However it should be also kept in mind, that EfI based family of methods assume that a number of first few modes is sufficient in description of structure's dynamics and identification of structural parameter modifications resulting from damage. Such an approach might not be necessarily optimal for damage detection methods which do not utilize identification of modal properties and are based on structural response itself.

As a result, new methods for optimal sensor placement, which are sensitive to potential damage localization, are needed. In this study we propose the Virtual Distortion Method (VDM) as a tool to achieve this goal. The VDM is a fast structural reanalysis technique allowing for analytical gradient computation. Therefore, it can be efficiently applied for damage identification defined as an optimization problem, in which the objective function utilizes responses of the structure obtained for both: an intact and a faulty state. We begin our work by recalling the VDM basics. Then, we will mention its successful application to mass and stiffness identification in skeletal structures, leakage localization in water distribution networks or defect identification in electrical circuits.

The proposed approach in this study is focused on optimal arrangement of strain gauges. First, we determine the sensitivity of the structural responses with respect to stiffness parameters. Next, based on the above results we calculate the average sensitivity of a particular sensor location for all potential damages. Using this average sensitivity the candidate sensor location is ranked and the most sensitive locations are selected as the optimal ones. Finally, the theoretical considerations introduced in sections 2 and 3 are demonstrated on an example of typical 6-bay truss structures subjected to windowed sine wave excitation.

2 Optimal sensor placement for damage identification

The proper identification of an existing damage within a structure depends on three different aspects, namely: damage location, sensor placement, and applied forces. Mathematically, it can be expressed as a set of equations. First of these equations expresses relation between the applied forces and the response of the structure:

$$\mathbf{M}(\boldsymbol{\theta})\ddot{\mathbf{q}}(\boldsymbol{\theta},t) + \mathbf{C}(\boldsymbol{\theta})\dot{\mathbf{q}}(\boldsymbol{\theta},t) + \mathbf{K}(\boldsymbol{\theta})\mathbf{q}(\boldsymbol{\theta},t) = \mathbf{f}(t), \tag{1}$$

where t denotes time, $\ddot{\mathbf{q}}, \dot{\mathbf{q}}, \mathbf{q}$ are acceleration, velocity and displacement vectors, respectively, and $\mathbf{M}, \mathbf{C}, \mathbf{K}$ are mass, damping and stiffness matrices, respectively. The right hand side $\mathbf{f}$ is the excitation vector.

The second equation represents observed quantities and depends on the type of transducers used:

$$\mathbf{y}(\boldsymbol{\theta},t) = \mathbf{C}_q\mathbf{q}(\boldsymbol{\theta},t) + \mathbf{C}_v\dot{\mathbf{q}}(\boldsymbol{\theta},t) + \mathbf{C}_a\ddot{\mathbf{q}}(\boldsymbol{\theta},t) + \mathbf{w}(t), \tag{2}$$

where $\mathbf{C}_q, \mathbf{C}_v, \mathbf{C}_a$ denote displacement, velocity and acceleration output matrices, respectively, and $\mathbf{w}(t)$ is measurement noise.

Finally, the third equation represents a measure for quality of identified damage. For that purpose we define performance index:

$$J = \min_{\mathbf{S}} \|(\boldsymbol{\theta} - \hat{\boldsymbol{\theta}})^T(\boldsymbol{\theta} - \hat{\boldsymbol{\theta}})\|, \tag{3}$$

where $\mathbf{S}$ is the vector of discrete variables that represent the location of the sensors, $\boldsymbol{\theta}$ represents structural parameters to be identified, $\hat{\boldsymbol{\theta}}$ denotes the estimate of $\boldsymbol{\theta}$. Symbol $\|.\|$ represents a norm of the covariance matrix of the estimation error. To be able to detect damage at the earliest possible stage, we postulate that this norm should be understood as the maximal element in the covariance matrix. In other words, the optimal placement problem considered in this study can be stated as follows: we are looking for such a location of the given number of sensors that the maximal element of the covariance of the estimation error is minimal.

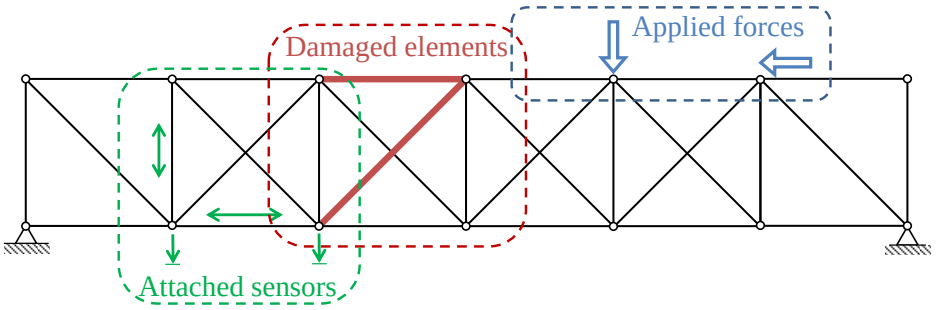


Figure 1: Three aspects associated with a successful damage identification

3 The Virtual Distortion Method and its Applications

3.1 Introduction to the VDM

The Virtual Distortion Method (VDM) was originally presented in [6] for statically loaded structures with application to modelling structural modifications, physical properties (including non-linearities) and optimal material redistribution. The idea of an extension of the VDM-approach for dynamic problems with application to damage detection was firstly discussed in [8]. In this work authors presented a concept of damage identification in truss structures utilising analysis of perturbation of an elastic wave, where the damage is defined as Young modulus modification of the structural element. The identification problem was formulated as a gradient-based optimization task. Other examples utilising this approach for element stiffness assessment for dynamically loaded structures can be found in [12, 21] or for steady-state problems in [18, 19]. Optimal design of adaptive structures exposed to impact loads are considered in [22] and – including elasto-plastic material behaviour – in [23]. Other developed applications of the VDM are related to modelling and identification of elastic element connections in frame structures [17], progressive collapse analysis [20] and detection of delamination in composite structures [13]. It is worth to notice, that the VDM-approach was adapted to water networks [7] and electrical circuits [11] by utilising some analogies to truss-like structures.

3.2 Concept of the Virtual Distortion Method

In this section, the idea and the basics of the VDM will be briefly presented focusing on statically loaded truss structures. The *virtual distortion* is an initial strain introduced in a structural element which causes *pre-stressed state* of the statically indeterminate structure, whereas for determinate structures there is stress-free state. The virtual distortion, depending on formulation (definition), can be used in different ways e.g. for modelling of element stiffness or plastic deformations. The *unit virtual distortion* is the virtual distortion that would cause a *unit strain* in this out-of-structure element (unconstrained element). The corresponding, self-equilibrated load to the unit distortion is called the *compensating load*. Effect of imposing of the virtual distortion for a structural element is analogous to a geometric imperfection or uniform heating in that element. Imposing consecutively the unit distortions on all (or selected) structural elements the strain responses are determined and formed into columns (vectors) of a square matrix, and finally, the *influence matrix* is created. It is important to notice, the strain responses are stored for the elements which parameters are to be modelled.

For a more detailed explanation of the influence matrix building process let us consider a simply supported 6-bay truss structure shown in Figure 2(a) with square sections. The vertical and horizontal lengths are equal to $L_x = L_y = 1.52\,m$. The cross-section areas and Young moduli are assumed to be identical in each element, namely $A = 2 \cdot 10^{-5}\,\mathrm{m}^2$ and $E = 70\,\mathrm{GPa}$, respectively. To generate the influence matrix for the selected set of elements (1, 2, 16, 30) the unit distortions have to be independently imposed in those elements as indicated in Figures 2(b)–2(e). For each of the distortion states, the strain responses for the selected elements have to

be computed and grouped into the influence matrix:

$$\mathbf{D} = \begin{bmatrix} 0.895312 & -0.104688 & -0.001027 & 1.3 \cdot 10^{-6} \\ -0.104688 & 0.895312 & -0.001027 & 1.3 \cdot 10^{-6} \\ -0.001027 & -0.001027 & 0.810466 & -0.001027 \\ 1.3 \cdot 10^{-6} & 1.3 \cdot 10^{-6} & -0.001027 & 0.895312 \end{bmatrix}. \tag{4}$$

The largest values occur on the diagonal of the matrix $\mathbf{D}$, however, the condition has to be fulfilled $0 < D_{ii} < 1$. The introduced unit distortion has only a little influence for distant elements (see the last column of the influence matrix $\mathbf{D}$).

The VDM-approach can be applied for linear structures and extensively exploits the superposition principle. Firstly, let us assume an indeterminate structure (so-called *initial* or *original structure*) without any loading, but with an imposed distortion field $\boldsymbol{\varepsilon}^{\mathbf{0}}$ in structural elements. Thus, the vector of the residual strains $\boldsymbol{\varepsilon}^{\mathbf{R}}$ and stresses $\boldsymbol{\sigma}^{\mathbf{R}}$ in the prestressed structure can be expressed by the following formulas:

$$\boldsymbol{\varepsilon}^{\mathbf{R}} = \mathbf{D}\,\boldsymbol{\varepsilon}^{0}, \qquad \boldsymbol{\sigma}^{\mathbf{R}} = \mathbf{E}(\mathbf{D} - \mathbf{I})\,\boldsymbol{\varepsilon}^{\mathbf{0}}, \tag{5}$$

where $\mathbf{D}$ is the influence matrix, $\mathbf{E}$ is the diagonal matrix of element Young moduli and $\mathbf{I}$ is the identity matrix. Considering the initial structure only under the external loading we get the elastic strains $\boldsymbol{\varepsilon}^{\mathbf{L}}$ and stresses $\boldsymbol{\sigma}^{\mathbf{L}}$. Now, we can superpose those two above mentioned states:

$$\boldsymbol{\varepsilon} = \boldsymbol{\varepsilon}^{\mathbf{L}} + \boldsymbol{\varepsilon}^{\mathbf{R}}, \qquad \boldsymbol{\sigma} = \boldsymbol{\sigma}^{\mathbf{L}} + \boldsymbol{\sigma}^{\mathbf{R}} = \mathbf{E}\left(\boldsymbol{\varepsilon} - \boldsymbol{\varepsilon}^{\mathbf{0}}\right). \tag{6}$$

In this way, we obtain the *structure modelled by the virtual distortions* with the strains and stresses described by Equations (6). Independently, let us introduce a modification of the Young modulus in an element i from the value E_i to $\hat{E}_i$. This leads to the so-called *modified structure* with strains $\hat{\boldsymbol{\varepsilon}}$ and stresses $\hat{\boldsymbol{\sigma}}$. Now, we postulate, that *the structure modelled by the virtual distortions and the modified one are equal in the sense of their generalized strains and stresses*. Based on this postulate and using Equation (6), we can write

$$\boldsymbol{\varepsilon} = \hat{\boldsymbol{\varepsilon}}, \qquad \mathbf{N} = \mathbf{A}\mathbf{E}\left(\boldsymbol{\varepsilon} - \boldsymbol{\varepsilon}^{\mathbf{0}}\right) = \mathbf{A}\hat{\mathbf{E}}\,\boldsymbol{\varepsilon} = \hat{\mathbf{N}}. \tag{7}$$

where $\mathbf{N}$ and $\hat{\mathbf{N}}$ are the axial forces of the modelled structure and the modified one, $\mathbf{A}$ is the diagonal matrix of element cross section areas (assumed in this example to remain intact). Equation (7 b) can be rewritten:

$$\boldsymbol{\varepsilon} - \boldsymbol{\varepsilon}^{\mathbf{0}} = \boldsymbol{\mu}\,\boldsymbol{\varepsilon}, \tag{8}$$

where μ is the diagonal matrix with i-th element on the diagonal defined as the modification parameter:

$$\mu_i = \frac{\hat{E}_i}{E_i}. \tag{9}$$

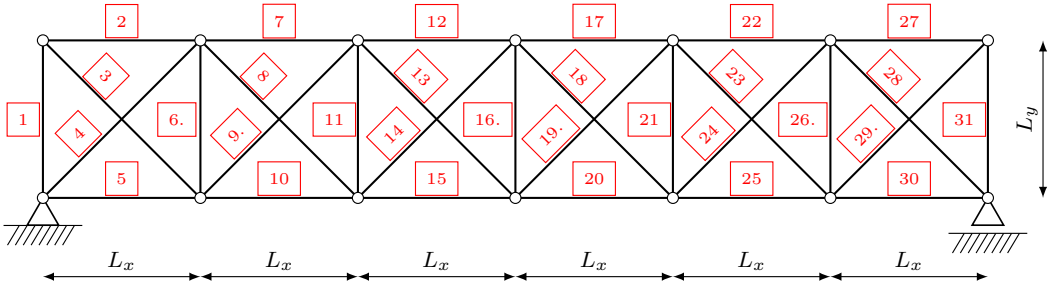
Substituting Equation (5 a) and (6 a) to Equation (8), we get a set of equations for determination of the virtual distortion $\boldsymbol{\varepsilon}^{\mathbf{0}}$:

$$\left[\mathbf{I} - \left(\mathbf{I} - \boldsymbol{\mu}\right)\mathbf{D}\right]\boldsymbol{\varepsilon}^{\mathbf{0}} = \left(\mathbf{I} - \boldsymbol{\mu}\right)\,\boldsymbol{\varepsilon}^{\mathbf{L}}. \tag{10}$$

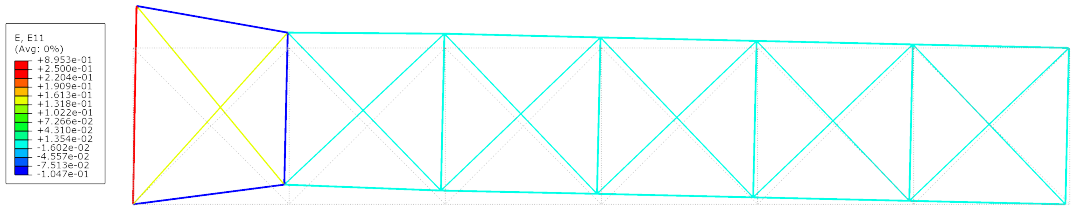
Let us notice, in Equation (10), the virtual distortion $\boldsymbol{\varepsilon}^{\mathbf{0}}$ depends on the external loading.

For dynamic loaded structures the virtual distortions $\boldsymbol{\varepsilon}^{\mathbf{0}}(t)$ and influence matrix $\mathbf{D}(t)$ are time-dependent. Therefore, firstly the influence matrix $\mathbf{D}(t)$ has to be determined for each time-step using the Newmark integration method. This can be done by imposing the unit virtual distortions on structural elements at the first time step. Knowing the distortion functions $\boldsymbol{\varepsilon}^{\mathbf{0}}(t)$ corresponding to the structural modifications, the updated strain and stress field, analogously to Equations (6), can be rewritten:

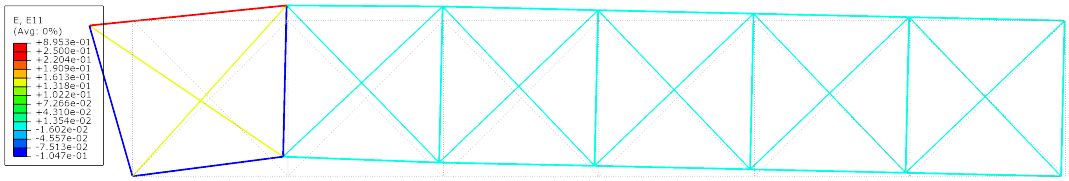
$$\boldsymbol{\varepsilon}(t) = \boldsymbol{\varepsilon}^{L}(t) + \sum_{\tau=1}^{t} \mathbf{D}(t-\tau)\boldsymbol{\varepsilon}^{\mathbf{0}}(\tau), \qquad \boldsymbol{\sigma}(t) = \mathbf{E}\left(\boldsymbol{\varepsilon}(t) - \boldsymbol{\varepsilon}^{\mathbf{0}}(t)\right). \tag{11}$$



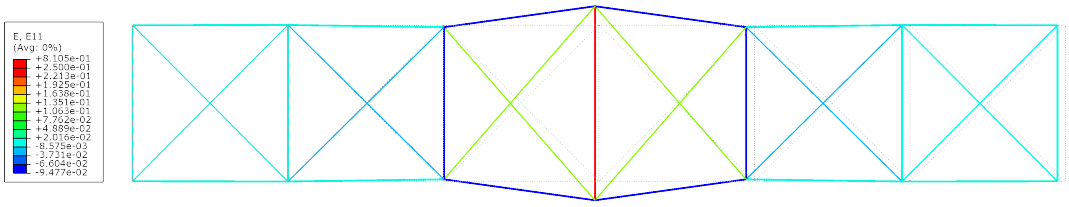
(a)



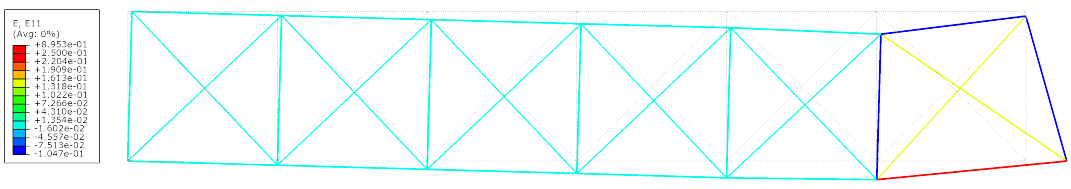
(b)



(c)



(d)



(e)

Figure 2: Tested 6-bay truss structure: (a) Scheme of the structure; Deformations caused by the unit virtual distortion introduced in: (b) element no. 1, (c) element no. 2, (d) element no. 16, (e) element no. 30.

By demanding the equality of strains $\boldsymbol{\varepsilon}(t)$ and generalized stresses $\mathbf{N}(t)$ for the modelled and modified (determined by the modification parameters μ_i) structures at each time step, similarly to Equation (10), we get the system of equations which has to be iteratively solved for each time step:

$$\mathbf{B}\,\boldsymbol{\varepsilon}^{\mathbf{0}}(t) = \begin{cases} \left(\mathbf{I} - \boldsymbol{\mu}\right)\boldsymbol{\varepsilon}^{\mathbf{L}}(0) & \text{for } t = 0\,, \\ \left(\mathbf{I} - \boldsymbol{\mu}\right)\left[\boldsymbol{\varepsilon}^{\mathbf{L}}(t) + \sum\limits_{\tau=0}^{t-1}\mathbf{D}(t-\tau)\,\boldsymbol{\varepsilon}^{\mathbf{0}}(\tau)\right] & \text{for } t > 0\,, \end{cases} \tag{12}$$

where the left-hand side matrix $\mathbf{B}$ does not depend on time:

$$\mathbf{B} = \mathbf{I} - \left(\mathbf{I} - \boldsymbol{\mu}\right)\mathbf{D}(0)\,. \tag{13}$$

3.3 The VDM-based structural parameter identification

The identification of the structural stiffness parameter μ_i can be defined as a gradient-based optimization problem. To this end, the mean-square distance $\mathbf{d}$ between the strain responses $\boldsymbol{\varepsilon}^{\mathbf{M}}(t)$ collected for the modified structure and the modelled responses $\boldsymbol{\varepsilon}(\boldsymbol{\varepsilon}^{\mathbf{0}}, t)$ (or equivalently $\boldsymbol{\varepsilon}(\mu_i, t)$) has to be minimized:

$$F(\mu_i) = \mathbf{d}^{\mathbf{T}} \cdot \mathbf{d} \tag{14}$$

where

$$\mathbf{d} = \sum_t \left(\boldsymbol{\varepsilon}(\mu_i, t) - \boldsymbol{\varepsilon}^{\mathbf{M}}(t)\right). \tag{15}$$

The objective function expressed by Equation (14) can be differentiated using the chain rule with respect to the design parameter μ_i:

$$\nabla F = \frac{\partial F}{\partial \boldsymbol{\varepsilon}}\frac{\partial \boldsymbol{\varepsilon}}{\partial \boldsymbol{\varepsilon}^{\mathbf{0}}}\frac{\partial \boldsymbol{\varepsilon}^{\mathbf{0}}}{\partial \mu_i} \tag{16}$$

The first term of Equation (16) can be calculated using Equations (14) and (15), the next one from Equation (12 a). The last component can be obtained by differentiating Equation (12).

Knowing the gradient of the objective function expressed by the Equation (16) e.g. steepest descent method can be applied. At each iteration k, the new design variable μ_i^{k+1} is computed according the formula:

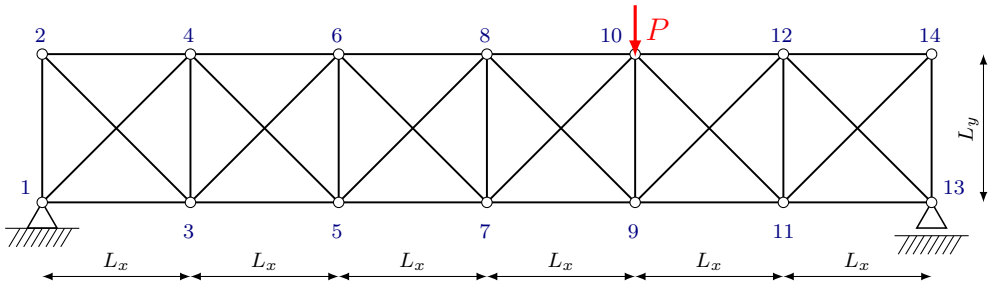
$$\mu_i^{k+1} = \mu_i^k - \alpha F^k \frac{\nabla F}{(\nabla F^k)^T\,\nabla F^k}, \tag{17}$$

The optimization step size α can be defined as constant from the interval of $(0.1, 0.3)$ or it can be preferably determined at each iteration (line search method). In Equation (17) F^k and ∇F^k denote the value of the objective function and its gradient in the k-th iteration. The optimization process is terminated if the objective function reaches either the pre-determined level or the number of iterations.

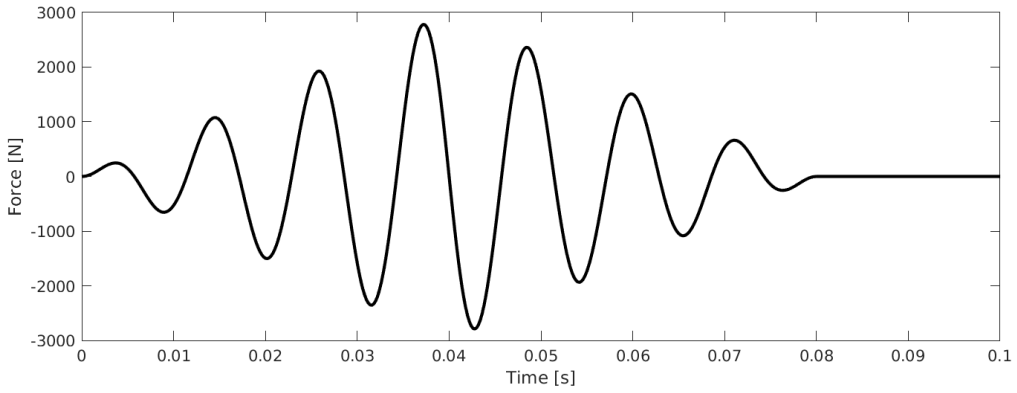
4 Numerical example

The numerical test was preformed using the two-dimensional truss structure shown in Figure 3(a). Element numbering is analogous to the example presented in Figure 2(a). However, the currently analysed steel elements with length of $L_x = L_y = 51$ cm have the cross sections areas $A = 1 \cdot 10^{-4}$ m^2, density $\varrho = 7850\ \frac{\text{kg}}{\text{m}^3}$ and Young's modulus $E = 200$ GPa. The test loading applied at node 10 is shown in Figure 3(b).

At the first step, in order to pre-select the strain sensor locations, strain responses for all element of the original structure caused by the external load were computed. The dynamic analysis was performed using



(a)



(b)

Figure 3: (a) Tested truss structure with the location of the excitation; (b) Test loading function.

the Newmark integration method with the number of $n = 501$ time steps ($\Delta t = 2 \cdot 10^{-4}$ s). Then, for independently introduced in each element i the testing stiffness modification parameter $\mu_i^t = 0.9$ objective functions F_i according to formula (14) were computed. By ascending sorting the obtained values F_i, a ranking for contributions of introduced modifications for the objective function is created. The ordered set of elements R corresponding to the ordered values F_i has the following form:

$$R = \{16, 26, 19, 21, 11, 14, 18, 13, 9, 1, 27, 2, 31, 24, 8, 4, 3, 30, 29, 23, 28, 25, 5, 20, 7, 22, 17, 10, 12, 15\} \quad (18)$$

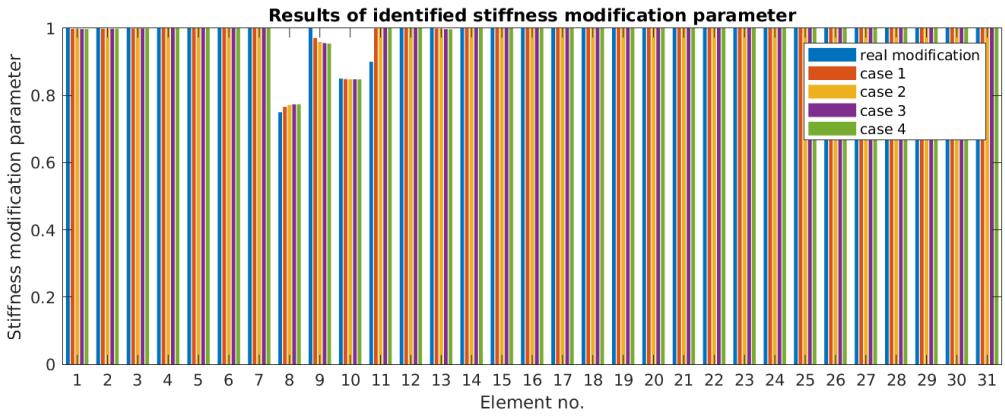
The five high-ranked elements (the last ones) from set (18) were chosen for the sensor locations, i.e. elements: 22, 17, 10, 12, 15, and let us denote it as *case 1*. For comparison purposes, the other scenarios of sensor locations were considered:

- *case 2* – elements: 13, 14, 16, 18, 19;
- *case 3* – elements: 8 ,9, 21, 23, 24;
- *case 4* – elements: 3, 9, 24, 28, 13.

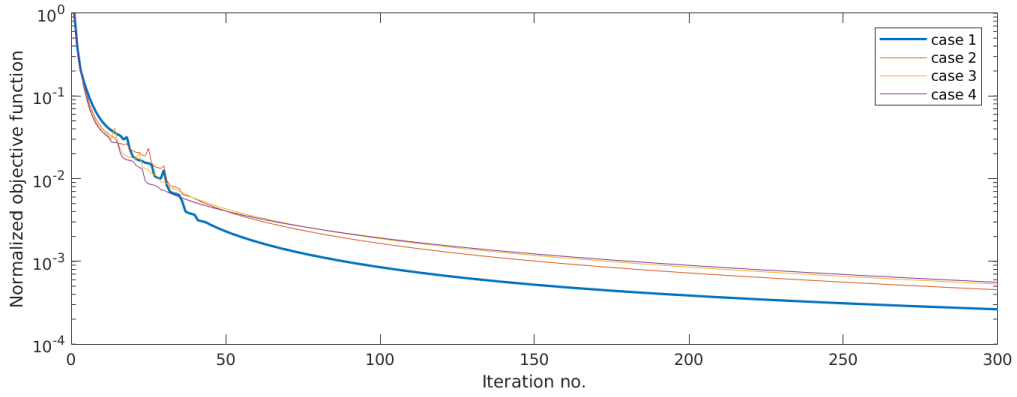
In the modified structure, the following stiffness modification parameters to be identified were randomly assumed: $\mu_8 = 0.75$, $\mu_{10} = 0.8$, $\mu_{11} = 0.9$. The optimization procedure (steepest descent method with line search) was applied using the responses collected for the original and modified structure from the sensors for each case of sensor locations. The optimization procedures were terminated as the total number of iterations has reached 300.

Results of the stiffness modification parameter identification with comparison to the real values are presented in Figure 4(a). The modifications for elements 8 and 10 were correctly determined for all scenarios of sensor

locations. Some discrepancies are present for element 11, due to the slight influence of its modification on the sensor responses. Evolutions of the objective functions during iteration processes are shown in Figure 4(b). One can notice, that the applied excitation does not induce any significant strain level in element no. 11 in comparison to high-loaded members, e.g. element 15 ($\frac{\max|\varepsilon_{11}(t)|}{\max|\varepsilon_{15}(t)|} \approx \frac{1}{20}$).



(a)



(b)

Figure 4: (a) Real and identified stiffness modification parameters; (b) Values of the objective functions during the iteration process.

For cases that require identification of stiffness of low-loaded elements, either additional sensors have to be used or another test loading has to proposed to avoid low-level responses.

5 Conclusions

In this paper, a method for identification of stiffness modification parameters, defined as Young modulus reduction, was presented. This problem is formulated as a gradient-based optimization task utilizing the Virtual Distortion Method for computation of updated structural responses.

A vital part of a successful parameter identification is an appropriate selection of either sensor locations or test loadings. We have shown, that the structural responses can be insensitive for member modification of the structure using some test loadings. Therefore, such loadings can be insufficient for the identification problem and some additional sensors or test excitations have to be used.

An idea of preselection of sensor locations taking into account the current test loading was discussed. It was shown that for the applied loading structural parameters in the vertical members (columns) are poorly identifiable. To avoid such problems in engineering practice one needs to optimize not only sensor location, but also properly select the excitation signal.

The research is ongoing to extend the presented approach to the case of modular structures [1], [25] and local substructural analysis [4], [3], [9], as well as to investigate the possibilities of its application in the problem of optimum placement of actuators for semi-actively controlled structures [15].

Acknowledgements

The authors gratefully acknowledge the support of the National Science Centre, Poland, granted through the project Re-Con (DEC-2017/25/B/ST8/01800).

References

[1] Y. An, B. Blachowski, Y. Zhong, P. Holobut, and J. Ou. Rank-revealing QR decomposition applied to damage localization in truss structures. *Structural Control and Health Monitoring*, 24(2):e1849–1–15, 2017.

[2] R. Barthorpe and K. Worden. Sensor placement optimization. In C. Boller, F. Chang, and Y. Fujino, editors, *Encyclopedia of Structural Health Monitoring*, chapter 70. John Wiley & Sons, 2009.

[3] B. Blachowski, Y. An, and B. Spencer Jr. Substructure-level based method for damage quantification in determinant trusses. In *Proc. of ISMA 2016 / USD 2016, International Conference on Noise and Vibration Engineering / International Conference on Uncertainty in Structural Dynamics*, pages 3283–3294, Leuven, Belgium, 19-21 September 2016.

[4] B. Blachowski, Y. An, B. Spencer Jr., and J. Ou. Axial strain accelerations approach for damage localization in statically determinate truss structures. *Computer-Aided Civil and Infrastructure Engineering*, 32(4):304–318, 2017.

[5] B. Blachowski, A. Świercz, P. Gutkiewicz, J. Szelążek, and W. Gutkowski. Structural damage detectability using modal and ultrasonic approaches. *Measurement*, vol. 85:201–221, 2016.

[6] J. Holnicki-Szulc. *Virtual Distortion Method*. Springer Berlin Heidelberg, 1991.

[7] J. Holnicki-Szulc, P. Kolakowski, and N. Nasher. Leakage detection in water networks. *Journal of Intelligent Material Systems and Structures*, 16(3):207–219, March 2005.

[8] J. Holnicki-Szulc and T. G. Zieliński. Damage identification method based on analysis of perturbation of elastic waves propagation. In F. Chang, editor, *Structural Control and Health Monitoring 2000*, pages 881–890, 1999.

[9] J. Hou, L. Jankowski, and J. Ou. Frequency-domain substructure isolation for local damage identification. *Advances in Structural Engineering*, vol. 18(1):137–153, 2015.

[10] D. Kammer. Sensor placement for on-orbit modal identification and correlation of large space structures. *Journal of Guidance, Control, and Dynamics*, vol. 14(2):251–259, 1991.

[11] M. Kokot and J. Holnicki-Szulc. Defect identification in electrical circuits via the virtual distortion method. part 1: Steady-state case. *Journal of Intelligent Material Systems and Structures*, 20(12):1465–1473, June 2009.

[12] P. Kolakowski, T. G. Zielinski, and J. Holnicki-Szulc. Damage identification by the dynamic virtual distortion method. *Journal of Intelligent Material Systems and Structures*, 15(6):479–493, June 2004.

[13] A. Orłowska, P. Kołakowski, and J. Holnicki-Szulc. Modelling and identification of delamination in double-layer beams by the virtual distortion method. *Computers & Structures*, 86(23-24):2203–2214, dec 2008.

[14] C. Papadimitriou. Optimal sensor placement methodology for parametric identification of structural systems. *Journal of Sound and Vibration*, vol. 278(4-5):923–947, 2004.

[15] B. Poplawski, G. Mikułowski, A. Mroz, and L. Jankowski. Decentralized semi-active damping of free structural vibrations by means of structural nodes with an on-off ability to transmit moments. *Mechanical Systems and Signal Processing*, vol. 100, 2018.

[16] P. Shah and F. Udwadia. A methodology for optimal sensor locations for identification of dynamic systems. *Journal of Applied Mechanics - Transaction of the ASME*, vol. 45:188–196, 1978.

[17] A. Świercz, J. Holnicki-Szulc, and P. Kołakowski. Impact loads for structural damage identification. In *Proceedings of the 7th European Workshop on Structural Health Monitoring*, pages 2115–2122, Nantes, France, July 8-11 2014.

[18] A. Świercz, P. Kołakowski, and J. Holnicki-Szulc. Identification of damage using low frequency harmonics in trusses and beams. In *Proc. of the International Conference on Noise and Vibration Engineering ISMA'06*, Leuven, Belgium, 18-20 September 2006.

[19] A. Świercz, P. Kołakowski, and J. Holnicki-Szulc. Damage identification in skeletal structures using the virtual distortion method in frequency domain. *Mechanical Systems and Signal Processing*, 22(8):1826–1839, November 2008.

[20] A. Świercz, P. Kołakowski, and J. Holnicki-Szulc. Monitoring of progressive collapse of skeletal structures. In *9th Int Conf. on Damage Assessment of Structures – DAMAS'11*, volume 305(1), page 012133, St. Anne's College, Oxford UK, 11-13 July 2011.

[21] A. Świercz and T. G. Zieliński. Software tools for structural damage identification. In *4th European Congress on Computational Methods in Applied Sciences and Engineering*, volume II, pages 1–16, Jyvaskyla, Finland, 2004.

[22] M. Wiklo and J. Holnicki-Szulc. Optimal design of adaptive structures: Part I. remodeling for impact reception. *Structural and Multidisciplinary Optimization*, 37(3):305–318, March 2008.

[23] M. Wiklo and J. Holnicki-Szulc. Optimal design of adaptive structures: Part II. adaptation to impact loads. *Structural and Multidisciplinary Optimization*, 37(4):351–366, April 2008.

[24] Y. Xu and J. He. Multi-type sensor placement. In Y. Xu and J. He, editors, *Smart Civil Structures*, chapter 8. Taylor & Francis Group, 2017.

[25] M. Zawidzki and L. Jankowski. Optimization of modular Truss-Z by minimum-mass design under equivalent stress constraint. *Smart Structures and Systems*, vol. 21(6), 2018.

Pseudo-faults (or damage metaphors) for SHM: a discussion on their practical use

E. Papatheou [1], **G. Manson** [2], **K. Worden** [2]
[1] College of Engineering, Mathematics and Physical Sciences,
University of Exeter, North Park Road, Exeter, EX4 4QF, UK
e-mail: **e.papatheou@exeter.ac.uk**

[2] Dynamics Research Group, Dept. of Mechanical Engineering,
University of Sheffield, Mappin Street, Sheffield, S1 3JD, UK,

Abstract

Pattern recognition (PR) has been successfully applied to many structural health monitoring (SHM) projects. Although, it has several advantages, PR relies heavily on data from structures in order to create the models for their monitoring. Especially, if supervised learning approaches are employed, then data from all possible damaged states of the structure will be required. For inexpensive structures, destructive means of acquiring those data under laboratory conditions may be possible, but for more expensive structures it may become prohibitively expensive, and other approaches will be required. Pseudo-faults, or damage metaphors in general, such as added masses, or loosened bolts, used experimentally to acquire damage sensitive features without actually damaging the structure may be a possible solution. This paper discusses the concept of using such damage metaphors for feature selection in pattern recognition-based SHM and attempts to explore their suitability for practical monitoring applications through a small laboratory study.

1 Introduction

Monitoring the state of structures is vital for their safe operation, and also for the efficient management of their maintenance. Traditional Non-Destructive Evaluation (NDE) methods [1] are the main inspection tools for structures. These methods can be highly accurate, but can be very expensive, they demand a high degree of expertise and usually work in a small region of the structure. In addition, they usually require the disruption of the structure's normal service and operation. Structural Health Monitoring (SHM) refers essentially to any process of damage identification in structures, and has been largely motivated by the effort to deal with the challenges and drawbacks of most NDE methods. Comprehensive reviews on SHM can be found here [2, 3].

Among the various approaches to SHM, data-based methods are becoming very popular - possibly because of the constant effort by researchers to apply their algorithms on real data from real structures. In fact, the concept of 'data-based' or 'data-centric' is becoming more prevalent in engineering (e.g. [4]) lately, even though it has probably been around for a lot longer (e.g. [5]). In general, most data-based approaches will try to apply a form of Pattern Recognition (PR) - which is usually done through machine learning algorithms [6]. It is perhaps then easy to see that one of the main challenges of any data-based approach is the availability, as well as the reliability of data.

Pattern Recognition, relies heavily on data from structures in order to create the models for their monitoring. Especially, if supervised learning approaches are employed, then data from all possible damaged states of the structure will be required. For inexpensive structures, destructive means of acquiring those data

under laboratory conditions may be possible, but for more expensive structures it may become prohibitively expensive, and other approaches will be required. Pseudo-faults, or damage metaphors in general, such as added masses, or loosened bolts, used experimentally to acquire damage sensitive features without actually damaging the structure may be a possible solution. Some of those, like the added mass, have been shown to work, at least partially and compare to more realistic types of damage [7], and also being able to create a set of surrogate data which can be used to train supervised learning algorithms [8].

In more detail, added masses have been applied based on the simple principle that damage on an elastic structural member will most commonly reduce its natural frequencies. Consequently then, the blithe extrapolation of a SDOF formula for its natural frequency ($\omega = \sqrt{k/m}$) allows for an assumption that perhaps an added mass could cause an equivalent effect and therefore be suitable for the feature selection for damage identification. A loosened bolt on a truss-type structure could have an equivalent effect and has therefore been used in various works as a proxy for the testing of new algorithms. Pseudo-faults, have also been shown to be limited, especially in cases of damage severity - for example, even if different levels of added mass can be identified, there is no consistent proof that they will correspond to equivalent levels of 'damage' (such as loss of stiffness or length of saw-cuts [7]).

The purpose of this paper is to present common experimental approaches which can be applied as damage metaphors, and simply discuss their practical application and limitations. A small laboratory structure which can be easily modelled as a 3-DOF system is used to demonstrate pseudo-faults of the type of added mass, loosened bolt, a short localised temperature increase [9], and are compared with a saw-cut (representing a more realistic form of damage) on one of the structure's elastic members. In previous studies [7, 8] it was shown that added masses can be used for the feature selection of damage sensitive features, and a rigorous comparison was done. This work does not do a similar rigorous study here, but simply demonstrates the application of the pseudo-faults in order to incite a discussion.

The layout of the paper is as follows: the next section describes the structure and a short theoretical analysis. The third section describes the experimental demonstration of all the examined pseudo-faults. Section four discusses the results and attempts to present a short discourse on the main idea of damage metaphors and of their suitability and limitations including some suggestions/discussion points. Finally, a short conclusion recaps the work in order to round off the paper.

2 Structure and theoretical analysis

In order to demonstrate a few of the most common pseudo-faults, a simple laboratory structure is considered here (see Figure1). The structure can be seen as a model of a 3-floor building, if standing vertically, or a standard 3-DOF spring-mass-damper system when arranged horizontally. The choice of the structure was such that it would be easy to model theoretically and also test experimentally.

2.1 Theoretical model

A theoretical model of the structure can be easily derived if it is considered as a 3-DOF spring-mass-damper system (see Figure 2). In fact, the equations of motion can be found easily into any vibration textbook e.g. [10] and will not be fully presented here, however it is easy to show that they will be in the form of,

$$[M]\{\ddot{x}\} + [C]\{\dot{x}\} + [K]\{x\} = \{F\} \tag{1}$$

where

$$M = \begin{bmatrix} m & 0 & 0 \\ 0 & m & 0 \\ 0 & 0 & m \end{bmatrix} \text{ and } K = \begin{bmatrix} 2k & -k & 0 \\ -k & 2k & -k \\ 0 & -k & 2k \end{bmatrix} \tag{2}$$

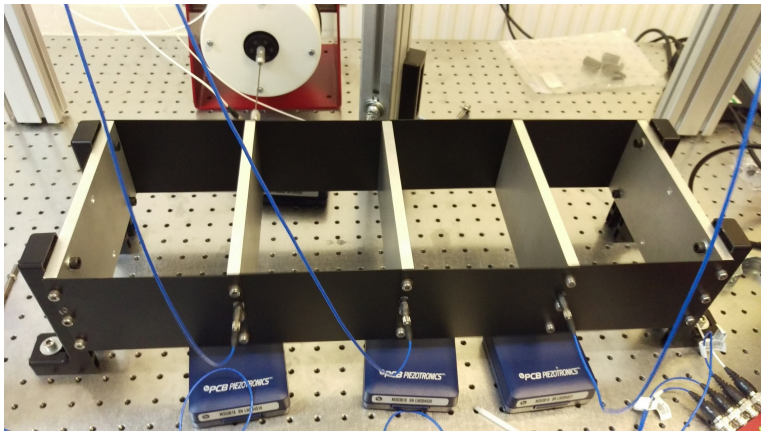


Figure 1: Laboratory structure representing a 3-DoF system.

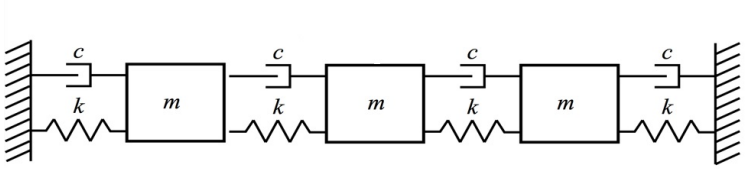


Figure 2: 3-DOF spring-mass-damper system.

assuming all masses have an equal value of m and all springs an equal value of stiffness k. Getting values for $m = 0.7257\,kg$ and a value for an equivalent spring stiffness calculated by the standard formula for a leaf spring: $k = 2 \cdot 12EI/l^3$, where $I = bh^3/12$, $b = 0.1\,m, l = 0.13\,m$ and $h = 0.001\,m$, it is easy to calculate from equation (2) the natural frequencies of the system as $f_1 = 18.81\,Hz$, $f_2 = 34.75\,Hz$ and $f_3 = 45.4\,Hz$. Note that the damping matrix can be selected with some guidance from an experimental test of the structure if one requires realistic values. This study is only using the theoretical model to calculate the effect of mass and stiffness changes on the frequencies of the system, and does not make use of any damping values.

2.2 Stiffness reduction and added mass on the theoretical model

If the concept of realistic damage as a form of stiffness reduction is assumed here, then it is easy to use the theoretical model and see the effect of any such reduction on the modal features of the system. Figure 3 shows how the natural frequencies of the system will drop with a change of the stiffness. Stiffness values for the spring constants are denoted with k_n, where $n = 1...4$ (see Figure 2). Since the structure is clamped at both ends, it is symmetric and therefore there are only two distinct cases of stiffness reduction. It should be noted that the stiffness value here is dropped directly as an absolute number, one could just drop the Young's modulus value for a potentially more realistic simulation.

A similar analysis may be performed for the increase of the mass. Figure 4 shows the change in the natural frequencies of the system when the second and third masses were increased up to three times their original size. It can be seen that the frequencies do drop, as would be expected, and it would be possible to use features for the location of the 'damage' as when the mass is added on the second floor it does not change the second mode at all - whereas the mass on 'floor' 3 changes it. Immediately, it can be seen by looking at Figure 3 that the loss in stiffness is not entirely equivalent (all modes are affected). This is expected as

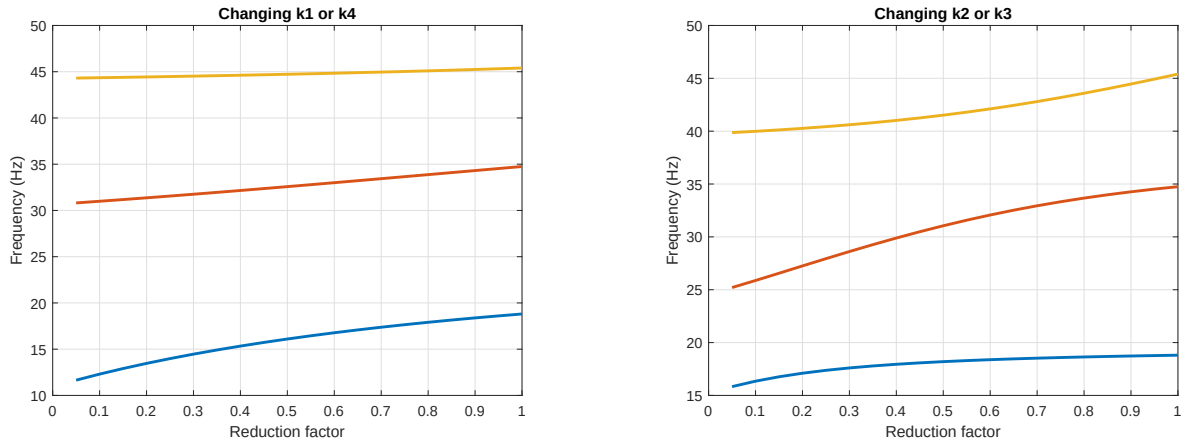


Figure 3: Theoretical change of the natural frequencies when the stiffness of springs k_1 or k_4 drops (left) and k_2 or k_3 drops (right).

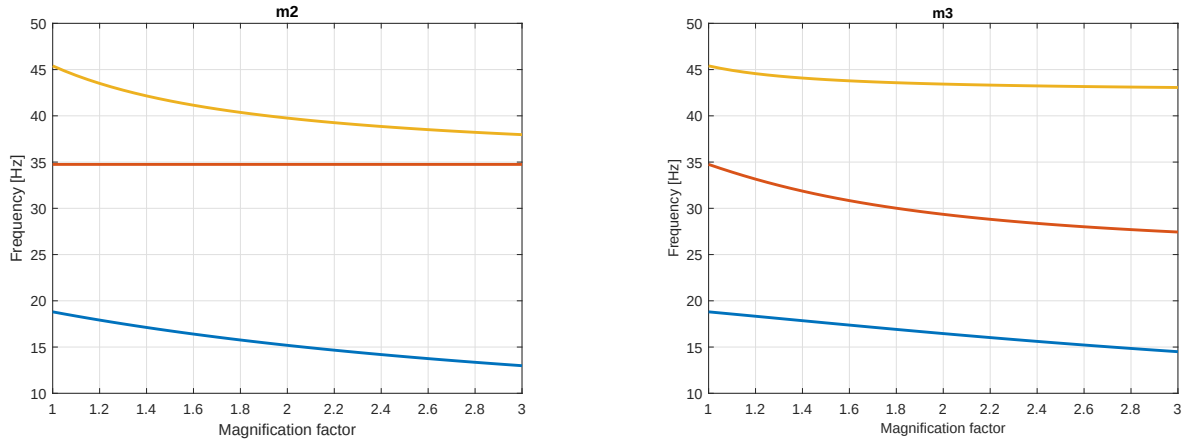


Figure 4: Theoretical change of the natural frequencies when the size of the masses increases.

the system when clamped at both ends, is symmetric and when the mass is applied on the second floor it is located exactly at the centre of the structure.

3 Experimental demonstration

The structure of interest was tested with the help of a Data Physics electromagnetic shaker, while its response was recorded through uniaxial accelerometers of the PCB type, attached directly on the structure as seen in Figure 1. The excitation force was recorded through a force transducer and the DAQ system used was a Data Physics Quattro Ace. No calibration factors were used during the measurement, so the FRFs units are simply voltage over voltage (although they should correspond to equivalent values of acceleration over force - after an appropriate conversion). FRFs were recorded from all three sensors and can be seen in Figure 5. The frequency bandwidth of the measurement was 125 Hz with a frequency resolution of 0.156 Hz, while random excitation was used and 30 averages were acquired for the estimation of the FRFs.

Since the laboratory structure has bolted components, care was taken during its assembly to use a controlled torque setting. A torque wrench was used and all bolts were tightened to the maximum allowed (based on their size) torque value. In addition, several FRFs were recorded when the bolts applied on the three aluminium plates (representing the 'floors' - see Figure 1) were tightened with lower values. It was found

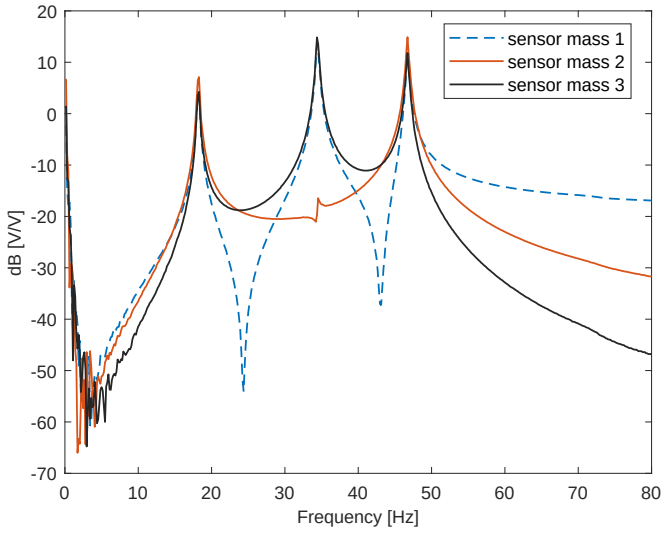


Figure 5: FRFs recorded from the experimental structure - normal state.

that settings between 2 Nm and 6 Nm did not produce any change on the first three modes. Of course the laboratory structure has higher modes than the theoretical model, and changes could be seen in higher frequencies. This can be discussed at a later section, however, it can be noted here that the aluminium plates (which represent the floors) contain threaded holes - which should explain the limited effect of the torque settings on the lower frequencies.

Through curve fitting (rational fraction polynomials) with the help of MATLAB, the first three frequencies of the experimental structure were identified. Table 1 shows a comparison between the theoretical and the experimental natural frequencies. In terms of percentage difference, the first and third mode are a bit further away, however, if the properties of the material are altered, then the absolute difference can change - although it will be a compromise between the three modes. Nevertheless, the theoretical model can be considered accurate enough to be used at least as a guide.

Theoretical freqs. [Hz]	Experimental freqs. [Hz]	Abs. Difference [%]
18.8	18.21	3.2
34.75	34.44	0.89
45.4	46.71	2.89

Table 1: Natural frequencies of the 3-DOF structure

3.1 Added mass on the experimental structure

The first pseudo-fault applied on the structure was the added mass. It is very convenient and easy to use and it is a non-destructive way of introducing a local change on the system. The added mass was firstly added on the second 'floor' (mass) of the structure and progressively increased from $66g$ to $216g$. Subsequently, the process was repeated to add the mass on the third 'floor'. Figure 6 shows the effect of the added mass on the frequency response of the system. A careful look at the theoretical analysis (Figure 4) shows that the mass on the centre would not affect at all the second mode - and the experimental results agree. The added mass on the third 'floor' is changing all three modes.

Added masses were also added directly on the spring leaf (see Figure 8), where the saw-cut was also applied (to be described in a following sub-section), to be in-line with previous studies [7] where the added mass was

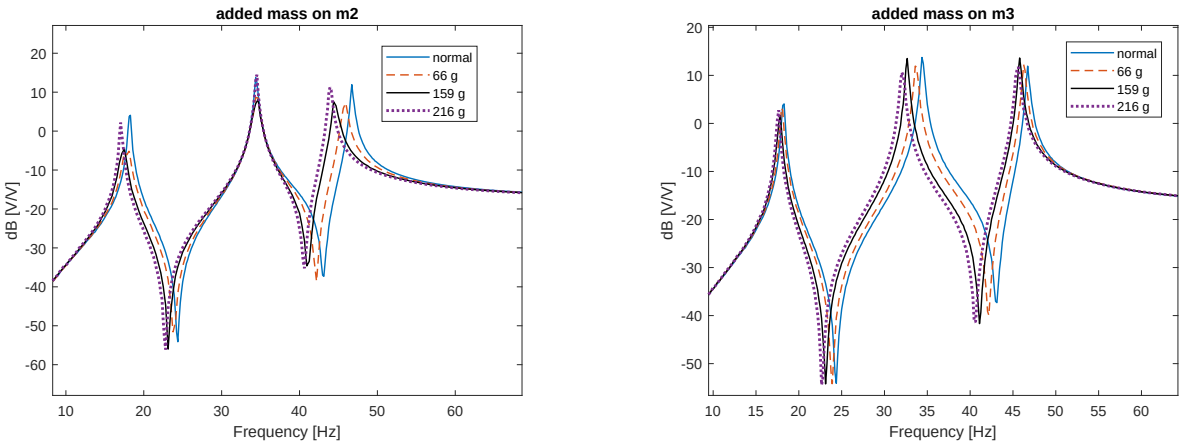


Figure 6: FRFs recorded with an added mass on m_2 (left) and m_3 (right).

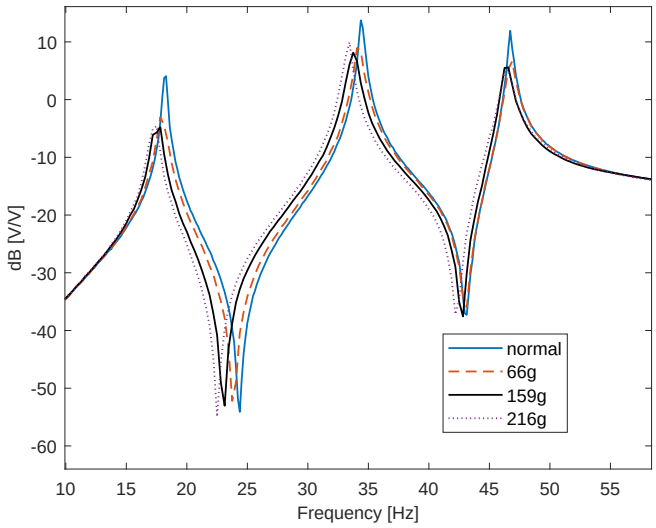


Figure 7: FRFs recorded when added mass was added directly on the leaf spring - where the saw-cut was later added.

added directly on the same location as the actual 'fault'. When the mass is added on the leaf spring, then the theoretical model cannot be used directly for comparison, as the mass of the leaf spring and its inertia have been changed. Figure 7 shows the FRFs when the mass was added on the leaf spring.

3.2 Loosened bolts

Another type of pseudo-fault which was tested was the simple case of loosening a bolt. This scenario is commonly applied to truss-like structures. Since the experimental rig here contained joints with bolts, it was a straight-forward choice to be examined. It is already mentioned in a previous section that torque settings may have an effect on the frequency response of the structure. A short study which used low torque settings showed that in a low frequency range, where the first three modes of the structure are, there was no effect. However, when a bolt was loose - to the extent that it could be turned by hand, but not 'rattle' during the test, the effect on the frequencies was evident.

Figure 8 shows the bolts which were used in this part of the study numbered, so that it would be easier for

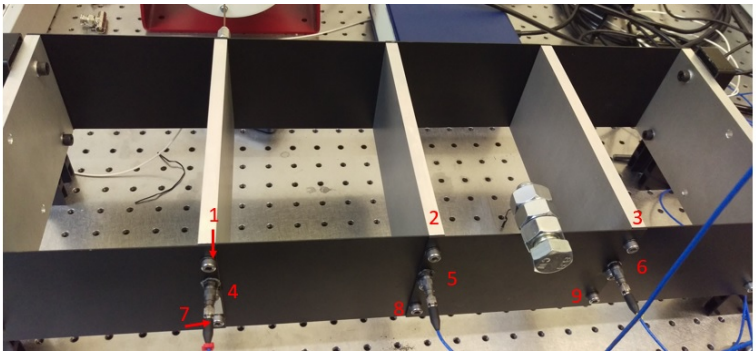


Figure 8: Indexing of bolts which were loosened during the study. An added mass can also be seen. Note that added masses were also applied directly on the central masses/plates (representing the floors of the 3DOF structure).

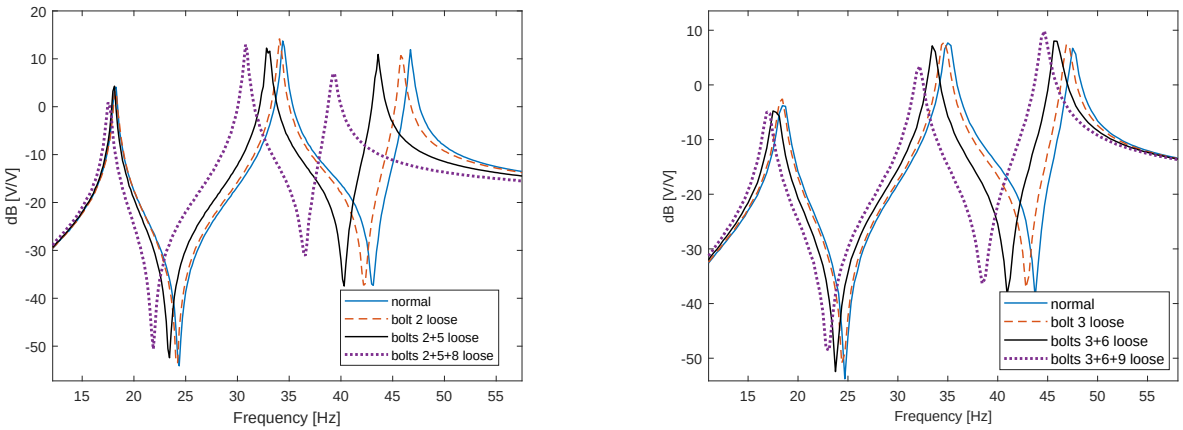


Figure 9: FRFs recorded when bolts in the joints of the structure were loosened. Please refer to Figure 8 for the location of the bolts.

the reader to understand which bolt was loosened every time. Several repeat tests with loosened bolts were performed, including the bolts residing at both sides of the structure. However, here two standard cases are presented: when bolts clamping the central mass (floor), and subsequently the third mass, were sequentially loosened. Even a single bolt was enough to produce a change in the frequencies as seen in Figure 9. It can also be seen that with three bolts the effect is as high as a substantial loss in stiffness (see Figure 3 from the theoretical model).

3.3 Local temperature increase - Heat gun

A localised increase on the temperature of a structure will change locally its properties and thus affect its natural frequencies. This has been used as a pseudo-fault before in [9]. A heat gun was used here as well to increase the temperature on the third leaf spring (representing stiffness value k_3 in the theoretical model), and subsequently on the fourth leaf spring. In order to have a consistent approach the heat gun was held at a distance of 15 cm and was used for 10 sec before any measurements were taken. It was immediately apparent that a prolonged application time of the heat gun would overheat the element (also burn the paint of the specimen) and transfer the heat to the neighboring plates (leaf springs). Overall, this meant that the FRFs recorded contained only 4 averages - as a longer time would create inconsistent results due to the heat conductivity of the metal plates. Figure 10 shows the comparison of the FRFs before the heat gun was applied, and after. It is clear that a change in the natural frequencies, more prominent on the third and second

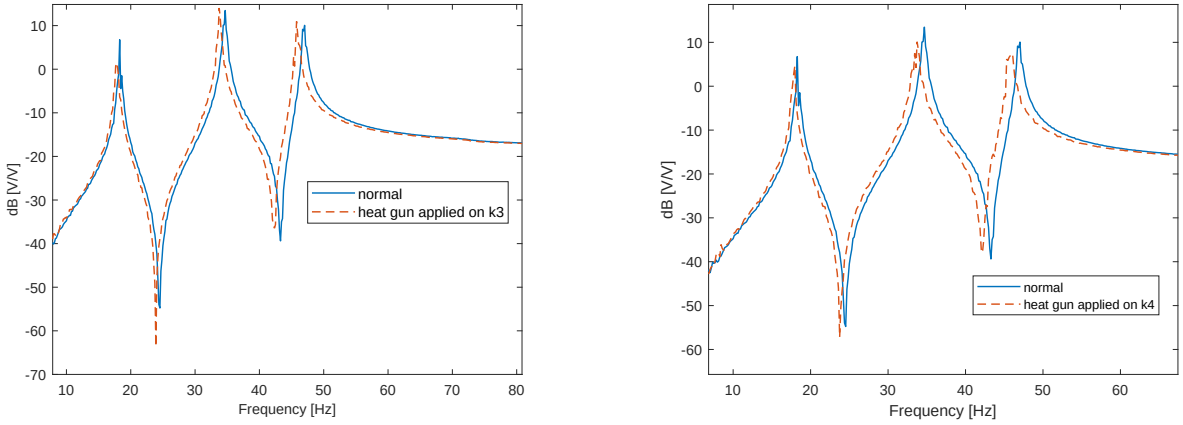


Figure 10: Heat gun applied locally on the plate representing k_3 (left) and k_4 (right). These FRFs were recorded with only four averages.

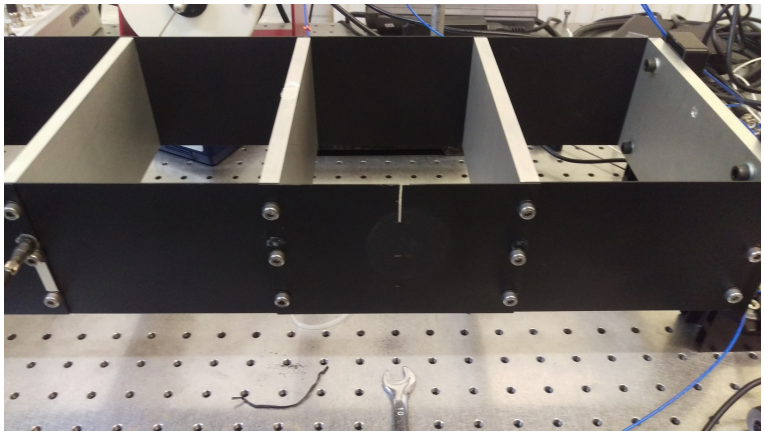


Figure 11: Saw-cut introduced to one of the plates (leaf spring) of the structures

mode (as was expected though the theoretical model - see Figure 3) was evident. It is interesting that the location of the local heat increase changes the magnitude of the FRFs (in the case of k_4 there is a drop in frequency and magnitude), although based on the few averages recorded this result should not be considered highly reliable.

3.4 Saw-cut

A saw-cut is a form of destructive type of damage which can be introduced on a structure - it is of course irreversible, so it is not recommended for high value specimens, however, it is generally considered a more realistic form of damage when compared to added masses or loosened bolts. Although, there are arguments against a saw-cut being realistic damage (e.g. it is visible by naked eye or it would not be easily created through the structure's normal operation), but most vibration-based approaches may include it as it will cause a local drop in the stiffness of the structure. Figure 11 shows the structure with a saw cut on one of its leaf springs.

Five different levels of 'damage' in the form of saw-cut lengths were gradually introduced: 10%, 25%, 50%, 75% and 100% (full removal of the leaf spring). Note that this was introduced only on one leaf spring (representing less stiffness reduction than if it were applied to both sides). It was seen that the first two levels (lengths) did not produce any change on the first three modes. In Figure 12 it can be seen that the

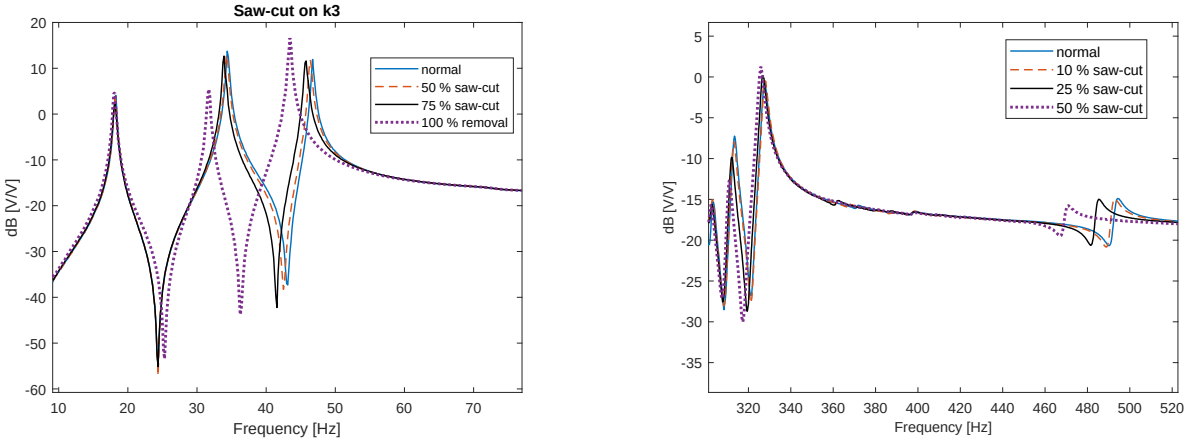


Figure 12: FRFs recorded when a saw-cut was introduced on one of the leaf springs representing k3 stiffness. Short lengths of saw-cut did not have an effect on the first three modes of the structure.

introduction of the saw-cut affects the first three frequencies of the structure after its length reaches 50% and above, with a complete removal of the panel causing the most significant frequency shift. The complete removal of the panel should be approximately equivalent to a 50% reduction of the stiffness value, however, there is a small mass change as well. Figure 12 also shows that in higher frequencies there will be features available for shorter saw-cuts.

A careful look at all the FRFs from all cases will show that although similar trends can be found, and the experiment agrees with the theory, it is not straight forward to equate stiffness loss with added mass (theory), or added mass with a saw-cut in the experiment. The location influences the effect, and added mass and stiffness reduction cannot be modeled exactly at the same location in theory. In practice, only the case where an added mass was added on the same leaf spring as the saw-cut has the exact same location for both types of damage. Table 2 shows some comparison of an absolute change, in %, of the first three modes of the structure when compared to the normal state. It can be seen that in the case of the 100 % saw-cut (full removal), the same trend can be seen as in the theory, however, the added mass, although it does reduce the third mode, it displays a different pattern (progression of change from one mode to the rest is reverse - third mode shows the least change).

	Saw-cut 50%	Saw-cut 75%	Saw-cut 100%	Theory 50 % k_3 reduction	Added mass 159g	Added mass 216g
f_1	0	0.4	0.9	3.2	3.4	4.7
f_2	0.4	1.5	8	10.6	2.2	3.3
f_3	0.7	2.1	7	8.5	1.5	1.6

Table 2: Absolute difference of changes of the first three modes of the structure when compared with normal state, under saw-cut and added mass (applied on the same location as the saw-cut).

4 Discussion points on damage metaphors

4.1 Added mass

This type of pseudo-fault is very common, and easy to implement. It has been shown that it works well, albeit at a small extent. Attempts to equate an increase of mass with loss in stiffness is challenging and will likely end up having the drawbacks of inverse problem approaches (like a non unique mapping between feature changes and the cause of those changes).

4.2 Loosened bolts

If a test structure contains bolts, then it is highly recommended to change its torque settings or loosen it completely, as it will certainly cause a visible change in the frequency response of the system. Care needs to be taken during any testing, as joints may introduce nonlinearities, especially with higher excitation levels. Again, a severity study may be challenging, unless it includes just the identification of the location (in order to assess partially the severity of the damage case).

4.3 Local temperature increase

This is an interesting choice of damage metaphor. It is shown here that it works by lowering the frequencies of the structure. In more complex structures though, it was shown [9] that not all features selected from the local heat increase are going to be adequate for the 'real' damage. There are also several practical limitations in its application.

4.4 Saw-cut

This was used as a benchmark for real damage introduced on the structure. It was shown that short saw-cuts do not cause an immediate effect in the low frequencies of the system. In general, this is expected in a vibration-based approach, as higher modes contain more local information about the structure. Of course, measurements in a higher frequency range can still be used for feature selection.

In addition, it can be considered ambiguous whether a saw-cut represents real damage - although it is generally applied to structural elements in order to cause a local loss in their stiffness. Ultimately, the choice of whether to be used or not will depend on the requirements of the SHM approach.

4.5 Open questions - suggestions

From the above a few discussion points can be raised:

- It is very common to require the need for a non-destructive way of introducing damage in an SHM attempt or validation of SHM algorithms. This may be necessary in data-based approaches.
- A pseudo-fault may be used as a guide for feature selection, but it cannot be damage - by its definition.
- A comparison of the pseudo-fault with 'real' damage will almost certainly be required. This perhaps, presents an irony - as the point of the pseudo-fault is to avoid real damage. Here, saw-cuts were used, but this has raised questions, and so the choice of the 'real' damage is crucial.
- The choice of pseudo-fault and consequently the choice of the 'real' damage to be used for comparison, will largely depend on the operational evaluation of the whole SHM system, i.e. the requirements of the monitored structure. This leads to the following point.
- The choice of the pseudo-fault should be guided by the features one is attempting to use. All the damage metaphors shown here are expected to be used in conjunction with modal features, if one, for example, is attempting to use strain gauges to monitor strain, then added masses will probably not be an appropriate choice.

5 Conclusions

The purpose of this paper was to go though common types of pseudo-faults or damage metaphors, which are very often necessary when dealing with damage identification on expensive structures. A laboratory structure was used to experimentally demonstrate added masses, loosened bolts, local temperature increase and compare them with saw-cuts. The latter is generally considered a more 'realistic' type of damage introduction as it forms an irreversible scenario. The work clearly showed that considering modal features, such as changes in natural frequencies and frequency response functions, all pseudo-faults can be used to extract damage-sensitive features. The attempt, however, to correlate the changes caused into the system in a damage severity study will likely prove very challenging. In other words, the absolute differences of the changes produced in the structure may not be necessarily useful (unless perhaps in special cases such as this laboratory structure), but the trends or the patterns observed should be informative for any SHM study. A few discussion points and suggestions were raised here, including how realistic is the 'real' damage scenario (saw-cut), and it is hoped that the work will inspire a debate on the use of damage metaphors among the SHM community.

References

[1] J. E. Doherty, *Nondestructive Evaluation*, in Chapter 12, *Handbook on Experimental Mechanics*, S. Kobayashi Edt., Society for Experimental Mechanincs, Inc. (1987).

[2] S. W. Doebling, C. R. Farrar, M. B. Prime, D. W. Shevitz, *Damage Identification and Health Monitoring of Structural and Mechanical Systems from Changes in their Vibration Characteristics: A Literature Review*, Los Alamos National Laboratory LA-13070-MS (1996).

[3] H. Sohn, C. R. Farrar, F. M. Hemez, D. D. Shunk, D. W. Stinemates, B. R. Nadler, J. J. Czarnecki, *A Review of Structural Health Monitoring Literature: 1996-2001*, Los Alamos National Laboratory LA-13976-MS (2004).

[4] F. Din-Houn Lau, N. M. Adams, M A. Girolami, L. J. Butler, M. Z.E.B. Elshafie, *The role of statistics in data-centric engineering* Statistics and Probability Letters, Vol. 136, (2018), pp. 5862.

[5] C. R. Farrar, S. W. Doebling, D. A. Nix, *Vibration-based structural damage identification*, Philosophical Transactions Of The Royal Society Of London Series A-Mathematical Physical And Engineering Sciences, Vol. 359, No. 1778, (2001), pp. 131-149.

[6] C.R. Farrar, K. Worden, *Structural Health Monitoring, A Machine Learning Perspective* John Wiley & Sons, (2013).

[7] E. Papatheou, G. Manson, R. J. Barthorpe, K. Worden, *The use of pseudo-faults for novelty detection in SHM*, Journal of Sound and Vibration, Vol. 329, No. 12, Academic Press (2010), pp. 2349-2366.

[8] E. Papatheou, G. Manson, R. J. Barthorpe, K. Worden, *The use of pseudo-faults for damage location in SHM: An experimental investigation on a Piper Tomahawk aircraft wing*, Journal of Sound and Vibration, Vol. 333, No. 3, Academic Press (2012), pp. 971-990.

[9] G. Manson and M. Matzakou, *SHM feature selection using damage metaphors*, *Proc. Int. Conf. Noise Vib. Eng. ISMA 2012*, Leuven (2012), pp. 3345-3358.

[10] S. R. Rao, *Mechanical Vibrations*, Prentice Hall, SI Edition (2005).

A methodology using health and usage monitoring system data for payload life prediction

P. Nalliah[1], A. Lewis[1], C. Lomax[2], C. Hawkins[3]
[1] University of Hertfordshire, School Of Engineering And Technology
College Lane, Hatfield AL10 9AB, United Kingdom
e-mail: **p.nalliah2@herts.ac.uk**

[2] MBDA (UK) Ltd, Six Hills Way, Stevenage SG1 2DA, United Kingdom

[3]Defence Science Technology Laboratory, Platform Systems Division
Dstl Porton Down, Salisbury, SP4 OJQ, United Kingdom

Abstract
This paper presents a methodology to monitor the fatigue life of aerospace structures and hence the remaining allowable fatigue life. In fatigue clearance, conservative load assumptions are made. However, in reality, a structure may see much lower loads and so would be usable for much longer. An example of this is air carried guided missiles. In the UK, missiles must be decommissioned after a period of carriage. The implementation of a system that can monitor the usage of a missile during its time in service is advantageous to the military customer and provides a competitive advantage for the missile manufacture in export markets where reduced through-life costs, longer in-service lives and increased safety are desired. The proposed methodology provides a means to monitor the service life of a missile. This paper describes how machine learning algorithms can be used with accelerometers to determine loads on a missile structure which would then be used to predict how long the missile has left in service.

1 Introduction

Current aircraft increasingly incorporate a Health and Usage Monitoring System (HUMS). HUMS is a data collection system that records inputs from the aircraft such as speed, other flight parameters, power and voltages of electrical systems [1]. Health and Usage Monitoring Systems (HUMS) come under the category of Damage Detection. The use of damage detection has become increasingly important for existing structures and mechanical systems. Existing structures such as bridges and systems such as aircraft have become more and more expensive to maintain. By introducing damage detection for structures and mechanical systems, it will be possible to extend their operational use beyond their designed service life [2] and prevent failure during service.

Distinguishing the two meanings behind health and usage monitoring is essential.

- Health Monitoring: the process of identifying aspects of data obtained through sensory measurement from a system over time and quantifying the extent of the damage.
- Usage Monitoring: the process of recording data during the structure's or system's operation. The data measured can include environmental variables such as temperature and moisture and operational variables such as speed and altitude [3].

The application of health and usage monitoring systems was first applied to rotary aircraft; however, it originated from the methodology of structural health monitoring (SHM) [2]. SHM is the process of damage detection for aerospace, civil and mechanical engineering infrastructure. In the aerospace industry, SHM has been predominant with rotor aircraft during early stages of HUMS development both in commercial and military sectors. The implementation of HUMS into aircraft has now been increasingly common practice

since the 1990's. It has been proven to lead to both improved safety and provide economic benefits [4]. While safety aspects are an important issue and a reason to implement the HUMS, the cost was the deciding factor. The typical cost and upkeep for a helicopter can be broken down into five categories. 36% for depreciation, 29% to insurance, 24% to maintenance, 6% to the flight crew and 5% to fuel [4]. The drive behind implementing HUMS in helicopters was to reduce the cost of insurance and maintenance. The reasoning behind this was cost saving in areas of replacement parts. The HUMS data would be used to identify parts which are damaged or reached their safe-life. Therefore, there was a reduced number of spares used for unnecessary removals of healthy parts and an increased time of the helicopter in-service. However. Guided weapons are typically safe-life structures and as such detectable damage is unlikely to be permitted while in-service. Hence, in this case, Damage Detection is less applicable than Operational Monitoring techniques.

The use of machine learning in the aerospace industry has been researched by Homes et al. [5], who used Gaussian Process Regression (GPR) to predict the loading on the landing gears during landing, taxiing and take off using onboard data recording systems. Previous research has used machine learning for fault and damage detection such as Baskaya et al.[6] and Bondyra et al.[7] whom both used Support Vector Machine (SVM), a machine learning algorithm, on a small Unmanned Aerial Vehicles (UAV) for fault diagnosis. The notable benefit of using supervised machine learning is that it only requires two sets of data, the inputs and output. This eliminates the problem of prior knowledge of the model, in this case, the dimensions and structural properties of the missile. This makes the methodology versatile since the process can be applied to any aircraft to predict any characteristic, whether it is loads, flight manoeuvres or damage detection. However, the potential downside of this methodology is that a machine learning model must be created for every eventual scenario. For example, if an aircraft is carrying one missile on either end of the wing, data would have to be collected, and a machine learning model would have to be created for that scenario. If there were two missiles on either end of the wing, then new data would potentially have to be collected, and a new model would have to be produced. If the missile type was changed but used the same layout configuration then the process has to be repeated. Every change could potentially require a specific model for the prediction to reliable and accurate. This process may be cumbersome. However, the same process would have been used to test a non-machine learning methodology to validate the algorithms.

The machine learning approach in this article utilises Gaussian Process Regression (GPR) along with Neural Network (NN) and Support Vector Machine methodologies in order to predict loads in the attachments of an air-carried missile to the aircraft, or hangers. Machine learning is a computer-based program which uses mathematics to predict and identify outcomes based on the properties of data. The information from the data would later be used to predict future data. Machine Learning works because it can learn patterns from non-random data such as simulations, experiments and surveys. It learns these patterns by generalising the data. Generalising the data is a method for the program to understand the data. The first step when creating a machine learning algorithm is selecting the raw data which will be used for the inputs. This is known as the input space. Each set of inputs which makes up the input set is known as features. For example, if an input space had recordings from one temperature sensor, one accelerometer and two strain gauges, then the data set would have four features. The next stage is pairing the input space with the output data. The output data are target output which one is trying to predict. The input space and the target output form together the training data. The next step is selecting the classifier which is the machine learning algorithm that forms a predictive algorithm based on patterns between the known input space and known target output data [8]. This process is known as the training stage. This stage takes up the most computational time since it is going through many iterations to obtain the optimal prediction algorithm to fit the data. The training data can consist of any statistical data whether it is numerical or categorical. Testing is the final stage where the classifier is tested to try to predict unknown output data using unknown input space data which has not been used in the training stage. The classifier is using patterns learnt from the training stage to predict the unknown targets. This stage is used to test the performance of the predictions and optimise the parameters to improve accuracy.

The ultimate goal of this methodology is to provide a process which results in a system that can determine the fatigue damage and thus remaining life of a missile. The process begins with load prediction using GPR. With this loads data in principle, stress time histories could then be determined and fatigue damage calculated making use of Cycle Counting, S-N curve data, and the Palmgren-Miner rule. Over time, this

process can be refined so that the cycle counting method and S-N curve data would not be longer be required and the system would only require the data from the HUMS and the machine learning algorithm to provide a prediction yielding the remaining life of a missile.

2 Theory - Overview of GP Regression

GP is a supervised machine learning algorithm which can solve complex datasets which traditional parametric methods may not be able to handle [9]. The algorithm used for this project was developed by Carl Rasmussen [10]. GP regression works by having a training dataset which contains the observed response data, in this project the strain, and the input vector data which are the accelerations. GP creates a prediction based on the dataset by forming a family of functions to fit the data and provides a predictive distribution as opposed to a single prediction [5]. What makes GP beneficial compared with other machine learning algorithms is its ability to show uncertainty estimates with predictions. It does not require cross-validation because the kernel and regulation parameters can be learned directly from the data. Also, feature selections can be used during the training stage [9]. Features are the input data used in prediction, such as acceleration, temperature and speed. Feature selection is an algorithm which removes features so that the optimal prediction algorithm can be created.

The Gaussian process is defined by two functions in the form of:

$$f(x) \sim GP(m(x), k(x, x')) \tag{1}$$

where

$$m(x) = \mathbb{E}[f(x)] \tag{2}$$

$$k(x, x') = \mathbb{E}\big[\big(f(x) - m(x)\big)\big(f(x') - m(x')\big)\big] \tag{3}$$

The mean function, $m(x)$, represents the expected value of the function $f(x)$ at the input x. The mean function is generally set as zero because little is known about the input data when it is the first time training the prediction model. The covariance function, $k(x, x')$, determines the covariance of the two predictions at any two specific points and can be considered as a measure of the confidence level for $m(x)$.

The GP then forms the following algorithm:

$$y = f(x) + \eta \tag{4}$$

Where y represents the observed response, x represents an input vector, η represents the noise.

When it comes to deciding on which covariance function should be used, the most common one is the squared exponential. This is used as a standard when first using GP regression on new data. The general form is written as follows [10]:

$$k(x, x') = {\sigma_f}^2 exp\left(\frac{1}{2l^2}|x - x'|^2\right) + {\sigma_n}^2 \delta_{pq} \tag{5}$$

Where ${\sigma_f}^2$ and ${\sigma_n}^2$ are signal and noise variances, respectively, and l is the characteristic length scale.

3 Missile Loads Testing Setup

The Structural Health and Usage Monitoring System (SHUMS) data was collected via a test rig to which a representative missile structure was mounted, via two of the hangers, by attachments providing simple support conditions. The structure was representative of an air carried complex weapon in terms of geometry, inertial characteristics and body bending stiffness. Excitation was provided by a shaker on which the test rig was mounted. To record the load acting on the hangers during the vibration test, two strain gauges were attached to each support, making four in all. The mean strain was calculated for each support giving two sets of axial strain recordings for the hangers. Seven tri-axial accelerometers were placed at specific positions along the length of the missile structure.

In this study, the dataset collected contained 810442 by 11 data points over a time of 100 seconds of excitation. Seven columns contained the acceleration data, and the last four contained the strain data.

4 Results

The following section shows the results predicting strains on the attachments under vibrational loads using Gaussian Process Regression, Neural Network and Support Vector Machine. Figure 1, Figure 2 and Figure 3 are the results from GPR predictions. Figure 1 is the overview of the full data between 0 and 100 seconds, Figure 2 is the view between 0 and 4.5 seconds and Figure 3 is the view between 80 and 80.5 seconds. Figure 4 shows the equivalent results for NN and SVM. Figure 5 shows the scatter plots for all three machine learning algorithms showing the actual strain against predicted strain. The last of the results is shown in Tables 1 and 2 which provide measures of the performance of the three algorithms.

All three machine learning algorithms were programmed to use 70 percent data training and 30 percent testing. Therefore after 70 seconds, the algorithms were predicting unseen data. In each Figure are two more graphs that represent the strain data from the two hangers, for example as shown in Figure 1. Figure 5 gives scatter graphs representing the actual strain against the predicted strain.

In each of Figures 1 to 3, there are three crucial pieces of information being shown, the predicted strain, true strain and confidence level. The predicted strain was calculated using the GP algorithm. The true strain is the recorded strain from the hangers. The confidence interval uses the 95 percent approach from a normal distribution.

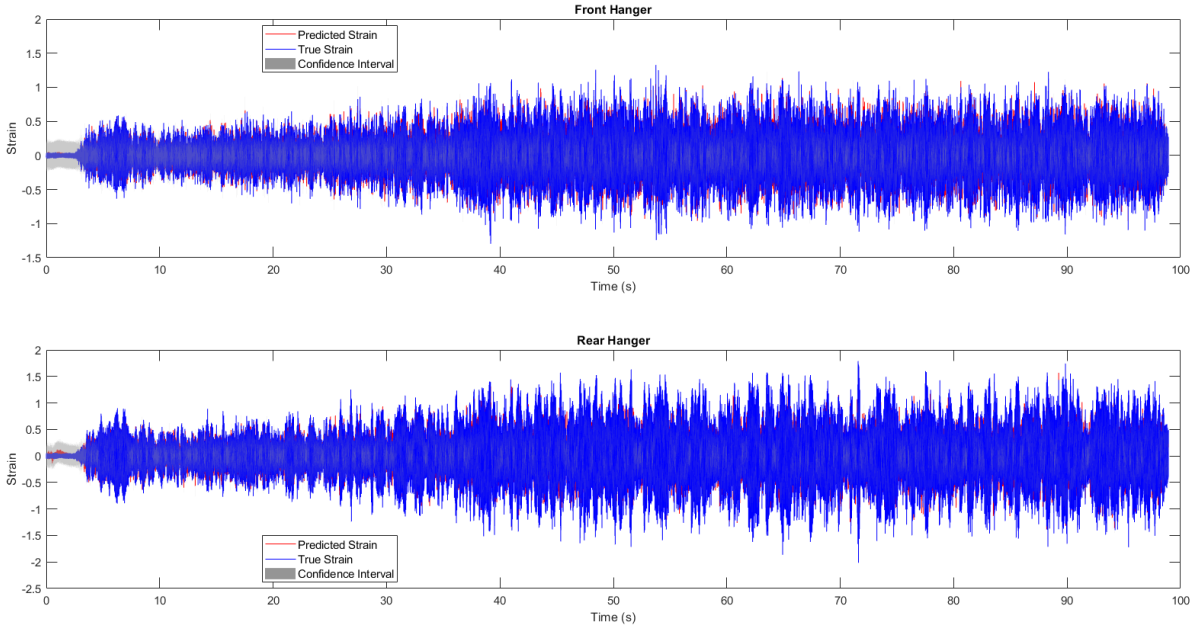


Figure 1: GP prediction graph for stains in the Front and Rear Hanger between 0 and 100 seconds.

A critical part of the load prediction is predicting peak loads, especially where these points are essential to extract data that will be important for later analysis such as Cycle Counting. Figure 2 and Figure 3 shows a magnified view of Figure 1. It is challenging to analyse large amounts of data, so the figures mentioned provide a small window of the load prediction. The purpose of showing the first 5 seconds was to demonstrate reconstruction during low loads and then higher loads. During flight, an aircraft will experience long hours of steady flight and the model would have to be capable of predicting these levels accurately.

It can be seen in Figure 2 during the first 3 seconds that the predicted strain deviates away from the true strain especially for the rear hanger between 0.2 and 2 seconds. This is corroborated by the confidence interval being much higher. This may be due to the acceleration data or the positions of the accelerometers. When it transitions to higher loads after 3 seconds the predictions become more accurate and the confidence interval shrinks which tells that the model recognises the data. The predictions for the testing data, shown in Figure 3, also shows accurate predictions. One of the problems that occurs with GPR is the predicted strain undershooting the true strain. For example, in Figure 3, the front hanger, at peak 80.32 seconds the predicted strain undershoots the true strain. There maybe a few undershoots in this graph but when the time increases these undershoots accumulate. As mentioned previously, undershooting is not ideal if the peaks are going to be used for Cycle Counting because it is safer if a missile has to be decommissioned early from service due to predictions overshooting rather than staying in service longer due to undershooting where the missile structure could be prone for failure.

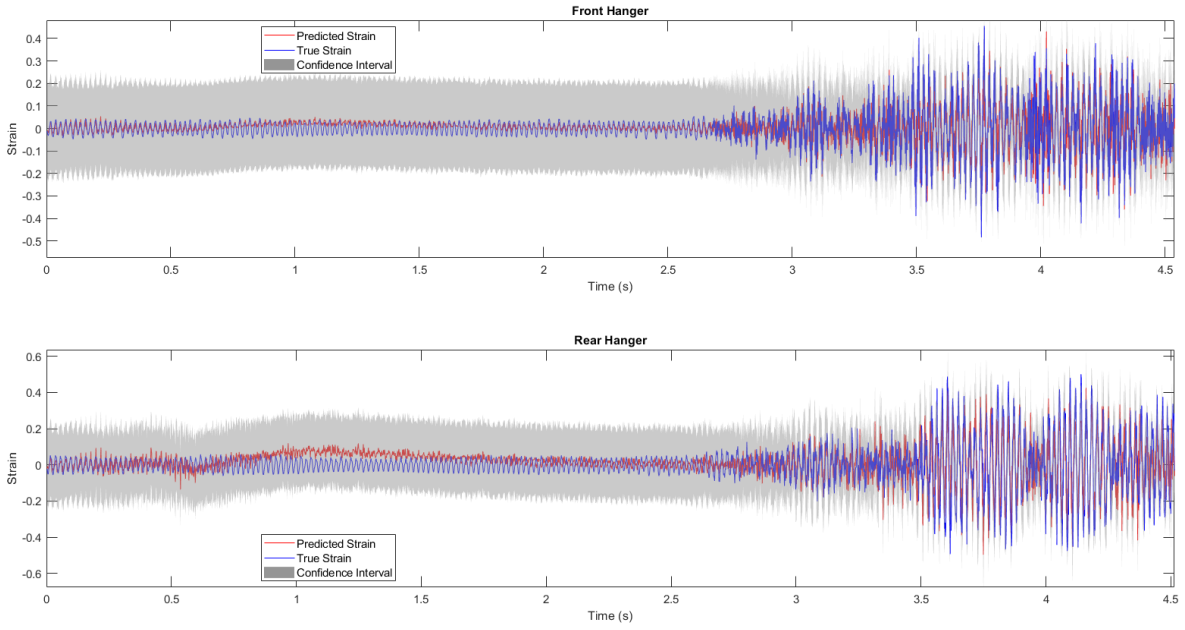


Figure 2: GP prediction for stains in the Front and Rear Hanger between 0 and 4.5 seconds.

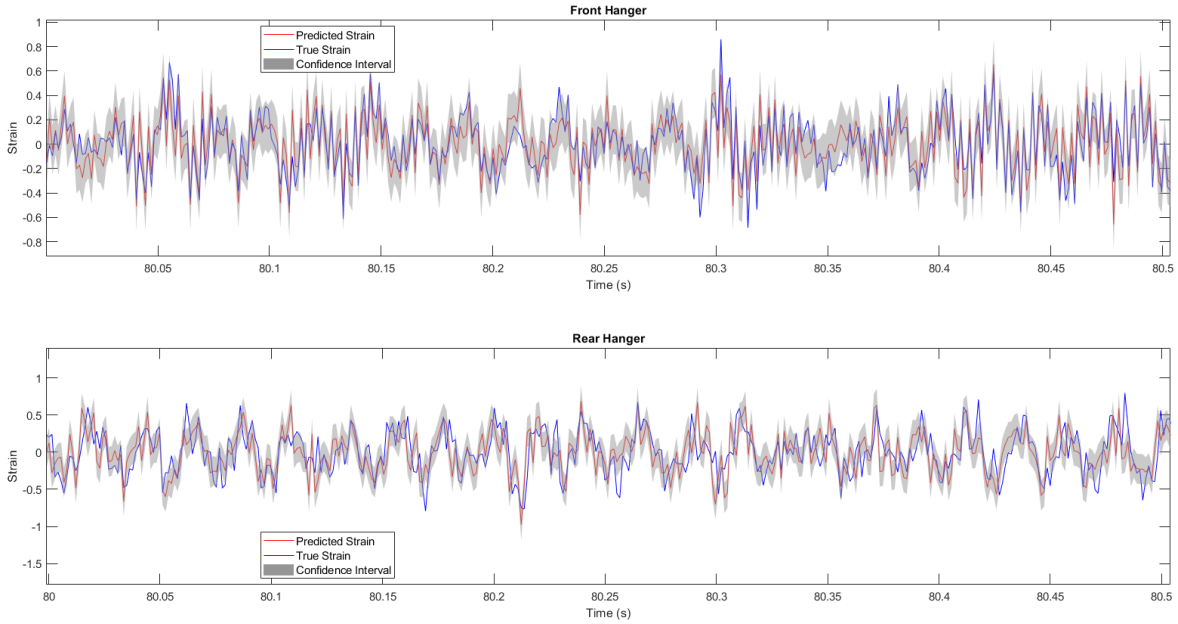
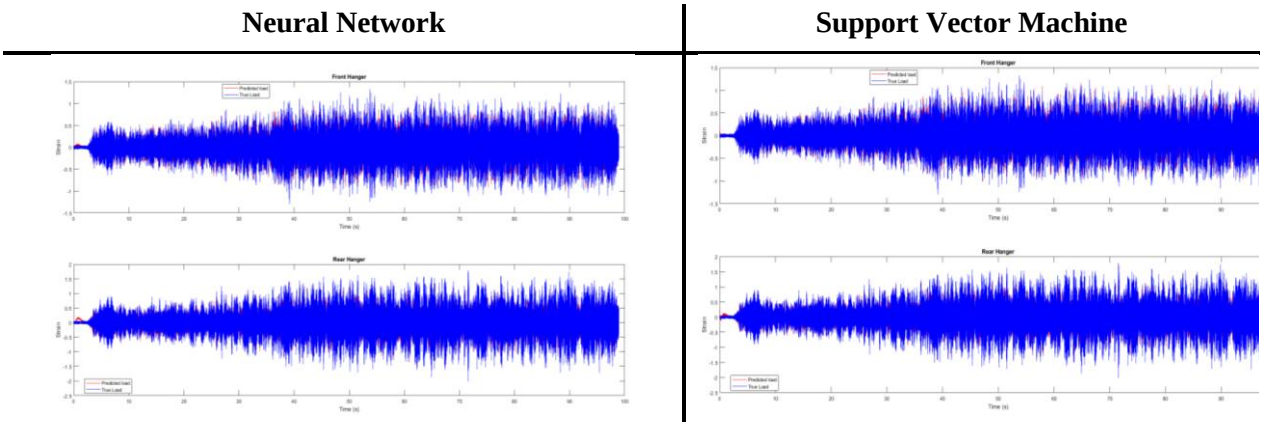


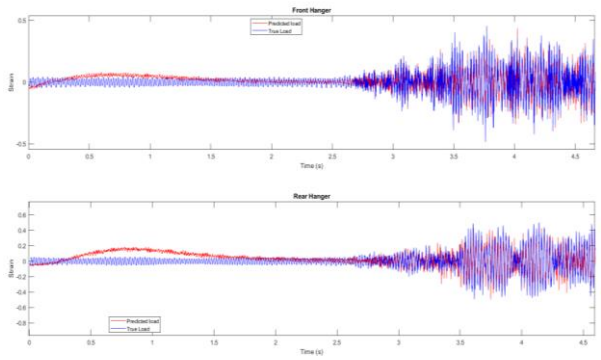
Figure 3: GP prediction for stains in the Front and Rear Hanger between 80 and 80.5 seconds.

Neural Network and Support Vector Machine approaches have a disadvantage, and that is that the model cannot show the extent to which it recognises the data through the confidence interval [11], as shown when using GPR. There are other methods to compensate for this by improving accuracy such as cross-validation and training with more data. What is noticeable in Figure 4 (c) is the first 2 seconds. The predicted strain forms a 'bump' in the line plot. This is greater than that seen in the GPR Figure 2. This prediction error may be due more to the acceleration data than the model itself. For the test data results, shown in Figure 4 (d), they are very similar to the GPR. The NN scatter plot in Figure 5 (a) and (b) show similar shape to GP scatter plot.

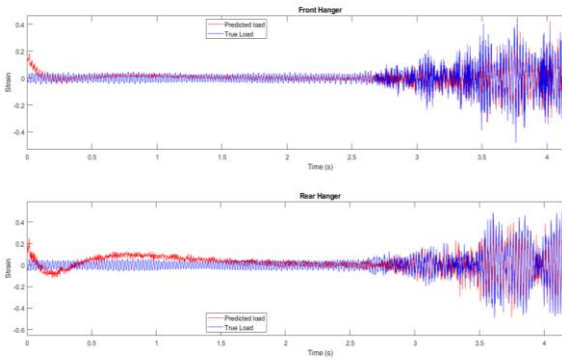
Figure 4 (b), (d) and (f) show the load predictions using SVM. This model shows almost identical results to GP and NN. However, for the front hanger, there is a difference during the first 2 seconds where the prediction begins with a strain value higher than the true strain, and then it normalises after 0.2 seconds. This does not occur with the rear hanger where the predicted strain undershoots and then overshoots before normalising at 2 seconds. Since these discrepancies occur during the first 2.5 seconds for the three models, the cause may be due to the recorded data rather than the model setup.



Front and Rear Hanger between 0 and 100 seconds

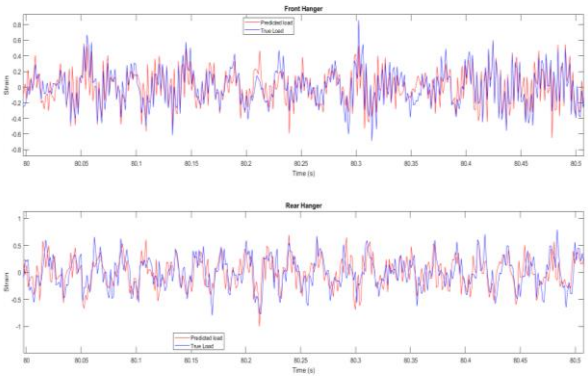


(c)

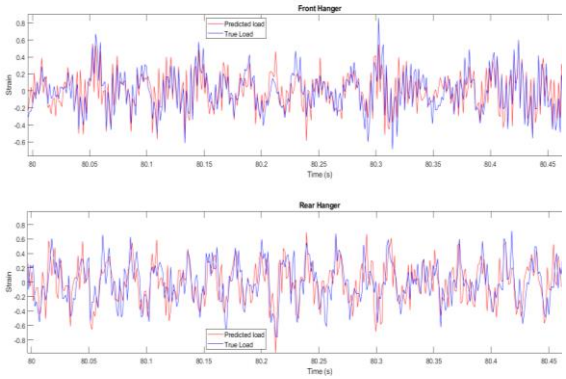


(d)

Front and Rear Hanger between 0 and 4.5 seconds.



(e)

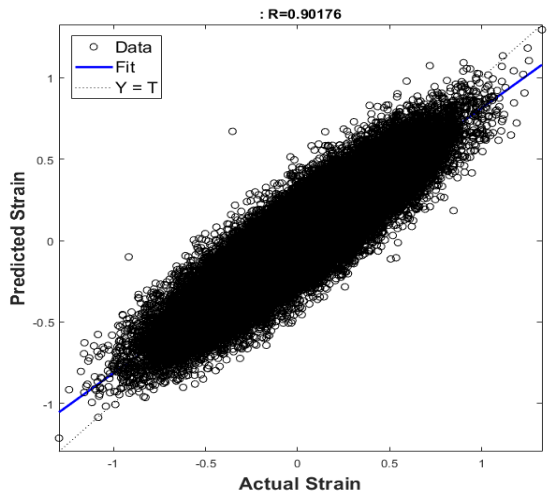


(f)

Front and Rear Hanger between 80 and 80.5 seconds

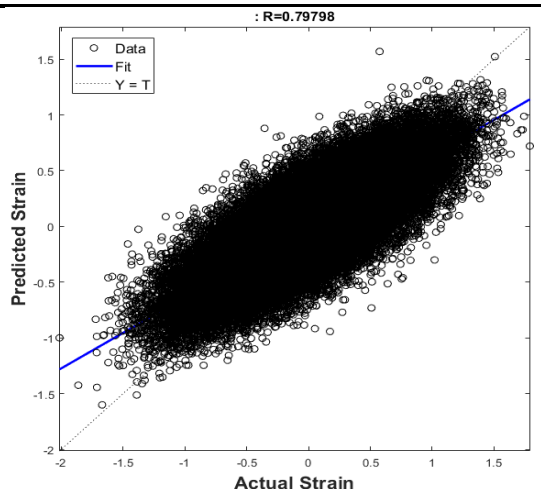
Figure 4: NN and SVM prediction graph for stains in the Front and Rear Hanger.

Front Hanger



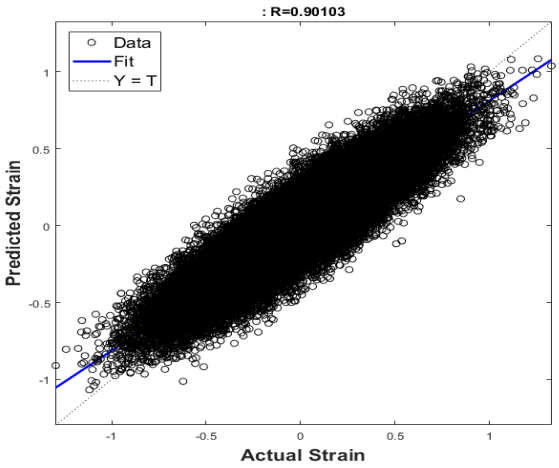
(a)

Rear Hanger

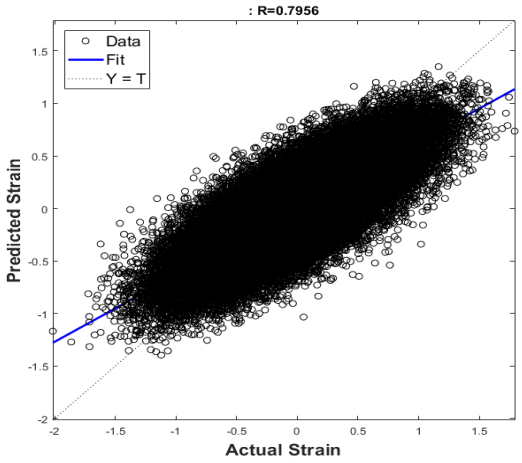


(b)

GPR scatter plots of Actual Strain against Predicted Strain

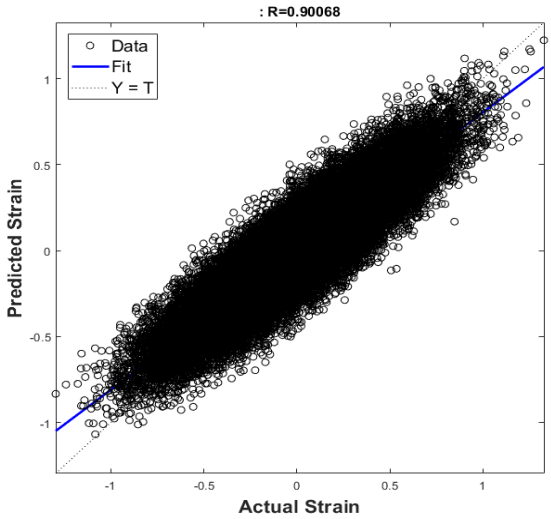


(c)

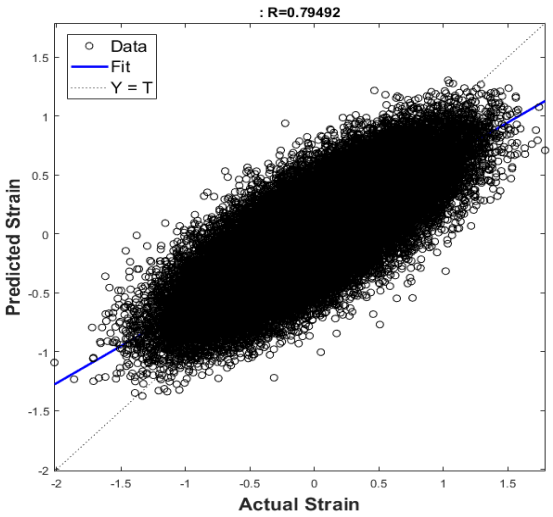


(d)

NN scatter plots of Actual Strain against Predicted Strain



(e)



(f)

SVM scatter plots of Actual Strain against Predicted Strain

Figure 5: GPR, NN and SVM scatter plots of Actual Strain against Predicted Strain.

Scatter plots of actual strain against predicted strain for the overall GPR used on both hangers are shown in Figure 5 (a) and (b). The closer a data point is to the Actual Strain versus Predicted Strain line the more accurate the prediction.

An overall evaluation of the performance of the models is given in Table 1 and Table 2 for the front and rear hangers respectively. In each table there are three evaluation columns: mean absolute error (MAE), root mean squared error (RMSE) and Pearson correlation coefficient (R). Furthermore, evaluation data for training, testing and overall is provided with a comparison of prediction when the model is shown seen and unseen data. The evaluation equations used to measure the performance of the classifiers for MAE, RMSE and R are as follows:

$$MAE = \frac{1}{N}\sum_{i=1}^{N}|y_i - \bar{f}_i| \tag{6}$$

$$RMSE = \sqrt{\frac{1}{N}\sum_{i=1}^{N}\left(y_i - \bar{f}_i\right)^2} \tag{7}$$

$$R = \frac{\sum_{i=1}^{N}(y_i - \bar{y})\left(\bar{f}_i - \bar{\bar{f}}\right)}{\sqrt{\sum_{i=1}^{N}(y_i - \bar{y})^2\left(\bar{f}_i - \bar{\bar{f}}\right)^2}} \tag{8}$$

where

$$\bar{y} = \sqrt{\frac{1}{N}}\sum_{i=1}^{N} y_i \text{ and } \bar{\bar{f}} = \sqrt{\frac{1}{N}}\sum_{i=1}^{N} \bar{f}_i \tag{9}$$

where N represents the size of the dataset, y_i is the target output and $\bar{f}_i$ is the predicted output of the GPR prediction model.

In Figure 1, is the overall strain prediction using GPR. One of the noticeable discrepancies is in the performance values between front and rear hangers, as shown in Table 1 and Table 2. For example, the R value for the front hanger was 0.90176, and the rear hanger was 0.79798. This same difference can also be observed with the other two models. It would have been expected that these values would have been roughly the same since they were using the same model and inputs dataset. The only difference is the strain targets values and the position of the strain gauges. This may be the reason why the rear hanger performance value is not as good as the front hanger value. The current position and the number of the accelerometers may not be ideal for the rear hanger. Therefore, changing the accelerometer locations may influence the results of the predictions.

Front	**Training (70%)**			**Testing (30%)**			**Overall**		
Model	MAE	RMSE	R	MAE	RMSE	R	MAE	RMSE	R
GPR	0.0924	0.1227	0.90179	0.1200	0.1507	0.90171	0.1007	0.1317	0.90176
NN	0.0939	0.1243	0.899	0.1188	0.1489	0.90416	0.1014	0.1322	0.90103
SVM	0.0935	0.1243	0.89917	0.1195	0.1497	0.90301	0.1013	0.1324	0.90068

Table 1: Performance comparison of GPR, NN and SVM for the Front Hanger.

Rear	**Training (70%)**			**Testing (30%)**			**Overall**		
Model	MAE	RMSE	R	MAE	RMSE	R	MAE	RMSE	R
GPR	0.1926	0.2539	0.80319	0.2551	0.3196	0.78981	0.2113	0.2752	0.79798
NN	0.1961	0.2575	0.79683	0.2529	0.3170	0.79371	0.2131	0.2767	0.7956
SVM	0.1954	0.2575	0.79675	0.2540	0.3181	0.79206	0.2130	0.2771	0.79492

Table 2: Performance comparison of GPR, NN and SVM for the Rear Hanger.

5 Discussion

One of the limitations in using GP is that it is necessary to invert a large N by N matrix, where N is the number of data points in the training dataset. For this study, the total dataset contained 8914862 data points. The ability to do this is affected by a computer's hardware due to the size of the RAM. The larger the matrix, the more RAM and computational processing time are required. To reduce the demand on the RAM sub-sampling of every 11th data point from the dataset was implemented. One of the problems in using this approach is the likely chance of losing critical data especially at the peaks where strain is at maximum or minimum. While this approach was not ideal, it was necessary to overcome hardware limitations. However, there are ways to circumvent these problems. New studies in handling big data sets have emerged with regards to GP [12], [13]. The benefit of machine learning is once the classifier has been trained, the prediction process or testing stage is not limited by matrix size and computational time is greatly reduced to a few minutes.

Overall, the results show promising predictions when using machine learning for load predictions. All three models provided accurate prediction. For the rear hanger improvements to the hanger positions and the number of accelerometers will be researched to improve the performance of the methodologies. As for which was the best model for load predictions, GPR did yield the highest correlation coefficient for both hangers but only by a small amount. Deciding which is the best machine learning model is not only decided by which provides the best results. As shown in the tables all three models showed similar results. What decides which model is the best is how much resources are needed to get a good prediction such as computational power and time to process and how much data is required. Also by what form of assurances can be provided to obtain the optimal predictive model, such as cross-validation and the confidence interval. Each model has its advantages and disadvantages. One of the issues which occur with machine learning is overfitting and underfitting. Overfitting occurs when the prediction results are identical to the actual results. This may be ideal; however, if unknown data is introduced, then the predictive model would be unable to produce accurate results, as found in [5]. Underfitting is the opposite to overfitting where the predictive results are poor and are not close to the actual results. There has to be a balance between the two and the confidence interval provides information as to whether the predictive model is balanced and optimal.

When using the GPR and SVM both had problems dealing with large datasets, the computational time was 8 and 6 hours for training, respectively, when using supercomputers. The GPR required 192 GB of RAM to complete training. However, NN was able to complete the training in 1 hour. NN can handle large datasets while GPR and SVM cannot. What makes GPR advantageous is its prediction of the confidence interval, its accessibility to different variations of covariance functions that can influence the prediction and the ability to modify the model to suit the problem. NN is accessible however it is a complex system in comparison with GPR.

The paper presented has focused on the use of machine learning algorithms for the load predictions of a missile supported by two hangers. It is common for missiles to be supported by two hangers, but some missiles require three hangers. It is necessary that GPR be capable of predicting loads for three hangers. During the development of GPR for two hanger load predictions, the three hanger problem was also tested using data obtained from a Finite Element Analysis (FEA) model which generated response data for given input loads. The purpose of using such FEA software rather than using experimental data was to test the capability of GPR and identify any potential problems before proceeding to an experimental setup which requires money, resources, time and validation data to confirm that the missile is setup correctly. After training the model to predict three loads through the hangers and then testing, the results were promising; the prediction resembled the results from the presented two hanger load predictions. A problem that load predictions has for a three hanger missile is it being ill-posed which was identified in research by Vishwakarma et al [14]. Using the pseudo-inverse method for load predictions, he proposed that to overcome the ill-posedness problem, regularisation was required. However, for GPR it appears that based on the initial results regularisation was not required.

6 Conclusion

The purpose of the paper was to show the potential application of Gaussian Process Regression to extend the life of an air-carried missile. Load predictions using GPR is part of the process for extending the life by monitoring the usage of a missile during its time in service. Using machine learning for monitoring the usage of a missile means that it does not rely on the use of a model which may have limitations. The only necessary data are the inputs and output, in this project, the acceleration and strain data, respectively. The machine learning algorithm forms a predictive model based on these two sets of data without requiring any knowledge of the structure. The disadvantage of this process is that it is computationally expensive in time and resources and requires a large dataset to obtain the optimal prediction model. Also, there may have to be multiple predictive models for every structural change to the missile and aircraft. However, once the predictive model has been obtained, it is capable of calculating prediction results rapidly, and the process is not limited by the data size and computational power available.

Using GPR has its advantages and disadvantages, it is computationally more expensive than NN due to the large inverse matrix which is required to process the data. However, there has been research into how to enable GPR to handle large data better. The important feature which GPR has is the confidence interval which provides information on the accuracy of the prediction. NN and SVM do not have this feature.

As for the GPR used in this missile load prediction study, it is necessary to implement improvements to the model and the training dataset, especially for the rear hanger. While the front hanger predictions were better, the peaks were not always well predicted. Further research is required to remove or reduce the noise to improve the accuracy of the prediction. It may only require the number and the position of the accelerometers to be changed to improve the results. Another possibility is that it requires the model's covariance function to be changed.

NN and SVM were used as a comparison for GPR. NN and SVM have proven to be more than capable for load prediction and making them possible alternatives. If there were no prospect to enable the use of GPR to handle large data without the requirement for large computational resources and NN had the ability recognise that the model is making inaccurate predictions, then NN would have been the ideal choice. However, GPR has accessibility to the code which makes it versatile for modification to suit the user requirements.

Using GPR is only one part of the system to predict Payload Life. Once this part has been optimised to perform to the user requirements, it can be implemented with standard methods for usage monitoring such as Cycle Counting Analysis. More research is required for HUMS since it has a wide range of accessible data to exploit other than accelerations, but GPR has shown it is capable of predict loads on a missile.To enable GPR to handle large data and reduce computer resources without changing the current GPR algorithm, one approach might be to create a logical method whereby the HUMS is only activated during manoeuvres where loads would be large. During flights where the aircraft will be flying straight and steady these can be classified as benign flight conditions, and fatigue damage could be assumed to accumulate at some pre-determined rate. Another algorithm or secondary machine learning algorithm can identify manoeuvres that go over a pre-determined threshold and filter out the benign flights which are only used for the load predictions training process.

7 Acknowledgements

The authors from the University of Hertfordshire would like to thank DSTL and MBDA for sponsoring this project and providing their invaluable assistance on the project. The authors would also like to include thanks to R Vishwakarma, RJ Amos, A Whitelaw, and MA Hussain for providing the foundation for the work.

References

[1] Cleveland, G. and C. Trammel. *An integrated health and usage monitoring system for the SH-60B helicopter*, in G. Cleveland, *Proceeding of The 52nd Annual Forum of the American Helicopter Society, Washington, DC, USA, 1996 June 4-6* (1996), pp. 1767-1787.

[2] Farrar, C.R. and K. Worden, *Structural Health Monitoring: A Machine Learning Perspective*: John Wiley & Sons, Incorporated, Chichester, West Sussex, U.K. (2012).

[3] Shull, P.J., *Nondestructive Evaluation: Theory, Techniques, and Applications*: Marcel Dekker, 270 Madison Avenue, New York, NY, USA (2002).

[4] Land, J. and C. Weitzman. *How HUMS systems have the potential of significantly reducing the direct operating cost for modern helicopters through monitoring*, in J. Land, *Proceeding of The 51st Annual Forum and Technology Display of the American Helicopter Society (AHS), Fort Worth, TX, USA, 1995 May 9-11*, American Helicopter Society (1995), pp. 744-757.

[5] Holmes, G., P. Sartor, S. Reed, P. Southern, K. Worden, and E. Cross, *Prediction of landing gear loads using machine learning techniques.* Structural Health Monitoring, Vol. 15, No. 5, SAGE Publications (2016), pp. 568-582.

[6] Baskaya, E., M. Bronz, and D. Delahaye. *Fault detection & diagnosis for small UAVs via machine learning*, in E. Baskaya, *Digital Avionics Systems Conference (DASC), St. Petersburg, FL, USA, 2017 September 17-21*, IEEE (2017), pp. 1-6.

[7] Bondyra, A., P. Gasior, S. Gardecki, and A. Kasiński. *Fault diagnosis and condition monitoring of UAV rotor using signal processing*, in A. Bondyra, *Signal Processing: Algorithms, Architectures, Arrangements, and Applications (SPA), Poznan, Poland, 2017 September 20-22*, IEEE (2017), pp. 233-238.

[8] Theodoridis, S., *Machine Learning: A Bayesian and Optimization Perspective*: Elsevier Science, San Diego, CA, USA (2015).

[9] Moore, C.J., A.J.K. Chua, C.P.L. Berry, and J.R. Gair, *Fast methods for training Gaussian processes on large datasets.* Royal Society Open Science, Vol. 3, No. 5, The Royal Society Publishing (2016), pp. 160125.

[10] Rasmussen, C.E. and C. Williams, *Gaussian Processes for Machine Learning*: MIT Press, Cambridge, Massachusetts (2006).

[11] Kong, D., Y. Chen, and N. Li, *Gaussian process regression for tool wear prediction.* Mechanical Systems and Signal Processing, Vol. 104, Science Direct (2018), pp. 556-574.

[12] Hensman, J., N. Fusi, and N. D. Lawrence. *Gaussian Processes for Big Data*, in A. Nicholson and P. Smyth, *Proceedings of the 29th Conference Uncertainty in Artificial Intelligence (UAI), Bellevue, WA, USA, 2013 July 11-15*, AUAI (2013), pp. 282-290.

[13] Das, S., S. Roy, and R. Sambasivan, *Fast Gaussian Process Regression for Big Data.* CoRR, Vol. 1509.05142, ArXiv (2015).

[14] Vishwakarma, R., D. Turner, A. Lewis, Y. Chen, P. Houghton, and Y. Xu. *Load reconstruction on a missile structure using the Pseudo-Inverse methods*, in R. Vishwakarma, *Proceedings of the 2010 International Conference on Modelling, Identification and Control, Okayama, Japan, 17-19 July 2010*, IEEE (2010), pp. 100-105.

Multi-level damage identification in operational condition

S. Milana[1], G. Acunzo[2], S. Gabriele[3], A. Culla[1], G. R. Argento[3]
[1] University of Rome La Sapienza, Department of Mechanical and Aerospace Engineering
Via Eudossiana 18, I-00184, Roma, Italy
e-mail: **silvia.milana@uniroma1.it**

[2] University Roma Tre, Department of Mathematics and Physics
Via della Vasca Navale 84, I-00146 Roma, Italy

[3] University Roma Tre, Department of Architecture
Via della Madonna dei Monti 40, I-00184, Roma, Italy

Abstract
Aim of this paper is the description and the comparison of two Structural Health Monitoring (SHM) techniques to identify a structural damage of a tower crane. First technique considers the natural frequencies and the mode shapes. Consequently, the damage is localized and quantified exploiting well-known techniques, implemented in a Multi-Level Damage Identification Platform (MuDI). The second approach considers the displacement of some points of the crane due to the excitation of a running load. In this case, Continuous Wavelet Transform (CWT) is performed and, by analyzing the CWT coefficients, only the damage position is identified. This second approach requires few sensors and optimizes cost that is a relevant parameter in operational conditions. The obtained results of these two techniques are compared, together with their efficiency.

1 Introduction

Collapse of civil or industrial structures and malfunctioning of machines could have serious consequences. Structural Health Monitoring (SHM) is a procedure that aims at providing an efficient and continuous information, about the condition and the efficiency of the supervised structure. Many monitoring strategies have been proposed regarding both the experimental setup (i.e. choice, number and positioning of transducers, kind of excitation, etc.) and the measured data management. In this paper, two techniques are taken into consideration to localize a structural damage of a tower crane.

The first approach considers natural frequencies and mode shapes to localize the damage and by a modal updating technique quantify its amplitude. A Multi-Level Damage Identification Platform (MuDI) performs the identification procedure. Multi-Level means that, each level of a damage identification process is informed by the previous, in order to decrease the number of the sought damage parameters. As an example, the concurrent application of different localization procedures leads to possible damage zones of the crane, then a model updating of possible damaged parameters (e.g. stiffness of some elements) obtains the damage quantification. The possible damage parameters are selected as a subset of all the possible model parameters, and this selection is informed by the localization level. In other words, the application of different localization methods makes the localization process more robust, with the consequence of limiting the number of parameters to be updated in the damage quantification [1-5].

The second approach is based on the Continuous Wavelet Transform (CWT) of the structure response signal. CWT highlights the singularities of a signal, because its coefficients show a maximum in

correspondence of these singularities. Since, the response of a structure excited by a running load shows anomalies when the load crosses the damage, because the elastic waves are reflected by the structure discontinuity, this irregularities can be detected analyzing the CWT coefficients [6-11].

In this paper, a finite element model (FEM) allows to calculate natural frequencies and mode shapes of the damaged and undamaged test structure. The first technique uses directly the modal parameters so obtained. However, we must consider that in operative conditions mode shapes and natural frequencies have to be identified by some modal identification techniques (e.g. OMA) and it involves the use of a large number of sensors.

The second approach uses natural frequencies and mode shapes to calculate the response at some observation points when a running load, the carriage movement along the jib, is simulated. The analysis of the CWT coefficients allows identifying the damage position, but it does not allow quantifying the damage size. The convenience of this approach, in operative conditions, lies on the use of few sensors, because it needs the structure responses and not the modal parameters of the structure. This one optimizes cost that is a relevant parameter.

2 MuDI approach

First of the two approaches employed in this paper for damage identification consists in using a Multilevel Identification Platform, named MuDI [1]. Damage identification using MuDI is a process based on three steps corresponding to the first three levels of damage identification defined by Ritter [2]:

- level 1: damage presence;
- level 2: damage localization;
- level 3: damage quantification.

First level is approached by the frequency shift technique proposed by G. Hearn and R.B. Testa [3]. The required data are the natural frequencies of both damaged and undamaged structure together with the mode shapes of the undamaged one. The fundamental assumption of this formulation, correct for most of the civil and industrial structures, is that degradation of a structure has significant effect on its stiffness, but negligible variation of its mass. For each element of the structure, the characteristic ratio of equation (1) is calculated: it represents a prediction of modal frequencies change occurring when that element is damaged:

$$\frac{\Delta\omega_i^{\,2}}{\Delta\omega_j^{\,2}} = \frac{\frac{\varepsilon_N^T(\Phi_j)K_N\varepsilon_N(\Phi_j)}{\Phi_j^T M\Phi_j}}{\frac{\varepsilon_N^T(\Phi_i)K_N\varepsilon_N(\Phi_i)}{\Phi_i^T M\Phi_i}} \tag{1}$$

In equation (1) $\Delta\omega_i$ is the variation of the i^{th} natural frequency, K_N is the stiffness matrix of the N^{th} element, M is the mass matrix and $\varepsilon_N(\Phi_i)$ are the displacements induced by the i^{th} mode shape in the N^{th} element.
Presence of damaged elements is verified by comparing this characteristic ratio with the ones calculated from the measured frequency shift in the structure.

Through the minimization of the mean square error defined in equation (2), the presence of the damage is estimated for each element:

$$E_N = \frac{1}{M}\sum_{i,j}\left[\left(\frac{\Delta\omega_i^{\,2}}{\Delta\omega_j^{\,2}}\right)_{N\ measured} - \left(\frac{\Delta\omega_i^{\,2}}{\Delta\omega_j^{\,2}}\right)_{N\ characteristic}\right]^2 \tag{2}$$

where M is the total number of elements.

Besides the presence of damage, a first approximation of damage location is also obtained.

The second method implemented corresponds to level 2 and is based on the formulation of A. K. Pandey et al. [4]. Since, different damages can cause the same frequency shift, this method is supposed to give a better estimate of damage position than the estimate valued by the techniques based on natural

frequencies. The authors proposed the use of a parameter based on mode shape, the mode curvature, in order to identify the correct position of the structural damage. Once this parameter for both damaged and undamaged structure is known, this method allows localizing the damage.

The mode shape curvature is numerically computed at each monitored point, using a central difference approximation with the displacements of the adjacent points:

$$v_i'' = \frac{(v_{i+1} - 2v_i + v_{i-1})}{h^2} \tag{3}$$

h is the length of the element. The damage is then localized near the points that maximizes the difference

$$\Delta = |v_{iD}'' - v_{iU}''| \tag{4}$$

where the subscripts *D* and *U* mean damaged and undamaged, respectively.

The third implemented method, level 3, quantify the damage. It requires a FE model of the undamaged structure in order to perform an updating of a selected group of parameters. The goal of this procedure is to minimize the difference between the damaged structure modal data set and the corresponding undamaged one. The implemented formulation is the one given in [5] for iterative least squares procedures.

3 Case of study: multilevel damage identification of a tower crane

In this section, the MuDI damage identification procedure is performed on a tower crane. The structure consists of 105 steel pipes with a square cross section of 0.1 m side length and thickness of 0.01 m. The steel type is classified as S355, according to the National Italian Code.

The FEM of the crane consists of 105 frame elements, modeling the steel bars, and 55 nodes (figure 1).

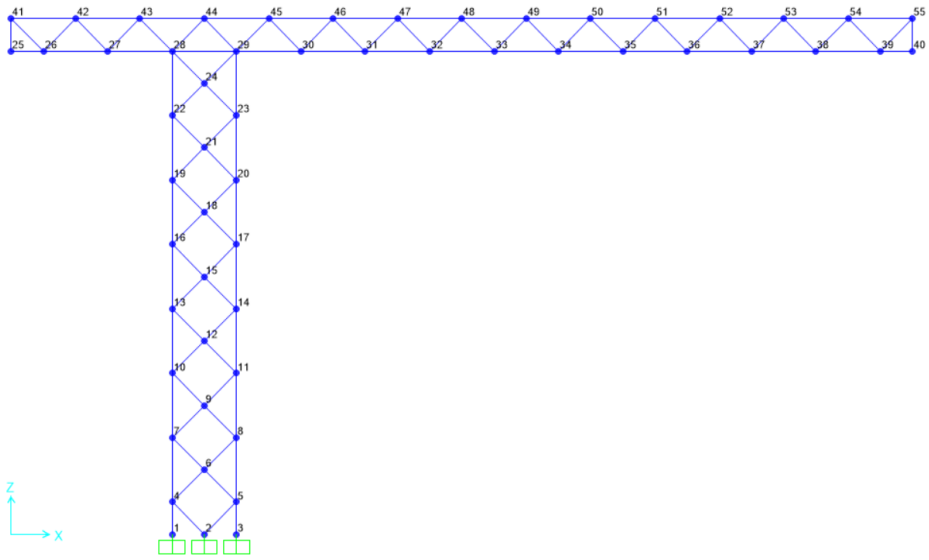


Figure 1: Finite Element Model of the tower crane

The monitored nodes, assembled in the Group 1 inside of the FE model, are those on the upper current of the cantilever truss beam, as shown in figure 2.

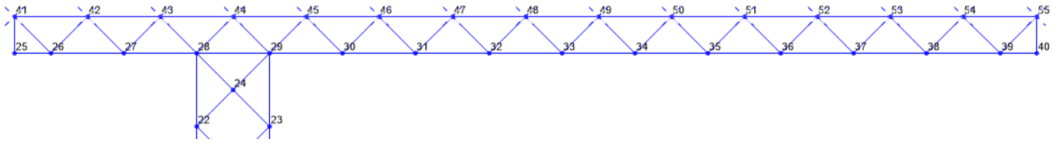


Figure 2: Selection of the monitored points

The FEM model of the crane tower is imported in MuDI software, so that its data can be correctly acquired by the platform.

In order to start with damage identification, natural frequencies and mode shapes of undamaged structure were calculated. A damage is simulated in the frame 98, between the nodes 47 and 48 (figure 3), by reducing its cross-section area of 20%. Then, natural frequencies and mode shapes of the damaged structure are calculated also for this new damaged configuration of the crane model.

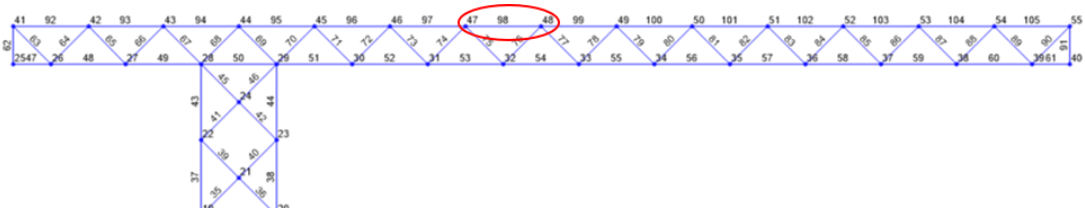


Figure 3: Damaged element

The result of the damage identification level 1 shows that the area around the seventh element, which corresponds to the frame 98, is the one with the highest damage index. As said before, the result is obtained by comparing the measured ratios (Fig. 4) and the characteristic ratios (Fig. 5) of the first three vibration modes, related to the first frequency.

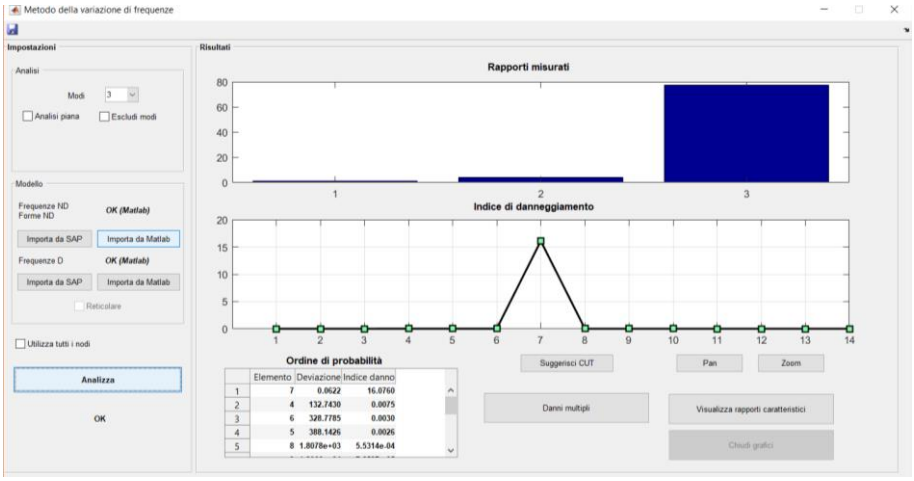


Figure 4: Result of the damage identification level 1

After, also damage identification level 2 is performed and the node 48, belonging to the Group 1 (the monitored points), is identified as that damaged.

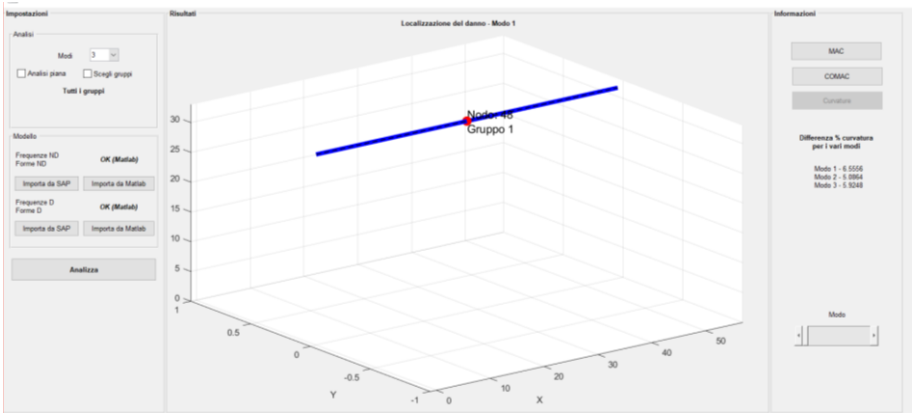


Figure 5: Result of the damage localization level 2

The MAC index between damaged and undamaged mode shapes is calculated for the first three vibration modes. It can be noticed that the same order modes are perfectly correlated. The correlation between the first and the second mode is very high ad almost equal to one, because the two mode shapes of the monitored side of the structure are very similar (see figure 6).

MAC

Damaged modes	1	2	3
1	1	0.98	0.43
2	0.98	1	0.42
3	0.42	0.41	1
	1	2	3

Undamaged modes

Table 1: MAC index for the first three vibration modes

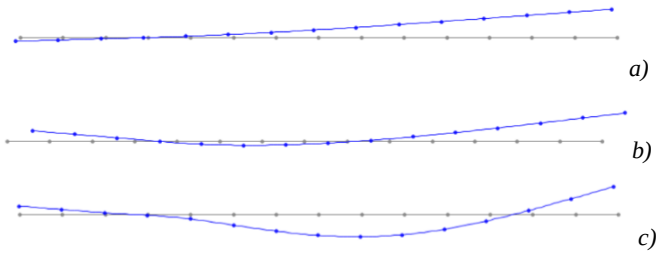


Figure 6: *a)* first, *b)* second and *c)* third mode shape

The two levels performed allowed to select the most likely damaged elements. These elements were renamed as Group1, Group2, Group3, Group4, Group5 (figure 7). Damage quantification is performed through an iterative process: it consists in updating a multiplier parameter of the cross section area of each selected element and making a comparison between the natural frequencies and mode shapes of the damaged structure model and of the updated model. The process of model updating is stopped once a combination of parameters that minimizes the difference between the two models is reached.

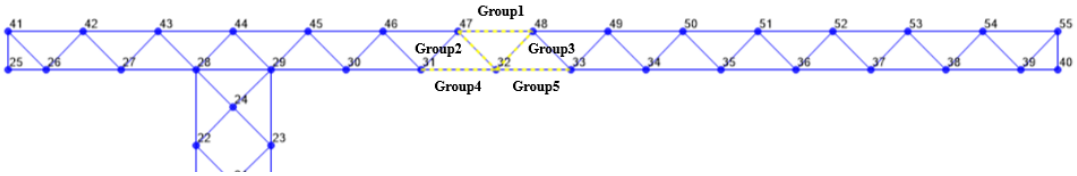


Figure 7: Most probable damaged elements

As shown in figure 8, modal updating is able to find the multiplier that reduces the cross section area of the imposed percent reduction.

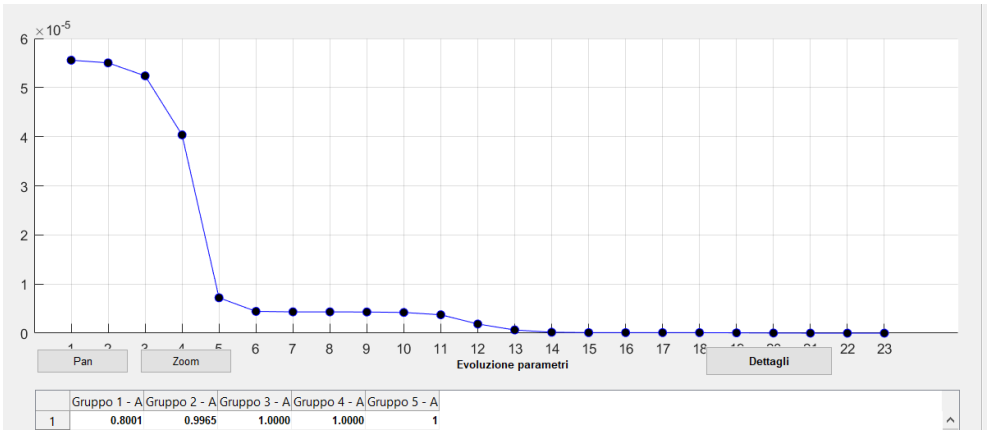


Figure 8: Results of model updating

In order to test the sensitivity of the proposed method, the 98th frame is divided into four sections (figure 9) and a damage is imposed in the first of them by reducing its cross section area of 20%. The process of damage identification is performed again. The results of the first two levels of damage identification show negligible differences respect to the previous test case.

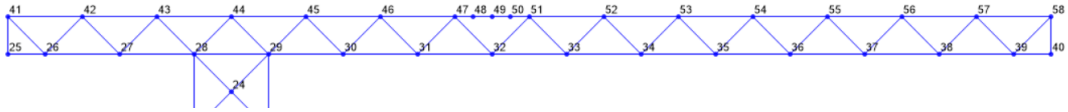


Figure 9: Structure with the divided 98th frame

After model updating is performed on a group of possible damaged elements (figure 10).

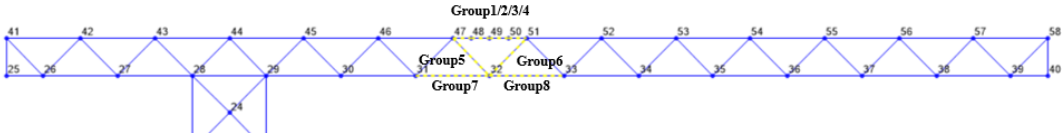


Figure 10: Defined groups for model updating of the second test case

Damage quantification results are less precise with respect to the previous case. Nevertheless, the damaged frame is identified and the reducer multiplier is estimated. This estimation is 0.9352, by using an error tolerance of 1x10^{-6} and 0.8542 with an error tolerance of 1x10^{-10}. This happens because the software stops to update the model when the error is smaller than the tolerance.

MuDI approach is performed again with a damage of 10%. In addition, in this case the level 1 and level 2give almost the same results of the previous cases and the model updating shows a good estimation of the reducer multiplier: 0.9367.

4 CWT theoretical background: wavelet analysis and damage detection method

In this section, the background of the damage identification method based on CWT is discussed.

CWT of a one-dimensional signal *f(t)* is defined by the following equation [7]:

$$C_{s,\tau} = C(s,\tau) = |s|^{-p} \int_{-\infty}^{+\infty} f(t)\bar{\psi}\left(\frac{t-\tau}{s}\right) dt \tag{5}$$

where $\psi(t)$ is called mother wavelet, $\bar{\psi}$ is its complex conjugate, and it has the following two properties:

$$\int_{-\infty}^{+\infty} \psi(t)dt = 0 \ , \int_{-\infty}^{+\infty} |\psi(t)|^2 \, dt < \infty \tag{6}$$

The mother wavelet function can be scaled and expanded by the parameter *s* and it can be translated by the parameter τ:

$$\psi_{s,\tau}(t) = |s|^{-p} \, \psi\left(\frac{t-\tau}{s}\right) \tag{7}$$

Symbol $C_{s,\tau}$ indicates the wavelet coefficient, which depends on the *s* and τ parameters.

Wavelets are band-limited functions and the convolution integral is equivalent to a band-pass filter. The parameter τ localizes the wavelet and the parameter *s* is proportional to the inverse of the wavelet Fourier spectrum central frequency.

Wavelet analysis allows detecting instantaneous changes in a signal. In fact, a relationship exists between the number of vanishing moments of a particular wavelet and the identification of a discontinuity in a function, or within any of its derivatives [6-11].

The identification of damage is carried out identifying the maxima of the wavelet coefficients at different scales. The elastic waves travelling in a structure are partly reflected by the local structural variation due to a localized damage. A perturbation in the structure response is observed and it appears as a peak of the wavelet coefficients: its time duration is correlated to the adopted scale parameter. Unfortunately, a general and robust procedure cannot be based only on a peak finder algorithm, because boundary effects and other disturbances can be appear and corrupt the analysis result.

The damage identification procedure based on CWT needs the response of the structure at certain observation points. Here, these responses are not measured, but they are calculated by the normal modes obtained by a FEM. In our case, the number of modes used to find the physical response is very relevant. In fact, the singularities in the signal of the structure displacement due to the presence of a damage can emerge only if the normal modes combined to construct the response show these singularities. Therefore, it is essential to arrange a suitable FEM mesh and a linear combination of modes up to a convenient order. More simply, the linear combination can be stopped not before the first mode showing these singularities and the FEM mesh must be sufficiently thick to be representative of this higher order mode. Clearly, these considerations are necessary having to work with numerical models and they would be transparent to an analysis of experimental responses.
Hence, the eigenvalues and the eigenvectors, φ_n, are computed by an FE model quiet similar to that used by the MuDI approach and they are employed to compute the response, *w(xo,t)*, when the structure is excited by a running load [12].

The considered load travels on the upper elements of the crane with velocity *v* = 0.025 m/s and it is simulated by a Gaussian distribution as follows:

$$F = a \cdot e^{-\frac{[x-(vt)]^2}{c^2}} \tag{8}$$

with amplitude a =5 and width c = 0.5

The generalized coordinates of the response, q_n, are calculated by the set of independent equations below:

$$\ddot{q}_n + 2\delta_n\omega_n\dot{q}_n + \omega_n^2 q_n = a \cdot \int_0^L \varphi_n(x) e^{-\frac{[x-(vt)]^2}{c^2}} dx \tag{9}$$

and the physical displacement is:

$$w(x_0, t) = \sum_{n=1}^{N_m} \varphi_n(x_o) q_n(t) \tag{10}$$

The displacement of equation (10) is polluted by a numerical random noise proportional to the 10% of the standard deviation of the signal.

5 CWT results

The CWT analysis is performed using ®MATLAB Wavelet Analyzer tool in correspondence of the four observation points of table 2.

Point	**O_1**	**O_2**	**O_3**	**O_4**
Position	16 m	21.6 m	27.2 m	32.8 m

Table 2: Observation points in CWT analysis.

The analysis is performed considering the load travelling on the upper elements of the crane (from the beginning to 52 m) and the simulated damage is a reduction of 20% of the cross-section area between the nodes at 24 m and 28 m (as shown in figure 3). As can be notice from the CWT analysis results of the undamaged and damaged structure, shown respectively in figure 11 and figure 12, the presence of damage can be easily identified for almost all the observation points without the knowledge of the undamaged structure.

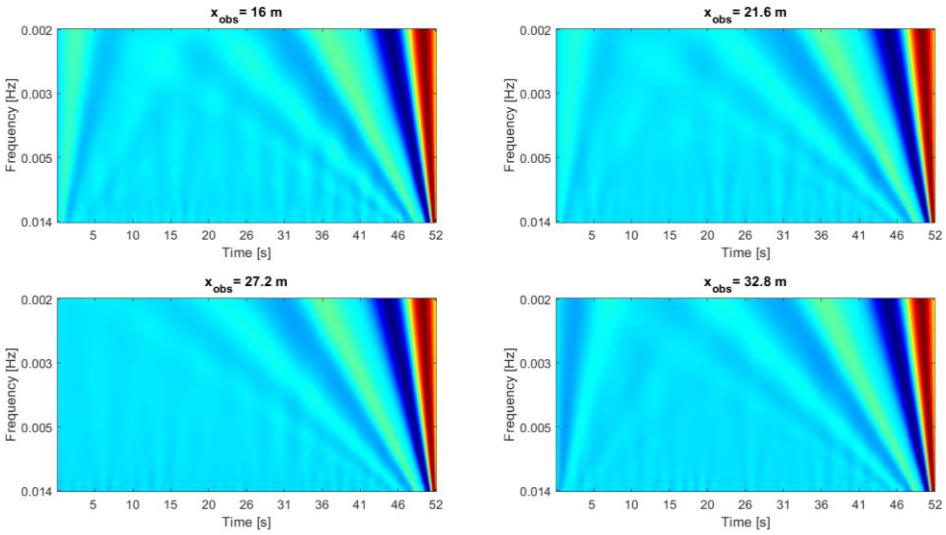


Figure 11: CWT analysis of undamaged structure

The analysis is performed in correspondence of the frequency range excited by the considered load, indeed in this range of scales the CWT transform highlight the discontinuity introduced by the presence of the damage.

The results in figure 12 show that the needed number of observation points is lower compared to the MuDI method shown in the previous sections, but cannot be less than two. In fact, considering only the first observation point the CWT analysis does not allow to identify the presence of the damage.

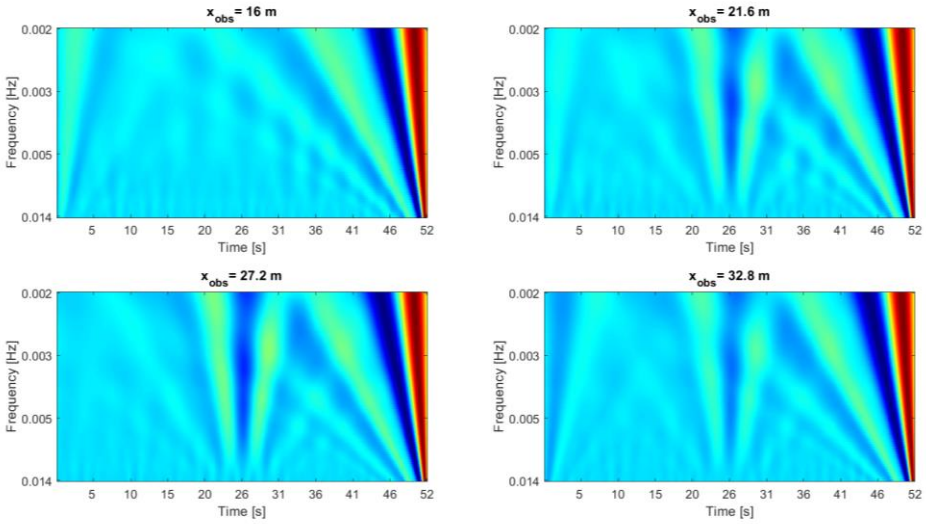


Figure 12: CWT analysis of damaged structure

Figure 13 shows the comparison of the coefficient lines, of all considered scales, calculated in three different conditions: the undamaged structure, the structure with a reduction of cross-section area equal to the 10% and with a reduction of cross-section area equal to 20%.

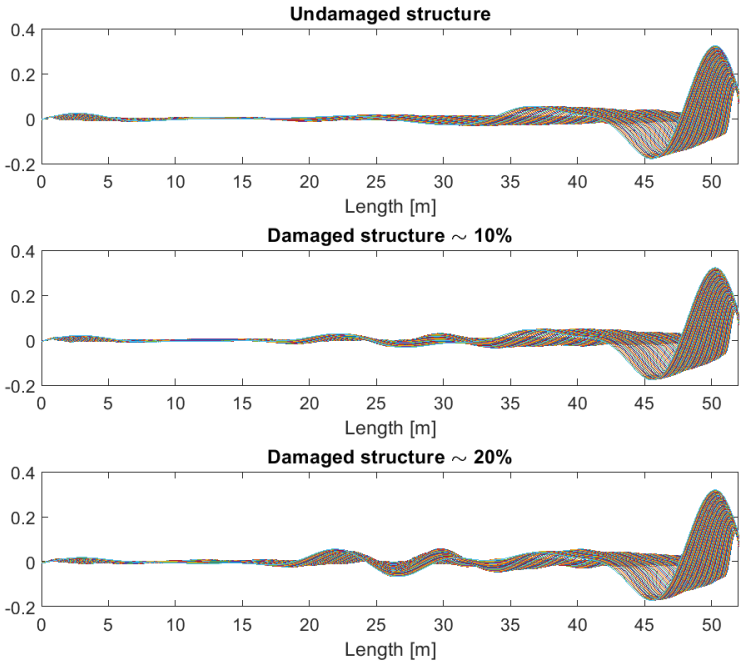


Figure 13: Comparison of the coefficient lines of the undamaged and damaged structure obtained from the CWT analysis of the response measured at 21.6 m.

As expected, the amplitude of the coefficients in correspondence of the damage increases with the severity of the damage itself.

6 Conclusions

Two structural damage identification techniques are studied. The MuDI approach uses natural frequencies, mode shapes and an updating technique to localize the damage and to quantify its severity. The CWT approach allows identify the damage position by the response of the structure. The analysis is performed by numerical data, the results of a test structure FEM. Both the approaches give good results and they are compared together with their efficiency.

It is important to focus on some limitations and advantages of the two methods. MuDI gives a complete identification of the damage, localization and quantification. On the contrary, in operative conditions it needs a high number of sensors to identify the natural modal parameter of the structure by an operational modal analysis technique. CWT localizes the damage and it does not quantify its severity, but in operative conditions, it needs a few number of sensor, because this approach uses the structure response and it does not need natural frequencies and mode shapes. This observation leads to consider the possibility of using the two approaches in cascade: CWT localizes the damage more efficiently; MuDI can take advantage of the CWT localization in order to quantify it.

Acknowledgements

This research is supported by grants from University of Rome “La Sapienza” and University Roma Tre.

References

[1] G. Acunzo, S. Gabriele, D. Spina, C. Valente, MuDI: A Multilevel Damage Identification Platform, in B.H.V. Topping, P. Iványi, (Editors), Proceedings of the Twelfth International Conference on Computational Structures Technology, Civil-Comp Press, Stirlingshire, UK, Paper 123, 2014. doi:10.4203/ccp.106.123

[2] A. Rytter, Vibration based inspection of civil engineering structures, Department of Building Technology and Structural Engineering, Aalborg University, Denmark, 1993

[3] G. Hearn, R.B. Testa, Modal Analysis for Damage Detection in Structures , Journal of Structural Engineering, 1991

[4] A.K. Pandey, M. Biswas, M.M. Samman, Damage Detection from Changes in Curvature Mode Shapes, Journal of Sound and Vibration, 1991

[5] M.I. Friswell, J.E. Mottershead, Finite Element Model Updating in Structural Dynamics, Kluwer Academic Publishers, 1995

[6] N. Roveri, A. Carcaterra. Unsupervised identification of damage and load characteristics in time-varying systems. Continuum Mechanics and Thermodynamics, 27.4-5: 531-550, 2015.

[7] N. Roveri, A. Carcaterra. Damage detection in structures under traveling loads by Hilbert–Huang transform. Mechanical Systems and Signal Processing, 28: 128-144, 2012.

[8] W.J. Staszewski, Structural and mechanical damage detection using wavelets. The Shock and Vibration Digest; 30, 6, 457–472, 1998.

[9] M. Rucka, K. Wilde, Application of continuous wavelet transform in vibration based damage detection method for beams and plates. Journal of Sound and Vibration, 297, 536-550, 2006.

[10] G.Kaiser, A Friendly Guide To Wavelets, New York, Birkhäuser, 1994

[11] S. Milana, N. Roveri, A. Culla, A. Carcaterra, Structural health monitoring of a plate by continuous wavelet transform, Proceeding of Novem2018, 7-9 May 2018 Ibiza.

[12] Meirovitch, Leonard. Elements of vibration analysis. McGraw-Hill Companies, 1975.

Transmissibility based structural assessment using deep convolutional neural network

S. Cofré[1], P. Kobrich[1], E. López Droguett[1],V. Meruane[1]
[1] Universidad de Chile, Department of Mechanical Engineering
Beauchef 851, Santiago, Chile
e-mail: **vmeruane@ing.uchile.cl**

Abstract

This article presents novel deep Convolutional Neural Networks (CNN) approach for transmissibility based damage assessment in structures. The proposed approach operates on images that are generated from the structure's transmissibility functions so to exploit the CNNs' image processing capabilities and thus to automatically extract and select relevant features to the structure's degradation process. These feature maps are then fed into a multi-layer perceptron to achieve damage assessment. The proposed approach is validated and exemplified by means of two case studies involving a mass-spring system and a structural beam where training data is generated from finite element models that have been calibrated on experimental data. The results indicate that the proposed CNN based approach delivers satisfactory damage localization and quantification and thus being an appropriate tool for accurate damage assessment.

1 Introduction

One of the main challenges in vibration-based damage assessment is the selection of an appropriate metric of the system response that is sufficiently sensitive to small damage. This metric can be constructed in the time, frequency or modal domains, being the latter two the most broadly used. The idea of directly using the transmissibility functions (TF) has attracted many researchers [1]–[19]. TF relate the responses between two points of the structure. Among all dynamic responses, transmissibility functions are the easiest to obtain in real-time because the in-situ measurement is straightforward. The advantage is that no modal extraction is necessary, thus contamination of the data with modal extraction errors is avoided and they are identified from response only data. Therefore, it does not involve the measurement of excitation forces.

Worden [1] presented the first investigation of TF as indicators of structural damage, where it was shown that for a simple lumped-parameter system, transmissibilities are able to detect small stiffness changes. Since then, the research group headed by Worden and Manson has done extensive research in this topic. In [2], Worden et al. used a representative aircraft skin panel to investigate the sensitivity of transmissibilities to damage. Damage detection was realized via a statistical outlier analysis. Manson et al [3], [4] verified the performance of the outlier analysis technique to detect damage in a Gnat aircraft inspection panel. Damage was simulated by holes and saw-cuts across the panel. About the same time as Worden, Zhang et al [20] proposed a procedure to detect structural damage using changes in the TF, which were derived from structural translations and curvatures, being the latter the most sensitive to damage. Johnson and Adams [6] also studied the use of TF for detecting, locating and quantifying damage. They demonstrated that since transmissibility functions are determined solely by the system zeroes (antiresonant frequencies), they are potentially better indicators of localized damage. These results were employed to develop a framework for transmissibility-based damage identification using smart sensor arrays [7]. Maia et al. [8] presented a methodology for computing the transmissibility matrix from responses only. They showed that TF are sensitive to damage, making them a possible approach for damage assessment. Sampaio et al. [9] implemented a similar approach to explore the ability of transmissibilities in detecting and localizing damage. They concluded that it is possible to detect sensitive changes to damage, but further research is needed. In a later work, Maia et al. [10] compared two damage indicators constructed with TF and with

frequency response functions (FRF). They concluded that the method based on transmissibility measurements is much more sensitive to damage.

The most successful applications of vibration-based damage assessment are model updating methods based on global optimization algorithms [21]–[24]. The basic assumption is that damage can be directly related to a decrease in stiffness in the structure. Nevertheless, these algorithms are exceedingly slow, making them impractical for real-time applications. As an alternative to these methods, Neural Networks (NN) have been proposed as a tool for damage identification [25]–[27]. In recent years, the interest in applying machine learning algorithms for transmissibility-based damage assessment has increased [28], being NN the most frequently used. However, the number of spatial response locations and spectral lines in transmissibility measurements is overly large for traditional NN applications. The direct use of transmissibilities leads to NN with many input variables and connections, thus rendering them until now impractical. Hence, it has been necessary to extract features from the transmissibilities and then use these features as inputs to the NN. Indeed, Worden [12] trained an auto-associative NN for damage detection (novelty detection). The feature vector was constructed from transmissibility data, selecting spectral lines centered at a particular peak and then using PCA to reduce the dimension of the data set. Chen et al. [13] used a comb data sampling technique to acquire amplitude and phase data of transmissibility functions randomly. These data were the input to a damage classification NN, which was validated using simulated data of a sandwich beam and a frame structure. Pierce et al. [14] and Worden et al. [29] identified spectral line windows with the largest variations due to damage as features to train a NN-based damage classifier. In both cases, the classifier was evaluated with experimental data of the aircraft (Gnat) wing. Lai and Perera [16] trained a damage classification NN using damage indicators extracted from the power spectrum density transmissibility. This methodology was evaluated using simulated data of a beam. Meruane [17] trained an online sequential extreme learning machine (OS-ELM) algorithm to detect, locate and quantify structural damage using antiresonant frequencies extracted from transmissibility measurements. The approach is illustrated with two experimental cases: an eight-degree-of-freedom (DOF) mass-spring system and a beam under multiple damage scenarios. Meruane and Ortiz-Bernardin [18] presented another algorithm for real-time damage assessment that uses a linear approximation method in conjunction with antiresonant frequencies that are identified from transmissibility functions. The performance is validated by considering three experimental structures: an eight DOF mass-spring system, a beam, and an exhaust system of a car.

All the aforementioned works rely on identifying and extracting proper features. Nonetheless, the feature extraction process requires specialized knowledge of the problem under investigation and the best selection is case sensitive. It is here where deep learning techniques have been proposed for automatic feature extraction and fault diagnostic analysis. Indeed, since 2015, deep learning techniques have proven to be competitive with traditional machine learning techniques when dealing with fault diagnosis of rotating machines such as in [30]–[40].

In this paper, we propose a novel deep CNN based approach for the detection, localization and quantification of structural damage that operates on transmissibility functions. The main advantage over previous investigations is that this approach makes automatic feature extraction. Therefore, the input to the proposed algorithm are the full transmissibility functions. The proposed CNN based approach is validated and exemplified by means of two case studies: an eight degree of freedom (DOF) mass-spring system and a beam under multiple damage scenarios.

2 Deep Learning and Convolutional Neural Networks

Deep learning is representation learning commonly used as supervised learning to analyze previously labeled data through either regression or classification. Since 2012, deep learning has become a popular approach for numerous tasks involving image recognition and computer vision, due to its high performance which rivals and surpasses human accuracy. Deep learning techniques have shown superior performance in image classification [41], natural sentence classification [42] and image segmentation [43] than previous state of the art methods mainly based on shallow architectures.

To understand how convolutional neural network works, first it is important to know how a one-layer Feed Forward Network (FFN) works. Consider, for example, the neural network shown in Figure 1. A FFN takes the input data vector $\boldsymbol{x}$, a weight matrix $\boldsymbol{W}^1$ (for the input layer) and a bias vector $\boldsymbol{b}^1$ to obtain a vector of values for the hidden layer. This is represented by using Equation 1, where f is an activation function such as the sigmoid function or a rectifier linear unit (ReLU) function. Then, the output vector $\boldsymbol{y}$ is computed from the hidden unit's vector $\boldsymbol{h}$ and an additional weight matrix $\boldsymbol{W}^2$ and bias vector $\boldsymbol{b}^2$ (characterizing the connections between the hidden and the output layers) using Equation 2.

$$\boldsymbol{h} = f(\boldsymbol{W}^1\boldsymbol{x} + \boldsymbol{b}^1) \tag{1}$$

$$\boldsymbol{y} = f(\boldsymbol{W}^2\boldsymbol{h} + \boldsymbol{b}^2) \tag{2}$$

The weights and biases are then obtained by minimizing the error between the predicted value and the real value based on a training dataset. The error is represented by a cost function, where regression models usually use the mean squared error. The minimization is usually done with gradient descent method and the gradients are calculated with the backpropagation algorithm [44].

The FFN architecture can be expanded for use in deep learning problems by adding additional hidden layers or increasing the number of hidden units. Deeper FFNs allow for a higher level of abstraction but require more computational resources.

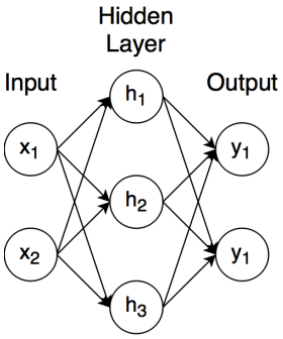


Figure 1: Feed Forward Neural Network with 3 hidden units and 2 output values.

A CNN is a deep learning neural network that uses convolution operations instead of matrix multiplication in its layers. The convolution is performed using a weights matrix $\boldsymbol{K}$, also known as filter or kernel. The kernel is used to obtain a feature map $\boldsymbol{S}$ from the input vector **A** using the convolution operation as shown in Equation 3.

$$\boldsymbol{S} = \boldsymbol{A} * \boldsymbol{K} \quad \text{where} \quad \boldsymbol{S}(i,j) = \sum_n \sum_m \boldsymbol{A}(i-m, i-n) \cdot \boldsymbol{K}(m,n) \tag{3}$$

Figure 2 shows a representation of the convolution operation using a 2x2 kernel and a 3x3 input data matrix to obtain a 2x2 output matrix. A bias matrix $\boldsymbol{B}$ is added to the convolution and an activation function is applied to the result to form the feature map $\boldsymbol{H}$ as shown in Equation 4. The training of the weights and biases can be interpreted as a feature extraction. If a value in the feature map gets activated, it indicates that an important learned feature is in that position. In the case of image analysis, an activation in the feature map can indicate the location of features like edges or specific shapes. In the context of vibration analysis, these local features identification capabilities can be used to locate peaks in the transmissibility functions which are later used to characterize the damage state of a system.

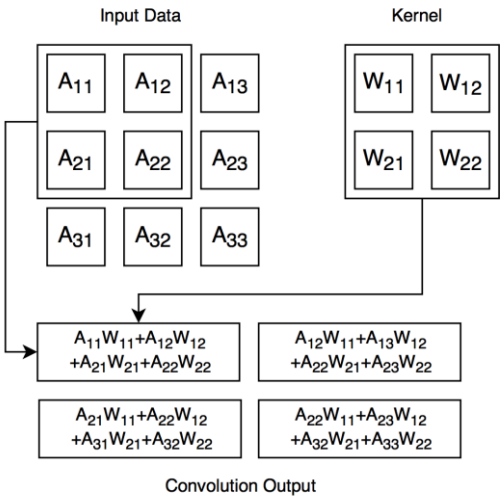


Figure 2: Convolution operation of a 3x3 input matrix and a 2x2 kernel.

A convolution layer in a CNN consists of several kernels and biases applied to a single input matrix to generate a set of feature maps in a hidden layer. Every component in the feature map is computed using the same kernel thus reducing the amount of weights that need to be calculated. Also, each component of the output feature map is calculated only from a subset of the input matrix reducing the amount of connections and, therefore, decreasing the required computation resources. To achieve higher levels of abstraction and more complex relations between features, feature maps can be used as input to adjacent convolution layers.

$$\boldsymbol{H} = f(\boldsymbol{A} * \boldsymbol{K} + \boldsymbol{B}) \tag{4}$$

The last section of a CNN is a feed forward neural network that is responsible for generating the predicted labels as the output vector. Figure 3 shows an architecture of a CNN with three 5x5 convolutional filters as the first layer, one 2x2 pooling layer and a fully connected feed forward layer. The CNN is trained in the same way as a FFN defining a cost function and then preforming gradient descent to minimize the cost.

Due to the usually high degrees of freedom of CNN architectures, one should prevent overfitting, i.e., over adjustment of the weights to the training data resulting in poor generalization performance to unseen data. This can be accomplished via regularization techniques. One of commonly used such techniques to tackle overfitting when training CNN architectures is dropout [20]. Furthermore, another regularization technique is early stopping, which stops the training cycle when training and validation errors begin to diverge. These two techniques together greatly reduce overfitting and prevent the network from identifying noise and use it as a distinguishing feature.

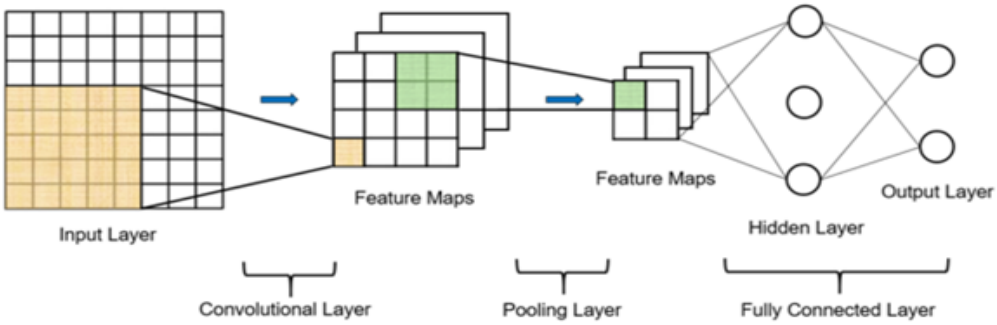


Figure 3: CNN architecture illustration.

3 Proposed CNN Approach for Structural Damage Localization and Quantification

The proposed approach is intended to analyze any structure that can be divided into a determined number of elements for identifying and quantifying the damaged elements by processing transmissibility functions. In the following sections, we discuss the different modeling choices made for the damage representation, input data format and the proposed CNN architecture.

3.1 Structural Damage

Damage is represented as a reduction in the stiffness of an element of the structure. This is a simple representation of structural damage, but has demonstrated good results in damage identification algorithms [45]. If the element's stiffness reaches zero, it is considered to have catastrophic failure. Defining y_i as the stiffness reduction of element i, undamaged and completely damaged states can be represented by y_i=0 and y_i=1, respectively. This definition can be expressed in Equation (5), where $\mathbf{K}_i$ and $\mathbf{K}_i^d$ are the undamaged and damaged stiffness of the i-th element, respectively.

$$\mathbf{K}_i^d = (1 - y_i)\mathbf{K}_i . \tag{5}$$

3.2 Transmissibility Function Images as Input Data

In vibration analysis, transmissibility functions (TFs) are defined as the ratio in the frequency domain between two responses when an excitation force is applied. TFs have shown a strong relation with a system's damage and have been previously used for damage assessment in different studies [1]–[4], [6]–[10], [12]–[14], [16]–[20], [28], [29]. TFs can be computed from experimental measurements or from a numerical model of the structure. Since it is not feasible to produce large enough data sets to train a CNN from experiments, the CNN have been trained with data generated from numerical models of the structures and then have been validated with experimental data.

To fully take advantage of the CNNs capabilities local feature extraction, the TFs are represented by small sized images which include the information of the TF represented by the intensity of each pixel. The images only contain the values of the logarithmic magnitude of the TF at a given frequency range. Figure 4 (a) shows 10 different transmissibility functions measured on a structural beam on a 0-2000 Hz frequency range.

In Figure 4 (b) these measurements were converted to image format. The image has a size of 10x96 pixels, were each row is a distinct TF and the frequency range was converted from 2000 to 96 frequencies using a bi-cubical interpolation. The proposed CNN model is trained to use the TF in this image format to localize and quantify damage.

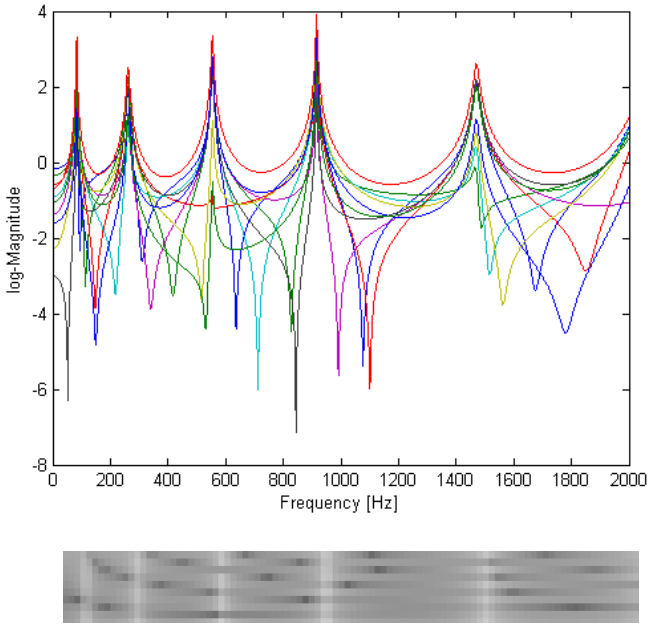


Figure 4: Ten TFs measured in a structural beam (a) and the image representation of the TFs used as input by the CNN (b).

3.3 The Proposed Convolutional Neural Network Architecture

The proposed architecture encompasses a two-layer CNN that is used for automatic feature extraction purposes. For the first convolutional layer, 32 different filters are used, whereas 64 filters are used in the second layer. The first convolutional layer's filters sizes are 1 pixel wide with a height equal to the number of transmissibility functions' pixels. Padding, where the filter is bounded within the image matrix when computing the convolution, is not applied. The aim of this architecture is to have the first layer extracting meaningful relations between different transmissibility functions at a given frequency; the second convolutional layer, with filter size of 1x5 pixels, is designed to detect peaks and dips in the input feature maps that are related to the anti-resonant frequencies. After each convolution, a ReLU (Rectified Linear Unit) function is applied as the activation function.

The assessed structure is divided into elements, and each element can have an amount of damage represented by a real number. Therefore, the proposed architecture also has a feed forward neural network that processes the feature maps provided by the last convolutional-pooling layers. Each output node of the neural network provides an estimate of the amount of damage in the corresponding structural element.

Figure 5 shows a diagram of the proposed deep CNN architecture where 10 different TF measurements are used. Notice that the input data consists of 10x96 pixels images. Using this architecture, the model requires training a total of 5.98×10^6 weights and biases.

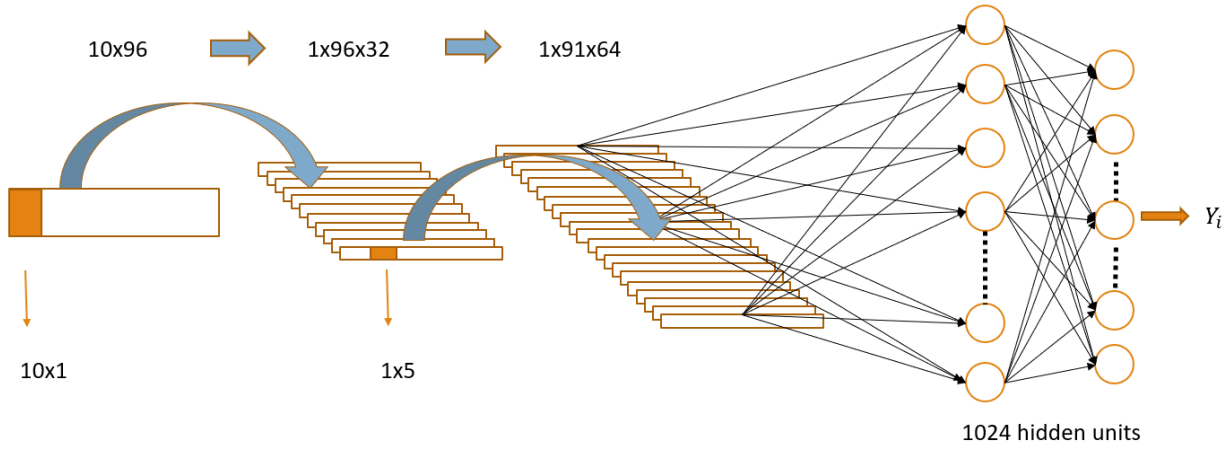


Figure 5: Deep CNN architecture for damage localization and quantification.

4 Case Study 1: Spring-Mass Structure

Los Alamos National Laboratory (LANL) designed a structure to study different vibration based damage identification techniques [46]. The setup consists of an 8-DOF spring-mass system where identical masses are separated by identical springs as shown in Figure 6. Each mass consists of an aluminum disk with a 76.2 mm diameter and 25.4 mm thickness. The first mass is also connected to a shaker that provides the excitation force. Each mass has an accelerometer that measures the horizontal acceleration data that is used to obtain the transmissibility functions. Experimental data is acquired in a frequency range from 10 Hz to 110 Hz with a frequency resolution of 0.125 Hz. Note that the possible rotation of the masses is not included when obtaining the transmissibility functions. The physical properties of the structure used in the finite element model for generating the training datasets are shown in Table 1.

Table 1 Experimental setup mass and strength values

Mass 1	559.3 g
Masses 2-8	419.4 g
Spring Young Modulus k	56.7 kN/m

The FE model is built using concentrated masses for the discs and linear spring elements for the springs, it considers only horizontal displacement and has a total of seven spring elements and eigth degrees of freedom (see Figure 6). In this system, damage is represented by a spring's stiffness reduction (e.g., change of one of the spring for a softer one). Thus, each spring represents one element of the system, hence, a stiffness reduction in one of the springs is equivalent to the damage level y_i described in Section 3.1. For instance, a 20% reduction on the *i*-th spring's stiffness would correspond to a damage level $y_i = 0.2$.

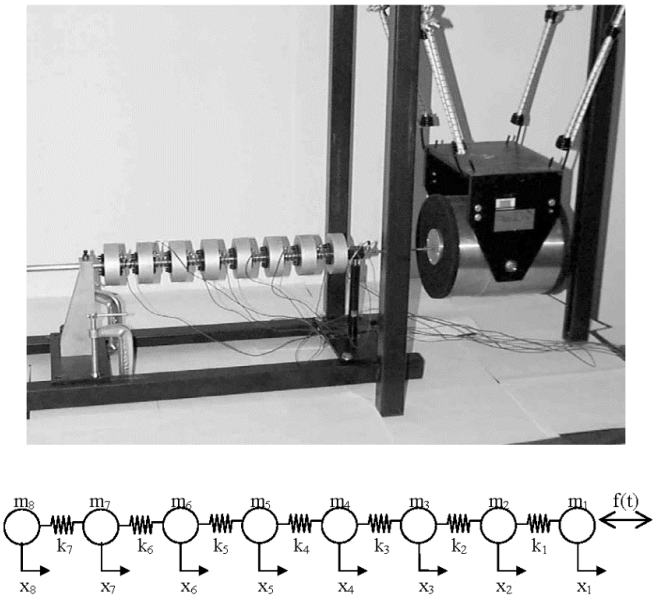


Figure 6: 8-DOF Mass-Spring system at Los Alamos National Laboratory.

4.1 Results

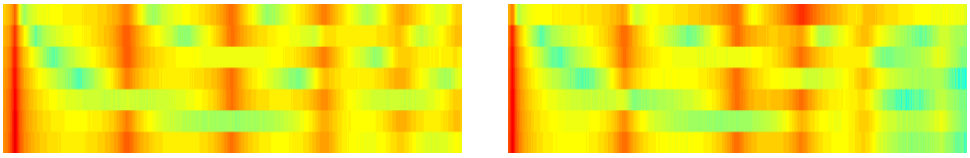
The numerical model of the mass-spring system has been calibrated with experimental data, so the model can satisfactorily reproduce the experimental measurements. This model is then used to generate large amounts of training data with different damaged elements and corresponding damage magnitudes. To deal with the problem of randomness in real measurements and to improve the robustness of the proposed models to randomness, random amounts of noise were added to the input signal generated by the FE models. The noise was applied as a percentage of the magnitude of the TF and the amount of noise added was randomly selected from 0 to 6 percent uniformly distributed.

The proposed damage assessment algorithm was trained considering up to one damaged element, using a total of 74,000 images. In this case, the system possesses eight elements, and transmissibility functions were obtained by exciting the first mass of the system with a shaker and measuring the response from the seven remaining masses, thus resulting in a total of seven transmissibility functions.

An example of the images generated from the transmissibility functions is shown in Figure 7, where Figure 7 (a) shows an image representation of the seven transmissibility functions corresponding to the system with no damaged elements, whereas Figure 7 (b) illustrates a representation of the these transmissibility functions when one element is randomly damaged. The colors represent the logarithm of the magnitude of the transmissibility functions at each frequency.

Three different metrics are implemented to evaluate the model's performance: Mean Sizing Error (MSE), Damage Missing Error (DME) and False Alarm Error (FAE), which are all defined in [47]. Table 2 presents the overall values obtained for the MSE, DME and FAE, whereas Figure 8 show the DME and FAE for ranges of 10% damage when evaluating the trained models on the test set. The results show that that all false alarms and missing damages lie strictly in the range between 0% and 10%. Thus, the results obtained when evaluating the test set show that the trained models are reliable when predicting damage level over 10% as these are detected with 100% accuracy.

For validation purposes, the damage localization and quantification performance of the proposed approach is evaluated using experimental data corresponding to the spring-mass system with a 55% damage level in the fifth element. These results are presented in Figure 9. We can see that the algorithm accurately predicts a 54% damage at the fifth element. Moreover, no false alarms where detected. These results were expected given the metrics presented in Table 2.



(***a***) **(b)**

Figure 7: Images for the spring-mass system with no damaged elements (a) and one randomly damaged element (b).

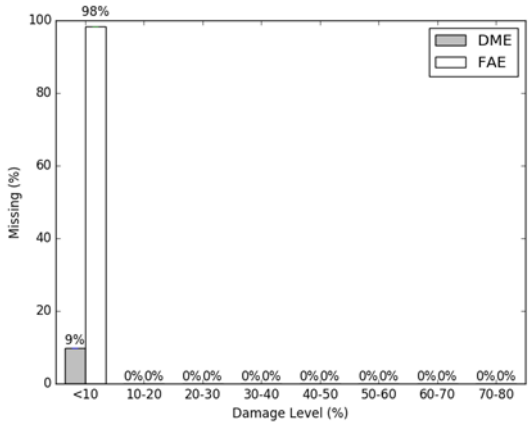


Figure 8: DME and FAE, spring series case study.

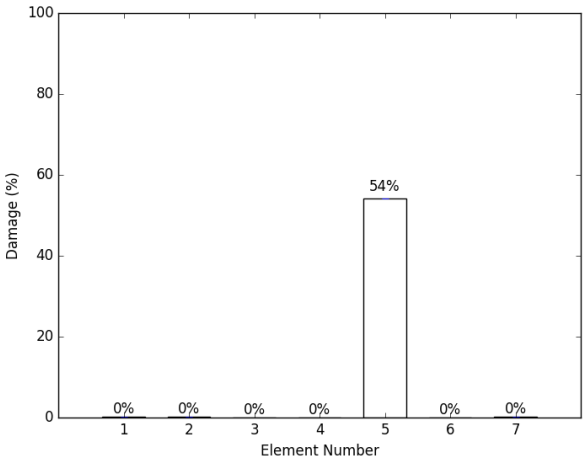


Figure 9: Predicted damage for the spring-mass system. Expected damage level of 55% at the fifth element

Table 2: Training results summary for the spring-mass system when evaluating the test set.

MSE [%]	DME [%]	FAE [%]
0.271	0.916	32.548

5 Case Study 2: Structural Beam

Meruane et al. [27] proposed an experimental setup to identify damage in a structural beam through transmissibility data and antiresonant frequencies. For this work, the experiment was implemented at the Laboratory of Mechanical Vibrations and Rotordynamics at the University of Chile. The experiment consists of a structural beam where damage is generated by saw cutting the beam. The transmissibility data is recorded with accelerometers along the structural beam.

Figure 10 presents the experimental beam of 1-meter longitude and a rectangular cross-section area of 25x10 mm2. Both ends of the beam are suspended on soft springs to simulate a "free-free" boundary condition. The excitation force is generated by a shaker at one end of the structure and the response is measured with 11 accelerometers (therefore 10 transmissibility functions are obtained). Experimental data is acquired for a frequency range from 1 to 2000 Hz with a frequency resolution of 1 Hz.

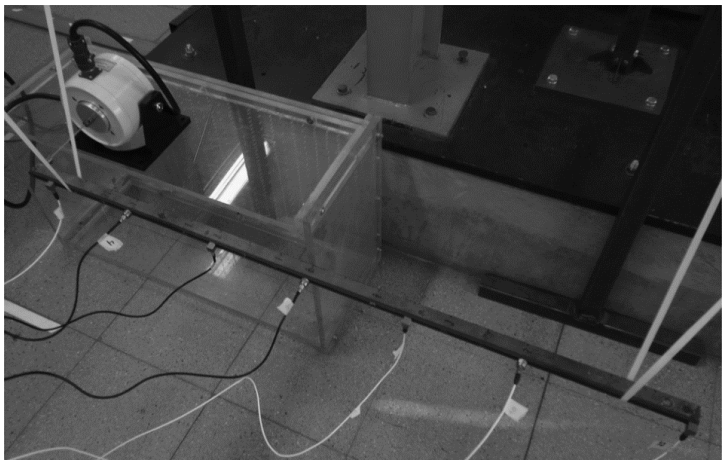


Figure 10: Experimental beam setup [18].

The beam is modelled using unidimensional beam elements with two nodes per element and two degrees of freedom (DOF) per node. The beam (and its finite element model) was divided into 20 elements of 5 cm each, as shown in Figure 11, resulting in a FE model with 42 DOF. The transmissibilities are computed using the translational DOF at nodes 1, 3, 5, ..., 21, being node 1 the reference.

To simulate stiffness reduction (i.e., damage), saw cuts of different lengths were inflicted in a set of beams. Four damage scenarios are studied, where damage scenarios 1 and 2 correspond to two different beams with one saw cut each (i.e., one damaged element), whereas damage scenarios 3 and 4 consist of two different beams with two and three damaged elements, respectively.

Since there is no direct relationship between saw cuts and stiffness reduction of the structure, as there was for the spring-mass series system discussed in the previous section, the damage level is represented by the saw cuts' length. Details for each scenario are provided in Table 3.

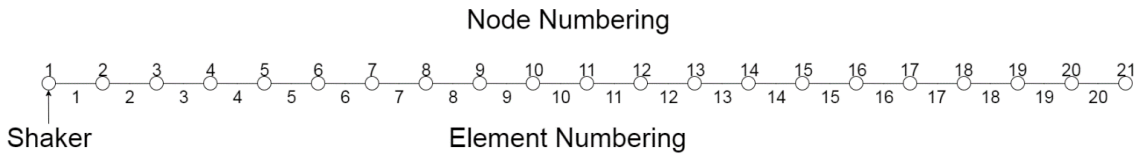


Figure 11: FEM element and node numbering.

Table 3: Experimental beam damage scenarios.

Damage Scenario	Number of cuts	Distance from the left side [mm]	Damaged Element	Cut depth [mm]
1	1	313	7	7
2	1	637	13	9
3	2	361	8	8
		812	17	15
4	3	363	8	13
		574	12	8
		696	14-15	6

5.1 Results

Similarly to the previous case study the finite element model is first calibrated with experimental data of the undamaged beam and then is used to generate large amounts of training data with different damaged elements and corresponding damage magnitudes. To simulate experimental measurements, the TFs generated with the numerical model are polluted with up to 6% random noise. The proposed damage assessment algorithm was trained considering up to three simultaneous damaged elements, using a total of 100,000 images model. In this case, there are 10 transmissibility functions available for 20 possible damage elements.

Figure 12 shows two examples of the generated images with ten transmissibility functions, where Figure 12 (a) represents a beam with no damage, and Figure 12 (b) is obtained from a beam with three randomly damaged elements.

The testing results are presented in Table 4, which shows the overall MSE, DME and FAE when evaluating the test set. Figure 8, on the other hand, shows the DME and FAE for ranges of 10% damage. From the results we can say that every element with a damage level above 20% can be accurately detected and quantified. Furthermore, the FAE values are higher than the DME for all the damage ranges, which indicates that false positives are more recurrent than false negatives for low damage levels, making the proposed CNN based approach a conservative one.

Now we turn our attention to the validation of the proposed approach in the context of the structural beam by using the experimental results shown in Table 3. Indeed, Figure 14 shows the predicted damage for every damaged scenario. The algorithm predicts the true damaged locations for all scenarios, but they tend to yield small false damages, all of them lower than 15% damage. Also, the algorithm tends to propagate the damage to adjacent elements.



(***a***) **(b)**

Figure 12: Images for Structural Beam with (a) no damaged elements and (b) three randomly damaged elements.

Table 4: Training results summary for the experimental beam.

MSE [%]	DME [%]	FAE [%]
1.334	6.70	57.55

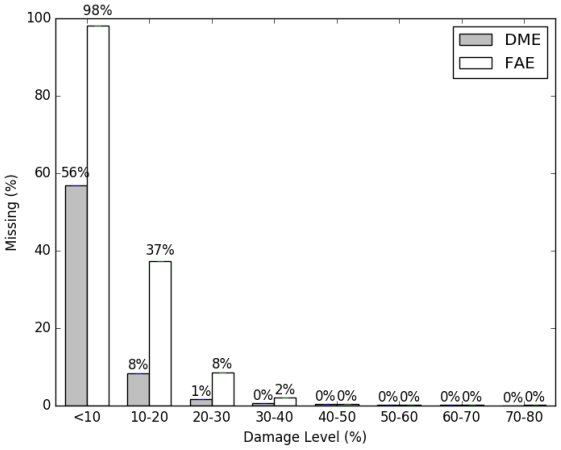


Figure 13: DME and FAE versus damage level for the structural beam

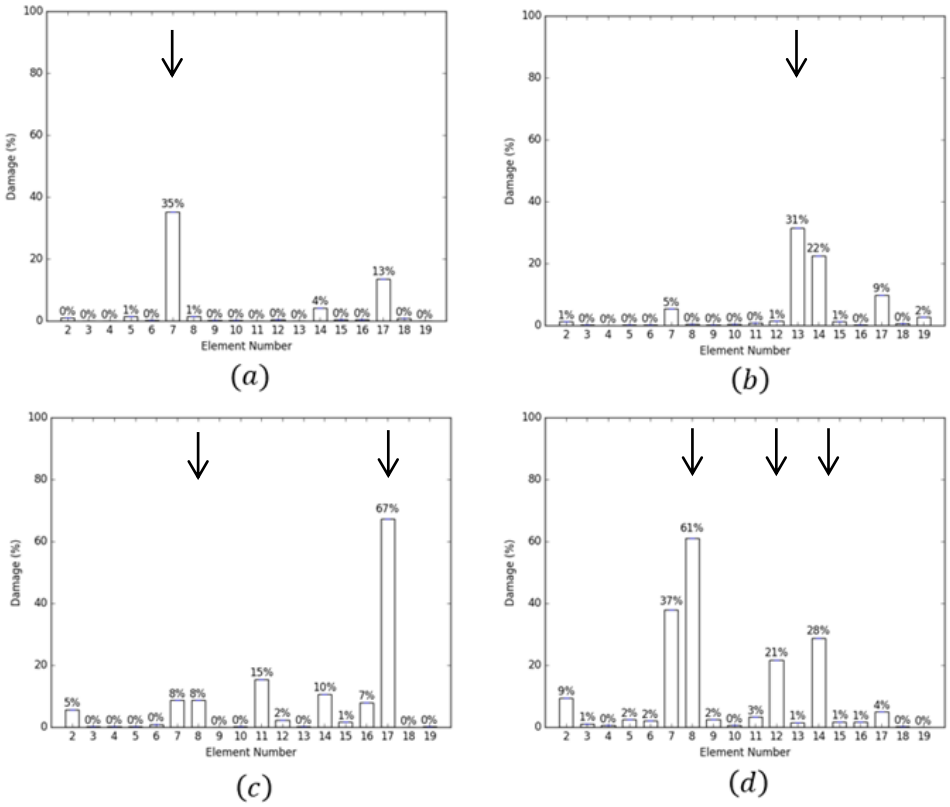


Figure 14: Predicted damage for (a) scenario 1, (b) scenario 2, (c) scenario 3 and (d) scenario 4.

6 Concluding Remarks

Early damage detection has become an essential task in structural health monitoring, allowing engineers to prevent sudden failures in structures, thus reducing costs by taking safety precautions. However, it is not always straightforward to analyze the available data since many times relevant features must be manually extracted requiring expert knowledge and time to process. In this paper, we have proposed a new approach for structural damage assessment based on deep convolutional neural networks that processes transmissibility functions-based images from monitored structures.

The usefulness of the proposed CNN based approach in damage assessment was evaluated and validated by means of two case studies. The first involved an eight-degree of freedom mass-spring system and the second case study involved a structural beam. Based on the resulting performance metrics, the proposed CNN based approach delivers accurate assessments for damage levels above 10%. This was corroborated by the predictions of the trained CNN based models for the experimental spring mass system with a 55% reduction of stiffness (damage level) at the fifth element that resulted in a predicted 54% damage level for that same element. Though it is not possible to have experimental quantification for the inflicted damage in the case of the structural beams, the CNN based approach provides satisfactory results at localizing the damaged elements and at assigning greater damage level to those elements with deeper saw cuts (i.e., greater damage level). These results can also be attributed to the ability of the CNN architecture to successfully and automatically extract relevant features from the transmissibility functions.

A disadvantage of using transmissibility measurements is their dependency on the force location. Therefore, in a real application a requisite is to have the structure excited always on the same location, which can be a problem in structures where the input excitations are not controlled, such as ambient or seismic excitations. A solution is to use the value of the transmissibility measurements evaluated only at the natural frequencies, which has been demonstrated to be independent on the force location, or in narrows bands around these frequencies [20]. In addition to the force variability it should be noted that the proposed models has been evaluated in simple structures under controlled conditions. Therefore, a topic of future research is to evaluate the proposed models with more complex structures considering variable environmental and excitation conditions.

References

[1] K. Worden, “Structural Fault Detection using a Novelty Meassure,” *J. Sound Vib.*, vol. 201, no. 1, pp. 85–101, 1997.

[2] K. Worden, L. Cheung, and J. Rongong, “Damage detection in an aircraft component model,” in *Proceedings of the International Modal Analysis Conference, IMAC XIX*, 2001, pp. 1234–1241.

[3] G. Manson, K. Worden, and D. Allman, “Experimental validation of a structural health monitoring methodology: Part III. Damage location on an aircraft wing,” *J. Sound Vib.*, vol. 259, no. 2, pp. 365–385, 2003.

[4] G. Manson, K. Worden, and D. Allman, “Experimental validation of a structural health monitoring methodology. Part II. Novelty detection on a Gnat aircraft,” *J. Sound Vib.*, vol. 259, no. 2, pp. 345–363, 2003.

[5] M. J. Sc. and F. F. H.Zhang, “Structural Health Monitoring Using Transmittance Functions,” *Mech. Syst. Signal Process.*, vol. 13, no. 5, pp. 765–787, 1999.

[6] T. J. Johnson and D. E. Adams, “Transmissibility as a differential indicator of structural damage,” *J. Vib. Acoust.*, vol. 124, no. 4, pp. 634–641, 2002.

[7] T. J. Johnson, R. L. Brown, D. E. Adams, and M. Schiefer, “Distributed structural health monitoring with a smart sensor array,” *Mech. Syst. Signal Process.*, vol. 18, no. 3, pp. 555–572, 2004.

[8] N. M. M. Maia, J. M. M. Silva, and A. M. R. Ribeiro, “The transmissibility concept in multi-degree-of-freedom systems,” *Mech. Syst. Signal Process.*, vol. 15, no. 1, pp. 129–137, 2001.

[9] R. P. C. Sampaio, N. M. M. Maia, A. M. R. Ribeiro, and J. M. M. Silva, “Transmissibility techniques for damage detection,” in *Proceedings of SPIE, the International Society for Optical Engineering*, 2001, vol. 4359, pp. 1524–1527.

[10] A. P. V. Urgueira, R. A. B. Almeida, and N. M. M. Maia, “On the use of the transmissibility concept for the evaluation of frequency response functions,” *Mech. Syst. Signal Process.*, vol. 25, no. 3, pp. 940–951, 2011.

[11] K. Worden and G. Manson, “The application of machine learning to structural health monitoring,” *Philos. Trans. R. Soc. A Math. Phys. Eng. Sci.*, vol. 365, no. 1851, pp. 515–537, 2007.

[12] K. Worden, G. Manson, and D. Allman, “Experimental validation of a structural health monitoring methodology: Part I. Novelty detection on a laboratory structure,” *J. Sound Vib.*, vol. 259, no. 2, pp. 323–343, 2003.

[13] Q. Chen, Y. W. Chan, and K. Worden, “Structural fault diagnosis and isolation using neural networks based on response-only data,” *Comput. Struct.*, vol. 81, no. 22–23, pp. 2165–2172, 2003.

[14] S. G. Pierce, K. Worden, and G. Manson, “A novel information-gap technique to assess reliability of neural network-based damage detection,” *J. Sound Vib.*, vol. 293, no. 1–2, pp. 96–111, 2006.

[15] K. Worden, G. Manson, and T. Denœux, “An evidence-based approach to damage location on an aircraft structure,” *Mech. Syst. Signal Process.*, vol. 23, no. 6, pp. 1792–1804, 2009.

[16] Z. Lai and R. Perera, “Transmissibility based damage assessment by intelligent algorithm 1,” no. July, pp. 2443–2448, 2014.

[17] V. Meruane, “Online Sequential Extreme Learning Machine for Vibration-Based Damage Assessment Using Transmissibility Data,” *J. Comput. Civ. Eng.*, vol. 30, no. 3, 2016.

[18] V. Meruane and A. Ortiz-Bernardin, “Structural damage assessment using linear approximation with maximum entropy and transmissibility data,” *Mech. Syst. Signal Process.*, vol. 54, 2015.

[19] S. Chesné and A. Deraemaeker, “Damage localization using transmissibility functions : A critical review,” *Mech. Syst. Signal Process.*, vol. 38, pp. 569–584, 2013.

[20] H. Zhang, M. J. Schulz, and F. Ferguson, “Structural health monitoring using transmittance tunctions,” *Mech. Syst. Signal Process.*, vol. 13, no. 5, pp. 765–787, 1999.

[21] Y. J. Yan, L. Cheng, Z. Y. Wu, and L. H. Yam, “Development in vibration-based structural damage detection technique,” *Mech. Syst. Signal Process.*, vol. 21, no. 5, pp. 2198–2211, 2007.

[22] M. I. Friswell, “Damage identification using inverse methods.,” *Philos. Trans. A. Math. Phys. Eng. Sci.*, vol. 365, no. 1851, pp. 393–410, Feb. 2007.

[23] V. Meruane and V. Del Fierro, “An inverse parallel genetic algorithm for the identification of skin/core debonding in honeycomb aluminium panels,” *Struct. Control Heal. Monit.*, vol. 22, no. 12, 2015.

[24] V. Meruane, “Model updating using antiresonant frequencies identified from transmissibility functions,” *J. Sound Vib.*, vol. 332, no. 4, 2013.

[25] C. González-Pérez and J. Valdés-González, “Identification of Structural Damage in a Vehicular Bridge using Artificial Neural Networks,” *Struct. Heal. Monit. An Int. J.*, vol. 10, no. 1, pp. 33–48, Jan. 2011.

[26] J. L. Zapico, M. P. González, and K. Worden, “Damage assessment using neural networks,” *Mech. Syst. Signal Process.*, vol. 17, no. 1, pp. 119–125, 2003.

[27] V. Meruane and J. Mahu, “Real-time structural damage assessment using artificial neural networks and antiresonant frequencies,” *Shock Vib.*, vol. 2014, 2014.

[28] K. Worden and G. Manson, “The application of machine learning to structural health monitoring,” *Philos. Trans. R. Soc. A Math. Phys. Eng. Sci.*, vol. 365, no. 1851, pp. 515–537, 2007.

[29] K. Worden, G. Manson, and T. Denœux, “An evidence-based approach to damage location on an aircraft structure,” *Mech. Syst. Signal Process.*, vol. 23, no. 6, pp. 1792–1804, 2009.

[30] X. Guo, L. Chen, and C. Shen, "Hierarchical adaptive deep convolution neural network and its application to bearing fault diagnosis," *Meas. J. Int. Meas. Confed.*, vol. 93, pp. 490–502, 2016.

[31] J. Wang, "2016 International Symposium on Flexible Automation A MULTI-SCALE CONVOLUTION NEURAL NETWORK FOR FEATURELESS FAULT DIAGNOSIS," pp. 1–3, 2016.

[32] D. Lee, V. Siu, R. Cruz, and C. Yetman, "Convolutional Neural Net and Bearing Fault Analysis," *Int'l Conf. Data Min. | DMIN'16 |*, pp. 194–200, 2016.

[33] O. Janssens *et al.*, "Convolutional Neural Network Based Fault Detection for Rotating Machinery," *J. Sound Vib.*, vol. 377, pp. 331–345, 2016.

[34] Z. Chen, C. Li, and R.-V. Sanchez, "Gearbox Fault Identification and Classification with Convolutional Neural Networks," *Shock Vib.*, vol. 2015, pp. 1–10, 2015.

[35] C. Zhang, P. Lim, A. K. Qin, and K. C. Tan, "Multiobjective Deep Belief Networks Ensemble for Remaining Useful Life Estimation in Prognostics," *IEEE Trans. Neural Networks Learn. Syst.*, vol. PP, no. 99, pp. 1–13, 2016.

[36] L. Liao, W. Jin, and R. Pavel, "Enhanced Restricted Boltzmann Machine with Prognosability Regularization for Prognostics and Health Assessment," *IEEE Trans. Ind. Electron.*, vol. 63, no. 11, pp. 7076–7083, 2016.

[37] G. Sateesh Babu, P. Zhao, and X.-L. Li, "Deep Convolutional Neural Network Based Regression Approach for Estimation of Remaining Useful Life," *Lect. Notes Comput. Sci. (including Subser. Lect. Notes Artif. Intell. Lect. Notes Bioinformatics)*, vol. 9642, pp. 214–228, 2016.

[38] L. Guo, H. Gao, H. Huang, X. He, and S. Li, "Multifeatures Fusion and Nonlinear Dimension Reduction for Intelligent Bearing Condition Monitoring," *Shock Vib.*, vol. 2016, 2016.

[39] F. Zhou, Y. Gao, and C. Wen, "A Novel Multimode Fault Classification Method Based on Deep Learning," vol. 2017, 2017.

[40] H. Liu, L. Li, and J. Ma, "Rolling Bearing Fault Diagnosis Based on STFT-Deep Learning and Sound Signals," *Shock Vib.*, vol. 2016, 2016.

[41] A. Krizhevsky, I. Sutskever, and G. E. Hinton, "ImageNet Classification with Deep Convolutional Neural Networks," *Adv. Neural Inf. Process. Syst.*, pp. 1–9, 2012.

[42] Y. Kim, "Convolutional Neural Networks for Sentence Classification," Aug. 2014.

[43] C. Farabet, C. Couprie, L. Najman, and Y. Lecun, "Learning hierarchical features for scene labeling," *IEEE Trans. Pattern Anal. Mach. Intell.*, vol. 35, no. 8, pp. 1915–1929, Aug. 2013.

[44] N. Srivastava, G. Hinton, A. Krizhevsky, I. Sutskever, and R. Salakhutdinov, "Dropout: A Simple Way to Prevent Neural Networks from Overfitting," *J. Mach. Learn. Res.*, vol. 15, pp. 1929–1958, 2014.

[45] M. I. Friswell and J. E. T. Penny, "Crack modeling for structural health monitoring," *Struct. Heal. Monit.*, vol. 1, no. 2, pp. 139–148, 2002.

[46] T. A. Duffey, S. W. Doebling, C. R. Farrar, W. E. Baker, W. H. Rhee, and S. W. Doebling, "Vibration-Based Damage Identification in Structures Exhibiting Axial and Torsional Response," *Trans. ASME-L-Journal Vib. Acoust.*, vol. 123, no. 1, pp. 84–91, 2001.

[47] C. B. Yun, J. H. Yi, and E. Y. Bahng, "Joint damage assessment of framed structures using a neural networks technique," *Eng. Struct.*, vol. 23, no. 5, pp. 425–435, 2001.

Embedded optical sensors for vibration monitoring of large structures

M. Pinto[1], N. Roveri[1], G. Pepe[1], A. Nicoletti[2], G. Balconi[3], A. Carcaterra[1]
[1] Dep. of Mechanical and Aerospace Engineering, Sapienza University of Rome
e-mail: **manuel.pinto@uniroma1.it**

[2] BASF Italy Spa

[3] SIREG GEOTECH srl

Abstract
The paper illustrates the technique to handle optical signals coming from optical fiber lines equipped with Fiber Bragg Grating (FBG) strain sensors. The case of interest is that of vibration monitoring of very large structures equipped with Glass Fibers Reinforced Polymers (GFRP) with an embedded set of optical fiber sensors. Due to the production process of such elements, it is difficult to locate precisely the FBG along the reinforcement bar, therefore it is difficult to recover the actual position of the measurement points knowing the acquired strain signals only. A technique for the identification of the placements of these sensors is here proposed, which relies on two main algorithms. The first one is based on a modal approximation of the elastic shape of the beam, allowing a theorical estimation of the sensor placements; the second algorithm is based on an Artificial Neural Network, which is able to predict the robustness of the previous estimation. Numerical results are shown to illustrate the methodology.

1 Introduction

The use of vibration measurements for structural health monitoring has attracted significant research attention during the last three decades [1-6]. Traditional strengthened concrete members, such as beams, are composed of concrete included cement and steel bars reinforcement. In such structures, the main function of concrete is to provide resistance to compressive loads. Steel bars embedded in the concrete, instead, provide resistance to tensile and shear loads. Nevertheless, the problem of corrosion associated with the steel bars reduced its live time. Recent technologies have resulted in alternative reinforcing materials such as Glass Fibers Reinforced Polymer materials [7] that can be embedded in concrete members to satisfy several desired properties.

GFRP represents an attractive opportunity in the field of new concrete constructions as well as in the field of restoration of old ones. Their weight and resistance properties provide good chances of replacement of traditional steel reinforcements in many applications for civil and mechanical structures [8-11].

This project started as a collaboration between the department of Mechanical and Aerospace Engineering of Sapienza University of Rome, BASF Italy Spa and SIREG GEOTECH srl. The main task of such project is to perform a structural restoration on a train bridge, located over Bormida river, in northern Italy. Instead of using traditional steel bars reinforcements, for this structure the mentioned GFRP bars with embedded FBG sensors, will be adopted, as shown in Fig. 1. The research is focused on using GFRP (i) as a reinforcement material, with embedded optical fibers, equipped with Fiber Bragg Grating sensors, also (ii) to monitor the structural health of the reinforced existing structure.

FBG sensors allow indeed distributed sensing over significant areas by multiplexing a large number of sensors on a single fiber, which are immune to electromagnetic interference and have compact size. Due to

all these advantages, they have been widely used in many applications for the structural health monitoring [12,13].

The paper is organised as follow: section 2 is devoted to discuss the main technological limitation of embedding FBG optical sensors within GFRP bars, which does not allow an accurate placement of such sensors along the beam. A general mechanical model of the GFRP/FBG system is presented in section 3, where a technique for the identification of the placements of the FBG sensors is also introduced. The performance of the technique are tested in section 4, where an Artificial Neural Network algorithm is also introduced, to predict the robustness of the estimation with an index that forecasts the maximum error involved in the identification process.

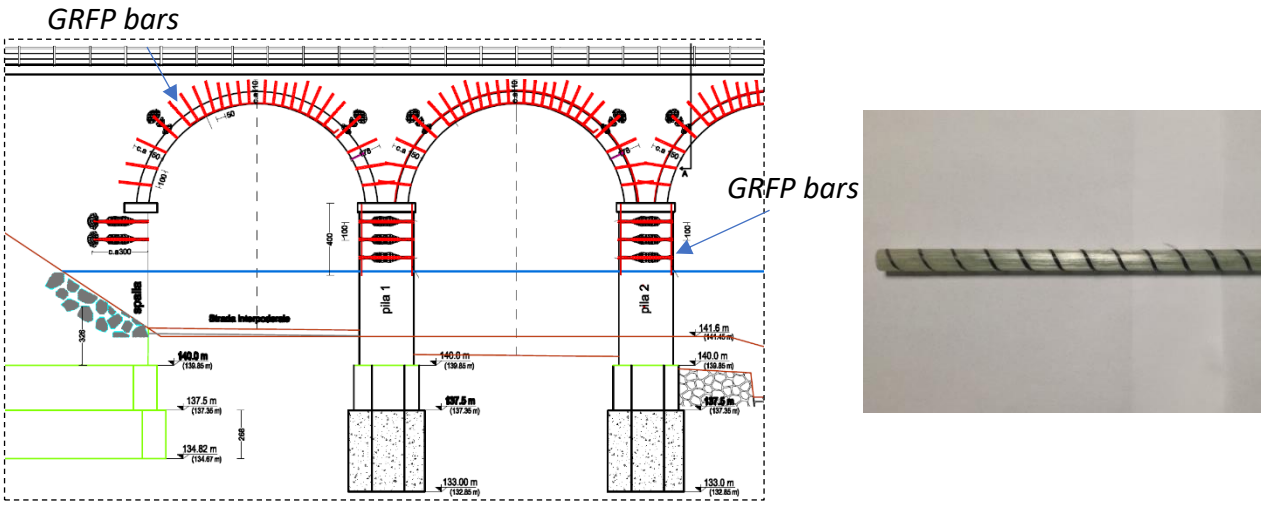


Figure 1: Schematics of the restoration blueprint (left) and picture of a GFRP bar (right).

2 Technological limitation of embedding FBG optical sensors within GFRP

A general difficulty with fiber glass reinforcement bars is related to the poor localization of the actual sensor position along the bar. The production of the GFRP/FBG bars [14-15], as shown in Fig. 2, involves a classic pultrusion process in which glass fibers, impregnated with epoxy resin, and optical fibers with the FBG sensors, are pulled together through a heated stationary die to perform the polimerization of the resin.

The final bar issued from the production line is cut into several pieces of a certain length L, depending on the product specification. As a consequence of the cutting procedure, the actual localization of the sensors along the line is unkonwn.

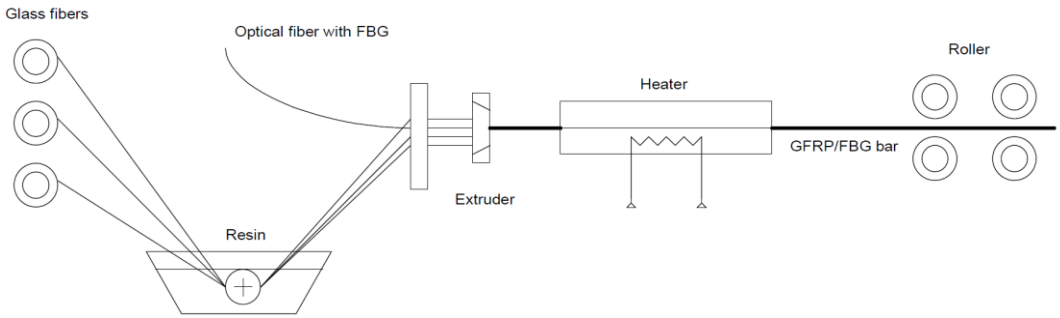


Figure 2: Schematic of the pultrusion process for the production of GFRP bar with embedded FBG sensors.

Each bar should be equipped with three embedded optical lines, each one equipped with at least one sensor. This configuration, as it comes out from the following considerations, permits to solve the under-determinacy intrinsically related to: (i) the axial positioning of the sensors on each line along each bar, (ii) the angular positioning of each bar inside the beam.

However, since the radius of each bar is small with respect to the characteristic size of the beam section, and the radius of the circle over which the optical lines are placed is even smaller, we can approximate the nominal optical line positioning on each section as it is identified by the centre of each bar. In this way the only unknown parameter of the sensors placements is related to their axial positions.

3 Analytical model for predicting the system deformation

Task of the proposed method is to estimate the elastic shape of the beam through the measurements of axial deformations in several points along the beam, whose positions are unknown. This method [16] is applied to a beam subjected to bending deformation according to the Euler-Bernoulli hypothesis. The unknown elastic shape of the beam can be expressed in form of an expansion of known eigenfunctions $\phi_k(x)$, combined through a set of weighting unknown time-dependent coefficients, that are the modal coordinates $A_k(t)$. Since the distributed-parameter system has infinitely many vibration modes, the general response is a linear combination from all vibration modes:

$$w(x,t) = \sum_{k=1}^{\infty} A_k(t)\phi_k(x) \tag{1}$$

where $w(x,t)$ is the transverse displacement of the neutral axis (at the point *x* and the time *t*) due to bending. Let us analyze first the static case: from the theory of Euler beam, we can deduce that the *j-th* optical fiber embedded within the GFRP beam (generally we have three fibers within each beam as explained in the previous section) has an axial deformation, the one measured by the the *i-th* FBG sensor, that is simply proportional to the curvature of the beam at that position (*x*):

$$\varepsilon_i^{(j)} = -z_i^{(j)} \frac{d^2 w}{dx^2}\left(x_{si}^{(j)}\right) = -z_i^{(j)} \sum_{k=1}^{\infty} A_k \frac{d^2\phi_k}{dx^2}\left(x_{si}^{(j)}\right) \tag{2}$$

Where $x_{si}^{(j)}$ is the longitudinal position of the *i-th* sensor along the *j-th* fiber, and $z_i^{(j)}$ is the distance with respect to the neutral axis. However, since the radius of the circumference at which the three optical lines are placed is small with respect to the characteristic size of the beam, the following approximation holds: $z_i^{(j)} \sim z^{(j)}$, i.e. the distance from the neutral axis only depends on the centre of the bar we consider.

However, if the positions $x_{si}^{(j)}$ are unknown, together with the unknown coefficients A_k, an undetermined set of conditions is produced, since the number of unknowns is larger than the number of equations. A simple trick to proceed at the identification of the sensor location is to produce a fiber in which the sensors are placed at constant known distance *d*. This requirement does not affect at all the production process, and it is only related the layout of the FBGs that is ordered to the fiber supplier. In this case, eq. (2) becomes:

$$-\frac{\varepsilon_i^{(j)}}{z_i^{(j)}} = \sum_{k=1}^{\infty} A_k \frac{d^2\phi_k}{dx^2}\left(x_{so}^{(j)} + (i-1)\,d\right) \tag{3}$$

where now only the *line offset* $x_{so}^{(j)}$ is unknown for each fiber.

The information balance is easily analyzed: using N_B fibers, each one carrying N_S sensors, the total number of available signals is $N_B N_S$. On the right hand side of eq. (3), *N+1* unknowns appear, i.e. the *N* coefficients A_k and the offsets $x_{so}^{(j)}$. To solve the system of equations it is necessary to satisfy the balance $N_B N_S = N+1$.

The problem of determining the elastic shape of the beam is simultaneously solved, since the solution of the previous system provides also the coefficients A_k, i.e. through $w(x) = \sum_{k=1}^{\infty} A_k \phi_k(x)$ one can determine the elastic shape.

3.1 Algorithm for the identification of the coefficients A_k

Let us assume that the elastic shape is represented only by two coefficients A_1 A_2 and considering the beam simply supported, we can write the mode shape in harmonic form as:

$$w(x,t) = A_1(t)\sin\left(\frac{\pi x}{L}\right) + A_2(t)\sin\left(\frac{2\pi x}{L}\right) \tag{4}$$

where the two mode shapes have different wavenumbers, the first completing one cycle along *2L*, the second one cycle along *L*. Eq. (3) becomes:

$$-\frac{\varepsilon_i^{(j)}(t)}{z_i^{(j)}} = -\sum_{k=1}^{N}\left(k\frac{\pi}{L}\right)^2 A_k(t) sin\left[\frac{k\pi\left(x_{so}^{(j)} + (i-1)\,d\right)}{L}\right] \tag{5}$$

with *N=2*. An algorithm for the solution of these nonlinear equations can now be set. Note that in terms of the A_k coefficients the system is linear, and the nonlinearity is only related to the offsets $x_{so}^{(j)}$. In order to solve the problem recursively, let introduce a first guess for the offsets $x_{so}^{(j)}$, the linear system is defined:

$$\boldsymbol{b} = \left\{\frac{\varepsilon_i^{(j)}(t)}{z_i^{(j)}}\right\}, \qquad \boldsymbol{U} = \left\{\left(k\frac{\pi}{L}\right)^2 sin\left[\frac{k\pi\left(x_{so}^{(j)} + (i-1)\,d\right)}{L}\right]\right\} \tag{6}$$

Where $\boldsymbol{b}$ is the column vector of the acquired strains and $\boldsymbol{U}$ is an $N_s \times N$ matrix. In matrix form, the previous equation reads:

$$\boldsymbol{U}\left(x_{so}^{(j)}\right)\boldsymbol{A} = \boldsymbol{b} \quad \rightarrow \quad \boldsymbol{A} = \boldsymbol{U}^{+}\left(x_{so}^{(j)}\right)\boldsymbol{b} \tag{7}$$

Where $\boldsymbol{U}^{+}$ is the pseudo-inverse matrix.

The estimation error for the set of coefficient A_k is now introduced:

$$e = \left\|\boldsymbol{A} - \boldsymbol{U}^{+}\left(x_{so}^{(j)}\right)\boldsymbol{b}\right\| \tag{8}$$

Now, fixed an initial guess for the offsets $x_{so}^{(j)}$, an optimal set of coefficient $\boldsymbol{A}$ is obtained, then the problem is iterated varying $x_{so}^{(j)}$, to find the minimum point $\bar{x}_{so}^{(j)}$ so that a suitable error function will be minimised and $\bar{x}_{so}^{(j)}$ will be the estimated offset for the fiber *j*.

3.2 A practical example of application

Let's now consider the following setup: assume we use a single GFRP bar of a certain length *L*, i.e. N_B=1, with embedded a number of FBG sensors equal to seven, that means N_S=7, all sensors are equally spaced of a distance *d*. As explained, the uncertainty related to the location of the array of FBG sensors is reduced only to the placement of the first sensor, that is the *line offset*. That means that the maximum error for the identification of such offset is equal to the spacing *d*, which can be written as $d = \frac{L}{N_s}$. This setup is represented in Fig. 3.

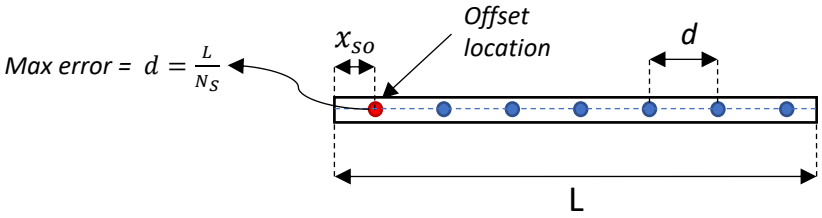


Figure 3: Schematics of the FBG sensors embedded within a GFRP beam. The red dot is the offset of the optical line, while the blue dots are the remaining six sensors.

In order to provide an example of application of the algorithm, for the sake of simplicity it is here analysed a static problem, considering a punctual load. In fact, the calibration of the measurement apparatus, e.g. the GFRP with embedded FBG sensors inserted into the mechanical/civil structure, can be easily carried out employing suitable static loads.

Considering seven FBG sensors, eq. (5) becomes:

$$\begin{cases} \dfrac{\varepsilon_1^{(1)}}{z_1^{(1)}} = \left(\dfrac{\pi}{L}\right)^2 A_1 \sin\left(\dfrac{\pi x_{so}^{(1)}}{L}\right) + \left(\dfrac{2\pi}{L}\right)^2 A_2 \sin\left(\dfrac{2\pi x_{so}^{(1)}}{L}\right) \\ \dfrac{\varepsilon_2^{(1)}}{z_2^{(1)}} = \left(\dfrac{\pi}{L}\right)^2 A_1 \sin\left(\dfrac{\pi x_{so}^{(1)} + \pi d}{L}\right) + \left(\dfrac{2\pi}{L}\right)^2 A_2 \sin\left(\dfrac{2\pi x_{so}^{(1)} + 2\pi d}{L}\right) \\ \vdots \\ \dfrac{\varepsilon_7^{(1)}}{z_7^{(1)}} = \left(\dfrac{\pi}{L}\right)^2 A_1 \sin\left(\dfrac{\pi x_{so}^{(1)} + 6\pi d}{L}\right) + \left(\dfrac{2\pi}{L}\right)^2 A_2 \sin\left(\dfrac{2\pi x_{so}^{(1)} + 12\pi d}{L}\right) \end{cases} \tag{9}$$

Therefore, we have two unknown coefficients A_1 A_2 and the line offset $x_{so}^{(1)}$, i.e. three unknowns in seven equations that can be solved in terms of A_1 A_2 and $x_{so}^{(1)}$ in two steps.

As explained, the error function $e(x_{so}^{(j)})$ defined in eq. (8) depends on the initial guess of the offset. We can set a first guess for $x_{so}^{(1)}$, for example $x_{so_{guess}}^{(1)} = \frac{L}{M}$, where M is a given positive integer, thus we obtain an overdetermined set of seven equations in two unknowns A_1 A_2 that can be solved in a least square sense (by using the pseudo-inverse), and evaluate the corresponding error $e(x_{so}^{(j)})$.

Now we are able to introduce another error function *err*, slightly different than eq. (8), which is defined as the mean error between the strains measured by the FBG sensors and the strains estimated by eq.(5) having used the optimal set of coefficients A_1 A_2:

$$err(x_{so}) = \sum_{i=1}^{s} \frac{\varepsilon_i - \varepsilon_i(x_{so})}{s\varepsilon_i} \tag{10}$$

Then we can modify the value, as $x_{so}^{(1)} = \frac{2L}{M}$, and solve again in the least square sense for A_1 A_2, and compute again the error. Let us proceed in this way evaluating the set of errors for $x_{so}^{(1)} = \frac{kL}{M}$, *k=1,2,3,...,M*.

The value of k for which the equation error (10) is minimum identifies the estimated value of the offset $x_{so}^{(1)}$, at which are associated the optimal values for A_1 A_2.

Therefore, in this way we can to each strain measurement the related position along the longitudinal axis, i.e. $x_{so\,i}^{(1)} = x_{so}^{(1)} + (i-1)d$.

The algorithm has been tested varying the position of the same load P all over the length of the beam, between 0 and L, for a fixed value of the actual line offset. Then the same set of loads have been applied varying the position of the offset in the range of the maximum error of location, namely between 0 and d.

The simulation has been carried out considering 39 positions for the load, equally spaced over the entire length of the beam, for a number of fixed offsets equal to 28; the results of the test are represented in Fig. 4. Note that, for explanatory purpose, the results reported in Fig. 4 refer to just one fixed value of the line offset x_{so}. In this graphic, each curve is the error function, eq. (10), related to a single load applied in a specific position. The error function curves have the same trend and most of them have a minimum in the neighbourhood of the actual offset. However among these curves, there are some that provide a better estimation of the offset, while other provide larger errors. The estimation error is therefore introduced, namely the relative error between the actual and the estimated offset:

$$e_c = \left| \frac{x_{os} - x_{os_{est}}}{x_{os}} \right|. \tag{11}$$

Where, for the sake of notation, the dependence on the load position x_p, e.g. $e_c(x_p)$, has been omitted.

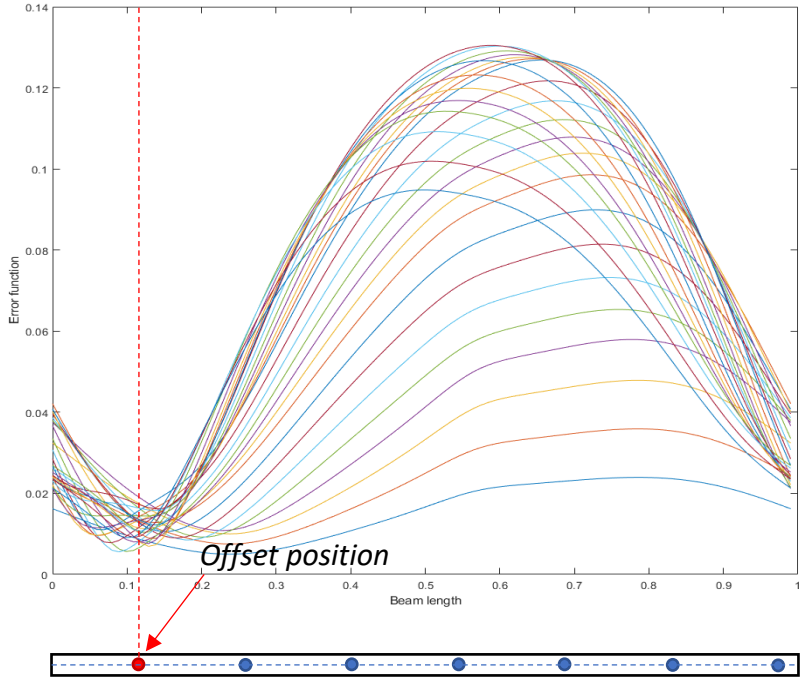


Figure 4: Simulation results: trend of the $err(x_{so})$ functions for one fixed offset ($x_{so} = 0.115$) and 39 loads. Schematics of the beam is reported on the lower side of the picture.

Over the entire set of obtained curves, only for certain positions of the load the optimal solution provides a relative error close to zero.

The reasons behind this behaviour may depend on the generality of the model, which relies only on a few periodic eigenfunctions adopted to model the mechanical system; however this limits the reliability of the algorithm introduced so far. An *Artificial Neural Network* algorithm will be indeed implemented, to classify the reliable curves, which provide a good localization of the line offset, from the other curves that, on the contrary, provide wrong estimations.

4 Data post processing with an ANN algorithm

The algorithm previously introduced works under rather general hypothesis, so that it is able to provide an estimate of the flexural deformation without requiring an accurate mechanical model of the structure. As a

result, the algorithm can be applied to a wide set of structures, the trade-off is that the accuracy of the offset estimation is affected by the actual placement of the offset and of the load that is exciting the structure. For a specific placement of the offset, the proposed technique shows indeed good accuracy for certain load positions, while it is not effective for others, as shown in Fig. 4.

The objective of the present section is to develop an Artificial Neural Network [17], which is able to predict the robustness of the estimated offset, providing an index that forecasts the error involved in the estimation process. This is obtained designing a multilayer artificial neural network, which will use the deformation signal measured by the sensors embedded into the structure.

For each actual placement of the offset and of the load, the input vector that feeds the neural network will be composed by the following features:

1. A set of g-error values $err\left(x_{so_{guess}j}\right)$, defined in eq. (10), evaluated on an array of initial guess, $x_{so_{guess}j}$, uniformly distributed within the interval $[0, d]=[0, \Delta x, \ldots, j\Delta x, \ldots, (g-1)\Delta x]$, where $d<L$, being L the length of the structure, with $g=51$;
2. the estimated offset value $x_{os_{est}}$;
3. the prominence value of the error function, e. g. $\frac{err(x_{os_{est}})}{\overline{err}\left(x_{so_{guess}j}\right)}$; where $\overline{err}\left(x_{so_{guess}j}\right)$ is the mean value of the error.
4. the total number of minima.

To each input vector is associated a target value, which is the relative error e_c involved in the estimation of the offset position, previously introduced in eq. (11).

In order to train the net, a dataset is generated by the iteration of the process above, considering n-different positions for the offset, uniformly distributed within the interval $[0, d]$, and m-different positions for the load, uniformly distributed within $[0, L]$, with $n=2848$ and $m=191$. To summarize, the generated dataset will contain a total number of records $n \times m = 543968$; each record is composed by $g+3=54$ variables, which form the input of a column vector V. The target vector T has only one value, which ranges from 0 to 1.

One of the problems with the data set is that the number of records needed for good estimations, i.e. the value of the function e smaller than 0.1, is smaller than the ones for bad estimations, i.e. $e>0.5$, respectively true and false cases, for notation. If we train the network using a higher number of false cases, the network will be biased to indicate false events. A simple solution is to select an equal number of good and bad estimates in the dataset dedicated to the training.

After the data has been collected and divided, an important step is the data normalisation, which makes it easier for the neural network training to extract the relevant information. The input and output data is normalized so that they fall into a standard range, typically -1 to 1.

When coding the target values we also need to consider the transfer function that is used in the output layer of the network. For pattern recognition problems, sigmoid functions are generally adopted: log-sigmoid or tangent-sigmoid, the latter is used in the present document so target values range from -1 to 1, which represent the asymptotes of the function.

However, this tends to cause difficulties for the training algorithm, which tries to saturate the sigmoid function to meet the target value. It is better to assign target values at the point where the second derivative of the sigmoid function is maximum. For the tangent-sigmoid function, this occurs when the net input is -1 and 1, which corresponds to output values of -0.76 and +0.76, therefore the targets are set to values of -0.76 and +0.76 instead of -1 and 1.

Fig.5 shows the network architecture, which consists of two hidden layers with 54 and 2 neurons and the tangent-sigmoid transfer function is used in all the layers. This architecture, which is rather standard for pattern recognition, has been determined starting from one hidden layer with 10 neurons and then testing the network performance after training.

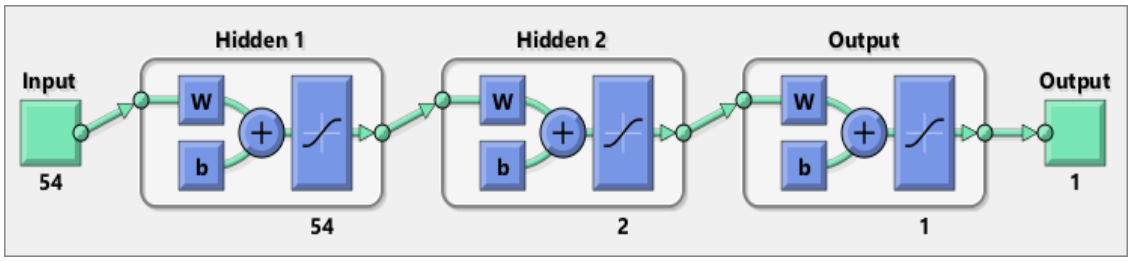


Figure 5: Actual architecture of the Feedforward Network used in the proposed algorithm.

The training data consist of 6350 samples of good estimations and 6350 of bad ones, for a total of 12700 records dedicated to the training. To guarantee a better learning of the network, a larger training set is generated, by randomly selecting, 4 times, one (good-bad) pair at the time from the original data set. The final datasets will be composed of 50800 of record, 75 % (38100) of which will be used for training. The program is implemented in *Matlab* where the function *train* is used, which automatically set aside 15% of the training data for validation and 15% for testing. The network is trained using the scaled conjugate gradient algorithm, which is very efficient for pattern recognition problems.

After the network has been determined, its performance are tested using the remaining 12700 records at disposal. Results will be discussed in the devoted section.

4.1 Testing the Network

Results of the network testing are here reported in the left side of Fig.6: red circles represent the actual values of the normalised target used for testing, while the blue dots are the predictions made by the developed ANN. In detail, in the lower side of the graph there are the good estimations while in the upper side there are the false cases. The network is able to properly classify the vast majority of the cases: there is an almost perfect fit between the false cases and the output of the net, while for what concerns the true cases, ANN roughly provides a mean value between less (-0.6) and more (0.8) accurate estimations of the expected target, demonstrating that the reliability of the dataset processing performed by the ANN is high. In the right side of Fig. 6, same results are reported in terms of probability density function: target and ANN predictions have indeed the same shape, mean value and variance.

In the end, with reference to Fig. 7, it is reported the relative Network error, as the relative error between the target values and the predictions performed by the ANN algorithm, that is: $e_{net} = \left|\frac{Target-Output}{Target}\right| \cdot 100$.

As shown, the network is able to classify both true and false cases with an error which is, except some few cases over the entire dataset, below 10%.

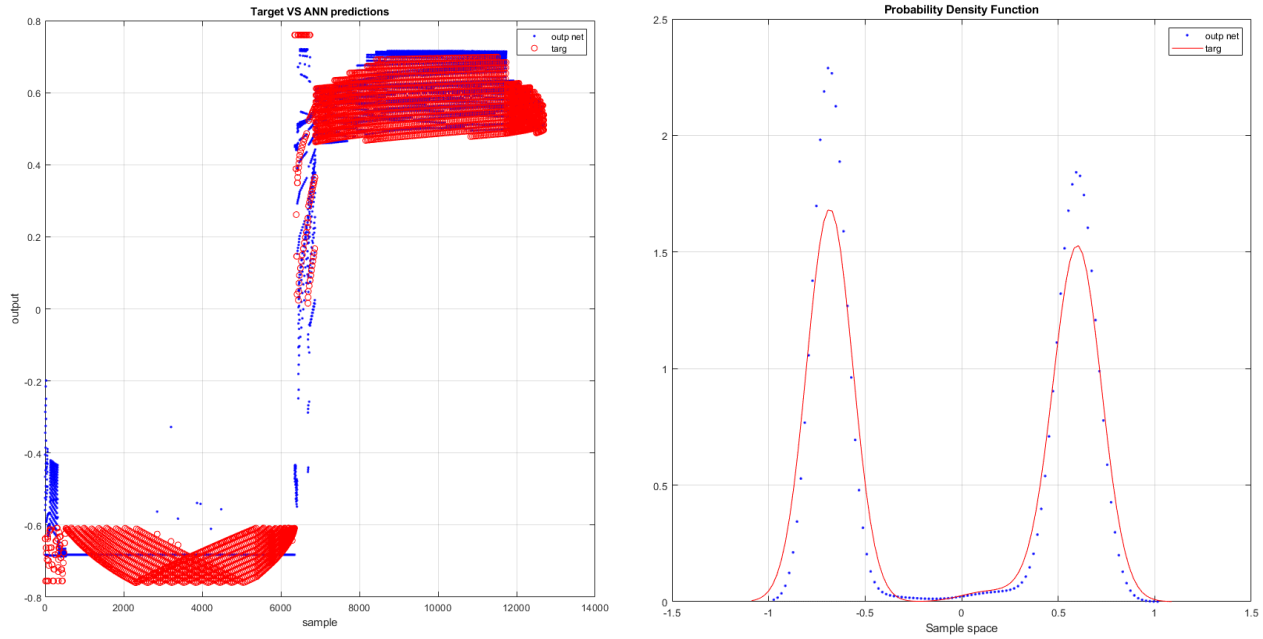


Figure 6: Network testing results (left) and Probability Density function (right).

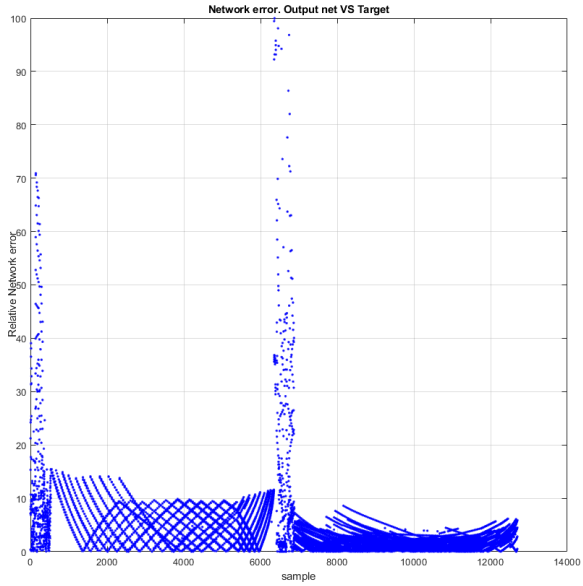


Figure 7: Relative network error: $e_{net} = \left|\frac{Target - Output}{Target}\right| \cdot 100$.

Concluding Remarks

The production process does not allow an accurate placements of FBG sensors along a Glass Reinforced Fibers beam. A technique for the identification of the placements of these sensors has been proposed, which relies on two main algorithms. The first algorithm is based on a modal approximation of the elastic shape of the beam, allowing a theorical estimation of its deformation, to be compared with the one arising from the strain measurements, which permits a first estimation of the sensors placements.

The accuracy of the estimation is however affected by the combination of the actual placement of the sensors and of the load that is exciting the structure. Since the calibration of the measurement apparatus, e.g. the

GFRP with embedded FBG sensors inserted into the structure, can be carried out employing a number of suitable loads, a set of estimations will be at disposal but, among them, only some unknown trials, will provide good results, while other will provide larger errors.

The problem of classify good from bad estimations is solved with a second algorithm, which is based on an Artificial Neural Network, and is able to predict the robustness of the estimation, providing an index that forecasts the error involved in the estimation process, for each position of the exciting load.

Numerical results shows that the proposed technique is able to locate properly the actual position of the sensors with good accuracy, performing a relative error as high as 10%.

Acknowledgements

This work was carried out by the Department of Mechanical and Aerospace Engineering, Sapienza, University of Rome, in collaboration with BASF Italy Spa., and SIREG GEOTECH srl.

References

[1] O.S. Salawu, Detection of structural damage through changes in frequency: a review, Engineering Structures 19 (9) (1997) 718–723.

[2] S.W. Doebling, C.R. Farrar, M.B. Prime, A summary review of vibration-based damage identification methods, The Shock and Vibration Digest 30 (2) (1998) 91–105.

[3] J.N. Yang, P.C. Chang, H. Fujitani, H. Li, B.F. Spencer Jr., Y.L. Xu, F.G. Yuan, Structural control and health monitoring, Proceedings of International Conference on Advances and New Challenges in Earthquake Engineering Research 3 (2002) 9–14.

[4] J.W. Lee, J.D. Kim, C.B. Yun, J.H. Yi, J.M. Shim, Health-monitoring method for bridges under ordinary traffic loadings, Journal of Sound and Vibration 257 (2) (2002) 247–264.

[5] J. Li, M. Su, Resonant vibration for a simply supported girder bridge under high-speed trains, Journal of Sound and Vibration 224 (5) (1999) 897–915.

[6] N. Roveri, A.Carcaterra, Damage detection in structures under traveling loads by Hilbert–Huang transform, Mechanical Systems and Signal Processing 28(2012)128–144.

[7] Patrícia Escórcio, Paulo M.França, Experimental study of a rehabilitation solution that uses GFRP bars to replace the steel bars of reinforced concrete beams, Engineering Structures, Volume 128, 1 December 2016, Pages 166-183.

[8] M. Kemp, D. Blowes Concrete Reinforcement and Glass Fibre Reinforced Polymer Queensland Roads Edition, no. 11 (2011), pp. 40-48.

[9] V.R. Patil Experimental Study of Behavior of RCC Beam by Replacing Steel Bars with Glass Fiber Reinforced Polymer and Carbon Reinforced Fiber Polymer (GFRP) (2014).

[10] M. Kemp, D. Blowes, Concrete Reinforcement and Glass Fibre Reinforced Polymer, Queensland Roads Edition, no. 11 (2011), pp. 40-48.

[11] N. Roveri, A.Carcaterra, A.Sestieri, Real-time monitoring of railway infrastructures using fibre Bragg grating sensors, Mechanical Systems and Signal Processing 60-61(2015)14–28.

[12] B. Glisic, D. Inaudi, Fibre Optic Methods for Structural Health Monitoring, Wiley, New York, 2007.

[13] F. Vestroni,J. Ciambella, F. Dell'Isola, S. Vidoli, Damage detection with auxiliary subsystems, CIMTEC 2008 – in: Proceedings of Third International Conference on Smart Materials, Structures and Systems – Emboding Intelligence in Structures and Integrated Systems, vol. 56, pp. 401–413.

[14] Z. Zhou, J.P. Ou & B. Wang, Smart FRP-OFGB bars and their application in reinforced concrete beams.

[15] Zhi Zhou, Thomas W. Graver, Luke Hsu, Jin-ping Ou, Techniques of Advanced FBG sensors: fabrication, demodulation, encapsulation and their application in the structural health monitoring of bridges, Pacific Science Review, vol. 5, 2003, pp.116~121.

[16] N. Roveri, M. Pinto, G. Pepe, A. Carcaterra, Sensors Placement identification in long optical fibers for vibration monitoring, submitted to MSSP, Mechanical Systems and Signal Processing –June 2018

[17] Neural Network Design (2nd Edition) – 1 set 2014 di Martin T Hagan, Howard B Demuth, Mark H Beale, Orlando De Jesús.

Vibration-based structural damage identification using sparsity constrained Extended Kalman Filter concept

C.-P. Fritzen [1,2]**, D. Ginsberg** [1]**, O. Loffeld** [2]
[1] University of Siegen, Department of Mechanical Engineering,
Paul-Bonatz-Strasse 9-11, 57076 Siegen, Germany
e-mail: **claus-peter.fritzen@uni-siegen.de**

[2] University of Siegen, Center of Sensor Systems (CESS),
Paul-Bonatz-Strasse 9-11, 57076 Siegen, Germany

Abstract
Structural health monitoring (SHM) systems are necessary to achieve smart predictive maintenance and repair planning as well as they lead to a safe operation of mechanical structures. In the context of vibration-based SHM the measured structural responses are employed to draw conclusions about the structural integrity. This usually leads to an inverse problem which needs regularization. Compared to the undamaged state usually only a few local stiffness changes occur while the other areas remain unchanged. These changes can be described by a sparse damage parameter vector. Such a sparse vector can be identified by employing L_1-regularization techniques. This paper presents a novel framework for damage parameter identification by combining sparse solution techniques with an Extended-Kalman Filter. In order to ensure sparsity of the damage parameter vector the measurement equation is expanded by an additional non-linear L_1-minimizing observation. For verification, a proof-of-concept example on a quadratic aluminum plate is presented.

1 Introduction

Structural health monitoring (SHM) is a methodology to ensure safe operation of mechanical structures and to reduce life cycle cost by replacing schedule-driven inspections by Condition-Based Maintenance (CBM). One major task of SHM systems is the detection and identification of damage in an early stage of structural damage evolution. For vibration-based SHM an integrated sensor network is required to measure the structural vibrations excited either by an artificial or a natural source, e.g. wind and traffic loads. By means of the integrated sensor system the effect of the damage on the structural vibration response can be measured.

SHM systems need smart data processing algorithms in order to draw conclusions about the exact cause for the measured effect. Thus, vibration-based damage identification can be seen as the inversion of the principle of cause and effect. This leads to a mathematical inverse problem. If there are many causes which will lead to the same measurable effect, the inverse problem is additionally ill-posed. Ill-posedness means that either the existence, the uniqueness or the stability of the solution is violated.

In the last decades many methods have been developed and a considerable amount of literature has been published on the inverse problem of structural damage identification, an overview on this topic can be found for example in [1]. Damage identification techniques can be classified as frequency or time domain or time-frequency domain methods. Classical frequency domain approaches consider the changes of the natural frequencies, modal damping and mode shapes or changes of Frequency Response Functions (FRFs) due to damage. As these quantities provide information on a global level, they are often insensitive to small local structural damage, especially if only lower structural modes are used. In the medium or higher frequency

range problems may occur to identify these modes since this requires a very dense sensor network. Time domain approaches seem to be comfortable, as raw time data can be used directly.

Several time domain approaches have already been proposed, such as least-squares estimation methods [2, 3] or methods using particular filters [4, 5, 6, 7]. For the latter the Extended Kalman Filter (EKF) is the most well-known system parameter estimation method [8, 9, 10]. EKF-based system parameter identification belongs to the class of model-based approaches. Here, a reference model of the undamaged structure is tested against the actual system in each filter step. In the filter process the state vector of the Kalman Filter equations is typically augmented [10] or sometimes even replaced [11] by the system parameter to be estimated. By making use of the input-output signal, an estimation of the system parameters is obtained in each filter step. Even so the original Kalman Filter is known as optimal linear filter, EKF-based damage identification is still facing some challenges, e.g. high computational effort for complex structures and intrinsic ill-posedness of the inverse problem [12]. To overcome ill-posedness usually the damage parameter space is reduced by considering only damage hot spots or by a drastic increase of the number of sensors. In order to perform damage monitoring on the whole structure and to keep the required number of sensors low, a sparsity-constrained Extended Kalman Filter concept is proposed.

Therefore, a priori information about the damage properties is used to solve the inverse problem and to obtain meaningful solutions. For example, cracks can be interpreted as spatial singularities, which cause only a very local structural stiffness reduction. Thus, a system parameter vector which describes the change in structural stiffness has only a few non-zeros elements corresponding to the actual damage location. Such a vector is called sparse. In many fields of applied mathematics, L_1-regularizing techniques have been proven to promote such kind of sparse solutions (e.g. Compressive Sensing [13, 14]). The proposed damage identification method links the concept of L_1-regularization with the Extended Kalman Filter by expanding the measurement equation by an additional non-linear L_1-minimizing observation.

The paper is structured as follows: Section 2 describes the L_1-minimizing sparse solution strategy for inverse problems. The problem of damage parameter estimation using a non-linear state-space description is formulated in section 3. In section 4 the concept of sparse solution is incorporated in the Extended Kalman Filter concept. A proof-of-concept simulation study is carried out in section 5. Here the functionality of the proposed identification method is demonstrated by analyzing different damage scenarios on a quadratic aluminum plate structure. Finally, concluding remarks are presented in section 7.

2 Sparse solution of inverse problem

Most ill-posed inverse problems can be formulated by a linear algebraic equation system of the form:

$$\mathbf{y} = \mathbf{H} \cdot \mathbf{A} \tag{1}$$

or can be transformed into such a system. In Eq. (1) $\mathbf{y} \in \mathbb{R}^M$ is a vector which contains all measurable output information and $\mathbf{A} \in \mathbb{R}^N$ all possible causes. The transition matrix $\mathbf{H} \in \mathbb{R}^{M \times N}$ describes the linear causes-effect relationship. If the dimension of $\mathbf{y}$ is smaller than the dimension of $\mathbf{A}$ $(M < N)$ the linear system of equations is called underdetermined. In this case Eq. (1) has an infinite number of possible solutions, which means an infinite number of different causes will result in the same effect. The challenge of solving such an equation system is the determination of the right one.

In order to close the gap of information and to obtain a solution additional constraints $\Omega(\mathbf{A})$ need to be formulated, which regularize the problem. The most common regularization is the *Tikhonov-Regularization* [15],

$$\hat{\mathbf{A}}_2 = \underset{\mathbf{A} \in \mathbb{R}^N}{\arg\min} \left\{ \|\mathbf{y} - \mathbf{H} \cdot \mathbf{A}\|_2^2 + \lambda \|\mathbf{A}\|_2^2 \right\} . \tag{2}$$

with the constraint $\Omega(\mathbf{A})$:

$$\Omega(\mathbf{A}) = \|\mathbf{A}\|_2^2 \quad \text{and} \quad \|\mathbf{A}\|_2 = \sqrt{\sum_i A_i^2} \tag{3}$$

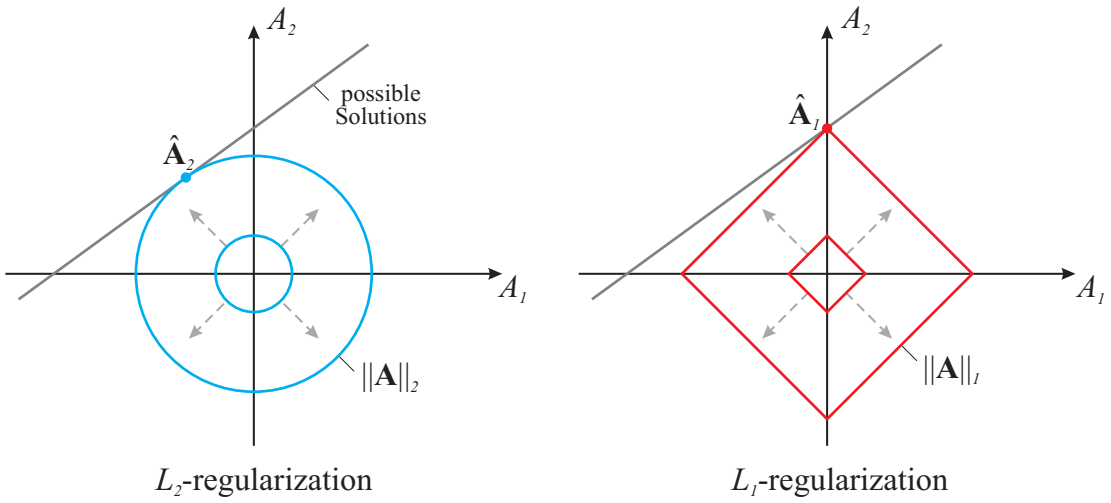


Figure 1: Comparison of L_2- and L_1-regularization of underdetermined equation systems

Here, the solution of Eq. (1) is generated via an optimization problem. The constraint can be interpreted as additional information which regularize the inverse problem and forces the L_2-norm of the solution vector $\hat{\mathbf{A}}_2$ to be minimal. Furthermore, for Tikhonov-Regularization $\mathbf{y}$ is not necessarily equal to $\mathbf{H} \cdot \mathbf{A}$ so that the solution is stabilized if $\mathbf{y}$ is polluted by noise. However, for most applications the choice of L_2-minimization as constraint is not suitable to close the gap of information and to obtain meaningful results.

In recent years, new reconstruction strategies for solving underdetermined linear systems of equations have been proposed, pushed forward by the developments in the field of Compressive Sensing (CS) [13, 14]. For these reconstruction methods it is assumed that the solution vector has just a few nonzero elements or can be transformed to such a sparse vector by using some other coordinate spaces. This assumption holds for most vectors which describe some real world phenomena (e.g. images, sounds, forces); the elements inside such vectors are not completely arbitrary and have some kind of internal structure. Such a structure is always used for compressing data, e.g. wavelet transformation of images or Fourier transformation of sounds. So the information carried by these vectors is mostly a lot smaller than the dimension of the vectors itself suggests. However, it is not known in advance which elements are nonzero, but the information that the solution vector is sparse can be included as additional information in the reconstruction strategy.

The number of nonzero elements s inside the vector $\mathbf{A}$ can be expressed by means of the L_0-norm

$$s = \|\mathbf{A}\|_0 = |\text{supp}\,(\mathbf{A})| \ , \tag{4}$$

where $\text{supp}\,(\mathbf{A}) := \{i : \ A_i \neq 0\}$ denotes the support set of the vector $\mathbf{A}$ and $|\circ|$ the cardinality of this set. If the dimension N of the vector $\mathbf{A}$ is much bigger than the number of nonzero elements s $(N \gg s)$, then $\mathbf{A}$ is a sparse vector.

The sparsest solution which agrees with our measurements could be obtained by minimizing the following expression:

$$\hat{\mathbf{A}}_0 = \underset{\mathbf{A}\in\mathbb{R}^N}{\arg\min} \|\mathbf{A}\|_0 \quad \text{subject to} \quad \mathbf{y} = \mathbf{H} \cdot \mathbf{A} \tag{5}$$

Unfortunately, solving Eq. (5) requires a combinatorial search, which makes it nearly impossible to solve computationally. Under the assumption of a sparse solution, e.g. in [14] is shown shown that by replacing the L_0-norm with the L_1-norm almost the same solution can be obtained as solving Eq. (5):

$$\hat{\mathbf{A}}_1 = \underset{\mathbf{A}\in\mathbb{R}^N}{\arg\min} \|\mathbf{A}\|_1 \quad \text{subject to} \quad \mathbf{y} = \mathbf{H} \cdot \mathbf{A} \tag{6}$$

The L_1-norm is the sum of all absolute values of the vector entries A_j,

$$\|\mathbf{A}\|_1 = \sum_j |A_j| \,. \tag{7}$$

Eq. (6) is now a convex optimization Problem which can by solved be some linear programming techniques. The reason why L_1-regularization also delivers sparse solutions, is illustrated in Fig. 1. It can be seen that L_2-regularization leads to a solution closest to the origin while L_1-regularization finds a solution on the coordinate axes, with just a few nonzero elements.

3 Problem Statement

In general, the dynamics of a non-linear, time-varying structure can be described similar to [1] as:

$$\mathbf{M}\left(\boldsymbol{\Theta}_k, \mathbf{x}_k, k\right) \ddot{\mathbf{x}}_k + \mathbf{g}\left(\boldsymbol{\Theta}_k, \mathbf{x}_k, \dot{\mathbf{x}}_k, k\right) = \mathbf{u}_k \tag{8}$$

$$\boldsymbol{\Theta}_{k+1} = \boldsymbol{\Gamma}\left(\boldsymbol{\Theta}_k, \mathbf{x}_k, \dot{\mathbf{x}}_k, k\right) \tag{9}$$

$$\mathbf{y}_k = \mathbf{h}^*\left(\boldsymbol{\Theta}_k, \mathbf{x}_k, \dot{\mathbf{x}}_k, \mathbf{u}_k, k\right) \tag{10}$$

Eq. (8) is the non-linear equation of motion in discrete time $t_k = k\Delta t,\ k \in \mathbb{N}$. $\mathbf{M}\left(\cdot\right) \in \mathbb{R}^{m\times m}$ is the mass matrix and $\mathbf{g}\left(\cdot\right) \in \mathbb{R}^m$ the force vector of elastic and damping forces. These can depend on the nodal displacement $\mathbf{x} \in \mathbb{R}^m$, the nodal velocity $\dot{\mathbf{x}} \in \mathbb{R}^m$ and the time step k. The damage parameter $\boldsymbol{\Theta} \in \mathbb{R}^p$ describes the change of structural integrity (loss of stiffness, loss of mass, etc.) by location and damage extent. For Structural Health Monitoring this is the parameter which needs to be reconstructed. Moreover, the damage parameter $\boldsymbol{\Theta}$ usually has also influence on the equation of motion. $\mathbf{u} \in \mathbb{R}^m$ is the vector of the external acting loads on the structure. The number of degrees of freedom (DOF) is m. The non-linear function $\boldsymbol{\Gamma}\left(\cdot\right) \in \mathbb{R}^p$ describes the evolution of the damage parameter in Eq. (9). Eq. (10) is the measurement equation which links the model quantities (displacement, velocities and system parameters) with the output $\mathbf{y} \in \mathbb{R}^n$ of the measurement device by means of the function $\mathbf{h}^*\left(\cdot\right) \in \mathbb{R}^n$. The number of measurements equals n.

If the structure can be assumed to be linear, the equation of motion becomes:

$$\mathbf{M}\left(\boldsymbol{\Theta_k}\right) \ddot{\mathbf{x}}_k + \mathbf{C}\left(\boldsymbol{\Theta_k}\right) \dot{\mathbf{x}}_k + \mathbf{K}\left(\boldsymbol{\Theta_k}\right) \mathbf{x}_k = \mathbf{u}_k \tag{11}$$

Here, the structural mass $\mathbf{M}$, the structural stiffness $\mathbf{K}$ and the damping $\mathbf{C}$ still depend on the damage parameter $\boldsymbol{\Theta}$.

Mostly the evolution of the damage parameter $\boldsymbol{\Theta}$ and the structural dynamic vibrations occur on two different time scales. Compared to the structural vibrations, the evolution of damage usually is a rather slow process. Thus, the damage parameter $\boldsymbol{\Theta}$ seems to remain constant during a short time span of data acquisition [1].

Now, a state space model can be defined, in which the unknown damage parameter vector is the state vector. The evolution of it is modeled by a Gaussian Markov process, also called as random walk process [11]

$$\boldsymbol{\Theta}_{k+1} = \boldsymbol{\Theta}_k + \mathbf{w}_k \tag{12}$$

$$\mathbf{y}_k = \mathbf{h}\left(\boldsymbol{\Theta}_k, \left[\mathbf{U}\right]_k, \mathbf{x}_0, \dot{\mathbf{x}}_0, k\right) + \mathbf{v}_k \,, \tag{13}$$

where $\mathbf{w}_k \in \mathbb{R}^p$ is zero-mean white process noise with covariance $\mathbf{Q}_k$, $\mathbf{w}_k \sim N\left(\mathbf{0}, \mathbf{Q}_k\right)$. Here, the measurement equation in Eq. (13) is defined slightly different as above. Unlike Eq. (10), the output measurement data are obtained depending on the initial nodal displacement and velocity $\mathbf{x}_0$ and $\dot{\mathbf{x}}_0$ and vector $\left[\mathbf{U}\right]_k = \left[\mathbf{u}_1,\, \mathbf{u}_2, \ldots,\, \mathbf{u}_k\right]^T$, which describes the external load input from the time step 1 to the current time step k. So the equation of motion is implicitly included in the non-linear measurement equation $\mathbf{h}\left(\cdot\right) \in \mathbb{R}^n$. $\mathbf{v}_k \in \mathbb{R}^n$ represents the measurement noise with covariance $\mathbf{R}_k$, $\mathbf{v}_k \sim N\left(\mathbf{0}, \mathbf{R}_k\right)$. For reasons of clarity and without loss of generality, in the remainder of this paper it is assumed that $\mathbf{x}_0 = \mathbf{0}$ and $\dot{\mathbf{x}}_0 = \mathbf{0}$.

4 Extended L_1-minimizing Kalman Filter

In the following, the concept of L_1-minimizing sparse reconstruction is incorporated into an Extended Kalman Filter framework. Loffeld et al. were the first to propose an L_1-minimizing Kalman filter approach for solving underdetermined sparse problems [16]. Here, this idea is adopted to stabilize the extended Kalman Filter parameter estimation process for a large damage parameter space p and a low number of sensors n.

As already pointed out, structural damages due to e.g. cracks lead to a stiffness reduction in a very local area of the system. Thus, it can be assumed that the unknown damage parameter vector $\mathbf{\Theta}$ is sparse. The sparsity will be considered as a constraint, which will be part of the state space model as an additional, non-linear observation. It is promoted by the L_1-norm of the state vector:

$$\hat{\mathbf{y}}_k = \gamma_k = \|\mathbf{\Theta}_k\|_1 = \sum_{j=1}^{p} |\Theta_{j,k}| \tag{14}$$

Starting from $\gamma_0 = \|\mathbf{\Theta}_0\|_1$ the fictive measurement γ_k can now successively be decreased in each time step k by a scaling factor $\alpha < 1$,

$$\gamma_k = \alpha \|\mathbf{\Theta}_{k-1}\|_1 \tag{15}$$

The scalar Eq. (14) pushes down the L_1-norm of the state vector and thus leads to a sparse estimation of $\mathbf{\Theta}$. The now obtained augmented observation vector $\tilde{\mathbf{y}}_k$ reads as follows:

$$\tilde{\mathbf{y}}_k = \begin{bmatrix} \mathbf{y}_k \\ \gamma_k \end{bmatrix} = \begin{bmatrix} \mathbf{h}\left(\mathbf{\Theta}_k, [\mathbf{U}]_k, k\right) \\ \|\mathbf{\Theta}_k\|_1 \end{bmatrix} + \begin{bmatrix} \mathbf{v}_k \\ \nu_k \end{bmatrix} \tag{16}$$

$\nu_k \in \mathbb{R}$ reflects the uncertainty of the additional L_1-minimizing observation equation.

For estimating the states of the now obtained non-linear state space model an Extended-Kalman Filter is used. The EKF linearizes the non-linear model in each time step around the *a posteriori* estimated state vector, using a first-order Taylor series approximation. After linearization the traditional prediction-correction algorithm of the Kalman Filter can be applied.

Starting from the initial conditions $\hat{\mathbf{\Theta}}_{0|0}$ and $\mathbf{P}_{0|0}$, a forecast of the state is made in the prediction step:

$$\hat{\mathbf{\Theta}}_{k|k-1} = \hat{\mathbf{\Theta}}_{k-1|k-1} \tag{17}$$

$$\mathbf{P}_{k|k-1} = \mathbf{P}_{k-1|k-1} + \mathbf{Q}_k \tag{18}$$

In the corrector step the actual measurements $\mathbf{y}_k$ and the fictive measurements $\tilde{\mathbf{y}}_k$ are considered and compared with the prediction. The residual $\Delta\tilde{\mathbf{y}}_k$ is weighted by the Kalman gain matrix $\mathbf{K}_k$ and added to the prediction $\hat{\mathbf{\Theta}}_{k|k-1}$:

$$\Delta\tilde{\mathbf{y}}_k = \tilde{\mathbf{y}}_k - \tilde{\mathbf{h}}\left(\mathbf{\Theta}_{k|k-1}, [\mathbf{U}]_k, k\right) \tag{19}$$

$$\mathbf{K}_k = \mathbf{P}_{k|k-1}\mathbf{H}_k^T \left(\mathbf{H}_k \mathbf{P}_{k|k-1} \mathbf{H}_k^T + \tilde{\mathbf{R}}_k\right)^{-1} \tag{20}$$

$$\hat{\mathbf{\Theta}}_{k|k} = \hat{\mathbf{\Theta}}_{k|k-1} + \mathbf{K}_k \Delta\tilde{\mathbf{y}}_k \tag{21}$$

$$\mathbf{P}_{k|k} = \left(\mathbf{I} - \mathbf{K}_k \mathbf{H}\right) \mathbf{P}_{k|k-1} \tag{22}$$

For the proposed damage parameter estimation strategy only the measurement equation is non-linear and needs to be linearized:

$$\mathbf{H}_k = \begin{bmatrix} \left.\frac{\partial \mathbf{h}\left(\mathbf{\Theta}_k, [\mathbf{U}]_k, k\right)}{\partial \mathbf{\Theta}}\right|_{\mathbf{\Theta}=\hat{\mathbf{\Theta}}_{k|k-1}} \\ \left.\frac{\partial \|\mathbf{\Theta}_k\|_1}{\partial \mathbf{\Theta}}\right|_{\mathbf{\Theta}=\hat{\mathbf{\Theta}}_{k|k-1}} \end{bmatrix} \tag{23}$$

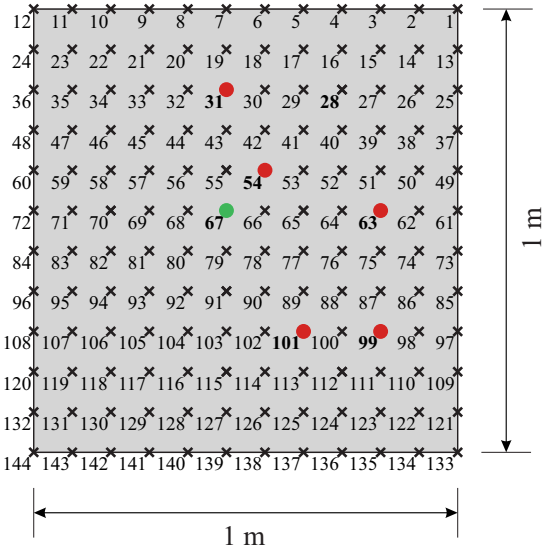


Figure 2: Node numbering of the finite element plate model; node 31, 54, 63, 99 and 101 are acceleration measurement positions; node 67 is the excitation position

The derivative of $\mathbf{h}(\cdot)$ with respect to $\boldsymbol{\Theta}$ can be either approximated by the finite difference method or determined analytically by using the system-output sensitivity for linear structures. A detailed description of the output-sensitivity calculation can be found e.g. in [17].

The Jacobian matrix of the L_1-minimizing constraint

$$\frac{\partial \|\boldsymbol{\Theta}\|_1}{\partial \boldsymbol{\Theta}} = \left[\frac{\partial \|\boldsymbol{\Theta}\|_1}{\partial \Theta_1} \frac{\partial \|\boldsymbol{\Theta}\|_1}{\partial \Theta_2} \cdots \frac{\partial \|\boldsymbol{\Theta}\|_1}{\partial \Theta_p} \right] , \tag{24}$$

can be obtained by:

$$\frac{\partial \|\boldsymbol{\Theta}\|_1}{\partial \Theta_j} = \operatorname{sign}(\boldsymbol{\Theta}_j) \tag{25}$$

The determination of the partial derivative in each time step k is computationally very expensive. In order to save computing time, this can be performed just in every 2nd or 3rd step. This also helps to stabilize the filter process in the beginning.

As usually structural damage has no direct impact on the measurements at the same specific time step k, it is advisable to extend the physical measurement $\mathbf{y}_k$ and to process a block of l physical measurements in each Kalman Filter step:

$$\begin{bmatrix} \mathbf{y}_k \\ \mathbf{y}_{k+1} \\ \mathbf{y}_{k+2} \\ \vdots \\ \mathbf{y}_{k+l} \end{bmatrix} = \mathbf{h}^l \left(\boldsymbol{\Theta}_k, [\mathbf{U}]_k, k, l \right) + \mathbf{v}_k^l \tag{26}$$

By this *en bloc* processing, the filter is no longer operating in real time but with a time lag $t_l = l\Delta t$ in the past.

5 Proof-of-Concept

In order to demonstrate the functionality of the proposed damage identification strategy a proof-of-concept simulation study is performed. The observed mechanical structure is a simple square aluminum plate of

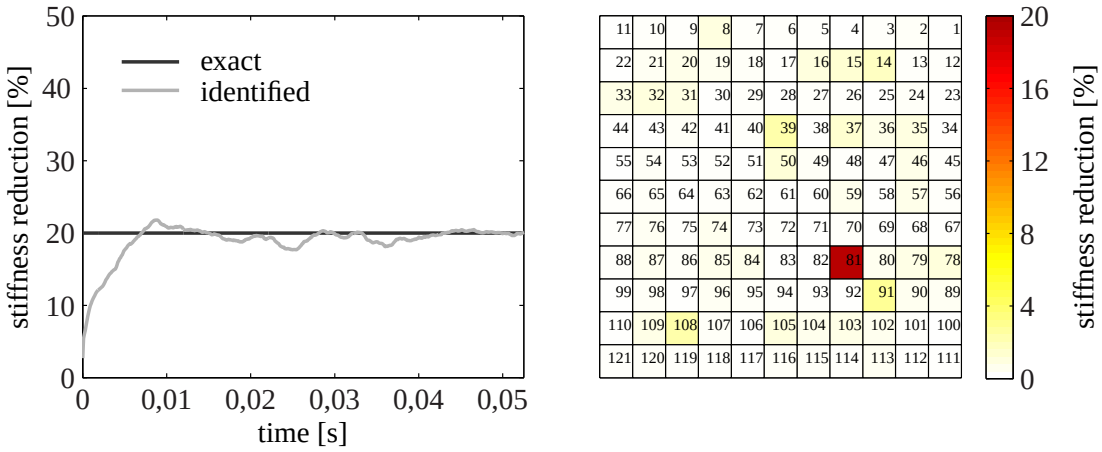


Figure 3: Damage identification result; left: evolution of damage parameter no. 81; right: estimated stiffness reduction for all elements at the end of simulation time

1m $\times$ 1m edge length and 2mm thickness. It is clamped on all sides. The structural dynamics of the plate due to external forces are described by a finite element model. The plate is modeled by 121 quadratic shell elements and 144 nodes (each with 6 degrees of freedom), see Fig. 2. The employed structural responses are simulated acceleration measurements perpendicular to the plate plane. The obtained simulated measurement signals are low-pass filtered by a cut-off frequency of 200Hz. Thus, for damage detection only the low frequency content of the time signals is employed. White Gaussian noise, with a standard deviation of three percent of the maximum measurement value, is added to the simulated outputs to imitate real acceleration measurement data. Only five accelerometers are used for damage identification.

A widely used approach to introduce structural damage on a substructure or element level which represents the changes of the structural stiffness $\Delta\mathbf{K}$ compared to a reference model $\mathbf{K}_0$ is:

$$\Delta\mathbf{K} = \sum_j \mathbf{K}_j \boldsymbol{\Theta}_j \tag{27}$$

where $\mathbf{K}_j$ is the jth substructure or element stiffness matrix, respectively with appropriate dimension. By determination of the unknown correction parameters $\boldsymbol{\Theta} = [\Theta_1, \Theta_2, \ldots, \Theta_p]$ the damage can be localized and quantified.

5.1 Single and multiple damage scenarios

In a first simulation study the stiffness of element no. 81 has been decreased by 20%. The plate is excited by an impulse force load perpendicular to the surface at node no. 67 of known time history. The obtained simulated acceleration time data are now used for structural damage identification. Fig. 3 shows the identification result in the left part. Here, the evolution of the damage parameter corresponding to element no. 81 is plotted over time. It can be seen that starting from initial conditions (all damage parameters zero) the parameter of the damage element tends to the true value of stiffness reduction. The right part of Fig. 3 shows that for all the other elements the corresponding damage parameters are close to zero. Thus, the damage is localized and quantified.

Fig. 4 compares the damage parameter estimation results for the proposed Extended Kalman Filter method with and without additional L_1-minimizing observation. It is obvious that no clear damage estimation result can be achieved without L_1-minimizing observation. Even though the reconstructed damage parameter error for the damage element no. 81 is not too big, many more element stiffness changes (reduction and increase) are identified. On the other hand, it can be clearly distinguished between damaged and undamaged elements if the additional observation is used, as L_1-minimization promotes this sparse solution.

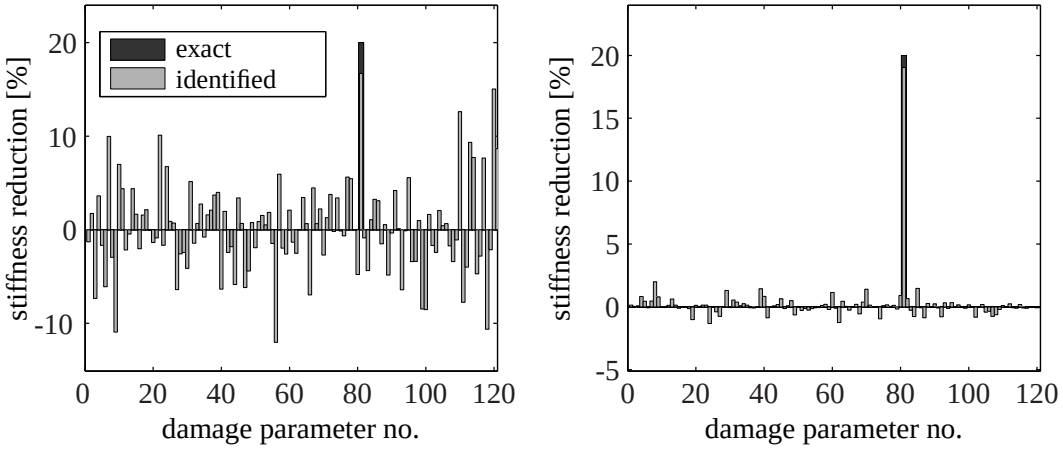


Figure 4: Comparison of damage parameter estimation; left: Kalman filter estimation without additional L_1-observation; right: Estimation result with L_1-minimizing observation

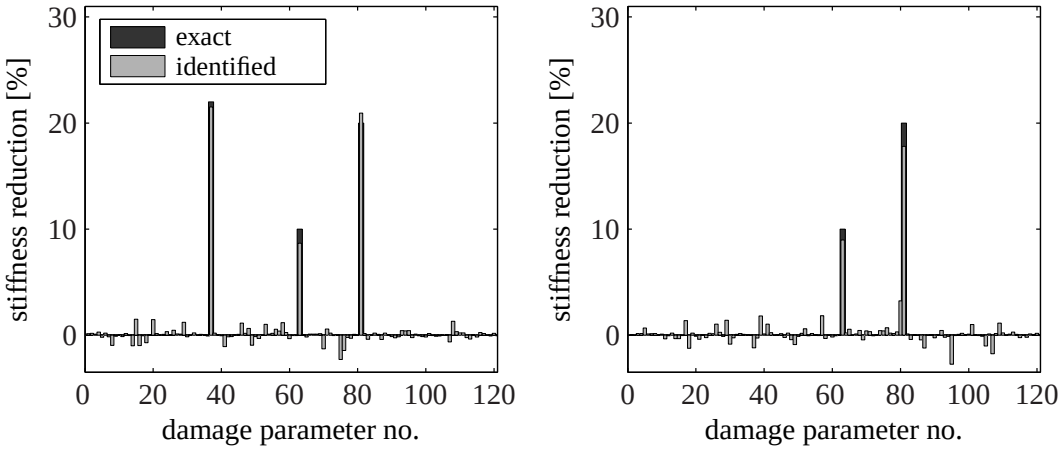


Figure 5: Multiple damage scenarios both identified with additional L_1-observation: three damaged elements no. 37, no. 63 and no. 81 (left); two damaged elements no. 63 and no. 81 (right)

In a next step a multiple damage scenario is investigated. Here the plate structural damage is modelled by a stiffness reduction of various elements with different amount. Which means the damage parameter vector needs to be less sparse than in the case of a single element stiffness change. Fig. 5 shows the damage identification results at the end of the simulation time for two and three damaged elements. In both cases a similar clear damage identification as before is obtained.

5.2 Monte Carlo simulation

In section 5.1 some selected damage identification results have been shown. However, for a statistical validation several Monte Carlo simulations are performed. In a first simulation study 5000 Monte Carlo trials with different damage scenarios are carried out. In each of the 5000 trials a single damage is introduced in the structure by reducing the stiffness of one element. The damage location is chosen randomly with uniform distribution over all elements. The damage extent is also a random parameter with Gaussian distribution (mean value: 25% stiffness reduction; standard deviation: 5%).

The obtained results by using the proposed algorithm are displayed in Fig. 6. For each element, Fig. 6 shows on the right hand side the mean value of the relative deviation for damage extent estimation. The

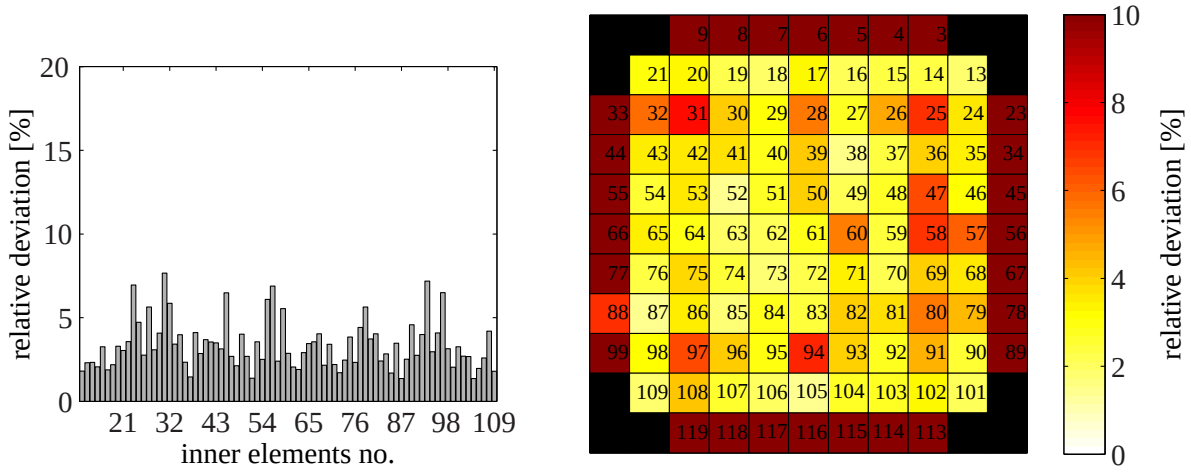


Figure 6: Result of the Monte Carlo simulation for a single damaged element: Right: Representation of the averaged deviation; Left: Mean deviation of the inner structural elements

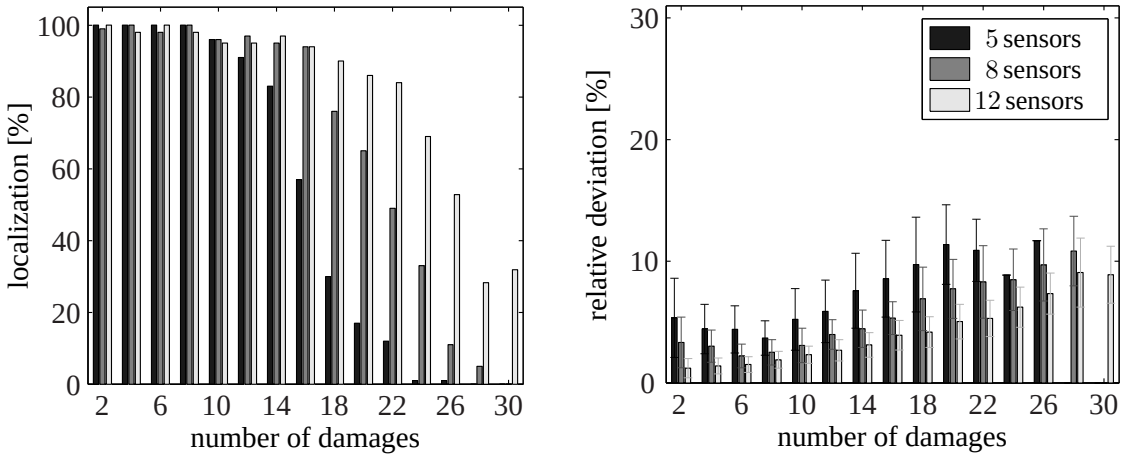


Figure 7: Monte Carlo simulation: Influence of the sensors and damage number on the localization reliability (left) and the reconstruction of the extent of damage (right)

results indicate clearly a bad performance of estimating a damage, which is introduced in an element along the bounderies. As the plate is clamped on all sides, vibration-based damage detection is very difficult for such elements placed at the clamped edges. Nevertheless, the damage extends estimation for the inner plate elements are very reliable. The mean estimation error is distinctly under 10% (see Fig. 6 left). Moreover, the damage location for an inner plate element stiffness reduction is always detected correctly.

The second Monte Carlo simulation analyses the influence of the employed sensor network and the number of damaged elements. In this study three different sensor setups (5, 8 or 12 sensors) are compared. For each setup 5000 Monte Carlo trials with different damage scenarios are carried out. In each of the 5000 trials multiple damages are introduced in the structure by reducing the stiffness of various elements. Again, the damage locations are chosen randomly with uniform distribution over all elements.

The obtained damage identification results are displayed in Fig. 7. On the left hand side the damage localization reliability is plotted against the number of damaged elements. An estimated damage pattern is only defined as correct if all stiffness-reduced elements have been detected correctly. It can be seen that for a larger number of damages the localization reliability decreases. However, if more sensors are used this reliability can be improved. The relative deviations of damage extend estimation shows a similar behavior

(see Fig. 7 right). Here, the relative deviation is calculated only if the damage pattern is localized correctly.

5.3 Model error compensation

As the proposed damage identification strategy is a model-based approach, modeling errors will have an impact on the reconstruction results. For most practical applications there are some modeling parameters which are subject to uncertainties, e.g. the global modulus of elasticity, the mass density or the correct definition of the boundary conditions.

In order to compensate possible modeling errors, such model parameters can also be integrated in the estimation process. Thus, the algorithm will fit the unknown model parameters to the measurement output data. To this end, the parameter vector $\boldsymbol{\Theta}$ needs to be extended by these model parameters:

$$\tilde{\boldsymbol{\Theta}} = \left[\Theta_1, \Theta_2, \cdots, \Theta_p, \Theta_1^m, \cdots, \Theta_n^m\right] \tag{28}$$

Here the first p values are the damage parameters as previously defined. The last n parameters describe now the global model parameters.

Fig. 8 shows in the left part a damage reconstruction result by using an incorrect structural model. The model used in the reconstruction process varies from the one, which is employed to create the measurement data, not only in terms of the structural damage but also in terms of a modulus of elasticity and mass density. The deviation is 7% in mass density and 10% in modulus. However, a very clear estimation of the damage pattern can be obtained. The damage elements no. 41 and 85 are identified correctly and also the damage extent is reconstructed properly. Additionally, the model parameters mass density and modulus of elasticity have been identified, as shown in the right part of Fig. 8.

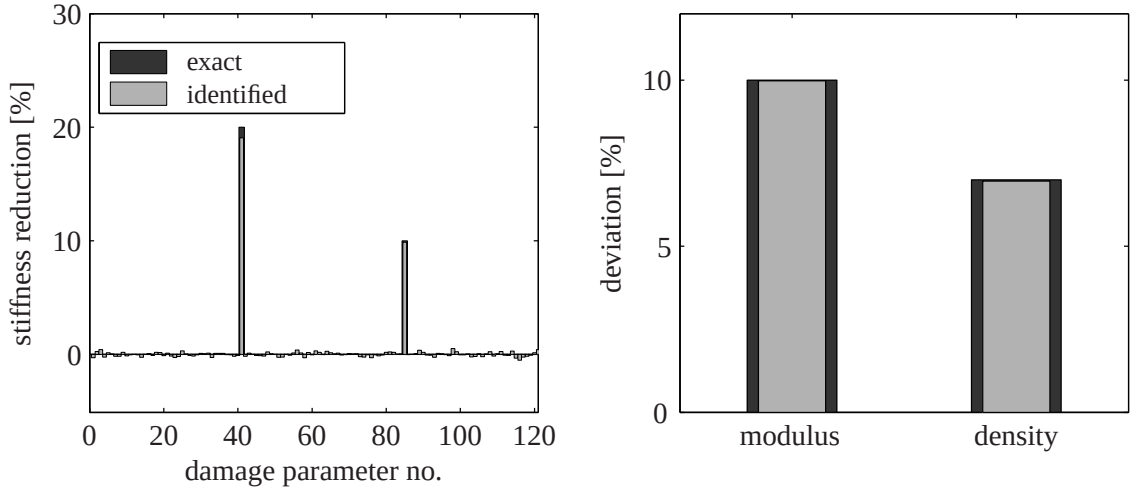
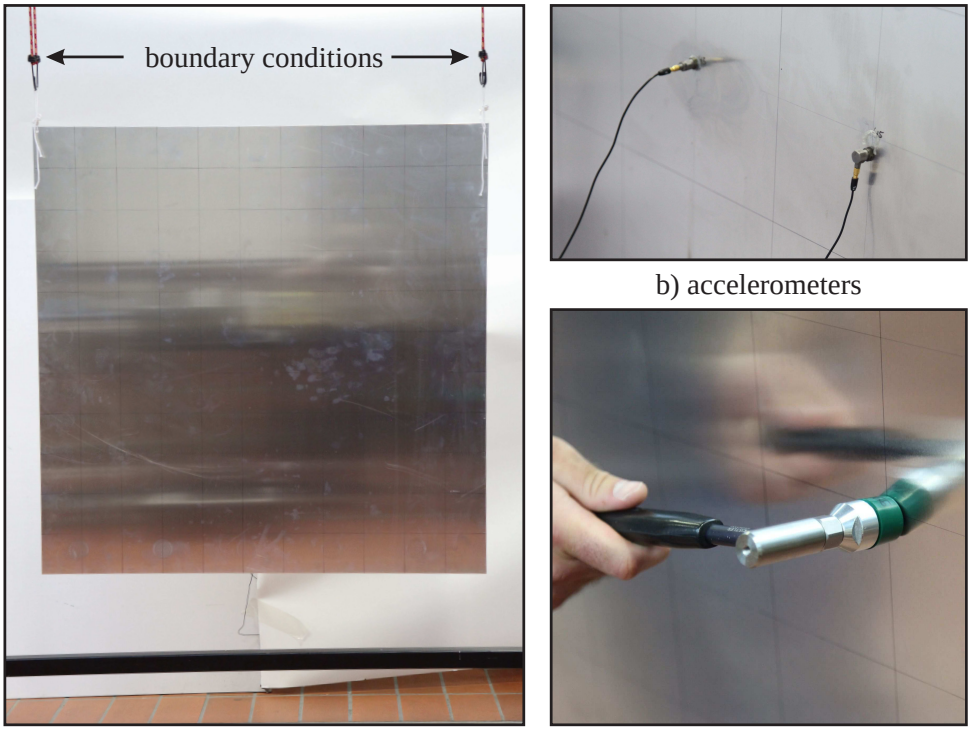


Figure 8: Left: Damage identification by using an incorrect structural model; Right: Estimation of initially wrong model parameters (Young's modulus and mass density)

6 Experimental results

For experimental validation a test bench analogous to the simulation model (with the same plate properties) is set up. Seven piezoelectric accelerometers are mounted on the plate back side. The plate is excited by an impact hammer, which has a built-in force sensor (compare Fig. 9). The analogy of test bench and simulation allows using the same reference FE-model as before. The sampling rate for acquisition of the measurement



a) aluminum plate

b) accelerometers

c) impact hammer

Figure 9: Experimental validation on aluminum plate; a) plate structure, b) piezoelectric accelerometers applied on plate, c) impact excitation by means of impact hammer

data throughout all experimental investigations is 2kHz. These data are filtered by a 500Hz analog low-pass filter.

Two magnets, each weighing 0.12 kg, are attached to both sides of the plate at different nodes. Thus, damage is modeled as a mass increase of 0.24 kg. As the plate weighs 5.4 kg in total, this corresponds to a punctual additional mass of 4.44%.

Fig. 10 displays two reconstruction results. On the left hand side the reconstructed and the actual damage parameter vector can be seen. The right part shows the identified damage pattern. The experimental results show that a strong emphasis on L_1-minimizing observations is needed to obtain meaningful experimental results. This emphasis on L_1-minimization stabilizes the EKF, but also leads to a significant underestimation of the additional mass. On average, the deviation of the reconstructed mass is 37.2%. Nevertheless, the simulated damage can be localized correctly.

7 Conclusion

In this contribution a new time domain method for damage detection has been proposed. The local character of damage justifies the use of sparse reconstruction strategies for the ill-posed inverse problem. Sparsity of the estimated state vector of damage parameters is ensured within the Extended Kalman Filter by adding a fictive non-linear L_1-minimizing observation.

It has been shown that the proposed reconstruction method is able to determine the damage location and extent simultaneously. In contrast to the Extended Kalman Filter process without additional L_1-observation a clear damage pattern is obtained. This was shown for single damage scenarios as well as for multiple damage events. A statistical validation has been performed by means of a Monte Carlo simulation. Considering the damage parameter space of size 121 in the demonstrated study, the number of sensors using only 5

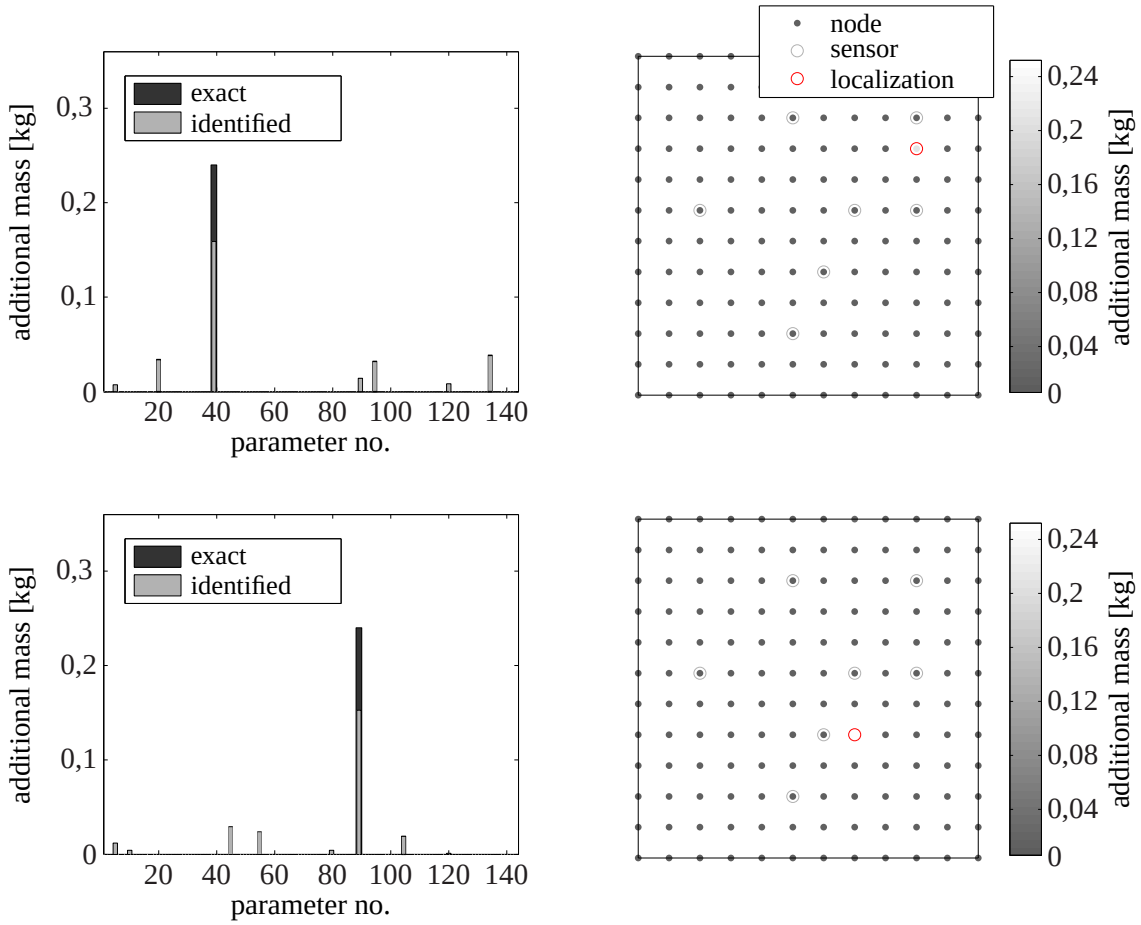


Figure 10: Experimental reconstruction results for the detection of an additional mass of 0.24 kg at two different plate positions; left: Identified and exact parameter vector; right: Reconstructed damage pattern

to 12 accelerometers is significantly lower than the parameter space. Moreover, modeling error can be compensated by including those model parameters, which are subject to uncertainties. Besides the unknown model parameter, this approach can also be used to reconstruct damage under changing environmental and operational conditions (EOC), if the EOC sensitive parameters are also included in the parameter vector.

References

[1] D. Balageas, C.-P. Fritzen, A. Güemes, *Structural Health Monitoring*, Hermes Science Publishing (2006).

[2] A. W. Smyth, S. F. Masri, A. G. Chassiakos, T. K. Caughey, *On-line parametric identification of MDOF nonlinear hysteretic systems*, Journal of Engineering Mechanics, Vol. 125, No. 2, (1999), pp. 133-142.

[3] J. N. Yang, S. Lin, *Identification of parametric variations of structures based on least squares estimation and adaptive tracking technique*, Journal of Engineering Mechanics, Vol. 131, No. 3, (2005), pp. 290-298.

[4] B. Wu, T. Wang, *Model updating with constrained unscented Kalman filter for hybrid testing*, Smart Structures and Systems, Vol. 14, No. 6, (2014), pp. 1105-1129.

[5] C. Wan, T. Sato, Z. Wu, J. Zhang, *Damage identification using chaotic excitation*, Smart Structures and Systems, Vol. 11, No. 1, (2013), pp. 87-102.

[6] J. Ching, J. L. Beck, K. A. Porter, *Bayesian state and parameter estimation of uncertain dynamical systems*, Probabilistic Engineering Mechanics, Vol. 21, No. 1, (2006), pp. 81-96.

[7] T. Sato, K. Qi, *Adaptive H_∞ filter: its application to structural identification*, Journal of Engineering Mechanics, Vol. 124, No. 11, (1998), pp. 1233-1240.

[8] Y. Ding, L. Guo, *Structural identification based on incomplete measurements with iterative Kalman filter*, Structural Engineering and Mechanics, Vol. 59, No. 6, (2016), pp. 1037-1054.

[9] A. Corigliano, S. Mariani, *Parameter identification in explicit structural dynamics: performance of the extended Kalman filter*, Computer Methods in Applied Mechanics and Engineering, Vol. 193, No. 36, (2016), pp. 3807-3835.

[10] X. Liu, P. J. Escamilla-Ambrosio, N. A. J. Lieven, *Extended Kalman filtering for the detection of damage in linear mechanical structures*, Journal of Sound and Vibration, Vol. 325, No. 4, (2009), pp. 1023-1046.

[11] H. Ebrahimian, R. Astroza, J. P. Conte, *Extended Kalman filter for material parameter estimation in nonlinear structural finite element models using direct differentiation method*, Earthquake Engineering and Structural Dynamics, Vol. 44, No. 10, (2015), pp. 1495-1522.

[12] C. Zhang, J.-Z. Huang, G.-Q. Song, L. Dai, H.-K. Li, *Detection of structural damage via free vibration responses by extended Kalman filter with Tikhonov regularization scheme*, Structural Monitoring and Maintenance, Vol. 3, No. 2, (2016), pp. 115-127.

[13] E. J. Candès, M. B. Wakin, *An introduction to compressive sampling*, IEEE Signal Processing Magazine, Vol. 25, No. 2, (2016), pp. 21-30.

[14] D. L. Donoho, X. Huo, *Uncertainty principles and ideal atomic decomposition*, IEEE Transactions on Information Theory, Vol. 47, No. 7, (2001), pp. 2845-2862.

[15] A. N. Tikhonov, V. I. A. Arsenin, *Solutions of Ill-Posed Problems*, Scripta Series in Mathematics, Winston (1977).

[16] O. Loffeld, A. Seel, M. Heredia Conde, L. Wang, *A Nullspace Based L_1 Minimizing Kalman Filter Approach to Sparse CS Reconstruction*, *Proceedings of the 11th European Conference on Synthetic Aperture Radar, Hamburg, Germany, 2016*.

[17] C.-P. Fritzen, D. Jennewein, D. Buchen, *Model based damage detection from vibration data*, *Proceedings of The International Seminar on Modal Analysis 1996*.

Transmissibility *versus* damage detection

N. M. M. Maia[1], M. M. Neves[1], T. A. N. Silva[2]
[1] LAETA, IDMEC, Instituto Superior Técnico, Universidade de Lisboa
Av. Rovisco Pais, 1049-001, Lisboa, Portugal
e-mail: **nuno.manuel.maia@tecnico.ulisboa.pt**

[2] NOVA UNIDEMI, Department of Mechanical and Industrial Engineering, Faculty of Science and Technology, Universidade NOVA de Lisboa
Campus de Caparica, 2829-516 Caparica, Portugal

Abstract
The generalization of the motion transmissibility to multiple degrees of freedom systems establishes the linear relationship between two sets of responses, when a set of loads is applied at some given coordinates. In previous works, the authors have developed algorithms based on the transmissibility that allow for the identification of the applied loads. Such an identification includes the determination of the quantity of loads, their localization and also their magnitude. In damage detection, one is also interested in determining the number of defects, their localization and to quantify their extent. If one thinks of a defect as a local structural modification, one can show that it may be interpreted as an alteration of the dynamic load at that location. In this paper, one presents a transmissibility-based force identification technique as a means to detect, localize and quantify structural damages. Some numerical examples are presented to illustrate the performance of the proposed procedure.

1 Introduction

In this paper the detection of damage is addressed as a force identification problem. A very brief summary on the force identification issue is given next.

In some engineering applications it may be important to estimate operational forces at inaccessible locations of installed machinery [1, 2], forces transmitted to the supports [3,4], aerodynamic loads on a rotorcraft blade [5], or on turbine blades [6]. This is normally a difficult problem, namely when one has a limited amount of response data. The search for unknown forces from a set of measured responses is an inverse problem, which is often ill-posed [4], due to lack of information. There are techniques that help overcoming some of these problems, like regularization techniques [4], pseudo-inversion [7], data filtering [8], singular value decomposition (SVD) and Tikhonov regularization [9-11].

When the location of the forces is known, the objective is their reconstruction, as in [12, 13]. In other cases, one has to estimate the location, magnitude and phase of the forces acting on the structure, as in [14].

The main objective of this paper is to identify structural damage using a force identification method, based on the displacement transmissibility [15-20], as explained in Section 3.

2 Damage identification

The dynamic equilibrium equation of a linear viscoelastic structure with *n dofs*, is given by:

$$\boldsymbol{M}\ddot{\boldsymbol{y}} + \boldsymbol{C}\dot{\boldsymbol{y}} + \boldsymbol{K}\boldsymbol{y} = \boldsymbol{f} \tag{1}$$

where $\boldsymbol{M}$, $\boldsymbol{C}$ and $\boldsymbol{K}$ are the $n \times n$ mass, damping and stiffness matrices of the structure, respectively; $\boldsymbol{y}$, $\dot{\boldsymbol{y}}$, and $\ddot{\boldsymbol{y}}$ are the nodal displacement, velocity and acceleration, respectively and $\boldsymbol{f}$ is the applied force vector. When a damage occurs, there will be a modification that can happen in the mass, in the stiffness, or in the damping, or still in a combination of those three properties. For instance, a crack will decrease the stiffness locally and will increase the damping due to the increase of the friction, but will not change significantly the mass. A decrease in mass due to corrosion will also cause a decrease in the stiffness, but probably will not affect much the damping. In general, after some kind of damage has happened, we may say that the structure will be governed by a new equation, where the new properties are expressed by $\boldsymbol{M} + \Delta\boldsymbol{M}$, $\boldsymbol{C} + \Delta\boldsymbol{C}$, and $\boldsymbol{K} + \Delta\boldsymbol{K}$; applying the same force, the response will be different and the new equilibrium equation will be

$$\left(\boldsymbol{M} + \Delta\boldsymbol{M}\right)\ddot{\boldsymbol{y}}_{\Delta} + \left(\boldsymbol{C} + \Delta\boldsymbol{C}\right)\dot{\boldsymbol{y}}_{\Delta} + \left(\boldsymbol{K} + \Delta\boldsymbol{K}\right)\boldsymbol{y}_{\Delta} = \boldsymbol{f} \tag{2}$$

or

$$\boldsymbol{M}\ddot{\boldsymbol{y}}_{\Delta} + \boldsymbol{C}\dot{\boldsymbol{y}}_{\Delta} + \boldsymbol{K}\boldsymbol{y}_{\Delta} = \boldsymbol{f} - \left(\Delta\boldsymbol{M}\ddot{\boldsymbol{y}}_{\Delta} + \Delta\boldsymbol{C}\,\dot{\boldsymbol{y}}_{\Delta} + \Delta\boldsymbol{K}\,\boldsymbol{y}_{\Delta}\right) \tag{3}$$

If the damage occurs at coordinates "*D*", the new force corresponding to those coordinates is:

$$\boldsymbol{f}_D = -\left(\Delta\boldsymbol{M}\ddot{\boldsymbol{y}}_D + \Delta\boldsymbol{C}\dot{\boldsymbol{y}}_D + \Delta\boldsymbol{K}\boldsymbol{y}_D\right) \tag{4}$$

Equation (4) means that the change in the dynamic behavior of the structure due to the existence of damage is equivalent to applying additional forces at coordinates "*D*", the ones where the modification of the properties due to the damage has occurred. Assuming harmonic excitation, $\boldsymbol{f}_D = \boldsymbol{F}_D e^{i\omega t}$ and $\boldsymbol{y}_D = \boldsymbol{Y}_D e^{i\omega t}$ (in steady-state conditions), we can re-write (4), as

$$\boldsymbol{F}_D = -\left(\Delta\boldsymbol{K} - \omega^2\Delta\boldsymbol{M} + i\omega\Delta\boldsymbol{C}\right)\boldsymbol{Y}_D \tag{5}$$

From eq. (5), we conclude that the damage identification problem can be reduced to a force identification problem. As far as we be able to identify the location and the magnitude of the forces, the damage will be localized and we will be able to quantify its extent by evaluating $\Delta\boldsymbol{M}$, $\Delta\boldsymbol{C}$ and $\Delta\boldsymbol{K}$. We shall see in the next section how to identify the forces. Assuming for the moment that we have already done that, let us see how to evaluate the structural modifications: separating (5) into its real and imaginary parts, we obtain:

$$Re\boldsymbol{F}_D + iIm\boldsymbol{F}_D = -\left(\Delta\boldsymbol{K} - \omega^2\Delta\boldsymbol{M} + i\omega\Delta\boldsymbol{C}\right)\left(Re\boldsymbol{Y}_D + iIm\boldsymbol{Y}_D\right) \tag{6}$$

and thus,

$$\begin{aligned} Re\boldsymbol{F}_D &= -\left(\Delta\boldsymbol{K} - \omega^2\Delta\boldsymbol{M}\right)Re\boldsymbol{Y}_D + \omega\Delta\boldsymbol{C}\,Im\boldsymbol{Y}_D \\ Im\boldsymbol{F}_D &= -\left(\Delta\boldsymbol{K} - \omega^2\Delta\boldsymbol{M}\right)Im\boldsymbol{Y}_D - \omega\Delta\boldsymbol{C}\,Re\boldsymbol{Y}_D \end{aligned} \tag{7}$$

Assuming that the structural modifications are concentrated at the nodal *dofs*, i.e., the matrices $\Delta\boldsymbol{M}$, $\Delta\boldsymbol{C}$ and $\Delta\boldsymbol{K}$ are diagonal and so, for each nodal change j ($j = 1 \ldots p$), it follows that

$$\begin{Bmatrix} ReF_D \\ ImF_D \end{Bmatrix}_j = \begin{bmatrix} -ReY_D & \omega^2 ReY_D & \omega ImY_D \\ -ImY_D & \omega^2 ImY_D & -\omega ReY_D \end{bmatrix}_j \begin{Bmatrix} \Delta K \\ \Delta M \\ \Delta C \end{Bmatrix}_j \tag{8}$$

or

$$\underset{(2\times1)}{\left\{F_D(\omega)\right\}_j} = \underset{(2\times3)}{\left[Q(\omega)\right]_j} \underset{(3\times1)}{\begin{Bmatrix} \Delta K \\ \Delta M \\ \Delta C \end{Bmatrix}_j} \qquad j = 1,..,p \tag{9}$$

The problem is undetermined, as for each entry j we have two equations and three unknowns. We need more equations. Taking L frequencies, we can write an over-determined set of equations:

$$\underset{(2L\times1)}{\begin{Bmatrix} \left\{F_D(\omega_1)\right\} \\ \vdots \\ \left\{F_D(\omega_L)\right\} \end{Bmatrix}_j} = \underset{(2L\times3)}{\begin{bmatrix} \left[Q(\omega_1)\right] \\ \vdots \\ \left[Q(\omega_L)\right] \end{bmatrix}_j} \underset{(3\times1)}{\begin{Bmatrix} \Delta K \\ \Delta M \\ \Delta C \end{Bmatrix}_j} \qquad j = 1,..,p \tag{10}$$

In a more compact form,

$$\boldsymbol{F}_{D_{T_j}} = \boldsymbol{Q}_{T_j} \boldsymbol{\Delta}_j \qquad j = 1,..,p \tag{11}$$

where the index *"T"* stands for total. This can be solved in a least-squares sense, as:

$$\boldsymbol{\Delta}_j = \boldsymbol{Q}_{T_j}^{+} \boldsymbol{F}_{D_{T_j}} \qquad j = 1,..,p \tag{12}$$

where $\boldsymbol{Q}_{T_j}^{+}$ is the Moore-Penrose pseudo-inverse of $\boldsymbol{Q}_{T_j}$, given by $\boldsymbol{Q}_{T_j}^{+} = \left(\boldsymbol{Q}_{T_j}^T \boldsymbol{Q}_{T_j}\right)^{-1} \boldsymbol{Q}_{T_j}^T$.

3 Force identification

The force identification problem will be addressed through the use of the displacement transmissibility applied to multiple degree-of-freedom (*MDOF*) systems.

3.1 Transmissibility in *MDOF* systems

The extension of the classical displacement transmissibility has been presented in [15] and developed in [16]. In a different context, the application of the transmissibility to the force identification problem was also studied in [17-20]. A brief summary is given in what follows: we define three sets of *dofs* as illustrated in Fig. 1, two distinct sets *U* and *K* where the responses are measured and the set *A* where the

forces can be applied (and that may overlap some *dofs* of the other sets). Some of these forces may be zero, but the corresponding *dofs* have to be included in the set *A*.

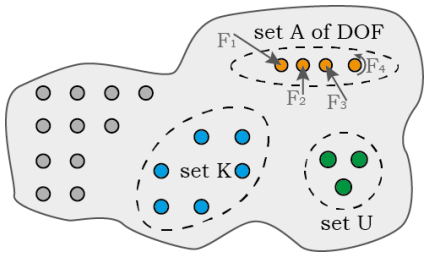


Figure 1: Illustration of the three sets *A*, *U* and *K*

The responses $\boldsymbol{Y}_U$ and $\boldsymbol{Y}_K$ can be related to the applied forces $\boldsymbol{F}_A$ through

$$\begin{aligned} \boldsymbol{Y}_U &= \boldsymbol{H}_{UA}\boldsymbol{F}_A \\ \boldsymbol{Y}_K &= \boldsymbol{H}_{KA}\boldsymbol{F}_A \end{aligned} \tag{13}$$

where $\boldsymbol{H}_{UA}$ is the truncated *FRF* matrix relating the sets of *dofs U* and *A*. Likewise, $\boldsymbol{H}_{KA}$ relates sets *K* and *A*. Eliminating $\boldsymbol{F}_A$ between eqs. (13), one obtains the transmissibility between $\boldsymbol{Y}_U$ and $\boldsymbol{Y}_K$. This involves the pseudo-inverse of $\boldsymbol{H}_{KA}$, i.e.,

$$\boldsymbol{Y}_U = \boldsymbol{T}_{UK}^{A}\boldsymbol{Y}_K = \boldsymbol{H}_{UA}\left(\boldsymbol{H}_{KA}\right)^{+}\boldsymbol{Y}_K \tag{14}$$

where $\boldsymbol{T}_{UK}^{A} = \boldsymbol{H}_{UA}\left(\boldsymbol{H}_{KA}\right)^{+}$ is the transmissibility matrix relating the displacement amplitudes of *U* and *K* for the forces at set *A*. This pseudo-inversion requires the size of set *K* to be larger or equal to the size of the set *A* ($\#K \geq \#A$). As $\boldsymbol{F}_A$ has been eliminated between eqs. (13), the transmissibility depends on the *dofs A*, where the forces can be applied, but not on their amplitudes; in other words, the transmissibility is invariant with respect to the amplitudes of the forces.

3.2 Methodology

The force identification consists of two steps, (i) the determination of the number and position of the forces and (ii) the evaluation of their magnitudes.

The methodology based on the transmissibility requires the knowledge of the response amplitudes $\tilde{\boldsymbol{Y}}_K$ and $\tilde{\boldsymbol{Y}}_U$ (the superscript "~" stands for "measured quantity"). The idea is to find the correct transmissibility matrix $\boldsymbol{T}_{UK}^{A}$, that when applied to $\tilde{\boldsymbol{Y}}_K$ produces an estimated value for $\boldsymbol{Y}_U$ that should be close enough to the measured $\tilde{\boldsymbol{Y}}_U$. As the transmissibility depends on the location of the forces, one has to search for the

right set *A*. When the correlation between $\boldsymbol{Y}_U$ and $\tilde{\boldsymbol{Y}}_U$ happens, it means that the set *A* has been correctly found. Once again, it should be noted that the transmissibility depends only on the location of the forces (set *A*) but not on their amplitudes. For each possible combination of locations A_i, one has:

$$\boldsymbol{Y}_U = \boldsymbol{T}_{UK}^{A_i} \tilde{\boldsymbol{Y}}_K \tag{15}$$

where the index $i = 1,\ldots$, refers to the number of combinations of *dofs* of *A*. The resulting $\boldsymbol{Y}_U$ is compared with the measured $\tilde{\boldsymbol{Y}}_U$, using the following estimation error for each component *j*:

$$error_j = \sum_{\omega} \left(\log \left| \tilde{Y}_{U_j} \right| - \log \left| Y_{U_j} \right| \right)^2, \quad j = 1, \ldots \text{length of } \left(\tilde{\boldsymbol{Y}}_U \right) \tag{16}$$

The accumulated error of each combination is defined as the norm of the vector $\boldsymbol{\varepsilon} = \boldsymbol{error}$. When this error has an absolute minimum, the correct combination of *dofs* A_i has been found. Naturally, the number of loads applied to the structure is not known *a priori*, so we start with one force, then in combinations of two forces, etc. The number of forces that this method can find is limited by the size of the set *K*, as $\#K \geq \#A$. For a specific combination A_i, the reconstructed force is obtained from eq. (13) with the values $\tilde{\boldsymbol{Y}}_K$, as:

$$\boldsymbol{F}_{A_i} = \left(\boldsymbol{H}_{KA_i} \right)^{+} \tilde{\boldsymbol{Y}}_K \tag{17}$$

It is desirable that the finite element model of the original structure is updated enough, to represent as accurately as possible the experimental results of the unmodified structure.

Often, it happens that the combinations involve locations with applied forces together with locations without any force; in those situations the additional locations have near-zero force amplitudes and a near-zero value of accumulated error is expected. This makes the process less efficient and some kind of modification must be sought.

To avoid this issue, a modification has been introduced, consisting of computing both the reconstructed force amplitudes for every combination and the root mean square (*RMS*) in frequency for the forces at each *dof* of A_i. Whenever the accumulated error indicates a location where a load has a near-zero *RMS* amplitude, its respective error is artificially increased. Such a modification improves considerably the efficiency of the force location method. Once the forces are identified, we can reconstruct the magnitude of the damage using eq. (12).

4 Numerical examples

In this section, we shall explore the possibilities of the proposed approach for detecting damage. The test item is a free rectangular plate, whose properties are given in Tab. 1; the plate is modelled using Kirchhoff-Love plate theory for finite elements with 4 nodes, each with 3 *dofs* (1 displacement and 2 rotations), in a 20×20 rectangular mesh. The stiffness and mass matrices are assembled and the damping is considered as negligible for the model, and of the proportional type to simulate the measurements; the proportionality is taken with respect to the stiffness matrix, with a coefficient $\beta = 10^{-9}\ s^{-1}$. The code builds the dynamic stiffness matrices (with and without damping) and consequently their inverses, the *FRF* matrices $\boldsymbol{H}$ and $\tilde{\boldsymbol{H}}$.

Five cases will be considered, (i) a loss of stiffness, (ii) a loss of mass, (iii) increase in damping, (iv) combined loss of stiffness and mass and (v) combined loss of stiffness and increase in damping.

Mass Density	7850 kg/m^3
Young Elasticity Modulus	210 GPa
Thickness	1.9 mm
Width	470 mm
Height	348 mm

Table 1: Plate properties

4.1 Identification of a single force

Before studying the damage cases, it is advisable to verify whether we are able to identify (localize and quantify) just the applied forces. Thus, we apply a transversal harmonic force of *1 N* at node *225* of the *FE* model (Fig. 2), with a frequency range between *1* and *70 Hz* in intervals of *1 Hz*. We can compute the whole *FRF* matrix, but as the force is acting along the axis *Oy*, only the transversal displacement *dofs* along this direction are considered at the nodes where the displacements are "measured".

The "measured" displacements will be $\tilde{Y}_K = \tilde{Y}_{120}$ and $\tilde{Y}_U = \tilde{Y}_{324}$ (*Y* refers to the displacement along *Oy* and the subscript to the node), according to Fig. 2; *#K = 1*, therefore it is only possible to identify a single applied force. There are *441* possible locations for the force. The accumulated error (eq. (16)) for each combination is shown in Fig. 3. The minimum value of the error correctly identifies the force, at node *225*.

In this example the amplitude of the reconstructed force presents a maximum error of $3.7\text{x}10^{-10}$ *%* . When there is no guarantee that the number of forces is just one, we can enlarge the *K* set, allowing the maximum number of possible locations to be *2*, and looking for the combination of the force at node *225* with all the other nodes.

Any other relative minima besides the correct combination, include the correct node *225* with another location where the force presents near-zero amplitude (after reconstruction).

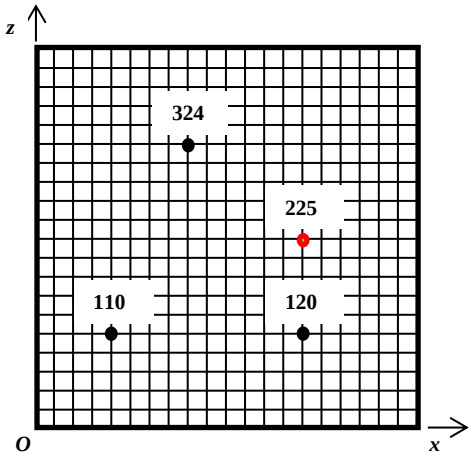


Figure 2: Finite element model of a plate with some representative nodes

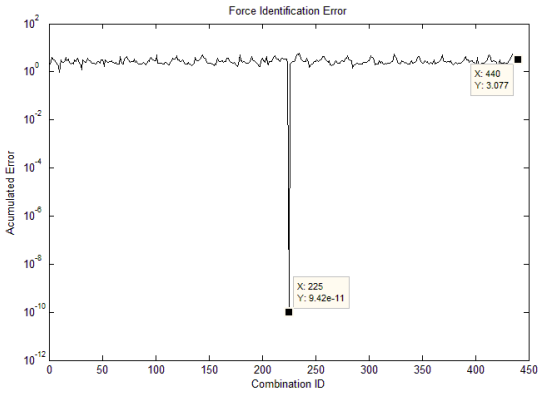


Figure 3: Accumulated error in frequency vs force combination for one applied force (#K=1)

4.2 Identification of a single force

4.2.1 Case 1 – Loss of stiffness

To simulate a crack, we shall consider a decrease of 10% in the stiffness at node *110*. The original values of the stiffness, mass and damping at node 110 are $1.20805x10^{7}$ *N/m*, $3.32452x10^{-3}$ *kg* and $1.20805x10^{-2}$ *Ns/m*, respectively. Only perpendicular displacements are considered. We have considered both the cases without any noise and with some added random (normal) noise to the real and imaginary parts of the "measured" data, to simulate more realistic conditions and to test the sensitivity of the method. Two levels of noise are added: 1% and 3%.A known harmonic force with an amplitude of *1 N* is applied at node *225*. The unmodified model is used to identify the two forces (*#A=2*) using eqs. (14) and (17) and, for example, the "measured" vectors $\tilde{\boldsymbol{Y}}_K = \left\{\tilde{Y}_{120}, \tilde{Y}_{324}\right\}^T$ and $\tilde{\boldsymbol{Y}}_U = \tilde{Y}_{225}$.

The accumulated error has the minimum at the right combination (nodes *225* (applied force) and *110* (force generated by the reduced stiffness). Eq. (17) is used for the force reconstruction. The stiffness reduction is obtained from eq. (12), with a relative error of only $3.5x10^{-8}$ *%* for -10% of damage and no added noise (Tab. 2); Y_{110} is calculated from eq. (15), using one of the "measured" outputs (nodes *120* or *324*) and the transmissibility involving one of those output nodes and node *110*, for the applied force at node *225* and no force applied at node *110*. It should be stressed that we can put the force at node *110* to zero because one of the fundamental transmissibility properties is that the transmissibility is invariant with respect to the magnitude of the applied forces. This means that Y_{110} may be calculated (using eq. 15) from:

$$Y_{110} = T^{225}_{110,120}\tilde{Y}_{120} \tag{18}$$

or

$$Y_{110} = T^{225}_{110,324}\tilde{Y}_{324} \tag{19}$$

4.2.2 Case 2 – Loss of mass

Undertaking a similar study with a variation in the mass, again at node *110*, considering once more a decrease of *10%*, we obtained the results shown in (Tab. 3). The same "measured" vectors $\tilde{\boldsymbol{Y}}_K = \left\{\tilde{Y}_{120}, \tilde{Y}_{324}\right\}^T$ and $\tilde{\boldsymbol{Y}}_U = \tilde{Y}_{225}$ have been used.

Damage (%)	Imposed ΔK [N/m]	Added noise level (%)	Localization	Identified ΔK [N/m]	Relative error (%)
-10	-1.20805E+06	0	Y (node 110)	-1.20805E+06	3.50E-08
		1	Y (node 110)	-1.76911E+06	4.64E+01
		3	N (node 187)	---	---

Table 2: Identification of a loss of stiffness

Damage (%)	Imposed ΔM [kg]	Added noise level (%)	Localization	Identified ΔM [N/m]	Relative error (%)
-10	-3.324500E-04	0	Y (node 110)	-3.324500E-04	7.90E-05
		1	N (node 189)	---	---
		3	N (node 165)	---	---

Table 3: Identification of a loss of mass

4.2.3 Case 3 – Increase of damping

Here we impose an increase of ten times (1000%) in the damping, again at node *110*. The results are given in (Tab. 4), always using the "measured" vectors $\tilde{\boldsymbol{Y}}_K = \left\{\tilde{Y}_{120}, \tilde{Y}_{324}\right\}^T$ and $\tilde{\boldsymbol{Y}}_U = \tilde{Y}_{225}$.

Damage (%)	Imposed ΔC [Ns/m]	Added noise level (%)	Localization	Identified ΔC [Ns/m]	Relative error (%)
+1000	+1.20805E-01	0	Y (node 110)	+1.20226E-01	4.80E-01
		1	Y (node 110)	+2.67367E-01	1.21E+02
		3	N (node 109)	---	---

Table 4: Identification of an increase in damping

4.2.4 Case 4 – Simultaneous loss of stiffness and mass

Here, we introduced a variation of 10% in both the stiffness and mass in node *110*. The results are presented in Tab. 5, using the "measured" vectors $\tilde{\boldsymbol{Y}}_K = \left\{\tilde{Y}_{120}, \tilde{Y}_{324}\right\}^T$ and $\tilde{\boldsymbol{Y}}_U = \tilde{Y}_{225}$.

Damage (%)	Imposed ΔK [N/m] and ΔM [kg]	Added noise level (%)	Localization	Identified ΔK [N/m] and ΔM [kg]	Relative error (%)
-10	-1.20805E+06 -3.324500E-04	0	Y (node 110)	-1.20805E+06 -3.324642E-04	6.30E-08 4.27E-03
		1	Y (node 110)	-1.75934E+06 -1.23978E+01	4.56E+01 --
		3	Y (node 110)	-1.36993E+06 -4.65631E+00	1.34E+01 --

Table 5: Identification of a loss of stiffness and mass

4.2.5 Case 5 – Simultaneous loss of stiffness and increase in damping

Now, we introduce a decrease of 10% in the stiffness and a 1000% increase in the damping, always at node *110* and for the same "measured" vectors $\tilde{\boldsymbol{Y}}_K = \left\{\tilde{Y}_{120}, \tilde{Y}_{324}\right\}^T$ and $\tilde{\boldsymbol{Y}}_U = \tilde{Y}_{225}$. The results are presented in Tab. 6.

Damage (%)	Imposed ΔK [N/m] and ΔC [Ns/m]	Added noise level (%)	Localization	Identified ΔK [N/m] and ΔC [Ns/m]	Relative error (%)
-10 in K +1000 in C	-1.20805E+06 +1.20805E-01	0	Y (node 110)	-1.20805E+06 0.82239E-02	6.30E-08 9.32E+01
		1	Y (node 110)	-2.84822E+06 +7.6455E-02	1.36E+02 3.67E+01
		3	Y (node 165)	---	---

Table 6: Identification of a loss of stiffness and increase in damping

5 Discussion

The results of these numerical simulations without added noise show that in almost all the situations the localization of the damage is achieved with good accuracy; When the data is "perfect", i.e., without any added noise, the quantification of damage is always correct, except when the change in the damping is considered. When noise is added to the "measured" responses, the results show a very high sensitivity of the method to this parameter, as it is common in such inverse problems. Up to 1% of added random noise the localization of the damage still worked well in most cases. However, the quantification of the damage

exhibited very high errors, as the noise strongly affects the reconstruction of the forces. The stiffness is the property that better "resists" to the existence of noise in the data, namely for the localization step. The most sensitive is the damping.

These results still have space for some improvements. Note that none of the known tools to deal with noisy signals have been used in this work; the authors will be addressing this in future work.

6 Conclusions

It has been shown that it is possible to establish a relation between the identification of damage and the identification of dynamic forces. While the damage is modeled through the variation of the structure properties (mass, stiffness and damping), the force identification is accomplished by a methodology that uses the displacement transmissibility between groups of coordinates. Whenever a damage occurs, new forces directly related to the changes in the dynamic properties appear and those additional forces are then identified using the transmissibility.

In principle, and in the context of damage identification, the procedure seems potentially suitable for the detection, localization and also quantification of a structural modification, or even more than one. The results without any added noise illustrate the effectiveness of the method. The simulations with added random noise up to 1% and damages of 10% in the stiffness and mass and 1000% in the damping show that the method works reasonably well in the detection and localization steps concerning changes only in the stiffness, but fails in the quantification, mainly when it comes to damages due to mass and damping variations. Although not shown in this work, the choice of different frequency ranges does not seem to have a significant effect on the results, something that was not anticipated initially. Further research from both the numerical and experimental points of view will be necessary to improve the procedure.

Acknowledgements

The authors thank the Portuguese Science Foundation, FCT, through IDMEC, under LAETA, project no. UID/EMS/50022/2013 and under the project UNIDEMI Pest-OE/EME/UI0667/2014.

References

[1] Mas, P., Sas, P., Indirect force identification based on impedance matrix inversion: a study on statistical and deterministic accuracy, *Proceedings of 19th ISMA*, (1994), pp. 1049-1065.

[2] Dobson, B. J., Rider, E., A review of the indirect calculation of excitation forces from measured structural response data, *J. of Mechanical Engineering Science* , 204(2), (1990), pp. 69-75.

[3] Tao, J. S., Liu, G. R., Lam, K. Y., Excitation Force Identification of an Engine with Velocity Data at Mounting Points, *J. of Sound and Vibration*, 242(2), (2001), pp. 321-331.

[4] Uhl, T., The inverse identification problem and its technical application, *Archive of Applied Mechanics*, 77(5), (2007), pp. 325-337.

[5] McColl, C., Palmer, D., Chierichetti, M., Bauchau, O., Ruzzene, M., Comprehensive UH-60 loads model validation, *Proceedings of 66th Annual Forum - American Helicopter Society*, (2010), pp. 1531-156.

[6] Vyas, N. S., Wicks, A. L., Reconstruction of turbine blade forces from response data, *Mechanism and Machine Theory*, 36, (2001), pp. 177-188.

[7] Lage, Y. E., Maia, N. M. M., Neves, M. M., Ribeiro, A.M.R., A Force Identification Approach for Multiple-Degree-of-Freedom Systems, *Proceedings of IMAC-XXVIII*, (2010), pp. 53-61.

[8] Ma, C. K., Ho, C. C., An inverse method for the estimation of input forces acting on non-linear structural systems, *Journal of Sound and Vibration*, 275, (2004), pp. 953-971.

[9] Choi, H. G., Thite, A. N., Thompson, D. J., A threshold for the use of Tikhnov regularization in inverse force determination, *Applied Acoustics*, 67, (2006), pp. 700-719.

[10] Thite, A. N., Thompson, D. J., The quantification of structure-borne transmission paths by inverse methods. Part1: improved singular value rejection methods, *Journal of Sound and Vibration*, 264, (2003), pp. 411-431.

[11] Thite, A. N., Thompson, D. J., The quantification of structure-borne transmission paths by inverse methods. Part 2: use of regularization methods, *Journal of Sound and Vibration*, 264, (2003), pp. 433-451.

[12] Chang, C., Sachse, W., Analysis of elastic wave signals from an extended source in a plate," *Journal of the Acoustical Society of America*, 77(4), (1985), pp. 1335-1341.

[13] Michaels, J. E., Pao, Y.-H., The inverse source problem for an oblique force on an elastic plate," *Journal of the Acoustical Society of America*, 77(6), (1985), pp. 2005–2011.

[14] D'Cruz, J., Crisp, J. D. C., Ryall, T. G., On the Identification of a harmonic force on a viscoelastic plate from response data, *Journal of Applied Mechanics*, 59, (1992), pp. 722-729.

[15] Maia, N. M. M., Silva, J. M. M., Ribeiro, A. M. R., The transmissibility concept in multi-degree-of-freedom systems, *Mechanical Systems and Signal Processing*, 15 (1), (2001), pp.129-137.

[16] Maia, N. M. M., Urgueira, A. P. V., Almeida, R. A. B., Whys and wherefores of transmissibility, in *Vibration Analysis and Control - New Trends and Developments*, Dr. Francisco Beltran-Barbajal, InTech, (2011), pp. 197-216.

[17] Lage, Y. E., Maia, N. M. M., Neves, M. M., Ribeiro, A. M. R., Force identification using the concept displacement transmissibility, *Journal of Sound and Vibrati*on, 332(7), (2013), pp. 1674-1686.

[18] Neves, M. M., Maia, N. M. M., Estimation of applied forces using the transmissibility concept, *Proceedings of ISMA2010*, (2010), pp. 3887-3897.

[19] Maia, N. M. M., Lage, Y. E., Neves, M. M., Recent advances on force identification in structural dynamics, in *Advances in Vibration Engineering and Structural Dynamics*, InTech, (2012), pp. 103-132.

[20] Lage, Y. E., Neves, M. M., Maia, N. M. M., Tcherniak, D., Force transmissibility *versus* displacement transmissibility, *Journal of Sound and Vibration*, 333(22), (2014), pp. 5708-5722.

On the quality of identified parameters of prestressed concrete catenary poles in existence of uncertainty using experimental measurements and different optimization methods

F. Alkam [1], **T. Lahmer** [1]
[1] Bauhaus University Weimar, Institution of Structural Mechanics,
Marienstr. 15, DE-99423, Weimar, Germany
e-mail: **feras.alkam@uni-weimar.de**

Abstract
Prestressed concrete catenary poles are widely used in train systems. To trace the dynamic behavior of these poles, we installed a structural monitoring system on three of them along one of the high-speed train tracks in Germany. The efficient analysis of the recorded measurements by this system requires a well-known data covering the entire properties of the given structure. In this paper, we inversely identify the material properties of the poles using the deterministic and probabilistic approaches. In the deterministic approach, the uncertainty of the identified parameters is quantified using a Markov Estimator. Bayesian inference is utilized in the probabilistic approach for better estimation of the probability distribution of the parameters. Both approaches successfully estimated the parameters' mean values. The Bayesian method, even though computationally more demanding, is more suitable for estimating the variances of the identified parameters and the correlations between each pair of them.

1 Introduction

The catenary systems of the electric trains are suspended by structural members, called poles, installed at equal-spaced distances along the train-track. They play a vital role in the entire train system as any damage to one of these members leads to troubles in the functionality of the whole system.
These poles are mainly affected by a combination of several actions. Besides, the static actions, seasonal ambient temperature and the wind effects; the train passing near the poles causes a transient excitation. Due to this transient excitation, the poles vibrate frequently in a complex form. There are mainly three sources of such transient vibrations: The vibrations transmitted from the waving of the catenary cables due to the interaction between them and the pantograph of the train; the vibration caused by the air pressure wave generated by the train; and the vibrations that traveling through the foundation by cause of the interaction between the train wheels and the sub-base of the track.
Each of the aforementioned sources of the transient excitation is separately well-studied by many researchers. In the case of the train-induced ground vibrations, some research focus on the nature of the wave that transmitted through the soil and how to use them to detect the train speed [12, 7]. Other research study the effect of the train-induced vibrations on the adjacent building but not the poles that carry the catenary system. Additionally, due to the collapse of some of the noise protection walls, Ampunant et. al investigates the effect of the aerodynamic pressure loads on them when high-speed trains are passing by [1]. The interaction of the train's pantograph and the catenary cables are investigated for various types of the pantographs and different train types and speeds. Some of these research replace the pole by fixed connection in the numerical model, where others assume some stiffness by using elastic springs to simulate the connection [10, 17]. This is valid

to study the behavior of the catenary as an isolated system without taking the actual interaction between it and the poles. Pombo et. al provides a detailed model of the catenary system including the poles themselves. However, they study the changes in the behavior of the catenary cables without addressing the effects on the poles [15].
Right now, the poles have not received the adequate attention compared to their importance to the entire train system. This means that further research and investigations are needed to detect the actual behavior of the poles and their interaction with the catenary system and surrounding soil.
The high-strength prestressed concrete poles have been recently used in the catenary systems. They replace the classical poles, i.e. the timber and steel ones, because they are more feasible and supposed to have a longer service-life. Thousands of this type of the poles carry the catenary system of the new high-speed train tracks and the electric transmission lines in Germany. Working with the prestressed concrete poles increases the complexity of tracing the behavior of the poles along the high-speed train tracks. The properties of the pole change visibly over time due to different effects i.e. the degradation of concrete because of the shrinkage, creep, and low-cycle fatigue; and the increase in the prestressing losses. This, besides the high importance of the poles to the whole catenary system, increases the necessity to trace the behavior of the poles under various actions i.e. the static, environmental and dynamic actions; considering the long-term changes in the material of the pole. In this aim, we installed a Structural Health Monitoring (SHM) system on three poles along the high-speed train track.
Having the actual values of the material properties is necessary for the analysis and the validation processes of the output of the monitoring system. In this case study, the only available information is the characteristic properties that derived from the datasheet of the structure. Moreover, testing small specimens of the poles is not available in our case, but we had the opportunity to test a full-scale structure. In this paper, we describe the parameter identification process as a first and essential step for detecting the behavior of the given structures. We inversely identify the parameters of the poles using the available experimental measurements and a numerical model considering the different sources of the uncertainty. The parameters are identified using two different approaches: The deterministic approach by means of minimizing the least square errors using nonlinear optimization algorithm; and the probabilistic approach using Bayesian inference. To assure the quality of the identified parameters, we compared the convenience of the applied approaches. In the deterministic approach, the covariance matrix is derived by applying the Markov estimator, but in the case of the probabilistic approach, it is implicitly included in the Bayesian updating process.

2 Problem and Formulation

The parameter identification requires solving the inverse problem using the experimental measurements, called observation, and the output of the numerical model considering the noise errors. We assume the forward model [2, 3]

$$\mathbf{d} = \mathbf{G}(\mathbf{m}) + \varepsilon\,, \tag{1}$$

where $\mathbf{d}$ is the set of observations, $\mathbf{d} = \{d_1, d_2, \ldots, d_n\}^T$; n is the number of observations; $\mathbf{m}$ is the vector of model parameters, $\mathbf{m} = \{m_1, m_2, \ldots, m_k\}^T$; k is the number of parameters of the model $\mathbf{m}$; ε is the noise of measurements, $\varepsilon = (\varepsilon_1, \cdots, \varepsilon_n)$. Different methods are available for solving the inverse problem. In this paper, we choose two different approaches: The deterministic approach based on minimizing the least square errors, and the probabilistic approach based on Bayesian inference.

When comparing the results of the selected approaches, we shall keep in mind that the probability has a different interpretation in each approach. Markov estimator, as a frequentist approach, uses the confidence intervals (CIs). For a selected confidence interval, let us say $95\ \%$, this means that when repeating the event many times, $95\ \%$ of the cases of the computed confidence interval will contain the true value of the parameter. On the other hand, the Bayesian approach uses the credible region (CIs). It means that for the observed data of the events, there is a $95\ \%$ probability that the true value of the parameter lies within the credible region [18].

2.1 Deterministic Approach

In this approach, we solve the inverse problems using the least squares concept by minimizing the residuals between the model predictions and the observations to get the most probable solution. The residuals are weighted by the variance of the observations σ_i^2 for considering the effect of the uncertainties in the measurements [11]

$$\min_{\mathrm{m}} \left\| \frac{\mathbf{G}(\mathbf{m}) - \mathbf{d}}{\sigma_i} \right\|_2^2 . \tag{2}$$

The mean values of the parameters are identified by solving the Eq. 2 using the simplex algorithm according to Nelder-Mead [16]. However, the covariance matrix of the parameters can be evaluated by the estimation of the confidence intervals by linearization $\widehat{\mathbf{G}}'(\mathbf{m})$ of the nonlinear relation between the parameters and the observation at the optimal point, or the so-called Markov Estimator [13]. The confidence of the parameters is proportional to the entries on the main diagonal of the so-called information matrix M or sensitivity matrix, then the higher the value of M, higher is the confidence.

$$M := \sum_{i=1}^{n} \widehat{\mathbf{G}}'(\mathbf{m})^T \, W^{-1} \, \widehat{\mathbf{G}}'(\mathbf{m}) \, , \tag{3}$$

where W is the covariance matrix of the observations. It can also be estimated by the inverse of the information matrix M^{-1}, and applying Cramér-Rao-Inequality the so-called variance-covariance matrix

$$C \succeq \left(\sum_{i=1}^{n} \widehat{\mathbf{G}}'(\mathbf{m})^T \, W^{-1} \, \widehat{\mathbf{G}}'(\mathbf{m}) \right)^{-1} , \tag{4}$$

then, the confidence intervals of the parameters are proportional to the diagonal entities C_{ii} of the covariance matrix C. Then, the probability that

$$\mid \mathrm{m}_i^{exact} - \mathrm{m}_i^{computed} \mid \; \leq \sqrt{C_{ii} \chi_k^2 (1-\alpha)}, i = 1, \cdots, k \tag{5}$$

is larger than $(1-\alpha)$, where $\chi_k^2(1-\alpha)$ denotes the $(1-\alpha)$ of the χ_k^2 probability distribution. The smaller the right-hand side of the Eq. 5 the more reliable the identified parameter can be assumed.

2.2 Bayesian Approach

The Bayesian approach considers all quantities as random variables and describes them as probability distributions. One of the advantages of using this approach is to identify the parameters in form of probability distributions that reflect the uncertainty of the estimated parameters and concurrently, incorporates any available prior information of the considered problem [5, 11].
The Bayesian approach is based on Bayes' rule which is the conditional probability of the model parameters given the observations [8]

$$q(\mathbf{m}|\mathbf{d}) = \frac{f(\mathbf{d}|\mathbf{m}) \cdot p(\mathbf{m})}{p(\mathbf{d})} = c^{-1} \cdot f(\mathbf{d}|\mathbf{m}) \cdot p(\mathbf{m}) \, , \tag{6}$$

where $p(\mathbf{m})$, $f(\mathbf{d}|\mathbf{m})$ and $p(\mathbf{d})$ are the so-called Prior, Likelihood and Evidence, respectively. Supposing the parameters in Eq. 6 are continuous

$$c = p(\mathbf{d}) = \int f(\mathbf{d}|\mathbf{m}) \cdot p(\mathbf{m}) d\mathbf{m} \, , \tag{7}$$

c is a constant that normalizes the posterior distribution to have an integral of one in the model space. As a result, the Eq. 6 can be written as a statement of proportionality [2]

$$q(\mathbf{m}|\mathbf{d}) \propto f(\mathbf{d}|\mathbf{m}) \cdot p(\mathbf{m}) \, . \tag{8}$$

The prior distribution $p(\mathbf{m})$ includes all the available information or the current knowledge about the parameters before incorporating the observations. Assuming the errors of the observation $\mathbf{d}_i$ are independent and normally distributed with zero expected value and standard deviation σ_i, i.e. $\varepsilon_i \sim N(0, \sigma_i)$. Consequently, the likelihood function $f(\mathbf{d}|\mathbf{m})$ for the complete data set follows the normal distribution i.e. $L(\mathbf{m}|\mathbf{d}) \sim N(\mathbf{G}(m), \sigma)$. For more efficiency of the Bayesian updating method, the process can be applied consequently in j steps. The likelihood of each step of model updating becomes

$$L^j(\mathbf{m}^j|\mathbf{d}^j) = \frac{1}{\prod_{i=1}^{n^j} \sigma_i^j (\sqrt{2\pi})^{n^j}} \quad e^{-\sum_{i=1}^{n^j} \frac{(\mathbf{G}(m_i^j) - d_i^j)^2}{2(\sigma_i^j)^2}}, \tag{9}$$

where $\mathbf{d}^j = \{d_1^j, d_2^j, \cdots, d_{n^j}^j\}^T$ is the observations' vector; $\mathbf{m}^j = \{m_1^j, m_2^j, \cdots, m_{k^j}^j\}^T$ is the vector of the parameters; $\sigma^j = \{\sigma_1^j, \cdots, \sigma_{n^j}^j\}$ is the standard deviation of the observations $\mathbf{d}^j$; n^j is the number of the observations $\mathbf{d}^j$; k^j is the number of the parameters of the model $\mathbf{m}^j$; $j = 1, \cdots, K$.

The posterior distribution $q(\mathbf{m}|\mathbf{d})$ can be estimated based on the sampling technique in terms of Markov Chain Monte Carlo (MCMC) method [9, 14]. In this study, the Transitional Markov Chain Monte Carlo (TMCMC) algorithm is implemented as it is a recommended tool in the case of complex conditions. It is usually considered for solving the problems with high-dimensional PDFs, multi-modal PDFs, very peaked PDFs, etc. Besides, it is suitable for parameters which are highly correlated [6].

3 Description of the Pole and Tests

3.1 Dimensions and Materials

The poles are made from high-strength prestressed concrete. They are made of 10 m height with tapered hollow circular sections. The spinning method is used in the production resulting in a variation of the wall thickness. The nominal material properties and geometry of the structure are extracted from the data sheet provided by the manufacturer and summarized in Table 1.

Dimensions and Materials	**Nominal value**
Dimensions	
Length, L [m]	10
Outer diameter at bottom, d_{bot} [mm]	400
Outer diameter at top, d_{top} [mm]	250
Wall thickness at bottom, t_{bot} [mm]	62
Wall thickness at top, t_{top} [mm]	52
Materials	
Concrete grade	C80/95
Prestressing strands	7/16" St 1680/1880
Number of strands, n	10
Area of strand , A_{PT} [mm^2]	70
Prestressing initial stress, σ_{PT} [MPa]	975

Table 1: The nominal properties of the poles.

3.2 Experimental Programme

A set of experimental tests was conducted at the Bauhaus-Universität Weimar within the DFG research training group 1462. In the frame of this work, two types of experiments were selected. The first test is

a vibration test from which the system identification is achieved. The second test is a 3-point bending test which represents the linear and non-linear behavior of the structure.

3.2.1 Vibration Test

A pole was tested through a vibration test in free-free setup by hanging it in a horizontal position using two ropes as shown in Figure 1. A set of twelve sensors were attached to the pole in order to measure the acceleration in the horizontal and vertical directions. Two of the sensors were fixed to the top end of the pole and considered as reference sensors where the rest were configured in two measurement setups to increase the quantity and quality of the identified mode shapes and natural frequencies. Moreover, an appropriate impact hammer was used for exciting the structure in three positions, horizontally and vertically for each, and repeated for each sensor-setup. In the first sensor-setup, the sensors were attached with an in-between distance of 2 m, then these sensors were moved 1 m to form the second measuring setup as shown in Figure 1. The natural frequencies of the first fifth mode shape in the horizontal and vertical direction were calculated using the Stochastic Subspace Identification method. The results of the vibration test are summarized in Table 2.

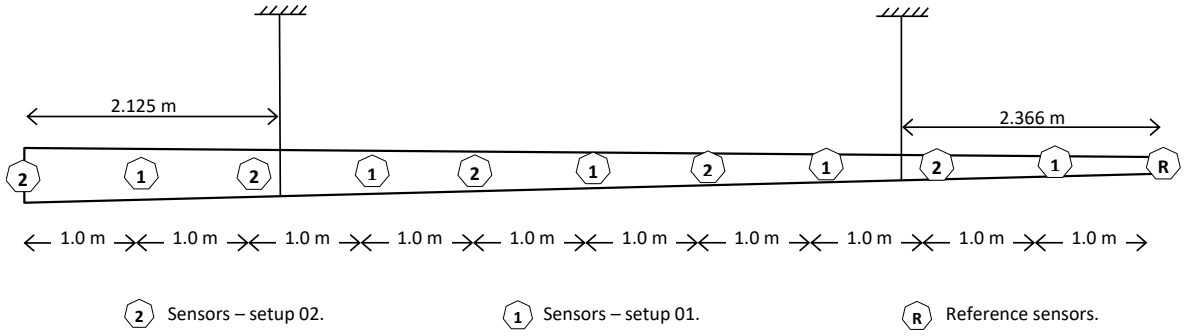


Figure 1: Experimental setup (vibration test).

Mode shape	1 - h	1 - v	2 - h	2 - v	3 - h	3 - v	4 - h	4 - v	5 - h	5 - v
Natural frequency [Hz]	15.28	15.39	41.64	42.63	80.45	81.51	130.64	131.48	191.14	192.58

Table 2: The results of the vibration test in vertical (v) and horizontal (h) directions.

3.2.2 3-Point Bending Test

A displacement-based 3-point bending test was conducted to the same pole in a simply supported setup in the horizontal position. The supports were located at 1.5 m from both ends, see Figure 2. The displacements were applied in steps at the mid-span till the pole was crushed.

During the test, the deflection and load were recorded continuously at middle and quarters of the $7\,\mathrm{m}$ span i.e. at points P1, P2 and P3 shown in Figure 2. The load-displacement curve at point P1 is displayed in Figure 3. The non-linear behavior of the pole can be clearly seen. The spun-cast concrete pole behaves linearly up to a force of 25 kN, corresponding to a mid-displacement of 8 mm. Along with the cracking in the center region of the concrete pole, the stiffness of the pole decreases, leading to higher deformations for load levels above the linear range. The maximum load was 81 kN corresponding to deflection of 110 mm at the mid-span (i.e. at point P1). This corresponds to the failure point of the pole, where the concrete at the most upper fiber at mid-span failed under compression.

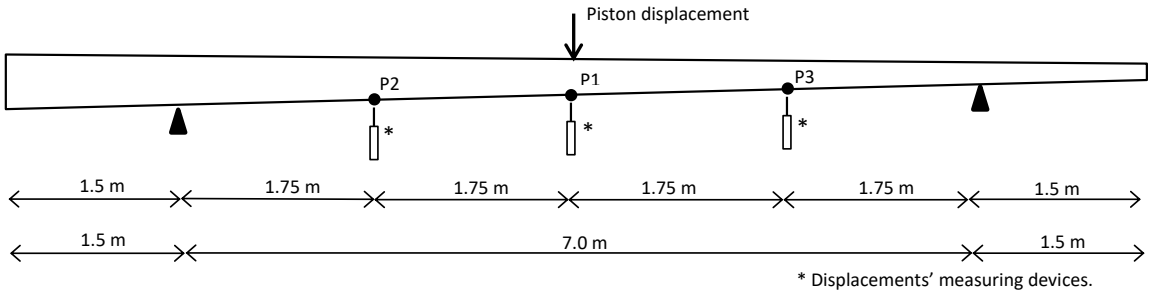


Figure 2: Experimental setup (bending test).

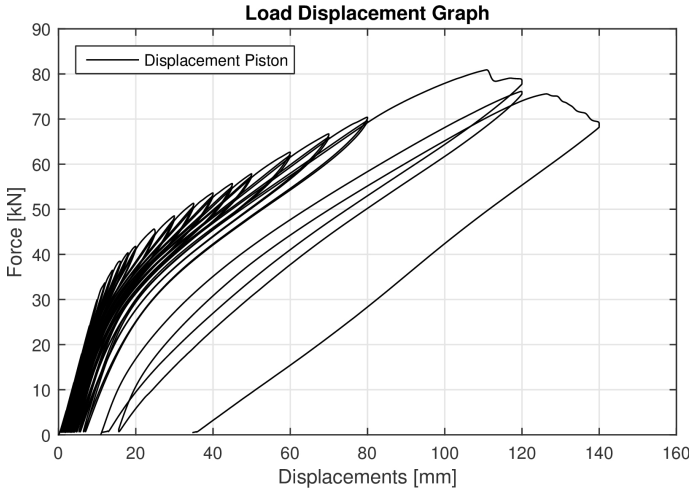


Figure 3: Load-displacement curve at point P1.

4 Parameter Identification

The deterministic and Bayesian approaches are implemented to identify the parameters of the given structure. The vector of parameters are build from five parameters $\mathbf{m} = \{\varepsilon_{PT}, f_{cm}, \varepsilon_c, E_c, f_{ctm}, \rho_c\}^T$, where ε_{PT} is the prestressing initial strain; f_{cm} is the compression strength of the concrete; ε_c is the concrete strain at maximum compressive stress; E_c is the concrete modulus of elasticity; f_{ctm} is the concrete tensile strength; and ρ_c is the concrete density. The parameters are bounded during the identification process depending on the available datasheet and the engineering prejudgment based on the values recommended by FIB Model Code 2010 [4] as shown in Table 3. For the selected case study, the measurements are considered as observations $\mathbf{d}^i$. Where, the observations $\mathbf{d}^1$ of the vibration test are formed from the first ten natural frequencies of the structure. On the other hand, the load-deflection curves at mid-span and quarters of the span are considered as the observations $\mathbf{d}^2$ of the bending test. Conversely, FEM models, corresponding to each experimental test, are playing the role of models $\mathbf{G}(\mathbf{m})$.

For using the deterministic approach we assume the probability distribution of the identified parameters as a normal distribution. The parameters are estimated to 95 % confidence level ($\alpha = 0.05$). The results of this approach are summarized in Table 4.

The histograms in Figure 4 shows the distributions of the identified parameters using Bayesian approach. Additionally, the correlations between each pair of the parameters are shown in the scatter plots on the

Parameter	Range
Prestressing initial strain, ε_{PT} [‰]	2.7 - 3.7
Concrete compressive strength, f_{cm} [MPa]	80 - 120
Concrete strain at maximum compressive stress, ε_c [‰]	2.5 - 3.0
Concrete Modulus of Elasticity, E_c [GPa]	43 - 53
Concrete tensile strength, f_{ctm} [MPa]	4.0 - 6.0
Concrete density, ρ_c [$\mathrm{g\,cm^{-3}}$]	2.1 - 2.5

Table 3: The intervals of selected parameters.

Parameter	ε_{PT} [‰]	f_{cm} [MPa]	ε_c [‰]	E_c [MPa]	f_{ctm} [GPa]	ρ_c [$\mathrm{g\,cm^{-3}}$]
Mean value	3.16	105.08	2.70	48.19	5.07	2.27
Std. [%]	2.82	1.19	0.60	3.05	0.25	2.04

Table 4: Summary of the identified parameters (deterministic approach).

same figure. The parameters E_c and ρ_c are well-correlated as shown in the sub-plots because of the natural frequencies are proportional to the square root of the ratio between the stiffness and the mass. Moreover, a negative correlation between f_{ctm} and ε_{PT} can be seen. This is also understandable from the engineering point of view as increasing the prestressing stresses raises the load corresponding to the first crack and hence decreases the inferred tensile strength of the concrete as a solution of the inverse problem. Supplementary, to get an overview of the whole applied process, the mean values and the standard deviations are listed in Table 5.

Figure 5 shows a comparison between the results of the applied approaches. A perfect match can be

Parameter	ε_{PT} [‰]	f_{cm} [MPa]	ε_c [‰]	E_c [MPa]	f_{ctm} [GPa]	ρ_c [$\mathrm{g\,cm^{-3}}$]
Mean value	3.16	105.12	2.70	48.38	5.00	2.33
Std. [%]	2.82	2.03	3.83	1.63	3.25	2.17

Table 5: Summary of the identified parameters (Bayesian approach).

recognized in the mean values of the identified parameters except for the mean values of the concrete density ρ_c and the concrete tensile strength f_{ctm} where a small bias of 3% and 2% respectively appeared. However, the variance of the identified parameters differ considerably and has no specific trend, but in most the cases the variances in Bayesian approach have higher values. Considering the complexity and the computation efforts, we conclude that Markov estimator can be simply implemented to have, to a good accuracy compared to Bayesian approach, the mean values and to some limits an indicator of the parameters' uncertainty. The Bayesian approach, in comparison, needs heavier efforts but it can precisely draw the probability distributions of the identified parameters. Besides, Bayesian approach gives a good overview of the correlation between the parameters, which leads to better understanding of the studied problem.

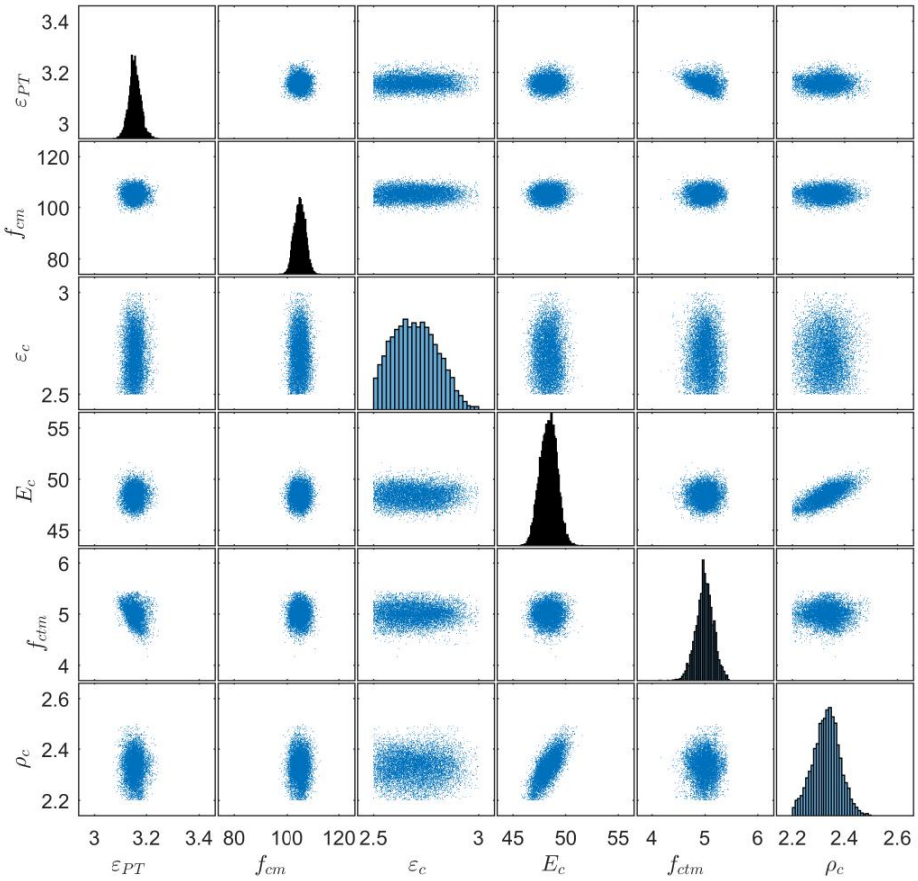


Figure 4: Identified parameters (Bayesian approach).

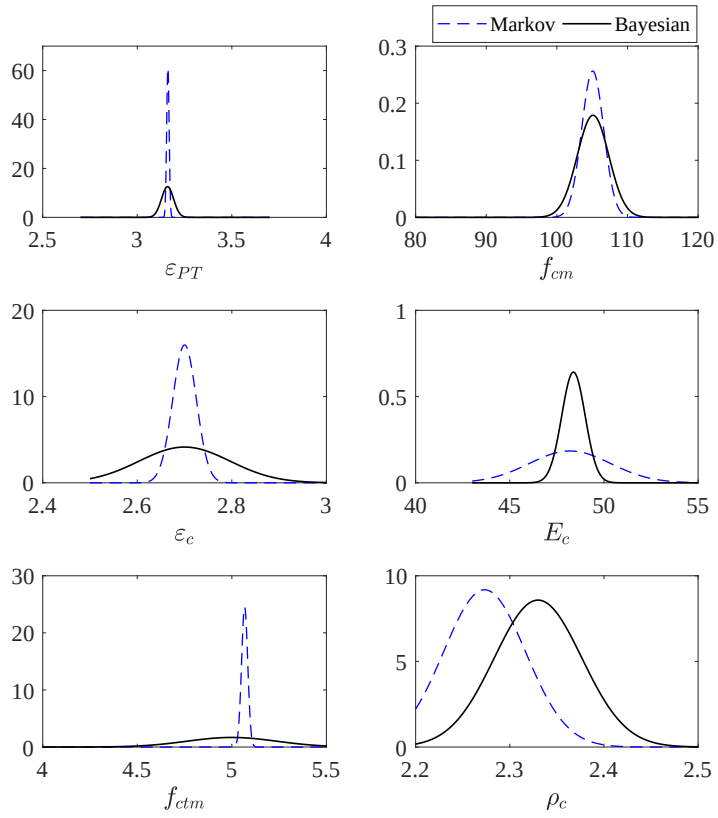


Figure 5: Identified parameters (Markov estimator vs. Bayesian).

To validate the above-mentioned values, the mean values of the identified parameters by the Bayesian approach are used as input for the FEM models. However, the results of the FEM are compared with the corresponding observations. In the case of the bending test, the results of the finite element are plotted against the hysteresis loops of the force-deflection derived from the measurements. Figures 6 and 7 show the agreement between the experimental measurements of the bending test, which were measured at the mid-span and quarters, and the FEM using the identified parameters. Furthermore, the first five natural frequencies in horizontal and vertical direction, according to the test setup, are derived from the FEM model using the inferred parameters and listed in Table 6. These results show that the FEM model using the inferred parameters conforms with the experimental observations of the vibration test to a high accuracy.

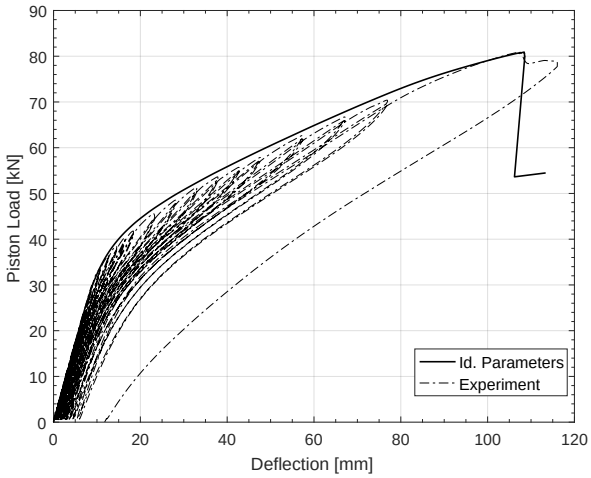


Figure 6: Validation of the results - bending test at P1.

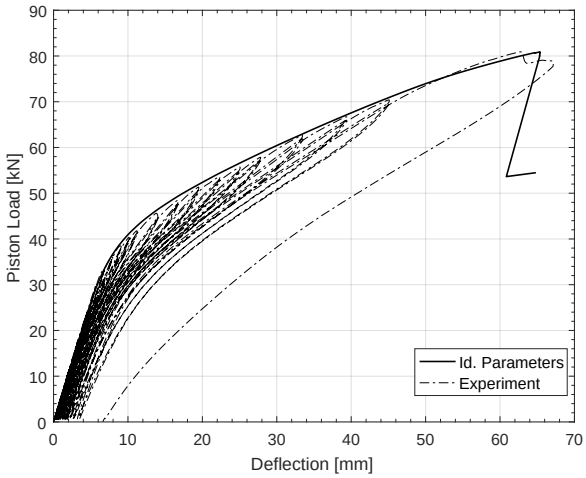


Figure 7: Validation of the results - bending test at P2.

Mode shape	1 - h	1 - v	2 - h	2 - v	3 - h	3 - v	4 - h	4 - v	5 - h	5 - v
Natural frequency [Hz]	15.37	15.54	41.65	42.09	80.35	81.16	130.48	131.76	191.04	192.83
Tolerance [%]	0.60	1.00	0.00	1.30	0.10	0.40	0.10	0.20	0.10	0.10

Table 6: Validation of the results - vibration test.

5 Conclusion

In this paper, we achieved the preliminary step for analyzing the measurements of the structural monitoring system. This system is attached to the prestressed concrete catenary poles located along the high-speed train track in Germany. Through this step, we identified the material properties of the poles to be utilized later as priors in the assessment and validation steps of the SHM system. The identification process is attained using deterministic and probabilistic approaches. In the first one, Markov Estimator is involved to quantify the uncertainty of the identified parameters. Bayesian inference is implemented to identify the parameters in the case of the probabilistic approach. In this approach, the uncertainty of the parameters can be easily identified by calculating the statistical moments of the parameter's distributions. Both approaches identically estimated the mean values of the parameters. The Bayesian approach estimates the variances of the identified parameters in a more effective and accurate manner. Moreover, it describes the correlation between the different parameters, and then, we recommend to implement it when the parameters' uncertainty is the main subject of interest. In the future step, we are going to trace the changes in the mechanical behavior of catenary poles on site using Signal Processing, Operational Modal Analysis method, and Model Updating.

Acknowledgements

This work was done under a support of Deutsche Forschungsgemeinschaft (DFG) through Research Training Group 1462, which is greatly acknowledged by the authors. Another acknowledgement goes to the German Academic Exchange Service (DAAD) for supporting the main author through the scholarship program "Leadership for Syria".

References

[1] P. AMPUNANT, F. KEMPER, I. MANGERIG, AND M. FELDMANN, *Train–induced aerodynamic pressure and its effect on noise protection walls*, in 9th International Conference on Structural Dynamics, A. Cunha, E. Caetano, P. Ribeiro, and G. Müller, eds., EURODYN 2014, July 2014, pp. 3739–3743. ISBN: 978-972-752-165-4.

[2] R. C. ASTER, B. BORCHERS, AND C. H. THURBER, *Parameter Estimation and Inverse Problems*, Academic Press, second edition ed., 2013.

[3] J. V. BECK AND K. J. ARNOLD, *Parameter Estimation in Engineering and Science*, Wiley, New York, 1977.

[4] P. BEVERLY, ed., *fib Model Code for Concrete Structures 2010*, Wiley-VCH Verlag GmbH & Co. KGaA, 2013.

[5] D. CALVETTI AND E. SOMERSALO, *An Introduction to Bayesian Scientific Computing: Ten Lectures on Subjective Computing*, vol. 2, Springer Science & Business Media, 2007.

[6] J. CHING AND Y.-C. CHEN, *Transitional Markov Chain Monte Carlo Methods for Bayesian Model Updating, Model Class Selection, and Model Averaging*, Journal of engineering mechanics, 133 (2007), pp. 816–832.

[7] D. CONNOLLY, G. KOUROUSSIS, P. WOODWARD, P. A. COSTA, O. VERLINDEN, AND M. FORDE, *Field testing and analysis of high speed rail vibrations*, Soil Dynamics and Earthquake Engineering, 67 (2014), pp. 102–118.

[8] A. GELMAN, J. B. CARLIN, H. S. STERN, AND D. B. RUBIN, *Bayesian Data Analysis*, vol. 2, Chapman & Hall/CRC Boca Raton, FL, USA, third edition ed., 2014.

[9] P. GREEN AND K. WORDEN, *Bayesian and Markov Chain Monte Carlo Methods for Identifying Nonlinear systems in The Presence of Uncertainty*, Phil. Trans. R. Soc. A, 373 (2015), p. 20140405.

[10] D. HE, Q. GAO, AND W. ZHONG, *A numerical method based on the parametric variational principle for simulating the dynamic behavior of the pantograph-catenary system*, Shock and Vibration, 2018 (2018).

[11] J. IDIER, *Bayesian Approach to Inverse Problems*, John Wiley & Sons, 2013.

[12] G. KOUROUSSIS, O. VERLINDEN, D. P. CONNOLLY, AND M. C. FORDE, *Estimation of railway vehicle speed using ground vibration measurements*, Beijing, China, July 2014, 21st International Congress on Sound and Vibration (ICSV21), pp. 1–8.

[13] T. LAHMER AND E. RAFAJŁOWICZ, *On the optimality of harmonic excitation as input signals for the characterization of parameters in coupled piezoelectric and poroelastic problems*, Mechanical Systems and Signal Processing, 90 (2017), pp. 399–418.

[14] Y. M. MARZOUK, H. N. NAJM, AND L. A. RAHN, *Stochastic Spectral Methods for Efficient Bayesian Solution of Inverse Problems*, Journal of Computational Physics, 224 (2007), pp. 560–586.

[15] J. POMBO AND J. AMBRÓSIO, *Influence of pantograph suspension characteristics on the contact quality with the catenary for high speed trains*, Computers & Structures, 110 (2012), pp. 32–42.

[16] A. TARANTOLA, *Inverse Problem Theory and Methods for Model Parameter Estimation*, Society for Industrial and Applied Mathematics, 2005.

[17] O. V. VAN, J.-P. MASSAT, AND E. BALMES, *Waves, modes and properties with a major impact on dynamic pantograph-catenary interaction*, Journal of Sound and Vibration, 402 (2017), pp. 51–69.

[18] J. VANDERPLAS, *Frequentism and Bayesianism: A python-driven primer*, arXiv preprint arXiv:1411.5018, (2014).

Continuous wavelet transform for structural health monitoring of a pipe

S. Milana[1], N. Roveri[1], A. Carcaterra[1], A. Culla[1]
[1] University of Rome La Sapienza-Department of Mechanical and Aerospace Engineering
Via Eudossiana, 18, I-00184, Roma, Italy
e-mail: **silvia.milana@uniroma1.it**

Abstract
In this paper, a Structural Health Monitoring (SHM) procedure, based on the Continuous Wavelet Transform (CWT) applied on a pipe excited by a flow that carries a travelling load, is presented. The proposed procedure allows the early stage localization of damages along the structure. The basic idea is to take advantage of time-space relation given by a traveling load of which speed is known, because wavelet analysis may highlight the singularities of a signal related with the damage. The displacement of the pipe excited by the traveling load shows singularities when the load crosses the damages, because the elastic waves are reflected in correspondence of the structure discontinuity. An index, based on the analysis of the CWT coefficients, is defined to identify these singularities in time and the load velocity law allows finding their correspondent position. A numerical test is performed to validate the performance of the proposed technique.

1 Introduction

Pipelines are ever-present in industrial and civil structures, because they carry fluids and gasses in chemical or power plants, or more commonly in civil buildings. Collapse of this pipelines can provoke serious ecological pollution and economic losses. Monitoring of these structures is essential to optimize maintenance and repair in order to maximize performances and minimize losses. SHM is a process allowing preventing collapse and it consists of continuous recording and analysis of data. [1-6].

In this paper, the potentiality of a SHM approach based on CWT [7-9] is investigated. Wavelet transform of a signal allows isolating those instants where discontinuities exists. The displacement signal of a point of the pipe excited by the traveling load shows singularities when the load crosses discontinuities of the structure. They can depend on the designed shape or on the damages. In the first case, their positions are known, in the second one CWT allows localizing these damages.

The coefficients of the Continuous Wavelet Transform (CWT) of the displacement are conveniently post-processed and an index is obtained, allowing an automatic localization procedure. The considered displacements are calculated using the numerical model built considering eigenvalues and eigenvectors extracted from the Finite Element Model (FEM) of the damaged structure and it is polluted by a noise.

The identification is performed considering three different damage extensions and five different positions on the pipe. Two analyses on this set of data are proposed: the first one allows establishing the minimum number of sensors for a correct damage localization, the second one provides the relationship between the position of the sensors and the damage location.

2 Theoretical background

In this section the background of the damage identification method based on CWT is discussed.

2.1 Wavelet analysis

The Continuous Wavelet Transform of a one-dimensional signal *f(t)* is defined as follows[7-9]:

$$C_{s,\tau} = C(s,\tau) = |s|^{-p} \int_{-\infty}^{+\infty} f(t)\bar{\psi}\left(\frac{t-\tau}{s}\right) dt \quad (1)$$

where $\psi(t)$ is the mother wavelet, the symbol $\bar{\psi}$ denotes its complex conjugates and $C_{s,\tau}$.is the wavelet coefficient.

The mother wavelet has two properties:

$$\int_{-\infty}^{+\infty} \psi(t)dt = 0 \ , \int_{-\infty}^{+\infty} |\psi(t)|^2 \, dt < \infty \quad (2)$$

It is used for generation of other functions:

$$\psi_{s,\tau}(t) = |s|^{-p} \, \psi\left(\frac{t-\tau}{s}\right) \quad (3)$$

The parameter τ and *s* localise the wavelet and define its width in time and frequency, respectively. It can be shown [9] that the modulus of the wavelet transform $|C_{s,\tau}|$ is the cross correlation at lag τ between the signal *f*(*t*) and the wavelet function, so the higher $|C_{s,\tau}|$, the higher the correlation or similarity between the template function $\psi_{s,\tau}(t)$, at that time and that scale, and the signal *f*(*t*).
Wavelet analysis allows identifying instantaneous changes within the signal. In fact, signal singularities can be detected by finding the abscissa where the maxima of the wavelet transform modulus converge at fine scales [7].

2.2 Damage detection method

The CWT analysis is a useful tool in a damage identification procedure. The reflection of the elastic waves in correspondence of the local structural variation, due to the presence of the damage, induces a perturbation in the structure response. The coefficient line exhibits a local extremum, especially in the scale range that is sensitive to the damage characteristic wavelength. Unfortunately, many other reasons can be at the origin of the presence of the coefficient lines peaks (e.g. end effects, boundary conditions, noise in the signal, etc.) and these are spurious peaks in this identification analysis. For this reason, a reliable and automatic procedure cannot be based only on a peak finder algorithm.

The automatic procedure here presented consists indeed of two steps.

First, a specific range of scales is selected, so that the CWT of the system response is restricted to this range. In correspondence of this scales band, the envelopes of the wavelet coefficient lines are calculated and the upper envelopes, $s_{eup_{ij}}$, are averaged over the scales range. Let *Ns* be the number of the considered scales, N_t the number of time samples, N_o the number of observation points, *i* the scale index, *j* the observation point index and *n* the time sample index. The average of the upper envelopes is computed by the following equation [10]:

$$A_j(t_n) = \frac{1}{N_s} \sum_{i=1}^{N_s} s_{eup_{ij}}(t_n) \quad (4)$$

The use of the envelope limits the fluctuation of the coefficient lines around the zero (as shown in the second subplot of Fig. 3) and the average operation reduces the effects of the spurious peaks highlighting the presence of the damage.

Then, since the distance between the position of the damage and of the observation point is affecting the accuracy of the identification process, an additional index *J* is introduced. It is defined as the average of $A_j(t_n)$ over the considered observation points. Hence, *J* can be calculated as follows:

$$J(t_n) = \frac{1}{N_o} \sum_{j=1}^{N_o} A_j(t_n) \quad (5)$$

Therefore, the time instant t^*, at which the load crosses the damage, is identified by the local maximum of J with the highest prominence, excluding the maxima given by the boundary effects. The corresponding damage position can be easily computed when the velocity is known.

In order to evaluate the effect of the relative distance between the position of the damage and the observation point, it is analyzed the maximum value of the prominence of the index A for all considered observation points and several damage positions.

3 Numerical model of the load and of the structure

The considered test bed, shown in figure 1, is a steel pipe of radius 0.2 m, 5 m long and 0.01m thick, the pipe is clamped at both the extremity. The structure is excited by a load that runs over the length of the pipe with a speed of 1 m/s.

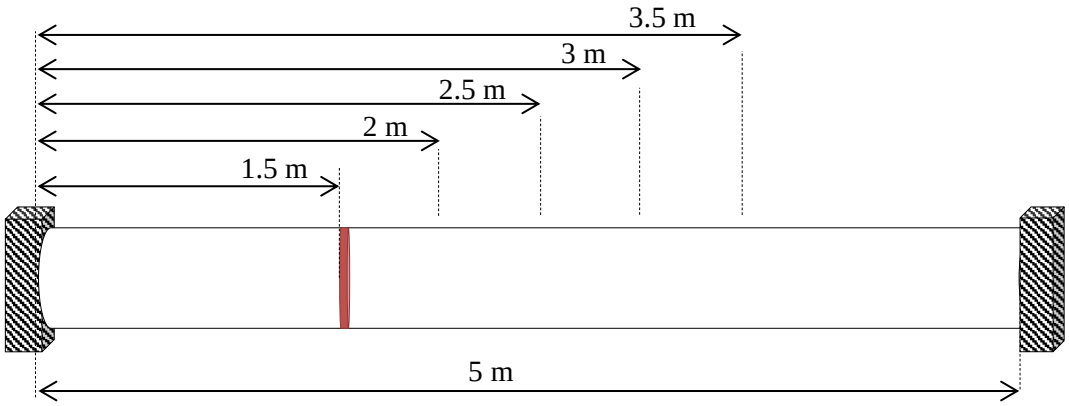


Figure 1: Test bed: position of the damage

As shown in figure 2, six observation points are chosen, uniformly distributed along the structure.

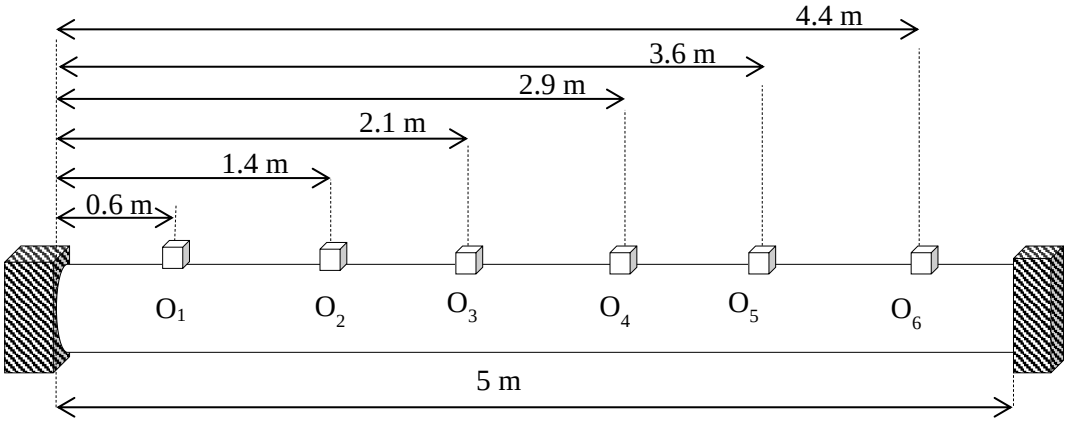


Figure 2: Test bed: observation points position

The damage is simulated by three different thickness reductions at five positions. The considered test cases are summarized in table 1.

Test	Damage location	Thickness reduction

1	**1.5 m**	**30** %
2	**1.5 m**	**20** %
3	**1.5 m**	**10** %
4	**2.0 m**	**30** %
5	**2.0 m**	**20** %
6	**2.0 m**	**10** %
7	**2.5 m**	**30** %
8	**2.5 m**	**20** %
9	**2.5 m**	**10** %
10	**3.0 m**	**30** %
11	**3.0 m**	**20** %
12	**3.0 m**	**10** %
13	**3.5 m**	**30** %
14	**3.5 m**	**20** %
15	**3.5 m**	**10** %

Table 1: Test cases

A FEM of the studied structure is created and employed to calculate N_m natural frequencies, ω_n, and eigenvectors, φ_n. The response, $w(x_o,t)$, at each measurement point is calculated by modal analysis. Modal coordinates are the result of the following set of independent equations [11-12]:

$$\ddot{q}_n + 2\delta_n\omega_n\dot{q}_n + \omega_n^2 q_n = F\int_0^L \frac{\varphi_n(x_o)}{\left[r_0^2+(x_0-Ut)^2\right]^2}dx_o \tag{6}$$

and the physical displacement is calculated by the following linear transformation:

$$w(x_0,t) = \sum_{n=1}^{N_m}\varphi_n(x_o)q_n(t) \tag{7}$$

The response computed by equation (7) is polluted by a random noise proportional to the 5% of the standard deviation of the signal.

By ®MATLAB Wavelet Analyzer the CWT analysis of the response is carried out and the result is shown in figure 3.

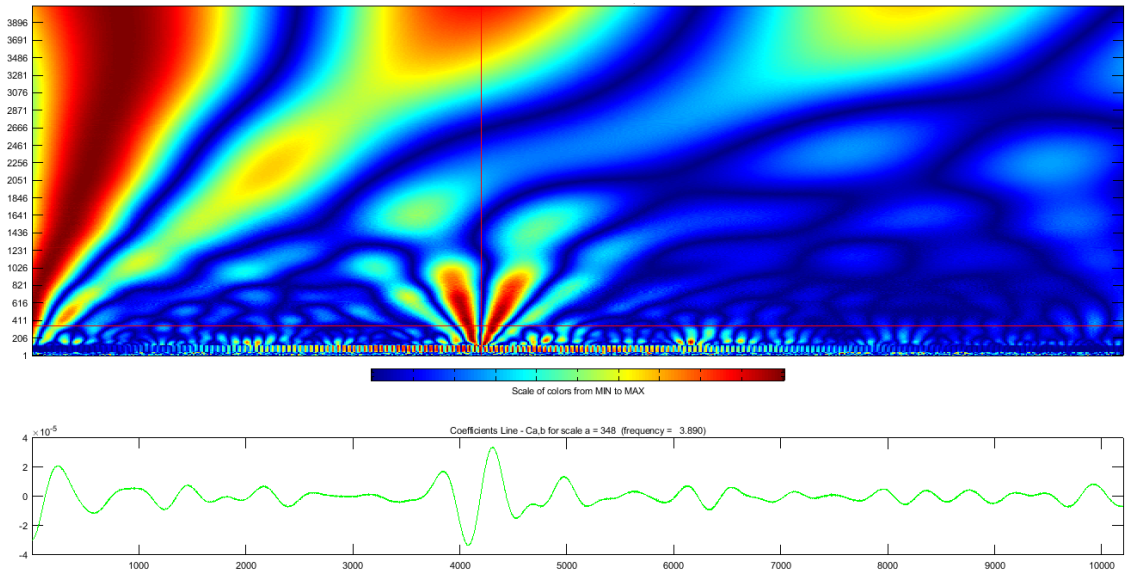


Figure 3: CWT Analysis of the response measured on O_2 of the pipe damaged at 2 m

The analysis is performed using the dmay basis function. The figure shows that only in correspondence of a reduced set of scales, i.e. from 200 to 1000, corresponding to the frequencies excited by the imposed load, the CWT highlights the presence of the damage (positioned at 2 m).

4 Results: discussion and validation

The CWT analysis is performed for the 15 tests of table 1. As shown in figure 4, while in correspondence of the observation points close to the damage the CWT plot highlight the time instant at which the load crosses the damage, the analysis performed on the other observation points does not guarantee a clear identification of the damage position.

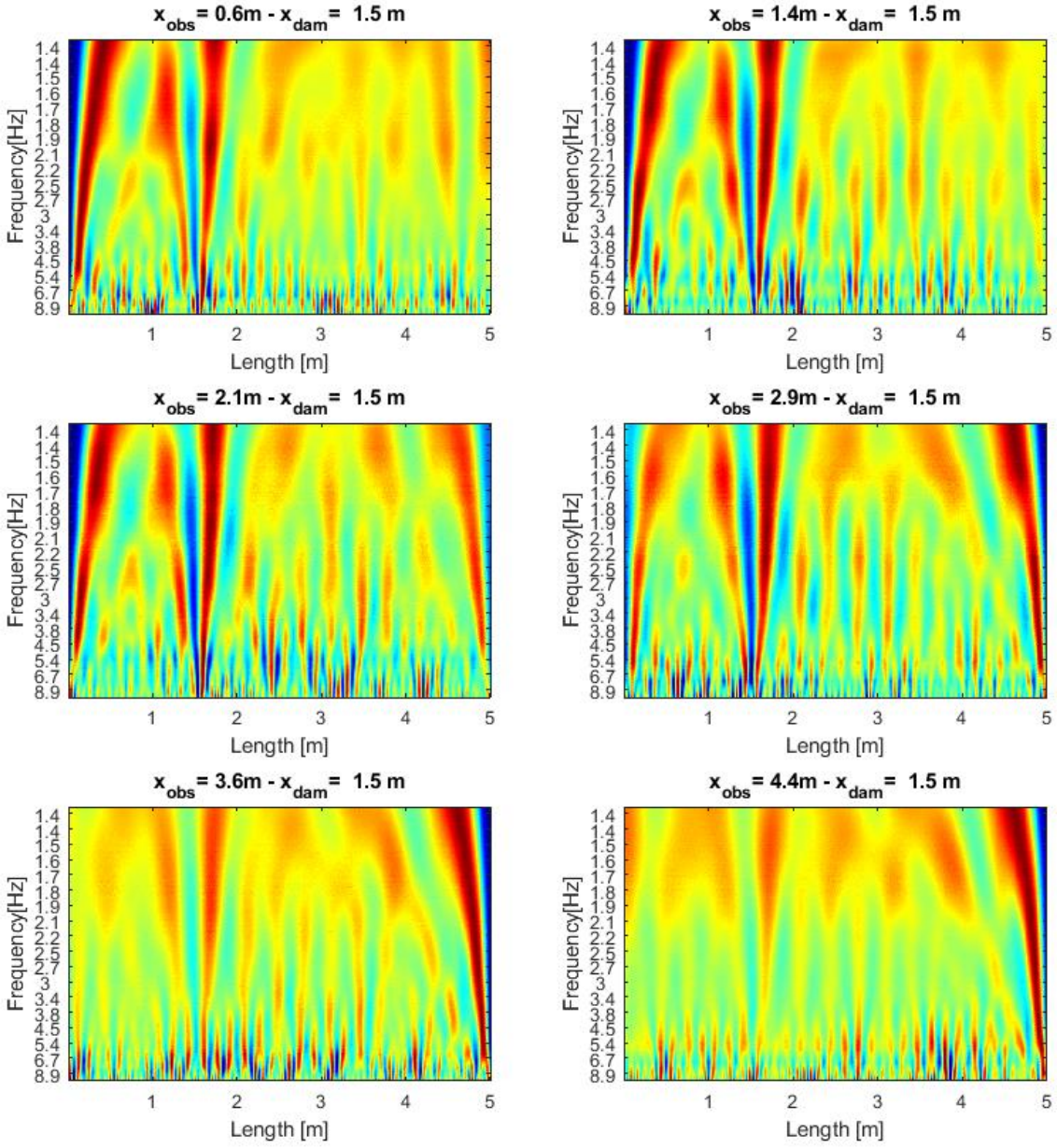


Figure 4: CWT analysis of the responses of test 3 for the six considered observation points in correspondence of the selected frequency range.

Figure 5 shows the indices *A* and *J* (equations (4) and (5)) for the considered test case. As expected the *A* index mitigates the effect of the spurious components, but it does not give good result in correspondence of the observation points O_5 and O_6 (see figure 2), where also a visual analysis of a human operator cannot

provide the damage position. Instead, the use of index *J* allows to identify correctly the damage position, in fact it can be noticed that also considering only the two observation points close to the boundary, whose signal is characterized by a lower energy content, it is possible to perform the identification.

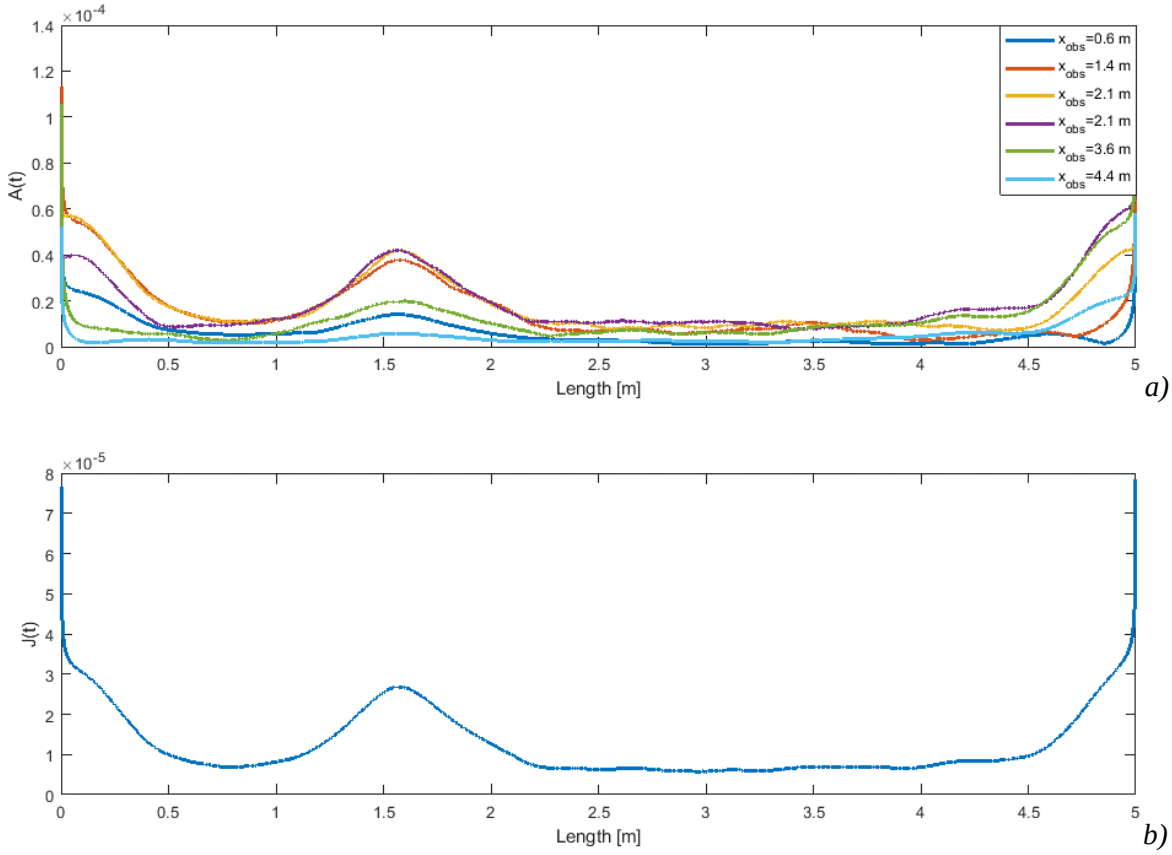


Figure 5: *a)* comparison of index *A* computed for each measurement point (test 3); *b)* index *J* (test 3)

The results obtained for each considered test are shown if figure 6, where the red line highlight the local maximum of *J* that has the highest prominence. For all considered cases, *J* provides the correct position of the damage.

In order to evaluate the effects of the relative position between the damage and the observation points it is analyzed the maximum value of the prominence of the index *A* computed for all considered observation points.

Figure 7 shows the prominence value related to the distance between the observation points and the damage, for a damage amplitude of 10%. Since, the position of the damage and of the observation points are both symmetric, the trends of the first and the last graph and of the second and third one are quite similar, respectively. The prominence grows with the shift of the damage along the direction of the running load, a result in line with a previous work [6].

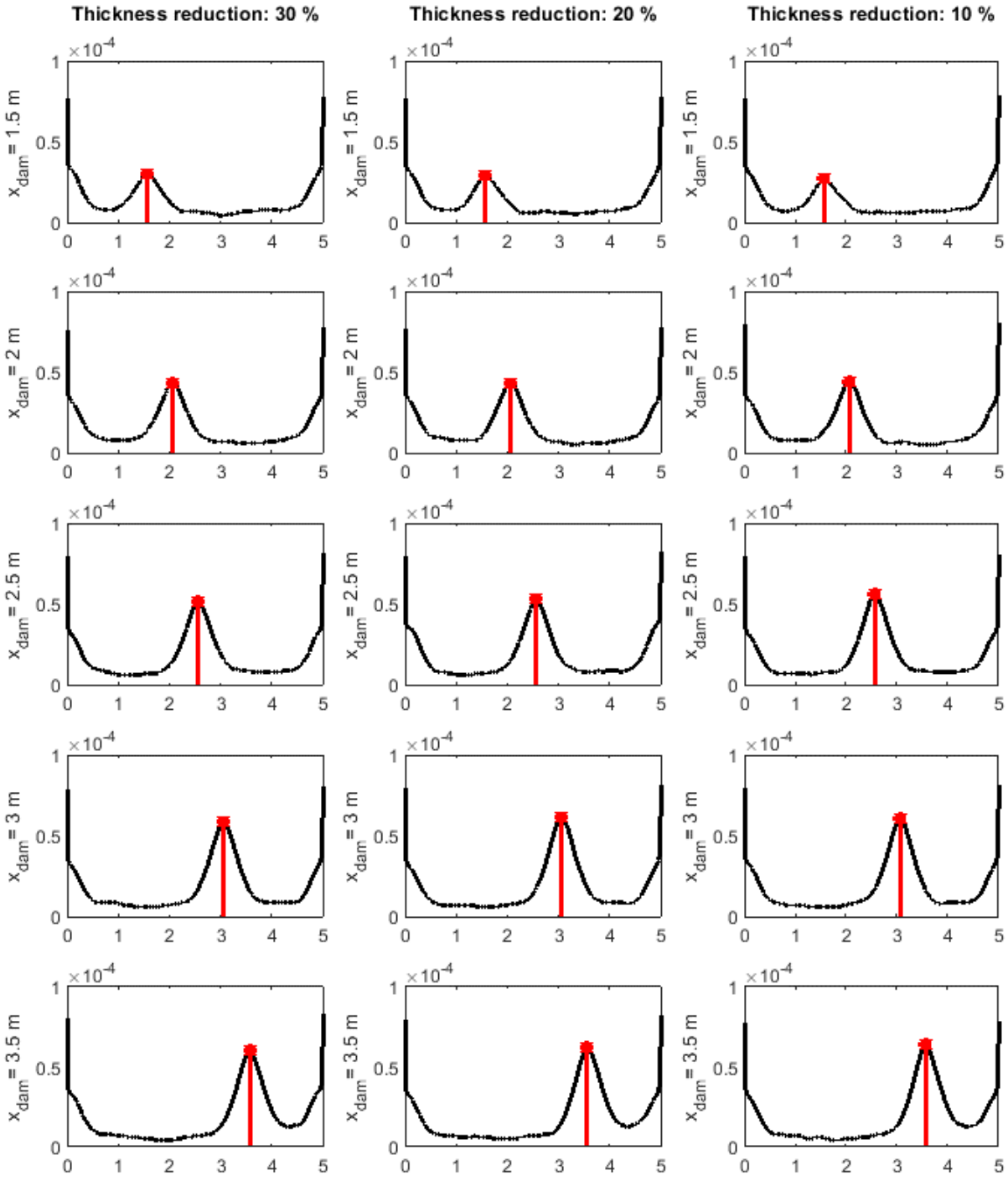


Figure 6: *J* index computed for all considered tests of table 1.

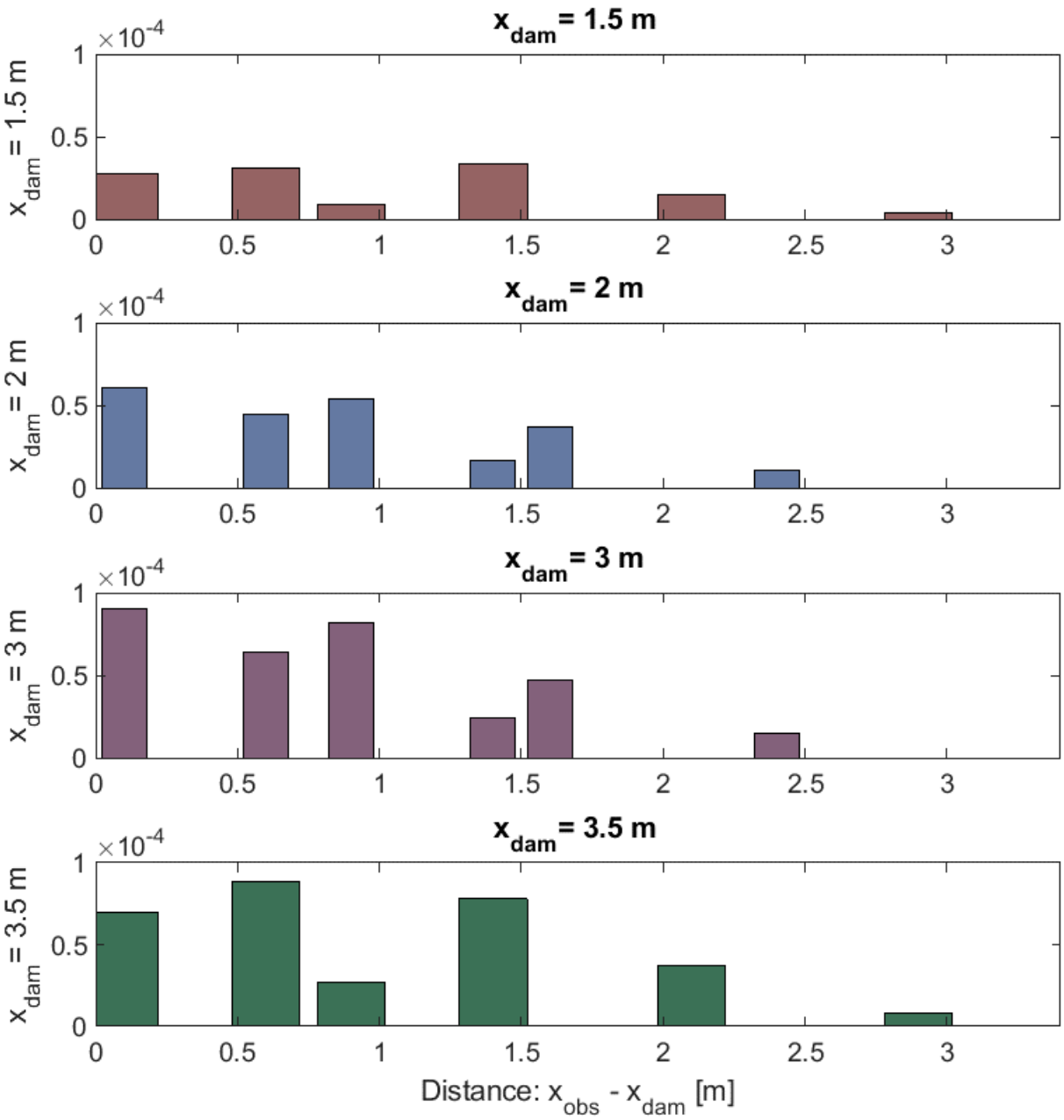


Figure 7: Comparison of the prominence value related to the distance between the observation points and the damage

5 Conclusions

In this paper, a SHM procedure applied on a pipe charged by a flow is presented. An index obtained through the postprocessing of the CWT coefficients is here proposed, since the inspection of the CWT spectrogram does not guarantee a clear, robust and general localization of the damage. As shown, the proposed index is indeed able to highlight the instant in which the load cross the damaged section, and provides good results for all considered test cases (for

thickness reduction from 10% to 30% and different positions on the pipe length), also for a reduced number of measurement points, as low as 2.

Unfortunately, the index does not allow quantifying the amplitude of the damage, as shown by the analysis developed for three different damage thickness, which is however a common problem of many SHM algorithms [2].

The analysis of the prominence related to relative distance between the observation points and the damage points out that the proposed index is sensitive to this distance and highlights that the results are sensitive to the position of the damage, in respect to the travelling direction of the running load. The amplitude of the index grows indeed with the shift of the damage along the direction of the travelling load: the closer the damage to end of the beam, the larger the index.

Acknowledgements

This research is supported by grants from University of Rome “La Sapienza”.

References

[1] O. S.Salawu, Detection of structural damage through changes in frequency: a review, Eng. Struct. 1997; 19, 9, 718–723.

[2] S. W. Doebling, C. R. Farrar, M. B. Prime, A summary review of vibration-based damage identification methods, *Shock Vib.* Dig.; 30, 2, 91–105, 1998.

[3] C.R. Farrar, D.A. Jauregui, Comparative study of damage identification algorithms applied to a bridge: I. Experiment. *Smart Materials and Structures*; 7, 704–719, 1998.

[4] J.N. Yang, P.C. Chang, H. Fujitani, H. Li, Jr. B.F. Spencer, Y.L. Xu, F.G. Yuan, Structural control and health monitoring, *Proceedings of International Conference on Advances and New Challenges in Earthquake Engineering Research*; 3, 9–14, 2002.

[5] N. Roveri, A. Carcaterra. Unsupervised identification of damage and load characteristics in time-varying systems. *Continuum Mechanics and Thermodynamics*, 27.4-5: 531-550, 2015.

[6] N. Roveri, A. Carcaterra. Damage detection in structures under traveling loads by Hilbert–Huang transform. *Mechanical Systems and Signal Processing*, 28: 128-144, 2012.

[7] W.J. Staszewski, Structural and mechanical damage detection using wavelets. *The Shock and Vibration Digest*; 30, 6, 457–472, 1998.

[8] M. Rucka, K. Wilde, Application of continuous wavelet transform in vibration based damage detection method for beams and plates. *Journal of Sound and Vibration*, 297, 536-550, 2006.

[9] G.Kaiser, A Friendly Guide To Wavelets, New York, Birkhäuser, 1994

[10] S. Milana, N. Roveri, A. Culla, A. Carcaterra, Structural health monitoring of a plate by continuous wavelet transform, Proceeding of Novem2018, 7-9 May 2018 Ibiza.

[11] Meirovitch, Leonard. Elements of vibration analysis. McGraw-Hill Companies, 1975.

[12] P.K. Kundu, I. M. Cohen, D. R. Dowling, Fluid mechanics (5th ed.). Waltham, MA Academic Press, 2012.

Damage phenomena characterization in RCF tests using image analysis and vibration-based machine learning

M. Lancini [1], I. Bodini [1], C. Petrogalli [1], L. Provezza [1], M. Faccoli [1], G. Sansoni [1], L. Solazzi [1], A. Mazzù [1]
[1] University of Brescia, Department of Mechanical and Industrial Engineering
via Branze, 38 I-25123, Brescia, Italy
e-mail: **luca.provezza@unibs.it**

Abstract
Rolling Contact Fatigue (RCF) tests are a common effective method to study the behavior of wheel- and rail-steels. The measurements usually performed are discrete and destructive: they can only be performed at each intermediate stop of a test and they result in the alteration or destruction of the examined specimens. This work aims to assess the damage level steel samples during RCF tests, making continuous, non-destructive, and contactless measurements. A machine-learning technique based on vibration and torque measurements, together with 2D image was applied to RCF-dry tests carried out on different railway wheel steels tested according to the same operating parameters.

The proposed algorithm was able to quantitatively estimate the damage level of the samples by calculating the current data distance from specific references, e.g. a defined final damaged state. The used approach ensures a good degree of reliability both in terms of specificity and sensitivity

1 Introduction

At least 10% of the 2000 train accidents recorded in the EU per year are likely caused by problems related to the rolling contact fatigue (RCF) phenomenon [1]. Victims, investigations, maintenance and replacement are just a few of the high costs involved. These, as well as the need of faster and more reliable railway material, constitute a strong push towards a better characterization of the materials used, and a more detailed study of the evolution of the damage mechanism.

The damage assessment in railway application is, in fact, still an open question. Many parameters affect the assessment in a wheel/rail contact: materials, load history, climatic condition, and sliding ratio. Different damage mechanism can also occur along with wear and rolling contact fatigue, the two principal players [2,3] that can interact and influence each other, even in competition.

The aim of this study is to add new tools and technologies to study wear and fatigue damages due to wheel-rail contact. One of the most common test that can be performed to characterize the wheel and rail steel material involves a twin-disk test bench, where specimens are used to simulate the real operating conditions of wheels and rails, with controlled operating conditions: rotation speed, slip ratio and load [3]. More and less accurate modelling of the damage can be found in the literature: some studies have focused on the mechanical and metallurgical characterization of different steels for wheels and rails, to identify the types of damage phenomena involved; while other researches focused on the development of analytical models.
A typical test procedure [16] using this test bench is to stop the machine at predefined cycles numbers, remove the samples, clean them, and perform some non-destructive tests, such weighing, magnetic measurement and image analysis; then resume the test. Destructive measurements can be taken only at the

end of the test, to identify the damage that let to failure, if any, and measure the cracks, where present. The need to stop the test to perform assessments and the impossibility of repeating a test after a destructive measurement is the main limitation to the study of damage evolution, since staircase approaches are time and resources consuming. Moreover, the interruption of the test, dismounting and mounting of the specimen could lead to different damage evolution, introducing relaxation phases.
The objective of the proposed study is to quantitatively estimate the damage status of the specimens using a continuous non-contact measurement system. This activity is based on the use of k-means clustering, a non-supervised Machine Learning technique, fed with vibration and torque measurement data, suitably pre-processed. Similar techniques have already been used to identify possible variations in the frequency responses of a particular mechanical model of the samples [23], but that approach required extensive post-processing of all tests data and operator-based manual tuning, while the proposed method is fully automated.
In the present work, k-means clustering method is implemented by combining three in different signals in time (two vibrations and one torque) in wheel-rail contact on RCF tests carried out by using a twin-disk bench. With the extraction of statistical and spectral features and a PCA analysis to reduce the number of features, K-means is applied to determine the damage in time on wheel specimens. The damage assessment is obtained with the clustering of the three signals. The novelty of the propose work is that there is a constant evaluation of damage in time with the possibility to have a characterization of materials in railway application with the use of an on-line method. In literature, there is only the determination of a fault condition with machine learning techniques. To have a confirm of the robustness of this method, a correlation with a R_b index, calculated from a binarization of images taken from a speed camera installed on twin-disk bench, it was given.

2 State of the art

Machine learning techniques have a wide use in many research field and they are used in signal vibrations in order to diagnose the health condition of rotary machines. The literature reports many works, in which several machine-learning techniques are used to classify different faults. Bearings of rotary machines are the most commonly studied parts, with research focused on detecting different defects. A lot of works in literature report Convolutional Neural Network (CNN) as a valid technique to extrapolate discriminative features to detect fault condition of beating parts [4-9]. Other works display a comparison with different machine learning methods (ANN, SVM, SOM, fuzzy method, Gaussian Process Regression), or using different machine learning languages with different features extractor algorithm to find higher accuracy in detection of fault conditions [10-13]. For example, Elfojani [14] correlates AE features with corresponding natural wear of slow speed bearing thought a series of laboratory experiments by using neural network model and Gaussian Process Regression. In [15], it was proposed a deep-hybrid model composed of the Convolutional Neural Network (CNN) and stacked denoising-autoencoder for unsupervised features learning and classification on multi-channel vibrations data. This deep hybrid model allows to obtain higher accuracy than single CNN. All these machine-learning techniques are used to handle big amounts of raw data and to detect fault conditions of rotary machines.

K-means algorithm is a simple machine learning technique that allows diagnostics of rotary machine through clustering. K-means is normally used when the number of data is not excessive. With the combination of an algorithm to reduce the number of features, there is the possibility to have a data clustering to find fault status in rotary machine. Several works in literature reports the use of k-means as an algorithm to detect abnormal or normal function of bearing elements in rotary machine [17-21]. In [22], k-means algorithm is used with a combination of vibration signal and thermal images features, to extract shape features using image segmentation.

To our current knowledge only few studies have been focused on quantifying the damage evolution, an improvement of the fault detection, especially without stopping the test.

3 Materials and Methods

3.1 Materials

Six different sets of railway-wheel samples supplied by Lucchini RS were analysed to verify and establish the robustness of the method. All these specimens, obtained directly from the real components, were tested on the twin-disk bench of the University of Brescia. The tests have the same duration in time with a number of cycles that corresponds to 130000 cycles. The tests ranging from 1 to 5 were performed with a periodically stop of the machine where the samples were dismounted, ultrasonically cleaned and weighted to evaluate their weight loss in time. The twin-disk bench was stopped at 10000, 20000, 50000 and 70000 cycles. Test 6 was performed without interruption. The test conditions, reported in Table 1, were the same for all the tests carried out and the considered specimens were reported in Table 2.

Specimens Diameter [mm]	***Specimens thickness [mm]***	***Specimens Speed [r.p.m.]***	***Contact Pressure [MPa]***	***Sliding Ratio [%]***	***Applied Load [N]***	***Lubrication***
60	15	500	1100	1	7557	Air

Table 1: Operative conditions of the tests.

Test Number	***Rail-Specimen material***	***Wheel-specimen material***
1	350HT	ER 8
2	350HT	ER 8
3	350HT	SANDLOS® S
4	350HT	SANDLOS® S
5	350HT	CLASS C
6	350HT	SANDLOS® H

Table 2: Considered Specimens.

The steel for the wheel specimens is different for every couple of the considered samples, while the steel for rail specimens is the same for all the tests. The steel considered for the rail specimens was 350HT EN13674-1 and it was a material typically used for rail applications. Three steels were considered for the wheel specimens and respectively are:

- ER8 EN13262
- SANDLOS® S, that is a modified AAR CLASS C
- CLASS C (AAR M107/M208 2004)
- SANDLOS® H, that is a modified AAR CLASS D.

The Principal steels properties are summarized in Table 3.

STEEL	***350HT***	***ER8***	***SANDLOS® S***	***CLASS C***	***SANDLOS® H***
Rupture Stress [MPa]	≥1175	940	1180	1120	1270
Yield Stress [MPa]		590	750	715	800
Elongation [%]	≥9	17	12	12	11
Brinell Hardness [HB]	345	203-255	347	355	354

Table 3: Principal properties of the steels considered.

3.2 Instrumentation

Figure 1 shows a schematic drawing of the twin-disk bench used in this work. The test bench was designed and developed internally and is deeply described in [16]: the specimens are positioned onto independent shafts, one of which can be displaced orthogonally to the shaft axis by a hydraulic cylinder that applies the imposed contact load. The rolling speed of the shafts is measured by encoders, and a load cell located at the piston head measures the contact load between specimens. The bench is equipped with a torque sensor with a full scale of 200 Nm positioned on the displaceable shaft, which can continuously acquire torque values at a synchronous sampling frequency of 5kHz. Piezo-accelerometers with a bandwidth of 26 kHz are fixed near each mandrel support, on the machine frame.

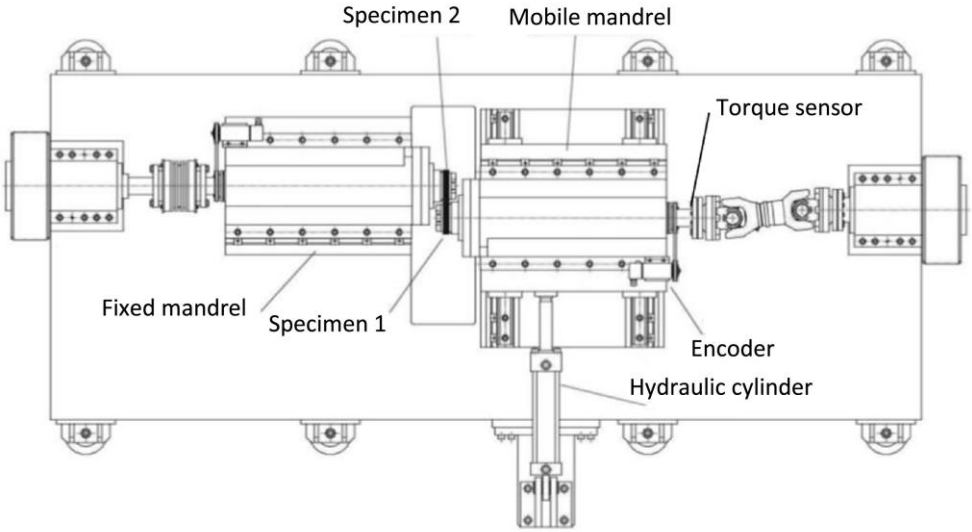


Figure 1: Schematic of the test bench

In addition to the signals of the torque and vibration, the twin-disc bench is equipped with a vision-based measurement system able to acquire frame with a high speed for the duration of all the test. The optical apparatus is based on the use of a speed camera (PROMON 501, AOS Technologies AG), and a system, composed with a defocused laser source and two laser stripes, for the illumination of the interested region (ROI). A detailed description of the optical apparatus for 2D and 3D surface analysis is given in [24]. The images are acquired at a frequency of 377 fps with an exposure time of 40 μs. In this way, there is the possibility to have three different ROI typologies: with the first one, there is the possibility to measure the 3D profile of the light stripe in axial direction of the specimen; with the second one can be measure the profile length of light that correspond at the encoder used for the angular position of the specimen, and the third ROI is used for the 2D elaboration of the surface.

3.3 Data processing

Data acquired from the two piezo-accelerometers and the torque sensor, are recorded in packets of 0.2 s having one thousand samples per channel. The next step in the preparation of the data is the features extraction: for the three sampled signals (two vibration and one torque), statistic-based and spectral-based features were extracted every 0.2 sec. This step is necessary to reduce the amount of data, from 3000 samples to 57 features.

The statistic-based features extracted from the three signals are: mean, standard deviation, variance, RMS, and quartiles. The spectral features are the centroid of the Power Spectrum Density and its quartiles. The signals where further combined to compute the maximum value of the cross-correlation and its associated time delay, the centroid of the Frequency Response Function and its frequency quartiles.

Some extracted features are redundant and were automatically removed by looking at the R^2 value: for each couple of features, the *coefficient of determination* was computed and the set of feature with the lower overall determination was chosen. After this second cleaning, the number of features was reduced to 44.

As a subsequent step, the features have been normalized with a z-score method, to compare different features with different units of measurements: subtracting the average of its value, and dividing it by its standard deviation.

To have a further reduction of the computation of the algorithm, a Principal Component Analysis, PCA, was employed. This analysis was chosen to allow a reduction of the dimensional data with the transformation of n possible variables in fewer q variables linearly correlated to the initial ones. The criterion adopted for the PCs was to consider the first PCs that are able to describe at least 90% of the variance explained. The result of this analysis is a matrix of the original data projected in the space of the PC's principal components chosen. In conclusion, the dataset described in the PCs space is ready to be processed by the K-means algorithm.

After the reduction, the z-score normalization and the PCA analysis, the dataset is imported in the k-means clustering algorithm. It is important to specify that the mean and standard deviation values used for the normalization derives from the considered test, so the dataset is normalized in relation to the features of the actual test. When the algorithm reaches the convergence, the outputs are different.

To translate the classification information provided by the k-means approach into a quantitative measurement, a probabilistic approach has been chosen. Following this approach the distance between the point (in n-space) identified by the PCs as coordinates X, associated with the current condition, and each cluster centres C_i detected by the algorithm, is used as an indication of similarity between the two states. The membership probability P_i is computed directly as the reciprocal value of the square of this distance, later normalized to guarantee that $\Sigma(Pi)=1$. An example of result can be seen in Figure 2. It is clearly visible how we can clearly detect the phases in which the test bench was offline (in red), and that the system gradually changes from a state similar to the one found at the beginning ("pristine") and the one found at the end of the test ("damaged").

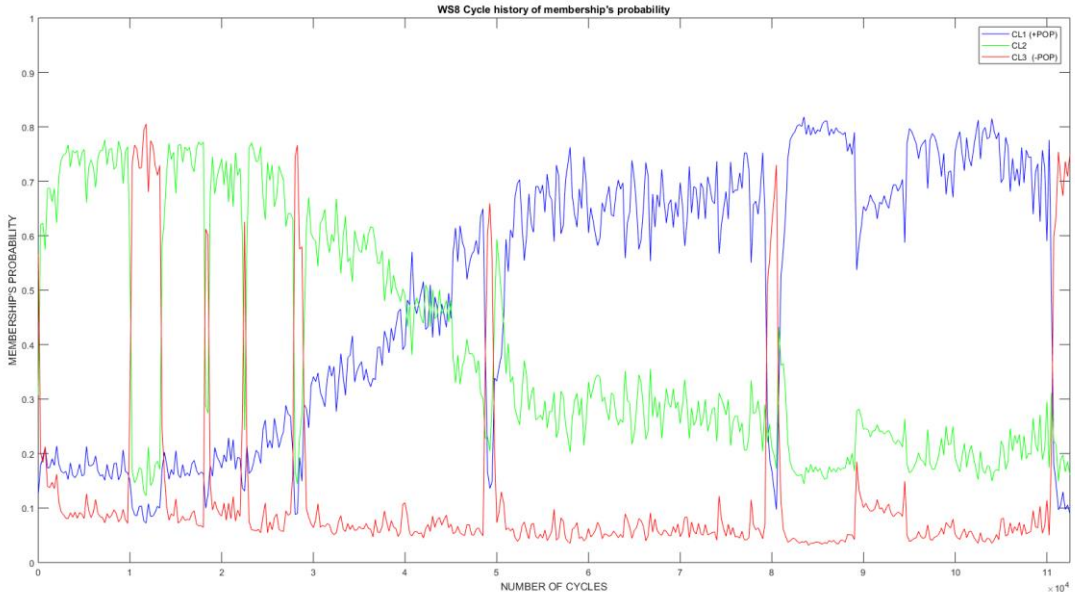


Figure 2: Example of Membership probability chart, for test number 1. In red the probability of belonging to the "test offline" cluster, in green the probability of belonging to the same cluster of the first cycles, and in blue the membership probability of belonging to the condition found at the end of the test.

The images acquired with the high-speed camera are analysed using different ROI. One of the ROI is used to perform a *blob analysis* to count small craters that form on the surface of the specimen during the test, likely due to fatigue and wear phenomena. The acquired images are elaborated with a binarization of the images to have images clearer and, after this elaboration, it can be calculated synthetic indices to evaluate the trend of these blob.

The most relevant index that is possible to correlate to the k-means probability graph is the R_b% calculated with this formulation:

$$R_b\% = \frac{\sum_{i=1}^{n} A_{bi}}{A_{ROI}} \times 100$$

where n is the number of blob found in the considered ROI, AROI is the total area of the interested region and the numerator is the sum of the n Area blob found in the ROI. This index is calculated for every frames acquired during the test and then, it is averaged at defined number of cycles in order to find an averaged index. This averaged R_b% represents the evolution of the damage ratio expressed as fraction. Figure 3 shows an example of how the surface image was analyzed and the R_b coefficient computed.

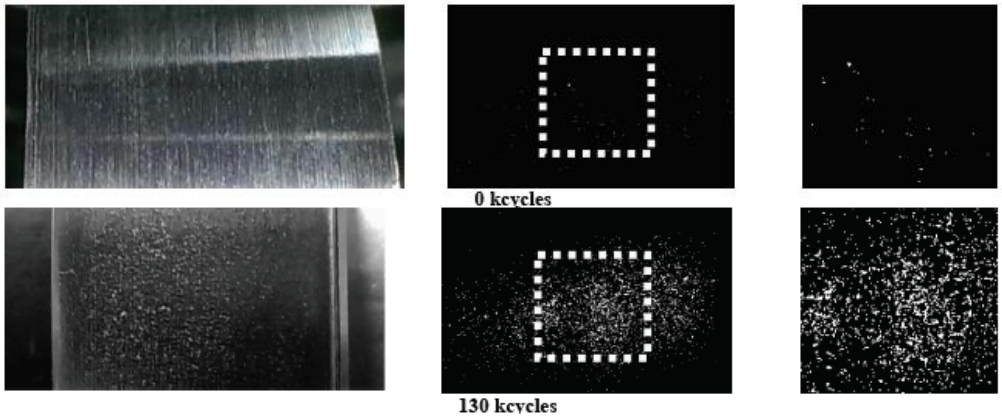


Figure 3: Example of images analysis of the specimen sample, at the beginning of the test (top) and at 130k cycles (bottom). On the left column a photo of the specimen, in the central column the particle analysis and in the right column the ROI zoomed in.

4 Results

4.1 Vibration analysis validation

As can be seen in Figure 2, the change between the pristine and damaged state of the specimen happens at a specific point in time, which could be associated with a change in the damage phenomena. The change is gradual, allowing to propose a quantitative evaluation of the phenomena progression. To demonstrate that the developed method is reliable during the clustering elaboration, a K-fold cross-validation was used. The datasets of two tests were divided in five parts and each part was used as ground-truth to validate the other parts. The fold used as groundtruth is the part used for the training and the other parts are used for the validation. The results of this cross-validation are positive, with values of sensitivity, specificity and accuracy in a range of 98% - 100%.

To demonstrate that the developed method is robust and not subjected to overfitting, an exhaustive cross-validation was used, taking into account all the tests under examination. In this cross-validation each test was used validated against each other, using as ground-truth the dataset used to train the system, obtaining the results shown in Table 4. The reliability of the algorithm in classifying states based on extracted features is good, in terms of sensitivity (min.19% - max.100%), specificity (min.25% – max.99%) and accuracy (min.59% – max.98%).

Status	Pristine / undamaged						Bench halted						Damaged					
Specimen	**1**	**2**	**3**	**4**	**5**	**6**	**1**	**2**	**3**	**4**	**5**	**6**	**1**	**2**	**3**	**4**	**5**	**6**
Sensitivity [%]	19	55	25	53	61	79	36	72	97	69	85	54	100	99	90	98	85	95
Specificity [%]	99	98	98	96	87	93	99	99	94	99	98	98	25	62	49	62	65	83
Accuracy [%]	64	83	85	80	76	86	92	97	94	94	98	97	59	83	79	80	76	88

Table 4**:** Exhaustive cross-validation results.

4.2 Comparison with image data

Out of the six trials, three where chosen and image data was also analysed, to get confirmation that the vibration-based machine-learning assessment was able to detect a phenomena whose effects could also be visible using an high speed camera focusing on the specimen.

The R_b coefficient was computed for every image available and plotted against the number of cycles. The membership probability was assigned a 63% level (using 1 sigma approximation) to be used as a threshold, and the data representing the machine stops was remove.

Figure 4, 5 and 6 respectively present the test number 5, 2 and 4. Except for test 2, where the variation in slope of the image-based index is less clear, the other charts clearly show a good superimposition between the change in state in the vibration state, and the change in the R_b image-based index.

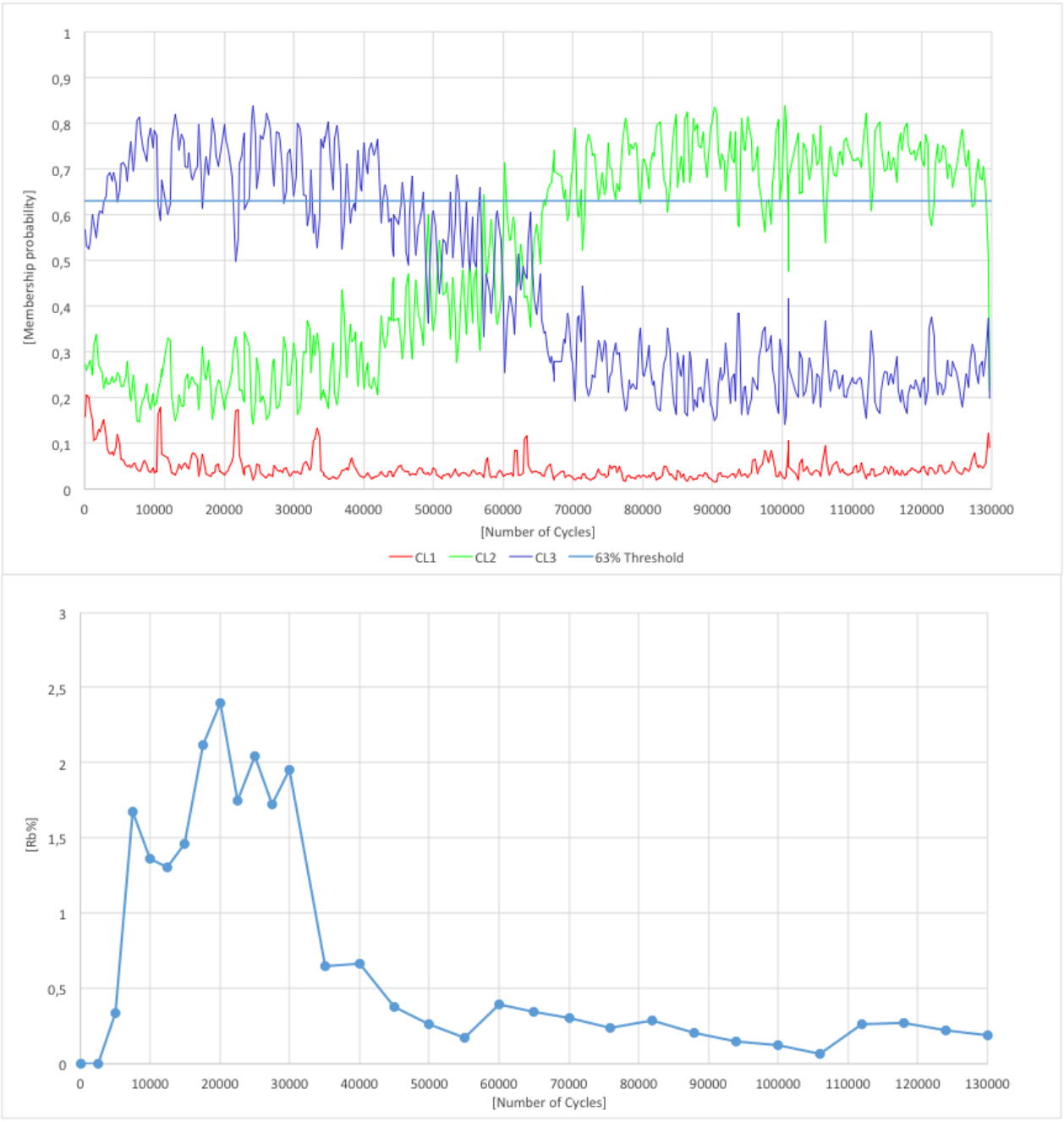


Figure 4: K-means clustering results for test number 5 (top) with blue indicating membership of the "pristine state" cluster, green the "damaged" cluster and red (removed here) the bench stops due to maintenance. R_b index for the same test (bottom).



Figure 5: K-means clustering results for test number 2 (top) with blue indicating membership of the "pristine state" cluster, green the "damaged" cluster and red (removed here) the bench stops due to maintenance. R_b index for the same test (bottom).



Figure 6: K-means clustering results for test number 4 (top) with blue indicating membership of the "pristine state" cluster, green the "damaged" cluster and red (removed here) the bench stops due to maintenance. R_b index for the same test (bottom).

5 Discussion

The vibration-based clustering method presented is consistent in terms of results, and portable between different material conditions, as the correlation validation pointed out. More tests are needed to understand if the image-based index will corroborate the results obtained. A proper validation could be achieved only by performing destructive tests at given intervals, but such solution will take time. For this reason a comparison between different continuous and non-destructive solutions could be sought.

This method, could lead to the ability to carry out a quick analysis of how the single test is performing in real time, which in turn will provide the ability to automatically detect the test bench working conditions, and to detect abnormalities, asymmetries or data structures that a traditional test could miss.

6 Conclusion

The method proposed is simple to implement and could greatly decrease the costs of fatigue characterization in wheel and rail steel. The membership probability obtained, if validated by further study, could prove to be a metric of interest to understand what damage phenomena is occurring and when. The ability to detect the change between different states will also open up the possibility of designing tests to be stopped at a particular state change, driven by the machine-learning information, to allow for destructive tests at a specific progression stage of the damage phenomena.
This work lays the ground for a more detailed study on the application of machine learning techniques in material characterization tests. The correlation of the presented results with traditional damage progression assessment (wear, cracks etc..) is not yet fully proven, although validation tests are currently under evaluation and preliminary results are positive.

Acknowledgements

Authors would like to thank Mr. Coffetti and Mr. Bonometti for their help in the experimental setup. Thanks also should be extended to Ing. Bini Chiesa for his support during the development of the algorithm.

References

[1] Eurostat, 2018, Annual number of accidents by type of accident

[2] A. Ekberg, E. Kabo, Fatigue of railway wheels and rails under rolling contact, Wear 258 (2005) 1288–1300.

[3] Bharat Bhushan (Ed.), Modern Tribology Handbook Vol. II, CRC Press, Boca Raton, Florida, USA, 2001, pp. 1271–1326.

[4] Kankar, P. K., Sharma, S. C., & Harsha, S. P. (2011). Rolling element bearing fault diagnosis using wavelet transform. *Neurocomputing*, *74*(10), 1638–1645.

[5] Elforjani, M. (2018). Diagnosis and prognosis of slow speed bearing behavior under grease starvation condition. Structural Health Monitoring, 17(3), 532–548.

[6] Janssens, O., Slavkovikj, V., Vervisch, B., Stockman, K., Loccufier, M., Verstockt, S., … Van Hoecke, S. (2016). Convolutional Neural Network Based Fault Detection for Rotating Machinery. Journal of Sound and Vibration, 377, 331–345.

[7] Hayashi, S., Asakura, T., & Zhang, S. Z. S. (2002). Study of machine fault diagnosis system using neural networks. *Proceedings of the 2002 International Joint Conference on Neural Networks. IJCNN'02 (Cat. No.02CH37290)*, *1*, 956–961.

[8] Kankar, P. K., Sharma, S. C., & Harsha, S. P. (2011). Fault diagnosis of ball bearings using machine learning methods. *Expert Systems with Applications*, *38*(3), 1876–1886.

[9] Prieto, M. D., Cirrincione, G., Espinosa, A. G., Ortega, J. A., & Henao, H. (2013). Bearing fault detection by a novel condition-monitoring scheme based on statistical-time features and neural networks. *IEEE Transactions on Industrial Electronics*, *60*(8), 3398–3407.

[10] Kankar, P. K., Sharma, S. C., & Harsha, S. P. (2011). Fault diagnosis of ball bearings using continuous wavelet transform. *Applied Soft Computing Journal*, *11*(2), 2300–2312.

[11] Wong, P. K., Yang, Z., Vong, C. M., & Zhong, J. (2014). Real-time fault diagnosis for gas turbine generator systems using extreme learning machine. *Neurocomputing*, *128*, 249–257.

[12] Yu, X., Dong, F., Ding, E., Wu, S., & Fan, C. (2017). Rolling Bearing Fault Diagnosis Using Modified LFDA and EMD with Sensitive Feature Selection. *IEEE Access*, *PP*(99), 1.

[13] Xie, J. P., Yang, Y., Li, T. R., & Jin, W. D. (2014). Learning Features from High Speed Train Vibration Signals with Deep Belief Networks. *Proceedings of the 2014 International Joint Conference on Neural Networks (Ijcnn)*, (2012), 2205–2210.

[14] Elforjani, M., & Shanbr, S. (2017). Prognosis of Bearing Acoustic Emission Signals Using Supervised Machine Learning. *IEEE Transactions on Industrial Electronics*, *PP*(99), 1.

[15] Shaheryar, A., Yin, X.-C., & Ramay, W. Y. (2017). Robust Feature Extraction on Vibration Data under Deep-Learning Framework: An Application for Fault Identification in Rotary Machines. *International Journal of Computer Applications*, *167*(4), 975–8887.

[16] G. Donzella, M. Faccoli, A. Mazzù, C. Petrogalli, R. Roberti (2011) Progressive damage assessment in the near-surface layer of railway wheel–rail couple under cyclic contact Wear, 271 (1–2), pp. 408-416

[17] Danner, C., Gov, K., & Xu, S. (n.d.). Condition Monitoring Using Accelerometer Readings. *Cs229.Stanford.Edu*.

[18] Amruthnath, N., & Gupta, T. (2018). Fault Class Prediction in Unsupervised Learning using Model-Based Clustering Approach. *2018 International Conference on Information and Computer Technologies (ICICT)*, 5–12.

[19] Jia, F., Lei, Y. G., Xing, S. B., & Lin, J. (2016). A Method of Automatic Feature Extraction from Massive Vibration Signals of Machines. *2016 Ieee International Instrumentation and Measurement Technology Conference Proceedings*, 714–719.

[20] Mai, C., & Engineering, I. (2016). A Comparative Investigation of the Robustness of Unsupervised Clustering Techniques for Rotating Machine Fault Diagnosis with Poorly-Separated Data, 165–172.

[21] Bouguerne, A. (2015). K- Means Clustering Based on Vibration Signal for Classification Induction Machine Faults, (2), 1–5.

[22] Hidayat, A. Y., Widodo, A., & Dwi Haryadi, G. (2018). Fault Diagnostic System Bearing Centrifugal Pump Using K-Means Method for Thermography Image and Signal Analysis Vibrations. *MATEC Web of Conferences*, *159*.

[23] A. Mazzù et al. (2015) An experimental procedure for surface damage assessment in railway wheel and rail steels. Wear 342-343 p 22–32

[24] I. Bodini et al. (2018) Evaluation of wear in rolling contact tests by means of 2D image analysis Wear 400-401 p 156-168

Model-based optimization of axisymmetric wave motion in buried plastic water distribution pipes

O. Scussel [1], **M. J. Brennan** [1], **J. M. Muggleton** [2], **F. C. L. de Almeida** [3], **A. T. Paschoalini** [1]
[1] Unesp − São Paulo State University, Department of Mechanical Engineering,
15385-000, Ilha Solteira, São Paulo, Brasil.
e-mail: **oscar.scussel@gmail.com**

[2] University of Southampton, Institute of Sound and Vibration,
Highfield, SO17 1BJ, Southampton, UK.

[3] Unesp − São Paulo State University, Department of Biosystems Engineering,
17602-496, Tupã, São Paulo, Brasil.

Abstract
This paper describes a model-based technique to determine the bulk and shear modulus of the soil from measured leak noise data, assuming that the pipe properties are known. Two water pipe systems which have different soil properties are considered: one is in the UK and the other one is in Brazil. The UK pipe system has sandy soil, where both compressional and shear wave propagate away from the pipe. The Brazilian pipe system has clay-like soil and only shear wave propagates away from the pipe. The results, based on optimising the soil properties to give a best fit for the leak noise speed and its attenuation, give soil properties that fall within the expected range for the different locations. These results are helpful in determining the fundamental limitations of acoustic correlators in various situations.

1 Introduction

Detection and location of leaks in buried pipelines are topics of great concern for water companies due to the wastage of drinking water in their distribution systems. Approximately 40% up to 50% of water is lost globally in developing countries mostly due to water leakage [1, 2], which in some extreme cases it may exceed 70% of the potable water supply resulting in social, economic and environmental effects.

If a leak occurs, the noise it generates will propagate along the pipe in the form of an acoustic wave, which is the axisymmetric ($n = 0$) fluid-borne wave ($s = 1$) [3]. The physical behaviour of this wave has been studied extensively because of its role in the detection of leaks in buried fluid-filled water distribution pipes. This fluid-dominated wave is strongly coupled to the pipe-wall, meaning that most of the energy is dissipated along the pipe-wall as well as into the surrounding soil where the pipe is buried.

A pipeline has many joints, and monitoring its integrity is crucial. Among several strategies and technologies for finding leaks, the acoustic correlation technique has been widely used to provide an accurate estimate of the position of a leak in order to reduce the wastage of water [4]. However, this technique depends on an accurate estimate of the wave propagation speed along the pipe, which is heavily dependent on the type of soil in which the pipe is buried. The soil also affects drastically the distance that leak noise will propagate along the pipe [3, 5, 6, 7, 8].

Muggleton et al. [3] validated experimentally the analytical model of the fluid-borne wave ($s = 1$) by taking into account the presence of soil. In this work, the soil was treated as a fluid supporting two different waves, each of which exerted normal dynamic pressure on the pipe wall. Although the shear coupling of the pipe

to the surrounding soil was not properly accounted for, the theoretical results and measurements for wave speed showed good agreement at low frequencies. At higher frequencies, however, the results matched the in-air case better than the buried pipe predictions due to possible uncertainties in the soil properties or even effects of the ground surface (which was not considered in the theoretical modelling). In summary, the soil was not modelled effectively, since it was treated as a fluid supporting elastic waves. These properties were considered in subsequent work by Muggleton and Yan [5]. However, the authors derived analytical expressions for the $s = 1$ wave through an incomplete model (pipe-soil interface under slip contact) in which the soil is connected to the pipe in the radial direction, but not connected in the axial direction. In effect, there is a lubricated contact between the pipe and the surrounding soil in such formulation. Later, Gao et al. [6] proposed a more complete model (pipe-soil interface under no-slip contact) in which the pipe connected to the soil both radially and axially. The authors carried out their investigation by an analytical method in which the effect of the soil loading on the pipe response is characterized by the soil loading matrix. Two years later, Brennan et al. [8] reformulated the model proposed by Muggleton and Yan [5] in which the analytical model is formulated in terms of dynamic stiffness of the fluid, pipe and soil. The investigation involved analytical modelling, numerical modelling, and experimental work on two very different test rigs, one in the UK and one in Brazil. The authors demonstrated that the dynamic stiffness approach facilitates physical insight into the effects of soil parameters on the leak noise propagation.

However, the works discussed hitherto did not propose a methodology for the choice of the soil parameters necessary in the prediction of wavenumber, wave attenuation and wave speed. Motivated by this, the present paper has two clear aims:

- To provide a methodology for the selection of soil parameters based on an optimization procedure by minimizing a cost function that calculates the difference between the measured wavenumber with the one predicted by an analytical model, either under slip contact or no-slip contact.
- To propose an alternative model for the $s = 1$ wave, based on the analytical expressions proposed by Gao et al. [6], but written in terms of dynamic stiffness in order to aid a physical insight into the features extracted from the model.

The paper is organized as follows. Section 2 presents two analytical models for wavenumber prediction. It is first assumed that the pipe-soil interface is under compact contact. Second, it is assumed that there is a lubricated contact, in which there is no axial connection between the pipe and the soil. Section 3 presents the optimization algorithm adopted. Following this, the models are validated in two different experimental test rigs in section 4. Finally, some conclusions are given in section 5.

2 Analytical models for wavenumber prediction

This section presents two analytical models for the prediction of axisymmetric waves in buried fluid-filled plastic pipe under different coupling conditions. At low frequencies, below the pipe ring frequency, the axisymmetric ($n = 0$) fluid-dominated ($s = 1$) wavenumber in a fluid-filled pipe surrounded by an elastic medium given by the no-slip coupling, where the pipe-soil interface is assumed to be under compact contact, and the slip coupling, where the pipe-soil interface is assumed to be under lubricated contact, were investigated recently by Muggleton and Yan [5]; Gao et al. [6, 7]. In order to aid physical insight, they can be rewritten in terms of dynamic stiffnesses as follows

$$k = k_{\text{water}}\left(1 + \frac{K_{\text{water}}}{K_{\text{pipe}} + K_{\text{soil}}}\right)^{\frac{1}{2}} \tag{1}$$

where $k_{\text{water}} = \omega(\rho_{\text{water}}/B_{\text{water}})^{\frac{1}{2}}$ is the free-field wavenumber of water, which is a function of the density ρ_{water} the corresponding bulk modulus B_{water} and the angular frequency ω. The term $K_{\text{water}} = 2B_{water}/a$

is the stiffness of the water and

$$K_{\text{pipe}} = \frac{K_{\text{pipe}}^{(\text{stiff})}}{(1-\nu_p^2)} + K_{\text{pipe}}^{(\text{inertia})} = \frac{E_p^* h}{a^2(1-\nu_p^2)} - \omega^2 \rho_p h \tag{2}$$

is the stiffness of the pipe-wall where a is the mean radius, h is the thickness, ρ_p, $E_p^* = E_p(1+j\eta_p)$ and ν_p are the density, Young's modulus and Poisson's ratio of the pipe, respectively. The term η_p is the loss factor of the pipe.

The term $K_{\text{pipe}}^{(\text{stiff})}$ denotes the stiffness component of pipe-wall and $K_{\text{pipe}}^{(\text{inertia})}$ corresponds to the inertial component. Additionally, the term K_{soil} in Eq. (1) denotes the stiffness of the surrounding soil. Note that the soil properties affect drastically the propagation characteristics of the fluid-borne $s = 1$ wave travelling on the pipe since part of its energy propagates into the soil. Thus, two different boundary conditions at the pipe-soil interface are considered: one that assumes the pipe-soil interaction under lubricated contact (slip coupling) where there is no frictional stress applied on the axial direction, and the other one that assumes the pipe-soil interaction under compact contact (no-slip coupling) with propagation on both axial and radial directions.

The soil dynamic stiffness for the slip coupling condition can be written as a combination of three components, so the term K_{soil} in Eq. (1) becomes [8]

$$K_{\text{soil}}^{\text{slip}} = K_1 + K_2 + K_3 \tag{3}$$

in which

$$K_1 = \left(B_s^* - \frac{2G_s^*}{3}\right)\frac{k_d^2}{k_d^r}\left(1 - 2\frac{k^2}{k_r^2}\right)\frac{H_0\left(k_d^r a\right)}{H_0'\left(k_d^r a\right)} \tag{4}$$

$$K_2 = -2G_s^* k_d^r \left(1 - 2\frac{k^2}{k_r^2}\right)\frac{H_1'\left(k_d^r a\right)}{H_1\left(k_d^r a\right)} \tag{5}$$

$$K_3 = -4G_s^* k_r^r \frac{k^2}{k_r^2}\frac{H_1'\left(k_r^r a\right)}{H_1\left(k_r^r a\right)} \tag{6}$$

For the no-slip coupling condition, the soil dynamic stiffness term K_{soil} in Eq. (1) becomes

$$K_{\text{soil}}^{\text{noslip}} = \frac{\mu_s}{a} K_a + \frac{E_p^* h}{a^2(1-\nu_p^2)} K_b \tag{7}$$

where

$$K_a = 2 + \frac{k_r^r a k_r^2 a^2 \left[\frac{H_0(k_r^r a)}{H_0'(k_r^r a)}\right]\left[\frac{H_0(k_d^r a)}{H_0'(k_d^r a)}\right]}{k_r^r a k_d^r a \left[\frac{H_0(k_r^r a)}{H_0'(k_r^r a)}\right] + k^2 a^2 \left[\frac{H_0(k_d^r a)}{H_0'(k_d^r a)}\right]} \tag{8}$$

$$K_b = -\frac{\nu_p^2}{\left(1 + \frac{S_1}{k^2 a^2}\right)} + \frac{j2\nu_p S_2}{ka\left(1 + \frac{S_1}{k^2 a^2}\right)} + \frac{S_2^2}{k^2 a^2 \left(1 + \frac{S_1}{k^2 a^2}\right)} \tag{9}$$

in which

$$S_1 = -\mu_s \frac{(1-\nu_p^2)a}{E_p h}\left[\frac{k_d^r a k_r^2 a^2}{k_r^r a^2 k_d^r \left[\frac{H_0(k_r^r a)}{H_0'(k_r^r a)}\right] + k^2 a^2 \left[\frac{H_0(k_d^r a)}{H_0'(k_d^r a)}\right]}\right] \tag{10}$$

$$S_2 = \frac{j\mu_s(1-\nu_p^2)ka^2}{E_p h}\left[2 - \frac{k_r^2 a^2 \left[\frac{H_0(k_d^r a)}{H_0'(k_d^r a)}\right]}{k_r^r a^2 k_d^r \left[\frac{H_0(k_r^r a)}{H_0'(k_r^r a)}\right] + k^2 a^2 \left[\frac{H_0(k_d^r a)}{H_0'(k_d^r a)}\right]}\right] \tag{11}$$

Moreover, the soil radial wavenumbers k_d^r and k_r^r, are given by $k_d^r = \sqrt{k_d^2 - k^2}$ and $k_r^r = \sqrt{k_r^2 - k^2}$ where k_d and k_r are the compressional and shear wavenumbers in the surrounding soil, respectively, given by $k_d^2 = \omega^2 \rho_s / (\lambda_s + 2\mu_s)$ and $k_r^2 = \omega^2 \rho_s / \mu_s$ in which ρ_s is the soil density and $\lambda_s = B_s^* - \frac{2}{3} G_s^*, \mu_s = G_s^*$ are the Lamé coefficients, which are function of bulk modulus $B_s^* = B_s(1 + j\eta_{\text{soil}})$ and shear modulus $G_s^* = G_s(1 + j\eta_{\text{soil}})$ of the soil. The terms H_0, H_1 are the Hankel functions of zero, first order and second kind, respectively, that describe the outgoing waves in the surrounding soil, and $'$ denotes the spatial derivative.

The attenuation of the fluid-borne wave in terms of dB/m is given by [3]

$$\text{Attenuation} = \frac{-20\text{Im}\{k\}}{\ln(10)} \tag{12}$$

For a fluid-filled pipe in-air there is no surrounding soil present in the model, so that $K_{\text{soil}} = 0$. Furthermore, note that in several practical situations involving buried pipes, the soil properties are usually unknown. Thus, an alternative method to identify soil parameters through an optimization algorithm is presented in section 3.

3 Identification of soil parameters based on optimization algorithm

This section presents a constrained optimization problem adopted to determine locally optimal solutions for to the soil properties from measured vibration data. The pipe geometry is assumed to be known, thus the optimization algorithm is used to identify a set of optimal parameters related to bulk modulus $\hat{B}_s$ and shear modulus $\hat{G}_s$ of the soil by minimizing a cost function that calculates the difference between the measured wavenumber with the one predicted by an analytical model, either under slip contact or no-slip contact as presented in section 2. This iterative procedure ends when the cost function reaches the stopping criteria, searching for the best solution from all feasible solutions subject to constraints on its variables in a certain local minimum.

The best value (also called local minimum) for the vector $\theta = \left[\hat{B}_s \;\; \hat{G}_s\right]$, can be found by solving the following optimization problem where the cost function is based on the normalized mean square error (NMSE) metric:

$$\underset{\theta \in \mathbb{R}}{\text{minimize}}\; F(\theta) = \frac{\left\| \text{Re}\left\{k_{H_{xy}}(\omega)\right\} - \text{Re}\left\{k(\theta, \omega)\right\} \right\|}{\left\| \text{Re}\left\{k_{H_{xy}}(\omega)\right\} \right\|} \tag{13}$$

subject to the bound constraints $\theta_{\text{low}} \leq \theta \leq \theta_{\text{up}}$ where θ_{low} and θ_{up} denote the lower and upper bounds, respectively. The term $k_{H_{xy}}(\omega)$ is the experimental wavenumber estimated through spectral estimator. It involves the ratio between the auto and cross-power spectrum density of two signals x and y measured through sensors connected at two access points [4]:

$$H_{xy}(\omega) = \frac{S_{xy}(\omega)}{S_{xx}(\omega)} \tag{14}$$

The real part of experimental wavenumber is computed based on the phase of the frequency response function in Eq. (14) divided by the distance d between the sensors

$$\text{Re}\{k_{H_{xy}}(\omega)\} = \frac{-\phi_{H_{xy}(\omega)}}{d} \tag{15}$$

The attenuation is given by [8]

$$\text{Attenuation} = \frac{-20\log_{10}\left(|H_{xy}(\omega)|\right)}{d} \tag{16}$$

The term $\mathrm{Re}\{k(\theta,\omega)\}$ in Eq. (13) denotes the wavenumber predicted by the analytical model from Eq. (1) with the vector θ that contains the corresponding optimal values for bulk and shear moduli of the soil. The symbol $\|\|$ denotes the Euclidean norm. This paper adopts the pattern search algorithm that was first introduced by Hooke and Jeeves [9]. This algorithm has a simple strategy for searching a current point in a predetermined direction for an enhanced cost function value. The pattern search algorithm is used to solve the optimization problem that starts with an initial guess $\theta^{(0)}$ and ends up when the stop criterion is met after n iterations, so that $F\left(\theta^{(n)}\right) < \varepsilon$. The whole procedure is then summarized into 4 steps as showed in Fig. 1.

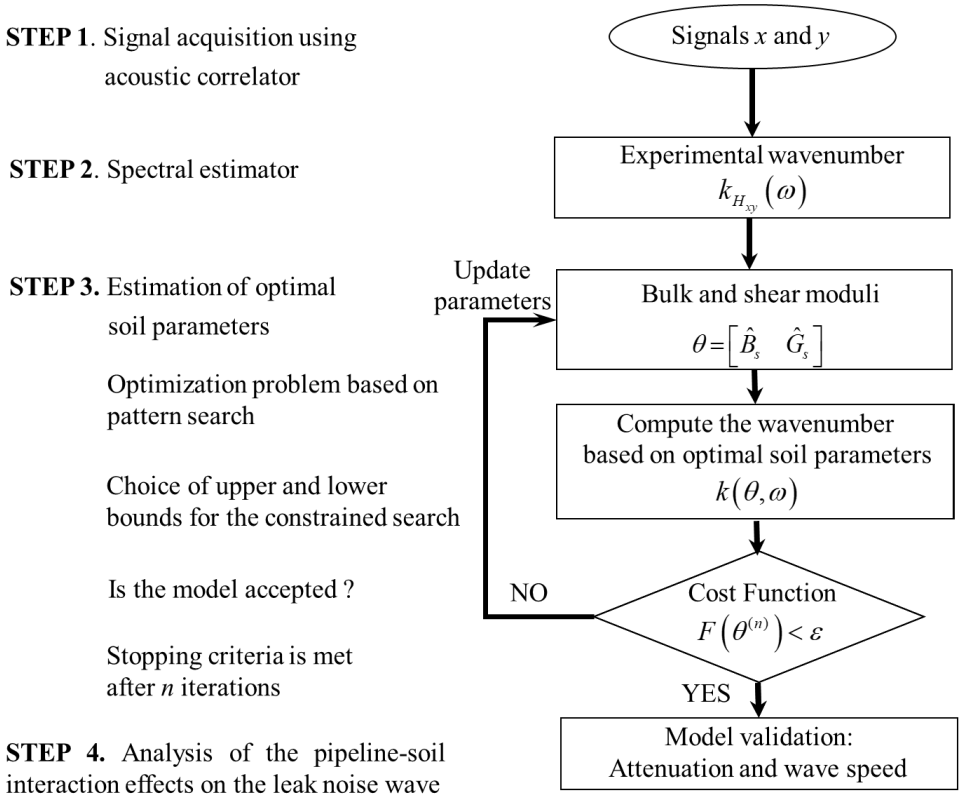


Figure 1: Computational flowchart for the identification of optimal soil parameters.

4 Results and discussion

Two experimental pipe systems, one in Brazil and the other one in UK, are considered to validate the method proposed in section 3. The systems have very different types of soil and geometry as showed in Tab. 1.

Table 1: Properties of the Brazilian and UK pipe systems.

Properties	UK	Brazil
Pipe Young's modulus E_p [N/m^2]	2×10^9	2×10^9
Pipe density ρ_p, ρ_s [kg/m^3]	900, 2000	900, 2000
Pipe loss factor η_p	0.06	0.06
Pipe radius [mm]	84.5	35.8
Pipe-wall thickness [mm]	11	3.4
Type of soil	Sandy	Clay

A schematic of both test rigs are shown in Fig. 2. The UK system consists of a 34 metres long test rig and

the static pressure is due to the 1.5 m head of water in the termination tanks. In this case, the fluid-dominated wave $s = 1$ was excited by an underwater loudspeaker using a stepped sine signal increasing frequency from 30 Hz to 1 kHz (1 Hz increment) and the dynamic pressure was measured using two hydrophones 2 metres apart. More details about the measurements done in UK can be found in Muggleton et al. [3]. The geometry of Brazilian pipe system, described in more detail in Brennan et al. [8], is much smaller than UK pipe system, which was pressurised with a centrifugal pump (3.4 bar). In this experimental test rig, the $s = 1$ wave was excited by opening a valve and the signals related to this leak noise wave were measured by using two accelerometers at two access points 7 metres apart.

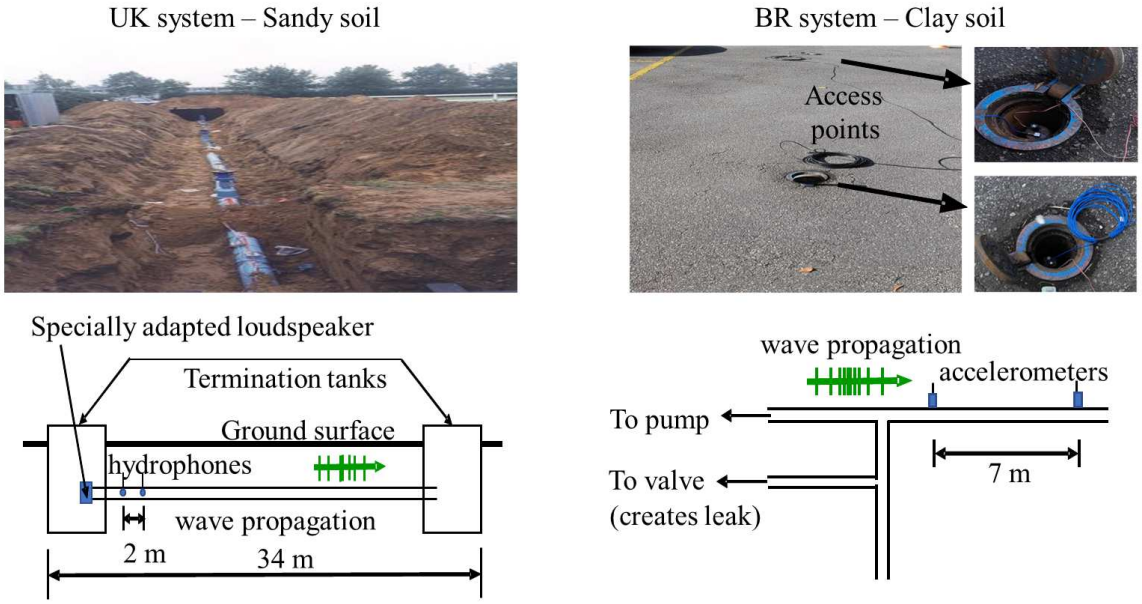


Figure 2: Experimental setup of the pipe systems adopted: UK pipe system on the left [3] and Brazilian pipe system on the right.

Before moving to the optimization procedure, illustrated in Fig. 1, an analysis of the surface plots based on the objective functions from Eq. (13) involving the wavenumber, wave attenuation and corresponding wave speed is carried out. Figure 3 shows the surfaces of objective functions for UK pipe system. It is possible to see that both bulk and shear modulus have an effect on the wavenumber, wave attenuation and wavespeed of the fluid-dominated ($s = 1$) wave generated by the leak. According to the surfaces, locally optimal solutions for values for bulk and shear modulus are within the range from 1×10^7 [N/m^2] to 6×10^7 [N/m^2] for both parameters.

In figure 4 it is possible to see that the bulk modulus has a marginal effect on the wavenumber for Brazilian pipe system, and the local minimum value for shear modulus, that has dominant contribution, is expected to be located within the range from 2×10^8 [N/m^2] to 3×10^8 [N/m^2]. This effect can also be seen in the surface plot of wave speed values in Fig. 5.

To solve the optimization problem in Eq. (13), the values of corresponding upper and lower bounds were chosen based on the soil where each pipe is buried. The UK pipe system is characterized by sandy soil, so that $\theta_{low} = \begin{bmatrix} 1 \times 10^7 & 1 \times 10^7 \end{bmatrix}$ and $\theta_{up} = \begin{bmatrix} 5 \times 10^7 & 6 \times 10^7 \end{bmatrix}$. On the other hand, Brazilian pipe system is characterized by clay-like soil, thus the corresponding values of bulk modulus and shear modulus are higher than sandy soil as $\theta_{low} = \begin{bmatrix} 1 \times 10^9 & 1 \times 10^8 \end{bmatrix}$ and $\theta_{up} = \begin{bmatrix} 5 \times 10^9 & 6 \times 10^8 \end{bmatrix}$. The starting point was chosen as the average of upper and lower bounds, with tolerances for objective function, step and optimality as factor of 1×10^{-10}. The value for both bulk and shear loss factor was used as $\eta_{\text{soil}} = 0.15$.

Tables 2 and 3 show the best values for soil parameters identified by optimization algorithm using model A

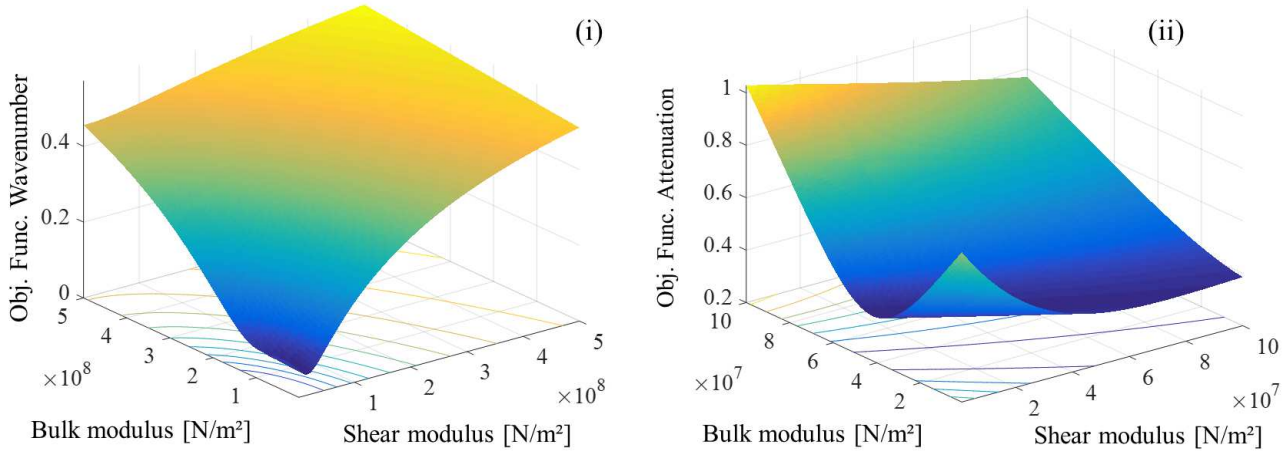


Figure 3: Behavior of the objective functions (i) Wavenumber and (ii) Wave attenuation calculated based on different values of bulk and shear moduli for the UK test rig that is characterized by sandy soil.

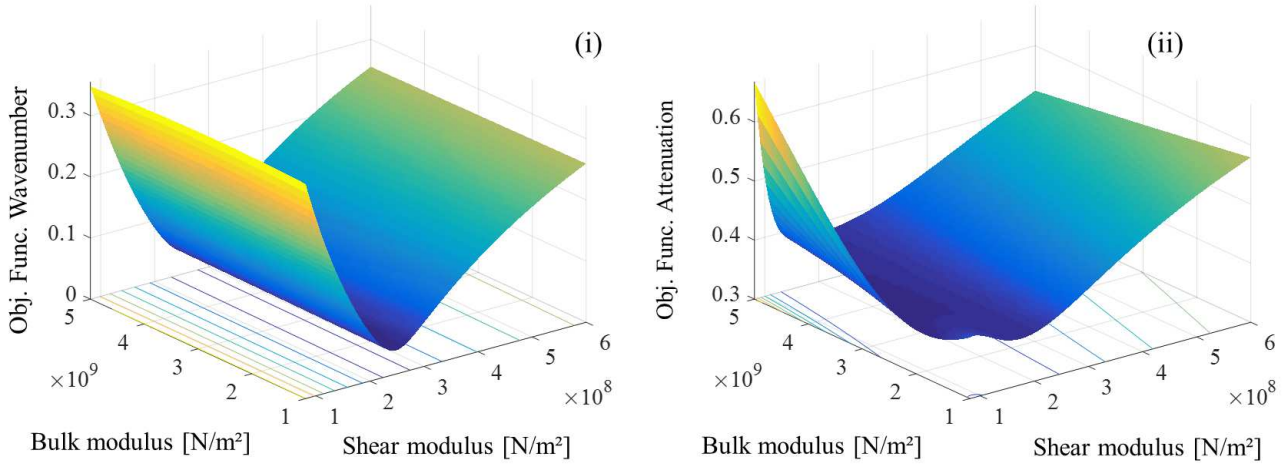


Figure 4: Behavior of the objective functions (i) Wavenumber and (ii) Wave attenuation calculated based on different values of bulk and shear moduli for the Brazilian test rig that is characterized by clay soil.

under slip contact and model B no-slip contact between the pipe-soil interaction. These values were then used to predict the wavenumber, wave attenuation and wave speeds, shown in Figs. 6, 7 and 8, where it is possible to see good agreement between the results.

Table 2: Best values for sandy soil properties identified through pattern search algorithm (UK system).

Optimization Parameters	Model A (Slip)	Model B (No-slip)
Bulk modulus $\hat{B}_s$ [N/m^2]	4.0032×10^7	4.0000×10^7
Shear modulus $\hat{G}_s$ [N/m^2]	1.5665×10^7	1.4903×10^7

Examination of Fig. 6 shows an agreement between the experimental wavenumber, from Eq. (15), with the ones predicted by model A and B, that assumes the pipe-soil interface under lubricated and compact contact, respectively. The real part of wavenumber reaches 10 m^{-1} at 600 Hz in the UK pipe system and is around 7 m^{-1} for the Brazilian system.

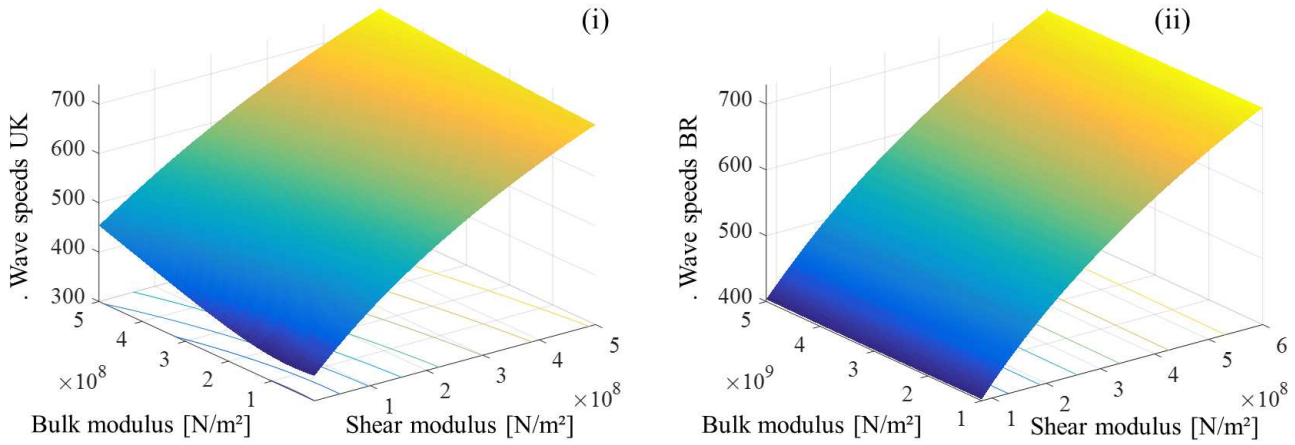


Figure 5: Behavior of the objective functions for the wavespeed of two different test rigs: (i) UK pipe system and (ii) Brazilian pipe system.

Table 3: Best values for clay soil properties identified through pattern search algorithm (BR system).

Optimization Parameters	Model A (Slip)	Model B (No-slip)
Bulk modulus $\hat{B}_s$ [N/m^2]	1.9400×10^9	4.0000×10^9
Shear modulus $\hat{G}_s$ [N/m^2]	0.2478×10^9	0.2359×10^9

Although the real part of wavenumbers predicted present similar behavior in both pipe systems, some differences are found in the attenuation and wave speed, as can be seen in Figs. 7 and 8.

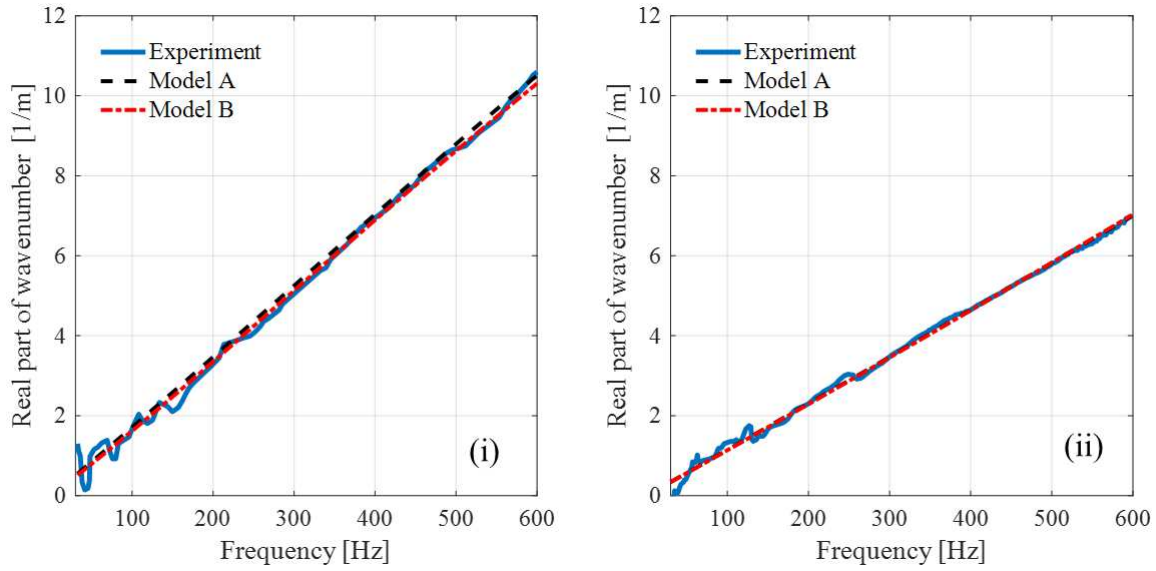


Figure 6: Measured wavenumber compared with the one predicted by model A (pipe-wall and soil with slip contact) and by model B (pipe-wall and soil with no-slip contact) for two different test rigs: (i) UK system with sandy soil and (ii) Brazilian system with clay-like soil.

The wave attenuation for the Brazilian pipe system and the UK system is shown in Fig. 7. It can be seen that for a typical Brazilian water pipe system, which is characterized by a clay-like soil, the coupling pipe-soil

in the radial direction has a much greater effect than coupling in the axial direction. Furthermore, it has a predominant effect on the wave motion in the pipe, mainly through the radial coupling. On the other hands, the axial coupling has a greater effect in the UK pipe system. Thus, the model B with non slip coupling is a better representation for such type of system. The wave attenuation is mostly due to material losses within the pipe wall plus radiation losses in the soil. Based on Fig. 7, it is possible to see that at 600 Hz, the attenuation is around 18 dB/m for UK system, whereas for the Brazilian system is around 6 dB/m.

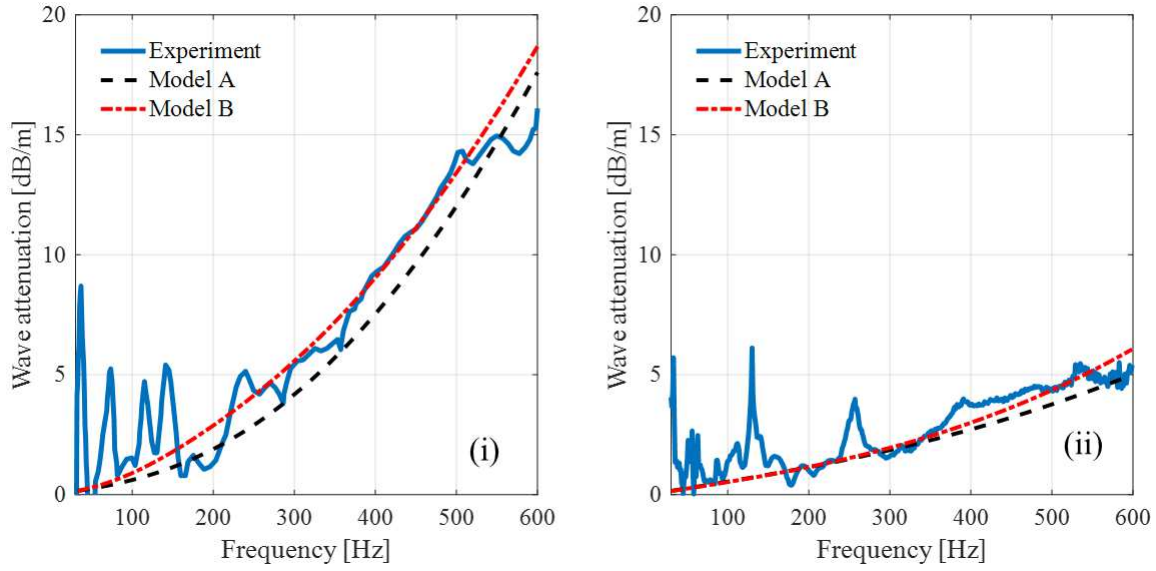


Figure 7: Measured wave attenuation compared with the one predicted by model A (pipe-wall and soil under slip contact) and by model B (pipe-wall and soil under no-slip contact) for two different test rigs: (i) UK system with sandy soil and (ii) Brazilian system with clay-like soil.

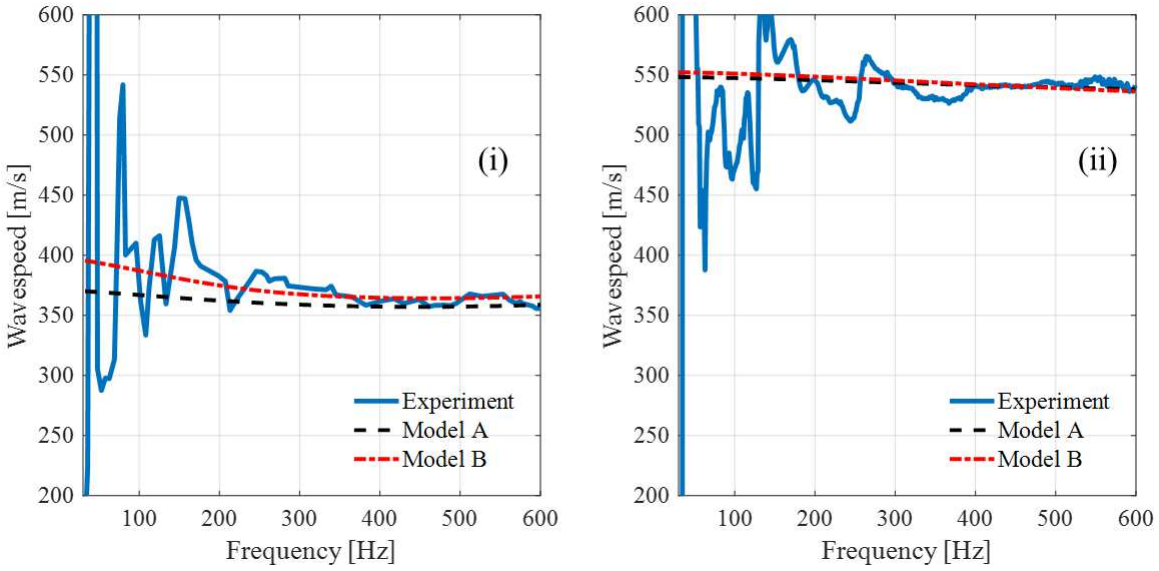


Figure 8: Measured wave speed compared with the one predicted by model A (pipe-wall and soil under slip contact) and by model B (pipe-wall and soil under no-slip contact) for two different test rigs: (i) UK system with sandy soil and (ii) Brazilian system with clay-like soil.

Figure 8 shows the predicted wave speeds, which are about 375 m/s for the UK pipe system and 540 m/s for Brazilian pipe system. The shear stiffness of the soil has a greater contribution and effect on the wave speed in the pipe compared to the bulk stiffness of the soil and is the main reason why the wave speed in the Brazilian system is much higher than in the UK pipe which is buried in sandy soil.

5 Final remarks

This paper has presented a methodology for the identification of soil parameters from measured vibration data. Together with a model, they have been used to give a better understanding into how the fluid-pipe-soil interface affects the propagations characteristics of the fluid-borne ($s = 1$) wave in two experimental test rigs with different geometry and soil properties. For a typical pipe and soil properties found in parts of Brazil, it has been found that coupling between the pipe and the soil in the radial direction has a much greater effect on the speed of leak noise propagation in the pipe, than coupling in the axial direction. In terms of the attenuation of leak noise in the pipe, it has been found that both radial and axial coupling pipe-soil have some effect. For a typical pipe and soil found in UK, it has been shown that both compressional and shear waves propagate away from the pipe adding to the damping effect in the pipe. Experimental results have showed the applicability of the method for automatically estimate the soil parameters aiming an enhanced leak noise detection in buried plastic pipes through acoustic techniques.

Acknowledgements

The authors would like to thank the financial support provided by the São Paulo Research Foundation (FAPESP) under Grant numbers 2013/50412-3 and 2017/14432-0.

References

[1] A.C.D. Royal, P.R. Atkins, M.J. Brennan, D.N. Chapman, H. Chen, A.G. Cohn, K.Y. Foo, K.F. Goddard, R. Hayes, T. Hao, P.L. Lewin, N. Metje, J. M. Muggleton, A. Naji, G. Orlando, S.R. Pennock, M.A. Redfern, A.J. Saul, S.G. Swingler, P. Wang and C.D.F Rogers, *Site assessment of multiple-sensor approaches for buried utility detection*. International Journal of Geophysics, (2011) Article ID 496123. doi: https://doi.org/10.1155/2011/496123.

[2] F.C.L. de Almeida, M.J. Brennan, P.F. Joseph, S. Dray, S. Whitfield and A. T. Paschoalini, *Measurement of wave attenuation in buried plastic water distribution pipes*, Journal of Mechanical Engineering, vol. 60, no. 5 (2014), pp. 298-306. doi: https://doi.org/10.5545/sv jme.2014.1830.

[3] J.M. Muggleton, M.J. Brennan and P.W. Linford, *Axisymmetric wave propagation in fluid-filled pipes: wavenumber measurements in in vacuo and buried pipes*, Journal of Sound and Vibration, vol. 270 (2004), pp. 171-190. doi: https://doi.org/10.1016/S0022-460X(03)00489-9

[4] Y. Gao, M.J. Brennan, P.F. Joseph, J.M. Muggleton and O. Hunaidi, *A model of the correlation function of leak noise in buried plastic pipes*. Journal of Sound and Vibration, vol. 277, no. 1-2 (2004), pp. 133-148. doi: https://doi.org/10.1016/j.jsv.2003.08.045.

[5] J.M. Muggleton and J. Yan, *Wavenumber prediction and measurement of axisymmetric waves in buried fluid filled pipes: Inclusion of shear coupling at a lubricated pipe/soil interface*. Journal of Sound and Vibration, vol. 332, no. 5 (2013), pp. 1216-1230. doi: https://doi.org/10.1016/j.jsv.2012.10.024.

[6] Y. Gao, F. Sui, J.M. Muggleton and J. Yang, *Simplified dispersion relationships for fluid-dominated axisymmetric wave motion in buried fluid-filled pipes*. Journal of Sound and Vibration, vol. 375 (2016), pp. 386-402. doi: https://doi.org/10.1016/j.jsv.2016.04.012.

[7] Y. Gao, Y. Liu and J.M. Muggleton, *Axisymmetric fluid-dominated wave in fluid-filled plastic pipes: Loading effects of surrounding elastic medium*. Applied Acoustics, vol. 116 (2017), pp. 43-49, doi: https://doi.org/10.1016/j.apacoust.2016.09.016.

[8] M.J. Brennan, M. Karimi, J.M. Muggleton, F.C.L de Almeida, F. K. de Lima, P.C. Ayala, D. Obata, A.T. Paschoalini and N. Kessissoglou, *On the effects of soil properties on leak noise propagation in plastic water distribution pipes*, Journal of Sound and Vibration, vol. 427 (2018), pp. 120-133. doi: https://doi.org/10.1016/j.jsv.2018.03.027.

[9] R. Hooke and T. A. Jeeves, *Direct search solution of numerical and statistical problems*, J. ACM, vol. 8, no. 2, (1961), pp. 212-229. url: https://dl.acm.org/citation.cfm?doid=321062.321069.

Substructuring approach and blocked forces method: application for structure-borne vibration prediction in heavy weight assemblies

D. Miguez[1, 2], O. Farrell[1], M.A. Bannister[1], R. Arbabi[1], A. T. Moorhouse[2], A. S. Elliott[2]
[1] Farrat Isolevel Ltd, Altrincham WA15 8HJ, United Kingdom
e-mail: **dm@farrat.com**

[2] Acoustics Research Centre, University of Salford, Greater Manchester M5 4WT, United Kingdom

Abstract
Prediction of vibration levels in heavy structures enables engineers to adopt vibration mitigation measures in the initial design stages, therefore reducing costs and time taken for construction or installation. Different strategies for achieving accurate predictions range from numerical methods, such as FEA and SEA, to methods incorporating measured data. Here, we present an experimental method that combines the sub-structuring approach with the in-situ blocked forces method to characterise the key elements of an assembly. In order to implement this methodology, the assembly is subdivided into the components vibration source, isolator and receiver. These three elements are characterised by performing mobility measurements on the individual substructures and the source is additionally characterised by the blocked force measured in-situ. Predictions made using the independent component characterisations are compared with measures obtained from a whole assembly composed of a heavy structure supported on resilient isolators.

1 Introduction

Vibration prediction is important in buildings designed for living, working, listening and for certain types of sensitive equipment. Unlike airborne, structure borne noise prediction is very challenging due to the complexity for characterising the elements involved. Besides an important increase on research studies for predicting structure borne noise in industries such as automobile or aircraft in recent years, that trend is not so noticeable within the building industry.

Different strategies used for prediction of ground/structure borne noise range from numerical methods, which discretise the problem domain into well-defined inputs expressed as equations or parametric studies (e.g. Finite Element Analysis, Statistical Energy Analysis); to measurement based methods, that reduce the problem to transfer functions between assembly elements [1].

Due to limitations of numerical methods such as the high computational requirements and their disagreement with field data [2], there has been an increase in the development of solutions on measurement based approaches such as dynamic sub-structuring for light structures [3].

The combination of *in situ* blocked forces and sub-structuring empirical methods (described in the following section) have been proven accurate for the prediction of structure borne noise from lightweight assemblies e.g. electric pumps [4] or engine parts [5] and heavier assemblies such as micro wind turbines [6]. In order to implement this methodology, the assembly is subdivided into the components: vibration source, isolator and receiver. These three elements are then characterised by performing mobility or impedance measurements on the individual sub-structures and the source is additionally characterised by the blocked force measured in-situ [7].

Besides the good agreement shown between predictions and *in situ* measurements with lighter structures, the accuracy of the aforementioned methods for heavier structures, more representative of realistic factory machinery or building situations, is yet to be assessed and will be the focus of this work.

2 Theory and Methods

In order to simplify the notation used throughout the present work and to also allow its application to other situations, the assembly is subdivided into three general elements namely source (S), isolator (I) and receiver (R). The source is defined as the object or structure that generates a vibration which is propagated to a final structure known as receiver. These two elements are connected via another structure defined as the isolator, which typically provides a resilient link in order to reduce structure-borne vibration.

Furthermore, Figure 1 describes the three aforementioned elements, together with four defined interfaces that comprise the different excitation/response positions: Internal mechanisms of the source which are not part of the interface with isolator (a), the source-isolator interface (b), the isolator-receiver interface (c), and response points on the receiver away from the interface (d).

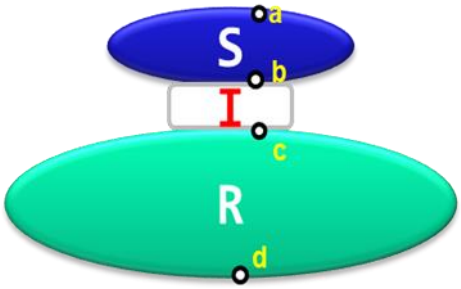


Figure 1: Source-Isolator-Receiver assembly diagram showing the different elements (S, I, R) and interfaces (a-d)

In the following sections a similar nomenclature is followed, consisting of the use of subscripts S, I, R and C for referring to the independent Source, Receiver, Isolator and the Coupled assembly respectively. Following this, two subscripts are used to denote the sets of degrees of freedom where response and excitation measurements are made respectively. As an example, Y_{Ccb} refers to the transfer mobility of the coupled assembly where the response is observed below the isolator (c) when exciting at (b).

2.1 Blocked Force Method for active source characterisation

Blocked forces of structure borne sound sources can be obtained *in situ* as demonstrated in [7], [8], and can be defined as:

$$\bar{\boldsymbol{f}}_{\boldsymbol{Sb}} = \boldsymbol{Y}_{\boldsymbol{S,bb}}{}^{-\mathbf{1}}\tilde{\boldsymbol{v}}_{\boldsymbol{Sb}} \tag{1}$$

where f_{Sb} is the blocked force of the source at interface b, Y_S is the source mobility and v_{sb} is the velocity of the free source. Over score and tilde denote blocked and free conditions respectively.

An alternative of the blocked force can also be obtained from coupled assembly measurements *in situ*, therefore not requiring free-free conditions:

$$\bar{\boldsymbol{f}}_{\boldsymbol{Sb}} = \boldsymbol{Y}_{\boldsymbol{C,bb}}{}^{-\mathbf{1}}\boldsymbol{v}_{\boldsymbol{Cb}} \tag{2}$$

where f_{Sb} is the blocked force of the source at interface b, $Y_{C,bb}$ is the coupled source mobility and v_{Cb} is the operational velocity of the coupled source at b.

Due to the fact of being an inherent characteristic of the source, the blocked force can also be used to predict the structure borne vibration when being part of different assemblies.

2.2 Dynamic sub-structuring

As detailed in [7], the dynamic substructuring method (DS) allows for the prediction of a coupled assembly behaviour as individual contributions of the different subsystems that are part of it. This methodology provides important advantages when faced with heavy weight structure limitations:

- It allows freedom for the characterisation of the different assembly elements, enabling the combination of approaches such as numerical methods (e.g. FEA or SEA); or empirical methods that incorporate directly measured data, which is the option presented in this work.

- A reverse application of dynamic sub-structuring, structure decoupling, allows the extraction of the properties of one of the sub-structures from data collected from the coupled assembly together with the remaining sub-structures. A useful application of this would be to avoid the need to mount an industrial press under free conditions obtaining its properties by subtracting the isolator and floor impedance from the coupled assembly.

However, the use of dynamic sub-structuring has implicit limitations that condition the reliability of the resulting predictions. To a large extent the uncertainties come from the fact that the application of matrix inversion is highly sensitive to errors, being able to affect the entire matrix when only one element is wrong before inversion [9].

Another important factor affecting the accuracy of predictions of sub-structuring is the number of degrees of freedom (DOF) accounted for. Due to the inherent complexity of interface dynamics, a lack of information regarding translational and rotational DOF can strongly influence the error between prediction and on board validation measurements, therefore justifying the need of accounting for all DOF. However, the use of resilient isolators has proven to reduce this effect in lower frequencies, being able to provide reasonably accurate predictions when neglecting rotational and in-plane forces [10].

In order to obtain the passive properties of the different sub-structures and predict their coupled behaviour, source, isolator and receiver were independently characterised (detailed in following section). The classical impedance procedure was applied [11] to the resulting accelerance matrices by constructing a block diagonal matrix which contains the independent assembly element impedance matrices:

$$\boldsymbol{Z_{BlDiag}} = \begin{bmatrix} \boldsymbol{Y_S^{-1}} & \mathbf{0} & \mathbf{0} & \mathbf{0} & \mathbf{0} \\ \mathbf{0} & \boldsymbol{Z_i} & \mathbf{0} & \mathbf{0} & \mathbf{0} \\ \mathbf{0} & \mathbf{0} & \boldsymbol{Z_i} & \mathbf{0} & \mathbf{0} \\ \mathbf{0} & \mathbf{0} & \mathbf{0} & \boldsymbol{Z_i} & \mathbf{0} \\ \mathbf{0} & \mathbf{0} & \mathbf{0} & \mathbf{0} & \boldsymbol{Y_R^{-1}} \end{bmatrix} \quad \textbf{(3)}$$

where Y_S is the source mobility (3 by 3 matrix), Z_i is the isolator impedance (2 by 2 matrix) and Y_R is the receiver mobility including the interface d FRFs (4 by 4 matrix).

The resulting diagonal matrix (13 by 13) is pre and post multiplied by two Boolean coupling matrices in order to assure conditions of equilibrium and compatibility:

The pre-multiplicative matrix L_f enforces equilibrium at the coupling DoFs, and the post-multiplicative matrix L_v enforces compatibility of the coupling DoFs, whilst also accounting for the remote reference DOFs. This way, the overall coupled mobility matrix result of the application of the dynamic sub-structuring method would be given by:

$$\boldsymbol{Y_C = \left(L_f Z_{BlDiag} L_v\right)^{-1}} \quad \textbf{(4)}$$

, where:

$$L_f = \begin{bmatrix} 1 & 0 & 0 & 1 & 0 & 0 & 0 & 0 & 0 & 0 & 0 & 0 & 0 \\ 0 & 1 & 0 & 0 & 0 & 1 & 0 & 0 & 0 & 0 & 0 & 0 & 0 \\ 0 & 0 & 1 & 0 & 0 & 0 & 0 & 1 & 0 & 0 & 0 & 0 & 0 \\ 0 & 0 & 0 & 0 & 1 & 0 & 0 & 0 & 0 & 1 & 0 & 0 & 0 \\ 0 & 0 & 0 & 0 & 0 & 0 & 1 & 0 & 0 & 0 & 1 & 0 & 0 \\ 0 & 0 & 0 & 0 & 0 & 0 & 0 & 0 & 1 & 0 & 0 & 1 & 0 \\ 0 & 0 & 0 & 0 & 0 & 0 & 0 & 0 & 0 & 0 & 0 & 0 & 1 \end{bmatrix}$$

and:

$$L_v = {L_f}^T$$

3 Methods

In order to be able to implement a methodology that combines the use of blocked forces for active source characterisation together with dynamic sub-structuring of the entire assembly, source and receiver were characterised under free-free conditions whereas the isolator was characterised both *in situ* and under dynamic compression (MTS) using a dynamic hydraulic testing machine. Despite the use of free mounting for the source and receiver characterisation, other mountings could have been used following Eq. (2). Furthermore, the source-isolator-receiver assembly was characterised and the resulting data used for validation of the different methods described in this section.

The different elements were characterised by obtaining the point and transfer accelerance frequency response functions (FRFs) derived from force excitations and acceleration responses of the individual substructures *in-situ*. The instrumentation used for these experiments consisted of 4507-B004 (B&K) single axis accelerometers as response sensors, and an 8206-001 instrumentation hammer (B&K) for performing the different structure excitations. The force and acceleration measures together with their Frequency Response Functions (FRFs) were synchronously collected using a SIRIUS acquisition card (DEWESOFT) at a sampling rate of 20000Hz with a frequency resolution of 0.6 Hz/data point.

3.1 Source and Receiver characterisation

The source used was a servo motor bolted to an aluminium plate, which at the same time is bolted to three steel feet used for the connection with the isolator mounts (Figure 2-top). Free-free conditions were implemented by suspending the source using elastic bungees.

Six single axis accelerometers were used for the characterisation of the source, two per foot and separated by 2.5 cm. Force excitations were applied on top of the three feet and at interface a.

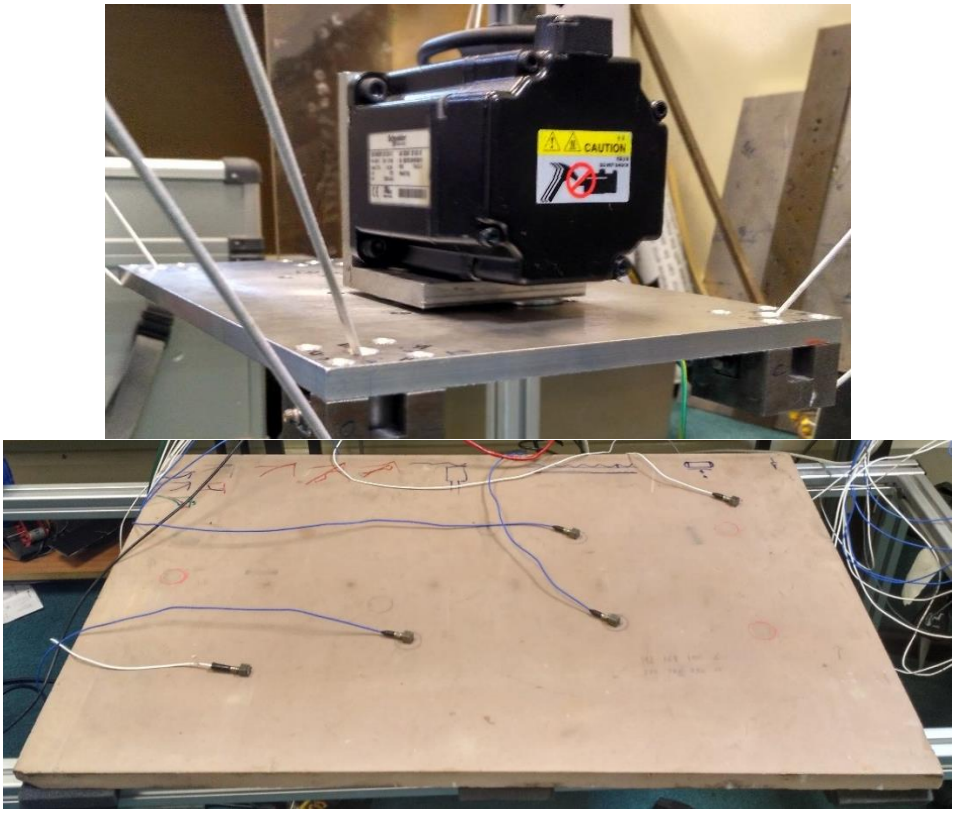


Figure 2: Free-free experiment view of Source (top) and Receiver (bottom).

A 900x600x20 mm construction slab (Figure 2-bottom) was used as the receiver structure for the presented work. Three accelerometers acquired the structure response below the three coupling points between the receiver and the isolators (Figure 4), together with two additional accelerometers positioned away from the connections (interface d). Three force excitations were applied on top of the three coupling points.

In order to proof that the blocked force method can predict the effect of the internal mechanism of a vibrating source (interface a) when coupled to a different assembly, the blocked force was calculated from the free-free independent source experiment by applying Eq. (1). The acceleration at response points d was then calculated using this blocked force together with the *in situ* accelerance obtained in the coupled experiment between interfaces b and d:

$$\boldsymbol{a_{C,d} = A_{C,db}\bar{f}_{Sb}} \quad \textbf{(5)}$$

The acceleration predicted at d using the blocked force method Eq. (1) (5) was compared with the *in situ* obtained from the coupled experiment, and can be observed in Figure 3 in terms of narrow band frequencies (top) and in third octave bands (middle).

In order to provide a numerical expression of the accuracy of the prediction, the error was calculated in the frequency domain by using Eq. 6, and is shown graphically in Figure 3-bottom.

$$error\ (dB) = 20\log\left({predicted_response}/{measured_response}\right) \quad \textbf{(6)}$$

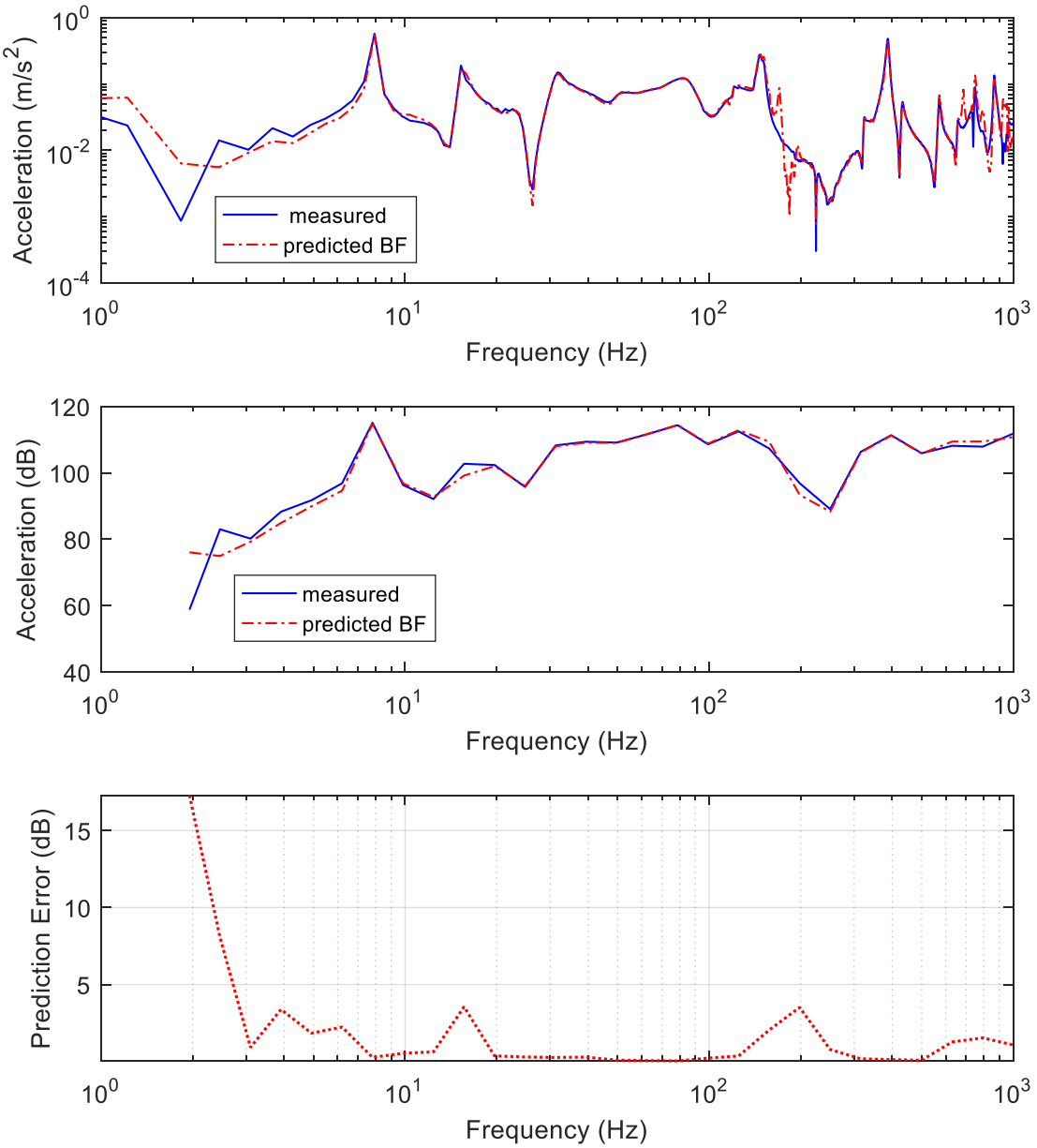


Figure 3: $a_{C,d}$ acceleration obtained in the coupled measurement (blue) vs prediction using the blocked force method (red-dashed) in narrow band frequency (top) in m/s^2 and per third octave band (middle) in decibels (ref. 1µm/s^2). Bottom: error between prediction and *in situ* obtained coupled acceleration (dB) in third octave bands.

Results show that predictions of the source response using the blocked force method provide a very accurate fit of the *in situ* measured data in terms of both narrow band and third octaves. Errors between these measures are below 3.5dB above 3 Hz. The error at 1Hz (16dB) is due to a lack of coherence in the FRFs obtained below 10Hz.

These results validate the use of the blocked forces method as a reliable independent active source characterisation which is also descriptive of its performance in new assemblies.

3.2 Isolator characterisation

The material chosen as resilient coupling between source and receiver was VIDAM (detailed datasheet can be found in [12]), a nitrile rubber and granulated cork composite material typically used as industrial equipment vibration isolator. The 40mm long and 30mm diameter cylindrical isolators were characterised using two different methods: dynamic compression (Figure4-left) and *in situ* method (Figure4-right).

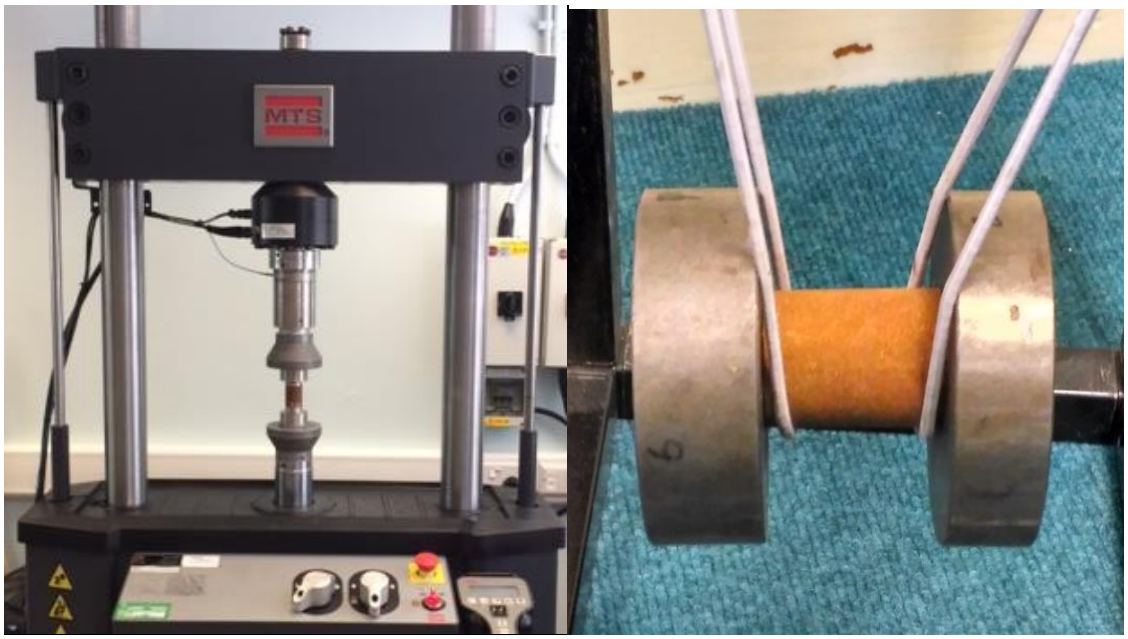


Figure 4: dynamic compression (left) and *in situ* (right) isolator characterisation experimental setups

The isolator was firstly characterised under dynamic compression at frequencies from 1 to 100 Hz using a dynamic hydraulic testing press (MTS, USA). The experimental conditions included an average static preload of 235.4N and a dynamic amplitude of 0.01mm. Preconditioning was applied to the sample prior to the experiment in order to obtain more accurate and repeatable results. As an outcome of this process, complex dynamic stiffness was obtained in eleven frequencies up to 100Hz.

In addition to the dynamic compression experiment, the isolator was also characterised using an *in situ* mass-isolator-mass procedure as described in [13]. It consisted of the acquisition of point and transfer mobilities above and below the material when connected to two known masses. Two single axis accelerometers were used for this experiment together with the application of forces above and below the two masses.

Dynamic stiffness was extracted from the accelerance FRFs acquired with the *in situ* method and then compared with the stiffness obtained using the dynamic hydraulic testing press in Figure 5.

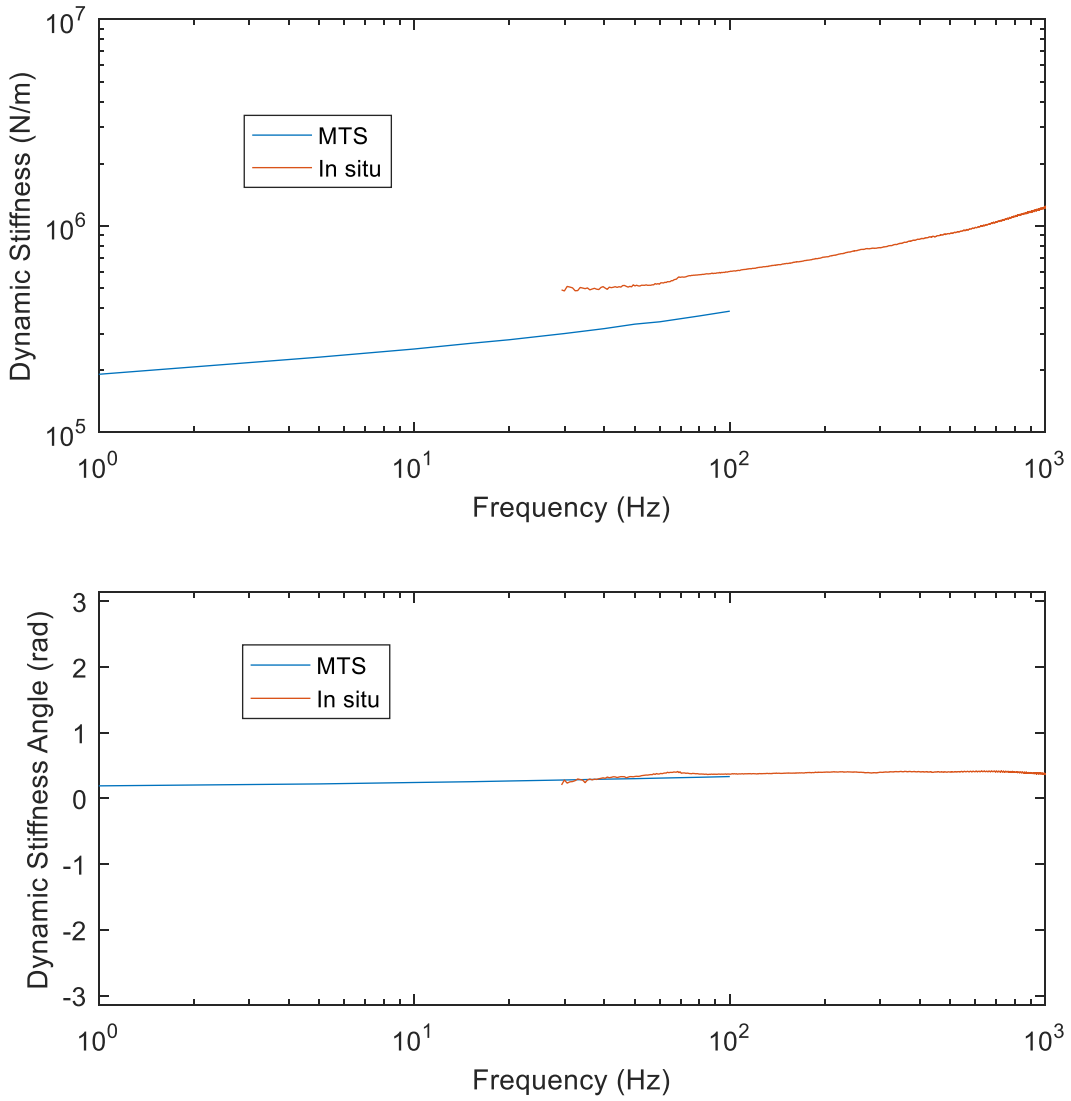


Figure 5: Dynamic stiffness of VIDAM isolator measured using the *in situ* Mass-isolator-mass procedure (red) vs. using Dynamic compression (blue) in both terms of magnitude (top) and phase (bottom).

Results show a similar trend followed by the two methods with some disagreement in terms of magnitude (Figure 5-top), which could be justified by the preload difference in the two experiments. Due to the lack of coherence in the accelerance FRFs obtained for the *in situ* method at the lowest frequencies (particularly below 10Hz), the isolator was characterised using dynamic compression results below 100Hz and the in situ experiment results for frequencies above.

3.3 Coupled Assembly

Once performed the assembly elements independent characterisations, a fourth experiment defined as the coupled assembly characterisation was performed by coupling the source and receiver via three isolators glued at the same time to the three steel feet of the source and the receiver slab in the positions shown in Figure 6.

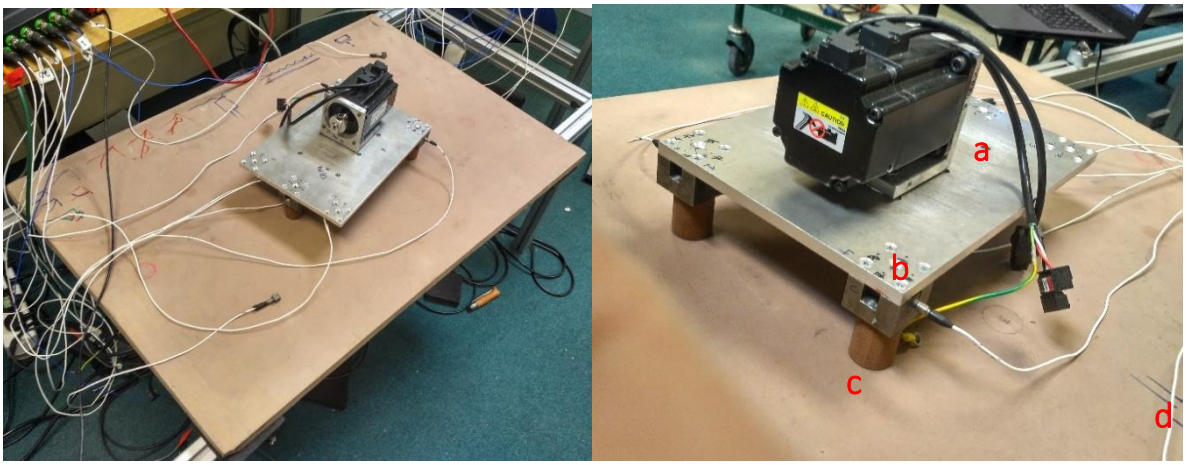


Figure 6: Left: Coupled Source-Isolator-Receiver assembly experimental setup. Right: Closer view of the assembly identifying the different interfaces (a-d) in red font.

A total of eleven accelerometers were used for the coupled experiment providing acceleration responses at both the source and receiver in identical positions to the independent experiments described previously. Excitations were applied to both the source (three on top of the isolator coupling points -b- and two internal to the source -a-) and the receiver structures (three below the isolator coupling points -c- and two external to the isolator-receiver interface -d-), obtaining this way a symmetric accelerance matrix as described in the theory section.

4 Results

As described in the theory section, dynamic sub-structuring is applied to the independently characterised source, isolator and receiver accelerance FRFs by mathematically coupling as described in Eq. (3). As an outcome of this, the predicted coupled accelerance at the external point in the receiver (interface d) is obtained after applying Eq. (4) to the resulting matrix and the two Boolean coupling matrices that assure conditions of equilibrium and compatibility.

4.1 Dynamic Sub-structuring predictions

Figure 7 graphically shows the comparison between the predicted coupled assembly accelerance and the *in situ* measured response of the coupled elements, in both terms of magnitude (Figure 7-top) and phase (Figure 7-bottom).

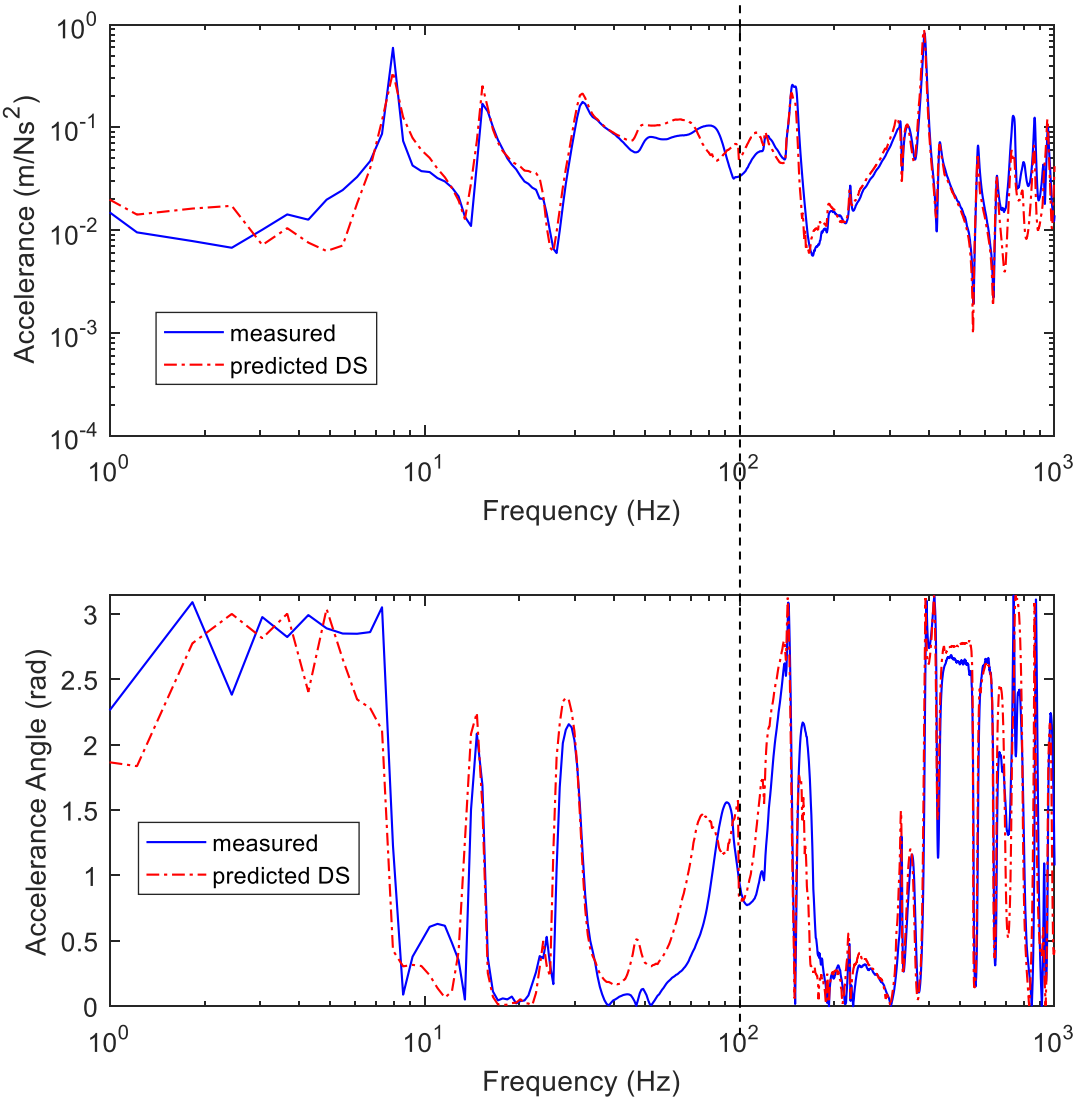


Figure 7: $A_{C,d}$ accelerance obtained in the coupled measurement (blue) vs prediction using the dynamic sub-structuring method (red-dashed) in terms of magnitude (top) and phase(bottom). Black dashed line divides the isolator characterisation between MTS (below 100Hz) and *in situ* methods.

Results show a very good agreement throughout the entire frequency range studied in terms of magnitude and phase, which includes isolator characterisation from two different methods detailed in the previous section (delimited by the black dashed line in Figure 7). Small disagreements were observed between 40 and 100Hz and below 10Hz, the latter being due to poor coherence in the FRFs obtained.

4.2 Blocked Forces and Dynamic Sub-structuring combined predictions

Once validated the individual application of blocked forces method and dynamic sub-structuring for the data collected in the different experiments, a combination of the two methods was implemented as described in Eq. (5), defining "$A_{C,db}$" as the DS prediction using the independent assembly element characterisations; and "f_{Sb}" as the blocked force extracted from the active source characterisation as detailed in section 3.1.

Figure 8 graphically compares the predicted acceleration at the interface d when exciting an internal part of the source (interface a) with the same acceleration measured *in situ* extracted from the coupled experiment.

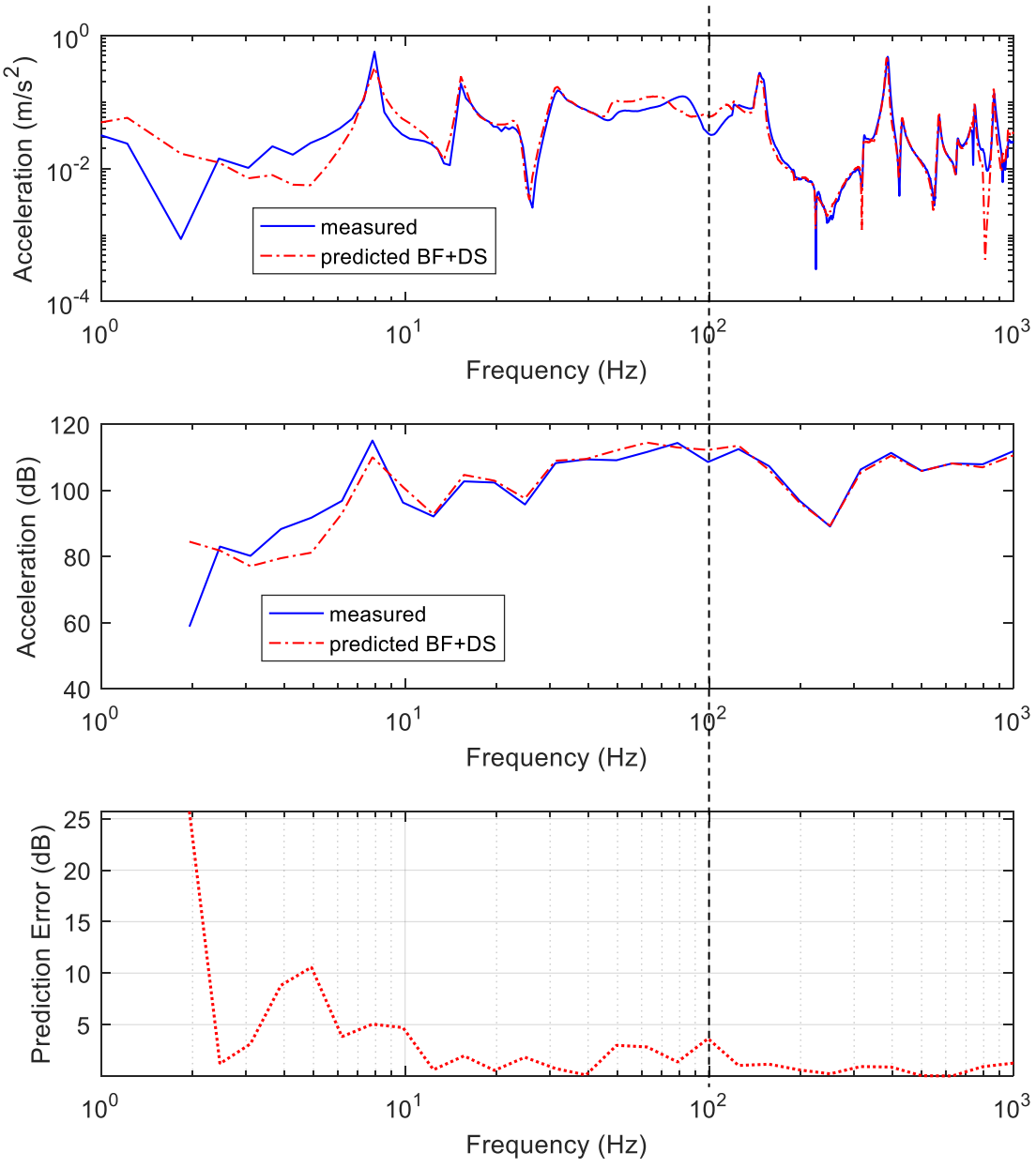


Figure 8: $a_{C,d}$ accelerance obtained in the coupled measurement (blue) vs prediction using the blocked forces method combined with dynamic sub-structuring (red-dashed) in terms of narrow band frequency (top) in m/s² and per third octave band (middle) in decibels (ref. 1µm/s²). Bottom: error between prediction and *in situ* obtained coupled acceleration (dB) in third octave bands. Black dashed line divides the isolator characterisation between MTS (below 100Hz) and *in situ* methods.

The resulting curves exhibit a good agreement in both terms of narrow band frequencies and octave bands, exhibiting noticeable error peaks of 25.7 and 10.6dB at 1.9Hz and 4.9Hz respectively. Errors were always lower than 5dB after the latter frequency.

5 Conclusions

The work presented here demonstrates that the behaviour of a coupled assembly can be predicted using data from independent experiments performed on its elements. In order to achieve this, the source was characterised by its blocked force and, together with the mobility matrices obtained for the resilient isolators and receiver, the coupled assembly FRF is constructed by applying the sub-structuring method.

Besides showing very good overall agreements, the methodology proposed provided some noticeable errors in the lowest frequencies studied. Measures that could compensate for these errors include the use of accelerometers with better low frequency response and the use of a bigger instrumentation hammer for better excitation of the low frequency structural modes in order to increase the coherence of the different FRFs acquired.

Future work includes the validation of this methodology to heavier structures more representative of realistic situations such as industrial equipment and concrete floors as well as its posterior application to real building vibration isolation. Alternatively, the use this methodology also allows the use of non-empirical data for the definition of independent measures of the assembly elements (such as FEA and/or SEA models) and therefore its implementation should be studied in more detail.

Furthermore, the application of structure decoupling could be used to extract independent assembly element properties by using coupled experiment data together with independent characterisation of the remaining assembly elements (either *in situ* or by the use of numerical methods).

Acknowledgements

This work was supported by an Innovate UK Knowledge Transfer Partnership between Farrat Isolevel and University of Salford.

The dynamic compression isolator characterisation experiments described in section 3.2 were performed by Dr Zyad Haji and Dr Kian Samami at Farrat Isolevel R&D facilities.

References

[1] D. Davis, “A Review of Prediction Methods for Ground-Borne Noise due to Construction Activities,” *Proc. 20th Int. Congr. Acoust.*, no. August, pp. 23–27, 2010.

[2] G. Kouroussis, K. E. Vogiatzis, and D. P. Connolly, “A combined numerical/experimental prediction method for urban railway vibration,” *Soil Dyn. Earthq. Eng.*, vol. 97, no. March, pp. 377–386, 2017.

[3] D. De Klerk, D. J. Rixen, and S. N. Voormeeren, “General Framework for Dynamic Substructuring: History, Review and Classification of Techniques,” *AIAA J.*, vol. 46, no. 5, pp. 1169–1181, 2008.

[4] A. S. Elliott, J. W. R. Meggitt, and A. . Moorhouse, "Blocked forces for the characterisation of structure borne noise," *Internoise Noise-Con Congr. Conf. Proc.*, vol. 250, no. 1, pp. 5798–5805, 2015.

[5] D. Lennström, M. Olsson, F. Wullens, and A. Nykänen, "Validation of the blocked force method for various boundary conditions for automotive source characterization," *Appl. Acoust.*, vol. 102, pp. 108–119, 2016.

[6] A. S. Elliott and A. . Moorhouse, "In-situ characterisation of structure borne noise from a building mounted wind turbine," *Proc. ISMA2010*, pp. 2055–2068, 2010.

[7] A. S. Elliott, "Characterisation of structure borne sound sources in-situ," University of Salford, 2009.

[8] A. . Moorhouse, A. S. Elliott, and T. A. Evans, "In situ measurement of the blocked force of structure-borne sound sources," *J. Sound Vib.*, vol. 325, no. 4–5, pp. 679–685, 2009.

[9] B. Jetmunsen, "On frequency domain methodologies for prescribed structural modification and subsystem synthesis," ProQuest Dissertations Publishing, 1986.

[10] J. W. R. Meggitt and A. . Moorhouse, "the in-Situ Decoupling of Resiliently Coupled Sub-," no. July, pp. 1–8, 2017.

[11] J. W. R. Meggitt, "On In-situ Methodologies for the Characterisation and Simulation of Vibro-Acoustic Assemblies," University of Salford, 2017.

[12] F. Isolevel, "Vibration Isolation and Damping Materials - Farrat Vidam (VM)." [Online]. Available: http://www.farrat.com/anti-vibration-materials-washers-bushes/vidam-vm#9. [Accessed: 27-Jun-2018].

[13] J. W. . Meggitt, A. S. Elliott, and A. . Moorhouse, "In-situ determination of dynamic stiffness for resilient elements," *J. Mech. Eng. Sci.*, vol. 0, no. 0, pp. 1–8, 2015.

Characterization of dynamic forces generated by an active component: experimental validation of the Block Sensor Method

X. Carniel[1], J. Champain[1], T. Gardin[1], G. Pavic[2]
[1] Cetim/MAV
52 avenue Félix Louat F-60304 Senlis, France
e-mail: **xavier.carniel@cetim.fr**

[2]INSA/LVA
20 rue Albert Einstein F-69621 Villeurbanne, France

Abstract
Characterizing the vibroacoustic contribution of an active component, which has to be integrated in a mechanical assembly, concerns three types of noise generation: air, fluid and structure borne sound. If the basic techniques of airborne noise analysis are well standardized, difficulties arise with fluid and structure borne sounds. Measurements results depend on the dynamic characteristics of the receiving structures.

In this paper, the Blocked Force/Impedance have been chosen as descriptors to characterize experimentally structure borne noise of mechanical components. The method used, named as "Block-Sensor", allows to obtain these descriptors which can be used to predict the structure borne noise of an assembly .

The paper recalls the principle of the method and details the different steps of the experimental approach. An analysis of the results is provided, giving advantages, drawbacks and limits of the method.

The method is now in a process of standardization, within prISO 21955.

1 Introduction

The need to characterize the vibroacoustic behavior of mechanical assemblies is increasing, due to health, quality or comfort requirements. These constraints are generally governed by application of the standards or statutory texts in force (Machinery directive, or Physical agents (noise and vibration) directive), but also by the publication of customer requirements with increasingly demanding specifications, taking into account the needs with regard to current and future technological developments.

For suppliers, in terms of marketing, it may also be advisable to promote products featuring better acoustic performance than the competition. Acoustics can be a shop window demonstrating the know-how of the manufacturers, and represent a quality descriptor that may be primordial depending on the application.

Lastly, suppliers want to participate in the dimensioning of low-noise systems, and would logically like to be involved and intervene in the acoustics of the systems, and of their products in particular, as far upstream as possible in the development cycle of new projects. Taking the vibration and acoustic aspect of the suppliers' components into account in the early stages of system design increases chances that in the end the noise of the assembled product is satisfactory. If this is not the case, only late and expensive corrections or adaptation measures can be taken, and may not be as effective as the ones taken on time (technical¬economic constraint).

A technical dialogue should therefore be established early in the project between the supplier, knowing well its component, and the integrator, knowing well the entire product. The problem that then arises can be expressed in these terms: what can their exchange be based on? Are they at the same technical level on

dealing with vibration and acoustics? What technical data must they share in order to reach a satisfactory solution?

This problem can be addressed by an approach named acoustical synthesis. The present paper covers one of several aspects of acoustical synthesis: the characterization of a vibration source. The technique used, the block sensor methods, has been conceived to respond to the conditions of an industrial user.

2 Prediction of noise emission: Acoustic synthesis approach

The noise emitted by noise sources in units, buildings, ships and vehicles (on road and off road) is often accompanied by the vibrations of their components. From the noise control viewpoint each component can be considered as a "black box" that emits acoustic and vibrational energy in three forms (Figure 1):

- Airborne noise: acoustic radiation from the source and the nearby structures, propagating in the surrounding air; it is measured using microphones or sound intensity probes.
- Hydraulic or fluid-borne noise generated in the piping systems and radiated: it originates in the pressure pulses emitted by the source in the liquid columns of the system which are broadly responsible for the noise emission by the piping. It is generally evaluated using flush-membrane pressure sensors.
- Structure-borne noise: vibration transmitted from a source through its coupling to the surrounding and further radiated as airborne noise. .

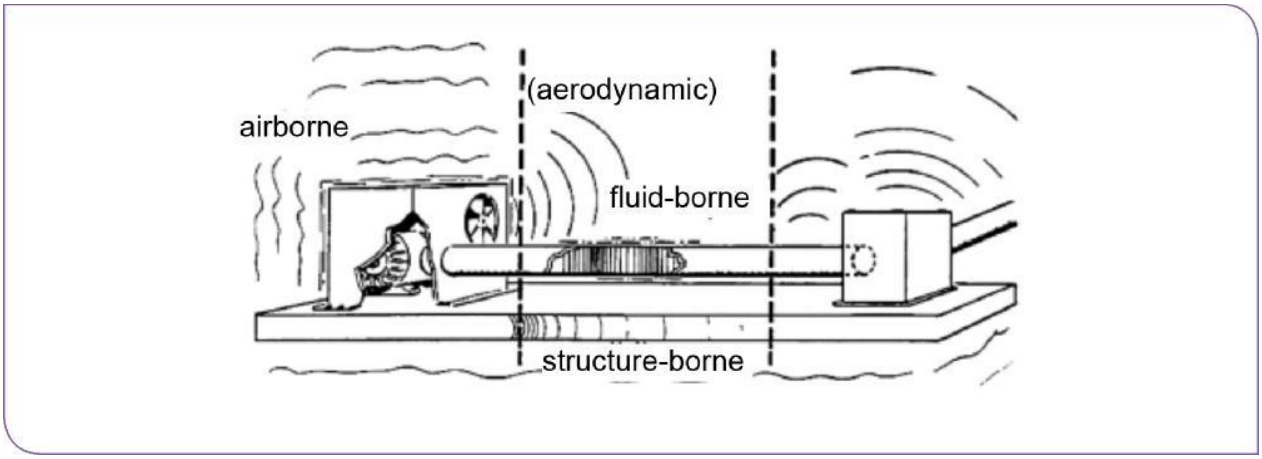


Figure 1 – Different forms of noise generating mechanisms

Acoustic synthesis is an approach for design or diagnosis consisting in breaking down a system into noisy or vibrating components (sources) and into passive ones (transmission paths), in order to control its vibration and acoustic behaviour at a required reception point (Figure 2).

Each component should be described by experimental and/or numerical data or by analytical or empirical formulations.

Modelling of the active components, treated as sources in the acoustic synthesis approach, is fairly complex, and several approaches can be considered:

- on the basis of a source design data, using numerical methods
- on the basis of measurements, characterizing the source according to operating parameters.

Modelling of the passive components, treated as transfer functions in the acoustic synthesis approach, necessitates a non-trivial experimental validation approach.

For the sake of acoustical synthesis, each component of the assembly is described fully at the interfaces with other components, using continuity conditions and taking into account any interaction between the active and passive substructures

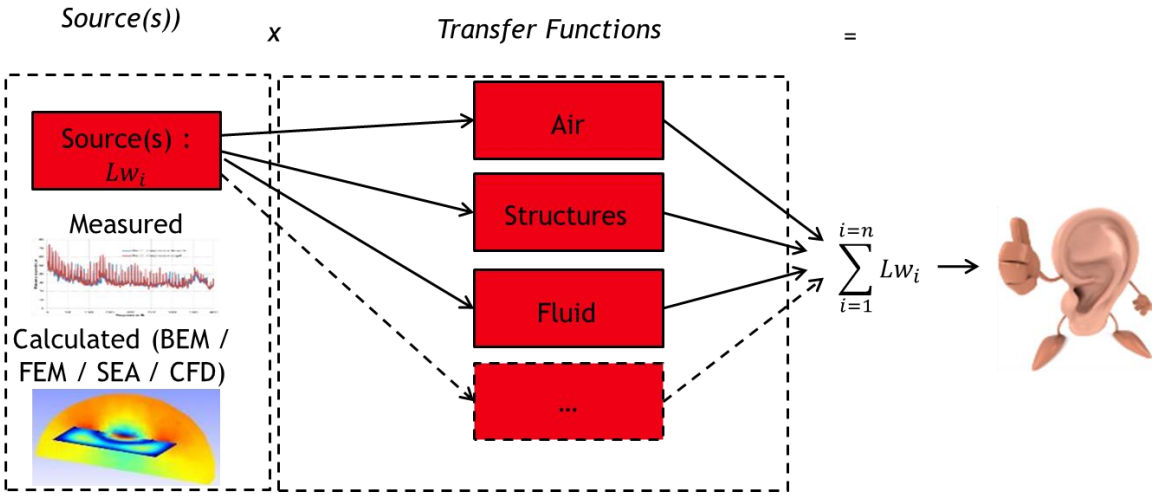


Figure 2 – Noise synthesis approach

3 Characterization of the structure-borne noise of a source

The characterisation of structure-borne noise by measurement has been of concern in recent decades [1-2]. A simple characterization technique applicable to resiliently suspended vibration sources has been standardized [3]. The passive way of characterizing a mechanical structure requires the use of either mobility or impedance [4]. The latter being difficult to measure directly, the impedance is obtained by the measurement of mobility and subsequent inversion. The mobility and impedance approaches, are strictly equivalent as mobility can be obtained from the impedance by inversion and vice versa, the measurement of mobility is inherently easier [5-6].

A typical vibration source has multiple connection points with the support. In order to measure mobility at each connection point an external excitation should be applied to each degree of freedom at a time, while leaving all the other points free in all degrees of freedom. This is achieved in practice using a flexible suspension of the source.

The transmission of vibrations at the coupling points is achieved by both forces and moments. The importance of moments, especially at high frequencies, has been clearly established. Moreover, the movements which contribute to the vibration transmission are both translations and rotations. Such a complex mechanism of transmission is difficult to properly control during measurements. This is why the moments and rotations are usually ignored in practice. The excitation torque is difficult to create in a controlled way. Different methods have been attempted so far to measure the mobility components involving torque and rotation [7-13], most in well controlled laboratory conditions.

Mounting a mechanical source to its support often leads to static deformations which can affect a lot the source vibration. The source mounting conditions during characterization should be as close as possible to true operational conditions. Two theoretical approaches have been developed to this end [14], [15], the latter being extended to several applications. A source can be alternatively characterized in terms of its "apparent force", suggested for building engineering applications, [16].

Most of the developed approaches of structure-borne noise measurements suffer from uncertainty of results linked to poor conditioning due to multi-connection / multi degrees-of-freedom drawbacks. A recent technique applicable to small vibration sources has the objective of increasing the robustness of the characterization procedure through some simplifications [17]. This technique uses the notion of “equivalent

force" which has been already investigated in [18]. The present paper demonstrates the use of the technique in an industrial environment using a particular way of measuring the needed quantities.

4 Equivalent force torsor and "block-sensor method

The "equivalent force torsor" method has been developed to characterize and predict the noise of a component. This inverse method is based on the principle of determination of the descriptors according to the characterization by source impedance/blocked forces. The two descriptors can be useful if experimental hierarchization of sources is needed, but are also necessary in numerical models for source modelling and in particular for optimization of source connection with its intended support.

4.1 General overview

The source impedance and blocked forces depend on the number of connection points between the component and its receiving structure as well as on the number of effective degrees of freedom per point. To limit the volume of data, the equivalent force torsor method replaces the interactions between source and receiver at several points by a resultant interaction applied to a single point. Such a replacement results in the equivalent force torsor and the equivalent reduced impedance.

To identify the reduced descriptors, an elastically-suspended rigid mass is used as receiver.

4.2 Theoretical principles

The principle of this method can be illustrated by the behaviour in a linear electrical circuit, for which a complete analogy can be established with linear vibratory systems (Figure 3).

With the switch open, the voltage V between terminals A and B is V, as no current is flowing. In the coupled state (circuit closed), the current has to flow through resistances RS and RR in series, and the voltage V between A and B drops to the value given by Ohm's law for the current iC:

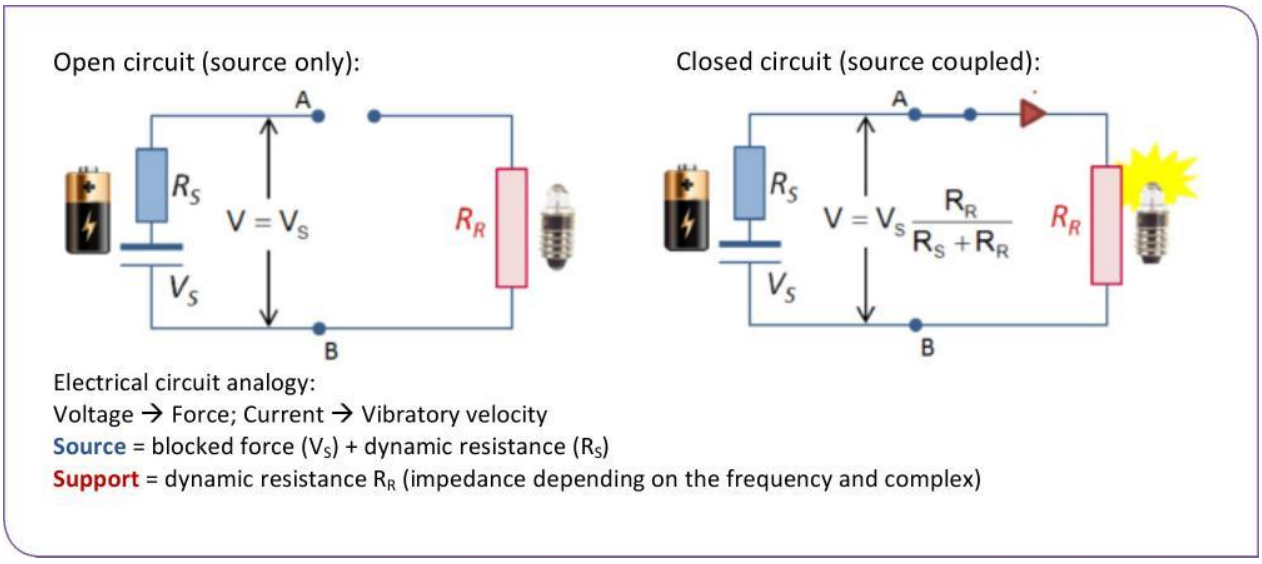


Figure 3 – Electrical analogy for structure coupling

This imples that the blocked force F_B of a vibratory system (V in Figure 3) can be accessed without being really connected to its support. During the process of force identification the source can stay connected with its actual support or, alternatively, with a specific receiver (RR).

Thus, if the coupled impedance Z_C (i.e. source/receiver coupling) is known and the vibratory velocity V_C (or acceleration in practice) is also known, the blocked force F_B can be obtained by Eq. 1. Moreover, the coupled impedance is the sum of the impedances of the receiver and the isolated source, Eq. 2.

$$F_B = -Z_C V_C \tag{1}$$

$$Z_C = Z_S + Z_R \tag{2}$$

Note:

It must be remembered that a system with N connections is governed by a multi-point force torsor F_B, i.e. a vector of 6N complex components F_i (three translation forces and three moments) and that the complex impedances Z_{ij} in Eq. (2) are placed in matrices Z with [6N x 6N] components.

4.3 Equivalent force torsor concept

A way to limit the volume of data is to use an equivalent force torsor, replacing the interactions between source and receiver at several points by a resultant interaction applied to a single point.

At this single point, referred to as the coupling point, the component under study can be described by the six degrees of freedom (three translations, three rotations) of a non-deformable solid. The six components of torsor F_{BS} that have to be identified are ranked in a vector as follows:

$$F_{BS} = \left[F_x\ F_y\ F_z\ M_x\ M_y\ M_z\right]^t \qquad \text{(at the coupling point, t - transpose)} \tag{3}$$

Similarly, the size of the reduced impedance matrix of the component at the coupling point is 6 x 6 (36 values of which 21 independent by the symmetry of the system $Z_{ij} = Z_{ji}$).

The main advantage of the equivalent force torsor is to reduce the number of source data representative of the source. The mutually nearer the coupling points (compact source) and the stiffer the receiver in the coupling area the closer this approximation to reality.

4.4 Specific receiver for identification – the “block-sensor”

4.4.1 Principle

In order to identify the equivalent force torsor and the reduced impedance of the source, the component in the coupled state is installed on a rigid mass as support. This support, also referred to as “block-sensor” or calibration block, is suspended elastically through flexible means (e.g. resilient mounts, elastic straps) ensuring freedom of vibratory movements of the different points of the block, Figure 3. It must enable easy measurements of the mobilities of the coupled and uncoupled system (to ultimately identify Z_C and Z_R) and of the accelerations in operation of the coupled system (to identify V_C) in Eq. 1 and Eq. 2.

The advantage of using a rigid receiver with a simple geometry is threefold:

- to easily identify its impedance by different means (measurements, analytical calculation or finite element model.)
- to access the six vibration components at an arbitrary point on the basis of any six known independent components of vibration on the block.
- to easily translate an applied external force from any point of the block to any other point by adding a compensating torque.

All of the three mentioned advantages simplify the identification ofthe blocked forces F_B using Eq. 1 and the source impedance Z_S using Eq. 2.

In order to provide six independent vibration components the block is instrumented with accelerometers placed judiciously to record the vibrations according to the six degrees of freedom of a non-deformable solid (refer to § 4.4.4).

The role of the "block-sensor" can be summarized as follows:

- It provides the system with a reference or "calibration" impedance Z_R that is simple and known (identifiable by measurements and/or calculations).

- It acts as acceleration transducer by measuring the six independent components. Measurement of the accelerations at different points on the block provides the data necessary at the coupling point (Eq. 1).

- It acts as a force transducer. Measurement of an externally applied force on the block coupled to a source provides the (inaccessible) forces and moments acting in the coupling point.

4.4.2 Position of the equivalent coupling point

To obtain the equivalent reduced impedance of the pump, the impedances of the support Z_R and the impedance of coupled system Z_C must be measured at the same point. This point may be real and accessible (for placing a transducer there, for example), or virtual.

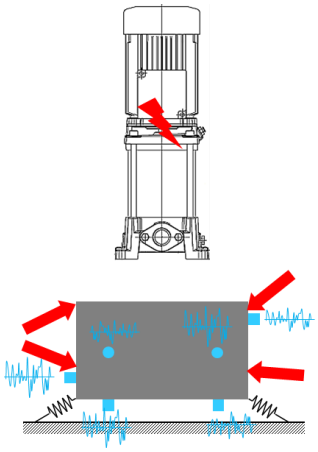
The simplest way to provide an external excitation needed for the measurement of impedance is to apply impacts, e.g. by an impact hammer. However, it is often not possible to measure the accelerations nor to apply the impacts directly at the coupling point. The transducer block is then used as a measuring device which, by means of kinematic transfer matrices, determines the accelerations at the coupling point, based on the measurement of the six degrees of freedom at other places on the block.

But the strong underlying assumption, on which the equivalent torsor method is based, is that the coupling points have fixed positions with respect to each other and in particular with respect to the equivalent coupling point. Consequently, the coupling point should be positioned in a rigid area so that the transposition of the vibrations measured at the distant points is governed only by a frequency-invariant kinematic transfer matrix.

Similarly owing to the rigidity of the transducer block an excitation applied at an impact point can be easily translated to the coupling point. Lastly, the mobility at the coupling point can be deduced from the transfer function between the accelerations grouped in vectors $\ddot{\tau}_{mes}$ and the forces F_{meas} at the chosen measurement points.

In order to simplify data handling the impedances will be redefined with respect to the classical definition of the type force/velocity. In this work the impedance is the ratio between the force or couple and the acceleration rather than velocity.

4.5 Measurement procedure



Soft suspension of bloc sensor

Installation of 6 accelerometers to get the 6 dof

Coupling of source and mass

Artificial sollicitation of the mass (impact hammer)

Identification of coupled impedance Z_c

Calculate the impedande of the mass Z_R

Obtain source impedance: $Z_S = Z_C - Z_R$

Operate the source and measure the vibrations $\ddot{u}_C$

Obtain the blocked forces torsor $F_b = -Z_C \ddot{u}_C$

Figure 4: The measurement procedure

5 Application case: Characterization of a compressor

5.1 Set-up and experiment

A "scroll" compressor has been tested in different operational points, Table 1. The compressor was supported by its 4 feet either rigidly, by bolts, or softly, via resilient rubber mounts. A solid steel block was used as a sensor-receiver, Fig. 6.

Table 1: Operating points of the source**Operational Point**	**Rotation frequency (Hz)**	**Connections**
Chiller	35, 50, 65, 80	Rigid
HeatPump	35, 50, 65, 80	Rigid
Rooftop	35, 50, 65, 80	Rigid
Rooftop	65	Soft
Rooftop	65	Soft



5.2 Results

5.2.1 Receiver impedance identification (Z_R)

The first step is to determine the impedance of the block sensor Z_R and the transfer matrix between measurement points and impact excitation points ($Y_{ij}(f) = X_i(f)/F_j(f)$), Figure 5. Results are shown Figure 6

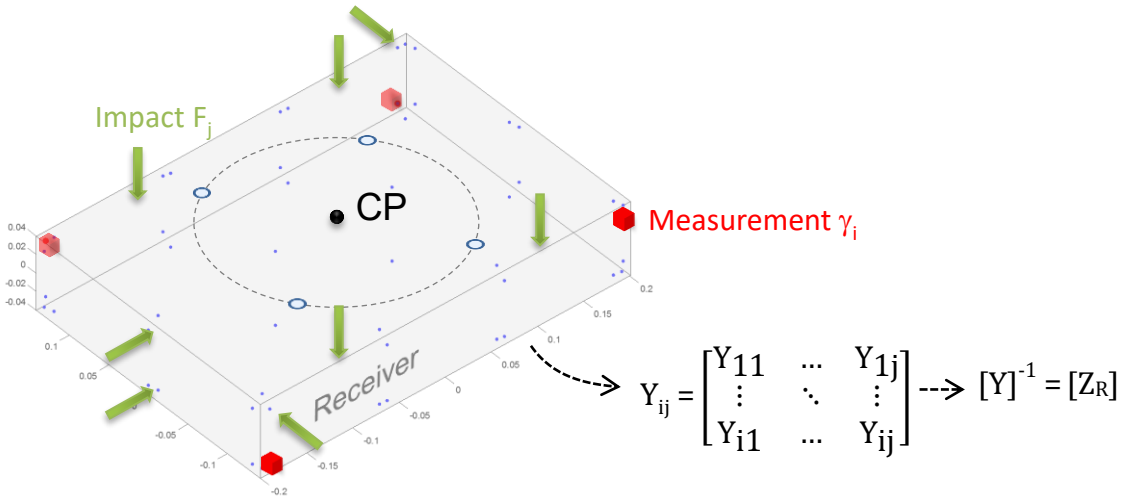


Figure 5 – Measurement of block sensor impedance Z_R.

Below 50 Hz, the block suspension system, in spite of being very soft, does influence the behavior of the block considered free. On the other hand the block can be considered rigid below 1800 Hz. The frequencies of analysis were thus limited to a 50-1800 Hz band.

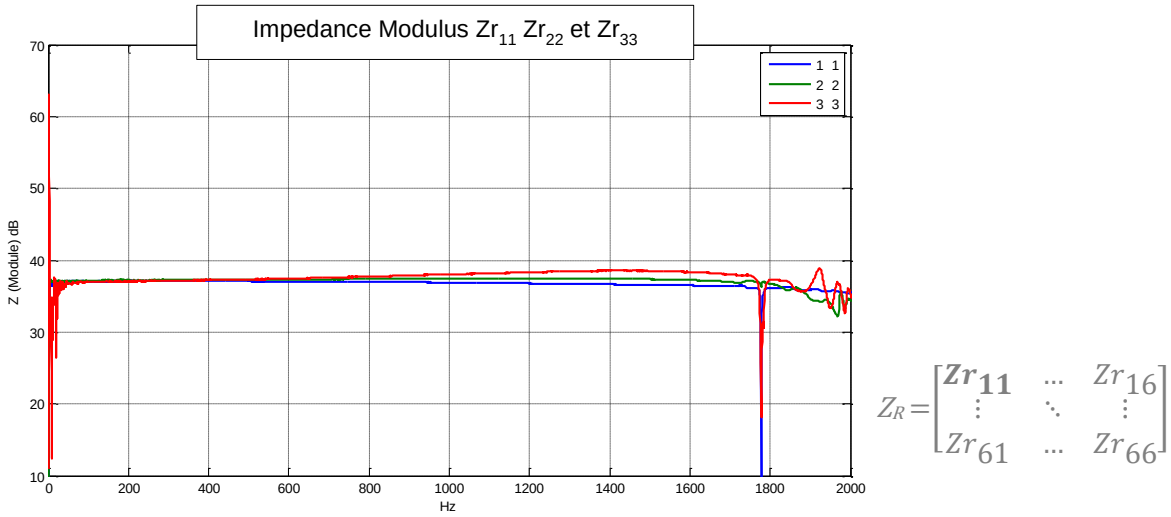
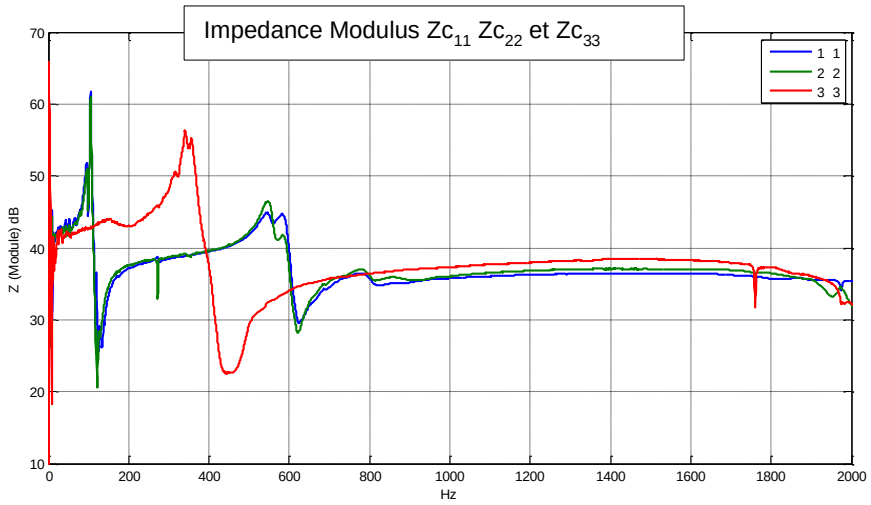


Figure 6 – Impedance Z_R of receiving block alone

5.2.2 Coupled impedance identification (Z_C)

The second step is the determination of the coupled impedance at the coupling point, the component being installed on the block. Modulus of the impedance in the 3 directions (11 = X, 22= Y, 33 = Z=Z) are shown on Figure 7.

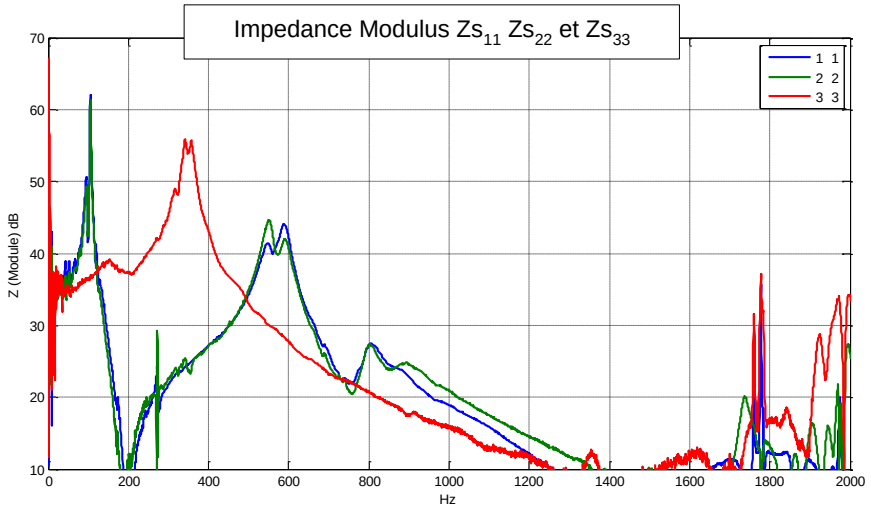


$$Zc = \begin{bmatrix} \boldsymbol{Zc_{11}} & \cdots & Zc_{16} \\ \vdots & \ddots & \vdots \\ Zc_{61} & \cdots & Zc_{66} \end{bmatrix}$$

Figure 7 – Coupled impedance Z_C

5.2.3 Source impedance identification (Z_S)

It is now possible to calculate Z_S using $Z_C = Z_R + Z_S$ at the coupling point. This quantity may be used in a numerical model to set the compressor vibroacoustic behavior.



$$Zs = \begin{bmatrix} \boldsymbol{Zs_{11}} & \cdots & Zs_{16} \\ \vdots & \ddots & \vdots \\ Zs_{61} & \cdots & Zs_{66} \end{bmatrix}$$

Figure 8 – Compressor impedance Zs

5.2.4 Blocked force torsor determination (F_B)

The blocked force torsor is obtained using $F_B = - Z_C.V_C$ Figure 9 shows blocked force spectra (Fx, Fy, Fz) for the 3 operating modes « Chiller », « Rooftop » and « PAC » with rotation speed of 65 Hz.

Efforts are dominant in horizontal plan (X Y).

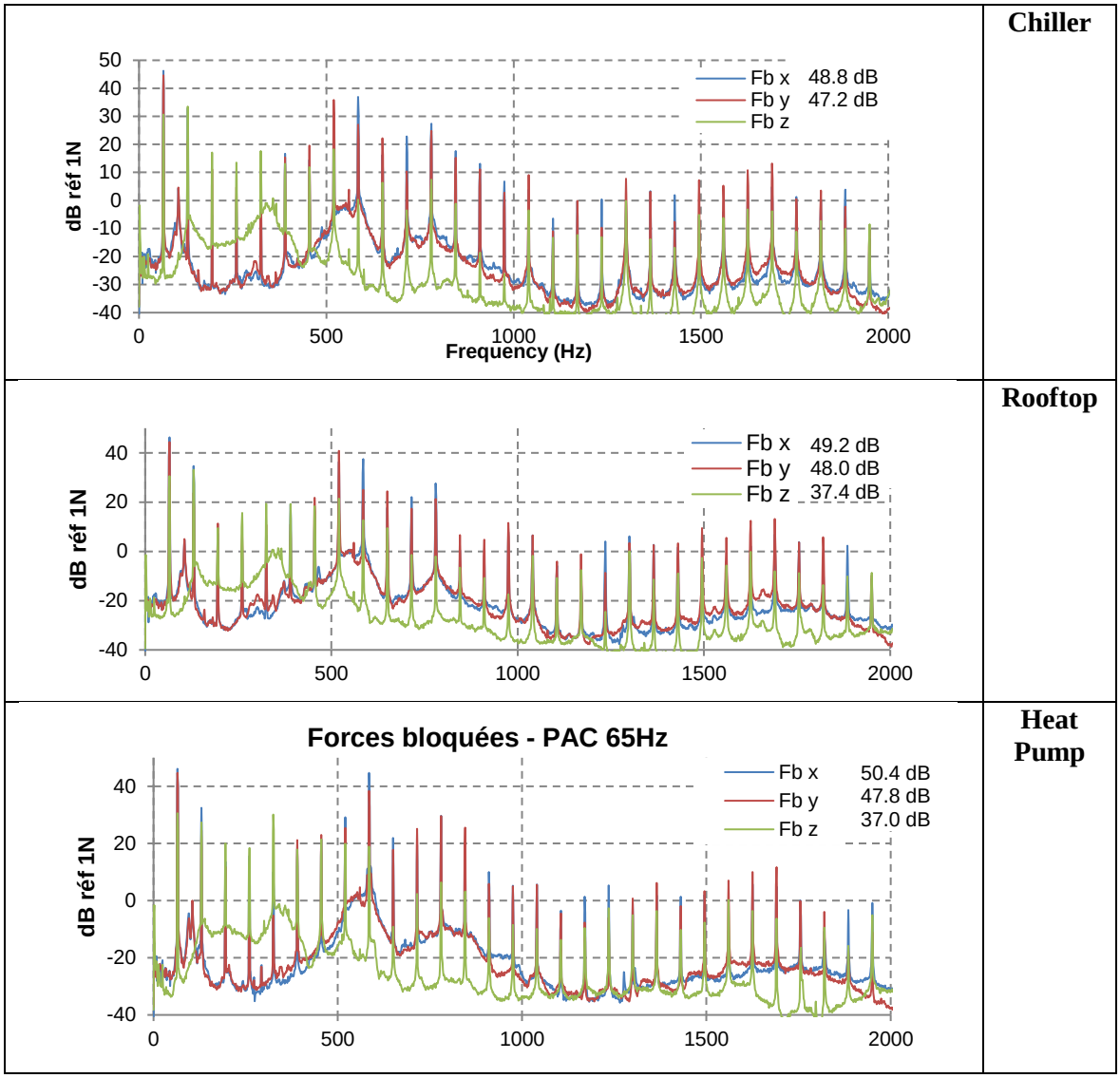


Figure 9 – Blocked force torsor at coupling point. Components Fx, Fy, Fz for 3 operational modes @65Hz

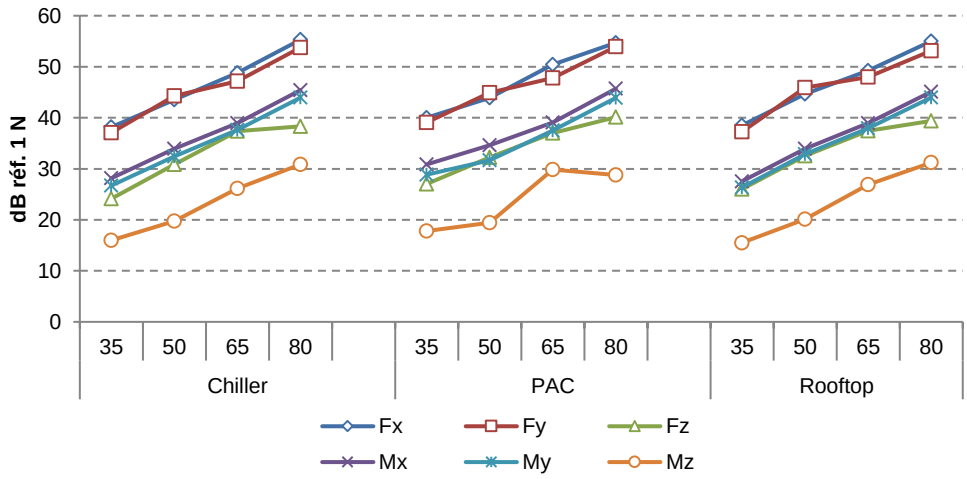


Figure 10 –Blocked force torsor F_b Overall level, RMS [0-2kHz] 3 Operational modes, 4 rotation speeds.

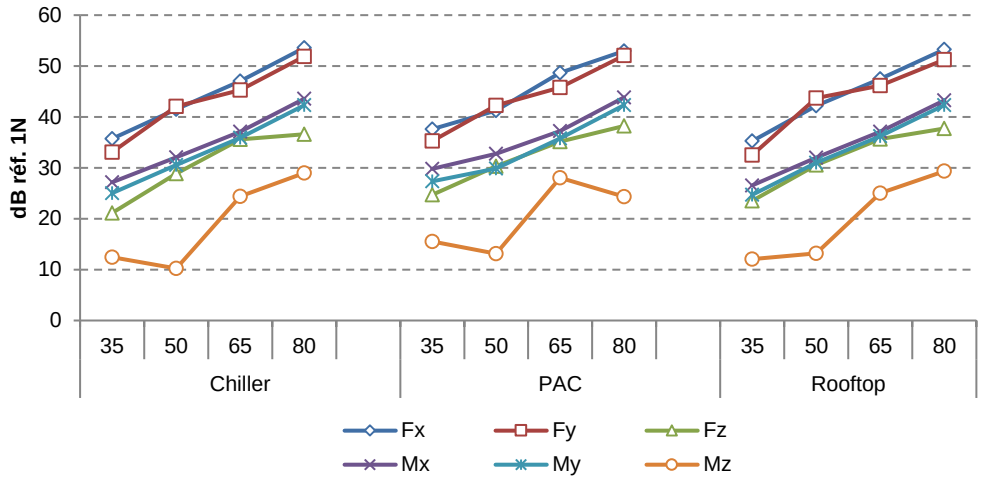
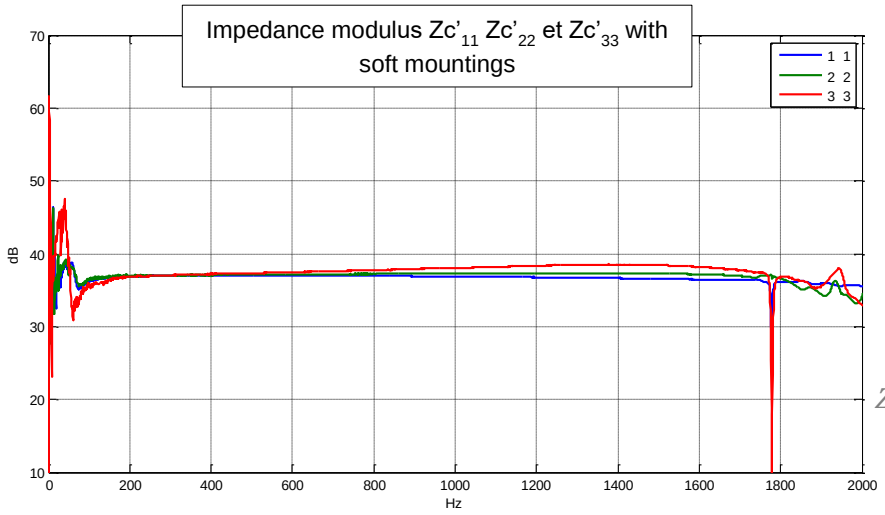


Figure 11 –Blocked force orsor F_b Overall level, order 1 to 12. 3 Operational modes, 4 rotation speeds.

Figure 10 and Figure 11 show the overall levels in 3 directions obtained on the frequency range [0-2kHz] and on the first 12 harmonic of rotation for the 3 operating mods.

5.2.5 Set-up with soft mountings

Two types of mountings have been tested: a stiff one (compressor screwed directly on the block) and soft mounting (using isolators-see figure 12). Results are shown in operational mode "Rooftop 65Hz". A new impedance Zc is calculated with isolators. Zc is now similar to Z_R, showing the efficiency of the isolators.





coupledcoupled system with elastomeric mounts

$$Zc_plots = \begin{bmatrix} Zc'_{11} & \cdots & Zc'_{16} \\ \vdots & \ddots & \vdots \\ Zc'_{61} & \cdots & Zc'_{66} \end{bmatrix}$$

Figure 12 - Impédance Zc_(Block+Compressor with isolators)

Comparison of components Fx and Mx are shown on figure 14 in configuration Rooftop 65 Hz. Figure 14 shows also the results of overall level [0-2 kHz] on the 6 components.

Most of the harmonics levels are decreased, but some may be amplified (see H1 Mx) Nevertheless, overall levels are drastically reduced.

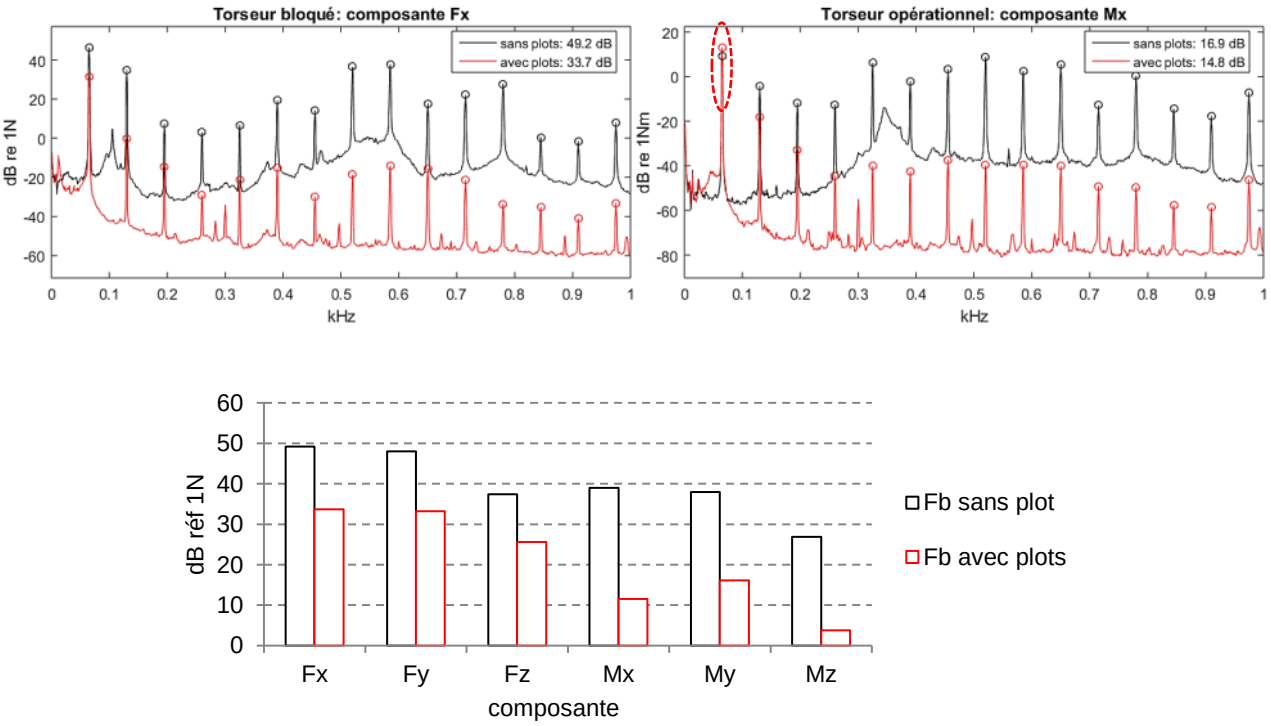


Figure 13 – Blocked forces Fb on mode « Rooftop 65Hz » – Fx et Mx with/without isolators. Spectra and overall level [0-2 kHz]

5.3 Conclusion and further work

The "block-sensor" method has been developed to characterize sources of structure-borne noise using intrinsic descriptors (independent of the receiver): the equivalent blocked forces and source impedance.

On their own, these descriptors are useful to the manufacturers for understanding or clarifying the operation of their products, for performing comparative tests or obtaining a ranking of the products, or for use as calibration for vibration calculations.

However, with the objective of prediction within a vibration/acoustic scheme, the model must include the passive characteristics of the receiver or of the active component connected to it (impedance), which only the suppliers are entitled to know and communicate.

There is thus a need to work transparently between suppliers and integrators to optimize mechanical assemblies.

The method has been applied to a compressor in different operating conditions, showing results that allow to understand its vibroacoustic behavior.

The method is now in a process of standardization. Repeatability and reproducibility have to be tested and quality indicators have to be defined.

Acknowledgements

This work has been developed in cooperation with the Working Group “Noise” of French Mechanical Industries: Pumps, Cooling Machines

References

[1] T. Ten Wolde, G. Gadefelt, *Development of standard measurement methods for structure-borne sound emission*, Noise Control Engineering Journal Vol. 28, (1987), 5-14.

[2] O. Doutres, A. C. l'Ecuyer, T. Kathirchelvan, M. Etchessahar, *Experimental assessment of the structure-borne noise in an aircraft cabin due to vibrating equipment*, Proc. INTERNOISE 2015, San Francisco, (2015), pp. 4304-5299.

[3] International Standards Organisation ISO 9611: Acoustics – characterisation of sources of structure-borne sound with respect to sound radiation from connected structures – *Measurement of velocity at the contact points of machinery when resiliently mounted* (1996).

[4] J. O'Hara, *Mechanical impedance and mobility concepts*, Journal of the Acoustical Society of America, Vol. 41, (1967), pp. 1180-1184.

[5] B. A. T. Petersson, J. Plunt, *On effective mobilities in the prediction of structure-borne sound transmission between a source structure and a receiving structure – Part I: Theoretical background and basic experimental studies*, Journal of Sound and Vibration, Vol. 82, (1982), pp. 517-529.

[6] S. Jianxin, A. T. Moorhouse, B. M. Gibbs, *Towards a practical characterization for structureborne sound sources based on mobility techniques*, Journal of Sound and Vibration, Vol. 185, (1995), pp. 737-741.

[7] B. A. T. Petersson, *On the use of giant magnetostrictive devices for moment excitation*, Journal of Sound and Vibration, Vol. 115, (1987), pp. 191-194.

[8] Y. Champoux, V. Cotoni, B. Paillard, O. Beslin, *Moment excitation of structures using synchronized impact hammers*, Journal of Sound and Vibration, Vol. 263, (2003), pp. 515-533.

[9] S. S. Sattinger, *A method for experimentally determining rotational mobilities of structures*, Shock and Vibration Bulletin Vol. 50, (1980), pp. 17–28.

[10] M. A. Sanderson, *Direct measurement of moment mobility, part II: An experimental study*. Journal of Sound and Vibration, Vol. 179, (1995), pp. 685-696.

[11] S. Jianxin, B. M. Gibbs, *Measurement of point moment mobility in the presence of non-zero cross mobility*, Applied Acoustics, Vol. 54, (1998), pp. 9-26.

[12] L. H. Ivarsson, M. A. Sanderson: *MIMO technique for simultaneous measurement of translational and rotational mobilities*, Applied Acoustics, Vol. 61, (2000), pp. 345-370.

[13] A. S. Elliott, A. T. Moorhouse, G. Pavić, *Moment excitation and the measurement of moment mobilities*, Journal of Sound and Vibration Vol. 331, (2012), pp. 2499-2519.

[14] G. Pavić, A. S. Elliott, *Structure-borne sound characterization of coupled structures – Part II: Feasibility study*, Journal of Vibration and Acoustics, Vol. 132, (2010), pp. 041009-1/13.

[15] A. T. Moorhouse, A. S. Elliott, T. A. Evans, *In situ measurement of the blocked force of structure-borne sound sources*, Journal of Sound and Vibration, Vol. 325, (2009), pp. 679–685.

[16] M. H. A. Janssens, J. W. Verheij, *A pseudo-forces methodology to be used in characterization of structure-borne sound sources*, Applied Acoustics, Vol. 61 (2000), pp. 285-308.

[17] G. Pavić, C. Sandier, X. Carniel, *Characterisation of a small vibration source*, Proc. ISMA 2014, Leuven, (2014), pp. 2077-2085.

[18] M Thivant, A Carbonelli, P. Bouvet, *Derivation of the force interaction within strongly coupled systems – application to diesel engine oil pumps*, Proc. ISMA 2010, Leuven (2010), pp. 2013-2115.

Contact problems in the framework of dynamic substructuring

J. Brunetti [1], **W. D'Ambrogio** [1], **A. Fregolent** [2]
[1] Università dell'Aquila, Dipartimento di Ingegneria Industriale e dell'Informazione e di Economia,
Via G. Gronchi 18, I-67100, L'Aquila (AQ), Italy
e-mail: **walter.dambrogio@univaq.it**

[2] Università di Roma La Sapienza, Dipartimento di Ingegneria Meccanica e Aerospaziale,
Via Eudossiana, 18, I-00184, Roma, Italy

Abstract
Typical applications of dynamic substructuring deal with time-invariant systems. An interesting extension of the dynamic substructuring can be to consider, among time-variant systems, those built from time-invariant component subsystems subjected to time-variant coupling conditions, such as those encountered in contact problems. Specifically, a time-varying interface due to a frictional sliding contact is considered. The link between substructuring and contact problems can lead to interesting perspectives, for instance, in the macroscopic analysis of the time-frequency behaviour of bodies in relative sliding with friction. The problem can be tackled in time domain using both primal and dual assembly. In the former case classical numerical time integration techniques can be used; in the latter case to avoid singularities forward increment Lagrange multiplier method can be adapted to dual assembly. The methods are applied to discrete models of substructures. In both cases, the assumption of sliding contact can be verified at the end of the computation.

1 Introduction

Dynamic substructuring is typically applied to time-invariant systems [1]. An interesting subset of time variant systems is represented by those built from time-invariant component subsystems subjected to time-variant coupling conditions. For such systems, the classical techniques developed for time invariant systems can be adapted with few modifications. Typical examples of such time variant systems are those encountered in contact problems (e.g. when a sliding velocity exists between two contacting bodies).

The analysis of contact problems in the framework of dynamic substructuring can provide interesting results with relatively low computational effort. For instance, the macroscopic analysis of the time-frequency behaviour of bodies in relative sliding with friction can benefit of the substructuring approach.

Since time-variant coupling conditions are involved, the time domain approach is the most appropriate. Substructuring in time domain has been considered by Rixen and van der Valk [2, 3], by using impulse response functions. However, the coupling conditions (compatibility and equilibrium) are considered as time-invariant.

In this paper, the general framework for dynamic substructuring is extended to time-variant interfaces among connecting substructures. Specifically, a time-variant interface due to a sliding contact is considered by introducing time dependent compatibility and equilibrium conditions. The sliding contact can be without or with friction. With friction, the set of degrees of freedom to which equilibrium conditions apply includes tangential directions at the contact interface, which are not considered in the compatibility conditions because of sliding. This is in fact a non collocated interface as defined in decoupling problems [4, 5].

The problem can be tackled in the time domain using primal assembly and numerical time integration. In a previous work [6], the authors proposed a time-frequency domain approach using dual assembly to avoid singularity problems in numerical integration, thus obtaining Time Dependent Frequency Response Functions (TD-FRFs) of the assembled structure. In this work, singularity problems are overcome by adapting the forward increment Lagrange multipliers method [7] to dual assembly.

The approach is applied to a lumped parameter model in order to evaluate its feasibility and effectiveness. The approach can be extended to simple finite element models under the assumption that the relative sliding motion at the contact interfaces is known a-priori, at least approximately.

2 Theoretical background

2.1 Substructuring

Let us consider a structural system consisting of n coupled subsystems. The equation of motion of a linear time-invariant subsystem r may be written as:

$$[M]^{(r)}\{\ddot{u}(t)\}^{(r)} + [C]^{(r)}\{\dot{u}(t)\}^{(r)} + [K]^{(r)}\{u(t)\}^{(r)} = \{f(t)\}^{(r)} + \{g(t)\}^{(r)} \tag{1}$$

where:

$[M]^{(r)}$, $[C]^{(r)}$, $[K]^{(r)}$ are the mass, damping and stiffness matrices of subsystem r;
$\{u(t)\}^{(r)}$ is the vector of displacements of subsystem r;
$\{f(t)\}^{(r)}$ is the vector of external forces on subsystem r;
$\{g(t)\}^{(r)}$ is the vector of connecting forces with other subsystems (internal constraint forces).

The equation of motion of the n subsystems to be coupled can be written in a block diagonal format as:

$$[M]\{\ddot{u}(t)\} + [C]\{\dot{u}(t)\} + [K]\{u(t)\} = \{f(t)\} + \{g(t)\} \tag{2}$$

with

$$[M] = \begin{bmatrix} [M]^{(1)} & & \\ & \ddots & \\ & & [M]^{(n)} \end{bmatrix}, \quad [C] = \begin{bmatrix} [C]^{(1)} & & \\ & \ddots & \\ & & [C]^{(n)} \end{bmatrix}, \quad [K] = \begin{bmatrix} [K]^{(1)} & & \\ & \ddots & \\ & & [K]^{(n)} \end{bmatrix} \tag{3}$$

$$\{u(t)\} = \begin{Bmatrix} \{u(t)\}^{(1)} \\ \vdots \\ \{u(t)\}^{(n)} \end{Bmatrix}, \quad \{f(t)\} = \begin{Bmatrix} \{f(t)\}^{(1)} \\ \vdots \\ \{f(t)\}^{(n)} \end{Bmatrix}, \quad \{g(t)\} = \begin{Bmatrix} \{g(t)\}^{(1)} \\ \vdots \\ \{g(t)\}^{(n)} \end{Bmatrix} \tag{4}$$

The compatibility condition implies that any pair of matching DoFs at time t, i.e. DoF l on subsystem r and DoF m on subsystem s must have the same displacement, that is $u_l^{(r)}(t) - u_m^{(s)}(t) = 0$.

This condition can be generally expressed as:

$$[B_C(t)]\{u(t)\} = \{0\} \tag{5}$$

where each row of $[B_C(t)]$ corresponds to a pair of matching DoFs at time t. Note that $[B_C(t)]$ is, in most cases, a signed Boolean matrix and it can be written by distinguishing the contribution of the different subsystems:

$$[B_C(t)] = \begin{bmatrix} [B_C(t)]^{(1)} & \cdots & [B_C(t)]^{(n)} \end{bmatrix}$$

The equilibrium condition for internal constraint forces, arising from the compatibility conditions and eventually from sliding friction, implies that the sum of connecting forces at a pair of matching DoFs must be zero, i.e. $g_l^{(r)}(t) + g_m^{(s)}(t) = 0$: this holds for any pair of matching DoFs at time t. Furthermore, if DoF k on subsystem q is not a connecting DoF at time t, it must be $g_k^{(q)}(t) = 0$: this holds for any non-connecting DoF at time t. In presence of friction, the set of degrees of freedom to which the equilibrium condition applies includes tangential directions at the contact interface, which are not considered in the compatibility conditions due to sliding. This is in fact the definition of a non collocated interface.

Overall, the above conditions can be expressed as:

$$[L_E(t)]^T \{g(t)\} = \{0\} \tag{6}$$

where the matrix $[L_E(t)]$ is a Boolean localisation matrix. Note that the number of rows of $[L_E(t)]^T$ is equal to the number of non-interface DoFs plus the number of pairs of equilibrium interface DoFs.

Eqs. (2-6) can be put together to get the three field formulation, i.e the total system describing the coupling between any number of substructures:

$$\begin{cases} [M]\{\ddot{u}(t)\} + [C]\{\dot{u}(t)\} + [K]\{u(t)\} = \{f(t)\} + \{g(t)\} \\ [B_C(t)]\{u(t)\} = \{0\} \\ [L_E(t)]^T \{g(t)\} = \{0\} \end{cases} \tag{7}$$

Therefore, the three field formulation is very similar to the classical one for a stationary interface, except for $[B_C]$ and $[L_E]$ which now depend on time t.

2.2 Solution approach in time domain

In principle, both primal assembly and dual assembly could be used [1, 8].

2.2.1 Primal assembly in time domain

In the primal assembly, a unique set of interface DoFs is defined and the interface forces are eliminated by automatically satisfying the interface equilibrium. This is obtained by stating that:

$$\{u(t)\} = [L_C(t)]\{q(t)\} \tag{8}$$

where $\{q\}$ is the unique set of DoFs, including also non-interface DoFs, and $[L_C(t)]$ is different from the localisation matrix $[L_E(t)]$ introduced previously, when friction forces are exchanged at the interface. Since Eq. (8) states that the DoFs of all subsystems are obtained from the unique set $\{q\}$, the compatibility condition holds for any set $\{q\}$, i.e.

$$[B_C(t)]\{u(t)\} = [B_C(t)][L_C(t)]\{q(t)\} = \{0\} \qquad \forall \{q\} \tag{9}$$

Hence, $[L_C(t)]$ represents the nullspace of $[B_C(t)]$:

$$[L_C(t)] = \text{null}\left([B_C(t)]\right) \tag{10}$$

Since the compatibility condition in Eq. (7) is satisfied by the choice of the unique set $\{q\}$, the system of equations is:

$$\begin{cases} [M]\,[L_C(t)]\,\{\ddot{q}(t)\} + [C]\,[L_C(t)]\,\{\dot{q}(t)\} + [K]\,[L_C(t)]\,\{q(t)\} = \{f(t)\} + \{g(t)\} \\ [L_E(t)]^T\,\{g(t)\} = \{0\} \end{cases} \tag{11}$$

Pre-multiplying the dynamic equilibrium equation by $[L_E(t)]^T$ and noting that $[L_E(t)]^T\{g(t)\} = \{0\}$, the assembled system reduces to:

$$[L_E(t)]^T[M][L_C(t)]\{\ddot{q}(t)\}+[L_E(t)]^T[C][L_C(t)]\{\dot{q}(t)\}+[L_E(t)]^T[K][L_C(t)]\{q(t)\}=[L_E(t)]^T\{f(t)\} \tag{12}$$

i.e.

$$\left[\tilde{M}(t)\right]\{\ddot{q}(t)\} + \left[\tilde{C}(t)\right]\{\dot{q}(t)\} + \left[\tilde{K}(t)\right]\{q(t)\} = \left\{\tilde{f}(t)\right\} \tag{13}$$

where

$$\begin{aligned} \left[\tilde{M}(t)\right] &= [L_E(t)]^T\,[M]\,[L_C(t)] & \left[\tilde{C}(t)\right] &= [L_E(t)]^T\,[C]\,[L_C(t)] \\ \left[\tilde{K}(t)\right] &= [L_E(t)]^T\,[K]\,[L_C(t)] & \left\{\tilde{f}(t)\right\} &= [L_E(t)]^T\,\{f(t)\} \end{aligned} \tag{14}$$

Eq. (13) can be recast in state space form:

$$\begin{Bmatrix} \{\dot{q}(t)\} \\ \{\ddot{q}(t)\} \end{Bmatrix} = \begin{bmatrix} [0] & [1] \\ -\left[\tilde{M}(t)\right]^{-1}\left[\tilde{K}(t)\right] & -\left[\tilde{M}(t)\right]^{-1}\left[\tilde{C}(t)\right] \end{bmatrix} \begin{Bmatrix} \{q(t)\} \\ \{\dot{q}(t)\} \end{Bmatrix} + \begin{Bmatrix} \{0\} \\ \left[\tilde{M}(t)\right]^{-1}\left\{\tilde{f}(t)\right\} \end{Bmatrix} \tag{15}$$

i.e.

$$\{\dot{y}(t)\} = [A(t)]\,\{y(t)\} + \{F(t)\} \tag{16}$$

where

$$\{y\} = \begin{Bmatrix} \{q\} \\ \{\dot{q}\} \end{Bmatrix} \qquad [A] = \begin{bmatrix} [0] & [1] \\ -\left[\tilde{M}\right]^{-1}\left[\tilde{K}\right] & -\left[\tilde{M}\right]^{-1}\left[\tilde{C}\right] \end{bmatrix} \qquad \{F\} = \begin{Bmatrix} \{0\} \\ \left[\tilde{M}\right]^{-1}\left\{\tilde{f}\right\} \end{Bmatrix} \tag{17}$$

having omitted the explicit dependence on t in the last equation for the sake of simplicity.

Since $[A(t)]$ is time dependent, Eq. (16) can not be solved analytically but needs numerical time step integration.

2.2.2 Dual assembly in time domain

In the dual assembly, the total set of DoFs is retained, i.e. each interface DoF is present as many times as there are substructures connected through that DoF. The equilibrium condition $g_l^{(r)} + g_m^{(s)} = 0$ at a pair of interface DoFs is ensured by choosing, for instance, $g_l^{(r)} = -\lambda$ and $g_m^{(s)} = \lambda$. Therefore, the overall interface equilibrium can be ensured by writing the connecting forces in the form:

$$\{g(t)\} = -\left[B_E(t)\right]^T \{\lambda(t)\} \tag{18}$$

where $\{\lambda\}$ are Lagrange multipliers corresponding to connecting force intensities and $[B_E(t)]$ is different from the signed Boolean matrix $[B_C(t)]$ used to enforce the compatibility condition, because $[B_E(t)]$ must also account for friction forces at the interface.

The interface equilibrium condition (6) is thus written:

$$\left[L_E(t)\right]^T \{g(t)\} = -\left[L_E(t)\right]^T \left[B_E(t)\right]^T \{\lambda(t)\} = \{0\} \tag{19}$$

Hence $[B_E]^T$ represents the nullspace of $[L_E]^T$:

$$\left[B_E(t)\right]^T = \text{null}\left(\left[L_E(t)\right]^T\right) \tag{20}$$

Since Eq. (19) is always satisfied, Eq. (7) becomes:

$$\begin{cases} [M]\{\ddot{u}(t)\} + [C]\{\dot{u}(t)\} + [K]\{u(t)\} + \left[B_E(t)\right]^T \{\lambda(t)\} = \{f(t)\} \\ [B_C(t)]\{u(t)\} = \{0\} \end{cases} \tag{21}$$

and in block matrix form:

$$\begin{bmatrix} [M] & [0] \\ [0] & [0] \end{bmatrix} \begin{Bmatrix} \{\ddot{u}(t)\} \\ \{\ddot{\lambda}(t)\} \end{Bmatrix} + \begin{bmatrix} [C] & [0] \\ [0] & [0] \end{bmatrix} \begin{Bmatrix} \{\dot{u}(t)\} \\ \{\dot{\lambda}(t)\} \end{Bmatrix} + \begin{bmatrix} [K] & [B_E]^T \\ [B_C] & [0] \end{bmatrix} \begin{Bmatrix} \{u(t)\} \\ \{\lambda(t)\} \end{Bmatrix} = \begin{Bmatrix} \{f(t)\} \\ \{0\} \end{Bmatrix} \tag{22}$$

Eq. (22) is singular and cannot be explicitly solved in the time domain. To overcome the singularity problem of Eq. (22), an approach similar to the Forward increment Lagrange multipliers method [7] can be used.

2.2.3 Forward increment dual assembly in time domain

This formulation relates constraints at time $t_{n+1} = t_n + h$ with Lagrange multipliers at time t_n, and the equation of motion becomes:

$$\begin{cases} [M]\{\ddot{u}\}_n + [C]\{\dot{u}\}_n + [K]\{u\}_n + [B_E]_{n+1}^T \{\lambda\}_n = \{f\}_n \\ [B_C]_{n+1}\{u\}_{n+1} = \{0\} \end{cases} \tag{23}$$

In this notation the subscripts n and $n+1$ indicate the functions at time t_n and t_{n+1}.

The first equation of (23) can be rewritten as:

$$\{\ddot{u}\}_n = [M]^{-1}\left[\{f\}_n - [C]\{\dot{u}\}_n - [K]\{u\}_n - [B_E]_{n+1}^T \{\lambda\}_n\right] \tag{24}$$

For explicit integration of the equation, the Newmark β_2 scheme can be used, that for $\beta_2 = 0.5$ reduces to the central difference scheme:

$$\{\ddot{u}\}_n = \frac{1}{h^2}\left(\{u\}_{n+1} - 2\{u\}_n + \{u\}_{n-1}\right) \tag{25}$$

By substituting the central difference expression of $\{\ddot{u}\}_n$ in the equation of motion (24), and by using $\{\dot{u}\}_n = \left(\{u\}_n - \{u\}_{n-1}\right)/h$ one obtains:

$$\begin{aligned}\{u\}_{n+1} =& h^2 [M]^{-1}\left[\{f\}_n - \frac{1}{h}[C]\left(\{u\}_n - \{u\}_{n-1}\right) - K\{u\}_n\right] + 2\{u\}_n - \{u\}_{n-1} + \\ &- h^2 [M]^{-1} [B_E]^T_{n+1} \{\lambda\}_n\end{aligned} \tag{26}$$

Therefore, by substituting Eq. (26) in the second line of Eq. (23) one obtains:

$$\begin{aligned}&[B_C]_{n+1}\left\{h^2 [M]^{-1}\left[\{f\}_n - \frac{1}{h}[C]\left(\{u\}_n - \{u\}_{n-1}\right) - K\{u\}_n\right] + 2\{u\}_n - \{u\}_{n-1}\right\} = \\ &= [B_C]_{n+1}\, h^2 [M]^{-1} [B_E]^T_{n+1} \{\lambda\}_n\end{aligned} \tag{27}$$

Hence, the contact forces $\{\lambda\}_n$ can be computed as:

$$\begin{aligned}\{\lambda\}_n = &\left(h^2 [B_C]_{n+1} [M]^{-1} [B_E]^T_{n+1}\right)^{-1} [B_C]_{n+1} \cdot \\ &\cdot\left\{h^2 [M]^{-1}\left[\{f\}_n - \frac{1}{h}[C]\left(\{u\}_n - \{u\}_{n-1}\right) - K\{u\}_n\right] + 2\{u\}_n - \{u\}_{n-1}\right\}\end{aligned} \tag{28}$$

Finally, by substituting $\{\lambda\}_n$ in Eq. (26) $\{u\}_{n+1}$ is obtained.

3 Numerical model

The considered system (Fig. 1) consists of two subsystems connected through a sliding interface with a constant friction coefficient μ. Subsystem 1 is a bar of length l and mass m_1, suspended by two vertical springs k_1 and k_2, and one horizontal spring k_3. The bar is modeled as a 2 node bar element with lumped mass matrix ($m_1/2$ at each end), and an axial stiffness k_6. Subsystem 2 is a lumped mass m_2 connected, by a vertical spring k_4 and a horizontal spring k_5, to a support moving with constant velocity v in the horizontal direction. A vertical preload F_2 acts on the lumped mass m_2 to push it on the bar.

k_1	k_2	k_3	k_4	k_5	k_6		m_1	m_2		l	F_2	v
50	200	3000	200	1e5	6.41e6	N/m	1	0.3	kg	2 m	10 N	9.77 mm/s

Table 1: Values of the physical parameters of the model.

Subsystem 1 has 4 DoFs $\{u\}^{(1)} = [u_1 \;\; u_2 \;\; u_3 \;\; u_4]^T$, and the mass and stiffness matrices are:

$$[M]^{(1)} = \begin{bmatrix} m_1/2 & 0 & 0 & 0 \\ 0 & m_1/2 & 0 & 0 \\ 0 & 0 & m_1/2 & 0 \\ 0 & 0 & 0 & m_1/2 \end{bmatrix} \qquad [K]^{(1)} = \begin{bmatrix} k_3 + k_6 & 0 & -k_6 & 0 \\ 0 & k_1 & 0 & 0 \\ -k_6 & 0 & k_6 & 0 \\ 0 & 0 & 0 & k_2 \end{bmatrix} \tag{29}$$

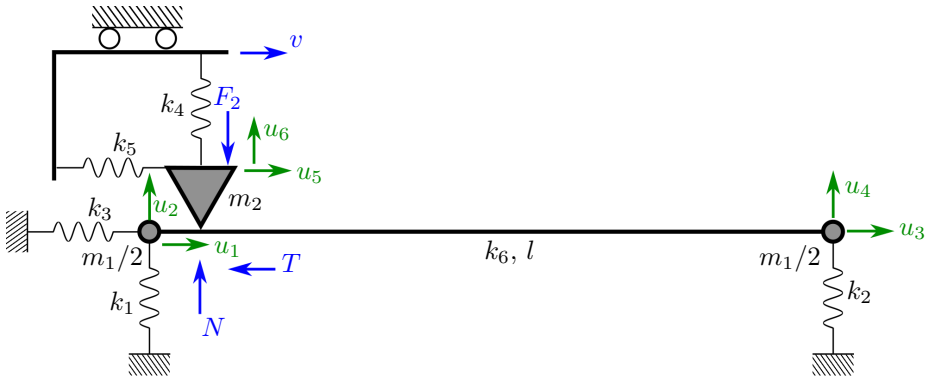


Figure 1: Sketch of the system model: N and T acting on mass 2.

The vector of external forces $\{f\}^{(1)}$ acting on subsystem 1 (DoFs u_1-u_4) is zero.

Subsystem 2 has 2 DoFs $\{u\}^{(2)} = [u_5 \;\; u_6]^T$, and the mass and stiffness matrices are:

$$[M]^{(2)} = \begin{bmatrix} m_2 & 0 \\ 0 & m_2 \end{bmatrix} \qquad [K]^{(2)} = \begin{bmatrix} k_5 & 0 \\ 0 & k_4 \end{bmatrix} \tag{30}$$

The vector of external forces acting on u_5 and u_6 of subsystem 2 is $\{f\}^{(2)} = [k_5 vt \quad -F_2]^T$.

The block diagonal mass and stiffness matrices of the whole system are expressed according to Eq. (3), while the vectors of the full set of DoFs and of the external forces are expressed according to Eq. (4). A proportional viscous damping matrix is defined as $[C] = \beta[K]$ with $\beta = 1e-4$ s. .

When the two subsystems are connected together, it is assumed that mass m_2 is always in contact with the bar (i.e. $N > 0$ where N is the normal contact force between the bar and the moving mass) and that the relative velocity between the moving mass and the bar is positive ($v_r = \dot{u}_5 - \dot{u}_c > 0$, where u_c is the horizontal component of the velocity of the contact point on the bar). Therefore, the tangential force is $T = -\mu N$. These assumptions can be verified at the end of the computation.

3.1 Compatibility and equilibrium matrices for primal assembly

To perform the primal assembly, the independent set of DoFs is selected as $\{q\} = [u_1 \;\; u_2 \;\; u_3 \;\; u_4 \;\; u_5]^T$. Therefore:

$$[L_C(t)] = \begin{bmatrix} 1 & 0 & 0 & 0 & 0 \\ 0 & 1 & 0 & 0 & 0 \\ 0 & 0 & 1 & 0 & 0 \\ 0 & 0 & 0 & 1 & 0 \\ 0 & 0 & 0 & 0 & 1 \\ 0 & n_1(t) & 0 & n_2(t) & 0 \end{bmatrix} \qquad [L_E(t)] = \begin{bmatrix} 1 & 0 & 0 & 0 & 0 \\ \mu & 1 & 0 & 0 & 0 \\ 0 & 0 & 1 & 0 & 0 \\ 0 & 0 & \mu & 1 & 0 \\ 0 & 0 & 0 & 0 & 1 \\ 0 & n_1(t) & 0 & n_2(t) & \mu \end{bmatrix} \tag{31}$$

where

$$n_1(t) = 1 - vt/l \qquad n_2(t) = vt/l \tag{32}$$

are time dependent coefficients used in $\{u\} = [L_C]\{q\}$ to obtain the vertical position u_6 of mass m_2 as functions of the vertical positions u_2 and u_4 of the end nodes of the bar, and in $[L_E]^T\{g\} = 0$ to satisfy the equilibrium of constraint forces in the vertical direction, e.g.

$$g_2 + n_1(t)g_6 = 0 \qquad g_4 + n_2(t)g_6 = 0 \tag{33}$$

Note that the relation between the friction force and the normal force ($T = \mu N$) is also accounted in $[L_E]^T\{g\} = 0$ as

$$g_1 + \mu g_2 = 0 \qquad g_3 + \mu g_4 = 0 \qquad g_5 + \mu g_6 = 0 \tag{34}$$

3.2 Compatibility and equilibrium matrices for dual assembly

To perform the dual assembly, the matrices $[B_C(t)]$ and $[B_E(t)]$ to be used in the compatibility equation $[B_C(t)]\{u\} = 0$ and in the equilibrium equation $\{g\} = -[B_E(t)]^T\{\lambda\}$ are

$$\begin{aligned}[B_C(t)] &= \begin{bmatrix} 0 & n_1(t) & 0 & n_2(t) & 0 & -1 \end{bmatrix} \\ [B_E(t)] &= \begin{bmatrix} -\mu n_1(t) & n_1(t) & -\mu n_2(t) & n_2(t) & \mu & -1 \end{bmatrix}\end{aligned} \tag{35}$$

where $n_1(t)$ and $n_2(t)$ are defined as above. Note that, from Eq. (35) and Eq. (31), it can be verified that $[B_C][L_C] = 0$ and $[L_E]^T[B_E]^T = 0$, as stated by Eqs. (9) and (19).

4 Results

Two values of the friction coefficient μ are used: $\mu = 0$ and $\mu = 0.2$.

4.1 Time domain results using primal assembly

The problem defined by Eq. (15) is solved numerically by using the Matlab function `ode45`, using fourth order Runge Kutta time step integration. The simulation is performed for the time employed by the mass m_2 to slide along the total length of the bar, i.e. 204.75 s.

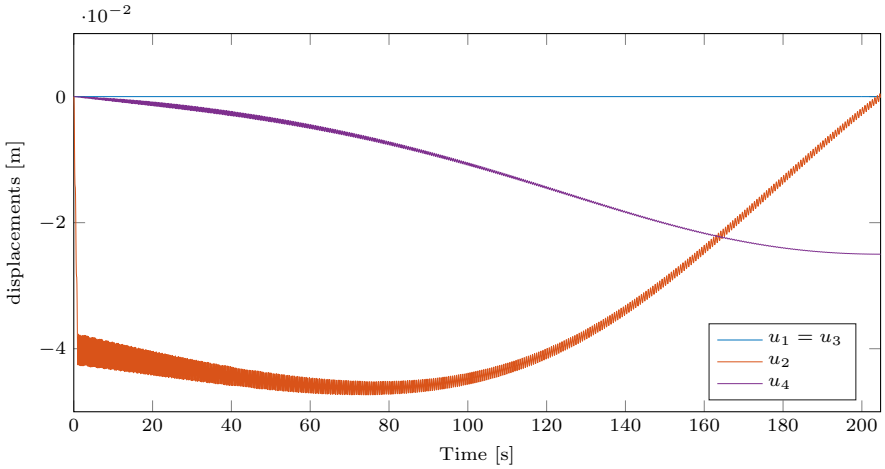
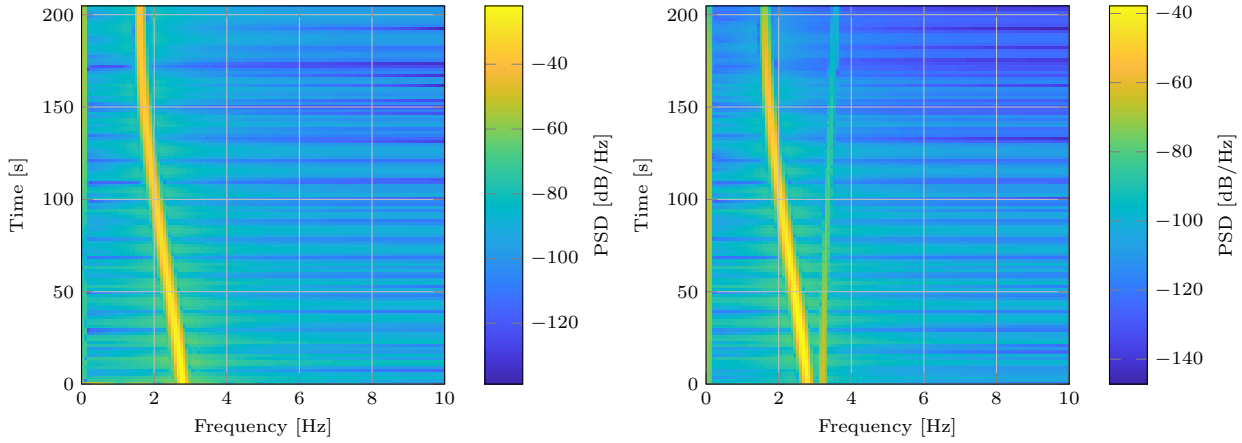


Figure 2: Time histories of displacements at the ends of the bar for $\mu = 0$ (primal assembly).

The sampling time chosen to observe the results is $\Delta t = 0.05$ s. The physical displacements u can be obtained using Eq. (8). Time histories of displacements u_1, u_2, u_3, u_4 at the ends of the bar are shown in Fig. 2 for $\mu = 0$. Without friction, the horizontal displacements u_1, u_3 are equal to zero, because the horizontal motion is not excited by the moving mass m_2. Vertical displacements u_2, u_4 behave as expected.

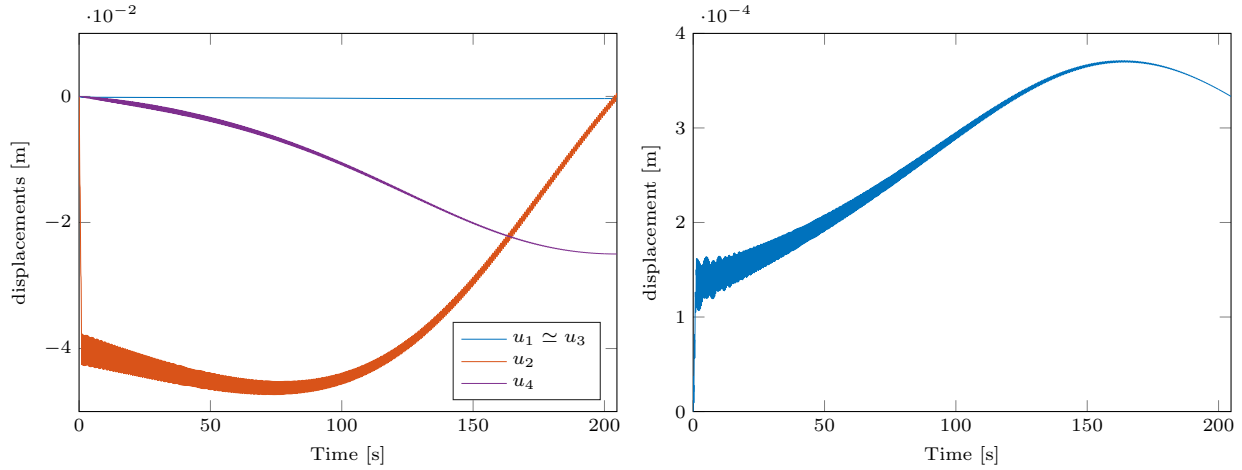
Spectrograms of vertical velocities $\dot{u}_2$, $\dot{u}_4$ are shown in Figs. 3(a) and 3(b). It can be noticed that the first natural frequency of the system goes from 2.81 Hz to 1.59 Hz when the mass m_2 moves from left to right, while the second natural frequency increases from 3.18 Hz to 3.55 Hz.



(a) $\dot{u}_2$. (b) $\dot{u}_4$.

Figure 3: Velocity spectrograms for $\mu = 0$ (primal assembly).

Time histories of displacements u_1, u_2, u_3, u_4 at the ends of the bar are shown in Fig. 4(a) for $\mu = 0.2$. With friction, the horizontal displacements u_1, u_3 in Fig. 4(b) are very low but not equal to zero, because the horizontal motion is excited by the friction force exerted by the moving mass m_2. Vertical displacements u_2, u_4 are very similar to the frictionless case.



(a) DoFs u_1, u_2, u_3 and u_4. (b) DoF $u_1 \simeq u_3$.

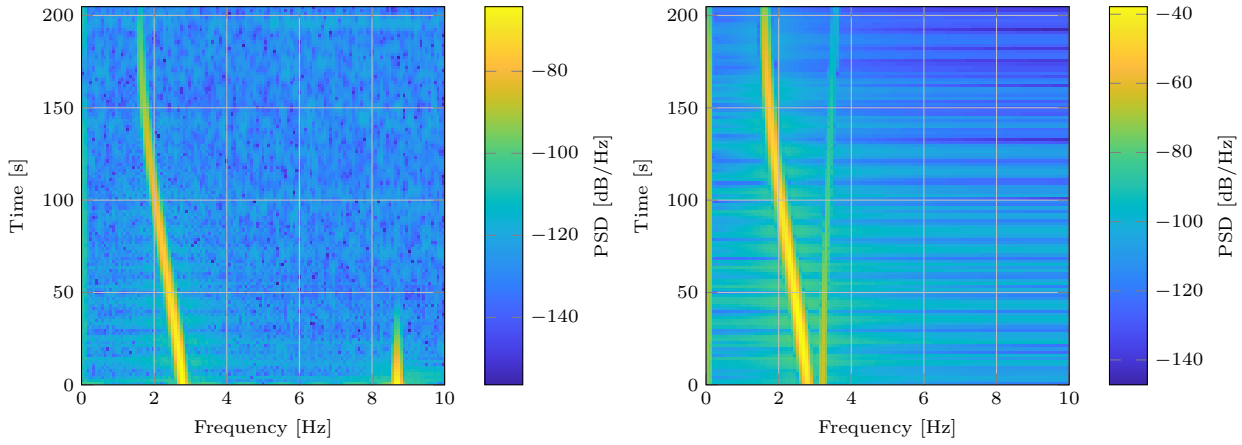
Figure 4: Time histories of displacements at the ends of the bar for $\mu = 0.2$ (primal assembly).

Spectrograms of velocities $\dot{u}_3$, $\dot{u}_4$ are shown in Figs. 5(a) and 5(b). The spectrogram of the horizontal velocity $\dot{u}_3$ shows a third natural frequency corresponding to horizontal motion of the bar. The spectrogram of the vertical velocity $\dot{u}_4$ is very similar to the frictionless case.

The contact assumption can be verified computing the contact forces acting on the moving mass. According to Eq. (1) with $r = 2$, the connecting forces can be expressed as:

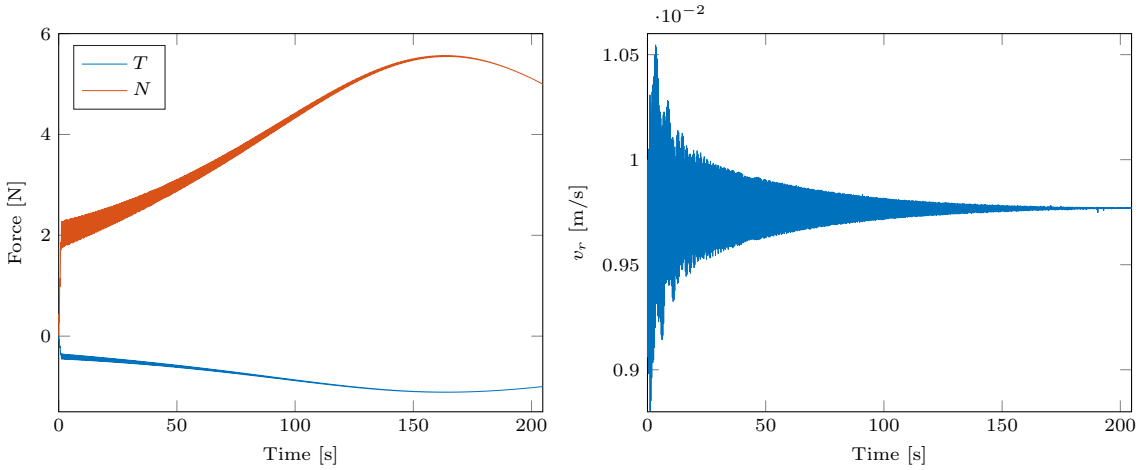
$$\{g(t)\}^{(2)} = \begin{Bmatrix} T \\ N \end{Bmatrix} = [M]^{(2)} \{\ddot{u}(t)\}^{(2)} + [C]^{(2)} \{\dot{u}(t)\}^{(2)} + [K]^{(2)} \{u(t)\}^{(2)} - \begin{Bmatrix} k_5\, v\, t \\ -F_2 \end{Bmatrix} \tag{36}$$

Moreover, the sliding assumption can be verified by computing the relative velocity using the time dependent



(a) $\dot{u}_3$. (b) $\dot{u}_4$.

Figure 5: Velocity spectrograms for $\mu = 0.2$ (primal assembly).



(a) Contact forces acting on the moving mass. (b) Relative velocity between the moving mass and the bar.

Figure 6: Verification of contact assumption (primal assembly).

coefficients in Eq. (32):

$$v_r = \dot{u}_5 - \dot{u}_c = \dot{u}_5 - \left(n_1(t)\,\dot{u}_1 + n_2(t)\,\dot{u}_3\right) \tag{37}$$

The contact forces and the relative velocity are shown in Fig. 6. The sign of the normal contact force N confirms that the mass is in contact with the bar. Furthermore, the sign of the relative velocity v_r confirms the sliding assumption.

4.2 Time domain results using dual assembly

The explicit integration scheme described in section 2.2.3 is used to solve in time domain the equation (23). As for the primal assembly case the simulation is performed for the time employed by the mass m_2 to slide along the total length of the bar, i.e. 204.75 s. By looking at eigenfrequencies and eigenvectors, the time step chosen to perform the explicit integration is Δt = 1e-4 s. This value allows to correctly estimate the oscillations along vertical DoFs (u_2, u_4 and u_6) that are essential to impose the compatibility condition. Note that the horizontal displacements do not affect the solution since there is no compatibility condition defined along this direction.

Time histories of displacements u_1, u_2, u_3, u_4 at the ends of the bar and the vertical displacement of the moving mass u_6 are shown in Fig. 7 for $\mu = 0.2$. Displacements are practically the same as those obtained by primal assembly. In fact, the physical problem is the same, therefore it is expected that the solutions are practically the same. However, the assembly techniques and the integration methods are substantially different so the coincidence of the solutions cannot be taken for granted.

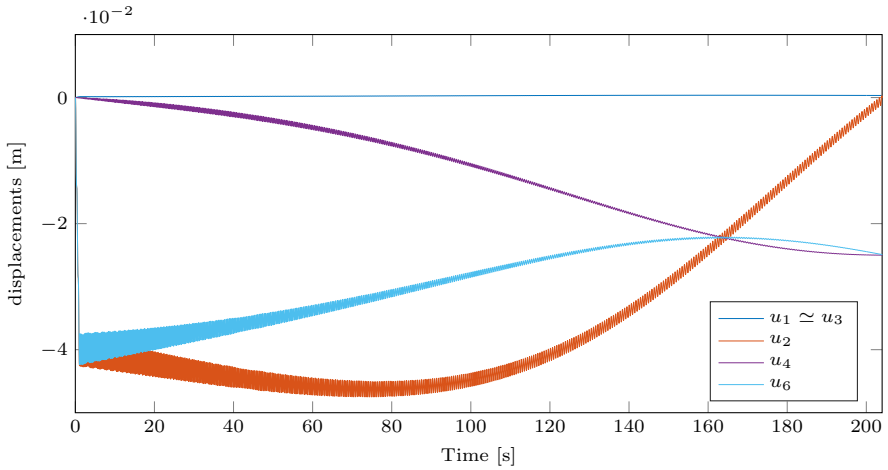
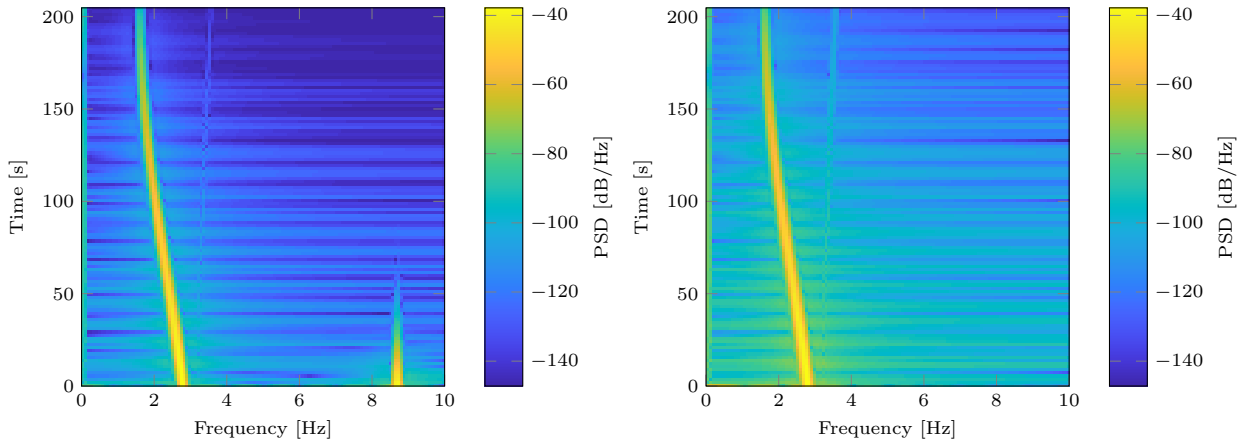


Figure 7: Time histories of displacements (u_1 to u_4) at the ends of the bar and vertical displacement (u_6) of the moving mass for $\mu = 0.2$ (dual assembly).

Spectrograms of velocities $\dot{u}_3$, $\dot{u}_6$ are shown in Figs. 8(a) and 8(b). Also using dual assembly in presence of friction the spectrogram of the horizontal velocity $\dot{u}_3$ shows a third natural frequency corresponding to horizontal motion of the bar.



(a) $\dot{u}_3$. (b) $\dot{u}_6$.

Figure 8: Velocity spectrograms for $\mu = 0.2$ (dual assembly).

The contact assumption can be verified observing the time histories of $\{g\} = -[B_E]^T \lambda$. In Fig. 9, the time history of g_6 is shown. The positive sign of g_6 confirms the contact assumption because the normal contact force acting on the mass m_2 is directed upwards.

5 Conclusions

In this paper, the general framework for dynamic substructuring is extended to time-variant interfaces among connecting substructures. Specifically, a time-variant interface due to a sliding contact is considered by

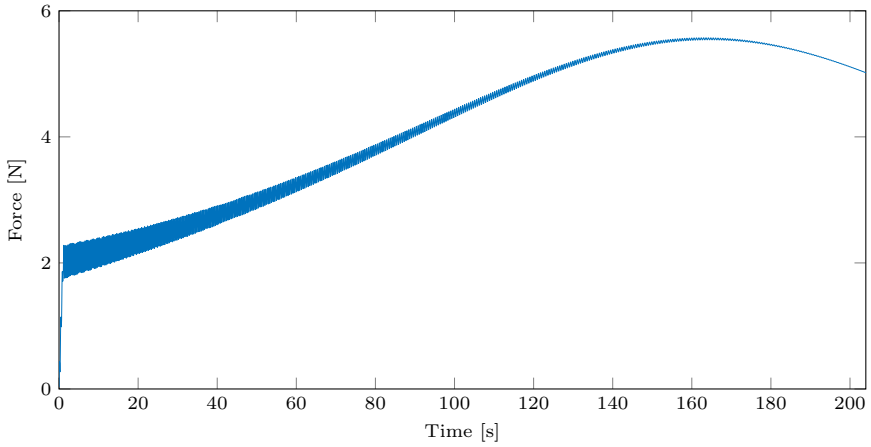


Figure 9: Verification of contact assumption, Normal contact force g_6 for $\mu = 0.2$ (dual assembly).

introducing time dependent compatibility and equilibrium conditions. The sliding contact can be without or with friction. In presence of friction, equilibrium conditions involve tangential directions at the contact interface, that do not appear in the compatibility conditions.

The solution approach in time domain can use both primal and dual assembly. In the former case classical numerical time integration is used (`ode45`); in the latter case the forward increment Lagrange multiplier method is adapted to dual assembly.

Results on a lumped parameter model show the feasibility and effectiveness of the proposed approaches. The assumption of sliding contact is verified at the end of the computation.

Future developments involve the extension of the approach to simple finite element models under the assumption that the relative sliding motion at the contact interfaces is known a-priori, at least approximately.

Acknowledgements

This research is supported by University of Rome La Sapienza and University of L'Aquila.

References

[1] D. de Klerk, D. J. Rixen, and S. Voormeeren, "General framework for dynamic substructuring: History, review, and classification of techniques," *AIAA Journal*, vol. 46, pp. 1169–1181, May 2008.

[2] D. J. Rixen and P. L. van der Valk, "An impulse based substructuring approach for impact analysis and load case simulations," *Journal of Sound and Vibration*, vol. 332, no. 26, pp. 7174 – 7190, 2013.

[3] P. L. van der Valk and D. J. Rixen, "An impulse based substructuring method for coupling impulse response functions and finite element models," *Computer Methods in Applied Mechanics and Engineering*, vol. 275, no. Supplement C, pp. 113 – 137, 2014.

[4] S. N. Voormeeren and D. J. Rixen, "A family of substructure decoupling techniques based on a dual assembly approach," *Mechanical Systems and Signal Processing*, vol. 27, pp. 379–396, Feb 2012.

[5] W. D'Ambrogio and A. Fregolent, "Inverse dynamic substructuring using direct hybrid assembly in the frequency domain," *Mechanical Systems and Signal Processing*, vol. 45, no. 2, pp. 360–377, 2014.

[6] J. Brunetti, W. D'Ambrogio, and A. Fregolent, "Dynamic substructuring with a sliding contact interface," in *Dynamics of Coupled Structures, Volume 4* (A. Linderholt, M. S. Allen, R. L. Mayes, and D. Rixen, eds.), pp. 105–116, Cham: Springer International Publishing, 2018.

[7] N. J. Carpenter, R. L. Taylor, and M. G. Katona, "Lagrange constraints for transient finite element surface contact," *International Journal for Numerical Methods in Engineering*, vol. 32, no. 1, pp. 103–128, 1991.

[8] W. D'Ambrogio and A. Fregolent, "Direct decoupling of substructures using primal and dual formulation," in *Conference Proceedings of the Society of Experimental Mechanics Series, Volume 4, Linking Models and Experiments*, vol. 2, (Jacksonville, Florida USA), pp. 47–76, Springer, January 31-February 3 2011.

Comparison of substructuring techniques for experimental identification of rubber isolators dynamic properties

M. Haeussler [1], **S.W.B. Klaassen** [1], **D.J. Rixen** [1]
[1] Technical University of Munich, Faculty of Mechanical Engineering,
Chair of Applied Mechanics, Boltzmannstr. 15, 85748 Garching, Germany
e-mail: **michael.haeussler@tum.de**

Abstract
Hydraulic testing machines can be used to obtain dynamic stiffnesses of rubber isolators in translational degrees of freedom (DoF) up to a few hundred Hertz. Substructuring methods may identify the dynamic properties also in rotational DoF while requiring only standard vibration testing equipment. Results of two substructuring methods will be compared to those from a hydraulic machine. Both use rigid fixtures, mounted to the bottom and top of the isolators. *Frequency based substructuring* requires knowing the rigid fixtures dynamics to decouple them. *Inverse Substructuring* does not require the fixtures dynamics, but is assuming negligible mass and a special stiffness matrix topology of the isolator. Both methods produce accurate results for translational and rotational DoF up to the kilo Hertz range. Nevertheless, frequency based substructuring does not rely on specific isolator assumptions, which could not be justified.

Keywods*: rubber isolators, frequency based substructuring, inverse substructuring, virtual point transformation.*

1 Introduction

Optimizing the vibration behavior of a mechanical system frequently requires knowledge about rubber isolators' dynamic properties. These depend on many different factors, such as static preload, temperature and vibration amplitude [1]. Many researchers investigated methods for identifying the frequency dependent modulus and damping of the rubber material. In [2], the authors compare different formulations for the complex modulus whose parameters are fitted to transmissibility measurements. Approaches of this kind are very valuable if the intent is to model and modify the geometry of the rubber mount for a specific application. However, the intent in this paper is not to model the material of the rubber, but more globally, to identify the

dynamic properties of readily available isolator elements with different materials and geometries. The authors of [3] perform shaker and hammer measurements on a mass sitting on top of the rubber mount. They compare different methods for identifying the complex stiffness of the mount in this single degree of freedom (DoF) configuration. It is proposed to use a complex stiffness, which is a piecewise frequency depended polynomial, fitted to the measurement data. Recently, some research was focused on identifying isolator properties from pure frequency response function (FRF) measurements of an assembly containing the rubber elements [4] via a method which we think was first published under the name of "inverse substructuring" [5, 6]. This method assumes a special topology of the isolator matrix and negligible mass of the rubber isolators. In [7] the authors use the same assumptions to identify the properties of the structures connected by the isolators. However, they reformulate the equations so that only a smaller submatrix needs to be inverted, which makes the operation less sensitive to measurement errors. In this paper, we describe and compare a classic substructuring approach and the inverse substructuring method for obtaining rubber isolators dynamic stiffnesses up to the kilo-hertz frequency range in translational and rotational DoF.

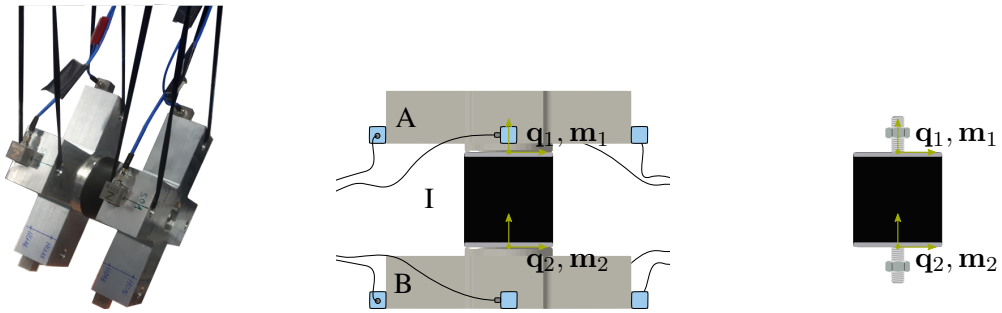
2 Experimental modeling

This section gives an overview of the performed measurements and introduces the notation used throughout the paper. This includes the derivation of 6-DoF dynamic models from standard measurements with hammer impacts and triaxial accelerometers, via virtual point transformation (section 2.1), the modeling of the fixtures as rigid bodies (section 2.2) and an explanation of the validation measurements performed on a servo hydraulic testing machine (section 2.3).

2.1 Six degree of freedom model of rubber isolators

As hammer impacting directly at the end of a rubber isolator I is practically infeasible, it was attached to two fixtures in the form of crosses. An upper cross A and a lower cross B, resulting in the assembly AIB (see figure 1b).

The crosses were designed so that one can apply hammer impacts that excite all translations and rotations at the connection to the rubber isolator. The sensors are mounted at well-defined positions which can observe all translations and rotations of the cross (cf. figures 1a and 2). During the impact measurements on the freely suspended assembly AIB (cf. figure 1a), 16 points on the upper cross A and 16 points on the lower cross B were excited with hammer impacts. Responses were measured with 4 triaxial accelerometers on either cross, resulting in a 24×32 FRF matrix $\mathbf{Y}_{uf}^{AIB}(\omega)$, where u indicates the responses in the measurement channels of the sensors, f indicates the hammer impacts and ω denotes the frequency dependence. The explicit frequency dependence of FRF matrices $\mathbf{Y}$ and dynamic stiffness matrices $\mathbf{Z}$ will be omitted in the rest of the paper. The measurements were performed on a Mueller-BBM MK2 data acquisition system and the rubber temperature was at 21°C. Each FRF was estimated from at least 3 averages with



(a) (b) (c)

Figure 1: (a) Measurement setup: rubber isolator between upper and lower fixture hung up with rubber bands. (b) Schematic: free-free measurement of isolator I between fixutures A and B, resulting in the FRF matrix of the assembled system $\mathbf{Y}^{AIB}$. (c) Admittance $\mathbf{Y}^{I}$ of the sole rubber isolator which is to be determined. Vectors $\mathbf{q}_1$ and $\mathbf{q}_2$ describe the rigid body responses at the top and bottom of the rubber isolator respectively. Vectors $\mathbf{m}_1$ and $\mathbf{m}_2$ contain the translational and rotational excitations.

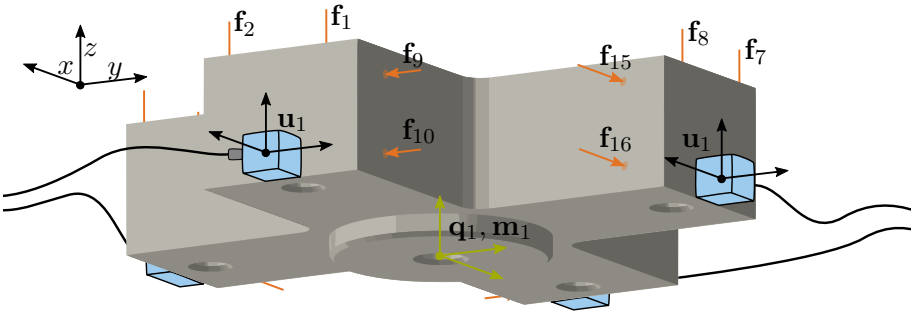


Figure 2: Upper fixture A with measured sensor accelerations $\mathbf{u}$, applied hammer impacts $\mathbf{f}$, transformed rigid body DoF $\mathbf{q}_1$ and forces and moments $\mathbf{m}_1$ around virtual point 1 (indicated as green point).

an H1-estimator. The DoF on the upper cross will be given the subscript $(\star)_1$ and the ones on the lower cross the subscript $(\star)_2$. The measured FRF can thus be partitioned as:

$$\mathbf{Y}_{uf}^{AIB} = \begin{bmatrix} \mathbf{Y}_{11} & \mathbf{Y}_{12} \\ \mathbf{Y}_{21} & \mathbf{Y}_{22} \end{bmatrix}_{uf}^{AIB} . \tag{1}$$

The measured FRF matrix $\mathbf{Y}_{uf}^{AIB}$ shall be transformed to a matrix $\mathbf{Y}_{qm}^{AIB}$ which contains translational and rotational responses (contained in the vector $\mathbf{q}$) to applied loads and moments (contained in the vector $\mathbf{m}$),

$$\mathbf{q} = \begin{bmatrix} \mathbf{q}_1 \\ \mathbf{q}_2 \end{bmatrix}, \qquad \mathbf{m} = \begin{bmatrix} \mathbf{m}_1 \\ \mathbf{m}_2 \end{bmatrix}. \tag{2}$$

The rotations and moments are defined around a so-called 'virtual point'. The positions of sensors and hammer impacts with respect to the virtual point on the upper cross A are shown in

figure 2. For given rigid body motions $\mathbf{q}$, it is straightforward to derive the resulting motion in each of the sensor channels $\mathbf{u}$ (provided the position and orientation of the sensors with respect to the virtual point is known. The assumed sensing position is in the center of the sensor housing.):

$$\mathbf{u} = \mathbf{R}_u \mathbf{q}, \tag{3}$$

where the matrix $\mathbf{R}_u$ contains the information about position an orientation of each sensor channel with respect to the virtual points. For more information on how to create $\mathbf{R}_u$ see e.g. [8]. Similarly, for a given vector of applied forces at the hammer impact points $\mathbf{f}$, it is possible to calculate the resulting forces and moments around the virtual points $\mathbf{m}$:

$$\mathbf{m} = \mathbf{R}_f^T \mathbf{f}, \tag{4}$$

where the matrix $\mathbf{R}_f$ contains the information about position and orientation of each hammer impact with respect to the virtual point (see [8]). In order to transform the measured $\mathbf{Y}_{uf}^{AIB}$ to $\mathbf{Y}_{qm}^{AIB}$, it is necessary to derive the inverse relationships of equations (3) and (4), which can be done with e.g. a least squares projection for the displacements and a constrained minimization for the forces:

$$\mathbf{q} = \underbrace{(\mathbf{R}_u^T \mathbf{R}_u)^{-1} \mathbf{R}_u^T}_{\mathbf{T}_u} \mathbf{u} \qquad \mathbf{f} = \underbrace{\mathbf{R}_f (\mathbf{R}_f^T \mathbf{R}_f)^{-1}}_{\mathbf{T}_f^T} \mathbf{m}, \tag{5}$$

where $\mathbf{T}_u$ and $\mathbf{T}_f$ are the transformation matrices for the displacements and forces respectively. See [9] for an explanation of the minimizations involved in the derivation of the transformation matrices (including the possible use of weightings for single sensor channels and force inputs). With the above relationships, the measured FRF matrix $\mathbf{Y}_{uf}^{AIB}$ can be transformed to an FRF matrix containing the rigid body motions around the virtual points $\mathbf{Y}_{qm}^{AIB}$:

$$\mathbf{Y}_{qm}^{AIB} = \mathbf{T}_u \mathbf{Y}_{uf}^{AIB} \mathbf{T}_f^T. \tag{6}$$

For the rest of the paper the subscript $(\star)_{qm}$ will be dropped. Implicitly, it will be assumed that all DoF are in the form of rigid body motions in the two virtual points.

Remark 1: *When using* (6) *with measured data, it is mandatory to ensure high quality of the measurements. One way of doing so is to use the consistency metrics defined in [8]. Before performing the measurement, one should also check the noise level in the single sensor channels. Recording just the noise floor in the channels, it was found that the noise in one sensor channel was around* $50dB$ *higher than for all others. Interchanging cables and connectors on the data acquisition system led to the conclusion that it was actually a broken channel of the sensor itself. The FRFs measured with this sensor*

channel reflected the significantly higher noise level. In figure 3, two different FRFs that should be equal (due to symmetry of the assembly AIB) are compared: one measured with the broken channel and the other with an intact sensor. Due to over determination of the transformation, it is not necessary to keep the noisy sensor channel in the transformation. In this case, it is recommended to take the noisy channel completely out of the transformation (deleting the corresponding row from $\mathbf{Y}_{uf}^{AIB}$ and $\mathbf{R}_u$). The result of a transformed FRF which is particularly influenced by the response in the broken channel is shown in figure 4, for keeping and neglecting the data of this channel.

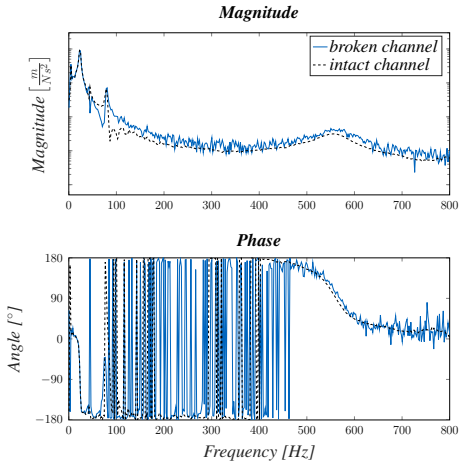


Figure 3: FRF measured with the broken channel compared to intact channel.

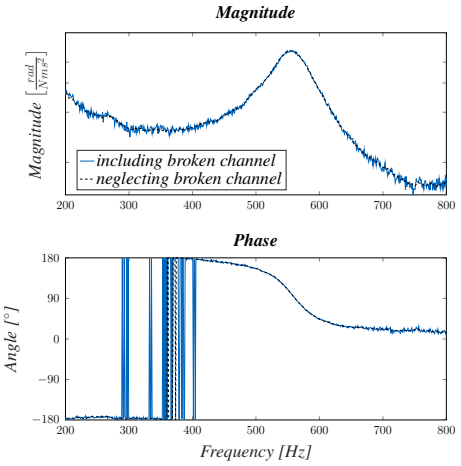


Figure 4: Virtual point transformed FRF for a rotational DoF which is particularly affected by the broken channel.

2.2 Analytical model of the crosses

The crosses where designed to behave like a rigid body in the frequency range of interest. Their first flexible mode is found at 4489Hz. The crosses dynamics where modeled by their mass and rotational inertia from the CAD model, and an additional correction for the mass of the sensors. The rigid body assumption was found to be reasonable up to 2000Hz. It is also important to note that the virtual point V does not correspond to the center of gravity G (cf. figure 5). The dynamic stiffness of a freely suspended, rigid cross $\mathbf{Z}$ is given by:

$$\mathbf{Z} = -\omega^2\mathbf{M} = -\omega^2 \begin{bmatrix} m_{tot}\mathbf{I} & -m_{tot}\tilde{\mathbf{r}}_{V,G} \\ m_{tot}\tilde{\mathbf{r}}_{V,G} & \mathbf{\Theta}_V \end{bmatrix}, \tag{7}$$

where $\mathbf{M}$ is the mass matrix of the cross plus sensors, for the six rigid body degrees of freedom around virtual point V. $\mathbf{I}$ is a 3×3 identity matrix, $\mathbf{r}_{V,G}$ is the vector from the virtual point V to

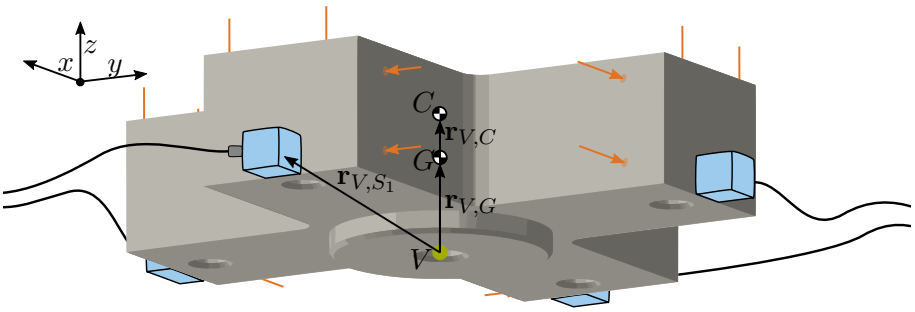


Figure 5: Position of total center of gravity G, center of gravity for the cross without the sensor masses C, the sensor positions S_i and the virtual Point V. Connecting vectors are indicated as $\mathbf{r}$.

the center of gravity G and $\mathbf{\Theta}_V$ is the rotational inertia of the cross plus sensors. The notation $\tilde{\mathbf{r}}$ is the matrix representation for the cross product with the vector $\mathbf{r}$. Note that $\tilde{\mathbf{r}}^T = -\tilde{\mathbf{r}}$ and thus the mass matrix $\mathbf{M}$ is symmetric.

The total mass m_{tot} and the rotational inertia $\mathbf{\Theta}_V$ are given by:

$$m_{tot} = m_c + 4m_s, \tag{8}$$

$$\mathbf{\Theta}_V = \underbrace{\mathbf{\Theta}_C^{cross} + m_c(||\mathbf{r}_{V,C}||^2\mathbf{I} - \mathbf{r}_{V,C}\mathbf{r}_{V,C}^T)}_{\text{rot. inertia of cross around } V} + \underbrace{\sum_{i=1}^{4} m_s(||\mathbf{r}_{V,S_i}||^2\mathbf{I} - \mathbf{r}_{V,S_i}\mathbf{r}_{V,S_i}^T)}_{\text{rot. inertia of sensors}}, \tag{9}$$

where m_c is the mass of the cross and m_s is the mass of one sensor. The mass of the sensors with cable-connector was measured on a fine scale to 7.51 gram. The sensors where all PCB Model TLD356A32. The rotational inertia of the cross around its center of gravity $\mathbf{\Theta}_C^{cross}$ and the position of its center of gravity C, was taken from the CAD software. The vector from the virtual point to the total center of gravity of cross plus sensors is:

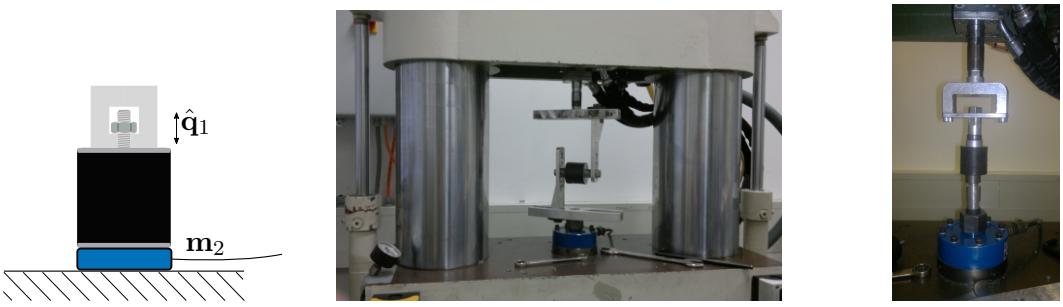
$$\mathbf{r}_{V,G} = \frac{1}{m_{tot}}\left[m_c\mathbf{r}_{V,C} + \sum_{i=1}^{4} m_s\mathbf{r}_{V,S_i}\right]. \tag{10}$$

2.3 Validation measurements on hydropulse

For validation of the two methods, the rubber isolators where tested on a servo hydraulic testing machine, or in short: "hydropulse". The machine controls the vibration amplitude and frequency on the upper connection bolt of the rubber, and measures the reaction force on the lower connection (see figure 6a for a schematic depiction of the measurement principle). The controlled vibration amplitude is measured within the hydraulic cylinder at the top of the machine. The fixtures needed for mounting the rubber isolators in the machine are considered to be rigid in the

	freq. range [Hz]	freq. resolution [Hz]	vibration amplitude [mm]
lower	$3-200$	1	0.1
medium	$20-400$	10	0.03
higher	$100-900$	20	0.01

Table 1: Test cycles performed on the rubber isolator with the hydropulse machine.



(a) (b) (c)

Figure 6: Overview of the hydropulse measurements. (a) Measurment principle with controlled vibration $\hat{\mathbf{q}}_1$ on the top and force measurement $\mathbf{m}_2$ at the bottom. This corresponds to measuring single entries in the off-diagonal stiffness matrix $\mathbf{Z}_{21}$. (b) Measurement setup for radial stiffness measurement. (c) Measurement setup for axial stiffness measurement.

frequency range of interest. If this assumption holds, then the displacement of the upper isolator connection bolt is the same as the one controlled in the hydraulic cylinder. The stiffnesses were measured in the axial (z-direction in figure 5) and radial direction (since the rubber mount is axis-symmetric, any direction in $x-y$ plane in figure 5). The setups for the radial and axial measurements can be seen in figure 6b and figure 6c respectively. During the measurements, the preload of the rubber isolators can be adjusted, so that the dynamic stiffnesses are measured around this operating point. In all reference measurements shown, the preload was $20N$. Depending on the frequency range of interest, the vibration amplitude was adjusted. In total 3, different frequency ranges where tested (see table 1).

3 Substructuring methods for identification of rubber isolator properties

The goal of this section is to introduce the two methods that were investigated for obtaining the dynamic properties of a rubber isolator from the virtual point transformed FRF matrix $\mathbf{Y}^{AIB}$. Therefore, we review the (de-)coupling process in the primal formulation in section 3.1. In section 3.2, the specific assumptions for the inverse substructuring method are explained and the results are compared to the hydropulse measurements. In section 3.3, these assumptions are tested for validity by comparing them to the results of the primal decoupling method, which does not rely on any assumptions about the isolator.

3.1 Primal (dis-)assembly of dynamic stiffness matrices

Assume the dynamic stiffness matrix of the rubber isolator $\mathbf{Z}^I$ shall be coupled to the upper cross $\mathbf{Z}^A$. In the coupled configuration, there will be connection forces $\mathbf{g}_1$ acting on the interface between both substructures:

$$\begin{bmatrix} \mathbf{Z}_{11}^A & \mathbf{0} & \mathbf{0} \\ \mathbf{0} & \mathbf{Z}_{11}^I & \mathbf{Z}_{12}^I \\ \mathbf{0} & \mathbf{Z}_{21}^I & \mathbf{Z}_{22}^I \end{bmatrix} \begin{bmatrix} \mathbf{q}_1^A \\ \mathbf{q}_1^I \\ \mathbf{q}_2^I \end{bmatrix} = \begin{bmatrix} \mathbf{m}_1^A + \mathbf{g}_1^A \\ \mathbf{m}_1^I + \mathbf{g}_1^I \\ \mathbf{m}_2^I \end{bmatrix}. \tag{11}$$

When coupling any two structures to each other the following conditions must be fulfilled: *Compatibility* of displacements and *Equilibrium* of forces. Compatibility states in the above case that $\mathbf{q}_1^A = \mathbf{q}_1^I$. When using the so called 'primal' assembly, the two separated variables on either side of the interface are replaced by one global variable $\mathbf{q}_1^{AI} := \mathbf{q}_1^A = \mathbf{q}_1^I$, so that the compatibility condition is automatically fulfilled:

$$\begin{bmatrix} \mathbf{Z}_{11}^A & \mathbf{0} \\ \mathbf{Z}_{11}^I & \mathbf{Z}_{12}^I \\ \mathbf{Z}_{21}^I & \mathbf{Z}_{22}^I \end{bmatrix} \begin{bmatrix} \mathbf{q}_1^{AI} \\ \mathbf{q}_2^I \end{bmatrix} = \begin{bmatrix} \mathbf{m}_1^A + \mathbf{g}_1^A \\ \mathbf{m}_1^I + \mathbf{g}_1^I \\ \mathbf{m}_2^I \end{bmatrix}. \tag{12}$$

Remark 2: *The notion of 'primal' assembly is related to the fact that the displacements* $\mathbf{q}$ *are usually the 'primal' variables for which the equations are being solved in mechanics. The 'dual' variables are the connection forces, which can be solved for in a post procesing step. For an interesting discussion regarding the distinction between primal and dual variables in engineering generally, see [10, chapter 2.5].*

The next coupling condition is the equilibrium, requiring that the coupling forces on either side of the interface are equal in magnitude, but have opposite sign (*actio est reactio*): $\mathbf{g}_1^A = -\mathbf{g}_1^I$. Adding the first two lines of (12) and considering the equilibrium condition yields the coupled stiffness matrix:

$$\underbrace{\begin{bmatrix} \mathbf{Z}_{11}^I + \mathbf{Z}_{11}^A & \mathbf{Z}_{12}^I \\ \mathbf{Z}_{21}^I & \mathbf{Z}_{22}^I \end{bmatrix}}_{\mathbf{Z}^{AI}} \begin{bmatrix} \mathbf{q}_1^{AI} \\ \mathbf{q}_2^I \end{bmatrix} = \begin{bmatrix} \mathbf{m}_1^I + \mathbf{m}_1^A \\ \mathbf{m}_2^I \end{bmatrix}, \tag{13}$$

which corresponds to the stiffness matrix assembly well known from e.g. finite element modeling. Coupling also the lower cross B then yields the stiffness matrix of the whole assembly,

$$\mathbf{Z}^{AIB} = \begin{bmatrix} \mathbf{Z}_{11}^A + \mathbf{Z}_{11}^I & \mathbf{Z}_{12}^I \\ \mathbf{Z}_{21}^I & \mathbf{Z}_{22}^B + \mathbf{Z}_{22}^I \end{bmatrix}. \tag{14}$$

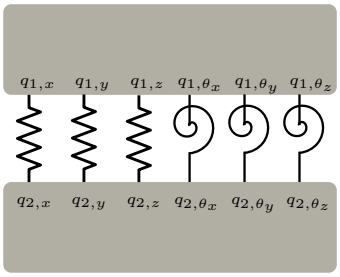


Figure 7: Schematic depiction of the assumed "DoF to DoF " topology of the joint elements for the inverse substructuring approach.

Formulated loosely, when coupling dynamic stiffness matrices, the coupling process comes down to just "*adding the overlapping matrix parts*". As can be seen from (14), the uncoupled stiffness $\mathbf{Z}^I$ of the rubber isolator alone can be found from "*subtracting the dynamic stiffness of the structures A and B*" from $\mathbf{Z}^{AIB}$.

3.2 Inverse Substructuring

The description in this section is following [11]. When coupling two substructures via a resilient isolator, the assembled $\mathbf{Z}^{AIB}$ will always have the form of (14). Experimentally, we can measure the FRF matrix and invert it to obtain the dynamic stiffness of the assembly $\mathbf{Z}^{AIB} = (\mathbf{Y}^{AIB})^{-1}$. Inverse substructuring uses the fact that the off-diagonal terms in (14), are a property of the rubber isolator alone:

$$\mathbf{Z}_{21}^{AIB} = \mathbf{Z}_{21}^{I}, \qquad \mathbf{Z}_{12}^{AIB} = \mathbf{Z}_{12}^{I}. \tag{15}$$

Assume the isolator connects the DoF of the two virtual points with the special topology shown in figure 7, i.e. each DoF on one side of the interface is only coupled to one DoF on the other side and there are no cross couplings with any other DoF . The depiction of springs in figure 7 is just for didactic purposes. Of course there can be any kind of frequency dependent stiffness and damping properties inherent in the links depicted as mere springs. Additionally, it is assumed that the joint element (i.e. the rubber) has negligible mass. If these assumptions hold, then the stiffness matrix of the rubber isolator has the following properties:

$$\mathbf{Z}_{11}^{I} = -\mathbf{Z}_{12}^{I} = -\mathbf{Z}_{21}^{I} = \mathbf{Z}_{22}^{I}, \tag{16}$$

where in the general case $\mathbf{Z}_{11}^{I}$ and therefore also $\mathbf{Z}_{12}^{I}$ have to be diagonal matrices. Thus, by simply *inverting* the measured FRF matrix of the assembly, the whole rubber isolator can be identified from just taking the off-diagonal blocks of the matrix (provided that the above stated assumptions hold). Hence, the name "inverse substructuring". In this case it is trivial to derive the dynamic stiffnesses of the two separate substructures A and B from the measurements:

$$\begin{bmatrix} \mathbf{Z}_{11}^{A} & \mathbf{0} \\ \mathbf{0} & \mathbf{Z}_{22}^{B} \end{bmatrix} = \begin{bmatrix} \mathbf{Z}_{11}^{A} + \mathbf{Z}_{11}^{I} & \mathbf{Z}_{12}^{I} \\ \mathbf{Z}_{21}^{I} & \mathbf{Z}_{22}^{B} + \mathbf{Z}_{22}^{I} \end{bmatrix} - \begin{bmatrix} \mathbf{Z}_{11}^{I} & \mathbf{Z}_{12}^{I} \\ \mathbf{Z}_{21}^{I} & \mathbf{Z}_{22}^{I} \end{bmatrix}. \tag{17}$$

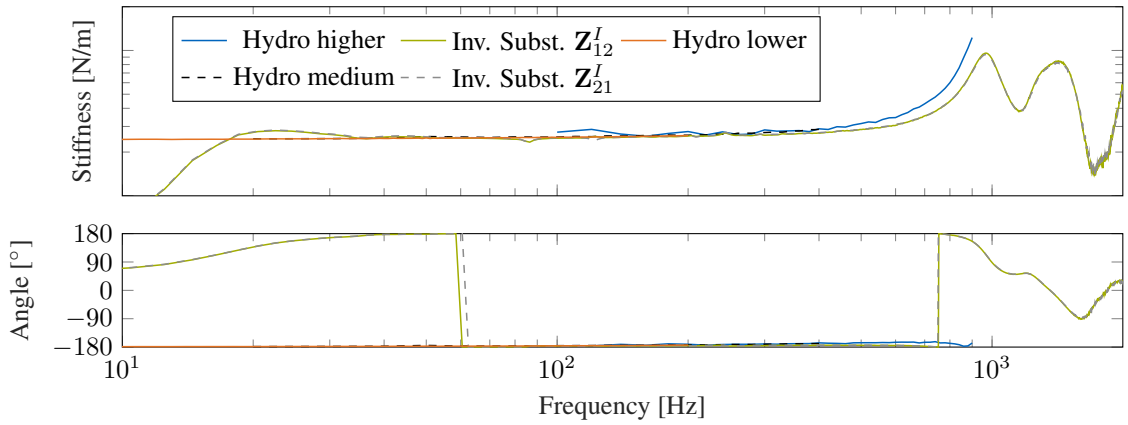


Figure 8: Axial direction: Comparison of hydropulse with inverse substructuring results.

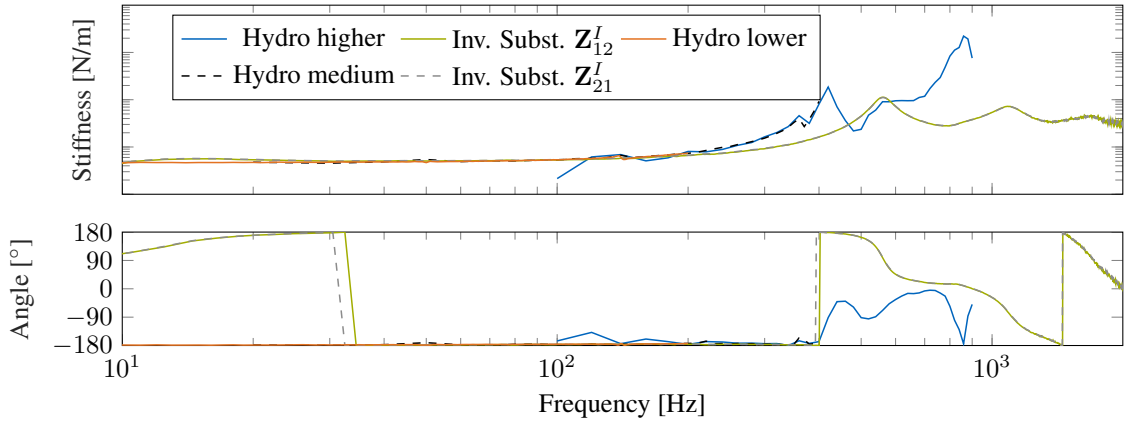


Figure 9: Radial direction: Comparison of hydropulse with inverse substructuring results.

This comes with the great practical advantage that it is not necessary to know anything about the dynamic properties of the two structures A and B which are coupled by the isolator. Thus, one is able to identify the dynamic properties of all involved substructures A, B and I separately from only one set of measurements performed on the assembly AIB.

Just as with inverse substructuring, the hydropulse identifies the off-diagonal stiffness terms $\mathbf{Z}_{21}^I$ (see figure 6) of the isolator in the axial and radial direction. In figure 8, the hydropulse measurements (details listed in table 1) are compared to the results from the inverse substructuring approach in axial direction. In the figure, both entries containing the axial-axial stiffness from the two off diagonal matrices $\mathbf{Z}_{12}$ and $\mathbf{Z}_{21}$ are shown. In figure 9, the results in the radial direction are compared.

As can be seen in figure 8 the magnitude of the axial stiffness identified from the inverse substructuring fits the hydropulse measurements well for frequencies higher than 30Hz. The phase, which is important for a good damping estimate, is more difficult. This is assumed to be due to slight phase errors in the acceleration sensors. The same argument for the magnitude and phase

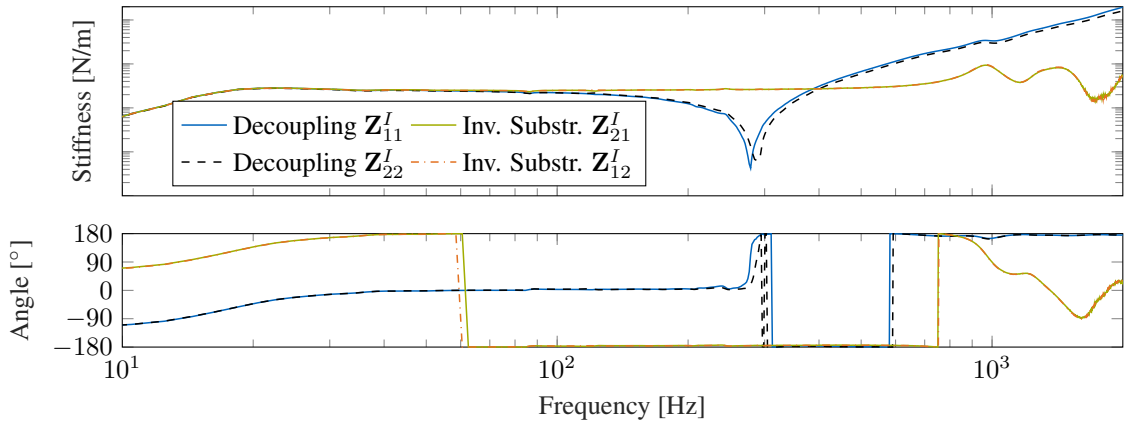


Figure 10: Axial direction: Comparison of off-diagonal ($\mathbf{Z}^I_{12}$, $\mathbf{Z}^I_{21}$) and diagonal ($\mathbf{Z}^I_{11}$, $\mathbf{Z}^I_{22}$) entries.

can be made for the radial direction in figure 9. However, for higher frequencies the deviation of stiffness magnitude between hydropulse and the inverse substructuring is higher.

3.3 Validation of the inverse substructuring assumptions

The dynamic stiffness of upper and lower cross, $\mathbf{Z}^A$ and $\mathbf{Z}^B$ respectively, is known from (7). Therefore, it is straightforward to perform the decoupling of both crosses in the primal formulation:

$$\begin{bmatrix} \mathbf{Z}^I_{11} & \mathbf{Z}^I_{12} \\ \mathbf{Z}^I_{21} & \mathbf{Z}^I_{22} \end{bmatrix} = \begin{bmatrix} \mathbf{Z}^A_{11} + \mathbf{Z}^I_{11} & \mathbf{Z}^I_{12} \\ \mathbf{Z}^I_{21} & \mathbf{Z}^B_{22} + \mathbf{Z}^I_{22} \end{bmatrix} - \begin{bmatrix} \mathbf{Z}^A_{11} & \mathbf{0} \\ \mathbf{0} & \mathbf{Z}^B_{22} \end{bmatrix}. \tag{18}$$

Obviously, the entries on the off-diagonals are unchanged by the decoupling, but it is now possible to investigate the assumptions underlying the inverse substructuring approach by comparing the main- and off-diagonal entries. For other decoupling formulations see [12].

In figure 10, the axial stiffness values taken from the diagonal ($\mathbf{Z}^I_{11}$ and $\mathbf{Z}^I_{22}$) are compared to those from the off diagonal terms. If the assumption of negligible rubber mass holds, then they should be the same apart from a negative sign, i.e. a 180° phase shift (see (16)). This is true for the low frequency spectrum up to around 100Hz. For higher frequencies there is a clear resonance (showing as a dip in the stiffness magnitude) visible in the entries of the main diagonal.

A quick investigation of this resonance can be done assuming the rubber isolator to be a lumped mass and stiffness model. When using the static axial stiffness and half of the rubber isolator mass (including bolts and nuts, see figure 1c), one can compute the resonance of a single DoF oscillator resulting in 257Hz. The actual resonance appearing in figure 10 is at 278Hz. The higher value may be attributed to dynamic stiffening of the rubber and the fact that the mass of the rubber is not lumped but continuously distributed. The slope of the main diagonal entries for higher frequencies in figure 10 is indicating a quadratic increase of stiffness with frequency,

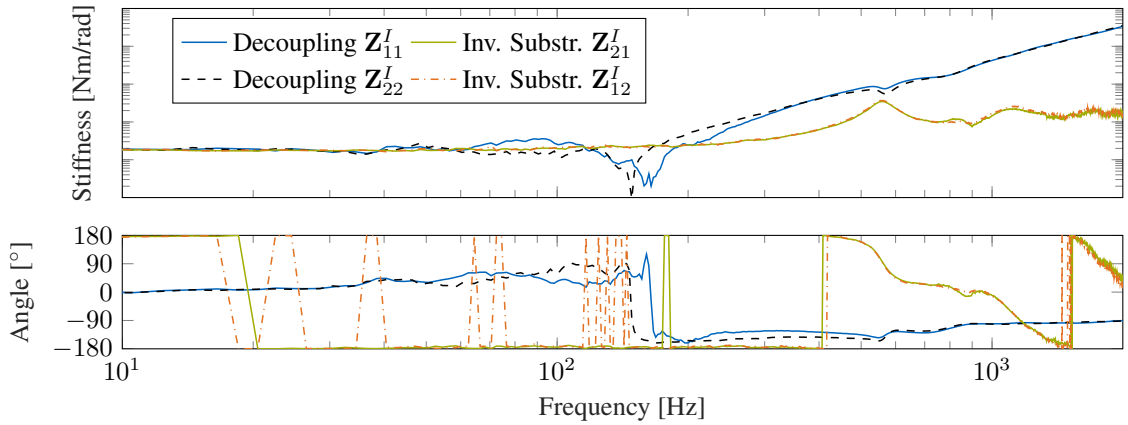


Figure 11: Rotation around z: Comparison of off-diagonal ($\mathbf{Z}^I_{12}$, $\mathbf{Z}^I_{21}$) and diagonal ($\mathbf{Z}^I_{11}$, $\mathbf{Z}^I_{22}$) entries.

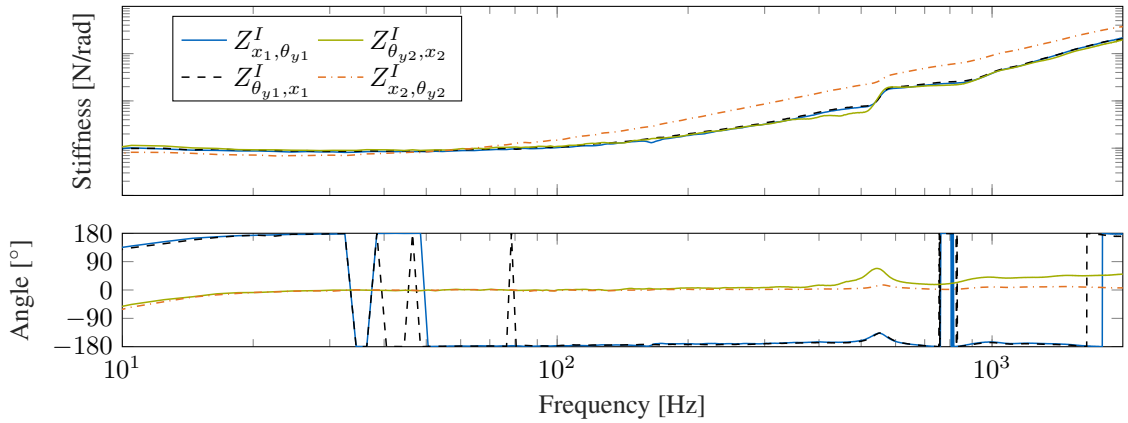


Figure 12: Coupling stiffness between translations in y direction and rotations around x axis.

typical for a "mass line". The results for the radial directions show similar behavior. So it may be argued that the rubber isolator mass *does* play a significant role for the rubber stiffness at higher frequencies.

The phase of the main diagonal terms should be between $0°$ and $180°$ for a rubber isolator with positive damping [13]. Again, there seems to be an error of a few degrees in the phase, which is assumed to be due to a phase error in the acceleration sensors.

In figure 11, the off-diagonal and main diagonal entries for the rotational stiffness around the z-axis are compared. Similar effects can be observed here: up to around 100Hz, the off-diagonal terms deviate only in a $180°$ phase shift from the main diagonal entries, as expected. For higher frequencies, clear influences of the isolator mass can be observed. The phase error here is more apparent and the magnitude seems more affected by noise than in the axial direction.

In figure 12, the coupling stiffness between the x-translation and y-rotation in the main diagonal matrices $\mathbf{Z}_{11}$ and $\mathbf{Z}_{22}$ are compared. In the experiments, one can observe that there is a clear

coupling between the radial directions and the rotation around the axis perpendicular to it. This is by no means surprising since it is the normal behaviour of e.g. a beam. However, this violates the no-cross coupling assumption of the inverse substructuring (see figure 7).

4 Discussion

Non-linear effects in dynamic behaviour of rubber isolators
As has been mentioned in section 2.3, the measurements on the hydropulse have been performed with a static preload of 20N. They have also been tested with 120N preload, which did not yield significantly different results. However, there is a nonlinear effect depending on the maximum displacement during the vibration in the *time domain*. Rubber generally behaves stiffer if the maximum transient displacement in time is small, e.g. in a harmonic test with only one excitation frequency like on the hydropulse (see table 1). When excited by a broad spectrum of frequencies, like real operating conditions in a car or in the case of an impact like in the tests performed in this paper, the rubber material behaves softer. In these cases the maximum transient displacement is higher due to the superposition of multiple frequency components. The softening with higher transsient displacements can be attributed to the elastomer molecule chains in the material, which start to unfold from a compact packaging in the idle position, to a more flexible structure when subjected to larger dynamic displacements. For a detailed discussion of this effect see [14]. In [15], it is shown that this change of stiffness is more prominent for higher frequencies than for lower frequencies. This effect might explain the higher stiffness measured with the hydropulse in the high-frequency-range when compared to the inverse substructuring (see figure 8 and 9).

Rigidity of Hydropulse fixtures
It is not sure whether the fixture for holding the rubber isolators in the hydropulse is behaving rigidly in the whole frequency-range. This may be another explanation for the deviations between the inverse substructuring results and the hydropulse measurements at higher frequencies. Especially the rigidity of the fixture that holds the rubber isolator during the radial measurements seems to be questionable (see figure 6b and the results in figure 9).

Phase errors in acceleration sensors
Apparently, the phase in the identified stiffness is not stable and not physically meaningful for frequencies out of a band of approximately $80 - 300$ Hz. The untransformed FRFs are also showing these errors in the identified phase. An accelerance driving point FRF should always have a positive phase [13]. A negative phase would indicate negative damping, which is impossible in a passive system. A quick check on a driving point FRF in the measured matrix $\mathbf{Y}_{uf}^{AIB}$ (impact f_{10} and the coressponding channel of the adjacent sensor, see figure 2), shows a negative phase of about 2° at 500Hz which is growing to approximately 7° at 2000Hz. The virtual point transformation seems to be helpfull by averaging out the different phase errors of single sensors, but also here some driving point FRFs in $\mathbf{Y}_{qm}^{AIB}$ have a negative phase (growing from about -0.8° at 500Hz to -2° at 2000Hz). Different sensor manufacturers specify different maximum phase error for their sensors. However, we could not yet find manufacturer specifications for the sensors used in this paper. The decoupling of the cross masses amplifies slight errors

in the phase even more. When the cross masses are decoupled the ratio of purely real stiffness ($k - \omega^2 m$) to the damping terms ($i\omega d$) is even lower. This might explain the bigger deviations in phase for those entries where the rubber has negligible effective mass of its own (see e.g. the rotation around the z-axis in figure 11).

5 Conclusion

This paper investigated the performance of experimental techniques for identifying 6-DoF dynamic models of rubber isolators. The results suggest that it is possible to achieve a good agreement in the stiffness magnitudes up to the kilo-Hertz frequency range. It is thereby possible to obtain dynamic stiffness values of rubber isolators in more degrees of freedom and up to a higher frequency range than usually possible, even with an expensive hydropulse testing machine. However, the estimation of good damping values from the measurements is currently hindered by phase errors in the FRF measurements. Furthermore, the stiffness values on the off-diagonal obtained with the inverse substructuring approach have been successfully validated against the hydropulse measurements. Nevertheless, the underlying assumptions of the inverse substructuring method could not be validated. First, the mass of the rubber isolators seems to be not negligible. The influence of the neglected rubber mass however, would depend on the mass of the assembly in which rubber isolators shall be included later. Second, the assumption of no cross couplings between different DoF over the interface was shown to be untrue (see figure 12). It is therefore recommend to use a full decoupling to obtain rubber element properties that can be used for modeling a larger assembly.

Acknowledgments

We want to thank the BMW Group for funding this research as well as supporting it with measurement equipment and know-how. We also want to thank Mueller-BBM and VIBES.technology for their technical support.

References

[1] A. D. Nashif, D. I. G. Jones, and J. P. Henderson. *Vibration damping*. 1985, pp. 61–68.

[2] D. Koblar and M. Boltežar. “Evaluation of the Frequency-Dependent Young’s Modulus and Damping Factor of Rubber from Experiment and Their Implementation in a Finite-Element Analysis”. In: *Experimental Techniques* (Nov. 2013).

[3] T. R. Lin, N. H. Farag, and J. Pan. “Evaluation of frequency dependent rubber mount stiffness and damping by impact test”. In: *Applied Acoustics* 66.7 (2005), pp. 829–844.

[4] A. Moorhouse, A. S. Elliot, and Y. Heo. “Intrinsic characterisation of structure-borne sound sources and isolators from in-situ measurements.” In: *Proceedings of Meetings on Acoustics* 19 (2013), pp. 1–9.

[5] J. Zhen, T. C. Lim, and G. Lu. "Determination of system vibratory response characteristics applying a spectral-based inverse sub-structuring approach. Part I: analytical formulation". In: *International journal of vehicle noise and vibration* (2004).

[6] J. Wang et al. "General Formulation of Inverse Substructuring Method for Multicoordinate Coupled System". In: *Advances in Mechanical Engineering* 6 (2014), p. 475128.

[7] L. Keersmaekers et al. "Decoupling of mechanical systems based on in-situ frequency response functions: The link-preserving, decoupling method". In: *Mechanical Systems and Signal Processing* 58 (2015), pp. 340–354.

[8] M. V. van der Seijs et al. "An improved methodology for the virtual point transformation of measured frequency response functions in dynamic substructuring". In: *4th ECCOMAS Thematic Conference on Computational Methods in Structural Dynamics and Earthquake Engineering* June (2013).

[9] M. Haeussler and D. J. Rixen. "Optimal transformation of frequency response functions on interface deformation modes". In: *Dynamics of Coupled Structures, Volume 4. Conference Proceedings of the Society for Experimental Mechanics Series*. Ed. by R. D. Allen M., Mayes R. Springer, Cham, 2017, pp. 225–237.

[10] G. Strang. *Computational Science and Engineering*. First Edit. Wellesley-Cambridge Press, 2007.

[11] J. Meggitt and A. Moorhouse. "The in-situ decoupling of resiliently coupled sub-structures". In: *ICSV - International Congress on Sound and Vibration, London* (2017). Ed. by B. Gibbs.

[12] S. N. Voormeeren and D. J. Rixen. "A family of substructure decoupling techniques based on a dual assembly approach". In: *Mechanical Systems and Signal Processing* 27.1 (2012), pp. 379–396.

[13] P. Sjövall and T. Abrahamsson. "Component system identification and state-space model synthesis". In: *Mechanical Systems and Signal Processing* 21.7 (2007), pp. 2697–2714.

[14] J. A. Harris. "Dynamic Testing under Nonsinusoidal Conditions and the Consequences of Nonlinearity for Service Performance". In: *Rubber Chemistry and Technology* 60.5 (Nov. 1987), pp. 870–887.

[15] P. Hinsch. "Einige Untersuchungen zum Messen dynamischer Moduln von Elastomeren". In: *Kautschuk + Gummi Kunststoffe* 42.9 (1989), pp. 752–756.

Vibration response of a solid volume of arbitrary shape using the Boundary Forming Approach

G. Pavić
INSA-Lyon, Vibrations and Acoustics Laboratory
Avenue Jean Capelle 25 bis, F-69621, Villeurbanne, France
e-mail: **goran.pavic@insa-lyon.fr**

Abstract

A semi-analytical approach is presented which uses the known Green's function for the displacements and stresses of an infinite, elastic, homogeneous and isotropic solid to reconstruct the response of a finite body of arbitrary shape. To this end a closed "boundary surface" is defined within the infinite solid, identical to the external surface of the finite body. The response is obtained by superposing two complementary excitations which act simultaneously on the infinite solid: a primary and a secondary one. The primary excitation is identical to the one driving the finite body. The secondary excitation, located at the exterior of the boundary surface, has the role of re-creating across this surface the boundary conditions of the finite body. The physical side of approach is discussed first, the corresponding mathematical procedure is then outlined and an example is provided to demonstrate the validity of this approach.

1 Introduction

The prediction of vibration response of a mechanical object in a given point is usually done by a numerical approach, such as one of Galerkin methods, e.g. the Finite Element Method. Analytical solutions exist only for objects of extremely simple geometrical shapes and boundary conditions, such as a simply-supported beam or shell. Yet an analytical solution is often useful, in particular when the physical insight into the nature of the vibration is needed.

In this paper a particular approach, named the boundary forming, will be used to compute the response of a 3D solid body made of a homogeneous isotropic material. This approach, applied to beams, plates and shells, has been studied by the author almost two decades ago, [1], and has since been developed in more depth in plate applications, [2]. The boundary forming approach has close links with the technique called the Distributed Point Source Method (DPSM) which has been used for the modelling of ultrasonic and electromagnetic fields [3]. The basic idea is to employ the known Green's function of a simple body, usually an infinite medium, and to reconstruct the targeted boundary conditions of one section of such a body using a (large) number of point sources external to this section. In such a case the section of the body inside of the boundary, artificially created by the point sources, will behave exactly as if this section was independent of the rest of the main body, Fig. 1. The elastic waves created by a given vibration source, the primary source, will superpose with the waves created by the external, secondary sources. In steady state motion the interference between the primary and secondary waves will create in a number of points particular field conditions, such as zero displacement or zero stress. Providing the positions of secondary sources are conveniently selected and their strengths correctly identified the interference between the primary and secondary waves will create the required boundary conditions exactly at points located across the contour of the targeted section. If these points, named control points, are sufficiently close to each other the boundary conditions in between control points will closely match the required conditions too.

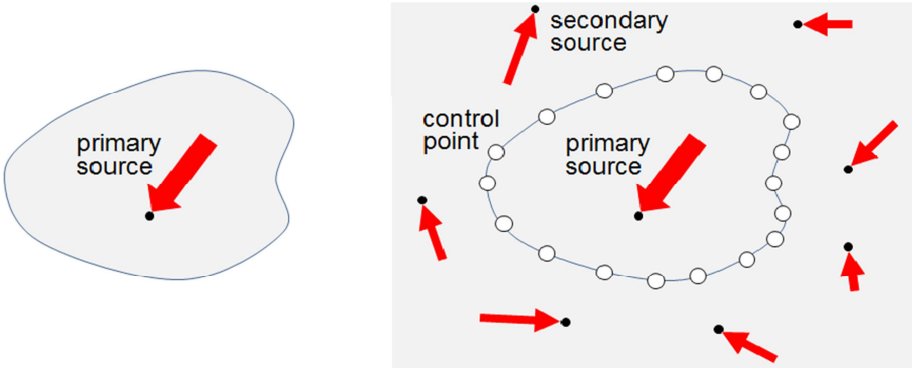


Figure 1. Principle of the boundary forming approach. Left: original; right: model.

Following the basic relationships the boundary forming approach will be demonstrated using an infinite elastic solid in order to predict the vibration response of a prismatic section within the solid.

2 Basic relationships

2.1 The field in an infinite solid

The medium is an elastic, homogeneous, isotropic solid of mass density ρ, Young's modulus E and Poisson's factor ν. Harmonic motion at a frequency ω will be assumed; the common time factor $\exp(j\omega t)$ will be omitted. The displacement response vector $\mathbf{u}(t) = [u_1(t), u_2(t), u_3(t)]^t$ at a point $\mathbf{d} = [d_1, d_2, d_3]^t$ and the excitation force vector $\mathbf{f}(t) = [f_1(t), f_2(t), f_3(t)]]^t$ at a point $\mathbf{e} = [e_1, e_2, e_3]^t$ will be fully represented by their complex amplitudes: $\mathbf{U} = [U_1, U_2, U_3]^t$ and $\mathbf{F} = [F_1, F_2, F_3]^t$ respectively:

$$\mathbf{U} = \mathbf{G}(\mathbf{d}, \mathbf{e})\mathbf{F} \tag{1}$$

Here **G** stands for the 3×3 Green's function for the solid, [4]:

$$G_{mn} = \frac{\xi^p_{mn} + \xi^s_{mn}}{4\pi\rho\omega^2}, \quad m,n = 1,2,3 \tag{2}$$

with

$$\begin{aligned}
\xi^p_{mn} &= \frac{e^{jk_p r}}{r}\left[k_p^2\gamma_{mn} + (3\gamma_{mn} - \delta_{mn})\left(\frac{jk_p}{r} - \frac{1}{r^2}\right)\right] \\
\xi^s_{mn} &= \frac{e^{jk_s r}}{r}\left[k_s^2(\delta_{mn} - \gamma_{mn}) - (3\gamma_{mn} - \delta_{mn})\left(\frac{jk_s}{r} - \frac{1}{r^2}\right)\right] \\
r &= |\mathbf{d} - \mathbf{e}|, \quad \gamma_{mn} = \frac{(d_m - e_m)(d_n - e_n)}{r^2}, \quad k_p = \frac{\omega}{c_p}, \quad k_s = \frac{\omega}{c_s}
\end{aligned} \tag{2a}$$

The symbols stand for: δ-Kronecker delta, c_p - speed of dilatational waves, c_s – speed of shear waves.

Using the differential relationship between stress and displacement, [5], the stress tensor in the point **d** can be expressed in terms of displacement derivatives. By denoting strain components by $u_{mn} = \partial u_m/\partial x_n$ and assuming summation over repeating indices the components of stress tensor read:

$$\sigma_{mn} = \frac{E}{1+\nu}\left(u_{mn} + \frac{\nu}{1-2\nu}u_{ii}\delta_{mn}\right) \tag{3}$$

The boundary conditions will be expressed in terms of displacements and stresses at the contour surface of the body section considered. Eqs. 1-3 provide thus the mathematical background of the technique.

2.2 The model

The contour of the segment to be subjected to the required boundary conditions is identical to the physical surface of the modelled body. The number and the positions of control points on the contour and of the secondary sources around it need to be selected. Unfortunately the positions of these points do not result from any explicit physical considerations and the choice of positions has to be done by intuition or by a convenient search procedure.

Once the C control positions and S secondary positions have been selected the strengths of secondary sources can be obtained in a rather straightforward way. Assuming that the number of field variables which define the boundary conditions per point is B the following procedure may be applied:

- Define the boundary conditions via either displacements, stresses or both at the control points. E.g. if the boundary variables are surface stresses, three stress components have to be taken into account per each control point: the out-of-plane normal stress and two in-plane shear stresses. If instead the variables are the displacements, there will be three displacement components per boundary point. Thus in both cases $B = 3$.
- Specify the targeted values of boundary variables. The targeted values can be arranged into a vector **T** the size of which is thus BC. E.g. if the body has free boundaries, the three components of surface stresses will have to vanish across the contour surface. If instead the boundaries are clamped the three displacement components per boundary point have to vanish. In both cases the **T** vector will be zero.
- Compute the values of the boundary variables at all the control points due to the primary source. A vector of primary boundary variables $\mathbf{V}_0$ can be thus formed, the length of which is the product between the number of control points and the number of boundary variables per point, i.e. BC.
- Compute the transfer functions between the boundary variables and all of the secondary sources. Since there are S secondary sources and three force components per source a transfer matrix **H** is thus obtained of size $BC \times 3S$.
- Compute the strengths of secondary sources set in a vector **Q** through the relationship:

$$\mathbf{V}_0 + \mathbf{HQ} = \mathbf{T} \tag{4}$$

The vector **Q** is of size $3S$. It contains the three orthogonal complex force amplitudes per each secondary point. Once the vector **Q** has been found, the response of the vibrating object either in its interior or at its surface can be simply obtained by superposing the fields created by primary and secondary excitations.

The technique will be demonstrated via the next example.

3 Example

A simple example will demonstrate the principle of the method. The object considered is a beam of moderate thickness. The beam will be driven by a normal force. The choice of a beam as a demonstrator was made in view of its simplicity and the well-known dynamic behaviour. A classical Euler-Bernoulli solution will be used for comparing it with that obtained by the boundary forming approach.

3.1 Input parameters

The beam is made of steel: $E = 2\times10^{11}$ Pa, $\rho = 7800$ kg/m^3, $\nu = 0.3$. The dimensions are: length 0.6m, width 12cm, thickness 2cm.

In the present case the contour surface, identical to the surface of the beam, is a simple parallelepiped. The spacing between control points was selected at 5mm, which resulted in 6800 control points. The secondary sources were placed across two surfaces of shape similar to that of the contour surface but displaced from it outwards by 25mm and 100 mm with the spacing between source points of 20 and 50mm respectively.

The selected positions and spacing between the secondary sources produced the total number of 1274 source points. The layout of different points is shown on Fig. 2.

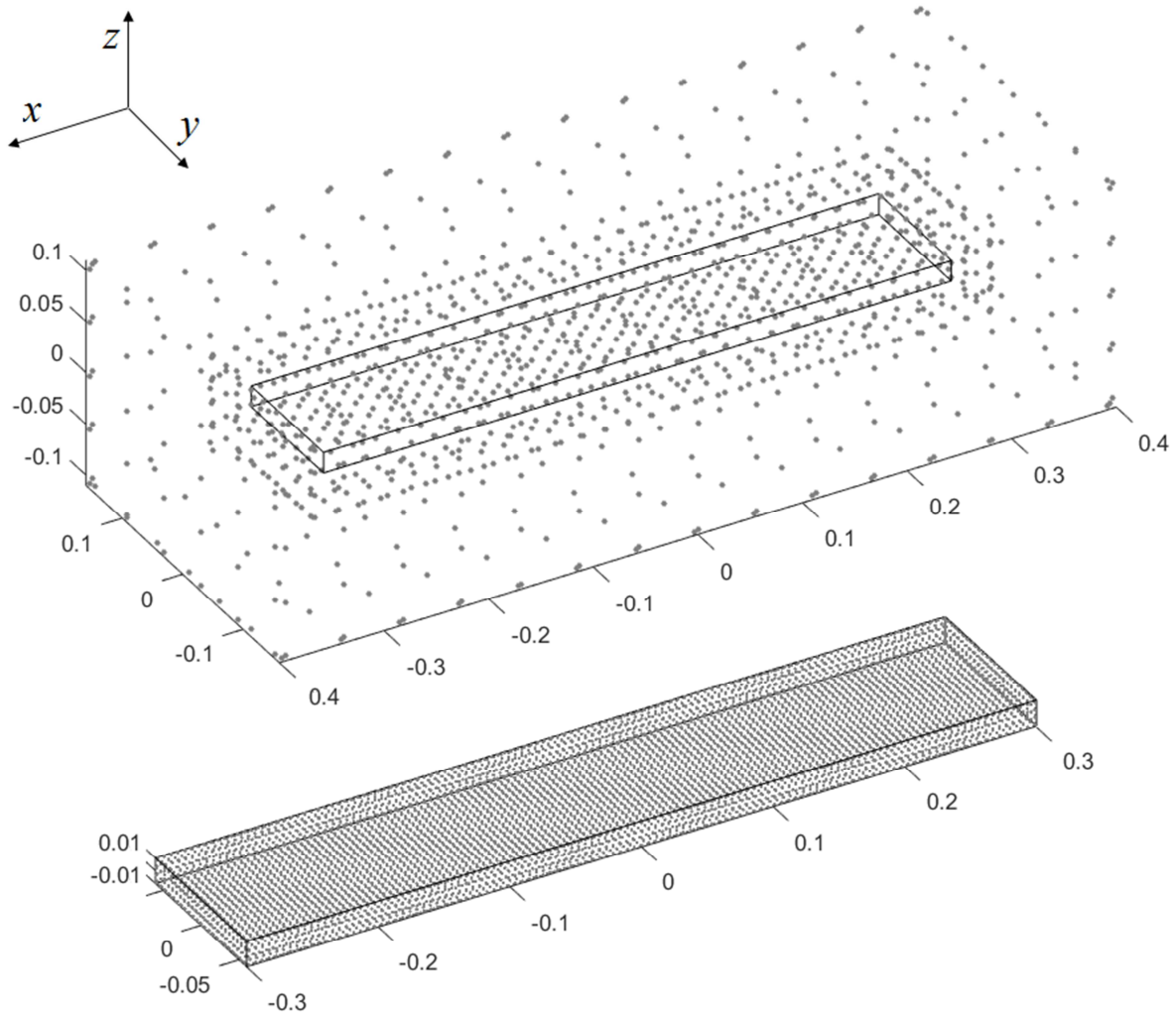


Figure 2. Secondary source points (top) and control points (bottom) of the beam model.

The selected parameters of the model, i.e. $C = 6800$ and $S = 1274$, resulted in a system matrix **H**, Eq. (4), of size $3C \times 3S = 20400 \times 3822$. In order to obtain the source strengths **Q**, i.e. the complex amplitudes of 3 force components at each point, the matrix **H** has to be inverted. In view of the problem being overdetermined, the inversion had to be replaced by pseudo-inversion. It has been already found in the resolution of similar problems, such as shown in [2], that the over-determination in the computation of source strengths gives much more accurate results than the application of strictly determined conditions, resulting is a square system matrix $BC = 3S$.

3.2 Results

Free-free boundary conditions were applied, known to be the most difficult ones to model using analytical techniques. In order to validate the results obtained by the boundary forming approach, the classical Euler-Bernoulli model was employed to provide a comparative solution. Using this model the result for a free-free beam driven by a normal point force was obtained in closed form. The classical model is based on simplifications which hold only if the beam thickness is much smaller than the wavelength.

The excitation was provided by a point force located lengthwise at 10cm from the left beam edge and in the axis of lateral symmetry. In the boundary forming model the excitation was taken to act in the middle of beam height. The force amplitude and the material loss factor were taken 1kN and 1% respectively.

Figure 3 shows the maps of the instantaneous normal displacement of the upper beam surface obtained by two models at two frequencies: 500Hz and 1kHz. At 500 Hz the classical model produces a result almost identical to the boundary forming one. On the contrary, at 1 kHz the two results visibly diverge.

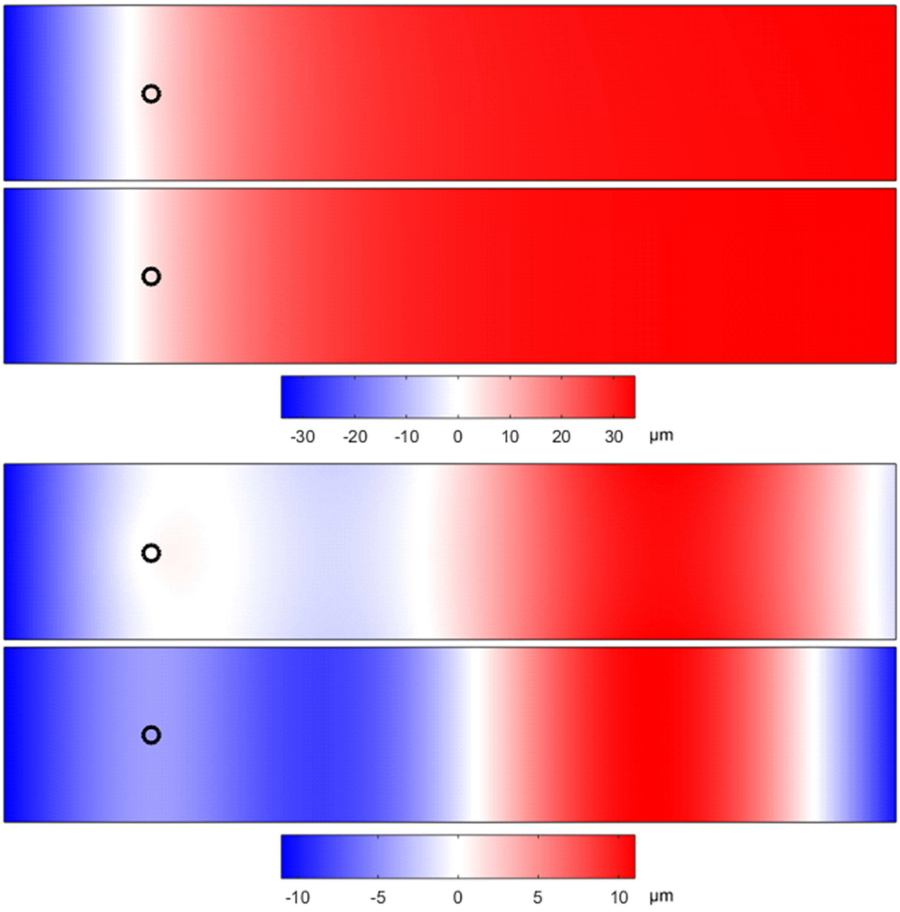


Figure 3. Instantaneous beam displacement. Top: 500 Hz, bottom: 1 kHz. Upper map: boundary forming model; lower map: Euler-Bernoulli model. Circle: excitation force.

Figure 4 shows the effect of the lateral offset of driving point on vibration distribution across the beam surface at 1kHz. The result was obtained by the boundary forming approach only since the classical model cannot provide analytical solution for this case. Not shown here are the displacements of beam sides which are distributed in a non-uniform manner, as expected.

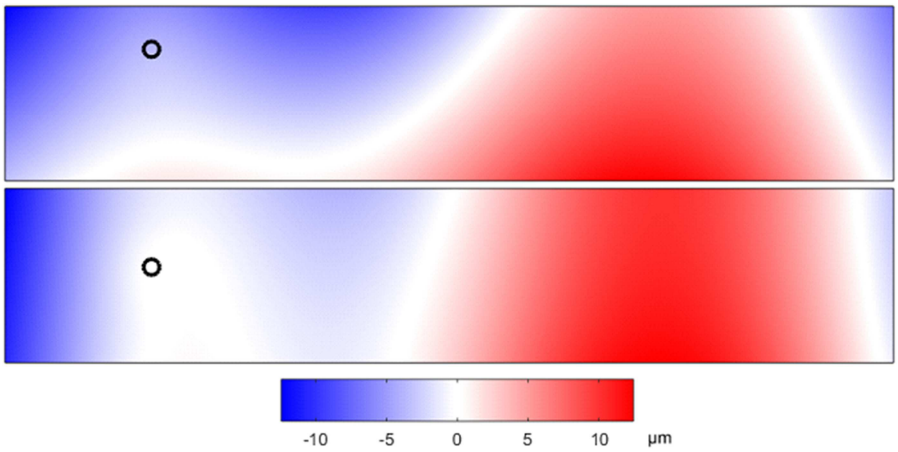


Figure 4. Instantaneous beam displacement by the boundary forming model. Lateral offset of driving point in width percentage: lower map 5%; upper map 25%. Frequency 1kHz.

4 Conclusions

The boundary forming approach, applied to the vibration of an elastic body, has been validated via the example of a free-free beam. The approach uses the analytical solution to the point force excitation of an infinite elastic solid. The validation was done by comparing the results of forced vibration obtained in two ways: by a 3D boundary forming model of a slender parallelepipedic body and by the classical Euler-Bernoulli model of the same body considered to be a beam vibrating in flexure. Good matching was obtained at a sufficiently low frequency at which the classical model provides satisfactory results.

References

[1] G. Pavić, *Hybrid vibration modelling of structures using analytical formulations*, *Proceedings of International Conference on Structural Dynamics Modelling, Funchal, Portugal, 2002 June 3-5*, pp. 25-32.

[2] G. Pavić, *Analytical modelling of flexural vibrations of arbitrary flat plates by boundary forming approach*, Journal of Sound and Vibration, Vol. 346, (2015), pp. 376-401.

[3] D. Placko, T. Kundu (editors), *DPSM for modelling engineering problems*, Wiley Interscience, Hoboken (2007).

[4] A. K. Mal, S. J. Singh, *Deformation of Elastic Solids*, Prentice Hall, Englewood Cliffs (1991).

[5] L. D. Landau, E. M. Lifshitz, *Theory of Elasticity*, Pergamon Press, Oxford, (1970).

Experimental-analytical state-space synthesis of passenger car components

A. Bylin [1,2], **M. Gibanica** [1,2], **T.J.S. Abrahamsson** [1]
[1] Mechanics and Maritime Sciences, Chalmers University of Technology,
Hörsalsvägen 7A, SE-412 96 Göteborg, Sweden

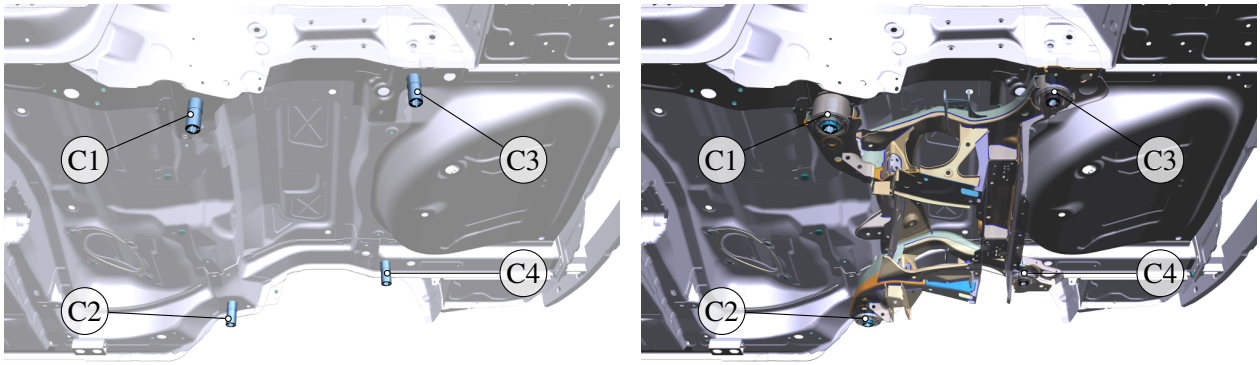
[2] Volvo Car Corporation, SE-405 31 Göteborg, Sweden
e-mail: **mladen.gibanica@chalmers.se**

Abstract
In this paper an experimental model of a Volvo XC90 body-in-white and a finite element model of a rear subframe are coupled for vibration assessment using a state-space synthesis method. This problem is challenging due to the complex structures considered. They are exhibiting high modal densities, high damping and the coupling is through four rubber bushings. The models are connected through four virtual points created at each coupling position. The state-space synthesis method relies on a system identification procedure for the experimental model, which in itself pose a significant challenge for the modally dense body-in-white. In this paper a newly proposed system identification technique focusing not to the least on direct accelerances, based on a subspace state-space method, is used. It also aims to fulfil physically motivated constraints. Results from the coupled system are shown to agree well with experimental data of the system assembly, and the method outperforms a finite element based coupling.

1 Introduction

The noise and vibration characteristics of a car are very important factors for customers. To understand the noise and vibration problems simulation tools are used, mainly based on finite element (FE) models, along with experimental data. Many times the simulation models (also denoted analytical models) have poor predictive capability, which is especially true for very complex models such as the body-in-white (BIW). One possibility to improve the analytical models is to use FE model updating, e.g. [1]. The updating procedure assumes that experimental data of the model are available. For smaller components, model updating can provide physical insight into uncertain parameters and it is many times possible to improve the models significantly. However, for very complex systems, such as the BIW, model updating can be very time consuming. Also, the parameter space can be very large possibly leading to poor physical insight after update is done. Synthesis of analytical models with mixed predictive capability is expected to yield poor results of the coupled system. Therefore, there is an interest in experimental-analytical substructuring techniques where hard-to-model components, such as the BIW, can instead be modelled from experimental data and coupled to analytical components that are more simple to model accurately. It is assumed that the experimental model represent the true system better than could be obtained with an updated FE model. Therefore the experimental-analytical synthesised system is expected to give better predictive capability than a purely analytical system.

Many different methods for substructuring exist. Component mode synthesis (CMS) [16] methods are common in analytical substructuring, but less suited for experimental substructuring. Frequency response function (FRF) based substructuring methods [12] have been developed mainly for experimental substructuring. Usually FRFs are obtained from measurements and these can then directly be used in a synthesis. In practice



(a) Attached cylinder placement on BIW

(b) Subframe BIW assembly

Figure 1: Cylinder placement on the four coupling locations on the BIW in (a) and the subframe coupled to the BIW in (b) with virtual point numbering

this is not so simple due to measurement noise in the measured FRFs, causing ill-conditioned FRF matrices, that need to be inverted. Another substructuring method is based on first order form, denoted state-space synthesis [19]. The rationale behind the method is that many times an identified system of the substructured system is desirable. It is easier to identify systems of the individual subcomponents compared to the more complex assembled system. Therefore, it is easier to assemble the identified systems of subcomponents to obtain a model of the substructured system. Furthermore, state of the art FRF system identification techniques, such as N4SID [15], identify systems on first order form. Hence these systems can directly be assembled without conversion to other forms.

There have been a few successful applications of the state-space method on fairly simple structures with simple connections, e.g. [17, 14]. In this paper the state-space synthesis method will be used on considerably more complicated components and connection types. The considered components are the BIW and rear subframe from a Volvo XC90 (2015). The BIW is modelled experimentally while the rear subframe is modelled with FE. The rear subframe FE model has been updated towards data of the same subframe used in the experimental system assembly, see [7]. The two components are connected through four rubber bushings, situated on the rear subframe FE model. On the BIW aluminium cylinders, resembling the inner bushing aluminium cylinders, are attached with the same bolt used to attach the subframe, see Figure 1. This makes the coupling region mass loaded and also allows for easier positioning of sensors. A virtual point is then created from three triaxial accelerometers and three orthogonal inputs on each of the four connection positions. System identification of the BIW experimental model was performed using a newly developed method which not to the least estimates the drive point channels with good accuracy, see [8, 9]. Such accuracy is essential in coupling applications. The substructured system is compared to measured data of the assembled BIW and rear subframe. The results are also compared to the synthesised FE counterpart, i.e. BIW modelled with FE. Further analysis of the considered problem can be found in [4].

This paper is organised as follows. First the state-space synthesis theory is restated in Section 2 followed by the system identification method and the virtual point transformation used in Sections 3 and 4, respectively. In Section 5 the FE and experimentally derived models are explained. Section 6 presents the results and Section 7 concludes the paper.

2 State-space synthesis

A linear time-invariant system of some component (s) can be written on first order form as

$$\dot{\boldsymbol{x}}^{(s)}(t) = \boldsymbol{A}^{(s)}\boldsymbol{x}^{(s)}(t) + \boldsymbol{B}^{(s)}\boldsymbol{u}^{(s)}(t) \tag{1a}$$

$$\boldsymbol{y}^{(s)}(t) = \boldsymbol{C}^{(s)}\boldsymbol{x}^{(s)}(t) + \boldsymbol{D}^{(s)}\boldsymbol{u}^{(s)}(t) \tag{1b}$$

where $\boldsymbol{A}^{(s)} \in \mathbb{R}^{n^{(s)}\times n^{(s)}}$, $\boldsymbol{B}^{(s)} \in \mathbb{R}^{n^{(s)}\times n_{\mathrm{u}}^{(s)}}$, $\boldsymbol{C}^{(s)} \in \mathbb{R}^{n_{\mathrm{y}}^{(s)}\times n^{(s)}}$ and $\boldsymbol{D}^{(s)} \in \mathbb{R}^{n_{\mathrm{y}}^{(s)}\times n_{\mathrm{u}}^{(s)}}$ represent the state, input, displacement output and direct feedthrough matrices, respectively. Explicit time dependence will here on be dropped for brevity. Here $\boldsymbol{x}^{(s)} \in \mathbb{R}^{n^{(s)}\times 1}$ is the state vector, $\boldsymbol{u}^{(s)} \in \mathbb{R}^{n_{\mathrm{u}}^{(s)}\times 1}$ the input vector and $\boldsymbol{y}^{(s)} \in \mathbb{R}^{n_{\mathrm{y}}^{(s)}\times 1}$ the displacement output vector. A synthesis procedure for such systems with $\boldsymbol{D}^{(s)} = \boldsymbol{0}^{(s)}$ is presented in [19]. Assuming that $(s) = \{\mathrm{I}, \mathrm{II}\}$ the system input and output vectors are partitioned as

$$\boldsymbol{y}^{(s)} = \begin{Bmatrix} \boldsymbol{y}_{\mathrm{c}}^{(s)} \\ \boldsymbol{y}_{\mathrm{b}}^{(s)} \end{Bmatrix} \quad \text{and} \quad \boldsymbol{u}^{(s)} = \begin{Bmatrix} \boldsymbol{u}_{\mathrm{c}}^{(s)} \\ \boldsymbol{u}_{\mathrm{b}}^{(s)} \end{Bmatrix} \tag{2}$$

where $\boldsymbol{y}_{\mathrm{c}}^{(s)}, \boldsymbol{u}_{\mathrm{c}}^{(s)} \in \mathbb{R}^{n_{\mathrm{c}}^{(s)}\times 1}$ represent the system outputs and inputs used in coupling. Further, $\boldsymbol{y}_{\mathrm{b}}^{(s)}$ and $\boldsymbol{u}_{\mathrm{b}}^{(s)}$ represent the remaining system outputs and inputs not used in the coupling. Subscripts c and b denote coupling and non-coupling degrees-of-freedom (DOFs), respectively. Arranging the coupling DOFs in the same order for both subsystem the response and excitation of the synthesised system can be written as

$$\begin{Bmatrix} \boldsymbol{y}_{\mathrm{c}}^{\mathrm{I}} \\ \boldsymbol{y}_{\mathrm{c}}^{\mathrm{II}} \end{Bmatrix} = \begin{bmatrix} \boldsymbol{I} \\ \boldsymbol{I} \end{bmatrix} \bar{\boldsymbol{y}}_{\mathrm{c}} \quad \text{and} \quad \bar{\boldsymbol{u}}_{\mathrm{c}} = \begin{bmatrix} \boldsymbol{I} & \boldsymbol{I} \end{bmatrix} \begin{Bmatrix} \boldsymbol{u}_{\mathrm{c}}^{\mathrm{I}} \\ \boldsymbol{u}_{\mathrm{c}}^{\mathrm{II}} \end{Bmatrix}. \tag{3}$$

Before coupling, the system in (1) must be transformed to coupling form using the transformation

$$\tilde{\boldsymbol{x}}^{(s)} = \boldsymbol{T}^{(s)}\boldsymbol{x}^{(s)} = \begin{Bmatrix} \dot{\boldsymbol{y}}_{\mathrm{c}}^{(s)} \\ \boldsymbol{y}_{\mathrm{c}}^{(s)} \\ \boldsymbol{x}_{\mathrm{b}}^{(s)} \end{Bmatrix}. \tag{4}$$

The transformation matrix $\boldsymbol{T}^{(s)}$ is initialised with

$$\boldsymbol{T}_0^{(s)} = \begin{bmatrix} \boldsymbol{C}_{\mathrm{c}}^{(s)}\boldsymbol{A}^{(s)} \\ \boldsymbol{C}_{\mathrm{c}}^{(s)} \\ \boldsymbol{N}^{(s)} \end{bmatrix} \triangleq \begin{bmatrix} \boldsymbol{T}_1^{(s)} \\ \boldsymbol{T}_2^{(s)} \\ \boldsymbol{T}_{0,3}^{(s)} \end{bmatrix} \tag{5}$$

where $\boldsymbol{Z}_0^{(s)} = \boldsymbol{T}_0^{(s)^{-1}}$ and then

$$\boldsymbol{T}^{(s)} = \begin{bmatrix} \boldsymbol{C}_{\mathrm{c}}^{(s)}\boldsymbol{A}^{(s)} \\ \boldsymbol{C}_{\mathrm{c}}^{(s)} \\ \boldsymbol{N}^{(s)}\left(\boldsymbol{I}^{(s)} - \boldsymbol{A}^{(s)}\boldsymbol{Z}_{0,1}^{(s)}\boldsymbol{C}_{\mathrm{c}}^{(s)}\right) \end{bmatrix} \triangleq \begin{bmatrix} \boldsymbol{T}_1^{(s)} \\ \boldsymbol{T}_2^{(s)} \\ \boldsymbol{T}_3^{(s)} \end{bmatrix} \tag{6a}$$

$$\boldsymbol{Z}^{(s)} = \boldsymbol{T}^{(s)^{-1}} \triangleq \begin{bmatrix} \boldsymbol{Z}_1^{(s)} & \boldsymbol{Z}_2^{(s)} & \boldsymbol{Z}_3^{(s)} \end{bmatrix}. \tag{6b}$$

Here $\boldsymbol{N}^{(s)}$ is an arbitrarily selected subspace of the nullspace of $\boldsymbol{B}_{\mathrm{c}}^{(s)}$ such that $\boldsymbol{N}^{(s)}\boldsymbol{B}_{\mathrm{c}}^{(s)} = \boldsymbol{0}^{(s)}$ and $\boldsymbol{T}^{(s)}$ is non-singular. Matrices $\boldsymbol{C}_{\mathrm{c}}^{(s)}$ and $\boldsymbol{B}_{\mathrm{c}}^{(s)}$ are the partitions of $\boldsymbol{C}^{(s)}$ and $\boldsymbol{B}^{(s)}$ pertinent to output and input at

the coupling DOFs, respectively. It is then possible to transform $\boldsymbol{A}^{(s)}$, $\boldsymbol{B}^{(s)}$ and $\boldsymbol{C}^{(s)}$ to coupling form

$$\tilde{\boldsymbol{A}}^{(s)} = \boldsymbol{T}^{(s)}\boldsymbol{A}^{(s)}{\boldsymbol{T}^{(s)}}^{-1} \triangleq \begin{bmatrix} \boldsymbol{A}_{\mathrm{vv}}^{(s)} & \boldsymbol{A}_{\mathrm{vd}}^{(s)} & \boldsymbol{A}_{\mathrm{vb}}^{(s)} \\ \boldsymbol{I}^{(s)} & \boldsymbol{0}^{(s)} & \boldsymbol{0}^{(s)} \\ \boldsymbol{0}^{(s)} & \boldsymbol{A}_{\mathrm{bd}}^{(s)} & \boldsymbol{A}_{\mathrm{bb}}^{(s)} \end{bmatrix} \tag{7a}$$

$$\tilde{\boldsymbol{B}}^{(s)} = \boldsymbol{T}^{(s)}\boldsymbol{B}^{(s)} \triangleq \begin{bmatrix} \boldsymbol{B}_{\mathrm{vv}}^{(s)} & \boldsymbol{B}_{\mathrm{vb}}^{(s)} \\ \boldsymbol{0}^{(s)} & \boldsymbol{0}^{(s)} \\ \boldsymbol{0}^{(s)} & \boldsymbol{B}_{\mathrm{bb}}^{(s)} \end{bmatrix} \tag{7b}$$

$$\tilde{\boldsymbol{C}}^{(s)} = \boldsymbol{C}^{(s)}{\boldsymbol{T}^{(s)}}^{-1} \triangleq \begin{bmatrix} \boldsymbol{0}^{(s)} & \boldsymbol{I}^{(s)} & \boldsymbol{0}^{(s)} \\ \boldsymbol{C}_{\mathrm{bv}}^{(s)} & \boldsymbol{C}_{\mathrm{bd}}^{(s)} & \boldsymbol{C}_{\mathrm{bb}}^{(s)} \end{bmatrix}. \tag{7c}$$

Using Eq. (3) the synthesised system is then

$$\begin{Bmatrix} \ddot{\bar{\boldsymbol{y}}}_{\mathrm{c}} \\ \dot{\bar{\boldsymbol{y}}}_{\mathrm{c}} \\ \dot{\boldsymbol{x}}_{\mathrm{b}}^{\mathrm{I}} \\ \dot{\boldsymbol{x}}_{\mathrm{b}}^{\mathrm{II}} \end{Bmatrix} = \begin{bmatrix} \bar{\boldsymbol{A}}_{\mathrm{vv}} & \bar{\boldsymbol{A}}_{\mathrm{vd}} & \bar{\boldsymbol{A}}_{\mathrm{vb}}^{\mathrm{I}} & \bar{\boldsymbol{A}}_{\mathrm{vb}}^{\mathrm{II}} \\ \boldsymbol{I} & \boldsymbol{0} & \boldsymbol{0} & \boldsymbol{0} \\ \boldsymbol{0} & \boldsymbol{A}_{\mathrm{bd}}^{\mathrm{I}} & \boldsymbol{A}_{\mathrm{bb}}^{\mathrm{I}} & \boldsymbol{0} \\ \boldsymbol{0} & \boldsymbol{A}_{\mathrm{bd}}^{\mathrm{II}} & \boldsymbol{0} & \boldsymbol{A}_{\mathrm{bb}}^{\mathrm{II}} \end{bmatrix} \begin{Bmatrix} \dot{\bar{\boldsymbol{y}}}_{\mathrm{c}} \\ \bar{\boldsymbol{y}}_{\mathrm{c}} \\ \boldsymbol{x}_{\mathrm{b}}^{\mathrm{I}} \\ \boldsymbol{x}_{\mathrm{b}}^{\mathrm{II}} \end{Bmatrix} + \begin{bmatrix} \bar{\boldsymbol{B}}_{\mathrm{vv}} & \bar{\boldsymbol{B}}_{\mathrm{vb}}^{\mathrm{I}} & \bar{\boldsymbol{B}}_{\mathrm{vb}}^{\mathrm{II}} \\ \boldsymbol{0} & \boldsymbol{0} & \boldsymbol{0} \\ \boldsymbol{0} & \boldsymbol{B}_{\mathrm{bb}}^{\mathrm{I}} & \boldsymbol{0} \\ \boldsymbol{0} & \boldsymbol{0} & \boldsymbol{B}_{\mathrm{bb}}^{\mathrm{II}} \end{bmatrix} \begin{Bmatrix} \bar{\boldsymbol{u}}_{\mathrm{c}} \\ \boldsymbol{u}_{\mathrm{b}}^{\mathrm{I}} \\ \boldsymbol{u}_{\mathrm{b}}^{\mathrm{II}} \end{Bmatrix} \tag{8a}$$

$$\begin{Bmatrix} \bar{\boldsymbol{y}}_{\mathrm{c}} \\ \boldsymbol{x}_{\mathrm{b}}^{\mathrm{I}} \\ \boldsymbol{x}_{\mathrm{b}}^{\mathrm{II}} \end{Bmatrix} = \begin{bmatrix} \boldsymbol{0} & \boldsymbol{I} & \boldsymbol{0} & \boldsymbol{0} \\ \boldsymbol{C}_{\mathrm{bv}}^{\mathrm{I}} & \boldsymbol{C}_{\mathrm{bd}}^{\mathrm{I}} & \boldsymbol{C}_{\mathrm{bb}}^{\mathrm{I}} & \boldsymbol{0} \\ \boldsymbol{C}_{\mathrm{bv}}^{\mathrm{II}} & \boldsymbol{C}_{\mathrm{bd}}^{\mathrm{II}} & \boldsymbol{0} & \boldsymbol{C}_{\mathrm{bb}}^{\mathrm{II}} \end{bmatrix} \begin{Bmatrix} \dot{\bar{\boldsymbol{y}}}_{\mathrm{c}} \\ \bar{\boldsymbol{y}}_{\mathrm{c}} \\ \boldsymbol{x}_{\mathrm{b}}^{\mathrm{I}} \\ \boldsymbol{x}_{\mathrm{b}}^{\mathrm{II}} \end{Bmatrix} \tag{8b}$$

with

$$\boldsymbol{K} = \left(\boldsymbol{B}_{\mathrm{vv}}^{\mathrm{I}} + \boldsymbol{B}_{\mathrm{vv}}^{\mathrm{II}}\right)^{-1} \tag{9a}$$

$$\bar{\boldsymbol{A}}_{\mathrm{vv}} = \boldsymbol{B}_{\mathrm{vv}}^{\mathrm{I}}\boldsymbol{K}\boldsymbol{A}_{\mathrm{vv}}^{\mathrm{II}} + \boldsymbol{B}_{\mathrm{vv}}^{\mathrm{II}}\boldsymbol{K}\boldsymbol{A}_{\mathrm{vv}}^{\mathrm{I}} \tag{9b}$$

$$\bar{\boldsymbol{A}}_{\mathrm{vd}} = \boldsymbol{B}_{\mathrm{vv}}^{\mathrm{I}}\boldsymbol{K}\boldsymbol{A}_{\mathrm{vd}}^{\mathrm{II}} + \boldsymbol{B}_{\mathrm{vv}}^{\mathrm{II}}\boldsymbol{K}\boldsymbol{A}_{\mathrm{vd}}^{\mathrm{I}} \tag{9c}$$

$$\bar{\boldsymbol{A}}_{\mathrm{vb}}^{\mathrm{I}} = \boldsymbol{B}_{\mathrm{vv}}^{\mathrm{II}}\boldsymbol{K}\boldsymbol{A}_{\mathrm{vb}}^{\mathrm{I}} \tag{9d}$$

$$\bar{\boldsymbol{A}}_{\mathrm{vb}}^{\mathrm{II}} = \boldsymbol{B}_{\mathrm{vv}}^{\mathrm{I}}\boldsymbol{K}\boldsymbol{A}_{\mathrm{vb}}^{\mathrm{II}} \tag{9e}$$

$$\bar{\boldsymbol{B}}_{\mathrm{vv}} = \boldsymbol{B}_{\mathrm{vv}}^{\mathrm{I}}\boldsymbol{K}\boldsymbol{B}_{\mathrm{vv}}^{\mathrm{II}} \tag{9f}$$

$$\bar{\boldsymbol{B}}_{\mathrm{vb}}^{\mathrm{I}} = \boldsymbol{B}_{\mathrm{vv}}^{\mathrm{II}}\boldsymbol{K}\boldsymbol{B}_{\mathrm{vb}}^{\mathrm{I}} \tag{9g}$$

$$\bar{\boldsymbol{B}}_{\mathrm{vb}}^{\mathrm{II}} = \boldsymbol{B}_{\mathrm{vv}}^{\mathrm{I}}\boldsymbol{K}\boldsymbol{B}_{\mathrm{vb}}^{\mathrm{II}}. \tag{9h}$$

For the synthesis procedure to work some physical requirements exist on the models [19]. From Newton's second law it follows that there is no direct relation between force input and displacement and velocity output. Therefore, the direct feedthrough matrix $\boldsymbol{D}^{(s)} = \boldsymbol{0}^{(s)}$ as the utilized systems must be on displacement output form. It also follows that $\boldsymbol{C}^{(s)}\boldsymbol{B}^{(s)} = \boldsymbol{0}^{(s)}$. Furthermore, the system must be reciprocal meaning that a partition of the FRF matrix with collocated and co-oriented sensor-actuator pairs should be symmetric. Also, the system must be stable and passive. Passivity will not be treated here, but has been addressed in [13].

For a mechanical system (s) modelled with FE and with $\boldsymbol{q}^{(s)} \in \mathbb{R}^{m^{(s)}\times 1}$ the physical DOF vector a common form of the state vector is $\boldsymbol{x}^{(s)} = \left\{ {\boldsymbol{q}^{(s)}}^{\mathrm{T}}, {\dot{\boldsymbol{q}}^{(s)}}^{\mathrm{T}} \right\}^{\mathrm{T}}$. Then the state, input and displacement output matrices are

$$\boldsymbol{A}^{(s)} \triangleq \begin{bmatrix} \boldsymbol{0}^{(s)} & \boldsymbol{I}^{(s)} \\ -\boldsymbol{M}^{-1^{(s)}}\boldsymbol{K}^{(s)} & -\boldsymbol{M}^{-1^{(s)}}\boldsymbol{V}^{(s)} \end{bmatrix}, \quad \boldsymbol{B}^{(s)} \triangleq \begin{bmatrix} \boldsymbol{0}^{(s)} \\ \boldsymbol{M}^{-1^{(s)}}\boldsymbol{P}_{\mathrm{u}}^{(s)} \end{bmatrix}, \quad \boldsymbol{C}^{(s)} \triangleq \begin{bmatrix} \boldsymbol{P}_{\mathrm{y}}^{(s)} & \boldsymbol{0}^{(s)} \end{bmatrix} \tag{10}$$

where $\boldsymbol{M}^{(s)} \in \mathbb{R}^{m^{(s)}\times m^{(s)}}$, $\boldsymbol{V}^{(s)} \in \mathbb{R}^{m^{(s)}\times m^{(s)}}$ and $\boldsymbol{K}^{(s)} \in \mathbb{R}^{m^{(s)}\times m^{(s)}}$ represent the mass, damping and stiffness matrices, respectively. It follows that $n^{(s)} = 2m^{(s)}$. Furthermore, $\boldsymbol{P}_{\mathrm{u}}^{(s)} \in \mathbb{R}^{m^{(s)}\times n_{\mathrm{u}}^{(s)}}$ and

$\boldsymbol{P}_{\mathrm{y}}^{(s)} \in \mathbb{R}^{n_{\mathrm{y}}^{(s)} \times m^{(s)}}$ are input and output localisation matrices, respectively. Such a system obtained from first-principles fulfils the required conditions stated above, and is physical. Therefore no further action is required on such models. However for experimentally identified systems this is not necessarily true and constraints must be enforced for physically consistent systems. Below the superscript (s) will be dropped for brevity.

3 System identification

For successful coupling, accurate models must be obtained from the system identification. In this paper a state of the art system identification procedure N4SID [15] is used to obtain a state-space system from frequency response data. However, it has been observed [8] that the direct accelerances (or drive point channels) are often poorly estimated. Because these channels are used as coupling DOFs it is of great importance that they are well estimated. A procedure has been proposed in [8, 9] that significantly improves such channels by introducing a complementary residual mode above the frequency range of interest.

A receptance FRF matrix $\boldsymbol{H}^{\mathrm{R}}(\omega) \in \mathbb{C}^{n_{\mathrm{y}} \times n_{\mathrm{u}}}$ of an undamped system for a frequency $\omega \in [\underline{\omega}, \overline{\omega}]$ can be approximated in modal parameters for $j = 1, \ldots, n_{\mathrm{y}}$ and $k = 1, \ldots, n_{\mathrm{u}}$ as

$$H_{jk}^{\mathrm{R}}(\omega) \approx -\frac{1}{\omega^2 M_{jk}^{\mathrm{R}}} + \sum_{r=n_1}^{n_2} \frac{R_{jk}^{(r)}}{\omega_r^2 - \omega^2} + \frac{R_{jk}^{(\mathrm{S})}}{\omega_{\mathrm{S}}^2 - \omega^2} + \frac{R_{jk}^{(\mathrm{K})}}{\omega_{\mathrm{K}}^2 - \omega^2} \tag{11}$$

where ω_r is the eigenfrequency of the rth mode in ordered sequence and $R_{jk}^{(r)}$ the residue factor for mode r. Here M_{jk}^{R}, $R_{jk}^{(\mathrm{S})}$ and $R_{jk}^{(\mathrm{K})}$ are the residual mass and the complementary and stiffness residue factors. From [8] it is concluded that a good choice of $\omega_{\mathrm{S}} = 1.43\overline{\omega}$ and $\omega_{\mathrm{K}} \gg \overline{\omega}$.

It was proposed in [8, 9] that the N4SID algorithm be used on augmented FRF data where the residual influences M_{jk}^{R}, $R_{jk}^{(\mathrm{S})}$ and $R_{jk}^{(\mathrm{K})}$ had been removed from test data. The system containing only the three residuals is denoted the residual system. The N4SID identified system on augmented test data is then added in parallel to the residual system producing the sought $\{\boldsymbol{A}, \boldsymbol{B}, \boldsymbol{C}\}$. In a last step the $\boldsymbol{B}$ and $\boldsymbol{C}$ matrices were iteratively re-estimated to improve the model fit to data, further described below. The complementary residual ω_{S} was seen to greatly improve the identified model's drive point channels. However, for coupling applications the constraint $\boldsymbol{CB} = \boldsymbol{0}$ must hold, which is introduced in the procedure here. A state-space system can be transformed to the frequency domain, with discrete frequencies $\Omega_m \in \left[\underline{\Omega}, \overline{\Omega}\right]$ for $m = 1, \ldots, M$, as

$$\boldsymbol{G}(\Omega_m) = \boldsymbol{C}\left(i\Omega_m \boldsymbol{I} - \boldsymbol{A}\right)^{-1} \boldsymbol{B} \triangleq \boldsymbol{C}\boldsymbol{Q}_m\boldsymbol{B} \in \mathbb{C}^{n_{\mathrm{y}} \times n_{\mathrm{u}}} \tag{12}$$

where $i^2 = -1$ defines the imaginary number i. Now a minimisation problem can be formulated with $\boldsymbol{H}_m^{\mathrm{R}} \triangleq \boldsymbol{H}^{\mathrm{R}}(\Omega_m)$

$$\underset{\substack{\boldsymbol{B},\boldsymbol{C} \\ \text{s.t. } \boldsymbol{CB}=\boldsymbol{0}}}{\arg\min} \sum_{m=1}^{M} \left\| \boldsymbol{H}_m^{\mathrm{R}} - \boldsymbol{C}\boldsymbol{Q}_m\boldsymbol{B} \right\|_{\mathrm{F}} \tag{13}$$

with $\|\cdot\|_{\mathrm{F}}$ the Frobenius norm. Note that the problem in (13) is bilinear, i.e. given that $\boldsymbol{A}$ and $\boldsymbol{B}$ are fixed, the problem is linear in $\boldsymbol{C}$. It is also linear in $\boldsymbol{B}$ if $\boldsymbol{A}$ and $\boldsymbol{C}$ are fixed. A sequential solution is shown to produce good results [10]. The constraint is enforced weakly and solved in a linear least-squares sense as

$$\boldsymbol{C}^{p+1} = \underset{\boldsymbol{C}}{\arg\min} \sum_{m=1}^{M} \left\| \begin{bmatrix} \boldsymbol{H}_m^{\mathrm{R}} & \boldsymbol{0} \end{bmatrix} - \boldsymbol{C} \begin{bmatrix} \boldsymbol{Q}_m\boldsymbol{B}^p & w\boldsymbol{B}^p \end{bmatrix} \right\|_{\mathrm{F}} \tag{14a}$$

$$\boldsymbol{B}^{p+1} = \underset{\boldsymbol{B}}{\arg\min} \sum_{m=1}^{M} \left\| \begin{bmatrix} \boldsymbol{H}_m^{\mathrm{R}} \\ \boldsymbol{0} \end{bmatrix} - \begin{bmatrix} \boldsymbol{C}^{p+1}\boldsymbol{Q}_m \\ w\boldsymbol{C}^{p+1} \end{bmatrix} \boldsymbol{B} \right\|_{\mathrm{F}} \tag{14b}$$

with w a weighting factor. These equations are iterated $p = 0, \ldots, P-1$ times until convergence is reached.

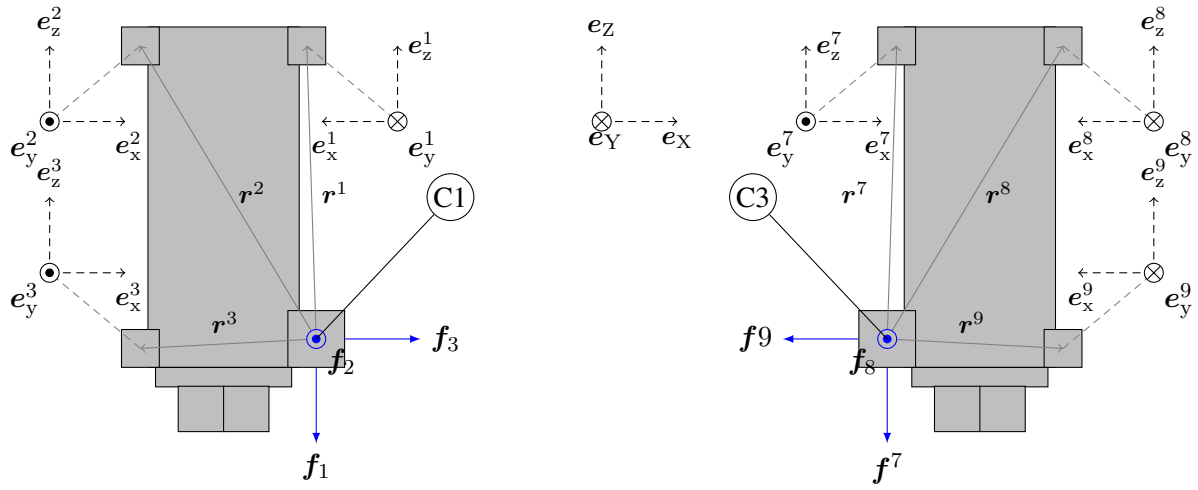


Figure 2: Virtual point (C1 and C3) transformation for two of the four cylinders. To the left (on the left side of the BIW point towards the front) is C1 and to the right C3, see Figure 5b. The global coordinate system is shown in the middle

4 Virtual point transformation

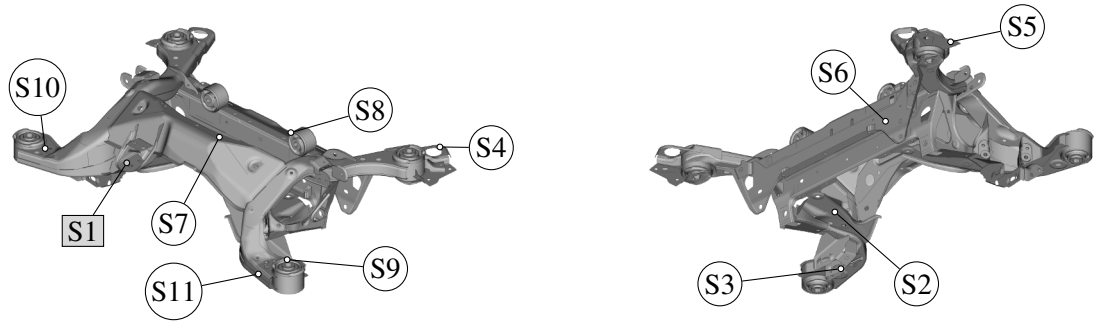
Many times it is hard to place sensors and actuators at the desired coupling position. It is also hard to measure rotations and apply pure moment excitation. Therefore, to make the coupling feasible, sensors and actuators can be placed around the coupling position and a 6 DOF virtual point created from these measured positions. This virtual point is then used in the synthesis. At least six accelerometers and actuators are needed to describe the motion of an arbitrary point that is rigidly connected to the accelerometers. These arbitrary points are denoted virtual points. Here the actuator positions coincide with the virtual points, further explained below. Three triaxial accelerometers are used at each of the four coupling positions. Hence an overdetermined system is obtained at each coupling position, which can be solved in a linear least-squares sense. One way of formulating this transformation is the virtual point transformation [18]. A schematic of two such transformations is shown in Figure 2. In that figure f denote force and it can be seen that three orthogonal force inputs are used. Two of the virtual points, C1 and C3, are marked in Figure 2. See Figures 1 and 5b for virtual point numbering.

For a triaxial accelerometer k, with the local output $\hat{\boldsymbol{y}}^k$, the motion $\boldsymbol{y}^v$ at the virtual point v can be expressed as

$$\begin{Bmatrix} \hat{y}^k_{\mathrm{x}} \\ \hat{y}^k_{\mathrm{y}} \\ \hat{y}^k_{\mathrm{z}} \end{Bmatrix} = \begin{bmatrix} e^k_{\mathrm{x,X}} & e^k_{\mathrm{x,Y}} & e^k_{\mathrm{x,Z}} \\ e^k_{\mathrm{y,X}} & e^k_{\mathrm{y,Y}} & e^k_{\mathrm{y,Z}} \\ e^k_{\mathrm{z,X}} & e^k_{\mathrm{z,Y}} & e^k_{\mathrm{z,Z}} \end{bmatrix} \begin{bmatrix} 1 & 0 & 0 & 0 & r^k_{\mathrm{Z}} & -r^k_{\mathrm{Y}} \\ 0 & 1 & 0 & -r^k_{\mathrm{Z}} & 0 & r^k_{\mathrm{X}} \\ 0 & 0 & 1 & r^k_{\mathrm{Y}} & -r^k_{\mathrm{X}} & 0 \end{bmatrix} \begin{Bmatrix} y^v_{\mathrm{X}} \\ y^v_{\mathrm{Y}} \\ y^v_{\mathrm{Z}} \\ y^v_{\Theta_{\mathrm{X}}} \\ y^v_{\Theta_{\mathrm{Y}}} \\ y^v_{\Theta_{\mathrm{Z}}} \end{Bmatrix} \triangleq \boldsymbol{E}^{k^{\mathrm{T}}} \overline{\boldsymbol{R}}^{kv} \boldsymbol{y}^v \triangleq \boldsymbol{R}^{kv} \boldsymbol{y}^v \quad (15)$$

where r^k_i is the distance from the virtual point v to the sensor k:s position in the global coordinate system. Here $\boldsymbol{e}^k$ defines the triaxial accelerometers direction of measurement. The left matrix $\boldsymbol{E}^{k^{\mathrm{T}}}$ is a transformation matrix from the global coordinate system to the local system of the triaxial accelerometers. For $k = 1, \ldots, K$ accelerometers the relation can be expressed as

$$\begin{Bmatrix} \hat{\boldsymbol{y}}^1 \\ \vdots \\ \hat{\boldsymbol{y}}^K \end{Bmatrix} = \begin{bmatrix} \boldsymbol{R}^{1v} \\ \vdots \\ \boldsymbol{R}^{Kv} \end{bmatrix} \boldsymbol{y}^v \triangleq \boldsymbol{R} \boldsymbol{y}^v. \quad (16)$$



(a) Top view (b) Bottom view

Figure 3: Top view of rear subframe in (a) and bottom view in (b), from [8]. Circle markings indicate accelerometer locations and the rectangular marking indicate a sensor and input force position (normal to the surface)

The transformation from the triaxial sensors local output $\hat{\boldsymbol{y}}$ to the virtual point v global output $\boldsymbol{y}^v$ is thus

$$\boldsymbol{y}^v = \left(\boldsymbol{R}^{\mathrm{T}}\boldsymbol{W}\boldsymbol{R}\right)^{-1}\boldsymbol{R}^{\mathrm{T}}\boldsymbol{W}\hat{\boldsymbol{y}} \tag{17}$$

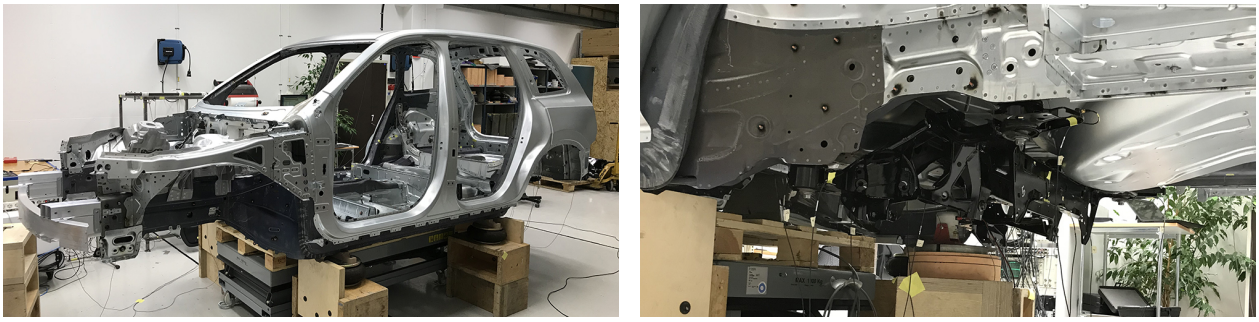
where $\boldsymbol{W}$ is a weighting matrix. It is necessary that $\boldsymbol{R}$ is full column rank, thus a minimum of six output channels are required. Worth mentioning is that two triaxial accelerometers with six channels are not sufficient since rotation around a straight line between the centre of the sensors cannot be detected by these accelerometers. In a similar manner the inputs can also be transformed to the same virtual point. However, this requires at least six inputs, as is explained in [18]. Here the virtual point is created at the location of force inputs, and therefore only outputs need to be transformed to this point. To expand the model for unmeasured inputs (moment inputs) at the virtual point the modal model is used. The modally based expansion is valid under the assumption of reciprocity. This requires that collocated input output pairs are known at the virtual point, see [2] for further details.

5 Models

Here the rear subframe FE model is explained followed by the experimental process and system identification procedure.

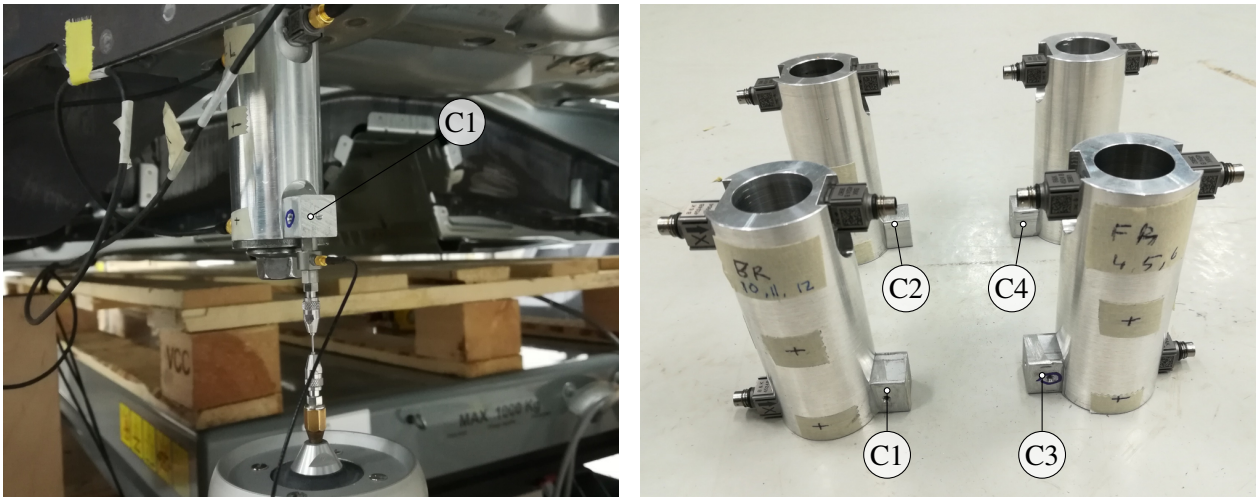
5.1 Rear subframe finite element model

The rear subframe is modelled with FE, and is shown in Figure 3. The subframe is connected to the BIW through four rubber bushings. In Figure 1 the connection is shown. Note that the innermost bushing cylinder, seen in that figure, has here been removed from the FE model because approximately the same cylinder is attached to the BIW in experiments to allow for easier sensor positioning. Note also that the coupling point is not located in the cylinder centres, see virtual point in Figure 2, and this is also reflected in the rear subframe FE model. Furthermore, the rear subframe has been studied extensively in [7]. In that paper the FE model was updated towards experimental data with focus on identifying each individual bushing stiffness parameter. In a second step other model parameters were updated to achieve a better overall model fit to data. Here the updated model is used in both the experimental-analytical and analytical coupling. Experimentally identified modal damping is used from that model for modes up to approximately 250 Hz and the remaining modes were assigned a damping of 0.5 %.



(a) BIW (b) Assembly

Figure 4: BIW in (a) and BIW and rear subframe assembly in (b)



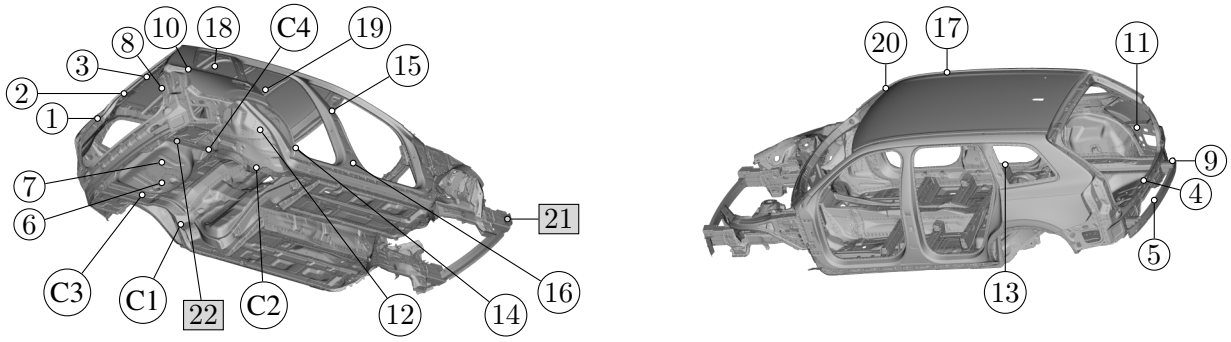
(a) Example of force input (b) Four cylinders with mounted accelerometers

Figure 5: Shaker excitation in (a) and accelerometer configuration on cylinders and virtual point numbering in (b)

5.2 Measurements

Vibration experiments were performed on the BIW and the BIW and rear subframe assembly, which are shown in Figure 4. In both scenarios the structures were supported on four soft air springs. The highest quasi-rigid body mode was at approximately 7 Hz while the first flexible mode was at 32 Hz, which is close to recommendations for a soft support system, see Ewins [5]. The measurements were performed using the open source AbraDAQ software [6]. Brüel & Kjær triaxial and uniaxial accelerometers were used, type 4524-B and 4507-B, respectively. The excitation force was measured using a Brüel & Kjær force transducer type 8203 with an IEPE converter 2647B. A shaker of Ling Dynamic Systems make and of type V201 was used as force input, with an approximately 5 mm long metal stinger.

For the BIW measurement a total of 12 triaxial sensors and 22 uniaxial accelerometers were used. All triaxial sensors were placed on the cylinders, seen in Figure 5b. The cylinders were mounted in this configuration on the BIW, see also Figure 1. The uniaxial sensors were placed on the BIW according to Figure 6. The structure was excited with 3 orthogonal force inputs at each cylinder resulting in 12 inputs. One such input is seen in Figure 5a. Further, two more force inputs were used for validation purpose, placed according to Figure 6, so that in total 14 inputs were had. In the BIW and rear subframe assembly measurement 10 triaxial and 1 uniaxial accelerometers were placed on the subframe, and 22 uniaxial accelerometers on the same BIW positions as in the BIW measurement. However, only the normal measurement direction was used in the analysis from the triaxial sensors. Force inputs were according to Figure 6 and Figure 3. Hence,



(a) Rear bottom view

(b) Side view

Figure 6: Rear bottom view of BIW in (a) and side view in (b). Circle markings indicate uniaxial accelerometer locations and rectangular markings indicate a sensor and input force position (normal to the surface)

two inputs were on the BIW (21 and 22) and one on the rear subframe (S1). The experimental procedure is further explained in [4].

5.3 Body-in-white experimental model

The coupling channels were first transformed on the raw FRF data to four virtual points with three translations and rotations each, see Figure 2. All channels from the three triaxial sensors for each coupling point were selected for the virtual point transformation. To impose reciprocity the corresponding FRF matrix partition was made symmetric on this data. The experimental model of the BIW was identified on this data with the procedure stated in Section 3. The considered frequency range was $\omega \in [30, 200]$ Hz. Within this range 136 modes were identified. However, data were collected up to 300 Hz and further 90 modes were identified in the frequency range $[200, 300]$ Hz. These modes were included in the used model. To increase the model fit further two residual modes, at $\omega_{\mathrm{S}} = 1.43\overline{\omega}$ and $\omega_{\mathrm{K}} \gg \overline{\omega}$ with $\overline{\omega} = 300$ Hz, for each input ($n_{\mathrm{u}} = 14$) above the considered frequency range were included. Also six rigid body modes were added to the system, taken from the FE model which accounted for the air springs boundary condition. The experimentally identified system consisted of $m = 260$ modes ($n = 520$ states). The model fit, according to the frequency response assurance criterion (FRAC) [11], for each channel can be seen in Figure 7. Here 1 (white) indicate perfect fit while numbers decreasing towards 0 indicate an increasingly bad fit. In that figure the horizontal axis represent outputs and the vertical axis inputs. On the horizontal axis $\{\mathrm{C1}, \mathrm{C2}, \mathrm{C3}, \mathrm{C4}\}$ indicate translation and rotation outputs $(\mathrm{X}, \mathrm{Y}, \mathrm{Z}, \Theta_{\mathrm{X}}, \Theta_{\mathrm{Y}}, \Theta_{\mathrm{Z}})$ while for the vertical axis only translation inputs $(\mathrm{X}, \mathrm{Y}, \mathrm{Z})$. From the procedure $\|\boldsymbol{CB}\|_2 \approx 10^{-13}$ which was good enough for the coupling form transformation to work. To extract rotational inputs from the identified model reciprocity is assumed. However, the identified model was not fully reciprocal outside the considered frequency range meaning that the expanded rotation inputs must be considered much poorer than the other channels.

In Figure 8 the receptance for one channel for the identified BIW (input 22 and output 6) is shown. It can be seen that the identified model fit is good over the whole frequency range.

6 Results

Here the experimental-analytical system with only translation DOFs coupled at the four coupling locations is denoted T while the system with translation and rotation DOFs coupled is denoted TR. The FE coupled system is denoted FE T and FE TR for coupled translation DOFs only and translation and rotation DOFs, respectively. The considered frequency range is $\omega \in [30, 200]$ Hz.

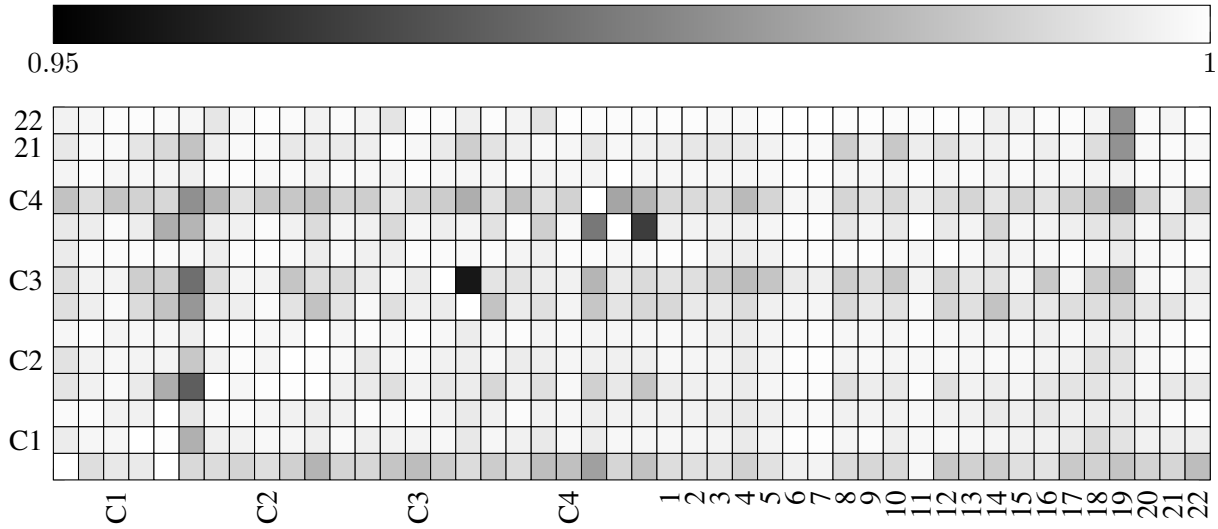


Figure 7: Identified model fit (FRAC) to test data for $\omega \in [30, 200]$ Hz

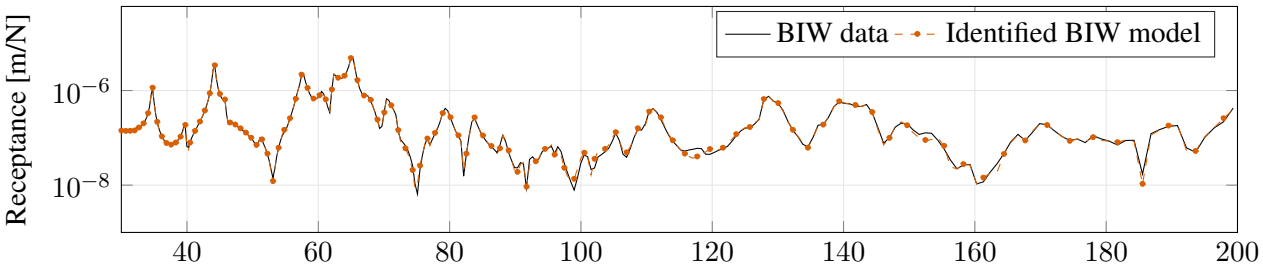
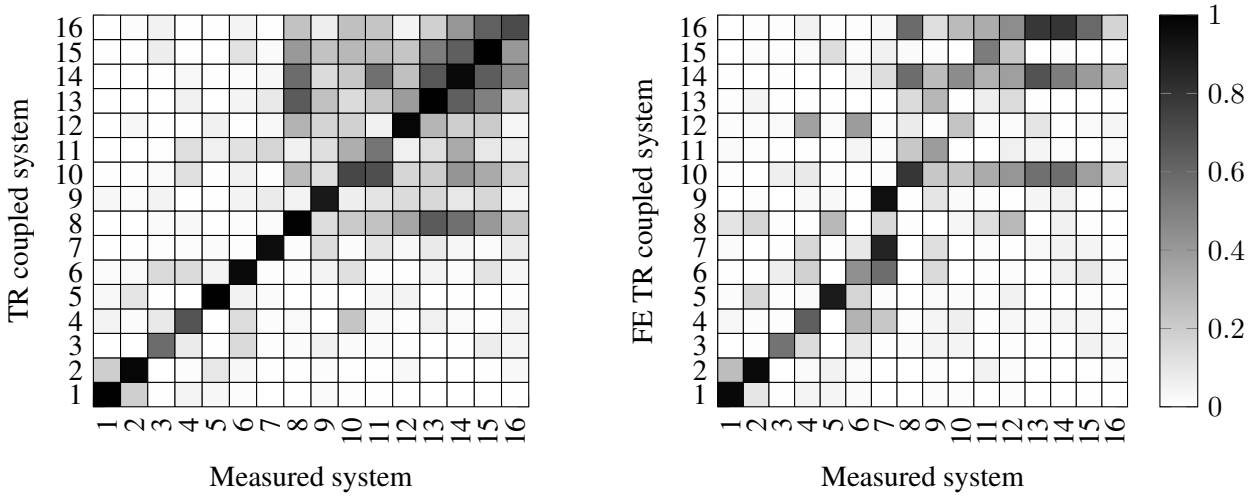


Figure 8: Identified BIW model fit at input 22 output 6

Figure 9 shows the modal assurance criterion (MAC) [3] for the experimental-analytical and FE coupled models TR and FE TR for the 16 first flexible modes. The experimental-analytical model TR shows higher correlation. In Table 1 the first 16 flexible eigenfrequencies are shown for the experimentally coupled system (Data), experimental-analytical coupled system (TR) and FE coupled system (FE TR). It can be seen that the TR model gives better estimations of eigenfrequencies. Note that the FE TR model seem to introduce more modes around mode 8 or 9, with the MAC also indicating this. This was not further investigated.

In Figure 10 the FRAC is shown for all non-coupling outputs on the BIW and rear subframe for inputs 21 and 22 on the BIW and input S1 on the rear subframe. Note that here 1 (black) indicate perfect fit. Note also that only numbers indicate sensor and actuator positions on the BIW while an S prefix indicate sensors and actuators on the subframe. It can be seen that in general the TR model gave best results, especially for the BIW inputs and outputs. The FE models generally give poorer results compared to the experimental-analytical coupled system. However, 0.5 % damping was used for all modes for the BIW FE model, which might have had an effect on the results.

In Figure 11 the receptance at input 22 and output 12 (both on the BIW) which gave best fit (and was not a drive point channel), for model TR, is shown for the four considered models. It can be seen that the experimental-analytical model TR gave a good fit over the whole frequency range, and captured the low frequency well. On the other hand the experimental-analytical model T has some spurious modes appearing in the low frequency range, but also gave an overall good fit. The two corresponding coupled FE models show much poorer results, especially higher up in frequency. In Figure 12 the worst channel (input at S1 and output at 21), for the TR model, is again shown for all four models. It can be seen that the low frequency range is captured well with model TR. However, here the translation DOFs only coupled models, T and FE T, produce poor results in the low frequency range. This is caused by the spurious modes.



(a) MAC between TR and data

(b) MAC between FE TR and data

Figure 9: MAC for the 16 first flexible modes of models with experimentally identified BIW model in (a) and FE BIW model in (b)

Table 1: First 16 flexible eigenfrequencies (Hz) of the identified experimentally coupled system (Data), experimental-analytical coupled system (TR) and FE coupled system (FE TR)

Mode	1	2	3	4	5	6	7	8
Data	31.86	34.35	39.40	42.78	45.72	50.86	54.76	56.92
TR	31.85	34.34	39.44	42.80	45.74	50.90	54.98	56.91
FE TR	31.71	34.29	39.70	42.75	45.53	48.95	55.08	55.58
Mode	9	10	11	12	13	14	15	16
Data	57.31	59.17	59.37	62.03	62.39	64.22	67.31	70.01
TR	57.28	59.21	59.34	62.04	62.40	64.10	67.44	70.14
FE TR	56.67	57.34	57.67	58.64	59.44	60.55	61.40	63.43

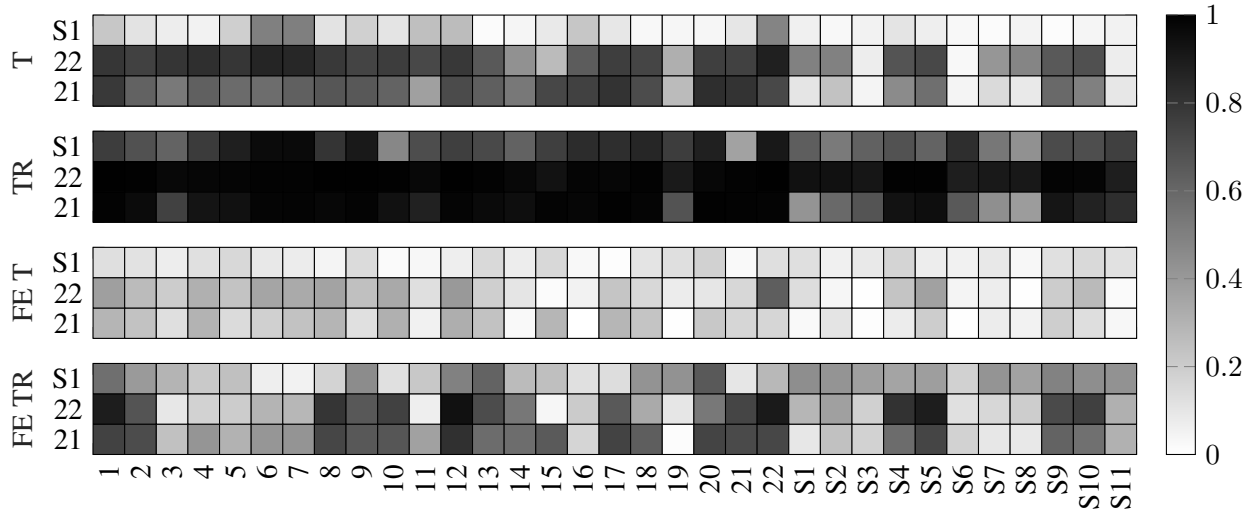
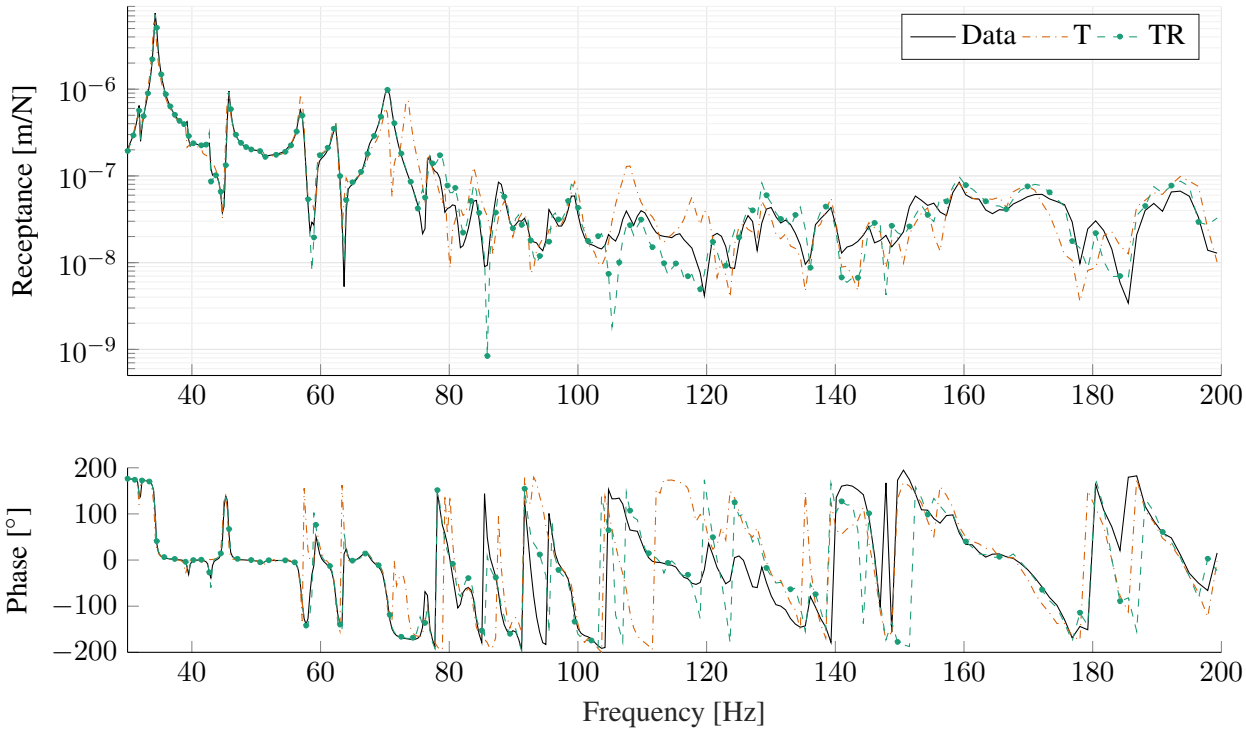
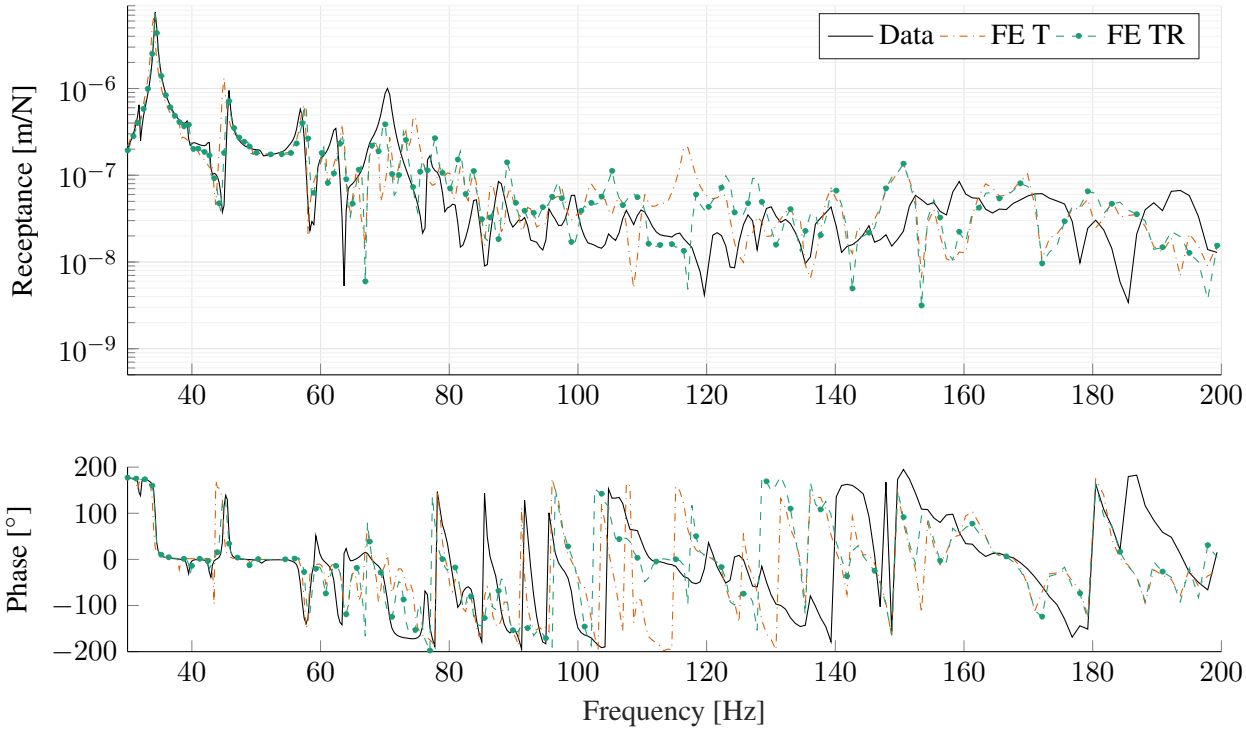


Figure 10: Coupled model fit (FRAC) to test data for $\omega \in [30, 200]$ Hz

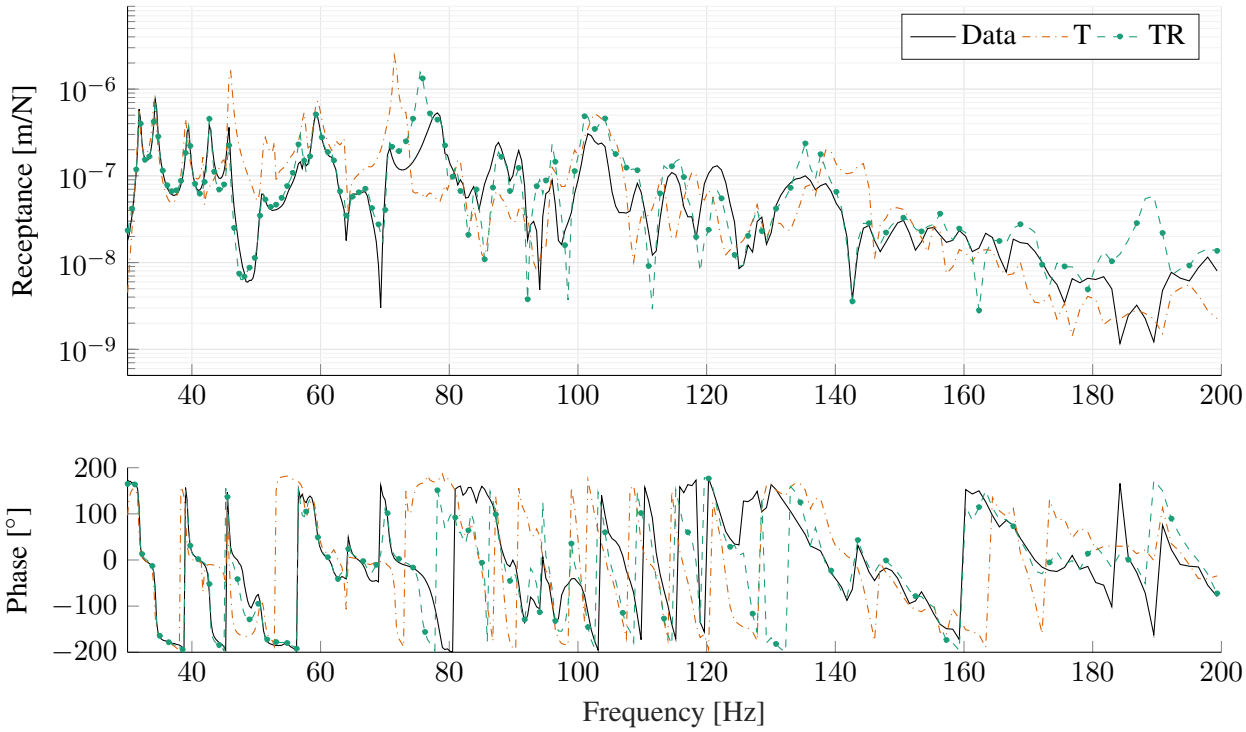


(a) Coupled systems with experimental BIW model

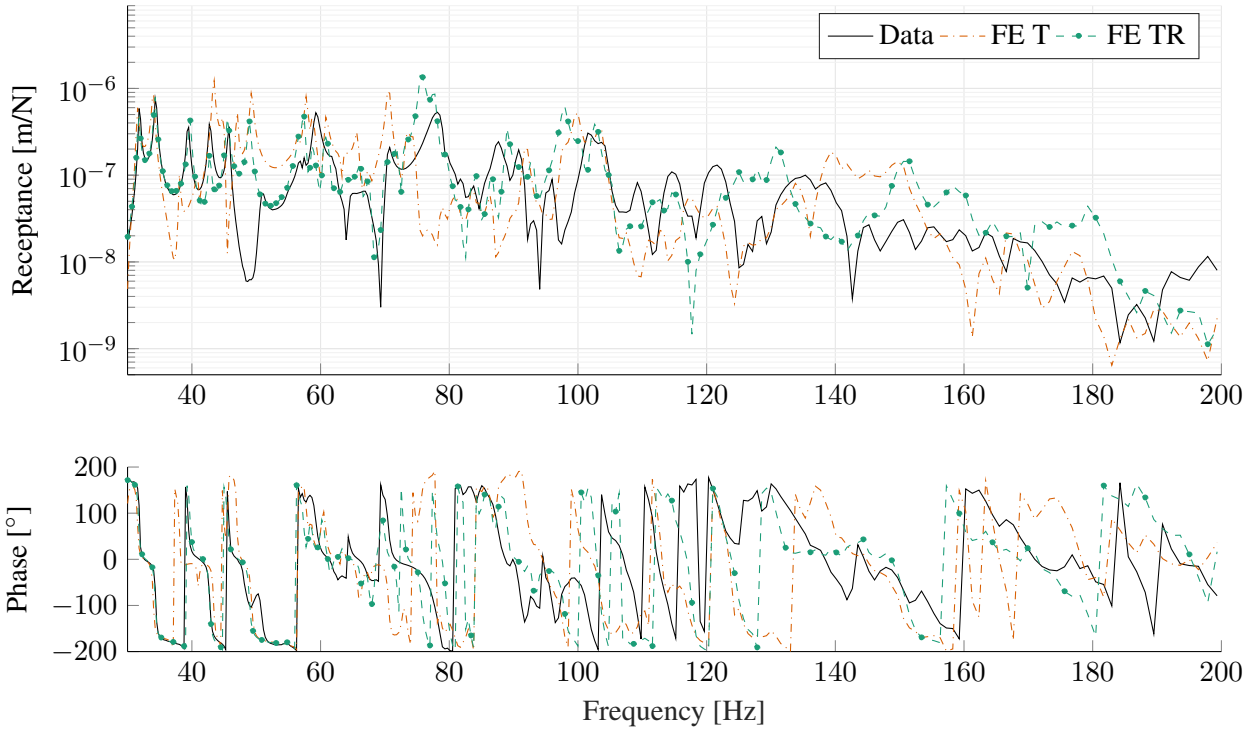


(b) Coupled systems with FE BIW model

Figure 11: Channel with best fit (not drive point) showing receptance at input 22 and output 12, both on BIW



(a) Coupled systems with experimental BIW model



(b) Coupled systems with FE BIW model

Figure 12: Channel with worst fit showing receptance at input S1 and output 21, input on subframe and output on BIW

7 Conclusion

Experimental-analytical substructuring of an experimentally modelled BIW and FE rear subframe has been performed. The synthesised model is shown to outperform an FE assembly counterpart based on CMS. The considered industrial systems are complex and show high modal densities. A new system identification technique has been used to obtain good models of the hard-to-model drive point channels. The constraint $\boldsymbol{CB} = \boldsymbol{0}$ was solved without changing the model considerably, i.e. only decreasing the model fit slightly. It was shown that it is necessary to couple all 6 DOFs at the 4 coupling locations. A coupling using only translation DOFs introduced spurious modes, not seen in the experimental data of the assembly. This was observed in both the analytical and experimental-analytical synthesis. Moment inputs were estimated using a modal model, assuming reciprocity. Since the experimental model is not fully reciprocal the FRFs associated with moment input must be seen as less trustworthy. However, it is seen that good results are obtained. One possible explanation to this could be that the translation DOFs are more important in the frequency range of interest, compared to the rotation DOFs. Although, some channels show poor fit which could be related to the poor estimation of the rotation inputs. See [4] for a longer discussion on this subject.

Acknowledgements

Volvo Car Corporation is gratefully acknowledged for providing the funding for this paper.

References

[1] T. J. S. Abrahamsson, and Kammer, D. C., *Finite element model calibration using frequency responses with damping equalization*, Mechanical Systems and Signal Processing, Vol. 62–63, Elsevier (2015), pp. 218-234.

[2] T. Abrahamsson, *Modal-parameter extraction for nonproportionally damped linear structures*, International Journal of Analytical and Experimental Modal Analysis, Vol. 3, No. 2, (1988), pp. 62-68.

[3] R. J. Allemang, D. L. Brown, *A correlation coefficient for modal vector analysis*, *Proceedings of the 1st IMAC, Orlando, FL, USA, 1982*, Orlando (1982), pp. 110-116.

[4] A. Bylin, *Substructuring using hybrid experimental-analytical state-space models of automotive components*, Chalmers University of Technology, Department of Mechanics and Maritime Sciences, Göteborg (2018).

[5] D. J. Ewins, *Modal Testing: Theory, Practice and Application*, 2nd edition, Wiley-Blackwell, Baldock, Hertfordshire, (2000).

[6] M. Gibanica, T. J. S. Abrahamsson, *AbraDAQ*, https://github.com/mgcth/abraDAQ, (Visited on 2018-01-15).

[7] M. Gibanica, T. J. S. Abrahamsson, *Parameter Estimation and Uncertainty Quantification of a Subframe with Mass Loaded Bushings*, Model Validation and Uncertainty Quantification, Vol. 3, Springer International Publishing (2017), pp. 61-76.

[8] M. Gibanica, T. J. S. Abrahamsson, R. J. Allemang, *Residual states for modal models identified from accelerance data*, in, *Proceedings of the 36th IMAC, Orlando, FL, USA, 2018 February 12-15*, Orlando (2018). In press.

[9] M. Gibanica, T. J. S. Abrahamsson, T. McKelvey, *Physically motivated rank constraint on direct throughput of state-space models*, in, *Proceedings of 18th IFAC Symposium on System Identification, SYSID 2018, Stockholm, Sweden, 2018*, Stockholm (2018). In press.

[10] S. Gumussoy, A. A. Ozdemir, T. McKelvey, L. Ljung, M. Gibanica, R. Singh, *Improving linear state-space models with additional iterations*, in, *Proceedings of 18th IFAC Symposium on System Identification, SYSID 2018, Stockholm, Sweden, 2018*, Stockholm (2018). In press.

[11] W. Heylen, S. Lammens, *FRAC: a consistent way of comparing frequency response functions*, in M. I. Friswell, J. E. Mottershead, editors, *Proceedings of the Conference on Identification in Engineering Systems, 1996*, Swansea (1996), pp. 48-57.

[12] D. de Klerk, D. J. Rixen, S. N. Voormeeren, *General Framework for Dynamic Substructuring: History, Review and Classification of Techniques*, AIAA Journal, Vol. 46, No. 5, AIAA (2008), pp. 1169-1181.

[13] A. Liljerehn, T. Abrahamsson, *Dynamic sub-structuring with passive state-space components*, in, *Proceedings of the 26th ISMA International Conference on Noise and Vibration Engineering, Leuven, Belgium, 2014 August 15-17*, Leuven (2014), pp. 3879-3890.

[14] A. Liljerehn, *Machine Tool Dynamics - A constrained state-space substructuring approach*, Chalmers University of Technology, Department of Applied Mechanics, Göteborg (2016).

[15] T. McKelvey, H. Akcay, L. Ljung, *Subspace-based multivariable system identification from frequency response data*, IEEE Transactions on Automatic Control, Vol. 41, No. 7, IEEE Control Systems Society (1996), pp. 960-979.

[16] R. R. Craig Jr., A. J. Kurdila, *Fundamentals of Structural Dynamics*, 2nd edition, Wiley, Hoboken, N.J (2006).

[17] M. Scheel, A. T. Johansson, *State-Space Substructuring with Transmission Simulator*, Dynamics of Coupled Structures, Vol. 4, Springer International Publishing (2016), pp. 91-103.

[18] M. V. van der Seijs, D. D. van den Bosch, D. J. Rixen, D. de Klerk, *An improved methodology for the virtual point transformation of measured frequency response functions in dynamic substructuring*, in M. Papadrakakis, V. Papadopoulos, V. Plevris, editors, *Proceedings of 4th ECCOMAS Thematic Conference on Computational Methods in Structural Dynamics and Earthquake Engineering, Athens, Greece, 2014 June 12-14*, Athens (2014), pp. 4334-4347.

[19] P. Sjövall, T. Abrahamsson, *Component system identification and state-space model synthesis*, Mechanical Systems and Signal Processing, Vol. 21, No. 7, Elsevier (2007), pp. 2697-2714.

Application of System Equivalent Model Mixing (SEMM) to model the structural dynamic properties of a complex vehicle component using numerical and experimental data

E. Pasma[1], **S. Klaassen**[2], **L. Nieuwenhuijse**[1,3], **M. van der Seijs**[1,3], **D. Lennström**[4]
[1] VIBES.technology
Molengraaffsingel 14, 2629 JD, Delft, The Netherlands,
e-mail: **epasma@vibestechnology.com**

[2] Technische Universität München, Faculty of Mechanical Engineering, Institute of Applied Mechanics, Boltzmannstr. 15, 85748 Garching, Germany

[3] Delft University of Technology, Department of Precision and Microsystems Engineering
Mekelweg 2, 2628CD, Delft, The Netherlands

[4] VOLVO CAR GROUP,
91610, Torslanda PV32, SE-405 31, Göteborg, Sweden

Abstract
A popular strategy in structural dynamic modelling is breaking the structure down into separable, manageable substructures. One can choose the most efficient way of modelling the substructures, before synthesizing the full system model. System Equivalent Model Mixing (SEMM) is a new method that allows mixing of frequency-based models, either of numerical or experimental nature, to form a hybrid structural dynamic model. The method expands measured data onto a numerical mode manifold using Lagrange-Multiplier Frequency Based Substructuring (LM-FBS). Hence, SEMM combines the DoF-space of the numerical model with the dynamic properties of the measured substructure. In this paper, SEMM is applied to a complex vehicle component. Frequency Response Function (FRF) measurements on the component are used to enrich the uncalibrated Finite Element Model of the component. The resulting hybrid model comprises interfaces in six degrees of freedom, which is required for the connectivity to neighboring structures in the FBS framework.

Introduction

Engineers in the automotive industry are faced with numerous challenges. First of all, the demand for shorter product development cycles and fewer physical prototypes is rising, whilst the number of products (or variants) is growing. Moreover, the complexity, functionality and attribute demands (such as NVH, emissions, weight, durability, safety, handling) are increasing.

One of the ways to keep up with these trends, is adopting a modular way of working. For the particular field of sound and vibration engineering, Dynamic Substructuring (DS) is an often-chosen approach. This technique allows the combination of component models coming from different sources (test or numerical), in order to simulate the sound and vibration performance of the full product. Using DS, optimisation of the individual components is possible, while simultaneously respecting the NVH signature of the full vehicle.

Secondly, automotive electrification is becoming more and more prevalent. In traditional vehicles, the internal combustion engine masks the bulk of NVH-problems. On the other hand – in electric vehicles – tonal components become more dominant at higher frequencies (> 1 kHz) [1]. Full (virtual) vehicle simulations

with (deterministic) numerical approaches (e.g. Finite Element Analysis) are pushed towards their limits. Due to this increasing frequency band and desired accuracy, a trend towards test-based modelling strategies is unavoidable.

One recently developed and promising method that fits both in the modular modelling approach and is able to capture complex dynamic behaviour of a structure, is System Equivalent Model Mixing (SEMM). This method allows mixing of frequency-based models, either of numerical or experimental nature, to form a hybrid structural dynamic model. The method expands measured data onto a numerical mode manifold, using theory derived from Lagrange-Multiplier Frequency Based Substructuring (LM-FBS). Therefore, SEMM exploits the best of both domains, by combining the DoF-space of the numerical model with the dynamic properties of the measured substructure.

Paper goal & outline

The main goal of this paper is to show how SEMM is used to model the structural dynamics of the subframe of a vehicle. This subframe hosts an electric drive unit (EDU) which is used for the propulsion of a hybrid vehicle. The second goal is to show how this model is used in the experimental Dynamic Substructuring (DS) Framework. The components considered in this DS application are depicted in figure 1.

The first part of the paper covers the theory on LM-FBS, SEMM and the Virtual Point Transformation. In the second part, the subframe is modelled according to the SEMM method, whereafter it is coupled with LM-FBS to four rubber decoupling elements and a test-based model of the EDU. The test-based modelling of the EDU and the characterisation of the rubber decoupling elements is beyond the scope of this paper.



Figure 1: On the left, a picture of the SEMM measurement set-up. On the right, an overview of the FBS case. The red arrow indicates the force excitation, the blue circle the location of the validation sensor.

1 Theory

The contents of this section is divided into three parts. The first section will briefly explain the dual solution of experimental dynamic substructuring in the frequency domain along with the definition and inclusion of weak interfaces. The second part covers the theory of the SEMM-method, tailored to the envisioned application. Last, a short recap on the virtual point transformation is provided.

1.1 Lagrange Multiplier Frequency Based Substructuring

DS is applied in this work with the Lagrange Multiplier Frequency Based Substructuring (LM-FBS) method [2]. As the name implies, LM-FBS is applied in the frequency domain and its main strength lies in the fact

that it works in the admittance space; this allows for direct implementation of experimental measurement results. This makes it the preferred DS method when working with experimental models.

The equation of motion to couple two arbitrary systems with LM-FBS is as follows:

$$\mathbf{u} = \mathbf{Y}\left(\mathbf{f} + \mathbf{g}\right), \quad \text{with} \quad \mathbf{Y} = \begin{bmatrix} \mathbf{Y}^{\mathrm{A}} & \\ & \mathbf{Y}^{\mathrm{B}} \end{bmatrix}, \quad \mathbf{f} = \begin{bmatrix} \mathbf{f}^{\mathrm{A}} \\ \mathbf{f}^{\mathrm{B}} \end{bmatrix}, \quad \mathbf{g} = \begin{bmatrix} \mathbf{g}^{\mathrm{A}} \\ \mathbf{g}^{\mathrm{B}} \end{bmatrix} \tag{1}$$

Where $\mathbf{u}$ is the vector of dynamic displacements, $\mathbf{Y}$ is an admittance FRF matrix, $\mathbf{f}$ is a vector of applied forces and $\mathbf{g}$ is a vector of interface forces. The displacement and force vectors can contain rotations and moments, respectively. Equation (1) is subject to two sets of constraints: the compatibility and equilibrium conditions. First, the compatibility condition states:

$$\mathbf{u}_b^{\mathrm{A}} - \mathbf{u}_b^{\mathrm{B}} = \mathbf{0} \quad \rightarrow \quad \mathbf{B}\mathbf{u} = \mathbf{0} \tag{2}$$

Where $\mathbf{B}$ is a signed Boolean matrix explicitly stating a relation between the boundary DoF. It has the form:

$$\mathbf{B} = \begin{bmatrix} \mathbf{0} & \mathbf{I} & \mathbf{0} & -\mathbf{I} \end{bmatrix} \tag{3}$$

Where the columns of $\mathbf{B}$ refer to the elements in $\mathbf{u} = \begin{bmatrix} \mathbf{u}_i^{\mathrm{A}} & \mathbf{u}_b^{\mathrm{A}} & \mathbf{u}_i^{\mathrm{B}} & \mathbf{u}_b^{\mathrm{B}} \end{bmatrix}^T$ and the rows refer to number of compatibility equations. The equilibrium condition enforces force equilibrium on the boundary:

$$\mathbf{g}_b^{\mathrm{A}} = \mathbf{g}_b^{\mathrm{B}} = \boldsymbol{\lambda} \quad \rightarrow \quad \mathbf{B}^T\boldsymbol{\lambda} = -\mathbf{g} \tag{4}$$

Where the same coupling matrix in definition (3) is used. Equation (1) is solved by inserting the compatibility equation (2) and the equilibrium equation (4) and solving for $\boldsymbol{\lambda}$. Equation (5) is then re-applied into equation (1) to find the coupled dynamics.

$$\boldsymbol{\lambda} = \left(\mathbf{B}\mathbf{Y}\mathbf{B}^T\right)^{-1}\mathbf{B}\mathbf{Y}\mathbf{f} \tag{5}$$

$$\mathbf{u} = \mathbf{Y}\mathbf{f} - \mathbf{Y}\mathbf{B}^T\left(\mathbf{B}\mathbf{Y}\mathbf{B}^T\right)^{-1}\mathbf{B}\mathbf{Y}\mathbf{f} \tag{6}$$

The coupled model thus becomes:

$$\mathbf{Y}^{\mathrm{AB}} = \mathbf{Y} - \mathbf{Y}\mathbf{B}^T\left(\mathbf{B}\mathbf{Y}\mathbf{B}^T\right)^{-1}\mathbf{B}\mathbf{Y} \tag{7}$$

1.1.1 Interface weakening in LM-FBS

Equation (2) assumes a rigid connection since it requires a 1-to-1 relation. Yet the connection can also be weakened by allowing a gap to exist in the boundary displacements [3]. This means that a gap is allowed in the compatibility, i.e. equation (2) is reformulated:

$$\mathbf{B}\mathbf{u} = \boldsymbol{\Delta}\mathbf{u}_b \tag{8}$$

The gap $\boldsymbol{\Delta}\mathbf{u}_b$ is maintained by joint stiffness $\mathbf{K}^{\mathrm{J}}$ and damping $\mathbf{C}^{\mathrm{J}}$ when enforced by the boundary forces described by $\boldsymbol{\lambda}$. Note that sithese terms only denote the connection stiffness and damping between the interfaces of both sides. Mathematically, they represent the off-diagonal terms of the joint.

$$\mathbf{C}^{\mathrm{J}}\boldsymbol{\Delta}\dot{\mathbf{u}}_b(t) + \mathbf{K}^{\mathrm{J}}\boldsymbol{\Delta}\mathbf{u}_b(t) = \boldsymbol{\lambda}(t) \quad \rightarrow \quad \mathbf{Z}^{\mathrm{J}}\boldsymbol{\Delta}\mathbf{u}_b(\omega) = \boldsymbol{\lambda}(\omega) \quad \rightarrow \quad \boldsymbol{\Delta}\mathbf{u}_b(\omega) = \mathbf{Y}^{\mathrm{J}}\boldsymbol{\lambda}(\omega) \tag{9}$$

Note that in the weakening assumption no mass terms exist in the joint; the inertial forces from a mass contribution would mean equation (4) no longer holds.

The weakened LM-FBS can then be derived by first deriving the boundary forces $\boldsymbol{\lambda}$ and then solving the constrained equation of motion (1) like before (for the full derivation, see [3]):

$$\boldsymbol{\lambda} = \left(\mathbf{B}\mathbf{Y}\mathbf{B}^T + \mathbf{Y}^{\mathrm{J}}\right)^{-1}\mathbf{B}\mathbf{Y}\mathbf{f} \tag{10}$$

$$\mathbf{Y}^{\mathrm{AJB}} = \mathbf{Y} - \mathbf{Y}\mathbf{B}^T\left(\mathbf{B}\mathbf{Y}\mathbf{B}^T + \mathbf{Y}^{\mathrm{J}}\right)^{-1}\mathbf{B}\mathbf{Y} \tag{11}$$

Where the addition of the superscript $(\bullet)^{\mathrm{J}}$ to $\mathbf{Y}^{\mathrm{AJB}}$ in equation (11) indicates that the joint dynamics have been included in the formulation.

1.2 System Equivalent Model Mixing

For SEMM, a few "building blocks" are needed. First, the **parent** models $\mathbf{Y}^{\text{par}}$ are the models of the system which will be mixed. In the proposed case they are the numerical FE-model and the experimental measurements of the component. The FE-model, which could potentially contain any desired DoF, acts as the manifold composed of the equivalent-experimental-DoFs and the expansion DoF-set. The experimental measurements are deemed a more accurate representation of the complex component's physics and will be considered the more trusted information source throughout the frequency range.

Next, the overlay and removed model are defined. The **overlay** model $\mathbf{Y}^{\text{ov}}$ is the model which will determine the dynamic properties of the hybrid model and is therefore a trusted (sub)set of the **experimental** model. The **removed** model $\mathbf{Y}^{\text{rem}}$ is a (sub)set of the **numerical** manifold which contains the DoFs overlapping with the overlay model.

Translating this to classic DS notations, the expanded DoF are internal DoF unique to the numerical parent model which will be denoted by $\mathbf{u}_i$; following this conjecture the shared DoFs are boundary DoFs which are denoted by $\mathbf{u}_b$. Therefore the previously introduced building blocks become:

$$\mathbf{Y}^{\text{par, Num.}} = \mathbf{Y}^{\text{rem}} = \begin{bmatrix} \mathbf{Y}_{ii} & \mathbf{Y}_{ib} \\ \mathbf{Y}_{bi} & \mathbf{Y}_{bb} \end{bmatrix}^{\text{Num.}}, \qquad \mathbf{Y}^{\text{par, Exp.}} = \mathbf{Y}^{\text{ov}} = \begin{bmatrix} \mathbf{Y}_{bb} \end{bmatrix}^{\text{Exp.}} \tag{12}$$

Generally the removed model must contain, but is not limited to the boundary DoF. In the case of a full system decoupling, as applied in this work, the removed model is equal to the numerical parent model; more information can be found in [4]. Likewise, the overlay model and experimental parent model are identical; assuming the entirety of the experimental measurements DoF is deemed a trusted set. In light of this, since the experimental parent model is no longer needed, the parent model will now refer to the numerical parent model throughout this work:

$$\mathbf{Y}^{\text{par}} = \mathbf{Y}^{\text{par, Num.}} = \mathbf{Y}^{\text{rem}}, \qquad \mathbf{Y}^{\text{ov}} = \mathbf{Y}^{\text{Exp.}} \tag{13}$$

SEMM is based on DS on an abstract level; the problem is solved by solving (1) for the SEMM abstract system:

$$\mathbf{u} = \mathbf{Y}\left(\mathbf{f} - \mathbf{g}\right), \quad \text{with} \quad \mathbf{Y} = \begin{bmatrix} \mathbf{Y}^{\text{par}} & & \\ & -\mathbf{Y}^{\text{rem}} & \\ & & \mathbf{Y}^{\text{ov}} \end{bmatrix}, \quad \mathbf{f} = \begin{bmatrix} \mathbf{f}^{\text{par}} \\ \mathbf{f}^{\text{rem}} = \mathbf{0} \\ \mathbf{f}^{\text{ov}} = \mathbf{0} \end{bmatrix}, \quad \mathbf{g} = \begin{bmatrix} \mathbf{g}^{\text{par}} \\ \mathbf{g}^{\text{rem}} \\ \mathbf{g}^{\text{ov}} \end{bmatrix} \tag{14}$$

Note that the external forces are only applied on the parent model. There is no physical force exerted on the removed and overlay model as they are merely used to apply boundary conditions on the parent model to update its dynamics.

To solve (14) the compatibility and equilibrium constraints are applied as in LM-FBS. Compatibility requires:

$$\mathbf{u}^{\text{par}} - \mathbf{u}^{\text{rem}} = \mathbf{0} \tag{15a}$$

$$\mathbf{u}_b^{\text{rem}} - \mathbf{u}^{\text{ov}} = \mathbf{0} \tag{15b}$$

Note that the relationship is explicit between the parent and removed model, and then between the removed and overlay model. The removed model essentially acts as a conduit, yet note that implicitly a relationship between the overlay model and parent model also exists. Equation (15) can be rewritten in matrix form as in equation (2) with the signed Boolean matrix defined as (using $\mathbf{u} = \begin{bmatrix} \mathbf{u}_i^{\text{par}} & \mathbf{u}_b^{\text{par}} & \mathbf{u}_i^{\text{rem}} & \mathbf{u}_b^{\text{rem}} & \mathbf{u}_b^{\text{ov}} \end{bmatrix}^T$):

$$\mathbf{B} = \begin{bmatrix} \mathbf{I} & \mathbf{0} & -\mathbf{I} & \mathbf{0} & \mathbf{0} \\ \mathbf{0} & \mathbf{I} & \mathbf{0} & -\mathbf{I} & \mathbf{0} \\ \mathbf{0} & \mathbf{0} & \mathbf{0} & \mathbf{I} & -\mathbf{I} \end{bmatrix} \tag{16}$$

This matrix is also used in the equilibrium condition as in equation (4). In this case the equilibrium enforces the following:

$$\mathbf{g}_i^{\text{par}} + \mathbf{g}_i^{\text{rem}} = \mathbf{0} \tag{17a}$$

$$\mathbf{g}_b^{\text{par}} + \mathbf{g}_b^{\text{rem}} + \mathbf{g}^{\text{ov}} = \mathbf{0} \tag{17b}$$

It is apparent that the problem follows the LM-FBS notation as described before. The SEMM problem can therefore be solved with equation (7). It is shown that from this solution the single line of SEMM can be obtained. The derivation is omitted in this paper, the interested reader is recommended to read [4]:

$$\mathbf{Y}^{\text{SEMM}} = \mathbf{Y}^{\text{par}} - \mathbf{Y}^{\text{par}} \left(\mathbf{Y}_{bg}^{\text{rem}}\right)^{+} \left(\mathbf{Y}_{bb}^{\text{rem}} - \mathbf{Y}_{bb}^{\text{ov}}\right) \left(\mathbf{Y}_{gb}^{\text{rem}}\right)^{+} \mathbf{Y}^{\text{par}} \tag{18}$$

Where the subscript $(\bullet)_g$ denotes the global set of DoF, i.e. $g = [i; b]$

1.3 Virtual Point Transformation

The compatibility and equilibrium conditions require that substructures have collocated DoFs: the boundary DoFs. Acquiring collocated DoF in experiments is not trivial since it is often not possible to measure at connection locations.

In order to still create these collocated DoF, the virtual point transformation can be used to create virtual nodes with DoF shared by both sides of a structure. The virtual node is created by rigid transformation of a set of DoF to a 6-DoF (three translations and three rotations) point in space, preferably at the location of the contact [5].

$$\mathbf{u} = \mathbf{R}_{\text{u}}\mathbf{q}, \qquad \mathbf{m} = \mathbf{R}_{\text{f}}^{T}\mathbf{f} \tag{19}$$

Where $\mathbf{R}_{\text{u}}$ and $\mathbf{R}_{\text{f}}$ are rigid transformation matrices transforming from the virtual displacements and forces $\mathbf{q}, \mathbf{m}$ to the measured displacements and forces $\mathbf{u}, \mathbf{f}$. In order to create a full-rank 6-DoF virtual node, at least 6 linear independent functions are needed, i.e. 6 or more displacement and force DoF are required in the input vectors $\mathbf{u}, \mathbf{f}$. Next, $\mathbf{R}_{\text{u}}$ and $\mathbf{R}_{\text{f}}$ are (least-square) inverted and used as the transformation matrices to the virtual locations such that the VP transformed model becomes:

$$\mathbf{Y}^{\text{VP}} = \left(\mathbf{R}_{\text{u}}{}^{T}\mathbf{R}_{\text{u}}\right)^{-1} \mathbf{R}_{\text{u}}\mathbf{Y}\mathbf{R}_{\text{f}} \left(\mathbf{R}_{\text{f}}{}^{T}\mathbf{R}_{\text{f}}\right)^{-1} = \left(\mathbf{R}_{\text{u}}\right)^{+} \mathbf{Y} \left(\mathbf{R}_{\text{f}}^{T}\right)^{+} \tag{20}$$

Where $\mathbf{Y}^{\text{VP}}$ is the virtual point transformed FRF matrix.

Note that the rigid transformation inherently means that a rigid interface assumption is made. If flexibility exists between the virtual node and the input DoF the rigid transformation will no longer adequately describe the correct dynamics [6]. It is therefore important to choose input DoF close to the connection point, such that the rigid interface assumption holds.

2 Application

In this section the test case is presented. The ultimate goal is to obtain a full system FRF model comprising models of the EDU, the rubber decoupling mounts and the subframe through the Frequency Based Substructuring coupling procedure. This model should provide the transfer functions such that the vibration transmission from the EDU to a point of interest can be studied. In NVH engineering, the structure-borne noise at the driver's ears originating from the source is of great concern/interest. To achieve this goal, first accurate individual subsystem FRF models have to be obtained separately, with correct coupling interfaces. This is achieved by building 6 Cartesian translational and rotational DoFs by using the virtual point transformation (section 1.3). This is a prerequisite for successful FBS in the 0 - 2 kHz frequency range of interest [7]. In the following, the modelling techniques for the sub-components are listed:

- *Electric drive unit*: A test-based FRF model by application of the virtual point transformation [5] on the four coupling points of the motor;
- *Rubber decoupling mounts*: The transfer stiffnesses of the four rubber decoupling elements are obtained by an in-situ characterisation approach [8];
- *Subframe*: An FRF model is obtained through SEMM, see section 1.2.

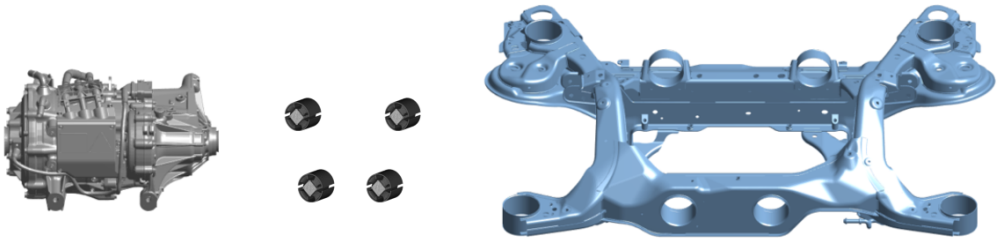


Figure 2: Overview the components in the test case. The EDU connects through four decoupling mounts to the subframe. From left to right: the electric drive unit, the rubber mounts and the subframe.

In this paper, only the SEMM application on the subframe is shown. Using SEMM for the subframe is driven by basically two factors. Firstly, the subframe is a complex system (high modal density), for which the mode shapes can be obtained easily, but the exact eigen-frequencies and damping factors are more challenging. Secondly, there is a limit on the available measurement equipment (for e.g. a full test based model, see section 1.3). In section 2.1.1 a more elaborate motivation for using SEMM is discussed.

2.1 SEMM Application

2.1.1 Motivation to use SEMM

The subframe is a relatively complex DS case as it includes components with up to eight connecting interfaces. Using the virtual point method on each interface would therefore require either up to 24 different sensors, or exhausting roving sensor measurements, in order to create enough linearly independent functions in the FRF-matrix.

In such cases, expansion techniques become an interesting alternative. A few methods exist, all of which would require some notion of an expansion matrix; which, in turn, is mostly extracted out of numerical data. Even fewer are the methods that work well with experimental FRF-data: SEREP, its expansion VIKING and SEMM are the most notable examples.

In order to create per-point linear independent FRF (As required for the virtual points) there are some restrictions: namely that for each point a minimum of 6 linearly independent functions exist in the FRF-subset used in virtual point minimization, i.e. the rank of the said FRF matrix is ≥ 6. Additionally, in order to observe the dynamics of the 8×6 point connections, a minimum of $8 \times 6 = 48$ linearly independent functions should exist in the expanded model. For SEREP, this would mean that a minimum of 48 sensor channels must exist, even more to obtain clean filtered results [9]. VIKING can include numerical data in the expansion and therefore would not require as many sensors per se [10]. It would then however, require a modal fitting of the experimental data; with the modal density of the subframe's FRF, this is an ardous process to this date. SEMM includes the numerical data from the numerical parent model implicitly, consequently the hybrid model's rank is equal to the numerical model's rank (generally full rank). In conclusion, the hybrid model's expanded DoFs can not only be used in the virtual point creation, but also in the DS coupling.

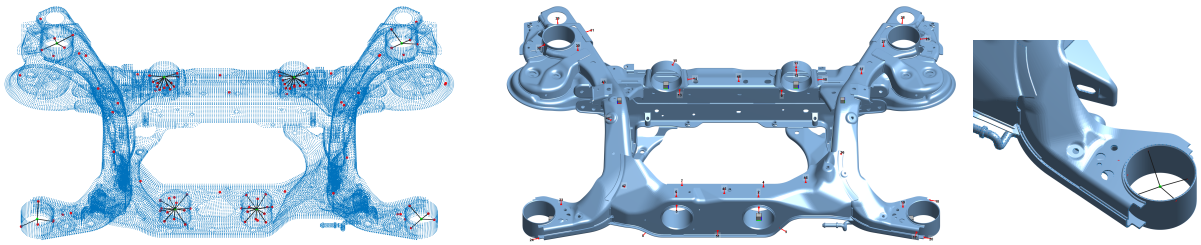


Figure 3: The parent, overlay and resulting SEMM model.

2.1.2 Practical considerations

For the successful application of SEMM, one has to consider some practicalities concerning the placement of the sensors. These sensor locations determine the nature of the trust-set; thus it is important to locate the sensors relatively close to the expansion locations.

Yet bundled sensor locations will negatively affect the conditionality of the numerical removed model, which must share the boundary DoF locations. In equation (18) it is clearly seen that the removed model (part of the numerical parent model) is inverted in a least-squares sense. The noise characteristic of the hyrbid model is therefore affected by the conditionality of the numerical model.

It is clear that an optimum must be found between bundling the sensors near the expanded DoF locations and spreading them around the structure for a better removed model conditioning.

2.1.3 The setup

For SEMM two sets of FRFs of the same subframe are required, a parent model and an overlay model. The parent model comprises the DoF-set for the expansion and the same DoF-set as the overlay model. The parent FRF-model is obtained from a Finite Element model of the subframe of which FRFs are synthesized by mode-superposition of 500 modes, which corresponds to roughly 4.5 kHz. The overlay model provides the accurate dynamics. These FRFs are obtained by an impact test on the physical subframe. In the following, an overview of the three models used in the SEMM calculation is shown:

1. *Parent model*: The FE-based FRF model $\left(\mathbf{Y}^{\text{parent}} \in \mathbb{C}^{198\times219}\right)$. This model has the larger DoF set on which the overlay model is expanded and can be seen as the provider for the high spatial resolution in the SEMM model;

2. *Overlay model*: These FRFs provide the accurate dynamics or 'trust-set FRFs'. The subframe is instrumented with nine triaxial accelerometers, one on every coupling point and one on another (random) position. In total 48 impact locations were distributed over the structure. From this measurement set-up, a subset of measured FRFs were chosen ($\mathbf{Y}^{\text{ov}} \in \mathbb{C}^{20\times33}$);

3. *Removed model*: This subset from the parent model and makes place for the overlay model.

DoFs	**Channels**	**RefChannels**	
Measurement	20	33	
Coupling	96	96	$(8 \times 4 \times 3 = 96)$
Conditioning	75	75	
Validation	7	15	
Total	**198**	**219**	

Table 1: Overview of the SEMM measurement set-up.

Now that the sub-systems have been defined, the actual construction of the SEMM model is done according to equation (18).

As can be read in table 1, there is a set of FRFs which are *not* used in the overlay model. These measured FRFs are independent from the updated SEMM FRFs and can therefore be used for validation.

2.2 Results

In this section the results of the SEMM process are shown. In the left plot of figure 4, a subframe FRF from the FE model and a measured FRF is shown. It can be observed that even the first resonance does not match the measurement. In the right plot, a trust-set FRF (i.e. from the overlay model) is displayed. It can observed that the updated parent model follows the overlay model exactly as required by the method.

In figure 5, two SEMM FRFs are shown against a validation measurement. It can be observed that the SEMM expanded DoF adhere to the validation FRF in the low frequency regime very well. At higher frequencies, although the resonance frequencies themselves are accurate, the FRF from the SEMM model diverge from the validation measurements. At these frequencies the delta between the implicit numerical and experimental mode-shapes is too large, and the hybrid model can no longer properly match the FRF due to the inadequate numerical manifold. Nevertheless the FRF are deemed satisfactory for the virtual point method in DS.

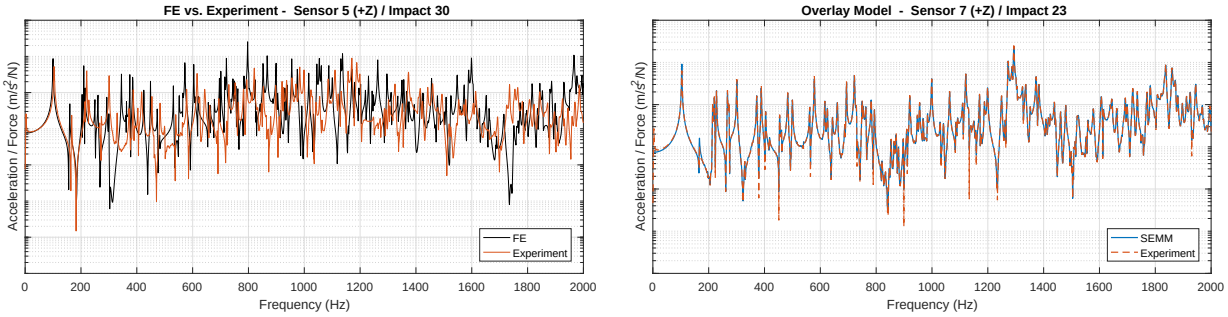


Figure 4: In the left figure a synthesized FRFs is shown against a measured FRF. In the right figure, boundary DoF SEMM FRF from the overlay model is shown. A clear 1-to-1 match to the measurement is observed as required by the method.

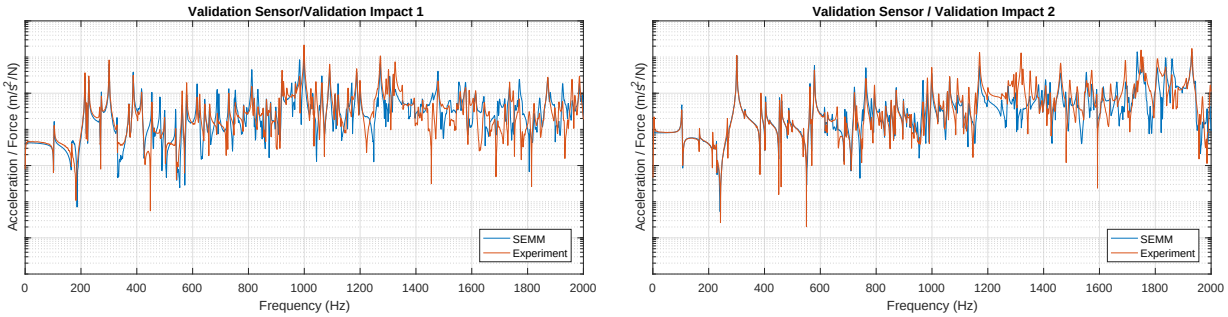


Figure 5: SEMM Results: In the left and right figures, internal validation DoF FRFs are shown; a close match is apparent at lower frequencies, yet the SEMM model diverges when the numerical parent model is no longer representative of the measured structure.

As a side-note; note the high frequency density of the subframe. It becomes apparent that expansion methods whose expansion basis is that of a limited set of numerical modes, such as SEREP and VIKING, would have a hard time capturing the number of modes present in a relatively low frequency band.

2.3 Part 2: Frequency-Based Substructuring

In section 2.1 an FRF model of the vehicle's subframe has been obtained. As mentioned, the test-based modelling of the EDU and the characterisation of the rubber decoupling mounts are not shown in this paper. The transfer dynamic stiffness rubber decoupling elements are obtained using the in-situ approach as described in [8]. This cannot be used as a subsystem in the LM-FBS equation (7), as the point stiffness is not available. Therefore, to use this transfer stiffness correctly, it is used in the weakened LM-FBS relation (11).

In figure 6 the coupling results are shown for a force excitation on the EDU to a response on the subframe validation sensor. The main tendency of the assembled FRFs shows that the global trend is captured very well, which is especially well depicted in the graphs below of the same transfer functions, shown in 12^{th} octave bands. The assembled system shows a very damped response, although the subframe does clearly not, as can be seen in the figures 5. This can be explained by the coupling to neighboring substructures which are very heavily damped.

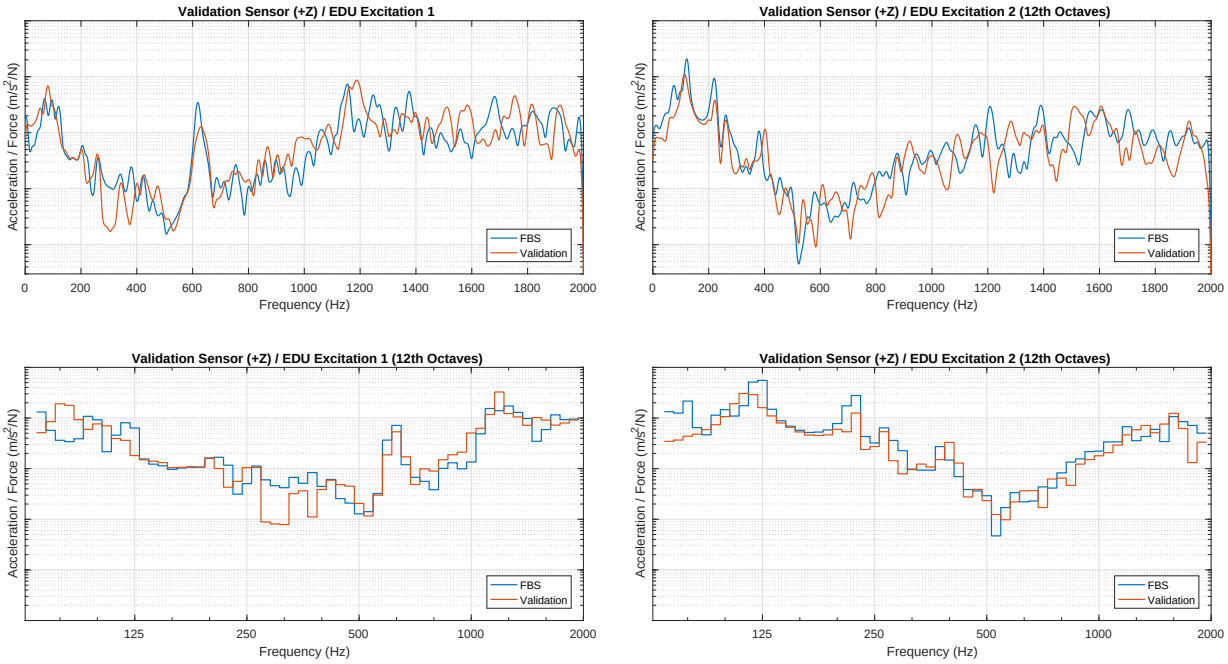


Figure 6: FBS Results compared with validation, the excitation and response locations are shown in fig. 1.

2.4 Discussion

The sensor and impact locations were chosen based on a "best guess" of the optimum in the matrix conditioning vs. interface observability problem stated in section 2.1.2. Furthermore, the number of sensor and impact channels was limited by the equipment and time available. The quality of the SEMM model is case specific; finding an optimum in resources (time or otherwise) vs. model accuracy is still largely a grey area. This holds for determining the optimum in both the number and location of sensor/impacts. More research is warranted to find an optimal resources vs. accuracy curve which will, in turn, enhance the practical applicability of SEMM.

3 Conclusions

This paper is concerned with the application of the System Equivalent Model Mixing (SEMM) method on a subframe of a hybrid vehicle. Practical considerations are stipulated on how the method is applied successfully. It is demonstrated how the obtained FRF-model of the subframe can be applied in the LM-FBS

framework along with its neighbouring substructures to construct an assembly. To establish the connectivity between all components in the translational and rotational degrees of freedom the virtual point transformation is used. It is shown that the various modelling strategies result in a full-system prediction of structural vibrations well into the kHz-range.

For future vehicle engineering, this DS assembly can be extended with noise transfer functions (NTFs) from the subframe coupling points to microphones in the cabin of the vehicle. For prediction of in-vehicle noise levels, the DS assembly can by combined with a description of the active source (EDU), such as blocked forces or free-velocities [11].

Acknowledgments

This project has been a collaboration between Volvo Car Group and VIBES.technology.

References

[1] D. Lennström, A. Nykänen, "Interior sound of today's electric cars: Tonal content, levels and frequency distribution", Technical Report 2015-01-2367, SAE Technical Paper, 2015, DOI: 10.4271/2015-01-2367.

[2] D. de Klerk, D. J. Rixen, S. N. Voormeeren, "General framework for dynamic substructuring: History, review and classifcation of techniques", *AIAA Journal*, 46(8):1169–1181, 2008, DOI: 10.2514/1.33274.

[3] E. Barten, M. V. van der Seijs, D. de Klerk, "A complex power approach to characterise joints in experimental dynamic substructuring", in: *Dynamics of Coupled Structures*, *Proceedings of the 32nd IMAC, A Conference and Exposition on Structural Dynamics*, volume 1, chapter 27, 281–296, Springer New York, 2014, DOI: 10.1007/978-3-319-04501-6_27.

[4] S. W. Klaassen, M. V. van der Seijs, D. de Klerk, "System equivalent model mixing", *Mechanical Systems & Signal Processing*, 105:90 – 112, 2018, DOI: https://doi.org/10.1016/j.ymssp.2017.12.003.

[5] M. V. van der Seijs, D. D. van den Bosch, D. J. Rixen, D. de Klerk, "An improved methodology for the virtual point transformation of measured frequency response functions in dynamic substructuring", in: M. Papadrakakis, V. Papadopoulos, V. Plevris (eds.), *4th ECCOMAS Thematic Conference on Computational Methods in Structural Dynamics and Earthquake Engineering (COMPDYN)*, 4334–4347, Kos Island, Greece, 2013, DOI: 10.7712/120113.4816.C1539.

[6] E. A. Pasma, M. V. van der Seijs, S. W. B. Klaassen, M. W. van der Kooij, "Frequency Based Substructuring with the Virtual Point Transformation, Flexible Interface Modes and the Transmission Simulator", in: *Proceedings of the XXXV International Modal Analysis Conference (IMAC), Orlando, FL*, 2018.

[7] D. de Klerk, D. Rixen, S. Voormeeren, F. Pasteuning, "Solving the RDoF problem in experimental dynamic substructuring", in: *Proceedings of the XXVI International Modal Analysis Conference (IMAC), Orlando, FL*, Society for Experimental Mechanics, Bethel, CT, 2008.

[8] J. Meggit, A. Elliot, A. Moorhouse, "In-situ determination of dynamic stiffness for resilient elements", *Journal of Mechanical Engineering Science*, 230(6):986–993, 2015.

[9] J. C. O'Callahan, P. Avitabile, R. Riemer, "System equivalent reduction expansion process (SEREP)", in: *Proceedings of the VII International Modal Analysis Conference (IMAC), Boston, MA*, volume 1, 29–37, Society for Experimental Mechanics, Bethel, CT, 1989.

[10] L. Thibault, A. Butland, P. Avitabile, "Variability improvement of key inaccurate node groups – viking", in: R. Allemang, J. De Clerck, C. Niezrecki, J. Blough (eds.), *Topics in Modal Analysis II, Volume 6*, 603–624, Springer New York, New York, NY, 2012.

[11] M. V. van der Seijs, D. de Klerk, D. J. Rixen, "General framework for transfer path analysis: History, theory and classification of techniques", *Mechanical Systems & Signal Processing*, 68–69:217–244, 2016, DOI: 10.1016/j.ymssp.2015.08.004.

Design of Particle Dampers for Lightweight Structures Using Frequency Based Substructuring

J. Oltmann[1], T. Hartwich[1], D. Krause[1]
[1] Hamburg University of Technology,
Institute for Product Development and Mechanical Engineering Design
Denickestr. 17, 21073 Hamburg, Germany
e-mail: **j.oltmann@tuhh.de**

Abstract
In this paper a new approach to predict the particle damping using a frequency based substructuring approach is presented. With this linear approach the consideration of particle dampers (PD) is possible without modelling its complex dynamic behaviour in detail with e.g. the discrete element method. The frequency response of the particle system - as one substructure - is determined experimentally. Finally, with a hybrid frequency based assembly, using test (particle damper) and simulation (honeycomb sandwich panel) results, is used to determine the dynamic behaviour of the entire system. In the paper the influence of the particle mass, the position of the damper, different test set-ups and sandwich panels with different composite lay-ups are investigated and compared to test results.

1 Introduction

The reduction of vibrations or noise plays an important role for the design of many applications. Especially lightweight structures are prone to strong vibrations disturbances. Particle damping was found to be an efficient way to reduce vibrations of lightweight structures since not much weight has to be added. Particles of different shape, size or material are used to fill cavities with a certain filling ratio. Dissipation of energy occurs due to particle-to-wall and particle-to-particle collisions caused by any dynamic excitation. However, for particle damping it is difficult to define an efficient modelling technique to predict the dynamic behaviour of a mechanical structure. Either simplified equivalent models or detailed simulation models but with higher computational time (e.g. using the Discrete Element Method) are used. Additionally, in both cases extensive experimental testing is required. Firstly, due to the non-linear behaviour of particle damping, depending on e.g. excitation amplitude, frequency or damper design. But still a validity of equivalent models is not given for a generalized simulation. Secondly, for a valid design approach for systems with dynamic loadings it is necessary to carry out tests on the final product design, which are possibly large and complex assemblies, because damping mechanisms can still not be determined from specimens of smaller scales. In this paper a new approach to predict the influence of particle damping on lightweight structures using Frequency Based Substructuring (FBS) is presented. Moreover, the aim is to set up a design approach in order to find not only the optimal placement, but also the best filling ratio, area of application and possible weight savings for the base structure and to allow at the same time an engineering design at an affordable level.

The investigated system consists of a sandwich structure of glass fibre prepregs and a Nomex© honeycomb core, as it is used especially for aircraft cabin interior. Particle cavities are glued to the sandwich panel to apply the damping. The FBS modelling is carried out according to the dual coupling approach. For the simulation of the honeycomb sandwich panel a finite element (FE) model is used and frequency response functions (FRF) are calculated with a commercial FE-solver. Substructure FRFs of the particle cavity are determined experimentally. The modelling approach is analysed with respect to a nonlinear particle damping

behaviour. Moreover, the damping efficiency of various particle cavities on the assembled system is investigated using FBS-coupling and compared to experimental results.

2 State of the Art

When it comes to resonance of lightweight structures as a result of stationary dynamic loading, damping can play a major role to reduce vibration and noise amplifications [1]. However, the consideration of damping in product design is difficult. Despite the increasing accuracy of the constitutive models and the constant enhancement of the computational tools they do not solve the problem of identifying the dynamic model parameters and the uncertainties associated with their estimation for dynamic models [2]. Methods like the FEM are only capable of predicting dynamic properties such as eigenfrequencies and mode shapes to a certain degree. However, damping is often modelled by global structural damping parameters despite the presence of different dissipation sources [3]. Therefore, still a lot of experimental testing is necessary to determine dynamic characteristics like damping. In order to reduce the testing effort for the design of these structures and its associated costs and development time, the industry generally shifts to virtual design and simulation.

Generally, damping is defined as the phenomenon in which the mechanical vibration energy is dissipated and converted into other forms, e.g. internal thermal energy, in dynamic systems [8]. Damping dissipation is essentially a nonlinear and still not fully modeled and understood phenomenon [4].

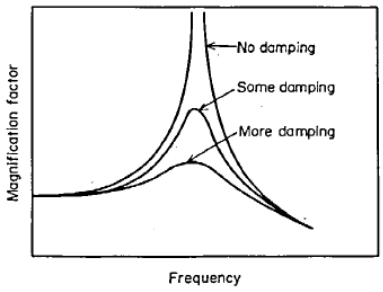


Figure 1 Damping effect on the magnification at resonance [5]

For the consideration of damping or even to design damping properties trial-and-error is still a common way. On the other hand linear modelling, can be used to approximate the structural dynamics of especially large structures, for which testing is very time consuming and expensive [6]. A FBS approach using the advantages of modular product structures is presented in [7]. For the particle damping the applicability of such a linear approach is investigated in this paper.

2.1 Particle Damping

Particle damping is a passive technology to reduce vibrations. Especially for lightweight structures particle damping can be a good measure since the added mass can be very small compared to the overall mass of the system [8]. Particle dampers are usually cavities partially filled with small particle of variable material. They are directly filled into existing enclosures of the base structure or they can be attached to a vibrating structure at a location with high displacement amplitudes [9]. For the design of particle dampers exist numerous studies over the last decades. A few of them are presented here, which cover working principles, modelling and experimental testing.

For particle damping, a few physical damping mechanisms are relevant to describe the overall dissipation. In the first place there are non-elastic particle-particle and particle-wall collisions that induce damping, as indicated in Figure 2. Furthermore, friction between particles and particle-wall friction adds more dissipation. But all these physical mechanism at such small scale are the reason that the dissipation behaviour of granular materials is still not fully understood [10].

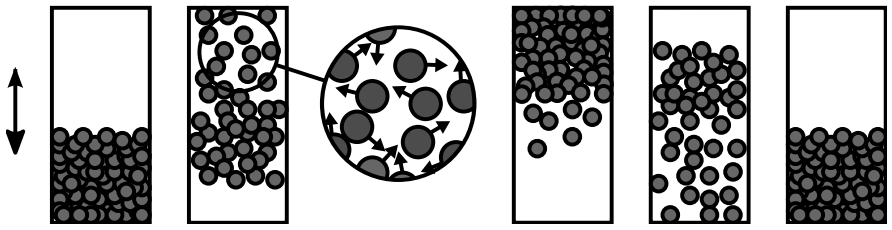


Figure 2: Particle damping – working principle and dissipation mechanism

For particle there are some qualitative findings that are stated in literature. First of all the damping behaviour of granular materials is a highly nonlinear due to impacts and sliding between the particles [11,12]. A few research papers state that for typical particles (e.g. metal and sand) the damping performance of particle dampers is independent on the environmental conditions, like temperature. In comparison to viscoelastic dampers in many applications this can be an advantage. It is found that particle dampers with properly selected mass ratios and space of movement can effectively attenuating several modes with one damper design over a wide frequency range [9,13].

However, the modelling of particle damping is still difficult [8]. Initially, Sun et al. (1986) used a static energy analysis to calculate the transmission loss of sand-filled structures. Whereas others developed equivalent SDOF models to predict the damping behaviour [9,13,14]. For the simplified parametric models, the problem so far is the high number of design parameters for particle damping compared to the number of variables exiting for this type of modelling approach [15]. Another approach to predict particle damping follows a hydrodynamic approach based on the similarities of molecular or gas liquid behavior to particle movement. However, the approach greatly varies with the choice of identification system (box-division) to estimate the flow field values and is therefore still very uncertain [15]. Today the three dimensional (3-D) discrete element method is focused by many researchers to exactly model single particle behaviour [16]. However, this method is limited by e.g. the number of particles, because of the increasing computing effort. Therefore, it is not yet an efficient tool for vibration problems and especially not for design optimisation since this requires multiple runs of different particle damper configurations. Furthermore, Pourtavakoli et al. 2016 [10] remarked recently that the dissipative properties of granular materials are still poorly understood. Consequently, besides the modelling investigations trial-and-error experimental studies to optimize the particle damping design are still very common [8,9,17]. Fowler et al. [12] present a list of basic “rules-of-thumb” for the design of particle dampers, including mass, material coefficient of friction, gravity and excitation frequency.

For the proposed models, except from DEM, the validity is only given for a restricted range of operating conditions, although the PD performance varies with changing operating conditions. Therefore, using the models for engineering decision making either the amount of information is limited, the computational time is so high that optimization is not feasible or an extensive amount of experimental work for dynamic characterization at the final product stage must be done.

Only a few papers so far investigated the potential of damping honeycomb structures with particle damping. Liu 2011 [8] studied experimentally the effect of particle damping in comparison to other damping methods and with respect to its weight gain. There, particle damping was proven to be an efficient measure to damp lightweight structures. Michon et al. 2013 [9] demonstrated the damping potential of particles within metallic honeycomb structures. Specifically, they investigated the optimal filling ratio of the honeycomb cells and their placement. For that they proposed a simplified equivalent viscous damping model, which was derived by least square approximation of test data. Recently, Koch et al. 2017 [18] proved the potential of defined partial fillings of a honeycomb structure by granular materials of an oil pan bottom of an engine in order to reduce sound emissions.

2.2 Frequency Based Substructuring

The Frequency Based Substructuring (FBS) is a frequency domain method to solve linear vibration problems by decomposing a structure into several smaller parts, the so-called substructures. FBS theory was already published in the 1960s-1980s [19]. The FBS assumes that a reduced number of DoF are sufficient to describe the dynamic behaviour of a system. Each substructure can individually be characterized by its frequency response functions (FRF), that can be determined via simulation or experimental testing. This so-called experimental substructuring is one of the major advantages of this approach if experiments are carried out appropriately. Thus, real (non-linear, frequency dependant) physical effects, that cannot be modelled in an appropriate manner, can be incorporated into a frequency based assembled system response. However, only in 2006 De Klerk et al. [20] published a new systematic notation, called dual assembly, that facilitates the handling for numerical calculation. Following the dual assembly according to [20], the overall frequency response function matrix can be derived from the general equation of motion of subsystems Eq. 1 in the time domain. The interface compatibility is defined in Eq. 2 with the boolean matrix B and the equilibrium of connection forces in Eq. 3 with the Boolean localization matrix L [20].

$$\mathbf{M\ddot{u} + C\dot{u} + Ku} = \mathbf{f} + \mathbf{g} \quad \textit{(Local Equilibrium)} \tag{1}$$

$$\mathbf{Bu} = \mathbf{0} \quad \textit{(Interface compatibility)} \tag{2}$$

$$\mathbf{L}^T\mathbf{g} = \mathbf{0} \quad \textit{(Equilibrium of connecting forces)} \tag{3}$$

With the Structural Impedance Matrix

$$\mathbf{Z}(j\omega) \triangleq -\omega^2\mathbf{M} + j\omega\mathbf{C} + \mathbf{K}$$

the transformation to the frequency domain is carried out to

$$\mathbf{Z}(\mathrm{w})\mathbf{u}(j\omega) = \mathbf{f}(\omega) + \mathbf{g}(\omega) \tag{4}$$

$$\mathbf{Bu}(\omega) = \mathbf{0} \tag{5}$$

$$\mathbf{L^T g}(\omega) = \mathbf{0.} \tag{6}$$

Introducing the Lagrange Mutliplier $\boldsymbol{\lambda}$ such that $\mathbf{g} = -\mathbf{B}^T\boldsymbol{\lambda}$, one gets the so-called dual assembly in matrix form as following.

$$\begin{bmatrix} \mathbf{Z} & \mathbf{B}^T \\ \mathbf{B} & \mathbf{0} \end{bmatrix} \begin{bmatrix} \mathbf{u} \\ \boldsymbol{\lambda} \end{bmatrix} = \begin{bmatrix} \mathbf{f} \\ \mathbf{0} \end{bmatrix} \tag{7}$$

The Lagrange mutliplier λ respectively represents the internal connection forces. Solving the first equation for u with $\mathbf{Z}^{-1} = \mathbf{Y}$ yields

$$\mathbf{u} = \mathbf{Y}(\mathbf{f} - \mathbf{B}^T\boldsymbol{\lambda}) \tag{8}$$

Y is the uncoupled admittance matrix of the whole mechanical system in block diagonal form. Inserting Eq.8 in Eq. 7 one finds

$$\mathbf{B}(\mathbf{Yf} - \mathbf{YB}^T\boldsymbol{\lambda}) = \mathbf{0} \tag{9}$$

$$\Rightarrow \boldsymbol{\lambda} = (\mathbf{BYB}^T)^{-1}\mathbf{BYf}$$

Which leads to the coupled transfer function matrix $\mathbf{Y_C}(\omega)$

$$\mathbf{u} = \mathbf{Yf} - \mathbf{YB^T}\left(\mathbf{BYB^T}\right)^{-1}\mathbf{BYf}$$

$$\mathbf{u} = \underbrace{(\mathbf{Y} - \mathbf{YB}^T(\mathbf{BYB}^T)^{-1}\mathbf{BY})}_{\mathbf{Y_C}(\omega)}\mathbf{f} \tag{10}$$

Using the FBS approach the particle damping is predicted for the described sandwich structure and shall also be applied to lager structures, where trial-and-error testing is not possible or too expensive. The

consideration of particle dampers without modelling its complex dynamic behavior in detail shall be investigated. With this first step, the design of particle dampers is facilitated because a reduced number and smaller tests are needed to determine a damper design.

3 Experimental Study

For the experimental tests a sandwich panel is clamped at one end and excited with classical base point excitation at different excitation levels. It is the same system as investigated in [21]. The testing is carried out with and without particle damper. The investigated system in this paper consists of a typical honeycomb sandwich panel typically used in the aircraft cabin for mostly all lightweight structures like lavatories, galleys and lining component etc. The vibration testing is carried out as impedance sweep tests on a hydraulic shaker. The test set-up is shown in Figure 3. Vibration tests are carried out as a frequency sweep at constant 0.35 g (3,4335 m/s^2) within a frequency range of 5 - 25 Hz. The sweep velocity is 0.5 octave/min.

The panel is clamped with an aluminum fixture at one end and freely vibrating at the top. The acceleration is measured as input and output signal by triaxial ICP acceleration sensors. The input signal is measured on the fixture at the bottom of the panel. The acceleration output is measured at the top of the panel. The excitation load is also measured at the fixture by a 5kN 6D load cell. All measurements are done with a sampling rate of 600 Hz. The evaluation of the test data is done in the frequency domain in the out of plane direction of the panel to calculate the resonance frequency and the acceleration amplification as well as to determine the damping factor for FE-simulation via half-power-bandwidth method.

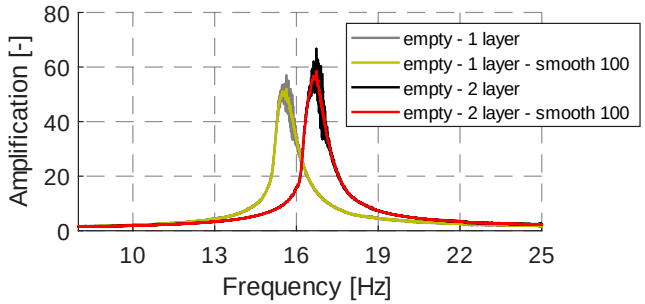


Figure 3: Test set-up for vibration testing of honeycomb sandwich panel

3.1 Honeycomb Sandwich

A sandwich panel design is chosen, as shown in Figure 3, in order to have the first resonance frequency within the defined frequency range. The size of the panel is 950 x 190 x 19 mm. The investigated material is a typical aircraft interior sandwich panel consisting of glass fibre fabric reinforced phenolic resin prepreg face sheets (PHG600-68-50/44) and a Nomex honeycomb core (cell size 3.2 mm, density 48 kg/m³). Two sandwich panels are tested with 1 and 2 prepreg layers in order to have different level of acceleration at the coupling point. The so-called panel with 1 layer has a thin cover layer, the PHG600-68-44, with 0.09 mm thickness on top, because this is necessary for the surface finish for cabin interior due to of the telegraphing effect. Nonetheless, for simplicity, the investigated layups are differentiated as 1 and 2 prepreg lay-ups. Furthermore, it can be shown that a simple stiffening of a panel does not shift the frequency considerably higher than with 1 layer, as shown in Figure 4. Based on these test results a structural damping ratio is determined via half-power-bandwidth method from 3 tests of each panel, because still today modelling the dynamic behavior requires an experimentally derived damping value. For this reason, additionally a moving

average smooth with an averaging interval of 100 steps is also shown, since this is the underlying FRF for the determination of the structural damping coefficients



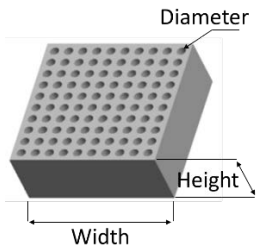
Structural damping D

Prepreg layer	D_{mean} [%]
1 layer	1,52
2 layer	1,33

Figure 4: FRF derived from vibration test of honeycomb sandwich panels with 1 and 2 prepreg layers and evaluation of damping coefficient via half-power-bandwidth method

3.2 Particle Damped Honeycomb Panel

Different particle dampers are then mounted to honeycomb sandwich panels with 1 and 2 prepreg layers and the same frequency sweep is carried out, as described above. For the particle damper 3 sizes are used, small, medium and large size cavities with 4 mm drill holes distributed equally in excitation direction. The area orthogonal to the excitation direction doubles with increasing dimensions. The cavities are 3D-printed. The particle used is commercial quartz sand with defined particle size of 0.1 - 0.4 mm. A filling ratio of 50 % is realized for every PD. To close the particle cavity strong adhesive tape is used. This certainly influences the damping performance - it lowers the particle damping - but it should not be important for the qualitative research presented in this paper.



Height [mm]	Dimensions [mm]		Drill hole [mm]	Particle mass - 50 % filling ratio [g]	Mass of particle cavity [g]
26	72.5	49	4	24	60
26	102.5	69,3	4	46	116
26	145	98	4	99	236

Figure 5: Dimensions of the particle damper including the filling ratio and the associated mass

For the evaluation of the measurement results the magnitude of the transmissibility, the amplification, is shown in Figure 6 for all PDs compared to the panel without damping treatment. In all FRFs a large decrease of amplification of up to 30 % of the reference tests can be seen. With increasing particle damper and particle mass the amplification can be reduced more, as expected and already stated in literature. The effect is a little bit less for the sandwich panel with 2 layers since this system is much stiffer, but still extraordinary high. In the first place, however, the comparison of two different sandwich facesheets shall demonstrate that the FBS approach can be suitable for particle damping predictions on structures with different mechanical properties in the following paragraphs. The frequency shift mainly due to the mass increase towards a lower resonance frequency is about 7-8 Hz from 16 Hz to a minimum of 9 Hz for 1 layer panel and from 17 Hz to 11 Hz for the 2 layer panel. One of the main reasons for the large frequency shift is the amount of mass only added by the empty particle cavity. However only the mass of the cavity does not lower the amplification a lot – only from 58 to 53 for the 1 layer panel, so that the particle can be accounted for the damping effect.

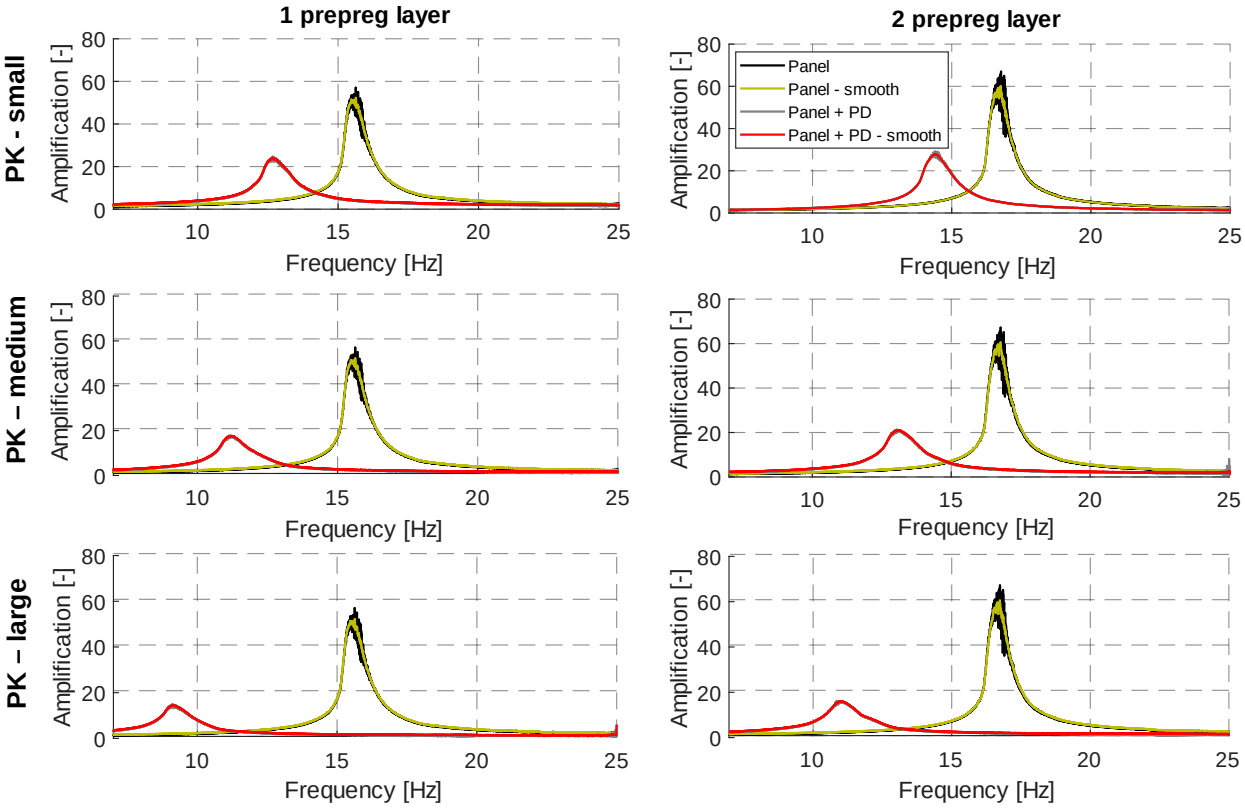


Figure 6: Test results for particle damping at panel top

4 Experimental Substructuring for Particle Damping

For the FBS-substructuring the system is partitioned into the two main components (Figure 7). The sandwich panel plus its fixture are one substructure and the particle damper - the particle cavity plus the particle filling - the other. In this way it is possible to exchange the particle damper easily to estimate the FRF for a variety of different damper configurations.

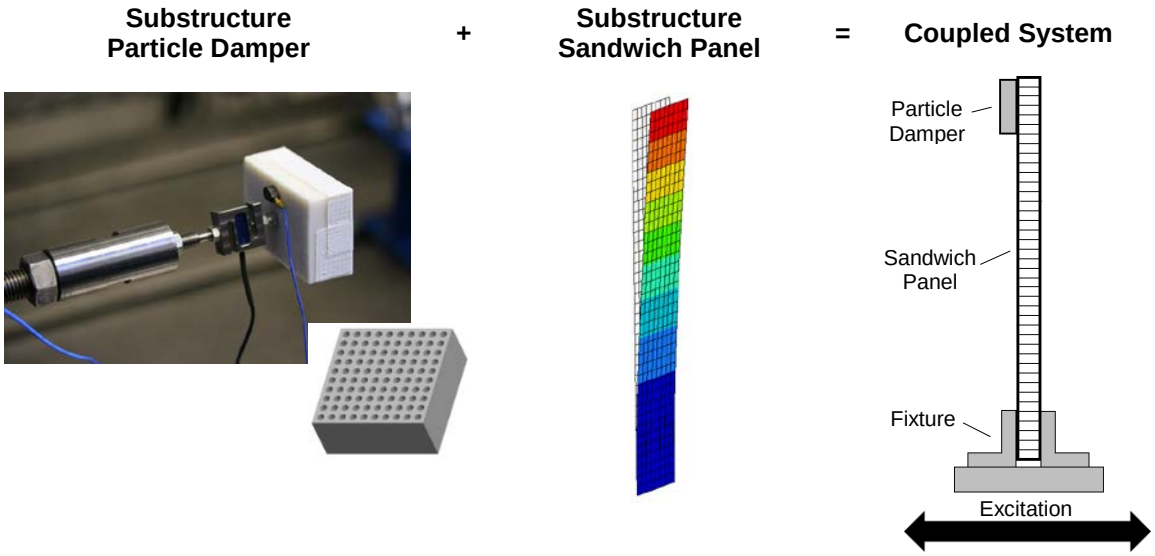


Figure 7: Substructuring approach for particle damping

The frequency response of the sandwich panel is derived from a linear FE-model. The frequency response of the particle system - as one substructure - is determined experimentally. Finally, with a hybrid frequency

based assembly using test (particle cavity) and simulation (lightweight structure) results is used to determine the dynamic behaviour of the entire system. In this way the consideration of particle dampers is possible without modelling its complex dynamic behaviour in detail.

For the coupling of the particle damper to the panel a rigid multipoint connection is used, via interpolation constraint elements (RBE2) in the FE-model. In this way, the particle damper is only linked to the FE-model at one single node, the master node of the rigid connection. The interface definition is shown in Figure 8. There also the 4 dof of the coupled system are indicated in the Figure with respect to the acceleration outputs in Eq. 15.

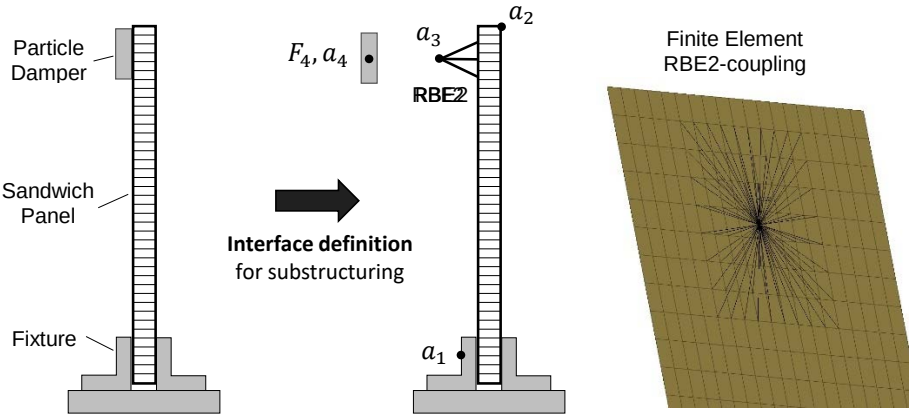


Figure 8: Interface definition between sandwich panel and particle damper via rigid link with interpolation constraint elements

For the interface definition it is assumed that the particle damper can be represented through a 1D frequency response in the direction of main particle movement, along the thin drilling holes. Following this approach, the uncoupled FRF matrix Y can be written as

$$\mathrm{Y} = \begin{bmatrix} \mathrm{Y}_{\mathrm{Panel}} & 0 \\ 0 & \mathrm{Y}_{\mathrm{PD}} \end{bmatrix} = \begin{bmatrix} \mathrm{Y}_{11} & \mathrm{Y}_{12} & \mathrm{Y}_{13} & 0 \\ \mathrm{Y}_{21} & \mathrm{Y}_{22} & \mathrm{Y}_{23} & 0 \\ \mathrm{Y}_{31} & \mathrm{Y}_{32} & \mathrm{Y}_{33} & 0 \\ 0 & 0 & 0 & \mathrm{Y}_{\mathrm{PD}} \end{bmatrix} \quad , \mathrm{Y} \in \mathbb{R}^{4x4} \tag{11}$$

where Y_{PD} is the measured FRF of the particle damper. For the coupling matrix B follows

$$\mathrm{B} = [0 \quad 0 \quad 1 \quad -1]. \tag{12}$$

The coupled FRF-matrix Y_C can be calculated with Eq. 10

$$\mathrm{Y}_C = \mathrm{Y} - \mathrm{Y}\mathrm{B}^T(\mathrm{B}\mathrm{Y}\mathrm{B}^T)^{-1}\mathrm{B}\mathrm{Y} \tag{13}$$

Inserting Y and B leads to

$$\mathrm{Y}_C = \begin{bmatrix} \mathrm{Y}_{11} & \mathrm{Y}_{12} & \mathrm{Y}_{13} & 0 \\ \mathrm{Y}_{21} & \mathrm{Y}_{22} & \mathrm{Y}_{23} & 0 \\ \mathrm{Y}_{31} & \mathrm{Y}_{32} & \mathrm{Y}_{33} & 0 \\ 0 & 0 & 0 & \mathrm{Y}_{\mathrm{PD}} \end{bmatrix} - \frac{1}{\mathrm{Y}_{33} + \mathrm{Y}_{\mathrm{PD}}} \begin{bmatrix} \mathrm{Y}_{13}\mathrm{Y}_{31} & \mathrm{Y}_{13}\mathrm{Y}_{32} & \mathrm{Y}_{13}\mathrm{Y}_{33} & -\mathrm{Y}_{13}\mathrm{Y}_{\mathrm{PD}} \\ \mathrm{Y}_{23}\mathrm{Y}_{31} & \mathrm{Y}_{23}\mathrm{Y}_{32} & \mathrm{Y}_{23}\mathrm{Y}_{33} & -\mathrm{Y}_{23}\mathrm{Y}_{\mathrm{PD}} \\ \mathrm{Y}_{33}\mathrm{Y}_{31} & \mathrm{Y}_{33}\mathrm{Y}_{32} & \mathrm{Y}_{33}\mathrm{Y}_{33} & -\mathrm{Y}_{33}\mathrm{Y}_{\mathrm{PD}} \\ -\mathrm{Y}_{\mathrm{PD}}\mathrm{Y}_{31} & -\mathrm{Y}_{\mathrm{PD}}\mathrm{Y}_{32} & -\mathrm{Y}_{\mathrm{PD}}\mathrm{Y}_{\mathrm{PD}} & \mathrm{Y}_{\mathrm{PD}}\mathrm{Y}_{\mathrm{PD}} \end{bmatrix}. \tag{14}$$

For a linear system with a unit load the acceleration output can be computed with

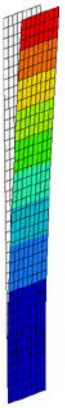
$$\begin{bmatrix} a_1^C \\ a_2^C \\ a_3^C \\ a_4^C \end{bmatrix} = (\mathrm{Y}_C) \begin{bmatrix} 0 \\ 1 \\ 0 \\ 0 \end{bmatrix}, \tag{15}$$

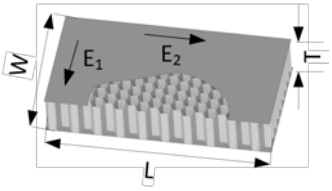
so that the acceleration transmissibility T of the coupled system from the input to the output acceleration can be derived

$$\mathrm{T}_{\mathrm{Panel+PD}} = \frac{a_2^C}{a_1^C}. \tag{16}$$

4.1 FE-Modelling of Honeycomb Sandwich Structure

As the vibration tests the simulations are carried out for a frequency range of 5 - 25 Hz with harmonic excitation derived from typical aircraft cabin dynamics. The FE-simulation is carried out with MSC.Nastran Sol 108, to recieve the direct frequency response. The sandwich panel is modelled with 1805 2D CQUAD4 shell elements. The element size is 10 mm. The clamping at the bottom is realized with single point constraint elements. The macroscopic elastic material properties of the honeycomb core are given by the manufacturer and where slightly adjusted by experimental modal analysis in a previous study [21].

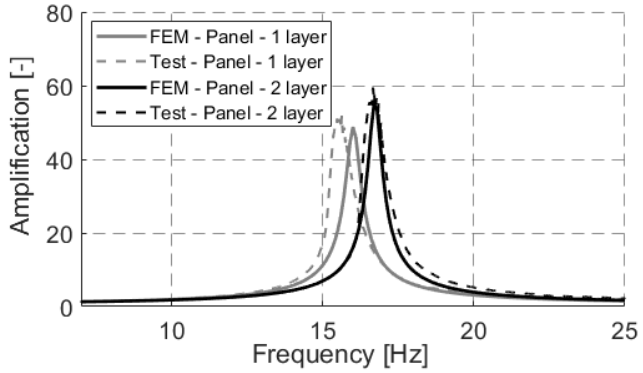
Face sheet		Honeycomb core		FE-model
E_1 [MPa]	24000	E [MPa]	200	
E_2 [MPa]	22000	G [MPa]	83	
G_{12} [MPa]	7500	ν	0.2	
G_{1T} [MPa]	2900			
G_{2T} [MPa]	3700	Thickness [mm]	18.5	
ν_{12}	0.2			



2D-shell elements

Table 1: Simulation of base point excitation for the panel design

Using the material parameters in Table 1, the FRF of the sandwich panels with 1 and 2 prepreg layers are shown in Figure 9. There is a good agreement between simulation and test results. However, the resonance frequency of the 2 layer panel slightly deviates from the test results, but the deviations are less than 5 % with the simple 2D-shell model. Therefor the model is assumed to be valid and taken for the FBS.



	Panel with 1 layer		Panel with 2 layers	
	FEM	Test	FEM	Test
Resonance Frequency [Hz]	15.2	15.6	16.6	16.7
Amplification	49	51	58	59

Figure 9: Comparison between simulation and test results for sandwich panel without damping

4.2 Experimental Characterisation of Particle Damper

The test set up for the experimental determination of the FRF of the particle damper is depicted in Figure 10. The test was also carried out as frequency sweep with constant acceleration in the same frequency range. The interface load is measured by a 1D-100N load cell and the acceleration is measured with a lightweight (0.8 g) 50g-ICP acceleration sensor.

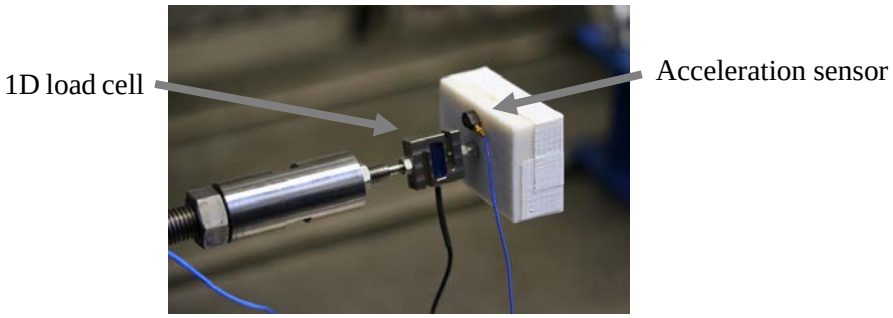


Figure 10: Test set-up for experimental substructure characterization of the particle damper.

The measured time signals are transformed into the frequency domain. An excerpt of the results - the accelerance - is shown in Figure 11 in a detailed view. The amplitude is nearly constant in the whole frequency range, whereas the phase is slightly decreasing. Furthermore, the results are depicted with a moving average smooth (intervals: 100 and 1000). The amplitude of the raw measurement data is not considerably different to the moving average smooth 100. In the raw data of the phase, however, there are some spurious peaks. But, with the reduced data set, that is necessary for the coupling with the FE-model, because of the lower frequency step than the measurement sampling rate, these peaks are eliminated.

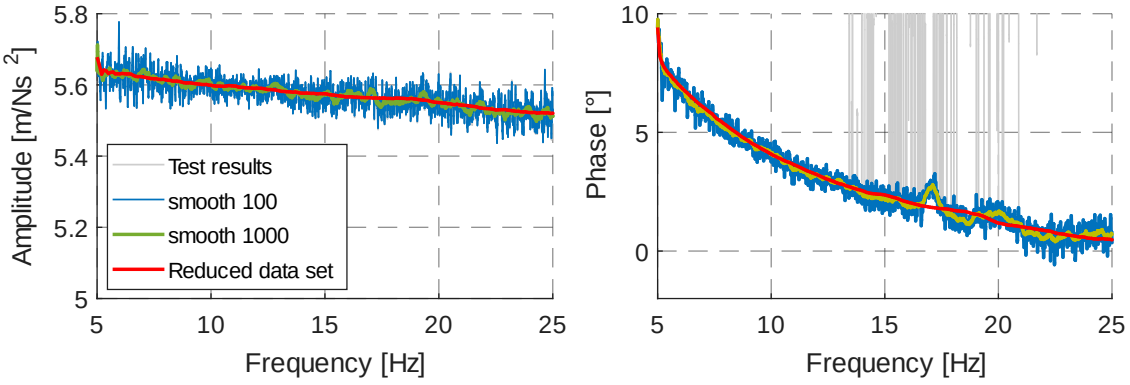


Figure 11: Reduction of measurement data of medium particle damper – Comparison of smoothed and reduced data set for coupling

The results of all three particle dampers used in this study are shown in Figure 12, for the small medium and large particle damper in the reduced data set format, which is used for the coupling with the FE-model. Each particle damper was tested with 3 different sweep excitations of 0.5 g, 1 g and 2 g. As expected the amplitude decreases with increasing particle mass and the trend for all dampers is very similar. Therefore, a strong nonlinearity cannot be seen at this stage. However, the 2 g result is always slightly higher than the other two. The phase differences are more obvious. For 2 g excitation the phase angle is in every case more than 30 % higher. However, the phase seems to be independent of the filling ratio since there are no obvious differences between the 3 dampers.

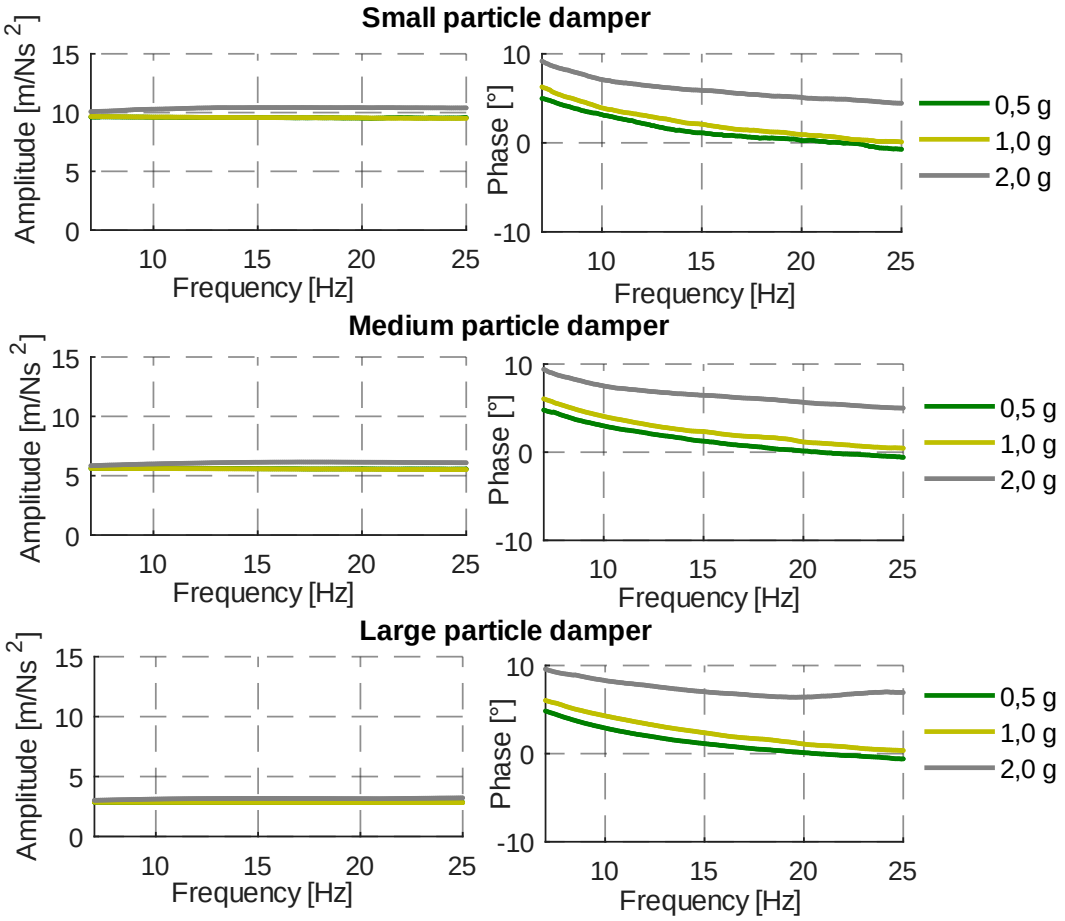


Figure 12: Experimentally determined substructure FRFs (accelerance) of particle damper in reduced data set format

5 Results and Discussion

For the coupling, the FE-model of the honeycomb sandwich panel (Figure 9) and the experimentally determined FRF for the particle damper (Figure 12) are coupled according to the interface definition and the derived equation 14. Besides the 3 different particle dampers with increasing particle mass at 50 % filling ratio of quartz sand, the influence of different composite layups, accelerations sensors, sweep excitations and positions of the PD are investigated. Using the measured PD-FRFs with different sweep excitations, the FBS-coupling is shown in Figure 13 for a sandwich panel with 1 and 2 layers. Between the FE-models the only difference is the structural damping coefficient which is determined by experimental testing of the panels without damping treatment (Figure 4).

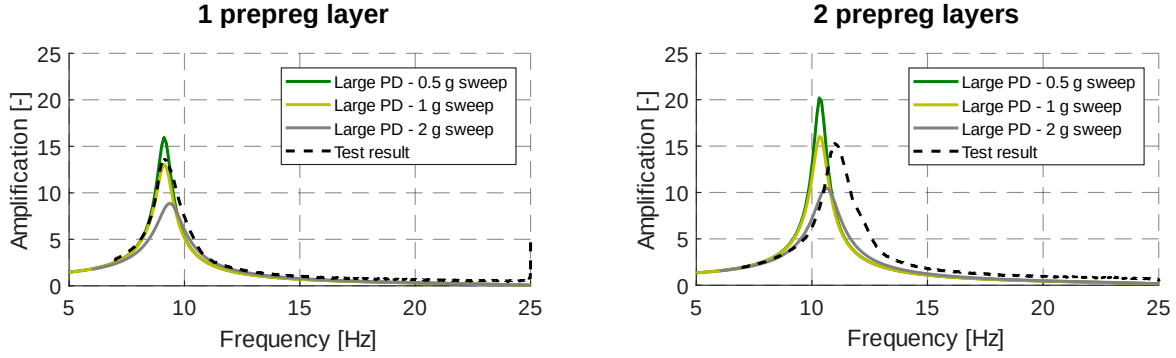


Figure 13: FBS-coupling with PD-FRFs at panel top from different sweep excitations

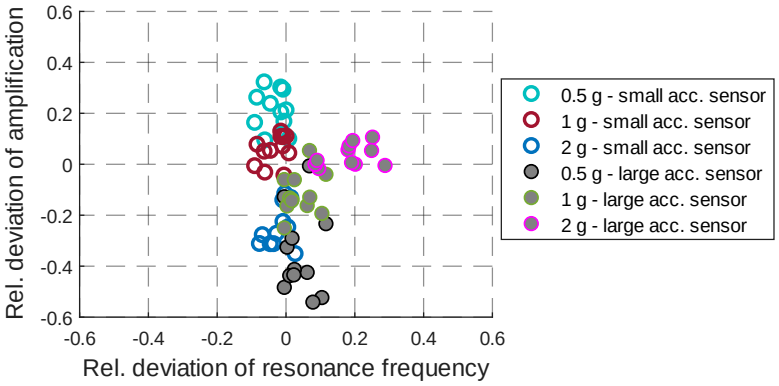


Figure 14: Rel. deviations of resonance frequency and amplification dependent on the acceleration sensor

For the 1 g excitation the results match very good with the test results (see Figure 13 and Figure 14). There is, however, an influence of the acceleration level of the sweep tests, as expected, since particle damping is amplitude dependent. For 0.5 g the amplification is overestimated by 20 % and on the other side for 2 g the deviation is underestimated with more than 20 %. But few more aspects must be considered. For 0.5 g the particle movement might not be high enough to result in sufficient interface load acting on the sandwich panel. For the 2 g excitation the measurement data of the sweep test was noisier than the others and the magnitude compared to the two other tests was higher. Furthermore, using a larger acceleration sensor leads to increasing deviations from the reference tests as indicated in Figure 14. The mass increase 1.8 g to 10 g can be the reason as well as the inertia of a non-centred additional mass with respect to the moving direction. Generally, it must be concluded that the coupling is very sensitive to measurement errors, because only the slight inaccuracies lead to larger deviations. But only considering the amplitude reduction with respect to the undamped system the linear predictions deviate not more than 12 % from the test results.

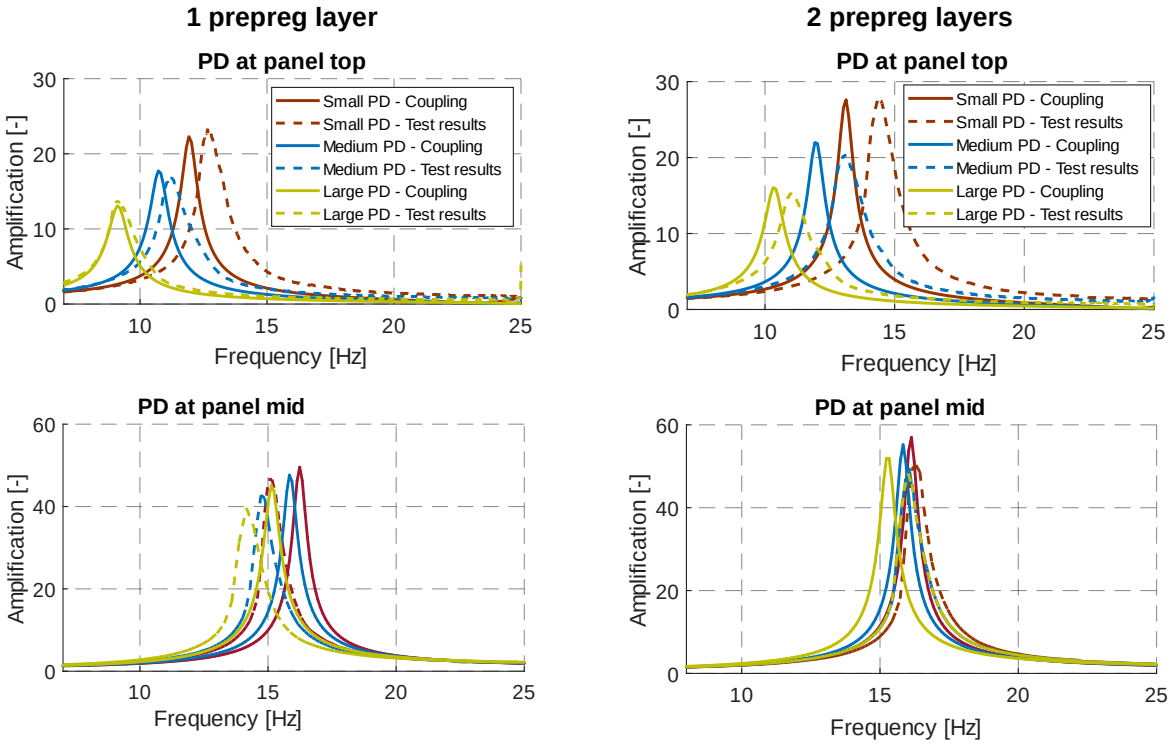


Figure 15: Coupling results for particle dampers at top and mid position

In this study, the PD-FRF determined at 1 g was further taken to analyze the coupling in more detail. The amplification of the FBS-coupling for the particle damper at top and mid position of the panel dependent on

the composite lay-up is shown in Figure 15. For these configuration, the prediction of the particle damping is very good. The amplitudes and the resonance frequency for the top position are within 5 % deviation to test results for both positions. For the sandwich with 2 layers the amplitudes deviate slightly more within 7 % compared to test results. The frequency deviations are only within 9 %. That can also be reduced with improved material data for the composite lay-up and above all with the mass decoupling of the mounting screw from the experimentally determined damper FRF, since the frequency predictions are below the test results. As expected the influence of the particle at the panel mid position damper on the amplification is not very strong but the damping predictions are still accurate. The deviations in percentage become larger with increasing particle mass due to the decrease in reference amplification, but the absolute deviations are smaller than in every other case.

6 Conclusion and Outlook

In this paper a new approach to predict the particle damping using a frequency based substructuring approach. In this way the consideration of particle dampers (PD) is possible without modelling its complex dynamic behaviour in detail as with e.g. the discrete element method. The frequency response of the particle system - as one substructure - is determined experimentally. Finally, with a hybrid frequency based assembly, using test (particle damper) and simulation (honeycomb sandwich panel) results, is used to determine the dynamic behaviour of the entire system. In the paper the influence of the particle mass, the position of the damper, different test set-ups and two sandwich panels with different stiffness are investigated.

Generally, despite of the nonlinear behavior of particle damping the predictions using the frequency based substructuring approach are within a reasonable amount of deviations for the investigated system. Moreover, the trend of all results matched the experimental tests. Therefor using a linear approximation to predict the damping can be a valid approach for other problems especially if the effort for testing of large structures can be reduced in this way. For small structures and cases where more particle material is added to a structure than in this case it might be not feasible to measure interface forces, or the damping nonlinearity is too high for accurate linear predictions. Moreover, the experimental characterization of the particle is very sensitive to the test set-up and the testing must be carried out with care. In the future this study shall be expanded to more parameters, to find out more about the validity of the approach. Besides, the aim is to set up an optimization in order to find not only the optimal placement, but also the best filling ratio, area of application and possible weight savings for the base structure to allow an engineering design at an affordable level.

References

[1] C. F. Beards, *Structural vibration*: *Analysis and damping*, Arnold; Halsted Press, London, New York, 1996.

[2] R. Ibrahim and C. Pettit, "*Uncertainties and dynamic problems of bolted joints and other fasteners"*, Journal of Sound and Vibration, No. 279 (2005), pp. 857–936.

[3] A. Brandt, *Noise and vibration analysis*: *Signal analysis and experimental procedures*, Wiley, Chichester, Hoboken, N.J., 2011.

[4] G. Kerschen, K. Worden, A. F. Vakakis et al., "*Past, present and future of nonlinear system identification in structural dynamics"*, Mechanical Systems and Signal Processing, Vol. 20, No. 3 (2006), pp. 505–592.

[5] C. W. Bert, "*Material damping"*, Journal of Sound and Vibration, Vol. 29, No. 2 (1973), pp. 129–153.

[6] R. Seemann, B. Plaumann, J. Oltmann et al., "*FE-Modelling Guidelines for the Dimensioning of Aircraft Cabin Interior Under Stationary Dynamic Loads", in 29th Congress of the International Council of Aeronautical Sciences (ICAS),* St. Petersburg (2014).

[7] B. Plaumann, *Systemanalyse und -synthese für die Auslegung varianter Leichtbaustrukturen unter dynamischen Lasten,* ph.D., Technischen Universität Hamburg-Harburg, 2015.

[8] Y. Lui, *Damping Technologies for Automotive Panel Structures*, ph.D., ETH Zurich, 2011.
[9] G. Michon, A. Almajid, and G. Aridon, "*Soft hollow particle damping identification in honeycomb structures*", Journal of Sound and Vibration, Vol. 332, No. 3 (2013), pp. 536–544.
[10] H. Pourtavakoli, E. J. R. Parteli, and T. Pöschel, "*Granular dampers:* Does particle shape matter?", New Journal of Physics, Vol. 18, No. 7 (2016).
[11] F. Duvigneau, S. Koch, E. Woschke et al., "*An effective vibration reduction concept for automotive applications based on granular-filled cavities*", Journal of Vibration and Control, Vol. 24, No. 1 (2016), pp. 73–82.
[12] B. L. Fowler, E. M. Flint, and S. E. Olson, "*Design Methodology for Particle Damping*", *in SPIE Conference on Smart Structures and Materials*, Newport Beach, CA (2001).
[13] I. Yokomichi, Y. Araki, Y. Jinnouchi et al., "*Impact Damper With Granular Materials for Multibody System*", Journal of Pressure Vessel Technology, Vol. 118, No. 1 (1996).
[14] R. D. FRIEND and V. K. KINRA, "*PARTICLE IMPACT DAMPING*", Journal of Sound and Vibration, Vol. 233, No. 1 (2000), pp. 93–118.
[15] C. X. Wong, M. C. Daniel, and J. A. Rongong, "*Energy dissipation prediction of particle dampers*", Journal of Sound and Vibration, Vol. 319, 1-2 (2009), pp. 91–118.
[16] M. SAEKI, "*Impact Damping with Granular Materials in a Horizontally Vibrating System*", Journal of Sound and Vibration, Vol. 251, No. 1 (2002), pp. 153–161.
[17] M. Sánchez, G. Rosenthal, and L. A. Pugnaloni, "*Universal response of optimal granular damping devices*", Journal of Sound and Vibration, Vol. 331, No. 20 (2012), pp. 4389–4394.
[18] S. Koch, F. Duvigneau, R. Orszulik et al., "*Partial filling of a honeycomb structure by granular materials for vibration and noise reduction*", Journal of Sound and Vibration (2017).
[19] B. Jetmundsen, R. Bielawa, and W. G. Flannelly, "*Generalized Frequency Domain Substructure Synthesis*", Journal of the American Helicopter Society, Vol. 33, No. 1 (1988), pp. 55–65.
[20] D. de Klerk, D.J. Rixen, and J. de Jong, "*The Frequency Based Substructuring (FBS) Method Reformulated According to the Dual Domain Decomposition Method*", *in Proceedings of the XXIV International Modal Analysis Conference (IMAC)*, St. Louis, MO (2006).
[21] J. Oltmann, R. Seemann, and D. Krause, "*Experimental Investigation on Damping for Honeycomb Sandwich Panels under Different Support Conditions*", *in Workshop on Aircraft System Technologies (AST)*, Hamburg (2015), pp. 207–216.

Reduced order modeling for forced response prediction of structures with large contact interfaces

G. Battiato [1*], **C. M. Firrone** [1]
[1] Politecnico di Torino, Department of Mechanical and Aerospace Engineering,
Corso Duca degli Abruzzi, 24, 10129 Torino, Italy
*e-mail: **giuseppe.battiato@polito.it**

Abstract
Real structures consist of components assembled together by means of joints whose behavior may result nonlinear. Modeling the contact interactions at the interface between neighboring components is thus essential for a precise prediction of the structure's response. One of the categories of joints that are widely used in mechanical applications are the lap joints and flanged joints. The two types of joints usually share two features: the contact regions are generally large and can not be considered localized with respect to the volume of the assembled bodies and bolted joints are used as a removable joint and distributed over the contact equally spaced. In this paper an efficient method to deal with large contact interface is presented in order to run fast nonlinear simulations taking into account the friction forces occurring at the contact.

1 Introduction

Structural dynamic applications exhibiting a clear linear behavior are rare exceptions. Real structures generally consist of components assembled together by means of joints whose behavior may result highly nonlinear. Depending on the nature of the excitation, joints might strongly affect the structure's dynamics, which therefore is far away from being linear. Modeling the interfaces interaction is thus an essential task to be accomplished for a more precise prediction of the structure's response in order to preserve integrity when safety margins are adopted during design based on intrinsic uncertainties.

Among all the possible sources of nonlinearities taking place at the contact interfaces of joints, friction phenomena are the commonest. The high interest in modeling and evaluating the effects of friction on the dynamics of structures is proven by recent academic studies and industrial applications [4, 5, 6, 8, 7, 9]. In this regard, the typical approach consist in creating the finite element (FE) models of components in contact having compatible meshes at the contact interfaces. In this way classic node-to-node contact elements based on the Coulomb friction law can be applied and the nonlinear forced response of the system finally evaluated. The mentioned approach is nowadays well-established and appears as convenient when applied to structures featuring small contact regions. However, it involves large computational times when extended contact interfaces with refined mesh are present between substructures.

Most of the well-established reduction methods in the class of the component mode synthesis (CMS) aims at reducing the substructure's dynamics to few master degrees-of-freedom (DoFs). For nonlinear dynamic analyses involving contact phenomena, such set of master DoFs has to include the contact DoFs, i.e. the physical DoFs where the nonlinear contact forces act. When the number of contact DoFs is a substantial percentage of the total number of DoFs, the application of the common CMS methods loses its efficiency in terms of reduction of the computational costs. On the other hand, interface reduction methods can be employed to reduce the number of DoFs at the contact regions in order to make the evaluation of the nonlinear contact forced response faster [19].

Several methods for the interface reduction have been proposed in the past few years [10, 11, 12, 13, 14, 15]. Among them, the *Gram-Schmidt Interface* (*GSI*) reduction method appears one of the most promising [16]. In this research, the *GSI* method is combined with a layer of macroslip contact elements in order to predict the effect of friction on the nonlinear forced response of two beam-like structures interacting through a large contact interface. The goodness of the proposed methodology is evaluated both in terms of solution accuracy and time costs savings on the calculation of nonlinear forced responses by using the Harmonic Balance Method.

2 Mathematical Background

In this section the *GSI* reduction method developed in [16] is briefly summarized and the numerical procedure employed to solve the reduced nonlinear equations of motion (EQM) of a structure featuring extended contact interfaces is discussed.

2.1 *GSI* reduction method

The *GSI* reduction method is an upgrade of the pre-existing technique based on the Characteristic Constraint Modes (*CC* modes) by Castainer et al. [10]. Similar to the classic CMS methods, the *GSI* technique allows for the reduction of a subset of master DoFs (either interface or contact DoFs) by means of a truncated basis of modes known as *GSI* modes. The starting point for this method is represented by the FE models of a linear substructures s whose DoFs can be partitioned as follows:

$$\boldsymbol{x}^s = \begin{Bmatrix} \boldsymbol{x}_i^s \\ \boldsymbol{x}_a^s \\ \boldsymbol{x}_r^s \end{Bmatrix} \tag{1}$$

where:

- $\boldsymbol{x}_i^s$ is the vector listing the n_i *interface* DoFs, i.e. the DoFs that are at the frontiers between substructures where compatibility is not guaranteed (as in the presence of joints that are characterized by a certain level of looseness);
- $\boldsymbol{x}_a^s$ is the vector of n_a *active* DoFs, i.e. the DoFs used either for the external force application or the response monitoring;
- $\boldsymbol{x}_r^s$ is the set of n_r *remaing* DoFs, i.e. those that are neither $\boldsymbol{x}_i^s$ nor $\boldsymbol{x}_a^s$.

Henceforth in this section the superscript s will be omitted to simplify the notation.

Although several CMS schemes exist to condense the substructure dynamics into a small set of master DoFs, the *GSI* method starts with the *Craig-Bampton* (CB-CMS) reduced EQM for the generic substructure [1, 2]:

$$\begin{bmatrix} \tilde{\boldsymbol{M}}_{mm} & \tilde{\boldsymbol{M}}_{mk} \\ \tilde{\boldsymbol{M}}_{km} & \boldsymbol{I}_{kk} \end{bmatrix} \begin{Bmatrix} \ddot{\boldsymbol{x}}_m \\ \ddot{\boldsymbol{q}}_k \end{Bmatrix} + \begin{bmatrix} \tilde{\boldsymbol{K}}_{mm} & \boldsymbol{0} \\ \boldsymbol{0} & \boldsymbol{\Omega}_{kk}^2 \end{bmatrix} \begin{Bmatrix} \boldsymbol{x}_m \\ \boldsymbol{q}_k \end{Bmatrix} = \begin{Bmatrix} \boldsymbol{f}_m \\ \boldsymbol{\phi}_k \end{Bmatrix} \tag{2}$$

where $\boldsymbol{x}_m = [\boldsymbol{x}_i^T \ \boldsymbol{x}_a^T]^T$ is the vector of $n_m = n_i + n_a$ master DoFs collecting the interface and active DoFs, $\boldsymbol{q}_k$ represents the reduced set of $n_k \ll n_r$ fixed-interface modal coordinates, $\boldsymbol{f}_m = [\boldsymbol{f}_i^T \ \boldsymbol{f}_a^T]^T$ is the $n_m \times 1$ vector including the contact and externally applied forces, while $\boldsymbol{\phi}_k$ is the $n_k \times 1$ vector of modal forces corresponding to the retained fixed-interface normal modes.

By taking the master DoFs partitions of the CB-CMS mass and stiffness matrices, the following eigenproblem is found:

$$(\tilde{\boldsymbol{K}}_{mm} - \omega_{m,j}^2 \tilde{\boldsymbol{M}}_{mm}) \boldsymbol{\varphi}_{m,j} = \boldsymbol{0} \qquad \forall\, j = 1, \ldots, n_m \tag{3}$$

where $\boldsymbol{\varphi}_{m,j}$ and $\omega^2_{m,j}$ are the j^{th} mass normalized *CC* mode and the corresponding eigenvalue respectively. The complete set of *CC* modes can be arranged (for increasing eigenvalues) as the columns of the following modal matrix:

$$\boldsymbol{\Phi}_{mm} = \begin{bmatrix} \boldsymbol{\varphi}_{m,1} & \dots & \boldsymbol{\varphi}_{m,n_m} \end{bmatrix} \tag{4}$$

The modal matrix of Eqn. 4 would allow for a coordinate transformation involving all the master DoFs. If a coordinate transformation is desired for only the interface DoFs, $\boldsymbol{\Phi}_{mm}$ has to be partitioned as follows:

$$\boldsymbol{x}_m = \begin{Bmatrix} \boldsymbol{x}_i \\ \boldsymbol{x}_a \end{Bmatrix} = \boldsymbol{\Phi}_{mm} \begin{Bmatrix} \boldsymbol{q}_i \\ \boldsymbol{q}_a \end{Bmatrix} = \begin{bmatrix} \boldsymbol{\Phi}_{ii} & \boldsymbol{\Phi}_{ia} \\ \boldsymbol{\Phi}_{ai} & \boldsymbol{\Phi}_{aa} \end{bmatrix} \begin{Bmatrix} \boldsymbol{q}_i \\ \boldsymbol{q}_a \end{Bmatrix} \tag{5}$$

where $\boldsymbol{q}_i$ and $\boldsymbol{q}_a$ are two arbitrary set of modal coordinates with size n_i and n_a respectively. By solving the second equation for $\boldsymbol{q}_a$ and substituting the result into the first, Eqn. 5 becomes:

$$\boldsymbol{x}_m = \begin{Bmatrix} \boldsymbol{x}_i \\ \boldsymbol{x}_a \end{Bmatrix} = \begin{bmatrix} \boldsymbol{\Phi}_{ii} - \boldsymbol{\Phi}_{ia}\boldsymbol{\Phi}_{aa}^{-1}\boldsymbol{\Phi}_{ai} & \boldsymbol{\Phi}_{ia}\boldsymbol{\Phi}_{aa}^{-1} \\ \mathbf{0}_{ai} & \boldsymbol{I}_{aa} \end{bmatrix} \begin{Bmatrix} \boldsymbol{q}_i \\ \boldsymbol{x}_a \end{Bmatrix} \tag{6}$$

which clearly shows the coupling between $\boldsymbol{x}_i$ and $\boldsymbol{x}_a$.

According to Eqn. 4 the modal matrix $\boldsymbol{\Phi}_{mm}$ has been built by ordering the eigenvectors $\boldsymbol{\varphi}_{m,j}$ for increasing eigenvalues. Therefore, the reduction of master DoFs' can be achieved by performing the modal truncation of the eigenvectors corresponding to the highest eigenvalues. Under this consideration, the coupling between $\boldsymbol{x}_i$ and $\boldsymbol{x}_a$ might be removed by truncating the last n_a columns of $\boldsymbol{\Phi}_{mm}$, which corresponds to neglect the submatrices $\boldsymbol{\Phi}_{ia}$ and $\boldsymbol{\Phi}_{aa}$ into the Eqn. 5. Hence, the coordinates transformation of Eqn. 6 becomes:

$$\boldsymbol{x}_m = \begin{Bmatrix} \boldsymbol{x}_i \\ \boldsymbol{x}_a \end{Bmatrix} \approx \begin{bmatrix} \boldsymbol{\Phi}_{ii} & \mathbf{0}_{ia} \\ \mathbf{0}_{ai} & \boldsymbol{I}_{aa} \end{bmatrix} \begin{Bmatrix} \boldsymbol{q}_i \\ \boldsymbol{x}_a \end{Bmatrix} \tag{7}$$

The columns of the submatrix $\boldsymbol{\Phi}_{ii}$ in general are not linearly independent to each other. In order to avoid this drawback they are orthonormalized by using the *Gram-Schmidt* algorithm [3]:

$$\boldsymbol{\Phi}_{ii} \xrightarrow{\textit{Gram-Schmidt}} \hat{\boldsymbol{\Phi}}_{ii} \tag{8}$$

The columns of the resulting matrix $\hat{\boldsymbol{\Phi}}_{ii}$ are called *GSI* modes and represent a good basis for the modal reduction of the interface. By keeping a reduced set with $n_w \ll n_i$ *GSI* modes, the interface DoFs $\boldsymbol{x}_i$ can be approximated as:

$$\boldsymbol{x}_i \approx \hat{\boldsymbol{\Phi}}_{iw}\boldsymbol{q}_w \tag{9}$$

Henceforth in this paper the "hat" is omitted and the Gram-Schmidt orthonormalization is always applied unless otherwise specified. By applying the transformation of Eqn. 9, the CB-CMS generalized coordinate vector of Eqn. 2 finally becomes:

$$\begin{Bmatrix} \boldsymbol{x}_i \\ \boldsymbol{x}_a \\ \boldsymbol{q}_k \end{Bmatrix} \approx \begin{bmatrix} \boldsymbol{\Phi}_{iw} & \mathbf{0}_{ia} & \mathbf{0}_{ik} \\ \mathbf{0}_{aw} & \boldsymbol{I}_{aa} & \mathbf{0}_{ak} \\ \mathbf{0}_{kw} & \mathbf{0}_{ka} & \boldsymbol{I}_{kk} \end{bmatrix} \begin{Bmatrix} \boldsymbol{q}_w \\ \boldsymbol{x}_a \\ \boldsymbol{q}_k \end{Bmatrix} \tag{10}$$

Note that the interface reduction performed by the *GSI* method does not necessary require the application of a prior reduction. In fact, Eqn. 7 is still to be consider valid even when dealing with non-reduced FE models. In this case the set of master DoFs coincides with $\boldsymbol{x}$ and *GSI* modes can be computed by following the mathematical procedure from Eqn. 3 to Eqn. 8. As a general rule, the generalized coordinate vector $\boldsymbol{x}$, either reduced or not, has just to be partitioned into $\boldsymbol{x}_i$ and $\boldsymbol{x}_o$, with the latter including all the *other* DoFs, i.e. those not belonging to the interface. On the fulfillment of this condition Eqn. 10 can be rewritten as:

$$\begin{Bmatrix} \boldsymbol{x}_i \\ \boldsymbol{x}_o \end{Bmatrix} \approx \begin{bmatrix} \boldsymbol{\Phi}_{iw} & \mathbf{0}_{io} \\ \mathbf{0}_{ow} & \boldsymbol{I}_{oo} \end{bmatrix} \begin{Bmatrix} \boldsymbol{q}_w \\ \boldsymbol{x}_o \end{Bmatrix} \tag{11}$$

2.2 Nonlinear Equations of Motion

The nonlinear EQM for a structure with contact interfaces can be written in the following form:

$$\boldsymbol{M}\ddot{\boldsymbol{x}}(t) + \boldsymbol{C}\dot{\boldsymbol{x}}(t) + \boldsymbol{K}\boldsymbol{x}(t) = \boldsymbol{f}_e(t) - \boldsymbol{f}_{nl}(\boldsymbol{x}, \dot{\boldsymbol{x}}, t) \tag{12}$$

where $\boldsymbol{M}$, $\boldsymbol{C}$ and $\boldsymbol{K}$ are the mass, damping and stiffness matrices, $\boldsymbol{x}$ is the vector of displacement, $\boldsymbol{f}_e$ is the vector of the external harmonic loads and $\boldsymbol{f}_{nl}$ is the vector of the nonlinear contact forces. When the steady state response is of interest, it is a common practice to solve the former EQM in the frequency domain. Due to the periodicity of $\boldsymbol{f}_e$, the displacements and nonlinear contact forces can be written according to the following Fourier series:

$$\boldsymbol{x}(t) = \Re\left(\sum_{f=0}^{n_h} \boldsymbol{X}^{(f)} \cdot e^{if\omega t}\right) \qquad \boldsymbol{f}_{nl}(\boldsymbol{x}, \dot{\boldsymbol{x}}, t) = \Re\left(\sum_{f=0}^{n_h} \boldsymbol{F}_{nl}^{(f)} \cdot e^{if\omega t}\right) \tag{13}$$

where $\boldsymbol{X}^{(f)}$ and $\boldsymbol{F}_{nl}^{(f)}$ are the f^{th} order complex amplitudes of the displacements and contact forces respectively, ω is circular frequency and n_h is the number of retained harmonics. The differential equations in Eqn. 12 can then be turned into the following set of nonlinear, complex, algebraic equations:

$$\boldsymbol{D}^{(f)}(\omega)\boldsymbol{X}^{(f)} = \boldsymbol{F}_e^{(f)} - \boldsymbol{F}_{nl}^{(f)}(\boldsymbol{X}) \qquad \forall\, f = 0, 1, 2, \ldots, n_h \tag{14}$$

where $\boldsymbol{D}^{(f)} = \boldsymbol{K} + if\omega\boldsymbol{C} - (f\omega)^2\boldsymbol{M}$ is the f^{th} order dynamic stiffness matrix. By assuming the 1^{st} order approximation for $\boldsymbol{x}$ and $\boldsymbol{f}_{nl}$ (SHBM approximation), Eqn. 14 can be rewritten as:

$$\boldsymbol{D}(\omega)\boldsymbol{X} - \boldsymbol{F}_e + \boldsymbol{F}_{nl}(\boldsymbol{X}) = 0 \tag{15}$$

with the superscript $^{(1)}$ omitted in order to simplify the notation. Note that Eqn. 14 can not be solved analytically due to its nonlinear nature. It has to be solved iteratively for the unknown amplitudes $\boldsymbol{X}$.

Without loss of generality, assume the structure consisting of two substructures identified by the superscript (1) and (2). Moreover, let the number of DoFs at the contact interfaces be the same, i.e. $n_i^{(1)} = n_i^{(2)} = n_i$. Under these assumptions, the global mass and stiffness matrices and the vectors of Eqn. 15 can be expressed as:

$$\boldsymbol{M} = \begin{bmatrix} \boldsymbol{M}_{ii}^{(1)} & \boldsymbol{M}_{io}^{(1)} & \boldsymbol{0} & \boldsymbol{0} \\ \boldsymbol{M}_{oi}^{(1)} & \boldsymbol{M}_{oo}^{(1)} & \boldsymbol{0} & \boldsymbol{0} \\ \boldsymbol{0} & \boldsymbol{0} & \boldsymbol{M}_{ii}^{(2)} & \boldsymbol{M}_{io}^{(2)} \\ \boldsymbol{0} & \boldsymbol{0} & \boldsymbol{M}_{oi}^{(2)} & \boldsymbol{M}_{oo}^{(2)} \end{bmatrix} \qquad \boldsymbol{K} = \begin{bmatrix} \boldsymbol{K}_{ii}^{(1)} & \boldsymbol{K}_{io}^{(1)} & \boldsymbol{0} & \boldsymbol{0} \\ \boldsymbol{K}_{oi}^{(1)} & \boldsymbol{K}_{oo}^{(1)} & \boldsymbol{0} & \boldsymbol{0} \\ \boldsymbol{0} & \boldsymbol{0} & \boldsymbol{K}_{ii}^{(2)} & \boldsymbol{K}_{io}^{(2)} \\ \boldsymbol{0} & \boldsymbol{0} & \boldsymbol{K}_{oi}^{(2)} & \boldsymbol{K}_{oo}^{(2)} \end{bmatrix}$$

$$\boldsymbol{x} = \begin{Bmatrix} \boldsymbol{X}_i^{(1)} \\ \boldsymbol{X}_o^{(2)} \\ \boldsymbol{X}_i^{(1)} \\ \boldsymbol{X}_o^{(2)} \end{Bmatrix} \qquad \boldsymbol{f}_e = \begin{Bmatrix} \boldsymbol{0} \\ \boldsymbol{F}_{e,o}^{(1)} \\ \boldsymbol{0} \\ \boldsymbol{F}_{e,o}^{(2)} \end{Bmatrix} \qquad \boldsymbol{f}_{nl} = \begin{Bmatrix} \boldsymbol{F}_{nl,i}^{(1)} \\ \boldsymbol{0} \\ \boldsymbol{F}_{nl,i}^{(2)} \\ \boldsymbol{0} \end{Bmatrix} \tag{16}$$

It must be pointed out that the external and contact forces are applied to the active and interface DoFs respectively. Since $\boldsymbol{F}_{nl}$ only depends on the relative displacements at the contact interface, the number of nonlinear algebraic equations can be halved by employing the coordinate transformation linking the absolute to the relative interface displacements:

$$\begin{Bmatrix} \boldsymbol{X}_i^{(1)} \\ \boldsymbol{X}_o^{(2)} \\ \boldsymbol{X}_i^{(1)} \\ \boldsymbol{X}_o^{(2)} \end{Bmatrix} = \begin{bmatrix} \boldsymbol{I} & \boldsymbol{I} & \boldsymbol{0} & \boldsymbol{0} \\ \boldsymbol{0} & \boldsymbol{0} & \boldsymbol{I} & \boldsymbol{0} \\ \boldsymbol{0} & \boldsymbol{I} & \boldsymbol{0} & \boldsymbol{0} \\ \boldsymbol{0} & \boldsymbol{0} & \boldsymbol{0} & \boldsymbol{I} \end{bmatrix} \begin{Bmatrix} \boldsymbol{X}_i^{(r)} \\ \boldsymbol{X}_i^{(2)} \\ \boldsymbol{X}_o^{(1)} \\ \boldsymbol{X}_o^{(2)} \end{Bmatrix} = \boldsymbol{R}\boldsymbol{X}^{(r)} \qquad \text{where} \quad \boldsymbol{X}_i^{(r)} = \boldsymbol{X}_i^{(1)} - \boldsymbol{X}_i^{(2)} \tag{17}$$

where $\boldsymbol{R}$ is the coordinate transformation matrix. By substituting the Eqn. 17 into the Eqn. 15 and pre-multiplying both sides by $\boldsymbol{R}^T$, the following system of equation is obtained:

$$\boldsymbol{R}^T\boldsymbol{D}\boldsymbol{R}\boldsymbol{X}^{(r)} - \boldsymbol{R}^T\boldsymbol{F}_e + \boldsymbol{R}^T\boldsymbol{F}_{nl}(\boldsymbol{X}^{(r)}) \approx 0 \quad \Rightarrow \quad \boldsymbol{D}^{(r)}\boldsymbol{X}^{(r)} - \boldsymbol{F}_e^{(r)} + \boldsymbol{F}_{nl}^{(r)}(\boldsymbol{X}^{(r)}) \approx 0 \tag{18}$$

Although the pre-multiplication by $\boldsymbol{R}$ leaves $\boldsymbol{F}_e$ unchanged, more attention has to be paid on the term $\boldsymbol{F}_{nl}^{(r)}$:

$$\boldsymbol{F}_{nl}^{(r)} = \boldsymbol{R}^T\boldsymbol{F}_{nl} = \begin{bmatrix} \boldsymbol{I} & \boldsymbol{0} & \boldsymbol{0} & \boldsymbol{0} \\ \boldsymbol{I} & \boldsymbol{0} & \boldsymbol{I} & \boldsymbol{0} \\ \boldsymbol{0} & \boldsymbol{I} & \boldsymbol{0} & \boldsymbol{0} \\ \boldsymbol{0} & \boldsymbol{0} & \boldsymbol{0} & \boldsymbol{I} \end{bmatrix} \begin{Bmatrix} \boldsymbol{F}_{nl,i}^{(1)} \\ \boldsymbol{0} \\ \boldsymbol{F}_{nl,i}^{(2)} \\ \boldsymbol{0} \end{Bmatrix} = \begin{Bmatrix} \boldsymbol{F}_{nl,i}^{(1)} \\ \boldsymbol{F}_{nl,i}^{(1)} + \boldsymbol{F}_{nl,i}^{(2)} \\ \boldsymbol{0} \\ \boldsymbol{0} \end{Bmatrix} \tag{19}$$

The contact forces at the contact interface are equal in amplitude but opposite in sign, meaning that the term $\boldsymbol{F}_{nl,i}^{(1)} + \boldsymbol{F}_{nl,i}^{(2)}$ is null:

$$\boldsymbol{R}^T\boldsymbol{f}_{nl} = \begin{bmatrix} \boldsymbol{I} & \boldsymbol{0} & \boldsymbol{0} & \boldsymbol{0} \\ \boldsymbol{I} & \boldsymbol{0} & \boldsymbol{I} & \boldsymbol{0} \\ \boldsymbol{0} & \boldsymbol{I} & \boldsymbol{0} & \boldsymbol{0} \\ \boldsymbol{0} & \boldsymbol{0} & \boldsymbol{0} & \boldsymbol{I} \end{bmatrix} \begin{Bmatrix} \boldsymbol{F}_{nl,i}^{(1)} \\ \boldsymbol{0} \\ \boldsymbol{F}_{nl,i}^{(2)} \\ \boldsymbol{0} \end{Bmatrix} = \begin{Bmatrix} \boldsymbol{F}_{nl,i}^{(1)} \\ \boldsymbol{0} \\ \boldsymbol{0} \\ \boldsymbol{0} \end{Bmatrix} \tag{20}$$

In this way the number of nonlinear EQM finally decreases from $2 \times n_i$ to n_i.

For structures featuring large interfaces, a further reduction of the nonlinear DoFs (i.e. those corresponding to the nonlinear contact forces) can be achieved by employing the *GSI* method introduced in section 2.1. If $\boldsymbol{\Phi}_{iw}$ is a reduced basis with $n_w \ll n_i$ *GSI* modes, the vector of complex relative displacements $\boldsymbol{X}^r$ can be expressed as:

$$\boldsymbol{X}_i^{(r)} = \begin{Bmatrix} \boldsymbol{X}_i^{(r)} \\ \boldsymbol{X}_i^{(2)} \\ \boldsymbol{X}_o^{(1)} \\ \boldsymbol{X}_o^{(2)} \end{Bmatrix} \approx \begin{bmatrix} \boldsymbol{\Phi}_{iw} & \boldsymbol{0} & \boldsymbol{0} & \boldsymbol{0} \\ \boldsymbol{0} & \boldsymbol{I} & \boldsymbol{0} & \boldsymbol{0} \\ \boldsymbol{0} & \boldsymbol{0} & \boldsymbol{I} & \boldsymbol{0} \\ \boldsymbol{0} & \boldsymbol{0} & \boldsymbol{0} & \boldsymbol{I} \end{bmatrix} \begin{Bmatrix} \boldsymbol{Q}_w^{(r)} \\ \boldsymbol{X}_i^{(2)} \\ \boldsymbol{X}_o^{(1)} \\ \boldsymbol{X}_o^{(2)} \end{Bmatrix} = \boldsymbol{G}\boldsymbol{X}_{GSI}^{(r)} \tag{21}$$

where $\boldsymbol{Q}_w^{(r)}$ is the vector of the complex displacements of the modal coordinates $\boldsymbol{q}_{iw}$. By projecting the Eqn. 18 onto the space spanned by the columns of $\boldsymbol{G}$, the following relationship is obtained:

$$\boldsymbol{G}^T\boldsymbol{D}^{(r)}\boldsymbol{G}\boldsymbol{X}_{GSI}^{(r)} - \boldsymbol{G}^T\boldsymbol{F}_e^{(r)} + \boldsymbol{G}^T\boldsymbol{F}_{nl}^{(r)}(\boldsymbol{X}_{GSI}^{(r)}) \approx 0 \tag{22}$$

with:

$$\boldsymbol{G}^T\boldsymbol{F}_{nl}^{(r)} = \begin{Bmatrix} \boldsymbol{\Phi}_{iw}\boldsymbol{F}_{nl,i}^{(1)} \\ \boldsymbol{0} \\ \boldsymbol{0} \\ \boldsymbol{0} \end{Bmatrix} \tag{23}$$

where the term $\boldsymbol{\Phi}_{iw}\boldsymbol{F}_{nl,i}^{(1)}$ represents the vector of the modal contact forces. Although the contact forces $\boldsymbol{F}_{nl,i}$ are always estimated in the space of the physical DoFs, these are introduced into the equilibrium equations through the reduced set of modal coordinates $\boldsymbol{q}_w^{(r)}$. This procedure allows for a fast solution of the nonlinear partition of Eqn 22, that otherwise would be computationally expensive as in the case of Eqn. 18.

The strategy used to built the reduced basis of $\boldsymbol{\Phi}_{iw}$ is discussed later on in the section 3, since it strictly depends on the physics behind the contact phenomena occurring at the interfaces between the substructures.

2.3 Contact Model

The one-dimensional Jenkins contact element with normal load variation is used to compute the periodic contact forces for a given periodic relative displacement, by taking into account possible separation of the

normal contact [21]. Hence, three possible contact states can be modeled: stick, slip and separation. A schematic view of this contact model can be found in Figure 1, where the two dimensional relative displacement is decomposed into two perpendicular directions: two in-plane tangential component denoted by u and w components, and one out-of-plane normal component v.

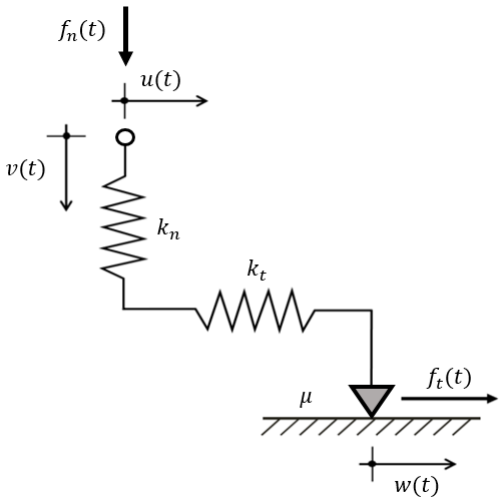


Figure 1: 1-D contact model with normal load variation.

The contact model's parameters are represented by the tangential and normal contact stiffnesses, which are modeled by two springs with stiffness k_t and k_n respectively, the coefficient of friction μ and the normal preload f_0 (see Figure). At every time instant the normal contact force $f_n(t)$ is defined as:

$$f_n = \max(f_0 + k_n \cdot v, 0) \tag{24}$$

If f_0 is positive, the bodies are in contact before vibration starts, while if f_0 is negative an initial gap $g_0 = -\frac{f_0}{k_n}$ exists between the two bodies.

Along the tangential direction, the contact force is defined as:

$$f_t = \begin{cases} k_t \cdot (u - w) & \text{sticking mode} \\ \text{sgn}(\dot{w}) \cdot \mu f_n & \text{slipping mode} \\ 0 & \text{lift-off mode} \end{cases} \tag{25}$$

Since the EQM are formulated in the frequency domain, the Fourier coefficients of the nonlinear contact forces $\boldsymbol{F}_{nl,i}^{(1)}$ have to be computed from the Fourier coefficients of the corresponding relative displacement $\boldsymbol{X}_i^{(r)}$. This is done by using the so called *Alternating Frequency Time* (AFT) method [22, 23].

3 Application

The reduction method presented in the previous section was applied to two beam-like structures denoted with A and B (Figure 2). Each structure consists of two cantilever beams with equal dimensions (2 mm $\times$ 20 mm $\times$ 100 mm and 5 mm $\times$ 100 mm $\times$ 500 mm for A and B respectively), interacting through an extended contact interface.

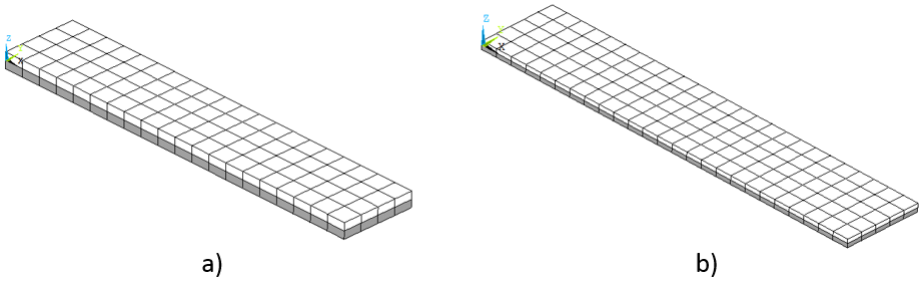


Figure 2: Finite element models of the structures A (a) and B (b).

Each beam is discretized with the 8-nodes hexahedral element. The total numbers of DoFs for the structure A and B are 1260 and 1872. The beams are made of a standard steel with Young's modulus $E = 200$ GPa, Poisson's ratio $\nu = 0.33$ and density $\rho = 7800$ kg/m^3. The constraint is on the same end for both beams.

Due to the limited number of DoFs, the choice to work with the full FE models was pursued. For each beam the whole set of DoFs was partitioned as:

$$\boldsymbol{x}^{(s)} = \begin{Bmatrix} \boldsymbol{x}_i^{(s)} \\ \boldsymbol{x}_o^{(s)} \end{Bmatrix} \qquad s = 1, 2 \tag{26}$$

where the size of the partitions $\boldsymbol{x}_i^{(s)}$ and $\boldsymbol{x}_o^{(s)}$ are $n_{i_A}^{(s)} = n_{o_A}^{(s)} = 315$ for the s^{th} beam of the structure A and $n_{i_B}^{(s)} = n_{o_B}^{(s)} = 468$ for s^{th} beam the structure B.

Before showing the applications of the *GSI* method, some considerations on the contact state at the interface are needed. Depending on the nature of the external excitation, preload and contact parameters, the system's response usually follows the typical trend of the slip-stick nonlinear phenomenon (Figure 3).

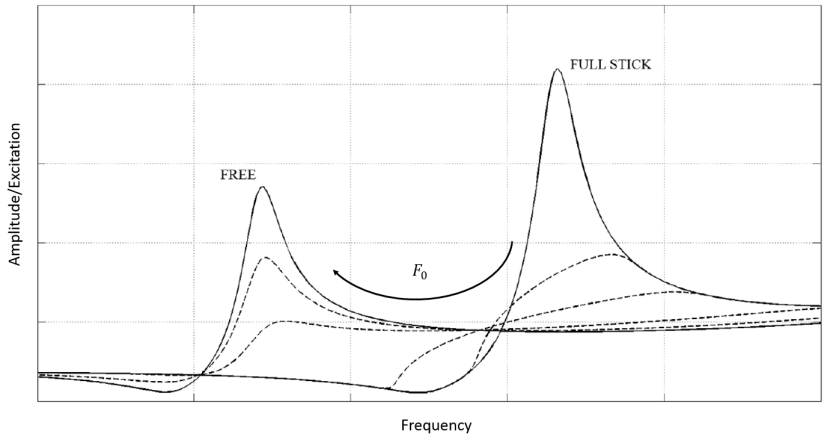


Figure 3: Stick-slip phenomenon in the frequency domain: for a fixed value of the normal preload an increase of the excitation amplitude F_0 shifts the resonance towards the free response.

For a fixed value of the external load, an increase of the contact preload has the effect of shifting the resonant frequency towards higher values, moving from the *free* configuration (i.e. no contact occurs during the whole vibration cycle) to the *full-stick* configuration. Oppositely, for a fixed value of the static preload, the system response moves from the full-stick to the free configuration when the amplitude of the external load increases. It is also quite crucial understanding the nature of the structure's mode shapes for these two extreme configurations: in the free case, the mode shapes coincide to those of the isolated substructures, while in the fully stick case the mode shapes are close to those of the assembled structure.

According to the previous observations, the contact DoFs can be approximated with a basis of *GSI* modes that has to well represent the interface motion for both the free and full-stick configurations. Such basis can be obtained by applying the mathematical procedure described in section 2 for two sets of linear matrices:

- the free matrices, $\boldsymbol{M}_{fr}^{(r)}$ and $\boldsymbol{K}_{fr}^{(r)}$, obtained by just applying the coordinate transformation of Eqn. 17 to the mass and stiffness matrix of Eqn. 16;
- the full-stick matrices, $\boldsymbol{M}_{fs}^{(r)}$ and $\boldsymbol{K}_{fs}^{(r)}$, defined as:

$$\boldsymbol{M}_{fs}^{(r)} = \boldsymbol{M}_{fr}^{(r)} \qquad \begin{cases} \boldsymbol{K}_{fs}^{(r)} = \boldsymbol{R}^T \boldsymbol{K}_{fs} \boldsymbol{R} \\ \boldsymbol{K}_{fs} = \boldsymbol{K} + \boldsymbol{K}_{link} \end{cases} \tag{27}$$

where $\boldsymbol{K}_{link}$ performs the assembly of the matrices $\boldsymbol{K}^{(1)}$ and $\boldsymbol{K}^{(2)}$ by means of a set of node-to-node springs having the same stiffness assumed for the contact elements. In this way, two bases of *GSI* modes are obtained ($\boldsymbol{\Phi}_{ii}^{fr}$ and $\boldsymbol{\Phi}_{ii}^{fs}$, corresponding to the free and full-stick models respectively) and the reduction of the relative interface DoFs finally performed. In this preliminary research, the strategy adopted to accomplish the mentioned task is based on the definition of a reduction basis collecting $n_w \ll n_i$ *GSI* modes from the bases $\boldsymbol{\Phi}_{ii}^{fr}$ and $\boldsymbol{\Phi}_{ii}^{fs}$:

$$\boldsymbol{\Phi}_{iw} = \left[\boldsymbol{\Phi}_{iw_{fr}}^{fr} \; \boldsymbol{\Phi}_{iw_{fs}}^{fs} \right] \tag{28}$$

with the subscript w_{fr} and w_{fs} denoting the number of *GSI* modes retained from each basis, i.e. $n_{w_{fr}}$ and $n_{w_{fs}}$ for $\boldsymbol{\Phi}_{ii}^{fr}$ and $\boldsymbol{\Phi}_{ii}^{fs}$ respectively. The choice of the numbers $n_{w_{fr}}$ and $n_{w_{fs}}$ is discussed in the application presented in the following.

Before performing the dynamic analyses and testing the reduction method, it was decided to calculate the normal preload distribution at the contact interface by solving a nonlinear static analysis. In this regards, the Jenkins contact element with variable normal load described in section 2.3 was implemented for each pair of nodes in contact, by assuming the following contact parameters: $k_n = 10^8$ N/m, $k_t = 10^7$ N/m and $\mu = 0.5$.

The beams of the structures A and B were pressed one against the other for two different patterns of static forces (Figure 4).

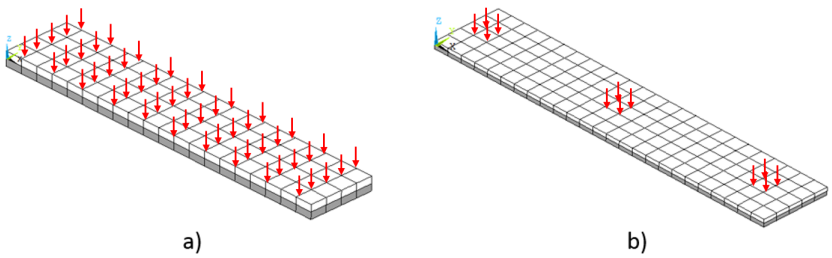


Figure 4: Static force pattern for the structure A (a) and B (b).

As expected, for the structure A the distribution appears uniform, meaning that all the pairs of contact nodes have similar value of the normal preload ($\sim$ 50 N per contact node pair). While for the case B, two sharp

peaks ($\sim$ 2000 N) are present in the regions where the forces are applied. In between the two peaks negative values of the normal preload were obtained taking into account the gap $g_0 = -\frac{f_0}{k_n}$, meaning that separation occurs for the corresponding pairs of nodes in contact.

Two sets of benchmark frequency response functions (FRFs) were computed in order to test the performances of the *GSI* reduction. For the structure A, the compatibility conditions of displacements in the normal direction at the contact interface were enforced. In this case the contact model acts like a pure Jenkins contact model since the relative normal displacement is forbidden for the compatibility condition. Two in-phase harmonic forces were applied at the free end of both beams. While for the structure B two in-phase harmonic forces were used to force the free end of the beam 1 (Figure 5). Both loading conditions aim to excite the first bending mode shape of the beam assemblies.

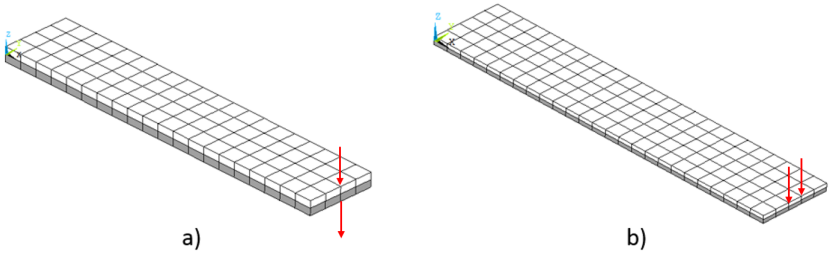


Figure 5: Harmonic force on the structure A (a) and B (b).

Figure 6 shows the FRFs for the structures A and B. For the structure A no separation can occur and the stick-slip phenomenon previously described takes place. For the structure B separation may occur and the so-called jump phenomenon typical of nonlinear structures appears [20].

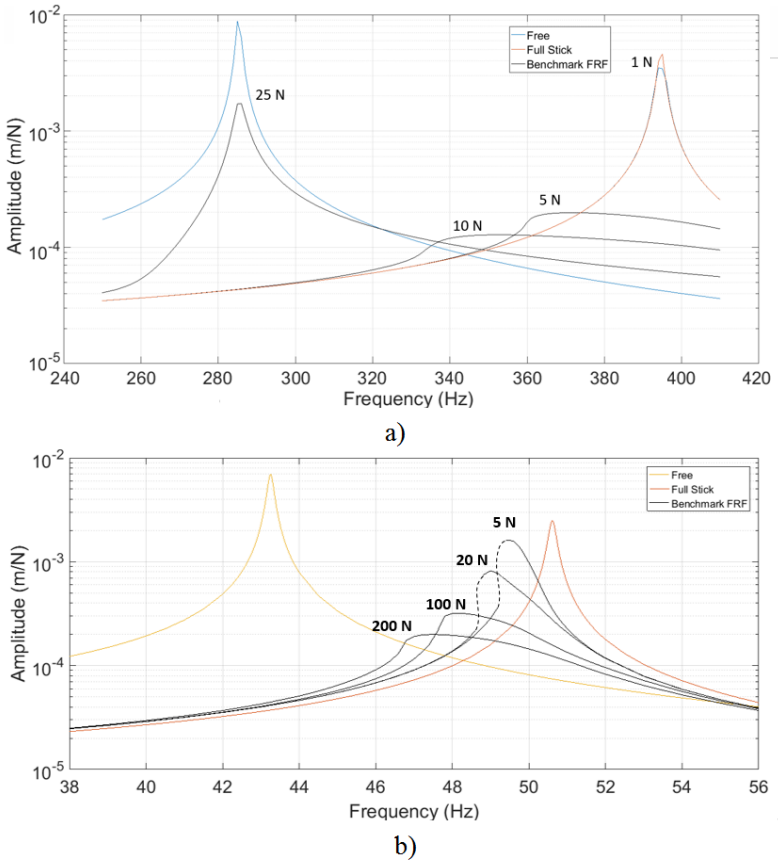


Figure 6: Benchmark FRFs for the structure A (a) and B (b).

In the same Figure it is also shown the full-stick response that is obtained by connecting the whole contact surface with a node-to-node springs having the same stiffness assumed for the contact elements. The value of the resonance frequency of the full-stick FRF is higher than the actual FRFs with the localized normal preload, since some regions are always characterized by the separation state due to the receding contact. Note that the amplitude of the external excitation for the case b) has been set in order to allow the stick-slip phenomenon and test the *GSI* method in such working conditions. No further considerations on the safety margins of the structure B will be made in the following.

In Figure 7 the nonlinear FRFs evaluated by using the *GSI* reduction method are shown and compared with the benchmark calculations of Figure 6.

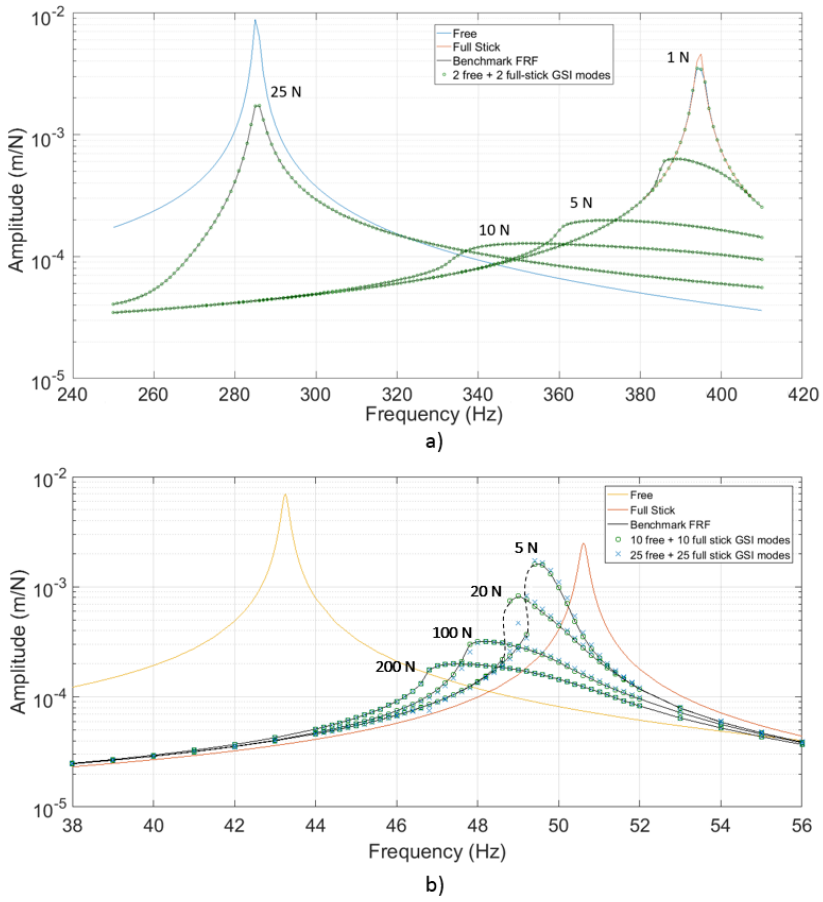


Figure 7: FRFs of the reduced order models of structure A (a) and B (b).

Figure 7 (a) clearly shows a perfect match between the benchmark FRFs with those obtained from the reduced model with just 4 *GSI* modes, i.e. 2 computed in free condition and 2 in the full-stick. This result makes the reduced model preferable when the nonlinear calculation have to be performed. The best performance of the *GSI* reduced model can be easily justified in terms of size of the model (1260 DoFs of the FE model vs 622 DoFs of the *GSI* reduced model) and time spent in the computation of each nonlinear forced response (i.e. the calculation performed with the non- reduced contact interface is 24 times slower than the calculation performed after the application of the *GSI* reduction technique). Note that the remarkable reduction of the computational time is strictly related to the reduction on the nonlinear DoFs (300 of the full model vs 4 of the *GSI* model.

Similar considerations can be carried out from the comparison of Figure 7 (b). It can be noted that even when the jump phenomenon occurs, the *GSI* method still captures with a good accuracy the structure's response. Due to the complex dynamics of the system, a perfect match of the FRFs can be achieved by employing 50 *GSI* modes, i.e. 25 computed with models in the free condition and 25 in the full-stick condition. Even in

this case a strong reduction of the computational time has been achieved (i.e. 33 times faster using the *GSI* reduction technique), thanks to the notable reduction of the nonlinear DoFs (468 of the full model vs 50 of the *GSI* model). The computational time can be further decreased when using the basis with 20 *GSI* modes (Figure 7) (b). In this regard, although the response approximation remains acceptable, the good accuracy of the solution is partially lost.

4 Conclusions

The current trend in the design process is the simulation of large complex systems made by a large number of components. The ambitious task of the whole system simulation relies, first, on a suitable tuning of the single components FE model participating to the full structure and, second, on a suitable modeling of the interface between components. When such interfaces can not be considered as localized with respect to the physical domain of the components, reduction techniques based on retaining a set of physical master nodes are no more efficient in terms of computational time. For this reason, dedicated reduction techniques for the contact interfaces have to be developed in particular when the uncertainty of loose contacts is taken into account. In this paper a method to overcome the long computations of the frictionally damped nonlinear response of systems with lap joints is presented. It is based on the *Gram-Schmidt Interface method* developed in [16]. Two preliminary tests with two beams in contact, preloaded with a uniform load and a localized load that mimics the presence of bolted joints and producing receding contact, are presented. Results show promising good accuracy for applying the method to more complex structures in spite of a strong reduction of the computational efforts.

References

[1] Hurty, W. C. *Dynamic Analysis of Structural Systems Using Component Modes*, AIAA Journal 3.4 (1965): 678-685.

[2] Craig R. and Bampton M. *Coupling of Substructures for Dynamic Analyses*, AIAA Journal 6.7 (1968): 1313-1319.

[3] Gilbert Strang. *Introduction to linear algebra*. Wellesley, MA: Wellesley-Cambridge Press, 1993.

[4] P. Pennacchi, S. Chatterton, N. Bachschmid, E. Pesatori, G. Turozzi. *A model to study the reduction of turbine blade vibration using the snubbing mechanism*. Mechanical Systems and Signal Processing 25 (2011), 1260–1275. doi:10.1016/j.ymssp.2010.10.006.

[5] Szwedowicz, J., Visser R., Sextro W., Masserey P.A. *On Nonlinear Forced Vibration of Shrouded Turbine Blades*. Journal of Turbomachinery 2007, 130.

[6] Gu, W., Xu Z., Liu Y. *A method to predict the nonlinear vibratory response of bladed disc system with shrouded dampers*. In Proceeding of the IMechE Vol. 226 Part C: Journal of Mechanical Engineering Science, 2011

[7] Firrone, C.M., Zucca S. *Underplatform dampers for turbine blades: the effect of damper static balance on the blade dynamics*. Mechanics Research Communications, 36:515–522, 2009

[8] Panning L., Popp K., Sextro W., Gotting F., Kayser A., Wolter, I. *Asymmetrical Underplatform Dampers in Gas Turbine Bladings: Theory and Application*. Proceedings of ASME Turbo Expo 2004, 269-280

[9] Lavella M.; Botto D.; Gola M.M., *Test rig for wear and contact parameters extraction for flat-on-flat contact surfaces*. ASME/STLE 2011 International Joint Tribology Conference (IJTC 2011), Los Angeles, California, USA, Oct 24-26, 2011. pp. 307-309. https://doi.org/10.1115/IJTC2011-61234

[10] Castanier M. P., Yung-Chang T., and Pierre C. *Characteristic constraint modes for component mode synthesis*, AIAA journal 39.6 (2001): 1182-1187.

[11] Lindberg Eskil, Nils-Erik Horlin, and Peter Goransson. *Component mode synthesis using undeformed interface coupling modes to connect soft and stiff substructures*. Shock and Vibration 20.1 (2013): 157-170.

[12] P. Holzwarth, P. Eberhard. *Interface reduction for CMS methods and alternative model order reduction*. IFAC-PapersOnLine, 2015, 48.1: 254-259.

[13] Kuether R. J., Allen M. S., and Hollkamp J. J. (2017). *Modal substructuring of geometrically nonlinear finite element models with interface reduction*. AIAA Journal, 1-12.

[14] Krattiger, Dimitri, et al. *Interface reduction for Hurty/Craig-Bampton substructured models: review and improvements.* Mechanical Systems and Signal Processing 114 (2019): 579-603

[15] G. Battiato, C.M. Firrone, T.M. Berruti, and B.I. Epureanu. *A General Method for Sub-Systems Coupling for the Dynamic Analysis*, Proceedings of ISMA Conference, 2016. Leuven, Belgium.

[16] Battiato, G., Firrone C. M., Berruti T. M., and Epureanu B. I. (2018). *Reduction and coupling of substructures via Gram Schmidt Interface modes*. Computer Methods in Applied Mechanics and Engineering, 336, 187-212

[17] G. Battiato, C.M. Firrone, T.M. Berruti, and B.I. Epureanu. Reduced Order *Modeling for Multi-Stage Coupling of Cyclic Symmetric Structures*, Proceedings of ISMA Conference, 2016. Leuven, Belgium.

[18] Firrone C. M., Battiato G., and Epureanu B. I. *Modeling the Microslip in the Flange Joint and Its Effect on the Dynamics of a Multistage Bladed Disk Assembly*. Journal of Computational and Nonlinear Dynamics 13.1 (2018): 011011.

[19] Battiato G., Firrone C. M., Berruti T. M., and Epureanu B. I. (2018). *Reduced Order Modeling for Multistage Bladed Disks With Friction Contacts at the Flange Joint*. Journal of Engineering for Gas Turbines and Power, 140(5), 052505

[20] Yang B.D., Chu M.L., Menq C.H. (1998) *Stick-Slip-Separation Analysis and Non-Linear Stiffness and Damping Characterization of Friction Contacts Having Variable Normal Load*. J. Of Sound and Vibration 210(4), 461-481.

[21] Firrone, C.M.; Zucca, S. *Modelling friction contacts in structural dynamics and its application to turbine bladed disks. In: Numerical Analysis-Theory and Application*. InTech, 2011.

[22] Cameron, T. M., Griffin, J. H. *An Alternating Frequency Time Domain Method for Calculating the Steady-State Response of Nonlinear Systems*, Journal of Applied Mechanics, Vol. 56, pp. 149-154, 1989

[23] Petrov, E. P., Ewins, D. J. *Analytical Formulation of Friction Interface Elements for Analysis on Nonlinear Multi-Harmonic Vibrations of Bladed Discs Discs*, ASME-Paper GT-2002-30325, Proceedings of the ASME Turbo Expo 2002, Amsterdam (Netherlands), 2002

Use cases for vehicle TPA: from shock absorbers to electric drive

J. Freund[1], T. Vöhringer[1]
[1] ZF Friedrichshafen AG, Research & Development – NVH & Dynamics, Graf-von-Soden-Platz 1, 88046 Friedrichshafen, Germany
e-mail: **johannes.freund@zf.com**

Abstract
Several use cases for vehicle transfer path analysis (TPA) by an automotive supplier and its wide range of products are presented here, thus showing, that the TPA method has made it to a standard development tool. The pure structure-borne TPA models are based on common matrix inversion for the determination of operational forces. Good experiences are made with just one to two times matrix overestimation. Matrix data is collected simultaneously with the relevant transfer functions, to the interior target location, via hammer impacts. TPA model verification is made by means of artificial excitation. The calculations are carried out with an in-house Matlab software and the results are closely communicated with the customer in order to optimize the products and possibly the surrounding system in the most efficient way.

1 Introduction

The transfer path analysis has become more and more established in the field of vehicle acoustics. With its help, dominant transfer paths between a source and a receiver can be located and quantified and critical frequency ranges can be identified. Studying the critical paths in detail, dedicated measures for optimization can be designed and defined subsequently. In this paper some use cases are presented that demonstrate a broad application range: transient noise phenomena like shock absorber bumps or clatter noise in electro-mechanic actuators (electric roll control or rea axle steering) can be handled as well as quasi-stationary phenomena like whining of gears or electric machines.

The established procedure is presented in section 2 and some use cases of the transfer path analysis of an automotive supplier in section 3.

2 Method

2.1 System boundary

The reduced transfer path analysis used in this case only considers the translational structure-borne sound transmission paths [1]. Noise radiated by the unit and the acoustic-acoustic transmission paths (ATF) are neglected ad well as all rotational degrees of freedom. As a transfer path, the interface between the unit and the body is defined for the passenger compartment and considered in all spatial directions. As a result of this triaxle consideration of the intersection points and the resulting high number of channels, only one to two times over determination of the matrix can take place compared with the recommended triple over determination ([2], [3], [4]).

2.2 Transfer path analysis using the inverse matrix method

In practice, the transfer path analysis using the inverse matrix method has proven itself. Here, all measurements are measured in-situ, i.e. in the assembled state. This has proven its worth in practice due to the rapid and simplified measurement of weakly coupled systems. Internal investigations showed that the influence of the coupled system is present, but can be neglected in soft couplings. Figure 1 shows the basics of a transfer path analysis. It is used to identify and classify dominant transfer paths to several receivers.



Figure 1: TPA basics

In the first step, the inertance matrix (1) and the vibro-acoustic transfer functions (VTFs) (2) are determined by impact hammer measurement in a laboratory measurement.

$$I_{ij} = \frac{a_i}{F_j} \tag{1}$$

I_{ij} ..... inertance matrix

a_i ..... acceleration at point i

F_j ..... force at point j

$$H_{kj}^{VTF} = \frac{p_k}{F_j}\bigg|_{Q_j=0} \tag{2}$$

H ..... vibro-acoustic transfer function

k ..... microphone position

Q ..... volume flow

In the second step, operating measurements are carried out under real conditions in order to determine the disturbing noise. More information is provided in section 2.4. By correctly changing the equations (1) and (2), the operational force (3) introduced into the vehicle body can now be calculated by means of the measured operational acceleration.

$$F_{j(road)} = I_{ij}^{-1} * a_{i(road)} \tag{3}$$

By linking the calculated force with the vibro-acoustic transfer function, the partial sound pressure components of each path can be calculated (4). By summing them, the interior noise can be synthesized (5).

$$p_{kj} = H_{kj}^{VTF} * F_{j(road)} \tag{4}$$

$$p_k = \sum_j p_{kj} \tag{5}$$

2.3 In-house Matlab-Software

For an efficient and fast creation of the matrices and calculation of the transfer path analysis, an in-house Matlab software was created, which is constantly being optimized and extended.

2.3.1 Import / Export

The interface data format was Universal File Format 58 (UFF58). The UFF 58 format has a relatively simple standardized structure with 12 so-called records, which contains a complete record for descriptive data.

2.3.2 Impact-Tool

An in-house tool (Figure 2, left) is used for an optimized and fast selection of suitable impacts from the laboratory measurement. This evaluates the best combinations of multiple impacts based on the coherence criterion over defined channels and a defined frequency range. There are further investigations to insert further criterions based on auto- and cross-power-spectra. The output includes the optimized inertance matrix and vibro-acoustic transfer functions.

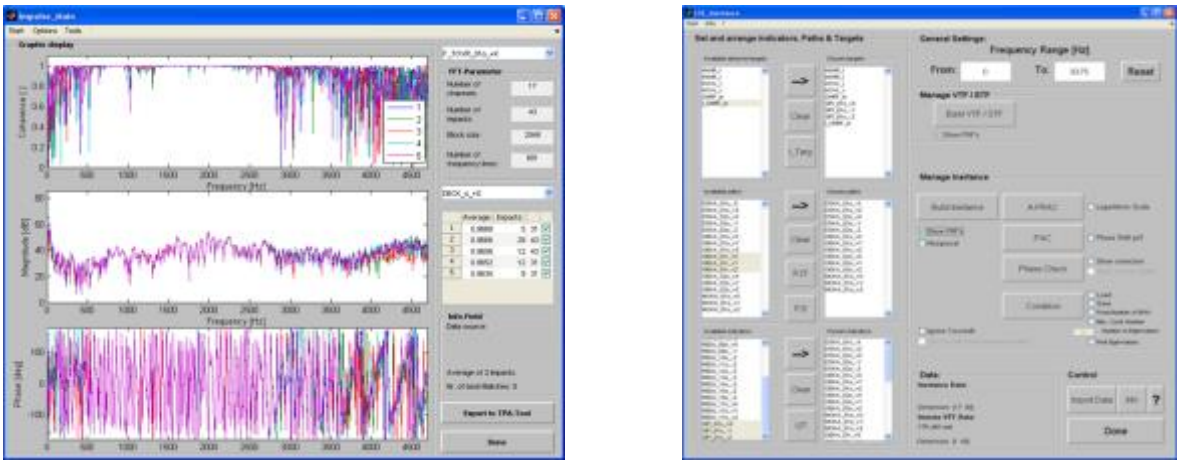


Figure 2: Impact-Tool (left), Matrix-Tool (right)

2.3.3 Matrix-Tool

With the help of the matrix tool (Figure 2, right), the inertance matrix and the VTF matrix can be constructed and generated with just a few clicks. Also it is possible to assess the inertance matrix by several criteria (FRAC, PAC, phase check, coherence).

2.3.4 Synthesize-Tool

The Synthesize-Tool is used to compare the measured and synthesized data (Figure 3, left). There are two 2D diagrams showing the magnitude and phase of the measured and synthesized target. In the lower part, the Campbell diagram shows the partial components of each path considered. In addition, it is possible to use a polar diagram to display the magnitude and phase of all paths of a specific frequency with pointers. To identify individual transmission path segments it is possible to get an overview using calculated force,

measured VTF and synthesized partial sound pressures (Figure 3, right). The upper diagram shows the calculated forces from the load case measurement. The middle diagram shows the transfer functions to the target. The lower diagram shows the calculated partial components calculated from the force and the transfer functions.

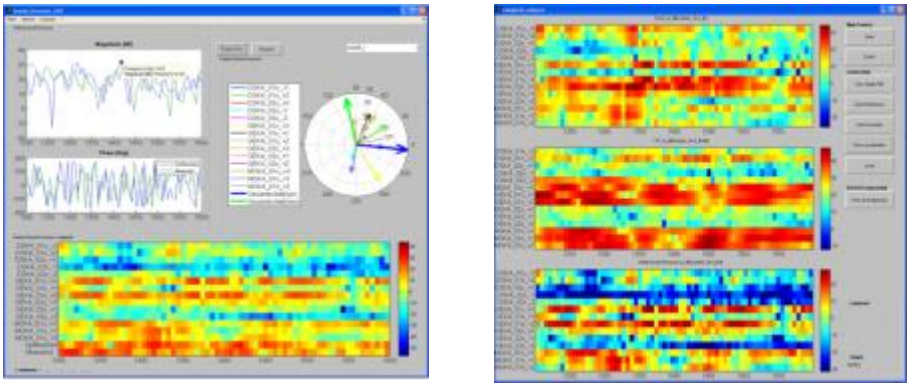


Figure 3: Synthesize-Tool

2.4 Load cases

2.4.1 Continuous noise

To generate a load case for quasi-stationary noises such as gear whining, pumps or electrical machines, depending on the application, speed ramps are run at different loads in all relevant shifted gear positions. This happens on a factory test track (Figure 4) as well as on public roads and highways. In order to obtain higher loads at low speeds it is possible to use sloped hills. The road must be as quiet, clean, and dry as possible for the measurements.



Figure 4: testing track

2.4.2 Transient noise

Rubber mats (Figure 5) are used to generate defined impacts in the respective axis (vehicle side left, right) and simulates the passage of cobblestones or potholes. Due to the defined distances, the noises of the front and rear axles can be precisely assigned. One to six layers of 5mm thick mats allow the consideration of different amplitudes.

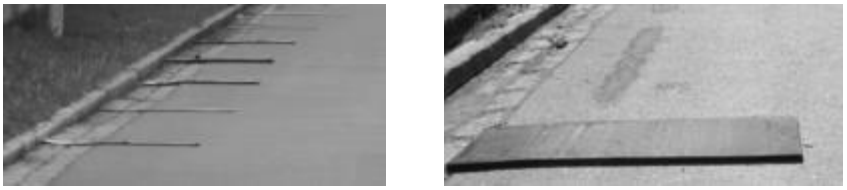


Figure 5: rubber mats

3 Results and discussion

3.1 Shock absorber

Due to internal investigations concerning possible transfer paths of shock absorber noise, a transfer path analysis was performed. Figure 6 shows the sensor setup.

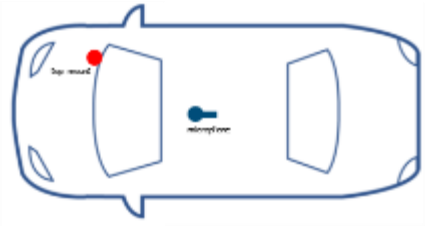


Figure 6: shock absorber sensor setup

Focus was on the top mount in the rumble frequency range of 200-400Hz (Figure 7). The load case was created by driving over the rubber mats. Triggering in a proper way aligned with the subjective impression when listening to interior noise is critical here. At the top mount sensor as well as in the cabin, the rumbles are identified and correlate well.

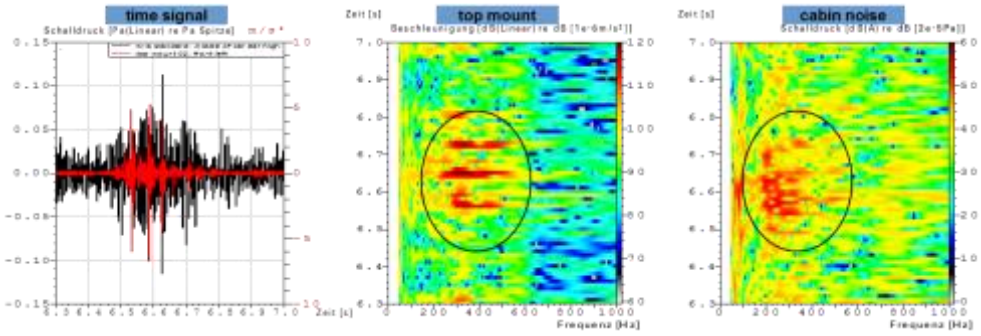


Figure 7: shock absorber rumble noise

Using this load case for transfer path analysis we can see (Figure 8), that the high acceleration in Z-direction leads to just a small force input. The dominant path (top mount z-direction) results from on the high transfer function to the cabin in this point.

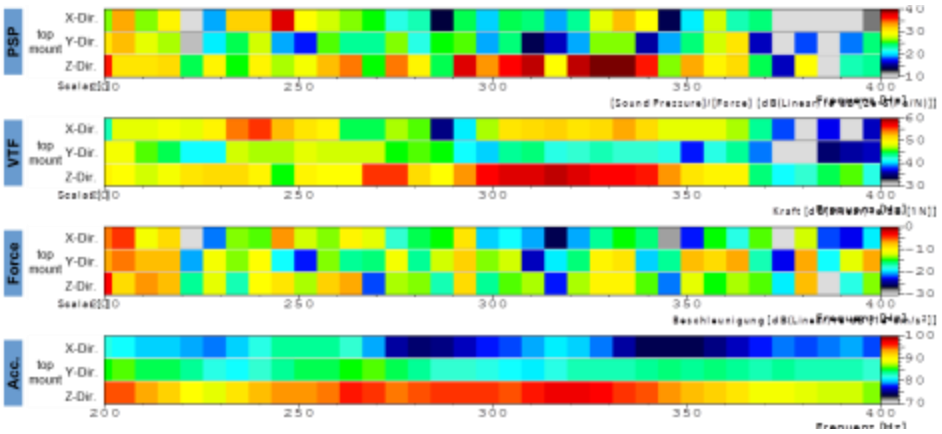


Figure 8: TPA results shock absorber

3.2 Active kinematic control (AKC)

Also due to internal investigations concerning possible transfer paths of knocking or running noise, a transfer path analysis was performed. Previous assumptions of the main transfer path were on the AKC mount in Y-Direction. Figure 9 shows the setup of the sensors and mounting points.

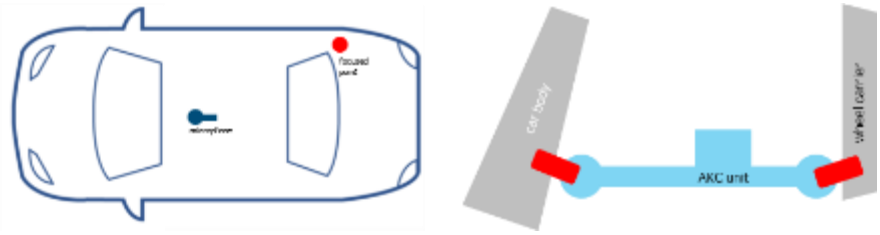


Figure 9: active kinematic control sensor setup

Focus was on the AKC mount in the clacking frequency range of 150-600Hz (Figure 10). The load case was created by driving over the rubber mats. Triggering in a proper way aligned with the subjective impression when listening to interior noise is critical here. The clacking noise is measureable at the AKC mount sensor as well as in the cabin.

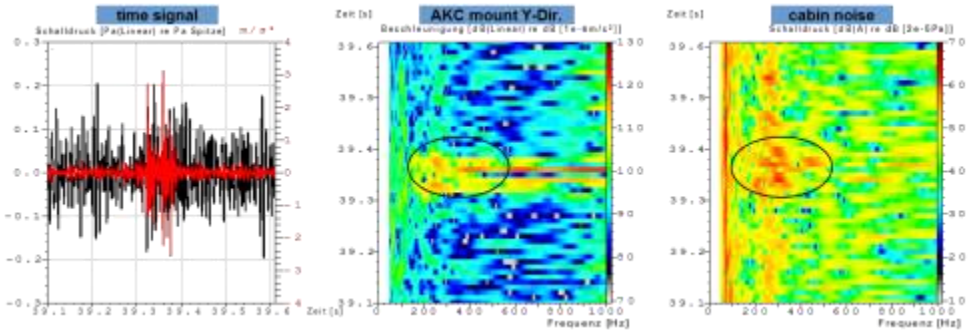


Figure 10: active kinematic control clacking noise

Using this load case for transfer path analysis we can see (Figure 11), that the high acceleration in Y-direction at the AKC mount and at one of the control arms leads to a high force input. The dominant path (AKC mount and partial a control arm in y-direction) results from the high force input at these points.

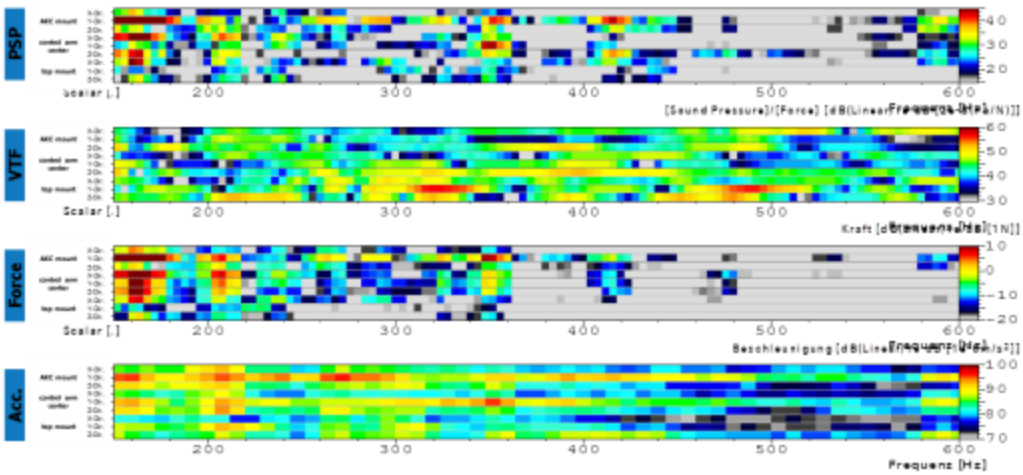


Figure 11: TPA results active kinematic control

3.3 Gear whining

Based on internal optimization suggestions, a transfer path analysis was carried out regarding gear whining for an automatic transmission. The aim of this study was to identify and optimize the dominant transfer paths. Figure 12 shows the used sensor setup.

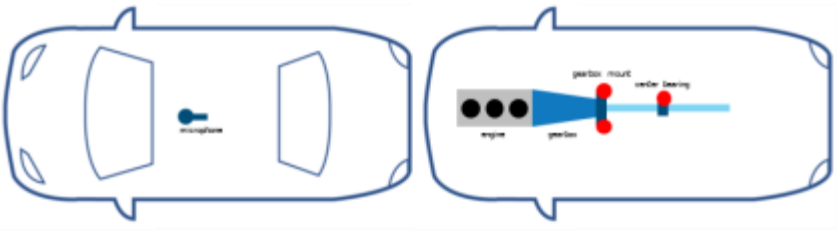


Figure 12: gear whining sensor setup

From a run up measurement with medium load on a test track the critical frequency range for gear whining could be identified between 1200Hz and 1800Hz (Figure 13) with a good signal-noise-ratio.

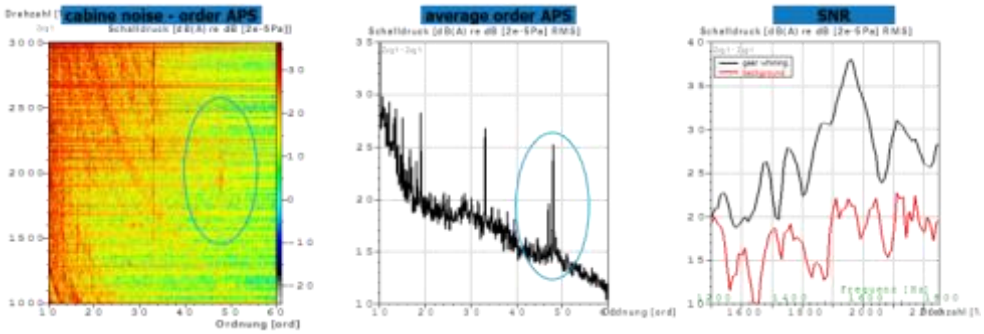


Figure 13: gear whining noise

Using this load case for transfer path analysis we can see (Figure 14), that the high acceleration in Y-direction at the gearbox mounts and the center bearing leads to a high force input. The dominant path (gearbox mount left and center bearing in y-direction) results from the combination of high force input and good transfer to cabin at these points.

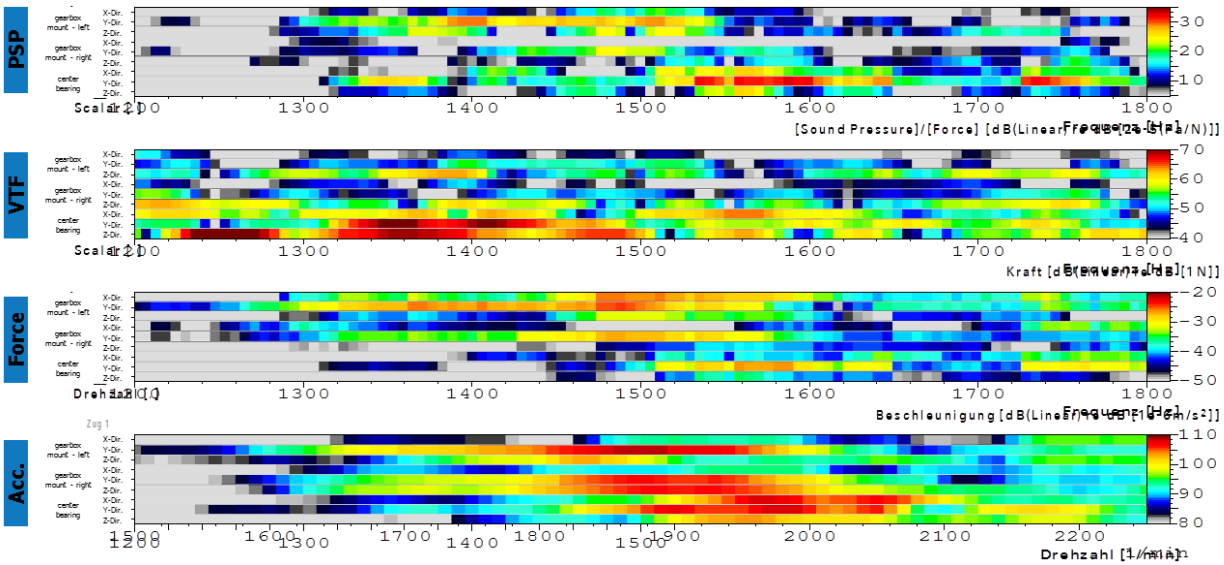


Figure 14: TPA results gear whining

3.4 Electric Drive

Based on an internal benchmark, a transfer path analysis was carried out regarding electric drive noise at an electric vehicle. The aim of this study was to identify and classify the dominant transfer paths. Figure 15 shows the used sensor setup.



Figure 15: electric drive sensor setup

From a run up measurement with high load on a test track the critical frequency range for electric drive noise could be identified in a first range between 250Hz and 550Hz (Figure 16) and in a second range between 650Hz and 850Hz with a good signal-noise-ratio.

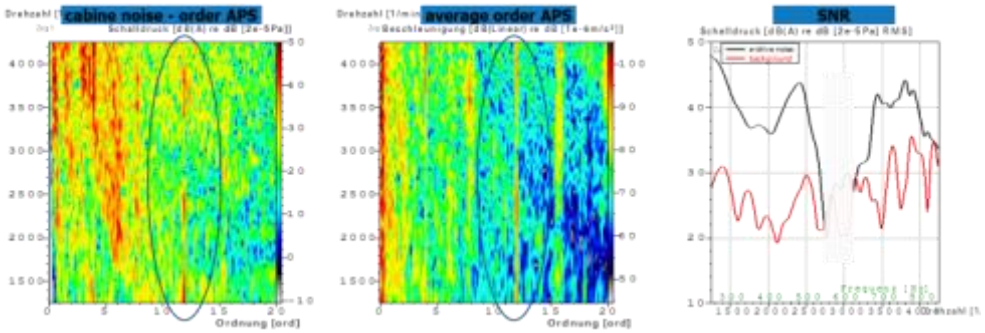


Figure 16: electric drive noise

Using this load case for transfer path analysis we can see (Figure 17), that there is just a low acceleration level for the lower frequency range and a high acceleration in the upper frequency range. The dominant path at the lower frequency range are the both front mounts in Z-direction due to a high force input and at the higher frequency range all mounts in Z-direction due to a good transfer to the cabin at these points.

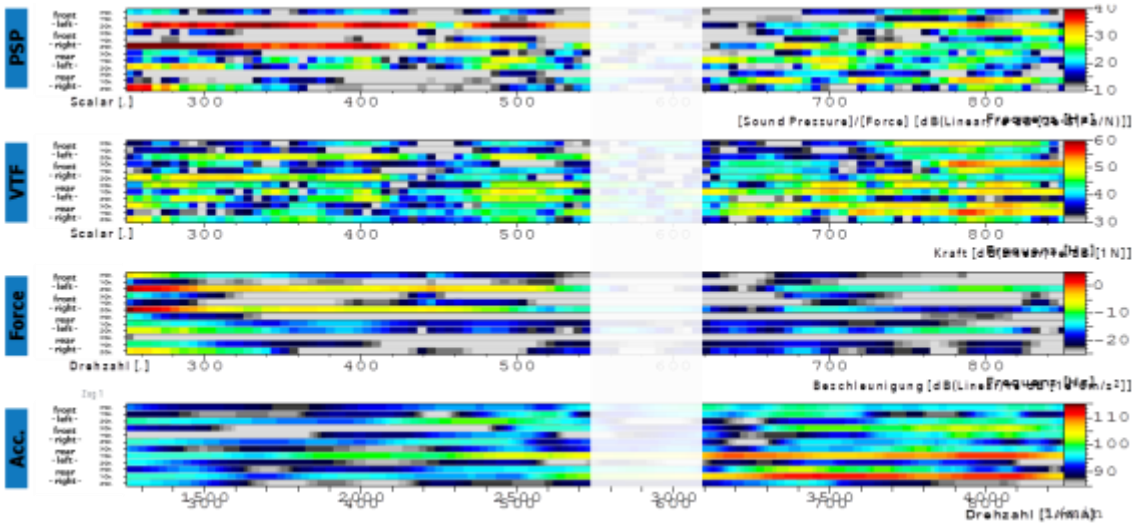


Figure 17: TPA results electric drive

4 Conclusion & Outlook

Structure-borne transfer path analysis is a very suitable tool for identifying and optimizing dominant noise transfer paths. Both impulsive and continuous noises can be examined by a suitable setup for the collection of operational data. The load cases can be specifically excited and extracted from overall noise for analysis. Based on the results, system weaknesses can be localized and displayed.

Further investigations and developments are ongoing within ZF in order to enhance the common matrix inversion abroad in frequency and time domain and to implement the blocked forces approach [5] in the in-house Matlab software.

References

[1] F. Gries, *Transferpfadanalyse in der Praxis: Parameterstudien an Beispielstrukturen*, Friedrichshafen: Diplomarbeit ZF-Friedrichshafen AG, 2011

[2] J. Neveling, *Transferpfadanalyse mit Fokus auf Getriebegeräusche in Front-Quer-Anwendungen*, Friedrichshafen: Bachelorarbeit ZF Friedrichshafen AG, 20.02.2013

[3] T. Vöhringer, *Inverse Ermittlung der mechano-akustischen Transferfunktion bei Getriebegeräuschuntersuchungen*, Friedrichshafen: Diplomarbeit ZF-Friedrichshafen AG, 2000

[4] R. Höldrich, A. Sontacchi, *Verfahren zur Berechnung von richtungskorrigierten Übertragungsfunktionen und/oder richtungskorrigierten Impedanzgrößen in einer Transferpfadanalyse einer schwingenden Struktur"*, Deutschland Patent 102008023094, 9 Mai 2008

[5] L. Trampus, T.Bischof, *Improvement of the Blocked Force method by considering the cross & moment mobilities*, in Proceedings of the 43th German Annual Conference on Acoustics (DAGA) Conference on Acoustics (2017)

Empirical formula for the vibration reduction index of junctions with different coplanar walls

C. Crispin[1], C. Mertens[1], A. Dijckmans[1]
[1] Belgian Building Research Institute, Acoustic division
Rue du Lombart 42, B-1000, Brussels, Belgium
e-mail: **charlotte.crispin@bbri.be**

Abstract

The vibration reduction index K_{ij} is a normalized quantity related to the vibrational power transmission over a structural junction in a building. Its measured or predicted value is used in prediction models in order to determine the contribution of the flanking transmission in the global sound transmission between rooms.

The predicted values provided in the standard ISO 12354-1 concern mainly rather simple junctions. This article suggests new engineering approximations for junctions of which the coplanar walls are different. These types of junction are roughly addressed in the standard. The empirical formulas, easy to use, are derived from a large number of numerical simulations and some measurements.

1 Introduction

The vibration reduction index, $K_{ij,}$ expresses the vibrational power transmission over a junction between two physically connected building elements in function of the frequency. The K_{ij} can be evaluated by measurement according to the standard ISO 10848 [1] or by prediction formulas presented in the annex E of the standard ISO 12354-1[2].

This article studies the K_{ij} for particular junctions named, here, rigid mixed cross-junctions that means cross-junctions composed of two different coplanar walls. The annex J of the standard 12354 proposes a rather simplistic interpretation to address these particular junctions: It proposes to replace the two different coplanar walls by two identical walls whose surface mass is the average of the surface mass of these walls (Figure 1). This article therefore supplies more relevant formulas which are derived from numerical simulations based on the finite element method (FEM, software Actran 15), statistical energy analysis (SEA) and the wave based method (WBM) [5].

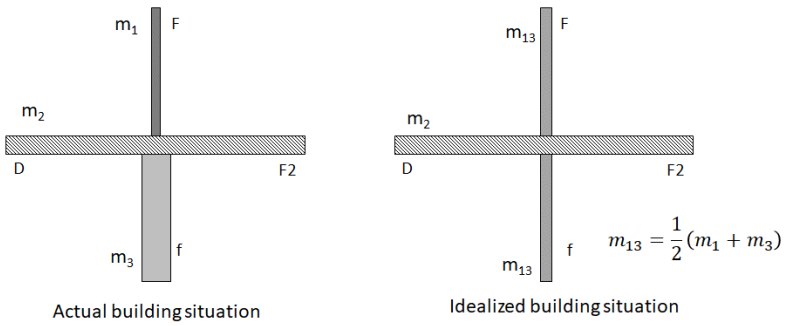


Figure 1: Interpretation for cross-junction with more than 2 element types according to annex J of the standard 12354-1 [2]

2 The vibration reduction index K_{ij} and its single-values

According to the measurement method (ISO 10848 [1]), the K_{ij} is estimated by the average of the velocity level differences $D_{v,ij}$ and $D_{v,ji}$ normalized to the junction length and the equivalent sound absorption length according to following formula:

$$K_{ij} = \overline{D}_{v,ij} + 10\lg\frac{l_{ij}}{\sqrt{a_i a_j}} \quad [\text{dB}] \tag{1}$$

$\overline{D}_{v,ij}$ is the direction averaged velocity level difference. It is obtained from the mean value of the velocity level differences $D_{v,ij}$ (when wall i is excited) and $D_{v,ji}$ (when the j is excited). It is expressed in decibels:

$$\overline{D}_{v,ij} = \frac{1}{2}\left(D_{v,ij} + D_{v,ji}\right) \quad [\text{dB}] \tag{2}$$

a_i (a_j, resp.) is the equivalent absorption length of wall i (wall j, resp.). It is expressed in meters.

$$a_i = \frac{2.2\pi^2 S_i}{c_0 T_{si}}\sqrt{\frac{f_{ref}}{f}} \quad [\text{m}] \tag{3}$$

where, S_i is the surface area of wall i [m²];
$T_{s,i}$ is the structural reverberation time of wall i [s];
c_0 is the speed of sound in air [m/s];
f is the current frequency [Hz];
f_{ref} is the reference frequency [f_{ref} = 1000 Hz].

The measured K_{ij} can be expressed by a single value $\overline{K_{IJ}}$ which is the arithmetic average of K_{ij} within the frequency range 200 Hz- 1250 Hz.

Annex E of the standard ISO 12354-1[2], for its part, proposes two methods to predict the K_{ij} for heavy structures. The first method considers that the K_{ij} is frequency-independent and gives a constant value for all frequencies. The empirical data are deduced from standardized measurements, theory or both and are expressed in terms of the ratio of the surface masses of the elements in the junction.

The data of the second method come from simulations [3]. These data are more difficult to use but more traceable. Futhermore, the K_{ij} is given in three different frequency ranges because in practice, it is shown that the K_{ij} is not really frequency independent:

- $K_{ij,low}$ is the arithmetic average of the one-third octave band values from 50 Hz to 200 Hz;
- $K_{ij,mid}$ is the arithmetic average of the one-third octave band values from 250 Hz to 1000 Hz;
- $K_{ij,high}$ is the arithmetic average of the one-third octave band values from 1250 Hz to 5000 Hz.

According to this method, the K_{ij} is determined by the characteristic moment-impedance, named the PC ratio (see section 5).

To be consistent with this annex the new prediction formulas dedicated to rigid mixed cross-junctions are given for the two approaches in sections 4 and 5, respectively.

3 Numerical simulations

Details of the FEM, SEA and WBM models developed to predict the vibration transmission across rigid plate junctions can be found in previous publications [4, 5, 13, 14]. All the models assume homogeneous, acoustically thin plates and unpinned junction lines. They take into account the finite dimensions of the plates and include both in-plane and bending wave vibration. The main difference between WBM and FEM are the plate boundary conditions: while the FEM model incorporates free plate boundary conditions, the WBM assumes simply supported plates. The frequency-dependent loss factor needed to evaluate the damping of the walls is set equal to $1/\sqrt{f}$. The dimensions of the floor F1 (and F2) used in the WBM and SEA models are 5m x 4m. The dimensions of the wall Wh (and Wl) used in the WBM and SEA models are 3.5 m x 4 m. For the FEM simulations, the floor dimensions are 4 m x 2.74 m and the wall dimensions 4 m x 2.38 m.

The material properties used in the simulations are given in tables 1 and 2.

Surface mass of the concrete floor $m'_{F1\text{-}F2}$ [kg/m²]	Surface mass of the heavy wall m'_{Wh} [kg/m²]	Surface mass of the 10 cm lightweight wall m'_{Wl} [kg/m²]	Numerical simulation used to study these combinations
276 (h=12 cm, ρ=2300kg/m³)	230 (h=10 cm, ρ=2300kg/m³)	40, 80, 140, 175, 180, 200, 220, 230	WBM, SEA
276 (h=12 cm, ρ=2300kg/m³)	345 (h=15 cm, ρ=2300kg/m³)	40, 80, 140, 175, 180, 200, 220, 230, 276 (12 cm), 345 (15 cm)	WBM, SEA
460 (h=20 cm, ρ=2300kg/m³)	230 (h=10 cm, ρ=2300kg/m³)	40, 80, 140, 175, 180, 200, 220, 230	WBM, SEA, FEM
460 (h=20 cm, ρ=2300kg/m³)	345 (h=15 cm, ρ=2300kg/m³)	40, 80, 140, 175, 180, 200, 220, 230, 276 (12 cm), 345 (15 cm)	WBM, SEA
644 (h=28 cm, ρ=2300kg/m³)	230 (h=10 cm, ρ=2300kg/m³)	40, 80, 140, 175, 180, 200, 220, 230	WBM, SEA
644 (h=28 cm, ρ=2300kg/m³)	345 (h=15 cm, ρ=2300kg/m³)	40, 80, 140, 175, 180, 200, 220, 230, 276 (12 cm), 345 (15 cm)	WBM, SEA

Table 1: Studied combinations for the rigid mixed cross-junctions

The Poisson's ratio is 0.2 and the Young's modulus in function of the density is given in table 2.

ρ [kg/m³]	E_{dyn} [N/m²]
400	1.32×10^9
800	2.51×10^9
1400	6.56×10^9
1750	1.22×10^{10}
1800	1.24×10^{10}
2000	1.71×10^{10}
2200	2.36×10^{10}
2300	2.6×10^{10}

Table 2: Young's modulus used for the numerical simulations

4 Empirical formula for K_{ij} in function of the surface mass ratio

4.1 Path F1-F2

For this path, it is expected that the vibration reduction index of the mixed junction is between the value of the rigid T-junction when the surface mass of the lightweight wall tends towards zero, $K_{F1\text{-}F2,T,Wh,}$ and the value of the rigid cross-junction when the surface mass of the lightweight wall is equal to the heavy wall, $K_{F1\text{-}F2,X,Wh}$. The expected form of the K_{ij} for the mixed junction is then:

$$K_{F1-F2,mixed} = p * K_{F1-F2,X,Wh} + (1-p) * K_{F1-F2,T,Wh} \quad (4)$$

where p is the weight factor to evaluate.

To this end, a large number of numerical simulations was carried out. The $K_{F1\text{-}F2,mixed}$ were determined numerically for the combinations given at table 1 with the corresponding $K_{F1\text{-}F2,X,Wh}$ and $K_{F1\text{-}F2,T,Wh}$. For each combination, the factor p was calculated with Eqn. (4). By plotting the data on a chart, the linear relationship between p and the ratio of the surface masses of the two walls is well observed (Figure 2). While ensuring that p equals 1 for m'_{wl} equals m'_{wh} and that p equals 0 for m'_{wl} equals 0, it can be approximated by:

$$p = \left(\frac{m'_{Wl}}{m'_{Wh}}\right) \quad (5)$$

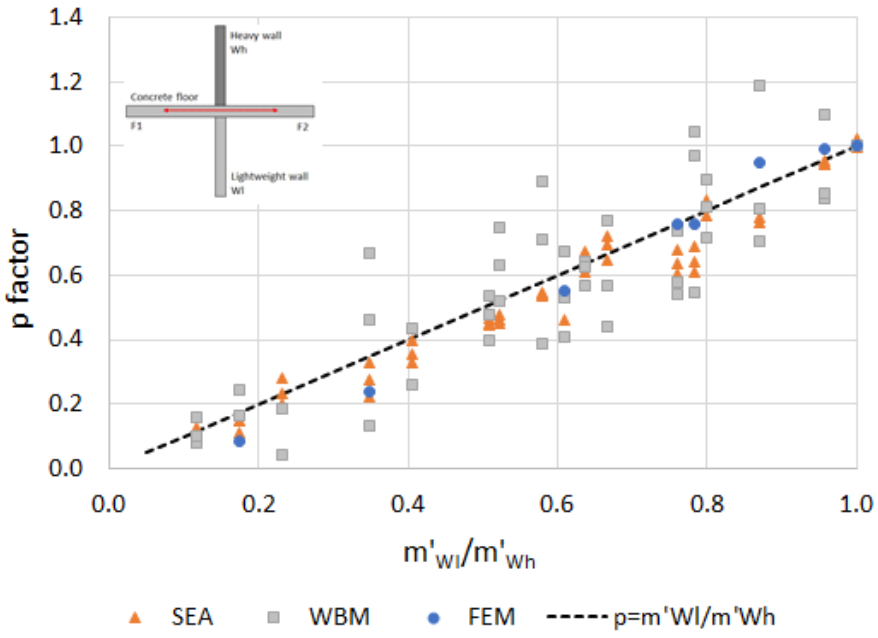


Figure 2: Weight factor p obtained by simulations for the transmission path F1-F2

The coefficient of determination, R^2, for this trendline is 0.99 for FEM data, 0.95 for SEA data and 0.77 for WBM data. The WBM data are more scattered than the SEA data due to the significant influence of the plate modal behavior in a broad frequency range [9,14]. While the FEM also incorporates the modal behavior, the variation seen in the eight test cases is smaller.

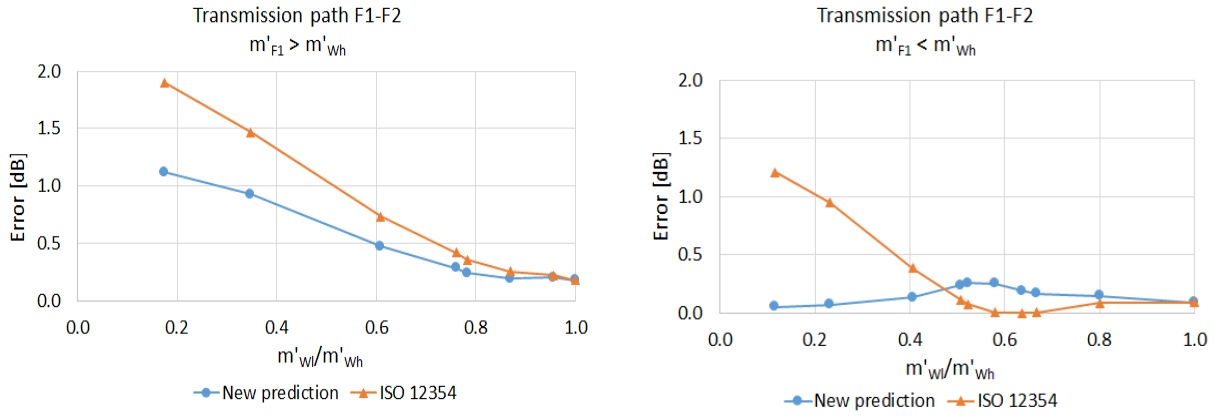
The new prediction according to Eqn. (4) is more accurate than the prediction proposed in annex J of the standard ISO 12354-1 where the mixed junction is replaced by an idealized junction (see figure 1). The

accuracy of Eqn. (4) and the ISO 12354-1 prediction was evaluated on some SEA simulations (Figure 3a and 3b).

These figures present the calculation error obtained with the new prediction (the absolute difference between the expected values and the new prediction) and with the 12354 prediction (the absolute difference between the expected values and the 12354 prediction) for different surface mass ratio's between the walls. All data (expected values, new prediction values and 12354 values) come from SEA simulations.

For a floor having a surface mass higher than the heavy wall, an error close to 2 dB can be observed with the 12354 prediction when the surface mass ratio is low. With the new prediction, this error falls to approximately 1 dB.

For the other case ($m'_{F1}<m'_{Wh}$) the error is close to zero with the new prediction. The calculations errors obtained with the 12354 prediction is 1.2 dB for m'_{Wl}/m'_{Wh} equal to 0.12. As expected, the larger the difference in surface mass of the walls is, the larger the calculation errors obtained with the 12354 prediction is.



(a) (b)

Figures 3a and 3b: Transmission path F1-F2: Comparison between the calculation error [dB] of the new prediction and of the 12354 prediction obtained by SEA simulations in function of the surface mass ratio's between the walls. (a) for $m'_{F1}> m'_{Wh}$ and (b) for $m'_{F1}< m'_{Wh}$

4.2 Path Wh-Wl

This transmission path crosses the two coplanar walls with different properties. In this case, the following equation can be expected:

$$K_{Wh-Wl,mixed} = p * K_{Wh-Wl,X,Wm} \quad (6)$$

Where $K_{Wh\text{-}Wl,X,Wm}$ is the vibration reduction index of the simple rigid cross-junction of which the surface mass of the coplanar walls is the average of the surface mass of the walls Wh and Wl. As before, the $K_{Wh\text{-}Wl,mixed}$ of different combinations and the corresponding $K_{Wh\text{-}Wl,X,Wm}$ were obtained from the three numerical methods from which the p factor could be calculated. Figure 4 presents this factor in function of the ratio of the surface masses of the two walls.

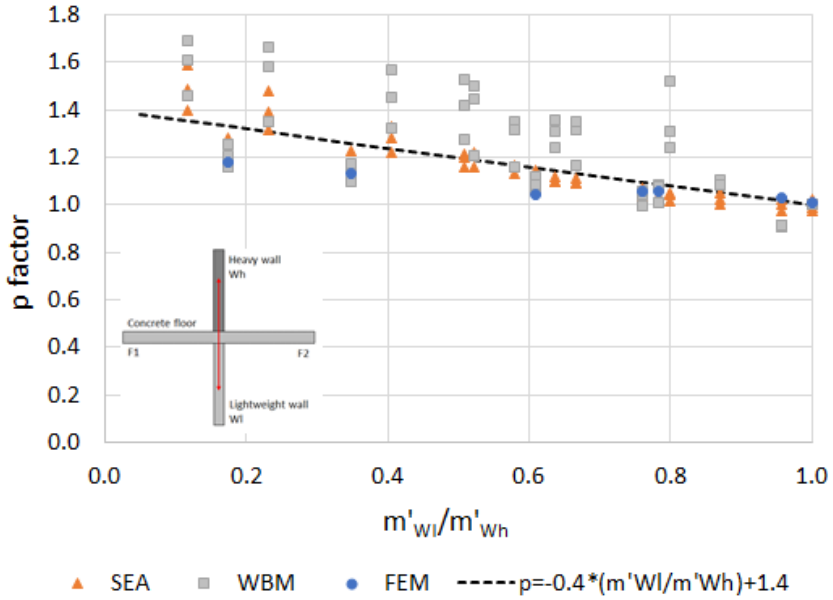
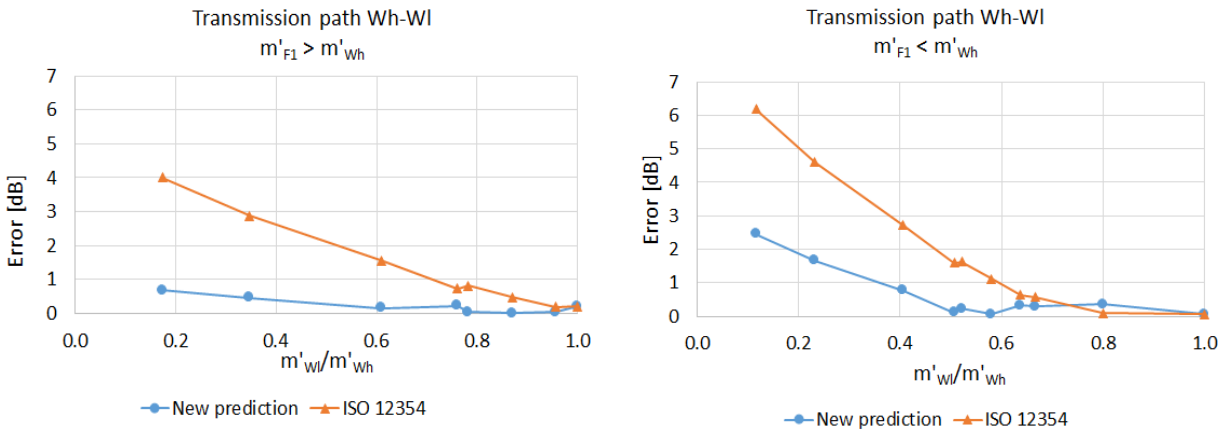


Figure 4: Weight factor *p* obtained by simulations for the transmission path Wh-Wl

Again, the WBM data are more scattered than the SEA data. The FEM data for the 10cm concrete heavy wall agree well with the WBM data. The WBM data for the 15cm concrete heavy wall are higher than the SEA data. The slope given by the FEM data is the lowest. While ensuring that *p* equals 1 for m'_{Wl} equals m'_{Wh}, the best trendline for all data is given by:

$$p = -0.4 * \left(\frac{m'_{Wl}}{m'_{Wh}}\right) + 1.4 \tag{7}$$

The coefficient of determination, R^2, for the SEA data is 0.77, for the FEM data, 0.92 and for the WBM, 0.48. As before, the calculation errors of the new prediction and of the 12354 prediction were evaluated by SEA simulations (Figures 5a and 5b).



(a) (b)

Figures 5a and 5b: Transmission path Wh-Wl : Comparison between the calculation error [dB] of the new prediction and of the 12354 prediction obtained by SEA simulations in function of the surface mass ratio's between the walls. (a) for $m'_{F1} > m'_{Wh}$ and (b) for $m'_{F1} < m'_{Wh}$

For $m'_{F1}>m'_{Wh}$, an error of 4 dB can be reached for a low surface mass ratio with the 12354 prediction. This error decreases when the surface mass ratio tends towards 1. The error of the new prediction is lower than 1 dB. For the case $m'_{F1}<m'_{Wh}$, the calculation errors obtained with the 12354 prediction can be higher than 6 dB, while the maximum error for the new prediction is 2.5 dB.

4.3 Path F1-Wh

For this transmission around the corner and involving the heaviest wall (Figure 6), it is expected that the $K_{F1\text{-}Wh,mixed}$ will be between two limit values: the value of the rigid T-junction , $K_{F1\text{-}Wh,T,Wh}$, when the surface mass of the lightweight wall tends towards zero, and the value of the rigid cross-junction, $K_{F1\text{-}Wh,X,Wh}$, when the surface mass of the lightweight wall is equal to the heavy wall:

$$K_{F1-Wh,mixed} = p * K_{F1-Wh,X,Wh} + (1-p) * K_{F1-Wh,T,Wh} \quad (8)$$

The weight factors p were calculated from several $K_{F1\text{-}Wh,mixed}$, $K_{F1\text{-}Wh,X,Wh}$ and $K_{F1\text{-}Wh,T,Wh}$ obtained by the three numerical simulations. The results are presented in figure 6 in function of the ratio of the surface masses of the walls W_l and W_h. The WBM method gives again widely scattered points due to the different modal behavior of the different junctions modeled. The best selected trendline is a polynomial relationship:

$$p = 0.4 * \left(\frac{m'_{Wl}}{m'_{Wh}}\right)^2 + 0.6\left(\frac{m'_{Wl}}{m'_{Wh}}\right) \quad (9)$$

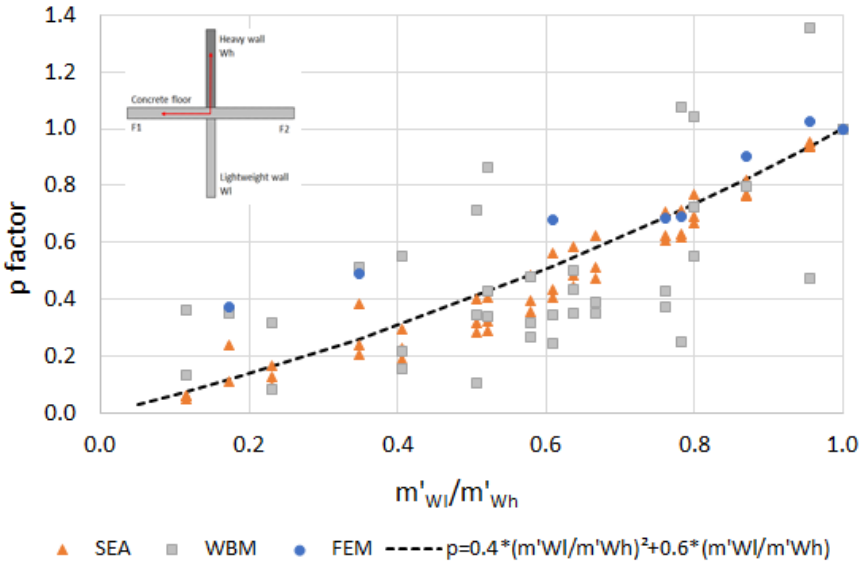
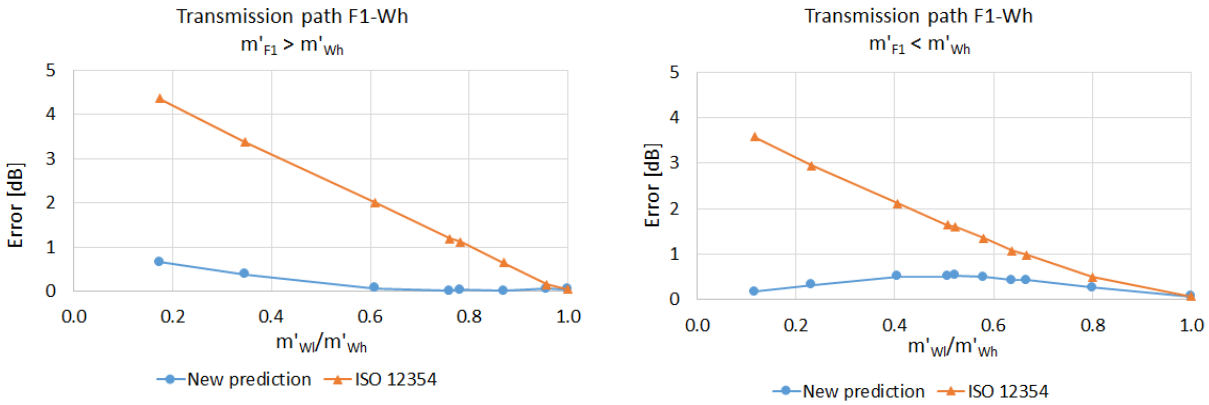


Figure 6: Weight factor p factor obtained by simulations for the transmission path F1-Wh

The coefficient of determination, R^2, for the SEA data is 0.96, for the FEM data, 0.93 and for the WBM, 0.55.

Figures 7a and 7b confirm that this new proposition is more accurate than the K_{ij} obtained by the 12354 prediction which uses the mean of the walls. The calculation errors obtained by the 12354 prediction increases significantly when the contrast between the surface masses increases. For example, a deviation of ± 4 dB is observed around a surface mass ratio of 0.2. The error for the new prediction is smaller than 1 dB.



(a) (b)

Figures 7a and 7b: Transmission path F1-Wh : Comparison between the calculation error [dB] of the new prediction and of the 12354 prediction obtained by SEA simulations in function of the surface mass ratio's between the walls. (a) for $m'_{F1} > m'_{Wh}$ and (b) for $m'_{F1} < m'_{Wh}$

4.4 Path F1-Wl

In this case, the $K_{F1\text{-}Wl,mixed}$ is calculated from the $K_{F1\text{-}Wl,X,Wl}$ which represents the vibration reduction index of the rigid cross-junction of which the coplanar walls are identical and composed of the lightest walls W_l.

$$K_{F1-Wl,mixed} = p * K_{F1-Wl,X,Wl} \tag{10}$$

The p factors obtained with the numerical simulations are presented in figure 8. While the FEM method gives a slope close to zero, the WBM and SEA simulations follow the selected trendline (ensuring that p=1 for $m'_{Wl}=m'_{Wh}$), given by:

$$p = -0.4 * \left(\frac{m'_{Wl}}{m'_{Wh}}\right) + 1.4 \tag{11}$$

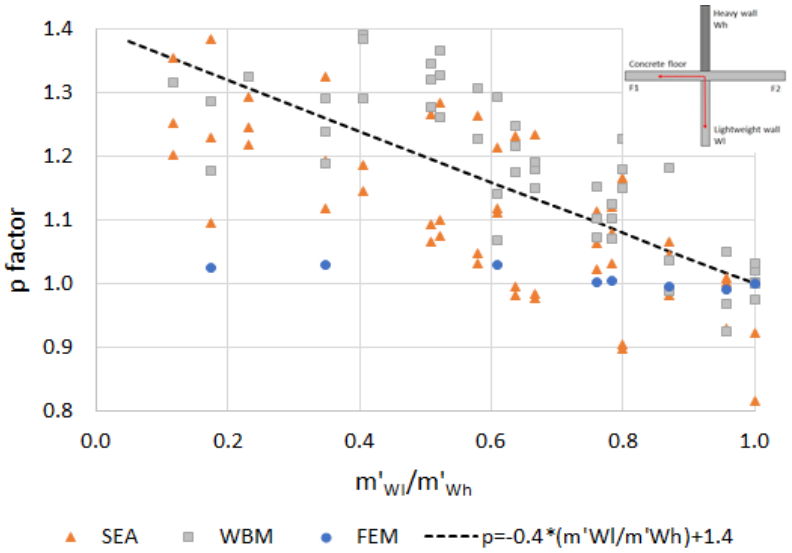
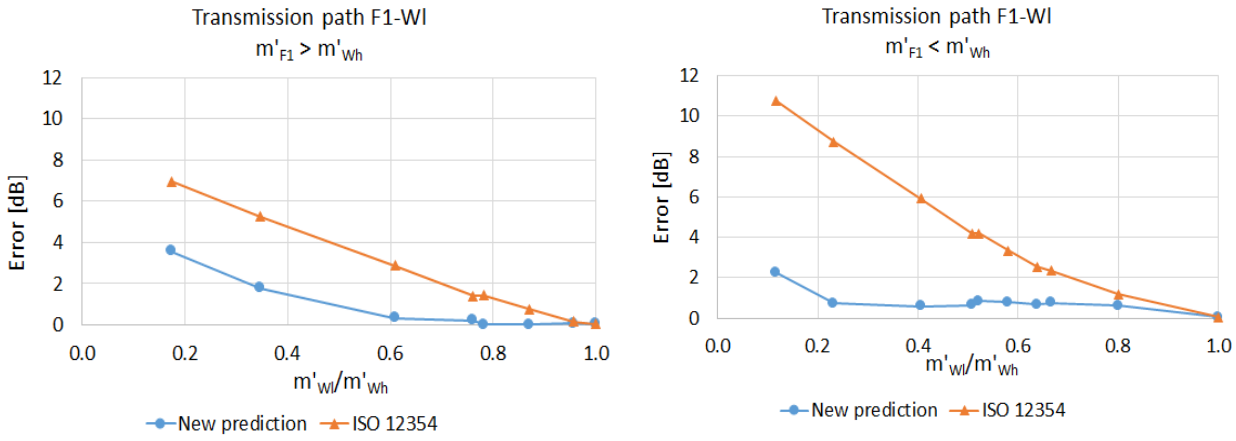


Figure 8: Weight factor p factor obtained by simulations for the transmission path F1-Wl

The coefficient of determination, R^2, for the SEA data is 0.75, for the FEM data, 0.70 and for the WBM, 0.74 giving mitigated results but nevertheless gives, according to some SEA results (figures 9), a quite good prediction compared to the prediction which uses the mean of the walls. For example, an error higher than 5 dB is already observed between the actual mixed junction value and the 12354 prediction value for a surface mass ratio around 0.5. This error can increase if the surface mass ratio tends towards 0. The error is smaller than 1 dB with the new prediction and remains relatively constant in terms of the surface mass ratio.



(a) (b)

Figures 9a and 9b: Transmission path F1-Wl : Comparison between the calculation error [dB] of the new prediction and of the 12354 prediction obtained by SEA simulations in function of the surface mass ratio's between the walls. (a) for $m'_{F1} > m'_{Wh}$ and (b) for $m'_{F1} < m'_{Wh}$

5 Empirical formula for K_{ij} in function of the characteristic moment-impedances ratio

In the new version of the standard ISO 12354-1 [1], more accurate and traceable formulas are now available. These formulas come from numerical simulations and concern, for the time, only rigid L-, T- and X-junctions of homogeneous, isotropic plates. We propose here to extend these formulas to rigid cross-mixed junctions in the same way.

In this case, the prediction of K_{ij} must be given in three different frequency ranges in order to take into account the effect of in-plane waves as well as bending waves: a low-frequency range (50 Hz to 200 Hz), a mid-frequency range (250 Hz to 1k Hz) and a high-frequency range (1.25 kHz to 5 kHz). Furthermore, the K_{ij} is expressed as a function of the ratio of the characteristic moment-impedances (PC ratio) instead of the surface masses [3, 4]. That is why the weight factor p mentioned above will be in this case a function of this ratio too.

$$PC\ ratio = \sqrt[4]{\frac{m'_{\perp i} B^3_{\perp i}}{m'_i B^3_i}} = \left(\frac{\rho_{\perp i}}{\rho_i}\right)^{1/4} \left(\frac{h_{\perp i}}{h_i}\right)^{5/2} \left(\frac{E_{\perp i}}{E_i}\right)^{3/4} \tag{12}$$

Figures 10a to 10d present the $K_{ij,low}$, $K_{ij,mid}$ and $K_{ij,high}$ per transmission path for the three different frequency ranges. On each graph, the distinction between the three numerical simulations is not visible anymore but the three ranges are highlighted as well the selected trendline for p.

The results in the low frequency range are very scattered. This is not surprising because in low frequency the determination of the single value is less accurate due to the low number of modes. The dispersion of the results increases as the PC ratio decreases.

It seems that a single trendline could be appropriate for the three frequency ranges. It is advantageous to avoid the risk of errors when calculating the predictions.

The coefficients of the determination are not very high, especially for the low frequency range but these propositions of prediction offer better results than the ones reached by the predictions which use the mean of the PC ratio of the walls.

In conclusion, the weight factor p for the transmission path F1-F2 (Figure 10a) is given by:

$$p = -0.9 * \left(\sqrt[4]{\frac{m'_{Wl} B^3_{Wl}}{m'_{Wh} B^3_{Wh}}} \right)^2 + 1.9 * \left(\sqrt[4]{\frac{m'_{Wl} B^3_{Wl}}{m'_{Wh} B^3_{Wh}}} \right) \tag{13}$$

This factor is applied in Eqn. (4) where the $K_{F1\text{-}F2,mixed}$, $K_{F1\text{-}F2,X,Wh}$ and $K_{F1\text{-}F2,T,Wh}$ are replaced by the corresponding values at low (mid and high, resp.) frequencies for a prediction in the low (mid and high, resp.) frequency range.

For the transmission path Wh-Wl (Figure 10c), the weight factor p that has to be applied in Eqn. (6) is:

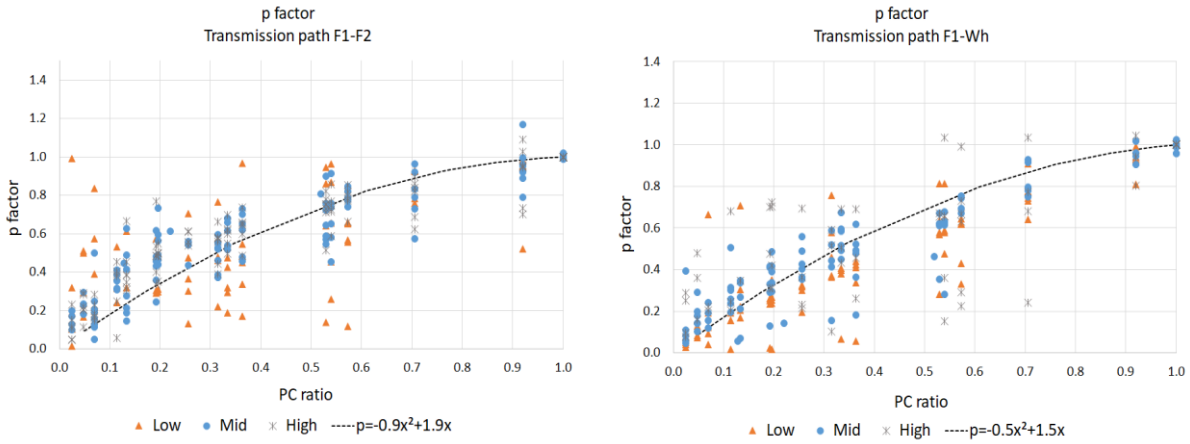
$$p = 0.8 * \left(\sqrt[4]{\frac{m'_{Wl} B^3_{Wl}}{m'_{Wh} B^3_{Wh}}} \right)^2 - 1.5 * \left(\sqrt[4]{\frac{m'_{Wl} B^3_{Wl}}{m'_{Wh} B^3_{Wh}}} \right) + 1.7 \tag{14}$$

For the transmission path F1-Wh (Figure 10b), the weight factor p that has to be applied in Eqn. (8) is:

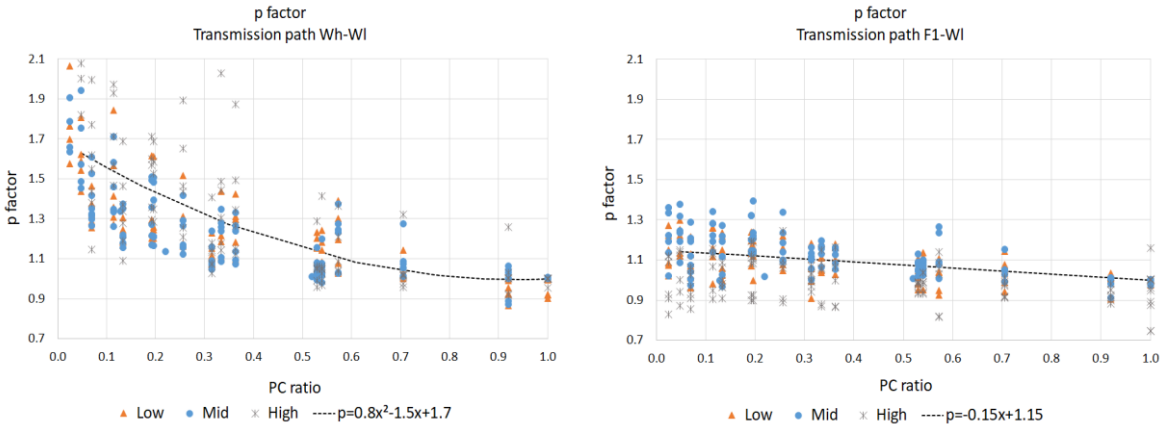
$$p = -0.5 * \left(\sqrt[4]{\frac{m'_{Wl} B^3_{Wl}}{m'_{Wh} B^3_{Wh}}} \right)^2 + 1.5 * \left(\sqrt[4]{\frac{m'_{Wl} B^3_{Wl}}{m'_{Wh} B^3_{Wh}}} \right) \tag{15}$$

For the transmission path F1-Wl (Figure 10d), the weight factor p that has to be applied in Eqn. (10) is:

$$p = -0.15 * \left(\sqrt[4]{\frac{m'_{Wl} B^3_{Wl}}{m'_{Wh} B^3_{Wh}}} \right) + 1.15 \tag{16}$$



(a) (b)



(c) (d)

Figure 10: Weight factor *p* in function of the PC ratio obtained by simulations for (a) the transmission path F1-F2 (b) the transmission path F1-Wh (c) the transmission path Wh-Wl (d) the transmission path F1-Wl

6 Experimental validation

6.1 Test constructions and measurement procedure

The assessment of the vibration transmission reduction through rigid mixed cross-junctions was carried out on a junction where the floor, F1-F2 (100 mm), was composed of a reinforced concrete plate, the heavy wall was composed of solid concrete blocks (90 mm) and the lightweight wall was composed of cellular concrete blocks (70 mm). The experimental results have been obtained according to the specifications of the standard 10848 but on a half scaled test bench (Figure 11) [5, 6, 7].



Figure 11: pictures of the measurement setup

The properties of the walls are given at table 3.

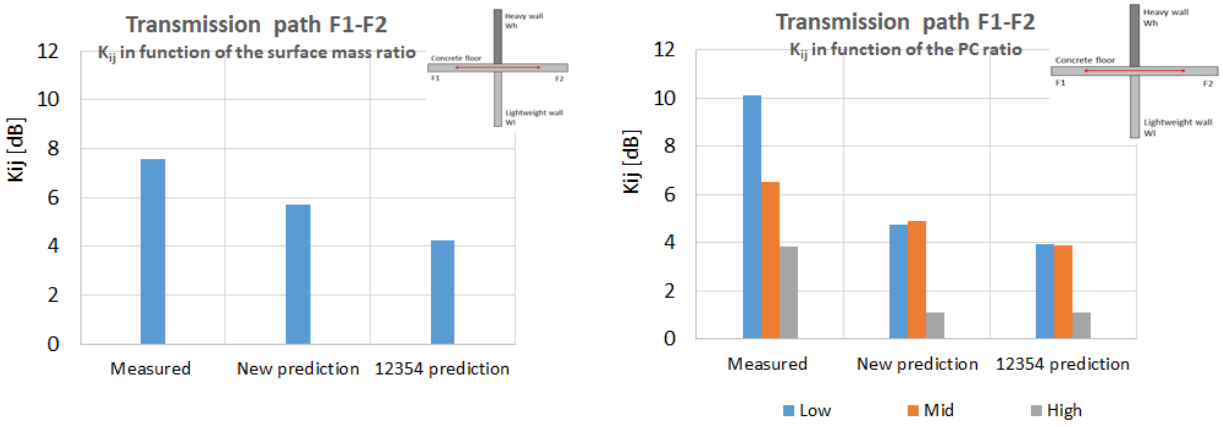
Material	Thickness [mm]	Density [kg/m³]	Surface mass [kg/m²]	c_L [m/s]	fc [Hz]	Edyn [N/m²]
reinforced concrete	100	2300	230	3400	190	2.60E+10
Concrete blocks	90	2300	207	3400	210	2.60E+10
Cellular concrete blocks	70	666	47	1650	563	1.74E+09

Table 3: properties of the materials

6.2 Results

The idea, here, is:

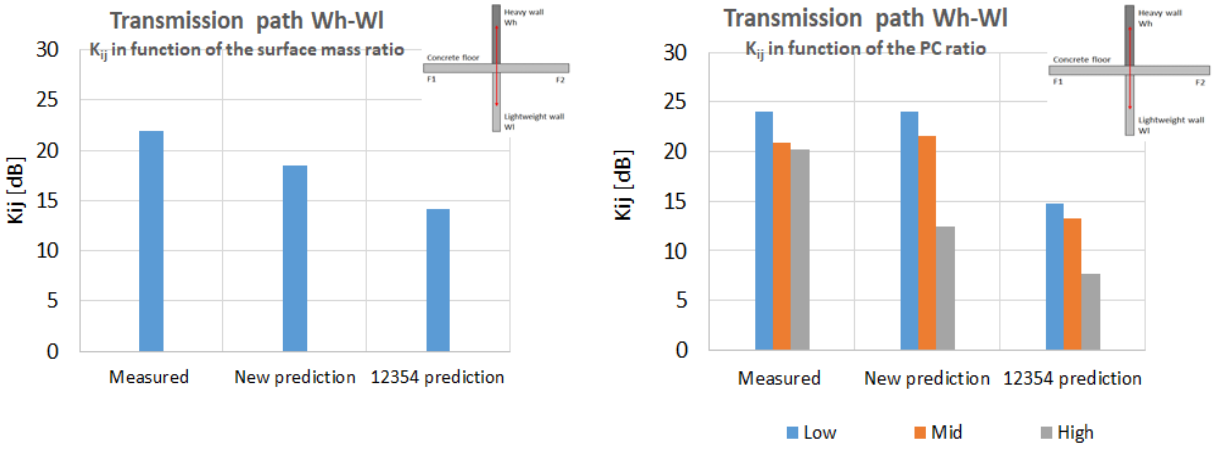
- To calculate the prediction of rigid mixed cross-junction on the basis of the new weight factor *p* applied on the K_{ij} (or $K_{ij,low}$, $K_{ij,mid}$, $K_{ij,high}$) proposed in the standard ISO 12354-1 [1];
- To calculate the prediction according to annex J of the standard 12354 where the surface mass is the average of the walls Wh and Wl (or the average of the characteristic moment impedance);
- To compare these results with the measured values.



(a) (b)

Figure 12: Path F1-F2: Comparison between the measured results, the new prediction results and the prediction results obtained according to the annex J of the standard 12354. (a) for K_{ij} expressed in terms of the surface mass ratio, (b) for K_{ij} expressed in terms of PC ratio.

Overall, we find, for the path F1-F2 (figures 12a and 12b) an improvement of the new prediction with the use of the weight factor *p*. The predictions are still lower than the measured results. This is due to the fact that the initial prediction formulas of the standard 12354-1 underestimate the $\overline{K_{ij}}$ for this path. The measured $K_{ij,low}$ is unduly high because there is a lack of modes in this frequency range.

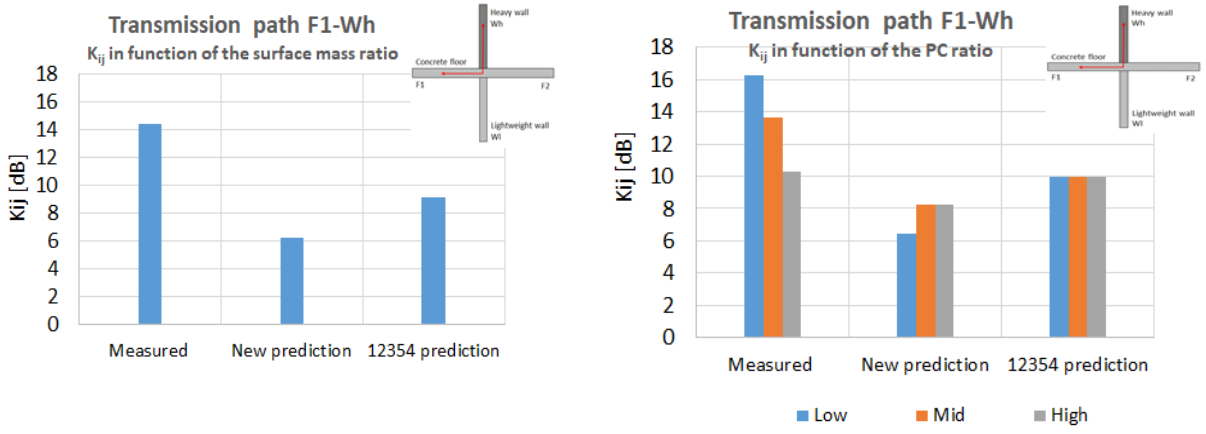


(a) (b)

Figure 13: Path Wh-Wl: Comparison between the measured results, the new prediction results and the prediction results obtained according to the annex J of the standard 12354. (a) for K_{ij} expressed in terms of the surface mass ratio, (b) for K_{ij} expressed in terms of PC ratio.

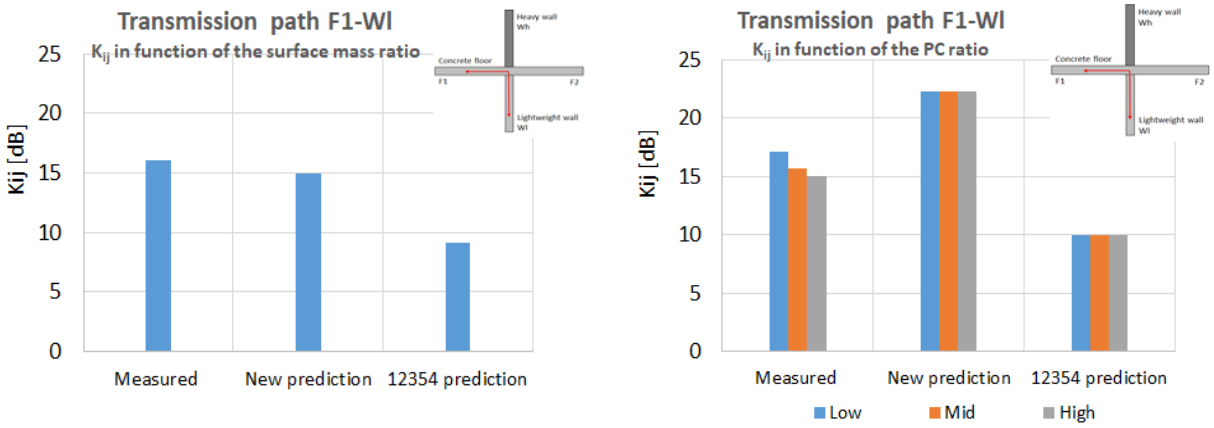
For the path Wh-Wl (Figure 13a and 13b), the improvement with the new prediction is significant. Particularly, the results obtained with the new prediction are very close to the expected values for the estimation of the $K_{ij,mid}$ and $K_{ij,low}$ expressed in terms of the PC ratio.

The results for the path F1-Wh (Figures 14) are somewhat disappointing. A degradation of the prediction is observed but it is attributed to the fact that the K_{ij} values of the cross-junction and the T-junction given by the standard 12354 are underestimated. Indeed, a previous testing program carried out on simple cross-junctions and T-junctions showed that the 12354-1 prediction values were ± 5 dB lower than the measured values [16].



(a) (b)

Figure 14: Path F1-Wh: Comparison between the measured results, the new prediction results and the prediction results obtained according to the annex J of the standard 12354 (Wmean prediction). (a) for K_{ij} expressed in terms of the surface mass ratio, (b) for K_{ij} expressed in terms of PC ratio.



(a) (b)

Figure 15: Path F1-Wl: Comparison between the measured results, the new prediction results and the prediction results obtained according to the annex J of the standard 12354. (a) for K_{ij} expressed in terms of the surface mass ratio, (b) for K_{ij} expressed in terms of PC ratio.

For the path F1-Wl, a best estimation is obtained with the new prediction for the K_{ij} expressed in terms of the surface mass ratio (Figure 15a). However, an excessive overestimation is observed for the estimation of the K_{ij} expressed in terms of the PC ratio which is not on the safe side as preferred for the predictions (Figure 15b).

7 Conclusion

This article proposes new prediction formulas to evaluate the vibration reduction index K_{ij} for rigid mixed cross-junctions. These formulas which were derivated from a large number of numerical simulations are relatively simple. They are based on the weighting of K_{ij} of simple rigid cross- and T- junctions. The weight factor p is expressed by the ratio of the surface masses or the PC ratio according to both approaches that recently appeared in the standard ISO 12354-1.

The numerical simulations have shown an obvious improvement of the new prediction compared to the proposition which idealizes the junction by averaging the surface masses of the two different coplanar walls (annex J of the standard 12354). The calculations errors obtained with this idealization can be very high and increases significantly when the contrast between the surface masses increases while the new prediction results remain very close to the expected results.

The comparison between measurement and prediction results shows, in general, the best agreement if the weight factor p is used. An excessive overestimation of the vibration reduction index is however observed for a few cases, which is not on the safe side as preferred for predictions.

Acknowledgements

The authors wish to acknowledge the financial assistance of the Federal Public Service Economy of Belgium.

References

[1] ISO 10848-1 to 4 (2017). Acoustics - Laboratory and field measurement of flanking transmission for airborne, impact and building service equipment sound between adjoining rooms;
[2] ISO 12354-1 (2017) Building Acoustics — Estimation of acoustic performance of buildings from the performance of elements — Part 1: Airborne sound insulation between rooms;
[3] Hopkins C., Crispin C., Poblet-Puig J., Guigou-Carter C., Regression curves for vibration transmission across junctions of heavyweight walls and floors based on finite element methods and wave theory, *Applied Acoustics* 113 (2016) 7-21.
[4] Crispin C., De Geetere L., Ingelaere B., Extensions of EN 12354 vibration reduction index expressions by means of FEM calculations, *Proceedings of Internoise*, Melbourne, Australia, 16-19 November(2014).
[5] Crispin C., Mertens C., Dijckmans A., Detailed analysis of measurement results of flanking transmission across a junction composed of double walls carried out on a half scaled test bench, *Proceedings of* ICSV24, 23-27 July 2017, London.
[6] Kling C., Miniaturising a wall test facility, *Journal of Building Acoustics*, Vol. 14, N°4, 2007, 243-266.
[7] Wittstock V., Schmelzer M., Kling C., On the use of scaled models in building acoustics, *Proceedings of Euronoise*, Paris, France, 29 June-4 July(2008).
[8] Crispin C., Mertens C., Dijckmans A. Integrating lightweight concepts in acoustical standardization. BBRI Technical Report, DIVA2018/CCR001 (2018)
[9] Dijckmans A. , "Structure-borne sound transmission across junctions of finite single and double walls", *Proceedings of Inter-Noise 2015,* San Francisco, USA, (2015)
[10] Gerretsen, E., "Calculation of sound transmission between dwellings by partitions and flanking structures", Applied Acoustics 12 (1979), 413-433.
[11] C. Hopkins, Sound insulation, Butterworth-Heineman, Amsterdam e.d., 2007
[12] Poblet-Puig J., Guigou-Carter C., Amplified catalogue of vibration reduction index formulas for junction based on numerical simulations, *Proceedings of Internoise*, Hamburg, Germany, 21-24 August, (2016).

[13] Dijckmans A., Vibration transmission across junctions of double walls using the wave approach and statistical energy analysis, *Acta Acustica united with Acustica*, Vol. 102 (2016) 488-502.
[14] Dijckmans A. Wave based modelling of vibration transmission across junctions composed of rectangular single and double walls, *Acta Acustica united with Acustica*, Vol. 102 (2016) 1011-1026.
[15] Poblet-Puig J., Guigou-Carter C., Using spectral finite elements for parametric analysis of vibration reduction index of heavy junctions oriented to flanking transmissions and EN-12354 prediction method, *Applied Acoustics* 99 (2015), 8-23.
[16] BBRI, Integrating lightweight concepts in acoustical standardization (A-Light). Research projet (2016-2018)

A hybrid numerical and experimental approach for structural intensity analysis of stiffened lightweight structures

J. Biedermann [1], **R. Winter** [1], **M. Norambuena** [1], **M. Böswald** [1]
[1] Deutsches Zentrum für Luft- und Raumfahrt e.V. (DLR), Institute of Aeroelasticity,
Bunsenstraße 10, 37073 Göttingen, Germany
e-mail: **joern.biedermann@dlr.de**

Abstract
Aircrafts are lightweight structures and as such they are prone to vibrations, which make them susceptible to structure-borne noise. Especially, engine induced vibration and their transmission as structure-borne noise towards the aircraft cabin are of interest. In order to implement optimal noise treatments for cabin comfort improvement it is essential to identify the transfer path from the engines through the wings and fuselage into the cabin. On the numerical side Structural Intensity Analysis is a established method to identify the energy transfer paths. With the help of Finite Element models, rather complex structures can be investigated because detailed mathematical models are provided. In this paper a hybrid method is proposed in order to estimate the energy transfer paths of complex structures using experimental response data obtained from a laboratory structure and a full-sized aircraft fuselage. This method combines experimentally determined velocities and numerical methods known from the Finite Element Analysis.

1 Introduction

Lightweight structures like an aircraft fuselage are designed for low mass and high stiffness. They are usually stiffened in longitudinal and circumferential direction to provide the necessary amount of structural stiffness. Such a design with discrete stiffeners (i.e. stingers in longitudinal and frames in circumferential direction) covered with a thin layer metal sheet (i.e. skin) enables a high efficiency and low operation costs, but are disadvantageously to acoustic passenger comfort because structure-borne noise can easily propagate though the aircraft structure. This problem gets magnified by modern engine designs like recent Ultra High Bypass Ratio (UHBR) engines or possible Boundary Layer Ingestion (BLI), which are directly attached to the aircraft fuselage. In order to allow optimal placed noise reduction treatments a better understanding of the actual transfer paths of vibrational energy along the aircraft fuselage is necessary.

Estimating the transfer paths of vibrational energy through a complex structure like an aircraft fuselage is no easy task. While established methods of Transfer Path Analysis (TPA) work well for describing the source contribution of multi-component systems and give a coarse description between the transfer path of source-receiver, such methods do not provide a detailed characterization of how the vibrational energy flows from the source to different parts of the structure.

In June of 2016 DLR performed an extensive vibration measurement campaign at the Acoustic Flight-LAB, a full-sized aircraft fuselage demonstrator, with the goal of conducting cabin acoustics measurements previously limited to flight tests on the ground. A three-week campaign resulted in an unprecedented set of vibration and acoustic data acquired at a combined 12000 measurement positions that served as key dataset for the further development of the new hybrid methods of energy transfer path estimation presented here and in [1], but also for frequency range classifications of low-, mid- and high-frequency ranges [2].

The motivation of this work is to measure and to understand the energy transfer paths through complex aircraft structures and individual components without solving a full numerical model.

Therefore, the presented approach to Structural Intensity Analysis (STI) combines experimental data with only the numerical analysis methods transferred from Finite-Element (FE) procedures. When successfully applied, STI results in map of energy flows through the analysed structure and thus getting closer to the goal of mapping the transfer path of vibrational energy through an aircraft fuselage.

The proposed method is demonstrated on a complex stiffened plate structure in an laboratory environment for the high-frequency range where the plate structure shows a strong local dynamic behaviour of the skin fields and on the full-sized fuselage of the Acoustic Flight-LAB for the low- to mid-frequency range where the fuselage shows a global dynamic behaviour.

2 Theory of Structural Intensity

In order to identify the energy transfer path from an source through the aircraft fuselage the Structural Intensity is used, which is a vectorial quantity describing the change of energy density in an infinitesimal volume [3]. In the time domain the Structural Intensity describes the instantaneous energy flow and in the frequency domain the net energy flow per frequency for steady state random vibrations.

In general, it is defined as the matrix vector product of the stress tensor $\left[\sigma\right]$ and the conjugate complex velocity vector $\left\{v\right\}$ at an arbitrary point of the structure. The velocity vector is rotated and amplified by the stress tensor.

$$\begin{Bmatrix} I_x(\omega) \\ I_y(\omega) \\ I_z(\omega) \end{Bmatrix} = -\frac{1}{2}\Re\left(\begin{bmatrix} \sigma_{xx}(i\omega) & \sigma_{xy}(i\omega) & \sigma_{xz}(i\omega) \\ \sigma_{yx}(i\omega) & \sigma_{yy}(i\omega) & \sigma_{zz}(i\omega) \\ \sigma_{zx}(i\omega) & \sigma_{zy}(i\omega) & \sigma_{zz}(i\omega) \end{bmatrix} \begin{Bmatrix} v_x(i\omega) \\ v_y(i\omega) \\ v_z(i\omega) \end{Bmatrix}^* \right) \tag{1}$$

2.1 Structural Intensity of plates

Due to the thin-walled nature of aircraft fuselages, the Structural Intensity is discussed in the following based on the theory of plates of Reissner [4] and Mindlin [5]. It uses the assumption that the normal to the mid-surface remains straight for all deformations. Then it is applicable for small displacements u of the plate

$$u_x = z\varphi_y \qquad u_y = -z\varphi_x \tag{2}$$

with the in-plane coordinates x and y, the perpendicular coordinate of the plate z and the rotation of the normal to the undeformed mid-surface φ_x and φ_y.

Integrating the Structural Intensity over the thickness h of the plate and dividing by the thickness gives the averaged net energy flow I' of the plate along the mid-surface

$$I' = \frac{1}{2h}\int_{-\frac{h}{2}}^{\frac{h}{2}} I dz \tag{3}$$

In this case the Structural Intensity can be described with the stress resultants: shear forces Q and the internal moments M

$$I'_x = -\frac{1}{2h}\Re\left(M_x\dot{\varphi}_y^* - M_{xy}\dot{\varphi}_x^* + Q_x v_z^*\right) \tag{4}$$

$$I'_y = -\frac{1}{2h}\Re\left(-M_y\dot{\varphi}_x^* + M_{yx}\dot{\varphi}_y^* + Q_y v_z^*\right) \tag{5}$$

with

$$Q_x = \int_{-\frac{h}{2}}^{\frac{h}{2}} \sigma_{xz} dz = \frac{Eh}{2(1-\nu^2)}\epsilon_{xz}, \quad Q_y = \int_{-\frac{h}{2}}^{\frac{h}{2}} \sigma_{yz} dz = \frac{Eh}{2(1-\nu^2)}\epsilon_{yz},$$

$$M_x = \int_{-\frac{h}{2}}^{\frac{h}{2}} \sigma_{xx}\, z\, dz = \frac{Eh^3}{12(1-\nu^2)}(\epsilon_x + \nu\epsilon_y), \quad M_y = \int_{-\frac{h}{2}}^{\frac{h}{2}} \sigma_{yy}\, z\, dz = \frac{Eh^3}{12(1-\nu^2)}(\epsilon_y + \nu\epsilon_x),$$

$$M_{xy} = \int_{-\frac{h}{2}}^{\frac{h}{2}} \sigma_{xy}\, z\, dz = \frac{Eh^3(1-\nu)}{12(1-\nu^2)}\epsilon_{xy}.$$

E is the Young's modulus and ν is the Poission's ratio. The z-component of the Structural Intensity is neglected under the assumption that the displacement of the thickness of the plate is constant. I'_x and I'_y describe the out-of-plane energy flow. The in-plane energy flow of the membrane is neglected because the bending of the aircraft fuselage dominates the dynamic response. Note, the local z-axis of the shell elements of the fuselage skin coincide with the radial direction of the aircraft fuselage. In order to take this into account for complex structures, a conversion is performed by a transformation matrix from local to global coordinates.

2.2 Approximation of bending and shear strains with shape functions

For the estimation of the bending and shear strains at the discrete measured point of the structure element shape functions known from the Finite Element Method [6] are used. The bending strains are defined as

$$\epsilon_x = -\frac{\partial\varphi_y}{\partial x}, \quad \epsilon_y = \frac{\partial\varphi_x}{\partial y}, \quad \epsilon_{xy} = \frac{\partial\varphi_x}{\partial y} - \frac{\partial\varphi_y}{\partial x} \tag{6}$$

and the shear strains as

$$\epsilon_{xz} = \frac{\partial u_z}{\partial x} + \varphi_y, \quad \epsilon_{yz} = \frac{\partial u_z}{\partial y} - \varphi_x \tag{7}$$

under the assumption that the strains are constant through the thickness. There are several shape functions N available from linear, bilinear, quadratic and more. It depends on how the discrete points of the structure are connected. In general, M points of the structure are connected with M shape functions. In order to approximate the bending and shear strains at each measured point the derivatives of the shape functions and the local displacements and rotations are used

$$\begin{Bmatrix} \epsilon_x \\ \epsilon_y \\ \epsilon_{xy} \\ \epsilon_{xz} \\ \epsilon_{yz} \end{Bmatrix} = \begin{bmatrix} 0 & 0 & -\frac{\partial N_1}{dx} & \cdots & 0 & 0 & -\frac{\partial N_M}{dx} \\ 0 & \frac{\partial N_1}{dy} & 0 & \cdots & 0 & \frac{\partial N_M}{dy} & 0 \\ 0 & \frac{\partial N_1}{dy} & -\frac{\partial N_1}{dx} & \cdots & 0 & \frac{\partial N_M}{dy} & -\frac{\partial N_M}{dx} \\ \frac{\partial N_1}{dx} & 0 & N_1 & \cdots & \frac{\partial N_M}{dx} & 0 & N_M \\ \frac{\partial N_1}{dy} & -N_1 & 0 & \cdots & \frac{\partial N_M}{dy} & -N_M & 0 \end{bmatrix} \begin{Bmatrix} u_{z,1} \\ \varphi_{x,1} \\ \varphi_{y,1} \\ \vdots \\ u_{z,M} \\ \varphi_{x,M} \\ \varphi_{y,M} \end{Bmatrix} \tag{8}$$

2.3 Approximation of rotation degree of freedom

Knowing that the bending dominates the aircraft fuselage response, the rotation degree of freedom can be derived directly by the measured bending response. Under the assumption of small displacements the rotation can be approximated by the derivatives of the shape functions and the bending u_z

$$\varphi_x = \frac{\partial u_z}{\partial y} = \left\{ \frac{\partial N_1}{\partial y} \quad \cdots \quad \frac{\partial N_M}{\partial y} \right\} \left\{ u_{z,1} \quad \cdots \quad u_{z,M} \right\}^T \tag{9}$$

$$\varphi_y = -\frac{\partial u_z}{\partial x} = -\left\{ \frac{\partial N_1}{\partial x} \quad \cdots \quad \frac{\partial N_M}{\partial x} \right\} \left\{ u_{z,1} \quad \cdots \quad u_{z,M} \right\}^T \tag{10}$$

2.4 Structural Intensity of beams

Similar to the Structural Intensity of plates, it is possible to estimate the energy flow along the centre line of a beam. In this particular case of a radial bending dominated fuselage, the axial and perpendicular components of the z-direction are neglected. Note, the local z-axis of the fuselage beams (stringer,frames) coincide with the radial direction of the aircraft fuselage.

$$I'_x = -\frac{1}{2h} \Re \left(Q_z v_z^* + M_x \dot{\varphi}_x^* + M_y \dot{\varphi}_y^* \right) \tag{11}$$

with

$$Q_z = -EJ_y \frac{\partial^3 u_x}{\partial x^3}, \quad M_x = GJ_x \frac{\partial \varphi_x}{\partial x}, \quad M_y = -EJ_y \frac{\partial^2 u_z}{\partial z^3},$$

J_x, J_y, J_z are the moments of inertia and G the shear modulus. From Eq. 11 it is possible to note that the beam only transfers energy along the centre line of the beam.

2.5 Divergence Structural Intensity flow field

Calculating the divergence of the Structural Intensity field $\nabla \cdot \vec{I}$ allows an identification of energy sources or sinks at any point of the structure [7]. This information can be a desirable additional information to the estimated energy transfer paths. Where, $\nabla \cdot \vec{I} > 0$ defines a source and $\nabla \cdot \vec{I} < 0$ a sink.

2.6 Discrete Hodge-Helmholz field decomposition

Most of the structures show areas of local energy exchange, for example between two neighbouring eigenmodes. This energy exchange creates local vortices in the intensity flow field. So, the identification of the irrotational intensity flow field has significant advantages because it describes the energy flow without the masking effects of energy vortices that are related to the rotational intensity flow field [8].

The intensity vector field $\vec{I}$ can be separated into an irrotational (curl-free) ∇E and rotational (divergence-free) $\nabla \times \vec{W}$ part using a discrite Hodge-Helmholz field decomposition [9]

$$\vec{I} = (\nabla E) + \left(\nabla \times \vec{W} \right) + \vec{R}. \tag{12}$$

$\vec{R}$ is the harmonic remainder part.

3 Procedure of Structural Intensity estimation

The procedure of the STI estimation based on measured dynamic response consists of seven steps and two additional steps if an analysis of divergence and vector field decomposition is intended.

First step is to measure the surface velocity of the structure at discrete points either, e.g. either using a Laser Doppler Vibrometer or accelerometers.

Second step is to separate the structure and the measured velocities into structural components.

Third step is to connect the measuring points of these individual components, e.g. with lines or triangles, in order to use shape functions for the approximation of the needed variables.

Fourth step is to approximate the rotation degrees of freedom using the derivatives of the shape functions.

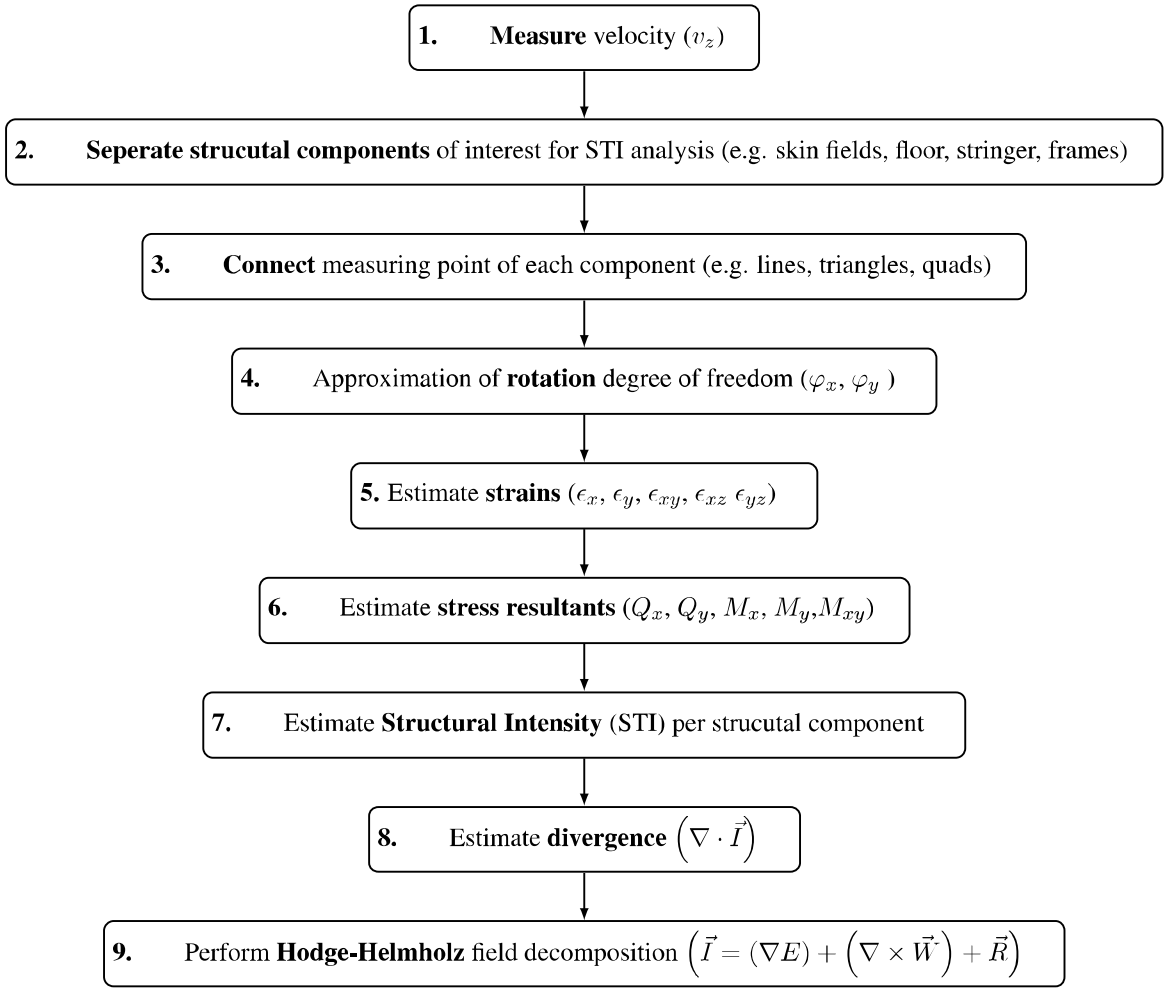
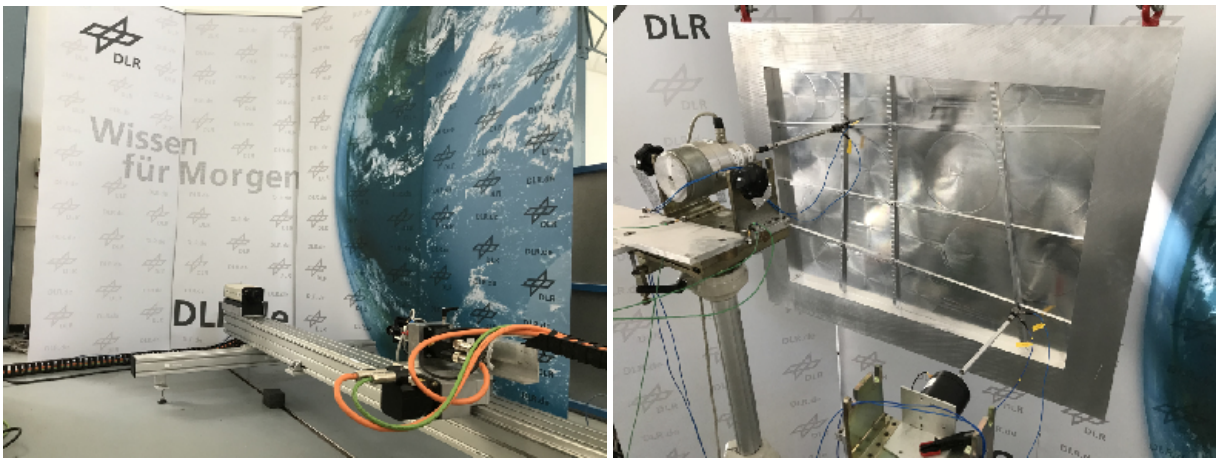


Figure 1: Procedure of Structural Intensity estimation

Fifth step is to estimate the strain based on the measured deformation and the derivatives of the shape functions.

Sixth step is to estimate the shear forces and internal moments, which can be calculated by the strains, thickness and material parameters.

The final step is to estimate the STI using the stress resultants and the measured velocities.



(a) (b)

Figure 2: (a) DLR developed LDV-scanning unit (b) Stiffened plate at DLR in Göttingen.

This approach enables an energy flow analysis of each structural component independent of all the rest. For lager structures this procedure has the advantage to focus on smaller local areas of interest disregarding a measurement of the whole structure, which saves time and effort.

In addition, the divergence of the STI can be calculated in order to identify energy sources or sinks and a Hodge-Helmholz field decomposition can be performed to remove local energy vortices.

4 Laboratory test of a complex stiffened plate

Before discussing the full-sized aircraft fuselage, a laboratory test-structure will be addressed. This test-structure is a plate with an asymmetrical set of stiffeners attached to the skin, as seen in Fig. 2 (b). This layout generates a certain level of complexity in the geometrical setup and in the dynamic response pattern.

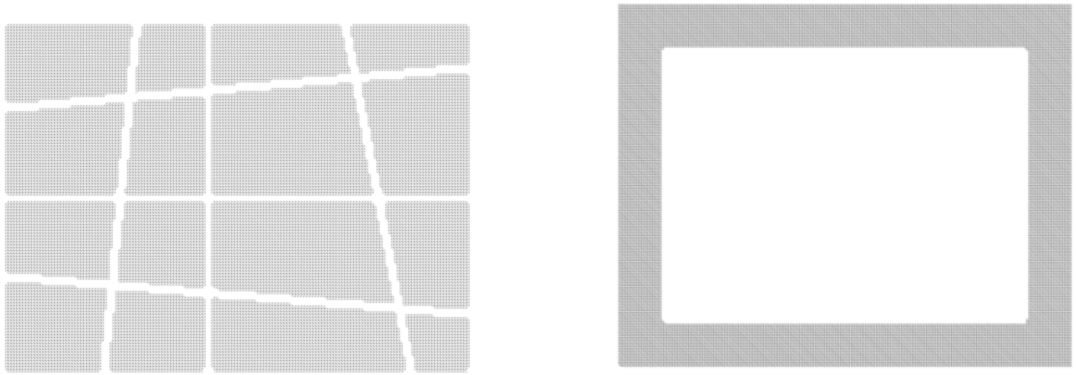
The plate hangs with two bungee cords to a rigid frame, providing in this way an almost free-free boundary condition. This test-setup allows the plate to response almost unconstrained in normal direction. In order to provide the necessary amount of measuring points for an accurate estimation of high-resolution energy transfer paths over the skin fields and the stiffeners a Laser Doppler Vibrometer with a DLR developed scanning unit is used, shown in Fig. 2 (a). This laser scanning unit allows an automated measurement of the test-structure. Since it is assumed that the normal velocity response is the most dominant, all other degrees of freedom are neglected. This means that only the energy transport of bending waves is considered in the analysis process. The normal velocity response of this test-structure is measured at 32365 equally spaced measuring points.

In this test a two exciter setup was chosen in order to force an energy flow in the highly undamped plate. The exciters are attached at two stiffeners crossings in the upper left and lower right corner of the plate, shown in Fig. 2 (b).

The frequency range of interest, from 30 Hz to 4000 Hz, was excited with two uncorrelated random signals. In this frequency range the test-structure exhibits a global as well as strong local dynamic behaviour.

5 Structural Intensity flow field of a complex stiffened plate

In order to estimate the STI at all 32365 measurement points based on the measured surface velocities, the plate structure is meshed with triangular elements. Note that all plate components are meshed separately



(a) (b)

Figure 3: (a) 16 skin field meshes (b) frame mesh.

and independent from each other. This results into 40 meshes of 16 skin fields and 24 stiffener sections with different thicknesses, which has to be considered for estimating the stress resultants. The resulting 63999 triangular elements were evaluated using linear shape functions for the presented analysis. The 16 skin field meshes are shown in Fig. 3 (a) and the mesh of the outer frame in Fig. 3 (b).

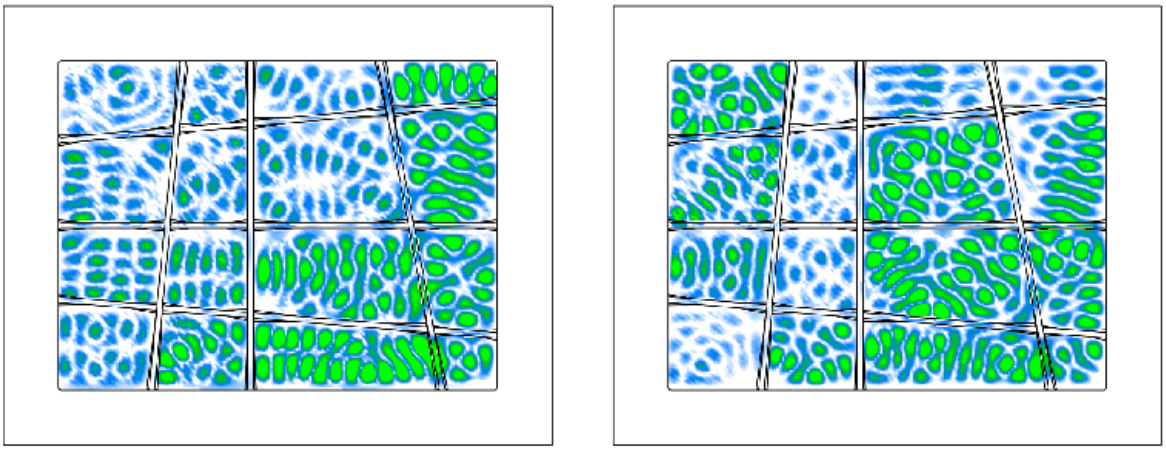
The STI is estimated directly from the ODS data. Fig. 4 shows the measured Operational Deflection Shape (ODS) of the surface velocity at 3700 Hz (a) and 4000 Hz (b). Both figures indicate a strong local dynamic response of the skin fields, whereas the areas of the stiffeners seem to be in rest.

Fig. 5 (a) shows the estimated STI flow at 3700 Hz. The energy flows from the lower right stiffener crossing to the left and upper part of the plate passing several skin fields. The energy paths are indicated by the strong intensities (green cones). From the lower right stiffener crossing, where one of the energy sources is attached to the structure, the energy flows down the vertical stiffener and then into both neighbouring skin fields. In the lower right skin field the energy flows into a vortex and returns back to the stiffener, where it coalesces with the energy flow of the stiffener and continues to flow through the neighbouring skin field to left part of the structure. The second major energy path follows the vertical stiffener up and into the right horizontal stiffener in the middle. From this horizontal stiffener the energy flow continues to the upper part of the plate.

Fig. 5 (b) shows a strong energy path in diagonal direction towards the second energy source at 4000 Hz. Whereas the energy paths of the STI at 3700 Hz seem uninterrupted, some of the skin field energy at 4000 Hz seems to pop up. This indicates that non-considered energy paths are present like in-plane paths, which were not measured.

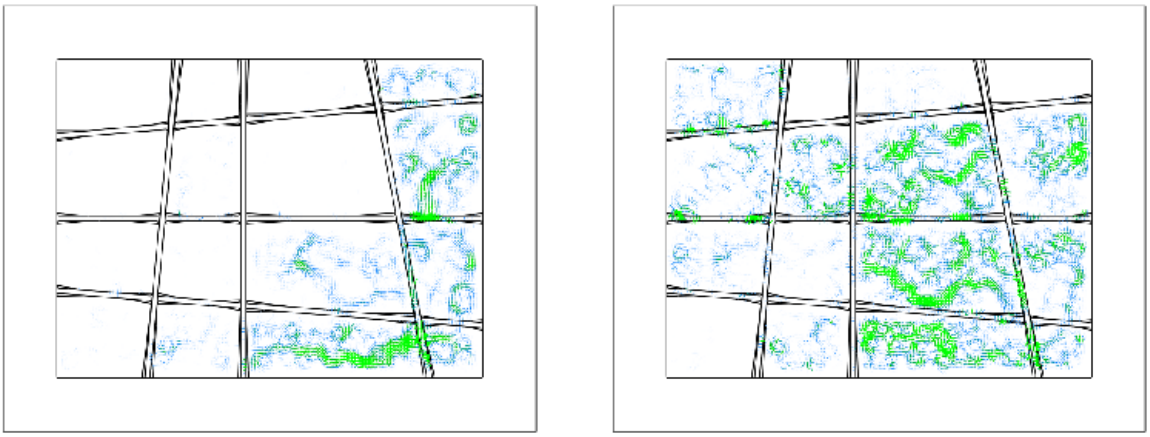
Comparing Fig. 5 (a) and (b) shows that the skin fields are dominated by several vortices, suggesting local energy exchange between two eigenmodes. A separation of the STI flow field into a irrotational and rotational field helps to remove these vortices for further analysis. Fig. 6 (a) and (b) show the irrotational STI flow fields at 3700 Hz and 4000 Hz. The vortices vanish and only the translational flow is left. The results confirm the previous observations. The dominant energy path at 3700 Hz is to the left and upper part of the plate and the energy path at 4000 Hz dominates the diagonal direction.

In this section a high-resolution energy path analysis was demonstrated in the high-frequency range. Due to the strong local behaviour of the skin filed the identified energy paths are not straight forward into one direction, this can be improved by applying the Hodge-Helmholz field decomposition.



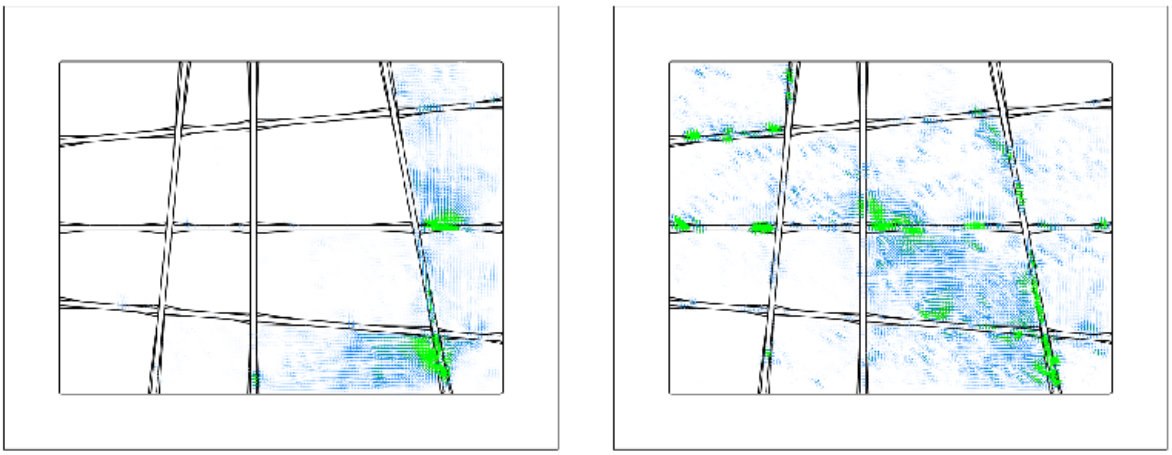
(a) (b)

Figure 4: Measured Operational Deflection Shape at (a) 3700 Hz (b) 4000 Hz (colour range of abs. values).



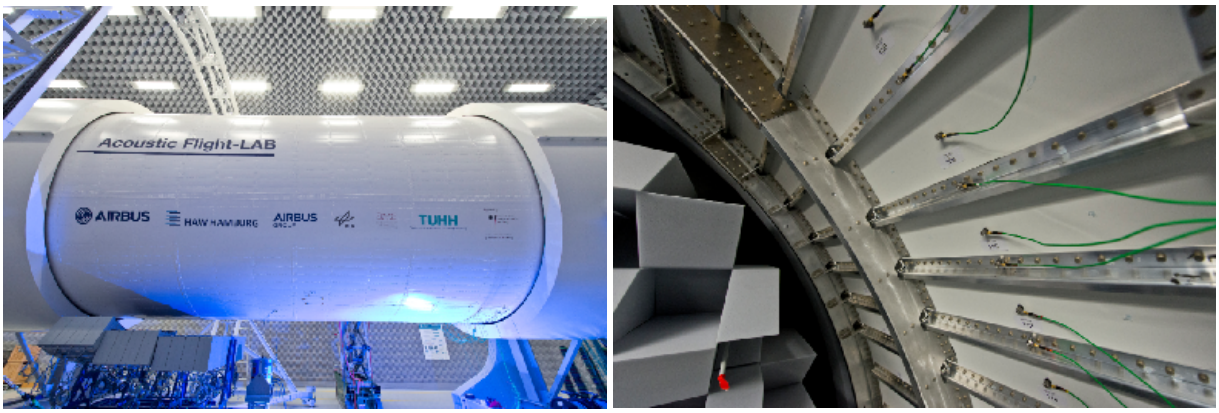
(a) (b)

Figure 5: Measured Structural Intensity flow field at (a) 3700 Hz (b) 4000 Hz (colour range of abs. values).



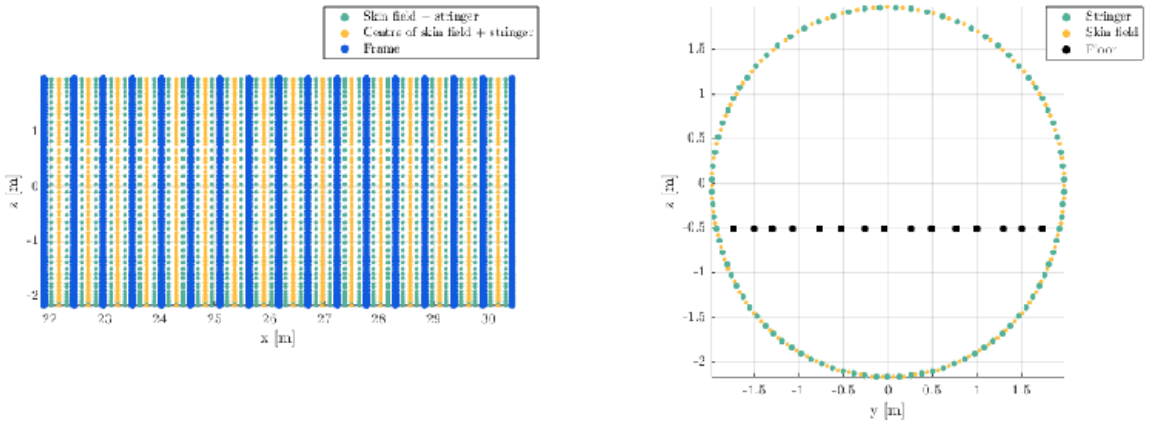
(a) (b)

Figure 6: Measured irrotational Structural Intensity flow field at (a) 3700 Hz (b) 4000 Hz (colour range of abs. values).



(a) (b)

Figure 7: (a) Acoustic Flight-LAB demonstrator at ZAL in Hamburg. (b) Inside the demonstrator cabin showing frames, stringers, accelerometers and acoustic absorber.



(a) (b)

Figure 8: (a) Sensor grid (xz-plane). (b) Sensor grid (yz-plane).

6 Acoustic Flight-LAB demonstrator

The second test-structure used in this paper is a an aircraft fuselage mock-up build to structurally mimic a section of an actual commercial short range aircraft. The section of the aircraft fuselage demonstrator, which is installed in a dedicated suspension system in a testing hall at the ZAL TechCenter in Hamburg, is about $8.5\,\mathrm{m}$ long and has a diameter of about $4\,\mathrm{m}$.

The fuselage demonstrator, which is shown in Fig. 7 (a), is mounted between two portals on four nitrogen springs, which provide a soft suspension so that the vibrations of the demonstrator are fully decoupled from the environment. This test setup allows the fuselage to response almost unconstrained in radial direction on both ends. Additionally, both ends of the fuselage section are not only insulated but also treated with acoustic absorbers, which are necessary for acoustic measurements in the cabin cavity with known acoustic boundary conditions. These absorbers are shown in the lower left area of Fig. 7 (b). There, it is also possible to observe the underlying rip structure (17 frames and 87 stringers) of the fuselage and the accelerometers, which were used to measure the dynamic response of the fuselage due to a point force excitation. The electro-dynamic exciter is radially attached under the fuselage to a stiff structural point, i.e. crossing of frame and stringer, in order to better distribute the excitation energy all over the structure, instead of vibrating just one skin field. In Fig. 7 (a) it is possible to observe the shaker in the middle of the fuselage.

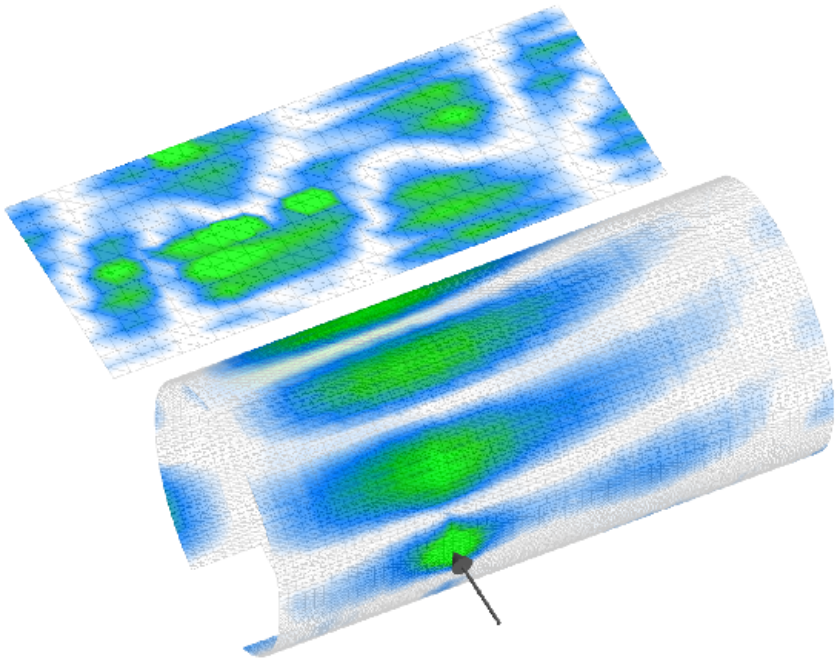


Figure 9: Measured Operational Deflection Shape of Acoustic Flight-LAB demonstrator at 69 Hz

The frequency range of interest, from 8 Hz to 1000 Hz , was chosen to cover the regions where the structure exhibits global as well as strong local dynamic behaviour.

For the dynamic tests on the FlighLAB fuselage a highly dense configuration of sensor positions is used since an accurate observation of local behaviour is only possible if the spatial resolution of the observation points is high enough. Figure 8 shows the sensor grid of the vibration tests. In total, the dynamic response of the fuselage is measured on about 11310 points, including positions on the skin fields (yellow), frames (blue), stringers (green) and cabin floor (black).

7 Structural Intensity flow field of Acoustic Flight-LAB demonstrator

In order to perform STI, the positions of the 11406 measurement points included in the data of the Acoustic Flight-LAB was used to create a surface mesh of triangular elements. As the cross beams connecting the fuselage to the cabin floor were not part of the original measurement grid there is no connection between the floor and fuselage grids. The resulting 23516 triangular elements were evaluated using linear shape functions for the presented analysis. The frames and stringers are connected with 13578 line segments and the STI is estimated with Hermite polynomials.

Fig. 9 shows the ODS of the Acoustic Flight-LAB demonstrator at 69 Hz, which is used to estimated the STI. A global bending wave is propagating away from the point force, which is marked with a grey arrow. Also the floor shows still a global behaviour. Note that the longitudinal stiffeners of the floor are clearly visible in the deflection shape as straight lines. This is an indication that the global behaviour starts to transition into a local behaviour.

In Fig. 10, the STI of the individual fuselage components is separated into skin (a), floor (b), frames (c) and stringers (d). From the data shown in Fig. 10 (a), it is possible to interpret that the dominant energy flow starts at the shaker position (grey arrow) and runs along the surface over the upper fuselage section to the opposite side and down directly into the floor (compare Fig (a) and (b)). The floor creates a bypass in the fuselage. The energy is bounded in the upper part of the fuselage and the floor. Almost no energy is transferred into the cargo area of the fuselage. On the floor, the energy flows to the opposite side of the point

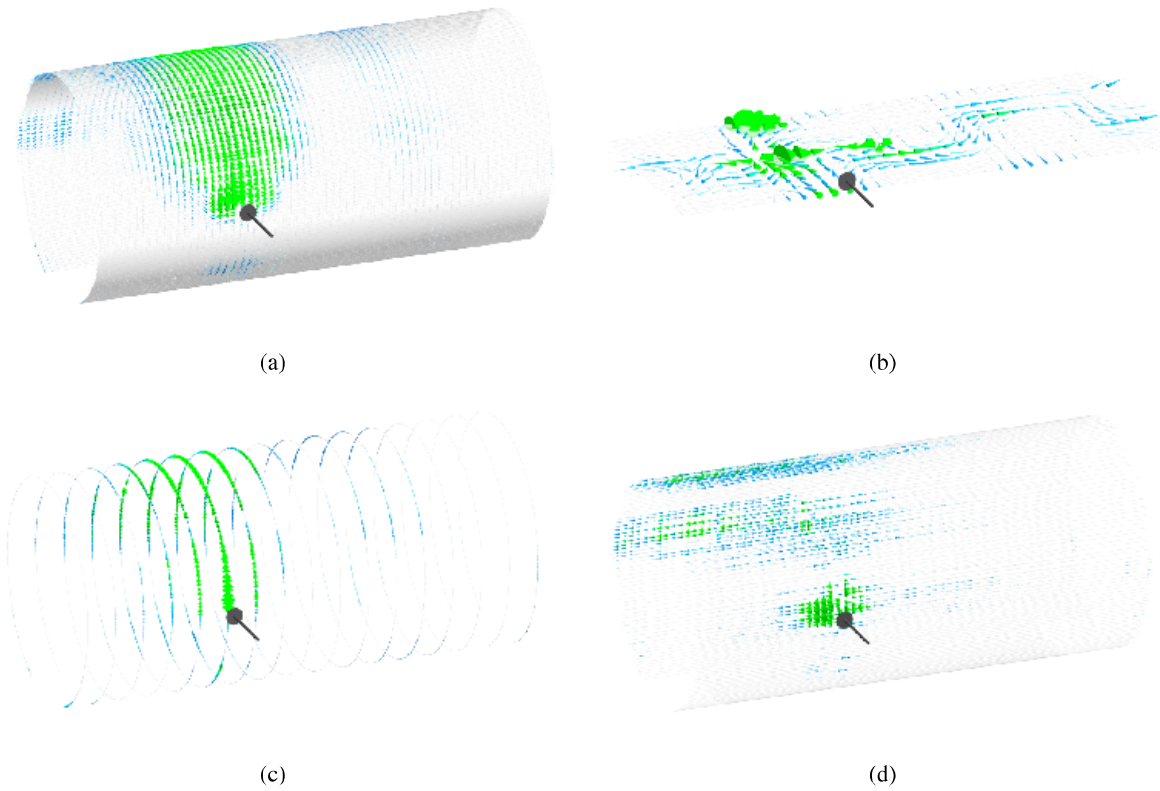


Figure 10: Measured Structural Intensity flow field at 69 Hz (a) skin (b) floor (c) frames (d) stringers.

force, where it coalesces with the energy flow from fuselage and continues to flow to the left opening of the cylinder. In the middle of the floor the energy dissolves into three directions, the aforementioned path to the opposite side and two paths to both openings of the fuselage. It seems that the energy flows to the suspension system positions at the first and last cross beam at the ends of the fuselage. At these points the energy can flow out of the structure.

In Fig. 10 (c) strong intensities can be observed in the five frames in the closest vicinity of the point force. This indicates that the primary energy flow in circumference direction is over these frames to the opposite side. This observation coincides with the previously discussed observations of the fuselage skin. The energy flows from the exciter over the stringers into these five frames, indicated by the strong intensities in Fig. 10 (d). The four areas of energy flow over the stringers, which can be observed also in Fig 10 (d), coincides with the vibration antinode of the ODS (see Fig. 9). Due to the antinodes, the stingers are stretched and energy flows in longitudinal direction.

Fig. 11 shows the divergence distribution of the STI over the fuselage. In order to determine derivatives of the STI, linear shape functions are used again. The highest divergence can be observed in the area around the point force indicating the presents of an energy source, which is obviously the point force. The positions of the suspension system, which are assumed to be energy sinks, cannot be identified because there was no sensor placed in the vicinity of the springs in this test-setup.

In this section a high-resolution energy path analysis was demonstrated on an full-sized aircraft fuselage and the energy path over the curvature was identified. And it is shown that a separated analysis of structural components is possible because each component can be meshed independent from each other.

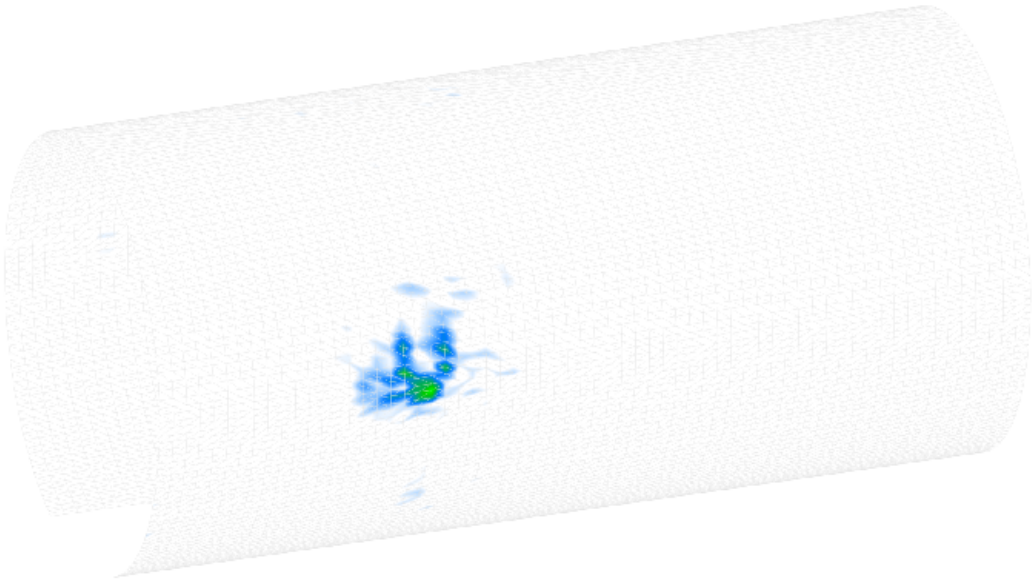


Figure 11: Measured divergence of Structural Intensity flow field at 69 Hz

8 Conclusion

The novel hybrid method of estimating Structural Intensity was introduced and described. its applicability was demonstrated by means of two experimental setups. A small scale laboratory structure and a real scale fuselage section where used to exemplify the quality of results obtained. These results show the potential of being able to estimate the energy flow on complex structures.

The hybrid method proved helpful as a post-processing for the calculation of STI of complex structures in the low- to high-frequency range. It is possible to identify detailed energy paths for global as well as strong local dynamic response pattern if the measured spatial resolution is high enough. The interpretation of the resulting energy paths calculated by the STI method presented here are intuitive.

In the high-frequency range, where the skin fields of the stiffened plate show a strong local behaviour, several high detailed energy paths over the stiffeners and through the skin fields can be identified, including several energy vortices inside the skin fields.

In the low-frequency range, where the full-sized aircraft fuselage shows a global behaviour, the energy flows from the excitation point through the cabin floor and along the fuselage stiffeners towards the suspension points.

A separated analysis of the energy flow per structural component is possible, this allows to put emphasis on particular areas of interest. This approach can save time and efforts since a measurement of the whole structure is not necessary.

Also the energy path through the enclosed air cavity is not considered and will be part of future work, where the Sound Intensity will be measured in the 'Acoustic Flight-LAB'.

While the work introduced here demonstrates the usability of the method for a qualitative estimation of the energy flow presented on large scale data, a quantitative validation is not performed. Further work is aiming on the validation of the method by considering all three spatial direction of the dynamic response in order to capture also the in-plane and longitudinal structural wave propagation.

ACKNOWLEDGEMENTS

The experimental results of the Acoustic Flight-LAB fuselage were conducted in the COCLEA project, which was funded by the German Federal Ministry for Economic Affairs and Energy (BMWi). The authors would like to express their gratitude to all people, who contributed to this project.

References

[1] R. Winter, J. Biedermann, M. Norambuena, *High-Resolution Vibration Measurement And Analysis Of The Flight-LAB Aircraft Fuselage Demonstrator, in Proceedings of Inter-Noise 2018, USA, 2018 August 26-29, Chicago (2018).*

[2] J. Biedermann, R. Winter, M. Norambuena, M. Böswald, *Classification of the mid-frequency range based on spatial Fourier decomposition of Operational Deflection Shapes, in Proceedings of 24th International Congress on Sound and Vibration, United Kingdom, 2017 July 23-27, London (2017).*

[3] L. Gavrić, G. Pavić, *A finite element method for computation of Structural Intensity by the normal mode approach*, Journal of Sound and Vibration, Vol. 164, No. 29 (43), (1993).

[4] E. Reissner, *The effect of transverse shear deformation on the bending of elastic plates*, Journal of Applied Mechanics, Vol. 67, No. 69 (77), (1945).

[5] R. D. Mindlin, *Influence of rotatory inertia and shear on flexural motion of isotropic elastic plates*, Journal of Applied Mechanics, Vol. 18, No. 31 (38), (1951).

[6] K.-J. Bathe, *Formulation and Calculation of Isoparametric Finite Element Matrices*, Chap. 5 in Finite Element Procedures, edited by W. Strenquist and M. Peterson, PRENTICE HALL, New Jersey, (1996).

[7] B. Lamarsaude, Y. Bousseau, A. Jund, *Structural Intensity analysis for car body design: going beyond interpretation issues through vector field processing, in Proceedings of ISMA2014 including USD2014, Belgium, 2014 Septemper 15-17, Leuven (2014).*

[8] N.B. Roozen, J.L. Guyader, C. Glorieux, *Measurement-based determination of the irrotational part of the Structural Intensity by means of test functional series expansion*, Journal of Sound and Vibration, Vol. 356, (2015).

[9] Q. Guo, M. K. Mandal, M. Y. Li, *Efficient Hodge- Helmholtz decomposition of motion fields*, Pattern Recognition Letters , Vol. 26, (2005).

Application of operational test data and transfer path analysis to a test bench for optical systems

C. Schedlinski[1], C. Marzok[2], U. Wiesendahl[2]
[1] ICS Engineering GmbH
Am Lachengraben 5, 63303 Dreieich, Germany
e-mail: **sched@ics-engineering.com**

[2] Carl Zeiss SMT GmbH
Rudolf-Eber-Str. 2, 73447 Oberkochen, Germany

Abstract
In this paper the application of operational test data analysis and transfer path analysis to a test bench for optical systems is presented. Especially data of vibration and acoustic measurements are investigated and spectral analysis is employed next to TPA in order to identify the driving sources of occasional failures of test runs.

1 Introduction

Carl Zeiss SMT GmbH is known for high precision optics. In order to assure the required high level of fidelity of its products, various quality assurance steps are employed.

A special test bench is utilized to verify certain performance parameters of a specific optical product. Occasionally, under distinct environmental conditions, non-expected performance was determined during performance tests, that has subsequently been attributed to external perturbations rather than to performance deviations of the product. In these cases, a repetition of the performance tests yielded results as expected proving the conformity of the investigated system.

Since a repetition of performance tests is both time and cost consuming and reduces the overall throughput of the test bench, vibration and acoustic measurements have been conducted as a basis for identifying the driving sources for deviations of the test runs. Especially operational data were investigated with the help of spectral and transfer path analyses.

This paper highlights the main results and outcome of the test campaign and shows how an intelligent combination of state of the art experimental techniques can aid in optimizing the performance of modern technical systems.

2 Conducted Tests

Vibration (acceleration) and acoustic (sound pressure) measurements were taken at and in the vicinity of a test bench for specific optical components in a clean room environment. The test bench itself is comprised of a heavy, resiliently mounted, base granite that carries a test item next to measurement appliances. During the conducted vibration and acoustic tests the test bench was under operation and performance parameters (e.g. control errors) were measured synchronously.

In addition to defined transfer path measurements (see e.g. [1]) by means of force (modal hammer) and airborne sound excitations (two sound sources, one for low frequencies up to about 400 Hz – LFM – and one for higher frequencies – HFM, see also [3]), realistic operating vibration tests were also carried out. Figure 1 shows typical force and sound source excitations while figure 2 highlights a representative

operational excitation scheme with a loaded lifter traveling back and forth along the path passing by the test bench.

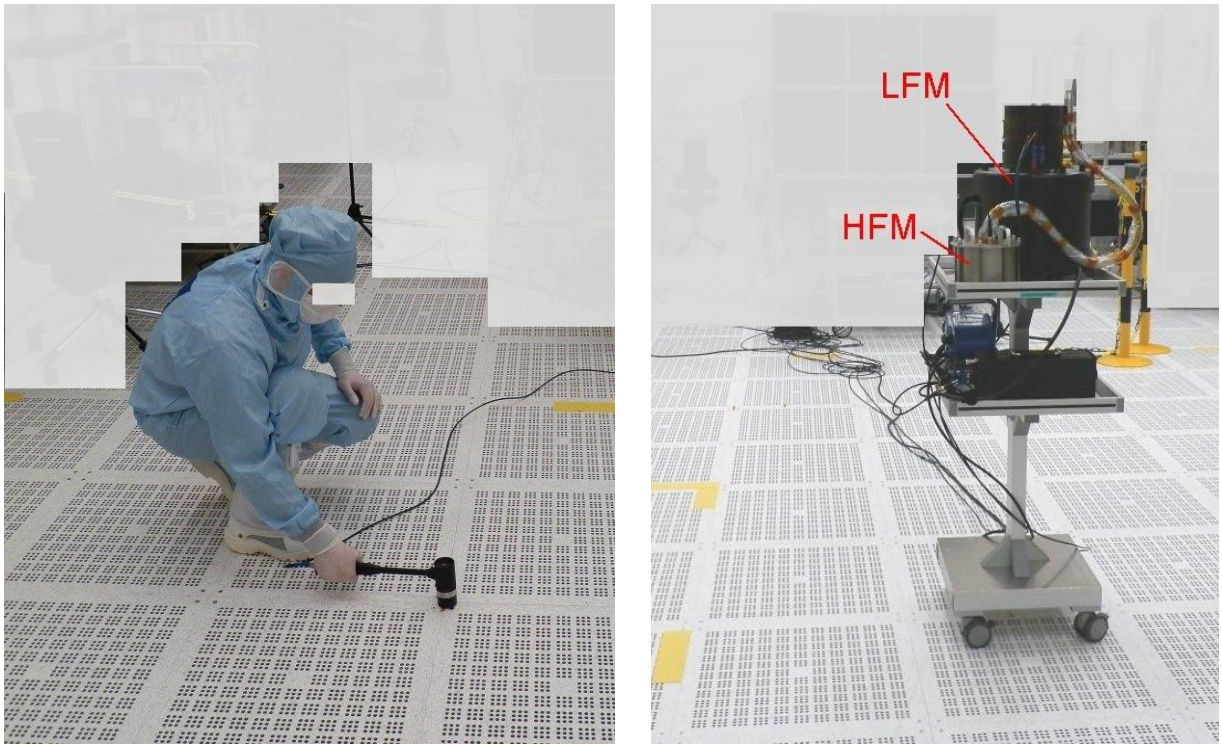


Figure 1: Excitation with modal hammer (left) and sound sources (right)



Figure 2: Operational excitation (lifter with loaded pallet)

3 Data Analysis

Due to the high complexity of the relations between force and sound excitation as well as to the resulting structural responses and performance parameters, the evaluation of the obtained data was divided into three phases:

1. General assessment of time data and spectral information
2. Level and Spectral Analysis
3. TPA

The general evaluation of time data and spectral information is dealt with in Section 3.1 and is used for the basic analysis of the signal contents for the operational tests on the basis of selected measurement signals. On one hand, a first evaluation of the interference effects resulting from the mocked-up operating conditions was carried out directly on the basis of the time signals. On the other hand, a global screening of the spectral contents was done on the basis of averaged power spectral densities (PSD).

Level and spectral analyses according to Section 3.2 were subsequently carried out for the defined excitations and for the operational measurements respectively in order to be able to further assess the vibration behavior. In particular, temporal changes of the signal contents were identified and related to the mocked-up operating situations. Specifically, level analyses over time, third-octave analyses as well as Campbell diagrams over time for the respective signals were generated.

In addition to the level and spectral analyses, a TPA was performed, which is presented in Section 3.3. For TPA a matrix inversion technique was applied (see e.g. [1], [2]). Here, frequency response functions of selected potential transmission paths (or "paths" for short) are measured first, from which excitation forces can subsequently be identified (via an inversion of the frequency response function matrix) with the aid of measured operational responses. Based on these forces, it is possible to determine individual response components, finally allowing an assessment of the significance of individual paths.

3.1 General assessment of time data and spectral information

Figure 3 shows the time responses of two representative acceleration sensors (one on the floor in the vicinity of one foot of the test bench support frame and one on the granite base of the test bench itself that is resiliently decoupled from the floor), one microphone, and a typical performance parameter (control error, measured over 100s only instead of 152s) enforced by operational excitation from a moving lifter with loaded pallet.

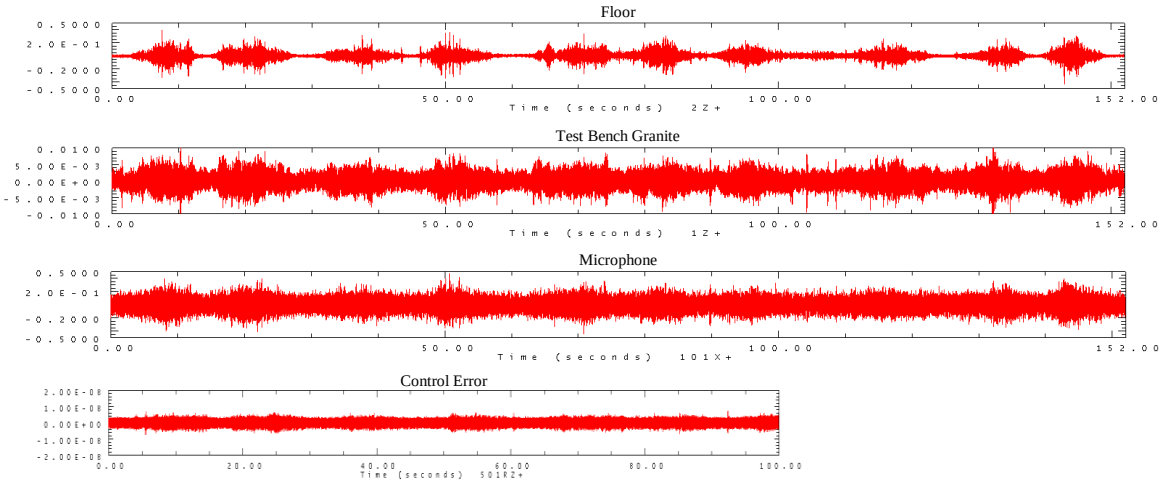


Figure 3: Time responses enforced by loaded lifter operation

It can be noted that on the ground and on the granite as well as at the microphone significant responses can be seen that can directly be correlated to the disturbances by the lifter passing by back and forth. For the control error similar behavior can be noticed, however, less pronounced due to the noise level.

In Figure 4 a comparison between an idle measurement and two lifter excitation runs is shown. It is particularly observable here that in the lower frequency range a clear increase in the spectrum takes place due to the lifter motion (see also marking in red).

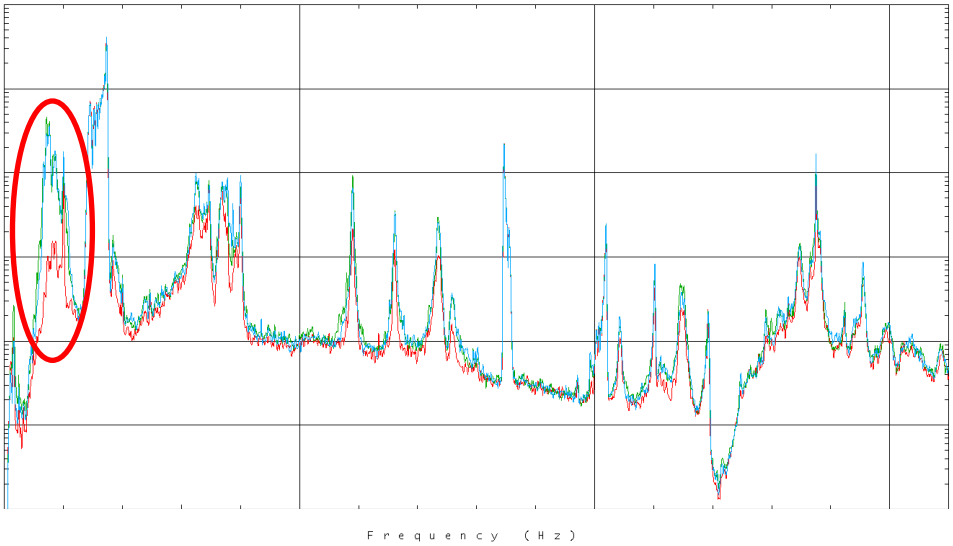


Figure 4: Control error PSDs of idle measurement (red) vs. moving lifter (green/blue)

3.2 Level and Spectral Analysis

To obtain further insight, dedicated level and short time spectral analyses were conducted. In a first step, the measurements with known excitation (force excitation with hammer on the ground and sound excitation with sound source in the area of the travel path) were compared to idle measurements in order to assess the basic effects of both excitation variants (force excitation see Figures 5-10, sound excitation see Figures 11-16). Here, the following observations can be made:

For force excitation, the hammer impulses are clearly visible on the ground in the vicinity of the test bench (Figure 5) and still – in a weakened manner – on the base granite of the test bench (Figure 6). On the test item mounted on the test bench effects can rather be noted for sensor 1 than for sensor 2 (Figures 7, 8). For a representative microphone (Figure 9) practically no effects can be observed. The control error (Figure 10), however, again shows the hammer pulses relatively clearly.

The effects of sound excitation are only weakly recognizable on the ground (Figure 11). The main elevation occurs in the lower frequency range, as already noticed above from the general spectral information (see also PSD in Figure 4). The granite of the test bench (Figure 12) shows practically no effects. For the test item mounted on the test bench effects can rather be noted for sensor 2 than for sensor 1 (Figures 13, 14), in contrast to force excitation. For the microphone (Figure 15) and the control error (Figure 16), however, the sound excitation leads to relatively clear interferences in the complete frequency range.

A closer look reveals that a signature of residual controller noise in the upper frequency range can also be recognized at sensor 2 on the test item (compare pictures 8 and 10 as well as 14 and 16). There is thus a recognizable transmission path. As a result, disturbances on the test item due to base excitation over the granite or via sound excitation over air are in principle possible.

Figures 17 to 22 finally show a comparison of an idle measurement with the operating measurement with loaded lifter passing by. Here, the signatures of the lifter passing by are more or less clearly visible on all measured signals.

Hammer Excitation (Ordinate: Frequency in Hz, Abscissa: Time in s):

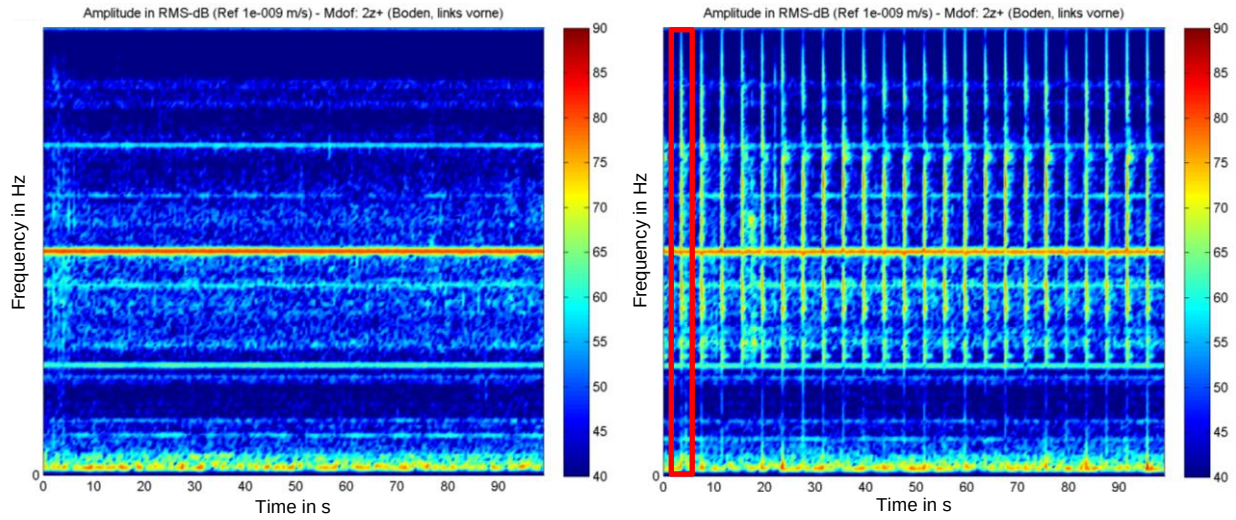


Figure 5: Sensor on ground, left: idle measurement/right: hammer excitation on ground

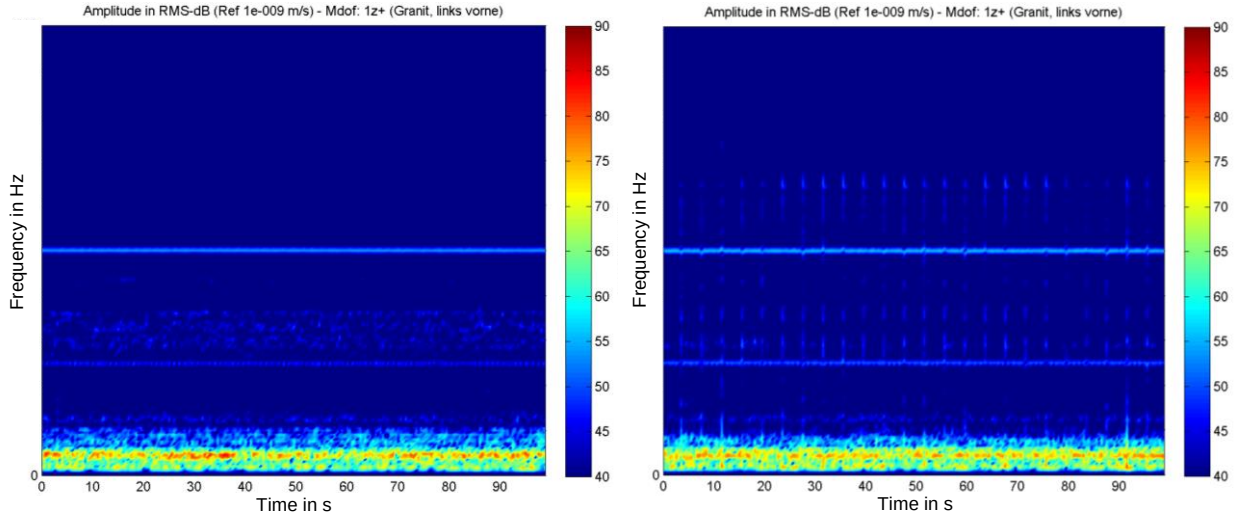


Figure 6: Sensor on granite, left: idle measurement/right: hammer excitation on ground

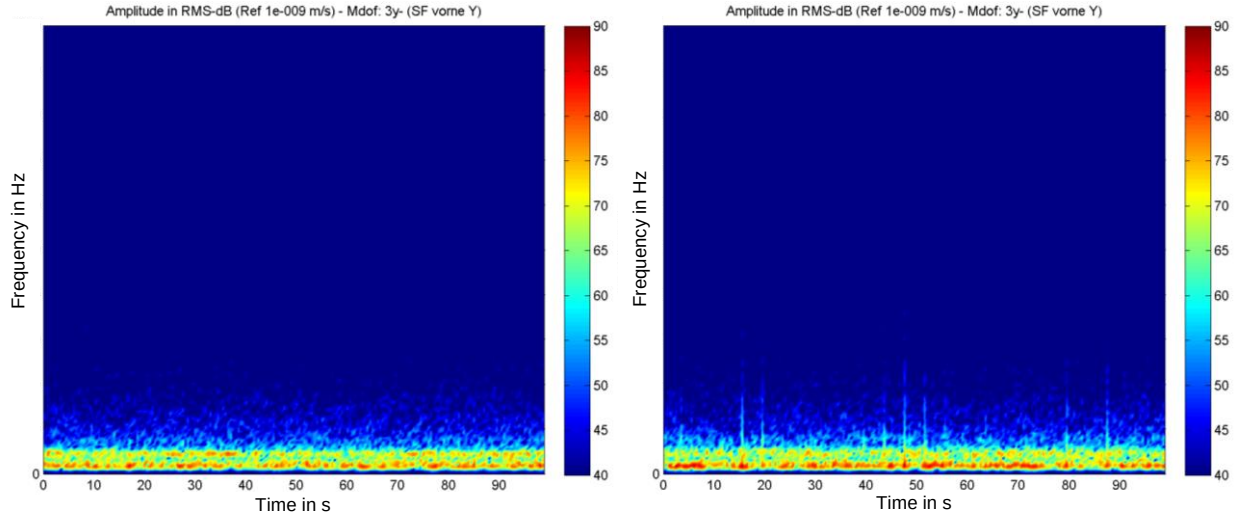


Figure 7: Sensor 1 on test item, left: idle measurement/right: hammer excitation on ground

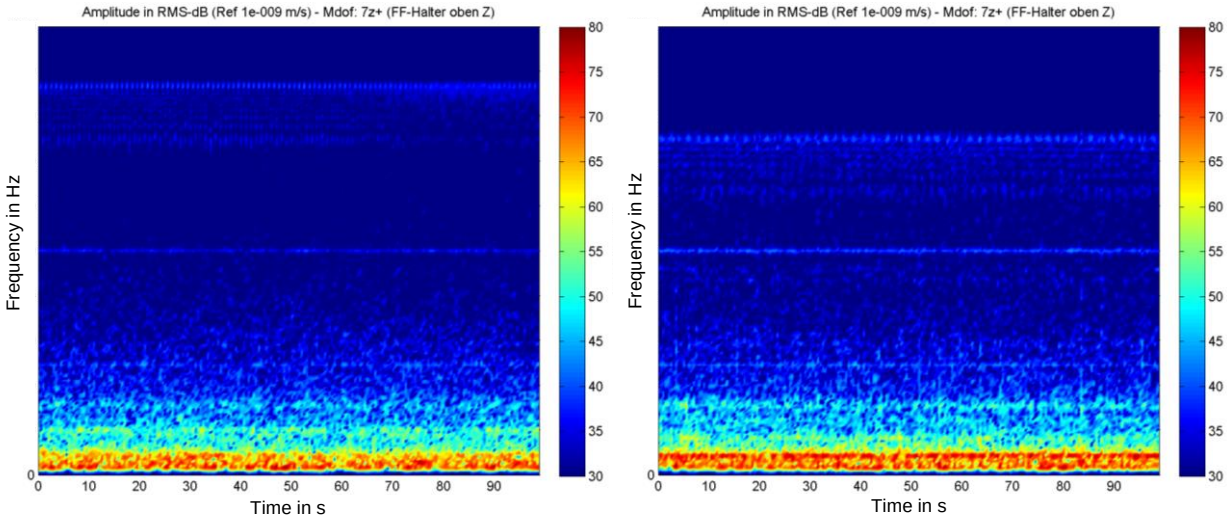


Figure 8: Sensor 2 on test item, left: idle measurement/right: hammer excitation on ground

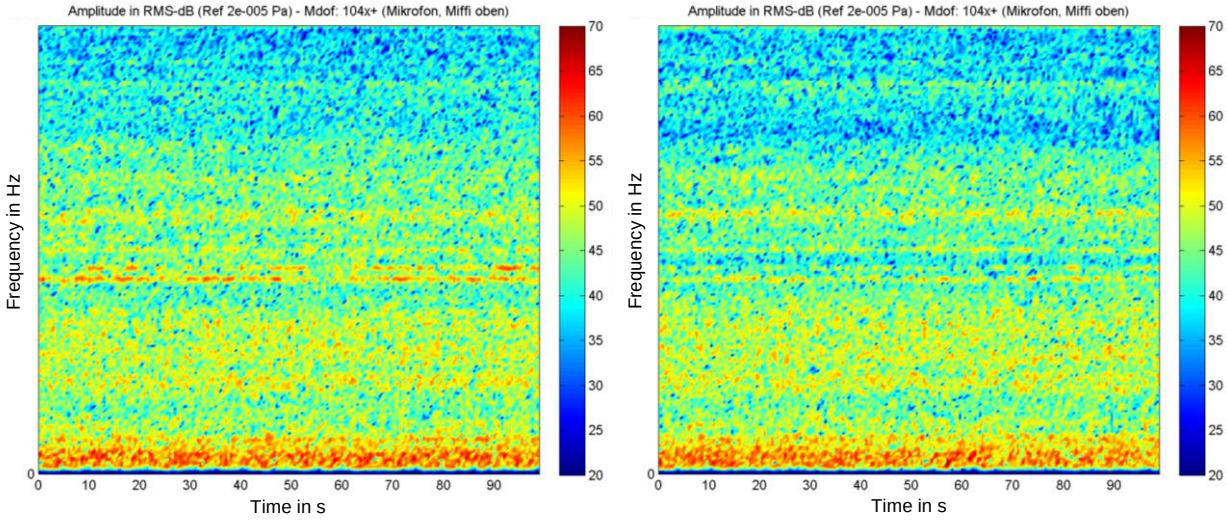


Figure 9: Microphone, left: idle measurement/right: hammer excitation on ground

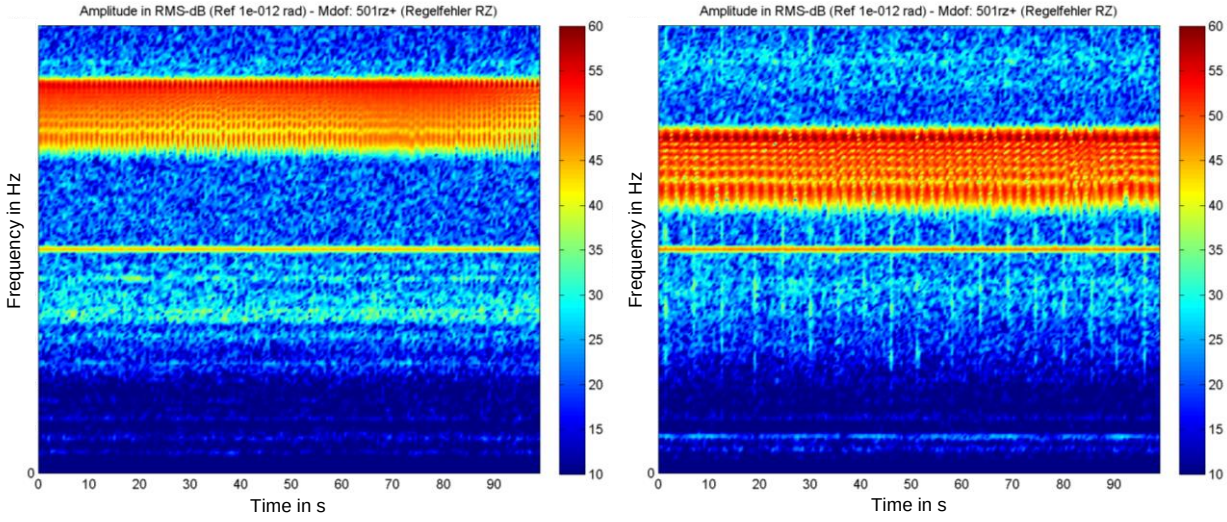


Figure 10: Control Error, left: idle measurement/right: hammer excitation on ground

Sound Excitation (Ordinate: Frequency in Hz, Abscissa: Time in s):

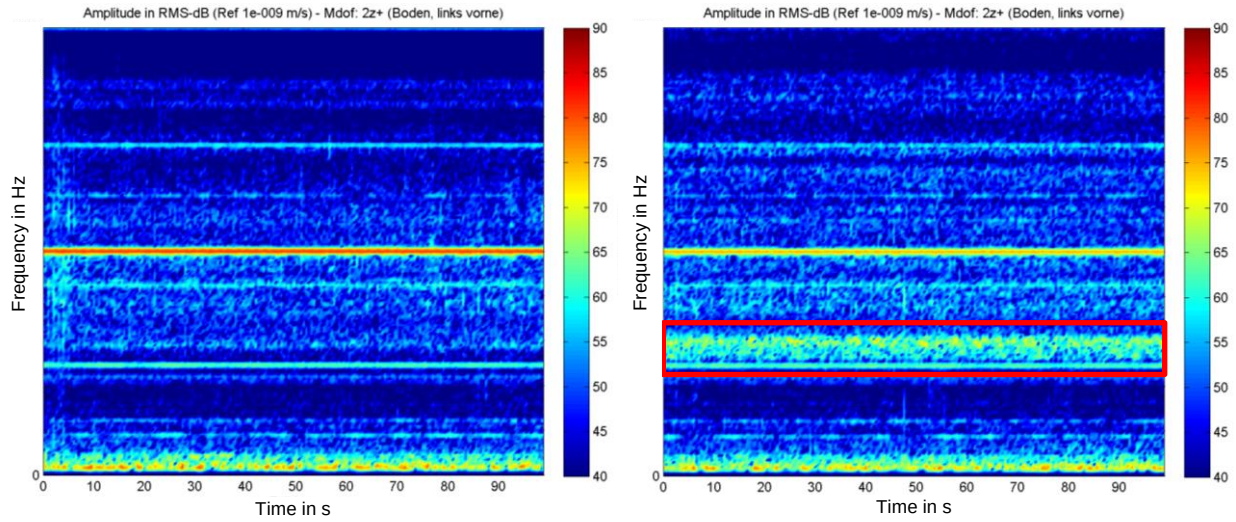


Figure 11: Sensor on ground, left: idle measurement/right: sound excitation

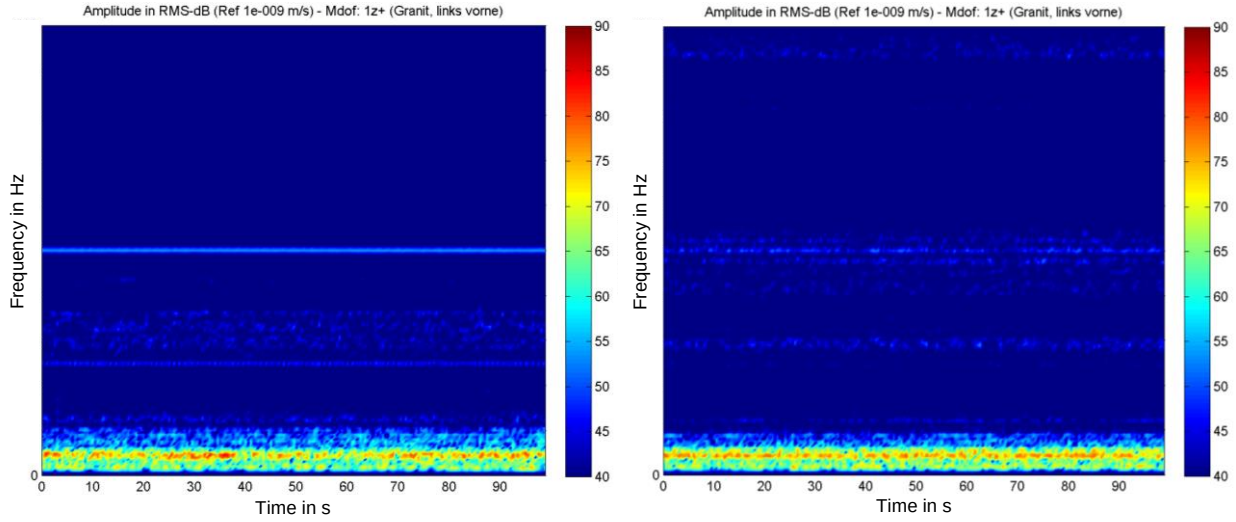


Figure 12: Sensor on granite, left: idle measurement/right: sound excitation

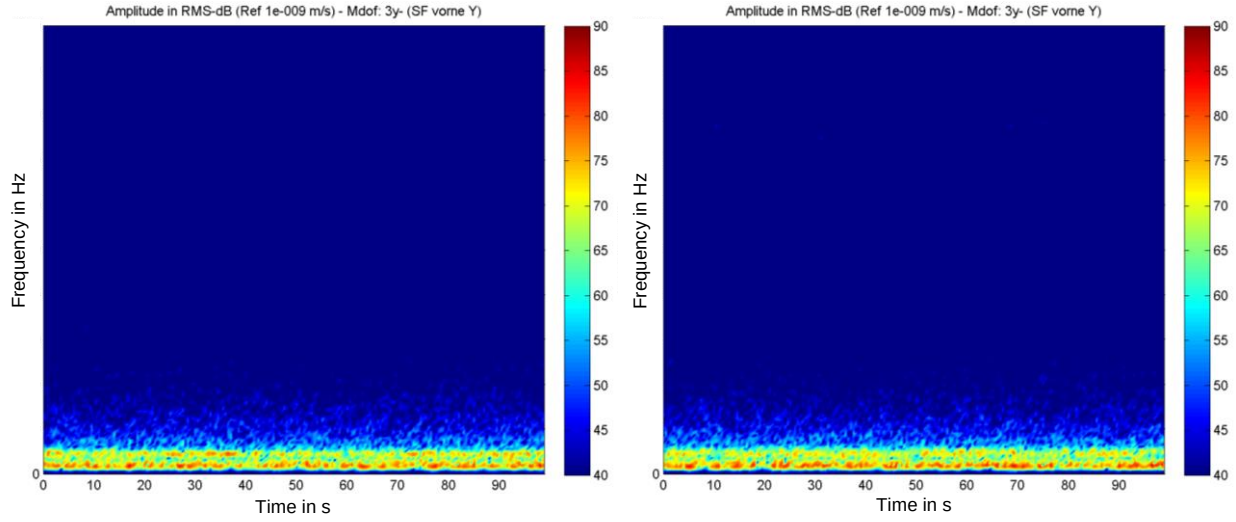


Figure 13: Sensor 1 on test item, left: idle measurement/right: sound excitation

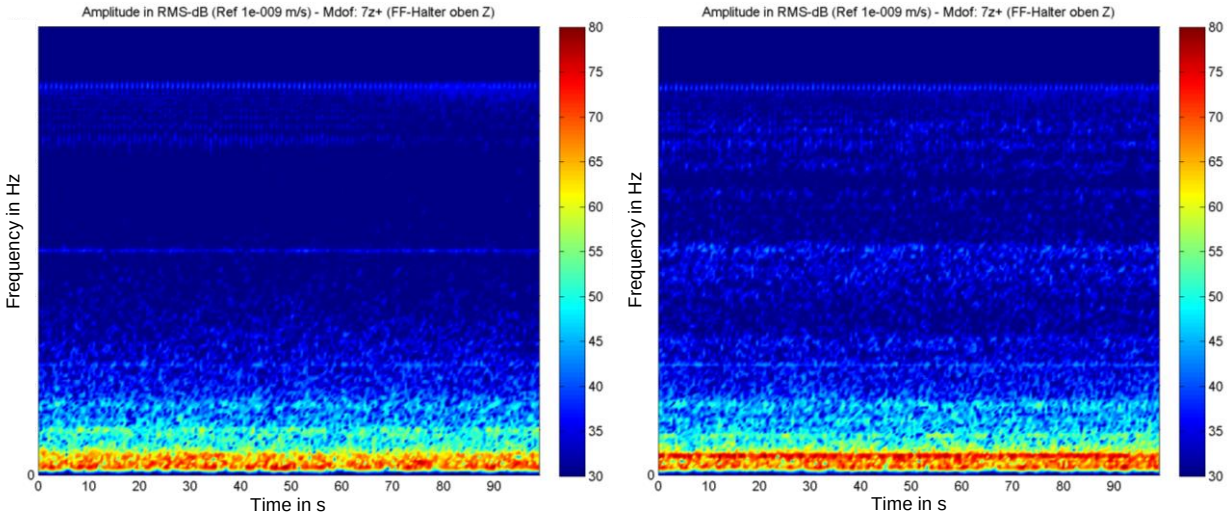


Figure 14: Sensor 2 on test item, left: idle measurement/right: sound excitation

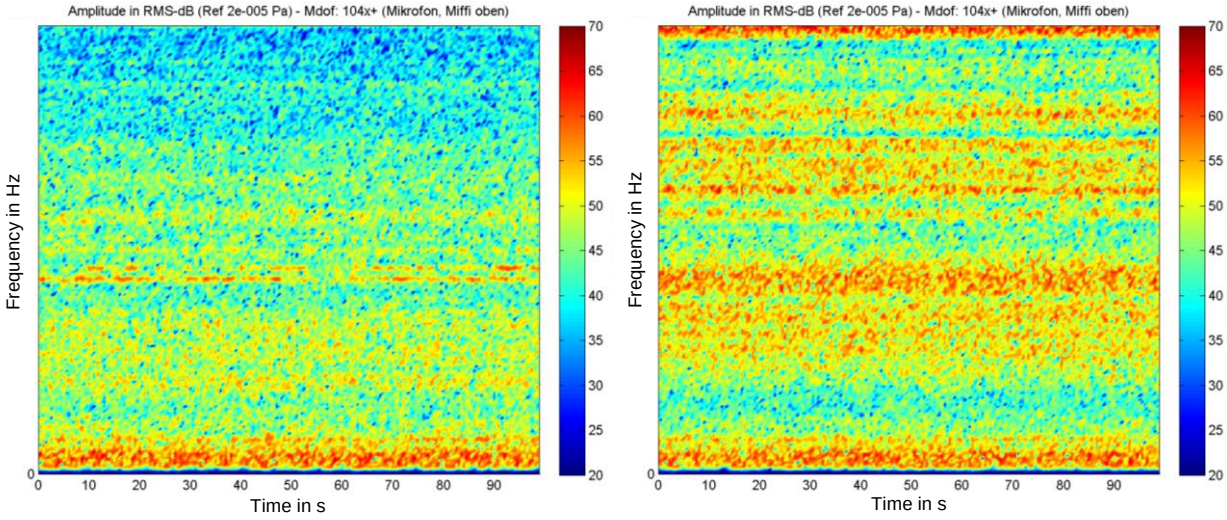


Figure 15: Microphone, left: idle measurement/right: sound excitation

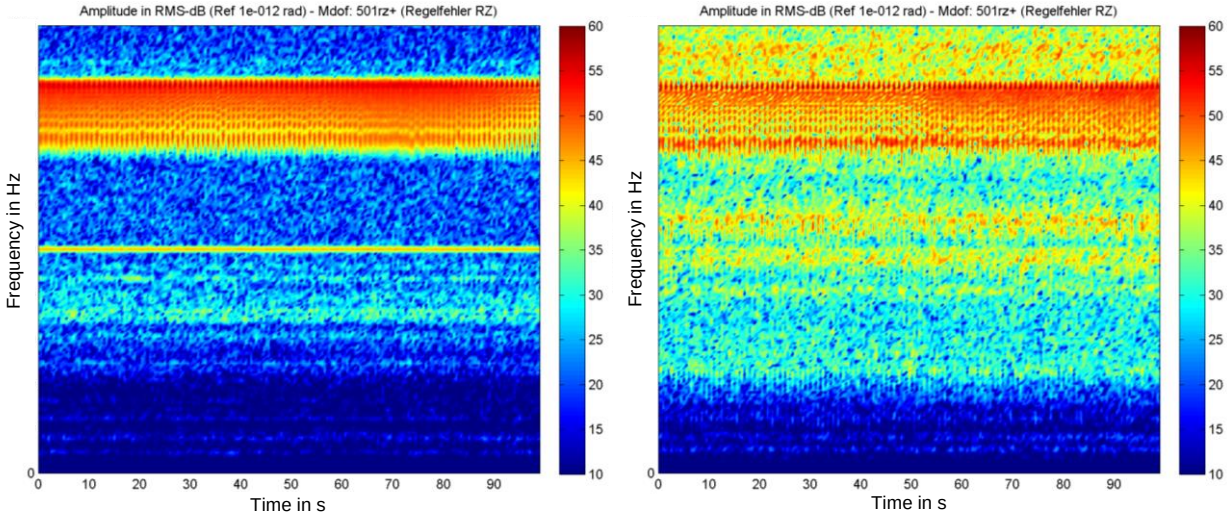


Figure 16: Control Error, left: idle measurement/right: sound excitation

Operational Excitation (Ordinate: Frequency in Hz, Abscissa: Time in s):

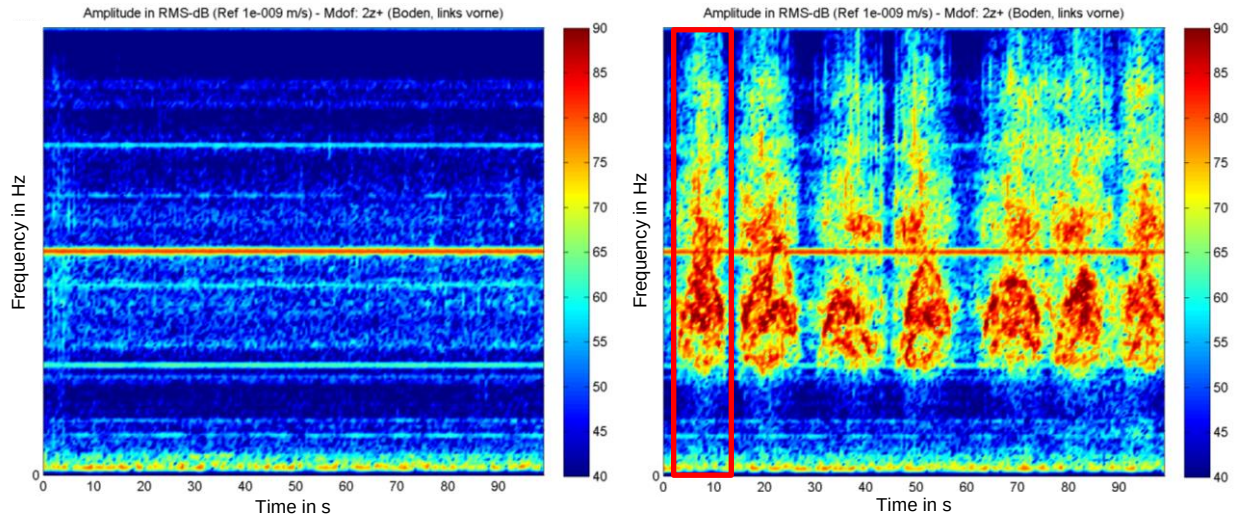


Figure 17: Sensor on ground, left: idle measurement/right: operational excitation with loaded lifter

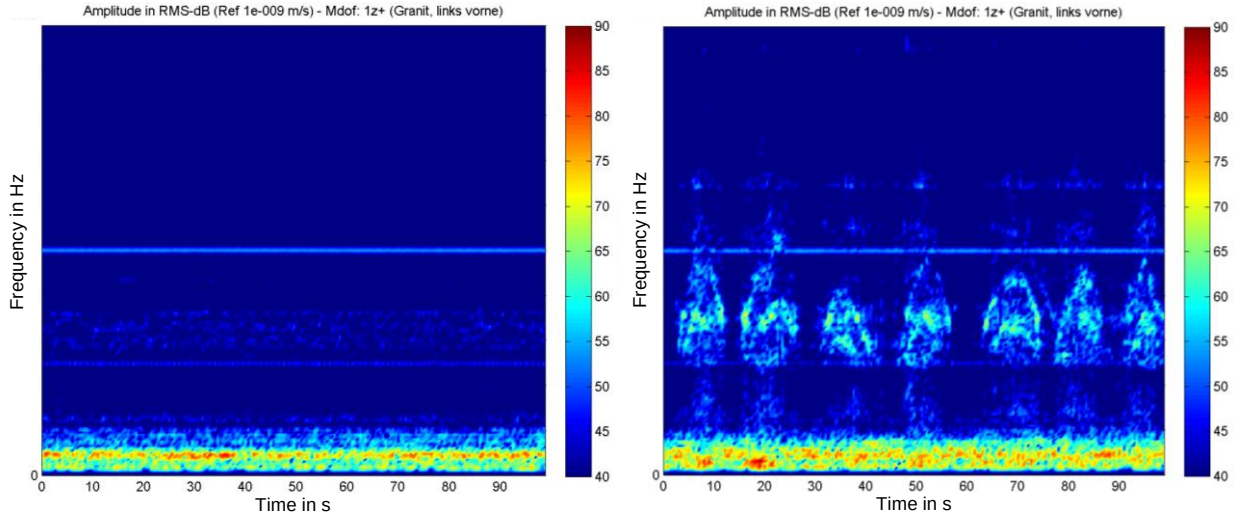


Figure 18: Sensor on granite, left: idle measurement/right: operational excitation with loaded lifter

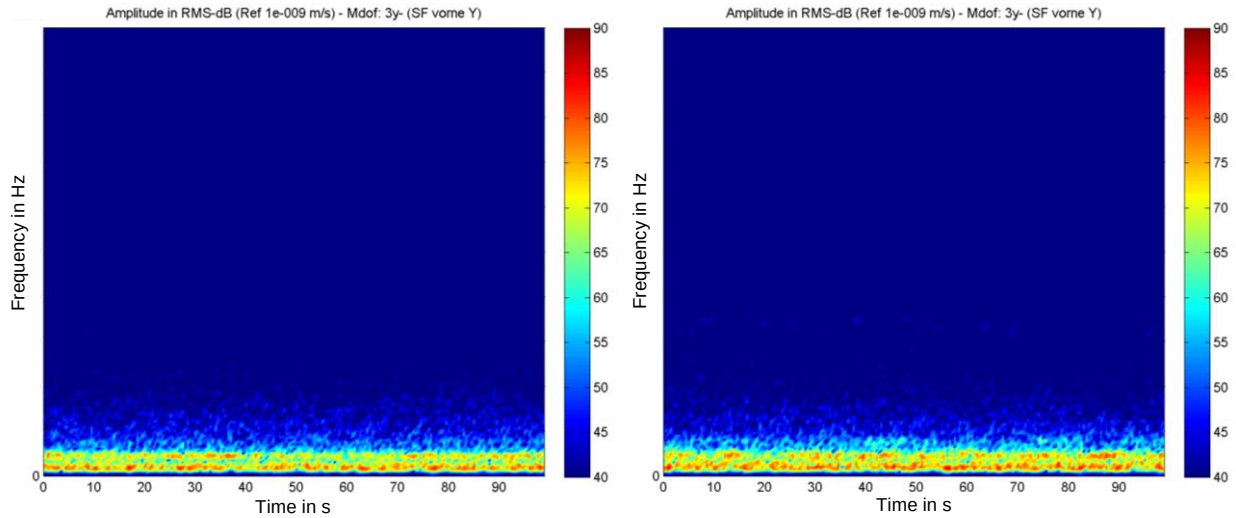


Figure 19: Sensor 1 on test item, left: idle measurement/right: operational excitation with loaded lifter

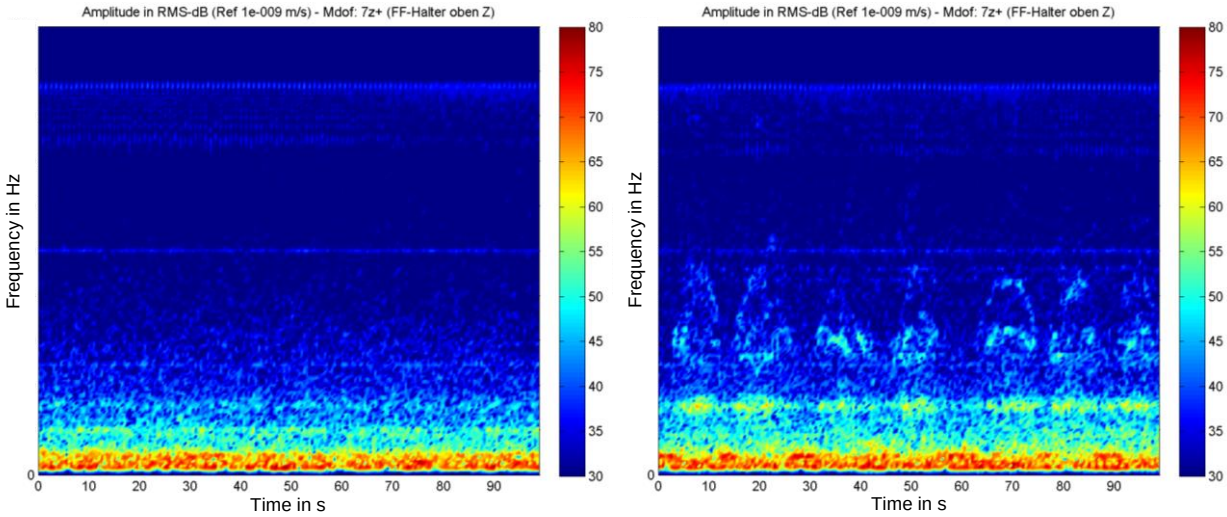


Figure 20: Sensor 2 on test item, left: idle measurement/right: operational excitation with loaded lifter

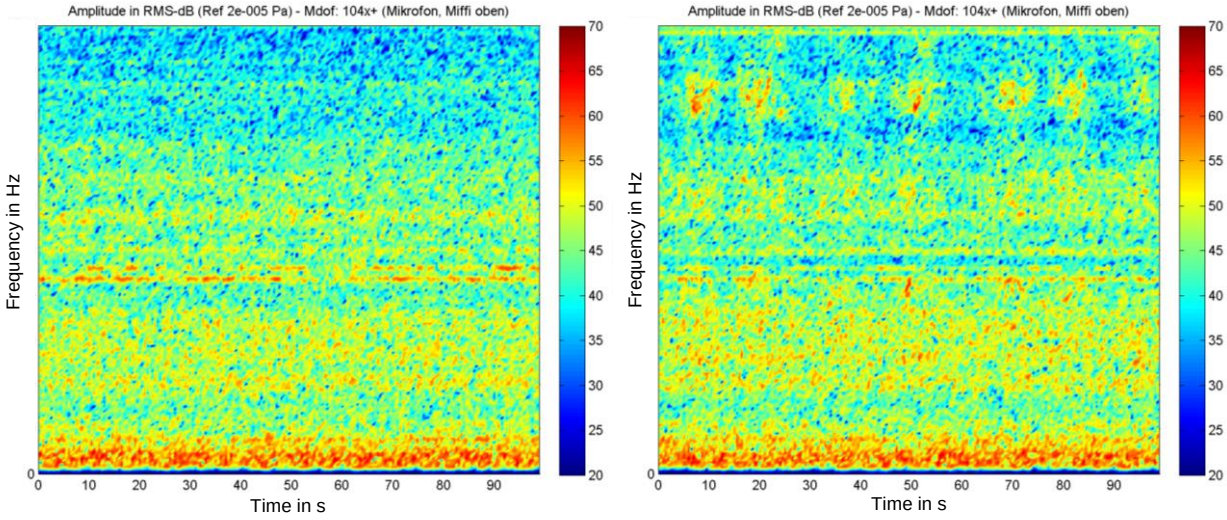


Figure 21: Microphone, left: idle measurement/right: operational excitation with loaded lifter

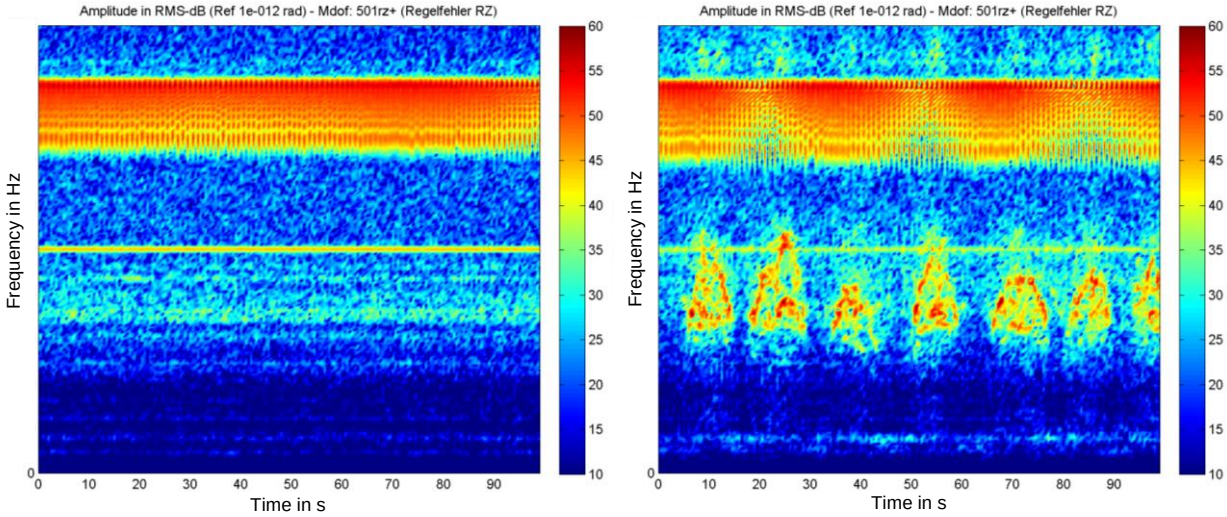


Figure 22: Control Error, left: idle measurement/right: operational excitation with loaded lifter

3.3 TPA

For TPA of the test bench, paths and operating data according to section 2 were used. The challenge was here that not all planned sound excitation paths could be measured because of failure of the sound source particle sensor before the end of the test campaign. Thus only a reduced base of paths was available. From the finally available paths, the following subset was selected for the TPA:

1. Hammer excitation, ground near left front foot of test bench support frame
2. Hammer excitation, ground near right front foot of test bench support frame
3. Hammer excitation, ground on travel path left
4. Hammer excitation, ground on travel path right
5. Sound Source, on travel path
6. Sound Source, in front of test bench
7. Sound Source, on left side of test bench
8. Sound Source, behind of test bench

As operational input data for the TPA force identification, a subset of the measuring points and directions ("indicators") was selected from the measurement with loaded lifter. The recalculation of the measured input data by means of the path frequency response functions and the identified forces was finally conducted for selected target measurement points and directions.

Figure 23 shows the forces identified with the TPA model described above. The recalculations for the targets sensors 1 and 2 on the test item and the control error are presented in Figures 24 to 26. For the control error Figure 27 additionally illustrates the individual path contributions to the overall response.

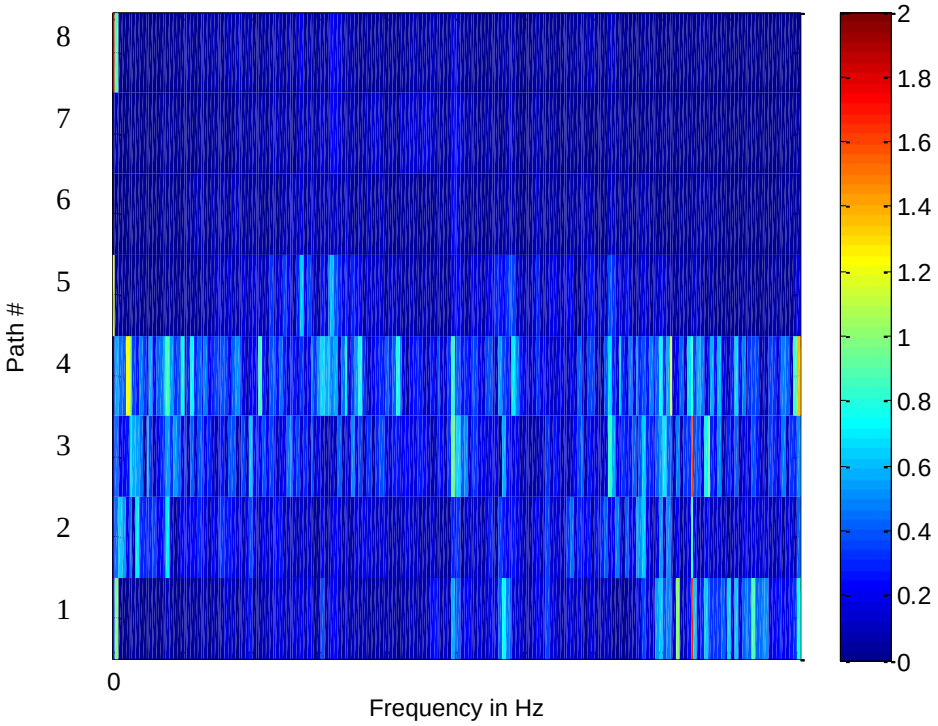


Figure 23: TPA results – identified forces

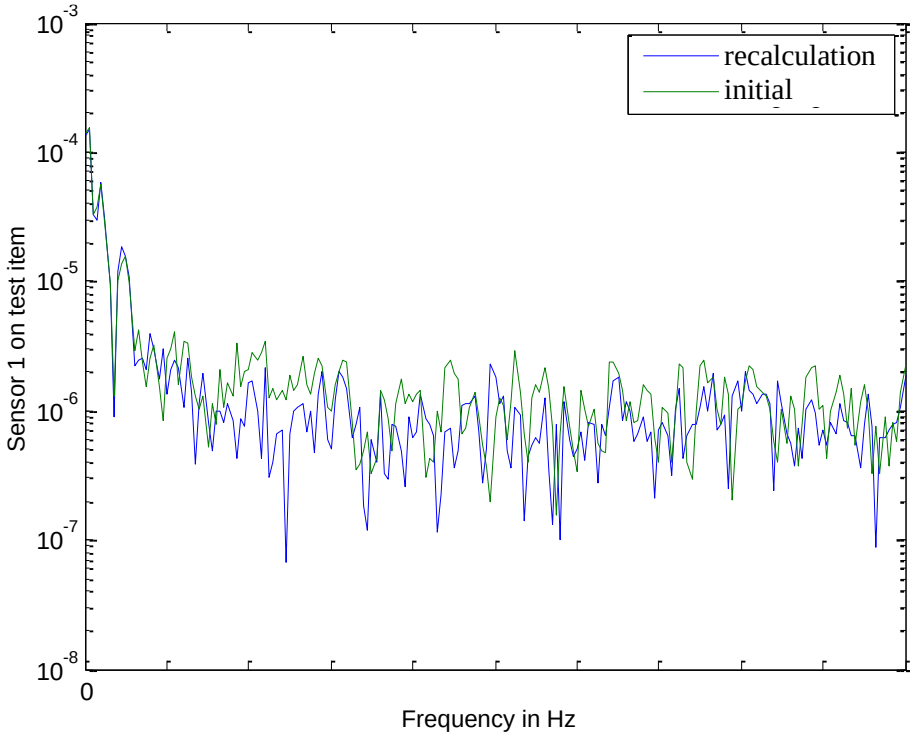


Figure 24: TPA results – comparison measured vs. recalculated signal for sensor 1 on test item

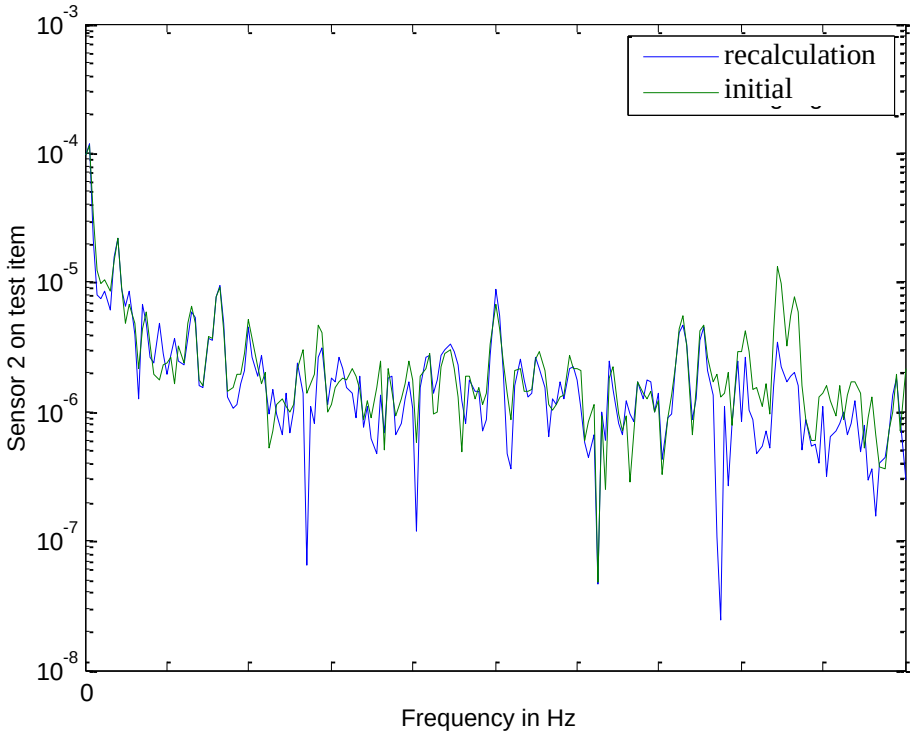


Figure 25: TPA results – comparison measured vs. recalculated signal for sensor 2 on test item

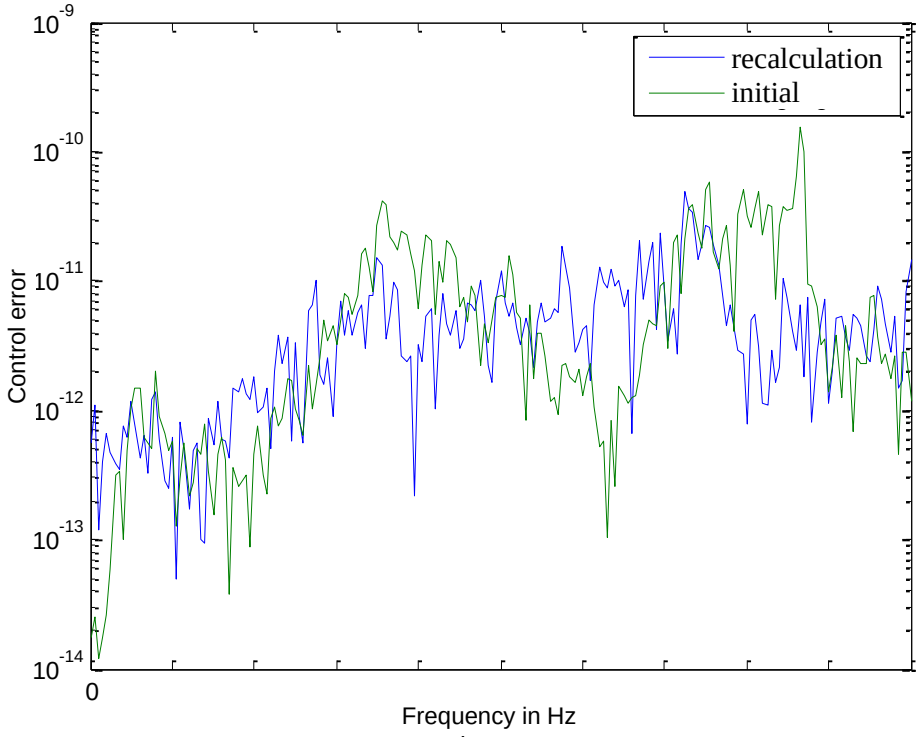


Figure 26: TPA results – comparison measured vs. recalculated signal for control error

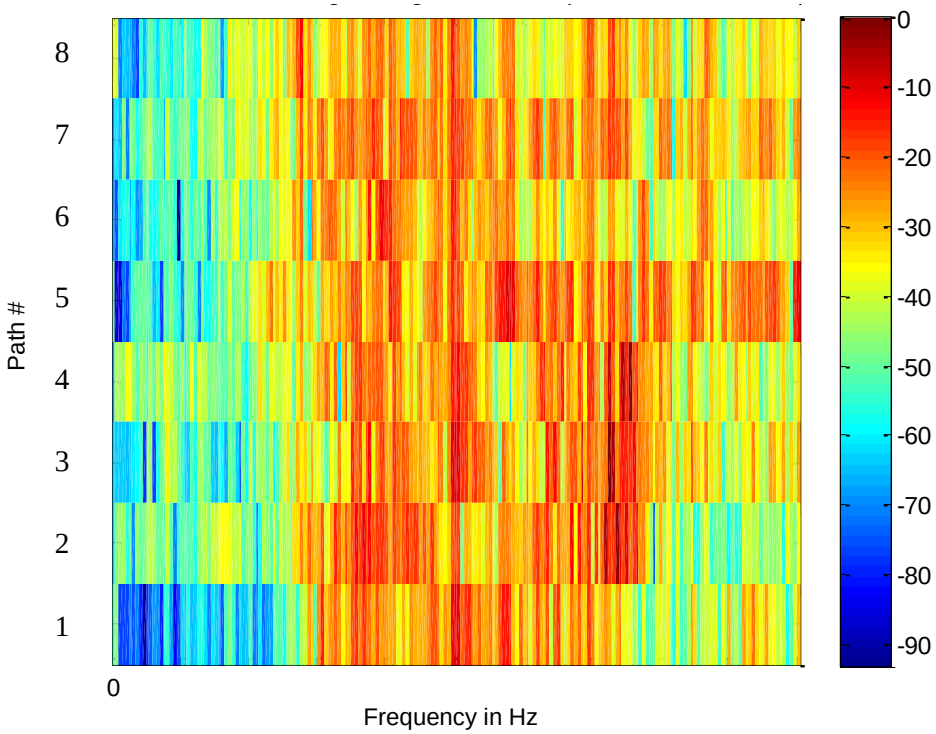


Figure 27: TPA results – path contributions to overall signal

First of all, it should be noted that the recalculations reproduce the characteristics of the initially measured signals very well. For the control error according to Figure 26 larger deviations can be observed in the upper frequency range that can be explained by the residual controller noise in this frequency range. Since the controller noise can be regarded as non-structural, it cannot be mapped by the TPA model.

Furthermore, it can be observed that none of the paths stands out from the others in particular. From this no preference for either structural or sound excitation can be concluded. One reason could be that both excitation variants can lead to control errors, which is why they can – in principle – be excited in either case via corresponding paths and associated forces (→ non-unique force identification).

Finally, it should be noted that a force excitation with hammer always produces a (pulsed) sound excitation as well and that sound excitation can always cause a structural vibration. Thus, in both cases, in case of doubt, energy is transmitted via both transmission paths, albeit with different intensity.

4 Test Results

To summarize, it can be stated that control errors can be triggered by typical operating situations in the vicinity of the test bench. This can clearly be seen on both time and spectral data, e.g. in case of pass-bys with a loaded lifter. Especially in the lower frequency range significant PSD increases occur.

Furthermore, by temporal resolution of the signal contents using short-term spectral analyses, typical operating signatures can be identified. These signatures can, depending on the type of excitation, be observed with varying intensity on the individual components of the test bench itself as well as on sound pressures, and, finally, on the control errors.

With predominant force excitation disturbances seem to be transferred primarily over the foundation in the test bench. Since the excitation signatures can also be detected on test item at location 1, this can have a direct effect on the control errors. With predominant sound excitation the disturbances are to be recognized first of all on the test item at location 2 as well as on the microphones. The assumption is therefore obvious that the disturbances, which can also be found on the control errors, can result from an excitation of the test item via air.

With combined force and sound excitation, as it occurs for example when passing by with a lifter, in principle both phenomena described above are basically recognizable. However, the disturbance signatures on the test item at location 1 are virtually undetectable (as for pure sound excitation), whereas they stand out clearly in the test item at location 2. From this, a primary disturbance due to sound excitation may be concluded.

5 Summary and Conclusions

Vibration and acoustic measurements were carried out on a test bench. Accelerations on the ground and on the test bench, sound pressures in the immediate vicinity, and control errors were measured. In particular, the control errors can be regarded as a measure of the impact of external disturbances. The excitation was carried out successively both by defined force and sound excitation at several points, as well as by typical operating loads.

It was found that day-to-day operation in front of the test benches can cause clearly detectable effects on the control errors. These disturbances are also found on the measured structural accelerations and (partly) on the sound pressures. In this case, a clear separation of the individual excitation pathways (structurally or by air) via TPA is not completely possible – in principle, both path variants have the potential to cause the disturbances individually and also in combination. However, a certain preference on the airborne path can be concluded.

Therefore, for a reduction of the occurring disturbances primary measures for decoupling the test stand from the acoustic environment may be required. To achieve this, an enclosure for the test bench with sufficient acoustic decoupling of external disturbances is currently under development. Later, to check the effectiveness of the enclosure, additional measurements are planned.

Acknowledgements

The authors wish to thank the Carl Zeiss SMT GmbH for the support of this work and the permission to present the results.

References

[1] D. J. Ewins, Modal testing: theory, practice and application, 2nd edition, Research Studies Press Ltd. (2000).

[2] M. V. van der Seijs, D. de Klerk, D. J. Rixen, General framework for transfer path analysis: History, theory and classification of techniques, MSSP 68-69 (2016), pp. 217-244

[3] Microflown Technologies, Products|Sources, Website: http://microflown.com/products/sources/ (2018)

Predicting vibration levels on an experimental test case by using invariant loads (e.g. blocked forces) as source characterization

J. Ortega Almirón[1,2], F. Bianciardi[1], P. Corbeels[1], W. Desmet[2,3]
[1] Siemens Industry Software NV,
Interleuvenlaan 68, B-3001 Leuven, Belgium
e-mail: **jesus.ortega@siemens.com**

[2] KU Leuven, Department Mechanical Engineering,
Celestijnenlaan 300 B, B-3001, Heverlee, Belgium

[3] DMMS core lab, Flanders Make,
Celestijnenlaan 300c, 3001 Leuven, Belgium

Abstract
Component-based TPA is a relatively new TPA approach that allows to characterize a structureborne source component independently from the receiver structure (as opposed to classical TPA) and to predict its behavior when coupled to different receivers. This approach would allow to frontload the development process and considerably increase the flexibility during the design process. However, there are a number of challenges affecting its applicability, such as a proper modelling of the coupling degrees of freedom at the interface, the difficulty to access the interface connection points and the conditioning of the equations. A number of innovative methods were developed to address these issues, that will be investigated by means of measurements on a laboratory test bench. A systematic analysis will be performed through which the accuracy and applicability of the component-based TPA will be analyzed and assessed.

1 Introduction

Classical Transfer Path Analysis (TPA) is a well-established technique that successfully identifies the transmission paths of noise and vibration problems [1][2][3]. One of the requirements of classical TPA is the physical availability of the vehicle to estimate the structural and acoustic loads from operational measurements.

Due to the increasing vehicle variants, shorter development cycles, the trend to reuse the same components on all vehicle variants and the limited availability of prototypes, the automotive industry is seeking for alternative technologies to predict the contribution of vehicle components (engine, intake, exhaust, tyres, etc.) upfront, early in the development process. In that sense, it is necessary the development and validation of techniques that allow the prediction of the contributions from the different sources, without actually being assembled in the final vehicle. However, even though in theory it would be possible to calculate those contributions from the internal load and structural data of the vehicle, in practice is a challenging procedure whether because of the high complexity of the internal load generation mechanisms inside the source or the difficulty to access it to obtain the data in a proper and accurate way. With this purpose, the sources (components that comprise the basic internal load generator mechanisms) are characterized by a set of pseudoforces or blocked forces [4], [5]. These quantities represent in a unique way the load exerted by the source and transmitted to any receiver structure. As opposed to classical TPA, component-based TPA tries to characterize those quantities. This procedure can be performed with the source installed on a test bench or directly on a vehicle, namely in-situ source characterization [6].

The characterization of the source is combined with the structural data of both, source and receiver, for the contribution prediction. Frequency Based Substructuring (FBS) is a method used to calculate the acoustic and structural behavior of the assembly using FRF data from the source and receiver structures separately [7]. FBS was first introduced by Bishop and Johnson [8] and became widely known with the approach of Jetmundsen et al. [9].

FBS requires to access the defined DOFs of the connections, this can be achieved by applying geometrical reduction. This technique allows to obtain the required DOFs without actually measure in the exact locations [10], what would be useful when the locations are difficult or impossible to access, and when moments and rotations are needed (especially important for rigid connections), but at the expense of using more impacts and responses for the modelling.

This paper aims to validate every step of this full process, from the source characterization on a test-bench to the structural vibration prediction in a simplified vehicle receiver. Strengths and weaknesses of its practical implementation are highlighted in an academic setup.

2 Methods for source characterization and vibration prediction

2.1 Source characterization: pseudoforces and blocked forces

To characterize a source is necessary to obtain a quantity that, by itself, allows the full description of the source for a given operational condition, as well as the prediction of its behavior when coupled to any known receiver structure. Classical TPA can identify the contact forces that are transmitted between the source and the receiver, however, these forces are dependent on the assembled structure (source + receiver) and cannot be transferred to different receivers. Therefore contact forces don't successfully identify the source independently [11].

Component-based TPA is a relatively new TPA technique aiming to independently characterize a source by a set of forces (pseudoforces or blocked forces), based on the hypothesis of a finite number of connecting DOFs between source and receiver [12].

It's known that a certain source with an input force $\boldsymbol{F}_i$ will generate a field of accelerations $\boldsymbol{a}_r$ in the receiver that it is connected to, that depends on both, source and receiver, according to eq. (1).

$$\boldsymbol{a}_r = \boldsymbol{Y}_{rs_i}^{SR}\boldsymbol{F}_i \tag{1}$$

Where $\boldsymbol{Y}_{rs_i}^{SR}$ is the frequency response function of the coupled system between the input forces of the source and any point r in the receiver. (Variables are expressed in the frequency domain). The system is depicted in figure 1.

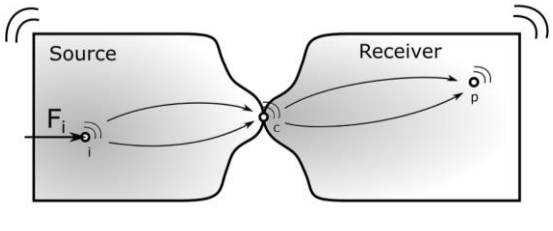


Figure 1: Source and receiver system model

Input forces are used here to refer the external or internal forces that the basic source mechanism exerts on the source component. If we assume that those input forces $\boldsymbol{F}_i$ are always independent from the receiver, these forces would already be a valid characterization of the source. However, this way is discarded in practice, as most of the sources generate an input force that is infeasible or impossible to measure accurately

because of the complexity of the multiple mechanisms that might be involved and the impossibility to access them.

To tackle that problem one may use the general concept of pseudoforces. For a source assembled on a receiver with a finite number of connecting DOFs, n, a set of n forces can be calculated for a certain set of n points in the source, such that it would generate the same accelerations in the n DOFs of the connection when the source is turned off, as the source would do when active (fig 2(a)) [13]. Those forces can be easily calculated with matrix inversion of a square matrix, as long as it is well conditioned (eq. (2)).

$$\boldsymbol{F}_{ps} = \boldsymbol{Y}_{cs_{ps}}^{SR\ -1}\boldsymbol{a}_c = \boldsymbol{Y}_{cs_{ps}}^{SR\ -1}\boldsymbol{Y}_{cs_i}^{SR}\boldsymbol{F}_i \tag{2}$$

Where $\boldsymbol{F}_{ps}$ is the set of pseudoforces, $\boldsymbol{a}_c$ is the set of accelerations in the connection DOFs, $\boldsymbol{Y}_{cs_{ps}}^{SR}$ is the frequency response function of the coupled system between the pseudoforces and the connection, and $\boldsymbol{Y}_{cs_i}^{SR}$ is the frequency response function of the coupled system between the input forces and the connection. When the calculated set of forces act in the opposite way, the generated accelerations in the connections would also be the opposite to the ones generated by the source. Therefore when both, source and the opposite set of calculated forces, act at the same time, the accelerations at the connection DOFs are cancelled, resulting on the connection DOFs remaining still (fig 2(b)). As the receiver is only connected through those DOFs, not having any additional source, all the points of the receiver will also remain still, hence the accelerations of the receiver can be generated by the same set of forces, namely pseudoforces. This only holds for receiver accelerations and cannot be extended to accelerations in the source.

That means that pseudoforces can be calculated using the accelerations of any DOF that belongs to the receiver, either in the connection or not, for any connected receiver. Therefore, they can also be calculated using the accelerations of the connections of the uncoupled source in operational conditions, as it can be assumed to be coupled to a massless, infinitely flexible receiver, according to eq. (3).

$$\boldsymbol{F}_{ps} = \boldsymbol{Y}_{rs_{ps}}^{SR\ -1}\boldsymbol{a}_r = \boldsymbol{Y}_{rs_{ps}}^{SR\ -1}\boldsymbol{Y}_{rs_i}^{SR}\boldsymbol{F}_i = \boldsymbol{Y}_{cs_{ps}}^{S\ -1}\boldsymbol{Y}_{cs_i}^{S}\boldsymbol{F}_i \tag{3}$$

Where $\boldsymbol{Y}_{rs_{ps}}^{SR}$ is the frequency response function of the coupled system between the pseudoforces and any point r in the receiver, $\boldsymbol{Y}_{cs_{ps}}^{S}$ is the frequency response function of the decoupled source between the pseudoforces and the connection, and $\boldsymbol{Y}_{cs_i}^{S}$ is the frequency response function of the decoupled source between the input forces and the connection. It can be noticed that all the possible sets of pseudoforces would generate the same acceleration field in the receiver but not in the source. Also different sets of pseudoforces would generate different acceleration fields in the source.

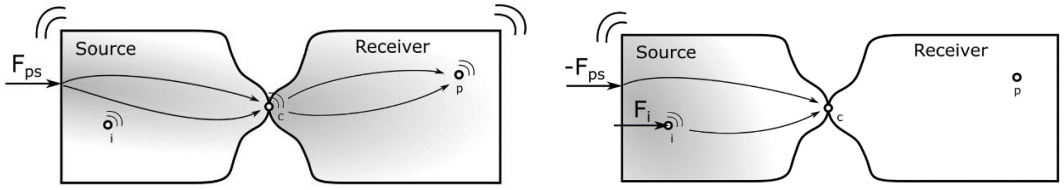


Figure 2: (a) Pseudoforces acting alone; (b) opposite pseudoforces acting with the source in operation

When the pseudoforces are calculated in the connection DOFs, they are called blocked forces [14]. Therefore blocked forces are a particular case of pseudoforces with the same properties (fig 3(a) and 3(b)).

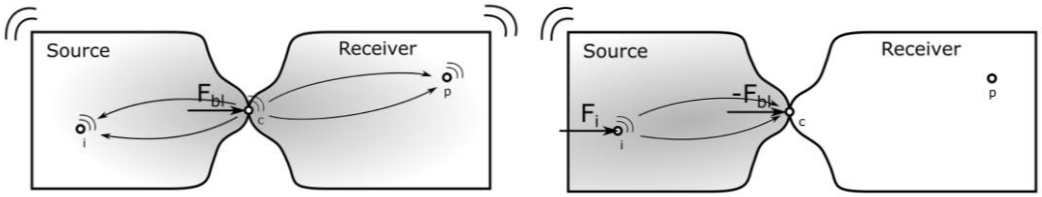


Figure 3: (a) Blocked forces acting alone; (b) opposite blocked forces acting with the source in operation

As they are calculated in the connection (eq. (4)), they are the same forces that the source would exert to a blocking restriction in the connection DOFs. However, this theoretical definition is not a feasible way to measure them in practice, as the ideal blocking restriction is physically impossible to reproduce for most sources, especially without affecting the source dynamics. Thus, in order to calculate blocked forces, $\boldsymbol{F}_{bl}$, of a source mounted on a receiver structure, either in-situ characterization or bench dynamics compensation has to be applied [15].

$$\boldsymbol{F}_{bl} = \boldsymbol{Y}_{rc}^{SR\,-1}\boldsymbol{a}_r \tag{4}$$

Where $\boldsymbol{Y}_{rc}^{SR}$ is the frequency response function of the coupled system between the connection and any point r in the receiver.

2.2 Frequency based substructuring

The pseudoforces or blocked forces need to be combined with coupled FRF data, experimental or simulated, in order to predict the final contribution in the vehicle. Coupled FRFs can be experimentally measured, if the components are physically available. When only the uncoupled components are available, FBS is applied to calculate the FRFs of the coupled setup from the FRFs of the uncoupled source and receiver [16].

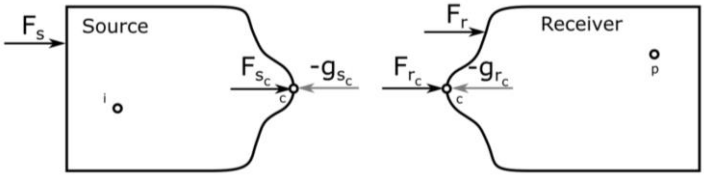


Figure 4: Frequency based substructuring model

Let us take the subsystem's FRF matrices and model them as an uncoupled system in eq. (5). In this system, the effect of the coupling is represented with a set of external forces $\boldsymbol{g}$ acting in the connections of both bodies as contact forces, as shown in fig 4. The contact forces must guarantee the compatibility condition of the connection DOFs, represented in eq. (6), and the equilibrium condition of eq. (7).

$$\boldsymbol{a} = \begin{bmatrix} \boldsymbol{a}_s^S \\ \boldsymbol{a}_{s_c}^S \\ \boldsymbol{a}_{r_c}^R \\ \boldsymbol{a}_r^R \end{bmatrix} = \begin{bmatrix} \boldsymbol{Y}_{ss}^S \boldsymbol{Y}_{sc}^S & \boldsymbol{0} & \boldsymbol{0} \\ \boldsymbol{Y}_{cs}^S \boldsymbol{Y}_{cc}^S & \boldsymbol{0} & \boldsymbol{0} \\ \boldsymbol{0} & \boldsymbol{0} & \boldsymbol{Y}_{cc}^R \boldsymbol{Y}_{cr}^R \\ \boldsymbol{0} & \boldsymbol{0} & \boldsymbol{Y}_{rc}^R \boldsymbol{Y}_{rr}^R \end{bmatrix} \left(\begin{bmatrix} \boldsymbol{F}_s \\ \boldsymbol{F}_{s_c} \\ \boldsymbol{F}_{r_c} \\ \boldsymbol{F}_r \end{bmatrix} + \begin{bmatrix} \boldsymbol{0} \\ \boldsymbol{g}_{s_c} \\ \boldsymbol{g}_{r_c} \\ \boldsymbol{0} \end{bmatrix} \right) = \boldsymbol{Y}(\boldsymbol{f} + \boldsymbol{g}) \tag{5}$$

$$\boldsymbol{a}_{r_c}^R - \boldsymbol{a}_{s_c}^S = [\boldsymbol{0} \quad -\boldsymbol{I} \quad \boldsymbol{I} \quad \boldsymbol{0}]\boldsymbol{a} = \boldsymbol{B}\boldsymbol{a} = \boldsymbol{0} \tag{6}$$

$$\boldsymbol{g} = \boldsymbol{B}^T\boldsymbol{\lambda} \tag{7}$$

In these and following equations of this section the subscripts make reference to the DOFs (s: any source DOFs, s_c: connection in source side, r_c: connection in receiver side, r: any receiver DOFs, c: connection, s_i: input forces, s_{ps}: pseudoforces) and the superscripts make reference to the component (S: source, R: receiver, SR: coupled source and receiver). The equilibrium equation uses $\boldsymbol{\lambda}$ as the Lagrange multipliers in order to guarantee the condition. Substituting eq. (7) in (5) and in (6) an expression for $\boldsymbol{\lambda}$ can be obtained in eq. (8).

$$\boldsymbol{\lambda} = -(\boldsymbol{B}\boldsymbol{Y}\boldsymbol{B}^T)^{-1}\boldsymbol{B}\boldsymbol{Y}\boldsymbol{f} \tag{8}$$

Using this expression in eq. (7) and (5) leads to the general FBS equation, eq. (9).

$$\boldsymbol{Y}^{\boldsymbol{SR}} = \boldsymbol{Y} - \boldsymbol{Y}\boldsymbol{B}^T(\boldsymbol{B}\boldsymbol{Y}\boldsymbol{B}^T)^{-1}\boldsymbol{B}\boldsymbol{Y} \tag{9}$$

When the connection between source and receiver is not rigid, but relative displacements are allowed by means of a mount of certain stiffness, a similar derivation can be carried out, with a different equation (eq. (10)) in the place of the previous compatibility and equilibrium conditions.

$$\boldsymbol{g} = -\boldsymbol{B}^T\boldsymbol{K}\left(\boldsymbol{a}_{r_c}^R - \boldsymbol{a}_{s_c}^S\right) = -\boldsymbol{B}^T\boldsymbol{K}\boldsymbol{B}\boldsymbol{a} \tag{10}$$

Where $\boldsymbol{K}$ is the stiffness of the mount. The new coupled accelerance matrix for this case is shown in eq. (11).

$$\boldsymbol{Y}^{\boldsymbol{SR}} = \boldsymbol{Y} - \boldsymbol{Y}\boldsymbol{B}^T(\boldsymbol{K}^{-1} + \boldsymbol{B}\boldsymbol{Y}\boldsymbol{B}^T)^{-1}\boldsymbol{B}\boldsymbol{Y} \tag{11}$$

We can expand those expressions to look at the equations in terms of DOFs as in eq. (5), obtaining eq. (12).

$$\boldsymbol{Y}^{\boldsymbol{SR}} = \begin{bmatrix} \boldsymbol{Y}_{ss}^S & \boldsymbol{Y}_{sc}^S & \boldsymbol{0} & \boldsymbol{0} \\ \boldsymbol{Y}_{cs}^S & \boldsymbol{Y}_{cc}^S & \boldsymbol{0} & \boldsymbol{0} \\ \boldsymbol{0} & \boldsymbol{0} & \boldsymbol{Y}_{cc}^R & \boldsymbol{Y}_{cr}^R \\ \boldsymbol{0} & \boldsymbol{0} & \boldsymbol{Y}_{rc}^R & \boldsymbol{Y}_{rr}^R \end{bmatrix} - \begin{bmatrix} -\boldsymbol{Y}_{sc}^S \\ -\boldsymbol{Y}_{cc}^S \\ \boldsymbol{Y}_{cc}^R \\ \boldsymbol{Y}_{rc}^R \end{bmatrix} [\boldsymbol{Y}_{cc}^S + \boldsymbol{Y}_{cc}^R + \boldsymbol{K}^{-1}]^{-1} [-\boldsymbol{Y}_{cs}^S \quad -\boldsymbol{Y}_{cc}^S \quad \boldsymbol{Y}_{cc}^R \quad \boldsymbol{Y}_{cr}^R] \tag{12}$$

Let us take the first column of the coupled FRFs and particularize it to the DOFs of the input forces of the source mechanism to calculate accelerations in the coupled system (eq. (13)). When the input force is substituted by the definition of pseudoforce (eq. (3)) eq. (14) is obtained.

$$\begin{bmatrix} \boldsymbol{a}_s^S \\ \boldsymbol{a}_{s_c}^S \\ \boldsymbol{a}_{r_c}^R \\ \boldsymbol{a}_r^R \end{bmatrix} = \begin{bmatrix} \boldsymbol{Y}_{ss_i}^{SR} \\ \boldsymbol{Y}_{cs_i}^{SR} \\ \boldsymbol{Y}_{cs_i}^{SR} \\ \boldsymbol{Y}_{rs_i}^{SR} \end{bmatrix} \boldsymbol{F}_i = \begin{bmatrix} \boldsymbol{Y}_{ss_i}^S - \boldsymbol{Y}_{sc}^S[\boldsymbol{Y}_{cc}^S + \boldsymbol{Y}_{cc}^R + \boldsymbol{K}^{-1}]^{-1}\boldsymbol{Y}_{cs_i}^S \\ \boldsymbol{Y}_{cs_i}^S - \boldsymbol{Y}_{cc}^S[\boldsymbol{Y}_{cc}^S + \boldsymbol{Y}_{cc}^R + \boldsymbol{K}^{-1}]^{-1}\boldsymbol{Y}_{cs_i}^S \\ \boldsymbol{Y}_{cc}^R[\boldsymbol{Y}_{cc}^S + \boldsymbol{Y}_{cc}^R + \boldsymbol{K}^{-1}]^{-1}\boldsymbol{Y}_{cs_i}^S \\ \boldsymbol{Y}_{rc}^R[\boldsymbol{Y}_{cc}^S + \boldsymbol{Y}_{cc}^R + \boldsymbol{K}^{-1}]^{-1}\boldsymbol{Y}_{cs_i}^S \end{bmatrix} \boldsymbol{Y}_{cs_i}^{S\ -1}\boldsymbol{Y}_{cs_{ps}}^S\boldsymbol{F}_{ps} \tag{13}$$

$$\begin{bmatrix} \boldsymbol{a}_s^S \\ \boldsymbol{a}_{s_c}^S \\ \boldsymbol{a}_{r_c}^R \\ \boldsymbol{a}_r^R \end{bmatrix} = \begin{bmatrix} \boldsymbol{Y}_{ss_i}^{SR} \\ \boldsymbol{Y}_{cs_i}^{SR} \\ \boldsymbol{Y}_{cs_i}^{SR} \\ \boldsymbol{Y}_{rs_i}^{SR} \end{bmatrix} \boldsymbol{F}_i = \begin{bmatrix} \boldsymbol{Y}_{ss_i}^S\boldsymbol{Y}_{cs_i}^{S\ -1}\boldsymbol{Y}_{cs_{ps}}^S - \boldsymbol{Y}_{sc}^S[\boldsymbol{Y}_{cc}^S + \boldsymbol{Y}_{cc}^R + \boldsymbol{K}^{-1}]^{-1}\boldsymbol{Y}_{cs_{ps}}^S \\ \boldsymbol{Y}_{cs_{ps}}^S - \boldsymbol{Y}_{cc}^S[\boldsymbol{Y}_{cc}^S + \boldsymbol{Y}_{cc}^R + \boldsymbol{K}^{-1}]^{-1}\boldsymbol{Y}_{cs_{ps}}^S \\ \boldsymbol{Y}_{cc}^R[\boldsymbol{Y}_{cc}^S + \boldsymbol{Y}_{cc}^R + \boldsymbol{K}^{-1}]^{-1}\boldsymbol{Y}_{cs_{ps}}^S \\ \boldsymbol{Y}_{rc}^R[\boldsymbol{Y}_{cc}^S + \boldsymbol{Y}_{cc}^R + \boldsymbol{K}^{-1}]^{-1}\boldsymbol{Y}_{cs_{ps}}^S \end{bmatrix} \boldsymbol{F}_{ps} \tag{14}$$

It can be noticed that the resultant set of FBS equations also supports the pseudoforces assumptions described in the previous section. The last 3 lines of eq. (14) are the exact same FBS equations of the coupled FRF system with the pseudoforces as input. Moreover, the last 2 lines prove that the accelerations in the receiver of the coupled system can be calculated using pseudoforces combined with coupled FRFs. As expected, the first line of eq. (14) indicates that is not possible to calculate the accelerations in the source using pseudoforces combined with coupled FRFs, neither is to obtain pseudoforces using source accelerations as indicators. Unique exception is to use source accelerations at the connections, as proven in the second line of eq. (14).

2.3 Geometrical reduction

The coupling of the components using FBS and the blocked forces calculation usually require the access to input and output DOFs that cannot be directly measured, whether because of feasibility issues or just nonexistence of the material point. Also a finite number of DOFs is required by FBS and blocked forces practicability. For that purpose the surrounding region of the point of interest is assumed to exhibit a rigid behavior, creating a rigid body dependence between the DOFs contained by the region. A schematic geometrical reduction (GR) is shown in fig 5.

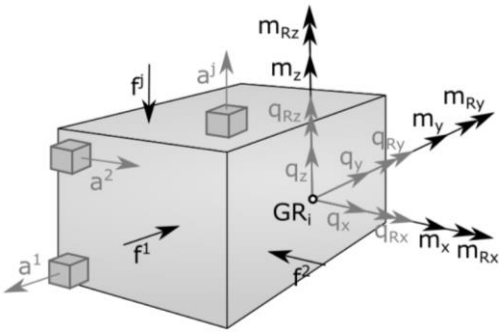


Figure 5: Geometrical reduction model

That dependence allows to transform the measured forces and accelerations into the forces and accelerations of any geometrical point that is assumed to fulfill the rigid behavior of the region, which is used to represent a rigid body. Note that it is not required that the representing point exists as a real point of the body or is positioned within its boundary. The number of measured DOFs is reduced to the final point by using geometrical relationships.

Let us consider the measured accelerations, $\boldsymbol{a}_i$, in the region of interest assumed to be rigid. This region will be reduced to the point GR_i, that represents the geometrical reduction i. There will be a set of 6 geometrically reduced rigid DOFs $\boldsymbol{q}_i$ which allow to approximate the measured DOFs with eq. (15).

$$\boldsymbol{a}_i = \boldsymbol{R}_{\boldsymbol{a}_i}\boldsymbol{q}_i = \begin{bmatrix} a_i^1 \\ \vdots \\ a_i^{N_{a_i}} \end{bmatrix} = \begin{bmatrix} \boldsymbol{R}_{\boldsymbol{a}_i}^{\ 1} \\ \vdots \\ \boldsymbol{R}_{\boldsymbol{a}_i}^{\ N_{a_i}} \end{bmatrix} \boldsymbol{q}_i \tag{15}$$

Where a_i^j is the acceleration of the DOF j for the geometrical reduction i and $\boldsymbol{R}_{\boldsymbol{a}_i}^{\ j}$ is a matrix that contains the geometrical relationships of the rigid body behavior of the acceleration DOF j. N_{a_i} is the number of acceleration DOFs used for the geometrical reduction i. Each acceleration can be calculated using the expanded expression of eq. (16).

$$a_i^j = \boldsymbol{R}_{\boldsymbol{a}_i}^{\ j}\boldsymbol{q}_i = \begin{bmatrix} e_x^j & e_y^j & e_z^j & r_y^j e_z^j - r_z^j e_y^j & r_z^j e_x^j - r_x^j e_z^j & r_x^j e_y^j - r_y^j e_x^j \end{bmatrix} \begin{bmatrix} q_x^i \\ q_y^i \\ q_z^i \\ q_{Rx}^i \\ q_{Ry}^i \\ q_{Rz}^i \end{bmatrix} \tag{16}$$

Where r^j are the distances of the acceleration DOF j respect to GR_i for each direction, and e^j are the projections of the DOF j direction to each of the unitary vectors. It can be noticed that to be able to calculate $\boldsymbol{q}_i$ in an inverse manner, a minimum number of 6 equations are needed to construct the $\boldsymbol{R}_{\boldsymbol{a}_i}$ matrix, however, a higher number is recommended in order to overdetermine the system [17]. Those singular equations are assembled for every individual geometrical reduction, which in turn can be assembled to form the global geometrical reduction system of the component, as shown in eq. (17).

$$\boldsymbol{a} = \boldsymbol{R}_{\boldsymbol{a}}\boldsymbol{q} = \begin{bmatrix} \boldsymbol{a}_1 \\ \vdots \\ \boldsymbol{a}_{N_i} \end{bmatrix} = \begin{bmatrix} \boldsymbol{R}_{\boldsymbol{a}_1} & \cdots & \boldsymbol{0} \\ \vdots & \ddots & \vdots \\ \boldsymbol{0} & \cdots & \boldsymbol{R}_{\boldsymbol{a}_{N_i}} \end{bmatrix} \begin{bmatrix} \boldsymbol{q}_1 \\ \vdots \\ \boldsymbol{q}_{N_i} \end{bmatrix} \tag{17}$$

Where N_i is the number of individual geometrical reductions. This equation system allows to calculate the reduced acceleration DOFs $\boldsymbol{q}$ by matrix inversion using the pseudoinverse of $\boldsymbol{R}_{\boldsymbol{a}}$ with eq. (18).

$$\boldsymbol{q} = \left(\boldsymbol{R}_{\boldsymbol{a}}^{\ T}\boldsymbol{R}_{\boldsymbol{a}}\right)^{-1}\boldsymbol{R}_{\boldsymbol{a}}^{\ T}\boldsymbol{a} = \boldsymbol{T}_{\boldsymbol{a}}\boldsymbol{a} \tag{18}$$

A similar reasoning can be applied to the input DOFs. When a set of forces is applied on a region that is assumed to be rigid, the resultant force reduced to any point can be calculated using analogous geometrical relationships, as shown in eq. (19).

$$\boldsymbol{m}_i = \boldsymbol{R}_{\boldsymbol{f}_i}\boldsymbol{f}_i = \begin{bmatrix} \boldsymbol{R}_{\boldsymbol{f}_i}^{1} & \cdots & \boldsymbol{R}_{\boldsymbol{f}_i}^{N_{f_i}} \end{bmatrix} \begin{bmatrix} f_i^1 \\ \vdots \\ f_i^{N_{f_i}} \end{bmatrix} \tag{19}$$

With $\boldsymbol{R}_{\boldsymbol{f}_i}^{j}$ being a matrix that contains the geometrical relationships of the rigid body behavior for the input DOF j and $\boldsymbol{m}_i$ being the resultant reduced forces for the geometrical reduction i. N_{f_i} is the number of force DOFs for the geometrical reduction i. Every force f_i^j generates a set of 6 resultant forces in the region according to eq. (20).

$$\boldsymbol{m}_i = \begin{bmatrix} m_x^i \\ m_y^i \\ m_z^i \\ m_{Rx}^i \\ m_{Ry}^i \\ m_{Rz}^i \end{bmatrix} = \sum_{j=1}^{N_{f_i}} \boldsymbol{R}_{\boldsymbol{f}_i}^{j} f_i^j = \sum_{j=1}^{N_{f_i}} \begin{bmatrix} e_x^j \\ e_y^j \\ e_z^j \\ r_y^j e_z^j - r_z^j e_y^j \\ r_z^j e_x^j - r_x^j e_z^j \\ r_x^j e_y^j - r_y^j e_x^j \end{bmatrix} f_i^j \tag{20}$$

It can be noticed that to be able to calculate $\boldsymbol{f}_i$ in an inverse manner, a minimum number of 6 equations are needed to construct the $\boldsymbol{R}_{\boldsymbol{f}_i}$ matrix, however, a higher number is recommended in order to overdetermine the system. Those singular equations are assembled for every individual geometrical reduction, which in turn can be assembled to form the global geometrical reduction system of the component, as shown in eq. (21).

$$\boldsymbol{m} = \boldsymbol{R}_{\boldsymbol{f}}\boldsymbol{f} = \begin{bmatrix} \boldsymbol{m}_1 \\ \vdots \\ \boldsymbol{m}_{i_N} \end{bmatrix} = \begin{bmatrix} \boldsymbol{R}_{\boldsymbol{f}_1} & \cdots & \boldsymbol{0} \\ \vdots & \ddots & \vdots \\ \boldsymbol{0} & \cdots & \boldsymbol{R}_{\boldsymbol{f}_{N_i}} \end{bmatrix} \begin{bmatrix} \boldsymbol{f}_1 \\ \vdots \\ \boldsymbol{f}_{N_i} \end{bmatrix} \tag{21}$$

This equation system allows to calculate one possible set of $\boldsymbol{f}$ that could generate the resulting reduced forces $\boldsymbol{m}$ by matrix inversion using the pseudoinverse of $\boldsymbol{R}_{\boldsymbol{f}}$, as shown in eq. (22).

$$\boldsymbol{f} = \boldsymbol{R}_{\boldsymbol{f}}^{T}\left(\boldsymbol{R}_{\boldsymbol{f}}\boldsymbol{R}_{\boldsymbol{f}}^{T}\right)^{-1}\boldsymbol{m} = \boldsymbol{T}_{\boldsymbol{f}}\boldsymbol{m} \tag{22}$$

Both acceleration and forces geometrical reductions can be applied to the FRF matrix of the system to calculate $\boldsymbol{Y}_{\boldsymbol{GR}}$, the reduced FRF matrix, according to eq. (23).

$$\boldsymbol{a} = \boldsymbol{Y}\boldsymbol{f} = \boldsymbol{R}_{\boldsymbol{a}}\boldsymbol{q} = \boldsymbol{Y}\boldsymbol{T}_{\boldsymbol{f}}\boldsymbol{m} \rightarrow \boldsymbol{q} = \boldsymbol{T}_{\boldsymbol{a}}\boldsymbol{Y}\boldsymbol{T}_{\boldsymbol{f}}\boldsymbol{m} = \boldsymbol{Y}_{\boldsymbol{GR}}\boldsymbol{m} \tag{23}$$

This technique will be applied in the experimental setup to both forces and accelerations, in the connections, to properly accomplish the FBS (fig. 6) and to calculate blocked forces.

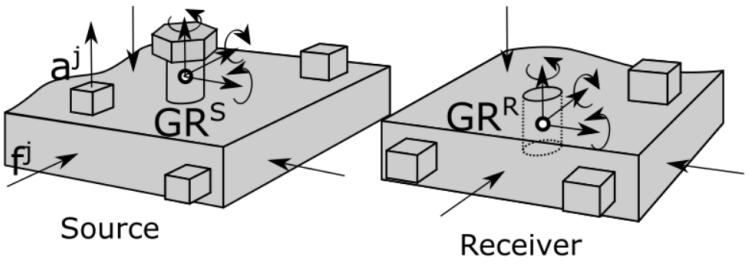


Figure 6: Geometrical reduced DOFs for an FBS

3 Experimental results

3.1 Test setup

For the experimental validations, three components are combined and tested in two setups. One component is used as a vehicle resemblance structure, made mainly by steel bars and a cavity. A second component is considered as a test bench to characterize the source. A star shaped aluminum plate constitutes the source. The sensors and bolts are considered part of the components in order to avoid mass loading effects. For all the components the FRFs are measured in coupled and uncoupled conditions using and impact hammer.

The first setup, consisting of the source on the test bench (fig 7(a)), is used to characterize the source by a set of blocked forces. The second setup, consisting of the source assembled with the vehicle structure (fig 7(b)), is used to validate the results of the component-based TPA process. As input force, a closed loop controlled mini shaker (resembling the source mechanism) exciting frequencies between 20 and 1500 Hz, is used.

The FRFs used to calculate the blocked forces are obtained by applying geometrical reduction from the impact points close to the connection to the center of each connection. However, in both setups and the uncoupled source, the impact points for FRFs measurement at the connection are in the same locations, so the geometrical reduction to calculate the blocked forces is the same for both setups. This means that the blocked forces transfer is equivalent to a pseudoforces transfer, as this geometrical reduction doesn't have an influence on the prediction.

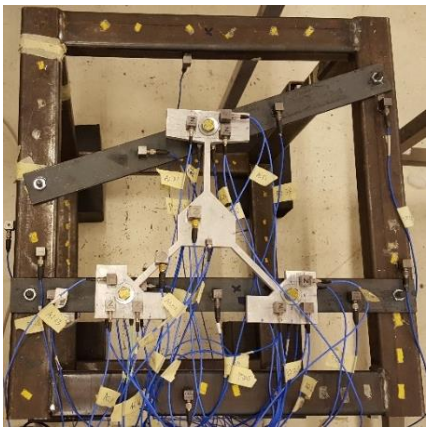
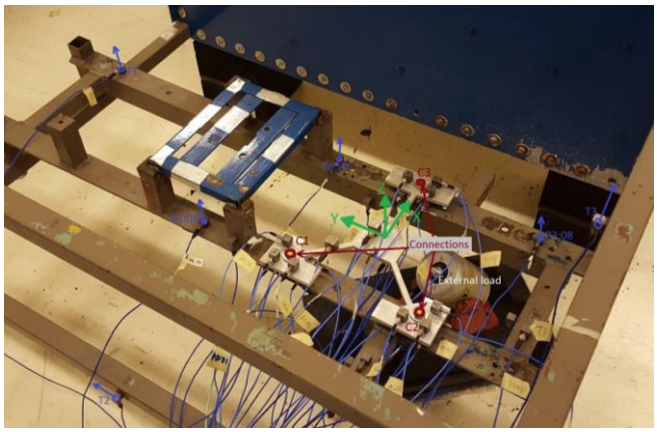
a)  b) 

Figure 7: Experimental setups. (a) Test bench. (b) Vehicle setup.

The source is connected with each receiver with 3 bolted connections, which are modelled as punctual connections. As the connections are rigid and restrict all the displacements, 6 DOFs per connection are considered in the coupling. In this way we try to characterize the complete coupling interface, which is needed for an adequate model [18]. To calculate reduced forces and accelerations, in each connection of both, source and receiver structures, 3 triaxial accelerometers and 6 impact points are used per connection (fig 8(a) and 8(b)). Additionally, 9 extra indicators are instrumented in the uncoupled test bench for a total of 36 indicators, to achieve an overdetermination of 2 in the blocked forces calculation. 3 targets instrumented in the vehicle structure (T1, T2, T3 in fig 7(b)) are used for validation purposes. The steps to validate the process are schematically depicted in figure 9.

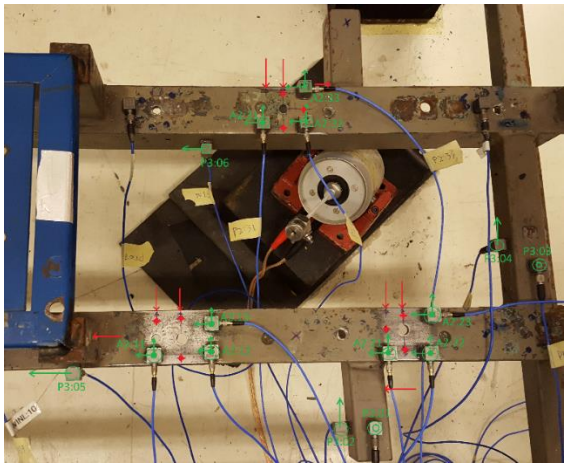
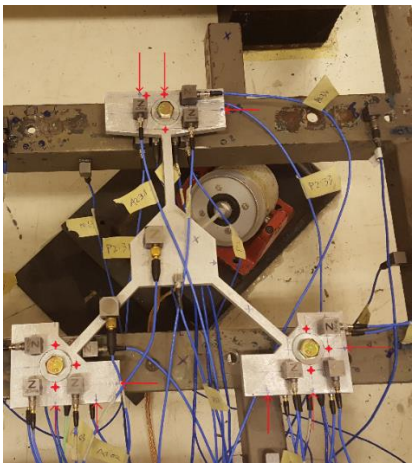
a)  b) 

Figure 8: Vehicle setup impacts (red dots and lines) and accelerometers location close to the connections. (a) Uncoupled. (b) Coupled.

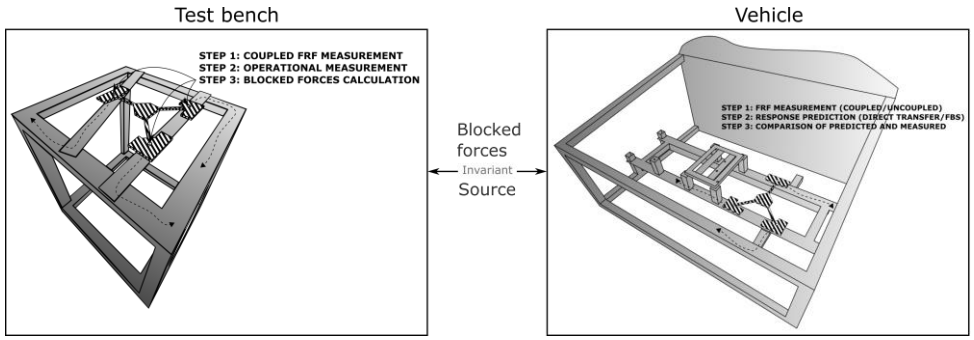


Figure 9: Schematic description of the component-based TPA process steps. (left) Test bench. (right) Vehicle structure.

To properly validate the results, improve stability and optimize the method, different sets of DOFs (presented in table 1) are used to calculate the blocked forces, and the obtained results are compared.

Label	Description
All indicators	The 36 DOFs indicators in the receiver, not GR
Without Rz	Excluding the DOFs of moments in Z direction for each connection
Without Rx Ry Rz	Excluding the DOFs of all the moments for each connection
Only Passive Connections	Indicators only at the connections of the receiver (18 GR DOFs)
Active and passive	Indicators in the source close to the connections and indicators in the receiver (theoretically wrong)
Only active	Indicators in the source only, close to the connections (theoretically wrong)

Table 1: Sets of DOFs used for the inversion.

The exclusion of Rz is done because of its lower contribution compared with other DOFs. Exclusion of moments is done as well to check negligibility of certain DOFs and the degree of translational DOFs sufficiency when characterizing a lowly damped and rigidly coupled structure.

The inclusion of source indicators pursues the improvement of the condition number and the overdetermination of the system. To reduce the error, the accelerometers of the source are in a region close to the connection that is assumed to behave rigidly together with the receiver side of the connection. Even though strictly speaking this is theoretically wrong, the error made by its inclusion may be lower compared to the potential numerical errors of an ill-conditioned system.

3.2 In-situ validation

The first validation consists of the in-situ validation. The blocked forces are calculated and then used to predict the response in the same structure, in targets that were not used for the inversion, as shown in eq. (24).

$$\boldsymbol{F}_{bl}^{SR_1} = \boldsymbol{Y}_{rc}^{SR_1\,-1}\boldsymbol{a}_{r}^{SR_1} \rightarrow \boldsymbol{a}_{r_T}^{SR_1} = \boldsymbol{Y}_{r_Tc}^{SR_1}\boldsymbol{F}_{bl}^{SR_1} \tag{24}$$

Where r_T refers to the target DOFs. Fig 10 shows a very good match between the measured and predicted target spectra over the entire frequency range. This validation can give an idea of the quality of the blocked forces calculation for the structure but is not really helpful with respect to assess the performance when transferred to a different one. Being the indicators and targets in the same structure, the dominant mechanisms of vibration transmission are very similar, and the matching of the predicted acceleration shows too optimistic results. Moreover it doesn't provide any validation for the FBS since the inversion is made using measured coupled FRFs.

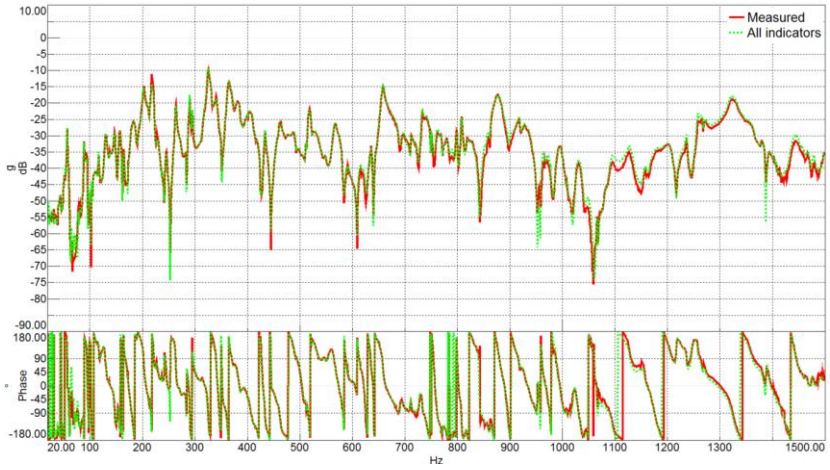


Figure 10: In-situ validation in target T3.

However, already in this validation some differences between the different sets of DOFs explained before can be observed. The results of the Frequency Response Assurance Criterion (FRAC), applied in the whole frequency range to the measured and predicted spectra for every different set of DOFs, are shown in table 2. For instance, the best matches are achieved when using indicators located only in the receiver, whether in the connections or not. While the performance worsens when excluding moments and when using active side indicators. The worst results are obtained if all the moments are excluded and if only active side indicators are used.

Label	FRAC value
All indicators	0.9801
Without Rz	0.9770
Without Rx Ry Rz	0.7942
Only Passive Connections	0.9784
Active and passive	0.9753
Only active	0.8311

Table 2: FRAC for each set of indicators in the in-situ validation.

3.3 Transferability validation

The second step in the validation is the transferability validation. The blocked forces are calculated in the test bench structure, and then used to predict responses in the vehicle structure, using again measured coupled FRFs, as shown in eq. (25).

$$\boldsymbol{F}_{bl}^{SR_1} = \boldsymbol{Y}_{rc}^{SR_1\,-1}\boldsymbol{a}_r^{SR_1} \rightarrow \boldsymbol{a}_r^{SR_2} = \boldsymbol{Y}_{rc}^{SR_2}\boldsymbol{F}_{bl}^{SR_1} \tag{25}$$

Where R_1 and R_2 refer to the two different receiver structures. From the figure 11 it can be noticed that the accuracy of the prediction is very good up to 500 Hz, and it lowers in general from 500 Hz toward the high frequencies.

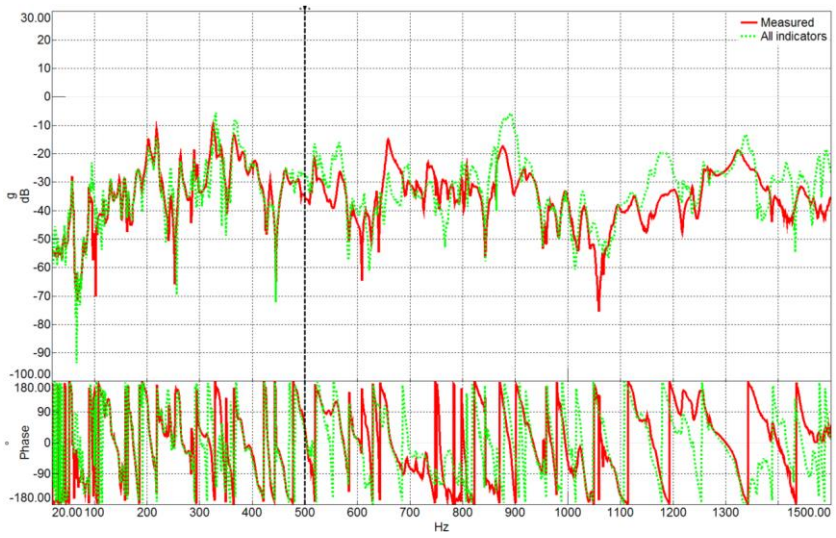


Figure 11: Transferability validation in target T3.

Again, similarly to the in the in-situ validation, the best results are achieved for the cases using indicators available on the receiver.

As well as for the in-situ validation, excluding moments (figure 12) or including source indicators performs generally worse and at least with no improvement compared to the usage of indicators only in the receiver, observation supported by the FRAC, when evaluated in regions without numerical problems, as shown in table 3.

Label	FRAC value
All indicators	0.8475
Without Rx Ry Rz	0.0275
Only Passive Connections	0.8626
Only active	0.7370

Table 3: FRAC for each set of indicators in the transferability validation.

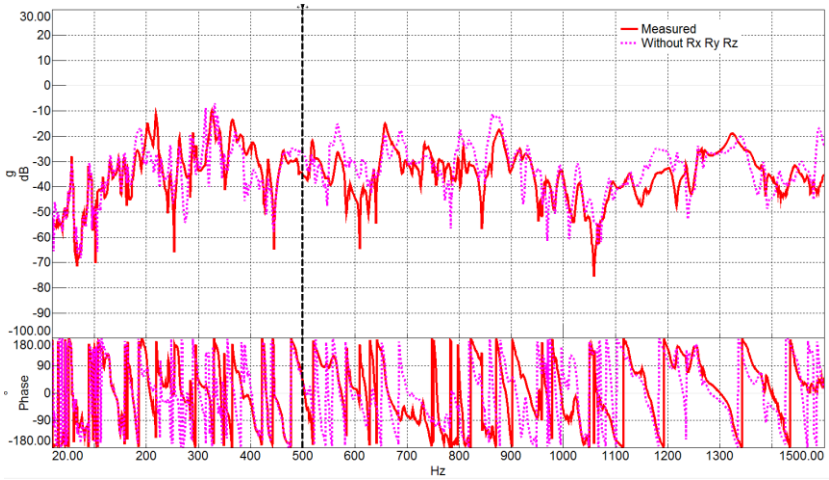


Figure 12: Transferability validation excluding moments in target T3.

3.4 Transferability with FBS validation

Finally, the transferability of blocked forces using FBS is evaluated as well. The blocked forces are calculated in the test bench structure, and then used to predict responses in the vehicle structure, using coupled FRFs calculated with FBS, as shown in eq. (26).

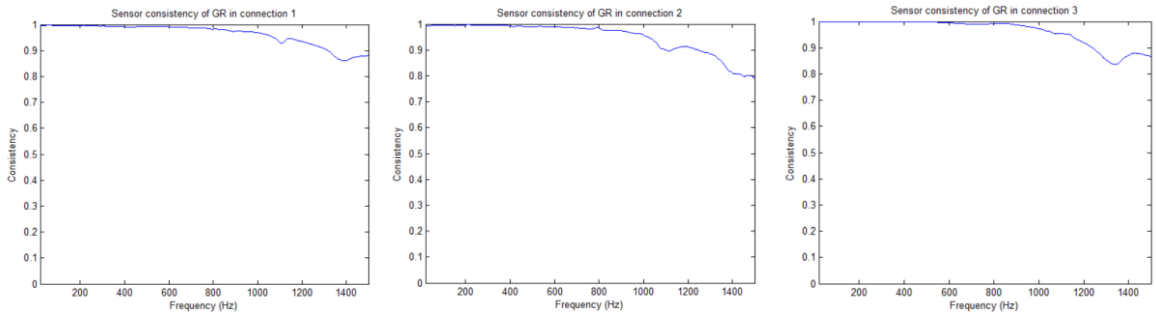
$$\boldsymbol{F}_{bl}^{SR_1} = \boldsymbol{Y}_{rc}^{SR_1}{}^{-1}\boldsymbol{a}_r^{SR_1} \rightarrow \boldsymbol{a}_r^{SR_2} = \boldsymbol{Y}_{rc}^{R_2}\left[\boldsymbol{Y}_{cc}^{S} + \boldsymbol{Y}_{cc}^{R_2}\right]^{-1}\boldsymbol{Y}_{cc}^{S}\boldsymbol{F}_{bl}^{SR_1} \tag{26}$$

In this way, this validation takes into account the effects of the transferability and the FBS coupling. Geometrical reduction is applied to the connections of source and receiver in order to make the coupling, so the rigidity hypothesis will play a determining role in the validation at higher frequencies.

In order to assess the quality of the geometrical reduction the concept of sensor consistency [19] is introduced. This sensor consistency evaluates the similarity between the theoretical rigid behavior and the real measured behavior of the geometrical points where the accelerometers are, for a given force DOF, using a MAC between both acceleration vectors:

$$\rho^2 = \mathrm{MAC}(\boldsymbol{R}_{\boldsymbol{a}}\boldsymbol{q}, \boldsymbol{a}) = \mathrm{MAC}(\tilde{\boldsymbol{a}}, \boldsymbol{a}) = \frac{(\tilde{\boldsymbol{a}}^H\boldsymbol{a})(\boldsymbol{a}^H\tilde{\boldsymbol{a}})}{(\tilde{\boldsymbol{a}}^H\tilde{\boldsymbol{a}})(\boldsymbol{a}^H\boldsymbol{a})} \tag{27}$$

Where ρ^2 is the consistency value, ranging from 0 to 1. According to that, a decrease of accuracy would be expected as the frequency increases, which would be added to the effects of the transferability. The product of the consistency for every force DOF is plot in figure 13 for each connection.



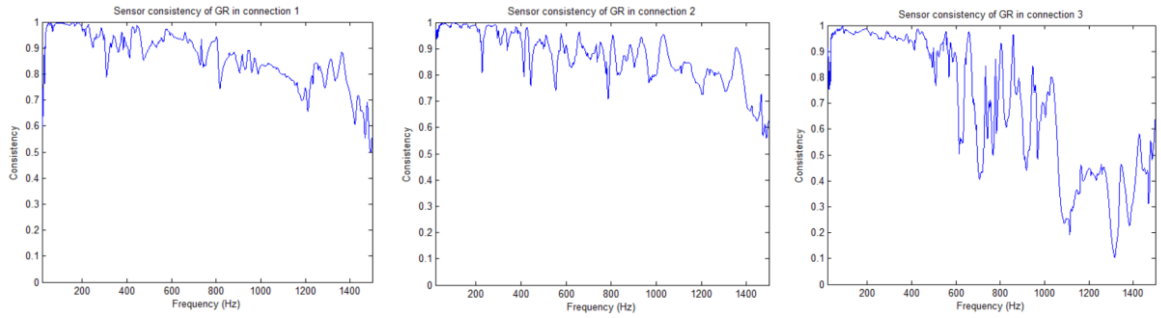


Figure 13: Product of sensor consistency for the source (up) and for the vehicle structure (down).

A comparison between the measured target acceleration and the predicted values using transferability with FBS is shown in figure 14.

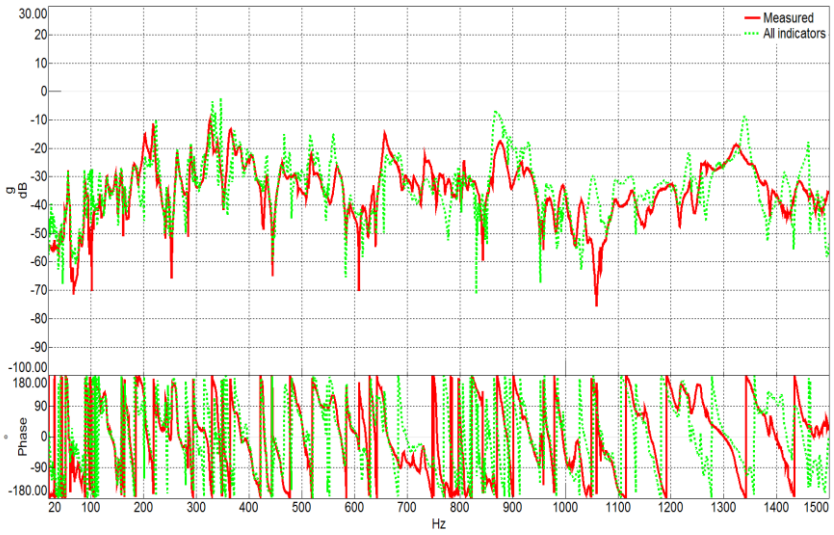


Figure 14: Transferability with FBS validation in target T3.

As expected, the highest predictive value is again obtained up to 500 Hz. However, the predicted vibration spectrum seems to be slightly more noisy when compared to the prediction obtained by transferability of blocked forces using measured coupled FRFs, as shown in figure 11.

In this case the differences between the different sets of indicators might be less noticeable due to the accumulated errors in load characterization, geometrical reduction and FBS calculation, and for this reason are not presented.

4 Conclusions

This work has investigated the joint application of techniques that allow the prediction of the behavior of a source in a given receiver, going from source characterization to the calculation of the response. This methodology has already shown some value in similar rigidly connected and low damped structures, in either academic setups [20] or industrial applications [21][22][23]. In this paper the prediction process steps, including the use of FBS equations, have been validated in an academic setup.

For this setup, the vibration prediction using transferability of blocked forces performs slightly better before the FBS application. However, it is found that in the whole frequency range the additional error of the FBS application is considerably lower than the error already made by the calculation of blocked forces and their transferability using measured coupled FRFs. This leads to the conclusion that the main challenge of the

method could be the correct blocked forces estimation (in a stable and complete system) for its transferability, and not mostly the FBS itself. Furthermore, using FBS for blocked forces transferability has the following advantages: i) it allows to couple a source with a receiver not manufactured yet, by means of simulated data of the receiver; ii) it allows to calculate the coupled FRFs of the assembly and the exerted contact forces between source and receiver without being physically coupled.

For this case, theory and experience support consistently the idea of using as many indicators as possible being in the receiver only. In addition, due to its low excitation and contribution, Rz could be neglected from the connection DOFs without detriment to the result, but without a clear improvement either. However, neglecting moments should only happen in the case that the setup and operational condition strongly and reasonably advice to, and not in a general way. As shown in this experimental case of rigid connections, neglecting moments clearly worsen the prediction results.

The accuracy of the prediction is in general good up to 500 Hz, taking into account that is a low damped structure, with a very light and flexible source compared to the receiver, and a rigid connection. Results and conclusions could be carefully extrapolated to similar structures (e.g. steering system) but might vary for others with different conditions of coupling, mass and stiffness (e.g. combustion engine). A future validation of interest would be trying to expand the applicability to assembled structures connected with rubber mounts, which for now remains out of the reach of this work.

Acknowledgements

The authors gratefully acknowledge the European Commission for its support of the Marie Sklodowska Curie program through the ETN PBNv2 project (GA 721615).

References

[1] Van der Auweraer, H. Wyckaert, K. Hendricx, W. and van der Linden, *Noise and vibration transfer path analysis, Lecture series-van Kareman Institute for fluid dynamics*, 2, pp.I1-I22.

[2] P. Van de Ponseele, H. Van der Auweraer, K. Janssens, *Source-Transfer-Receiver approaches: a review of methods, Proceedings of ISMA2012, International Conference on Noise and Vibration Engineering, Leuven, Belgium, 2012*, Leuven (2012).

[3] H. Van der Auweraer, P. Mas, S. Dom, A. Vecchio, K. Janssens and P. Van de Ponseele, *Transfer path analysis in the critical path of vehicle refinement: the role of fast, hybrid and operational path analysis. Proc. SAE N&V Conf., 2007 May 14-17*, paper 2007-01-2352.

[4] H. A. Bonhoff, B. A. T. Petersson, *Towards a structure-borne sound source characterization for low-noise design, Institute of Fluid Mechanics and Engineering Acoustics, TU Berlin, Berlin, Germany*, D-10587.

[5] M. H. A. Janssens, J. W. Verheij, *A pseudo-forces methodology to be used in characterization of structure-borne sound sources*, Applied Acoustics, Vol. 61, Elsevier Science (2000), pp. 285-308.

[6] A. Elliott, *Characterisation of structure borne sound sources in-situ*, University of Salford, Acoustics Research Centre, School of Computing, Science and Engineering, United Kingdom (2009).

[7] D. de Klerk, D. J. Rixen, S. N. Voormeeren, *General framework for dynamic substructuring: history, review and classification of techniques*, AIAA J. 46 (5) (2008) pp. 1169-1181.

[8] R. E. D. Bishop and D. C. Johnson, *The Mechanics of Vibrations*, Cambridge University Press, United Kingdom (1960).

[9] B. Jetmundsen, R. L. Bielawa, W. G. Flannelly, *Generalized Frequency Domain Substructure Synthesis*, Journal of the American Helicopter Society 33.1 (1988), pp. 55–64.

[10] M. Häußler, D. J. Rixen, *Optimal transformation of frequency response functions on interface deformation modes, International Modal Analysis Conference IMAC, Bethel, USA, 2017 January*, Bethel (2017).

[11] M. V. van der Seijs, et al., *General framework for transfer path analysis: History, theory and classification of techniques*, Mechanical Systems and Signal Processing (2015).

[12] E. A. Pasma, M. V. van der Seijs, D. D. van den Bosch, M. W. F. Wernsen, *A Benchmark Structure for Validation of Blocked Force Transfer Path Analysis Techniques, 24th International Congress on Sound and Vibration, London, United Kingdom, 2017 July 23-27*, London (2017).

[13] A. S. Elliott, A. T. Moorhouse, T. Huntley, S. Tate, *In-situ source path contribution analysis of structure borne road noise*, Journal of Sound and Vibration, Vol. 332, Elsevier (2013), pp. 6276-6295.

[14] D. J. Rixen, et al., *Vibration source description in substructuring: A theoretical depiction*, Mechanical Systems and Signal Processing (2015).

[15] D. de Klerk, D. J. Rixen, *Component transfer path analysis method with compensation for test bench dynamics*, Mechanical Systems and Signal Processing, Vol. 24, Elsevier (2010), pp. 1693-1710.

[16] Sakai T., Terada M., Ono S., et al. *Development procedure for interior noise performance by virtual vehicle refinement, combining experimental and numerical component models, SAE International, Warrendale, Pennsylvania, 2001*, Warrendale (2001).

[17] M. V. van der Seijs, *Experimental Dynamic Substructuring, Analysis and Design Strategies for Vehicle Development*, Delft University of Technology, The Netherlands (2016).

[18] J. W. R. Meggitt, A. T. Moorhouse, A. S. Elliott, *On the Problem of Describing the Coupling Interface Between Sub-structures: An Experimental Test for 'Completeness'*, A. Linderholt et al. (eds.), *Dynamics of Coupled Structures, Volume 4, Conference Proceedings of the Society for Experimental Mechanics Series, 2018*.

[19] M. V. van der Seijs, D. D. van den Bosch, D. J. Rixen, D. de Klerk, *An improved methodology for the virtual point transformation of measured frequency response functions in dynamic substructuring*, M. Papadrakakis, V. Papadopoulos, V. Plevris (eds.), *4th ECCOMAS Thematic Conference on Computational Methods in Structural Dynamics and Earthquake Engineering, Kos Island, Greece, 2013 June 12-14*, Kos Island (2013).

[20] G. Banwell, R. Faventi, *Assessment of experimental techniques to characterize the vibration source strength of a motor radially mounted with resilient elements, Proceedings of International Conference on Noise and Vibration Engineering ISMA 2016, Leuven, Belgium, 2016 September*, Leuven (2016).

[21] M. van der Seijs, E. Pasma, D. de Klerk, D. Rixen, *A robust Transfer Path Analysis method for steering gear vibrations on a test bench, Proceedings of ISMA2014 International Conference on Noise and Vibration Engineering, Leuven, Belgium, 2014 September*, Leuven (2014), pp. 4027-4040.

[22] M. Sturm, T. Alber, A. T. Moorhouse, D. Zabel, Z. Wang, *The in-situ blocked force method for characterization of complex automotive structure-borne sound sources and its use for virtual acoustic prototyping, Proc. Int. Conf. On Noise & Vibr. Engineering (ISMA), Leuven, Belgium, 2016*, Leuven (2016).

[23] M. Sturm, C. Marchand, M. Priebe, A. T. Moorhouse, *Robust NVH Development of Steering Systems Using In-Situ Blocked Forces from Measurements with Low-Noise Driver Simulators, Noise-Con 2017, Grand Rapids, MI, 2017 June 12-14*, Grand Rapids (2017).

Passive multi-mode piezoelectric shunt damping: an approach based on matrix inequalities

M. Berardengo[1], S. Manzoni[2], M. Vanali[1], A.M. Conti[2]
[1] Università degli Studi di Parma - Department of Engineering and Architecture
Parco Area delle Scienze, 181/A – 43124 Parma (Italy)
e-mail: **marta.berardengo@unipr.it**

[2] Politecnico di Milano - Department of Mechanical Engineering
Via La Masa, 34 – 20156 Milan (Italy)

Abstract
Piezoelectric shunt damping is a well-known technique for suppressing vibrations in light mechanical systems. The method is based on the connection of a properly designed electrical network (shunt circuit) to a piezoelectric actuator bonded to the vibrating structure. This network can be either passive (i.e. made from resistances, capacitances and inductances) or active. When active shunts are used, possible problems related to instability of the system can raise. This paper addresses a new approach for designing shunt electrical circuits allowing to damp more than one mechanical mode of the structure at the same time with a single piezoelectric actuator. Moreover, the method assures to design passive shunt impedances, thus avoiding instability problems. Starting from a state space description of the electro-mechanical system, the definition of the shunt circuit is achieved using an approach based on matrix inequalities, which allows to design shunt circuits with different goals by expressing the desired target as a single or a system of matrix inequalities.

1 Introduction

The use of piezoelectric shunt is a renewed approach for damping vibrations [1]. Many approaches are possible: from the use of passive shunt networks (e.g. [2–6]), to the use of negative capacitances for enhancing the damping performance (e.g. [7–13]), from the employment of non-linear impedances (e.g. [14–16]), to the use of networks of piezoelectric actuators (e.g. [17–22]).

Here, the discussion is focused on shunt methods which allow to use even a single piezoelectric actuator for controlling more than one mode at the same time and ensure the passivity of the electro-mechanical system (EMS, composed by the vibrating structure, the piezoelectric actuator bonded to the structure and the shunt electric impedance). Indeed, such an approach, based on the EMS passivity, plays an important role, especially in the industrial and aerospace fields, thanks to its passivity, lack of instability, and lack of additional devices.

When the aim of the control system is to act on several modes, using a single piezoelectric actuator, there are different methods to design proper passive shunt electrical networks.

Hollkamp firstly proposed an impedance design technique employing a single piezoelectric patch working on different modes at the same time [23]. The proposed network design is made from as many branches connected in parallel as the number of modes to be damped. The main problems related to this method are the cross-talk between the branches of the circuit, which requires perfectly decoupled modes, and the complexity of the procedure to fix the values of all the electric components.

Wu [24] and Behrens et al. [25] introduced the current blocking (CB) and current flowing (CF) methods, respectively. Again, the shunt impedance is made from as many branches as the number of modes to control, and all the branches are connected in parallel.

Although the CB was proposed to simplify somewhat the design of the shunt impedance, the complexity of the circuit is evident, especially when the number of modes to be damped increases. Another problem with the CB method is that there are some degrees of freedom in the tuning of the network: the values of some electric components must be fixed arbitrarily without any guidelines, which often results in non-optimal damping actions.

As for the CF technique, each branch is made from three elements: a resistance, a capacitance, and an inductance and the values of the resistances in the shunt impedance must be fixed by numerical minimization. Furthermore, there are some degrees of freedom that lead to a non-optimal solution in this case as well, although some guidelines to overcome this problem were proposed [26]. There are also cross-talk effects that are not accounted for in the tuning procedure and can be solved just by using numerical minimizations.

Fleming et al. [27] proposed a method that can be seen as a mix of CB and CF. The shunt network is a combination of cells connected in series and parallel but, like in other approaches, the main drawback of the method is that there are some degrees of freedom in the tuning of the network wich have to be arbitrarily fixed.

Despite all the described tuning strategies provide good damping performances, the values of some electric components must be fixed arbitrarily without any guidelines; as mentioned, this often results in non-optimal damping actions. Moreover, these approaches often do not allow for a specific control target to be set. Therefore, the aim of this paper is to present a new general approach to multi-mode vibration reduction which can be applied to any generic structure. Furthermore, the proposed approach is aimed at finding the optimal controller for given control applications, and it relies on the matrix inequality (MI) theory. The MI approach allows for a control target to be set (e.g. H_2 or H_∞ on acceleration, velocity, or displacement) and for constraints to be imposed on the control features. The particular focus is on passive control. Therefore, the method allows an expression of the shunt impedance to be found that satisfies the fixed control target, assuring that it can be realized by a passive physical network.

The paper structure is as follows: Section 2 presents the model used to describe the EMS and its state space expression. Such a way to express the system behavior is needed for using the matrix inequality approach, as explained in Section 3. Finally, Section 4 presents some experimental tests to show the reliability and effectiveness of the proposed approach.

2 Model of the system

The model of the EMS describes both the mechanical and the electrical dynamics. A generic structure excited by an external forcing $\mathbf{F}_{\text{ext}}$ is taken into account; the piezoelectric actuator used for damping is shunted by an impedance Z (see Figure 1a). Q_{p} is the charge in the upper electrode ($-Q_{\text{p}}$ in the lower electrode), and V_{p} is the voltage between the electrodes. The displacement W of any point x of the structure at time t can be expressed as a modal summation:

$$W(x,t) = \sum_{r=1}^{N} \Phi_r(x) q_r(t) \tag{1}$$

where q_r is the r^{th} modal coordinate, N is the number of modes considered (theoretically $N \to \infty$), and Φ_r is the rth eigenmode, scaled to the unit modal mass, of the structure. The modal coordinates are the solutions of the following problem [10,28–30]:

$$\ddot{q}_r + 2\xi_r\omega_r\dot{q}_r + \omega_r^2 q_r - \chi_r V_\mathrm{p} = F_r \qquad \forall\, r\epsilon\,\{1,\dots,N\} \tag{2}$$

$$C_\infty V_\mathrm{p} - Q_p + \sum_{l=1}^{N}\chi_l q_l + \frac{\int V_\mathrm{p}}{R_\mathrm{p}} = 0 \tag{3}$$

where ω_r is the r^{th} eigenfrequency of the EMS in short-circuit (SC, i.e. $Z = 0$), ξ_r is the associated non-dimensional damping ratio, and F_r is the harmonic modal force. χ_r is a modal coupling coefficient that describes the energy transfer between the piezoelectric patch and the r^{th} mode. Therefore, the behaviour of the EMS is described by two equations: Equation (2) and Equation (3). Equation (2) describes the equations of motion of the system. The term χ_r couples these equations of motion to Equation (3), which models the electric behaviour of the EMS (see Figure 1b, where the term $\sum_{l=1}^{N}\chi_l\dot{q}_l$ is abbreviated as $\dot{Q}_{\mathrm{cs}}$). R_p is the resistance associated with the piezoelectric patch, which is usually very high [31]. $\int V_\mathrm{p}$ is intended as an integral in time (i.e. $\int V_\mathrm{p}\mathrm{d}t$). C_∞ is the electrical capacitance of the piezoelectric patch with blocked structure, which also corresponds to the value of the capacitance at infinite frequency [10].

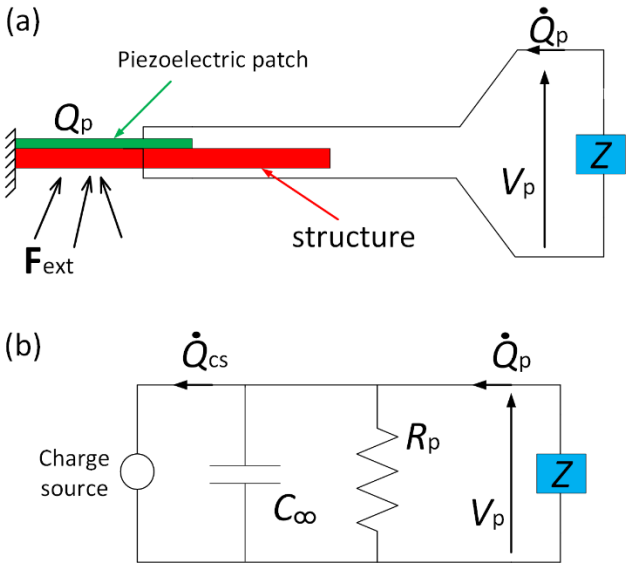


Figure 1: A generic structure with a shunted piezoelectric patch (a) and electric model of the EMS (b).

The terms χ_r can be found analytically [30], through a finite element model [29], or experimentally by measuring the effective coupling coefficients associated with each mode [32]. In case of low modal density, if only the modes between the u^{th} (i.e. $r = u$) and the h^{th} modes (i.e. $r = h$, with $h > u$) are considered, Equations (2) and (3) can be rearranged as:

$$\ddot{q}_r + 2\xi_r\omega_r\dot{q}_r + \omega_r^2 q_r - \chi_r V_\mathrm{p} = F_r \qquad \forall\, r\epsilon\,\{u,\dots,h\} \tag{4}$$

$$C_\infty V_\mathrm{p} - Q_\mathrm{p} + \sum_{l=u}^{h}\chi_l q_l + \frac{\int V_\mathrm{p}}{R_\mathrm{p}} + MV_\mathrm{p} = 0 \tag{5}$$

where M is a term that accounts for the contribution of the modes higher than the h^{th} mode. According to[10,11]:

$$M = \sum_{n=h+1}^{N} \frac{\chi_n^2}{\omega_n^2} \tag{6}$$

Therefore, Equation (5) can be written as:

$$C_{\text{p}} V_{\text{p}} - Q_{\text{p}} + \sum_{l=u}^{h} \chi_l q_l + \frac{\int V_{\text{p}}}{R_{\text{p}}} = 0 \tag{7}$$

with:

$$C_{\text{p}} = C_{\infty} + \sum_{n=h+1}^{N} \frac{\chi_n^2}{\omega_n^2} \tag{8}$$

C_{p} can be found by measuring the value of the capacitance of the piezoelectric actuator midway between ω_h and ω_{h+1} [32]. Thus, the dynamics of the EMS in the frequency range of interest is described by Equations (4) and (7). To use the matrix inequality approach to solve a given control problem, the EMS model needs to be represented in terms of state space variables. The state space representation provided in this paper plays a key role since it also allows the shunt impedance to be seen as a controller. Indeed, expressing Z as a controller allows the passivity requirement to be imposed directly on the impedance Z in the matrix inequality problem, which is one of the targets of the proposed control approach.

According to Equations (4) and (7), the following system of equations can be written:

$$\begin{cases} \ddot{q}_r + 2\xi_r \omega_r \dot{q}_r + \omega_r^2 q_r - \chi_r V_{\text{p}} = F_r & \forall\, r \epsilon \{u, \dots, h\} \\ \dot{q}_r = \dot{q}_r & \forall\, r \epsilon \{u, \dots, h\} \\ C_{\text{p}} V_{\text{p}} - Q_{\text{p}} + \sum_{l=u}^{h} \chi_l q_l + \frac{\int V_{\text{p}}}{R_{\text{p}}} = 0 \end{cases} \tag{9}$$

By defining:

$$\bar{V} = V_{\text{p}} \sqrt{C_{\text{p}}} \quad \text{and} \quad \bar{Q} = \frac{Q_{\text{p}}}{\sqrt{C_{\text{p}}}} \tag{10}$$

and defining the vector **g** of the state variables:

$$\mathbf{g} = \begin{bmatrix} \dot{q}_u \\ q_u \\ \vdots \\ \dot{q}_h \\ q_h \\ \int \bar{V} \end{bmatrix} \tag{11}$$

the system described by Equation (9) can be written in state space notation:

$$\begin{cases} \dot{\mathbf{g}} = \mathbf{A}\mathbf{g} + \mathbf{B}_{\mathrm{w}}\bar{Q} + \mathbf{B}_{\mathrm{f}}\mathbf{F}_{\mathrm{ext}} \\ z_{\mathrm{o}} = \mathbf{C}_{\mathrm{z}}\mathbf{g} + \mathbf{D}_{\mathrm{zw}}\bar{Q} + \mathbf{D}_{\mathrm{zf}}\mathbf{F}_{\mathrm{ext}} \\ y = \mathbf{C}_{\mathrm{y}}\mathbf{g} + \mathbf{D}_{\mathrm{yw}}\bar{Q} + \mathbf{D}_{\mathrm{yf}}\mathbf{F}_{\mathrm{ext}} \end{cases} \tag{12}$$

where z_{o} is the target variable of the control (e.g. the displacement W, velocity $\dot{W}$, and acceleration $\ddot{W}$ of the system computed at a given point x_{m} of the structure); y is the output of the system, which is $-\int \bar{V}$ in this case ($\int \bar{V}$ is intended as an integral in time $\int \bar{V}\mathrm{d}t$). Finally, $\bar{Q}$ is seen as a control action provided to the vibrating system. More details on the way to express the matrices of the state space expression can be found in [33].

The state space model describes the EMS as a controlled system via a feedback loop. The transfer function of the controller K can be expressed as:

$$K = \frac{\bar{Q}}{-\int \bar{V}} = \frac{\dot{Q}_{\mathrm{p}}}{-C_{\mathrm{p}}V_{\mathrm{p}}} = \frac{1}{C_{\mathrm{p}}Z} = \frac{Y}{C_{\mathrm{p}}} \tag{13}$$

where the admittance Y is $1/Z$. Thus, the model presented can describe the EMS as a system controlled by a feedback loop, and the controller is the electric admittance shunted to the piezoelectric actuator (divided by C_{p}). This control problem is an output feedback problem. It is now possible to set the control targets and the constraints on the controller structure. The next section discusses how to translate these requirements to matrix inequality problems and how to find the most suitable transfer function of Z.

3 The matrix inequality approach

In this section, the H_∞ control (chosen as an example) as well as the passivity of the controller are formulated as linear matrix inequality (LMI) problems. Control specifications for the closed-loop transfer function T_{zF} linking the disturbance F_{ext} (considering a single force F_{ext} acting as disturbance; however, this assumption does not cause any loss of generality) and the target variable of the control z_{o} are taken into account. Referring to Equation (12), T_{zF} can be expressed in the Laplace domain as:

$$T_{\mathrm{zF}} = \mathbf{C}_{\mathrm{z}}(s\mathbf{I} - [\mathbf{A} + \mathbf{B}_{\mathrm{w}}K\mathbf{C}_{\mathrm{y}}])^{-1}\mathbf{B}_{\mathrm{f}} + \mathbf{D}_{\mathrm{zw}}K\mathbf{C}_{\mathrm{y}}(s\mathbf{I} - [\mathbf{A} + \mathbf{B}_{\mathrm{w}}K\mathbf{C}_{\mathrm{y}}])^{-1}\mathbf{B}_{\mathrm{f}} + \mathbf{D}_{\mathrm{zf}} \tag{14}$$

where s is the Laplace operator, and $\mathbf{I}$ is the identity matrix. All the matrices that are always null in Equation (11) (i.e. regardless of whether the target variable is displacement, velocity, or acceleration) are neglected in Equation (14).

Formulating the controller K with a state space representation, the state space representation of the closed-loop system is then obtained:

$$\begin{cases} \dot{\mathbf{g}}_{\mathrm{cl}} = \mathbf{A}_{\mathrm{cl}}\mathbf{g}_{\mathrm{cl}} + \mathbf{B}_{\mathrm{cl}}F_{\mathrm{ext}} \\ z_{\mathrm{o}} = \mathbf{C}_{\mathrm{cl}}\mathbf{g}_{\mathrm{cl}} + \mathbf{D}_{\mathrm{cl}}F_{\mathrm{ext}} \end{cases} \tag{15}$$

where the closed-loop state vector is:

$$\mathbf{g}_{\mathrm{cl}} = \begin{Bmatrix} \mathbf{g} \\ \mathbf{g}_{\mathrm{k}} \end{Bmatrix} \tag{16}$$

$\mathbf{g}_{\mathrm{k}}$ is the vector of state variables of the controller. Refer to [33] for more details about the way to calculate the matrices $\mathbf{A}_{\mathrm{cl}}$, $\mathbf{B}_{\mathrm{cl}}$, $\mathbf{C}_{\mathrm{cl}}$, and $\mathbf{D}_{\mathrm{cl}}$. Therefore, the transfer function T_{zF} of Equation (14) can be expressed as a function of the closed-loop matrices using Equation (15):

$$T_{\mathrm{zF}} = \mathbf{C}_{\mathrm{cl}}(s\mathbf{I} - \mathbf{A}_{\mathrm{cl}})^{-1}\mathbf{B}_{\mathrm{cl}} + \mathbf{D}_{\mathrm{cl}} \tag{17}$$

In the MI approach, each control target or specification is expressed as a constraint on the admissible Lyapunov functions for the internally stable closed-loop system [34]:

$$\exists \quad V(\mathbf{g}_{\mathrm{cl}}) = \mathbf{g}_{\mathrm{cl}}^{\mathrm{T}}\mathbf{P}\mathbf{g}_{\mathrm{cl}}, \quad \mathbf{P} > 0 \quad : \quad \mathbf{A}_{\mathrm{cl}}^{\mathrm{T}}\mathbf{P} + \mathbf{P}\mathbf{A}_{\mathrm{cl}} < 0 \tag{18}$$

where V is a quadratic Lyapunov function, $\mathbf{P}$ the Lyapunov matrix, $\mathbf{A}_{\mathrm{cl}}$ is the state matrix of the system, and $\mathbf{g}_{\mathrm{cl}}$ is the closed-loop state-space vector. The superscript T indicates the transposed matrix.

Since the additional constraints are related to targets on the transfer function T_{zF} of Equation (17), the related MI formulation will be thus expressed as a function of the closed-loop matrices $\mathbf{A}_{\mathrm{cl}}$, $\mathbf{B}_{\mathrm{cl}}$, $\mathbf{C}_{\mathrm{cl}}$, and $\mathbf{D}_{\mathrm{cl}}$ (see Equation (19) further in the paper). Therefore, the solution of the MI problem will provide state matrices that satisfy the given specifications. Then, the controller K transfer function can be derived [33].

As for H_∞ control, the objective is to find a controller K such that $\|T_{\mathrm{zF}}\|_\infty$ is minimised. As shown in [35] and [34], there exists a controller K such that $\|T_{\mathrm{zF}}\|_\infty < \gamma$ and $\mathbf{A}_{\mathrm{cl}}$ is stable if and only if the following problem is feasible for some symmetric $\mathbf{P} > 0$, $\gamma > 0$, and $\mathbf{A}_{\mathrm{k}}$, $\mathbf{B}_{\mathrm{k}}$, $\mathbf{C}_{\mathrm{k}}$, and $\mathbf{D}_{\mathrm{k}}$ of compatible dimensions [36]:

$$\begin{bmatrix} \mathbf{A}_{\mathrm{cl}}^{\mathrm{T}}\mathbf{P} + \mathbf{P}\mathbf{A}_{\mathrm{cl}} & \mathbf{P}\mathbf{B}_{\mathrm{cl}} & \mathbf{C}_{\mathrm{cl}}^{\mathrm{T}} \\ \mathbf{B}_{\mathrm{cl}}^{\mathrm{T}}\boldsymbol{P} & -\gamma\mathbf{I} & \mathbf{D}_{\mathrm{cl}}^{\mathrm{T}} \\ \mathbf{C}_{\mathrm{cl}} & \mathbf{D}_{\mathrm{cl}} & -\gamma\mathbf{I} \end{bmatrix} < 0 \tag{19}$$

It follows that the solution of the problem requires minimising γ.

Other objectives can be set, alternatively or in parallel with the previous H_∞ control requirement (e.g. H_2 [34]). In this paper, special focus is related to the passivity of the controller and thus on the passivity of the shunt impedance (see Equation (13)), as previously mentioned.

Passivity can be expressed as an LMI as well, where the unknown variables are the controller matrices $\mathbf{A}_{\mathrm{k}}$, $\mathbf{B}_{\mathrm{k}}$, $\mathbf{C}_{\mathrm{k}}$, and $\mathbf{D}_{\mathrm{k}}$. If passivity is satisfied, then the transfer function of the controller is positive real.

Therefore, the controller passivity can be expressed as an LMI constraint using the positive real lemma [35]. It follows that a controller $K(s)$ is positive real if and only if there exists $\mathbf{P} > 0$ such that:

$$\begin{bmatrix} \mathbf{A}_{\mathrm{k}}^{\mathrm{T}}\mathbf{P} + \mathbf{P}\mathbf{A}_{\mathrm{k}} & \mathbf{P}\mathbf{B}_{\mathrm{k}} - \mathbf{C}_{\mathrm{k}}^{\mathrm{T}} \\ \mathbf{B}_{\mathrm{k}}^{\mathrm{T}}\mathbf{P} - \mathbf{C}_{\mathrm{k}} & -\mathbf{D}_{\mathrm{k}}^{\mathrm{T}} - \mathbf{D}_{\mathrm{k}} \end{bmatrix} \leq 0 \tag{20}$$

where $\mathbf{P}$ is the Lyapunov matrix.

Actually, Equations (19) and (20) are not LMIs since the dependence on the decision variables is not linear. As an example, referring to Equation (19), the expression $\mathbf{A}_{\mathrm{cl}}^{\mathrm{T}}\mathbf{P} + \mathbf{P}\mathbf{A}_{\mathrm{cl}}$ is not affine in the variables $\mathbf{P}$ and $\mathbf{A}_{\mathrm{cl}}$ because it involves the product between the Lyapunov matrix $\mathbf{P}$ and the controller variables which are included in the $\mathbf{A}_{\mathrm{cl}}$ expression. Hence, these problems are non-linear and cannot be solved by LMI optimisation (e.g. using the ellipsoid method or the interior-point method [37,38]). However, for the state feedback case and even for the output feedback systems (which is the case considered in this paper), there exists a change of variables that makes all the inequalities affine in a new set of unknowns, making the constraints linear and easily solvable [34].

Even multi-objective problems [34,39] can be solved, e.g. H_∞ control together with controller passivity. In this case Equations (19) and (20) must be fulfilled at the same time. This makes the multi-objective output feedback control problem a non-linear matrix inequality problem; more specifically, it becomes a bilinear matrix inequality (BMI) problem. One suitable approach to solve such a problem is the use of non-linear solvers [40,41]; refer to [33] for more details about the procedure to be used and the algorithms, and to the next section for the experimental validation of passive multi-objective controllers (i.e. BMI controllers).

4 Experimental tests

The experimental setup was made from an aluminum cantilever beam with one piezoelectric patch bonded at its clamped end. The beam was 25 mm wide, 161 mm long, and 1.1 mm thick; the piezoelectric patch was 25 mm wide, 51 mm long, and 0.38 mm thick. The structure was excited by means of a contactless actuator composed of a coil and a magnet bonded to the beam near its tip. The current flowing in the coil results in a proportional force exerted on the beam [42]. The current was measured using a current clamp, and the response of the structure was measured through a laser Doppler velocimeter in a co-located position with the exerted force (on the other side of the beam). The third and fourth eigenmodes were considered, and their modal data are gathered in Table 1. The eigenfrequencies and non-dimensional damping ratios were estimated by an experimental modal analysis with the piezoelectric patch short-circuited. χ_r was estimated by means of measurements of the r^{th} coupling coefficient $k_r^{\mathrm{eff}} = \sqrt{(\omega_{r,\mathrm{oc}}^2 - \omega_r^2)/\omega_r^2}$ ($\omega_{r,\mathrm{oc}}$ is the r^{th} eigenfrequency with the piezoelectric patch in open-circuit (OC)) and then performing the following computation [10]:

$$\chi_r = k_r^{\mathrm{eff}}\omega_r\sqrt{C_{\mathrm{pr}}}. \tag{21}$$

where C_{pr} is the measured piezoelectric capacitance value after the r^{th} eigenfrequency.

Mode number	$\omega_r/(2\pi)$ [Hz]	ξ_r [%]	k_r^{eff}
3	500.98	0.40	0.0400
4	1004.39	0.44	0.0924

Table 1: Modal parameters identified experimentally

Many tests have been carried out to validate the proposed approach based on matrix inequalities, but only two are described here for brevity. The first test was carried out without synthetizing a real passive shunt impedance (i.e. one made from resistances, capacitances, and inductances). Instead, a synthetic device was used to simulate the shunt impedance [43]. This approach allowed the authors to avoid any possible uncertainty on the values of the electric elements composing the shunt impedance and thus enabled to test the MI approach without additional errors from external factors (i.e. uncertainty on the values of the electrical parameters). Thus, the use of this synthetic system was useful for testing the reliability of the MI approach. The test was carried out on the third and fourth modes, having displacement as target variable to be decreased. The type of control imposed was a mixed H_2/H_∞ control, together with the passivity constraint. Figure 2a shows both the experimental and numerical results. They match satisfactorily, and the damping action is effective, evidencing the reliability of the proposed method.

The second test was instead a H_2 control on displacement, together with the passivity constraint. Again, the modes taken into account are the third and fourth. This time the shunt impedance was built physically. The way to synthetize the impedance from the controller layout resulting from the matrix inequality problem was based on the Brune's method [44,45]. Again, the control action is evident and experimental and numerical results match (see Figure 2b).

More details about these tests can be found in [33].

5 Conclusion

This paper has dealt with vibration attenuation by means of piezoelectric shunt. The paper proposed an approach for designing passive shunt impedances to be used for multi-mode vibration damping. Such an approach is based on matrix inequality problems, which allow to set both performance targets and impedance passivity.

The experimental tests carried out on a cantilever beam confirmed the reliability of the approach and the accuracy of the analytical model used to develop the work.

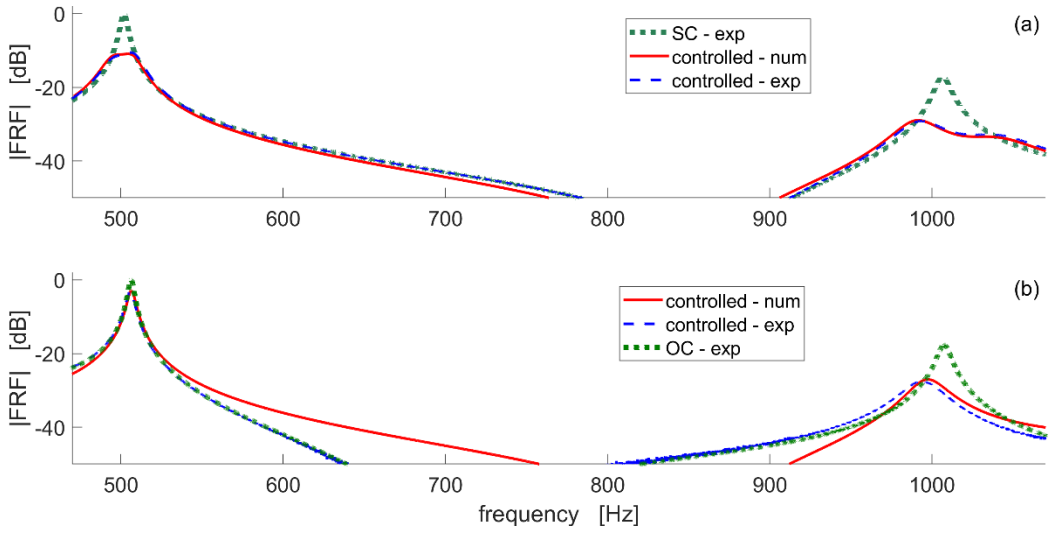


Figure 2: Amplitude of Frequency Response Functions (FRF) for the first test (that performed simulating the shunt impedance with a synthetic device) (a) and for the second test (that carried out building the shunt impedance) (b)

References

[1] N. Hagood, A. von Flotow, Damping of structural vibrations with piezoelectric materials and passive electrical networks, J. Sound Vib. 146 (1991) 243–268.

[2] G. Caruso, A critical analysis of electric shunt circuits employed in piezoelectric passive vibration damping, Smart Mater. Struct. 10 (2001) 1059–1068. doi:10.1088/0964-1726/10/5/322.

[3] M. Berardengo, A. Cigada, S. Manzoni, M. Vanali, Vibration Control by Means of Piezoelectric Actuators Shunted with LR Impedances: Performance and Robustness Analysis, Shock Vib. 2015 (2015) ID 704265. doi:10.1155/2015/704265.

[4] M. Berardengo, S. Manzoni, M. Vanali, The Behaviour of Mistuned Piezoelectric Shunt Systems and Its Estimation, Shock Vib. 2016 (2016) 9739217. doi:10.1155/2016/9739217.

[5] V.P. Matveenko, N.A. Iurlova, D.A. Oshmarin, N. V Sevodina, M.A. Iurlov, N.A. Iurlova, D.A. Oshmarin, N. V Sevodina, An approach to determination of shunt circuits parameters for damping vibrations, Int. J. Smart Nano Mater. 9 (2018) 135–149. doi:10.1080/19475411.2018.1461144.

[6] J. Høgsberg, S. Krenk, Balanced calibration of resonant piezoelectric RL shunts with quasi-static background flexibility correction, J. Sound Vib. 341 (2015) 16–30. doi:10.1016/j.jsv.2014.12.006.

[7] B. de Marneffe, a Preumont, Vibration damping with negative capacitance shunts: theory and experiment, Smart Mater. Struct. 17 (2008) 035015. doi:10.1088/0964-1726/17/3/035015.

[8] O. Heuss, R. Salloum, D. Mayer, T. Melz, Tuning of a Vibration Absorber with Shunted Piezoelectric Transducers, Arch. Appl. Mech. 86 (2016) 1715–1732. doi:10.1007/s00419-014-0972-5.

[9] M. Pohl, Increasing the performance of negative capacitance shunts by enlarging the output voltage to the requirements of piezoelectric transducers, J. Intell. Mater. Syst. Struct. 28 (2017) 1379–1390. doi:10.1177/1045389X16666181.

[10] M. Berardengo, O. Thomas, C. Giraud-Audine, S. Manzoni, Improved resistive shunt by means of negative capacitance: new circuit, performances and multi-mode control, Smart Mater. Struct. 25 (2016) 075033. doi:10.1088/0964-1726/25/7/075033.

[11] M. Berardengo, O. Thomas, C. Giraud-Audine, S. Manzoni, Improved shunt damping with two negative capacitances: an efficient alternative to resonant shunt, J. Intell. Mater. Syst. Struct. 28 (2017) 2222–2238. doi:10.1177/1045389X16667556.

[12] M. Berardengo, S. Manzoni, O. Thomas, C. Giraud-Audine, A new electrical circuit with negative capacitances to enhance resistive shunt damping, in: Proc. ASME 2015 Conf. Smart Mater. Adapt. Struct. Intell. Syst. - SMASIS 2015 - Sept. 21-23 2015, Colorado Springs (CO, USA), 2015: p. ID 8836.

[13] B. Götz, R. Platz, T. Melz, Effect of static axial loads on the lateral vibration attenuation of a beam with piezo- elastic supports, Smart Mater. Struct. 27 (2018) 035011.

[14] M. Lallart, A. Badel, D. Guyomar, Nonlinear Semi-active Damping using Constant or Adaptive Voltage Sources: A Stability Analysis, J. Intell. Mater. Syst. Struct. 19 (2008) 1131–1142. doi:10.1177/1045389X07083612.

[15] A. Badel, G. Sebald, D. Guyomar, M. Lallart, E. Lefeuvre, C. Richard, J. Qiu, Piezoelectric vibration control by synchronized switching on adaptive voltage sources: Towards wideband semi-active damping, J. Acoust. Soc. Am. 119 (2006) 2815–2825.

[16] B. Bao, W. Tang, Semi-active vibration control featuring a self-sensing SSDV approach, Meas. J. Int. Meas. Confed. 104 (2017) 192–203. doi:10.1016/j.measurement.2017.03.018.

[17] L. Yan, B. Bao, D. Guyomar, M. Lallart, Periodic structure with interconnected nonlinear electrical networks, J. Intell. Mater. Syst. Struct. 28 (2017) 204–229. doi:10.1177/1045389X16649448.

[18] M. Collet, M. Ouisse, M.N. Ichchou, Structural energy flow optimization through adaptive shunted piezoelectric metacomposites, J. Intell. Mater. Syst. Struct. 23 (2012) 1661–1677. doi:10.1177/1045389X12449915.

[19] B. Lossouarn, J. Deü, M. Aucejo, K.A. Cunefare, Multimodal vibration damping of a plate by piezoelectric coupling to its analogous electrical network, Smart Mater. Struct. 25 (2016) 115042. doi:10.1088/0964-1726/25/11/115042.

[20] U. Andreaus, F. Dell'Isola, M. Porfiri, Piezoelectric passive distributed controllers for beam flexural vibrations, J. Vib. Control. 10 (2004) 625–659. doi:10.1017/CBO9781107415324.004.

[21] I. Giorgio, A. Culla, D. Del Vescovo, Multimode vibration control using several piezoelectric transducers shunted with a multiterminal network, Arch. Appl. Mech. 79 (2009) 859–879. doi:10.1007/s00419-008-0258-x.

[22] L. Airoldi, M. Ruzzene, Wave Propagation Control in Beams Through Periodic Multi-Branch Shunts, J. Intell. Mater. Syst. Struct. 22 (2011) 1567–1579. doi:10.1177/1045389X11408372.

[23] J.J. Hollkamp, Multimodal passive vibration suppression with piezoelectric materials and resonant shunts, J. Intell. Mater. Syst. Struct. 5 (1994) 49–57.

[24] S. Wu, Method for multiple-mode shunt damping of structural vibration using a single PZT transducer, in: Proc. SPIE 3327, Smart Struct. Mater. 1998 Passiv. Damping Isol., San Diego (USA), 1998.

[25] S. Behrens, S.O.R. Moheimani, a. J. Fleming, Multiple mode current flowing passive piezoelectric shunt controller, J. Sound Vib. 266 (2003) 929–942. doi:10.1016/S0022-460X(02)01380-9.

[26] A. Cigada, S. Manzoni, M. Redaelli, M. Vanali, Optimization of the current flowing technique aimed at semi-passive multi-modal vibration reduction, J. Vib. Control. 18 (2012) 298–312. doi:10.1177/1077546311407537.

[27] A.J. Fleming, S. Behrens, S.O.R. Moheimani, Reducing the Inductance Requirements of Piezoelectric Shunt Damping Systems, Smart Mater. Struct. 12 (2003) 57–64. doi:10.1088/0964-1726/12/1/307.

[28] O. Thomas, J. Ducarne, J.-F. Deü, Performance of piezoelectric shunts for vibration reduction, Smart Mater. Struct. 21 (2012) 015008. doi:10.1088/0964-1726/21/1/015008.

[29] O. Thomas, J. Deü, J. Ducarne, Vibrations of an elastic structure with shunted piezoelectric patches: efficient finite element formulation and electromechanical coupling coefficients, Int. J. Numer. Methods Eng. 80 (2009) 235–268. doi:10.1002/nme.

[30] J. Ducarne, O. Thomas, J.-F. Deü, Placement and dimension optimization of shunted piezoelectric patches for vibration reduction, J. Sound Vib. 331 (2012) 3286–3303. doi:10.1016/j.jsv.2012.03.002.

[31] E. Doebelin, Measurement Systems: application and design, McGraw-Hill, New York, 2003.

[32] M. Berardengo, S. Manzoni, O. Thomas, M. Vanali, Piezoelectric resonant shunt enhancement by negative capacitances: Optimisation, performance and resonance cancellation, J. Intell. Mater. Syst. Struct. 29 (2018) 2581–2606. doi:10.1177/1045389X18770874.

[33] M. Berardengo, S. Manzoni, A.M. Conti, Multi-mode passive piezoelectric shunt damping by means of matrix inequalities, J. Sound Vib. 405 (2017) 287–305. doi:10.1016/j.jsv.2017.06.002.

[34] C. Scherer, P. Gahinet, M. Chilali, Multiobjective Output-Feedback, IEEE Trans. Automat. Contr. 42 (1997) 896–911.

[35] G.-R. Duan, H.-H. Yu, LMIs in control systems - Analysis, design and applications, Press, CRC, Boca Raton (FL, USA), 2013.

[36] C. Papageorgiou, M. Smith, Positive real synthesis using matrix inequalities for mechanical networks: application to vehicle suspension, IEEE Trans. Control Syst. Technol. 14 (2006) 423–435.

[37] S. Boyd, L. El Ghaoui, E. Feron, BalakrishnanV., Linear matrix inequalities in system and control theory, Society for Industrial and Applied Mathematics, 1994.

[38] F.A. Potra, S.J. Wright, Interior-point methods, J. Comput. Appl. Math. 124 (2000) 281–302. doi:10.1016/S0377-0427(00)00433-7.

[39] F. Li, M. de Oliveira, R. Skelton, Integrating information architecture and control or estimation design, SICE J. Control. Meas. Syst. Integr. 1 (2011) 120–128.

[40] M. Stingl, On the solution of nonlinear semidefinite programs by augmented Lagrangian methods, PhD thesis, University of Erlangen-Nurnberg, 2006.

[41] A. Conn, N. Gould, P. Toint, Trust region methods, Society for Industrial and Applied Mathematics, 2000.

[42] O. Thomas, C. Touzé, a. Chaigne, Asymmetric non-linear forced vibrations of free-edge circular plates. Part II: experiments, J. Sound Vib. 265 (2003) 1075–1101. doi:10.1016/S0022-460X(02)01564-X.

[43] S. Moheimani, A. Fleming, Piezoelectric transducers for vibration control and damping, Springer, London, 2006.

[44] O. Brune, Synthesis of a Finite Two-terminal Network whose Driving-point Impedance is a Prescribed Function of Frequency, J. Math. Phys. 10 (1931) 191–236.

[45] E.A. Guillemin, Synthesis of Passive Networks, John Wiley & Sons, New York, 1957.

Optimization of tuned mass damper parameters based on numerical optimization and model reduction

M. Soubeyroux [1], **C. Dumoulin** [2] **and A. Deraemaeker** [2]
[1] ENSTA ParisTech
828, boulevard des Marchaux, 91120 Palaiseau, France

[2] Université Libre de Bruxelles, BATir,
50 Av F.D Roosevelt, CP 194/02, B-1050, Brussels, Belgium
e-mail: **aderaema@ulb.ac.be**

Abstract
Optimal parameters of tuned mass dampers (TMD) can be obtained using analytical expressions by reducing the discrete model of the host structure to a sdof system. This simplification leads however to suboptimal solutions, especially when the order of the mode to which the TMD is tuned increases. An alternative is to use numerical optimization based on the full model of the host structure and the TMD. For large finite element models representative of real applications, the costs are prohibitive. We therefore propose an efficient model reduction strategy based on model reduction and substructuring. The methodology is validated on a simple cantilever beam model and a complex finite element model of a 30-storey building.

1 Introduction

Mass-spring tuned mass dampers (TMDs) are used in civil engineering to passively mitigate the vibrations of tall structures, bridges and buildings. They consist in a one-degree-of-freedom (dof) system with a specific mass, spring and damper. The mass of the device is limited in practice to a few percents of the total mass of the structure, so that when the device is tuned to a specific mode of a structure, it results in a significant increase of the damping of this mode, while keeping the other modes unaffected. For a fixed mass of the TMD, there exist optimal values of stiffness and damping which allow to minimize a certain response quantity, depending on the targeted application.

Analytical expressions of these optimal parameters can be derived when the main structure is represented by a single degree-of-freedom (dof) system. The first author to derive such analytical expressions was probable Den Hartog [1] in 1956. He found the analytical expressions of the optimal stiffness and damping of a TMD attached to a one dof system which is excited by a harmonic force, considering the maximum of the displacement frequency response function of the host structure as the target response quantity to be minimized. The expressions are a function of the chosen mass ratio between the TMD and the host structure. Obviously, with a higher mass ratio, the efficiency of the TMD is increased. Since then, many authors have derived analytical expressions of the optimal stiffness and damping parameters of the TMD attached to a one dof system considering different types of excitations (harmonic and random, including base excitation) and different output quantities (displacement, velocity, acceleration, relative displacement) of which either the maximum of the FRF is minimized for the case of the harmonic excitation, or the variance of the response in the time domain is minimized in the case of random excitation. A very comprehensive summary of the different cases is given in [2]. These analytical expressions can only be used when the host structure is represented by a sdof system with zero damping. When the structure is more complex, a simple approach can be used to compute

equivalent mass and stiffness parameters of the host structure and reduced it to a sdof system. Due to the approximation introduced, the parameters derived with the analytical expressions are however suboptimal, especially when the order of the mode to which the TMD is tuned increases, when there is another mode in the frequency vicinity of the targeted mode, and when the damping in the host structure is non zero.

For complex structures, optimal parameters can be obtained using numerical optimization instead of analytical tuning rules. The strategy consists in defining a cost function depending on the excitation and output quantity of interest, as in the analytical case, and to minimize it using numerical optimization procedures which require to compute the response of the system several times until the minimum of the cost function is reached. The structure is discretized with the finite element method, and for large models representative of real structures, the computational costs associated to this technique can become prohibitive.

The idea presented in this paper is to use an efficient model reduction technique in order to strongly lower the computational costs. The first section of this paper presents the analytical approach to derive optimal parameters of TMDs attached to complex structures. The second part details the numerical optimization strategy together with the model reduction approach. The third section deals with the application of the two techniques to a simple model of a cantilever beam. The numerical approach is performed both with the full model and with the reduced order model in order to show the excellent performances of the model reduction technique applied. The results also illustrate how the optimal values obtained with the numerical approach deviate from the values obtained with the analytical approach when the order of the mode to which the TMD is tuned increases. In the last section, the numerical optimization procedure is applied to a large finite element model of a 30 stories building, and the optimal parameters are obtained for a harmonic input force and the displacement of the top of the building as an output to be minimized.

2 Analytical tuning rules for TMDs attached to a SDOF system

Consider a sdof system with mass M, stiffness K and damping B. A TMD with stiffness k, mass m and damping b is attached to the sdof system, resulting in a two dofs system represented in Figure 1.

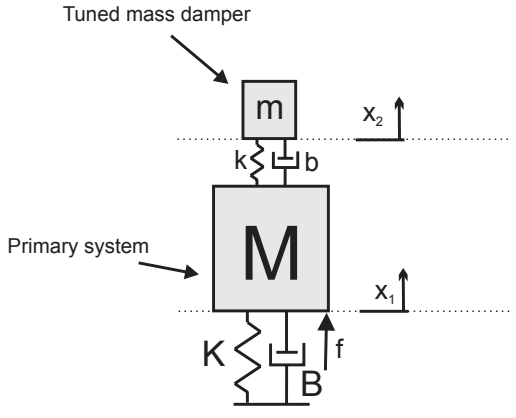


Figure 1: SDOF system with tuned mass damper attached

The equations of motions of this 2 dofs system are:

$$\begin{bmatrix} M & 0 \\ 0 & m \end{bmatrix} \begin{Bmatrix} \ddot{x_1} \\ \ddot{x_2} \end{Bmatrix} + \begin{bmatrix} B+b & -b \\ -b & b \end{bmatrix} \begin{Bmatrix} \dot{x_1} \\ \dot{x_2} \end{Bmatrix} \begin{bmatrix} K+k & -k \\ -k & k \end{bmatrix} \begin{Bmatrix} x_1 \\ x_2 \end{Bmatrix} = \begin{Bmatrix} f \\ 0 \end{Bmatrix} \tag{1}$$

In the frequency domain, we have $x_1(t) = X_1 e^{j\omega t}$, $x_2(t) = X_2 e^{j\omega t}$, and $f(t) = F e^{j\omega t}$ which leads to:

$$\begin{bmatrix} K + k + j\omega(B + b) - \omega^2 M & -(k + j\omega b) \\ -(k + j\omega b) & k - \omega^2 m + j\omega b \end{bmatrix} \begin{Bmatrix} X_1 \\ X_2 \end{Bmatrix} = \begin{Bmatrix} F \\ 0 \end{Bmatrix} \tag{2}$$

which can be solved in order to compute the FRF of the main system X_1/F.

We define

$$\omega_n = \sqrt{\frac{k}{m}}, \quad \Omega = \sqrt{\frac{K}{M}} \tag{3}$$

$$\nu = \frac{\omega_n}{\Omega}, \quad \mu = \frac{m}{M} \tag{4}$$

Figure 2a shows the response of the system for different values of b and for $\nu = 1$. The mass ratio μ is equal to 3%.

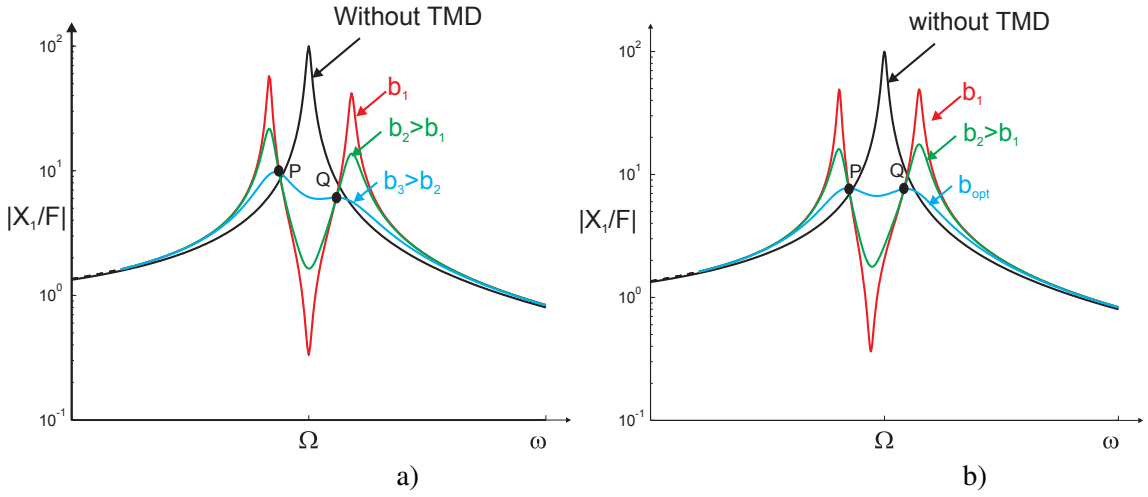


Figure 2: a) Effect of damping in the TMD for $\nu = 1$ and $\mu = 0.03$, b)Optimal TMD for $\mu = 0.03$

Note the existence of two points P and Q where all the curves for the different values of b cross. The optimal tuning of a TMD consists in finding the parameters k and b for a given mass m such that the two points P and Q are at the same height, and such that the response X_1 is maximum at these two points.

The tuning rules of Den Hartog [1] are given as a function of μ:

$$\nu = \frac{1}{1 + \mu} \tag{5}$$

$$\xi = \sqrt{\frac{3\mu}{8(1 + \mu)}} = \frac{b}{2\sqrt{km}} \tag{6}$$

This optimal solutions aims at minimizing the maximum of the X_1/F transfer function in the frequency band around the natural frequency of the primary system. Other input/output quantities can be considered, but are not discussed in the present paper [2]. The methodology presented is however applicable to all of these situations.

3 Reduction of a complex structure to a SDOF system

For real life applications, the host structure is never a sdof system, and has theoretically an infinite number of eigenfrequencies and mode shapes. The TMD has a very narrow-band effect on the dynamic response, so

that it only makes sense to tune it in order to damp a single eigenfrequency of this system. As the response of a structure is governed by the related mode shape around this eigenfrequency, it is possible to approximate the continuous system with a single degree of freedom system taking into account a single mode.

We first consider the equations of motion of the host structure without TMD with a force applied at the position and in the direction of the TMD (Figure 3).

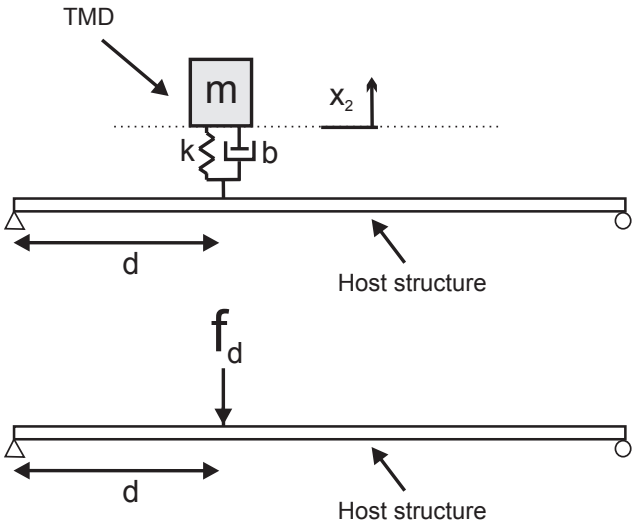


Figure 3: TMD attached to a continuous system, and host structure without TMD with force applied at the position and in the direction of the TMD

The host structure is discretized with the finite element method leading to the equations of motion:

$$M_0\ddot{x} + K_0 x = f \tag{7}$$

where M_0 and K_0 are the NxN mass and stiffness matrices obtained from the finite element discretization, x is the Nx1 vector of displacements at the dofs of the structure and f is a Nx1 column vector with zeros everywhere except at the dof corresponding to the position and direction of the TMD to be attached to the structure where the value is f_d. N is the number of dofs of the finite element model. Note that no damping is considered here as Den Hartog's rules are only derived for the case when the host structure is undamped. Note also that the TMD needs to be attached to a node of the finite element model for this approach to be valid.

Projection of these equations in the modal basis of real mode shapes consists in writing

$$x = \sum_{i=1}^{N} \psi_i z_i \tag{8}$$

where z_i are the modal amplitudes and ψ_i are the mode shapes of the host structure. This leads to a set of N uncoupled equations of the type

$$\mu_i \ddot{z_i} + \mu_i \omega_i^2 z_i = \psi_i(d) f_d \tag{9}$$

where μ_i is the modal mass and ω_i the natural frequency of mode i and we have used the fact that f is zero at all dofs except the dof where the TMD is attached for which the value if f_d. If we now make the assumption that around the eigenfrequency ω_j, the displacement can be approximated with a single mode:

$$x = \sum_{i=1}^{N} \psi_i z_i \simeq \psi_j z_j \tag{10}$$

The displacement at the position of the TMD is therefore

$$x(d) = \psi_j(d) z_j \tag{11}$$

and we can write

$$z_j = \frac{x(d)}{\psi_j(d)} \tag{12}$$

Replacing in (9) for mode j we obtain:

$$\frac{\mu_j}{\psi_j^2(d)} \ddot{x}(d) + \frac{\mu_j \omega_j^2}{\psi_j^2(d)} x(d) = f_d \tag{13}$$

which can be written

$$M_{eq} \ddot{x}(d) + K_{eq} x(d) = f_d \tag{14}$$

with

$$M_{eq} = \frac{\mu_j}{\psi_j^2(d)}, \quad K_{eq} = \frac{\mu_j \omega_j^2}{\psi_j^2(d)} \tag{15}$$

Equations (5,6) can now be used to tune the parameters of the TMD to a specific mode using the values of M_{eq} and K_{eq} to define the mass ration μ and the natural frequency of the host structure reduced to a sdof system Ω. The determination of the optimal parameters of the TMD only require to compute the mode shapes of the host structure without the TMD using a finite element package and extract the values of μ_j, ω_j and $\psi_j(d)$.

4 Numerical optimization of TMDs using model reduction

The mass and stiffness matrices of the host structure can be augmented in order to take into account the TMD attached to a specific dof by assembling the 2x2 mass, stiffness and damping matrices of the TMD element with the host structure matrices M_0, K_0 and B_0. Here B_0 is added to the system matrices of the host structure in order to accurately model the damping inevitably present in real structures. The new matrices K, B and M correspond to the finite element matrices of the host structure with the TMD attached, and the vector of displacements x is augmented with a single dof corresponding to the motion of the mass of the TMD.

The equations of motion in the frequency domain ($x(t) = Xe^{j\omega t}$, $f = Fe^{j\omega t}$) read :

$$(K - \omega^2 M + j\omega B)X = F \tag{16}$$

In this paper, the finite element matrices K, M and B and the force vector F are obtained with the Matlab toolbox SDT (Structural Dynamics Toolbox []). In order to optimize the parameters b and k of the TMD, a cost function is defined as the maximum of $|X/F|$ computed in a frequency band around the natural frequency of the mode shape to which the TMD is tuned, with a certain frequency resolution. This cost function is parameterized as a function of b and k and the Matlab function $fminsearch$ is used to find the parameters which minimize the maximum of $|X/F|$. We have found that a good choice for the frequency band is $\omega = [0.9 - 1.3]\omega_j$ where ω_j is the frequency of the mode of interest, and the solution of equation (16) is computed at 2048 frequencies in this frequency band. The starting point of the optimization is taken as the parameters obtained with the analytical procedure described in sections 2 and 3. As this solution is not too far from the optimum, this ensures fast convergence of the optimizer which, in our calculations typically converges after 30-50 evaluations of the cost function. This leads to solving $\simeq$ 50x2048 times

equation(16) to find the optimal parameters. For large finite element models, this is clearly prohibitive in terms of computational costs, which calls for efficient model reduction. The approach considered in this paper is to use substructuring and model reduction. As the host structure's parameters do not vary during the optimization, it can be efficiently reduced using a CMS-type approach. The TMD model however is not reduced as its parameters vary during the optimization procedure. The two models are then coupled to compute the full model response and optimize the TMD parameters.

4.1 Model reduction and static corrections

A very general approach for model reduction is the Ritz formalism [3] in which the solution X is written as the linear combination of shape vectors arranged in a reduction matrix T:

$$X = TX_r \tag{17}$$

The size of T is Nxn where N is the initial number of dofs, and $n < N$ in order to reduce the size of the problem.

Replacing (17) in (16) and premultiplying by T^T, we have:

$$(T^T KT - \omega^2 T^T MT + j\omega T^T BT)X_r = T^T F \tag{18}$$

which we write:

$$(K_r - \omega^2 M_r + j\omega B_r)X_r = F_r \tag{19}$$

where

$$K_r = T^T KT \tag{20}$$
$$M_r = T^T MT \tag{21}$$
$$B_r = T^T BT \tag{22}$$
$$F_r = T^T F \tag{23}$$

If T is taken as the matrix of real mode shapes, this corresponds to projecting the solution on the subspace of the normal modes. Matrices K_r and M_r are diagonal, but B_r is diagonal only if a modal damping model is adopted (or in the case of the Rayleigh damping model which is a specific case of modal damping). The modal damping approach is valid in the case of proportional damping or for structures with low levels of damping, which will be the case of the host structures studied in this paper. Modal truncation consists in keeping in T only a set of $n < N$ modeshapes. A common rule is to retain all the modes which have a natural frequency lower than 1.5 ω_{max} (the maximum frequency at which the solution needs to be computed). The main advantages of taking such a Ritz basis are (i) the decoupling of the equations (if B_r is diagonal), and (ii) the reduction of the number of dofs from the initial number of dofs N to only a few dofs corresponding to the n lower mode shapes. The approach is therefore very efficient when the frequency band of interest contains only a few mode shapes. It is well known that this approach leads however to relatively important truncation errors due to the effect of the higher order modes which are neglected.

The static correction method, also known as the modal truncation augmentation method [4] aims at reducing the truncation error. The high order modes which are responsible for the truncation error have a frequency ω_i larger than the frequency of computation ω, so that one can approximate their contribution by a static term (not depending on the frequency ω). This can be done by using the following Ritz basis:

$$T = \left[\psi_1 ... \psi_n \, K^{-1}F\right] \tag{24}$$

where F is a matrix whose columns represent the different possible excitation patterns on the structure. In practice, if one uses (23) to compute the reduced matrices K_r, M_r and B_r, this will lead to numerical conditioning problems because there is a certain degree of collinearity between the mode shapes and the static responses $K^{-1}F$. This can be solved by performing an orthogonalization of T with respect to the matrices M and K.

4.2 Model reduction and CMS

We are interested in computing the dynamic response of a structure which is decomposed into several substructures. For each substructure, a dynamic model reduction is performed. This approach is commonly referred to as component mode synthesis (CMS). The derivations in this section will be made for the case of two substructures but can be extended to any number of them. Let us therefore assume that the equations of motion in substructure 1 are given by

$$(K_1 - \omega^2 M_1 + j\omega B_1)X_1 = F_1 \tag{25}$$

where the matrices are of size N_1xN_1, where N_1 is the number of dofs in substructure 1. and in substructure 2 by:

$$(K_2 - \omega^2 M_2 + j\omega B_2)X_2 = F_2 \tag{26}$$

Similarly N_2 is the number of dofs in substructure 2. The uncoupled equations can be written in the general form

$$\left(\begin{bmatrix} K_1 & 0 \\ 0 & K_2 \end{bmatrix} - \omega^2 \begin{bmatrix} M_1 & 0 \\ 0 & M_2 \end{bmatrix} + j\omega \begin{bmatrix} B_1 & 0 \\ 0 & B_2 \end{bmatrix} \right) \begin{Bmatrix} X_1 \\ X_2 \end{Bmatrix} = \begin{Bmatrix} F_1 \\ F_2 \end{Bmatrix} \tag{27}$$

We will restrict this analysis to the case where the meshes of substructures 1 and 2 are conforming (Figure 4), i.e all nodes on the interface of the two substructures are present in the two substructures. Let us assume that there are n_{int} dofs on the interface. Displacement continuity at the interface imposes that

$$X_{2,int} = X_{1,int} \tag{28}$$

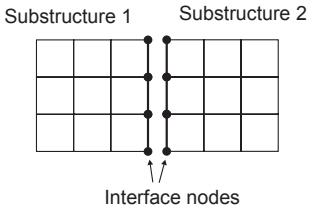


Figure 4: Substructures 1 and 2 and interface nodes for a conforming mesh

Let us define the operator L which extracts $X_{1,int}$, the displacements of substructure 1 restricted to the interface dofs, from X_1, we get:

$$X_{1,int} = LX_1 \tag{29}$$

where L is a n_{int}xN_1 operator. Enforcing the constraint (28) we have

$$X_{2,int} = LX_1 \tag{30}$$

The vector of displacements can now be written :

$$\begin{Bmatrix} X_1 \\ X_2 \end{Bmatrix} = \begin{Bmatrix} X_1 \\ X_{2,int} \\ X_2^* \end{Bmatrix} = \Lambda \begin{Bmatrix} X_1 \\ X_2^* \end{Bmatrix} \tag{31}$$

with

$$\Lambda = \begin{bmatrix} I_1 & 0 \\ L & 0 \\ 0 & I_2 \end{bmatrix} \tag{32}$$

where I_1 is a N_1xN_1 identity matrix and I_2 is a $(N_2 - n_{int})$ x $(N_2 - n_{int})$ identity matrix, and X_2 has been reordered so that

$$X_2 = \begin{Bmatrix} X_{2,int} \\ X_2^* \end{Bmatrix} \tag{33}$$

and X_2^* corresponds to the displacements at the dofs which are not on the interface of substructure 2. Equation (31) reduces the $(N_1 + N_2)$-size displacement vector to a $(N_1 + N_2 - n_{int})$-size displacement vector in which the continuity constraints are enforced.

Equation (31) is then used in (27) which is premultiplied by Λ^T to give :

$$\Lambda^T \left(\begin{bmatrix} K_1 & 0 \\ 0 & K_2 \end{bmatrix} - \omega^2 \begin{bmatrix} M_1 & 0 \\ 0 & M_2 \end{bmatrix} + j\omega \begin{bmatrix} B_1 & 0 \\ 0 & B_2 \end{bmatrix} \right) \Lambda \begin{Bmatrix} X_1 \\ X_2^* \end{Bmatrix} = \Lambda^T \begin{Bmatrix} F_1 \\ F_2 \end{Bmatrix} \tag{34}$$

which is written:

$$\left(K_c - \omega^2 M_c + j\omega C_c \right) X_r = F_c \tag{35}$$

where

$$K_c = \Lambda^T \begin{bmatrix} K_1 & 0 \\ 0 & K_2 \end{bmatrix} \Lambda, \quad M_c = \Lambda^T \begin{bmatrix} M_1 & 0 \\ 0 & M_2 \end{bmatrix} \Lambda, \quad B_c = \Lambda^T \begin{bmatrix} B_1 & 0 \\ 0 & B_2 \end{bmatrix} \Lambda \tag{36}$$

which gives after a little algebra :

$$K_c = \begin{bmatrix} K_1 & 0 \\ 0 & 0 \end{bmatrix} + \begin{bmatrix} L^T & 0 \\ 0 & I_2 \end{bmatrix} K_2 \begin{bmatrix} L & 0 \\ 0 & I_2 \end{bmatrix} \tag{37}$$

and

$$M_c = \begin{bmatrix} M_1 & 0 \\ 0 & 0 \end{bmatrix} + \begin{bmatrix} L^T & 0 \\ 0 & I_2 \end{bmatrix} M_2 \begin{bmatrix} L & 0 \\ 0 & I_2 \end{bmatrix} \tag{38}$$

and

$$C_c = \begin{bmatrix} B_1 & 0 \\ 0 & 0 \end{bmatrix} + \begin{bmatrix} L^T & 0 \\ 0 & I_2 \end{bmatrix} B_2 \begin{bmatrix} L & 0 \\ 0 & I_2 \end{bmatrix} \tag{39}$$

The stiffness, mass and damping matrices of the coupled system K_c, M_c and B_c are the sum of the contributions of the submatrices of the two subsystems where the different coefficients have been relocated due to the Λ matrix. This corresponds to the standard assembly procedure for finite elements. K_c, M_c and B_c correspond therefore to the stiffness, mass and damping matrices of the coupled subsystems.

Assume now that model reduction is performed in each substructure separately :

$$X_1 = T_1 X_{1r} \tag{40}$$

$$X_2 = T_2 X_{2r} \tag{41}$$

where T_1 is the matrix of n_1 ($n_1 < N_1$) Ritz vectors for substructure 1 and T_2 is the matrix of n_2 ($n_2 < N_2$) Ritz vectors for substructure 2. We have also

$$X_2^* = [0 \quad I_2]\, X_2 = [0 \quad I_2]\, T_2 X_{2r} = T_2^* X_{2r} \tag{42}$$

where

$$T_2^* = [0 \quad I_2]\, T_2 \tag{43}$$

which is the reduced matrix T_2 from which the first n_{int} lines corresponding to the interface dofs have been removed. Equation (31) then becomes

$$\left\{ \begin{array}{c} X_1 \\ X_2 \end{array} \right\} = \Lambda \left\{ \begin{array}{c} X_1 \\ X_2^* \end{array} \right\} = \Lambda \left[\begin{array}{cc} T_1 & 0 \\ 0 & T_2^* \end{array} \right] \left\{ \begin{array}{c} X_{1r} \\ X_{2r} \end{array} \right\} = \Lambda_r \left\{ \begin{array}{c} X_{1r} \\ X_{2r} \end{array} \right\} \tag{44}$$

with

$$\Lambda^r = \Lambda T \tag{45}$$

with

$$T = \left[\begin{array}{cc} T_1 & 0 \\ 0 & T_2^* \end{array} \right] \tag{46}$$

The reduced stiffness matrix becomes :

$$K_r = \Lambda_r^T \left[\begin{array}{cc} K_1 & 0 \\ 0 & K_2 \end{array} \right] \Lambda_r = T^T \Lambda^T \left[\begin{array}{cc} K_1 & 0 \\ 0 & K_2 \end{array} \right] \Lambda T = T^T K_c T \tag{47}$$

and in the same way we can show that

$$M_r = T^T M_c T \quad , B_r = T^T B_c T \tag{48}$$

The model reduction strategy consists in defining the basis of Ritz vectors T_1 and T_2 in each substructure, and to build the Ritz basis T for the coupled system. The reduced matrices are then computed based on the coupled matrices M_c, K_c and B_c and the Ritz basis T.

4.3 Specific case of a TMD

Assume that a TMD is attached to a cantilever beam as shown in Figure 5. Substructure 1 is the cantilever

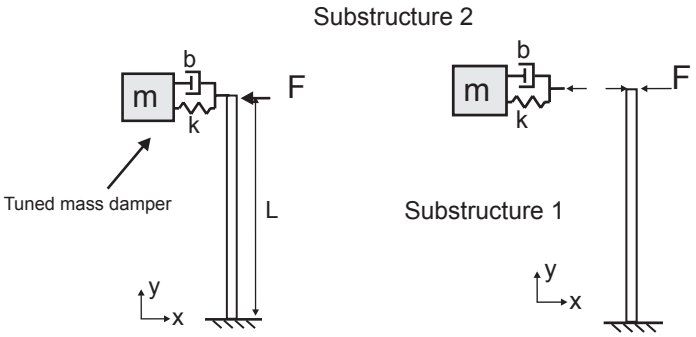


Figure 5: Cantilever beam with a tuned mass damper (TMD) attached at the tip, and definition of the two substructures

beam (without the TMD) and substructure 2 is the TMD. There is only one interface dof. During the optimization process, only the parameters of the TMD (stiffness, damping) will vary. We choose therefore to perform a dynamic reduction of substructure 1 using a Ritz basis T_1 containing n mode shapes and static corrections to forces acting on the host structure as explained in section 4.1. Here, the external force and the TMD act at the same position, so that only one static correction for a force acting horizontally on the top is needed. In CMS, this approach is usually referred to as the McNeal's method [5, 6]. For the TMD, as there are only two degrees of freedom, it is not necessary to perform a reduction so that

$$T_2 = \left[\begin{array}{cc} 1 & 0 \\ 0 & 1 \end{array} \right] \tag{49}$$

In addition, as we would like to vary the parameters of the TMD, it is important to keep the 'full' model of this substructure to have a very high accuracy solution. This is the main interest of the substructuring here. Matrix T_2^* is obtained by removing the first line and the first column of T_2 corresponding to the interface dof, resulting in $T_2^* = 1$. The reduction matrix is then given by

$$T = \begin{bmatrix} T_1 & 0 \\ 0 & 1 \end{bmatrix} \tag{50}$$

The stiffness, damping and mass matrices of the TMD are given by :

$$K_2 = k \begin{bmatrix} 1 & -1 \\ -1 & 1 \end{bmatrix}, M_2 = m \begin{bmatrix} 1 & 0 \\ 0 & 1 \end{bmatrix}, B_2 = b \begin{bmatrix} 1 & -1 \\ -1 & 1 \end{bmatrix} \tag{51}$$

The coupled matrices are then

$$K_c = \begin{bmatrix} K_1 & 0 \\ 0 & 0 \end{bmatrix} + k \begin{bmatrix} L^T & 0 \\ 0 & 1 \end{bmatrix} \begin{bmatrix} 1 & -1 \\ -1 & 1 \end{bmatrix} \begin{bmatrix} L & 0 \\ 0 & 1 \end{bmatrix} \tag{52}$$

$$M_c = \begin{bmatrix} M_1 & 0 \\ 0 & 0 \end{bmatrix} + m \begin{bmatrix} L^T & 0 \\ 0 & 1 \end{bmatrix} \begin{bmatrix} 1 & 0 \\ 0 & 1 \end{bmatrix} \begin{bmatrix} L & 0 \\ 0 & 1 \end{bmatrix} \tag{53}$$

$$B_c = \begin{bmatrix} B_1 & 0 \\ 0 & 0 \end{bmatrix} + b \begin{bmatrix} L^T & 0 \\ 0 & 1 \end{bmatrix} \begin{bmatrix} 1 & -1 \\ -1 & 1 \end{bmatrix} \begin{bmatrix} L & 0 \\ 0 & 1 \end{bmatrix} \tag{54}$$

which are written

$$K_c = K_{1c} + k\, K_{2c} \tag{55}$$
$$M_c = M_{1c} + m\, M_{2c} \tag{56}$$
$$B_c = B_{1c} + b\, B_{2c} \tag{57}$$

The reduced matrices are then given by

$$\begin{aligned} K_r &= T^T K_{1c} T + k\, T^T K_{2c} T = K_{1r} + k\, K_{2r} \\ M_r &= T^T M_{1c} T + m\, T^T M_{2c} T = M_{1r} + m\, M_{2r} \\ B_r &= T^T B_{1c} T + b\, T^T C_{2c} T = B_{1r} + b\, B_{2r} \end{aligned} \tag{58}$$

Matrices K_{1r}, K_{2r}, M_{1r}, M_{2r} and B_{1r}, B_{2r} can be computed once and for all before the optimization. When parameters k, m and b are varied, the reduced matrices can be recomputed in a very efficient manner using Equation (58).

4.4 Application to a cantilever beam

The proposed strategy is illustrated for the example of a cantilever beam equipped with a TMD at the top. The beam model is made of 20 beam elements in SDT and represents a tall building of height L =140 m made of concrete ($E = 30GPa$, $\nu = 0.2$, $\rho = 2200kg/m^3$), with a hollow box cross section of external width and height of $20m$ and a thickness of $30cm$. A small damping is introduced in the beam model through the use of a loss factor $\eta = 0.02$ for the concrete material. The excitation is a force in the horizontal direction at the location of the TMD and the displacement is measured at the same location in order to compute the magnitude of the frequency response function $H = |X_{top}/F|$.

The TMD parameters are optimized for different values of μ (from 1 to 10 $\%$) and for different target modes (first four bending modes). The strategy for building T_1 consists in using modeshapes corresponding to all

the natural frequencies below or equal to the natural frequency of the target mode, as well as a static correction to a horizontal force at the top of the cantilever beam. The numerical optimization is performed for the full model, as well as for the reduced order model in order to check the accuracy of the model reduction technique adopted. The full order model contains 40 degrees of freedom for the cantilever beam and one additional dof for the TMD. For the reduced model, the size varies as a function of the target mode shape. We are here considering modes 1 through 4, for which the size of the Ritz basis is respectively from 3 to 6. Because the initial finite element model is of very low size (40 dofs), the interest of model reduction here is not obvious, but this example is used to validate the strategy. The advantage of the technique presented will become obvious for the example presented in section 5.

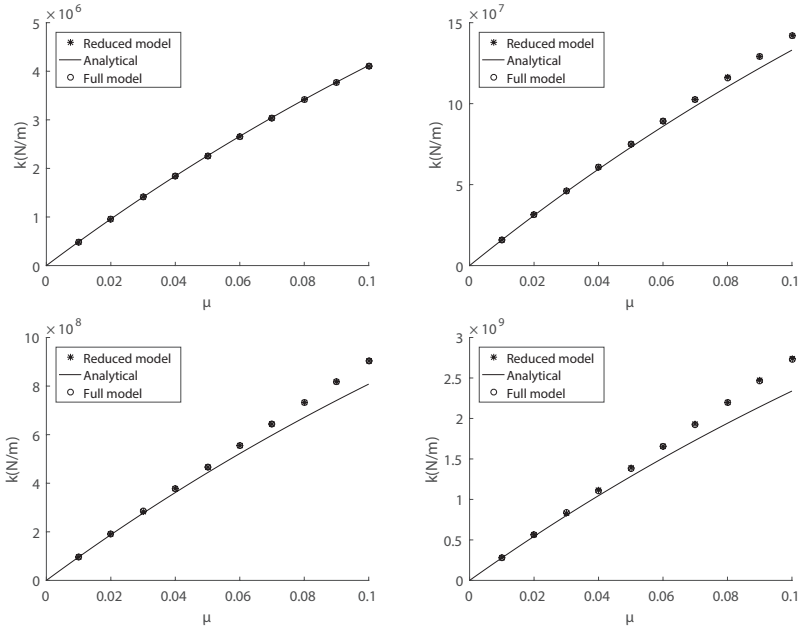


Figure 6: Value of the optimal stiffness of the TMD for different values of μ for modes 1 through 4. Comparison of optimal values obtained with the analytical approach, and the numerical approach with the full and reduced models

The optimal parameters are compared to the parameters obtained with the analytical approach detailed in section 2 in Figures 6 and 7. The figures show that the numerical optimums tend to deviate from the analytical value when the mode order increases, and for the higher values of μ, showing the interest of the numerical approach. The optimum values obtained with the numerical approach with the full and reduced order models are in very good agreement. There is only a slight difference on the optimum damping for mode 4 and high values of μ.

The maximum of the FRF resulting from these optimal values is plotted in Figure 8. As expected, the numerical approach leads to lower values of the maximum of $|X/F|$, in particular for the higher order modes. The reduced and full model lead to almost exactly the same value of this minimum, confirming the efficiency of the approach.

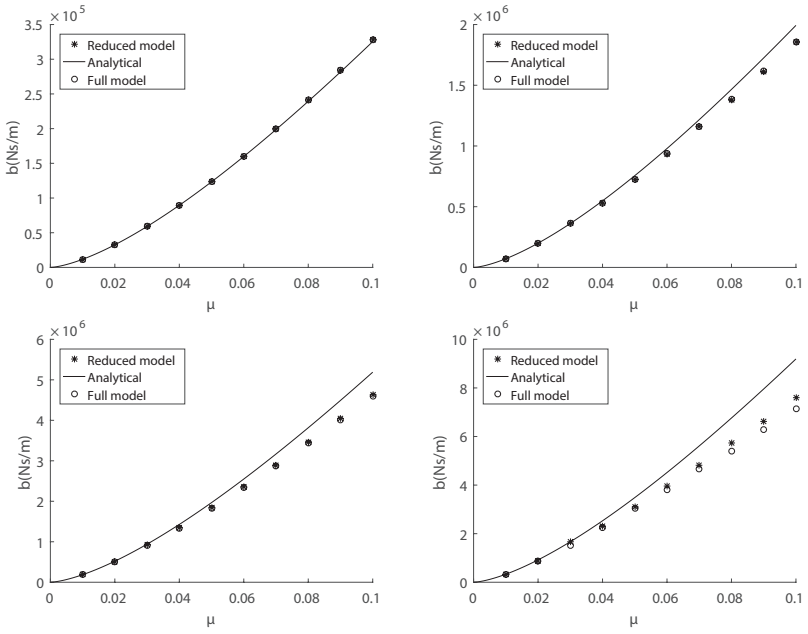


Figure 7: Value of the optimal damping of the TMD for different values of μ for modes 1 through 4. Comparison of optimal values obtained with the analytical approach, and the numerical approach with the full and reduced models

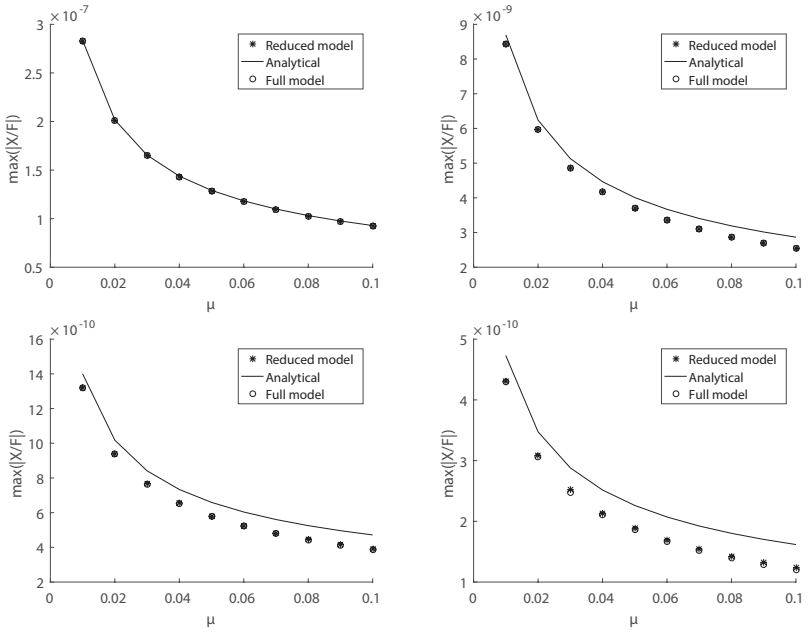


Figure 8: Maximum of $|X/F|$ for the optimal values obtained with the analytical approach, and the numerical approach with the full and reduced models

5 Application to a large building model

In order to show the interest of the proposed method, we consider a large finite element of a 30 story building also modelled in SDT. The three first bending mode shapes in direction x are represented in Figure 9. The model contains $\simeq$ 55 000 dofs and is made of plate and beam elements.

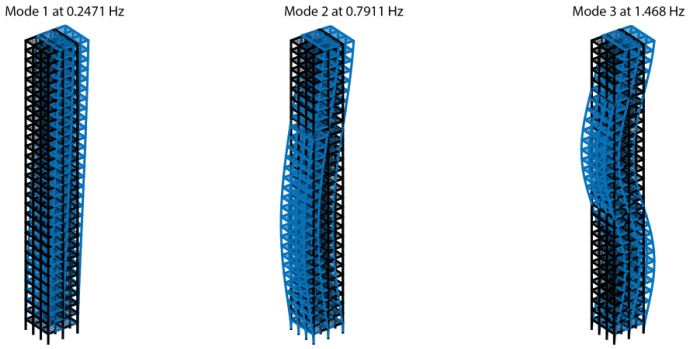


Figure 9: First three bending modes of a 30 story building with main motion in the x direction

A TMD acting in the x direction is attached to the top of the building. The optimal parameters are compared to the analytical values in Figures 10 and 11. The maximum of $|X/F|$ is plotted in Figure 12. The conclusions are similar to the ones for the cantilever beam.

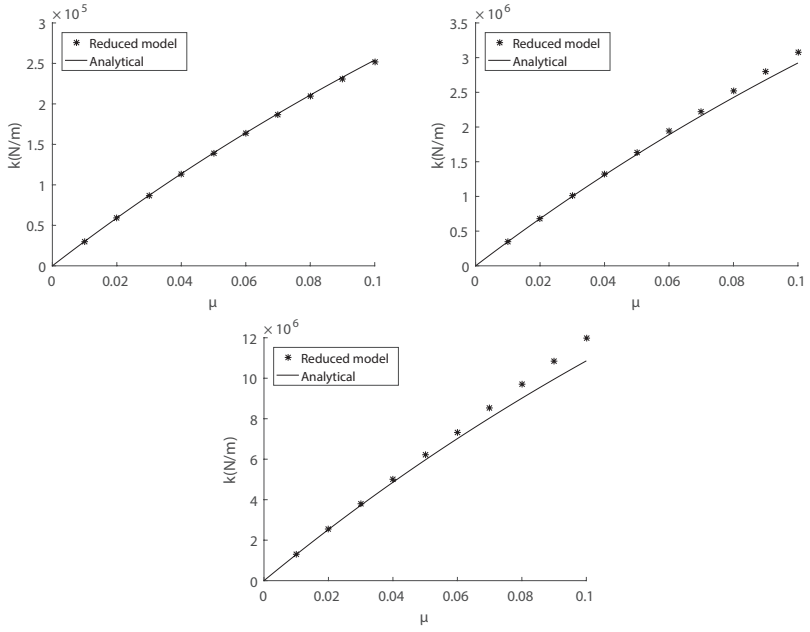


Figure 10: Value of the optimal stiffness of the TMD for different values of μ for modes 1 through 3. Comparison of optimal values obtained with the analytical approach, and the numerical approach with the reduced model

Figure 13 shows a zoom of $|X/F|$ around the third natural frequency of the building for a TMD tuned to this natural frequency using the analytical and numerical optimum k and b values. The numerical approach leads to equal peaks whereas the analytical approach leads to a suboptimal solution with non-equal peaks and a higher amplitude (increase of about 20% with respect to the numerical optimum).

In terms of computational costs, all computations have been performed on a laptop computer HP Probook 430 G3 with 16Gb of memory with SDT. The reduced basis are computed using the pre-programmed routines for model reduction in SDT. For the full order model, one evaluation of the cost function is performed in approximately 1h. One can expect therefore the optimisation with such a full model to last between 1 and 2 full days. For the reduced order model, the first step consists in computing the reduced matrices which for all

target modes of interest, takes slightly less than 1 minute. For mode 1, the optimization procedure then lasts in average for 1.5 seconds, for mode 2, 3 seconds, and for mode 3, 3.2 seconds. This clearly demonstrates the huge improvement in terms of computational costs by using the proposed strategy detailed in this paper. With such an approach, optimisation of TMD parameters on large finite element models of host structures can be performed in less than 2 minutes, while it would last for 1 to 2 days with a full model.

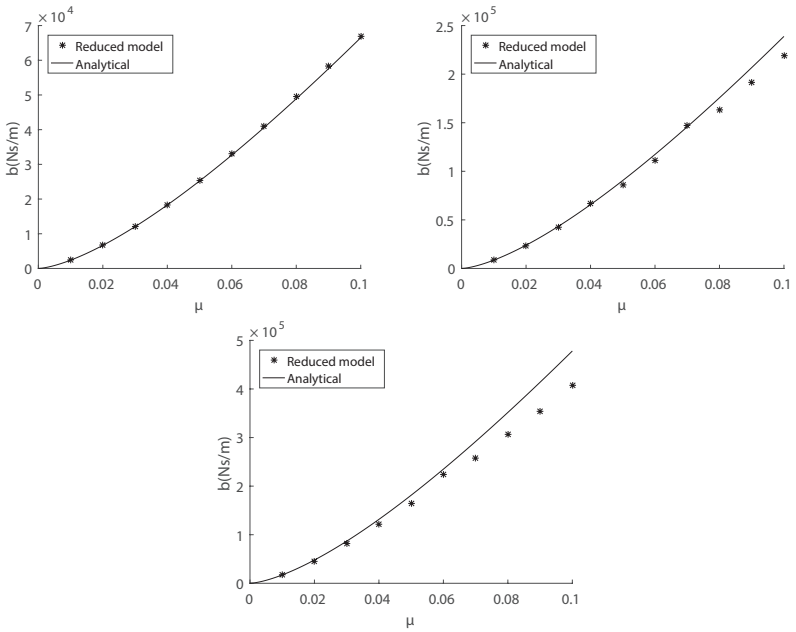


Figure 11: Value of the optimal damping of the TMD for different values of μ for modes 1 through 3. Comparison of optimal values obtained with the analytical approach, and the numerical approach with the reduced model

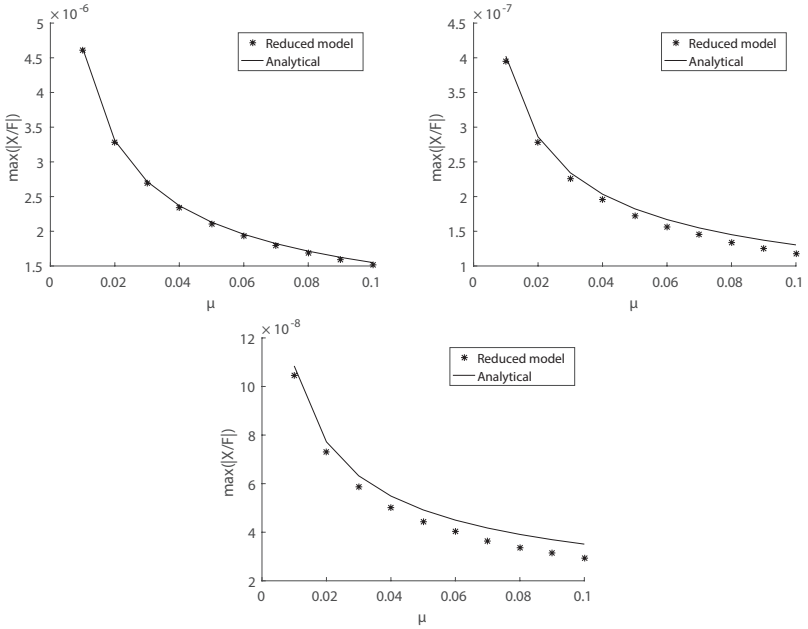


Figure 12: Maximum of $|X/F|$ for the optimal values obtained with the analytical approach, and the numerical approach with the reduced model

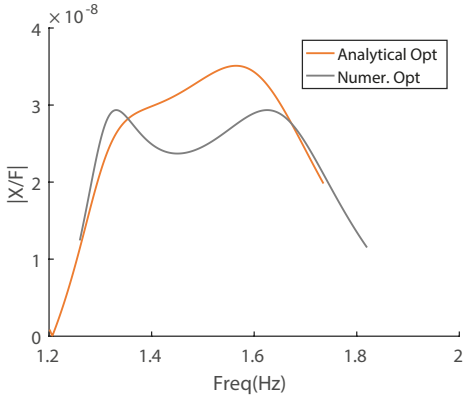


Figure 13: $|X/F|$ for the optimal values obtained with the analytical approach, and the numerical approach for the third bending mode with $\mu = 0.1$

6 Conclusions

The methodology presented in this paper allows to find optimal parameters of TMDs attached to host structures discretized with a large number of dofs using the finite element method. It leads to true optimal parameters on the contrary to the approaches based on analytical expressions for equivalent sdof systems. Due to the very efficient model reduction strategy adopted, the optimal parameters can be computed in only a few minutes on a laptop computer, rather than a few days for the full model. The technique has been applied for the minimization of the maximum of the transfer function between an applied harmonic force and the displacement of the host structure at the location of the TMD, but can be applied to any other target response under harmonic or random excitation [2]. Future developments of the technique will deal with the case of random and base excitation problems, as well as the optimization of the parameters of pendulum tuned mass dampers (PTMD).

References

[1] JP Den Hartog. *Mechanical vibrations*. McGraw-Hill Book Company, 1956.

[2] G.B. Warburton. Optimum absorber parameters for various combinations of response and excitation parameters. *Earthquake Engng and Struct. Dynamics*, 10:381–401, 1982.

[3] A.W. Leissa. The historical bases of the rayleigh and ritz methods. *Journal of Sound and Vibration*, 287:961–978, 2005.

[4] B. Besselink, A. Lutowska, N. van de Wouw, H. Nijmeijer, D.J. Rixen, M.E. Hochstenbach, and W.H.A.Schilders. A comparison of model reduction techniques from structural dynamics, numerical mathematics and systems and control. *Journal of Sound and Vibration*, 332:4403–4422, 2013.

[5] R.R. Craig and A.J. Kurdila. *Fundamentals of Structural Dynamics*. John Wiley & Sons, 2nd edition, 2006.

[6] R.H. MacNeal. A hybridg method of component mode synthesis. *Journal of Computers and Structures*, 1(4):581–601, 1971.

Dynamics of torsional vibration damper (TVD) pulley: implementation of elastomeric constitutive law

C. A. F. Silva[1], L. Manin[1], R. G. Rinaldi[2], E. Besnier[1], M. –A. Andrianoely[1], J. Ameil[3]
[1] Univ Lyon, INSA-Lyon, CNRS UMR5259, LaMCoS, F-69621, Villeurbanne France
* e-mail:**ferreira.silva.ca@gmail.com**

[2] Univ Lyon, INSA-Lyon, UMR5521, Mateis, F-69621, Villeurbanne, France

[3] Volvo Trucks Technology - Powertrain Engineering, 69806, Saint Priest, France

Abstract
In this work, the TVD-ring viscoelastic-material properties of the elastomeric constituents are determined based on Dynamical Mechanical Analysis (DMA) measurements and master curves reconstructions using thermo-simplicity principle. The elastomeric constitutive behavior is then implemented in the damper's equation of motion and the frequency response is simulated so that more accurate physical representation of the TVD dynamics can be achieved. At last, important difference in the TVD response are highlighted and analyzed whether or not the viscoelastic material properties (i.e. modulus and damping) are considered constant or frequency/temperature-dependent.

1 Introduction

The Torsional Vibration Damper (TVD) is an essential component of power transmission systems such as the Front Engine Accessory Drives (FEAD). The FEAD of a vehicle is a system composed of individual accessories such as the compressor, the alternator, the water and steering pumps, etc. These accessories are coupled to pulleys driven in rotation by a poly-V belt, itself driven by the crankshaft pulley. This driving pulley is commonly used as a torsional vibration damper for the crankshaft since rotational vibrations are harmful to the system performance [1] and may cause fatigue failure of structural components. The TVD is composed of an inner ring (hub) mounted on the crankshaft extremity, an intermediate viscoelastic rubber ring and an outer ring used as a poly-V pulley (Fig. 1). Generally, in simulation and for sake of simplification, the TVD dynamic properties – stiffness and damping – are chosen to be constant [1], although these properties depend on the operating temperature, the shear strain amplitude and the frequency to which the TVD is subjected because of its intermediate ring which is made of a viscoelastic material [2].

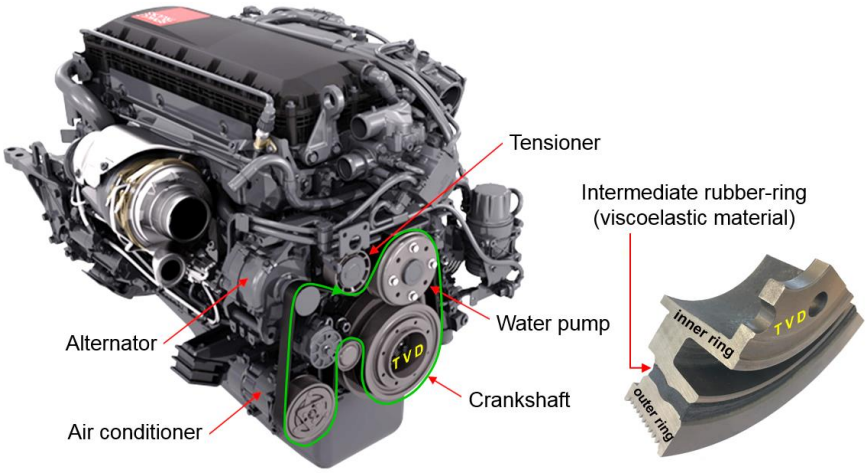


Fig. 1. Serpentine belt drive system with its TVD pulley

In the literature, most of the works related to the account for the rubber viscoelastic behavior in the structural components (belt, pulley, dampers) of the FEAD are about the impact of the poly-V belt viscoelasticity on its different vibration modes [3-7]. The viscoelasticity of the rubber used in vibration dampers such as the TVD has rarely been explored. Recently, Bhatti [8] indirectly compared viscoelastic dampers with Magnetorheological dampers. Also, the TVD behavior was speedily investigated by Jauregui [9] through a case study of a complicated model. A particularity of these studies is that they consider rheological models such as Maxwell [8], Kelvin [9, 10], etc. Yet, such rheological models significantly increase the complexity of the differential equations which are usually solved using complex schemes.

Other authors analyzed the dynamic characteristics of the stiffness and the damping from an experimental point of view (see Wakabayashi [11] and Kinoshita [12] who studied the TVD experimentally). However, in the first work reported the results were fitted to a specific engine case. Recently, Manin et al. [13] proposed a methodology to easily characterize the pulley torsional vibration damper.

The objectives of this paper are: (1) to propose a methodology based on the TVD-elastomer master curves to predict the temperature/frequency viscoelastic response of the TVD (2) then to simply and directly consider the viscoelastic properties of the constituting rubber-ring in the damper's equation of motion; (3) to highlight the influence of taking into consideration the viscoelastic properties of the elastomer when computing the TVD dynamic response; (4) to evaluate the coefficients of the equation of motion, stiffness and damping, as a function of the engine operating conditions.

In turn, this work aims at accurately calculating the viscoelastic TVD response which is of key importance in order to provide a realistic and accurate representation of the system dynamics, which is in accordance with Jauregui work and conclusions [9].

2 Torsional Vibration Damper

2.1 Torsional damper model

The torsional vibration damper can be modeled by a one degree-of-freedom (DOF) mass-spring-damper system as in [14], it is also similar to the base excitation one DOF harmonically excited system in [15], however, in this case, the single DOF is the rotation around z-axis as shown in Fig. 2.

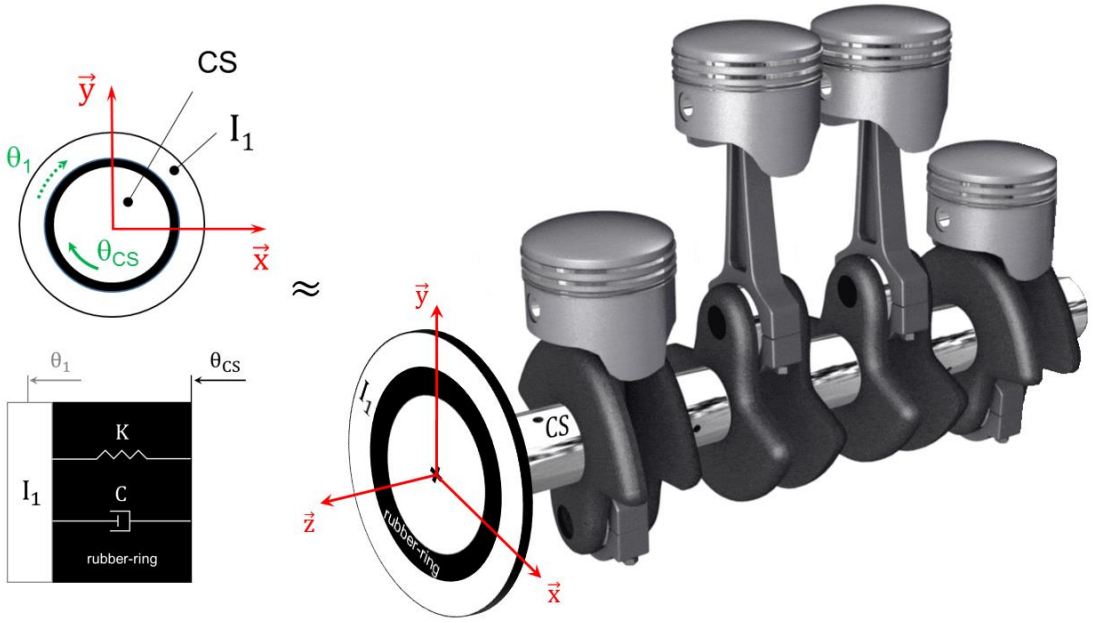


Fig.2. Tensioner vibration damper and its schematic diagrams

Supposing the engine at idling, the driving torque fluctuation usually contains 2 harmonics $(\omega, 2\omega)$. However, in this paper, only the prevailing harmonic generally represented as $\theta_{CS} = \theta_{amp} \sin(\omega\, t)$ (Fig. 2) is considered. The difference between the torque experienced by the TVD outer-ring and the driving torque imposed by the crankshaft results in an angular lag of θ_1 with respect to the excitation θ_{CS}, and is due to the viscoelastic properties of the TVD intermediate rubber-ring.

To evaluate the impact of considering the intermediate rubber-ring viscoelastic properties influenced by temperature and frequency and leading to varying TVD stiffness K and damping C coefficients, let us consider the equation of motion in Eq. (1) for the system shown in Fig. 2.

$$I_1\, \ddot{\theta_1} + C\, \dot{\theta_1} + K\, \theta_1 = C\, \theta_{amp}\, \omega \cos(\omega\, t) + K\, \theta_{amp} \sin(\omega\, t) \tag{1}$$

Where I_1 is the outer-ring inertia, K the stiffness and C the damping of the rubber-ring. The angle θ_1 is the DOF considered, θ_{amp} and ω are, respectively, the amplitude and the excitation radian frequency of the fluctuations (engine acyclism) in angular displacement.

The steady-state response of θ_1 have an amplitude and phase as in Eq. (2) ([15]). This is the Frequency Response Function (FRF) of one DOF base excitation system with the frequency ratio r, natural frequency ω_n and damping ratio ξ as in Eq. (3).

$$\text{FRF}: \left\{ \frac{\theta_1}{\theta_{CS}} = \frac{\sqrt{1 + (2\,\xi\, r)^2}}{\sqrt{(1 - r^2)^2 + (2\,\xi\, r)^2}} \;\middle|\; \varphi_{\theta_1} = \tan^{-1}\left(\frac{2\,\xi\, r^3}{1 - r^2 + (2\,\xi\, r)^2}\right) \right\} \tag{2}$$

$$r = \frac{\omega}{\omega_n} \qquad \omega_n = \sqrt{\frac{K}{I_1}} \qquad \xi = \frac{C}{2\sqrt{K\, I_1}} \tag{3}$$

Equations (2) and (3) were chosen because they are part of a classical formulation in the frequency-domain and the frequency domain is the one in which the TVD elastomer is characterized via DMA.

2.2 TVD rubber-ring viscoelastic properties

The TVD intermediate ring is made of rubber which can be described as a viscoelastic material. For this type of material, an intermediate between purely elastic and purely viscous materials [2] a complex modulus E^* is usually defined. Thus, in this paper, the Eq. (4) is defined to represent the viscoelastic properties of the TVD rubber-ring. The real part of E^* (storage modulus, E') relates to the elastic behavior of the ring, and defines the capacity of its material to store energy. The imaginary part of E^*(loss modulus, E'') relates to the material's viscous behavior, and defines the energy dissipative ability of the rubber-ring to dampen the crankshaft torque fluctuations.

$$E^* = E' + i\, E'' = f\,(T_{exp}, f_{exp}, \varepsilon_{exp}) \tag{4}$$

The complex modulus E^* is obtained via DMA characterization and varies as a function of the temperature T_{exp}, , the loading frequency f_{exp} and the dynamic strain ε_{exp} experienced by the rubber-ring.

The TVD intermediate ring material data shall be acquired to coincide with the engine-range of operating conditions (speed, temperature). To this aim, the rubber-ring was tested at conditions, i.e. a dynamic strain, various temperatures and discrete frequencies as in Fig. 3, representative of industrial applications (Fig. 1).

Next, the thermo-simplicity principle can be used (see [16]) to predict the viscoelastic behavior of the rubber-ring at the temperature in the engine room (T_{ref} in Fig. 3) over a broad range of frequencies by shifting the data obtained via DMA for several testing temperatures (a_T in Fig. 3, left).

As a result, a master curve is obtained (Fig. 3, right). It will be further fitted (Tab. (1)) in order to be used in the TVD viscoelastic model as explained in the coming paragraphs.

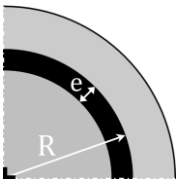
2.3 Viscoelastic torsional damper model

When the viscoelasticity of the TVD rubber-ring is considered the equation of motion Eq.(1) becomes Eq.(5) with variable stiffness K_{var} and damping C_{var} since they depend on the temperature, the frequency and the dynamic strain as the complex modulus E^* in Eq. (4).

$$I_1 \ddot{\theta_1} + C_{var}\, \dot{\theta_1} + K_{var}\, \theta_1 = C_{var}\, \theta_{amp}\, \omega \cos(\omega t) + K_{var}\, \theta_{amp} \sin(\omega t) \tag{5}$$

Actually, K_{var} and C_{var} are deduced from E^*. Let us examine the dependency of these terms on E^* and point out the way to determine them.

The torsional stiffness K of a rubber ring in Fig. 2 can be estimated by Eq. (6) which was demonstrated by Blanc in [14].



$$K = \frac{2\,\pi\, R^3 L\; G'}{e} \tag{6}$$

Where R , L , e are the rubber-ring radius, width and thickness, respectively. Also, G' is the shear modulus of the rubber-ring which is assumed here to be a homogeneous and isotropic material. Thus, Eq. (7) is valid to calculate G' from E' obtained via DMA with the Poisson ratio of the rubber $\nu \approx 1/2$.

$$G' = \frac{E'}{2\,(1+\nu)} \quad \rightarrow \quad K_{var} = \frac{\pi\, R^3 L}{e\,(1+\nu)}\, E' \tag{7}$$

As E' in Eq. (4), K_{var} varies as a function of the temperature T_{exp}, , the frequency f_{exp} and the strain ε_{exp} experienced by the TVD rubber-ring.

In parallel, the damping C in Fig. 2 can be calculated using the third term of Eq. (3) where the only unknown is the damping ratio ξ (Eq. (8)).

$$C = 2\sqrt{K\, I_1}\, \xi \tag{8}$$

However, according to [17, 18] the structural loss factor η is equal to twice the damping ratio ξ, i.e. $\eta = 2\xi$ (at resonance [19]) and $\eta = E''/E'$ for viscoelastic materials (rubber-ring) leading to Eq. (9).

$$C_{var} = \sqrt{K\, I_1}\, \frac{E''}{E'} \tag{9}$$

Similarly, C_{var} depends on the temperature T_{exp}, , the frequency f_{exp} and the strain ε_{exp} experienced by the TVD rubber-ring.

In the next paragraphs, the differences between Eqs. (1) and (5) can be evaluated thanks to the TVD response (FRFs) for several operating conditions (temperature, frequency). The differences between the constant (K, C) and varying (K_{var}, C_{var}) stiffness and damping are also discussed.

3 Results

Results are presented for the TVD geometrical characteristics as in Tab. (1). This is a torsional vibration damper TVD used in a FEAD of a six-cylinder truck engine.

Table 1. TVD geometrical parameters

I_1 (Kg mm^2)	R (mm)	L (mm)	e (mm)
31344.2	90	35	7

In the next sections, data from Tab. (1) with the rubber-ring material properties (stiffness, damping) calculated from DMA characterization are used in Eqs. (2), (3), (7) and (9) for several TVD operating conditions (temperature, frequency) producing the Figs. 4, 5, 6 and 7. The difference of results obtained with constant and varying coefficients for the equations of motion (1) and (5), respectively, are discussed through Figs. 8 and 9. Finally, the results are summarized and discussed in the last section.

3.1 Dynamical Mechanical Analysis

In Eqs. (7) and (9) the storage and loss $E^{'}$, $E^{"}$, and therefore, the complex E^{*} moduli (Eq. (4)) can be obtained via DMA measurements of the TVD rubber-ring. Indeed, Dynamical Mechanical analysis (DMA) is an experimental technique which consists in applying a cyclic and controlled strain ($\varepsilon_{exp} = 0.2\%$), to a sample at different frequencies (0.2, 2, 20Hz) and testing temperatures, from -10 to 120°C, as in Fig. 3 (left). Then, master curves (e.g. Fig. 3, right) are built to predict the mechanical behavior of the TVD rubber-ring under the engine operating conditions, a given master curve corresponding to a given reference temperature. Master curves were obtained and fitted (Tab. (2)) for the engine room temperature $20, 40, \ldots, 100°C$. Further details about the DMA apparatus, principle, and the companion master curve reconstruction methodology can be found in [16].

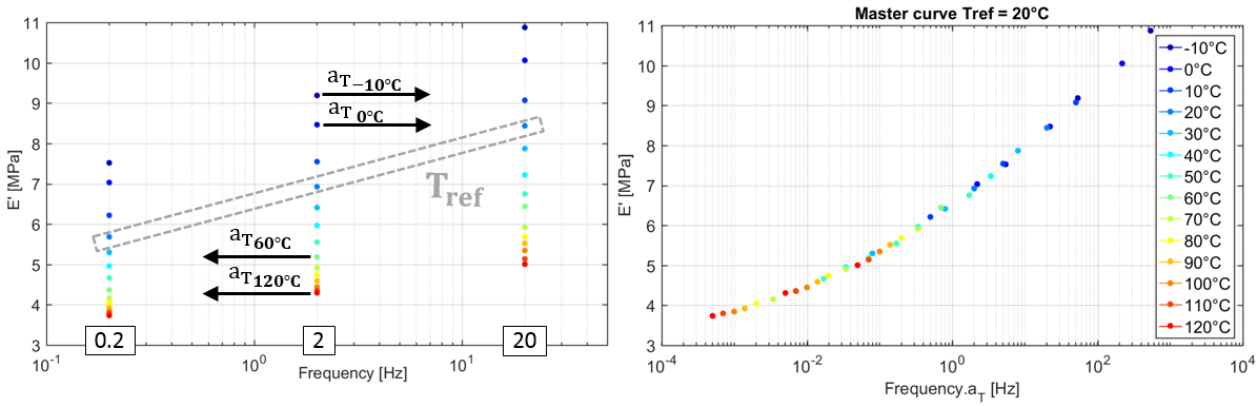


Fig. 3. TVD rubber-ring DMA data (left) and correspondent master curve (right)

Table 2. Empirical equations describing the TVD rubber-ring moduli as F ($T_{ref}, f_{req}, 0.002$)

T_{ref} (°C)	Storage modulus $E^{'}$(MPa)	Loss modulus $E^{"}$ (MPa)
20	$6.55\ f_{req}{}^{0.0814}$	$5.79\ f_{req}{}^{0.0156} - 4.81$
40	$5.68\ f_{req}{}^{0.0815}$	$5.41\ f_{req}{}^{0.0163} - 4.58$
60	$5.02\ f_{req}{}^{0.0820}$	$6.17\ f_{req}{}^{0.0141} - 5.47$
80	$4.49\ f_{req}{}^{0.0808}$	$6.07\ f_{req}{}^{0.0139} - 5.49$
100	$4.27\ f_{req}{}^{0.0835}$	$6.34\ f_{req}{}^{0.0137} - 5.81$

3.2 Simulations

Table 3. TVD characteristics at $T_{exp} = 60°C$ (average), used to trace the constant FRF in Figs. 4 and 5

K (N m/rad)	C (N m s/rad)	Resonance (Hz)	Damping ratio ξ
58000	6.4	216.5	0.075

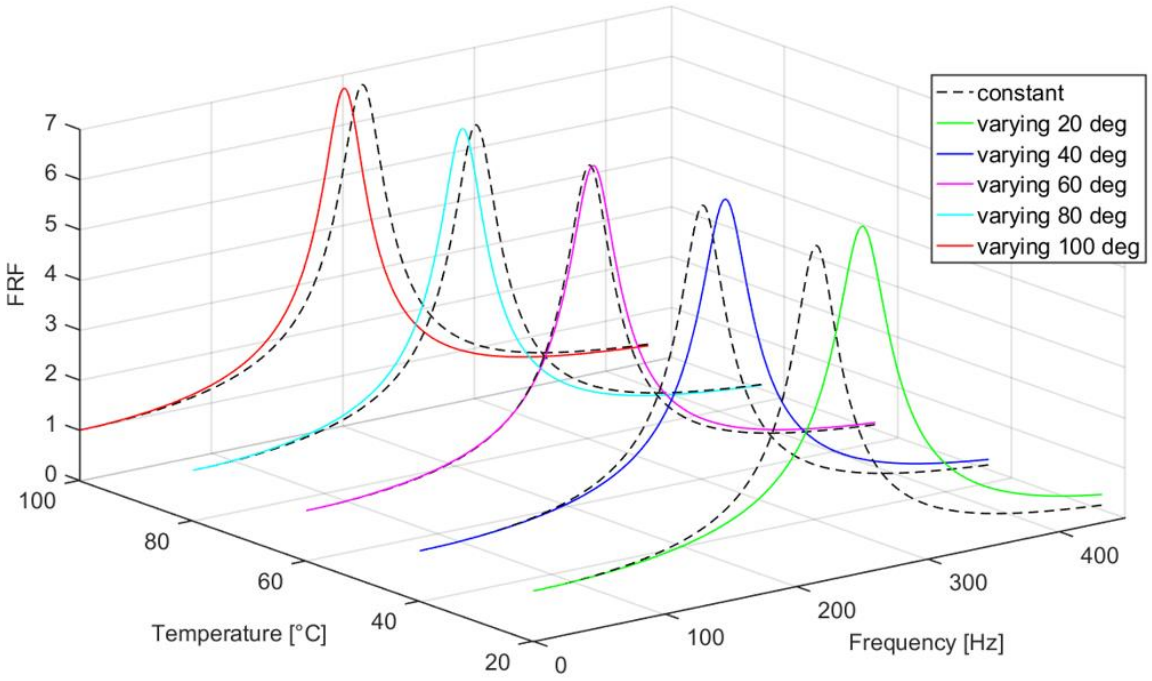


Fig. 4. TVD amplitude, frequency response for several temperatures

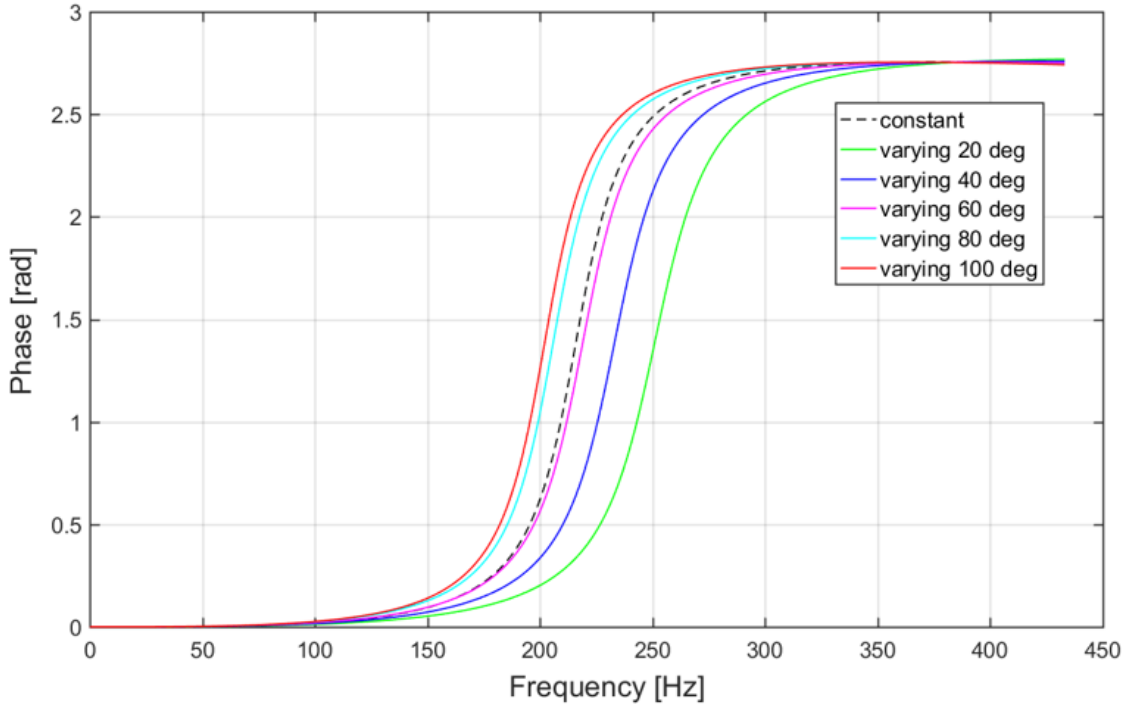


Fig. 5. TVD phase, frequency response for several temperatures

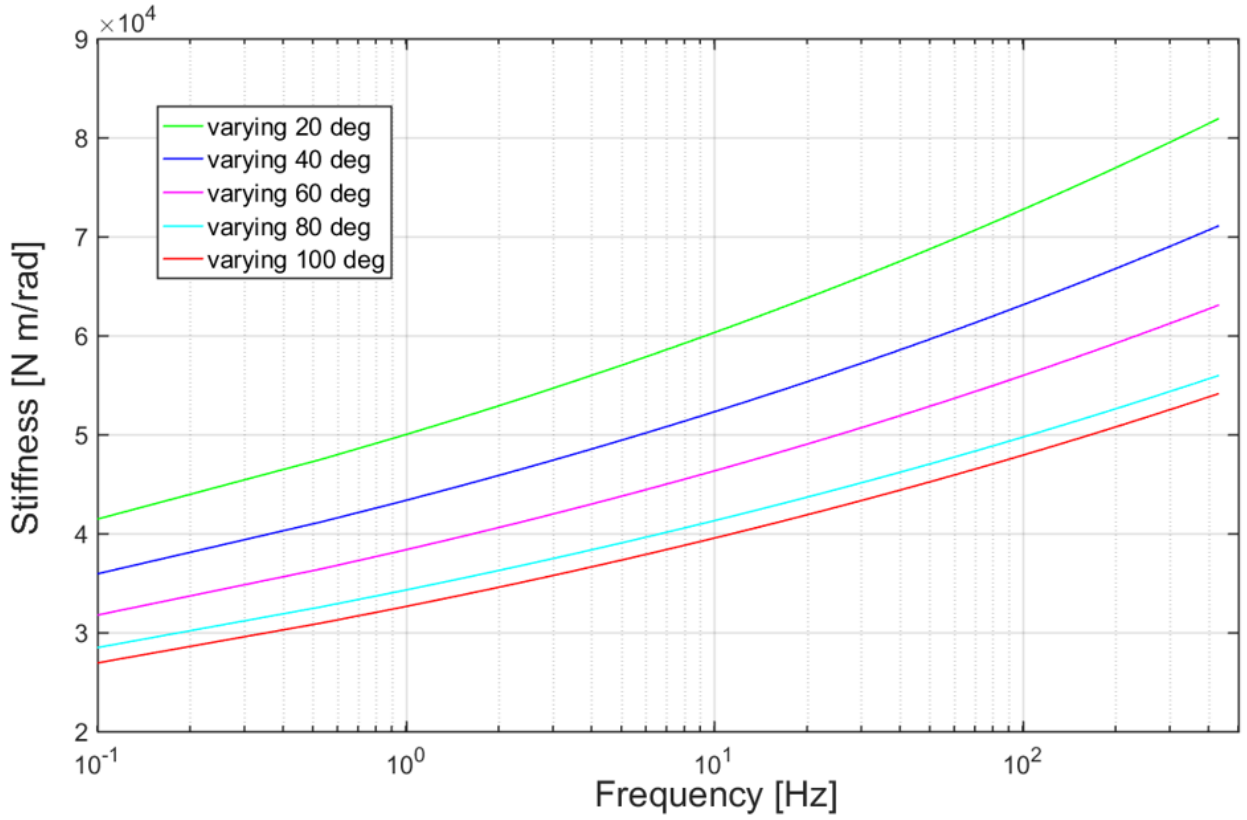


Fig. 6. TVD rubber-ring stiffness K_{var} for several temperatures

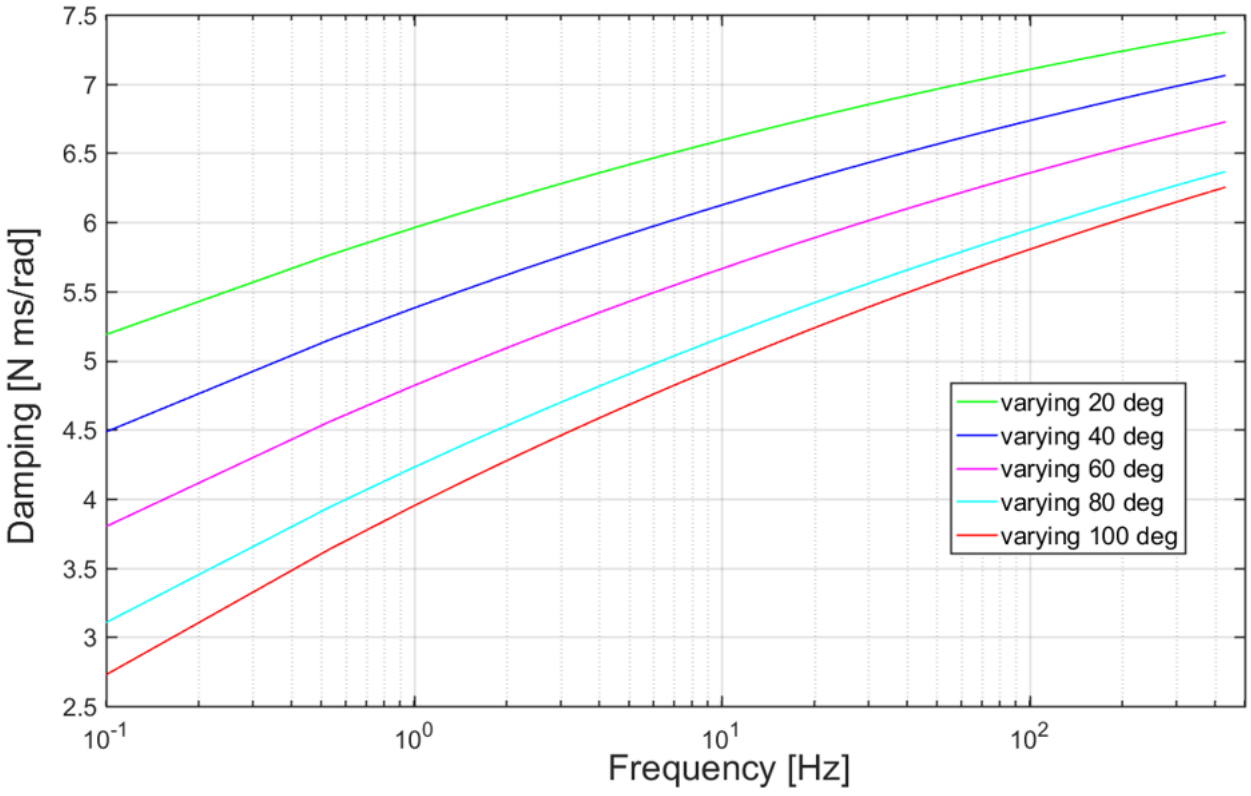


Fig. 7. TVD rubber-ring damping C_{var} for several temperatures

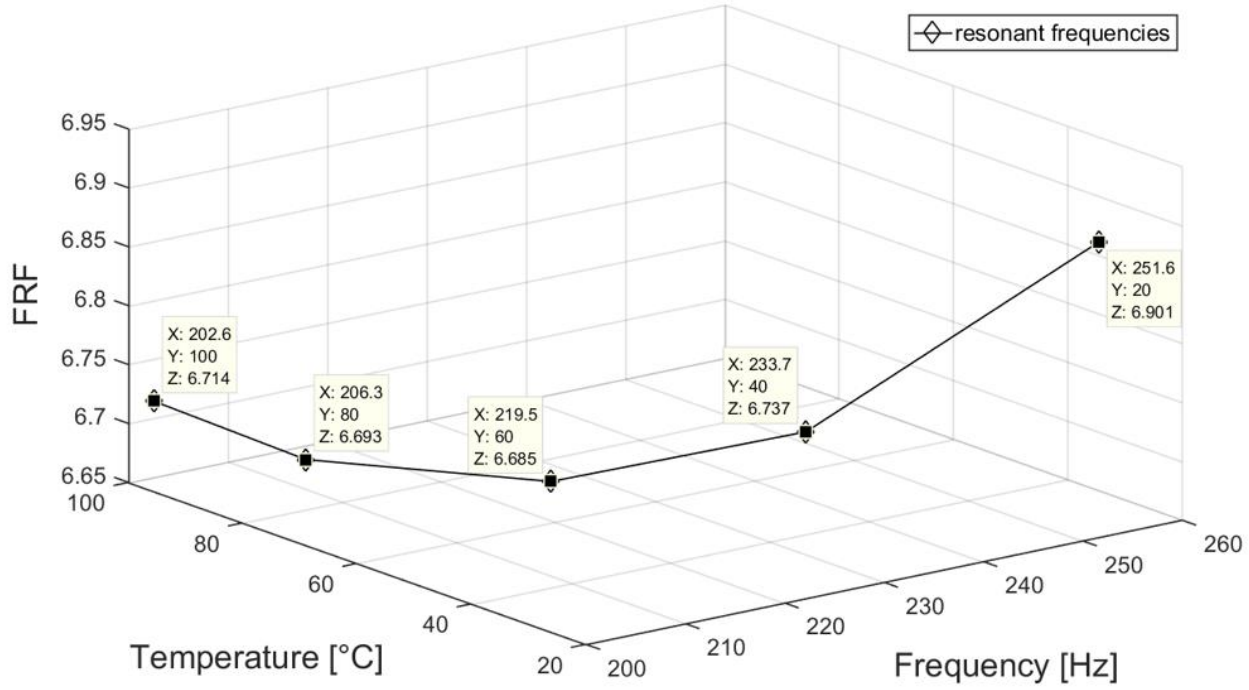


Fig. 8. FRFs maximum peaks when K and C are assumed to be constant

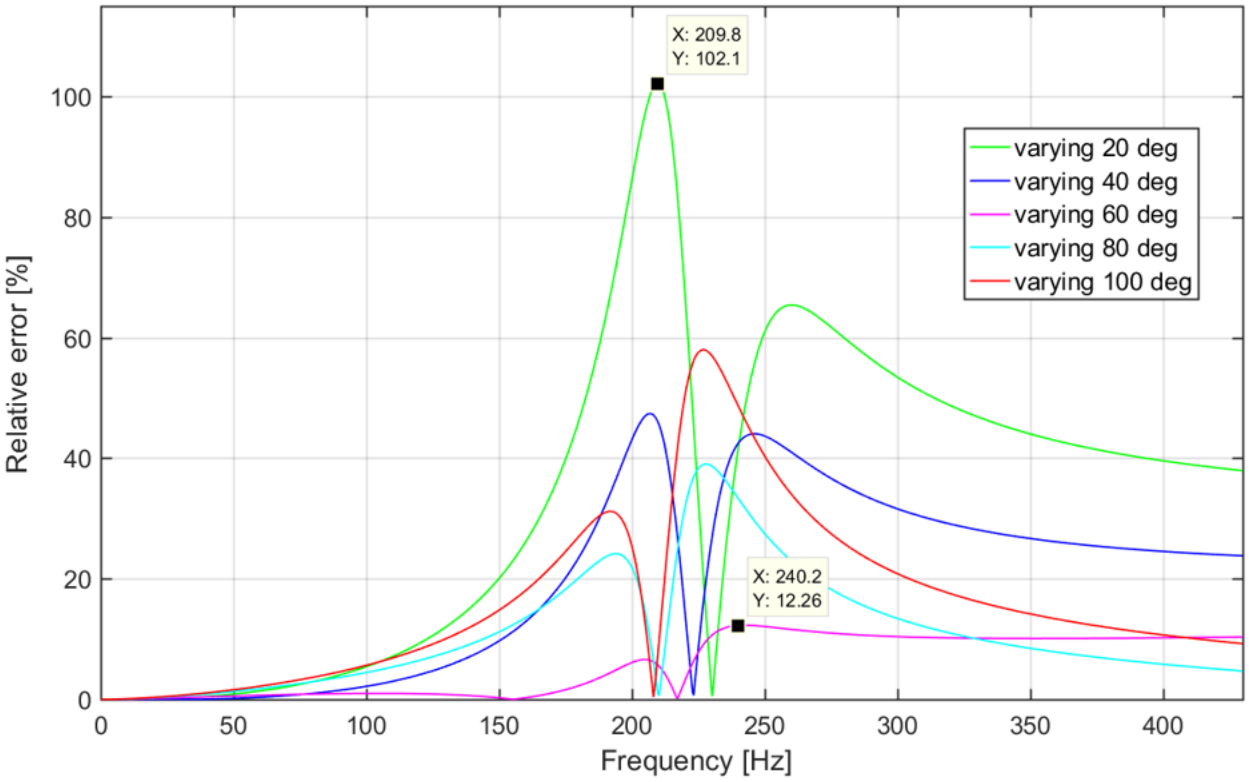


Fig. 9. FRFs relative error when K and C are assumed to be constant

Table 4. TVD resonance frequencies as a function of the frequency $T_{exp} = T_{ref}$

Temperature (°C)	20	40	60	80	100
Frequency (Hz)	251.6	233.7	219.5	206.3	202.6

4 Discussion and conclusion

Constant parameters stiffness K and damping C are considered in Tab. (3). Sometimes, these average values are used to represent the TVD operating at steady conditions, e.g. $T_{exp} = 60°C$, $\varepsilon_{exp} = 0.2\%$ and f_{exp} coinciding with the engine acyclism ($\sim 30Hz$), and throughout the engine operation point. In practice, constant K and C are often used in straightforward models (Eq. (1)), whereas in this paper, they are used to highlight the variation of the TVD response (Eq. (2)) as a function of the temperature and frequency. Moreover, the TVD response is analyzed as a function of its operating conditions (temperature, frequency) because it is assumed here that the moduli in Eq. (4) and, consequently, the TVD rubber-ring properties K_{var} and C_{var} depend exclusively on the temperature and the frequency (no Payne effect) [16], thus for the constant strain $\varepsilon_{exp} = 0.2\%$, different operating conditions lead to different responses as in Figs. 4 and 5.

The differences between the FRFs in the Figs. 4 and 5 are proportional to the rubber-ring stiffness and damping variations in the Figs. 6 and 7 since the FRFs are generated from K_{var} and C_{var} using Eqs. (2) and (3). Thus, both the FRFs and the rubber-ring properties from DMA vary proportionally with the TVD operating conditions (temperature, frequency) and the empirical equations in Tab. (2).

In Fig. 4 when the TVD working temperature is changed, e.g. from $T_{exp} = 60°C$ to 80°C, the maximum amplitude (peak) value of its FRF slightly changes (Fig. 8), i.e. it changes by a few percent with a maximum of 3.3% at $T_{exp} = 20°C$ when compared to the constant case in Tab. (3) ($T_{exp} = 60°C$).

Assuming constant K and C ($FRF_{constant}$ in Fig. 4) for the same temperature ($T_{exp} = 60°C$) seem to be good approximations of the realistic K_{var} and C_{var} ($FRF_{60\,deg}$ in Fig. 4) with a maximum relative error of around 12.3 % (Fig. 9). However, throughout the engine operating point with f_{exp} ranging from $0Hz$ (engine at rest) to 2 times the TVD resonant frequency ($\sim 430Hz$) in Fig. 9, the relative error increases substantially when the temperature is changed. For example, comparing the $FRF_{20\,deg}$ obtained at $T_{exp} = 20°C$ (K_{var} and C_{var} as in Eqs. (7, 9)) and $FRF_{60\,deg}$ (K and C as in Tab. (3)) at $T_{exp} = 60°C$ the relative error $(FRF_{20\,deg} - FRF_{constant})/FRF_{20\,deg}$ between these TVD responses can reach around one hundred percent, more precisely, 102.1% as in Fig. 9.

Another interesting point when considering the viscoelasticity of the TVD rubber-ring is the different resonant frequencies in Tab. (4) accordingly with the operating conditions, i.e. the strain, the temperature and the frequency to which the rubber-ring might be subjected. When the temperature is increased the TVD resonance peak is shifted to the left. This is because the stiffness K in Eq. (6) depends on G' which depends on E' as in Eq. (4), thus the TVD resonant frequency calculated by the second term of Eq. (3) also depends on the TVD operating conditions.

Future work will consist in developing an experimental set-up to characterize the behavior of the TVD and thus validate the simulation results obtained through the present approach.

Nomenclature

FEAD	Front Engine Accessory Drive	TVD	Torsional Vibration Damper
FRF	Frequency Response Function	DMA	Dynamical Mechanical Analysis

Acknowledgements

The authors are very grateful to the Auvergne Rhone Alpes regional council and Volvo-Renault Trucks Corporation who supported this work.

References

[1] D. Ewins, S. S. Rao, S.S. Braun, *Encyclopedia of vibration*, pp. 165-174. Academic Press, Oxford (2001), doi: http://dx.doi.org/lO. 1006/rwvb.2001

[2] R.S. Lakes, *Viscoelastic materials*, Cambridge University Press (2009).

[3] J. Zhang, J. W. Zu, *Non-linear vibrations of viscoelastic moving belts*, Journal of Sound and Vibration, Vol. 216, Toronto (1998), pp. 93-105, doi: https://doi.org/10.1006/jsvi.1998.1689

[4] H. Ding, L. -Q. Chen, *Nonlinear models for transverse forced vibration of axially moving viscoelastic beams*, Shock and Vibration, Vol. 18, IOS Press (2011), pp. 281-287, doi: 10.3233/SAV20100586

[5] L. -Q. Chen, H. Ding, *Steady-state transverse response in coupled planar vibration of axially moving viscoelastic beams*, ASME, Vol. 132, New York (2010), doi: 10.1115/1.4000468

[6] Marynowski, K., *Non-Linear Dynamic Analysis of an Axially Moving Viscoelastic Beam*, J. Theor. Appl. Mech., Vol. 40 (2002), pp. 465–482.

[7] Marynowski, K, Kapitaniak, T, *Zener Internal Damping in Modelling of Axially Moving Viscoelastic Beam with Time-Dependent Tension*, J. Non-Linear Mech., Vol. 42 (2007), pp. 118–131.

[8] A. Q. Bhatti, H. Varum, *Comparison between the visco-elastic dampers and magnetorheological dampers and study the effect of temperature on the damping properties*, WCEE, Lisboa (2012).

[9] J. C. Jauregui, J. A. Becerril, A. L. Guzman, *Viscoelastic torsional damper model*, in Power Transmission and Gearing Conference, ASME, Vol. 88, New York (1996), pp. 777-780.

[10] J. M. Kelly, *Moving load problems in the theory of viscoelasticity*, Ph.D Diss., Stanford (1962).

[11] K. Wakabayashi, Y. Honda, T. Kodama, K. Shimoyamada, *Torsional vibration damping of diesel engine with rubber damper pulley*, JSME, Serie C, Vol. 38, No. 4, (1995), pp. 670-678.

[12] M. Kinoshita, T. Sakamoto, *An experimental study of a torsional/bending damper pulley for an engine crankshaft*, Society of Automotive Engineers, SAE Paper n. 891127 (1989).

[13] L. Manin, R. Dufour, S. Schultz, *Pulley torsional vibration damper characterization*, Mechanics & Industry, Vol. 14, AFM, EDP Sciences (2013), pp. 151-155, doi: 10.1051/meca/2013057

[14] H. Blanc, *Dynamique des rotors en torsion Etude des amortisseurs de torsion*, Techniques de l'Ingenieur (2000), Ref.: BM5124 V1.

[15] R. N. Jazar, *Advanced Vibrations A Modern Approach*, pp. 197-209, Springer, New York (2013), doi: 10.1007/978-1-4614-4160-1

[16] C. A. F. Silva, L. Manin, R. G. Rinaldi, D. Remond, E. Besnier, M. –A. Andrianoely, Modeling of power losses in poly-V belt transmissions: hysteresis phenomena (enhanced analysis), Mech. Mach. Theory, Vol. 121 (2018), pp. 373-397, doi: https://doi.org/10.1016/j.mechmachtheory.2017.10.008

[17] P. P. Hujare, A. D. Sahasrabudhe, Experimental investigation of damping performance of viscoelastic material using constrained layer damping treatment, AMME Procedia Materials Science Vol. 5 (2014), pp. 726-733, doi: https://doi.org/10.1016/j.mspro.2014.07.321

[18] A. G. Piersol, T. L. Paez, Harris' Shock and Vibration Handbook, McGraw Hill, New York (2010)

[19] M. Thomas, F. Laville, Simulation des vibrations mécaniques, Presses de l'Université du Québec, 2007.

Effect of temperature on the tuning of a piezoelectric resonant shunt composed of variable inductance or variable capacitance

R. Darleux [1], **B. Lossouarn** [1], **J.-F. Deü** [1]
[1] Laboratoire de Mécanique des Structures et des Systèmes Couplés (LMSSC),
Conservatoire national des arts et métiers (Cnam),
292 rue Saint-Martin, 75003 Paris, France
e-mail: **robin.darleux@lecnam.net**

Abstract

The piezoelectric resonant shunt is an electromechanical device that can significantly damp mechanical vibrations if it is finely tuned. However, temperature may influence the electrical components of the shunt and the mechanical parameters of the vibrating structure, and deteriorate the damping performance as a consequence. The objective of this work is to describe how inductive and capacitive components can be chosen so that the shunt tuning is maintained in the case of temperature variations. Two solutions of fully passive adaptive shunts are developed, tested and compared. The first solution includes a variable inductance. In contrast, the second solution includes a variable capacitance and intends on keeping the shunt inductance as constant as possible. Experiments validate the concept of a resonant shunt that autonomously adapts to temperature variations.

1 Introduction

Mechanical vibrations can be mitigated by bonding piezoelectric patches on the surface of a vibrating structure, as it allows transferring part of the vibration energy to an electrical circuit where it can be dissipated in a resistive component. A well documented electrical circuit is the resonant shunt [1], which is the electromechanical equivalent of a tuned mass damper (also called dynamic vibration absorber). The vibration damping induced by this device is mainly owed to a precise tuning of the electrical parameters [2, 3, 4]. Besides, electrical parameters and mechanical characteristics of the system may strongly evolve with environmental parameters such as temperature. Several studies have highlighted the dependence in temperature of piezoelectric properties [5, 6]. While solutions have been proposed for an online tuning of the resonant shunt, they are either limited to a few decibels of vibration damping [7], or active solutions that require external power [8]. Recently, the choice of the magnetic material of the considered inductor has been highlighted as a way to passively counterbalance the tuning variations of a resonant shunt [9].

The objective of this work is to validate the concept of an autonomous resonant shunt, whose tuning is maintained in case of temperature variations. To do so, an electromechanical model of the structure is developed in section 2. Two solutions, denoted solutions A and B, are proposed: the adapting component is a variable inductance in the solution A, while it is a variable capacitance in the solution B. Then in section 3, we describe the experimental setup of a vibrating cantilever beam covered with a pair of piezoelectric patches. From there, the design of electrical components for both solutions is performed. Finally, experimental results in section 4 show that both solutions sustain the tuning up to at least $50\,^{\circ}\mathrm{C}$. In the end, the concept of a reliable and fully passive resonant shunt adpating to temperature variations is validated.

Mechanical quantity		Electrical quantity
Force	$\leftrightarrow$	Voltage
Velocity	$\leftrightarrow$	Electrical current
Compliance	$\leftrightarrow$	Capacitance
Mass	$\leftrightarrow$	Inductance
Viscous damping	$\leftrightarrow$	Resistance

Table 1: Direct electromechanical analogy

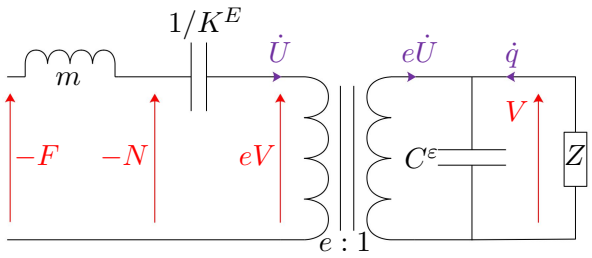


Figure 1: Equivalent electrical circuit of the shunted structure

2 Electromechanical model of a piezoelectric resonant shunt

2.1 Piezoelectric shunt damping

Piezoelectric shunt damping consists in bonding a vibrating structure with piezoelectric transducers, and connecting them to an electrical circuit. The electrical energy transferred to this circuit is dissipated in a resistive component, and mechanical vibrations are mitigated as a consequence. In this article, we consider the case of two piezoelectric patches covering opposite faces of a cantilever beam. Three stages are needed to describe the dynamics of the system: developing an electromechanical model of the piezoelectric transducer, developing a mechanical model of the structure, and defining the shunt components.

We propose a one-dimensional model of a piezoelectric transducer:

$$\begin{aligned} N &= K^E U - eV, \\ q &= C^\varepsilon V + eU, \end{aligned} \tag{1}$$

where N is the normal force applied to the transducer, q is the electric charge on an electrode, U is the displacement in the longitudinal direction, and V is the voltage between the electrodes of the piezoelectric device. The constants e, K^E and C^ε are the coupling coefficient, the structural stiffness when the piezoelectric transducer is short-circuited (i.e. when $V = 0$), and the piezoelectric capacitance under no displacement (i.e. when $U = 0$), respectively. The mechanical structure is then modeled as an undamped one degree-of-freedom system, whose dynamics can be expressed by

$$m\ddot{U} + K^D U = F + \frac{e}{C^\varepsilon} q, \tag{2}$$

where m is the mass, F is the excitation force, and $K^D = K^E + e^2/C^\varepsilon$ is the stiffness in open-circuit. Equation (2) highlights the equivalent mechanical quantities on its left side, and the external forces applied to the structure on its right side. Finally, the structure is shunted with an impedance Z. Ohm's law applied to the shunt impedance gives

$$V = -Z\dot{q}. \tag{3}$$

The use of a direct electromechanical analogy, summed up in Table 1, allows to define the equivalent electrical circuit of the electromechanical system based on equations (1), (2) and (3). It is represented in Figure 1. These equations can also be combined to obtain the dimensionless transfer function between the displacement and the excitation at angular frequency Ω:

$$\frac{U}{F/K^D} = \frac{1 + \mathrm{j}\Omega C^\varepsilon Z}{\left[1 - \left(\frac{\Omega}{\Omega_\mathrm{O}}\right)^2\right](1 + \mathrm{j}\Omega C^\varepsilon Z) - \frac{k_{c0}^2}{1+k_{c0}^2}}, \tag{4}$$

with $\mathrm{j}^2 = -1$. In this last equation, k_{c0} is the coupling factor, and Ω_O and Ω_S are the mechanical resonance angular frequencies in open-circuit (i.e. when $q = 0$) and in short-circuit (i.e. when $V = 0$), respectively. These quantities are defined by

$$\Omega_\mathrm{O} = \sqrt{\frac{K^D}{m}}, \qquad \Omega_\mathrm{S} = \sqrt{\frac{K^E}{m}}, \qquad k_{c0} = \sqrt{\frac{\Omega_\mathrm{O}^2 - \Omega_\mathrm{S}^2}{\Omega_\mathrm{S}^2}}. \tag{5}$$

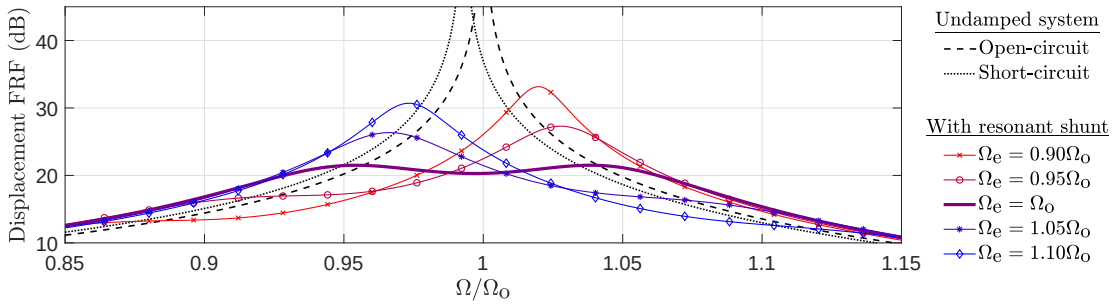


Figure 2: Displacement FRF around the resonance for $k_{c0} = 0.12$ and $\xi_e = (\xi_e)_{opt}$

2.2 Adaptive tuning of a resonant shunt in case of temperature variations

2.2.1 Solution A: Resonant shunt with variable inductance

A basic resonant shunt is first considered. The impedance Z consists of a resistance R and an inductance L connected in series:

$$Z = R + \mathrm{j}\Omega L. \tag{6}$$

The transfer function in equation (4) then becomes

$$\frac{U}{F/K^D} = \frac{1 + 2\mathrm{j}\frac{\xi_e}{\Omega_e}\Omega - \left(\frac{\Omega}{\Omega_e}\right)^2}{\left[1 - \left(\frac{\Omega}{\Omega_O}\right)^2\right]\left[1 + 2\mathrm{j}\frac{\xi_e}{\Omega_e}\Omega - \left(\frac{\Omega}{\Omega_e}\right)^2\right] - \frac{k_{c0}^2}{1+k_{c0}^2}}, \tag{7}$$

with Ω_e the electrical resonance angular frequency and ξ_e the electrical damping defined by

$$\Omega_e = \frac{1}{\sqrt{LC^\varepsilon}}, \qquad \xi_e = \frac{R}{2}\sqrt{\frac{C^\varepsilon}{L}}. \tag{8}$$

The main drawback of the resonant shunt is the need for a precise tuning [2, 3, 4]. The transfer function criterion detailed in [2] states that the optimal values of these electrical parameters are:

$$(\Omega_e)_{opt} = \Omega_O, \qquad (\xi_e)_{opt} = \sqrt{\frac{3}{8}}k_{c0}. \tag{9}$$

The frequency response function (FRF) in equation (7) is represented in Figure 2. Variations of the electric damping ξ_e are not considered since it has little influence on the vibration mitigation when compared to Ω_e variations [2, 3, 4]. Figure 2 shows that the damping performance drops as soon as the electrical resonance differs from its optimal value: for $k_{c0} = 0.12$, a difference of 10 % between Ω_e and its optimal value adds nearly 10 dB to the transfer function peak. Hence, the tuning condition in equation (9) should be verified in any situation to maintain the vibration damping. However, mechanical and electrical parameters of the system may vary when temperature changes. If the evolutions with temperature of the mechanical resonance and the piezoelectric capacitance are given data, then the inductance is the control parameter. That means the value of L should be adapted so that it always verifies

$$\Omega_O^2(T) = \frac{1}{L(T)\,C^\varepsilon(T)}. \tag{10}$$

In this work, we suppose that Ω_O, C^ε and L evolve linearly over the considered temperature range, and the associated temperature coefficients are noted α_{Ω_O}, α_{C^ε} and α_L, respectively. Room temperature is noted T_0.

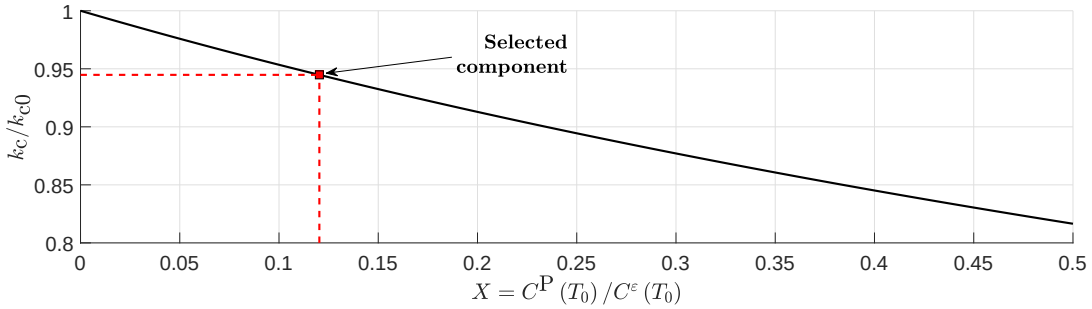


Figure 3: Evolution of the coupling coefficient in case of an added parallel capacitance

The evolutions with temperature of these quantities can be written as follows:

$$\begin{aligned} \Omega_O(T) &= \Omega_O(T_0)\left[1+\alpha_{\Omega_O}(T-T_0)\right], \\ C^\varepsilon(T) &= C^\varepsilon(T_0)\left[1+\alpha_{C^\varepsilon}(T-T_0)\right], \\ L(T) &= L(T_0)\left[1+\alpha_L(T-T_0)\right]. \end{aligned} \tag{11}$$

A linear approximation of equation (10) gives the relation between the temperature coefficients that should be verified to keep the resonant shunt tuned:

$$\alpha_L = -\left(2\alpha_{\Omega_O} + \alpha_{C^\varepsilon}\right). \tag{12}$$

This solution for a passive temperature adjustment of the resonant shunt tuning, denoted solution A, requires to design the inductor according to temperature characteristics of the system. A limit of this solution would be that the inductance of the passive inductors may depend on the electrical current, as Legg reported in [10]. Since the electrical current in the shunt is generated by mechanical vibrations, the shunt inductance may strongly depend on the amplitude of the mechanical excitation. Furthermore, the temperature and electrical current characteristics of these inductors are interdependent, because they both depend on the magnetic circuit properties. As a consequence, designing inductors with large variations of inductance with temperature may lead to large variations with the excitation amplitude as well. For this reason, another solution is developed below.

2.2.2 Solution B: Resonant shunt with additional variable capacitance

For this second proposed solution, the objective is first to design an inductor that is as stable as possible with respect to temperature and electrical current. Then, a capacitance C^P is added in parallel with a series RL shunt. This added capacitance should be designed to maintain the damping performance when temperature evolves. In this case, the impedance Z is

$$Z = \frac{R + \mathrm{j}\Omega L}{1 + \mathrm{j}\Omega R C^P - L C^P \Omega^2}. \tag{13}$$

The system FRF is still expressed by equation (7). The only differences are that the piezoelectric capacitance C^ε is replaced by $C^\varepsilon + C^P$, and that the coupling factor k_{c0} is replaced by a lower coupling factor k_c. Indeed, using the parameters defined in (5) allows to express the equivalent coupling coefficient k_c:

$$\frac{k_c}{k_{c0}} = \frac{1}{\sqrt{1+\frac{C^P}{C^\varepsilon}}}. \tag{14}$$

The evolution of the coupling coefficient with the additional capacitance is represented in Figure 3. It shows that adding some capacitance to the shunt deteriorates the electromechanical coupling, and thus the damping

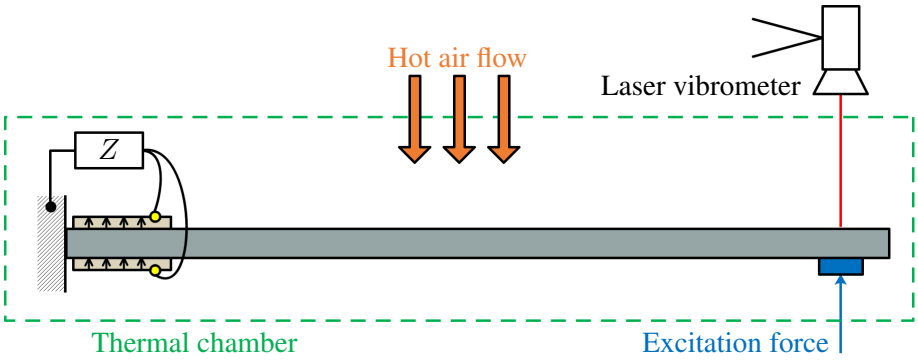


Figure 4: Sketch of the experimental setup inside the thermal chamber

performance [2, 11]. In this situation, the tuning condition derived from equation (10) becomes

$$\Omega_{\mathrm{O}}^2(T) = \frac{1}{L(T)\left[C^{\varepsilon}(T) + C^{\mathrm{P}}(T)\right]}. \tag{15}$$

If the evolutions with temperature of the mechanical resonance, the piezoelectric capacitance and the inductance are given data, then the control parameters are the added capacitance and its temperature characteristics. We assume that C^{P} evolves linearly over the considered temperature range, which means $C^{\mathrm{P}}(T) = C^{\mathrm{P}}(T_0)\left[1 + \alpha_{C^{\mathrm{P}}}(T - T_0)\right]$ with $\alpha_{C^{\mathrm{P}}}$ its temperature coefficient. A linear approximation of equation (15) shows that the tuning condition becomes

$$\alpha_{C^{\mathrm{P}}} = -\left[\left(\alpha_L + 2\alpha_{\Omega_{\mathrm{O}}} + \alpha_{C^{\varepsilon}}\right)\frac{C^{\varepsilon}(T_0)}{C^{\mathrm{P}}(T_0)} + \alpha_L + 2\alpha_{\Omega_{\mathrm{O}}}\right]. \tag{16}$$

Using dimensionless quantities, the tuning condition can also be written:

$$Y = -\left(\frac{a}{X} + b\right), \qquad \text{with} \quad Y = \frac{\alpha_{C^{\mathrm{P}}}}{\alpha_{C^{\varepsilon}}}, \quad X = \frac{C^{\mathrm{P}}(T_0)}{C^{\varepsilon}(T_0)}, \quad b = \frac{\alpha_L + 2\alpha_{\Omega_{\mathrm{O}}}}{\alpha_{C^{\varepsilon}}}, \quad a = b + 1. \tag{17}$$

This solution for a passive temperature adaptation of the resonant shunt is denoted solution B. Solution B may offer a more stable solution than solution A. Indeed, the electrical current should have little influence on the inductance, since it has been designed to this end. However, more stability is achieved at the expense of the damping performance. For this reason, the added capacitance should be as small as possible.

3 Design of electrical components

3.1 Experimental setup

The experimental setup consists of a cantilever beam covered with two piezoelectric patches close to the clamped end. The duralumin beam is 170 mm long, 25 mm large and 2 mm thick. The PIC 151 PZT patches are 25 mm long, 20 mm large and 0.5 mm thick. The excitation and the velocity measurement are both made at the free end of the beam. The setup is eventually heated with a heat gun inside a thermal chamber, in which measurements are made with an infrared thermometer in steady thermal state. A sketch of the setup is represented in Figure 4.

The evolutions with temperature of the mechanical resonance Ω_{O} and of the piezoelectric capacitance C^{ε} are plotted in Figure 5. The estimated temperature coefficients are $\alpha_{\Omega_{\mathrm{O}}} = -0.5 \cdot 10^{-3}\mathrm{K}^{-1}$ and $\alpha_{C^{\varepsilon}} = 3.1{\cdot}10^{-3}\mathrm{K}^{-1}$. The evolution with temperature of the piezoelectric capacitance is in rough agreement with the manufacturer data. The main reason for the remaining difference is the variations of the structural properties, as it leads to piezoelectric capacitance variations because of the electromechanical coupling.

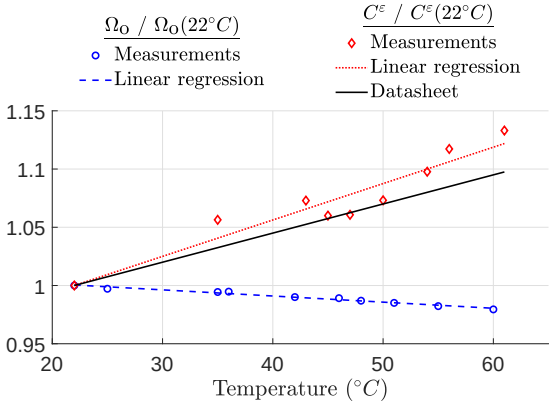


Figure 5: Evolution with temperature of the piezoelectric capacitance and the mechanical resonance angular frequency in open-circuit divided by their respective values at room temperature

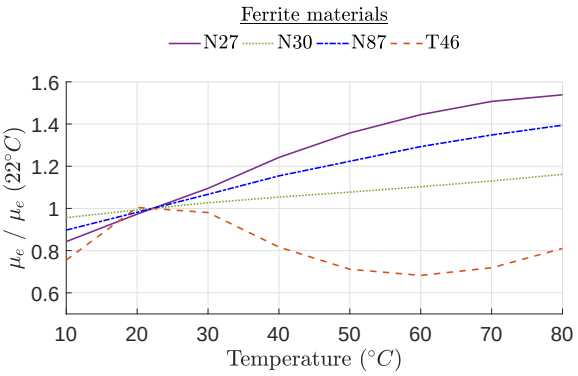


Figure 6: Effective permeability evolution with temperature of available ferrite materials in ungapped E 16/8/5 core geometry, extracted from datasheets

3.2 Variable inductor for solution A

Optimized inductors for piezoelectric shunt damping usually require large inductance and small resistance values. Passive inductors meeting these requirements can be made following the method described in [12]. Inductors are produced by winding N turns of conductive wire around magnetic cores of effective permeability μ_e. This permeability depends on the properties of the magnetic circuit [13]. The obtained inductance value is proportionnal to N^2 and μ_e, with a geometry depending constant β:

$$L = \beta \mu_e N^2. \tag{18}$$

Equation (12) shows the inductance has to vary with temperature to keep the resonant shunt tuned. Since β and N do not depend on temperature, equation (18) shows the temperature coefficient of the effective permeability α_{μ_e} is equal to α_L. For practical reasons related to ferrite materials availability, the ungapped E 16/8/5 core geometry from core manufacturer Epcos TDK has been selected. The temperature characteristics of several available ferrite materials are compared in Figure 6. According to equation (12) and measurements in subsection 3.1, designing a resonant shunt adapting to temperature variations requires an inductor whose inductance decreases when temperature rises. In an other work [9], we have shown that the T46 ferrite material is the one that should be selected among the available ones.

We measure that $C^\varepsilon = 38.3$ nF and $\Omega_O/2\pi = 322$ Hz, so the required inductance is estimated at $L = 6.38$ H using equation (10). Since data from manufacturers give $\beta = 0.672$ nH and $\mu_e = 1410$, we calculate $N = 2600$ turns using equation (18). The produced inductor is then tested with an LCR-meter at 322 Hz. Inductance variations with temperature and electrical current are plotted in Figure 7. When available, data from manufacturers are represented as well.

In Figure 7(a), the available datasheet do not accurately predict the inductance evolution from 22 °C to 60 °C. Moreover, the predicted decrease of the inductance is only obtained at low levels of excitation and below 42 °C. In Figure 7(b), our measurements show as well a decrease of the inductance under 40 µA and 42 °C. However, as soon as the environmental parameters are outside this range of low temperature and low levels of excitation, the inductance increases. In hindsight, this practical characterization highlights the correlation that can exist between temperature and excitation effects on the inductance. For this reason, it can be difficult to design an inductor whose characteristics meet our requirements over a wide range of both temperature and excitation amplitude. This is the reason why the solution B has been developed.

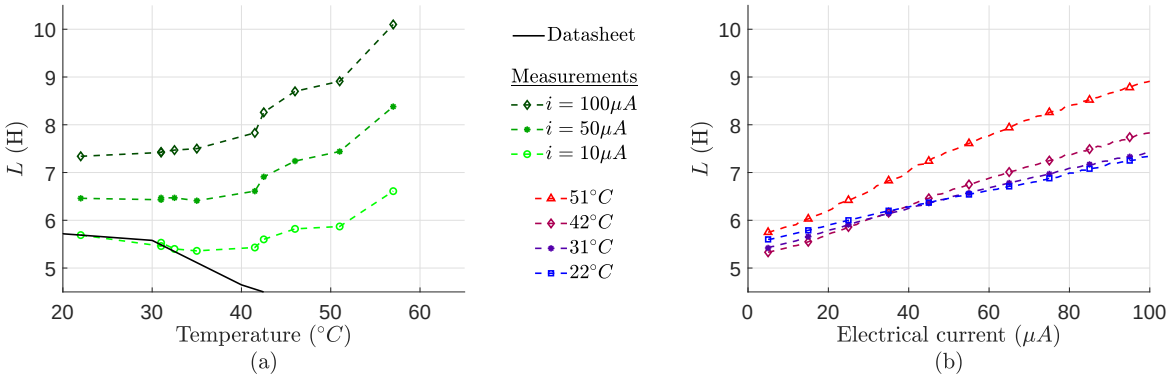


Figure 7: Effect of (a) temperature and (b) electrical current on the T46 ferrite-based inductor.

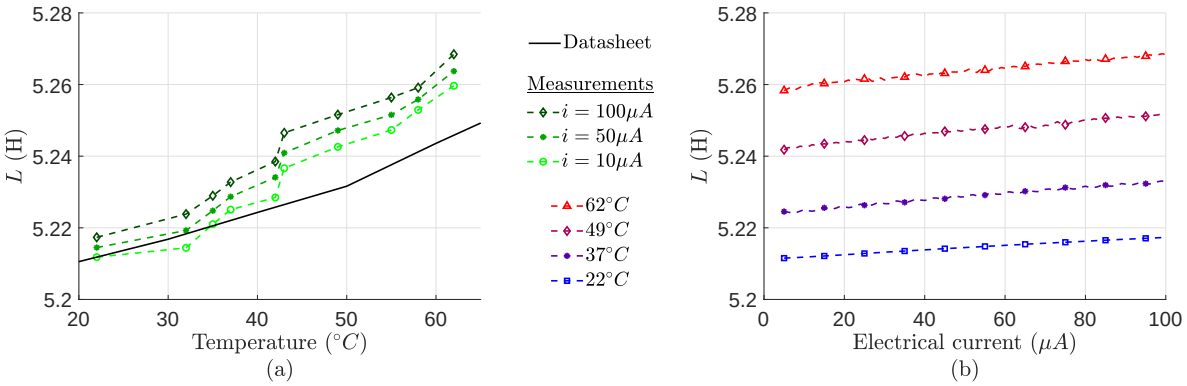


Figure 8: Effect of (a) temperature and (b) electrical current on the N48 ferrite-based inductor. Notice the scale of the y-axis.

3.3 Variable capacitor for solution B

In the case of solution B, the objective is first to design an inductor whose variations with electrical current and temperature are as small as possible. Equation (18) is still considered. Obtaining the required inductance value while minimizing α_{μ_e} is possible by adding an air gap in the magnetic circuit of the component [13]. The N48 ferrite material with the gapped RM10 core geometry from Epcos TDK has been selected. In this case, $\beta = 2.48$ nH, $\mu_e = 254$ and $N = 2870$ turns.

Figure 8 shows the characteristic of the produced inductor. Data from core manufacturers do not precisely predict the inductance evolution with temperature, which may be due to a smaller air gap than anticipated. The estimated temperature coefficient for L is $(\alpha_L)_{\mathrm{B}} = 2.5 \cdot 10^{-4}\mathrm{K}^{-1}$. This value is nearly thirty times smaller than $(\alpha_L)_{\mathrm{A}}$ from subsection 3.2. Moreover, electrical current and temperature effects do not seem strongly correlated. Hence, the produced inductor meet our requirements by having a nearly constant inductance when environmental parameters evolve.

The next step is to select the added capacitance C^{P}. Given the decrease of k_{c} expressed in equation (14) and plotted in Figure 3, the goal is to add the smallest possible value of C^{P}. Figure 9 represents the optimal tuning possibilities for solution B, as expressed in equation (17). Values of $\alpha_{\Omega_{\mathrm{O}}}$ and $\alpha_{C^{\varepsilon}}$ are estimated in subsection 3.1. The graph shows that the smaller C^{P} is, the bigger its variations have to be to maintain the tuning. As a consequence, we selected ceramic capacitors of class 2 [14], which are characterized by large variations of capacitance with temperature over their working range. Characteristics of some of the dielectrics that vary the most with temperature are extracted from datasheets and added to Figure 9. The selected capacitor is a Y5V $4.7\,\mathrm{nF}$ capacitor, as it is the closest component to the optimal curve among the available ones. Its measured characteristics is rougly in agreement with its datasheet. Both are placed

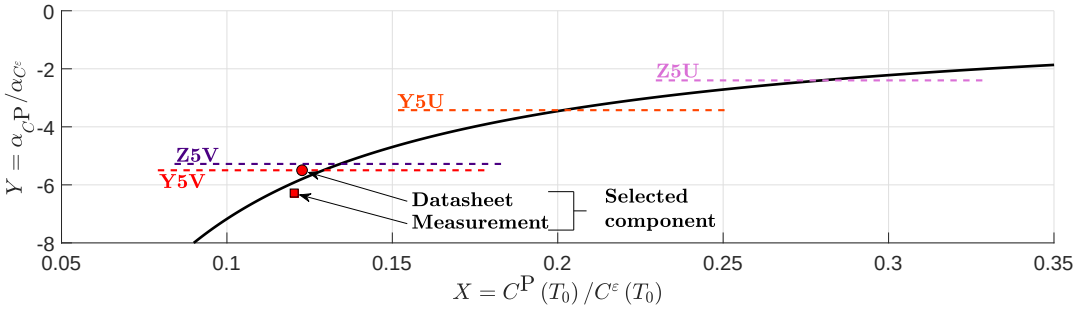


Figure 9: Solid line: Optimal characteristics of the added capacitance. Dashed lines: Usual temperature variations of several class 2 dielectrics. Red points: selected capacitor.

on Figure 9. The selected component is added to Figure 3 as well, and it shows that trading off some of the damping performance for more stability makes sense, since the coupling coefficient k_{c} is only 6 % lower than $k_{\mathrm{c}0}$.

4 Vibration damping of a clamped beam

4.1 Adaptive resonant shunt using solution A

The solution A is considered for passive vibration damping of the second bending mode of a clamped beam. The inductance of the resonant shunt is the T46 ferrite-based inductor designed in subsection 3.2. At room temperature, the shunt resistance is intentionally set under its theoretical optimal value [2, 4]. The evolution of the shunt tuning is thus more easily detected. Experiments are conducted at low levels of excitation to benefit from the inductance decrease spotted on Figure 7. The experimental setup is represented in Figure 4.

Experimental FRFs are compared at different temperatures in Figure 10. The shunt tuning is preserved from room temperature to around 51 °C. It appears that the system benefits from a larger decrease of the inductance value than what had been anticipated by looking at Figure 7. Moreover, it is experimentally noticed that the shunt gets mistuned at steady thermal state if the excitation amplitude increases. This is a consequence of the strong mutual dependence between electrical current and temperature effects on the inductance, spotted in Figure 7. For this reason, the solution A might keep the shunt tuned only if the mechanical excitation is stable enough over time. This could be a restrictive condition in some practical applications.

4.2 Adaptive resonant shunt using solution B

The solution B is now considered to damp bending vibrations of a clamped beam. The inductance of the resonant shunt is the N48 ferrite-based inductor designed in subsection 3.3. The shunt resistance is also set under its optimal value to spot tuning variations more easily.

Experimental FRFs are compared at different temperatures in Figure 11. The shunt seems to get slightly mistuned from room temperature to 50 °C, before coming back to a better tuning at 62 °C. This can be explained by the nonlinear variations with temperature of the added capacitance. Its variations are more important below 50 °C, which explains the initial mistuning. The reduction of the height between the initial peaks at 304 Hz and 334 Hz and the initial valley at 322 Hz may be explained by the increase of the electrical damping with temperature. Moreover, changing the excitation amplitude at steady thermal state do not get the shunt mistuned as much as with solution A. In the end, the shunt tuning is preserved from room temperature to 62 °C, so these results are promising. The electromechanical coupling is reduced when compared to solution A, which leads to a slightly lower damping performance, but stability over a wider range of temperature is achieved.

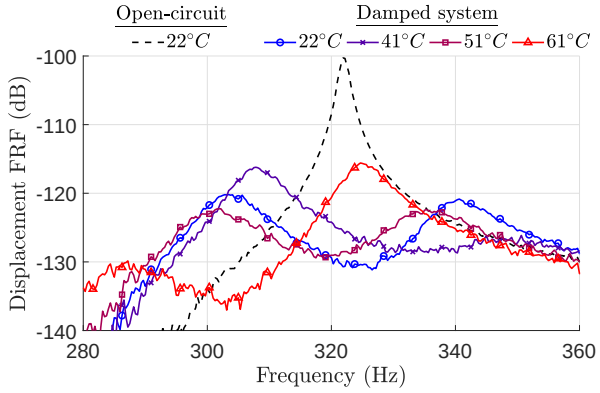


Figure 10: Experimental displacement FRFs at different temperatures with solution A

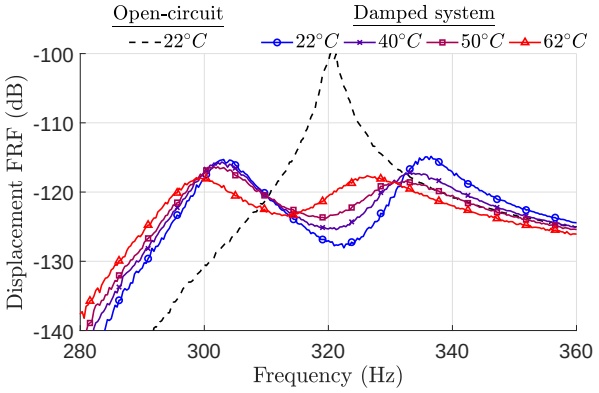


Figure 11: Experimental displacement FRFs at different temperatures with solution B

5 Conclusions

The objective of this work is to design a piezoelectric resonant shunt that passively adapts to temperature variations. Two solutions are developed: the first one (denoted solution A) involves a variable inductance, while the second one (denoted solution B) keeps the shunt inductance constant and uses a variable parallel capacitance. An electromechanical model of the vibrating structure connected to the resonant shunt leads to a tuning criterion for each solution. Electrical components are then designed to meet these criteria by taking into account temperature characteristics of the system parameters. When it comes to inductors, we produce them with magnetic circuits. The evolution with temperature of such components depends on the geometry and the material of the magnetic circuit. When it comes to the added parallel capacitance, the class 2 capacitors are selected since they are the ones that vary the most with temperature. All these components are tested, and then used to damp bending vibrations of a cantilever beam. Experimental results show that the shunt tuning is vaguely maintained from room temperature to around 50 °C for solution A, and more precisely maintained from room temperature to more than 60 °C for solution B.

The design of a fully passive and adaptive resonant shunt over a wider range of temperature would require predictive models of electrical components evolutions with temperature. For this matter, solution A would be quite complex to implement, because of the mutual dependence of electrical current and temperature characteristics of the produced inductors. Solution B seems easier to design and implement, but this more predictable and stable solution comes at the expense of the electromechanical coupling. If the slight induced drop of damping performance is acceptable, then solution B may be recommended.

References

[1] N. W. Hagood and A. Von Flotow, *Damping of structural vibrations with piezoelectric materials and passive electrical networks*, Journal of Sound and Vibration, Vol. 146, No. 2, Elsevier BV (1991), pp. 243–268.

[2] O. Thomas, J. Ducarne, J.-F. Deü, *Performance of piezoelectric shunts for vibration reduction*, Smart Materials and Structures, Vol. 21, No. 1, IOP Publishing (2012), pp. 015008.

[3] J.-W. Park, J.-H. Han, *Sensitivity analysis of damping performances for passive shunted piezoelectrics*, Aerospace Science and Technology, Vol. 33, No. 1, Elsevier BV (2014), pp. 16–25.

[4] M. Berardengo, A. Cigada, S. Manzoni, M. Vanali, *Vibration Control by Means of Piezoelectric Actuators Shunted with LR Impedances: Performance and Robustness Analysis*, Shock and Vibration, Vol. 2015, Hindawi Limited (2015), pp. 1–30.

[5] M. W. Hooker, *Properties of PZT-based piezoelectric ceramics between -150°C and 250°C*, NASA (1998).

[6] C. Miclea, C. Tanasoiu, L. Amarande, C. F. Miclea, C. Plavitu, M. Cioangher, L. Trupina, C. T. Miclea, C. David, *Effect of temperature on the main piezoelectric parameters of a soft PZT ceramic*, Romanian Journal of Information Science and Technology (2007), Vol. 10, No. 3, pp. 243–250.

[7] D. Niederberger, M. Morari, *An autonomous shunt circuit for vibration damping*, Smart Materials and Structures, Vol. 15, No. 2, IOP Publishing (2006), pp. 359–364.

[8] J. J. Hollkamp, T. F. Starchville, *A Self-Tuning Piezoelectric Vibration Absorber*, Journal of Intelligent Material Systems and Structures, Vol. 5, No. 4, SAGE Publications (1994), pp. 559–566.

[9] R. Darleux, B. Lossouarn, J.-F. Deü, *Passive self-tuning inductor for piezoelectric shunt damping considering temperature variations*, Journal of Sound and Vibration, (Accepted for publication), Elsevier BV (2018).

[10] V. E. Legg, *Magnetic Measurements at Low Flux Densities Using the Alternating Current Bridge*, Bell System Technical Journal, Vol. 15, No. 1, IEEE (1936), pp. 39–62.

[11] A. J. Fleming, S. Behrens, S. O. R. Moheimani, *Reducing the inductance requirements of piezoelectric shunt damping systems*, Smart Materials and Structures, Vol. 12, No. 1, IOP Publishing (2013), pp. 57–64.

[12] B. Lossouarn, M. Aucejo, J.-F. Deü, B. Multon, *Design of inductors with high inductance values for resonant piezoelectric damping*, Sensors and Actuators A: Physical, Vol. 259, Elsevier BV (2017), pp. 68–76.

[13] E. C. Snelling, *Soft ferrites*, 2nd edition, CRC Press (1969).

[14] M. J. Pan, C. A. Randall, *A brief introduction to ceramic capacitors*, IEEE Electrical Insulation Magazine, Vol. 26, No. 3, IEEE (2010), pp. 44–50.

Optimization of multi-modal targeted energy transfer performance of nonlinear passive vibration absorbers

K. Dekemele [1], **P. Van Torre**[2], **M. Loccufier** [1]
[1] Ghent University, Department of Electrical Energy, Metals, Mechanical Construction and Systems,
Tech Lane Ghent Science Park - Campus A 914, 9052, Ghent, Belgium
e-mail: **kevin.dekemele@ugent.be**

[2] Ghent University, Department of Information Technology,
Tech Lane Ghent Science Park - Campus A 15, 9052, Ghent, Belgium

Abstract
Nonlinear energy sinks (NES) are use to passively mitigate vibrations of mechanical systems. The NES is connected to system with a nonlinear spring, such that NES has no fixed natural frequency. A linear absorber only mitigates a single frequency while a NES engages in resonance capture cascade (RCC), sequentially mitigating the modal frequencies of the vibrating system for transient vibrations. Recently, three performance measures for NES were defined. 1) energy dissipation, the vibration energy dissipated by NES 2) pumping time , the time for the NES to absorb a single mode 3) cascading time, the time the NES engages in RCC. All three performance measure are algebraic, requiring no numerical simulation to compute. In other research, NES coefficients are optimized by performing many numerical simulations. Here, the NES coefficients are determined with the pumping or cascading time. The result is a quick and practical optimizing procedure based on the algebraic performance that results in a robust and multi-modal vibration absorber.

1 Introduction

To passively reduce vibrations in mechanical systems, the linear tuned mass spring damper (TMD), is locally added to the vibrating structure, serving as a vibration absorber. The vibrations in the mechanical system are greatly mitigated if the TMD is tuned such that its natural frequency equals the vibration frequency of the mechanical system [1]. The performance of the TMD in mitigating vibrations is significantly reduced if the vibrating frequency of the mechanical system shifts. This is caused by changes in the mechanical system: reduced stiffness or reduces/increased mass. A TMD also fails to significantly reduce vibrations consisting of several different frequencies. A mechanical system typically vibrates significantly with a combination of its vibration modes, characterized by the modal or eigenfrequencies and modeshapes or eigenvectors.

To counter these downsides, a vibration absorber with nonlinear connecting stiffness has been proposed, a so-called nonlinear energy sink (NES)[2]. As opposed to the TMD which has a fixed natural frequency determined by its mass and connecting linear stiffness, the nonlinear stiffness of a NES has no fixed vibration frequency [3]. Because of this, a well-tuned NES is able to mitigate several different frequencies and is more robust to detuning. The mechanism of vibration mitigation of a NES is called targeted energy transfer (TET). It is defined as a sudden one-way irreversible transfer of energy from source (mechanical system) to a donor (NES) [2]. For the NES to engage in TET, the vibration energy has to be above a certain threshold, as opposed to a TMD, which has the same behavior regardless of vibration energy. A major advantage the NES has over the linear TMD is the capability to dissipate multiple frequencies for transient vibrations, [2], through the resonance capture cascading (RCC) mechanism. An impulsive loaded mechanical system

vibrates according to its eigenfrequencies, which NES mitigated sequentially from high frequency to low frequency (hence cascades). This sequential mode mitigation is easily observed in the NES, which initially vibrates with a single frequency, even though the mechanical system vibrates with multiple frequencies. If enough energy of this mode has been dissipated, the NES will start to vibrate with the modal frequency just below the initial mode. This continues until all modes have been dissipated.

In [4], Nyugen proposed a tuning method for an impulsively loaded mechanical system by finding the energy threshold above which TET ensues, and derived an algebraic measure of performance of the NES, the pumping time, granted the mass ratio of NES and main system is small. This was only done for single-mode vibrating systems. In a preliminary work, the author extended the tuning and pumping time to RCC [5]. The multi-modal pumping time was dubbed cascading time and was determined through modal decomposition of the vibration energy into separate modes. Besides the duration of TET and RCC, an other important aspect of NES performance is the residual vibration energy. Contrary to the linear TMD, a NES is not capable to completely reduce the vibrations of the mechanical system. A residual amount is left after NES and RCC, and is dissipated very slowly. This residual energy was expressed in [4] in the so-called energy dissipation for single-mode vibrations and is extended here to a multi-modal equivalent, the cascade dissipation. To complement the preliminary work of the author,[5], the developed algebraic performance measures are effectively employed to develop a simple optimization of a NES, both for single and multi-modal vibrations.

This paper is structured as follows: In section 2 the dynamics of the compound system, (mechanical system + NES) are described, while assuming single-mode vibration. Then the nonlinear differential equations are solved by using semi-analytic techniques in section 3, which yield the slow flow dynamics, describing the nonlinear dynamics on a slow time scale. The results of section 3 are used in section 4 to derive the tuning of the NES and its performance measures. Then, the pumping time, energy dissipation and their multi-frequency equivalents are used to optimize a NES for both TET (section 5) and RCC (section 6). The performance of the NES is also compared to an optimally tuned TMD, both in the single and multi-modal case.

2 System dynamics

The vibrating mechanical system is linear chain of mass spring dampers with n-degrees of freedom, $x \in \mathbb{R}^n$. On coordinate x_ℓ, a single NES is attached. This compound system is shown on Figure 1a. By performing modal decoupling, modal coordinates $q \in \mathbb{R}^n$, n eigenfrequencies ω_i and the eigenvector matrix, $E = [e_1 \quad e_2 \quad \dots \quad e_n] \in \mathbb{R}^{n\times n}$ are obtained with $x = Eq$. The modal dynamics are:

$$\begin{cases} M_q\ddot{q} + C_q\dot{q} + K_q q + m_{na}e_*(\ell)^T\ddot{x}_{na} = E^T F \\ m_{na}\ddot{x}_{na} + c_{na}(\dot{x}_{na} - \dot{x}_\ell) + k_{na}(x_{na} - x_\ell)^3 + k_{lin}(x_{na} - x_\ell) = 0 \end{cases} \tag{1}$$

with $e_*(\ell) \in \mathbb{R}^{n\times 1}$ the ℓ-th row of E, $M_q \in \mathbb{R}^{n\times n}$ the modal mass, $C_q \in \mathbb{R}^{n\times n}$ the modal damping, $K_q \in \mathbb{R}^{n\times n}$ the modal stiffness matrix and $F \in \mathbb{R}^{n\times 1}$ the force vector applied to coordinates x. To simplify the analysis, it is assumed that the system vibrates with a single vibration mode $i : x(t) = \sum_{k=1}^{n} e_k q_k(t) = e_i q_i(t)$ and that there is no external forcing, $F = 0^{n\times 1}$. The physical coordinate $x_\ell = e_i(\ell)q_i$ is reintroduced:

$$\begin{cases} \ddot{x}_\ell + \epsilon\lambda\dot{x}_\ell + \omega_i^2 x_\ell + \epsilon\ddot{x}_{na} = 0 \\ \epsilon\ddot{x}_{na} + \epsilon\lambda_{na}(\dot{x}_{na} - \dot{x}_\ell) + \epsilon\Omega_3\omega_i^4(x_{na} - x_\ell)^3 + \epsilon\kappa\omega_i^2(x_{na} - x_\ell) = 0 \end{cases} \tag{2}$$

with

$$\epsilon\lambda = \frac{c_{q,i}}{m_{q,i}} \quad \omega_i^2 = \frac{k_{q,i}}{m_{q,i}} \quad \epsilon = \frac{m_{na}e_i^2(\ell)}{m_{q,i}} \quad \kappa = \frac{k_{lin}}{m_{na}\omega_i^2} \quad \lambda_{na} = \frac{c_{na}}{m_{na}} \quad \Omega_3 = \frac{k_{na}}{m_{na}\omega_i^4}$$

It is assumed that the mass ratio $\epsilon \ll 1$, implying that the coefficient of each NES term in (1) is small. The $n+1$ DOF problem is reduced to a 2DOF problem because of the single mode assumption, depicted on Figure 1b. For the single mode assumption to hold, both ϵ and κ should remain small to have a weak

coupling between NES and mechanical system. Later, it will be seen that multi-modal vibrating main system can be decoupled into single-mode vibrating main system. The differential equation in (2) does not allow an exact analytic solution because of the nonlinearities. Therefore, semi-analytic techniques are used in the next section yielding an approximate solution.

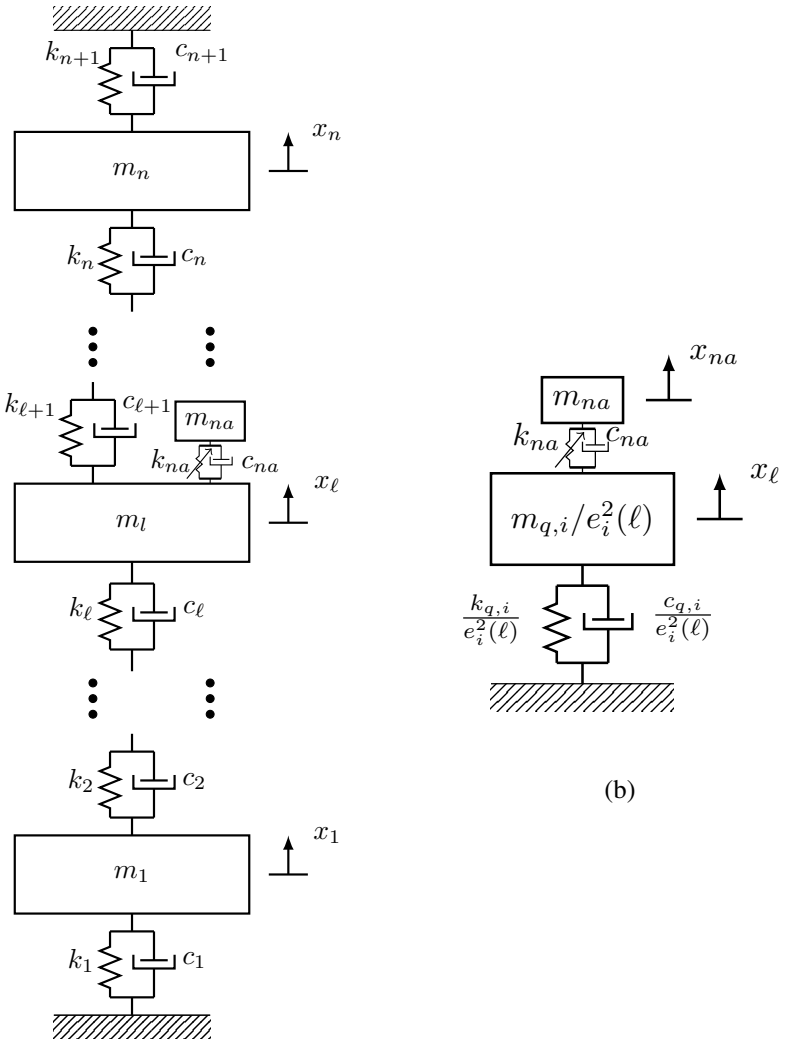


Figure 1: The studied compound system, an MDOF linear system, with a NES attached to coordinate ℓ (a). Single mode assumption of compounds system results in a 2DOF problem (b).

3 Semi-analytic

In this section, the slow flow dynamics are derived through a semi-analytic reduction. These slow flow dynamics are used to state algebraic performance measures. New variables are introduced, $u = x_l + \epsilon x_{na}$, the center of mass of modal/absorber system , and $v = x_l - x_{na}$, the relative absorber movement. In the new coordinates (2) becomes (while omitting terms $\mathcal{O}(\epsilon^2)$ and with $\epsilon\ddot{u} = -\epsilon\omega_i^2 u + \mathcal{O}(\epsilon^2)$)

$$\begin{cases} \ddot{u} + \omega_i^2 u + \epsilon\Big(\lambda\dot{u} + \omega_i^2(v-u)\Big) + \mathcal{O}(\epsilon^2) = 0 \\ \epsilon(\ddot{v} + \omega_i^2 v) + \epsilon\omega_i^2(u-v) + \epsilon\lambda_{na}\dot{v} + \epsilon\Omega_3\omega_i^4 v^3 + \epsilon\kappa\omega_i^2 v + \mathcal{O}(\epsilon^2) = 0 \end{cases} \tag{3}$$

Then, (3) is semi-analytic reduced as in [5] in three steps; 1) Complexification of u and v to $\varphi(t)e^{j\omega_i t} = \dot{u} + j\omega_i u$ and $\varphi_{na}(t)e^{j\omega_i t} = \dot{v} + j\omega_i v$, φ_{na} and $\varphi \in \mathbb{C}$ the amplitude/phase modulating part and $e^{j\omega_i t}$ the single-mode vibrating part, 2) the nonlinear behavior is seen as a perturbation on the linear dynamics; by expanding both complexified variables in a major $\mathcal{O}(\epsilon^0)$ and minor contribution $\mathcal{O}(\epsilon)$: $\varphi = \varphi_0 + \epsilon\varphi_1$ and $\varphi_{na} = \varphi_{na0} + \epsilon\varphi_{na1}$, 3) the dynamics are assumed to behave on two time separate time scale, a fast $T_0 = t$ and slow $T_1 = \epsilon t$, $u(t) = u(T_0, T_1)$, $v(t) = v(T_0, T_1)$. This way, d/dt now is a total derivate, $\frac{d}{dt} = \frac{\partial}{\partial T_0} + \epsilon\frac{\partial}{\partial T_1}\mathcal{O}(\epsilon^2)$. It is vital for both the perturbation analysis as the two-timing that the mass ratio is small. These three operations on (3) results in:

$$\begin{cases} \dfrac{\partial\varphi_0}{\partial T_0} + \epsilon\dfrac{\partial\varphi_0}{\partial T_1} + \epsilon\dfrac{\partial\varphi_1}{\partial T_0} + \epsilon\lambda\dfrac{\varphi_0}{2} + \epsilon\dfrac{\omega_i^2}{2j\omega_i}\big(\varphi_{na0} - \varphi_0\big) + \Big(\epsilon\lambda\dfrac{\bar{\varphi}_0}{2} - \epsilon\dfrac{\omega_i^2}{2j\omega_i}\big(\bar{\varphi}_{na0} - \bar{\varphi}_0\big)\Big)e^{-2j\omega_i t} = 0 \\ \epsilon(\dfrac{\partial\varphi_{na0}}{\partial T_0}) + \epsilon\dfrac{\omega_i^2}{2j\omega_i}\big(\varphi_0 - \varphi_{na0}\big) + \epsilon\lambda_{na}\dfrac{\varphi_{na0}}{2} + \dfrac{\epsilon\kappa\omega_i^2}{2j\omega_i}\varphi_{na0} + \dfrac{\epsilon\Omega_3\omega^4}{\big(2j\omega_i\big)^3}\displaystyle\sum_{k=0}^{3}(-1)^k\binom{3}{k}\varphi_{na}^{3-k}\bar{\varphi}_{na}^{k}e^{j(3-2k-1)\omega_i t} \\ \quad - \Big(\epsilon\dfrac{\omega_i^2}{2j\omega_i}\big(\bar{\varphi}_0 - \bar{\varphi}_{na0}\big) - \epsilon\lambda_{na}\dfrac{\bar{\varphi}_{na0}}{2} + \dfrac{\epsilon\kappa\omega_i^2}{2j\omega_i}\bar{\varphi}_{na0}\Big)e^{-2j\omega_i t} = 0 \end{cases} \tag{4}$$

with bar sign the complex conjugate. To ensure the assumption of harmonic vibration and to remove secular terms (terms which may cause an infinite large response), the oscillating terms in (4) are omitted. Then, the remaining terms are collecting according to ϵ.

$$\begin{cases} \dfrac{\partial\varphi_0}{\partial T_0} = 0 \quad \Rightarrow \quad \varphi_0(T_1) \\ \dfrac{\partial\varphi_0}{\partial T_1} + \dfrac{\partial\varphi_1}{\partial T_0} + \dfrac{\lambda\varphi_0}{2} + \dfrac{\omega_i^2\varphi_{na0}}{2j\omega_i} - \dfrac{\omega_i^2\varphi_0}{2j\omega_i} = 0 \\ \dfrac{\partial\varphi_{na0}}{\partial T_0} + \dfrac{\lambda_{na}\varphi_{na0}}{2} + \dfrac{\omega_i^2\varphi_0}{2j\omega_i} - \dfrac{\omega_i^2(1-\kappa)\varphi_{na0}}{2j\omega_i} \\ \qquad -j\dfrac{\Omega_3\omega_i^4}{\omega_i^3}\left(\dfrac{3}{8}|\varphi_{na0}|^2\varphi_{na0}\right) = 0 \end{cases} \tag{5}$$

$$\begin{cases} \dfrac{\partial\varphi_0}{\omega_i\partial T_1} = -\dfrac{\xi\varphi_0}{2} + \dfrac{j\Phi_{na0}}{2} - \dfrac{j\varphi_0}{2} \\ 0 = -\dfrac{j(1-\kappa) + \xi_{na}}{2}\Phi_{na0} + \dfrac{j\varphi_0}{2} \\ \qquad + \dfrac{j3\Omega}{8}(|\Phi_{na0}|^2\Phi_{na0}) \end{cases} \tag{6}$$

The first equation of (5) tells us that φ_0 is constant for a fast time scale T_0. Gendelman shows in [6] that both φ_{na0} and φ_1 evolve towards a steady state as $T_0 \to \infty$; $\lim_{T_0\to\infty}\varphi_{na0} = \Phi_{na0}$ and $\lim_{T_0\to\infty}\varphi_1 = \Phi_1$; so that the other two equations of (5) can be written in steady state form of T_0, only dependent of the slow time scale T_1. This results in (6), with $\xi = \frac{\lambda}{\omega_i}$ and $\xi_{na} = \frac{\lambda_{na}}{\omega_i}$. Next, the complexified variables are put in polar form; $\varphi_0(T_1) = R_0(T_1)e^{j\delta_0(T_1)}$ and $\Phi_{na0}(T_1) = R_{na}(T_1)e^{j\delta_{na}(T_1)}$, R_0, R_{na}, δ_0, $\delta_{na} \in \mathbb{R}$. Splitting (6) in real and imaginary parts results in (7).

$$\begin{cases} \dfrac{\partial R_0^2}{\partial T_1} = -\xi R_0^2 - \xi_{na}R_{na}^2 \\ R_0^2 = \left[\xi_{na}^2 + \left(1 - \kappa - \dfrac{3}{4}\Omega R_{na}^2\right)^2\right]R_{na}^2 \end{cases} \tag{7}$$

$$\boxed{\begin{array}{l} \dfrac{\partial Z_0}{\partial T_1} = -\lambda Z_0 - \lambda_{na}Z_{na} \\ Z_0 = \left[\xi_{na}^2 + \left(1 - \kappa - \dfrac{3}{4}Z_{na}\right)^2\right]Z_{na} \end{array}} \tag{8}$$

By introducing the energy-like variables $E_0 = R_0^2$ and $E_{na} = R_{na}^2$ and in dimensionless form $Z_0 = \Omega R_0^2 = \Omega|\varphi_0|^2$ and $Z_{na} = \Omega R_{na}^2 = \Omega|\Phi_{na0}|^2$ (8) is obtained which describes the dynamics of the vibration energy

on a slow time scale. The first equation states that Z_0 always decreases, and the second a static relation, a slow invariant manifold (SIM) on which Z_{na} and Z_0 are confined. A collection of SIMs are shown on Figure 2a and 2b. The SIM has two extrema as long as $\xi_{na} < \frac{(1-\kappa)}{\sqrt{3}}$:

$$\begin{cases} Z_{na\pm} = \frac{4}{9}\left(2(1-\kappa) \pm \sqrt{(1-\kappa)^2 - 3\xi_{na}^2}\right) \\ Z_0^{\pm} = \left[\xi_{na}^2 + \left(1 - \kappa - \frac{3}{4}Z_{na\mp}\right)^2\right] Z^{na\mp} \end{cases} \tag{9}$$

It is shown in [4] that the existence of these extrema determines the existence of TET and whether or not significant vibration mitigation is possible.

4 Tuning and performance

Different from linear TMD's, both tuning and performance of a NES depend on the initial conditions. Although the tuning and performance is based on the formulas of the previous section that assume single-mode vibrations, the tuning and performance is easily extended to multi-modal vibrating systems by considering the initial *modal* conditions $\dot{x}(0) = \sum_{k=1}^{n} \dot{x}^{[k]}(0) = \sum_{k=1}^{n} e_k \dot{q}_k(0)$, with $\dot{x}^{[k]}(0) = e_k \dot{q}_k(0) \in \mathbb{R}^n$ the hypothetical initial speed as if only mode k is present. The initial displacements can similarly be expressed as $x^{[k]}(0) = e_k q_k(0) \in \mathbb{R}^n$. This decomposition of initial conditions makes sense as the NES only interacts with one mode at a time.

4.1 Tuning

To tune the NES for single-modal systems, the nonlinear coefficient has to be chosen such that $Z_0(0) \geq Z_0^+$, otherwise no TET occurs [4]. This means that initially, Z_0 should be above the maximum value on the SIM, Figure 2a and 2b

$$k_p \geq \frac{m_{na}\omega_i^4(Z_0^+)}{\dot{u}^2(0) + \omega_i^2 u^2(0)} \tag{10}$$

TET is fastest [5] for if it equals this expression. It is often taken a bit higher to ensure attraction to the SIM, see simulations. In the multi-modal case, the mode i which initiates the RCC has to be chosen. The initial conditions in (10) then corresponds to the modal initial conditions of mode i, $x^{[i]}(0)$ and $\dot{x}^{[i]}(0)$.

4.2 Performance

4.2.1 Energy dissipation during TET and RCC

If TET is initiated, it will persist until the slow dynamics reach the minimum of the SIM, [5]. At this point, not all of the vibration energy has been dissipated. The amount energy that has been dissipated during TET is:

$$E_{TET} = 1 - \frac{Z_0^-}{Z_0(0)} = 1 - \frac{E_0^-}{E_0(0)} \tag{11}$$

with a residual amount of vibration energy remaining. In simulation it will be seen this residual part is dissipated very slowly. In the multi-modal case, a $E_{TET}^{[k]}$ can be calculated for each mode by using the modal initial conditions. As each mode has different amount of initial vibration energy $E_0^k(0)$ and dissipated energy $E_{TET}^{[k]}$, a total, weighted cascading dissipation can be calculated as:

$$E_{RCC} = \frac{\sum_{i=1}^{k} E_{TET}^{[i]} E_0^{[i]}(0)}{\sum_{i=1}^{k} E_0^{[i]}(0)} \tag{12}$$

4.2.2 Pumping and cascading time

The SIM equation and slow flow dynamics (7) can be combined yield an expression for $\frac{\partial Z_{na}}{\partial T_1}$. By assuming an undamped main system, $\xi = 0$, separation of variables allows for integration, resulting in:

$$\frac{27}{32}Z_{na}^2 - 3(1-\kappa)Z_{na} + \Big((1-\kappa)^2 + \xi_{na}^2\Big)ln(Z_{na}) = C - \omega_i \xi_{na} T_1 = I(Z_{na}) \tag{13}$$

From this relation, the time (in slow time) it takes for the dynamics between two states of Z_{na} on the SIM can be calculated. If TET is initiated, the SIM will be descended from $Z_{na}(0)$ until Z_{na}^+. The duration of TET, called pumping time, is then:

$$\epsilon T_{pmp} = \frac{1}{2\pi\xi_{na}}\Big(I(Z_{na}(0)) - I(Z_{na}^+)\Big) \tag{14}$$

with T_{pmp} relative to the period of the modal frequency and $T_{pmp}\frac{\omega_i}{2\pi}$ the time in seconds. By considering each modal initial condition separately, a pumping time can be calculated for each mode partaking in the cascade. The total time for resonance capture is simply the sum of all of these pumping times:

$$T_{cascade} = \sum_{k=1}^{i} T_{pmp}^{[k]} \cdot \frac{\omega_k}{2\pi} \tag{15}$$

Both the pumping and cascading time have been extended to damped mechanical systems in [5].

5 SDOF optimization

The SDOF mechanical system considered has mass $m = 1$ kg, stiffness $k = 1$ N/m and no damping and with an initial speed of $\dot{x}(0) = 0.1$ m/s. The absorber mass is $m_{na} = 0.02$ kg. The nonlinear stiffness is tuned for several κ and ξ_{na} in this section. With these parameters, the energy dissipation and pumping time are already calculated before any simulation is made, and can be found on Table 1.

NES	$T_{pmp}\frac{\omega_i}{2\pi}$ [s]	E_{TET}
$\xi_{na} = 0.05 \wedge \kappa = 0.0$	131	0.986
$\xi_{na} = 0.20 \wedge \kappa = 0.0$	29	0.778
$\xi_{na} = 0.05 \wedge \kappa = 0.2$	83	0.976
$\xi_{na} = 0.10 \wedge \kappa = 0.2$	40	0.908
$\xi_{na} = 0.05 \wedge \kappa = 0.4$	46	0.95
$\xi_{na} = 0.05 \wedge \kappa = 0.5$	32	0.94

Table 1: Performance of the NES tuned for an SDOF system

5.1 Design space

O Figure 2c, the pumping time in shades of red and energy dissipation contours in function of ξ_{na} and κ are plotted for NES tune with (10), taken 10 % higher than the threshold. Clearly, the higher κ and ξ_{na}, the lower the pumping time, yet comes at a cost, a lower energy dissipation. The white area is unfeasible, where the condition $\xi_{na} < \frac{(1-\kappa)}{\sqrt{3}}$ is not met, where no E_{TET} and T_{pmp} can be calculated. In optimization terminology, T_{pmp} is the objective function and E_{TET} an inequality constraint, as we wish to dissipate sufficient vibration energy. Although an optimization algorithm would find the smallest T_{pmp} for a lower boundary of E_{TET}, further on in this section it is seen that simply increasing κ and ξ_{na} results in the slow flow (from which the T_{pmp} and E_{TET} is derived) not representing the actual vibrations.

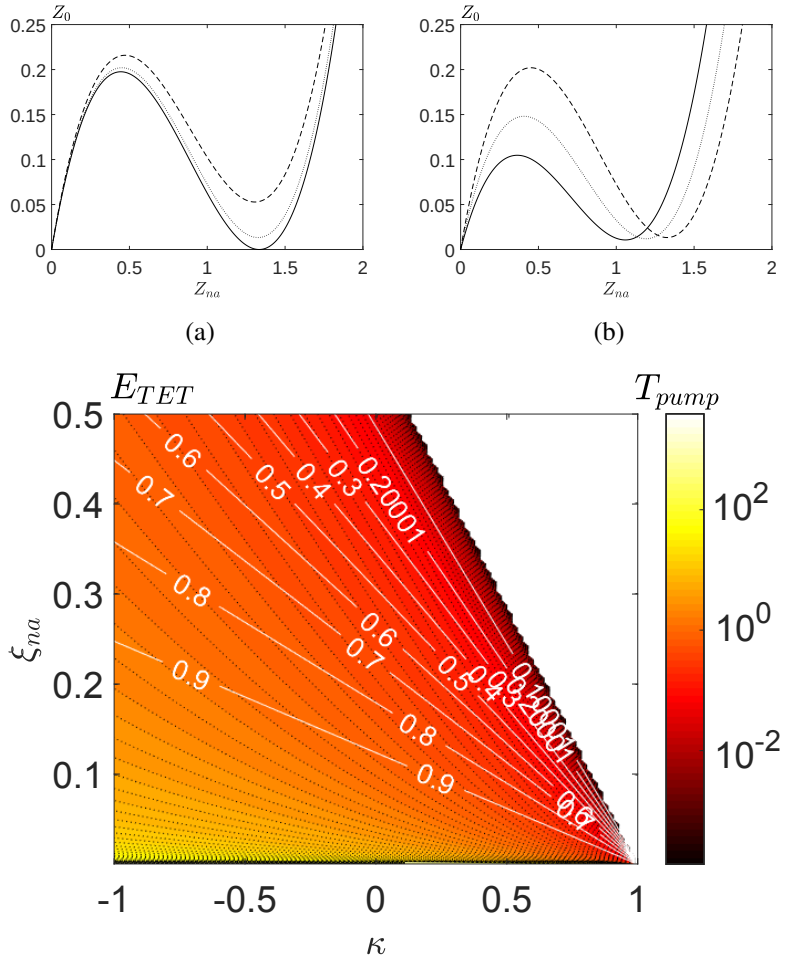


Figure 2: The SIM for $\kappa = 0$ and $\xi_{na} = [0, 0.1, 0.2]$ (full, dotted, dash) (a), $\kappa = [0, 0.1, 0.2]$ (full, dotted, dash) and $\xi_{na} = 0.1$ (b) and T_{pmp} (red shade) and E_{TET} (white contour lines) in function of ξ_{na} and κ (c).

5.2 A first simulation

A first simulation is presented here to illustrate concepts of slow flow, pumping time, energy dissipation and the actual numerical simulation of (1). Figure 3a and 3b are the main system's vibration and the vibration of the relative NES coordinate. TET happens as the NES vibrates heavily until a certain point in time. It is this time we try to estimate with the pumping time (14). After TET, a small part of the vibration energy stays in the main system, which we want to estimate with the energy dissipation (11). The slow flow dynamics (8) are simulated as well. To show that the slow flow is representative for the actual dynamics, it is compared with the envelope of the actual vibration, obtained with the *Hilbert* transform, Figure 3c and 3g, as the slow flow energy variables E_0 and E_{na} are the slow time envelopes. On average, the enveloppe of the actual dynamics follow the slow dynamics. Either the sudden change op slope for E_0 or the sudden jump in E_{na} signify the end of TET and thus happen at the pumping time. This point in time exactly equals the pumping time. The actual vibrations are not able to follow the sudden change of E_{na}, yet clearly decrease significantly after the jump. Plotting both Z_0, Z_{na} and their respective Hilbert transform on Figure 3h show that the actual dynamics don't start on the SIM. After an *attraction* phase (about 20 s), the real dynamics follow the SIM on average. This attraction phase plus the pumping time are the total time the actual dynamics engage in TET. The right branch of the SIM is traversed until the minimum of $\{Z_{na}^+, Z_0^-\}$ after which the dynamic fall back to the left branch of the SIM. The Hilbert transform needs some time to completely fall to this left side.

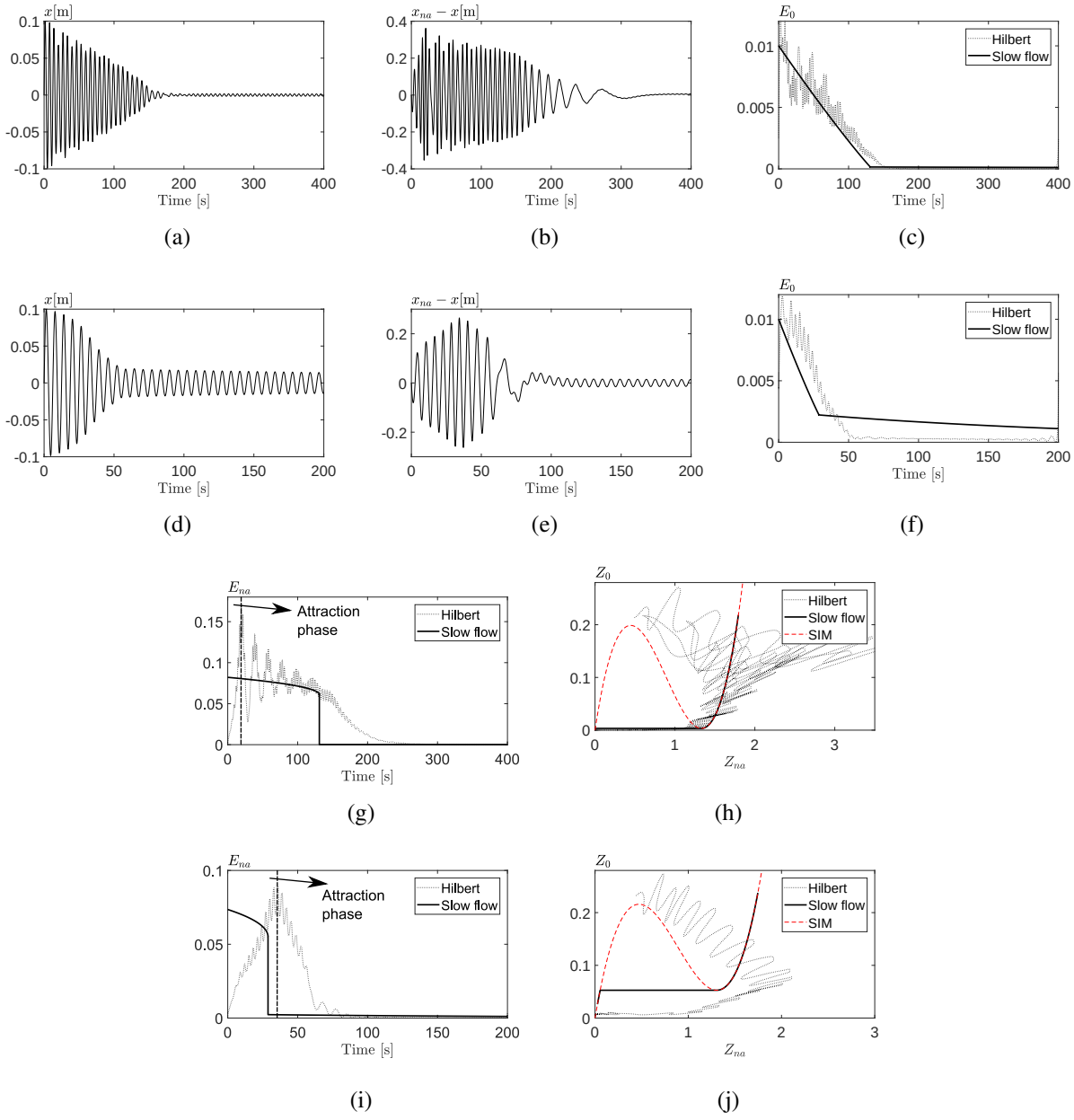


Figure 3

5.3 Exploring the design space

Increasing the damping to $\xi_{na} = 0.2$ decreases the pumping time but has a downside a reduced energy dissipation according to Table 1. This is reflected in the vibrations Figure 3d and 3e. However, the predicted pumping time of 29 s does not reflect the actual TET time. This is because the attraction phase is even longer (40 s) than the pumping time, Figure 3i. However, it is still a lot faster than when $\xi_{na} = 0.05$ but with a clear downside the increased residual vibration energy. An increase in pumping time is now attempted by again lowering $\xi_{na} = 0.05$, to reduce the attraction phase, and increasing κ. From now, only the envelopes of the actual vibration and slow flow are compared, together with the SIM, as this conveys all information about the vibrations. For $\xi_{na} = 0.05$ and $\kappa = 0.2$, a pumping time of 83 s is predicted and followed well by the Hilbert transforms, Figure 4a, 4b and 4c. The same κ but with $\xi_{na} = 0.10$ has a pumping time of 40 s yet the attraction phase here is long resulting in a badly predicted pumping time, Figure 4d, 4e and 4f. To again have a short attraction phase, damping is put on $\xi_{na} = 0.05$ again but this time $\kappa = 0.4$, Figure 4g,

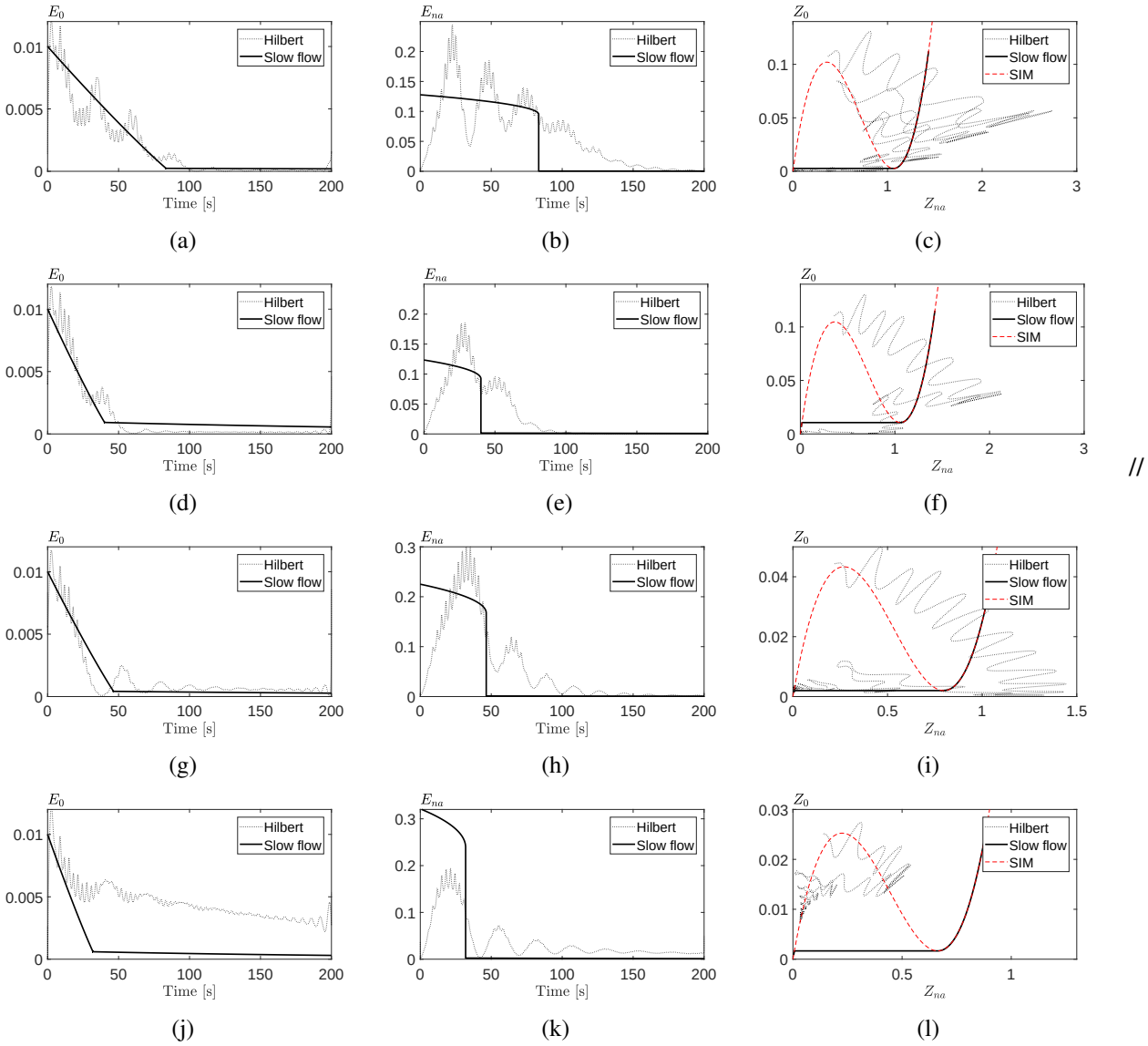


Figure 4: Exploring the design space by tuning several NES

4h and 4i. The pumping time of 46 s is well followed but there is some beating seen in the vibrations. By increasing κ, the NES is more linear, resulting in the beating phenomena, associated with linear TMDs. If κ is increased to 0.5, Figure 4g, 4h and 4i, the actual vibrations fail to be attracted to the right side of the SIM, and only a small fraction of the energy is dissipated.

Increasing the damping will lengthen the initial attraction phase, resulting in longer than predicted TET, and increasing κ makes the NES more linear. One of the assumptions was that both κ and ξ_{na} remain small, and that the NES and main system vibrate according to the mode of the mechanical system. By adding a significant linear stiffness to the compound main-NES system, a second linearized eigenfrequency will appear. So although according to Figure 2c increasing κ and ξ_{na} decreases pumping time, the assumptions made to determine pumping time and dissipated energy are not as strong, causing bad predictions, or simply no TET at all.

5.4 Comparison to linear absorber

The NES with $\xi_{na} = 0.1$ and $\kappa = 0.2$ is compared to an optimally tuned TMD for transient vibrations. The tuning methodology is by pole placement and taken from [3]. It is seen that the vibrations are reduced at roughly the same rate, Figure 5a, but that the NES clearly causes a residual amount of vibration energy, which the TMD does not cause. Note that before in [3] and [2], it was claimed that the TMD was a lot faster in mitigating the vibration energy of the main system, yet here, by increasing the NES performance with the pumping time, this apparent downsides is gone. The NES also vibrates longer than the TMD, because of the jump in the SIM, Figure 5b. As mentioned in the introduction, a NES should be able to deal with detuning better than the TMD. During operation, the vibrating system main frequency may shift because of aging construction. To simulate this, the same system but with $3/4$th the stiffness is fitted with the same NES and TMD, Figure 5c and Figure 5d. Clearly the NES is better suited to handle this detuned situation, while the TMD is not.

6 MDOF optimization

The MDOF mechanical system considered has three masses, $m_i = 1$ kg and stiffness connecting the masses $k_i = 1$ N/m, $i \in \{1, 2, 3\}$ with no stiffnes connecting the third mass to the ground. There is no damping and only an initial speed on the first mass of $\dot{x}_1(0) = 0.1$ m/s, which can be seen as an impulsive base excitation. Modal decomposition leads to the following eigenvectors and eigenfrequencies:

$$E = \begin{bmatrix} 0.328 & -0.737 & 0.591 \\ 0.591 & -0.325 & -0.737 \\ 0.737 & 0.591 & 0.328 \end{bmatrix} \quad \omega_i = \begin{bmatrix} 0.445 \\ 1.247 \\ 1.802 \end{bmatrix} \frac{rad}{s} \tag{16}$$

The absorber mass is $m_{na} = 0.06$ kg (2% of the total mechanical system's mass) and is put on x_2. The nonlinear stiffness is tuned such that RCC starts at mode 3,such that all modes are captured. The modal decomposition of the initial conditions is found with with $E^{-1}\dot{x}(0) = \dot{q}(0)$ and is for mode 3 $\dot{x}^{[3]}(0) = e_3\dot{q}_3(0) = [0.0349 \;\; -0.0436 \;\; 0.0194]^T$, which is used in tuning of the NES (10). It is also used to calculate the pumping time and together with the initial conditions of mode 1 and 2 the cascading time and the cascading dissipation can be calculated. For several κ and ξ_{na} in this section, the cascading time and cascading dissipation is shown on figure 6a. Here, the damping has a large influence while κ has only little influence on the cascading time, first slightly decreasing and then increasing for decreasing κ. For a set of parameters, the compound system will be simulated to asses performance. The modal pumping times, cascading times, energy dissipation and cascading dissipation are calculated before the simulation on Table 2.

6.1 A first simulation

A first simulation is performed for $\xi_{na} = 0.1$ and $\kappa = 0$. It is seen that the vibration at the attachment point x_2 slowly decrease, Figure 6b. The cascading is best seen in the sequential dissipation of the modal coordinates, Figure 6c. First, the third mode is dissipated. Roughly after the pumping time for mode 3, the vibrations of mode 2 decrease. After TET for mode 2, the final mode engages in the cascade after which a residual amount of vibrations remain. This sequential dissipation of the modes is seen in the relative NES vibration, which vibrates according to different frequencies, depending which mode is engaging in the RCC, Figure 6d. The wavelet transform of the NES vibrations is more suitable to visualize this time depending frequency. Each mode is dissipated in roughly the estimated pumping time. The total cascading time is larger then the estimated, attributed to an attraction phase for each mode.

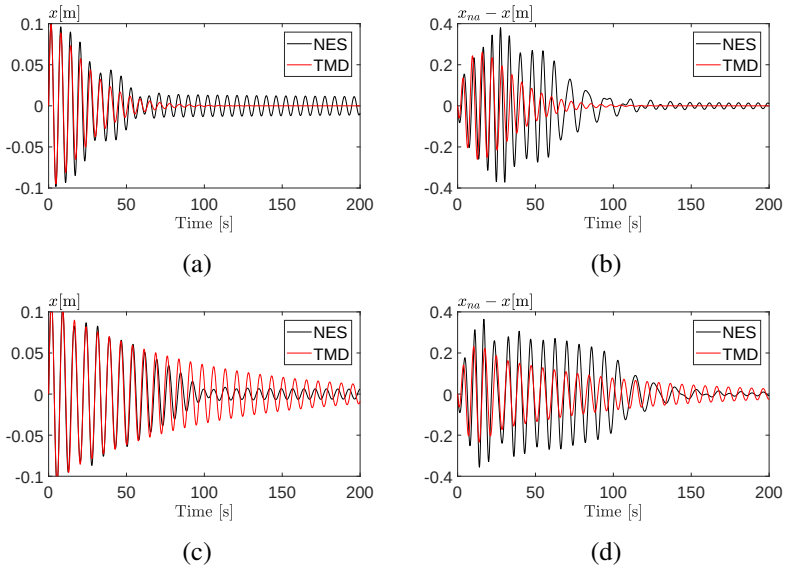


Figure 5: Comparison the TMD and a NES. Main system vibration, (a) for perfectly tuned and (b) for detuned, and relative absorber vibration, (b) for perfectly tuned and (d) for detuned,

NES	$T^{[3]}_{pmp}\frac{\omega_3}{2\pi}$ [s]	$T^{[2]}_{pmp}\frac{\omega_2}{2\pi}$	$T^{[1]}_{pmp}\frac{\omega_1}{2\pi}$	T_{csc}	$E^{[3]}_{TET}$	$E^{[2]}_{TET}$	$E^{[1]}_{TET}$	E_{RCC}
$\xi_{na} = 0.1 \wedge \kappa = 0.0$	22	140	1067	1228	0.94	0.90	0.98	0.93
$\xi_{na} = 0.1 \wedge \kappa = 0.01$	21	138	1118	1277	0.94	0.91	0.99	0.93
$\xi_{na} = 0.1 \wedge \kappa = -0.1$	26	158	807	991	0.96	0.92	0.95	0.93
$\xi_{na} = 0.2 \wedge \kappa = -0.1$	12	65	392	469	0.81	0.68	0.86	0.75
$\xi_{na} = 0.3 \wedge \kappa = -0.1$	7	27	252	286	0.61	0.36	0.73	0.49

Table 2: Performance of the NES tuned for an MDOF system

6.2 Exploring the design phase

According to Figure 6a, for $\kappa > 0$, as long as its feasible, actually increases the pumping time, an opposite effect compared to the SDOF case. For $\xi_{na} = 0.1$ and $\kappa = 0.01$, the simulation show just that, an increase of the cascading time, Figure 7a for the modal coordinates and Figure 7b and Figure 7c for the wavelet transform of the NES vibrations. By decreasing κ slightly to -0.1 it is predicted that the NES dissipates the modes faster. This is confirmed by simulation, Figure 7d, 7e and 7f where the cascade halts after about 1000 s, close to the predicted 991 s. From now on κ is held at -0.1 while ξ_{na} is increased. Decreasing κ has no significant benefit on Figure 6a while a too negative κ has other issues al together, as chaotic vibrations [7]. For $\xi_{na} = 0.2$, the cascading is predicted to halt at 469 s. However, the actual cascading, while decreasing in time, only halts after about 700 s, Figure 7g, 7h and 7i . The culprit is the second mode, which only has a energy dissipation of only 0.68. This causes a long attraction time from mode 2 to 1, as there still a lot of residual vibration energy left in mode 2, seen in the wavelet transform. After a two-frequency regime, the NES vibrates for another 400 s with mode 1, about the pumping time of mode 1, Table 2. Although the prediction is off, the NES is remarkably faster then before. By increasing the damping even more to $\xi_{na} = 0.3$, the cascading time is predicted to decrease to a low of 252 s, but the small dissipation of mode 2 (0.36) again results in a two-frequency regime for the NES, Figure 7j, 7k and 7l. However, the NES still is significantly faster, managing to cascade in less then 600 s, more than twice as fast as for $\xi_{na} = 0.1$ and $\kappa = 0$

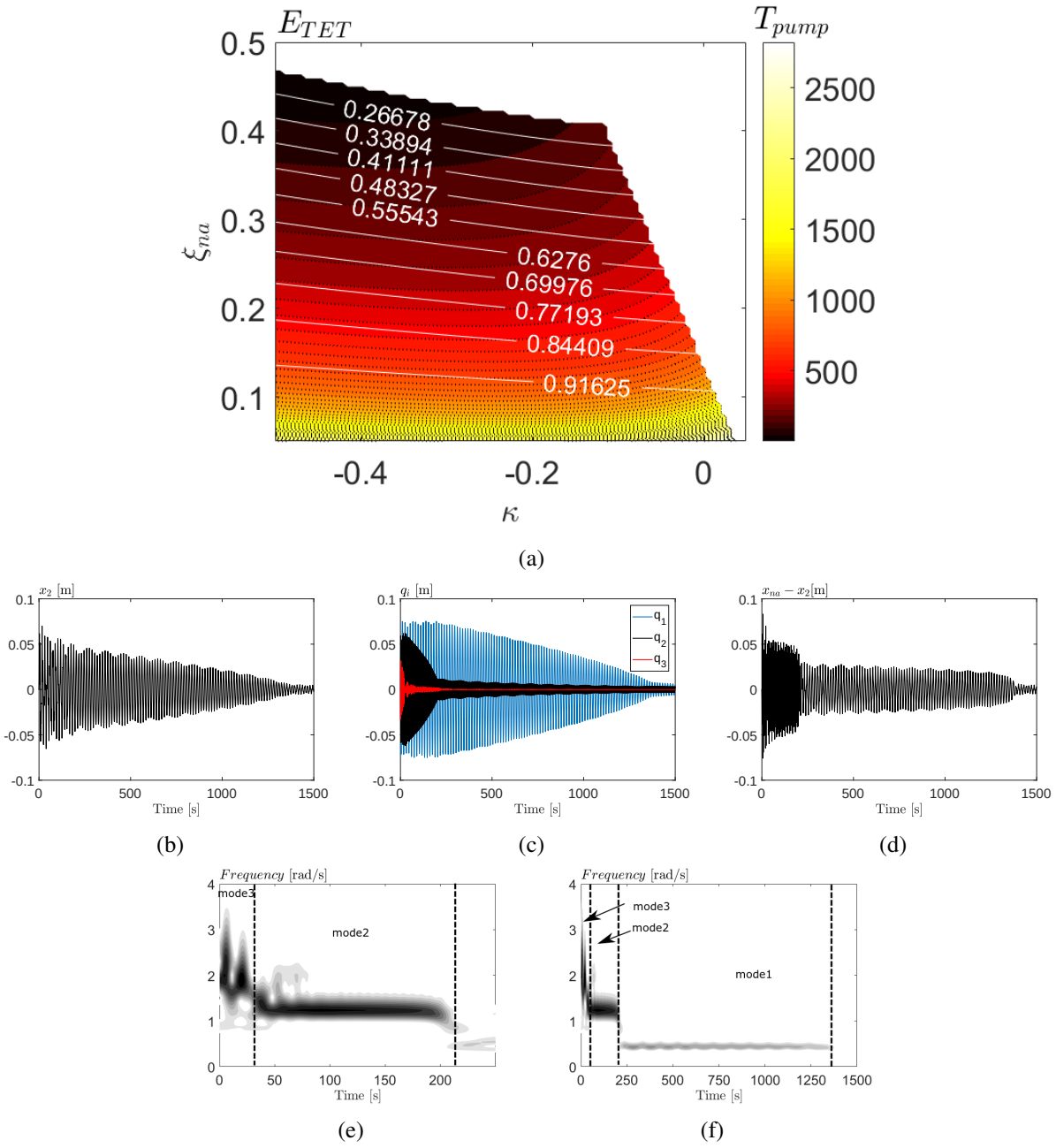


Figure 6

6.3 Comparison to linear absorber

The same mechanical system is fitted with a TMD instead of an NES on x_2. It is tuned to mode 3 according to tuning rules in [3]. As seen in the relative absorber motion Figure 8a and the evolution of the modal coordinates Figure 8b, the TMD is only capable of mitigating vibration of the 3rd mode, where it was tuned for. When comparing the TMD with the NES with $\xi_{na} = 0.1$ and $\kappa = 0$, not even the fastest NES shown previously, the NES is clearly superior because of RCC, Figure 8d for the cascading NES and Figure 8e for the modal coordinates. The vibrations of physical coordinate x_2 are shown for the TMD, Figure 8c and the NES Figure 8f, with again the NES vastly superior because of its capability to mitigate different modal frequencies.

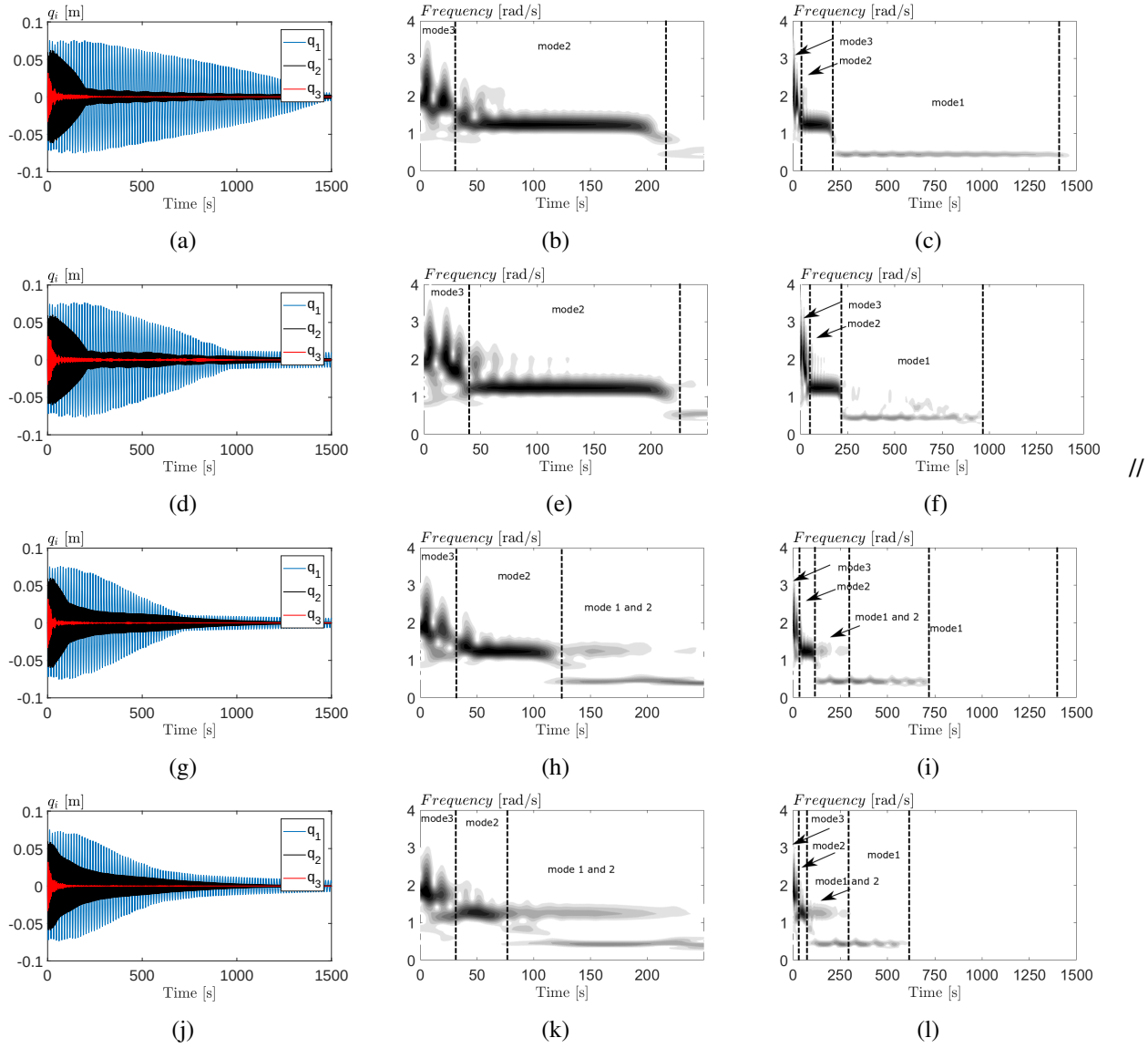
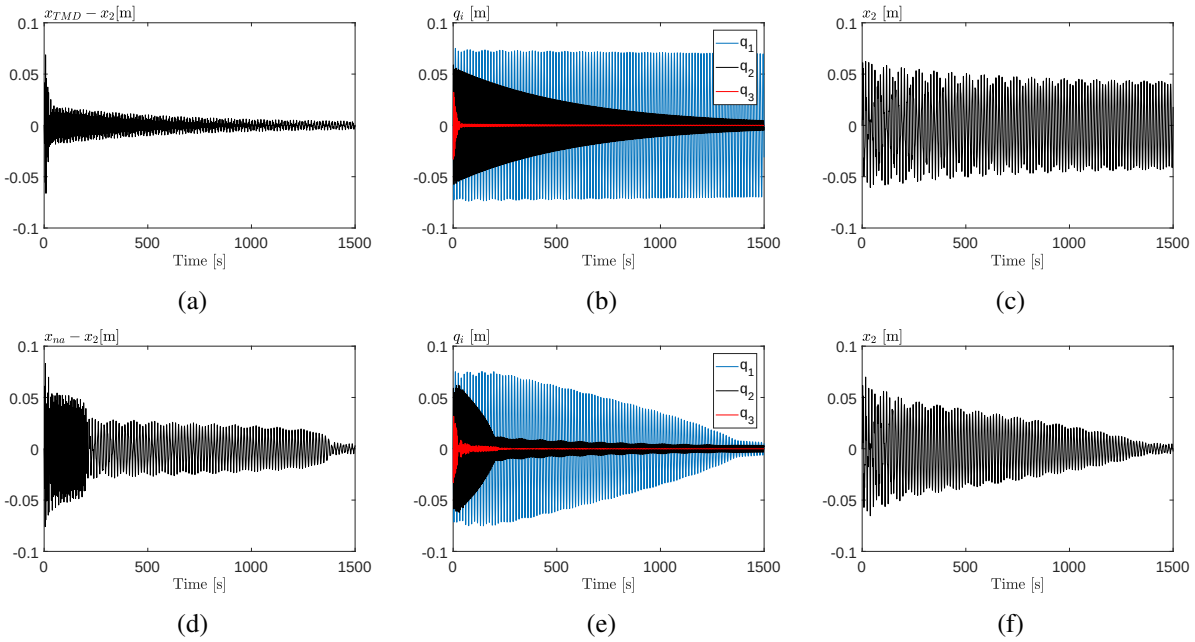


Figure 7: Exploring the design space by tuning several NES for RCC

7 Conclusion

In this paper the nonlinear energy sink (NES) was optimized for both single and multi-modal vibrations using the framework of pumping time, cascading time and energy/cascading, which are algebraic performance measures, allowing us to asses the performance without simulation. In the SDOF case, increasing the linear stiffness part and damping of the NES increases the speed in which the NES is capable of dissipating vibration energy. As a downside, there is an increased amount of residual vibration energy, expressed in the energy dissipation. The NES was compared to the standard solution linear tuned mass damper (TMD). Although an optimized NES and TMD are equally capable of mitigating vibration, the NES is more able to deal with a detuned main system, because the NES lacks a fixed natural frequency. When the a single NES is tuned to deal with MDOF vibrations, it is able to dissipate all modal frequencies through resonance capture cascades (RCC). Increasing the NES damping significantly increased the speed of the RCC, the cascading time, just as in the single mode case, yet a negative linear part of the NES stiffness improves the performance, opposite as in the SDOF case. A single NES is vastly superior in damping multi-modal vibration compared to a single TMD. A single TMD is only able to reduce vibration of the mode it is tuned for, while a NES reduces all modes. While the pumping time and cascading time is able to predict the actual dissipation time



in the SDOF and MDOF cases well, the faster the prediction the more off the actual dissipation time. Still, an increased performance is observed, making the pumping and disspation time valid measure for optimizing a NES.

References

[1] Den Hartog, J. P, *Mechanical vibrations*, Courier Corporation (1985)

[2] A.F. Vakakis, O.V. Gendelman, L.A. Bergman, D.M. McFarland, G. Kerschen, and Y.S. Lee, *Nonlinear targeted energy transfer in mechanical and structural systems*, Springer Science & Business Media (2008)

[3] F. Petit, M. Loccufier, D. Aeyels *Feasibility of nonlinear absorbers for transient vibration reduction*, Proceedings of ISMA 2010 (2010), pp. 1-15

[4] T.A. Nguyen, S. Pernot. *Design criteria for optimally tuned nonlinear energy sinks part 1: transient regime*, Nonlinear Dynamics, Vol. 69, No. 2, Springer (2012), pp. 1-19

[5] K. Dekemele, R. De Keyser, M. Loccufier, *Performance Measures for Energy Transfer and Resonance Capture Cascading in Nonlinear Energy Sinks*, Nonlinear Dynamics, Vol. 93, No. 2, Springer (2018), pp. 259284

[6] O.V. Gendelman, *Bifurcations of nonlinear normal modes of linear oscillators with strongly nonlinear damped attachment*, Nonlinear Dynamics, Vol. 37, No. 2, Springer (2004), pp. 115-128.

[7] F. Romeo, L. I. Manevitch, L.A. Bergman, A.F. Vakakis, *Transient and chaotic low-energy transfers in a system with bistable nonlinearity*, Chaos: An Interdisciplinary Journal of Nonlinear Science, Vol. 25, No. 5, AIP Publishing (2015), 053109.

Modeling the the amplitude and magnetic dependency to the vibration isolation effect for magneto-sensitive rubber isolation system by assessing the energy flow

B.C. Wang [1], **L. Kari** [1]
[1] KTH Royal Institute of Technology, The Marcus Wallenberg Laboratory for Sound and Vibration Research (MWL)
Teknikringen 8, 100 44 Stockholm, Sweden
e-mail: **bochao@kth.se**

Abstract

A highly nonlinear model which consider the impact of the frequency, amplitude and magnetic field dependency for MS rubber and mobility for the foundation is developed for a MS rubber isolation system. Harmonic loadings ranging from 60 to 160 Hz with different levels of force magnitude are applied for the system. Vibration isolation effect is evaluated by assessing the energy flow into the foundation. It is found that the energy flow into the system and the vibration isolation effect for MS isolator are highly related to the amplitude and magnetic field dependency for MS rubber. Furthermore, by comparing the energy flow to the foundation under zero and saturation magnetic field, a control strategy to reduce the energy flow to the foundation by changing the magnetic field is obtained. After applying the control strategy it is found that the energy flow into the foundation can be reduced by about 20% by changing the magnetic field compared to traditional passive rubber isolators.

1 Introduction

Magneto-sensitive (MS) rubber is a kind of smart material which mainly consists of rubber matrix and polarized iron particles. By applying magnetic field, a rapid, continuous and reversible change of its modulus can be reached. Compared to vibration reduction components based on traditional rubber, MS rubber-based vibration reduction devices have the ability to change its mechanical properties. Thus, an adaptability to various loading conditions and an improved vibration reduction effect is available for MS rubber-based vibration reduction devices.

Many studies have focused on the constitutive model for MS rubber. Initially, Jolly et al. [1] developed a model by using the concept of dipoles in electromagnetism to represent the magnetic related mechanical properties for MS rubber. Later, Dorfmann et al. [2, 3] developed a model for MS rubber by combine Maxwell equation and continuum mechanics. After those work, model with considering the viscoelastic properties is developed [4]. For the work mentioned above, the amplitude dependency for MS rubber are rarely considered. However, according to the work by Blom and Kari [5], there is an unneglectable amplitude dependency for MS rubber even for small strain and the amplitude dependency for MS rubber is strongly related to the magnetic field applied. Therefore, a constitutive model which has the ability to depict the mechanical properties of MS rubber properly is needed. Although Blom and Kari [6] have developed a constitutive model with amplitude, frequency and magnetic field dependency for MS rubber, the vibration reduction effect for MS rubber-based devices has not been fully studied.

In addition to the study of the constitutive model for MS rubber, large investigations dedicated to explore the possibility of using MS rubber in vibration reduction area have been performed. Initially, Ginder et al.

[7] designed an MS rubber-based bushing. Gong et al. [8, 9] developed a MS rubber tuned vibration absorbers(TVAs) and focused on the frequency shift property for the MS rubber-based adaptive tuned vibration absorber. In addition to TVAs application area, application of using MS rubber to sandwich beam and the effect of boundary conditions [10] and changing magnetic field [11] to the dynamic properties of MS rubber sandwich beam were studied.

It is worth noting that, compared to the studies on the application of MS rubber in TVA and sandwich beams, the research about MS rubber's application in vibration isolation is not enough. Although the vibration isolation problem based on MS rubber were investigated, but those researches [12, 13] are only focused on base isolation problem. Another important type of vibration isolation problem, the isolation of machine vibration is not included in their study. However, in reality vibration caused by rotating machine is often encountered.

Based on the research status about MS rubber, a MS rubber isolation system which consists of a block mass supported by four MS rubber isolators placed on an infinite extend foundation is studied in this paper. The machine vibration is simulated by a harmonic force applied on the block mass. Subsequently, a nonlinear model which consider the impact of the amplitude, frequency, magnetic field dependency of MS rubber and the stiffness for the foundation is developed for this MS rubber isolation system. Energy flow is used to serve as the indicator to assess the vibration isolation effect for this MS rubber isolation system. The impact of the amplitude and magnetic field dependency for MS rubber to the isolation effect is investigated. The outcome of this research facilitates the development of the adaptive MS rubber isolation devices with nonlinear features considered. Meanwhile, the control strategy about the magnetic field applied can be applied to other MS rubber-based devices where variable mechanical properties is needed.

2 Model and method

2.1 Composition and parameters for the model

The schematic diagram for the whole system is in Figure 1. External force F_{ext} is applied at the center for the block mass and the force provided by each MS rubber isolator is F_{MS}. The displacement for the block mass and the foundation are u and u_{f}, respectively. The geometrical dimensions and material parameters for this system are set to be: distance between MS isolator in y-direction $2l_{\mathrm{y}}= 0.3\,\mathrm{m}$, distance between MS isolator in z-direction $2l_{\mathrm{z}}= 0.4\,\mathrm{m}$, thickness for each MS rubber element $h_{\mathrm{MS}} = 0.002\,\mathrm{m}$, area for each MS rubber element $A = 0.025 \times 0.025\,\mathrm{m}^2$ and the thickness for the infinite extent concrete foundation $h_{\mathrm{f}} = 0.35\,\mathrm{m}$. The total mass for the solid mass block is $m = 40\,\mathrm{kg}$. The density, Poisson's ratio and Young's modulus for the concrete foundation is set to $\rho_{\mathrm{f}} = 2300\,\mathrm{kg\,m^{-3}}$, $\nu_{\mathrm{f}} = 0.2$ and $E_{\mathrm{f}} = (1 + 0.02\mathrm{j}) \times 2.6 \times 10^{10}\,\mathrm{kg\,m^{-3}}$, where j is the imaginary unit.

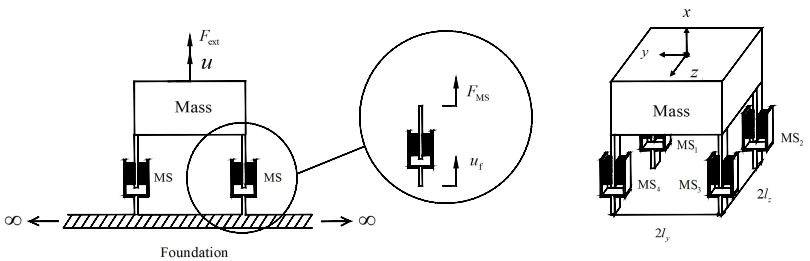


Figure 1: Schematic diagram for the MS rubber isolation system.

2.2 Governing equation for the model

The governing equation for this model is

$$m\ddot{u} + 4 \cdot g_{\mathrm{MS}}(u - u_{\mathrm{f}}) = F_{\mathrm{ext}}, \tag{1}$$

where $\ddot{(\cdot)}$ denotes the second time derivative and $g_{\mathrm{MS}}(\cdot)$ is the nonlinear function representing the relation between F_{MS} and displacement $(u - u_{\mathrm{f}})$ for each MS rubber isolator.

Based on the work by Alberdi et al. [14], it is assumed that the foundation is much more rigid than the MS isolator, thus $u_{\mathrm{f}} \ll u$. The governing equation is simplified as

$$m\ddot{u} + 4 \cdot g_{\mathrm{MS}}(u) = F_{\mathrm{ext}}. \tag{2}$$

This second order nonlinear equation can be solved numerically based on Newmark's method [15].

After obtaining u and F_{MS}, the displacement u_{f} can be obtained by the mobility matrix for the foundation

$$\tilde{v}_{\mathrm{f}(i)} = (\mathrm{j}2\pi f) \cdot \tilde{u}_{\mathrm{f}(i)} = Y_{ik}\tilde{F}_{\mathrm{MS}(k)}, \quad i,k = 1,2,3,4, \tag{3}$$

where $\tilde{(\cdot)}$ is the Fourier transform for the signals. Parameters $\tilde{v}_{\mathrm{f}(i)}$ and $\tilde{u}_{\mathrm{f}(i)}$ represent the velocity and displacement for the point connected to the i^{th} MS rubber isolator, frequency is f and Y_{ik} represents the mobility on point k to the velocity on point i.

The mobility [16] for the transfer point with a distance of r to the driving point is

$$Y(r) = \frac{\omega}{8Bk_B^2}\left[H_0^{(2)}(k_B r) - j\frac{2}{\pi}K_0(k_B r)\right], \tag{4}$$

where ω is the angular frequency for the force, $B = EI/(1-\nu^2)$ is the bending stiffness for the plate, $I = h^3/12$ is the cross-sectional second moment of per unit width. Parameters E, ν, h and ρ are the Young's modulus, Poisson's ratio, thickness and density for the concrete foundation, respectively. The mass per unit area for the foundation is $m = \rho h$. Lastly, $H_0^{(2)}$ is the zero order Hankel function of the second kind, K_0 is the zero order modified Bessel function of the second kind and $k_B = \sqrt[4]{m/B}\sqrt{\omega}$ is the bending wave number.

2.3 Constitutive model for MS rubber

According to the research by Blom and Kari [6] the absolute value of shear modulus of MS rubber is strongly related to the amplitude, frequency and magnetic field applied; while the impact for the magnetic field dependency to the loss factor is relatively neglectable. A constitutive model describes the relation between the strain γ and stress τ is developed. The rheological model is shown in Figure 2.

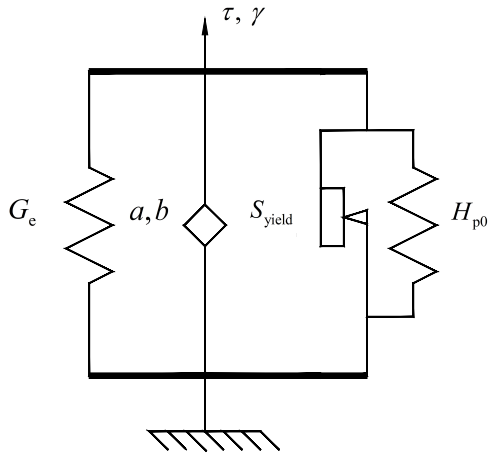


Figure 2: Rheological model for MS rubber.

The total stress τ splits up to three parts: τ_{e}, τ_{ve} and τ_{f}. The elastic shear stress is linearly related to shear strain by the elastic shear modulus G_{e}

$$\tau_{\mathrm{e}}(t) = G_{\mathrm{e}} \cdot \gamma(t). \tag{5}$$

The viscoelastic shear stress and shear strain is connected by a relaxation convolution integral [17]

$$\tau_{\mathrm{ve}}(t) = \frac{b}{\Gamma(1-a)} \frac{\mathrm{d}}{\mathrm{d}t} \int_0^t \frac{\gamma(s)}{(t-s)^a} \mathrm{d}s, \tag{6}$$

where a and b are the parameters in the relaxation convolution integral and Γ is the gamma function.

The relation between frictional stress τ_{f} and shear strain γ is described by bounding surface model. For the details of bounding surface model, the reader is referred to Ref. [18]. The main idea about bounding surface model is that two surfaces which includes a yield surface and a bounding surface are used to calculate the frictional stress. For one dimensional case with a vanishing size of yield surface for bounding surface model [19], it can be visualized in Figure 3. Symbols $\mathrm{X} - \mathrm{X}' - \mathrm{Y}' - \mathrm{Y}$ represent the bounding surface and the curve inside is the yield surface. The evolution laws are

$$\dot{\tau}_{\mathrm{f}} = \dot{\alpha} = H\dot{\gamma} \tag{7}$$

and

$$\dot{\bar{\tau}}_{\mathrm{f}} = \dot{\beta} = H_{\mathrm{p}}\dot{\gamma}, \tag{8}$$

where H and H_{p} are plastic modulus for the yield surface and the bounding surface. A bar over τ_{f} means the stress on the bounding surface, α and β are the back stresses which serve as the center for the bounding surface and yield surface, respectively.

The expression for H is

$$H = H_{\mathrm{p}} \left(1 + \frac{\delta}{\delta_{\mathrm{in}} - \delta}\right), \tag{9}$$

where δ is the distance between the stresses on yield surface and bounding surface at present, parameter δ_{in} is the distance to the bounding surface at the previously turning point for τ_{f}. Initially, it is set that $\delta_{\mathrm{in}} = S_{\mathrm{yield}}$. With the development of the strain, the values of δ, δ_{in} and H are continuously update in the subsequent calculation .

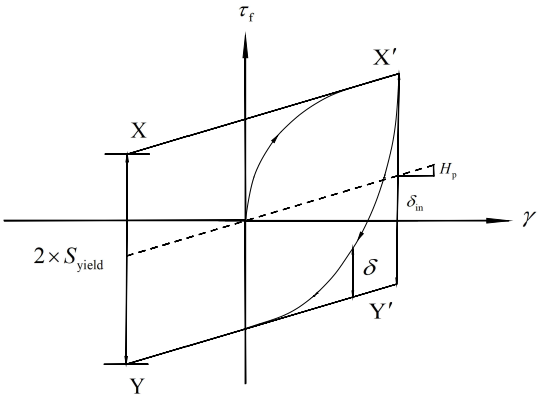


Figure 3: One dimensional case for bounding surface model with a vanishing size of yield surface.

Based on the work by Blom and Kari [6], the magnetic field sensitivity is introduced for the elastic and frictional part in the model as

$$G_{\mathrm{e}} = G_{\mathrm{e}}^{0}\left[1+\left(\frac{M}{M_{\mathrm{s}}}\right)^{2}\delta_{1}\right], \tag{10}$$

$$S_{\mathrm{yield}} = S_{\mathrm{yield}}^{0}\left[1+\left(\frac{M}{M_{\mathrm{s}}}\right)^{2}\delta_{2}\right] \tag{11}$$

and

$$H_{\mathrm{p0}} = H_{\mathrm{p0}}^{0}\left[1+\left(\frac{M}{M_{\mathrm{s}}}\right)^{2}\delta_{3}\right], \tag{12}$$

where G_{e}^{0}, S_{yield}^{0} and H_{p0}^{0} are parameters at zero magnetic field for MS rubber. The parameter M_{s} represents the upper limit for the applied magnetic field. Physically, it is the saturation magnetic field for the MS rubber. Parameters δ_1, δ_2 and δ_3 represent the magnetic influence factors.

2.4 Fundamentals about energy flow

Energy flow which is the time averaged product for the force and velocity, describes the change rate of energy for dynamic system. The fundamentals of this method is based on energy conservation law. Compared with other indicators like force and displacement transmissibility, energy flow can assess the vibration isolation effect more properly [20]. The time averaged energy flow is expressed as

$$\langle P\rangle = \lim_{\mathrm{T}\to\infty}\frac{1}{\mathrm{T}}\int_{-\mathrm{T}/2}^{\mathrm{T}/2}F(t)v(t)\mathrm{d}t, \tag{13}$$

where $F(t)$ and $v(t)$ are the force and velocity for the measured structure. According to signal analysis theory [21], the averaged energy flow can be obtained by calculating the zero time delayed cross-correlation

function R for velocity and force as

$$\langle \mathrm{P} \rangle = \lim_{T\to\infty} \frac{1}{T} \int_{-T/2}^{T/2} F(t) v(t+\tau) \mathrm{d}t|_{\tau=0} = R(F,v)|_{\tau=0}. \tag{14}$$

The relation between the zero time delayed cross-correlation function and cross-spectrum S is

$$R(F,v)|_{\tau=0} = \int_{-\infty}^{\infty} S(F,v) \mathrm{d}f. \tag{15}$$

Lastly, the cross-spectrum can be obtained by Fourier transform as

$$S(F,v) = \lim_{T\to\infty} \frac{1}{T} E\left[\tilde{F}(f)\tilde{v}^*(f)\right], \tag{16}$$

where $(\cdot)^*$ represents the complex conjugate operator, $\tilde{(\cdot)}$ is the Fourier transform and $E[\cdot]$ denotes the expected value operator.

3 Numerical study

3.1 Shear modulus for MS rubber

Based on the measurement results by Lejon and Kari [22]. Firstly, the parameters for zero magnetic field are identified by the nonlinear least square method using the "*lsqnonlin*" command in Matlab® (MATLAB Release 2015b, The MathWorks, Inc.,Natick, Massachusetts, United States). The results are $G_{\mathrm{e}0}$= 3.0712 × $10^6\,\mathrm{N\,m^{-2}}$, $S^0_{\mathrm{yield}0} = 0.4531 \times 10^5 \mathrm{Nm^{-2}}$, $H^0_{\mathrm{p}0} = 0.1026 \times 10^6 \mathrm{Nm^{-2}}$, $a = 0.2997$ and $b = 0.2709 \times 10^6\,\mathrm{N\,s^a\,m^{-2}}$. After obtaining the parameters for zero magnetic field, a second time of nonlinear least square method is applied and it is obtained δ_1= 0.2594, δ_2= 0, δ_3= 0.7576 and M_{s}= 0.5615 T. The comparison between the simulation results and the measurement results are shown from Figure 4 to 6. It reveals that the simulation results fit well with the measurement results in most part of the measurement frequency range. The jump for the measurement results between 600 and 700 Hz is caused by the resonance for the machine. Therefore, the constitutive model developed for MS rubber in this paper is capable of prediction the amplitude, frequency and magnetic field dependency for MS rubber. After identifying the material parameters for MS rubber, the mechanical behavior of MS rubber is extrapolated to a low frequency range from 20 to 100 Hz. Since the frequency dependency for MS rubber is relatively small in low frequency range and the main goal for this paper is to investigate the impact of the amplitude, magnetic field dependency to the isolation effect, the extrapolation does not affect the feasibility for this MS rubber isolation model.

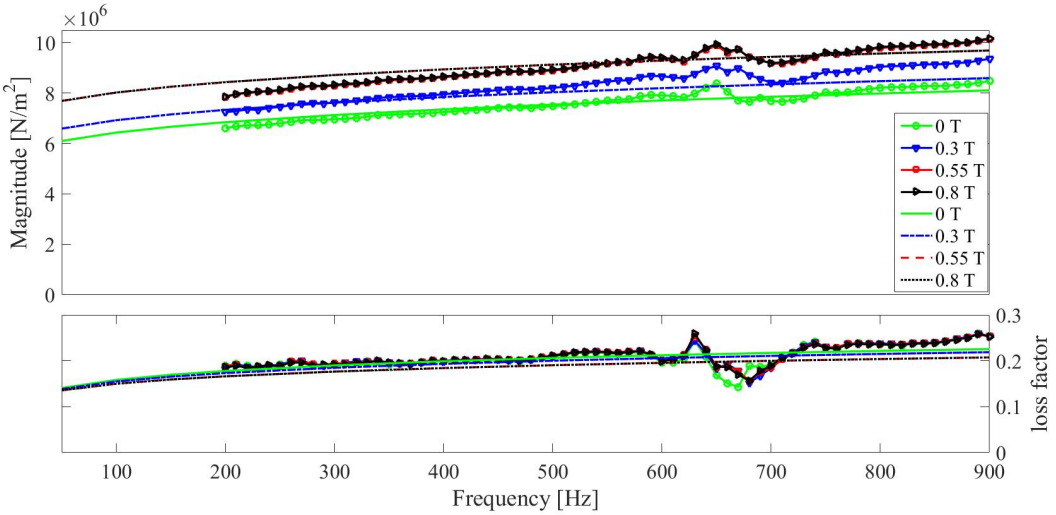


Figure 4: Measured (symbols) and simulated (lines) dynamic stiffness for MS rubber versus frequency with shear strain of 0.0005.

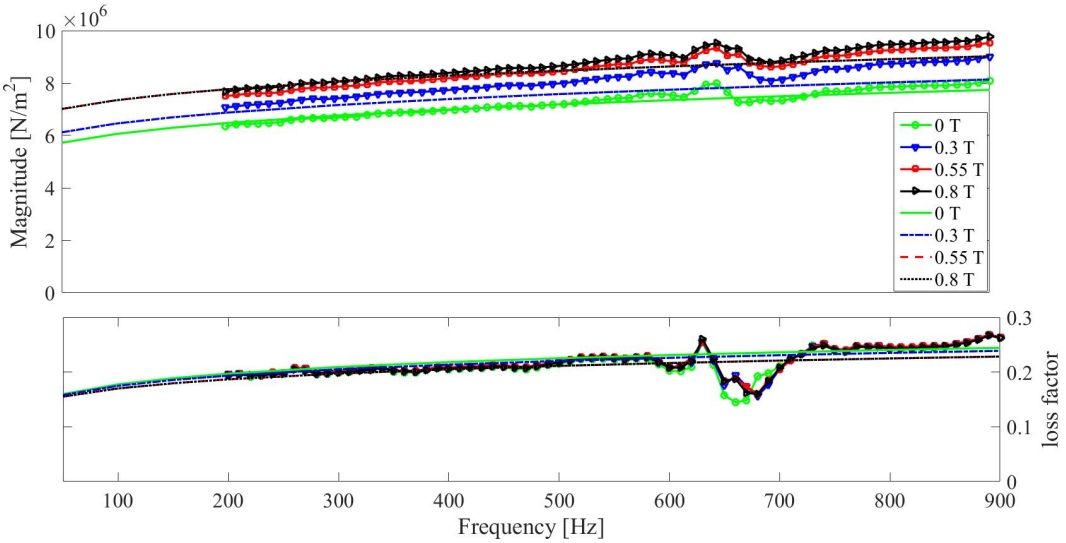


Figure 5: Measured (symbols) and simulated (lines) dynamic stiffness for MS rubber versus frequency with shear strain of 0.0015.

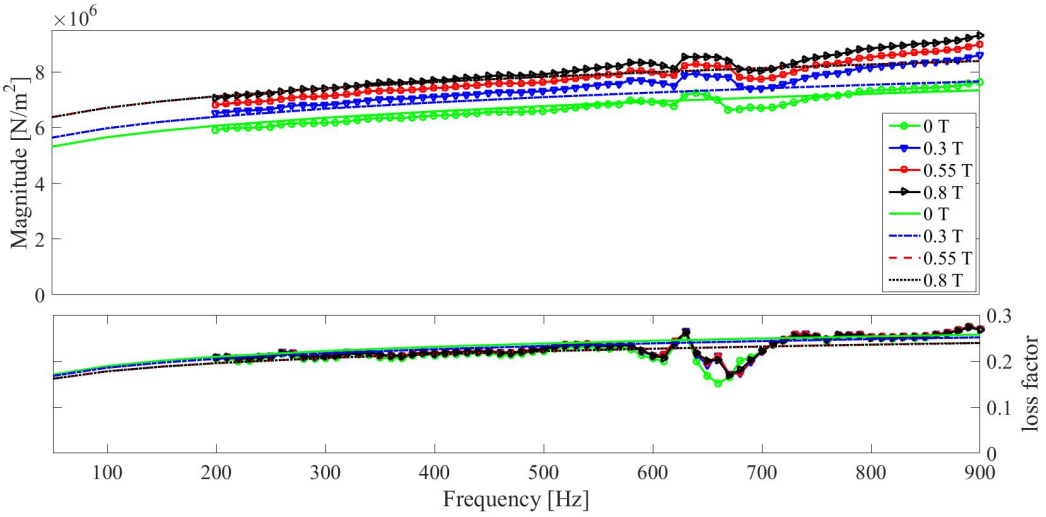


Figure 6: Measured (symbols) and simulated (lines) dynamic stiffness for MS rubber versus frequency with shear strain of 0.005.

3.2 Energy flow

Harmonic force ranging from 60 to 160 Hz with magnitude of 3, 10 and 30 N are applied at the center for the block mass. The energy flow to the whole system and foundation are plot from Figure 7 to 9. It is found that the energy flow reaches a peak at the resonance frequency for the system. After applying the magnetic field, the value for the resonace frequency increases. This is caused by the magnetic field dependency for MS rubber. In addition to this, the energy transmitted to the foundation is much smaller than the energy flow into the whole system. It means that most part of the energy is dissipated by the MS isolator and the assumption $u_{\mathrm{f}} \ll u$ is reasonable. Furthermore, by comparing the energy flow for different magnitude of the harmonic loading, it is found that difference between the energy flow for zero and maximum magnetic field case becomes smaller as the increase of the magnitude for the harmonic loading. It is caused by the fact the magnetic field dependency is stronger for smaller amplitude case for MS rubber.

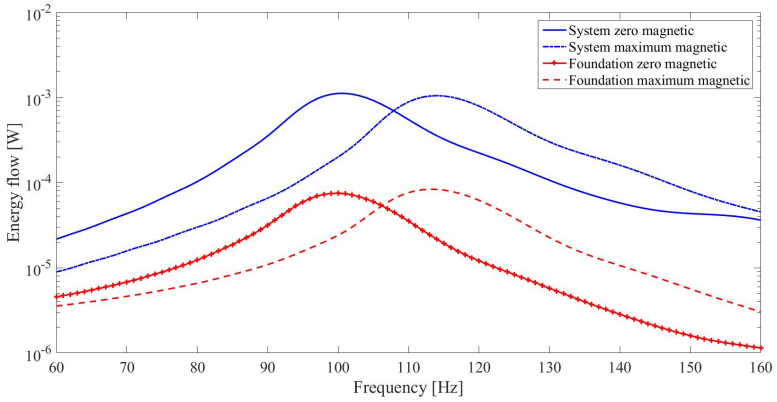


Figure 7: Energy flow to the whole system and foundation with force magnitude equals 3 N.

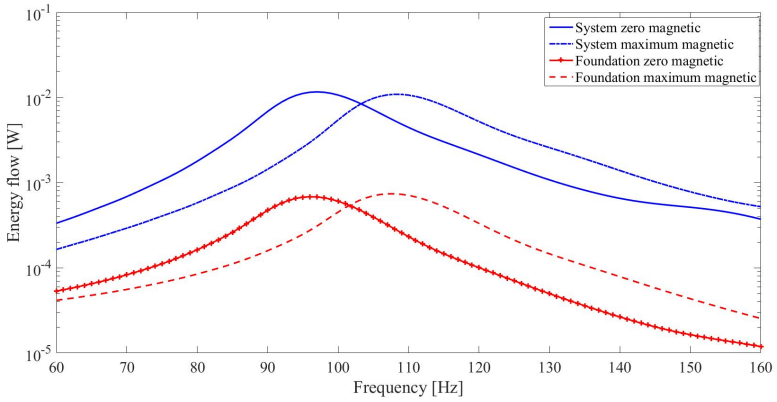


Figure 8: Energy flow to the whole system and foundation with force magnitude equals 10 N.

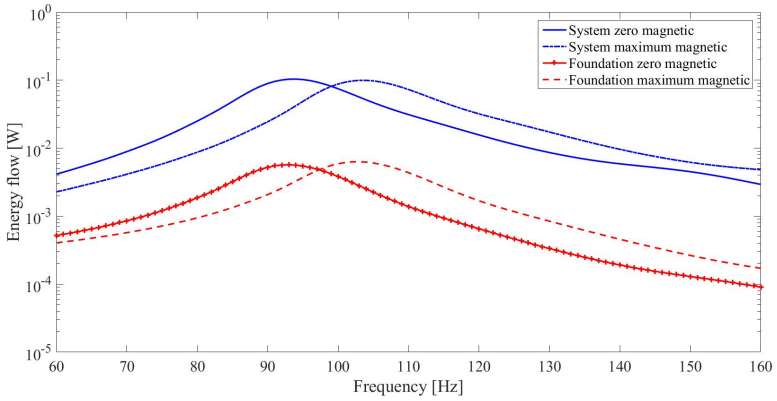


Figure 9: Energy flow to the whole system and foundation with force magnitude equals 30 N.

Furthermore, by comparing the energy flow to the foundation under zero and maximum magnetic field, it is found that a reduced energy flow into the foundation can be reached by changing the magnetic field applied for different frequency. Assuming that the frequency for which the two energy flow have the same value (zero magnetic field and maximum magnetic field) is called the coincidence frequency (f_c), the control strategy to change the magnetic field for MS rubber is listed in Table 1. The frequency for the harmonic loading is f. For example, when the magnitude for the excitation force is 3 N, the coincidence frequency is found to be 103 Hz. In order to reach a reduced energy flow to the foundation, the switch of the magnetic field applied should follow the control strategy shown in Figure 10. The energy flow peaks for zero, maximum and switching magnetic field cases to the foundation are shown in Table 2 . It is found that after applying the control strategy, the energy flow into the foundation is reduced by more than 20% for switching magnetic filed case compared to zero and maximum magnetic field cases.

Criteria	Magnetic field applied
$f < f_c$	Maximum magnetic field
$f \geq f_c$	Zero magnetic field

Table 1: Control strategy for the harmonic loading case.

F_{ext} [N]	f_{c} [Hz]	Maximum energy flow [W]		
		Zero magnetic	Maximum magnetic	Switched magnetic
3	106	7.510×10^{-5}	8.369×10^{-5}	5.193×10^{-5}
10	103	6.836×10^{-4}	7.398×10^{-4}	5.234×10^{-4}
30	97	5.696×10^{-3}	6.314×10^{-3}	4.666×10^{-3}

Table 2: Energy flow to the foundation for different magnetic field

Lastly, it is found that the coincidence frequency for the control strategy is strongly related to the force magnitude. The energy flow to the foundation for three levels of harmonic loading after implementation of control strategy is shown in Figure 11. Combining with the results in Table 2, it is found that for an increased force, the coincidence frequency (f_{c}) decreases. This is caused by the amplitude dependency for MS rubber. An increased force leads to an increased strain and a decreased modulus for MS rubber, thus the coincidence frequency increases in frequency domain.

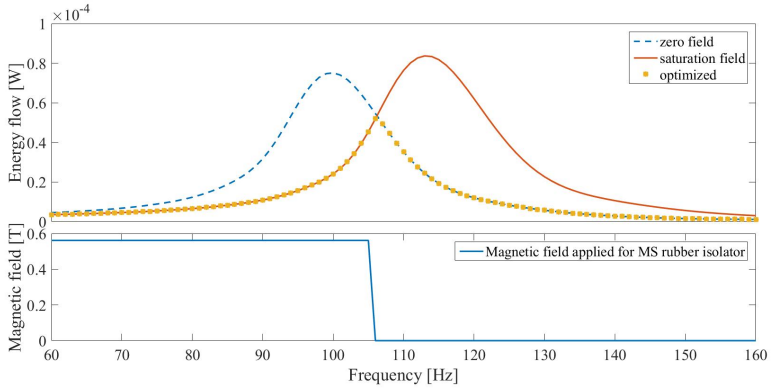


Figure 10: Energy flow to the foundation and the magnetic field required in frequency range.

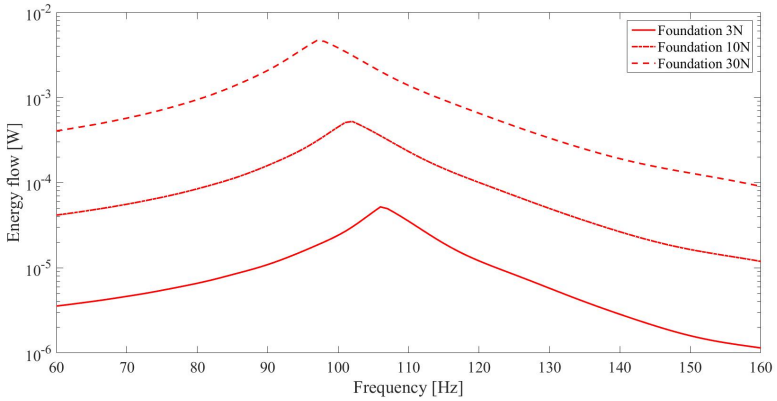


Figure 11: Energy flow to the foundation after application of control strategy for different level of force.

4 Conclusion

A highly nonlinear model aimed at predicting the dynamic behavior for MS rubber isolation system and optimizing the vibration isolation effect is developed in this paper. The amplitude, frequency and magnetic field dependency for MS rubber, the stiffness for the infinite foundation to the isolation effect are incorporated in this model. Energy flow is used to serve as the indicator to evaluate the vibration isolation effect for MS rubber isolator. Simulation results for harmonic loading case reveal that by changing the applied magnetic field for different frequency range, the resonance for the MS isolation system can be avoided to some extent and the energy flow into the foundation can be reduced. In addition to this, it is found that the amplitude dependency for MS rubber has a great impact on the isolation effect for this MS rubber isolation system. Thus, for the achievement of good vibration isolation effect, the amplitude dependency for MS rubber should take into consideration at the design stage. The control strategy developed in this paper provides guidance for the design of the control strategy for MS rubber isolators and other MS rubber-based devices.

Acknowledgements

The authors would like to acknowledge the work previously perfomed by Ane Alberdi-Muniain and Nere Gil-Negrete in this line of research, which has been a helpful starting point for the development of the present paper.

References

[1] M. R. Jolly, J. D. Carlson, B. C. Muoz, *A model of the behaviour of magnetorheological materials*, Smart Materials and Structures, Vol. 5, No. 5, (1995), pp. 607-617.

[2] A. Dorfmann, R. Ogden, *Magnetoelastic modelling of elastomers*, European Journal of Mechanics - A/Solids, Vol. 22, (2003), pp. 497-507.

[3] A. Dorfmann, I. Brigadnov, *Constitutive modelling of magneto-sensitive cauchy-elastic solids*, Computational Materials Science, Vol. 29, (2004), pp. 270-282.

[4] R. Li, L. Z. Sun, *Dynamic viscoelastic modeling of magnetorheological elastomers*, Acta Mechanica, Vol. 225, (2014), pp. 1347-1359.

[5] P. Blom, L. Kari, *Amplitude and frequency dependence of magneto-sensitive rubber in a wide frequency range*, Polymer Testing, Vol. 24, (2005), pp. 656-662.

[6] P. Blom, L. Kari, *A nonlinear constitutive audio frequency magneto-sensitive rubber model including amplitude, frequency and magnetic field dependence*, Journal of Sound and Vibration, Vol. 330, (2011), pp. 947-954.

[7] J. M. Grinder, M. E. Nichols, L. D. Elie, J. L. Tardiff, *Magnetorheological elastomers properties and applications*, Proceedings of SPIE, Vol. 3675, (1999), pp. 131-138.

[8] H. X. Deng, X. L. Gong, *Adaptive tuned vibration absorber based on magnetorheological elastomer*, Journal of Intelligent Material Systems and Structures, Vol. 18, (2007), pp. 1205-1210.

[9] G. L. Liao, X. L. Gong, C. J. Kang, S. H. Xuan, *The design of an active-adaptive tuned vibration absorber based on magnetorheological elastomer and its vibration attenuation performance*, Smart Materials and Structures, Vol. 20, No. 7, (2011), 075015(10pp).

[10] B. Nayak, S. Dwivey, K. Murthy, *Dynamic analysis of magnetorheological elastomer-based sandwich beam with conductive skins under various boundary conditions*, Journal of Sound and Vibration, Vol. 330, (2011), pp. 1837-1859.

[11] B. Dyniewicz, J. M. Bajkowski, C. I. Bajer, *Semi-active control of a sandwich beam partially filled with magnetorheological elastomer*, Mechanical Systems and Signal Processing, Vol. 60-61, (2015), pp. 695-705.

[12] H. J. Jung, S. H. Eem, D. D. Jang, J. H. Koo, *Seismic performance analysis of a smart base-isolation system considering dynamic of MR elastomers*, Journal of Intelligent Material Systems and Structures, Vol. 18, (2007), pp. 1205-1210.

[13] Y. C. Li, J. C. Li, *A highly adjustable base isolator utilizing magnetorheological elastomer: experimental testing and modelling*, Journal of Vibration and Acoustics, Vol. 137, (2015), 011009.

[14] A. Alberdi-Muniain, N. Gil-Negrete, L. Kari, *Modelling energy flow through magneto-sensitive vibration isolators*, International Journal of Engineering Science, Vol. 65, (2013), pp. 22-39.

[15] M. Géradin, D. Rixen, *Mechanical Vibrations: Theory and Application to Structural Dynamics*, Wiley, Chichester (1994).

[16] L. Cremer, M. Heckl, *Structure-Borne Sound*, Springer, Berlin Heidelberg (1988).

[17] S. Kempfle, I. Schäfer, H. Beyer, *Fractional calculus via functional calculus: Theory and applications*, Nonlinear Dynamics, Vol. 29, (2002), pp. 99-127.

[18] Y. F. Dafalias, E. P. Popov, *Cyclic loading for materials with a vanishing elastic region*, Nuclear Engineering and Design, Vol. 41, (1977), pp. 293-302.

[19] R. Österlöf, H. Wentzel, L. kari, N. Diercks, D. Wollscheid, *Constitutive modelling of the amplitude and frequency dependency of filled elastomers utilizing a modified boundary surface model*, International Journal of Solids and Structures, Vol. 51, (2014), pp. 3431-3438.

[20] C. M. Mark, Y. Yun, *A study of power transmissibility for the vibration isolation of coherent vibratory machines on the floor of a building*, Applied Acoustics, Vol. 71, (2010), pp. 368-372.

[21] J. S. Bendat, A. G. Piersol *Engineering applications of correlation and spectral analysis*, Wiley-Interscience, New York (1980).

[22] J. Lejon, L. Kari, *Measurements on the temperature, dynamic strain amplitude and magnetic field strength dependence of the dynamic shear modulus of magnetosensitive elastomer in a wide frequency range*, Journal of Vibration and Acoustics, Vol. 135, (2013), 064506.

Suppression of the wind-induced vibration of high-rise buildings with inerter systems

Y. Xia [1], **R. Zhang** [2], **M.I. Friswell** [1], **Y. Cao** [2]
[1] Swansea University, College of Engineering,
Fabian Way, Swansea SA1 8EN, UK
e-mail: **yuying.xia@swansea.ac.uk**

[2] Tongji University, Research Institute of Structural Engineering and Disaster Reduction,
Siping Road, 200092, Shanghai, China

Abstract
The inerter concept is able to significantly enhance the capability of vibration suppression compared to conventional vibration absorbers. The inerter is acceleration-dependent, which enhances the effective mass. Inspired by the innovative applications of the inerter in mechanical and automotive engineering, a vibration suppression system for civil structures is developed. In this study, a performance-based optimal design method is proposed to determine the inerter system parameters by minimizing both the vibration response of the structure and the cost as a multi-objective optimization problem. Numerical examples for the suppression of the wind-induced vibration of a single degree of freedom oscillator, and an MDOF high-rise structure with the inerter system on the top floor, have been investigated. The results show that the proposed system can substantially improve the wind induced vibration suppression performance. Compared to the traditional tuned mass damper system, the mass of the vibration control device is significantly reduced.

1 Introduction

Structural control is an efficient approach to suppress the dynamic response of civil structures under external excitations, such as wind or seismic loadings. High rise buildings, due to the vortex shedding effect, are very sensitive to wind excitations. Turned mass dampers (TMDs) have been widely used in civil structures for vibration suppression for decades. However, it is also well-recognized that the vibration suppression capability of TMDs is highly dependent to the additional mass in the TMD system. The efficiency and robustness of TMDs increases with the increase of mass [1]. Relatively large additional mass is generally required for high-rise buildings due to the high effective mass [2]. For example, the additional mass of the TMD in the Taipei 101 building is about 660 tonnes. In practical structures and architecture, there are constraints for the mass and volume of the vibration suppression system. These constraints are particularly critical for tall buildings due to the trend of constructing lighter, slender structures with high flexibility. The inerter concept offers a good solution for lighter vibration suppression systems for high rise buildings. Although there is limited literature on the inerter-based vibration suppression systems for wind-induced vibration control [3, 4], some researchers have studied the seismic response reduction in building structures using the inerter concept. Saito et al. [5] proposed an inerter-based damper called a tuned viscous mass damper (TVMD). The optimal response control method has been proposed and verified by vibration experiments of a single degree of freedom system with a TVMD. Sugimura et al. [6] applied the TVMD system to a steel structure built in Japan and investigated the seismic response control effect of this system. In this study, the mass amplification effect and a significant increase in the modal damping have been observed. On the other hand, the lack of design methods for inerter-based systems has restricted the realisation of industry applications.

In most cases, the classical tuning optimal theories (for example, the so-called 'fixed-point theory') are not suitable any more. Pan et al. [7] proposed a demand-based optimal design method for an oscillator with a parallel layout viscous inerter damper, followed by an easy to use method for the practical design of single degree of freedom (SDOF) structures with inerter systems under seismic excitation [8]. This method adopts the stochastic vibration response mitigation ratio as the design index, and expressions of the closed-form stochastic response are used to evaluate the structural response and optimize the design parameters.

The motivation of this research is to explore the requirement-driven, performance based design and optimisation strategy of inerter vibration suppression systems for wind-induced vibration control. In this study, a constitutive model for the proposed inerter based system is established. The dynamic behaviour of the inerter system is then derived based on random vibration theory. A performance-based optimal design method is proposed for designing the inerter system by minimizing both the response and the cost. Then the design problem of the inerter system is transformed into a multi-objective optimization problem with the performance requirement as a key constraint. This is followed by a numerical example for the suppression of the wind-induced vibration of a single degree of freedom oscillator by adding an additional inerter system to show the efficacy of the proposed method. Finally, an MDOF high-rise structure, with the proposed inerter system on the top floor, has been investigated. The results show that the proposed system significantly improved the wind induced vibration suppression performance. Compared with the traditional tuned mass damper system, the mass of the vibration control device was significantly reduced, which offers advantages in manufacture, cost and installation. This requirement-driven, performance-based design and multi-objective optimisation method of the proposed inerter-based vibration suppression system is proved to be effective by obtaining the design parameters of the inerter system, which can meet the performance requirements and minimize the cost.

2 Problem Statement

The wind-induced vibration of high-rise buildings can be modelled as an n degrees of freedom linear vibration system under random excitation. Consider the equation of motion of a linear dynamic system with n degrees of freedom and viscous damping given by

$$\mathbf{M}\ddot{\mathbf{x}}(t) + \mathbf{C}\dot{\mathbf{x}}(t) + \mathbf{K}\mathbf{x}(t) = \mathbf{f}(t) \tag{1}$$

where $\mathbf{M}$, $\mathbf{C}$ and $\mathbf{K}$ are the mass, damping and stiffness matrices, respectively, and $\mathbf{f}(t)$ is the random wind load vector. Due to the structural integrity and residential comfort requirements in the structure design, it is essential to ensure the structural response, especially the peak floor acceleration, is below a certain threshold:

$$\max|\ddot{\mathbf{x}}| \leq a_{th} \tag{2}$$

The widely used method is to mitigate the vibration by incorporating additional devices into the primary structure for supplemental damping. In practical engineering design of vibration mitigation devices, it is not reasonable to just minimize the response without considering the cost. There should always be a trade-off between performance and cost. In another words, a good design of a vibration mitigation device should satisfy the performance requirement, at a relatively low cost. The performance-based design of a vibration mitigation system optimizes the characteristic parameters of the system by solving a multi-objective optimization problem to achieve the performance requirement, as well as minimizing the cost.

Based on the classic theory of random vibration [9], the variances of acceleration can be obtained by either time domain methods or frequency domain methods. For time domain methods, the response history can be obtained by solving Eq. (1) directly with the input of the wind excitation history. Then the variance of the responses are calculated statistically from the response solution over the time history of duration T_{wind}. For frequency domain methods, the power spectral density of the displacement, velocity and acceleration response can be obtained as

$$\mathbf{S_{xx}}(\omega) = \mathbf{H}(\omega)^{*}\mathbf{S_{ff}}(\omega)\mathbf{H}(\omega) \tag{3}$$

$$\mathbf{S}_{\dot{\mathbf{x}}\dot{\mathbf{x}}}(\omega) = \omega^2 \mathbf{H}(\omega)^* \mathbf{S}_{\mathbf{ff}}(\omega) \mathbf{H}(\omega) \tag{4}$$

$$\mathbf{S}_{\ddot{\mathbf{x}}\ddot{\mathbf{x}}}(\omega) = \omega^4 \mathbf{H}(\omega)^* \mathbf{S}_{\mathbf{ff}}(\omega) \mathbf{H}(\omega) \tag{5}$$

where $\mathbf{S}_{\mathbf{ff}}$ is the power spectral density (PSD) matrix of the wind load, and $\mathbf{H}(\omega)$ is the transfer matrix given by

$$\mathbf{H}(\omega) = [\mathbf{K} - \omega^2 \mathbf{M} + j\omega \mathbf{C}]^{-1} \tag{6}$$

Then the variances of the displacement, velocity and acceleration of the k-th DOF can be obtained as

$$\sigma_{x_k}^2 = \int_0^\infty S_{x_k x_k}(\omega) \mathrm{d}\omega \tag{7}$$

$$\sigma_{\dot{x}_k}^2 = \int_0^\infty S_{\dot{x}_k \dot{x}_k}(\omega) \mathrm{d}\omega \tag{8}$$

$$\sigma_{\ddot{x}_k}^2 = \int_0^\infty S_{\ddot{x}_k \ddot{x}_k}(\omega) \mathrm{d}\omega \tag{9}$$

The peak acceleration of the k-th DOF can be estimated by,

$$\max |\ddot{x}_k| = g \sqrt{\sigma_{\ddot{x}_k}^2} \tag{10}$$

where g is the peak factor which can be estimated by using the empirical formula proposed by Davenport [14]. The peak acceleration of the k-th DOF can be estimated by,

$$g = \sqrt{2 \ln(\eta T_{wind})} + 0.577 / \sqrt{2 \ln(\eta T_{wind})} \tag{11}$$

where $\eta = 2\pi/\omega_1$ is the effective structural response frequency and ω_1 is the fundamental angular frequency of the primary structure. T_{wind} is the time duration during which the peak response is quantified.

The variance of the relative velocity response $\sigma_{(\dot{x}_k - \dot{x}_q)}^2$ between two different DOFs k and q, can be obtained as

$$\sigma_{(\dot{x}_k - \dot{x}_q)}^2 = \sigma_{\dot{x}_k}^2 + \sigma_{\dot{x}_k}^2 - 2 \int_0^\infty S_{\dot{x}_k \dot{x}_q}(\omega) \mathrm{d}\omega \tag{12}$$

3 Modelling of the dynamic systems

3.1 Mechanical model for two-terminal inerter

Smith [10] proposed a two-terminal inertial element concept in 2002, as shown in Figure 1. Unlike a typical mass element with a reaction force that is proportional to the absolute acceleration, the reaction force of an inerter is proportional to the relative acceleration between its two terminals,

$$p = b(\ddot{u}_1 - \ddot{u}_2) \tag{13}$$

where b is the inerter coefficient and measured in mass units; p is the axial force of the inerter; $\ddot{u}_1$ and $\ddot{u}_2$ are the accelerations of the two terminals of the inerter, respectively.

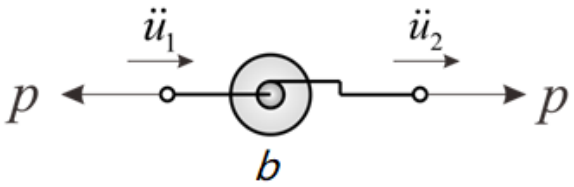


Figure 1: Mechanical model of a two-terminal inerter element

3.2 Dynamic model of the uncontrolled primary system under wind excitation

A high rise building can be modelled as an n-DOF lumped-mass system, as shown in Figure 2(a), where m_i, c_i and k_i represent the mass, damping coefficient, and shear stiffness of the ith story, respectively. The equation of motion for the uncontrolled primary structure can be written as

$$\mathbf{M}_p\ddot{\mathbf{x}}_p(t) + \mathbf{C}_p\dot{\mathbf{x}}_p(t) + \mathbf{K}_p\mathbf{x}_p(t) = \mathbf{f}_w(t) \tag{14}$$

where $\mathbf{M}_p$, $\mathbf{C}_p$, and $\mathbf{K}_p$ are the $n \times n$ mass, damping and stiffness matrices of the uncontrolled primary structure; $\mathbf{x}_p(t)$, $\dot{\mathbf{x}}_p(t)$ and $\ddot{\mathbf{x}}_p(t)$ are the displacement, velocity and acceleration vectors of the primary system; and $\mathbf{f}_w(t)$ is the wind excitation vector. The matrices are given by

$$\mathbf{M}_p = \begin{bmatrix} m_1 & 0 & \dots & 0 \\ 0 & m_2 & & \vdots \\ \vdots & & \ddots & 0 \\ 0 & \dots & 0 & m_n \end{bmatrix} \tag{15}$$

$$\mathbf{K}_p = \begin{bmatrix} k_1+k_2 & -k_2 & 0 & \dots & 0 \\ -k_2 & k_2+k_3 & -k_3 & & \vdots \\ 0 & -k_3 & \ddots & -k_{n-1} & 0 \\ \vdots & & -k_{n-1} & k_{n-1}+k_n & -k_n \\ 0 & \dots & 0 & -k_n & k_n \end{bmatrix} \tag{16}$$

$$\mathbf{C}_p = \begin{bmatrix} c_1+c_2 & -c_2 & 0 & \dots & 0 \\ -c_2 & c_2+c_3 & -c_3 & & \vdots \\ 0 & -c_3 & \ddots & -c_{n-1} & 0 \\ \vdots & & -c_{n-1} & c_{n-1}+c_n & -c_n \\ 0 & \dots & 0 & -c_n & c_n \end{bmatrix} \tag{17}$$

If $\mathbf{C}_p$ is assumed to be Rayleigh damping (proportional damping), the fundamental angular frequency of the primary structure ω_1^p can be obtained by standard modal analysis.

3.3 Dynamic model of controlled system with TMD under wind excitation

Tuned mass dampers (TMDs) have been widely used in practice for vibration mitigation. Figure 2(b) shows the model of a typical tall building with a TMD attached to the top floor. m_T, c_T and k_T represent the mass,

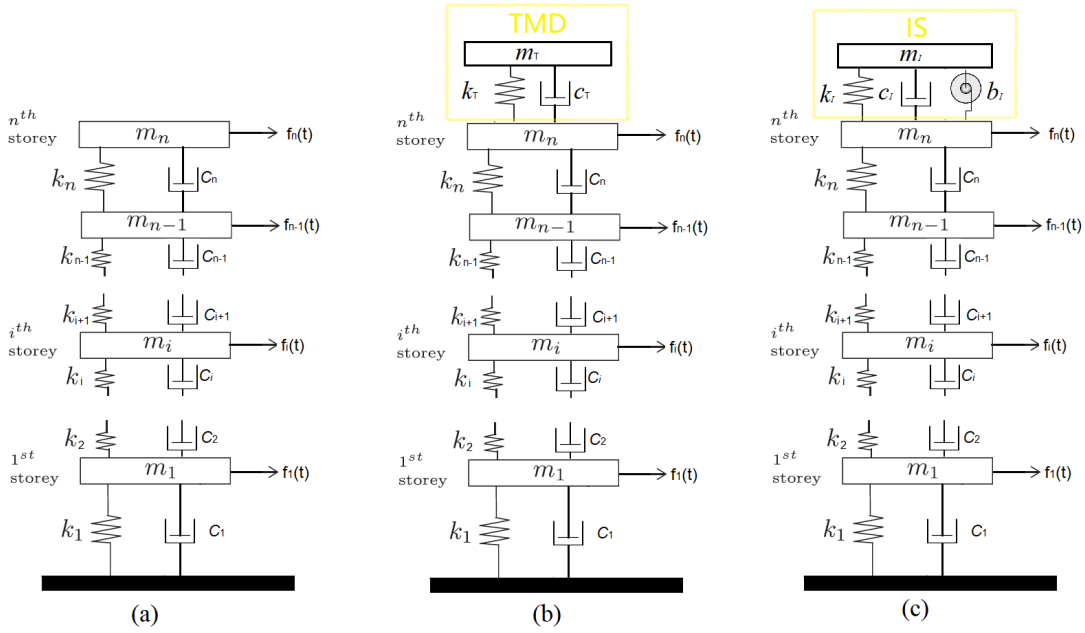


Figure 2: Lumped-mass model of an n storey high rise building under wind excitation

damping and stiffness of the TMD system. Then the mass, damping and stiffness matrices, $\mathbf{M}$, $\mathbf{C}$ and $\mathbf{K}$ in Eq. (1), become

$$\mathbf{M} = \begin{bmatrix} \mathbf{M}_p & 0 \\ 0 & m_T \end{bmatrix} \tag{18}$$

$$\mathbf{K} = \begin{bmatrix} \mathbf{K}_p & 0 \\ 0 & 0 \end{bmatrix} + \begin{bmatrix} \mathbf{O}^{(n-1)\times(n-1)} & & \\ & k_T & -k_T \\ & -k_T & k_T \end{bmatrix} \tag{19}$$

$$\mathbf{C} = \begin{bmatrix} \mathbf{C}_p & 0 \\ 0 & 0 \end{bmatrix} + \begin{bmatrix} \mathbf{O}^{(n-1)\times(n-1)} & & \\ & c_T & -c_T \\ & -c_T & c_T \end{bmatrix} \tag{20}$$

and the excitation vector $\mathbf{f}(t)$ is

$$\mathbf{f}(t) = \begin{bmatrix} \mathbf{f}_w(t) \\ 0 \end{bmatrix} \tag{21}$$

The additional mass ratio, μ_T, the nominal damping ratio, ξ_T, and the nominal stiffness ratio, κ_T, of the attached TMD system are defined as,

$$\mu_T = m_T/M \tag{22}$$

$$\xi_T = \frac{c_T}{2M\omega_1^p} \tag{23}$$

$$\kappa_T = \frac{k_T}{M(\omega_1^p)^2} \tag{24}$$

where M is the total mass of the primary structure and ω_1^p is the fundamental angular frequency of the primary structure.

3.4 Dynamic model of controlled system with inerter under wind excitation

Due to the mass amplification effect, the inerter system (IS) offers another solution for vibration mitigation, which may potentially reduce the mass of traditional TMD systems. Figure 2(c) shows the model of a typical tall building with an inerter system (IS) attached to the top floor. m_I, c_I and k_I represent the mass, damping and stiffness of the IS system, and b is the inerter coefficient. Then the mass, damping and stiffness matrices, $\mathbf{M}$, $\mathbf{C}$ and $\mathbf{K}$ in Eq. (1), become

$$\mathbf{M} = \begin{bmatrix} \mathbf{M}_p & 0 \\ 0 & m_I \end{bmatrix} + \begin{bmatrix} \mathbf{O}^{(n-1)\times(n-1)} & & \\ & b_I & -b_I \\ & -b_I & b_I \end{bmatrix} \tag{25}$$

$$\mathbf{K} = \begin{bmatrix} \mathbf{K}_p & 0 \\ 0 & 0 \end{bmatrix} + \begin{bmatrix} \mathbf{O}^{(n-1)\times(n-1)} & & \\ & k_I & -k_I \\ & -k_I & k_I \end{bmatrix} \tag{26}$$

$$\mathbf{C} = \begin{bmatrix} \mathbf{C}_p & 0 \\ 0 & 0 \end{bmatrix} + \begin{bmatrix} \mathbf{O}^{(n-1)\times(n-1)} & & \\ & c_I & -c_I \\ & -c_I & c_I \end{bmatrix} \tag{27}$$

and the excitation vector $\mathbf{f}(t)$ is

$$\mathbf{f}(t) = \begin{bmatrix} \mathbf{f}_w(t) \\ 0 \end{bmatrix} \tag{28}$$

The additional mass ratio, μ_I, the inertance ratio, ν_I, the norminal damping ratio, ξ_I, and the norminal stiffness ratio, κ_I, of the attached inerter system are defined as,

$$\mu_I = m_I/M \tag{29}$$

$$\nu_I = b_I/M \tag{30}$$

$$\xi_I = \frac{c_I}{2M\omega_1^p} \tag{31}$$

$$\kappa_I = \frac{k_I}{M(\omega_1^p)^2} \tag{32}$$

4 Performance-based optimal design for suppression of the wind-induced vibration

As discussed in the previous section, a good design of a vibration mitigation device should satisfy the performance requirement, at a relative low cost, which needs to optimize the characteristic parameters of the system by solving a multi-objective optimization problem to achieve the performance requirement, as well as minimizing the cost.

The performance requirement should be chosen based on building codes and guidelines, with consideration of a reasonable design redundancy. For high-rise buildings, the absolute value of peak acceleration of the top floor, $|\ddot{x}_n|\, g\sqrt{\sigma^2_{\ddot{x}_n}}$, is usually chosen as the performance indicator which needs to be below a threshold value, a_{th}. In another words, the variance of the acceleration of the top floor should satisfy,

$$\sigma^2_{\ddot{x}_n} \leq (a_{th}/g)^2 \tag{33}$$

We can also set the performance requirement by using the response mitigation ratio, which is defined as the ratio of the response of the controlled system to the response of the primary system, as follows,

$$\gamma = \sqrt{\frac{(\sigma^2_{\ddot{x}_n})_{Controlled}}{(\sigma^2_{\ddot{x}_n})_{Primary}}} \leq \gamma_t \tag{34}$$

where γ_t is the target response mitigation ratio.

The cost of the vibration mitigation device is mainly related to the energy dissipation force in the device, f_d, which is a function of the damping efficiency of the energy dissipation device and the velocity difference between the two terminals (the top floor and the additional mass),

$$f_d = c_T(\dot{x}_{n+1} - \dot{x}_n) \quad \text{(for the TMD)}$$
$$f_d = c_I(\dot{x}_{n+1} - \dot{x}_n) \quad \text{(for the Inerter System)}$$

Therefore, to minimize the force in the dissipation device, the objective function should set up to minimize the variance of the relative velocity $\sigma^2_{\dot{x}_{n+1}-\dot{x}_n}$ between the additional mass and the top floor, which can be obtained as

$$\sigma^2_{(\dot{x}_{n+1}-\dot{x}_n)} = \sigma^2_{\dot{x}_{n+1}} + \sigma^2_{\dot{x}_n} - 2\int_0^\infty S_{\dot{x}_{n+1}\dot{x}_n}(\omega)\mathrm{d}\omega \tag{35}$$

4.1 Performance-based optimal design of traditional TMD for suppression of the wind-induced vibration

Classical tuning theory [11], also known as fixed-point theory, was proposed by Den Hartog and is a well-known method for designing a dynamic absorber. However, this method does not consider the damping of the main structure. Recently, researchers [12, 13] have proposed some methods with consideration of the damping of the main structure. In these methods, the tuned stiffness ratio, κ_T, and the tuned damping ratio, ξ_T, are expressed as functions of the additional mass ratio, μ_T. However, this method is based on a pre-set additional mass ratio, μ_T, which is not based on the performance requirement and is not the global optimal solution.

In this paper, a performance based method tor optimize the TMD system, with consideration of the cost, is proposed and shown in Table 1. The optimal parameters μ_T, ξ_T and κ_T will be obtained by solving this multi-objective optimization problem.

Objective functions	$\min \mu_T$ $\min \sigma^2_{(\dot{x}_{n+1}-\dot{x}_n)}$
Variables	μ_T, ξ_T, κ_T
Constraints	$\sigma^2_{\ddot{x}_n} \leq (a_{th}/g)^2$ or $\gamma \leq \gamma_t$

Table 1: Optimization for the MDOF dynamic system with a TMD

4.2 Performance-based optimal design of an inerter system for suppression of wind-induced vibration

The optimization of the inerter system for suppression of the wind-induced vibration is similar to the optimization method proposed in the previous sub-section for the TMD system, although the design variables are the additional mass ratio, μ_I, the inertance ratio, ν_I, the nominal damping ratio, ξ_I, and the nominal stiffness ratio, κ_I. The objectives will be to minimize the additional mass and the energy dissipation force for the device, and also satisfy the performance requirement. The optimal parameters μ_I, ξ_I, κ_I and ν_I will be obtained by solving the multi-objective optimization problem summarized in Table 2.

Objective functions	$\min \mu_I$ $\min \sigma^2_{(\dot{x}_{n+1}-\dot{x}_n)}$
Variables	$\mu_I, \xi_I, \kappa_I, \nu_I$
Constraints	$\sigma^2_{\ddot{x}_n} \leq (a_{th}/g)^2$ or $\gamma \leq \gamma_t$

Table 2: Optimization for an MDOF dynamic system with Inerter

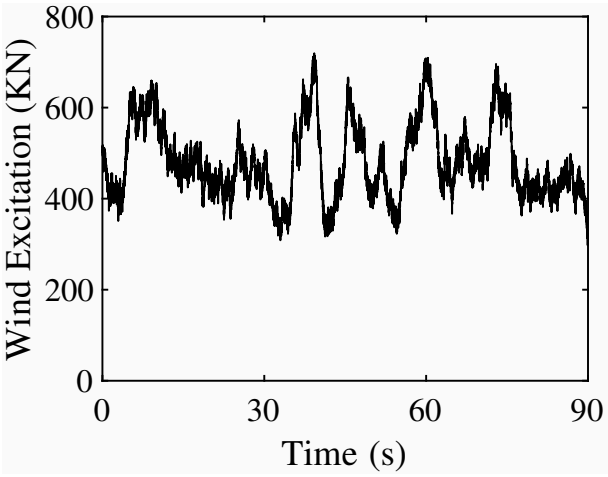


Figure 3: Wind excitation for the SDOF system

5 Case study

5.1 Performance-based optimal design for suppression of the wind-induced vibration of an SDOF system

The key parameters of the single degree of freedom structure are as follows: mass $m = 1.8\times10^5$ kg, stiffness $k = 1.7 \times 10^6$ N/m, and the damping ratio $\zeta = 0.01$. The wind excitation is shown in Figure 3 in the time domain. From the modal analysis of the primary structure, the fundamental angular frequency is 3.0732 rad/s. The performance requirement is that the mitigation ratio of the peak acceleration of the oscillator is no more than 0.7. Based the optimization methods proposed in the previous section, the optimal parameters of the TMD and Inerter systems are summarized in Table 3.

The accelerations of the oscillator in the uncontrolled primary system, the controlled system using a TMD and the controlled system using Inerter system, is shown in Figures 4, 5 and 6, respectively.

TMD	μ_T	κ_T	ξ_T		mitigation ratio of peak acceleration
	0.011	0.012	0.065		0.700
IS	μ_I	κ_I	ξ_I	ν_I	mitigation ratio of peak acceleration
	0.0068	0.0834	0.0187	0.0089	0.700

Table 3: Optimal parameters of the TMD and Inerter System for an SDOF dynamic system

5.2 Performance-based optimal design for suppression of the wind-induced vibration of an MDOF system

A benchmark model of a typical slender building is used to illustrate the efficiency of the proposed methods. This structure has 22 storeys and the total mass is 184×10^3 kg. The total height of the building is 61.8m.

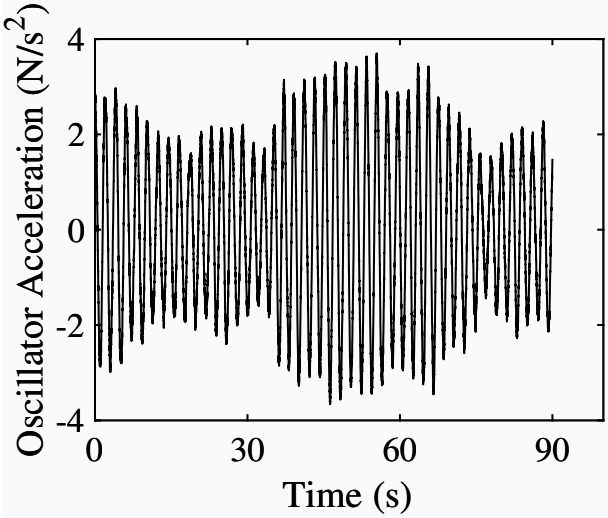


Figure 4: The acceleration of the SDOF uncontrolled primary system

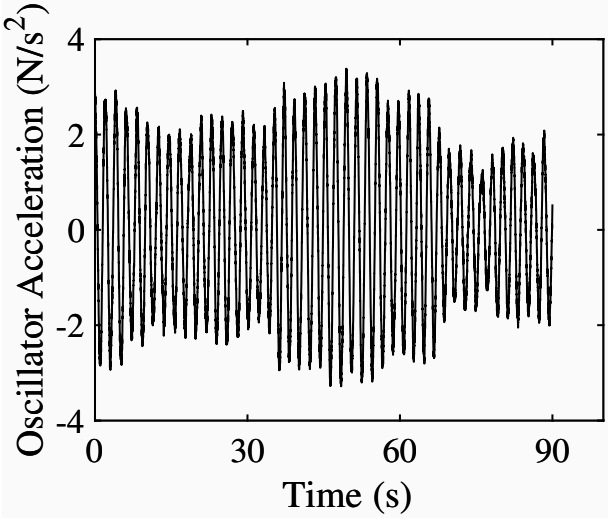


Figure 5: The acceleration of the controlled SDOF system using a TMD

The wind excitation on each storey are integrated by the time history of the pressure distributions from the wind tunnel test. Figure 7 shows the time history of the wind excitation on the top floor. From the modal analysis of the primary structure, the fundamental angular frequency is 3.031 rad/s.

The performance requirement is that the acceleration mitigation ratio of the top floor is no more than 0.7. Based the optimization methods proposed in the previous section, the optimal parameters of the TMD and Inerter systems are summarized in Table 4.

6 Discussion and conclusion

From the results of the two case studies, we can draw the conclusion that the proposed performance-based design and multi-objective optimisation methods are working properly for both the TMD and Inerter systems. The optimal parameters of the attached system for the vibration suppression system (TMD or IS) can be obtained by solving multi-objective optimisation problems. Unlike other parameter design methods, such as

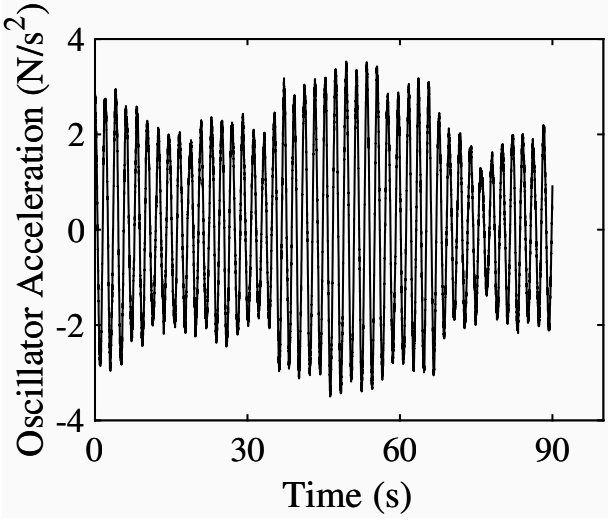


Figure 6: The acceleration of the controlled system using an Inerter

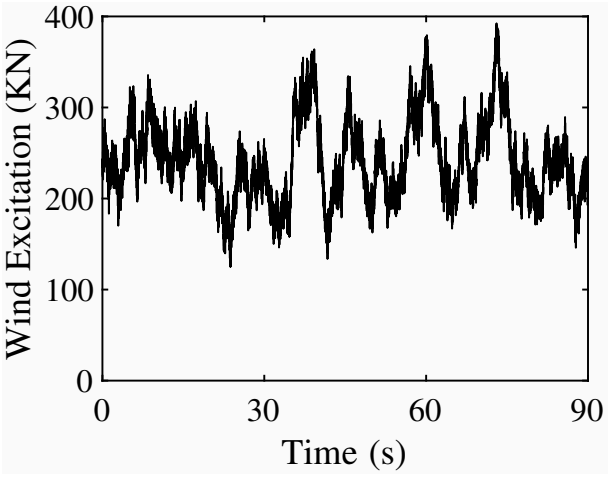


Figure 7: Wind excitation on top floor of the high rise building

the Fixed-point Theory, the proposed method has also considered the damping of the primary system. This requirement-driven, performance-based design and multi-objective optimisation method is demonstrated to be effective in obtaining a vibration suppression device which can meet the performance requirements and minimize the cost. The results also show that the additional mass can be significantly reduced compared to the traditional TMD, if the inerter system is adopted, which offers advantages in manufacture, cost and installation. In practical structures and architecture, there are constraints for the additional mass and the volume of the vibration suppression system. These constraints are particularly critical for tall buildings due to the trend of constructing lighter and slender structures with high flexibility. Therefore, there are advantages in using inerter systems instead of the traditional TMDs due to the mass amplification effect of the inerter device.

TMD	μ_T	κ_T	ξ_T		mitigation ratio of peak acceleration
	0.014	0.010	0.072		0.700
IS	μ_I	κ_I	ξ_I	ν_I	mitigation ratio of peak acceleration
	0.006	0.0852	0.0211	0.0072	0.700

Table 4: Optimal parameters of the TMD and Inerter System for an MDOF dynamic system

References

[1] M. De Angelis, S. Perno, A. Reggio, *Dynamic response and optimal design of structures with large mass ratio TMD*, Earthquake Engineering and Structural Dynamics, Vol. 41, Wiley (2012), pp. 41-60.

[2] R. Mcnamara, *Tuned mass dampers for buildings*, Journal of the Structural Division, Vol. 103, No.9, ASCE (1977), pp. 1785-1798.

[3] A. Giaralis, F. Petrini, *Wind-induced vibration mitigation in tall buildings using the tuned mass-damper-inerter*, Journal of the Structural Engineering, Vol. 143, No.9, ASCE (2017), paper 04017127.

[4] A. Giaralis, F. Petrini, *Optimum design of the tuned mass-damper-inerter for serviceability limit state performance in wind-excited tall buildings*, Procedia Engineering, Vol. 199, ASCE (2017), pp. 17731778.

[5] K. Saito, Y. Sugimura, S. Nakaminami, H. Kida, N. Inoue, *Vibration Tests of 1-story Response Control System using Inertial Mass and Optimized Softy Spring and Viscous Element*, The 14th World Conference on Earthquake Engineering, Beijing, China (2008).

[6] Y. Sugimura, W. Goto, H. Tanizawa, K. Saito, T. Ninomiya, *Response Control Effect of Steel Building Structure Using Tuned Viscous Mass Damper*, The 15th World Conference on Earthquake Engineering, Lisbon, Portugal (2012).

[7] C. Pan, R. Zhang, H. Luo, C. Li, H. Shen, *Demandbased optimal design of oscillator with parallel-layout viscous inerter damper*, Structural Control Health Monitoring, Vol. 25, No.1, Wiley (2017), paper e2051.

[8] C. Pan, R. Zhang, *Design of structure with inerter system based on stochastic response mitigation ratio*, Structural Control and Health Monitoring, Vol. 25, No.6, Wiley (2018), paper e2169.

[9] C. Lalanne, *Mechanical Vibration and Shock Analysis. Volume 3: Random Vibration*, 3rd Edition, Wiley-ISTE (2014).

[10] M. C. Smith, *Synthesis of mechanical networks: the inerter*, IEEE Transactions on Automatic Control, Vol. 47, No. 10, IEEE (1995), pp. 1648-1662.

[11] J. P. Den Hartog, *Mechanical Vibrations*, 4th Edition, McGraw-Hill (1956).

[12] R. Rana, T. T. Soong, *Parametric study and simplified design of tuned mass dampers*, Engineering Structures, Vol. 20, No. 3, Elsevier (1998), pp. 193-204.

[13] R. Rana, T. T. Soong, *Optimal design of wind-induced vibration control of tall buildings and high-rise structures*, Wind and Structures, Vol. 2, No. 1, Techno-Press (1999), pp. 69-83.

[14] A. G. Davenport, *Note on the distribution of the largest value of a random function with application to gust loading*, Proceedings of the Institution of Civil Engineers, Vol. 28, No. 2, ICE (1964), pp. 187-196.

Uneven vane spacing design for reducing noise emission in a variable displacement vane oil pump

L. Benzoni[1], **F. Braghin**[1], **L. Marchetti**[2], **F. Tramaglia**[2]
[1] Politecnico di Milano, Department of Mechanical Engineering,
via Giuseppe La Masa 1, 20156, Milano, Italy

[2]Bosch VHIT Spa, R&D Pump Development,
Strada Vicinale delle Sabbione 5, 26010, Offanengo (CR), Italy

Abstract
The variable displacement vane pump is part of the engine lubrication system, and is subjected to strict oil flow requirements, wide range of temperatures and different aerations levels. In this context, the target of the designer consists in the development and implementation of energy efficient devices able to ensure the necessary NVH targets. In this work it has been developed a strategy to improve the pump's tonal noise. This has been achieved introducing a specific vane spacing in the pump core. That was a great challenge due to high oil pressure pulsations, created by this device design, which are the main excitation energy within the lubricating system. First was developed a numerical model of the system, accounting for aeration, engine permeability and oil dynamics. Then different rotor designs have been studied with the focus of NVH performance and tonal prominences. For validation purposes, numerical and experimental results will be compared, in order to evaluate the best vane spacing logic among the prototypes.

1 Introduction

Nowadays, the environmental impact generated by vehicles and their NVH performance are one of the major design criteria, when developing a new vehicle. The scope of this work is the numerical and experimental analysis of the pressure ripples inside the vane pump with the aim to provide a design method for minimizing the tonal noise. Experimental data was collected in order to support the model calibration and to validate simulation results. This reliable model was in fact used to implement different changes in the pump core. The variable displacement vane pump regulates the oil flow according to the engine request [1]. This provides a significant reduction of power absorption but an increase in term of noise, reason for which the acoustic research has recently become necessary. In this work the noise emission problem related to the pump pressure pulsation is studied through the prominence criteria which is described in the standard ECMA-74 [4]. A design solution based on an asymmetric rotor will be proposed with the target of altering the noise spectrum of the pump, achieving an optimization of the noise generation. From this assumption, experimental and numerical activities have been done. In the design phase the pressure traces were analysed and in the testing procedure all pressures, vibrations and noise data have been collected. A dedicated testing procedure was adopted during the experimental phase. As showed in the figure 1 the need to measure the pressure inside the pump core was met with the use of a piezoelectric transducer in the delivery kidney. Moreover when the different proposed solutions were tested, an additional accelerometer on the pump cover and a microphone were added. In figure 2 is reported an example of pressure time history at the delivery kidney, collected during the test. This typical behaviour can be explained by following the chamber during its rotation in the pump core. A chamber volume at the inlet of the vane pump is mostly filled with oil and a certain amount of trapped air. When connecting to the delivery channel, the volume encounters an higher pressure domain which leads to a sudden compression of air bubbles. At this stage, all the air initially present is converted into

molecules dispersed in oil and a pressure peak is generated. Eventually this pressure wave will propagate in the hydraulic system and structures. The described process occurs every time a chamber is connected to the outlet, giving rise to a pulsed phenomena as a whole.

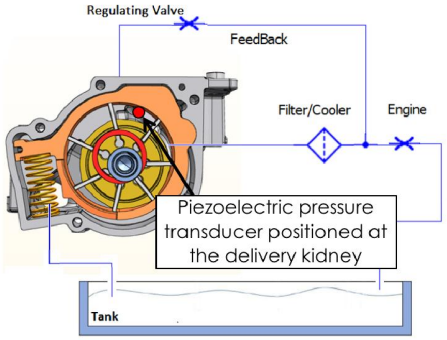


Figure 1: Vane pump's circuit and position of the pressure tranducer inside the pump's core

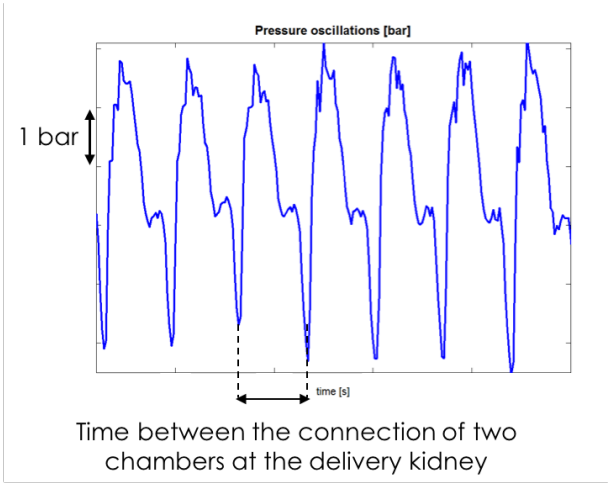


Figure 2: Typical pressure oscillations collected inside the pump core

2 Model regulation

The Amesim software is capable of model gas transport and dynamics inside the oil. The adopted 1D numerical model was initially regulated through the experimental test. The most important parameters for the model validations were the dissolution time constant (τ_d), saturation pressure (P_{sat}) , and the undissolved gas mass fraction (X_u) , the terms which leads the pressure oil's pressure oscillation inside the pump core. For regulating these variables it was essential to monitor the aeration level inside the oil of the circuit. The sensor used in our test can directly measure the X_u and its correlated volumetric one ($V\%_{undissolved}$) at the ambient pressure. Then for set the correct value of P_{sat} it was necessary to use the well known Henry-Dalton-law that is showed in figure 3. This law defines the volumetric air content that can be dissolved in the oil at difference reference pressure. The slope of this relation is given by the Bunsen coefficient (B). This term is different for every bi-phase fluid, and the available literatures [5], [6] state that for the oil-air combination, can be approximated around 9 [vol.%/bar] which means that the dissolved air fraction at the

reference pressure ($V\%_{dissolved}$) is 9%. So knowing that the saturation pressure is the threshold value by which all the air is dissolved inside the oil, it can be easily obtained through the following equation 1:

$$P_{sat} = \frac{V\%_{undissolved} + V\%_{dissolved}}{B} \tag{1}$$

Then a reasonable value of τ_d was settled trying to match the experimental pressure amplitude oscillations at different working speeds.

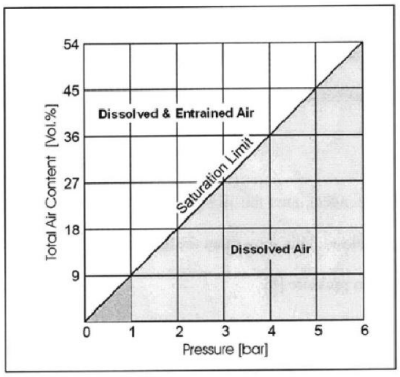


Figure 3: Henry-Dalton diagram

In figure 4 is shown a schematic representation of the adopted model. From the hydraulic model, in output it can be obtained the pump flow rate at different engine permeability and also the pressure profile inside each single chamber. The theoretical model at the base of the hydraulic one, takes in consideration all the interested bi-phase fluid dynamic parts and the pump functioning. As it is represented in the following figures is interesting to notice that the model in consideration is able to reproduce the magnitude of the amplitude of the oscillations on the pump's core itself in the time domain. That is well reflected also looking at the results in the PSD as are represented in figure 5 and 6. It is clear that the model is reliable in reproducing the pump's order magnitude and trend, which are the main frequencies components that are equally spaced in the frequency domain. In our case the pump has seven chambers and so the pump's orders are multiples of the 7x revolution. For this reason it was decided to use the considered model to study the changes inside the pump's core, changing the angular chamber's amplitude in order to break these strong pump's orders.

3 NVH Improvements

From the frequency analysis is noticeable that in the pump core are present clear and discrete tones. These pulsations excite the pump structure, in particular the cover, which can act as resonance box. This last, vibrating, generates noise that is perceived by the human hear, as amplified or decreased dependently on the oscillation frequency. From this analysis, we can distinguish three different main blocks (see figure 7). In the following section it developed a design method for reducing the source of the audible prominent tones, so the excitation input. The main idea is to change the chamber dimension for spreading the energy of the multiples of the pump's order over other frequencies to decrease the maximum excitation at each interested bandwidth and the tones audibility. In the design phase the prominence criteria was applied directly on the pressure trace data. In this way, looking directly at the pressures obtained by the regulated model, we can have reasonable fast and reliable results on what happens changing the angular amplitude of the chambers.

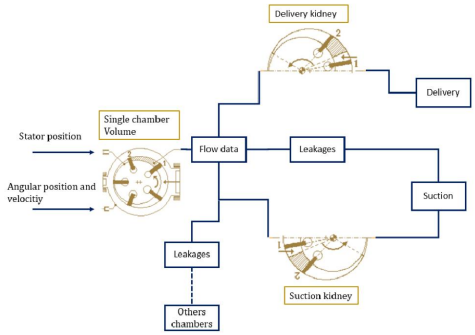


Figure 4: scheme of the adopted model

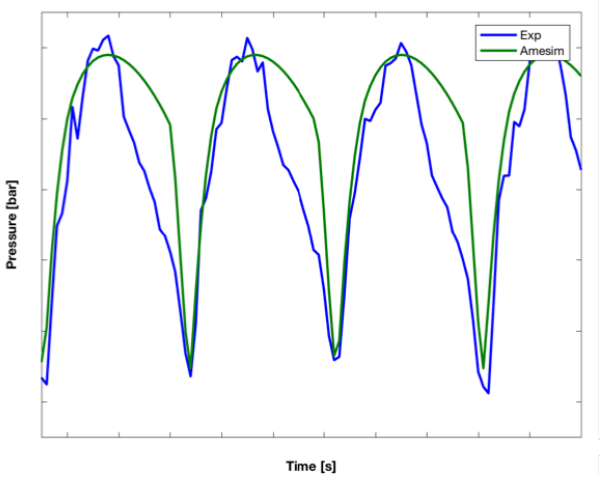


Figure 5: Numerical and experimental pressure trace comparison in the time domain

3.1 Identification and evaluation of prominent tones

An important parameter for the noise improvement of the pump over the total sound emission is the tonal prominence evaluation. In fact, even a low amplitude tone can be very irritating. A tone is typically a single frequency that is audible by the human hear [2]. Using a traditional measure of sound like a decibel is not enough to characterize tones. Instead the metric of Prominence Ratio can be used to quantify the presence of distinctly tones in a signal. Rather than using the absolute level of the tone, these metrics look at the level of the tone relative to the background sound level to determine how prominent, or noticeable, the tone is to a listener [2]. Even if a single frequency is visible in a sound spectrum, it does not mean that it can be heard as distinct tone. If the tone is not high enough relative to the background, it will not be perceived by the listener as represented in figure 8. Referring to the standard ECMA-74 [4], the prominence ratio method can provide to readily automated to handle multiple tones within the same critical band [4]. This method is suitable to our application because knowing that the main core pump excitations are all multiples to the pumps order and so dependent to the rotation speed, some tones may fall in the same critical region. For this standard, when using the prominence ratio method, a discrete tone is classified as prominent if the difference between the level of the critical band centred on the tone and the average level of the adjacent critical bands is equal to or greater than 9 dB for tone frequencies of 1000 Hz and higher [4], and by a greater amount for tones at lower frequencies. The width of a critical band is a function of frequency . Critical bands are used to quantify the

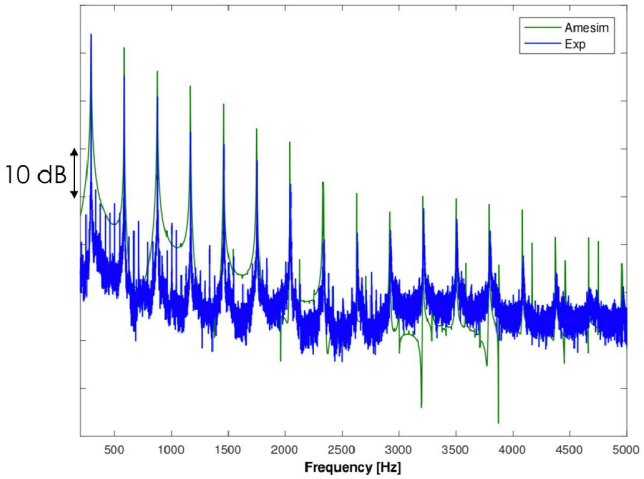


Figure 6: Numerical and experimental pressure trace comparison in the frequency domain



Figure 7: Main system blocks

ability of the human ear to distinguish between individual frequency tones. The human ear can hear from 20 to 20,000 Hz, but the ability to distinguish individual tones varies as a function of frequency. At low frequencies, the human ear can distinguish changes in frequency more easily than at high frequencies. For example, the ear can distinguish a 20 Hz difference between 500 and 520 Hz tones more readily than a 5000 and 5020 Hz tones [3]. As a result, the ear tends to have hearing bands. These bands increase in bandwidth from low to high frequency as shown in figure 9. In figure 10 is reported the prominence evaluation of the even vane pump on the sound data collected from a ramp up speed test. Here is noticeable that are present strong prominent tones, especially the first four pump's orders.

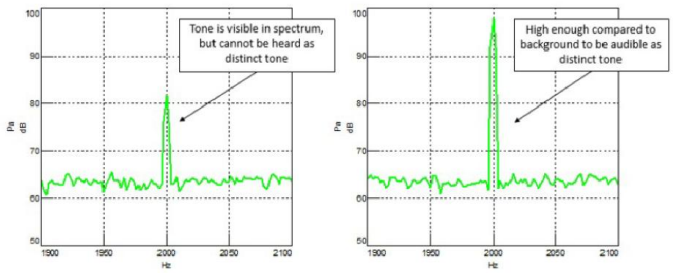


Figure 8: Examples of audible and not audible tone

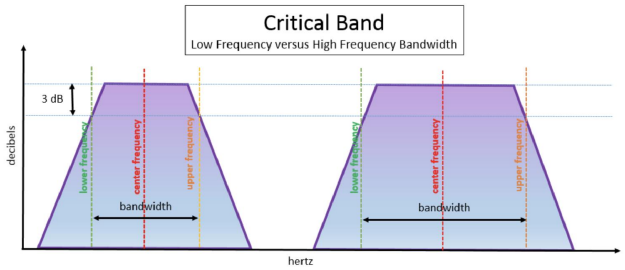


Figure 9: Bandwidth of critical band

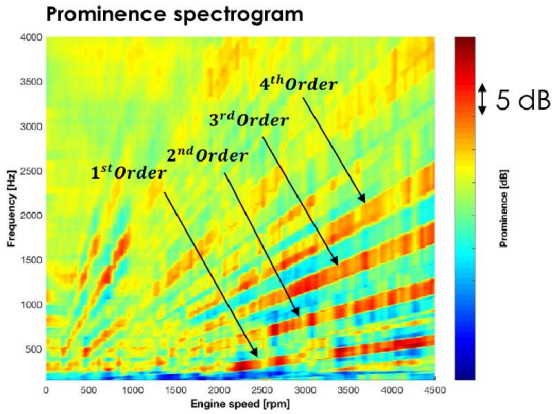


Figure 10: Example of prominence evaluation from a microphone data collection during a speed ramp up test

3.2 Best vane lag

As previously mentioned, an efficient tool to spread the energy far from the main peaks, reducing in this way the prominence and the maximum excitation in each interested frequency band, is the vane displacement with respect to the original position. The vane displacement is aimed to the variation of the chamber angular amplitude, in this way the compression and decompression phase are changed causing the resulting delivery pressure pulsation to be no more constant in time. In the frequency domain, the vane displacements, have the effect to move energy content to other frequencies. During our work, many configurations were simulated, but in this thesis are reported only two logics that have accounted better results through batch simulations. These two logics are called ”square” and ”alternated”. They take their names by the disposition of the chamber amplitude variation around the rotor. In figure 11 the dispositions of the chambers are visible in terms of amplitude variation. It has to be noted that the chamber number one is standard, so its angular amplitude is not changed. The other six chambers change their amplitude according to the logic adopted and respecting the constraint that the superposition of all chambers amplitude must be equal to 360 degree. Another constraint is that the maximum chamber’s angular variation that is strongly dependent on the pump’s geometry. In fact, if too big, the pre- compression phase became too inefficient, causing undesired pressure drop and back flow rate. Instead, if too little, the pre-compression phase can be too efficient and cause, in certain working condition, undesired pressure peaks, decreasing in this way the pump’s sound performance

and fatigue life. For studying the logics effect, it was performed a batch process, where each test was conducted with an increased chamber amplitude variation, until the limit condition was reached (five degree in our case). For respecting the constraint of a totality of 360 degree, summing all chamber's amplitudes, the six chambers were paired in two group of three. The members of both group have the same angular variation in module, but are opposite in sign. Doing in this way, the constraint over the totality of the chamber amplitude is easily satisfied. In our batch analysis we have seen that ,for both alternated and square logic, the best results in terms of prominence evaluation are obtained at the maximum allowable chamber's angle variation performed (in order to not encounter the problem discussed above). In figure 12 is reported a zoom in the PSD spectrum in which are compared the alternated logic and the even spaced vane one. Here the prominence bands are also reported and centred in the pump order under analysis (red rectangle) . According to the standard ECMA 74 are also reported the bands in which fall the tones that contribute to the order masking (green rectangles). As it can be seen from figure 12 the alternated logic is able to shift the pump's order energy greatly inside the masking bands. So it can be said that this logic can provide an effective prominence reduction. In figure 13 is repeated the previous analysis but with the square logic. It can be seen that in this case the energy shift is nearer to the pump order but the energy related to this last is sensibly reduced. So it can be said that both logics can provide an effective prominence reduction acting in a different way on the energy spreading.

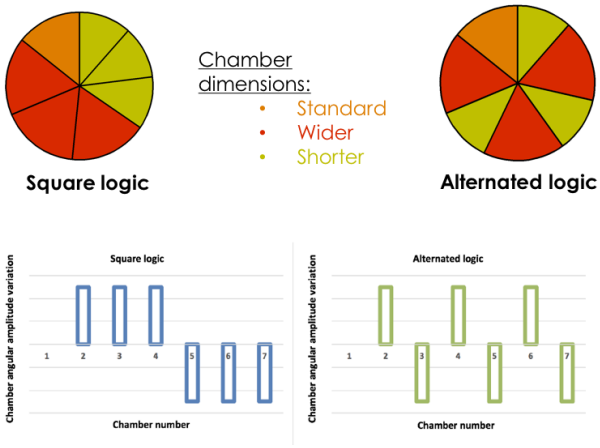


Figure 11: Developed logics

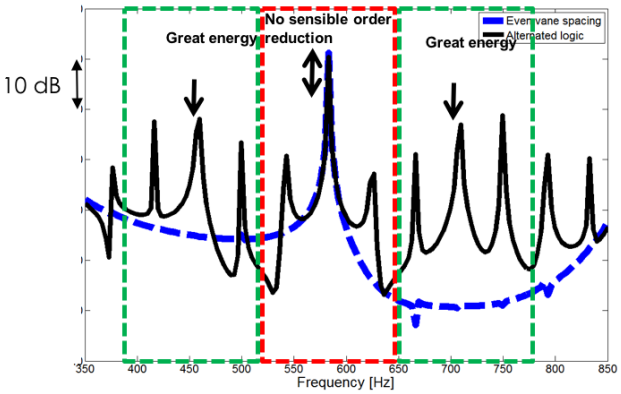


Figure 12: Zoom comparison in the PSD spectrum between the Alternated solution and the base one with the prominence band centred in the pump order

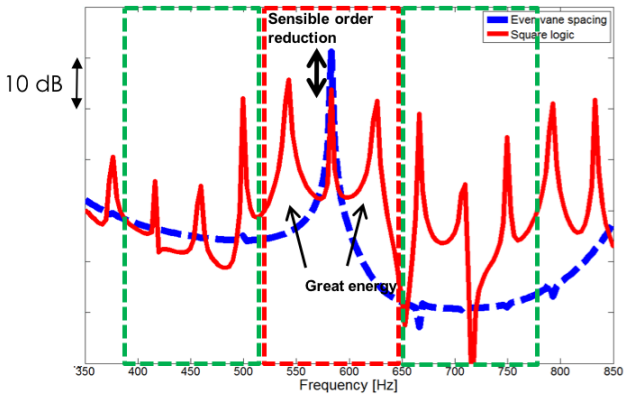


Figure 13: Zoom comparison in the PSD spectrum between the Square solution and the base one with the prominence band centred in the pump order

4 Experimental results

In order to validate the logics previously discussed it was performed an experimental campaign by which delivery pressure, cover acceleration and sound pressure were collected simultaneously by the respective transducer (see figure 14). With the sake of simplicity here are discussed only the data acquired with the microphone as reported by figure 15. Here, with the aim to have a wide vision on the obtained results, are reported the results from the speed ramp up test of the sound data already processed under the prominence criteria. In particular, in the figure under consideration, are reported the six spectrograms divided in three columns (even spaced case, square logic, alternated logic) From each column we can identify two types of spectrogram:

- An upper one with reported the absolute level of prominence.
- A lower one with marked only the areas with the tones over the prominence limit.

Looking to these results (see figure 15), it is clear that the two developed logics can provides huge improvements with respect the even case. The main difference between the alternated and the square logic it can be seen analysing the spectrogram where are marked only the tones over the prominence limit. Looking at the previous spectrogram (figure 15) it can be noted that the 1^{st} pump's order is the hardest to hide, especially at high frequencies. In particular it became prominent at frequencies dependently on the chosen masking logic. For better understanding the differences regarded to the masking capability of the 1^{st} pump's order between the logics adopted, figures 16, 17 were reported: they describe the distance between the logics orders respect to the pump's one and the width of the tone and noise bands defined by the standard and centred in the 1^{st} pump's order. Looking at figure 16 it can be noted that the higher orders developed by the alternated logic (black lines) start to go out from the noise bands for engine speeds over the 3000 rpm. That means that the alternated logic is not more effective to hide the 1^{st} pump's order. In other hands, seeing figure 17 we have an opposite trend, so the square logics became more effective in hiding the 1^{st} pump's order at speeds higher than 3000 rpm.

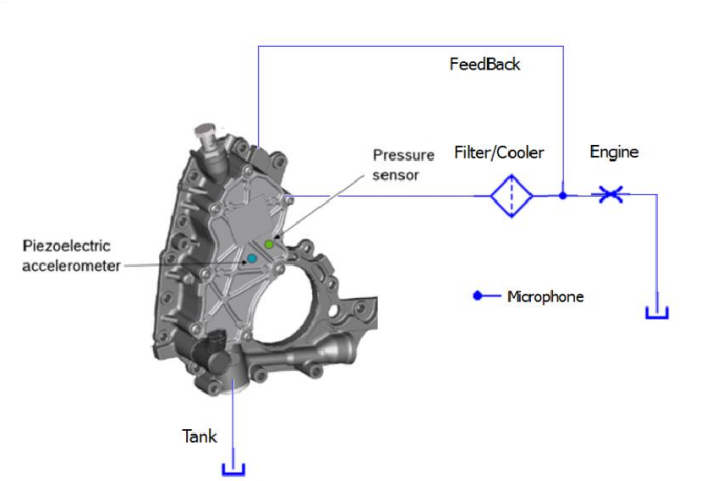


Figure 14: Experimental set up

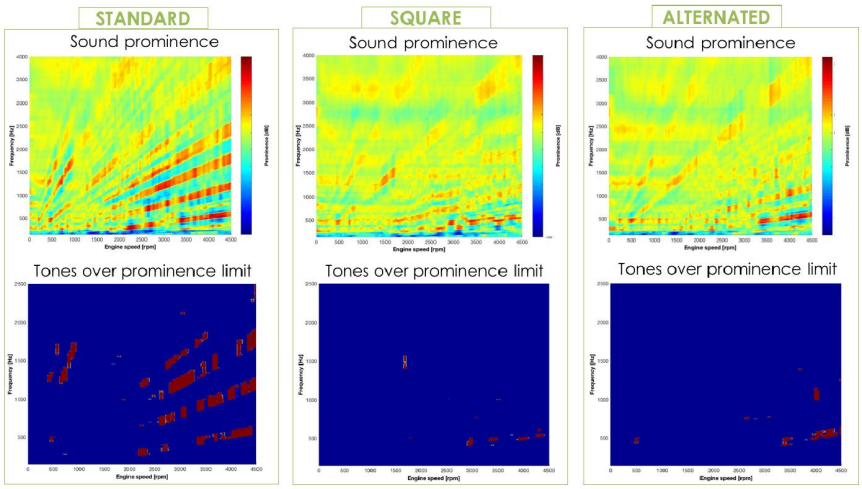


Figure 15: Experimental spectrograms of the prominence evaluation obtained by the collection of acceleration pressure and sound data from the rump up test

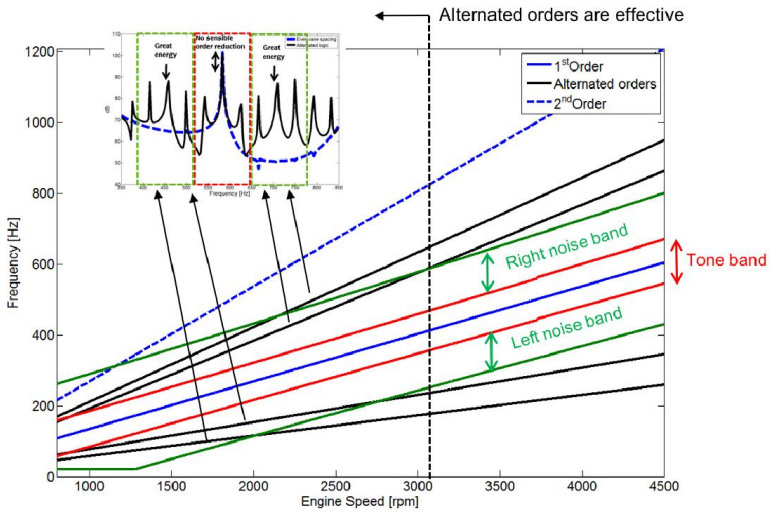


Figure 16: Scheme of the trend of alternated pumps orders with respect to the tone and noise bands defined by the standard with increasing frequency

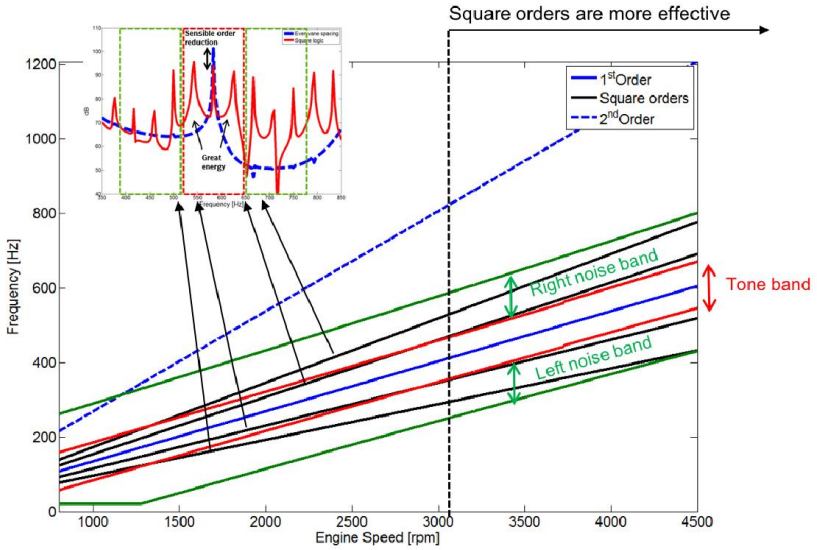


Figure 17: Scheme of the trend of square, pumps orders with respect to the tone and noise bands defined by the standard with increasing frequency

5 Conclusions

In this work, starting from the analysis of a vane pump, it was studied the role of aeration in the pressure peaks generation. In particular, several numerical simulations were performed in order to find a correlation between aeration parameters and pressure pulsations at pump delivery kidney obtained from the experimental tests. Then it was described the concept of the ear bandwidth which is recalled in the standard ECMA 74 that define the tone prominence criteria. This criteria was used to design and select an efficient modification of the pump rotor. Each specific pattern of uneven vane spacing was numerically evaluated in terms of its capacity to spread the energy among the frequency spectrum. From these simulations were selected and reported here only the logics with the best results, so the alternated and squared ones. The best logics chosen previously were physically realised and tested. It was verified with success that the induced harmonic components spread presents the same shape of the one predicted numerically. From the obtained experimental results is it clear that the alternated logic is better at medium velocities and the square one at high. At low velocities the pressure pulsations are too low and pump harmonic orders too near to each other that no tonal prominence is noticed. It can be concluded that there is not a best logic for all speed, but the logic choice depends on which is the critical pump's speed and so where there are the major noises problems. Moreover, the critical pump's speed depends also on the environment noise. In fact, the tone prominence is dependent on the level of the masking noise. In the real application the major contribution to the masking noise is given by the engine sound. Therefore, for a correct choice of the best solution, additional data on the environment noise must be collected.

References

[1] Sara Gronchi, Riccardo Maccherini, Raffaele Squarcini, Fabio Guglielmo, and Emanuela Ligar. Analysis of the Acoustic Emission of an Oil Pump:Experimental and Numerical Activities. SAE Technical Paper 2014-32-0120;

[2] Tone-to-Noise Ratio and Prominence Ratio - Siemens PLM Community, community.plm.automation.siemens.com;

[3] Human-hear-cochlea - Siemens PLM Community, community.plm.automation.siemens.com;

[4] ECMA-74 12th Edition / December 2012 Measurement of Airborne Noise emitted by Information Technology and Telecommunications Equipment;

[5] Ben Ni and John Pieprzak.Transportation and Transformation of Air Bubbles in Aerated Oil through an Engine Lubrication System. SAE Technical Paper. 2004-01-2915;

[6] Maassen, F., F. Koch, and F. Pischinger, Connecting Rod Bearing Operation with Aerated Lube Oil. SAE, 1998;

Estimation of steering gear running noise using simulated excitations and measured noise transfer functions

A. Scholz[1], P. Marinova[1], N. Schmidt[1], D. Vieker[1], S. Orlando[2], B. Van Genechten[2]
[1] ZF Friedrichshafen AG, Department CAE Structural Dynamics & Acoustics
Hansaallee 190, 40547 Düsseldorf, Germany
e-mail: **andreas.scholz1@zf.com**

[2] Siemens Industry Software NV, Department Simcenter Engineering & Consulting
Interleuvenlaan 68, 3001 Leuven, Belgium

Abstract
In this paper we present a hybrid approach for estimating in-vehicle steering gear running noise during a parking maneuver. The approach is based on a simulation model that provides the structural dynamic excitations from the steering gear, and experimentally measured transfer functions that map these excitations to interior sound pressure level. Providing realistic excitations requires simulating the steering gear in a power-on condition. To this end, we use a multibody model of the gear mechanics in co-simulation with models of the steering torque controller, the torque and angle sensor, and the electric drive. Our results show that the presented approach is a useful tool for frontloading NVH-driven design decisions in the development process of steering gears.

1 Introduction

Running noise of electrically powered steering systems (EPS) is an essential assessment criterion in today's automotive development because modern drivetrains are so silent that steering gear noise becomes audible in the vehicle. A classic Noise, Vibration, and Harshness (NVH) assessment of steering gear running noise requires a physical integration of the steering system into the vehicle, yet physical components of both these systems are only available in late stages of the development process. As a result, NVH-driven design changes are often time consuming and expensive. It is therefore desirable to characterize running noises of steering gears as early as possible, even prior to the availability of physical parts.

Full vehicle noise and vibration performance is depending on the interaction between many subsystems, such as powertrain, subframe, body, and suspension. For an effective design improvement procedure, it is of paramount importance to identify the contribution of each of these subsystems and to clearly assess the NVH improvement potential for single component modifications. The traditional compromise solution relies on iterative component improvements and the validation of several physical prototypes throughout the vehicle development process. Especially for steering system development this poses significant challenges as the final in-vehicle performance depends as strongly on the acoustic sensitivity of the car body as on the excitations generated by the steering system operation. The core of advanced NVH design process management is a predictive vibro-acoustic full vehicle analysis model, used to support concept decisions, monitor component performance, and evaluate cabin noise targets at any design stage, thus reducing the total development time and costs. The predictive full vehicle modeling as proposed in this paper makes use of test-based component models for existing parts and pure finite element component models for newly designed components.

At early design stages the model is built based on predecessor dynamic data. It then offers the engineers the analysis environment to quantify, directly at the level of the final cabin noise performance:

- the contribution of every subsystem, and
- the effect of subsystem or component design changes.

The target is to provide the vehicle NVH team with qualitative and quantitative insight in major causes for interior noise, at any stage or time in the design cycle, and to set clear responsibilities and targets for every component design team (both internal for the steering system and external for the subframe and body design teams). The proposed analysis model allows for quick evaluation of the effects on interior noise of design modification requirements from any vehicle development section. Throughout the design cycle the individual component characteristics and input loads in the full vehicle analysis model can be flexibly updated to match as-build parts, from prototype until mass production. In this way the model provides an easy way to monitor the NVH progression of the vehicle at each step of the development process.

The rest of this paper is structured as follows: In section 2 we give some generic background on steering gear running noise assessment based on physical parts. We then explain what is required to perform the same analysis virtually, describe the structure of the underlying prediction process, and provide briefly some theoretical background about the used methods. Section 3 explains the overall topology of electric power steering systems (EPS) and continues with describing the structure of the mechatronic system model that provides the noise-generating excitations. In the following section 4 we explain the necessary steps to compute interior noise from the calculated excitations, which involves building up a structural assembly model and incorporating measured noise transfer functions. Section 5 contains an application example that shows the influence of different connections between steering gear and vehicle. We finish the paper with conclusions and outlook in section 6.

2 Method

Running noise is classically evaluated during emulated parking maneuvers. These maneuvers are performed in a semi anechoic chamber with zero vehicle speed and different constant handwheel speeds in clockwise (CW) and counterclockwise (CCW) direction. The resulting interior sound pressure level is then recorded with a binaural head and the frequency content of the recorded signal is extracted for evaluation. Note here that constant handwheel speed is necessary to operate the system in a quasi-steady state condition so that results are comparable and order-driven excitations from the electric drive or other subsystems do not corrupt the measurements.



Figure 1 Semi anechoic chamber for in-vehicle steering gear running noise assessment. Asphalt on the ground ensures realistic resistance forces during emulated parking maneuvers.

For the simulation-based prediction of running noise it is necessary to operate a virtual model of the steering gear in the target environment, i.e., the vehicle. The gear model must replicate the parking maneuver load

case and provide the resulting noise-generating excitations while the vehicle model must contain the noise-transmitting properties from the gear to the driver ear. In this section we describe the overall structure of the underlying noise prediction process and show how the individual models are combined.

2.1 Noise prediction process

Figure 2 shows the overall structure of the interior noise prediction process. The prediction is based on a mechatronic excitation model that comprises the mechanical components of the gear, the electric drive, the torque sensor, and the steering torque controller. A more detailed description of the model structure is given in section 3. To create the excitations, the mechatronic model is run for multiple load cases that correspond to parking maneuvers with different constant handwheel speeds from 30 to 90 rotations per minute (rpm) and a constant rack load, e.g., 4 kilonewtons (kN). This procedure is in line with standard NVH in-vehicle and on-bench test procedures so that simulation results are comparable when physical parts become available.

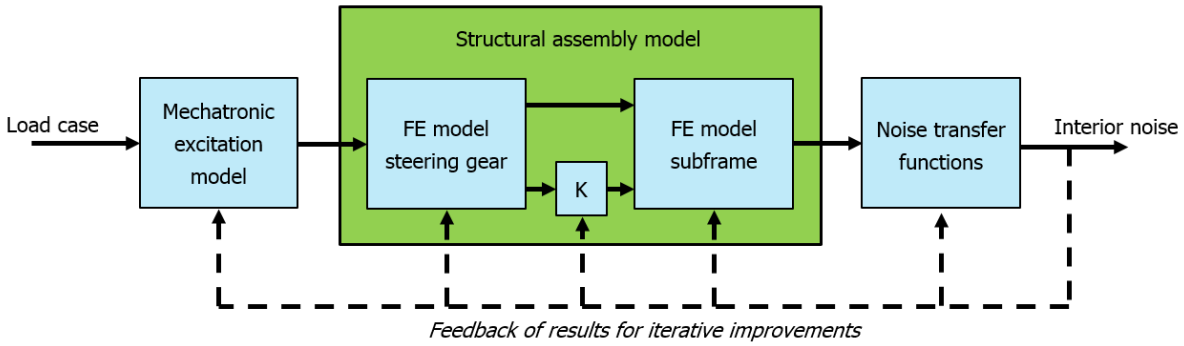


Figure 2 Interior noise prediction process. Virtual excitations and measured noise transfer functions yield predicted interior noise as an output.

The excitation model outputs time domain data of loads at various internal interfaces between moving and static parts. Simulation in the time domain is required to capture the load-dependent non-linear behavior of the system as well as to allow the full rack travel of approximately 150 mm for a typical belt drive EPS. The dynamic loads are then transformed into the frequency domain and fed into an assembly model which comprises two substructure models of the steering gear and the vehicle subframe, as well as the connection stiffnesses at the mounting points between the gear and the subframe, labeled as K in Figure 2. Including both the gear and the subframe as coupled substructures allows for identifying their individual influence on the full-system behavior, which is key to improving running noise later in the process. For instance, assembly modes exist that are either dominated by the modal behavior of the gear or by the modal behavior of the subframe. This is important when the manipulation of such system modes is necessary and highlights the value of the virtual integration process described in this article. More details on the structural model are given below.

Feeding the structural assembly model with the virtual excitations from the mechatronic system model yields forces at the mounting feet, which are the main connection points to the integration target, i.e., the vehicle. Accordingly, the last step towards predicting interior noise in the vehicle consists of using noise transfer functions (NTFs) that map dynamic mounting point forces to interior sound pressure levels. NTFs are typically obtained experimentally by tapping the point of excitation with an impact hammer while measuring the sound pressure level response with a binaural head in the vehicle. Note here that in early development stages, measured NTFs of the vehicle are not available, so that predictions or NTFs from a previous version of the vehicle must be used as approximations.

2.2 Theoretical background

The modeling technique used for the assembly modeling is Frequency Response Function (FRF) based substructuring (FBS). The basic principles are briefly reviewed in this section, for more details see [1]. The basic idea of the FBS method is to predict the global frequency response function matrix between forces acting at specific operational excitation degrees of freedom (DOF) on a substructure and selected response DOF in any substructure of the assembly. Note that no limitations are set on the type of response signals: sound pressure and vibrations are treated in the same way. From a component designers point of view, the exploitation of a FBS model to calculate force transmissibility spectra is very interesting. The operational reaction forces at the component coupling interfaces can be estimated for every set of external force spectra acting on any component or part of the assembled structure. These interface reaction forces are of interest in case of hybrid FBS models because they implicitly contain all effects that the coupling has on the structural dynamics behavior. They can thus be applied as input to the original, uncoupled, finite element component models for design optimization.

Prior to the assembly calculations, each component is represented by its FRF matrix $[H_{ij}]$, relating a response vector $\{x_i\}$ to an excitation vector $\{F_j\}$:

$$\{x_i\} = [H_{ij}]\{F_j\} \tag{1}$$

This matrix describes the frequency dependent interaction between the force input DOF, the general (vibration or noise) response DOF and the DOF connecting that component to other vehicle components. For coupling calculations, these FRF matrices of the uncoupled components are reorganized in submatrices. The submatrix dimensions are determined by the number of coupling DOF, the number of excitation DOF and the number of response DOF on each subsystem. The interface DOF from both substructures can either be rigidly coupled or, in the general case, joined by flexible elements, characterized by a stiffness block matrix [Ks]. The FRF of the assembled structure are then derived from the compatibility conditions for the displacements and the equilibrium conditions for the forces. Each component is modeled by a measured FRF matrix or by a synthesized FRF matrix based on a FE model of the component. To guarantee the accuracy of the predictions on the assembly model, the component FE model must be validated and updated using experimental modal analysis on a physical prototype as soon as it becomes available.

The steering system predictive model described in this paper includes the main structural components: the steering system structure (including housing, motor, gear and BNA) and the vehicle subframe. Measured FRF matrices are used to characterize the car body attachment stiffness and acoustic sensitivity. Depending on the steering system configurations the steering system and subframe components are connected through rigid or bushing mounts. An overview of the assembly layout is given in Figure 3.

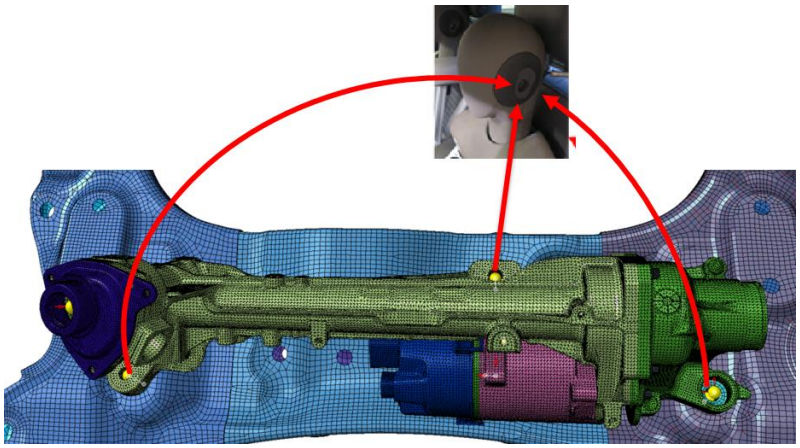


Figure 3 Steering system interior noise assembly model.

The input forces applied to the full vehicle model in the scope of the work presented here are motor and internal bearing forces inside the steering system. They are calculated using a co-simulation model that includes a MBS steering system model and a motor torque control model. The details of the calculation of these forces are discussed in the next section of the paper.

3 Mechatronic excitation model

3.1 Steering-gear topology

Steering systems of vehicles are commonly built around the steering column assembly and the steering rack (see Figure 4). The steering column is a chain of shafts and joints that provide the mechanical connection of the steering wheel to the actual steering gear. The driver's hand wheel torque is transformed to a linear force by a pinion that drives the steering rack. Assisted steering, so called power steering, has been used for decades in the automotive industry. While the initial concept of providing steering assist was originally based on hydraulically powered systems (HPS), electrically powered systems (EPS) are now state-of-the-art. Among other reasons, this is because EPS consume less power, which helps reduce fuel consumption. EPS are available today in different designs, depending on system packaging requirements, costs, and required steering assist.

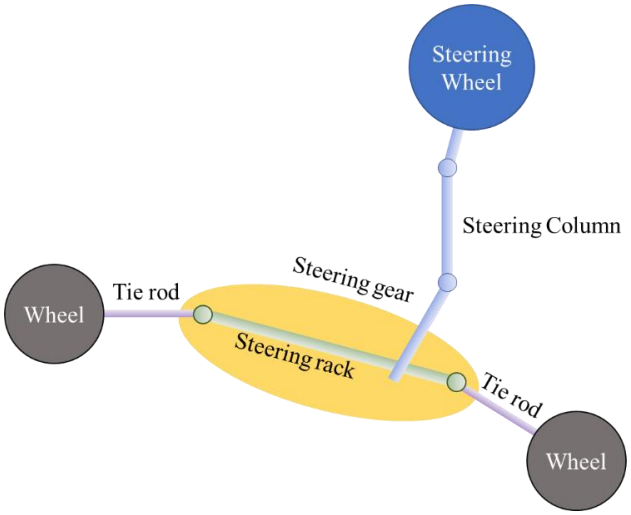


Figure 4 General schematic of an automotive steering gear. Steering wheel torque is transmitted along the column and transformed to a linear rack force that actuates the wheels.

In this article, we will only discuss so-called belt drive EPS. Belt drive systems are a subset of steering gear topologies that provide steering assist by driving a ball nut on the steering rack, which is connected to the electric drive with a belt. The ball nut transforms torque from the motor to linear rack force and provides radial support of the steering rack. Due to their complexity, belt drive steering systems contain various sources of running noise. In the following paragraph, we will briefly describe the excitation sources: the electric drive, the belt-and-pulley assembly, and the ball nut assembly.

The electric drive is a source of running noise because of two main reasons. First, it contains a discrete number of permanent and electro magnets that cause low-amplitude ripple in the torque output of the motor. Second, the rotating electromagnetic field in the stator excites the motor housing periodically when generating assist torque. Torque from the electric drive is transmitted to the ball nut by a timing belt which produces excitations due to tooth engagement with the pulleys. Belt resonances may also become audible depending on the preloading, the speed, and the transmitted torque. A further contributor to running noise is the ball nut assembly (BNA) which contains multiple balls that interact dynamically with the surfaces of the ball nut body and the steering rack. In general, the balls do not always roll at the same speed and can collide when entering or leaving the return path of the ball nut. Because of the complex contact situation

inside the BNA, the resulting excitations show a broadband behavior that cannot be related precisely to its rotational speed.

3.2 Model topology

We use a multi physical excitation model to simulate the forces of a steering gear at the interfaces between static and moving parts. It contains subsystem models of the steering gear mechanics, the torque and angle sensor, the steering torque controller, and the electric drive. Figure 5 shows the structure of the simulation model, where the interfaces between subsystem models as well as inputs and outputs are displayed by the connecting arrows.

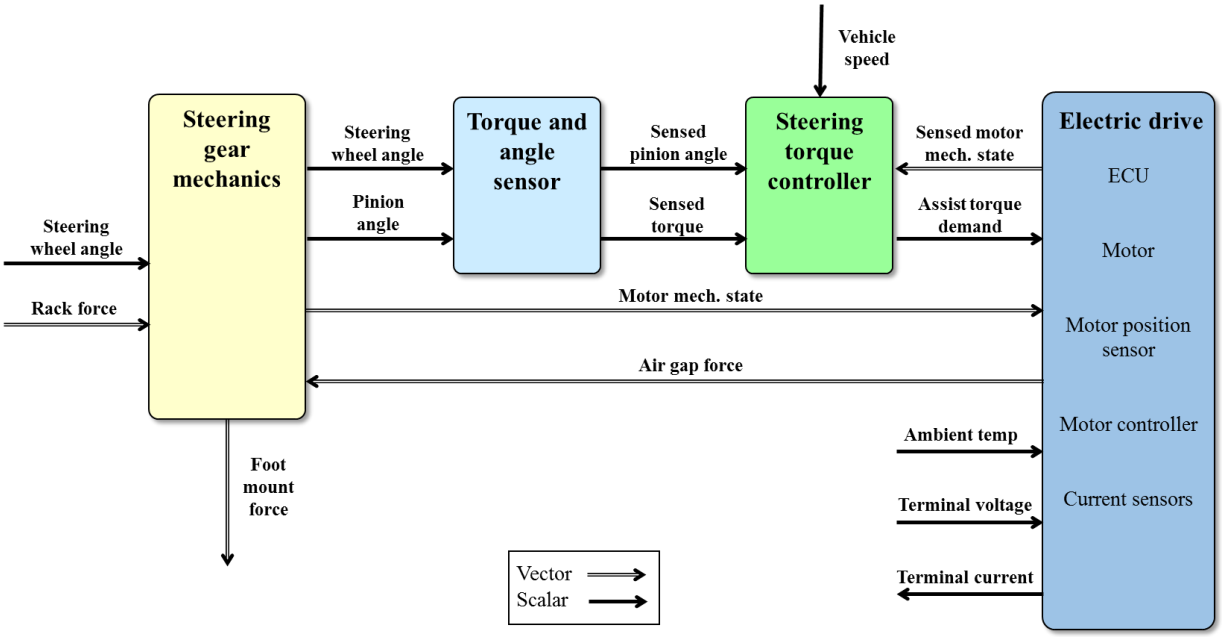


Figure 5 Schematic of the mechatronic excitation model.

Modeling and simulation of the excitation model is a complex task. This is because (a) different physical domains and software algorithms are required to run in co-simulation so that the complete model renders high frequency excitations, and (b) each part of the model must fulfill requirements that trace back to the requirements of the full system model. We use Matlab/Simulink as the host software to run the full system model. In our current implementation, the steering gear mechanics is first modeled in a multibody simulation environment, which allows us to render large relative motions of parts such as the full rack travel of approximately 150mm for a common belt drive system. It also gives us the possibility to represent some parts as flexible bodies, while keeping other parts rigid for computational efficiency. Other advantages are the straightforward implementation of constant and variable gear ratios, and the incorporation of nonlinear interfaces. Figure 6 shows our mechanics model in MSC Adams. Note here that Adams supports a model export to Matlab/Simulink so that the mechanical portion can be run in co-simulation with the other subsystem model.

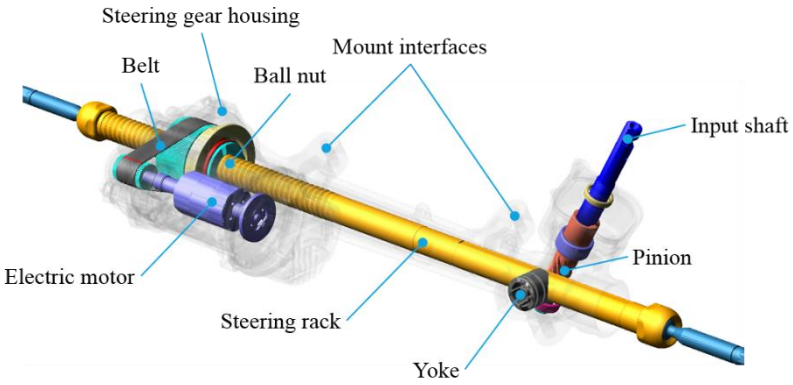


Figure 6 Belt drive EPS model. The assist torque from the electric motor is transmitted with a belt to a ball nut on the rack, which transforms torque to axial rack force.

Both the torque and angle sensor and the steering torque controller were directly modeled in Matlab/Simulink. The main purpose of the sensor model is to compute the driver input torque by measuring the angular difference of the steering wheel and the input shaft, which is straightforward since the rotational stiffness of the connecting torsion bar is known. It then discretizes the "continuous" torque signal at a certain sample rate before handing it over to the steering torque controller. The steering torque controller (STC) calculates the torque demand to assist the driver in powered steering systems. To this end, it requires the mechanical state of the system as well as the sensed steering torque and the current vehicle speed, which is zero for the running noise load case described in this paper. The purpose of the electric drive model is to provide the magnetic air gap forces between the rotor and the stator. These air gap forces are then fed back to the mechanics model, where they are used to compute the resulting rotor torque and the respective loads on the housing. In our current implementation the magnetic forces of the electric drive are computed in Matlab/Simulink using look up-tables that were created from a finite element simulation in Ansys Maxwell. Thereby, the dynamic behavior of the system can be simulated without the need for a parallel finite element simulation.

4 Structural assembly model and interior noise estimation

To describe the noise transferring mechanisms between the virtual excitation points already defined in the mechatronic model and the noise pressure level at the driver's / passenger's ear a model combining finite element simulation and measured data is utilized. The finite element structural model accounts for the frequency response of an assembly that consists of two subassemblies: the vehicle's subframe and the steering gear. The noise transfer functions represent the noise transmission between the gear mounting point on the subframe and the noise pressure level at the driver's ear. Considering the complexity of a car body model with respect to structure- and air-borne noise transmission, measured data is used to obtain the response of the car body structure in this case.

4.1 System assembly via dynamic substructuring

The assembly structural model is built by applying the dynamic substructuring (DS) technique. The technique is not limited to, but preferably used in the frequency domain, due to easier obtaining and combining of frequency response functions (FRFs) from both simulation and physical measurements. The approach is called frequency based substructuring (FBS) and relies on clear definitions of the coupling points between the separate components. In the current contribution the subassemblies are dynamically coupled at the mounting points, labeled as MNT1, MNT2, and MNT3, as shown in Figure 7. The coupling points are represented by virtual points that are compatible with the nodes in the FE models, which also correspond to the measured dynamics from the experiments.

At each coupling point the system dynamics at the interfaces is condensed to nodes with six degrees-of-freedom. These points are also very often called interface points, since within one connection there is a point that belongs to each of the components. In this way the interconnection between the subassemblies is reduced to a nodal connection, which needs to be further defined. The nodal connection could be rigid, with prescribed dynamical stiffness etc. In the example presented measured complex stiffness curves describe the bushing mounts of the steering system to the subframe.

The FBS allows explicit modelling of the interface dynamic stiffnesses between the different components of the systems and facilitates further optimizations on a component level. It offers at the same time also the possibility to incorporate both simulated and experimentally obtained data, when available. As a result, the assembly model is flexible and provides frame-like model structure with exchangeable components. Such model composition comes very handy for quick assembly-level evaluation of componentwise improvements.

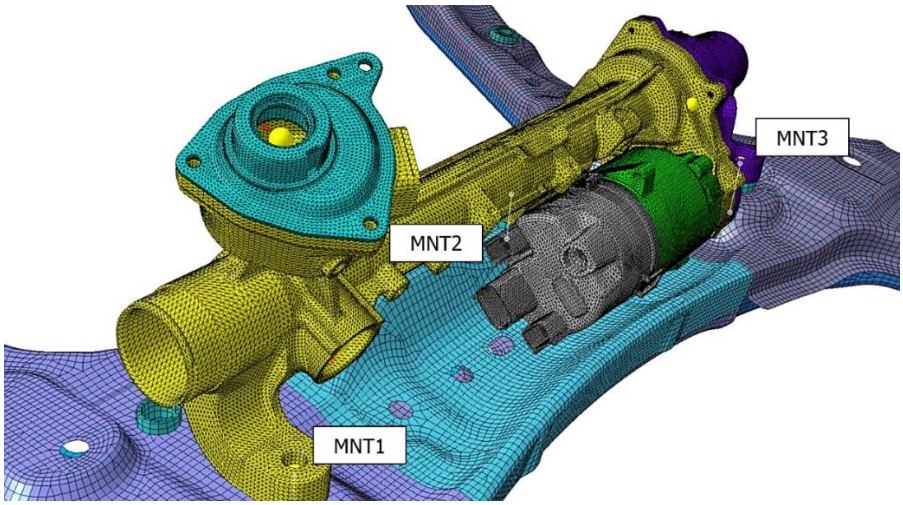


Figure 7 The FRF assembly comprises reduced-order models of the steering gear and the subframe.

4.2 Modal analysis of the substructures and FRF synthesis

Each substructure is accounted for in the assembly through its decoupled FRFs. The FRFs of the substructures are synthesized based on data from modal analysis. Performing the modal analysis there is a general rule, regarding the boundary conditions valid for the substructures. The component modes should be calculated, taking into consideration the component installation on the car level, except the boundary conditions at the coupling interfaces, which must be left free-free. In this particular case this means that for the subframe appropriate boundary conditions are required at the mounting points of the subframe to the car chassis and no boundary conditions at the mounting points of the steering gear as shown in Figure 8. The FRFs for each of the components are then established and then used for describing the dynamic behaviour of the created assembly.

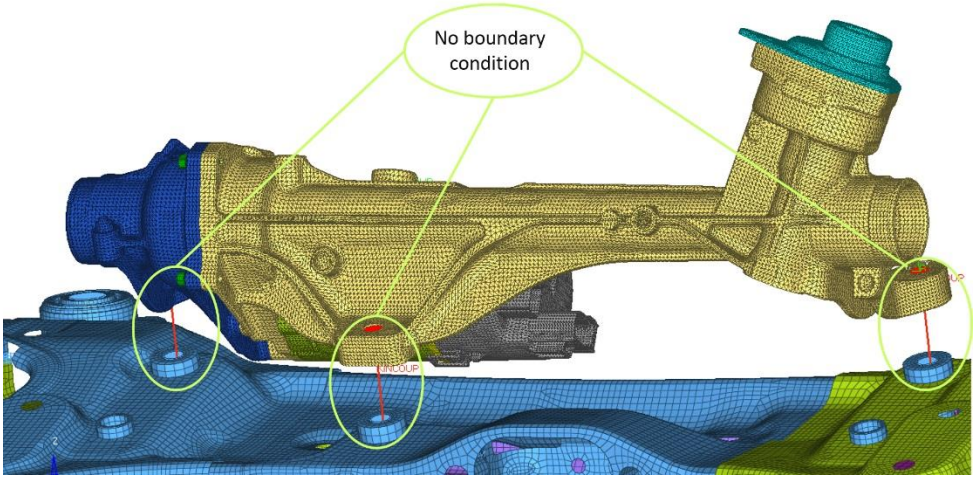


Figure 8 Modal analysis boundary conditions.

4.3 Forced frequency response analysis

A modal-based frequency response analysis of the structure is used to map the excitation forces into dynamic forces at the coupling points. Within this type of analysis, the modal behavior of the investigated subassemblies is evaluated by means of decoupled frequency response functions. The frequency-based substructuring (FBS) technique combines the independent frequency response functions (FRFs) of the substructures to FRFs of the entire assembly. The forced frequency response of the full assembly is then simulated by combining the assembly FRFs, established by the FBS and the virtual excitations provided by the mechatronic excitation model. Following the above described process the interface forces from the steering gear to the subframe are determined. These forces are then used as virtual excitations of the next level frequency response, which estimates the noise pressure level at the driver's ear.

4.4 Interior noise calculation

The calculation of the interior noise, caused by the forces transmitted from the steering gear to the subframe, is basically a forced frequency response procedure. In this case it stays for the full car acoustic response, excited by the forces, resulting at the gear-subframe interface. To achieve this the FRF matrix characterizing the car body stiffness and acoustic sensitivity also described as a noise transfer matrix is multiplied by the interface forces acting on the subframe at the coupling points with the steering gear. (MNT1, MNT2 and MNT3).

5 Case study

This section demonstrates the application of the described procedure in a decision-making process, regarding the choice of the type of mounting connections between the steering gear unit and the subframe. The task is to find the optimal position for a "soft" mount, i.e., a bushing, so that the resulting interior noise is improved compared to all other configurations. Note here that interior noise improvement implies a certain amount of freedom by the interpretations of the scope and the target, as shown below.

The optimization prerequisites are as follows:

a) the soft mount can be placed at each of the three coupling points (MNT1, MNT2, or MNT3) between the housing of the steering gear and the vehicle subframe,

b) there can only be one soft connection among the three options, the rest of the connections must be "hard",
c) the frequency-dependent dynamic stiffness of the bushing element is already known through measurements.

After positioning the soft connection and assigning the measured stiffness, the remaining two connection points are considered as rigid. For this case study we used one set of excitations, resulting from the mechatronic model, which was evaluated for equal stiffness parameters at all three coupling points. The motivation behind this choice is to make sure that the differences observed at the noise pressure level are only caused by the changes in the matrix [Ks] and are not influenced by the excitation. The resulting noise pressure levels are shown in Figure 9.

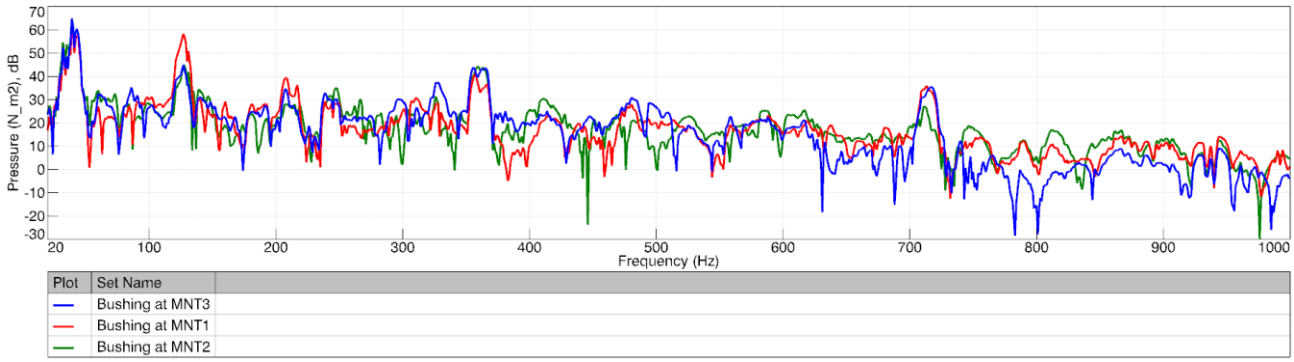


Figure 9 Noise pressure levels for the three different bushing positions.

The results show that identifying a "good" solution is often a challenging task. This is because each bushing position decreases the interior noise in a certain frequency range while increasing it in another frequency range. For example, using a soft mount at MNT2 or at MNT3 can decrease the peak at about 125 Hz. However, both these options increase the amplitudes at about 400Hz. In this example, using a bushing at MNT3 has the highest impact on frequencies above 500Hz.

From our experience, it is hardly possible to decrease the interior noise along the whole frequency range of interest of 0Hz – 1kHz only with bushings. A complete simulation-driven design optimization process must therefore include more "design parameters", such as the housing geometry, electric drive tunes etc., as described in section 2. Additionally, it may also include customer-specific requirements and preferences.

6 Conclusions and outlook

This paper described a process for predicting steering gear running noise using simulated gear excitations and measured transfer paths that represent the vibro-acoustic characteristics of the vehicle. The process offers insights into the noise generating and noise transmitting mechanisms on a full system level. Hence it provides the possibility to make objective design decisions early in the development process. Due to the multi-disciplinary nature of the process, including multibody and finite element models, as well as co-simulation to replicate realistic power-on conditions, the creation and evaluation of the overall model is a challenging task.

The individual steps of the presented process are typically performed in independent analysis environments. As a result, good prediction accuracy requires adequate transferring and processing of geometrical and load/response data. In our current implementation, we used about five different software packages to generate and process data. Further progression of computer simulation tools will reduce this number by providing integrated simulation environments that allow for a more straightforward and automated data handling.

References

[1] WYCKAERT K., McAVOY G., MAS P. – Flexible Substructuring Based on Mixed Finite Element and Experimental Models: A step ahead of Transfer Path Analysis. Proceedings 14th International Modal Analysis Conference, Michigan, 1996.

Towards a high-fidelity simulation approach for predicting coarse road dynamic tire/road contact forces using an ALE-formulation and a-priori nonlinear hyper-reduction

D. De Gregoriis [1,2], **F. Naets** [2,3], **P. Kindt**[1], **W. Desmet**[2,3]
[1] Vibration Mechanics, Goodyear Innovation Center* Luxembourg
Avenue Gordon Smith, L-7750 Colmar-Berg, Luxembourg
e-mail: **daniel_degregoriis@goodyear.com**

[2] KU Leuven, Department of Mechanical Engineering,
Celestijnenlaan 300 B, B-3001, Heverlee, Belgium

[3] Member of Flanders Make

Abstract
Currently no industrially applicable fully predictive high fidelity numerical approach is available in literature to model a car tire rolling over a coarse road surface. Therefore, a fully predictive high fidelity numerical approach for the calculation of tire/road contact forces and hub forces during rolling with a constant angular velocity over a coarse road surface is presented in this work. A nonlinear structural finite element (FE) tire model in combination with an ALE formulation is used to describe both the rotational tire dynamics as well as the coarse road excitation. No measurement data taken from a physical tire is used in the proposed approach, thus keeping it fully predictive. A novel nonlinear projection-based model order reduction (MOR) technique is applied to the proposed approach to greatly reduce the associated computational costs. The proposed predictive high fidelity approach is shown to predict dynamic tire/road contact forces and hub forces with good accuracy, thereby showcasing its use in virtual tire design exploration and design assessment.

1 Introduction

When optimizing the design of a passenger car tire, typically over 50 different performance criteria have to be taken into account. These are related to (but not limited to) e.g. energy efficiency, handling, wear and noise. Due to the complex structure of a typical passenger car tire, most of these criteria are coupled: trying to enhance one performance will often decrease other performances. In order to cope with the increasing need to optimize multiple tire performance criteria simultaneously, predictive numerical simulation techniques could be used, rather than time-consuming experiments. A numerical approach offers the possibility to perform various virtual studies and virtual assessment of different tire designs in a more efficient and cost-effective manner than building and testing physical tires.

In this work, the prediction of structure-borne interior noise due to a tire rolling over a coarse road surface is of interest. More specifically, the vertical hub force, resulting from the tire/road contact forces, is of interest as it excites the vehicle suspension and results in the structure-borne interior noise. The structure-borne noise due to tire/coarse road interaction tends to be dominant over airborne noise inside the passenger cabin in the 0 – 500Hz frequency range [1]. Being able to predict the structure-borne noise of a specific tire design is therefore valuable in an overall performance assessment during design exploration. Several approaches to numerically predict the structure-borne tire/road noise have been suggested in literature. An extensive overview can be found in e.g. the work by Hoever [2]. The numerical approaches to predict tire/road noise

typically consist of a mathematical tire model and a tire/(coarse) road contact model. The tire models used in the numerical approaches can generally be divided into two categories: reduced-order models (analytical and semi-analytical) and high-fidelity models. Reduced-order models tend to be based on analytical descriptions and physical insights, yielding computationally efficient numerical models that can be evaluated in a fast and efficient manner. Examples of these models can be found in the works by Graham [3], Kindt et al. [4], Kropp [5], Larsson et al. [6] and Pinnington [7], [8], amongst others. Linking parameters of these models to physical tire design parameters, such as reinforcement material fiber angles, tire cross-section geometry, rubber compound properties etc., is typically not possible. Furthermore, inherent nonlinear tire behavior (due to e.g. the rubber compounds and reinforcement materials) is typically not included in these models, unless the models are tuned to a specific configuration of a physical tire using measurements. Therefore, the use of reduced-order models in a purely predictive numerical design optimization approach, where no measurements and/or physical tires are available, is very limited. The use of high fidelity tire models, where the models are built in a rigorous, mathematical analogous way to the real physical tire, appears to be more appropriate. Physical design parameters, such as e.g. reinforcement material fiber angles, are typically mapped one-to-one to the numerical model parameters. Different material properties can be described by dedicated constitutive models, using material test data rather than system-level tire measurements. The tire geometry can be replicated, given an adequate discretization of the tire cross-section and circumference domains. These properties enable the use of the high-fidelity models in a predictive numerical design optimization approach. High-fidelity tire models are typically described using a nonlinear finite element (FE) formulation. Using a FE formulation allows to include all sorts of nonlinearities, thereby allowing to model all of the relevant physical effects such as nonlinear large strain behavior, incompressible material behavior, time and/or frequency dependent viscous material behavior, embedded reinforcement behavior etc. Examples of the use of high-fidelity FE tire models to predict tire/road interaction can be found in the works by Brinkmeier et al. [9], Lopez Arteaga [10] and Nackenhorst [11]. A major drawback of using these high-fidelity FE tire models however, is the large computational cost associated with the evaluation of these models, thereby limiting their use in a design exploration context.

Several tire/coarse road surface contact models have been proposed in literature. The convolution approach for tire/road contact, as proposed by Kropp [12], uses Green's functions which describe the tire response, convolved with contact force inputs. In this approach the tire is considered to be a linear time-invariant (LTI) system that can be represented by a set of Green's functions. The tire/road contact problem is solved iteratively in the time domain, to allow for any contact nonlinearities. The method was further expanded and combined with different types of tire models by e.g. Andersson et al.[13], Larsson et al. [14] and Wullens et al. [15]. Lopez-Arteaga combined the Green's function convolution approach with a high-fidelity FE model in order to include large deformations [10]. Brinkmeier et al. [9] proposed to use measured road surface data to generate equivalent time-harmonic contact forces that excite the rolling tire. All of these approaches have in common that they cannot be used in a fully predictive nonlinear approach, as they either make assumptions regarding the tire model (LTI models and constant Green's functions) or tire/road contact forces (fitting contact stifnesses and/or using measurement data). As the tire/road contact forces are the result of a coupled problem, the proposed tire/road contact models are not usable in a fully predictive approach.

To the authors' knowledge, a fully predictive high-fidelity approach has not been proposed in literature before. Therefore, such a predictive high-fidelity numerical approach for the calculation of tire/road contact forces during rolling with a constant angular velocity over a coarse road surface is proposed and described in this work. A high-fidelity nonlinear structural finite element (FE) tire model, in combination with an Arbitrary Lagrangian Eulerian (ALE) formulation [16] is used to describe both the rolling tire dynamics as well as the coarse road excitation. The use of the ALE-formulation is limited to slick and ribbed slick (i.e. a tire with only circumferential grooves) tire designs, as these have a constant circumferential geometry, which is required by the ALE-formulation. As coarse road excitation and structure-borne interior noise is of interest, this approximation of the tire design is justified, as there is little to no contribution of the tread pattern induced airborne noise in the 0-500Hz frequency range [1]. The tire/road surface interaction is modeled using the physics-based contact mechanics formulation, rather than non-predictive, semi-empirical approaches. More

specifically, the tire/road contact is modeled by means of imposing geometrical contact constraints, which is the classical computational contact mechanics approach [17]. Tire/road contact forces are calculated by solving the constrained fully nonlinear tire/road problem. These contact forces are the forces necessary for the tire to meet the geometrical contact constraints imposed in the footprint area (the coarse road roughness asperities). As such, the contact forces are the result of imposing constraints rather than imposing displacements. Therefore, the tire/road contact modeling can be considered as a physics-based high-fidelity approach rather than the reduced-order approaches described before. The numerical costs related to evaluating the proposed high-fidelity approach quickly rise with the complexity of the nonlinear FE tire model and contact problem and typically even surpass the costs of physical experiments. Therefore, a nonlinear projection-based model order reduction (MOR) technique, the Multi-Configuration Multi-Expansion point Modal method (MCMEM) [18], is applied to the proposed predictive high-fidelity approach. This nonlinear MOR technique belongs to a class of hyper-reduction techniques, which are nonlinear MOR techniques developed specifically for nonlinear structural FE problems. Applying the proposed hyper-reduction method drastically reduces the numerical costs associated with the use of the high-fidelity approach, while still retaining a high level of accuracy. The overall hyper-reduced, predictive high-fidelity approach allows to perform a fully-predictive numerical virtual assessment of different tire designs, i.e. ranking, as an alternative to performing the equivalent physical assessment using prototype tires.

2 Equations of motion

The equations of motion of a tire rolling with a constant velocity over a coarse road surface can be expressed as follows:

$$\mathbf{M}\ddot{\mathbf{x}} + \mathbf{G_{ALE}}\left(\mathbf{x}\right)\dot{\mathbf{x}} + \mathbf{f}\left(\mathbf{x},\dot{\mathbf{x}}\right) - \mathbf{f_{ALE}}\left(\mathbf{x}\right) = \mathbf{f_p}\left(\mathbf{x},p_a\right) + \mathbf{f_c}\left(\mathbf{x},\mathbf{x_r}\right) + \mathbf{f_e} \tag{1}$$

Here $\mathbf{M} \in \mathbb{R}^{n\times n}$ is the configuration-independent mass matrix, $\mathbf{G_{ALE}}\left(\mathbf{x}\right) \in \mathbb{R}^{n\times n}$ is the ALE skew-symmetric Gyroscopic matrix and $\mathbf{f_{ALE}}\left(\mathbf{x}\right) \in \mathbb{R}^{n}$ the ALE rotational inertia force vector [16] which describe the constant rolling. The steady-state tire material flow is modeled using a Eulerian formulation in a fixed frame of reference. Conceptually a spatial mesh (which coincides with the tire domain) is used to describe the motion of tire material particles passing through spatial points (which are part of the spatial mesh), rather than tracking the tire material particles individually. The deformation of the spatial mesh is described using a Lagrangian formulation. This yields a time-independent description of the steady-state rolling behavior of the tire. Mass and Gyroscopic matrices arise to describe the dynamic response during constant velocity rolling due to excitation by e.g. road surface asperities. Furthermore, $\mathbf{f}\left(\mathbf{x},\dot{\mathbf{x}}\right) \in \mathbb{R}^{n}$ is the internal force vector which includes the nonlinear strain-displacement behavior and nonlinear nearly-incompressible (visco-) hyperelastic constitutive behavior, $\mathbf{f_p}\left(\mathbf{x},p_a\right) \in \mathbb{R}^{n}$ the air cavity air-pressure force vector and p_a the applied inflation air pressure, $\mathbf{f_c}\left(\mathbf{x},\mathbf{x_r}\right) \in \mathbb{R}^{n}$ the tire/road contact force vector which is described using a penalty method formulation [17], $\mathbf{x_r}$ the current road surface contact constraints (described in more detail in section 2.1) and $\mathbf{f_e} \in \mathbb{R}^{n}$ the configuration-independent external force vector. The current configuration is defined as $\mathbf{x} = \mathbf{x_0} + \mathbf{u} \in \mathbb{R}^{n}$, where $\mathbf{x_0}$ is the reference configuration and $\mathbf{u}$ the total displacement at time t with respect to the reference configuration. The time dependency is omitted from notation for clarity. The first and second derivatives of the current configuration with respect to time are denoted as $\dot{\mathbf{x}}$ and $\ddot{\mathbf{x}}$ respectively. In order to describe the nearly-incompressible behavior of the (visco-)hyperelastic constitutive models, a mixed displacement-pressure (u/p) formulation is used [19]. A variant of the implicit generalized-α discrete time integration method, proposed by Arnold and Brüls [20], is chosen to time-discretize the equations of motion (1). This variant of the generalized-α method has second-order accuracy for the acceleration field variables. Theory and implementation details can be found in [20]. An implicit rather than an explicit time integration scheme is chosen, as this allows to use larger timesteps. This results in less timesteps to be evaluated and in general lower overall computational costs. As an implicit scheme is used, the nonlinear equations of motion (1) are consistently linearized in the spatial domain around the current configuration $\mathbf{x}$.

This yields the following set of equations:

$$\mathbf{M}\ddot{\mathbf{x}} + \mathbf{G_{ALE}}\dot{\mathbf{x}} + (\mathbf{K} - \mathbf{K_p} - \mathbf{K_c} - \mathbf{K_{ALE}})\,\boldsymbol{\Delta}\mathbf{u} = \mathbf{f_p} + \mathbf{f_c} + \mathbf{f_e} - (\mathbf{f} - \mathbf{f_{ALE}}) \tag{2}$$

Here $\mathbf{K} \in \mathbb{R}^{n\times n}$ is the internal force tangent stiffness matrix, $\mathbf{K_p} \in \mathbb{R}^{n\times n}$ is the pressure load force tangent stiffness matrix, $\mathbf{K_c} \in \mathbb{R}^{n\times n}$ is the contact force tangent stiffness matrix and $\mathbf{K_{ALE}} \in \mathbb{R}^{n\times n}$ is the ALE inertia matrix [16]. The interested reader is referred to the work by Nackenhorst [16] for more information about the ALE formulation for rolling bodies in contact. Solving the set of linearized equations of motions (2) per iteration step quickly becomes very costly as the amount of degrees of freedom increases. For industrial-sized design problems, e.g. the tire/road contact problem discussed in this work, the total computational cost becomes too large and the simulations are no longer feasible to use in a design context. Therefore, the MCMEM hyper-reduction method [18] is applied to the linearized equations of motion (2), yielding:

$$\tilde{\mathbf{M}}\ddot{\mathbf{q}} + \bar{\mathbf{G}}\dot{\mathbf{q}} + \bar{\mathbf{K}}\boldsymbol{\Delta}\mathbf{q} = \bar{\mathbf{f}} \tag{3}$$

Here the reduced and hyper-reduced terms are:

$$\bar{\mathbf{G}} = \sum_{i=1}^{|E^s|} s_i \mathbf{V}_i^T \mathbf{G}_{i,\mathbf{ALE}} \mathbf{V}_i$$

$$\bar{\mathbf{K}} = \sum_{i=1}^{|E^s|} s_i \mathbf{V}_i^T \left(\mathbf{K}_i - \mathbf{K}_{i,\mathbf{ALE}}\right) \mathbf{V}_i - \sum_{i=1}^{|E_p^s|} s_{i,\mathbf{p}} \mathbf{V}_i^T \mathbf{K}_{i,\mathbf{p}} \mathbf{V}_i - \mathbf{V}^T \mathbf{K_c} \mathbf{V}$$

$$\bar{\mathbf{f}} = \sum_{i=1}^{|E_p^s|} s_{i,\mathbf{p}} \mathbf{V}_i^T \mathbf{f}_{i,\mathbf{p}} + \mathbf{V}^T \mathbf{f_c} + \mathbf{V}^T \mathbf{f_e} - \sum_{i=1}^{|E^s|} s_i \mathbf{V}_i^T \left(\mathbf{f}_i - \mathbf{f}_{i,\mathbf{ALE}}\right)$$

Element force- and stiffness terms are denoted by the subscript i, element weights are denoted by s_i. A subset of elements of the finite element mesh is denoted by E. The constant reduction space basis is denoted as $\mathbf{V}$. Details about its construction, the choice of the element subsets E and more information about the MCMEM method can be found in [18]. The tire configuration and its derivatives with respect to time are approximated as:

$$\mathbf{x} \approx \tilde{\mathbf{x}} = \mathbf{x_0} + \mathbf{V}\mathbf{q} \tag{4}$$

$$\dot{\mathbf{x}} \approx \dot{\tilde{\mathbf{x}}} = \mathbf{V}\dot{\mathbf{q}} \tag{5}$$

$$\ddot{\mathbf{x}} \approx \ddot{\tilde{\mathbf{x}}} = \mathbf{V}\ddot{\mathbf{q}} \tag{6}$$

2.1 Dynamic ALE contact constraints

Following the ALE approach, the road surface can be considered to be flowing through the spatial tire mesh as well. This results in time-dependent road surface contact constraints $\mathbf{x_r}$ which are applied to spatial points rather than material points. As a time-discretized dynamic problem (2) is solved, the time-dependent contact constraints $\mathbf{x_r}$ are discretized as well. Given the maximal temporal frequency of interest due to the road coarseness excitation, f_{max}, the minimal discrete sampling timestep Δt used to sample/discretize the contact constraints can be determined by applying the Nyquist sampling theorem:

$$\Delta t = \frac{1}{2 f_{max}} \tag{7}$$

Defining the set of contact constraints, by means of sampling a real road surface or by defining an analytical equivalent road surface, the minimal discrete spatial sampling length/wavelength needs to be determined. Given a material particle velocity v_m and using the Nyquist sampling theorem again, the corresponding minimal discrete spatial sampling length $\Delta\lambda$ can be determined as:

$$\Delta\lambda = \frac{v_m}{2 f_{max}} \tag{8}$$

Here $\Delta\lambda$ is in fact the wavelength which for a given material particle velocity v_m results in a temporal frequency $2f_{max}$. The spatial sample length can be considered as the spatial equivalent of the discrete timestep Δt. The relationship between the temporal and spatial sampling lengths can thus be given as:

$$\Delta\lambda = v_m \Delta t \tag{9}$$

A schematic overview of the dynamic ALE contact constraints formulation is shown in Figure 1. An example of contact constraints applied in a spatial point is shown in Figure 2, where a duration of 1 second is considered.

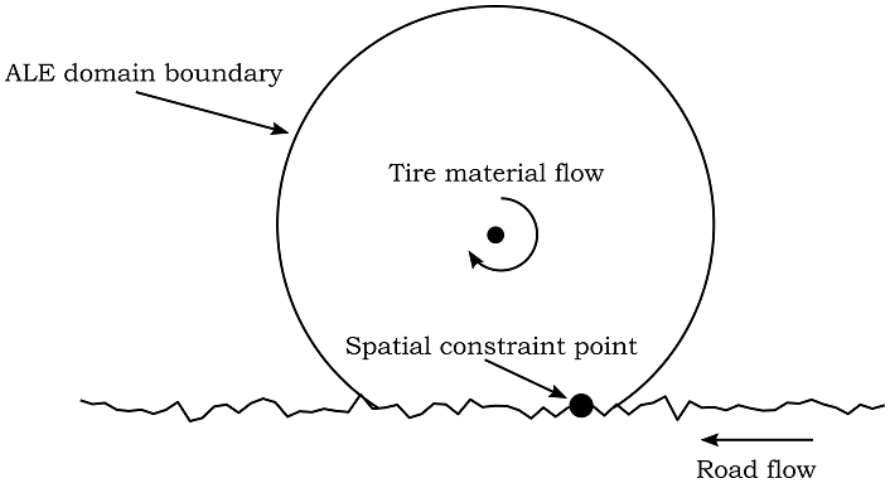


Figure 1: Schematic overview of applying dynamic contact constraints in the ALE-formulation

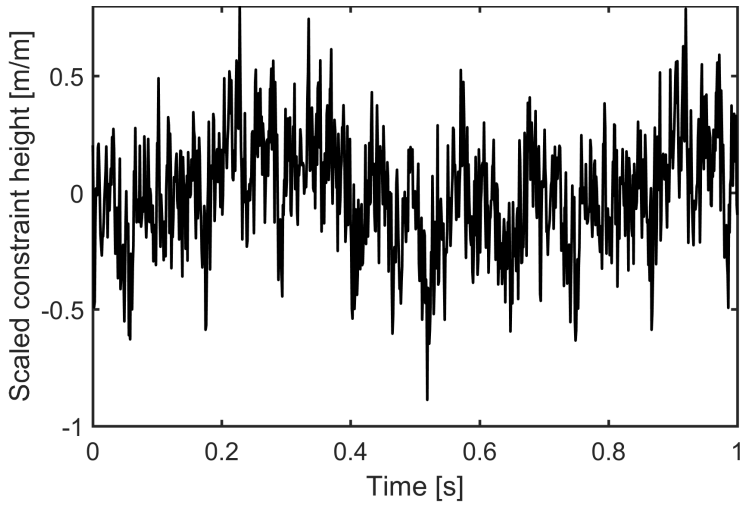


Figure 2: Example of dynamic contact constraints applied in a spatial point

2.2 Persistency contact condition in dynamic ALE contact

As dynamic contact is considered, an additional contact condition needs to be taken into account. Apart from the Karush-Kuhn-Tucker (KKT) [17] contact conditions, the so-called persistency condition [21] needs to be included as well. This condition states that two points that are in contact need to have the same velocity as long as they are in contact (and thus be in persistent contact). For the tire/road contact problem, a tire material point is in persistent contact with a road surface asperity as long as said road asperity travels through the tire footprint. Not enforcing the persistency condition results in tire material points coming into and out of

contact with the road surface, during the travel of the road asperities through the tire footprint. As discussed by Suwannachit et al. [22], using an adapted integrator (as proposed by e.g. Laursen [21]) or having enough numerical dissipation in the integrator leads to enforcement of the persistency constraint. Therefore, in this work the ρ_∞ parameter is set to a low value to ensure the persistency condition. Furthermore, contact constraints are applied and held constant for *multiple smaller timesteps*, in order to ensure that the persistency condition can be met. Not doing so would lead to violation of the persistency condition, as impact-effects are not allowed to decay in one timestep, but need multiple to do so (in order to meet the persistency condition).

3 Numerical test setup

A nonlinear high-fidelity FE tire model of a ribbed slick tire design consisting of over 100,000 finite elements and 300,000 DOFs is used in this work. While not large by today's standards, this model is fully nonlinear: nonlinear visco-hyperelastic and hyperelastic constitutive models are used to model the rubber compounds and reinforcement materials, while nonlinear large strain behavior and nonlinear follower and contact forces are included as well. As per iteration step every element needs to re-evaluated to construct the force vectors and stiffness matrices in equation (2), the computational costs quickly rise with the model size. Therefore, even relatively small models (as the one used in this work) result in very large computational costs. Material parameters are extracted from a material database and the geometry of the numerical tire model is based on the tire design drawings. The tire is mounted on a rigid rim and inflated to a specific air pressure p_a. The numerical test-setup consists of the tire being loaded force-controlled on a rotating drum with a coarse road surface. The external loading force is held constant. An example of a high-fidelity ribbed slick tire model and a set of road surface contact constraints is shown in Figure 3:

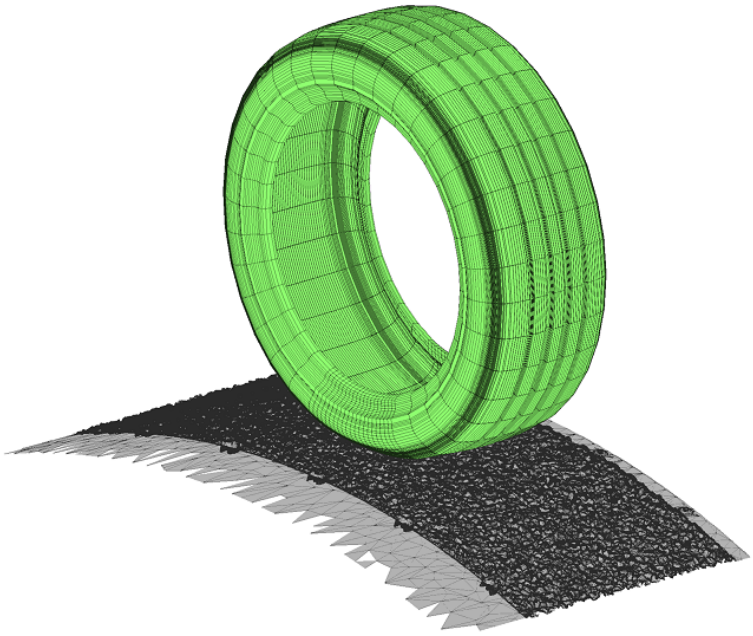


Figure 3: A high fidelity tire model and set of a road surface contact constraints

The drum angular velocity corresponds to a surface velocity of $13.89\frac{\mathrm{m}}{\mathrm{s}}$ (which results in a tire rolling speed of 50 $\frac{\mathrm{km}}{\mathrm{h}}$) and drives the rotation of the tire. The tire can thus be considered to be in a free-rolling regime. Given the maximum excitation frequency of interest, this leads to a minimal timestep and sampling length, as discussed in section 2.1. The applied road surface contact constraints correspond to a maximum excitation frequency of 500 Hz. The corresponding minimal sampling frequency is 1 kHz, leading to a minimal timestep $\Delta t = 0.001s$ and minimal sampling length $\Delta\lambda = 0.0139$m. The minimal sampling length is used

as a criterion for the footprint mesh density. As discussed before, the hyper-reduced discretized equations of motion (3) are solved using a generalized-α integrator [20]. A smaller timestep is used to ensure stability, as the unconditional stability property does not hold for nonlinear problems [20]. A total of 1 seconds of constant rolling is simulated, using a discrete timestep $\Delta t = 0.0001s$. This yields a frequency resolution of 1Hz, which is sufficient for the assessment and ranking of the tire structure-borne interior noise performance. The MCMEM method is applied to the predictive high-fidelity approach, which results in computational speedups of a factor 300 and higher [18], while still maintaining a good accuracy with respect to the unreduced problem. More specifically, application of the MCMEM method results in computational times of hours instead of weeks.

4 Numerical results

In order to validate the proposed predictive high-fidelity approach, measurement data is taken from a physical tire corresponding to the numerical tire model. Similarly as in the numerical setup, the physical tire is inflated to a specific air pressure p_a and loaded onto a drum rotating at $13.89\frac{\mathrm{m}}{\mathrm{s}}$ with a coarse road surface. This coarse road surface is used to generate the dynamic ALE contact constraints which are applied to the high-fidelity tire model. One second of vertical hub force data is taken from both the experimental setup and numerical approach. The frequency spectra of the experimental and numerical vertical hub force are compared and shown in Figure 4:

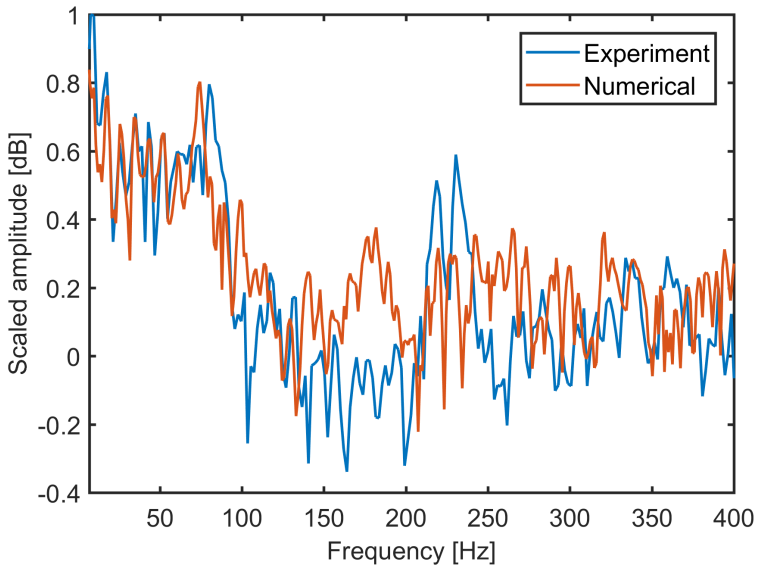


Figure 4: Comparison of the vertical hub force frequency spectra of experimental data and numerical data obtained via the proposed high-fidelity approach

A relatively good match between the experimental and numerical data can be observed. The accuracy of the fully predictive high-fidelity approach could be further improved by fine tuning the tire model such that the dynamic properties of the tire model perfectly match with the dynamic properties of the tested tire and including the vibro-acoustic coupling with the air cavity, as the air cavity resonance peak is missing from the simulation results (but clearly visible in the experimental results). This showcases the potential of the proposed fully predictive high-fidelity approach, as the nonlinear high-fidelity tire model can be created a-priori for any new tire design and any type of road surface can be applied as well. Furthermore, the effect of the nonlinear filter behavior of the tire can be observed when comparing the frequency spectra of the total vertical contact force and the resultant hub force, as shown in Figure 5:

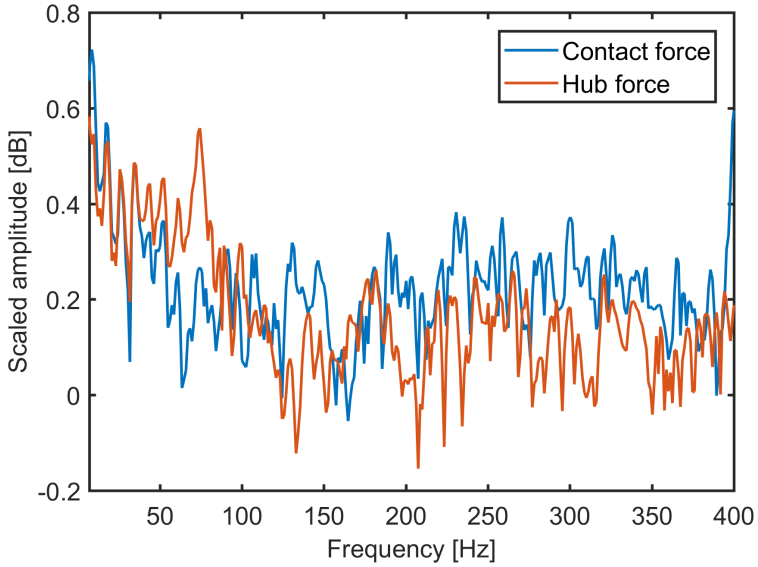


Figure 5: Comparison of the frequency spectra of the total numerical vertical contact force and numerical vertical hub force

As the contact forces arise as part of the solution of the nonlinear equations of motion (1), they are dependent on the nonlinear structural behavior of the tire and boundary conditions. Figure 5 shows the relation between the dynamic contact forces in the footprint and the resulting hub forces. The tire clearly shows nonlinear behavior between the road surface texture and the hub forces. An additional benefit of the proposed predictive high-fidelity approach is the availability of the dynamic contact forces resulting from rolling over a road surface texture. These dynamic contact forces are very hard to retrieve experimentally. The influence of different tire design parameters onto the dynamic contact forces offers an increased insight during the tire design process.

5 Conclusion

In this work, a fully predictive high-fidelity numerical approach for the calculation of tire/road contact forces during rolling with a constant angular velocity over a coarse road surface is proposed and described. The approach combines a high-fidelity nonlinear FE tire model, an ALE-formulation and a computational contact mechanics description of the tire/road contact to numerically predict the time-varying dynamic tire/road contact forces and the corresponding hub forces. These dynamic tire/road contact forces and hub forces are used to e.g. assess the structure-borne interior noise performance of a specific tire design. No measurement data, obtained from physical tires, is needed for the proposed approach. Other approaches presented in literature typically need some form of measurements or are not predictive due to other restrictions. Therefore, these approaches cannot be used in virtual tire design exploration. Also different from other approaches, is the application of contact constraints to calculate the contact forces, rather than imposing displacements or contact forces (calculated seperately) to the tire. Key to making the proposed approach feasible to use in a design exploration context, is the application of the MCMEM hyper-reduction method. Overall simulation times are drastically lowered using the MCMEM method, effectively making the high-fidelity predictive approach more efficient and cost-effective than building and testing physical tires.

When comparing the numerical hub force results, obtained with the proposed approach, with experimental hub force data, a good correspondence between both results can be observed, especially given the fact that no tuning of the numerical tire model was performed. The potential of the proposed fully predictive high-fidelity approach is showcased, as the nonlinear high-fidelity tire model can be created a-priori for any new tire design and any type of road surface can be applied as well. The proposed approach also allows to directly

compare the contact forces arising for different tire designs and/or road surfaces, which is very hard to do so in an experimental setting. Future research will be dedicated to e.g. including more complex contact conditions, boundary conditions and performing an extensive case study to further showcase the use of the proposed fully predictive high-fidelity approach.

Acknowledgments

The research of Daniel De Gregoriis is funded by an AFR-PhD grant supported by the Fonds National de la Recherche, Luxembourg (AFR PhD Grant Agreement PhD 2015-1, Project Reference 10222097). The Fund for Scientific Research - Flanders (F.W.O.) is gratefully acknowledged for the support of the postdoctoral research of Frank Naets. The Industrial Research Fund KU Leuven is gratefully acknowledged for its support.

References

[1] Vercammen, S., *Tyre/road noise due to road surface texture excitations: Experimental and numerical analyses*, PhD thesis, KU Leuven, Leuven, Belgium (2017).

[2] Hoever, C., *The simulation of car and truck tyre vibrations, rolling resistance and rolling noise*, PhD thesis, Chalmers University of Technology, Goteborg, Sweden, (2014).

[3] Graham, W. R., *Tyre rolling simulation using a state-space formulation*, in *Proceedings of ISMA2014 including USD2014, Leuven, Belgium, 2014 September 14-17*, Leuven (2014), pp. 1731-1746.

[4] Kindt, P., Sas, P., and Desmet, W., *Development and validation of a three-dimensional ring-based structural tyre model*, Journal of Sound and Vibration, Vol. 326, No. 3, Elsevier (2009), pp. 852-869.

[5] Kropp, W., *Structure-borne sound on a smooth tyre*, Applied Acoustics, Vol. 26, No. 3, Elsevier (1989), pp. 181-192.

[6] Larsson, K., and Kropp, W., *A high-frequency three-dimensional tyre model based on two coupled elastic layers*, Journal of Sound and Vibration, Vol. 253, No. 4, Elsevier (2002), pp. 889-908.

[7] Pinnington, R., *A wave model of a circular tyre. part 1: belt modelling*, Journal of Sound and Vibration, Vol. 290, No. 1, Elsevier (2006), pp. 101-132.

[8] Pinnington, R., *A wave model of a circular tyre. part 2: side-wall and force transmission modelling*, Journal of Sound and Vibration, Vol. 290, No. 1, Elsevier (2006), pp. 133-168.

[9] Brinkmeier, M., Nackenhorst, U., Petersen, S., and Von Estorff, O., *A finite element approach for the simulation of tire rolling noise*, Journal of Sound and Vibration, Vol. 309, No. 1, Elsevier (2008), pp. 20-39.

[10] Lopez Arteaga, I., *Greens functions for a loaded rolling tyre*, International Journal of Solids and Structures, Vol. 48, No. 25, Elsevier (2011), pp. 3462-3470.

[11] Nackenhorst, U., *Finite element analysis of tires in rolling contact*, GAMM-Mitteilungen, Vol. 37, No. 1, Wiley (2014), pp. 27-65.

[12] Kropp, W., *Ein Modell zur Beschreibung des Rollgeräusches eines unprofilierten Gürtelreifens auf rauher Straßenoberfläche*, VDI-Verlag (1992).

[13] Andersson, P., and Kropp, W., *Time domain contact model for tyre/road interaction including nonlinear contact stiffness due to small-scale roughness*, Journal of Sound and Vibration, Vol. 318, No. 1, Elsevier (2008), pp. 296-312.

[14] Larsson, K., Barrelet, S., and Kropp, W., *The modelling of the dynamic behaviour of tyre tread blocks*, Applied Acoustics, Vol. 63, No. 6, Elsevier (2002), pp. 659-677.

[15] Wullens, F., and Kropp, W., *A three-dimensional contact model for tyre/road interaction in rolling conditions*, Acta Acustica, Vol. 90, No. 4, S. Hirzel (2004), pp. 702-711.

[16] Nackenhorst, U., *The ALE-formulation of bodies in rolling contact: Theoretical foundations and finite element approach*, Computer Methods in Applied Mechanics and Engineering, Vol. 193, No. 39, Elsevier (2004), pp. 4299-4322.

[17] Wriggers, P., *Computational Contact Mechanics: Second Edition*, Springer-Verlag, Berlin (2006).

[18] De Gregoriis, D., Naets, F., Kindt, P., and Desmet, W., *A nonlinear a-priori hyper-reduction method for the dynamic simulation of a car tire rolling over a rough road surface*, in *Proceedings of the Sixth European Conference on Computational Mechanics (ECCM 6), Glasgow, UK, 2018 June 11-15*, Glasgow (2018).

[19] Bathe, K.-J., *Finite Element Procedures*, Prentice Hall, Inc., Upper Saddle River (1996).

[20] Arnold, M., and Brüls, O., *Convergence of the generalized-α scheme for constrained mechanical systems*, Multibody System Dynamics, Vol. 18, No. 2, Springer (2007), pp. 185-202.

[21] Laursen, T. A., *Computational Contact and Impact Mechanics*, Springer-Verlag, Berlin (2003)

[22] Suwannachit, A., Nackenhorst, U., and Chiarello, R., *Stabilized numerical solution for transient dynamic contact of inelastic solids on rough surfaces*, Computational Mechanics, Vol. 49, No. 6, Springer (2012), pp. 769-788.

Analysis of experimental MT clunk with STFT and CWT to observe mode participation and reduction

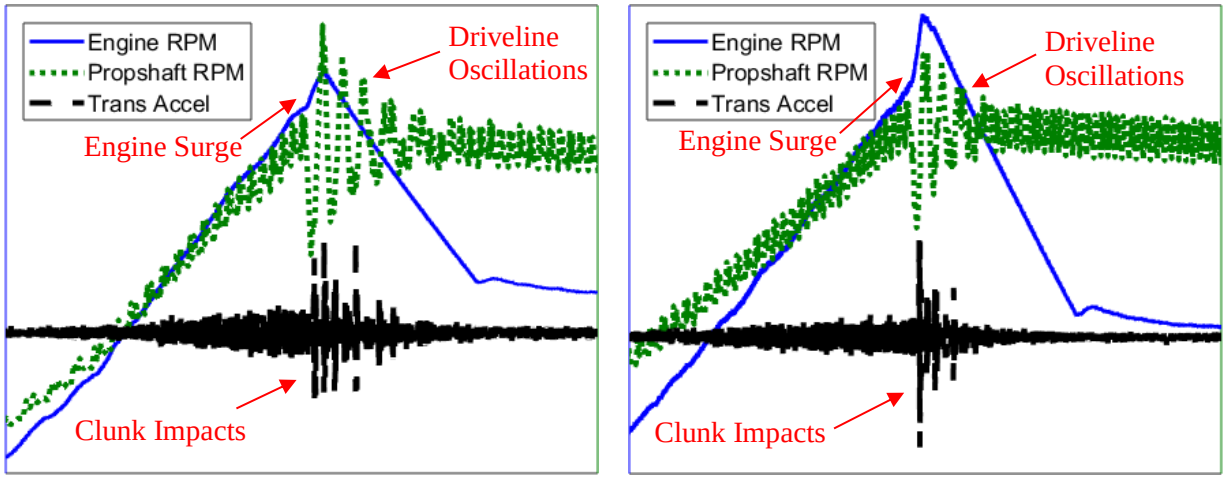
J. Furlich[1], J. Blough[1], D. Robinette[1]
[1] Michigan Technological University, Department Mechanical Engineering
815 R.L. Smith MEEM Building, 1400 Townsend Drive, Houghton MI, 49931, USA
e-mail: **jefurlic@mtu.edu**

Abstract
Clunk is a phenomenon observed with MT vehicles during high torque transient conditions after uncoupling the driveline from the engine. Decoupling of the clutch plate and flywheel in a step relaxation manner releases the stored potential energy within the driveline inducing clunk. This transient condition is observed in operating data of a six speed MT vehicle and post processed with both STFT and CWT. Each post processing condition struggles to highlight key features in the data due to time and frequency resolution compromises. These compromises will be compared and contrasted to develop an optimal strategy for processing operating clunk data. The resulting observations from STFT and CWT processed clunk data highlight specific frequency bands near powertrain rigid body modes and high frequency impulses due to the rate of step relaxation. It is shown that a modification of the step relaxation torque function modifies the resulting response with optimal relaxation time close to the shuffle mode period.

1 Introduction

Personal vehicle transportation has become the norm in developed countries and with increased demand comes high competition between vehicle manufacturers for higher market capitalization. Manufacturers must meet a large number of stakeholder needs, including demands for lower interior noise levels, which according to B. Wyerman et. al. shows a 0.3 dBA reduction per year between 1980-2000 [1]. There are several noise sources associated with passenger vehicles including the engine, transmission, differential, road, etc. which may excite phenomena such as boom, shuffle, clunk, whine, etc. [1] [2]. This study is interested in clunk transient vibrations that propagate from the manual transmission (MT). The noise is perceived as unnatural by operators, thus reducing stakeholder satisfaction of a particular manufacturer.

The clunk transient analyzed in this study is driven by a geometric non-linearity due to gear tooth backlash [3] that excites clunk through a torque reversal within the vehicle driveline [4], as shown in Figure 1. This non-linearity is described by a Hertz contact stiffness model similar to that used in [5]. A torque reversal occurs when the torsional input to the driveline switches between the engine and the brakes/road. The engine provides torque during acceleration events while the brakes/road provide torque during coast or deceleration events. A rapid succession of torque reversal occurs in MT vehicles when a fixed gear shift is demanded, which decouples the torque input from the engine to allow for a gear shift. This creates a torque reversal due to road contact while the engine is decoupled from the transmission. Decoupling of the clutch also releases any stored potential energy due to windup of the driveline, which influences the impact amplitude [6]. Initiation of clunk, shown in Figure 1, during vehicle acceleration was achieved by decoupling the clutch thus inducing a surge in Engine RPM and release of driveline windup. The release of potential energy led to driveline oscillations in the Propshaft causing impact excitation through the gear components as depicted by the Trans Accell in both First and Second gear. It is well known that impact excitation has broadband frequency content [7]. Thus broadband excitation has the potential to induce modal response of nearby components if there is low mechanical impedance and sufficient energy transfer.



a) b)

Figure 1: Operating Clunk Data Captured in a) First Gear and b) Second Gear

Clunk was observed in vehicle operating conditions, as shown in Figure 1, which comes with many hurdles to overcome when data post processing. Due to the non-stationary condition, time data was collected during operation and post processed with Time-Frequency Analysis (TFA) techniques to better understand frequency content, modal participation, and correlation between transducers, similar to Transfer Path Analysis (TPA). TFA techniques such as the Short Time Fourier Transform (STFT) and Continuous Wavelet Transform (CWT) are used to identify frequency content excited during the non-linear clunk event from operating data [8] [9]. Similar applications of TFA were done to predict piston slap [10], engine knock [11], estimate Frequency Response Functions (FRF's) [12], predict damping [13], and perform modal analysis [14]. Each technique was applied to the same data set, but with differing results due to shortcomings of each transform which will be discussed in Sections 2 and 3. There will also be proposed criteria to use when computing TFA, particularly with the STFT due to data processing requirements.

To acquire data for this analysis, a test sedan equipped with a V8 engine, six-speed MT, and Rear Wheel Drive (RWD) similar to that modeled in Figure 2 was retrofitted with accelerometers and microphones to capture operating data. Two accelerometers were mounted on the transmission, two were mounted on the differential, a tachometer was mounted on the propshaft, and a microphone was placed in the vehicle cabin near the driver's ear. Previous studies on this vehicle were able to identify some of the low frequency modes of the vehicle shown in Table 1 [4]. TFA was applied to the data and used to identify participation during vehicle operation. This led to a better understanding of which modes the clunk event excites and indicates further analysis of the excitation forcing function.

Mode	Natural Frequency
1st Gear Driveline Shuffle	7.0 Hz
2nd Gear Driveline Shuffle	10.0 Hz
Transmission Roll	19.5 Hz
Differential Roll	63.5 Hz
Differential Pitch	55.0 Hz
Front Propshaft 1st Torsional	1111 Hz
Rear Propshaft 1st Torsional	1557.5 Hz

Table 1: Truncated List of Known Modes and Natural Frequencies of the Test Vehicle

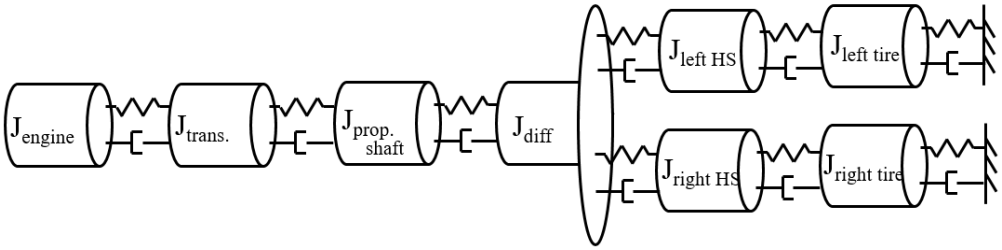


Figure 2: Example RWD Lumped Parameter Model of Test Vehicle Drivetrain

In Section 2, the background for TFA including STFT and CWT formulations are presented along with processing considerations when applied to a clunk dataset. In Section 3, the processing considerations are compared and contrasted for improved identification of participating modes of the passenger vehicle during clunk. Further discussion is made in Section 4 to the application and techniques. Section 4 also includes analysis based on an understanding of the TFA results and implied torque excitation. Analytical results are shown based on the torque excitation when applied to a lumped parameter model for improved vehicle response.

2 Time-Frequency Analysis

2.1 Short Time Fourier Transform (STFT)

The STFT is the application of the familiar Discrete Fourier Transform (DFT) in multiple successions when applied to a continuous time signal. The result of this transform projects from the time domain to the frequency domain which contains spectral information contained in the period of the transformed time signal. The complex DFT for a single sided, positive frequency spectrum is described below in Equation 1 as [7]:

$$G(k\Delta f) = \frac{2}{N}\sum_{n=0}^{N-1} g(k\Delta t)e^{-2j\pi kn/N} \tag{1}$$

When applied to a signal with time longer than $N\Delta t$, a unity window function, Uniform window, is convolved in the time domain with the time signal and Fourier kernel described in Equation 2 as:

$$G(k\Delta f, \tau) = \frac{2}{N}\sum_{n=0}^{N-1} g(k\Delta t)w(k\Delta t - \tau)e^{-2j\pi kn/N} \tag{2}$$

With any signal subjected to the DFT, there are signal processing limitations for time and frequency resolution dictated by sampling parameters chosen for acquisition and processing. In the analysis performed on the previously mentioned clunk data, the sampling frequency was selected when acquiring data and was therefore fixed (consequently fixing the time resolution as shown in Equation 3). Thus the only parameter left to choose is either the frequency resolution, sampling period of the STFT, or number of samples to compute each STFT. These are a product of the DFT development and described in Shannon's Sampling Equations presented in Equations 3-4:

$$\Delta t = \frac{1}{F_s} = \frac{T}{N} = \frac{1}{N\Delta f} \tag{3}$$

$$\Delta f = \frac{F_s}{N} = \frac{1}{T} = \frac{1}{N\Delta t} \tag{4}$$

From Equations 3-4 the relationship of frequency resolution and time resolution are shown to be dependent of one another when the sampling frequency has been previously fixed. This limitation further shows that with the STFT, there is a compromise in frequency and time resolution. The compromise is similar in theory

to the Heisenberg uncertainty principle due to wave-particle duality. This similarity results in the Gabor limit [15] as described by Equation 5:

$$\sigma_t \sigma_f \geq \frac{1}{4\pi} \approx 0.08 \tag{5}$$

The Gabor limit provides a fundamental principal causing strain on the desire for both improved time and frequency resolution, however several other factors cause error in the STFT from non-stationary data. This is ever present in operating data of rotating machinery, i.e. passenger vehicle. During operation, many orders of the engine sweep up or down in frequency with time causing non-periodic frequency content, or in the case of clunk, where non-linearities are present and therefore cause leakage. An example of signal leakage is depicted in Figure 3 along with signal processing applied to reduce these effects.

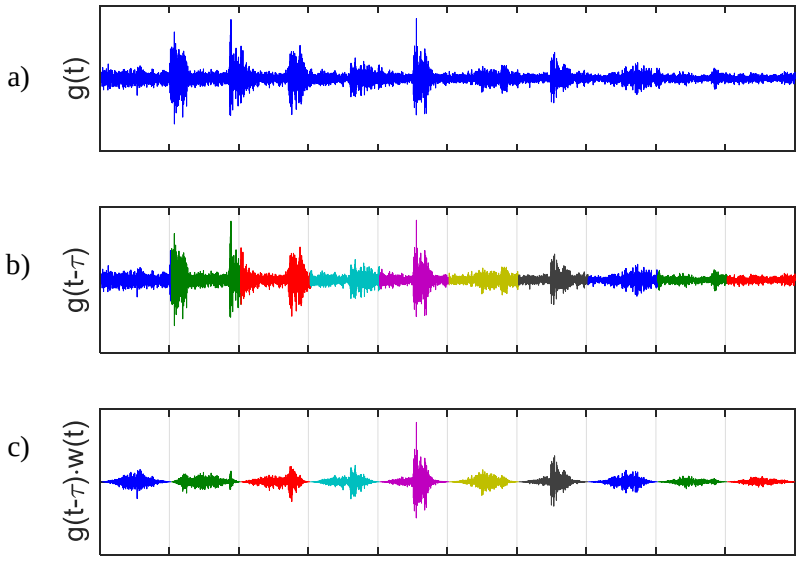


Figure 3: Transmission Accelerometer Response During Clunk Transient

2.1.1 Windowing

Leakage due to non-periodic frequency content in the operating data can never be eliminated, only reduced by the window functions applied. A uniform window should only be used with extreme caution on operating data however, hanning, flattop, and other windows can be applied with ease during the STFT as described by Equation 6:

$$g^w(t) = g(t) * w(t) \tag{6}$$

The choice of which window function should be applied is up to the data processor based upon the measured signal. The data shown in Figure 3a is raw data from one of the accelerometers mounted to the transmission (previously depicted in Figure 1) and is a truncated dataset during the clunk event. The data is sectioned into several separate periods in Figure 3b that will be used for individual DFT processing to develop the STFT. In Figure 3c, a window is applied to the data to enforce periodicity and reduce leakage. Notice that the choice of window for clunk application is important to capture the entire transient event without truncating the peak amplitude of each consecutive impact from gears completely traversing their lash zone.

It is further noted from Figure 3c that not each windowed period is able to capture clunk in the center of the period, causing truncation of the amplitude and in some cases the impact is eliminated by application of the window. It might then be desirable to choose a trigger time that captures the first impact after which all other impacts should fall in the center of each STFT sample period, however due to the non-linear nature of clunk this is not possible without a dynamic trigger event. After every consecutive impact, non-conservative

forces dissipate energy and the time between impacts increases over time such that a dynamic period length would be required to achieve this goal and is not achieved in classical implementation of the STFT.

2.1.2 Overlapping

One technique to overcome the amplitude truncation is through the use of overlapping periods of the STFT as shown in Figure 4. The application of overlapping assures that when the clunk impact amplitudes are truncated by windowing an arbitrary period of the STFT, consecutive windows nearby have a better chance of capturing the complete impact event with minimal truncation.

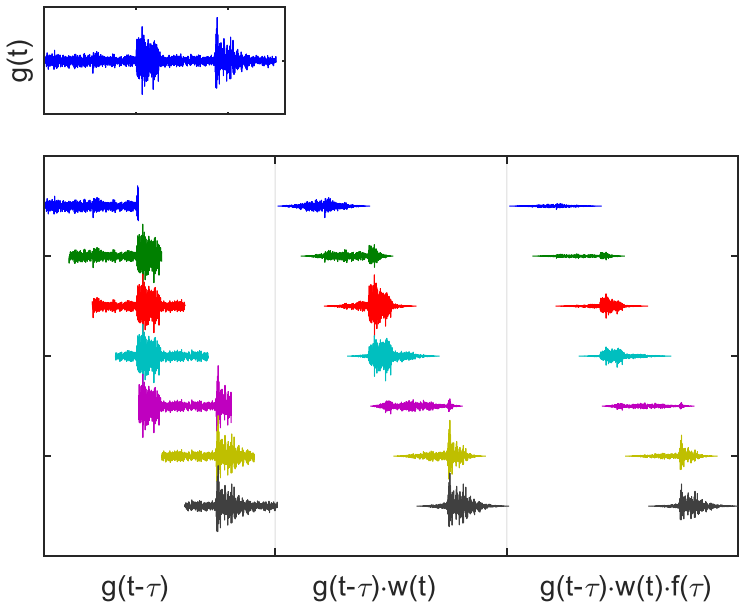


Figure 4: Truncated Acceleration Trace with a) Overlapping Applied b) Overlapping and Windowing Applied c) Overlapping, Windowing, and Weighting Applied to Consecutive Periods for Averaging

2.1.3 Averaging with Overlap

Application of the overlapping periods during the STFT implies a need for averaging consecutive periods that overlap in the time domain, $t_{overlapped}$. It is noted in Figure 4 that a relationship exists between number of periods and amount of overlap applied, $T_{overlap}$. This criterion is described by Equation 7 as:

$$t_{overlapped} \geq \frac{1}{1-T_{overlap}} \tag{7}$$

Hence, when averaging overlapped data sets, the number of periods to average together should not exceed the inequality proposed in Equation 7. Note that when averaging with unity weighting applied to all averages, this technique replicates that of a smoothing function.

Commercial application of the windowing and overlapping of data is available in several software packages with internal functions such as MATLAB's spectrogram(), Mathmatica's spectrogram[], and LMS.Test Lab's TFA, STFT plugin. However, these functions currently do not have available averaging and weighting abilities applied to the overlapped data. One additional advantage of averages with the time data allows for development of cross-spectral information and pseudo-coherence measurements of the STFT results.

2.2 Continuous Wavelet Transform (CWT)

The application of the CWT is defined by convolving a mother wavelet with the time domain signal described in Equation 8 as:

$$WT(a,\tau) = \frac{1}{\sqrt{|a|}} \int_{-\infty}^{\infty} g(t)\psi\left(\frac{t-\tau}{a}\right)dt \tag{8}$$

Application of the CWT with the Morlet Kernel will be used in this paper described by Equation 9:

$$\psi(t) = e^{-j\pi t/T} e^{-t^2/2T^2} \tag{9}$$

Use of the Morlet-CWT is likened to applying a band pass filter to the time signal. The result is a signal representing the solution presented at the band pass center frequency. This can be a computationally demanding process, however the CWT captures both time and frequency tradeoffs with one result. The band pass center frequencies of the CWT increase logarithmically, therefore the bandwidth increases respectively. Thus at low frequency there is low time resolution but high frequency resolution while the converse occurs at higher band pass center frequencies. To achieve improved frequency resolution at low band pass center frequency, more "filters" are applied (referred to as voices per octave). There becomes a limit at such high number of voices per octave that the practical filter design or implementation of the Morlet Kernel will result in overlapping of the band pass frequencies and thus no further advantage is achieved with increasing voices per octave.

3 Clunk Analysis with TFA

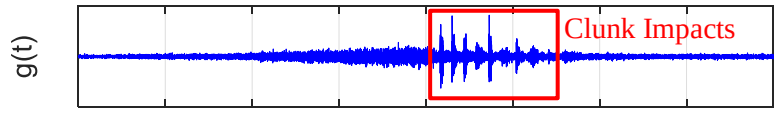


Figure 5: Truncated Section of Time Data for TFA to Identify Mode Participation

One sample of data collected is presented in Figure 5 which represents the acceleration response of the transmission during clunk excitation. There are several impact events that occur around with high amplitude that are of interest. Prior to the impact events, there will be many engine orders participating in the frequency spectrum. Apart from engine orders, it is desired to observe which frequencies/modes are not participating prior to the clunk impacts but begin to participate due to clunk excitation.

3.1 STFT: Influence of windowing

It is shown in Figure 6 that the resulting spectrogram with no overlapping begins to show broadband impulsive data with the excitation of clunk. A majority of the response is not visually appealing, however, and there is not an appreciable amount of information to be extracted from a non-overlapped STFT. The application of windowing begins to highlight certain orders in the low frequency range along with decisive impact events instead of one large smeared impact.

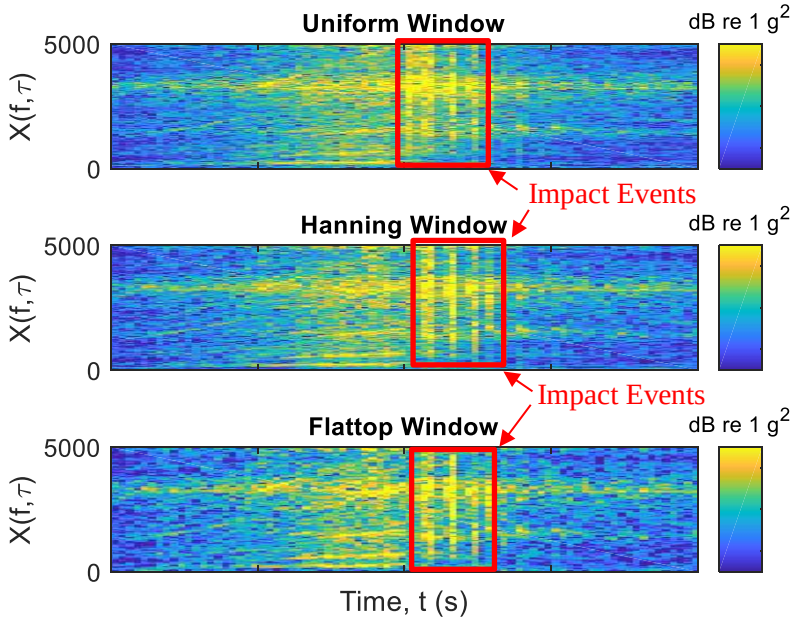


Figure 6: STFT with Common Window Functions Applied

3.2 STFT: Influence of overlapping with windows

The spectrogram observed in Figure 7 applies overlapping along with application of a window function from Figure 6 to reduce leakage and improve data post processing of the STFT. Figure 7 reveals that with increased overlapping, an increase in time resolution is gained in the spectrogram even without modifying the time resolution of the individual DFT itself. With high overlapping, the impulse responses are clear, along with several engine orders. This is observed not only in the low frequency range but in the mid 2-3 kHz range as well. Overlapping further shows how upon excitation of the clunk transient, there is a high amplitude broadband response from 500-5000 Hz that dominates the overall response of clunk. This depicts why clunk is perceived audibly as unpleasant due to the impulsive nature. One drawback is the identification of low frequency modes is desired but not separated by only overlapped and windowed STFT results and will be discussed further in Section 4.

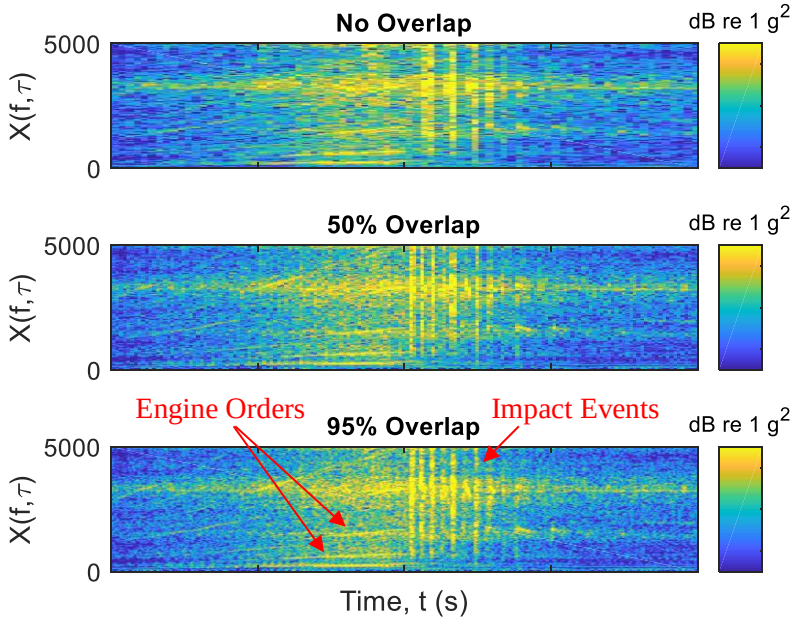


Figure 7: STFT Continued with Overlapping Periods Applied.

3.3 STFT: Influence of averaging with overlapping and windows

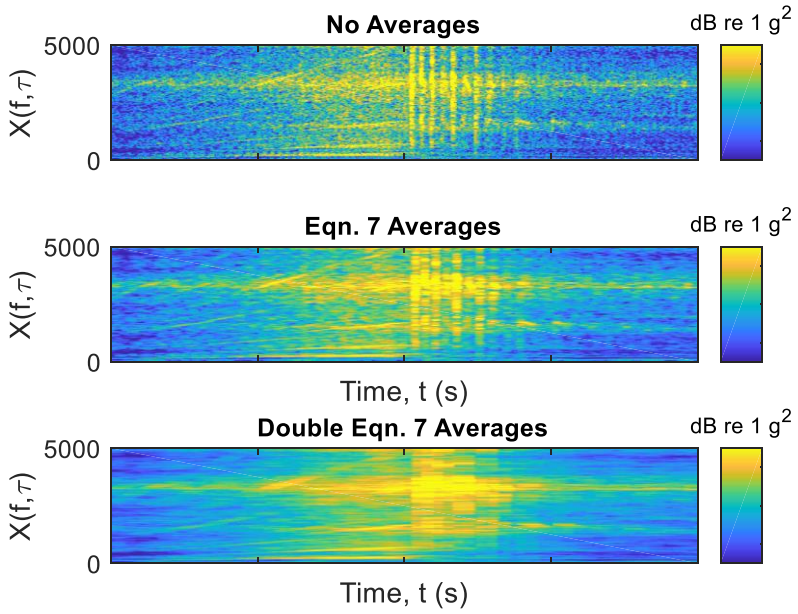


Figure 8: STFT Continued with Averaging of Overlapped Periods

Windowing and overlapping of the STFT is further post processed in Figure 8 with the addition of averaging several periods of the spectrogram together as a way to ensure each measurement fully captures any impulsive data in nearby periods. The application of averaging appears to act as smoothing of the spectrogram, which makes the impulsive data smear across the time spectrum when the inequality described by Equation 7 is exceeded. Thus when averaging is applied to STFT analysis, the inequality should not be surpassed.

3.4 STFT: Influence of Weighted Averages

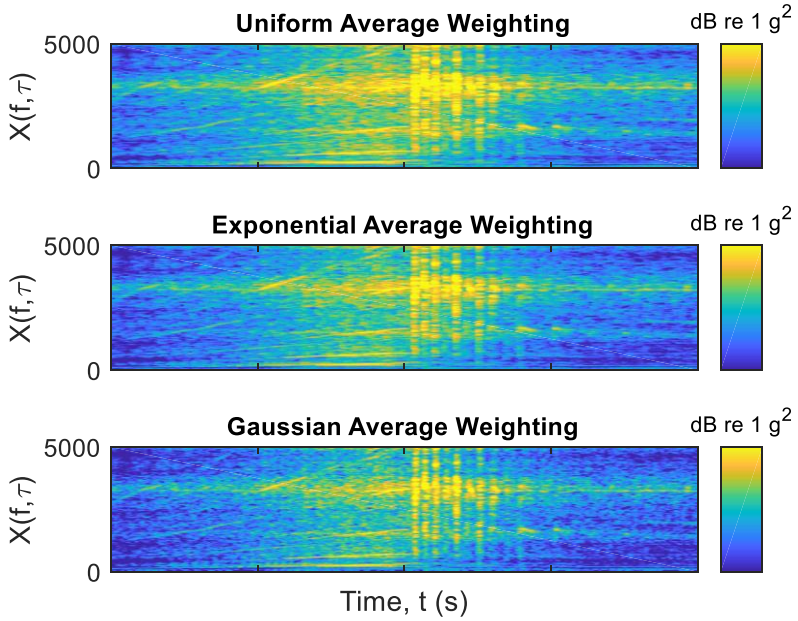


Figure 9: STFT Continued with Weighted Averaging

The application of averaging is further improved by creating a weighted average of the periods used in averaging. There are many approaches to averaging such as uniform, linear, logarithmic, exponential, Gaussian, etc. The choice of exponential averaging is due to the non-linear and impulsive behavior of the data. With an exponential window, the very last period of data observed has the highest weighting applied and is therefore emphasized most. In the event that the final average period contains a majority of the impact event information, it will be windowed and emphasized with less smearing of impacts, as shown in Figure 9, and consequently is the weighting scheme applied in Figure 4c.

When considering the convolution to compute the STFT function, similar to the data truncation in Figure 4a, it is observed that a peak transient event lands in the center of a sample period once or twice during a number of averaged periods. The periods in which it lands in the center will occur near the middle of the averaged periods, thus intuition would lead to emphasizing the middle samples and not the final sample as done with exponential averaging. It is shown in Figure 9 that the application of a Gaussian weighting function that will emphasize the middle periods does improve impact smearing and an overall better looking spectrogram above those computed with no averages in Figure 8. One caveat is that the time stamp applied to the time averaging must be modified to reflect the new emphasis on the middle periods used for averaging the spectral content.

3.5 CWT: Influence of VPO

The CWT shown in Figure 10 shows similar results to that of the STFT with mixed tradeoff of frequency and time resolution. It is also observed that the increase in number of voices per octave increases the appearance of the CWT but in the current implementation it does not capture the impulse events effectively. It also shows that at low frequency there appears to be significant band pass filter overlap. This results in low frequency resolution of the frequency content analyzed for vehicle modal response during clunk excitation. The CWT is often useful in NVH implementation; however, it does not appear to have clear benefits over STFT when applied to non-linear clunk transients.

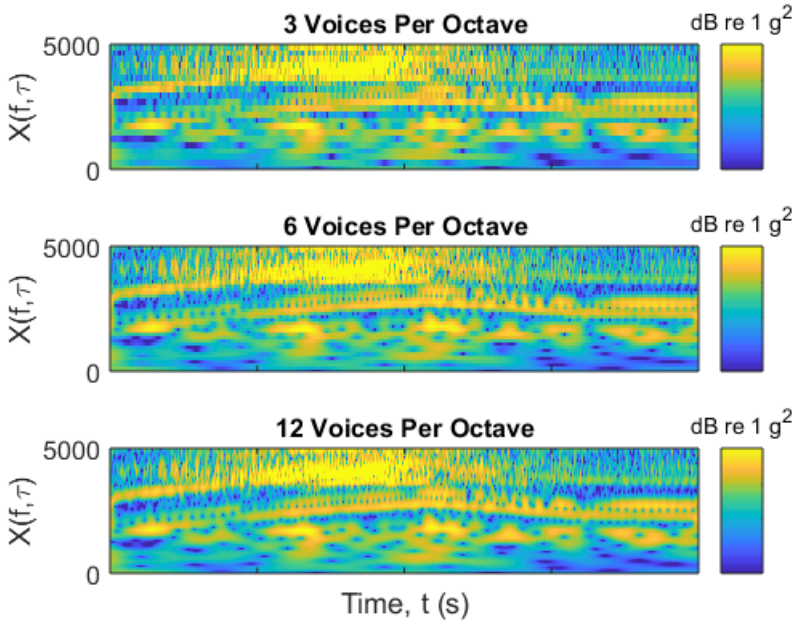


Figure 10: Analytical Morlet-CWT with Varying Voices per Octave

4 Results and Discussion

4.1 TFA Results and Discussion

A summarized development of STFT improvements is observed in Figure 11 while focused on low frequency content. Note that the frequency scaling decreased from 0-5000 Hz to 0-100 Hz. To create the image shown in Figure 11, the time resolution was decreased while frequency resolution was increased in accordance with the Gabor limit and Shannon's Sampling Equations. The original spectrogram with no overlapping, windowing, or weighted averaging is very poor and slightly indicates first order of the engine sweeping up in frequency and poor indication of low frequency (0-50 Hz) participation. The application of windowing and overlapping improves the spectrogram resolution, however the addition of a weighted average with Gaussian weighting and number of averages in accordance with Equation 7 further refines the spectrogram.

Figure 11 with windowing, overlapping, and weighted averages indicates low frequency excitation near 20 Hz. This corresponds to the transmission roll mode from Table 1. This mode participates slightly during acceleration during half engine order excitation, followed by excitation after the clunk impulses. Similar application to the differential accelerometer trace reveals peak excitation near 36 and 48 Hz, lower than expected for the differential modes. However, the modes presented in Table 1 were measured in a laboratory setting where ambient temperatures were much lower than operating temperatures. Thus the elastomer mounts of the RDM were expected to decrease in stiffness with increase in temperature lowering the differential modes.

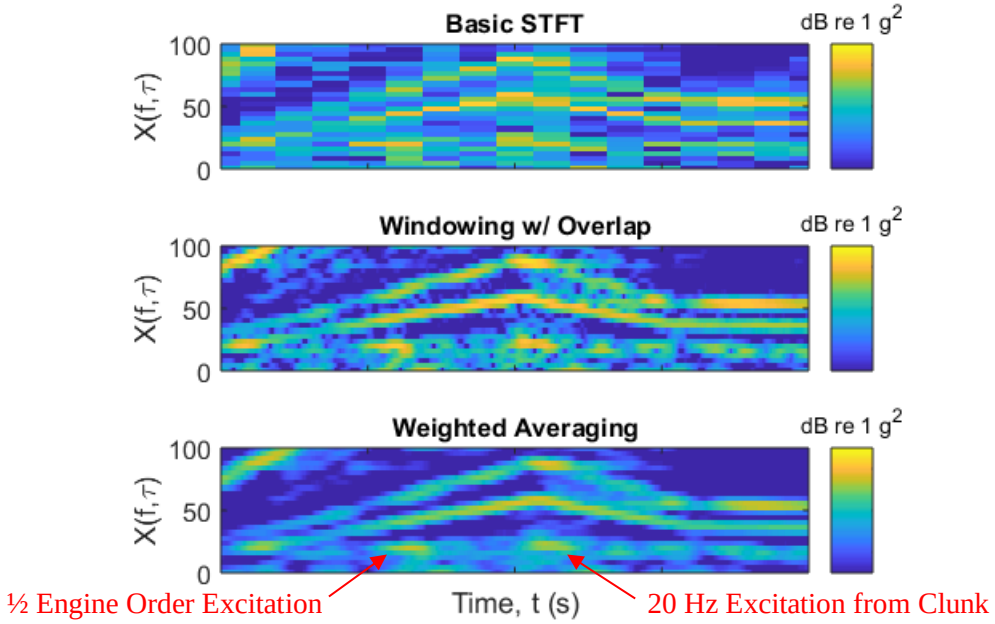


Figure 11: Low Frequency Analysis with Improved STFT Results

Overall the STFT and CWT both indicate how different frequencies are present over time when processing non-linear data. Application of the CWT was shown to be ill fitting to the non-linear data as shown in Figure 10. Further understanding of the Morlet Kernel illustrates that it is suitable for linear systems because the Kernel itself is similar to that of a burst chirp sinusoid. Future analysis of clunk data with CWT should investigate additional Kernals with better application to non-linear data.

It was shown through Section 3 that data post processing methods applied to the STFT improve the results obtained and assist in identifying impact events along with low frequency excitation of non-linear time varying data. The application of windows reduces leakage of the individual DFT computations and should always be used in best practice with non-stationary data as shown in Figure 6. Further refinement of period

overlapping improves the spectrogram time resolution without effecting the DFT time resolution depicted in Figure 7. It also reduces the amount of amplitude truncation caused by windowing that occurs when impulsive behavior in the time domain is near the beginning or end of a period and forced to zero for periodicity by the window function as observed in Figure 3. Implementation of an averaging technique smooths out the spectrogram in Figure 8, however too many averages leads to high smearing and thus a decrease in appearance of the resulting STFT. A weighting function applied along with the averaging technique and corresponding Equation 7 yields the best results as shown in Figure 9 and Figure 10 when used with all other STFT refinements previously identified.

4.2 Improved Vehicle Response with Modified Forcing Function

Observing the improved TFA results provides an indication of both the high and low frequency content during clunk as shown in Figure 6-Figure 11. The signal processed depicts the receiver's response to the operating forcing function. It is understood that the excitation was driven by a decoupling of the engine torque input as a type of step relaxation function. To understand the implications of the step relaxation function, three analytical torque signals were developed in Figure 12.

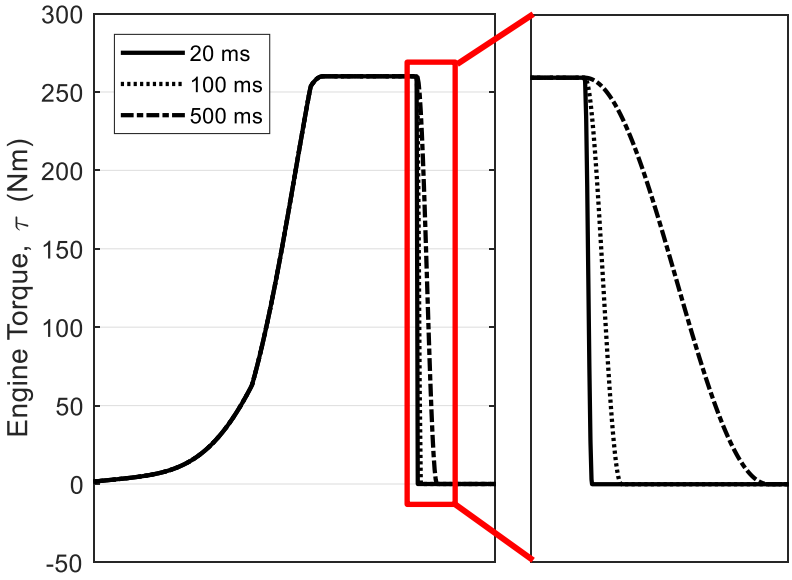


Figure 12: Clutch/Engine Torque Input and Step Relaxation

The individual torque signals in Figure 12 are similar with increasing torque during vehicle acceleration, however they differ in rapid relaxation time of the torque input. The time it takes for torque to fully decay to zero occurs in 20, 100, and 500 ms as shown in Figure 12. This correlates to real world application of the clutch pedal, which decouples the engine and driveline causing a step relaxation of torque input. TFA of the varying torque relaxation functions reveals how a rapid clutch decoupling induces broadband frequency content as shown in Figure 13. The 20 ms relaxation shown results in the shortest transient of frequency content, however, it has more excitation propagating into higher frequencies. The opposite occurs with the 500 ms relaxation which results in drawn out low frequency excitation over time with less high frequency excitation. Thus, Figure 13 shows, in theory, slower step relaxation of the clutch pedal and torque decoupling results in less high frequency content induced in a clunk transient.

An analytical implementation of this technique was performed on a lumped parameter model of the test vehicle used during data acquisition, similar to Figure 2. The output of the lumped parameter model was given in pk-pk driveshaft oscillations which were shown to correlate with increased pk-pk transmission and differential accelerometer measurements in [4] and depicted in Figure 1. The results for varying clutch step relaxation time is depicted in Figure 14, and concludes that longer step relaxation times result in lower pk-pk oscillations. This correlates to lower acceleration excitation previously observed during clunk in Figure

6-Figure 11. It is further noted from Figure 14 that there is a dip in pk-pk oscillations noted at the 86 ms step relaxation time which is equivalent to an 11.6 Hz frequency of relaxation. Recall from Table 1 that this dip occurs near the driveline shuffle mode frequency. This highlights that as the relaxation of the clutch torque is released at a period approaching the shuffle mode frequency, there is a reduction in shuffle leading to lower clunk transient in the vehicle driveline.

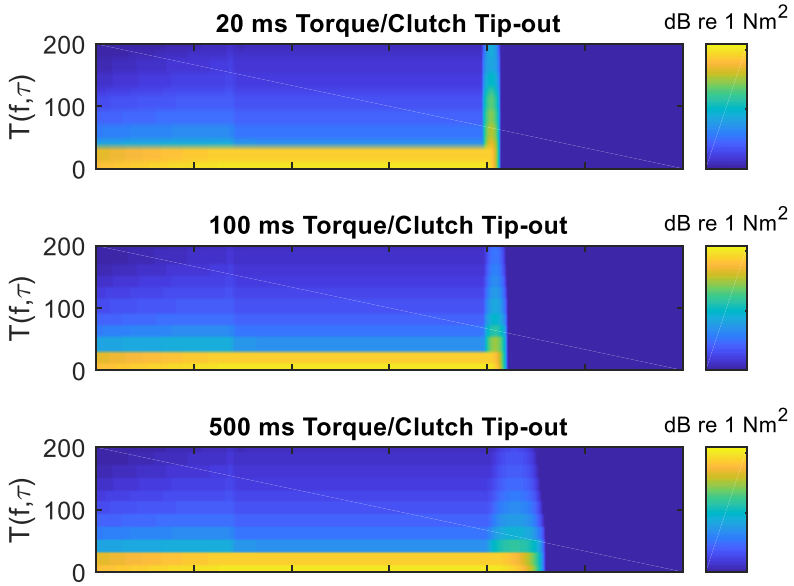


Figure 13: STFT of Engine/Clutch Torque Step Relaxation

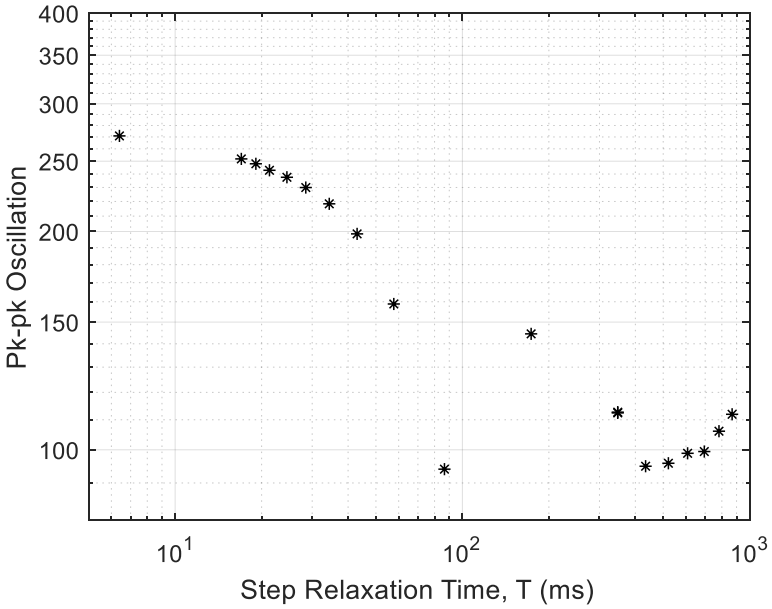


Figure 14: Pk-pk Driveshaft Oscillations Induced by Varying Engine/Clutch Torque Step Relaxation

5 Conclusions

This study showed how both STFT and CWT can be applied to extract frequency content from long time traces of non-stationary operating data. It revealed several strategies for the STFT common in signal processing such as windowing, overlapping and weighted averaging to improve the resulting spectrogram. An inequality was developed for the maximum number of weighted averages to be used when applied to the STFT and should not be exceeded during application of averaging. Results were compared when applied

to real life clunk transient data which revealed participation of the transmission roll mode as well as differential pitch and roll modes excited by the impulses. The impulses also indicated broadband frequency excitation of 500-5000 Hz, the metal to metal impact events that create a negative perception on vehicle quality.

The results of TFA also indicated low frequency content excited during clunk by release of the clutch pedal during operation. The clutch pedal release was modeled as a step relaxation function with varying time to achieve full relaxation and analyzed through TFA for its implications on operating data. It was shown that rapid step relaxation induces more broadband frequency content in the system, which correlates well with the measured response data analyzed. The various step relaxation functions were applied to a lumped parameter model of the test vehicle and shown to reduce the effects of clunk with lower pk-pk driveshaft oscillations. The optimal response was observed when the relaxation time approached the period of the driveline shuffle mode.

Acknowledgements

This research was completed with funding provided by our sponsor Ford Motor Company and we would like to thank them for their support and contributions.

References

[1] B. Wyerman, M. Dinsmore, P. Saha, B. Baker, A. Carey, R. Hadi, *Automotive Noise and Vibration Control Practices in the New Millennium*, *SAE Technical Paper 2003-01-1589* (2003).

[2] T. Wellmann, K. Govindswamy, E. Braun, K. Wolff,. *Aspects of Driveline Integration for Optimized Vehicle NVH Characteristics, SAE Technical Paper 2007-01-2246* (2007).

[3] A. Crowther, C.. Janello, R. Singh,. *Quantification of clearance-induced impulsive sources in a torsional system*. Journal of Sound and Vibrations, Vol. 307, Elsevier (2007), pp. 428-451.

[4] J. Furlich, J. Blough, D. Robinette, *Torsional Vibration Analysis of Six Speed MT Transmission and Driveline from Road to Lab, SAE Technical Paper 2017-01-1845* (2017).

[5] R. Kalantari, and M. Saadat Foomani, *Backlash Nonlinearity Modeling and Adaptive Controller Design for an Electromechanical Power Transmission System*, Transaction B: Mechanical Engineering, Vol. 16, No. 6, Scientia Iranica (2009) pp. 463-469.

[6] C. Chae, Y. Lee, K. Won, K. Kang, *Experimental and Analytical Approach for Identification of Driveline Clunk Source & Transfer Path, SAE Technical Paper 2004-01-1231* (2004).

[7] W. Heylen, S. Lammens, P. Sas, *Modal Analysis Theory and Testing*, Katholieke Universiteit Leuven, Departement Werktuigkunde, Leuven (1997).

[8] I. Suh. *Application of Time-Frequency Representation Techniques to the Impact-Induced Noise and Vibration from Engines, SAE Technical Paper 2002-01-0453* (2002).

[9] X. Zhu, J. Kim,. *Application of the Analytic Wavelet Transform for Time-Frequency Analysis of Impulsive Sound Signals, SAE Technical Paper 2005-01-2391* (2005).

[10] M. Buzzoni, E. Mucchi, G. Dalpiaz, *Piston slap noise reduction in IC engines: design, Proceedings of the 2016 International Conference on Noise and Vibration Engineering, ISMA, KU Leuven* (2016).

[11] J. Z. Szabó, P. Bakucz, *Wavelet based knocking combustion analysis of vibration. Proceedings of the 2016 International Conference on Noise and Vibration Engineering, ISMA, KU Leuven* (2016).

[12] K. Dziedziech, W. J. Staszewski, T. Uhl, *Input-output time-frequency analysis of time-variant. Proceedings of the 2012 International Conference on Noise and Vibration Engineering, ISMA, KU Leuven* (2012).

[13] M. Mihalec, J. Slavic, Miha Boltezar, *Damping identification using synchrosqueezed wavelet transform. Proceedings of the 2016 International Conference on Noise and Vibration Engineering, ISMA, KU Leuven* (2016).

[14] M. Fortuna, A. Klepka, K. Dziedziech, W. J. Staszewski, T. Uhl. *Time-variant modal analysis of a CanSat rocket. Proceedings of the 2016 International Conference on Noise and Vibration Engineering, ISMA, KU Leuven* (2016).

[15] D. Gabor. *Theory of communication. Part 1: The analysis of information*. in Electrical Engineers - Part III: Radio and Communication Engineering, Journal of the Institution of, vol. 93, no. 26, pp. 429-441, November (1946).

Optimising geometry and asymmetrical damping ratio to reduce vehicle vertical acceleration under stochastic road profile

J. C. M. Fernandes [1], **M. Silveira** [1]
[1] São Paulo State University (UNESP), School of Engineering, Bauru
Av. Eng. Luiz Edmundo C. Coube 14-01, Vargem Limpa, 17033-360, Bauru, São Paulo, Brazil
e-mail: **julio.fernandes@unesp.br**

Abstract

This work presents a study on the dynamic behaviour of a vehicle suspension system with asymmetrical viscous damping, with stochastic road profile. The geometrical configuration of a double-wishbone suspension system is taken into account, so as to include geometrical nonlinearities. It is known that the use of asymmetrical damping can diminish the sprung mass acceleration, and causes a shift of the mean position of the sprung mass. The optimum configuration of the geometrical parameters and the asymmetry ratio that minimises the vertical acceleration of the vehicle body is seeked. The lengths of the lower and upper arms and the inclination of the spring-damper assembly are the geometrical parameters considered in the optimisation. Numerical simulations showed that the optimised system presents a reduction close to 30 % in the RMS acceleration. The optimised parameters depend on the chosen asymmetry ratio of the damper, in agreement with previous result showing the influence of asymmetry ratio on the acceleration of the sprung mass.

1 Introduction

All ground vehicles are subject to vibrations induced by the road, which directly affect the comfort of the passengers. Suspension systems are designed to minimise these unwanted effects to improve comfort, while also providing good handling [1]. Regarding ground vehicles, improving one of these objectives can compromise the other [2]. Generally, comfort is associated with a softer suspension, and good handling associated with a stiffer suspension [3].

The limitations regarding the classical passive suspensions have motivated research of controlled suspension systems as semi-active and active systems [4]. Compared to passive systems, semi-active suspensions provide a high level of comfort and employ electro- or magneto-rheological dampers [5, 6, 7]. According to [9], active suspension systems can provide up to 60% more comfort than passive suspension system and much effort has been put to improve such systems [9, 12, 13, 14]. Although semi-active and active suspension systems provide good comfort, its use implies an increase in the global cost of the vehicle and has been used only in high performance vehicles [8].

In order to reduce the overall cost of the vehicle without compromising the level of passenger comfort, engineers have sought alternatives to this question. A solution found was to develop passive dampers, whose damping forces act asymmetrically. Some studies involving the dynamic analysis of asymmetrical damping shows satisfactory results when applying this type of damping in suspension systems [2, 15, 16, 17]. Asymmetrical dampers have different damping coefficient during the extension and the compression phases. Suspension systems which employs asymmetrical damping can change the mean equilibrium position of the vehicle sprung mass. This effect is called jacking down or packing [16]. Numerical simulations and analytic solutions have been used to analyse the behaviour of the system employing asymmetrical damping [18].

The geometry of the suspension system is an important factor to be considered in vehicle design. In medium passenger vehicles, different types of suspension are used in the front and rear. The McPherson suspension type is the most used on the front of vehicles, since it presents some advantages such as simplicity of construction, reduced weight and volume [19]. Another common type of suspension is the double wishbone, which has significant effect on the handling and comfort of the vehicle if compared to McPherson and other suspension systems [20]. It has been shown that better comfort can be achieved when considering the suspension geometry while using asymmetrical damping [21]. Previous studies have shown that asymmetrical damping can diminish the amplitude of displacement and acceleration of the sprung mass, when the parameters of suspension geometry are combined with the asymmetrical damping [22].

Optimisation methods can be used to design vehicle suspension system with good compromise between comfort and handling. An optimisation process related to ride comfort, suspension travel and road holding of the vehicle was used to find the most important suspension stiffness and damping parameters [23]. Optimisation with asymmetrical damping were also investigated by [24], which the main objective was apply a methodology leading to optimum combinations of the suspension damping and stiffness parameters.

According to ISO 2631 standard, the intensity of the vibration must be evaluated by the RMS value of acceleration in order to assess its effect on the human body. In occupational vibration evaluation, several factors influence the risk characterization, among which are: vibration amplitude, frequency, its direction and the exposure time [25].

In this paper, we investigate the influence of asymmetrical damping in the response of the system, and the role of the geometrical parameters on the RMS acceleration of sprung mass. With the aim of analysing the combined effects of asymmetrical damping and geometric nonlinearities, the road profile characteristics are shown in section 2 ; a two-degree-of-freedom quarter-car model with stochastic base excitation considering the suspension geometry is presented in section 3 ; the parameters and the objective function considered in the optimisation process are shown in the section 4 ; results of RMS accelerations for the system considering the suspension geometry are shown in section 5 . Finally conclusions are drawn in section 6.

2 Road profile

The ISO 8608:1995 standard proposes a classification of the road roughness (Class A - H) based on the power spectral density (PSD) of to the longitudinal profile. According to [25], random road profiles can be approximated by a PSD as follows:

$$\Phi(\Omega) = \Phi(\Omega_0) \left(\frac{\Omega}{\Omega_0} \right)^{-w} \tag{1}$$

in which $\Omega = 2\pi/L$ rad/m denotes the spatial frequency (wavenumber) and L is the wavelength. The PSD of the road presents a constant drop in its magnitude according to the spatial frequency [26]. The value of PSD at $\Omega_0 = 1$ rad/m is given by $\Phi_0 = \Phi(\Omega_0)$. The values of $\Phi(\Omega_0)$ are shown in Table 1. The drop in the magnitude is modelled by the roughness coefficient of waviness w (according to ISO 8608:1995, $w = 2$). The integral of the PSD over a given frequency band calculates the average power of the signal over this frequency band.

According to this standard, roads, whether paved or not, can be classified from A to H, the classes are defined by Φ_0. For example, a class A road has $\Phi_0 = 1 \times 10^{-6}$ m^3, which is smooth, while a class H road has $\Phi_0 = 256 \times 10^{-6}$ m^3, and is rougher [26, 27].

3 Geometric vehicle suspension system

Figure 1 shows the parameters the double wishbone suspension system considered in this study. The elastic and damping forces are related to the geometry and are clearly nonlinear [28]. The double wishbone suspension is a four-bar mechanism, and the classical theory of mechanisms can be used to determine the positions

Table 1: Degree of roughness expressed in terms of Ω_0 accordind to the standard ISO 8608:1995 [25]

Road class	**Degree of roughness** $\Phi\ (\Omega_0)^1$ $10^-6\ m^3$		
	Lower limit	Geometric mean	Upper limit
A (very good)	-	1	2
B (good)	2	4	8
C (average)	8	16	32
D (poor)	32	64	128
E (very poor)	128	256	512
F	512	1024	2048
G	2048	4096	8192
H	8192	16384	-
$\Omega_0 = 1$ rad/m			

of all the links and angles. The equivalent 2-DOF model, with an asymmetrical damping considered between the sprung and unsprung mass, is shown in Fig. 2, with its characteristic. The parameters of interest for the calculation of the suspension kinematics are defined in Table 2. The initial configuration is considered when $z_r = 0$.

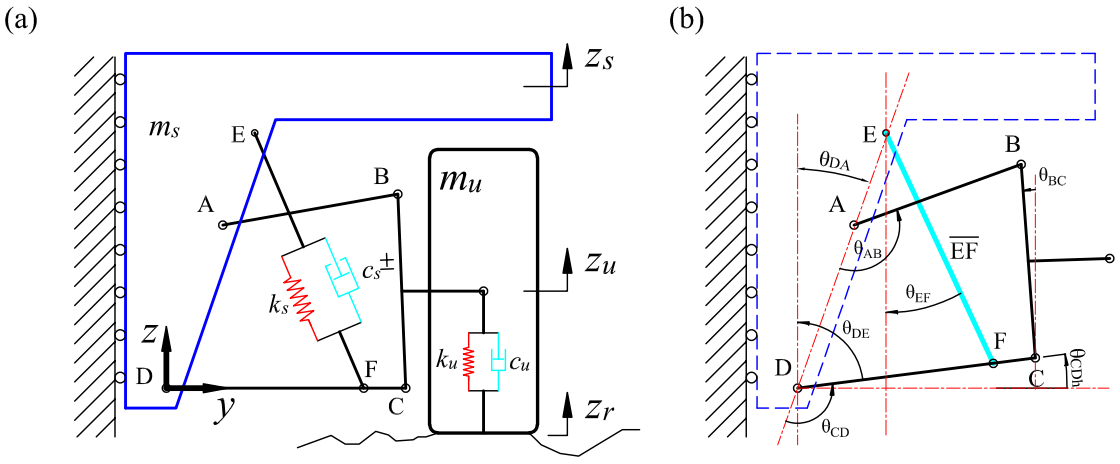


Figure 1: Representation of quarter-car model with asymmetrical damping considering geometrical nonlinearities (a); definition of geometrical parameters (b).

The $\overline{EF}$ segment represents the length of the spring-damper assembly and it is calculated as follows:

$$\overline{EF} = \sqrt{\overline{DF}^2 + \overline{DE}^2 - 2\overline{DF}\ \overline{DE}\cos(\theta_{DE} - \theta_{DA})} \tag{2}$$

The vertical component of the relative displacement is defined as:

$$a = (\overline{EF}_0 - \overline{EF})\cos(\theta_{EF}) \tag{3}$$

The angle of the spring-damper assembly, θ_{EF}, is defined by:

$$\theta_{EF} = \cos^{-1}\left(\frac{\overline{DE}^2 + \overline{EF}^2 - \overline{DF}^2}{2\overline{DE}\ \overline{EF}}\right) - \pi \tag{4}$$

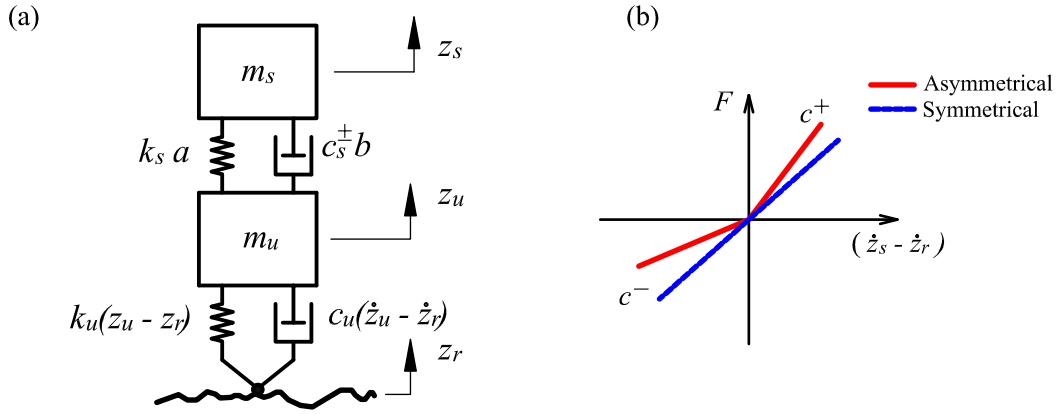


Figure 2: Equivalent 2-DOF model (a); characteristic of asymmetrical damping (b).

Table 2: Parameters values of the double wishbone suspension [29].

Parameter	Description	Value
$\overline{AB}$	Length of upper suspension arm	146.05 mm
$\overline{CD}$	Length of lower suspension arm	228.6 mm
$\overline{DA}$	Distance from the lower arm joint to upper arm joint	221.43 mm
$\overline{DF}$	Distance from the lower arm joint to lower damper joint	177.80 mm
$\overline{DE}$	Distance from the lower arm joint to upper damper joint	310.31 mm
A_y	Coordinate y of the joint A	75.18 mm
A_z	Coordinate z of the joint A	208.28 mm
$\overline{DE_h}$	Horizontal distance between the joints D and E	105.36 mm
$\overline{DE_v}$	Vertical distance between the joints D and E	291.88 mm
θ_{DA}	Angle of the segment $\overline{DA}$	19.84°
$B_{z,0}$	Initial position of the joint B	25.36 mm

The angular velocity of the upper arm is given by:

$$\dot{\theta}_{AB} = \frac{(\dot{z}_u - \dot{z}_s)}{\overline{AB}\sqrt{1 - \frac{(B_{z,0}+z_u-z_s)^2}{\overline{AB}^2}}} \tag{5}$$

The angular velocity of the lower arm is calculated as:

$$\omega_{CD} = -\frac{\dot{\theta}_{AB}\overline{AB}\cos\left(\theta_{BC} - \sin^{-1}\left(\frac{B_{z,0}+z_u-z_s}{\overline{AB}}\right)\right)}{\overline{CD}\sin\left(\theta_{BC} - \theta_{CD}\right)} \tag{6}$$

The vertical component of the relative velocity ($b = \dot{z}_s$ - $\dot{F}_y$) is obtained by:

$$\dot{F}_y = \omega_{CD}\overline{DF}\ \cos(\theta_{CDh}) \tag{7}$$

Finally, the damping force is calculated by the product of the asymmetrical damping coefficient and the relative velocity, and the asymmetrical damping coefficients during the extension and the compression cycles are defined by Eq. (8).

$$F_{cs}^{\pm} = c_s^{\pm}\ b \qquad\qquad c_s^{\pm} \Rightarrow \begin{cases} c_s^+ & \text{if } b \geq 0 \\ c_s^- & \text{if } b < 0 \end{cases} \tag{8}$$

The asymmetry ratio β is defined by:

$$\beta = \frac{c_s^+}{c_s^-} \tag{9}$$

Finally, the equations of motion for the suspension system with asymmetrical damping and taking into account the geometrical nonlinearities are given by:

$$\begin{aligned} m_u\,\ddot{z}_u + k_u\,(z_u - z_r) + c_u\,(\dot{z}_u - \dot{z}_r) - k_s\,a - c_s^{\pm}\,b = 0 \\ m_s\,\ddot{z}_s + k_s\,a + c_s^{\pm}\,b = 0 \end{aligned} \tag{10}$$

Different values of β are used, and for each value, c_s^+ and c_s^- are chosen to maintain the same dissipated energy for compression and expansion. The damping coefficients used are: for $\beta = 3$, $c_s^+ = 6000$ Ns/m and $c_s^- = 2000$ Ns/m, for $\beta = 1$, $c_s^+ = 4000$ Ns/m and $c_s^- = 4000$ Ns/m and for $\beta = 1/3$, $c_s^+ = 2000$ Ns/m e $c_s^- = 6000$ Ns/m. A class B road profile is considered with vehicle speed $v = 40$ km/h. The segments $\overline{CD}$, $\overline{AB}$ and $\overline{DF}$ are the decision variables for the optimisation process. The PSD of sprung mass acceleration, $PSD(\ddot{z}_s)$, is obtained by the *Welch* method [30].

4 Optimisation

The optimisation problem of the suspension system can be written as follows:

$$\text{Find} \qquad X = \left\{ \begin{array}{c} x_1 \\ x_2 \\ x_3 \end{array} \right\} = \left\{ \begin{array}{c} \overline{CD} \\ \overline{AB} \\ \overline{DF} \end{array} \right\} \qquad \text{which minimises} \qquad f(X)$$

In order to improve comfort, the objective function considered is the RMS value of the acceleration of the suspended mass, given by:

$$f(X) = RMS(\ddot{z}_s) \tag{11}$$

subject to the constraints

$$\begin{aligned} -x_1 + 177.8 \leq 0 \\ x_1 - 250 \leq 0 \\ -x_2 + 130 \leq 0 \\ x_2 - 160 \leq 0 \\ -x_3 + 105 \leq 0 \\ x_3 - 177.8 \leq 0 \end{aligned} \tag{12}$$

The system defined by Eq. (10) is nonlinear because of the asymmetrical damping and geometrical nonlinearities. In this study, the response of the system is obtained through numerical simulation, and a nonlinear programming solver was used to find the minimum of the constrained nonlinear multivariable optimisation problem described by Eq.(11) and Eq. (12). Several values are considered as initial guesses for the decision variables, in order to verify the convergence of the method. It was observed that the solver found solutions in a very small number of iterations, regardless of the initial guess. The optimum values found were: $\hat{x}_1 = 250$ mm, $\hat{x}_2 = 160$ mm and $\hat{x}_3 = 105$ mm.

5 Sprung mass acceleration

Figure 3 presents the $PSD(\ddot{z}_s)$ comparing the optimised and non-optimised system with $\beta = 1/3$, $\beta = 1$ and $\beta = 3$. For all frequencies, regardless of the asymmetry ratio, the optimised system presents a decrease of amplitude. It is also found that the the use of asymmetrical damping presents another peak of resonance.

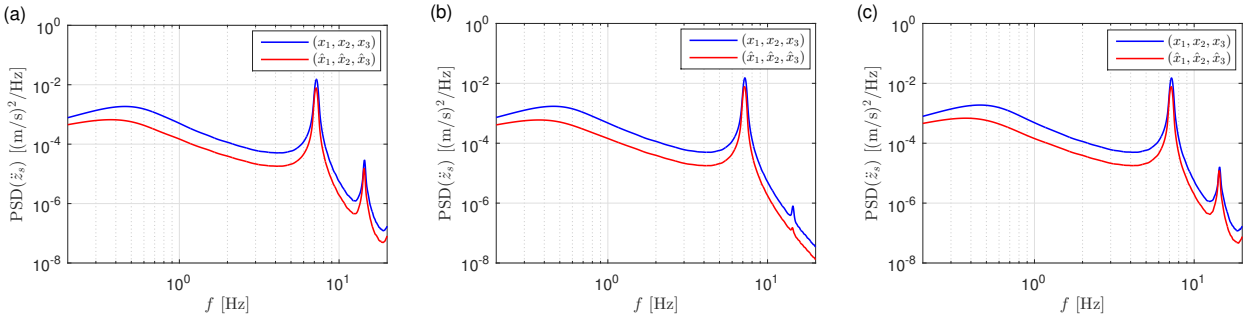


Figure 3: Comparison between the PSD of the sprung mass acceleration of the optimised and non-optimised system using $\beta = 1/3$ (a); $\beta = 1$ (b); $\beta = 3$ (c).

There are ranges where the optimised system presents larger acceleration. The PSD ratio (PSD_R) is defined as the PSD of the optimised system (PSD_o) divided by the PSD of the non-optimised system (PSD_n), and is defined as:

$$PSD_R = \frac{PSD_o}{PSD_n} \tag{13}$$

By analysing the PSD_R, it is possible to verify the improvement achieved with the optimised system (Fig. 4). Values above 1 show that the optimised system has RMS acceleration amplitude greater than the non-optimised system. The asymmetry ratio has low influence at low frequency, between 0 and 10 Hz. After this value, β close to 1 diminishes the RMS acceleration, and β far from 1 results in increase of acceleration.

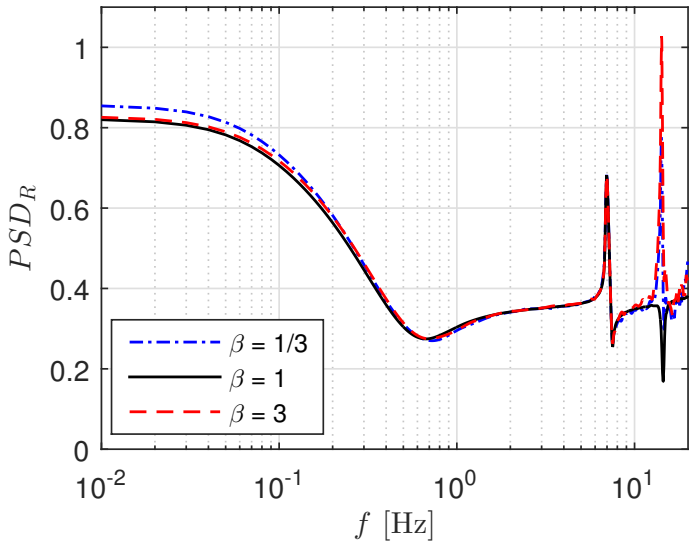


Figure 4: PSD ratio, PSD_R, in relation to the frequency f with $\beta = 1/3$, $\beta = 1$ and $\beta = 3$.

Considering only the optimised system, Fig. 5 shows the $PSD(\ddot{z}_s)$ for several values of β. At low frequencies, close to the first and second resonance peaks, it is shown that the asymmetry ratio β has low influence on the acceleration. After the second peak, due the geometrical nonlinearities and the asymmetry, a third resonance peak appears. The PSD does not present the third peak if β values are close to 1.

Through the analyses shown above it is possible to verify the influence of the optimised parameters ($\hat{x}_1$, $\hat{x}_2$, $\hat{x}_3$) individually, using asymmetry ratio $\beta = 3$. Figure 6-a shows the $PSD(\ddot{z}_s)$ for the systems with: (x_1, x_2, x_3); ($\hat{x}_1$, x_2, x_3); (x_1, $\hat{x}_2$, x_3); (x_1, x_2, $\hat{x}_3$), ($\hat{x}_1$, $\hat{x}_2$, $\hat{x}_3$). It is observed that both x_1 and x_2 are responsible for small decrease in the amplitude at the first and second peaks. However, varying only x_3 results in a decrease of amplitude in the entire range of frequencies.

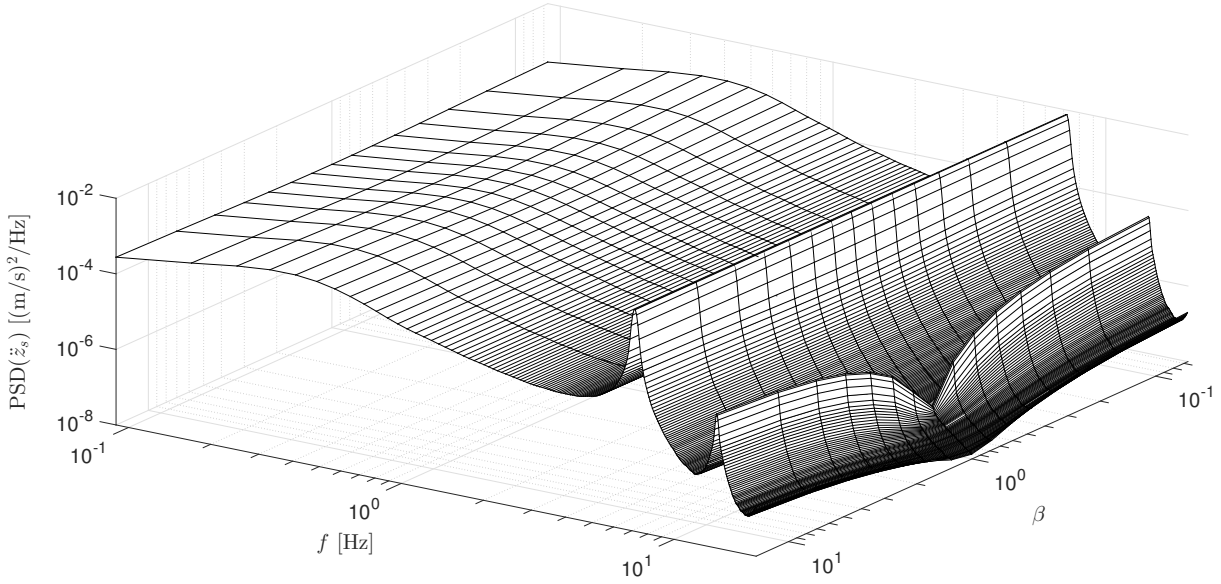


Figure 5: Surface graph of PSD of sprung mass acceleration for different values of asymmetry ratio β.

Figure 6-b shows the $RMS(\ddot{z}_s)$ for different β, comparing the optimised and non optimised suspension systems. It is shown that the geometrical parameter, specifically x_3, have more influence than the asymmetry ratio β. For example, for $\beta = 3$, the $RMS(\ddot{z}_s)$ with (x_1, x_2, x_3) is 0.087 m/s ^{2}, with ($\hat{x}_1$, x_2, x_3) is 0.086 m/s ^{2}, with (x_1, $\hat{x}_2$, x_3) is 0.085 m/s ^{2}, with (x_1, x_2, $\hat{x}_3$) is 0.062 m/s^2, and ($\hat{x}_1$, $\hat{x}_2$, $\hat{x}_3$) is 0.059 m/s ^{2}.

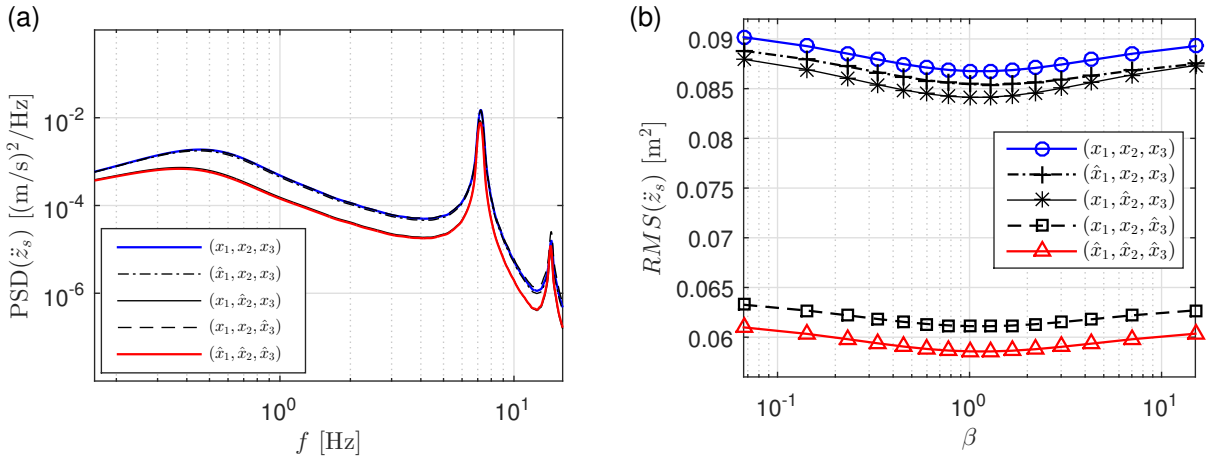


Figure 6: Comparison between the PSD of the sprung mass acceleration of the optimised and non-optimised system using for $\beta = 3$ (a); RMS acceleration of sprung mass in relation to β (b).

6 Conclusions

This work presented a study on the dynamic behaviour of a vehicle suspension system that employs asymmetrical viscous damping and considering geometrical parameters. Focusing on the improvement of comfort for the passengers, an optimisation technique were applied to find the best configuration for the suspension system geometry and asymmetry ratio. The shift in the mean position is also observed if the road profile considered is stochastic. It was showed that in low frequencies, close to the first and second resonance peaks, the asymmetry ratio has low influence.

The parameter that present more influence is $\overline{DF}$, which is the inclination of the spring-damper assembly. The use of asymmetrical damping with β different from 1 and geometrical non-linearities involves the appearance of a third resonance peak.

Results obtained through numerical simulation shows a reduction in the RMS acceleration of the sprung mass when compared to the optimised and non-optimised system. The simulations showed that the optimised system using asymmetrical damping presents a reduction close to 30 % in the RMS acceleration. However, in a narrow band close to the third resonance, the optimised system has higher acceleration.

Acknowledgements

The authors thank the Brazilian funding agency CAPES for financial support during this project.

References

[1] P. S. Els, N. J. Theron, P. E. Uys, M. J. Thoresson, *The ride comfort vs. handling compromise for off-road vehicles*, Journal of Terramechanics, Vol. 44, No. 4, (2007), pp. 303-317.

[2] M. Silveira, B. R. Pontes Junior, J. M. Balthazar, *Use of nonlinear asymmetrical shock absorber to improve comfort on passenger vehicles*, Journal of Sound and Vibration, Vol. 333, No. 7, (2014), pp. 2114-2129.

[3] Q. H. Nguyen, S. B. Choi, Y. G. Park, *An analytical approach to optimally design of electrorheological fluid damper for vehicle suspension system*, Meccanica, Vol. 47, No. 7, (2012), pp. 1633-1647.

[4] E. Guglielmino, T. Sireteanu, C. W. Stammers, G. Ghita, M. Giuclea, *Semi-active Suspension Control: Improved Vehicle Ride and Road Friendliness*, Springer London, (2008).

[5] A. M. Tusset, M. Rafkov, J. M. Balthazar, *An intelligent controller design for magnetorheological damper based on a quarter-car model*, Journal of Vibration and Control, Vol. 15, No. 12, (2009), pp. 1907-1920.

[6] M. Zapateiro, F. Pozo, H. R. Karimi, N. Luo, *Semiactive control methodologies for suspension control with magnetorheological dampers*, Mechatronics, IEEE/ASME Transactions on, Vol. 17, No. 2, (2012), pp. 370-380.

[7] M. El-Kafafy, S. M. El-Demerdash, A.-A. M. Rabeih, *Automotive ride comfort control using mr fluid damper*, SCIRP Journal of Engineering, Vol. 4, No. 4, (2012), pp. 179-187.

[8] M. Bouazara, M. J. Richard, S. Rakheja, *Safety and comfort analysis of a 3-d vehicle model with optimal non-linear active seat suspension*, Vol. 43, No. 2, (2006), pp. 97-118.

[9] B. L. J. Gysen, J. J. H. Paulides, J. L. G. Janssen, E. A. Lomonova, *Active electromagnetic suspension system for improved vehicle dynamics*, Vehicular Technology, IEEE Transactions, Vol. 59, No. 3, (2010), pp. 1156-1163.

[10] D. Hrovat, *Survey of advanced suspension developments and related optimal control applications*, Automatica, Vol. 33, No. 10, (1997), pp. 1781-1817.

[11] W. F. Milliken, D. L. Milliken, *Race Car Vehicle Dynamics*, Warrendale, PA: Society of Automotive Engineers, (1995).

[12] T. Yoshimura, K. Nakaminami, M. Kurimoto, J. Hino, *Active suspension of passenger cars using linear and fuzzy-logic controls*, Control Engineering Practice, Vol. 7, No. 1, (1999), pp. 41-47.

[13] D. Fischer, R. Isermann, *Mechatronic semi-active and active vehicle suspensions*, Control Engineering Practice, Vol. 12, No. 11, (2004), pp. 1353-1367.

[14] V. S. Deshpande, B. Mohan, P. Shendge, S. Phadke, *Disturbance observer based sliding mode control of active suspension systems*, Journal of Sound and Vibration, Vol. 333, No. 11, (2014), pp. 2281-2296.

[15] A. K. W. Ahmed, S. Rakheja, *An equivalent linearization technique for the frequency response analysis of asymmetric dampers*, Journal of Sound and Vibration, Vol. 153, No. 3, (1992), pp. 537-542.

[16] C. Rajalingham, S. Rakheja, *Influence of suspension damper asymmetry on vehicle vibration response to ground excitation*, Journal of Sound and Vibration, Vol. 266, No. 5, (2003), pp. 1117-1129.

[17] M. Silveira, B. R. Pontes Jr, J. M. Balthazar, *Reducing Vertical and Angular Accelerations With Nonlinear Asymmetrical Shock Absorber in Passenger Vehicles*, Proceedings of ASME 2013 International Design Engineering Technical Conferences - IDETC, 2013, Vol. 8.

[18] M. Silveira, P. Wahi, J. Fernandes, *Effects of asymmetrical damping on a 2 dof quarter-car model under harmonic excitation*, Communications in Nonlinear Science and Numerical Simulation, Vol. 43, (2017), pp. 14-24.

[19] J. Hurel, A. Mandow, A. Garcia-Cerezo, *Nonlinear two-dimensional modeling of a mcpherson suspension for kinematics and dynamics simulation*, Advanced Motion Control (AMC), 2012, 12th IEEE International Workshop, 2012 March 25-27, pp. 1-6.

[20] K. P. Balike, *Kineto-dynamic analyses of vehicle suspension for optimal synthesis*, Ph.D. thesis, Concordia University (September 2010).

[21] K. P. Balike, S. Rakheja, I. Stiharu, *Kineto-dynamic performance analysis of vehicle with an asymmetric suspension damper using a roll-plane model*, International Journal of Vehicle Performance, Vol. 1, No. 1, (2013), pp. 69-91.

[22] J. C. M. Fernandes, M. Silveira, B. R. Pontes Jr, J. M. Balthazar, *Effects of asymmetrical damping ratio and damper inclination on vertical dynamics of a suspension system*, Mathematics in Engineering, Science & Aerospace (MESA), Vol. 6, No. 3, (2015), pp. 391-398.

[23] G. Georgiou, G. Verros, S. Natsiavas, *Multi-objective optimisation of quarter-car models with a passive or semi-active suspension system*, Vehicle System Dynamics, Vol. 45, No. 1, (2007), pp. 77-92.

[24] G. Verros, S. Natsiavas, C. Papadimitriou, *Design optimization of quarter-car models with passive and semi-active suspensions under random road excitation*, Journal of Vibration and Control, Vol. 11, No. 5, (2005), pp. 581-606.

[25] International Organization for Standardization, *Mechanical Vibration and Shock-Evaluation of Human Exposure to Whole-body Vibration - Part 1: General Requirements*, International standard, The Organization, 1997.

[26] G. Rill, *Road Vehicle Dynamics: Fundamentals and Modeling*, Ground vehicle engineering series, Taylor & Francis, (2011).

[27] F. Tyan, Y. F. Hong, S. H. Tu, W. S. Jeng, *Generation of random road profiles*, Journal of Advanced Engineering, Vol. 4, No. 2, (2009), pp. 1373-1378.

[28] V. Cherian, N. Jalili, V. Ayglon, *Modelling, simulation, and experimental verification of the kinematics and dynamics of a double wishbone suspension configuration*, Proceedings of the Institution of Mechanical Engineers, Part D: Journal of Automobile Engineering, Vol. 223, No. 10, (2009), pp. 1239-1262.

[29] C. Campbell, *Automobile suspensions*, Springer Science & Business Media, (2012).

[30] P. Welch, *The use of fast fourier transform for the estimation of power spectra: a method based on time averaging over short, modified periodograms*, IEEE Transactions on audio and electroacoustics, Vol. 15, No. 2, (1967), pp 70-73.

Validation experiment for structural power

R. Ullmann [1,2]**, S. Sicklinger** [1]**, G. Müller** [2]
[1] BMW Research, New Technologies, Innovations
Parkring 19, 85748 Garching, Germany
e-mail: **rupert.ullmann@bmw.de**

[2] Chair of Structural Mechanics, Technical University of Munich
Arcisstr. 21, 80333 München, Germany

Abstract
The evaluation of structure-borne sound power is an effective analysis tool for the analysis of the structure-borne sound transmission in mechanical structures like vehicles, but also for the characterization of components. However in the case of measurement-based methods in particular the phase-accuracy becomes challenging for lightly damped systems vibrating at non-resonant frequencies. In order to enable the measurement of power quantities for such cases a method is discussed incorporating a frequency-dependent phase correction. The latter is predetermined in a small test setup solely for the impedance heads as these introduce the largest phase errors in the measurement chain. The evaluated impedance heads are used for the evaluation of power quantities at an example structure afterwards. Applying the phase correction a significant improvement of the resulting power quantities is finally achieved.

1 Introduction

Due to electric mobility and autonomous driving, requirements for acoustic vehicle quality are increased significantly. So the vibroacoustic assessment and optimization of vehicle components at the early stage of the complete vehicle development is an essential future competitive factor. For acoustic evaluations of the structural components, a representative and robust physical key performance indicator is needed as sound pressure levels at the passenger ears are not available at this stage of the development process. Besides the assessment of primary variables like displacements or forces the evaluation of energy flows can be a promising approach also in the lower frequency range. Power as the indicator for energy flow combines phase-correct force and velocity measures in one real scalar.

Although the acoustic assessment of the mechanical system must be mostly simulation-based at the early stage of vehicle development, there are some vehicle parts which are difficult to model numerically. Therefore energetic quantities have to be assessed by measurements at in- and outputs of mechanical subsystems like rubber bearings. As the latter ones usually have a rather low modal density one must be able to measure power quantities outside resonance. However this task is not state of the art in normal engineering practice.

Starting from a mechanical point of view, power is the scalar product of the normal and the intensity vector integrated over the surface [14]. The intensity vector is the multiplication of the stress tensor and the velocity vector. For discretized systems, however, the power calculation is simplified as it can be calculated from the vectors of discrete forces and velocities. For the harmonic vibration of a discretized linear system, the vectors of discrete forces and velocities are described by complex quantities in the frequency domain, resulting in the complex power [2]

$$P = \frac{1}{2}\boldsymbol{f}^H\boldsymbol{v} \tag{1}$$

H is the Hermitian transpose. While the imaginary part of the complex power is equal to the product of excitation frequency and the Lagrange energy $\bar{U} - \bar{K}$ [2]

$$\Im\left(P\right) = 2\omega(\bar{U} - \bar{K}) \tag{2}$$

especially the real part is of interest for the energetic analysis of vibroacoustic structures

$$\Re\left(P\right) = \bar{P}_{\mathrm{diss}}. \tag{3}$$

Following Equation 3 the real part of the complex power quantity is equal to the vibration cycle averaged dissipated power $\bar{P}_{\mathrm{diss}}$. Rewriting the latter equation results in

$$\bar{P}_{\mathrm{diss}} = \frac{1}{2}|\boldsymbol{f}||\boldsymbol{v}|\cos(\Delta\varphi_{\mathrm{fv}}). \tag{4}$$

This trigonometric form illustrates that besides the amplitudes of forces and velocities the relative phase between these $\Delta\varphi_{\mathrm{fv}}$ is included in the power calculation

$$\Delta\varphi_{\mathrm{fv}} = \arctan\frac{\Im\left(\boldsymbol{f}^H\boldsymbol{v}\right)}{\Re(\boldsymbol{f}^H\boldsymbol{v})}. \tag{5}$$

However, if the damping in the system becomes smaller, the relative phase $\Delta\varphi_{\mathrm{fv}}$ approaches $(2n-1)\cdot\pi/2$ for non-resonant frequencies, while $n \in \mathbb{Z}$. Following Equation 4 the cosinus-term is sensitive for even small errors in the phase for such values, thus the correct measurement of power becomes challenging. Each element of the measurement chain introduces a phase error. Especially impedance heads can exhibit an absolute phase error approaching $\varepsilon_{\Delta\varphi} = 5^\circ$ [1], the relative phase errors between force and acceleration channel are not documented in many cases.

Even so the measurement of power quantities is established in literature for some decades, there is no discussion available regarding phase errors for the limiting case of light damping, up to the authors knowledge. Therefore a method for the phase-correction in the frequency domain is investigated in the following by means of a lightly damped structure. In the latter power is measured at the inputs and outputs of single subcomponents.

Approaches to measure mean power at inputs and outputs of arbitrary parts are already presented for impedance heads [13], for more complex parts a six degree of freedom sensor was developed by [6]. This contrasts the many approaches in literature starting from the 1970's, in which structure-borne sound power quantities are determined not at inputs or outputs, but inside basic mechanical systems like trusses, beams or plates [12, 19, 5, 8, 3, 16, 4, 11, 17, 20, 18]. An overview is provided in [10]. These references are limited to analytical systems but not to complex geometric structures, as the displacement function, known from the analytical solution of the idealized mechanical system, is used to calculate the power from an acceleration sensor array.

The below example structure is vibrating in uniaxial vibration. The general methodology for phase-correct measurements and subsequently meaningful power values is therefore based on impedance heads. Corresponding test setups are presented in order to identify a correction factor for the phase deviation of the sensors. It will be shown how the power results can be improved in the frequency domain by this factor. Nevertheless the below discussion is more general and can be adapted for any sensor combination.

2 Phase-Correct Power Measurement

2.1 Concept of Phase Correction in the Frequency Domain

Each element of the measurement chain introduces a phase error into the experiment (compare for example [7]). This includes phase errors from the leakage in the time-to-frequency transformation, the influence of

cables, the DAQ (Data Aquisition) interface, or the sensors. Especially the impedance heads, as mentioned above can have a phase lag, which is significantly higher than the phase deviation which must be identified for lightly damped systems.

It will be shown in the following that if the phase errors of the impedance head only are considered, already physically meaningful power values can be obtained, although the phase errors of the DAQ-interface, the post processing et cetera are neglected. In order to compensate the phase error in the frequency domain a complex-valued and frequency dependent correction factor $\boldsymbol{C}_{\varphi}$ is determined. Therefore, the errors in the relative phase are identified for distinct channel pairs, though not the absolute phase error of single channels is determined. For the measurement of power the correction factor is included in the measured frequency response of the cross power spectrum at the two impedance heads

$$S_{\mathrm{fv}}^{\mathrm{c}} = \boldsymbol{f}(\boldsymbol{C}_{\varphi,\mathrm{IH}} \circ \boldsymbol{v})^{H}. \tag{6}$$

The $^{\mathrm{c}}$ indicates the correction for the phase error of the measurement chain. The mean power is directly obtained from the cross power spectrum

$$P^{\mathrm{c}} = \frac{1}{2} S_{\mathrm{fv}}^{\mathrm{c}} \tag{7}$$

as well as the relative phase

$$\Delta\varphi_{\mathrm{fv}}^{\mathrm{c}} = \arctan \frac{\Im(S_{\mathrm{fv}}^{\mathrm{c}})}{\Re\big(S_{\mathrm{fv}}^{\mathrm{c}}\big)} \tag{8}$$

2.2 Phase Errors in Impedance Heads

Prior to determining the phase error between the force and acceleration signal of the impedance heads, assumptions are made regarding the sources for the sensor's phase lag. In the following it will be shown that with these assumptions the power results can be improved significantly. Two classes of error sources are assumed for the impedance heads. One resulting from the mechanical interaction of the impedance head with the attached test structure, which is therefore test-object dependent, one resulting from test-object independent sources like electronic amplifiers inside the sensors.

In order to calculate the error resulting from the first class of test-object dependent errors, one needs information of the attached system, like the input impedance. Subsequently the error cannot be determined a priori. Additional phase shifts are introduced in the test setup, if the resonance of the MDOF-system of the impedance head is decreased to values near the frequency measurement range. However, assuming that the sensors are build sufficiently stiff, this error source is neglected for the benchmark structure.

The relative phase error, which is independent of the test structure, however, is determined and included in the correction factor. Therefore a top-mass setup is introduced (see Figure 1), known from calibration experiments for the amplitudes of impedance heads [15].

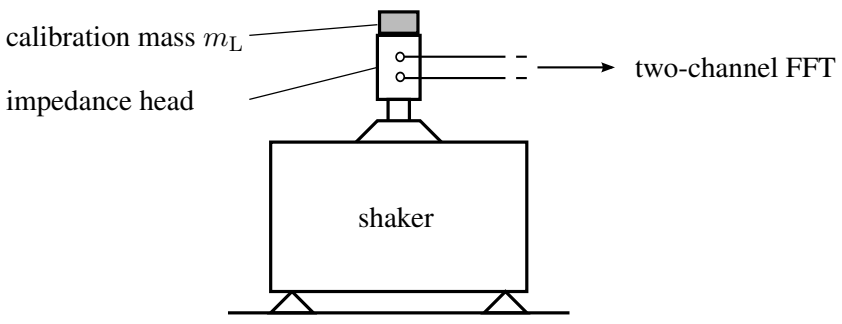


Figure 1: scheme of the top mass setup for the impedance head phase measurement

Following Figure 1 the impedance head is mounted on a vertically aligned shaker, on top of the impedance head a mass is screwed. The ideal mass has a purely imaginary impedance

$$\hat{Z} = i\,\omega\,m_{\mathrm{L}} \tag{9}$$

the relative phase between the acceleration and force channel therefore should be $\Delta\varphi_{\mathrm{IH}} = 0°$, according to the model assumptions. The resulting frequency dependent complex correction value of the impedance head C_{IH} is directly calculated from the measured phase difference

$$C_{\mathrm{IH}} = \frac{fa^*}{|fa^*|}. \tag{10}$$

The phase error of the DAQ-interface is assumed to be negligible.

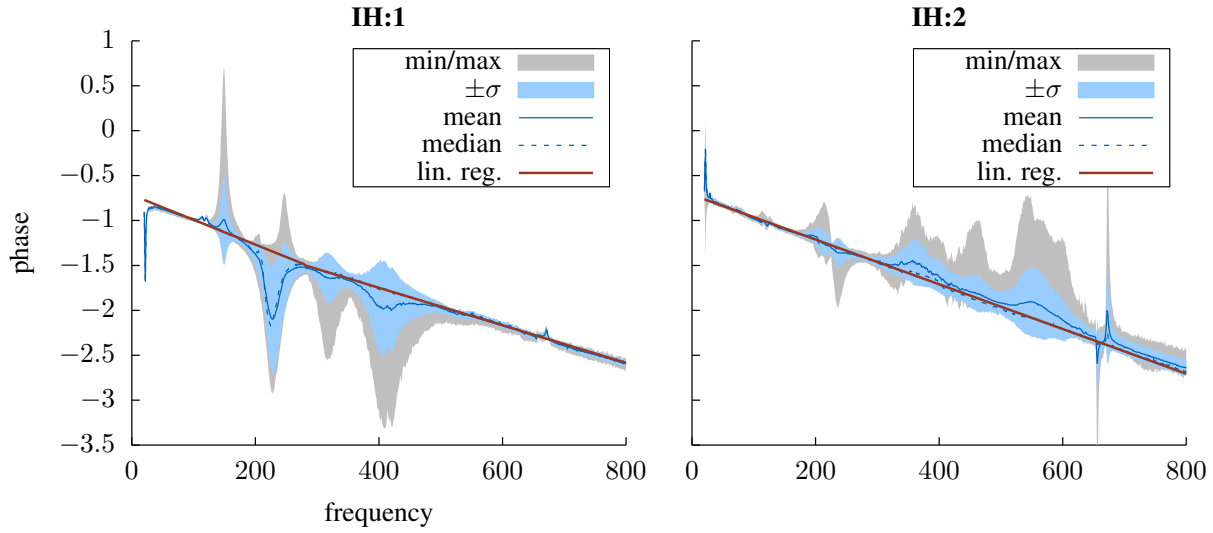


Figure 2: relative phase in degrees of the two impedance heads used for the power measurement obtained by the top-mass setup. Three different masses are used, four measurements are performed for each mass.

Naturally the mechanical MDOF-system of the impedance head is also influenced by the impedance of the mass in this setup. Therefore different top-masses are used in order to evaluate the variance of the phase results with respect to the mass. In the case of a small variance of the measured relative phase the latter is assumed to be independent of the attached mass, subsequently to be independent of the benchmark structure. The top-masses chosen for the experiment are rather high, otherwise the test setup is not capable to identify the phase lag also in the low frequency range. This results in three different masses from $m = 76.3g$ to $610g$.

A chirp excitation is chosen and twelfe measurements, four for each mass, are performed and evaluated. The results are shown in Figure 2. Following the latter, the median value of the measured phases is an almost linear function of frequency. A linear regression is therefore performed for the correction value. The resulting phase correction for the impedance heads is rather large and approaches $\Delta\varphi_{\mathrm{IH}} = 3°$ for a frequency of $f = 800\mathrm{Hz}$. The standard deviation is approximately $0.1°$ and is small compared to the median value, allowing for the assumption of a mass independent correction value as discussed above. Subsequently this correction factor is also assumed to be independent of the following example case.

Nevertheless there are frequency ranges, in which the mean in particular deviate from the linear phase function and the standard deviation σ is large. This, however, is not opposed to the above conclusions, as it can be explained by resonances of the test setup resulting from imperfections. These imperfections distort the desired phase results for a theoretically perfect longitudinal excitation. The resonances are shifted in frequency for the setups with different masses m_T, resulting in rather small effect of the resonances on the median value but a rather large one on the mean and standard deviation.

3 Lightly Damped Example

3.1 Experimental and Numerical Setup

In order to determine power quantities and relative phases between force and acceleration in a longitudinal direction only while limiting the vibration in the other directions to a minimum, a truss is suspended in the center of a beam. The latter is clamped at its ends. Realizing the clamping condition two identical pyramidal supports are manufactured. This provides a clamp condition for the beam and a clearance under the beam of $h = 720\mathrm{mm}$, so that the truss, sensors and a LMS Qsources Integral Shaker for the excitation can be suspended (see Figure 3).

The test rig should ensure the measurement of the relative phases and power quantities up to a frequency up of $f = 800\mathrm{Hz}$, the pyramids must have a first resonance above that frequency. Therefore the pyramids are manufactured from $32\mathrm{mm}$ thick aluminum plates which are screwed together. A plate is added in the horizontal center plane in order to stiffen the structure in addition.

At both sides of the truss a impedance head IH:1, respectively IH:2 is placed for the concurrent measurement of forces and accelerations from which the power can be calculated in the postprocessing. As there is damping in the system, there is mean energy flow from the source, which is the excitation at the lower end of the truss into the truss, from the latter in the beam, resulting in a mean power larger than zero in the positive direction of y. Correspondingly the phase shift between velocities and forces $\Delta\varphi_{\mathrm{fv}}$ is deviating - although just slightly - from $\pm\pi/2$.

All parts are manufactured from aluminium alloy EN AW-6060. For the evaluated frequency range $f = 1..800\mathrm{Hz}$ the structure should have a low modal density in order to analyze structure-borne power at non-resonant frequencies. Nevertheless there should be three resonances with symmetric mode shapes in the $x-y$ plane, for which the two impedance heads are excited in the longitudinal axis alone. This can be achieved by the geometrical parameters of the truss and beam according to Table 1 and Figure 3. In the following all values are given in millimeters, Newton, seconds and tons. In addition a steel mass is mounted between the truss and the shaker, resulting in the resonances analyzed in the next section.

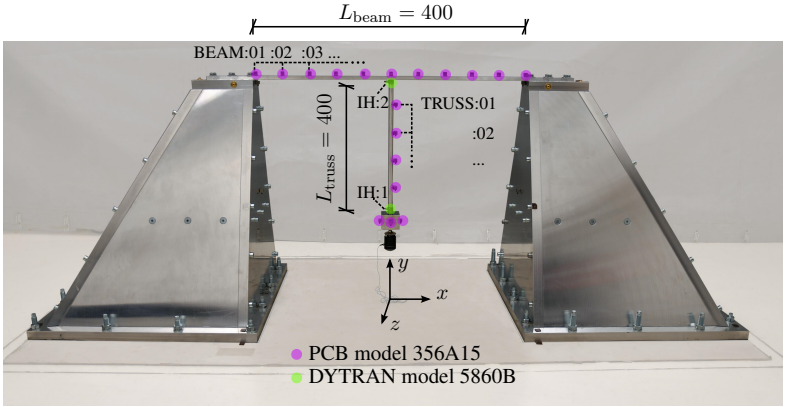


Figure 3: hardware realization of the benchmark structure, including the sensor instrumentation for the uniaxial, longitudinal phase and power measurement.

part	profile		value
truss	circular	D	16
beam	rectangular	b	60
		h	10

Table 1: values for the cross sections of the beam and the truss.

Besides the impedance heads, triaxial accelerometers PCB model 356A15 are installed (see Figure 3). This enables the identification of mode shapes, which can be correlated to the simulation as well as the evaluation of the amount of out of plane and asymmetrical deflection shapes resulting from geometrical imperfections. The latter results in an energy flow not only in the longitudinal direction of the truss but in additional degrees of freedom.

For the measurement setup a three dimensional linear FE-model incorporating tetrahedron, brick and shell elements, all using linear shape functions, is considered. The material parameters are chosen according to Table 2. The connection technique is modeled by tie contacts. The impedance heads are considered through spring elements with a translational and rotational stiffness of $k_{\mathrm{T}} = 1.1 \cdot 10^6$ respectively $k_{\mathrm{R}} = 4.5 \cdot 10^6$, connecting reference points of the corresponding parts. The mass of the impedance heads is considered via point masses of $m = 1.2 \cdot 10^{-5}$.

Firstly the modeling of the impedance heads by means of connector elements allows for a straightforward calculation of the internal forces in the postprocessing, which are needed for the power calculation following Equation 1. Some more general discussion of the calculation of power quantities as a postprocessing for FE-displacement solutions can be found for example in [9] . Secondly the power quantity can be separated for the different element degrees of freedom. This is beneficial for the comparison with the experimental results, as the frequency responses are measured in the longitudinal direction only at the impedance heads.

material	E-modulus	Poisson number	density	structural damping
aluminum	70500	0.3	$2.65\,10^{-9}$	0.025
steel	210000	0.3	$7.86\,10^{-9}$	0.025

Table 2: material properties for the FE-model

The FE-model is correlated via a modal analysis to the hardware realization. Therefore for both the experimental and numerical setup the resonant frequencies, mode shapes and modal dampings are determined and compared in Table 3. There is a good correlation between the resonant frequencies of the FE-model and the experimental setup, the error is below seven percent for all resonances. Evaluating the diagonal MAC-values between the experimental mode shapes Ψ_j and the numerical ones Φ_i

$$\mathrm{MAC} = \frac{|\boldsymbol{\Phi}_i^H \cdot \boldsymbol{\Psi}_j|^2}{\boldsymbol{\Phi}_i^H \boldsymbol{\Phi}_i \boldsymbol{\Psi}_j^H \boldsymbol{\Psi}_j} \tag{11}$$

there is also a good correlation.

Nr.	f_{eig}			mode shapes	ξ		
	EMA (Hz)	FEM (Hz)	error (%)	MAC	EMA (%)	FEM (%)	remarks
1		8.5				0.125	
2		9.6				0.125	
3	33.6	35.5	-5.4	0.99	0.18	0.125	1st symmetric mode shape
4		111.7				0.125	
5	136.2	141.8	-3.9	0.98	0.54	0.125	
6	143.2	147.7	-3.0	0.98	0.20	0.125	
7	201.8	205.3	-1.7	0.93	0.04	0.125	
8	281.0	284.6	-1.3	0.99	0.15	0.125	2nd symmetric mode shape
9	319.0	339.1	-5.9	0.96	1.1	0.125	
10	378.0	405.4	-6.8	0.96	0.93	0.125	
11	393.0	413.2	-4.9	0.92	0.35	0.125	
12	606.6	607.3	-0.1	0.65	0.1	0.125	
13	669.3	688.4	-2.7	0.90	0.42	0.125	
14	730.0	741.7	-1.6	0.95	0.1	0.125	3rd symmetric mode shape

Table 3: natural frequencies and modal dampings for the benchmark structure.

Analyzing the damping modeling of the FE-model, Table 3 shows that the assumption of a frequency-independent structural damping value of $\eta = 0.025$ coincides with the modal damping values of the ex-

perimental setup for the mode shapes 4, 8 and 14 which are symmetric in the $x - y$ plane and therefore are mainly excited in the later operational experiments (Figure 4). For the non symmetric mode shapes the damping values are underestimated by the FE-model, however, this mode shapes should contribute only little to the overall vibration response. Summarizing the above results, the FE-model can be appropriately correlated with the hardware realization, providing a well examined basis for the following discussion of the measurement of structure-borne sound power.

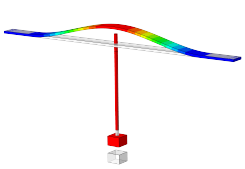
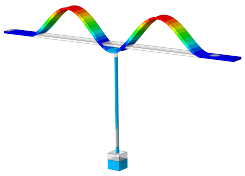
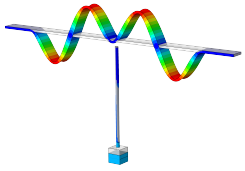
mode shape 4	mode shape 8	mode shape 14
		

Table 4: first resonant frequencies in longitudinal direction of the beam-truss system.

4 Results

Using the above measurement methodology for phase-correct power measurement, 12 measurement runs are performed on the validated example structure. In order to minimize leakage, a pseudo-random excitation profile is chosen for the vertically suspended shaker. Again, for all measurement quantities the mean value is calculated, the standard deviation is evaluated and the experimental results are compared to the numerical results for the FE-representation.

Analyzing exemplary the phase at impedance head IH:1 at first, one recognizes that as long as no phase correction is applied to the measurement data, the relative phases differ from the FE-simulation. The deviation gets larger the more the frequency is increased, partly switching the quadrant in the imaginary plane, finally resulting in a maximum difference of three degrees (see Figure 4). Applying the phase correction Equation 8, the deviation from the FE-results is decreased significantly, resulting in a maximum difference of $0.2°$. This error is equal to $2 \cdot \sigma$ from the impedance head phase phase measurement in Section 2.2.

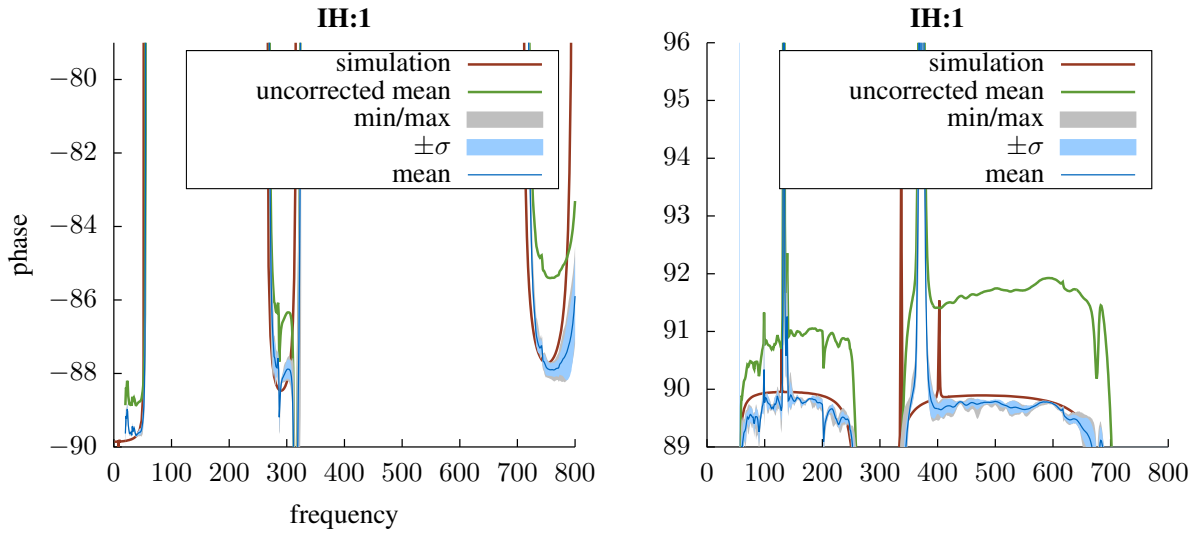


Figure 4: relative phases between force and velocity $\Delta\varphi_{\mathrm{f}}$ at IH:1, evaluated statistically for the experiment and compared to the simulation.

As a consequence, calculating power quantities from measurement without incorporating the phase correction, the mean power only has physically meaningful value around the resonances for the lightly damped example. Out of resonance, however, the values approach negative values, which is in contrast to the results from the FE-calculations.

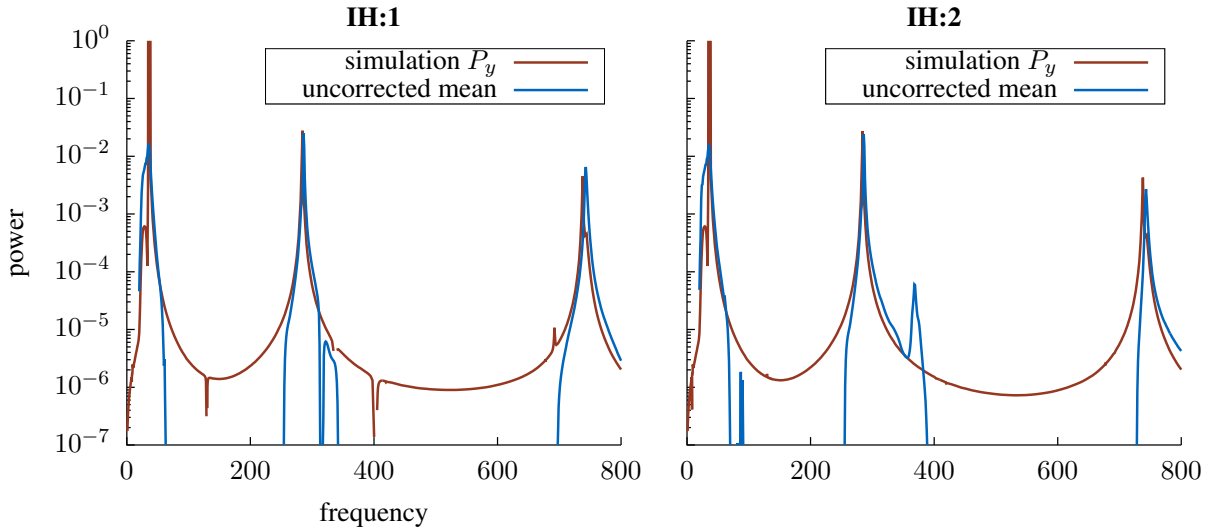


Figure 5: power results at the impedance heads from simulation and measurement, the latter without phase correction for the measurement chain. Left: IH1; right: IH2

Applying the phase correction the mean power becomes mainly positive as predicted by the FE-model. In addition the amplitudes coincide well, except for the lowest resonant frequency as the shaker is not capable to bring in the energy as requested. Excluding this frequency range, the experimental and numerical results for the mean power coincide with a maximal deviation of $5 \cdot 10^{-7}$.

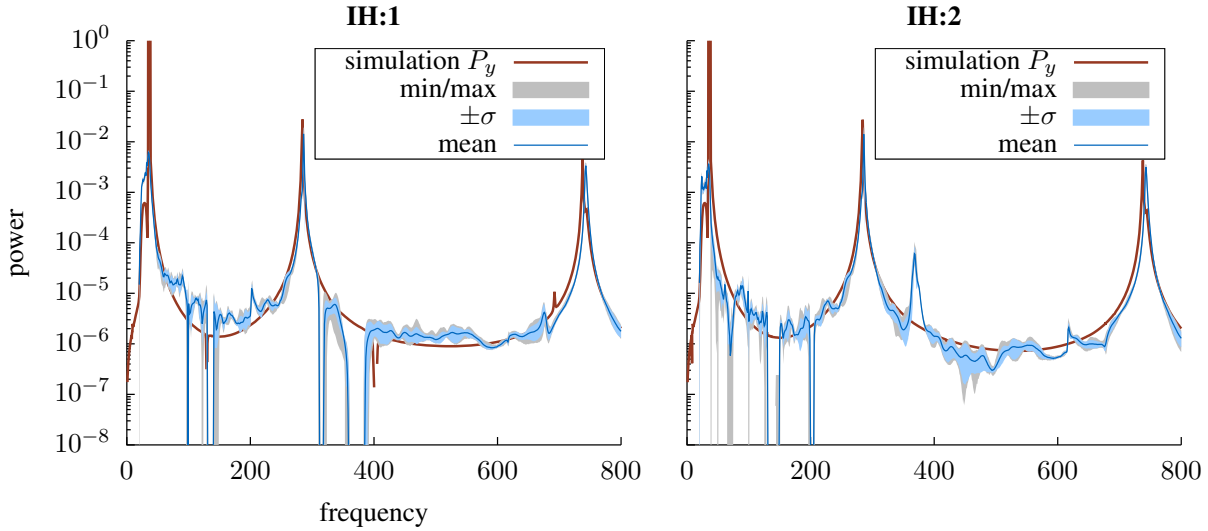


Figure 6: power results at the impedance heads from simulation and measurement, the latter with phase correction for the measurement chain. Left: IH1; right: IH2

However there are still frequency ranges, in which the phase-corrected mean power has negative values, indicating energy flow towards the shaker. Nevertheless this is not necessarily related to measurement errors. As [13] already discussed theoretically, impedance heads capture the energy flow for the longitudinal degree of freedom, but neglect the contributions of the remaining translational and rotational degrees of freedom. If the power of the non-measured degrees of freedom is larger than the power in the longitudinal direction,

the summed up overall power would be positive although the measured longitudinal power is negative. Consequently there are some frequency ranges in which also the FE-model has negative values for the mean power in longitudinal direction, however the power, summed up over all degrees of freedom, is positive (compare Figure 7 for impedance head IH:1). Such frequency ranges are for example around $f = 340\text{Hz}$ and $f = 404\text{Hz}$. These frequencies can be directly linked to resonances of the numerical model with mode shapes having mainly rotations at the locations of the impedance heads.

By means of the MAC of the benchmark structure, one can link the above resonances to the measured ones at $f = 319\text{Hz}$ and $f = 378\text{Hz}$. The validated benchmark structure therefore allows for an unambiguous explanation of these negative power values, which is the first time to the author's knowledge. They do not result from the phase error introduced by the measurement chain but are a physical property of the mechanical system due to the fact that impedance heads just capture the energy in one degree of freedom.

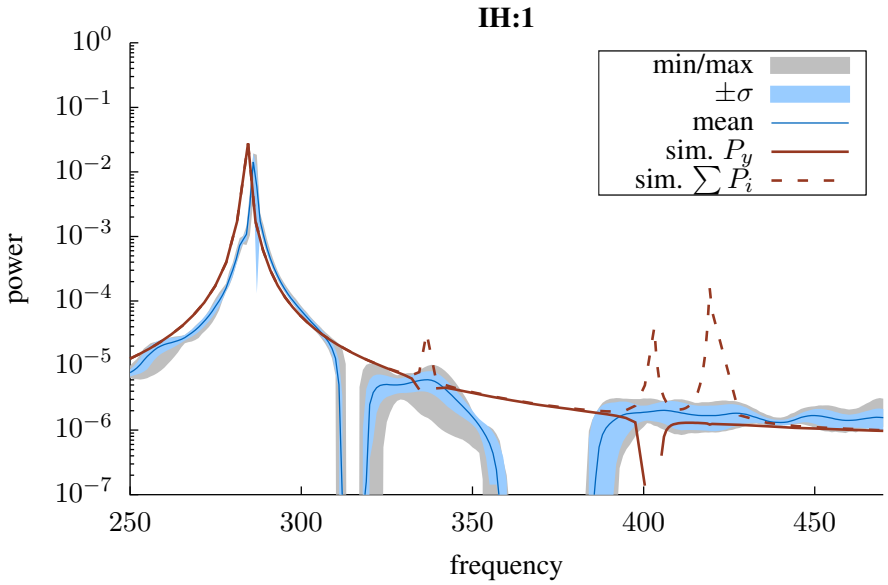


Figure 7: power results at IH:1 for the frequency range of resonances which load the impedance head with a moment. For the simulation once the power is evaluated solely for the longitudinal degree of freedom (sim. P_y), once for the sum of all degrees of freedom of the impedance head element (sim. $\sum P_y$).

5 Conclusion

Determining structure-borne sound power quantities is a challenging task for non-resonant frequencies of lightly damped structures. An experimental technique is therefore discussed for the determination of structure-borne sound power including a phase-correction in the frequency domain. By means of a lightly damped structure it is shown that measuring power without a compensation for the relative phase errors of the measurement chain leads to physically not meaningful results. Therefore the test-structure independent phase error is analyzed for the impedance head, which introduces the largest relative phase error in the measurement chain.

An example structure is introduced with a correlated hardware realization and FE-representation. The phase correction is applied to the corresponding cross power spectra of the impedance head signals, improving the power results significantly for the example structure. The final difference in the relative phases between experiment and simulation is smaller $\varepsilon_\varphi < 0.2°$.

In addition, the fact that besides the experimental setup also a validated FE-model is available for the example structure provides a basis for the detailed investigation of the results for the measured power quantities obtained by impedance heads. The negative power quantities observed for specific frequency ranges at the impedance heads can be related to out-of-plane modes, therefore the negative values can be explained by

the fact that power is measured in the longitudinal direction of the impedance heads only but are no artifact resulting from phase errors in the measurement chain.

References

[1] PCB Model 288d01 data sheet.

[2] Alfredsson, K. S. Use of the energy flow concept in vibration design. *AIAA Journal*, 34(6):1250–1255, June 1996.

[3] J. R. F. Arruda, J. P. Campos, and J. I. Piva. Experimental determination of flexural power flow in beams using a modified prony method. *Journal of Sound and Vibration*, 197(3):309–328, 1996.

[4] A. A. Freschi, A. K. Pereira, K. M. Ahmida, J. Frejlich, and J. R. F. Arruda. Analyzing the total structural intensity in beams using a homodyne laser doppler vibrometer. *Shock and Vibration*, 7(5):299–308, 2000.

[5] C. R. Halkyard and B. R. Mace. Structural intensity in beams - waves, transducer systems and the conditioning problem. *Journal of Sound and Vibration*, 185(2):279–298, 1995.

[6] C. Howard and C. Hansen. Six-axis vibrational power transducer for active vibration isolation. *Proceedings of ACOUSTICS 2005*, pages 9–11, 2005.

[7] ISO 16063-1:1998(E) Methods for the calibration of vibration and shock transducers - Part 1: Basic concepts. Standard, International Organization for Standardization, Geneva, CH, Oct. 1998.

[8] Linjama and Lahti. Estimation of bending wave intensity in beams using the frequency response technique. *Jourrnal of Sound and Vibration*, 153:21–36, 1992.

[9] B. Mace and P. Shorter. Energy flow models from finite element analysis. *Journal of Sound and Vibration*, 233(3):369–389, 2000.

[10] N. K. Mandal. Vibration power flow: A critical review. *The Shock and Vibration Digest*, 37(1):3–11, 2005.

[11] Nirmal K. Mandal. One transducer method for quantifying vibration power flow in orthotropic plates for both general and far-field conditions. *Trends in Applied Sciences Research*, pages 1–8, 2006.

[12] G. Pavić. Measurement of structure borne wave intensity, part I: Formulation of the methods. *Journal of Sound and Vibration*, 49(2):221–230, 1976.

[13] B. Qiao, T. Zhao, X. Chen, and J. Liu. The assessment of active vibration isolation performance of rotating machinery using power flow and vibrational energy: Experimental investigation. *Proceedings of the Institution of Mechanical Engineers, Part C: Journal of Mechanical Engineering Science*, 230(2):159–173, 2016.

[14] T. D. Rossing, editor. *Springer handbook of acoustics*. Springer, Dordrecht, 2nd ed edition, 2014.

[15] D. A. Scott, L. P. Dickinson, and T. J. Bell. Traceable calibration of impedance heads and artificial mastoids. *Measurement Science and Technology*, 26(12):125013, 2015.

[16] R. P. Szwerc, C. B. Burroughs, S. A. Hambric, and T. E. McDevitt. Power flow in coupled bending and longitudinal waves in beams. *The Journal of the Acoustical Society of America*, 107(6):3186–3195, 2000.

[17] R. P. Szwerc and S. A. Hambric. The calculation and measurement of flexural and longitudinal structural power flow on a tee-shaped beam. Technical report, DTIC Document, 1996.

[18] Troshin. Structural energy flow in a resilently coupled t-shaped beam by wave intensity. 1990.

[19] J. W. Verheij. Cross spectral density methods for measuring structure borne power flow on beams and pipes. *Journal of Sound and Vibration*, 70(1):133–138, 1980.

[20] E. G. Williams, H. D. Dardy, and R. G. Fink. A technique for measurement of structure-borne intensity in plates. *The Journal of the Acoustical Society of America*, 78(6):2061–2068, 1985.

Multiple-order excitation and response of centrifugal pendulum vibration absorbers

E. R. Gomez [1,2]**, I. Lopez Arteaga** [2,3]**, L. Kari** [2]
[1] Scania CV AB, Transmission Development, SE 151 48, Södertälje, Sweden
e-mail: **gomez@kth.se**

[2] KTH Royal Institute of Technology,
The Marcus Wallenberg Laboratory for Sound and Vibration Research (MWL), SE 100 44, Stockholm, Sweden.

[3] Eindhoven University of Technology,
Department of Mechanical Engineering, Section Dynamics and Control, P.O Box 513, 5600 MB, Eindhoven, The Netherlands.

Abstract
The multiple-order response of a rotor equipped with a centrifugal pendulum vibration absorber (CPVA) is investigated in this study. CPVAs have been used in the abatement of torsional vibrations since the 1930s and have been extensively researched but seldom with a focus on the full multiple-harmonic response. Although the firing order in reciprocating engines dominates in amplitude, the higher-order harmonics have impact on driveline-related noise issues. This investigation is conducted in order to understand if an higher-order amplification can stem from the design of the CPVA or if this phenomenon is due an interaction between other powertrain components. Therefore, an isolated rotor-CPVA system is studied. The investigated rotor is subjected to an oscillating torque consisting of single- and multiple-order harmonics. The equations of motion are derived by Kane's method and the multiple-harmonic response of the system is analyzed. The linear steady-state response is compared with numerical time integration of the equations of motion.

1 Introduction

Torsional dampers integrated in the clutch disc are conventionally used to decouple the driveline from torsional vibrations of the internal combustion engine (ICE) of heavy trucks. This method of decoupling will not be sufficient with future ICEs. Environmental legislation on CO_2 drive the development of the ICE and the traditional driveline of heavy trucks in the same manner as for passenger cars [1]. To fulfill CO_2 regulations, manufacturers are lowering operating rotational speeds of the ICE by appropriate gearing of the driveline, increasing the combustion pressure and downsizing the engines, without sacrificing the power output. Unfortunately, these measures to fulfill CO_2 regulations increase driveline torsional vibration and thus increase the emitted noise such as gear rattle from the transmission. The higher levels of torsional vibration also affect the fatigue life of the powertrain components negatively. These issues must be addressed to fulfill future noise legislation, vehicle comfort requirements and fatigue life expectations of the powertrain.

The centrifugal pendulum vibration absorber (CPVA) is a passive device designed to absorb torsional vibration in oscillating rotating systems. Appropriate tuning of the CPVA counteracts the oscillatory torsional motion of the rotor caused by the engine combustion and crank motion. The CPVA commonly consists of several pendulums attached to a rotor, for example, attached to an engine flywheel or located on other rotating parts of the powertrain depending on the need to abate certain torsional vibration modes. The CPVA is an order-tuned absorber which allows absorption of the engine torsional vibration order over all rotational

speeds. This is due to the pendulum's centrifugal force dependency where the pendulum's eigenfrequency is proportional to the rotational speed. The tuning order is commonly adjusted to absorb the main firing order of the combustion engine. For a four-stroke engine this order is half the number of cylinders since a full combustion cycle is completed every two revolutions of the crankshaft. A schematic of a rotor-CPVA is shown in Figure 1. The rotor spins about point O and the pendulum rotates about the pivot at point Q. This type of absorber is a compound pendulum absorber where the center of mass of the pendulum follows a circular path. This fundamental absorber type is the base model of this investigation.

Single rotor-CPVA models have been extensively researched since the 1930s. An early overview of different pendulum absorber types and their main linear characteristics can be found in Ref. [2], containing references to the first patents on rotational pendulum absorbers. Non-linear studies show that the circular path pendulum absorber possesses bifurcation jumps that may, contrary to what is desired, amplify the vibrations [3]. A type of epicycloidal pendulum path, the tautochronic epicycloidal path, has shown to reduce the risk of the bifurcation jump [6]. An overtuning with cycloidal pendulum paths may also help the stability of the pendulums' unison response at a small cost of decreasing its efficiency to absorb the vibration [4, 5]. The gained interest from the automotive industry in this century has led to more research on the tautochronic and general path pendulum absorber with a focus on the non-linear response and stability [4, 5]. Further, the theory has been extended to other CPVA types other than point mass models [7, 8].

A commonly used perturbation method for analyzing the non-linear behavior of CPVAs has been the method of averaging [9]. The method of averaging does not capture the multiple-harmonic response since it assumes a single-harmonic response [10]. It is of great interest to capture the multiple harmonics since higher engine orders may cause gear rattle in the transmission. Also, heavy vehicle combustion engines always produce significant harmonics which may be amplified by the CPVA configuration. This is observed in numerical simulations and measurements in Ref. [11] and is further investigated in this study.

The equations of motion of rotor-CPVA systems have commonly been derived using Lagrange's method. However, the Hamiltonian formulation is also used in Refs. [7, 8]. Here, the equations of motion are derived by means of Kane's method, also known as the method of generalized speeds [12, 13]. The advantage with Kane's method is that the governing equations fall out directly as compact first-order ODEs suitable for numerical integration. Also, the use of generalized speeds to define the kinematics appears more natural for rotating systems rather than generalized coordinates. The method of generalized speeds is also suitable for implementation in a Computer Algebra System (CAS), assisting the bookkeeping of the equations, minimizing the risk for manual error and maintaining repeatability through coding which is highly desirable in an industrialized simulation process [14, 15, 16].

In this investigation the equations of motion of a rotor-CPVA depicted in Figure 1 is derived by Kane's method. The linear characteristics of the system are investigated and the full non-linear equations are analyzed by time integration showing the multiple-harmonic response while excited by single- and multiple-harmonic excitation. The analytically derived model is validated against simulations performed in the multibody software Adams by MSC Software. The purpose of this investigation is to gain understanding of CPVAs in the context of a heavy vehicle powertrain to further enhance the virtual product development process.

2 Mathematical Model

In this section, Kane's equations and the equations of motion of the rotor-CPVA system in Figure 1 are presented. The full derivation and the procedure of Kane's method may be found in Appendix A. The full non-linear equations are linearized about an operating rotational speed and the main linear characteristics of the system are investigated. Only one pendulum attached to the rotor is considered but the procedure can easily be extended to several pendulums. The single pendulum is equivalent to several pendulums if one assumes synchronous pendulum response while maintaining the total pendulum mass [6]. Also, gravity is neglected.

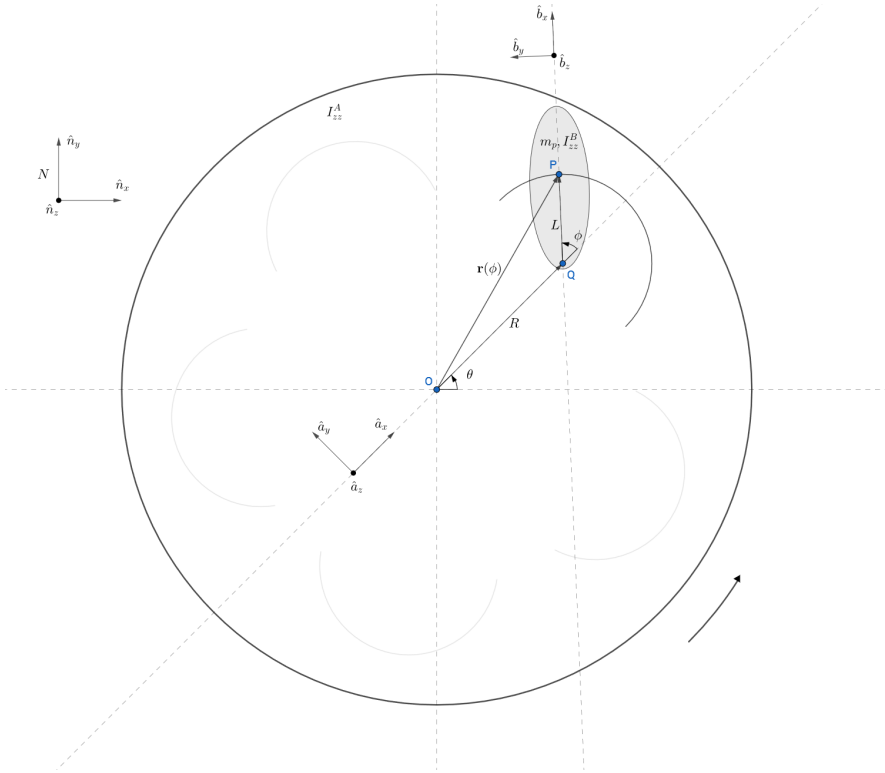


Figure 1: Rotor-CPVA model.

2.1 Method of generalized speeds (Kane's Method)

Several methods are commonly used to derive the equations of motion of mechanical multibody systems. Kane's method, also called the method of generalized speeds, is one of the most recent methods published in 1965 by Kane and Wang [17]. The relationship between Newton's, Kane's and Lagrange's equations can be shown by projecting Newton's equations onto suitable tangent coordinate vectors [18]. In this section, bold symbols represent vectors and an over-dot represents the time derivative of the vector relative to the inertial reference frame N. Kane's equation states the balance between inertial forces f_i^* and the applied forces f_i as

$$f_i = f_i^*, \tag{1}$$

where the projected inertial forces are expressed as a sum over all nr rigid bodies as

$$f_i^* = \sum_{j=1}^{nr} \left[\dot{\mathbf{p}}^{B_j} \cdot \mathbf{v}_i^{B_j} + \dot{\mathbf{L}}^{B_j} \cdot \boldsymbol{\omega}_i^{B_j} \right], \tag{2}$$

where

$$\dot{\mathbf{p}}^{B_j} = m_j \, \mathbf{a}^{B_j}, \tag{3}$$

is the time derivative of the linear momentum of the center of mass of body B_j,

$$\dot{\mathbf{L}}^{B_j} = \mathbf{I}^{B_j} \cdot \dot{\boldsymbol{\omega}}^{B_j} + \boldsymbol{\omega}^{B_j} \times \mathbf{I}^{B_j} \cdot \boldsymbol{\omega}^{B_j} \tag{4}$$

is the time derivative of the angular momentum about the center of mass of body B_j and $\mathbf{I}^{B_j}$ is the inertia

tensor about the center of mass of body B_j. Further, the partial velocities are

$$\begin{aligned} \mathbf{v}_i^{B_j} &= \frac{\partial \mathbf{v}^{B_j}}{\partial u_i}, \\ \boldsymbol{\omega}_i^{B_j} &= \frac{\partial \boldsymbol{\omega}^{B_j}}{\partial u_i}, \end{aligned} \tag{5}$$

where u_i are the generalized velocities as an affine function of the time derivative of the generalized coordinates, $\dot{q}_i$.

The projected generalized forces are also expressed as a sum over all nr rigid bodies as

$$f_i = \sum_{j=1}^{nr} \left[\mathbf{F}^{B_j} \cdot \mathbf{v}_i^{B_j} + \mathbf{T}^{B_j} \cdot \boldsymbol{\omega}_i^{B_j} \right], \tag{6}$$

where $\mathbf{F}^{B_j}$ is the force and $\mathbf{T}^{B_j}$ is the torque acting on the center of mass of body B_j.

The overall procedure is in three main steps. First, choose an appropriate set of generalized speeds, u_i, describing the kinematics. Second, calculate the linear and angular momentum of the bodies in terms of the generalized speeds to further project them onto the partial velocities. Third, after projecting the applied forces onto to the partial velocities, evaluate the summation over all bodies of the system. This is performed in detail in Appendix A for the compound pendulum system analyzed in this investigation.

2.2 The governing equations

From Appendix A, the equations of motion of the rotor-CPVA system depicted Figure 1 are

$$\begin{aligned} \left(I_{zz}^A + m_p R^2\right) \dot{u}_1 + m_p RL\dot{u}_2 \cos(\phi) - m_p RL u_2^2 \sin(\phi) &= c_p(u_2 - u_1) + T_o - c_r u_1, \\ \left(I_{zz}^B + m_p L^2\right) \dot{u}_2 + m_p RL\dot{u}_1 \cos(\phi) + m_p RL u_1^2 \sin(\phi) &= -c_p(u_2 - u_1), \end{aligned} \tag{7}$$

where the viscous loss coefficient of the rotor is c_r and the viscous loss coefficient about the pivot point of the pendulum is c_p. The inertia about the center of mass of the rotor is I_{zz}^A, I_{zz}^B is the inertia about the center of mass of the pendulum that has a mass of m_p. R is the distance from the rotor's center to the pendulum pivot point Q and L is the distance from the pivot point to the center of mass of the pendulum body. Further, the generalized velocities are

$$u_1 = \dot{\theta}, \qquad u_2 = \left(\dot{\phi} + \dot{\theta}\right). \tag{8}$$

The complete system is thus fully described as a compact first-order differential equation system. The applied rotor torque, T_o, for different load cases is described in the following sections.

2.3 Linearization about an rotational operating point

In Kane's method it is possible to linearize the system before forming the equation of motions [13]. This is not unique for Kane's method. For example, the linearized equations of motion may be formed from the Lagrangian of the system by expanding the expressions to second order and then applying Lagrange's equation [18]. However, since the full nonlinear equations are already formed, the linearization about a constant rotational velocity with small pendulum motion is performed directly on the equations of motion (7).

We assume that the rotor has a steady rotational velocity Ω together with a perturbation $\dot{\theta}^*$. The first perturbed generalized velocity may then be expressed as

$$u_1^* = \Omega + \dot{\theta}^* \tag{9}$$

and the time derivative becomes

$$\dot{u}_1^* = \ddot{\theta}^*. \tag{10}$$

If we also assume a small pendulum motion in ϕ we can write the second generalized velocity as

$$u_2^* = u_1^* + \dot{\phi}^* = \left(\Omega + \dot{\theta}^*\right) + \dot{\phi}^* \tag{11}$$

and the time derivative becomes

$$\dot{u}_2^* = \ddot{\theta}^* + \ddot{\phi}^*. \tag{12}$$

Inserting the new generalized velocities into (7) yields the following linearized equations of motion about a rotational velocity Ω as

$$\begin{aligned} \left(I_{zz}^A + m_p R^2\right)\dot{u}_1^* + m_p RL\dot{u}_2^* - m_p RL\Omega^2\phi^* &= c_p(u_2^* - u_1^*) + T_o - c_r u_1^*, \\ \left(I_{zz}^B + m_p L^2\right)\dot{u}_2^* + m_p RL\dot{u}_1^* + m_p RL\Omega^2\phi^* &= -c_p(u_2^* - u_1^*). \end{aligned} \tag{13}$$

If we further assume that the rotor spins at constant rotational velocity without any oscillatory motion, the latter equation in (13), which is the equation of the pendulum, may be written in canonical form as

$$\ddot{\phi}^* + \tilde{c}_p\dot{\phi}^* + n_t^2\Omega^2\phi^* = 0, \tag{14}$$

where

$$n_t^2 = \frac{m_p RL}{(I_{zz}^B + m_p L^2)}, \tag{15}$$

is the linear tuning order of the pendulum absorber and

$$\tilde{c}_p = \frac{c_p}{(I_{zz}^B + m_p L^2)}. \tag{16}$$

Solving the eigenvalue problem of the characteristic equation of (13), without damping and applied torque, yields the rotor eigen-order n_r as a function of the linear tuning order n_t :

$$n_r^2 = \frac{n_t^2\left(\tilde{I} + 2n_t^2 + 1\right)}{\tilde{I} - n_t^4}, \tag{17}$$

where

$$\tilde{I} = \frac{\left(I_{zz}^A + m_p R^2\right)}{(I_{zz}^B + m_p L^2)}. \tag{18}$$

If the pendulum is assumed to be a point mass guided on a circular path we can see that the pendulum linear tuning order in Equation (15) is purely based on the geometrical parameters R and L since the inertia term vanishes. This is not the case when the pendulum body has significant inertia.

3 Solving the equations of motion

3.1 Linear frequency domain

The linearized equations in (13) may be put into matrix form

$$\mathbf{M}\dot{\mathbf{x}} + \mathbf{A}\mathbf{x} = \mathbf{T}, \tag{19}$$

where $\mathbf{M}$ is the mass matrix, $\mathbf{A}$ is the combined damping and stiffness matrix, $\mathbf{x}$ is a column vector of the system states $[\theta, \phi, u_1, u_2]^T$ and $\mathbf{T}$ is the torque column vector. The system may be solved by the anzats solution

$$\mathbf{x} = \hat{\mathbf{x}} e^{i\Omega n t}, \tag{20}$$

and the exciting torque as

$$\mathbf{T} = \hat{\mathbf{a}} e^{i\Omega n t}, \tag{21}$$

were $\hat{\mathbf{x}}$ and $\hat{\mathbf{a}}$ are complexed valued amplitude column vectors. Omitting the time dependency, the resulting linear response becomes

$$\hat{\mathbf{x}} = \left(i\Omega n \mathbf{M} + \mathbf{A}\right)^{-1} \hat{\mathbf{a}}. \tag{22}$$

3.2 Time-domain integration

Numerical time integration of the full non-linear equations of motion in (7) were performed by means of the SciPy odeint function using the default lsoda solver. The solver is an automatic method, switching between an implicit Adams method and based on backward differentiation formulas [19]. In order to validate the analytical model an equivalent model was built in the multi-body software Adams from MSC Software. The model is described in Appendix B. The GSTIFF SI2 time integrator in Adams was used as the solver method. The solver settings in both cases where refined until results converged to final values.

4 Load cases

4.1 Single-order excitation sweep

For the first study, the full non-linear equations where excited by a mean torque T_m and a single-order oscillating torque

$$T_o = T_m + T_n \sin(n\Omega t), \tag{23}$$

while sweeping the order n between 2.9 and 3.3 upward and downward for different oscillating amplitudes T_n at a mean rotational rotor speed of 1000 RPM. The mean torque, with a magnitude of the viscous loss torque of the rotor, was chosen to maintain a constant mean rotational velocity. The oscillating part of the excitation was initially ramped up with a polynomial step function with a duration of 2 seconds to minimize initial transients. The total length of the order sweep was 240 seconds to allow the amplitude to grow to full response.

The short Fourier transform of the time signals was then calculated using a Hanning window and the main- and second-order traces were extracted by means of the 5-frequency-bin summation method [20].

4.2 Multiple-order excitation

In the second investigation, the main- and second-order harmonic torques were extracted for a typical 6-cylinder heavy truck engine. This oscillating torque together with the mean torque was applied to the rotor at steady discrete mean rotational velocities in a typical operating range of a heavy truck engine. The torque is described as

$$T_o = T_m + T_n \sin(n\Omega t + \alpha_n) + T_{2n} \sin(2n\Omega t + \alpha_{2n}). \tag{24}$$

The torque amplitudes are shown in Table 1 for the different mean rotational velocities. The phase values are $\alpha_n = 0$ and $\alpha_{2n} = -0.32$ [rad]. For simplicity, the phases are held constant for every rotational velocity. The order harmonics were then extracted from the FFT of the time signals in the same manner as for the order sweep described above.

RPM	600	800	1000	1200	1400	1600	1800
T_n	670	945	1600	1600	1600	1600	1500
T_{2n}	430	570	900	900	838	627	406

Table 1: Oscillatory torque amplitudes for different mean rotor rotational velocities.

5 Results and Discussion

The numerical parameter values of the rotor-CPVA system used in this study are presented in Table 2. Figure 2 shows the linear steady-state angular acceleration response of the rotor normalized with the acceleration response of a rotor with a locked pendulum for the single-order excitation load case. Values below unity show a reduction in torsional vibration while values above unity show an amplification compared to the locked pendulum rotor. The response is shown as a function of the torque excitation order normalized with the tuning order at a mean rotational velocity of 1000 RPM for different values of the pendulum damping coefficient.

The minimum of the rotor response occurs when the excitation order and the tuning order are equal. In this region, the oscillations are efficiently absorbed by the pendulum absorber. With increased damping the performance of the absorber is decreased in this region. By further increasing the excitation order the response grows to a maximum at n_r, then falls down to a asymptotic level above unity. With the linear model, one may already conclude that all excitation orders above $n/n_t \approx 1.015$ are amplified.

The time integrated non-linear response is shown in Figure 3 and Figure 4 for two excitation amplitudes, 40 Nm and 500 Nm respectively, when subjected to the single-order excitation load case. The solid lines represent an upward sweep of the excitation order and the dashed lines represent a downward sweep. The main- and second-order harmonic of the response are present even though the excitation consists of a single frequency component. The first harmonic exists even at low excitation amplitudes. For high excitation amplitudes the first harmonic exceeds the main order around the tuning order. We can also observe a downward shift of the tuning order compared to the linear tuning order for high excitation amplitudes. This is known as a non-linear softening effect commonly associated with high amplitude pendulum responses. It is clear that the rotor-CPVA system also has several solution branches depending on the path of excitation. For the case in Figure 3, the upper solution branch falls back down to the lower solution branch at a lower excitation order, that is not the case for the high amplitude excitation case.

The ripple near the rotor eigen-order in the upward sweep is probably due to the instability in this region. One can observe that the response here has not reached steady state in comparison to the linear response. A slower sweep speed in this region can be a way to further resolve the response in this region.

Figure 6 in Appendix B shows the same graphs as in Figure 3 and Figure 4 together with the results from the Adams model as dot-dashes lines. The results are identical except for small deviations near instability regions. The analytical model may be considered validated since the two independent methods yield the same results.

The steady-state response of the rotor subjected to the multiple-harmonic excitation for different rotational velocities are presented in Figure 5. The dotted lines represent the response of the rotor with a locked pendulum and the solid lines represent the rotor-CPVA angular acceleration. As expected, the main-order response of the CPVA-equipped rotor is remarkably reduced while the second-order harmonic is amplified compared to the locked pendulum rotor, at and above 800 RPM. An increased level of the main order is evident at 600 RPM. This is due to the fact that the response has jumped up to the upper solution branch that was observed in the downward sweep in the response study. At lower rotational velocities the centrifugal stiffness of the pendulum is lower and the amplitude of the pendulum increases, facilitating the jump to this branch.

Parameter	Value
$\tilde{I}$	2255
n_t	3.11
m_p	6.0 [kg]
c_p	$5E^{-4}$ [Nms/rad]
c_r	$5E^{-3}$ [Nms/rad]

Table 2: Parameter values used in the simulation of the rotor-CPVA system.

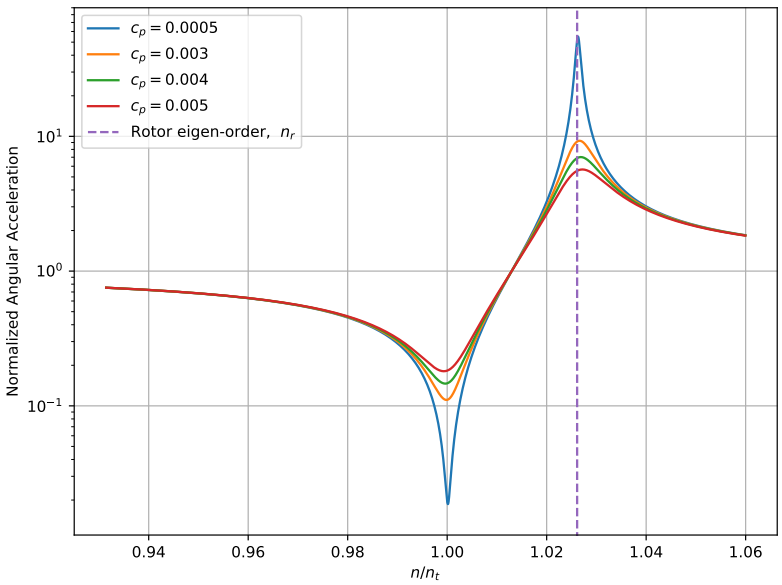


Figure 2: Linear steady-state normalized angular acceleration response of the rotor for different pendulum damping coefficients at 1000 RPM. Values below unity show a decrease in the response compared to a rotor with locked pendulum.

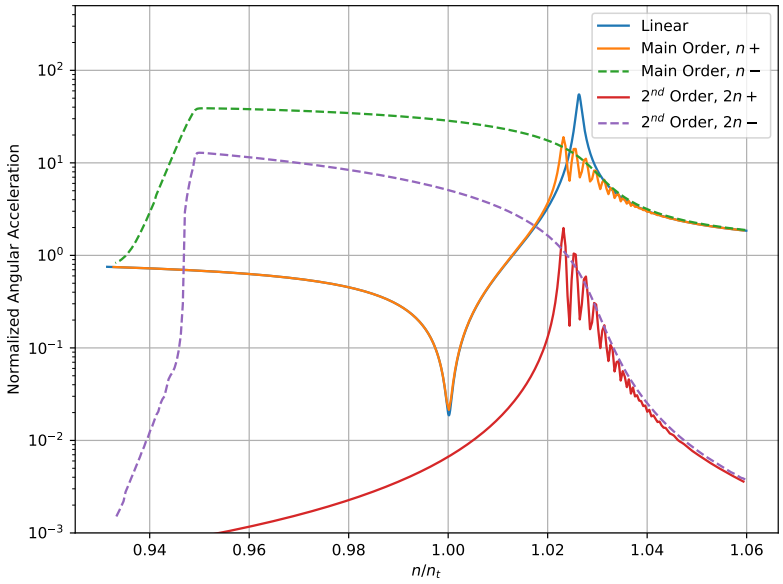


Figure 3: The non-linear angular acceleration response of the rotor for an excitation amplitude of 40 Nm. The solid lines represent an upward sweep of the excitation order and the dashed lines represent a downward sweep.

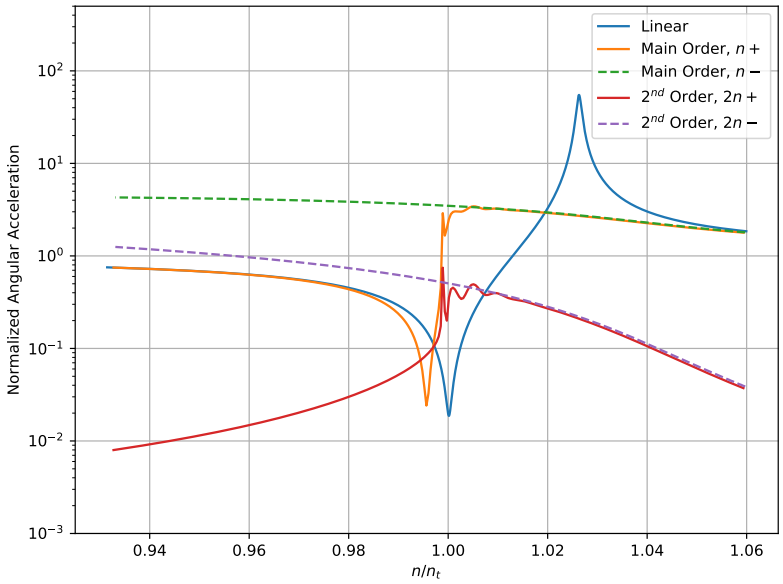


Figure 4: The non-linear angular acceleration response of the rotor for an excitation amplitude of 500 Nm. The solid lines represent an upward sweep of the excitation order and the dashed lines represent a downward sweep.

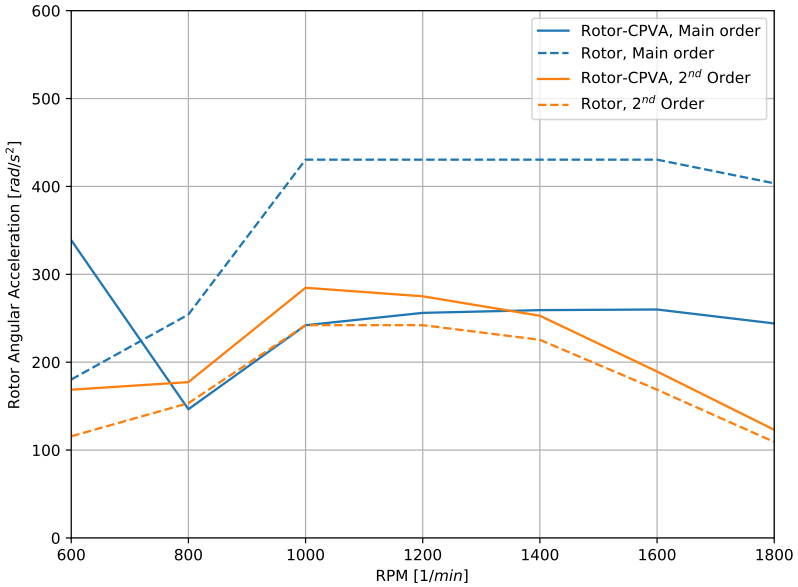


Figure 5: The steady-state responses of the rotor subjected to the multiple-harmonic excitation over a typical operating rotational speed range of a heavy truck.

6 Conclusions

The equations of motion of a rotor-CPVA system are derived by Kane's method yielding compact first-order differential equations and are validated against an Adams model. By linear and non-linear analysis we show the main characteristics of the rotor-CPVA system. We conclude that the rotor-CPVA system excited by a single-harmonic torque produces a multiple-harmonic response. This is evident for higher levels of oscillating torque amplitudes and becomes more apparent near the tuning order of the pendulum absorber since the main excitation order is significantly reduced. Also, when exciting the rotor-CPVA system with a multiple-harmonic torque we show that the higher harmonics above the rotor eigen-order are amplified by the pendulum absorber arrangement. Further, we show that the system possesses different solution branches depending on the previous state of the system due to non-linearities. A jump between these solution branches may occur. This jump occurs in the low rotational velocity range yielding an increase of torsional vibration. An important conclusion is that the low rotational speeds must be considered in the design of the pendulum absorber. Higher torsional vibrations at vehicle creeping conditions can cause poor noise quality issues. We show that it is possible to extract the different solution branches and the harmonic response from time-domain simulations by subsequent frequency analysis of the time signals. However, the time-domain integration to find the steady-state response can be time consuming, especially in the analysis of larger powertrain models. Therefore, future investigations will expand to other analysis methods such as the Harmonic Balance Method as in [10].

Acknowledgements

The author would like to thank Scania CV AB and the people in Transmission Cluster Network for supporting this work. Great thanks also to Arne Nordmark at KTH Royal Institute of Technology, Department of Mechanics, for interesting discussions on modern methods in mechanics during the course in Rigid Body Dynamics.

References

[1] Roland Seebacher. *Mission CO2 Reduction*. CONAT 2016 International Congress of Automotive and Transport Engineering, pages 451–461. Springer International Publishing, Cham, 2017.

[2] R W Zdanowich and T S Wilson. *The elements of pendulum dampers*. ARCHIVE: Proceedings of the Institution of Mechanical Engineers 1847-1982 (vols 1-196), 143(1940):182–210, jan 1940.

[3] D. E. Newland. *Nonlinear Aspects of the Performance of Centrifugal Pendulum Vibration Absorbers*. Journal of Engineering for Industry, 86(3):257, 1964.

[4] A.S. ALSUWAIYAN and S.W. SHAW. *Performance and Dynamic Stability of General-Path Centrifugal Pendulum Vibration Absorbers*. Journal of Sound and Vibration, 252(5):791–815, 2002.

[5] Steven W. Shaw and Bruce Geist. *Tuning for Performance and Stability in Systems of Nearly Tautochronic Torsional Vibration Absorbers*. Journal of Vibration and Acoustics, 132(4):041005, 2010.

[6] H.H. Denman. *Tautochronic bifilar pendulum torsion absorbers for reciprocating engines*. Journal of Sound and Vibration, 159(2):251–277, 1992.

[7] J. Mayet and H. Ulbrich. *Tautochronic centrifugal pendulum vibration absorbers: General design and analysis*. Journal of Sound and Vibration, 333(3):711–729, 2014.

[8] J. Mayet and H. Ulbrich. *First-order optimal linear and nonlinear detuning of centrifugal pendulum vibration absorbers*. Journal of Sound and Vibration, 335:35–54, 2015.

[9] Steven W. Shaw. *Designing Nonlinear Torsional Vibration Absorbers*. Exploiting Nonlinear Behavior in Structural Dynamics, pages 135–169. Springer Vienna, Vienna, 2012.

[10] Mustafa A. Acar and Steven W. Shaw. *Application of the harmonic balance method to centrifugal pendulum vibration absorbers*. Conference Proceedings of the Society for Experimental Mechanics Series, volume 6, pages 243–252. Springer International Publishing, 2016.

[11] Emma Smith. *Analysis and simulation of centrifugal pendulum vibration absorbers*. TRITA-AVE 1651-7660, KTH, Skolan för teknikvetenskap (SCI), Farkost och flyg, MWL Marcus Wallenberg Laboratoriet, 2015.

[12] Thomas R Kane and David a Levinson. *Dynamics Theory and Applications*. 2005.

[13] Carlos M. Roithmayr and Dewey H. Hodges. *Dynamics : Theory and Application of Kane's Method*. 2016.

[14] Richard H. Rand. *Topics in Nonlinear Dynamics with Computer Algebra*. Gordon and Breach Science Publishers, Inc., Newark, NJ, USA, 1994.

[15] Gilbert Gede, Dale L. Peterson, Angadh S. Nanjangud, Jason K. Moore, and Mont Hubbard. *Constrained Multibody Dynamics With Python: From Symbolic Equation Generation to Publication*. Volume 7B: 9th International Conference on Multibody Systems, Nonlinear Dynamics, and Control, page V07BT10A051. ASME, aug 2013.

[16] Aaron Meurer, Christopher P. Smith, Mateusz Paprocki, Ondřej Čertík, Sergey B. Kirpichev, Matthew Rocklin, AMiT Kumar, Sergiu Ivanov, Jason K. Moore, Sartaj Singh, Thilina Rathnayake, Sean Vig, Brian E. Granger, Richard P. Muller, Francesco Bonazzi, Harsh Gupta, Shivam Vats, Fredrik Johansson, Fabian Pedregosa, Matthew J. Curry, Andy R. Terrel, Štěpán Roučka, Ashutosh Saboo, Isuru Fernando, Sumith Kulal, Robert Cimrman, and Anthony Scopatz. *SymPy: symbolic computing in Python*. PeerJ Computer Science, 3:e103, jan 2017.

[17] T. R. Kane and C. F. Wang. *On the Derivation of the Equations of Motion*. Journal of the Society for Industrial and Applied Mathematics, 13(2):487–492, jun 1965.

[18] Essén Hanno and Arne Nordmark. *The Theory of Lagrange's Method*. Course Material in Rigid Body Dynamics at the Royal Institute of Technology. Department of Mechanics. 2006.

[19] Scipy. *scipy.integrate.odeint — SciPy v1.1.0 Reference Guide*.

[20] Anders Brandt. *Noise and Vibration Analysis: Signal Analysis and Experimental Procedures*. John Wiley & Sons, Ltd, Chichester, UK, 2010.

A Derivation of the equation of motions

Even though Kane's method is suitable to implement in a Computer Algebra System (CAS), such as in Refs. [15, 16], the equations of motion of the rotor pendulum system depicted in Figure 1 are manually derived to show the procedure of the method.

Bold symbols represent vectors and an over-dot represents the time derivative of the vector relative to the inertial reference frame N. Unit direction vectors are represented in bold and with a hat as $\hat{\mathbf{a}}_\mathbf{x}$.

A.0.1 Inertial forces

The total angular velocity of the rotor body A and the pendulum body B in the inertial reference system N are

$$\boldsymbol{\omega}^A = \dot{\theta}\hat{\mathbf{a}}_\mathbf{z}, \qquad \boldsymbol{\omega}^B = (\dot{\phi} + \dot{\theta})\hat{\mathbf{b}}_\mathbf{z}. \tag{25}$$

An appropriate set of generalized velocities may then be chosen from the expressions of the angular velocities in (25) as

$$u_1 = \dot{\theta}, \qquad u_2 = \left(\dot{\phi} + \dot{\theta}\right). \tag{26}$$

The velocity of the pendulum body may then be written in terms of these generalized velocities,

$$\mathbf{v}^B = Ru_1\hat{\mathbf{a}}_\mathbf{y} + Lu_2\hat{\mathbf{b}}_\mathbf{y}. \tag{27}$$

The partial velocities defined in (5) then become

$$\boldsymbol{\omega}_1^A = \hat{\mathbf{a}}_\mathbf{z}, \quad \mathbf{v}_1^A = \mathbf{0}, \quad \boldsymbol{\omega}_1^B = \mathbf{0}, \quad \mathbf{v}_1^B = R\hat{\mathbf{a}}_\mathbf{y}, \tag{28}$$

$$\boldsymbol{\omega}_2^A = \mathbf{0}, \quad \mathbf{v}_2^A = \mathbf{0}, \quad \boldsymbol{\omega}_2^B = \hat{\mathbf{b}}_\mathbf{z}, \quad \mathbf{v}_2^B = L\hat{\mathbf{b}}_\mathbf{y}. \tag{29}$$

Further, the time derivative in the inertial frame N of the velocity vector, $\mathbf{v}^B$, yields the acceleration of the pendulum center of mass and thus the time derivative of the linear momentum becomes

$$\dot{\mathbf{p}}^B = m_pR\left(-u_1^2\hat{\mathbf{a}}_\mathbf{x} + \dot{u}_1\hat{\mathbf{a}}_\mathbf{y}\right) + m_pL\left(-u_2^2\hat{\mathbf{b}}_\mathbf{x} + \dot{u}_2\hat{\mathbf{b}}_\mathbf{y}\right). \tag{30}$$

The time derivative of the angular momentum of the pendulum body and the rotor about their center of mass are

$$\dot{\mathbf{L}}^B = I_{zz}^B\dot{u}_2\hat{\mathbf{b}}_\mathbf{z}, \tag{31}$$

$$\dot{\mathbf{L}}^A = I_{zz}^A\dot{u}_1\hat{\mathbf{a}}_\mathbf{z}. \tag{32}$$

The components of the summation of the inertial forces f_i^* for each body in (2) may now be evaluated for each set of partial velocities (28), (29). For each body and for the first set of partial velocities the summation components are

$$\begin{aligned}
f_{1,A}^* &= \dot{\mathbf{p}}^A \cdot \mathbf{v}_1^A + \dot{\mathbf{L}}^A \cdot \boldsymbol{\omega}_1^A = I_{zz}^A\dot{u}_1, \\
f_{1,B}^* &= \dot{\mathbf{p}}^B \cdot \mathbf{v}_1^B + \dot{\mathbf{L}}^B \cdot \boldsymbol{\omega}_1^B = \\
&= \left(m_pR\left(-u_1^2\hat{\mathbf{a}}_\mathbf{x} + \dot{u}_1\hat{\mathbf{a}}_\mathbf{y}\right) + m_pL\left(-u_2^2\hat{\mathbf{b}}_\mathbf{x} + \dot{u}_2\hat{\mathbf{b}}_\mathbf{y}\right)\right) \cdot R\hat{\mathbf{a}}_\mathbf{y} = \\
&= m_pR^2\left(-u_1^2\hat{\mathbf{a}}_\mathbf{x} \cdot \hat{\mathbf{a}}_\mathbf{y} + \dot{u}_1\hat{\mathbf{a}}_\mathbf{y} \cdot \hat{\mathbf{a}}_\mathbf{y}\right) + m_pRL\left(-u_2^2\hat{\mathbf{b}}_\mathbf{x} \cdot \hat{\mathbf{a}}_\mathbf{y} + \dot{u}_2\hat{\mathbf{b}}_\mathbf{y} \cdot \hat{\mathbf{a}}_\mathbf{y}\right) = \\
&= m_pR^2\dot{u}_1 + m_pRL\left(-u_2^2\sin(\phi) + \dot{u}_2\cos(\phi)\right),
\end{aligned} \tag{33}$$

where the definition of the dot product between two vectors is used.

For each body and the second set of partial velocities, the summation components are

$$\begin{aligned} f^*_{2,A} &= \dot{\mathbf{p}}^A \cdot \mathbf{v}^A_2 + \dot{\mathbf{L}}^A \cdot \boldsymbol{\omega}^A_2 = 0, \\ f^*_{2,B} &= \dot{\mathbf{p}}^B \cdot \mathbf{v}^B_2 + \dot{\mathbf{L}}^B \cdot \boldsymbol{\omega}^B_2 = \\ &= \left(I^B_{zz} + m_p L^2\right) \dot{u}_2 + m_p RL\dot{u}_1 \cos(\phi) + m_p RL u_1^2 \sin(\phi). \end{aligned} \tag{34}$$

Finally, the equations of motion without any applied forces are then formed by evaluating the sum as

$$f^*_1 = f^*_{1,A} + f^*_{1,B} = \left(I^A_{zz} + m_p R^2\right) \dot{u}_1 + m_p RL\dot{u}_2 \cos(\phi) - m_p RL u_2^2 \sin(\phi) = 0, \tag{35}$$

$$f^*_2 = f^*_{2,A} + f^*_{2,B} = \left(I^B_{zz} + m_p L^2\right) \dot{u}_2 + m_p RL\dot{u}_1 \cos(\phi) + m_p RL u_1^2 \sin(\phi) = 0. \tag{36}$$

A.0.2 Applying Torques

A viscous loss torque about point O in the rotor frame A, is applied together with an applied torque T_o, representing the engine torque. The two torques may be written in vector form as

$$\mathbf{T}^A = (T_o - c_r u_1)\hat{\mathbf{a}}_\mathbf{z}, \tag{37}$$

where c_r is a the viscous damping coefficient.

A viscous damping torque acting on the pendulum frame B, proportional to the angular velocity difference between frame A and B, is applied to represent the viscous loss of the pivot bearing about point Q. This loss is described in terms of generalized velocities as

$$\mathbf{T}^B = -c_p(u_2 - u_1)\hat{\mathbf{b}}_\mathbf{z}, \tag{38}$$

where c_p is the viscous damping coefficient. This torque also acts on the rotor frame but with opposite sign. The generalized active forces for each degree of freedom becomes

$$\begin{aligned} f_{1,A} &= (\mathbf{T}^A - \mathbf{T}^B) \cdot \boldsymbol{\omega}^A_1 = c_p(u_2 - u_1) + T_o - c_r u_1, \\ f_{1,B} &= \mathbf{T}^B \cdot \boldsymbol{\omega}^B_1 = 0, \end{aligned} \tag{39}$$

and for the second degree of freedom

$$\begin{aligned} f_{2,A} &= (\mathbf{T}^A - \mathbf{T}^B) \cdot \boldsymbol{\omega}^A_2 = 0, \\ f_{2,B} &= \mathbf{T}^B \cdot \boldsymbol{\omega}^B_2 = -c_p(u_2 - u_1). \end{aligned} \tag{40}$$

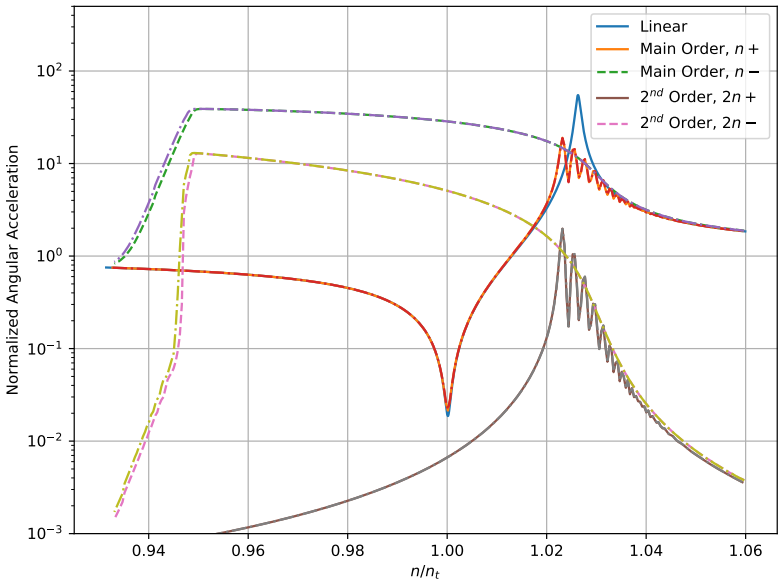
Collecting the inertial terms, (35), (36) and the generalized active forces, (39), (40) into $f^*_i = f_i$ results in the equations of motion in terms of generalized coordinates and velocities with applied torques as

$$\begin{aligned} \left(I^A_{zz} + m_p R^2\right) \dot{u}_1 + m_p RL\dot{u}_2 \cos(\phi) - m_p RL u_2^2 \sin(\phi) &= c_p(u_2 - u_1) + T_o - c_r u_1, \\ \left(I^B_{zz} + m_p L^2\right) \dot{u}_2 + m_p RL\dot{u}_1 \cos(\phi) + m_p RL u_1^2 \sin(\phi) &= -c_p(u_2 - u_1). \end{aligned} \tag{41}$$

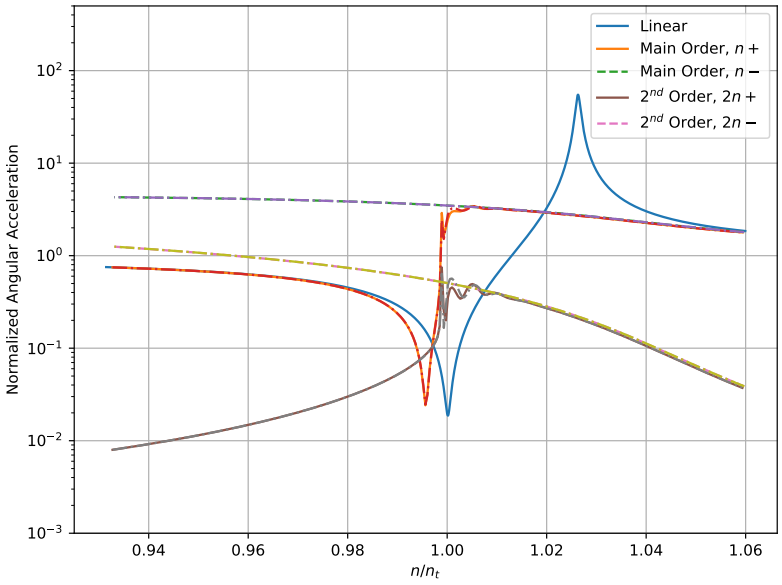
Together with the kinematical differential equations, (26), the complete system is described as a first-order differential equation system.

B Model validation against Adams

The Adams model consists of a rotor body attached to the ground with a rotational joint. A torsional damper element without stiffness was applied between the rotor and ground to represent the viscous loss c_r. Further, a rotational joint is attached between the rotor and pendulum body at the pivot point Q. A torsional damper element without stiffness was applied between the pendulum and rotor to represent the viscous loss c_p. The applied forces and load cases are the same as for the analytical model.



(a)



(b)

Figure 6: The non-linear angular acceleration response of the rotor. The solid lines represent an upward sweep of the excitation order and the dashed lines represent a downward sweep using the analytical model. The dot-dashed lines are results from the Adams model.

Structural power as an acoustic design criterion for the early phase of product design

S. Sicklinger, [1]**, R. Ullmann** [1]
[1] BMW AG, Research, New Technologies, Innovations
Parkring 19, 85748 Garching, Germany
e-mail: **stefan.sicklinger@bmw.de**

Abstract
The vibroacoustic assessment and optimization of vehicle components at the early stage of complete vehicle development is an essential. This is because only at the early phase it is possible to change concepts. Therefore, it is necessary to focus on analysis methods which can work with a limited set of information in contrast to the high-fidelity methods. Hence a representative and robust physical structural key performance indicator is needed as sound pressure levels at the passenger ears are not available at the early stage of the design process. A performance comparison of accelerations, forces and powers is performed within this work. A numerical model where the transfer functions form the excitation, over to the structural component, then over to the sound pressure level is available forms the basis for the presented study. The applicability of different structural key performance acoustic indicators (e.g. accelerations, forces and powers) for this model is discussed. We will present the significance of each indicator for the conceptual design phase.

1 Introduction

For the conceptual design phase it is particularly challenging to apply analysis techniques which have an acceptable level of prediction on the one hand and can work with a limited set of information on the other hand. For structure-borne sound problems the concept [1, 2] of power-flow is a promising candidate to fulfill the requirements of conceptual design. In vehicle design the conceptual design of vibroacoustics

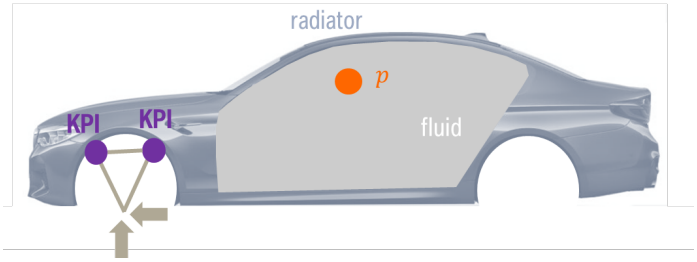


Figure 1: Acoutics transfer from excitation to cabin

performance is challenging as the modelling of the acoustic transfer path from the excitation (i.e. tire, powertrain etc.) into the cabin is mostly not possible to an acceptance level of accuracy due to the lack of information. Therefore, it is crucial to find structural key performance indicators (KPIs) which have a good correlation to the sound pressure level inside the cabin (e.g. Figure 1 point p). If and only if such a KPI can be found the conceptual design decisions can be made by the performance measured with the particular structural KPI. In the following it will be demonstrated with the help of representative example that structural power-flow is a promising candidate to solve that challenge in contrast to primal (velocity) oder dual (force) structural variables.

2 Power-flow Workflow

The detailed concept of the workflow is presented in [3]. The core idea is to quantify the energy which is transmitted from the sender structures (i.e. chassis, powertrain, mechatronic system) to the receiving structure (i.e. body-in-white (BIW)) which finally radiates fractions of that energy into the cabin where the driver and passengers are affected. The energy transfer is thereby quantified via the structural active power which is given by

$$\bar{P} = \frac{1}{2} \Re \left(\hat{\boldsymbol{f}}^H \cdot \hat{\boldsymbol{v}} \right). \tag{1}$$

H is the Hermitian transpose.

3 Representative Example

With the help of the following example it is demonstrated that insertion loss of structural active power shows a better correlation to the insertion loss of the sound pressure level than the insertion losses of velocities or forces. The problem setup of the representative example is shown in Figure 2. The problem is considered

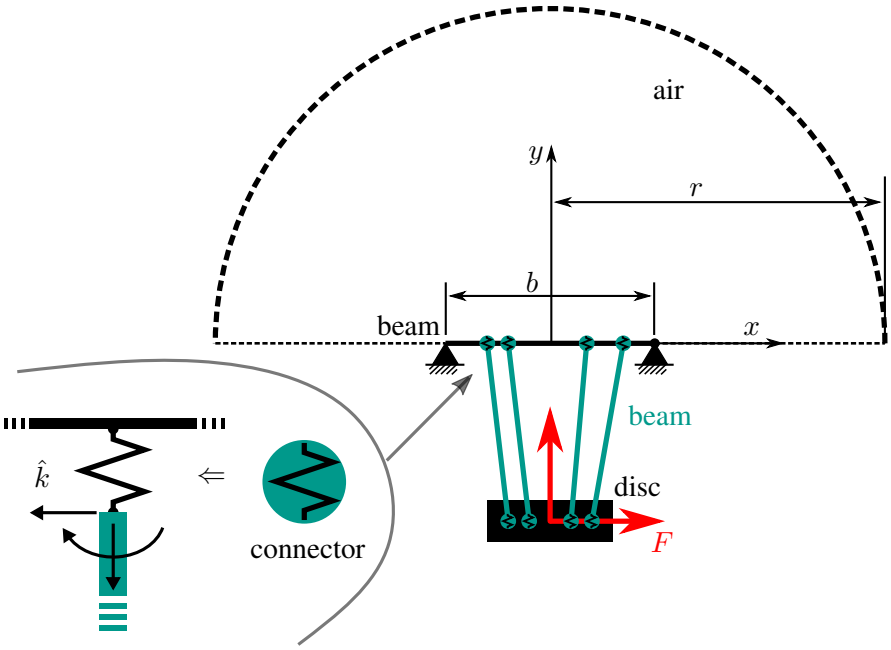


Figure 2: Problem layout

two-dimensional. With this problem it is possible to analyse the complete acoustic transfer path from the excitation to the sound pressure level (SPL) in the air.

The excitation is applied to an elastic disc which is connected with four connectors (rubber bushings) to four slender steel beams. These (”legs”) are connected again with four connectors to a simple supported beam which radiates into a half space (see Figure 2). The connectors are modeled by springs with complex stiffnesses $\hat{k} = k(1 + j \cdot \eta)$. Inside the half space the SPL is spatial averaged on two different circular arcs r_{inner} and r_{outer} each sampled with elven point probes (see Figure 3). The spatial averaged SPL in the acoustic medium (air) are abbreviated with $\hat{p}_{\text{inner}}$ and $\hat{p}_{\text{outer}}$. At each connector $i = 1...4$ force $\hat{\boldsymbol{f}}_i$, velocity $\hat{\boldsymbol{v}}_i$ and active power $\bar{P}_i$ are evaluated. Afterwards each KPI (force, velocity and active power) is accumulated for

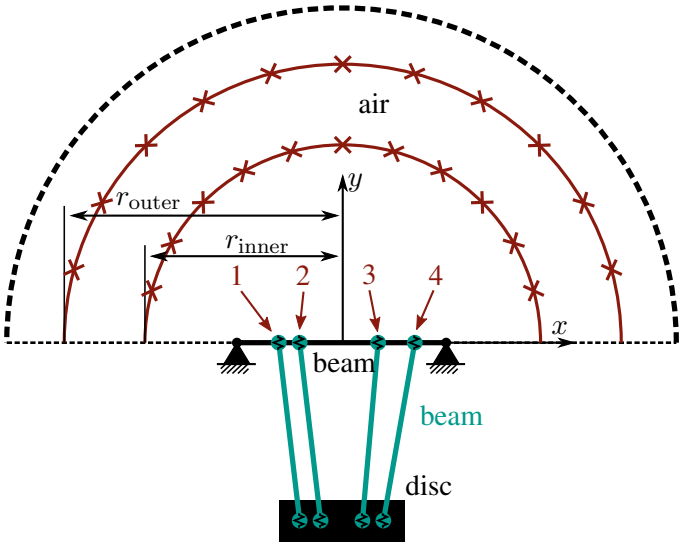


Figure 3: SPL probes

all connectors $i = 1...4$. For active powers this a straight forward procedure as all three degree of freedoms of each connection point between radiating beam and connector $i = 1...4$ are summed up.

$$\bar{P}_{\text{sum}} = P = \sum_{n=1}^{4} \bar{P}_i \tag{2}$$

For velocities the rotational contribution needs to neglected (no physical meaning mixing translational and rotational velocities)

$$v_{\text{sum}} = \sum_{n=1}^{4} |\hat{\boldsymbol{v}}_{\text{translation}_i}| = \sum_{n=1}^{4} |\hat{v}_{\text{x}_i}| + |\hat{v}_{\text{y}_i}| \,. \tag{3}$$

For forces the vector and the arithmetic sum are distinguish

$$f_{\text{sum}_{\text{ari}}} = f_{\text{sum}} = \sum_{n=1}^{4} \left| \hat{\boldsymbol{f}}_{\text{translation}_i} \right| = \sum_{n=1}^{4} \left| \hat{f}_{\text{x}_i} \right| + \left| \hat{f}_{\text{y}_i} \right| \tag{4}$$

$$f_{\text{sum}_{\text{vec}}} = f_{\text{vec}} = \left| \sum_{n=1}^{4} \hat{\boldsymbol{f}}_{\text{translation}_i} \right| = \left| \sum_{n=1}^{4} \begin{pmatrix} \hat{f}_{\text{x}_i} \\ \hat{f}_{\text{y}_i} \end{pmatrix} \right| . \tag{5}$$

4 Results

For different conceptual designs the structural KPIs are computed and compared to the insertions losses of the SPLs. For two different designs (baseline and modification) of the system the SPL insertion loss is computed as follows

$$D_{p_{\text{inner}}} = -10 \cdot \log_{10} \left(\frac{|p_{\text{inner}_{\text{mod}}}|}{|p_{\text{inner}_{\text{base}}}|} \right) \tag{6}$$

$$D_{p_{\text{outer}}} = -10 \cdot \log_{10} \left(\frac{|p_{\text{outer}_{\text{mod}}}|}{|p_{\text{outer}_{\text{base}}}|} \right) . \tag{7}$$

For the baseline design the spatial averaged magnitude of the SPLs is plotted in Figure 4

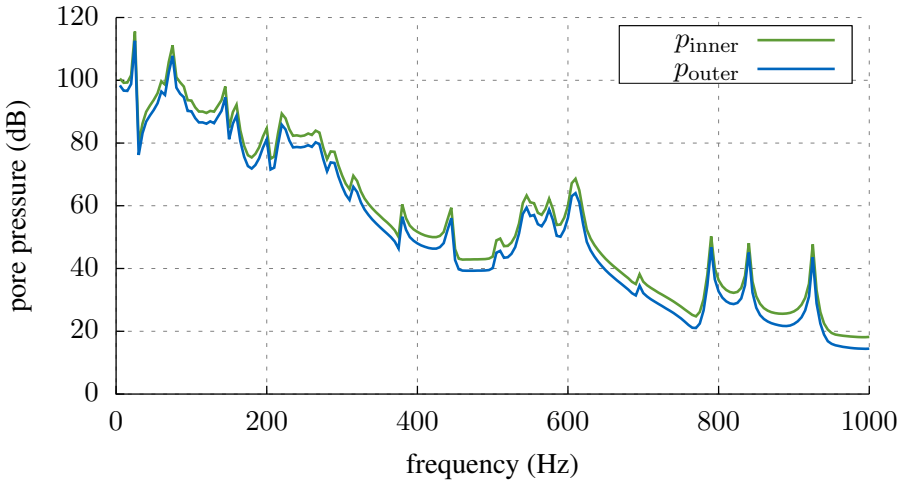


Figure 4: Spatial averaged magnitude of the SPLs for inner and outer probes

The insertion losses can also be computed for each individual structural KPI

$$D_l = -10 \cdot \log_{10}\left(\frac{|l_{\text{mod}}|}{|l_{\text{base}}|}\right) l \in \ P,\ v_{\text{sum}},\ f_{\text{sum}},\ f_{\text{vec}}. \tag{8}$$

For a material change aluminium (base) to steel (mod) for the legs the structural insertion losses are plotted in Figure 5.

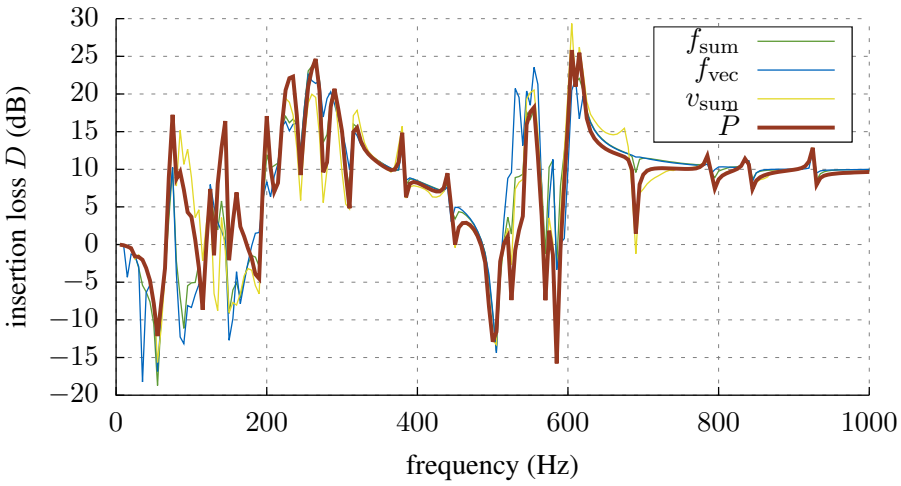


Figure 5: D_l for material change of legs: aluminium $\rightarrow$ steel

As the $D_{p_{\text{inner}}}$ and $D_{p_{\text{outer}}}$ are very similar the insertion losses of the structural KPIs are comapred to $D_{p_{\text{outer}}}$ only. The deviation of the each structural KPI to the truth $D_{p_{\text{outer}}}$ is given by

$$\text{DEV}_l = \text{sign}\left(\frac{D_l}{D_{p_{\text{outer}}}}\right) \cdot |D_l - D_{p_{\text{outer}}}|\,. \tag{9}$$

For a material change aluminium (base) to steel (mod) for the legs of the structure this is given by Figure 6 from $f = 0\,\text{Hz}$ to $1\,\text{kHz}$. Note that a negative value of DEV_l reflects a wrong trend in the prediction of the analysis with respect to the behavior of the SPL.

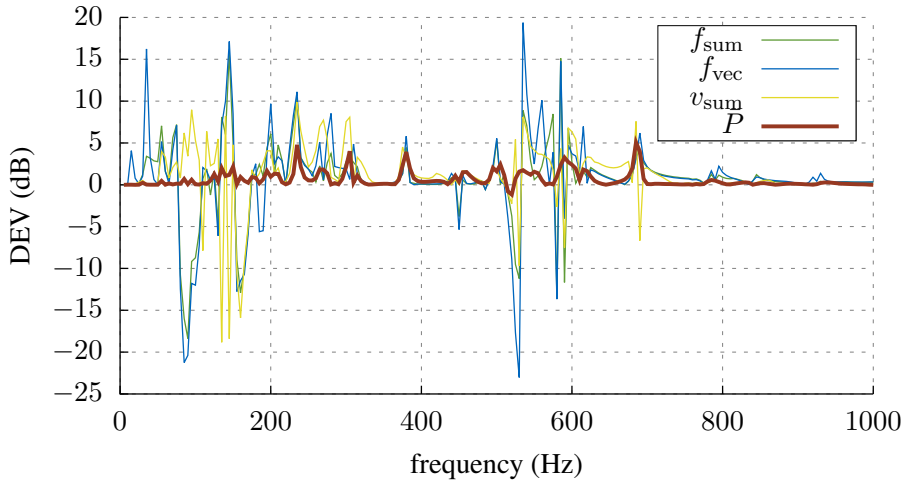


Figure 6: DEV_l for material change of legs: aluminium $\rightarrow$ steel

For the representative example six more design modifications are benchmarked by this methodology. The results are presented in Figure 7.

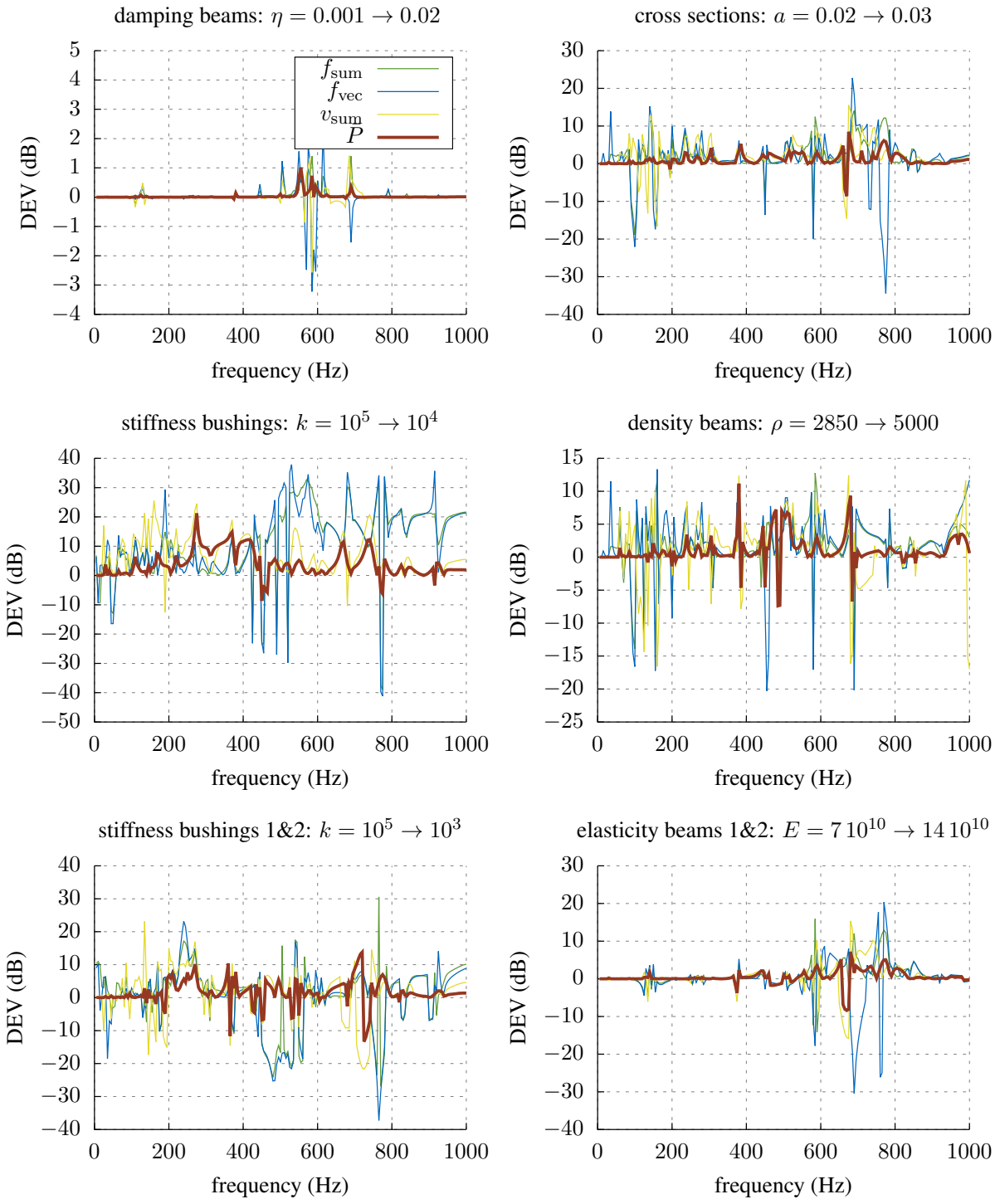


Figure 7: DEV_l for different modification

5 Conclusion

With a representative example it has been demonstrated that power as a structural key performance (KPI) indicator shows a better correlation for various design modifications of the example than primal or dual variables inside the structure. Furthermore, a methodology is presented which allows for a comparison between different structural KPIs.

References

[1] S. A. Hambric. Power flow and mechanical intensity calculations in structural finite element analysis. *Journal of Vibration and Acoustics*, 112:542–550, 1990.

[2] S. A. Hambric. Comparison of experimental and finite element Structure-borne flexural power measurements for a straight beam. *Journal of Sound and Vibration*, 170(5):595–605, 1994.

[3] R. Ullmann, S. Sicklinger, M. Buchschmid, and G. Müller. Power-based approach for assessment of structure-borne sound in mechanical networks of vehicle structures. *Procedia Engineering*, 199:1386–1391, 2017.

A robust design approach to optimize the vibrational comfort of automotive seats

R. Barbeau [1] [2], **T. Weisser** [1], **R. Dupuis** [1], **E. Aubry** [1], **S. Baudu** [2]
[1] IRIMAS, Université de Haute-Alsace,
12 rue des frères Lumière, F-68093, Mulhouse Cedex, France
e-mail: **romain.barbeau@uha.fr**

[2] Faurecia Automotive Seating,
ZI Brières les Scellés BP89, 91152 Etampes Cedex, France

Abstract
Automotive seats are designed to provide the best driving comfort to the occupant while ensuring high safety levels. Static comfort aims to provide an optimal body support and safety requirements. Dynamic comfort tends to strengthen these features and to provide an optimal vibrational environment, under riding conditions. However, considering a typical seat design process, dynamic comfort is usually adjusted once an accurate static comfort has been determined. The purpose of this study is to propose and to illustrate a robust design methodology to optimize the dynamic behaviour of a human-seat coupled system while still verifying a targeted static behaviour. A two-dimensional multi-body model is presented and the impact of the variability of both seat and human body parameters is discussed, emphasizing the need to handle these uncertainties through the optimization procedure. A robustness analysis is finally performed to assess the performance of the derived optimal solutions, highlighting some crucial trade-offs faced by seat manufacturers.

1 Introduction

Automotive seats are designed to provide the best driving comfort to the occupant while ensuring high safety levels. This complex notion of comfort is usually inversely handled by considering discomfort sources and distinguishing different types of physical solicitations, as proposed by Bubb [7] in his pyramid of discomfort. From a mechanical point of view, postural comfort aims to provide an optimal body support to lower numbness, fatigue or pain issues; while vibrational comfort tends to strengthen these features and to provide an optimal dynamic environment, by considering time varying inputs under riding conditions. Considering a typical seat design process, one fundamental rule is to design a seat around the hip point (H-point) of the driver, to ensure a proper driving position. Then, vibrational comfort is usually adjusted by taking into account the vibrations at the seat base, resulting from the tyre/road interaction and the thermal engine.

Automotive seats have become very complex systems as they gather lots of technical solutions aiming to improve the interface between the occupant and its environment, during riding. Focusing on their mechanical behaviour, seats are usually simplified from more than eighty components to four main sub-components, namely the frame structure, the suspension mat, the foam pad and the cover. The mechanical interactions between these components still remain very complex, leading seat manufacturer to assess the vibrational comfort only once a prototype has been built. Hence, the achievable dynamic behaviour of the seat and thus its vibration isolation performances may be limited due to some previous design solutions. Its improvement using iterative test/modification steps may also turn out to be both time consuming and costly. To handle these issues, seat manufacturers are more and more interested in developing virtual prototyping tools. These

would allow investigating the evolution of the mechanical behaviour of the seat with regard to multiple design parameters and simulating untested configurations. Therefore, future design processes could rely on a stronger parallel between static and dynamic comforts.

In order to help seat manufacturers anticipate innovation stakes that could derive from such a parallel process, a robust design methodology is presented in this paper to optimize the dynamic response of a multi-body human-seat coupled system. In section 2, a quick overview of the approaches available in the literature to model human-seat systems is first presented. The considered multi-body model is further introduced and validated with regard to an experimental transmissibility measurement. The variability of this dynamic response is also discussed, emphasizing the impact of the human body parameters on the assessment of the vibrational comfort. In section 3, robust design tools are proposed to optimize the dynamic behaviour of a human-seat system with regard to the seat impacting design parameter, while taking into account the variability of the seated human body. Both deterministic and reliability-based optimization procedures are presented and the derived solutions are finally compared through an Info-gap robustness analysis.

2 Human-seat model

2.1 Modelling approach

Lots of mathematical models have been developed in the literature to predict the dynamic responses of a human-seat coupled system. These models can be broadly divided into three groups: lumped parameter models, multi-body models and finite element models (not detailed in this study). Preliminary investigations were performed by the authors on a simple lumped parameter model in vertical direction [1]. The derived results showed some strong prediction limitations and the need to develop a more complex model with additional directions to take into account the backrest contribution and internal dynamic interactions of the human-seat coupled system.

Since the 2000s, multi-body dynamic models have been widely developed allowing a better representation of the human body motions, as well as of the human-seat coupled system behaviour. Such models are classically composed of several rigid bodies connected by rotational and/or longitudinal springs and/or dampers. These bodies are part of an equivalent system representing the human anatomy. Each body has three Degrees Of Freedom (DOF) in the sagittal plane: vertical, fore-aft and rotational directions.

The first multi-body model describing the human-seat coupled system was introduced by Cho and Yoon to evaluate the ride quality inside a vehicle [8]. Four different biomechanical models were studied based on nine DOFs in order to evaluate the transmissibilities to the head, to the back and to the hip, resulting from vertical vibrations. To validate their model, the authors measured acceleration responses on ten subjects under vertical vibration excitations, obtaining a good matching of the transmissibilities at resonance frequencies. A fourteen DOFs multi-body dynamic model was further proposed by Liang and Chiang [15] based on Cho's model [8] to evaluate the impact of the backrest inclination on both apparent mass and head transmissibility. This linear model was composed of five rigid bodies representing thighs, pelvis, upper-body, head and viscera in the sagittal plane. Three different cases were considered (*i.e.* without backrest, with backrest at 12 ° and 21 °), and were validated by comparison to various experimental data. The results showed that fewer vibrations were transmitted with a 21 ° backrest angle. Finally, this model was extended by Kumbhar [13] who added six DOFs to describe more accurately the dynamic behaviour of the seat and its sub-components. Three seat configurations were studied (rigid, traditional and suspension seats) and transmissibilities and absorbed powers were computed to rank the filtration performance in each case.

Furthermore, a study was conducted by Kim *et al.* to develop a tool for car seat designers [14]. The occupant and the seat were modelled by three bodies (torso, buttocks and legs) and two bodies (backrest and cushion), respectively. Based on natural frequencies and mode shapes the authors performed a parametric study, highlighting the influence of particular mechanical parameters on the dynamic behaviour. A good cor-

relation between simulated frequency responses and experimental ones was achieved, in terms of locations of resonances and deflection shapes.

In view of these studies, it can be emphasized that the modelling hypothesis and the purpose of the various proposed models are very different, making it difficult to compare their ability to help improving the vibrational comfort. Some authors attempted to evaluate the ride quality computing transmissibilities [8]; other focused on the mode shapes of the human body [14]; others investigated the impact of seat properties (e.g. foam properties, backrest inclination, additional suspension) on some vibration responses [15, 13]. Moreover, while some authors considered a linear behaviour of the human-seat coupled system [8, 15, 13], others developed non-linear models of foam [14]. It can also be noticed that all the studied vibration responses are deterministic, although human body variability and its impact on these responses has already been observed experimentally [19].

2.2 Model description

The seat design approach proposed in this study is based on the twenty DOFs model initially proposed by Kumbhar [13] and depicted in figure 1. It is composed of five rigid bodies, with their respective masses and centres of gravity, representing the occupant: the thighs (m_1, G_1), the pelvis (m_2,G_2), the torso (m_3, G_3), the head (m_4, G_4) and the viscera (m_5, G_5). Three additional bodies represent the seat: the seat frame (m_{st}), the cushion (m_c) and the backrest (m_{bc}). Each mass except m_5, has two translational motions (fore-aft and vertical ones) and one rotational motion. The viscera have only two translational motions. All masses except mass m_5 are connected to each other by joints ($J_{(i=1,\ldots,4)}$) formed by translational and torsional sets of springs (K_i, K_{ri}) and dampers (C_i, C_{ri}). The viscera are connected by a fore-aft and vertical set of springs and dampers. The contacts between seat masses and body masses are represented by points $c_{(i=1,2,3,25,35)}$. The fore-aft (K_{hi}, C_{hi}) and vertical (K_{vi}, C_{vi}) springs and dampers are associated to their respective masses.

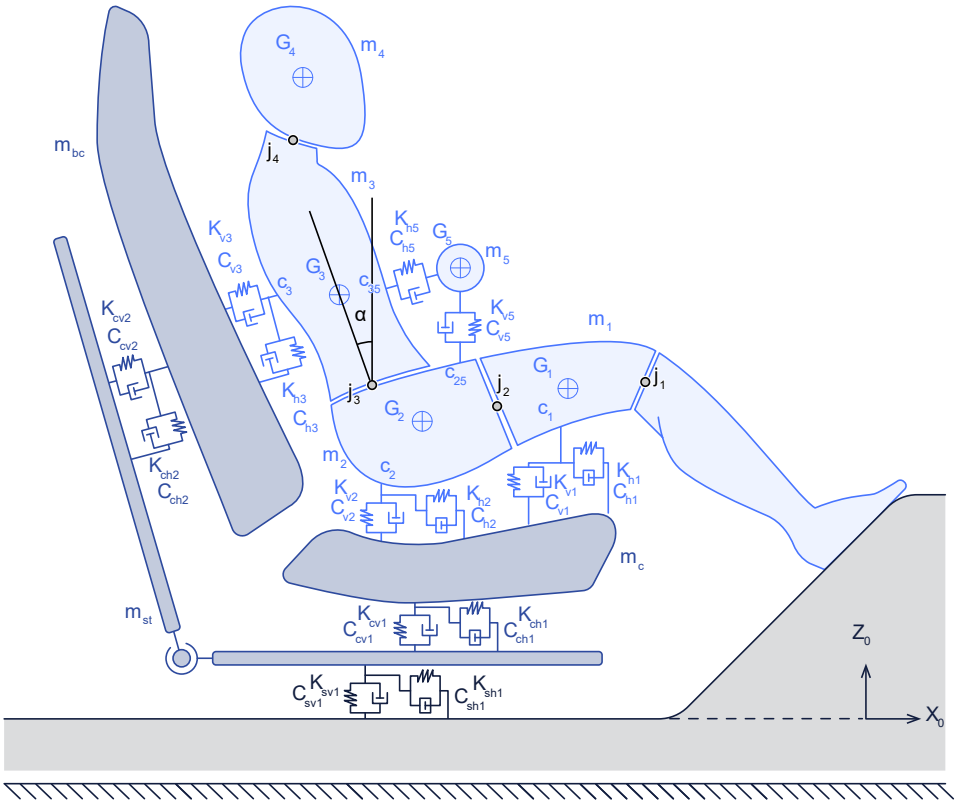


Figure 1: Human-seat model adapted from the Kumbhar's study [13]

The coordinates of each human body (depending on the backrest angle α) and the human body parameters are directly extracted from Liang and Chiang's study [15], representing a mean human (*i.e.* 71.3 kg total mass). A second set of masses has been derived in the present study to reach a 80 kg total mass. A traditional seat design is chosen, with suspension parameters (K_{sv1} and K_{sh1}) considered as rigid. The cushion parameters, given in table 1, are derived from measurements presented in a previous study [1].

Seat parameters	Suspension	Cushion
$m\ (kg)$	$m_{st} = 16.8$	$m_c = 1.3$
$K_h\ (N/m)$	$K_{sh1} = 1e8$	$-$
$K_v\ (N/m)$	$K_{sv1} = 1e8$	$K_{cv1} = 85866$
$C_v\ (N.s/m)$	$-$	$C_{cv1} = 448$

Table 1: Seat parameters

The twenty equations of motion associated to each DOF of the model, are derived using Newton's second law. Under both steady-state and harmonic excitation assumptions, this can be expressed in the frequency domain under matrix form as:

$$\left[-\omega^2 M + j\omega C + K\right] x(\omega) = f(\omega) \quad , \tag{1}$$

where $M \in \mathbb{R}^{(20;20)}$, $C \in \mathbb{R}^{(20;20)}$, $K \in \mathbb{R}^{(20;20)}$ represent the mass, damping and stiffness matrices, respectively; $x \in \mathbb{R}^{(20;1)}$ is the displacement vector and $f \in \mathbb{R}^{(20;1)}$ the input excitation vector (ω is the excitation frequency and $j^2 = -1$).

2.3 Test-model comparison

To ensure that the nominal values of the model input parameters are relevant, this computed response is compared to a previous transmissibility measurement with a human subject weighting 80 kg [1], as depicted in figure 2. Calculations are performed considering the second set of masses (80 kg total mass), a 21° backrest angle (*i.e.* automotive posture), and applying a unitary input displacements to the seat base. Among the twenty derived responses, only the cushion transmissibility in the vertical direction is considered, which is a commonly used response in the automotive industry. It is observed that the first resonance around 4.3 Hz is estimated with a 5 % error in frequency and a 29 % error in amplitude, with regard to the experimental data. The second resonance is also predicted and the filtration area is well fitted.

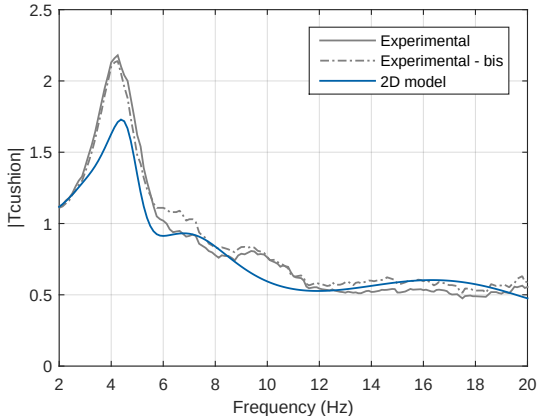


Figure 2: Test-model comparison of vertical cushion transmissibility

While these results seem encouraging for a direct computation, it can be noticed that some modifications could be performed to improve these predictions, by complementing the considered physical phenomena

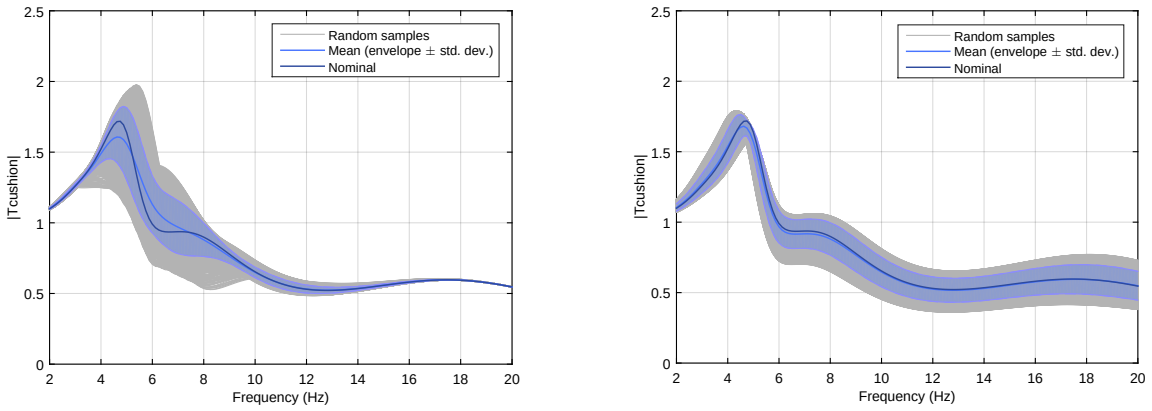
(e.g. reaction forces due to feet friction) and/or by updating the value of all or part of the model parameters. The former would mean modifying the initial modelling hypothesis, which is out of the scope of this study. The latter would need either complementary experimental characterizations (e.g. of each of the seat sub-component), or some computations to minimize the distance between both experimental and numerical responses. While this numerical approach has been preferred, it has been decided to handle the unknown variability of the human body rather than to determine some averaged parameters. Indeed, Toward and Griffin [19] showed that the variability between different mean-subjects can impact up to 30 % of the seat transmissibility response levels. Hence, it would be more accurate to compare sets of experimental/numerical responses, by taking these associated parametric uncertainties into account.

2.4 Transmissibility evolution

In order to help identifying the impact of these uncertainties on the dynamic behaviour of the human-seat coupled system, a global sensitivity analysis was performed by the authors [2]. While the complete methodology is out of the scope of this study, it seems interesting to visualize the evolution of the transmissibility involved by the variation of the most impacting factors identified, namely both stiffness K_{v5} and mass m_5 parameters of the viscera and the vertical stiffness of the cushion K_{cv1}.

Sample-based analyses using Monte Carlo simulations are usually performed for this purpose [10]. In a first step, probability distributions are specified for each input parameter; then, a high number of samples are generated accordingly; finally, the model is evaluated for each set of input parameters. Various algorithms are available to generate these samples, so as to cover most of the design space. In this study, Latin Hypercube sampling (stratified sampling) is subsequently used.

Figure 3 (a) depicts 1000 computed cushion transmissibilities where only the identified important input parameters from the human body (m_5 and K_{v5}) are varying. The blue shaded area represents the standard deviation of these transmissibilities, quantifying the dispersion of the response at each frequency. A low standard deviation indicates that the transmissibilities tend to be close to the mean (blue curve) of the set, while a high standard deviation indicates that the output responses are spread out over a wider range of values. The dark blue curve represents the nominal transmissibility.



(a) (b)

Figure 3: Evolutions of vertical cushion transmissibilities: (a) impact of human-body parameters; (b) impact of the seat parameter

Then, the input parameters associated to the human body are blocked to their nominal values, and only the influent seat parameter (K_{cv1}) is varying. A new sampling is performed to illustrate its impact on the vertical cushion transmissibility, as depicted in figure 3 (b). It is observed that while the evolution range induced by the variation of K_{cv1} is lower between 3 and 9 Hz, it is higher from 9 Hz than the evolution induced by

the variation of human body parameters (which is also confirmed by the narrower corridor defined by the standard deviation).

Therefore, it can be concluded that the input parameters of the human body have more impact than the seat ones on the transmissibility around the resonance frequency and that only the seat parameter has some impact on the filtration area.

3 Robust design methodology

Based on the previously described observations, the goal of this section is to propose a procedure to optimize the seat design while taking into account the lack of knowledge associated to the occupant's variability, in order to guarantee the robustness of the targeted notion of comfort.

3.1 Uncertainty quantification

According to the literature [5, 17], uncertainties in engineering sciences are often classified into two main categories:

- random uncertainties coming from the physical variability of the system and its environment (physical properties, assembly and operating conditions,...). These uncertainties can be related to model parameters or to the model itself and could be characterized;
- epistemic uncertainties coming from a lack of knowledge of the system (wrong values of parameters, unknown probability laws,...). These uncertainties are related to modeling issues or lack of experimental data. These uncertainties could be reduced by increasing the amount of available information on the system.

In this study, the variability of the coupled system is first considered as deriving from random uncertainties associated to the most impacting factors K_{v5}, m_5 and K_{cv1}. Such parametric approaches (as opposed to non-parametric ones [18]) are characterized by a mean value and a standard deviation or by a Probability Density Function (PDF) associated to each parameter considered as uncertain. Their nominal values are generally determined by measurements and the uncertainties are propagated through the computations using Monte Carlo based sampling methods [6]. For each independent sample, the deterministic response is calculated considering the probability distribution. The main drawback of these methods is the slow convergence of the solutions because an important number of random samples is needed [20]. Then, considering that a probabilistic approach may not be suitable to represent the high lack of knowledge on the human body parameters, an Info-Gap approach as initially proposed by Ben-Haim [3], is also proposed in this study to assess the robustness of a reliability-based (*i.e.* probabilistic) approach.

3.2 Deterministic optimization

As indicated in the introduction, the vertical cushion transmissibility is classically referred to as the most relevant feature to characterize the vibrational comfort: the main purpose is to lower the main resonance frequency and to increase the filtration area (*i.e.* $|T_{cushion}| < 1$). Hence, optimizing the dynamic response of the human-seat coupled system comes down to minimizing both the frequency resonance f_r and the area A under the cushion transmissibility curve. Regarding the results depicted in figure 3 (b), this would mainly require to decrease the K_{cv1} parameter, representing the stiffness of the cushion. However, it is easy to understand that this parameter corresponds to the material properties of the constitutive foam pad, whose static and dynamic behaviour are highly related [22].

3.2.1 Design constraint and objective definition

Therefore, a static design constraint is defined, corresponding to the maximum allowed sinking of the occupant in the seat, so as to guarantee an acceptable postural comfort. As the developed 2D-model does not handle such detailed geometrical aspects, a proportionality rule between the static displacement of the centre of gravity of the pelvis G_2, denoted d_{stat}, is used to define the constraint function D_{max}, as follows:

$$D_{max} = d_{stat} - d_0 \leq 0 \,, \tag{2}$$

where d_0 is a constant associated to the real maximum sinking as illustrated in figure 4.

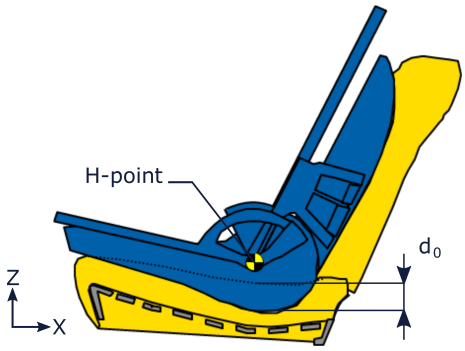


Figure 4: Illustration of the design constraint

Using the previous performance criteria f_r and A, a normalized cost function F_{cost} to minimize is further defined:

$$F_{cost} = \frac{1}{2}\left(\frac{A}{A_{nom}} + \frac{f_r}{f_{r\,nom}}\right) \,. \tag{3}$$

It can be noted that as none of the above observations tend to justify the use of different weightings on these features, an equal one is considered for the study.

The optimization problem thus consists in minimizing F_{cost} while still ensuring that D_{max} is verified, using a constrained non-linear optimization algorithm, with regard to the dynamic stiffness of the cushion K_{cv1}. Several numerical methods allow solving this kind of optimization problems among which constrained non-linear optimization algorithms are often used and implemented in commercial software. Thereafter, all the numerical computations are handled using *SIMBAD* software whose procedures are based on the Matlab Optimization Toolbox.

3.2.2 Deterministic optimal design (DO)

At first, the following simple mono-objective optimization problem is considered:

$$\begin{cases} \min\limits_{x\in\mathbb{R}} F_{cost}(x) \,,\ F_{cost} \in \mathbb{R} \\ \text{with:} \\ D_{max}(x) \leq 0 \,,\ D_{max} \in \mathbb{R} \end{cases} \,, \tag{4}$$

where x represents the considered design variable, namely the cushion dynamic stiffness K_{cv1}. It is solved using the *fmincon* Matlab function. For each transitional solution of this iterative procedure, the algorithm seeks the direction in the design space having the highest slope to converge to the nearest solution, potentially leading to a local minimum of the cost function. As observed in figure 5, the procedure converges after 19 iterations to an optimal design (DO) associated to an 8 % improvement of the performance, also corresponding to a 28 % reduction of the initial value of the cushion stiffness.

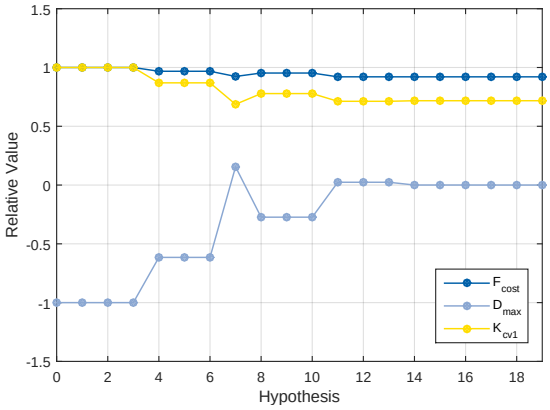


Figure 5: Evolution plots of the active design parameter, constraint and performance functions

While this solution does verify the optimization problem, it remains closely related to the considered occupant's parameters: as an example, a heavier occupant would inevitably lead to a lower performance and would not satisfy the static constraint requirement anymore. It is therefore necessary to go beyond such deterministic approaches to derive solutions whose performances are less sensitive to a variation of some uncontrolled input parameters.

3.3 Reliability-based approach

The next step is thus to perform a probabilistic reliability analysis, to define the probability for which the static constraint is guaranteed considering a given variability of the seat occupant.

3.3.1 Estimation of the probability of failure

A design is considered as reliable if it meets all the performance targets in the presence of parameter variations, *i.e.* if the system has a low chance of failure. In our case, the failure is directly related to the limit state of the constraint function, defined as:

$$D_{max}(x, \mathbf{u}) = 0 \,, \tag{5}$$

where $\mathbf{u}$ is the random variation of the uncertain human-body parameters, namely K_{v5} and m_5 as identified in a previous study [2]. The reliability R is thus defined as:

$$R = 1 - P_{fail} = P\left\{D_{max} < 0\right\} \,, \tag{6}$$

where the probability of failure P_{fail} is given by:

$$P_{fail} = \int_{D_{max}>0} f_u(\mathbf{u}) du \,, \tag{7}$$

where f_u is the Probability Density Function (PDF) of u.

It must be emphasized that, due to the complexity of the underlying problem, this integration is usually handled using numerical methods, as transformation methods or Monte Carlo simulations. Concerning transformation methods, the probability of failure is commonly estimated based on the First Order Reliability Method (FORM) or the Second Order Reliability Method (SORM). These initially require some iso-probabilistic transformations to convert the given random variables into standard normal ones. Based on the Rosenblatt transformation [16], the probability of the vector $\mathbf{u}$ (physical space) is thus transformed into

a vector $\mathbf{U}$, constituted of normal centred variables where the mean (μ) and the unitary standard deviation (σ) are dimensionless (standard space):

$$u = \mu + \sigma U \ . \tag{8}$$

In this study, a normal distribution $\mathcal{N}$ is assumed for random variation of both K_{v5} and m_5, whose parameters are arbitrarily fixed to $\mu = 1$ and $\sigma = 0.5$ (with regard to the nominal value of each parameter), because no information have been found in the literature on the variability of the viscera (or internal body parts) dynamic behaviour. Therefore, the probability of P_{fail} can be expressed, in the standard space, as:

$$P_{fail} = \int_{D_{max}>0} \Phi_U(\mathbf{U}) dU \ , \tag{9}$$

where Φ_U is the PDF of $U \propto \mathcal{N}(\mu, \sigma)$. Regarding the FORM method, the limit state function is approximated, using a first order Taylor expansion, by a plane tangent to the failure domain at the so-called Most Probable Point (MPP) $\mathbf{U}^*$. The probability of failure can thus be re-expressed as:

$$P_{fail} = \Phi(-\beta) \ , \tag{10}$$

where $\beta = \|\mathbf{U}^*\|$ is the distance between the centre of the PDFs and the MPP.

In this study, the reliability R associated to both nominal and deterministically optimized designs is computed, resulting in $R = 1$ and $R = 0.49$, respectively. In the former case, the design is far enough from the limit state to satisfy the constraint within the considered variability of the human-body. In the latter case, the MPP is located on the border between both safe and failure regions: regarding the chosen normal distributions, there is a 50 $\%$ chance of failure. It is concluded that the optimized design has a better performance but is less reliable than the nominal one.

3.3.2 Probabilistic Reliability-Based Design Optimization (RBDO)

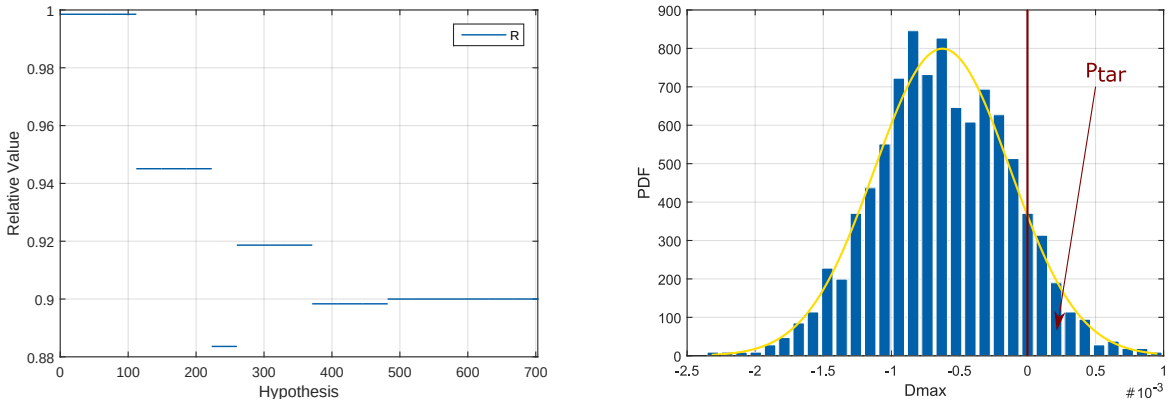
Following this reliability analysis, a new optimization problem is defined by considering an additional reliability constraint, arbitrarily fixed at $R_{tar} = 0.9$ (*i.e.* $P_{tar} = 1 - R_{tar}$):

$$\begin{cases} \min\limits_{x \in \mathbb{R}} F_{cost}(x) \ , \ F_{cost} \in \mathbb{R} \\ \text{with:} \\ D_{max}(x, \mathbf{u}) \leq 0 \ , \ D_{max} \in \mathbb{R} \\ P_{fail}(x, \mathbf{u}) \leq P_{tar} \end{cases} . \tag{11}$$

The purpose is to determine optimal values of the seat parameter leading to the best dynamic performance possible while ensuring that in 90 $\%$ of cases, the static constraint is also verified, when the human-body characteristics are allowed to vary in the considered intervals.

As observed in figure 6 (a), the procedure converged after 700 iterations. Using the optimal values of the parameter resulting from the last iteration, a Monte Carlo sampling analysis is performed to check if the reliability target is reached. The derived estimated PDF of D_{max} illustrated in figure 6 (b) further confirms the expected target.

The derived reliability-based optimal design (RBDO) leads to a 4 $\%$ improvement of the performance, compared to the nominal one, as summarized in table 2. It can be concluded that the RBDO procedure could allow taking into account some probabilistic information about the human-body variability through the dynamic comfort design process.



(a) (b)

Figure 6: (a) Evolution plot of the reliability function; (b) Probability Density Function of D_{max}

Output feature	Nominal	DO	RBDO
Cushion stiffness (K_{cv1})	1	0.72	0.84
Reliability (R)	1	0.49	0.90
Performance (F_{cost})	1	0.92	0.96

Table 2: Comparison of the optimal solutions (relative values)

3.3.3 Discussion

Figure 7 compares the vertical transmissibilities obtained using both derived optimal solutions to the nominal response. It is observed that the progression margin to optimize the transmissibility of a standard seat is very low. However, while such procedures give reliable designs, the way their performance will evolve with regard to variations of the occupant is still unknown. Indeed, as these solutions are optimal ones, their associated performance will inevitability get worse as the allowed variability on the human-body characteristic increases. It is thus necessary to investigate the robustness of each of theses solutions.

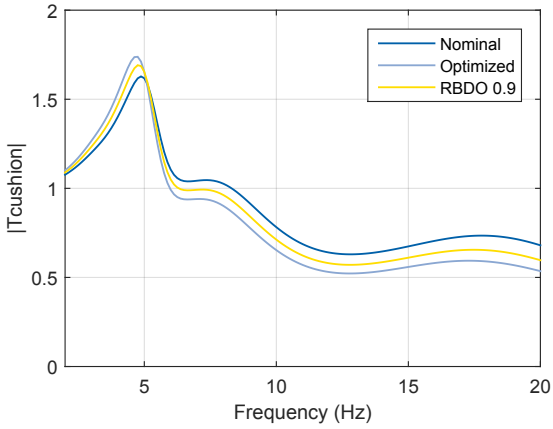


Figure 7: Comparison of optimized transmissibilities

3.4 Robustness assessment

Finally, a robustness analysis is performed, to observe the impact of lack of knowledge (concerning the variability of the viscera parameters) on the system performance.

3.4.1 Info-Gap formulation

The Info-Gap theory aims to quantify the robustness of model-based decisions to lack of knowledge in the system model [4]. This approach provides a useful framework to investigate the trade-off between performance and robustness but also to compare different candidate design solutions. Considering its general formulation, it has been used in a variety of fields, and in particular in structural dynamics concerning, for example, model updating [11], reliability analysis [9], robust design [12].

This type of analysis aims to quantify the difference (*i.e.* the gap) between the information that is known, e.g. the nominal value of a parameter, and the information that has to be known in order to ensure an *a priori* defined critical level of performance. In this study, the main idea is to handle the strong lack of knowledge on the viscera parameters K_{v5} and m_5 by assuming that the vector of the mean values $\boldsymbol{\mu}$ of the associated normal distributions, as initially (and arbitrarily) chosen for the reliability analysis, may vary from their nominal (*i.e.* best estimated) values $\tilde{\boldsymbol{\mu}}$ according to the following relation:

$$\mathcal{U}\left(\tilde{\boldsymbol{\mu}}, h\right) = \left\{\boldsymbol{\mu} \ : \ |\boldsymbol{\mu} - \tilde{\boldsymbol{\mu}}| \leq h\tilde{\boldsymbol{\mu}}\right\} \ , h \geq 0 \, . \tag{12}$$

This quantity is usually referred to as the "uncertainty model" and consists in a collection of nested sets of uncertain values of $\boldsymbol{\mu}$, centred on $\tilde{\boldsymbol{\mu}}$, whose size is controlled by a dispersion parameter h called the "horizon of uncertainty": the larger the horizon, the more inclusive the uncertainty.
The robustness function $\hat{h}$ is further defined as the greatest value of h up to which a chosen criterion $\mathcal{C}$ (e.g. the probability of failure P_{fail} or the performance criterion F_{cost} in what follows) is satisfied for all realization of the uncertainty model:

$$\hat{h} = \max\left\{h \ : \ \left(\max_{\mu \in \mathcal{U}(\tilde{\mu}, h)} \left(\mathcal{C}(x, \boldsymbol{\mu}) \leq \mathcal{C}_{crit}\right)\right)\right\} \ , \tag{13}$$

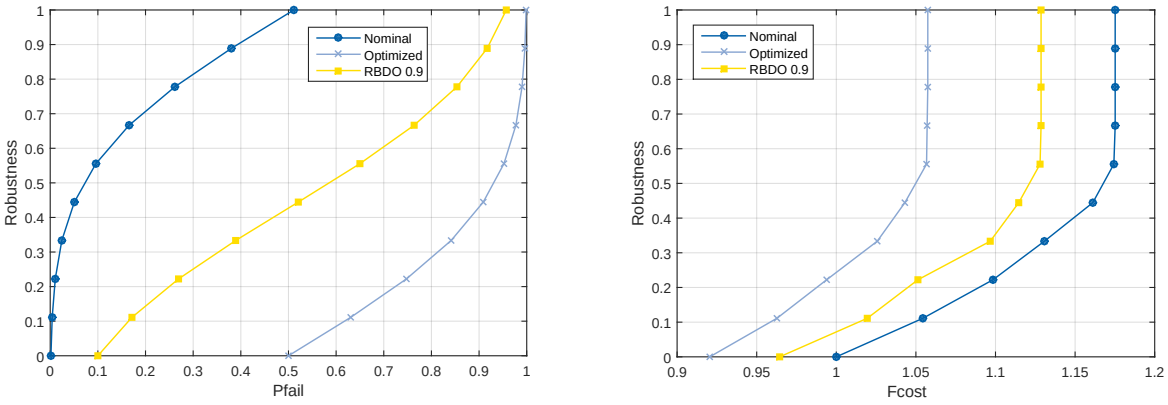
where $\mathcal{C}_{crit}$ is the maximum allowable value of the considered criterion. According to this definition, determining this robustness function comes down to numerically solve a complex non-linear optimization problem. In practice, the robustness is derived by determining the worse value of $\mathcal{C}$ for a given level of uncertainty h_i:

$$C_{crit,h_i} = \max_{\mu \in \mathcal{U}(\tilde{\mu}, h)} \mathcal{C}(x, \boldsymbol{\mu}) \, . \tag{14}$$

3.4.2 Discussion

Figure 8 shows the robustness curves associated to both the probability of failure P_{fail} (figure (a)) and the previously defined performance F_{cost} (figure (b)). Each figure considers three cases corresponding to the solutions given in table 2. It is observed, figure 8 (a), that the nominal design is the most robust from a reliability point of view (highest slope of the curve) but this solution is only designed for a mean human. This can be explained by the fact that: the initial design point is not an optimal value; the static design constraint corresponds to an extreme configuration where the weight of the occupant is a lot heavier than the reference weight considered for the design. Moreover, the reliability-based design has a better robustness than the deterministically optimized one: indeed, this design fulfils the static constraint in 90 $\%$ of the cases and has a lower deterioration due to uncertainties than the optimal design. It is observed, figure 8 (b), that the performance decreases (*i.e.* F_{cost} increases) as the uncertainty increases, which illustrates that optimal solutions are not robust. However, the performance of both reliability-based design and deterministically optimized design remain better than the nominal one, the latter being the best one.

In view of these results, it can be concluded that a trade-off has to be made between reliability and performance of the design (as their robustness curves are conversely ranked), depending on the lack of knowledge that the seat manufacturer is ready to tolerate.



(a) (b)

Figure 8: Info-Gap robustness curves: (a) probability of failure P_{fail}; (b) performance F_{cost}

4 Conclusion

The main contribution of this study is the presentation of a robust design procedure taking into account the lack of knowledge associated to the occupant's variability in order to optimize the vertical cushion transmissibility. The derived solutions illustrate that a compromise between a reliable design and an optimal one is necessary. However, the performance improvement of these solutions still remains limited by the considered multi-body model. Hence, complementing the multi-body model by a more complex description of the foam behaviour could lead to significant modifications of the transmissibility. Finally, the Info-gap analysis emphasized the need to handle the variability of the seat occupant through the whole design procedure, allowing to assess the robustness level of a given design, for a tolerated lack of knowledge on the human body properties. Such tools could thus help seat manufacturers to provide not only "comfort for all" but also a "personalized comfort".

Acknowledgements

The authors would like to thank Dr. Scott Cogan from FEMTO-ST Institute, University of Franche-Comté, Besançon, France, for allowing to use SIMBAD software version 1.0.0, Copyright © 2010-2016 by CNRS.

References

[1] R. Barbeau, T. Weisser, R. Dupuis, E. Aubry & S. Baudu, *Caractérisation expérimentale du comportement dynamique d'un siège automobile*, Congrès Français d'Acoustique, Le Mans, (2016).

[2] R. Barbeau, T. Weisser, R. Dupuis, E. Aubry & S. Baudu, *Optimization of the dynamic comfort of automotive seats: Investigation of the impact of human body variability*, 52nd Human Response to Vibration Conference, Shrivenham, United Kingdom, (2017).

[3] Y. Ben-Haim, S. Cogan & L. Sanseigne, *Usability of mathematical models in mechanical decision processes*, Mechanical Systems and Signal Processing, Vol. 12(1), pp. 121-134, (1998).

[4] Y. Ben-Haim, *Info-Gap Decision Theory: Decision Under Severe Uncertainty*, second ed., Academic Press, Oxford, United Kingdom, (2006).

[5] H. G. Beyer & B. Sendhoff, *Robust optimization - a comprehensive survey*, Computer methods in applied mechanics and engineering, Vol. 196(33), pp. 3190-3218, (2007).

[6] G. Blatman, B. Sudret, & M. Berveiller, *Quasi random numbers in stochastic finite element analysis*, Mechanics & Industry, Vol. 8(3), pp. 289-297, (2007).

[7] H. Bubb, H. Strasser, K. Kluth & H. Rausch, *Quality of Work and Products in Enterprise of the Future*, Proceedings of the Annual Spring Conference of the GfA and the XVII Annual Conference of the International Society for Occupational Ergonomics & Safety, ergonomia Verlag oHG, (2003).

[8] Y. Cho Y & Y. Yoon, *Biomechanical model of human on seat with backrest for evaluating ride quality*, International Journal of Industrial Ergonomics, Vol. 27.5, pp. 331-345, (2001).

[9] M. Guedri, S. Cogan & N. Bouhaddi, *Robustness of structural reliability analyses to epistemic uncertainties*, Mechanical Systems and Signal Processing, Vol. 28, pp. 458-469, (2012).

[10] J. C. Helton & F. J. Davis, *Sampling Based Methods*, Mathematical and Statistical Methods for Sensitivity Analysis of Model Output, Chapter 6, (2000).

[11] F. Hemez, & Y. Ben-Haim, *Info-gap robustness for the correlation of test and simulations in non-linear transient*, Mechanical Systems and Signal Processing, Vol. 18, pp. 1443-1467, (2004).

[12] A. Hot, T. Weisser & S. Cogan, *An info-gap application to robust design of a prestressed space structure under epistemic uncertainties*, Mechanical Systems and Signal Processing, Vol. 91, pp. 1-9, (2017).

[13] P. B. Kumbhar, *Simulation-Based Virtual Driver Fatigue Prediction and Determination of Optimal Vehicle Seat Dynamic Parameters*, Master thesis, Texas Tech University, (2013).

[14] T. Kim, Y. Cho & Y. Yoon, *Dynamic Ride Quality Investigation and DB of Ride Values for Passenger and RV cars*, SAE Technical Paper 2001-01-0384, (2001).

[15] C. C. Liang & C. F. Chiang, *Modeling of a Seated Human Body Exposed to Vertical Vibrations in Various Automotive Postures*, Industrial Health, Vol. 46, pp. 125-137, (2008).

[16] M. Rosenblatt, *Remarks on a multivariate transformation*, The annals of mathematical statistics, Vol. 23(3), pp. 470-472, (1952).

[17] G. I. Schuëller & H. A. Jensen, *Computational methods in optimization considering uncertainties - an overview*, Computer Methods in Applied Mechanics and Engineering, Vol. 198(1), pp. 2-13, (2008).

[18] C. Soize, *A comprehensive overview of a non-parametric probabilistic approach of model uncertainties for predictive models in structural dynamics*, Journal of sound and vibration, Vol. 288(3), pp. 623-652, (2005).

[19] M. GR. Toward & M. J. Griffin, *The transmission of vertical vibration through seats: Influence of the characteristics of the human body*, Journal of Sound and Vibration, Vol. 330.26, pp. 6526-6543, (2011).

[20] B. Yu & P. Mykland, *Looking at Markov samplers through cusum path plots: a simple diagnostic idea*, Statistics and Computing, Vol. 8(3), pp. 275-286, (1998).

[21] L. A. Zadeh, *Fuzzy sets*, Information and control, Vol. 8(3), pp. 338-353, (1965).

[22] X. Zhang, *Measurement and modelling of seating dynamics to predict seat transmissibility*, PhD thesis, University of Southampton, (2014).

Assessment of the potential of trim parts to reduce structure-borne noise in the interior of vehicles

R. Stelzer[1], T. Delpero[1], R. D'Amico[1]
[1] Autoneum Management AG
Schlosstalstrasse 43, 8406 Winterthur, Switzerland
e-mail: **rainer.stelzer@autoneum.com**

Abstract
The selection of the appropriate bills of materials for NVH trims for vehicle interiors, like carpets or inner dashes, is usually based on a trade-off between light weight and insulation performance generally with respect to airborne excitations. This paper is focused on understanding how the reduction of structure-borne noise could be also taken into account as metrics for bills of materials selection. Especially in early stage development phases, it would be preferable to take decisions for the bill of materials based on rather simple test cases, such as small flat samples of the trim. In order to link sample to vehicle-level performance, this paper investigates different scenarios both at experimental and simulation level while discussing the relation between the structure-borne insertion loss and the SPL in the passenger cabin of a vehicle. Experimental data are obtained with tailored test setups that allow estimating the structure-borne performance either of flat samples or from vehicle-level.

1 Introduction

A system like a car is excited by different sound sources, which are mainly split into two categories, airborne and structure-borne. When the structure of a system is excited by sound waves travelling in air, one talks about airborne noise. Instead, when the same structure is directly excited on its surface by an attached structural part or by an impact from another structure, like a hammer, one talks about structure-borne noise. For most of the cars, which are nowadays on the market, it is said that the structure-borne noise is more a low frequency issue up to about 800/ 1000 Hz [1] and the air-borne noise is more an issue at frequencies higher than 400/500 Hz.

To reduce the noise in the passenger compartment due to these sources, trim parts are placed on top of the main structural panels, like a carpet system on the floor or some layers of trim on the inner side of the dash. The main requirements to such trims are that they are as light as possible and that their ability to reduce noise is as high as possible. However, when it comes to the performance, an easy-to-measure quantity that characterizes the acoustics in the vehicle is necessary to rank different trims and to select the one that fits best to acoustic requirements.

In the automotive industry the investigation of the structure borne performance of trims is not as popular as the one of the airborne performance, and there is only a limited number of articles about it. In [1] this topic is mainly discussed on the basis of measurements and simulation for flat small plates, which are partly coupled to a small reverberant box. Additionally, simulations are shown for a point-force excited floor mock-up which is coupled to the air-filled passenger compartment of a car. Several indicators are used to rank the performances of trims. Velocities and accelerations of the underlying structures and of the top of the trim are compared as well as sound pressure levels (SPL) in the air. In [2] the structure-borne performance of trims and their dependence on different underlying structural materials for the main floor, steel or CFRP, are compared using the mobility on the floor structure and on the top layer of the trim. Another possible quantity to compare the structure-borne acoustic performance of a trim is the structure-borne insertion loss. In the articles of Bertolini [3], Nelisse [4] and Lu [5] measurements and simulations

of it are shown for flat plates. Based on this data also the relation between the Airborne Insertion Loss (ABIL) and the Structure-borne Insertion Loss (SBIL) is discussed.

The aim of this paper is not to add another quantity to characterize the structure borne performance, but rather to discuss the relation between all these quantities and to investigate the possibility to transfer results obtained for the structure-borne performance on the level of small flat plates to vehicle level. For the first topic, the definition of the SBIL and the acoustic radiation from a vibrating panel are discussed in chapter 3. As the sound radiation is independent from the excitation, the ABIL is exploited instead of the SBIL in examples. The ABIL and the related transmission loss are quantities, which are commonly accepted and easily interpreted. A key question here is whether the acoustic performance at vehicle level - in terms of SPL but also ranking of different trim materials - is reflected on the performance at flat sample level. If at least the ranking would be the same, the main design choices for the acoustic trims could be done based on flat samples, leading to drastic reduction of time consumption when measuring or simulating vehicle level performance. For this purpose, the measurement and simulation results for two experimental set-ups are compared in chapter 4. The numerical and experimental set-ups used for this investigation are described in chapter 2.

2 Setup and models for SBIL assessment

Two measurement setups have been used for studying the structure-borne acoustic performance of passive treatments. The first consists of a heavy and stiff frame with a table-like shape on which different flat plates can be fixed on the top (see Figure 1). The dimensions of the plate are about 70x80 cm, and a shaker is placed close to one of the corners of the plate to excite it directly as a point force. The velocities of the plate or, in the trimmed configuration, of the top layer of the trim are measured on a grid of 195 points with a laser vibrometer. Additionally, accelerations at selected points are measured from below on the surface of the plate using accelerometers. A similar setup is also used for a floor mockup. As shown in Figure 2 the top of a body in white of a car is cut so that mainly the dash, the floor and the lower part of the trunk remain. The chosen excitation points for the shaker are located on the front beam, at one of the engine attachment points, and in the rear on the trunk floor, at one of the rear axle attachment points. These points are among the typical structure-borne excitation points in a real car. The velocities on the different surfaces are measured again by a laser vibrometer from the bottom and the top of the floor. Up to now, the used measurements procedure is only able to measure the velocities of impervious surfaces like steel or heavy layer.

Similarly to the two measurement set-ups two simulation models have been created (see Figure 3). The chosen excitations in the simulations are the same as in the measurements and the used simulation software is Actran. Besides the velocities on points similar to those in the measurements the software can automatically calculate the radiated sound power from surfaces and many other indicators. Additionally, to the two simulation models for the structure borne excitation, the model of a car is used for airborne simulations in the next chapter. An engine bay is coupled here through a dash structure to the passenger compartment. The excitation, a simplified vibrating engine, is located in the engine bay and the radiation towards the passenger compartment is simulated.

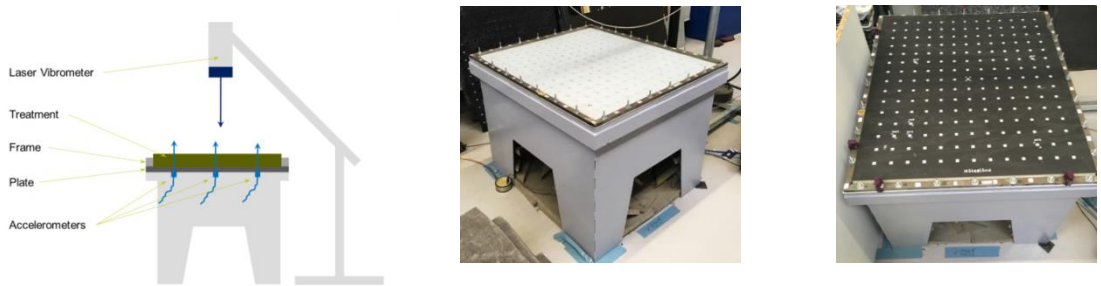


Figure 1: Measurement set-up to investigate the behavior of trims on top of flat plates

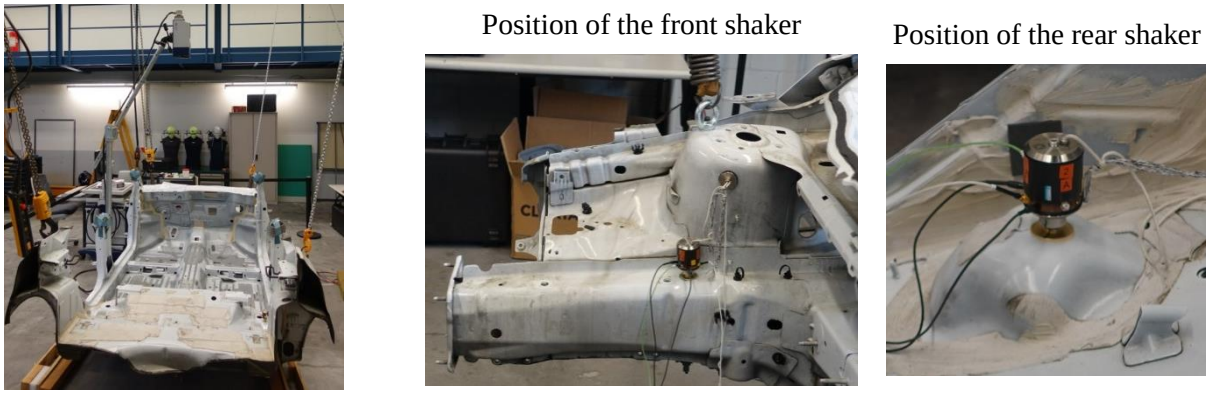


Figure 2: Measurement set-up to investigate the behavior of trims on top of a real floor mock-up

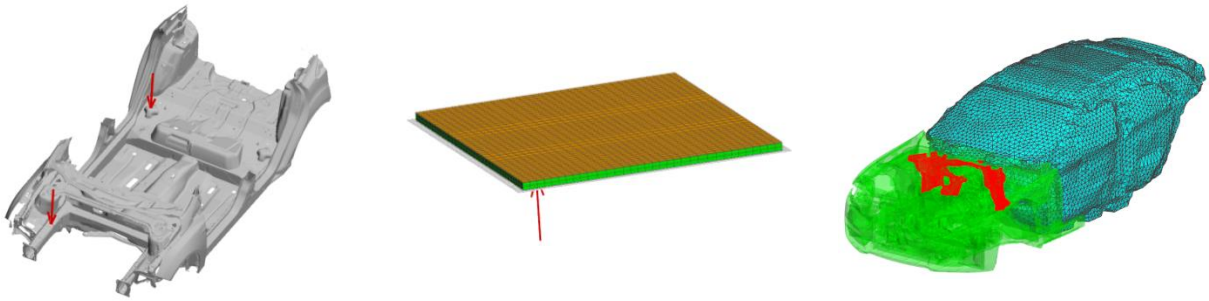


Figure 3: Used simulation models: floor mock-up, clamped flat plate and engine bay coupled to a passenger compartment through a dash structure

3 Insertion losses and relation to other acoustic measurable

The ideal comparison of the acoustic performance of different trims would be based on one single and unique value or curve for each trim that is independent from the environment around. A very common indicator in acoustics for whole partitions is the Transmission Loss (TL). For this quantity, it is assumed that the excitation is airborne, the partition is excited by sound waves in a fluid. TL is defined as follows, using the ratio between the incident power P_i and the transmitted power P_t:

$$TL = 10\log_{10}\frac{1}{\tau} = 10\log_{10}\frac{P_i}{P_t} \tag{1}$$

where τ is the transmission coefficient. To get a describing quantity just for the additional trim on top of wall/ partition, the difference between the transmission loss with and without a trim is taken. This difference is called Insertion Loss (IL) or, more precisely, the Airborne Insertion Loss (ABIL) [6].

$$ABIL = TL_{with\ trim} - TL_{bare} \tag{2}$$

A similar definition for insertion loss can be used under the assumption of structure-borne noise excitation. Instead of the incident power the input power into the structure is used. In this way, the Structure Borne Insertion Loss SBIL can be defined like that [6]:

$$SBIL = SBTL_{with\ trim} - SBTL_{bare} = 10\log_{10}\left(\frac{P_{in}}{P_{rad}}\right)_{with\ trim} - 10\log_{10}\left(\frac{P_{in}}{P_{rad}}\right)_{bare} \tag{3}$$

where the transmitted power P_t is renamed as radiated power P_{rad} and minuend and subtrahend can be called structure-borne TLs [3] or vibro-acoustic power transfer functions.

Main practical important questions are: what does such an IL, airborne or structure borne, mean for the people that are sitting in a closed room like inside a car? In terms of measurable, what is the relation to the sound pressure level (SPL)? Another question that matters for simulations and measurements is the relation between the surface velocity and the IL. Is it possible to measure/ simulate just the velocity of the top surface of a structure in untrimmed and trimmed condition and to determine in a simple way the IL? These questions can be answered by discussing the possibilities to measure and to calculate the airborne transmission loss and by investigating the sound radiation under different conditions.

3.1 Diffuse sound field

One way to obtain the TL is the usage of a double room suite. A room that is acoustically excited by loudspeakers (sending room) is coupled only through a window to a second receiving room. In the window the partition is placed which should be investigated regarding its TL. Assuming that the sound field is diffuse in the sending room, which is true above a certain frequency and depending on the room size, the incident power P_i can be expressed as a function of the mean squared sound pressure p_S^2 in this room [7].

$$P_i = \frac{S p_S^2}{4\rho c} \tag{4}$$

where S is the surface of the partition mounted in the window and ρ and c are respectively the density and the speed of sound of air in the room. The radiated/ transmitted power can be determined as follows from the mean quadratic pressure p_R^2 in the receiving room under the same assumptions and the relation that the radiated power is equal to the power dissipated in this room:

$$P_t = \frac{A_R p_R^2}{4\rho c} \tag{5}$$

where A_R is the equivalent absorption area of the receiving room. The TL can be written using equations 1, 4 and 5 therefore as [7]

$$TL = 10\log_{10}\frac{S p_S^2}{A_R p_R^2} = SPL_S - SPL_R - 10\log_{10}\frac{A_R}{S} \tag{6}$$

where SPL_S and SPL_R are the sound pressure levels in the sending and the receiving room. Thus, when the absorption area of the receiving room is known, the TL can be determined simply by measuring the mean quadratic pressures in both rooms. That means that the ABIL is equal to the difference between the SPLs of the receiving room without and with the trim when the absorption of the receiving room remains the same (or similar) in these two cases and as long as the excitation in the sending room stays equal.

$$ABIL = TL_{with\ trim} - TL_{bare} \approx SPL_{R,bare} - SPL_{R,with\ trim} \tag{7}$$

Inserting equation 5 for the transmitted/ radiated power of the structure-borne insertion loss SBIL into equation 3, and under the same assumptions made for the validity of formula (7) it follows that:

$$\begin{aligned} SBIL &= 10\log_{10}\left(\frac{P_{in}}{P_{rad}}\right)_{with\ trim} - 10\log_{10}\left(\frac{P_{in}}{P_{rad}}\right)_{bare} \\ &\approx 10\log_{10}\left(\frac{P_{in\ with\ trim}}{P_{in\ bare}}\right) + SPL_{R,bare} - SPL_{R,with\ trim} \end{aligned} \tag{8}$$

If we can further assume that the input power is the same in trimmed and bare conditions (which actually happens in many cases of interest, as explained in following sections), also the SBIL is equal to the difference between the SPLs in bare and trimmed conditions That raises the question if there is such a direct link between the IL, both SBIL and ABIL, and the delta SPL in general and not only under the condition of a diffuse field on the radiation side.

3.2 Radiation of sound into free acoustic field

For this purpose, it is necessary to start again from the basic equation for the TL and the definition of the radiated power P_{rad}. This leads to the intensity I and its relation with the sound particle velocity v and sound pressure p on the surface S of the partition that is radiating the sound.

$$P_{rad} = \frac{1}{2}\, Re\left(\int_S \vec{I}\,\vec{n}\, dS\right) = \frac{1}{2} Re\left(\int_S p\,\overrightarrow{v^*}\,\vec{n}\, dS\right) \tag{9}$$

Where * denotes the complex conjugate of a quantity and n is the normal vector of the surface. Using the fact that the sound particle velocity v and sound pressure p are coupled with an acoustic impedance

$$Z = \frac{p}{v} \tag{10}$$

The previous equation for the radiated sound power/ intensity can be written as follows:

$$P_{rad} = \frac{1}{2} Re\left(\int_S p\,\overrightarrow{v^*}\,\vec{n}\, dS\right) = \frac{1}{2} Re\left(\int_S \frac{pp^*}{Z} dS\right) = \frac{1}{2} Re\left(\int_S Z\,\vec{v}\overrightarrow{v^*}\, dS\right) \tag{11}$$

Inserting this equation in equation 2 it follows for example for the ABIL written as a function of the pressure ("trim" denotes partition with trim on top):

$$ABIL = 10\log_{10}\left(\frac{P_{i,trim}}{P_{i,bare}}\right) + 10\log_{10} Re\left(\frac{1}{2}\int_S \frac{pp^*}{Z} dS\right)_{bare} - 10\log_{10} Re\left(\frac{1}{2}\int_S \frac{pp^*}{Z} dS\right)_{trim} \tag{12}$$

Or as a function of the velocity it gives

$$ABIL = 10\log_{10}\left(\frac{P_{i,trim}}{P_{i,bare}}\right) + 10\log_{10} Re\left(\frac{1}{2}\int_S Z\vec{v}\overrightarrow{v^*}\, dS\right)_{bare} - 10\log_{10} Re\left(\frac{1}{2}\int_S Z\vec{v}\overrightarrow{v^*}\, dS\right)_{trim} \tag{13}$$

When the incident power stays the same and when the acoustic radiation impedance is independent from the location and the configuration of the partition, with and without trim, the ABIL is just given by

$$ABIL = TL_{with\ trim} - TL_{bare} = SPL_{R,bare} - SPL_{R,with\ trim} \tag{14}$$

Or it can be written in terms of velocity as

$$ABIL = 10\log_{10}\left(\overline{v^2}\right)_{bare} - 10\log_{10}\left(\overline{v^2}\right)_{with\ trim} = PVL_{R,bare} - PVL_{R,with\ trim} \tag{15}$$

where $\overline{v^2}$ is the mean square velocity of the surface of the partition. Similar to the SPL its logarithmic value is named here as Particle Velocity Level (PVL). The same relations between IL and SPL and PVL are valid for the structure-borne sound, when the input power for the partition is equal with and without trim.

As demonstrated before this is the case for a diffuse field on the radiation side. Another very often assumed case is the plane wave radiation to a free/ semi-infinte sound field. This is assumed for example for the Transfer Matrix Method or in the mass law for the TL in which the partition is also assumed to be infinite so that the boundary conditions play no role [6]. Here, the radiation impedance is only depending on the fluid density and the sound of the speed in the fluid.

$$Z = \rho c \tag{16}$$

Thus, the equalities shown in equations 14 and 15 are valid also in this case. For a general small plate that is baffled in rigid wall and radiating in the free sound field the radiation impedance becomes more complicate. The relation between the velocity of the panel and the acoustic pressure on the surface can be described by the Rayleigh-Integral in which it is assumed that each point of the panel is a point source radiating to a semi-infinite space [8].

$$p(r) = \frac{i\omega\rho}{2\pi}\int_S \frac{\mathrm{v}(r_s)e^{-ikR}}{R}dS \tag{17}$$

where k is the wavenumber of air, ω is the angular frequency and R is the distance between an arbitrary position on the surface and the position r_S of the source point. Equation 17 can be written in of terms of structural mode shapes φ_n[8]:

$$p = \sum_n \frac{i\omega\rho v_n}{2\pi}\int_S \frac{\Phi_n e^{-ikR}}{R}dS \tag{18}$$

where v_n is the modal amplitude of the velocity for the mode n. Thus, it can be stated that there is a radiation impedance Z_n for each mode.

$$Z_n = \frac{p_n}{v_n} = \frac{i\omega\rho}{2\pi}\int_S \frac{\Phi_n e^{-ikR}}{R} \tag{19}$$

This demonstrates that the radiation impedance and the radiation to the fluid are in general depending on the partition and its vibrational behavior that is related to the size and the material properties. To show the consequence of this result on an illustrative example the sound radiation efficiency, σ, is used instead of the radiation impedance. The real radiated power P_{rad} is in this quantity compared to the power which would be radiated in case of a plane wave radiation and is defined as follows [9]:

$$\sigma = \frac{P_{rad}}{\rho c S \overline{v^2}} \tag{20}$$

where $\overline{v^2}$ is the mean square velocity of the surface of the partition. That means in case of a plane wave radiation, Z=ρc, σ is equal to one. In all other cases σ is in general smaller than 1. Equation 2 for the IL can be rewritten using the radiation efficiency instead of the impedance:

$$ABIL = 10\log_{10}\left(\frac{P_{i,trim}}{P_{i,bare}}\right) + 10\log_{10}\left(\overline{v^2}\right)_{bare} - 10\log_{10}\left(\overline{v^2}\right)_{with\ trim} + 10\log_{10}\left(\frac{\sigma_{bare}}{\sigma_{with\ trim}}\right) \tag{21}$$

When introducing a trim on top of the plate, its presence influences the radiation efficiency to the free field. Such a change is quantified by the fourth component of equation (21). To show its relevance in the overall sum, the radiation efficiency can be quantified for a plate with and without trim, as shown in Figure 4. When including the trim, the radiation efficiency is also impacted around the mass-spring resonance of the trim. Similar experimental analysis has been carried out by Devaux and Dauchez [10]. The ratio between the radiation efficiency of the top layer with and without trim for this specific case is quantified in Figure 4. It can reach 20dB and therefore it is not negligible. Consequently, in free field there is no equality between IL, delta SPL and delta PVL.

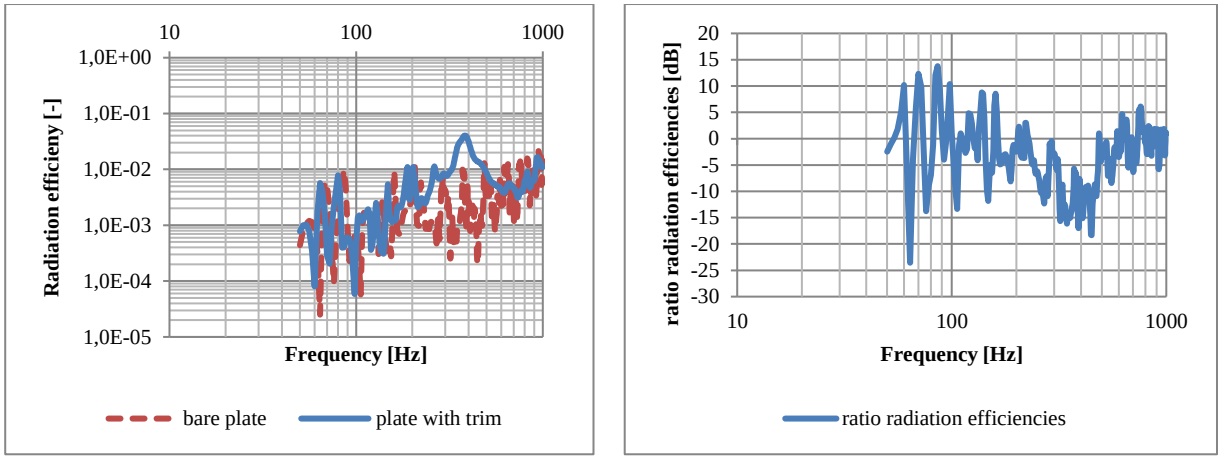


Figure 4: Radiation efficiencies of a plate with and without a foam heavy layer trim and their delta

3.3 Radiation into a passenger compartment of a car

In case of a vehicle compartment there is neither a free field radiation nor necessarily a diffuse field in the frequency range up to about 1000 Hz in which the structure-borne sound has an important contribution to the overall noise. The sound field is not yet diffuse enough but dominated by a reverberant sound field which has a low modal density. As explained in [11] room/ cavity modes are at the end plane waves, but the modal shapes of the partition and the fluid are not matching and they are not exactly at the same frequency. This interaction can be described for example with the modal interaction work [12]. Because of that and simply the fact that the modal density is much smaller than in an ideal diffuse field (infinite modal density), the radiation/ acoustic energy transfer is also much less efficient than in the diffuse field. But of course the sound field becomes more and more diffuse with increasing frequency, because the modal density μ is increasing quadratically with the frequency f and is approximately given by [11]:

$$\mu = \frac{4\pi f^2 V}{c^3} \tag{22}$$

where V and the c are the volume and the speed of sound of the air of the room/ passenger compartment.

To further analyze the in-situ situation for cars the example of a simplified structure of a dash is taken, which is excited from the engine bay and radiating towards the passenger compartment (see Figure 3). Figure 5 shows the simulated TL for a dash structure of a vehicle in bare and trimmed conditions (foam-heavy layer) under different radiation conditions. When the dash structure is radiating in a closed passenger compartment of a car, the TL is higher than radiating into a free field especially at low frequencies. But with an increasing frequency the two results are going towards each other especially for the bare dash and towards the result which is obtained using the transfer matrix method (infinite flat panel and plane wave radiation). In contrast to that the two ABIL curves for free field and closed-cavity radiation (Figure 6) are very similar and the differences between them are small in the whole frequency range. The difference to the ABIL simulated with TMM is quite big around the spring-mass resonance of the trim. For the sake of completeness it has to be said that the trim has been placed here towards the radiation side and the ABIL is even more independent from the radiation condition, free field or closed cavity, when it is placed towards the source side (see Figure 6). It demonstrates also that under realistic conditions the TL and IL are not fully invariant against the transposition of source and receiving side as it is the case for infinite flat structures with a plane wave radiation as assumed for the TMM.

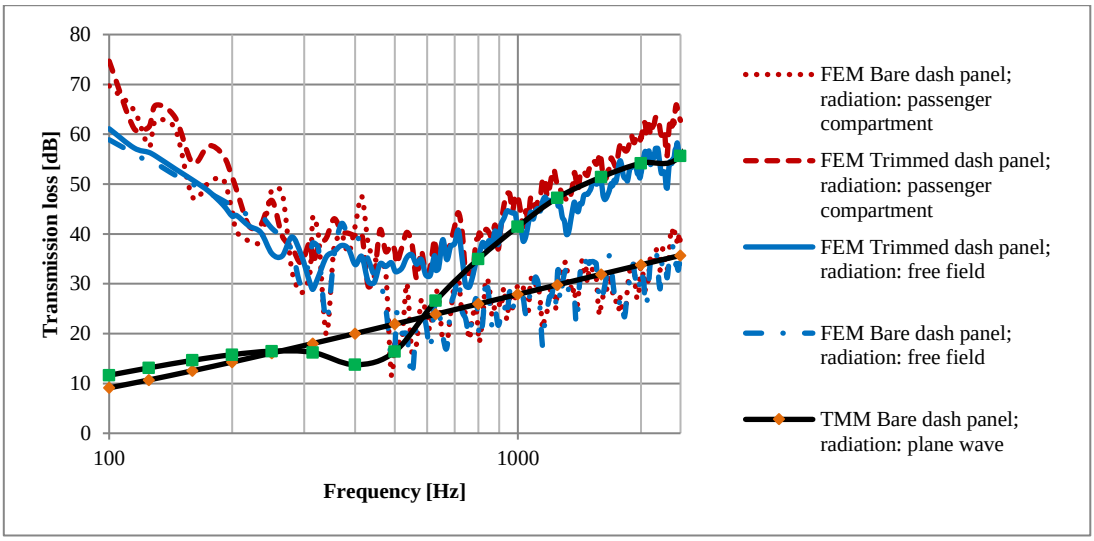


Figure 5: Transmission loss under different radiation conditions

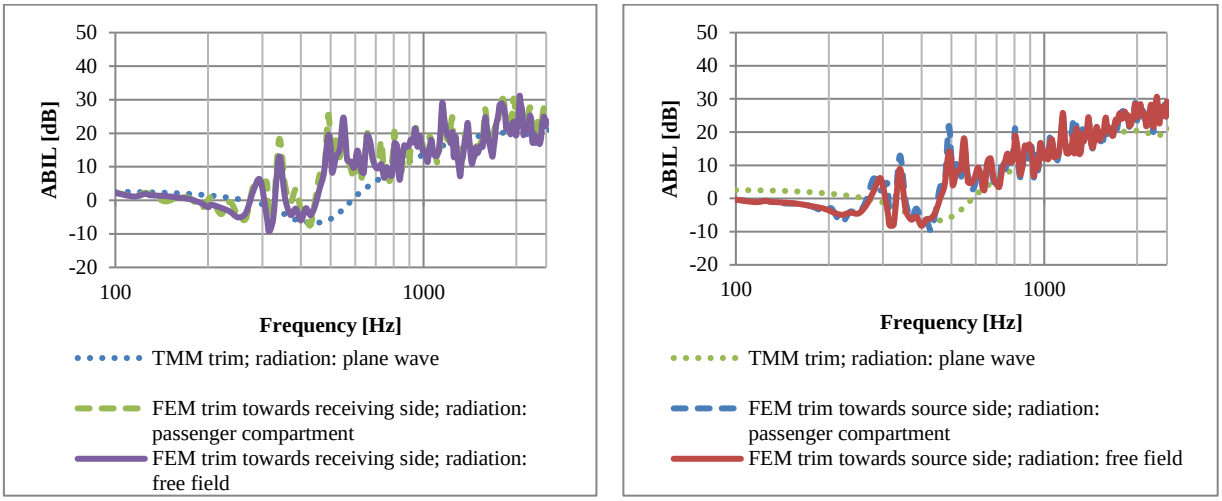


Figure 6: IL for the trim placed once towards the receiving side and once towards the source side

In Figure 7 it is demonstrated that the equality between the IL and delta of the averaged SPL (based on the mean squared pressure) is already approximately given for a passenger compartment, closed fluid space, in which the sound field is maybe far away from to be diffuse at low frequencies. There are only differences up to 1.5 dB at single frequencies between the IL for a dash trim (same as in Figure 6) and the delta SPL and the difference becomes smaller at higher frequencies. Thus, as long as the excitation stays the same it can be stated that the equality between the IL, ABIL or SBIL, the SPL and the particle velocity level PVL as shown in equations 14 and 15 is already at least approximately given for a passenger compartment although the sound field is not so diffuse. It has to be noted that because of the problematic of a probably non-diffuse sound field and because of practical reasons the TLs for this dash example are not obtained from the FE-simulation results using the standard formula, equation 6. Instead the following alternative formula has been used for the TL that has been developed for low frequencies for which the assumption of the diffuse field in a room cannot be considered as valid anymore [13].

$$TL = SPL_{S,i} - L_{in,S,rad} - 9 - 10\log_{10}\frac{S_m}{S} = SPL_{S,i} - L_{in,S,rad} - 9 \tag{23}$$

where $SPL_{S,i}$ is the mean sound pressure level on the surface S of the partition on the side of the source room and $L_{in,S,rad}$ is the sound intensity level measured over an area S_m near to the partition in the receiving room. For the post-processing of the simulations here S and S_m are equal. For higher frequencies the results are becoming the same as those of equation 6, which is assuming diffuse sound fields [13].

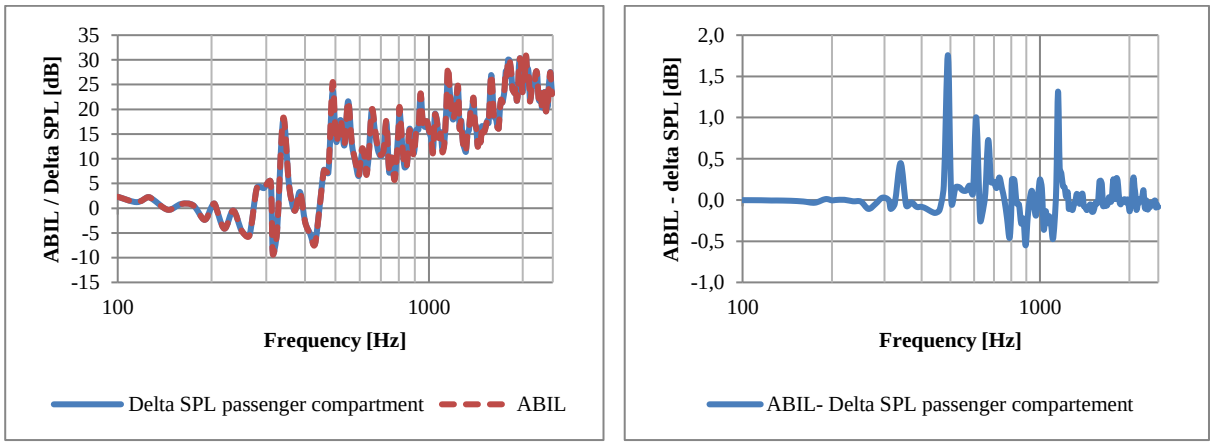


Figure 7: ABIL of a foam-heavy layer trim and the corresponding delta SPL in a passenger compartment

3.4 Input/ Incident power

As shown in the previous chapters there is equality between the IL, the delta SPL and the delta PVL under certain radiation conditions, but one requirement is always that the incident or input power is equal for a panel with and without trim. For the airborne excitation this is always true when the trim is placed on top of the partition towards the receiving room and as long as the same source is used. But placing a highly absorbing trim towards the emitting room is changing there the SPL used in equations 6 and 23. One practical example for this problematic is for example a trim put on the outer side of a dash of a vehicle (see Figure 3). In the case of the engine noise the engine bay becomes the source room and the passenger cabin the receiving room. As long as the trim is very reflective the ABIL is equal to delta SPL in the passenger compartment (see Figure 8). But in case of a highly absorbent trim the pressure inside the engine bay is also reduced and the delta SPL with and without trim becomes bigger inside the car than the ABIL. From this example it can be seen that the IL is always only describing the influence on the transmission. Thus, for the extrapolation from the ABIL to the interior SPL change it is necessary to keep in mind the excitation side.

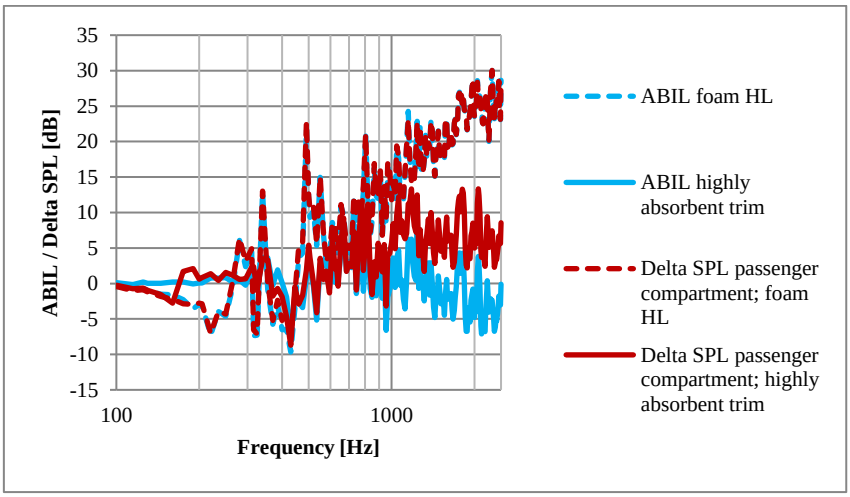


Figure 8: ABIL for a very reflective (--- ; foam HL) and a very absorptive trim (—) in comparison with the respective delta SPLs in the passenger compartment in case that the trim is placed on the source side

In contrast to the airborne excitation, it is quite obvious for a structure like a small flat plate which is excited by a point force as described in chapter 2 that it is very difficult to get the same input power under bare and trimmed conditions. The input power P_{in} is calculated as follows from the force and the velocity at the excitation point [14]:

$$P_{in} = \frac{1}{2} Re(F v_e^*) \tag{24}$$

where F is the force vector and v_e^* is conjugate complex of the velocity vector at the excitation point. The velocity v at a position X of a structure can be expressed using a modal description [9] by

$$v(X) = \sum_{i=1}^{n} \frac{i\omega F \phi(X)_n^2}{M_n(\omega_n^2 - \omega^2 + i\eta_n\omega_n\omega)} \tag{25}$$

where M_n , ω_n, η_n and φ_n are the modal mass, the angular eigenfrequency, the modal damping and modal shape of a mode n. As it can be seen from this equation the velocity at the excitation point e will change by adding some trim on top of the plate even when the force is kept constant, because at least the damping coefficient is changing and so the real part of the velocity, too.

$$Re\big(v(e)\big) = \sum_{i=1}^{n} \frac{\eta_n\omega_n\omega^2 F \phi(X)_n^2}{M_n[(\omega_n^2 - \omega^2)^2 + (i\eta_n\omega_n\omega)^2]} \tag{26}$$

In the case of a vehicle it is not easy to judge if the input power stays the same or not, because the main structural excitations are not like a point force at a specific part like the floor. A car is mainly excited structurally at stiff parts that are not part of the areas of interests to put acoustic trims. Thus, it is like exciting a plate through its frame. The excitations are for example on the front beams in the engine bay on which the engine is mounted or on the points where the axes are connected to the body. On the example of the floor mock-up described in chapter 2 it is demonstrated by measurements and simulations that the common trims have no significant influence on the input power (see Figure 9). Only at very low frequencies the input power is slightly changing at single frequencies.

It has to be mentioned that, in measurement conditions, it is complicated to have always exactly the same force for measurements with shakers and so the input power is changing. But for a linear elastic system the velocity is changing by the same factor as the force. Using this fact it follows from equations 3 and 24, when the trim has no influence on the input power:

$$SBIL = 10\log_{10}\left(\frac{\overline{v^2}}{\overline{F^2}}\right)_{bare} - 10\log_{10}\left(\frac{\overline{v^2}}{\overline{F^2}}\right)_{with\ trim} \tag{27}$$

The ratio between the velocity and the force is the well-known quantity mobility.

$$Mobility = \frac{v}{F} \tag{28}$$

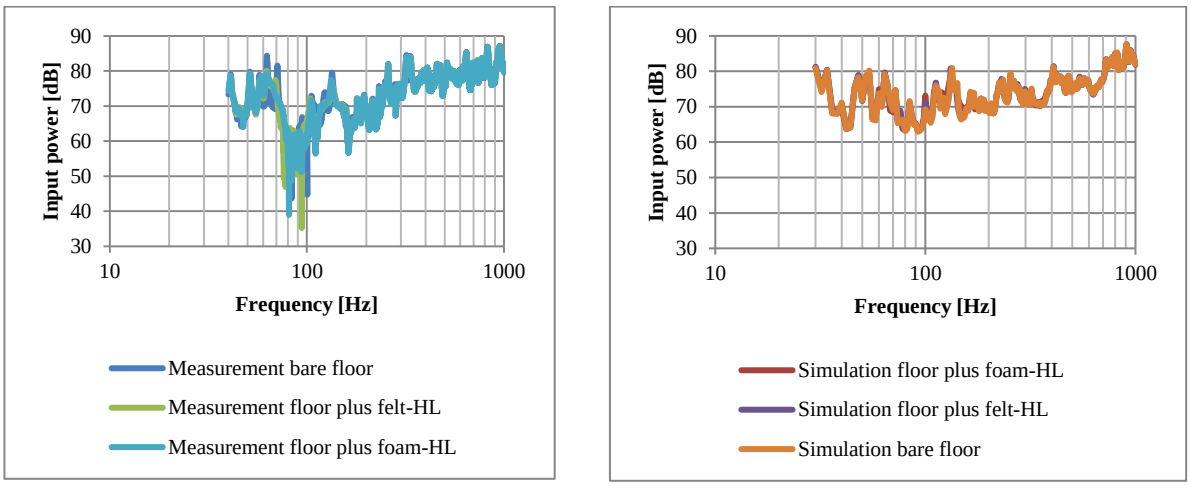


Figure 9: Input power of the point-force excited floor mock-up (see chapter 2; excitation point in the front) in case of bare and trimmed floor (left: measurement; right: simulation)

3.5 Consequences for measurements and simulations

First, for vehicles it can be assumed at least approximately that the IL of a typical trim, dash insulator or floor carpet, is equivalent to the average SPL change in the passenger compartment and to the change of the mean square velocity (as logarithmic value in dB) of the top layer of a panel. Thus, it makes sense to use this fact even for a floor mock-up as described in chapter 2 and to evaluate the structure borne performance only with the measured/ simulated velocities or mobilities using equation 15 or 27. But of course, the equality of these quantities is only true when a certain panel is the only transfer path to the passenger compartment. To get to know the exact influence on a specific car under a specific excitation situation it is necessary to make simulations with a complete vehicle model which contains all the trims and seats. On full vehicle level also the other main characteristic quantity of a trim, the absorption, becomes then important beside the IL. The reason is that the noise transfer from the exterior to the interior through a certain panel can become much less important in comparison to the one through other panels. Thus, its capability to absorb and to dissipate and to reduce so the acoustic energy inside is becoming its main function.

The second consequence is that it is in general not possible to use directly the delta of the mean quadratic velocity of the top layer for measurements on small plates like the one described in chapter 2, because the input power is normally not equal under bare and trimmed conditions. And the radiation efficiency/ impedance strongly depends on the configuration in case of the radiation to a free field. The velocities measured all over the plate are taken better as input data for a post-processing routine that is solving numerically the integral for the radiation to a semi-infinite sound field (equation 17) and to calculate so the radiated power, equation 11. The second necessary quantity to obtain in this case the SBIL, the input power, can be obtained by using equation 24.

Third, the IL, SBIL or ABIL, for a certain trim is unfortunately not a unique absolute value/ frequency dependent curve and it is not possible to get such a global indicator. The influence of a trim on its environment, vibration of a structure or SPL, is depending also on this environment like the radiation condition. Thus, it might be that the absolute values for the SBIL gained from measurements or simulations for the table-system (free field condition) are not fully transferable to the situation in car.

4 SBIL on flat sample and vehicle level in comparison

The findings of the last chapter are applied to calculate the SBIL of three trims that are typical for car floors. For the floor the measured or simulated velocities are directly used to obtain the SBIL that is equal to the difference between the logarithmic mobility of the bare structure and the logarithmic mobility of the top layer of the trimmed floor (equation 27). For the plate excited by a point force the radiated power and input power are calculated as described in the previous chapter to get the SBIL. The chosen trims consist of a foam plus heavy layer, a felt plus heavy layer and a double layer felt trim. The trims used for the flat plate have a constant thickness of 22mm in case of heavy layer or 25mm in case of felt as top layer. Contrary, the bottom layers of the investigated trims for the floor mock-up, which are touching the floor structure, have -as usual in cars - a variable thickness. The main/mean thickness of the bottom layer is about 20mm and the variation of the thickness is between 10 and 40mm.

The aim of the following subchapters is to investigate two main questions. First, if at least the ranking of the different trims in terms of ability to reduce the radiated noise stays the same on vehicle and flat sample level even so the trims have not the same thickness distribution. Second, if the location of the point force or the material of the underlying structure has an influence on this ranking.

4.1 Influence of the variation of the location of the excitation point on the SBIL

Three different locations for the point force are selected on the flat small steel plate to investigate this influence on the SBIL. Besides the original location in one corner which is used also for measurements, a point in the mid of the plate and one point in between the two is chosen for the point excitation (see Figure 10). As shown in Figure 10 the SBILs of the foam plus heavy layer trim and of the double layer felt are depending on the location of the point force, because of course different modes are excited and this can be even seen in third octave band values. But the differences are not huge and the most important, the ranking between the two trims stays globally the same, because the change of the location has a similar influence on the SBILs of the two configurations. That does not mean that the ranking for each frequency is the same. For example, in Figure 10 the ranking is changing for the 630Hz-centered band. In average, the double layer felt trim has the higher SBIL and is thus bringing a higher noise reduction. The same observation can be made for measured and simulated SBILs of the trims of the car floor shown in Figure 11. The SBIL for the different trims is also here depending on the location of the excitation, front and rear excitation as shown in Figure 2. And the ranking regarding their performance to reduce the sound is overall always the same.

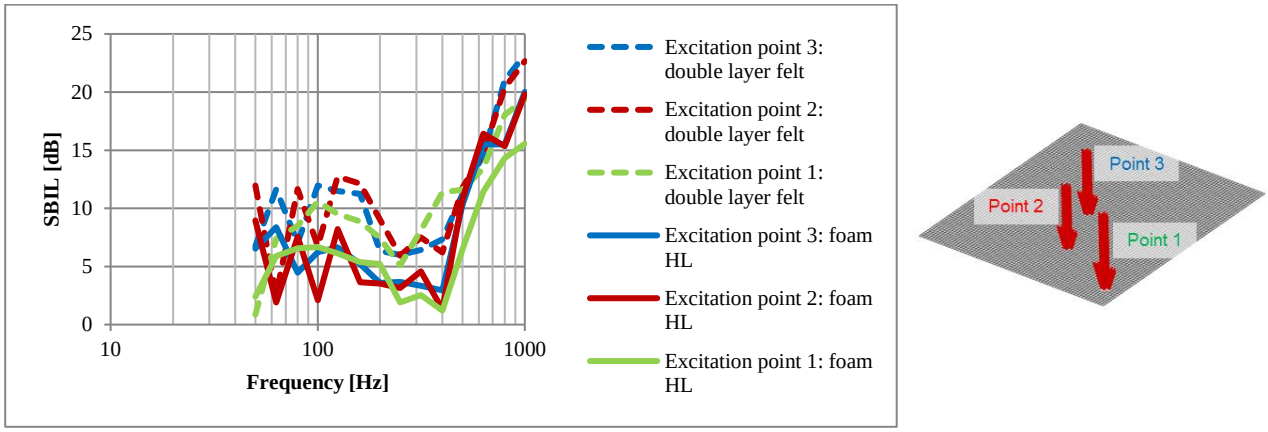


Figure 10: SBIL for different excitations on the flat plate (---: double layer felt; ——: foam HL)

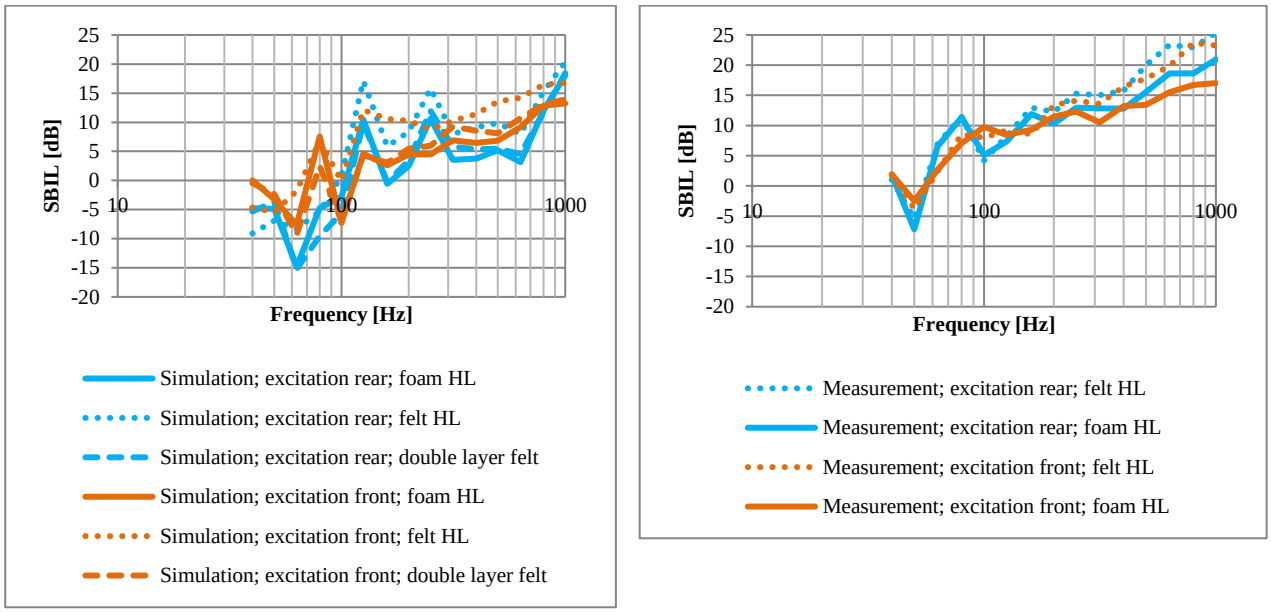


Figure 11: SBIL for the front (brown lines) and rear excitation (blue lines) on the floor mock-up (---: double layer felt; ——: foam HL,·····: felt HL)

4.2 Influence of the material of the underlying structure on the SBIL

The investigated structures are made out of steel and CFRP (Carbon Fiber Reinforced Polymer). In case of the plate simply the whole plate is changing from 1mm of steel to 2.6mm of CFRP. For the floor three different configurations have been created: one original floor completely out of steel, one for which the steel tunnel and one steel side beam are replaced by CFRP and one for which the right steel floor is replaced by CFRP (see Figure 13). More details about these floor structures are described in [2]. As demonstrated in Figure 12 the simulated SBILs for the different trims are depending on the material of the flat plate at low frequencies. At higher frequencies they are becoming similar. The reason is certainly the modal density, the modes, the eigenfrequencies and the damping of the respective plate, because the SBIL is at low frequencies very sensitive to the damping factor of the plate as shown in [3] and [6]. Anyhow, the ranking of the three trims stays - maybe not at each frequency but overall- the same independent from the material of the plate. On the contrary, the simulated and measured SBILs for the three different floor constructions are more similar in the whole shown frequency range (see Figure 13 and 14). But none of them is also made completely out of CFRP. All these Figures for flat plates and different floor constructions are demonstrating additionally that the ranking of the different trims with respect to the

potential of reducing the radiated sound is overall always similar independent of the shape, size and material of the underlying structure. Thus, the trims can be ranked just by measurements or simulations for flat small samples.

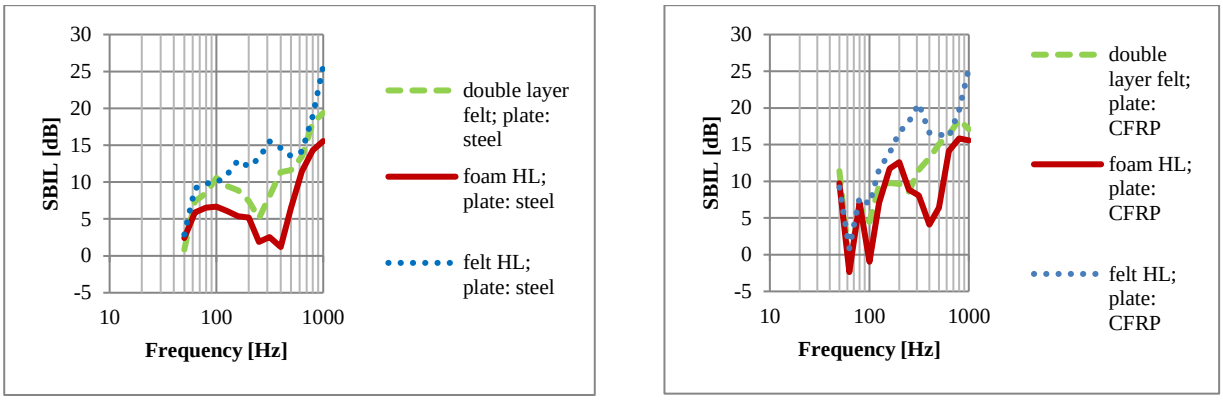


Figure 12: Simulated SBIL of three example trims put on top of a steel (left) and a CFRP (right) plate

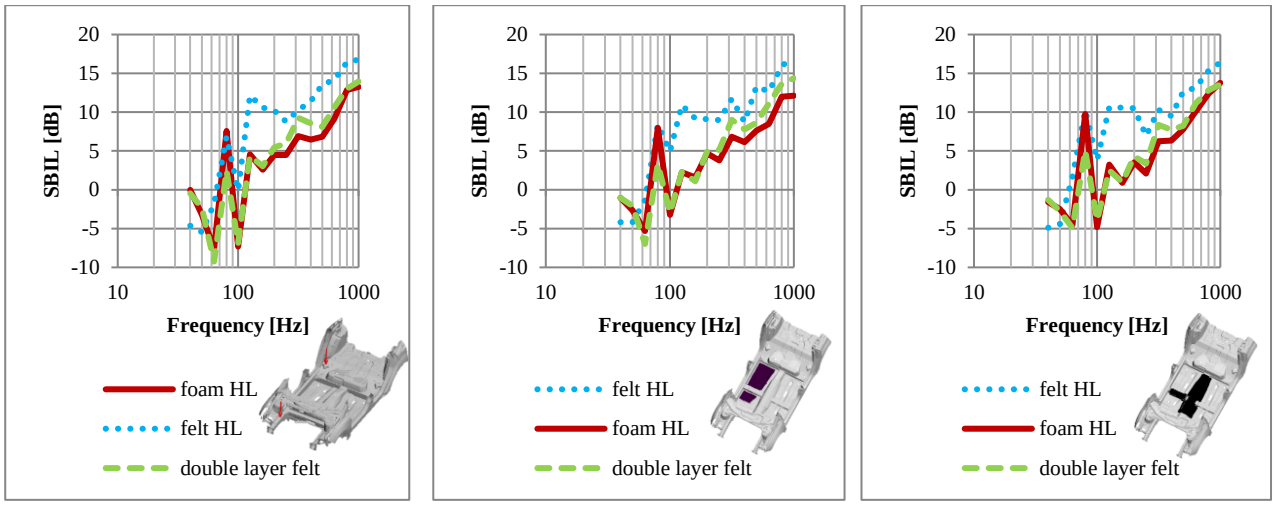


Figure 13: Simulated SBILs of three example trims put on top of three different floor constructions (gray: steel; black: CFRP)

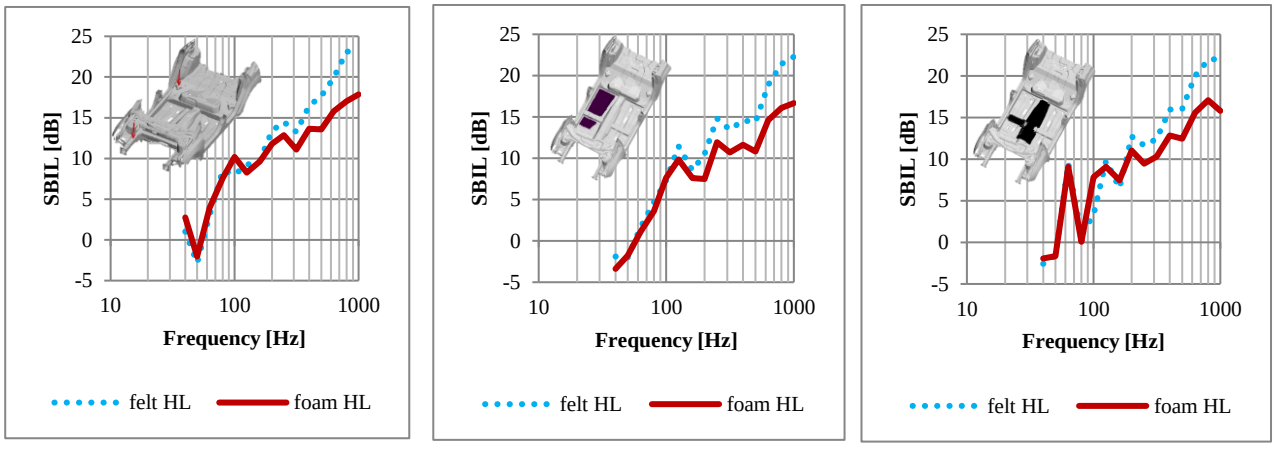


Figure 14: Measured SBILs of three example trims put on top of three different floor constructions (gray: steel; black: CFRP)

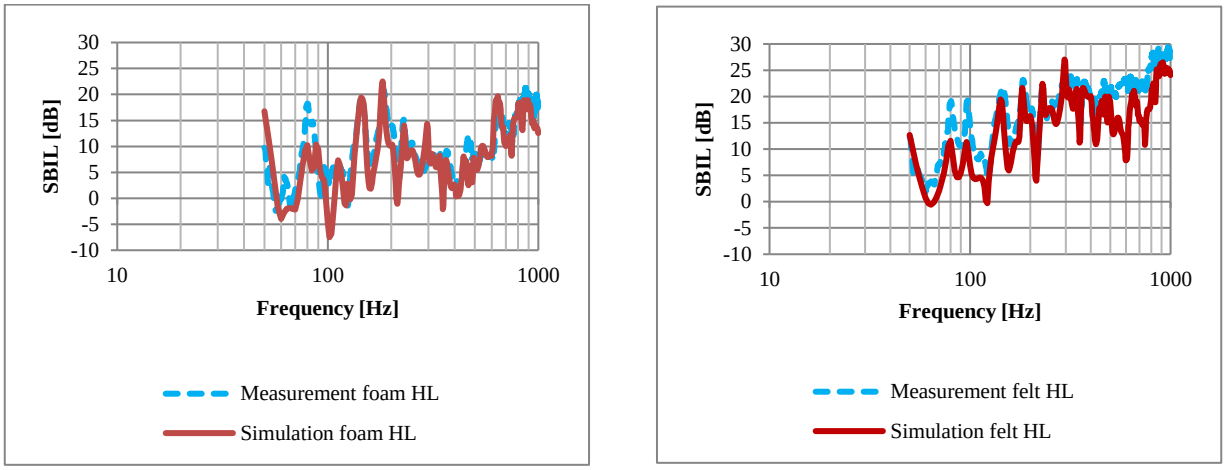


Figure 15: Measured and simulated SBILs for two different trims on the flat plate in comparison

It is expected that it will work with measurements on the plate as good as with simulations, because first correlations between measured and simulated SBILs are good (see Figure 15). But as it can be seen in comparing Figure 13 and 14, the correlation between measured and simulated SBILs is worse in case of the floor. Possible reasons are the coupling conditions of the trims to the floor and the material properties of the porous material. All these things are more difficult to describe for complex 3D shapes and for variable thicknesses of the trim. Anyhow, that does not matter for the scope of the chapter which is the ranking of the different trims.

5 Conclusion

The findings of the paper can be summarized in four main statements, which are answering the questions raised in the introduction.

First, when the input/ incident power stays the same, the IL is equal under certain radiation conditions to the delta SPL in air and equal to the delta mobility on the radiating surface measured or simulated for the bare and the trimmed condition of a structure. This is the case for a plane wave radiation and a radiation into a diffuse sound field, when the absorption of the trim does not influence substantially the receiving environment. For a vehicle this relation between the quantities can be used as a very close and good approximation.

Second, according to the investigated configurations, a ranking of trims for vehicles can be done on flat sample level regarding their performance to reduce the sound radiation, as the overall averaged ranking is not influenced by the environment around the trims, like the location of the excitation, the underlying structural material and the type of the structure, car floor or flat plate. But at specific single frequencies the ranking may change under certain conditions.

Third, the absolute values of the ILs from the flat small sample level can be used only as very approximate orientation, because the absolute values will change for each vehicle, depending on the structural design and the excitation condition.

Fourth, that means also that the acoustic performance of a trim cannot be characterized by one unique absolute value/ frequency dependent curve, like the ABIL or SBIL, as the absolute amount of reduction of noise due to a trim is always depending on the environment in which it is placed. These statements are valid for structure-borne as well as for airborne sound.

Acknowledgements

The authors gratefully thank the two the trainees M. Położyńska and M. Galante for designing the table-shaped measurement set-up (see chapter 2) and for creating the related post-processing computer tools.

References

[1] T. Courtois, M. Seppi, F. Ronzio, L. Sangiuliano, T. Yano, *Importance of the evaluation of the structure borne NVH performance for light weight trim design, Proceedings of Automotive Acoustics Conference 2015,* Zurich, Switzerland (2015).

[2] T. Courtois, O. Chesa, R. Stelzer, D. Golombowski, M. Zogg, *Feasibility of the NVH simulation of representative CFRP automotive body structures, Proceedings of 21st International Conference on Composite Materials,* Xi'an, China (2017).

[3] C. Bertolini, *Numerical Investigations on Structure-Borne and Air-Borne Insertion Loss of Acoustical Multilayers used in the automotive industry, Proceedings of AIA-DAGA 2013 Conference on Acoustics*, Merano, Italy (2013).

[4] H. Nelisse, T. Onsay, N. Atalla, *Structure Borne Insertion Loss of Sound Package Components*, SAE Technical Paper 2003-01-1549, 2003.

[5] Z. LU, Z. Hao, X. Zheng, J. Yang, *Research on the Insertion Loss of Sound Package under Structure-borne and Airborne Excitation in Mid-frequency Using Hybrid FE-SEA Method*, Journal of Computational Information Systems 7:4 (2011), pp. 1190-1197.

[6] J. F. Allard, N. Attala, *Propagation of Sound in Porous Media: Modelling Sound Absorbing Materials,* Wiley, 2nd edition (2009).

[7] M. Möser, *Technische Akustik*, Springer, 7th edition (2007).

[8] F. J. Fahy, P. Gardonio, *Sound and Structural Vibration: Radiation, Transmission and Response*, Elsevier, 2nd edition (2007).

[9] L. Cremer, M. Heckl, B. A. T. Petersson, *Structure-Borne Sound*, Springer, 3rd edition (2005)

[10] C. Devaux, N. Dauchez, *Acoustic radiation of a structure covered by porous layer, Proceedings of CFA/DAGA '04 conference,* Strasbourg, France (2004).

[11] F. J. Fahy, *Foundations of Engineering Acoustics*, Elsevier (2007).

[12] R. Stelzer, *An energy based method for coupled vibro-acoustic systems*, PhD Thesis, INSA Lyon, France (2012).

[13] W. Maysenhölder, W. Scholl, S. Koch, M. Nicolai, *Wie soll man die Schalldämmung bei tiefen Frequenzen unterhalb 100 Hz messen?*, IBP Mitteilung 325, Fraunhofer Institute for Building Physics IBP, Stuttgart, Germany (1997)

[14] F. G. Kollmann, T. F. Schösser, R. Angert, *Praktische Maschinenakustik*, Springer (2006)

Active damping of automotive driveline oscillations and its interactions with engine suspension

A. Gaudin[1]
[1] PSA Group, Scientific and future technologies department
Route de Gizy, 78943 Vélizy Villacoublay, France
e-mail: **arnaud.gaudin@mpsa.com**

Abstract

Strong variations of driving torque coming from the driver may excite driveline first torsional mode located at a very low frequency (comprised between 2 and 8Hz depending on gearbox ratio). It may induce cabin longitudinal oscillations uncomfortable for the driver and its passengers. To investigate this phenomenon, vehicle vibrational behavior has to be modeled at very low frequency. Special attention has been put on its interaction with the engine block and mounts including their non-linearities.

To prevent oscillations, an active damping is added through an engine torque control. This control is introduced in a simplified manner on proposed models. A multi-objectives optimization is formulated to improve comfort through oscillations reduction and, at the same time, to keep a good driveability. Some constraints must also be respected and among them are stability criteria of the feedback loop. Eventually, the impact of the coupling with engine suspension on the final result is presented.

1 Introduction

Studying vehicle vibrational behavior at low frequency, driveline first torsional mode is one of the first modes appearing (between 2 and 8Hz depending on gearbox ratio). It is located just above vehicle suspension modes (bounce, pitch and roll modes) which are related to the resonances of vehicle mass and inertias on the vertical stiffnesses of the suspension springs. It is just below the 6 engine suspension modes associated with the resonances of engine-gearbox unit mass and inertias on the stiffnesses of the upper right and left mounts and lower mount (see Figure 1).

As for all the other modes, a sufficiently low positioning of its natural frequency allows a good filtering of the excitations above the resonance. However, passing on the resonance could be critical. For vehicle suspension modes, dampers with specifically tuned force-speed laws are required. For engine suspension modes, even if frequencies associated to engine speed harmonics are beyond all natural frequencies, hydromounts are designed to reduced amplifications under road excitation. For driveline first torsional mode, the solution is an active control of the oscillations using a feedback loop on engine applied torque.

For all those modes, fine tuning is a trade-off between many important vehicle attributes. Regarding driveline mode, it is a trade-off between driveability (especially during take-off) and passenger comfort (with no perceived oscillation in the cabin).

In order to reduce fuel consumption and emissions, 3-cylinder engines are massively introduced into vehicles. The resulting drop of excited frequencies at idle or at low engine speeds –even more important without balance shaft- makes engine suspension design more complicated. An important point becomes interactions between loaded suspension modes and engine harmonics.

Thus, special attention has been put on the interactions between engine suspension and the first driveline torsional mode. In this approach, we will use a simple mechanical model with a limited number of non linearities. The control will also be introduced in a simplified way to validate the effect of the engine suspension on the driveline torsional mode.

2 Driveline mechanical model

To describe driveline torsional modes and their interactions with engine suspension, driveline has to be modeled in torsion by giving the main flexibilities and inertias. A very detailed description of the driveline components modelizations is given in [1]. A linearized model is deduced to analyze driveline torsional modes. Non linearities due to multi staged clutch and gear backlash are introduced in [2]. A visualization of the different parts of a front wheel drive vehicle driveline and their connections with the rest of the vehicle is shown on Figure 1.

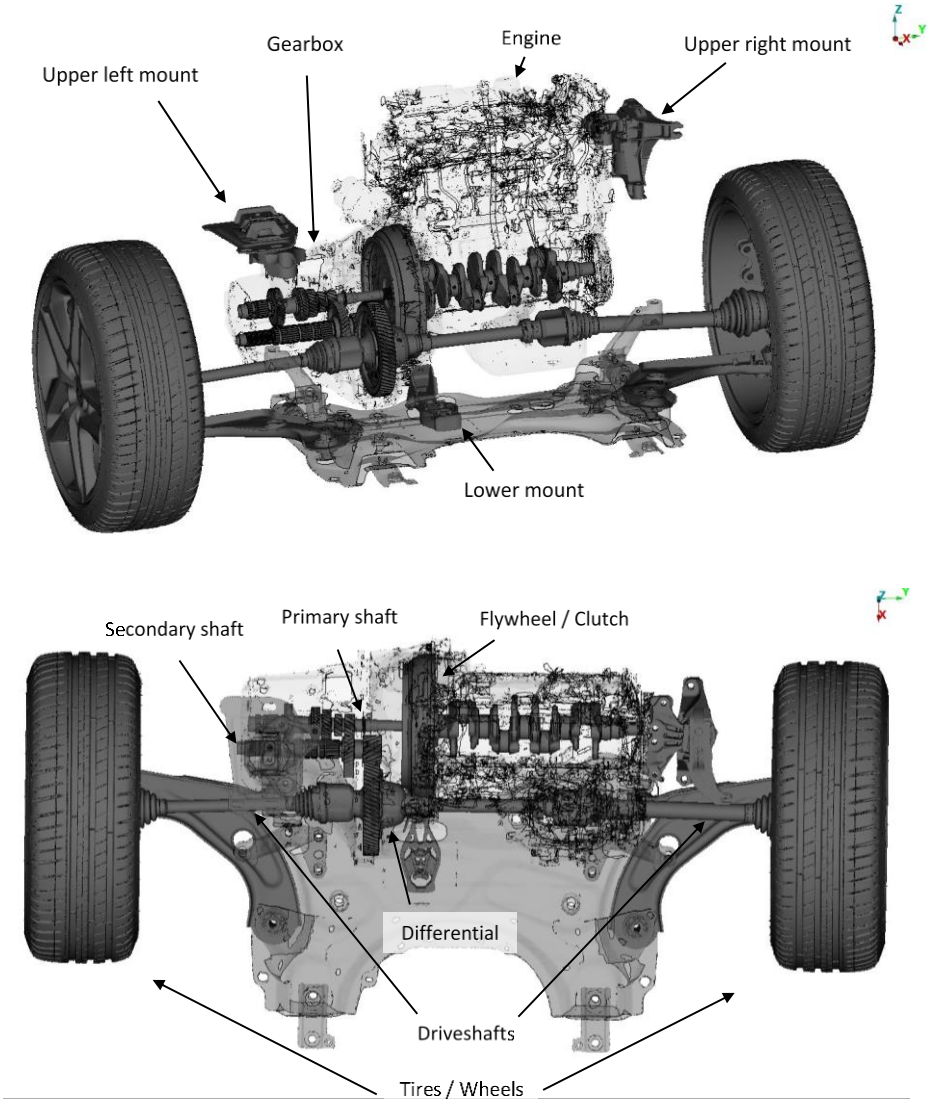


Figure 1: Different parts of a front wheel drive vehicle driveline and its environnement

We take the same type of model starting from the inertia of the flywheel and the crankshaft. This is linked to the primary shaft of the gearbox by a stiffness representing the flexibility of the clutch in torsion (case of a simple flywheel). This flexibility depends on the deflection angle in a non-linear manner with a stiffness around 0 which is similar to a play. The link from the primary shaft to the secondary shaft of the gearbox and to the front drive axle can be represented by a gear ratio depending on the gear engaged. Gear backlash is neglected. Differential angular displacement θ_{diff} is related to primary shaft angular displacement θ_{prim} through the global gear ratio r. Both are turning in the same direction.

$$\theta_{diff} = r.\theta_{prim} \tag{1}$$

In this paper we mainly considered the first gear which is most of the time the most critical.

For the differential, the rotation of the gears $\theta^L_{drivSh}$and θ^R_{drivSh} linked to left and right driveshafts have to be related to the rotation of the satellite gear θ_{sat}. As the differential could be turning, its rotation θ_{diff} has to be taken into account writing :

$$\theta^L_{drivSh} - \theta_{diff} = r_{diff/sat}.\theta_{sat} = \theta_{diff} - \theta^R_{drivSh}$$
$$\theta^L_{drivSh} + \theta^R_{drivSh} = 2\theta_{diff} \quad (2)$$

Left and right driveshafts flexibilities have to be modelized. Transmission joints are supposed to be perfect. A torque applied to the wheel center is then transformed by the tires into a longitudinal force in the axle depending on the radius of the tire. To represent tire, a longitudinal flexibility is positioned at the wheel base. A deeper understanding of tire modeling is proposed in the following paragraph. There is a coupling with the longitudinal mass of the car body through the longitudinal flexibility of the suspension. Since this flexibility is done with elastomeric mounts, a hysteretic damping is added to complete its behavior. A simplified equivalent modelization in terms of mass/inertias and stiffnesses is given on Figure 2, differential being supposed to be blocked.

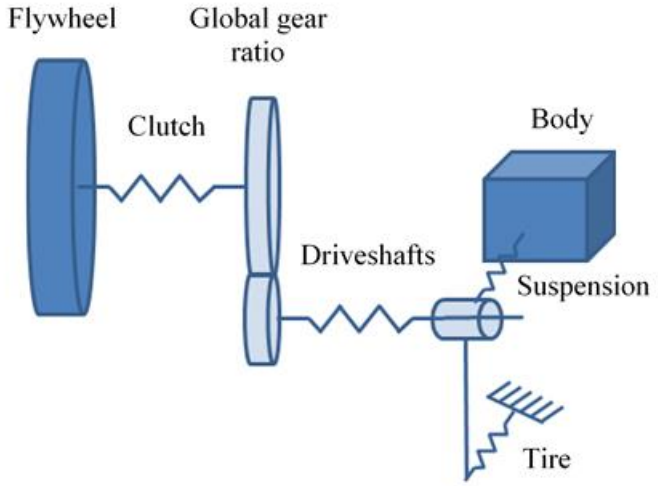


Figure 2 : Front driveline vibrational model in torsion

The first driveline torsional mode corresponds to the movements in opposite directions of the flywheel inertia $I_{flywheel}$ and the car body mass m_{body} (represented in dark blue on Figure 2) so that all the stiffnesses between them are solicited. By linearizing clutch stiffness k_{clutch} around a working point, the natural frequency can be estimated with a good approximation using stiffnesses of driveshaft $k_{drive\ shafts}$, tire k_{tire} and suspension $k_{susp.}$. The tire radius R_{tire} allows to convert rotation into longitudinal translation.

$$f_{driveline\ 1st\ torsional} = \frac{1}{2\pi}\sqrt{\frac{k_{driv.;susp.}}{I_{flywheel;body}}}$$
$$\frac{1}{k_{driv.;susp}} = \frac{1}{k_{clutch}} + \frac{1}{r^2}\left(\frac{1}{k_{drive\ shafts}} + \frac{1}{R^2_{tire}}\left(\frac{1}{k_{tire}} + \frac{1}{k_{susp.}}\right)\right) \quad (3)$$
$$\frac{1}{I_{flywheel;body}} = \frac{1}{I_{flywheel}} + \frac{1}{m_{body}R^2_{tire}r^2}$$

3 Interaction with the rest of the vehicle

First of all, to take into account the interaction with the engine block and its suspension, it must be considered that the internal combustions generate a torque applied to the flywheel but also a reaction torque applied on the engine block.

Furthermore, it is necessary to rewrite the relation (1) between the rotation of the primary shaft and the rotation of the differential. In fact, engine block reaction and the induced rotational movement must be considered. To do so, engine block rotation angle θ_{block} must be introduced. The previous relation is now between $(\theta_{diff} - \theta_{block})$ and $(\theta_{prim} - \theta_{block})$ and leads to :

$$\begin{aligned} \theta_{diff} - \theta_{block} &= r.(\theta_{prim} - \theta_{block}) \\ \theta_{diff} &= r.\theta_{prim} + (1-r).\theta_{block} \end{aligned} \tag{4}$$

Besides shafts rotation, engine-gearbox unit is assumed to be rigid and can be represented by its mass and inertia. It is connected to car body through 3 elastic mounts defined by their translational stiffnesses in the 3 directions. The lower mount stiffness in the lateral and vertical directions can be neglected. Along longitudinal direction, a nonlinear behavior for the 3 mounts must be used. As far as those mounts are elastomeric mounts, some hysteretic dampings are associated to their linear stiffnesses.

By linearizing around an operating point the resulting stiffness $k_{engine\ roll}$ of engine suspension in rotation around lateral (or engine roll) axis, the driveline first torsional mode natural frequency can take into account this interaction in the following formula :

$$\begin{aligned} f_{driveline\ 1st\ torsional} &= \frac{1}{2\pi}\sqrt{\frac{k_{driv.;susp.;eng.susp.}}{I_{flywheel;body}}} \\ \frac{1}{k_{driv.;susp.;eng.susp.}} &= \frac{1}{k_{driv.;susp}} + \left(1-\frac{1}{r}\right)^2 \frac{1}{k_{engine\ roll}} \end{aligned} \tag{5}$$

Another stiffness is added in series to the previous ones.

To assess the coupling effect between driveline and engine block on engine roll mode, it can be assumed that, for those frequencies, flywheel and tire/wheel angles are blocked. Then, engine roll mode natural frequency can be estimated by adding the stiffness $\left(1-\frac{1}{r}\right)^2 k_{driv.;susp}$ coming from the driveline in parallel of engine roll stiffness :

$$\begin{aligned} f_{engine\ roll} &= \frac{1}{2\pi}\sqrt{\frac{\tilde{k}_{driv.;susp.;eng.susp.}}{I_{engine\ roll}}} \\ \tilde{k}_{driv.;susp.;eng.susp.} &= k_{engine\ roll} + \left(1-\frac{1}{r}\right)^2 k_{driv.;susp} \end{aligned} \tag{6}$$

For a rolling tire, the effects due to the scrolling of contact patch are well described in H.B. Pacejka book [6]. Considering a steady-state movement, lateral (resp. longitudinal) tire forces are coming from the treads that are stretching progressively as they are moving forward in the contact patch. Summing all those contributions leads to an effort proportional to lateral (resp. longitudinal) velocity. This is valid for sufficiently low movements regarding the time for a tread to go through the contact patch. On the other hand, if the movements are fast then all the treadband stretches instantaneously and tire behaves as a spring. To represent tire behavior in lateral or longitudinal direction, a stiffness and a viscous damper have to be put in serie as shown in Figure 3. The damping factor is inversely proportional to vehicle speed which make it nonlinear. The tire is in fact the main source of damping for the first driveline torsional mode.

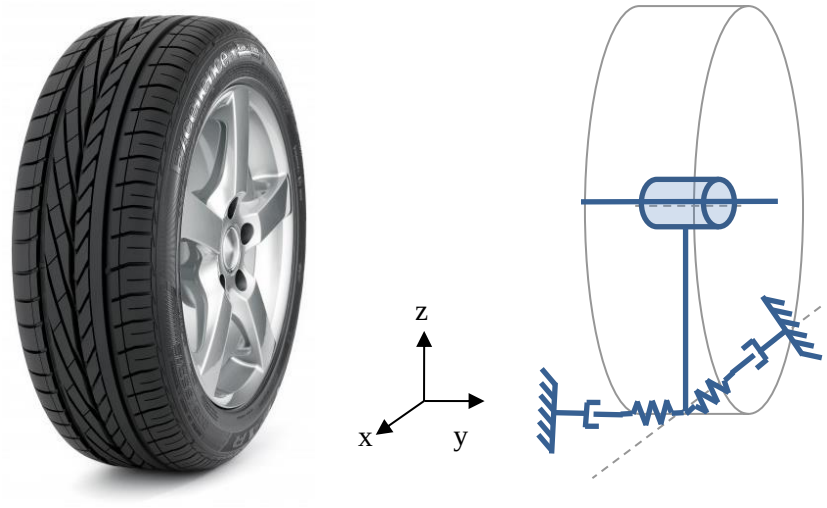


Figure 3 : Lateral and longitudinal tire modelization

In order to work in the time domain, hysteretic dampings have to be converted in equivalent viscous dampings. Most significatives values are associated with elastomeric mounts and are therefore coming from engine and suspension mounts. Modes whose dissipation is driven by engine mounts are engine suspension modes with natural frequencies comprised between 7 and 20Hz. Therefore, equivalence with viscous damping is made at 10Hz according to expression (7). Regarding vehicle suspension, natural frequencies are between 15 and 20Hz and the equivalence is done at 20Hz still according to (7). Other hysteretic dampings in the model are low as they come from metallic parts. For them the equivalence is done close to driveline first torsional natural frequency.

$$c_{visq\ eq.} = \frac{1}{2\pi f_{ref}} c_{hyst} \tag{7}$$

All the previously mentioned components are introduced in a 3D model in which car body and engine-gearbox unit are assumed rigid. Some visualization elements are introduced. The 3D model is presented on Figure 4.

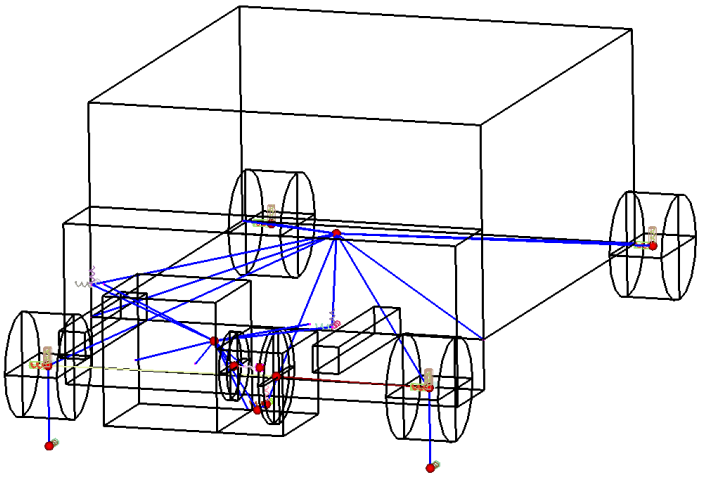


Figure 4 : 3D model visualization

4 Calculation and analysis of the mechanical system responses

At first, a torque excitation is applied on the flywheel and its opposite on the engine block. The definition of time varying torque is taken from the one applied experimentally on a vehicle in [4] without feedback. Curves are given on Figure 5. The variation of calculated engine speed is compared with the measured one on Figure 6. Cabin longitudinal accelerations are compared on Figure 7. Measured and modeled vehicle have significant differences in their characteristics. Therefore, calculated results are not supposed to reproduce accurately measurements but we can simply notice the general shapes are effectively similar. Without any feedback, strong oscillations due to first driveline torsional mode appear on cabin longitudinal accelerations.

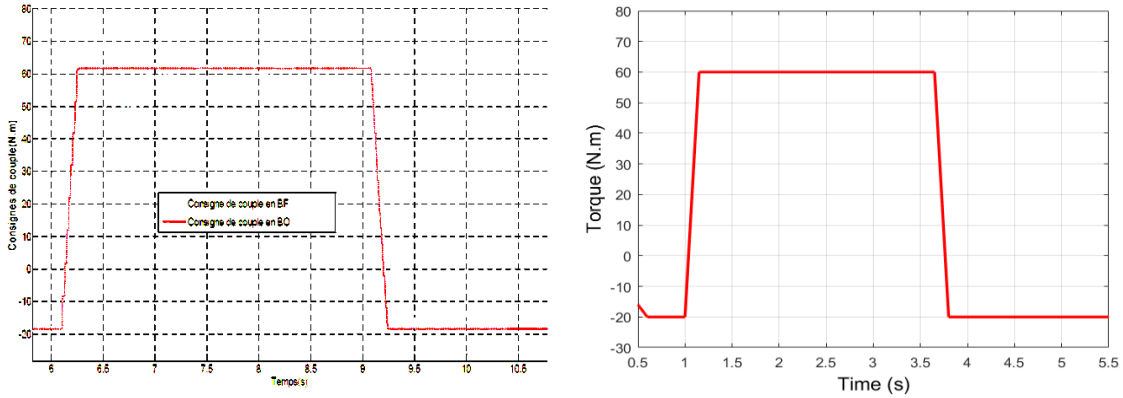


Figure 5 : Torque step applied (left : measurements ; right : calculations)

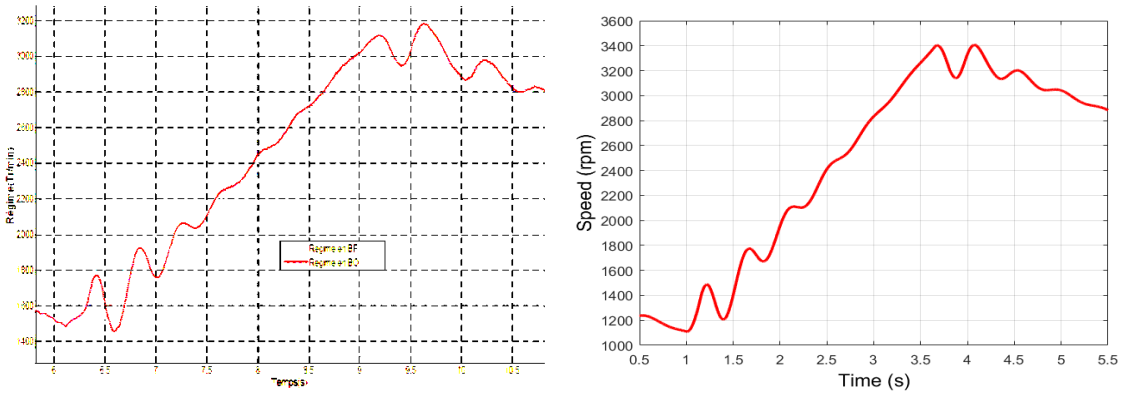


Figure 6 : Engine speed variations (left : measurements ; right : calculations)

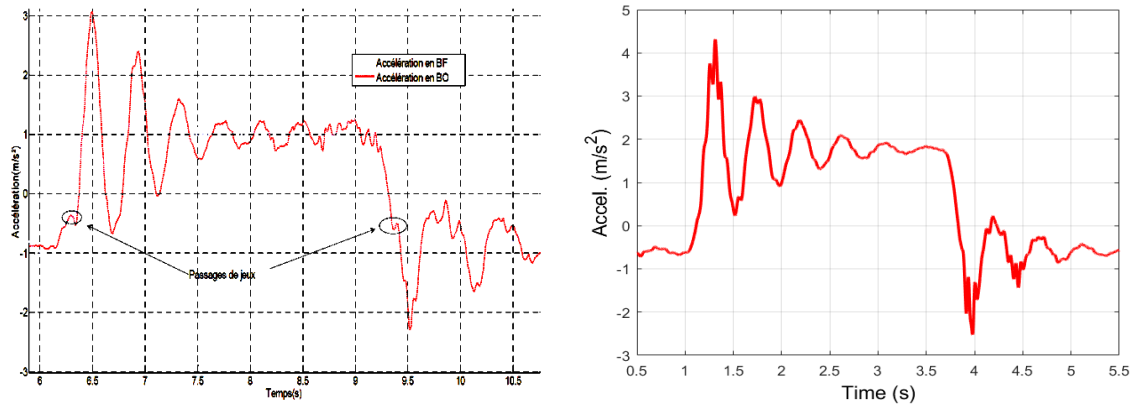


Figure 7 : Cabin longitudinal acceleration (left : measurements ; right : calculations)

The effect of the coupling between driveline and engine block as introduced in (4) is examined on Figure 8. Without coupling, the blue curve exhibits a higher frequency for first driveline torsional mode. Discrepancies on frequencies are deeper analyzed in the following but the coupling seems to add a flexibility as suggests by expression (5). It also appears that the response is smoother, suggesting that the non linearities of the engine suspensions are naturally more solicited with the coupling. Higher frequencies seem to be excited by those non linearities.

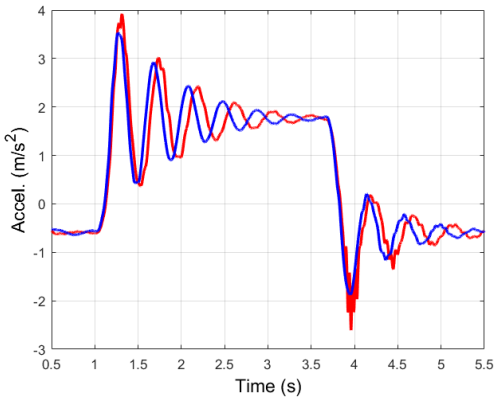


Figure 8 : Effect of the coupling between driveline and engine block on cabin longitudinal acceleration (red : with coupling; blue : without coupling)

Three non linearities are introduced in th 3D model. The first one concerns engine mounts stiffnesses on the longitudinal directions. The second one is the clutch rotational stiffness and the third one is the tire viscous damping inversely proportional to vehicle speed. Linearizations around the operational point of 60Nm torque are proposed on Figure 9:

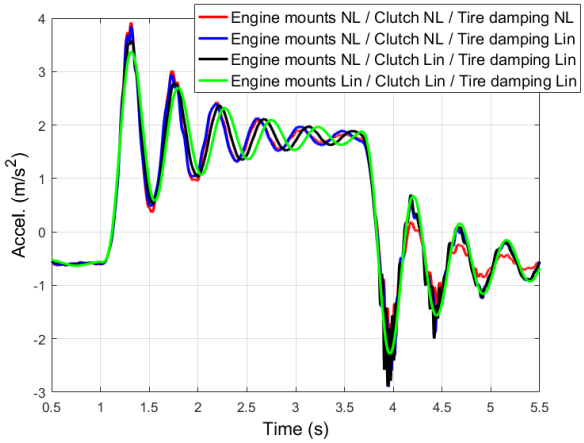


Figure 9 : Effect of the 3 non linearities of the model on cabin longitudinal acceleration

The effect of tire damping is felt on the second torque step at -20Nm. The linearization of the clutch slightly increases the period of resonance at the end of the first torque step. For the engine suspension, the maximum levels are different with a smoother curve in linearized version.

Using the linearized model, frequency responses are calculated up to 50Hz with a unit torque applied only on flywheel, then on engine block and finally on both. Accelerations are calculated on flywheel, tire/wheel, body and engine block. Results are shown on Figure 10. Several resonances are excited. The first one is the driveline 1st torsional mode at 2.1Hz. Engine roll mode has a natural frequency of 11.6Hz and can be also seen on cabin longitudinal acceleration. Engine pitch is at 15.9Hz whereas engine yaw is at 18.1Hz. Suspension 1st longitudinal mode is positioned at 16,6Hz and appears on cabin longitudinal acceleration.

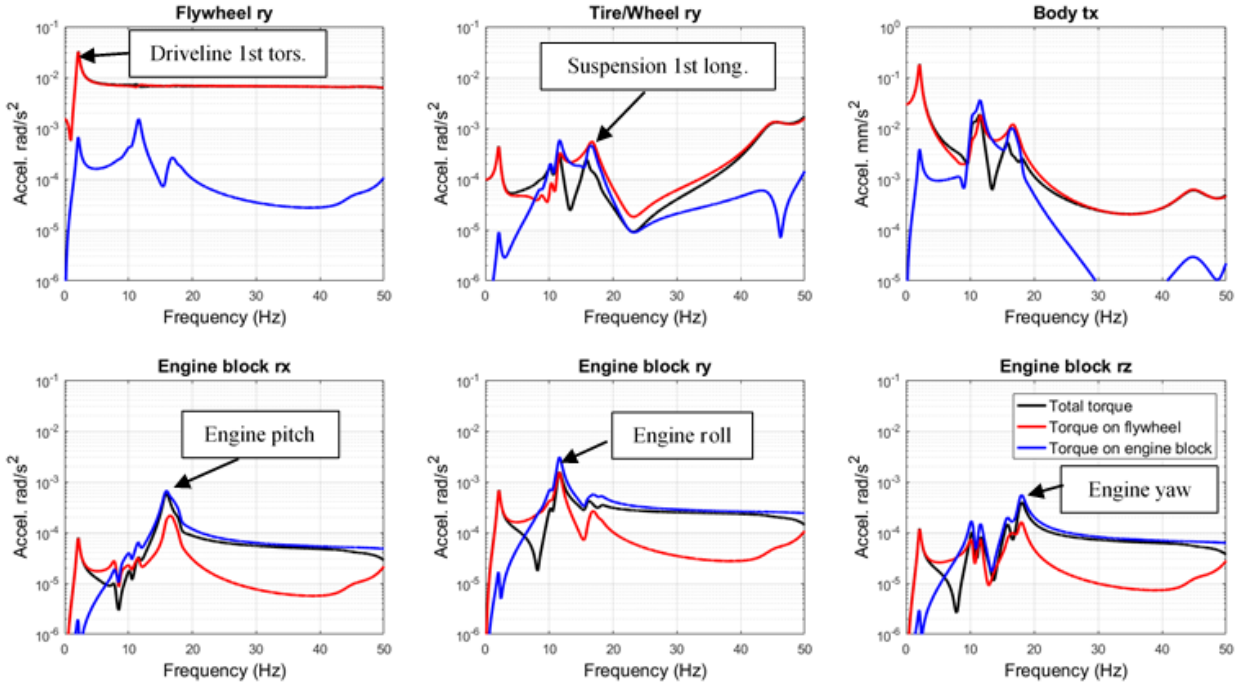


Figure 10 : Torques contributions and main resonances on frequency responses

Assumptions made to convert hysteretic dampings to viscous dampings in the time domain are assessed on Figure 11. Black curve corresponds to real hysteretic dampings and the red one to equivalent viscous dampings. A good agreement validate the assumptions made.

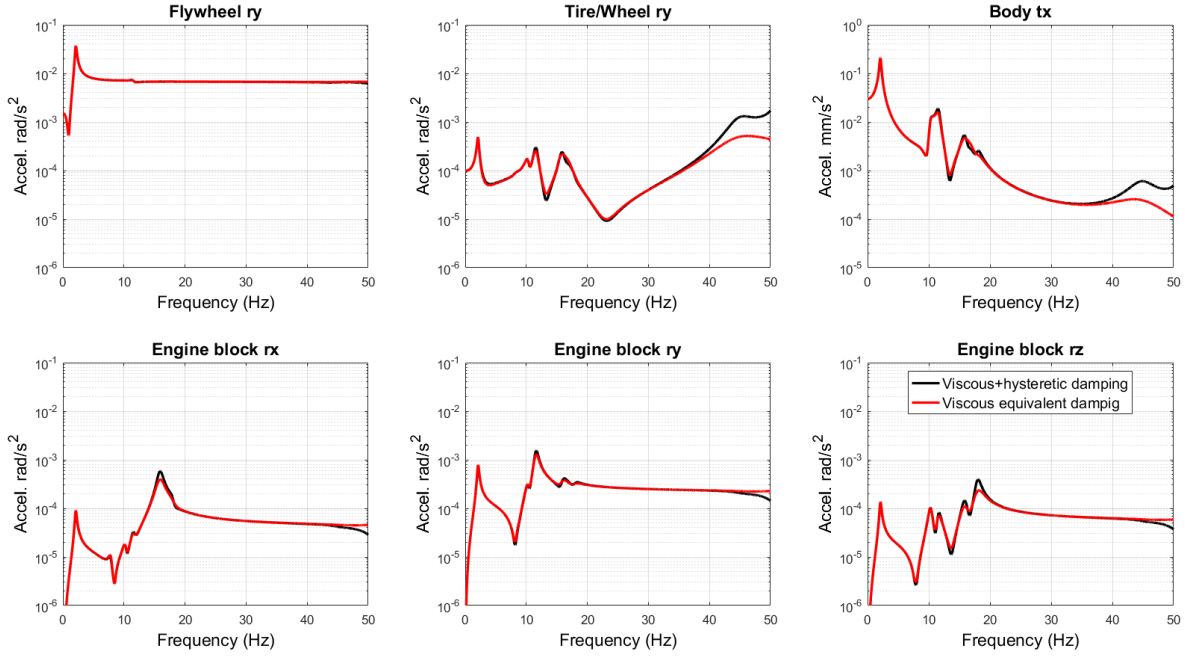


Figure 11: Assessments of damping assumptions

Natural frequencies obtained with the linearized 3D model can be compared to those obtained from formulas (3), (5) and (6). Stiffnesses values are extracted from the linearized model. Engine roll stiffness must be calculated from the engine mounts stiffnesses and positions. The relation between angular displacements of primary shaft and differential can be given without link with engine suspension as in (1) or considering this link according to (4). Results are presented in the following tables:

	Driveline 1st torsional mode		
	With link	Without link	
3D model	2,09	2,39	Hz
Formulas	2,14	2,40	Hz

	Engine roll mode		
	With link	Without link	
3D model	11,61	10,05	Hz
Formulas	11,72	10,45	Hz

Table 1 : Natural frequencies comparisons in 1st gear between 3D model and formulas

The agreement is considered very satisfactory on the frequency of the driveline 1st torsional mode. The coupling with engine suspension significantly changes the frequency of the mode. Stiffness contributions to 1st torsional mode can be analyzed by calculating the ratio between total stiffness and component stiffness:

$\frac{k_{driv.;susp.;eng.susp.}}{k_{clutch}}$	$\frac{k_{driv.;susp.;eng.susp.}}{r^2.k_{drive\ shafts}}$	$\frac{k_{driv.;susp.;eng.susp.}}{r^2R_{tire}^2.k_{tire}}$	$\frac{k_{driv.;susp.;eng.susp.}}{r^2R_{tire}^2k_{susp.}}$	$\left(1-\frac{1}{r}\right)^2\frac{k_{driv.;susp.;eng.susp.}}{k_{engine\ susp}}$
11%	55%	7%	7%	20%

Table 2 : Contribution of all the components to driveline 1st torsional stiffness

Main flexibility is coming from driveline shafts with 55% but engine suspension can't be neglected with 20%.

For the engine roll mode, the fact the engine modes are not purely along one canonical direction makes the analysis harder but frequencies estimates remain correct and the coupling with driveline not negligible.

5 Driveline oscillations control

Active damping of driveline oscillations through a feedback loop on engine torque is described more precisely in [3] and [4]. In [5], a mechanical model is used for the simulation and the control of an automotive dry clutch. In this paper, driveline oscillations control is addressed in a simplified manner in order to assess engine suspension impact.

A torque is applied on the flywheel. As we have seen previously, this torque can excite the 1st driveline torsional mode. The frequency of engine explosions that drive the engine torque is large enough in front of the frequency of the mode and it is possible to modify the excitations around the frequency of the mode so that the torque transmitted to the kinematic chain do not excite the mode.

To estimate this torque on the vehicle, we know the engine torque applied Γ_{eng} and the engine rotation speed ω_{eng}. Transmitted torque Γ_t is the opposite of reaction torque and can be expressed writing dynamic equilibrium on the flywheel :

$$I_{flywheel}\dot{\omega}_{eng} = \Gamma_{eng} - \Gamma_t \tag{8}$$

In the frequency domain, assuming that the system is linear, the transfer function between Γ_t and Γ_{eng} without feedback loop is denoted t_{nf} and defined by:

$$\Gamma_t(\omega) = t_{nf}(\omega)\Gamma_{eng}(\omega) \tag{9}$$

Then, the feedback loop is introduced by filtering the signal (possibly including a gain factor) defined by the function $t_{filt}(\omega)$. The filter is intended to select the torque's part which excits the 1st driveline torsional mode and to prevent the transmission to the rest of the vehicle.

$$\Gamma_{tfilt}(\omega) = t_{filt}(\omega)\Gamma_t(\omega) \tag{10}$$

The associated flow chart is the following:

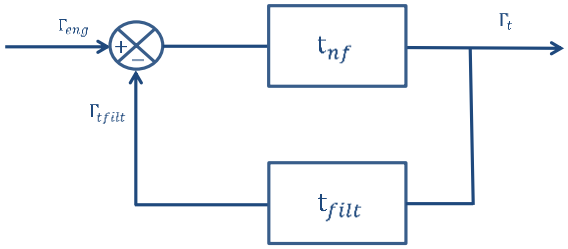


Figure 12 : Control simplified flow chart

The transmitted torque is related to the applied torque through:

$$\Gamma_t(\omega) = t_{nf}(\omega)\left(\Gamma_{eng}(\omega) - t_{filt}(\omega)\Gamma_t(\omega)\right)$$
$$\Gamma_t(\omega) = \frac{t_{nf}(\omega)}{1 + t_{filt}(\omega)t_{nf}(\omega)}\Gamma_{eng}(\omega) \quad (11)$$

To eliminate oscillations due to the 1st driveline torsional mode, the maximum of the new transfer function must be as low as possible.

Moreover, the torque application and engine speed rise must not be disturbed to keep a good driveability. Given characteristic times, this implies that the new transfer function (11) is almost identical to the reference one (9) below 1Hz.

Finally, the addition of a feedback loop raises the question of the stability of the response. Open loop mechanical system is stable as it doesn't have any eigenvalue with a positive real part. It implies that $t_{nf}(\omega)$ doesn't have any zero or pole with a positive real part. The question of stability is then to make sure that the term $\left(1 + t_{filt}(\omega)t_{nf}(\omega)\right)$ does not have any zero with a positive real part. The Nyquist stability criterion can be simplified by checking that the function $t_{filt}(\omega)t_{nf}(\omega)$ in the Nyquist plane is leaving the point (-1,0) on his left. A margin is defined so that the distance between the curve described by $t_{filt}(\omega)t_{nf}(\omega)$ and the point (–1,0) is sufficient.

All those criteria can be analyzed on the followings 2 plots with the linearized transfer function of the mechanical system $t_{nf}(\omega)$ and an optimal filter $t_{filt}(\omega)$ which is a 1st order Butterworth bandpass filter.

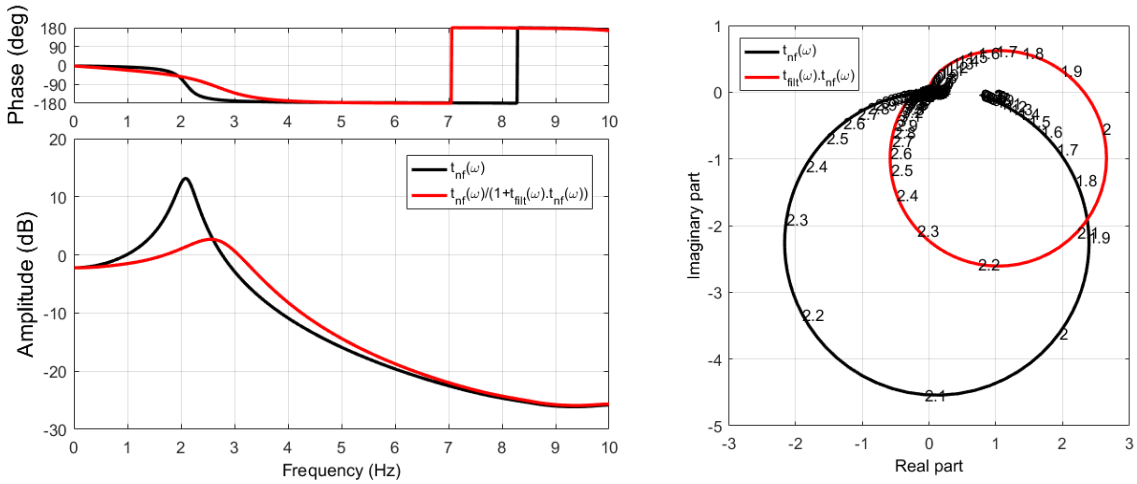


Figure 13 : Feedback loop filtering perfomances

On the left, the Bode plot exhibits a lower maximum response for the new transfer function (in red) compared to the reference one (in black). Below 1Hz, the 2 transfer functions are almost the same. On the right, the Nyquist plot shows the distance between the function $t_{filt}(\omega)t_{nf}(\omega)$ (in red) and the point (-1,0).

In the time domain, filtered torque $\Gamma_{t\ filt}$ is obtained using the state-space representation of the filter with the matrix A, B, C, D. New variables x are introduced:

$$\dot{x} = A.x + B.\Gamma_t(t)$$
$$\Gamma_{t\ filt}(t) = C.x + D.\Gamma_t(t) \quad (12)$$

The feedback torque is then added in the 3D model. The result can be seen on Figure 14 to Figure 16. Responses with feedback loop (in blue) are compared with responses in open loop (in red). Once again, measurements in the reference [4] are given for comparison on the left column. It is recalled that measured and modeled vehicle have significant differences in their characteristics and calculated results are not supposed to reproduce accurately measurements but the general shapes are effectively similar.

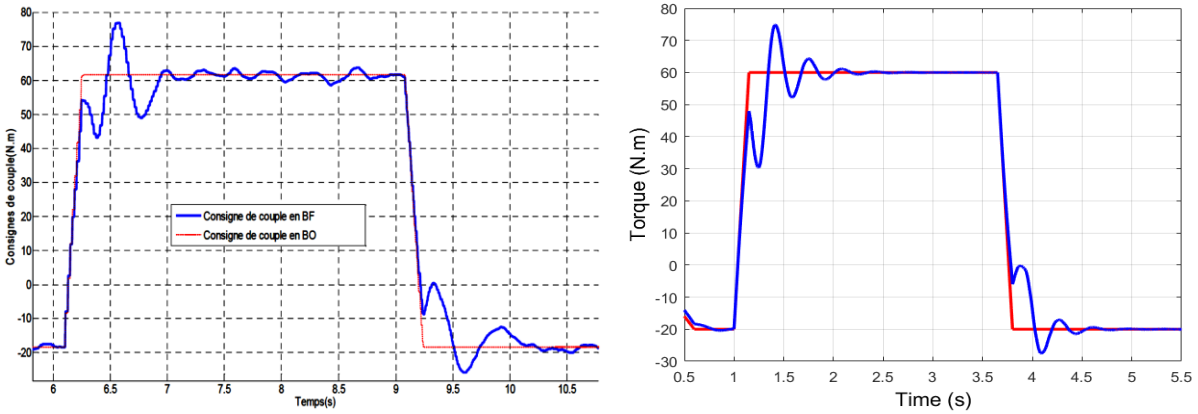


Figure 14 : Torque step applied with feedback loop (left : measurements ; right : calculations)

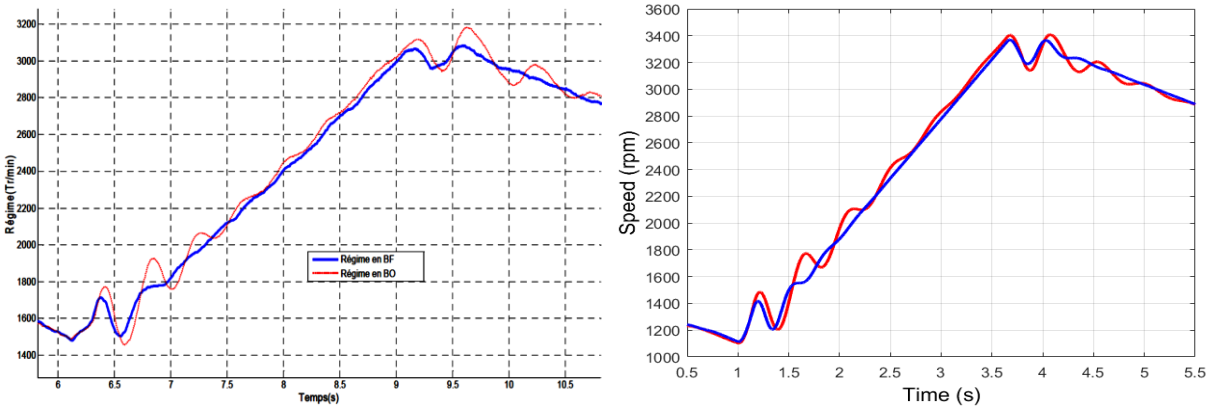


Figure 15 : Engine speed variations with feedback loop (left : measurements ; right : calculations)

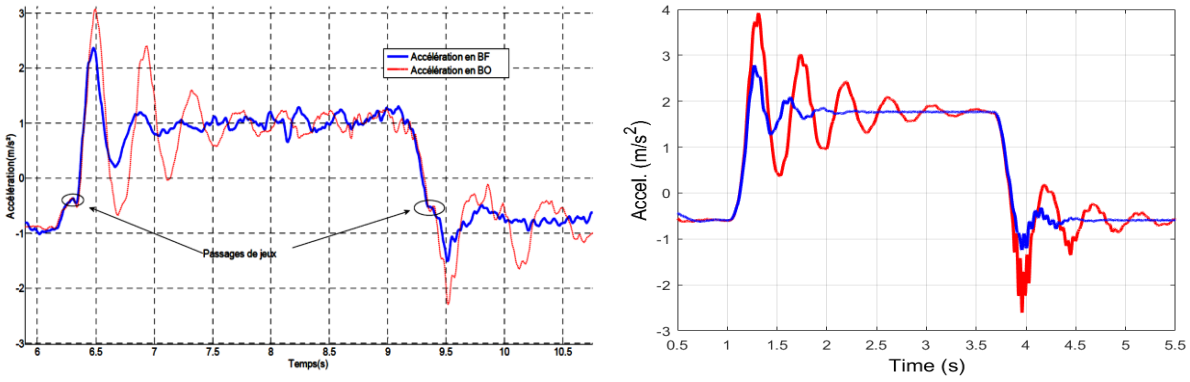


Figure 16 : Cabin longitudinal acceleration with feedback loop (left : measurements ; right : calculations)

On Figure 16, the treatment of the oscillations due to the 1st driveline torsional mode is very effective. Moreover, the engine speed rise does not seem affected by the feedback loop (see Figure 15).

The effect of the engine mounts non-linearities on the active damping of the oscillations can be estimated by comparing the answer taking into account these non-linearities to the one obtained with a linearized behavior around an operational point. Both results are compared on Figure 17, the red curve including non-linearities. Slight differences appear but the attenuation of the oscillations remains the same.

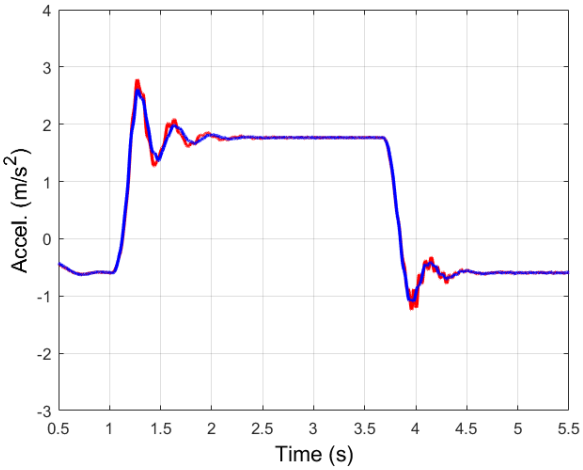


Figure 17 : Engine mounts non linearities effect on cabin longitudinal acceleration

6 Conclusions

Strong variations of driving torque may excite driveline first torsional mode located at a very low frequency. A simple mechanical model with a limited number of non linearities is described to reproduce this phenomenon. An analytical formula (3) is given for the mode natural frequency and shows a good agreement with the 3D model.

To investigate the interactions with engine suspension, it is necessary to rewrite the relation between the rotation of the primary shaft and the rotation of the differential. Engine block reaction and the induced rotational movement must be considered. Flexibility induced by the 3 engine mounts can be added in series and leads to an new analytical formula (5). In 1st gear, the natural frequency goes from 2.4Hz to 2.1Hz. The contributions of all the components to the total stiffness has been evaluated. The main flexibility is coming from driveline shafts with 55% but engine suspension can't be neglected with 20%.

The coupling between driveline and engine block on the engine roll mode has been estimated. This time a stiffness coming from the driveline is added in parallel of the one from engine mounts. In 1st gear, the engine roll mode natural frequency passes from 10Hz to 11.6Hz.

To prevent oscillations, an active damping is added through an engine torque control. Driveline oscillations control is addressed in a simplified manner in order to assess the final engine suspension impact. The main objectives are to eliminate oscillations due to the 1st driveline torsional mode and to keep a good driveability while respecting the stability criteria for the feedback loop. Optimization process is done using a linearized transfer function of the mechanical system at a relevant operational point. The resulting feedback loop is applied in time domain on the 3D model with all the non linearities considered. The treatment of the oscillations due to the 1st driveline torsional mode is still very effective.

References

[1] Sheng-Jiaw Hwang, Jer-Shi Chen, Li Liu, Ching-Chung Ling, *Modeling and simulation of a powertrain-vehicle system with automatic transmission*, International Journal of Vehicle Design, Vol. 23, No1/2 (2000).

[2] Ph. Couderc, J. Callenaere, J. Der Hagopian, G. Ferraris, A. Kassai, Y. Borjesson, L. Verdillon, S. Gaimard, *Vehicle driveline dynamic behaviour: experimentation and simulation*, Journal of Sound and Vibration, Vol. 218, No1, pp133-157 (1998).

[3] D. Lefebvre, P. Chevrel, S. Richard, *Control analysis tools for active attenuation of vehicle longitudinal oscillations*, Conference on control application, Mexico, pp5-7 (2001).

[4] M. Berriri, P. Chevrel, D. Lefebvre, M. Yagoubi, *Active damping of automotive powertrain oscillations by a partial torque compensator*, Control Engineering Practice, Vol. 16, No 7, pp874-883 (2008).

[5] A.F.A. Serrarens, M. Dassen, and M. Steinbuch, *Simulation and Control of an Automotive Dry Clutch*, Proceedings of the American Control Conference (2004).

[6] H.B. Pacejka, *Tyre and Vehicle Dynamics*, 2nd Ed., Butterworth-Heinemann (2006).

Investigation of the influence of DC-bus voltage on switched reluctance machines regarding noise and vibrations

Y. Mollet [1,2], **F. Chauvicourt** [1,2,3], **J. Pelletier** [2], **M. Sarrazin** [1], **C. Faria** [1], **H. van der Auweraer** [1], **J. Gyselinck** [2]
[1] Siemens Industry Software NV,
Interleuvenlaan 68, 3001 Leuven, Belgium
e-mail: **yves.mollet@siemens.com**

[2] ULB, BEAMS Energy Department,
Avenue Franklin Roosevelt 50 (CP165/52), B-1050, Brussels, Belgium
e-mail: **yves.mollet@ulb.ac.be**

[3] KU Leuven, Department of Mechanical Engineering,
Celestijnenlaan 300 box 2420, B-3001, Heverlee, Belgium

Abstract
Switched reluctance machines (SRMs) benefit from simple and cheap design and inherent fault tolerance, but still suffer from torque ripple and noise, vibration and harshness (NVH) issues. This paper aims at experimentally investigating the influence of the DC-bus voltage on NVH aspects of a 15 kW 8/6 SRM. Spectrograms of current, vibration and acoustic noise, as well as the evolution of loudness and sharpness are presented for DC-bus-ramp tests. It turns out that a higher DC-bus voltage combined with a hysteresis control leads to the excitation of higher frequencies and therefore to the generation of a sharper noise. This trend is essentially remarkable in hard-chopping mode. Furthermore, the sound becomes also louder as the DC-link voltage increases, probably due to the discrete character of the controller, responsible for overshoots outside the current-hysteresis band, becoming more important as the switching frequency increases. Finally, similar trends, but highly different values of loudness are found depending on the position of the microphone.

1 Introduction

In SRMs torque is produced by successively supplying with current the concentrated coils on its salient stator poles to attract the nearest salient rotor poles. As the torque is produced by the maximum-flux principle, neither winding nor permanent magnet is present in the rotor, which is only made of stacked soft-iron sheets. Each of the phase activations in this step-by-step process is called 'stroke'. SRMs, previously limited to very specific applications, have gained attention in the last decades, since the development of power converters allows for their use in various state-of-the-art drive configurations, such as in automotive, [1] aerospace [2] and energy-conversion applications (high-speed gas turbines) [3].

The main assets of SRMs are the simplicity of their stator construction and their permanent-magnet- and winding-free rotor, allowing for low-cost production [1, 4, 5, 6], robustness [4, 5, 6, 7] and suitability for severe environments [2, 7, 8] and high-speed applications [2]. SRMs also benefit from a high torque density [5] and very suitable torque-speed characteristics for electrical vehicles (EVs). The absence of permanent magnets also avoids depleting the limited available reserves of rare-earth elements [2, 9]. SRMs are also inherently tolerant to electrical faults, since the magnetic coupling between phases is negligible [2, 5, 7,

10], allowing for fault-tolerant operation, when combined with a modular design [11], converter [12] and optimized control [13].

However, an accurate knowledge of the rotor position (via a hardware or software measurement) is required for the control of the machine [6, 14] and the fringing effect and the high magnetic saturation level during operation make control strategies complex [2]. Compared to PMSMs, SRMs are also less efficient, since they have to be magnetized from the stator and need higher current amplitudes at equal torque [7]. Finally, the discontinuous character of the currents [7] and the excitation of structural resonance modes of the stator [9] are the origin of torque ripple and noise, vibration and harshness (NVH) issues [1, 2, 4, 5, 6, 7, 9, 13]. Due to these NVH [15, 16] and control-related issues [17] conventional induction machines and PMSMs are still generally preferred to SRMs in automotive applications.

Consequently, the investigation of NVH concerns in SRMs and their resolution are of high importance to allow for a more extensive use in various applications. A better understanding of the problem can be completed using modelling approaches, first with analytical equations [4, 5, 18, 19], then by combining analytical and FEA models [8] to compute magnetic forces and their resulting vibrations and acoustic noise. Experimental approaches can also support and strengthen the understanding process. For instance [1] shows a modal analysis and run-up tests on a 12/8 SRM, and [20] run-ups on a 12/8 and a 8/6 SRMs, as well as on two PMSMs. Both papers show the influence of speed, geometry (via the generation of forces and the resonance phenomena) and control on NVH issues and additionally consider sound quality metrics as relevant criteria for the definition of solutions.

Obviously, geometrical design solutions, such as a larger air gap or a skewed rotor may also be considered, yet with their drawbacks, i.e. a reduction of torque density and the production of torsional vibrations and associated noise in larger machines [13]. Manufacture refinements are also proposed in order to reduce noise of electric machines due to resonances [21]. Nevertheless, these last techniques are only achievable while the machine is under its first designing phases. On the other hand, when the machine is already built, control optimization algorithms, using e.g. torque-sharing functions or advanced converter topologies [13], can be considered and apply on the electronic side of the energy flow chain (from electric energy to mechanical energy). In particular the DC-bus voltage has an influence on the time derivative of the flux inside the SRM, as well as on the switching frequency of the converter if hysteresis control is used [22]. This reference investigates the effects of halving the DC-bus voltage through the comparison of run-ups with the use of soft instead of hard chopping and similar behaviours are observed at medium speed. However, at low and high speeds the hard chopping technique combined with a halved DC-link voltage results in an increase and in a reduction of the switching components in current respectively, due to the influence of the pseudo-electromotive force.

This paper experimentally investigates the effect of the DC-bus voltage of the converter on noise and vibrations in an 8/6 SRM, based on vibration, acoustic noise and current signals. Contrary to the more classical speed-frequency spectrograms showing run-up condition experiments [1, 20, 22], tests are performed at constant speed with a continuously increasing DC-bus voltage in order to visualize the DC-bus voltage effect on the vibration and acoustic spectra. Section 2 describes the main characteristics of the investigated SRM and the main origins of vibrations. The test bench and its measurement set-up, as well as the implementation of the control are presented in Section 3, while results are shown and discussed in Section 4.

2 Typical waveforms and NVH aspects of the investigated SRM

2.1 Main characteristics and typical waveforms

The rated and peak power, peak torque and peak current of the investigated 8/6 SRM are 15 kW, 30 kW, 200 Nm and 200 A respectively, while its maximum speed is 10 krpm. Further characteristics of the SRM can be found in [22].

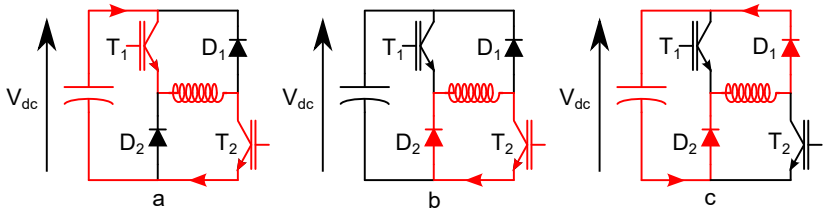


Figure 1: Asymmetric H-bridge feeding one phase of the SRM: possible current paths. Depending on the states of both power switches T_1 and T_2, the applied voltage may be $+1$, 0 or -1 times the DC-bus voltage V_{dc} (cases a, b and c respectively).

The phases of the SRM behave as RL circuits whose inductances highly vary with rotor position and current due to the saliency of stator and rotor poles, and to magnetic saturation respectively. Therefore, the voltage equation of each phase can be written as the sum of the ohmic voltage drop and the time derivative of the flux linkage ψ_{ph}:

$$v_{ph} = R_{ph} i_{ph} + \frac{\mathrm{d}\psi_{ph}\left(i_{ph}, \theta_r\right)}{\mathrm{d}t}, \tag{1}$$

with v_{ph} the voltage applied to the phase terminals, i_{ph} the current, R_{ph} the phase resistance, θ_r the rotor position and t the time. If the mutual coupling between phases is neglected, the time derivative of the flux linkage can be decomposed in two terms related to the variation of stored magnetic energy and to the production of mechanical power respectively [23]:

$$\frac{\mathrm{d}\psi_{ph}\left(i_{ph}, \theta_r\right)}{\mathrm{d}t} = \frac{\partial \psi_{ph}}{\partial i_{ph}} \frac{\mathrm{d}i_{ph}}{\mathrm{d}t} + \frac{\partial \psi_{ph}}{\partial \theta_r} \frac{\mathrm{d}\theta_r}{\mathrm{d}t} = \left(L_{ph}(\theta_r, i_{ph}) + i_{ph} \frac{\partial L_{ph}}{\partial i_{ph}} \right) \frac{\mathrm{d}i_{ph}}{\mathrm{d}t} + e_{ph}, \tag{2}$$

with L_{ph} the phase inductance. This last term e_{ph} corresponds to a pseudo-electromotive force (pseudo-EMF), as it contains a small part linked with stored magnetic energy if the machine is saturated [3].

In the frame of this work, one phase is activated at a time, when the nearest rotor pole is approaching (i.e. when the inductance is increasing) in motor mode. The current reference is set so that the desired torque is produced in average during the stroke (average-torque control, ATC). This is achieved at low speed by chopping each phase current by means of a dedicated asymmetrical H-bridge converter, comprising two insulated-gate bipolar transistors (IGBTs) and two free-wheeling diodes, as shown in Figure 1. A hysteresis control is here used to keep the current in a desired band Δi^*_{ph} around the reference i^*_{ph}.

When hard chopping is used, both IGBTs are simultaneously turned on and off and the current is maintained in the defined hysteresis band around its set-point value by applying successively V_{dc} and $-V_{dc}$ on the phase, the current path being represented in Figure 1 a and c respectively. In case of soft chopping, one switch remains closed during the whole stroke, while the other one is switched to chop the current, its path being successively represented in Figure 1 a and b. At the end of the stroke both IGBTs are turned off and the magnetic energy stored in the phase is sent back to the DC-bus through both diodes according to Figure 1 c.

The current waveforms at low and medium speeds are presented along with mechanical angle for soft chopping in Figure 2. Current ripple due to chopping can be seen in both cases, inducing oscillations in the generated torque. According to equations (1) and (2) the decay slope of the current is much lower in soft chopping, as a zero voltage is applied to the phase at that time. Combined with hysteresis control, this leads to an important reduction of the switching frequency, as it is shown in the next section.

At medium speeds the pseudo-EMF partially balances the supply voltage, leading to less sharp rising edges and fewer switching instants within a stroke, as shown in Figure 2. The turn-on θ_{on} and turn-off θ_{off} angles of the phase also have to be moved forward to ensure the current sufficiently rises at the beginning of the stroke and has the time to fall down to zero and the end to avoid production of negative torque. Beyond the base speed the pseudo-EMF overcompensates the supply voltage and no more chopping can be performed; θ_{on} and θ_{off} are then used to control the current, only allowing to maintain the rated power, while the maximum torque decreases as an inverse function of speed.

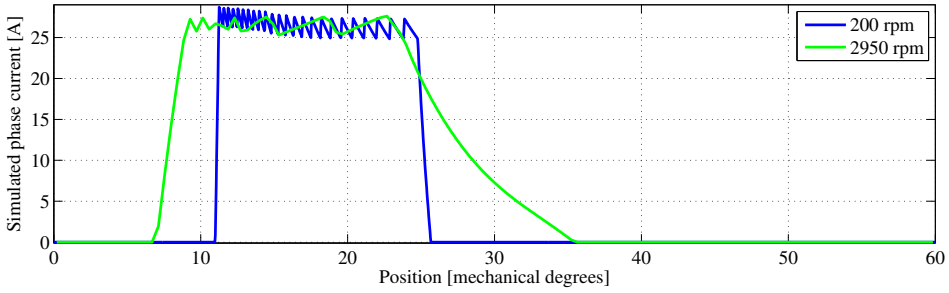


Figure 2: Simulated current waveforms corresponding to one phase of the investigated 8/6 SRM with 10 Nm load at low and medium speeds in soft chopping. The 0° and 60° and 30° rotor angles correspond to the unaligned and aligned positions respectively.

2.2 Influence of the DC-bus voltage on the waveforms

As a hysteresis controller is used, the DC-bus voltage is essentially expected to have an influence on the switching frequency of the converter, as the general waveform of the current is determined by the control structure. Supposing that the current follows a triangular path between the lower and upper boundary within a stroke (i.e. neglecting the variation of the time derivative of the current between two switching instants), as suggested in Figure 2, the instantaneous switching frequency can be computed as the inverse of the sum of the rising and falling periods $t_{rise} = \frac{\Delta i^*_{ph}}{\mathrm{d}i_{ph}/\mathrm{d}t}$ and $t_{fall} = -\frac{\Delta i^*_{ph}}{\mathrm{d}i_{ph}/\mathrm{d}t}$ respectively.

The slope of the current can be computed according to equations (1) and (2):

$$\left(\frac{\mathrm{d}i_{ph}}{\mathrm{d}t}\right) = \frac{v_{ph} - e_{ph} - R_{ph}i_{ph}}{\frac{\partial \psi_{ph}}{\partial i_{ph}}}, \tag{3}$$

with v_{ph} equal to V_{dc}, 0 and $-V_{dc}$ for the rising slope in both cases and for the falling slope in soft and hard chopping respectively.

Neglecting the voltage drop on the phase resistance, approximative expressions of the switching frequency can then be derived for soft and hard chopping respectively:

$$f_{sw,soft} = \frac{e_{ph} - e_{ph}^2/V_{dc}}{\frac{\partial \psi_{ph}}{\partial i_{ph}}\Delta i^*_{ph}}, \tag{4}$$

$$f_{sw,hard} = \frac{V_{dc} - e_{ph}^2/V_{dc}}{2\frac{\partial \psi_{ph}}{\partial i_{ph}}\Delta i^*_{ph}}, \tag{5}$$

According to equations (4) and (5), plotting the switching frequency with respect to DC-bus voltage would result in a hyperbola with a horizontal and an oblique asymptote in soft and hard chopping respectively. Comparing both expressions it can also be shown that $f_{sw,soft} < f_{sw,hard}$ for $e_{ph} < V_{dc}$, i.e. when the current has to be chopped. However, as e_{ph} and $\frac{\partial \psi_{ph}}{\partial i_{ph}}$ fluctuate during the stroke due to the non-linear relationship between flux linkage and both current and position, the switching frequency is not constant during the stroke. In consequence, equations (4) and (5) have to be considered as giving trend lines around which the frequency components are distributed. Furthermore, equations (4) and (5) also show the dependency of switching frequency on the hysteresis bandwidth Δi^*_{ph}, and on speed through the pseudo-EMF e_{ph}.

2.3 NVH aspects

The torque delivered by the SRM is produced by the tangential components of the magnetic forces generated between stator and rotor when activating the phases. These forces have also radial components, which are

responsible for most of the vibrations in the machine, due to the pulsating character of the attraction between poles coming from the succession of strokes on the one hand, and from the chopping on the other hand. These radial components essentially deform the stator yoke and its surrounding pieces [1, 4, 5, 24], leading to the production of acoustic noise in the surrounding air. As shown in [4], vibrations are essentially produced during the commutations and their amplitudes increase with the flux present at that time in the activated poles.

While the successive activation of the phases generates components in the phase currents, air-gap forces and torque at multiples of the mechanical speed, that is, speed orders, the chopping of the current at low speed adds supplementary components at the switching frequency [1].

Furthermore, resonance modes of the stator and of other components (e.g. cooling jacket) can be excited by the radial pulsating forces [1, 4, 20, 24]. The corresponding resonance frequencies can be estimated in a first approach by considering the circumferential modes of the stator, modelled as a cylindrical shell without constraints at both ends [24]. For a more accurate computation, the poles, end caps, coils, and the motor mounting have to be taken into account, as they affect stiffness of the system and thus the modes and associated frequencies [1, 24]. According to the working principle of the motor, the order m of the dominant circumferential mode corresponds to the ratio between the number of stator poles and phases [7], i.e. $m = 2$ (ovalization mode, as each phase consists of a pair of opposite poles) in the case of the 8/6 SRM. Furthermore, the contribution of phases 1 and 3 to this mode shape are in opposition with each other, while phases 2 and 4, act similarly on an independent and 45-degree-sifted mode shape, as they are situated on nodes of the deflection shape related to phases 1 and 3 [25]. Consequently, the mode is excited by odd multiples of the fundamental frequency of the phases, while the even multiples generate in-phase actions of phases 1 and 3 and therefore tend to cancel the displacement.

3 Measurement set-up, simulation model and implementation of the control

3.1 Measurement set-up and AMESim model

This paper investigates the influence of DC-bus-voltage ramps on current, radial vibration and acoustic-noise spectra of the SRM (in no-load condition and for a 5 Nm load torque). The investigated SRM is controlled using a home-made dedicated converter and is loaded with a 37 kW DC machine associated with a commercial double thyristor bridge. A system of pulleys and synchronous belts with a speed ratio of 4 is used as the speed of the DC machine cannot exceed 4000 rpm. The schematic of the bench is presented in Figure 3 a, comprising the electrical sensors, the speed and torque measurements and the position of accelerometers and microphones (represented as numbered green and blue squares respectively). The small dimensions of the SRM compared to its power normally requires water cooling, while air is forced into the DC machine by an external fan. The short duration of the tests permits, however, not activating the cooling system of the SRM, while the one of the DC machine is only started for the loaded tests. In that way the addition to the spectrum of frequencies from other sources than the SRM is avoided when possible.

In order to verify the behaviour of the currents, the investigated SRM, its converter and control have been modelled in AMESim software. The model with the implementation of soft chopping is presented in Figure 3 b, a constant load torque playing the role of the DC machine.

3.2 Structure and implementation of the control

The SRM is controlled in Matlab/Simulink environment via an 1103 dSPACE fast-prototyping platform. In the present case average-torque control (ATC) is used, that is, the reference current i_{ph}^{*} is computed so that the desired torque T^{*} is produced in average within the stroke by one phase at a time. This reference

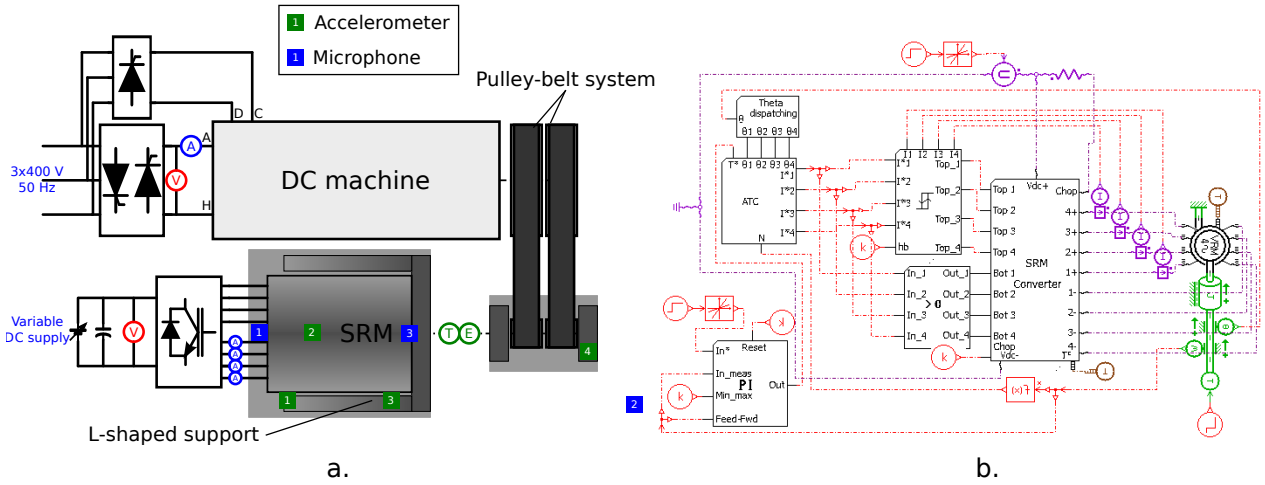


Figure 3: a. General schematic of the SRM test bench. b. Overview of the AMESim model with soft-chopping implementation.

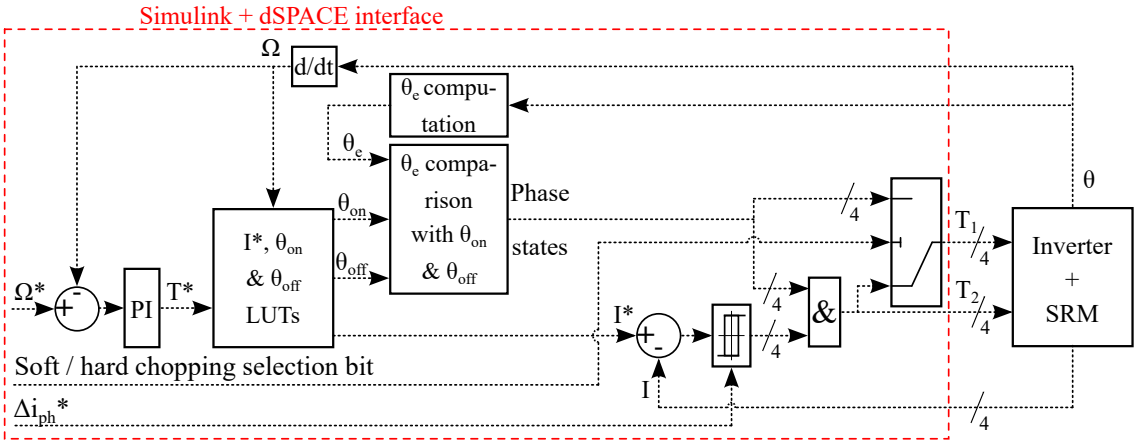


Figure 4: SRM test-bench control structure. The T_1 and T_2 inputs of the 'Inverter + SRM' block refer to the gate signals of the upper and lower power switches in Figure 1.

current, as well as the turn-on and turn-off angles of the phases (θ_{on} and θ_{off}), are computed from the actual speed and set-point torque by means of look-up tables, as shown in Figure 4. A comparison between the measured electrical rotor angle θ_e, computed as the remainder from the division of the mechanical angle θ by the number of rotor poles, and the turn-on and turn-off angles permits sending the reference current to the active phase, while the hysteresis controller maintains the actual current in the defined band Δi^*_{ph}. Hard or soft chopping are selected, using a Boolean variable, resulting in synchronizing both gate signals T_1 and T_2 and in maintaining T_2 at one for the whole stroke respectively. Finally, a classical (proportional-integral) speed controller sets the torque reference. This control structure runs at a 30 kHz sampling frequency. The DC machine is controlled with a four-quadrant commercial rectifier (Alstom WNTC).

The same control structure is modelled in AMESim: the look-up tables are implemented together with the comparison between electrical angle and turn-on and -off angles in the "ATC" block in Figure 3. For the soft-chopping implementation, the top IGBTs of the converter are controlled through a hysteresis block, while the bottom IGBTs are closed as soon as the reference current of the corresponding phase is non-zero. The classical speed PI controller is also visible in the bottom left of Figure 3 b. A variable-step solver is used for the simulations and the sampling frequency of the hysteresis control is not limited to 30 kHz in this case.

4 Experimental and simulation results

Before the main results are shown, the current, vibration and acoustic-noise spectra are presented for a run-up test to allow distinguishing the main different frequency components (depending or not on speed) that appear in the plots and exciting a large range of frequencies [1]. The global impact of the DC-bus voltage on current waveforms, vibration and acoustic noise is then investigated in a similar way by measuring these quantities while performing DC-bus-voltage ramps while the SRM is running. In all tests the SRM is speed controlled with a constant hysteresis bandwidth of 2.5 A, while the load torque is imposed by the DC machine. Simulation results are stored with the same sampling frequency as measurements, i.e. 40.96 kHz.

4.1 Run-up test and general observations

Current, vibration and acoustic noise are measured in the present case while the speed reference of the SRM is linearly increased from 150 to 3000 rpm and the load torque of the DC machine is set to 10 Nm. Soft-chopping mode is used for the present test.

Using a sliding window, the measured signals from the sensors represented in Figure 3 are decomposed into a succession of short-time ones on each of which an FFT is performed, similarly to [26]. The quarter of the window length is used as time shift between two consecutive windows and each obtained spectrum is associated to the time and speed at the middle point of its corresponding window.

Due to possible speed oscillations present in the original signal, these results are, in practice, sorted by increasing speed and interpolated according to a regularly growing speed profile. The processed data are presented as spectrograms in Figure 5 for the simulated current and in Figures 6 and 7 for experimental results regarding different sensors of Figure 3. The frequency and speed resolutions of the spectrograms are 10 Hz and 1 rpm respectively. RMS values are considered for the computation of the decibels.

In this kind of figure speed orders appear as oblique lines with their origin at $\{0\text{ Hz}, 0\text{ rpm}\}$, while structural resonances and other speed-independent frequency content have the form of vertical lines. On the spectrogram of simulated currents in Figure 5, speed orders multiple of 6 (crossing multiples of 100 Hz at 1000 rpm) appear, since the successive activation of the SRM phases has to be repeated six time per revolution due to the presence of six poles in the rotor. Below 1500 rpm it can further be noted that the amplitudes of orders multiple of 24 (corresponding to frequencies multiple of 400 Hz at 1000 rpm) are reduced. A simple Fourier analysis of a square signal with a fundamental being six times the rotation frequency and with a 0.25 duty-cycle, i.e. close to the blue current waveform presented in Figure 2, effectively results in the absence of harmonics multiple of 4. From about 3 to 6 kHz, a series of inverted-C shapes can also be remarked. These zones of relative higher amplitude have to be related to the switching frequency as already attested in [1]. As shown in equation (4), the switching frequency in soft-chopping mode follows a quadratic trend with respect to speed and e_{ph}. At low speeds, when the pseudo-EMF is low, the quadratic term of equation (4) can be neglected and the switching frequency grows linearly with speed. However, at medium and high speeds, this quadratic terms grows up to completely cancelling the linear terms, such that the switching frequency goes through a maximum before decreasing back to zero at the base speed, i.e. when the pseudo-EMF compensates the supply voltage.

The same comments can be made for the experimental current plot of Figure 6, except that the inverted C-shape is not present, due to the limited (30 kHz) sampling frequency of the hysteresis controller implemented in dSPACE. As the switching instant cannot take place within a sampling period, the switching process is highly affected as delays between the crossing of the hysteresis-band limits and the reaction of the controller are generated, causing reduced and more random sampling frequencies and overshoots of the current outside the hysteresis band [27].

Speed orders are also found in the acoustic-noise and vibration plots in Figures 6 and 7 respectively, since the radial forces generated by the current act as vibration sources. The amplitude of these orders are, however,

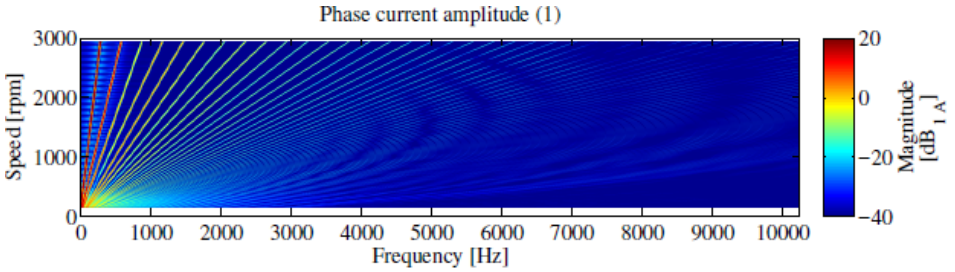


Figure 5: Phase current (run-up simulation, soft chopping, 10 Nm load). The 0 dB reference is 1 A.

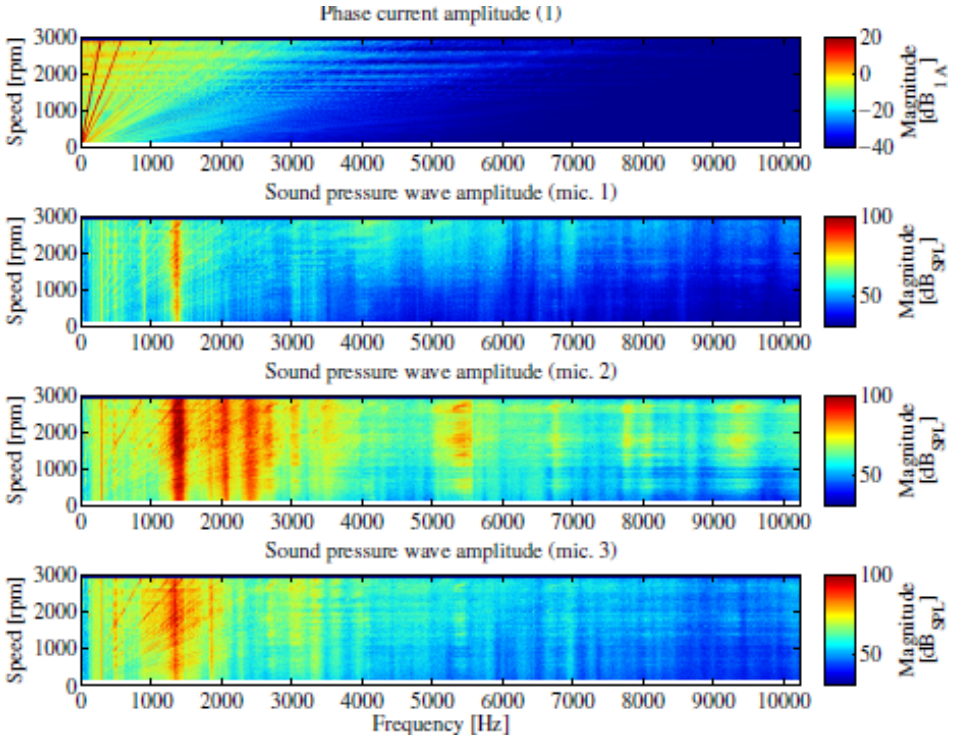


Figure 6: Phase current and acoustic-noise frequency content measured by the three microphones represented in Figure 3 (run-up test, soft chopping, 10 Nm load). The 0 dB references are 1 A and 20 μPa respectively.

modulated by the activation of specific structural resonances of the SRM, and particularly the dominant ovalization (second circumferential) mode close to 1375 Hz [8, 22], resulting from the activation at each stroke of two opposite poles. This process may also excite in a lesser extent the zero (breathing) and fourth (square) circumferential modes of the SRM. According to different analytical methods and FE results gathered in [22], the eigenfrequencies associated to the square (without bending of the poles) and breathing modes are situated between 5.5 and 7.5 kHz and between 7 and 8 kHz respectively. This suggests that the relatively higher vibration amplitudes appearing in the spectrograms of the three first accelerometers (glued on the SRM) in Figure 7 around 6550 Hz and 7100 Hz may correspond to the square and breathing modes. On the contrary, no straightforward explanation can be given regarding the vertical lines between 2.5 kHz and 4 kHz. Possible explanations may be the excitation of other eigenmodes of the SRM or of its accessories.

Regarding the acoustic noise, the spectrograms coming from the three microphones presented in Figure 6 show rather different frequency contents. Much more content seems to be caught by microphone 2, positioned at a few tens of centimetres from the bench. On the contrary, both other microphones are placed very close to some parts of the bench, which can act as shields and prevent sound coming from other bench parts to reach the microphone. This is especially the case for microphone 1, positioned near the end plate of the SRM and whose corresponding graph shows low amplitudes, except for the dominant ovalization mode.

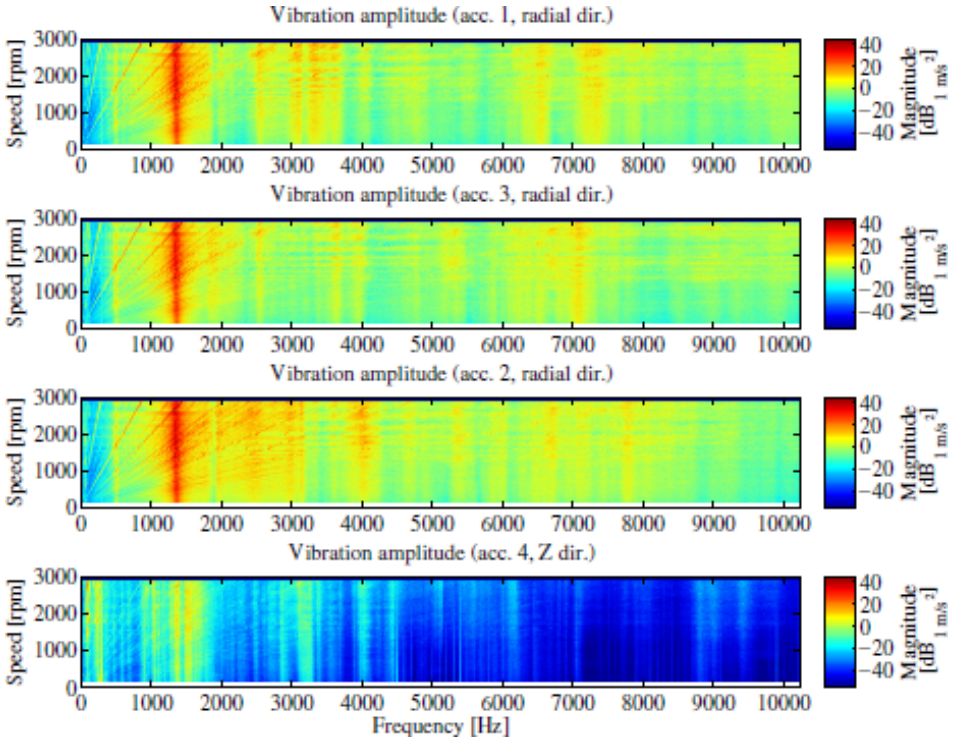


Figure 7: Frequency content of the radial vibration measured by accelerometers 1, 2 and 3 and vertical vibration from accelerometer 4 (run-up test, soft chopping, 10 Nm load). The 0 dB reference is 1 m/s^2.

4.2 DC-bus-voltage ramp tests in soft and hard chopping

The DC-bus-voltage ramp tests are performed for both hard- and soft-chopping cases at no-load and at load. Each time the SRM is maintained at 1000 rpm while the DC-bus voltage is progressively increased from 150 to 450 V by applying a 2.5 V/s ramp on the programmable DC-power supply feeding the SRM converter. The plots are obtained using the same technique as for run-ups, except that the FFTs are neither sorted nor interpolated, since they are plotted in function of the voltage reference of the DC-power supply, which is directly proportional to time. The resulting frequency and DC-link-voltage resolutions of the spectrograms are 10 Hz and 0.0625 V respectively.

The spectrogram of the simulated phase current and the ones of experimental phase current, radial vibration and acoustic noise corresponding to a DC-bus-voltage ramp in soft-chopping mode with 5 Nm load are presented in Figures 8 and 9. Since the speed is now constant during the test, the corresponding orders become vertical lines and the detection of the resonance frequencies is less obvious. Similar comments as above can be formulated concerning the orders multiple of 6 and 24.

In Figure 8 the switching frequency seems to globally follow the trend specified by equation 4 with respect to DC-bus voltage, i.e. hyperbolas tending to constant frequency values. In the measured current these hyperbolas do not appear due to the limited sampling frequency of dSPACE, but a general rise of amplitudes (orders and background) is observed in the current spectrogram, especially between 2 kHz and 4 kHz, as the voltage increases from 150 to 450 V.

This general rise of amplitudes and frequencies with DC-link voltage can also be observed in the acoustic-noise plot and especially in the vibration one, exciting also more and more the main eigenmodes of the SRM.

The spectrogram of the simulated phase current and the ones of experimental phase current, radial vibration and acoustic noise corresponding to the same test as before, but in hard-chopping mode are presented in Figures 10 and 11.

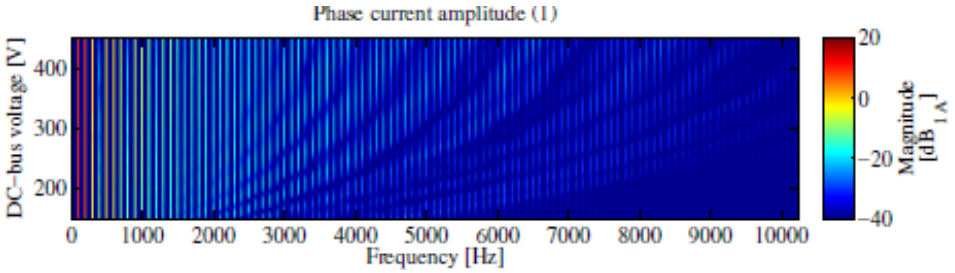


Figure 8: Phase current (simulation of DC-bus-voltage-ramp, soft chopping, 5 Nm load). The 0 dB corresponds to 1 A.

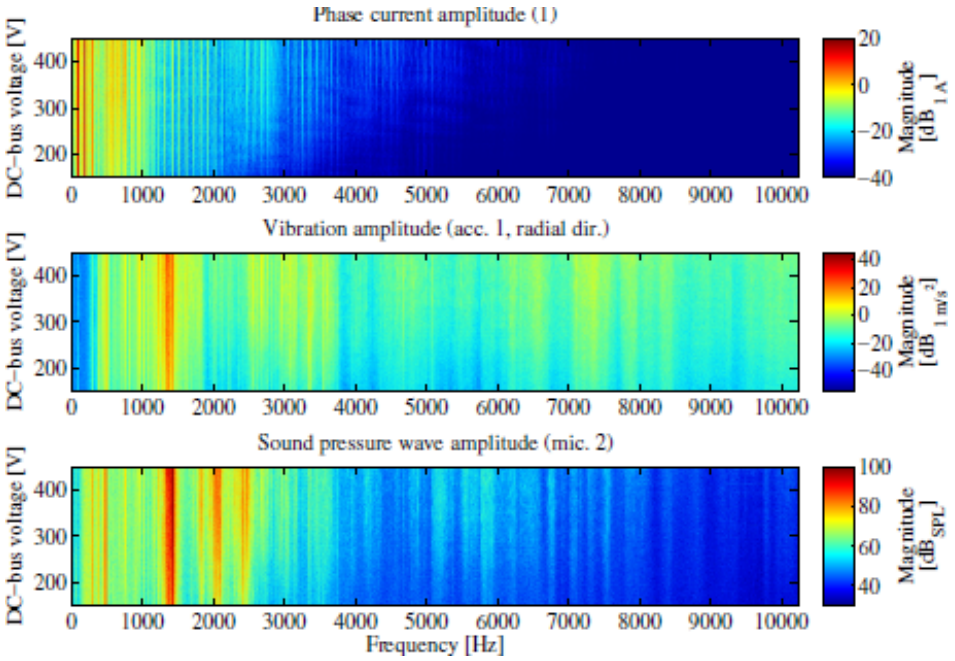


Figure 9: Phase current, radial vibration and acoustic-noise frequency content (DC-bus-voltage-ramp test, soft chopping, 5 Nm load). The 0 dB references are 1 A, 1 m/s^2 and 20 μPa respectively.

In Figure 10 the switching frequency seem to follow a much more linear trend than in Figure 8 and therefore reach higher frequencies. This corroborates equation (5), as the hyperbola tends to a linear behaviour for high DC-bus voltages. In practice, with the reduced sampling frequency of the controller, similar observations to the ones of the soft-chopping case can be made, but the effect of the ramp is more visible due to increased ripple amplitude and shifted to higher frequencies. Nearly no change in amplitude with DC-bus voltage is observed below 2 kHz, while a fast grow rate in the dB values is observable on an oblique line from {2 kHz, 150 V} to {5 kHz, 450 V}.

The effect of the rise of amplitudes and frequencies in the current on vibration and acoustic-noise is also more visible than in soft chopping. Due to the globally higher switching frequency similar and much higher amplitudes are observed below and above 2 kHz respectively. The ovalization mode even seems less excited with hard chopping, while the opposite can be said for the other modes.

4.3 Sound quality measurements

The evolution of sound quality with DC-bus voltage is presented in the next figures, based on the measurements from the three different microphones. This allows showing the impact of the location of the microphone on the computation of these psychoacoustic indices. The loudness and sharpness computed

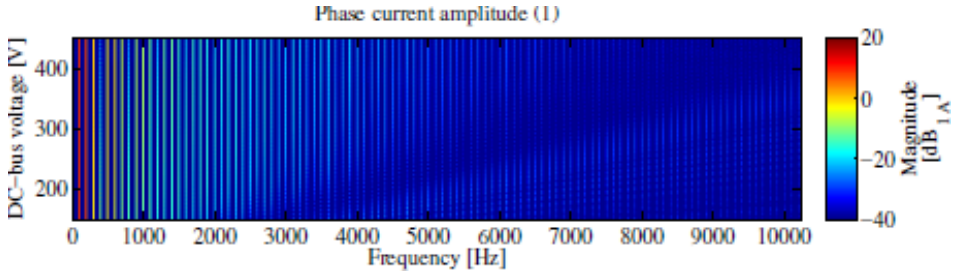


Figure 10: Phase current (simulation of DC-bus-voltage-ramp, hard chopping, 5 Nm load). The 0 dB corresponds to 1 A.

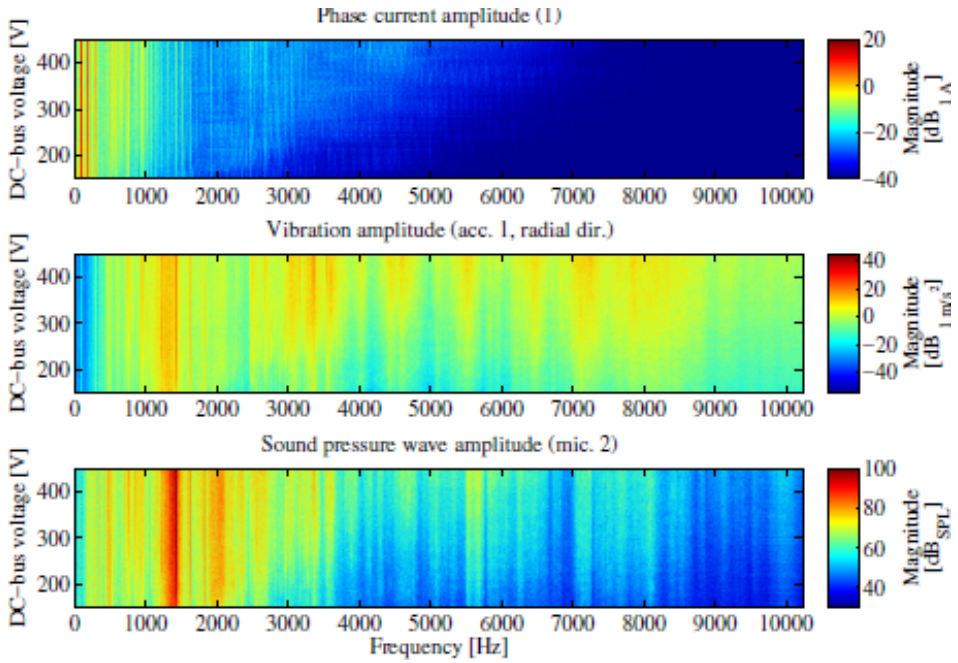


Figure 11: Phase current, radial vibration and acoustic-noise frequency content (DC-bus-voltage-ramp test, hard chopping, 5 Nm load). The 0 dB references are 1 A, 1 m/s^2 and 20 μPa respectively.

from microphone 1 in Figure 3 are plotted in Figure 12 as a function of DC-bus voltage for both soft and hard chopping cases, with and without load.

The loudness appears to increase relatively linearly with DC-bus voltage, a higher rate being observed in no-load case. Furthermore, the loudness increases less rapidly for high values of the DC-link voltage. The relative linear increase of loudness with voltage corroborates [4], which shows that the vibrations that are produced in the SRM are proportional to the time rate of change of power fed to the phase in unsaturated conditions. Consequently, the most important vibration are produced at switching instants when the flux (or the current) is non-zero in the phase. As the reference current is constant in the present test, the vibration amplitude, and therefore the loudness are effectively expected to grow with DC-bus voltage. As also mentioned in [4], magnetic saturation tends to mitigate vibrations; this could explain the observed reduced slopes for load compared to no-load cases.

However, when comparing soft and hard chopping, the former technique turns out to be louder than the latter, even with a halved voltage rate of change at switching instants. This has to be related to the lower switching frequency of soft chopping, which excites much more the ovalization mode of the SRM, which is particularly dominant in the spectrum acquired with microphone 1 as shown in Figure 6. As the switching frequency also increases with DC-link voltage, the less important excitation of the ovalization mode and of other relatively dominant frequencies in the spectrum may explain the reduction of the increasing rate of loudness at high

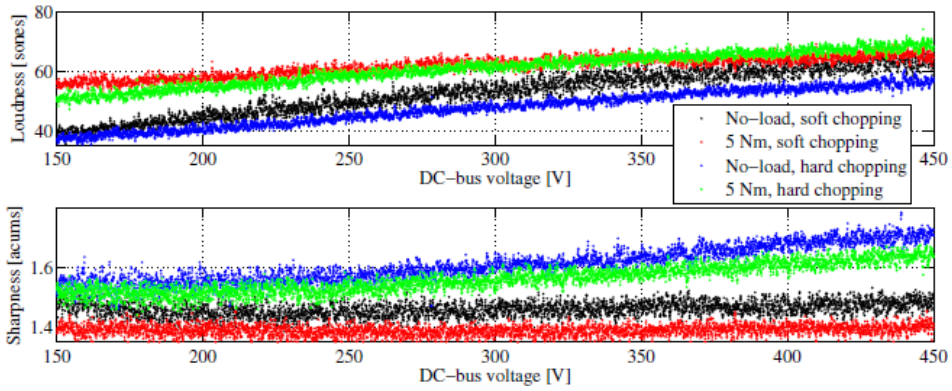


Figure 12: Loudness and sharpness computed from microphone 1 in function of the DC-bus voltage for no-load and load cases with both soft and hard chopping.

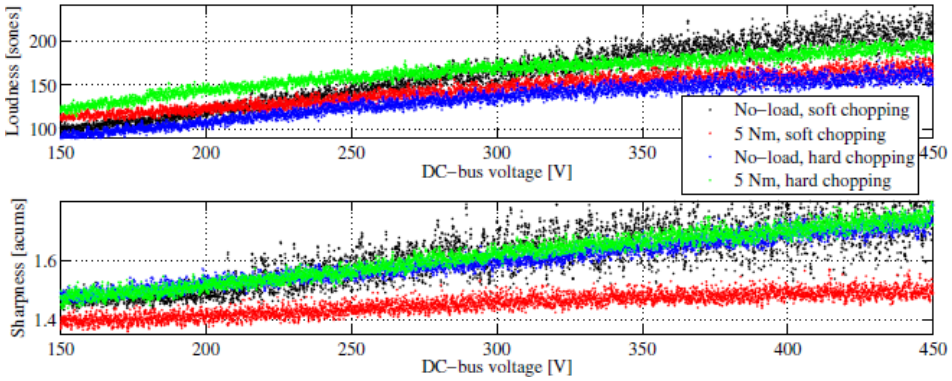


Figure 13: Loudness and sharpness computed from microphone 2 in function of the DC-bus voltage for no-load and load cases with both soft and hard chopping.

DC-bus voltages.

Regarding sharpness, only a little increase can be observed in Figure 12 for hard chopping at high DC-link voltage, while values are always higher than in soft chopping mode. The explanation is the higher switching frequency (and the reduced excitation of the ovalization mode) in hard chopping and its higher dependence on DC-link voltage as it can be remarked comparing Figures 9 and 11. The comparable or higher sharpness for no-load case can also be explained by a higher proportion of switching harmonics compared to speed orders coming from the strokes, as the current amplitude is higher in load case.

Similarly to microphone 1, the loudness and sharpness computed from microphone 2 in Figure 3 are plotted in Figure 13 as a function of DC-bus voltage for both soft and hard chopping cases, with and without load. Results are similar to the ones presented in Figure 12, except a much higher loudness, as expected from the comparison of spectrograms in Figure 6. Some other little differences can also be observed, essentially in the sharpness plot, where an increasing sharpness is also visible in soft-chopping mode at no-load. The probable reason is the much more important high-frequency content observed in the case of microphone 2 compared to microphone 1 in Figure 6. This second microphone, placed a bit further from the bench can then receive sounds (related to vibrations) from most of the parts of the bench, contrary to the first one, which is situated on the end plate of the SRM, acting as a shield.

Finally, the loudness and sharpness computed from microphone 3 in Figure 3 are plotted in Figure 14 in the same way as for the other microphones. Once again, results are similar to both previous figures, with an intermediate value of loudness, as expected from Figure 6. The evolution of sharpness with DC-bus voltage is also intermediate comparing with Figures 12 and 13, with only a little increase of the sharpness in soft-chopping mode at no-load. The last microphone is effectively situated just on the top of the support of

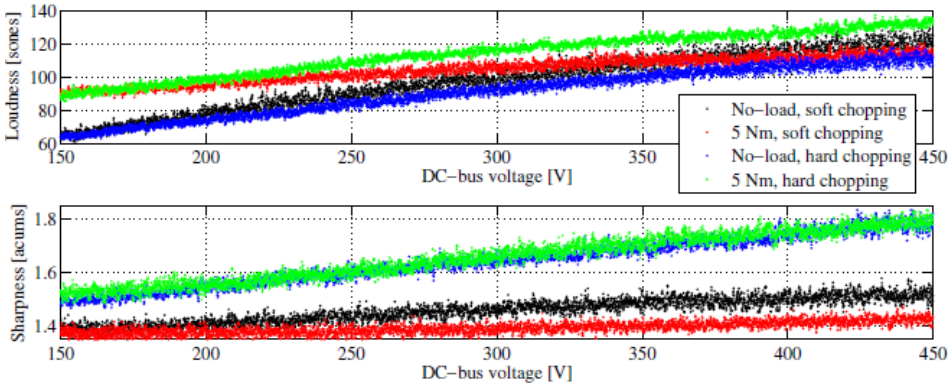


Figure 14: Loudness and sharpness computed from microphone 3 in function of the DC-bus voltage for no-load and load cases with both soft and hard chopping.

the SRM, resulting in a less ideal location compared to microphone 2 (but better than for microphone 1) to receive sounds from most of the parts of the bench.

5 Conclusion

This paper has investigated the effect of DC-bus voltage on current frequency components as well as on noise and vibration aspects in an 8/6 SRM. Experimental results have been compared with simulated currents and derived expressions of switching frequency. Spectrograms of current, vibration and acoustic noise have first been presented for a run up to explain the origin of the various frequency components. Similar plots, as well as the computed loudness and sharpness have then been shown for DC-bus voltage ramps, in order to highlight the impact of this voltage on the spectra and on the quality of the sound produced by the SRM. The influence of the position of the microphone on the measurement has also been briefly discussed.

It turns out that increasing the DC-link voltage globally increases the switching frequency, especially in hard chopping, as a hysteresis controller is used to chop the current. The production of vibrations at higher frequencies is then the origin of a sharper acoustic noise, considered as less pleasant. The noise becomes also louder, probably because of increasing overshoots of the current outside the predefined hysteresis band linked to the discrete character of the hysteresis controller. However, the higher frequencies generated in case of hard chopping may limit the excitation of the main resonance mode of the SRM around 1375 Hz.

Furthermore, it has to be noted that, even if the general trend of loudness and sharpness hardly depends on the used microphone, important differences in loudness from one microphone to another can be mentioned, probably due to the distances between the microphones and the various noise sources (e.g. parts vibrating at their eigenfrequencies, etc.) and the orientation of the microphones with respect to these sources.

Acknowledgements

The authors would like to thank the Wallonia-Brussels Federation and the National Authority for Research of the Romanian Government for supporting this research via the cooperation project Hardware-in-the-loop testing of variable reluctance machines for low-noise automotive applications.

References

[1] M. Sarrazin, S. Gillijns, K. Janssens, H. Van Der Auweraer, K. Verhaeghe, *Vibro-acoustic measurements and techniques for electric automotive applications*, INTER-NOISE and NOISE-CON Congress and Conference Proceedings. Institute of Noise Control Engineering (2014), pp. 5128-5137.

[2] S. Faid, P. Debal, S. Bervoets, *Development of a Switched Reluctance Motor for Automotive Traction Applications*, The 25th World Battery, Hybrid and Fuel Cell Electric Vehicle Symposium & Exhibition (2010), pp. 1-5.

[3] I. Boldea, *Switched Reluctance Generators and Their Control*, The Electric Generators Handbook, Boca Raton, FL, USA: CRC Press, Taylor & Francis Group, LLC, (2006).

[4] C. Lin, B. Fahimi, *Prediction of Radial Vibration in Switched Reluctance Machines*, Ind. Electron. Soc. IECON 2013-39th Annu. Conf. IEEE, vol. 28, no. 4 (2013), pp. 1072-1081.

[5] C. Lin, S. Wang, B. Fahimi, *Efficient Multiphysics Modelling of Vibration and Acoustic Noise in Switched Reluctance Motor Drives*, Industrial Electronics Society, IECON 2014 - 40th Annual Conference of the IEEE (2014), pp. 542-548.

[6] P. Rafajdus, A. Peniak, D. Peter, P. Makys, L. Szabo, *Optimization of switched reluctance motor design procedure for electrical vehicles*, Optimization of Electrical and Electronic Equipment (OPTIM), 2014 International Conference on (2014), pp. 397-404.

[7] Z. Yang, F. Shang, I. P. Brown, M. Krishnamurthy, *Comparative Study of Interior Permanent Magnet, Induction, and Switched Reluctance Motor Drives for EV and HEV Applications*, IEEE Trans. Transp. Electrif., vol. 1, no. 3 (2015), pp. 245-254.

[8] F. L. M. dos Santos, J. Anthonis, F. Naclerio, J. J. C. Gyselinck, H. Van Der Auweraer, L. C. S. Góes, *Multiphysics NVH Modeling : Simulation of a Switched Reluctance Motor for an Electric Vehicle*, Ind. Electron. IEEE Trans., vol. 61, no. 1 (2014), pp. 469-476.

[9] C. T. Faria, F. Santos, F. Chauvicourt, S. Orlando, *Noise emissions on switched reluctance motors : evaluation of different structural models*, EVS28 International Electric Vehicle Symposium and Exhibition (2015), pp. 1-8.

[10] J. F. Marques, J. O. Estima, N. S. Gameiro, A. J. Marques Cardoso, *A New Diagnostic Technique for Real-Time Diagnosis of Power Converter Faults in Switched Reluctance Motor drives*, IEEE Trans. Ind. Appl., vol. 50, no. 3 (2014), pp. 1854-1860.

[11] L. Szabó, R. Terec, M. Ruba, *Reconfigurable Fault Tolerant Control System for Switched Reluctance Motors*, Electr. Power Eng. Front., vol. 1, no. 1 (2012), pp. 1-8.

[12] L. Szabó, M. Ruba, *On fault tolerance increase of switched reluctance machines*, IEEE EUROCON 2009, EUROCON 2009 (2009), pp. 734-739.

[13] P. Moreno-Torres, M. Lafoz, M. Blanco, G. Navarro, J. Torres, G. Navarro, J. Torres, L. Garca-tabars, *Switched Reluctance Drives with Degraded Mode for Electric Vehicles*, Modeling and Simulation for Electric Vehicle Applications, M. A. Fakhfakh, Ed. InTech (2016), pp. 97-124.

[14] M. Ehsani, B. Fahimi, *Elimination of position sensors in switched reluctance motor drives: state of the art and future trends*, IEEE Trans. Ind. Electron., vol. 49, no. 1 (2002), pp. 40-47.

[15] D. Panda and V. Ramanarayanan, *DC-Bus-Voltage-Based Sensorless Switched Reluctance Motor Drive for HVAC Applications*, IEEE Trans. Ind. Electron, vol. 54, no. 4 (2007), pp. 2065-2078.

[16] L. Chen and W. Hoffman, *Speed Regulation Technique of One Bearingless 8/6 Switched Reluctance Motor With Simpler Single Winding Structure*, IEEE Trans. Ind. Electron, vol. 59, no. 6 (2012), pp. 2592-2600.

[17] J. Zheng, S. Zhao and S. Wei, *Application of self-tuning fuzzy PID controller for a SRM direct drive volume control hydraulic press*, Control Engineering Practice, vol. 17, no. 12 (2009), pp. 1398-1404.

[18] G. Myrria, F. Chauvicourt and C. Faria, *Evaluation of the influence of the control strategy of the electric vehicles motor on its radiated noise using 1D simulation*, European Acoustic Conference - EuroRegio (2016).

[19] J. Le Besnerais, *Réduction du bruit audible d'origine magnétique dans les machines asynchrones alimentées par MLI - règles de conception silencieuse et optimisation multi-objectif*, PhD thesis at Ecole Centrale de Lille (2008).

[20] M. Sarrazin, J. Anthonis, H. Van Der Auweraer, C. Marţiş, J. Gyselinck, *Signature analysis of Switched Reluctance and Permanent Magnet electric vehicle drives*, Proceedings - 2014 International Conference on Electrical Machines, ICEM 2014 (2014), pp. 1831-1837.

[21] F. Chauvicourt, *Vibro-acoustics or rotating electric machines: Prediction, validation and solution*, PhD thesis at Katholieke Universiteit Leuven and Université Libre de Bruxelles (2018).

[22] Y. Mollet, *Fault-tolerance and noise and vibration aspects of electrical drives - Application to wind turbines and electrical vehicle traction*, PhD Thesis Université Libre de Bruxelles, Brussels, Belgium, (2017).

[23] G. Gallegos-Lopez, J. Walters, K. Rajashekara, *Switched Reluctance Machine Control Strategies for Automotive Applications*, Proceedings of SAE 2001 World Congress (2001).

[24] D. Fodorean, M. Sarrazin, C. S. Marţiş, J. Anthonis, H. Van der Auweraer, *Characterizing the motorization of a light electric vehicle through FEM and NVH tests*, Proceedings - 2014 International Conference on Electrical Machines, ICEM 2014 (2014), pp. 2404-2409.

[25] J. O. Fiedler, K. A. Kasper and R. W. De Doncker, *Calculation of the Acoustic Noise Spectrum of SRM Using Modal Superposition*, IEEE Trans. Ind. Electron, vol. 57, no. 9 (2010), pp. 2939-2945.

[26] E. Cabal-Yepez, A. G. Garcia-Ramirez, R. J. Romero-Troncoso, A. Garcia-Perez, R. A. Osornio-Rios, *Reconfigurable monitoring system for time-frequency analysis on industrial equipment through STFT and DWT*, IEEE Trans. Ind. Informatics, vol. 9, no. 2 (2013), pp. 760-771.

[27] Y. Mollet, M. Sarrazin, H. van der Auweraer, J. Gyselinck, *Noise and vibrations of switched reluctance machine drives - influence of the current hysteresis control*, Electroteh. Electron. Autom., vol. 64, no. 1 (2016), pp. 33-42.

Experimental applications of Bayesian Focusing in an industrial context

T. Le Magueresse[1], O. Minck[1], J. Antoni[2]
[1]MicrodB
28 Chemin du petit bois- BP 36 – 69131 ECULLY - France
e-mail: **thibaut.le-magueresse@microdb.fr**

[2] Univ Lyon, INSA-Lyon, Laboratoire Vibrations Acoustique - 69621 Villeurbanne, France

Abstract
Sound source localization using microphone arrays is largely applied in industrial engineering to diagnose acoustic issues appearing on complex machineries. An important number of algorithms have been developed to enhance the source identification procedure in terms of spatial resolution and quantification capabilities, such that engineers have to understand a lot of methods to cover the majority of industrial applications. Recently, it has been proven that a Bayesian approach can generalize some of these methods by automatically calculating the optimal basis functions depending on the geometrical experimental set-up. Moreover, the probabilistic way of solving the acoustic inverse problem offers the opportunity to introduce prior knowledge about the source, the noise and the propagation model. The aim of this publication is to apply the method to experimental cases and to show how the results can be exploited in practice to help the acoustics engineer to better characterize sound sources.

1 Introduction

Acoustic imaging techniques represent an effective tool to both localize and quantify sound sources using pressure measurements done by a microphone array. The main difficulty lies in recovering continuous sources based on noisy and discrete number of microphone measurements and an approached model. In general case, the solution of the problem is not unique and constraints must be defined to reach satisfactory results. Then, a large number of methods have been developed for decades to respond to specific needs depending on the application. Leclère *et al.* [1] attempt to classify every method by analyzing their main assumptions, their priors and their algorithms to resolve the obtained cost functions. Authors separate the methods into two large categories: (i) beamforming-based methods, which aims at reconstruct uncorrelated sources, and (ii) inverse methods, which look for the distribution of the sources at once without considering any assumptions about the correlation of sources. Deconvolution methods (CLEAN [2], DAMAS [3] …), extensively used in aeroacoustics field, fall within the first category whereas holography methods (NAH [4], HELS [5], SONAH [6], iBem [7]…) belongs to the second. Putting aside the algorithm considerations, the beamforming-based methods may be defective in low frequencies, where the uncorrelated assumption is frequently violated. Inverse methods, on the other hand, suffer from an unstable behavior coming from the innate ill-posed problem characteristic. To tackle this issue, the Tikhonov regularization [8] [9] process is often used and its efficiency has been largely demonstrated. This technique implicitly aims at recovering the solution as the compromise between the fidelity to the measured data and the minimal energy of the sources. This compromise is found by the estimation of the regularization parameter. Even if this parameter is well-tuned, researchers observed that the given solution becomes quantitatively non-satisfactory in high frequencies when the spatial sampling of the array is not sufficient [10] [11].

In that context, Bayesian Focusing (BF) has been introduced by Antoni [12]. This method considers both the source and the measurement as random variables. The probabilistic formalism and the use of the Bayes rule are exploited to derivate solutions depending on explicit priors about the source and the noise perturbing

the measurements. Then, it has been demonstrated that if the noise and the source are *a priori* modelled as Gaussian laws, the optimal solution can be written as the general-form Tikhonov solution. By the way, the superiority of the Bayesian estimation of the regularization parameter have been proven in different types of applications [13] [14] [15]. In order to improve quantitative results in high frequencies and to go beyond the limitations of the Tikhonov solution, one can play with the prior probability density function (pdf). The most intuitive way to add some physical information to the problem is to define a spatial aperture function that acts as a lens to focus on a particular zone of the space. Both spatial resolution and quantification performances may be improved by the definition of that prior [16] [17] [10]. The process of focusing and its definition in terms of pdf is largely described in an upcoming submitted paper [18]. Moreover, it can be shown that this Bayesian formalism is general enough to consider the cases of NAH or beamforming as a special case [12]. This flexibility in terms of (i) geometry, (ii) explicit prior definition and (iii) validity of the solutions in a wide frequency range makes the method attractive but yet not applied enough in practical cases.

The goal of the present communication is to apply BF on experimental cases and to show how one can exploit the wealth of information obtained.

2 Bayesian focusing: theory

2.1 Forward problem

The aim of the inverse problem is to reconstruct the finite source distribution over the object of interest using:

1. The cross-spectral matrix measured by an array composed of M microphones;
2. The acoustical model relating the radiation of sources placed on the surface of the object and the sound pressure measurement at the positions of the microphones of the array;
3. Any kind of prior information about the source (correlation length of sources, initial idea of the localization pattern, spatial sparsity of the sources…)

The classical forward problem is written as a matrix form, at a given frequency f:

$$\mathbf{p} = \mathbf{G}\mathbf{q} + \mathbf{b}, \tag{1}$$

with $\mathbf{p}$ the measured vector of dimensions of [MX1], with M the number of microphones, $\mathbf{q}$ the vector of the volume velocity of the sources placed on the nodes of the object of dimensions of [NX1] with N the number of nodes and $\mathbf{G}$ the transfer function relating the volume velocity of the sources and the sound pressure measured by the array. As a remark, one can write the forward problem as a function of the parietal pressure or the normal velocity if the transfer function between these quantities and the measured sound pressure is available (by Boundary Element Method for instance). In the case studies of this work, the propagation is considered in the free-field:

$$\mathbf{G} = -\frac{\mathrm{i}\omega\rho \mathrm{e}^{\mathrm{j}k\mathbf{R}}}{4\pi\mathbf{R}}, \tag{2}$$

with $\boldsymbol{R}$ the matrix of distances between the microphones and nodes. It is usual in imagery technique to decompose the acoustic field into basis functions. Depending on the geometrical configuration, the user has to choose the adapted basis to its problem. The direct problem expressed in eq. (1) could be re-written by introducing the decomposition of the source distribution into the basis $\boldsymbol{\Phi}$:

$$\mathbf{p} = \mathbf{G}\boldsymbol{\Phi}\mathbf{c} + \mathbf{b}, \tag{3}$$

with $\boldsymbol{c}$ the basis coefficients and $\boldsymbol{q} = \boldsymbol{\Phi}\boldsymbol{c}$.

2.2 Bayesian formalism

If one considers the measured spectra as random variables, the goal consists in finding the conditional pdf $\mathbf{q}$ given $\mathbf{p}$, written $[\mathbf{q}|\mathbf{p}]$. This pdf is unknown but it can be estimated according to the Bayes rule which expresses the searched posterior probability as:

$$[\mathbf{q}|\mathbf{p}] = \frac{[\mathbf{p}|\mathbf{q}][\mathbf{q}]}{[\mathbf{p}]}, \tag{4}$$

where [X] represents the pdf of the random variable X and [X|Y] the conditional probability of X given Y. The density $[\mathbf{p}|\mathbf{q}]$ represents the likelihood function i.e. the probability of observing the measurements $\mathbf{p}$ knowing the spectrum of the source. The prior probability $[\mathbf{q}]$ is the probability of the sources before knowing the measurements. Finally, the quantity $[\mathbf{p}]$ expresses the probability for all possible sources considered.

Experimental errors caused by measurement noise are modelled by a Gaussian pdf because experimental errors have many different origins. Additive noise then follows a complex zero-mean Gaussian law $\mathcal{N}_c(0, \beta^2\mathbf{\Omega_b})$ where β^2 stands for the unknown energy of noise and $\mathbf{\Omega_b}$is a known structure matrix defining the nature of the noise (an identity matrix is generally chosen to enforce the zero correlation of noise between microphones) :

$$[\mathbf{b}|\beta^2] = \mathcal{N}_c(0, \beta^2\mathbf{\Omega_b}) \tag{5}$$

In practice, $\mathbf{\Omega_b}$ is usually equal to the identity matrix. For the next developments, $\mathbf{\Omega_b} = \mathbf{I}$.The likelihood function $[\mathbf{p}|\mathbf{q}]$ is derived using the direct problem of eq. (1). The measurements are perturbed by the additive noise defined above:

$$[\mathbf{p}|\mathbf{q}, \beta^2] = \mathcal{N}_c(\mathbf{Gq}, \beta^2\mathbf{I}). \tag{6}$$

Lastly, prior information about nature of sound sources is also chosen as a Gaussian distribution. This hypothesis is mathematically convenient and other choices could be adopted [19] however these will not be investigated in this paper. The pdf of sources is finally written:

$$[\mathbf{q}|\alpha^2\,\mathbf{\Omega_q}] = \mathcal{N}_c(0, \alpha^2\,\mathbf{\Omega_q}) \tag{7}$$

with $\mathbf{\Omega_q}$a known structure matrix defining spatial correlation of sources. As a summary of this section where all the pdf have been defined, the following figure illustrates the studied system.

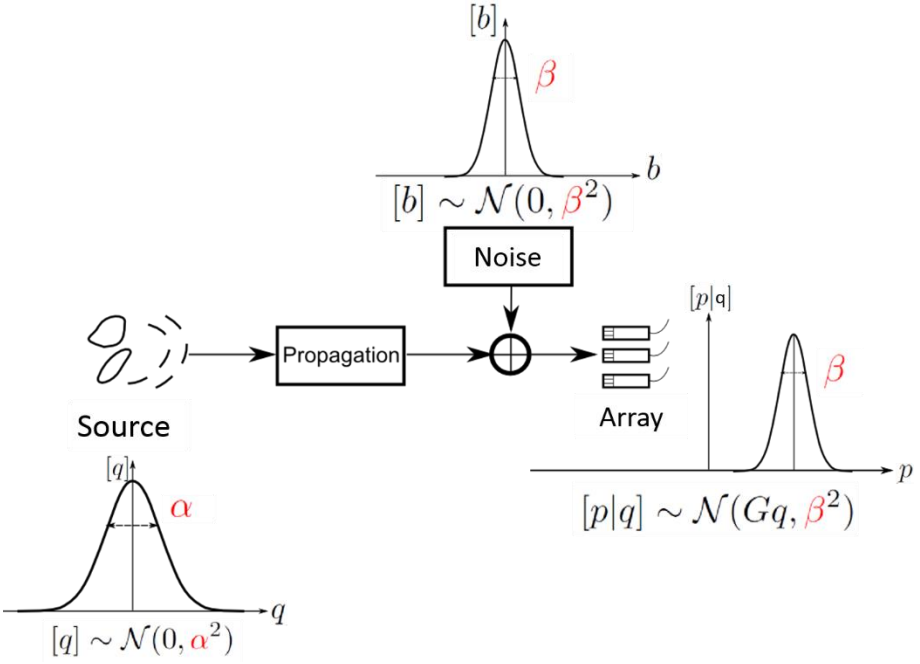


Figure 1 : Illustration of the studied acoustical direct problem

The result of the inverse problem is given by the maximum a posteriori estimator which is the most probable solution of the posterior pdf (from eq. (4)):

$$\boldsymbol{q}_{map} = Argmax[\boldsymbol{p}|\boldsymbol{q}][\boldsymbol{q}]. \tag{8}$$

The most probable source distribution will be estimated passing through the estimation of the basis coefficients. Then, the basis functions can be derived using the Bayes rule [12] :

$$\boldsymbol{\Phi} = \boldsymbol{\Omega}_{\mathbf{q}}^{\mathbf{1/2}}\boldsymbol{G}^{*}\boldsymbol{S}^{-\mathbf{1}}\boldsymbol{\Omega}_{\boldsymbol{b}}^{\mathbf{-1/2}}\boldsymbol{U} \tag{9}$$

with $\boldsymbol{U}$the singular matrix of the singular value decomposition of the propagation matrix G and $\boldsymbol{S}$ its singular values :

$$\boldsymbol{\Omega}_{\boldsymbol{b}}^{\mathbf{-1/2}}\boldsymbol{G}\boldsymbol{\Omega}_{\mathbf{q}}^{\mathbf{1/2}} = \boldsymbol{U}\boldsymbol{S}\boldsymbol{V}^{H}. \tag{10}$$

As a remark, $\boldsymbol{\Phi}$ can be replaced by known basis function as plane waves of spherical harmonics if the set-up is convenient.

The most probable solution of the inverse problem is called the maximum a posteriori estimator. This value is given by maximizing the numerator of the Bayes equation:

$$\mathrm{J} = \ \mathrm{Argmax}\ \{\ [\mathbf{c}, \alpha^2\ , \beta^2\ |\ \mathbf{p}]\ \}$$

$$\mathrm{J} = \ \mathrm{Argmin}\ \{\ -\ln\ [\mathbf{c}, \alpha^2, \beta^2\ |\ \mathbf{p}]\ \}$$

Enforcing the derivative of this cost function to zero with respect to the solution $\mathbf{c}$ bring us to an analytical expression of the sources:

$$\tilde{\boldsymbol{c}} \ = \ \frac{\mathbf{s}}{\mathbf{s}^2 \ + \ \eta^2}\mathbf{U}^{\mathrm{H}}\mathbf{p} \tag{11}$$

with $\tilde{\boldsymbol{c}}$ the regularized form solution, and $\eta^2 = \frac{\beta^2}{\alpha^2}$ the regularization parameter. It is noteworthy that this solution is similar to the well-known Tikhonov solution. Then the regularization parameter is determined by marginalizing the joint pdf $[\alpha^2, \beta^2|\mathbf{p}]$. Interested readers can refer to [20].

From the estimation of the regularization parameter and the knowledge of the basis functions, the inverse filter can be calculated as:

$$\boldsymbol{H}_{inv} = \boldsymbol{\Phi}\frac{\boldsymbol{S}}{\boldsymbol{S}^2 + \eta^2}\boldsymbol{U}^{H}, \tag{12}$$

and the final cross spectral matrix of the sources is then deduced:

$$\boldsymbol{S}_{qq} \ = \ \boldsymbol{H}_{inv}\boldsymbol{S}_{pp}\boldsymbol{H}_{inv}^{H}. \tag{13}$$

From this matrix, the information of the energy of each node is driven by the diagonal of the matrix.

2.3 “Focusing” iterative process

The quantification and localization performance of the method can be improved by iteratively enforcing the algorithm to concentrate the reconstructed energy on a particular zone. This process is largely explained in [18]. The covariance matrix of the prior pdf can be iteratively updated:

$$\boldsymbol{\Omega}_{q}^{1/2} = \mathrm{diag}(\boldsymbol{S}\boldsymbol{q}\boldsymbol{q})_{[n-1]}^{1-\frac{p}{2}} \tag{14}$$

with $\mathrm{diag}(\boldsymbol{S}\boldsymbol{q}\boldsymbol{q})_{[n-1]}$ the squared-volume velocity of each node of the mesh for the previous iteration and p the norm with $1<p\leq2$. The choice of p=2 leads to reaching the standard Tikhonov solution. Setting p to 1 enforces the sparsity of the sources. The sparsity constraint means that the reconstructed acoustic field can be explained using a few number of sources. The convergence of this algorithm can be observed and a stopping criterion has to be adjusted by the user.

2.4 Sound power estimation

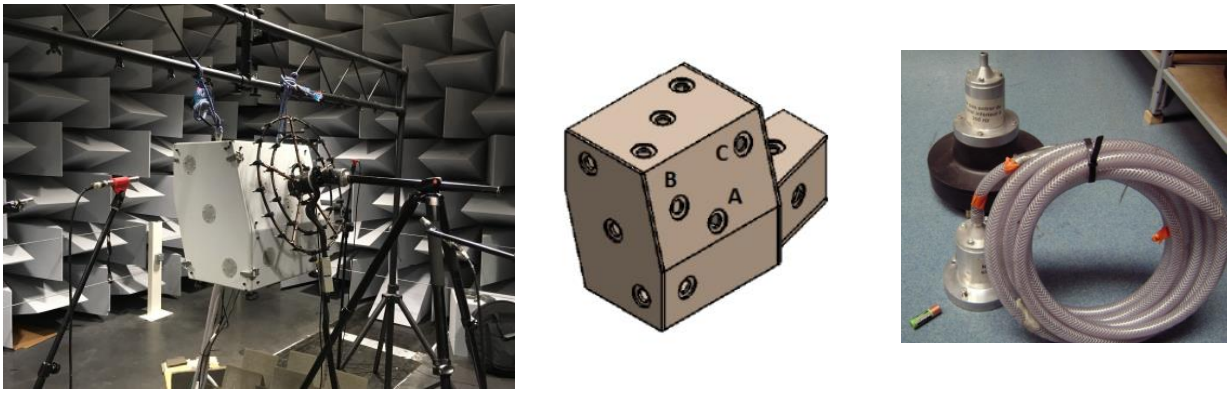
In practice, the acoustic quantity of interest is the sound power that can be expressed from the volume velocity cross spectral matrix:

$$\boldsymbol{W}_{eq} = \frac{\rho c k^2 diag\left(\boldsymbol{S}_{\boldsymbol{qq}}\right)}{4\pi} \tag{15}$$

As a remark, this expression describes the sound power of each equivalent source taken independently. Another expression can be used to model the interference created between the identified sources [10].

3 Experimental validations

A first experimental and academic case is proposed. The considered object is a rigid wooden box equipped with holes where point sources can be flush mounted on the panels. The mock-up has been built with the dimension range of an automotive engine. For the considered case, two fully correlated sources (denoted A and C) and one other uncorrelated source (B) are placed on the same panel. One microphone is mounted inside each of these sources to be able to measure the true coherence criterion as a function of the frequency. Then, a 36 microphones array is placed at 12cm of the source plane. The measurements have been carried out in the semi-anechoic room of the Laboratoire Vibrations Acoustique, University of Lyon. The ground has been locally treated with acoustic foam. The full experimental set-up is displayed in Figure 2.



(a) (b) (c)

Figure 2 : a) Photography of the array in front of the object inside the semi-anechoic room, b) position of the sources in the object and c) photography of the used source

Sound power maps have been calculated using BF on the 3-dimensions mesh of the box. The distribution of sources is assumed to propagate in the space as baffled sources. The norm of the equation (14) has been fixed at p=1.1 and the iterative process stops when two successive iterations give less than 0.1dB of deviation on the global reconstructed sound power. Figure 3 presents the results at 1.5 kHz.

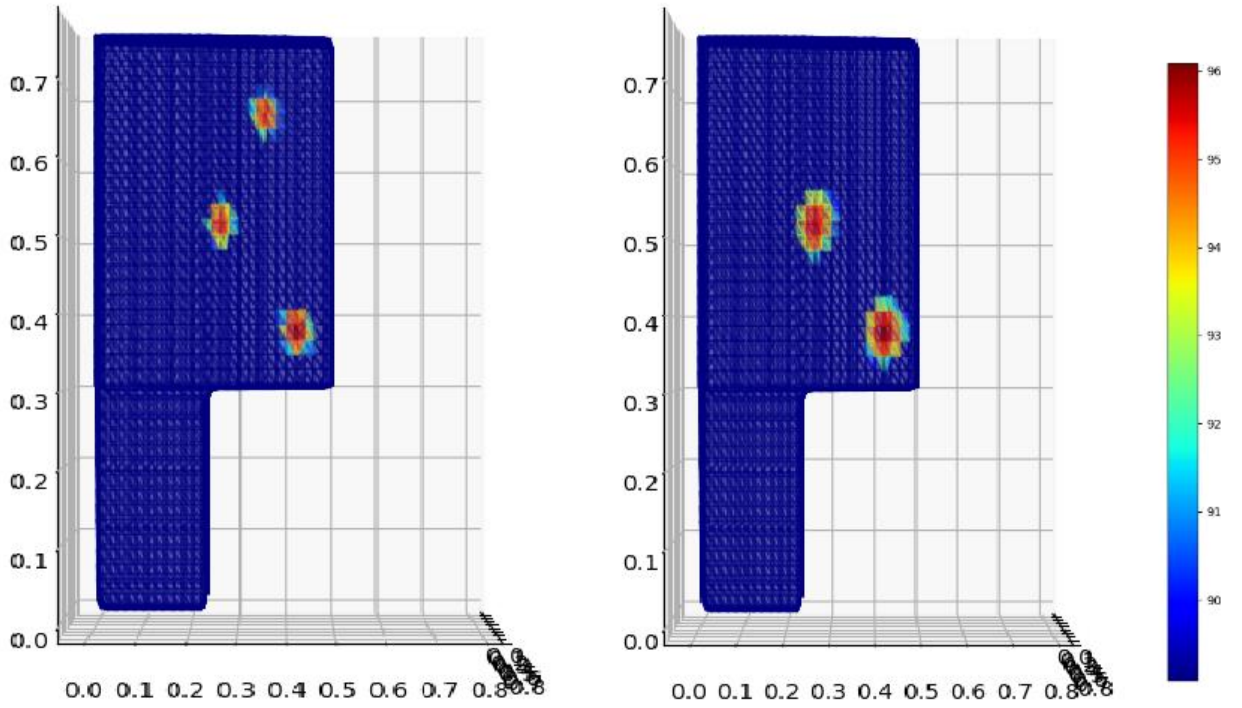


Figure 3 : Classical sound power map given by Bayesian focusing (on the left) and sound power map correlated with the identified source A (on the right) in dB (ref. 1e-12W) with a display dynamic of 8 dB

The three sources are well-localized with a satisfactory spatial resolution. Generally speaking, users of imaging techniques consider this result as the final one, whereas this result only represents a partial information about the sources, namely the diagonal of the sources cross-spectral matrix. The sound power map of the right side of Figure 3 represents the map correlated with the identified source A defined as:

$$\boldsymbol{W}_{coh} = \frac{\rho c k^2 \left|\boldsymbol{S_{qq}}(:, r_{ref})\right|}{4\pi}, \tag{16}$$

with r_{ref} the index of source A. It is interesting to note that the uncorrelated source B disappears from the map (given with a dynamic display of 8dB). This type of map could be useful in order to understand the mutual origin of identified sources.

The cross spectral matrix of the sources may also be used to estimate the coherence function between two nodes of the map. Figure 4 depicts this quantity measured by the microphones situated inside the sources (ground truth) and this same criterion reconstructed by BF when source B switched on or off.

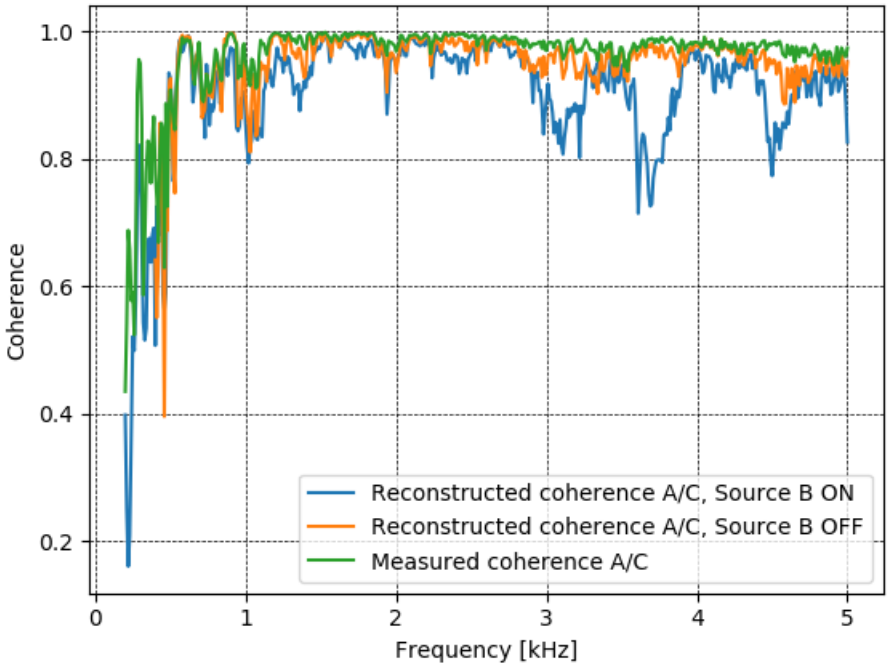


Figure 4 : Coherence between sources A and C measured directly inside the source (green), and reconstructed by Bayesian Focusing when source B is OFF (orange) and ON (blue)

The coherence function is well-recovered especially if source B is switched off. At around 3 kHz and 3.5 kHz, the source B radiates more energy than the two other and it perturbs the estimation of the coherence.

For design engineers, it also can be useful to propagate the identified sources in the space in order to estimate the directivity or to predict the sound pressure level at 1m for example and act on it if necessary (to improve the acoustic comfort). Theoretically, BF is able to recover these quantities by simply applying eq. (1). To experimentally validate this point, a quarter-of-sphere array has been placed in front of the source plane. The radiation of the three sources has been measured by two positions of this array to catch the total directivity pattern of the sources (see Figure 5).

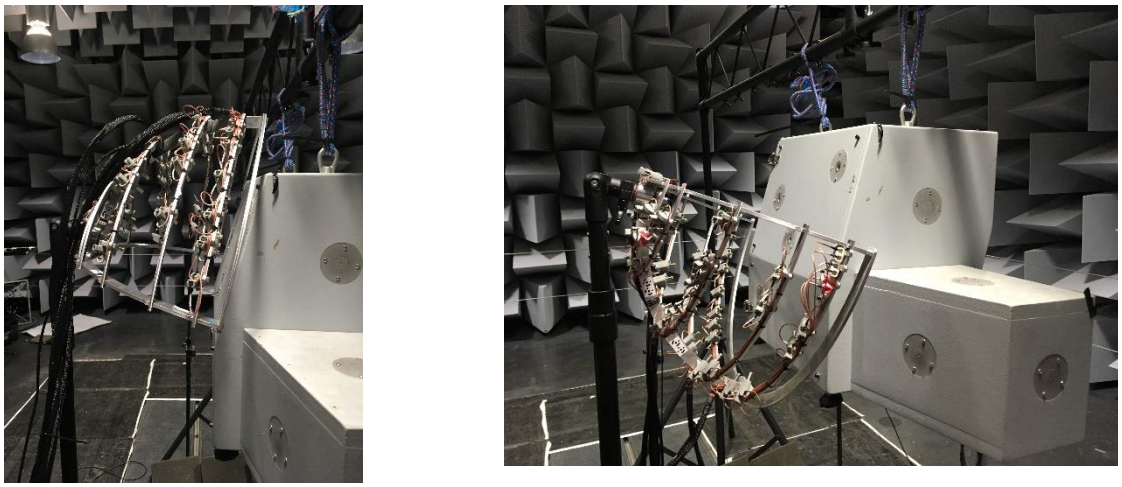


Figure 5 : Positions of the quarter-of-sphere array around the three sources

Figure 6 shows the spatial measured field and the recovered field by propagation of the identified sources to the microphones at 1.5 kHz. The spatial patterns are similar.

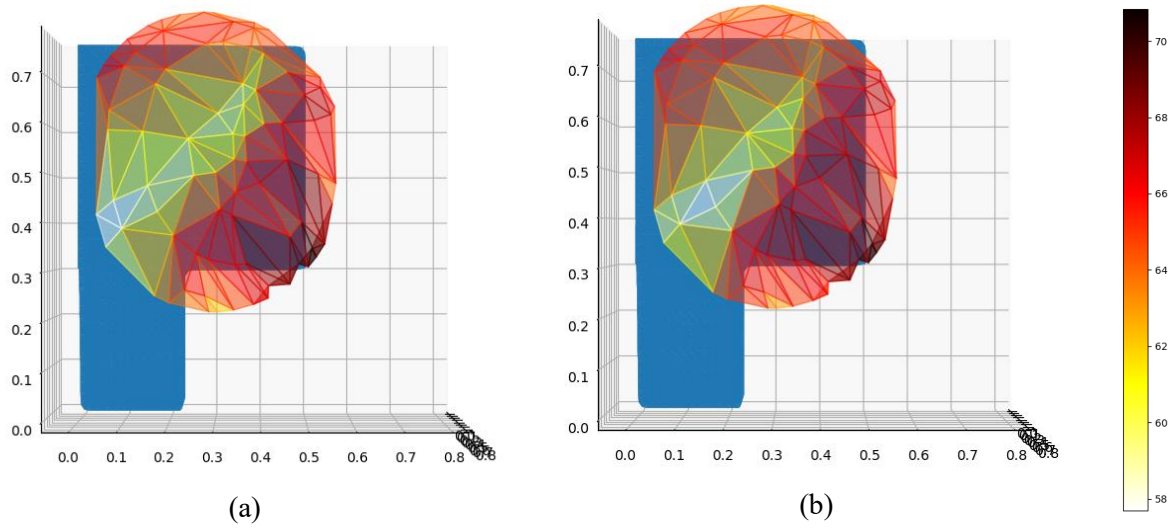


Figure 6 : a) Measured pressure field radiated from sources A, B and C and b) recovered pressure field by propagation of the sources identified by Bayesian Focusing at 1.5 kHz with 12dB display dynamic

The same process has been applied to predict the sound pressure level at 0.5m from the source plane. Figure 7 shows the comparison between the measured sound field at this location and the estimation by BF and classical beamforming. The estimation from classical beamforming has been obtained by propagating the acoustic field based on the three sources amplitudes since phase relationship is by essence neglected in beamforming.

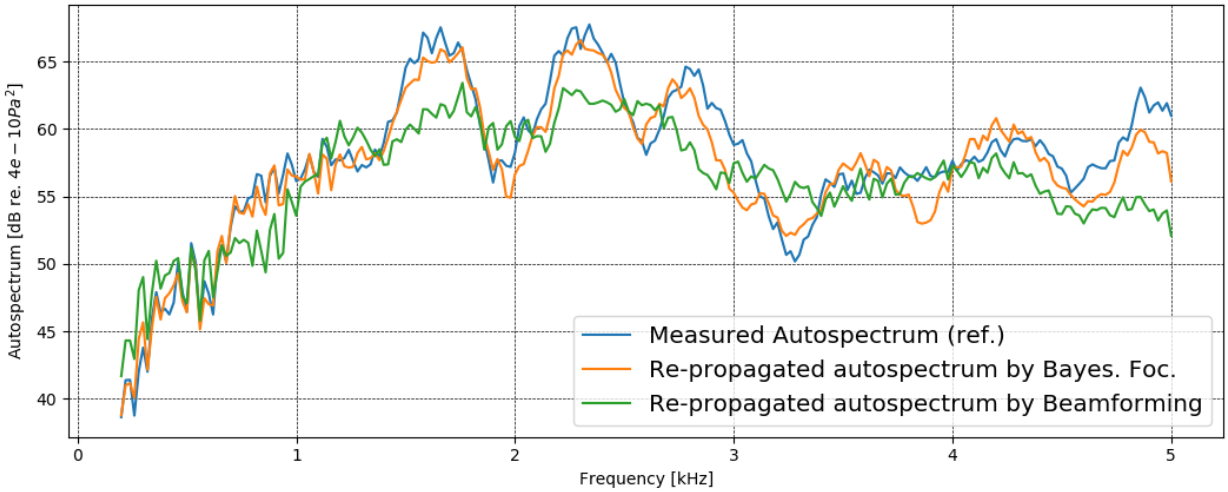


Figure 7 : Autospectra measured by the far-field microphone (in blue), and synthetized by the propagation of the identified sources by Bayesian Focusing (orange) and Beamforming (Green)

The propagation of the sources identified by BF respects the frequency evolution of the measured sound field. In particular, the three “humps” at 1.8 kHz, 2.3 kHz and 2.8 kHz are well-predicted. These shapes have probably been created by the wave interferences between the two correlated sources. In the other hand, the propagation of the source identified by beamforming does not reproduce this behavior because it assumes uncorrelated sources. Moreover, the prediction at low frequencies is not as accurate as provided by BF. This observation is probably due to the fact that the spatial support of the point spread function of the two correlated sources is not disjoint in this frequency range [1] (in that case, the two sources are not separated by beamforming). As a remark, Clean-SC will provide the same results as beamforming since it is based on the same assumptions.

4 Industrial application: windtunnel tests

The academic case validates the consistency of the reconstructed quantities with the physical reality (given by the ground truth coherence measurements or the directivity measurements). However, the interest would be limited if the method was only applied to artificial point sources.

To go further than previous validations, wind tunnel array-based measurements have been exploited. The measurement data was carried out at the Daimler Wind Tunnel Centre in Sindelfingen. The automobile is the current C-class Coupe subjected to the wind speed of 140 km/h with 0° yaw angle. The acoustic radiation has been recorded by a microphone array system which is located 6m from the ground.

The sources have been reconstructed on a 2D grid assuming a free-field propagation modified by the convection phenomenon due to the presence of the wind. It is well-known that the autospectra of the array measurements are critically corrupted by the generation of a “pseudo-sound” produced by the interaction between the rigidity of the microphone cartridge and the wind. Methods have been developed to de-noise the cross-spectral matrix [20] [21] [22] but these considerations are not on the scope of this paper. As a consequence, noisy cross-spectra are considered in that case.

Sound power maps given by Clean-SC and BF are shown in Figure 7 for the frequency of 2kHz. Additionally, the sound power maps correlated with 2 points of the left mirror have been plotted.

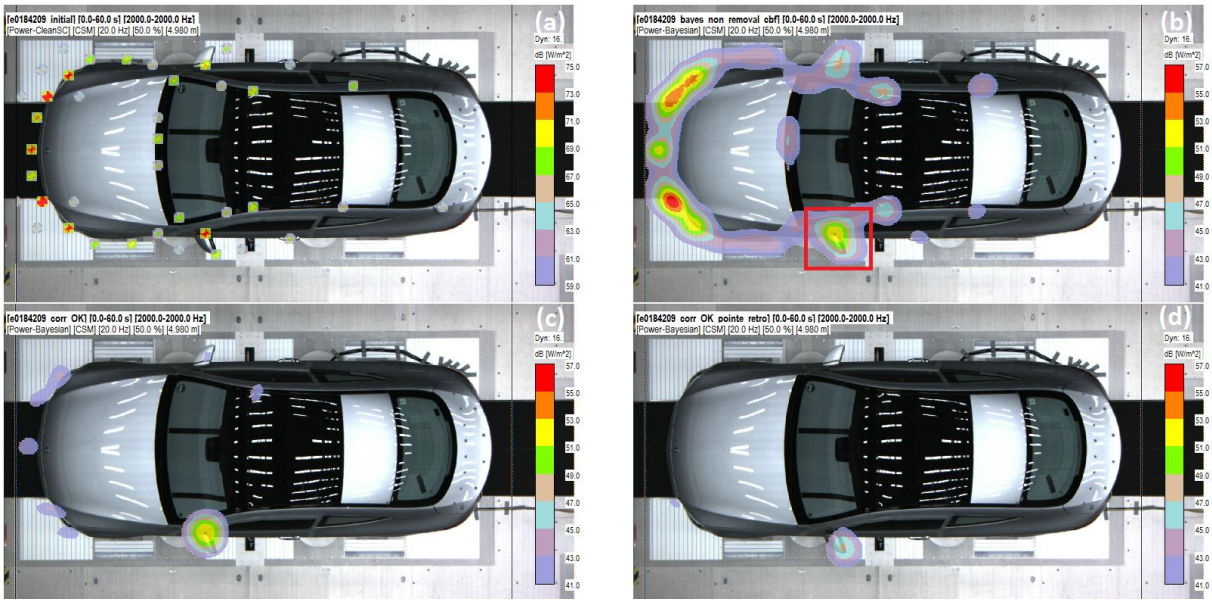


Figure 8 : Sound power maps given by Clean-SC (a) and BF (b). Sound power maps correlated with the maximum amplitude point recovered on the left mirror (c) and with the source recovered at the tip of the left mirror (d) at 2kHz with a dynamic display of 16dB.

Both Clean-SC and BF results are consistent, highlighting the same location of sources. However, the correlation information between sources given by the methods is different: Clean-SC recovers only uncorrelated sources whereas BF respects and keeps the spatial correlation relation between identified sources. This property can be exploited by displaying the sound power map correlated with one source pointed by the user. As an example, Figure 8 displays the sound power map correlated with two locations of the left mirror: the tip and the maximum amplitude location recovered by Bayesian focusing. Clean-SC identified these two locations as uncorrelated sources, as does the Bayesian focusing.

As a remark, the spatial correlation distance between sources is “smoothed” by the regularization process of the inverse method. Then, the recovered spatial correlation function is probably blurred.

To go beyond the classical localization maps, the reconstructed phase relationship between sources could be exploited by re-propagating the sources in the volume around the vehicle. Figure 8 shows the propagation over two cross-sections of the sources identified on a 2D grid. Moreover, the sources belonging to the red

square zone (displayed on the Figure 8 (b)) have also been propagated over a hemisphere in the nearfield of the mirror.

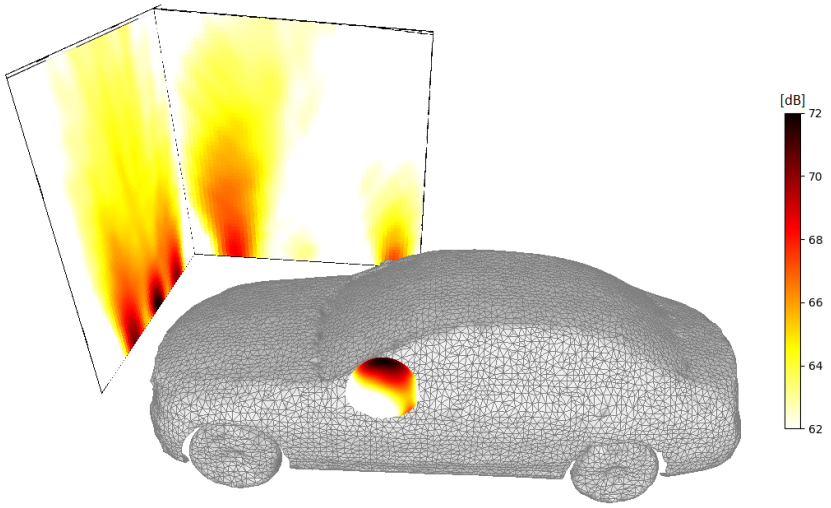


Figure 9 : Sound field propagated over two cross-sections (from the whole cross-spectrum matrix of the identified sources) and over a hemisphere in the nearfield of the mirror (from the sources belonging to the red square zone)[1]

The re-propagated pressure field could be used by the manufacturer in order to optimize the design of the vehicle to reach a certain sound level given by automotive standards for example.

These results are based on measurements recorded on the top of the vehicle. The sound pressure seems to foster the radiation towards the array. The complete directivity of each acoustic component present in the vehicle would be better estimated if the radiation was measured all around the vehicle. Moreover, the scattering effect of the vehicle, the real 3D geometry and the convection effect should be taken into account to improve the prediction of the propagation of the acoustic field in the volume.

5 Conclusions

Imaging techniques and more specifically inverse methods provide more information about sources than expected localization maps. The output of the method may inform the user about the coherence complexity of the source distribution as well as its directivity or about the sound level propagated anywhere in the space (from the source to the ears of the user of the machine for example). Then, imaging techniques coupled with a precise propagation model could play a major role in the design of the machineries.

To illustrate this point, Bayesian focusing has been applied on experimental data for its flexibility in terms of geometry, frequency range of validity and stability in regards with noise. Moreover, this method is able to provide statistical criteria that reflect the quality of the reconstruction. This formalism could offer to the users confidence intervals associated to the estimated quantities for example [17] [10].

Acknowledgements

Authors would like to thank Daimler AG for providing us the measurements data recorded in the Daimler Wind Tunnel Centre in Sindelfingen. This research was supported by the LUG2 project funded by the Région Auvergne Rhône-Alpes and the BPI France (grant FUI22). Authors would also like to thank Charles

[1] Remark : the 3D mesh is only used to give a spatial visual reference to the reader

Vanwynsberghe, Laurent Gilquin and Simon Bouley for their kind help regarding measurement campaign on the mock-up.

References

[1] Q. Leclère, A. Pereira, C. Bailly, J. Antoni and C. Picard, "A unified formalism for acoustic imaging," in *Bebec*, Berlin, 2016.

[2] P. Sijtsma, "CLEAN based on spatial source coherence," *International journal of aeroacoustics*, vol. 6, pp. 357-374, 2007.

[3] T. F. Brooks and W. M. Humphreys, "A deconvolution approach for the mapping of acoustic sources (DAMAS) determined from phased microphone arrays," *Journal of Sound and Vibration*, vol. 294, pp. 856-879, 2006.

[4] E. G. Williams, J. D. Maynard and E. Skudrzyk, "Sound source reconstructions using a microphone array," *The Journal of the Acoustical Society of America*, vol. 68, p. 340, 1980.

[5] S. F. Wu, "On reconstruction of acoustic pressure fields using the Helmholtz equation least squares method," *The Journal of the Acoustical Society of America*, vol. 107, p. 2511, 2000.

[6] J. Hald, "Basic theory and properties of statistically optimized near-field acoustical holography," *The Journal of the Acoustical Society of America*, vol. 125, pp. 2105-2120, 2009.

[7] M.-R. Bai, "Application of BEM (boundary element method)-based acoustic holography to radiation analysis of sound sources with arbitrarily shaped geometries," *The Journal of the Acoustical Society of America*, vol. 92, p. 533, 1992.

[8] A. Tikhonov, "Solution of incorrectly formulated problems and the regularization method," in *Soviet Math. Dokl.*, 1963.

[9] P. C. Hansen, "Analysis of discrete ill-posed problems by means of the L-curve," *SIAM review*, vol. 34, pp. 561-580, 1992.

[10] A. Pereira, "Acoustic imaging in enclosed spaces," 2013.

[11] J. Hald, "Wideband Acoustical Holography," in *Internoise*, 2014.

[12] J. Antoni, "A Bayesian approach to sound source reconstruction: Optimal basis, regularization, and focusing," *The Journal of the Acoustical Society of America*, vol. 131, pp. 2873-2890, 2012.

[13] A. Pereira, J. Antoni and Q. Leclère, "Empirical Bayesian regularization of the inverse acoustic problem," *Applied Acoustics* , vol. 97, pp. 11-29, 2015.

[14] C. Faure, C. Pézerat, J. Antoni and F. Ablitzer, "IDENTIFICATION OF VIBRATION SOURCES FROM MEASUREMENTS OF TRANSVERSE DISPLACEMENT, FROM A BAYESIAN POINT OF VIEW.".

[15] T. Le Magueresse, J. Thomas, J. Antoni and S. Paillasseur, "Instantaneous Bayesian regularization applied to real-time near-field acoustic holography," *JASA*, 2017.

[16] Q. Leclère, A. Pereira and J. Antoni, "Une approche bayésienne de la parcimonie pour l'identification de sources acoustiques," in *CFA*, Le Mans, 2014.

[17] T. Le Magueresse, Approche multidimensionnelle du problème d'identification acoustique inverse, Ph.D. thesis, INSA de Lyon, 2016.

[18] J. Antoni, Q. Leclère, T. Le Magueresse and P. Simard, "Sparse acoustical holography from iterated Bayesian focusing," *[submitted]*, 2018.

[19] P. M. Lee, Bayesian statistics: an introduction, John Wiley & Sons, 2012.

[20] A. P. Q. L. A. Finez, "Broadband Mode Decomposition of Ducted Fan Noise using Cross-Spectral Matrix Denoising," *Fan Noise 2015*.

[21] J. Hald, "Removal of incoherent noise from an averaged cross-spectral matrix," *The Journal of the Acoustical Society of America* , vol. 142, 2017.

[22] R. Dougherty, "Cross spectral matrix diagonal optimization," in *Proceedings of Berlin Beamforming Conference*, Berlin, 2016.

MOR for friction induced self-excitation in jointed structures based on substructuring for nonlinear interfaces – a review of methods with application to brake squeal

M. Zacharczuk [1,2]**, O. Stump** [1]**, H. Hetzler**[2]
[1] Daimler AG, Research and MBC Development ,
Benz-Straße, 71063, Sindelfingen, Germany
e-mail: **martin.zacharczuk@daimler.com**

[2] University of Kassel, Department of Mechanical Engineering, Engineering Dynamics Group
Mönchebergstraße 7, 34125, Kassel, Germany

Abstract
The modelling and simulation of friction induced NVH-problems is still a challenging task due to the high complexity and sensitivity of the problem. Today, linear stability analyses of large-scales FE-models have become state of the art in industrial applications. However, the so-called *Complex-Eigenvalue-Analysis* (CEA) provides information for steady states without considering the nonlinear impact of e.g. joints or contacts. Thus it has become evident that reliable analyses include nonlinearities. To assess nonlinear systems it is necessary to reduce the models to a practicable size. This contribution aims on comparing different substructuring techniques with regard to their applicability to stability problems appearing in the field of friction-induced vibrations. To this end a model structure under frictional self-excitation and employed dynamic substructing is investigated by comparing results from a linearized approach via eigenvalue analysis to those from direct time integration of the nonlinear model.

1 Introduction

Brake noise problems have been a challenging task for engineers in the industry for a long time. There are various studies on the matter [21, 20] with the focus on underlying mechanisms that cause the noise. It is commonly accepted that friction induced oscillations are responsible for different brake noise phenomenons like brake squeal, groan or moan. Self-exited vibrations can occur when a HOPF bifurcation occurs and the stability of a steady state is lost. When a HOPF bifurcation occurs the stability of a steady state may be lost and self-exited vibrations can occur. Two mechanisms, that are commonly considered responsible for the loss of stability in terms of LYAPUNOV [14] regarding brake systems are flutter and negative effective damping. Regarding the flutter mechanism, the circulatorical contact forces excite the system [22, 23]. It is commonly agreed, that flutter may be associated with brake squeal. Negative damping on the other hand can occur when the gradient of the velocity-depended friction coefficient characteristic of a joint or contact is negative [17, 12]. This effect can lead to negative effective damping unless the viscous damping is less than the friction gradient.

The CEA is used for analysing the dynamical behaviour of different operation conditions and is state of the art in industrial application. This method allows to assess the linear stability behaviour in a small domain around the linearized operation state, assuming the HARTMANN-GROBMAN theorem for equivalent topological flow in this region [8]. Nonetheless, this analysis technique can deviate or over-predict instabilities

when the results are compared to measured data. Numerous reasons that can be responsible for this issue besides modelling errors. One of the influential issues is non-consideration of nonlinearities in the brake model, which are responsible for limiting the amplitude. To obtain limit cycle amplitudes time integration approaches are applicable to extend the consideration of nonlinear behaviour but pose an impediment due to high computational cost.

To overcome the computational effort *model order reduction* (MOR) is employed. A widely used model order reduction technique is *component mode synthesis* (CMS), also known as *dynamic substructuring*, and applied for systems that consist of multiple components, that can be partitioned into an assembly of subcomponents. The earliest utilization of substructuring were in 1960 by HURTY [5] and later introduced as the first CMS technique by combining rigid body modes, constraint modes and fixed-interface modes [11]. That approach was later simplified by CRAIG and BAMPTON in 1968 [1] and up until this day it is one of the most used CMS methods in academia and the industry, referred as the HURTY/CRAIG-BAMPTON (HCB) approach. The HCB method uses a truncated set of fixed-interface modes, which are computed via CEA whilst fixing all interface degrees of freedom (DOF). The fixed-interface modes are ought to represent the interior dynamic of a substructure. A set of constraint modes, where each deformation shape is calculated by applying an unit displacement on one interface DOF whilst fixing the other interface DOF, is ought to represent the interface influences on the substructure. These two mode sets combined represent the HCB transformation matrix. HCB reduced-order-models (ROM) then are assembled to the whole system by enforcing exact compatibility by the interface displacements, called primal assembly.

Another family of CMS techniques employs a basis of free-interface modes. To form a complete representation it is needed to include interface attachment modes as well as rigid-body modes if the substructure is not constrained. The transformation matrix of this reduction method, called CRAIG-CHANG (CC) approach [6], consists of the rigid-body modes, a set of free interface modes and inertia-relief residual-flexibility attachment modes. Similar methods that use free-interface modes are described in [3, 4]. In a more recent publication RIXEN [10] proposed the dual assembly of free-interface modes and residual-flexibility attachment modes, called DUAL CRAIG-BAMPTON-method, using interface forces and therefore resulting in a weakly enforced compatibility when compared to a primal assembled structure. A wider overview of substructuring techniques can be found in [9].

Commonly CMS techniques focus in the reduction of the interior of a substructure while retaining all physical interface DOF. Often the size of a CMS-ROM size is prevailed by the number of interface DOF, hence, there is a demand for efficient interface reduction techniques. Interface reduction techniques are not the scope of this contribution but a review of methods is provided in [18].

The goal of this contribution is to investigate the impact of dynamic substructuring on stability problems by comparing in the first step the linear stability characteristic of a reduced model structure to the unreduced model when affected by friction induced self-excitation and secondly comparing results obtained by numerical time integration. In the next chapters an academic model is presented and after a brief description of the HCB- and the CC-reduction methods, the stability characteristics is presented and discussed in respect to the influence of MOR on structures under friction induced self-excitation, finally concluding and providing an outlook for future research.

2 A multiple DoF model problem with friction induced self-excitation

In the following a well-known academic problem of mass on a belt [15, 13, 12] is extended to a chain of masses to obtain a structure with multiple deflection shapes. Then the generic equations of motions are derived with an impinging self-excitation due to negative damping.

The model is outlined in Fig. 1 and consists of a simple mass-damper-spring system, which is pressed onto a belt, coupled with a multiple mass-spring system. Between the belt and the mass sliding friction is present with a friction coefficient that is a function of the relative velocity v_{rel}. The self-excited oscillator is subjected

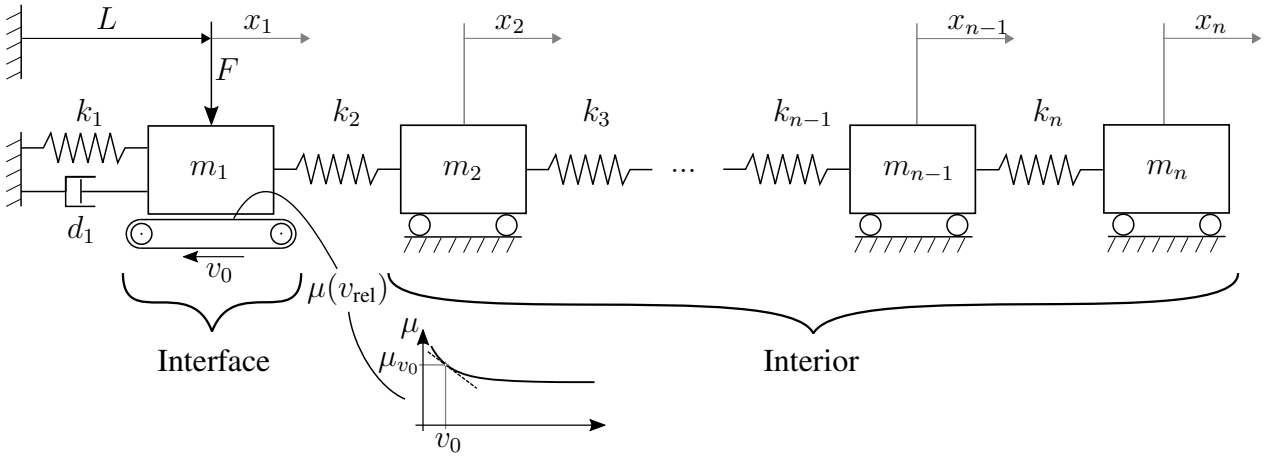


Figure 1: Chain of masses connected with springs and damper, partitioned into interface and interior parts, with an exemplary belt with a friction coefficient, that depends on the relative velocity.

to linear structural damping. The equations of motion read

$$\mathbf{M}\ddot{\mathbf{x}} + \mathbf{P}\dot{\mathbf{x}} + \mathbf{Q}\mathbf{x} + \mathbf{f}_{\text{nl}}(\mathbf{x}, \dot{\mathbf{x}}) = \mathbf{0}, \tag{1}$$

where the nonlinear forces are described as

$$\mathbf{f}_{\text{nl}} = \mathbf{w}F\mu(v_{\text{rel}}), \qquad v_{\text{rel}} = v_0 - \mathbf{w}^T\dot{x}, \qquad \mathbf{w} = [1, 0, ..., 0]^T \in \mathbb{R}^n$$

with the vector $\mathbf{w}$ specifying the location of the belt. With introducing the relation $\omega_1 = \sqrt{k_1/m_1}$ and the characteristic length L the dimensionless quantities read

$$\begin{aligned} \mathbf{u} &= \mathbf{x}/L, \qquad & \mathbf{u} &= [u_1, ..., u_n]^T, \\ \tau &= \omega_1 t, \qquad & \tilde{v}_{\text{rel}} &= v_{\text{rel}}/\omega_1 L, \\ \tilde{m}_n &= \frac{m_n}{m_1}, \qquad & \tilde{k}_n &= \frac{k_n}{k_1}. \end{aligned} \tag{2}$$

As a result the equations of motion read

$$\mathbf{M}\mathbf{u}'' + \tilde{\mathbf{P}}\mathbf{u}' + \mathbf{Q}\mathbf{u} + \frac{\mathbf{w}F\mu(\tilde{v}_{\text{rel}})}{\omega_1^2 m_1 L} = 0, \tag{3}$$

with $()' = d/d\tau$ describing the differentiation with respect to the dimensionless time τ. Linearizing with respect to the rest position $\mathbf{u}_0 = [u_1, 0, ..., 0]^T$ leads to the matrices

$$\mathbf{M} = diag(1, \tilde{m}_2, ..., \tilde{m}_n), \qquad \mathbf{D} = \begin{bmatrix} \frac{d_1 - F\mu(\tilde{v}_{\text{rel}})}{m_1\omega_1^2 L} & \mathbf{0} \\ \mathbf{0} & \mathbf{0} \end{bmatrix}, \tag{4}$$

$$\mathbf{K} = \begin{bmatrix} 1+\tilde{k}_2 & -\tilde{k}_2 & 0 & \dots & & 0 \\ & \tilde{k}_2+\tilde{k}_3 & -\tilde{k}_3 & \ddots & & \vdots \\ & & \ddots & \ddots & & \\ & & & & -\tilde{k}_{n-1} & 0 \\ & sym. & & & \tilde{k}_{n-1}+\tilde{k}_n & -\tilde{k}_n \\ & & & & & \tilde{k}_n \end{bmatrix}, \tag{5}$$

and the resulting equations of motion

$$\mathbf{M}\mathbf{u}'' + \mathbf{D}\mathbf{u}' + \mathbf{K}\mathbf{u} = \mathbf{0}. \tag{6}$$

To be able to assess the nonlinear behaviour the velocity dependent friction law was regularized and fitted to a characteristic, where the transition from static friction to sliding friction shows a negative gradient. Therefore the friction coefficient μ is written as

$$\mu(v_{\text{rel}}) = (0.3)\frac{2}{\pi}\arctan(v_{\text{rel}}/\epsilon) + 0.2e^{(-2|v_{\text{rel}}|)}, \tag{7}$$

where ϵ is a constant, that changes the transition characteristic from static to sliding friction. Fig. 2 shows the resulting nonlinear force as a function of v_{rel} with the different values for ϵ.

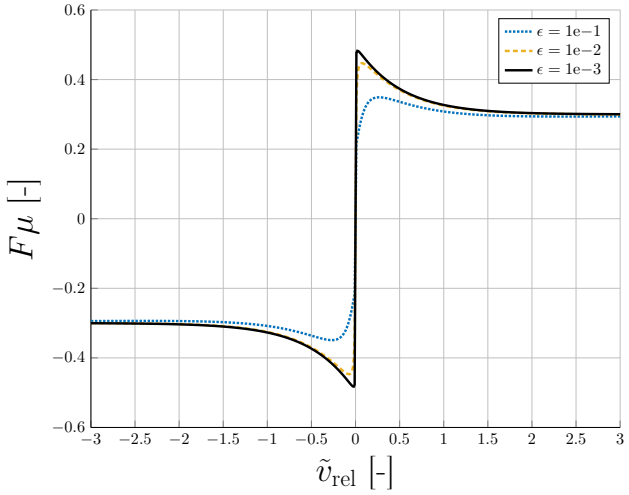


Figure 2: Regularized, velocity dependent force curve.

For the presented cases in the next chapters $\epsilon = 0.001$ is used.

3 Model order reduction

This section presents two different substructuring techniques which are considered in this contribution. The HCB- and the CC-methods will then be applied to the model structure (Fig. 1).

3.1 Hurty/Craig-Bampton Method

The system of equations of motion for a substructure reads

$$\mathbf{M}\ddot{\mathbf{u}} + \mathbf{D}\dot{\mathbf{u}} + \mathbf{K}\mathbf{u} = \mathbf{f}. \tag{8}$$

The substructure equations of motion are partitioned into interior (subscript i) and interface (subscript b) DOF, as

$$\begin{bmatrix}\mathbf{M}_{bb} & \mathbf{M}_{bi}\\ \mathbf{M}_{ib} & \mathbf{M}_{ii}\end{bmatrix}\begin{pmatrix}\ddot{\mathbf{u}}_b\\ \ddot{\mathbf{u}}_i\end{pmatrix} + \begin{bmatrix}\mathbf{D}_{bb} & \mathbf{D}_{bi}\\ \mathbf{D}_{ib} & \mathbf{D}_{ii}\end{bmatrix}\begin{pmatrix}\dot{\mathbf{u}}_b\\ \dot{\mathbf{u}}_i\end{pmatrix} + \begin{bmatrix}\mathbf{K}_{bb} & \mathbf{K}_{bi}\\ \mathbf{K}_{ib} & \mathbf{K}_{ii}\end{bmatrix}\begin{pmatrix}\mathbf{u}_b\\ \mathbf{u}_i\end{pmatrix} = \begin{pmatrix}\mathbf{f}_b\\ \mathbf{0}\end{pmatrix} \tag{9}$$

where the indices b and i are relating to the interface and internal component of the system matrices and vectors. The static response of the substructure interior is computed by prescribing a unit displacement at one interface DOF at a time while holding all the other interface DOF fixed. These CMs are given as

$$\mathbf{\Psi} = \begin{bmatrix}\mathbf{I}\\ -\mathbf{K}_{ii}^{-1}\mathbf{K}_{ib}\end{bmatrix}. \tag{10}$$

The CMs form a static condensation that leads to a reduced model. This leads to a representation where all interior DOF are eliminated and the physical interface DOF are retained. To enhance the capability of the

reduced representation to capture the dynamic behaviour of the model, the internal dynamic of the model has to be taken into consideration. The set of CMs is then complemented with a set of dynamic modes by assuming a harmonic solution for the interior DOF where the interface DOF are held fixed. The modes are given as

$$\left(\mathbf{K}_{ii} - \omega_r^2 \mathbf{M}_{ii}\right)(\boldsymbol{\phi}_i)_r = 0, \tag{11}$$

where $(\boldsymbol{\phi}_i)_r$ is the eigenvector to the corresponding eigenfrequency ω_r^2. These eigenvectors are referred to as fixed-interface modes. The modes are mass normalized and a selected number of these eigenvectors will then provide a basis for the interior representation of the substructure, which are formed as

$$\boldsymbol{\Phi} = \begin{bmatrix} \mathbf{0} \\ (\boldsymbol{\phi}_i)_1, \ldots, (\boldsymbol{\phi}_i)_n \end{bmatrix} = \begin{pmatrix} \mathbf{0} \\ \boldsymbol{\Phi}_i \end{pmatrix}. \tag{12}$$

The combination of the constraint modes and the fixed-interface modes then shape the HCB transformation matrix as

$$\mathbf{T}_{\text{HCB}} = \begin{bmatrix} \boldsymbol{\Psi} & \boldsymbol{\Phi} \end{bmatrix}. \tag{13}$$

The HCB reduction matrix provides a transformation from the physical DOF to HCB generalized DOF, expressed as

$$\mathbf{u} = \begin{pmatrix} \mathbf{u}_b \\ \mathbf{u}_i \end{pmatrix} \approx \begin{bmatrix} \mathbf{I} & \mathbf{0} \\ -\mathbf{K}_{ii}^{-1}\mathbf{K}_{ib} & \boldsymbol{\Phi}_i \end{bmatrix} \begin{pmatrix} \mathbf{u}_b \\ \mathbf{q}_i \end{pmatrix} = \mathbf{T}_{\text{HCB}} \begin{pmatrix} \mathbf{u}_b \\ \mathbf{q}_i \end{pmatrix}. \tag{14}$$

$\mathbf{q}_i$ are the modal coordinates linked to the fixed-interface modes. This transformation matrix can be used to transform the mass, damping and stiffness matrices into their HCB representations.

$$\mathbf{M}_{\text{HCB}} = \mathbf{T}_{\text{HCB}}^{\text{T}} \mathbf{M} \mathbf{T}_{\text{HCB}}, \qquad \mathbf{D}_{\text{HCB}} = \mathbf{T}_{\text{HCB}}^{\text{T}} \mathbf{D} \mathbf{T}_{\text{HCB}}, \qquad \mathbf{K}_{\text{HCB}} = \mathbf{T}_{\text{HCB}}^{\text{T}} \mathbf{K} \mathbf{T}_{\text{HCB}}. \tag{15}$$

The coupling of two HCB models is conducted by a primal assembly. With a constraint equation a transformation matrix can be formed to couple the models. As this contribution in particular investigates the influence of MOR on one substructure, the coupling of substructures won't be illustrated. More details on the assembly of HCB reduced order systems are found in [18].

3.2 Craig-Chang Method

While the HCB reduction method utilizes fixed interface modes, there are also various methods employing free-interface modes. One of these techniques is the Craig-Chang reduction method. The free-interface vibration modes are shapes of the structure when the interface DOF are unconstrained. The modes are obtained solving the eigenvalue problem of the whole system (Eq. 8):

$$\left(\mathbf{K} - \omega_r^2 \mathbf{M}\right)(\boldsymbol{\phi}_{\boldsymbol{f}})_r = 0. \tag{16}$$

The free vibration modes contain the full vibration content of the substructure and are referred to as $\boldsymbol{\Phi}_f$ in the further context. The free vibration modes are not enough to meet static completeness. Hence, by augmenting $\boldsymbol{\Phi}_f$ with two additional mode sets the problem is addressed. First the rigid-body modes are computed, if the system is not fully constrained, written as

$$\mathbf{K}\boldsymbol{\Phi}_{\mathbf{r}} = \mathbf{0}. \tag{17}$$

The rigid-body modes $\boldsymbol{\Phi}_{\boldsymbol{r}}$ represent the substructure's displacement without deformations. Whereas constraint modes are defined by a unit displacement at one boundary DOF while fixing the rest, attachment modes are defined by a unit force at one interface DOF while letting the other DOF free. Due to disadvantageous properties attachment modes are discarded in favour of residual attachment modes (RAM). However, in order to obtain RAMs, attachment modes computed first, defined as

$$\boldsymbol{\Psi}_{am} = \mathbf{K}^{+} \begin{bmatrix} \mathbf{I} \\ \mathbf{0} \end{bmatrix} = \mathbf{G}\mathbf{F}, \tag{18}$$

where $\mathbf{K}^+$ denotes the generalized inverse or pseudo-inverse of the stiffness matrix, which is the definition of the flexibility matrix $\mathbf{G}$. If the structure is fully constrained by the boundary conditions, $\mathbf{K}^+ = \mathbf{K}^- = \mathbf{G}$ is valid and the computation is obtained from Eq. (18). In the case that the substructure is not fully constrained, $\mathbf{K}$ is singular and there is a special procedure for computing attachment modes with the elastic flexibility matrix $\mathbf{G}_f$. In [19] it is shown, that for an unconstrained system with n DOF and n_r rigid body modes, the spectral expansion of $\mathbf{G}_f$ is

$$\mathbf{G}_f = \sum_{j=n_r+1}^{n} \frac{\boldsymbol{\phi}_{f,j}\boldsymbol{\phi}_{f,j}^T}{\omega_{f,j}^2}, \tag{19}$$

where $\boldsymbol{\phi}_{f,j}$ is a free vibration mode. The spectral expansion shows, that the flexibility of the free vibration modes will then be accounted for twice. That poses a disadvantage in regards to convergence reasons, therefore RAMs are introduced. The residual flexibility matrix reads

$$\mathbf{G}_r = \mathbf{G}_f - \sum_{j=n_r+1}^{n_f} \frac{\boldsymbol{\phi}_{f,j}\boldsymbol{\phi}_{f,j}^T}{\omega_{f,j}^2}, \tag{20}$$

where n_f denotes the number of free vibration modes that are included in the reduction basis. Hence, $\mathbf{G}_r$ stores the information of the $n_d = n - n_f$ discarded modes. With the obtained matrix, the RAMs are computed as

$$\boldsymbol{\Psi}_{ram} = \mathbf{G}_r\mathbf{F}. \tag{21}$$

After the computation of the three mode sets the CC transformation matrix can be assembled to

$$\mathbf{T}_{\text{CC}} = \begin{bmatrix}\boldsymbol{\Psi}_r & \boldsymbol{\Phi}_f & \boldsymbol{\Psi}_{ram}\end{bmatrix} \tag{22}$$

and it provides the transformation from physical DOF to CC generalized DOF, expressed as

$$\mathbf{u} \approx \begin{bmatrix}\boldsymbol{\Psi}_r & \boldsymbol{\Phi}_f & \boldsymbol{\Psi}_{ram}\end{bmatrix} \begin{pmatrix}\mathbf{q}_r \\ \mathbf{q}_f \\ \mathbf{q}_{ram}\end{pmatrix} = \mathbf{T}_{\text{CC}} \begin{pmatrix}\mathbf{q}_r \\ \mathbf{q}_f \\ \mathbf{q}_{ram}\end{pmatrix}. \tag{23}$$

$\mathbf{q}_r, \mathbf{q}_f$ and $\mathbf{q}_{ram}$ are the modal coordinates linked to the complete substructure. The transformation matrix then can be used to transform the system matrices into their CC representations

$$\mathbf{M}_{\text{CC}} = \mathbf{T}_{\text{CC}}^{\text{T}}\mathbf{M}\mathbf{T}_{\text{CC}}, \qquad \mathbf{D}_{\text{CC}} = \mathbf{T}_{\text{CC}}^{\text{T}}\mathbf{D}\mathbf{T}_{\text{CC}}, \qquad \mathbf{K}_{\text{CC}} = \mathbf{T}_{\text{CC}}^{\text{T}}\mathbf{K}\mathbf{T}_{\text{CC}}. \tag{24}$$

The CC reduced order model can be coupled via primal assembly. Similar to HCB-ROMs a constraint equation leads to a transformation matrix for the full coupled system of substructures. As already mentioned in the previous subsection, this will be neglected in this contribution.

4 Results

To assess the propensity for a system to loose the stability of the rest position the so-called CEA is used, as already mentioned in the introduction. Therefore the system equations are linearized around the rest position. The eigenvalue problem for the chain of oscillators (Fig. 1) is written as

$$(\lambda^2\mathbf{M} + \lambda\tilde{\mathbf{P}} + \mathbf{Q})\boldsymbol{\phi} = \mathbf{0}, \tag{25}$$

where λ are the complex eigenvalues and $\boldsymbol{\phi}$ are the eigenvectors of the unreduced reference system. Accordingly the complex eigenvalues of the HCB-reduced model are computed with

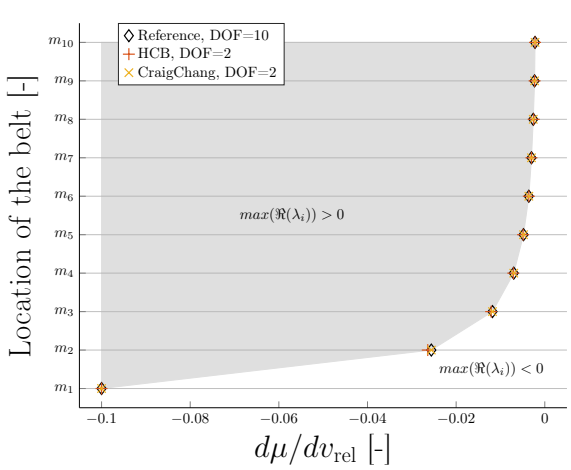
$$(\lambda_{\text{HCB}}^2(\mathbf{T}_{\text{HCB}}^{\text{T}}\mathbf{M}\mathbf{T}_{\text{HCB}}) + \lambda_{\text{HCB}}(\mathbf{T}_{\text{HCB}}^{\text{T}}\tilde{\mathbf{P}}\mathbf{T}_{\text{HCB}}) + (\mathbf{T}_{\text{HCB}}^{\text{T}}\mathbf{K}\mathbf{T}_{\text{HCB}}))\boldsymbol{\phi}_{\text{HCB}} = \mathbf{0} \tag{26}$$

and for the CC-reduced model

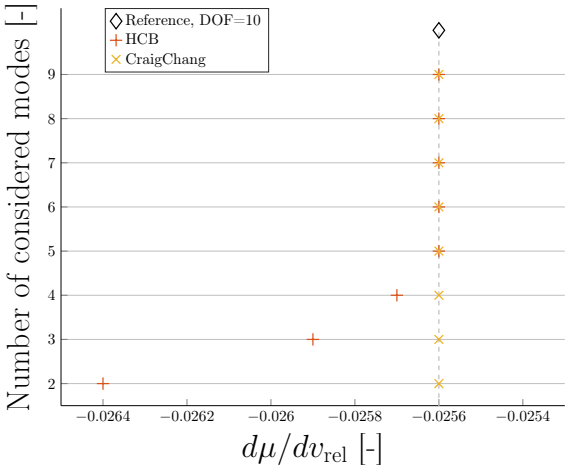
$$(\lambda_{\mathrm{CC}}^2(\mathbf{T}_{\mathrm{CC}}^{\mathrm{T}}\mathbf{M}\mathbf{T}_{\mathrm{CC}}) + \lambda_{\mathrm{CC}}(\mathbf{T}_{\mathrm{CC}}^{\mathrm{T}}\tilde{\mathbf{P}}\mathbf{T}_{\mathrm{CC}}) + (\mathbf{T}_{\mathrm{CC}}^{\mathrm{T}}\mathbf{K}\mathbf{T}_{\mathrm{CC}}))\boldsymbol{\phi}_{\mathrm{CC}} = \mathbf{0} \tag{27}$$

respectively.

For the comparison of the stability behaviour of the models the location of the belt and the number of considered modes is of high interest. Therefore a varation of the belt location and the number of considered modes of the ROM were done. The model structure (Fig. 1) was set to a size of ten masses. The reduced representations of the model always discard the modes in ascending order, beginning with the highest corresponding frequency.



(a) Comparison of $max(\Re(\lambda)) = 0$ for different belt locations with respect to the friction gradient $d\mu/dv_{\mathrm{rel}}$.



(b) Comparison of $max(\Re(\lambda)) = 0$ for a different number of considered modes of a mass-chain with 10 DOF and a belt under m_2.

Figure 3: Linear stability results for different belt locations and various reduced model sizes.

While variating also the friction gradient, the location of the belt shows little to none influence for the reduction methods on the bifurcation point (Fig. 3a). The highest deviation for the bifurcation point is seen for the HCB-method, when the belt is located under the mass m_2. With increasing the number of modes in the reduction basis for this case (m_2) of the HCB-ROM, the difference to the full model decreases and its influence on the stability border seems to be neglectable(Fig. 3b).

The results of the reference model are compared to the reduced models, where the model sizes are reduced from ten to five DOF. The nonlinear results (Fig. 5) show, that there is a difference in terms of occurring frequencies in the time signals. The reduced representations capture a different behaviour in the considered frequency range.

5 Conclusion and outlook

This contribution aimed at the question, if model order reduction of a structure is stability-preserving. Two different model order reduction techniques and a multiple DOF structure were presented and the stability characteristics of the original structure and the reduced structures were compared. The linear results show good agreement and indicate, that the reduction methods do not change the location of the bifurcation point significantly in the examined case. The bifurcation point is independent to the location of the belt and the number of considered modes in the reduction basis. Moreover the CC-method shows better agreement than the HCB-method.

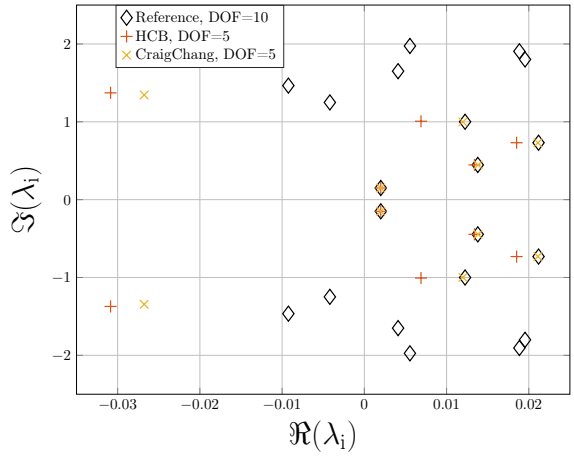
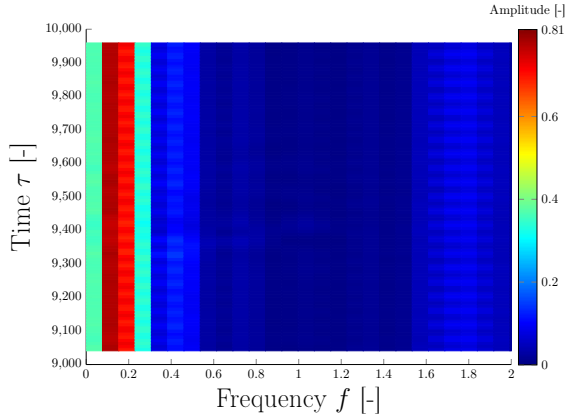
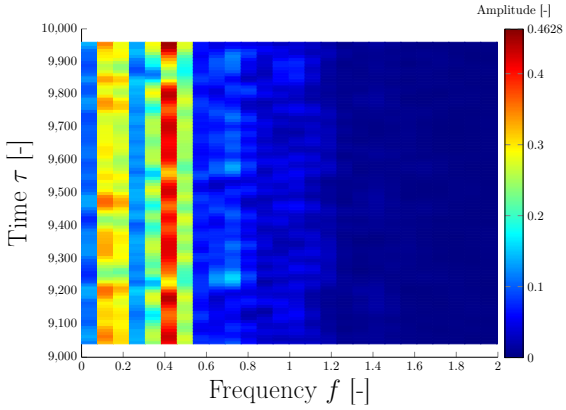


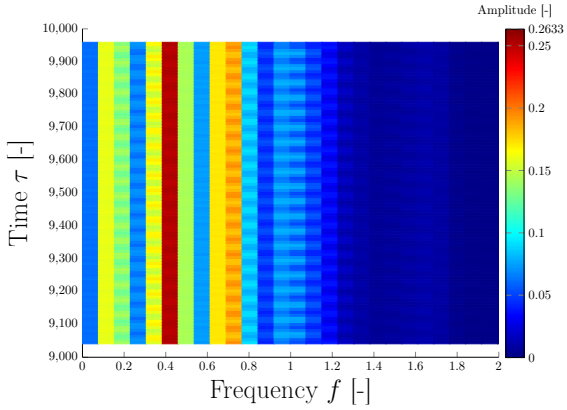
Figure 4: Eigenvalues of the linearized state with the belt under m_2 and $d\mu/dv_{\text{rel}} = -0.2677$.



(a) Fast fourier transform (FFT) over time for the unreduced oscillator-chain after 10000 time steps.



(b) FFT over time for the HCB-reduced oscillator-chain after 10000 time steps.



(c) FFT over time for the CC-reduced oscillator-chain after 10000 time steps.

Figure 5: FFTs over time for the unreduced, the HCB-, and the CC-representation with the belt under m_2.

The nonlinear results do not allow a clear conclusion. On one hand the findings show an unstable system behaviour for all models, on the other hand there are significant differences between the occurring frequencies. There a extended study is needed, where the result can be discussed in regards to the reduced-model size.

In future studies further model order reduction techniques, e.g. the *Dual Craig-Bampton*-method, will be investigated and applied to a extended model structure, where the influence of different interfaces between

substructures can be examined. Moreover interface reduction techniques will be evaluated in conjunction with self-excitation. Also the nonlinear consideration has to be explored to find appropriate criteria in order to assess the quality of the reduced order model. In addition it is intended to implement different analysis methods with direct approximation of the limit cycle via *Harmonic Balance*.

References

[1] Bampton, M. C. C. and Craig, Jr R. R., *Coupling of substructures for dynamic analyses*, AIAA Journal, Vol. 6, No. 4, American Institute of Aeronautics and Astronautics (1968), pp. 1313-1319.

[2] Craig, Jr R. R., Roy R and Chang, C.-J., *Coupling of substructures for dynamic analyses*, Report, National Aeronautics and Space Administration (1977).

[3] Macneal, R. H., *A hybrid method of component mode synthesis*, Computers & Structures, Vol. 1, No. 4, Elsevier (1971), pp. 581-601.

[4] Rubin, S., *Improved Component-Mode Representation for Structural Dynamic Analysis*, AIAA Journal, Vol. 13, No. 8, American Institute of Aeronautics and Astronautics (1975), pp. 995-1006.

[5] Hurty, W. C., *Vibrations of structural systems by component mode synthesis*, Journal of the Engineering Mechanics Division, Vol. 86, No. 4, American Society of Civil Engineers (1960), pp 81-70.

[6] Craig, Jr R. R., Roy R and Chang, C.-J., *On the use of attachment modes in substructure coupling for dynamic analysis*, *Proceedings of the 18th Structures*, Structural Dynamics and Material Conference, AIAA/ASME, San Diego (1977), pp.89-99

[7] Craig, Roy R. and Kurdila, A. J., *Fundamentals of structural dynamics*, John Wiley & Sons (2006).

[8] Wiggins, S., *Introduction to Applied Nonlinear Dynamical Systems and Chaos*, Vol.2, Springer Science & Business Media (2003).

[9] Craig, R. R., *Coupling of substructures for dynamic analyses: an overview*, Structures, Structural Dynamics and Material Conference, 41st AIAA/ASME/ASCE/AHS/ASC, Atlanta (2000), pp. 1573-158.

[10] Rixen, D., *A dual Craig–Bampton method for dynamic substructuring*, Journal of Computational and Applied Mathematics, Vol. 168, No. 1-2, Elsevier (2004), pp 383-391.

[11] Hurty, W. C., *Dynamic analysis of structural systems using component modes*, AIAA Journal, Vol. 3, No. 4, American Institute of Aeronautics and Astronautics (1965), pp 383-391.

[12] Hetzler, H., *On the effect of nonsmooth Coulomb friction on Hopf bifurcations in a 1-DoF oscillator with self-excitation due to negative damping*, Nonlinear Dynamics, Vol. 69, No. 1, (2012), pp 601-604.

[13] Hagedorn, P., Stadler, W., *Non-linear oscillations*, Clarendon (1988).

[14] A. H. Nayfeh, B. Balachandran, *Applied nonlinear dynamics: analytical, computational and experimental methods*, John Wileys & Sons (2008).

[15] DenHartog, J. P., *Mechanical vibrations*, Dover (1985).

[16] Hetzler, H., Schwarzer, D., Seemann, W., *Steady-state stability and bifurcations of friction oscillators due to velocity-dependent friction characteristics*, Journal of Multi-body Dynamics, Vol. 221, No. 3, Proceedings of the Institution of Mechanical Engineers (2007), pp 401-412.

[17] Fulcher, L. P., Scherer, R. C., Melnykov, A., Gateva, V., Limes, M. E., *Negative Coulomb damping, limit cycles, and self-oscillation of the vocal folds*, American Journal of Physics, Vol. 74, No. 5, (2006), pp 386-393.

[18] D. Krattiger, L. Wu, M. Zacharczuk, M. Buck, R.J. Kuether, M.S. Allen, P. Tiso, M.R.W. Brake, *Interface reduction for Hurty/Craig-Bampton substructured models: Review and improvements*, Mechanical Systems and Signal Processing, Vol. 114, Elsevier (2019), pp 579-603.

[19] M. Géradin, D.J. Rixen, *Mechanical vibrations: Theory and application to structural dynamics*, Wiley (2015).

[20] S. Kruse, M. Tiedemann, B. Zeumer, P. Reuss, H. Hetzler, N. Hoffmann, Norbert, *The influence of joints on friction induced vibration in brake squeal*, Journal of Sound and Vibration, Vol. 340, Elsevier (2015), pp 239-252.

[21] Papinniemi, Antti and Lai, Joseph C.S. and Zhao, Jiye and Loader, Lyndon, *Brake squeal: A literature review*, Applied Acoustics, Vol. 63, No. 4, Elsevier (2002), pp 391-400.

[22] H. Hetzler, *On moving continua with contacts and sliding friction: Modeling, general properties and examples*, International Journal of Solids and Structures, Vol. 46, No. 13, Elsevier (2009), pp 2556-2570.

[23] H. Hetzler, *On the effect of non-smooth Coulomb damping on flutter-type self-excitation in a non-gyroscopic circulatory 2-DoF-system*, Nonlinear Dynamics, Vol. 73, No. 3, Springer (2013), pp 1829-1847.

Real-time assignment method of resonance frequency by change of coupling stiffness for improving road induced noise

Masashi Komada[1,3], Yuichi Matsumura[2], Ichiro Kido[2] Eiji, Nakatsugawa[1] and Hironori Ozaki[3]

[1] Toyota Motor Corporation Vehicle Dynamics Technology Development Department
1, Toyota-cho, Toyota, Aichi, 471-8572, Japan
e-mail: **masashi_komada@mail.toyota.co.jp**

[2] Gifu University
1-1, Yanagido, Gifu-shi, Gifu, 501-1193, Japan

[3] Graduate School of Gifu University
1-1, Yanagido, Gifu-shi, Gifu, 501-1193, Japan

Abstract
This paper proposes a method for natural frequency assignment by semi-actively changing coupling stiffness matrix. This method can decide the coupling stiffness basically in one-time calculation to assign natural frequency. For two vibration systems connected with springs at multi-points, the compliance matrix which is sum of two system's compliance matrixes and the inverse matrix of coupling stiffness matrix at coupling degrees of freedom becomes rank deficient at natural frequencies, and consequently the condition for resonance occurrence is equivalent that all column vectors of the matrix exist in a hyperplane. The coupling stiffness is obtained to meet this condition by inner product calculation between a column vector in the compliance matrix and the normal vector of a hyperplane at required frequency. In a feasibility study, the method was applied to two beams connected with three translational springs.

1 Introduction

In the vehicle development for noise and vibration, it is necessary to design the vibration characteristic of the body for various kinds of operational force. In recent years, it has become difficult to design the vibration characteristics of the vehicle body with many natural frequencies, while satisfying these severe requirements, as the demand for the improvement of the collision safety performance and weight reduction. In the future, the engine sound is eliminated by the electric motor drive vehicle, and the road induced noise is especially important. In addition to the change of road profile, the operational input to the vehicle is changed during the driving by the effect of nonlinearity of the tire and suspension, such as the amplitude dependence of tire rubber characteristics. Therefore, it is necessary to reduce the road induced noise in response to the changing input, instead of the conventional body structure optimization for further performance improvement requirements. The active noise control which reduces the sound pressure of the car in the opposite phase is an effective method. However, it is difficult to widely reduce the noise because the cost is high to achieve sufficient effect in a wide frequency band [1].

From these background, assumed that the semi-active control is generally low in cost for active control, and considered that a sub system as a body part or an attachment module of the main body, we are researching a technique to reduce the road induced noise by controlling the coupling spring which connects the main and sub systems while suppressing the mass increase and cost of countermeasure. Road induced noise is wide band frequency phenomena and operational force to the body changes in response to road surface and vehicle speed, therefore it is necessary both to reduce the noise peak level and to make

the noise level smooth against target line in frequency range. If there is a steep peak in the noise but it's not so high level, the peak is very noticeable for driver. Therefore, the purpose of this study is to smooth the interior sound pressure level of a vehicle in frequency range. For smoothing, it is necessary to control the vibration level of the body in response to the input from the suspension to the body. To achieve this, it can be considered that the method of controlling the anti-resonant frequency of the body's response point to assign close to the peak frequency of the input, and controlling the resonance frequency of the body to assign to lower level of input separating from the peak frequency of it. To further smooth the response, it is also possible to control the resonance level of the body. In this paper, we examine the control method of the resonance frequency. In addition, because there are several resonances in the tire and suspension and the body, it is desirable that the resonance control of the body can control multiple resonance at the same time. Therefore, for the development of this research in the future with the intention of increasing the control degree of freedom, the coupling spring between the main and sub systems is assumed to be a multi-degree-of-freedom connection.

In semi-active control, it is necessary to determine the change of the characteristic of the coupling spring which is controlled. Conventionally, the following passive methods have been used to analyze vehicle noise and vibration problem and to make clear change amounts of dynamic characteristics of vehicle's parts. First, we measure the actual vibration and frequency response function of the body and perform the transfer pass analysis [2-6]. Next, we focus on the main transfer path contribution, and analyze the experiment mode analysis of the body, the panel contribution analysis, and the analysis that considers the coupling between the body structure system and the room acoustic system [7]. In addition, the sensitivity analysis is performed on the transfer function of the body, and the stiffness addition and the mass addition to the parts where the influence is large are done by the reduction of the body sensitivity [8,9]. However, in order to obtain an optimal solution these methods need iterative computation and it is not suitable to calculate and apply the control to the phenomenon that the input changes at any moment. Therefore, in this paper, we propose a simple method that can calculate the coupling stiffness to shift the resonant frequency from peak frequency of input within a suitable calculation load for sequential computation.

For a simple method, we think it is important to grasp the vibration coupling relation between the two systems of the main system and the sub system. In the coupling analysis of the vibration system, there is a study using the transfer function synthesis method [10,11]. They define the *kernel* compliance matrix that contains information of the vibration coupling relation at connection points, and they proposed a method to analyze coupling relation by making the *kernel* compliance matrix a diagonal using eigenvalues and eigenvectors Furthermore, in order to derive analytical solution of the relation between them, the coupling degree of freedom is reduced to two degrees of freedom, and it is applied to the analysis of one resonance that the tire and the suspension are coupled.

From above, in this paper, it is intended to smooth the response of the frequency domain to the two vibration systems combined with multiple degrees of freedom, it is assumed a semi-active control, to create a simple method of assigning a coupled resonance to a target frequency. Therefore, the coupling springs which connect the main and sub systems are independent of each other. In particular, the coupling spring is connected at only one degree of freedom of the same connection point of the two systems, and not to connect it across the connection point. This means that the matrix of the coupling stiffness in the *kernel* compliance matrix becomes a diagonal matrix, and the column vectors in the *kernel* compliance matrix can be controlled independently. In addition, we clarify the condition expression of the resonance generation by analyzing the relation of these column vectors as a geometric vector. By using this condition expression, we propose a method which can easily calculate the coupling stiffness to assign the resonance to the target frequency by changing only one coupling stiffness. We also propose a method to use this method for structural design semi-active control systems.

2 Assignment Method of Resonance Frequency of Coupled Two Systems

In this chapter, firstly, the condition of resonance generation is cleared by the analysis for coupling relation between two systems connected at multi-points, then, simple method for assigning the resonance frequency using coupling spring is explained.

2.1 Condition of resonance generation for coupled two systems

2.1.1 Equation about coupling relation of two systems

Fig.1 shows vibration system diagram. Main system A and sub system B are connected at multi-points with coupling springs. Main system A assumes body and sub system B assumes part of the body or attachment module. Coupling stiffness is control object. Character 1 and 3 in main system A mean each input region and response region. Character 2 in main system A and sub system B mean connection region.

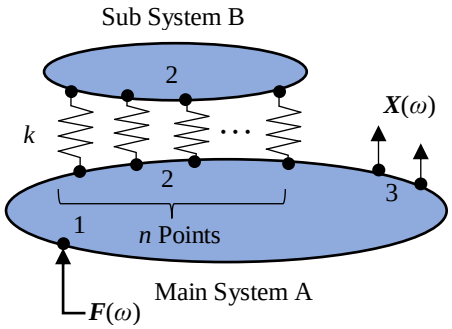


Figure 1: Vibration System diagram. Main system A and sub system B are coupled at multi-point with coupling springs. Here $\boldsymbol{F}(\omega)$ indicates input force. $\boldsymbol{X}(\omega)$ indicates response of main system A. Input region, connection region and response region are respectively indicated by 1, 2 and 3.

Based on the sub-structuring method, the response $\boldsymbol{X}$ in region 3 by operational force $\boldsymbol{F}$ in region 1 can be written as

$$\boldsymbol{X} = \{\boldsymbol{G}_{31}^{\mathrm{A}} - \boldsymbol{G}_{32}^{\mathrm{A}}\left(\boldsymbol{G}_{22}^{\mathrm{A}} + \boldsymbol{G}_{22}^{\mathrm{B}} + \boldsymbol{K}^{-1}\right)^{-1}\boldsymbol{G}_{21}^{\mathrm{A}}\}\,\boldsymbol{F} \tag{1}$$

$\boldsymbol{G}$ is compliance matrix. The left of lower subscripts of matrix shows response region, the right of lower subscripts shows input region and upper subscript shows main or sub system. $\boldsymbol{G}_{22}^{\mathrm{A}}$ is the compliance matrix of main system A at connection region and $\boldsymbol{G}_{22}^{\mathrm{B}}$ is the compliance matrix of sub system B at connection region. $\boldsymbol{K}^{-1}$ is the inverse matrix of coupling stiffness matrix. The sum of $\boldsymbol{G}_{22}^{\mathrm{A}}$, $\boldsymbol{G}_{22}^{\mathrm{B}}$ and $\boldsymbol{K}^{-1}$ named *kernel* compliance matrix $\boldsymbol{G}_{ker}$ [10] and the *kernel* compliance matrix is a matrix that quantitatively expresses the vibration coupling between the main system A and the sub system B through coupling spring. Further, sum of $\boldsymbol{G}_{22}^{\mathrm{A}}$ and $\boldsymbol{G}_{22}^{\mathrm{B}}$ is expressed by $\boldsymbol{G}_{22}^{\mathrm{AB}}$ and $\boldsymbol{K}^{-1}$ is replaced by $\boldsymbol{J}$ named as coupling stiffness compliance matrix. Using $\boldsymbol{G}_{22}^{\mathrm{AB}}$ and $\boldsymbol{J}$, the *kernel* compliance matrix $\boldsymbol{G}_{ker}$ is defined as,

$$\boldsymbol{G}_{ker} = \boldsymbol{G}_{22}^{\mathrm{A}} + \boldsymbol{G}_{22}^{\mathrm{B}} + \boldsymbol{K}^{-1} = \boldsymbol{G}_{22}^{\mathrm{AB}} + \boldsymbol{J} \tag{2}$$

If the coupling degrees of freedom of main system A and sub system B are n, the *kernel* compliance matrix $\boldsymbol{G}_{ker}$ is represented by $n \times n$ matrix as follows. When each coupling spring connects only between the degree of freedom in the same direction of the two systems at same connection point, the coupling

stiffness matrix $\boldsymbol{K}^{-1}$ becomes a diagonal matrix, then coupling stiffness compliance matrix $\boldsymbol{J}$ is also a diagonal matrix which diagonal elements are the inverse of coupling stiffness.

$$\boldsymbol{G}_{ker} = \begin{bmatrix} G_{22}^{\mathrm{A}}(1,1)+G_{22}^{\mathrm{B}}(1,1) & \cdots & \overbrace{G_{22}^{\mathrm{A}}(1,j)+G_{22}^{\mathrm{B}}(1,j)}^{\boldsymbol{G}_{22}^{\mathrm{AB}}(:,j)} & \cdots & G_{22}^{\mathrm{A}}(1,n)+G_{22}^{\mathrm{B}}(1,n) \\ G_{22}^{\mathrm{A}}(2,1)+G_{22}^{\mathrm{B}}(2,1) & \cdots & G_{22}^{\mathrm{A}}(2,j)+G_{22}^{\mathrm{B}}(2,j) & \cdots & G_{22}^{\mathrm{A}}(2,n)+G_{22}^{\mathrm{B}}(2,n) \\ \vdots & \ddots & \vdots & \ddots & \vdots \\ \vdots & \ddots & G_{22}^{\mathrm{A}}(j,j)+G_{22}^{\mathrm{B}}(j,j) & \ddots & \vdots \\ \vdots & \ddots & \vdots & \ddots & \vdots \\ G_{22}^{\mathrm{A}}(n,1)+G_{22}^{\mathrm{B}}(n,1) & \cdots & G_{22}^{\mathrm{A}}(n,j)+G_{22}^{\mathrm{B}}(n,j) & \cdots & G_{22}^{\mathrm{A}}(n,n)+G_{22}^{\mathrm{B}}(n,n) \end{bmatrix} + \begin{bmatrix} \boldsymbol{J}(1,1) & \cdots & \overbrace{0}^{\boldsymbol{J}(:,j)} & \cdots & 0 \\ 0 & \cdots & 0 & \cdots & 0 \\ \vdots & \ddots & \vdots & \ddots & \vdots \\ \vdots & \ddots & \boldsymbol{J}(j,j) & \ddots & \vdots \\ \vdots & \ddots & \vdots & \ddots & \vdots \\ 0 & \cdots & 0 & \cdots & \boldsymbol{J}(n,n) \end{bmatrix} \tag{3}$$

Here, $\boldsymbol{J}(:,j)$=1/k_j .In addition, the *kernel* compliance matrix $\boldsymbol{G}_{ker}$ consists of the following $n \times 1$ column vector $\boldsymbol{G}_{ker}(:,j), j = 1, \cdots, n$.

$$\boldsymbol{G}_{ker}(:,j) = \boldsymbol{G}_{22}^{\mathrm{AB}}(:,j) + \boldsymbol{J}(:,j) = \begin{bmatrix} G_{22}^{\mathrm{A}}(1,j)+G_{22}^{\mathrm{B}}(1,j) \\ G_{22}^{\mathrm{A}}(2,j)+G_{22}^{\mathrm{B}}(2,j) \\ \vdots \\ G_{22}^{\mathrm{A}}(j,j)+G_{22}^{\mathrm{B}}(j,j) \\ \vdots \\ G_{22}^{\mathrm{A}}(n,j)+G_{22}^{\mathrm{B}}(n,j) \end{bmatrix} + \begin{bmatrix} 0 \\ 0 \\ \vdots \\ 1/k_j \\ \vdots \\ 0 \end{bmatrix} \tag{4}$$

Here, in accordance with the notation of the literature [12], the j column vectors in $\boldsymbol{G}_{ker}$, $\boldsymbol{G}_{22}^{\mathrm{AB}}$ and $\boldsymbol{J}$ of eq. (2) are respectively represented as $\boldsymbol{G}_{ker}(:,j)$, $\boldsymbol{G}_{22}^{\mathrm{AB}}(:,j)$ and $\boldsymbol{J}(:,j)$.

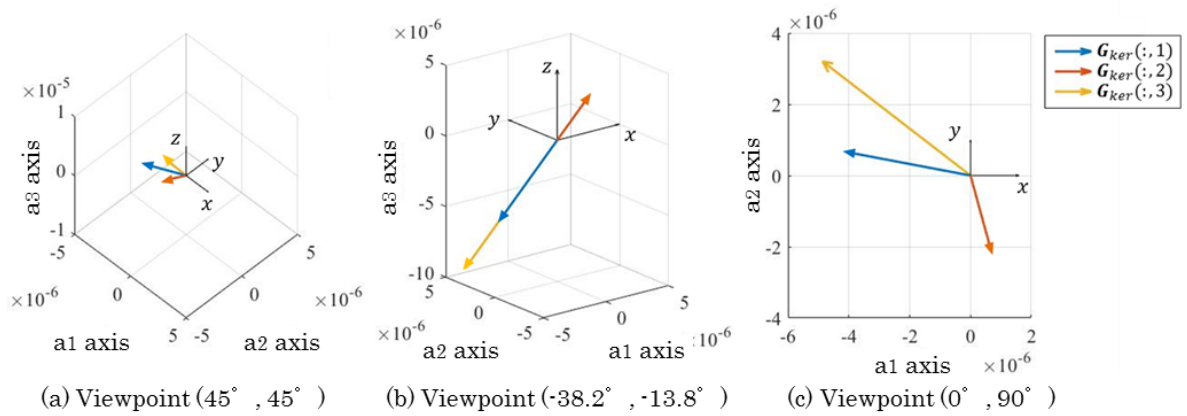
2.1.2 Condition of resonance generation

We clarify the condition of the resonance that the main system A coupled with the sub-system B through coupling spring by the analysis of the *kernel* compliance matrix $\boldsymbol{G}_{ker}$. The resonance frequency is called the coupled resonance frequency of the resonance that the main system A and the sub-system B are coupled.

In the case of the non-damping system, the coupled resonance occurs in the condition that the *kernel* compliance matrix $\boldsymbol{G}_{ker}$ has zero eigenvalues. $\boldsymbol{G}_{ker}^{-1}$ has the infinity eigenvalues, and the response of all systems is an infinite level. The conditional expression with zero eigenvalues is $\det(\boldsymbol{G}_{ker}) = 0$, which is used to determine the coupling stiffness value. However, in the case of multi-degree-of-freedom connection in this paper, since the computation of the determinant is complicated, we derive the condition of resonance in the form of a simple expression by analyzing the column vectors of the *kernel* compliance matrix $\boldsymbol{G}_{ker}$ as geometric vectors.

In the condition that $\boldsymbol{G}_{ker}$ has zero eigenvalues, at least one column vector is dependent on the column vector $\boldsymbol{G}_{ker}(:,j)$ that constitutes the *kernel* compliance matrix, and the rank deficient of the matrix occurs. The dependency of the column vectors in the case of coupled resonance is shown in Fig. 2 as an example of a 3×3 *kernel* compliance matrix. In this example, since the column vector of the *kernel* compliance matrix is a number vector of three dimensions, the starting point is the coordinate origin, and the first to third line components of $\boldsymbol{G}_{ker}(:,j)$ are drawn in the standard base. Here, the base vector of the standard

base is represented by $\boldsymbol{e}_1 = [1,0,0]^T, \boldsymbol{e}_2 = [0,1,0]^T, \boldsymbol{e}_3 = [0,0,1]^T$. Fig. 2 shows that the zero eigenvalue is one, and three column vectors exist on the same plane. In Fig. 2 (a) (c), we saw this plane from a slant, it is unclear that there are three vectors in the plane, but in Fig. 2 (b) seen from the side of this plane, three vectors can be confirmed to be aligned. In the case of two zero eigenvalues, three vectors exist on the same line and can be expressed in one-dimensional space.



(a) Viewpoint (45˚ , 45˚) (b) Viewpoint (-38.2˚ , -13.8˚) (c) Viewpoint (0˚ , 90˚)

Figure 2: Relation among three column vectors $\boldsymbol{G}_{ker}(:,j), j = 1,2,3$. In this case study, the size of the *kernel* compliance matrix $\boldsymbol{G}_{ker}$ is 3×3 and it has zero eigenvalue. If one column vector is dependent on other two column vectors, then three vectors are on a same plane. Here, viewpoint is indicated by azimuth angle θ_{Az} and is elevation angle θ_{El}.

Therefore, it is necessary for the *n*×*n kernel* compliance matrix to have one or more zero eigenvalues if the coupling point is *n* degrees of freedom. One column vector of the *kernel* compliance matrix is dependent on other $n-1$ column vectors. This is equal that *n* column vectors constituting the *kernel* compliance matrix exist on the $n-1$ dimensional hyperplane. Therefore, the condition for coupled resonance generation is that one column vector $\boldsymbol{G}_{ker}(:,j)$ and normal vector $\boldsymbol{n}$ of the $n-1$ dimensional hyperplane spanned by the remaining $n-1$column vector $\boldsymbol{G}_{ker}(:,i)$, $i \neq j$ are under orthogonal condition. This is expressed by the following equation.

$$\boldsymbol{n}^T \cdot \boldsymbol{G}_{ker}(:,j) = 0 \tag{5}$$

Here, we describe one of the ways to obtain the normal vector $\boldsymbol{n}$ of the $n-1$ dimensional hyperplane. If the *kernel* compliance matrix $\boldsymbol{G}_{ker}$ has zero eigenvalues, determinant of $\boldsymbol{G}_{ker}$ is 0 : $\det(\boldsymbol{G}_{ker}) = 0$. The following equation is obtained when the determinant of $\boldsymbol{G}_{ker}$ is expanded with cofactor expansion regarding j column.

$$\det(\boldsymbol{G}_{ker}) = \boldsymbol{G}_{ker}(1,j) \cdot C_{1j} + \boldsymbol{G}_{ker}(2,j) \cdot C_{2j} + \cdots + \boldsymbol{G}_{ker}(n,j) \cdot C_{nj} \tag{6}$$

Here, C_{ij} is (i, j) cofactor of $\boldsymbol{G}_{ker}$. The right side of Eq. (6) is inner product of the column vector $\boldsymbol{G}_{ker}(:,j)$ and the vector $[C_{1j}, C_{2j}, \cdots, C_{nj}]^T$ composed of cofactor of $\boldsymbol{G}_{ker}$. Therefore, vectors $[C_{1j}, C_{2j}, \cdots, C_{nj}]^T$ can be regarded as the normal vector $\boldsymbol{n}$ of equation (5). In other words, the normal vector $\boldsymbol{n}$ of the $n-1$ dimensional hyperplane can be determined from the cofactor of $\boldsymbol{G}_{ker}$.

In this way, the normal vector $\boldsymbol{n}$ of the $n-1$ dimensional hyperplane is important to the condition of the coupled resonance, but also includes information to determine the level of the response. The purpose of this paper is to propose the method to assign a resonant frequency, but for future research, here, we simply arrange the relationship between the response level and the normal vector $\boldsymbol{n}$. When the $\boldsymbol{G}_{ker}$ has a zero eigenvalue and the eigenvector $\boldsymbol{\Psi}$ corresponding to a zero eigenvalue $\boldsymbol{G}_{ker} \cdot \boldsymbol{\Psi} = 0$ is established [10]. For this expression, the following equation is obtained when considering that $\boldsymbol{G}_{ker}$ is a symmetric matrix.

$$\boldsymbol{\Psi}^T \boldsymbol{G}_{ker} = \boldsymbol{0}, \qquad \therefore \boldsymbol{\Psi}^T \cdot \boldsymbol{G}_{ker}(:,j) = 0 \tag{7}$$

Therefore, from the formulation (5) and (7), the relation between the normal vector $\boldsymbol{n}$ of the $n-1$ dimensional hyperplane and eigenvector $\boldsymbol{\Psi}$ of $\boldsymbol{G}_{ker}$is the following expression.

$$\boldsymbol{n} = \boldsymbol{\Psi} \tag{8}$$

Here, from the equation (1), since the internal force vectors generated at the connection points of the main system A and sub system B are represented by $\boldsymbol{G}_{ker}^{-1}\boldsymbol{G}_{21}^{\mathrm{A}}\boldsymbol{F}_{1}^{\mathrm{A}}$, the eigenvector $\boldsymbol{\Psi}$ and the eigenvalue of $\boldsymbol{G}_{ker}$ are proportional to the internal force vector [10]. Therefore, from the equation (8), the normal vector $\boldsymbol{n}$ is also proportional to the inner force vector generated at the connection points. In addition, the internal force vector of the connection point is one of the factors which determines the response level because it acts on the compliance matrix $\boldsymbol{G}_{32}^{\mathrm{A}}$ of the main system A of the equation (1). From the above, the normal vector $\boldsymbol{n}$ is important for the control of the response level.

2.2 Control method for assigning a coupled resonance frequency by coupling stiffness change

2.2.1 Calculation method to identify a coupling stiffness

In order to assign a coupled resonant frequency to the target frequency, the column vector $\boldsymbol{G}_{ker}(:,j)$ is controlled based on Eq. (5). The simply method by controlling the column vector $\boldsymbol{G}_{ker}(:,j)$ independently is explained.

For controlling the column vector $\boldsymbol{G}_{ker}(:,j)$, it is necessary to change the vector of j column of $\boldsymbol{G}_{22}^{\mathrm{AB}}$ or coupling stiffness compliance matrix $\boldsymbol{J}$ from the equation (4). For example, if you change $\boldsymbol{G}_{22}^{\mathrm{AB}}$ to change the sub system B, all the elements of the column vector $\boldsymbol{G}_{22}^{\mathrm{AB}}(:,j)$ are changed and $\boldsymbol{G}_{ker}(:,j)$ cannot be independently controlled. On the other hand, when focusing on coupling stiffness compliance matrix $\boldsymbol{J}$ is a diagonal matrix, it is possible to control only the diagonal component of $\boldsymbol{G}_{ker}$ by changing coupling stiffness because the coupling stiffness which is the diagonal component of matrix $\boldsymbol{J}$ can be changed independently. The column vector $\boldsymbol{G}_{ker}(:,j)$ in Eq. (5) contains only the coupling stiffness k_j, if you seek the normal vector $\boldsymbol{n}$ at target frequency you want to assign the coupled resonance, coupling stiffness k_j can be obtained from eq. (5). In other words, it is possible to assign coupled resonance to a target frequency by changing only the coupling stiffness.

Next, we show a procedure for determining a specific coupling stiffness for assigning the coupled resonant frequency to any frequency using a single coupling stiffness.

When the coupling stiffness k_i at connection point j is changed only Δk_i, assume that vector $\boldsymbol{J}(:,j)$of j column in the coupling stiffness compliance matrix $\boldsymbol{J}$ and the *kernel* compliance matrix $\boldsymbol{G}_{ker}$ changes to $\boldsymbol{J}'(:,j)$ and $\boldsymbol{G}'_{ker}(:,j)$ respectively. The relation between $\boldsymbol{J}'(:,j)$ and $\boldsymbol{G}'_{ker}(:,j)$ is represented by the following equation.

$$\boldsymbol{G}'_{ker}(:,j) = \boldsymbol{G}_{22}^{\mathrm{AB}}(:,j) + \boldsymbol{J}'(:,j) \tag{9}$$

Here,

$$\boldsymbol{J}'(:,j) = \begin{bmatrix} 0 \\ 0 \\ \vdots \\ 1 \\ \hline k_j + \Delta k_j \\ \vdots \\ 0 \end{bmatrix} \tag{10}$$

Now, before coupling stiffness change, in target frequency to generate the coupled resonance, if $\boldsymbol{n}$ is the normal vector of $n-1$ dimension hyperplane composed by $n-1$ column vectors in $\boldsymbol{G}_{ker}$ except for

column vector $\boldsymbol{G}_{ker}(:,j)$ related to the connection point j, the conditional expression of the coupled resonance occurs is the following equation from eq. (5) (9).

$$\boldsymbol{n}^T \cdot \boldsymbol{G}'_{ker}(:,j) = \boldsymbol{n}^T \cdot \{\boldsymbol{G}_{22}^{\mathrm{AB}}(:,j) + \boldsymbol{J}'(:,j)\} = 0 \qquad \therefore\ \boldsymbol{n}^T \cdot \boldsymbol{J}'(:,j) = -\boldsymbol{n}^T \cdot \boldsymbol{G}_{22}^{\mathrm{AB}}(:,j) \tag{11}$$

Here, $\boldsymbol{J}'(:,j) = [0,\ \cdots,\ \boldsymbol{J}'(j,j),\ \cdots, 0]^T$, $\boldsymbol{n} = \left[n_1,\ \cdots,\ n_j,\ \cdots, n_n\right]^T$, the following equation is obtained when the target frequency is ω_T.

$$\boldsymbol{J}'(j,j) = -\frac{\boldsymbol{n}^T|_{\omega=\omega_T} \cdot \boldsymbol{G}_{22}^{\mathrm{AB}}(:,j)\big|_{\omega=\omega_T}}{n_j\big|_{\omega=\omega_T}} \tag{12}$$

Compliance $\boldsymbol{J}'(j,j)$ is transferred to stiffness by the relation of $\boldsymbol{J}'(j,j) = 1/(k_j + \Delta k_j)$.

$$k_j + \Delta k_j = -\frac{n_j\big|_{\omega=\omega_T}}{\boldsymbol{n}^T|_{\omega=\omega_T} \cdot \boldsymbol{G}_{22}^{\mathrm{AB}}(:,j)\big|_{\omega=\omega_T}} \tag{13}$$

We can easily calculate the coupling stiffness which can assign coupling resonance to target frequency ω_T.

2.2.2 The way to select of coupling stiffness to change

Next, we show the way for selecting coupling stiffness which should be controlled from multiple coupling stiffness. The ratio of the coupling stiffness $(k_j + \Delta k_j)/k_j$ is calculated from the following equation, and this ratio of the coupling stiffness that the value is closest to 1 is chosen. When the ratio is closer to 1, the amount to change by semi-active control is small. It is useful for the reduction of the power for control and the responsiveness of control. In this paper, $(k_j + \Delta k_j)/k_j$ is called the change ratio of coupling stiffness.

$$\frac{k_j + \Delta k_j}{k_j} = -\frac{n_j\big|_{\omega=\omega_T} / k_j}{\boldsymbol{n}^T|_{\omega=\omega_T} \cdot \boldsymbol{G}_{22}^{\mathrm{AB}}(:,j)\big|_{\omega=\omega_T}} \tag{14}$$

From the above, the procedure to assign the coupled resonance frequency to target frequency by changing a coupling stiffness is as follows.

1: In the target frequency ω_T, calculate the amount of coupling stiffness required to assign the coupled resonance frequency by Eq. (13) for all coupling stiffness.

2: Calculate the change ratio of coupling stiffness $(k_j + \Delta k_j)/k_j$ by Eq. (14) and select a coupling stiffness which the change ratio is closest 1.

2.2.3 The amount of change in the column vector

To analyze the *kernel* compliance matrix $\boldsymbol{G}_{ker}$ as a geometric vector, we explain the relationship between the change of the column vectors of $\boldsymbol{G}_{ker}$ and the compliance matrix $\boldsymbol{J}$. When coupling stiffness is changed by Δk, the amount of change in the column vectors of the compliance matrix $\boldsymbol{J}$ is expressed as $\Delta\boldsymbol{J}(:,j)$**.** In this case, the change in the column vectors of the *kerne*l compliance matrix can be written as

$$\boldsymbol{G'}_{ker}(:,j) = \boldsymbol{G}_{ker}(:,j) + \Delta\boldsymbol{J}(:,j) \tag{15}$$

Here

$$\Delta \boldsymbol{J}(:,j) = \boldsymbol{J}'(:,j) - \boldsymbol{J}(:,j) = \begin{bmatrix} 0 \\ 0 \\ \vdots \\ \frac{1}{k_j+\Delta k_j} - \frac{1}{k_j} \\ \vdots \\ 0 \end{bmatrix} \tag{16}$$

From equation (16), we can understand that in the case of $\Delta k_j \to \pm\infty$, $\Delta \boldsymbol{J}(j,j)$ is asymptotic to $-1/k_j$, in the case of $\Delta k_j \to -k_j \pm 0$, $\Delta \boldsymbol{J}(j,j)$ is asymptotic to $\pm\infty$.

3 Application to Beam Structure

In this chapter, we apply the theory of the preceding chapter to the beam structure, and assign the coupled resonance frequency by changing the coupling stiffness. The relation between the coupled resonance frequency and eigenvalue, and the dependency among column vectors in the *kernel* compliance matrix are confirmed as a geometric vector. Finally, we analyze the relationship between coupling stiffness and coupled resonance frequency, and describe the way to utilize it for structural design of coupling spring.

3.1 Analysis model and its vibration characteristics

A schematic diagram and the specifications of the analysis model are shown in Fig. 3. The main system A and sub-system B are respectively lengths of 1.0 m and 0.3 m. In order to take advantage of the mutual interference between elastic vibration modes of main and sub systems, the two beams are spring-coupled in three places. The degree of freedom of the coupling stiffness is only in the x-direction translation, and the coupling stiffness is k_1, k_2, k_3 = 250 N/mm, and the specifications of beam: Young's modulus = 2.058×10^{11} Pa, Density = 7.8×10^{3} kg/m^3, Second moment of area = 6.75×10^{-11} m^4, Cross-section area = 9.0×10^{-5} m^2. The frequency response characteristics of the main system A and sub system B were determined by the finite element method, and the frequency response characteristics of the coupled system were determined using the equation (1). In Fig. 4, the rightmost x-directional response displacement of the main system A for the leftmost x-direction excitation is shown as a blue line, and the frequency response characteristics of only main system A are indicated by the green dashed line. At about above 70 Hz, the resonance frequency of main system A is changed by the addition of sub-system B, and it is understood that both are strongly coupled. Especially, the influence of the sub-system B is large for all systems above 280Hz.

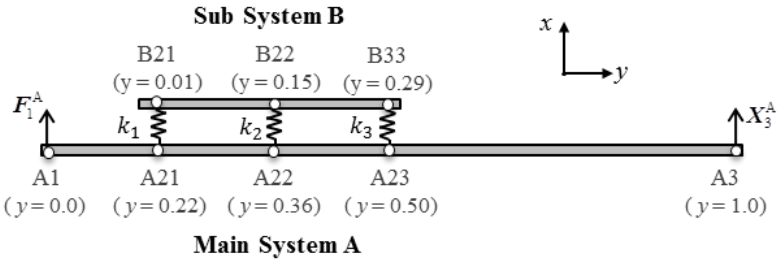


Figure 3: Analysis model diagram. Main system A and sub system B are modeled by beam elements. The number of connection DOFs is three and DOF of connection points is only x direction. Coupling stiffness: k_1, k_2, k_3 = 250 N/mm. Specifications of beam: Length of Main System A = 1.0 m; Length of Sub System B = 0.3 m, Density = 7.8×10^{3} kg/m^3, Young's modulus = 2.058×10^{11} Pa, Second moment of area = 6.75×10^{-11} m^4, Cross-section area = 9.0×10^{-5} m^2

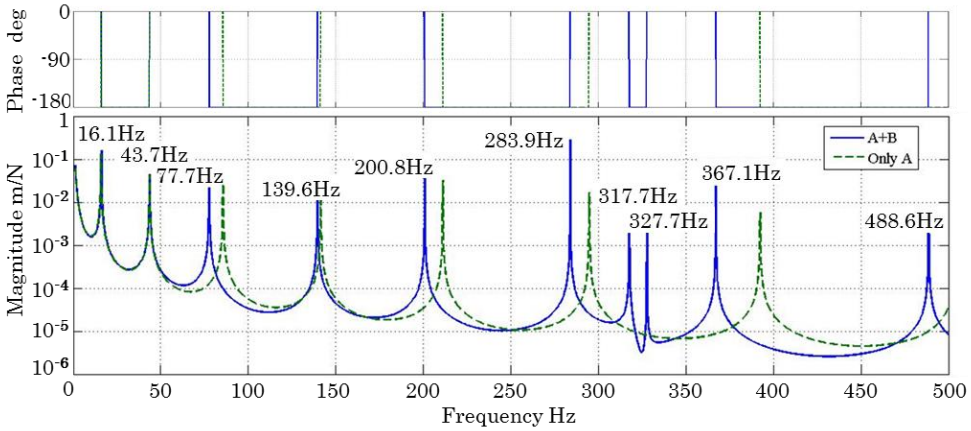


Figure 4: Magnitude and phase of the compliances of the whole system. Solid line: main system A with sub system B which is coupled with springs. Dashed line: only main system A.

3.2 Relation between eigenvalues and column vectors in the kernel matrix

We confirm the relation between the eigenvalues and the column vectors of the *kernel* compliance matrix at the coupled resonance frequency. To clarify the size of eigenvalues, Fig. 5 shows the singular value of the *kernel* compliance matrix. In the resonance frequency, it is understood that one singular value is minimized (almost 0) corresponding to the zero eigenvalue. The singular value does not become completely 0 because of the effect of the frequency resolution of the analysis and because of a small damping in calculation. The relation between the three column vectors constituting the *kernel* compliance matrix $\boldsymbol{G}_{ker}$ at resonance frequency 283.9 Hz and non-resonant frequency 250.0 Hz is shown in Fig. 6. From Fig. 6 (a), three column vectors exist in the same plane at the resonance frequency, and one vector can be confirmed to be dependent on the other two vectors. On the other hand, from Fig. 6 (b), it can be confirmed that three column vectors do not exist in the same plane at the non-resonance frequency.

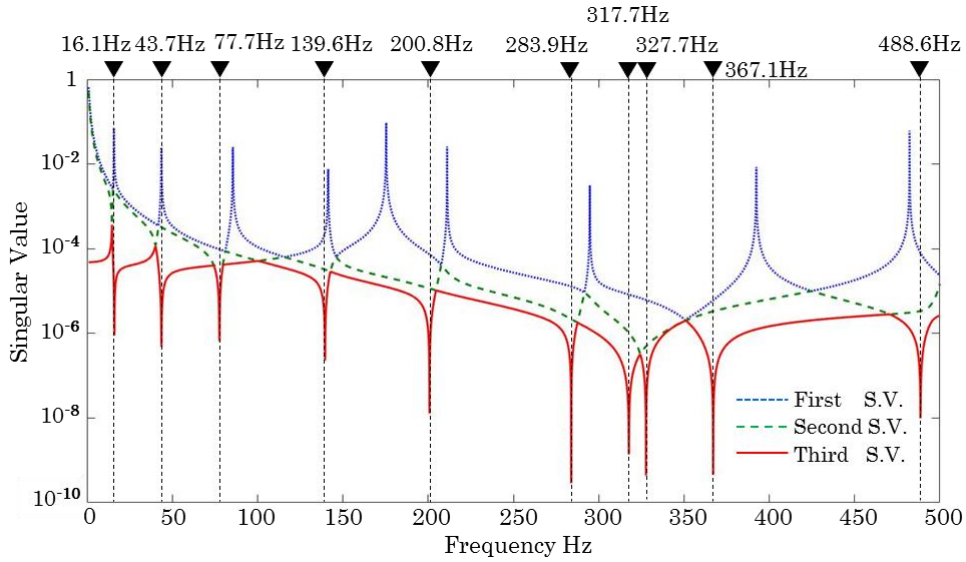
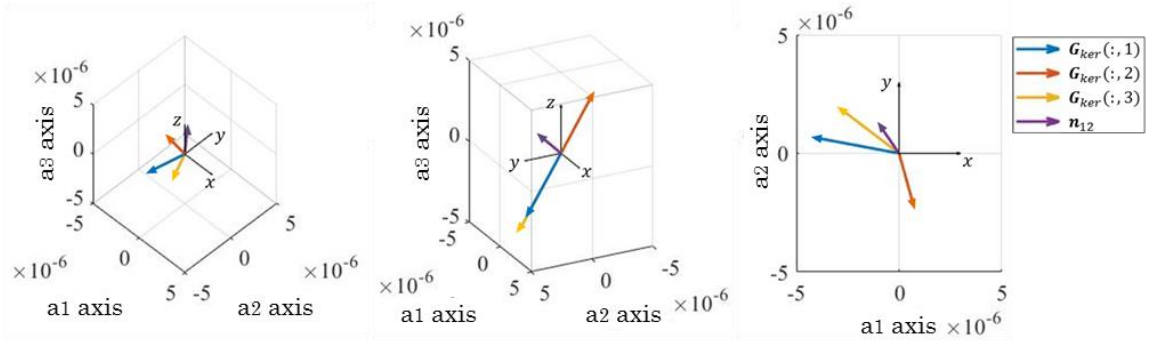
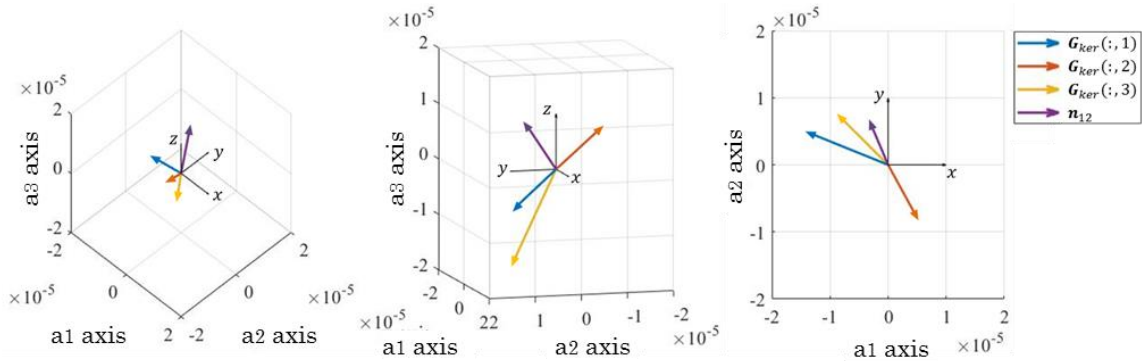


Figure 5: Three singular values of $\boldsymbol{G}_{ker}$ of Fig. 4. One singular value almost equals zero at each resonance frequency.



(a-1) Viewpoint (45˚ , 45˚) (a-2) Viewpoint (-63.0˚ , -19.0˚) (a-3) Viewpoint (0˚ , 90˚)

(a) Relation among three column vectors $\boldsymbol{G}_{ker}(:, j)$ at resonance frequency: 283.9Hz



(b-1) Viewpoint (45˚ , 45˚) (b-2) Viewpoint (-74.6˚ , -7.8˚) (b-3) Viewpoint (0˚ , 90˚)

(b) Relation among three column vectors $\boldsymbol{G}_{ker}(:, j)$ at non-resonant frequency: 250.0 Hz

Figure 6: Relation among the *kernel* matrix's column vectors $\boldsymbol{G}_{ker}(:, j)$. Column vectors $\boldsymbol{G}_{ker}(:,1)$, $\boldsymbol{G}_{ker}(:,2)$ and $\boldsymbol{G}_{ker}(:,3)$ are respectively plotted with blue, red and orange arrow. Normal vector $\boldsymbol{n}_{12}$ to the hyperplane spanned by $\boldsymbol{G}_{ker}(:,1)$ and vector $\boldsymbol{G}_{ker}(:,2)$ is plotted with purple arrow. (a) Three vectors at resonance frequency 283.9 Hz exist in a same plane. (b) Three vectors at non-resonance frequency don't exist in a same plane.

3.3 Calculation of coupling stiffness and its change ratio

3.3.1 Coupling stiffness

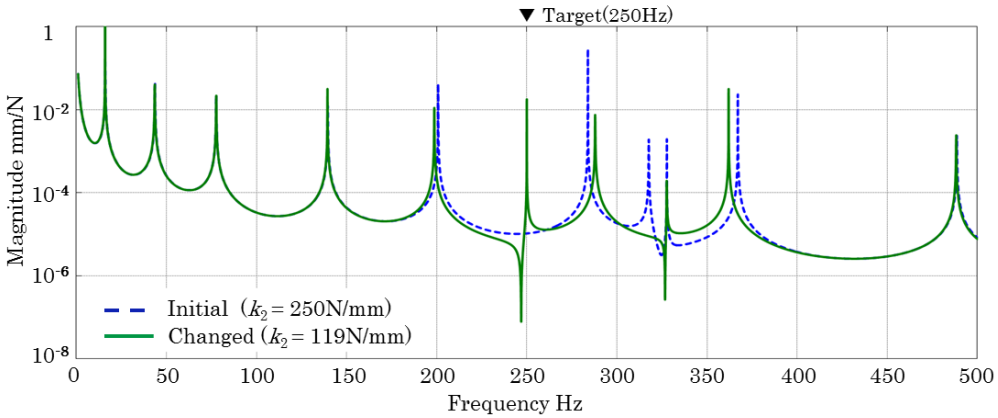
Next, we show an example of assigning a coupled resonance frequency to the target frequency by changing one of the three coupling stiffness k_1, k_2 and k_3.

The target frequency is 250 Hz, and a coupled resonance is generated by moving the three column vectors shown in Fig. 6 (b) to the same plane. The value after the change of the coupling stiffness obtained from equation (13) is shown in table 1. For the coupling stiffness in table 1, the frequency response characteristics of all systems is shown in Fig. 7. For example, in Fig. 7 (a), the coupling stiffness k_2 is changed from 250 N/mm to 119 N/mm, and the other coupling stiffness k_2 and k_3 are using the initial value of 250 N/mm. From Fig. 7, it is possible to assign resonance to the target frequency of 250 Hz by change one coupling stiffness k_j. In addition, focusing on the response level of 200Hz-280Hz, when the coupling stiffness k_2 is changed, the anti-resonance frequency occurs below 250Hz, when the coupling

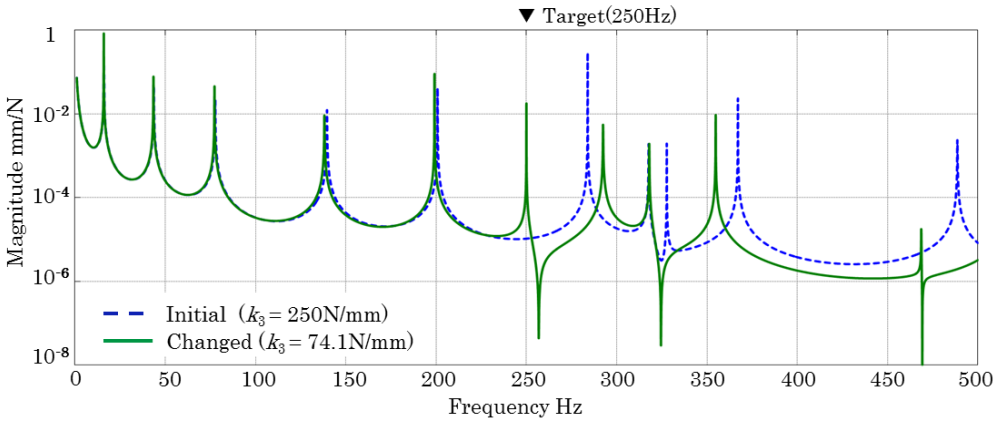
stiffness k_3 are changed, the anti-resonance frequency is generated more than 250Hz. For this factor analysis, the normal vector $\boldsymbol{n}$ described in section 2-1-2 is important.

Coupling stiffness $k_j + \Delta k_j$ [N/mm]	$k_1 + \Delta k_1$	$k_2 + \Delta k_2$	$k_3 + \Delta k_3$
	76.1	119	74.1

Table 1. The coupling stiffness to assign the coupled resonance to 250 Hz.



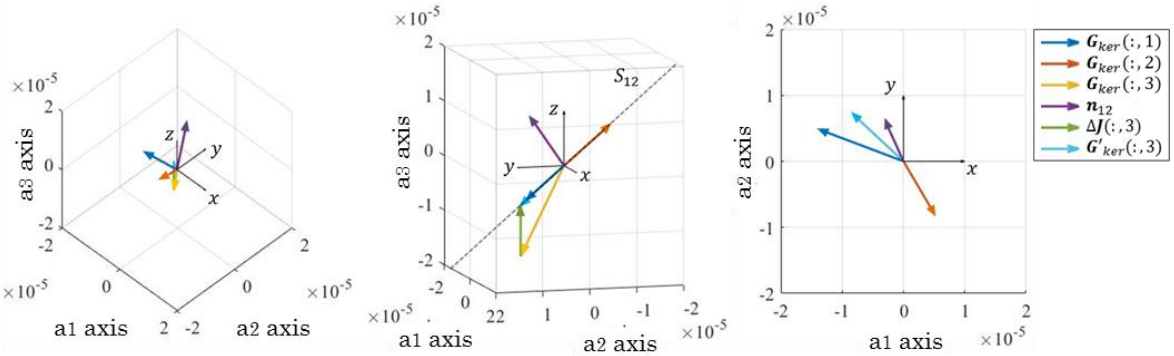
(a) k_2 is changed, Solid line (changed): k_2 = 119 N/mm, dashed line(initial): k_2 = 250 N/mm



(b) k_3 is changed, Solid line (changed): k_3 = 74.1 N/mm, dashed line(initial): k_3 = 250 N/mm

Figure 7: Frequency response function of the whole structure. Solid line: k_j is changed to assign the coupled resonance to 250 Hz by Eq. 13. Dashed line: k_j is initial value.

Next, Fig. 8 shows the column vectors of the *kernel* compliance matrix at 250 Hz, as shown in Fig. 7 (b), which changed the coupling stiffness k_3. For $\boldsymbol{G}_{ker}(:,3)$, we plotted the $\boldsymbol{G}'_{ker}(:,3)$ and $\Delta\boldsymbol{J}(:,3)$ using the Eq. (15) (16). From Fig. 8 (b), it can be confirmed that the initial state of the column vector $\boldsymbol{G}_{ker}(:,1)$, $\boldsymbol{G}_{ker}(:,2)$ and $\boldsymbol{G}_{ker}(:,3)$ do not exist in the same plane. In Fig. 8 (b), it also confirmed that a new column vector$\boldsymbol{G}'_{ker}(:,3)$ is generated by adding $\Delta\boldsymbol{J}(:,3)$ to the initial state of the column vector $\boldsymbol{G}_{ker}(:,3)$, and three column vectors $\boldsymbol{G}_{ker}(:,1)$, $\boldsymbol{G}_{ker}(:,2)$ and $\boldsymbol{G}'_{ker}(:,3)$ exit in the same plane.



(a) Viewpoint (45˚ , 45˚) (b) Viewpoint (-74.6˚ , -7.8˚) (c) Viewpoint (0˚ , 90˚)

Figure 8: Relation among the *kernel* matrix's column vectors $\boldsymbol{G}_{ker}(:,j)$ and coupling stiffness compliance vector$\Delta\boldsymbol{J}(:,3)$. Initial vector $\boldsymbol{G}_{ker}(:,3)$ is changed to vector $\boldsymbol{G}'_{ker}(:,3)$ by adding vector$\Delta\boldsymbol{J}(:,3)$. $\Delta\boldsymbol{J}(:,3)$ is calculated from Eq.16. These figures show that three vectors, $\boldsymbol{G}'_{ker}(:,3)$, $\boldsymbol{G}_{ker}(:,1)$ and $\boldsymbol{G}_{ker}(:,2)$, exist in one plane at resonance frequency 250 Hz by the change of coupling stiffness k_3.

3.3.2 Calculation of the change ratio of coupling stiffness

We select a coupling stiffness to change after the calculation of the change ratio of coupling stiffness $(k_j + \Delta k_j)/k_j$ from eq. (14). The change ratio of the coupling stiffness for the target resonance frequency of 250 Hz is shown in table 2. The change ratio of coupling stiffness of k_2 is closest to 1, therefore coupling stiffness k_2 is selected to change.

Change Ratio of Coupling Stiffness $(k_j + \Delta k_j)/k_j$	$(k_1 + \Delta k_1)/k_1$	$(k_2 + \Delta k_2)/k_2$	$(k_3 + \Delta k_3)/k_3$
	0.304	0.476	0.296

Table 2: The coupling stiffness by eq.14 to assign the coupled resonance to 250 Hz.

3.4 Relation analysis between the coupling stiffness and the assignment range of resonant frequency for the structural design of coupling spring

We analyze the assignment range of resonance frequencies by changing the coupling stiffness and propose to utilize it for the structural design for coupling spring to realize the coupling stiffness necessary for semi-active control.

The relation between the change ratio of coupling stiffness and coupled resonant frequency is shown in Fig. 9 to confirm the assignment range of coupled resonant frequencies. Each of the three line-types is a case of changing a coupling stiffness. For example, the legend $(k_1 + \Delta k_1)/k_1$ is the case that the only coupling stiffness k_1 is changed, but k_2 and k_3 did not changed. The initial resonant frequency is shown on the right vertical axis so that the resonance frequency and the initial resonant frequency can be understood after the coupling stiffness change. It is noted that there is a region that is not plotted under the influence of the analysis resolution. From Fig. 9, if the change ratio of coupling stiffness is controlled between -1 ~ 2, the resonance can be assigned to the desired frequency below 500Hz by changing only one coupling stiffness. On the other hand, there is a region where the coupled resonance frequency is hardly assign even if the coupling stiffness is changed, and the tendency is different at each coupled resonance. Therefore, there is a difference in the change ratio of coupling stiffness which is necessary for the assignment of the resonance frequency, and the following relationship is arranged. Below 150Hz: the change ratio of coupling stiffness = about -0.1 ~ 0.3, 150Hz ~ 300Hz: the change ratio of coupling

stiffness = about 0 ~ 1, 300Hz ~ 400Hz: the change ratio of coupling stiffness = about 0 ~ 2, 400Hz ~ 500Hz: the change ratio of coupling stiffness = about-1 ~ 1. In addition, the sensitivity of the resonance frequency change for the change ratio of coupling stiffness is different at each coupled resonance. The sensitivity below 200Hz tends to be higher than the sensitivity above 200Hz. This information will be calculated at the stage when the compliances of the body are obtained, and it is factored into the performance requirements of the coupled spring structural design of the semi-active control system. In addition, we assume the assignment frequency range for smoothing from the relation between the frequency of the suspension transmitted force and the resonance frequency of the vehicle body predicted at the vehicle development stage and reflect it into the coupling spring structure design.

When the coupled resonant frequency of the coupling stiffness k_2 is changed, from the intersection of the dashed line of Fig. 7 $(k_2 + \Delta k_2)/k_2$ and the horizontal axis of the change ratio of coupling stiffness 0.476 ($k_2 + \Delta k_2 = 119$ N/mm in Fig. 7 (a)), the resonance generated at 250 Hz is found to have occurred by shifting the initial resonant frequency 283.9 Hz. Similarly, other resonance frequencies are related to the following. The ratio of the initial resonant frequency (Hz) and the resonant frequency (Hz) after k_2 change is 16.1/16.0, 43.7/43.5, 77.7/77.7, 139.6/139.4, 200.8/198.6, 283.9/249.7, 317.7/287.9, 327.7/327.7, 367.1/362.0, and 488.6/488.2.

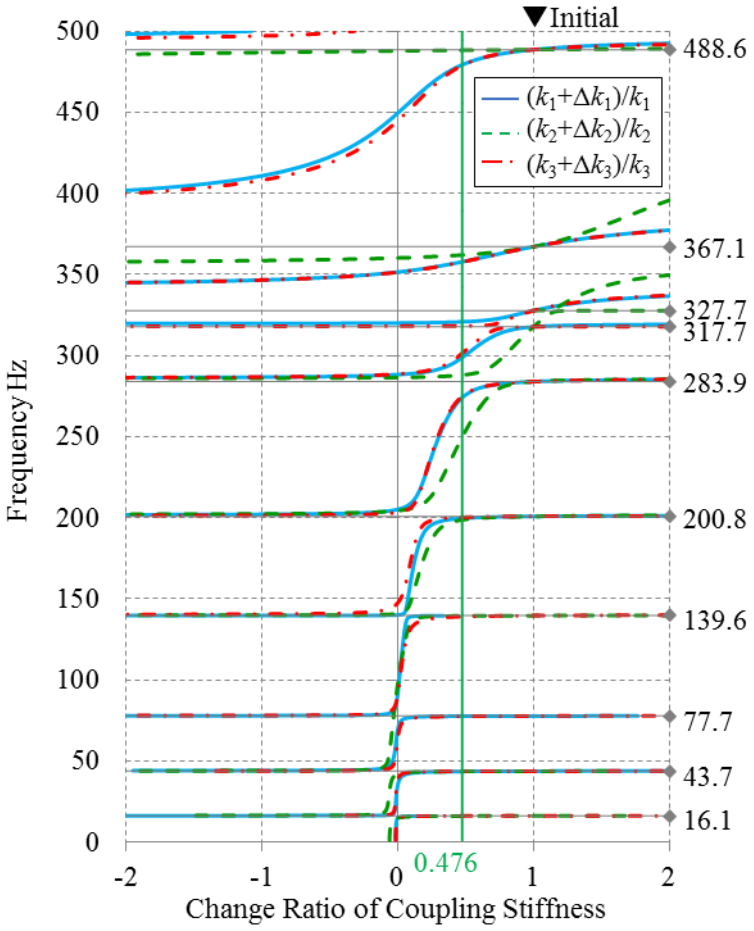


Figure 9: Relation between the change ratio of coupling stiffness $(k_j + \Delta k_j)/k_j$ and resonance frequency calculated from Eq. 14. Blue solid line: only k_1 is changed. Green dashed line: only k_2 is changed, Red dot chain line: only k_3 is changed.

Conclusion

For smoothing the response in the frequency domain of two vibration systems coupled with multiple degrees of freedom, we developed a method of assigning the coupled resonance frequency to the target frequency without repeated calculation assuming the use it in semi-active control.

(1) This method is based on moving the column vectors constituting the *kernel* compliance matrix to the same hyperplane in order to occur rank deficient the kernel compliance matrix at the target frequency. Using the normal vector of this hyperplane, we clarified that the condition expression of the resonance generation is equivalent that inner product of the normal vector and the column vector equals to zero. As a result, the amount of change of the column vector can be obtained without repeated calculation.

(2) In order to change the column vectors shown in the above (1) independently by the semi-active structure change, we proposed that only the coupling stiffness with independent freedom from each other connecting the two systems can be changed. If the structure of the sub system itself is changed, each column vector changes at the same time, but if the coupling stiffness is changed, only the diagonal component of the *kernel* compliance matrix is changed, and each column vector can be manipulated individually. We realized a method to assign the coupled resonance to the target frequency by changing one of the coupling stiffness by using the conditional expression of the resonance generation of the above (1). It is possible to calculate the coupling stiffness using only the compliance of the connection point and the normal vector of the above (1). We propose a method to select a coupling stiffness which should be controlled from multiple connection points using the all calculated coupling stiffness.

(3) As a numerical example, we applied this method to two beam structures which were connected in three places by a translational one-degree-of-freedom spring and confirmed the validity of this method. We analyzed the assignment range of the coupled resonance frequency for the ratio of the initial coupling stiffness and the changed coupling stiffness, then we propose to use this result as a performance requirement for the structural design of the coupling spring in semi-active control system.

References

[1] Toshio Inoue, Hisashi Sano, Akira Takahashi, Tsuyoshi Yamashita, Dai Ishihara, Mitsuo Nakamura, Kenichi Terai and Yoshio Nakamura, *Development of active control system for low frequency road noise*, SAE Technical Paper, 2000-08-0147 (2000).

[2] Katrien Wyckaert and Herman Van der Auweraer, *Operational Analysis, Transfer Path Analysis, Modal Analysis: Tools to Understand Road Noise Problems in Cars*, SAE, 951251 (1995), pp. 139-143.

[3] P.J.G van der Linden and K. Wyckaert, Modular Vehicle Noise and Vibration Development, SAE, 1999-01-1689 (1999), pp. 1-13.

[4] Ichiro Kido, Akeru Nakamura, Masashi Komada, Makoto Asai, *Vibration coupling analysis of tire/wheel and suspension*, Proc. of 3rd Darmstadter Reifenkolloquium 2000, VDI Reihe12 Nr.437 (2000), pp41-50.

[5] Kazuyoshi Takahashi, Takuya Yoshimura, *Variability Evaluation of Measured FRF and the Effect on Force Identification*, SAE Technical Paper 2012-08-0104 (2012).

[6] Maarten V. van der Seijs, Dennis de Klerk and Daniel J. Rixen, *General framework for transfer path analysis: History, theory and classification of techniques*, Mechanical Systems and Signal Processing, 68-69 (2016), pp. 217-244.

[7] Shinichi Maruyama, Tetsuya Arai, Kinichi Tanuma, Tadayoshi Fukushima and Yoshiaki Koshikawa, *A Study on Reduction in Low-Frequency Road Noise of Passenger Cars*, SAE Technical Paper 1999-08-0084 (1999).

[8] Kohei Furuya, Takuya Yoshimura, Akira Suto and Seiya Narikuni, *Optimality Condition for Sound Pressure Minimization in Vibro-Acoustic Problem and Structural Optimization*, SAE Technical Paper 2006-08-0254 (2006).

[9] Keisuke Terada, Takuya Yoshimura, *Sensitivity Analysis for Noise Reduction under Operational State*, SAE Technical Paper 2010-08-0256 (2010).

[10] Ichiro KIDO and Atsuo SUEOKA, *Analytical Approach for Strongly Coupled Vibration System Composed of Two Substructures (1st Report, Theory and Its Application to Vibration of Vehicle Suspension)*, Transactions of the Japan Society of Mechanical Engineers. C, Vol. 71, No. 712 (2005), pp. 3335-3342.

[11] Ichiro KIDO, Sagiri UEYAMA and Atsuo SUEOKA, *Coupled Vibration Analysis of Tire and Wheel for Road Noise Improvement*, Proc. of the Noise and Vibration Conference, SAE Paper 2005-01-2260 (2005).

[12] Gene H. Golub, Charles F. Van Loan, *Matrix Computations*, The Johns Hopkins University Press (1983).

Nonlinear modelling and simulation of impact events and validation with physical data

M. Bayani[1,2], A. P. Szekely[3], N. Alhanna[3], H. Viktorsson[1], C. Wickman[1,2], R. Söderberg[2]
[1] Volvo Cars Corporation, SE-405 31, Göteborg, Sweden
e-mail: **mohsen.bayani@volvocars.com**

[2] Chalmers University of Technology, Department of Industrial and Materials Science, SE-412 96, Göteborg, Sweden

[3] KTH Royal Institute of Technology, School of Engineering Sciences, Stockholm, Sweden

Abstract
Squeak and Rattle are nonstationary sounds that imply quality deficiency in premium cars. In order to enhance prediction and verification capabilities of squeak and rattle problems upfront in product development phases, robust and accurate virtual models are required. In this research, a modelling approach is employed to simulate the nonlinear response of impact events from a rattle-producing machine by finite element analysis. The model comprises nonlinear contact interactions to capture the system response at impact events and is correlated versus experimental data considering the modal and time domain response. A sensitivity study is performed on the parameters of the contact model. System response is formulated in the form of impact kinematic and kinetic components, which are well correlated with rattle sounds in impact events. The parameters with high impact factor are identified. These results can be used to estimate the response with higher accuracy and enhance rattle event prediction capability.

1 Introduction

Squeak and rattle sounds have always been among the top quality concerns in automotive industries, even in early decades of the past century [1]. Squeak and rattle, in the view of car users, denote a failure mode and the need for a workshop visit. This burdens high warranty costs on car manufacturers [2]. However, the “find-and-fix” approach has remained the most common treatment in automotive industry to deal with squeak and rattle problems [3]. In practice, using tapes and greases in problematic areas is the number one solution in car production lines. This indicates a huge amount of workload in late development phases and often demands the availability of physical complete vehicle prototypes. Needless to say that each physical prototype demands considerable project resources both in terms of material and man-hour costs. While automakers try to shift product development engineering activities from late phases to early phases, measures should be taken into account to ensure reliable product verification methods. Simulation by computer aided engineering (CAE) has been widely used in different industries and for different disciplines for design and verification purposes.

Computer simulation has been used as an early phase development tool to predict and eliminate rattle problems in automotive industry. Her and colleagues used a single degree of freedom mass damper model to predict the rattle sounds [4]. They used a threshold method as a function of relative impact velocity to predict the impact sound pressure level. The method subjected to periodically excited systems and results showed good accordance with physical data for the frequencies outside the resonance regions. In another study, Choi and co-workers worked on the idea of using Rayleigh integral equation to estimate the emitted sound from a flat vibrating panel [5]. In this method, surface velocity of impacting parts was used to calculate the sound pressure as a function of distance from the impact point. The proposed method was

applied for a glove box in a cockpit assembly of a car and the results correlated well with experiment in time and frequency domains.

In [6] and [7] two methods for rattle prediction are presented, both applicable to industry today since they both use ordinary NVH models (Noise, Vibration and Harshness). A linear simulation approach and added elements in the critical interfaces is common for both methods. The added elements called "Virtual sensors" in [7] and "SAR-LINE™" in [8], are used differently between the two methods since one method is evaluating rattle in frequency domain [7] and the other in time domain [8], but they serve the same purpose, store information about relative displacement between the parts in the studied interface. According to [7], the "Virtual sensors" were automatically generated and their location was chosen based on clearances in the structure. An alternative approach to find the suitable locations for the additional elements is to use the contact point analysis method, described in [8].

Arun and colleagues gave a good example for nonlinear modelling of rattle events [9]. Although it is not an NVH problem, it seeks for an accurate modelling approach of dynamic response of suspended parts subjected to dynamic loading conditions. The virtual model was compared to a random excitation experiment, and showed the significance of non-linear time domain modelling of the vibration problem, as linear motion transmissibility could not capture the vibration phenomenon and predict acceleration levels in the parts. They established a soft constrained penalty formulation based contact with static and dynamic friction coefficient and viscous damping. It also gives a good way to reduce computational cost of long duration simulations while maintaining accurate contact modelling, by employing a dynamic sub-structuring strategy. This strategy is based on dividing the structure to parts that behave linearly and nonlinearly, and then reduce the linear substructures' degree of freedom to speed up the computation.

The linearity in the finite element analysis (FEA) is defined by the mathematical stiffness and load components of the modelled structure. In linear FEA, these dataset remain constant during the simulation. There is no need for the software to re-calculate stiffness and load components when deformation occurs. In nonlinear analyses, which may result from geometry, material properties, or like this case, contact, the stiffness or load components vary constantly. A time increment is then needed, since the stiffness and force components are needed to be updated at every step of simulation. This is due to the fact that the nonlinear phenomena present in the event cause the previously defined parameters unable to describe the structure accurately. In finite element tools, contact modelling can be described by preventing (kinematic method) or eliminating (penalty method) the penetration of the parts involved using different methods. These methods are further described in section 4.1.

Akay reviewed the process of impact noise generation [10]. He mentioned that there exists a relation between peak flow velocity of the sound wave and the relative impact velocity of colliding bodies. He also pointed out that for the rigid body radiation part of the impact sound, acceleration of the impacting part relates to the peak sound pressure. In addition, it is discussed that the peak sound pressure and the momentum of impacting parts are related. In lower frequencies, this relation can be linear, but at higher frequencies due to inefficient energy transfer, the relation turns to be nonlinear. For plane vibrations in impact events, in low frequencies the radiated sound pressure and normal velocity of impact surface are linearly related, while in high frequency the sound pressure is more proportional to surface acceleration.

According to [10] and [4], impact sound is highly related to relative velocity, impact acceleration and momentum of impacting parts and using the surface velocity to estimate the severity of rattle events has shown promising results, [5]. However, the finite element approach used for simulating rattle events in automotive industry, currently relies on linear models, [6] and [7]. Therefore, in order to further advance the assessment criterion for rattle evaluation, nonlinear models capable of predicting impact kinetics and kinematics with higher accuracy are required.

In this study, a nonlinear modelling approach will be used to simulate impact events. For this purpose, contact parameters in a finite element model of a rattle producing beam will be investigated. The finite element model will be correlated against experimental data and a sensitivity analysis will be conducted to identify the important model parameters in contact interaction that have high impact on system response and the results will be discussed.

2 Methodology

Figure 1 gives an overall view of the method followed in this work to conduct the study. In this research, a physical test setup that was previously built for studying characteristics of rattle sounds was taken as the case study. Further details about the physical setup will be given in the next section. Experiments were done utilising the rattle test setup. A representative finite element model of the setup was developed. The modelling information including, the geometrical dimensions and material properties were obtained from the drawings of the physical setup [11]. The finite element model was correlated in three stages. Firstly, correlation of eigenvalue analysis of the setup, without the connection to the shaker, was performed versus physical measurement. Afterwards, an explicit time domain simulation of the setup was done, while it was excited by the shaker and in absence of impact event and results were compared to empirical data. Lastly, correlation of an impact event while the test setup was excited by the shaker was performed, utilising explicit time domain finite element simulation method. By this, the validity of the model was checked against physical data in three steps prior to conducting contact parameter study. Thereafter, the finite element model of the setup was used to perform a parameter study, to investigate the parameters in contact region that affect the system response. The findings from the parameter study is planned to be examined for a car subsystem in future and the results of the computer simulation be compared with experimental data for validation purpose.

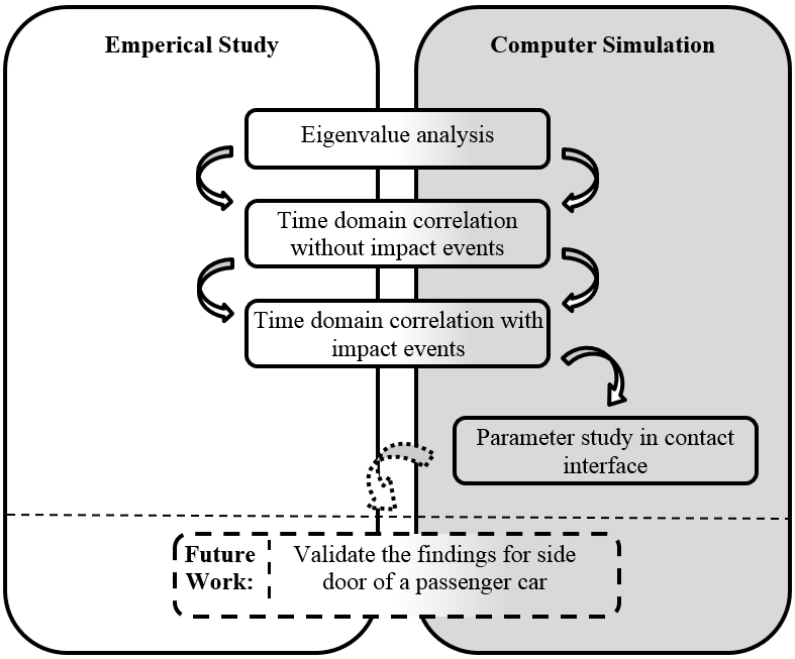


Figure 1: Research methodology

3 Modelling and simulation method

3.1 Experimental Setup

The test stand used as the case study is depicted in Figure 2. The setup consisted of an aluminium beam (1) with 320 [mm] length and 20×6 [mm] rectangular cross-section that was fully clamped to a stand at one end (2). On the other end, a material sample (3) with 1.6 [mm] thickness and a circular cross-section of 16 mm diameter and with a flat surface was mounted. The material sample was located just in front of another material sample (4) fixed to an impact hammer. For this study, both of the material samples were chosen to be steel. However, it is possible to repeat the experiment for other metallic and non-metallic

material pairs in future. The gap between the two material samples could be adjusted between 10 [mm] gap to -5 mm pretention. The beam was connected to a silent shaker by a connecting threaded rod of M6 size (5). The rod was fastened by nuts (6 and 7) to both the beam and shaker. For further details about the setup design please refer to [11]. The experiments were performed in the modal laboratory at room temperature. Acceleration data were acquired from two accelerometers and impact force was collected by the impact hammer that held the counterpart. Data acquisition was done at 48 [kHz] sampling rate using SQuadriga II front end from Head Acoustics, as shown in Figure 2. One accelerometer was mounted at the impact point on the tip of the beam (8) and the other at the excitation point on the shaker (9).

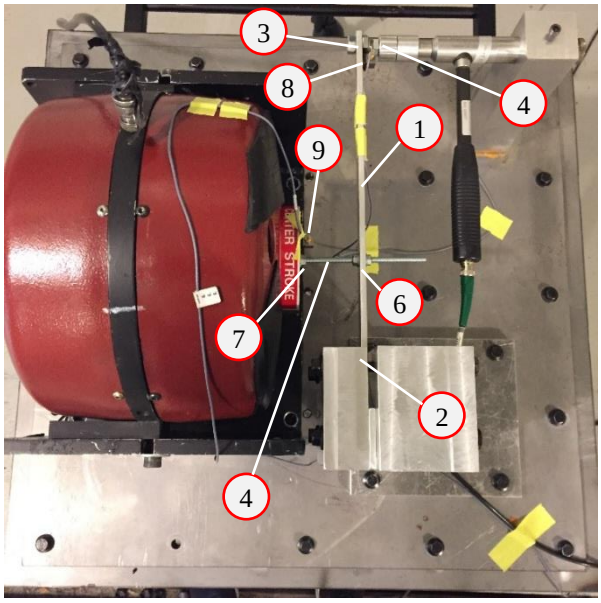


Figure 2: Rattle test setup

3.2 Setup virtual model

The finite element model was built as a representation of the physical test setup that had been developed for rattle sound studies. This model was used and evolved through the described model correlation steps in methodology section. It was a goal to have the simplest possible model, while keeping the required details in this model for sensitivity analysis of the interesting parameters. Simplicity in modelling will facilitate further industrial application of the findings from this work. The finite element model and the boundary conditions are presented in Figure 3 (left). The beam elements used to model the shaker connecting rod are shown by thick elements for the sake of better visibility. In Figure 3 (right), the impact area at the tip of the beam, where material samples are installed, is magnified. The following subsections detail the features of the baseline model upon which the parameter study, as described in section 4, was then performed.

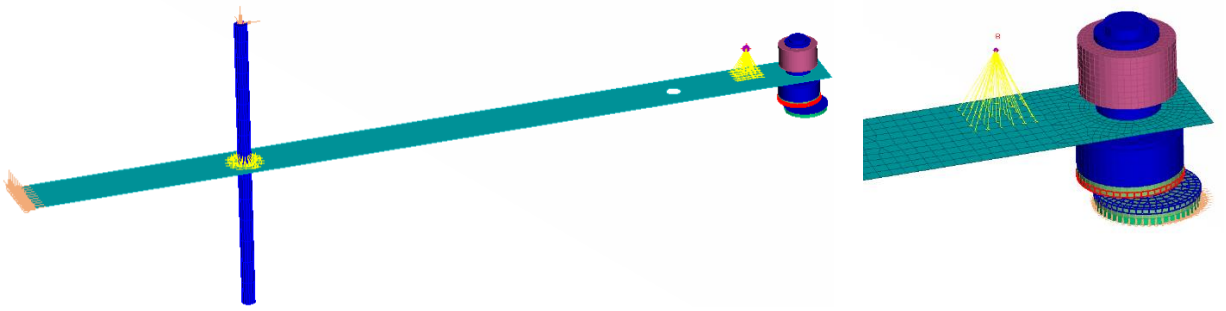


Figure 3: Complete finite element model of the setup (left) and impact area (right)

3.2.1 Mesh

The finite element model was built in Ansa software with a mixture of solid, shell and beam elements, all of them being first order. The mesh size varied between 1 and 2 mm. The type and size of elements were chosen based on similar models from the field of NVH. An aim was set to change these parameters, only if they were required for the sake of correlation with physical measurements. The model totally consisted of 1833 shell elements and 6350 solid elements and it was prepared for running the solutions with Abaqus solver. Below is a detailed explanation of the elements used for modelling different parts of the model. For information regarding the of element types please refer to [12].

- The beam was modelled with 2D shell elements (S3, S4). Using 3D elements gave no higher accuracy, while increasing the CPU time.
- The bolt and nut pair, holding the samples and the samples itself were modelled with 3D brick (C3D8) and Penta (C3D6) elements. Since small details of these parts were neglected, the density was scaled up to match the original mass.
- The threaded rod that connected the beam to the shaker was modelled with 1D beam elements (Abaqus B31).
- Small parts with negligible contributing geometry, like accelerometers and nuts of the shaker connector rod were modelled as point masses. The equivalent mass values were based on measurements and they were validated within the first steps of the model correlation to check if they properly represented the parts.
- The connection between the shaker connector rod and the beam was modelled with rigid elements. The mass point representing the accelerometer was connected to the beam with MPC boundary condition (multi-point boundary condition).

3.2.2 Boundary conditions

The boundary conditions in the model were defined accordingly to the experimental setup.

- The end of the beam at the support was constrained in all 6 DoF (Degrees of Freedom) since it was rigidly clamped in the test setup (point 2 in Figure 2).
- The nodes of the counterpart sample on the hammer side (point 4 in Figure 2) were constrained in all 3 DoF (solid elements were used for these parts). The effect of elasticity coming from the hammer support was investigated and was neglected due to its minor effect on the results.
- The shaker connector rod, at the end where it was fixed to the shaker (point 6 in Figure 2), was constrained in all DoF, except the Z direction, which was the excitation direction in the FEA model. The Z direction had a prescribed displacement as the input signal that will be discussed later.

3.2.3 Material and property cards

The finite element model consisted of three types of property cards. One shell property for the beam, describing its thickness of 6 [mm], solid properties with the corresponding material cards and the beam property for the shaker connector. For the beam, the material and cross sectional properties were also included in the property as: 7.85e-9 [t/mm^3] density, 2.5 [mm] radius of circular cross section, 210 000 [MPa] elasticity modulus and 80 796 [MPa] shear modulus.

Since the modelled part of the setup consisted of only steel and aluminium parts, two groups of materials were used. The steel with 210 000 [MPa] elasticity modulus and 0.3 [-] Poisson’s ratio, and varying density, as it was required to scale the mass of parts because of geometric simplifications. The baseline

density was 7.85e-9 [t/mm^3]. The aluminium parts had only one material property with 68 900 [MPa] elasticity modulus, 0.33 [-] Poisson's ratio and 2.609e-9 [t/mm^3] density. These values were based on 6061 aluminium alloy, and were validated by the eigenvalue analysis.

3.2.4 Contact modelling

In this study three main groups of contact interaction were employed.

- Contact pair surface definition with hard kinematic contact method.
- Contact pair surface definition with penalty contact method.
- General formulation with penalty contact method.

These contact interaction variations, as well as further contact interface parameters that were studied and considered during the parameter study will be explained in section 4.1.

3.2.5 Solver and settings

During the study two solvers were used [12]: Abaqus/Standard for the eigenvalue extraction, using the Lanczos method and extracting the first 10 modes; and Abaqus/Explicit was used for the time domain simulations. The stable time increments were chosen automatically based on the critical element in each increment. No mass scaling and other settings were used in the solver.

3.3 Eigenvalue analysis

As mentioned in the methodology section, a step-by-step approach was taken for model validation. In the first place, a modal experiment was performed while the connection rod between the beam and the shaker, as well as the impact counterpart were removed. The physical setup for modal experiment is depicted in Figure 4. An excitation in the form of an initial displacement was applied at the tip of the beam and the acceleration signals at the tip of the beam and the connection point to the rod in the free vibration event were recorded. Fourier transformation of the empirical acceleration data is shown in Figure 5 (up) and it can be observed that the fundamental eigenvalue of the beam was measured at 31.27 [Hz].

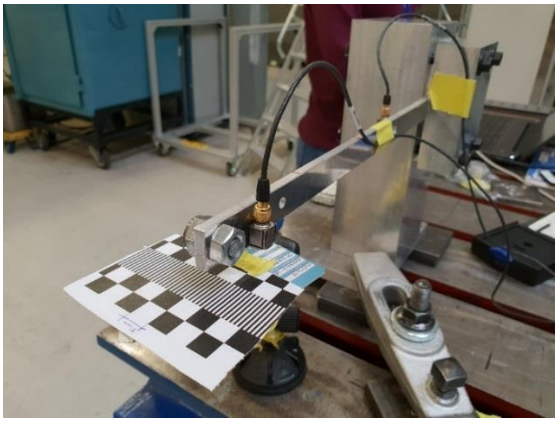


Figure 4: simplified setup for modal analysis

Similarly, an eigenvalue analysis was performed for the finite element model while the connection rod between the beam and the shaker was removed. First eigenmode of the beam, from finite element analysis results, is presented in Figure 5 (down) with the scale factor of 2. The fundamental frequency of the beam

was computed at 31.94 [Hz]. A good agreement between results of finite element modal analysis and experimental data was achieved with an error of 2.14 %. While conducting the modal correlation, where required model parameters like mass and mass distribution of simplified parts and Young's modulus and Poisson's ratio of the beam were calibrated.

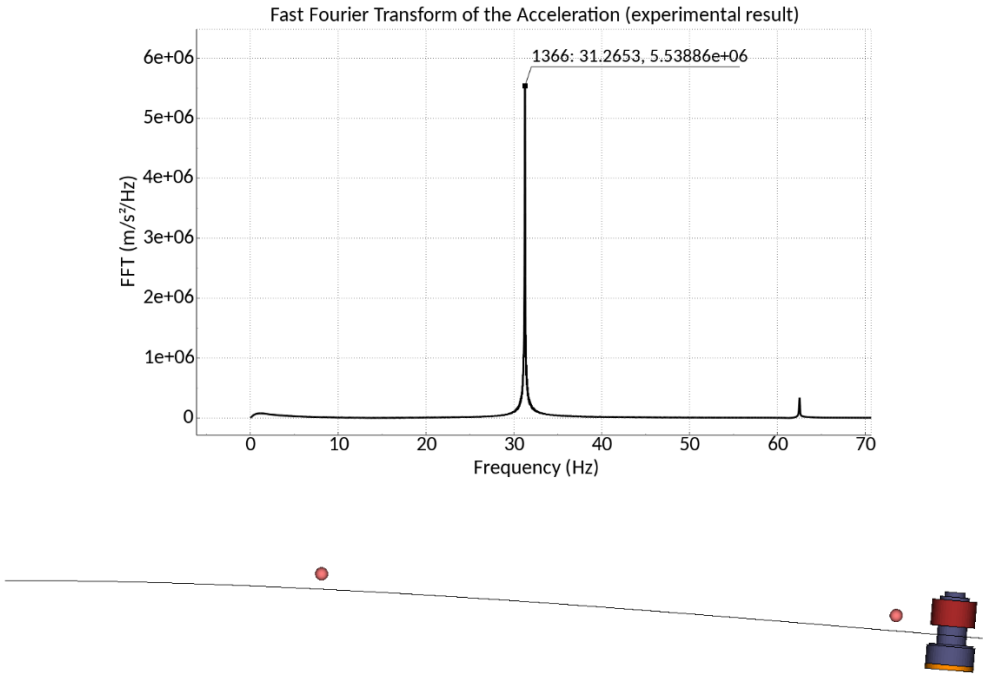


Figure 5: Experimental eigenvalue analysis result (up), First eigenmode from computer simulation with scale factor of 2 (down)

3.4 Model correlation in time domain

After analysing the modal behaviour of the disconnected beam from the shaker, dynamic behaviour of the system when exposed to shaker excitation was experimentally tested and simulated. The dynamic correlation in time domain was performed in two steps: firstly, for no impact condition and afterwards for impact events.

3.4.1 Time domain correlation before impact event

In the first step, the counter material insert was dismounted from the hammer tip and the system was exposed to a sine input of 10 Hz by the shaker. A single wavelength from the measured input sine wave at the shaker point was chosen as the input excitation signal for the computer simulation. The excitation signal, CAE result and experimental measurement for displacement at impact point are presented in Figure 6. Results show that the finite element model is capable of predicting the system response accurately. By having a closer look at the curves in Figure 6, a shift of 1.7 [milliseconds] in time can be seen between the experimental data and simulation results. The source for this difference could be the simplified modelling details. The boundary condition at the connection point of the beam to the shaker rod showed to have an impact on the shape of the displacement curve. Specifically, a connection with low stiffness at this point could lead to a buckling behaviour of the rod, which was reflected as some breakpoints and distortion in the displacement curve at the tip of the beam. The other source for this difference could be the difference in input signal, since in simulation the input signal was defined in the form of a displacement curve that was calculated from measured acceleration data. This will be discussed further in section 3.4.2. However,

for the purpose of performing a parameter study and sensitivity analysis, the shape of system response agrees with the experimental data. In fact, the CAE model was capable of capturing the interesting response details that were needed for the parameter study as will be introduced in section 4.2.

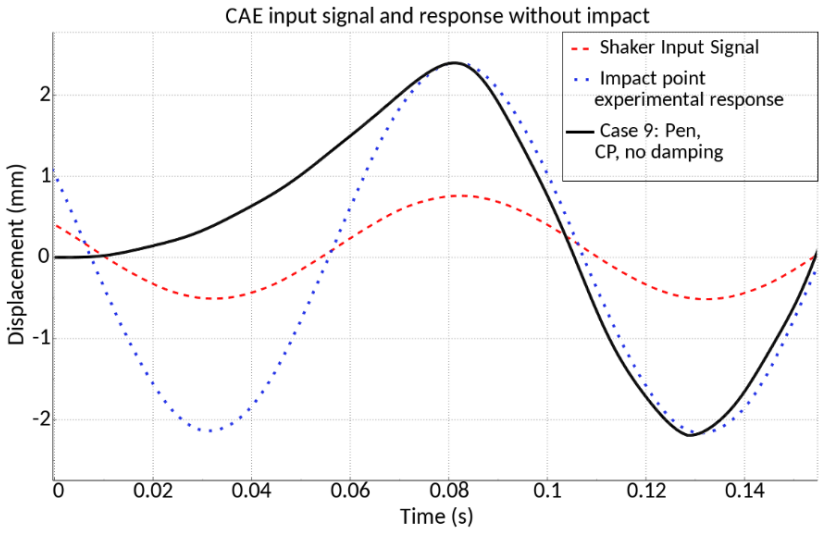


Figure 6: excitation signal, CAE (case 9 in Table 1) result and experimental measurement for displacement at impact point

In section 3.4.2, the signal processing approaches used to minimise the effect of noises on the calculated displacement from measured acceleration signals, are described.

3.4.2 Signal processing

In experiment, accelerometers were used to measure acceleration data at shaker connection point and tip of the beam (points 3 and 9 in Figure 2). The displacement data were obtained by double integrating the acceleration data. This caused introduction of a drift in the displacement curves as a result of accumulated errors imposed by noises present in the measured data. The noise sources could be electromagnetic interferences in the test environment between the measurement cables, data acquisition device, power sources, shaker amplifier and the shaker itself, the impact hammer used for measuring the force data and computers used in the experimental event. Different signal processing approaches were employed to avoid drift in calculated displacement signals as a result of accumulated errors. After trying several filters, omega arithmetic method proved to give the best results with the least drifted and distorted data.

- Mean removal only removed the DC offset, but the signal had a varying drift.
- 3rd order high-pass Butterworth filter could remove the drift, but distorted the shape of the signal near impacts and introduced phase shift.
- Moving average filter (high pass filtering) gave the second best result, but still resulted minor drift
- Finally, the omega arithmetic method [13], which allows the elimination of unwanted frequencies in the frequency domain before transferring the signal to the time domain again, was found to be the best solution. By eliminating the frequencies causing the obvious distortions in the time domain curve, displacement signals without drift were obtained.

In order to speed up the simulations for parameter study, the starting point of the input signal was taken at a time instance close to the first impact and directly before the last “no impact inducing” cycle. To avoid a “jerk” at the beginning of the simulation, the input signal was smoothened at the start by a sine wave with a local minimum at zero. Using a MATLAB script, it was secured that there was no breakpoint in derivative (velocity) and double derivative (acceleration) of the resultant signal at the joint between the

measured signal and the sine wave. Finally, in order to make the data handling easier, the signal was downsampled to one seventh of the original sample rate, 6.86 [kHz]. This signal was used for both the validation and parameter study purpose.

3.4.3 Time domain correlation for the impact event

As the next step for validating the finite element model, the same 10 Hz sine input signal, as presented in Figure 6, was applied to the model, by including the impacting pairs. In Figure 7, system response for a wavelength of the results from the experiment and simulation are illustrated. The results for simulation are plotted for different initial gaps between the impacting pairs. As stated before, the rattle producing test machine was built in a way to allow changes in initial mounting gap between the two samples, in order to study the different mounting interfaces in a car cabin. In the apparatus, gap adjustment was done by a bolt gage mechanism. Therefore, the accuracy of the resulted gap was not less than 0.1 [mm]. This could result in a deviation from the nominal gap. This uncertainty source, in addition to the uncertainties imposed by signal measurement, filtration and finite element modelling uncertainties resulted in a deviation in absolute displacement results between the experimental data and simulation results. This can be seen in Figure 7. To investigate sensitivity of the system with respect to gap variation, displacement at impact point for different installation gaps (2.3, 2.4 and 2.5 [mm]) were simulated. The model setup for this simulation was similar to case 9 of the parameter study in Table 1 (section 5). By looking at the curves in Figure 7, although the simulation results show a deviation from measured data, it is observed that the finite element model is capable of predicting the shape of the signal at the impact point compared to the experiment. As discussed before, different sources of uncertainty in data acquisition, signal processing and virtual modelling could cause this deviation. Considering the fact that the model is capable of capturing impact response details that were used in the parameter study, which is describe in detail in section 4.2, it was assumed that the virtual model was valid enough for performing the sensitivity analysis.

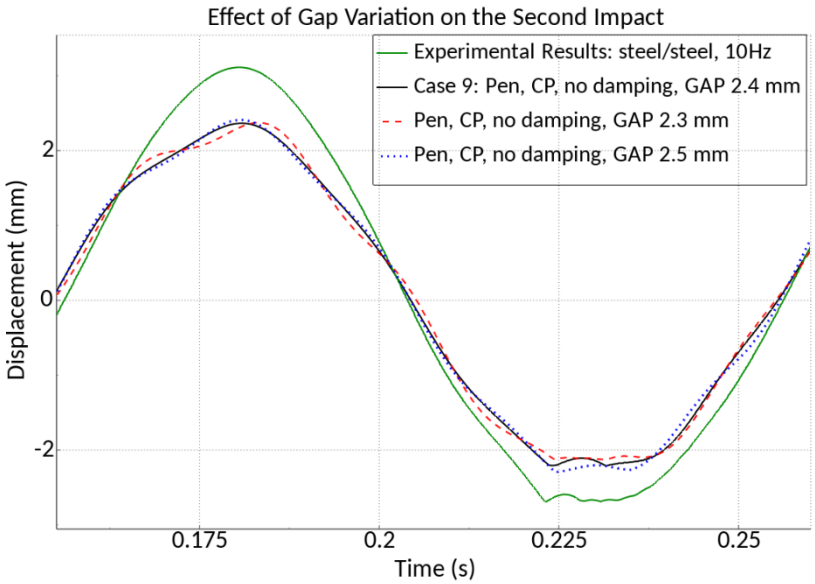


Figure 7: System response for an impact event: experimental vs simulation (case 9 in Table 1) for varied gaps of 2.3, 2.4 and 2.5 [mm].

4 Parameter study in contact interface

In order to identify the effect of parameter variations in contact interface on system response, a parameter study was planned and performed.

4.1 Nominated parameters and the ranges

The model parameters investigated throughout the parameter study are listed in the left section of Table 1. Following is a description of these parameters.

4.1.1 Contact interaction definition

Two different definitions of 'contact pair' and 'general contact' were studied in the parameter study. Contact pair surface definition requires the user to manually select the surfaces that are expected to come in contact. Whereas, the general contact formulation allows the definition of an area of, or the whole, model and locates any contact within that region as the simulation runs.

4.1.2 Contact mechanics

Contact mechanics were chosen either in the form of 'hard kinematic' or 'penalty contact'. Hard kinematic contact method "uses a kinematic predictor/corrector contact algorithm to strictly enforce contact constraints (for example, no penetrations are allowed)" [12]. Penalty contact method searches for penetrations and applies forces, which are calculated as a function of penetration, to the slave nodes to eliminate penetration.

4.1.3 Damping

During the study, damping was studied in two different ways. Rayleigh damping was defined for the material card of the beam. Three different options were investigated: one with no damping; one damped model with only mass-proportional part of Rayleigh damping; and one only with stiffness-proportional part of Rayleigh damping. The mass-proportional damping coefficient was calculated from the damping ratio captured during the eigenvalue test described in section 3.3, giving a value for α of 0.8418. The stiffness proportional damping was calculated as 5% of the target time step based on a suggestion in [14], giving a value for β of 6.627e-9. The other employed damping type was contact damping and it was given as a fraction of critical damping coefficient between 0 and 0.2.

4.1.4 Small sliding

The effect of small sliding formulation was also studied. In case of employing this option, the pairing of dependent and independent nodes takes place only once per increment, opposed to the default setting where it is done for every iteration. This should speed up the computation run time, but should only be used for contacts with small relative lateral motion, which was the case in this study [12].

4.1.5 Friction

Friction at the contact interface was also investigated. A simple Coulomb friction with a coefficient of 0.2 was included in the parameter study.

4.2 Evaluation criteria

In order to perform the sensitivity analysis, metrics formulated based on the kinematic and kinetic response of the system around the impact time were defined and used. These metrics were defined based

on the previous studies [10] on correlation between impact sound and impact dynamics and are described below.

4.2.1 Peak impact force

The absolute value of the impact force contributes to the impact power and relates to impact momentum and acceleration. These parameters all affect the peak sound pressure of generated sound [10]. Therefore, the peak impact force was chosen as an evaluation criterion.

4.2.2 Impact power

It was stated [10] that relative impact velocity between the impacting bodies relates to peak flow velocity of the sound wave. In addition, both impact momentum and acceleration correlate well with peak sound pressure. Resultantly, impact power formulated as impact force times impact velocity was taken as a metric from the system response. In fact, this metric equals to multiplication of impact momentum by acceleration.

4.2.3 Ratio of height of bounce to impact velocity

Another phenomenon that influence the generated impact sound is the bouncing effect at an impact event [10]. To study the bounce characteristics just after the impact, height of the bounce was chosen as an evaluating response parameter. In order to track and compare the changes of bounce characteristics among different run cases, it was decided to normalise the bounce height with respect to the impact velocity. This way, the shape of the bounce can be compared throughout parameter study independent from varying impact velocity.

4.2.4 Frequency of biggest bounce

Similar to height of bounce at an impact event, the duration of the bounce denotes the shape of it as well. The bouncing frequency for the first bounce was calculated and listed as an evaluation criterion.

5 Results of the parameter study and discussion

Results of the parameter study are summarised in Table 1. The left part of the table gives the nominated parameters and their levels in each run case. On the right side of the table, the calculated values for the evaluation criteria are given. For the sake of readability, the following abbreviations are employed in the presented results and in the result discussion.

- Contact definition: Contact Pair (CP), General contact (Gen)
- Contact mechanics: Kinematic (Kin), Penalty (Pen)
- Rayleigh damping: stiffness component(Stiff), mass component (Mass)
- Contact damping [value of critical damping fraction]: Con [value]

Case number	Contact definition: CP: contact pair, Gen: General contact	Contact mechanics: Kin: Kinematic, Pen: Penalty	Damping Stiff: Rayleigh, stiffness component Mass: Rayleigh, mass component Con [value]: contact damping with a critical damping fraction	Small Sliding	Friction: with friction coefficient of 0.2	Frequency of biggest bounce [Hz]	Ratio of height of bounce to impact velocity [mm/mm/s]	Peak impact force [N]	Impact power = Impact force times impact velocity [N.mm/s]
1	CP	Kin		×	×	244.50	0.001254	105.90	8969.54
2					×	243.31	0.001255	105.30	8918.29
3			Stiff			242.72	0.001275	88.34	7438.86
4				×		243.31	0.001324	88.31	7434.48
5						242.13	0.001324	87.88	7387.63
6*						242.72	0.001322	87.88	7397.47
7			Mass			245.70	0.001375	85.70	7195.45
8	CP	Pen	Stiff; Con [0.2]		×	244.50	0.001289	82.54	-6982.52
9						241.55	0.001164	71.64	-6138.49
10			Stiff			241.55	0.001154	71.67	-6143.95
11			Con [0.05]			241.55	0.001164	71.64	-6139.00
12			Con [0.1]			241.55	0.001163	71.64	-6140.12
13			Con [0.2]			241.55	0.001161	71.64	-6142.09
14			Mass			242.72	0.001284	69.24	-5929.06
15					×	264.55	0.001280	82.58	-6870.29
16	Gen	Pen				246.31	0.001390	84.21	-7098.09
17			Stiff			245.70	0.001366	84.34	-7168.12
18			Mass			243.31	0.001299	81.02	-6904.45

Table 1: Parameter design space and system response from sensitivity analysis of the contact model. * In case 6, contact interface was defined by a nodal surface against an element face.

In Table 1, cases are clustered for the three sets of contact type combinations: [CP + Kin], [CP + Pen] and [Gen + Pen]. In general, it is observed that the peak impact force and the impact power (in absolute value) are lowest for [CP+Pen] and highest for [CP+Kin]. It can also be seen that ratio of height of bounce to impact velocity and bounce frequency is the lowest for [CP+Pen] but higher in the two other combinations. By looking at the effect of adding 'small sliding' (in cases 1 and 4), no significant influence is detected. However, results in Table 1 indicate that including friction in contact interface has a significant impact on the system response. If cases 9 and 15 with the only difference in contact friction are compared, 15.27% higher peak impact force and 11.92% higher impact power when friction is introduced (case 15) are detected. The same applies for cases 2 and 5, where the difference for peak impact force and impact power is 19.82% and 20.72% higher in presence of friction, respectively. Moreover, including contact friction gives the highest peak impact force and impact power in each set of combinations ([CP + Kin] and [CP + Pen]).

In this parameter study, contact interaction was defined between two element faces at the contact interface. However, it is possible to define a contact interface by a nodal surface against an element face. This was investigated in case 6 for [CP+Kin] combination. The results indicated no significance impact

when nodal-element contact interaction was used. Therefore in the parameter study, only element-element contact interactions were considered. In cases 11, 12 and 13, the critical damping fraction of 0.05, 0.1 and 0.2 were added as the contact damping in [CP+Pen] combination. Results show that adding contact damping did not change the response metrics chosen for response evaluation purpose.

In order to study the effect of adding damping to the model, a comparison is made for the results from cases with and without damping as presented in Table 2. For each combination, the stiffness and mass components of Rayleigh damping were added to the model and system response was calculated. With adding Rayleigh mass damping (cases 7, 14 and 18), the peak impact force and impact power are respectively 3.21% and 2.91% lower compared to no damping condition (cases 5, 9 and 16). On the other hand, the ratio of height of bounce to impact velocity and bounce frequency increases by introducing mass component of Rayleigh damping in cases with 'contact pair' definition. Whereas, in cases with 'general contact' interaction the effect is adverse. Rayleigh stiffness damping (cases 3, 10 and 17), has negligible effect on peak impact force, impact power and bounce frequency. While when it comes to the ratio of height of bounce to impact velocity, the stiffness damping has a relatively bigger effect, always producing a lower ratio. In fact, the case that include Rayleigh mass damping, give the lowest peak impact force and impact power in each set of combinations.

Case Number	Contact definition (CP: Contact Pair, Gen: General Contact, Kin: Kinematic, Pen: Penalty)	Rayleigh Damping (Stiff: stiffness component, Mass: mass component)	Frequency of biggest bounce [Hz]	Difference percent %	Ratio of height of bounce to impact velocity [mm/mm/s]	Difference percent %	Peak impact force [N]	Difference percent %	Impact power [Nmm/s]	Difference percent %
5	CP+Kin		242.13		0.001324		87.88		7387.63	
3		STIFF	242.72	+0.24	0.001275	-3.67	88.34	+0.52	7438.86	+0.69
7		MASS	245.70	+1.47	0.001375	+3.88	85.70	-2.48	7195.45	-2.60
9	CP+Pen		241.55		0.001164		71.64		6138.49	
10		STIFF	241.55	0.00	0.001154	-0.91	71.67	+0.04	6143.95	+0.09
14		MASS	242.72	+0.48	0.001284	+10.25	69.24	-3.35	5929.06	-3.41
16	Gen+Pen		246.31		0.001390		84.21		7098.09	
17		STIFF	245.70	-0.25	0.001366	-1.75	84.34	+0.15	7168.12	+0.99
18		MASS	243.31	-1.22	0.001299	-7.06	81.02	-3.79	6904.45	-2.73

Table 2: Impact response sensitivity analysis for introducing Rayleigh damping in FE model. The percent difference for each response metric is calculated with respect to the corresponding no damping condition

The displacement results for all cases in the parameter study are illustrated in Figure 8. It can be observed that how each parameter variation can affect the shape of the displacement curve at vicinity of impact point. To find the parameter variation details for each case in Figure 8, please refer to Table 1.

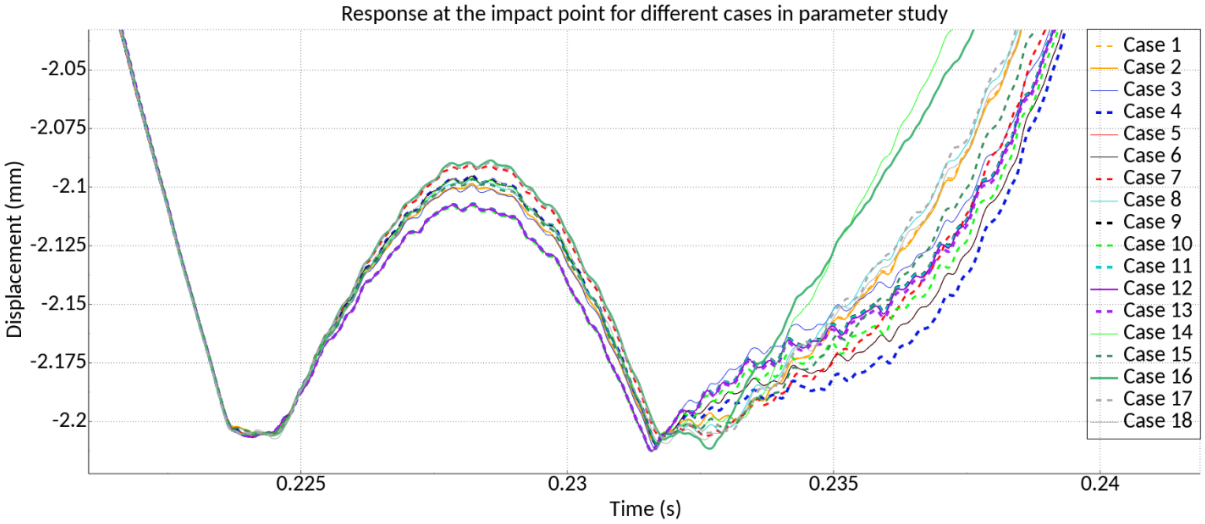


Figure 8: Displacement results at impact point for all cases in parameter study from simulation. To realise model details for each case please refer to Table 1.

6 Conclusion

In this research a parameter study was performed on the model parameters of a nonlinear finite element model aiming at identifying the important contact parameters contributing to the system response. The evaluation criteria were chosen as response metrics that relate to generated impact sound. It was shown that using the contact interaction in the form of 'contact pair' combined with 'penalty' method results in lowest response values compared to other contact interaction combinations, while combination of 'contact pair' and 'hard kinematic' gives the highest response values. Moreover, it was detected that including friction in damping interface has a significant impact on the results. In addition, it can be concluded that introducing Rayleigh mass damping in the finite element model, gives the lowest peak impact force and impact power in each set of combinations considered in the parameter study. In contrary, the ratio of height of bounce to impact velocity and bounce frequency increases by introducing mass component of Rayleigh damping in cases with 'contact pair' definition. It can also be seen that including 'small sliding' or 'contact damping' in contact interface or adding stiffness component of the Rayleigh damping to the model did not affect the system response considerably.

It is of importance to mention that during the validation loop for virtual model with respect to empirical data, some uncertainty sources were identified and proved to introduce errors in experimental data analysis and computer simulation results. However, it was decided to continue the parameter study work with the virtual model, since the model proved to be capable of capturing the response trends, although there were discrepancies in the absolute results.

The authors are currently continuing the work by conducting a similar study for a shell mesh model of the test setup instead of the solid model that was used in this work. Furthermore, similar studies will be performed by adding other dimensions to the parameter study, like doing the sensitivity analysis for other metallic and non-metallic material pairs, initial contact gap and pretention conditions, as well as applying different sine and stochastic input signals for system excitation. For the purpose of verifying the findings of this research, the proposed conclusions will be tested for a car subsystem. This will be done by nonlinear finite element modelling of the subsystem and comparing the results with experimental data

The evaluation criteria in this study were defined based on the literature. In order to get more reliable results, a future research on how impact sound is related to impact dynamics will be required. Furthermore, it will be invaluable to investigate the uncertainty sources more and repeat the study with the calibrated virtual model. In addition, performing the parameter study with other solvers for the contact problem and comparing the results with this work to check the accuracy, robustness and performance of the modelling approach will be valuable.

The findings of this research can be used when approaching nonlinear simulation of rattle events in car cabin. Simulating impact in rattle events by modelling contact in finite element method, enables the estimation of response metrics to be done with higher accuracy. This will in turn, result in an enhanced capability in predicting and treating rattle events by virtual models upfront in product development phases.

Acknowledgements

The work was carried out in Volvo Car Corporation in Gothenburg, Sweden. The authors would like to gratefully acknowledge the help from engineers and staff in modal and durability labs for the support during the experimental studies.

References

[1] W. D. Appel, *Aspects of Frameless Car Design*, SAE Technical Paper 390184 (1939).

[2] M. Trapp and F. Chen, *Automotive buzz, squeak and rattle : mechanisms, analysis, evaluation and prevention*, Butterworth-Heinemann/Elsevier (2012).

[3] F. Kavarana and B. Rediers, *Squeak and Rattle - State of the Art and Beyond*, SAE Technical Paper 1999-01-1728 (1999).

[4] J. Her, S.-R. Hsieh, W. Li, and A. Haddow, *Quantitative Prediction of Rattle in Impacting System*, SAE Technical Paper 972059 (1997).

[5] J. M. Choi, S. J. Lyu, Y. S. Seol, I. K. Jun, and C. Yi, *A BSR Analytical Evaluation Method Considering the Sound Quality Perception*, SAE Technical Paper 2013-01-1913 (2013).

[6] E. Caamaño, I. Lama, A. Rousounelos, and J. Viñas, *Improved Methodology For Squeak & Rattle Analysis With Abaqus And Correlation With Test Results*, in *SIMULIA Customer Conference* (2011).

[7] J. Weber and I. Benhayoun, *Squeak & Rattle Correlation in Time Domain using the SAR-LINE™ Method*, SAE International Journal of Passenger Cars - Mechanical Systems, Vol. 5, No. 3, SAE International (2012), pp. 1124–1132.

[8] H. Daams, *Squeak and Rattle Prevention in the Design Phase Using a Pragmatic Approach*, SAE Technical Paper 2009-26-0051 (2009).

[9] A. Ramanathan, S. Noll, E. Dehoff, and R. Rittenhouse, *An Investigation into Modeling Approaches for the Dynamic Response of a Shipping Container Cart and Suspended Automotive Parts Under Random Base Excitation using LS-DYNA ®*, in *11th European LS-DYNA Conference* (2017).

[10] A. Akay, *A Review Of Impact Noise*, The Journal of the Acoustical Society of America, Vol. 64, No. 4, Acoustical Society of America (1978), pp. 977–987.

[11] A. Svensson and J. Hasselström, *Fundamental physical testing of rattle - Design and evaluation of a rattle producing test rig*, Chalmers University of Technology, Göteborg (2017).

[12] *Abaqus 16.4 Documentation*, Dassault Systèmes Simulia Corp. (2016).

[13] C. Mercer, *Acceleration, Velocity and Displacement Spectra – Omega Arithmetic*, Prosig Signal Processing Tutorials (2006).

[14] *RADIOSS 2017 Documentation*, Altair Hyperworks (2017).

Alternative lamination stacking technique of stator cores for improved structural damping of electric machines

F. Chauvicourt [1,2,3], **C.T. Faria** [1], **J.C. Gyselinck** [3], **H. van der Auweraer** [1,2], **W. Desmet** [2]
[1] Siemens Industry Software NV
ResearchPark 1237, Interleuvenlaan 68, 3001 Leuven
e-mail: **fabien.chauvicourt@siemens.com**

[2] KU Leuven, Department of Mechanical Engineering (PMA)

[3] Université Libre de Bruxelles, Department of Bio, Electro And Mechanical Systems (BEAMS)

Abstract
The search for cheaper bring the industry to consider permanent magnet less or even free electrical machines. However extremely high and prohibitive level of acoustic noise might occur from these designs due to the large magnetic forces acting on their stator, essentially due to stator core resonance phenomena. Being axially laminated, the stator core shows non trivial mechanical behavior. The frictional contacts between laminations play a significant role in the energy transfers inside the entire core. Hence they give the possibility to tune the manufacturing and stacking process of the core to dissipate this energy. Firstly, a novel lamination stacking technique is thoroughly hypothesized. Then experimental validations jointed with result significance evaluations are carried out and show damping capabilities of critical modes responsible for high vibrations and acoustic noise of electric machines. The hypotheses made earlier to motivate the implementation of the novel stacking technique are finally validated and confirm the potentials of the technique.

1 Introduction

The growing interests in electrification of transportation to cope with the new regulations imposed, bring the need for cheaper designs. In particular the powertrain has lately been extensively studied to that purpose. Eventually rare-earth free electrical machines are good candidates to reduce manufacturing cost, and research activities follow this trend [19]. However, those designs might show higher levels of acoustic noise compared to conventional designs already used in current Electric Vehicles (EV). Several noise categories define the signature of an electric machine noise: aerodynamic, mechanical, electronic and magnetic [8, 26]. But because of its tonal characteristic, the latter is often considered to be the major contributor to unappreciated sound.

It is caused by an electro-magneto-mechanical phenomenon, largely studied in literature [8, 24, 7]. The rotating magnetic flux density induced at the air gap of the machine produces magnetic forces acting on the stator teeth. These time-varying forces excite the stator that consequently vibrates and generates acoustic pressure waves that travel outwards through the air, i.e. sound is produced. Hence the signature of this noise depends directly on the force profile and the vibrating transfer structure. Design optimization for noise mitigation can therefore be addressed from the source side (force) and/or from the transfer side.

Important features of the radiated magnetic noise typically include order lines and resonance phenomena [12]. The order lines represent high amplitudes which frequency vary with the rotational speed. They are directly related to the current profiles which fundamental and sub-harmonics are affected by several features

such as machine geometry, topology, number of phases, etc. The resonance phenomena however show high amplitudes at fixed frequencies, independently of the rotational speed, which indicates a correspondence to structural mode vibration of the system [15]. Any structure can be decomposed in an infinite set of orthogonal modes that have unique shape (space distribution) and frequency (time distribution). In the case when both space and time distribution of the magnetic forces and modes match, large levels of vibration and acoustic occur, one refers to as resonance phenomenon. From a psycho-acoustic point of view, these induced high tonal noises can be perceived quite annoying [13].

Several solutions can be adopted address this problem. Part of which, one has degrees of freedom on the current waveforms that can be optimized [21, 22] through control refinements and/or machine topology optimization. Optimum number of rotor poles and stator slots can also change drastically the acoustic behavior of a machine [10]. Rotor/stator skewing are common methods to reduce acoustic noise; in the first case it shapes the forces such that the modes are not excited, and in the second case it affects the mode shapes which are not activated by axially-independent forces [30, 6]. Furthermore machine efficiency is reduced by skewed designs, which has to be avoided in general. Overall, these techniques can be beneficial but with the high constraint of re-optimizing the control algorithms due to changes in machine concept design.

In this paper, an alternative solution to resonance mitigation is proposed and benefits from not changing the concept design of the electric machine, thus not increasing design costs. It proposes a novel lamination stacking technique that permits to reduce resonance vibration of targeted modes from the laminated stator core. It essentially uses a different distribution of welds that permits to enhance vibration damping phenomena. Section 2 explains and formulates hypotheses why this technique should improve structural damping. Section 3 describes the experimental campaign carried out to prove the concept, and Section 4 presents the experimental results, with a particular emphasis on validating and/or invalidating certain hypotheses priorly made.

2 Methodology

2.1 Fundamentals of structural dynamics

A linear vibrating structure transferring energy from an exciting source to the surrounding medium (e.g. air) can be uniquely characterized by three modal characteristics: the mode shape $\{X_k\}$, the natural frequency ω_k and the modal damping ratio ξ_k. A finite number of Frequency Response Functions (FRF) representative of vibration paths relating an input source to output vibrations, permit to build the transfer function matrix $[H(\omega)]$ derived as [9],

$$\begin{aligned} [H(\omega)] &= \sum_{k=1}^{N} \frac{[A_k]}{j\omega - \lambda_k} + \frac{[A_k]^*}{j\omega - \lambda_k^*} \\ \text{where} \quad \lambda_k &= -\xi_k\omega_k + j\sqrt{1-\xi_k^2}\omega_k \end{aligned} \tag{1}$$

where the terms $[A_k]$ and $[A_k]^*$ are the residues which depend on the scaling factor Q_k and the modal vectors $\{X_k\}$,

$$\forall k \in [1..N], \quad A_k = Q_k\{X_k\}\{X_k\}^t \tag{2}$$

The output displacement $X(\omega)$ which is the forced response to harmonic excitation is simply derived from the multiplication of the FRF matrix $[H(\omega)]$ with the excitation force vector $\{F(\omega)\}$. First it is clear that in the case of harmonic excitation $F(\omega)$ at frequency $\omega = \omega_k$, a large response $X(\omega = \omega_k)$ is generated when damping is low: referred to as resonance. Second, it is interesting to note that the columns of $[A_k]$ are proportional to each other, i.e. each column j is sufficient to reconstruct the full matrix, except if this column

coincides with a null modal coefficient $\{X_k\}_j$ [9]. The corresponding row and column of $[A_k]$ will then be zero. This presupposes that a mode cannot be detected if the excitation is applied at a node point (null modal vector coefficient) of a mode. Generally the modal participation factor matrix $[L]$ is defined,

$$[L] = [Q_1\{X_1\} \ldots Q_N\{X_N\} \quad Q_1^*\{X_1\}^* \ldots Q_N^*\{X_N\}^*]^t \tag{3}$$

It is a measure of the excitation efficiency of each DOF for each mode, and can be used extensively to know the best excitation location to (de)activate certain modes. Ultimately, the resonance effect coming from the match of the force distribution with the modal characteristics of the structure is attenuated by large modal damping values. As such, dedicated damping strategies are welcome for reducing the acoustic noise radiation.

2.2 Application to the laminated stator core

Resonance phenomena that occur in rotating electric machines essentially come from structural mode excitation and can be particularly annoying due to their tonal characteristics at high frequencies, i.e. at the order of a few kilo Hertz. In general, it is agreed that the modal characteristics of an electric machine for EV application are dominated by the laminated stator core [8, 29, 28, 18].

As being very close geometrically to thick cylinders, the stator cores have similar modal characteristics, including mode shapes. They are commonly defined by particular combinations (n_r, n_z) of radial mode order n_r and axial mode order n_z. Besides there exist modes with azimuthal, torsion, shear and axial deformations but usually do not contribute significantly to the acoustic noise of a machine. For instance, the first flexible mode shapes (n_r, n_z) are illustrated in Fig. 1. Two sets of highly recurring modes are referred to as the pure radial $A(n_r, 0)$ and radial with transverse anti-symmetry $B(n_r, 1)$ modes. For the sake of consistency, symmetries are defined as follows: the axial symmetry represents the symmetry around the z axis, and relates to the independence of the object parameter upon azimuthal direction θ, the radial symmetry represents the condition of having similar object parameter parts regularly arranged around the central axis z, and the (perpendicular) transversal symmetry is the symmetry related to the middle plane parallel to the cross-section of the stator core.



(a) Undeformed stator core (b) $B(0,1)$ (c) $A(2,0)$ (d) $B(2,1)$



(e) $A(3,0)$ (f) $B(3,1)$ (g) $A(4,0)$ (h) $B(4,1)$

Figure 1: Illustration of the typical modes of an stator core (n_r, n_z)

Because of their occurrence at the lowest frequencies, their transversal symmetry similar to the force excitation and the fact that they are acoustically efficient, the pure radial modes $A(n_r, 0)$ are generally the most critical modes responsible for high acoustic noise from resonances. However, for the exact same stator geometry, reducing the stator vibrations at the corresponding resonances is not trivial. Damping which plays a significant role in the output vibrations and acoustic pressure of the system, is hard to be estimated by computational means since it involves a variety of unquantifiable phenomena e.g. friction, viscous damping [1].

But in the case of the stator core, the structure is composed of hundreds of thin lamination (steel sheets) that are attached through different stacking techniques. One common approach is to glue the laminations

together [5]. A second approach consists in welding the sheets along different lines to attach them together [5]. These manufacturing techniques can affect the output vibration responses, as it was shown in [23]. Based on physical insights and engineering thinking, three hypotheses are formulated here to explain the phenomenon when comparing glued stators with welded stators.

Hypothesis 1: a change in stiffness distribution. The welding event during manufacture of the core involves very high temperatures, hence inducing residual stresses σ_{res} at the welding locations. These residual stresses tend to attract the core yoke back to its equilibrium position. Fig 2 shows these effects for pure radial deformations of modes $A(2,0)$ and $A(3,0)$, while Fig. 3 shows the phenomenon for the anti-symmetric mode $B(2,1)$. The residual stresses have a stiffening effect which depends on the welding distribution, and thus can generate vibration amplitude reduction if large stiffness variations are developed.

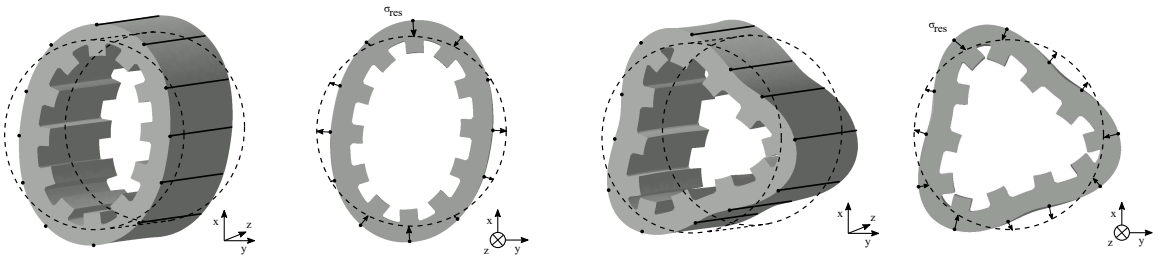


Figure 2: Residual stresses effects on mode $A(2,0)$ (a) and $A(3,0)$ (b)

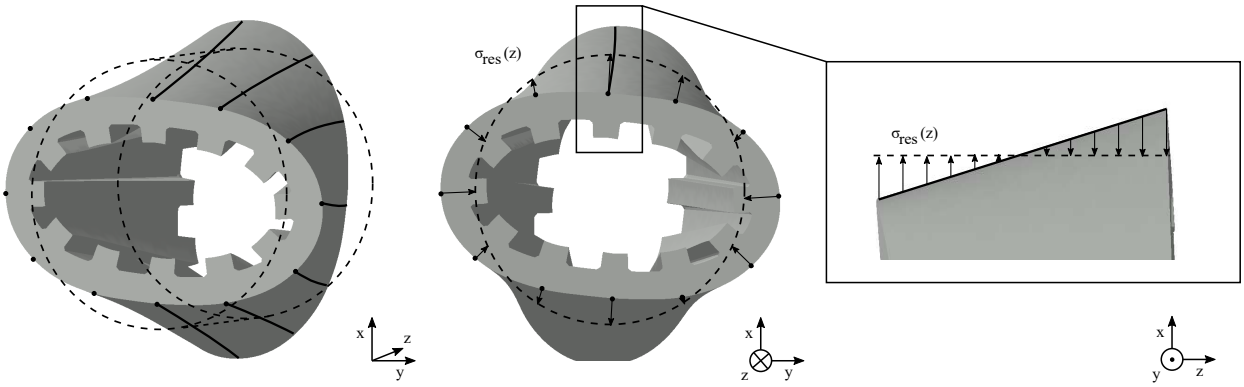


Figure 3: Residual stresses effects on mode $B(2,1)$

Hypothesis 2: a change in inter-laminar contact nature. When comparing welding to gluing, there is a significant difference in the contact properties of neighboring laminations, referred to as inter-laminar contact. Viscous damping is induced within the contact area for glued stators, as depicted in Fig. 4a, and glue compound is subjected to shear, thus inducing vibration damping. For the welded stators, Coulomb (or friction) damping is activated via sliding friction between laminations [14], as shown in Fig. 4b. It is important to note that these phenomena should only happen when there is relative motion of the neighboring laminations, i.e. mainly accentuated for $(n_r, 1)$ modes. On the other hand for $(n_r, 0)$ modes, the laminations deform in phase with each other such that it does not activate this friction, as depicted in Fig. 5.

Hypothesis 3: a change in mode shape. The change in stiffness distribution due to welding events, (related to hypothesis 1), also has a direct impact on the mode shapes, which immediately affects the transformation of the exciting force wave to the modal domain. This relates to variations in the modal participation factor from Eq. (3), ultimately translated as vibration reduction at resonances.

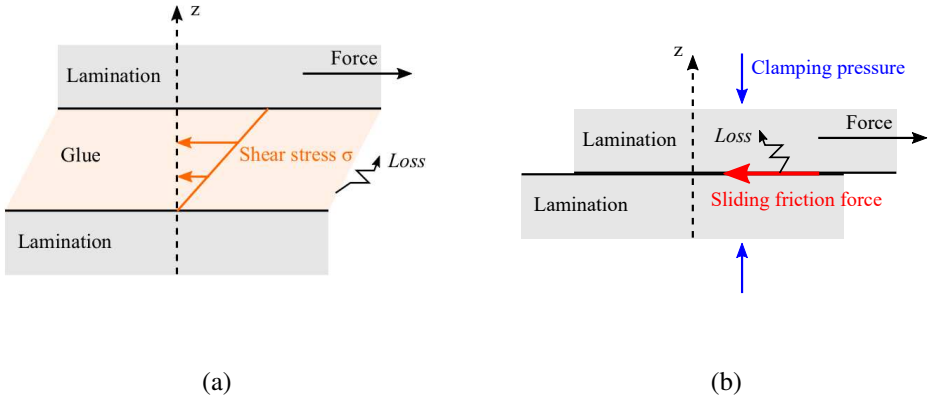


Figure 4: Illustration of viscous (a) and Coulomb (b) damping in the case relative displacement occurs

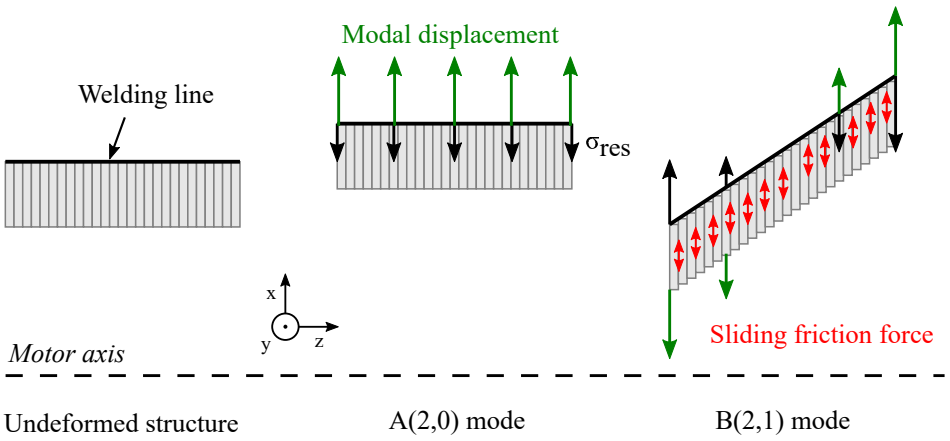


Figure 5: Illustration of the damping occurrence for specific modes - NB: Vector amplitudes are informative

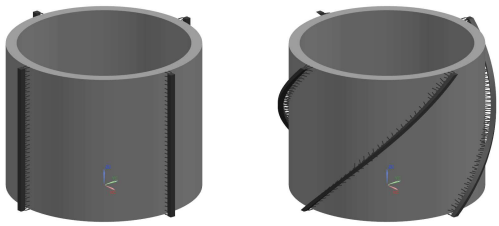
2.3 Alternative solution description

Based on the three hypotheses formulated in the previous Section 2.2, and recognizing the importance of reducing resonance from pure radial mode vibrations as mentioned in Section 2.2, an alternative solution can be expressed further. Since the ultimate purpose is to damp resonance phenomena coming from vibrations of pure radial modes (which are transversally-symmetric), the idea of the proposed technique is to introduce manufacturing asymmetry to the geometrically symmetric laminated stator core. Although it might involve different attachment techniques (gluing, welding, interlocks), skew welding lines along the shaft axis of the machine are proposed and implemented in this paper as it is an interesting and alternative manufacturing example of bringing asymmetry, yet holding the laminations together. This original stacking technique is pictorially compared to the common welding approach in Fig. 6.

This stacking technique is expected to reduce vibrations of $A(n_r, 0)$ modes for the three reasons enumerated previously. The skewed distribution of stiffness brought by diagonal welding lines are directly related to hypotheses 1 and 2, and sliding friction may be introduced for $A(n_r, 0)$ modes with this technique as can be seen in Fig. 7, which was not the case for common welding approaches, see Fig. 5,

The advantages of this technique are three-fold:

- Keep the same cross-section geometry, such that changes on the electromagnetic properties nor housing designs have to be adapted. The stator core stays axially, radially and transversally symmetric.
- Force the structure to behave non-symmetrically, such that the vibration modes are either damped or deleted. Transversally-asymmetric stiffness is introduced.



(a) Common welding (b) Novel attachment method

Figure 6: Illustration of the novel lamination attachment method for welding with four weld lines

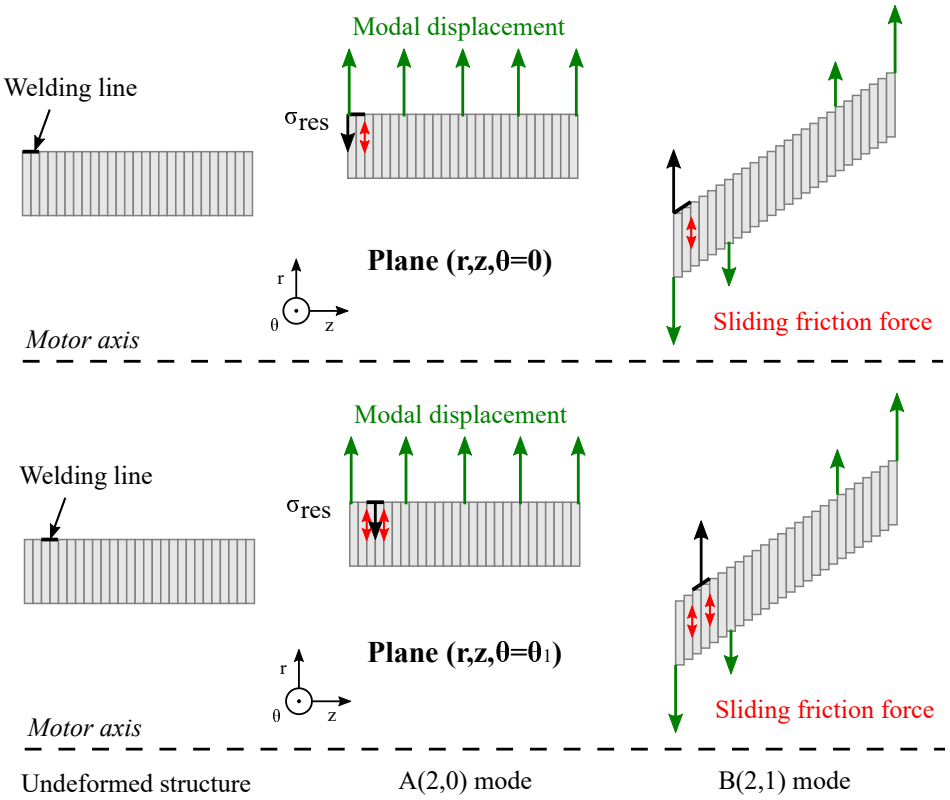


Figure 7: Illustration of the damping occurrence when using skew-weld - NB: Vector amplitudes are informative

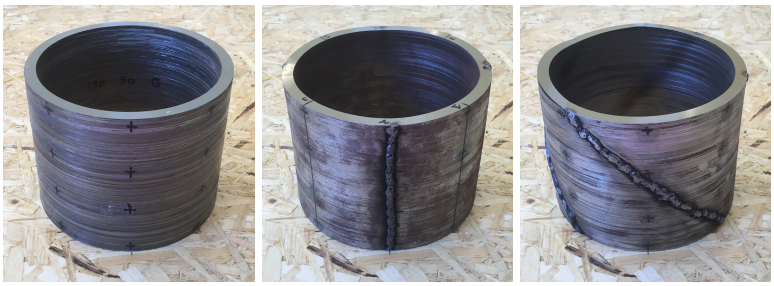
- Use production technique already implemented in chain-manufacturing, e.g. gluing and welding, thus making it not more expensive to realize than common techniques

3 Experimental campaign

3.1 Testing setup and procedure

Several specimens were built in order to validate the alternative stacking technique. The specimens represent laminated stator cores without teeth, i.e. simple cylinders, which is not a large assumption stretch since teeth effects can be neglected in terms of damping []. They stand within the size of stators used in EVs, i.e. they have an outer diameter of 180 mm, an inner diameter of 160 mm and a stack length of 140 mm, and are composed of 400 M330-35A steel laminations. Different stacking techniques are implemented for

comparison purposes. A glued sample, referred to as 180_g, serves as the reference sample, a welded sample with four welding lines, referred to as 180_w, and a skew-welded samples with four skewed welding lines, referred to as 180_sw, are constructed and shown in Fig. 8. It is important to mention that the manufacturing of these specimens were done manually, thus involving uncertainties in the repeatability of the samples. Hence a statistical analysis was performed in Section 3.2 to allocate for manufacturing uncertainties.



(a) 180_g - 5.31 kg (b) 180_w - 5.34 kg (c) 180_sw - 5.38 kg

Figure 8: Test specimens under study

The modal parameters (natural frequencies, modal damping and mode shapes) of each specimen are collected experimentally through Experimental Modal Analyses (EMA). A specific test setup is defined to reproduce free-free conditions in order to capture the intrinsic dynamics of the specimen while eliminating the interference of rigid body modes. Flexible ropes hang the test specimen to that end. Output/Input FRFs $H_{O/I}$ are measured by exciting from a miniature shaker (LMS Qsource SN045) the structure and by measuring at 32 points (PCB Piezotronics SN 356A22 accelerometers): 8 along the circumference and 4 along the stacking axis. The shaker generates a white noise input from 100 Hz to 8 kHz as a burst random signal (80% burst time, 0.025 s burst ramp time) and 50 averaged measurements are used to estimate non-noisy FRFs through H1 algorithm [9]. With this setup, one can ensure consistent, repeatable and coherent measurements up to 5.5 kHz with a frequency resolution of 0.78 Hz.

Every measured FRF $H_{O/I}$ is curve-fitted to the linear mathematical parametric model of Eq. (1) to extract the modal parameters. The sine qua non condition for this processing step is to have a linear structure. Hence reciprocity and linearity checks [9] were performed and permit to assume the linearity of every specimen. PolyMAX [16] implemented in Simcenter Test.lab is the curve-fitting technique used for high quality modal parameter estimation capabilities. In parallel beside modal damping, another indicator of the vibration reduction potential from different manufacturing technique can be calculated: the peak amplitude $G_k = |S_H(\omega_k)|$ of the sum of all acceleration/force FRFs S_H at each natural frequency ω_k where,

$$S_H(\omega) = \frac{1}{32 \times 3} \sum_{32\times3} |\Re(H_{O/I}(\omega))| + j|\Im(H_{O/I}(\omega))| \tag{4}$$

Similarly as in the previous Section, the uncertainties in realizing perfectly repeatable experiments is coped by the statistical analysis of Section 3.2.

3.2 Significance evaluation

Statistical approaches are necessary to define the significance of the different manufacturing processes in terms of natural frequency, damping and FRF-sum amplitude for each mode. Given that a perfect repeatability of the manufacturing, testing and post-processing are not always guaranteed, a pooled variance σ_m is calculated [27]. It represents the variance of different populations when the mean of each population might be different, under the assumption that each population variance is the same. It is applied to the glued specimen 180_g which serves as the basis to deviation calculations for other specimens, under the assumption that

the variances are equal between manufacturing techniques, and is calculated by,

$$\sigma_m^2 = \frac{(n_1-1)\sigma_1^2 + (n_2-1)\sigma_2^2 + (n_3-1)\sigma_3^2}{n_1+n_2+n_3-3} \tag{5}$$

where σ_j^2 ($j = 1,2,3$) are the variances allocating for the uncertainty respectively due to manufacturing ($n_1 = 2$ samples of the 180_g are built and compared), to testing ($n_2 = 2$ tests of the same 180_g are carried out) and to modal parameter estimation processing ($n_3 = 10$ different EMAs for the same specimen 180_g and the same test are performed). The interesting variances are applied to the following modal metrics: the natural frequencies $f_{A(2,0)}$, $f_{A(3,0)}$, $f_{A(4,0)}$, the modal damping $\xi_{A(2,0)}$, $\xi_{A(3,0)}$, $\xi_{A(4,0)}$ and the peak FRF-sum amplitude $G_{A(2,0)}$, $G_{A(3,0)}$, $G_{A(4,0)}$.

From these pooled variances, an ANalysis Of VAriances (ANOVA) [27] is performed to conclude on the significance of the different stacking techniques, referred to as factors in ANOVA. In short, the probability (P-value) of obtaining equal means from all populations is calculated [27] and compared to the maximum allowed value of 0.05 that suggests that at least one factor is more significant than the others. The ANOVA assumes that the populations follow a normal distribution, that the population variances are all equal and that the quantities are taken randomly inside the populations. Here, 9 ANOVAs were carried out: one study that investigates the significance of skew-welding against welding and gluing strategy, which itself incorporates analyses on 3 natural frequency variances, 3 modal damping variances and 3 FRF-sum peak amplitude variances.

4 Results

4.1 Damping improvements

The results of the EMAs together with the ANOVAs are presented in this Section. Table 1 shows the averaged natural frequencies (in Hz), the modal damping and FRF-sum for every $A(n_r, 0)$ modes (which are the only observable modes within the testable frequency bandwidth), their corresponding pooled standard deviation and the P-value from the ANOVAs. Fig. 9 illustrates particularly the damping obtained.

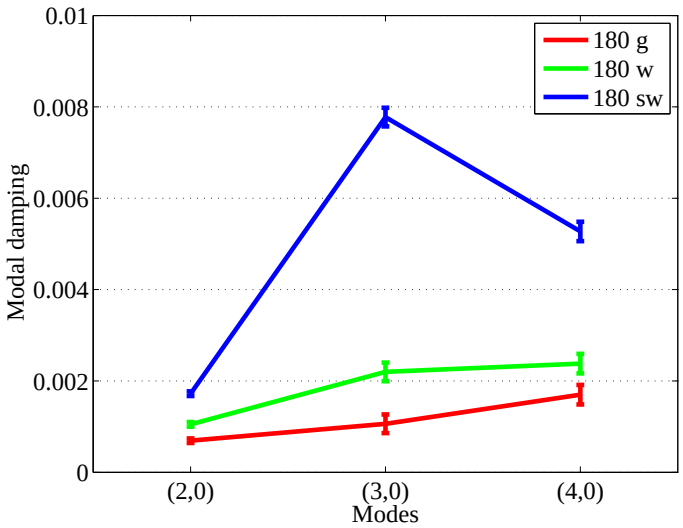


Figure 9: Modal damping comparison for glued, welded and skew-welded cores

It is shown that the natural frequencies are not significantly affected by the stacking technique. However, the modal damping is greatly impacted when looking at the P-values, and especially for mode $A(3,0)$. Welding

	180_g	180_w	180_sw	Pooled standard deviation σ_m	P-value
Natural frequency f_k (Hz)					
$f_{A(2,0)}$	856	853	855	0.1	7.77e-8
$f_{A(3,0)}$	2394	2387	2385	1.0	3.05e-5
$f_{A(4,0)}$	4530	4519	4526	1.0	7.87e-5
Modal damping ξ_k					
$\xi_{A(2,0)}$	0.0007	0.0011	0.0017	0.0001	4.39e-5
$\xi_{A(3,0)}$	0.0011	0.0022	0.0078	0.0002	2.94e-8
$\xi_{A(4,0)}$	0.0017	0.0024	0.0053	0.0002	1.33e-6
Peak Amplitude G_k (g/N) in dB					
$G_{A(2,0)}$	20.0	18.3	12.5	3.4	7.5e-2
$G_{A(3,0)}$	20.5	14.5	11.7	3.1	3.2e-2
$G_{A(4,0)}$	24.7	21.9	15.9	1.9	3.9e-3

Table 1: Significance levels for the samples tested, skew-welding effect

seems to increase damping in comparison with gluing, as suggested by the hypotheses. in parallel, the developed original technique proposed in this paper, i.e. skew-welding, exhibits the best vibration damping performances up to 700% of the original damping value (from glued stator) and close to 10 dB reduction in acceleration FRF at the resonances. It demonstrates the potential of the novel stacking technique for vibration reduction purposes at resonances of laminated cores.

The natural frequencies are not much impacted by the attachment technique used. However, modal damping is affected drastically and also significantly given the P-value obtained, especially for mode $A(3,0)$. From gluing (180_g) to welding (180_w), there is an overall damping increase, but more important for $A(3,0)$. Here, the 4 welding lines are spread such that they correspond exactly to 4 vibration nodes of $A(2,0)$ while they bring stiffness to the nodes of $A(3,0)$. On the other hand from welding (180_w) to skew-welding (180_sw), one can note a drastic difference of damping values. Actually similarly to the previous conclusions, the skew distribution of the welding lines adds stiffness to non-nodal points which is translated in higher damping. In that sense, mode $A(3,0)$ is 7 times more damped from 180_g to 180_sw compared to $A(2,0)$ that is 2.4 times more damped. The FRF-sum peak amplitudes do show significant changes for $A(3,0)$ and $A(4,0)$ but not for $A(2,0)$. Yet the trend shown on damping previously is strengthened by acceleration transfer reductions of close to 10 dB for the modal peaks, which is another great indicator that the novel lamination technique is valuable.

4.2 Hypotheses validation

Now that the skew-welding concept was proved experimentally to reduce vibration at resonances, it is important to understand if the hypotheses formulated previously in Section 2.2 are coherent.

Hypothesis 1: a change in stiffness distribution. As mentioned in Table 1 of the previous Section, the natural frequencies are not drastically affected by the stacking technique, while the specimen mass is not changed either. Therefore it is reasonable to accept that, although being skewly distributed, the stiffness is not significantly affected, especially to the purpose of vibration reduction. Moreover, vibration damping due to extra stiffness is very limited in general [9], because it would require large differences in stiffness values.

Hypothesis 2: a change in inter-laminar contact nature. Another explanation to increased damping was supposedly related to the dry friction occurring between neighboring laminations. Nevertheless it is well known that friction phenomena are nonlinear, composed of static and dynamic features [17]. When a sliding force is applied to a lamination, it sticks to the neighboring sheet (static friction) until a threshold is found and laminations exhibit relative motions (static friction). This threshold depends on hardly determined parameters alike normal force, surface roughness, etc. Here the hypothesis 2 supposes relative motion between laminations occur, thus an activation of dynamic friction.

In order to verify this assumption, it is sufficient to justify on the linearity of the test specimens. This check was actually performed in Section 3, although not presented earlier. For hypothesis validation, an example of such linearity check is given in Fig. 10 with four different input force levels leading to four different FRFs. This time, damping ratios are estimated using the half-power technique [9] and shown in Table 2.

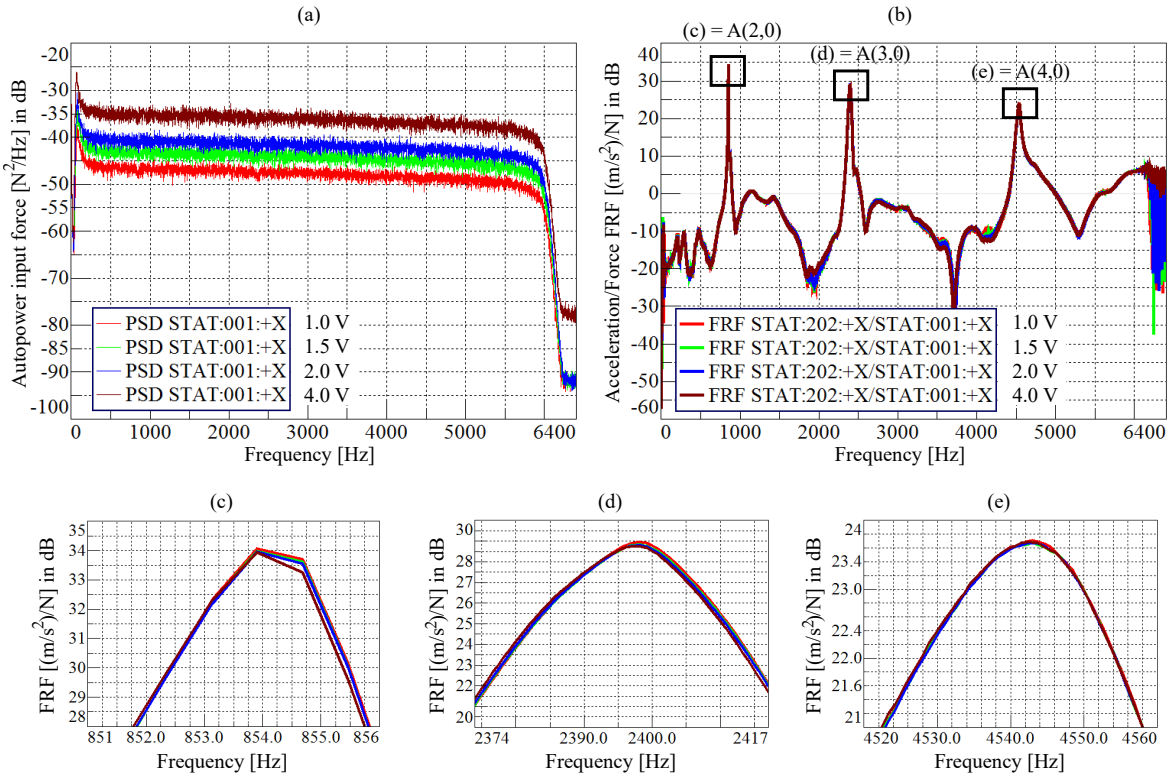


Figure 10: Example of a linearity check for the skew-welded core: (a) input autopower (RMS) spectrum, (b) FRF results for different input levels, (c-d-e) zooms on the FRF peaks

The linearity checks show that damping is affected to some degree by the level of force input. It eventually indicates that energy is also lost by friction phenomena as it was hypothesized. Nevertheless the variations are minor (below 6%) compared to the ones observed by changing the stacking technique (up to 700%). That is one of the reasons why the structure was previously assumed linear for further EMAs, and it confirms that nonlinearities from dynamic friction forces are not the major contributor to higher damping values. Yet it is important to mention that the hardware limitations constrained the linearity analysis: the maximum force level applicable by the miniature shaker is 2 newtons (here where voltage input to the shaker is 4V), so it would be valuable in the future to apply larger forces, such as the electromagnetic ones going up to 300 newtons, to activate more effectively dry-friction.

Hypothesis 3: a change in mode shape. The transformation of the exciting force wave to the modal domain through the modal participation factor of Eq. (3) is done using mode shapes $\{X_k\}$. In parallel, it is expected to see variations in mode shapes coming from the welding lines that distribute uniformly the stiffness of cores. The comparison of mode shapes is possible by analysing MAC matrix between two mode shapes. The

Mode	Voltage input [V]	Modal damping ξ_n	Difference [%]
	1.0	0.003162	ref.
$A(2,0)$	1.5	0.003185	+0.74
	2.0	0.003197	+1.11
	4.0	0.003349	+5.93
	1.0	0.009852	ref.
$A(3,0)$	1.5	0.009998	+1.48
	2.0	0.010015	+1.65
	4.0	0.010202	+3.55
	1.0	0.008310	ref.
$A(4,0)$	1.5	0.008305	-0.05
	2.0	0.008354	+0.53
	4.0	0.008433	+1.48

Table 2: Modal damping estimations (half-power technique) for skew-welding core and different input voltage levels to the shaker (equivalent to force levels)

MAC matrix to correlate two mode shapes $\{X_r\}$ and $\{X_s\}$ is derived as [9],

$$MAC\Big(\{X_r\},\{X_s\}\Big) = \frac{|\,\{X_r\}\{X_s\}\,|^2}{\big(\{X_r\}^{*T}\{X_r\}\big)\big(\{X_s\}^{*T}\{X_s\}\big)} \tag{6}$$

It varies between 0 and 1 and represents how much two mode sets correlate with each other; a perfect correlation would show a MAC number of 1, while a 0 value means no correlation. Two different MAC analyses can be carried out to understand how skew-weld is beneficial in terms of vibration damping. On the one hand, the MAC analysis can be performed on the full stators where different manufactures are compared. On the other hand, the influence of the manufacture can be investigated by doing a MAC analysis for different cross-sections along the stator, referred to as layer.

At first, a MAC analysis is performed for the entire glued, welded and skew-welded cores under study, and is shown in Fig. 11. Every specimen is compared to the reference glued stator.

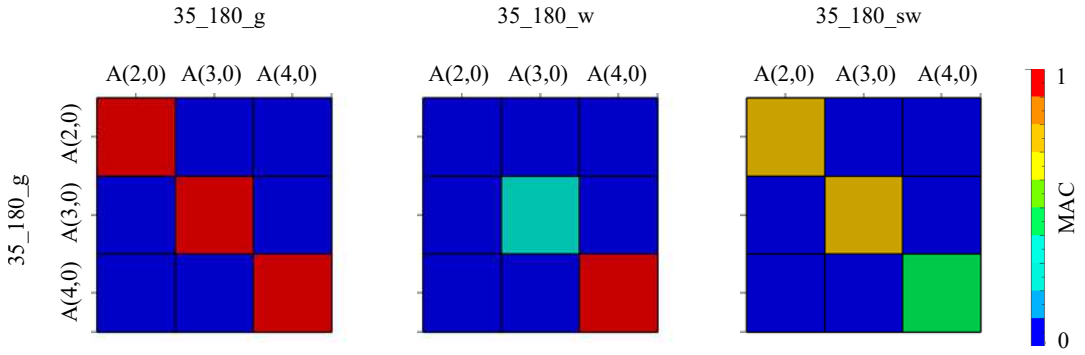
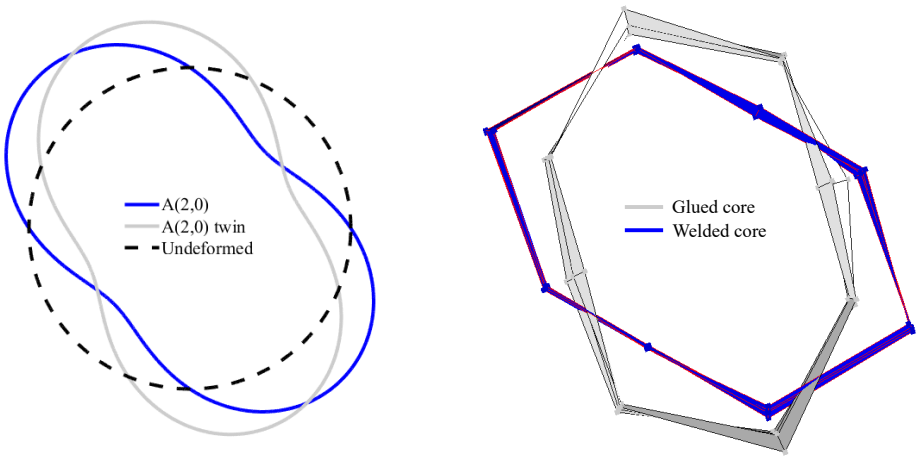


Figure 11: Complete MAC analysis for different stator manufactures - matrices

Auto-correlation between the two same test specimens (left matrix) gives the maximum MAC number of 1 and the cross-correlation values are very low, which confirms the uniqueness of the modes extracted (orthogonality of the modal basis). Looking at the middle matrix, the $A(2,0)$ mode does not correlate between the glued and welded cores. This is due to the fact that twin modes occur at each natural frequency and

that measurements cannot distinguish these two modes. For the glued and welded cores, the captured modes exactly correspond to twin modes, as seen in Fig. 12, which are by essence orthogonal [4] thus leading to poor correlation. The $A(3,0)$ mode is not well correlated as well but this is a direct consequence of welding in comparison with gluing. Last regarding the right matrix, every mode is poorly correlated with the reference glued mode shapes. In the end, this MAC analysis presupposes that mode shapes are affected such that vibrations are reduced through modal participation factor variations. However the influence of transverse asymmetry on the mode shapes is hardly comprehensible by solely performing this analysis.



(a) (b)

Figure 12: Illustration of (a) a twin mode in theory for $A(3,0)$, and (b) the experimentally identified mode shape for $A(3,0)$

As a consequence in order to reinforce the claims, another set of MAC analyses are performed. This time, the mode shapes for different layers along the stator axial axis are correlated. EMAs were performed to estimate the mode shapes of each layer. The reference mode set corresponds to the layer 1.

Looking at the two first rows of Fig. 13, the correlation between each layer is acceptable with MAC values above 0.8. For these two specimens (glued and welded), the transverse symmetry is kept and therefore the mode shapes are not varying along the axial axis. However when transverse asymmetry is introduced (third row) in the skew-welded core, significant mode shape discrepancies occur between layers. This suggests that, originally transversally symmetric, the pure radial modes $A(n_r,0)$ become transversally asymmetric by skew-welding; thus shaping the modal participation factor presupposing vibration amplitude reduction.

5 Conclusions

An alternative lamination stacking technique of stator cores is developed in this paper for vibration damping purposes, with the ultimate goal of mitigating noise coming from resonance effects. The technique exploits the laminated nature of the stator core by connecting the laminations with a skewed distribution of the welding lines. Based on fundamental physical insights, three hypotheses on the vibration damping occurrence explanation are formulated and validated experimentally for different test specimens. It is shown that welding compared to glue-bonding provides slight damping improvements while the novel skew-welding technique demonstrates impressive damping increases up to 7 times higher than the glues specimen, leading to 9 dB reduction capabilities. These results mainly confirm the hypotheses that motivated the experimental implementations. It is principally shown that the mode shape changes are responsible for vibration attenuation at resonance frequencies, rather than inter-laminar friction or stiffness distribution variations. This work finally suggests that particular welding line profiles lead to specific modes damping, hence it would be interesting to investigate optimized skew-welding patterns for particular critical modes damping.

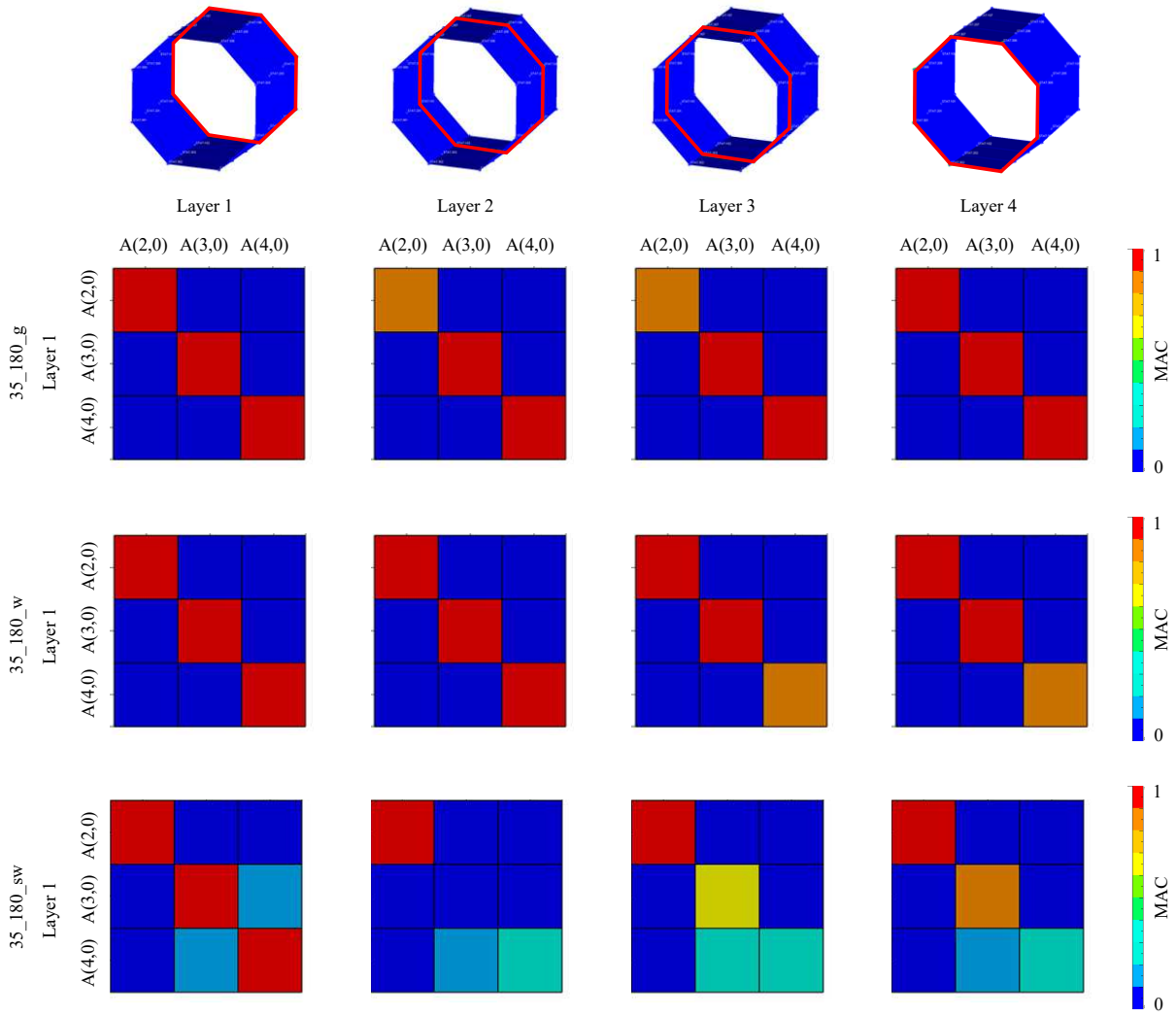


Figure 13: Layered MAC analysis for different stator manufactures

Acknowledgements

The authors would like to acknowledge the financial support of the European Commission via the EU funded Marie Curie ITN project called ADvanced Electric Powertrain Technology (ADEPT), grant number 607361 [19].

References

[1] S. Adhikari. *Damping models for structural vibration*. PhD thesis, University of Cambridge, 2001.

[2] D. Belkhayat, D. Roger, and J. F. Brudny. Active reduction of magnetic noise in asynchronous machine controlled by stator current harmonics. In *Eighth International Conference on Electrical Machines and Drives (Conf. Publ. No. 444)*, pages 400–405, Sep 1997.

[3] W. Cai and P. Pillay. Resonant frequencies and mode shapes of switched reluctance motors. *Energy Conversion, IEEE Transactions on*, 16(1):43–48, 2001.

[4] F. Chauvicourt. *Vibro-acoustics of rotating electric machines: Prediction, validation and solution*. PhD thesis, Katholieke Universiteit Leuven and Université Libre de Bruxelles, 2018.

[5] A. Crow. Stator and rotor laminations from prototype to volume production. In *UKMAG seminar Advances in Machine Manufacture*, Newcastle University, 2013.

[6] C. Gan, J. Wu, M. Shen, S. Yang, Y. Hu, and W. Cao. Investigation of Skewing Effects on the Vibration Reduction of Three-Phase Switched Reluctance Motors. *IEEE Transactions on Magnetics*, 51(9):1–9, Sept. 2015.

[7] J. F. Gieras, C. Wang, and J. C. Lai. *Noise of polyphase electric motors*. Number 129 in Electrical and computer engineering. CRC/Taylor & Francis, Boca Raton, Fla., 2006.

[8] J. R. Hendershot. Causes & Sources of audible noise in elecric motors. In *22nd Incremental Motion Control Systems and Devices Symposium*, pages 259–270, Champaign IL, 1993. B.C. Kuo Ed.

[9] W. Heylen, S. Lammens, and P. Sas. *Modal analysis theory and testing*. Katholieke Universiteit Leuven, Faculty of Engineering, Department of Mechanical Engineering, Division of Production Engineering, Machine Design and Automation, 2 edition, 1997.

[10] Jian Li, Xueguan Song, and Yunhyun Cho. Comparison of 12/8 and 6/4 Switched Reluctance Motor: Noise and Vibration Aspects. *IEEE Transactions on Magnetics*, 44(11):4131–4134, Nov. 2008.

[11] R. Krishnan and P. Vijayraghavan. State of the art: acoustic noise in switched reluctance motor drives. In *Industrial Electronics Society, 1998. IECON'98. Proceedings of the 24th Annual Conference of the IEEE*, volume 2, pages 929–934. IEEE, 1998.

[12] J. Le Besnerais. *Réduction du bruit audible d'origine magnétique dans les machines asynchrones alimentées par MLI - règles de conception silencieuse et optimisation multi-objectif*. PhD thesis, Ecole Centrale de Lille, 2008.

[13] F. Lin, S. Zuo, W. Deng, and S. Wu. Noise Prediction and Sound Quality Analysis of Variable-Speed Permanent Magnet Synchronous Motor. *IEEE Transactions on Energy Conversion*, 32(2):698–706, June 2017.

[14] V. Luchscheider, K. Willner, and M. Maidorn. A material model for lamination stacks based on rough contacts. In *Electric Drives Production Conference (EDPC), 2014 4th International*, pages 1–6. IEEE, 2014.

[15] P. Millithaler. *Dynamic behaviour of electric machine stators*. PhD thesis, Université de Franche-Comté, 2015.

[16] B. Peeters, H. Van der Auweraer, P. Guillaume, and J. Leuridan. The PolyMAX frequency-domain method: a new standard for modal parameter estimation? *Shock and Vibration*, 11(3-4):395–409, 2004.

[17] M. Pirnat, G. Čepon, and M. Boltežar. Introduction of the linear contact model in the dynamic model of laminated structure dynamics: An experimental and numerical identification. *Mechanism and Machine Theory*, 64:144–154, June 2013.

[18] C. Schlensok, M. van der Giet, M. Herranz Gracia, D. van Riesen, and K. Hameyer. Structure-Dynamic Analysis of an Induction Machine Depending on Stator – Housing Coupling. *IEEE Transactions on Industry Applications*, 44(3):753–759, 2008.

[19] A. Stefanskyi, A. Dziechciarz, F. Chauvicourt, G. Sfakianakis, K. Ramakrishnan, K. Niyomsatian, M. Curti, N. Djukic, P. Romanazzi, S. Ayat, S. Wiedemann, W. Peng, S. Stipetic, and A. Tamas. Researchers within the EU funded Marie Curie ITN project ADEPT, grant number 607361, 2013.

[20] H. Stemmler and T. Eilinger. Spectral analysis of the sinusoidal PWM with variable switching frequency for noise reduction in inverter-fed induction motors. In *Power Electronics Specialists Conference, PESC'94 Record., 25th Annual IEEE*, volume 1, pages 269–277. IEEE, 1994.

[21] I. Takahashi and H. Mochikawa. Optimum PWM waveforms of an inverter for decreasing acoustic noise of an induction motor. *IEEE transactions on industry applications*, (5):828–834, 1986.

[22] M. Takiguchi, H. Sugimoto, N. Kurihara, and A. Chiba. Acoustic Noise and Vibration Reduction of SRM by Elimination of Third Harmonic Component in Sum of Radial Forces. *IEEE Transactions on Energy Conversion*, 30(3):883–891, Sept. 2015.

[23] A. Tan-Kim, N. Hagen, V. Lanfranchi, S. Clnet, T. Coorevits, J.-C. Mipo, J. Legranger, and F. Palleschi. Influence of the manufacturing process of a claw-pole alternator on its stator shape and acoustic noise. In *XXIIth International Conference on Electrical Machines (ICEM),*, pages 2273–2279. IEEE, 2016.

[24] P. Timar. *Noise and Vibration of electrical machines*, volume 34. Elsevier, 1989.

[25] G. Verez, G. Barakat, and Y. Amara. Influence of slots and rotor poles combinations on noise and vibrations of magnetic origins inu'-core flux-switching permanent magnet machines. *Progress In Electromagnetics Research B*, 61:149–168, 2014.

[26] P. Vijayraghavan and R. Krishnan. Noise in electric machines a review. *IEEE Transactions on Industry Applications*, 35(5):1007–1013, Oct. 1999.

[27] C. Walck. *Handbook on statistical distributions for experimentalists*. University of Stockholm Internal Report SUF-PFY/96-01, 2007.

[28] Wei Cai, P. Pillay, and Zhangjun Tang. Impact of stator windings and end-bells on resonant frequencies and mode shapes of switched reluctance motors. *IEEE Transactions on Industry Applications*, 38(4):1027–1036, July 2002.

[29] B. Weilharter, M. Mair, H. Lang, K. Ellermann, and O. Birox. Experimental investigation of the vibration behaviour of a laminated stack with winding. In *Industrial Electronics Society, IECON 2013-39th Annual Conference of the IEEE*, pages 2816–2820. IEEE, 2013.

[30] H.-Y. Yang, Y.-C. Lim, and H.-C. Kim. Acoustic Noise/Vibration Reduction of a Single-Phase SRM Using Skewed Stator and Rotor. *IEEE Transactions on Industrial Electronics*, 60(10):4292–4300, Oct. 2013.

[31] S. Yang. *Low-Noise electric motors*. Oxford University Press, Oxford, 1981.

Composite phononic crystals modelling and its application in vehicle noise control

C. Jin[1], T.P. Zhang[1]
[1] Tongji University, School of Automotive Studies
4800 Caoan Rd., Shanghai, China
e-mail: **bryan_jin_1@hotmail.com**

Abstract

This paper presents the work of modelling a locally resonant type composite phononic crystals which has vibration forbidden band gap in low frequency range. Composite phononic crystals of 5×8 period on aluminum plate was modelled by FEM and the result was verified by experimental test. Vibration band gaps below 1k Hz on the panel were observed, which meant composite phononic crystals with multiple periods were capable of suppressing low frequency panel vibration. Acoustic responses of vehicle interior cavity with 5×18 period composite phononic crystals deployed on vehicle roof was then simulated by means of a FEM-BEM coupled technique. Experimental test on vehicle was also carried out with same phononic crystals structure on the roof as in simulation. Both results from simulation and experiment show decreased vehicle interior noise in mid-low frequency range, which makes locally resonant composite phononic crystals an applicable measure for vehicle noise control.

1 Introduction

Phononic crystals (PCs) are composite materials made of periodic distribution of inclusions that constituted by two or more compounds with different elastic properties embedded in a matrix [1-3]. When the elastic wave propagates within the crystal structure, a special dispersion curve is formed as a result of its internal periodic structure, which may exhibit absolute band gaps in certain frequency range. Acoustic or elastic wave propagation is inhibited or prohibited in this band gap which can be designed through the change in periodic structure and material of PCs. Therefore PCs structures have several potential applications, such as wave guiding, filtering, sound isolation and vibration damping [4-8]. It is for this reason that they have been gaining much attention over the past two decades.

There are two kinds of gap formation mechanism for PCs, Bragg scattering mechanism [9-10] and locally resonant (LR) mechanism [11-13]. For the Bragg type, the periodic scale and the magnitude of acoustic or elastic wave length are in the same order. Locally resonant PCs contain elastic resonators composed of a heavy core, called scatter, surrounded by a soft coating. The lattice constant of locally resonant PCs is two times smaller than that of Bragg PCs, which can exist in a frequency range of two orders of magnitude lower than the one resulting from the Bragg scattering. Therefore it is suitable for controlling low- and medium-frequency vibration or noise. References [14,15] illustrate the current situation of studies in the field of vibration and noise control, particularly the anti-vibration and anti-noise of vehicles.

In this paper, a LR composite PCs plate was firstly modelled for the potential use in vehicle engineering application. The result was verified by experimental test. Then LR PCs deployed on vehicle roof was modelled and the acoustic responses of vehicle were computed numerically. Experimental test on vehicle was also carried out with same PCs structure on the roof in computation.

2 Modelling and verification of a LR PCs plate

A locally resonant composite PCs aluminum plate was modelled in order to investigate its potential use in vehicle panel vibration control application. Vibration test was carried out to verify the numerical result

2.1 Unit cell of LR PCs

The unit cell of a LR PCs is composed of high-density scatter, matrix, and coating of elastically soft material. The distance between two neighboring scatters is referred to as the lattice constant *a* (Figure 1). Individual scatters produce resonances under the excitation of elastic waves in a certain frequency range. This causes interaction with incident waves, which impedes the propagation. The formation of band gaps relies on the structure of individual scatters and their interaction with elastic waves.

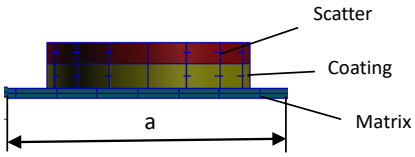


Figure 1: Unit cell of LR PCs

2.2 Vibration response of modeled LR PCs plate

The LR PCs plate is modeled based on unit cells, arranged in five rows along the x direction, eight columns along the y direction on an aluminum plate as shown in Figure 2, which forms 5×8 period. The size of aluminum matrix is 600×400×2 mm and the coating layer, which is 5 mm in thickness and 40 mm in diameter, is made of silicone rubber with damping rate of 0.1. The steel resonators are 4 mm in thickness and 40 mm in diameter. The lattice constant is set to 50 mm. Finite element method (FEM) is used to compute the vibration response of LR PCs plate under a free-free boundary condition. The material properties of LR PCs plate are listed in table 1. A vertical unit force excites the PCs plate up to 1k Hz at PCs side of the plate and response is picked up on the other side as shown in Figure 2.

Material	Density （kg/m^3）	Elastic modulus (Pa)	Poisson's ratio
Steel	7840	2.16e11	0.28
Silicone rubber	1300	1.37e5	0.47

Table 1: Material properties of LR PCs used in FEM

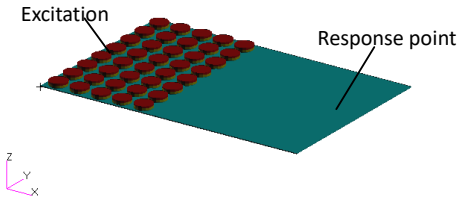


Figure 2: Model of LR PCs plate in FEM

Vibration response was computed by Nastran code, the results are shown in figure 3, in which vibration response of plate with and without PCs are shown respectively. A distinct forbidden band gap exists in LR PCs plate. The major band gap is from 240Hz to 560Hz with maximum attenuation of 49dB.

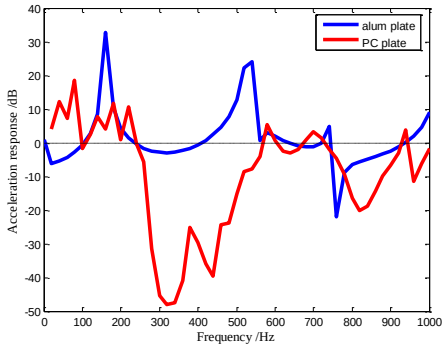


Figure 3: Vibration responses of plate with and without PCs

2.3 Experimental verification of modeled LR PCs plate

A LR PCs plate sample of same structure as modeled (Figure 4) was made in order to experimentally verify the vibration response computed by FEM. The position of excitation and response measuring point were the



Figure.4 : sample of PCs plate

same as in the FEM. The entire test system, as shown in figure 5, includes excitation system, LR PCs plate, response system and data acquisition system. The excitation system contains shaker, power amplifier and force transducer. The accelerometer of response system was positioned on the response point of PCs plate to measure the vibration response. During the test the plate was suspended by soft elastic ropes at four corners to ensure its free-free boundary condition as in FEM. The suspension frequency was around 5Hz, which was far below the first modal frequency of the plate and would not affect its dynamic behavior. The plate was excited by the shaker with 1k Hz bandwidth white noise signal of unit force amplitude. The SCIII 305 data acquisition system and signal processing software Test.Lab from LMS recorded and processed the vibration signal.

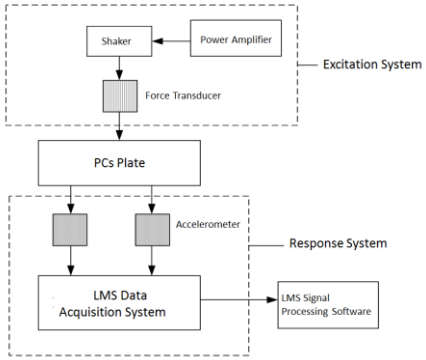


Figure.5 : Experimental test system for PCs plate

Figure 6 shows the comparison of vibration response acquired numerically and experimentally. A band gap in the same frequency range is also observed from the result of experimental test, which coincides with the major one from FEM. Therefore both numerical and experimental results verify that multiple periods LR PCs has the capability of controlling mid-low frequency panel vibration which is one of the root causes inducing vehicle interior noise.

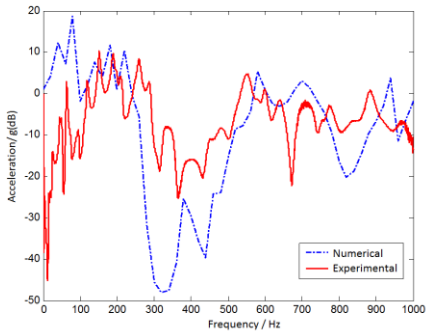


Figure.6 : Experimental and numerical results of vibration response

3 LR PCs Modelling on vehicle body panel

For the application of LR PCs in vehicle noise control, vehicle body structure was modeled with multiple periods LR PCs on the body panel and acoustic responses of vehicle interior cavity were computed numerically by means of a FEM-BEM coupled technique.

3.1 Modeling and modal analysis of vehicle body structure

Finite element model of a sedan body structure was built with doors and glasses on it (Figure 7). The doors were mounted to the body through rigid connections while the front and rear glasses were mounted through glue connections. The material properties used in FEM is listed in table 2. Body trim and seats were not taken into account for the simplifying of computation.

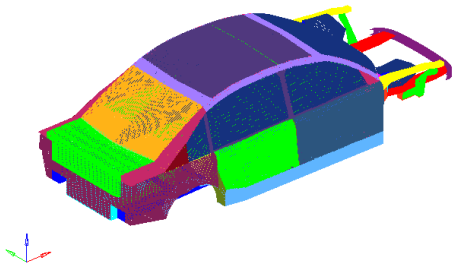


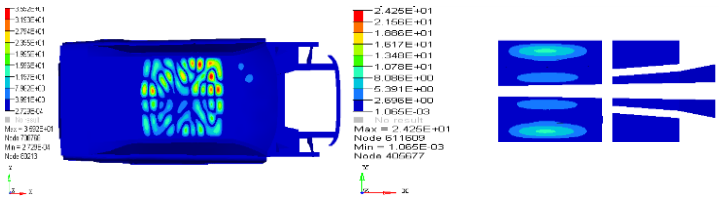
Figure. 7: FE model of a sedan body structure

Material	Elastic modulus (MPa)	Shear modulus (MPa)	Poisson's ratio	Density (kg/m^3)
Steel	2.16e5	8.3e4	0.266	7850
Glass	2.0e4	8.73e3	0.145	2530
Glue	3.6e3	2.5e3	0.35	1200

Table 2.Material properties of body structure used in FEM

Modal is the natural dynamic behavior of structures, which indicates the vibration mode of structure at each modal frequency. For vehicle body which is mainly composed of panels, vibration of panel mode will generate radiation noises in the vehicle cavity [16-19]. Therefore controlling of vehicle panel modes can lead to the reduction of interior noise. Modal analysis finds all the vibration modes of vehicle body including panel modes and shows their vibration energy in the form of mode shape.

In this work modal analysis of vehicle body was carried out. Two panels, roof and floor, were focused due to their large area that several local modes could emerge. Figure 8 shows the vibration mode shapes from two panels, in which the vibration energy of roof is much higher than that of floor. This means that vibration of roof may bring about more radiation noise than that of floor and should be controlled with priority. Modal analysis provided a guide for identifying the most effective panel for noise control.



(a) Roof mode (b) Floor mode

Figure 8. Panel modes of vehicle body

3.2 Numerical computation for acoustic responses of vehicle cavity with LR PCs on roof

The roof of vehicle body was selected for LR PCs deployment due to its high energy of vibration mode. The unit cell and lattice constant of LR PCs on the roof were kept same as in PCs plate, that was 5mm thick silicone rubber coating layer, 4mm thick steel resonator and 50mm lattice constant. The roof itself was also the matrix for PCs. According to the size of roof and the weight of PCs, 5×18 period which was 5 rows along x direction, 8 columns along y direction was arranged on the rear of roof (Figure 9). The connection between PCs and roof matrix shared the same nodes in FE model.

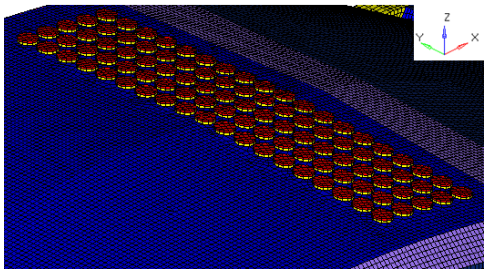


Figure. 9 : FE model of LR PCs on vehicle roof

The acoustic response of vehicle is in a cavity enclosed by vehicle body, so an acoustic cavity needs to be modeled. This was realized by boundary element method (BEM) which modeled the acoustic boundary of vehicle cavity. The acoustic responses were computed by a FEM-BEM coupled technique which referred to as Modal Acoustic Transfer Vector (MATV) technique. The principle of MATV is in equation (1) and (2) [20]

$$p(\omega) = \{ATV(\omega)\}^T \cdot \{v_n(\omega)\} \tag{1}$$

$$\{v_n(\omega)\} = j\omega \cdot [\Phi_n] \cdot \{MRSP(\omega)\} \tag{2}$$

The acoustic response $p(\omega)$ is the results of normal structure vibration velocities $v_n(\omega)$ transferred by $ATV(\omega)$ which is the system matrix relating input of unit vibration velocity and output of corresponding acoustic response.

Equation (2) presents how structure vibration is projected onto the normal direction with respect to the acoustic boundary and converted from displacement into velocity, Where $[\Phi_n]$ represents a matrix whose columns are composed of the structural modal vectors projected onto the normal direction with respect to the acoustic boundary, $\{MRSP(\omega)\}$ is the column vector containing the modal participation factors for the given excitation frequency, and $j\omega$ is the frequency domain multiplication factor for the conversion of the modal vector data expressed in terms of vibration displacements into vibration velocities.

Therefore MATV is essentially a combination of FEM modal analysis and BEM analysis to calculate sound pressure radiated from a structure based on the normal vibration velocity coming from the forced response of the structure. First step is obtaining a structural FEM modal analysis, and secondly to calculate a Forced Response, to get modal participation factors. In second part structural vibration modes are projected into the acoustic boundary element model, the modal participation factors are also taken in account and the ATV are computed from the acoustic model to the points of acoustic response. Finally the sound pressure is obtained at each acoustic response point.

In this work acoustic boundary element of vehicle cavity was modeled with mesh size of 80mm (Figure 10). The fluid inside the cavity was air of 1.225kg/m^3 density and the sound speed in the cavity was 340m/s at room temperature. There were no acoustic treatments on the cavity model, which made the boundary acoustically rigid. Four acoustic response points were defined as passenger position of front left (FL), front right (FR), rear left (RL) and rear right (RR).

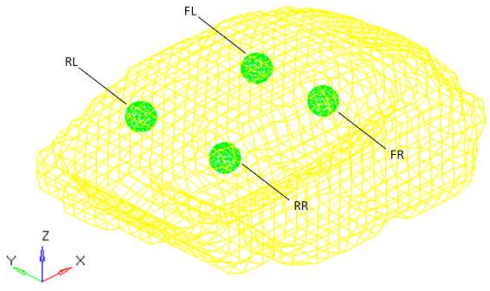


Figure. : 10 Acoustic BE model of vehicle cavity

The force excitation inputs on the vehicle body were selected at four engine mount connection points (Figure 11). The spectrum of white noise signals which simulated the engine forces excited the vehicle body at four

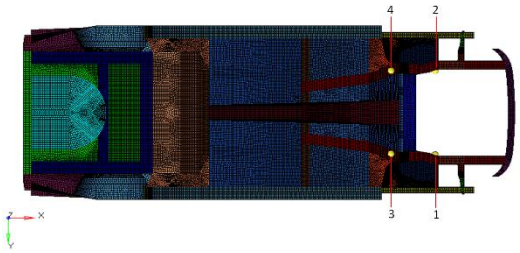
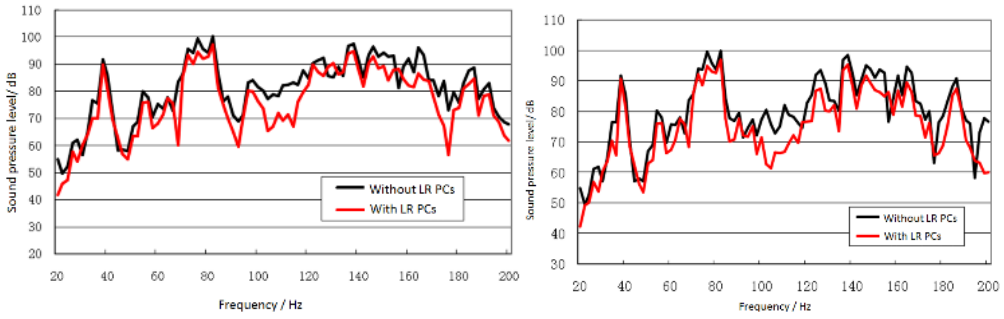


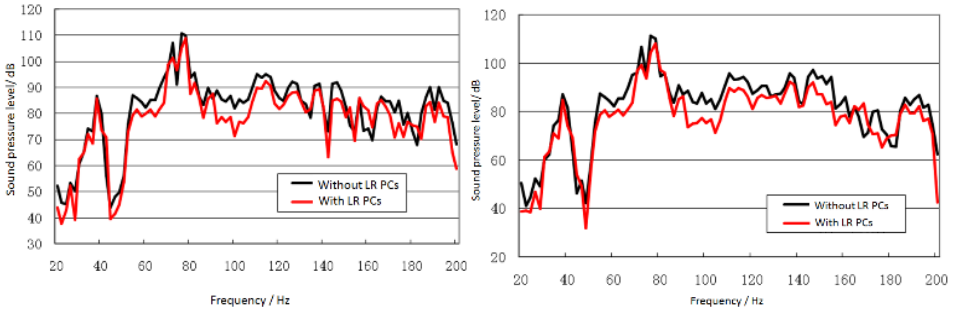
Figure. 11: Excitation points at vehicle body

connection points. FEM-BEM coupled computation of acoustic responses were carried out LMS Virtual.Lab solver. The frequency range was set to 200Hz due to large computation complexity of vehicle body.

The four acoustic responses computed with and without LR PCs on roof are shown in Figure 12. The results are relative comparisons of LR PCs effect because the excitations were not under real operational condition. The employment of LR PCs on roof resulted in noise reductions at four acoustic response points especially in the frequency range of 100 to 200Hz in which possibly local panel modes of roof generates.



(a) FL position (b) FR position



(c) RL position (d) RR position

Figure. 12 : Four numerically computed acoustic responses

4 LR PCs application test on vehicle

Experimental test on vehicle under operational condition was carried out to verify the application of LR PCs for vehicle interior noise control. To ensure the consistency of the results the test was conducted on chassis dynamometer inside a semi-anechoic chamber. The vehicle which is the same sedan as in numerical computation was fixed on the roller bench of chassis dynamometer (Figure 13). The chassis dynamometer provided road load simulation for vehicle and the semi-anechoic chamber ensured a free field acoustic environment for the measurement.



Figure. 13: Vehicle test on chassis dynamometer inside semi-anechoic chamber

The configuration of LR PCs on vehicle roof was the same as in numerical computation: 5×18 period with 5mm thick silicone rubber coating layer, 4mm thick steel resonator and 50mm lattice constant. One 1/2-inch microphone and four uni-axis accelerometers were positioned on left ear of driver and on roof to measure interior noise and roof normal vibrations respectively (Figure 14).



(a) Microphone position (b) Accelerometers position

Figure. 14 : Location of measurement points

During the test the vehicle was running under stationary operational condition of 3000rpm engine speed in D gear (with automatic transmission). The signals from microphone and accelerometers before and after employing LR PCs were recorded respectively with 30 seconds duration by LMS SCIII 305 data acquisition system and processed by Test.Lab software.

The normal vibration response on middle of the roof (Acc-4) before and after employing LR PCs is shown in Figure 15. It can

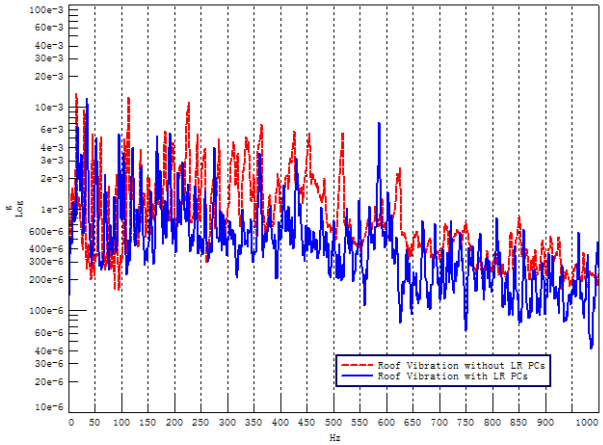


Figure. 15 : Normal vibration response on middle of the roof (Acc-4) before and after employing LR PCs

be seen that there is a distinct decrease of vibration on the roof in the range of 220~520Hz after employing LR PCs. This vibration attenuation was caused by the band gap of 5×18 period LR PCs. The overall vibration on middle of roof decreased from 0.05g to 0.03g. Vehicle interior noise at driver left ear reduced as well after employing LR PCs (Figure 16). The frequency range of noise reduction coincided with that

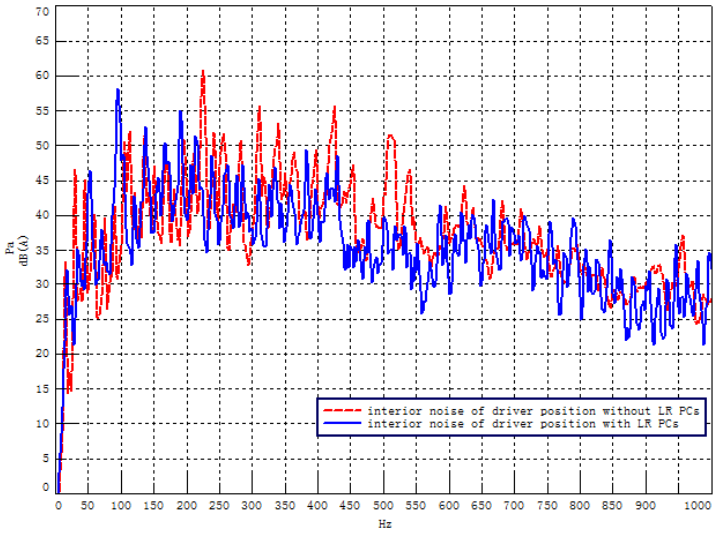


Figure. 16 : Vehicle interior noise at driver left ear before and after employing LR PCs

of vibration attenuation, which matched the band gap effect of LR PCs. The overall interior noise level at driver left ear reduced by 2.7 dB(A) from 69.4 dB(A) to 66.7 dB(A). The experimental test on vehicle shows the potential of composite LR PCs in the field of vehicle noise control application.

5 Conclusions

In this paper, composite LR PCs was modeled for the control of vehicle interior noise caused by body panel vibration. A multiple periods LR PCs plate with unit cell made of steel and silicon rubber was firstly modeled numerically and verified experimentally. The vibration response of PCs plate shows attenuation at mid-low frequency, which is a desired feature that can be utilized for the control of vehicle panel vibration.

Furthermore, the LR PCs was modeled on vehicle body structure. Modal analysis was conducted to identify the most effective body panel of vehicle which will radiate more interior noise. LR PCs on the rear of vehicle roof was modeled and the acoustic responses in the vehicle interior were computed by means of a FEM-BEM coupled technique MATV. The numerical results shows noise reductions at acoustic response points especially in the frequency range of 100 to 200Hz in which possibly generates local panel modes of roof.

Finally, experimental test on vehicle under operational condition was carried out to verify the application of LR PCs for vehicle interior noise control. After employing LR PCs the vibration on vehicle roof decreased distinctly in the mid-low frequency range of multiple period LR PCs band gap. Vehicle interior noise at driver left ear also reduced in the corresponding frequency range and overall level reduced by 2.7dB(A).

The present work provides evidence that composite LR PCs structure, as a metamaterial, has potentials to be used in the field of vehicle noise control.

References

[1] Yan Pennec, Bahram Djafari-Rouhani, Hocine Larabi, et al, "Phononic crystals and manipulation of sound," Phys. Status Solidi C6, No.9:2080-2085, 2009, DOI: 10.1002/pssc.200881760.

[2] M.S.Kushwaha，P.Halevi, L.Dobrzynski, "Acoustic Band Structure of Periodic Elastic Composites," Physical Review Letter, Vol.17, 1993, p. 2022-2025.

[3] Sigalas M M., Economou E N., "Band structure of elastic waves in two-dimensional systems," Solid State Commun., Vol.86, 1993, p.141-143.

[4] J.S. Jensen., "Phononic band gaps and vibrations in one- and two-dimensional mass–spring structures," Journal of Sound and Vibration, Vol.266, 2003, p.1053-1078.

[5] Martin Hirsekorn., "Small-size sonic crystals with strong attenuation bands in the audible frequency range," Applied Physics Letters. Vol.84, 2004, p.3364-3366.

[6] J.O. Vaseurt, B. Djafari-Rouhani, L. Dobrzynski et al., "Complete acoustic band gaps in periodic fibre reinforced composite materials: the carbon/epoxy composite and some metallic systems," Phys.: Condens. Matter 6, 1994, p.8759-8770.

[7] R.Martinez-Sala, J.Sancho, J. V.Sanchez et al., "Sound attenuation by sculpture," Nature, Vol.378, 1995, p. 241.

[8] C. Yilmaz, N. Kikuchi., "Analysis and design of passive band-stop filter-type vibration isolators for low-frequency applications," Journal of Sound and Vibration, Vol.291, 2006, p.1004-1028.

[9] M.S. Kushwaha, P. Halevi, G. Martinez, L. Dobrzynski, B. Djafari-Rouhani, "Theory of acoustic band structure of periodic elastic composites," Physical Review B 49 (1994) 2313-2322.

[10] M.M. Sigalas, E.N. Economou, "Elastic and acoustic wave band structure," Journal of Sound and Vibration 158 (1992) 377-382.

[11] J.H. Wen, G. Wang, D.L. Yu, et al., "Theoretical and experimental investigation of flexural wave propagation in straight beams with periodic structures: application to a vibration isolation structure," Journal of Applied Physics 97 (2005) 114907.

[12] D.L. Yu, Y.Z. Liu, J. Qiu, G. Wang, H.G. Zhao, "Complete flexural vibration band gaps in membrane-like lattice structures," Physics Letters A 357 (2006) 154-158.

[13] D.L. Yu, Y.Z. Liu, H.G. Zhao, G. Wang, J. Qiu, "Flexural vibration band gaps in Euler–Bernoulli beams with two-degree-of-freedom locally resonant structures," Physical Review B 73 (2006) 064301.

[14] Shu'en Zhao, Yinong Li, Ling Zheng, et al., "Phononic Crystals and Automotive Noise and Vibration Control," Materials Review, Vol. 21, Issue 4, 2007, p.84-86.

[15] Xiaoxiong Jin, Jianwang Shao, Wei Peng. "Vehicle Interior Noise Study Based on Phononic Crystals," Vibration and Shock. Vol.28, Issue12, 2009, p.107-109.

[16] Teik C. Lim, "Automotive panel noise contribution modeling based on finite element and measured structural-acoustic spectra," Applied Acoustics, 60 (2000), 505-519.

[17] Gregor Koners, "Panel Noise Contribution Analysis: An Experimental Method for Determining the Noise Contributions of Panels to an Interior Noise," SAE Technical Paper 2003-01-1410.

[18] Oliver Wolff, Roland Sottek, "Panel Contribution Analysis - An Alternative Window Method," SAE Technical Paper 2005-01-2274.

[19] Yuksel Gur, Sanjay Abhyankar, David Wagner, "Radiating Panel NVH Performance Evaluations for Vehicle Design," SAE Technical Paper 2013-01-1991.

[20] André de Oliveira, Thiago A. Fiorentin, Marcelo G. Silva, "Design of System and Components - NVH view - Test and Simulation," SAE Technical Paper 2008-36-0239.

Test and improvement of drive axle whine for a light bus

W. Shi[1], G. Liu[1], C. Gao[1], H. Shi[1,2], Z. Chen[1]
[1]State Key Laboratory of Automotive Simulation and Control, Jilin University, Changchun 130022, China.
e-mail: **shiwk@jlu.edu.cn**

[2]Department of Mechanical Engineering, KU Leuven, Celestijnenlaan 300 B, B-3001, Heverlee, Belgium

Abstract
Aiming at identifying and reducing the drive axle whine of a light bus, the vehicle test and the modal test were performed. The test results show that the vehicle interior noise is mainly composed of the 2nd order and 4th order noise of the engine. But the drive axle whine is obvious in some conditions, especially when the bus speed is 90km/h. And the reason is that the meshing excitation of the rear axle gear leads to the resonance of the drive axle. By the improvement of the axle housing structure, the modal frequency related to the axle whine was changed. Then the radiation noise of the axle housing before and after the structure improvement was simulated by finite element analysis and boundary element analysis. The simulation results show that the reduction of the drive axle noise at 90km/h is about 4dB(A) after the structure improvement.

1 Introduction

The drive axle is an important component of the drivetrain, which is also the main contributor to the vibration and noise of the vehicle. For new energy vehicles, especially the increasingly popular electric vehicles, the rear axle noise is particularly obvious because of the disappearance of the cover of engine noise [1, 2]. The noise of the drive axle mainly consists of the whine and the knocking noise [3], among which the whine noise is more common and disgusting for consumers. Hence, there are numerous scholars researching the axle whine all over the world.

Meng Qinghua [4] analyzed the noise signal of the drive axle, and he found that the source of the drive axle noise was caused by the meshing impact force of the spiral bevel gear of the drive axle. Guo Niancheng [5] studied the noise of the drive axle of a bus by means of testing and finite element analysis, and the drive axle noise could be reduced by the structure improvement and the application of dynamic vibration absorber. Lu Lei [6] studied the whine of rear axle for a car at the high speed, researched the dynamic meshing characteristics of the hypoid gears by finite element method, and analyzed the influence of pressure angle and bias distance on the noise. Li Zhuan [7] adopted the method of the finite element and boundary element to analyze the rear axle noise, and reduced it by reinforcing the surface of the axle housing. In the case of gear whine, most scholars focused on the transmission error, which could result the meshing impact of the gears [8-10]. Choi B - J [11-12] studied the excitation of hypoid gear meshing, and analyzed the influence factors of the drive axle noise.

He found that the optimization of the hypoid tooth shape and temperature could influence both the transmission error and noise. Koronias[13] analyzed the rear axle whine of a light truck by establishing the

multi-body dynamics model of the drive axle including the leaf springs and drive shaft, and the influence of oil temperature and other factors on the axle whine was also studied.

This paper analyzed the rear axle whine of a light bus by the vehicle test and modal test, taking into account both the passenger's subjective feeling and the objective data. Then the improvement measure was proposed to reduce the noise. Finally, the effect of the improvement measure was verified by the finite element method and the boundary element method.

2 Vehicle test of drive axle whine

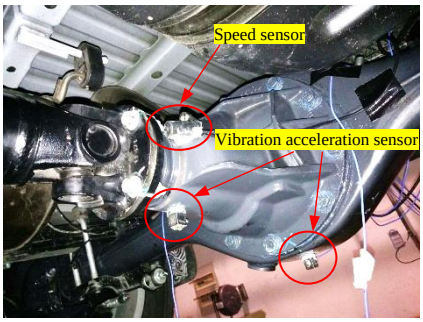
2.1 Test program

A light bus was studied in this paper, which has a four-cylinder engine. In order to analyze the reason of the rear axle whine and resolve it, the vehicle test of the drive axle whine was performed in a standard testing ground. The test instruments mainly include LMS data acquisition system, acoustic microphone, vibration acceleration sensor and magneto-electric speed sensor. The details about the number and layout of the sensors are shown in Table 1.

Type	location	Number	Number of channels
Speed sensor	Input shaft of the rear axle	1	1
Acoustic microphone	The driver's right ear	1	1
	Rear passenger's right ear	1	1
Vibration acceleration sensor	Driver's seat	1	3
	Rear cover of the axle housing	1	3
	Bearing seat of the input shaft	1	3
	Leaf spring seat	1	3
	Bottom of the rear axle	1	3
Total		8	18

Table 1: Arrangement of the sensors.

Figure 1 shows the locations of some sensors. For the acoustic microphones, the location in the bus were in accord with GB / T18697 [14]. The speed sensor is positioned near to the input shaft of the rear axle to monitor the real time rotation speed. The test conditions include accelerating, uniform speed and coasting.



(a) Drive axle



(b) The driver's position



(c) Driver’s seat rail

Figure 1: Positions of sensors

2.2 Analysis of test results

According to the subjective evaluation of both the driver and passengers, when the car is in 4th gear at 90Km/h (the speed of the rear axle input shaft is 2700rpm), there is an obvious axle whine noise in the bus. Especially in the coasting condition, the axle whine is obvious because the engine noise is smaller than that of the acceleration, so the engine’s "masking effect" is weak which leads to the appearance of axle whine noise.

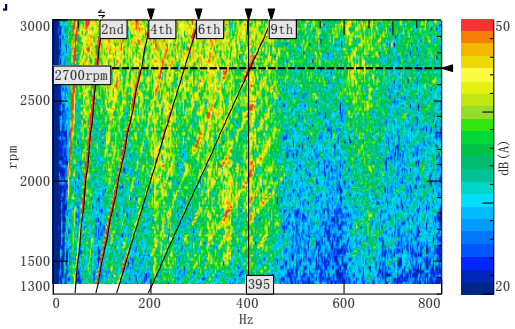


Figure 2: Order tracking graph of the noise (driver’s right ear)

Figure 2 is the order tracking diagram of the interior noise of the bus in 4th gear, i.e. the direct gear, when the bus is accelerating. The speed of the input shaft of the drive axle is taken as the reference speed, and it can be seen that the 2nd, 4th and 6th order noises of the engine are obvious. The transmission ratio of the rear axle’s main reducer is 41/9 (the ring gear has 41 teeth while the pinion 9 teeth). With each rotation of the pinion shaft, the meshing gears will produce 9 impact force, therefore the 9th order noise is the basic frequency of the rear axle.

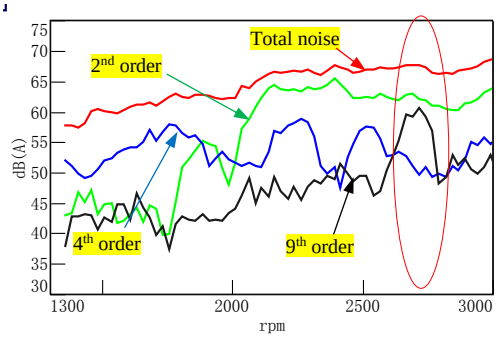


Figure 3: Order section of the noise (driver's right ear)

Figure 3 shows the order sections of the noise inside the bus. It can be seen from the figure the total inner noise increases gradually with the increase of the rotational speed. When the engine speed is below 2000rpm, the 4th order noise of the engine makes the greatest contribution to the total noise inside the bus. In contrast, the 2nd order engine noise makes up the largest component of the total noise when the speed is higher than 2000rpm. In general, the 9th order noise of the rear axle is not evident except that at 2700rpm when the amplitude of the it increases sharply. Specifically, the difference between the 9th order noise and the total noise is less than 6dB (A) at 2700rpm. In consequence the axle whine could be heard easily in the bus, especially for the passengers whose position is more close to the axle than the driver. At other speeds, the difference between the axle noise and the total noise is larger than 10dB (A), so the axle noise can hardly be recognized in the bus.

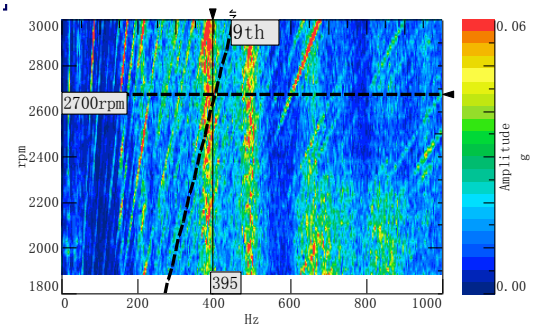


Figure 4: Order tracking of the vibration on the rear axle housing

Figure 4 is the order tracking map of the vibration of axle housing's rear cover, and there is an obvious resonance band at 395Hz. When the 9th order excitation of the gear intersects with the resonant band at 2700rpm, the resonance of axle housing could be produced, leading to the increasing of the axle whine noise. So it could be heard by both driver and passengers, consistent with the results of figure 2 and figure 3.

3 The modal analysis of the drive axle

In order to determine the mode which causes the axle whine at 395Hz, a finite element model of the drive axle is established. Its modal shapes and frequencies are simulated and modal tests are also performed by LMS.Scadas.

3.1 Finite element analysis

The finite element model of the drive axle assembly is established by Hypermesh and ABAQUS software. The Lanczos algorithm is used to simulate the mode of the driving axle in ABAQUS software.

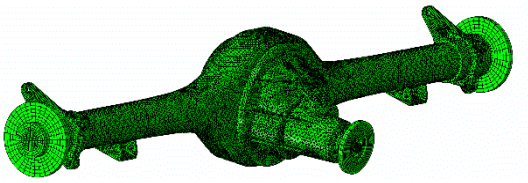


Figure 5: Finite element model of drive axle

3.2 Modal test

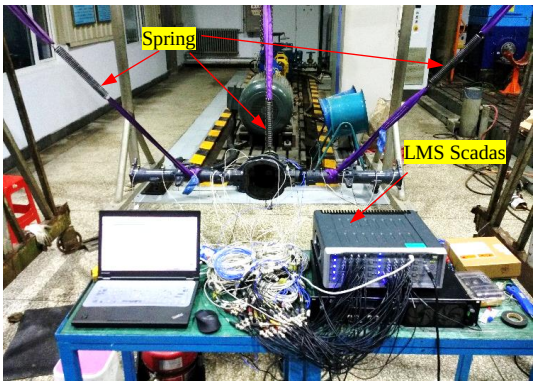


Figure 6: Modal test rear axle

Figure 6 is the modal test of the drive axle, using LMS data acquisition system, PCB acceleration sensor and PCB hammer. Drive axle is hanged by ropes connected with springs, so that its free modes and structure modes could be separated apparently, with the difference between them larger than 10 times. The number of vibration pick-up points on the drive axle is 43 points, and a three-directional vibration acceleration sensor is put at each point. The total number of channels is 129, while the whole number of channels of the LMS Scadas is 72, so it is necessary to divide the measured points into two groups and test them respectively.

Order	Simulation values(Hz)	Test values(Hz)	Error（%）
1st	78.89	73.57	7.23
2nd	104.7	99.03	5.72
3rd	270.37	281.88	-4.08
4th	337.56	343.44	1.72
5th	410.06	402.31	1.93
6th	514.35	493.68	-4.19

Table 2: Comparison of experimental and simulation modes

Table 2 shows the result of modal test and simulation of the drive axle. The errors are within 8%, which meet the needs of the project. And the finite element model can be considered accurate. The 5th order modal frequency of the drive axle is about 400Hz, which is consistent with the resonance frequency of the drive axle at 2700rpm, indicating that the rear axle whine is caused by the 5th order mode of the rear axle aroused by the meshing excitation of the gear.

4 Refinement of the rear axle whine

4.1 Mechanism of the rear axle whine

As mentioned above, the rear axle noise is mainly divided into two components: air transmission noise and structure transmission noise. Air transmission noise refers to the gear meshing noise transmitted directly through the air to the passengers. Structural transmission noise is that the gears' meshing force is transmitted through the bearing to the drive axle housing, causing its structural vibration and radiated noise. Because the hypoid gears are completely wrapped by the metal axle housing, it is difficult for the gear meshing noise to be transmitted to the outside directly, so the noise of drive axle is mainly the structural transmission noise [15].

It is known from the vehicle test that the axle whine is obvious at 90Km/h (the speed of input shaft is 2700rpm). And it is caused by the resonance of the 5^{th} order mode of the rear axle, which is aroused by the gear meshing force of the main reducer.

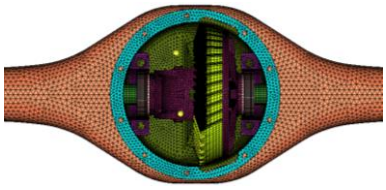
Based on the above results, the axle whine can be solved from the following aspects: (1) Reduce the meshing excitation of the main reducer of the rear axle, so it could reduce the whine noise of the drive axle from the root. However, due to the complex machining technology of hypoid gears, there is little room for the improvement of the hypoid gears. (2) Lower the vibration response value of the axle housing without changing the excitation source. (3) Improve the bus's sound insulation by the acoustic packaging, which could reduce the noise in the sound transmission path, but it will increase the cost.

4.2 Improvements

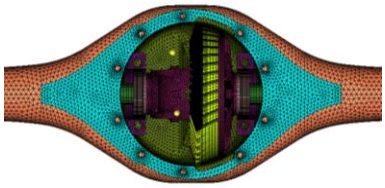
Taking into account both the practicality and the cost, in this paper, the axle whine is reduced by improvement of the axle housing's structure, which could reduce the vibration response of the axle housing.

When the bus is in 4^{th} gear, the commonly used speed range is 40Km/h~98Km/h. When the bus speed is 98Km/h the rear axle input speed is 2940rpm, and the frequency of the gears meshing force is 2940/60*9 = 441Hz. Hence, it is necessary to improve the 5^{th} modal frequency from 400Hz to more than 441Hz in order to avoid resonance in common condition.

The axle housing is welded by two pieces of stamped steel plates. As shown in Figure 7 (a), the connection position between the original axle housing and the main reducer is the annular stiffening ring welded to the axle housing, and the thickness of the stiffening ring is larger than that of the axle housing. In order to increase the stiffness of the connecting position between the main reducer and the axle housing, the shape of the structure is modified to the structure shown in Figure 7 (b). ABAQUS software is used to simulate the modal frequency of the improved structure. It is found that the modal frequency has been improved to 453Hz.



(a) Original structure



(b) Improved structure

Figure 7: The improved structure

4.3 Effect evaluation

Based on the finite element model of the drive axle, the dynamic characteristic of the driving axle is simulated by ABAQUS software with the dynamic implicit analysis method [16]. The rotation speed is applied to the input shaft, while the load torque is applied to the both sides of the axle shafts to simulate the real working condition. As shown in Figure 8, the vibration of the housing surface is simulated.

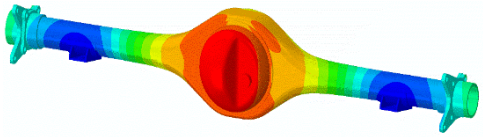


Figure 8: Vibration of the drive axle surface

Then the vibration data of the axle housing surface is imported into the LMS. Virtual. Lab software, and the radiated noise field of the drive axle is calculated by the boundary element analysis. As shown in Figure 9, the noise level at the selected position, 300mm above the drive axle referring to QC/T 533-1999[17], is extracted from the radiated noise field.

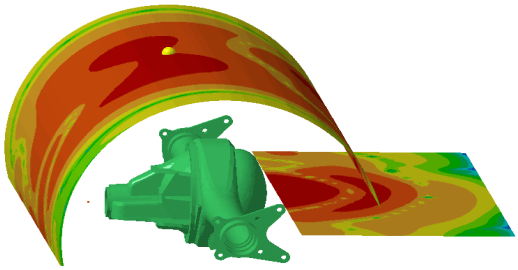


Figure 9: Radiated noise of the drive axle surface

Figure 10 shows the radiation noise of the drive axle before and after structural improvement, and it can be found that the noise of the improved drive axle at 90Km/h is obviously reduced, which is about 4dB (A) lower than that of the original structure.

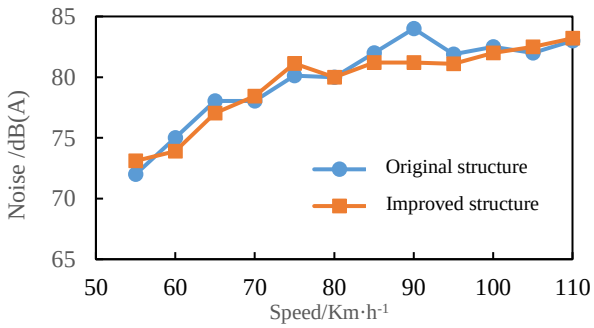


Figure10: Comparison of noise before and after the structural improvement

5 Conclusion

1) The driving axle whine is caused by the meshing excitation of the hypoid gears in the main reducer, and the order of the rear axle noise is related to the number of teeth of the pinon.

2) When the meshing excitation of the hypoid gears intersects with the inherent frequency of the drive axle, the drive axle resonates, which causes the axle whine.

3) Through the structure improvement, the resonant frequency was moved away from the common conditions. From the simulation result, the axle noise of the improved structure could be reduced by approximate 4dB (A) compared with the original structure at 90Km/h.

References

[1] RANJBAR A H, FAHIMI B. AC, Machines: Permanent Magnet Synchronous and Induction Machines. Encyclopedia of Sustainability Science and Technology, New York: Springer, 2012.
[2] Yu Peng, He Lizhao, Zhang Tong, NVH performance study of centralized motor driven vehicle power train, Journal of Machine Design, 2014, 31 (3):1-6.
[3] Guo Dong, Sound quality evaluation and control method of automotive driveline, Phd Thesis, Southwest Jiaotong University, 2015.
[4] Meng Qinghua, Zhou Xiaojun, Pang Mao, Analysis and investigation on vehicle driver axle's noise, Journal of vibration and shock, 2006, 25(1):136-139.
[5] Guo Niancheng, SHI Wenku, LIU Wenjun, Analysis and Optimization of Vibration and Noise for Driving Axle of a Light Bus, Journal of Vibration, Measurement & Diagnosis, 2012, 32(4):608-613.
[6] Lu Lei, Research and realization of noise reduction of cross-over rear axle during high-speed coasting, PhD Thesis, Wuhan University Of Technology, 2014.
[7] Li Zhuan, Study on NVH analysis of a certain type of vehicle rotary drive axle, PhD Thesis, Hefei University of Technology,2016.
[8] Litvin F L, Fuentes A, Gear Geometry and Applied Theory, Camaxle University Press, 2004.
[9] Platten M, Troubleshooting gear noise, Gear Solutions, 2011, 9(94): 34-44.
[10] Remond D, Jean Y, Simulation and experimental measurement of the transmission error of real hypoid gears under load, BOOK REVIEW, 2000: 109.
[11] Yoon J H, Choi B J, Yang I H, Deflection test and transmission error measurement to identify hypoid gear whine noise, International Journal of Automotive Technology, 2011, 12(1): 59-66.
[12] Choi B J, Yoon J H, Oh J E, A study on axle gear whine noise reduction with deflection test, Proceedings of the Institution of Mechanical Engineers, Part D: Journal of Automobile Engineering, 2012, 226(2): 225-233.
[13] Koronias G, Theodossiades S, Rahnejat H, Axle whine phenomenon in light trucks: a combined numerical and experimental investigation, Proceedings of the Institution of Mechanical Engineers, Part D: Journal of Automobile Engineering, 2011, 225(7): 885-894.
[14] General Administration of Quality Supervision, Inspection and Quarantine of the People's Republic of China(AQSIQ), GB/T 18697-2002, GB/T 18697-2002, Acoustic vehicle interior noise measurement method [S]. Beijing: Standards Press of China, 2002.
[15] Li Runfang, Wang Jianjun, Gear system dynamics, Science Press, 1999.
[16] Shi Yiping, Zhou Yurong, Detailed examples of finite element analysis of ABAQUS, Mechanical Industry Press, 2006.
[17] QC / T 533-1999. Bench test method of vehicle drive axle, Beijing: Standards Press of China, 1999.

Mechatronic suspension design for vehicle dynamic performance enhancement

H. Yuan [1], **Y. Li** [1], **J.Z. Jiang** [1], **P.H. Mellor** [2]
[1] University of Bristol, Department of Mechanical Engineering,
Queen's Building, University Walk, Bristol, United Kingdom
e-mail: **z.jiang@bristol.ac.uk**

[2] University of Bristol, Department of Eelecitrical and Electronic Engineering,
Merchant Ventures Building, Woodland Road, Bristol, United Kingdom

Abstract
This paper investigates the performance advantages of an mechatronic suspension strut for a road vehicle. Mechatronic struts have attracted growing research interest since the interior electrical circuit has the potential to realise the high-order impedances with sensible size and weight to achieve desirable performance. To deal with different driving conditions, it is straightforward to adjust electrical element values in real-time compared with changing pure mechanical elements. To obtain the optimal mechatronic suspension design, a methodology is proposed by considering all possible design parameters and constraints such as nominal voltage and current of motors, maximum force on the ball-screw shaft, and size and weight of electrical elements. Based on a qualitative analysis, it provides brief guidelines for ball-screw and motor selections. Case studies are carried out with a quarter-car model using two electrical candidate layouts, which show potential performance advantages of the mechatronic strut using a motor with sufficiently large nominal current.

1 Introduction

Mechatronic suspension struts attract wide attentions with great potential in realising complex networks and performance enhancement. Different realisations of mechatronic strut have been studied recently. In Sijing's paper [1], two different types of Energy Harvesting Shock Absorbers (EHSAs), one with mechanical motion rectifier (MMR) and one without it, have been compared on different vehicles. It has been shown that MMR-EHSAs provide better rider performances and road handling simultaneously over the traditional shock absorber when installed on light-damped, heavy-duty vehicles. The EHSAs translate the up-and-down suspension vibration into a bidirectional rotation of the generator using a rack-pinion mechanism. A ball-screw mechanism can also be applied to translate linear motion to rotational motion in mechatronic struts, which is presented in [2]. Furthermore, a prototype of an electro-hydraulic semi-active damper was designed and manufactured, and a series of experimental tests were conducted to demonstrate its effectiveness to generate the damping characteristic for enhanced performance in Yuxin's paper [3]. Apart from rotary motors, linear motor is also employed in the mechatronic strut. For example, in Songye's paper [4], a novel application of electromagnetic damper using a linear motor is studied on structural vibration control, and it presents a theoretical and experimental study of linear electromagnetic dampers connected with four representative circuits. A good match between the modelling and testing results clearly demonstrates that the described model can predict the performance of the linear electromagnetic damper very well.

In mechatronic struts, rotary motors are commonly used with a mechanism to translate linear motion to translational such as ball-screw and rack-and-pinion. Rotary motors and these mechanisms bring inertia effects

to the strut, which is considered and can be realised as an inerter in a mechanical network. Since the inerter [5] was proposed to substitute the mass element in the mechanical-electrical analogy, the abundant electrical theorems can be directly applied to the analysis and synthesis of mechanical networks which can be used in designing mechanical systems to achieve enhanced performance. The more high-order passive impedance, the further enhanced system performance is obtained [6]. In this analogy, the physical characteristics of inerters, dampers and springs correspond to the electrical characteristics of capacitors, resistors and inductors, respectively. The mechatronic strut, combined of mechanical and electrical networks, can be translated to a equivalent mechanical network using this analogy. The synthesis of a high-order pure mechanical system is difficult due to the limitation on the size and weight of the system. Therefore, in [2], a high-order passive impedance can be easily realised by a basic mechanical network with a high-order electrical network, where a prototype of the mechatronic strut was proposed and applied to vehicle suspension systems. Although considerable research effects have been made, some challenges still exist which hinder the large scale application of mechatronic vibration suppression devices. Firstly, a systematic optimum design approach has not been established to identify the optimum designs for both the mechanical and electrical parts, in terms of the topology and element values. Secondly, realistic considerations, such as weight, size and robustness of the whole system, have not been fully explored.

In this paper, a design methodology for mechatronic struts is presented. Based on qualitative analysis, some guidelines for ball-screw and motor selection are drawn. Case studies have shown that the mechatronic strut has a potential to achieve enhanced performance for road vehicles. This paper is arranged as follows: Section 2 introduces the principles of the mechatronic strut and represents its corresponding mechanical network and admittance function. In Section 3, the design methodology of suspension systems is presented. Furthermore, the qualitative analysis of the mechatronic strut is carried out. Section 4 presents the quarter-car model and the case studies of the mechatronic strut for different motors and suspension networks. In Section 5, some conclusions are drawn.

2 The mechatronic strut

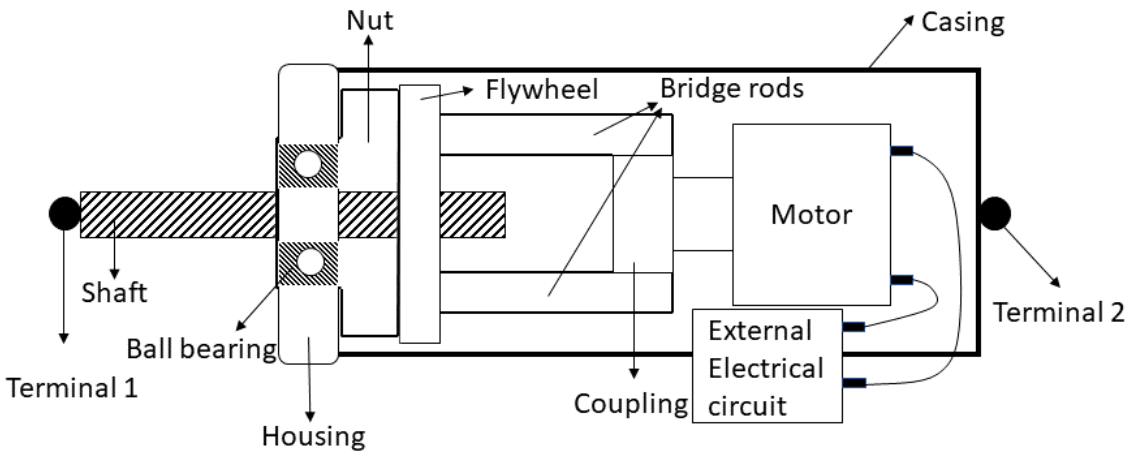


Figure 1: The schematic diagram of the mechatronic strut system

A schematic diagram of the mechatronic strut is shown in Figure 1. The proposed mechatronic strut consists of a ball-screw mechanism, a permanent magnetic electrical motor (PMEM) and an external electrical circuit. The relative linear motion between the two terminals of the strut results in the rotational motion of the ball-screw mechanism, which in turn drives the motor to generate an inductive voltage. To provide desirable performance, a suitable external electrical circuit is connected to the motor to generate corresponding torque in the rotor. The torque acts back to the ball-screw mechanism, and hence change the force-velocity

behaviour across terminals 1 and 2. Furthermore, the external electrical circuit is connected to the PMEM terminals.

The working principle and electrical model of a PMEM is introduced, and then the principle of a ball-screw mechanism is presented. In Section 2.3, the admittance and equivalent mechanical network of the mechatronic strut is introduced.

2.1 The permanent magnet electric motor

In a PMEM, the armature can be modelled as a resistor R_m and inductor L_m in series in electrical circuits. R_m is the coil resistance of the armature and the inductance L_m for the armature is produced once the armature rotates. Figure 2 presents the schematic electrical circuit diagram of a PMEM with an external electrical circuit connected.

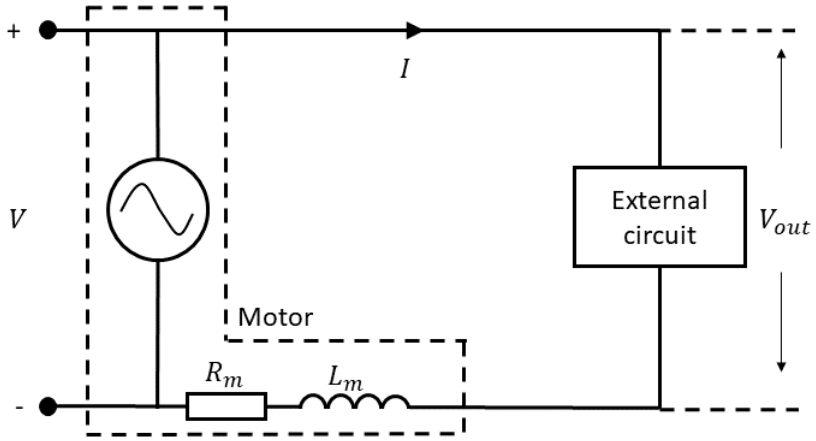


Figure 2: The schematic electrical circuit diagram for a PMEM model connected with an external electrical circuit.

The inductive voltage V and inductive torque T_m are generated by the motor simultaneously while the armature rotates. If the armature rotates with an angular velocity ω, the inductive voltage V can be represented as:

$$V = k_e \cdot \omega, \tag{1}$$

where k_e is the voltage constant (Vs/rad). The armature current I can then be calculated from the inductive voltage V and electrical admittance $Y_e(s)$, with the latter determined by the external electrical circuit and armature model. The expressions of I in the Laplace domain and $Y_e(s)$ are given as follows:

$$\widetilde{I} = Y_e(s) \cdot \widetilde{V}, \tag{2}$$

$$Y_e(s) = \frac{\widetilde{I}}{\widetilde{V}} = \frac{1}{R_m + s \cdot L_m + Z_{ex}(s)}, \tag{3}$$

where $Z_{ex}(s)$ is the external circuit impedance. Then the inductive torque T_m is calculated by the following equation:

$$T_m = k_t \cdot I, \tag{4}$$

where k_t is the motor torque constant with unit $\mathrm{N} \cdot \mathrm{m/A}$. The inductive voltage constant k_e and inductive torque constant k_t are identical and are determined by the magnetic flux, the number of the armature coils and poles of a PMEM. Therefore, the dynamics of the motor in rotational direction can be represented as:

$$T_E = J_m \frac{d\omega}{dt} + T_m + B_m \omega, \tag{5}$$

where T_E is the total torque generated by the motor and J_m the moment of inertia for the rotor. B_m is the damping coefficient of the motor strut.

2.2 Ball-screw mechanism

A ball-screw mechanism is used to convert linear motions into rotational motions to drive the motor. The relation between the force F_M on the ball-screw and the torque T_M is shown as follows:

$$F_M = (\frac{2\pi}{P}) T_M, \tag{6}$$

where P is the pitch of a ball-screw mechanism. The relation between the angular velocity ω on the ball-screw and the linear velocity v is presented as follows:

$$\omega = (\frac{2\pi}{P}) v, \tag{7}$$

If the ball-screw mechanism is ideal, for example, by ignoring friction and backlash, the torque T_M can be expressed as follows:

$$T_M = J_T (\frac{d\omega}{dt}), \tag{8}$$

where J_T is the total moment of inertia of the nut and the flywheel in a ball-screw mechanism, which can produce an inertance effect for the strut. Substituting Equations 7 and 8 into 6, the force F_M is given as:

$$F_M = (\frac{2\pi}{P})^2 J_T (\frac{dv}{dt}) = b \cdot a, \tag{9}$$

where $b = (\frac{2\pi}{P})^2 J_T$ is the ball-screw inertance and a the relative acceleration across its two terminals. The total ball-screw mechanism inertance b can be easily adjusted by tuning the flywheel.

2.3 Mechanical admittance of the mechatronic strut

To determine the admittance and equivalent mechanical network of the mechatronic strut, the dynamics of the motor in rotational direction is transferred to translational direction. As the torque T_E is acting through the ball-screw mechanism to the system, the dynamics of the motor in translation direction can be written by substituting Equation 7 and $F = \frac{2\pi}{P} T$ into Equation 5 and simplified as follows:

$$F_E = \frac{2\pi}{P} T_E = b_e \cdot a + F_m + (\frac{2\pi}{P})^2 B_m v, \tag{10}$$

where F_E is the force produced by the motor, the inertance, b_e, generated by the rotor equals $(\frac{2\pi}{P})^2 J_m$, and the inductive force, F_m, equals $\frac{2\pi}{P} T_m$. The total force F generated by the mechatronic strut is the sum of mechanical force F_M and electrical force F_E as given by:

$$F = F_M + F_E. \tag{11}$$

Substituting Equations 9 and 10 into 11, the dynamics equation of the mechatronic strut can be rewritten as follows:

$$F = (b_e + b) \cdot \frac{dv}{dt} + F_e + (\frac{2\pi}{P})^2 \cdot B_m \cdot v \tag{12}$$

Substituting Equation 1 - 4 and 6 - 7 into Equation 12 to obtain the admittance Y_{ms} of the mechatronic strut:

$$Y_{ms} = \frac{F(s)}{v(s)} = (b_e + b)s + (\frac{2\pi}{P})^2 B_m + \frac{(\frac{2\pi}{P})^2 k_e k_t}{R_m + s \cdot L_m + Z_{ex}(s)} \tag{13}$$

For simplification, the following parameters are defined:

$$\begin{cases} c_e = (\frac{2\pi}{P})^2 B_m \\ G_m = (\frac{2\pi}{P})^2 k_t k_e \end{cases}$$

Therefore, Equation 13 can be rewritten as follows:

$$Y_{ms} = (b_e + b)s + c_e + \frac{G_m}{R_m + sL_m + Z_{ex}(s)}. \tag{14}$$

From the admittance Y_{ms}, the mechatronic strut can be divided into two parts: the first part $(b_e + b)s + c_e$ is considered as the mechanical inerter and damper of the motor structure, and $G_m/(R_m + sL_m + Z_{ex}(s))$ is regarded as the admittance of an external electrical circuit and motor. Using the analogy of mechanical and electrical systems, the equivalent mechanical network of the strut is presented in Figure 3, where k_m, c_m and G_m/Z_{ex} represent the corresponding internal inductor, internal resistor and external circuit, respectively. The corresponding relationships between electrical and mechanical elements are presented as follows:

$$\begin{cases} k_m = \frac{G_m}{L_m} \\ c_m = \frac{G_m}{R_m} \end{cases}$$

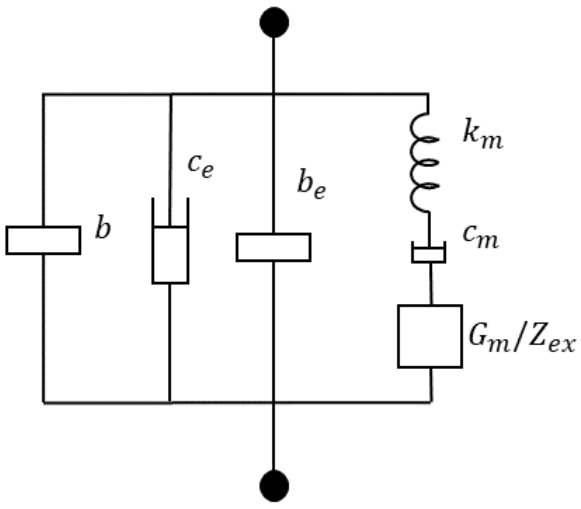


Figure 3: Simplified equivalent network for the mechatronic strut

3 Suspension design

3.1 Optimisation methodology

In the optimisation methodology, design parameters and physical constraints for the ball-screw mechanism, electrical motor and electrical elements are considered. These design parameters and constraints for the strut are listed in Table 1.

	Ball-screw	Motor	Electrical elements
Design parameters	P, J_M	$k_e, k_t, J_m, B_m, R_m, L_m$	R, L, C
Constraints	$\delta x_{max}, F_{max}, b$	$V_{peak}, I_{rms}, \omega$	physical range of c, k, b

Table 1: Selected parameters and constraints considered for the optimisation process.

For a ball-screw mechanism, pitch P is one of the most important design parameters as analysed in Section 2.2 and 2.3. Furthermore, the nut inertia, J_M is another design parameter to represent the minimum inertia of a ball-screw mechanism. As the values of P and J_M is interact, the corresponding J_M for each value of P is different. For a motor, parameters $k_e, k_t, J_m, B_m, R_m, L_m$ are constant properties, but values of them may vary for different motors and can be found from its specification. Based on these parameters and pitch, the value of mechanical elements b_e, k_m and c_m are determined for the mechanical network. In the external circuit, three basic electrical elements may be used which are resistors R, inductors L and capacitors C. The values of their corresponding mechanical elements can be determined from the relations shown as follows:

$$\begin{cases} k = \frac{G_m}{L} \\ c = \frac{G_m}{R} \\ b = G_m \cdot C. \end{cases}$$

Physical constraints for the mechatronic strut have to be determined and implemented into the optimisation process to check if the optimal values of these elements are feasible in physical realisation. For a ball-screw mechanism, δx_{max} and F_{max} are the maximum relative displacement between two terminals and maximum force applied to the ball-screw mechanism, respectively. In the specification, the maximum force F_{max} of a ball-screw mechanism is listed for each set value of P. The minimum inertia of a ball-screw mechanism J_M produces a minimum inertance for the system, which is used as the lower boundary of b for the ball-screw mechanism. If the optimal value of b is bigger than the lower boundary, the rest inertance can be easily adjusted by tuning the attached flywheel. For a motor, to make sure the mechatronic strut system working normally in a long time, the value of V, I and ω calculated in the optimisation process for the motor have to be smaller than its nominal voltage V_{nom}, current I_{nom} and velocity ω_{nom}, respectively. For physical realisation, each electrical element should be considered within its achievable physical range. From these ranges, the constraints for their corresponding mechanical elements can be calculated. Therefore, these constraints are used in the optimisation to obtain the optimum values for these corresponding mechanical elements and meet the physical realisation requirements of electrical elements.

The optimisation methodology can be simplified as some design parameters and constraints may not able to be determined from their specifications. The simplified optimisation methodology is used to for the case studies later on. For motors used in case studies, the damping coefficient B_m is not able in their specifications. Therefore, the value of c_e can not be calculated for the suspension network, and then the element c_e is neglected for the optimisation process. However, the value of B_m can be identified through experiment and implemented into the system. Moreover, it is assumed that all values of electrical elements can be physically realised in the optimisation so the constraints of electrical elements can be neglected in optimisation. Therefore, the general network can be simplified as in Figure 3 without c_e.

3.2 Qualitative analysis

In this section, it provides an analysis to qualitatively discuss what the preferred properties required of the ball-screw mechanism and motor for the mechatronic strut.

3.2.1 Ball-screw mechanism

The total ball-screw inertance $b = b_M + b_{flywheel}$ can be adjusted by adding or removing the flywheel, but there is a lower boundary, which is the inertance b_M dominated by the nut with inertia J_M and pitch P for a

ball-screw mechanism and the relation between them is given as follows:

$$b_M = (\frac{2\pi}{P})^2 \cdot J_M \tag{15}$$

Therefore, the total equivalent inertance b_{total} of the mechatronic strut should be larger than b_M and the relation is presented as follows:

$$b_{total} \geq b_M \tag{16}$$

To increase the possibility of achieving more admittance functions for the strut, the value of b_M should be as small as possible only considering the ball-screw mechanism. To have small b_M, the ball-screw mechanism requires large P and small J_M. However, there is a trade-off between pitch P and lower boundary inertia J_M. Sometimes, there is no detailed information available on the trade-off, a specific ball-screw for case studies in Section 4 is picked. Furthermore, the constraint of F_{max} should be as large as possible to enhance the capability of force acting through the ball-screw shaft.

3.2.2 Electrical motor

Inertance b_e in Figure 3, which is fixed once the motor is selected, is dominated by the motor inertia J_m and pitch P and its relation is given as follows:

$$b_e = (\frac{2\pi}{P})^2 \cdot J_m \tag{17}$$

Therefore, combining Equations 15 and 17, b_{total} should be larger than the sum of b_M and b_e and its relation is shown as follows:

$$b_{total} \geq b_M + b_e \tag{18}$$

To increase the possibility of achieving more admittance functions for the strut, the value of b_e should be as small as possible. As b_e is determined by Equation 17, it shows that the large pitch it has with small inetias J_m, the small b_e it will have. Conclusively, the selected motor should have a small inertia to achieve small inertance b_e for a mechatronic strut.

The internal resistance R_m and internal inductance L_m of the selected motor is modelled as a spring k_m and damper c_m in mechanical network which are in series with an external circuit shown in Figure 3. From Equation 3, to increase possibility of obtaining optimum transfer function for a system, the value of R_m and L_m should be as small as possible. For that reason, the values of c_m and k_m should be as large as possible to demonstrate this by applying translation relationships between mechanical and electrical elements. Conclusively, small values of R_m and L_m of a motor is more suitable for the proposed mechatronic strut.

In Section 2.3, the inductive force F_m equals $\frac{2\pi}{P}T_m$. By substituting it into Equation 4, the relation of F_m and I is given as follow:

$$I_{nom} \geq I = \frac{F_m \cdot P}{2\pi \cdot k_t}. \tag{19}$$

From Equation 1 and 7, the relation of V and v is given:

$$V_{nom} \geq V = 2\pi \frac{k_e}{P} v. \tag{20}$$

For each motor, there is a set of corresponding nominal voltage V_{nom} and current I_{nom}. To make sure the optimisation results are feasible, the optimised voltage and current in the electrical circuit must meet these constraints of nominal voltage and current. Furthermore, it is assumed that all optimised electrical elements' values can be realised. Then Equations 19 and 20 can be combined and rearranged as follows:

$$\frac{F_m}{2\pi \cdot I_{nom}} \leq \frac{k_e}{P} \leq \frac{V_{nom}}{2\pi \cdot v} \tag{21}$$

To expand the possible solutions of $\frac{k_e}{P}$, the nominal voltage and current of a motor have to be as large as possible. In conclusion, a optimum motor for the proposed mechatronic strut should have small inertia J_m, internal resistance R_m, internal inductance L_m and large nominal voltage V_{nom} and current I_{nom}.

4 Case studies

The potential performance in ride comfort J_1 of the mechatronic strut is presented in a quarter-car model. A commonly used ball-screw mechanism is selected for the mechatronic strut. Using simplified optimisation procedure, case studies are carried out with specific motors and candidate external electrical circuits.

4.1 Quarter-car model and Performance index

A quarter-car model in Figure 4 (a) is applied to illustrate the performance benefits of the proposed mechatronic strut for vehicle dynamics, where m_s and m_u are the sprung and unsprung masses, x_r the displacement of road excitation, x_s and x_u the corresponding displacement of the sprung and unsprung masses, k_t the tyre stiffness. Figure 4 (b) presents the conventional suspension system for the quarter-car model. In this paper, the parameters of the quarter-car model are fixed as follows: $m_s = 250$kg, $m_u = 35$kg, $k_t = 150$kN/m [7]. Furthermore, $k_s = 30000\mathrm{N/m}$ is set to represent a normal passenger vehicle.

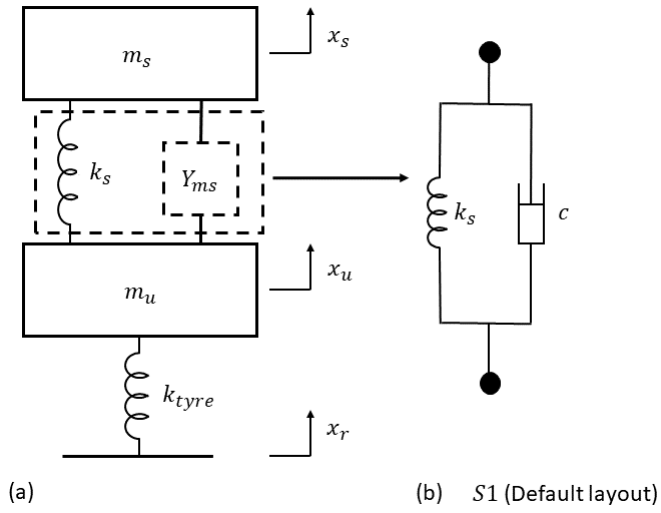


Figure 4: The schematic diagram of the quarter-car model.

To design a suspension system, there are a number of practical design requirements to meet such as passenger comfort, handling, tyre normal loads, limits on suspension travel etc. Although suspension design usually involve a trade-off between various performance requirements, it is useful to consider first how much improvement can be obtained in individual performance measures for various configurations. To compare the performance benefits, ride comfort J_1 index is selected as follows [7]:

$$J_1 = 2\pi\sqrt{V\kappa}||sT_{\widetilde{x}_r\to\widetilde{x}_s}||_2 \tag{22}$$

where $||sT_{\widetilde{x}_r\to\widetilde{x}_s}||_2$ is the H_2 - norm of $sT_{\widetilde{x}_r\to\widetilde{x}_s}$, V the driving velocity of the vehicle, while κ is the road roughness parameter. Values of V and κ are referred in [7].

The road input in time domain is also used to determine the system transient response such as V_{peak} and I_{rms}. The procedure to generate the time domain signal is referred in [8].

4.2 Selected ball-screw

Based on qualitative analysis, the ball-screw mechanism should have small inertia and large force constraints. In Yilun's paper [9], a common ball-screw mechanism, which the inertia and pitch are $0.02\mathrm{kgcm}^2$ and $6\mathrm{mm}$,

respectively, is was proposed for a novel shock absorber. The value of maximum force constraint was not presented in Yilun's paper so it is taken from common ball-screw mechanism specification where its value is 26.5kN [10].

4.3 Selected motors

The qualitative analysis in Section 3.2 gives a brief guidelines for motor selection. Furthermore, the maximum terminal voltage of motors must be below 48V considering automotive 48V system [11]. As a result, two specific motors are selected with maximum available terminal voltage (48 V) and their parameter values are presented in Table 2. Comparing Motor-1 and Motor-2, Motor-1 has a small inertia J_m while Motor-2 has large nominal I and small R_m and L_m. Two candidate external electrical circuits E_1 and E_2 are proposed, with the corresponding mechanical networks shown in Figure 5. The proposed two electrical circuits are used to replace the G_m/Z_e part in Figure 3.

	$V_{nom}(\text{V})$	$I_{nom}(\text{A})$	$R_m(\Omega)$	$L_m(\text{mH})$	$J_m(\text{gcm}^2)$	$k_t(\text{Nm/A})$	$k_e(\text{Vs/rad})$
Motor-1	48	1.41	2.95	0.514	21.2	0.0429	0.0428
Motor-2	48	2.17	1.40	0.473	75.9	0.0585	0.0586

Table 2: Parameters values for different motors.

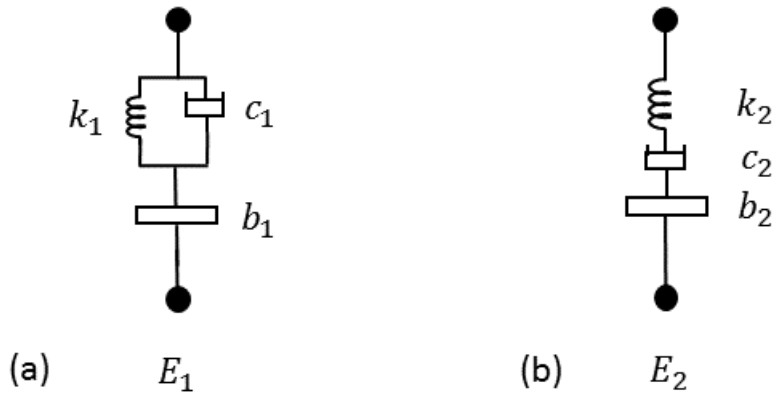


Figure 5: The corresponding mechanical networks of two external electrical circuits E_1 and E_2.

Table 3 shows the optimisation results of four cases for two different motors in two different suspension networks using E_1 and E_2. In comparison with the optimal J_1 obtained by the conventional suspension network S_1 shown in Figure 4 (b), the dynamic performance J_1 of four cases are much worse. It also can be seen from Table 3 that current in motors reaches the upper boundary of constraints I_{nom} for all cases. To explore the impacts of the constraints on the cost function, a further investigation of J_1 to the change of constraint values is necessary. As the terminal voltage of motors has not reached the safe level, here only the constraint I_{nom} is considered.

	J_1			$V_{peak}(\text{V})$		$I_{rms}(\text{A})$	
	Optimal, S_1	E_1	E_2	E_1	E_2	E_1	E_2
Motor-1	1.24	41.4	41.4	10.6	10.8	1.41	1.41
Motor-2	1.24	27.2	12.6	13.2	41.2	2.17	2.17

Table 3: Results of two different motors.

If the constraint I_{nom} is released for both specific motors, the optimal J_1 can be further improved. Table 4 presents the optimal results of J_1 and their corresponding required current I_{rms} and voltage V_{peak} in the electrical circuit for all cases. In comparison with the optimal J_1 obtained by the conventional suspension system S_1, a maximum 14.5 % enhanced performance in ride comfort can be achieved if I_{nom} of Motor-2 using network E_1 is large enough. Furthermore, a 13.7% improvement of J_1 is obtained with Motor-2 using network E_2. Comparing these two cases, Motor-2 using E_1 is better for the system as it has smaller required current and larger improvement. As improvements for Motor-1 using both networks are poor, Motor-2 with large I_{nom} and small R_m and L_m is more suitable the system.

Figure 6 presents the vertical acceleration of m_s in frequency domain for all cases. Furthermore, the vertical acceleration of m_s in time domain for the optimal case is shown in Figure 7 where only 25s response signal is shown. To clearly see improvements in time and frequency domain, the response of vertical acceleration of m_s is presented in both domains.

In conclusion, for these two specific motors, none of them can provide a better dynamic performance J_1 than the optimised conventional system. However, the investigation of constraint I_{nom} shows that both motors with large I_{nom} can obtain better dynamic performance J_1. Furthermore, Motor-2 with smaller internal resistance and inductance and large nominal current can have better performance.

	Optimal, S_1	Motor-1, E_1	Motor-1, E_2	Motor-2, E_1	Motor-2, E_2
J_1	1.24	1.23	1.23	1.06	1.07
I_{rms}(A)	-	3.3	3.4	3.4	4.1
V_{peak}(V)	-	48	48	48	48
Improvement (%)	-	0.8	0.8	14.5	13.7

Table 4: Optimal results of J_1 for four cases and their corresponding required current, voltage and improvement.

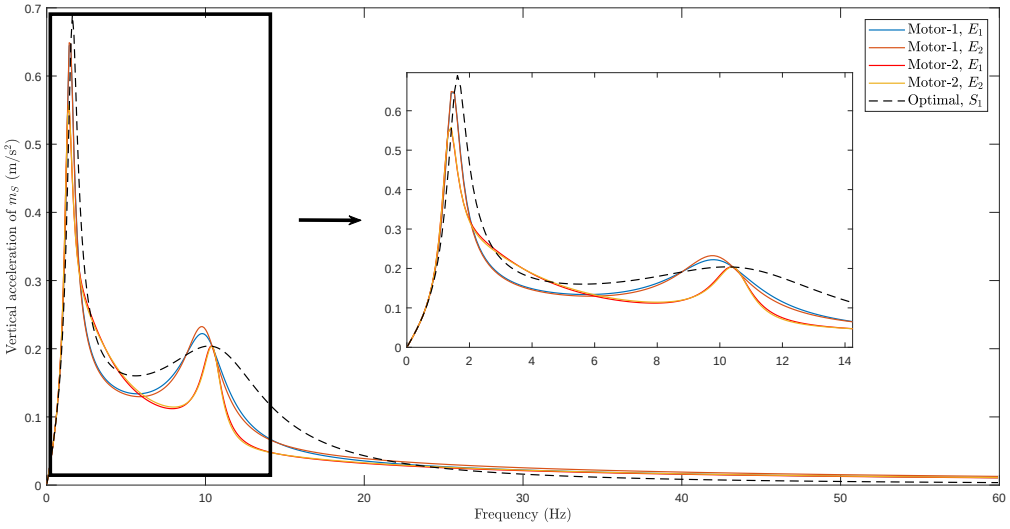


Figure 6: The vertical acceleration of m_s in frequency domain.

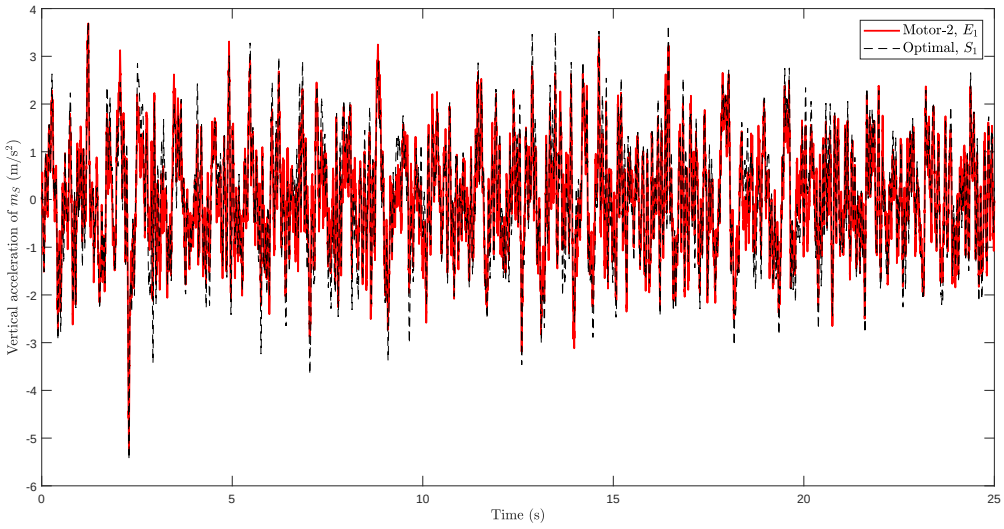


Figure 7: The vertical acceleration of m_s in time domain.

5 Conclusion

This paper investigated the potential of mechatronic strut for road vehicles and proposed a design methodology and qualitative analysis. Cases studies of the mechatronic vehicle suspension strut were carried out and it shows that the strut can provide improvements of ride comfort for a quarter-car model. To obtain the optimal mechatronic suspension design, an optimisation methodology is proposed by considering all possible design parameters and constraints such as nominal voltage and current for the motor, maximum force acting on the ball-screw mechanism and size and weight of the electrical elements. In the qualitative analysis of the mechantronic strut, an motor for the strut should have small inertia J_m, internal resistance R_m, internal inductance L_m and large nominal current I_{nom} and voltage V_{nom}. A ball-screw mechanism should have small initial inertance b_M and large bearable force F_{max}. Furthermore, to obtain the optimal J_1 for the system, the corresponding suitable ratio of $\frac{k_e}{P}$ can be only a value or within a range. Therefore, there may be multiple solutions of $\frac{k_e}{P}$ for the system. Simultaneously, there are multiple available choices for motor and ball-screw mechanism selections for each value of $\frac{k_e}{P}$. In case studies, the dynamic performance of suspensions using two specific motors are determined with two candidates external electrical circuits by using a simplified optimisation procedure. It shows obtained J_1 for all these motors are worse than J_1 obtained by conventional suspension system. This is because that J_1 becomes poor to meet those constraints in optimisation such as I_{nom} and V_{nom}. Then the impact of I_{nom} to J_1 was carried out as V_{nom} has not reached the safe level shown in Table 4. From the analysis for both motors, dynamic performance J_1 can be improved significantly if the constraint of I_{nom} is released. As Motor-2 has small internal resistance and inductance, optimal J_1 obtained using Motor-2 is better than that obtained with Motor-1 with up to 14.5% improvement.

Acknowledgements

The authors would like to acknowledge the support of the Royal Society, EPSRC and the China Scholarship Council: Jason Zheng Jiang is supported by an Royal Society (Reference: IE151194) and EPSRC grants (Reference: EP/P013456/1), Hui Yuan is supported by an EPSRC scholarship (Reference: EP/N509619/1) and Yuan Li is supported by a China Scholarship Council studentship.

References

[1] S. Guo, Y. Liu, L. Xu, X. Guo, and L. Zuo, *Performance evaluation and parameter sensitivity of energy-harvesting shock absorbers on different vehicles*, Vehicle System Dynamics, Vol. 54, No. 7, (2016), pp.918-942.

[2] F. C. Wang, H. Chan, *Vehicle suspensions with a mechatronic network strut*, Vehicle System Dynamics, Vol. 49, No. 5, (2011), pp. 811-830.

[3] Y. Zhang, H. Chen, K. Gao, X. Zhang, and S. E. Li, *Electro-hydraulic damper for energy harvesting suspension: Modeling, prototyping and experimental validation*, Applied energy, Vol. 199, (2017), pp. 1-12.

[4] S. Zhu, W. A. Shen, and Y. L. Xu, *Linear electromagnetic devices for vibration damping and energy harvesting: Modeling and testing*, Engineering Structures, Vol. 34, (2012), pp. 198-212.

[5] M. C. Smith, *Synthesis of mechanical networks: The inerter*, IEEE Transactions on automatic control, Vol. 47, No. 10, (2002), pp. 1648-1662.

[6] C. Papageorgiou, M. C. Smith, *Positive real synthesis using matrix inequalities for mechanical networks: application to vehicle suspension*, IEEE Transactions on Control Systems Technology, Vol. 14, No.3, (2006), pp. 423-425.

[7] M. C. Smith, and F. C. Wang, *Performance benefits in passive vehicle suspensions employing inerters*, Vehicle System Dynamics, Vol. 42, No. 4, (2004), pp. 235-257.

[8] J. Z. Jiang, A. Z. Matamoros-Sanchez, A. Zolotas, R. M. Goodall, and M. C. Smith, *Passive suspensions for ride quality improvement of two-axle railway vehicles*, Proceedings of the Institution of Mechanical Engineers, Part F: Journal of Rail and Rapid Transit, Vol. 229, No. 3, (2015), pp.315-329.

[9] Y. Liu, L. Xu, and L. Zuo, *Design, Modeling, Lab, and Field Tests of a Mechanical-Motion-Rectifier-Based Energy Harvester Using a Ball-Screw Mechanism*, IEEE/ASME Transactions on Mechatronics, Vol. 22, (2017), pp. 1933-1943.

[10] THK CO., LTD, *Precision Ball Screws DIN Standard Compliant Ball Screw*, https://tech.thk.com/upload/catalog_claim/pdf/335-2E.pdf, Access on 5th May 2018.

[11] M. Bikson, *A review of hazards associated with exposure to low voltages* New York: University of New York, (2004).

A parametric study and modal analysis of an acoustic black hole on a beam

K. Hook [1], **J. Cheer** [1], **S. Daley** [1]
[1] The Institute of Sound and Vibration Research, Faculty of Engineering and the Environment,
The University of Southampton, Southampton, United Kingdom
e-mail: **k.hook@soton.ac.uk**

Abstract
Acoustic black holes are structural features that have a varying thickness profile, and provide a potential lightweight damping solution for flexural vibrations. In practical applications, the length of an acoustic black hole will be constrained by the available space and the minimum tip height will be limited by both the manufacturing capabilities and strength requirements. Therefore, the power law of the taper is often the critical design parameter. In this paper, a parametric study of an acoustic black hole termination on a beam is presented with practical constraints on the length and tip height. The reflection coefficient of the acoustic black hole has been calculated for a range of power laws and it has been shown that, for a fixed power law, the reflection coefficient varies over frequency and exhibits bands of high and low reflection. These bands can be related to modes of the acoustic black hole. In addition, it has been found that an optimum power law exists for minimising the broadband average reflection coefficient for each acoustic black hole configuration.

1 Introduction

The acoustic black hole effect, as described by Mironov in 1988 [1], is a phenomenon that occurs when a beam or plate is tapered to a point, over a distance equal to or larger than the acoustic wavelength. Figure

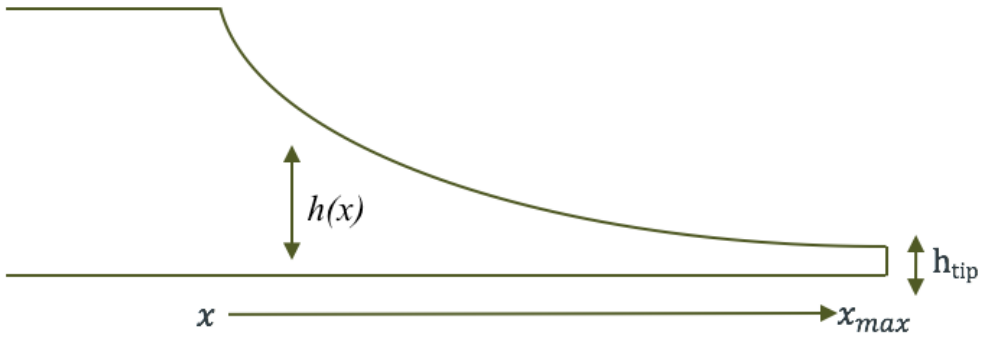


Figure 1: A diagram of an acoustic black hole taper.

1 shows an example of an acoustic black hole, seen as the tapering of the beam to a point via a power law curve. The behaviour of such an acoustic black hole can be explained by considering flexural vibrations travelling down a tapered Euler-Bernoulli beam. As the vibrations propagate towards the tip, their velocity is reduced following the relationship

$$c_b = \sqrt[4]{\frac{Eh^2(x)\omega^2}{12\rho}} \tag{1}$$

where E is the Young's modulus of the beam material, $h(x) = \varepsilon x^{\mu} + h_{tip}$ is the height function of the beam, ω is the angular frequency of the vibrations, ρ is the density of the beam material and ν is the poisson ratio [2,3]. For a tapered semi-infinite plate, the same equation may be used by the inclusion of the poisson ratio term: $1/(1-\nu^2)$ [4]. It can be seen, from equation 1, that the wave speed in a tapered beam is proportional to the square root of the beam height. It follows that, as the height function tends to zero, the velocity of a propagating wave converges to zero. Hence, the propagating wave will theoretically never reach the tip of the taper and therefore will not reflect back out of the taper. In reality, a perfect and infinite tapered beam cannot be manufactured and the structural integrity of the acoustic black hole is questionable for very thin tip heights. It has previously been shown that the acoustic black hole effect is negligible for practical tip heights, but that improvements could be made to the effectiveness by applying thin viscoelastic damping layers to either one or both sides of the taper, which results in a significant reduction in the reflection coefficient from the acoustic black hole [5–7]. It is clear that there is a tradeoff between practicality and performance in the design of acoustic black holes.

Over time, there has been an increase in the amount of literature modelling more practically dimensioned acoustic black holes. This has coincided with an increase in experimental studies, used to validate the models, which are limited by manufacturing restrictions on the tip height and length of the taper. The thickness tends to range from about a 10mm beam or plate height down to a 0.25mm tip height. The taper lengths are usually up to 10cm long and the power law of the taper tends to be between 2 and 4. Damping layers, applied to the acoustic black hole taper, have usually been thin but theory predicts that the thickness of the damping layer can be up to six times the thickness of the base layer before the increase in loss factor diminishes [8, 9].

So far, work has been done that examines the influence of the tip height and power law on the modal density of an acoustic black hole on a beam [10]. It has been shown that a smaller tip height significantly increases the modal density of an acoustic black hole. Higher power laws cause a slight increase in modal density. The modal density of the acoustic black hole on a beam was not found to be related to the modal density of a uniform beam [10]. In addition to this, band gaps have been observed in acoustic black holes. For an acoustic black hole cell, the mode shapes of the bounding frequencies of the band gaps have been matched to the mode shapes of the resonant frequencies [11]. These band gaps have also been shown to vary in range and frequency when the power law of the acoustic black hole taper is changed, and when the tip height is changed. The optimum thickness of damping has been investigated with the use of a laser as both an excitation and measurement device, which also allowed visualisation of wave propagation and small imperfections in the structure [7].

This paper will investigate the potential link between the reflection coefficient of an acoustic black hole, the band gaps mentioned in [11] and the different controllable parameters of an acoustic black hole. In this paper, a finite element model of a lightly damped acoustic black hole on a beam is presented and used to investigate the design tradeoff between the geometric parameters. The reflection coefficient for frequency dependant parameter sweeps and broadband frequency parameter tradeoffs is then shown and there is a discussion of the findings. A link between the modes of an acoustic black hole and the power law of the taper is presented alongside a discussion about optimising the power law for practical application. Finally, the conclusions of this work are presented.

2 The finite element model of an ABH on a beam

In order to carry out a parametric study of the acoustic black hole, a finite element model of an acoustic black hole on the end of a long beam has been developed. The beam was assigned a width of 4cm, a length of 3m and a height of 1cm. The acoustic black hole shared the same width and starting height as the beam. The beam and taper were both assumed to be constructed from aluminium and a small amount of isotropic damping ($\eta = 0.07$) was applied to the acoustic black hole taper in addition to the natural damping properties of aluminium. It should be noted that isotropic damping does not have frequency dependant characteristics and is therefore not the most accurate representation of a practical, thinly applied, damping layer. However,

isotopic damping was considered to be suitable for this investigation since it is the profile of the taper that is being investigated rather than the damping layer itself. The initial conditions of the acoustic black hole were set to stationary and the boundary conditions of all the edges were set to free. A point force of 10N was applied to the end of the beam furthest from the acoustic black hole. Finally, the two dimensional model was meshed using an edge element mesh. To determine the necessary mesh size, a convergence study was carried out which determined the number of elements required per wavelength for both the beam section and the acoustic black hole section. Although it is possible to mesh the acoustic black hole with a spatially varying element size, for simplicity the acoustic black hole was meshed in a uniform manner and the reference wavelength was taken from the tip so that there would be *at least* the required number of elements per wavelength to obtain accurate results. An example of the difference in mesh size for the

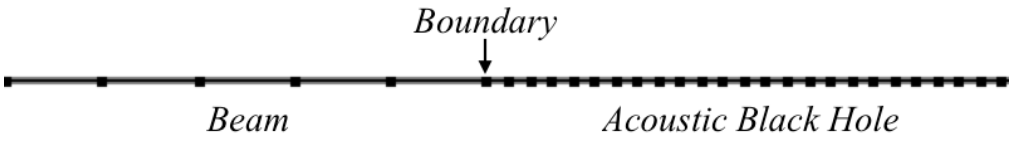


Figure 2: The meshing difference between the beam, on the left, and the acoustic black hole, on the right.

acoustic black hole and beam section is shown in Figure 2, where the difference in mesh resolution for the beam and taper sections is clear. The displacement of the acoustic black hole calculated by the model when it is being excited at 2kHz is shown in Figure 3. Note that, because the displacement has been magnified

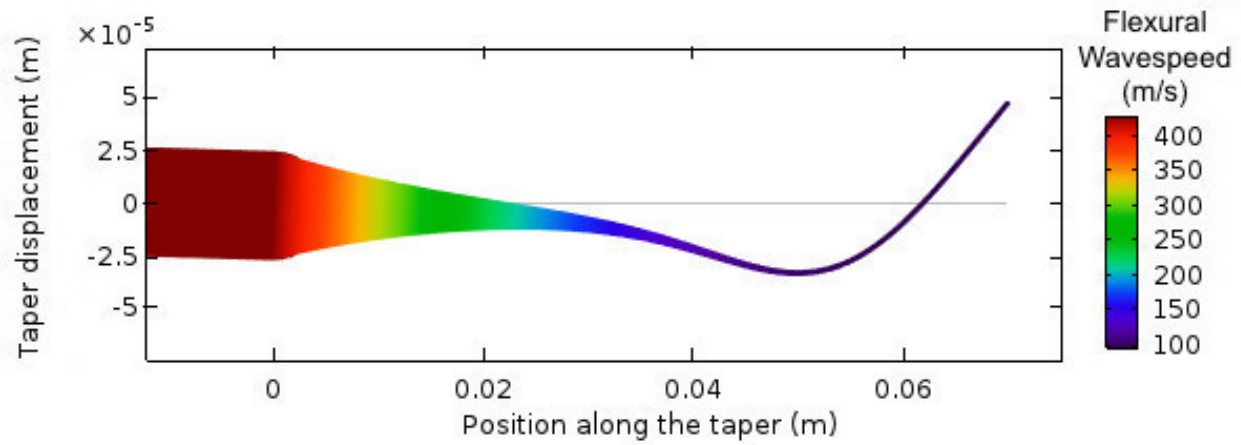


Figure 3: The position along the taper plotted against the displacement of the taper for an excitation of 10N at 2000Hz. The flexural wave speed is shown as a colour scale.

for clarity, the taper height in Figure 3 is not to scale. The flexural wave speed has also been included to demonstrate the acoustic black hole effect (ie the slowing of the wave speed) occurring towards the tip. For reference, the dimensions of the model can be found in the default column of Table 1 in Section 3.

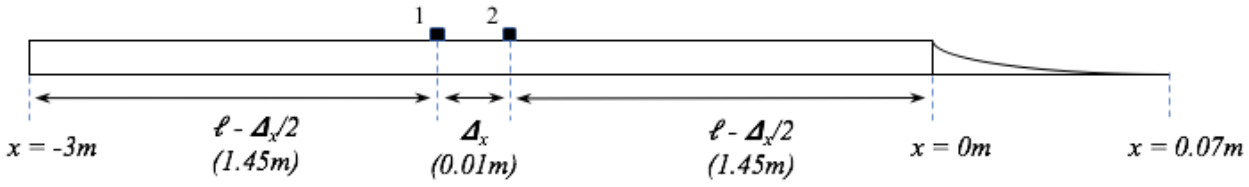


Figure 4: The evaluation points used on the beam for measurement of the acoustic black hole reflection coefficient.

Two evaluation points were added midway along the beam section, shown in Figure 4, at $x = -1.55$m and $x = -1.45$m to allow calculation of the reflection coefficient. The transverse acceleration of the beam was evaluated at these two points. Based on the sensor separation, an upper frequency limit can be been defined as

$$f_{max} = \frac{c_b}{2\Delta_x} \tag{2}$$

where Δ_x is the separation between the two sensor points and f_{max} is the upper frequency limit [12]. The influence of near field effects can be assumed negligible (max contribution ≈ 0.04) if the sensor array is at least half a wavelength away from the primary source and any significant changes in the structure (ie the ABH). Therefore, a lower frequency limit can be defined as

$$f_{min} = \frac{1}{8\left(\ell - \frac{\Delta_x}{2}\right)^2} \tag{3}$$

where f_{min} is the lower frequency limit and ℓ is the distance from the sensor array to the primary source [12]. The evaluation points were 1.45m from either the input force or the discontinuity in the beam formed by the taper and therefore near field effects could be neglected at frequencies above 0.06Hz. Therefore, assuming these limits are fulfilled, the wave amplitudes of the positive and negatively travelling propagating waves can be calculated as

$$A = \frac{i(a_1 e^{\frac{ik_B\Delta_x}{2}} - a_2 e^{\frac{-ik_B\Delta_x}{2}})}{2\omega^2 \sin(k_B\Delta_x)} \tag{4}$$

$$B = \frac{i(a_2 e^{\frac{ik_B\Delta_x}{2}} - a_1 e^{\frac{-ik_B\Delta_x}{2}})}{2\omega^2 \sin(k_B\Delta_x)} \tag{5}$$

where a is the measured acceleration at the data acquisition points 1 and 2 (shown in Figure 4), A and B are the complex amplitudes of the positive and negative travelling waves respectively, ω is the angular frequency and k_B is the bending wavenumber, calculated as

$$k_B = \sqrt[4]{\frac{\rho_s S}{E I_z}}\sqrt{\omega} \tag{6}$$

where ρ_s is the cross-sectional density, S is the cross-sectional area, E is the Young's modulus of the material and I_z is the cross-sectional moment of inertia. The reflection coefficient can then be calculated by taking the ratio of the reflected to the incident wave amplitudes,

$$R = \left|\frac{B}{A}\right|. \tag{7}$$

This technique has commonly been used for the calculation of the reflection coefficient for acoustic samples [12–15] and also for vibrational samples in acoustic black holes [16].

3 A parametric study and modal analysis of acoustic black holes

To investigate the effect that design parameters have on the acoustic black hole performance, a parametric study has been performed and the reflection coefficient has been evaluated as a function of the different parameters. The three parameters of interest: tip height, taper power and taper length were swept over the ranges specified in Table 1. The parameter ranges were chosen with a consideration of manufacturing restrictions. The acoustic black hole taper has been defined using the geometrical expression

$$h(x) = \varepsilon[(l - x)/l]^{\mu} + h_{tip} \tag{8}$$

Parameters		
Parameter	Range being swept	Default if not being swept
Power law (μ)	2 to 10	4
Taper length (l)	50mm to 500mm	70mm
Tip height (h_{tip})	0.5mm to 10mm	0.5mm
Frequency (f)	100Hz to 10000Hz	-
Beam height (h_{beam})	-	10mm
ABH / Beam width	-	40mm
ABH isotropic damping (η)	-	0.07
Structure material	-	Aluminium

Table 1: The range over which each parameter was swept in the finite element model and the default values for the structural parameters.

where $\varepsilon = h_{beam} - h_{tip}$. This expression Provides an exponentially decreasing taper, whilst allowing separate control over the taper length, tip height and power law, allowing each parameter to be changed independently.

The frequency was swept on a logarithmic scale from 100Hz to 10000Hz using the expression

$$f_{range} = 10^{\log_{10}(f_{min}) \,:\, 1/490 \,:\, \log_{10}(f_{max})} \tag{9}$$

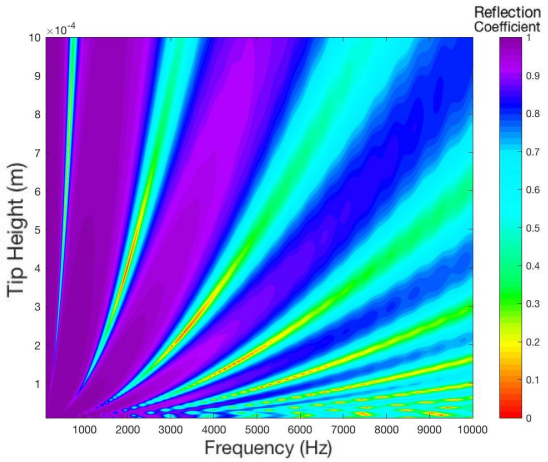
in order to account for the smaller bandwidths of low frequency resonances by increasing the frequency step density at the low end.

It is important to note that due to the low damping factor used, the reflection from the acoustic black hole is generally relatively high. This paper aims to provide insight into how the behaviour of an acoustic black hole can be related to its modal characteristics and this behaviour is clearer for low damping factors and, therefore, a low damping factor has been used to provide physical insight into the behaviour.

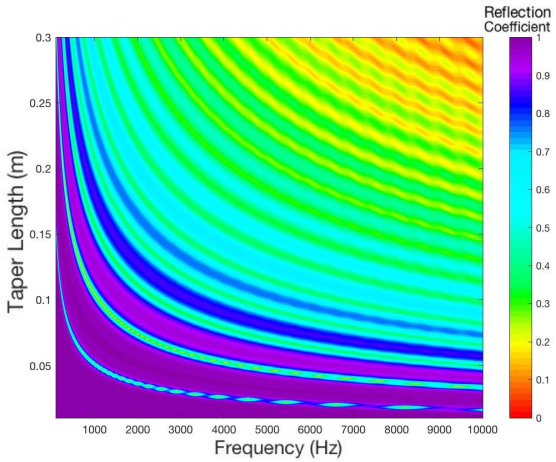
Figure 5a shows how the reflection coefficient of the acoustic black hole varies with different tip heights over a frequency range of 100Hz to 10000Hz. The results show that for smaller tip heights, the frequency bands of low reflection decrease in width but increase in density so that there is, in general, a lower amount of reflection from the tip. Also, at higher frequencies the bands of low reflection are wider and therefore there is less reflection from the tip at higher frequencies. These results demonstrate that there is periodic spectral variation in the reflection coefficient of an acoustic black hole that is dependant on the tip height.

Figure 5b shows how the reflection coefficient of the acoustic black hole varies with taper length over a frequency range of 100Hz to 10000Hz. The results show that at any frequency, a longer acoustic black hole taper produces a lower reflection coefficient. At higher frequencies, there is less reflection for any taper length. Considering the small damping coefficient used, a longer taper length appears to produce very low reflection, which indicates that the acoustic black hole effect is working well. These results are also consistent with the literature and demonstrate that the performance of an acoustic black hole is better for longer taper lengths and at higher frequencies. These results also show the spectral variation in the reflection coefficient of an acoustic black hole.

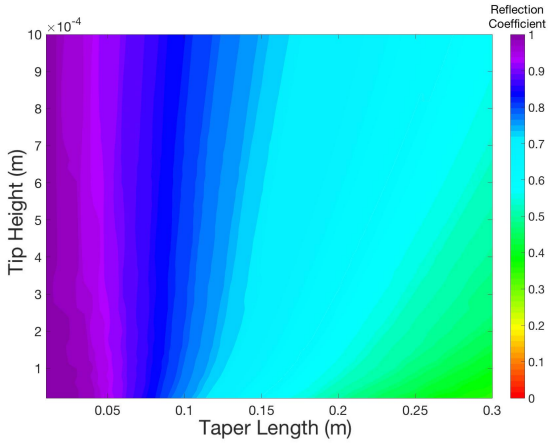
Figure 5c shows how the broadband average of the reflection coefficient varies with the taper length and tip height of an acoustic black hole. These results show that on average, the reflection decreases for longer tapers and for smaller tip heights. At a taper length shorter than 0.05m, the practical range of tip heights that were examined appeared to have no effect on the average broadband reflection coefficient. As the taper length increases above 0.05m, the tip height of the acoustic black hole has more influence on the average broadband reflection coefficient and a smaller tip height produces lower reflection. For any tip height examined, the average broadband reflection coefficient decreases as the taper length increases. There was a 0.12 average difference in the reflection coefficient between the smallest and largest tip height and, in contrast to this,



(a) Tip height plotted against frequency for an acoustic black hole with a taper length of 70mm and a power law of 4.



(b) Taper length plotted against frequency for an acoustic black hole with a tip height of 0.5mm and a power law of 4.



(c) The tradeoff between the tip height and the taper length of an acoustic black hole with a power law of 4.

Figure 5: The reflection coefficient, plotted on a scale of 0 to 1, as a function of frequency and a parameter (5a, 5b), and as a tradeoff between two parameters for a broadband frequency average (5c).

there was a 0.49 average difference in the reflection coefficient between the shortest and longest taper length.

Figure 6 shows how the reflection coefficient of an acoustic black hole varies with the taper power law over a frequency range of 100Hz to 10000Hz. These results show that as the power law of the taper increases for a single frequency, a particular range of power law values produces a low reflection coefficient. At higher frequencies, there are more power law values that produce a low reflection coefficient for a specific frequency. For any given power, at higher frequencies the bands of low reflection are wider. At low power laws, these bands become very wide and this results in a cut-on frequency for each power law, above which the acoustic black hole produces low reflection.

The white dotted lines shown in Figure 6 show how the frequencies of the first five modes of the acoustic black hole cell vary with the power law. The acoustic black hole cell is the acoustic black hole without the beam section (i.e. just the taper). From the results shown in Figure 6, it can be seen that the modes of the acoustic black hole occur at the same frequencies as the minima in the reflection coefficient. It can also be seen that as the power law increases, the modal frequencies decrease. The power law could, therefore, be used to tune the modal frequencies and thus the frequency bands of low reflection. In practice, this could be

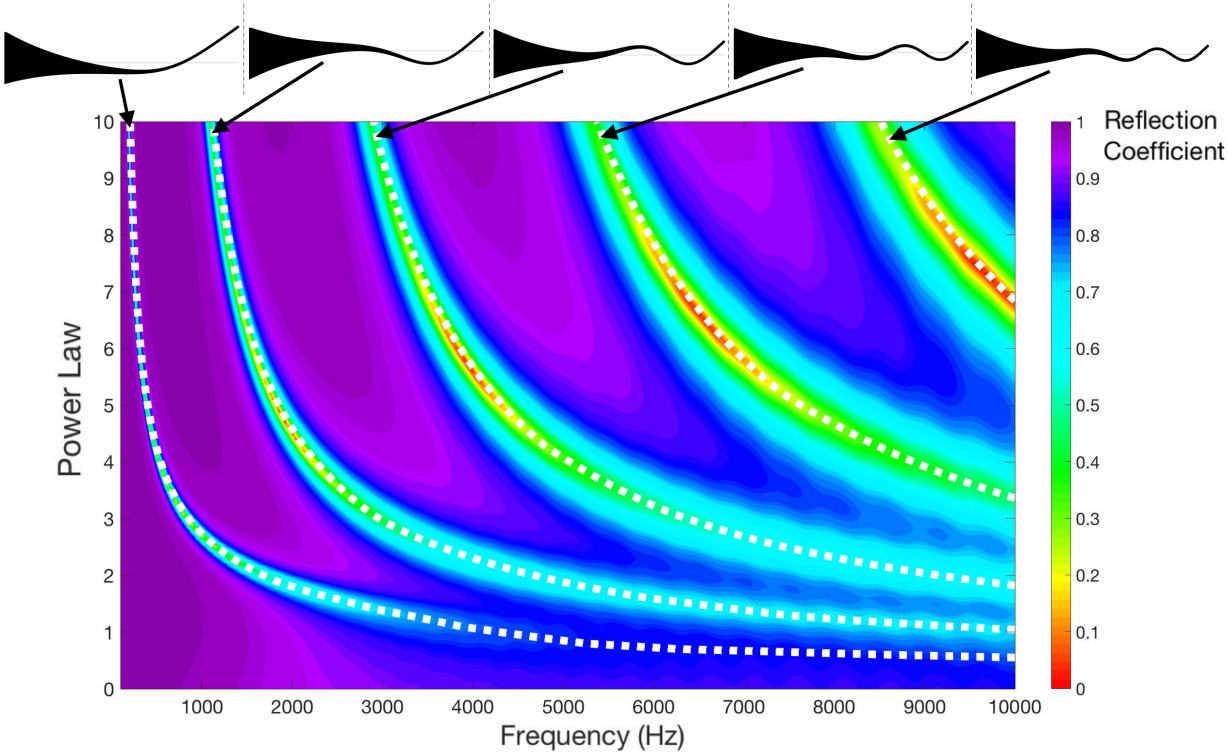


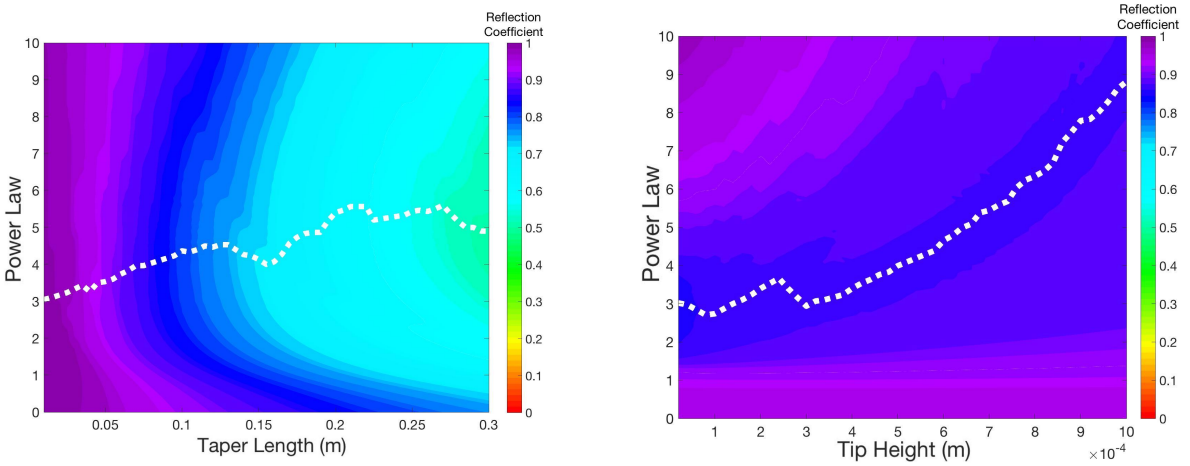
Figure 6: The power law of the taper plotted against frequency for an acoustic black hole with a tip height of 0.5mm and a taper length of 70mm. The reflection coefficient is represented by a colour scale from 0 to 1. An overlay of the first 5 modal frequencies for different power laws, and their shapes, are shown by the white dotted lines.

used to tune the bands of low reflection to the resonant frequencies of a structure.

Figure 7a shows the tradeoff between the power law of the acoustic black hole and the taper length. These results show that there is an optimum power law for the average broadband performance of an acoustic black hole at a specific taper length. For a longer taper length, the optimum power law is slightly higher than for a shorter taper length. The optimum power law at each taper length is shown by a dotted white line. This confirms that the power law, a key controllable parameter, can be optimised for a specific taper length. Figure 7b shows the tradeoff between the power law of the acoustic black hole and the tip height. These results show that there is an optimum power law that can be used to achieve a minimum average broadband reflection at a specific tip length. For a larger tip height, the optimum power law is higher than for a smaller tip height. The optimum power law at each tip height is shown by a dotted white line. The power law can therefore be optimised for a specific tip height. As seen earlier in Figure 5c, over a practical range with a small amount of damping, increasing the taper length appears to have more influence on the reflection coefficient than decreasing the tip height. However, both Figures 7a and 7b show that for an acoustic black hole of practical dimensions (shown as the default values in Table 1), the optimum power law is approximately 4. Optimising and tailoring the power law can be useful, for example, when the working environment of an acoustic black hole is restricted geometrically. In such a scenario, the power law can still be used to optimise the broadband reflection coefficient for the particular length and tip height of the acoustic black hole.

4 Conclusions

This paper presents an extended study of how the controllable parameters influence the reflection coefficient and broadband frequency average reflection coefficient of an acoustic black hole on a beam. An investigation



(a) The tradeoff between the power law of the taper and the taper length for an acoustic black hole with a tip height of 0.5mm.

(b) The tradeoff between the power law of the taper and the tip height of the acoustic black hole. The taper length was set at 70mm.

Figure 7: The broadband frequency average reflection coefficient, plotted on a scale of 0 to 1, as a tradeoff between the power law and the taper length (7a) and the power law and the tip height (7b). For both tradeoffs, the optimum power law for a minimum broadband reflection coefficient has been marked on with a dotted white line.

was carried out to determine how the power law of an acoustic black hole can be used as a key design parameter for acoustic black holes with practical dimensions and a modal analysis was performed to observe the modal band gaps in the reflection coefficient and their dependance on the power law of the taper.

It has been shown that an acoustic black hole has a higher performance if designed with a longer taper length and smaller tip height. The influence of these two parameters on the reflection coefficient of the acoustic black hole has been shown for a range of sweep values and a tradeoff between the two parameters has also been shown. The results are as predicted for individual cases in the literature: a longer taper and smaller tip height produces a better energy absorption and therefore a lower reflection coefficient. However, when designing acoustic black holes for practical applications, these two parameters are likely to be constrained, leaving the power law of the acoustic black hole taper as the key controllable parameter.

The reflection coefficient of an acoustic black hole has been shown to exhibit spectral variation over a range of power law values, present as frequency bands of low reflection. Raising the power law has been shown to shift the bands of low reflection down in frequency and also increase the width of the bands. The modal analysis has shown that the frequencies of an acoustic black hole's modes match the frequencies of the bands of low reflection coefficient. The frequency of the modes has been shown to change with the power law of the taper, making the power law a key controllable parameter when designing acoustic black holes, especially for practical applications where the length and tip height may be constrained. A tradeoff plot between the tip height and the taper length of an acoustic black hole has shown that, for the practical parameter range investigated, increasing the taper length had more influence on the reflection coefficient than decreasing the tip height. Tradeoff plots between the power law and both tip height and taper length have both shown that there exists an optimum power law for the geometry of an acoustic black hole that results in the lowest broadband refection coefficient. For the practically dimensioned acoustic black hole tested this was found to be around 4. When utilised in a practical application, an acoustic black hole might be used to damp particular frequency bands or provide an overall attenuation in a restricted space. Both of these cases can be optimised by changing the power law of the acoustic black hole taper.

Acknowledgements

This work was supported by an EPSRC iCASE studentship.

The authors acknowledge the use of the IRIDIS High Performance Computing Facility, and associated support services at the University of Southampton, in the completion of this work.

References

[1] M.A. Mironov *Propagation of a flexural wave in a plate whose thickness decreases smoothly to zero in a finite interval*, Soviet Physics: Acoustics, Vol. 34, No. 3, American Institute of Physics (1988), pp. 318-319.

[2] F.J. Fahy and J.G. Walker *Fundamentals of Noise and Vibration*, Spon Press (1998).

[3] L. Cremer, M. Heckl and B.A.T. Petersson *Structure Borne Sound*, 3rd edition, Springer (2005).

[4] A.N.Norris *Flexural waves on narrow plates*, The Journal of the Acoustical Society of America, Vol. 113, No. 5, Acoustical Society of America (2003), pp. 2647-2658.

[5] V.V. Krylov and F.J.B.S Tilman *Acoustic 'black holes' for flexural waves as effective vibration dampers*, Journal of Sound and Vibration, Vol. 274, No. 3-5, Elsevier (2004), pp. 605-619.

[6] L. Zhao *Passive vibration control based on embedded acoustic black holes*, Journal of Vibration and Acoustics, Vol. 138, No. 4, The American Society of Mechanical Engineers (2016), pp. 1-6.

[7] H. Ji, J. Qiu, J. Luo and L. Cheng *Investigations on flexural wave propagation and attenuation in a modified one-dimensional acoustic black hole using a laser excitation technique*, Mechanical systems and signal processing, Vol. 104, Elsevier (2018), pp. 19-35.

[8] E.M. Kerwin Jr. *Damping of plate flexural vibrations by means of viscoelastic laminae*, *ASME Annual Meeting Structural Damping*, New York (1959), pp. 49-87.

[9] M.R. Shepherd, P.A. Feutado and S.C. Conlon *Multi-objective optimization of acoustic black hole vibration absorbers*, The Journal of the Acoustical Society of America, Vol. 140, No. 3, Acoustical Society of America (2016), pp. 227-230.

[10] V. Denis, A. Pelat, F. Gautier and B. Elie *Modal overlap factor of a beam with an acoustic black hole termination*, Journal of Sound and Vibration, Vol. 333, No. 12, Elsevier (2014), pp. 2475-2488.

[11] L. Tang and L. Cheng *Broadband locally resonant band gaps in periodic beam structures with embedded acoustic black holes*, Journal of Applied Physics, Vol. 121, No. 19, AIP Publishing (2017), pp. 1-9.

[12] C.R. Halkyard and B.R. Mace *Feedforward adaptive control of flexural vibration in a beam using wave amplitudes*, Journal of Sound and Vibration, Vol. 254, No. 1, Elsevier (2002), pp. 117-141.

[13] S.J. Elliott C.R. Fuller and P.A. Nelson *Active Control of Vibration*, Academic Press (1996)

[14] B.H. Song and J.S. Bolton *A transfer-matrix approach for estimating the characteristic impedance and wave numbers of limp and rigid porous materials*, Journal of Sound and Vibration, Vol. 107, No. 3, Elsevier (2000), pp. 1131-1152.

[15] C.R. Halkyard and B.R. Mace *Structural intensity in beams - waves, transducer systems and the conditioning problem*, Journal of Sound and Vibration, Vol. 185, No. 2, Elsevier (1995), pp. 279-298.

[16] V. Denis, F. Gautier, A. Pelat, and J. Poittevin *Measurement and modelling of the reflection coefficient of an acoustic black hole termination*, Journal of Sound and Vibration, Vol. 349, Elsevier (2015), pp. 67-79.

Robust sound transmission modelling of finite-sized layered walls and floors

C. Decraene [1], **A. Dijckmans** [2], **E. P.B. Reynders** [1]
[1] KU Leuven, Department of Civil Engineering, Structural Mechanics Section,
Kasteelpark Arenberg 40, 3001 Leuven, Belgium
e-mail: **carolina.decraene@kuleuven.be**

[2] Acoustics Division, Belgian Building Research Institute,
Lombardstraat 42, B-1000 Brussels, Belgium

Abstract
An accurate design tool over a broad frequency range which replaces laboratory testing of multilayered structures, is the objective in this work as such systems are regularly applied in buildings. The main used methodology is the semi-analytical transfer matrix method. Two disadvantages will be tackled: (1) the finite size will be taken into account using a modal approach, allowing a detailed examination of the behaviour of the system in small frequency bands; (2) a hybridization is created in order to avoid the numerical integration of the plane wave sound transmission loss over all angles of incidence, and at the same time to allow the computation of the variance, inherent to the diffuse field assumption in the sending and receiving room. By modelling the wall or floor system deterministically using the modal transfer matrix method and the rooms carrying a diffuse field, a hybrid modal transfer matrix-statistical energy analysis approach is established by making use of the diffuse field reciprocity relationship. Different validation examples are examined.

1 Introduction

There is an increasing use of lightweight layered systems in buildings to achieve a high thermal performance. Because of their relatively low weight and complex vibro-acoustic behaviour, achieving sufficient sound insulation with such systems is, however, challenging. The goal in this work is thus to create an accurate sound transmission loss prediction method, which is fast enough to be used as a design tool for layered systems.

The framework of the hybrid finite element-statistical energy analysis (FE-SEA) approach [1, 2, 3] serves as a starting point for the new methodology. Using the diffuse field reciprocity relationship [4, 5], the hybrid framework allows modelling the rooms of the overall room-wall-room system as stochastic subsystems (like in statistical energy analysis, SEA), while treating the wall in a deterministic way with finite element (FE) analysis. Because of the statistical room models, the uncertainty of the sound transmission loss concerning the diffuse field assumption in the rooms can be assessed [3]. Therefore, not only the mean of the sound transmission loss but also its variance can be obtained. Note that the computation time of the FE-SEA method will increase at higher frequencies as a finer mesh is needed to capture the small wavelength deformations of the walls or floors.

To overcome this limitation, the finite element analysis is replaced by the semi-analytical transfer matrix method (TMM) [6, 7, 8], which allows to predict the behaviour of infinite walls and floors, consisting of homogeneous solid, fluid and/or poroelastic layers. However, assuming an infinite wall can cause important

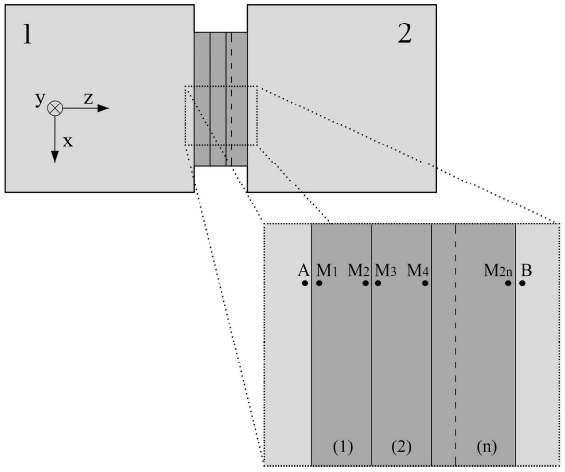


Figure 1: A room-wall-room system, in which the wall is a multilayered structure.

prediction errors at low and medium frequencies. Edge diffraction can be taken into account by using a fast and simplified spatial windowing technique [9, 10, 11], but then the modal behaviour is still neglected. Alternatively, the wall displacement can be projected onto a set of sinusoidal lateral basis functions, such that the wall impedance at a given frequency and for a given lateral basis function (hence lateral wavenumber) can be computed using the TMM [12, 13]. This approximate modal TMM (mTMM) accounts approximately for modal wall behaviour when the boundary conditions are simply supported.

The newly developed modal transfer matrix-statistical energy analysis (mTMM-SEA) approach contributes with respect to the conventional mTMM that integration of the plane wave transmission over all angles of incidence is avoided. This integration causes both numerical difficulties at grazing incidence and the limitation that only the ensemble mean of the sound transmission loss can be computed. Other statistics that are inherent to the diffuse sound field assumption, such as the variance of the sound transmission loss, can not be obtained by the several variations of the TMM. The hybrid mTMM-SEA methodology offers a solution to this problem.

The remainder of this article is organized as follows: The theory is summarized in section 2. Section 2.1 introduces the hybrid deterministic-SEA approach to sound transmission modelling in general. Section 2.2 elaborates the computation of the deterministic dynamic stiffness matrix using the mTMM. Subsequently, the performance of the hybrid mTMM-SEA approach is investigated in detail for two walls, by comparing the predicted sound insulation values with results of other hybrid approaches and with measured values. The considered wall types are a thick brick wall (§3.1), a double-leaf wall (§3.2) and a double glazing (§3.3). The conclusions are presented in Section 4. *The present paper is an abbreviated version of a more detailed analysis to be found in reference* [14].

2 A modal transfer matrix - statistical energy analysis framework

2.1 Modeling strategy

Throughout this article, a room-wall-room system is considered, where the rooms carry a diffuse wave field and the wall a deterministic wave field (cfr. Fig. 1). The out-of-plane displacement u_z of the partition wall is approximated using a finite set of N_m global basis functions ϕ (e.g. the in-vacuo modes) and corresponding generalized coordinates q. When the wall is thin, the transverse displacement of the wall in position $\mathbf{x} =$

(x, y) at frequency ω is independent of the z-coordinate:

$$u_{\mathrm{z}}(\mathbf{x}, \omega) \approx \sum_{p=1}^{N_{\mathrm{m}}} \phi_p(\mathbf{x}) q_p(\omega) \tag{1}$$

For a thick wall, the decomposition is performed for each of both outer surfaces A and B:

$$u_{\mathrm{z}}(\mathbf{x}, z_{\mathrm{A}}, \omega) \approx \sum_{p=1}^{N_{\mathrm{m}}} \phi_p(\mathbf{x}, z_{\mathrm{A}}) q_{p\mathrm{A}}(\omega) \qquad \text{and} \qquad u_{\mathrm{z}}(\mathbf{x}, z_{\mathrm{B}}, \omega) \approx \sum_{p=1}^{N_{\mathrm{m}}} \phi_p(\mathbf{x}, z_{\mathrm{B}}) q_{p\mathrm{B}}(\omega) \tag{2}$$

All generalized response degrees of freedom (DOFs) are collected in an amplitude vector $\mathbf{q}(\omega) \in \mathbb{C}^{N_{\mathrm{dof}}}$, so that the time-domain response is given by $\mathrm{Re}(\mathbf{q}\mathrm{e}^{\mathrm{i}\omega t})$, with i the imaginary unit. Similarly, the corresponding generalized harmonic loads are collected in the load amplitude vector $\mathbf{f}(\omega) \in \mathbb{C}^{N_{\mathrm{dof}}}$. Note that, when the wall is modelled as thin, then $N_{\mathrm{dof}} = N_{\mathrm{m}}$, but when it is thick, then $N_{\mathrm{dof}} = 2N_{\mathrm{m}}$. Since $\mathbf{q}$ contains all (generalized) interface degrees of freedom between the wall and the rooms, the equations of motion of the whole system (room-wall-room) can be written as

$$\mathbf{D}\mathbf{q} = \mathbf{f}, \tag{3}$$

with $\mathbf{D} \in \mathbb{C}^{N_{\mathrm{dof}} \times N_{\mathrm{dof}}}$ the dynamic stiffness matrix at frequency ω. $\mathbf{D}$ may be decomposed as the sum of the dynamic stiffness matrix of the wall, denoted as $\mathbf{D}_{\mathrm{d}}$ (subscript d stands for deterministic), and the dynamic stiffness matrices of the rooms, denoted as $\mathbf{D}_1$ and $\mathbf{D}_2$:

$$\mathbf{D} = \mathbf{D}_{\mathrm{d}} + \mathbf{D}_1 + \mathbf{D}_2 \tag{4}$$

Since the rooms are assumed to carry a diffuse field in this work, they are modelled as the random subsystems in the overall room-wall-room system. The dynamic stiffness matrix of each acoustic room volume k is decomposed as

$$\mathbf{D}_k = \mathbf{D}_{\mathrm{dir}}^{(k)} + \mathbf{D}_{\mathrm{rev}}^{(k)}, \qquad k = 1, 2 \tag{5}$$

where $\mathbf{D}_{\mathrm{dir}}^{(k)}$ denotes the mean of the subsystem's dynamic stiffness matrix $\mathbf{D}_{\mathrm{dir}}^{(k)} := \mathrm{E}\left[\mathbf{D}_k\right]$. This term describes the limiting response of subsystem k to the displacements of the deterministic boundary that would be observed at that boundary when the extent of the subsystem would be increased [4, 15]. $\mathbf{D}_{\mathrm{rev}}^{(k)}$ represents the response of the reverberant field in the subsystem, caused by the presence of random wave scattering boundaries or objects. With this decomposition, the equations of motion for a random subsystem are

$$\mathbf{D}_{\mathrm{dir}}^{(k)}\mathbf{q} = \mathbf{f}_k + \mathbf{f}_{\mathrm{rev}}^{(k)}, \tag{6}$$

where the reverberant forces are defined as $\mathbf{f}_{\mathrm{rev}}^{(k)} := -\mathbf{D}_{\mathrm{rev}}^{(k)}\mathbf{q}$, and $\mathbf{f}_k$ denotes the sum of the loads applied to subsystem k at its DOFs. The overall equations of motion (3) become

$$\mathbf{D}_{\mathrm{tot}}\mathbf{q} = \mathbf{f} + \mathbf{f}_{\mathrm{rev}}^{(1)} + \mathbf{f}_{\mathrm{rev}}^{(2)}, \tag{7}$$

where $\mathbf{D}_{\mathrm{tot}} := \mathbf{D}_{\mathrm{d}} + \sum_{k=1}^{2} \mathbf{D}_{\mathrm{dir}}^{(k)}$ is a purely deterministic matrix. When a diffuse field acts in both rooms, the reverberant forces $\mathbf{f}_{\mathrm{rev}}^{(k)}$ are related to $\mathbf{D}_{\mathrm{dir}}^{(k)}$ through the diffuse field reciprocity relationship [4]:

$$\mathrm{E}[\mathbf{f}_{\mathrm{rev}}^{(k)}\mathbf{f}_{\mathrm{rev}}^{(s)}] = \delta_{ks}\frac{4\hat{E}_k}{\omega\pi n_k}\mathrm{Im}\big(\mathbf{D}_{\mathrm{dir}}^{(k)}\big), \tag{8}$$

with n_k the modal density of subsystem k and δ_{ks} the Kronecker delta. Note that the hat symbol is employed here as shorthand notation for ensemble mean. From this equation, it is possible to obtain the mean time-averaged total energy $\hat{E}_k$ of room k from a stationary power balance which involves the other random subsystems as well as the deterministic master system, assuming the fields are statistically independent of

each other. For the case where the external loading acts solely on the random subsystems (rooms), this reads [1]:

$$\omega\left(\eta_k+\hat{\eta}_{\mathrm{d},k}\right)\hat{E}_k+\sum_{j=1}^{2}\omega\hat{\eta}_{kj}n_k\left(\frac{\hat{E}_k}{n_k}-\frac{\hat{E}_j}{n_j}\right)=\hat{P}_k,\qquad k=1,2. \tag{9}$$

In this expression, η_k is the damping loss factor of subsystem k, P_k the power input from external loading injected directly into the diffuse field of this subsystem, and

$$\hat{\eta}_{\mathrm{d},k}=\frac{2}{\omega\pi n_k}\sum_{r,s}\mathrm{Im}\left(D_{\mathrm{d},rs}\right)\left(\mathbf{D}_{\mathrm{tot}}^{-1}\mathrm{Im}\left(\mathbf{D}_{\mathrm{dir}}^{(k)}\right)\mathbf{D}_{\mathrm{tot}}^{-\mathrm{H}}\right)_{rs} \tag{10}$$

$$\hat{\eta}_{kj}=\frac{2}{\omega\pi n_k}\sum_{r,s}\mathrm{Im}\left(D_{\mathrm{dir},rs}^{(k)}\right)\left(\mathbf{D}_{\mathrm{tot}}^{-1}\mathrm{Im}\left(\mathbf{D}_{\mathrm{dir}}^{(j)}\right)\mathbf{D}_{\mathrm{tot}}^{-\mathrm{H}}\right)_{rs} \tag{11}$$

where the superscript H denotes Hermitian transpose and the integer subscripts r, s select an element in row r and column s of a matrix. If the wall provides sufficient sound insulation, $\hat{P}_k$ can be approximated as the ensemble mean of the power input into a hard-walled room. It can be noted that the power balance equation (9) has formally the same structure as in conventional SEA. Therefore the factors $\hat{\eta}_{kj}$ can be interpreted as coupling loss factors, and (11) provides a rigorous way to compute their ensemble mean. In a similar manner, (10) enables to rigorously estimate the power that is lost by energy dissipation in the wall. By solving for the mean coupling loss factor $\hat{\eta}_{12}$ between the two subsystems, the mean sound transmission coefficient $\hat{\tau}_{12}$ can be obtained from [10]

$$\hat{\tau}_{12}=\hat{\eta}_{12}\frac{4\omega V_1}{c_a S}, \tag{12}$$

with S the surface area of the wall, V_1 the volume of the sending room, and c_a the speed of sound.

The computation of the dynamic stiffness matrix of the wall, $\mathbf{D}_{\mathrm{d}}$ will be discussed in section 2.2. For the computation of the direct field dynamic stiffness matrices of the rooms as seen from the baffled wall, $\mathbf{D}_{\mathrm{dir}}^{(1)}$ and $\mathbf{D}_{\mathrm{dir}}^{(2)}$, the reader is referred to the wavelets approach [16]. Note that the combination of the hybrid method and the wavelet approach allows to take cross modal coupling into account, which is not possible when the sound transmission is integrated over all possible angles of incidence using a conventional modal based TMM [13].

An important advantage of the general deterministic-SEA framework described above, is that not only the mean, but also the variance of the transmission loss which is inherent in the diffuse field models of the rooms, can be obtained. It was demonstrated by Langley and Cotoni [2] that this variance can be computed by a first-order perturbation analysis of the power balance (9); Reynders et al. [3] then made the connection with the variance of the sound transmission loss. This variance of the sound transmission $\sigma_\tau^2=\mathrm{Relcov}[C_{12},C_{12}]\hat{\tau}_{12}^2$ can be computed in closed form by solving for the relative covariance $\mathrm{Relcov}[C_{12},C_{12}]$ [3, Eq. (15)].

2.2 Computing the deterministic dynamic stiffness matrix from finite wall impedances using the transfer matrix method

The transfer matrix method [6, 7, 8] is an efficient framework that allows computing the mechanical impedance matrix $\mathbf{Z}(k_x,\omega)$ for two-dimensional (x-z) wave propagation between both sides of an infinite wall consisting of solid, fluid and/or poroelastic layers for a given longitudinal wavenumber k_x and a given frequency ω (cfr. Fig. 1):

$$\begin{bmatrix}Z_{11}(k_x,\omega) & Z_{12}(k_x,\omega)\\ Z_{21}(k_x,\omega) & Z_{22}(k_x,\omega)\end{bmatrix}\begin{bmatrix}v_{\mathrm{zA}}(\omega)\\ v_{\mathrm{zB}}(\omega)\end{bmatrix}=\begin{bmatrix}p_{\mathrm{A}}(\omega)\\ p_{\mathrm{B}}(\omega)\end{bmatrix} \tag{13}$$

For finite walls, the normal displacement $u_{\mathrm{z}}(\mathbf{x}, z, \omega)$ can be approximated using a Ritz approach, i.e., by means of a finite set of shape functions $\phi_p(\mathbf{x})$ that satisfy the boundary conditions (e.g., simply supported):

$$u_{\mathrm{z}}(\mathbf{x}, z, \omega) \approx \sum_{p=1}^{N_{\mathrm{m}}} \phi_p(\mathbf{x}) q_p(z, \omega), \tag{14}$$

The plate velocities and the pressures at both sides of the wall can then be written as [12, 13]

$$\begin{bmatrix} v_{\mathrm{zA}}(\mathbf{x}, \omega) \\ v_{\mathrm{zB}}(\mathbf{x}, \omega) \end{bmatrix} = \sum_p \begin{bmatrix} V_{\mathrm{zAp}}(\omega) \\ V_{\mathrm{zBp}}(\omega) \end{bmatrix} \phi_p(\mathbf{x}) \qquad \text{and} \qquad \begin{bmatrix} p_{\mathrm{A}}(\mathbf{x}, \omega) \\ p_{\mathrm{B}}(\mathbf{x}, \omega) \end{bmatrix} = \sum_p \begin{bmatrix} P_{\mathrm{Ap}}(\omega) \\ P_{\mathrm{Bp}}(\omega) \end{bmatrix} \phi_p(\mathbf{x}) \tag{15}$$

The basis functions $\phi_p(\mathbf{x})$ are chosen to be the mode shapes of a thin simply supported plate with dimensions $L_x \times L_y \times t$:

$$\phi_p(\mathbf{x}) = \sin\left(\frac{p_x \pi x}{L_x}\right) \sin\left(\frac{p_y \pi y}{L_y}\right), \tag{16}$$

where p_x and p_y are the integer numbers of half wavelengths in the x and y directions, respectively, of mode p and with corresponding modal wavenumber $k_p = \sqrt{(p_x \pi / L_x)^2 + (p_y \pi / L_y)^2}$. The modal response of this homogeneous thin plate is obtained by imposing the modal wavenumber as trace wavenumber in an infinite plate model. Using the orthogonality property of the bending mode shapes when combining equations (13) and (15), one has the following exact relationship for a finite homogeneous thin plate:

$$\begin{bmatrix} Z_{11}(k_p, \omega) & Z_{12}(k_p, \omega) \\ Z_{21}(k_p, \omega) & Z_{22}(k_p, \omega) \end{bmatrix} \begin{bmatrix} V_{\mathrm{zAp}}(\omega) \\ V_{\mathrm{zBp}}(\omega) \end{bmatrix} = \begin{bmatrix} P_{\mathrm{Ap}}(\omega) \\ P_{\mathrm{Bp}}(\omega) \end{bmatrix} \tag{17}$$

This implies that (1) the impedances of the wall in the chosen generalized coordinates (i.e., simply supported thin plate modal coordinates) can be computed independently for each basis function, and (2) the impedance matrix between both sides of a finite wall in generalized coordinates can be evaluated as the impedance matrix of the corresponding infinite wall, evaluated for the wavenumber k_p of the basis function p. A relation between $\mathbf{Z}(k_p, \omega)$ and $\mathbf{D}_{\mathrm{d},p}$ is established by transforming the modal velocity into the modal displacement and the modal pressure into the modal force:

$$\mathbf{D}_{\mathrm{d},p}(\omega) = \frac{\mathrm{i}\omega L_x L_y}{4} \mathbf{Z}(k_p, \omega) \tag{18}$$

Eq. (18) is exact for a simply supported thin plate. Its validity for other wall types depends on the validity of approximation (14), which assumes that only waves with in-plane wavenumbers k_p can propagate through the wall.

3 Validation examples

In this section, the proposed mTMM-SEA approach is validated on wall systems of increasing complexity. The predicted sound transmission loss values are compared against experimental results and alternative prediction results, such as the wave based method (WBM) [20], which takes both the room and wall modes into account. A comparison is also made with the hybrid FE-SEA method, that has been discussed earlier in [3, 17]. Numerical results of the conventional TMM and the TMM using a simplified spatial windowing technique (FTMM) [11] as finite size correction are also shown.

In all but one example (the double-leaf wall of Section 3.2), the experimental results have been obtained at the KU Leuven Laboratory of Acoustics. More details concerning the Laboratory can be found in [20]. The measured values of the damping loss factors of the mounted walls are listed in Table 1. In all simulations, the reverberation time T, the air density ρ_a and the sound speed c_a in the rooms are taken to be $1.5\,\mathrm{s}$, $1.2\,\frac{\mathrm{kg}}{\mathrm{m}^3}$ and $343\,\frac{\mathrm{m}}{\mathrm{s}}$, respectively. Note that in the simulations, the walls are assumed to have simply supported boundary conditions; the accuracy of this assumption has been experimentally confirmed [17].

f [Hz]	50	63	80	100	125	160	200	250	315	400	500	...
η_{brick} [%]	3.8	6.7	7.0	4.6	4.3	3.9	5.3	3.5	1.7	2.4	2.2	...
$\eta_{\text{glass,6mm}}$ [%]	3.1	2.3	2.6	2.1	1.9	1.7	1.8	2.2	2.2	2.6	2.8	...
$\eta_{\text{glass,8mm}}$ [%]	3.4	3.5	3.0	2.7	2.7	2.4	2.2	2.3	2.3	3.0	2.9	...
f [Hz]	...	630	800	1000	1250	1600	2000	2500	3150	4000	5000	
η_{brick} [%]	...	3.2	2.1	1.5	2.3	1.4	1.2	1.4	0.7	0.9	0.8	
$\eta_{\text{glass,6mm}}$ [%]	...	2.7	2.0	1.6	1.7	1.6	1.7	1.1	3.4	2.7	2.2	
$\eta_{\text{glass,8mm}}$ [%]	...	2.6	2.0	1.9	1.6	1.7	2.0	4.0	4.3	3.4	2.3	

Table 1: Measured damping loss factors η for the partition walls tested in the KU Leuven Laboratory of Acoustics.

3.1 Hollow brick wall

In the first application, a perforated brick wall with dimensions $3.25\,\text{m} \times 2.95\,\text{m} \times 0.19\,\text{m}$ is considered. The wall is plastered at both sides. The acoustic behaviour of perforated brick walls is complex, given the inhomogeneities at three different scales: the fire clay material, the brick where small cavities are present in the fire clay because of the perforations, and the entire wall where the bricks are held together by mortar layers. When the inhomogeneities are small compared to the wavelength, and when the stiffness is not too different in different directions, the wall can be modelled as homogeneous and isotropic. The thickness effects, however, can not be neglected: not only is shear deformation important, thickness resonances (i.e., Lamb modes) are often observed in the audio frequency range [21]. Following [12], the equivalent Young's modulus, Poisson's ratio, density and thickness are taken as $E = 1825$ MPa, $\nu = 0.2$, $\rho = 613.5\ \frac{\text{kg}}{\text{m}^3}$ and $t = 0.2934$ m, respectively.

Fig. 2 shows the predictions of the hybrid mTMM-SEA method, of the conventional TMM, of the FTMM and of a hybrid FE-SEA model. In the hybrid FE-SEA model, the wall is modelled using 8-node solid linear elastic finite elements (of the SOLID45 element type in ANSYS) and only the boundary displacements in the middle plane of the wall are restrained. The hybrid mTMM-SEA and FE-SEA predictions agree well but they are not exactly the same, which is expected since the boundary conditions are slightly different

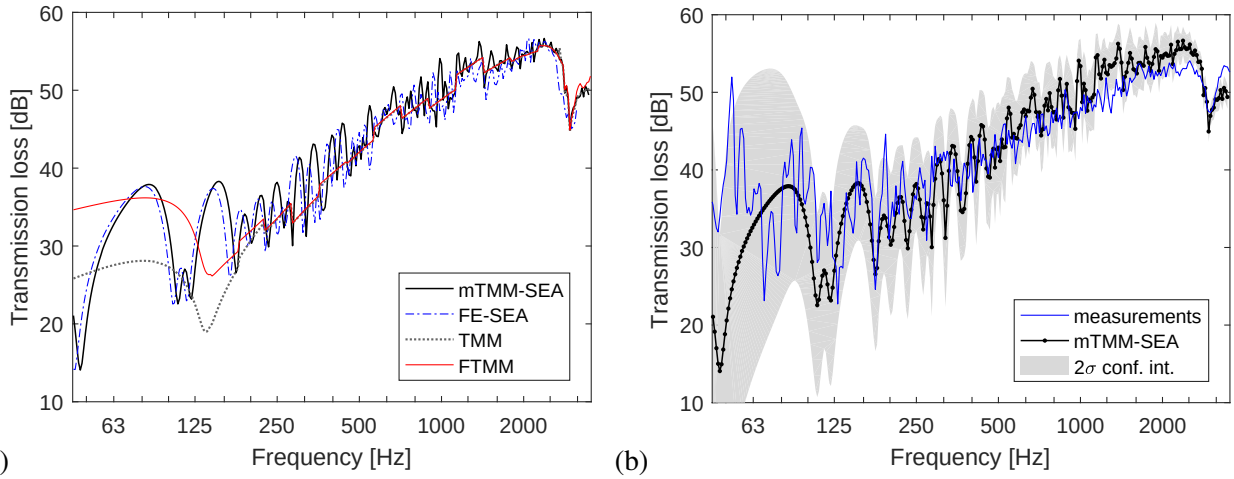


Figure 2: Harmonic sound transmission loss of a perforated brick wall (a) as predicted with the hybrid mTMM-SEA approach, the hybrid FE-SEA approach, the conventional TMM, the FTMM, and (b) as measured in the laboratory. The 2σ confidence interval, computed with the hybrid mTMM-SEA, is shown in the right figure.

and since (14) results in an approximation of the true wall behaviour for thick walls. Both models correctly predict the first thickness resonance of the wall at around 3000 Hz. The comparison with the conventional TMM and the FTMM predictions illustrates that the modal behaviour of the wall plays an important role up to about 500 Hz. The low modal density of the wall makes that the coincidence dip, which can be observed in the conventional TMM and the FTMM predictions between 125 Hz and 160 Hz, cannot develop. This is confirmed by the comparison of the hybrid mTMM-SEA results with measured values [3, 20]. A good agreement is observed between the measurements and the mTMM-SEA predictions.

The 95% confidence interval of the mTMM-SEA predictions is also plotted. As explained earlier, the related uncertainty is due to the assumption of a diffuse field in the rooms. This uncertainty is well captured by the mTMM-SEA predictions: at low frequencies, where the modal overlap of the rooms is low and their modal behaviour has a large influence on the transmission loss, the mTMM-SEA predictions have a large uncertainty, while they have a small uncertainty at high frequencies, where the modal overlap of the rooms is large.

Note that the computation cost of the mTMM-SEA model (71.5 s) is much lower than for the FE-SEA model (5651.5 s), because (1) the finite element model of the wall is a 3D solid model, and (2) the modal density of the wall is low. The FTMM (42.9 s) results in only half of the computation time of the mTMM-SEA approach, but shows deviations at lower frequencies.

3.2 Double-leaf wall

In this section a double-leaf wall, consisting of a steel plate, a mineral wool core with a flow resistivity of $34\mathrm{kNs/m}^4$ and a laminate plate, are considered. The different layers are glued onto each other. This validation example was adopted from the literature, as it is known to be a challenging example for modelling poro-elastic layers. The material properties and experimental results in 1/3 octave bands can be found in [9].

The mineral wool is a poro-elastic material. It may be modelled as an equivalent fluid, e.g., using the empirical model of Delany and Bazley [23]. In this model, the complex characteristic impedance Z_c and the propagation coefficient $\Gamma = \mathrm{i}k$ are derived from the flow resistivity. These complex parameters are then implemented in the transfer matrix of a fluid as explained in [24]. The advantage is that only the flow resistivity σ and thickness of the porous layer have to be known as input parameters. When using an equivalent fluid model, it is assumed that the frame is motionless and that only a compressional wave will

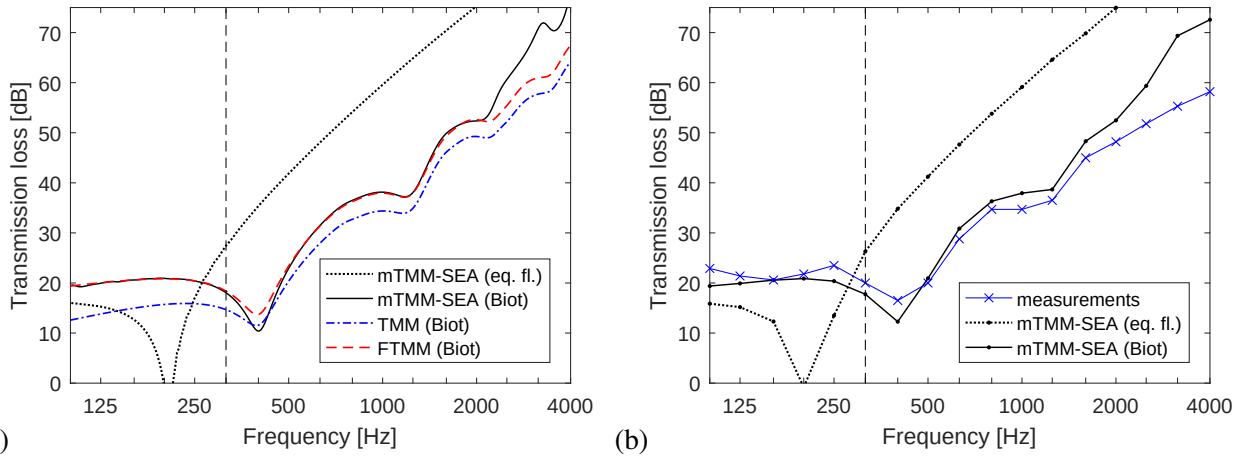


Figure 3: Harmonic sound transmission loss of a double-leaf wall with poro-elastic material in the cavity (a) as predicted with the hybrid mTMM-SEA approach using an equivalent fluid model or a Biot model, the conventional TMM, the FTMM and (b) as measured in [9]. The results in the right figure are band-averaged to 1/3 octave bands.

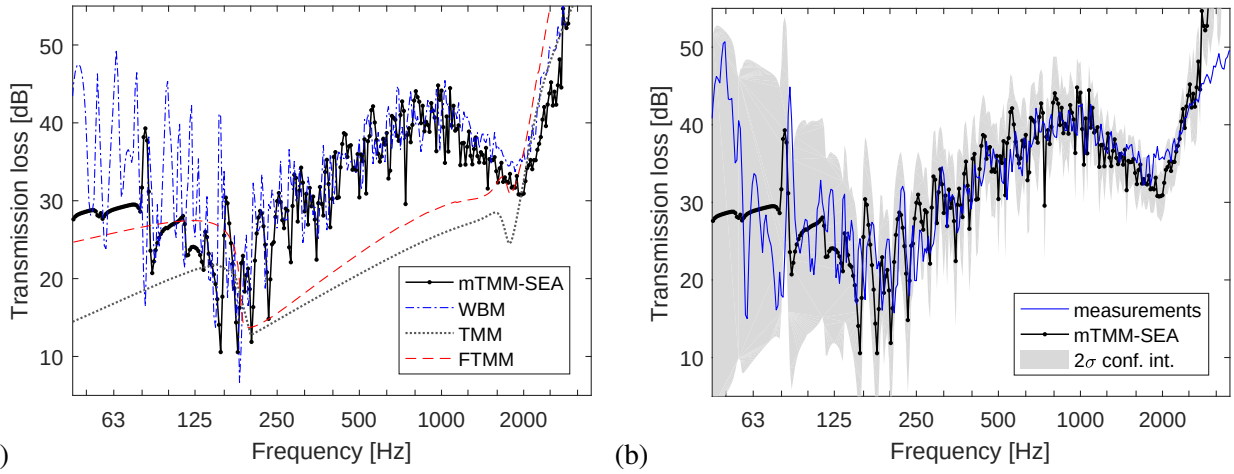


Figure 4: Harmonic sound transmission loss of a double glazing (a) as predicted with the hybrid mTMM-SEA approach, the hybrid WBM approach, the conventional TMM, the FTMM and (b) as measured in the laboratory. The 2σ confidence interval, computed with the hybrid mTMM-SEA, is shown in the right figure.

travel through the layer. However, in case of a poro-elastic material with a flexible frame a more elaborated model may be needed such as the Biot model [25, 26]. This model has been incorporated into the transfer matrix method [8]. While the Biot model is physically more accurate, it requires also more input parameters than the Delany-Bazley equivalent fluid model.

The Biot model and the equivalent fluid model are implemented in the TMM framework, allowing to examine possible differences. Numerical predictions of the TMM, FTMM and mTMM-SEA approach using a Biot model and results of the mTMM-SEA approach using an equivalent fluid model are displayed in Fig. 3. The band-averaged results of the mTMM-SEA approach using both models for the poro-elastic material, are also compared to experimental data. Note that the empirical formulae of Delany and Bazley [23] are only valid in the range $0.01 \leqslant \rho_a f/\sigma \leqslant 1$, which implies that the equivalent fluid model is valid from 315 Hz onwards. This is indicated by the vertical dashed line. A comparison with the experimental results shows that the equivalent model overestimates clearly the sound transmission loss in this example, unlike the Biot model, which is able to capture the behaviour of the mineral wool accurately.

3.3 Double glazing

The final structure is a double glazing with dimensions $1.25\,\mathrm{m} \times 1.50\,\mathrm{m} \times 0.026\,\mathrm{m}$ which consists of two glass panels with a thickness of $6\,\mathrm{mm}$ and $8\,\mathrm{mm}$, separated by an air cavity of $12\,\mathrm{mm}$. For the simulations, the following material properties for the glass panels are taken: density $\rho = 2500\,\frac{\mathrm{kg}}{\mathrm{m}^3}$, Young's modulus $E = 62\,\mathrm{GPa}$ and Poisson's ratio $\nu = 0.24$. The experimentally determined damping loss factor of both glass panels in mounted condition can be found in table 1. The air cavity is taken to be undamped.

The TMM cannot be used for estimating the sound insulation of layered walls containing both solid layers and undamped air layers, as the results will be less accurate [12, 13]. However, it is possible in the mTMM-SEA approach to model the glazing using a Rayleigh-Ritz approach, in which the air layer is modelled analytically, as a hard-walled cavity, while the glass panels are modelled as elastic thin plates using the mTMM. The resulting double glazing model is then again coupled to SEA models, describing the neighbouring rooms.

Fig. 4 displays the predictions of this modified mTMM-SEA method in comparison with results of the conventional TMM and of a WBM model. The results are also compared with measured values [3]. All models agree well, except for the conventional TMM and the FTMM which largely underestimate the sound transmission loss in between the mass-spring-mass resonance (around $160 - 200\,\mathrm{Hz}$) and the coincidence

dip (around $1600 - 2000$ Hz), as the empty cavity was modelled using a fluid layer in these approaches. Note that the WBM accounts for the modal behaviour of the rooms, and it is therefore computationally much more expensive than the hybrid mTMM-SEA. Above 2500 Hz the predictions overestimate the sound transmission loss in comparison with the measurements; this is probably due to the structural coupling between the edges of the glass panels at in the measurement setup, which is not accounted for in the prediction models.

4 Conclusions

A hybridization between the transfer matrix method and statistical energy analysis has been developed for the computation of the diffuse sound transmission through finite walls and floors that consist of layers of solid, fluid and/or poroelastic material. The modal behaviour of the wall is approximately accounted for. The sound insulation predictions for different examples have been compared with experimental data. An overall good agreement has been observed.

The detailed contributions of the hybrid mTMM-SEA framework that is presented in this paper are (1) with respect to the TMM and related approaches (1a) that the variance, which is inherent to the diffuse field models of the sound fields can be computed at low computational cost, (1b) that cross-modal coupling is accounted for, while keeping a similar computation cost as in the conventional mTMM and (1c) that numerical difficulties in evaluating the plane-wave transmission, related to grazing incidence, are avoided; and (2) with respect to the hybrid FE-SEA approach: a substantial increase in computational efficiency when the system is simple enough to be modelled with mTMM.

Acknowledgments

This research was supported by a PhD Fellowship (C. Decraene) and Postdoctoral Fellowships (E. Reynders and A. Dijckmans) from the Research Foundation - Flanders, and by an Assistant Professorship from KU Leuven (E. Reynders). The financial support of FWO and KU Leuven is gratefuly acknowledged.

References

[1] P.J. Shorter, R.S. Langley, *Vibro-acoustic analysis of complex systems*, Journal of Sound and Vibration, Vol. 288, No. 3 (2005), pp. 669-699.

[2] R.S. Langley, V. Cotoni, *Response variance prediction for uncertain vibro-acoustic systems using a hybrid deterministic-statistical method*, Journal of the Acoustical Society of America, Vol. 122, No. 6 (2007), pp. 3445-3463.

[3] E. Reynders, R.S. Langley, A. Dijckmans, G. Vermeir, *A hybrid finite element - statistical energy analysis approach to robust sound transmission modelling*, Journal of Sound and Vibration, Vol. 333, No. 19 (2014), pp. 4621-4636.

[4] P.J. Shorter, R.S. Langley, *On the reciprocity relationship between direct field radiation and diffuse reverberant loading*, Journal of the Acoustical Society of America, Vol. 117, No. 1 (2005), pp. 85-95.

[5] R.S. Langley, *On the diffuse field reciprocity relationship and vibrational energy variance in a random subsystem at high frequencies*, Journal of the Acoustical Society of America, Vol. 121, No. 2 (2007), pp. 913-921.

[6] W. Lauriks, P. Mees, J.F. Allard, *The acoustic transmission through layered systems*, Journal of Sound and Vibration, Vol. 155, No. 1 (1992), pp. 125-132.

[7] B. Brouard, D. Lafarge, J.F. Allard, *A general method of modelling sound propagation in layered media*, Journal of Sound and Vibration, Vol. 183, No. 1 (1995), pp. 129-142.

[8] J.F. Allard, N. Atalla, *Propagation of sound in porous media*, John Wiley & Sons, Chichester, UK (2009).

[9] M. Villot, C. Guigou, L. Gagliardini, *Predicting the acoustical radiation of finite size multi-layered structures by applying spatial windowing on infinite structures*, Journal of Sound and Vibration, Vol. 245, No. 3 (2001), pp. 433-455.

[10] L. Cremer, M. Heckl, *Structure-borne sound: Structural vibrations and sound radiation at audio frequencies*, Springer, Berlin (1988).

[11] T.E. Vigran, *Predicting the sound reduction index of finite size specimen by a simplified spatial windowing technique*, Journal of Sound and Vibration, Vol. 325, No. 3 (2009), pp. 507-512.

[12] A. Dijckmans, G. Vermeir, *Development of a hybrid wave based - transfer matrix model for sound transmission analysis*, Journal of the Acoustical Society of America, Vol. 133, No. 4 (2013), pp. 2157-2168.

[13] D. Rhazi, N. Atalla, *Acoustic and vibration response of a structure with added noise control treatment under various excitations*, Journal of the Acoustical Society of America, Vol. 135, No. 2 (2014), pp. 693-704.

[14] C. Decraene, A. Dijckmans, E. P.B. Reynders, *Fast mean and variance computation of the diffuse sound transmission through finite-sized thick and layered wall and floor systems*, Journal of Sound and Vibration, Vol. 442 (2018), pp. 131-145.

[15] R.S. Langley, J.A. Cordioli, *Hybrid deterministic-statistic analysis of vibro-acoustic systems with domain couplings on statistical components*, Journal of Sound and Vibration, Vol. 321, No. 3-5 (2009), pp. 893-912.

[16] R.S. Langley, *Numerical evaluation of the acoustic radiation from planar structures with general baffle conditions using wavelets*, Journal of the Acoustical Society of America, Vol. 121, No. 2 (2007), pp. 766-777.

[17] E. Reynders, C. Van hoorickx, A. Dijckmans, *Sound transmission through finite rib-stiffened and orthotropic plates*, Acta Acustica united with Acustica, Vol. 102, No. 6 (2016), pp. 999-1010.

[18] ISO 12999-1:2014: Acoustics Determination and application of measurement uncertainties in building acoustics - Part 1: Sound insulation, *International Organization for Standardization* (2014)

[19] ISO 10140:2010: Acoustics Laboratory measurement of sound insulation of building elements, *International Organization for Standardization* (2010)

[20] A. Dijckmans, *Wave based calculation methods for sound-structure interaction. Application to sound insulation and sound radiation of composite walls and floors*, PhD thesis, Ku Leuven (2011).

[21] G. Jacqus, S. Berger, V. Gibiat, P. Jean, M. Villot, S. Ciukay, *A homogenised vibratory model for predicting the acoustic properties of hollow brick walls*, Journal of Sound and Vibration, Vol. 330, No. 14 (2011), pp. 3400-3409.

[22] F. Fahy, P. Gardonio, *Sound and structural vibration: radiation, transmission and response*, Academic Press, Oxford, UK (2007)

[23] M.A. Delany, E.N. Bazley, *Acoustical properties of fibrous materials*, Applied Acoustics, Vol. 3, No. 2 (1970), pp. 105-116.

[24] T.E. Vigran, *Building Acoustics.*, Taylor & Francis, Oxon, UK (2008)

[25] M.A. Biot, *Theory of propagation of elastic waves in a fluid-saturated porous solid. I. low-frequency range.*, Journal of the Acoustical Society of America, Vol. 28, No. 2 (1956), pp. 168-178.

[26] M.A. Biot, *Theory of propagation of elastic waves in a fluid-saturated porous solid. II. high-frequency range.*, Journal of the Acoustical Society of America, Vol. 28, No. 2 (1956), pp. 179-191.

Validity of the transfer matrix method for modeling trim components in vibro-acoustic applications

B. Van Antwerpen, S. Corveleyn, G. Lielens, B. Van den Nieuwenhof [1]
[1] Free Field Technologies, MSC Software Belgium
Rue E. Francqui, 9, B-1435, Mont-Saint-Guibert, Belgium
e-mail: **bva@fft.be**

Abstract

NVH applications, both in the automotive and aerospace industries, resort to poro-elastic and visco-elastic materials, frequently configured in multiple and sandwiched layers, to improve the acoustic transmission properties of structural panels. In a numerical context, the evaluation of the transmission loss of such treated panels is commonly performed using finite element models. A computationally less expensive alternative consists in using a locally-reacting transfer matrix to model these composite trim components.

This paper presents the implementation inside a commercial finite element software of the transfer matrix method for trim component modelling, supporting a spatially variant thickness definition. The method validity in terms of addressable frequency range is demonstrated on multiple simple configurations and applied on an industrial model for the transmission loss evaluation of a trimmed firewall panel.

1 Introduction

NVH applications, both in the automotive and aerospace industries, resort to poro-elastic and visco-elastic materials, frequently configured in multiple and sandwiched layers, to improve the acoustic transmission properties of structural panels. In a numerical context, the evaluation of the transmission loss of such treated panels is commonly performed using finite element models. The trim component layers are modelled, for porous materials, through formulations based on the Biot theory and, for visco-elastic materials, through frequency-dependent complex material properties.

At component level, direct methods are practicable for the transmission loss evaluation of the trimmed panel. At system level, where the objective is the assessment of the full trim package impact on the vibro-acoustic response, the model size may become prohibitive for direct simulation and reduced impedance methods are advantageously selected. Though, an alternative to such strategies consists in using a locally-reacting transfer matrix to model these composite trim components. Indeed, such approach eliminates the need to mesh the trim component, therefore providing significant gains in engineering time at model setup, and allows to reduce the size of the vibro-acoustic model, leading to faster computations. Nevertheless, it assumes local reaction and normal incidence, which a priori precludes the use of transfer matrices over the whole frequency range.

This paper presents the implementation inside a commercial finite element software of the transfer matrix method for trim component modelling. The strategy relies on the analytical construction of the equivalent properties of a composite trim in the form of a total transfer admittance matrix, by combining the analytical transfer admittance matrices of the different layers. The transfer admittance matrix of each layer relates the degrees of freedom at the top and the bottom of that layer in the normal direction, the transverse coupling between degrees of freedom being neglected.

This paper also studies the method validity in terms of addressable frequency range. The transfer matrix method is demonstrated on simple configurations involving transmission through acoustic fluid layers, visco-elastic layers and poro-elastic layers. In each configuration, a comparison with a refined finite element model is presented and conclusions are drawn with respect to the validity of the method. Finally, the applicability and efficiency of the method is demonstrated on an industrial model for the transmission loss evaluation of a trimmed firewall panel.

2 Transfer matrix method implementation

The simple 1D Trim modelling use a variant of the classic Transfer Matrix Method (TMM [1]), based on Schur reduction instead of matrix multiplications.

The Trim is composed of a stacking of different layers that can be porous but also fluid or solid. Each layer is characterized by a frequency dependent Transfer matrix $\boldsymbol{T}(f)$, which represents a linear relation between top and bottom primary-variable (fluid pressure p, solid displacement u) and corresponding flux-variable (average normal velocity, total normal stress). Those linear relations can be expressed in different ways, by selecting main and dependent variables.The classic TMM method expresses top primary and flux variable as a function of bottom primary and flux variable, so that layers can be combined using simple matrix multiplications.

...	...
Layer $i+1$	σ_n^{t}, σ_t^{t}, u_n^{t}, u_t^{t} σ_n^{b}, σ_t^{b}, u_n^{b}, u_t^{b}
Layer i	v_n^{t}, p^{t} v_n^{b}, p^{b}
...	...

Figure 1: Trim made of stacked layer, described by top/bottom primary and flux variables

Our variant expresses top and bottom flux variables in function of top and bottom primary variables. As primary and flux variables have been chosen so that inter-layer coupling condition are as simple as possible (continuity of primary variable, cancelation of flux variables), layers be combined in a way similar to 1D finite element assembly. At each interface, the equality of the primary variables is trivially achieved by using a single DOF for both layers, and the sum of normal flux variables to be equal to 0. Each layer can be seen as a single element whose dynamic stiffness matrix is the transfer matrix, but contrary to classical finite element, the shape functions are frequency-dependent analytical solution of the layer wave equations.

To get the transfer matrix of the whole layer stacking, all the primary interface variables are eliminated, keeping only the topmost and bottommost variables. The Schur complement obtained after the elimination of the internal primary variable is the stacking transfer matrix, in a format (Primary-variable → Flux-variable) that is completely equivalent to the one used for describing a single layer.

Similarly to classic multiplicative TMM method, this method can thus be applied recursively, sets of layers being homogenized into a macro-layer that can itself be included in a macro-stacking.

The advantage compared to the multiplicative method is an easier coupling between different layers, especially when combining solids, fluids and porous types, together with easier treatment of alternative coupling conditions (impervious, sliding, glued, added mass and stiffness at the interface,…). Moreover,

because primary and flux variables are selected the same as classic Finite elements, both the layer transfer matrix and the final stacking transfer matrix can be directly used in a FE code as pseudo-elements.

Drawback is a slightly more costly Schur-reduction (compared to matrix multiplication) for layer homogenization, which however does not impact the global performance for our applications.

3 Validity of the method

The implemented method allows to model multiple layers of different materials, including fluid, solid or poro-elastic materials. It can couple either fluid or structural degrees of freedom on each side of the coupling interface. In order to cover the broad range of possible applications, four different configurations are assessed:

- The structural transmission of a foam between two structural plates (U-U coupling)
- The acoustic transmission of a rigid porous (P-P coupling)
- The acoustic radiation of a plate covered by a foam (U-P coupling)
- The acoustic radiation of a plate covered by a foam and a heavy septum (U-P coupling)

Each model is loaded using local point loads or incident plane waves to ensure sufficiently complex excitation with both normal and transverse components, to better asses 1D trim model validity when compared to a Finite Element modal.

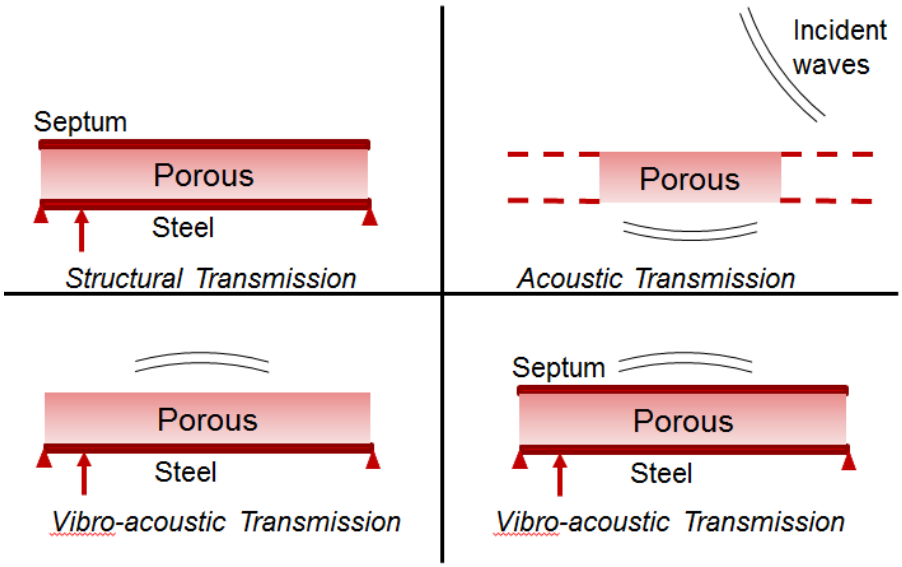


Figure 2: Covered configurations

3.1 Structural transmission

The handled configuration consists in a 3mm supported steel plate covered by a layer of foam of varying thickness and a 2.5mm heavy septum. The handled foam is a typical foam used in the automotive industry to insure structural decoupling with a heavy layer and is used for floor panels. The thickness of the intermediate porous layer is varying between 1cm to 4 cm. The foam and septum properties are the following:

	Foam	Septum
Airflow Resistivity: σ (kNs/m^4)	43.5	-
Porosity: Ω	0.921	-
Tortuosity: α_∞	1.74	-

Viscous Length: Λ (μm)	50	-
Thermal Length: Λ'(μm)	120	-
Solid density: ρ (kg/m³)	883	3800
Young modulus: E (kPa)	14.7	77400
Loss factor: η	0.35	0.21
Poisson ratio: ν	0	0.35

Table 1: Material properties of porous and solid materials

A 2D quadratic model of this configuration of a width of 2.4m is created to model the structural behavior of this coupling. Each solid layer is modeled using 1 element along their thickness, and a minimum of 16 elements is used along the porous layer to insure a convergence of the Finite Element model. A local point load is applied at 0.342m from the border insuring a non-normal behavior of the model. In the transfer Matrix model, the porous layer is replaced by an incongruent interface including the transfer matrix. In this configuration, both the steel plate and heavy septum remains modeled in finite elements. The transfer matrix used varies from point to point as local thickness is used in the procedure described in section 2.

When analyzing the structural response of the model both on the steel plate and the solid septum (as shown in Figure 3 and Figure 4), a first lower part of the spectrum shows the mass – spring – mass resonance behavior of the system that occurs. In this part of the spectrum, the structural deformation of both foam and septum follow the deformation of the steel. This generates global transverse damping effects which are not captured by the transfer matrix method.

$$f = \frac{1}{2\pi}\sqrt{\frac{\frac{K_a}{\Omega} + K_s}{h_p \rho_s h_s}} \tag{1}$$

Above this frequency, a structural decoupling between the steel plate and heavy layer is observed, shown by the decrease of velocity on the heavy septum.

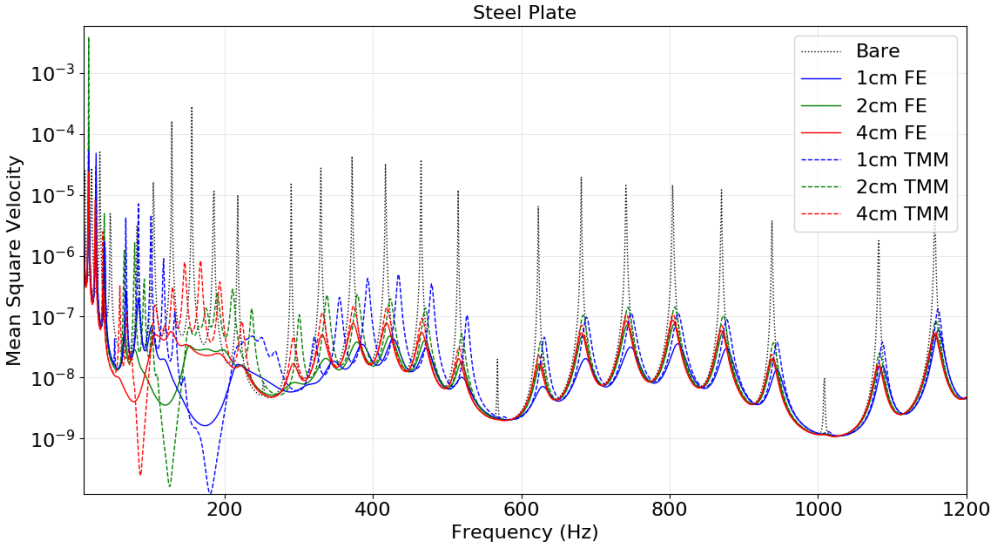


Figure 3: Structural response of the steel plate

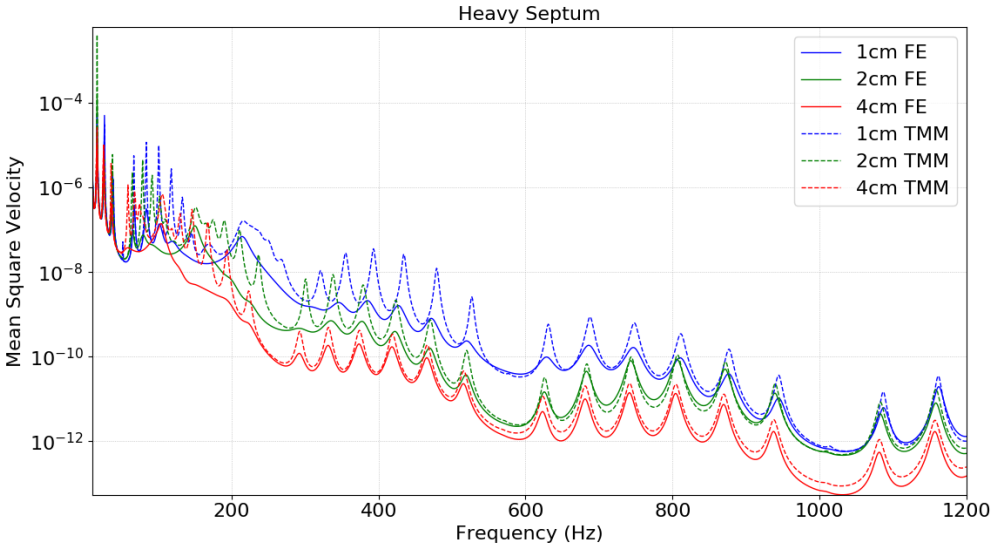


Figure 4: Structural response of the heavy septum

The comparison of Finite Elements models with Transfer Matrix models shows globally a good correlation in this frequency range. When modifying the thickness of the porous layer, the correlation between both methods tends to appear at lower frequencies for larger thicknesses. When computing the compressional wavelengths of the porous material analytically, we can observe that the correlation seems to correspond to the frequency where the thickness of the porous layer coincides with the 2nd compressional wavelength of the porous material. We assume that, starting from this frequency, the compression effect along the thickness direction of the porous layer (which is captured by the 1D transfer matrix method) becomes the most important contribution for dissipation. The in-plane effects (not captured by the 1D TMM) being relatively less important, the match becomes better.

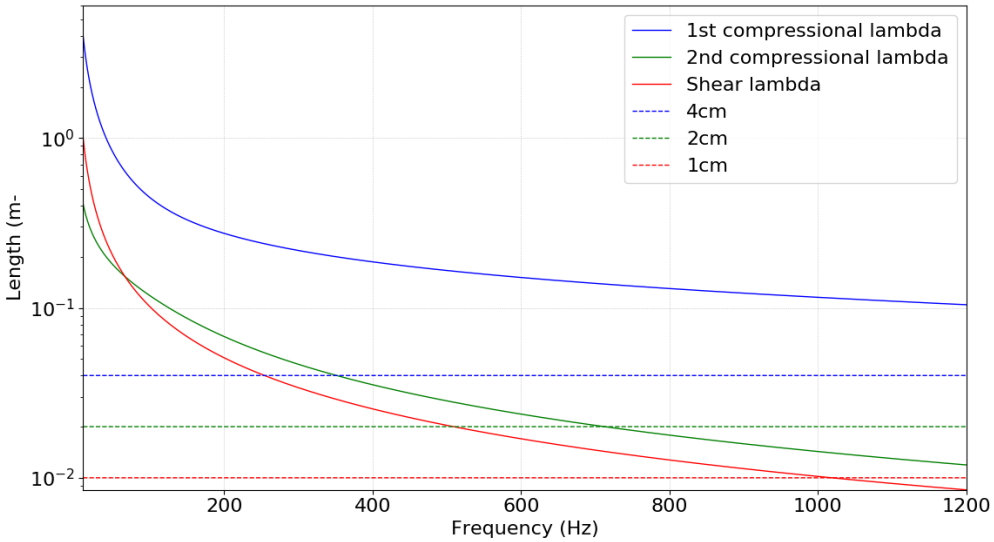


Figure 5: Compressional wavelengths of the porous material

3.2 Acoustic transmission

This configuration consists in a 2cm thick baffled layer of porous material subjected to an incident plane wave excitation, for which we evaluate the acoustic transmission on the other side. In such model, the

porous component is usually simplified by assuming that the skeleton is perfectly rigid and using an equivalent fluid rigid porous formulation. The acoustic medium is modeled on both sides of the porous material, and the acoustic radiated power on the opposite side is evaluated. Different sources are modeled using an incidence angle varying between 0 and 80°. In this presentation, an incidence angle of 0° is assumed to be normal to the component and does not affect the porous layer in the transverse direction. The discretization of the porous layer for the Finite Element model is similar to the previous configurations. When using the Transfer Matrix method, the porous layer is replaced by an incongruent interface including the transfer matrix, and both acoustic media remain.

The radiated power for an incident angle of 45° is shown in Figure 6. The difference between both models increases with the frequency. Figure 7 shows the variation of the radiated power when modifying the incidence angle. For a normal incidence, the relative error between Finite Element and Transfer Matrix method tends to be equal to zero, but it becomes large when increasing the incidence angle.

This difference between both methods for incident waves is explained by the transverse contribution of the incident wave. As the frequency increases, the acoustic wavelength becomes smaller and the damping mechanism inside the porous layer increases. When the incidence angle increases, the travelling path of the acoustic waves through the porous layer also increases due to the transverse contribution. This is not captured by the 1D TMM method, which considers the normal behavior of the porous layer only.

This configuration heavily differs from the previous configuration, in which the transverse behavior of the porous layer becomes predominant at higher frequencies. For pure acoustic transmission, the relative error for a random incidence increases with the frequency and its validity is restricted to low frequencies.

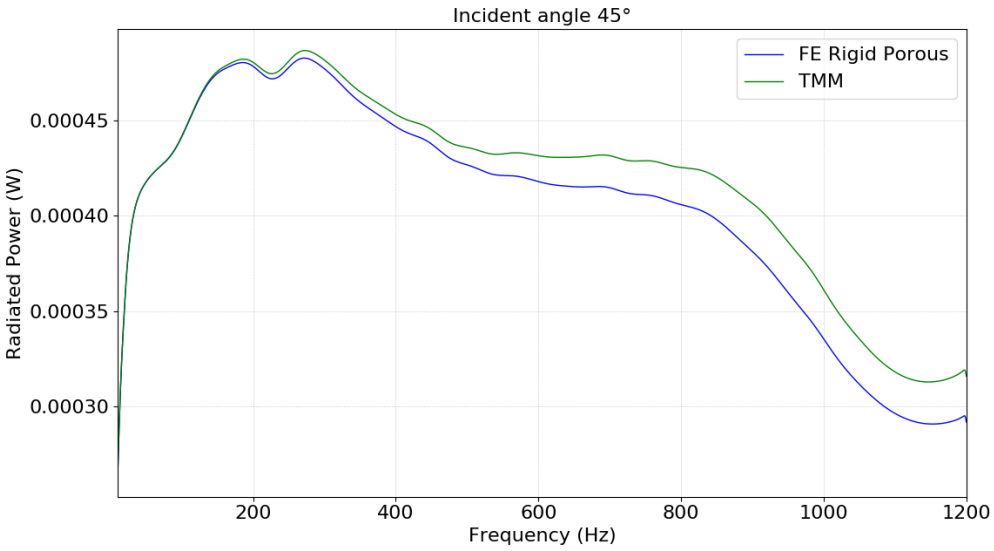


Figure 6: Radiated power on opposite side

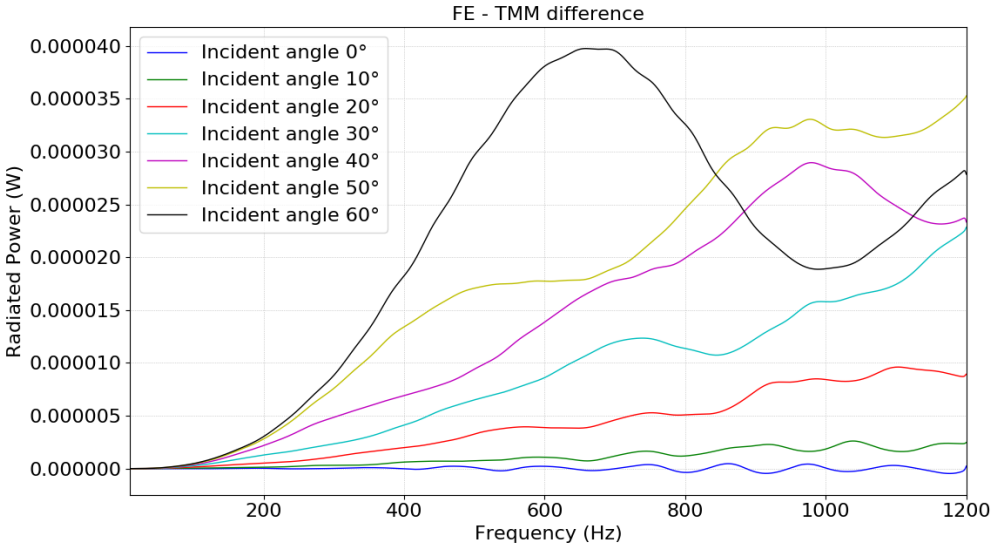


Figure 7: Influence of the angle of incidence (difference between the full FE model and the TMM-based model)

3.3 Vibro-acoustic transmission

3.3.1 Acoustic radiation through foam

This configuration is similar to the one detailed in section 3.1. To model the vibro-acoustic behavior, the heavy septum is replaced by an acoustic medium and the acoustic radiated power is evaluated. When using the 1D TMM method, the porous layer is replaced by an incongruent interface between the steel plate and the acoustic component using the transfer matrices.

The difference between both methods for multiple porous layer thicknesses is shown on Figure 8. When comparing to the bare configuration, the presence of the porous layer mainly affects the acoustic radiation at resonance frequencies, except when the porous layer becomes very large. The observed differences between both methods are similar to those observed in Section 3.2. The structural behavior of the steel plate producing transverse waves, the acoustic transmission through the porous layer is not accurately captured by the Transfer Matrix method, although the global trend of the porous treatment is captured.

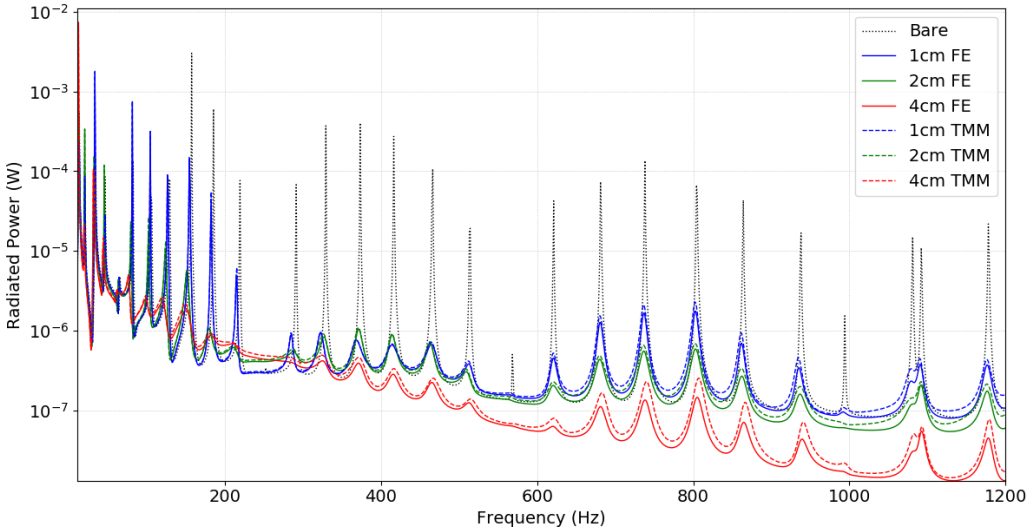


Figure 8: Radiated power through the porous layer

3.3.2 Acoustic radiation through a complex foam-septum

In this configuration, the acoustic medium is added on top of the heavy septum and the acoustic radiated power is evaluated. When using the 1D TMM method, both the porous layer and the heavy septum are replaced by an incongruent interface between the steel plate and the acoustic component. The transfer matrices contain the reduction of both the porous layer and the heavy layer, and are also coupling structural to fluid degrees of freedom.

The results in terms of radiated power for both methods and for the bare configuration are shown in Figure 9. The physical behavior is again very similar to those observed in section 3.1. As observed for the structural transmission, the accuracy of the 1D TMM method at the resonances becomes good as soon as the thickness of the foam layer corresponds to the second compressional wavelength.

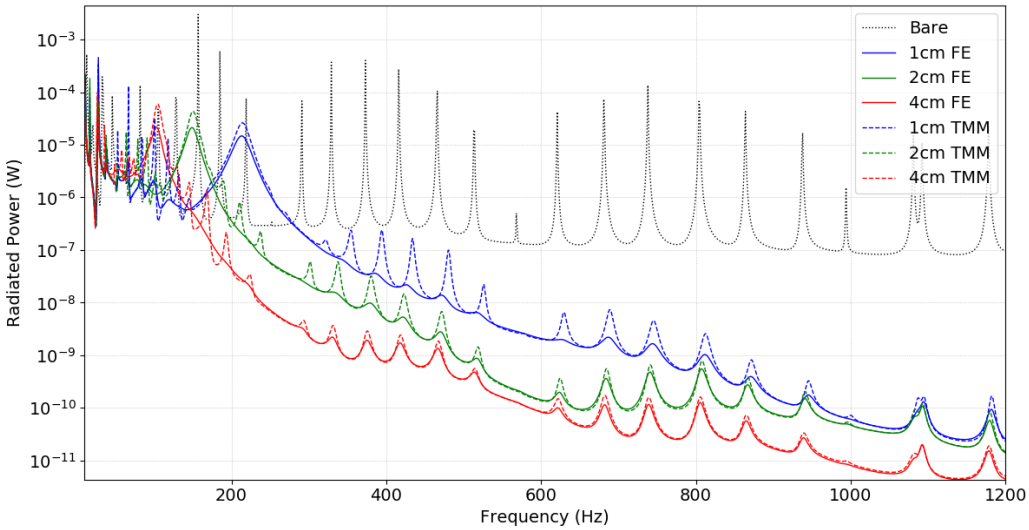


Figure 9: Radiated power through the complex foam-septum

4 Industrial model application

4.1 Model description

The handled configuration is a realistic model of trimmed firewall panel. The foam and heavy layer added on the firewall panels insure a correct acoustic insulation. The geometry of the structure is shown in Figure 10.

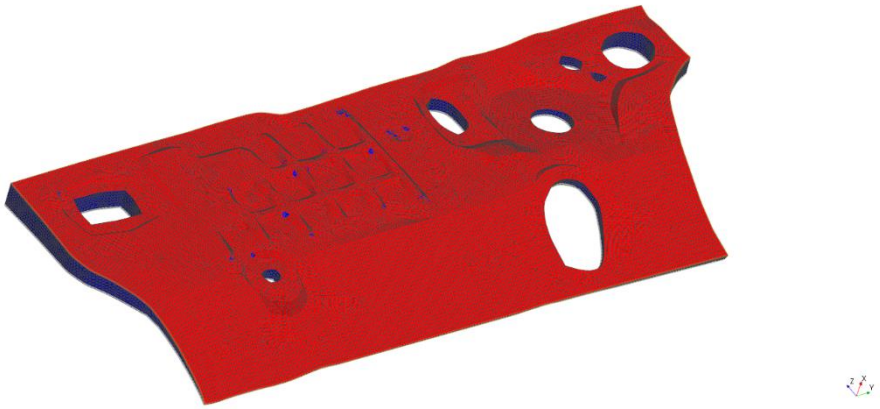


Figure 10: Firewall panel

The thickness of the trim component varies throughout the panel between 3cm and 1cm. The variation of the thickness is shown in Figure 11. The heavy layer has a constant thickness of 2mm. The material properties of both materials are provided in Table 2.

	Foam	Septum
Airflow Resistivity: σ (kNs/m^4)	55	-
Porosity: Ω	0.95	-
Tortuosity: α_∞	1.9	-
Viscous Length: Λ (μm)	-	-
Thermal Length: Λ'(μm)	-	-
Solid density: ρ (kg/m^3)	1300	450
Young modulus: E (kPa)	35	100000
Loss factor: η	0.2	0.022
Poisson ratio: ν	0.2	0.3

Table 2: Material properties of porous and solid materials

The thickness variation is handled by the 1D TMM method as the thickness between the firewall panel and the acoustic component is automatically evaluated in each grid point. The layer of each individual trim layer (respectively, the foam and heavy layer) is recomputed based on their relative thickness and their thickness scaling. In this model, no thickness scaling is applied on the heavy layer, and the porous layer will as such adapt its thickness while the heavy layer will be assumed of constant thickness.

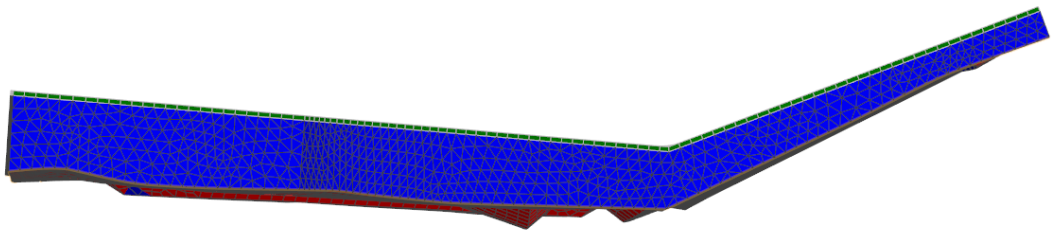


Figure 11: Thickness variation of the porous layer

The vibro-acoustic response corresponding to two excitations will be evaluated: a local point load and a diffuse sound field both applied on the firewall panel.

4.2 Results

4.2.1 Point load

Figure 12 shows the difference in terms of radiated power between a bare configuration in which no panel treatment is present and the treated configurations. The treated configurations are shown using FE method both in linear and quadratic interpolation, and using the Transfer Matrix method.

As shown in Section 3.3.2, the influence of the treatment is not entirely captured at lower frequencies using the 1D TMM method. Both the FE and the Transfer Matrix method start to correlate around 1250Hz, which corresponds approximately to the frequency where the mean thickness corresponds to the second compressional wavelength, as shown in Figure 13. After this frequency, both methods correlate, and the 1D TMM method is even more accurate than the Finite Element linear interpolation of the trim component.

However, above the first modes of the plate, the influence of the treatment seems correctly captured by both methods and the differences between them are acceptable when compared to the variation of the solution due to the uncertainty of the porous material properties in realistic conditions.

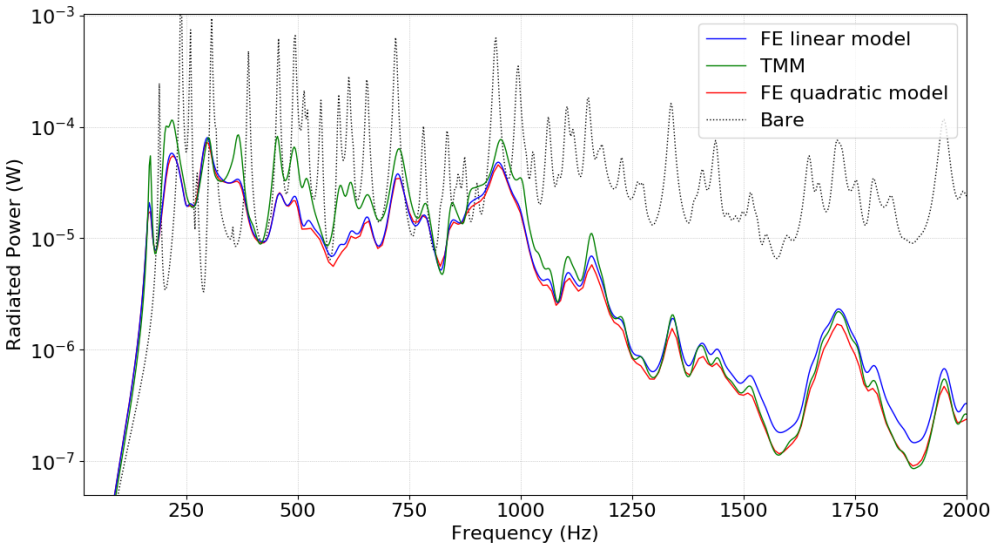


Figure 12: Radiated power of the treated and untreated panel

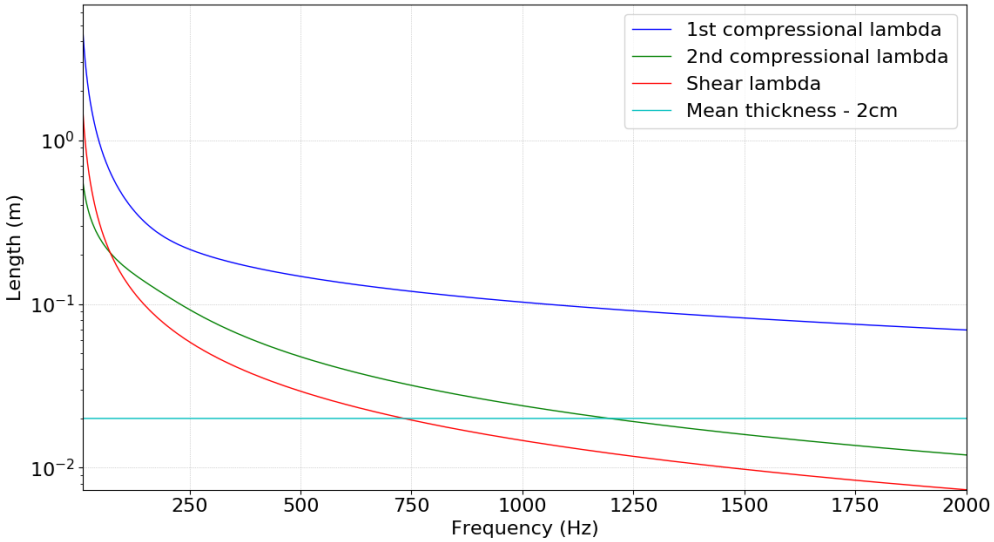


Figure 13: Compressional wavelengths of the porous material

4.2.2 Diffuse sound field

The transmission loss of the system subjected to a diffuse sound field is shown in Figure 14. The differences between the two different methods are, as in the previous section, mainly visible at very low frequencies and in the 500-800Hz range. A very good correlation is observed above 1250Hz. Again, the influence of the treatment is in both cases correctly captured.

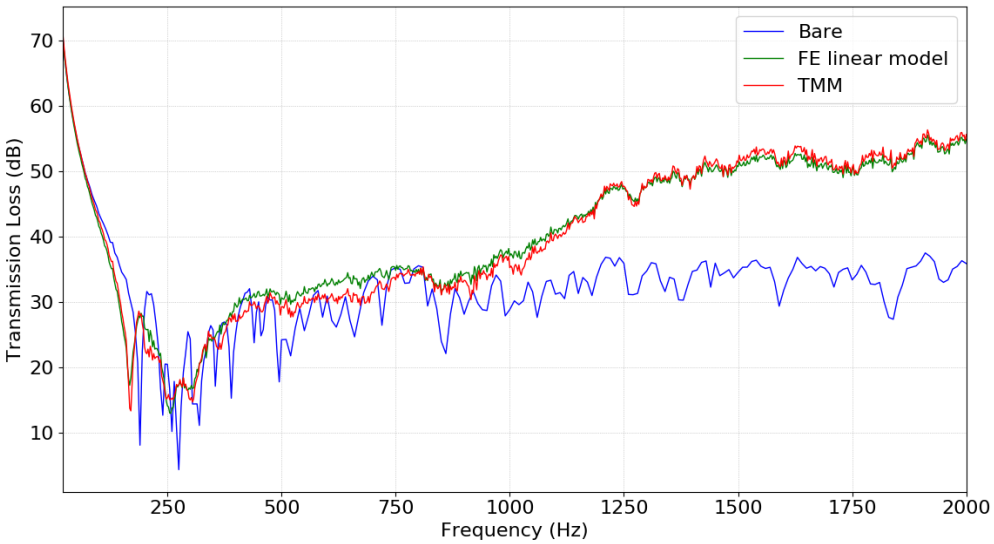


Figure 14: Transmission loss of the treated and untreated panel

4.3 Material variation

In this section, the comparison between Finite Element and 1D TMM method is performed for different porous materials applied on the same vibro-acoustic transmission model. Material 2 represents a lumped porous material while material 3 represents a porous material with a substantially rigid skeleton. Both

materials are used in the automotive industry. The material properties of both porous materials are provided in Table 3.

	Mat 2	Mat 3
Airflow Resistivity: σ (kNs/m^4)	23	57
Porosity: Ω	0.95	0.97
Tortuosity: α_∞	1	1.54
Viscous Length: Λ (μm)	54.1	24
Thermal Length: Λ'(μm)	162	73
Solid density: ρ (kg/m³)	1160	1500
Young modulus: E (kPa)	17	214
Loss factor: η	0.1	0.1
Poisson ratio: ν	0.01	0.3

Table 3: Material properties of additional porous materials

Figure 15 shows the comparison between both methods on the three different materials. As the second material is softer than the first handled material, the decoupling between both structural components is even more pronounced, whereas material 3 provides much less decoupling between both components. Globally, the general trends of each material are correctly captured even if some main differences occur.

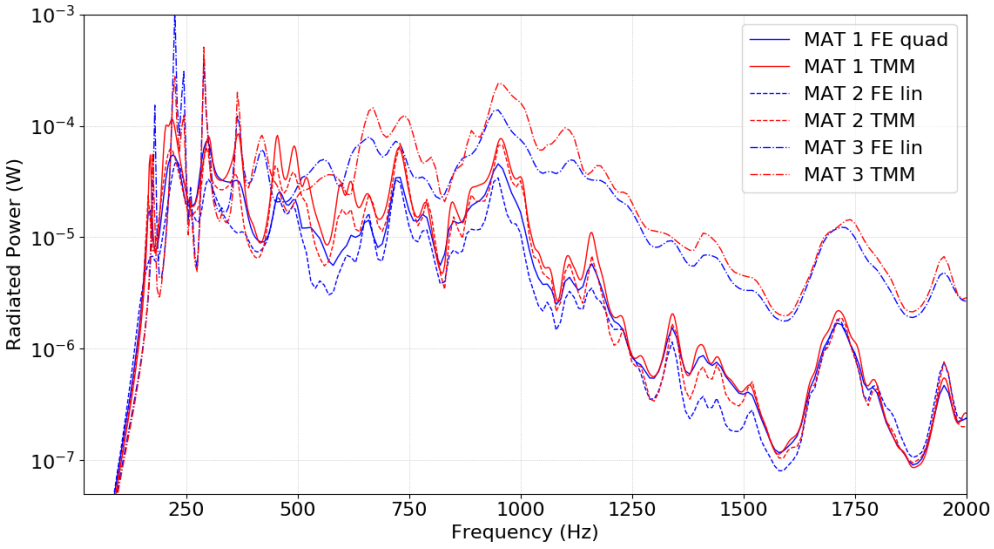


Figure 15: Radiated power FE-transfer matrices comparison for different materials

Figure 16 highlights the relative difference between Finite Element and the Transfer Matrix methods. These are shown for linear interpolation meshes only. As shown for material 1, this relative difference decreases above 1250Hz, and increases slightly above due to the linear interpolation. For lumped materials as material 2, the difference between both methods remains important up to 1750Hz, even with a very small compressional wavelength as shown in Figure 17. This could be explained by the very low Young modulus, which enables important transverse damping behaviors that cannot be captured using the Transfer Matrix method. For material 3, the relative differences at lower frequencies are smaller compared to the other materials, but are relatively important above 500Hz and are decreasing slowly at higher frequencies. For such stiff materials, the second compressional wavelength remains much higher than the average thickness of the complex structure, and damping mechanisms remain mainly structure based. For such materials, the transverse behavior remains important and the Transfer Matrix method cannot entirely capture the complete behavior.

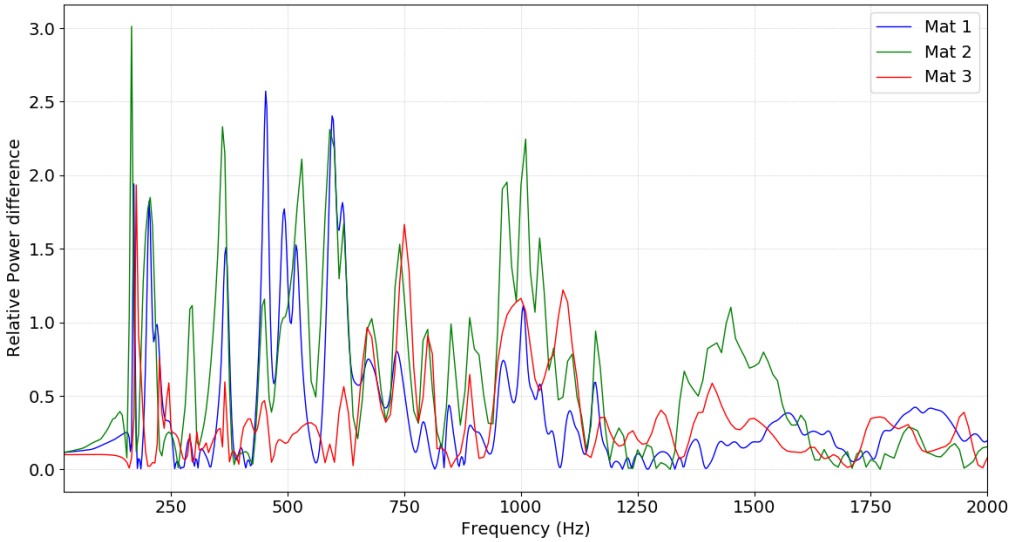


Figure 16: Relative power difference between finite element and transfer matrices

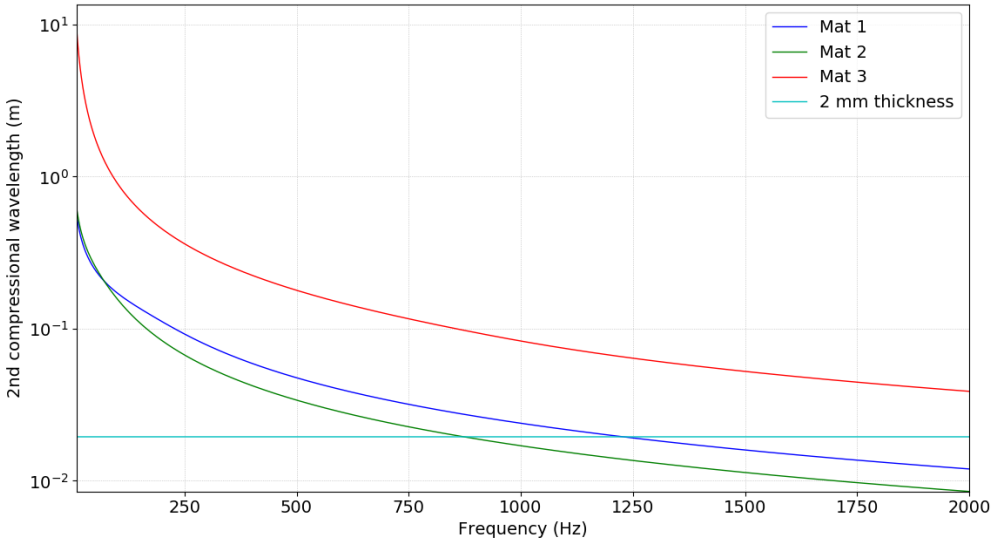


Figure 17: Second compressional wavelengths for the different porous materials

4.4 Performance

Both the CPU time and the memory consumption of the handled computations are shown in Table 4.

The bare configuration, including no damping mechanism, consumes less memory and CPU time than the methods including damping mechanisms. Despite having the same number of degrees of freedom as the bare configuration, the Transfer Matrix method consumes more memory and CPU time as the number of contributions within the system heavily increases, which reduces the sparsity of the impedance matrix. However, this method is three times faster than using a linear interpolation Finite Element mesh for modelling the porous layer and septum. Its memory consumption is about four times lower. As for using quadratic elements for the porous and heavy layer, it provides much more accurate results but remains expensive, being 40 times more expensive in CPU time.

	Bare	Linear FE	Quadratic FE	TMM
CPU Time / freq (s)	3	70	842	21
Memory consumption (Gb)	1.1	11.5	121	3

Table 4: Computational performance on industrial application

5 Discussion and further work

It has been shown that for high frequency, the 1D TMM methods works very well while introducing very small additional CPU cost compared to the no-trim case.

However, as expected, the approach is not as well suited for lower frequencies. In-plane behavior must be accounted for, which can be done using a finite element modelling, again with controlled additional CPU cost because low frequency allows for relatively coarse meshes.

In the future, we plan to develop a seamless way to combine the two approaches automatically, to offer a single method remaining accurate and efficient on the whole frequency range. This can be done in 3 ways:

1) By having a parametric description of the trim that will allow automatic meshing at low frequency and 1D modelling at higher frequency, the software automatically selecting the best method frequency per frequency.
2) The TMM method can be extended using a 1.5D approach, by accounting for in-plane field variation in the wavenumber space. All transfer matrices relations remain valid with an additional (k_x, k_y) parameter. Once the stacking transfer matrix $\boldsymbol{T}(k_x, k_y, f)$ is obtained, it is transformed back into physical space, with a local kernel so that cross-talk distance is kept finite [2]. We end up with a generalized transfer admittance that couples each dof of top surface to limited set of not-too-distant DOFs of the bottom surface.
3) Alternatively, the FE modelling of the trim can be improved using ideas from our version of the 1D TMM matrix: enriching shape function with the 1D wave solution of each layer and eliminating inner interface dofs should lead to a method with the same behavior as 1D trim in the normal direction, but accounting for slower variation in the in-plane direction. Those enriched FE should be extremely accurate, and CPU efficient (coarse trim mesh with 1 element in the thickness direction).

In addition to seamlessly cover a wide frequency range, approaches 2) and 3) should offer better prediction in the tricky mid-frequency region.

6 Conclusions

The implementation of the Transfer Matrix method inside a Finite Element software and its application on an industrial model have been demonstrated. The flexibility of this implementation allows to model multiple layers of varying materials between two incongruent surfaces with a varying thickness. It also offers the capability of coupling the trim component both with structural or fluid degrees of freedom, enabling various configurations covered in this paper.

The validity of the Transfer Matrix method to model porous components has been evaluated on different configurations. When modeling configurations including porous components integrated between structural components, the Transfer Matrix method tends to provide an accurate solution when the normal damping mechanisms become predominant. In our applications, we have observed this occurs mainly above the coincidence frequency with the second compressional wavelength and the thickness of the porous layer. We have also noticed that for extremely lumped materials, this conclusion seems not always sufficient. At very high frequencies, it has been shown that the accuracy of the Transfer Matrix method is even more

precise than the Finite Element method, whereas the Finite Element method is much more precise at lower frequencies.

In configurations involving a porous component directly coupled to an acoustic component (acoustic or vibro-acoustic transmission), the Transfer Matrix method is extremely sensitive to the in-plane component of the excitation, and the divergence with the Finite Element method increases at higher frequencies, as soon as the acoustic wavelength becomes of the size of the porous components.

The usage of both methods on an industrial model has shown the accuracy of the Transfer Matrix method to model such configurations as well as its interest in terms of performance.

References

[1] Allard J.F., *Propagation of Sound in Porous Media: Modelling Sound Absorbing Materials*, Elsevier Applied Science, London (1993).

[2] Alimonti L.,Attala N., Berry A. And Sgard F., *A hybrid modeling approach for vibroacoustic systems with attached sound packages,* Proc. Mtgs. Acoust. 19 (2013) .

Determination and optimisation of the sound reduction index of ship bulkheads through the wave propagation approach

E. A. Piana[1], U. Carlsson[2], L. Feng[2]
[1] University of Brescia, Applied Acoustics Laboratory
Via Branze 38, 25123, Brescia, Italy
e-mail: **edoardo.piana@unibs.it**

[2] MWL – Royal Institute of Technology
Teknikringen 8, 100 44 Stockholm, Sweden

Abstract
Lightweight composite structures are progressively replacing traditional materials like steel structures in the shipbuilding industry for their light weight and good mechanical characteristics. However, a lightweight composite structure has generally poor acoustic properties and is not suitable to shield noise. In this case some comfort issues may arise on board. Ships are also a source of underwater noise, which can seriously pollute the aquatic environment if a suitable form of shielding is not envisaged. It is therefore essential that some acoustic features are predicted and optimised. The paper presents the measurements carried out on two different types of bulkhead: a homogeneous ribbed fibreglass partition and a sandwich structure with two symmetrical fibreglass leaves plus a balsa core. The optimisation of such structures can be carried out following the simulations performed by using a code based on the wave propagation approach theory.

1 Introduction

Sound insulation is a relevant topic in the shipbuilding industry, involving safety of crew members, the comfort of passengers and the protection of marine ecosystems. Some applications where an accurate acoustic design is required are the attenuation of propeller and hydrodynamic noise transmission from the outside to the inside of the ship [1], the reduction of noise impact on the biological environment [2], and the insulation of critical bays, such as the engine room, with respect to cabins [3].

A key factor in the acoustical optimisation of ship interior is the accurate design of bulkheads, whose construction is conceived to ensure lightness, robustness and resilience, to fit limited space and to perfectly integrate with the surrounding structure and equipment. Bulkheads can be realised in a variety of materials, ranging from metals to wood and, in high-end applications, composites and resins. Their laboratory acoustic characterisation is often impossible due to their large size, and in-situ traditional measurements based on the use of sound sources are a challenging task because of the high flanking transmission due to the massive presence of connections, openings, hatches and pipes. Structural methods can be an alternative in this case.

The bending stiffness of a homogeneous or of a composite structure can be effectively used to describe the acoustic behaviour of an assembly [4]. For a homogeneous material the bending stiffness can be defined analytically based on the Young's modulus and the moment of inertia of the construction. If the structure has been already manufactured, the bending stiffness can be determined by means of simple measurements of the resonance frequencies on beams [5] or, in the field, through point mobility measurements [6]. In the following section, the basics of such theory will be explained. Subsequently, the application of the method to the acoustic characterisation of two types of ship bulkheads, corresponding to classical sandwich panels and to ribbed fibreglass panels, will be presented.

2 Theoretical background

Consider a homogeneous thin plate surrounded by air, Figure 1. A plane sound wave incident to one side of the plate causes the propagation of a bending wave. The bending wave excites a transmitted sound pressure wave on the other side of the plate in the receiving room. The ratio between the transmitted sound power over the incident sound power, the sound transmission coefficient τ, is a measure of the plate's ability to prevent sound transmission. Assume the plate is infinite and the incident plane sound pressure wave propagates in the *x*-*y* plane. The plate bending wave equation can then be expressed in terms of the total sound pressure acting on its sides as [7]:

$$\left(-\mu''\omega^2 + D_p \frac{\partial}{\partial y^4}\right) \boldsymbol{v}_x = i\omega[(\boldsymbol{p}_i + \boldsymbol{p}_r) - \boldsymbol{p}_t] \tag{1}$$

where μ'' is the mass per unit area of the plate and D_p is the plate bending stiffness.

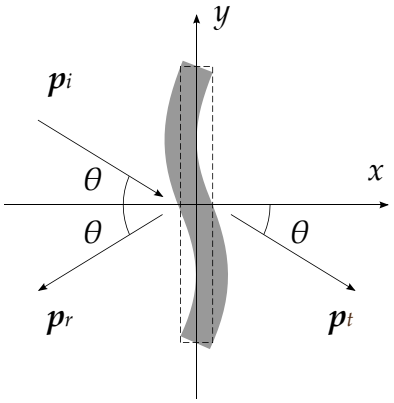


Figure 1: Transmission of a sound wave through a thin single leaf wall

Writing the velocities and the pressures at $x = 0$ as phasors,

$$\boldsymbol{p}_\alpha = \hat{\boldsymbol{p}}_\alpha e^{j(\omega t - k_y y)} \text{ and } \boldsymbol{v}_x = \hat{\boldsymbol{v}}_x e^{j(\omega t - k_y y)} \tag{2}$$

the previous relation (1) can be written as

$$\left(-i\omega\mu'' + D_p \frac{k_y^4}{i\omega}\right) \hat{\boldsymbol{v}}_x = [(\hat{\boldsymbol{p}}_i + \hat{\boldsymbol{p}}_r) - \hat{\boldsymbol{p}}_t] \tag{3}$$

where $k_y = k \sin\theta$. Since the normal velocities of all the fields at the plate are equal and considering that for a plane wave the particle velocity is identical to the pressure divided by the air impedance, one can write

$$(\hat{\boldsymbol{p}}_i - \hat{\boldsymbol{p}}_r) = \hat{\boldsymbol{p}}_t \tag{4}$$

and, as a consequence,

$$\left(-i\omega\mu'' + D_p \frac{k_y^4}{i\omega}\right) \frac{\hat{\boldsymbol{p}}_t cos\theta}{\rho_0 c} = 2(\hat{\boldsymbol{p}}_i - \hat{\boldsymbol{p}}_t) \tag{5}$$

From this equation the transmission coefficient can be derived as

$$\tau(\theta) = \frac{1}{1+\left(\frac{\omega\mu''\cos\theta}{2\rho_0 c}\right)^2 \left[1-\left(\frac{\omega \sin^2\theta}{\omega_c}\right)^2\right]^2} \qquad \omega_c = 2\pi f_c = c^2\sqrt{\frac{\mu''}{D_p}} \tag{6}$$

Here, f_c is the critical frequency, that is, the frequency at which the bending waves propagate in the structure with the sound speed in the surrounding medium, c. Equation (6) shows that the transmission coefficient is 1, and all the incident sound power is transmitted, at a frequency $f = f_c/\sin^2\theta$.

2.1 Determination of the bending stiffness: homogeneous ribbed panels

If structural characteristics must be guaranteed, the core or one part of the plate structure can be "ribbed", giving higher stiffness to the overall assembly. For certain types of composite ribbed plates, the acoustic properties can be very poor. The analysis of complex structures can be considerably simplified taking advantage of the concepts of impedance and mobility.

The vibration behaviour of finite structures can be derived from that of infinite plates. In an infinite plate, the bending waves excited by a point force can propagate indefinitely in the specimen. In a finite plate, the same bending waves reach the boundaries of the plate and are then reflected back. If a point force acts at a certain position of the plate, its velocity response depends upon the plate geometry and on boundary conditions, thus the point mobility will change with position and frequency. However, a space- and frequency-average of the real part of the point mobility for a finite structure is, in the mid- and high-frequency regions, equal to the real part of the point mobility of an infinite structure of the same material and thickness:

$$Re\langle \bar{Y}(\omega) \rangle = Re\, Y_{\infty}(\omega) \tag{7}$$

Consequently, the power input, injected in a finite panel by a force acting randomly in time and space, can be calculated as if the structure were infinite and excited by a point force with a power spectral density equal to the sum of the power spectral densities of all the sources acting on the finite structure. This assumption is valid if the modal density within a band is independent of boundary conditions, which is true for the medium and high frequency bands. To extend this assertion to the low-frequency range, a certain number of modes have to be included within each frequency band. It can be shown that the number of modes within a band should be at least 5 to have a fair accuracy. The mobility must be measured over a sufficiently large number of points, randomly distributed over the surface of the panel, in order to obtain a space average $\mathrm{Re}\langle Y \rangle$ of the mobility which is representative of the dynamic behaviour of the entire panel.

It can be demonstrated that, for a finite plate, far from the edges of the specimen, the point mobility is

$$Re\langle Y \rangle = \frac{1}{8\sqrt{D_p \mu''}} \tag{8}$$

This relation can be used to estimate the bending stiffness D_p of a plate starting from point mobility measurements. Using an average of the point mobility function measured on the panel surface over several measurement positions, the high stiffness of the points close to the ribs is averaged with the low stiffness of the central part of the sub-plates delimited by the ribs. In this way, the space- and frequency-average of the bending stiffness provides a good representation of the overall behaviour of the panel.

If the space-average is computed inside a specific frequency band, the bending stiffness per unit width of the panel at the central frequency of each band is obtained as

$$D_p = \frac{1}{64\, \mu'' \, [Re\langle \bar{Y} \rangle]^2} \tag{9}$$

For modes (m,n) having m = 0 or n = 0, and then for the modes in the low frequency range, it can be shown that

$$Re\langle \bar{Y} \rangle = \frac{2}{8\sqrt{D_p \mu''}} \tag{10}$$

This means that, for the first natural frequencies corresponding to such modes, the measured mobility should be divided by a factor 2.

2.2 Determination of the bending stiffness: sandwich panels

A sandwich panel cannot be considered a homogeneous or ribbed wall. For this reason, a different scheme must be applied in this case.

The static and dynamic performances of a panel can be greatly improved using sandwich constructions. For sandwich panels the bending stiffness is not constant, but it is rather frequency-dependent, ranging from a "static" bending stiffness in the low frequency region to the bending stiffness of the two laminates in the high frequency range. Let us consider a beam for which the width is b, mass per unit length μ' and mass per unit area μ''. The typical dimensions of the structure and its material parameters are indicated in Figure 2. It can be shown [8] that the bending stiffness per unit width D'_b of a sandwich beam is the real solution to the equation:

$$\frac{A}{f} D_b'^{3/2} - \frac{B}{f} D_b'^{1/2} + D_b' - C = 0 \tag{11}$$

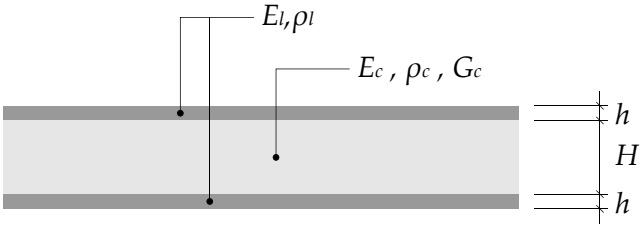


Figure 2: Sandwich structure made of laminates and core

Coefficients A, B and C in equation (11) can be computed analytically on the basis of some material parameters through the following equations:

$$A = \frac{G_c S}{\left(\sqrt{\mu'} 2\pi D_1'\right)}; \; B = \frac{G_c S}{\left(\sqrt{\mu'} 2\pi\right)}; \; C = 2D_2' \tag{12}$$

where S is the area of the cross section and D'_1 and D'_2 are the static bending stiffness of the entire beam and of a single laminate, respectively. Therefore, the coefficients can be calculated directly if the materials properties are known.

In case the parameters of the materials making the structure are not known, some measurements can be performed in order to compute the A, B and C parameters applying the least square method to a set of frequencies describing the normal modes of the specimen, according to the procedure described in [9].

If the bending stiffness D'_b for a beam, width b, is measured or estimated, then $D_p = D'_b/b$. As shown in the next section, the knowledge of D_p allows to calculate the sound transmission coefficient and, therefore, the sound reduction index of the structure.

2.3 Transmission coefficient and sound reduction index

Irrespective of the nature of the partition (ribbed or sandwich), the sound transmission coefficient can be computed in an accurate way according to the equations given in this section.

Cremer [10] derived the sound transmission coefficient $\tau(\theta)$ for a thin homogeneous plate as a function of the angle of incidence θ of the acoustic wave, see Figure 1. By introducing the definition of critical frequency, equation (6), in this expression, the transmission coefficient is obtained as:

$$\tau(\theta) = \left\{ \left[1 + \frac{\mu'' \omega}{2\rho c} \cos\theta \left(\frac{f}{\frac{c^2}{2\pi}\sqrt{\frac{\mu''}{D_p}}} \right)^2 \sin^4\theta \, \eta_{tot} \right]^2 + \left[\frac{\mu'' \omega}{2\rho c} \cos\theta \left(\frac{f}{\frac{c^2}{2\pi}\sqrt{\frac{\mu''}{D_p}}} \right)^2 \sin^4\theta - 1 \right] \right\}^{-1} \tag{13}$$

The parameters in equation (13) are: μ'' total mass per unit area of plate, f frequency, ω angular frequency, θ angle of incidence of acoustic wave, ρc wave impedance of the surrounding medium at room temperature,

and η_{tot} total loss factor of the structure. The sound reduction index R in decibels for a plate is $-10 \log \tau_d$, where τ_d is the sound transmission coefficient for diffuse incidence, defined as

$$\tau_d = 2 \int_0^{\pi/2} \tau(\theta) \cos\theta \sin\theta \, d\theta \tag{14}$$

A numerical integration of equation (13) gives the sound transmission coefficient and thus the sound reduction index R for a sandwich panel assuming a diffuse incident field.

2.3.4 Limiting angle of integration

The transmission coefficient can be estimated through equation (14) as the average over all the angles of incidence, thus including the so called "grazing angles" at which, in practical circumstances, sound is unlikely to reach the surface. Several researches examined what could be the best angle of integration for effectively modelling sound transmission in real cases. The existing sound insulation theories for infinite panels do not provide satisfactory predictions when the sound radiates at grazing angles. The radiation efficiency of an infinite flat panel, radiating a plane wave into half space, can be shown to be equal to the inverse of the cosine of the angle between the direction of propagation of the plane wave and the normal to the panel. The fact that this radiation efficiency tends to infinity as the angle tends to 90° causes discrepancies between the predictions carried out using simple theories of sound insulation and experimental results. Moreover, in real situations, sound waves are unlikely to reach the panel with grazing incidence. To simulate real situations, it has been shown that the angle of incidence must be limited to values between 85° and 78° [11].

2.3.5 Flanking transmission

The results of the simulations carried out according to the theory are valid if no flanking transmission takes place. Flanking transmission is the leakage of sound energy that occurs when two or more structures are coupled together. An example of the possible transmission paths due to the transmission of structure-borne sound is represented in Figure 3.

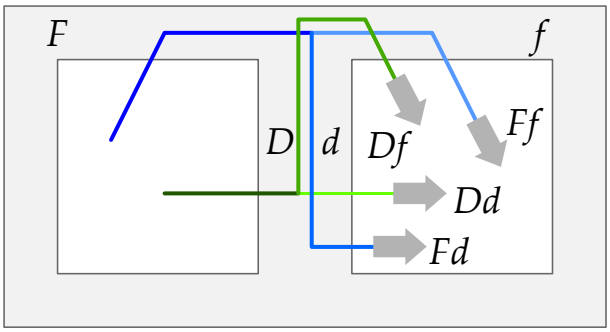


Figure 3: Transmission paths for structure borne sound in real structures

While in sound transmission suites the only possible transmission path is *Dd* (Direct-direct), in real cases the flanking transmissions must be added to consider also the other propagation paths through the joined structures (Direct-flanking, *Df*; Flanking-direct, *Fd*; Flanking-flanking, *Ff*). The overall sound reduction index is denoted by R', the prime superscript indicating that the flanking transmissions are considered. It is possible to simplify the analysis considering the overall weighted sound reduction index R'_W, that can be estimated using the following formula:

$$R'_W = -10 \log\left(10^{\frac{-R_{Dd,W}}{10}} + \sum_{F=f=1}^{n} 10^{\frac{-R_{Ff,W}}{10}} + \sum_{f=1}^{n} 10^{\frac{-R_{Df,W}}{10}} + \sum_{F=1}^{n} 10^{\frac{-R_{Fd,W}}{10}}\right) \tag{15}$$

where $R_{Dd,W}$ is the weighted sound reduction index of the main partition (obtained through laboratory tests) and the remaining terms are the weighted sound reduction indices associated to the other transmission paths, which depend on the ratio between the masses per unit area of the walls involved in the propagation path, the type of connection, the presence of resilient layers and the presence of additional layers on the floor or on the ceiling. The effect of the flanking transmissions can be described by the following formula:

$$R'_W = R_W - a \tag{16}$$

indicating that the laboratory value of the weighted sound reduction index must be reduced by a factor a, whose value depends on the characteristics and coupling degree of the structures

- $a > 5$ dB for strong flanking transmissions, as in the case of a heavy wall surrounded by lightweight structures;
- $2 < a \leq 5$ dB for medium flanking transmissions, as in the case of structures having the same mass per unit area;
- $a \leq 2$ dB for weak flanking transmissions, when the structures are decoupled from each other by means of resilient mountings.

In practice, formula (16) cannot be used except to have an estimation of R'_w because there is no direct method to obtain a. A solution is generally to follow the standards of the series ISO 12354 [12] to calculate R'_w. These standards have been specifically implemented to include the effect of the flanking transmissions.

2.4 Materials and methods

2.4.1 Instrumentation

The instrumentation needed to carry out mobility measurements consists of an FFT analyser, an impedance hammer and an accelerometer. Since mobility is essentially a transfer function between the vibration velocity response and the force excitation, the measurement system must be able to compute cross functions. The type of transducers depends on the weight of the structure under investigation and the frequency range of interest. Even if the final result is the mobility in one-third octave bands, the direct use of a CPB analysis is not applicable because of the corrections needed on the mobility values in the modal frequency range for the (n,0), (0,m) modes. In fact, it would be impossible to perform such corrections estimating the mobility values from a one-third octave band analysis.

2.4.2 Specimens under test

The partitions tested are of two types: a Glass Reinforced Plastic (GRP) panel with ribs, and a sandwich panel with 25.4-mm balsa core.

For the GRP panel, the collection of the required data is not straightforward, since the specimens are not homogeneous. This means that some information, like the mass per unit area and the moment of inertia, depends on the portion of the panel considered. Moreover, the thickness of the base structure varies with the position. For this reason, the uncertainty in the determination of the sound reduction index is expected to be higher for this type of panel than for the sandwich panel with balsa core. The nominal data considered for the simulations are relative to the small sample tested into the sound transmission suites, consisting in a flat 15-mm thick part of GRP and 2 ribs:

- E = 14 GPa
- μ'' = 23 kg/m^2
- $I = 4 \cdot 10^{-7}$ kg m^2

The data characterizing the sandwich panels with balsa core and used as an input for the simulation software have been determined from the beam specimens tested at KTH and from literature data. They are listed in the following Table 1.

Quantity	Meas. unit	Laminates	Core
h	m	0.0015	0.0225
ρ	kg/m^3	2700	200
E	GPa	70	3.7
G	GPa	-	0.12

Table 1: Geometric and material data for the sandwich specimen

2.5 Measurement results

2.5.1 In-situ measurements on GRP bulkheads

The GPR panel was tested both in-situ and in sound transmission rooms. The type of bulkhead which could be tested in-situ during the assembly stage was the GRP panel. In this case it was chosen to verify the dynamic and acoustic performances of the watertight bulkhead of Figure 4. The different hatches indicate that different thicknesses of GRP have been used during manufacturing (12.5 mm, 15.5 mm and 20 mm). The response of the bulkhead is obviously different depending on the boundary conditions. For this reason, the following conditions were considered:

- Free-free boundary conditions: in this case only mobility measurements have been performed since it was not possible to measure the sound reduction index according to the ISO 16283-1;
- Real fastening conditions of the edges: in this case three types of measurements have been carried out, consisting in mobility measurements, structural reverberation time measurements and sound reduction index measurements according to the ISO 16283-1 standard.

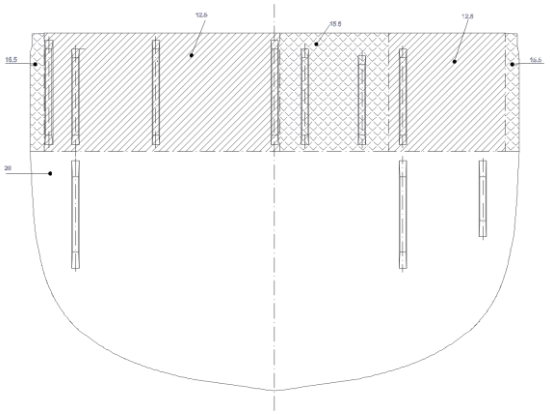


Figure 4: Schematic of the watertight GRP bulkhead under investigation

2.5.2 Mobility measurements on suspended bulkhead

The mobility measurements on the suspended bulkhead have been carried out by determining the average bending stiffness of the entire specimen. The bulkhead dimensions are approximately 10 m × 7 m and the thicknesses used are different depending on the distance from the bottom. For this reason, 30 measurement positions have been randomly distributed over the surface of the bulkhead, some of which inside the cavities

of the ribs, others between the ribs, and others on the lower flat surface of the bulkhead. After checking the frequency response function and the auto-spectra of the force and the velocity, a steel tip has been adopted to excite the panel. The accelerometer has been attached to the bulkhead surface by using cyanoacrylate glue. Once the bulkhead has been suspended, the accelerometer has been placed in the different positions and the mobility function has been acquired. It was found that the mobility is considerably lower on the ribs than on the panel. The resulting measured space-average of the bending stiffness is shown in Figure 5.

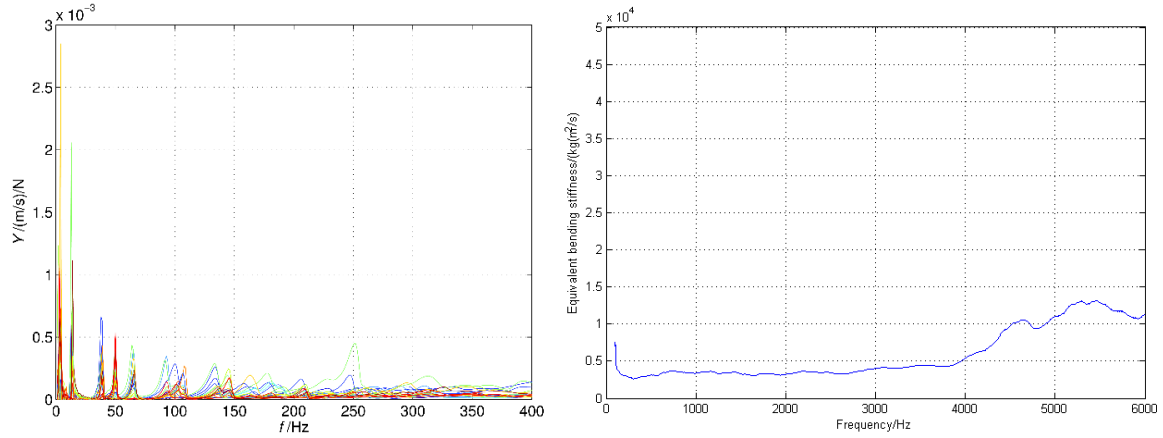


Figure 5: Measured point mobility function and apparent bending stiffness for the suspended bulkhead

It can be noted that the bending stiffness is relatively flat in the frequency range going from 100 Hz to 4 kHz. The fact that the apparent bending stiffness tends to increase at higher frequencies is arguably related to the increasing difficulty in injecting energy into the panel, due to the impedance difference between the tip of the hammer and the panel surface, rather than to a real change in the mobility of the bulkhead.

2.5.3 Mobility measurements on already mounted bulkhead

Using the same technique and the same instrumentation adopted for the measurements on the suspended bulkhead, a mobility measurement session has been performed on an already mounted panel. In this case, 12 measurement positions have been randomly distributed on a partition (dimensions 9 m × 2.7 m) dividing two rooms. Figure 6 represents the apparent bending stiffness computed on the basis of the point mobility space-average.

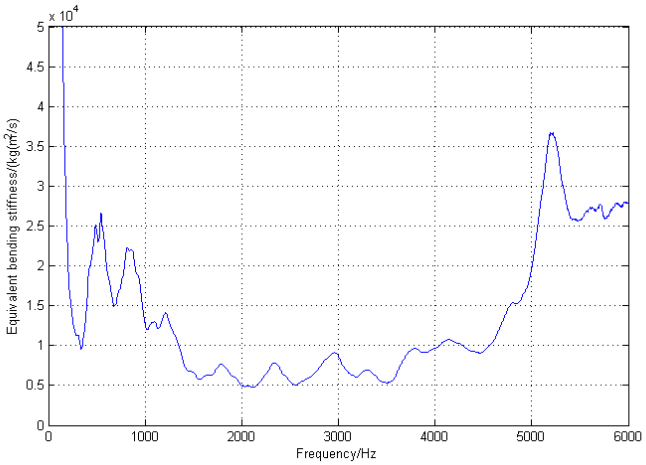


Figure 6: Equivalent bending stiffness for the already mounted bulkhead

It can be noted that the bending stiffness curve does not look flat anymore in the frequency range of interest, due to the modal behaviour of the bulkhead. Moreover, once it is mounted, the bulkhead undertakes a certain curvature and the stiffness in the low frequency range is shifted to higher values (below 1000 Hz). As already mentioned for the suspended panel, above 4000 Hz the apparent bending stiffness tends to increase with frequency as a consequence of an increasing difficulty in injecting energy into the panel.

2.5.4 Loss factor

The loss factor of a structure plays an important role on the sound reduction index at and above the coincidence frequency. Its determination is very important and must be carried out in real mounting conditions. If the loss factor is not correctly determined, the predicted sound reduction index in the high frequency range can be considerably different from the one measured according to ISO 16283. Since a panel has a strong modal overlap in the medium/high frequency range, it is not possible to apply the half-power bandwidth method on the mobility function and it is necessary to adopt the structural reverberation time method. For this reason, during the mobility measurements the time signals were recorded for both channels. The signal from the accelerometer was post-processed to determine the reverberation time and then the loss factor. In the case of the suspended panel, the loss factor derived from the measurements corresponds to the sum of the internal losses and the radiation losses. For the mounted panel the contribution of the adjoining structures is included. Figure 7 shows the loss factor curves for the suspended panel and for the mounted partition. It is evident that the losses due to the adjoining structures are particularly important below 500 Hz.

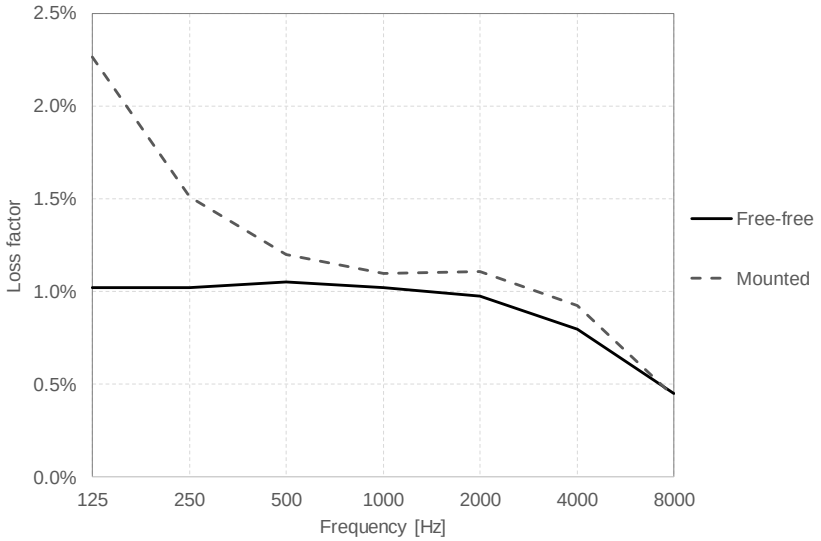


Figure 7: Loss factor measured for the suspended panel (solid line) and for the already mounted partition (dashed line)

2.5.5 Sound reduction index from mobility measurements

The real part of the space- and frequency-average of the point mobility function can be used to compute the apparent bending stiffness of the bulkhead. Together with the mass per unit area and the measured total losses, these data can be used to predict the sound reduction index of the bulkhead. The dashed line in Figure 8 represents the predicted sound reduction index derived from the mobility data measured on the suspended bulkhead. The coincidence region has a minimum at a frequency of 1250 Hz. The slope at frequencies above the coincidence dip is strongly influenced by the value of the total losses.

2.5.6 Sound insulation using pressure method (ISO 16283)

For a first comparison, some measurements have been carried out on board. The considered bulkhead was the same represented in Figure 4. The measurements have been carried out on the GRP bulkhead, without any additional layer. The compartments used for the tests are divided by a fibreglass partition with dimensions 9.62 m × 2.3 m. The volume of the receiving room is 86 m^3. The reverberation time of the receiving room was measured by post processing the impulse response of the room. The excitation was made by using a blank cartridge gunshot. To avoid sound leakages, all the openings have been closed by wooden frames both in the emitting and in the receiving rooms. An omnidirectional sound source generating pink noise has been placed in the bigger room. The resulting sound pressure level in the receiving room has been measured and corrected accounting for the dimensions of the partition and the sound absorption area of the receiving room. The in-opera sound reduction index is computed applying the following formula:

$$R'(f) = \bar{L}_{p1}(f) - \bar{L}_{p2}(f) + 10\log\left(\frac{S}{0.16\left(\frac{V}{T_R(f)}\right)}\right) \tag{17}$$

where $\bar{L}_{p1}$ is the space-average of the sound pressure level into the emitting room, $\bar{L}_{p2}$ is the space-average of the sound pressure level in the receiving room, S is the area of the partition dividing the emitting room from the receiving room, V is the volume of the receiving room and T_R is the acoustic reverberation time of the receiving room. Figure 8 shows a comparison between the sound reduction index values measured by applying the two techniques. The graph shows that the trend of the sound reduction index is predicted quite correctly, except for a local maximum at 160 Hz. The coincidence region starts from 800 Hz, with a minimum value at 1250 Hz.

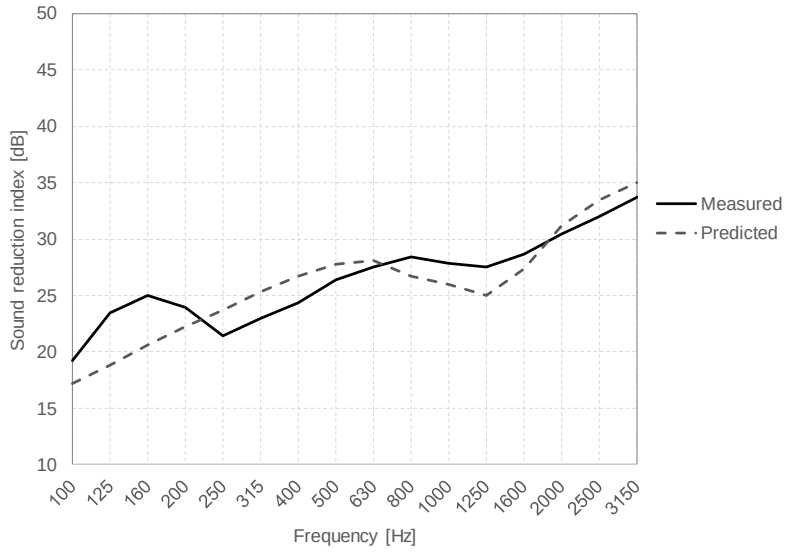


Figure 8: Comparison between the sound reduction index measured applying two different measurement techniques. The resulting value of the single-numbered weighted sound reduction index is R'_w = 29 dB (−1;−2)

The local maximum at 160 Hz in the measured curve is most likely due to the curvature the panel is undertaking when it is coupled to the hull. Such behaviour is typical for curved structures and, as it will be shown in the next section, is less evident for the small flat panels tested in sound transmission rooms.

2.6 Sound transmission suites measurements

The measurements have been carried out at the KTH – MWL facilities in Stockholm. The sound transmission suites used for the tests consists of a reverberant room coupled with a semi-anechoic room.

The samples to be tested have been placed in an opening between the two rooms. The determination of the sound reduction index of the panels have been performed with reference to the EN ISO 15186-1:2000 standard [13]. The sound reduction index, expressed in one-third octave bands, is calculated by using the formula

$$R = \bar{L}_{p1} - \bar{L}_{In} - 6 \tag{18}$$

where $\bar{L}_{p1}$ is the space-averaged sound pressure level in the source room, measured by a rotating microphone, and $\bar{L}_{In}$ is the average sound intensity level over the panel surface measured in the receiving room by using the scan method (ISO 9614-2:1994 [14]).

The tests have been carried out over two specimens. The size for all the specimens is about 1810 mm × 1010 mm. The samples (Figure 9) have been mounted in the opening between the anechoic and the reverberation room, taking care to seal the edges using high-density silicone and, in some cases, adding foil tape to further improve the insulation. The acoustic excitation has been applied in the reverberation room and the intensity measurement has been performed in the anechoic room. The measured sound reduction index in one-third octave band is shown in Figure 10.



Figure 9: Pictures of the panels mounted in the sound transmission rooms (left GRP, right sandwich)

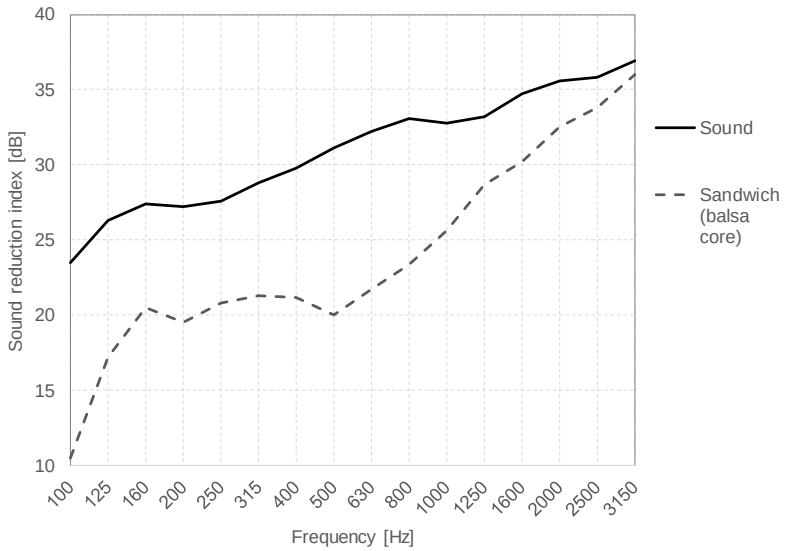


Figure 10: Sound reduction indices of the fibre-reinforced panel and of the sandwich panel tested in sound transmission rooms

Based on the described measurements, it is possible to perform a comparison between the sound reduction index curves obtained for two very different configurations of GRP panel: for the on-board measurements,

the sound reduction index is given by the sound insulation of the main partition and the flanking transmissions across the confining structures (bordering walls, ceiling and floor), while in the transmission suites the measurement is only relative to the small panel placed between the emitting and the receiving volumes. Figure 11 shows the comparison for the basic GRP fibre-reinforced panel measured on board and in sound transmission suites. The difference in the value of the weighted sound reduction index is 5 dB. With the exception of the local maximum placed at 160 Hz for the on-site measurements, the trend of the curves is quite the same for both the conditions, although the in-opera curve looks shifted down due to flanking transmissions.

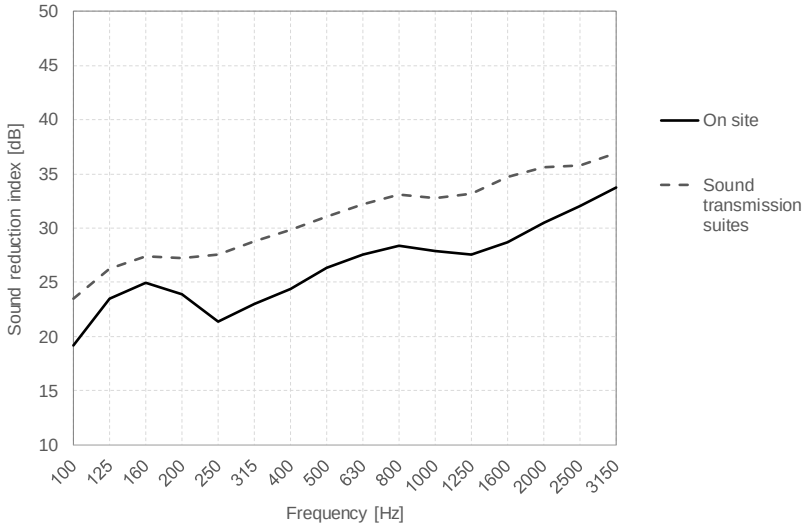


Figure 11: Comparison of the sound reduction indexes for the fibre-reinforced panels tested in sound transmission rooms and on-board

2.7 Validation: effect of the flanking transmissions

At the end of the experimental campaigns, the availability of results obtained on board and in sound transmission suites for the GRP panel allowed a comparison of the measured sound insulation performances with the predictions made through a software implementing the standards of the ISO 12354 series.

The proper prediction of the effect caused by the flanking transmission has been carried out using SuoNus, a software implementing the ISO 12354 standard series. As a first step, it is necessary to import the data for the sound reduction index of the horizontal and vertical partitions in the simulation software. In this simulation it was assumed that the ceiling and the floor have the same sound reduction index of the walls, being made of the same material and having a similar ribbed structure. The next step is to define the characteristics of the rooms for which the simulation must be carried out. The last step before computing the sound reduction index is to give the properties to the nodes connecting the different walls. All the junctions have been assigned the “T type” of node. Finally, the sound reduction index of the building system plus the flanking transmissions can be computed (Figure 12).

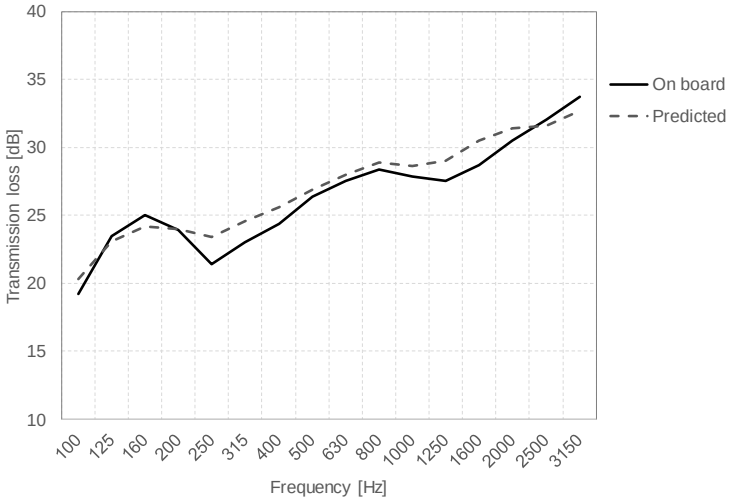


Figure 12: Comparison - SRI of the bulkhead measured on board vs simulations

The predicted value of R'_w is 30 dB, while the measured single-valued weighted sound reduction index measured in real conditions is 29 dB. Therefore, the comparison between the simulations and the measurements carried out on site for the GRP walls without additional layers is good.

2.7.1 Sandwich panel

The sandwich panel sound reduction index has been predicted by applying the wave propagation approach to a beam specimen and measured by testing the whole panel in sound transmission suites at KTH. A beam specimen, length 1.8 m, has been suspended by strings in free-free boundary conditions. An accelerometer has been placed at one end and the beam has been hit at the opposite side by using an impact hammer. The resulting frequency response function is shown in Figure 13a. For each maximum of the frequency response function, it is possible to compute the bending stiffness of the beam. Finally, from the set of the f_n, D_{xn} points derived from the measurements it is possible to compute the apparent bending stiffness function and the reduction index. Figure 13b shows the comparison between the sound reduction index measured in the transmission rooms (bullets) and the sound reduction index computed on the basis of the geometrical and material data plus the loss factor measured during the experimental session (solid line). The agreement between the two curves is fair, showing only a discrepancy below 160 Hz due to the finite dimensions of the tested panel and the baffle effect.

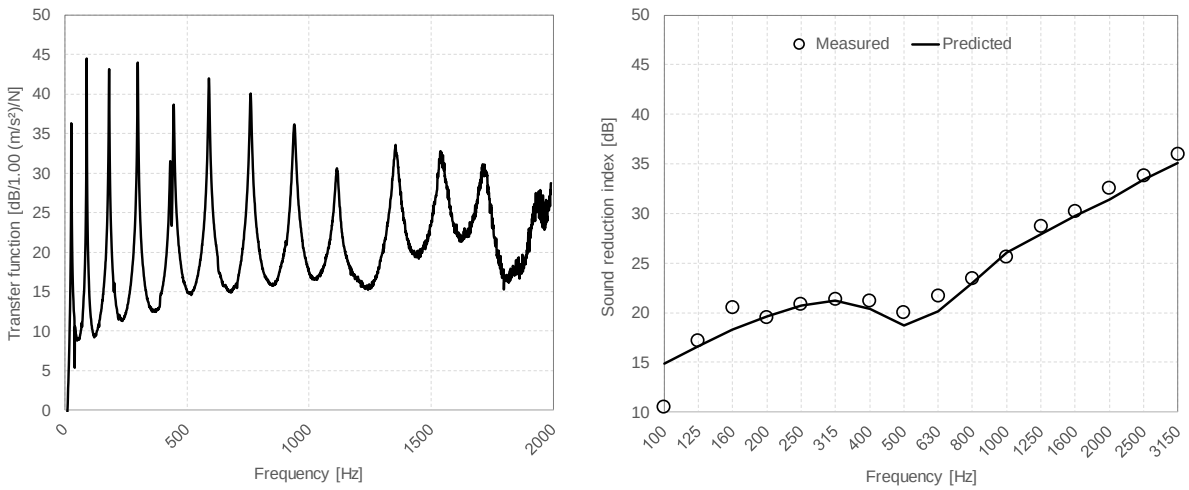


Figure 13: (a) Measured transfer function. (b) Comparison between the sound reduction indices measured in sound transmission rooms (solid line) and computed by using the prediction code (bullets)

2.8 Optimisation

Once the applicability of the theory has been demonstrated for the two types of bulkheads considered in this paper, it is possible to apply the model by only using the geometrical and materials parameters to predict the sound reduction index of bulkheads.

Considering equation (12), the three coefficients *A*, *B* and *C* can be computed starting from the mass per unit area, the cross section, the bending stiffness of the structure, the bending stiffness of a single laminate and the shear modulus of the core. Figure 14 shows an example of optimisation study based on a software for the prediction of the acoustic performances implemented in MATLAB environment.

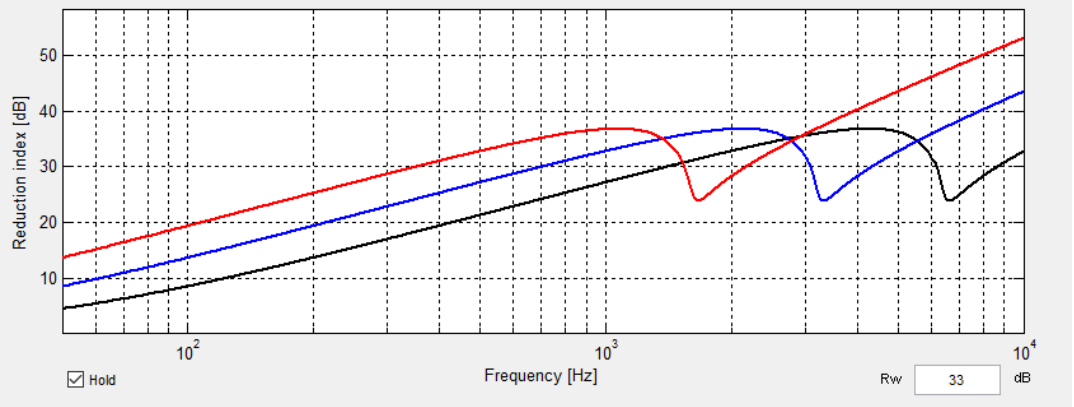


Figure 14: Example of reduction index predictions carried out for a GRP panel as a function of the thickness (black: 2 mm; blue: 4 mm; red: 8 mm)

Since the software takes into account the overall behaviour of the panel (low frequency range governed by the mass, coincidence region and total losses dominating in the medium high frequency range), different configurations can be easily evaluated to identify the most suitable solution.

3 Conclusions

This study compares measurements conducted on-site with laboratory measurements based on both standardised and innovative methods. It has been shown that, while standardised methods cannot be used on large bulkheads, measurements based on innovative methods can give excellent results on sandwich partitions and acceptable results on ribbed bulkheads. To obtain results comparable to those on site, the laboratory values must be corrected according to the provisions of the ISO 12354 series, in order to take into account the flanking transmissions. The resulting predictions are in good agreement with the experimental results obtained onboard.

The methodology allows the acoustic designers to identify “acoustically weak” frequency regions of a partition using laboratory and in-situ measurements or simulations, and then to suggest and discuss guidelines to improve the sound reduction properties, proposing enhancing treatments such as the use of additional absorptive layers.

References

[1] P.T. Arveson, D.J. Vendittis, *Radiated noise characteristics of a modern cargo ship*, Journal of the Acoustical Society of America, Vol. 107, No. 1 (2000), pp. 118–129.

[2] M.F. McKenna, S.M. Wiggins, J.A. Hildebrand, *Relationship between container ship underwater noise levels and ship design, operational and oceanographic conditions*, Scientific Reports, Vol. 3, No. 1 (2013).

[3] E.A. Piana, A. Marchesini, *How to lower the noise level in the owner's cabin of a yacht through the improvement of bulkhead and floor*, in *21st International Congress on Sound and Vibration 2014, ICSV 2014, Beijing, China, 2014 July 13–17*, IIAV (2014), pp. 3692–3699.

[4] E.A. Piana, A. Marchesini, A. Nilsson, *Evaluation of different methods to predict the transmission loss of sandwich panels*, in *20th International Congress on Sound and Vibration 2013, ICSV 2013, Bangkok, Thailand, 2013 July 7–11*, IIAV (2013), pp. 3552–3559.

[5] E.A. Piana, A.C. Nilsson, *Prediction of the sound transmission loss of sandwich structures based on a simple test procedure*, in *17th International Congress on Sound and Vibration 2010, ICSV 2010, Cairo, Egypt, 2010 July 18–22*, IIAV (2010), pp. 109–116.

[6] E.A. Piana, C. Petrogalli, L. Solazzi, *Dynamic and acoustic properties of a joisted floor*, in M.S. Obaidat, Y. Merkuryev, T. Oren, editors, *SIMULTECH 2016 - Proceedings of the 6th International Conference on Simulation and Modeling Methodologies, Technologies and Applications, Lisbon, Portugal, 2016 July 29–31*, SciTePress (2016), pp. 277–282.

[7] H.P. Wallin, U. Carlsson, M. Åbom, H. Bodén, R. Glav, R. Hildebrand, *Sound and Vibration*, KTH, Stockholm, Sweden (2014).

[8] E. Nilsson, A.C. Nilsson, *Prediction and measurement of some dynamic properties of sandwich structures with honeycomb and foam cores*, Journal of Sound and Vibration, Vol. 251, No. 3 (2002), pp. 409–430.

[9] E.A. Piana, C. Petrogalli, D. Paderno, U. Carlsson, *Application of the wave propagation approach to sandwich structures: Vibro-acoustic properties of aluminum honeycomb materials*, Applied Sciences (Switzerland), Vol. 8, No. 1 (2018).

[10] L. Cremer, M. Heckl, B.A.T. Petersson, *Structure-borne Sound: Structural Vibrations and Sound Radiation at Audio Frequencies*, Springer-Verlag, Berlin, New York (2005).

[11] B.H. Sharp, *Prediction methods for the sound transmission of building elements*, Noise Control Engineering, Vol. 11, No. 2 (1978), pp. 53–63.

[12] International Organization for Standardization, *ISO 12354-1:2017 -- Building Acoustics -- Estimation of Acoustic Performance of Buildings from the Performance of Elements -- Part 1: Airborne Sound Insulation between Rooms* (2017).

[13] International Organization for Standardization, *ISO 15186-1:2000 -- Acoustics -- Measurement of Sound Insulation in Buildings and of Building Elements Using Sound Intensity -- Part 1: Laboratory Measurements* (2000).

[14] International Organization for Standardization, *ISO 9614-2:1996 -- Acoustics -- Determination of Sound Power Levels of Noise Sources Using Sound Intensity -- Part 2: Measurement by Scanning* (1996).

Assessment of the vibro-acoustic performance of an all-electric light aircraft based on ground and in-flight measurements

R. Hallez[1], C. Colangeli[1], J. Cuenca[1], E. Di Lorenzo[1], U. Musella[1], J. Debille[1]
[1] Siemens Industry Software, Simulation and Test Solutions
Interleuvenlaan 68, B-3001, Leuven, Belgium
E-mail: **raphael.hallez@siemens.com**

Abstract
Vertical take-off and landing and reduced emissions are some examples of the great possibilities that electric propulsion offers and how it could disrupt air travel. However, important regulatory barriers still need to be overcome. One aspect of particular attention is the impact on environmental noise. Aero-elastic stability is another essential element to reach aircraft certification. This paper offers an overview of the experimental techniques required for the assessment of the vibro-acoustic performance of an all-electric light aircraft. The actual impact of electric propulsion on exterior radiated noise and cabin comfort has been quantified using two variants of the same airplane (conventional piston engine vs. electric motor). Results clearly highlight the different footprints of the two types of propulsion. In addition, structural dynamics performance of the all-electric aircraft was also investigated. The manuscript reports about the setup and execution of the test campaign; it describes the processing of the acquired data and discusses the major findings.

1 Introduction

Electric propulsion for aircrafts brings many new possibilities for more efficient, more flexible and greener air transportation. New concepts, such as flying taxies, based on all-electrical or hybrid propulsion are been studied to support urban air mobility in the future [1]. However, next to the many technological challenges associated with such new concepts, important regulatory barriers still need to be overcome to make flight in urban areas come true and one aspect of particular attention is the environmental noise impact. Air traffic is also expected to continue its unstoppable growth, not without damaging consequences on the environment. Beyond CO2 emissions and greenhouse effect, it is the noise pollution caused by air transportation, especially in the vicinity of airports, that is a source of concern. Thanks to electric propulsion systems, aircraft noise pollution could be significantly reduced. With lowered engine noise and improved sound quality, a passenger's flight experience could also become significantly more enjoyable.

Very few detailed experimental analyses have been performed so far to assess the impact of aircraft electric propulsion on exterior radiated noise and cabin comfort. Earlier work, see for instance [2] and [3], essentially concentrated on design and performance of propulsion systems but with no focus on the noise impact. Interesting work was recently performed by Rizzy [4], on the annoyance to noise produced by a distributed electric propulsion system. However, this analysis is based on simulated data only and does not contain experimental comparisons.

The objective of this paper is to experimentally assess the actual impact of electric propulsion on exterior aircraft noise and cabin comfort in the case of light aircrafts. The approach proposed here consists in comparing the acoustic performance of two variants of the same aircraft equipped with two different propulsion systems: in one case with a conventional piston engine, in the other case with an electric motor. To the authors' knowledge, this is the first time that such comparison is made. Both in-flight and on-ground measurements are performed to determine the acoustic footprint of the aircrafts and to get insight into noise generation mechanisms. Structural dynamics analysis of the all-electric aircraft is then performed based on

ground and in-flight measurements. The objective is to present the testing methods available to identify the main resonant modes of the aircraft, to be used for flutter prediction and to verify that the modes can also be correctly identified during flight.

The investigated airplane is the Magnus Fusion aircraft. The Magnus Fusion 212 is a multi-purpose 2-seater aircraft, see Figure 1. It has a length of 6.7m, height of 2.4m, and a wingspan of 8.3m including winglet, whereas the wing area is 10.59m². The eFusion is the all-electric version of the Fusion aircraft, first all-electric aerobatic training aircraft in the world. It is powered by a 60kW Siemens electric drive system. The aircraft is entirely battery-powered and has an endurance of approximately one hour. The aircraft has an empty weight of 410kg and a maximum take-off weight of 600kg. The stall and maneuvering speeds of the aircraft are 35kn and 104kn, respectively. The aircraft has a maximum range of up to 1,100km and a service ceiling of 12,000ft.



Figure 1: Magus Fusion aircraft tested with a conventional and all-electric propulsion system.

Fly-over noise levels, as used for aircraft noise certification, are first compared. Sound quality metrics are then used to highlight the differences between the two propulsion systems in terms of perceived noise and annoyance. Detailed acoustic analysis is performed using advanced sound source localization techniques. Finally, the ground vibration and flutter test results are presented.

2 Acoustic performance

2.1 Exterior noise

The objective of this first section is to compare the overall noise levels measured during fly-over, as typically used for noise certification of small aircrafts. The LASmax – maximum A-weighted noise level measured with slow time weighting – was computed according to the prescribed standard ICAO Annex 16 [5] using the Simcenter Testlab software [6]. The test set-up consists of a Simcenter SCADAS portable data acquisition system recording data from the ground microphone and from the adjacent weather station. A single microphone with wind protection positioned on the ground on a reflective plate is used for this measurement. The position of the aircraft is tracked in time to validate the trajectory and make sure that the two aircraft variants are measured in the same conditions.

Noise comparison results are shown in Table 1 for 2 different flight speeds. Significant noise reduction is observed in the case of the electric propulsion, especially at higher speeds (90 knots) and low altitude where the aircraft with combustion engine is particularly noisy. Noise reduction is also observed at high altitude but absolute noise levels are rather low in this case.

LASmax	Magnus Fusion 212 with combustion engine	Magnus eFusion with electrical motor	Noise reduction
60 knots – low altitude (50 feet)	**80.1**	**78.2**	**1.9 dB**
90 knots – low altitude (50 feet)	**84.4**	**80.8**	**3.6 dB**
60 knots – high altitude (1000 feet)	**57.6**	**56.5**	**1.1 dB**
90 knots – high altitude (1000 feet)	**61.7**	**51.4**	**10.3 dB**

Table 1: LASmax noise levels measured during fly-over for the Magnus Fusion Aircraft.

Sound quality metrics are used to quantify the differences in the perceived sound and annoyance. We will refer to the aircraft equipped with a piston engine propulsion with the names Fusion or Standard Aircraft in order to differentiate it from the one powered by an electric propulsion called eFusion or e-Aircraft in the text below. The flyover has been divided in three phases (Figure 2 (left)):

A. Aircraft approaching the ground microphone

B. Aircraft above the ground microphone

C. Aircraft leaving

The comparison between eFusion and Fusion Specific Loudness spectra reveals that the main loudness contributor for the eFusion aircraft is the aerodynamic noise induced by the propeller – Bark 1: 0-100 Hz – (Figure 2 (left)). Such a noise component is prominent in phases A and B, while it is severely reduced in phase C. In the Fusion case, besides the propeller aerodynamic noise, the main noise contributor is the piston engine, whose harmonics influence the specific loudness spectrum up to 5 kHz during phases B and C. The radar plot in Figure 2(right) reports the ratio between the metrics computed on the eFusion and on the Fusion during the phases A, B and C of their flyover at 50 ft altitude and at nominal speed of 90 kn. A value <1 means that the corresponding metric assumes a lower value in the case of the eFusion. The psychoacoustic attributes of the e-aircraft sound are systematically, and in the three phases, lower than the corresponding standard aircraft's ones. The absence of the piston engine noise, in fact, implies a dramatic reduction of roughness and tonality. Loudness is drastically reduced during phase C as well.

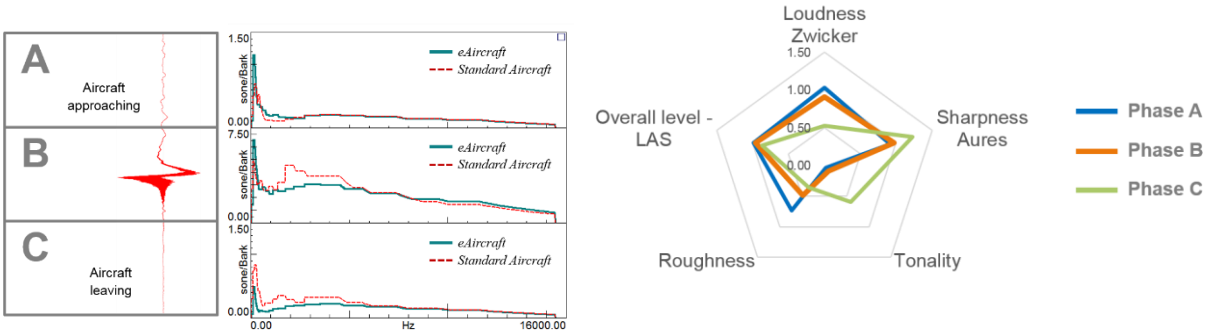


Figure 2: Comparison between the most salient psychoacoustic metrics computed during eFusion and Fusion flyover at 50 ft altitude and at nominal speed of 90 kn. (left) Specific Loudness spectra. (right) Ratio between the metrics computed on the eFusion and on the Fusion.

The just described overall psychoacoustic behavior of the two aircrafts during flyover can be further detailed by analyzing time-varying metrics related to loudness, tonality and modulation attributes. Figure 3 reports the comparison between the two aircraft versions in terms of loudness-related metrics. Such an analysis reveals a larger value of maximum loudness in the case of the piston engine aircraft flyover. Sharpness values are very similar in the two cases during phases A and B. eFusion maintains a higher sharpness in phase C. This can be attributed not to an actual increase of high frequency noise components in the case of e-motor propulsion, but rather to the fact that low frequency range noise produced by the piston engine remains loud also during phase C (Figure 2 (left)).

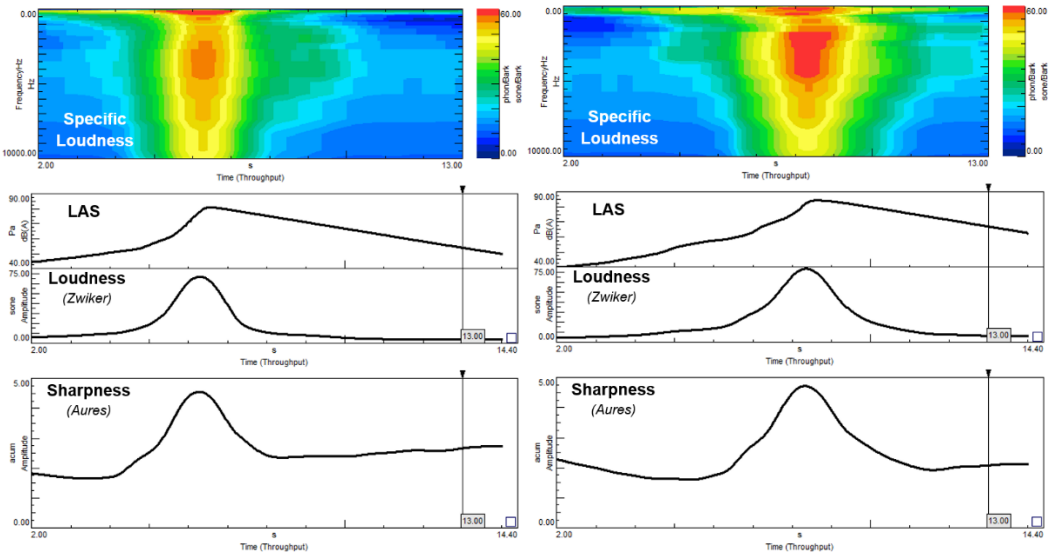


Figure 3: Loudness-related metrics. Comparison between: (left) eFusion and (right) Fusion.

Despite the fact that a larger value produced by the aircraft equipped with a piston engine is clearly observed, Loudness is not the main differentiator of the two variants. The absence of the internal combustion engine propulsion is even more clearly reflected on tonality and modulation-related sound quality aspects. As depicted by Figure 4, in fact, the Standard Aircraft flyover is perceived in all phases (and especially in phases A and B) as more tonal and reveals the appearance of distinguishable pitches. This is due to the presence of a large number of piston engine harmonics in the sound spectrum. In the eFusion case, instead, the e-motor noise contribution is not audible and the main noise source is represented by the propeller, mainly visible at the Blade Passing Frequency and its second harmonic.

The presence of the many harmonics of the piston engine propeller implies the Fusion sound to be rich of tones whose prominence makes the phase A of the Fusion noise characterized by a pitch at around 350 p.u. eFusion tonal noise, instead, is dominated by the Blade Passing Frequency (BPF) contribution at around 110Hz, but this does not impact pitch and tonality of this noise.

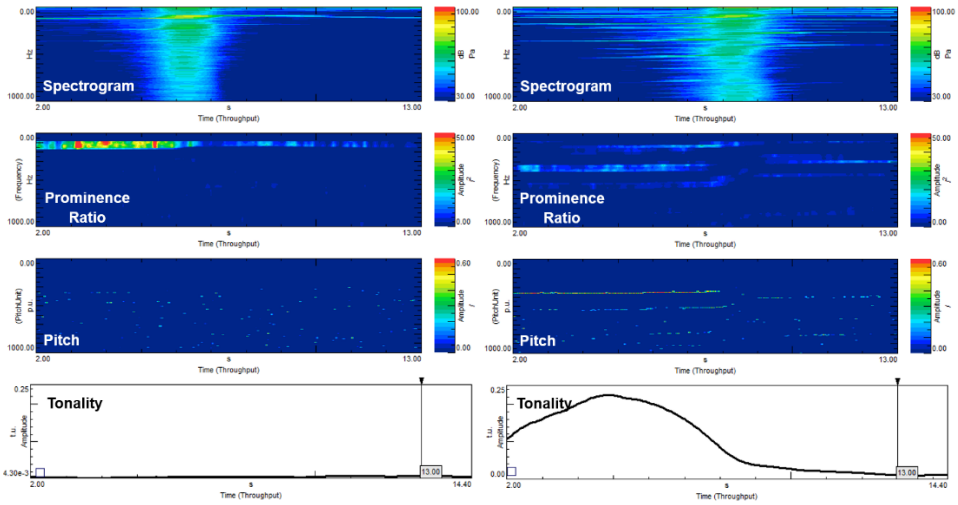


Figure 4: Tonality-related metrics, comparison between eFusion (left) and Fusion (right) in terms of Prominence Ratio, Pitch and Tonality.

The piston engine noise harmonics are also responsible for the appearance, in the Fusion case, of clearly audible modulation frequencies. The Modulation Maps reported in Figure 5 well explain such a difference revealing the appearance, in the Standard Aircraft case, of modulation over a large range of carrier frequencies. This is perceived as a combination of fluctuation and roughness. This latter metric considerably increases during phase B and the last part of phase A of the Fusion flyover. eFusion flyover sound, instead, is perceived as not rough. Such a modulation analysis can be further deepened by observing the Tracked Modulation Maps reporting the evolution of the modulation frequency over time, during the analyzed flyovers, per different carrier frequency ranges (critical bands). In the case of the eFusion flyover – Figure 6 – modulation is very limited. In fact, modulation frequencies appear only during phase B and mostly affecting a singular critical band (centered in 150 Hz). Due to the presence of the piston engine noise, instead, the Fusion flyover is strongly characterized by modulation patterns (Figure 6). Below 1000 Hz, the main modulation frequency is the first order of the piston engine. For higher carrier frequencies, the Fusion flyover noise is also modulated by higher harmonics.

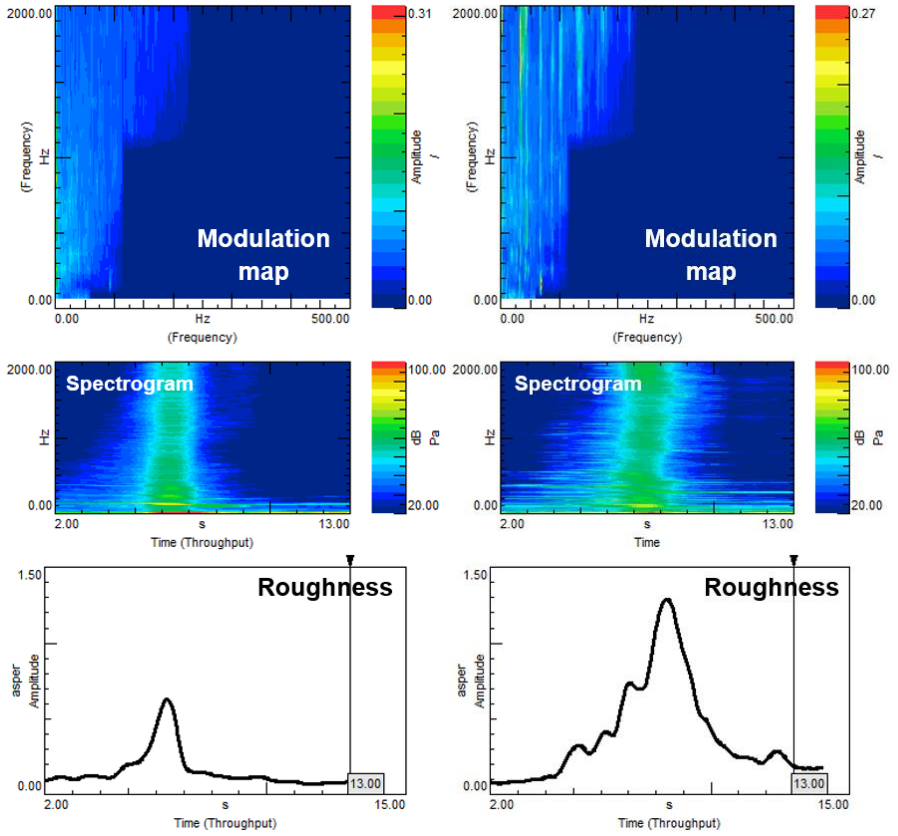


Figure 5: Interaction between piston engine and propeller aerodynamic noise harmonics generates, in the Fusion case (right), the occurrence of multiple audible tones closely spaced in frequency. In case of the eFusion aircraft (left), this is not the case because of the absence of the piston engine.

The flyover sound quality analysis of the two Fusion variants reveals that, despite a just exiguous reduction of loudness, the tonality, modulation and roughness attributes are greatly enhanced thanks to the electric propulsion, improving the pleasantness of the e-Aircraft flyover noise with respect to the Standard Aircraft case.

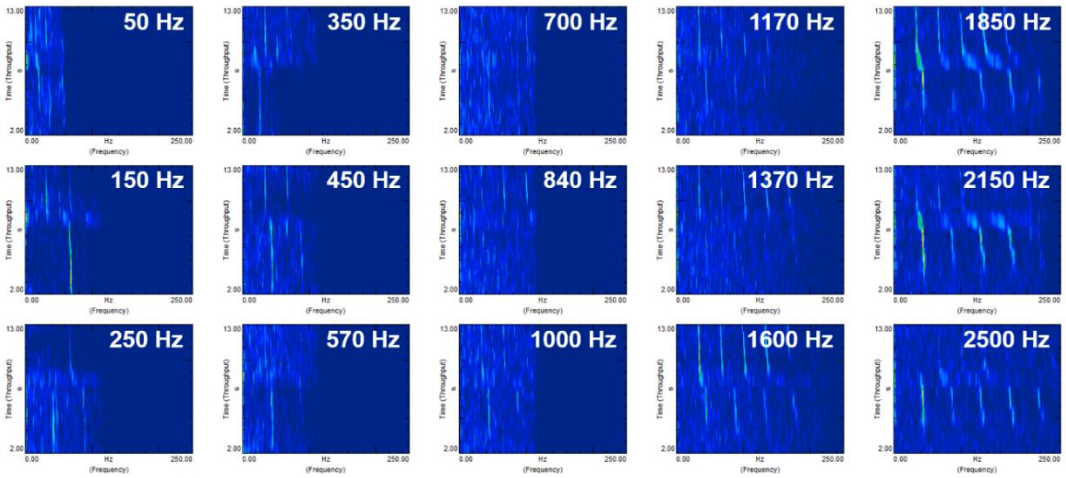


Figure 6: Tracked Modulation Maps (per critical bands in the range 50 – 2500 Hz) of the Fusion flyover.

2.2 Cabin comfort

Fusion and eFusion in-cabin noise was also studied adopting interior sound recordings acquired by a binaural headset worn by the co-pilot and the installation of accelerometers located in the proximity of the engine frame connection with the aircraft cabin body in order to capture the engine-induced vibrations transferred to the interior. Hereafter we report the results of the psychoacoustic analysis carried out on the two aircraft variants at cruising conditions and at two different nominal speeds: 60 knots and 90 knots.

The comparison between the eFusion and Fusion in-cabin noise Specific Loudness reported in Figure 7(left) reveals that the interior sound of both variants is dominated by the propeller noise, influencing the low frequency range (Bark 1 and Bark 2: 0-100 Hz and 100-200 Hz respectively). At higher nominal speed (90 kn) it is registered an increase of the eFusion specific loudness in the frequency range 2-10 kHz, while propeller noise contribution to the total loudness decreases. Such a behavior is not observed in the same conditions for the Standard Aircraft. The radar plot shown in Figure 7(right) reports the ratio between the metrics computed on the eFusion and on the Fusion aircrafts in the two speed conditions. A value <1 means that the corresponding metric assumes a lower value in the case of the eFusion. It can be observed that the two aircrafts interior sound performance do not differ in terms of overall loudness and speech-related metrics. On the contrary, the absence of the piston engine noise induces a drastic reduction of roughness at lower speeds (60 kn) in the eFusion in-cabin noise. The two aircrafts interior noise becomes very similar in terms of psychoacoustic behavior at higher speeds (90 kn). In this speed regime, in fact, it is observed a substantial equivalence between the two cases. As deductible from the specific loudness curves, the increase of sharpness of the eFusion sound with respect to the Fusion case at 90 kn is due to a reduction of the contribution of the propeller noise to the total loudness and an increase of the Turbulent Boundary Layer (TBL) noise contribution at higher frequency.

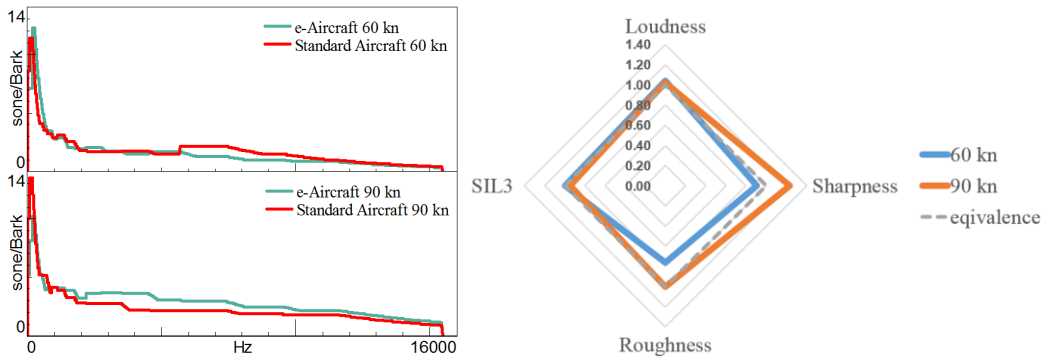


Figure 7: (left) eFusion and Fusion Specific Loudness spectra. (right) The radar plot reports the ratio between the metrics computed on the eFusion and on the Fusion aircrafts in the two speed conditions.

The spectrograms of the eFusion and Fusion in-cabin noise reported in Figure 8 show that the interaction between the piston engine and the propeller noise determines, in the Fusion case, the appearance of a large number of piston engine and propeller-related harmonics. These noise attributes, responsible for the increase of modulation phenomena and roughness in the case of the Standard Aircraft, are almost absent in the e-Aircraft in-cabin sound. Higher speed regimes imply a dramatic increase of the TBL excitation. Such a broadband noise contribution partially masks the higher harmonics of the Fusion interior noise. At higher speeds, therefore, results in Figure 8 confirm that the equivalence between the two aircrafts interior noise attributes increases.

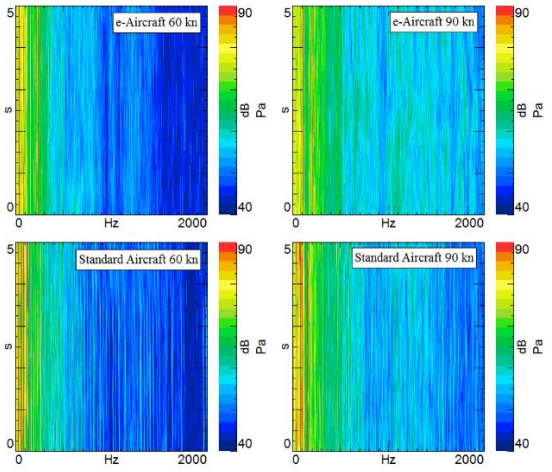


Figure 8: Spectrograms of the eFusion and Fusion in-cabin noise in stationary conditions.

Similarly to the fly-over case reported above in this paper, the analysis of tonality-related metrics reveals that the most prominent tones perceived in the eFusion cabin are the BPF and/or its first harmonic. Pitch perception is registered only in the 60 kn speed regime in the case of the Fusion in-cabin noise. At higher speed regimes the higher harmonic tones of the Fusion interior noise are partially masked by the more prominent TBL broadband noise.

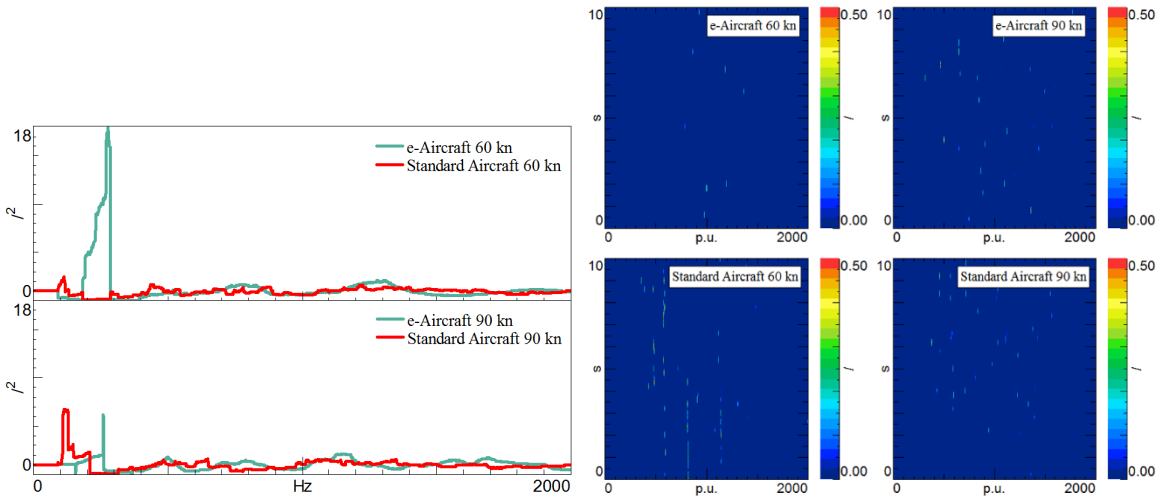


Figure 9: (left) eFusion and Fusion in-cabin noise Prominence Ratio, computed for two constant speed regimes: 60 kn and 90 kn, reveals the prominence of the BPF and/or its harmonics. (right) Pitch perception is registered only in the 60 kn speed regime in the case of the Fusion in-cabin noise

The comparison, reported in Figure 10, of the Auto-Power Spectra of pressure and vibration signals – computed respectively by: in-cabin microphone and accelerometer placed on the engine mounts (connection of the engine frame with the aircraft cabin) – discloses useful information for a first assessment of the mechanism of propagation of the exterior noise towards the interior of the aircrafts cabins. Observing Figure

10(left) , in fact, it can be noticed that e-motor excitation is limited to the frequency related to its rotational speed and a few harmonics. The e-Aircraft microphone spectrum reveals that its in-cabin noise is mainly influenced by airborne noise contributors due to the aero-acoustic sources generated by the propeller blades and to the TBL aerodynamic excitation, while only a minor part is transferred to the cabin through the engine frame mounts. The Fusion vibration pattern, instead, is composed by a large number of piston engine harmonics. Such harmonics are visible also in the in-cabin microphone spectrum suggesting, in this case, a major role of structure-borne noise transmission paths.

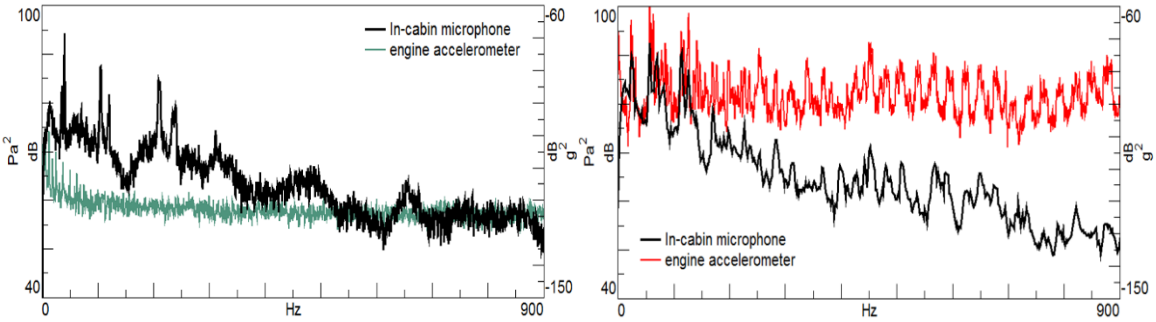


Figure 10: Comparison of the Auto-Power Spectra of pressure and vibration signals computed respectively by: in-cabin microphone (left channel of the binaural headset worn by the co-pilot) and accelerometer placed on the engine mounts (connection of the engine frame with the aircraft cabin). (left) eFusion. (right) Fusion.

Modulation maps reveal the presence of modulation phenomena – due to the interaction of piston engine noise and propeller noise – in the Fusion in-cabin noise. This is not the case for the eFusion interior noise, in which modulation patterns are almost not present (Figure 11).

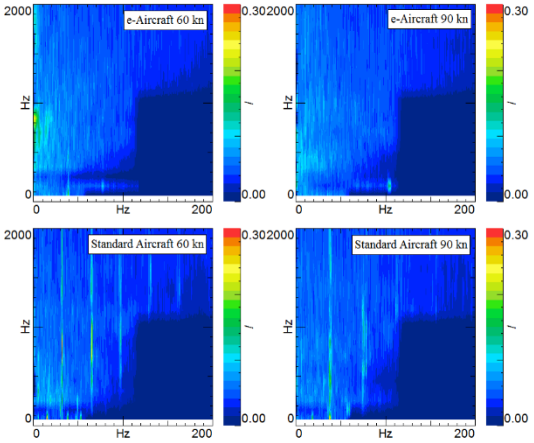


Figure 11: Modulation maps of the eFusion and Fusion in-cabin noise in stationary conditions.

From the in-cabin sound quality analysis of the two Fusion variants it can be concluded (confirming the results obtained in the flyover case) that the interior noise loudness levels are equivalent in the two variants, at the two analyzed speeds, while, on the contrary, modulation and roughness attributes are greatly improved thanks to the electric propulsion. It was moreover observed that the engine-related structure-borne excitation is drastically reduced in the eFusion case in which a major role is played by the aero-acoustic noise contributors such as propeller tonal noise and TBL broadband excitation.

2.3 Sound source localization

Sound source localization technique can help getting a better understanding of the main aircraft noise sources and how they are changing with electric propulsion. Results are presented below for the eFusion exterior radiated noise based on acoustic array measurements performed with the aircraft on the ground and also during flight.

In order to capture all aircraft noise sources including aerodynamic effects, the best is to measure the sound while the aircraft is flying. This requires to deploy an acoustic array with a large number of microphones on the ground and to synchronize the measurements with the position of the aircraft in-flight.

In this case, a relatively small array consisting of 100 microphone in a 5-arm star configuration with 10 meter diameter is used, as shown on Figure 12. This array is used to get a quick assessment of the source localization in flight. A larger array is typically required for obtaining detailed source localization and quantification during fly-over. Figure 12 also shows the Simcenter SCADAS data acquisition placed at the center of the array. This system is used to acquire and transfer the data from all microphones to a remote computer.



Figure 12: Ground array measurement set-up for source localization during fly-over (top and side view).

Simcenter Testlab software is used to process the microphone data. Beamforming and CIRA deconvolution techniques, see [7] and [8], are used to produce the source localization maps with improved spatial resolution and dynamic range. For this measurement, the aircraft is flying at an altitude of 50 feet at a speed of 70 knots.

Figure 13 shows a comparison of the two aircraft variants for the low frequencies, from 200 to 800 Hz, where most of the energy is concentrated. As expected, a dominant source is identified at the engine propeller in the case of the electric aircraft, whereas it is located at the engine exhaust in the case of the combustion engine aircraft.

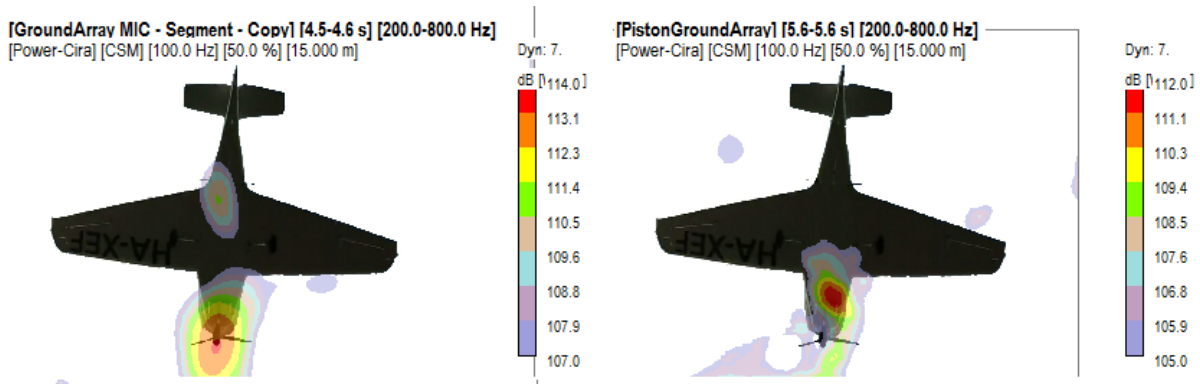


Figure 13: Source localization map on the eFusion all-electric aircraft (left) and Fusion combustion engine aircraft (right) at low frequency (200 to 800 Hz).

Figure 14 concentrates on noise at higher frequencies, from 800 to 1200 Hz. It is interesting to note that in the case of the piston engine aircraft, two dominant noise sources are identified, one at engine exhaust and one at the engine front part/propeller. This corresponds to the dominant sources also identified on the ground, as shown in next section. Results on the electric aircraft are more difficult to interpret, but also exhibit a noise source near the front landing gear attachment point to the fuselage.

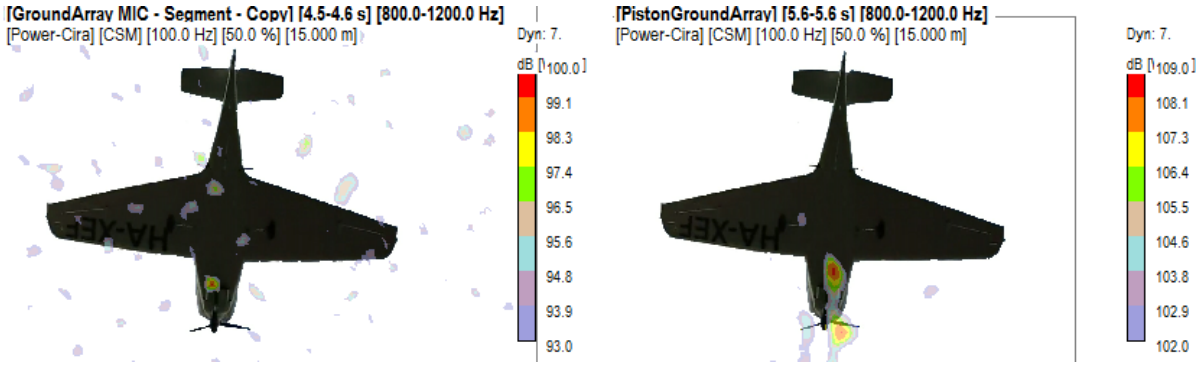


Figure 14: Source localization map on the eFusion all-electric aircraft (left) and Fusion combustion engine aircraft (right) at higher frequency (800 to 1200 Hz).

For these next measurements, the aircraft is maintained on the ground at a fixed position and an acoustic array is placed at a few meters from the engine, which allows to focus on the propulsion-related sources. The LMS sound camera, a high-quality acoustic array with 118 digital microphones, is used to localize and quantify the noise sources on the full frequency range, as shown in Figure 15(left).

Figure 15 shows a comparison of a measurement performed on the two aircraft variants for similar conditions (1000 RPM in the case of the combustion engine aircraft vs. 1150 RPM for the electric motor aircraft). It is interesting to note that most of the noise is radiated from the exhaust in the case of the combusting engine whereas propeller blade tip is the dominant noise source for the electric motor. Secondary sources appear at the air intake in the case of the electric aircraft and the front engine part for the conventional aircraft.

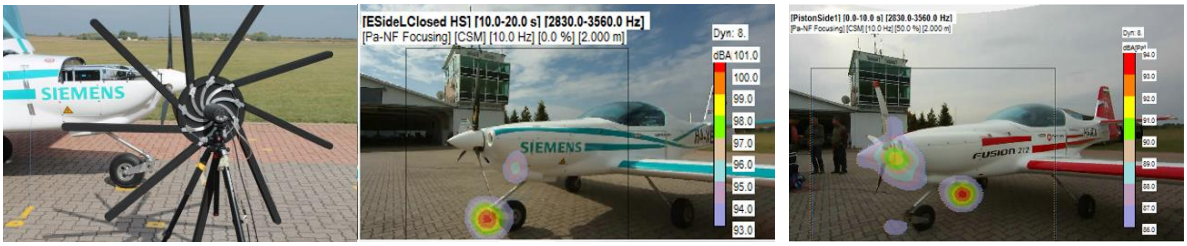


Figure 15: Measurement set-up for near-field sound source localization on the eFusion aircraft (Left). Sound source localization results with electric motor (middle) and conventional combustion engine (right).

There appears to be a strong interaction between the propeller wakes and the front landing gear leading to strong noise radiation. This is confirmed on Figure 16 where a dominant noise source is identified for most frequencies at the bottom part of the blade tip circle. This phenomenon is also observed on the conventional aircraft – although not shown here. This gives clear indication for potential noise reduction solutions.

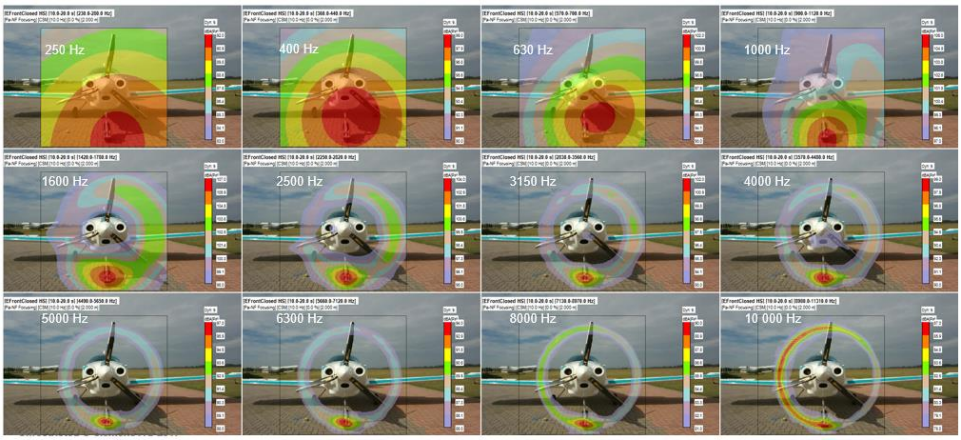


Figure 16: Sound source localization from the front for the eFusion Magnus aircraft.

3 Structural dynamics performance

3.1 Ground Vibration Testing

Ground Vibration Test (GVT) is part of the certification process and its purpose is to measure the aircraft dynamic characteristics (natural frequencies, mode shapes, structural damping coefficients and generalized mass). These results allow to update of the FEM (Finite Element Model) model of the structure used for flutter prediction.

Recently, more complex aircraft design raised additional testing requirements which are related to the increased use of composite materials, active systems and the need to quantify non-linear behavior. At the same time, a high time pressure exists on the test schedule due to limited availability of the fully assembled physical prototype aircraft so late in the design cycle.

In the past years, the so-called Normal Mode Testing has been almost exclusively used for GVT on aircrafts since this technique is very well suited for separating very closely spaced modes. Essentially it uses an excitation tuned at single frequency lines in correspondence of the modes of the aircraft. In this manner the vibration response only contains a contribution from the mode of interest. However this testing procedure is very time consuming and it has been replaced in the last years by techniques based on the estimation of modal parameters from broadband Frequency Response Functions (FRFs). Many excitation signals can be used to experimentally determine the system FRFs: periodic signals, stepped sine, burst random, swept sine. Recently swept-sine excitation received a lot of attention, as it represents a good compromise between magnitude of excitation level needed for large aircraft and testing time [10].

As the FE model is calculated supposing free-free boundary conditions, it is necessary to simulate the same boundary conditions during the test. For this purpose several alternatives are possible at this stage: bungees suspension system, deflated tires, pneumatic suspension.

In this paper the structural dynamics performance of the all-electric aircraft Magnus eFusion was investigated. The GVT campaign was performed at the Magnus facility in Hungary. The airplane's tires were deflated in order to reproduce the ideal free-free boundary conditions and two electrodynamic shakers were used in order to excite the system. They were placed at intermediate wing points as shown in Figure 17. The response accelerations were measured by using two Simcenter SCADAS systems in a Master-slave configuration. 58 monoaxial accelerometers and 11 triaxial accelerometers were used for a total of 91 measurement channels. The triaxial ones were distributed as follows: left and right wing tips (front node), left and right ailerons tips, front node of the fuselage, left and right tips of the horizontal tail, left and right elevators tips, front nodes on the top of the vertical tail and on the rudder.



Figure 17: GVT measurement setup

At first burst random tests were carried out at different force levels. In a second stage, logarithmic sine sweeps were used to excite the aircraft. Different sweep rates (0.3, 0.6, 1.2 and 2.4 oct/min), directions (sweep up and sweep down) and several force levels (10N, 15N, 20N) were used. Table 2 shows all performed tests.

Force (N)	Sweep Rate (oct/min)			
	slow (0.3)	medium (0.6)	fast (1.2)	very fast (2.4)
3	-	Up	-	-
10	-	up/down	up/down, +- 10 deg	-
15	Up	up/down	up/down	up/down
20	-	Up	-	-

Table 2: Test conditions performed during the Ground Vibration Test (GVT) campaign.

Several runs were performed in order to understand the different behavior at different force levels, which can be considered as an indicator for non-linear effects. The same is true for sweep-up and sweep-down tests which are commonly used in literature to identify the distorted FRF peaks due to the presence of non-linearity effects.

Mode #	Natural frequency [Hz]	Damping ratio (%)	Mode shape description
mode 1	11.185	1.38	1st wing bending
mode 2	15.377	1.75	tail torsion
mode 3	16.162	3.45	1st fuselage/wing bending
mode 4	17.224	3.22	aileron asymmetric
mode 5	18.348	1.80	tail bending
mode 6	20.436	1.84	1st horizontal tail bending
mode 7	21.764	4.98	ailerons symmetric
mode 8	23.230	1.70	rudder
mode 9	26.473	1.41	2nd wing bending
mode 10	27.416	1.65	vertical tail bending

Table 3: List of natural frequencies, damping ratios and mode shape descriptions for all modes up to 30 Hz

Table 3 shows the list of the identified natural frequencies and damping ratios of the first ten modes up to 30 Hz. A brief description of the identified modes is also given next to them. These modes have been

obtained by performing the conventional Multiple-Input-Multiple-Output (MIMO) method for FRFs estimation. The well-known Polymax modal parameters estimator has been used.

Figure 18 shows one of the Driving Point FRFs, where the Driving Point is the acceleration measurement channel placed next to the shaker excitation point. The sweep rate effect is considered by plotting the same FRF for the same force level (15 N) and with all the different sweep rates (as shown in Table 2). Increasing the sweep rate, the peaks have lower amplitude and become broader. Furthermore, a shift to higher frequency can also be highlighted.

Figure 19 shows the effect obtained by changing the force level from 3 N up to 20 N. If the system was linear, the same FRFs should be obtained, but some non-linear effects are present and for this reason a shift of the peaks towards higher frequencies can be underlined, especially around 20 Hz. This has also been confirmed from a further non-linear investigation by using innovative excitation techniques.

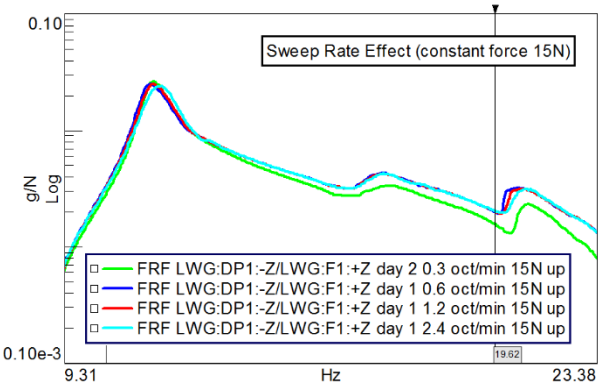


Figure 18: Driving Point FRF: sweep rate effect at constant force level (15 N).

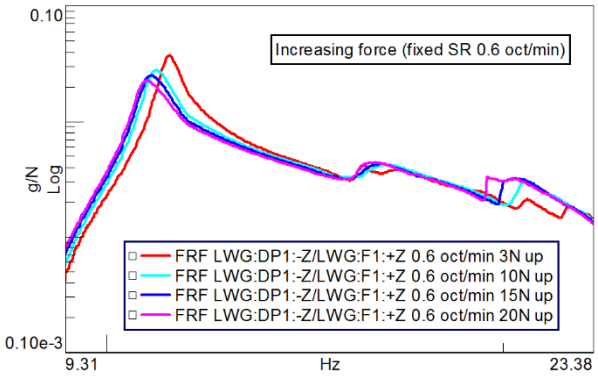


Figure 19: Driving Point FRF: force level effect at constant sweep rate (0.6 oct/min).

Figure 20 shows two of the main global modes of the eFusion aircraft, respectively mode #4 (aileron asymmetric) and mode #10 (vertical tail bending).

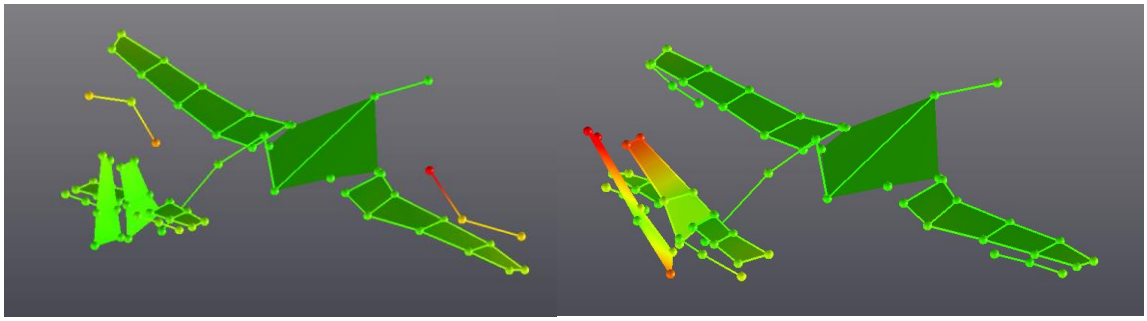


Figure 20: Ground Vibration Test modes: aileron asymmetric (mode #4, left); vertical tail bending (mode #10, right).

3.2 Flutter Analysis

Flutter is included in the broader term aeroelasticity, i.e. the study of the static and dynamic response of an elastic airplane. Since flutter involves the problems of interaction between aerodynamics and structural deformation, including inertial effects, at subcritical as well as critical speeds, it really involves all aspects of aeroelasticity [11] [12]. As already stated, the GVT results are used to perform flutter prediction by using

the correlated FE model of the aircraft. Despite all the efforts in developing flutter prediction tools, the only definitive method for clearing aircraft for flutter is flight testing. Aircraft certification procedures require that aerospace constructors demonstrate that the flight envelope of a new aircraft is clear of flutter with a high safety margin. Several possibilities exist for exciting the structural modes and performing a flutter test. In the eFusion case, the pilot was asked to impulsively excite the control surfaces and then bringing them back to zero position. Theoretically it is supposed to be a perfect impulse which should be able to excite all the structural modes, but practically it becomes difficult to excite high frequencies. Once the excitation is applied, the aircraft structure's response is measured at several locations. The aircraft was instrumented by means of 12 accelerometers as shown in Figure 21.

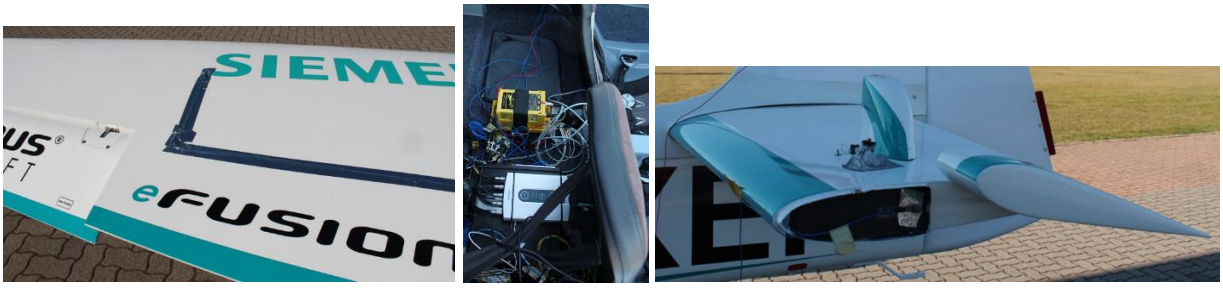


Figure 21: Aircraft instrumentation for flutter testing: Accelerometers placed on the left wing (left picture), Simcenter SCADAS XS measurement system in the cockpit (middle) and accelerometer inside the horizontal tail plane (right picture).

The Simcenter SCADAS XS system has been used in-flight to record 12 measurement channels which were placed at the same locations as during the GVT tests. Six different flights with different flight points (speed-altitude levels) were measured and the post-processing analysis allowed to identify some of the aircraft modes. The wing bending mode is plotted in Figure 22 (left picture) in which all measured points are represented by a sphere. On the right for comparison purposes it is reported the same mode measured during the GVT campaign where many points were measured on the ground. We can see that the 2 mode shapes correspond well.

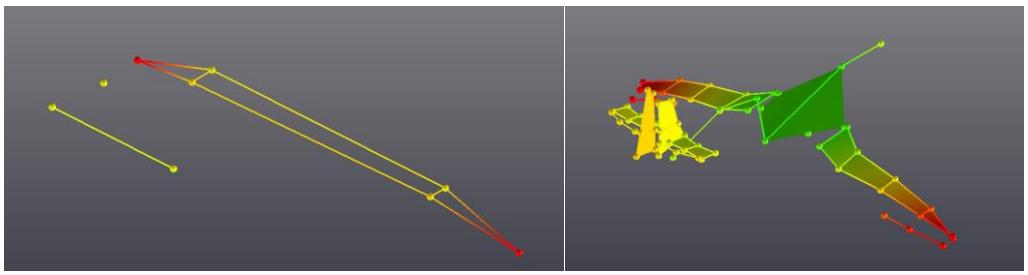


Figure 22: In-flight 1st wing bending (left picture) vs GVT 1st wing bending (right picture)

4 Conclusions

This paper aims at characterizing the vibro-acoustic performance of an all-electric aircraft. Acoustic performance was compared for two aircraft variants : one equipped with a conventional combustion engine, the other with an electric motor. Overall sound levels measured during fly-over show a significant reduction, with up to 10 dB difference measured. Sound quality metrics also help to prove that flying electric is not only quieter, but it also sounds more pleasant, both in fly-over conditions and in-cabin. Modulation (roughness and fluctuation) as well as tonality are greatly improved thanks to the electric propulsion system and the absence of low frequency engine order noise. Detailed sound source localization was also performed on the ground and during fly-over to pinpoint the dominant noise sources and understand how noise generation actually happens. As expected, engine intake and exhaust noise are the dominant noise sources in the case of conventional combustion engine whereas most noise is produced by the propeller and its interaction with the front landing gear in the case of the electric aircraft. Ground vibration testing allowed

to identify the main resonant modes of the aircraft structure. Different testing strategies were evaluated and non-linear phenomena were identified, especially by using different sine sweep parameters and by varying the excitation levels. In-flight vibration measurements were also performed to prepare for the flutter analysis. Corresponding mode shapes were identified from the ground and in-flight measurements.

Only a preliminary analysis of the GVT and flutter results is presented here. It is intended to present a more extensive analysis of the results in future publications. Future steps involve the development and validation of techniques to allow a better post-processing and modal parameters identification for Ground Vibration Test (GVT). Further studies will be conducted concerning the non-linearity issue underlined during the GVT tests. An estimate of the stability of each flight condition can be obtained if the damping ratio (related to a certain mode) is plotted against the dynamic pressure. Flutter plots can be drawn by analyzing different flight points acquired during an extensive measurement campaign. The damping ratio trends will be finally plotted for the critical modes in order to determine the flutter conditions which consist in a sudden drop of the damping ratio.

Acknowledgements

The authors would like to thank the Siemens eAircraft team as well as the Magnus personnel for their great support during these measurements in Germany and Hungary.

References

[1] UBER Elevate, Urban Air transportation white paper, “Fast-Forwarding to a Future of On-Demand Urban Air Transportation”.

[2] T. Wall and R. Meyer, "A Survey of Hybrid Electric Propulsion for Aircraft", 53rd AIAA/SAE/ASEE Joint Propulsion Conference, AIAA Propulsion and Energy Forum, (AIAA 2017-4700).

[3] R. Jansen, C. Bowman, A. Jankovsky, R. Dyson and J. Felder, "Overview of NASA Electrified Aircraft Propulsion (EAP) Research for Large Subsonic Transports", 53rd AIAA/SAE/ASEE Joint Propulsion Conference, AIAA Propulsion and Energy Forum, (AIAA 2017-4701).

[4] S. Rizzi, D. Palumb, J. Rathsam, A. Christian and M. Rafaelof, "Annoyance to Noise Produced by a Distributed Electric Propulsion High-Lift System", 23rd AIAA/CEAS Aeroacoustics Conference, AIAA AVIATION Forum, (AIAA 2017-4050).

[5] ICAO Annex16 Volume I, Chapter 8 Environmental protection - aircraft noise.

[6] Simcenter Testlab Release 17, User manual.

[7] R. Dougherty, Advanced Time-Domain Beamforming Techniques, AIAA 2004-2955, Proceedings of the 10th AIAA/CEAS Aeroacoustic Conference, Manchester, UK, 2004.

[8] T. F. Brooks and W. M. Humphreys, “A deconvolution approach for the mapping of acoustic sources (DAMAS) determined from phased microphone arrays,” J. Sound Vib. 294, 856–879 (2005).

[9] R. Hallez, S. Beebe, A. Finez, “Detection and analysis of interior and exterior noise sources in a MD902 helicopter”, AHS 72nd Annual Forum, West Palm Beach, Florida, 2016.

[10] B. Peeters. H. Climent, R. de Diego, J. de Alba, J. Rodriguez ahlquist, J. Martinez Carreno, W. Hendricx, A. Rega, G. Garcia, J. Deweer, J. Debille, “Modern solutions for Ground Vibration Testing of large aircraft’, 26th IMAC Conference and Exposition on Structural Dynamics – 2008, Orlando FL, US.

[11] S. Giclais, P. Lubrina, C. Stephan, “Aircraft Ground Vibration Testing at ONERA”, AerospaceLab Journal, ONERA, 2016, p. 1-18.

[12] J. E. Cooper, “Towards faster and safer flight flutter testing”, Defense Technical Information Center ADP014182, 2003.

Damping enhancement of sheet-metal components through shot peening process to improve vibro-acoustic performance

V. K. Balla [1,2], **F. Greco** [1,3], **E. Deckers** [1,3], **B. Pluymers** [1,3], **W. Desmet** [1,3], **G. Vadakkel** [1,2]
[1] KU Leuven, Department of Mechanical Engineering,
Celestijnenlaan 300 B, B-3001, Heverlee, Belgium
e-mail: **vamsikrishna.balla@kuleuven.be**

[2] Member R&D, TVS Motor Company Ltd. Hosur-635110, Tamilnadu, India

[3] DMMS Lab

Abstract
The vibration and noise amplitude levels at resonance frequency depends on the amount of damping present in the component. In this work, damping enhancement is achieved through a cold working process like shot peening. The residual stress measurements—using X-ray diffraction technique—and vibro-acoustic property measurements of a sheet metal plate is carried out in the original condition. The residual stress measurements are repeated on the plate after subjecting it to shot peening and found considerable increase in the stress levels in both longitudinal and transverse directions. The experimental modal testing of the plate confirmed the increase in the damping values of the system. The sound pressure levels of the shot-peened plate have reduced significantly. A brief simulation study of shot peening using ABAQUS is carried out to establish a transfer function between residual stress and shot peening process parameters. Further, attempts will be made to understand the relationship between residual stresses and damping in the system.

1 Introduction

In the automotive industry, steel material is widely used in the form of sheet metal components that are often manufactured through single stage or multi stage deep drawing process. The enhancement of structural worthiness without/with a minimum weight addition is highly desirable due to stringent regulatory needs related to mass-emission reductions and fuel-economy improvements. It is a common practice in the industry to increase the performance characteristics of the sheet metal components through either heat treatment processes such as annealing, induction hardening etc., or through cold working process such as shot peening. Cold working is used to increase the strength, especially in highly alloyed austenitic stainless steel [1]. The shot peening process affects the surface of the component and is often used to increase the hardness, fatigue strength of the material. In shot peening process, small spherical balls are impacted on the surface of the base metallic structure to induce residual compressive stresses [2, 3, 4]. The shot peened components can be subjected to higher operating stresses when compared to non-treated components, due to the presence of compressive stresses. This phenomenon will increase the fatigue life of the components significantly. By inducing residual compressive stress the inherent damping of the component may be increased. The damping factor may vary with the shot peening conditions and the depth of the material [5, 6]. However, the study of how such shot peening induced damping affects the noise and vibration characteristics of a component has not been widely studied. The residual compressive stress induced of the surface depends on a number of different parameters such as the shot intensity, shot coverage, angle, quality of shot etc. The damping induced in the material is characterized as damping ratio and it can be obtained either by the half-power bandwidth

method or experimental modal testing. The work presented in this paper explores how shot peening process of a plate affect the vibro-acoustic behaviour of the plate.

2 Component description

The vibro-acoustic performance variation of deep drawn components can be attributed to geometric profile and thickness deviations that occur during the manufacturing process. However, it is shown that these two factors can not explain the complete difference. The work hardening effects and variation of elastic modulus in the local regions also contribute to the total variation [7, 8]. It is also envisaged that residual stresses of the component play a key role in controlling the amplitude levels. Hence in the present work, four rectangular plates—two plates in the rolling direction and two plates in the transverse direction—are obtained from the blank sheet coil. The length, width and thickness of the plate considered are 300 mm, 50 mm and 1.5 mm respectively as shown in Figure 1. The two steel plates cut along the rolling radius of the steel roll are named R1 and R2 and the two steel plate cut perpendicular to the rolling radius of the steel roll are named T1 and T2. The thickness measurements of all these four plates are performed at 21 locations to ensure the consistency. The flatness measurements are carried out using a dial-guage in order to find out any geometrical profile deviation. The maximum variation found through these flatness measurements is approximately 10 microns. Hence, it can be stated that both the geometric profile and thickness variations of the four plates are negligible.

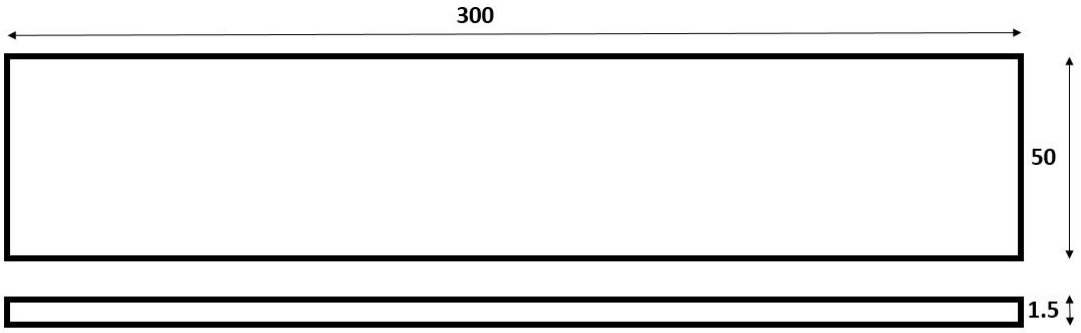


Figure 1: Top and front views of the rectangular plate (All dimensions are in mm).

3 Shot peening process

Shot peening process is commonly used surface treatment process to enhance the mechanical characteristics of metal components. The process uses high compressed gas along with spherical shots made from glass or metal beads. The size of the beads, angle of attack, duration, shot material properties and the velocity may be varied to induce required residual stress on the surface. The shot peening process changes the material phase of the base component from austenite to martensite. The percentage of retained austenite decreases with the increase in shot peening intensity. This process causes martensite formation and hence base component hardness increases. The reader is suggested to the reference [9] for a more detailed information regarding shot peening process. The shot peening intensity levels are measured using Almen scale. In the present study, the component is subjected to shot peening on both sides with an Almen intensity of 0.19 mm A.

4 Residual stress

4.1 Measurement set-up

The residual stress measurement is carried out using X-ray diffraction technique. In this method, residual stress are determined from the distance between crystallographic planes, i.e., d-spacing, as a strain gauge. The d-spacing of the material increases when material is in tension and decreases when material is under compression. The corresponding strains due to d-spacing changes can be related to stresses induced in the component. The reader is suggested to refer to [10] for a more detailed explanation of X-ray diffraction technique method to measure residual stresses. The shot peening intensity is measured using Almen scale.

The residual stress measurement set-up is shown in Figure 2. The residual stresses of all the plates are measured at three different locations. These points, as indicated in red boxed points of Figure 3, are represented as point-3, point-10 and point-20. The stresses in longitudinal (along Z direction) and transverse (along Y direction) are measured.



Figure 2: Measurement set-up used to determine the residual stress using X-ray diffraction technique.

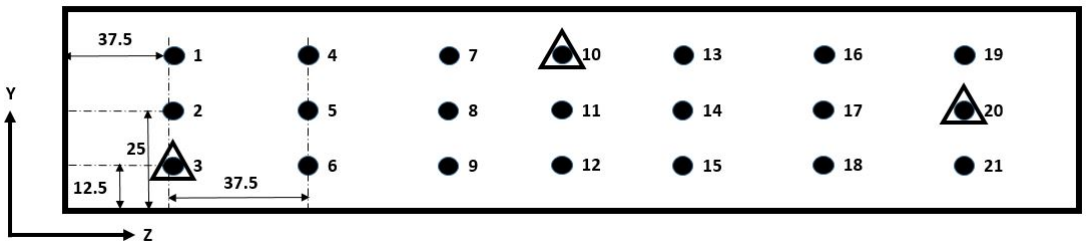


Figure 3: Measurement points of residual stresses (shown in triangles) and modal testing (shown in circles).

4.2 Stress measurement results—before and after shot peening

The residual stress measurements on the the blank sheet metal plates—that are obtained from transverse (T1 & T2) and rolling directions (R1 & R2) of the blank coil—are carried out after subjecting them to the shot peening process in order to find out the magnitude of induced stress levels. The shot peening operation is done with an Almen intensity of 0.19 mm A. Table 1 compares the change in residual stress at point 3 , 10 and 20 in both Y and Z directions. The comparison of residual stresses at point-10 of plates R2, T2 are shown in Figure 4. The stress values can not be measured exactly and hence some tolerance either on lower or higher side of the measured value is denoted. The accuracy of the stress measurement increases at higher stress values and hence the tolerance is reduced. However in the current measurement campaign, good care is taken to ensure a lower tolerance stress values. Results show two significant changes to the plates due to the

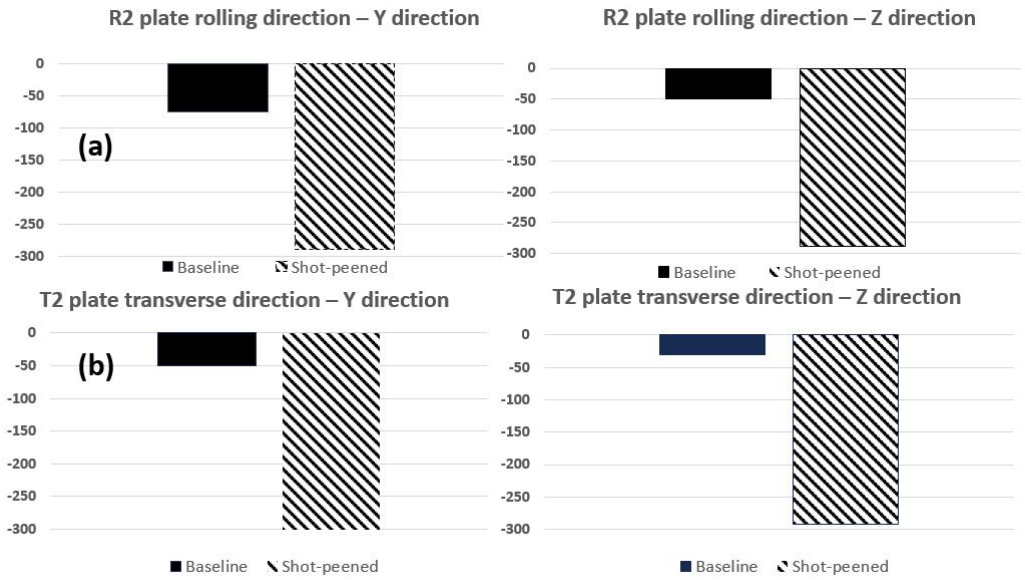


Figure 4: Comparison of residual stresses before and after shot peening at point-10 a) plates-R2 b) Plate- P2 respectively.

shot peening operation: i) There is considerable increase in compressive stresses in the plates ii) It induced uniform stresses in all the components in both longitudinal and transverse directions. Hence, the plates are more likely to exhibit a similar dynamic behaviour. The uniform stress field across the component helps in improving its dynamic behaviour. As there are no local stress concentrations due to secondary operations, it helps in increasing fatigue life of the component. The manufacturing process like deep drawing process often imparts some localized effects in the components and hence local damping can vary greatly. The shot peening operation can negate such adverse effects.

Plate	Point	Stress (MPa)			
		Before shot peening		After shot peening	
		Y direction	Z Direction	Y direction	Z Direction
P1	3	-98.5 ± 7.8	-44.6 ±9.5	-299.1 ±3.1	-313.1 ±7.2
	10	-53.9 ±9.9	-23.8 ±5.9	-292.0 ±2.6	-282.0 ±2.9
	20	-94.6 ±13.0	-50.3 ±17.1	-313.1 ±7.2	-287.8 ±3.1
R1	3	-56.1 ±12.7	-58.7 ±10.9	-290.2 ±4.7	-293.8 ±8.3
	10	-48.2 ±6.8	-18.8 ±7.5	-287.7 ±4.2	-287.7 ±4.2
	20	-55.7 ±11.7	-27.4 ±11.4	-254.1 ±14.0	-282.2 ±4.2

Table 1: Comparison of compressive residual stresses of P1 & R1 plates before and after shot peening process.

5 Experimental vibro-acoustic behaviour characterization

5.1 Measurement set-up

The natural frequencies of all the four plates R1, R2, T1, and T2 are obtained by performing an experimental modal testing in free-free boundary condition. The experimental test set-up is shown in Figure 5. The plate is suspended using soft springs from a rigid frame. A tri-axial accelerometer (PCB-356A08) is attached to the plate as shown in figure and a modal impact hammer (Onosokki-GK 3100) is used to excite the steel

plate. The plate test geometry consists of 21 points as shown in Figure 3. The points are placed 12.5 mm apart along the width and 37.5 mm apart along the length of the plate. The response points are chosen such that spacial aliasing effects are avoided in the frequency range of 0-1500 Hz. A sampling frequency of 1024 Hz and a 0.5 Hz frequency resolution is used to acquire vibration data. The windowing functions used on the reference impact force signal and the response signal are force-exponential window and an exponential window respectively. Additionally, a 1/2 inch (B&K-type 4940) microphone is placed at the center of the steel plate to measure the radiated noise due to an impact excitation. A sampling frequency of 4096 Hz along with 0.5 Hz frequency resolution is used to acquire noise data. The accelerometer, microphone and the impact hammer are all connected to a LMS SCADAS [11] data acquisition unit. The measurements are recorded and processed using the LMS Test.Lab software [12]. The impact direction is normal to the surface of the component at all locations, as component's out-of-plane dynamic behaviour is considered to be significant. A set of five averages are used, at all locations, to avoid noise contaminations in the response signals. The vibration and noise measurements are carried out for all four plates in a semi anechoic chamber to minimize the influence of any background noise.

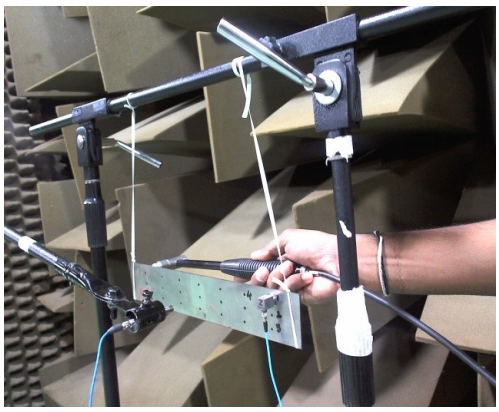


Figure 5: Structural and Acoustic FRF measurement set-up

The structural frequency response functions (FRF) are obtained by normalizing the vibration acceleration levels with reference to an input impact force. Hence, inertance a/F is obtained at all impact locations of the components. Similarly, the noise transfer functions (NTF) are obtained by dividing the acoustic sound pressure by the impact force. Hence, NTF is denoted as p/F. The experimental modal tests are carried out on all four plates and simultaneously NTFs are also obtained.

5.2 Structural FRF results—before and after shot peening

The natural frequencies of all the four plates are obtained from experimental modal testing as described in section 5. Table 2 shows the comparison of first ten natural frequencies between the two plates before and after shot peening process. It can be seen from the results that natural frequencies are reduced after shot peening process, although the percentage of reduction is not very significant. Figure 6a shows comparison of R2 plate at point-3. The solid line in the figure represents FRF of non-peened plate and dotted line represents FRF of shot peened plate. Figure 6b shows T2 plate FRF comparison at point-3. The solid line in the figure represents FRF of non-peened plate and dotted line represents FRF of shot peened plate. The FRF amplitude levels after the shot peening process are considerably reduced when compared to those of the base configuration.

5.3 Damping change due to shot peening

The damping values of the plates are obtained from the modal testing. Figure 7 a shows the average damping value results of plates T1 and T2 before and after the shot peening operation. Similarly, Figure 7 b shows the

Sl. No	Transverse direction				Rolling direction			
	T1	T1-SP	T2	T2-SP	R1	R1-SP	R2	R2-SP
1	87	84	88	85	88	85	88	86
2	249	241	249	243	250	243	250	243
3	319	304	322	305	322	299	319	302
4	489	475	492	478	492	477	493	478
5	661	634	666	638	662	628	662	634
6	809	786	813	791	812	789	814	791
7	1040	995	1045	1004	1038	994	1041	999
8	1206	1173	1213	1183	1209	1178	1214	1182
9	1452	1386	1463	1400	1449	1386	1457	1394
10	1684	1639	1693	1654	1687	1645	1694	1653

Table 2: Comparison of natural frequencies of plates before and after shot peening process

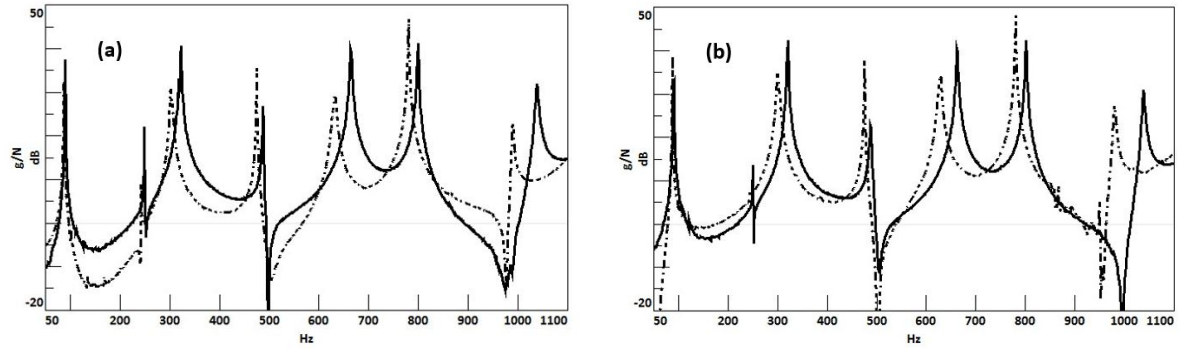


Figure 6: Comparison of structural FRFs of point-3 a) T2 plate b) R2 before and after shot peening process

average damping values of plates R1 and R2 before and after shot peening. The results from plates before shot peening is represented by solid black line whereas the results after shot peening is represented as

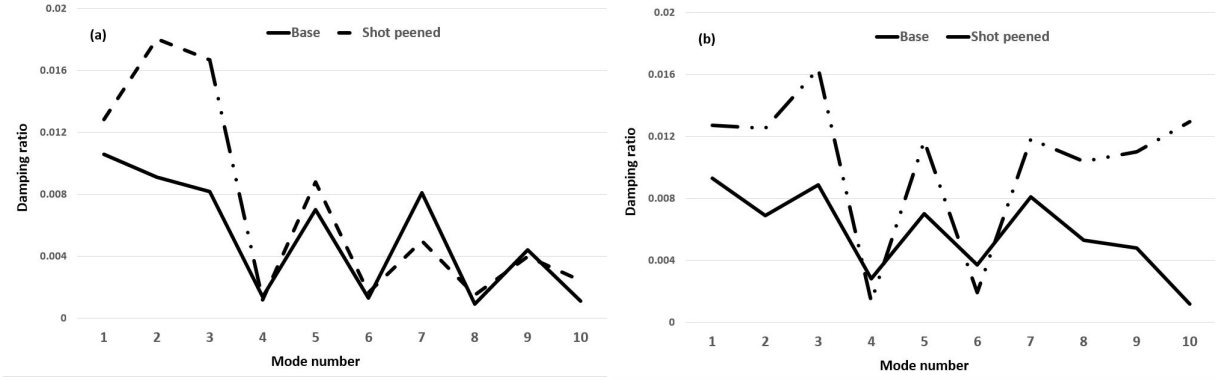


Figure 7: Comparison of averaged damping values in a) Transverse direction plate b) Rolling direction plate before and after shot peening process

dotted black line. The results show clear changes in the modal damping values of the plates. There is larger influence of shot peening operation on damping at the lower frequency modes compared to higher frequency modes. The changes in the damping are much larger for the torsional modes compared to the bending modes of the plate.

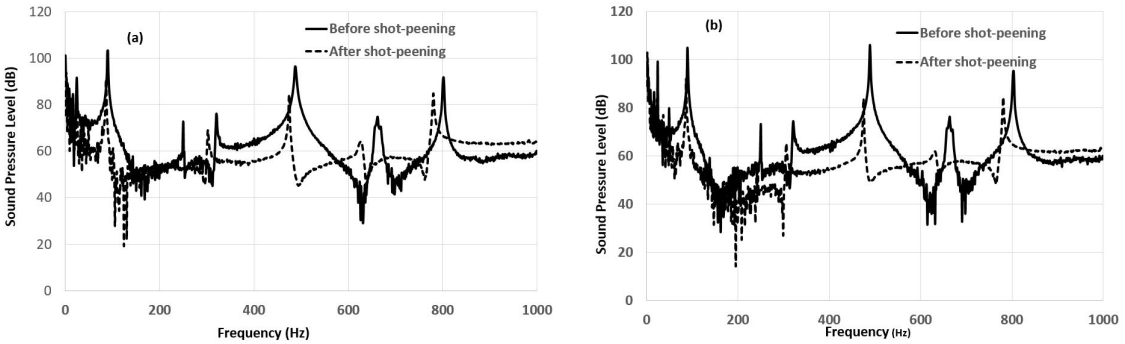


Figure 8: Comparison of acoustic transfer functions between point-3 and microphone in a) Transverse direction plate b) Rolling direction plate before and after shot peening process

5.4 Acoustic NTF results—before and after shot peening

Acoustic NTF is defined as the ratio of the radiated sound pressure and the impulse force input to the plate. The acoustic NTF gives an indication of the efficiency of the sound radiation at various frequencies. This can be compared between different plates as the output pressure is normalized by the input force. Figure 8a & Figure 8b show the acoustic NTF or acoustic response from the plates T1 and R1 respectively. The graphs compares the acoustic response measured before shot peening and after shot peening the plates. The results clearly show a significant reduction in the acoustic response from the plates after they are shot peened.

6 Simulation results

6.1 Vibro-acoustic behaviour—Before shot peening

The plate has a thickness of 1.5 mm and is made of IS 513 CR0 grade. The FE model of the plate is shown in Figure 9. The plate mesh consists of quadrilateral elements with an element size of 2.5mm. The mesh consists of 2541 nodes and 2400 quadrilateral elements. The density, modulus of elasticity and Poisson ratio of the blank material are 7850 kg/m^3, 2.1×10^5 MPa and 0.3 respectively.

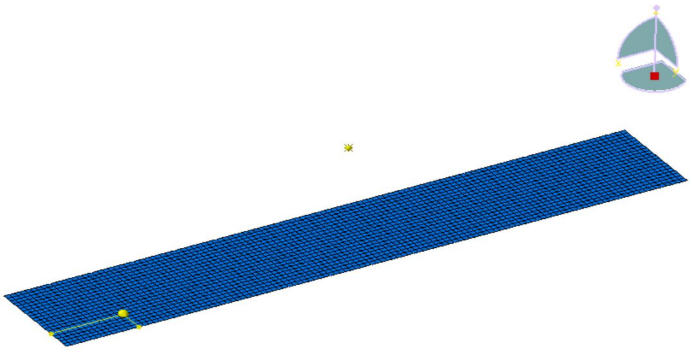


Figure 9: Schematic of FE & BEM model of the plate

The mass of each accelerometer (10.5 g) is considered using "CONM2" elements at the respective node location in the FE model, to account for the mass loading. The modal analysis of the component is carried out using LMS.Virtul Lab [13] software. The modal analysis is carried out in free-free conditions. The comparison of natural frequencies between simulation and experiments is shown in Table 3. It can be seen from the results that the correlation between results is good as the highest percentage difference is about 4.3, for the first ten natural frequencies. The harmonic analysis is carried out by exciting the plate in the normal direction at point-1(shown as yellow sphere in the Figure 9) by specifying a unit force. The harmonic analysis is carried out between 1-1000 Hz. and 1 Hz. frequency resolution.

Sl.No	Simulation	Experiment	% difference
1	88	87	1.1
2	250	244	2.5
3	322	318	1.3
4	492	481	2.3
5	662	649	2.0
6	812	798	1.8
7	1038	1002	3.6
8	1209	1196	1.1
9	1449	1389	4.3
10	1687	1674	0.8

Table 3: Comparison of natural frequencies between simulation and experiments before shot peening process

The acoustic transfer vectors are computed using boundary element method (BEM), using the same mesh. The surface velocities obtained using finite element harmonic analysis are mapped on to the acoustic mesh. The noise transfer function between point-1 and the filed mesh (shown as a yellow sphere in air medium) is computed for the same frequency range as described in harmonic response analysis. The comparison of experimental and simulation acoustic transfer functions is shown in Figure 10. The match between simulation and experimental results is good and hence FE model can be considered accurate.

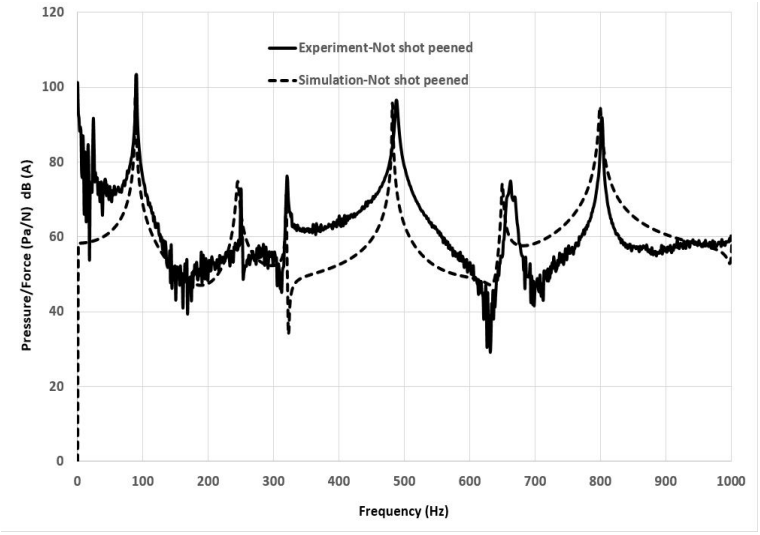


Figure 10: Comparison of acoustic FRF in non shot peened condition between point-1 and filed point of the plate

6.2 shot peening simulation results

6.2.1 Residual stress results

In order to understand the magnitude of compressive residual stresses and their distribution, a brief attempt is made to simulate the shot peening process. This simulation results will help to qualitatively characterise the impact of the shot peening process parameters on the residual stresses induced in the component. The analysis is carried out through explicit FE method using Abaqus software [14]. The plate is modelled using a four-noded S4R shell elements,as the stress distribution along the thickness is assumed to be negligible. The plate is fixed along the edges to represent the clamped boundary condition. The plate is impacted using steel balls of 2.5 mm radius. The steel balls are assumed to be rigid and hence no plasticity effects are considered. It is very cumbersome to model the impact of these balls using the finite element method. The discrete element method (DEM) [15] is used to simulate the dynamics of the steel balls on the metallic surface. The PD3D elements are used for simulating the projectile motion and collision against the parent metallic component of the steel balls. The Figure 11 shows the compressive residual stress distribution in the plate. The maximum stress value shown is 300 MPa, which is comparable to experimental value as shown in section 4.2. Hence, it can be concluded that the shot peening parameters chosen in the simulation study predicted stress values with a reasonable accuracy.

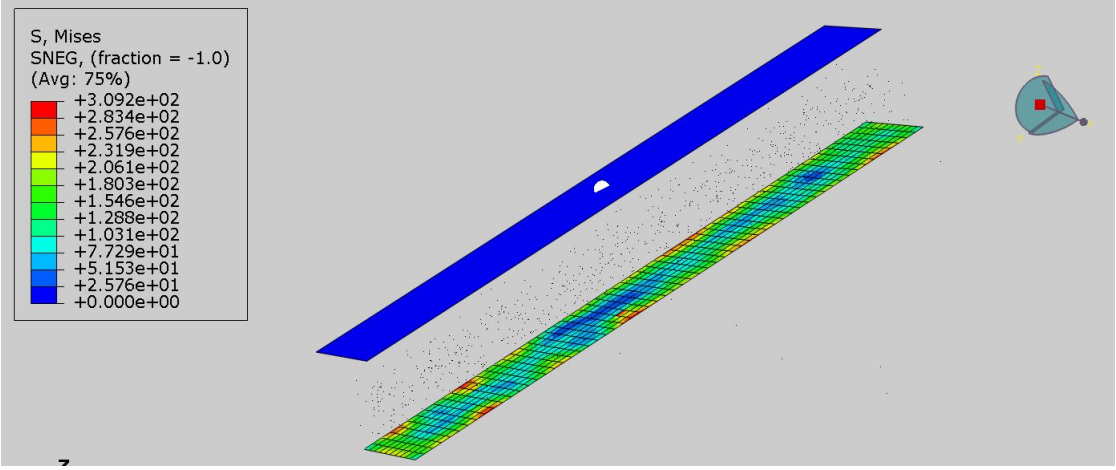


Figure 11: Residual stress distribution due to shot peening process.

6.2.2 Vibro-acoustic behaviour—After shot peening

This simulation model can be used for predicting stress values by varying the shot peening parameters. The results of this analysis can be used to arrive at different stress value by varying shot peening process parameters. These shot peening process parameters are in turn are used for carrying out actual shot peening process of the component. The experimental modal testing of these plates are carried out to establish a relationship between the stresses and the damping values. However, in the current study experiments are performed for only one particular stress state of the plate and damping values are obtained from experimental modal testing as described in section 5.3. These damping values are used for computing NTFs of the plate. The combination of FEM & BEM, as described in the section 6.1, are used for computing NTFs. The comparison of NTFs betwen simulation and experimental results of point-1 and field point mesh is shown in Figure 12. The result match can be considered reasonable and hence this methodology can be used for predicting NTFs of the plate.

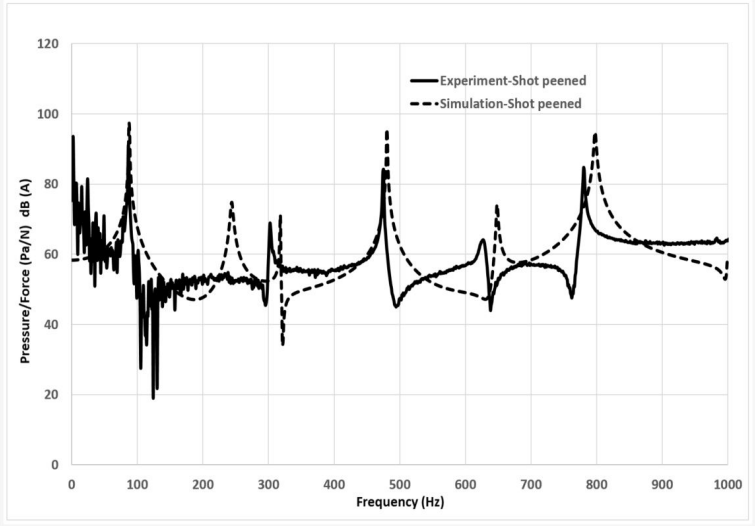


Figure 12: Comparison of acoustic FRF in non shot peened condition between point-1 and filed point of the plate

7 Conclusions

The shot peening process increases the residual compressive stresses significantly and creates a homogeneous stress field, when appropriate shot peening process parameters are used. The induced stress field changes the material phase and hence enhances the damping of the plates significantly. In the present work shot peening process increased the residual stress in both the longitudinal and transverse directions from approximately 50 MPa to about 300 MPa. The increase in stresses values results in significant increase in damping values. Hence, noise transfer functions after carrying out the shot peeing process reduced considerably. Also, a brief attempt to simulate the shot peening process using a combination FE and DEM is made. The results of this analysis can be used to arrive at shot peening process parameters to obtain the desired stress values. The experimental modal testing is carried using the shot peened plate to develop a relation between compressive stresses and damping values. This damping relationship can be used for computing and optimization of the component's noise transfer functions. The authors plan to carry out residual stresses inclusion—arising out of shot peening process—in the vibro-acoustic simulation,as future research work.

Acknowledgements

The authors gratefully acknowledge the help received from the colleagues at PMA section of KU Leuven and the members at Noise, Vibration and Harshness laboratory of TVS Motor Company. The KU Leuven research fund is gratefully acknowledged for its support. The research work of Elke Deckers is financed by a post-doctoral grant of the Research Foundation-Flanders (FWO). The authors would also like to sincerely thank Mr.R.Babu, Vice President of Research and Development, Mr.N.Jayaram (former Vice President of Research and Development) and Mr.Vinay Harne, President, New Product Introduction (NPI) of TVS Motor Company for providing support and facilities to carry out this work.

References

[1] R. L. Norton, Machine Design —an Integrated Approach, Pearson Education Asia, 2nd Edition, 2010.

[2] M. Ofsthun, When fatigue quality enhancers do not enhance fatigue quality, International Journal of Fatigue 25 (2003) 1223–1228.

[3] M. L. Aggarwal, V. P. Agrawal, R. A. Khan, A stress approach model for predictions of fatigue life by shot peening of en45a spring steel, International Journal of Fatigue 28 (2006) 1845–1853.

[4] M. L. Aggarwal, R. A. Khan, V. P. Agrawal, Influence of shot peening intensity on fatigue design reliability of 65si7 spring steel, Indian Journal of Engineering and Materials Sciences 12 (2005) 515–520.

[5] M. L. Aggarwal, Shot peened high nitrogen austenitic stainless steel: An alternate to ni rich austenitic steel for medical applications, International conference on materials for advanced technologies, Singapore, 2007, pp. 31–38.

[6] L. Singh, R. A. Khan, M. L. Aggarwal, Influence of residual stress on fatigue design of aisi 304 stainless steel, Journal of Engineering Research 8 (2011) 44–52.

[7] F. Greco, E. Deckers, J. Stroobants, S. V. Poppel, K. Linck, W. Desmet, Finite element simulation of the dynamic behaviour of deep drawn components with accurate thickness description, Finite Elements in Analysis and Design 138 (2018) 12–20.

[8] V. K. Balla, L. Coox, E. Deckers, B. Plyumers, W. Desmet, K. Marudachalam, Obtaining manufactured geometries of deep-drawn components through a model updating procedure using geometric shape parameters, Mechanical Systems and Signal Processing 98 (2018) 382–401.

[9] O. Unal, Optimization of shot peening parameters by response surface methodology, Surface & Coatings Technology 305 (2016) 99–109.

[10] SAE J784a, Residual Stress Measurement by X-Ray Diffraction, Handbook Supplement, Society of Automotive Engineers, Inc., 1971.

[11] LMS SCADAS, *LMS SCADAS brouchure*, Siemens PLM Software Inc (2015).

[12] LMS Test.Lab 15A , *LMS Test.Lab Signature Acquisition, User Guide*, Siemens PLM Software Inc (2015).

[13] LMS Virtual.Lab 15A , *LMS Virtual.Lab Theory Manual and User Guide*, Siemens PLM Software Inc. (2015).

[14] Abaqus CAE 2017, Abaqus Theory Manual and User Guide, Dassault systems Inc. (2017).

[15] P. A. Cundall, O. D. L. Strack, A discrete numerical model for granular assemblies, Geotechnique 29 (1979) 47–65.

Reflection from elastic wedges of different thickness profiles

A. Karlos [1], **S. Elliott** [1], **J. Cheer** [1]
[1] Institute of Sound and Vibration Research, University of Southampton,
Southampton, SO17 1BJ, United Kingdom
e-mail: **A.Karlos@soton.ac.uk**

Abstract
An elastic wedge whose thickness varies with axial position according to a power law can act as an absorber of incident flexural waves and thus as an anechoic termination. Ideally, if the wedge is tapered down to zero thickness, the incident wave slows down to zero propagation velocity at the edge, thus never reaching the boundary, and, so, not undergoing reflection. In practice, however, a small truncation of the wedge always occurs, due to manufacturing restrictions, leading to non-zero thickness at the edge, so that some reflection does occur. In this paper, alternative thickness profiles are examined, such as the power-cosine, the exponential and the Gaussian profile, the latter two inevitably having a truncation within a finite length. A method based on the WKB approximation is used in order to calculate the reflection coefficient of a structure comprising a wedge connected to a uniform plate. Higher-order WKB approximations are also applied. Results are compared with those from a Finite Element analysis.

1 Introduction

In various engineering applications, vibration damping is of great importance. A novel idea for attenuating structural vibrations was proposed by Mironov in [1]. In that article, it was theoretically predicted that a wedge-like plate which tapers according to a quadratic law down to zero thickness, undergoing one-dimensional bending, will cause incident waves to slow down to zero propagating velocity at the vicinity of the vanishing free edge; therefore, the waves will not reach the boundary and they will not be reflected. The energy carried by the waves will be dissipated by the arbitrarily weak damping of the material of the structure at the region near the free edge. This phenomenon has come to be known as the 'acoustic black hole' effect. It can be shown with the same type of analysis as the one carried out in [1] that this theoretical result holds for any non-uniform plate with a power-law thickness profile of order greater than or equal to two, that is, with thickness varying as $h_p = h_0 (1 - x/x_0)^n$, where h_0 is the thickness at the input end of the wedge and x_0 is the length of the wedge, the point $x = x_0$ corresponding to the edge of vanishing thickness, as depicted in Figure 1. The same qualitative conclusions hold for a beam of constant width, since the equation of motion of such a system is similar to that describing one-dimensional bending waves in a plate.

It was also demonstrated in [1] that even a small truncation at the edge of the plate, which inevitably occurs in practice due to manufacturing restrictions, introduces considerable reflection. In order to overcome this problem, Krylov and Tilman proposed applying thin layers of viscoelastic material on the sides of the wedge [2]. It was theoretically predicted in that article that the use of such damping layers greatly reduces the reflection from the truncated wedge, thus enhancing the damping effect due to the tapering geometry. This idea has been further elaborated on, both in terms of mathematical modelling and experimentally in a number of articles, as has been reviewed in [3].

The wedges examined in [1] and [2] are considered to be driven internally, that is, an incident flexural wave originating inside the wedge is travelling towards the free edge. Therefore, this approach only accounts

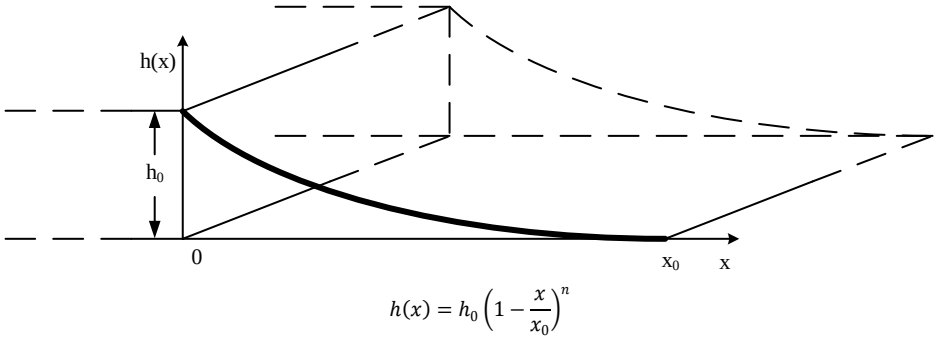


Figure 1: Elastic wedge of power-law thickness profile, ideally tapered down to zero thickness, terminating a uniform plate.

for reflection due to the edge. In practice, however, a wedge usually forms the termination of a uniform waveguide, so that there is an additional source of reflection due to the junction of the uniform and non-uniform parts of the system. Such composite systems have been examined in the literature using different mathematical modelling approaches. In [4], a rectangular uniform plate with one of its edges terminated as a power-law wedge is examined, using a matrix formulation for the various boundary conditions, including the continuity and equilibrium conditions at the junction of the uniform plate with the wedge. The vertical displacement in the wedge is represented by an approximate analytical solution of the two-dimensional equation of motion, so that oblique incidence is also accounted for. The analysis focuses on driving-point and transfer mobility. A numerical solution of the one-dimensional flexural wave equation is implemented in [5], where the impedance matrix method is employed for the formulation of the matrix equation to be solved numerically, thus yielding the reflection coefficient for a wave travelling towards the wedge from the uniform part. Yet another methodology was presented more recently in [6], where a wavelet expansion is used for the vertical displacement of the wedge, giving good correspondence with measurements. In all three of these articles, mathematical models for thin damping layers are included.

As regards mathematical models which are based on an analytical representation of the displacement field in the wedge, it is the first-order WKB approximation that is usually implicitly used in the literature. Such is the case in [1], as well as in [2], where it is referred to as the geometrical acoustics approximation, and in [4]. In the case where the reflection only due to the free end is considered, as in [1] and [2], the accuracy of the approximation is not easily assessed by comparison with experimental results. However, theoretically predicted results have been compared with experimental ones for example in [4], where the mathematical model includes the effect of the junction to the flexural wave. Even though the authors recognise qualitatively similar trends and some quantitative correspondence of the predicted and measured resonance frequencies in parts of the spectrum in that study, the use of different boundary conditions for the mathematical model and the experiment do not allow for a valid comparison between the two.

The validity of the WKB method is linked to a set of conditions that need to be satisfied so that the solution is an asymptotic solution to the differential equation under study [7]. Furthermore, an additional condition has to be satisfied, which is different for different orders of approximation, so that the truncation of the infinite-order solution up to a term of finite order form a valid approximation. In the literature of non-uniform flexural waveguides, for example in [1] and [2], only one of the validity conditions is typically used, which can be expressed as the requirement that the relative change of the wavenumber within the length of the order of a wavelength be negligible, usually expressed mathematically as

$$\left|\frac{k'}{k^2}\right| \ll 1, \tag{1}$$

where $k(x, \omega)$ is the space- and frequency-dependent wavenumber function within the waveguide and the prime denotes differentiation with respect to the spatial coordinate x. In [8] and [9], the quantity in the left side of condition (1) is used as a means of assessing the performance of a wedge in terms of reflection in correlation with the reflection coefficient predicted with a Finite Element model.

In the present article, an analytical method is used to calculate the reflection coefficient from a wedge driven from a semi-infinite uniform plate. It is shown that the usually employed first-order WKB approximation may give results that are significantly divergent from those obtained with a Finite Element model. Moreover, it is demonstrated that higher-order approximations may greatly improve the analytical prediction of the reflection coefficient.

Alternative profiles for the thickness variation may also be used, which still manifest the effect of suppressed reflection due to the decrease of propagation velocity towards the tapering edge of the non-uniform plate. An exponential profile with thickness varying as $h_e = h_0 e^{-\beta x}$, with $\beta > 0$, is considered, which forms the limit of a power-law profile with fixed length and maximum and minimum thickness as the order of the power tends to infinity, that is, $\lim_{n\to\infty} h_p(n) = h_e$, where $h_p = h_0 \left(1 - x/x_0\right)^n$ is the power-law profile of order n. An exponential wedge of finite length inevitably has a truncated edge, which does not pose a restriction to real applications, since the ideal taper of zero edge thickness is practically unrealisable. It can also be shown that the modulus of the inner reflection coefficient of the exponential wedge is smaller than any finite-length power-law wedge of the same dimensions, that is, the exponential produces less reflection due to truncation. Therefore, the exponential profile may be considered optimal in terms of inner reflection within the family of power-law thickness profiles. A practical disadvantage of the exponential wedge is that it becomes much thinner than a power-law profile before the edge, so that it is much acuter and thus harder to manufacture and more prone to damage.

In a wedge connected to a uniform plate, apart from the truncated edge, the junction of the two parts also introduces reflection, due to discontinuity of slope. Therefore, there is motivation to search for thickness profiles whose slope starts from zero, so that they may be smoothly connected to a constant profile. It was presented in [2] that a wedge with a sinusoidal thickness profile raised to a power equal to or greater than two also leads to propagation velocity which tends to zero towards the edge, if the wedge is ideally tapered down to zero thickness. In the present article, a sinusoidal profile in the form of a power-cosine is examined, that is, with its thickness varying as $h_{pc} = h_0 \cos^n\left(\pi x/(2x_0)\right)$, where x_0 is the length where the thickness becomes zero. Similarly to the power-law and exponential profiles, the Gaussian profile with thickness variation $h_g = h_0 e^{-\gamma x^2}$, with $\gamma > 0$, appears to form the limit of the power-cosine profile as the order of the power tends to infinity, that is, $\lim_{n\to\infty} h_{pc}(n) = h_g$, thus producing an inner reflection coefficient which is smaller than that of any power-cosine wedge throughout the spectrum. The power-cosine profiles have the advantage of not having a discontinuity of slope at the junction with a uniform plate, while producing a vanishing propagation velocity at their free edge in the ideally tapered case. The special characteristics of the various profiles are presented by means of the reflection coefficient calculated with Finite Element models as well as with WKB approximations of order up to three.

2 Methods

The system to be considered in this study is a truncated wedge-like non-uniform plate connected to a semi-infinite uniform plate. Incident waves are travelling on the x-direction from the uniform part towards the wedge, as depicted in Figure 2. The equation describing the one-dimensional flexural harmonic vibration of a thin plate with varying thickness, $h(x)$, is

$$\left[D(x)w''(x)\right]'' - \omega^2 \rho h(x) w(x) = 0, \tag{2}$$

where $w(x)$ is the vertical displacement amplitude of the midplane of the plate, ω is the angular frequency, ρ is the density of the material of the plate, $D(x) = \rho c_p^2 h^3(x)/12 = Eh^3(x)/\left(12(1-\sigma^2)\right)$ is the bending stiffness, E is Young's modulus, σ is Poisson's ratio, and c_p is the velocity of quasi-longitudinal waves

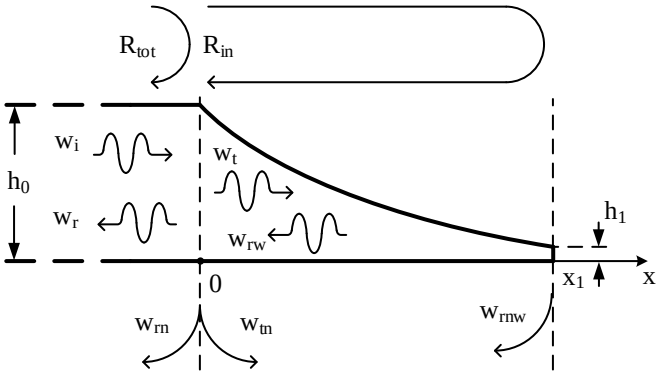


Figure 2: Truncated elastic wedge connected to a uniform plate. The various travelling and evanescent waves are shown, as well as the inner and total reflection coefficients.

in a thin plate, given by $c_p = \left[E/\left(\rho\left(1-\sigma^2\right)\right)\right]^{1/2}$ [10]. The prime denotes differentiation with respect to the spatial variable x. The harmonic time dependence of the displacement is assumed to be $e^{i\omega t}$. It should be mentioned that the displacement is also dependent on frequency. However, since the equation of motion involves differentiation only with respect to the spatial variable, the dependence on frequency may be omitted for notational convenience. In consequent analysis, the spatial dependence is also often omitted for simplicity; it should be remembered that the displacement and its derivatives, as well as the bending stiffness and the thickness, are spatially varying in the non-uniform part of the waveguide.

2.1 The WKB approximation

Equation (2) is not analytically solvable for an arbitrary variation of the thickness. Therefore, it either has to be solved by some numerical method or an analytical approximation may be used. The WKB is a method for analytical approximations of arbitrarily high order for differential equations; a systematic presentation of the method can be found, for example, in [7]. Usually in vibration literature, the first-order approximation is used, and it is commonly referred to simply as the WKB approximation. The first-order WKB approximation for beams and plates was derived by Pierce in [11], based on considerations of energy conservation. A more systematic approach, similar to the one in [7], is presented in [12], which readily allows for the use of higher-order approximations.

For the general formulation of the WKB approximation, a perturbation factor has to be included in the differential equation. In the case of Equation (2), a perturbation factor given by $\epsilon = \omega^{-1/2}$ may be included, so that the equation takes the form

$$\epsilon^4 \left[Dw''\right]'' - \rho h w = 0. \tag{3}$$

A trial solution for the vertical displacement is used, having the form

$$w = e^{\epsilon^{-1} \sum_{n=0}^{\infty} S_n \epsilon^n}, \epsilon \to 0, \tag{4}$$

where the functions S_n are spatially and spectrally variable. In strict mathematical notation, the sign of equality in relation (4) should be substituted by $\sim$, to express the fact that this relation is an asymptotic solution to the differential equation, as the perturbation factor tends to zero, and not an exact solution; a looser notational convention is followed in this analysis, following the engineering literature. The fact that when the perturbation factor tends to zero the frequency tends to infinity and vice versa implies that the WKB

solution (4) constitutes a better approximation at high frequencies and ceases to be a good approximation at low frequencies. As pointed out in [13], however, Equation (2) only applies below the frequencies where the rotational inertia is significant and so the WKB solution to Equation (2) only strictly applies over a given bandwidth.

Substitution of relation (4) into Equation (3) yields a polynomial equation for ϵ. For the polynomial equation to hold for any ϵ, all coefficients of the powers of ϵ have to be equal to zero, so that an infinite set of differential equations is obtained, the first four of which are

$$S_0'^4 = \frac{\rho h}{D} = \frac{12}{c_p^2 h^2}, \tag{5}$$

$$S_1' = -\frac{3}{2}\frac{S_0''}{S_0'} - \frac{1}{2}\frac{D'}{D}, \tag{6}$$

$$S_2' = -\frac{3}{2}\frac{S_1'^2}{S_0'} - \frac{3}{2}\frac{S_1''}{S_0'} - 3\frac{S_0''S_1'}{S_0'^2} - \frac{S_0'''}{S_0'^2} - \frac{3}{4}\frac{S_0''^2}{S_0'^3} - \frac{3}{2}\frac{D'}{D}\frac{S_1'}{S_0'} - \frac{1}{4}\frac{D''}{D}\frac{1}{S_0'} - \frac{3}{2}\frac{D'}{D}\frac{S_0''}{S_0'^2} \tag{7}$$

and

$$\begin{aligned} S_3' = &-\frac{S_1'^3}{S_0'^2} - \frac{3}{2}\frac{D'}{D}\frac{S_1'^2}{S_0'^2} - 3\frac{S_1'S_2'}{S_0'} - \frac{3}{2}\frac{D'}{D}\frac{S_2'}{S_0'} - \frac{3}{2}\frac{S_2''}{S_0'} - \frac{S_1'''}{S_0'^2} - \frac{1}{4}\frac{S_0''''}{S_0'^3} - \frac{1}{2}\frac{D''}{D}\frac{S_1'}{S_0'^2} - 3\frac{S_1'S_1''}{S_0'^2} - \\ &\frac{3}{2}\frac{D'}{D}\frac{S_1''}{S_0'^2} - \frac{S_0'''S_1'}{S_0'^3} - \frac{1}{2}\frac{D'}{D}\frac{S_0'''}{S_0'^3} - \frac{3}{2}\frac{S_0''S_1''}{S_0'^3} - \frac{1}{4}\frac{D''}{D}\frac{S_0''}{S_0'^3} - 3\frac{S_0''S_2'}{S_0'^2} - \frac{3}{2}\frac{S_0''S_1'^2}{S_0'^3} - \frac{3}{2}\frac{D'}{D}\frac{S_0''S_1'}{S_0'^3}. \end{aligned} \tag{8}$$

The WKB approximation of order N includes the first $N+1$ terms in the exponent of the solution (4), thus including the first $N+1$ WKB functions, that is, from S_0 up to S_N. Therefore, the first $N+1$ equations of the WKB formulation have to be serially solved, starting from the zeroth order. Equation (5), which is also called the eikonal equation, has four roots, namely

$$S_0' = \{\pm 1, \pm i\}\frac{12^{1/4}}{c_p^{1/2}h^{1/2}}, \tag{9}$$

where the factors defining the four distinct solutions are included in curly brackets. Integration with respect to x gives

$$S_0 = \{\pm 1, \pm i\}\int_0^x \frac{12^{1/4}}{c_p^{1/2}h^{1/2}}d\tilde{x}. \tag{10}$$

The lower limit of integration has been chosen to be at the junction of the uniform and non-uniform parts, where the origin for the x coordinate is set to be. Equation (6), also called the transport equation, may then be solved, giving

$$S_1 = \frac{3}{4}\ln\left(\frac{h_0}{h}\right). \tag{11}$$

The form of Equation (6) is such that the distinctive constant coefficients of S_0 cancel out, so that S_1 is the same for all four different solutions of the eikonal equation.

The first-order WKB solution to Equation (3) is found by including only the first two terms in the exponent of relation (4). Therefore, by virtue of Equations (10) and (11), the first-order WKB solution can be written as

$$w_1 = A\left(\frac{h_0}{h}\right)^{3/4} e^{\{\pm 1, \pm i\}\int_0^x k(\tilde{x})d\tilde{x}}, \tag{12}$$

where

$$k = \frac{12^{1/4}\omega^{1/2}}{c_p^{1/2}h^{1/2}}\left(1 - i\frac{\eta}{4}\right) \tag{13}$$

is the wavenumber function in the non-uniform plate, A is an arbitrary complex constant and η is the damping factor. The inclusion of the damping factor has been achieved by using a complex Young's modulus in the form of $E(1+i\eta)$, which, through the quasi-longitudinal velocity c_p and after appropriate simplifications due to the assumed small value of η, gives the complex wavenumber of Equation (13). The expected deviation of the WKB approximation at low frequencies mentioned earlier may be linked to the violation of the validity condition, relation (1), at low frequencies, as can be seen by use of the wavenumber function of Equation (13).

The second- and third-order WKB approximations may, accordingly, be written as

$$w_2 = A\left(\frac{h_0}{h}\right)^{3/4} e^{\{\pm 1,\pm i\}\int_0^x k(\tilde{x})d\tilde{x}+\omega^{-1/2}S_{2,j}} \tag{14}$$

and

$$w_3 = A\left(\frac{h_0}{h}\right)^{3/4} e^{\{\pm 1,\pm i\}\int_0^x k(\tilde{x})d\tilde{x}+\omega^{-1/2}S_{2,j}+\omega^{-1}S_{3,j}}, \tag{15}$$

respectively, where the subscript $j = \pm 1, \pm i$ denotes the different S_2 and S_3 functions corresponding to the four different S_0 functions; the S_2 and S_3 functions are obtained by integrating Equations (7) and (8), respectively. It should be noted that Equations (7) and (8) are in general not integrable analytically, so that numerical integration has to be applied.

2.2 Matrix formulation for calculating the reflection coefficients

The reflective behaviour of a wedge driven from a uniform plate, such as the one depicted in Figure 2, may be assessed by use of the ratio of the reflected wave, travelling in the negative-x direction in the uniform plate, to the incident travelling wave, evaluated at the junction of the uniform and non-uniform parts, where $x = 0$. This ratio is henceforth called the total reflection coefficient and is given by $R_{tot} = w_r(0)/w_i(0)$, in accordance with the notation shown in Figure 2.

The various wave components inside the wedge may be expressed in the form of WKB approximations of a specified order. The appropriate coefficient for the wavenumber has to be chosen to match with the direction and the qualitative type of each component; coefficients $-i$ and $+i$ correspond to positive-x and negative-x travelling waves, respectively, while coefficients -1 and $+1$ correspond to positive-x and negative-x evanescent waves, respectively. The wave components in the uniform part may be expressed as exponential functions with constant amplitude and constant wavenumber,

$$w_u = Ae^{\{+1,\pm i\}k_u x}, \tag{16}$$

where k_u is the spatially constant wavenumber in the uniform part; the appropriate one from the factors written in the curly brackets again needs to be chosen for each component. It should be noted that no incident nearfield wave is present in the uniform plate, since it is considered to be semi-infinite, and, hence, the factor of -1 is not included.

The displacement field in the uniform plate and in the wedge may be expressed as the superposition of the corresponding wave components, all of which will in general have different constant amplitude coefficients. The amplitude coefficients represent ratios of wave components evaluated at the coordinate origin, so that they may be thought of as reflection and transmission coefficients. These unknown coefficients may be calculated by applying the various boundary conditions of the system, which are the continuity of displacement and its slope and the equilibrium of bending moment and shear force at the junction, as well as the vanishing of bending moment and shear force at the free edge boundary, where the bending moment is given by $M = Dw''$ and the shear force by $V = -M'$ [10]. This procedure involves calculating up to the third derivatives of the wave components, which get increasingly complicated with increasing order of differentiation, and even more with increasing order of WKB approximation. Numerical differentiation has been used

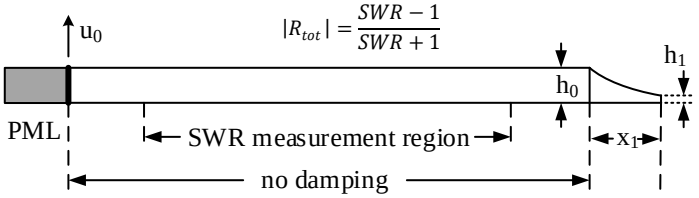


Figure 3: Schematic of a Finite Element model for a wedge connected to a semi-infinite uniform plate. A harmonic vertical velocity of constant amplitude u_0 is used as a source of excitation. A perfectly matched layer (PML) on the left end assures than no reflection occurs from that side. The standing wave ratio (SWR) is obtained by measuring the maximum and minimum displacement moduli over a region of the uniform plate away from sources of nearfield waves.

for the calculation of the second- and third-order derivatives of the second- and third-order WKB functions given in Equations (7) and (8). Solving the system of equations corresponding to the applied conditions yields, among others, the total reflection coefficient, R_{tot}, which is of primary interest, and the inner reflection coefficient, defined as $R_{in} = w_{rw}(0)/w_t(0)$, whose modulus is equivalent to the reflection coefficient used in [1] and [2].

A similar approach may be applied for a wedge ideally tapered down to zero thickness driven from a uniform plate. In this case, it is considered that all waves travelling or decaying towards the edge are completely attenuated, so that no reflected waves, either travelling or nearfield, are present in the wedge. Accordingly, no conditions need be applied at the vanishing edge, resulting in a four by four system of equations for the various reflection and transmission coefficients. In such a system, reflection occurs only at the junction, and the corresponding reflection coefficient, denoted by R_j in this analysis, expresses the reflective effect of the junction to incident waves.

2.3 Finite Element model

A Finite Element model was implemented in COMSOL Multiphysics 5.3 for calculating the modulus of the reflection coefficient of a wedge driven from a uniform plate. A qualitative illustration is given in Figure 3. The system is driven by applying a harmonic vertical velocity of constant amplitude to the uniform plate at a position away from the wedge. A perfectly matched layer is connected to the left end of the uniform plate in order to suppress reflections from this side, so that the model may simulate a semi-infinite system. Furthermore, the uniform plate is modelled as having no damping, so that travelling waves do not attenuate within it; damping is present only in the non-uniform part. The maximum and minimum displacement moduli are measured over a region of the uniform plate away from both the point of excitation and the junction with the wedge, in order to avoid measuring evanescent components. Therefore, the standing wave ratio is calculated from the relation $SWR = |w|_{max} \,/\, |w|_{min}$ [14]. Finally, the modulus of the total reflection coefficient is obtained from the following equation, [14],

$$|R_{tot}| = \frac{SWR - 1}{SWR + 1}. \tag{17}$$

It should be mentioned that, for accurate measurement of the maximum and minimum displacements, the region of measurement has to be long enough to include a wavelength of the lowest frequency examined. In the Finite Element simulations conducted here, 14456 two-dimensional solid elements were used for the uniform plate and 3939 to 8325 solid elements for the wedge, depending on the thickness profile.

3 Results and discussion

For the simulations of this study, wedges with properties as presented in Table 1 were used. The specific properties of the four different thickness profiles considered are summarised in Table 2, expressed with respect to given quantities. The quadratic profile constitutes the lowest-order power-law profile for which the propagation velocity vanishes at its ideal edge. A plot of the moduli of the inner and total reflection coefficients, along with the modulus of the junction reflection coefficient, which is present in an ideally tapered wedge of similar geometry, all calculated using the first-order WKB approximation, are shown in Figure 4. First of all, it can be seen that the total reflection coefficient fluctuates with frequency around the inner reflection coefficient. These fluctuations are the result of the frequency-varying interaction of an incident wave with the two sources of reflection, that is, the free edge and the junction. Secondly, the junction reflection coefficient retains high values at low frequencies, whereas it decreases down to very low values at higher frequencies. This may be linked to the fact that, at low frequencies, the discontinuity at the junction resembles a more abrupt thickness change, while at high frequencies, the flexural wavelength is smaller and can follow the change in thickness more easily, undergoing little reflection. Furthermore, the fluctuations of the total reflection coefficient around the inner reflection coefficient are greater in magnitude at lower frequencies, where reflection due to the junction is also strong. Moreover, the junction reflection coefficient in Figure 4 shows a peak at about 50 Hz, whereas it would be expected to decrease monotonically with increasing frequency. This result may be linked to the deteriorating validity of the WKB approximation as frequency decreases.

Geometrical properties	Value	Material properties	Value
Length of wedge (x_1)	0.3 m	Young's modulus (E)	$70 \cdot 10^9$ Pa
Thickness at junction (h_0)	0.01 m	Density (ρ)	2700 kg·m^{-3}
Thickness at edge (h_1)	10^{-4} m	Poisson's ratio (σ)	0.33
		Damping factor (η)	0.01

Table 1: Geometrical and material properties of the wedge model. Damping applies only to the non-uniform part of the waveguide.

Thickness profile type	Thickness variation	Length of ideal wedge	Decay parameter
Quadratic	$h_q = h_0 \left(1 - \frac{x}{x_0}\right)^2$	$x_0 = \frac{x_1}{1-\left(\frac{h_1}{h_0}\right)^{1/2}}$	-
Exponential	$h_e = h_0 e^{-\beta x}$	∞	$\beta = \frac{1}{x_1 \ln\left(\frac{h_0}{h_1}\right)}$
Power-cosine	$h_{pc} = h_0 \cos^n\left(\frac{\pi x}{2x_0}\right)$	$x_0 = \frac{\pi x_1}{2 \arccos\left(\left(\frac{h_1}{h_0}\right)^{1/n}\right)}$	-
Gaussian	$h_g = h_0 e^{-\gamma x^2}$	∞	$\gamma = \frac{1}{x_1^2 \ln\left(\frac{h_0}{h_1}\right)}$

Table 2: Formulas for different thickness profiles.

A set of plots with results based on the WKB approximation for the different thickness profiles presented above is shown in Figure 5; the thickness variation of the different profiles is illustrated in Figure 5a. In the following results, a seventh-order cosine is used, due to the fact that its inner reflection coefficient practically coincides with that of a quadratic wedge, as can be seen in Figure 5d. It should be noted that this correspondence holds for the specific geometrical properties used; different properties will lead to different order for the inner reflection coefficient of a power-cosine wedge to match with that of the corresponding quadratic one. The matching of the inner reflection coefficients of the quadratic and the seventh-order cosine may be linked to the fact that their thickness profiles seem to be very similar towards the narrow edge of the wedge, as can be seen in Figure 5a, where the propagation velocity becomes small and most of the energy is dissipated.

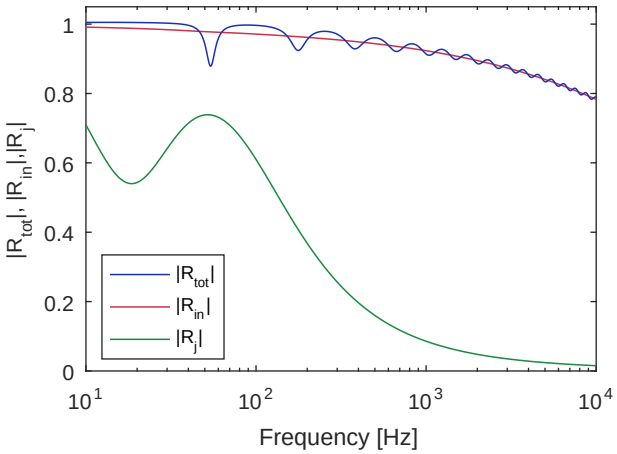


Figure 4: Moduli of the inner and total reflection coefficients of a truncated quadratic wedge, along with the modulus of the junction reflection coefficient of an ideally tapered quadratic wedge, using the first-order WKB approximation.

The phase velocity of a wave travelling in the wedge is given by $c_{ph} = \omega/\Re\{k\}$, where $\Re$ denotes the real part. The spatial variation of the phase velocity for the different profiles at 1000 Hz is shown in Figure 5c, where it can be seen that all profiles have a phase velocity of about 30 m·s^{-1} at the edge, where the thickness is 0.1 mm. The correspondence between thickness variation and phase velocity, through the wavenumber function of Equation (13), is apparent by comparison of Figures 5a and 5c.

The spectral variation of the modulus of the junction reflection coefficient for different profiles, calculated with the third-order WKB approximation, is plotted in Figure 5b. By inspection of the upper spectral region, it can be seen that the junction of the exponential wedge introduces more reflection than the junction of the quadratic wedge. This is expected, due to the fact that the exponential has greater absolute slope at the junction, thus introducing a more abrupt discontinuity. The power-cosine and Gaussian profiles, on the other hand, have junction reflection coefficients of modulus smaller than that of the quadratic at high frequencies, which may be related to the fact that the slope of these profiles at the junction is zero. At lower frequencies, however, it can be seen that the power-cosine and Gaussian profiles are predicted to produce greater reflection at the junction than the quadratic profile does, a result which contradicts the expected correspondence between slope and reflection at the junction. Nevertheless, this counter-intuitive result is verified by the Finite Element results, as can be seen in Figure 7, where the fluctuations of the power-cosine and Gaussian profiles are greater than those of the quadratic profile at low frequencies. This effect may be related to the presence of higher-order derivatives of the thickness variation in the solution.

Inconsistencies with the theory are present at low frequencies. The already mentioned violation of energy conservation, as well as fluctuations of the junction reflection coefficient, the latter occurring only for the exponential wedge at the currently used third-order of WKB approximation, are apparent. Such inconsistencies may again be linked to the issue of validity of the WKB at low frequencies.

Figure 5d shows the moduli of the inner reflection coefficients of the different thickness profiles. The inner reflection coefficient of the quadratic and the seventh-order cosine are practically indistinguishable, apart from the very low end of the spectrum, since the specific order of cosine was chosen with this criterion. Inspection of the corresponding thickness and phase velocity variations shown in Figures 5a and 5c, respectively, illustrates that the thinner part of the wedge is predominant in defining the inner reflection coefficient, since a slightly smaller thickness of the power-cosine in the thinner third of the wedge and, accordingly, a slightly smaller phase velocity, balance out the much greater thickness and phase velocity difference in the thicker two thirds. The inner reflection coefficient for the exponential wedge has an unexpected very narrow dip around 100 Hz; a plot of the same coefficient as calculated according to the analysis in [1] is also shown.

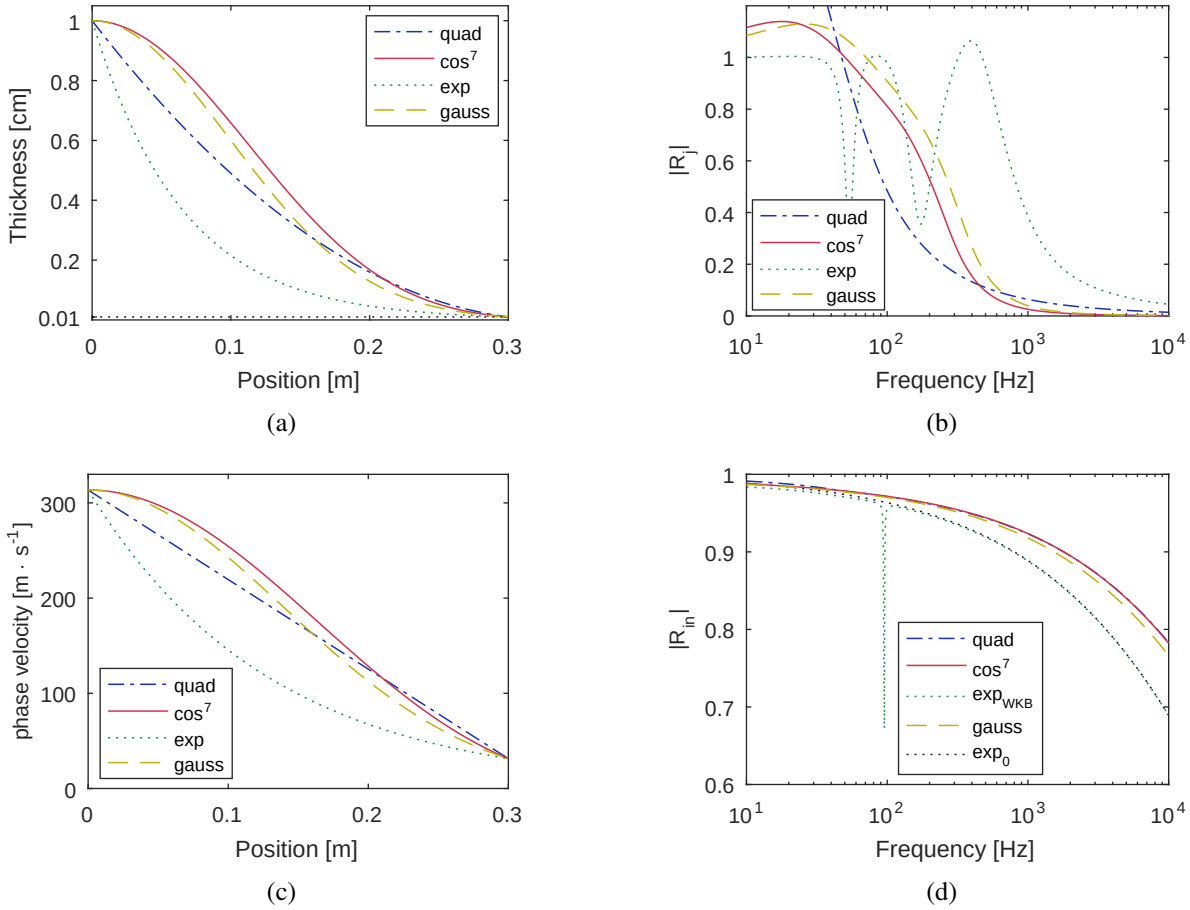


Figure 5: Properties of different profiles, namely a quadratic, a seventh-order cosine, an exponential and a Gaussian: (a) thickness variation, having a value of 0.1 mm at the thin edge, (b) spectral variation of the modulus of the junction reflection coefficient, calculated with the third-order WKB approximation, (c) spatial variation of the phase velocity at a frequnecy of 1000 Hz, (d) spectral variation of the modulus of the inner reflection coefficient, calculated with the first-order WKB approximation. The modulus of the inner reflection coefficient of the exponential wedge has an unexpected dip at around 100 Hz. A plot for the modulus of the inner reflection coefficient which is produced with the approach presented in [1], where the wedge is driven internally and evanescent waves are not taken into account, is therefore also shown for qualitative consistency with the rest of the results, labelled as exp_0.

It can be seen that the exponential clearly improves the inner reflection coefficient, as was mentioned earlier, which may also be illuminated by the fact that the phase velocity of the exponential acquires significantly smaller values than that of the quadratic. A similar conclusion was drawn in [2], where higher-order power-law wedges were found to produce less inner reflection. The Gaussian, on the other hand, presents a very small improvement compared to the quadratic and seventh-order cosine, which complies with the respective thickness and phase velocity variations.

A comparison of results for the modulus of the total reflection coefficient between the presented method based on the WKB approximation and Finite Element analysis for the different thickness profiles is shown in Figure 6. It may be generally observed that, for all the thickness profiles, the WKB results diverge from the Finite Element ones predominantly at lower frequencies, as is expected due to the deteriorating validity of the method. A second general observation is that the WKB results, especially from higher-order approximations, correspond well with those from Finite Elements as frequency increases, although a small deviation starts to be visible in the very upper end of the considered spectrum. Furthermore, the first-order WKB approximation does not give very good correspondence with Finite Element analysis for the total reflection coefficient, apart

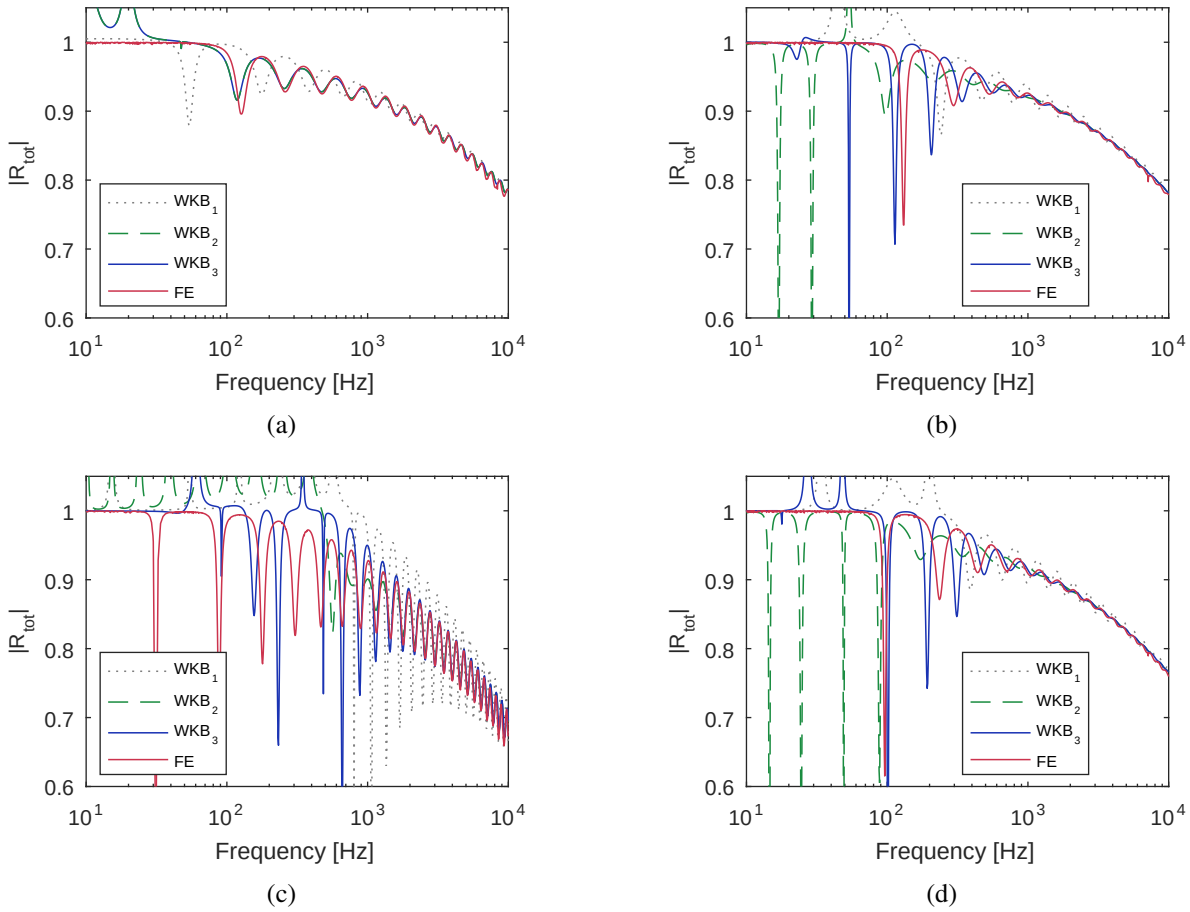


Figure 6: Comparison of the modulus of the total reflection coefficient calculated with the first three WKB approximations with corresponding results from Finite Element analysis, for different thickness profiles: (a) quadratic, (b) seventh-order cosine, (c) exponential and (d) Gaussian. For the quadratic, the third-order WKB solution is indistinguishable from the second-order one.

from frequencies at the upper end of the considered spectrum, failing in large part to predict similar resonance frequencies. On the other hand, the average level of the spectral fluctuations of the total reflection coefficient seems to be captured quite well, even by the first-order WKB approximation. This spectrally local average is linked to the inner reflection coefficient, as was mentioned earlier. Therefore, even though the inner reflection coefficient is not calculated by the current Finite Element model, the results for the total reflection coefficient imply that the former is well predicted even with first-order WKB considerations.

A central point of this analysis is the use of higher-order WKB approximations within the presented analytical model. A general overview of the results for all thickness profiles demonstrates the fact that higher-order approximations greatly improve the correspondence with the Finite Element model. In the case of the quadratic wedge, shown in Figure 6a, the second-order WKB already provides very good results in most of the spectrum, in this case above about 150 Hz, although correspondence is generally good even down to around 40 Hz. The third-order approximation does not produce any distinguishable improvement.

For the exponential wedge, shown in Figure 6c, inspection of the plots above about 400 Hz illustrates that the third-order WKB approximation provides significant improvement to the second-order one, which, in turn, greatly improves the first-order approximation. At lower frequencies, however, all WKB approximations up to third order fail to produce accurate results, also predicting values higher than one for the reflection coefficient. Furthermore, even for the higher-order approximations, the results are good above about 2 kHz. Interestingly, within the spectral region from about 900 Hz to roughly 1500 Hz, an oscillatory converging

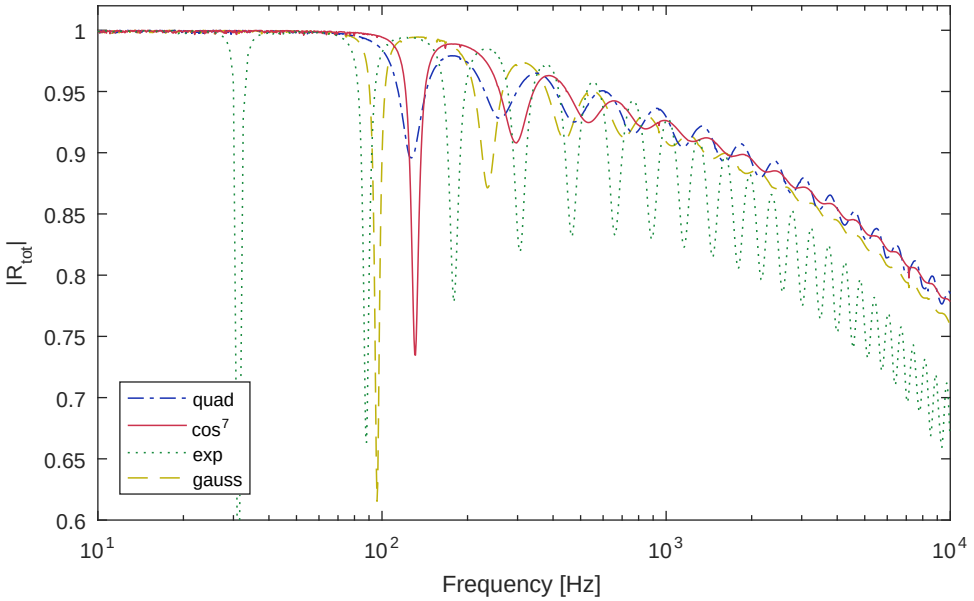


Figure 7: Modulus of the total refelction coefficient for different wedge thickness profiles, calculated from the Finite Element models.

trend for the solution seems to be followed, where consecutive orders of WKB approximation provide alternating overestimations and underestimations of the amplitude of spectral fluctuations of the total reflection coefficient. A similar behaviour is observed in Figures 6b and 6d for the power-cosine and Gaussian profiles, respectively. Finally, for the exponential as well as the power-cosine and Gaussian profiles, the third-order approximation seems to follow the Finite Element results starting from lower frequencies compared to the second-order approximation, thus providing better results in a greater part of the spectrum.

The seventh-order cosine and Gaussian wedges have similar reflection coefficients, as plotted in Figures 6b and 6d, respectively, which is expected due to the similarity of their thickness variation, as shown in Figure 5a. In the line of thought of the previous analysis for the quadratic and exponential wedges, the power-cosine and the Gaussian wedges seem to behave worse than the quadratic but much better than the exponential in terms of performance of the WKB method.

A comparative graph of the reflective behaviour of the different profiles is shown in Figure 7, where the moduli of the total reflection coefficients are plotted as calculated with Finite Element models. In the context of this comparative set-up, where all wedges are taken to have equal length and equal maximum and minimum thickness, the exponential wedge seems to provide considerably less reflection than the quadratic one over a large part of the spectrum. A power-cosine wedge with the same inner reflection coefficient as the quadratic comparatively reduces the fluctuation amplitude over most of the spectrum, above about 500 Hz in this case, though it increases it at low frequencies. The Gaussian wedge generally produces a small general decrease in the total reflection coefficient, again in compliance with the respective inner reflection coefficients shown in Figure 5d.

The reduction of the fluctuations that the power-cosine causes above some frequency, apart from being relatively small, does not improve the general level of reflection, since the order of the power of the cosine was chosen so as to give the same inner reflection as the quadratic. The Gaussian profile provides little improvement in that respect. Nevertheless, it should be noted that, in the considered context of comparison, the power-cosine and Gaussian wedges have considerably greater thickness than the quadratic along much of their length, as can be seen in Figure 5a. Apart from restrictions due to limitations in the realisability of very small thickness at the edge, which is taken to be the same for all wedges in this analysis, there are also

manufacturing restrictions on the acuteness of the wedge as represented by the length over which the wedge is very thin, a characterisation which is apparently of a qualitative nature. In light of this restriction, it can be commented that the exponential wedge is much acuter than the rest of the profiles. Therefore, longer Gaussian profiles may be manufactured, which would cause both less inner reflection, due to having a longer thin part in which the energy is dissipated, and less junction reflection, due to a longer thick part in which the slope varies more smoothly.

Two additional general comments need to be made. First, the reflection coefficients presented in this article generally have high values, due to the wedges being truncated, above 0.65 even at high frequencies. It is, however, well established in the literature, as reviewed in [3], that a combination of appropriate thickness variation and thin damping layers dramatically reduces reflection. Therefore, the current study focuses on one of the two main aspects of practically useful wedges. Second, all spectral results have been presented in a logarithmic scale for frequency, starting from a very low value of 10 Hz. The reason for this choice is that a key motivation for this study was to assess the behaviour of the WKB method in comparison with reference numerical results. Since it is known that the validity of results produced with the WKB method deteriorates with decreasing frequency, great resolution is required at low frequencies to facilitate comparison between the two methods. The fact that low frequencies cover a great part of the spectral plots might intuitively give a misleading impression that the less accurate results of the analytical method cover a wider spectrum than they actually do. In complement, it should be noted that the low end of the spectrum is less important in the study of wedges with absorbing properties, since, in general, their absorbing capability is poor at low frequencies.

4 Summary and Conclusions

A method has been presented for calculating reflection coefficients for a system consisting of a wedge connected to a semi-infinite uniform plate, which is based on the WKB approximation for the solution of the fourth-order equation of flexural vibrations of a thin plate. Four different thickness variation profiles for the wedge are considered, and the calculations are compared with those predicted from Finite Element models. The inner and junction reflection coefficients, obtained with the WKB-based method, are indirectly assessed through the above comparison of total reflection coefficients.

For all thickness profiles, the total reflection coefficient is found to fluctuate around the inner reflection coefficient along the spectrum. The amplitude of these fluctuations is related to the modulus of the junction reflection coefficient, so that, at low frequencies, where the junction reflection coefficient has high values, the fluctuations are great, whereas at higher frequencies, where the modulus of the junction reflection coefficient decreases, the amplitude of fluctuations also decreases.

The exponential profile produces less inner reflection due to the truncation but more reflection due to the junction than a quadratic wedge. Accordingly, the total reflection coefficient of the exponential fluctuates around a lower general level but with greater amplitude of fluctuations. In general, the effect of reduced inner reflection is found to be dominant, giving locally less total reflection in most of the spectrum compared to the quadratic. Furthermore, the power-cosine wedge, and, accordingly, its limit as the power tends to infinity, that is, the Gaussian, have the advantage of having zero slope at their thick end, so that they may be smoothly connected to a uniform plate. Such wedges are expected to produce less reflection at the junction compared to a power-law wedge. This appears to hold above some frequency; at low frequencies, however, the power-cosine wedge actually produces greater reflection at the junction than the quadratic.

The first-order WKB approximation is found to predict well the average level of reflection, represented by the inner reflection coefficient. However, it fails to predict the details of the fluctuations of the total reflection coefficient. Higher-order approximations are found to greatly improve the performance of the model, producing results that match the corresponding ones from Finite Element analysis very well above some frequency. The width of the spectrum over which correspondence with results from Finite Elements is good increases in accordance with the order of approximation, although this differs for the various profiles.

Acknowledgements

The authors would like to thank Kristian Hook for providing valuable help in the initial development of the Finite Element model, especially for the calculation of the SWR.

References

[1] M. A. Mironov, *Propagation of a flexural wave in a plate whose thickness decreases smoothly to zero in a finite interval*, Sov. Phys. Acoust., Vol. 34, No. 3 (1988), pp. 318-319.

[2] V. V. Krylov, F. J. B. S. Tilman, *Acoustic 'black holes' for flexural waves as effective vibration dampers*, Journal of Sound and Vibration, Vol. 274 (2004), pp. 605-619.

[3] V. V. Krylov, *Acoustic Black Holes: Recent Developments in the Theory and Applications*, IEEE Transactions on Ultrasonics, Ferroelectronics, and Frequency Control, Vol. 61, No 8 (2014), pp. 1296-1306.

[4] D. J. O'Boy, V. V. Krylov, V. Kralovic, *Damping of flexural vibrations in rectangular plates using the acoustic black hole effect*, Journal of Sound and Vibration, Vol. 329 (2010), pp. 4672-4688.

[5] V. B. Georgiev, J. Cuenca, F. Gautier, L. Simon, V. V. Krylov, *Damping of structural vibrations in beams and elliptical plates using the acoustic black hole effect*, Journal of Sound and Vibration, Vol. 330 (2011), pp. 2497-2508.

[6] Liling Tang, Li Cheng, Hongli Ji, Jinhao Qiu, *Characterization of acoustic black hole effect using a one-dimensional fully-coupled and wavelet-decomposed semi-analytical model*, Journal of Sound and Vibration, Vol. 374 (2016), pp. 172-184.

[7] Carl M. Bender and Steven A. Orszag, *Advanced Mathematical Methods for Scientists and Engineers*, McGraw-Hill, New York (1978).

[8] Philip A. Feurtado, Stephen C. Conlon and Fabio Semperlotti, *A normalized wave number variation parameter for acoustic black hole design*, J. Acoust. Soc. Am., Vol. 136, No 2 (2014), pp. 148-152.

[9] Philip A. Feurtado and Stephen C. Conlon, *Investigation of boundary-taper reflection for acoustic black hole design*, Noise Control Engineering Journal, Vol. 63, No 5 (2015), pp. 460-466.

[10] L. Cremer, M. Heckl and B. A. T. Petersson, *Structure-Borne Sound: Structural Vibrations and Sound Radiation at Audio Frequencies*, Springer-Verlag, Germany (2005).

[11] Allen D. Pierce, *Physical Interpretation of the WKB or Eikonal Approximation for Waves and Vibrations in Inhomogeneous Beams and Plates*, The Journal of the Acoustical Society of America, Vol. 48, No 1, Part 2 (1970), pp. 275-284.

[12] R. D. Firouz-Abadi, H. Haddadpour, A. B. Novinzadeh, *An asymptotic solution to transverse free vibrations of variable-section beams*, Journal of Sound and Vibration, Vol. 304 (2007), pp. 530-540.

[13] R. Nielsen, S. Sorokin, *The WKB approximation for analysis of wave propagation in curved rods of slowly varying diameter*, Proc. R. Soc. A, vol. 470 (2014)

[14] Lawrence E. Kinsler, Austin R. Frey, Alan R. Coppens and James V. Sanders, *Fundamentals of Acoustics, 4th Edition*, Wiley-VCH, United States of America (1999).

Optimization of perforated plates in interaction with acoustic waves

V. Lukeš, E. Rohan
Dept. of Mechanics, Faculty of Applied Sciences,
University of West Bohemia in Pilsen, Univerzitní 22, 306 14 Plzeň, Czech Republic
e-mail: **rohan@kme.zcu.cz**

Abstract
The paper deals with optimization of a perforated plate which interacts with acoustic waves propagating in an inviscid compressible fluid. In general, the aim is to influence the acoustic signal conducted through a waveguide in which the perforated plate is fitted. Nonlocal transmission conditions have been derived by homogenization of a problem describing vibroacoustic fluid-structure interactions in a fictitious layer in which the plate is embedded. The Reissner-Mindlin theory of plates is adopted for periodic perforations designed by arbitrary cylindrical holes For rigid plates, quite general types of perforations can be considered for which homogenized transmission coefficients reveal coupling of the transverse and tangential waves. For both the rigid and the deformable plates, the homogenized model of the vibroacoustic transmission has been derived using the two-scale asymptotic analysis. The design of the holes perforating the plate is parameterized by the B-spline representation of the reference periodic cell generating the transmission layer.

1 Introduction

We consider a problem of the acoustic wave propagation through vibrating perforated plates. The aim is to reduce the acoustic signal transmitted through the acoustic fluid and influenced by a perforated compliant plate. The acoustic problem is described by the Helmholtz equation and involves homogenized transmission conditions which we have developed with help of the asymptotic analysis, see [5]. The transmission conditions are imposed along a interface plane representing the compliant plate with a periodic structure. The perforation of the plate is designed by obstacles (holes) having arbitrarily shapes which can be parametrized by B-spline functions. The compliant plates were treated in [8], cf. [10] where the framework of the Reissner-Mindlin theory, cf. [3], was used to derive the vibroacoustic transmission conditions which take into account specific shapes of the holes in the plate.

The coefficients involved in the homogenized transmission equations were derived in [6]. These coefficients are calculated using the solutions of microscopic sub-problems defined in the reference cell. The above referenced paper also mentions the sensitivity relations for the homogenized coefficients, these are fundamental in the sensitivity analysis of an objective function. The sensitivity analysis employed in this paper is based on the approach of an adjoint system which leads to the adjoint problem solved on the macroscopic level, see Sec. 3. The presented optimization problem is aimed to minimize the transmission loss computed using values of the global acoustic field.

2 Homogenized model of the vibroacoustic interaction

In this section we present a homogenization based model which describes the vibroacoustic interaction on a perforated plate. In paper [9] we derive homogenized vibroacoustic transmission conditions using the

asymptotic analysis w.r.t. a scale parameter ε which has a double role: on one hand it deals with the thickness of an elastic (or rigid) plate, on the other hand it describes the size and spacing of holes perforating periodically drilled in the plate structure.

Monochromatic acoustic waves with frequencies ω propagate in a waveguide $\Omega^G \subset \mathbb{R}^3$ with embedded perforated elastic plate $\Sigma^\varepsilon \subset \mathbb{R}^3$; the acoustic fluid occupies the domain $\Omega^{*\varepsilon}$. We consider a fictitious transmission layer Ω_δ with a thickness $\delta > 0$, such that $\Sigma^\varepsilon \subset \Omega_\delta$. The plate thickness is $h^\varepsilon = \varepsilon\bar{h}$, while the layer thickness $\delta = \varkappa\varepsilon$ for a given fixed $\varkappa > 0$. Using a simplified notation (dropping the index ε) the problem is govern by the following equations,

$$\begin{aligned} c^2\nabla^2 p + \omega^2 p = 0 \quad &\text{in } \Omega^* \,, \\ \nabla\cdot\boldsymbol{\sigma}(\boldsymbol{u}) + \omega^2\rho\boldsymbol{u} = 0 \quad &\text{in } \Sigma \,, \end{aligned} \tag{1}$$

supplemented by the standard acoustic transmission conditions on the solid-fluid interface $\partial_*\Sigma = \partial\Sigma \cap \partial\Omega^*$,

$$\left.\begin{aligned} \mathrm{i}\omega\boldsymbol{n}\cdot\boldsymbol{u} &= \boldsymbol{n}\cdot\nabla p \\ \boldsymbol{n}\cdot\boldsymbol{\sigma}(\boldsymbol{u}) &= \boldsymbol{b}(p) = \mathrm{i}\omega\rho_0 p\boldsymbol{n} \end{aligned}\right\} \quad \text{on } \partial_*\Sigma \,, \tag{2}$$

whereby, in general, the following conditions can describe incident, absorbed, or reflected acoustic waves propagating in the fluid on the the external boundary of the domain Ω^G, and the clamped elastic solid structure on $\partial_{\boldsymbol{u}}\Sigma \subset \partial\Sigma$,

$$\begin{aligned} r\mathrm{i}\omega c p + c^2\frac{\partial p}{\partial n} = s2\mathrm{i}\omega c\bar{p} \quad &\text{on } \partial_{\mathrm{ext}}\Omega^G \setminus \partial_{\boldsymbol{u}}\Sigma \,, \\ \boldsymbol{u} = 0 \quad &\text{on } \partial_{\boldsymbol{u}}\Sigma \,. \end{aligned} \tag{3}$$

Above, c is the sound speed in the acoustic fluid, $\boldsymbol{\sigma}(\boldsymbol{u})$ is the stress in the lienar elastic solid, ρ_0 is reference fluid density, and by $\boldsymbol{n} = (n_i)$ we denote the normal vector. The plate is fixed to a rigid frame on the boundary $\partial_{\boldsymbol{u}}\Sigma$ and interacting with the fluid on the rest of the boundary $\partial_*\Sigma = \partial\Sigma \setminus \partial_{\boldsymbol{u}}\Sigma$. The constants $r, s \in \{0, 1\}$ and $\bar{p}$ are defined to describe incident waves, reflected, or absorbed acoustic waves in the fluid, according to a selected part of the boundary. In the example treated in section 4, we consider a waveguide with rigid walls Γ_w, where $r = s = 0$, with the input part Γ_{in}, where $r = s = 1$, and with the output part Γ_{out}, where $r = 1$ and $s = 0$.

This problem can be decomposed into two subproblems:

- The problem in a fictitious layer $\Omega_\delta = \Gamma_0\times]-\delta/2, \delta/2[\subset \Omega^G$ which is defined in terms of the plate mid-plane Γ_0. On the layer "upper" and "lower" faces, Γ_+^δ and Γ_-^δ, the acoustic field in the fluid is coupled with the outer acoustic field.
- The problem for the outer acoustic field defined in $\Omega_+^\delta \cup \Omega_-^\delta = \Omega^G \setminus \overline{\Omega_\delta}$.

In [9], see also [5] just for the rigid plate, we describe in detail homogenization of the problem imposed in the fictitious layer. The asymptotic analysi fro $\varepsilon \to 0$ (and thereby also $\delta = \varkappa\varepsilon \to 0$ with $\varkappa$ being fixed) leads to a reduced model defined on the interface Γ_0 in terms of PDEs describing acoustic pressure p^0, transversal momentum fluxes $G^\pm$, and kinematic variables (displacements and rotations) associated with plate deformation. The limit outer problem (when $\delta \to 0$) governs two acoustic pressure fields P defined in domain $\hat{\Omega}_\pm$. The two problems are coupled by additional constraint arising from an approximation of the natural transmission conditions imposed at the fictitious interfaces $\Gamma_+^{\delta_0}$ and $\Gamma_-^{\delta_0}$ which are equidistant with Γ_0, $\mathrm{dist}\left(\Gamma_0, \Gamma_\pm^{\delta_0}\right) = \delta_0$. Hence, the outer problem domains are $\hat{\Omega}_\pm = \Omega_\pm^{\delta_0}$.

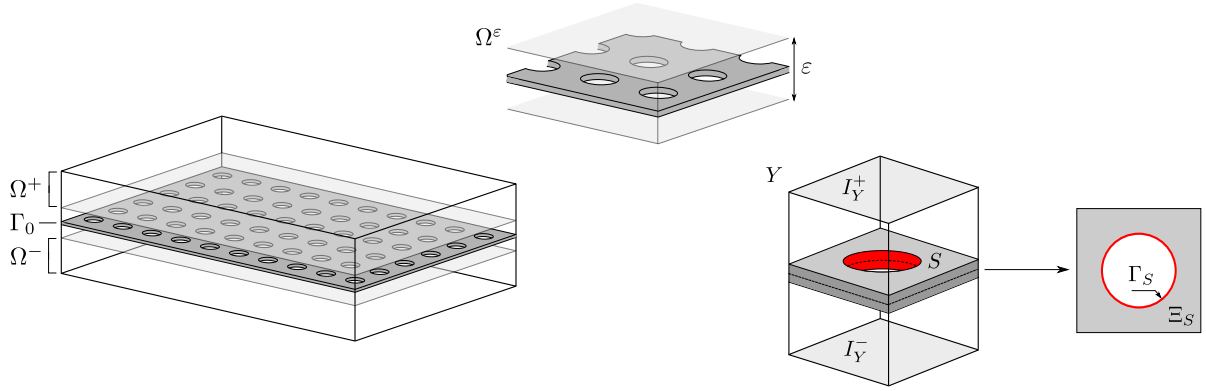


Figure 1: Perforated layer Ω^ε with the central plane Γ_0. The periodic structure is generated by the reference cell Y.

var. symbol	filed description	defined in / on	adjoint var.
P	acoustic pressure field	$\hat{\Omega}^+ \cup \hat{\Omega}^-$	Q
$P^\pm$	trace of acoustic pressure field on $\hat{\Gamma}^+$, $\hat{\Gamma}^-$	Γ^0	$Q^\pm$
$G^\pm$	acoustic momentum on $\hat{\Gamma}^+$, $\hat{\Gamma}^-$	Γ^0	φ, ψ
p	acoustic pressure field in the layer	Γ^0	q
$\boldsymbol{u}$	plate displacements	Γ^0	$\boldsymbol{v}$
$\overline{\boldsymbol{u}} = (u_\alpha)$	in-plane plate displacements	Γ^0	$\overline{\boldsymbol{v}}$
$\boldsymbol{\theta} = (\theta_\alpha)$	plate rotations	Γ^0	$\boldsymbol{\vartheta}$

Table 1: State and adjoint problem variables (fileds).

2.1 State problem

In this section we present weak formulation of the state problem which is defined in terms of the homogenized interface coupling conditions. The acoustic wave propagation coupled with the vibroacoustic transmission is described by the global acoustic potential defined in domain Ω and by fields defined on the interface Γ_0. Variables involved in the state problem are listed in Table 1. The in-plane displacements $\overline{\boldsymbol{u}} = (u_1, u_2)$ present the first two components of $\boldsymbol{u}$, *i.e.* $\boldsymbol{u} = (\overline{\boldsymbol{u}}, u_3)$. We can introduce the following generalized state variable: $\boldsymbol{U} = (P, p, G^+, G^-, \boldsymbol{u}, \boldsymbol{\theta}) \in \boldsymbol{\mathcal{U}} = H^1(\Omega, \Gamma_0) \times H^1(\Gamma_0) \times L^2(\Gamma_0) \times L^2(\Gamma_0) \times [H_0^1(\Gamma_0)]^5$.

To introduce the state problem equations, the following bilinear forms are needed which are expressed using the inner product $\langle \cdot, \cdot \rangle_{\Gamma_0}$ defined on the homogenized layer Γ_0,

$$
\begin{aligned}
\mathcal{A}(p,q) &= \langle \boldsymbol{A}\overline{\nabla} p, \overline{\nabla} q \rangle_{\Gamma_0} \ , \\
\mathcal{K}(p,q) &= \left\langle (\frac{\zeta^*}{c^2} + \rho_0 K) p, \, q \right\rangle_{\Gamma_0} \ , \\
\mathcal{D}(\overline{\boldsymbol{v}}, p) &= \langle \boldsymbol{D}\overline{\boldsymbol{v}}, \overline{\nabla} p \rangle_{\Gamma_0} \ , \\
\mathcal{H}(\overline{\boldsymbol{v}}, p) &= \bar{h} \left\langle \boldsymbol{H} : \overline{\nabla}^S \overline{\boldsymbol{v}}, \, p \right\rangle_{\Gamma_0} \ , \\
\mathcal{B}(p, \psi) &= \langle \boldsymbol{B} \cdot \overline{\nabla} p, \, \psi \rangle_{\Gamma_0} \ , \\
\mathcal{E}(\boldsymbol{\theta}, \boldsymbol{\vartheta}) &= \frac{\bar{h}}{\rho_0} \left\langle \mathbb{E}^H \overline{\nabla}^S \boldsymbol{\theta}, \, \overline{\nabla}^S \boldsymbol{\vartheta} \right\rangle_{\Gamma_0} \ , \\
\mathcal{M}(\overline{\boldsymbol{u}}, \overline{\boldsymbol{v}}) &= \left\langle (\frac{\bar{h}\overline{\rho}_S}{\rho_0} \overline{\boldsymbol{I}} + \overline{\boldsymbol{T}}) \overline{\boldsymbol{u}}, \, \overline{\boldsymbol{v}} \right\rangle_{\Gamma_0} \ ,
\end{aligned}
\tag{4}
$$

which are needed in (7), and

$$\begin{aligned}
\mathcal{F}(g,\psi) &= \langle Fg,\, \psi\rangle_{\Gamma_0}\ , \\
\mathcal{C}(u,\psi) &= \langle C_3 u,\, \psi\rangle_{\Gamma_0}\ , \\
\mathcal{N}(u,z) &= \left\langle \left(\bar{h}\frac{\overline{\rho}_S}{\rho_0} + T_{33}\right) u,\, z\right\rangle_{\Gamma_0}\ , \\
\mathcal{L}(\boldsymbol{\theta},\boldsymbol{\vartheta}) &= \frac{\bar{h}}{\rho_0}\left\langle \frac{\overline{\rho}_S}{\rho_0}\boldsymbol{\theta},\, \boldsymbol{\vartheta}\right\rangle_{\Gamma_0}\ , \\
\mathcal{S}((w,\boldsymbol{\theta}),(v,\boldsymbol{\vartheta})) &= \frac{\bar{h}}{\rho_0}\left\langle \boldsymbol{S}^{\mathrm{H}}(\overline{\nabla} w - \boldsymbol{\theta}),\, \overline{\nabla} v - \boldsymbol{\vartheta}\right\rangle_{\Gamma_0}\ ,
\end{aligned} \tag{5}$$

employed in (8). Homogenized transmission coefficients $\boldsymbol{A}, \boldsymbol{B}, F, \boldsymbol{H}, K, C_3, \boldsymbol{D}, \boldsymbol{T}, \boldsymbol{S}^{\mathrm{H}}$ and $\mathbb{E}^{\mathrm{H}}$ are obtained by solving local subproblems, see Sec. 2.2.

The global acoustic field $P \in H^1(\hat{\Omega}^+ \cup \hat{\Omega}^+)$ and the transversal acoustic momenta $G^+, G^- = L^2(\Gamma_0)$ satisfy

$$\begin{aligned}
&c^2 \int_{\hat{\Omega}^+\cup\hat{\Omega}^-} \nabla P\cdot\nabla Q - \omega^2 \int_{\hat{\Omega}^+\cup\hat{\Omega}^-} PQ + \int_{\partial_{\mathrm{ext}}\Omega^G} r\mathrm{i}\omega c PQ \\
&-\mathrm{i}\omega c^2\left(\left\langle G^+,\, Q^+\right\rangle_{\Gamma_0} - \left\langle G^-,\, Q^-\right\rangle_{\Gamma_0}\right) = \int_{\partial_{\mathrm{ext}}\Omega^G} s 2\mathrm{i}\omega c\bar{p} Q
\end{aligned} \tag{6}$$

for all $Q \in H^1(\hat{\Omega}^+ \cup \hat{\Omega}^-)$, whereby $Q^\pm$ denotes the trace of Q on $\partial\hat{\Omega}^\pm$.

Homogenization of the transmission layer Ω_δ in which the plate is embedded yields the interface coupling conditions involving functions $(P^\pm, p, \overline{\boldsymbol{u}}) \in [L^2(\Gamma_0)]^2 \times H^1(\Gamma_0) \times [H_0^1(\Gamma_0)]^2$ and $(G^\pm, u_3, \boldsymbol{\theta}) \in [L^2(\Gamma_0)]^2 \times H_0^1(\Gamma_0) \times [H_0^1(\Gamma_0)]^2$. They satisfy the following equations,

$$\begin{aligned}
\mathcal{A}(p,q) - \omega^2\mathcal{K}(p,q) + \mathrm{i}\omega\left(\mathcal{D}(\overline{\boldsymbol{u}},q) + \mathcal{H}(\overline{\boldsymbol{u}},q)\right) + \frac{\mathrm{i}\omega}{2}\mathcal{B}([G^+ + G^-],q) + \frac{\mathrm{i}\omega}{\varepsilon_0}\left\langle [G^+ - G^-],\, q\right\rangle_{\Gamma_0} = 0\ , \\
-\mathrm{i}\omega\left(\mathcal{D}(\overline{\boldsymbol{v}},p) + \mathcal{H}(\overline{\boldsymbol{v}},p)\right) + \mathcal{E}(\overline{\boldsymbol{u}},\overline{\boldsymbol{v}}) - \omega^2\mathcal{M}(\overline{\boldsymbol{u}},\overline{\boldsymbol{v}}) = 0\ ,
\end{aligned} \tag{7}$$

for all $(q, \overline{\boldsymbol{v}}) \in H^1(\Gamma_0) \times [H_0^1(\Gamma_0)]^2$, and

$$\begin{aligned}
\frac{\omega^2}{2}\mathcal{F}([G^+ + G^-],\psi) - \omega^2\mathcal{C}(u_3,\psi) + \mathrm{i}\omega\mathcal{B}(p^0,\psi) - \frac{\mathrm{i}\omega}{\varepsilon_0}\left\langle [P^+ - P^-],\, \psi\right\rangle_{\Gamma_0} = 0\ , \\
\frac{\omega^2}{2}\mathcal{C}([G^+ + G^-],v_3) - \omega^2\left(\mathcal{N}(u_3,v_3) + \frac{h^2}{12}\mathcal{L}(\boldsymbol{\theta},\boldsymbol{\vartheta})\right) \\
+\mathcal{S}((u_3,\boldsymbol{\theta}),(v_3,\boldsymbol{\vartheta})) + \frac{h^2}{12}\mathcal{E}(\boldsymbol{\theta},\boldsymbol{\vartheta}) = 0\ ,
\end{aligned} \tag{8}$$

for all $(\psi, v, \boldsymbol{\vartheta}) \in L^2(\Gamma_0) \times H_0^1(\Gamma_0) \times [H_0^1(\Gamma_0)]^2$. There is also the coupling equation:

$$\left\langle 2p - [P^+ + P^-],\, \varphi\right\rangle_{\Gamma_0} = 0 \quad \forall \varphi \in L^2(\Gamma_0)\ . \tag{9}$$

To introduce the optimization problem in Section 3, it is convenient to reformulate the state problem in the residual form: Find the generalized state variable $\boldsymbol{U} = (P, p, G^+, G^-, \boldsymbol{u}, \boldsymbol{\theta}) \in \boldsymbol{\mathcal{U}}$, which satisfies

$$\Psi(\boldsymbol{U},\boldsymbol{V}) = f(\boldsymbol{V}) \quad \forall \boldsymbol{V} = (q,\psi,z,\boldsymbol{\vartheta}) \in \boldsymbol{\mathcal{U}}_0 = \boldsymbol{\mathcal{U}}\ , \tag{10}$$

where

$$
\begin{aligned}
\Psi(\boldsymbol{U},\boldsymbol{V}) = {} & c^2 \int_{\hat{\Omega}^+\cup\hat{\Omega}^-} \nabla P\cdot\nabla Q|^* - \omega^2 \int_{\hat{\Omega}^+\cup\hat{\Omega}^-} PQ|^* + \int_{\partial_{\mathrm{ext}}\Omega^G} r\mathrm{i}\omega cPQ|^* \\
& - \mathrm{i}\omega c^2 \left(\left\langle G^+,\, Q^+ \right\rangle_{\Gamma_0} - \left\langle G^-,\, Q^- \right\rangle_{\Gamma_0} \right) \\
& + \mathcal{A}(p,q) - \omega^2 \mathcal{K}(p,q) + \mathrm{i}\omega \left(\frac{1}{2}\mathcal{B}(q,[G^+ + G^-]) + \mathcal{D}(\overline{\boldsymbol{u}},q) + \mathcal{H}(\overline{\boldsymbol{u}},q) \right) + \frac{\mathrm{i}\omega}{\varepsilon_0} \left\langle [G^+ - G^-],\, q \right\rangle_{\Gamma_0} \\
& - \mathrm{i}\omega \left(\mathcal{D}(\overline{\boldsymbol{v}},p) + \mathcal{H}(\overline{\boldsymbol{v}},p) \right) + \mathcal{E}(\overline{\boldsymbol{u}},\overline{\boldsymbol{v}}) - \omega^2 \mathcal{M}(\overline{\boldsymbol{u}},\overline{\boldsymbol{v}}) \\
& + \frac{\omega^2}{2}\mathcal{F}([G^+ + G^-],\psi) + \mathrm{i}\omega\mathcal{B}(p,\psi) - \omega^2\mathcal{C}(u_3,\psi) - \frac{\mathrm{i}\omega}{\varepsilon_0} \left\langle [P^+ - P^-],\, \psi \right\rangle_{\Gamma_0} \\
& + \frac{\omega^2}{2}\mathcal{C}([G^+ + G^-],v_3) - \omega^2 \left(\mathcal{N}(u_3,v_3) + \frac{h^2}{12}\mathcal{L}(\boldsymbol{\theta},\boldsymbol{\vartheta}) \right) \\
& + \mathcal{S}((u_3,\boldsymbol{\theta}),(v_3,\boldsymbol{\vartheta})) + \frac{h^2}{12}\mathcal{E}(\boldsymbol{\theta},\boldsymbol{\vartheta}) \\
& + \left\langle 2p - [P^+ + P^-],\, \varphi \right\rangle_{\Gamma_0} \,, \\
\text{and } f(\boldsymbol{V}) = {} & 2\mathrm{i}\omega \langle \bar{p},\, q \rangle_{\Gamma_{\mathrm{in}}} \,.
\end{aligned}
\tag{11}
$$

Above and in what follows, by $q|^*$ we mean the complex conjugate of q. All inner products and bilinear (sesquilinear) forms are considered in the complex Hilbertean spaces.

For the rigid plate, $\boldsymbol{u} = \boldsymbol{0}$ and $\boldsymbol{\theta} = \boldsymbol{0}$, thus $\boldsymbol{U}$ reduces to $\boldsymbol{U} = (P, p, G^+, G^-)$ and $\boldsymbol{V} = (Q, q, \varphi, \psi)$, whereby we consider the simplified problem with Ψ modified, as follows:

$$
\begin{aligned}
\Psi_R(\boldsymbol{U},\boldsymbol{V}) = {} & c^2 \int_{\hat{\Omega}^+\cup\hat{\Omega}^-} \nabla P\cdot\nabla Q|^* - \omega^2 \int_{\hat{\Omega}^+\cup\hat{\Omega}^-} PQ|^* + \int_{\partial_{\mathrm{ext}}\Omega^G} r\mathrm{i}\omega cPQ|^* \\
& - \mathrm{i}\omega c^2 \left(\left\langle G^+,\, Q^+ \right\rangle_{\Gamma_0} - \left\langle G^-,\, Q^- \right\rangle_{\Gamma_0} \right) \\
& + \mathcal{A}(p,q) - \omega^2 \mathcal{K}(p,q) + \mathrm{i}\omega \frac{1}{2}\mathcal{B}(q,[G^+ + G^-]) + \frac{\mathrm{i}\omega}{\varepsilon_0} \left\langle [G^+ - G^-],\, q \right\rangle_{\Gamma_0} \\
& + \frac{\omega^2}{2}\mathcal{F}([G^+ + G^-],\psi) - \omega^2\mathcal{B}(p,\psi) - \frac{\mathrm{i}\omega}{\varepsilon_0} \left\langle [P^+ - P^-],\, \psi \right\rangle_{\Gamma_0} \\
& + \frac{\mathrm{i}\omega}{\varepsilon_0} \left\langle 2p - [P^+ + P^-],\, \varphi \right\rangle_{\Gamma_0} \,.
\end{aligned}
\tag{12}
$$

We recall that by virtue of the microscopic local problems reported in the next section, the geometry of the perforation influences the homogenized coefficients involved in the bilinear forms (4).

2.2 Local state problems and homogenized coefficients

The homogenized transmission conditions described above are introduced in terms of characteristic response functions defined in the representative periodic cell $Y \subset \mathbb{R}^3$. Let us introduce the representative cell $\Xi \subset \mathbb{R}^2$ of the plate, $\Xi =]0, \ell_1[\times]0, \ell_2[$, where $\ell_1, \ell_2 > 0$ are given (usually $\ell_1 = \ell_2 = 1$). Further, we consider the hole representation $\Xi^* \subset \Xi$, then $\Xi_S = \Xi \setminus \overline{\Xi^*}$ defines the solid plate segment; for obvious reasons, $\overline{\Xi^*} \subset \Xi$ is required to guarantee the plate rigidity. Now the representative periodic cell Y embedding the solid plate part $S \subset Y$ are defined by

$$
\begin{aligned}
Y &= \Xi \times]-\varkappa/2, +\varkappa/2] \,, \\
S &= \Xi_S \times]-\bar{h}/2, +\bar{h}/2[\,,
\end{aligned}
\tag{13}
$$

where $\varkappa > 0$ is the dilated layer thickness and $\bar{h}$ is the relative plate thickness; for a given $\varepsilon > 0$ the plate thickness is $h^\varepsilon = \varepsilon\bar{h}$. The acoustic fluid occupies domain $Y^* = Y \setminus \overline{S}$, see Fig. 1. For the rigid plates, the shape of the holes can be quite arbitrary, therefore, also S is not restricted to the shapes defined by $(13)_2$. However, for elastic plates, because of the homogenization procedure applied to model the perforated plate [9, 6, 7], the geometry of the perforation is restricted by cylindrical holes "orthogonal" to the plate mid-plane.

Below we use the space $H^1_{\#(\Xi)}(Y^*)$ constituted by all Ξ-periodic functions in the Sobolev space $H^1(Y^*)$ (as the consequence, $H^1_{\#}(\Xi_S)$ is constituted by all Ξ-periodic functions). As the result of the homogenization, local problems for characteristic responses of the fluid and solid parts must be solved. The first group of the responses is associated with the fluid occupying the domain Y^*. Functions $\pi^\beta, \xi, \eta^k \in H^1_{\#(\Xi)}(Y^*)$ satisfy ($I^\pm_y = \{y \in \partial\overline{Y} |\ y_3 = \pm 1/2\}$)

$$\begin{aligned}
\Big(\nabla_y\pi^\beta,\, \nabla_y\psi\Big)_{Y^*} &= -\int_{Y^*} \partial^y_\beta\psi\ , \quad \beta = 1,2\ ,\\
(\nabla_y\xi,\, \nabla_y\psi)_{Y^*} &= -\left(\int_{I^+_y}\psi - \int_{I^-_y}\psi\right)\ ,\\
\Big(\nabla_y\eta^k,\, \nabla_y\psi\Big)_{Y^*} &= -\int_{\partial S} n_k\psi\ , \quad k = 1,2,3\ ,
\end{aligned} \tag{14}$$

for all $\psi \in H^1_{\#(\Xi)}(Y^*)$. The second group of the responses is associated with the elastic structure represented by the plate mid-surface Ξ_S. Functions $\overline{\boldsymbol{\chi}}^{rs} \in \mathbf{H}^1_{\#}(\Xi_S)/\mathbb{R}$, $\overline{\boldsymbol{\chi}}^* \in \mathbf{H}^1_{\#}(\Xi_S)/\mathbb{R}$ and $\chi^k \in H^1_{\#}(\Xi_S)/\mathbb{R}$, $k, r, s = 1, 2$, satisfy

$$\begin{aligned}
\fint_{\Xi_S} (\mathbb{C}\overline{\nabla}^S_y(\overline{\boldsymbol{\chi}}^{rs} + \boldsymbol{\Pi}^{rs})) : \overline{\nabla}^S_y\overline{\boldsymbol{v}} = 0 \quad \forall\overline{\boldsymbol{v}} \in \mathbf{H}^1_{\#}(\Xi_S)\ ,\\
\fint_{\Xi_S} (\mathbb{C}\overline{\nabla}^S_y\overline{\boldsymbol{\chi}}^*) : \overline{\nabla}^S_y\overline{\boldsymbol{v}} = \fint_{\partial\Xi_S} \overline{\boldsymbol{n}}\cdot\overline{\boldsymbol{v}} \quad \forall\overline{\boldsymbol{v}} \in \mathbf{H}^1_{\#}(\Xi_S)\ ,\\
\fint_{\Xi_S} \gamma\nabla_y(\chi^k + y_k)\cdot\nabla_y\tilde{z} = 0 \quad \forall\tilde{z} \in H^1_{\#}(\Xi_S)\ ,
\end{aligned} \tag{15}$$

where $\boldsymbol{\Pi}^{rs} = (\Pi^{rs}_i)$, $\Pi^{rs}_i = y_s\delta_{ri}$ with $i, r, s = 1, 2$. Using solutions of (14) and (15), the homogenized transmission coefficients can be computed:

$$\begin{aligned}
A_{\alpha\beta} &= \frac{1}{|\Xi|}\Big(\nabla_y(\pi^\beta + y_\beta),\, \nabla_y(\pi^\alpha + y_\alpha)\Big)_{Y^*}\ , \quad B_\alpha = \fint_{Y^*}\partial^y_\alpha\xi = \fint_{I^+_y}\pi^\alpha - \fint_{I^-_y}\pi^\alpha, \quad F = \fint_{I^+_y}\xi - \fint_{I^-_y}\xi\ ,\\
C_k &= \fint_{I^+_y}\eta^k - \fint_{I^-_y}\eta^k = \fint_{\partial S} n_k\xi\ , \qquad D^\beta_k = \fint_{Y^*}\partial^y_\beta\eta^k = \fint_{\partial S} n_k\pi^\beta\ , \qquad T_{kj} = -\fint_{\partial S}\eta^k n_j\ ,\\
H_{\alpha\beta} &= \fint_{\partial S}\overline{\boldsymbol{n}}\cdot\overline{\boldsymbol{\chi}}^{\alpha\beta}\ , \qquad K = \fint_{\partial S}\overline{\boldsymbol{n}}\cdot\overline{\boldsymbol{\chi}}^* + \fint_{\partial S} n_3\chi^*\ , \qquad \bar{\rho}_S = \fint_{\Xi_S}\rho\ ,\\
E^{\mathrm{H}}_{\alpha\beta\mu\nu} &= \fint_{\Xi_S}\mathbb{C}\overline{\nabla}^S_y(\overline{\boldsymbol{\chi}}^{rs} + \boldsymbol{\Pi}^{rs}) : \overline{\nabla}^S_y(\overline{\boldsymbol{\chi}}^{\alpha\beta} + \boldsymbol{\Pi}^{\alpha\beta})\ , \qquad S^{\mathrm{H}}_{\alpha\beta} = \int_{\Xi_S}\gamma\overline{\nabla}_y(\chi^\alpha + y_\alpha)\cdot\overline{\nabla}_y(\chi^\beta + y_\beta)\ .
\end{aligned} \tag{16}$$

The first three coefficients ($\boldsymbol{A}$, $\boldsymbol{B}$, F) are relevant also for the rigid plate.

3 The optimal perforation design

The design of periodic plate perforations can be controlled by distributed design variables $\mathbf{d}$ which describe the shape of the hole within the representative periodic cell Y. It is given by the design curve $\Gamma_S := \partial\Xi_S\setminus\partial\Xi$

which determines the simple cylindrical type of perforations, thus the shape of domain Y^*, see Fig. 1, so that $\mathbf{d}$ influences all the homogenized coefficients presented in Section 2.2.

In what follows, we shall consider the rigid plates, so that only three coefficients ($\boldsymbol{A}$, $\boldsymbol{B}$, F) parameterize the state problem by virtue of the residual function Ψ_R introduced in (12). We can define the *optimal perforation design problem*:

$$\begin{aligned} &\min_{\alpha\in\alpha_{adm}} \Phi(\boldsymbol{U}) \\ \text{subject to:}\quad &\boldsymbol{U} \text{ solves (10)}, \\ &\text{where } \boldsymbol{A}, \boldsymbol{B}, F \text{ are given by local solutions to (14)-(16).} \end{aligned} \tag{17}$$

Above α_{adm} is the set of admissible designs, constraining the shape regularity of ∂S and typically some other features, like porosity of the interface. For the "nearly-periodic" perforations, D_{adm} contains some smoothness constraints related to the scale ε_0. We considered the following objective function

$$\Phi(\boldsymbol{U}) = \Phi(P^a, P^b) = 20\, log\left(\frac{|P^a|}{|P^b|}\right) , \tag{18}$$

where P^a and P^b are acoustic pressures at given points of Ω.

3.1 The design parameterization

The design of a perforation is parametrized by control points of a B-spline box which embeds the whole representative cell Y, see Fig. 4. The perforation shape can be modified by varying positions of the control points $\boldsymbol{P}^i$ of the spline box which is expressed in terms of the B-spline basis function $\mathcal{B}^i$ as

$$\boldsymbol{y}(\boldsymbol{t},\boldsymbol{\alpha}) = \sum_i \boldsymbol{P}^i(\boldsymbol{\alpha})\mathcal{B}^i(\boldsymbol{t}), \qquad \boldsymbol{P}^i(\boldsymbol{\alpha}) = \hat{\boldsymbol{P}}^i + \mathbf{d}^i(\boldsymbol{\alpha}), \quad \mathbf{d}^i = \boldsymbol{Z}^i\boldsymbol{\alpha}, \quad \boldsymbol{t}\in Y , \tag{19}$$

where $\hat{\boldsymbol{P}}^i$ are the initial control points, $\boldsymbol{\alpha}$ are the design parameters and $\boldsymbol{Z}^i$ are transformation matrices, one for each control point. Now, we can introduce the design velocity field $\mathcal{V}$ established in Y using the definiton of the spline box (19) and the differentiation with respect to a scalar parameter: for any position $\boldsymbol{y}\in Y$ we define its perturbation $\delta y_j = \delta\tau\mathcal{V}_j$, so that

$$\delta\boldsymbol{y}(\boldsymbol{t},\delta\boldsymbol{\alpha}) = \sum_i \delta\mathbf{d}^i\mathcal{B}^i(\boldsymbol{t}) = \mathcal{V}\delta\tau, \qquad \text{where} \quad \delta\mathbf{d}^i = \boldsymbol{Z}^i\delta\boldsymbol{\alpha} . \tag{20}$$

To get the derivative of an objective function with respect to the k-th design parameter, *i.e.* $\frac{\partial\Phi}{\partial d_k}$, the shape derivatives δ_{sh} must be computed, see (26). For this the following design velocity field is introduced in terms of the B-spline basis functions and the transformation matrices,

$$\mathcal{V}_l^k = \sum_i \mathcal{B}^i(\boldsymbol{t})Z_{lk}^i . \tag{21}$$

The design velocity field is employed in (27) to express the shape sensitivity of the homogenized coefficients.

3.2 Sensitivity analysis

To compute the sensitivity of an objective function $\Phi(\boldsymbol{U})$, the adjoint problem must be solved:
Find $\tilde{\boldsymbol{V}} = (\tilde{Q}, \tilde{q}, \tilde{\varphi}, \tilde{\psi}, \tilde{\boldsymbol{v}}, \tilde{\boldsymbol{\vartheta}}) \in \boldsymbol{\mathcal{U}}_0$ such that

$$2\Psi(\boldsymbol{V},\tilde{\boldsymbol{V}}) = -\left[\delta_{\Re(\boldsymbol{U})}\Phi(\boldsymbol{U}) - \mathrm{i}\delta_{\Im(\boldsymbol{U})}\Phi(\boldsymbol{U})\right]\circ\boldsymbol{V} \quad \forall\boldsymbol{V}\in\boldsymbol{\mathcal{U}}_0 , \tag{22}$$

where $\Psi(\boldsymbol{V},\tilde{\boldsymbol{V}})$ is replaced by $\Psi_R(\boldsymbol{V},\tilde{\boldsymbol{V}})$, if the rigid plate problem is considered.

Thus, for the rigid plate, the adjoint problem reads, as follows:

$$\begin{aligned}
\int_{\hat{\Omega}^+\cup\hat{\Omega}^-}\left(c^2\nabla Q\cdot\nabla\tilde{Q}|^* - \omega^2 Q\tilde{Q}|^*\right) + \int_{\partial_{\mathrm{ext}}\Omega^G} r\mathrm{i}\omega c Q\tilde{Q}|^* \\
-\frac{\mathrm{i}\omega}{\varepsilon_0}\left\langle Q^+,\,\tilde{\varphi}+\tilde{\psi}\right\rangle_{\Gamma_0} - \frac{\mathrm{i}\omega}{\varepsilon_0}\left\langle Q^-,\,\tilde{\varphi}-\tilde{\psi}\right\rangle_{\Gamma_0} = -\frac{1}{2}\left[\delta_{\Re(P)}\Phi(P) - \mathrm{i}\delta_{\Im(P)}\Phi(P)\right]\circ Q \\
\forall Q\in H^1_{-1}(\Omega,\Gamma_0)\,, \\
\mathcal{A}(q,\tilde{q}) - \omega^2\mathcal{K}(q,\tilde{q}) - \omega^2\mathcal{B}(q,\tilde{\psi}) + \frac{\mathrm{i}\omega}{\varepsilon_0}\left\langle 2q,\,\tilde{\varphi}\right\rangle_{\Gamma_0} = 0 \quad \forall q\in H^1(\Gamma_0)\,, \\
-\mathrm{i}\omega c^2\left\langle\varphi,\,\tilde{Q}^+\right\rangle_{\Gamma_0} + \mathrm{i}\omega\frac{1}{2}\mathcal{B}(\tilde{q},\varphi) + \frac{\mathrm{i}\omega}{\varepsilon_0}\left\langle\varphi,\,\tilde{q}\right\rangle_{\Gamma_0} + \frac{\omega^2}{2}\mathcal{F}(\varphi,\tilde{\psi}) = 0 \quad \forall\varphi\in L^2(\Gamma_0)\,, \\
\mathrm{i}\omega c^2\left\langle\psi,\,\tilde{Q}^-\right\rangle_{\Gamma_0} + \mathrm{i}\omega\frac{1}{2}\mathcal{B}(\tilde{q},\psi) - \frac{\mathrm{i}\omega}{\varepsilon_0}\left\langle\psi,\,\tilde{q}\right\rangle_{\Gamma_0} + \frac{\omega^2}{2}\mathcal{F}(\psi,\tilde{\psi}) = 0 \quad \forall\psi\in L^2(\Gamma_0)\,,
\end{aligned} \tag{23}$$

This equation must be split into two parts according to the complex test functions $\boldsymbol{V} = \boldsymbol{V}_R + \mathrm{i}\boldsymbol{V}_I$. Note that $\tilde{\boldsymbol{V}}|^* = \tilde{\boldsymbol{V}}_R - \mathrm{i}\tilde{\boldsymbol{V}}_I$ is involved. The first set of equations is

$$\begin{aligned}
\int_{\hat{\Omega}^+\cup\hat{\Omega}^-}\left(c^2\nabla Q_R\cdot\nabla\tilde{Q}_R - \omega^2 Q_R\tilde{Q}_R\right) + \int_{\partial_{\mathrm{ext}}\Omega^G} r\omega c Q_R\tilde{Q}_I \\
-\frac{\omega}{\varepsilon_0}\left\langle Q_R^+,\,\tilde{\varphi}_I+\tilde{\psi}_I\right\rangle_{\Gamma_0} - \frac{\omega}{\varepsilon_0}\left\langle Q_R^-,\,\tilde{\varphi}_I-\tilde{\psi}_I\right\rangle_{\Gamma_0} = -\delta_{\Re(P)}\Phi(P)\circ Q_R\,, \\
\mathcal{A}(q_R,\tilde{q}_R) - \omega^2\mathcal{K}(q_R,\tilde{q}_R) - \omega^2\mathcal{B}(q_R,\tilde{\psi}_R) + \frac{\omega}{\varepsilon_0}\left\langle 2q_R,\,\tilde{\varphi}_I\right\rangle_{\Gamma_0} = 0\,, \\
-\omega c^2\left\langle\varphi_R,\,\tilde{Q}_I^+\right\rangle_{\Gamma_0} + \omega\frac{1}{2}\mathcal{B}(\tilde{q}_I,\varphi_R) + \frac{\omega}{\varepsilon_0}\left\langle\varphi_R,\,\tilde{q}_I\right\rangle_{\Gamma_0} + \frac{\omega^2}{2}\mathcal{F}(\varphi_R,\tilde{\psi}_R) = 0\,, \\
\omega c^2\left\langle\psi_R,\,\tilde{Q}_I^-\right\rangle_{\Gamma_0} + \omega\frac{1}{2}\mathcal{B}(\tilde{q}_I,\psi_R) - \frac{\omega}{\varepsilon_0}\left\langle\psi_R,\,\tilde{q}_I\right\rangle_{\Gamma_0} + \frac{\omega^2}{2}\mathcal{F}(\psi_R,\tilde{\psi}_R) = 0
\end{aligned} \tag{24}$$

for all $(Q_R, q_R, \varphi_R, \psi_R)\in H^1_{-1}(\Omega,\Gamma_0)\times H^1(\Gamma_0)\times L^2(\Gamma_0)\times L^2(\Gamma_0)$. The second set of equations is

$$\begin{aligned}
\int_{\hat{\Omega}^+\cup\hat{\Omega}^-}\left(c^2\nabla Q_I\cdot\nabla\tilde{Q}_I - \omega^2 Q_I\tilde{Q}_I\right) - \int_{\partial_{\mathrm{ext}}\Omega^G} r\omega c Q_I\tilde{Q}_R \\
+\frac{\omega}{\varepsilon_0}\left\langle Q_I^+,\,\tilde{\varphi}_R+\tilde{\psi}_R\right\rangle_{\Gamma_0} + \frac{\omega}{\varepsilon_0}\left\langle Q_I^-,\,\tilde{\varphi}_R-\tilde{\psi}_R\right\rangle_{\Gamma_0} = -\delta_{\Re(P)}\Phi(P)\circ Q_I\,, \\
\mathcal{A}(q_I,\tilde{q}_I) - \omega^2\mathcal{K}(q_I,\tilde{q}_I) - \omega^2\mathcal{B}(q_I,\tilde{\psi}_I) - \frac{\omega}{\varepsilon_0}\left\langle 2q_I,\,\tilde{\varphi}_R\right\rangle_{\Gamma_0} = 0\,, \\
\omega c^2\left\langle\varphi_I,\,\tilde{Q}_R^+\right\rangle_{\Gamma_0} - \omega\frac{1}{2}\mathcal{B}(\tilde{q}_R,\varphi_I) - \frac{\omega}{\varepsilon_0}\left\langle\varphi_I,\,\tilde{q}_R\right\rangle_{\Gamma_0} + \frac{\omega^2}{2}\mathcal{F}(\varphi_I,\tilde{\psi}_I) = 0\,, \\
-\omega c^2\left\langle\psi_I,\,\tilde{Q}_R^-\right\rangle_{\Gamma_0} - \omega\frac{1}{2}\mathcal{B}(\tilde{q}_R,\psi_I) + \frac{\omega}{\varepsilon_0}\left\langle\psi_I,\,\tilde{q}_R\right\rangle_{\Gamma_0} + \frac{\omega^2}{2}\mathcal{F}(\psi_I,\tilde{\psi}_I) = 0\,,
\end{aligned} \tag{25}$$

for all $(Q_I, q_I, \varphi_I, \psi_I)\in H^1_{-1}(\Omega,\Gamma_0)\times H^1(\Gamma_0)\times L^2(\Gamma_0)\times L^2(\Gamma_0)$.

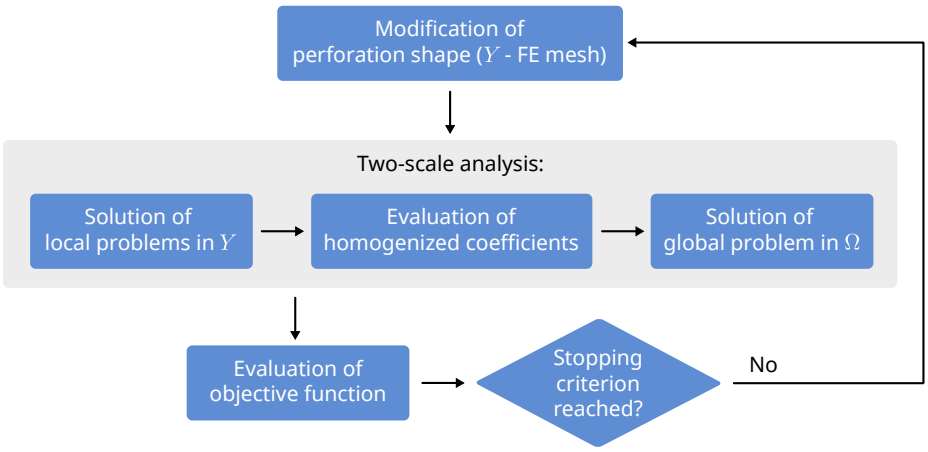


Figure 2: Scheme of the optimization process.

Consequently, the sensistivity can be evaluated by the formula

$$\begin{aligned}\delta\Phi(p) :=& 2\Re\Bigg\{\left\langle\delta_{\rm sh}\boldsymbol{A}\overline{\nabla}p,\,\overline{\nabla}\tilde{q}\right\rangle_{\Gamma_0}-\omega^2\left\langle(\frac{\delta_{\rm sh}\zeta^*}{c^2}+\rho_0\delta_{\rm sh}K)p,\,\tilde{q}\right\rangle_{\Gamma_0}\\&+\mathrm{i}\omega\left(\left\langle\delta_{\rm sh}\boldsymbol{D}\overline{\boldsymbol{u}},\,\overline{\nabla}\tilde{q}\right\rangle_{\Gamma_0}-\left\langle\delta_{\rm sh}\boldsymbol{D}\overline{\tilde{\boldsymbol{v}}},\,\overline{\nabla}p\right\rangle_{\Gamma_0}+\bar{h}\left\langle\delta_{\rm sh}\boldsymbol{H}:\overline{\nabla}^S\overline{\boldsymbol{u}},\,\tilde{q}\right\rangle_{\Gamma_0}-\bar{h}\left\langle\boldsymbol{H}:\overline{\nabla}^S\overline{\tilde{\boldsymbol{v}}},\,p\right\rangle_{\Gamma_0}\right)\\&+\mathrm{i}\omega\left(\frac{1}{2}\left\langle\delta_{\rm sh}\boldsymbol{B}\cdot\overline{\nabla}\tilde{q},\,[G^+ + G^-]\right\rangle_{\Gamma_0}+\left\langle\delta_{\rm sh}\boldsymbol{B}\cdot\overline{\nabla}p,\,\tilde{\psi}\right\rangle_{\Gamma_0}\right)\\&-\omega^2\left[\left\langle(\frac{\bar{h}\delta_{\rm sh}\overline{\rho}_S}{\rho_0}\boldsymbol{I}+\delta_{\rm sh}\boldsymbol{T})\boldsymbol{u},\,\tilde{\boldsymbol{v}}\right\rangle_{\Gamma_0}+\frac{h^2}{12}\frac{\bar{h}}{\rho_0}\left\langle\frac{\delta_{\rm sh}\overline{\rho}_S}{\rho_0}\boldsymbol{\theta},\,\tilde{\boldsymbol{\vartheta}}\right\rangle_{\Gamma_0}\right]\\&+\omega^2\left[\frac{1}{2}\left\langle\delta_{\rm sh}F[G^+ + G^-],\,\tilde{\psi}\right\rangle_{\Gamma_0}-\left\langle\delta_{\rm sh}C_3u_3,\,\tilde{\psi}\right\rangle_{\Gamma_0}+\frac{1}{2}\left\langle\delta_{\rm sh}C_3[G^+ + G^-],\,\tilde{v}_3\right\rangle_{\Gamma_0}\right]\\&+\frac{\bar{h}}{\rho_0}\left\langle\delta_{\rm sh}\boldsymbol{S}^{\rm H}(\overline{\nabla}u_3-\boldsymbol{\theta}),\,\overline{\nabla}\tilde{v}_3-\boldsymbol{\vartheta}\right\rangle_{\Gamma_0}+\frac{\bar{h}h^2}{12\rho_0}\left\langle\delta_{\rm sh}\mathbb{E}^H\overline{\nabla}^S\boldsymbol{\theta},\,\overline{\nabla}^S\tilde{\boldsymbol{\vartheta}}\right\rangle_{\Gamma_0}+\frac{\bar{h}}{\rho_0}\left\langle\mathbb{E}^H\overline{\nabla}^S\overline{\boldsymbol{u}},\,\overline{\nabla}^S\overline{\tilde{\boldsymbol{v}}}\right\rangle_{\Gamma_0}\Bigg\}.\end{aligned}\tag{26}$$

The scheme of the optimization loop including the two-scale computation is depicted in Fig. 2.

The shape sensitivity of the homogenized coefficients $\delta_{\rm sh}$ is given by the expressions derived in [6]. Here, just for illustration, we present the expression for coefficient $\mathbb{A}=(A_{\alpha\beta})$:

$$\begin{aligned}\delta_{\rm sh}A_{\alpha\beta}=&\int_{Y^*}(\partial^y_\beta\pi^\alpha+\partial^y_\alpha\pi^\beta+\delta_{\alpha\beta})\nabla_y\cdot\mathcal{V}-\int_{Y^*}\left(\partial^y_\beta(\mathcal{V}\cdot\nabla_y)\pi^\alpha+\partial^y_\alpha(\mathcal{V}\cdot\nabla_y)\pi^\beta\right)\\&+\delta^{\mathcal{V}}_\tau\left(\nabla_y\pi^\alpha,\,\nabla_y\pi^\beta\right)_{Y^*},\end{aligned}\tag{27}$$

where $\delta^{\mathcal{V}}_\tau$ is the shape derivative with respect to the design velocity field $\mathcal{V}$, for details on the concept of shape derivatives we refer to [1] and [2], see also [4].

4 Illustrative numerical simulation

We consider a 3D problem of acoustic waves in a waveguide devided by a perforated plated represented by the interface Γ_0, see Fig. 3. The boundary conditions are applied on $\partial_{ext}\Omega=\Gamma_{in}\cup\Gamma_{out}$, see Eq. (3), such

that: $r = 1$, $s = 1$ and $\bar{p}$ is prescribed on Γ_{in} and $r = 1$, $s = 0$ on Γ_{out}. The shape of perforations is given by the representative cell Y which geometry can be modified by the control points of the cubic B-spline box. We parametrize the perforation shape by two design parametres α_1, α_2 by which we move with the inner control points of the spline box symetrically in given directions, see Fig. 4. The control points can move only in the directions of plane Γ_0 and in such a way that all control points laying on a given line perpendicular to Γ_0 move equally. These assumptions preserve a cubic shape of the representative cell Y and ensure that the perforation is perpendicular to the central plane, see Fig. 4. If $\alpha_1 = \alpha_2$, we get the circular shape of the perforations. To avoid degeneration of the finite element mesh of the representative cell we assume the folowing lower and upper bounds of $\boldsymbol{\alpha}$: $\boldsymbol{\alpha}_L = [-0.7, -0.7]$ and $\boldsymbol{\alpha}_U = [0.5, 0.5]$.

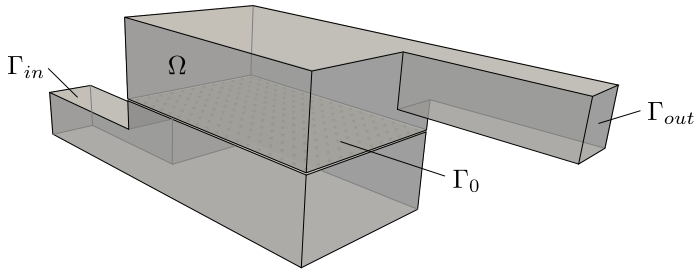


Figure 3: Geometry of a waveguide with the perforated plate represented by the interface Γ_0.

The optimization example started with the initial parameters $\boldsymbol{\alpha} = [0.5, -0.7]$, the corresponding shape is depicted in Fig. 5 left, and resulted in $\boldsymbol{\alpha} = [-0.078, -0.245]$, see Fig. 5 right. The values of the objetive function Φ and design parameters $\mathbf{d}$ during the optimization are shown in Fig. 6.

5 Conclusion

We presented a homogenized model of the vibroacoustic transmission problem a on perforated elastic plates. The model involves the homogenized transmission condition which is expressed in terms of the homogenized coefficients computed using solutions of the microscopic subproblems defined in the reference cell. In order to optimize shapes of the plate perforations, gradients of the objective function employed in optimization algorithms are needed. To compute them efficiently, the sensitivity analysis based on the adjoint problem was introduced. It is worth to note that two coupled adjoint problems must be solved for real and imaginary parts of the adjoint variables. The shape sensitivities of the homogenized coefficients involved in the resulting sensitivity formula were derived using techniques presented in [6]. These techniques allows us to find gradients of the objective function that are employed in optimization algorithms.

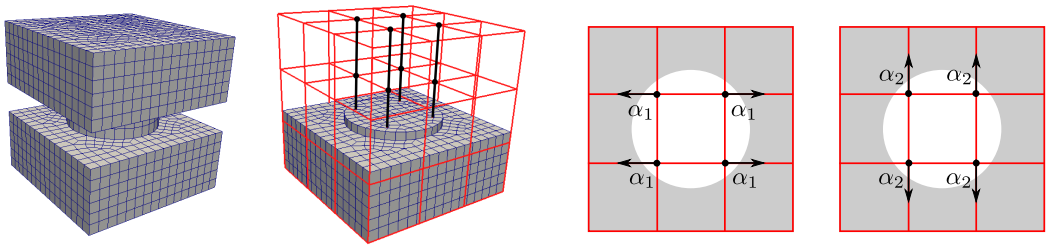
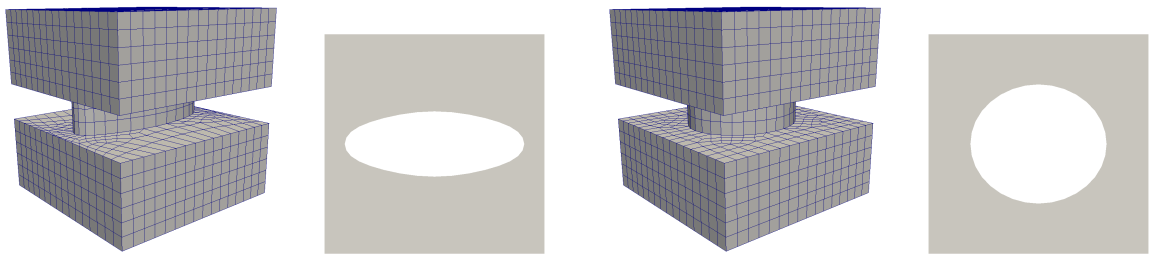


Figure 4: The FE mesh of the computational cell Y embedded in the B-spline box (left) and meaning of the design parameters α_1, α_2.



$\boldsymbol{\alpha} = [0.5, -0.7]$ $\boldsymbol{\alpha} = [-0.078, -0.245]$

Figure 5: Initial (left) and final (right) design of the perforations.

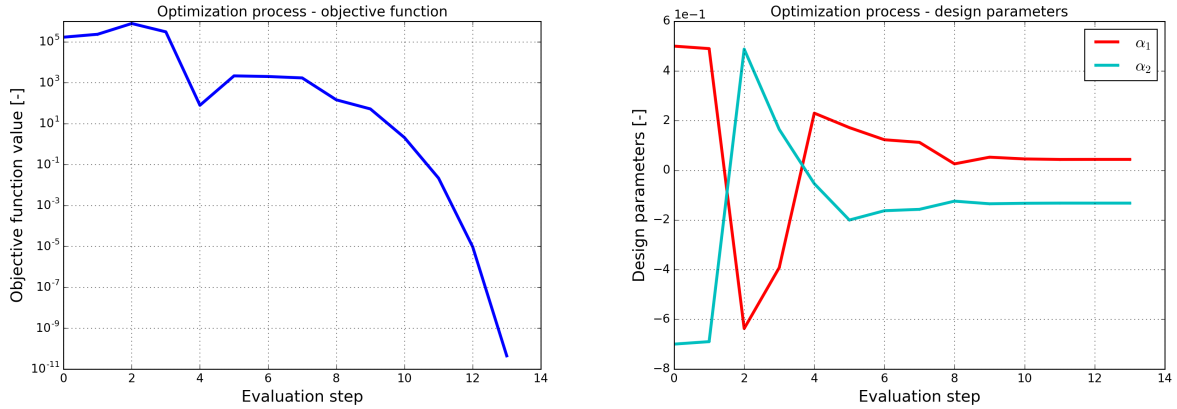


Figure 6: Evolution of the objetive function Φ and design parameters $\mathbf{d}$ during the optimization process.

The homogenized model including the shape sensitivity calculations is implemented in our Python based finite element software *SfePy* and the optimization is performed with help of *(Py)Ipopt* library using interior-point methods. We presented an illustrative numerical example in which we minimized the transmission loss in the acoustic waveguide. According to our numerical experiments, the obtained configuration of the perforation shape seems to be a local minimum related to a given initial shape configuration. Our further efforts are focused towards solving the optimization problems with the compliant plate and considering different optimality criteria. The proposed model can be extended easily for plates with locally modified perforations; such an option would lead to a better performance of the optimized design. Also we shall compare different optimization methods to select the one that could be suitable for our two-scale optimization problem.

Acknowledgments

The research of was supported by the Czech Scientific Foundation project GACR 17-01618S and in part by the project LO 1506 of the Czech Ministry of Education, Youth and Sports.

References

[1] J. Haslinger, P. Neittaanmäki, *Finite Element Approximation for Optimal Shape, Material and Topology Design*, 2nd ed. J. Wiley & Sons, Chichester, U.K., (1996).

[2] E.J. Haug, K.K. Choi, V. Komkov, *Design Sensitivity Analysis of Structural Systems*, Vol. 177, Math. in Sci. and Engrg., Academic Press (1986).

[3] P. Nardinocchi, P. Podio-Guidugli, *The Equations of Reissner-Mindlin Plates Obtained by the Method of Internal Constraints*, Meccanica 29 (1994), pp. 143–157.

[4] E. Rohan and B. Miara, *Homogenization and shape sensitivity of microstructures for design of piezoelectric bio-materials*, Mechanics of Advanced Materials and Structures 13 (2006), pp. 473-485.

[5] E. Rohan, V. Lukeš, *Homogenization of the acoustic transmission through perforated layer*, J. of Comput. and Appl. Math., Vol. 234(6), (2010) pp. 1876–1885.

[6] E. Rohan, V. Lukeš, *Sensitivity analysis for optimal design of perforated plates in vibro-acoustics: homogenization approach* Proceedings of ISMA 2012, Leuven (2012).

[7] E. Rohan, V. Lukeš, *Homogenized perforated interface in acoustic wave propagation – modeling and optimization*, in J. Náprstek etal, editors, *Proc. of the 10th International Conference on Vibration Problems, ICOVP 2011*, Springer Proceedings in Physics, Vol. 139 (2011), pp. 321-327.

[8] E. Rohan, V. Lukeš, B. Miara, *Homogenization of the vibro–acoustic transmission on perforated Reissner-Mindlin plate*, Proceedings of The 10th International Conference on Mathematical and Numerical Aspects of Waves (Waves 2011), Vancouver (2011), `http://www.sfu.ca/WAVES/proceedings/`

[9] E. Rohan, V. Lukeš *Homogenization of the vibro–acoustic transmission on perforated plates*, Submitted, 2018.

[10] E. Rohan, B. Miara, *Band gaps and vibration of strongly heterogeneous Reissner-Mindlin elastic plates*, Comptes Rendus Mathematique, Vol. 349 (2011), 777-781.

Investigation of the effect of stamping process on dimpled beams

V. Pendse [1], M. Ghazwani [1,2], K. Naghshineh [1]
[1] Western Michigan University, Department of Mechanical and Aerospace Engineering
Western Michigan University, Kalamazoo, MI 49008-5342 USA
E-mail: **koorosh.naghshineh@wmich.edu**

[2] Jazan University, Department of Mechanical Engineering, Jazan, 45142, KSA

Abstract
Creating dimples on beams has been proven to be an effective way of altering their vibroacoustic performance. This technique can change the structural natural frequencies and mode shapes and ultimately, the sound generated from these vibrating structures with no added mass. Our research, so far, has treated these dimples as having uniform thickness without considering the effects of the manufacturing process. However, after the stamping process, variations in thickness and width of the dimples are observed. The objective of this research is to model beams with such realistic dimples and analyze their performance to see if their natural frequencies and mode shapes, differ significantly from those obtained from previous work which assumed uniform dimple thickness and width. To this end, we have measured the geometry of actual dimpled beams using a scanning method and compared it to a finite element model of the process of stamping. These results were then compared to those of a uniform dimpled beam.

1 Introduction

Structures such as beams and plates are used heavily in structural design and commercial construction. These structures can produce unwanted noise and vibration. Researchers have investigated many methods to reduce the noise and vibrations in such structures. Shifting the natural frequencies of a structure away from the frequency range of the excitation force is a significant method to improve the dynamics of the structure. A method of improving the vibration and acoustic characteristics of beam based on introducing dimples on its surface is a topic of interest. This method focuses on creating one or more dimples on a structure's surface to shift its natural frequencies and change its mode shapes. In one study of changing the natural frequencies of beams using the dimpling technique, Cheng et al. [1] used a series of cylindrical dimples on the beam's surface to shift its fundamental frequency to prescribed values. In addition, Cheng et al. [2] studied the minimization of sound radiation from a vibrating beam.

Two studies were published by Alshabatat et al. [3], [4] on vibration and acoustic properties of dimpled beams and plates where the finite element method was used to calculate the beam and plate vibration natural frequencies and mode shapes. Myers et al. [5], [6] used the Boundary Value model (BVM) to compute the vibroacoustic properties, such as mode shapes in transverse and longitudinal directions, of dimpled beams. This method was also used to optimize shape and placement of dimples along a uniform beam.

Ghazwani et al. [7] published a study on the development of an analytical model for beams with two dimples in opposing directions. Their main goal was investigating the change in natural frequencies and mode shapes of a beam with two dimples in the same and opposing direction under different boundary conditions. Modeling and analysis of dimpled beams were performed using *MATLAB®* and *ANSYS®*. Furthermore, the beam dimpling approach was validated experimentally. A stamping technique was used to create dimples in order to change the vibration characteristics of beam structures. In this study, the dimple thickness was assumed to be uniform whereas in reality, the dimple is thicker at the center.

In all the research mentioned above, the dimple shape was assumed to be a part of an arc of a circle and its thickness was assumed to be uniform, while keeping the total beam mass constant. We realize that this may have been an unrealistic view since close examination of beams manufactured using the stamping process has shown that these beams exhibit non-uniform width and thickness near and along the dimple. The work presented in this paper seeks to take into account these real-world geometrical variations. The effect of these non-uniformities on beam natural frequency and mode shapes is also investigated. The goal of this study was to determine the importance of these variations and allow us to decide if these changes always need to be considered.

This paper is divided into 6 sections. In Section 2, we describe the fixture used to stamp the beam and the experimental method used to measure its natural frequencies. Section 3 explains the scanning method used to measure its width and thickness. These results will show that a manufactured dimpled beam exhibits non-uniform width and thickness. In Section 4, we describe the finite element model used to simulate the stamping process and the modal analysis of this deformed beam. To validate the accuracy of the FEA model, a comparison of its results will be made against the measured values in Section 5. The natural frequencies and mode shapes of the dimpled beam with uniform thickness are compared against those of the non-uniform beam in order to quantify the importance of the real-world manufacturing effects. Finally, in Section 6 we will summarize our results and provide concluding remarks and suggestions for future work.

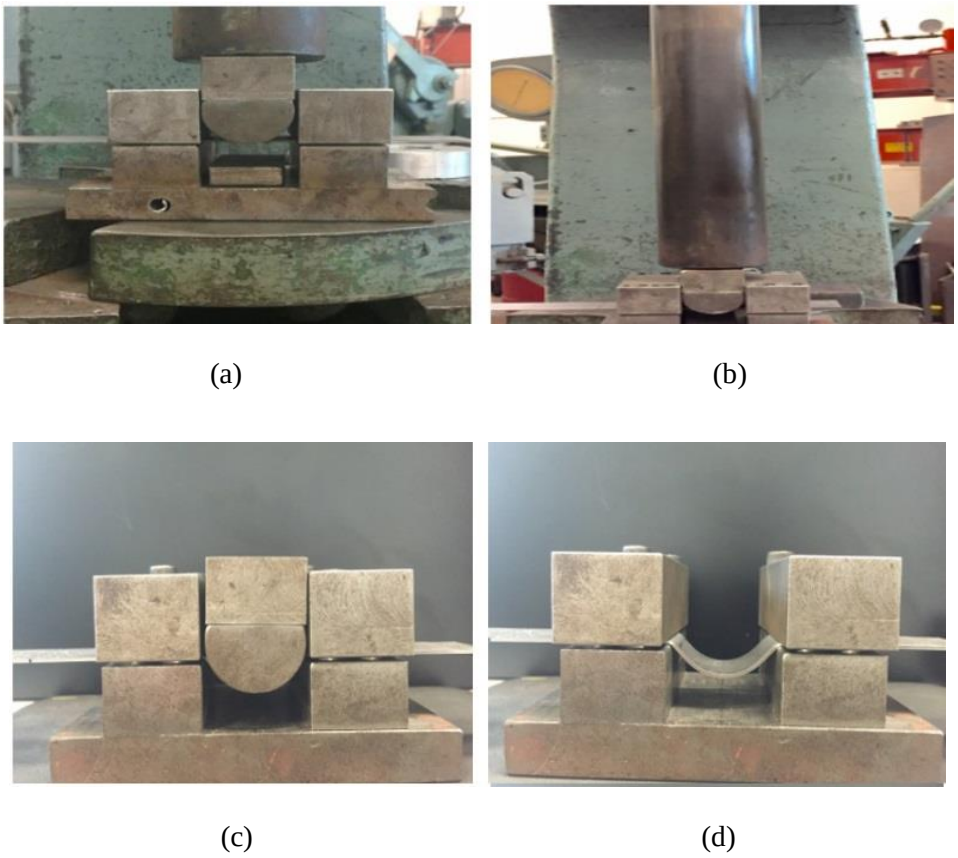
2 Experimental Procedure

The beams underwent the stamping process to create dimples on them at Western Michigan University's machine shop. A die and punch was used in the stamping process as shown in Fig. 1.



Figure 1: The die and the punch used in the manufacturing of the dimpled beams [8]

Two steps were used to create the dimples on the beam's surface [7]. First, the beam was clamped into the die to ensure that the clamped metal is not drawn (does not slip) during the stamping process. Second, the dimpled shape was pressed on the beam's surface. Figure 2 illustrates this process.



(a) (b)

(c) (d)

Figure 2: Manufacturing process of dimpled beam in four steps, (a), (b), (c), and (d) [9]

Table 1 shows equipment that was used to collect experimental data [9]. The National Instrument Data Acquisition system (NI DAQ) with the Smart Office (M+P International Smart Office) analyzer were used to collect and analyze the data. An impact hammer (PCB piezotronic /model 208C02) was used to generate the impulse force necessary to excite the beams at three different locations in order to extract the beam natural frequencies and mode shapes. The transverse vibration of each beam were measured using a single-axis accelerometer (PCB piezotronic/ model 352C22). The accelerometer was fixed onto the beam surface using the petro wax.

3 Scanning Method

Beam deformation results in *ANSYS*® can be exported in the form of nodal coordinates. To validate these results, the actual beam must be scanned at a set of discrete points with known coordinates. This is made possible by a 3D optical coordinate measuring technique. The digitization system Advanced Topometric Sensor (ATOS) is used to measure the beam with a high local resolution. The ATOS system consists of a sensor unit comprising of two cameras, a projector, a tripod, a control unit for the sensor head, and a high-performance computer. No additional hardware is required. The following section describes the measurement procedure.



Figure 3: The scanned beam with reference point stickers

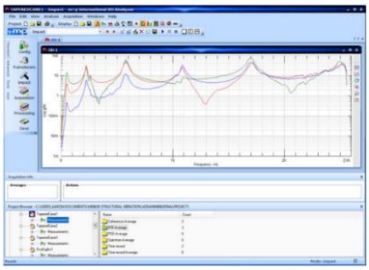
Equipment	**Function**
Two beam models. 	The material of the experimental model is steel and the uniform and dimpled beams have the same material properties.
Impact hammer model PCB piezotronic/model 208C02 with rubber tip. 	To generate the impulse force, that is used as the excitation to the beam.
A single axis accelerometer (PCB piezotronic/ model 352C22) and Petro wax.  	A single axis accelerometer is used to measure the acceleration. Petro wax is used to attach the accelerometer to the test beam.
A four-channel (NI -9234) data acquisition card and M+P International Smart Office Analyzer Software.  	A four-channel (NI -9234) data acquisition card to collect the data. M+P International Smart Office Analyzer Software to analyze the data collected.

Table 1: Experimental equipment [9]

The ATOS system is positioned in front of the beam and reference points are defined on the surface of the beam. These reference points are tiny stickers in the form of white circles inside black boxes as shown in Fig. 3. A striped pattern is projected onto the beam surface which is recorded by two cameras and 3D coordinates of the points on the surface are calculated by the software. All surfaces of the beam are exposed to the cameras at different angles, all the while keeping at least a few reference points in view. These partial images are then stitched together by the software with reference to the global coordinate system defined by the reference points. The beam is thus converted to a point cloud, which can be saved as equidistant sections normal to any of the principal axes of the global coordinate system.

4 Finite Element Modelling

Stamping is a metal forming process used to deform a part of the beam into a shape resembling a circular arc, referred to as a dimple. However, the principal premise of this study is to examine the effects of this process on the non-uniformity of thickness and width of the dimple and in turn, on the vibration characteristics of the beam. Therefore, it is necessary to simulate stamping first and then investigate the natural frequencies and mode shapes of the beams.

The software used for modelling and simulation was the *ANSYS®* Parametric Design Language (Mechanical APDL) module in *ANSYS®*. It was chosen due to its extensive library of elements, contact technologies, solvers and postprocessing capabilities. The overarching strategy followed here involves simulating stamping using a nonlinear static analysis to obtain a deformed beam, and then performing a modal analysis on this deformed shape. The nonlinear static analysis is executed as a series of consecutive load steps. Each load step involves a small amount of displacement of the plunger and consequently, a small amount of deformation of the beam. The simulation procedure consisted of the following salient points:

1. Creating a 3D parametric model
2. Assigning nonlinear material properties
3. Meshing the model
4. Setting up contact
5. Defining boundary conditions
6. Running a nonlinear static analysis to simulate stamping (results in a deformed beam shape)
7. Running a modal analysis using the output from the nonlinear static analysis

4.1 Creating a 3D parametric model

The setup used for stamping consists of a straight strip of cold drawn AISI 1018 steel, hereafter referred to as the beam, a plunger, four die blocks and a base plate. As shown in Fig. 1, the beam is held between two of the blocks on either side. Four bolts passing through each pair of blocks ensure that the beam is firmly clamped between them. This assembly, in turn, rests on the base plate.

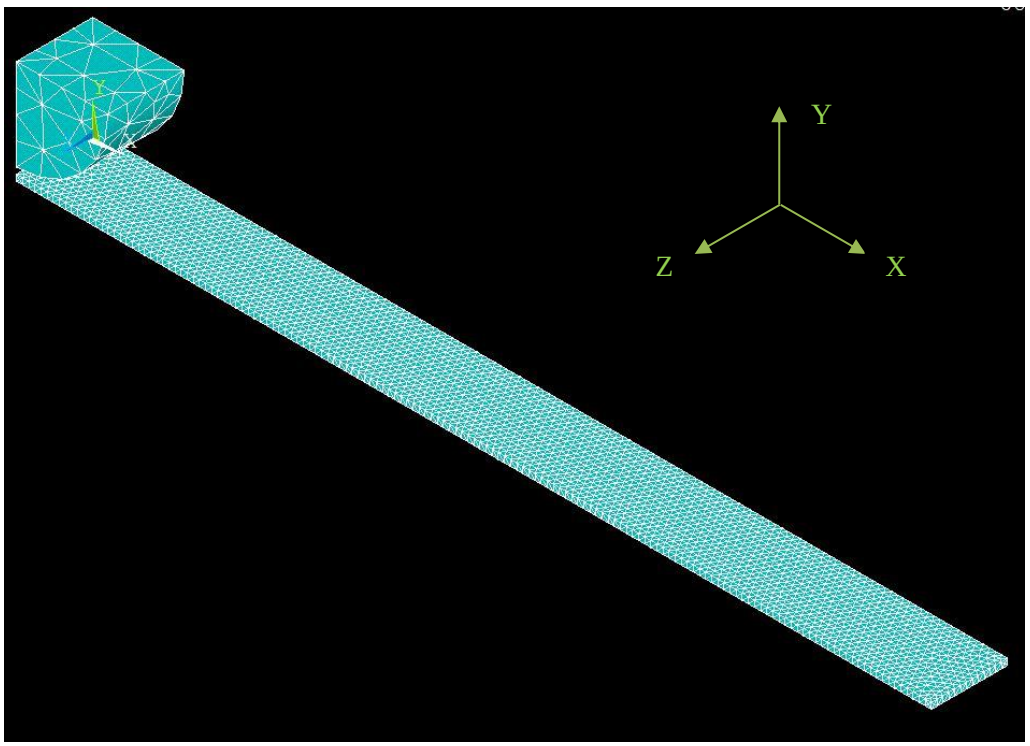


Figure 4: Finite element model with coordinate system (before beam truncation)

As shown in Fig. 4, in the coordinate system defined for the model, the X, Y and Z axes run along the length, thickness and width of the beam, respectively. The whole setup is symmetrical in the XY and YZ planes. Since in this study the dimple was located in the middle of the beam, it was decided to employ these symmetry conditions to better utilize time and computing resources. In addition, modelling the base plate and die blocks was avoided by implementing appropriate boundary conditions and parameters. An overhanging section of the beam outside the die blocks serves no meaningful purpose within the overall scope of the simulation for predicting the beam deflection. Hence, a truncated version of the beam with just a small overhang was included. Thus, the final model consisted solely of the plunger and the truncated beam.

To help ease modeling of beams/dimples of different size, parameters were used extensively to define the geometric characteristics of the model. Dimensions of the beam, dimple, plunger, and die blocks were some of the main quantities selected to be represented by parameters. Other model variables like material properties and the initial gap between the plunger and the beam were also defined this way.

4.2 Assigning nonlinear material properties

As this is a problem with plastic deformation, it is only logical that the material defined has nonlinear properties. Also, the material behavior after yielding corresponds to a bilinear kinematic hardening model, so a tangent modulus is specified to govern the post-yield stress-strain relationship. The beam is composed of cold drawn AISI 1018 steel, whose properties were obtained from MatWeb, as shown in Table 2.

Property	**Value**
Modulus of elasticity	200 GPa
Poisson's ratio	0.3
Coefficient of friction (with itself)	0.52
Density	7870 kg/m^3
Yield strength	250 MPa
Tangent modulus	1 GPa

Table 2: Material properties

4.3 Meshing the model

The model being three-dimensional, solid elements have been used to mesh it. The element selected is SOLID187 (*ANSYS®*16.1 element library), which is a higher order 3D, 10-node tetrahedral structural solid. It has a quadratic displacement behavior and is well suited to modelling irregular meshes. It is defined by 10 nodes having three degrees of freedom at each node (i.e. translation in the X, Y and Z directions). It also has plasticity, large deflection and large strain capabilities, all of which are required for our analysis. Another reason for selecting SOLID187 is a feature called mesh refinement that allows us to have a finer mesh in specific areas of interest that in turn, gives more in-depth results. For 3D solid models, a mesh refinement is possible only if the mesh is composed of tetrahedral elements. Using a higher order element allows us to capture a similar level of detail in a relatively coarser mesh as compared to a finer mesh consisting of lower order elements.

Meshing for the model has been done keeping in mind that the elements might get distorted by the end of the simulation due to large deflection and large strain. To avoid severe distortion, care must be taken that the elements do not have an aspect ratio greater than 2:1. To that end, the mesh settings have been specified so as to create elements that are roughly square in shape. Also, the plunger holds no interest for us, so its mesh is kept relatively coarse, while beam has a finer mesh to get as accurate results as possible.

4.4 Setting up contact

Defining contact correctly is a critical part of our analysis. Several important characteristics of this model, like the transfer of loads between the plunger and the beam, the elastic recovery of the beam, and the final shape of the dimple depend on how contact is set up. Our simulation requires that the plunger come down on the beam and deform it in a shape conforming to its own. However, this seemingly simple procedure cannot be replicated in *ANSYS®* as easily as it might seem at first glance. In *ANSYS®*, if the plunger is brought down on the beam, it will simply pass through it as the program does not understand that when two bodies coming in direct contact, one (or both) of them is (are) bound to deform. Hence, it is not sufficient to model the plunger and the beam alone but contact elements must be created as well.

The way this is accomplished is by designating the curved face of the plunger and the top face of the beam as surfaces coming into contact and populating them with contact elements of the appropriate kind. Contact elements fall into two main categories, namely target elements and contact elements. They are created on target and contact surfaces respectively, which together form the contact pair. There are several criteria for establishing and differentiating between contact and target surfaces, one of which is mesh or element size. If one surface has a fine surface mesh (small elements) and, in comparison, the other has a coarse mesh (large elements), the fine mesh should be the contact surface and the coarse mesh should be the target surface. In our case, the beam's mesh is finer than the plunger's. Hence, the top surface of the beam is designated as the contact surface and the curved face of the plunger is designated as the target surface.

The elements available for 3D surface to surface contact are TARGE170 for the target surface and CONTA173 and CONTA174 for the contact surface. CONTA173 and CONTA174 are functionally equivalent elements of lower and higher order respectively. The sole criterion for choosing between them is the order of underlying elements. Since the underlying elements are SOLID187, which are of higher order, CONTA174 is the element of choice for the contact surface. Thus, the beam and plunger surfaces were meshed with CONTA174 and TARGE170 elements, respectively.

4.5 Boundary conditions

Four sets of boundary conditions were implemented. The first set was used to implement the symmetry conditions along the X and Z directions (i.e. the YZ and XY planes respectively). The second set consisted of the initial boundary conditions and the first load step. The third and fourth sets consisted of load steps to move the plunger down on the beam and then back up again, respectively.

The symmetry conditions were enforced using commands built into *ANSYS®*. When symmetry in X direction is specified, displacement in the X direction is constrained. Similarly, when symmetry in the Z direction is specified, displacement in the Z direction is constrained.

In the second set, initial conditions are set. This involves a peculiar set of circumstances arising at the portion of the beam clamped between the die blocks. In the outer half of the blocks, displacements in X, Y and Z directions are constrained, while in the inner half of the beam, only displacement in the Y direction is constrained. The Y displacement is also constrained on the bottom surface of the beam. These conditions collectively enforce the displacement boundary conditions created by the die blocks and base plate, thereby making the inclusion of the actual components unnecessary. Additionally, the plunger is constrained to move only in the Y direction and is brought down to close up 90% of the initial gap between it and the beam. All this is saved as the first load step.

The third set of boundary conditions involves the plunger moving down on the beam in small displacement increments. This is achieved using a *DO loop, which is the *ANSYS®* equivalent of the more conventional 'for' loop. The fourth set has a similar loop, which then lifts the plunger back up, so that the beam can 'spring back' by recovering the elastic part of its deformation.

4.6 Nonlinear static analysis to simulate stamping

Since all the load steps have been defined and other data has been entered, starting the nonlinear static analysis is only a matter of issuing a few commands to specify some solver settings. The number of sub-steps in every time step is set and the program is instructed to save a 'restart' file at the last sub-step of the last successfully converged load step. Having a restart file saved is crucial for two reasons. The first is the scenario where the static analysis fails to complete successfully and the second is when the output from the static analysis needs to be available for further analysis. In either case, the restart file can be used as a starting point without having to repeat everything done up until that point.

The output from this analysis, shown in Fig. 5, corroborates several predictions regarding the final shape and size of the dimple. Firstly, it is clear that the dimple is not a perfect circular arc conforming to the shape of the plunger. Rather, its shape is a result of a combination of various factors such as the firmness of clamping provided by the die blocks, the lateral clearance of the plunger and die blocks, strain hardening of the beam material and elastic spring-back after load removal. The fundamental premise of this research, that the thickness and width of the dimple are not uniform, can also be validated visually.

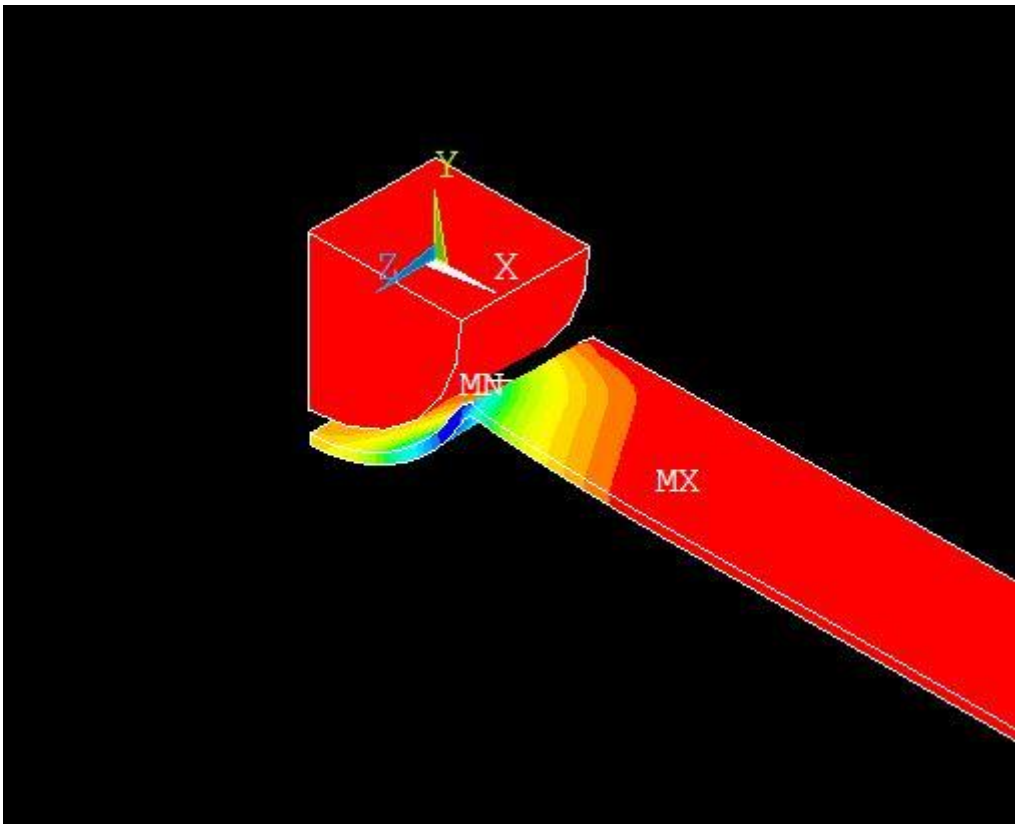


Figure 5: Deflected beam after stamping simulation

4.7 Modal analysis using the output from the nonlinear static analysis

Once the formation of a beam with a dimple having non-uniform thickness and width has been simulated, we can proceed to running a modal analysis of the deformed beam to look at its natural frequencies and mode shapes and compare them to the results achieved when the dimple was assumed to have uniform thickness and width. It is worth noting here that the truncated beam used for the stamping simulation cannot be used for the modal analysis, as it will have very different vibroacoustic characteristics rendering it unsuitable for comparison with previous results. To that end, the stamping simulation is run again with a full length beam, which is then input for the modal analysis. The first step is to delete all the constraints previously imposed on the model for the stamping simulation. Secondly, since the current study involves a

fixed-fixed beam, the fixed-fixed boundary conditions are applied. The first five natural frequencies and mode shapes are extracted for examination and are discussed in the following section. The first mode shape is shown in Fig. 6.

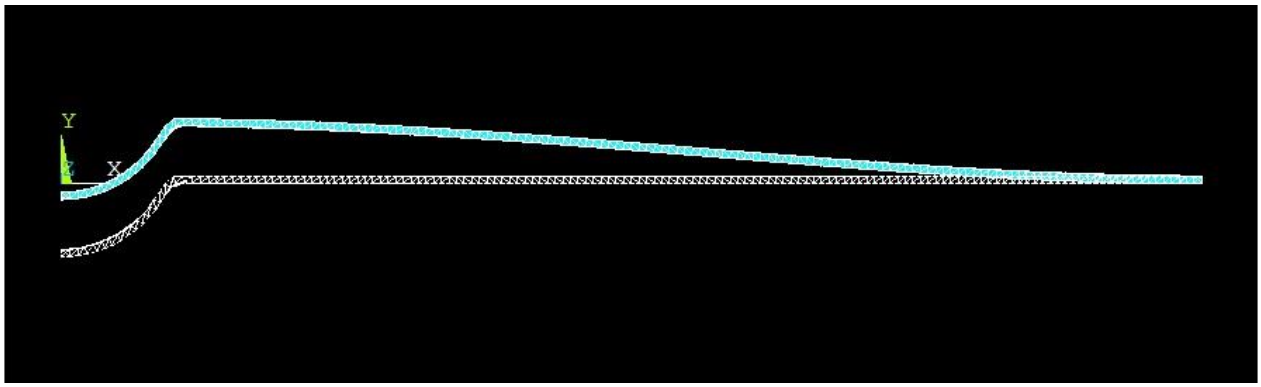


Figure 6: First mode shape corresponding to the simulated deformed beam (61.364 Hz)

5 Results and Discussions

At its most rudimentary level, creating a dimple can be characterized as simple elongation and bending of a straight beam. Since the material of the beam is elongated along its length, lateral strains cause contractions along its thickness and width. These lateral strains, however, vary as the deformation is in progress and this results in variable thickness and width along the length of the dimple. The section of the beam where the dimple starts is subjected to maximum strain while minimum strain occurs at the center of the dimple. Hence, the thickness and width reduce greatly at the start of the dimple. The least thickness and width are observed about halfway to the center. This trend is then reversed and some recovery can be observed as we get to the center. It should be noted, however, that the thickness and width never regain their original values. The presence of these nuances in the finite element model is clearly demonstrated in Figs. 7 and 8. In both the figures, the plot on top is the beam from the finite element model, while the one at the bottom is the scanned stamped beam. Visual inspection of these figures shows a close correlation between the simulation and the measured beam width and thickness.

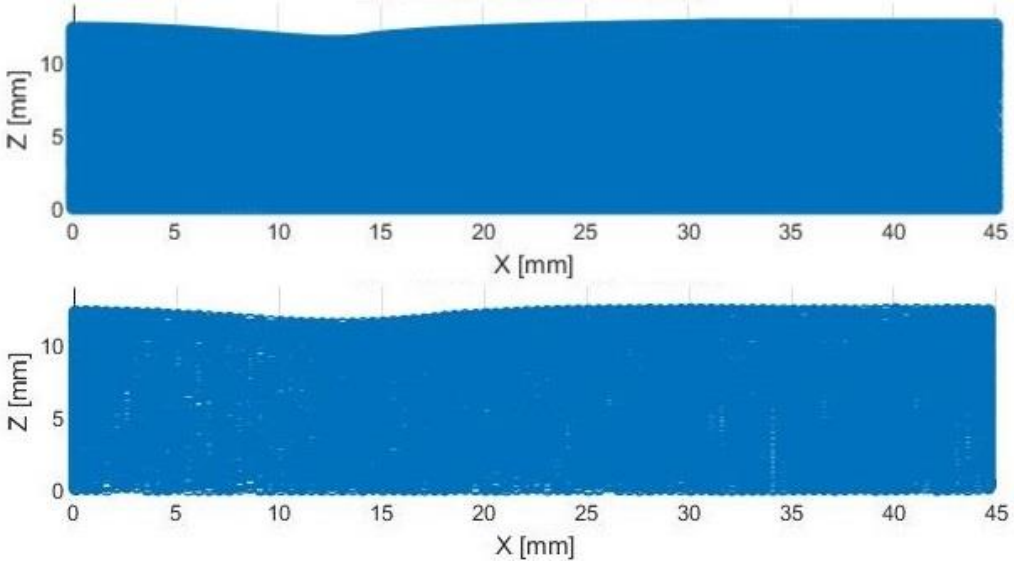


Figure 7: Width of finite element (top) and scanned (bottom) beams with a single dimple

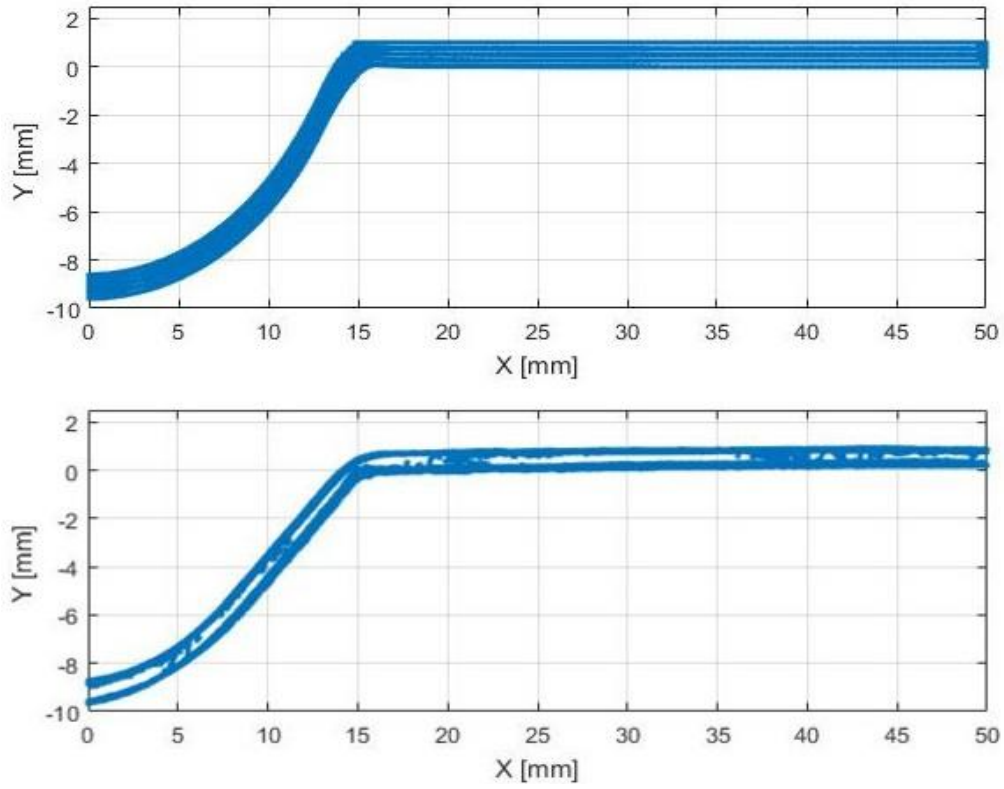


Figure 8: Thickness of finite element (top) and scanned (bottom) beams with a single dimple

Since the accuracy of the model has now been validated, natural frequencies for this model will now be evaluated against earlier work. It is very important to remember that the model for the current analysis consists of a quarter beam for the sake of symmetry, while previous analyses had a full beam. Consequently, the current model will exhibit only those natural frequencies whose mode shapes are symmetric. Hence, comparison of the two sets of results is valid and possible only for symmetric mode shapes. One such example is shown in Fig. 9.

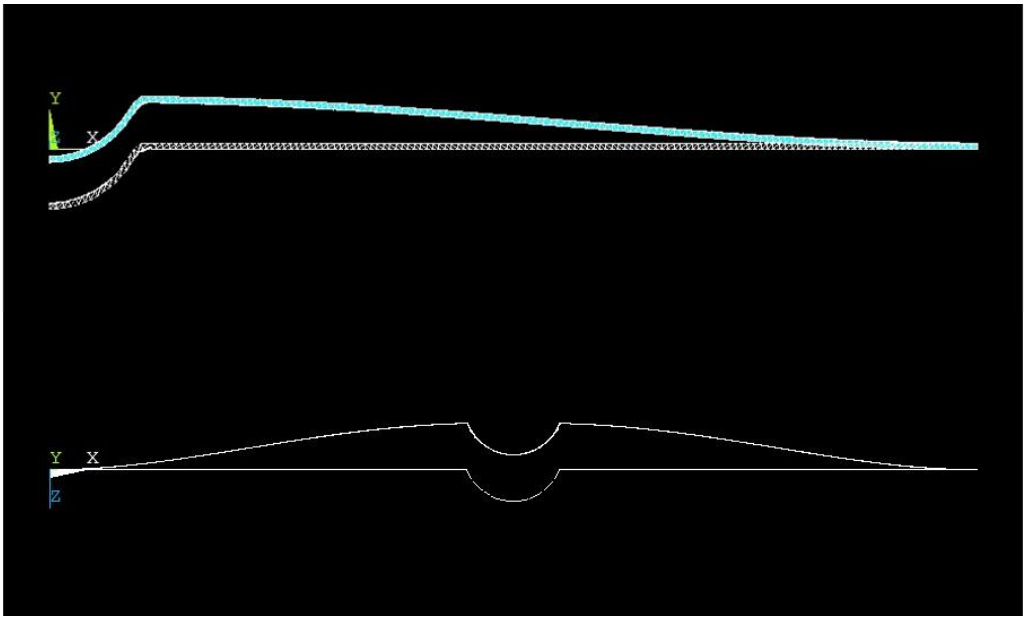


Figure 9: Comparison of the beam first mode shape (Top: variable thickness and width, bottom: uniform thickness and width)

Table 3 summarizes the first five natural frequencies of two beams with dimples having variable and uniform thickness and width. It can be seen that while the absolute difference in frequency increases as we proceed along the spectrum, the percent change remains more or less constant. The absolute and percent change in frequency have been calculated using the following equations:

$$\Delta f = f_v - f_u \tag{1}$$

$$\% \, \Delta f = \frac{\Delta f}{f_u} \times 100 \tag{2}$$

Where,

Δf is the absolute change in frequency

f_v is the frequency for the dimple with variable thickness and width

f_u is the frequency for the dimple with uniform thickness and width

Frequency	f_v (Hz)	f_u (Hz)	Δf (Hz)	% Δf
1st	61.364	58.793	2.571	4.374
2nd	339.840	325.653	14.187	4.356
3rd	848.290	812.626	35.664	4.389
4th	1596.300	1530.710	65.590	4.285
5th	2591.000	2487.730	103.270	4.151

Table 3: Natural frequencies for dimples with variable and uniform thickness and width

It is evident from Table 3 that the natural frequencies are affected by the variations in thickness and width. However, this change cannot be attributed solely to the variations. In fact, according to Myers [6, pp. 105-115], several factors such as boundary conditions, dimple angle, the variation of modal strain energy along the beam, dimple chord length etc. influence the natural frequencies of a dimpled beam.

6 Conclusions and Recommendations for Future Work

The stamping process which is used to create dimples was simulated using finite element software. To save time and computational resources, the symmetric nature of the model was utilized and just a quarter of it was created. The resulting shape of the beam, with varying thickness and width, was compared with a scan of an actual stamped beam and found to be accurate. Subsequent modal analysis of this beam showed that natural frequencies are indeed affected by the variations in the thickness and width of the beam.

Having said that, it must be remembered that these results have been obtained for a specific set of conditions and there are multiple avenues along which future work may progress. Further research may deal with changing key parameters of this study and seeing how the end results are affected.

Firstly, the boundary conditions of the beam in this study are fixed-fixed. It will be interesting to see if and how the effects on frequencies change when the boundary conditions are changed.

Secondly, it has been noted that natural frequencies having asymmetric mode shapes will be absent from the current model. Creation of a full model of the beam would allow us to investigate asymmetric mode shapes and frequencies. Further, this would also allow us to model dimples that are not at the center of the beam. This would be a step closer towards simulating real-life vibration control techniques, since the dimple may not always be placed in a symmetric position. Rather, its 'optimum' location is largely dependent on the variation of modal strain energy along the length of the beam.

Thirdly, it may be the case that addition of a single dimple to a beam will result in small changes to its vibration characteristics. In such a scenario, it might become necessary to employ multiple dimples. Further, each of these dimples may have different angles, chord lengths and orientations (i.e. pointing in the same or opposite directions). The cumulative effects of these factors and their interactions with each other will provide crucial insights into how and why dimples affect the natural frequencies and mode shapes of beams.

Lastly, learnings from this research can also be applied to create beads and dimples on plates to aid in the control of their vibrations and sound radiation.

References

[1] W. Cheng, C. Cheng and G. Koopmann, "Dynamic beam modification using dimples," *Journal of Vibration and Acoustics,* vol. 130, 2008.

[2] W. Cheng, C. Cheng and G. Koopmann, "A new design strategy for minimizing sound radiation of vibrating beam using dimples," *Journal of Vibration and Acoustics,* vol. 133, October 2011.

[3] N. Alshabatat and K. Naghshineh, "A design approach for improving the vibroacoustic characteristics of plate structures," in *Proceedings of the ASME 2011 International Mechanical Engineering Congress & Exposition,* Denver, CO, Nov. 11-17, 2011.

[4] N. Alshabatat and K. Naghshineh, "Optimization of the natural frequencies of beam via dimpling technique," *International Journal of Modelling and Simulation*, vol. 32, no. 2, pp. 134-144, 2012.

[5] K. Myers and K. Naghshineh, "Analytical model and numerical optimization of vibrating dimpled beam," *The 22nd International Congress of Sound and Vibration*, 2015.

[6] K. Myers, *Analysis of Vibroacoustic Properties of Dimpled Beams Using A Boundary Value Model,* A Dissertation Submitted to the Graduate College in Partial Fulfillment of the Requirements for the Degree of Doctor of Philosophy, Department of Mechanl and Aerospace Engineering,Western Michigan University, 2015.

[7] M. H. Ghazwani, K. Myers and K. Naghshin, "Development of an Analytical Model for Beams With Two Dimples in Opposing Direction," in *ASME 2017 International Mechanical Engineering Congress and Exposition*, Tampa, 2017.

[8] N. Alshabtat, Beading and dimpling techniques to improve the vibration and acoustic characteristics of plate structures, Western Michigan University, PhD Thesis, 2011.

[9] M. H. Ghazwani, *Development of an Analytical Model for Beams with Two Dimples in Opposing Directions,* Kalamazoo: http://scholarworks.wmich.edu/masters_theses/761, 2016.

Optimizing of acoustic doors using laser-spectro-vibrometry and finite element methods

C.C. van Dijk[1]
[1] Alara-Lukagro, R&D Department
Huijgensweg 3, 2964 LL, Groot-Ammers, the Netherlands
e-mail: **ch.van.dijk@alara-lukagro.com**

Abstract
Alara-Lukagro is a manufacturer of noise control solutions. One product range consist of acoustic door sets. The door sets are tailor made for projects and have more than just acoustic properties. Each individual Property implies size limitations depending on the legislation involved in the acquiring of the certificates. The manufacturing of these door sets is more labor intensive than mass produced door sets, the door sets are mostly used when acoustic isolation requirements are high in the lower frequencies. Despite the use of double walled structures, mass is an important ingredient for achieving these properties. Therefore the weights of the door sets is high, sometimes more than available ironmongery, or mechanics can handle. Therefore Alara-Lukagro started this year in conducting research in ways to achieve comparable properties with less weight. The evaluation in lower frequencies is sometimes unpredictable. While simulations become more viable. In this presentation Alara-Lukagro will share some of the experience gained by using FEM and Laser-Doppler-Spectro-Vibrometric measurements.

1 Introduction

As a door manufacturer there are a couple of phenomena that influence the design of doors. Certification, legislation and documentation play an ever more important role. There are more possibilities in access control, and even intensively used structures use more and more lightweight construction-elements. Alara-Lukagro is a steel works that is specialized in acoustics and vibration control. It therefore also produces steel doors. Doors are always built to order, and the development of adjustments is so, that several adjustments are introduced annually. Alara-Lukagro now has one of the most versatile doors in the world. But because of all these certifications, the restrictions on modifications are high. In order to stay ahead of the competition both the effect of drastic design changes for future doors, and small modifications need to be quantified acoustically. In order to do so in an acceptable timescale, the use of a finite element method is beneficial. These models are good in predicting improvements and impairments, but absolute values can be far from reality. Alara-Lukagro has asked the KU Leuven to perform Laser-Doppler-Spectro-Vibrometric measurements in order to help quantify its' models and eventually improve their modelling skills. So that the finite element method could better predict the effect of adjustments, and can be an essential aid in a complete design change.

In this paper the use of two dimensional and three dimensional models is compared with results from both laser-spectro-vibrometic measurements and acoustic measurements. The field in which we are mostly active requires insight between 25 and 400 Hz. By leaving out higher frequencies we can significantly reduce simulation times.

The aim of this paper was to show the correspondence between measurements and simulations. Especially because the predictability of the lower frequency of these frequencies is higher. The model still needs to

undergo significant changes. Therefore it is more a reflection on what changes need to be made, and why they are important in the specific modeling of a door structure. These reflections are important, because they bridge theory and practice.

2 Laser-Doppler-Spectro-vibrometric test

2.1 General

This test method analysis the vibration of an object. Since the radiated sound is directly related to the vibrations of a solid surface area that resolves in pressure fluctuations in air, this can be directly related to sound radiation of a surface. The laser doesn't influence the structural dynamics of the surface, because it doesn't change the mass or intervenes with the dynamics. In order to conduct such research reflective stickers need to be placed on the sample (see figure 1). The test was conducted in both directions. The stickers introduce a negligible change in mass. The excitation was done by a shaker, as seen in figure 1 on the right.



Figure 1. On the left and in the middle, measurement points on both directions. On the right the setup of the shaker.

Besides laser-Doppler-spectro-vibrometric measurements, ISO 10140 measurements were conducted. The sound reduction that is measured with laser-Doppler-spectro-vibrometry between 5 and 80 Hz is used, and the ISO 10140 measurements are used in higher frequencies. Two completely different door sets were measured the second door set is used to validate the robustness of the models. This report will focus on the most simple construction of the two doors.

2.2 Measurement results

First the results of all 91 observation points is averaged per excitation point. The excitation points are put in a grid of 3, times 6 point grid. Point 3,2 may seems like an anomaly, but may also be explained by its proximity next to a fixed locking point.

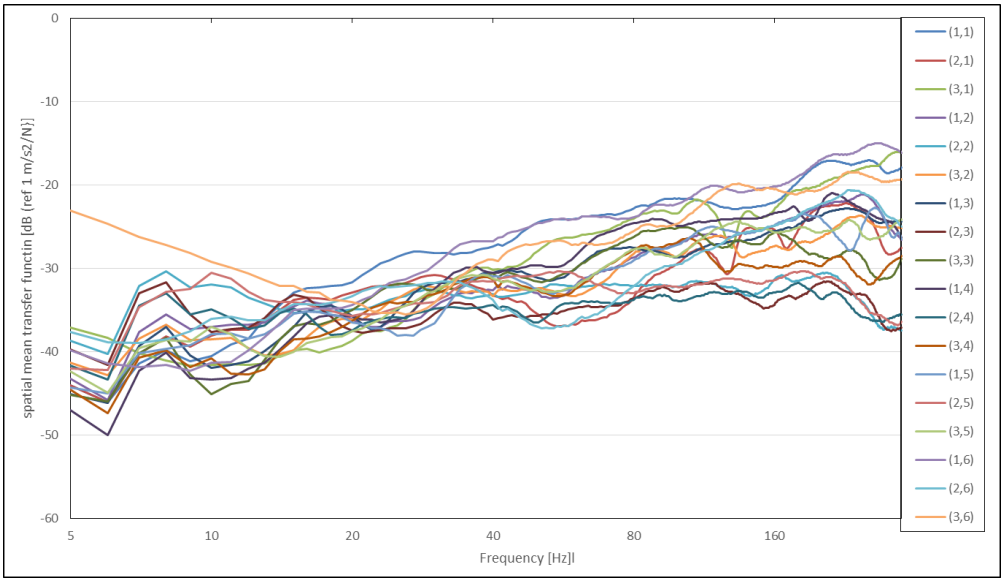


Figure 2. Mean transfer function per excitation point, the excitation points (horizontal direction, vertical direction).

From the transfer function as well as the ISO measurements a sound reduction value R may be derived. Values from both methods are plotted in figure 3.

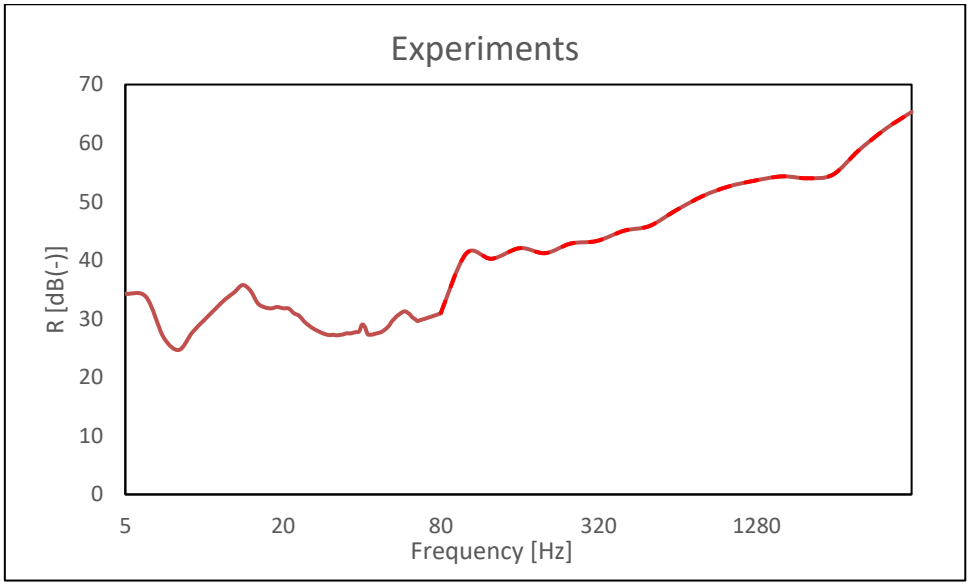


Figure 3 Continuous experimental results on the sound reduction favoring LDV till 80 Hz in single colored line and ISO 10140 from 80 Hz in dashed double colored line.

Bases on the transfer function, lower sound reductions between 80 and 350 Hz are expected than found based on ISO 10140 (see figure 2 and 3). It is not certain if this is due to interactions between the door and the wall, or if this is due to the method. A shaker has the benefits that it does not suffer from acoustic modes in the sending or receiving chamber, and is less effected by background noise than acoustic measurements. The influence of the point load of a shaker should be compared to an acoustic wave,especially in this frequency range.

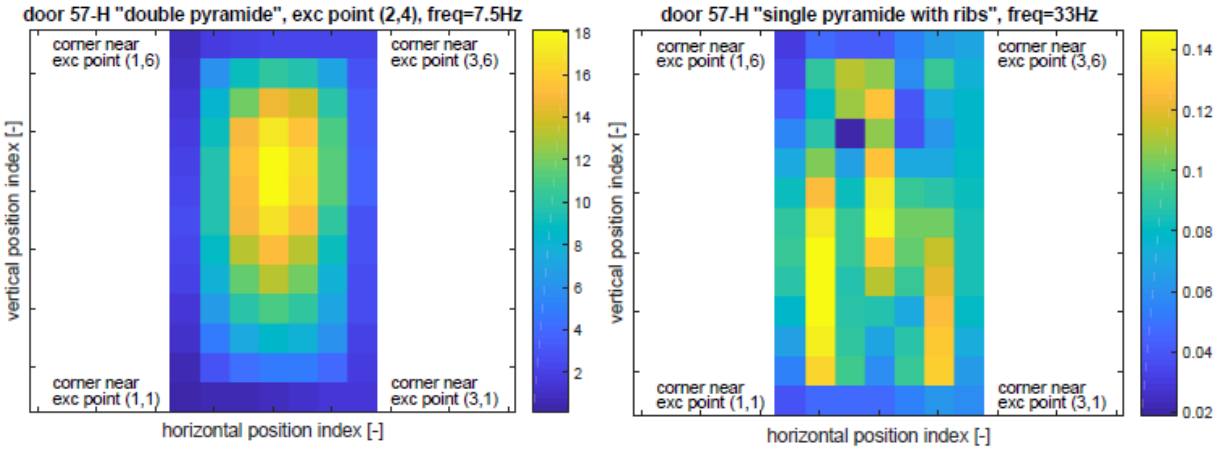


Figure 4. The vertical pressure index with respect to different frequencies

From figure 4 both at 7.5 and 33 Hz the modes of the door can be derived. At 7.5 Hz door acts as I n first mode, at 33 Hz the oscillation is split in six areas, of which three positive and three negative. One positive part at the upper half and two positive parts at the lower half near the sides. In time domain the positives and negatives interchange.

3 Finite Element Method

The sound reduction from figure 3 is compared to a 2-D simulation in figure 5 (left). In the 2-D simultion the optimum width was determined in order to reduce the probabillity of coincidences in a frequency domain where attenuation is so low, that could cause a risk on the ovrall sound reduction. Therefore the doorwidth was 1.3 m.
In figure 3 te lowest sound reduction is found just over 50 Hz. This dip cannot be found in the 3D model. This could be due to the fact that the height in the door will dominate the direction of the free sound field, which effect is not present in the 2D model. This height is roughly twice the width. Despite this logics this is a reminder of one great risk we can find in 2D modelling of such structures.

The sound reduction in dB equals:

$$R = 10 \cdot log \frac{P_{in}(f) - P_{out}(f)}{A} \quad (1)$$

Her $P_{in}(f)$ is the incoming sound power as a function of frequency, and $P_{out}(f)$ is the outgoing sound power as a function of frequency.

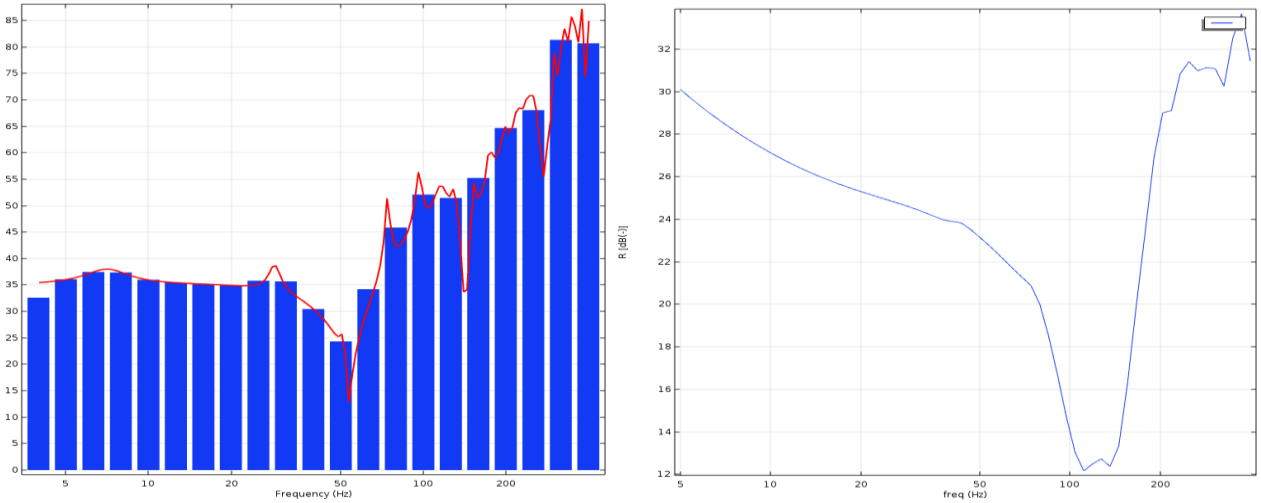


Figure 5. (left) sound reduction in 2D model (right) sound reduction in a 3D model.

3.1 2-Dimensional model

Another importnt issue with the 2D- model is the overestimation of the noise reduction. As a source a random wave field was used. In the gemetrical sound pressure level plots as shown in figure 6 can be seen that the perfectly matched layer at the outer shell of the acoustic field needs to conferge to quickly into zero. This is especially clear on the strong color variation on the loaded side. There was also no empty element placed between the random field and the door. This may result in an upstruction of the feedback/interaction of the door leaf on this pressure field. Because of the absence of the predominant diretin, namely the height of the door, the 2D model sould not be used for this frequency range anyway.

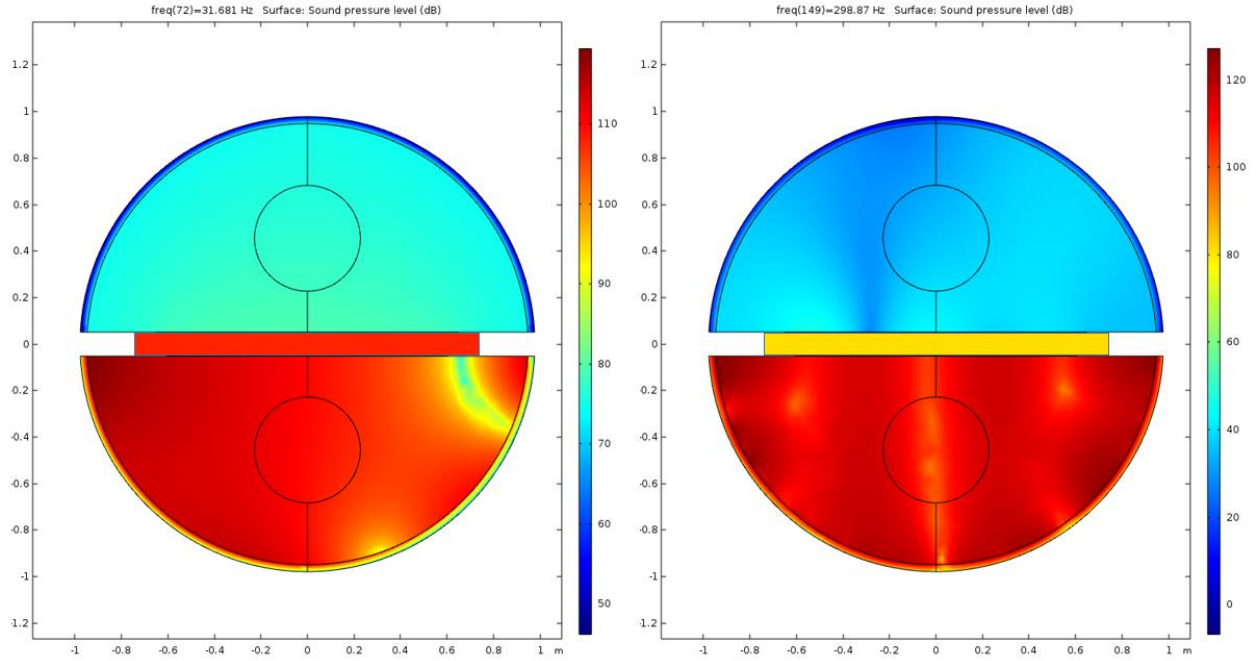


Figure 6. Sound pressure field around 31 and 300 Hz on both sides of te dividing structure according to a simple 2-D model.

3.2 Modes in the 3D model

The three dimensional model is more in line with the experiments, however the lower sound reduction values spread over a much wider range of frequencies. Than found in the experiments. The model used a plane wave radiation. When the isosurfaces in figure 7 are compared to the experimental results it can be seen that the behavior is similar in 7.5 Hz. Experiments point 7 Hz out as the eigen-frequency of the door, but that doesn't reflect the outcome of the simulations. In 33 Hz we don't find the third mode in the simulation, which doesn't correspond with the experiments. A similar pattern as in the experiments only disappears at 43 Hz, as can be seen on the right of figure 7. So even the shape patterns in the model are different from the experiments.

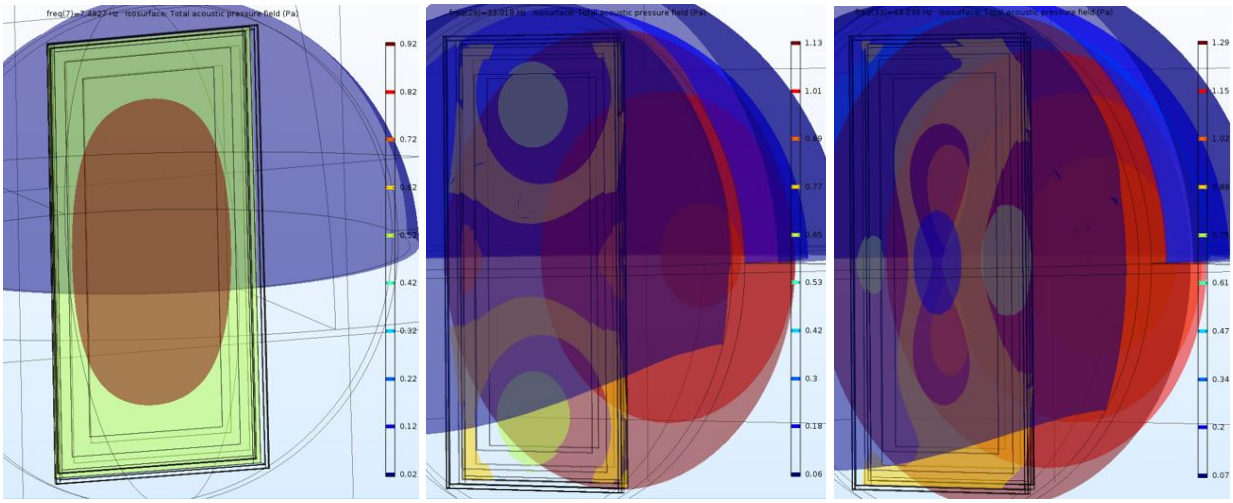


Figure 7. Isosurfaces of sound pressure levels in frequencies round 7.5, 33, and 43 Hz.

3.3 Reflections on comparison between experiment and the 3-D model

Simulations are always a simplification of the real world. In order to make these simplifications assumptions are made. Some assumptions have proven to be negligible others are new for this specific model and are reviewed in this section.

A. Excitation of the load side

18 excitation points were selected. The test door was not uniform on the inside of these positions. More excitation points may show better comparison with the excitation by an acoustic field. Although 18 points may also be sufficient. Making additional measurements is costly and time consuming. The effect of more excitation points could be best investigated in a simulation.

B. character of the load

Especially in low frequencies, the acoustic load has a wide area of comparable load, and can at the same time pose an equal opposite force at a significant distance. This has a different mechanical vibration dynamic with the plate work on the loaded side. As expressed earlier there are also benefits for a mechanical load, like the shaker that was used, noise in a laboratory in these frequencies can create standing waves in different modes, which can interact with the door surface by the positioning of the door surface in the room. Comparison of these measurements with such a model should be subject to the same load conditions, being point excitation rather that an acoustic load.

C. Interaction with frame, elasticity, hinges, lock and rubber

From figure 2 can be seen, the connection points can have a strong influence on the low frequency behavior of a door. This corresponds with field measurements that are not included in this paper. It does however show the importance of these connections in accordance with acoustical simulations. This may even be the strongest suspects why not all the coincidence frequencies from the measurement could be found in the simulation. These mechanisms should therefore be included in the model.

D. Leakage along door

The rubber sealing is in many cases the weakest point in the acoustic insulation of a door. Therefore interaction between the noise in the air between the door and the door frame can have a significant influence on the door leaf on the unloaded side. However since we don't use acoustic excitation this path can be assumed negligible.

E. simplification on bended curves in steel.

Steel doesn't deform in sharp angles, but is bended over a curvature. The radius of this curvature is small, typically below 2 mm. However bending also influences the mechanical properties of the steel. The model could be refined to take this local deviation into account.

F. Material properties not specifically verified

Some important material chooses of the internals of the door do not come with a full list of properties. Based on similar materials some properties such as the speed of sound had to be estimated. Furthermore the average speed of sound within porous material could differ from the speed of sound in air, because of the high viscosity. How the model deals with the interacting viscosity and the interaction with speed of sound has to be investigated, as well as some properties need to be verified.

G. Mesh accuracy

Convergence plots don't show the model to have any problems with convergence. Therefore the mesh must be assumed sufficiently refined. Since the model will need to be adjusted in a number of ways, this needs to be reinvestigated after each adjustment.

It should be clear that these models cannot just be built and expected to correspond with reality, even if the mesh is perfect, all material properties are known and implemented in the right way, and the physics is correct. Interactions with boundaries and the character of the load are important factors.

4 Conclusions

Both simulations and measurement result show phenomena around the coincidence frequencies that comply with logics. However the model is lacking a number of potential coincidences that are found in reality. It can safely be assumed the initial optimum dimensions were false. The 3D model has sound reduction values that are in the same order of magnitude as the experiment. However the 3D model seems to miss out on more potential coincidences than the 2D model. The model will need to be adjusted, it should include connections to the frame, and it should be excited in the same way as the experiment. After these adjustments the comparison should again be made before further refinement of the model.

Acknowledgements

This ongoing research is sponsored by Alara-Lukagro. The measurements were conducted and analyzed by Bert Roozen and Willy Bruyninckx from the KU Leuven.

Wave propagation in an auxetic core embedding resonators

M.A. Campana [1], **F. Scarpa** [1], **M. Ouisse** [2], **E. Sadoulet-Reboul** [2]
[1] Bristol Composites institute (ACCIS), CAME, University of Bristol,
University Walk, BS8 1TR Bristol, UK

[2] University Bourgogne Franche-Comté, CNRS/UFC/ENSMM,UTBM,FEMTO-ST, Department of Applied Mechanics,
24 Chemin de l'Epitaphe, Besancon 25000, France

Abstract
Stop bands in auxetic periodic structures including resonators are investigated in this paper. In aerospace field, sandwich panels like honeycombs are mainly used for their structural properties, and can present some advantages for vibroacoustics control. Auxetic structures seem to give enhanced properties for wave propagation control, and have been used here to perform the analysis. Resonators are included to open resonant band gaps in addition to the Bragg band gaps given by the periodicity of the core. Studies on the number of resonators inside the unit cell have been performed for a constant mass to identify the configuration which are able to open stop bands at low frequency range. Also, a parametric analysis on the resonator properties is done to compare the benefit concerning wave propagation while having a reasonable added mass for the core structure.

1 Introduction

Wave propagation in periodic structures has been investigated in many different fields of physics such as optics, acoustics or mechanics. More particularly, the study of crystal lattices known as phononic crystals as been highly investigated, representing a quantum vibrational of energy in an elastic medium, in order to create stop-bands for certain values of frequency, preventing the wave propagation through the periodic media due to an interaction between transmitted and reflected waves. Recently, periodic structure analyses have been extended to engineering structures such as honeycombs [1] in the aerospace field. One of the important aspects of introducing theory of periodic structures in engineering is the ability of describing behaviour of an entire structure just by analysing a part of it, called unit cell, instead of doing the analysis in the whole structure, earning a non negligible amount of computational time. Another interest, as it has been developed in the past with the phononic crystals, is the possibility of analysis of the band gaps linked to the periodicity. Unlike phononic crystals, many types of elastic waves exist inside elastic periodic structures (longitudinal, flexural, shear...) and some techniques can be used to cancel the propagation of specific type of waves. One of them consists in taking advantage of the Bragg band gaps, which are directly linked to the size of the unit cell constituting the whole structure. In this work, another type of band gap is investigated, called resonant band gap, created by adding some inserts such as resonators inside the structure. This approach make possible to improve the vibroacoustics performance of the structure by keeping its geometry and material properties constant, and so find a great interest in sandwich like structure as honeycombs, initially designed to improve the ratio stiffness over the mass of the structure, providing a good resistance for a low weight. Including resonators become on that way interesting since they do not modify the shape of the periodic structure, keeping all the structural characteristic of the honeycomb. Moreover, unlike the Bragg band gap, the resonant effect can open stop bands in the first modes of the structure, making the study more efficient to work in the low frequencies range. Resonators have been mainly investigated for chained

spring-mass systems [2], or beams [3] and plates including resonators [4], [5]. Many of these works have been also summarized covering several types of structure [6]. Among all these studies, it has been shown that the location of the band gap is narrowly linked to the eigenfrequency of the resonator while the bandwidth depends on the mass ratio between the resonator and the structure itself, allowing a predictable design of the resonators to target specific frequencies. However, this specificity is not true anymore when the structure has a complex shape like honeycombs. The shape of the media is not continuous as a plate or a beam, and the dynamic of the structure itself has to be taken in account in addition to the effect of the resonator, making the prediction of the cut-off frequencies more complex. Some analyses have been performed in an re-entrant core of a sandwich structure, to investigate how has to be tuned the resonators in order to obtain the widest band gaps in a relatively low range of frequency.

2 Periodic structures

A periodic structure is generally represented by a portion of the structure, called unit cell, representing the whole structure if it is repeated in one or several direction. We call 1D periodic structure if the repetition follows one direction, and so on for 2D and 3D periodic structure. To study the behaviour of the structure in an infinite way, Floquet-Bloch Theorem is applied to have access to the dispersion curve, giving the relation between the frequency and the wavenumber of the whole structure. Also, the Transfer Matrix Method is usually used in 1D case to compute the finite response of the full structure, choosing a fixed number of repetition of the unit cell.

2.1 Floquet-Bloch Theorem

The application of the Floquet-Bloch Theorem requires the a periodic structure to be applied. A simple representation for the 2D case is given in the figure 1. The unit cell is repeated along the x_p and y_p direction and its size (a_x, a_y). Each point P of a cell can be linked with the origin of the periodic structure thanks to the relation $r_p = r_{lp} + \boldsymbol{i}x_p + \boldsymbol{j}y_p$, with $\boldsymbol{i}$ and $\boldsymbol{j}$ the number of repetitions in each direction. Floquet Theorem has been introduced for the first time in the analysis of the solutions of periodic differential equations [7] in the 1D case. The Theorem stipulates that if $A(t)$ is a T-periodic matrix and $X(t)$ the fundamental matrix of solution of the ODE

$$\frac{\partial \mathbf{x}}{\partial t} = A(t)\mathbf{x} \tag{1}$$

then $X(t) = P(t)e^{Rt}$ is a solution of equation (1) with $P(t)$ a T-periodic matrix and R a $n \times n$ matrix. From this equation it comes that

$$X(t+T) = X(t)e^{RT} \tag{2}$$

In the field of mechanics, the Floquet theorem has been extended for 2D and 3D cases by the actual Floquet-Bloch Theorem for periodic structures

$$u(P) = u(O)e^{\mathbf{k}(\mathbf{i}x_p + \mathbf{j}y_p)} \tag{3}$$

with $\mathbf{k}$ the wavevector and $u(O), u(P)$ respectively the amplitudes of displacement at the origin and at the current point P.

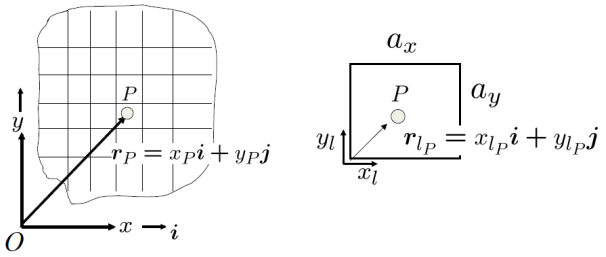


Figure 1: Representation of a 2D unit cell

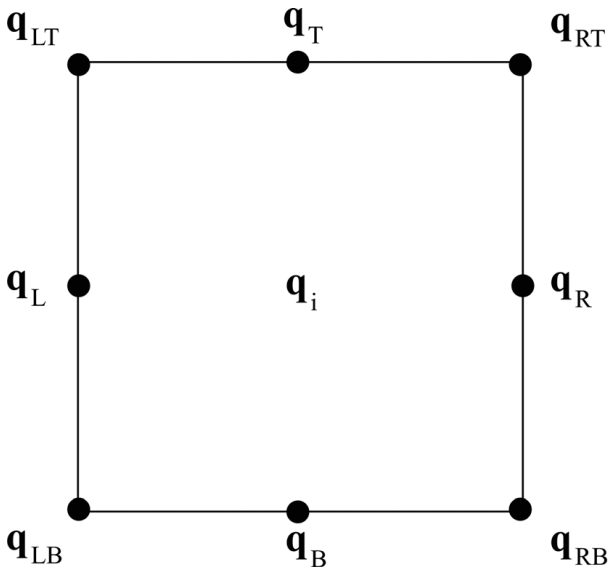


Figure 2: General representation of a unit cell using the finite element method in 2D

2.2 Application to periodic structures

The Floquet-Bloch Theorem can be applied in structures considered as continuous or discretised using the finite element method. Since the analytical expression become complex for honeycombs structures including resonators, the second option is used in this study. One of the most common tool used to study periodic structures involving the Floquet-Bloch theory is the Wave Finite Element Method (WFEM). Considering a discretisation of the structure as shown figure 2, all the boundaries of the unit cell can be linked using the Floquet relations, such as

$$\begin{array}{l} q_R = e^{j\mu_x} q_L,\ q_T = e^{j\mu_y} q_B,\ q_{RT} = e^{j(\mu_x+\mu_y)} q_{LB},\ q_{LT} = e^{j\mu_y} q_{LB},\ q_{RB} = e^{j\mu_x} q_{LB} \\ f_R = -e^{j\mu_x} f_L,\ f_T = -e^{j\mu_y} f_B,\ f_{RT} = -e^{j(\mu_x+\mu_y)} f_{LB},\ f_{LT} = -e^{j\mu_y} f_{LB},\ f_{RB} = -e^{j\mu_x} f_{LB} \end{array} \tag{4}$$

where $\mu_x = k_x L_x$ (respectively $\mu_y = k_y L_y$) is the reduced wavenumber, with k_x, k_y the wavenumber and L_x, L_y the length of the unit cell in the x or y direction, q is the vector of displacements on each node and f the vector of efforts. The letters L, B, R, T relate respectively to left, bottom, right and Top. The effect of damping is neglected here since some works have been done including it [8], so the dynamic equation is given by

$$([K] - \omega^2 [M])q = f \tag{5}$$

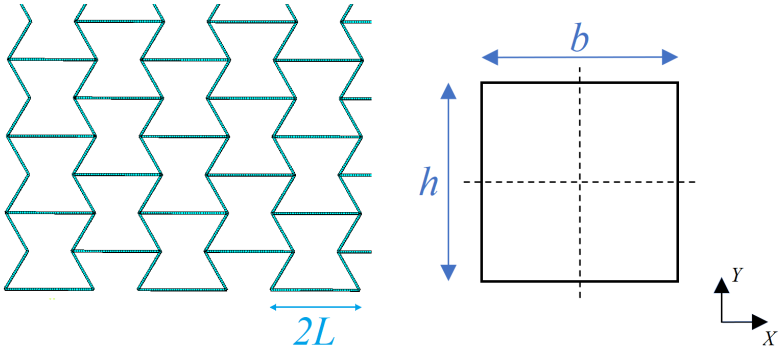


Figure 3: Part of the re-entrant structure

with $[K]$ and $[M]$ respectively the stiffness and mass matrix of the unit cell, q the vector of displacements on each node and f the vector of efforts. Including the Floquet relations into the equation (5), and assuming that all the internal efforts are equal to 0, it leads to a new dynamic relation given by

$$([K_r(\mu_x, \mu_y)] - \omega^2[M_r(\mu_x, \mu_y)])q_r = 0 \tag{6}$$

where $[K_r]$, $[M_r]$ and q_r are the reduced vectors. The equation (6) is an eigenvalue problem in ω^2 which leads, once solved for input values of μ_x and μ_y, to the dispersion curve giving the value of the group velocity inside the full structure, and also to the locations of the band gaps. The values of reduced wavenumber are chosen according to the First Brillouin Zone [9]. In this study, the First Brillouin Zone is given by $\mu_x = [0, \pi]$, $\mu_y = [0, \pi]$, and only the contour of the dispersion surface will be plot in order to identify the band gaps.

2.3 Model of the unit cell

For this study, a re-entrant and an hexagonal structure are studied as the core of the periodic structure. A Finite Element Model has been considered here, using Timoshenko beam elements with squared cross section. A representation of the Finite Element structure is shown in figure 3 and the geometric/material properties are listed in the table 1 for the auxetic configuration, where L refers to the length of one beam constituting the unit cell, b the thickness in X and h the thickness in Y direction. The hexagonal one has exactly the same properties, excepted the internal angle going from $-\frac{\pi}{6}$ to $\frac{\pi}{6}$.

The resonator used is also modelised as a Timoshenko beam, attached to the corners of the re-entrant unit cell in a fixed-free configuration. The properties of the resonators are the same as the unit cell, excepted for the length given by $L_r = 6.8$ mm. A representation of the unit cell with the resonator is shown in figure 4. This design of unit cell has already been used in the past [10], and is very convenient to include resonators. Indeed, in this configuration, it is possible to include two resonators by unit cell, which corresponds to exactly one resonator by ”butterfly” pattern. Also, configurations with four resonators by unit cell will be analysed to check the impact on vibroacoustics performances.

The Floquet conditions are applied to the border of the unit cell of the figure 4, leading to the following relations:

$$\begin{aligned} q_R &= e^{j\mu_x} q_L,\ q_{T_1} = e^{j\mu_y} q_{B_1},\ q_{T_2} = e^{j\mu_y} q_{B_2} \\ f_R &= -e^{j\mu_x} f_L,\ f_{T_1} = -e^{j\mu_y} f_{B_1},\ f_{T_2} = -e^{j\mu_y} f_{B_2} \end{aligned} \tag{7}$$

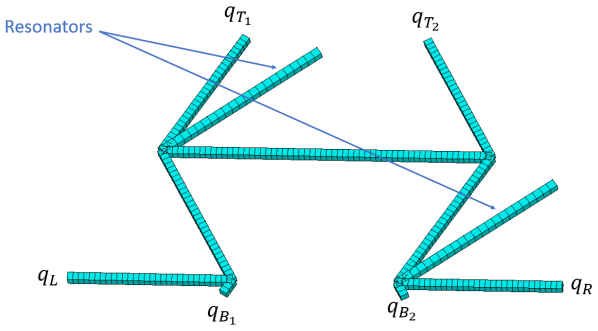


Figure 4: Re-entrant unit cell with resonator

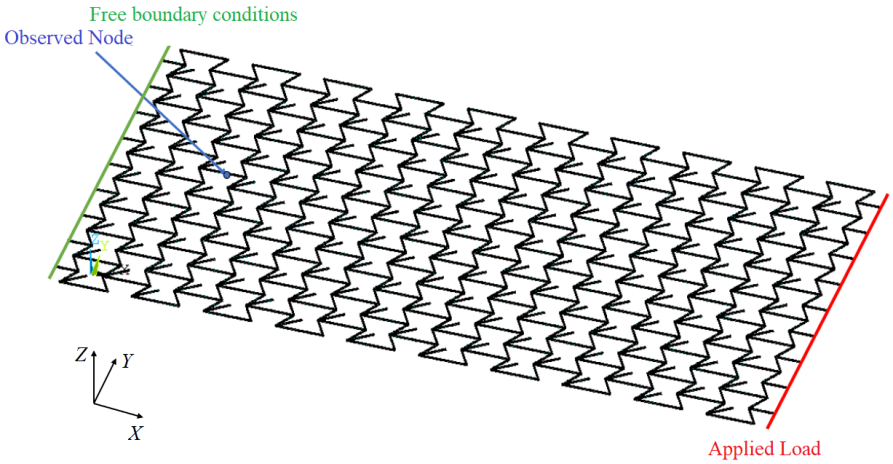


Figure 5: Periodic structure in finite configuration

2.4 Model of the finite structure

In parallel to the Floquet analysis, studies in finite structure are also performed. Harmonic analysis of a panel constituted of finite number of cells is performed, in order to compute the FRF at any node of the structure. A representation of this configuration is shown figure 5. The structure is composed with 9 unit cells in the Y direction, and 20 cells in the X direction. Free-free conditions are used, and, depending the type of analysis performed, an out-of-plane or an in-plane force is applied to excite the different type of waves and thereby observe the different band gaps on the FRF. The amplitude of the displacement is observed in a node picked just before the end of the structure in order to avoid the border effect we could have in the end of the periodic media.

Density, ρ $[kg.m^{-3}]$	1040	L [mm]	6
Young Modulus, E [GPa]	8.1	h [mm]	0.3
Poisson Ratio, ν	0.2	b [mm]	0.3

Table 1: Material and geometrical properties of the core

3 Simulations and Results

3.1 Selection of the core

Some analyses are done in infinite structure to compare several types of configurations of the studied core. The re-entrant and honeycomb configurations are chosen. For each curve, the segments [O-A-B-C-O] represent the values that μ_x and μ_y take along the contour, and are summarized in the table 2. The contour of the dispersion surfaces are represented figures 6 and 7.

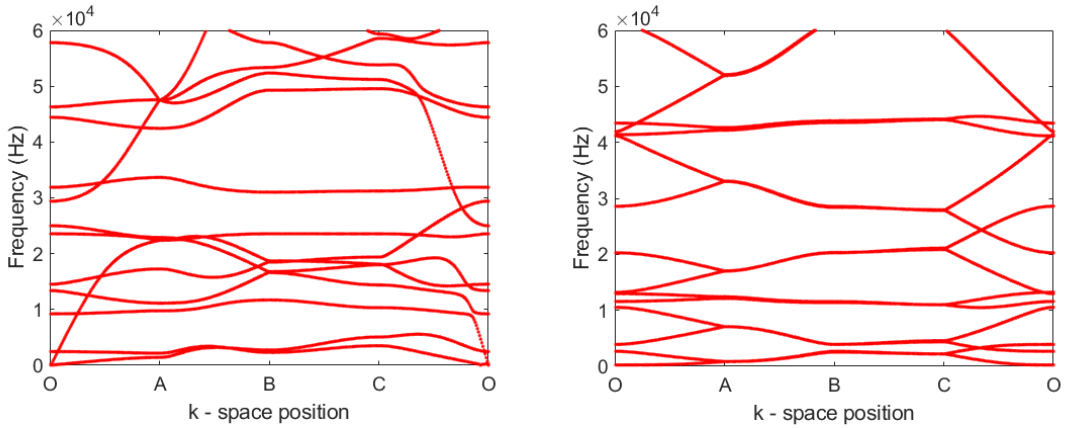
The first one represents the wave propagation in plane (degrees of freedom u_z, θ_x and θ_y blocked) while the second one out of plane (u_x, u_y and θ_z blocked), leading to a total of 4 different configurations. In the 4 configurations, only the fourth one exhibits Bragg band gaps and is selected as the core structure to continue the investigations including the resonators. The Resonators are then added to the re-entrant unit cell as shown in the figure 4, with the same material properties as the core. This resonator emplacement has been chosen for easier manufacturing. The dispersion diagram is plotted figure in 8. Around 20, 50 and 60 kHz, we can observe that some dispersion branches are opened to create a resonant band gap as shown if 8. This result is confirmed in the finite structure analysis, which is obtained by blocking in-plane degree of freedom and applying a force in the Z direction.

Segment	[O-A]	[A-B]	[B-C]	[C-O]
μ_x	$[0, \pi]$	π	$[\pi, 0]$	0
μ_y	0	$[0, \pi]$	π	$[\pi, 0]$

Table 2: Values of μ_x and μ_y for the dispersion contour

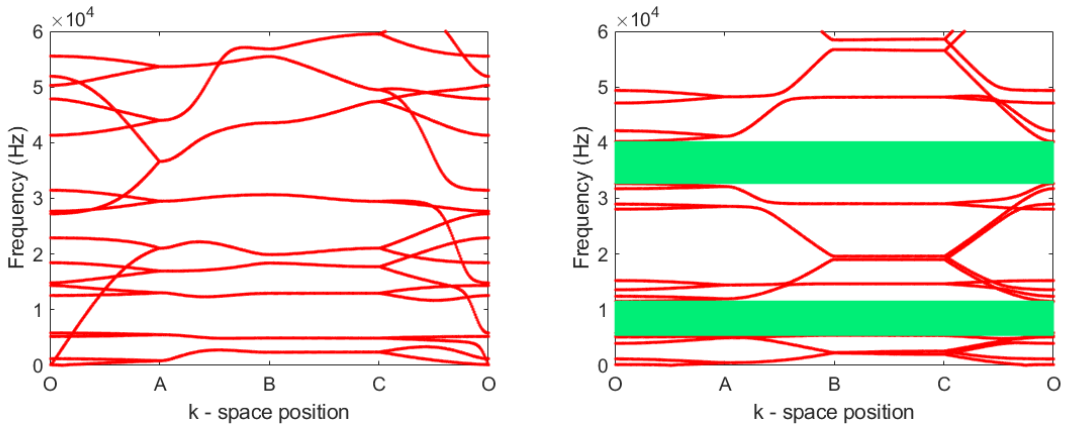
3.2 Number of resonators in the unit cell

To have a first look in the choice of the implementation of the resonator, an investigation has been done to know what is the optimal solution between putting 2 resonators or 4 resonators inside a unit cell, correspond-



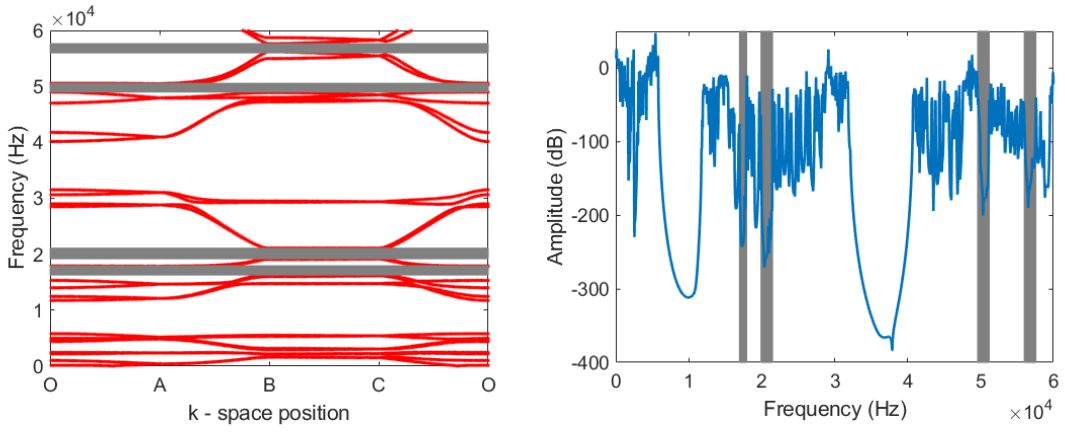
(a) In plane waves (b) Out of plane waves

Figure 6: Dispersion curve without resonator with hexagonal unit cell



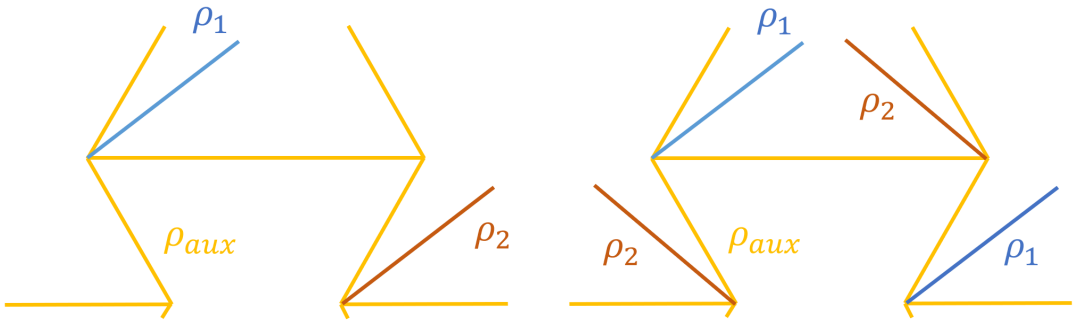
(a) In plane waves (b) Out of plane waves

Figure 7: Dispersion curve without resonator with re-entrant unit cell



(a) Dispersion curve with resonator (b) FRF with resonators

Figure 8: Dispersion curve without resonator with re-entrant unit cell



(a) 2 resonators (b) 4 resonators

Figure 9: Two different case of resonator implementation

ing to include respectively 1 or 2 resonators inside a "butterfly" pattern of the periodic structure. Two studies have been carried out making a variation of the density of each resonator, such as the total mass of the unit cell remain constant. The low frequencies are focused here, since the objective here is to put resonators is in order to open band gap for the first Floquet modes. To understand what are the low frequencies in that situation, we take as a reference the first mode of one of the beam constituting the unit cell, and we compute its first eigenfrequency in supported-supported boundary conditions. The value of the first eigenfrequency is $f_0 = 10505$ Hz. The unit cells are represented figure 9 and the evolution of the band gaps are shown in figure 10. Each configuration corresponding to the values of ρ_1 and ρ_2 are given in the table 3.

The results observed in figure 10 show that the optimal configuration to open band gaps in the lowest frequency correspond to the configuration number 10 for the case with 2 resonators, meaning that having the same density for the 2 resonators is more interesting than having two different densities. For the case with 4 resonators, it is the configuration 1 (or 19) which is the more interesting, and converge to the same result that the configuration number 10 for the case with 2 resonators. The similitude of the results is explained in the way that, for the configuration 1, one has $\rho_1 << \rho_2$ and $\rho_2 \simeq \rho_{aux}$, which tends to the case with 2 resonators. The configuration number 10 correspond to 4 equal densities for each resonator, and corresponds the worst result for a low frequency band gap opening in that situation.

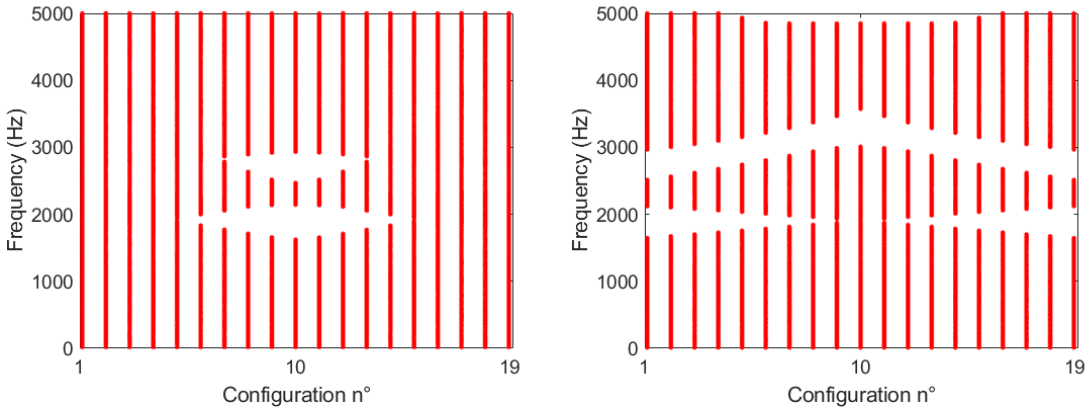
These results show that, for this type of unit cell, having 1 resonator per pattern is the best solution to have an interesting wave behaviour in low frequencies.

	Configuration n°	**1**	**2**	**3**	...	**10**	...	**19**
2 Resonators	$\frac{\rho_1}{\rho_{aux}}$	0.1	0.2	0.3	...	0.1	...	1.9
	$\frac{\rho_2}{\rho_{aux}}$	1.9	1.8	1.7	...	1	...	0.1
4 Resonators	$\frac{\rho_1}{\rho_{aux}}$	0.05	0.1	0.15	...	0.5	...	0.95
	$\frac{\rho_2}{\rho_{aux}}$	0.95	0.90	0.85	...	0.5	...	0.05

Table 3: Values of ρ_1 and ρ_2 for each configuration

3.3 Parametric Analysis

A parametric analysis is then performed by varying the material of the resonators. Since one of the main interest of creating a sandwich panel is the improvement of the ratio mass over the stiffness, the density of the resonator is chosen as a parameter. A comparison between the improvement band gap positioning and width versus the total added mass of the unit cell is checked. The evolution of the band gaps is represented figure 11 and is again focused on the low frequency range. The percentage of added mass is



(a) Study with 2 resonators (b) Study with 4 resonators

Figure 10: Band gap evolution analysis by varying the density of the resonators. Configurations are given table 3

.

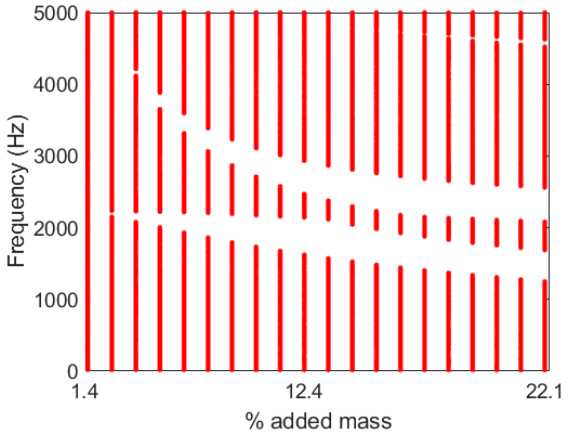


Figure 11: Band gaps investigation with variation of the mass of the resonator

$$a_m = 1 + \frac{2L_r\rho_{reso}}{8L_{aux}\rho_{aux}} \tag{8}$$

where ρ_{reso} represents the density of the resonator. Looking at the figure 11, we can observe that waves are naturally going to the low frequencies as we increase the value of the density of the resonator. For low values of added mass ($< 5\ \%$) no band gap is present in this frequency range. However, they start to open after that value in two different branches. Above about 15 $\%$, the width of the band gaps remain almost constant but continue to slowly going to lowest frequencies. By seeing this result and according to the frequency that we want to isolate and the maximum of added mass tolerated, it is possible to chose a value of the density for the resonator to create a stop band.

4 Conclusion

This work gives first investigations in wave behaviour of auxetic honeycombs including resonators. After a first look on different geometry of unit cell, the re-entrant one is selected for the better Bragg band gaps provided, and more specifically for waves travelling out of plane of the periodic structure. Beam resonators

have been introduced then, comparing the configurations with 2 resonators or 4 resonators in one unit cell. The results have shown that the best configuration on the analysed ones is having exactly one resonator by butterfly core cell, which corresponds to two resonators in the unit cell with the same density. Finally, since one of the most important parameter in the aerospace domain is the mass, a parametric study on the density of the resonator has been done in order to see what improvement can been obtained in a vibroacoustics versus a structural point of view. On the structure of interest, it has been shown that we need to have at least 5% added mass to open band gaps in low frequency range, while the bandwidth remains nearly constant after 15% added mass.

Acknowledgements

Thanks to everyone involved in the VIPER project. This project has received funding from the European Union's Horizon 2020 research and innovation programme under Marie Curie grant agreement No 675441. This work was performed in cooperation with the EUR EIPHI program (ANR 17-EURE-0002).

References

[1] M. Ruzzene, F. Scarpa *Control of Wave Propagation in Sandwich Beams with Auxetic Core*, Journal of Intelligent Material Systems and Structures, Vol. 14—July (2003)

[2] S. Yao, X. Zhou and G. Hu1 *Experimental study on negative effective mass in a 1D mass–spring system*, New Journal of Physics 10 (2008)

[3] J.S. Chen, B. Sharma, C.T. Sun *Dynamic behaviour of sandwich structure containing spring-mass resonators*, Composite Structures Volume 93, Issue 8, Pages 2120-2125, (2011)

[4] Y. Xiao, J. Wen and X. Wen *Flexural wave band gaps in locally resonant thin plates with periodically attached spring–mass resonators*, Journal of Physics D: Applied Physics, Volume 45, Number 19 (2012)

[5] C.C. Claeys, K. Vergote,P. Sas,W. Desmet *On the potential of tuned resonators to obtain low-frequency vibrational stop bands in periodicp anels*, Journal of Sound and Vibration 332, 1418–1436 (2013)

[6] A. Banerjee1, R. Das, E. P. Calius *Waves in Structured Mediums or Metamaterials: A Review*, Archives of Computational Methods in Engineering pp 1–30

[7] G. Floquet *Sur les équations différentielles linéaires à coefficients périodiques*, Annales scientifiques de l'E.N.S, 2e serie, tome 2 (1883), p. 47-48

[8] M. Collet, M. Ouisse, M. Ruzeene, M.N. Ichchou *Floquet–Bloch decomposition for the computation of dispersion of two-dimensional periodic, damped mechanical systems*, International Journal of Solids and Structures 48, 2837–2848 (2011)

[9] L. Brillouin *Wave propagation in periodic structure*, McGraw-Hill Book Company, New York, 1946

[10] M. Ruzzene, F. Scarpa *Directional and band-gap behavior of periodic auxetic lattices*, Phys. stat. sol. (b) 242, No. 3, 665–680 (2005)

Wavenumber identification technique for axial-symmetric structures

G. Tufano [1,2], **C. Droz** [1,2], **O. Bareille** [1], **A.-M. Zine** [3], **B. Pluymers** [2,4], **W. Desmet** [2,4], **M. Ichchou** [1]
[1] Vibroacoustic and Complex Media Research Group, LTDS, École Centrale de Lyon
36 Avenue Guy de Collongue, 69134, Écully, France
e-mail: **giovanni.tufano@ec-lyon.fr**

[2] Noise and Vibration Research Group, PMA, KU Leuven
Celestijnenlaan 300 B, B-3001, Heverlee, Belgium

[3] Institut Camille Jordan, Département de Maths-Info, École Centrale de Lyon
36 Avenue Guy de Collongue, 69134, Écully, France

[4] DMMS core lab, Flanders Make, Belgium

Abstract
This paper investigates the broadband vibro-acoustic and dynamic behavior of different structures, such as flat and curved panels and cylindrical shells. The aim of this work is to investigate propagation and dispersion features through the analysis of the wavenumber domain. The technique used to investigate the vibro-acoustic behavior is a wave propagation based technique, implemented to obtain the propagative and evanescent waves using a harmonic force excitation. The employed techniques are used to obtain the harmonic displacement field, given as primary input for the wavenumber domain analysis. To deeply investigate the dispersion features, a Discrete Fast Fourier Transform (DFFT) technique is used. The whole displacement field could be obtained by experimental tests or by numerical simulations; in our case, it is calculated using a classical Finite Element Analysis (FEA), by a commercial Finite Element package, or by an in-home algorithm, developed in a commercial numerical computing software.

1 Introduction

Flat and curved panels are widely used in the field of transportation engineering. In the aerospace engineering, the shape of the most employed structures for the aircrafts and for the space launchers can be considered to be axial-symmetric (the fuselage of the aircrafts, the first, the upper stages and the fairings of the launchers, for example).
The dynamic behavior and the vibro-acoustic response of these structures are a fundamental challenge for the industry. Indeed, the most important aspect is the understanding of the waves dispersion characteristics under different loading conditions. The identification of the propagation parameters is a fundamental issue in vibro-acoustics. In the last years, some analytical formulations were developed for flat and/or homogeneous structures and they can be found in [1], [2] and [3]. These analytical formulations are limited to the low-frequency domain, in which the mode are well defined; in the mid-high-frequency range classic analytical approach do not give a good estimation of the waves dispersion characteristics. In this bandwidth some statistical and energetic approaches were developed in [4], [5] and [6].
The identification of the wave propagation parameters is one of the most important challenges in vibro-acoustics. In literature several technique are available, especially for one-dimensional structures, mainly based on the loss factor identification, by the research of the complex wavenumber [7]. In their work, McDaniel et al. developed a strategy to estimate the frequency-dependent loss-factor in one-dimensional

structures, identifying the complex wavenumber of flexural and evanescent waves at each frequency.
In the last decades, some applications to two-dimensional structures have been proposed in literature. For example, Ferguson et al. [8] proposed a technique to identify the dominant wavenumber in a considered area, using a windowed field of the displacement of the structure, computing the correlation between the normal velocity measurement and an harmonic wave-field. Another method for the identification of the wavenumber was developed by Grosh et al. [9], based on Prony series.
An interesting algorithm for the identification of the complex wavenumber and of the damping loss factor was developed by Berthaut et al. [10]; the proposed method is called Inhomogeneous Wave Correlation (IWC) method and it allows to identify the complex flexural wavenumber in the broadband frequency range. An application of this method to one- and two-dimensional sandwich structures can be found in [11] and an application on ribbed plates was proposed by Ichchou et al. [12] and [13]; Cherif et al. [14] proposed the damping loss factor identification for flat plates; the identification of the material characteristics of the sandwich panels was proposed by Droz et al. [15]; Van Belle et al. [16] proposed the estimation of the flexural dispersion curve for a plate with local resonators; Van Damme et al. [17] applied this method to identify the mechanical properties of a classical timber plate.
This paper shows the comparison between the classical Discrete Fast Fourier Transform (DFFT) approach and the Inhomogeneous Wave Correlation (IWC) method in the *k-space* analysis. Both methods are applied on different structures: flat and curved panels and cylindrical structures. The wave field is obtained using either a full Finite Element Analysis (FEA) or a Wave Finite Element Method (WFEM) (this method is widely used in waves propagation investigations and it is well-described in [18], [19], [20], [21] and [22]).

2 Methodology

In this section, two different wavenumber identification techniques are presented. The classical approach in the wavenumber domain analysis is the Continuous Fourier Transform (CFT) and its equivalent in the discrete domain, the Discrete Fourier Transform (DFT). The second method adopted in this work is the Inhomogeneous Wave Correlation method (IWC). Both methods use the harmonic displacement field as primary input, usually defined in the (x, y) plane (see Eq. (1), in which the symbol $\hat{w}$ indicates that the displacement field is frequency-dependent), either from a harmonic excitation or from a temporal Fourier transform.

$$w(x, y, t) = \int_0^{+\infty} \hat{w}(x, y) e^{i\omega t} \, d\omega \tag{1}$$

The two methods are explained in the next sections; DFT and CFT are briefly described for the sake of clarity.

2.1 Spatial Fourier Transform

The DFT assumes two hypotheses:

1. the displacement field $\hat{w}$ is given in an uniform grid $(x_i = idx, y_j = jdy)_{(1 \leq i \leq N_1 - 1, 1 \leq j \leq N_2 - 1)}$, in which N_1 and N_2 are the number of the acquisition points along the axes x and y, respectively, dx and dy are the space increments along the axes x and y, respectively;

2. the field is assumed to be *2D-periodic*, i.e.:

$$\forall i, j \in \mathbb{N}^2, \hat{w}(idx, jdy) = \hat{w}((i/N_1)dx, (j/N_2)dy) \tag{2}$$

The spatial mesh has to be small enough to satisfy the Nyquist criterion, at the least half of the smallest wavelength of interest; on the other hand, the span of the measurement has to be large enough to have an acceptable resolution in the wavenumber domain.
In the discrete domain, we can assume $\Delta k_x = \frac{2\pi}{N_1 dx}$ and $\Delta k_y = \frac{2\pi}{N_2 dy}$ as a basis for the complex functions space; the family of exponential functions with discrete wavenumbers can be written: $(k_{xp} = p\Delta k_x, k_{yq} = q\Delta k_y)_{(1\leq p\leq N_1-1, 1\leq q\leq N_2-1)}$. Consequently, the displacement field can be written as:

$$\hat{w}(x_i, y_j) = \sum_{p=0}^{N_1-1} \sum_{q=0}^{N_2-1} \widehat{\hat{w}}(k_{xp}, k_{yq}) e^{i(k_{xp}x_i + k_{yq}y_j)} \tag{3}$$

The DFT $\hat{w} \longrightarrow \widehat{\hat{w}}$ assumes the following expression:

$$\widehat{\hat{w}}(k_{xp}, k_{yq}) = \frac{1}{N_1 N_2} \sum_{i=0}^{N_1-1} \sum_{j=0}^{N_2-1} \hat{w}(x_i, y_j) e^{-i(k_{xp}x_i + k_{yq}y_j)} \tag{4}$$

The periodicity condition, expressed in Eq. (2), imposes that also the DFT is periodic:

$$\widehat{\hat{w}}(k_x, k_y) = \widehat{\hat{w}}\left(k_x + \frac{2\pi}{dx}, k_y\right) = \widehat{\hat{w}}\left(k_x, k_y + \frac{2\pi}{dy}\right) \tag{5}$$

In this work, the DFT is performed in MATLAB and no additional windowing or signal processing was applied.

2.2 Inhomogeneous Wave Correlation method

Using the same displacement field as for the DFT, the dispersion relation can be found using a different approach: the Inhomogeneous Wave Correlation method. For a fixed frequency f_0, the spatial response is correlated with an inhomogeneous running wave (Eq. (6)), in which the terms $\theta, \gamma, \frac{2\pi}{k}$ are the heading angle, the attenuation factor and the apparent wavelength, respectively. The wave attenuation is strictly connected to the damping by this relationship: $\gamma = \frac{\eta c_\varphi}{2c_g}$, with η, c_φ, c_g being the damping loss factor, the phase velocity and the group velocity, respectively. This wave is defined as follows:

$$\hat{\sigma}_{k,\gamma,\theta}(x, y) = e^{-ik(\theta)(1+i\gamma(\theta))(x\cos\theta + y\sin\theta)} \tag{6}$$

The unknown wavenumber $k = k_\Re + ik_\Im$ can be found by the correlation between the inhomogeneous wave and the complete wave field, as the location of the maximum of the normalized correlation function:

$$IWC(k, \gamma, \theta) = \frac{\left|\iint_S \hat{w} \cdot \hat{\sigma}^*_{k,\gamma,\theta}\, dx\, dy\right|}{\sqrt{\iint_S |\hat{w}|^2\, dx\, dy \cdot \iint_S |\hat{\sigma}_{k,\gamma,\theta}|^2\, dx\, dy}} \tag{7}$$

where * denotes the complex conjugate. The identification of a complex wavenumber for a given direction θ leads to the maximization of the function $(k, \gamma) \longrightarrow IWC(k, \gamma, \theta)$; typically, the IWC has a well-defined maximum, denoting the point where the measured signal correlates best with the inhomogeneous wave $\hat{\sigma}_{k,\gamma,\theta}(x, y)$.
In practical applications, the wave field is measurable in discrete points, so the integration over the entire surface S in Eq. (7) is replaced by a finite weighted sum:

$$\iint_S dx\, dy \Longrightarrow \sum_{i=1}^{N} \rho_i S_i \tag{8}$$

where ρ_i is the coherence of the measured data at each point ($\rho_i = 1$ if the coherence is not available) and S_i is an estimation of the surface around the point i.

$$IWC(k,\gamma,\theta) = \frac{|\sum_{i=1}^{N} \hat{w}(x_i,y_i) \cdot \hat{\sigma}^*_{k,\gamma,\theta}(x_i,y_i) S_i|}{\sqrt{\sum_{i=1}^{N} |\hat{w}(x_i,y_i)|^2 S_i \cdot \sum_{i=1}^{N} |\hat{\sigma}_{k,\gamma,\theta}(x_i,y_i)|^2 S_i}} \tag{9}$$

Considering the well-known relationships between arcs and angles, and the transformation from the Cartesian coordinates reference system to the cylindrical one, the IWC method can be applied also on curved structure. Moving from the couple of coordinates (x, y) to the couple of coordinates (x, φ) and taking in account the circumferential wavenumber (Eq. (10)) instead of the one along the y axis, the new formulation of the IWC method can be easily developed.

$$k_\theta = k_x R = k_x \frac{\Delta x}{\Delta \theta} \tag{10}$$

where $\Delta\theta$ is the angular distance.

In this work, the IWC method is implemented in MATLAB, for both reference systems.

3 Numerical applications and results

In this section, the methods previously explained are applied to a flat (Fig. 1) and a curved (Fig. 2) panels and to a cylindrical shell (Fig. 3). The numerical models are built using a commercial Finite Element (FE) package. The numerical simulations of the two panels are obtained by a full FE analysis while the cylindrical shell is analyzed with a WFEM approach.

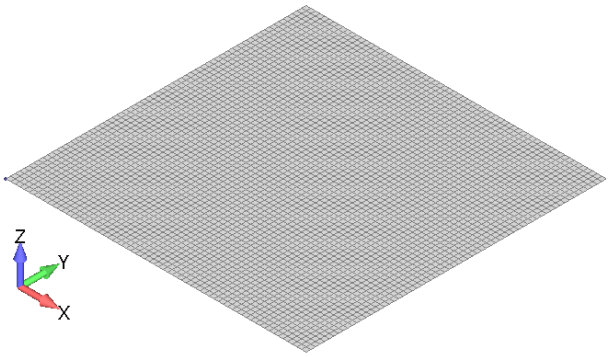


Figure 1: Flat panel: Finite Element Model

3.1 Flat panel

The first application is made on an isotropic flat panel. The employed material is a common alloy ($E = 70.0 \times 10^9\,\mathrm{Pa}$, $\nu = 0.33$ and $\rho = 2700.0\,\mathrm{kg}/\mathrm{m}^3$) and the geometric properties are: $L_x = L_y = 1.0\,\mathrm{m}$ and $t = 0.001\,\mathrm{m}$. The FE model of the panel is shown in Fig. 1.

The harmonic displacement field is obtained by numerical simulations using an *in-home* algorithm developed in MATLAB. The displacement field is calculated for different locations of the harmonic punctual excitation; in the specific case hereby shown, the force is located in the middle of the plate, on the bottom surface. The normal displacements are then extracted and used as primary input for the FFT and IWC calculations. All the simulations were performed considering with free-free boundary conditions. A constant structural damping is assumed and fixed at 1%; the dynamic matrix has the following expression: $D = K(1 + i\eta) - \omega^2 M$. The

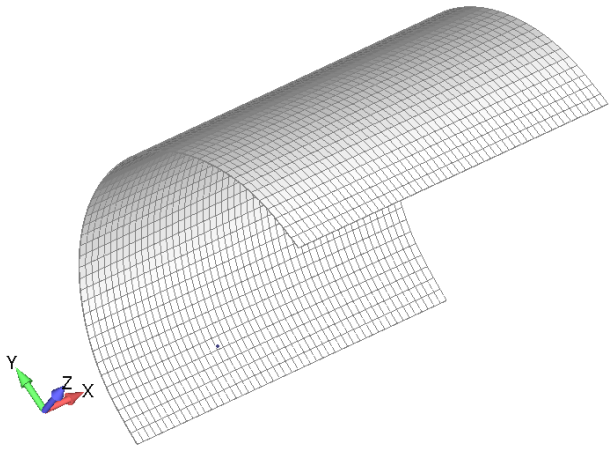


Figure 2: Curved panel: Finite Element Model

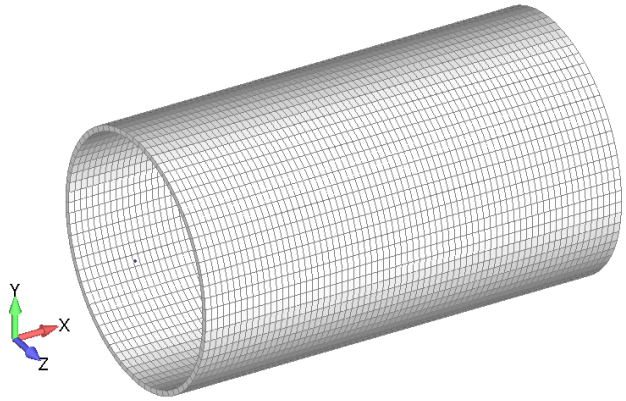
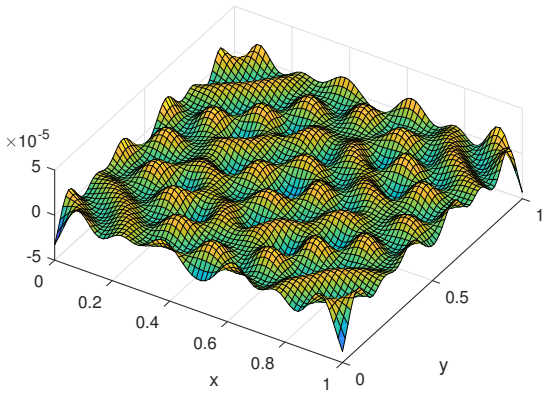


Figure 3: Cylinder: Finite Element Model

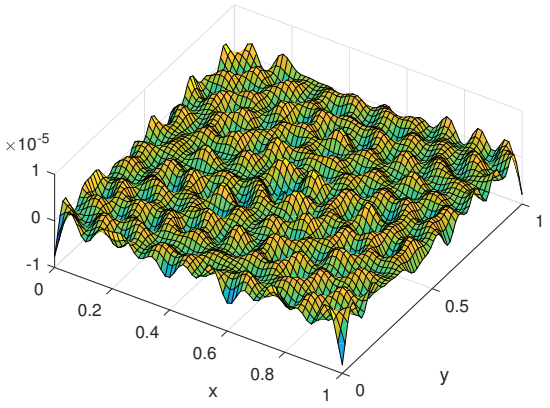
excitation covered a relatively large frequency broadband: from $50\,\mathrm{Hz}$ to $1200\,\mathrm{Hz}$.
Two different frequencies are shown in Fig. 4; in Fig. 4a and 4b the normal displacement fields are shown. These displacements are used both in the FFT and IWC method, in order to obtain the wavenumber domain; the *k-space* plots at these two different frequencies are shown in Fig. 4c and 4d, respectively. In these two figures, a perfect agreement in the peaks estimation is obtained between the two methods. At each heading angle of the inhomogeneous wave, the IWC method estimated the same value of (k_x, k_y) obtained with the FFT, predicting the classical ring shape expected for the isotropic panel.

3.2 Curved panel

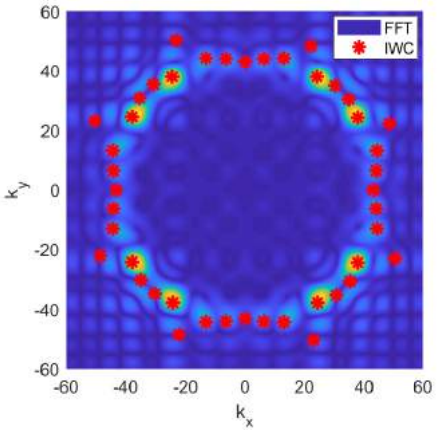
In this section, the previous methods are applied on a curved panel. The employed material is a common alloy ($E = 70.0 \times 10^9\,\mathrm{Pa}$, $\nu = 0.33$ and $\rho = 2700.0\,\mathrm{kg}\,/\mathrm{m}^3$) and the geometric properties are: $L_x = 1.0\,\mathrm{m}$, $R = 0.5\,\mathrm{m}$ and $t = 0.002\,\mathrm{m}$. The FE model of the curved panel is shown in Fig. 2. The FE model of the structure is assembled in a commercial FE software and the dynamic analysis is computed using an *in-home* algorithm developed in MATLAB. The excitation is punctual and located in the middle of the structure, normal to the inner surface; this location has been selected in order to excite many natural modes as possible. The forced responses and the wavenumber domain at two different frequencies are shown in Fig. 6. The transversal displacement field is obtained by projecting the displacement at each point from the global reference system of the structure into the local one; the *out-of-plane* displacements are shown in Fig. 6a and 6b, for the two considered frequencies.



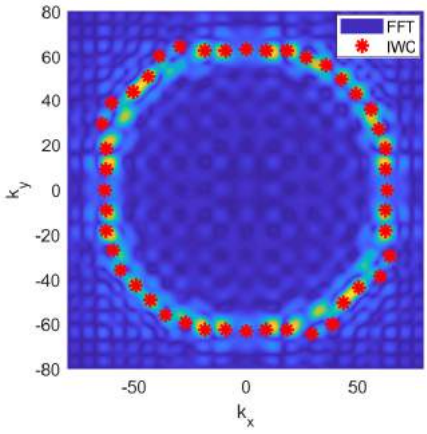
(a) 3D displacement field at 500.0 Hz.



(b) 3D displacement field at 1100.0 Hz.



(c) Comparison FFT-IWC at 500.0 Hz.



(d) Comparison FFT-IWC at 1100.0 Hz.

Figure 4: Flat panel: displacement field and wavenumber estimation at two different frequencies

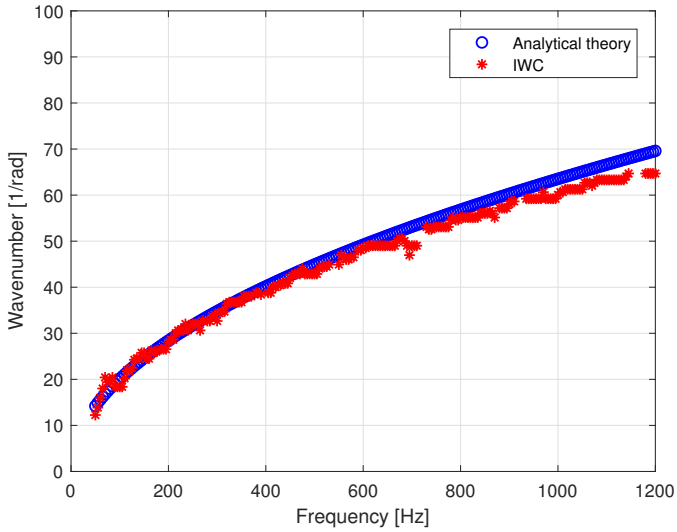
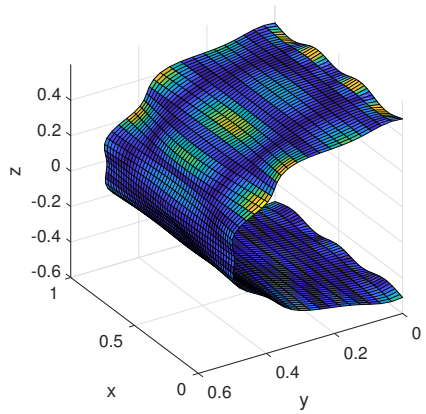
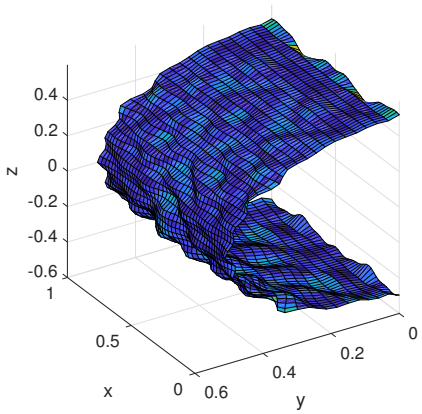


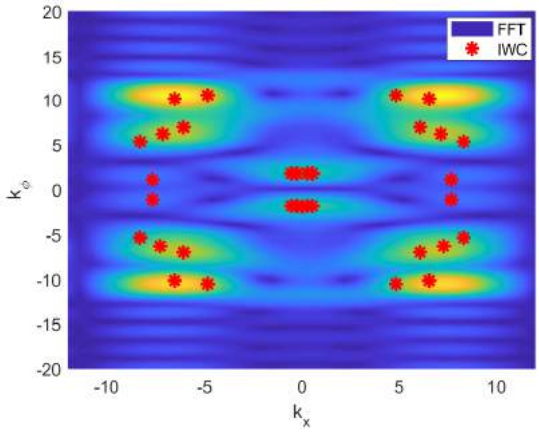
Figure 5: Flat panel: bending dispersion curve



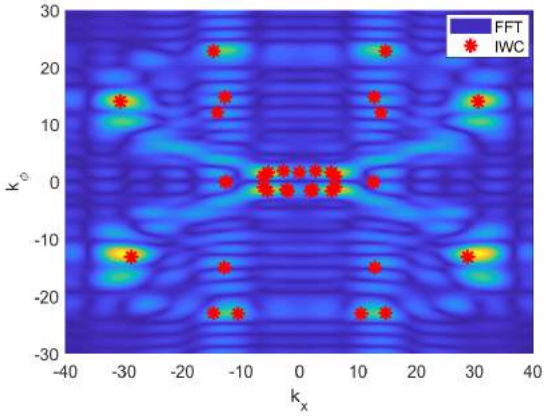
(a) 3D displacement field at 250.0 Hz.



(b) 3D displacement field at 1350.0 Hz.



(c) Comparison FFT-IWC at 250.0 Hz.



(d) Comparison FFT-IWC at 1350.0 Hz.

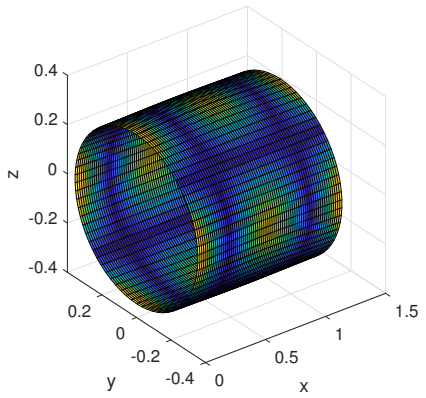
Figure 6: Curved panel: displacement field and wavenumber estimation at two different frequencies

3.3 Cylindrical shell

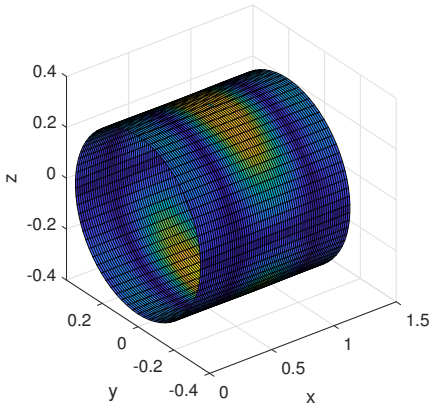
The last structure that has been investigated is a cylindrical shell. The cylinder is made of a classical isotropic alloy ($E = 70.0 \times 10^9$ Pa, $\nu = 0.33$ and $\rho = 2700.0\,\mathrm{kg}\,/\mathrm{m}^3$) and the geometric properties are: $L_x = 1.2\,\mathrm{m}$, $R = 0.35\,\mathrm{m}$ and $t = 0.0147\,\mathrm{m}$. The FE model of the cylinder is shown in Fig. 3. The FE model of the cylinder is built same as in the previous sections. The full displacement field is obtained implementing the WFEM. The harmonic excitation is located on the inner surface of the cylinder, locally normal to the surface and oriented along the radial direction. The normal displacement field and the wavenumber domain at two different frequencies are shown in Fig. 7. The normal displacement field is obtained by projecting the displacement of each node in the local reference system.

4 Conclusions

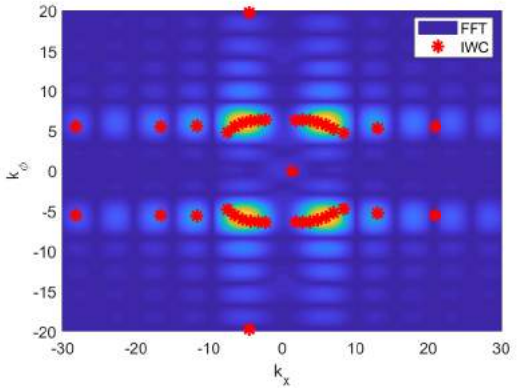
This paper compares two wavenumber identification techniques manly devoted to the the measurement of the dispersion of the bending waves in different structures. The IWC method shows a good agreement with the classical FFT approach and with the Kircchoff-Love theory in the estimation of the *k-space* and of the flexural dispersion curve.
The IWC method is also applied to curved and axial-symmetric structures, showing a good agreement with



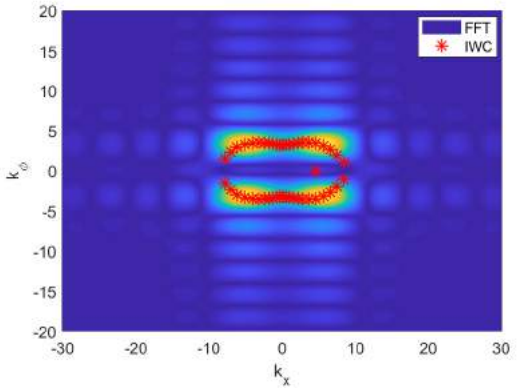
(a) 3D displacement field at 735.0 Hz.



(b) 3D displacement field at 4100.0 Hz.



(c) Comparison FFT-IWC at 735.0 Hz.



(d) Comparison FFT-IWC at 4100.0 Hz.

Figure 7: Cylinder: displacement field and wavenumber estimation at two different frequencies

the classical FFT approach, predicting the complex wavenumber at a fixed frequency and identifying the complete *θ-dependent dispersion curve*; the classical *8-shape* is also well identified, with a good estimation of the maxima in the wavenumber domain at different heading angles of the inhomogeneous wave. In the IWC algorithm, the introduction of the attenuation coefficient γ (with the associated damping loss factor coefficient) offers the possibility to separate near-field from far-field, reducing the effect of the finite size of the structures; the algorithm allows to identify and remove the wavenumbers with the imaginary part greater than the real part, which are associated to the near-field propagation and exhibiting a high apparent loss factor.

Acknowledgments

This project has received funding from the European Union Horizon 2020 research and innovation programme under the Marie Sklodowska-Curie grant agreement No. 675441.

References

[1] F.J. Fahy, E. Lindqvist, *Wave propagation in damped, stiffened structures characteristic of ship construction*, Journal of Sound and Vibration, Vol. 45, No. 1, (1976), pp. 115-138.

[2] A.W. Leissa, *Vibration of Shells*, Scientific and Technical Information Office, National Aeronautics and Space Administration, Ohio (1973).

[3] M. Qatu, *Vibration of Laminated Shells and Plates*, Academic Press, Oakland University, MI, USA (2004).

[4] R.H. Lyon, *Statistical Energy Analysis of Dynamical Systems: Theory and Applications*, MIT Press, Cambridge (1975).

[5] V. Cotoni, R.S. Langley, P.J. Shorter, *A statistical energy analysis subsystem formulation using finite element and periodic structure theory*, Journal of Sound and Vibration, Vol. 318, No. 4-5, (2008), pp. 1077-1108.

[6] D. Chronopoulos, M. Ichchou, B. Troclet, O. Bareille, *Predicting the broadband response of a layered cone-cylinder-cone shell*, Composite Structures, Vol. 107, (2014), pp. 149-159.

[7] J. McDaniel, P. Dupont, L. Savino, *A wave approach to estimating frequency-dependent damping under transient loading*, Journal of Sound and Vibration, Vol. 231, No. 2, (2000), pp. 433-449.

[8] N. Ferguson, B. Mace, C.R. Halkyard, K. Henon, *The estimation of wavenumbers in two dimensional structures*, *Proceedings of ISMA, International Conference on Noise and Vibration Engineering, Leuven, Belgium, 2002 September 16-18*, Leuven (2002), Vol. II, pp. 799-806.

[9] K. Grosh, E.G. Williams, *Complex wave-number decomposition of structural vibrations*, The Journal of the Acoustical Society of America, Vol. 93, No. 2, (1993), p. 836-848.

[10] J. Berthaut, M. Ichchou, L. Jezequel, *K-space identification of apparent structural behavior*, Journal of Sound and Vibration, Vol. 280, (2005), p. 1125-1131.

[11] M. Ichchou, J. Berthaut, M. Collet, *Multi-mode wave propagation in ribbed plates: Part I, wavenumber-space characteristics*, International Journal of Solids and Structures, Vol. 45, No. 5, (2008), p. 1179-1195.

[12] M. Ichchou, J. Berthaut, M. Collet, *Multi-mode wave propagation in ribbed plates. Part II: predictions and comparisons*, International Journal of Solids and Structures, Vol. 45, No. 5, (2008), p. 1196-1216.

[13] M. Ichchou, O. Bareille, J. Berthaut, *Identification of effective sandwich structural properties via an inverse wave approach*, Engineering Structures, Vol. 30, (2008), p. 2591-2604.

[14] R. Cherif, J.-D. Chazot, N. Atalla, *Damping loss factor estimation of two-dimensional orthotropic structures from a displacement field measurement*, Journal of Sound and Vibration, Vol. 356, (2015), p. 61-71.

[15] C. Droz, O. Bareille, M. Ichchou, *A new procedure for the determination of structural characteristics of sandwich plates in medium frequencies*, Composites Part B: Engineering, Vol. 112, (2017), p. 103-111.

[16] L. Van Belle, C. Claeys, E. Deckers, W. Desmet, *On the impact of damping on the dispersion curves of a locally resonant metamaterial: Modelling and experimental*, Journal of Sound and Vibration, Vol. 409, (2017), p. 1-23.

[17] B. Van Damme, A. Zemp, *Measuring dispersion curves for bending waves in beams: A comparison of Spatial Fourier Transform and Inhomogeneous Wave Correlation*, Acta Acustica united with Acustica, Vol. 104, No. 2, (2018), p. 228-234.

[18] D.J. Mead, *Wave propagation in continuous periodic structures: research contributions from Southampton*, Journal of Sound and Vibration, Vol. 190, No. 3, (1996), p. 495-524.

[19] E. Manconi, B.R. Mace, *Modelling wave propagation in two dimensional structures using finite element analysis*, Journal of Sound and Vibration, Vol. 318, No. 45, (2008), p. 884-902.

[20] J.M. Renno, B.R. Mace, *Calculating the forced response of cylinders using the wave and finite element method*, Journal of Sound and Vibration, Vol. 333, No. 21, (2014), p. 5340-5355.

[21] C. Droz, J.P. Lainé, M. Ichchou, G. Inquiété, *A reduced formulation for the free-wave propagation analysis in composite structures*, Composite Structures, Vol. 113, (2017), p. 134-144.

[22] F. Errico, M. Ichchou, S. De Rosa, O. Bareille, F. Franco, *The modelling of the flow-induced vibrations of periodic flat and axial-symmetric structures with a wave-based method*, Journal of Sound and Vibration, Vol. 424, (2018), p. 32-47.

Diffusion based homogenization method for one dimensional locally resonant system

S. Ahsani [1,2], **R. Boukadia**[1,2], **C. Droz**[3], **C. Claeys**[1,2], **E. Deckers**[1,2]
[1] KU Leuven, Department of Mechanical Engineering,
Celestijnenlaan 300 B, B-3001, Heverlee, Belgium
e-mail: **sepide.ahsani@kuleuven.be**

[2] DMMS lab, Flanders Make, Belgium

[3] École centrale de Lyon, France

Abstract
In recent years, extensive research has been carried out on dynamic homogenization approaches. Most of them are based on an analytical formulation of the equivalent medium and their validity is limited to low frequencies and avalibilty of a dynamic description of the heterogonous medium. In this paper, a two-step homogenization method is developed to derive a frequency dependent equivalent medium description for one-dimensional periodic systems. The first step focuses on the numerical calculation of the transmission and reflection coefficients at the interface of the unit cell of the original system and its equivalent medium representation. The second step is based on simultaneously minimising the reflection coefficients and maximising the transmission coefficients at the interface of the structure and its equivalent medium to retrieve the effective frequency dependent material properties. The method is validated by comparing the dispersion curves of a three-dimensional periodic tuned mass spring damper system and its equivalent model.

1 Introduction

Over the past decades, there has been extensive research on how waves propagate in metamaterials given their interesting properties such as stopband behavior in some targeted and tunable frequency ranges [1] which can be used to improve noise, vibration and harshness (NVH) behavior of lightweight material. Stopbands are frequency ranges in which certain types of waves cannot propagat and originate from interference caused by Bragg scattering (phononic crystals) for wavelengths of the lengthscale of the periodicity or by Fano-type interference between incoming and radiated waves by resonant cells around their resonance fequency when placed on a sub-wavelength scale [2].

Due to this intriguing property, there is an increasing interest in studying wave propagation in such structures. Taking advantage of the periodicity of locally resonant metamaterials, the wave propagation in the whole structure can be predicted by modelling a unit cell. While such an approach reduces the computation time by far, unit cells can be complex enough to trigger the motivation to use techniques to simplify the model. Additionally, these problems are frequency dependent and have to be solved per frequency and for each desired angle of propagation. An example of a unit cell is given in [3], where they use a duct with 16 to 32 resonator inclusions as unit cell, resulting in a model with lots of degrees of freedom. Moreover, if one wants to perform finite structure analysis, the whole structure needs to be modeled which results in models with considerable amount of degrees of freedom and higher computation time. Until now, different techniques have been developed to tackle this problem which can be divided in two groups. The first one

applies model order reduction strategies where they focus on reducing the size of the eigenvalue problem to be solved. In this category, recent developments by Boukadia et al.[4] can be cited where they use inverse Bloch approach to sample over the k-space and then apply the direct Bloch approach to solve over the sampled space resulting in a reduction factor above 1000 . The second category covers the methods that are specified as dynamic homogenization in literature, meaning replacing the original computtentionally expensive model with an equivalent one. A noticeable portion of these studies e.g. [5, 6, 7] are dedicated to asymptotic techniques which aim at including the micro-scale behavior in the elasto-dynamic equation of the system such that the solution contains both macro- and micro-scale components. These techniques are based on the main assumption that the characteristic length of the unit cell is much smaller than the wavelength in the medium. Although asymptotic techniques show a considerable amount of advantages, especially for Bragg scattering based metamaterials, they are weak in capturing the locally resonant metamaterial behavior since no closed analytical description is available for all the cases. More homogenization techniques can be found in literature such as Ensemble averaging [8] and Coherent Potential Approximation (CPA) [9]. The former technique, which was developed by Willis [10], yields exactly the whole dispersion curve but is only valid in low frequencies.Willis [10] considered an effective (average) response that relates the effective stress and momentum to effective strain and velocity of a medium under certain harmonic wave. The medium can be random or periodic [11], so the mean value of the elastic constant tensor is calculated accordingly using ensemble averaging definition. The later method (CPA) is an effective medium theory which goes beyond the quasi-static limit in metametrials and retrieves effective material properties in frequencies which are near the resonance frequency. Wu et al. [9] consider a cylindrical scatterer embedded in a solid host medium as their unit cell. Assuming that the unit cell is surrounded by an effective medium, they minimize the reflection at the interface to retrieve the effective material properties. The reason behind choosing such a system is that they can use the Mie-like scattering coefficients to determine frequency-dependent effective properties. The limitation of such a method is that firstly they can only compute the effective medium for systems that they have an analytical description for their scattering coefficients and secondly the wavelengths in both host and effective medium should be much larger than the size of the unit cell.

The limitation to a certain frequency range and dynamic description of the system in the stated methods, motivated the proposed approach of this paper that can compute effective frequency-dependent material properties based on finite element model of the unit cell. The diffusion based homogenization uses the CPA approach to calculate the equivalent material properties. The key point is to use the Diffusion method [12] to calculate the scattering coefficients numerically, therefore not being bound to certain geometries for the structure of the unit cell.

This paper is organized as follows. Section 2 explains the diffusion based homogenization methodology in detail. In Section 3, a case study is described and the homogenization results are shown in terms of dispersion curve and frequency response function (FRF) calculation. Furthermore, critical factors influencing the accuracy of the method are discussed. The paper concludes with a main summary in Section 4.

2 Methodology

This section consists of two parts. In the first part, a brief overview of wave finite element method for 1D waveguides and the Diffusion method are given. In the last part, a detailed description is provided on the combination of the CPA and the Diffusion method which is named the diffusion based homogenization method.

2.1 Wave Finite Element (WFE) for 1D waveguides

The method focuses on how wave propagates through a 1D periodic structure modelling only a single unit cell [13]. Let's consider a structure consisting of N unit cells along one direction (for example the z-axis) and its finite element model of the k^{th} unit cell as shown in Figure 1. The boundaries at the right($\bullet_R$) and

left($\bullet_L$) side of the unit cell can be discretized in n degrees of freedom. Therefore, the field variables of the boundaries can be written as below:

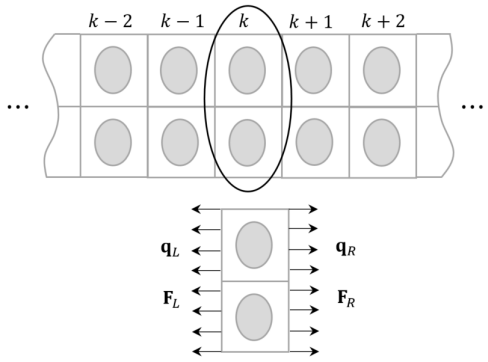


Figure 1: Schematic view a 1D periodic structure and its unit cell

$$\mathbf{u}_L^{(k)} = \begin{Bmatrix} \mathbf{q}_L^{(k)} \\ -\mathbf{F}_L^{(k)} \end{Bmatrix}, \qquad \mathbf{u}_R^{(k)} = \begin{Bmatrix} \mathbf{q}_R^{(k)} \\ \mathbf{F}_R^{(k)} \end{Bmatrix}, \tag{1}$$

where $\mathbf{q}$ corresponds to the $n \times 1$ vectors of displacements and $\mathbf{F}$ corresponds to the $n \times 1$ vectors of forces. Writing the equation of motion and by performing some mathematical manipulations, the field variables at the right boundaries can be linked to the ones of the left boundary:

$$\begin{Bmatrix} \mathbf{q}_R^{(k)} \\ \mathbf{F}_R^{(k)} \end{Bmatrix} = \begin{bmatrix} -(\mathbf{D}_{LR}^{(k)})^{-1}\mathbf{D}_{LL}^{(k)} & (\mathbf{D}_{LR}^{(k)})^{-1} \\ -\mathbf{D}_{RL}^{(k)} + \mathbf{D}_{RR}^{(k)}(\mathbf{D}_{LR}^{(k)})^{-1}\mathbf{D}_{LL}^{(k)} & -\mathbf{D}_{RR}^{(k)}(\mathbf{D}_{LR}^{(k)})^{-1} \end{bmatrix} \begin{Bmatrix} \mathbf{q}_L^{(k)} \\ -\mathbf{F}_L^{(k)} \end{Bmatrix}. \tag{2}$$

This can be reprented as:

$$\mathbf{u}_R^{(k)} = \mathbf{S}^{(k)}\mathbf{u}_L^{(k)}, \tag{3}$$

with $\mathbf{S}^{(k)}$ being the transfer matrix of the k^{th} unit cell.
In (2), $\mathbf{D}$ is the condensed dynamic stiffness matrix, defined as:

$$\mathbf{D}^{(k)} \begin{Bmatrix} \mathbf{q}_L^{(k)} \\ \mathbf{q}_R^{(k)} \end{Bmatrix} = \begin{Bmatrix} \mathbf{F}_L^{(k)} \\ \mathbf{F}_R^{(k)} \end{Bmatrix} \quad \text{with} \quad \mathbf{D}^{(k)} = \mathbf{K}^{(k)} + j\omega\mathbf{C}^{(k)} - \omega^2\mathbf{M}^{(k)}. \tag{4}$$

Using the coupling condition at the interface of the k^{th} and $(k-1)^{th}$ unit cells, the field variables of two consecutive cells can be related as follows:

$$\mathbf{u}_L^{(k)} = \mathbf{u}_R^{(k-1)}. \tag{5}$$

Subsituting the relation above in (3), we can arrive at:

$$\mathbf{u}_L^{(k)} = \mathbf{S}^{(k-1)}\mathbf{u}_L^{(k-1)}. \tag{6}$$

Applying the Bloch boundary condition, the left side field variables at two consecutive unit cells can be related to each other using a propagation constant (μ) that accounts for the phase change over the characteristic length of unit cell:

$$\mathbf{u}_L^{(k)} = \mu\mathbf{u}_L^{(k-1)}, \tag{7}$$

which in combination with (6) gives the following eigenvalue problem(EVP):

$$\mathbf{S}\boldsymbol{\phi}_i = \mu_i\boldsymbol{\phi}_i. \tag{8}$$

Where ϕ_i is the ith eigenvector , and is the basis of the field variables at each side e.g. $\mathbf{u}_L^{(k)} = \boldsymbol{\phi}\boldsymbol{Q}^{(k)}$, $\mathbf{u}_R^{(k)} = \boldsymbol{\phi}\boldsymbol{Q}^{(k+1)}$.
The EVP above yields $2n$ solutions, of which half represent positive going waves and the other half describe negative going waves. The positive($\bullet^+$) and negative($\bullet^-$) going waves can be separated using the criteria below:

$$|\mu^+| < 1 \qquad |\mu^-| > 1. \tag{9}$$

If the propagation constant is very close to 1, the waves can be separated using energy flow.

$$\text{if} \quad |\mu^+| \approx 1 \qquad Re(j\omega\boldsymbol{\phi}_q.\boldsymbol{\phi}_F) > 0. \tag{10}$$

Separating the waves, we can reorganize the wave basis in form of:

$$\boldsymbol{\Psi} = \begin{bmatrix} \boldsymbol{\phi}_q^+ & \boldsymbol{\phi}_q^- \\ \boldsymbol{\phi}_F^+ & \boldsymbol{\phi}_F^- \end{bmatrix}. \tag{11}$$

It is worth mentioning that the EVP above is ill-conditioned, and Zhong and Williams [14] proposed several reformulation to solve this problem. As a result, the EVP is altered to:

$$(\mathbf{N} - \mu_i \mathbf{L}) \begin{Bmatrix} \mathbf{q}_L^{(k)} \\ \mathbf{q}_R^{(k)} \end{Bmatrix} = \mathbf{0}. \tag{12}$$

The description of $\mathbf{N}$ and $\mathbf{L}$ can be found in [15].

2.2 Diffusion method

This method [12] investigates wave propagation through two waveguides coupled to an elastic junction (coupling element). A schematic view of such system is shown in Figure 2. Using continuity, one can easily

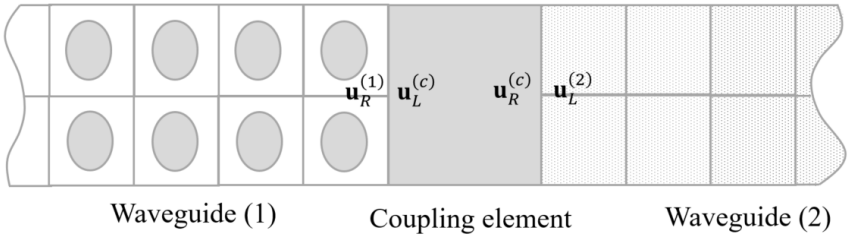


Figure 2: Schematic view of two semi-infinite waveguides coupled through a junction

relate the field variables at the right boundary of the last unit cell in waveguide (1) to the left boundary field variables of the coupling element:

$$\mathbf{u}_R^{(1)} = \mathbf{u}_L^{(c)}. \tag{13}$$

Using the same concept for the field variables at the right side of the coupling element, we can write:

$$\mathbf{u}_R^{(c)} = \mathbf{u}_L^{(2)}. \tag{14}$$

Substituting these in the equation of motion of the coupling element, we can relate the field variables at the interface boundaries of the two waveguides.

$$\mathbf{u}_L^{(2)} = \mathbf{S}^{(c)}\mathbf{u}_R^{(1)}, \tag{15}$$

where $\mathbf{S}^{(c)}$ is the transfer matrix of the coupling element. Now let's consider incident waves with certain amplitude at interface of waveguide (1) and coupling element ($\mathbf{Q}_{inc}^{(1)}$) or at the interface of waveguide (2) and the coupling element ($\mathbf{Q}_{ref}^{(2)}$). The field variables at each interface can be expanded as:

$$\mathbf{u}_L^{(2)} = \mathbf{\Psi}^{(2)} \begin{bmatrix} \mathbf{Q}_{inc}^{(2)} \\ \mathbf{Q}_{ref}^{(2)} \end{bmatrix}, \quad \mathbf{u}_R^{(1)} = \mathbf{\Psi}^{(1)} \begin{bmatrix} \mathbf{Q}_{inc}^{(1)} \\ \mathbf{Q}_{ref}^{(1)} \end{bmatrix}. \tag{16}$$

In the equation above, $\mathbf{Q}_{ref}^{(1)}$ and $\mathbf{Q}_{inc}^{(2)}$ represent the amplitude of reflected waves at the interface (1) and the amplitude of transmitted waves at the interface (2). Knowing the wave basis of each waveguide, the coupling equation, which gives the amplitude of the reflected and transmitted waves at the interfaces, is derived:

$$\mathbf{S}^{(c)}\mathbf{\Psi}^{(1)} \begin{bmatrix} \mathbf{Q}_{inc}^{(1)} \\ \mathbf{Q}_{ref}^{(1)} \end{bmatrix} = \mathbf{\Psi}^{(2)} \begin{bmatrix} \mathbf{Q}_{inc}^{(2)} \\ \mathbf{Q}_{ref}^{(2)} \end{bmatrix}, \tag{17}$$

which can be reformulated as:

$$(\mathbf{\Psi}^{(2)})^{-1}\mathbf{S}^{(c)}\mathbf{\Psi}^{(1)} \begin{bmatrix} \mathbf{Q}_{inc}^{(1)} \\ \mathbf{Q}_{ref}^{(1)} \end{bmatrix} = \begin{bmatrix} \mathbf{Q}_{inc}^{(2)} \\ \mathbf{Q}_{ref}^{(2)} \end{bmatrix}. \tag{18}$$

2.3 Difussion based homogenization method

The diffusion based homogenization method uses the concept behind CPA, and simultaneously applies the Diffusion method to be able to retrieve equivalent material properties for any given unit cell of which only the finite element model is available.
The unit cell of the waveguide to be homogenized is called the original unit cell original UC). Now two identical waveguides constructed from the same original unit cell are connected through a junction which is called the equivalent coupling element, see Figure 3.

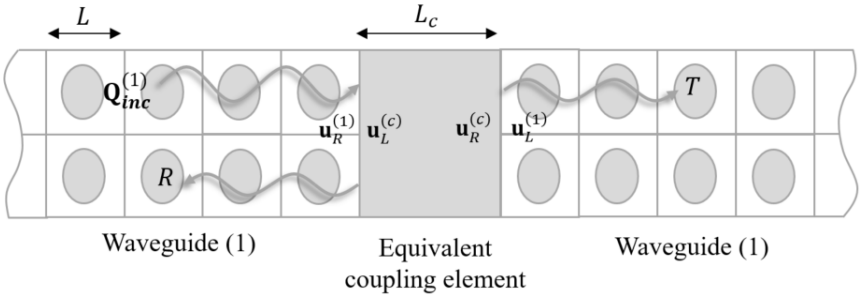


Figure 3: The configuration in which the coupling element is embedded between the targeted waveguides

Assuming that the coupling element is equivalent to the waveguide, an incoming wave with a given amplitude should be transmitted completely and have no reflection. Therefore, the equivalent material properties can be computed by minimizing the reflection and maximizing the transmission coefficients.
Rewriting the coupling equation for the system of Figure 3 and considering incident waves of unit amplitude from left hand side and no incident wave from the right hand side, equation (18) becomes:

$$\mathbf{\Psi}^{-1}\mathbf{S}^{(c)}\mathbf{\Psi} \begin{bmatrix} \mathbf{I} \\ \mathbf{R} \end{bmatrix} = \begin{bmatrix} \mathbf{T} \\ \mathbf{0} \end{bmatrix}. \tag{19}$$

In the equation above the wave basis is fixed, therefore the reflection and the transmission coefficients only depend on $\mathbf{S}^{(c)}$ which contains the material properties of equivalent coupling element.

As mentioned before the $\mathbf{S}^{(c)}$ matrix is not well-conditioned so we propose here another method to calculate it such that conditioning is improved, see Appendix A :

$$\mathbf{S}^{(c)} = \mathbf{A^{-1}B} \quad \text{with} \quad \mathbf{A} = \begin{bmatrix} \mathbf{D}_{LR}^{(c)} & \mathbf{O}_n \\ \mathbf{D}_{RR}^{(c)} & \mathbf{I}_n \end{bmatrix} \quad \text{, and} \quad \mathbf{B} = \begin{bmatrix} -\mathbf{D}_{LL}^{(c)} & \mathbf{I}_n \\ -\mathbf{D}_{RL}^{(c)} & \mathbf{O}_n \end{bmatrix}. \tag{20}$$

The target function for the optimization scheme is defined as follows:

$$f(p) = ||\mathbf{P_{out}^T} * \mathbf{T} * \mathbf{P_{in}} - \mathbf{P_{out}^T} * \mathbf{T_0} * \mathbf{P_{in}}||^2 + ||\mathbf{P_{out}^T} * \mathbf{R} * \mathbf{P_{in}}||^2, \tag{21}$$

where $\mathbf{P_{in}}$ defines which type of waves are excited, while $\mathbf{P_{out}}$ defines for which type of the waves, the material properties are optimized. And with $\mathbf{T_0} = (\boldsymbol{\mu}^+)^{\frac{L_c}{L}}$ describing the transmission coefficients matrix accounting for the difference in phase due to difference in unit cell size.

2.3.1 Model order reduction as wave basis selection scheme

If we look at equation (19), we notice that in order to calculate transmission and reflection coefficients, the wave basis should be well-conditioned. However, accounting for highly evanescent waves results in an ill-conditioned wave basis. To tackle this problem, the WFE method can be enriched with a model order reduction step, which contains the part of the wave basis with the relevant wave types, excluding the, not-required, highly evanescent waves.
The method used here for model order reduction is explained in [16] where they use part of the calculated wave basis at each frequency as the reduction basis to truncate the degrees of freedom to a reduced set of degrees of freedom:

$$\begin{Bmatrix} \mathbf{q}_L \\ \mathbf{q}_R \end{Bmatrix} = \begin{bmatrix} \boldsymbol{\Theta}_{red} & \boldsymbol{\Theta}_{red} \end{bmatrix} \begin{Bmatrix} \mathbf{q}_{Lsub} \\ \mathbf{q}_{Rsub} \end{Bmatrix}, \tag{22}$$

where $\boldsymbol{\Theta}_{red}$ is a $2n \times n_{red}$ submatrix of the wave basis($\boldsymbol{\phi}$) with n_{red} being the number of sub-modes considered in the reduction basis. Defining the truncated degrees of freedom as shown in (22), the dynamic stiffness matrix of the reduced set can be written as:

$$\mathbf{D}_{red} = \begin{bmatrix} \boldsymbol{\Theta}_{red} & \boldsymbol{\Theta}_{red} \end{bmatrix}^T \begin{bmatrix} \mathbf{D}_{LL} & \mathbf{D}_{LR} \\ \mathbf{D}_{RL} & \mathbf{D}_{RR} \end{bmatrix} \begin{bmatrix} \boldsymbol{\Theta}_{red} & \boldsymbol{\Theta}_{red} \end{bmatrix}. \tag{23}$$

The reduction method above is applied in two parts of the diffusion based homogenization method. First in the wave basis calculation of the original unit cell e.g. in equation (12). Second in the reduction of the dynamic stiffness matrix of the equivalent coupling element to match the number of the degrees of freedom of the equivalent coupling element and the original unit cell at the interfaces in equation (18).

3 Results and discussion

In this section the proposed method is evaluated on a case study. After evaluating the method on material identification of an isotropic homogenize beam and matching the shear, longitudinal, and bending behavior of the original beam with its equivalent model, a periodic beam with added TVAs is examined and discussed in this paper to verify the possibility of capturing more complex dynamic behavior, for instance stopband behavior.

A beam with added TVAs is one of the examples of locally resonant metamaterial structures often investigated in research. From an NVH perspective the out-of-plane bending motion is the most relevant since this wave couples to acoustic waves causing the structure to radiate noise. Consequently the main interest in the example given in this section is to duplicate as accurately as possible the out-of-plane bending behavior

using a homogenized equivalent model by optimising to two parameters: equivalent density and hysteresis damping.

This section is divided into four sub-sections. The first one describes the proposed example in detail, while the second one focuses on the importance and effect of wave type selection. To fully asses the proposed method and the effect of wave type selection, the dispersion curve of the the beam with TVAs(original UC) is compared with its homogenized models. The next sub-section higlights the advantage of the method, when finite structure analysis is considered. At last, homogenization variables are studied in the forth section, and the relation of the converged values for each variable with dynamic behavior is described.

3.1 Problem description

In this example an aluminum beam with added TVAs is investigated. The configuration used in the homogenization scheme including the finite element model of the original unit cell and the coupling element is shown in Figure 4. Both unit cells are meshed using CHEXA8 elements, and the TVAs are modeled using a Celas1 element with translation stiffness along x-axis. The material properties, dimensions of the unit cell, and characteristics of the TVAs are given in the tables 1 and 2.
Moreover, an unconstrained gradient free optimization in MATLAB and Optimization Toolbox Release 2016b is used to derive the material properties. The optimization variables are the density (ρ,) and the hysteresis damping (η).

Youngs modulus	Poissons ratio	Density	Dimension	Hysteresis damping
$68.9GPa$	0.27	$2700kg/m^3$	$25 \times 25 \times 50mm$	0.01

Table 1: Material properties of the beam and its unit cell dimension

Added mass	Tuned frequency	Hysteresis damping
$0.2m_{UC}$	$200\ Hz$	0.001

Table 2: Characteristics of TVAs

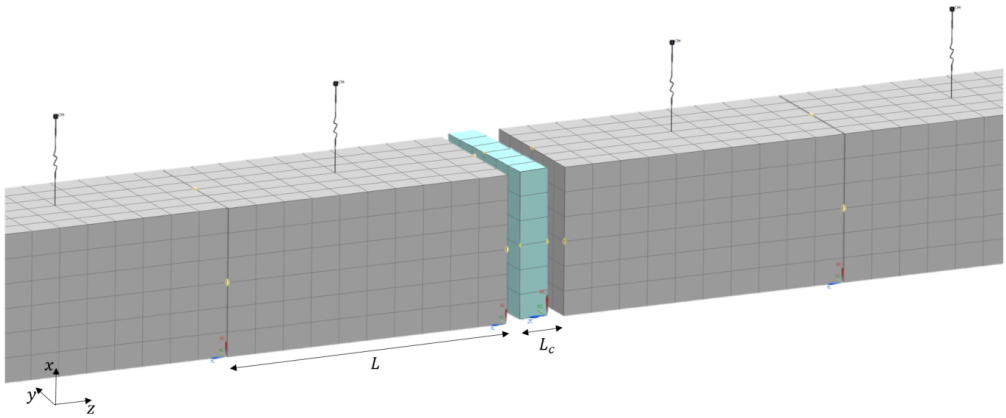


Figure 4: Finite element model of the beam with TVA and the coupling element

3.2 Influence of wave type selection

Due to the application of the considered system for NVH mitigation, the focus lies on matching the out-of-plane behavior of the beam with its equivalent model. Therefore, this section, which is divided in two

parts, is dedicated to investigating the effect of wave type selection on the accuracy of matching a wave type behavior. The first part evaluates the importance of using the wave basis reduction method, while the second one explains the impact of the correction matrices $\mathbf{P}_{in}$ and $\mathbf{P}_{out}$ on the optimization convergancy.

As mentioned earlier, in the coupling equation (equation (19)) the inverse of the wave basis is used, so the condition number of the wave basis is an important factor in the optimization process. Moreover, since in this example a certain wave type (bending mode) is targeted to be duplicated, it is necessary to distinguish between critical and unessential dynamics to be included in the homogenized model.
Therefore, a propagation ratio, which is the ratio between the real part of the wavenumber and the imaginary part of the wavenumber, is introduced as a strategy to choose reduction basis. The wave types are sorted according to the propagation ratio and the first desired number of the wave types with highest value of propagation ratio are chosen as reduction basis.
To prove this point, firstly the condition number of the complete wave basis over the frequency range is compared to the condition number of the reduced wave bases with different sizes in Figure 5. Looking at Figure 5, it is easy to realize that the inverse of the complete wave basis is very close to a singular matrix. As a result, a very high error in scattering coefficients calculation is expected, which is the reason behind complete failure of the optimization using the complete wave basis. Secondly, the dispersion curves of the

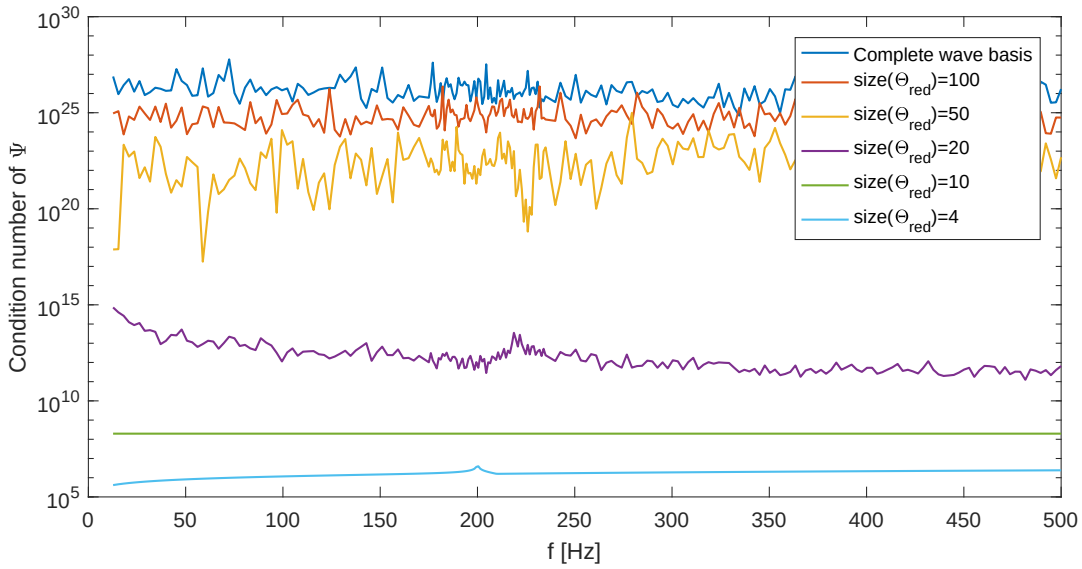


Figure 5: Condition number of the wave basis over frequency for different reduction bases

equivalent models obtained using different reduced wave bases are compared with the original UC dispersion curves in Figure 6. Moreover, To better undestand the difference in convergency accuracy, the relative error of both real and imaginary part of the wavenumbers between the original UC and the models with 10 and 4 modes as reduction basis, is shown in Figure 7, which proves the importance of the wave basis reduction in the optimisation process on the aspect of accuracy. Furthermore, the size of the equation to be solved at each iteration of the optimisation is reduced which results in computation time reduction.
Figure 6d shows a good agreement for both imaginary and real part of the wavenumber with a maximum relative error of 2% for the real part and 20% percent for the imaginary part in the stopband and mean value of 0.1% error for the real part and mean value of 2% for the imaginary one. It is expected that the higher error in the stopband is cause by the fact that higher order evanescent waves contribute to the behavior in this frequency zone which are not accounted for in this method due to the condition number of the wave basis.

In the next part, the effect of $\mathbf{P}_{in}$ and $\mathbf{P}_{out}$ on the optimization is evaluated by comparing two cases. In the first case all wave types are excited and the scattering coefficients of all wave types are optimised ($\mathbf{P}_{in} = \mathbf{I}$ and $\mathbf{P}_{out} = \mathbf{I}$), while in the second case only the bending wave around x-axis is excited and the scattering coefficients corresponding to the same wave type are optimised, which means only diagonal indices related

to the desired bending mode is non-zero in the $\mathbf{P}_{in}$ and $\mathbf{P}_{out}$ matrices. The dispersion curves of the equivalent model of these two case are compared to dispersion curves of the original UC in Figure 8.
It is worth mentioning that since in the previous part it was proven that considering only the first four propagating modes, which include shear, longitudinal, and two bending waves along two axis (x- and y-axis), is the best choice, in both of these cases the same reduced wave basis is chosen.

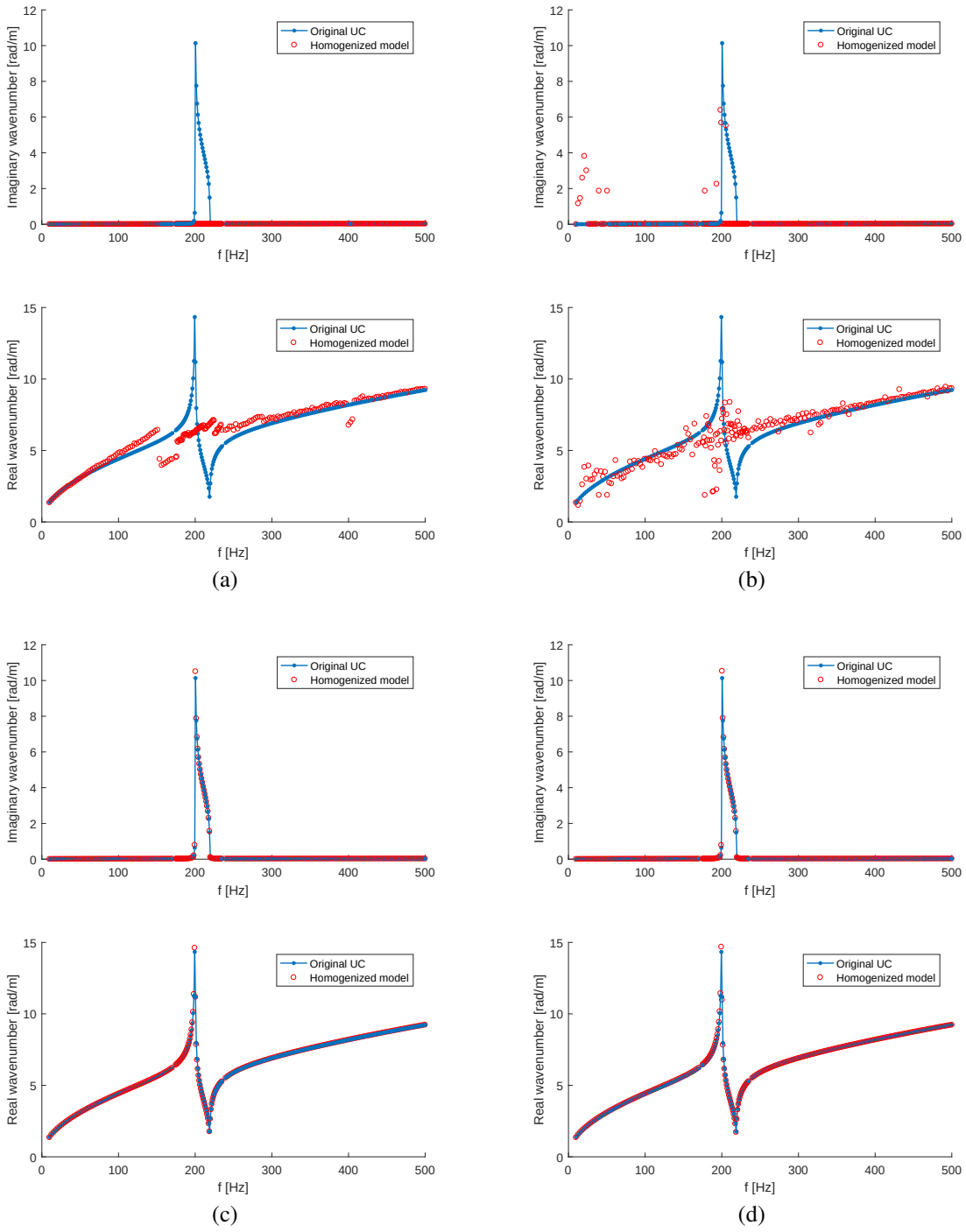


Figure 6: Dispersion curve comparison between the beam with TVAs and its equivalent model obtained using the first (a) 100 modes, (b) 50 modes, (c) 10 modes, (d) 4 modes of the wave basis as the reduction basis

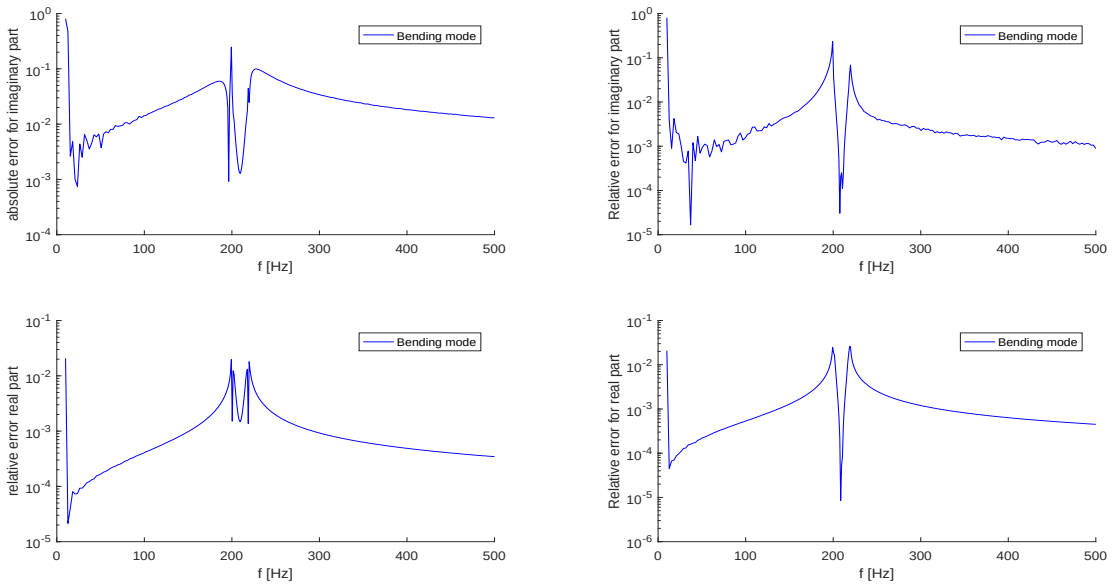


Figure 7: Relative error between the dispersion curves of the original UC and its equivalent model obtained using the first (a) 10 modes, (b) 4 modes of the the wave basis as the reduction basis

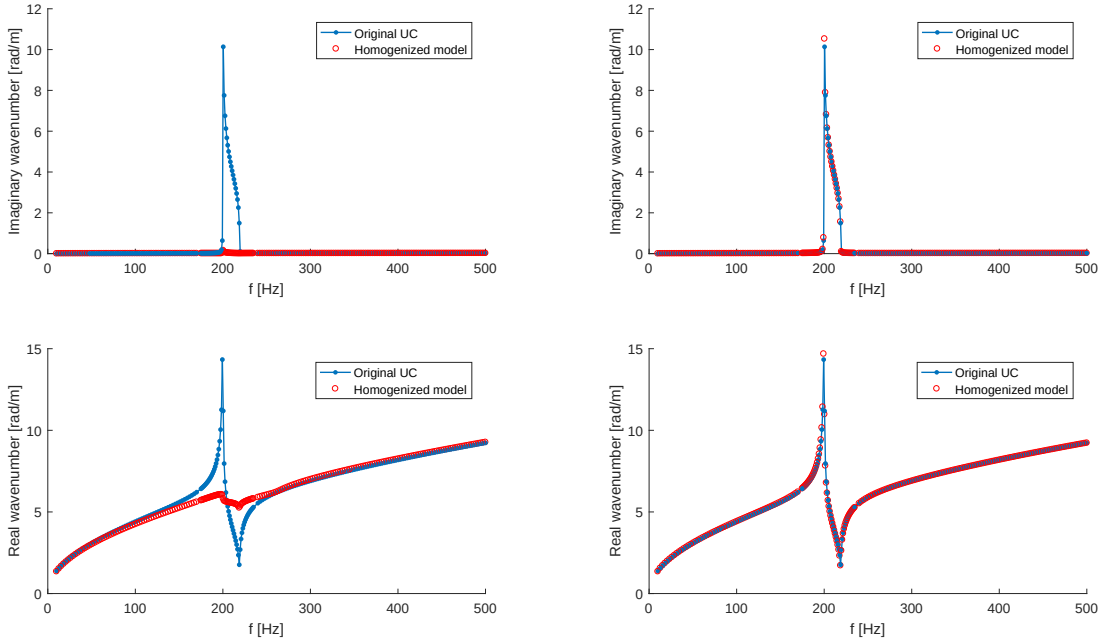


Figure 8: Dispersion curve comparison between the beam with TVAs and its equivalent model obtained exciting and optimizing all wave types (left), and exciting and optimizing only bending wave (right)

3.3 FRF analysis

In this section, the advantage of the diffusion based homogenization method when going to finite or semi-finite structures is evaluated by comparing the FRF of a semi-infinite beam constructed from the original UC and excited at its free end in out-of-plane direction to the FRF of a semi-infinite beam made by extension of the homogenized UC. In the Figure 9, the FRF of the semi-infinite beam with response location at 3,6,10,

and 20 (N) unit cells from the free edge is shown. Since the length of the original unit cell (L) is different from the homogenized unit cell (L_c), the number of homogenized unit cells (N_c) to have the same response location is calculated by scaling$N$ i.e. $N_c = \frac{L}{L_c} N$.

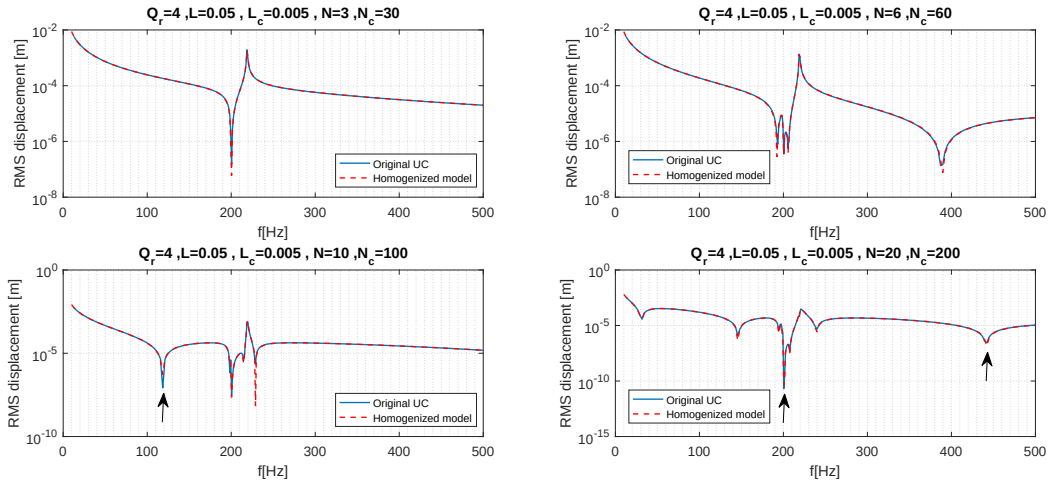


Figure 9: FRF of semi-infinite beam compared to its homogenized model at different response location

The TVA resonance frequency at 200 Hz is noticeable in both models, while some dips appear at both low and high frequencies when the response location is taken further away. These dips refer to nodal points and to clarify, the vibration pattern at some of these frequencies (the marked frequencies in Figure 9) are shown in Figure 10.

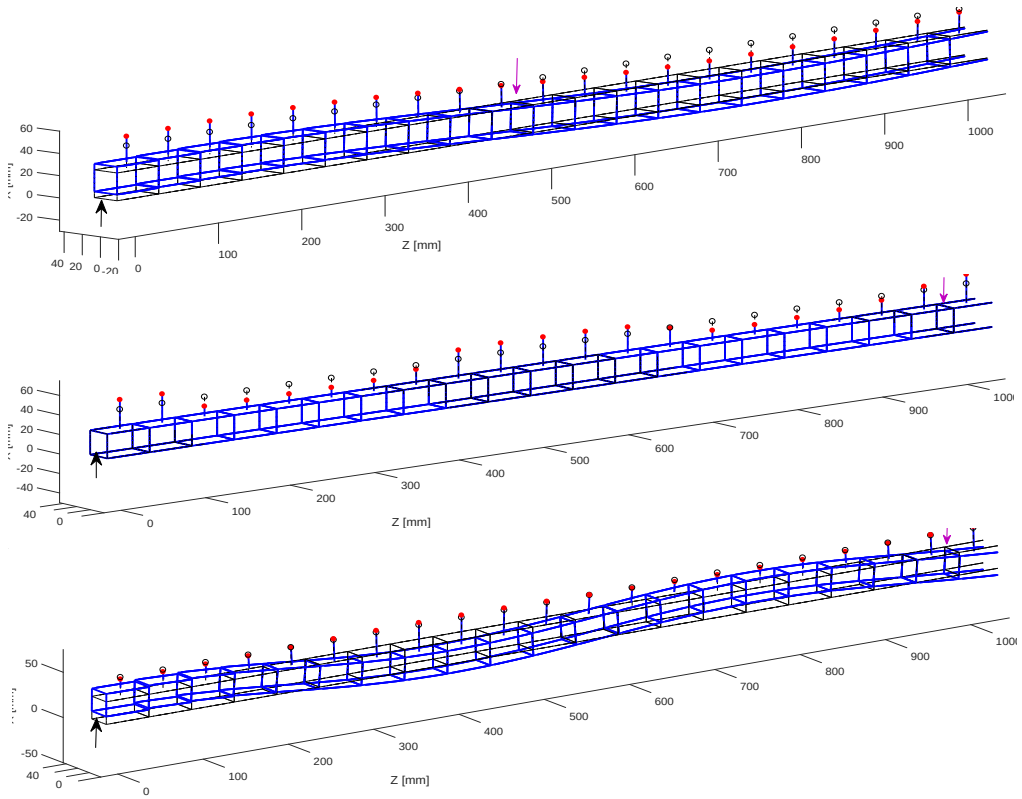


Figure 10: Vibration pattern of semi-infinite beam excited at its free end (black arrow) at 118.5Hz (top), 200Hz (middle), and 442.7 Hz (bottom). The pink arrow corresponds to the response location shown in Figure 9

3.4 Homogenization variable study

This section explains the physical meaning behind the converged values of the homogenization variables. The first variable is the equivalent density. It should be noted that these values cannot be compared to the nominal density of the beam (static mass). Instead the evaluation should be between the dynamic mass[17] and the equivalent densitiy resulting from the homogenization approach since the procedure used here is a dynamic homogenization. In this case, before the resonance frequency the structure behaves such that the mass is very high which explains no wave propagating at this frequency. Moreover, after the resonance frequency it behaves like the structure has a negative mass which is caused by the out-of-phase motion of the resonators and the host structure. This behavior can be noticed clearly in Figure 11. All values in Figure 11 are divided by static density of the host structure ($\rho = 2700 kg/m^3$). To have a better view, the density of the host structure and the TVA ($\rho_{tot} = 1.2\rho$) is plotted as well in Figure 11. Looking more closely at the Figure 11, two extremes are noticed which do not fit well with the dynamic density, that can be explained by the fact that the definition of the dynamic density given in [17] already takes into account the effect of damping in the resonator, whereas in the model of this paper, damping is added separately through the equivalent damping parameter. Therefore, causing the extremes of dynamic density to be pushed down.

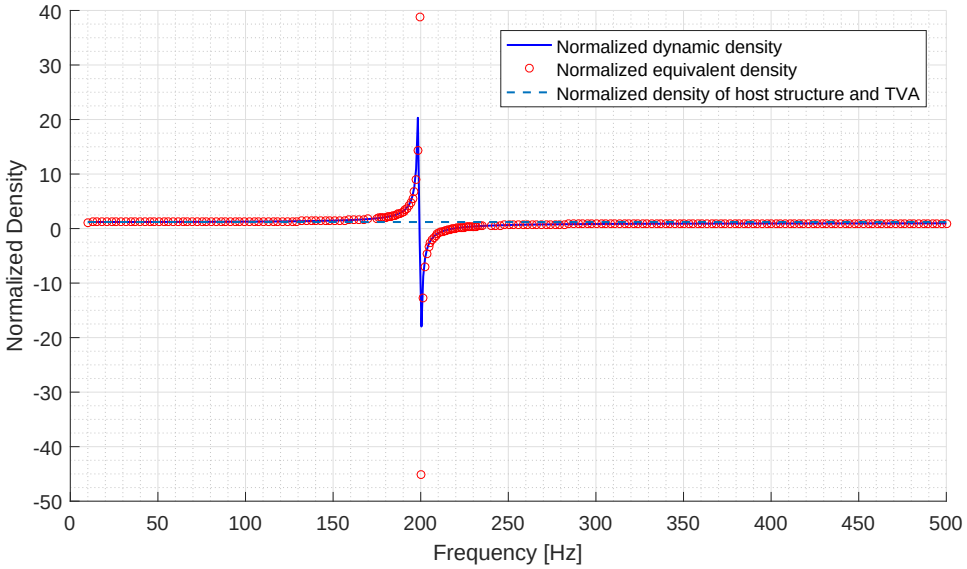


Figure 11: Dynamic mass and the converged value of density in the homogenization

The next variable is the equivalent hysteresis damping which represent the host structure's damping outside the stopband and the attenuation in the stopband. As a result, it is expected that inside the stopband higher value of equivalent damping is obtained, see Figure 12.

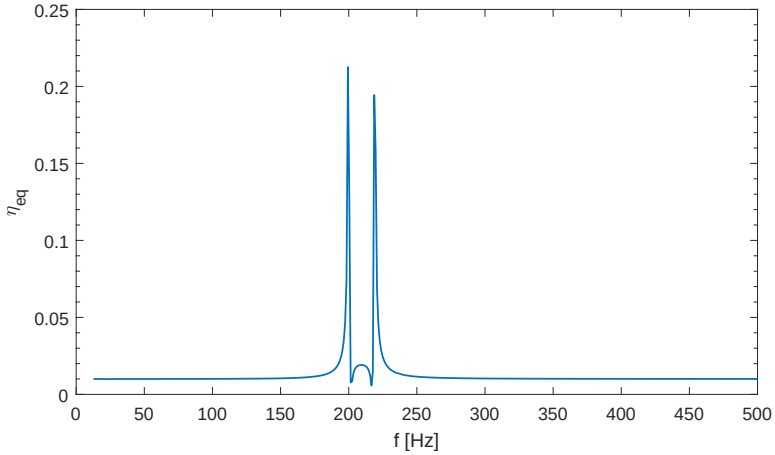


Figure 12: Absolute value of converged damping loss factor in the homogenization

4 Conclusion

This paper presents a computational homogenization approach for 1D periodic waveguides based on the finite element model of its unit cell. The homogenization strategy uses the Coherent Potential Approximation theory combined with the Diffusion method. Therefore, in this method the scattering coefficients are minimised at the interface of an equivalent coupling element embedded between two identical waveguides. Using the Diffusion method, the scattering coefficients can be calculated numerically which is one of the advantages of this method with respect to the others available in the literature. In this paper a beam with added TVAs was chosen to prove the ability of the method to capture complex dynamic behavior such as stopband behavior. Since one of the applications of locally resonant structures is NVH problems, where the out-of-plane behavior is of interest, a wave type selection scheme is proposed to capture the complex behavior as accuratly as possible with the most simple model possible i.e. isotropic homogenize medium. It was shown in the paper that this simple model is able to represent the original model with good accuracy in both unit cell analysis and FRF analysis which highlights the advantage of this model. Using such simple model is the trade off between capturing all possible behaviors i.e. longitudinal, shear, and bending behavior with more complex models and capturing the most dominant behavior in the problem setting, for example bending motion in NVH context, accurately with a very simple model.

Acknowledgement

The authors gratefully acknowledge the European Commission for their support through the VIPER research project (GA 675441). E. Deckers is a post-doctoral fellow of the research foundation - Flanders. The Research Fund KU Leuven is gratefully acknowledged for its support. This research was partially supported by Flanders Make, the strategic research centre for the manufacturing industry.

Appendix A Transfer matrix condition number

To demonstrate the improvement in the conditioning of the $\mathbf{S}$ matrix with new formulation proposed in this paper (equation (20)), the condition number of the transfer matrix of the beam with TVAs with both formulations is demonstrated over frequency, see Figure 13.

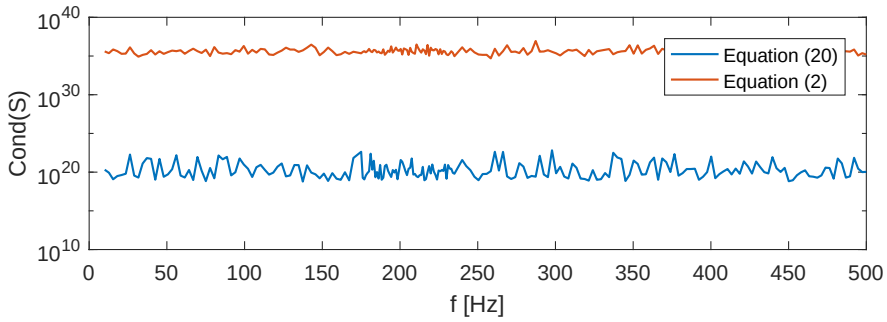


Figure 13: Condition number of the transfer matrix with two different formulation

References

[1] C. Claeys, E. Deckers, B. Pluymers, and W. Desmet, "A lightweight vibro-acoustic metamaterial demonstrator: Numerical and experimental investigation," *Mech. Syst. Signal Process.*, vol. 70-71, pp. 853–880, mar 2016.

[2] C. C. Claeys, K. Vergote, P. Sas, and W. Desmet, "On the potential of tuned resonators to obtain low-frequency vibrational stop bands in periodic panels," *J. Sound Vib.*, vol. 332, pp. 1418–1436, mar 2013.

[3] N. De Melo Filho, L. Van Belle, C. Claeys, E. Deckers, and W. Desmet, "Attenuation prediction in 1D waveguides using locally resonant metamaterials," *Proc. ISMA 2016 - Int. Conf. Noise Vib. Eng. USD2016 - Int. Conf. Uncertain. Struct. Dyn.*, 2016.

[4] R. F. Boukadia, C. Droz, M. N. Ichchou, and W. Desmet, "A Bloch wave reduction scheme for ultra-fast band diagram and dynamic response computation in periodic structures," *Finite Elem. Anal. Des.*, vol. 148, no. May, pp. 1–12, 2018.

[5] I. V. Andrianov, V. I. Bolshakov, V. V. Danishevs'kyy, and D. Weichert, "Higher order asymptotic homogenization and wave propagation in periodic composite materials," *Proc. R. Soc. A Math. Phys. Eng. Sci.*, vol. 464, no. 2093, pp. 1181–1201, 2008.

[6] C. Boutin, A. Rallu, and S. Hans, "Large scale modulation of high frequency waves in periodic elastic composites," *J. Mech. Phys. Solids*, vol. 70, no. 1, pp. 362–381, 2014.

[7] T. Antonakakis, R. V. Craster, and S. Guenneau, "Homogenisation for elastic photonic crystals and dynamic anisotropy," *J. Mech. Phys. Solids*, vol. 71, no. 1, pp. 84–96, 2014.

[8] J. R. Willis, "Effective constitutive relations for waves in composites and metamaterials," *Proc. R. Soc. A Math. Phys. Eng. Sci.*, vol. 467, no. 2131, pp. 1865–1879, 2011.

[9] Y. Wu, Y. Lai, and Z.-Q. Zhang, "Effective medium theory for elastic metamaterials in two dimensions," *Phys. Rev. B*, vol. 76, no. 20, p. 205313, 2007.

[10] J. R. Willis, "The construction of effective relations for waves in a composite," *Comptes Rendus - Mec.*, vol. 340, no. 4-5, pp. 181–192, 2012.

[11] S. Nemat-Nasser, J. R. Willis, A. Srivastava, and A. V. Amirkhizi, "Homogenization of periodic elastic composites and locally resonant sonic materials," *Phys. Rev. B - Condens. Matter Mater. Phys.*, vol. 83, no. 10, pp. 1–8, 2011.

[12] J. M. Mencik and M. N. Ichchou, "Multi-mode propagation and diffusion in structures through finite elements," *Eur. J. Mech. A/Solids*, vol. 24, no. 5, pp. 877–898, 2005.

[13] Y. Fan, M. Collet, M. Ichchou, L. Li, O. Bareille, and Z. Dimitrijevic, "Energy flow prediction in built-up structures through a hybrid finite element/wave and finite element approach," *Mech. Syst. Signal Process.*, vol. 66-67, pp. 137–158, jan 2016.

[14] W. X. Zhong and F. W. Williams, "On the direct solution of wave propagation for repetitive structures," *J. Sound Vib.*, vol. 181, pp. 485–501, mar 1995.

[15] J. M. Mencik, "New advances in the forced response computation of periodic structures using the wave finite element (WFE) method," *Comput. Mech.*, vol. 54, no. 3, pp. 789–801, 2014.

[16] D. J. Mead, "The forced vibration of one-dimensional multi-coupled periodic structures: An application to finite element analysis," *J. Sound Vib.*, vol. 319, no. 1-2, pp. 282–304, 2009.

[17] N. De Melo Filho, L. Van Belle, C. Claeys, E. Deckers, and W. Desmet, "On the use of the dynamic mass of metamaterials to calculate the transmission loss based on the acoustic mass law," *13th Int. Conf. Theor. Comput. Acoust. ICTCA 2017*, vol. 2017-July, 2017.

Modeling and experimental measurements of the sound transmission loss for multi-layer core topology systems

N. Guenfoud[1, 2], C. Droz[1], M. Ichchou[1], O. Bareille[1], B. Pluymers[2, 3] and E. Deckers[2, 3]
[1] Laboratoire de Tribologie et Dynamique des Systèmes, Ecole Centrale de Lyon
36 Avenue Guy de Collongue, 69134, Ecully, France
Email : **nassardin.guenfoud@ec-lyon.fr**

[2] Noise and Vibration Research Group, PMA, KU Leuven
Celestijnenlaan 300 B, B-3001, Heverlee, Belgium

[3] DMMS core lab, Flanders Make, Belgium

Abstract
In this paper, we focus on multi-layer core topology systems which consists in piling up layers made by different kind of cores and offers innovative solutions to periodic structures design. The main objective of this study is to analyze the phenomena occurring in these multilayer core topologies, and then compare the numerical models with experimental measurements while the effects of the phase shift on the STL will be investigated. The model is implemented using MATLAB and ANSYS apdl. The mass of the unit cell is taken as constraints to eliminate its influence on the STL and the compression modulus is calculated to verify the mechanical properties. To perform the experimental measurements, the samples are designed with CATIA and then made by an industrial 3D printer using the fused deposed model technic. An impedance tube is used to measure the STL and compare with the vibroacoustic phenomena.

1 Introduction

A great challenge of these last decades is to make lightweight structures with efficient acoustical and mechanical performances for many industrial applications (aeronautics, aerospace, building construction, automotive, …). Sandwich panels with laminates, composite structures as well as porous media have been developed to propose new solutions. Alternatively, periodic structures are widely used in aerospace industry since the stiffness to weight ratio is low. In terms of mechanical properties, the rigidity of the core enhances the tensile and compression modulus of the whole structure. The core geometry creates an anisotropic material with several main directions. Under wave excitations and at some frequencies it will make occur specific characteristics of the structure. Periodic structures can be easily characterized by the unit cell and many models can be applied to investigate their vibroacoustic properties.
The principle of the wave method firstly explained in [1] has been implemented using Finite Element Method and became the Wave Finite Element Method (WFEM) described in [2] for 1D and 2D periodicity. Analytical formulation combined with homogenized formulation can be used to determine the Sound Transmission Loss as it is done in [3] using the k-space obtained with the WFEM. Nevertheless, it is limited in terms of structure complexity due to the use of homogenized method. Besides, another approach using the Transfer Matrix Method ([4]) is proposed in [5] and reduce drastically the computational cost. In [6], the method is based on nodal surfaces and uses a simple formulation to obtain the acoustic properties. Similarly, [7] manipulates the shape functions associated with the displacement of the panel to develop the formulation to obtain the acoustic properties. Recently, the wave-based method has been used in [8] allowing to model any kind of acoustic excitations.

By exploiting these models, the study of design space is done by changing the geometry of the core and by analyzing the influence on the STL. In [9, 10], by computing a parametric survey as well as an optimization, they showed that modifying the shape of the core can improve the sound properties or by altering some parameters of the core and keeping the same geometry, leading to the possibility to optimize the structure. These effects have been investigated in [11, 12] as well. In [13], several core geometries (rectangular, triangular, hexagonal, …) are compared to optimize the transition frequency, corresponding to a vibroacoustic indicators.
Concerning multi-layer systems, [14, 15, 16, 17, 18, 19] have exploited the way to pill up several layers made of corrugated cores. These studies were mainly restricted for vibration and mechanical properties. In [20], the experimental measurement indicated the efficiency of a double-layer honeycomb panel compared to a single-layer especially in low frequency.

In this paper, a sandwich panel will be studied. By shifting the unit cell, it will offer the possibility to obtain a multi-layer that will be investigated in terms of mechanical and acoustic properties. Results will be validated by experimental measurements to conclude on the efficiency of making this type of structure.

2 Model

A sandwich panel with a standard rectangular core is used as a reference result. The principle is to make the new geometry by shifting a third of the unit cell in two directions x and y as illustrated in the Fig.1. This layout allows to keep the mass of the unit cell constant. The total thickness of the unit cell is 24 mm (y-direction), 15 mm in the x-direction and 15 mm in the z-direction. The thickness of the skins is 2 mm and the thickness of the core is 0,7 mm.
The following sandwich panels are made of ABS with E = 1,6 x 10^9 Pa, ρ = 985 kg/m^3 and ν = 0,33. The damping η is evaluated at 2 %. Theses values were obtained by characterizing the material.

A finite element analysis is made with the commercial software Ansys apdl. SHELL181 with a size of 1 mm is used to build the finite element model shown in Fig. 1.

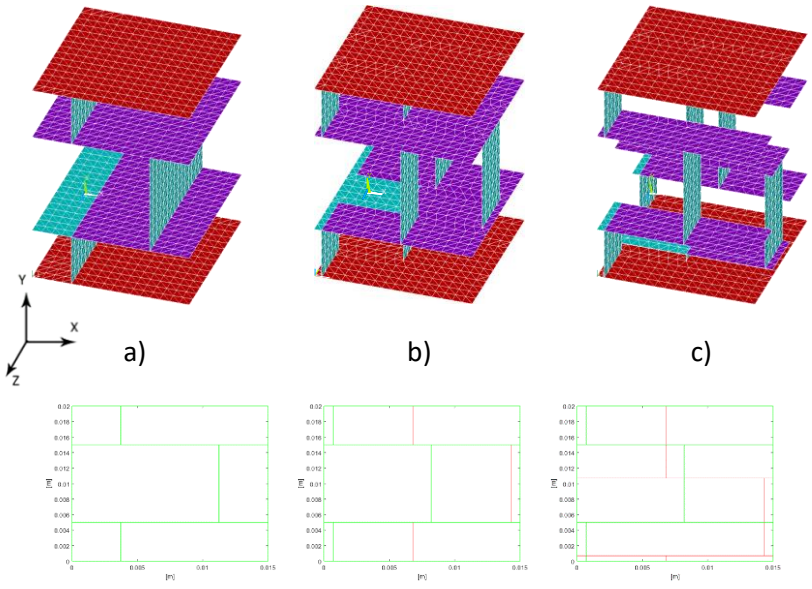


Figure 1 : a) Standard; b) x-Shift c) xy-Shift

2.1 Sound Transmission Loss

The studied structure is excited by normal incident waves considered as plane waves. It is then divided in three kind of acoustic plane waves: the reflected, the absorbed and the transmitted waves. The sandwich panel separates two semi-infinite fluids with $\rho 0 = 1{,}25$ kg/m^3 and $c0 = 343{,}6$ m/s.
Finally, the Sound Transmission Loss (STL) is obtained using the Eq.1:

$$STL = 10\log 10\left(\frac{W_i}{W_t}\right) \tag{1}$$

The method developed in [6] uses the following assumptions:

- The structure is assumed as an infinite panel.
- Only real wavenumbers are considered.
- The structure is excited by plane waves.
- The angles of incidence and reflection are equal.

A modal analysis is performed with Ansys apdl with free boundary conditions. The stiffness and mass matrix are extracted from the unit cell and allow to calculate the dynamic stiffness. The WFEM is then used to apply the Bloch-Floquet theory. The displacement on the incident and transmitted side and the external forces applied on the structure are linked with the dynamic stiffness and yields to Eq. 2:

$$\begin{bmatrix} b_{ii} & b_{it} \\ b_{ti} & b_{tt} \end{bmatrix}\begin{pmatrix} u_i \\ u_t \end{pmatrix} = \begin{pmatrix} e_i \\ e_t \end{pmatrix} \tag{2}$$

with u_i and u_t the node displacement on the incident and transmitted side whereas e_i and e_t are the external forces applied on the structure, respectively.
Considering the nodal surfaces of the incident and transmitted side (called S_i and S_t) of the unit cell, the external forces applied on the nodes can be rewritten as the product of the nodal surfaces multiply by the pressure evaluated on the node.

The continuity of normal particle velocity at the interfaces gives:

$$\begin{cases} \rho\omega^2 u_i = -ik_y(p_I - p_R) \\ \rho\omega^2 u_t = -ik_y p_T \end{cases} \tag{3}$$

k_y propagative constant in z-direction, p_i, p_r and p_t the incident pressure, the reflected and the transmitted wave, respectively.

Then, a matrix equation between the acoustic pressures of each side is obtained and becomes:

$$\begin{pmatrix} b_{ii} - \dfrac{S_i}{Y_0} \\ b_{ti} \end{pmatrix} p_I = \begin{bmatrix} b_{ii} + \dfrac{S_i}{Y_0} & -b_{it} \\ b_{ti} & -b_{tt} - \dfrac{S_t}{Y_0} \end{bmatrix}\begin{pmatrix} p_R \\ p_T \end{pmatrix} \tag{4}$$

Consequently, by solving the Eq. 4 the reflected and transmitted pressures are known and allow to calculate the STL. It is easy to implement the methodology with MATLAB since it consists on solving a matrix equation.
This method is applied for the three geometries and compared on the following Fig. 2. The frequency range is chosen from 100 Hz to 1600 Hz corresponding to the valid frequency range of the impedance tube.

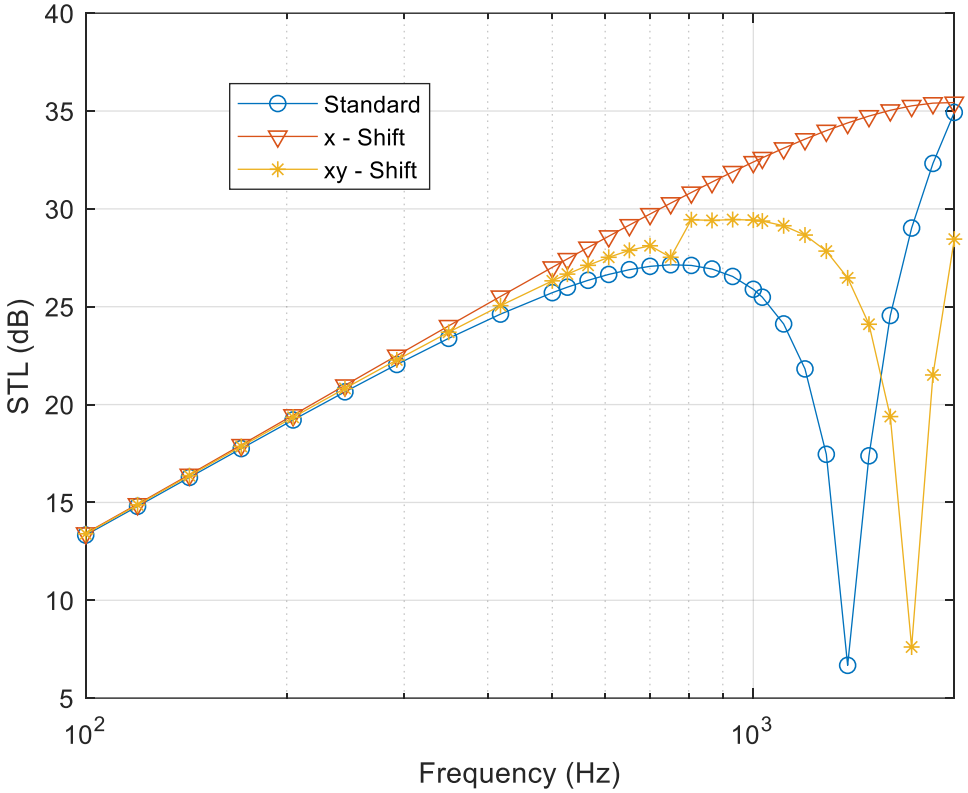


Figure 2 : Comparison of the Sound Transmission Loss of three sandwich panels made of three different unit cell

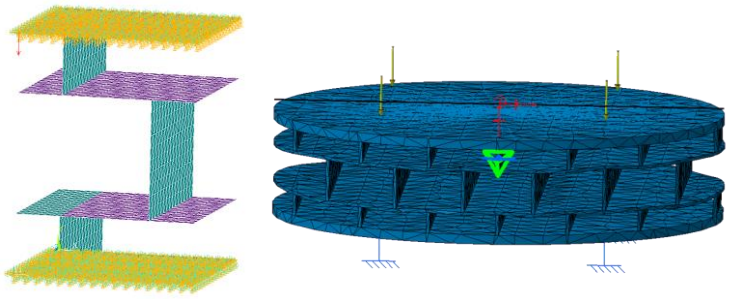
It is occurred that shifting the core improves the sound transmission loss and shifts the coincidence frequency to higher frequencies. The low mass is kept for a larger frequency band. The x-shift sample turns out being the best layout with the best acoustic performances. Indeed, the more the coincidence frequency will be in higher frequencies the more the structure will be efficient and reliable in terms of sound transmission loss. Finally, it seems that the shift in y-direction decrease the acoustic efficiency of the sandwich panel.

2.2 Compression Modulus

Since the geometry of the core changes, it has been chosen to calculate the compression modulus as a relevant indicator to verify the mechanical properties of the sandwich panel. The same boundary conditions as a compression machine are applied:

1. only the displacement in y-direction is free
2. A unit force is applied on the top skin
3. All nodes of the top skin are constraint to have the same displacement.

The commercial software Ansys apdl and CATIA are used to model the unit cell. SHELL181 is still used with Ansys apdl whereas Solid Elements are chosen for CATIA. The finite element models are illustrated in Fig. 3 and the result obtained shown in Table 1.



(a) (b)

Figure 3 : Finite element model a) Ansys apdl b) CATIA

	Ansys apdl (MPa)	CATIA (MPa)
Standard	$2{,}3 \times 10^5$	$5{,}7 \times 10^7$
x - Shift	$6{,}77 \times 10^6$	$1{,}08 \times 10^8$
xy - Shift	$7{,}3 \times 10^5$	$6{,}94 \times 10^7$

Table 1 : Calculation of the compression modulus

The differences between the two software could be mainly due to the element used since with solid elements the physics is better captured and closer to the reality. Nevertheless, the conclusion remains the same for both simulations: the x-Shift sample occurs to have the highest compression modulus. Indeed, adding the phase shift lead to well distribute the load on the skins and increase the rigidity of the whole sandwich panel. Shifting the unit cell in the y-direction creates nodes contact at some locations and drastically decrease the compression modulus.
Finally, the x-Shift sample appears to be the optimize structure to obtain the best acoustic and mechanical performances and keeping the mass constant. These results still need to be validated by measurements.

3 Experimental Measurements

3.1 Impedance tube

The experimental measurements were performed to verify the efficiency of the optimize structure as expected from the modeling part. A four microphones B&K standard wave tube (Fig. 4) with the two loads method was used. The loudspeaker is located at the end of the tube generating a random noise signal in the frequency range from 200 Hz to 1600 Hz. The B&K 4206 large tube with a diameter of 100 mm was chosen. The frequency response functions are measured with the four microphones and all transfer functions are computed. Two measurements are needed to calculate the sound transmission loss:

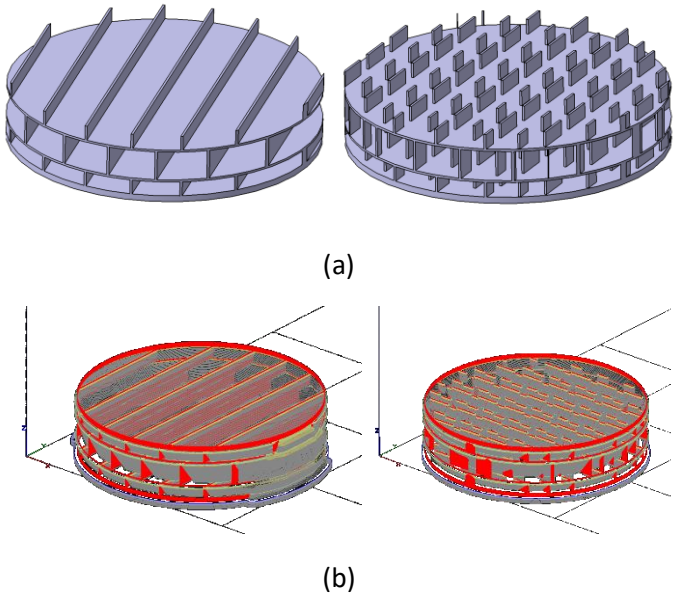
1. Measurement with an open tube termination
2. Measurement with an anechoic termination made using 4 standards sound absorbing samples with a 100 mm depth in total.



Figure 4 : Impedance tube (B&K)

3.2 Manufacturing process using the 3D printing technic

Both samples were made using a the FORTUS 250, a 3D printer using the fused deposed model technic making the structure layer by layer. The 3D printer can add two kinds of matter: the model material, corresponding to the material of the structure, and the support material helping to build the structure, but which will be removed after immerging the structure inside a solution.
The samples were firstly designed with CATIA and then preprocessed using INSIGHT as illustrated in Fig. 4. To improve the quality of the structure it is needed to add the support material. The thickness of the deposed rob is 0.3556 mm while the thickness of each layer is 0.1778 mm.



(a)

(b)

Figure 5 : (a) Samples designed using CATIA (b) Preprocessing using INSIGHT

The final samples are shown in Fig. 6. Since the structure is rigid and it is difficult to accurately reach 100 mm to fit inside the tube, it has been chosen to manufacture the sample with a diameter of 97 mm to overcome the uncertainty of the manufacturing process. Then, to set up the sample inside the tube, a circular joint made of rubber and scotch tape (Fig. 7) was made to avoid air leakage.

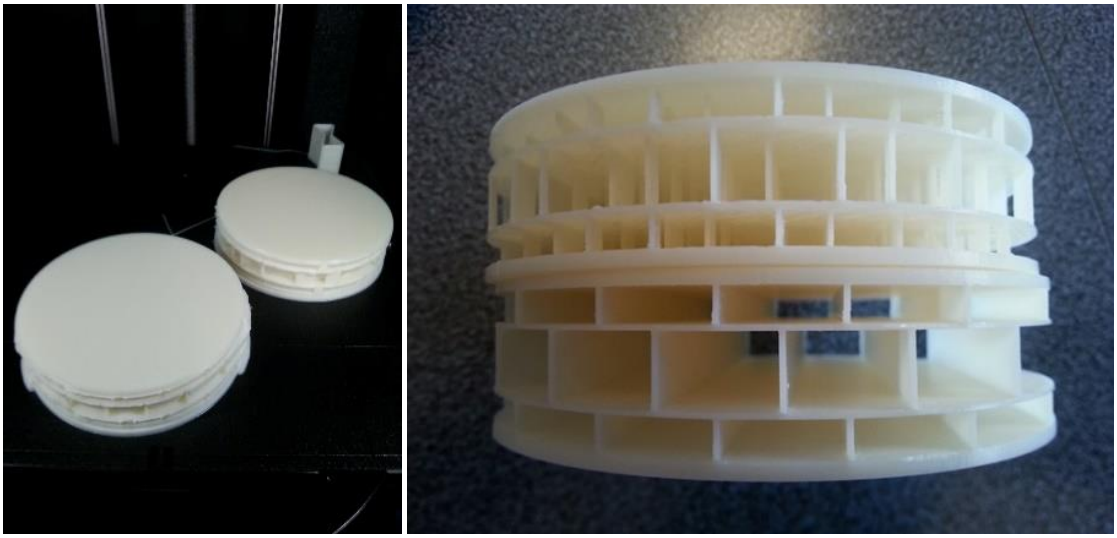


Figure 6 : Printed samples



Figure 7 : Joint made of rubber and scotch tape

The weight of both samples was measured and listed in Table 2.

	Without rubber joint	**With rubber joint**
Standard	47,29 g	69,93 g
x - Shift	47,80 g	68,72 g

Table 2: Samples weigth

Without the joint the difference between both samples is 1 % while adding the joint it reaches 1,7 %. These differences are neglectable and will not affect the mass low corresponding to low frequencies.

3.3 Results

The obtained result with the impedance tube are shown in Fig. 8. Three measurements were done with the standard case to verify the repeatability. As it was expected the x-Shift sample reveals the best acoustic performance. Before 1000 Hz, the difference is mainly due to the boundary conditions that are not perfectly respected and experimental conditions including measuring errors by microphones. After 1000 Hz, the x-Shift shows a great efficiency and reaches more than 7 dB better than the standard sandwich panel.

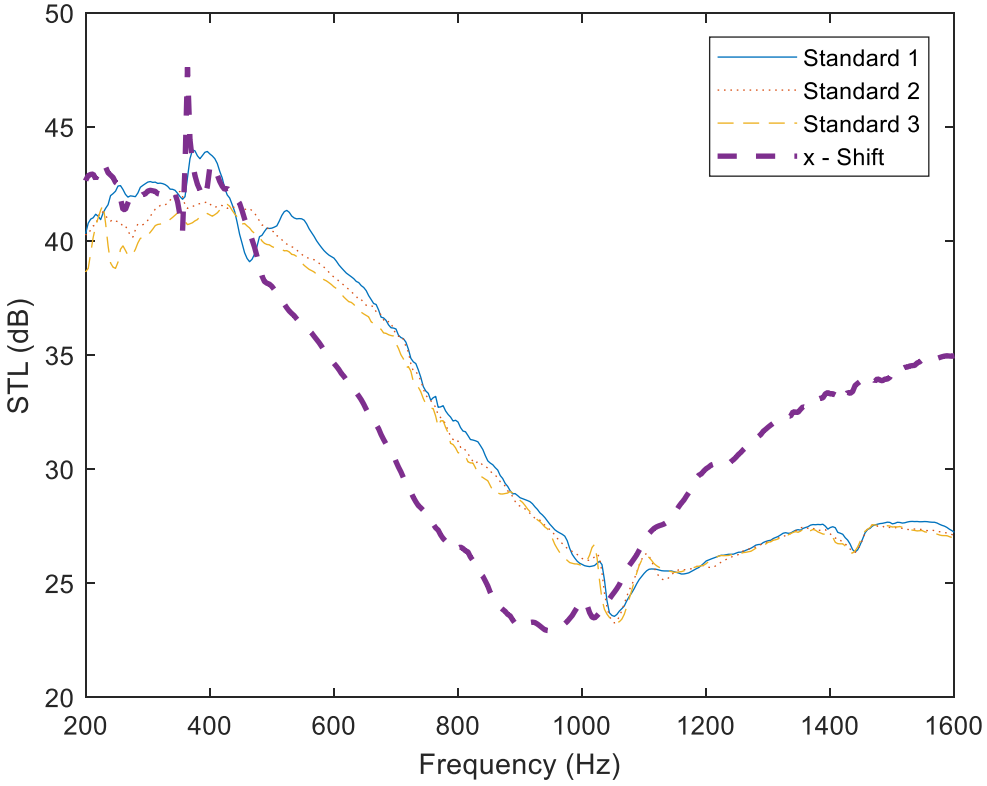


Figure 8 : Comparison of the sound transmission loss with the impedance tube (B&K)

4 Conclusion

This work proposes a new way to design sandwich panels creating multi-layer core topology systems. Three samples were designed by shifting a third of the unit cell in two directions. They were modeled under normal incident waves using the Wave Finite Element Method and then compared in terms of acoustic and mechanical properties. The sound transmission loss and the compression modulus were chosen as acoustic and mechanical relevant indicators.

The model revealed the possibility to increase the compression modulus of the sandwich panel as well as the sound transmission loss by shifting the unit cell in the x-direction and keeping the mass constant.

A 3D printer was used to manufacture the samples and then, a joint made of rubber was added to ensure the samples to fit inside the impedance tube without air leakage. The measurements were done using a Tube de Kundt from B&K with a diameter of 100 mm and shown the efficiency of shifting a part of the unit cell.

Further studies can be carried out to predict the efficiency of any type of unit cells and an optimize structure could be obtained.

Acknowledgments

This project has received funding from the European Union Horizon 2020 research and innovation program under the Marie Sklodowska-Curie grant agreement No. 675441. The author would like to acknowledge all the Institutions and Partners involved in the VIPER project.

References

[1] L. Brillouin, *Wave propagation in periodic structures*. Dover Publications, (1953).

[2] E. Manconi, *Modelling wave propagation in two-dimensional structures using a wave/finite element technique*, University of Parma, Italy, (2008).

[3] Z. Zergoune, M.N. Ichchou, O. Bareille, B. Harras, R. Benamar, B. Troclet, *Assessments of shear core effects on sound transmission loss through sandwich panels using two-scale approach*, Computer and Structure, Vol. 182., (2016), pp. 227-237.

[4] J.-F. Allard, N. Atalla, *Propagation of Sound in Porous Media: Modelling Sound Absorbing Materials*, Second Edition, John Wiley and Sons, Chichester, (2009).

[5] A. Parinello, G.L. Ghiringhelli, *Transfer Matrix representation for periodic planar media*, Journal of Sound and Vibration, Elsevier, Milano, Italy, (2016).

[6] J.-L Christen, *Acoustic transmission through composite shells with noise treatment: Modelling and sensitivity*, PhD Thesis, Ecole Centrale de Lyon, France, (2016).

[7] Y. Yang, B. Mace, M. Kingan, *Prediction of sound transmission through, and radiation from, panels using a wave and finite element method*, J. Acoust. Soc. Am. 141 (4) 2452–2460, (2017).

[8] E. Deckers, S. Jonckheere, L. Van Belle, C. Claeys, W. Desmet, *Prediction of transmission, reflection and absorption coeeficients of periodic structures using a hybrid Wave Based – Finite Element unit cell method*, Journal of Computational Physics, Vol 356, (2018), pp. 282-302.

[9] Z. Zergoune, *Meso-macro approach for modeling the acoustic transmission through sandwich panels*, Ecole Centrale de Lyon, France, (2016).

[10] O. Baho, *Conception de structures sandwiches à fort pouvoir d'atténuation acoustique : analyse de sensibilité et optimisation*, Ecole Centrale de Lyon, France, (2016).

[11] D. Griese, J.D. Summers, L. Thompson, The effect of honeycomb core geometry on the sound transmission performance of sandwich panels, Journal of Vibration and Acoustics, Vol. 137, (2015).

[12] M. S. Mazloomi, M. Ranjbar, L. Boldrin, F. Scarpa, S. Patsias, N. Ozada, *Vibroacoustic of 2D gradient auxetic hexagonal honeycomb sandwich panels*, Composite Structures, Vol. 187, (2018), pp. 593-603.

[13] C. Droz, Z. Zergoune, R. Boukadia, O. Bareille, M.N. Ichchou, Vibro-acoustic optimisation of sandwich panels using the wave/finite element method, Composite Structures, Vol. 156, (2016), pp. 108-114.

[14] E. Magnucka-Blandzi, Z. Walczak, L. Wittenbeck, P. Jasion, M. Rodak, W. Szyc, J. Lewinski, *Stability and vibrations of a metal seven-layer rectangular plate with trapezoidal corrugated cores*, Thin-Walled Structures, Vol. 114, (2017), pp. 154-163.

[15] J. Lewinski, E. Magnucka-Blandzi, W. Szyc, *Determination of shear modulus of elasticity for thin-walled trapezoidal corrugated cores of seven-layers sandwich panels*, Engineering transactions, Vol. 63, N° 4, (2015), pp. 421-437.

[16] P. Paczos, P. Wasilewicz, E. Magnucka-Blandzi, *Experimental and numerical investigations of five-layered trapezoidal beams*, Composite Structures, Vol. 145, (2016), pp. 129-141.

[17] E. Magnucka-Blandzi, Z. Walczak, L. Wittenbeck, *Strength of a metal seven-layer rectangular plate with trapezoidal corrugated cores*, Journal of Theoretical and Applied Mechanics, Vol. 55, N° 2, (2017), pp. 433-446.

[18] E. Magnucka-Blandzi, P. Jasion, Z. Walczak, L. Wittenbeck, *Buckling and vibrations of metal sandwich beams with trapezoidal corrugated cores – the lengthwise corrugated main core*, Thin-Walled Structures, Vol. 112, (2017), pp. 78-82.

[19] E. Magnucka-Blandzi, P. Paczos, P. Wasilewicz, A. Wypych, *Three-point bending of seven layers beams – theoretical and experimental studies*, Archives of Civil Engineering, Vol. LXII, Issue 2, (2016), pp.115-130.

[20] H. Wen-chao, N. Chung-fai, *Sound insulation improvement using honeycomb sandwich panels*, Applied Acoustics, Vol. 53, N° 1-3, (1998), pp. 163-177.

Model order reduction in unit cell modeling and its application to complex structures

R. F. Boukadia [1,2,3], C. Claeys [1,3], C. Droz [2], M. Ichchou [2], E. Deckers [1,3]
[1] KU Leuven, Department Mechanical Engineering
Celestijnenlaan 300 B, B-3001, Heverlee, Belgium

[2] Vibroacoustics and Complex Media Group
LTDS / Ecole Centrale de Lyon,
Bat. E6, 36 Avenue Guy de Collongue, 69134 Écully, France

[3] DMMS lab, Flanders Make, Belgium

Abstract
In this work, harmonic and temporal responses of structures composed of 1D periodic waveguides are computed using the wave finite element method framework (WFEM) in conjunction with model order reduction (MOR) methods. First, a model order reduction strategy at the unit cell level is introduced and extended to parametric model order reduction (PMOR) when the mesh does not depend of the interfaces. The method relies on a mode based MOR of the inner degrees of freedom of the unit cell combined with a wave based model order reduction of the interfaces' degrees of freedom by projecting them on a collection of wave shapes obtained through the inverse approach. A first example analyses the merits of the proposed PMOR. A second example exploits the MOR method to analyze guided-waves interactions with a 3D defect in the mid-frequency domain. The proposed methodology enables the computation of highly complex and detailed models while providing substantial time reduction when computations were already possible.

1 Introduction

Wave propagation in phononic crystals and metamaterials is the center of an extensive research effort to create novel lightweight solutions with good vibroacoustic behavior. Indeed, They allow to control acoustic and elastic wave propagation thanks to a feature called band gap that correspond to frequency bands in which only spatially decaying waves can propagate. To study this new type of structures, methods based on wave propagation have been developed over the years. The Semi-Analytical Finite Element method (SAFE) [1] , the spectral finite element method [2], the shift cell operator method [3] and the WFEM [4] are some of the most popular. In particular, the last one uses classical finite element modeling of the unit cell (UC) and applies Floquet-Bloch boundary conditions a posteriori to obtain free wave propagation properties by solving a symplectic eigenvalue problem quadratic in frequency and propagation constants. The main advantages of the method are its relatively low implementation cost and the number of application cases that were developed for it [5, 6, 7, 8]. Over the years, it has proved to be a relevant method for the design and validation of both phononic crystals and resonant metamaterials [9] as well as a competitive tool for the study of coupled homogeneous and periodic waveguides. Because it rests on the resolution of an eigenvalue problem at each frequency of interest, its asymptotic complexity suffers when dealing with very large unit cells. However, classical MOR methods like Krylov subspace methods or balance truncation are not compatible with the WFEM because the spatial structure of the UC need to be preserved during the reduction process. Several methods have been developed to try and address the issue [10] [11]. This text presents some of the most recent techniques for model order reduction in unit cell modeling of 1D periodic structures and applies them to models of complex structures.

2 Unit Cell Modeling with the Wave Finite Element Method

2.1 1D WFEM: Free wave propagation

Let us consider a periodic structure composed of a unit cell (UC) that is repeated in space. To compute the wave propagation properties of such a structure the WFEM uses a finite element model of the unit cell assuming that the left and right interfaces of the UC use the same mesh and type of shape functions so that primal assembly between them is possible. The UC's degrees of freedom are then partitioned in three sub-groups. The degrees of freedom (dof) of the left interface (L), the dofs of the right interface (R) and the inner dofs (I). From there, two paths can be followed. One can chose a wavenumber and find the different frequencies and wave shapes for which such a wavenumber is relevant. This is the inverse approach. The second option is to choose a frequency and compute the properties of all propagative and decaying waves at that frequency. That is the direct approach. While the first option is generally preferred to analyze wave propagation properties over the irreducible Brillouin contours of 2D periodic structures, the second one takes precedence for most other applications. Both methods are presented below.

2.1.1 The inverse approach

The inverse approach starts with choosing a wavenumber k and thus a propagation constant $\lambda = e^{-ikL}$ where L is the length of the UC in the direction of propagation. From there, Floquet-Bloch boundary conditions can be applied to the structure and are enforced using left and right projection matrices:

$$\begin{cases} U_R = \lambda U_L \\ F_R = -\lambda F_L \end{cases} \qquad P_U(\lambda) = \begin{bmatrix} I_n & 0 \\ \lambda I_n & 0 \\ 0 & I_m \end{bmatrix} \qquad P_F(\lambda) = \begin{bmatrix} I_n & \frac{1}{\lambda} I_n & 0 \\ 0 & 0 & I_m \end{bmatrix} \tag{1}$$

Modified mass, stiffness and damping matrices are then obtained:

$$K(\lambda) = P_F(\lambda) K P_U(\lambda), \qquad M(\lambda) = P_F(\lambda) M P_U(\lambda), \qquad C(\lambda) = P_F(\lambda) C P_U(\lambda) \tag{2}$$

Finally, wave shapes and eigenfrequencies are obtained by solving the eigenvalue problem (3):

$$[K(\lambda) + i\omega C(\lambda) - \omega^2 M(\lambda)]\phi = 0 \tag{3}$$

When a real wavenumber is chosen, the modified matrices are Hermitian hence the inverse approach can be understood as a form of modal analysis. The associated eigenvalue problem has good numerical properties and optimized eigenvalue solvers have been developed to solve it.

2.1.2 The direct approach

Following the opposite path, the direct approach starts by choosing the frequency of interest and forming the dynamic stiffness matrix:

$$G = K + i\omega C - \omega^2 M \tag{4}$$

From there, the condensed dynamic stiffness matrix is obtained by condensing the internal degrees of freedom leaving only those at the interfaces as in (5):

$$D = \begin{bmatrix} D_{LL} & D_{LR} \\ D_{RL} & D_{RR} \end{bmatrix} = G_{BB} - G_{BI} G_{II}^{-1} G_{IB} \tag{5}$$

Where the index (B) corresponds to the degrees of freedom of both left and right interfaces. This operation can be costly because it requires the inversion of the matrix G_{II} at each frequency of interest. Section 3.1 shows how this can be sped up using model order reduction. Then, wave shapes ψ and propagation constants λ satisfying the Floquet-Bloch conditions (1) are looked for leading to the eigenvalue problem (6).

$$\left[\frac{1}{\lambda}D_{LR} + (D_{LL} + D_{RR}) + \lambda D_{RL}\right]\psi = 0 \tag{6}$$

This eigenvalue problem is often extremely ill-conditioned but possess a symplectic structure. However, no mainstream eigenvalue solver was developed specifically for this class of problem. The problem (6) is therefore solved as a general eigenvalue problem after being put in quadratic form. To address these issues, another equivalent form was developed by Zhong [12] . It has better numerical properties and enables the use of iterative solvers when only a few solutions are desired. It should be noted that the solutions to the eigenvalue problem come in pairs $\left(\lambda, \frac{1}{\lambda}\right)$ and (ψ^+, ψ^-) of positive and negative going waves. The MOR technique presented in section 3.2 aims at reducing the computation time of the eigenvalue problem (6).

2.2 Forced response of finite waveguides

Using solutions from the direct approach, it is possible to compute the forced response of a finite periodic waveguide composed of *N* UCs by assuming that the displacement of the *p-th* section take the form:

$$U_p = \Psi^+\Lambda^p q^+ + \Psi^-\Lambda^{N-p} q^- \tag{7}$$

Where q^+ and q^- are the amplitude coefficients for the positive and negative going waves. For free-free boundary conditions, the following formula is derived:

$$\begin{bmatrix} F_0 \\ F_N \end{bmatrix} = \begin{pmatrix} D_{LL}\Psi^+ + D_{LR}\Psi^+\Lambda & D_{LL}\Psi^-\Lambda^N + D_{LR}\Psi^-\Lambda^{N-1} \\ D_{RL}\Psi^+\Lambda^{N-1} + D_{RR}\Psi^+\Lambda^N & D_{RL}\Psi^-\Lambda + D_{RR}\Psi^- \end{pmatrix}\begin{bmatrix} q^+ \\ q^- \end{bmatrix} \tag{8}$$

Where F_0 and F_N are efforts applied at the waveguide's extremities. Another formula is used to compute the forced response of two identical periodic waveguides coupled by an arbitrary substructure. Noting D^c the condensed dynamic stiffness matrix of the substructure, a formula can be derived for the whole waveguide with free-free boundary conditions:

$$\begin{pmatrix} D_{LL}\Psi^+ + D_{LR}\Psi^+\Lambda & D_{LL}\Psi^-\Lambda^N + D_{LR}\Psi^-\Lambda^{N-1} & 0 & 0 \\ D_{RL}\Psi^+\Lambda^{N-1} + (D_{RR} + D_{LL}^c)\Psi^+\Lambda^N & D_{RL}\Psi^-\Lambda + (D_{RR} + D_{LL}^c)\Psi^- & D_{LR}^c\Psi^+ & D_{LR}^c\Psi^-\Lambda^M \\ D_{RL}^c\Psi^+\Lambda^N & D_{RL}^c\Psi^- & (D_{RR}^c + D_{LL})\Psi^+ + D_{LR}\Psi^+\Lambda & (D_{RR}^c + D_{LL})\Psi^-\Lambda^M + D_{LR}\Psi^-\Lambda^{M-1} \\ 0 & 0 & D_{RL}\Psi^+\Lambda^{M-1} + D_{RR}\Psi^+\Lambda^M & D_{RL}\Psi^-\Lambda + D_{RR}\Psi^- \end{pmatrix}\begin{bmatrix} q_1^+ \\ q_1^- \\ q_2^+ \\ q_2^- \end{bmatrix} = \begin{bmatrix} F_0 \\ 0 \\ 0 \\ F_{N+M} \end{bmatrix} \tag{9}$$

In this formula, *N* and *M* are the numbers of unit cells contained in the first and second periodic waveguides. F_0 and F_{N+M}, the efforts applied on the full structure's extremities and q_i^+ and q_i^- are the amplitude coefficients for the positive and negative going waves in each periodic waveguide.

3 Model Order Reduction Strategy

3.1 Reduction of inner degrees of freedom

To reduce the internal degrees of freedom of a UC or coupling substructure, Craig-Bamptom model order reduction [13] is used as presented in [10]. The projection matrix has two essential components. The clamped modes and the static modes of the inner degrees of freedom. The first modes are simply solution of the eigenvalue problem (10):

$$\left(K_{II} + i\omega_j C_{II} - \omega_j^2 M_{II}\right)\phi_j = 0 \tag{10}$$

Modes up to at least 3 times the maximal frequency of interest should be introduced in the projection matrix. We note those Φ_d. The static modes are given by the formula (11):

$$\Phi_s = -K_{II}^{-1}K_{IB} \tag{11}$$

The final projection matrix is :

$$P_{CB} = \begin{pmatrix} I_n & 0 \\ \Phi_s & \Phi_d \end{pmatrix} \tag{12}$$

Leading to the expression for the reduced matrices :

$$X_{red} = P_{CB}^T X P_{CB} \tag{13}$$

Where X is the original mass, stiffness or damping matrix of the model and X_{red} the reduced one.

3.2 Interface degrees of freedom reduction

3.2.1 Single Waveguide

For this case, the model order reduction scheme used is presented in [14]. It is similar to the approximations used to study acoustic wave propagation in ducts of constant cross-sections. In essence, propagative modes with cut-on frequency lower than $n_f f_m$ are used in the projection basis where n_f is a security factor usually comprised between 1 and 3 and f_m the maximal frequency of interest. When one is only interested in far field computations, n_f=1 can be used. When near field is considered a greater value may be needed. The main difference with acoustic wave propagation comes from the fact that wave propagation in solids is dispersive in wavenumber and also in mode shape (wave conversion process and veering are two extreme examples of this happening). Therefore, it is not enough to sample modes at their cut-on frequencies, rather, a sampling of the K-space using the inverse approach is realized with several wavenumber's values. A parameter n_k, an integer greater or equal to one, governs the refinement of the sampling in the wavenumber domain. In order to get a real full rank orthogonal projection matrix two operations are performed on the sampled wave modes. First, real and imaginary parts of the wave modes are separated. This addresses the issue of a complex projection matrix and lead to the creation of a vector collection ψ_{coll}. Then, a singular value decomposition (SVD) is performed on ψ_{coll} keeping only the most important left singular vectors. The exact number of vectors kept is determined by a factor $\epsilon \in \mathbb{R}_+^*$ that should generally be smaller than 10^{-3}.This leads to an orthogonal local projection matrix $Proj_{LR}$. The final projection matrix of the model is given by the block diagonal projection matrix P_{LR} :

$$P_{LR} = \begin{pmatrix} Proj_{LR} & 0 & 0 \\ 0 & Proj_{LR} & 0 \\ 0 & 0 & I_n \end{pmatrix} \tag{14}$$

Again, the reduced matrices are given by :

$$X_{red} = P_{LR}^T X P_{LR} \tag{15}$$

Where X is the original mass, stiffness or damping matrix of the model and X_{red} the reduced one.

3.2.2 Multiple waveguides and PMOR

Herein, we extend the method presented in [14] in order to build a single projection matrix valid for a family of waveguides. This allows primal assembly of reduced models when considering the coupling of different waveguides. Moreover, it can also be understood as a form of parametric model order reduction when the waveguides considered belong to a parametric family. The main interest of the method comes from the fact that reduced order models can be created on the fly at no additional computational cost which is highly beneficial when conducting phenomenological studies or optimizing parametric designs. The downsides of this approach are that an offline computation time is required to build the global projection basis and that the dofs reduction and thus the time gains are lower than those obtained using a tailored projection matrix for each model. The idea of embedding a MOR Scheme in a PMOR one is described in details in [15]. What follows shows how it is implemented in the case at hand. To create the projection matrix, one must first have a list of sample parameter values $(p_i)_{i\in[\![1,n]\!]}$. For each of these values, the reduction process is carried out as described in section 3.2.1 up to the creation of the collection of wave shapes $\psi_{coll}^{(i)}$ for the parameter

p_i. Once all wave shapes collections have been computed, they are concatenated into a single wave shape collection :

$$\Psi_{\text{coll}} = \left[\psi_{coll}^{(1)}, \psi_{coll}^{(2)}, \dots, \psi_{coll}^{(\text{n})}\right] \tag{16}$$

Again, an SVD is performed on the matrix Ψ_{coll}. Only the most prominent singular vectors are retained and used to create a local projection matrix $Proj_{LR}$ valid for the whole parametric space.

4 Numerical Examples

This section introduces two numerical examples. The first one analyses the merits and drawbacks of PMOR over MOR in a worst case scenario (for PMOR) where parameter changes lead to a localization of waves in different parts of the waveguide's cross-section. The second example highlight the power of the (MOR) strategy in enabling fast computation of wave-defect interaction in time domain for a waveguide with a high number of dofs using only the WFEM framework.

4.1 Example 1 : Parametric Model Order Reduction of a Sandwich

In this section, we study a worst case scenario for the parametric model order reduction at the interfaces' degrees of freedom by introducing an heterogeneity in the cross-section of the waveguide. This is because simply varying the material properties of an homogenous section can be understood as a shift in the maximal frequency of interest and is therefore unchallenging. The change is controlled by a parameter α which represent a scaling of the material properties. For $\alpha = 1$ the waveguide is homogeneous while the asymptotic case $\alpha = 0$ can be understood as having two decoupled waveguides. In between, strong localization phenomena in wave propagation occur due to the contrast of material properties. The nature of the parameter α makes it evident that its logarithm should be considered and therefore a lower bound strictly superior to 0 should be chosen for PMOR lest the associated part of the cross-section cannot be reduced.

4.1.1 Presentation of the model

In this section, we consider a homogeneous sandwich waveguide comprised of two materials. The material of the skins is aluminum, while that of the core is variable in both density and young modulus. The whole section is 3 centimeters wide and 5 millimeters thick with a 3 millimeters thick core and a skin thickness of 1 millimeter. A model of the cross section is created using ANSYS APDL 17 and SOLID187 elements. The mesh corresponds to a perfect grid with cubic elements of side 0.25 millimeters to ensure 4 elements in the thickness of the skins. This results in a 15246 dofs model. An illustration of the mesh is provided in Figure 1.

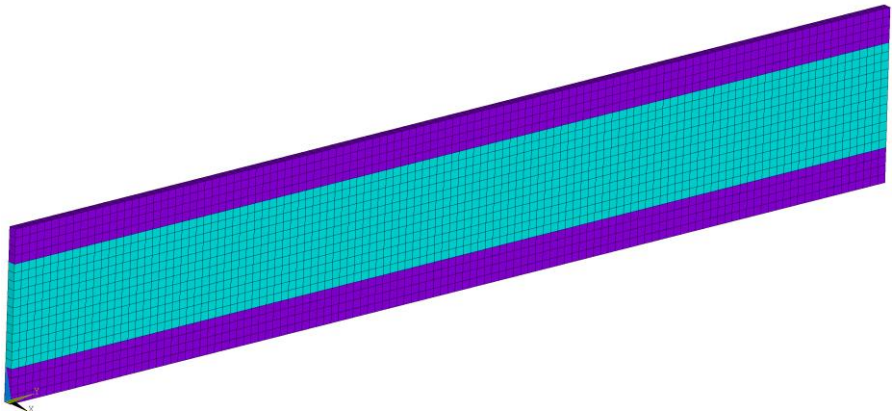


Figure 1 : Cross section of the parametric model. Material properties of the blue part are parametrized

The material properties of the skin are fixed and correspond to that of aluminum :

- Young Modulus : $E_0 = 69GPa$
- Poisson Ratio : 0.3
- Density : $d_0 = 2700\ kg.m^{-3}$
- Loss factor / hysteretic damping : $\eta = 3.10^{-3}$

The material properties of the core depend linearly on a parameter α taken in the interval $[2.10^{-1}, 1]$:

- Young Modulus : αE_0
- Poisson Ratio : 0.3
- Density : αd_0
- Loss factor / hysteretic damping : $\eta = 3.10^{-3}$

Because of this, the mass and stiffness matrices of the model can be expressed as linear combinations of 4 matrices :

$$\begin{cases} K(\alpha) = K_0 + \alpha K_1 \\ M(\alpha) = M_0 + \alpha M_1 \end{cases} \tag{17}$$

The dispersion curves obtained for extremal parameters values in the 0-60kHz frequency range are given in Figure 2. It can be observed that a low value of α accelerates the conversion of flexural waves from pure flexion to core shear. On the other hand, the compression waves and the shear wave are unaffected by the change of parameter value. This is because the mass to stiffness ratios are identical in the core and in the skins.

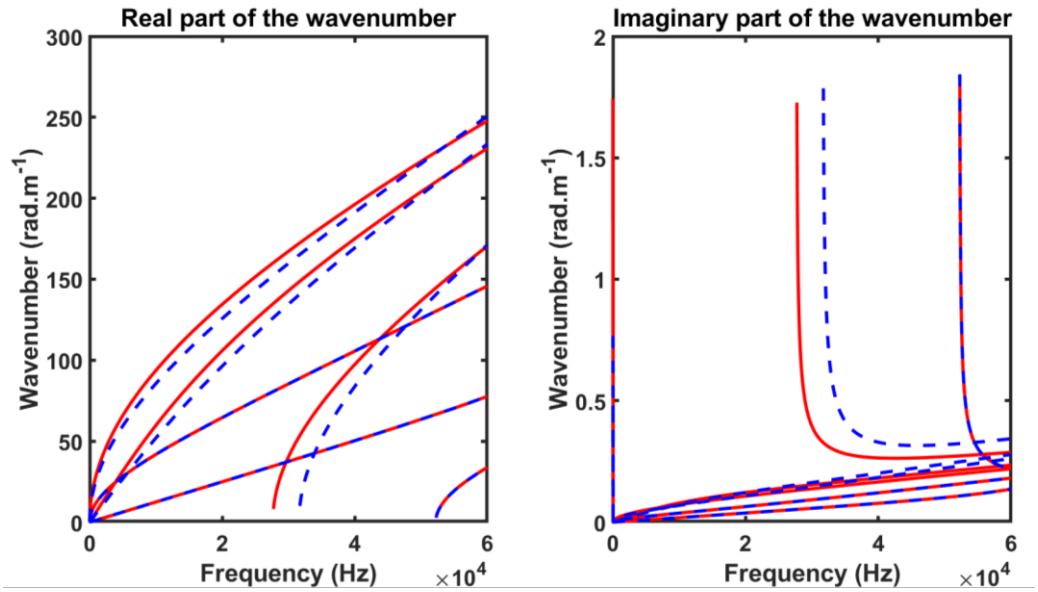


Figure 2 dispersion curves of the extremal models ($\alpha = 1$ blue ; $\alpha = 0.2$ red)

4.1.2 MOR and PMOR comparison

The MOR and PMOR strategies mostly work in the same manner with one difference. For MOR a projection basis must be created for each value of the parameter space while for PMOR a projection basis is created aggregating collections of vectors obtained at sampled values α_i. In our case, we chose a uniform logarithmic sampling for α with 10 values between 0.2 and 1. The reduced order models obtained by both strategies for a value $\alpha = 0.6003$ chosen randomly are compared in Table 1.

	MOR	PMOR
Building Reduced Model	253s	0s
Offline Computations	NA	2534s
dofs of the reduced order model	88	160
Time per eigenvalue problem	0.0094s	0.0417s

Table 1: MOR and PMOR time comparison

While creating a reduced order model using PMOR is instantaneous, there are two prices to pay for this. First, offline computations are required so that a global projection matrix can be formed. Secondly, the reduced order model obtained is bigger and therefore slower than the one obtained using MOR. Figure 3 compares the dispersion curves obtained by both methods. A perfect match is expected :

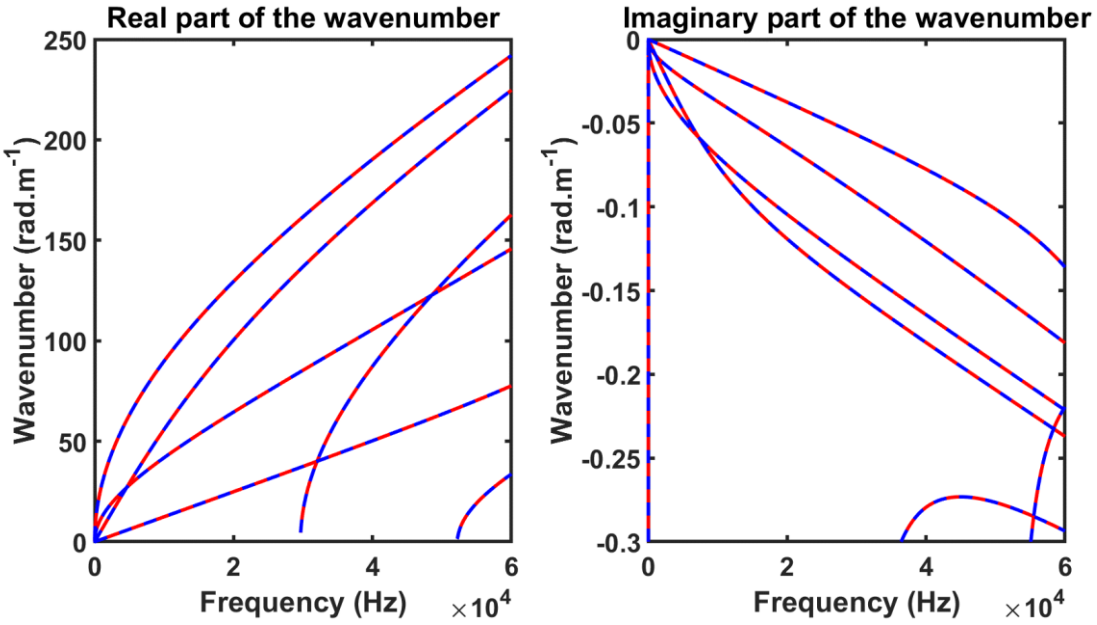


Figure 3 Dispersion curves for $\alpha = 0.6003$ MOR (red) PMOR (blue)

To complete the comparison, a forced response is computed with both models for a 40cm long waveguide with free-free boundary conditions as per the method described in section 2.2. A distributed vertical load is applied on the first section while no efforts are applied on the last one. The response is computed on the surface of the top skin on the middle of the first section ($X = 0,\ Y = 1.5\ cm,\ Z = 5\ mm$).

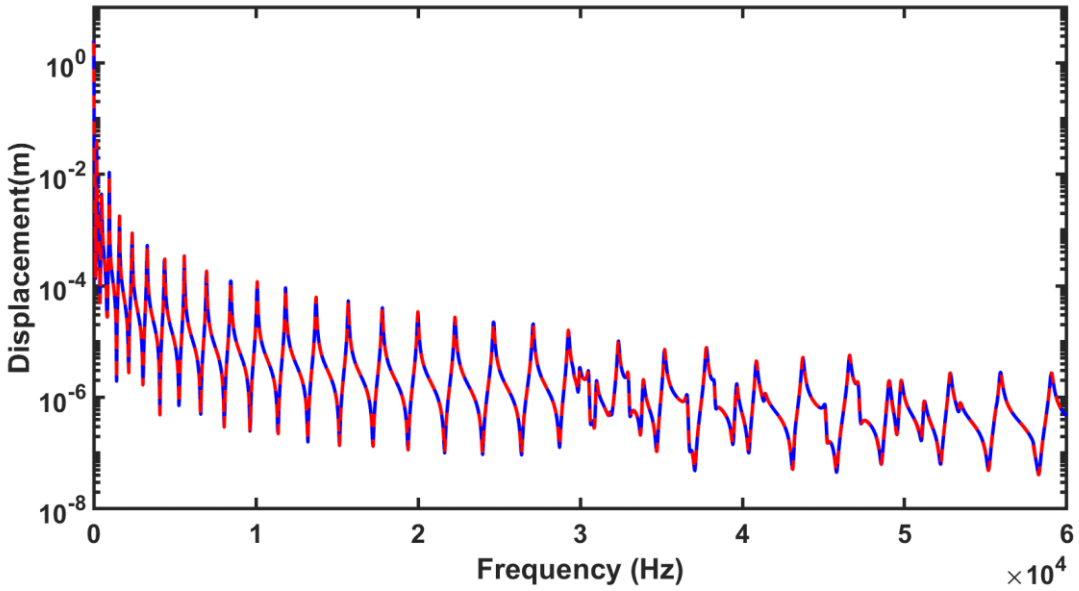


Figure 4 Forced response for $\alpha = 0.6003$ MOR (red) PMOR (blue)

4.1.3 Conclusion

The main advantage of the proposed PMOR scheme is that a reduced order model can be instantly created without having to go through the model order reduction process. There is an important possible drawback however. If completely different wave shapes are propagative for different parameters values, the global

projection basis still has to account for all of them. This may results in models several times bigger than those obtained using the simple model order reduction method. This point is important because WFEM computation time scales asymptotically with the third power of the number of degrees of freedom at the interfaces of the model. For PMOR to be a valid strategy, the increase in time computation must not offset the time required to reduce the model. Strategies are being developed to tackle this issue.

4.2 Example 2 : 3D modeling of damages in a pipe

In this section we consider a steel pipe with an inner radius of 194 millimeters and an outer radius of 203 millimeters similar to the experimental test set up in [16]. Effects of a 3D defect in the pipe are studied and analyzed using the WFEM framework in conjunction with the reduced order modeling strategies described in the previous sections. The global study strategy used is similar to that presented in [17] and the aim is medium to long range defect detection at low frequency.

4.2.1 Modeling of the cross-section

Modeling of the cross-section of the pipe was realized with ANSYS APDL 17. SOLID185 elements were used with an axisymmetric mesh with 4 elements in the wall thickness and 580 in the circumference. The elements are approximately cubic with side length of 2.25 millimeters. The model has 17400 dofs all located at its interfaces.

To model damping, we introduce a damping matrix C proportional to the stiffness matrix K. This is an elementary model which is causal and approximate hysteretic damping well when a narrow frequency band is considered. Both points are important modeling concerns when going form frequency to time domain.

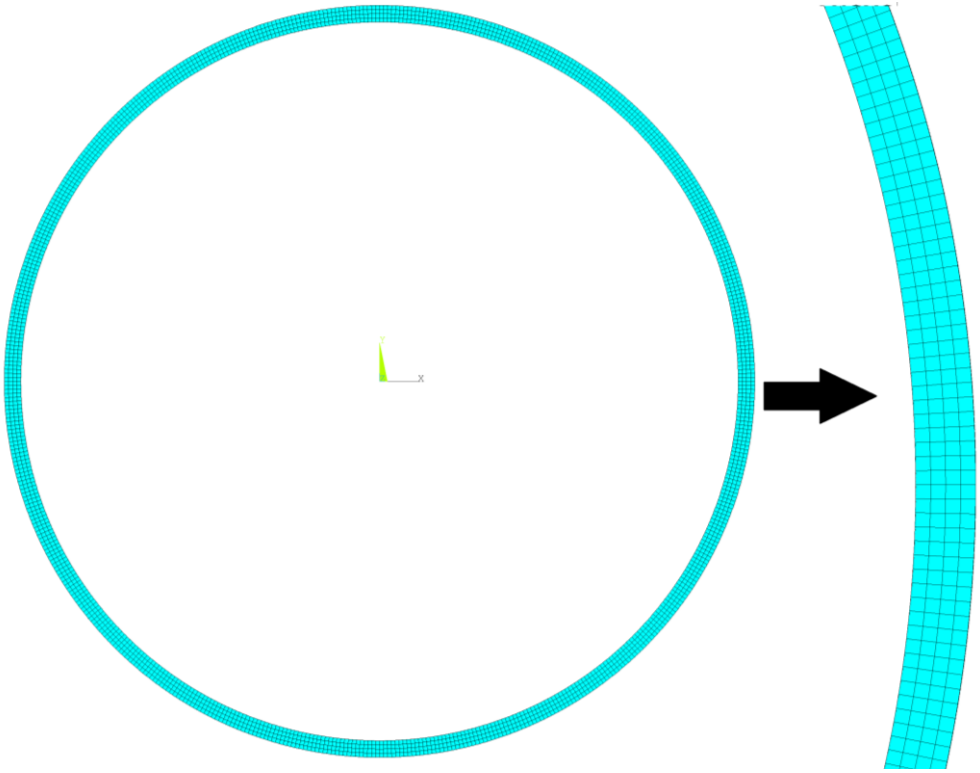


Figure 5: Mesh of the cross-section model

The material properties used are :

- Young Modulus : 210 GPa

- Poisson ratio : 0.3
- Density : 7850 $kg.m^{-3}$
- Damping stiffness ratio : $\eta_k = 10^{-3}$
- Damping stiffness frequency : $f_k = 6000\ Hz$

The damping matrix is thus given by :

$$C = \frac{\eta_k}{2\pi f_k} K \tag{18}$$

4.2.2 Modeling of the defect

We consider a defect in the cylinder in the form of a reduction of half of the wall thickness over angle θ of $\frac{\pi}{10}\ rad$ and a length of 4.5 cm. Undamaged sections are added at the beginning and the end of the defect as to make the coupling via the WFEM easier. An illustration of the model is provided in Figure 6.



Figure 6: Mesh of the defect

The model has 196908 dofs with 17400 at its interfaces. The damping and material properties used are identical to that of the cylinder.

4.2.3 Dispersion curves and choice of a wave mode

In order to get the dispersion curves of the pipe, the model order reduction strategy described above is used with $n_k = 2$ and $n_f = 1$ and $\epsilon = 10^{-4}$ to account for all propagative waves in the $[0\ ;\ 20kHz]$ frequency range. Table 2 briefly examines computation time differences between full and reduced order models.

	Original Model	**Reduced Model**
Degrees of Freedom	17400	516
Full eigenvalue problem resolution	NA (Estimated value of 39961s given $O(n^3)$ complexity)	1.11 s
Partial eigenvalue problem resolution	278 s	NA (Estimated value of 0.0073s given $O(n^3)$ complexity)
Model Order Reduction	NA	1030 s

Table 2 : Full and reduced order model comparison

Notably, a time factor of 250 is achieved even when comparing a full eigenvalue problem resolution for the reduced model to a partial resolution for the original model using Zhong's formulation [12]. The dispersion curves in Figure 7 are obtained using the reduced order model.

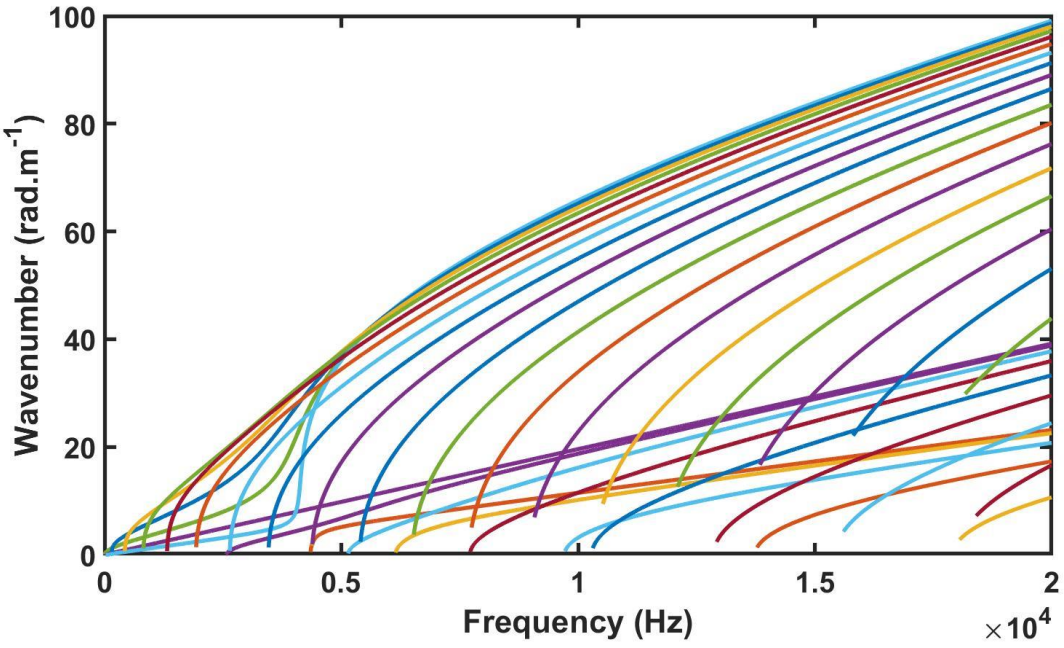


Figure 7: Dispersion curves of the pipe

We aim at detecting and if possible localizing a damaged part of the pipe at low frequency with a medium to long reach instead of at high frequency with a short reach as in [16]. Because of the respective dimensions of the pipe and defect, this means sub-wavelength detection may have to be used. In order to increase the wave-defect interactions, a high order wave mode is used as in [17] so that the circumferential size of the defect corresponds to the distance between two nodes.

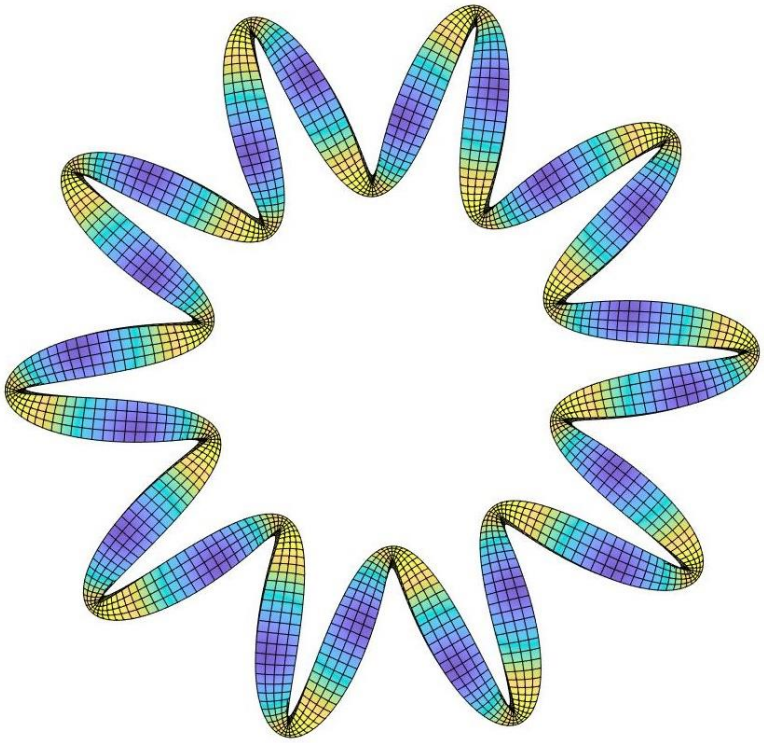


Figure 8: Chosen wave mode

The flexural mode of the 20th order (presented in Figure 8) is thus chosen for damage detection. Its cut-on frequency is slightly above $5kHz$.

4.2.4 Time domain simulations

4.2.4.1 Set up

A 36m long pipe is considered with Free-Free boundary conditions. For the simulation of the damaged pipe, the defect is located at the center of the pipe at 18m from the left end. In both cases, forces are applied on 20 points of the first cross-section to generate the 20th order flexural wave mode. The normal displacements at these points are also monitored. It is expected that the presence of the defect in the pipe leads to reflection, transmission and conversion phenomena. This can most easily be observed in time domain and is associated with a break in the spatial symmetry of the displacement field. Moreover, a premature echo due to reflection at the defect is expected. The response of the waveguide to a pulse centered at $8kHz$ is analyzed in section 4.2.4.3.

4.2.4.2 Reduced order modeling

For time domain simulations, another reduced wave basis is used for the waveguide by reducing the frequency range of interest as compared to section 4.2.3. It is obtained accounting for all propagative wave modes $[0\,;\,16kHz]$ frequency range using with parameters values $f_m = 16kHz$, $n_k = 1$, $n_f = 1$ and $\epsilon = 10^{-5}$. The reduced model of the waveguide is comprised of 524 dofs. For the defect, Craig Bampton model order reduction is used for the inner degrees of freedom. All 681 modes between 0 and 120kHz are kept. This ensures fidelity of the reduced order model without impacting computation times as the MOR process results in diagonal submatrices for the concerned dofs. The projection of the interfaces' degrees of freedom uses the same local projection basis as that of the waveguide. The model goes from 196908 to 1205 degrees of freedom. Using the WFEM framework, the frequency response functions of both waveguides are computed then time signals are obtained using a Non-uniform Discrete Fourier Transform (NDFT) with

Gaussian sampling and 8000 frequencies. The results are shown in Figure 9 and Figure 10 for a pulse of central frequency $f_c = 8000Hz$ with a Hanning window length of 100 periods. At that frequency, the group velocity of our wave mode is $930\ m.s^{-1}$. Thus, it should take $0.03871\ s$ for a pulse to travel form one side of the pipe to the other and the same amount of time for a return trip from one end to the center of the pipe.

4.2.4.3 Time signals

Figure 9 displays the normal displacements of all 20 points of the first section multiplied by a factor $(-1)^n$ to account for the spatial symmetry of the load.

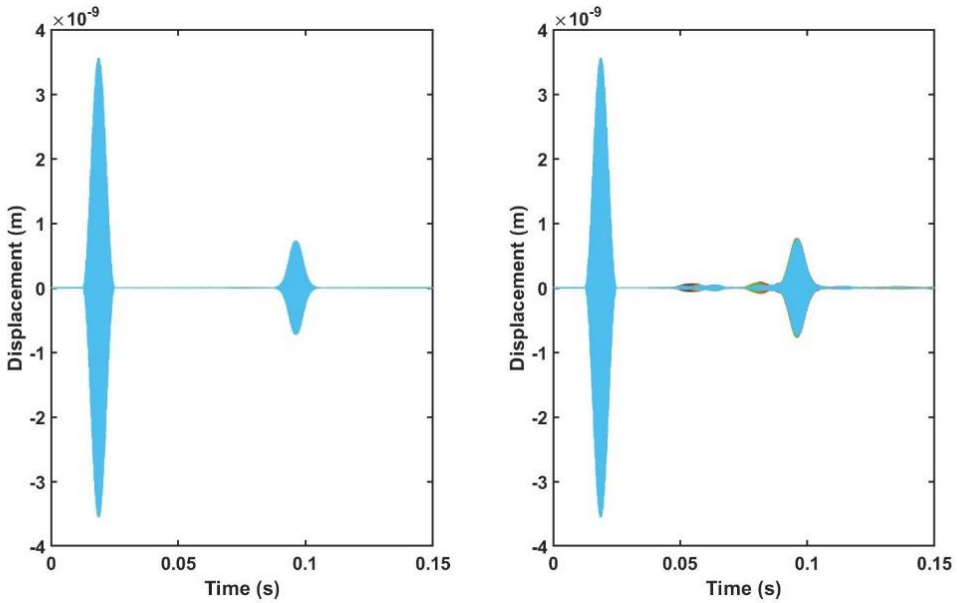


Figure 9 Time signal for all 20 points in the damaged (right) and undamaged (left) pipes

All signals are identical for the undamaged pipe but it is not the case for the damaged one. Monitoring the symmetry of the signal vector is therefore a good strategy to infer the presence of a defect. However, the asymmetric part of the vector does not allow to easily locate the defect. This is because of the conversion process in other wave modes which all have different group velocities. To solve this problem, we compute the average of all 20 signals. This is equivalent to filtering the signals to track only our wave mode since no other propagating wave shares the same symmetry. The result of this process is presented in Figure 10.

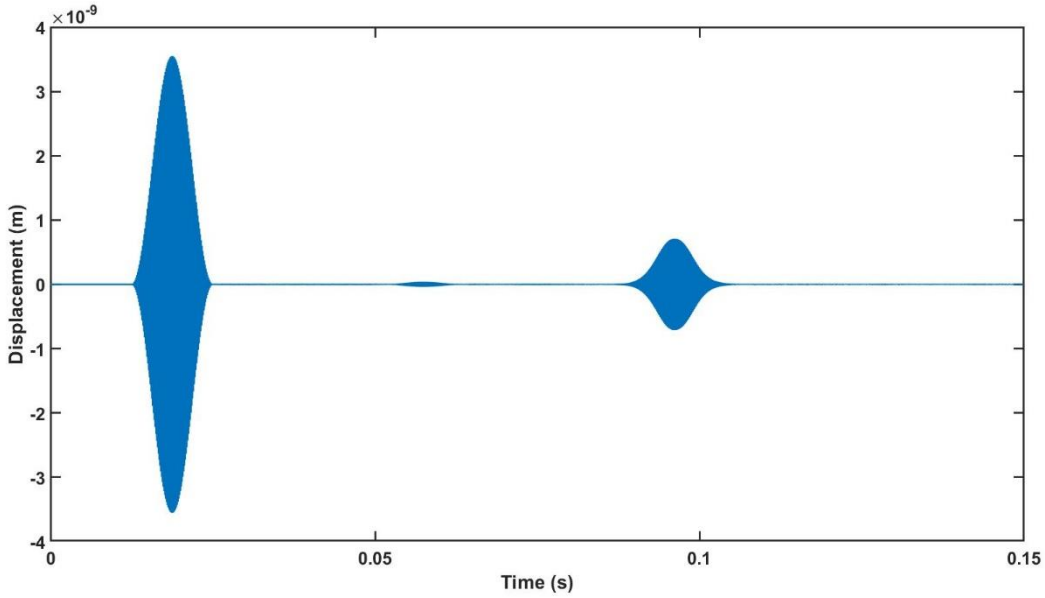


Figure 10 : average of all 20 signals in the damaged pipe

A small pulse of around 2% of the original amplitude is visible after 0.05s corresponding to wave reflection at the defect location. Indeed, the time difference between the centers of both pulses is $0.03871\ s$ which correspond to a return trip from the left end of the pipe to the defect: defect localization is achieved.

5 Conclusion

A methodology was described for reduced order modeling and parametric reduced order modeling in the WFEM framework. It was validated on a parametric sandwich model and used in the modeling of 3D wave-defect interactions in a pipe. The proposed strategy can be used to design a wave based damage-detection system by allowing fast computation of wave propagation in time domain. Lastly, some questions remain concerning the proposed PMOR scheme which will be the object of further developments.

Acknowledgements

The research of R. F. Boukadia is funded by an Early Stage Researcher grant within the European Project VIPER Marie Curie Initial Training Network (GA 675441). The research of E. Deckers is funded by a grant from the Research Foundation – Flanders (FWO). C. Claeys is a postdoctoral researcher supported through IMALIGHT. The Research Fund KU Leuven and the Flanders Make are also gratefully acknowledged for their support.

References

[1] I. Bartoli, A. Marzani, F. Lanza di Scalea and E. Viola, "Modeling wave propagation in damped waveguides of arbitrary cross-section," *Journal of Sound and Vibration*, vol. 295, pp. 685-707, 2006.

[2] U. Lee, Spectral Element Method In Structural Dynamics, Singapore: John Wiley & Sons, 2009.

[3] M. Collet, M. Ouisse and M. I. M. N. Ruzzene, "Floquet–Bloch decomposition for the computation of dispersion of two-dimensional periodic, damped mechanical systems," *International Journal of Solids and Structures,* vol. 48, pp. 2837-2848, 2011.

[4] D. J. Mead, "Vibration Response and Wave Propagation in Periodic Structures," *Transactions of the American Society of Mechanical Engineers, Journal of Engineering for Industry,* vol. 93, no. 3, pp. 783-792, 1971.

[5] J.-L. Christen, M. Ichchou, A. Zine and B. Troclet, "Wave Finite Element Formulation of the Acoustic Transmission Through Complex Infinite Plates," *Acta Acustica united with Acustica,* pp. 984-99, 2016.

[6] J. Mencik, "On the low- and mid-frequency forced response of elastic structures using wave finite elements with one-dimensional propagation," *Computers & Structures,* pp. 674-689, 2010.

[7] J. Mencik and M. Ichchou, "Multi-mode propagation and diffusion in structures through finite elements," *European Journal of Mechanics - A/Solids,* pp. 877-898, 2005.

[8] D. Duhamel, B. Mace and M. Brennan, "Finite element analysis of the vibrations of waveguides and periodic structures," *Journal of Sound and Vibration,* pp. 205-220, 2006.

[9] C. Claeys, N. G. R. de Melo Filho, L. Van Bell, E. Deckers and W. Desmet, "Design and validation of metamaterials for multiple structural stop bands in waveguides," *Extreme Mechanics Letters,* pp. 7-22, 2017.

[10] C. Zhou, J. Lainé, M. Ichchou and A. Zine, "Wave finite element method based on reduced model for one-dimensional periodic structures," *International Journal of Applied Mechanics,* 2015.

[11] C. Droz, Z. C, M. N. Ichchou and J. -P. Lainé, "A hybrid wave-mode formulation for the vibro-acoustic analysis of 2D periodic structures," *Journal of Sound and Vibration,* p. 285–302, 2016.

[12] W. X. Zhong and F. W. Williams, "On the direct solution of wave propagation for repetitive structures," *Journal of Sound and Vibration,* vol. 181, pp. 485-501, 1995.

[13] R. R. Craig and M. C. Bampton, "Coupling of substructures for dynamic analysis," *AIAA journal,* pp. 1313-1319, 1968.

[14] R. F. Boukadia, C. Droz, M. N. Ichchou and W. Desmet, "A Bloch wave reduction scheme for ultrafast band diagram and dynamic response computation in periodic structures," *Finite Elements in Analysis and Design,* 2018.

[15] P. Benner, S. Gugercin and K. Willcox, "A Survey of Projection-Based Model Reduction Methods for Parametric Dynamical Systems," *SIAM Review ,* vol. 57, no. 4, pp. 483-531, 2015.

[16] F. Schubert, B. Frankenstein, D. Hentschel, K.-J. Fröhlich, M. Küttner, B. Lamek, J. Schwenkkros and K. Kerkhof, "Structural Health Monitoring of Industrial Piping Systems Using Guided Elastic Waves," in *Deutsche Gesellschaft für Zerstörungsfreie Prüfung 2007*, 2007.

[17] C. Droz, O. Bareille, J. Lainé and M. N. Ichchou, "Wave-based SHM of sandwich structures using cross-sectional waves," *Structural Control and Health Monitoring,* vol. 25, p. e2085, 2018.

Investigation for the analysis of the vibrations of quasi-periodic structures

S. Timorian[1,2], F. Franco[1], M. Ouisse[2], S. De Rosa[1], N. Bouhaddi[2]
[1]Università degli Studi di Napoli Federico II, Department of Industrial Engineering, Aerospace section
Via Claudio, 21, 80125 Napoli, Italy

[2]Université Bourgogne Franche-Comté, Department of applied mechanics.
24 Rue de l'Épitaphe, 25000 Besançon, France
e-mail: **safiullah.timorian@femto-st.fr**

Abstract
Periodic structures are well known for the possibility to exhibit band gap effects. This work aims at investigating vibration behaviors of quasi-periodic structures. In this paper, the quasi-periodic structure is defined as a type of beam with an impedance mismatch generated by Fibonacci orders with non-symmetrical translation in geometry, acting as a waveguide. Two types of quasi-periodicity are considered, namely finite, and infinite Fibonacci sequences using super unit cell. Considering flexural elastic waves in above mentioned quasi-periodic models, the frequency ranges corresponding to band gaps are investigated, using either spectral analysis of infinite structures or frequency response functions of finite structures. Fibonacci beams exhibit multi stop bands with short widths in different frequency ranges, whereas periodic and its super unit cells-based structures have only one stop band frequency with larger frequency extension.

1 Introduction

The vibroacoustic response in many types of structures is complex. Structures are shaped continuous, periodic, aperiodic or random. These types of structures have different vibroacoustic responses with respect to their geometrical and materials properties. Some of them can be designed as periodic or quasi-periodic structures. The desirable periodic structures that have identical repetition can be modelled by using materials and geometrical periodicity [1].

Many research activities show that vibrations responses of periodic and quasi-periodic structures exhibit frequency band gap effects [1,2,3,4,5]. In periodic structures, the impedance mismatch generated by periodic discontinuities in the geometry, acting as a waveguide, and/or in the constituent material, causes destructive wave interference phenomena over specific frequency bands called “stop band” or “band gaps” [6]. For quasi-periodic structures, Fibonacci sequences are considered in several researches [7]. Spectral fragmentation of elastic waves represents the replication of primary and secondary gaps in Fibonacci sequence [7]. In other research paper, Gei. M. et al [8] claims that in an elementary repeated unit cell, generated adopting the Fibonacci sequence, in cases of axial and flexural vibration by higher order generation, the number of stop bands changes. The concern of the present paper is to model a quasi-periodic beam utilized by two different cross sections of 3D 2 node-beam finite element following the Fibonacci series.

The main issue is that the anti-symmetric condition of quasi-periodic structures cannot be applied by the wave-based approach using spectral analysis of Bloch-Floquet theorem, unless using an elementary cell/volume representative using Fibonacci lower order replications. In fact, the structural dynamics, model analysis and Frequency Response Function (FRF) of the structures are considered for understanding the dynamics structural behavior of the system to ensure a safe, efficient and affordable design.

In this research, an isotropic beam with a finite number of cells and a wave guide section with infinite number of cells is considered in the analysis. The quasi-periodicity of the span is translated according to the Fibonacci sequences [8]. The identical double cross sections (A) and (B) are translated using Fibonacci generating order from 4th to 10th orders (Figure 1).

The analysis has been carried out in two main sections. The first section presents the finite element analysis of Frequency Response Function [9,10], whereas the second section describes a wave guide section model, using combination of wave and finite element using transfer matrix method [11,12,13]. This wave guide section is modelled following super unit cell. Super unit cell is a cell hosting the first 4th generated order of Fibonacci sequence for Wave Finite Element Method (WFEM) analysis. Stiffness and mass matrix of the given unit super cell is extracted using MATLAB and APDL-ANSYS platform. Then, the extracted matrices are used into WFEM FRF and spectral analysis of Bloch-Floquet boundary conditions [14].

2 Theoretical approach

2.1 Spatial elastic waves

In infinite solid medium there are two types of waves that propagate with different velocities [15]. It is known from vector analysis that any vector field can be represented as sum of two vectors, one of which has a scalar potential and the other a vector one:

$$\mathbf{u} = \mathbf{u}_l + \mathbf{u}_t = \mathrm{grad}\varphi + \mathrm{rot}\boldsymbol{\Psi} \tag{2.1.1}$$

Taking into consideration that rot $u_l = \mathrm{div}\, u_t = 0$ and substituting equation (2.1.1) into the wave equation for elastic medium with the application of operations rot and div, we get

$$\frac{\partial^2 \mathbf{u}_l}{\partial t^2} - c_l^2 \nabla^2 \mathbf{u}_l = 0 \quad \mathrm{c}_l = \sqrt{(\Lambda + \frac{2\mu}{\rho}}, \tag{2.1.2}$$

and

$$\frac{\partial^2 \mathbf{u}_t}{\partial t^2} - c_l^2 \nabla^2 \mathbf{u}_t = 0 \quad \mathrm{c}_t = \sqrt{\frac{\mu}{\rho}} \tag{2.1.3}$$

$\mathbf{u}_l$ and $\mathbf{u}_t$ vectors correspond to the longitudinal and transversal waves, Λ and μ are Lame constants and ρ is a density. In the other hand c_l and c_t are the longitudinal and transversal wave velocities.

Hence the vector $\mathbf{u}_l$ in equation (2.1.2) is called a longitudinal wave or a wave of expansion-compression which, the vibration direction in it coincides with its propagation direction. The wave $\mathbf{u}_t$ in equation (2.1.3) in which the direction of vibrations is perpendicular to the direction of wave propagation and in which deformations are shear is called a transversal or shear wave.

2.2 Methods and tools

The modern tools for investigating the most significant impacts of quasi-periodic structures on the vibrational response of a given structure are codes based on conventional FE analysis, combination of wave and finite element, spectral finite element, and transfer matrix methods.
Theoretical background for modelling quasi periodicity and its significant impacts on wave analysis is carried out with mathematical series named Fibonacci sequence, Thue-Morse, Rodin-Shapiro and Penrose lattice. Spectral analysis of these types of subsystems are shown in phononic crystals, anisotropic beams, rods and Bravais lattices [16]. In this portion of work, a finite element beam with lower 4th and higher with

10^{th} generated order of Fibonacci sequence is modelled using MATLAB in parallel with APDL-ANSYS. The lower order is used as a super unit cell waveguide section for infinite structures, whereas the higher order is used as one span of finite beam in FE analysis [Table 1].

Fibonacci orders	**4^{th}**	**5^{th}**	**7^{th}**	**8^{th}**	**9^{th}**	**10^{th}**
Number of cells	5	8	21	34	55	89

Table 1: Geometrical distribution of cells according to Fibonacci generated orders.

Figure 1 shows a 2-node beam type 188 following Fibonacci orders. The geometrical characteristics of this beam is a combination of two different cross section. The distance between each key point is 100 mm, every segment between these two points are one of abovementioned two cross section with three finite elements. Section (A) and (B) can be seen in figure 1. Embedded Fibonacci sequence starts from $\boldsymbol{S_1}$ the first order and ends to $\boldsymbol{S_n}$ the $\boldsymbol{N_{th}}$ order of the sequence. The mathematical expressions following the Fibonacci sequences in this beam are defined in the following algorithm:

$$\boldsymbol{S_1 = \{A\}, \qquad S_2 = \{AB\},\ S_3 = \{ABA\},\ \ldots,\ S_n = S_{n\text{-}1}S_{n\text{-}2}}$$

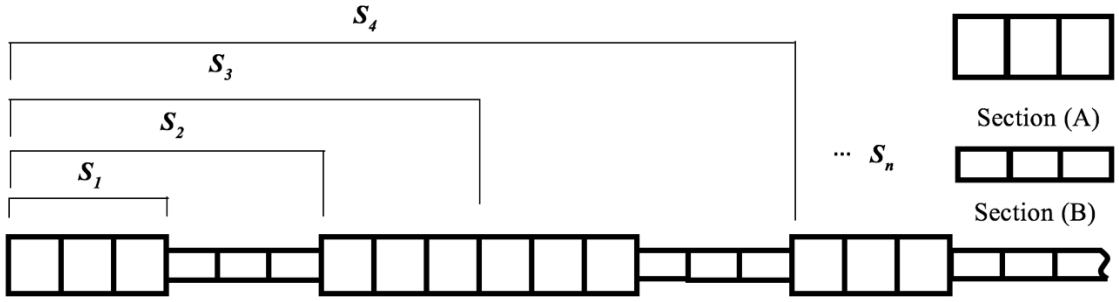


Figure 1: Numerical model of quasi-periodic model following Fibonacci sequence.

2.3 Finite Element Dynamic Analysis

Commercial FE software's APDL-ANSYS is used to perform the frequency response function of the quasi-periodic beam model. For damped structure, the dynamic finite element model is usually described by the system:

$$\mathbf{M}\ddot{\mathbf{x}} + \mathbf{C}\dot{\mathbf{x}} + \mathbf{K}\mathbf{x} = \mathbf{f}(\omega) \tag{2.3.1}$$

where $\mathbf{M}$, $\mathbf{C}$ and $\mathbf{K}$ in equation (2.3.1) are the mass, damping and stiffness matrices.

The associated eigenvalue problem is:

$$(\mathbf{K}\text{-}\omega_v^2\mathbf{M})\,\psi_v = 0, \quad v = 1, 2, \ldots \tag{2.3.2}$$

let $\boldsymbol{\Psi} = [\boldsymbol{\psi_1}, \boldsymbol{\psi_2}, \boldsymbol{\psi_3}, \ldots, \boldsymbol{\psi_N}]$ be the orthonormalized model basis, and $\boldsymbol{\Lambda} = \mathbf{diag}\,(\boldsymbol{\omega_v^2})$ the spectral matrix; the model projection $\mathbf{x} = \boldsymbol{\Psi}\,\mathbf{q}(\omega)$ and the mode superposition method allows to express, in the case of proportional damping, the dynamic response in the following form:

$$\mathbf{x}(\omega) = \sum_{i=1}^{N} \boldsymbol{\psi}_i \frac{\boldsymbol{\psi}_i^T \mathbf{f}(\omega)}{\omega_i^2\text{-}\omega^2 + 2j\xi\omega_i\omega}. \tag{2.3.3}$$

The FRF for displacement of the system is given by equation (2.3.4), where $\mathbf{x}(\omega)$ is the response of a system and $\mathbf{F}(\omega)$ is its excitation force.

$$\mathbf{H}(\omega) = \frac{\mathbf{x}(\omega)}{\mathbf{F}(\omega)} \tag{2.3.4}$$

The FRF for the k^{th} node degree of freedom with a single excitation force at j^{th} degree of freedom can be simulated by equation (2.3.5).

$$H_{kj}(\omega) = \sum_{i=1}^{N} \frac{\psi_{ik}\,\psi_{ij}}{\omega_i^2 - \omega^2 + 2j\xi\omega_i\omega} \tag{2.3.5}$$

Modal analysis and frequency response function of the quasi-periodic beam are computed. The aim is to investigate the frequency band gap like behavior in finite span with generating order of Fibonacci (number of cells) of beam type 2-node 188, by considering structural damping.

The conventional FE analysis is used for the frequency response function of the entire span with 10^{th} generated order of Fibonacci. The number of elements in numerical model are designed according to the known criteria which of one sixth of the wave-length. The description of the mechanical properties is provided in Table 2.

Material properties	**Aluminium**	**Polyethylene**
Modulus of elasticity	$2x10^{11}$ Pa	$7.2x10^{8}$ Pa
Poisson's ratio	0.3	0.3
Mass density	7800 kg/m^3	935 kg/m^3

Table 2: Mechanical properties of quasi-periodic bi-material beam.

2.4 Forced response analysis

In this section, the forced response function of a quasi-periodic beam is analysed. The analysis is done with a free-free Boundary Condition (BC). A white spectrum is applied in one end of the beam in the vertical direction and the response is simulated in the other end of the beam. The mesh size in this problem is optimized to a maximum frequency range of 5KHz. The choice of the free-free (BC) is interesting to visualize the energy transfer through the waveguide span. This type of wave guides is intended to use as a junction between two infinite mediums which the mechanics of those materials are not known. The results show band gaps in different ranges of frequencies. Multiple stop bands appear by the positioning of cross sections according to the Fibonacci sequence. The reason is that in this quasi-periodic structure the direction of elastic wave is considered in x direction, therefore an interference of reflected and incident waves creates frequency stop bands (i.e. in this frequency ranges the waves "cannot freely propagate"). This type of stop bands could be predicted as one type of passive wave filter in a quasi-periodic beam.
Figure 2 shows a Fibonacci super unit cell that contains 5 cross sections [ABAAB]. This cell shows the end of part of span with 50 cm length. The span is considered with (210,340, 550, and 890) cm long on the frequency ranges of [0-150] kHz. Using MATLAB and APDL-ANSYS the harmonic analysis is carried out. The allocated point response is received at the head of the span. The results of this dynamic analysis show that the full energy is transferred through the start and end of the span which can be represented as a junction between two infinite media. There is multiple frequency stop bands in different ranges of frequencies. Each frequency stop band has some localized wave modes that rapidly attenuates inside the band gap [Figure 3].

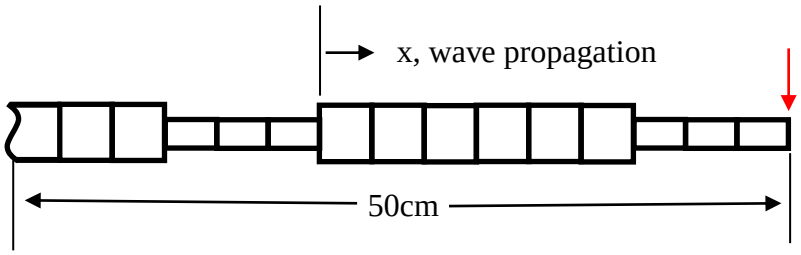


Figure 2: Quasi-periodic structure super unit cell; this cell is the N^{th} cell of the span with applied unit force at the end node.

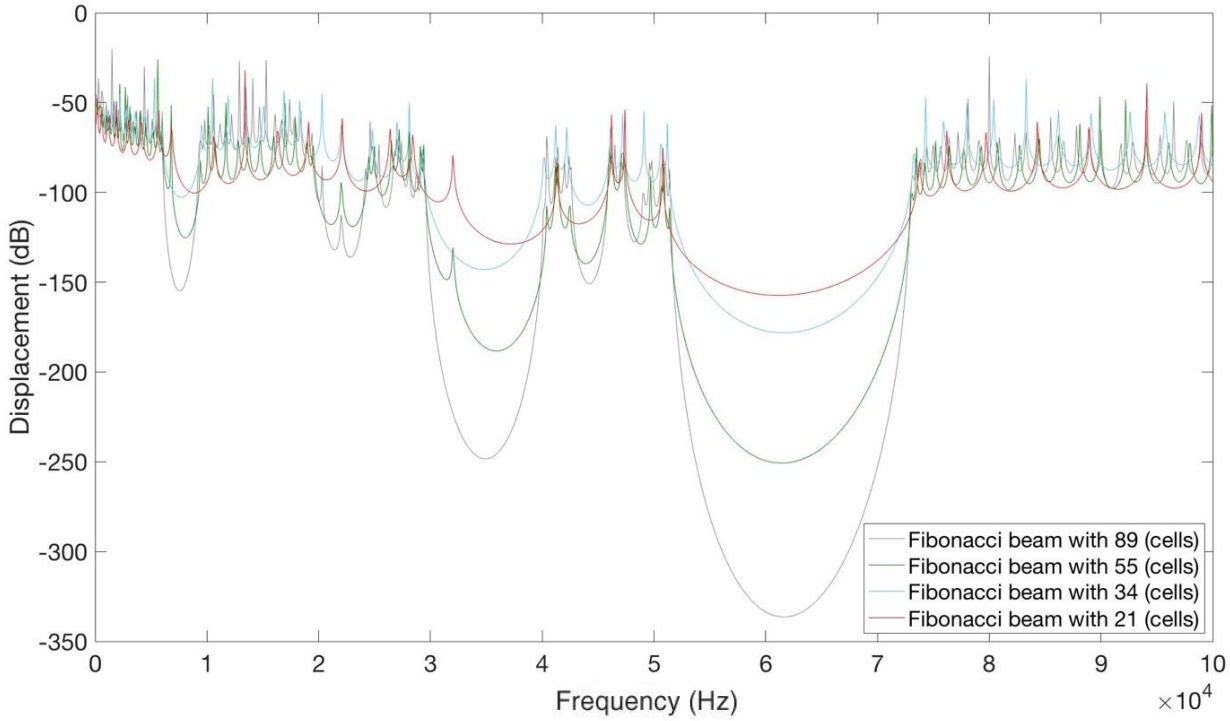


Figure 3: Frequency response function of a finite quasi-periodic beam with length increment.

3 Spectral Analysis of infinite structure

3.1 Substructures dynamics

A substructure (super unit cell) waveguide is considered as a unit cell of the periodicity pattern. In this part of an investigation carried out to obtain an algorithm for quasi-periodic function that permits to the repetition of unit cell with disturbance inside the periodicity.

The substructure in figure 4 is coded as a unit cell in MATLAB and the generated script is then run in APDL-ANSYS for extracting the transfer matrices. The extracted stiffness and mass matrices are used to generate results based on FRF and spectral analysis of Bloch-Floquet boundary condition.

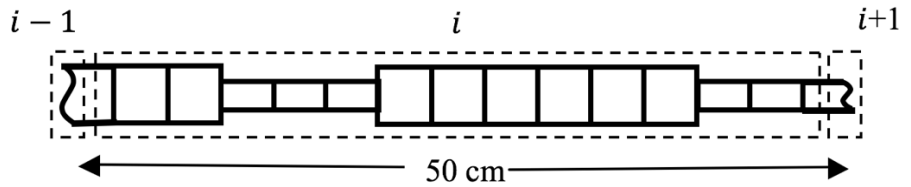


Figure 4: Waveguide section for spectral analysis of Floquet-Bloch boundary condition.

The FRF analysis is achieved in frequency range [0-5000] Hz, for a structural damping of $\eta = 0.001$. The dynamic response of the unit cell is described by:

$$\mathbf{Dq} = \mathbf{F} \tag{3.1.1}$$

Where $\mathbf{D}$, $\mathbf{q}$, and $\mathbf{F}$ define the dynamic stiffness matrix, displacement vector and force vector. The dynamic stiffness matrix, in equation (3.1.2), with complex modulus of elasticity becomes

$$\mathbf{D} = -\omega^2\mathbf{M} + (1 + i\eta)\mathbf{K} \tag{3.1.2}$$

$\mathbf{M}$, $\mathbf{K}$, and η are respectively the mass matrix, the stiffness matrix and the loss factor.

Dynamic stiffness matrix for the general case can be written for internal and external degrees of freedom. The internal degrees of freedom can be condensed and the left and right boundary displacements and forces are used in the analysis.

$$\begin{bmatrix} \tilde{\mathbf{D}}_{\mathbf{II}} & \tilde{\mathbf{D}}_{\mathbf{IL}} & \tilde{\mathbf{D}}_{\mathbf{IR}} \\ \tilde{\mathbf{D}}_{\mathbf{LI}} & \tilde{\mathbf{D}}_{\mathbf{LL}} & \tilde{\mathbf{D}}_{\mathbf{LR}} \\ \tilde{\mathbf{D}}_{\mathbf{RI}} & \tilde{\mathbf{D}}_{\mathbf{RL}} & \tilde{\mathbf{D}}_{\mathbf{RR}} \end{bmatrix} \begin{Bmatrix} \mathbf{q}_{\mathbf{I}} \\ \mathbf{q}_{\mathbf{L}} \\ \mathbf{q}_{\mathbf{R}} \end{Bmatrix} = \begin{Bmatrix} \mathbf{0} \\ \mathbf{f}_{\mathbf{L}} \\ \mathbf{f}_{\mathbf{R}} \end{Bmatrix} \tag{3.1.3}$$

3.2 Transfer matrix

A unit cell script file is coded and, then, transformed for post processing using commercial software's. The same procedure could be done directly through sub-structuring analysis (CMS) for extracting transfer matrices by utilizing commercial software's. Using MATLAB code, both mass and stiffness matrices of size [48x48] are extracted by 4th generated order of Fibonacci which has 5 unit cells and each cell has 3 elements. So, there a total of 15 elements in one super unit cell. Then the global matrices are extracted through APDL-ANSYS for wave finite element analysis.

$$\mathbf{S} = \begin{bmatrix} -\mathbf{D}^*_{\mathbf{LR}}{}^{-1}\mathbf{D}^*_{\mathbf{LL}} & -\mathbf{D}^*_{\mathbf{LR}}{}^{-1} \\ \mathbf{D}^*_{\mathbf{RI}}\text{-}\mathbf{D}^*_{\mathbf{RR}}\mathbf{D}^*_{\mathbf{I.R}}{}^{-1}\mathbf{D}^*_{\mathbf{I.I.}} & \mathbf{D}^*_{\mathbf{RR}}\mathbf{D}^*_{\mathbf{I.R}}{}^{-1} \end{bmatrix}. \tag{3.2.1}$$

$\mathbf{S}$ is the transfer matrix and $\boldsymbol{D}^*$ components inside the transfer matrix are the condensed internal degrees of freedom inside the unit cell that, defines, all the boundary internal nodes and boundary external nodes in equation (3.2.2)

$$\mathbf{D}^* = \mathbf{D}_{\mathbf{BB}}\text{-}\mathbf{D}_{\mathbf{BI}}\mathbf{D}_{\mathbf{I}}^{-1}\mathbf{D}_{\mathbf{IB}} \tag{3.2.2}$$

Equation (3.2.2) is condensed dynamic stiffness matrix. In equation (3.2.3) $\boldsymbol{S}$ is the transfer matrix which is symplectic and J is a 2nx2n matrix with real entries (non-singular matrix) or commonly called skew matrix.

$$\mathbf{S}^{\mathrm{T}}\mathbf{J}\mathbf{S} = \mathbf{J} = \begin{bmatrix} \mathbf{0} & \mathbf{I_n} \\ \mathbf{-I_n} & \mathbf{0} \end{bmatrix}. \tag{3.2.3}$$

4 Numerical Results

4.1 Frequency response function of finite structures

FRF of finite structure is analysed in two different parts. The first part corresponds to the conventional FE analysis of the quasi-periodic beam with isotropic and homogenous materials. Whereas the second part is analysed by considering inhomogeneous material variation including the Fibonacci cross section variation as in the first part. The quasi-periodicity in the first case is inscribed by cross section variations, according to the Fibonacci sequence.

4.1.1 FRF Results-geometrical variation

The first results are shown by finite element analysis of the FRF for the four different orders of the Fibonacci sequence beam. The 7^{th} order corresponds to 21 number of cells, whereas the 8^{th}, 9^{th}, and 10^{th} order follows the 34, 55, and 89 cells. The cells are in two different cross sections (A) and (B).

Figure 5 shows an FRF of the Fibonacci beam with increasing length by generated orders of the sequence. The results of flexural waves are plotted on the 1500 frequency steps in the range of [0-5000] Hz. The results show multiple stop bands alongside the frequency ranges for instance around [600-800] Hz, [2100-2500] Hz and followed a large frequency stop band around [3100-4200] Hz. There is also a medium band from [4500-4800].

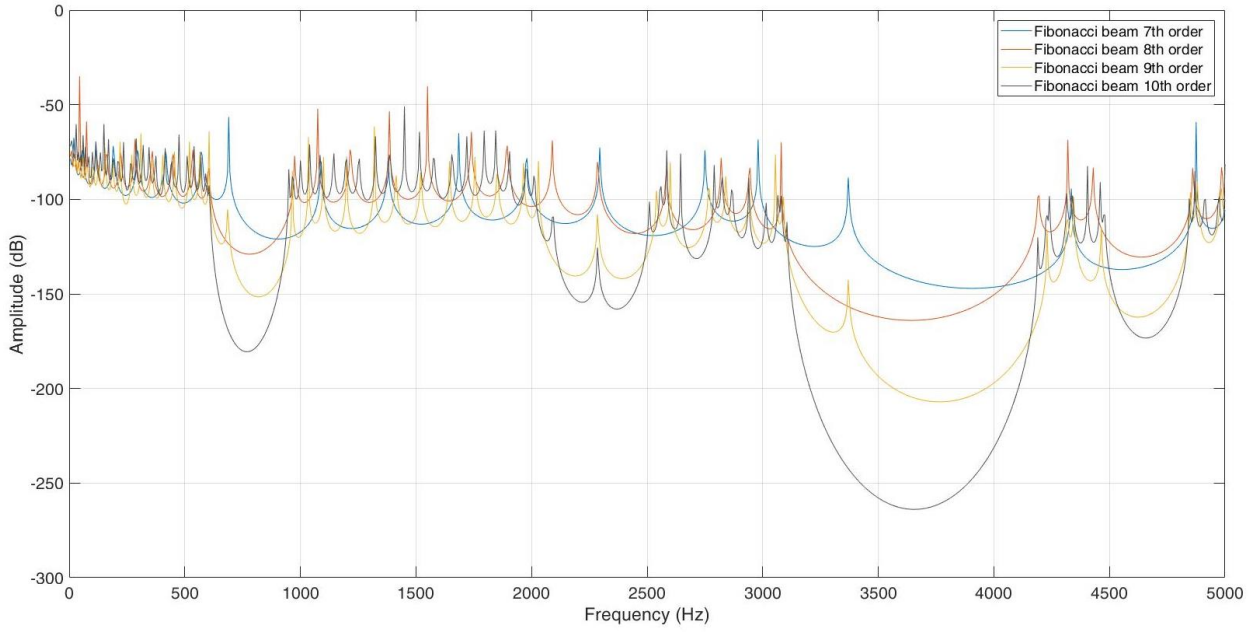


Figure 5: Finite element analysis of the FRF for fourth different orders of Fibonacci beam.

The number of frequency stop bands in the flexural wave analysis of finite quasi-periodic beam depends on the correspondence frequency range. It can be seen that four frequency stop bands are appearing in the frequency ranges of [0-5] kHz. These band gap like behaviours has narrow widths and if there is an

increase in the number unit cells, the depth of the stop band frequency grows deeper according to displacement decibels.

4.1.2 FRF Results of the beam with two materials

In this part of FRF analysis the same criteria of the Fibonacci beam are analysed with bi-material distribution all alongside the beam span. The first material is aluminium and the second is polyethylene. Cross section (A) is made of aluminium and cross section (B) is made of polyethylene.

The length of the structure starts from 2.1m span to 8.9 m explicitly ranging from [7^{th},8^{th},9^{th}, 10^{th}] orders of Fibonacci with [21,34,55,89] cells. The FRF analysis has been carried out with free-free boundary condition for all types of orders. A unit spectrum white force is applied in the head of the span (First node) and the response is simulated from the tip of the span (last node). Figure 6 shows two very wide frequency stop bands in the ranges of [0-5000] Hz. The first gap starts from [250-1750] Hz, following the second stop band from [1800-4100] Hz. These wider gaps are due to the bi-material distribution all over the span. The very promising results are the frequency stop bands and its depths by increasing the length of the span/the number of cells. The more increase in the generating orders of Fibonacci will give a result with more depth in the band gap of maximum order. In contrary lower orders has shorter frequency stop bands with low amplitude in (dB).

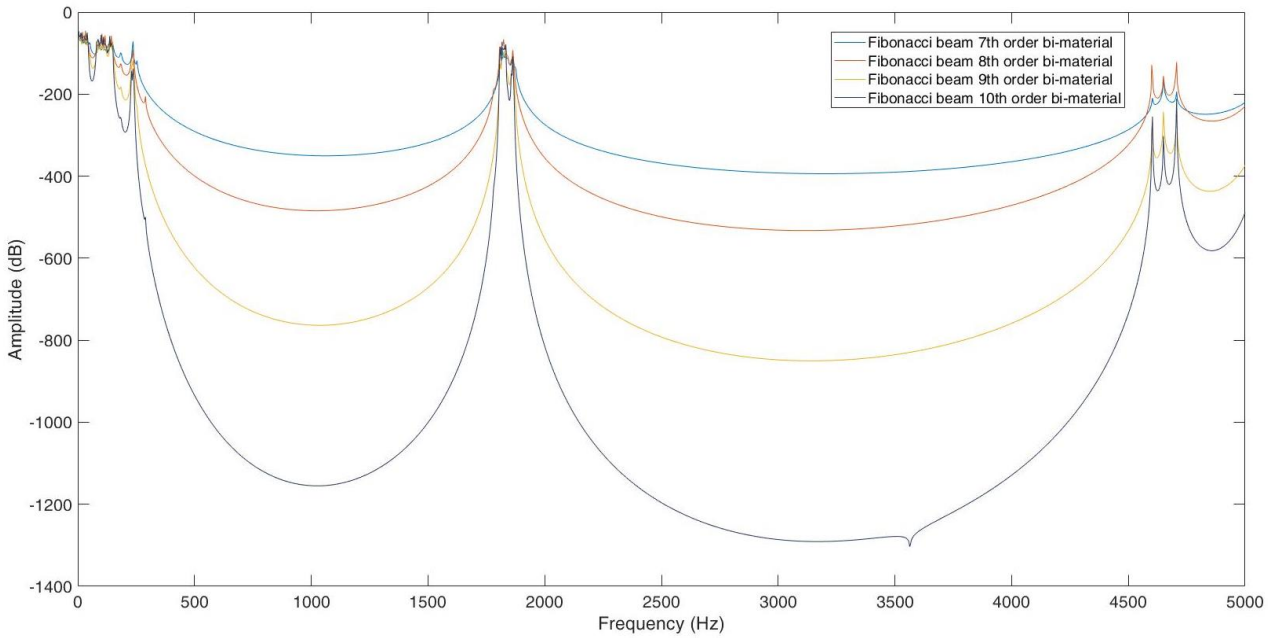


Figure 6: FRF of the Fibonacci beam with bi-materials using Finite element analysis.

4.2 Frequency response function using WFEM

These results correspond to the spectral analysis of the infinite structure. The mass and stiffness matrices are extracted and used as an input for the WFEM using transfer matrix method. The 4^{th} order of the abovementioned sequence is taken as a unit super cell and Floquet-Bloch boundary condition is applied to balance the left and right-side displacement and force vectors of the unit cell. The internal degrees of freedom are eliminated using condensation method and the transfer matrix is modelled with entrees from boundary-boundary and internal-boundary nodes. The super unit cell model can be seen in the Figure 7. The first result shows an FRF analysis of the unit cell by 20 replications of the same cell either in the right or left of the core cell.

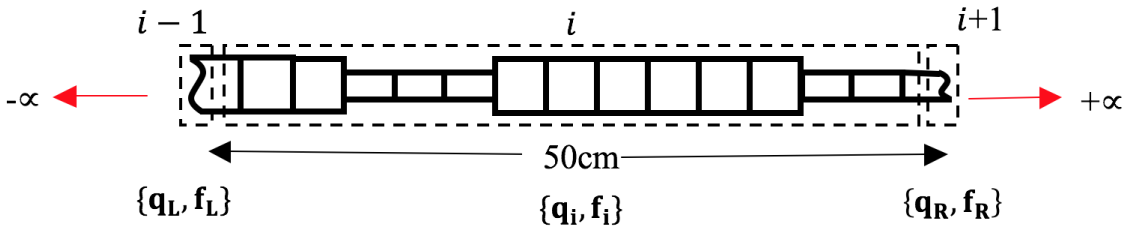


Figure 7: waveguide section of 4th order Fibonacci sequence

Flexural waves are investigated in this analysis. These types of waves can be visualized in the results of FRF using WFEM. Beside that, the findings in the spectral analysis also provide the longitudinal waves as well as flexural ones and for validating such kind of waves, WFEM analysis is used to plot the FRF of longitudinal wave and then compared with spectral analysis of Bloch-Floquet waves. Figure 8 shows a wave based finite element FRF of the Fibonacci 4th order. The repeated unit cell shows a promising filtering conditions in the different frequency ranges in the limit of [0-5000] Hz. Figure 9 shows a spectral analysis of the Floquet-Bloch boundary condition into a Fibonacci 4th order cell. The first branch of the plot in red describes the bending, and compressional waves. In contrary the second branch in blue shows the evanescent waves with curve shapes that corresponds to the stop bands of the real part of the wave numbers in the red branch of the plot. The red branch of the plot at Figure 9 starts with bending waves that propagates from [0-162] Hz and then a frequency stop band appears in [162-187] Hz frequency range. The waves are propagating until the next frequency stop band between the two portions of the bending waves. Another stop band appears between [653-1014] Hz, following the middle one around [1809-2298] Hz. The last frequency stop band is a combination of longitudinal/ compressional and flexural waves. The first mode starts form [3263-4557] Hz that belongs to the last flexural wave, whereas the following second blue curve with higher imaginary numbers in the negative zone of wave numbers corresponds to the longitudinal band gap [3523-4522] Hz.

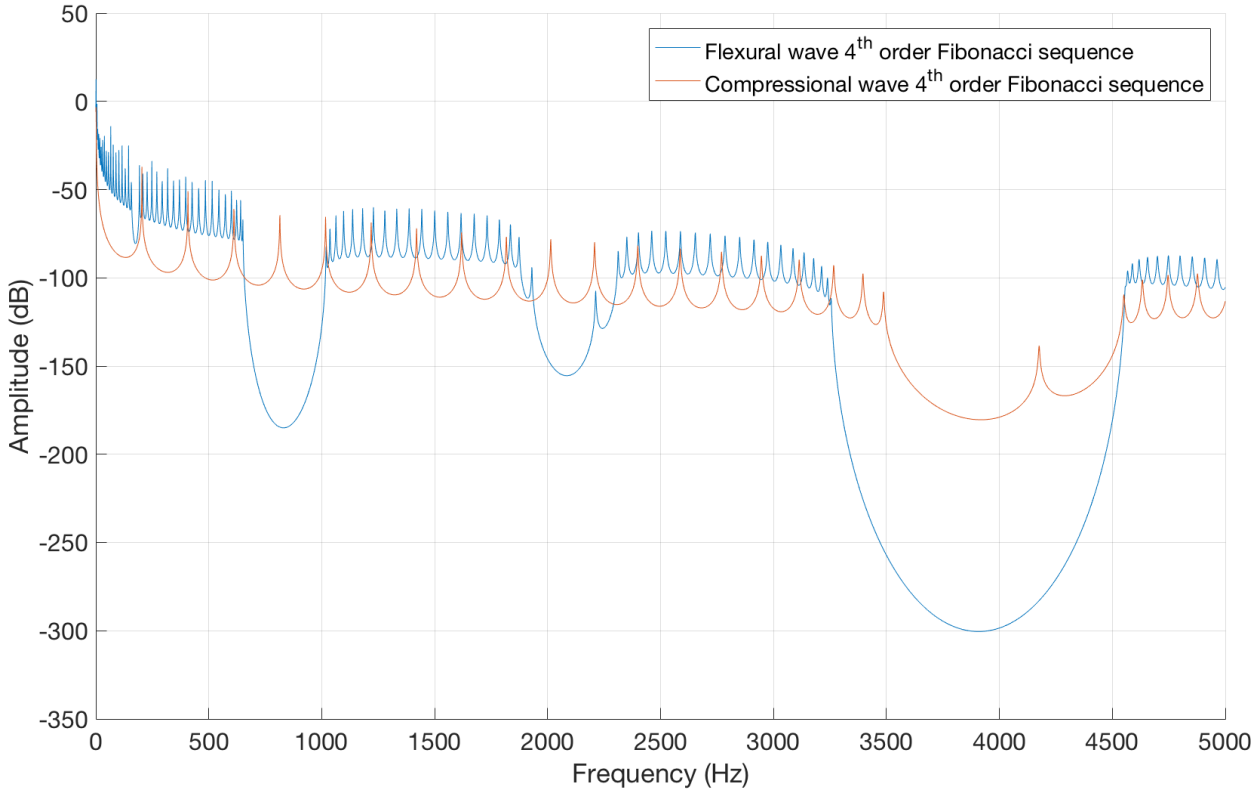


Figure 8: FRF of Fibonacci beam 4TH order analysis by (WFEM) using transfer matrix

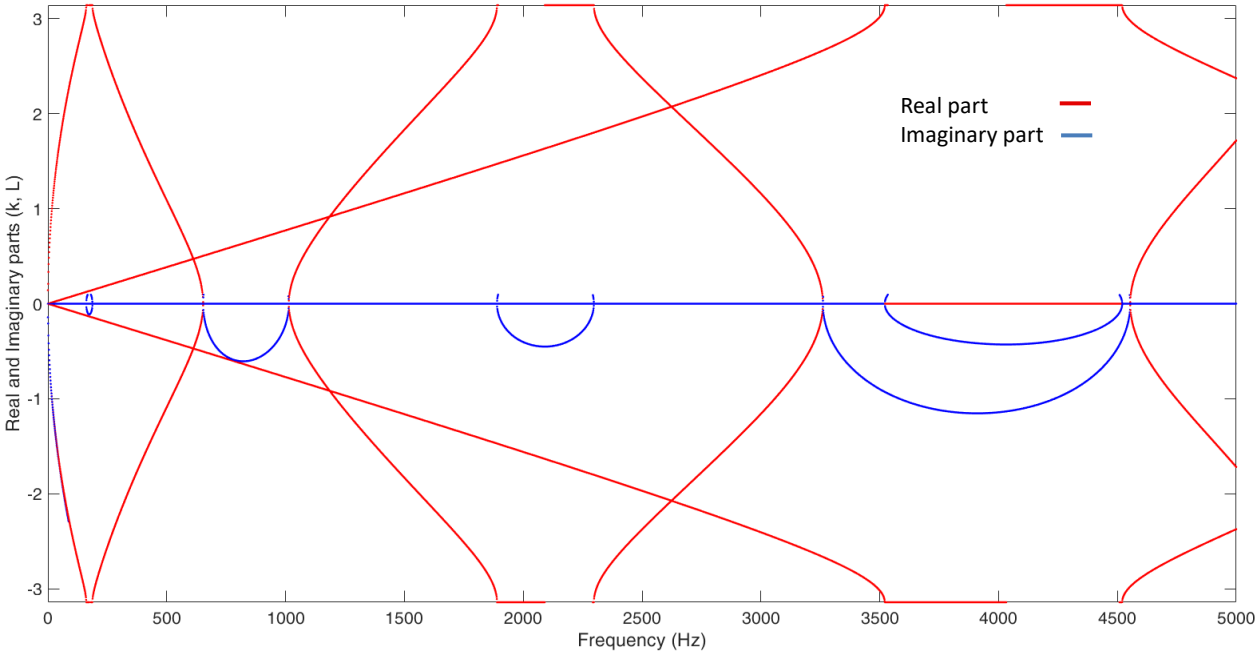


Figure 9: Spectral analysis of Floquet-Bloch boundary condition on the Fibonacci 4th order.

Table 3 shows CPU elapsed time of numerical simulation for three types of analysis; model FRF by FE analysis, model FRF by WFEM analysis and a spectral analysis of Floquet-Bloch waves. The three types of analysis are carried out using MATLAB®, APDL-ANSYS® and Intel® Core™ i7-6700 CPU @3.40GHz (8 CPUs). The elapsed time for maximum frequency 5kHz in spectral analysis of Bloch waves is expected to be very costly among the list. It seems that there is a huge difference almost around 52.7% between the spectral and FE analysis and 97.9% between spectral and WFEM analysis. All three types of analysis follow different frequency steps; thus, they are solved by two different solution methods, inverse and full VT (Variational Technology) harmonic analysis methods.

If we consider the spectral analysis as a reference in Table 3, the FE and WFEM are 47.3% and 2.1% of the CPU timing used in spectral analysis of Bloch waves. It is obvious that WFEM is one of the most useful technique for saving computation time, but still there are open topics in model order reduction to save more computational time.

Model FRF/Spectral analysis of Bloch waves	Methods	Steps number	Elapsed time (sec)	CPU ratio (%)
Spectral analysis of Bloch waves over the wave guide section	Inverse	1	266.1	100%
FE FRF analysis of wave guide section	VT Full	1500	126.22	47.3%
WFEM FRF analysis of a wave guide section	Inverse	1	5.61	2.1%

Table 3: CPU time of numerical simulations.

5 Conclusion

In a perfect periodic beam the effects of vibration are very different from the quasi-periodic one. In quasi-periodic beam, the impedance mismatch generated by four types of Fibonacci orders, causes destructive wave interference and thus generates the band gaps. The geometrical cross section variation, following Fibonacci sequence in the analysis, creates, multi frequency stop bands with narrow band gaps in which,

waves cannot freely propagate. These narrow band gaps not only appear in the medium frequency ranges as Bragg type frequency stop bands in periodic beams, but it also covers the lower and higher ranges of frequencies in between [0-5000] Hz.

By increasing the number of Fibonacci generated orders; the frequency stop bands ranges do not change, while in contrary the depth of the frequency stop bands grows deeper.

Using material variation in the quasi-periodic beam can significantly provide, frequency stop bands with larger widths. The effects of wider stop bands can help the structure to be a useful filter in real engineering problems. The very simple models herein presented allow continuing to study the configurations even considering the variation of the materials.

Acknowledgements

This paper containing intermediate investigation, carried out in the framework of the VIPER project (VIbroacoustic of PERiodic media). This project has received funding from the European Union's Horizon 2020 research and innovation program under Marie Curie grant agreement No 675441 and EUR EIPHI (ANR 17-EURE-0002) project.

References

[1] Bécus, G.A., 1978. Wave propagation in imperfectly periodic structures: a random evolution approach. *Zeitschrift für angewandte Mathematik und Physik ZAMP*, *29*(2), pp.252-261.

[2] Mester, S.S. and Benaroya, H., 1995. Periodic and near-periodic structures. *Shock and Vibration*, *2*(1), pp.69-95.

[3] Mead, D.J., 1973. A general theory of harmonic wave propagation in linear periodic systems with multiple coupling. *Journal of Sound and Vibration*, *27*(2), pp.235-260.

[4] Brillouin, L., 2003. *Wave propagation in periodic structures: electric filters and crystal lattices*. Courier Corporation.

[5] Billon, K., Zampetakis, I., Scarpa, F., Ouisse, M., Sadoulet-Reboul, E., Collet, M., Perriman, A. and Hetherington, A., 2017. Mechanics and band gaps in hierarchical auxetic rectangular perforated composite metamaterials. *Composite Structures*, *160*, pp.1042-1050.

[6] Spadoni, A., Gonella, S., Ruzzene, M. and Scarpa, F., 2007, September. Wave propagation and band-gap characteristics of chiral lattices. In *ASME 2007 International Design Engineering Technical Conferences &Computers and Information in Engineering Conference September* (pp. 4-7).

[7] Velasco, V.R. and Zárate, J.E., 2001. Elastic waves in quasiperiodic structures. *Progress in Surface Science*, *67*(1-8), pp.383-402.

[8] Gei, M., 2010. Wave propagation in quasiperiodic structures: stop/pass band distribution and prestress effects. *International Journal of Solids and Structures*, *47*(22-23), pp.3067-3075.

[9] Langley, R.S., 2017, January. The statistical properties of random frequency response functions. In *24th International Congress on Sound and Vibration, ICSV 2017*.

[10] Chen, A.L., Wang, Y.S., Guo, Y.F. and Wang, Z.D., 2008. Band structures of Fibonacci phononic quasicrystals. *Solid State Communications*, *145*(3), pp.103-108.

[11] Mencik, J.M. and Duhamel, D., 2016. A wave finite element-based approach for the modeling of periodic structures with local perturbations. *Finite Elements in Analysis and Design*, *121*, pp.40-51.

[12] Duhamel, D., Mace, B.R. and Brennan, M.J., 2006. Finite element analysis of the vibrations of waveguides and periodic structures. *Journal of sound and vibration*, *294*(1-2), pp.205-220.

[13] Miranda Jr, E.J.P.D. and Santos, J.M.C.D., 2018. Flexural Wave Band Gaps in Phononic Crystal Euler-Bernoulli Beams Using Wave Finite Element and Plane Wave Expansion Methods. *Materials Research*, (AHEAD), pp.0-0.

[14] Collet, M., Ouisse, M., Ruzzene, M. and Ichchou, M.N., 2011. Floquet–Bloch decomposition for the computation of dispersion of two-dimensional periodic, damped mechanical systems. *International Journal of Solids and Structures*, *48*(20), pp.2837-2848.

[15] Aki, K. and Richards, P., 1983. Kolichestvennaya seismologiya. *Teoriya i metody (Qualitative seismology. Theory and methods)*, *1*.

[16] Banerjee, A., Das, R. and Calius, E.P., 2018. Waves in Structured Mediums or Metamaterials: A Review. *Archives of Computational Methods in Engineering*, pp.1-30.

Inverse characterization method of viscoelastic materials using dispersion analysis

T. Bourgana [1,2,4], **R. F. Boukadia** [1,3,4], **S. Jonckheere** [1,4], **C. Claeys** [1,4], **G. Chevallier** [2], **M. Ouisse** [2], **E. Deckers** [1,4]

[1] KU Leuven, Department of Mechanical Engineering,
Celestijnenlaan 300 B, B-3001, Heverlee, Belgium
e-mail: **taoufikmohamed.bourgana@kuleuven.be**

[2] FEMTO-ST, Applied Mechanics Department, UMR-CNRS 6174,
24 chemin de l'épitaphe, 25000 Besançon, France.

[3] LTDS UMR-CNRS 5513, École Centrale de Lyon,
36 avenue Guy de Collongue, 69134 Écully, France.

[4] Flanders Make DMMS lab.

Abstract

This paper presents a dispersion-based method for identifying visco-elastic material properties by minimizing the residue between data of virtual experiments and data based on a viscoelastic model through the use of surrogate modeling. The dispersion data retrieved from a virtual experiment of a finite beam with constrained layer damping (the real and imaginary part of the wavenumber) is fitted with numerical dispersion data through an optimization scheme, which can be computationally expensive. In order to alleviate this issue, attention has been focused on the construction of a surrogate model that makes the optimization scheme cheaper without loosing much accuracy in the prediction. This paper uses an interpolation method based on radial basis functions. Once the surrogate model is constructed, the viscoelastic parameters can then be identified and results are compared to the reference parameters.

1 Introduction

Lightweight structures are increasingly used in many industrial sectors for their high stiffness to mass ratio. However, this comes with the price of deteriorated NVH performance. A common way to solve this issue is to use visco-elastic materials usually incorporated in two configurations : constrained and unconstrained visco-elastic layers, meaning that the visco-elastic core is bonded between a host and a constraining structure in the former case, in the latter case the visco-elastic core is directly put on the host structure. These materials are often desirable for their ability to dissipate part of the vibrational energy by heat when they are constrained in shear loading, e.g. when they are constrained by the host structure as well as the constraining layer [1].

In order to run numerical simulations to assess the performance of visco-elastic materials on a given vibrating structure, an accurate knowledge of its parameters is necessary. Several characterization techniques exist to identify the complex frequency-dependent properties of this class of materials, amongst them the dynamical mechanical analysis [3] and the Oberst beam test [4] are the most commonly used. The former is a quasi-static method (low frequencies) and the latter is a resonant method where only the first modes of the tested beam are taken into account. Both techniques are based on the assumption that the visco-elastic material

is rheologically simple, meaning that the time-temperature superposition[3] can be applied in order to extrapolate the storage and loss modulus of the viscoelastic material to higher frequencies. However, for some materials such as polymeric blends, the time-temperature superposition principle is no longer applicable, and thereby a new characterization technique which is not based on this principle is needed. In [2] several experimental identification methods were presented, ranging from quasi-static to higher frequencies, and were then compared to DMA measurements. It has been shown that although results using different methods were coherent, it is not easy to obtain a continuous description of the viscoelastic behavior of a material in the frequency range $[500, 5000]$ Hz. Another method has been presented in [5] and takes advantage of surface (Rayleigh) waves propagating in a infinite half-space visco-elastic material to retrieve experimentally, by means of an inverse technique, the material parameters. Two approaches have been proposed for the identification: on the one hand, a visco-elastic model type is assumed and updated in an optimization scheme such that numerical surface wave speed matches the measured one, on the other hand a similar model updating scheme is carried out but using frequency response function fitting instead. However, the theory is based on the premise that the visco-elastic material is considered as an infinite half-space whereas the experimental setup has finite boundaries, which explains the discrepancies noticed and stated by the authors. A reliable, simple, but not trivial, identification technique has been presented in [7] to characterize rod-like visco-elastic materials when they are subjected to longitudinal harmonic solicitation. It uses the Fourier Transform on experimental data of wave pulse propagating in a long 1D structure. This method provides very good results in determining visco-elastic properties in a wide frequency range, without making any assumption whether or not the material is rheologically simple. It is used when the rod is long enough and the attenuation of propagating waves is sufficiently high. Nonetheless, if right and left going waves are both contributing to the displacement field, meaning existence of reflected waves due to boundary conditions, the method will no longer be applicable. In [8] two techniques have been presented allowing the experimental identification of the equivalent complex frequency-dependent bending stiffness and damping of multi-layer plates : the force analysis technique [9] and a wave fitting technique by means of Hankel's function image source model [10], the output of these methods (equivalent material properties) were fitted with Guyader's homogenization model [11] or Ross, Kerwin and Ungar's model [12] in order to find the frequency-dependent properties of the damping layer.

Yet another inverse technique for the identification of linear visco-elastic material has been suggested in the literature. It is based on the minimization of the residual between measured data and numerical finite element model data. The latter is updated through an optimization scheme by varying the visco-elastic model parameters : Generalized Maxwell [13, 14], fractional derivatives [15]. The minimization can be modal-based [16] as well as frequency response function-based [17]. This technique has been widely applied in the literature, for instance in [17] for 1D structures, or in [18, 19, 20] for 2D structures. Although this type of method has several advantages, the hurdle comes up when dealing with highly damped structures where the identification of the modal parameters becomes really delicate, which is usually the case for high order modes where the behavior of the structure is local.

To amend to this issue, a new inverse characterization technique is hereby proposed. It is based on minimizing the distance between experimental and predicted dispersion curves from a wave finite element model through an optimization scheme. The experimental data in this case are replaced by numerical dispersion curves with added noise. The proposed method is applied to a highly damped beam treated with constrained layer damping, and the visco-elastic material parameters are identified using the proposed method over a broad frequency range.

This paper is structured as follows : in section 2, a viscoelastic model will be discussed, the latter will be used in section 3 in modeling the treated beam using the wave finite element method. McDaniel's method will be discussed as well in the same section. Finally, in section 4, an identification procedure will be presented through the use of surrogate modeling.

2 Linear viscoelastic behavior

Viscoelastic materials are known to dissipate vibrational energy, in particular when performing under shear stress. They possess both viscous and elastic behavior, and consequently their modulus is represented, in the frequency domain, by a complex quantity satisfying the following constitutive equation :

$$\tilde{\sigma}(\omega) = E_\nu(\omega)\tilde{\epsilon}(\omega), \tag{1}$$

where $\tilde{\sigma}$ and $\tilde{\epsilon}$ are the stress and strain expressed in the frequency domain, respectively. The frequency-dependent complex modulus of the visco-elastic material is written as :

$$E_\nu(\omega) = E'(\omega) + iE''(\omega) = E'(\omega)(1 + i\eta(\omega)), \tag{2}$$

The real part $E'(\omega)$, also known as the storage modulus, relates to the elastic behavior of the material, and defines its stiffness. The imaginary part $E''(\omega)$, also known as the loss modulus, relates to the material viscous behavior, and defines its energy dissipating ability of the material, the relationship between the storage modulus and the loss modulus can also be defined through the loss factor $\eta(\omega)$. One of the characteristics of viscoelastic materials is that their properties are influenced by many parameters, such as : frequency, temperature, dynamic strain rate, static pre-load, time effects such as creep and relaxation, aging and other irreversible effects [3]. The material complex modulus is dependent on all these factors. however, frequency and temperature are the most important.

Fractional derivative model:

The fractional derivative model is used to characterize the behavior of visco-elastic materials in frequency and time domain. The four-parameter fractional derivative model, also known as the generalized Zener model is given by the fractional differential equation as :

$$\sigma(t) + \tau^\alpha \frac{d^\alpha \sigma(t)}{dt^\alpha} = E_0\epsilon(t) + \tau^\alpha E_\infty \frac{d^\alpha \epsilon(t)}{dt^\alpha}, \tag{3}$$

where E_0 and E_∞ are the static and high frequency modulus respectively, τ is the relaxation time and α is the fractional parameter.

By applying a Fourier transform to equation (3), one can find the complex modulus of the viscoelastic material in the frequency domain, which is the ratio between the stress and the strain, as :

$$E_\nu(\omega) = \frac{E_0 + E_\infty(i\omega\tau)^\alpha}{1 + (i\omega\tau)^\alpha}. \tag{4}$$

This fractional derivative model is used in the following as it enables characterization of a wide variety of visco-elastic materials with only four parameters.

3 Modeling and numerical experiment

A modeling procedure and experimentation process are necessary for the parameter estimation. In the following, a wave finite element model of a segment of a treated beam will be presented as well as a specific numerical experimentation to identify dispersion curves.

The virtual test case is schematically represented in fig. 1 :



Figure 1: Representation of the clamped treated beam and excitation location

The constrained layer beam shown in fig. 1 is clamped at one end and excited at the other with a point force, the host structure as well as the constraining layer are in steel (shown in black in fig. 1), the viscoelastic material (shown in blue in fig. 1) parameters to be identified as well as the chosen steel properties are shown in table (1), the length of the beam in the $\vec{x}$ direction is $L = 0.6$ m, and $b = 0.03$ m in the $\vec{y}$ direction, the thickness in the $\vec{z}$ direction are $t_1 = 0.004$ m, $t_2 = 0.001$ m and $t_3 = 0.001$ m for the host structure, the viscoelastic core and the constraining layer respectively.

Parameters	Values	Units
E_0	10^6	[Pa]
τ	10^{-6}	[s]
α	0.6	[-]
E_∞	10^{10}	[Pa]
E_{steel}	$2.1\ 10^{11}$	[Pa]
ν_{steel}	0.3	[-]
ν_{visco}	0.37	[-]
ρ_{steel}	7850	[kg/m^3]
ρ_{visco}	990	[kg/m^3]

Table 1: Material properties of the three-layered beam

3.1 Wave finite element model

The Wave Finite Element method is a technique to investigate wave motion in periodic structures. It enables the dispersion analysis of a periodic structure by only studying one period or segment of it, which saves computation time.

A small segment of length $L = 0.01$ m of the treated beam previously shown in fig. 1, is considered and meshed using finite elements. Solid elements are used for the visco-elastic core and shell elements for the faces (see fig. 2).

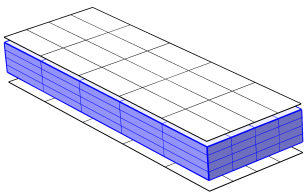


Figure 2: Finite element model of the unit cell of the treated beam

Once discretized, the equation of motion of the isotropic treated beam can be written as :

$$[\mathbf{K}^{(e)} + E_\nu(\omega)\mathbf{K}^{(\nu)} - \omega^2\mathbf{M}]\mathbf{q} = \mathbf{F}, \tag{5}$$

where $\mathbf{K}_e$, $\mathbf{K}_\nu$ and $\mathbf{M}$ are the global stiffness matrix associated with the elastic part of the structure, the global stiffness matrix associated with the viscoelastic part and evaluated at a unitary modulus and the global mass matrix, respectively. $E_\nu(\omega)$ is the complex modulus of the viscoelastic part from equation (4), and $\mathbf{q}$ and $\mathbf{F}$ are the displacement and the force vector respectively.

The equation of motion of the segment can be partitioned in the following manner :

$$\left\{ \begin{bmatrix} \mathbf{K}_{LL}^{(e)} & \mathbf{K}_{LR}^{(e)} & \mathbf{K}_{LI}^{(e)} \\ \mathbf{K}_{RL}^{(e)} & \mathbf{K}_{RR}^{(e)} & \mathbf{K}_{RI}^{(e)} \\ \mathbf{K}_{IL}^{(e)} & \mathbf{K}_{IR}^{(e)} & \mathbf{K}_{II}^{(e)} \end{bmatrix} + E_\nu(\omega) \begin{bmatrix} \mathbf{K}_{LL}^{(\nu)} & \mathbf{K}_{LR}^{(\nu)} & \mathbf{K}_{LI}^{(\nu)} \\ \mathbf{K}_{RL}^{(\nu)} & \mathbf{K}_{RR}^{(\nu)} & \mathbf{K}_{RI}^{(\nu)} \\ \mathbf{K}_{IL}^{(\nu)} & \mathbf{K}_{IR}^{(\nu)} & \mathbf{K}_{II}^{(\nu)} \end{bmatrix} - \omega^2 \begin{bmatrix} \mathbf{M}_{LL} & \mathbf{M}_{LR} & \mathbf{M}_{LI} \\ \mathbf{M}_{RL} & \mathbf{M}_{RR} & \mathbf{M}_{RI} \\ \mathbf{M}_{IL} & \mathbf{M}_{IR} & \mathbf{M}_{II} \end{bmatrix} \right\} \begin{bmatrix} \mathbf{q}_L \\ \mathbf{q}_R \\ \mathbf{q}_I \end{bmatrix} = \begin{bmatrix} \mathbf{F}_L \\ \mathbf{F}_R \\ \mathbf{0} \end{bmatrix}, \tag{6}$$

where coordinates $\mathbf{q}_L$,$\mathbf{q}_R$ and $\mathbf{q}_I$ denotes the physical degrees of freedom on the left boundary, on the right boundary and internal degrees of freedom respectively (as indicated by the corresponding subscripts). The internal degrees of freedom $\mathbf{q}_I$ are eliminated using a Guyan reduction [6], the relationship between the reduced and the original degrees of freedom can be written as:

$$\begin{bmatrix} \mathbf{q}_L \\ \mathbf{q}_R \\ \mathbf{q}_I \end{bmatrix} = \mathbf{B} \begin{bmatrix} \mathbf{q}_L \\ \mathbf{q}_R \end{bmatrix}, \tag{7}$$

where

$$\mathbf{B} = \begin{bmatrix} \mathbf{I} & \mathbf{0} \\ \mathbf{0} & \mathbf{I} \\ \mathbf{\Psi}_L & \mathbf{\Psi}_R \end{bmatrix}, \tag{8}$$

with $\mathbf{\Psi}_L = -\mathbf{K}_{II}^{-1}(\omega = 0)\mathbf{K}_{IL}(\omega = 0)$ and $\mathbf{\Psi}_R = -\mathbf{K}_{II}^{-1}(\omega = 0)\mathbf{K}_{IR}(\omega = 0)$ are the static boundary modes, and $\mathbf{K}(\omega = 0) = \mathbf{K}^{(e)} + E_0\mathbf{K}^{(\nu)}$, the latter is valid for the subscripts $LL, II, RR, LR, LI, RL, RI$ IR and IL.

Craig Bampton reduction followed by a dynamic condensation is generally more accurate than Guyan reduction when inertial forces exist, but requires inversions at each frequency step. Since the fixed interface modes of the beam section in our case are higher order modes with respect to the frequency range of interest (in this case from 10 Hz until 2000 Hz), the static condensation is more than sufficient for reducing the unit cell. In case the beam is not homogeneous along x direction, e.g. due to the presence of periodically placed resonators, Guyan reduction will no longer hold and a certain number of fixed interface modes must be taken into account in equations (7) and (8) in order for the reduced system to represent the same dynamics as the original one in the frequency range of interest, as for example applied in [21].

The condensed equation of motion can be written as :

$$\left\{ \begin{bmatrix} \tilde{\mathbf{K}}_{LL}^{(e)} & \tilde{\mathbf{K}}_{LR}^{(e)} \\ \tilde{\mathbf{K}}_{RL}^{(e)} & \tilde{\mathbf{K}}_{RR}^{(e)} \end{bmatrix} + E_\nu(\omega) \begin{bmatrix} \tilde{\mathbf{K}}_{LL}^{(\nu)} & \tilde{\mathbf{K}}_{LR}^{(\nu)} \\ \tilde{\mathbf{K}}_{RL}^{(\nu)} & \tilde{\mathbf{K}}_{RR}^{(\nu)} \end{bmatrix} - \omega^2 \begin{bmatrix} \tilde{\mathbf{M}}_{LL} & \tilde{\mathbf{M}}_{LR} \\ \tilde{\mathbf{M}}_{RL} & \tilde{\mathbf{M}}_{RR} \end{bmatrix} \right\} \begin{bmatrix} \mathbf{q}_L \\ \mathbf{q}_R \end{bmatrix} = \begin{bmatrix} \tilde{\mathbf{F}}_L \\ \tilde{\mathbf{F}}_R \end{bmatrix}, \tag{9}$$

where $\tilde{\mathbf{K}}^{(\mathbf{e})} = \mathbf{B}^T\mathbf{K}^{(e)}\mathbf{B}$, $\tilde{\mathbf{K}}^{(\nu)} = \mathbf{B}^T\mathbf{K}^{(\nu)}\mathbf{B}$, $\tilde{\mathbf{M}} = \mathbf{B}^T\mathbf{M}\mathbf{B}$ and $\tilde{\mathbf{F}} = \mathbf{B}^T\mathbf{F}$.

equation (9) can be written in terms of the dynamic stiffness matrix $\tilde{\mathbf{D}}$ as follows :

$$\begin{bmatrix} \tilde{\mathbf{D}}_{LL} & \tilde{\mathbf{D}}_{LR} \\ \tilde{\mathbf{D}}_{RL} & \tilde{\mathbf{D}}_{RR} \end{bmatrix} \begin{bmatrix} \mathbf{q}_L \\ \mathbf{q}_R \end{bmatrix} = \begin{bmatrix} \tilde{\mathbf{F}}_L \\ \tilde{\mathbf{F}}_R \end{bmatrix}, \tag{10}$$

where $\tilde{\mathbf{D}} = \tilde{\mathbf{K}}^{(\mathbf{e})} + E_\nu(\omega)\tilde{\mathbf{K}}^{(\nu)} - \omega^2\tilde{\mathbf{M}}$.

After applying Floquet-Bloch conditions, one obtains :

$$\mathbf{q}_R = \lambda \mathbf{q}_L, \tag{11}$$

and

$$\begin{bmatrix}\mathbf{q}_L & \mathbf{q}_R\end{bmatrix}^T = \mathbf{\Gamma}_R \mathbf{q}_L, \tag{12}$$

where $\mathbf{\Gamma}_R = \begin{bmatrix}\mathbf{I} & \lambda\mathbf{I}\end{bmatrix}^T$, $\mathbf{I}$ being the identity matrix and λ being the propagation constant.

The dynamic equilibrium of the segment holds the following equations :

$$\mathbf{\Gamma}_L \mathbf{F} = \mathbf{0}, \tag{13}$$

where $\mathbf{\Gamma}_L = \begin{bmatrix}\mathbf{I} & \frac{1}{\lambda}\mathbf{I}\end{bmatrix}$.

Pre-multiplying both sides of equation (10) by $\mathbf{\Gamma}_L$ and using equations (12) and (13), yields the classic quadratic eigenvalue problem of 1D wave propagation in terms of the propagation constant [23] :

$$[\lambda^2 \tilde{\mathbf{D}}_{LR} + \lambda(\tilde{\mathbf{D}}_{LL} + \tilde{\mathbf{D}}_{RR}) + \tilde{\mathbf{D}}_{RL}]\mathbf{q}_L = \mathbf{0}. \tag{14}$$

The frequency dependence is not an issue in this method as equation (14) is solved by fixing the frequency and calculating for the propagation constant.

3.2 Dispersion curves extraction method

A couple of works have been published to experimentally retrieve dispersion curves from vibrating structures. In [22] the in-homogeneous wave correlation method (IWC) was presented, that maximizes the correlation between the experimental displacement and a plane wave by adjusting the wave-number. This method has the edge of being applicable to 1D as well as 2D structures and has been compared to a spatial Fourier transform method for bending waves in beams in [25]. In the present paper, McDaniel's method [24] will be used to retrieve dispersion curves from a numerical noisy experiment. This method adjusts wave-numbers and wave-amplitudes of a postulated wave-field propagating in the structure with the reference response, and this is done at each frequency step. Contrary to other methods, the method does not require long structures with high damping so that a wave generated at one end is attenuated before it reaches the other end. However, it can be computationally expensive due to numerous parameters (wave numbers and wave amplitudes) that are optimized for. In the following, the latter method is applied to the treated beam depicted in fig. 1, the numerical displacements along the beam are polluted with noise and spatially sampled at 100 locations. The wave-field (to be fitted) in the structures is constructed by a finite set of waves that propagate back and forth and that decay due to the damping of the structure:

$$W(x,\omega) = \sum_r a_r(\omega) e^{-ik_r(\omega)x} + b_r(\omega) e^{-ik_r(\omega)(L-x)}, \tag{15}$$

where each r represents a distinct wave type that propagates in the structure with a complex valued wavenumber $k_r(\omega)$. The following minimization problem is run at each frequency step and provides the extracted dispersion curves :

$$\min_{k_r, a_r, b_r} \quad \sum_{samples} \left|\left| \frac{W - \tilde{W}}{\tilde{W}} \right|\right|^2 \qquad \forall r. \tag{16}$$

where $\tilde{W}$ are the reference displacements.

This method is applied to the cantilever treated beam case (see fig. 1). 2 percent of random noise (with respect to the wave's amplitudes) was added to the beam's displacement. Two wave types have been considered $r = 2$ corresponding to a propagating and evanescent wave (only two bending wave types exist in any 1D isotropic beam). The wave-number of the propagating wave is shown in fig. 3.

It is noteworthy that the treated beam is purposely chosen highly damped (see fig. 4) so as to show the advantages of the proposed viscoelastic parameter identification method. Starting from 600 Hz, the frequency response function shows a smoother behavior due to the high damping of the treated beam.

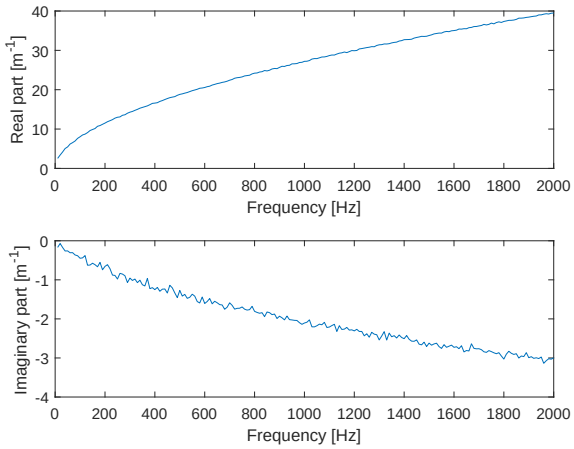


Figure 3: Real and imaginary wave-number of the propagating wave extracted from the treated beam using McDaniel's method

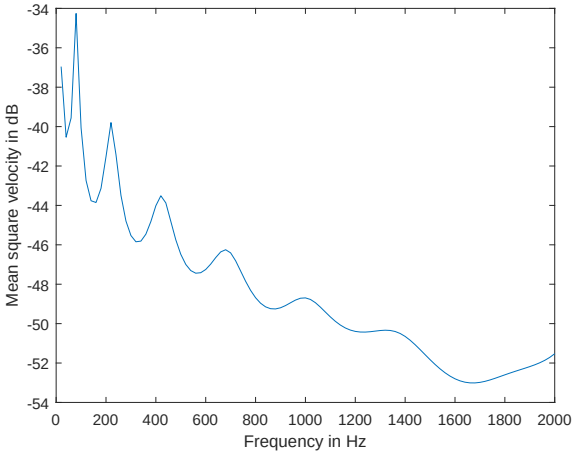


Figure 4: Mean square velocity of the treated beam shown in fig. 1 excited with a unit force.

4 Proposed identification inverse method

Solving the quadratic eigenvalue problem in equation (14) at multiple iterations can be computationally expensive, therefore, effort has been specifically focused on the construction of a surrogate model which will alleviate this issue. Surrogate models represent an approximation that is cheaper and more convenient to evaluate, than the underlying models they approximate. The most common use of surrogate models is to replace a known expensive computational model when a large number of repeated evaluations is required, e.g., for optimization or uncertainty quantification. Another common application is to obtain a continuous function from a fixed dataset, e.g., when the data is obtained experimentally. A third application is smoothing an underlying model with a lower order of continuity, perhaps to achieve differentiability for gradient-based optimization. In the following, a surrogate-based optimization is deployed to identify the viscoelastic parameters.

4.1 Surrogate model

Surrogate modeling approaches can be classified as interpolation (if the surrogate model matches the true function value at each point in the training dataset) or regression (if it does not). Regression methods smoothly approximate noisy data, and they include polynomials, splines, artificial neural networks (ANN), or

support vector regression (SVR). Interpolation methods attempt to smoothly and accurately fit non-spurious data, and they include inverse distance weighting (IDW), radial basis functions (RBFs), or kriging. These methods are extensively discussed in the literature in different applications e.g. see [26, 27, 28].

4.1.1 Radial basis functions

Radial basis functions (RBFs) are defined as linear combinations of basis functions, where each basis function depends on the distance from the prediction point to each training point. The coefficients in the linear combination are determined by solving a linear system that is typically dense. The radially varying basis functions are usually augmented with polynomial functions to capture the general trends.

In the following, the thin plate spline basis functions equation (17) are chosen because they have the edge of having no parameter that need to be tuned, whereas other basis functions do.

$$\psi_i(\mathbf{X}) = ||\mathbf{X} - \mathbf{X_i}||_2^2 \ln ||\mathbf{X} - \mathbf{X_i}||_2 \quad \forall i, \tag{17}$$

where $\mathbf{X_i}$ are the training points.

Prediction using the RBFs is given by :

$$k(\mathbf{X}) = \sum_i w_i \psi_i(\mathbf{X}) + \sum_j v_j p_j(\mathbf{X}), \tag{18}$$

where p_j is a polynomial function taken here as 1st degree polynomial, w_i and v_i are the unknown weights associated with the ith basis function and the ith polynomial trend function respectively.

In matrix notation, equation (18) can be written as :

$$\mathbf{k} = \mathbf{\Psi W} + \mathbf{PV}, \tag{19}$$

where $\mathbf{k}$ is a column vector of output training points $k(\mathbf{X_j})$ (wavenumbers), $\mathbf{W}$ and $\mathbf{V}$ are column vectors that consist of the coefficients w_j and v_j respectively, $\mathbf{\Psi}$ is the matrix $[\psi_i(\mathbf{X}_j)]_{ij}$, and $\mathbf{P}$ is the matrix $[p_i(\mathbf{X}_j)]_{ij}$, i denotes the row indices while j denotes the column indices. The training of RBFs consists of computing the weights by solving the following linear system :

$$\begin{bmatrix} \mathbf{k} \\ \mathbf{0} \end{bmatrix} = \begin{bmatrix} \mathbf{\Psi} & \mathbf{P} \\ \mathbf{P}^T & \mathbf{0} \end{bmatrix} \begin{bmatrix} \mathbf{W} \\ \mathbf{V} \end{bmatrix}. \tag{20}$$

A uniform sampling is used for the training points with a spacing of 10 points for each parameter.

It is note-worthy that we only focus on propagating waves with a decaying component (see fig. 3). The evanescent waves (their real part of the wave-number is smaller than their imaginary part) are not considered in the fitting.

4.2 Identification procedure

A set of three visco-elastic parameters (α, τ, E_∞) can be identified by solving the following minimization problem :

$$\begin{aligned} \min_{\mathbf{X}=(\alpha,\tau,E_\infty)} \quad & f(\mathbf{X}) = \sum_{frequencies} \left|\left| \frac{k'(\mathbf{X}) - \tilde{k}'(\mathbf{X})}{\tilde{k}'(\mathbf{X})} \right|\right|^2 + \left|\left| \frac{k''(\mathbf{X}) - \tilde{k}''(\mathbf{X})}{\tilde{k}''(\mathbf{X})} \right|\right|^2, \\ \text{subject to} \quad & 0 \leq \alpha \leq 1, \end{aligned} \tag{21}$$

where the prime and the double prime refer to the real and imaginary part of the wave-numbers respectively, k is the wave number constructed using the surrogate model presented in section 4.1, and $\tilde{k}$ is the propagating wave-number extracted from the numerical experiment explained in section 3.2.

The design variables that are optimized for are written in the following manner in order to efficiently span a broad range of values :

$$\begin{aligned} p_1 &= 10\alpha, \\ p_2 &= \log_{10}(\tau), \\ p_3 &= \log_{10}(E_\infty). \end{aligned} \tag{22}$$

It was noted during the numerical experiment that it is hard to identify the static modulus as the cost function, see equation (21), is not very sensitive to this parameter.

4.2.1 Two-parameter identification

In a first trial, the optimization is run on two parameters, the others being held constant. The cost functions with respect to two parameters are shown in fig. 5, fig. 6 and fig. 7. The results of the optimization are summarized in table 2, table 3 and table 4.

Parameters	Initial	Reference	Optimized
p_1	1.5	6	6.0001
p_2	-3.5	-6	-6.0011

Table 2: Numerical results for the case $\mathbf{X} = (\alpha, \tau)$

Parameters	Initial	Reference	Optimized
p_3	7	10	9.9981
p_2	-3.5	-6	-6.0001

Table 3: Numerical results for the case $\mathbf{X} = (E_\infty, \tau)$

Parameters	Initial	Reference	Optimized
p_3	7	10	9.9998
p_1	1.5	6	6.0011

Table 4: Numerical results for the case $\mathbf{X} = (E_\infty, \alpha)$

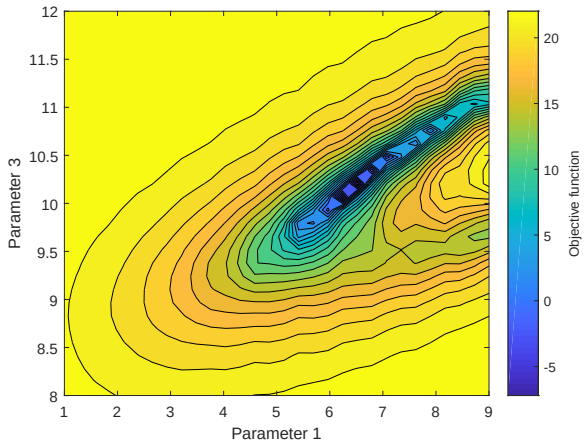


Figure 5: Logarithm of the objective function with respect to the parameters 1 and 3

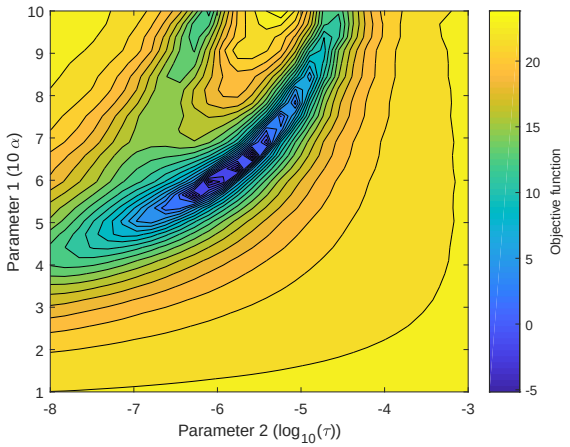


Figure 6: Logarithm of the objective function with respect to the parameters 1 and 2

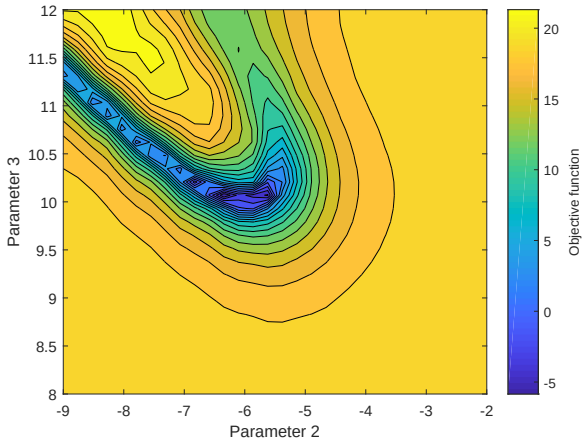


Figure 7: Logarithm of the objective function with respect to the parameters 2 and 3

A gradient-based optimization is deployed using Newton's method, the gradient and the Hessian are analytically calculated : exploiting the surrogate model previously built (see section 4.1). The present characterization technique has identified two-parameters at once in the frequency range of $[10\ 2000]$ Hz with 10 Hz increment, keeping the rest constant. The next section will treat the case of a three-parameter identification.

The cost function (see equation (21)), is not sensitive to the static modulus . This is depicted in figs. 8 to 10, showing horizontal or vertical lines indicating the value of the cost function is not considerably changing when varying the static modulus.

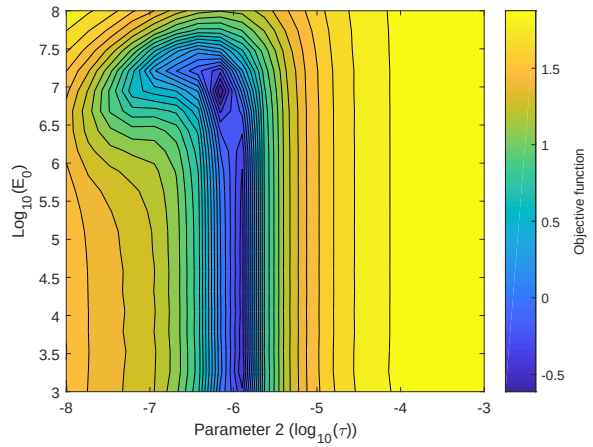


Figure 8: Logarithm of the objective function with respect to the parameters 1 and $\log_{10}(E_0)$

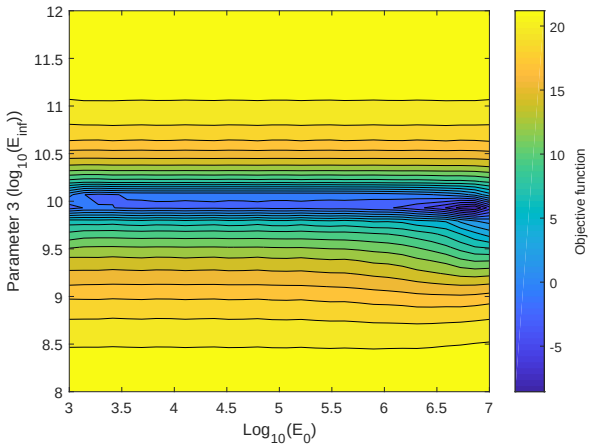


Figure 9: Logarithm of the objective function with respect to the parameters 3 and $\log_{10}(E_0)$

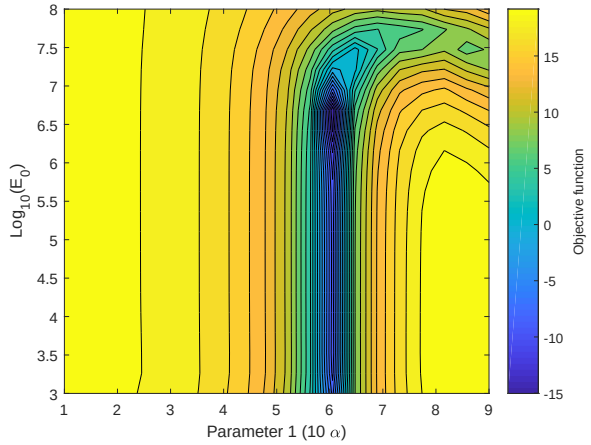


Figure 10: Logarithm of the objective function with respect to the parameters 2 and $\log_{10}(E_0)$

4.2.2 Three-parameter identification

Three parameters (E_∞, α, τ) can also be identified at once using this proposed method. The path of the optimization scheme is shown is fig. 11, the summarized results are given in table 5.

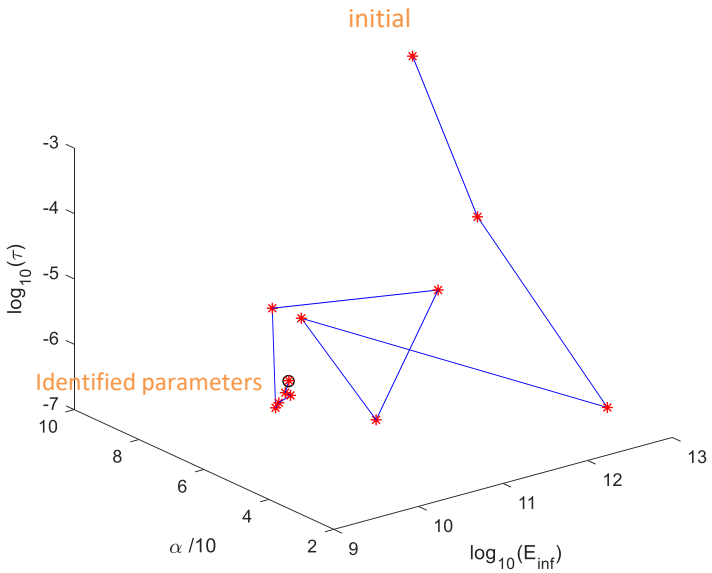


Figure 11: Path of the optimization convergence in the parameter space (E_∞, α, τ)

The identification of three parameters at once was successful using the proposed method. It is advisable to characterize E_0 first using static methods, and then plug it into this technique to retrieve the remaining parameters.

Parameters	Initial	Reference	Optimized
p_1	10	6	6.0001
p_2	-3	-6	-6.0011
p_3	13	10	9.9988

Table 5: Numerical results for the case $\mathbf{X} = (E_\infty, \alpha, \tau)$

5 Conclusion

This paper presents a dispersion-based characterization technique for identifying viscoelastic material properties. This method is applied to a highly damped beam and is able to characterize it over a wide frequency range. It is shown that, contrary to frequency response-function based inverse techniques, the proposed method does not loose its efficacy when dealing with highly damped structures. It actually makes the identification procedure easier as it is expected to capture more efficiently, the imaginary wave-number corresponding to the attenuation due to the added damping. Whereas the identification using the former method can become delicate because most of the material damping information is found at resonant frequencies levels, that most likely are not pronounced in case of high damping. However, the proposed method is not applicable to lightly damped structures as the signal to noise ratio of imaginary part of the extracted dispersion curves will be very low, which will make it difficult to extract the attenuating part of the propagating wave-number in a stable manner.

Acknowledgements

The research of T. Bourgana was funded by an Early Stage Researcher grant within the European Project VIPER Marie Curie European Joint Doctorates (GA 675441). The Research Fund KU Leuven is gratefully acknowledged for its support. E. Deckers is a post-doctoral fellow of the research foundation - Flanders. The research institute FEMTO-ST and Université de Bourgogne Franche-Comté, France, are gratefully acknowledged for their support. This research was performed in cooperation with EUR EIPHi (project ANR 17-EURE-0002).

References

[1] P. Butaud, E. Foltête, M. Ouisse. Sandwich structures with tunable damping properties: On the use of Shape Memory Polymer as viscoelastic core. *Composite Structures*, 153:401-408 , 2016.

[2] P. Butaud, M. Ouisse, V. Placet, F. Renaud, T. Travaillot, A. Maynadier, G. Chevallier, F. Amiot, P. Delobelle, E. Foltête, C. R. -Berriet . Identification of the viscoelastic properties of the tBA/PEGDMA polymer from multi-loading modes conducted over a wide frequency–temperature scale range. *Polymer Testing*, 69:250-258, 2018.

[3] J. D. Ferry. *Viscoelastic properties of polymers*. John Wiley and Sons, 1980.

[4] ASTM Standards E756-05. Standard test method for measuring vibration-damping properties of materials. American Society for Testing and Materials, West Consholocken, PA, 2010.

[5] T. J. Royston, Z. Dai, R. Chaunsali, Y. Liu, Y. Pend, L. R. Magin. Estimating material viscoelastic properties based on surface wave measurements: A comparison of techniques and modeling assumptions. *The Journal of the Acoustical Society of America*, 130(6):4126–4138, 2011.

[6] R. J. Guyan. Reduction of stiffness and mass matrices,*AIAA Journal*,3(2), 1965.

[7] Y. Sogabe, M. Tsuzuki. Identification of the dynamic properties of linear viscoelastic materials by the wave propagation testing. *Bulletin of JSME*, 29(254): 2410–2417, 1986.

[8] K. Ege, N.B. Roozen, Q. Leclere, R.G. Rinaldi. Assessment of the apparent bending stiffness and damping of multilayer plates; modelling and experiment. *Journal of sound and vibration*, 426:129–149, 2018.

[9] C. Pézerat, J.-L. Guyader. Force analysis technique: reconstruction of force distribution on plates. *Acta Acustica united with Acustica*, 86(2):322–332, 2000.

[10] N.B. Roozen, Q. Leclere, K. Ege, Y. Gerges. Estimation of plate material properties by means of a complex wavenumber fit using Hankel's functions and the image source method. *Journal of sound and vibration*,390:257–271, 2017.

[11] J.-L. Guyader, C. Cacciolati, Viscoelastic properties of single layer plate material equivalent to multilayer composite plate.*Proceedings of Inter-Noise*, 2007.

[12] D. Ross, E. E. Ungar, E. Kerwin, Damping of plate flexural vibrations by means of viscoelastic laminae.*Structural damping*,44-–87, 1959.

[13] D.A. Castello, F.A. Rochinha, N. Roitman, and C. Magluta. Constitutive parameter estimation of a viscoelastic model with internal variables. *Mechanical Systems and Signal Processing*,22:1840—1857, 2008.

[14] F. Renaud, J. -L. Dion, G. Chevallier, I. Tawfiq, R. Lemaire. A new identification method of viscoelastic behavior: Application to the generalized Maxwell model. *Mechanical Systems and Signal Processing*, 25(3):991–1010, 2011.

[15] S.-Y. Kim and D.-H. Lee. Identification of fractional-derivative model parameters of viscoelastic materials from measured frfs. *Journal of Sound and Vibration*, 324:570—586, 2009.

[16] Y. Shi, H. Sol, and H. Hua. Material parameter identification of sandwich beams by an inverse method. *Journal of Sound and Vibration*, 290:1234—1255, 2006.

[17] E. Zhang, J.D. Chazot, J. Antoni, and M. Hamdi. Bayesian characterization of young's modulus of viscoelastic materials in laminated structures. *Journal of Sound and Vibration*, 332:3654—3666, 2013.

[18] L. Rouleau, J.Deü, A. Legay. Inverse characterisation of frequency-dependent properties of adhesives. *Journal of Physics: Conference Series*, 744(1), 2016.

[19] L. Rouleau, B. Pluymers, W. Desmet. Characterisation of viscoelastic layers in sandwich lightweight panels through inverse techniques. *NOVEM - Noise and Vibration, Emerging Technologies*,2015.

[20] A. Van De Walle, L. Rouleau, E. Deckers, W. Desmet. Parametric model-order reduction for viscoelastic finite element models: an application to material parameter identifications. *Proceedings of the 22nd International Congress on Sound and Vibration*, 2015.

[21] R. F. Boukadia, C. Droz, M. N. Ichchou, W. Desmet. A Bloch wave reduction scheme for ultrafast band diagram and dynamic response computation in periodic structures. *Finite Elements in Analysis and Design*, 148:1-12, 2018.

[22] J. Berthaut, M.N. Ichchou, L. Jezequel, K-space identification of apparent structural behaviour, *Journal of Sound and Vibration*, 280(5):1125—1131, 2005.

[23] B. R. Mace, D. Duhamel, M. J. Brennan, L. Hinke, Finite element prediction of wave motion in structural waveguides, *The Journal of the Acoustical Society of America*, 117:2835–2843, 2005.

[24] J. G. McDaniel, W. S. Shepard, Estimation of structural wave numbers from spatially sparse response measurements, *The Journal of the Acoustical Society of America*, 108(4):1674–1682, 2000.

[25] B. Van Damme, A. Zemp, Measuring Dispersion Curves for Bending Waves in Beams: A Comparison of Spatial Fourier Transform and Inhomogeneous Wave Correlation, *Acta Acustica united with Acustica*, 104(2):228–234, 2018.

[26] D. Zhao, D. Liu, M. Zhu, A surrogate model for thermal characteristics of stratospheric airship, *Advances in Space Research*, 61(12):2989–3001, 2018.

[27] J. T. Hwang, J. R. R. A. Martins, A fast-prediction surrogate model for large datasets, *Aerospace Science and Technology*, 75:74–87, 2018.

[28] A. Nobari, H. Ouyang, P. Bannister, Uncertainty quantification of squeal instability via surrogate modelling, *Mechanical Systems and Signal Processing*, 60–61:887–908, 2015.

Design of a multi-scale reinforced sandwich panel with enhanced vibroacoustics performances

R. Palumbo[1], **D. Ivanov**[1], **C. Droz**[2], **O. Bareille**[2], **M. Ichchou**[2], **F. Scarpa**[1]
[1] University of Bristol, Bristol Composites Institute (ACCIS),
Queen's Building, University Walk, BS81TR, Bristol, United Kingdom

[2] Ecole Centrale de Lyon, Laboratoire de Tribologie et Dynamique des Systemes (LTDS)
69130, Ecully, France

Abstract
In the aerospace sector, cellular structures are widely used as cores of sandwich panels mainly because of their high stiffness-to-weight ratio. However, a small mass associated with a high stiffness usually leads to acoustic discomfort. Obtaining structures that provide both mechanical efficiency and good vibroacoustic performances is the reason why vibroacoustic constraints are being integrated in their design process. In this work, flax fibers in a polyethylene matrix are adopted as walls for a honeycomb core, replacing the metallic and polymeric materials historically used for this purpose. Viscoelastic inserts consisting of MWNT-reinforced resin are embedded within the core with the main goal of increasing the sandwich panel's shear transition frequency, which is the frequency at which the core's shear becomes important over the whole panels bending inducing bad vibroacoustic performances. A design procedure of the inserts is defined, taking into account both the added mass and the improvements aimed in terms of vibroacoustic performances.

1 Introduction

Sandwich panels have been widely used in industrial applications during the last decades. Their extraordinarly high stiffness-to-mass ratio given from the low-density core and the thin skin layers on its sides makes them attractive in a variety of fields such as in the aerospace industry, where weight-saving and mechanical performances are of primary importance. However, sandwich panels' great mechanical properties are often in conflict with their vibroacoustics performances: many researchers have been focusing their attention on sandwich panels sound insulation, as usually better acoustic performances correspond to a lower stiffness-to-mass ratio. In particular, sandwich panels' first transition frequency is an important vibroacoustic indicator for this kind of structures [1], as it provides information about their macro behaviour. Generally speaking, a transition frequency is the frequency at which the panel switches its current behaviour to another one. Referring to figure 1, showing a typical dispersion curve for sandwich panels, Fahy and Gardonio defined three main regions of vibroacoustic behaviour of these structures [1]. On the left, the area corresponding to $f < f_{t_1}$ is dominated by the panel's bending: this zone is controlled by the total section bending stiffness and the whole panel acts as homogeneous. In the middle region ($f_{t_1} < f < f_{t_2}$) the vibroacoustic behaviour is controlled by the core's shear stiffness, while the last zone ($f > f_{t_2}$) is dominated by the individual skin-face bending stiffness.

f_{t_1} is the first (or shear) transition frequency and defines the frequency at which the core's shear becomes important with respect to the whole panel's bending. It has been shown that usually a higher shear transition frequency reflects an improvement in the sound transmission loss through the panel at the mid frequencies [2], and this is why it is becoming of great interest [3] [4].

In this work, the focus is on the improvement of sandwich panels vibroacoustics performances by shifting

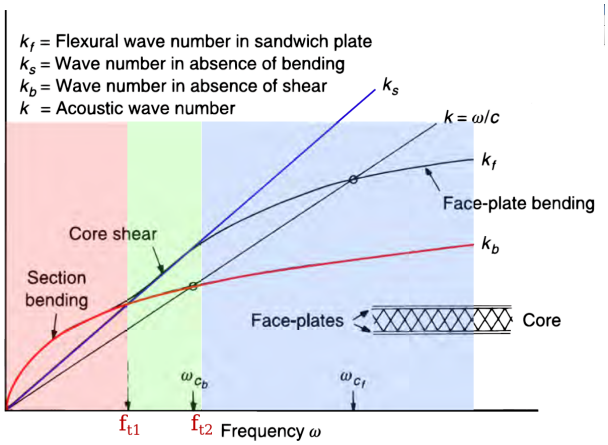


Figure 1: Typical dispersion curves of a sandwich panel [1]

the first transition frequency towards the high-frequency range, in which acoustic transparency can be controlled more easily, for instance by adding poroelastic inserts. This is done by working on the materials and manufacturing techniques of a square-cell honeycomb core equipped with reinforced viscoelastic inserts. The material adopted for the walls is a prepreg of unidirectional flax fibres (UD180-C003) of $180\,\mathrm{g/m^2}$ from Lineo, Belgium and Linear Low Density PolyEthylene (LLDPE) with a density of $0.91\,\mathrm{g/m^2}$. The viscoelastic inserts consist of an epoxy resin reinforced with Carbon Nanotubes. They are deposited at the junctions between perpendicular walls and are specifically designed with the aim of increasing f_{t_1} (from now on referred to simply as f_t) while keeping the percentage of added mass as small as possible at the same time. The position of the inserts is strategic also from another point of view, as not only it increases the core's toughness, but these are also the zones where the most of strain energy dissipation happens and the phenomenon is therefore enhanced by the introduction of the inserts precisely in these zones. As it will be better explained in section 4.3, Carbon Nanotube fillers are considered as an option to reinforce the resin and meet our goals.

2 Unit cell's effective mechanical characteristics

The software adopted for the numerical simulations is ANSYS® MECHANICAL APDL. Finite Element models were developed for the unit cell both in the base configuration - from now on indicating the standard honeycomb with no inserts - and the insert configuration. The geometric characteristics of the unit cell are shown in figure 2. Tables 1 and 2 show the epoxy resin and flax prepreg's materials properties respectively. The flax/PE mechanical properties derive from experimental tests carried out in [5], while the epoxy resin's characteristics are those of the pristine system - i.e. with no Carbon Nanotubes filler.

After a convergence study, a mesh with element size equal to 0.25 mm was chosen. The elements are SOLID185 (structural solid with eight three-degrees-of-freedom nodes) for both the insert and the honeycomb walls, with the difference that for the latter layered elements were adopted in order to model the orthotropic layered walls (lamination sequence of the unidirectional plies: $90^o/0^o/0^o/90^o$, where the fiber orientation is defined with respect to the z-axis of the model, figure 2).

2.1 Base configuration

Thanks to the symmetry of the unit cell with respect to the three orthogonal planes of the reference system shown in figure 2, only one octave unit cell was modeled.

E_{insert}	2.8 GPa
ν_{insert}	0.3
ρ_{insert}	1.15 g/cm^3

Table 1: Mechanical properties of the epoxy resin adopted for the inserts - Araldite® LY 3585 / Aradur® 3475 epoxy system

E_{11}	9.50 GPa	ASTM D 3039
E_{22}	1.30 GPa	ASTM D 3039
E_{33}	1.30 GPa	ASTM D 3039
G_{12}	0.55 GPa	ASTM D 4255
G_{13}	0.55 GPa	ASTM D 4255
G_{23}	0.40 GPa	ASTM D 4255
ν_{12}	0.40	ASTM D 3039
ν_{13}	0.40	ASTM D 3039
ν_{23}	0.60	ASTM D 3039
ρ	1.025 g/cm^3	

Table 2: Mechanical properties of the flax/PE composite adopted for the honeycomb's walls [5]

In-plane and out-of-plane virtual tensile and shear tests were simulated to evaluate the effective mechanical properties of the system. Figure 3 shows the boundary conditions applied for the in-plane tensile and shear tests. Analogous displacement fields were imposed in the out-of-plane direction.

The virtual tests were performed according to the procedure described in [6]. The outputs of the tensile test numerical simulation are the reaction R_x at $x = 0$ and the displacements v at $y = L$. Therefore, the expansion ratio and the effective elastic modulus are calculated as follows:

$$\chi = \frac{vL_x}{\Delta x L_y} = \frac{v}{\Delta x} \tag{1}$$

$$E_x^* = E_y^* = \frac{\sigma_x}{\epsilon_x} = \frac{R_x}{A_x}\frac{1}{\Delta x/L_x} = \frac{R_x}{L * h/2}\frac{L - t/2}{\Delta x} \tag{2}$$

Regarding the shear test, in principle there are several possibilities to simulate it - figure 4. However, only biaxial loading tests guarantee a deformation field which is as close as possible to pure shear. In this case, the outputs from the numerical simulations are the reactions R_x and R_y - sum of nodal forces along x at $x = 0$ and along y at $y = 0$ respectively. From these values it is possible to calculate the effective out-of-plane shear modulus:

$$G_{xy}^* = \frac{\tau_{xy}}{\gamma_{xy}} = \frac{\sigma_x - \sigma_y}{2(\epsilon_x - \epsilon_y)} = \frac{\frac{R_x}{A_x} - \frac{R_y}{A_y}}{2(\frac{\Delta x}{L} - \frac{\Delta y}{L})} \tag{3}$$

Performing the test in the out-of-plane direction, the remaining effective properties were evaluated and it was numerically verified that $G_{zy}^* = G_{yz}^* = G_{xz}^* = G_{zx}^*$. Table 3 summarizes the results.

2.2 Insert configuration

At the manufacturing level, the resin deposition is done from the top of the honeycomb by means of a modified 3D printer. Therefore, the most realistic shape to assume for the insert's profile is an hyperbole - figure 5. Due to the anisotropic nature of the insert along the z direction, in this case one-quarter unit cell

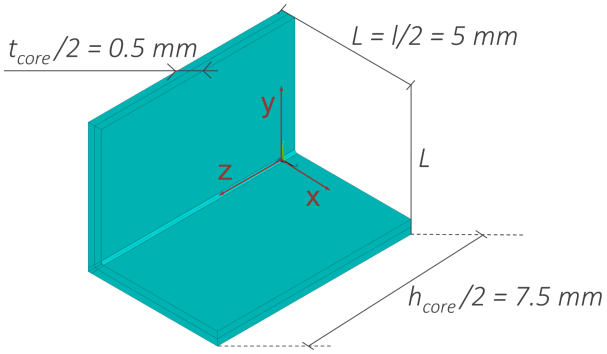
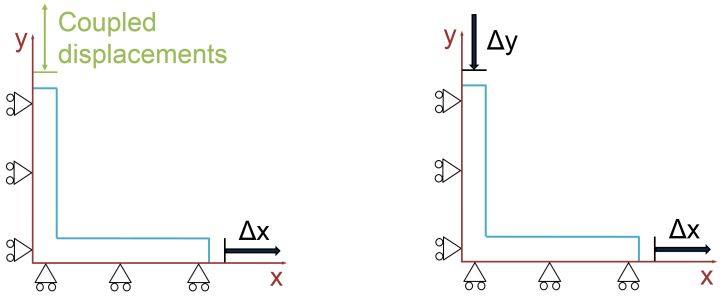


Figure 2: Geometry characteristics of one octave unit cell



(a) *In-plane tensile test* (b) *In-plane shear test*

Figure 3: Boundary conditions applied to simulate virtual in-plane tensile and shear tests

was modeled. The FE models in case of $A_{TOP} = A_{BASE} = 1$ mm and in the particular configuration of cylindrical profile ($A_{BASE} = 0$) are shown in figure 6 .

The shear modulus was evaluated following the same procedure as for the base configuration, but in this case a parametric study was performed in function of the geometric properties of the insert, figure 7 .

The shear modulus clearly increases as the insert's characteristic dimensions do. However, as the goal of this work is shifting the shear transition frequency of the sandwich panel towards higher values, it is fundamental to set some limits on the added mass given by the insert. In fact, not only one of the main advantages of sandwich panels is their reduced weight which should be preserved, but also the transition frequency depends on the shear stiffness as well as on the mass of the honeycomb - and therefore on the added mass given by the deposited resin.

3 Added mass design space

The percentage of added mass will be from now on indicated as m_{add} and was analytically evaluated as a function of the insert's geometric variables A_{TOP} and A_{BASE}. The resulting surface is shown in figure 8a, together with the constant-value surface corresponding to an arbitrary limit value of 20% added mass.

The intersection of the two surfaces generates the design space in figure 8b: to have a percentage of added mass smaller than 20%, the design point should be chosen within the yellow area. Finally, figure 8c shows the percentage mass in function of A_{TOP} in the particular case of cylindrical insert.

To have an idea of where it is better to choose the design point within this area, probabilistic design analyses were performed to establish which one between A_{BASE} and A_{TOP} has the biggest influence on the shear characteristics of the unit cell. The analyses were carried out by means of the Probabilistic Design

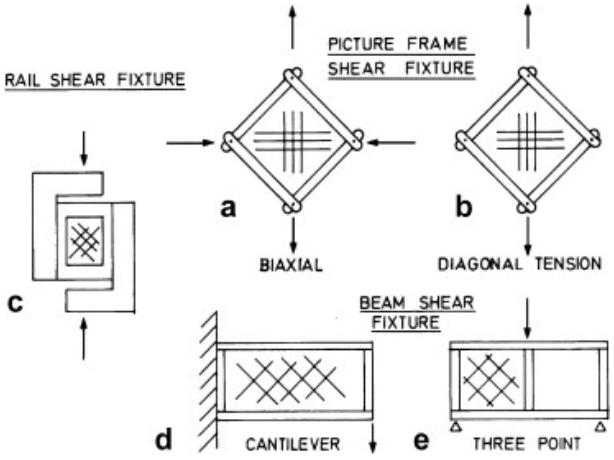


Figure 4: Shear test fixtures [6]

Tensile tests		Shear tests	
E^*_x	0.433 GPa	G^*_{xy}	0.187 GPa
χ^*_{xy}	-0.157		
E^*_z	1.30 GPa	G^*_{zy}	0.450 GPa
χ^*_{zy}	-0.454		

Table 3: Effective mechanical properties of the base configuration honeycomb unit cell

System module within ANSYS® MECHANICAL APDL. The random input (RI) variables of the problem are A_{BASE} and A_{TOP}, for which Gaussian distributions with mean values $\mu = 1\,mm$ and standard deviations $\sigma = 0.2\,mm$ were assumed, while the output parameter is the effective out-of-plane shear modulus of the unit cell. The analysis was performed by means of Monte Carlo simulations with Latin Hypercube sampling. The probabilistic sensitivities of the output parameter G^*_{ZY} show that, having set the significance level to 2.5%, only A_{TOP} is significant to the shear stiffness of the unit cell. For the sake of completeness, also the sensitivities of the effective in-plane shear modulus were evaluated. Here, both RI variables are significant, but A_{TOP} has a bigger impact (in terms of absolute values, the sensitivity to A_{TOP} is 0.96, while to A_{BASE} it is about 0.52). Therefore, for a certain value of added mass it is better to have a higher value of A_{TOP} rather than A_{BASE}, which means having the resin as uniformly distributed through the thickness as possible at the manufacturing level. Going back to figure 8b, the design point should be chosen in the left area to benefit the most of the insert's mass. For example, with $A_{TOP} = 1\,mm$ and $A_{BASE} = 0\,mm$ - cylindrical insert, added mass of 18.5% - G^*_{ZY} is $0.642\,GPa$, corresponding to an increase in the shear modulus value of about 43% with respect to the base configuration.

4 Shear transition frequency design space

While in the previous section the design area of the insert's geometry was defined in function of an arbitrary maximum value of percentage of added mass, from the shear transition frequency standpoint the relative importance between the added mass and the increase in the shear stiffness has to be considered. Therefore, in this section a new design space will be defined in terms of the material to adopt for the insert, according to the transition frequency requirements.

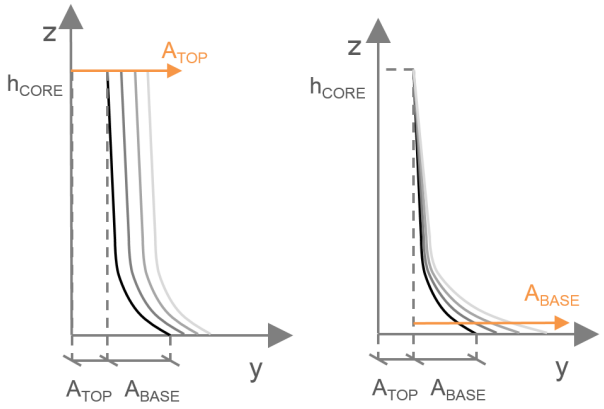
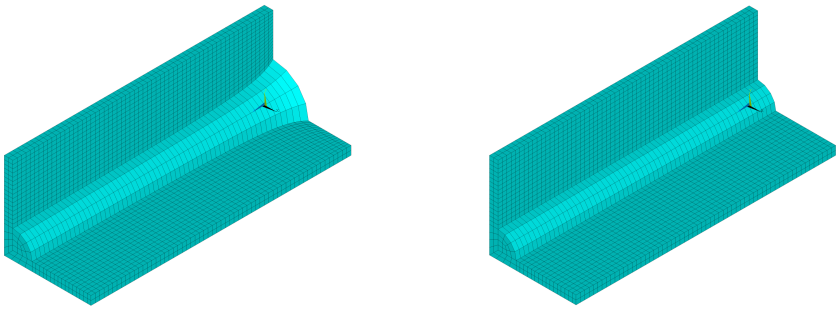


Figure 5: Hyperbolic insert's characteristic dimensions



(a) $A_{TOP} = A_{BASE} = 1$ *mm* (b) $A_{TOP} = 1$ *mm*, $A_{BASE} = 0$ *mm*

Figure 6: Insert configuration - FE model of one-quarter unit cell in case of hyperbolic and cylindrical profiles

4.1 Guillaumie's formulation

Guillaumie's work [7] provides an exact analytical expression for the transition frequency, derived using the inverse infinite mechanical impedance of the sandwich panel.

The global bending and shear impedances can be respectively written as:

$$(Z_\infty^D)^{-1} = \frac{1}{8\sqrt{D\rho_P}}; \tag{4}$$

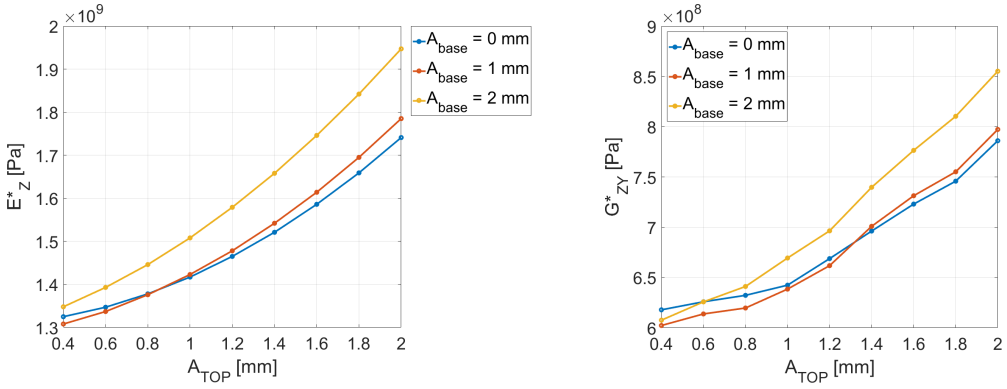
$$(Z_\infty^S)^{-1} = \frac{\omega}{4S}, \tag{5}$$

which are the inverse infinite mechanical impedances below and above the shear transition frequency. Therefore, equating (4) and (5) it is possible to find the exact formulation for the first transition frequency,

$$f_t = \frac{S}{4\pi}\sqrt{\frac{1}{\rho_P D}} \tag{6}$$

where,

$$S = G_{ZY}^* h_{core}\left(1 + \frac{h_{skin}}{h_{core}}\right)^2 \tag{7}$$



(a) *Effective tensile modulus* (b) *Effective shear modulus*

Figure 7: Insert configuration - Effective out-of-plane mechanical properties of the unit cell

is the equivalent shear modulus of the sandwich panel, G^*_{ZY} is the effective out-of-plane shear modulus of the core, h_{skin} and h_{core} are the thicknesses of the face-sheets and the core respectively, and ρ_P the mass per unit area [8];

$$D \approx \left(\frac{h_{core}^2}{2} h_{skin} + h_{core} h_{skin}^2 + \frac{2}{3} h_{skin}^3 \right) \frac{E_{skin}}{1 - \nu_{skin}^2} \tag{8}$$

is the equivalent isotropic behaviour bending stiffness of the sandwich panel. For standard sandwich panels, the bending stiffness is mainly given by the skins contribution and it can be calculated approximately with the expression as above. However, in the present case it was necessary to verify that this assumption was still valid, given the increase in the core's effective out-of-plane Young Modulus due to the inserts. The bending matrix of a sandwich panel with isotropic skins and orthotropic core can be written as:

$$D = \begin{pmatrix} D_{11} & D_{12} & D_{16} \\ D_{21} & D_{22} & D_{26} \\ D_{61} & D_{62} & D_{66} \end{pmatrix}$$

where the coefficients can be written in their exact formulations as:

$$D_{11} = \left(\frac{h_c^2}{2} h_s + h_c h_s^2 + \frac{2}{3} h_s^3 \right) \frac{E_s}{1 - \nu_s^2} + \frac{h_c^3}{12} \frac{E_x^c}{(1 - \nu_{xy}^c \nu_{yx}^c)}, \tag{9}$$

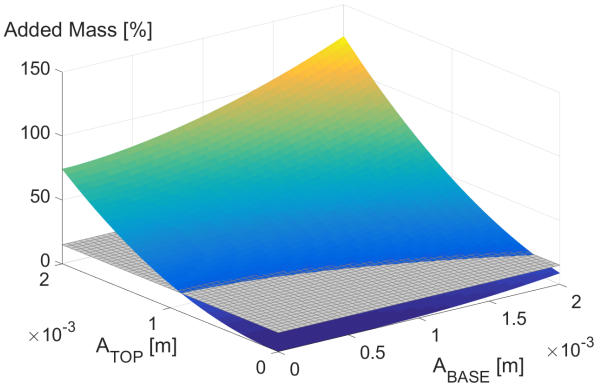
$$D_{22} = \left(\frac{h_c^2}{2} h_s + h_c h_s^2 + \frac{2}{3} h_s^3 \right) \frac{E_s}{1 - \nu_s^2} + \frac{h_c^3}{12} \frac{E_y^c}{(1 - \nu_{xy}^c \nu_{yx}^c)}, \tag{10}$$

$$D_{12} = \left(\frac{h_c^2}{2} h_s + h_c h_s^2 + \frac{2}{3} h_s^3 \right) \frac{\nu_s E_s}{1 - \nu_s^2} + \frac{h_c^3}{12} \frac{\nu_{xy}^c E_x^c}{(1 - \nu_{xy}^c \nu_{yx}^c)}, \tag{11}$$

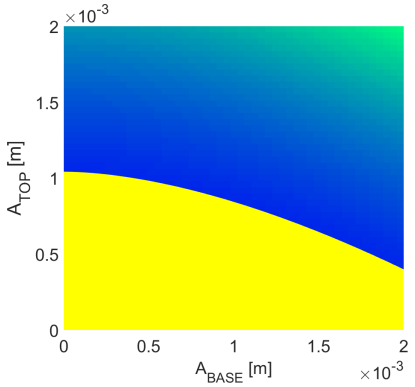
$$D_{66} = \left(\frac{h_c^2}{2} h_s + h_c h_s^2 + \frac{2}{3} h_s^3 \right) G_s + \frac{h_c^3}{12} G_{xy}^c. \tag{12}$$

in which the subscript s indicates the mechanical properties of the isotropic skins, and c the effective mechanical properties of the honeycomb core's unit cell. For all the coefficients, the increment with respect to the base configuration's value was evaluated as:

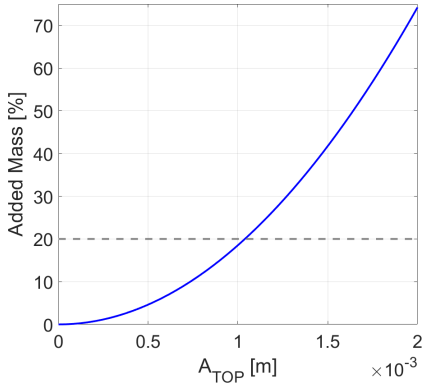
$$\Delta D_{ij} = \frac{D_{ij,\,ins} - D_{ij,\,bas}}{D_{ij,\,bas}} * 100.$$



(a) *Added mass vs insert's dimensions.*



(b) *Design space for a maximum added mass of* 20%



(c) *Cylindrical insert*

Figure 8: Added mass design space.

Considering isotropic alluminium skins - $E_s = 68.9\,GPa$, $\nu = 0.33$ - with a thickness $t_s = 1\,mm$ and cylindrical inserts:

$$\Delta D\,[\%] = \begin{pmatrix} 0.174 & 0.0012 & 0 \\ 0.0012 & 0.174 & 0 \\ 0 & 0 & 0.263 \end{pmatrix}$$

The increments are very small and can be neglected.

4.2 Effect of the insert on f_t

From equation (6), it is immediate to see that the transition frequency depends on both the effective out-of-plane shear modulus and the mass per unit area of the sandwich panel, ρ_P. Therefore,

$$\bar{f}_t = \frac{f_t}{f_{t,\,base}} = \frac{1 + \frac{\Delta S}{S_{bas}}}{\sqrt{1 + \frac{\Delta m_s}{m_{s,\,bas}}}}. \tag{13}$$

In equation (13), $\Delta S/S_{bas} = \Delta G^*_{zy}/G^*_{zy,\,bas}$ is evaluated from the results of numerical simulations of out-of-plane shear tests on the honeycomb's unit cell and Δm_s changes as the insert's area does.

Figure 9 shows $\bar{f}_t$ in function of the insert's thickness and stiffness for a cylindrical insert ($A_{BASE} = 0$).

It is immediate to observe that:

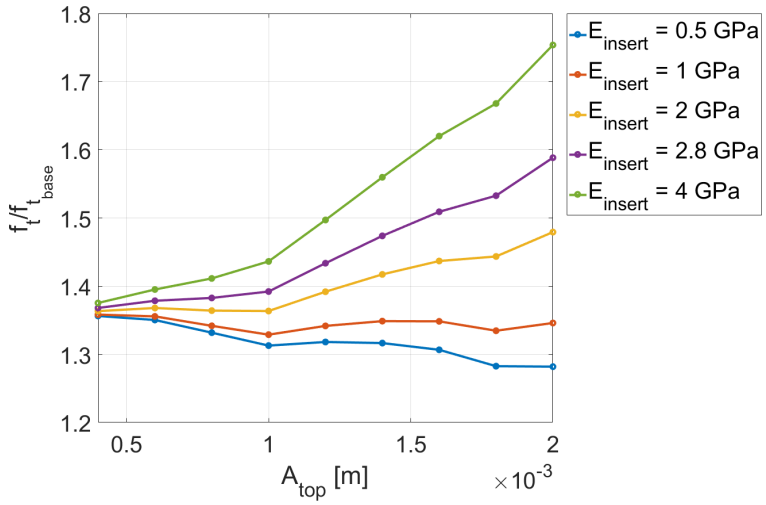


Figure 9: Transition frequency ratio in function of the insert's dimension and stiffness.

1. in the selected ranges of values, the transition frequency in presence of the inserts is always higher than the one given by the base configuration - $\bar{f}_t > 1$;
2. for small values of Young Modulus of the resin, as the insert's thickness increases the transition frequency becomes smaller, and this is due to the fact that $\sqrt{\Delta m_s}$ has a bigger impact on $\bar{f}_t$ than the shear stiffness term.

Therefore, once selected a resin with a sufficiently high stiffness, the shear transiton frequency is higher than the one in the base configuration and the bigger the insert's dimensions the better performances at the vibroacoustic level.

4.3 Analytic prediction of the insert's material effective properties

A solution to obtain the second type of behaviour just described is reinforcing the resin with Carbon Nanotube (CNT) inclusions. For random orientation of the CNTs, the effective Young's Modulus of the composite material E_{insert} can be expressed according to [9] as:

$$\frac{E_{insert}}{E_{resin}} = \frac{3}{8}\left[\frac{1+\zeta\eta_L V_{NT}}{1-\eta_L V_{NT}}\right] + \frac{5}{8}\left[\frac{1+2\eta_T V_{NT}}{1-\eta_T V_{NT}}\right] \tag{14}$$

and the so-called reinforcement dE_{insert}/dV_{NT} - in the assumption of small V_{NT} and $E_{insert} >> E_{resin}$ - as [10]:

$$\frac{dE_{insert}}{dV_{NT}} \approx \frac{3}{8}E_{resin}\eta_L(\zeta+1) + \frac{15}{8}E_{resin} \tag{15}$$

where:

$$\eta_L = \frac{E_{eff}/E_{resin} - 1}{E_{eff}/E_{resin} + \zeta}, \tag{16}$$

$$\eta_T = \frac{E_{eff}/E_{resin} - 1}{E_{eff}/E_{resin} + 2}, \tag{17}$$

$$\zeta = \frac{2L}{D}. \tag{18}$$

In the previous formulations, L and D are the length and outer diameter of the nanotubes respectively, E_{resin} is the matrix Young's Modulus and V_{NT} is the filler volume fraction, which can be expressed in function of the weight fraction w_{NT} through the CNTs and matrix densities, as:

$$V_{NT} = \left[\frac{\rho_r}{w_{NT}} - \rho_r + 1\right]^{-1};$$

$$\rho_r = \frac{\rho_{NT}}{\rho_{resin}}.$$

Finally, E_{eff} is the Young's Modulus of an equivalent effective fibre, which can be expressed according to [11] as:

$$E_{eff} = \frac{4t}{D} E_{NT}, \tag{19}$$

being t and E_{NT} respectively the wall's thickness and the Young's Modulus of the nanotubes .

4.4 Single-Walled Nanotubes

In case of Single-Walled Nanotubes (SWNTs), the wall's thickness was assumed to be $0.34\,nm$, the outer diameter $1\,nm$, the inner diameter $D-2t$, the CNT length $10\,\mu m$ and the Young's Modulus $1\,TPa$. According to [11], the nanotube density can be calculated as:

$$\rho_{NT} = \frac{\rho_g(D^2 - D_i^2)}{D^2}$$

being ρ_g the density of fully dense graphite, $2.25\,g/cm^3$.

With these assumptions, the Young's Modulus of the material composite and the reinforcement were calculated in function of the nanotubes volume fraction and the stiffness of the matrix - figures 10a and 10b, Y_C is the effective Young Modulus of the insert, so far indicated as E_{insert}.

4.5 Multi-Walled Nanotubes

In case of Multi-Walled Nanotubes (MWNTs), the outer layer thickness was still assumed to be $0.34\,nm$ and the length $10\,\mu m$, but this time an outer diameter of $15\,nm$ and an inner one of $5\,nm$ were assigned, and therefore a value of ρ_{NT}/ρ_{resin} of 1.74. The effective Young's Modulus and reinforcement of the composite material are shown in figures 10c and 10d.

Comparing the graphs, it is possible to notice how, in case of adoption of MWNTs, a higher filler volume fraction is needed to have a consistent increase in the Young Modulus of the composite material. In fact, its elastic properties are very sensitive to the nanotube diameter, since the larger the outer diameter is (i.e. the more layers it is made of) the lower the effective modulus is - [11], [12].

5 Design procedure

Putting together the content of the previous sections, a whole design procedure for the insert was developed. In fact, according to the requirements in terms of added mass and transition frequency it is possible to design the insert in terms of both geometry and material (i.e. resin and CNTs content).

Step zero is the assumption of a certain material for the insert. All the curves and surfaces are plotted assuming a certain initial value for the density of the insert's material, while its Young Modulus intervenes

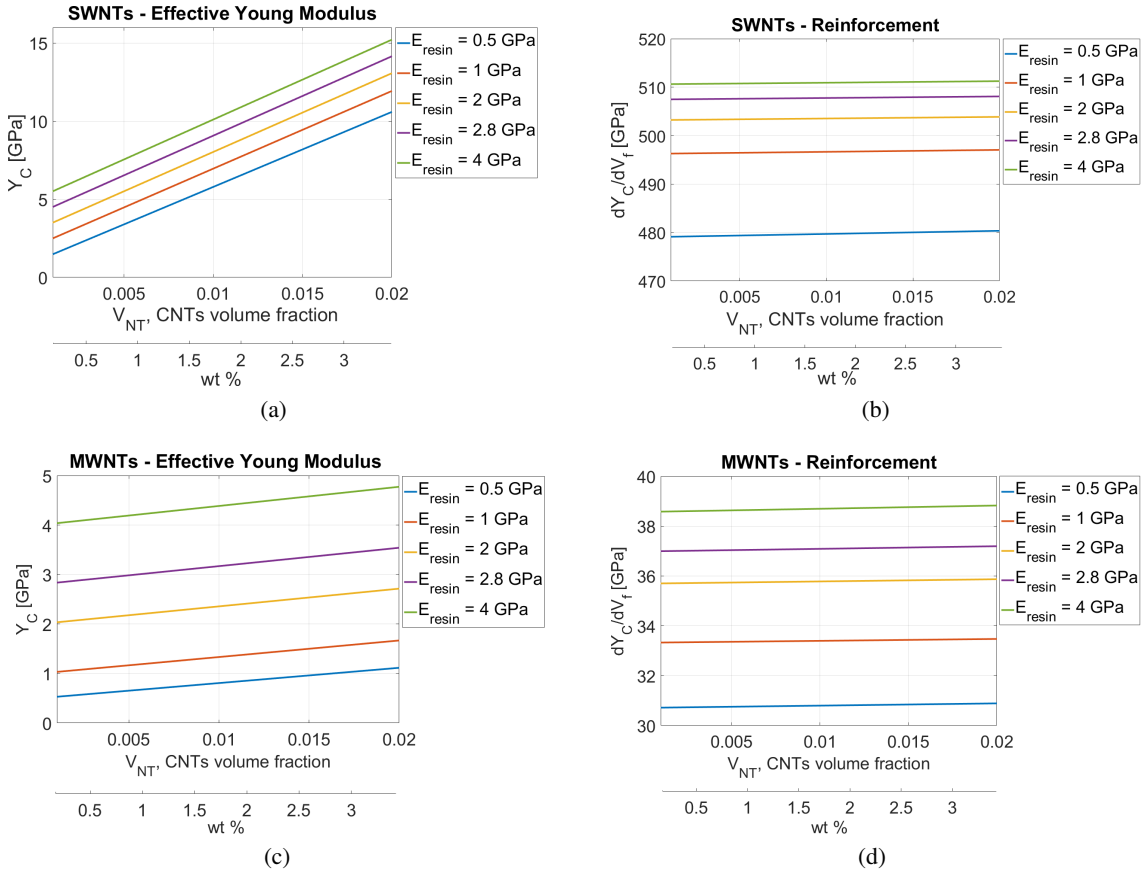


Figure 10: Effective Young Modulus and Reinforcement of the composite material - SWNTs and MWNTs

as a parameter only in the curves of E_{insert} in function of the filler volume fraction. Once an initial value of ρ_{resin} has been assumed, the following steps can be carried out.

1. First of all, choosing a design point in the space of the added mass in function of the geometric parameters, A_{TOP} and A_{BASE}. For example, a cylindrical insert - $A_{BASE} = 0\,mm$ and $A_{TOP} = 1.0\,mm$ with an added mass of $m_{add} = 18.5\%$ ($m_{insert} = 0.0542\,gr$, $m_{walls} = 0.292\,gr$) - figure 8b;

2. Secondly, establishing the increment in terms of transition frequency that is expected. For example, $\bar{f}_t = 1.4$ - 40% increment. In this case, with the geometry been set in the previous step, the Young's Modulus of the insert material should be $\sim 3\,GPa$ - figure 9;

3. Last step consists in evaluating different possible combinations of V_{NT} and E_{resin} that give such value of E_{insert}. In this case, very different solutions can be found in case of single-walled and multi-walled nanotubes - figure 10.

Once the material has been defined in terms of matrix stiffness and filler volume fraction, the composite material's density needs be calculated again and all the curves have to be updated in function of the new density value. Therefore, the procedure should be iterated till convergence considering updated curves.

However, while the insert's density effect on the added mass surface is definitely not negligible, it is not a significant variable to the shear stiffness of the panel, as PDS simulations with the insert's density as RI variable showed. Moreover, the transition frequency curves come from numerical parametric simulations so the computational and time costs would be very high if they had to be updated at each iteration. Therefore, they are kept constant even considering different values of ρ_{insert}.

Conclusions

In this paper, a procedure for the design of CNT-reinforced viscoelastic inserts for sandwich panels has been developed. Beyond the increase in the panel's toughness and strain energy dissipation due to the strategic location of the depositions at the walls junctions, the inserts provide improved vibroacoustics performances in terms of increase in the panel's characteristic shear transition frequency. However, not all configurations are convenient to adopt, as the increase of the core's shear stiffness is opposed by the augmented mass. Therefore, in order to have an increment in the transition frequency that also increases with the insert's dimension, there is a minimum value of Young's Modulus that the resin needs to have and this is one of the reasons why Carbon Nanotubes are adopted as a filler. The final design procedure takes into account the limits in terms of added mass, increment in the transition frequency and minimum value of the composite material Young's Modulus to define the inserts in terms of both geometry and material.

Acknowledgements

This work is part of a project that has received funding from the European Unions Horizon 2020 research and innovation programme under the Marie Skodowska-Curie grant agreement No 675441.

References

[1] F. Fahy, P. Gardonio, *Sound and Structural Vibration: Radiation, Transmission and Response*, Academic Press, second edition (2007).

[2] Z. Zergoune, M. Ichchou, O. Bareille, B.Harras, R. Benamar, B.Troclet, *Assessments of shear core effects on sound transmission loss through sandwich panels using a two-scale approach*, Computers & Structures, Vol. 182 (2017), pp. 227 - 237.

[3] O. Baho, Z. Zergoune, M. Ichchou, B. Harras, R. Benamar, B. Troclet, O. Bareille, *On global bending-shear core transition effects for the vibroacoustics of sandwich structures: Analytical and numerical investigations*, Composite Structures, Vol. 154 (2016), pp. 453 - 463.

[4] C. Droz, Z. Zergoune, R. Boukadia, O. Bareille, M. Ichchou, *Vibro-acoustic optimization of sandwich panels using the wave/finite element method*, Composite Structures, Vol. 156 (2016), pp. 108 - 114.

[5] G. Petrone, S. Rao, S. De Rosa, B.R. Mace, F. Franco, D. Bhattacharyya, *Initial experimental investigations on natural fibre reinforced honeycomb core panels*, Composites: Part B, Vol. 55 (2013), pp. 400 - 406.

[6] V. Salit, T. Weller, *On the feasibility of introducing auxetic behavior into thin-walled structures*, Acta Materialia, Vol. 57, Issue 1 (2009), pp. 125-135.

[7] L. Guillaumie, *Vibroacoustic flexural properties of symmetric honeycomb sandwich panels with composite faces*, Journal of Sound and Vibration, Vol. 343 (2015), pp. 71-103.

[8] K. Renji, P. S. Nair, *Modal density of composite honeycomb sandwich panels*, Journal of Sound and Vibration, Vol. 195(5) (1996), pp. 687 - 699.

[9] J. C. Halpin, S. W. Tsai, *Environmental factors in composite material design*, US Air Force Materials Laboratory Report (1969), AFML-TR 67 - 423.

[10] J. N. Coleman, U. Khan, W.J. Blau, Y.K. Gun'ko *Small but strong: A review of the mechanical properties of carbon nanotube-polymer composites*, Carbon, Vol. 44 (2006), pp. 1624 -1652.

[11] E. T. Thostenson, T. Chou, *On the elastic properties of carbon nanotube-based composites: modelling and characterization*, Journal of Physics D: Applied Physics, 36 (2003), pp. 573 - 582.

[12] Z. Tu, Z. Ou-Yang, *Single-walled and multiwalled carbon nanotubes viewed as elastic tubes with the effective Youngs moduli dependent on layer number*, Physical Review B, Vol. 65, 233407 (2002).

A load approximation for the vibroacoustic analysis of periodic structures to fluid excitation

F. Errico [1,2]**, M. Ichchou** [1]**, S. De Rosa** [2]**, O. Bareille** [1] **and F. Franco** [2]
[1] Laboratoire de Tribologie et Dynamique des Systémes, Ecole Centrale de Lyon, cully, 69134, France
e-mail: **fabrizio.errico@ec-lyon.fr**

[2] Pasta-Lab, Dipartimento di Ingegneria Industriale Sezione Aerospaziale - Universitá degli Studi di Napoli Federico II, Napoli, 80125, Italy

Abstract
Existing methods for the calculation of acoustic indicators, starting from periodic cells, are limited to very specific excitations. The present work investigates and validates a load approximation to deal and interface the periodic cell scale with more general stochastic and spatially-correlated loads. The method approximates the load using a summation of surface waves of aleatory amplitude and inclination, acting on the surface of the structure. The only required information is given by the wavemunber spectrum of the excitation desired: diffuse acoustic field (DAF) and turbulent boundary layer excitations (TBL) are considered within the present work. The load matrix, built using direct methods and the proposed approximation, is compared and used for the calculation of the sound radiation of finite and infinite panels subjected to stochastic load. A validation is performed with analytic and numerical results correlated and uncorrelated loads.

1 Introduction

Sandwich composite structures are used in modern aerospace as well as in the automotive, naval and civil industry because they are lighter and stronger than most advanced alloys. The anisotropy of such structures can be modelled by changing the geometry of the core, obtaining different wave propagation properties. However, these structures are also known for having poor vibroacoustic performances and, often, these can result in higher interior noise levels. At the same time, high computational costs arise, from the point of view of the numerical simulations, when sandwich panels are analysed using classical models as, for example, the finite element method (FEM). Some FEM applications for the vibroacoustic analysis of simple structures, under random aeroacoustic loads, are present in literature [1, 2, 3, 4].

An efficient alternative in terms of computational cost is, for example, the transfer matrix method (TMM). It is a general method used for the prediction of the propagation of monochromatic plane waves in planar and multi-layered structures of infinite extent in the lateral direction [5, 6, 7]. Finite size effects, important at low frequencies, can be included through appropriate corrections, leading to a broadband accuracy of the method [8, 9].

Alternatively, the wave finite element method (WFE), specifically for homogeneous and periodic structures, allows the modelling of just a single repetitive cell, applying the periodicity conditions for a correct description of the entire (infinite) waveguide [10, 11, 12, 13]. The use of finite elements, for the cells description, gives the possibility to describe any type of complex structural shape. The use of the WFEM for the sound transmission of periodic sandwich panels has been validated by many authors, under acoustic load [14, 15].

Periodic structures and meta-materials, on the other hand, can be used as frequency-selecting structures. The related waveguides, because of their complex shapes, require a higher computational cost for an accurate

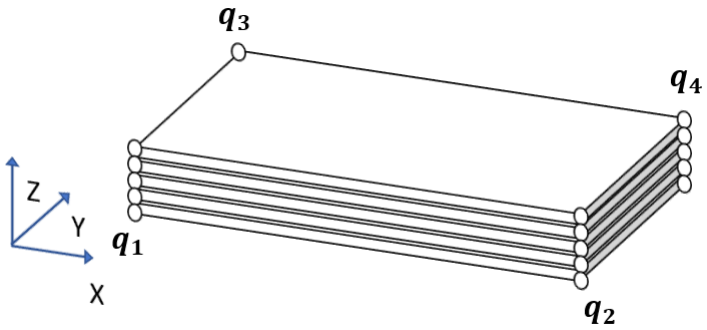


Figure 1: Example of a FE cell model with periodicity along the X-Y directions.

numerical simulation. In addition, the knowledge and the modelling of the correct operating conditions are fundamental in automotive and aerospace applications. For example, whenever a convective flow is present, boundary layer models should be included [16]. None of the models in literature, at this stage, allows the analysis of complex structural periodic shapes, under aeroacoustic excitations. The novelty of the present paper stands in overcoming these limits proposing a methodology for dealing with a wide range of industrially relevant case-studies. The method, thus, can be used as a tool for the analysis and the design of periodic complex structures under more realistic operating conditions, for example, superimposing boundary layer and acoustic excitations.

The paper is structured as follows: Section 2 and 3 presents the load approximation proposed and the wavenumber integration process, to take into account a general fluid excitation; Sections 4 and 5 show the numerical and experimental validations both for acoustic and aerodynamic load.

2 The Wave Finite element Method

A 2D periodic structure is composed by an assembly, along two arbitrary directions, of identical elementary cells. Using any FE commercial code, the mass and stiffness matrices of the cell, whenever complex, can be extracted and post-processed. With reference to Fig. 1, the dynamic stiffness equation of the segment can be written as:

$$[\mathbf{K} - \omega^2 \mathbf{M}]\mathbf{q} = \mathbf{D}\mathbf{q} = \mathbf{f} + \mathbf{e} \tag{1}$$

where **q**, **f** and **e** are respectively the nodal vectors of degrees of freedom (DoFs), internal and external forces; **K**, **M** and **D** are the stiffness, mass and dynamic stiffness matrices. Damping can be modelled by including, in Eq. 1, appropriate complex matrices and coefficients. Hereby, it is assumed that the vectors and matrices are ordered following the same sequence of the DoFs nodal vector: $\mathbf{q} = [\mathbf{q}_1, \mathbf{q}_2, \mathbf{q}_3, \mathbf{q}_4]$. The wave motion through a periodic media can be analysed by imposing the Bloch-Floquet conditions [10, 11] to the finite element (FE) of a periodic cell, assuming time and space harmonic excitation. The periodicity conditions are translated in complex propagating constant for each wave type. Displacements and forces at any point of the cell can be connected to the ones of a limited number of them, as follows:

$$\begin{bmatrix} \mathbf{q}_2 \\ \mathbf{q}_3 \\ \mathbf{q}_4 \end{bmatrix} = \begin{bmatrix} \mathbf{I}\lambda_X \\ \mathbf{I}\lambda_Y \\ \mathbf{I}\lambda_X\lambda_Y \end{bmatrix} \mathbf{q}_1 \tag{2}$$

with

$$\lambda_X = exp(-\mathrm{i}k_X L_X) \qquad \lambda_Y = exp(-\mathrm{i}k_Y L_Y) \tag{3}$$

where k_X and k_Y are wavenumbers of the propagating (or forcing) wave in the periodicity directions X and Y, while L_X and L_Y represent the cell lengths along the same directions. The matrix **I** is, instead, the

identity matrix. In a general form, thus, the total displacements and forces are connected to the reduced vectors (superscript r) through a periodicity matrix $\mathbf{\Lambda}$ (see Eq. 2):

$$\mathbf{q} = \mathbf{\Lambda}\mathbf{q}^r \qquad \mathbf{f} = -\mathbf{\Lambda}\mathbf{f}^r \qquad \mathbf{e} = -\mathbf{\Lambda}\mathbf{e}^r \tag{4}$$

Pre-multiplying Eq.1 by $\mathbf{\Lambda}^H$, where H stands for the hermitian operator, the dynamic stiffness matrix of the reduced model is given by Eq. 5.

$$\mathbf{D}^r = \mathbf{\Lambda}^H[\mathbf{K} - \omega^2\mathbf{M}]\mathbf{\Lambda}\mathbf{q}^r \tag{5}$$

At this stage, different eigenvalue problems can be solved, if the target is the estimation of the dispersion curves of the periodic structure, [12, 17]. The use of modal reduction is highly suggested for very fine meshes. In these cases, the internal degrees of freedom are substituted by the modal participation factors [17, 18].

2.1 Fluid-Structure Coupling

Let us assume a plane wave impinging on one face of the structure, with an amplitude p_I. The structure, as a result, transmits and reflects waves in the fluid adjacent to the top and bottom surfaces. On the excited side (subscript 1), the sound field is the superposition of the incident and reflected acoustic waves, while, in the receiver side (subscript 2), it is given by the transmitted waves.

Assuming the X-Y as the plane of reference (1 as example), an incident acoustic pressure wave can be defined, on the surface of the cell, omitting the time harmonic dependence, as:

$$p_I \mathrm{e}^{-\mathrm{i}(k_X X + k_Y Y - k_{Z,1} Z)}. \tag{6}$$

The reflected and transmitted pressure waves are, instead, given by:

$$\begin{array}{c} p_R \mathrm{e}^{-\mathrm{i}(k_X X + k_Y Y - k_{Z,1} Z)} \\ p_T \mathrm{e}^{-\mathrm{i}(k_X X + k_Y Y - k_{Z,2} Z)}. \end{array} \tag{7}$$

The wavenumber components k_X and k_Y are conserved along the structure and the only parameter which can vary with the nature of the fluid (and the excitation) is the k_Z component, derivable using the Helmholtz equation. Assuming a forced displacement field of the same nature, then, from continuity of the normal particle velocity on the excited and radiating surfaces, the dynamic stiffness of the fluids can be derived.

$$\begin{array}{rr} \rho_1\omega^2 q_{in} = \dfrac{\partial(p_I - p_R)}{\partial z}; & D_{f,1} = \dfrac{-\mathrm{i}\rho_1\omega^2}{k_{Z,1}} \\ \rho_2\omega^2 q_{rad} = \dfrac{\partial(p_T)}{\partial z}; & D_{f,2} = \dfrac{-\mathrm{i}\rho_2\omega^2}{k_{Z,2}} \end{array} \tag{8}$$

where ρ_1 and ρ_2 are the fluid densities, q_{in} and q_{rad} are the out-of-plane displacements and $D_{f,1}$ and $D_{f,2}$ the dynamic stiffness of the fluid in the incident and radiating domains, respectively. The load imposed on the plate, by the forcing surface waves of trace wavenumbers k_X and k_Y, can be derived from the two pressure fields, on both sides of the structure; it is lumped on the wetted nodes of the finite element model. As the forces act normal to the surfaces, the only excited degrees of freedom are the ones connected to the out-of-plane displacements. Consistent nodal forces can be calculated as follows:

$$e^r = S(p_I + p_R)q_{in} - S(p_T)q_{rad} \tag{9}$$

where S is the free nodal surface, p_I, p_R and p_T are the nodal pressure vectors, from Eqs. 6 and 7. A finer way to calculate consistent nodal forces, requires, however, the knowledge of the shape functions associated

with the out-of-plane displacements [15]. Exploiting the relationships in Eq. 8 in Eq. 9, the final system results in:

$$\mathbf{D}_S\mathbf{q}^r = \left[\mathbf{D}^r + \left(D_{f,1}\mathbf{w}_{in} + D_{f,2}\mathbf{w}_{rad}\right)\mathbf{S}\mathbf{\Lambda}^H\mathbf{\Lambda}\right]\mathbf{q}^r = 2p_I\mathbf{S}\mathbf{w}_{in}\mathbf{\Lambda}^H\mathbf{\Lambda} \tag{10}$$

where $\mathbf{w}_{in}$ and $\mathbf{w}_{rad}$ are the coupling matrices that give $\mathbf{q}_{in}$ and $\mathbf{q}_{rad}$ from multiplication with $\mathbf{q}^r$.

The algebraic system can be solved in $\mathbf{q}^r$ and Eq. 8 used to obtain the transmitted pressure. The power transmission coefficient τ associated with the couple of forcing wavenumbers k_X and k_Y is thus calculated:

$$\tau(k_X, k_Y) = \frac{(k_{Z,2}/\rho_2)\mathbf{S}|\mathbf{p}_T^2|}{(k_{Z,1}/\rho_1)\mathbf{S}|\mathbf{p}_I^2|}. \tag{11}$$

Finite size effects, can be included through correction factors, in order to increase the accuracy at low frequencies. While a formal and accurate spatial widowing approach is present in literature [8], the computational cost associated with this step might be high. For this reason, even losing some accuracy in the low frequency regime, the use of asymptotic formulas, as in [9], is here used to reduce the computational cost.

3 Stochastic Load Translation into Surface Waves

The sound transmission to plane wave excitation, as discussed in Sec. 2, is not sufficient for many applications. Herein, a method, to take into account a general type of excitation, is proposed. The idea is to use a forcing surface wave excitation for each couple of forcing wavenumbers k_X and k_Y, able to represent the desired excitation, once its wall pressure spectra in the wavenumber domain, is known. Using a vectorial form a sum of wall waves can be written as:

$$P(\bar{X}, \omega) = \sum_{j=1}^{N_W} A_j \mathrm{e}^{-\mathrm{i}\bar{K}_j \times \bar{X}}. \tag{12}$$

where $\bar{X}$ stands for the surface coordinates $X - Y$, $\bar{K}_j$ is the wavenumber vector associated with each wall surface wave of amplitude A_j, and N_W is the total number of waves constituting the pressure field. It is worth recalling that the surface coordinates can be global or local coordinates.

The description of the desired load needs the proper values of $\bar{K}_j$ and A_j (Eq. 12). They are obtained by equating the wavenumber spectra ϕ_{PP}, of the pressure field (Eq. 12), with the one of the fluid excitation model desired, Φ_{PP}, for a specific fluid wavenumber $\bar{K}$. Many fluid excitation models are investigated in the wavenumber domain in literature [19]. The cross correlation of the pressure field P is:

$$R_{PP}(\Delta\bar{X}_1, \Delta\bar{X}_2, \omega) = \sum_{j=1}^{N_W} A_j^2 \mathrm{e}^{-\mathrm{i}\bar{K}_j(\Delta\bar{X}_1 - \Delta\bar{X}_2)} + \sum_{j=1}^{N_W}\sum_{n=1;n\neq j}^{N_W} A_j A_n \mathrm{e}^{-\mathrm{i}(\bar{K}_j\Delta\bar{X}_1 - \bar{K}_n\Delta\bar{X}_2)} \tag{13}$$

where the auto and cross correlations have been divided in two different summations. Performing the Fourier transform of Eq. 13, the wavenumber spectra is obtained. Moving from summations to integrals, for sake of manageability of the Dirac functions, the final expression of ϕ_{PP} is the one of Eq. 14. The second term in Eq. 14 can be erased since, by definition, the correlation indices j and n must be different.

$$\begin{aligned}\phi_{PP}(\bar{K}, \omega) = \Phi_{PP}(\bar{K}, \omega) = \int 4\pi^2 \frac{A_j^2}{\Delta\bar{K}_j}\delta(\bar{K}_j - \bar{K})d\bar{K}_j \\ + \int\int 8\pi^4 \frac{A_j A_n}{\Delta\bar{K}_j\Delta\bar{K}_n}\delta(\bar{K}_j - \bar{K})\delta(\bar{K}_n - \bar{K})d\bar{K}_j d\bar{K}_n\end{aligned} \tag{14}$$

For each forcing k_X and k_Y, the desired loading model is simulated through the following surface wave:

$$P_W(X, Y, \omega) = \sqrt{\frac{\Phi_{PP}(k_X, k_Y, \omega)\Delta k_X \Delta k_Y}{4\pi^2}}\mathrm{e}^{-\mathrm{i}(k_X X + k_Y Y)}. \tag{15}$$

In conclusion, at each frequency and for each wavenumber of the fluid excitation model, a surface wave of specific wavenumbers and amplitudes can be used to simulate the load. No hypothesis on the correlation of the forcing waves is imposed as for the reference coordinates. The proposed approximation is thus valid for correlated and uncorrelated loads acting on the external surfaces, independently on the structural complexity.

3.1 Sound Transmission Loss

In order to simulate the sound transmission for a specific excitation, an integration of the transmission coefficient is performed, in the wavenumber domain. Thus, the total transmission coefficient can be calculated as follows:

$$\tau_{TOT}(\omega) = \frac{\int\int \tau(k_X, k_Y) \times W_A(k_X, k_Y, \omega) dk_X dk_Y}{\int\int W_A(k_X, k_Y, \omega) dk_X dk_Y} \tag{16}$$

where $\mathbf{W}_A$ is the matrix of the normalized amplitude function, of the wall surface waves, for all the wavenumber couples involved in the integration process. Within the framework of sound transmission, as identifiable from Eq. 11, the variation of waves amplitudes does not have an influence. The difference among different fluid loads is given by the integration. The choice of the integration limits can be changed depending on the type of load to be described. For example, for a diffuse acoustic field, at each frequency step, the wavenumber spectra Φ_{PP} is null outside the acoustic border, so, there is no need for the use of higher integration limits. The final transmission loss is, by definition:

$$TL(\omega) = -10 \log_{10}(\tau_{TOT}(\omega)) \tag{17}$$

The great advantage of the present approach relies in its generality and applicability to a wide range of test-cases both in terms of structural shapes and excitation models. The wall surface wave approximation releases the constraints to the plane waves angles of incidence, generally implied in literature.

4 Validation for Diffuse Field Transmission

In this section, using a diffuse acoustic excitation, some comparisons are presented for validation purposes, using well-established literature methods as a reference. In Fig. 2, a first comparison among the proposed method and the one of Christen et al., is shown [14]. The analysed sample is a $3\mathrm{mm}$ thick flat sandwich panel made of aluminium skins and isotropic core (E = 3 GPa, ν = 0.2, ρ = 48 $\mathrm{Kg/m^3}$). The cell is modelled using four ANSYS $HEXA-8$ elements through thickness and an excellent agreement is observed. Damping is set to 2%.

The second test-case proposed, in Fig 3, validates the method even for the case a fluid-structure interaction is present at the cell scale. A double glazing panel with two isotropic panes interconnected with an air cavity is considered, under a diffuse acoustic field. Each element is modelled using ANSYS $SOLID45$ elements for the structural part and $FLUID30$ elements for the fluid layers. Both the double wall resonance and the acoustic coincidence are correctly captured in frequency and amplitude. The comparison with the reference method ([14]), is total.

5 Validation for Boundary Layer Radiation and Transmission

The load approximation proposed in Sec.3, leading to Eq. 16, allows the simulation for loads of different nature. In this section, for example, the flow-induced transmission caused by turbulent boundary layer (TBL) excitation is considered since it is one of the main sources of radiated noise inside an aircraft cabin, in cruise flight conditions.

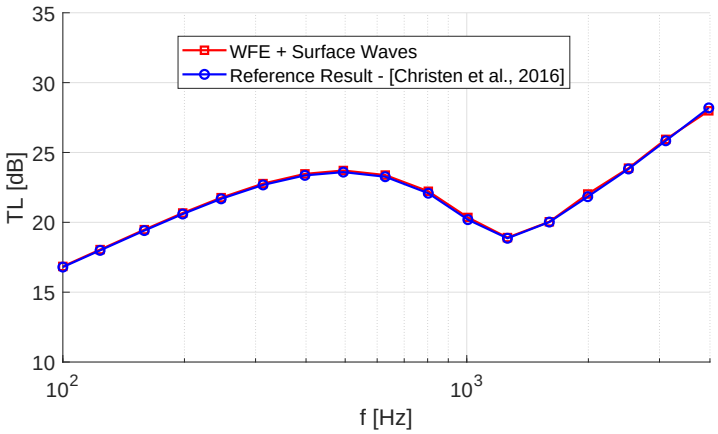


Figure 2: Transmission Loss comparison for a sandwich isotropic flat panel under diffuse acoustic field excitation

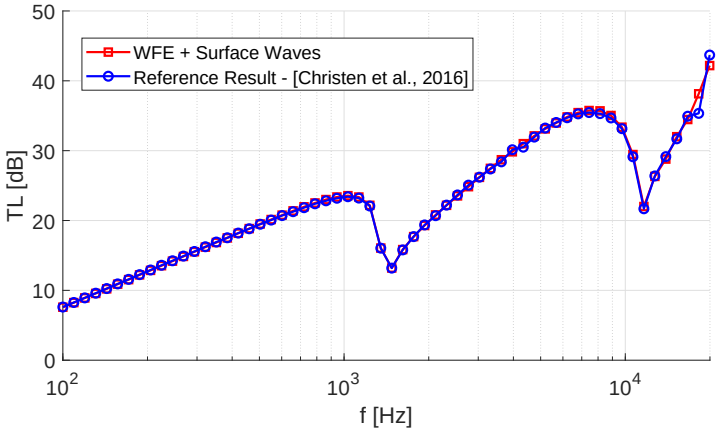


Figure 3: Transmission Loss comparison for double glazing panel under diffuse acoustic field excitation

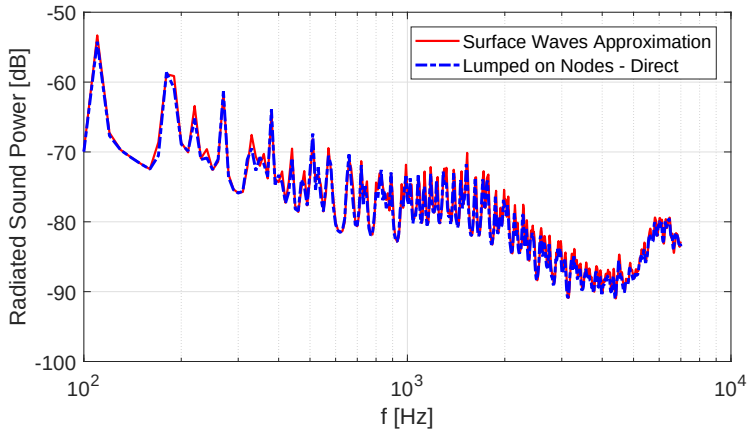


Figure 4: The radiated sound power of an isotropic plate under TBL excitation; numerical comparison using the proposed load approximation - U_c = 190 m/s; A = 0.8x0.55m^2

Many boundary layer models are proposed in literature; here, the characterisation of the wall pressure fluctuations proposed by Corcos is used [20]. No-gradients effects are considered and the TBL is assumed as fully developed. The wavenumber spectra, Φ_{PP}, proposed by Corcos, is here reported for completeness:

$$\Phi_{PP}(k_X, k_Y, \omega) = S_{pp}(\omega) \frac{4\alpha_X \alpha_Y}{\left[\alpha_Y^2 + \frac{U_c^2 k_Y^2}{\omega^2}\right]\left[\alpha_X^2 + \left(1 + \frac{U_c k_X}{\omega}\right)^2\right]} \tag{18}$$

where U_c is the convective flow speed, S_{pp} is the single-point auto spectral density of the wall pressure distribution. The stream-wise and cross-wise correlation coefficients, α_X and α_Y, are assumed to be 0.125 and 0.78, respectively, in all following test-cases. Since the boundary layer excitation represents a spatially-correlated random load, here, two different validations are proposed. First the sole load approximation will be tested, using, as a reference solution, the one calculated using a full stochastic FE method, as proposed, and validated, in many works in literature [3, 2]. In this first case the structural operator is described using the same approach, but the load matrices are build differently. In Fig. 4 the radiated power for a flat isotropic panel with simply-supported boundary conditions (edges), is compared using the surface waves approach and the classic one. The eigen-frequencies and the modal shapes of the reference panel are calculated using analytic solutions, while the load matrix is described using a direct method [3]. The agreement is very good broadband and both the aerodynamic and acoustic coincidences are properly described.

While the method proposed by Franco et al. ([3]) is used for the reference results, in a second test-case the whole procedure proposed in the present paper is used for the simulation of the sound transmission under boundary laer excitation. The incident power, for the transmission loss calculation, in the FEM cases (reference), is calculated using Eq. 19 as proposed in literature [6, 21]:

$$\Pi_{inc} = \frac{A S_{pp}(\omega)}{4\rho_1 c_1} \tag{19}$$

where A is the excited area and c_1 the speed of sound on the incident side. Even though a modal behaviour can not be described using the present method, Fig. 5 shows how the averaged TL are very well captured broadband. In both cases the aerodynamic and acoustic coincidences are at 1800 Hz and 6000 Hz. The finite size effects are accounted using a radiation efficiency formulation for flat panels, as proposed by Leppington [9]. Both the aerodynamic and acoustic coincidence are correctly identified, as the slopes in the acoustics and convective domains. As evident, the convective load induces a smoother and damped coincidence effect, with respect to the acoustic one.

The strong agreement in Fig.5, validates the proposed load approximation even for spatially-correlated random loads, as the TBL. It is worth underlying how the use of boundary layer excitation is here allowed even for infinite structures, differently from other methods in literature [6].

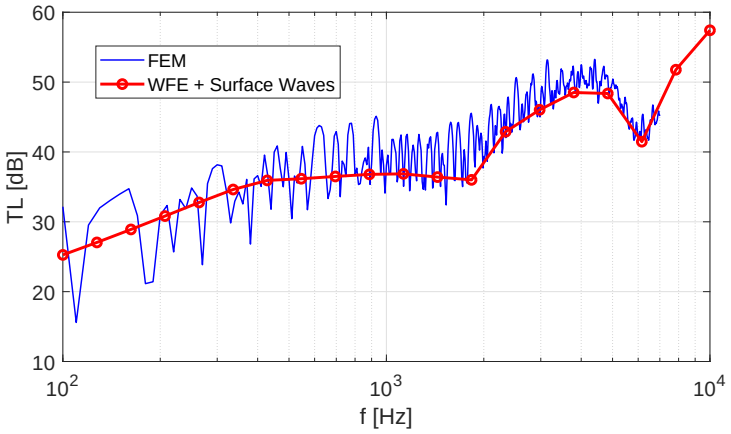


Figure 5: The transmission loss of an isotropic plate under TBL excitation; numerical comparison with full FEM method - U_c = 180 m/s; A = 0.7x0.5m^2

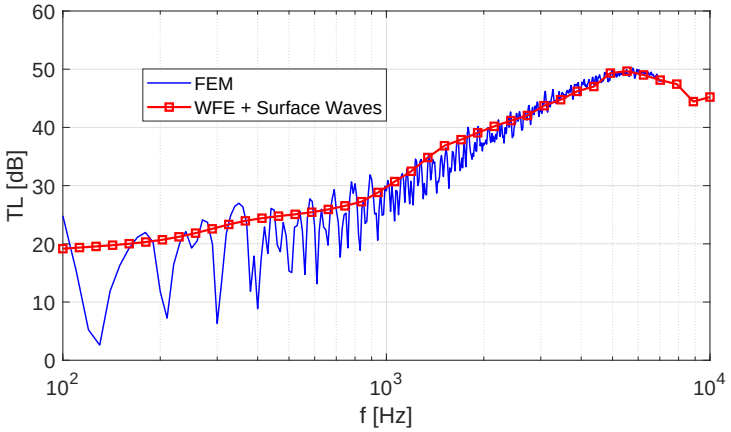


Figure 6: The transmission loss of an honeycomb sandwich plate under TBL excitation; numerical comparison with full FEM method - U_c = 152 m/s; A = 0.8x0.6m^2

Since much attention is placed on sandwich structures in many engineering areas, here, an honeycomb-cored sandwich panel is analysed under a turbulent boundary layer (Fig. 6). A Corcos model is used for the loading description and the proposed approximation into surface waves is used. The panel is made of $1\mathrm{mm}$-thick aluminium skins and a $10\mathrm{mm}$-thick hexagonal honeycomb core, homogenised in an equivalent isotropic model. Both the aerodynamic and acoustic coincidence are well predicted (Fig. 6). The first one is somewhat highly damped (700 Hz) while the second one is clearly visible (9 KHz). A full FEM calculation is used, again as a reference result.

6 Conclusions

This work proposes a numerical approach for the estimation of the sound transmission loss of complex flat periodic structures under any type of acoustic and aerodynamic load. The approach involves a wave-based method in a finite element framework, for the structural part, and proposes a load simulation into surface waves. The fluid-structure interaction is performed in analogy to the acoustic wave excitation, simulating the different forcing models, using a weighted wavenumber integration. The only requirement is the knowledge of the wavenumber spectra of the wall pressure fluctuation.

Finite size effects are accounted using the baffled window equivalence or asymptotic formulations, for flat

structures. Static and dynamic condensation can be applied if fine meshes are used in the modelling phase.

Both the accuracy and robustness of the present method are proved using analytic and well-established numerical references. Both uncorrelated (diffuse acoustic field) and spatially-correlated loads (turbulent boundary layer) are used for the validations. The convergence of the approach is assured by the one of the wavenumber integration process. The choice of the integration limits must be calculated on the base of the wavenumber spectra of the load. Moreover, the use of boundary layer excitation does not require the accounting of finite size effects and a comparison of the structural and acoustic design is possible, independently from the size of the analysed structure.

Acknowledgements

This project has received funding from the European Unions Horizon 2020 research and innovation programme under the Marie Sklodowska-Curie grant agreement No. 675441. The author would like to gratefully acknowledge everyone involved in the VIPER project. Dr. Giuseppe Petrone is acknowledged for the fruitful discussions.

References

[1] S. De Rosa, F. Franco, A scaling procedure for the response of an isolated system with high modal overlap factor, Mechanical Systems and Signal Processing 22 (2008) 1549–1565. doi:/10.1016/j.ymssp.2008.01.007.

[2] S. De Rosa, F. Franco, Exact and numerical responses of a plate under a turbulent boundary layer excitation, Journal of Fluids and Structures 24 (2008) 212–230. doi:/10.1016/j.jfluidstructs.2007.07.007.

[3] F. Franco, S. De Rosa, E. Ciappi, Numerical approximations on the predictive responses of plates under stochastic and convective loads, Journal of Fluids and Structures 42 (2013) 296–312. doi:/10.1016/j.jfluidstructs.2013.06.006.

[4] M. Ichchou, B. Hiverniau, B. Troclet, Equivalent rain on the roof loads for random spatially correlated excitations in the mid frequency range, Journal of Sound and Vibration 322 (2009) 926–940. doi:/10.1016/j.jsv.2008.11.050.

[5] J. Allard, N. Atalla, Propagation of sound in porous media: Modelling sound absorbing materials, John Wiley & Sonsdoi:/10.1002/9780470747339.

[6] N. Atalla, Modelling the sound transmission through complex structures with attached noise control materials, Wave Motion 51 (2014) 650–663. doi:/10.1016/j.wavemoti.2013.11.001.

[7] A. Parrinello, G. Ghiringhelli, Transfer matrix representation for periodic planar media, Journal of Sound and Vibration 371 (2016) 196–209. doi:/10.1016/j.jsv.2016.02.005.

[8] D. Rhazi, N. Atalla, A simple method to account for finite size effects in the transfer matrix method, J. Acoust. Soc. Am. 127 (2) (2010) EL30–EL36. doi:/10.1121/1.3280237.

[9] F. Leppington, E. Broadbent, K. Heron, The acoustic radiation efficiency from rectangular plates, Proc. R. Soc. 382 (1982) 245–271. doi:/10.1098/rspa.1982.0100.

[10] L. Brillouin, Wave propagation in periodic structures: Electric filters and crystal lattices, 2nd edition Dover Publications (Mineola, New York). doi:10.1016/S0031-8914(53)80099-6.

[11] D. Mead, Wave propagation in continuous periodic structures: research contributions from southampton, Journal of Sound and Vibration 190 (3) (1996) 495–524. doi:/10.1006/jsvi.1996.0076.

[12] E. Manconi, B. R. Mace, Modelling wave propagation in two dimensional structures using finite element analysis, Journal of Sound and Vibration 318(45) (2008) 884–902. doi:/10.1016/j.jsv.2008.04.039.

[13] F. Errico, M. Ichchou, S. De Rosa, O. Bareille, F. Franco, The modelling of the flow-induced vibrations of periodic flat and axial-symmetric structures with a wave-based method, Journal of Sound and Vibration 424 (2018) 32–47. doi:/10.1016/j.jsv.2018.03.012.

[14] J.-L. Christen, M. Ichchou, A. Zine, B. Troclet, Wave finite element formulation of the acoustic transmission through complex infinite plates, Acta Acustica united with Acustica 102(6) (2016) 984–991. doi:/10.3813/AAA.919013.

[15] Y. Yang, B. Mace, M. Kingan, Prediction of sound transmission through, and radiation from, panels using a wave and finite element method, J. Acoust. Soc. Am. 141 (4) (2017) 2452–2460. doi:/10.1121/1.4977925.

[16] M. Yang, M. Palodichuk, N. Murray, B. Jansen, Prediction of structural response in transonic flow using wavenumber decomposition of fluctuating pressures, 23rd AIAA/CEAS Aeroacoustics Conference (AIAA 2017-3202). doi:/10.2514/6.2017-3202.

[17] C. Droz, J.-P. Laine, M. Ichchou, G. Inquiete, A reduced formulation for the free-wave propagation analysis in composite structures, Composite Structures 113 (2014) 134–144. doi:/10.1016/j.compstruct.2014.03.017.

[18] C. Droz, O. Bareille, M. N. Ichchou, A new procedure for the determination of structural characteristics of sandwich plates in medium frequencies, Composites Part B: Engineering 112 (2017) 102–111. doi:/10.1016/j.compositesb.2016.12.023.

[19] W. Graham, A comparison of models for the wavenumber-frequency spectrum of turbolent boundary layer pressures, Journal of Sound and Vibration 206(4) (1997) 541–565. doi:/10.1006/jsvi.1997.1114.

[20] G. Corcos, Resolution of pressure in turbulence, Journal of the Acoustical Society of America 35 (1963) 192–199. doi:/10.1121/1.1918431.

[21] L. Barisciano Jr, Broadband transmission loss due to reverberant excitation, NASA/CR-1999-209687, Langley Research Center, Hampton, Virginia.

A study of structured uncertainties in wave characteristic of one-dimensional periodic structures

R.P. Singh[1,2], C. Droz [2], S. De Rosa [1], F. Franco [1], O. Bareille [2] ,M.N. Ichchou [2]
[1] Department of Industrial Engineering, University of Naples "Federico II", Via Claudio 21, 80125 Napoli, Italy

[2] Vibroacoustics & Complex Media Research Group, LTDS, Ecole Centrale de Lyon, 36 Avenue Guy de Collongue, F-69134 Ecully, France
e-mail: **ravipratap1428@gmail.com**

Abstract
Periodic structures have properties of controlling mechanical wave. These are used in aircraft, trains, submarines, space structures and demand high level of robustness, which can be ensured with consideration of the presence of uncertainty in the numerical models. The uncertainties, in terms of material properties and geometrical parameters, are mostly introduced in both the manufacturing and assembly process. In order to predict the wave characteristics of the periodic structures under the uncertainty, the stochastic wave finite element method has been extended to periodic structures; wave finite element method (WFEM) added with an additional dimension to model the uncertain parameter using the perturbation approach. Numerical experiments are performed to test the method with one-dimensional periodic rod and periodic beam with parametric uncertainty. The performance of the developed method is compared in terms of computational cost which offers computational advantages over the Monte Carlo Simulation.

1 Introduction

The vibroacoustic performance and dynamics of the structure are important subjects in aeronautics, transport, energy, and space where the periodic media can be used for vibration reduction, acoustic blocking, acoustic channeling and acoustic cloaking. Application for these unusual phenomena is mainly correlated to the inherent band gaps or frequency regions in which the propagation of acoustic/elastic waves in the periodic media can be manipulated. Inherent material inhomogeneity, manufacturing errors (ex. variation of geometry) and environmental influences are unavoidable.

To address this unavoidable actuality, the effects of uncertainties need to be considered when analyzing band structures (pass and stop band) and dynamics of the periodic structures. Also, to meet the regulatory compliance and user requirement, the designer accounts for variation in the input parameter at the design phase. For example, in the space industry designers consider the uncertainty in the system parameter to ensure that the during launch and orbital operation the vibration level are in a range that is acceptable.

Three different frequency ranges of analysis can be defined for the typical dynamic response of weakly dissipative structures. At the low-frequency range, FE-like approaches are applicable because of the low order modes and low sensitivity to variability, contrary the high frequency with many high order modes involved, energy-based methods (e.g. Statistical Energy Analysis (SEA)) are well suited. The mid-frequency range affected by variability of the model parameter and the wave-based approaches have been developed by increasing computational efficiency. However, most of them assume that waveguide properties are homogeneous in the direction of the travelling wave, which is the limitation of such approaches for variety of application where uncertainty can be considered. Also the analytical solutions are available but limited to the particular cases (e.g. acoustic horns, ducts, rods and beams) [1]. Manohar et al. [2] considered the randomness in the wave propagation in waveguides using spectral element analysis. Ichchou et al.[3] proposed a numerical approach using the Wave Finite Element Method (WFEM) [4] considering spatially

homogeneous variability in waveguides using a first order perturbation and extended with second order perturbation is proposed [5].

When dealing with layered structures the material or geometrical uncertainty often exhibits spatial correlation and random fields theory can be used to model spatially distributed variability with probability measure [6]. In addition, a Karhunen–Loeve (KL) expansion provides characterization of the random field in terms of deterministic eigenfunctions weighted by uncorrelated random variables. Also the (after Wentzel, Kramers and Brillouin) WKB approximation are employed in the modelling the random media [7]. The limitation of the method is that it does not consider the internal reflections which occur due to any local changes in the material or geometrical properties. This assumption can be mitigated if one considers a waveguide with piecewise constant material variability, where internal reflections due to local changes in the impedance can be taken into account at the junctions of the sections and the piecewise constant separated into a finite number of discrete sections [8]. Also, this would be an approximate representation for the spatially varying system [9].

The literature reveals that the effects of uncertainty in the material properties, geometry, loading condition and model play significant role in altering wave states. The work reported so far in the literature with the best of authors knowledge, is limited to wave propagation (with structured and unstructured uncertainty) in elastic media and random media only. In the present work, a Stochastic Wave Finite Element Method (SWFEM) [10], [11] is employed to analyze the complex band gap in 1D periodic structures. The results of the stochastic formulation are compared those obtained with analytical and Monte Carlo Simulation (MCS) for the bar and beam.

2 Formulation of SWFEM

One dimensional periodic structures are obtained by formulating the unit cell and then repeating in the propagation direction. Then, the study of this structure can be converted into study of unit cell based on the Floquet-Bloch theorem [3]. The schematic representation is shown in Fig. 1.

To consider the effect of the uncertainty on the response of the structure, the SWFEM is formulated which is extension of the classical WFEM to accommodate the uncertainty. The workflow of the SWFEM is depicted in Fig. 2.

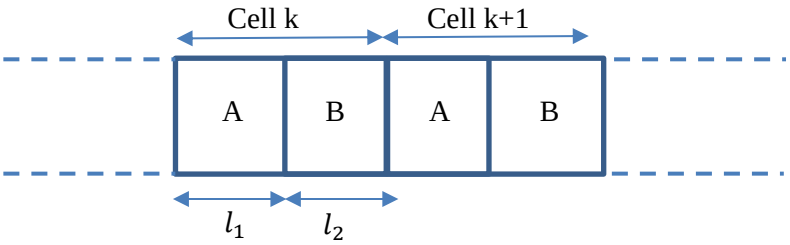


Figure 1: Schematic representation of periodic structure

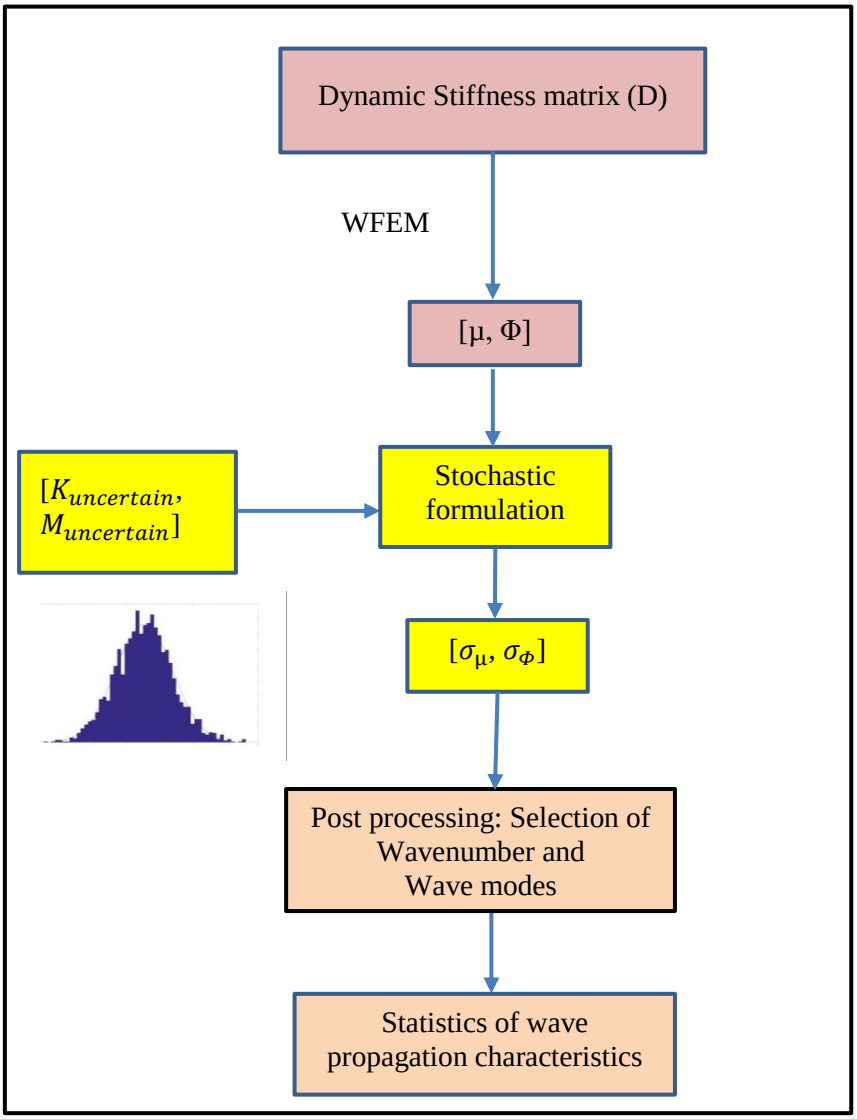


Figure 2: Flow diagram for SWFEM

To make the reader easily understand, the step in the formulation of SWFEM [3] is explained here.

The WFEM is used to study the behavior of periodic structures. This is extended to apply the WFEM for the uncertainty study. This starts with consideration of the random field as a supplementary dimension through the spatial discretization using the finite element steps. Which start from discretization of one sub-element of length (d). This discretization leads to stochastic dynamic equilibrium of any substructure in the following manner.

$$\left(\tilde{D}\right)\begin{pmatrix}\tilde{q}_L^k\\ \tilde{q}_R^k\end{pmatrix} = \begin{pmatrix}\tilde{F}_L^k\\ \tilde{F}_R^k\end{pmatrix} \tag{1}$$

Here $\left(\tilde{D}\right)$ is the stochastic complex dynamic stiffness matrix of the substructure, condensed on left and right boundaries degree of freedom at the pulsation ω:

$$\left(\tilde{D}\right) = -\omega^2\,\tilde{M} + \tilde{K}(1 + i\eta) \tag{2}$$

Here $\tilde{M}\ and\ \tilde{K}$ are stochastic mass and stiffness matrix respectively.

In the probabilistic tools, the parametric approach allows to consider the uncertain parameters (material, geometrical properties etc.) as random quantities. This is modeled using the stochastic finite element discretization approaches as expressed in [12].

The random variables are modeled using the first order perturbation, as Gaussian variables, such that the dynamical equilibrium is expressed as:

$$[-\omega^2(\bar{M}+\sigma_M\varepsilon)+(\bar{K}+\sigma_K\varepsilon)(1+i\eta)]\begin{pmatrix}\bar{q}_L^{(k)}+\sigma_{q_L}^{(k)}\varepsilon\\ \bar{q}_R^{(k)}+\sigma_{q_R}^{(k)}\varepsilon\end{pmatrix}=\begin{pmatrix}\bar{F}_L^{(k)}+\sigma_{F_L}^{(k)}\varepsilon\\ \bar{F}_R^{(k)}+\sigma_{F_R}^{(k)}\varepsilon\end{pmatrix} \tag{3}$$

The overbar $\bar{.}$ symbol denotes the mean of the random variable, σ; is standard deviation and ε is a Gaussian centered variable [13]. In the expression $\bar{M}, \bar{K}, \bar{q}, \bar{F}$ are the mean quantities of mass matrix, stiffness matrix, displacement vector and load. $\sigma_M, \sigma_K, \sigma_q, \sigma_F$ are their standard deviation.

As in the classical case, the stochastic problem in equation (1) can be partitioned in the following way:

$$\begin{pmatrix}\tilde{D}_{LL} & \tilde{D}_{LR}\\ \tilde{D}_{RL} & \tilde{D}_{RR}\end{pmatrix}\begin{pmatrix}\tilde{q}_L^k\\ \tilde{q}_R^k\end{pmatrix}=\begin{pmatrix}\tilde{F}_L^k\\ \tilde{F}_R^k\end{pmatrix} \tag{4}$$

It is to be noted that equation (4) is valid and can accommodate the stochastic behavior of the stiffness and mass matrix.

The stochastic kinematic variable, $\tilde{q}$ and $\tilde{F}$ are represented through stochastic state vector and related by the stochastic transfer matrix $\tilde{S}$.

$$\tilde{u}_R^k=\tilde{S}.\tilde{u}_L^k \tag{5}$$

Where $\tilde{S}=\bar{S}+\sigma_s\varepsilon$

$$\bar{S}=\begin{pmatrix}-\bar{D}_{LR}^{-1}\bar{D}_{LL} & \bar{D}_{LR}^{-1}\\ \bar{D}_{RL}-\bar{D}_{RL}\bar{D}_{LR}^{-1}\bar{D}_{LL} & -\bar{D}_{RL}\bar{D}_{LR}^{-1}\end{pmatrix}$$

$$\sigma_S=\begin{pmatrix}-\bar{D}_{LR} & 0\\ -\bar{D}_{RR} & 1\end{pmatrix}^{-1}\begin{pmatrix}\sigma_{D_{LL}} & \sigma_{D_{LR}}\\ \sigma_{D_{RL}} & \sigma_{D_{RR}}\end{pmatrix}\begin{pmatrix}1 & 0\\ -\bar{D}_{LR}^{-1}\bar{D}_{LL} & \bar{D}_{LR}^{-1}\end{pmatrix}$$

Following the steps of the deterministic development, a stochastic eigenvalue problem formulated as follows:

$$\begin{aligned}\tilde{S}\tilde{\phi}_i&=\bar{\mu}_i.\tilde{\phi}_i\\ \left|\tilde{S}-\tilde{\mu}_i I_{2n}\right|&=0\end{aligned} \tag{6}$$

The polynomial chaos projection of the eigenvalue problem leads to find their mean and standard deviation.

The standard deviation of the propagation constant μ_i (σ_{μ_i})

$$\begin{aligned}\sigma_{\mu_i}=&[(\bar{\phi}_i)^T\sigma_s^T(\bar{S}^T-\bar{\mu}_i I_{2n})^{-1}J_n(\bar{S}-(\bar{\mu}_i)^{-1}I_{2n})-(\bar{\phi}_i)^TJ_n\sigma_s)]\\ &\text{x }[(\bar{\phi}_i)^T(\bar{S}^T-\bar{\mu}_i I_{2n})^{-1}J_n(\bar{S}-(\bar{\mu}_i)^{-1}I_{2n})-(\bar{\mu}_i)^{-2}(\bar{\phi}_i)^TJ_n)]^{-1}\end{aligned} \tag{7}$$

similarly, the standard deviation of the eigenvectors (σ_{ϕ_i}) can be written as

$$\sigma_{\phi_i}=-[\bar{S}-\bar{\mu}_i I_{2n}]^+[\sigma_s-\sigma_{\mu_i}I_{2n}]\bar{\phi}_i \tag{8}$$

where + is pseudo inverse.

Using equation (7) and (8), the statistics of the wave characteristics can be expressed in the standard deviation of the propagation constant.

3 Results

This section shows the validation of SWFEM formulation considering binary periodic rod and binary periodic beam respectively. Binary rod and beam consist of section A of length l_1 and section B of length l_2 as depicted in the Fig. 3. Here cells A and B are made of different materials. In the first case, the longitudinal waves are studies while in the second case the flexural waves in beam of circular section are studied.

3.1 Longitudinal waves in binary periodic rod with uncertainty

In this subsection, the SWFEM is used to study the effect of parametric uncertainty on the dispersion relation of the longitudinal wave in binary periodic rod with sections A and B made of epoxy and aluminum respectively. The length of l_1 and l_2 are 1m each with circular cross section of radius of 0.0644m.

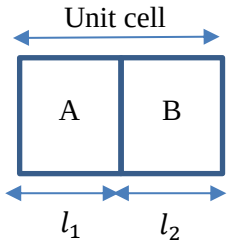


Figure 3: Symmetric unit cell

For the validation purpose SWFEM results is compared with the analytical solution of the wave number K expressed [14]:

$$\cos(Kl) = \cos\left(\frac{\omega}{c_a} l_a\right)\cos\left(\frac{\omega}{c_b} l_b\right) - \frac{1}{2}\left(\frac{\rho_a c_a}{\rho_b c_b} + \frac{\rho_b c_b}{\rho_a c_a}\right) sin\left(\frac{\omega}{c_a} l_a\right) sin\left(\frac{\omega}{c_b} l_b\right) \quad (8)$$

Where c_a, c_b is the wave velocity in the section A and B respectively and expressed as $c_a = \sqrt{\frac{E_a}{\rho_a}}$ and $c_b = \sqrt{\frac{E_b}{\rho_b}}$

The uncertainty effect is studied considering variation of the Young's modulus with four percentage. The study frequency range are up to 1800 Hz. The analytical results are treated as reference result for validation purpose. The sampling method with 10000 samples are used to get the wave characteristics of the analytical wave number obtained using equation (8).

In SWFEM formulation two-node rod elements are considered with the stiffness and mass matrices as following:

$$K_{rod} = \frac{ES}{d}\begin{pmatrix} 1 & -1 \\ -1 & 1 \end{pmatrix}$$

$$M_{rod} = \frac{\rho S d}{6}\begin{pmatrix} 2 & 1 \\ 1 & 2 \end{pmatrix}$$

Where E is the Young's modulus, S is cross sectional area and d is element length.

The global stiffness and mass matrices are assembled in the MATLAB environment with 100 elements in the unit cell of binary periodic rod. The material and geometric properties are shown in Table 1.

Geometry/Property	**Value**
Rod length (A)	1 m
Rod length (B)	1 m
Radius of rod	0.0644 m
Young's modulus (A)	4.35 Gpa
Young's modulus (B)	77.56 Gpa
Mass density (A)	1180 kg/m^3
Mass density (B)	2730 kg/m^3
Loss factor (A) and (B)	0.001

Table 1: Geometric parameters and material properties of binary periodic rod

Validation of SWFEM result in terms of dispersion equation is also computed using the MCS method with 10000 samples. As shown in Fig. 4, there exist one stop band in the considered frequency range according to the results obtained with SWFEM, analytical sampling and MCS in the considered frequency range. Also, the non-dispersive nature of propagation can be observed for the standard deviation. The comparison of the standard deviation is presented in the Fig. 5, obtained from analytical sampling, SWFEM and WFEM MCS. The results are in good agreement. The SWFEM standard deviation is computed considering loss factor on the contrary the analytical sampling is based on without damping.

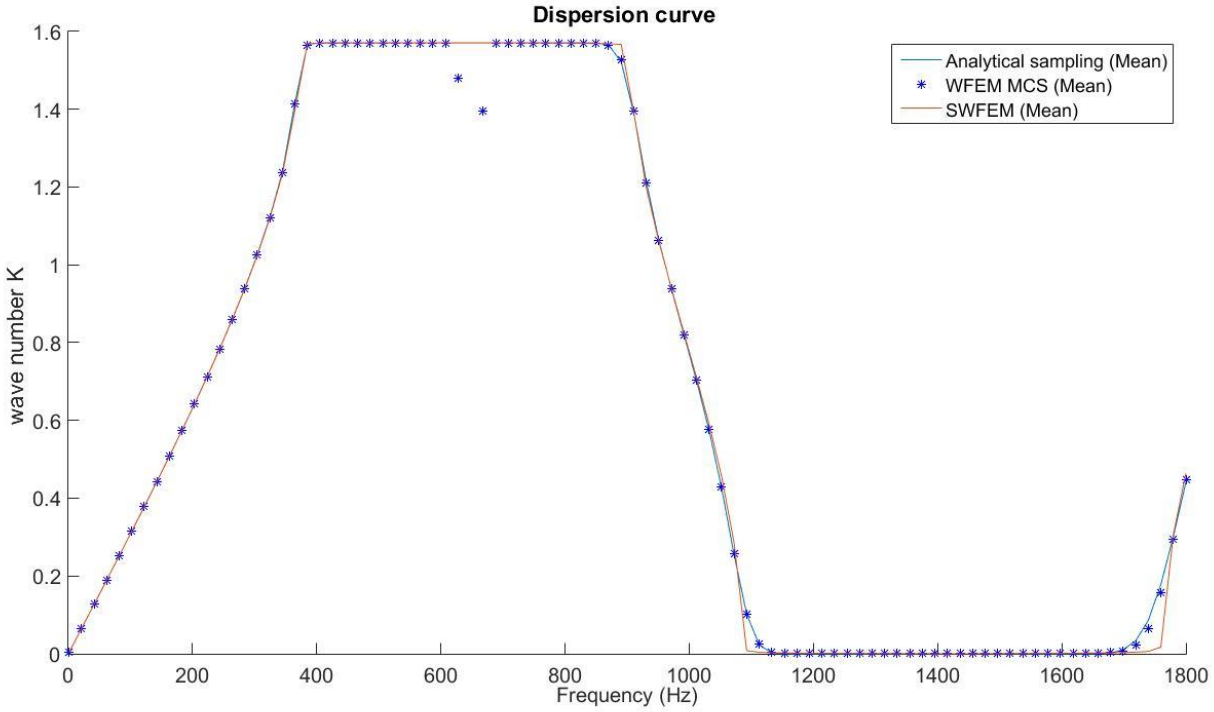


Figure 4: Comparison of mean of wave number

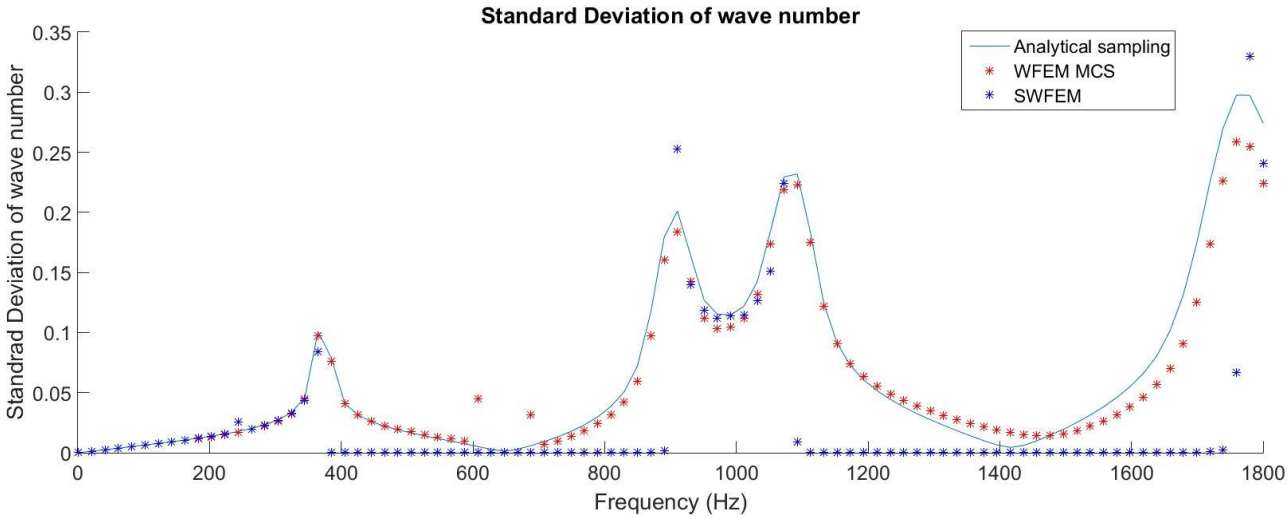


Figure 5: Comparison of the standard deviation of wave number

3.2 Flexural waves in binary periodic beam with uncertainty

In this subsection, the study of the uncertainty effect on the bending wave in binary periodic beam is performed. The Euler-Bernoulli beam theory is considered with material and geometrical properties listed in Table 2.

Geometry/Property	**Value**
Beam length	0.5m
Radius of beam	0.00945m
Young's modulus (A)	210 Gpa
Young's modulus (B)	0.72 Gpa
Mass density (A)	7800 kg/m^3
Mass density (B)	935 kg/m^3
Loss factor (A) and (B)	0.001

Table 2: Geometric parameters and material properties of binary periodic beam

For the numerical formulation the two-node beam element with two degrees of freedom per node is considered. The mass and stiffness matrices of the beam are as follows:

$$K_{beam} = \frac{EI}{d^3}\begin{bmatrix} 16 & 6d & -12 & 6d \\ 6d & 4d^2 & -6d & 2d^2 \\ -12 & -6d & 12 & -6d \\ 6d & 2d^2 & -6d & 4d^2 \end{bmatrix}$$

$$M_{beam} = \frac{\rho Sd}{420}\begin{bmatrix} 156 & 22d & 54 & -13d \\ 22d & 4d^2 & 13d & -3d^2 \\ 54 & -6d & 156 & -22d \\ -13d & -3d^2 & -22d & 4d^2 \end{bmatrix}$$

The frequency range of computation is 1-1500 Hz. Considering the uncertainty in the Young's modulus of the binary periodic beam with four percent about the nominal value, the numerical experiment is performed with SWFEM formulation. To validate the obtained result, MCS study is carried out with 10000 samples.

Fig. 6 shows the comparison of the mean value of the wave number obtained from SWFEM and MCS on the WFEM simulation. In Fig.7, the standard deviation comparison is shown from SWFEM and MCS results. The results are in good agreement which confirmed the validity of the SWFEM formulation applied to bending wave analysis.

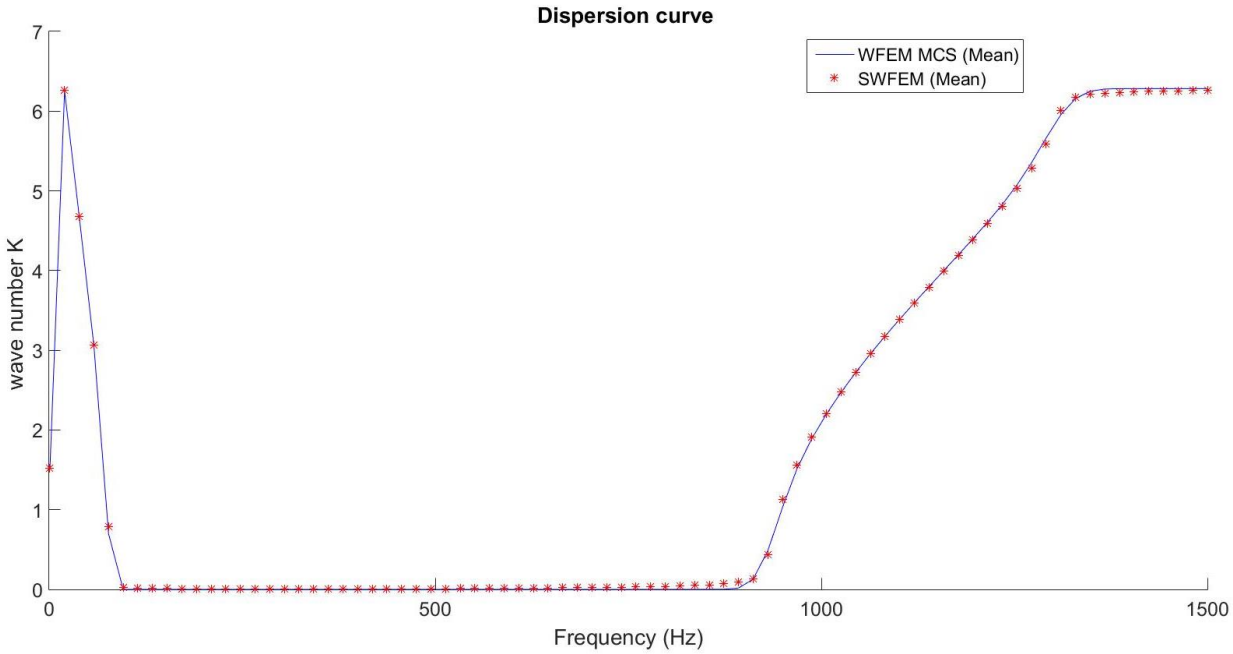


Figure 6: Comparison of mean of wave number

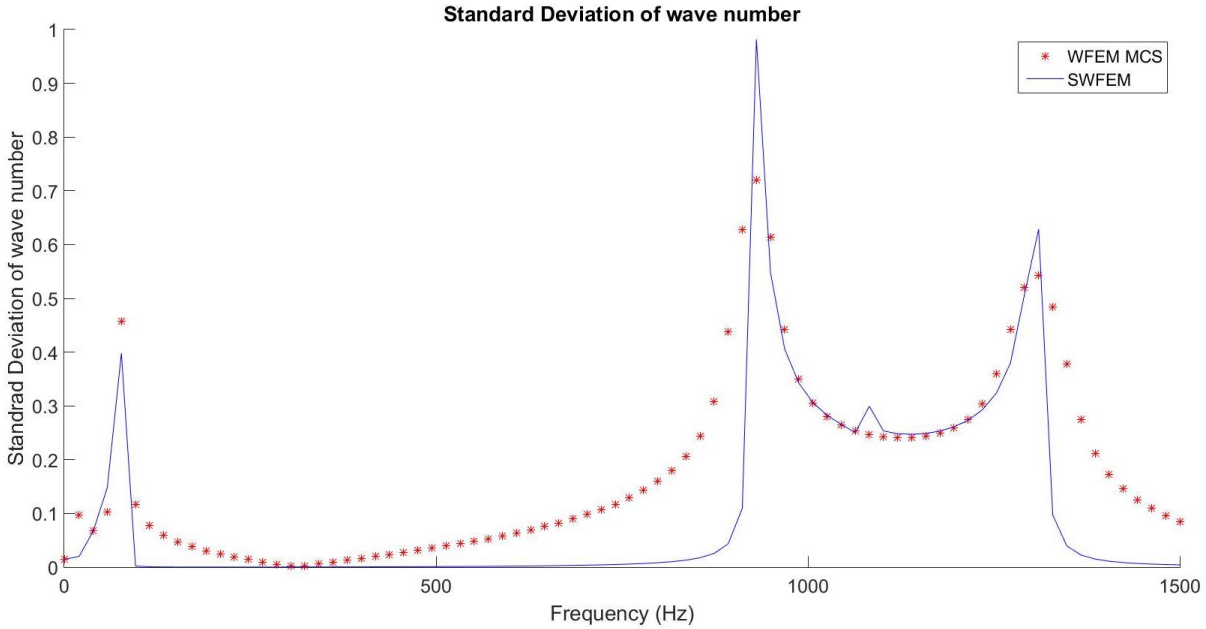


Figure 7: Comparison of the standard deviation

For the elapsed time computation, the MCS result obtained using homemade WFEM code which exploits the resources of the workstation with following characteristics, Intel® core™i7 7820 **HQ CPU@2.90GHz** with 32 GB RAM and data storage using solid state drive. The comparison is presented in the Table 3.

	WFEM MCS (10000 Sample)	SWFEM (single run)
Elapse time (Seconds)	3840	9.56

Table 3: Elapsed time comparison

4 Conclusion

This paper provides a computationally inexpensive stochastic numerical approach to study the uncertainty effect on free vibration of the 1D periodic structures. This formulation allows wave characteristic to be defined by stochastic finite element model using parametric probabilistic approach and which is easy to implement as it considers finite element model of the sample structural element. The SWFEM shows that the wave characteristic of the longitudinal and flexural wave can be obtained precisely. Main conclusion can be derived as follows:

(1) The formulation of the SWFEM is applied for the binary periodic rod and beam.
(2) Analytical sampling and numerical result showed the effectiveness of the formulation to predict the mean and standard deviation of the wave propagation.
(3) The SWFEM has computational advantage over MCS results.

The saving the computational cost can be a good point for the optimization and reliability study under uncertainties of complex waveguides. The statistics of the response can also be useful for the damage detection and sensitivity analysis. Future investigation is under progress for the forced response computation, using the present formulation.

Acknowledgements

This paper containing the work carried out in the framework of the VIPER project (VIbroacoustic of PERiodic media). This project has received funding from the European Union's Horizon 2020 research and innovation program under Marie Curie grant agreement No 675441.

References

[1] J. P. Arenas and M. J. Crocker, "*A note on a WKB application to a duct of varying cross-section*," Appl. Math. Lett., vol. 14, no. 6, pp. 667–671, 2001.

[2] C. S. Manohar and A. J. Keane, "*Axial vibrataion of a stochastic rod*," Journal of Sound and Vibration, vol. 165, no. 2, pp. 341–359, 1993.

[3] M. N. Ichchou, F. Bouchoucha, M. A. Ben Souf, O. Dessombz, and M. Haddar, "*Stochastic wave finite element for random periodic media through first-order perturbation*," Comput. Methods Appl. Mech. Eng., vol. 200, no. 41–44, pp. 2805–2813, 2011.

[4] Mead, D. J., *A general theory of harmonic wave propagation in linear periodic systems with multiple coupling,* Journal of Sound and Vibration, *27*(2), 235–260, 1973.

[5] F. Bouchoucha, M. N. Ichchou, and M. Haddar, "S*tochastic wave finite element method in uncertain elastic media through the second order perturbation*," J. Appl. Mech. Tech. Phys., vol. 58, no. 2, pp. 362–370, 2017.

[6] A. T. Fabro, N. S. Ferguson, and B. R. Mace, "*Wave propagation and response statistics of random waveguides with spatially correlated properties*," XVII International Symposium on Dynamic Problems of Mechanics, 2015.

[7] C. R. Steele, "*Application of the WKB method in solid mechanics*," Mechanics Today, vol. 3, pp. 243–295,1976.

[8] R. S. Langley, "*Wave Transmission Through One-Dimensional Near Periodic Structures: Optimum and To Random Disorder*," J. Sound Vib., vol. 188, no. 5, pp. 717–743, 1995.

[9] A. T. Fabro, D. Beli, J. R. F. Arruda, N. S. Ferguson, and B. R. Mace, "*Uncertainty analysis of band gaps for beams with periodically distributed resonators produced by additive manufacturing*," Proc. ISMA2016, no. November, pp. 2031–2042, 2016.

[10] Ben Souf, M. A., Ichchou, M., Bareille, O., Bouhaddi, N., & Haddar, M., *Dynamics of random coupled structures through the wave finite element method*, Engineering Computations: International Journal for Computer- Aided Engineering and Software, 32(7), 2020–2045, 2015.

[11] Ben Souf, M. A., Chronopoulos, D., Ichchou, M., Bareille, O., & Haddar, M., *On the Variability of the Sound Transmission Loss of Composite Panels Through a Parametric Probabilistic Approach*, Journal of Computational Acoustics, 23, 1550018-1–23, 2015.

[12] R. G. Ghanem and R. M. Kruger, "*Numerical solution of spectral stochastic finite element systems," Comput.* Methods Appl. Mech. Eng., vol. 129, no. 3, pp. 289–303, 1996.

[13] A. Sarkar and R. Ghanem, "*Mid-frequency structural dynamics with parameter uncertainty*," Comput. Methods Appl. Mech. Eng., vol. 191, no. 47–48, pp. 5499–5513, 2002.

[14] X. Sun, "*Elastic wave propagation in periodic structures through numerical and analytical homogenization techniques*," Ecole Centrale de Lyon, France, 2016.

Computation of wave dispersion characteristics in periodic porous materials modeled as equivalent fluids

D. Magliacano[1,2], M. Ouisse[1], A. Khelif[1], S. De Rosa[2], F. Franco[2], N. Atalla[3]
[1]Univ. Bourgogne Franche-Comté // FEMTO-ST Institute // CNRS/UFC/ENSMM/UTBM
Department of Applied Mechanics // 25000 Besançon, FRANCE
e-mail: **dario.magliacano@univ-fcomte.fr**

[2]Università degli Studi di Napoli "Federico II" (UniNa)
Corso Umberto I 40, 80138 Napoli, ITALY

[3]Université de Sherbrooke (UdeS)
2500 boul. de l'Université, Sherbrooke (Québec) J1K 2R1, CANADA

Abstract
This paper starts with the presentation of the shift cell technique, which allows the description of the propagation of all existing waves starting from the unit cell through a quadratic eigenvalue problem. Its major advantage is that it allows the implementation of any frequency dependence and damping in the problem: this is a fundamental advantage when computing the dispersion curves of a porous material modeled as an equivalent fluid. The second part of this work concerns the investigation of the link between the dispersion curves and the acoustic properties of the material. Deriving the equivalent acoustic properties of the unit cell from its dispersion characteristics, indeed, could be a very efficient approach for designing the sound packages with a simple a preliminary eigenvalue analysis.

List of symbols
- $\omega =$ angular frequency;
- $x, y, z =$ space variables;
- $j =$ imaginary unit;
- $p_0 =$ amplitude of the excitation mode (incident pressure);
- $\rho_0 =$ density of the interstitial fluid (air);
- $c_0 =$ sound speed in the interstitial fluid (air);
- $Z_0 =$ characteristic impedance of the interstitial fluid (air);
- $k_0 =$ wave number in the interstitial fluid (air);
- $\rho =$ density of the material;
- $Z_c =$ characteristic impedance of the material;
- $k =$ wave number in the material;
- $p =$ pressure;
- $K =$ bulk modulus;
- $\theta, \phi =$ angles of incidence;
- $p^* = conj(p)$;
- $\Omega =$ poro-elastic volume;
- $\Gamma =$ domain boundary;
- $I =$ flow of energy;
- $E =$ total energy;
- $E_k =$ kinetic energy;

- E_p = potential energy;
- v = istantaneous local velocity;
- v_E = energy transport speed;
- C_g = group velocity;
- s = side length;
- $\Pi_{incident}$ = incident power;
- $\Pi_{transmitted}$ = transmitted power;
- S = surface interested by incident pressure;
- d = thickness;
- τ_∞ = transmission coefficient;
- TL = transmission loss.

1 Introduction

The design based on the inclusion of vibroacoustic design rules at early stage of products development, through the use of porous media with periodic inclusions which exhibit proper dynamic filtering effects, is a powerful strategy for the achievement of lightweight sound packages and represents a convenient solution for manufacturing aspects.

The main advantage of designing sound packages with periodic arrangements is that they can provide a combination of absorption effects, resonance effects and wave interferences effects. This offers different applications in transportation (aeronautics, space, automotive, railway), energy and civil engineering sectors, where both weight and space, as well as vibroacoustic integrity and comfort, still remain as critical issues.

Indeed, although porous materials are commonly used for vibroacoustic applications, they suffer from a lack of absorption at low frequencies compared to their efficiency at higher ones. This difficulty is usually overcome by multi-layering. However, while reducing the impedance mismatch at the air-material interface, the efficiency of such devices relies on the allowable thickness. Instead, a more efficient way to enhance the low frequency performances of sound packages consists in embedding periodic inclusions in a porous layer. If the radius of these periodic inclusions is comparable with the acoustic wavelength, then an increase of the acoustical performances can be observed.

In order to develop efficient numerical techniques to handle the problem, the shift cell operator technique here is presented, providing details on its implementation [1]. Essentially, the shift cell technique consists of a reformulation of the Floquet-Bloch partial differential problem, in which the phase shift of the boundary conditions related to wave propagation is integrated into the derivation operator. Consequently, the periodicity is included in the overall behavior of the structure while the continuity conditions are imposed at the edges of the unit cell. Its major advantage is that it allows to implement any frequency dependence and damping in the problem; this is essential, if one needs to compute the dispersion curves of a porous material modelled as an equivalent fluid. In detail, it allows the description of the propagation of all existing waves from the description of the unit cell through the resolution of a quadratic eigenvalue problem. This is done through the $k(\omega)$ method, that allows to compute dispersion curves for frequency-dependent problems, instead of using the $\omega(k)$ one that leads to non-linear eigenvalue problems.

A validation of the implementation of this model in order to handle porous materials with periodic inclusions, together with a detailed explication of the meaning and the behavior of band gaps, can be found in literature [2].

Dispersion curves and acoustical characteristics for different numerical test cases are shown. In particular, they are obtained for a 3D melamine unit cell, with and without inclusion. The behavior of this porous material is described by JCA model in the following pages, but one can identically use any other equivalent fluid model.

The second part of this work concerns the investigation of the link between the dispersion curves and the acoustic properties of the material. In particular it's demonstrated that, starting from the wave numbers obtained as an output from the quadratic eigenvalue problem, it's possible to compute an equivalent transmission loss curve that, if compared to those obtained using classical methods, shows a very good agreement. Deriving the equivalent acoustic properties of the unit cell from its dispersion characteristics, indeed, could be a very efficient approach for designing sound packages with a simple a preliminary eigenvalue analysis.

All the results shown are related to a 3D melamine unit cell constituted by a cube with side equal to 2 [cm] (homogeneous case) and with a 0.5 [cm] radius cylindrical rigid inclusion (case with inclusion). The analyses are carried out in the frequency range 0 – 17000 [Hz]; this range of frequencies is interesting for acoustic applications and assures that the wavelength is much larger than the pore size, which is a necessary condition in order to use equivalent fluid models. Dispersion diagrams are computed along the direction that corresponds to $\phi = 0°$ and $\theta = 0°$ in the first Brillouin zone.

2 Shift cell operator technique

Considering a porous layer as an equivalent fluid [3], the starting equation for developing the associated shift cell formulation is

$$(\nabla + j\boldsymbol{k})^T \left(\frac{1}{\rho}(\nabla + j\boldsymbol{k})\boldsymbol{p}\right) = -\frac{\omega^2}{K}\boldsymbol{p}, \tag{1}$$

with $\rho = \rho(material, \omega)$ and $K = K(material, \omega)$.

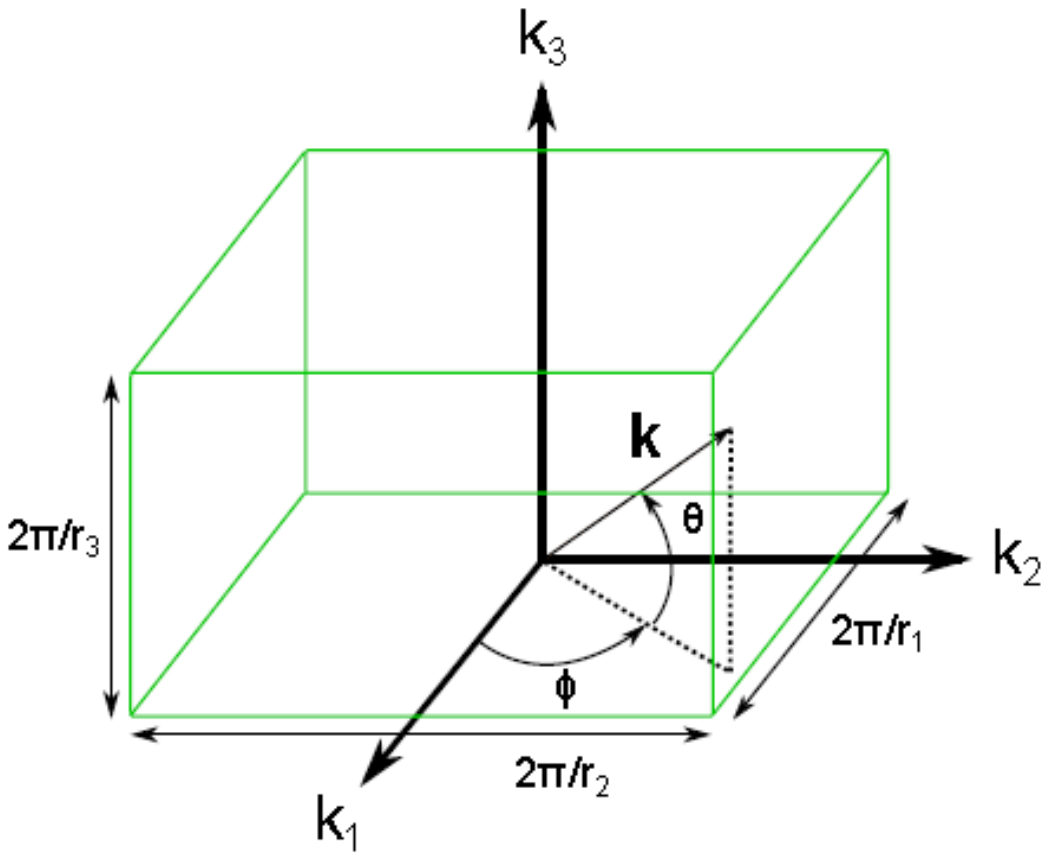


Figure 1: Reciprocal lattice vector in a 3D unitary cell [4].

By further developing the latter equation and considering $\boldsymbol{p} = pe^{j\boldsymbol{kx}}$ where $\boldsymbol{k}$, for a 3D application (Figure 1), is

$$\boldsymbol{k} = k\boldsymbol{\phi}, \boldsymbol{\phi} = \begin{pmatrix} cos\theta cos\phi \\ cos\theta sin\phi \\ sin\theta \end{pmatrix}, \tag{2}$$

one can obtain

$$\nabla^T \frac{\nabla(pe^{j\boldsymbol{kx}})}{\rho} + j\boldsymbol{k}^T \left(2\frac{\nabla(pe^{j\boldsymbol{kx}})}{\rho} + pe^{j\boldsymbol{kx}}\nabla\frac{1}{\rho}\right) - \boldsymbol{k}^T\boldsymbol{k}\frac{pe^{j\boldsymbol{kx}}}{\rho} + \frac{\omega^2}{K}pe^{j\boldsymbol{kx}} = 0. \tag{3}$$

2.1 Weak formulation

The weak formulation is calculated from the following equation, where $\tilde{p}$ is a weighting test function:

$$\int_\Omega \tilde{p}e^{-j\boldsymbol{k}^T\boldsymbol{x}}\left(\nabla^T \frac{\nabla(pe^{j\boldsymbol{kx}})}{\rho} + j\boldsymbol{k}^T \left(2\frac{\nabla(pe^{j\boldsymbol{kx}})}{\rho} + pe^{j\boldsymbol{kx}}\nabla\frac{1}{\rho}\right) - \boldsymbol{k}^T\boldsymbol{k}\frac{pe^{j\boldsymbol{kx}}}{\rho} + \frac{\omega^2}{K}pe^{j\boldsymbol{kx}}\right)d\Omega = 0 \tag{4}$$

$$\int_\Omega \left(\frac{1}{\rho}\nabla^T\tilde{p}\nabla p - j\boldsymbol{k}^T\frac{2}{\rho}(\tilde{p}\nabla p - \nabla\tilde{p}p) + \boldsymbol{k}^T\boldsymbol{k}\frac{4}{\rho}\tilde{p}p - \omega^2\frac{1}{K}\tilde{p}p\right)d\Omega = 0 \tag{5}$$

Considering that $\boldsymbol{\varphi}$ is the eigenvector, the equation can be written in its matrix form

$$(\boldsymbol{K} + jk\boldsymbol{L} + k^2\boldsymbol{H} - \omega^2\boldsymbol{M})\boldsymbol{\varphi} = 0 \tag{6}$$

with the following matrices:

- $\boldsymbol{K} \rightarrow \int_\Omega \frac{1}{\rho}\nabla\tilde{p}\nabla p\, d\Omega$;
- $\boldsymbol{L} \rightarrow \int_\Omega \frac{2}{\rho}(\nabla\tilde{p}p - \tilde{p}\nabla p)\, d\Omega$;
- $\boldsymbol{H} \rightarrow \int_\Omega \frac{4}{\rho}\tilde{p}p\, d\Omega$;
- $\boldsymbol{M} \rightarrow \int_\Omega \frac{1}{K}\tilde{p}p\, d\Omega$.

2.2 Right and left eigenvalue problems

The latter formulation leads to the following right eigenvalue problem:

$$\left[(\boldsymbol{K} - \omega^2\boldsymbol{M}) + \lambda_i\boldsymbol{L} - \lambda_i^2\boldsymbol{H}\right]\boldsymbol{\varphi}_i^r = 0 \tag{7}$$

where $\lambda_i = jk_i$ is the i-th eigenvalue, φ_i^r denotes the right eigenvector associated to λ_i, $\boldsymbol{M}$ and $\boldsymbol{K}$ are respectively the standard symmetric definite mass and symmetric semi-definite stiffness matrices, $\boldsymbol{L}$ is a skew-symmetric matrix and $\boldsymbol{H}$ is a symmetric semi-definite positive matrix. In this formulation, all matrices are frequency dependent.

For frequency-dependent systems, the estimation of the group velocity is not trivial. The equation (7) can be rewritten as

$$\boldsymbol{A}_1(\omega)\boldsymbol{\psi}_i^r = \lambda_i\boldsymbol{A}_2(\omega)\boldsymbol{\psi}_i^r \tag{8}$$

with

- $\boldsymbol{A}_1(\omega) = \begin{pmatrix} 0 & \boldsymbol{I_d} \\ \boldsymbol{K} - \omega^2\boldsymbol{M} & \boldsymbol{L} \end{pmatrix}$;
- $\boldsymbol{A}_2(\omega) = \begin{pmatrix} \boldsymbol{I_d} & 0 \\ 0 & \boldsymbol{H} \end{pmatrix}$;
- $\boldsymbol{\psi}_i^r = \begin{pmatrix} \boldsymbol{\varphi}_i^r \\ \lambda_i\boldsymbol{\varphi}_i^r \end{pmatrix}$.

where $\boldsymbol{I_d}$ is the identity matrix.

Conversely, a left-eigenvector for the same eigenvalue satisfies

$$\boldsymbol{\psi}_i^{l^T}\boldsymbol{A}_1(\omega) = \lambda_i\boldsymbol{\psi}_i^{l^T}\boldsymbol{A}_2(\omega), \text{ with } \boldsymbol{\psi}_i^l = \begin{pmatrix}\boldsymbol{A}\\ \boldsymbol{B}\end{pmatrix}. \tag{9}$$

$$\begin{cases}\boldsymbol{B} = \boldsymbol{\varphi}_{-i}^r = \boldsymbol{\varphi}_i^l\\ \boldsymbol{A}^T = \lambda_i\boldsymbol{\varphi}_{-i}^{r\,T}\boldsymbol{H} - \boldsymbol{\varphi}_{-i}^{r\,T}\boldsymbol{L} = \lambda_i\boldsymbol{\varphi}_i^{l^T}\boldsymbol{H} - \boldsymbol{\varphi}_i^{l^T}\boldsymbol{L}\end{cases} \tag{10}$$

In the resolution of the right eigenvalue problem, the i-th mode ($i \in N^+$) is defined by its $\lambda_i \geq 0$ and its eigenvector $\boldsymbol{\varphi}_i^r$. For each mode i, a mode $-i$ is associated with $\lambda_{-i} \leq 0$ such that $\lambda_{-i} = -\lambda_i$ and $\boldsymbol{\varphi}_{-i}^r = \boldsymbol{\varphi}_i^l$. by solving the right eigenvalue problem, the left solution is found too [4].

After some steps, one obtains the expression of the group slowness using $\lambda_i = jk_i$:

$$\frac{\partial k_i}{\partial\omega} = -j\frac{\boldsymbol{\varphi}_i^{l^T}\left[-2\omega\boldsymbol{M}+\frac{\partial\boldsymbol{K}}{\partial\omega}+\lambda_i\frac{\partial\boldsymbol{L}}{\partial\omega}-\lambda_i^2\frac{\partial\boldsymbol{H}}{\partial\omega}\right]\boldsymbol{\varphi}_i^r}{\boldsymbol{\varphi}_i^{l^T}[-\boldsymbol{L}+2\lambda_i\boldsymbol{H}]\boldsymbol{\varphi}_i^r} \tag{11}$$

The group velocity is the inverse of the group slowness [5]:

$$C_g = \frac{\partial\omega}{\partial k_i} = \frac{j\boldsymbol{\varphi}_i^{l^T}[-\boldsymbol{L}+2\lambda_i\boldsymbol{H}]\boldsymbol{\varphi}_i^r}{\boldsymbol{\varphi}_i^{l^T}\left[-2\omega\boldsymbol{M}+\frac{\partial\boldsymbol{K}}{\partial\omega}+\lambda_i\frac{\partial\boldsymbol{L}}{\partial\omega}-\lambda_i^2\frac{\partial\boldsymbol{H}}{\partial\omega}\right]\boldsymbol{\varphi}_i^r} \tag{12}$$

2.3 Classifying criteria to distinguish propagative and evanescent waves

Applying the shift cell operator technique to a sample modelled by an equivalent fluid, all the wave numbers are complex; consequently, there are not purely propagative solutions anymore. All waves are evanescent, with an evanescence rate that may be used to classify the branches in two categories: those that will be rapidly damped and those that will be slowly damped in space, with the latter that could be classified as propagative ones.

The distinction between the two is difficult and thus some classifying criteria are required:

1. the ratio between the real and the imaginary parts of every wavenumber → $C_1 = real(k)/imag(k)$;
2. the ratio between the real parts of the energy transport speed $v_E = I/E$ and the goup velocity C_g, where I is the flow of energy and $E = E_k + E_p = \int_\Omega \frac{1}{2}\left(\rho v^2 + \frac{p^2}{\rho c^2}\right)d\Omega$ is the total energy → $C_2 = real(v_E)/real(C_g)$.

Only the waves corresponding to $C_1 > \tau_1$ and $C_2 > \tau_2$ are considered as propagative ones. In practice, for the purpose of the following analysis, the thresholds τ are chosen such as $\tau_1 = 1$ and $\tau_2 = 0.7$. This is an arbitrary choice and these values are not meant to be considered as universal: for each different case, one may need to tune them [4]. In order to better appreciate the behavior of each branch in the frequency range of study in the following plots, dispersion and C_g curves are also colorized with a scale of colors that indicates the level of "propagativeness": the value 0 means that the wave at that specific frequency is totally spatially attenuated, while the value 1 represents a properly propagative behavior.

3 Calculation of group velocity and branch-tracking algorithm

In a dispersion diagram there is a set of points, forming branches, that one may wish to connect and follow according to the nature of each branch. Some solutions are proposed in literature, such as a MAC sorting criterion [6], but these methods require to store many data at every iteration. Instead, the group velocity constitutes a relevant indicator in order to follow the branches from a point of calculation to the next one [4]. The proposed technique consists in comparing $C_{g_i}(f)$ and $\boldsymbol{C_g}(f + \Delta f)$: from the group velocity

associated to a starting point, the routine compares the initial C_{g_i} with all the group velocities at the next frequency step and a minimization is made in order to identify the point at $f + \Delta f$ to which is associated the closest value of C_g. This point is defined as the new starting one and so on, step by step, the branch is identified.

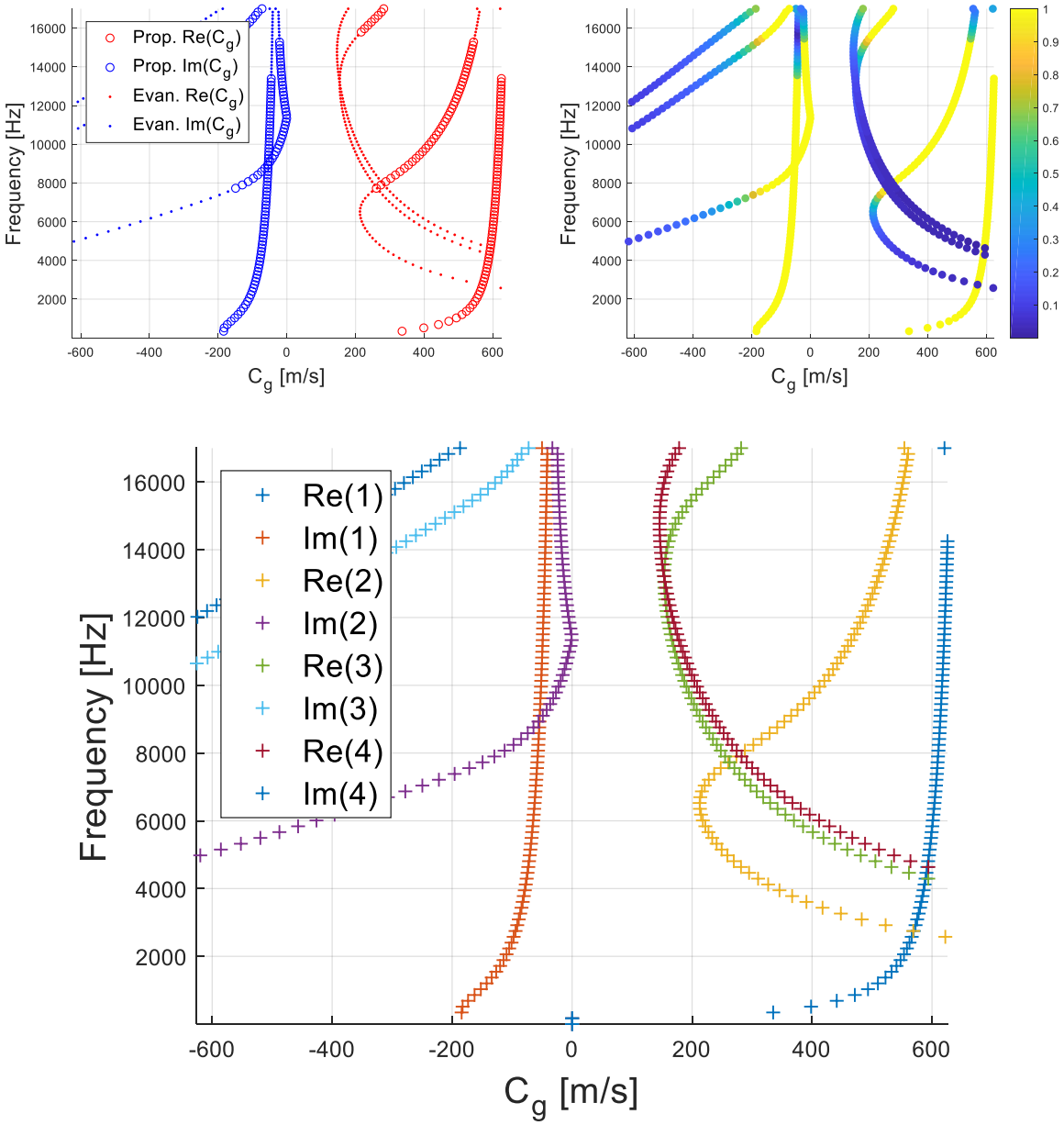


Figure 2: Evanescent and propagative (on the top) and branch-tracked (on the bottom) group velocity diagrams, for the case of a homogeneous unit cell.

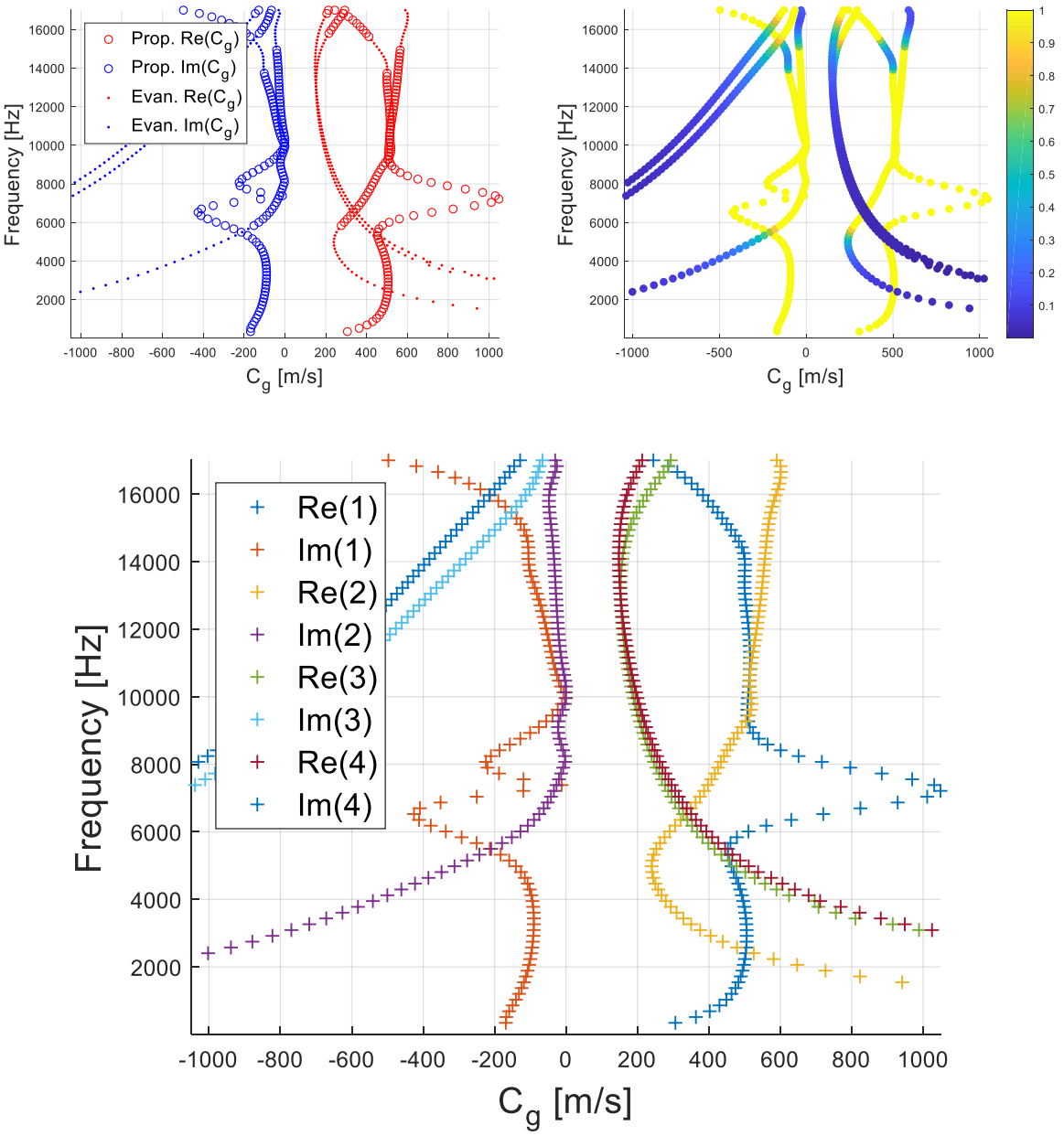


Figure 3: Evanescent and propagative (on the top) and branch-tracked (on the bottom) group velocity diagrams, for the case of an unit cell with an inclusion.

4 Dispersion curves

For each dispersion curve plot, three eigenvectors are reported in terms of acoustic pressure field (Figures 5 and 7). Only the real parts are shown, the imaginary parts being null. They are all extracted at the frequency of 8500 [Hz] (half of the range) and along the direction that corresponds to $\theta = \phi = 0°$ in the first Brillouin zone. Their branches are ordered as: at increasing frequencies, 1st is represented by the first real part that reaches the unitary value, 2nd is the second and so on. The fundamental acoustic parameters of the tested porous material have been experimentally determined in GAUS laboratory at University of Sherbrooke (Canada) and are: porosity $= 0.99$, tortuosity $= 1.02$, resistivity $= 8430 \left[\frac{Pa*s}{m^2}\right]$, viscous characteristic length $= 0.138\ [mm]$, thermal characteristic length $= 0.154\ [mm]$, density $= 5.73\ \left[\frac{kg}{m^3}\right]$.

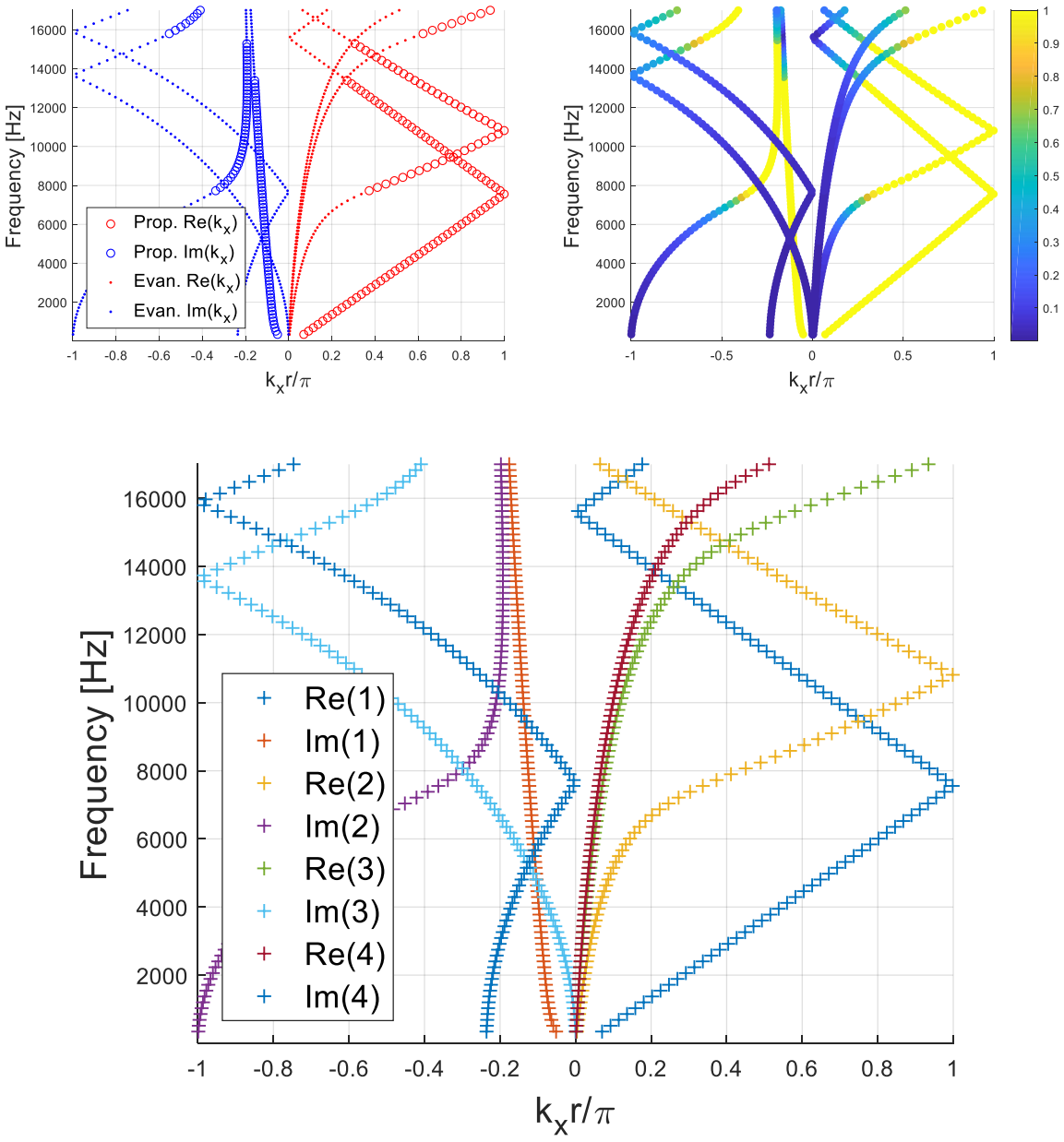


Figure 4: Evanescent and propagative (on the left) and branch-tracked (on the right) dispersion curves for a homogeneous melamine unit cell.

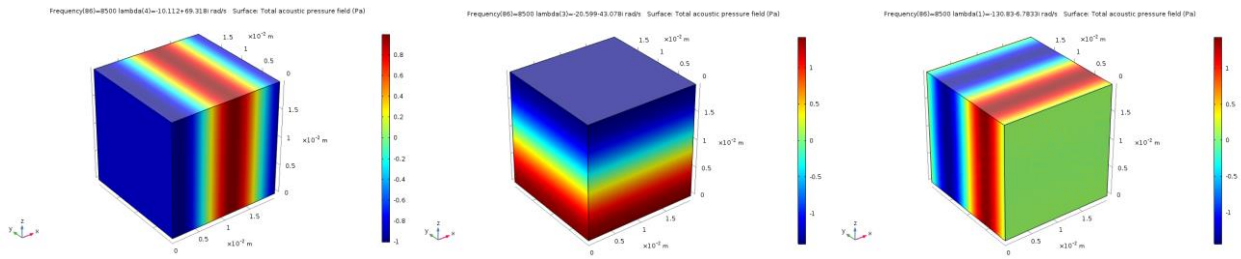


Figure 5: From left to right, real parts of the 1st, 2nd and 3rd branch eigenvectors for the homogeneous case.

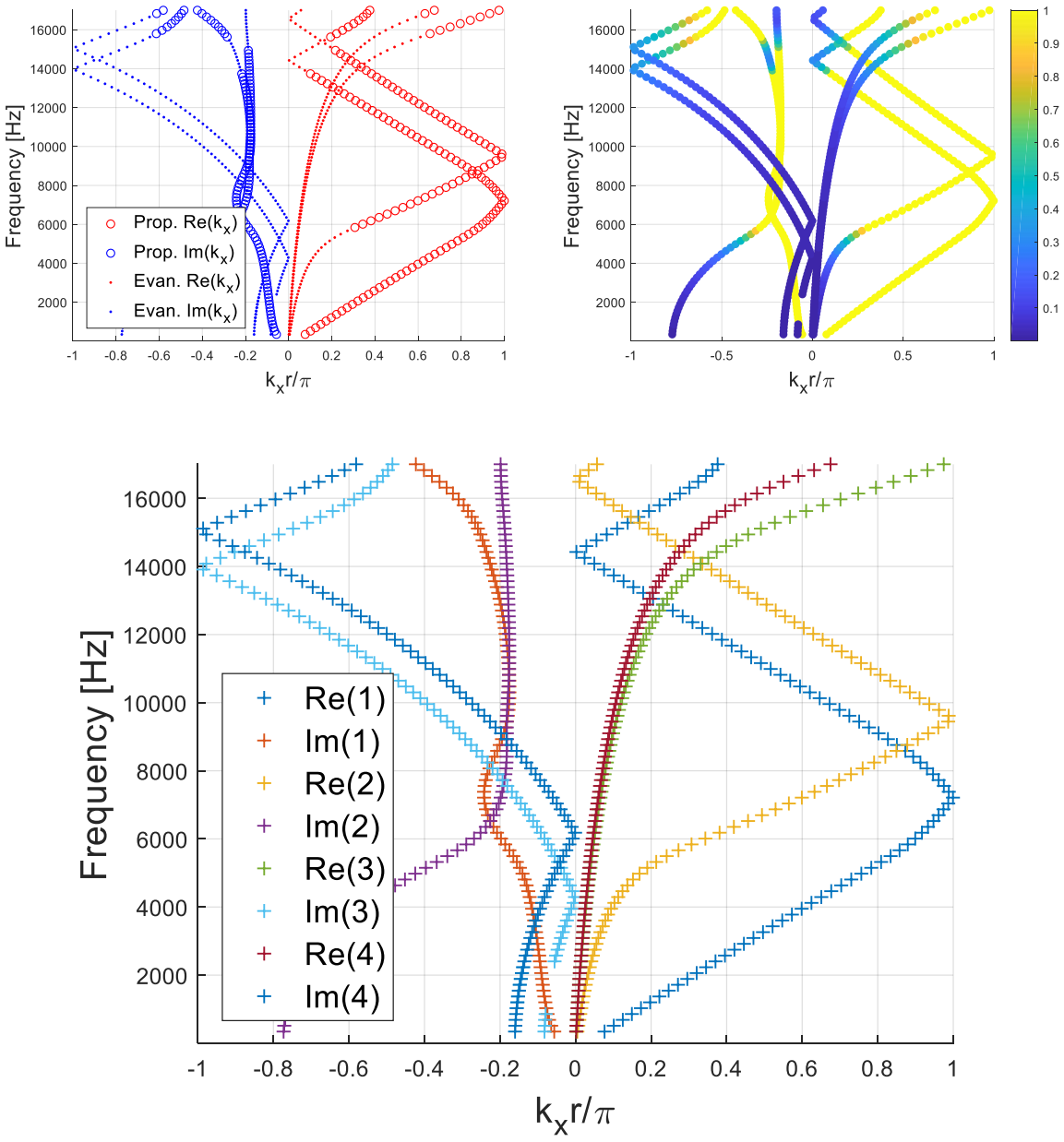


Figure 6: Evanescent and propagative (on the left) and branch-tracked (on the right) dispersion curves for a melamine unit cell with an inclusion.

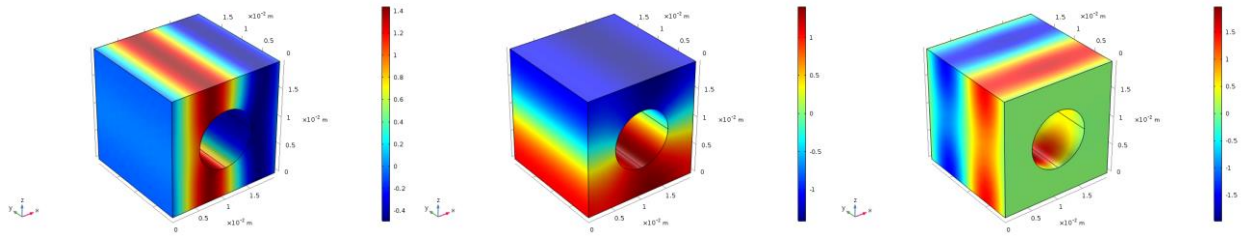


Figure 7: From left to right, real parts of the 1st, 2nd and 3rd branch eigenvectors for the case with an inclusion.

One may notice that there are some discontinuous curves: this is probably due to the fact that, as said, all waves are evanescent with different rates: a non-perfect tuning of the sorting criteria could lead to lines that disappears and reappears on the plots.

5 Transmission loss

While dispersion curves are computed for an infinite repetition of unit cells, transmission loss is calculated for a finite repetition of 5 unit cells, using the same domain and boundary conditions of the infinite periodic system. This, in a first approximation, allows to compare the dispersion relations and the acoustical characteristics of the equivalent finite medium. Indeed, a further increasing in the number of repeated cells would lead to a change in the mean value of absorption coefficient and transmission loss respectively below 2% and 20% respect to the usage of a repetition of 5 unit cells.

The transmission loss is numerically computed as

$$TL = 10\log_{10}\frac{\Pi_{incident}}{\Pi_{transmitted}} \tag{13}$$

where $\Pi_{incident}$ and $\Pi_{transmitted}$ represent the incident and transmitted power, respectively. For our plane wave configuration, the latter is compared, for homogeneous flat configurations, with the Transfer matrix method [7]:

$$TL = 10\log\left(\frac{1}{4}\left|T_{11} + \frac{T_{12}}{\rho_0 c_0} + \rho_0 c_0 T_{21} + T_{22}\right|^2\right), \tag{14}$$

$$\text{with } \begin{bmatrix} T_{11} & T_{12} \\ T_{21} & T_{22} \end{bmatrix} = \begin{bmatrix} \cos(kd) & j\sin(kd)\, Z_c \\ \frac{j\sin(kd)}{Z_c} & \cos(kd) \end{bmatrix} \tag{15}$$

For the inhomogeneous configuration, the validation is obtained using an implementation of the plane wave forced response of the periodic cell accounting for fluid loading [8].

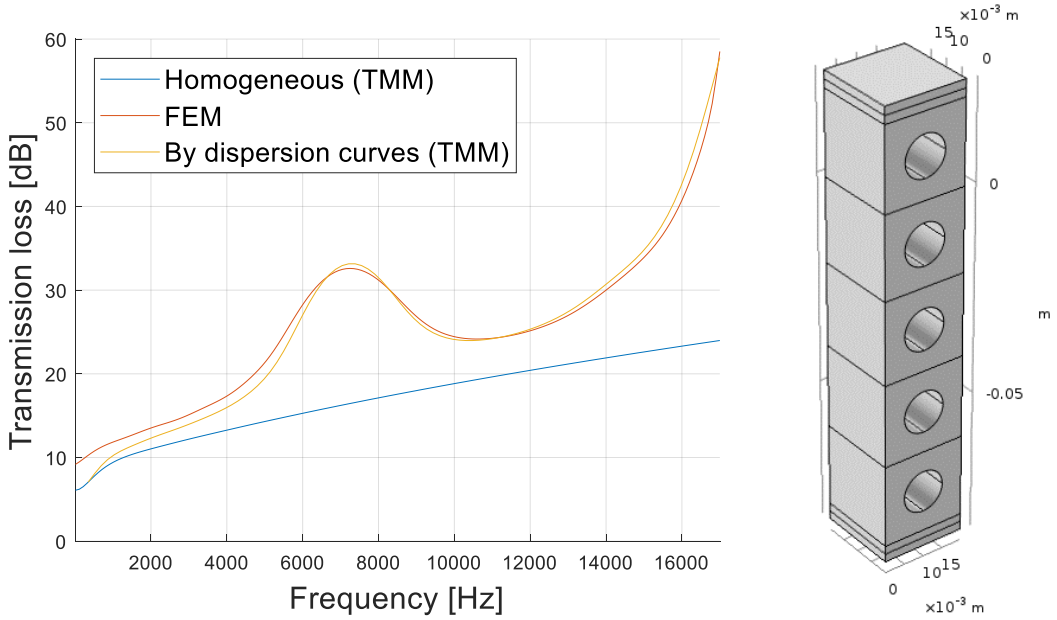


Figure 8: Transmission loss computed for a 3D repetition of 5 melamine unit cells.

Concerning the case with the inclusion, one can notice that an improvement of transmission loss properties, respect to the homogeneous case, is shown at all frequencies, in particular in correspondence of a peak at a frequency around 7 [kHz], in which it is equal to about 15 [dB], and at high frequencies. Note that, for the sake of comparison with the related dispersion curves, only their 1st branch is meaningful due to the fact that the correspondent mode is the only one that is actually excited during these transmission loss simulations. Indeed, the improvement peak exactly corresponds to the frequency range of the 1st branch of dispersion curves in which the wave is strongly spatially attenuated.

This is definitely encouraging, for the purpose of deriving more equivalent acoustic properties of the unit cell from its dispersion characteristics.

6 Conclusions

The shift cell technique has been presented, providing details on its numerical formulation. It has been necessary to introduce some classifying criteria and, consequently, the derivation of the group velocity expression. A branch-tracking criterion has been described, in order to clearly identify each branch in the dispersion diagram. Dispersion curves and transmission loss plots have then been computed for a JCA-modelled melamine unit cell. An equivalent transmission loss curve, obtained starting from the eigenvalues, has been compared to those obtained with classical methods, showing a very good agreement. Further developments of the work will include an estimation of the computational efficiency between the shift cell and the classical Floquet-Bloch approaches, as well as the implementation of the shift cell technique using Biot model.

Acknowledgements

This project has received funding from the European Union's Horizon 2020 research and innovation program under the Marie Skłodowska-Curie grant agreement No. 675441.

References

[1] D. Magliacano, M. Ouisse, A. Khelif, S. De Rosa, and F. Franco, "The shifted cell operator technique applied to equivalent fluids models for the computation of dispersion diagrams of periodic porous materials," in *SAPEM 2017 proceedings*, 2017.

[2] D. Magliacano *et al.*, "Validation of shift cell approach for the modelling of acoustic properties of porous materials embedding periodic inclusions," in *NOVEM 2018 proceedings*, 2018, pp. 1–11.

[3] O. Doutres, Y. Salissou, N. Atalla, and R. Panneton, "Evaluation of the acoustic and non-acoustic properties of sound absorbing materials using a three-microphone impedance tube," *Appl. Acoust.*, vol. 71, no. 6, pp. 506–509, 2010.

[4] K. Billon, "Composites periodiques fonctionnels pour l'absorption vibroacoustique large bande," *PhD thesis Univ. Fr.*, 2017.

[5] R. P. Moiseyenko and V. Laude, "Material loss influence on the complex band structure and group velocity in phononic crystals," *Phys. Rev. B - Condens. Matter Mater. Phys.*, vol. 83, no. 6, pp. 1–6, 2011.

[6] M. Collet, M. Ouisse, M. Ruzzene, and M. N. Ichchou, "Floquet-Bloch decomposition for the computation of dispersion of two-dimensional periodic, damped mechanical systems," *Int. J. Solids Struct.*, vol. 48, no. 20, pp. 2837–2848, 2011.

[7] J. F. Allard and N. Atalla, *Propagation of Sound in Porous Media: Modelling Sound Absorbing Materials*. 2009.

[8] N. Atalla, *NOVAFEM User's guide*. Sherbrooke (QC, Canada): Université de Sherbrooke, 2017.

Interlocked hybrid-cell Kirigami inspired cellular structures and their vibroacoustic performance

S. Del Broccolo[1], M. Ouisse[1], E. Foltete[1], F. Scarpa[2]
[1] Univ. Bourgogne Franche-Comté, FEMTO-ST Institute, CNRS/UFC/ENSMM/UTBM
Department of Applied Mechanics, 25000 BESANÇON-FR
e-mail: **simone.del.broccolo@gmail.com**

[2] Bristol Composites Institute (ACCIS), University of Bristol
Queen's Building, University Walk, Bristol BS8 1TR, United Kingdom

Abstract
Sandwich panels are widely used in applications where high stiffness and low weight structures have become an asset, such as the aerospace segment. The environment in which those panels are used produce uncomfortable vibrations in the low-mid range which also may induce inefficiency. This hybrid cellular core obtained with a Kirigami derived technique and intended to be used for sandwich panels, is investigated, parametrically, by performing numerical simulations and varying the topology. The vibration filtering characteristic of this innovative cellular core is compared to more classic configurations. The comparison is carried out using the Wave Finite Element Method (WFEM) by analysing only the unit cell thanks to the Floquet-Bloch theorem periodic conditions. Harmonic numerical simulations using commercial FEA software are also carried out to illustrate the validity of the bandgaps location and width. We will base the vibration performance evaluation analysing in-plane and out-of-plane bandgaps.

1 Introduction

Many efforts have been produced so far to better understand the dynamic behaviour of complex periodic structures. This is a direct consequence of the increase of such structures in the engineering domain. Some examples like train rails, bridges and skyscrapers can be encountered in everyday life but we can also find them in the Aerospace engineering field, where stiffened plates as well as composites sandwich panels are widely used. Those type of structures become convenient in terms of manufacturing as it is easier to produce a single item that can be used to create different final shapes rather than having to customize the manufacturing process to each application. The solicitations that an airplane fuselage or a space launcher undergoes, derives from various sources, and understanding the consequent perturbation propagation, is crucial to avoid catastrophic failures and lengthen its average service lifespan.

The Aerospace segment often requires light and stiff materials. This is mainly the reason why honeycomb sandwich panels are widely used there. They are well known to provide good static out of plane properties (compression) because of their high equivalent stiffness. However, the use of light cellular cores makes these structures possess a very high stiffness/mass ratio and therefore, their vibration frequency domain is usually in the high range. The solicitations mentioned before though, are in the mid-low range, and as engineered today, the periodicity possessed by sandwich panels, has not been fully exploited. Obtaining sandwich panels with improved vibroacoustic performances, at specific frequency ranges, is therefore an interesting research topic.

The response of periodic structures to external excitation has already been investigated starting from Brillouin's work [1] back in 1946. Mead et al. [2] have produced a document, summarizing almost thirty years of work carried out at the University of Southampton, demonstrating how spatial periodicity in terms of structure, material, inserts or boundary layers, interacts with travelling waves. Those periodic variations

cause some of the incident waves to be reflected and some to be transmitted. The destructive interaction, partial or full, between incident and reflected waves, causes attenuation (bandgaps) at certain frequency ranges, and therefore, periodic structures can act as passive filters. There is therefore, a relation between the geometrical dimensions of the periodic structure and the travelling wave characteristics.

Periodic structures thought, can exhibit two types of stop bands created by different phenomena: Bragg Scattering and Local Resonance. Bragg scattering stop band are consequence of the spatial periodicity just mentioned and it appears when wavelengths are on the same order as the period length. In contrary, local resonance stop bands do not necessarily require periodicity and only depend on the properties of the local resonator and therefore they can lie in the sub-wavelength regime. Each periodic structure therefore possesses bandgaps that depend upon the geometry and those are the ones we will focus on in this paper.

There are many different methods that have been developed in the years and that can be found in literature, to examine periodic structures. A good summary of those techniques which mostly are FEM derived can be found in the paper written by Hussein and Ruzzene [3].

Lately, the most commonly used one, is the Wave Finite Element Method (WFEM), where the Mass and Stiffness matrices of the single repetitive component of the periodic structure, are calculated with FEM commercial software, extracted, and used to calculate the dynamics of the structure by applying the periodicity conditions described by the Floquet-Bloch Theory. Scarpa et al. were, to the authors' knowledge, were the first ones to investigate wave propagation in a Kirigami lattice using WFEM [4].

Kirigami is an innovative way of producing cellular structures. It is an ancient Japanese form of art involving cutting and folding paper to produce tri-dimensional structures [5 - 6]. A previous work [5], attempted to produce, successfully, a cellular structure possessing zero in-plane Poisson's coefficient (AUXHEX). This was obtained using a hybrid tessellation which conferred the overall structure, the desired property. By hybrid, is intend a cellular core containing cells of different shapes. The geometrical constrain in term of final cell shape Kirigami imposes to the manufacturer though, pushed the authors to develop a new technique that overcomes the limitation and allows to produce new types of hybrid tessellation. The cellular structure analysed was named HEXHEX.

In this work, numerical simulations are carried out with the aim of investigating the vibration filtering properties of this new Kirigami structure firstly using 1DWFEM and subsequently 2WFEM methods.

The aim of this work is to detect the presence of the Bragg bandgaps possessed by the HEXHEX cellular structure, and attempt to enlarge existing or open new ones, by varying its geometrical parameters. The HEXHEX hybrid core will finally be compared with two classic tessellations, Hexagonal and Re-entrant. An overview of the investigation methods as well as some considerations on the results obtained are proposed.

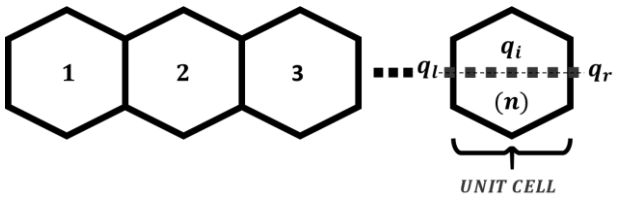
2 Wave propagation in periodic media

2.1 Periodic structures

A structure which exhibits some form of spatial periodicity is defined as a periodic structure. Such characteristic must be in its internal geometry, constituent material or the boundary conditions. Periodicity allows us to do some considerations about the behaviour of the full structure by carrying out analyses on just a portion of structure [4, 7-9], also known as the *unit cell*. By repeating this portion in space, we recreate the full structure (Figure 1).

2.2 Floquet-Bloch Theory

This theory is the core of the WFEM method and was firstly introduced for engineering investigations by Brillouin [1]. According to this theory, displacements and forces on the nodes on the extremities of a unit cell are related. This means that it is sufficient to analyse a small portion of our periodic structure to understand the overall dynamic behaviour.



$$q_r^{(n)} = \lambda q_l^{(n)} = e^{j\mu} q_l^{(n)} \quad (1)$$

$$-f_r^{(n)} = \lambda f_l^{(n)} = e^{j\mu} f_l^{(n)} \quad (2)$$

Figure 1 - Periodic structure unit cell and 1D Floquet Bloch periodic relations

The Floquet-Bloch relations for forces (f) and displacements (q) for 1D periodicity are shown in (1) and (2) respectively, where the subscripts l and r indicate the left or right of the unit cell, $\mu = kL$ is the reduced wave number, k is the wave number and L the length of the unit cell.

To understand the dynamic behaviour of a periodic structure, a dispersion curve, which represents the relation between the reduced wavenumber (μ) versus the frequency (ω) can be plotted. To produce a dispersion curve therefore, a relation between ω and $\lambda = e^{j\mu}$ is required. The starting point is represented by the Fundamental Dynamics Equation of the unit cell. Neglecting damping, such equation becomes:

$$(K_{uc} - \omega^2 M_{uc}) \begin{pmatrix} q_l \\ q_i \\ q_r \end{pmatrix} = \begin{pmatrix} f_l \\ f_i \\ f_r \end{pmatrix} \quad (3)$$

K_{uc} and M_{uc} are the stiffness and the mass matrix respectively of the unit cell, and the objective is to convert this relation into an eigenvalue problem, by cancelling the force vector on the right-hand side.

By applying the Floquet-Bloch conditions on forces and displacements into Equation (3) the following relation that describes the dynamics of the unitcell is obtained:

$$\Lambda_L (K_{uc} - \omega^2 M_{uc}) \Lambda_R \begin{pmatrix} q_l \\ q_i \end{pmatrix} = 0 \quad (4)$$

where $\Lambda_R = \begin{bmatrix} I & 0 \\ 0 & I \\ \lambda I & 0 \end{bmatrix}$ and $\Lambda_L = \begin{bmatrix} I & 0 & \frac{1}{\lambda} I \\ 0 & I & 0 \end{bmatrix}$

The right-hand side of equation (4) is equal to zero thanks to the Floquet-Bloch relation on the forces which assumes $f_i = 0$.

$$\left(K_r(\mu) - \omega^2 M_r(\mu)\right) q^{(r)} = 0 \tag{5}$$

Finally, the standard eigenvalue problem (5) is derived and by solving for $\mu \in [0; \pi]$, which represents the First Brillouin Zone, the frequency is obtained.

This procedure is usually followed when investigating periodic structures along their direction of periodicity and therefore it is known as 1DWFEM. In the case of cellular cores though, periodicity may happen along two directions.

Wave vectors can be expressed in terms of the reciprocal lattice basis which represents the Fourier transform of a periodic spatial function in real-space also known as the direct lattice. Since the reciprocal lattice is also periodic, one can restrict the wave vectors to a certain region called first Brillouin zone.

If there is symmetry in the reciprocal lattice, the wave vectors may be further restricted to the Irreducible Brillouin Zone (IBZ) (OABC), shown in Figure 1, where the wavenumbers are positive. In some descriptions of the wave propagation characteristics, only the contour of the IBZ (O-A-B-C-O) is considered, where the band extrema almost always occur [11].

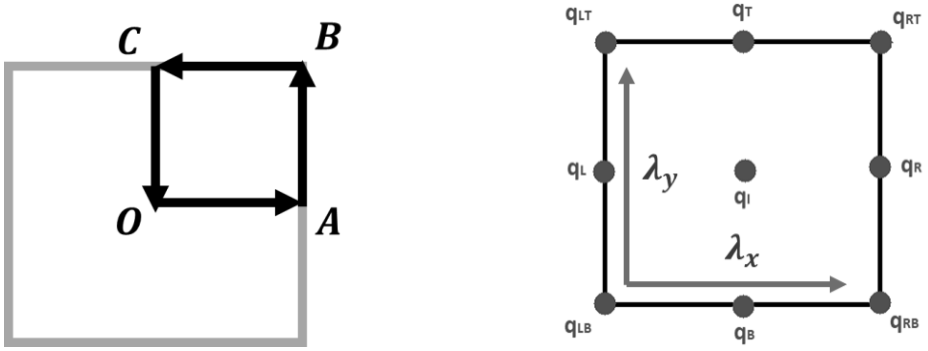


Figure 2 - Irreducible Brillouin Zone (left) and representative unit cell boundary nodes (right)

$$\begin{aligned} \lambda_x &= e^{j\mu_x} & \mu_x &= k_x L_x \\ \lambda_y &= e^{j\mu_y} & \mu_y &= k_y L_y \end{aligned} \tag{6}$$

$$\begin{aligned} q_T = \lambda_y q_B \;\; ; \;\; q_R = \lambda_x q_L \;\; ; \;\; q_{LT} = \lambda_y q_{LB} \\ q_{RB} = \lambda_x q_{LB} \;\; ; \;\; q_{RT} = \lambda_x \lambda_y q_{LB} \end{aligned} \tag{7}$$

$$\begin{aligned} f_{LB} + \lambda_x^{-1} f_{RB} + \lambda_y^{-1} f_{LT} + \lambda_x^{-1} \lambda_y^{-1} f_{RT} = 0 \\ f_L + \lambda_x^{-1} f_R = 0 \\ f_B + \lambda_y^{-1} f_T = 0 \end{aligned} \tag{8}$$

In Figure 2, a standard square 2D unit cell is represented and as the reader might have noticed, the nodes that need to be linked to analyse such periodicity are not just limited to the left and right boundaries of the cell, but also covers the bottom, top as well as the corner nodes. Equations (6) describes the 2D Floquet-Bloch relation while (7) and (8) link the cell extremities in terms of forces and displacements, just as it happened in the 1D case.

3 Hexhex pattern

Kirigami is an ancient Japanese art technique of cutting and folding paper to obtain a 3D structure. In the past [4-6] it has been used to produce cellular structures and the HEXHEX core, represents one of the many alternatives that the interlock concept is able to produce. The HEXHEX is a new interesting configuration that cannot be produced with classic Kirigami technique, due to the rhombohedral cells, but can be produced with the interlocking Kirigami derived technique.
By interlocking two hexagonal cores, we obtain the final structure which overall produces a hybrid cellular core made of different hexagonal cells as well as rhombohedral or parallelogram cells. The result of such interlocking is shown in Figure 3, where the side length of the hexagon is $l = 5\ mm$ and $t = 0.2\ mm$ the thickness of the squared cross-section beam.

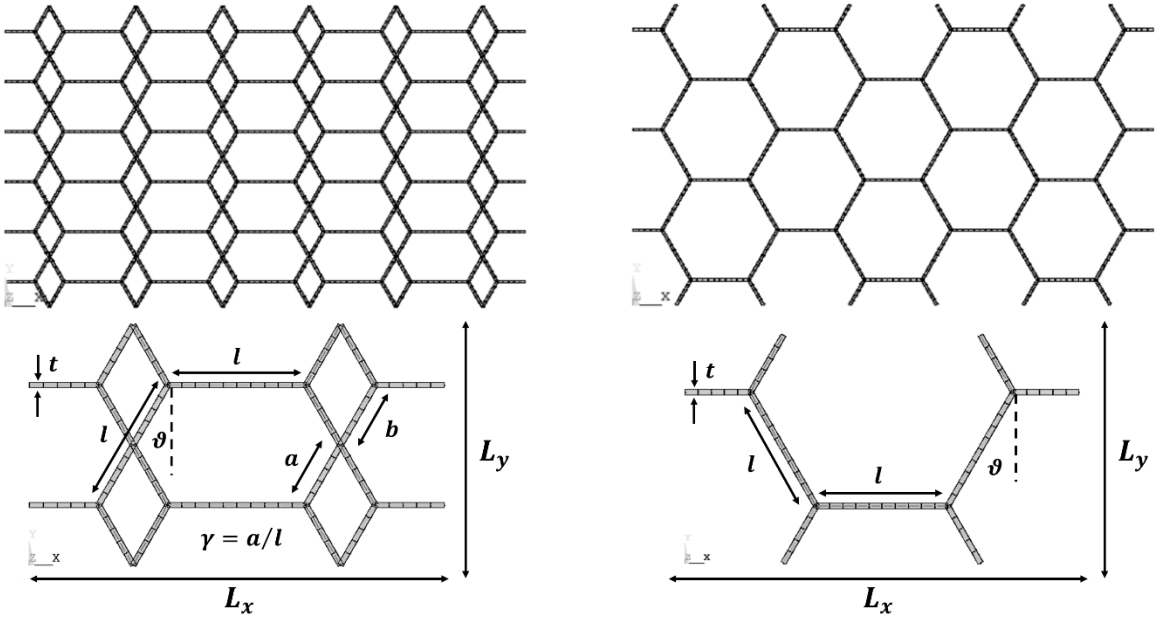


Figure 3 - HEXHEX lattice (top-left), Hexagonal lattice (top-right), HEXHEX unit cell (bottom-left), Hexagonal unit cell (bottom-right)

The investigation, both for 1D and 2D periodicity, was performed varying parameters like the shift ratio (which happens in the Y direction) between the two hexagonal cores $\gamma = a/l$, where $l = a + b$, and then the hexagonal internal angle ϑ. As shown in Figure 4, when the shift ratio is varied, the unit cell overall dimensions L_x and L_y are kept constant. This also means, since the core thickness in the Z direction is constant, that the overall relative density of the core will be constant and therefore the compression static properties in the Z direction will be equal [10].

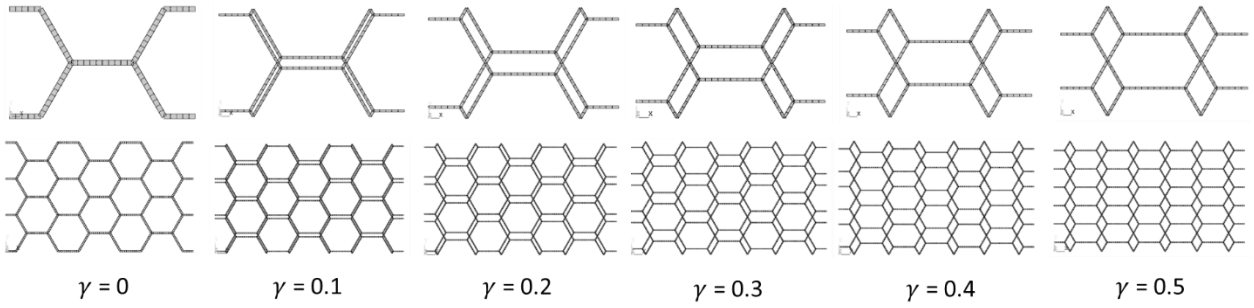


Figure 4 - HEXHEX unitcells (top) and respective representative lattices (bottom) for variable shift ratio

4 Investigation methods

As mentioned in the introduction, the objective is to perform vibration analyses on the HEXHEX topology to see whether it possesses in plane and/or out of plane Bragg bandgaps. The parameter taken into consideration to evaluate the topology performance is the presence and width of bandgaps.

Before proceeding with the actual bandgap evaluation, agreement between the bandgaps found using commercial software to produce FRF's and the ones found using Wave Finite Element Method (WFEM) will be carried out for the Hexagonal configuration, which has been chosen as the reference.

For the analysis, Timoshenko beam elements have been used as in this way, uncoupling of in-plane and out-of-plane behavior was possible. The element size for all the numerical simulations was set to 0.5mm and the material properties as well as variable parameters are listed in Table 1.

$\boldsymbol{Young's\ Modulus, E\ [GPa]}$	8.1
$\boldsymbol{Density, \rho\ [kg\ m^{-3}]}$	1040
$\boldsymbol{Poisson's\ Ratio, \upsilon}$	0.2
$\boldsymbol{Shift\ Ratio, \gamma}$	[0 - 1]
$\boldsymbol{Internal\ angle, \vartheta}$	[10° - 85°]

Table 1 - Numerical simulation parametric analysis variables and material properties

The Frequency response plot, obtained with a Harmonic simulation of the finite structure, is used to illustrate the validity of the bandgaps locations, as the amplitude drop of the plot increases with the increase of the number of unit cell repetitions.

The Harmonic analysis consisted in applying a compression force at one end of a truss structure created with repetition of unit cells along the periodicity direction. The out-of-plane degrees of freedom were blocked. The displacement amplitude of the selected nodes at the extremities of the truss was extracted and used to plot the FRF. The same type of harmonic study was carried out applying a bending (in-plane) force and recording displacements in the Y direction.

The 1D periodicity was analysed using the direct WFEM, which makes use of the Floquet Bloch theory to produce dispersion curves linking frequency (input) with the reduced wave number. For the 2D periodicity dynamic analysis, instead, the inverse WFEM form was used. In this method, the reduced wavenumber is imposed, and the output frequency calculated. In-plane and out-of-plane analysis was carried out.

4.1 Method validation (Hexagonal 1D)

The unit cell as well as a representation of the hexagonal topology are shown in Figure 5

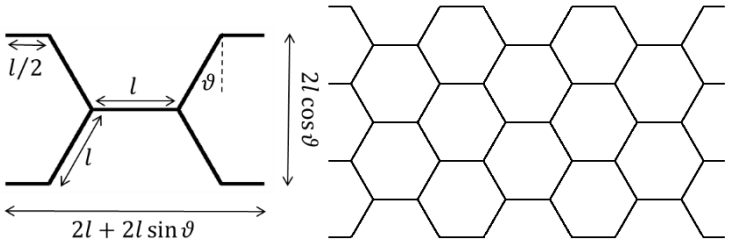


Figure 5 - Hexagonal unit cell and representative lattice

Figure 6 shows the FRF plots and the dispersion curves for the hexagonal topology. The graphs present vertical grey bands in correspondence of the bandgaps for clearness purposes. There is very good correspondence between dispersion curves (infinite structure) and the computed FRF plots (finite structure) and therefore from now on, we will only produce dispersion curves, as with a single simulation, we are able to identify the bandgaps without having to perform two different simulations.

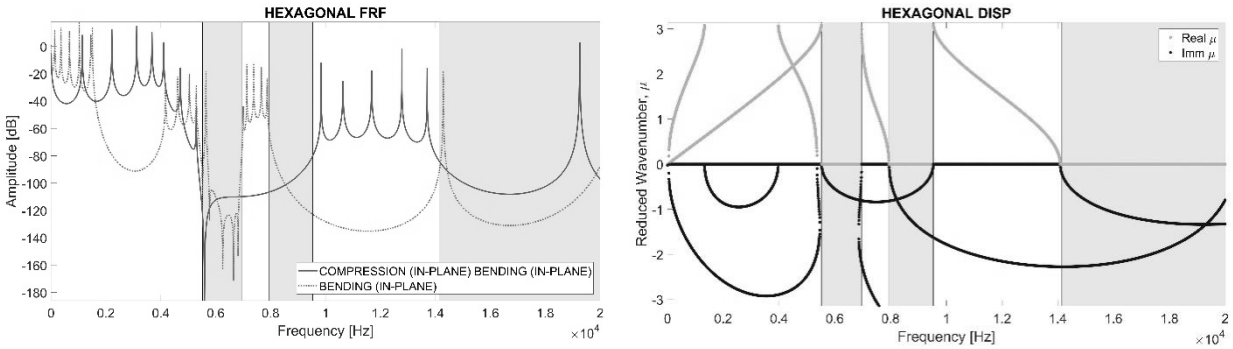


Figure 6 - Hexagonal lattice FRF (left) and Dispersion curves (right)

Since no damping was considered in the model, the amplitude scale of the FRF graph (Figure 6 left) loses its meaning. The intention here is just to use these plots as a visual tool to identify the frequency range of the bandgaps.

4.2 1DWFEM (in-plane)

Figure 7 shows the unit cells used for this type of analysis. In Figure 8 instead, two extreme configurations (for $\gamma = 0$ and $\gamma = 1$) representing regular hexagonal lattices are shown. To keep static out of plane properties constant, walls for those configurations were doubled where appropriate.

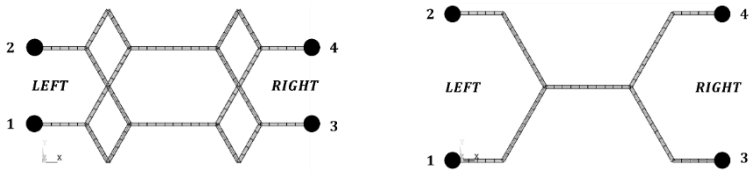


Figure 7 - 1DWFEM unitcells for HEXHEX (left) and HEXAGONAL (right) configurations

4.2.1 Variable shift ratio

The analysis will be carried out keeping $\vartheta = 30°$ and $l = 5mm$ constant. As consequence, a constant relative density is obtained since L_x and L_y do not vary, as shown in Figure 8. The shift only happens in the Y direction.

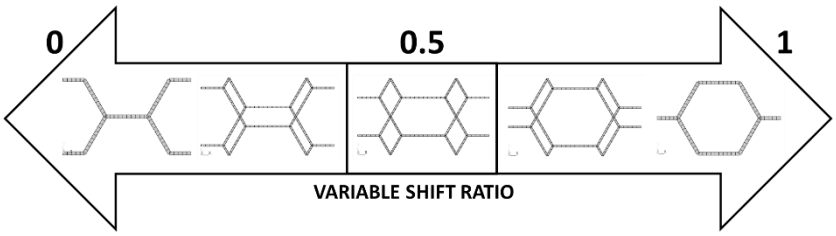


Figure 8 – HEXHEX unit cells according to the shift ratio variation

In Figure 9 (left) the dispersion plot for all the configurations are shown. Apparently, a minimum shift between the two initial hexagonal cores produces a bandgap that begins at 7410 Hz and has a bandwidth of 8910 Hz (see shift ratio $\gamma = 0.1$). For the latter shift ratio, we also obtain three very narrow bandgaps respectively starting at 4120 Hz, 17980 Hz and finally 18370 Hz. It is interesting also to point out how for $\gamma = 0$ and $\gamma = 1$ we obtain the same dispersion curves as their respective unit cell is the same one but simply shifted. Both unit cells maintain X and Y-axis symmetry and are therefore defined as being centrosymmetric.

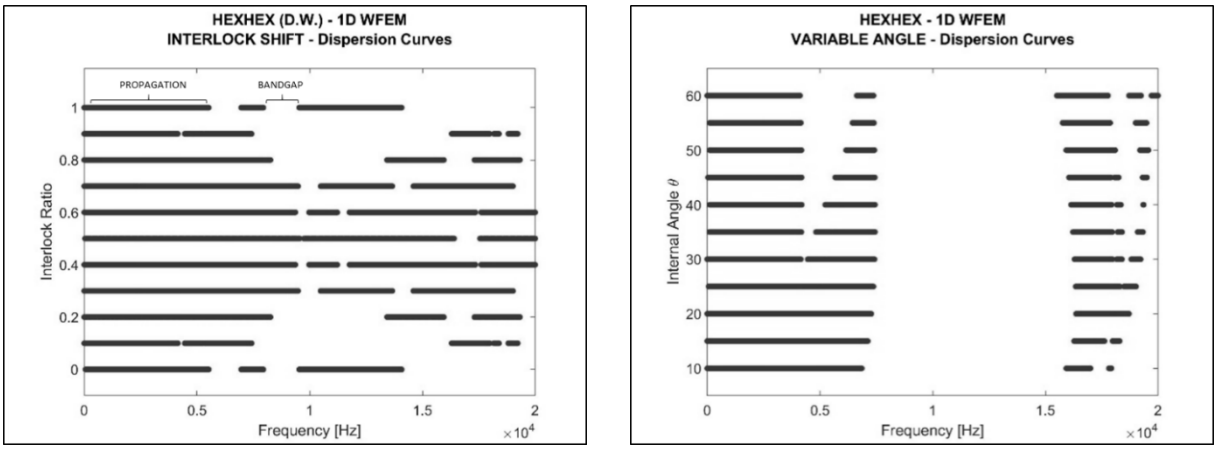


Figure 9 - 1DWFEM Dispersion curves for variable shift ratio (left) and variable internal angle with fixed shit ratio (right)

4.2.2 Variable internal angle

The variable angle analysis will be carried out keeping γ and l constant and the direct consequence is the change of relative density since L_x and L_y vary, as shown in Figure 10. The selected configuration to perform a variable angle analysis was the $\gamma = 0.1$ as it possessed the wider bandgap (8910 Hz) at lower frequencies (both aspects are within the investigation aim).

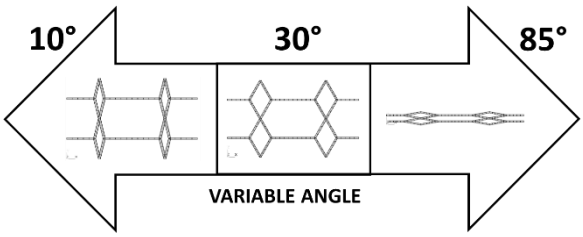


Figure 10 - HEXHEX unit cells according to internal angle variation

In Figure 9 (right) the dispersion plots for all the variable angle configurations are shown. The variation of the internal angle ϑ has a minimum effect upon the large bandgap which we observed during the shift ratio analysis (its width drops to 8170 Hz), but it opens up two of the minor bandgaps. The one starting at 4120 Hz, enlarges, keeping its left boundary roughly fixed and changing from an initial width of only 345 Hz to a width of 2580 Hz. The bandgap appearing at 17980 Hz tends to close as we increase ϑ, but the bandgap starting at 18370 Hz and finishing at 18830 Hz (width of 460 Hz) maintains the right boundary fixed and enlarges the left one reaching a width of 950 Hz.

4.3 2DWFEM

The unitcells used for the bidimensional periodicity analysis of the two cores are shown in Figure 11. We will perform both in-plane as well as out-of-plane analyses this time, contrary to the 1D periodicity case.

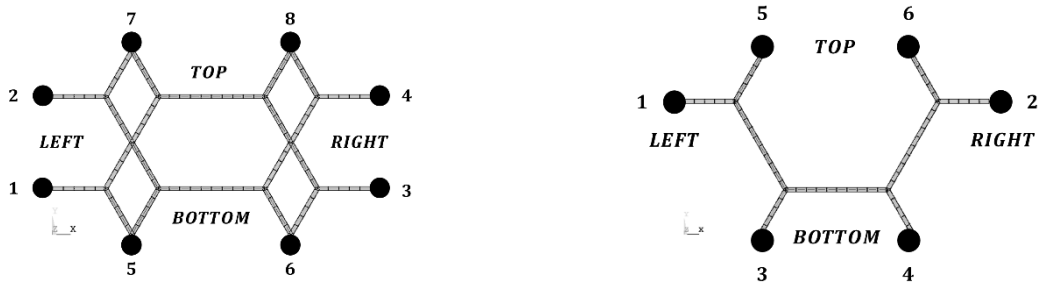


Figure 11 - 2DWFEM unitcells for HEXHEX (left) and HEXAGONAL (right) configurations

4.3.1 Hexagonal 2D

Figure 12 (top-left and top-right) shows respectively the 2D dispersion relation of a regular hexagonal lattice with $\vartheta = 30°$ and $l = 5mm$. Both in-plane and out-of-plane hexagonal configurations do not show presence of full bandgaps.

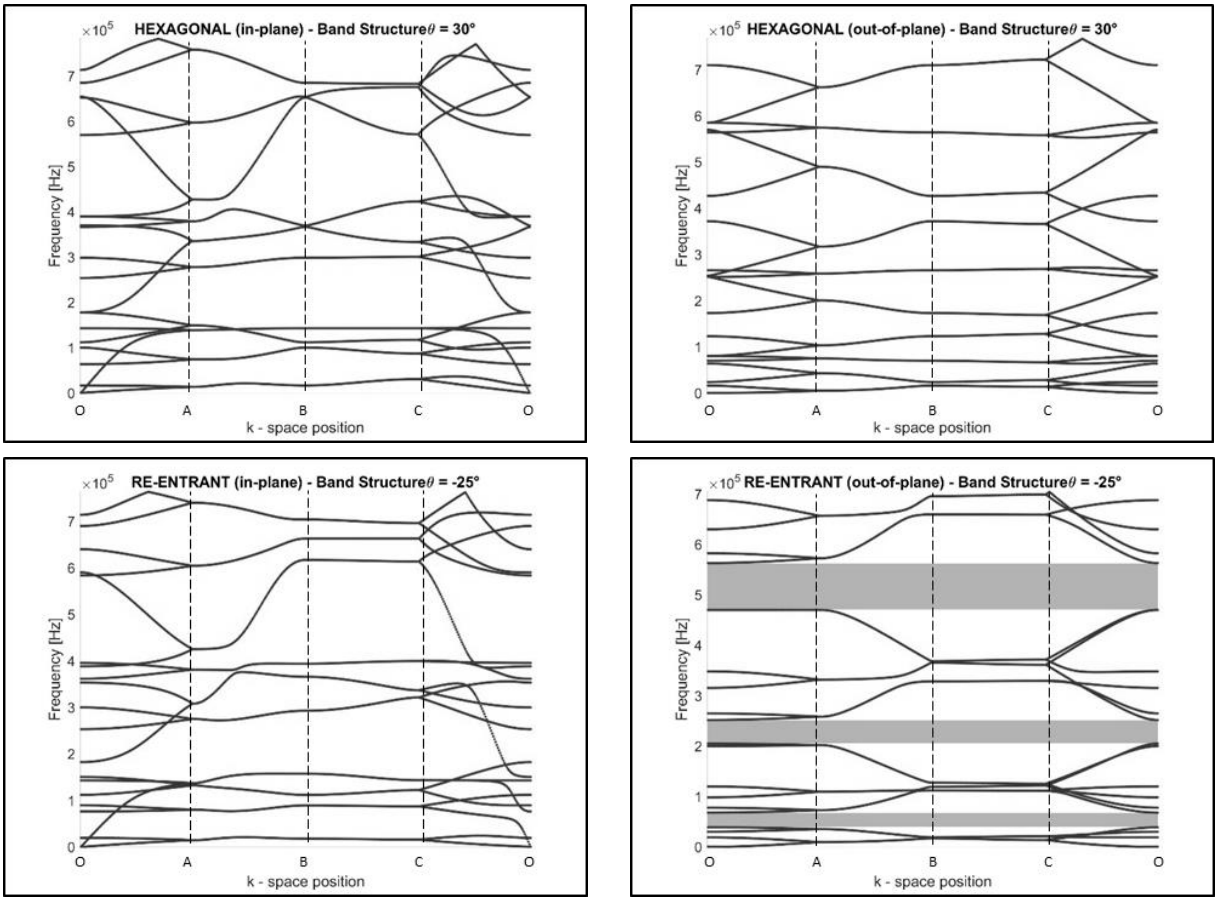


Figure 12 - 2DWFEM dispersion curves for Hexagonal/Re-entrant configuration (In-plane and out-of-plane)

When we vary the internal angle though shifting from a hexagonal to a re-entrant lattice, bandgaps in the out-of-plane analysis appear, as shown in Figure 12 (bottom-right). The respective bandgap widths starting from lower frequencies are: 29.12 kHz, 46.70 kHz and 92.90 kHz.

4.3.2 Hexhex

Figure 13 shows respectively the 2D dispersion relation in-plane and out-of-plane for the initial HEXHEX lattice with $\vartheta = 30°$, $\gamma = 0.5$ and $l = 5mm$. The in-plane configuration does not show presence of full bandgaps, just like the hexagonal case. The out-of-plane configuration instead does, and its bandwidth is 6.70 kHz.

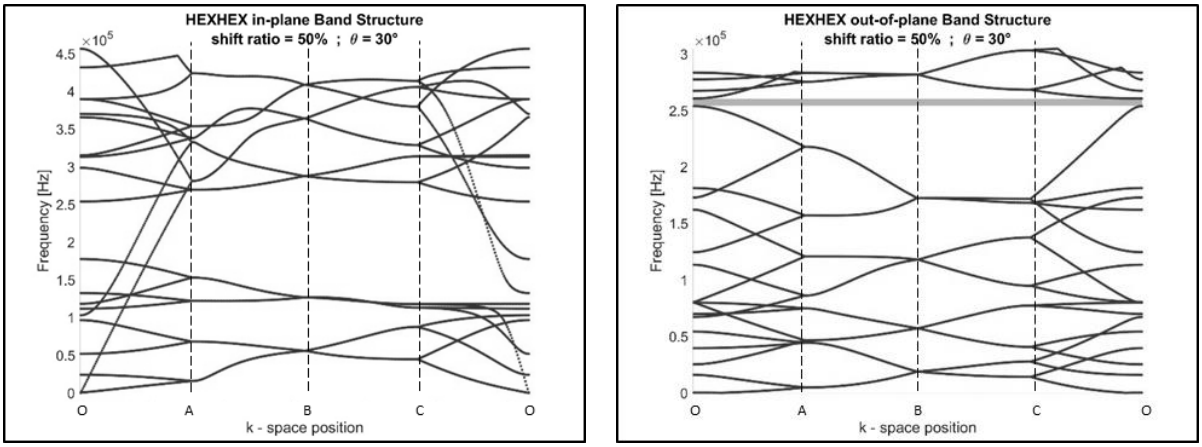


Figure 13 - 2DWFEM HEXHEX initial configuration dispersion curves (γ= 0.5; ϑ = 30°) in-plane and out-of-plane

Keeping in mind the initial objective, we varied ϑ and γ within the range listed in Table 1 and we obtained the following results, listed in Table 2 and Table 3. The variation of those parameters creates, and in some cases enlarges pre-existing bandgaps.

Figure 14 shows the configurations which exhibited the larger bandgaps. The widest in-plane full bandgap was obtained for $\vartheta = 35°$, $\gamma = 0.2$ (Figure 14 left) with a value of 9.90 kHz, whilst out of plane, for $\vartheta = 65°$ and $\gamma = 0.5$ (Figure 14 right) with a value of 16.40 kHz.

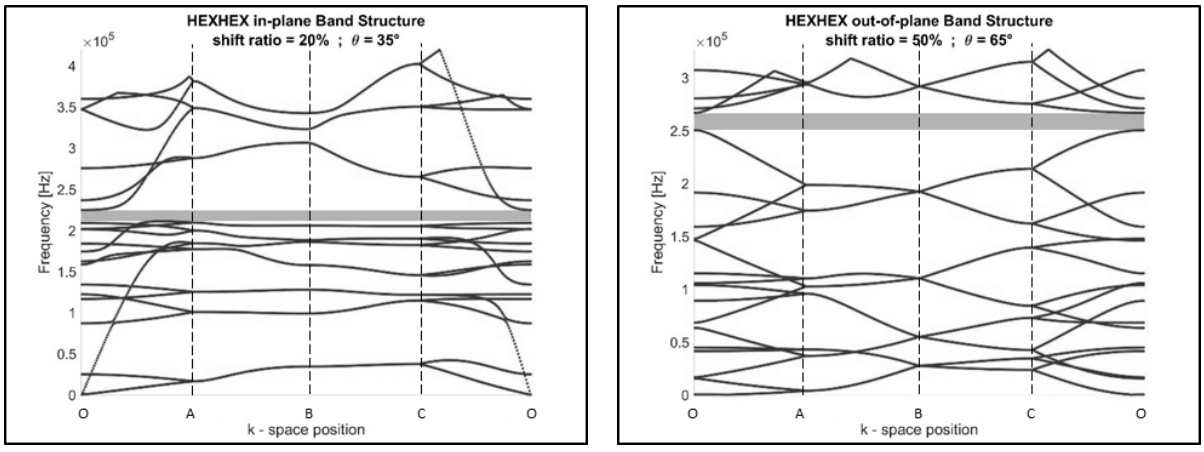


Figure 14 - 2DWFEM HEXHEX dispersion curves. In-plane and out-of-plane best performance obtained

It is worth to show (Figure 15) that for a combination of $\vartheta = 70°$ and $\gamma = 0.3$, there are 3 bandgaps, just like we obtain for the re-entrant configuration, although their width is considerably smaller if compared to those ones. The values from lower frequencies to higher ones are 5.40 kHz, 2.30 kHz and 7.60 kHz

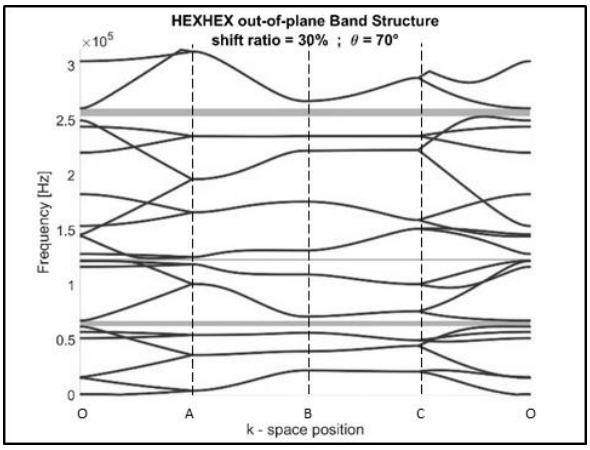


Figure 15 - 2DWFEM HEXHEX configuration (γ= 0.5; ϑ = 30°) with the highest number of bandgaps

5 Conclusions

The implementation of the Floquet-Bloch periodic boundary conditions through a transfer matrix method for 1D vibration bandgap prediction as well as for 2D periodicity is a valuable investigation resource, since the numerical results obtained agree with the ones obtained using commercial software.

The 1DWFEM analysis (Figure 9) shows that the HEXHEX lattice possesses bandgaps just like periodic mediums are supposed to do, and that the selected variables shift ratio (γ), and internal angle (ϑ), affect both the appearing of bandgaps as well as changing its width. In particular, for variable γ, the widest bandgap was produced when $\gamma = 0.1$ and $\vartheta = 30°$ was kept fixed. By selecting the latter configuration to vary ϑ this time, we observed that when $\vartheta = 60°$ the main bandgap keeps its width roughly constant the bandgap around 4500 Hz which is initially only 345 Hz wide, enlarges up to 2580 Hz as well as the one starting at 18370 Hz and finishing at 18830 Hz (width of 460 Hz) which reaches a width of 950 Hz.

The configuration that meets our goal for the 1DWFEM study is therefore $\gamma = 0.1$ and $\vartheta = 60°$.

The 2DWFEM analysis reveals that the regular hexagonal lattice does not possess full bandgaps both in-plane and out-of-plane. By varying the internal angle and reaching therefore the re-entrant configuration ($\vartheta = -25°$), three bandgaps appear with widths, starting from lower frequencies, of 29.12 kHz, 46.70 kHz and 92.90 kHz respectively.

The HEXHEX 2DWFEM analysis shows that this lattice is able to produce both in-plane and out-of-plane bandgaps. Figure 14 shows the configurations which exhibited the larger bandgaps. The widest in-plane full bandgap was obtained for $\vartheta = 35°$, $\gamma = 0.2$ (Figure 14 left) with a value of 9.90 kHz, whilst out of plane, for $\vartheta = 65°$ and $\gamma = 0.5$ (Figure 14 right) with a value of 16.40 kHz.

Although the largest bandgap recorded was obtained with the re-entrant configuration, the HEXHEX lattice represents a valid competitor for the classic hexagonal lattice.

6 Acknowledgements

I would like to express all my gratitude to [1]Université Bourgogne Franche Comté and [2]University of Bristol for hosting me during my research, and to my supervisor Morvan Ouisse[1] and Fabrizio Scarpa[2]. I would also like to thank my VIPER MSCA-ITN colleagues for constant feedback.

This project has received funding from the European Union's Horizon 2020 research and innovation programme under Marie Curie grant agreement No 675441 and was performed in collaboration with EUR EiPHi Project (ANR 17-EURE-0002).

7 References

[1] L. Brillouin. Wave propagation in periodic structures, electric filters and crystal lattices. Dover, 1953.
[2] D.J. Mead. Wave propagation in continuous periodic structures: research contributions from southampton 1964-1995. J. Sound Vib., 190(3):495-524, 1996.
[3] M I Hussein, M J Leamy, and M Ruzzene. Dynamics of phononic materials and structures: Historical origins, recent progress and future outlook. Applied Mechanics Reviews, 66(4):040802, 2014.
[4] F. Scarpa, M. Ouisse, M. Collet, K. Saito Kirigami Auxetic Pyramidal Core: Mechanical Properties and Wave Propagation Analysis in Damped Lattice. ASME. J. Vib. Acoust. 2013;135(4):041001-041001-11. doi:10.1115/1.4024433.
[5] S. Del Broccolo, S. Laurenzi, & F. Scarpa, 2017, 'AUXHEX – a Kirigami inspired zero Poisson's ratio cellular structure'. Composite Structures, vol 176., pp. 433-441.
[6] Neville, R.M., et al., Transverse stiffness and strength of Kirigami zero-ν PEEK honeycombs. Composite Structures, 2014. 114: p. 30-40.
[7] F. Scarpa, M. Ruzzene - Wave beaming effects in two-dimensional cellular structures, Smart Materials and Structures, 12 (2003) 363 – 372.
[8] Brian R. Mace, Denis Duhamel, Michael J. Brennan - Finite element prediction of wave motion in structural waveguides, The Journal of the Acoustical Society of America – 117 (2005) 2835-2843.
[9] Brian R. Mace, E. Manconi - Modelling wave propagation in two-dimensional structure using finite element analysis, Journal of Sound and Vib. 318 (2008) 844 – 902.
[10] Lorna J, Gibson MFA. Cellular Solids. 2nd Ed. Cambridge University Press, 1997.
[11] Kittel C. Introduction to Solid State Physics. Wiley, 8th edition. 11, 43.

8 Appendix

	HEXAGONAL $\vartheta \geq 0$		**HEXHEX** $\vartheta \geq 0$									
	In-plane	Out-of-plane	In-plane					Out-of-plane				
ϑ \ γ	0 & 1		0.1	0.2	0.3	0.4	0.5	0.1	0.2	0.3	0.4	0.5
10	0	2	0	0	0	0	0	0	0	0	0	1
15	0	1	0	0	0	0	0	0	0	1	0	1
20	0	0	0	0	0	0	0	0	0	1	0	1
25	0	0	0	0	0	0	0	0	0	1	1	1
30	0	0	0	1	1	0	0	0	0	0	1	1
35	0	0	0	1	1	0	0	0	0	0	0	1
40	0	0	0	1	1	0	0	0	0	0	0	0
45	0	0	0	1	0	0	0	0	0	0	0	0
50	0	1	0	0	0	0	0	0	1	0	0	0
55	0	1	0	0	0	0	0	0	1	0	0	1
60	0	1	0	0	0	0	0	1	0	0	0	1
65	0	1	0	0	1	0	0	1	0	2	1	1
70	0	1	1	0	1	0	0	1	0	3*	1	1
75	0	1	0	0	1	0	0	1	0	3*	1	1
80	0	1	0	0	0	0	0	1	0	2	1	1
85	0	1	0	0	0	0	0	1	0	1	0	0
* = Maximum number of bandgaps ; ___ = Maximum bandgap width reached												

Table 2 - 2DWFEM simulation summary

	HEXAGONAL $\vartheta \leq 0$ (Re-entrant configuration)									
	In-plane					Out-of-plane				
γ \ ϑ	-25	-20	-15	-10	0	-25	-20	-15	-10	-0
0 & 1	0	0	0	0	0	3 *	3*	3*	3*	3*
* = Maximum number of bandgaps ; ___ = Maximum bandgap width reached										
The HEXHEX configuration with this unit cell could not be used for $\vartheta \leq 0$										

Table 3 - 2DWFEM simulation summary bis

8.1 List of tables

Table 1 - Numerical simulation parametric analysis variables and material properties 6
Table 2 - 2DWFEM simulation summary 13
Table 3 - 2DWFEM simulation summary bis 13

8.2 List of figures

Figure 1 - Periodic structure unit cell and 1D Floquet Bloch periodic relations 3
Figure 2 - Irreducible Brillouin Zone (left) and representative unit cell boundary nodes (right) 4
Figure 3 - HEXHEX lattice (top-left), Hexagonal lattice (top-right), HEXHEX unit cell (bottom-left), Hexagonal unit cell (bottom-right) 5
Figure 4 - HEXHEX unitcells (top) and respective representative lattices (bottom) for variable shift ratio 5
Figure 5 - Hexagonal unit cell and representative lattice 6
Figure 6 - Hexagonal lattice FRF (left) and Dispersion curves (right) 7
Figure 7 - 1DWFEM unitcells for HEXHEX (left) and HEXAGONAL (right) configurations 7
Figure 8 – HEXHEX unit cells according to the shift ratio variation 7
Figure 9 - 1DWFEM Dispersion curves for variable shift ratio (left) and variable internal angle with fixed shit ratio (right) 8
Figure 10 - HEXHEX unit cells according to internal angle variation 8
Figure 11 - 2DWFEM unitcells for HEXHEX (left) and HEXAGONAL (right) configurations 9
Figure 12 - 2DWFEM dispersion curves for Hexagonal/Re-entrant configuration (In-plane and out-of-plane) 9
Figure 13 - 2DWFEM HEXHEX initial configuration dispersion curves (γ= 0.5; ϑ = 30°) in-plane and out-of-plane 10
Figure 14 - 2DWFEM HEXHEX dispersion curves. In-plane and out-of-plane best performance obtained 10
Figure 15 - 2DWFEM HEXHEX configuration (γ= 0.5; ϑ = 30°) with the highest number of bandgaps .. 11

Integrated dynamic testing and analysis approach for model validation of an innovative wind turbine blade design

M.M. Luczak[1], B. Peeters[2], S. Manzato[2], E. Di Lorenzo[2], P. Z. Csurcsia[2,5], K. Reck-Nielsen[3], P. Berring[1], P. U. Haselbach[1], K. Branner[1],V. Ruffini[4]
[1] Technical University of Denmark, Department of Wind Energy
Frederiksborgvej 399, 4000, Roskilde, Denmark
e-mail: **mluz@dtu.dk**

[2] Siemens Industry Software NV, RTD Test Division
Interleuvenlaan 68, 3001, Leuven, Belgium

[3] CEKO Sensors ApS
Diplomvej 381, DK-2800 Kgs. Lyngby, Denmark

[4] University of Bristol, Faculty of Engineering
Queen's Building, University Walk, Clifton BS8 1TR, UK

[5] Vrije Univeriteit Brussel, Department of Engineering Technology
Pleinlaan 2, 1050 Elsene, Belgium

Abstract
DTU Wind Energy continues the experimental investigation of the wind turbine blades to assess innovative designs of long and slender blades. This paper presents an experimental structural dynamics identification and structural model validation of the 14.3m long research blade. Unique feature of the blades is that its internal layup design has been highly optimized w.r.t. stretching the rotor and substantial mass reduction at the same time. As the result, the blade is more flexible than the traditional one. The results of the modal tests following analyses were performed: (i) Uncertainty Quantification of the experimental modal parameters for the blades, (ii) non-linearity assessment, (iii) numerical model correlation – frequencies and mode shapes of the experimental model comparison with those from Finite Element (FE). Finally, the outlook for the future experimental blade research activity is outlined.

1 Introduction

Modern wind turbine blades are expected to withstand the in-service and extreme loads for a lifetime of 25 years. The IEC 61400-23 standard [1] requires full-scale structural testing of wind turbine blades. The standard defines the static load, fatigue load and natural frequencies testing and interpretation of the results. Requirements for the structural dynamic identification are limited to measurements of the first and second flapwise and first edgewise frequencies. Remaining blade modal properties such as damping and mode shapes are listed under the optional tests.

The length of recently developed offshore wind turbine blades exceeds 100 meter [2]. In-depth understanding of the dynamic behavior of such slender and flexible structures requires detailed experimental investigation exceeding the current scope required by the standard since unstable vibrations of wind turbine

blade may lead to its failure. Adequate identification of the blade‘s mode shapes is critical for the analysis of stability problems. Experimental modal testing is a well-established tool [3-5] for the estimation of the modal model of a mechanical system. At DTU Wind Energy (former Risø National Laboratory), modal testing has been applied to full-scale wind turbine blades. The work of Larsen et al [6] and Pedersen et al [7] revealed some discrepancies between experimentally and numerically obtained mode shapes. Large differences were observed especially for torsional modes. Extensive and well documented activities on modal testing of research-scale blades was conducted at Sandia National Laboratory. Different support configurations for the investigated blades have been studied [8] followed by the uncertainty analysis of the obtained results [9]. Uncertainty quantification has been a subject of investigations for the modal test of helicopter rotor blades [10]. The test setup has been found to have a large effect on the performed tests, as the mass of the sensors or damping added from cables may significantly influence the values of the observed frequencies and damping. Furthermore, the influence of the support structure has also been taken into account in the parameter estimation and numerical model validation [11].

Progress in the development of measurement equipment has enabled application of different sensors for modal testing of wind turbine blades. Optical methods are commonly used for full-field blade response measurement [12-14]. One of the main advantages of the application of camera-based full field methods is the collection of strain and acceleration data combined in one measurement system. Strain modal analysis [15] is an attractive alternative for vibration acceleration measurements, as the blade is often instrumented with a dense network of strain gauges for static and fatigue testing. Alternative excitation methods are being investigated with the application of Piezoelectric Transducer (PZT) patches as actuators [16].

Characterization of blade dynamics is one area of the modal testing results application. The modal models are also used for the numerical model validation for the model improvement [17, 18] and damage detection [19].

This paper presents a study on the integrated dynamic testing and analysis for model validation of a research-scale wind turbine blade. Section 2 describes the experimental setup and measurement results. Section 3 provides information on the validation of the FE model of the blade. The final section concludes on the research done so far and sets the future outlook.

2 Numerical modal analysis

The blade was modelled using the commercial finite element package pre/post-processing software MSC Patran (version 2014). The model was generated by using Risø-DTU’s in-house software Blade Modeling Tool (BMT). MSC Marc was applied as the solver in all analyses.

The blade structure was discretized using 20-noded layered continuum solid elements, which requires a volume representation of the geometry. The entire blade geometry was modelled based on input data of 99 blade cross sections generated by DTU Wind Energy’s in-house Beam Cross section Analysis Software (BECAS) optimizing scheme [20]. The blade airfoil defines the outer cross-section geometry. An offset according to the layup and layer thickness of the composite material determines the element thickness. Finally, the individual cross-sections were connected by spline curves and interpolation surfaces to obtain a volume representation of the blade. This process was handled automatically by BMT, which uses 60 regions/solids to assign the different cross-sectional properties computed by the BECAS optimizing scheme. Figure 1 shows segments of the blade model.

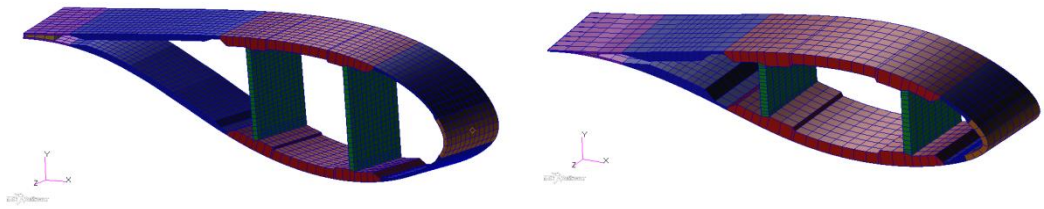


Figure 1: Left: Cross-section segment at radial position of around 5m, right: mid segment.

Depending on the region, the composite layup consists of 6 to 32 plies through the thickness. The properties of the composite, with its material, layup and ply orientations were assigned to 20-noded layered continuum elements defining the element stiffness matrix. The model was discretized with approximately 130,000 layered 20-noded continuum elements.

The blade manufacturer has not stated the exact properties for the fibers and matrix material, so properties from comparable materials described in the literature have been used to some extent. For this purpose, the elastic properties were calculated using Autodesk Simulation Composite tool, which uses a calculation scheme based on the Classical Laminate Theory. The estimated characteristic mechanical material properties and the estimated design material strengths applied in these studies are presented in Table 1.

Mechanical properties	**UNIAX**	**BIAX**	**TRIAX**	**Chop**	**Core**	**Glue**	**Gelcoat**
E1 [MPa]	37800	9550	18700	13600	48.5	3009	2000
E2 [MPa]	11100	9550	10900	13600			
G12 [MPa]	3270	10100	7720	5130			
ν_{12}	0.24	0.62	0.55	0.32	0.4	0.3	0.3
ϱ [kg/m^3]	1850	1780	1780	1684	80	1540	1500
Thickness [mm]	0.95	0.5	0.75	0.3	5-10	-	0.6
Design strength (PSF 2.205)							
X_T [MPa]	360.0	69.3	186.0	56.2	x	x	x
X_C [MPa]	257.0	64.9	152.0	56.2	x	x	x
Y_T [MPa]	24.8	69.3	30.5	56.2	x	x	x
Y_C [MPa]	63.5	64.9	51.5	56.2	x	x	x
S [MPa]	16.6	55.9	42.3	23.9	x	x	x

Table 1: Material properties

The natural frequencies and mode shapes of the blade are shown in Table 2:

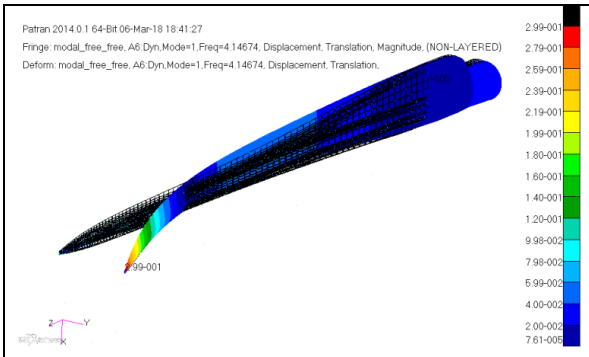
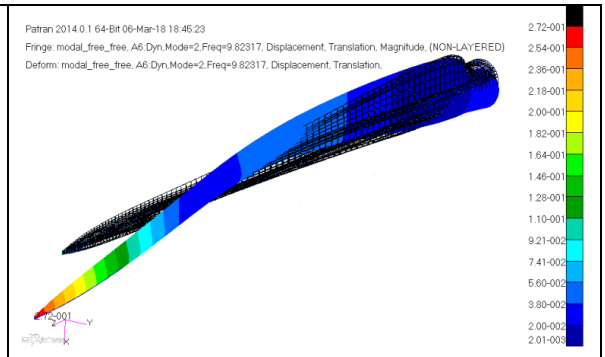
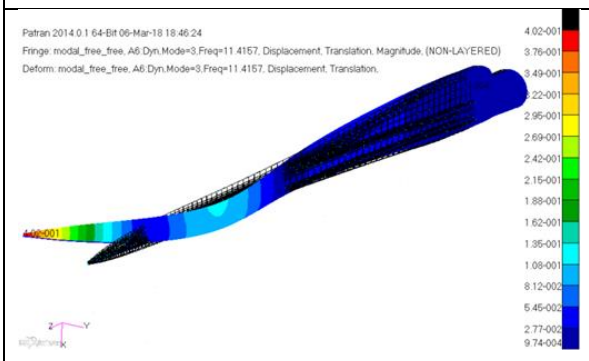
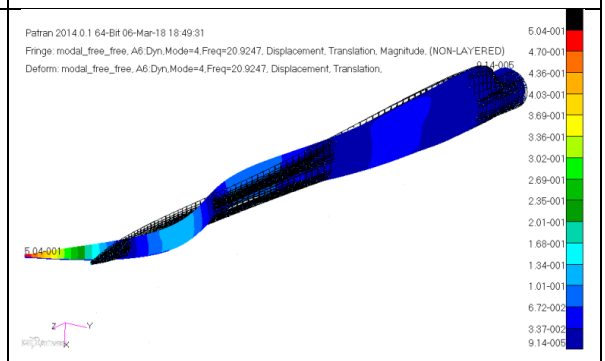
	
1st Flapwise FE mode 4.12 [Hz]	1st edgewise FE mode 9.87 [Hz]
	
2nd Flapwise FE mode 11.36 [Hz]	3rd Flapwise FE mode 20.81 [Hz]

Table 2 Mode shapes examples from FEM analysis

3 Experimental modal analysis

DTU Wind Energy department has recently commissioned a Large Scale Test Facility built for the experimental research of full-scale wind turbine blades and their subcomponents. The facility has three test rigs capable of accommodating blades of different lengths, ranging from 12 up to 45 meters, for static, fatigue and dynamic testing as shown in Figure 2.

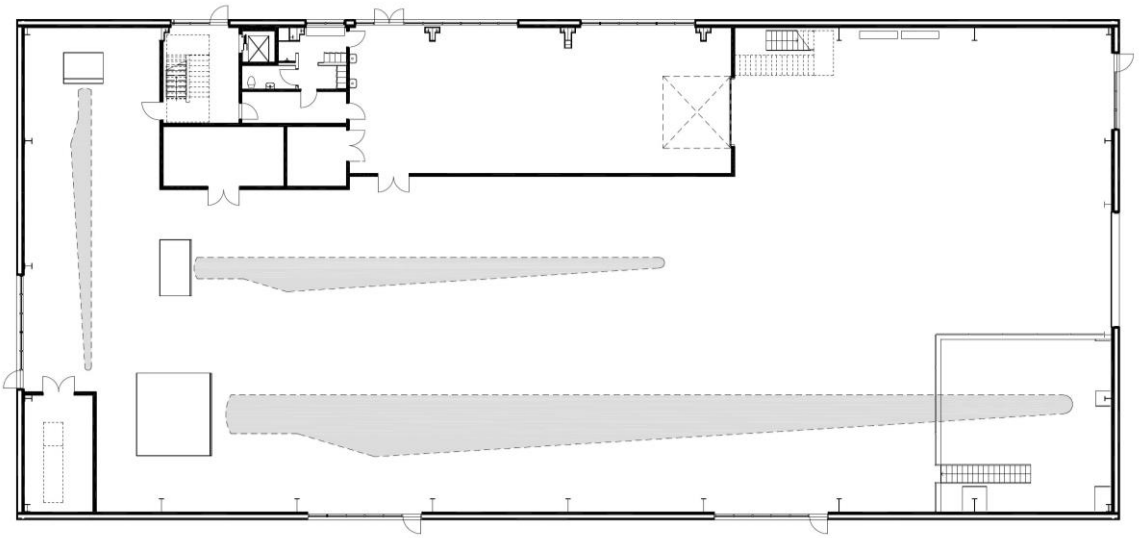


Figure 2 Large Scale Test Facility layout with three test rigs for a full scale blade tests.

The blade tested for this study is a research-scale blade, with a length of 14.3 m and a mass of approximately 530 kg. It has been entirely designed at the DTU Wind Energy department, and manufactured by Olsen Wings. Modal tests have been performed before destructive static and fatigue testing. An estimated modal model of the intact blade will serve as a reference data for the post-fatigue damage detection. After the fatigue testing, the modal tests will be repeated and the results will be compared to the initial modal analysis data. In addition, blade modal models will be analyzed in order to investigate the detection possibilities of damage in the blade.

3.1 Test setup

In the presented measurement campaign, the test blade was supported with two elastic cords in the edgewise direction to provide free-free boundary conditions as presented in Figure 3. This configuration is particularly convenient for the updating of the numerical model of the blade, as it does not require modelling of the boundary conditions.

The investigated blade has been simultaneously excited in the flapwise and edgewise directions with two electrodynamic shakers. As measurement grid, it was decided to split the blade into 15 equidistant “stations”, one every 1m. Additionally, each station was measured at 8 locations (Figure 4) , including: the trailing and leading edge, the point of maximum stiffness on the pressure and suction sides of the airfoil, plus 4 intermediate points between these. The high-fidelity finite element model presented in the previous section was used to simulate the test results and optimize sensor placement, in terms both of coordinates and orientation. Using the proposed locations, it was verified that the current measurement setup could guarantee a good description of the first 30 modes.

To ensure a consistent and repeatable excitation of the blade, and avoid damaging it, two relatively stiff points on the flap and edgewise directions were selected. As shown in Figure 3, the shaker along the edgewise direction was placed approximately in the middle of the blade, close to the expected nodal line of the first edgewise mode, to keep the maximum resonant response of the blade to safe levels. For the horizontal shaker, a point close to the center of gravity was selected. However, ensuring a good connection of the shaker to the blade in this direction has been more difficult, as in this direction the blade responds like a pendulum, causing the stinger to detach often from the blade. In addition, as the stingers were disconnected from the blade after each run before moving the accelerometers, a consistency check was performed to ensure the system remained invariant over the different test runs.

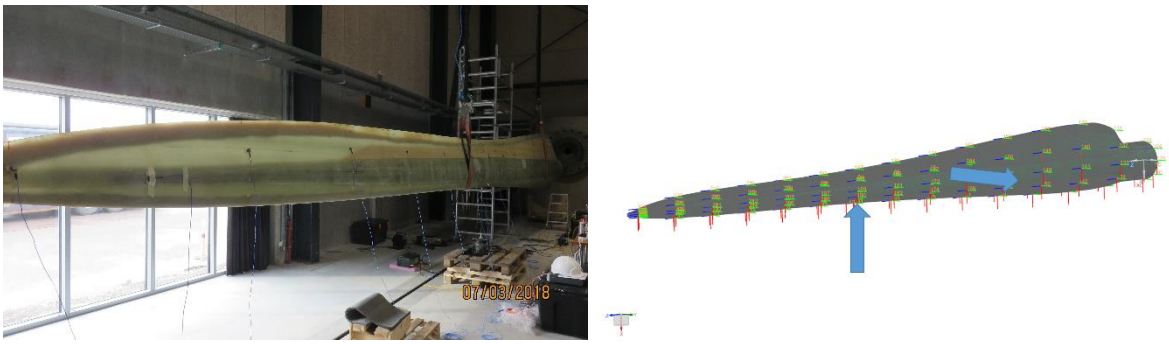


Figure 3 Instrumented blade on the test stand in the free-free support configuration (left) and geometry of the measurement and excitation points (right).

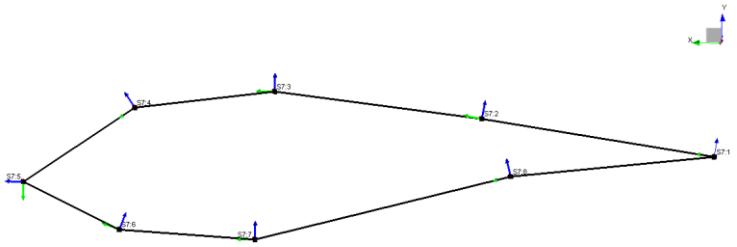


Figure 4: Sensor instrumentation along the airfoil.

The excitation forces and the corresponding driving-point Frequency Response Functions (FRFs) were measured by two impedance heads, which encapsulate force and acceleration sensors in one housing. The dynamic response of the blade was measured with 15 tri-axial piezoelectric accelerometers. Considering the total number of degrees-of-freedom on the measured grid (15 stations x 8 locations x 3 directions = 360 DOFs) it was decided to perform the measurement in a roving accelerometer configurations, so that the 15 sensors were moved over the 8 locations for each measurement station. As the driving-point FRFs at the excitation locations were measured for all runs, they are used as reference to recombine the different datasets and scale the mode shapes.

3.2 Uncertainty analysis

In this section, the main sources of uncertainties that were analyzed correspond to the measurement setup. As discussed in the previous section, the whole measurement grid was covered in 8 runs, where the excitation was applied always at the same location while the accelerometers were moved around the profile of the airfoil. Moreover, as the two stingers connecting the shakers to the blade were disconnected before moving the accelerometers, inconsistencies in the actual direction of application of the force could arise. Variations in modal parameters between the different runs can therefore be attributed to:

- Misalignment of the stinger axis,
- Loose connection between shakers and structure,
- Time of measurements (campaign was performed over a period of 3 days, with significantly different meteorological and temperature conditions),
- Mass loading effects due to accelerometers and cables (this is considered to be negligible considered the total mass of the blade),
- Change in the stiffness of the supporting elastic cords over time.

In Figure 5 the variability of the excitation over the 8 runs is shown. For the excitation in the edgewise direction, the Driving Point FRFs are highly repeatable and consistent. On the other hand, the corresponding flapwise Driving Points show much higher variability between the different runs, because of the difficulties in ensuring a good and reliable connection between the shaker and the blade.

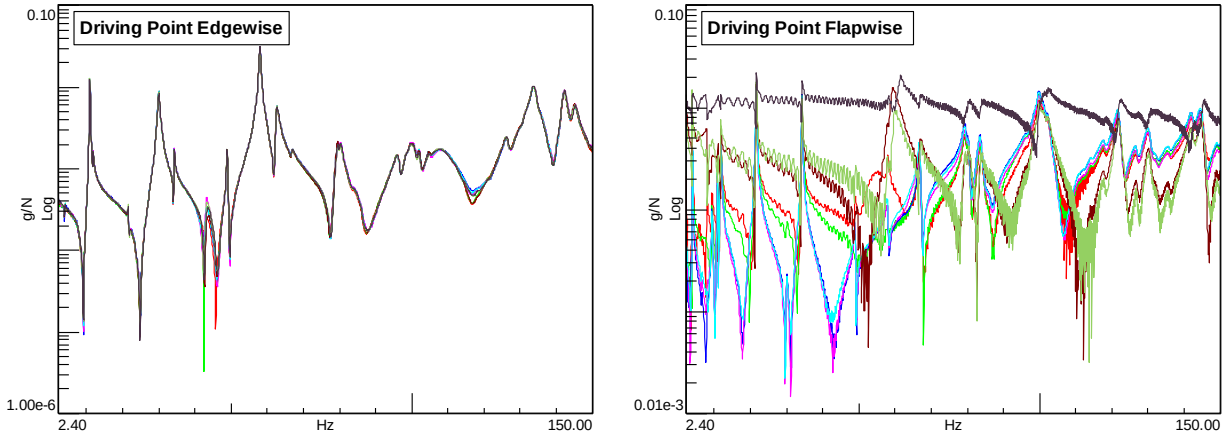


Figure 5: Driving Point FRF for the edgewise and flapwise excitation over the 8 different runs

Starting from these observations, modal analysis was performed on the 8 datasets and the individual estimates are compared. The following procedure was applied:

1. The Polymax modal parameter estimation was applied to the FRFs collected during each run using the same settings: (i) a maximum model order of 100 was set to estimate modes in the 2.5 to 150 Hz frequency band; (ii) upper and lower residuals were included; (iii) poles were selected manually; and (iv) modes were assumed to be complex.
2. Only modes consistently appearing in all modesets were included in the statistical calculation.
3. For each mode, the average and the standard deviation of the frequency and damping were computed.
4. Individual estimates were normalized to the corresponding average value to simplify visualization.
5. To correlate the results with the actual test, the average coherence on the edgewise driving point is also added to the plot.

The results of the analysis are displayed in Figure 6 both for the frequencies and damping. In general, the scatter of the estimates is very limited between the different runs. For the frequencies, we observed some higher variability in correspondence of the first mode (the 1st flapwise bending), the torsional mode around 43 Hz, and finally on a cluster of modes between 100 and 110 Hz. For the damping, a larger variability can also be observed at higher frequency, around 130 Hz. A higher uncertainty on the damping can generally be expected as damping estimates are more sensitive to inconsistencies in the data and on the selection of one specific pole in the stabilization diagram. In general, however, despite the difficulties in connecting the flapwise shaker to the structure, the actual duration of the test over few days and the roving of the accelerometers, the results are quite consistent and as a consequence, the FRFs from the different runs can be processed all together into a single database.

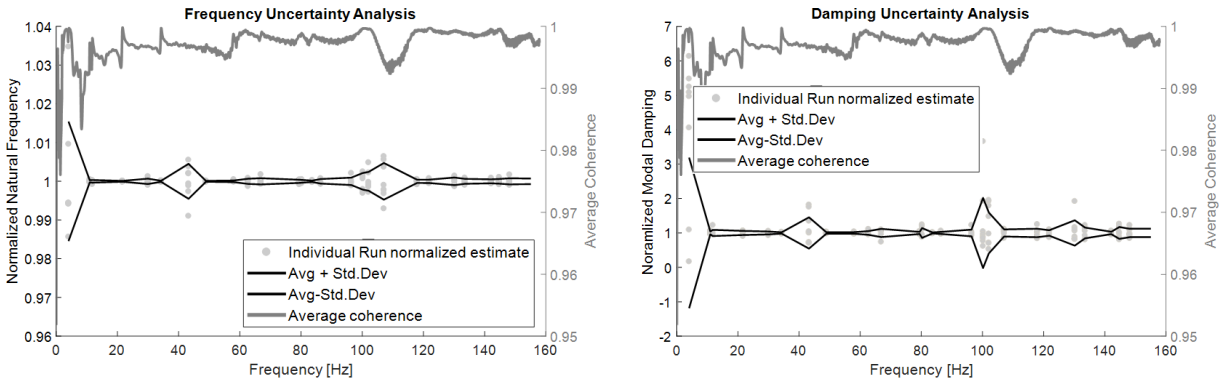


Figure 6: Modal Frequency and Damping uncertainty analysis results.

3.3 Nonlinearity assessment

In modern system identification special excitation signals are available to assess the underlying systems in a user-friendly, time efficient way [21]. In order to avoid any spectrum leakage, to reach full nonparametric characterization of the noise, and to be able to detect nonlinearities, a periodic signal is needed. Many users prefer noise excitations, because they are simple to implement, but in this case nonlinearities are not identifiable, and there is a possible leakage error.

3.3.1 Multisine excitation technique

The best signal that satisfies the properties listed above is the multi-sine signal (see Figure 7), which looks and behaves like Gaussian white noise, but is deterministic. It is important to highlight that multi-sine excitation is not equivalent to stepped sine excitation [22,23].

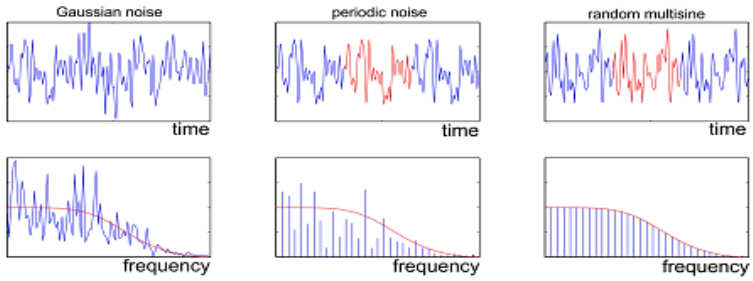


Figure 7 Different excitation signals in time and in frequency domain

3.3.2 Best Linear Approximation approach

The Best Linear Approximation (BLA) method has been widely used in the last decades to efficiently estimate FRFs [21, 24, 25]. The BLA of a nonlinear system minimizes the mean square error between the true output of a nonlinear system and the output of the linear model, see Figure 8. With this technique, instead of using the classical H1 estimate (cross-power spectral density estimate [21]) and its coherence function, a BLA model is estimated, and the coherence function is split into a) noise level and b) nonlinear contribution estimates.

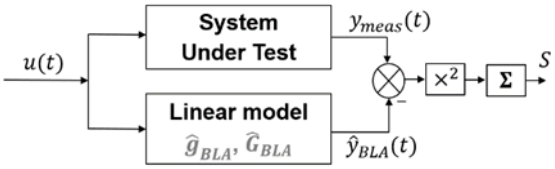


Figure 8 The baseline model and the cost function (S) of the best linear approximation framework

The proposed BLA technique makes use of the knowledge that the excitation signal has both stochastic and deterministic properties. In this work, random phase multi-sines are used and generated in the frequency domain such that the magnitude is set by the user, and the phases of the cosines are chosen randomly from a uniform distribution [26].

A further difference w.r.t. H1 estimation is that instead of directly using the averaged input and output data, a partial BLA estimate is calculated for each period of the excitation, and several different realizations of the excitation signal are repeated multiple times. A BLA FRF estimate, for a given signal, is then calculated

via the average of different BLAs. In this case it is possible to easily estimate the noise levels and standard deviation of the estimates at each frequency line. The difference between the total variance of BLA and the noise variance is an estimate of the variance of the stochastic nonlinear contributions. In [22] it has been shown that the above statements are only true when some additional assumptions are satisfied.

3.3.3 Measurement analysis

Multiple multisine experiments have been done at relatively low and high power levels as it is recommended for the BLA measurement procedure [24].

Figure 9 shows the magnitude spectrum of the flapwise measured excitation signal at low (left figure, grey line) and high (right figure, black line) levels (with an approximate overall signal level difference of 10 dB, i.e. factor of 3). The reference signal – a computer-generated ideal waveform – has a completely flat magnitude. The differences between the ideal flat and measured magnitude characteristic, and the level of nonlinearities w.r.t the noise level illustrate the dynamic behaviour of the shaker and its interaction with the underlying structure. Black dots show the corresponding noise level estimates, which gives a rough estimate of the SNR (around 46 dB at low level excitation at mid frequencies, and around 50 dB at high level excitation). Orange and blue dots refer to the odd and even nonlinearities on the non-excited detection lines (the frequency bins where the type of nonlinearities can be captured). The even nonlinearities – compared to the noise level – become dominant at the high-level excitation profile, especially above 60 Hz. A further interesting thing to mention is that the influence of electrical noise (harmonics of the mains frequency 50 Hz) is less significant at the higher level excitation. Apart from this, the nonlinearities have limited effect, as they are of the same order as noise.

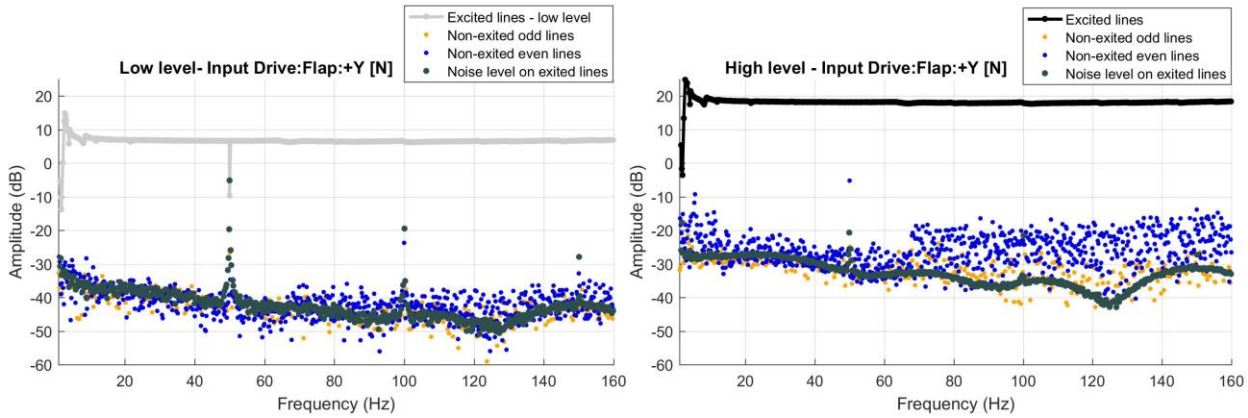


Figure 9 The measured excitation spectrum on the Y (flap) direction is shown for low level (gray line, on the left side) and high levels (black line, on the right side) together with the estimated noise level (black dots), even (blue dots) and odd (orange dots) nonlinearities.

Figure 10 shows the frequency response matrix estimate of the underlying system in the X and Y directions at the output channel S13, close to the wing tip. Black and grey lines show the high and low level FRFs with the corresponding noise (black and grey dots) and nonlinearity (red and orange dots) estimates. The low-level FRFs below -60 dB are quite noisy, and the nonlinearities have a limited effect (their level is approximately 5 dB higher than the noise). At the high excitation level, the SNR is significantly improved, but the level of the nonlinearities increases as well. From these results, it is also possible to see that the torsional mode at 42 Hz exhibits a particularly large difference in level between noise and nonlinearity, at both low and high excitation levels. In general, the nice overlay between the BLA and the measured FRFs is an indication that the system can be reasonably assumed to behave linearly. These results warrant further investigation of the behavior of this mode.

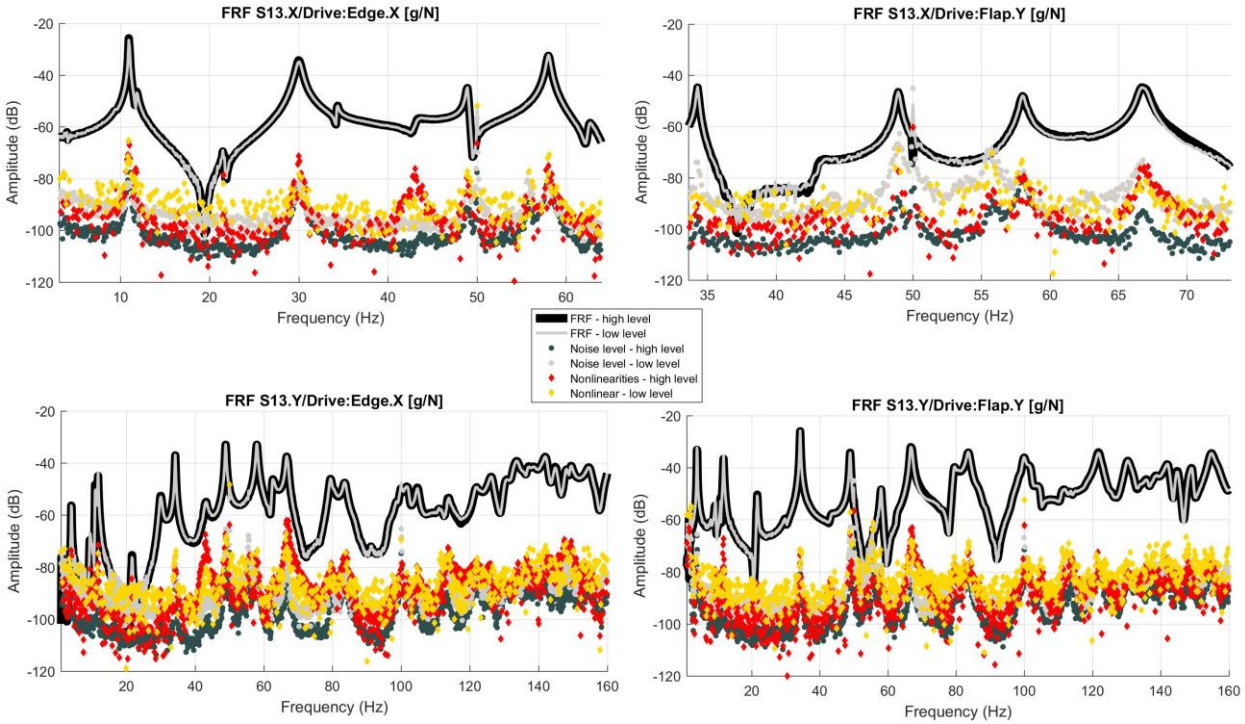


Figure 10 The best linear aproximation of the frequency response matrix is shown for low level (gray line) and high levels (black line) together with the estimated noise (grey and black dots) and nonlinearity (orange and red dots) levels at S13 channel.

3.4 Measurement results

Based on the preliminary observation and analysis performed in Sections 3.2 and 3.3, here a summary of the identified modes is given. Because of the repeatability between the different test runs, it was decided to fit a model including all FRFs at the same time, so that the fitted FRF and mode shapes can be more consistent to the actual blade behavior.

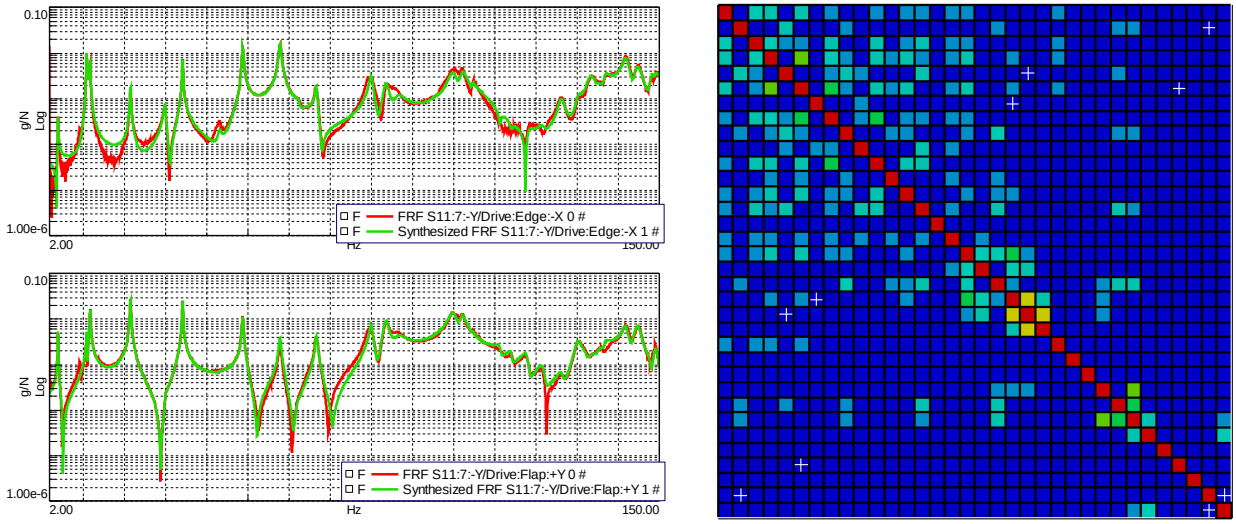


Figure 11: Validation of the identified modal model. Left: Comparison of measured (red) and synthesized (green) FRFs for a specific DOF (S11:7:-Y). Right: AutoMAC for the selected modeset.

In total, 33 modes have been reliably identified in the frequency range between 2 and 150 Hz. Figure 11 shows the validation of the modeset identified from the measured experimental data. On the left, the synthesized FRFs between one measured Degree of Freedom and the two excitations are displayed. In both cases, the correlation between the measured and reconstructed FRFs is very high, confirming that the identified model is able to correctly represent the structure in the frequency range of interest. On the right, the AutoMAC (autocorrelation between all mode shapes) is displayed: as the matrix has a dominant diagonal, the identified set contains independent vector and can thus be reliably used to validate (and later update) the numerical model from Section 2.

3.5 Optical accelerometer measurements



Mode	Frequency, Optical [Hz]	Frequency, Reference [Hz]	Deviation [%]
1	4.100	4.048	1.280
2	9.300	9.430	1.380
3	11.000	10.966	0.310
4	11.800	11.807	0.060
5	21.699	21.655	0.200
6	30.149	29.982	0.560
7	34.299	34.290	0.030

Figure 12 The optical accelerometer (CEKO OA1) was mounted flap-wise on the test blade. The accelerometer measures 27 mm in diameter. The first 7 resonance frequencies measured using the optical accelerometer and a reference piezoelectric accelerometer are shown in the table.

Two uniaxial all-optical MEMS accelerometers (CEKO Sensors, model OA1) were used to measure the transfer function of the test blade. The optical accelerometers are completely metal-free, thus immune to electromagnetic interference from e.g. lightning strikes, and therefore safe to operate on wind turbines under all conditions. They are based on refractive index modulation technology, which is a high sensitivity frequency modulated sensing principle. The accelerometers were mounted 12.5 m and 9 m from the root, respectively. Data was recorded using a CEKO Sensors S-DAS monitoring system operating at a 3000 Hz sampling rate. A piezoelectric accelerometer was located next to the optical accelerometer as reference. The measured transfer functions for the optical and piezoelectric accelerometer during pseudorandom excitation are seen in Figure 13. Figure 13 Comparison of measured transfer functions. Numerically calculated resonance frequencies are shown with dashed lines.Both the reference and the optical accelerometer detects practically all resonances below 100 Hz, though some have very low amplitudes due to the measurement locations. Differences in amplitudes are primarily due to the two accelerometers measuring along slightly different angles. At the 9 m position the amplitude of the fundamental mode is reduced compared to the resonances around 30 Hz. This is expected as this location is close to a node of the fundamental mode. The absolute error between resonance frequencies measured using the optical accelerometer and those of the piezoelectric reference, as well as the numerically calculated frequencies, is of the order of 1% or less.

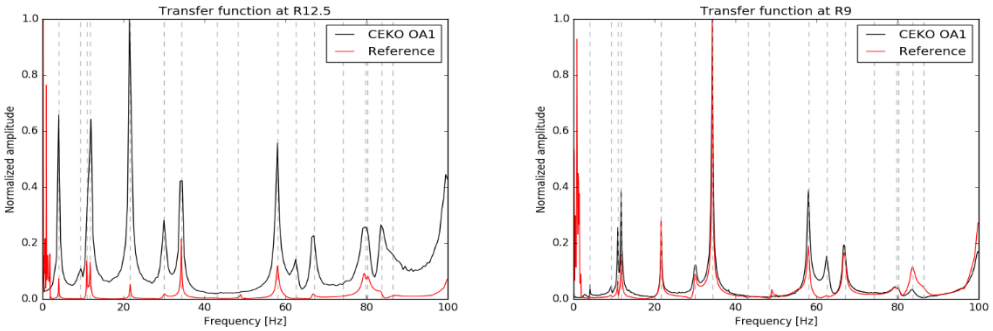


Figure 13 Comparison of measured transfer functions. Numerically calculated resonance frequencies are shown with dashed lines.

4 Test-simulation correlation

The numerical model described in Section 2 was validated with the experimental model identified in Section 3.4. As the experimental grid was derived from the numerical model, no geometric correlation is required as the measurement points already coincide with a node in the model. Consequently, the Modal Assurance Criterion between the numerical and experimental model can be calculated, and the results are displayed in Figure 14. Generally good correlation can be seen for the first 13 modes, while at higher frequencies the model and the experiments start to diverge. This is to be expected as the modal response at higher frequency is more localized and subject to uncertainties.

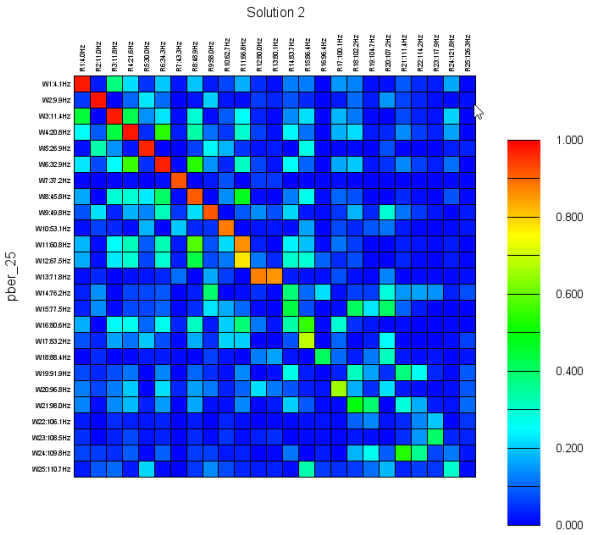


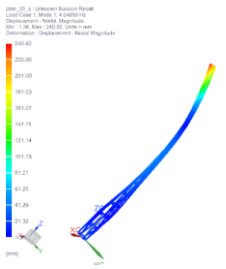
Figure 14 Modal Assurance Criterion between the numerical and experimental mode shapes

Test	FEM	MAC	Freq. % Error
4.05	4.13	0.98	2.14
10.96	9.87	0.98	-9.91
11.80	11.36	0.97	-3.71
21.65	20.81	0.98	-3.86
29.98	26.89	0.96	-10.31
34.28	32.86	0.97	-4.16
43.30	37.25	0.92	-13.98
48.93	45.76	0.91	-6.49
58.00	49.85	0.92	-14.06
62.67	53.14	0.88	-15.20
66.84	60.82	0.86	-9.00
80.00	71.75	0.87	-10.31
86.41	83.19	0.69	-3.73
100.10	96.78	0.66	-3.32
111.40	109.80	0.53	-1.44
133.59	110.73	0.59	-17.11

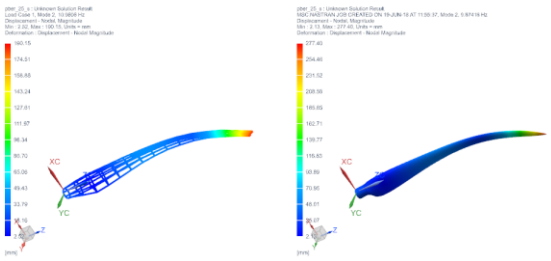
Table 3: Results of correlation analysis between test and simulation results

Based on the correlation between the modes, Table 3 compares the numerical and experimental natural frequency of matching modes. Here, only modes that show a correlation above 50% are compared and 16 pairs are reported. In general, very good agreement is found between all modes with a dominant flapwise direction, with errors between the natural frequencies ranging between 1 and 5%. Bigger discrepancies (with errors around 10%), on the other hand, are observed for the modes in the edgewise and torsional direction. Before drawing further conclusions, it is necessary to include the bungee cords used to suspend the blade in

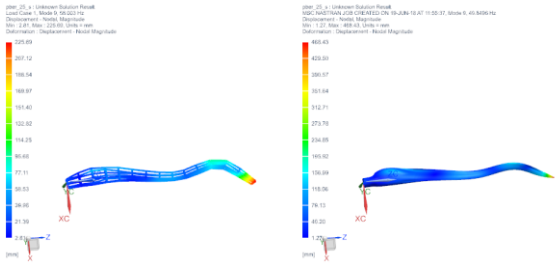
the model, as they add stiffness in the edgewise direction. Indeed, the natural frequencies of the numerical model in this direction are consistently softer than the experimental results. In general, the good correlation between the global modes at low frequencies gives confidence in the general validity of the model, and an update of the material properties is not deemed necessary at this stage. In Figure 15, a comparison of some of the mode pairs is given.



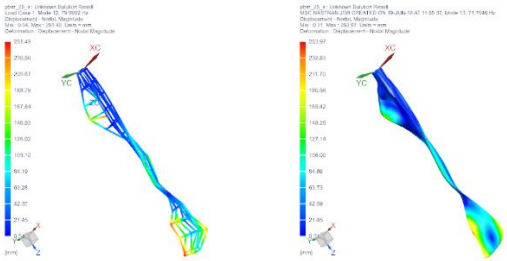
1st Flapwise Bending (4.05-4.12 Hz)



1st Edgewise Bending (10.96 – 9.87 Hz)



2 Edgewise Bending (58 – 49.85 Hz)



2nd Torsion (80 – 71.75 Hz)

Figure 15 Examples of experimental and numerical identified mode shapes.

5 Conclusions and future outlook

This paper presented dynamic testing and analysis for model validation of an innovative wind turbine blade design. Motivation for the work was to investigate the dynamic properties of the blade to a larger extent than required by a certification standard and apply the results for the blade model validation. An experimental modal analysis was implemented and provided an estimation of the full modal model parameters in the wide frequency band. Uncertainty quantification has confirmed high consistency in the experimental data collection. Based on this analysis result, the estimated experimental modal model was a credible reference for the validation of the numerical model. Performed tests did not show the presence of nonlinearity. Both uncertainty and nonlinearity analysis revealed problem with the precision of the identification of the torsional mode. Within the test campaign use of the innovative optical accelerometer has been successfully demonstrated. Future work will encompass use of the operational modal analysis for the blade bolted to the concrete block of the test rig. A certification standard requires static and fatigue testing with the use of the strain gauges. Therefore it is planned to use a test setup and the blade instrumentation for the vibration test.

Acknowledgements

The experimental work described herein has been conducted using mechanical testing and measurement equipment from Villum Center for Advanced Structural and Material Testing (CASMaT). The support from Villum Fonden (Award ref. 00007293) is gratefully acknowledged.

This work was supported by the Danish Centre for Composite Structures and Materials for Wind Turbines (DCCSM), Grant no. 09-067212 from the Danish Strategic Research Council.

The work is supported by the Danish Energy Agency through the Energy Technology Development and Demonstration Program (EUDP), Grant No. 64016-0023. The supported project is named ‘‘BLATIGUE: Fast and efficient fatigue test of large wind turbine blades”, and the financial support is greatly appreciated.

This work was funded by the VLAIO Innovation Mandate project number HBC.2016.0235.

References

[1] International Electrotechnical Commission. International standard iec 61400-23 Wind turbine generator systems – part 23: full-scale structural testing of rotor blades. Wind Turbines-Part 1: Design Requirements. (2014).

[2] GE Renewable Energy, GE announces Haliade-X, the world’s most powerful offshore wind turbine, (2018).

[3] P Avitabile, Modal testing : a practitioner's guide, John Wiley & Sons Ltd 2018.

[4] DJ Ewins, Modal testing: theory and practice, Research studies press Letchworth 1984.

[5] W Heylen, S Lammens, P Sas, Modal Analysis Theory and Testing, 2nd ed., Katholieke Universiteit Leuven, Departement Werktuigkunde, Leuven, 1998.

[6] GC Larsen, MH Hansen, A Baumgart, I Carlén, Modal analysis of wind turbine blades, Risø–R–1181(EN) (2002).

[7] HB Pedersen, OJD Kristensen. Applied modal analysis of wind turbine blades. (2003).

[8] DT Griffith, G Smith, M Casias, S Reese, TW Simmermacher. Modal Testing of the TX-100 Wind Turbine Blade, Sandia National Laboratories Technical Report, Report# SAND2005-6454. (2006).

[9] D Griffith, TG Carne. Experimental Uncertainty Quantification of Modal Test Data, Sandia National Laboratories (SNL-NM), Albuquerque, NM (United States). (No. SAND2006-6507C) (2006).

[10] MM Luczak, Uncertainty Quantification of the Main Rotor Blades Measurements, Recent Progress in Flow Control for Practical Flows, Springer, 2017, pp. 429-482.

[11] DT Griffith, TG Carne, Experimental modal analysis of 9-meter research-sized wind turbine blades, Structural Dynamics and Renewable Energy, Volume 1, Springer, 2011, pp. 1-14.

[12] US Paulsen, O Erne, M Klein, Modal analysis on a 500 kW wind turbine with stereo camera technique, International Operational Modal Analysis Conference. IOMAC. (2009).

[13] P Poozesh, J Baqersad, C Niezrecki, P Avitabile, E Harvey, R Yarala. Large-area photogrammetry based testing of wind turbine blades, Mechanical Systems and Signal Processing. 86 (2017) 98-115.

[14] P Poozesh, A Sarrafi, Z Mao, C Niezrecki. Modal parameter estimation from optically-measured data using a hybrid output-only system identification method, Measurement. 110 (2017) 134-145.

[15] FL dos Santos, B Peeters, Strain Modal Analysis, Recent Progress in Flow Control for Practical Flows, Springer, 2017, pp. 405-428.

[16] V Ruffini, T Nauman, C Schwingshackl, Impulse excitation of piezoelectric patch actuators for modal analysis, Topics in Modal Analysis & Testing, Volume 10, Springer, 2017, pp. 97-106.

[17] JR White, DE Adams, MA Rumsey, Modal analysis of CX-100 rotor blade and micon 65/13 wind turbine, Structural Dynamics and Renewable Energy, Volume 1, Springer, 2011, pp. 15-27.

[18] M Luczak, S Manzato, B Peeters, K Branner, P Berring, M Kahsin. Updating finite element model of a wind turbine blade section using experimental modal analysis results, Shock Vibrat. 2014 (2014).

[19] GC Larsen, P Berring, D Tcherniak, PH Nielsen, K Branner, Effect of a damage to modal parameters of a wind turbine blade, (2014).

[20] J Blasques, R Bitsche, V Fedorov, MA Eder, Applications of the beam cross section analysis software (becas), (2013) 46-49.

[21] J Schoukens, R Pintelon, Y Rolain, Mastering system identification in 100 exercises, John Wiley & Sons 2012.

[22] R Pintelon, J Schoukens, System identification: a frequency domain approach, John Wiley & Sons 2012.

[23] R Priemer, Introductory signal processing, World Scientific Publishing Company 1990.

[24] TP Dobrowiecki, J Schoukens. Linear approximation of weakly nonlinear MIMO systems, IEEE Transactions on Instrumentation and Measurement. 56 (2007) 887-894.

[25] P Guillaume, R Pintelon, J Schoukens. Accurate estimation of multivariable frequency response functions, IFAC Proceedings Volumes. 29 (1996) 4351-4356.

[26] P Csurcsia. Static nonlinearity handling using best linear approximation: An introduction, Pollack Periodica. 8 (2013) 153-165.

Virtual prototyping of an actuator-based structural health monitoring system of wind turbine blades

D. Garcia [1], **D. Tcherniak** [2], **K. Branner** [3]
[1] University of Strathclyde, Department of Mechanical and Aerospace Engineering,
75 Montrose Street, Glasgow, G1 1XJ, United Kingdom
e-mail: **david.garcia@strath.ac.uk**

[2] Brüel & Kjær Sound & Vibration Measurements, Innovation group,
Nærum, DK-2850, Denmark

[3] Technical University of Denmark, Department of Wind Energy,
Frederiksborgvej 399, 4000 Roskilde, Denmark

Abstract
Testing and evaluating the performance of a Structural Health Monitoring (SHM) system is a challenging and costly task. A proper experimental assessment of the system is not feasible in most cases. A possible solution is a virtual prototype of the monitored object together with the SHM system. This study presents the initial steps of creating a virtual prototype, namely simulation of the elastic wave propagation due to impact of the actuator. It is shown that even this very initial investigation helps to understand the complex vibration pattern of the blade and how the presence of the damage alters it. Similarly, for the same damage size and location, different actuations locations were studied. The location of the actuator affects the wave propagation, as the interaction with the structural parts of the blade significantly complicates the vibration pattern before it actually reaches the damage region. The results clearly indicate that the actuator-based SHM system has a good wave propagation and damage resolution ratio for damage diagnosis in large blades.

1 Introduction

In recent years, the research community has built up a wealth of knowledge in the field of Structural Health Monitoring for Wind Turbines [1, 2, 3]. To reduce the cost of energy the wind energy industry requires technologies that will act as the basics for full lifecycle asset management. The components in the wind turbines will develop different failures depending on the nature of each of them and therefore it is rather difficult to create an unique SHM system for monitoring all kind of failures. This is one of the reasons why, the importance of SHM system is a must in this kind of structures.

Thought in the last 25 years the concept of SHM has been in continuous development but there are still some challenges that should be taken under consideration as presented in [4]. One of the first aspects to have in mind is the tolerance of damage for each component. It is assumed that there is not a perfect material and hence damage will occur in one way or other. Therefore, it is needed to make a decision whether the tolerance of the damage is acceptable or not [5]. One of the most common methodologies for SHM is to compare the actual status of a component against a reference state, which determine the original conditions of the component to be monitored. These methodologies need to be robust to eventually create a reliable system that will help in the decision making by reducing the number of wrong decisions (i.e. reducing the number of false alarms by maximising the damage detection rate) [6]. As known in the research community, sensors do not directly measure damage but they provide the information from where to extract a feature that could be used to monitor any deviation from the reference state and therefore detect the presence of damage.

The selection of these features is not a simple task and they should be *smart* in the sense that they should not be affected by operations and environmental effects. The development of a SHM system should be robust and flexible to learn from the past and present towards successful damage diagnosis (i.e. damage detection, localisation and quantification) and hence to project the learning onto future decisions and thus predict the remaining lifetime of the component in monitoring (i.e. prognosis) [7]. As it can be deduced, a reasonable balance of all these aspects should be taken into account when a SHM system is to be designed. More or less emphasis will be dedicated to each of these aspects depending on the case. Thus, it is clear that there is not an unique SHM system but it depends on the study or object under consideration. On the other hand, there is other aspect to be considered that will contribute towards the development of SHM not only in the wind energy but also in other sectors of the engineering. The SHM system should be designed as such as it will awake the interest of business in different sectors of the industry. Therefore, as mentioned before, the SHM should be able to assist the evaluation of the full lifecycle asset management. This will arouse the interest of the industry, with inputs that variate from new product design to decision making for decommissioning or life extension of a structure. All these considerations come together in this early stage study for creating a virtual prototype as a platform where to test new SHM systems.

The study in this manuscript presents the initial steps towards creating such a virtual prototype, namely simulation of the elastic wave propagation due to impact of the actuator. For the same damage size and location, different actuations locations were studied. The fruitful results were discussed to set the foundations for further investigations.

2 The need of a virtual prototype with SHM system

Testing a Structural Health Monitoring (SHM) system and evaluating its performance is a challenging and costly task. A solution to this problem could be a virtual prototype of the monitored object together with the SHM system. A virtual prototype is a multiphysics model allowing simulation of an as-built structure, component, infrastructure, etc., to mirror the life of the real structure, component, infrastructure, etc. [8, 9]. The virtual prototype should simulate sensor data from the structure under study. The main aim of this virtual prototype is to evaluate new SHM methodologies in a realistic and robust environment towards life-cycle sustainability. Some of the challenges that indeed still need further investigation are discussed bellow in order to reflect the relevance of these virtual environments.

Testing and evaluating the performance of SHM systems has been always under study. SHM methodologies are tested, on their majority, on simulated structures with more or less accurately representation of the nature of the damage This simulations are very useful to understand the philosophy of the new system before they are extended for real implementation in large scale experiments. A realistic experimental assessment of the system against even few types of damage is an extremely expensive exercise as it requires introducing damage artificially, which is not even feasible in some scenarios. The benefit of having a virtual prototype will allow to test the SHM system for different scenarios, localisation, size, nature of the damage, even a combination of all, etc. Similarly, different SHM systems, which include hardware (e.g. different types of sensors, DAQ systems,...) and algorithms (e.g. model and non-model based, supervised and unsupervised,...) could be implemented in the same prototype. Moreover, new sensor technologies such as fibre-optic sensors could be tested for further development as well as combination of multiphysics environments that simulate a more realistic situations (i.e. operational and/or environmental effects). Similarly, a different set of sensor-array could be investigated to optimise the sensor locations for enhancing successful damage diagnosis. In [6], the relation of accelerometer location and damage detection for different damage locations and sizes was investigated. It was observed that sensors closer to the damage did not always provide a good detection of the damage. With virtual prototypes, the damage sensitivity ratio could be better studied by considering different sensors' distribution and therefore assess the performance towards damage diagnosis in a faster, easier and more affordable manner. In this case the sensor distribution could be optimised by defining areas with higher or lower density of sensors. All these aspects and more will be possible because virtual prototypes combine

adequate data fusion measured on real structures with high-fidelity models.

Reducing uncertainty and creating high reliability not only in the SHM methodology performance but also in an effective use of assets. One of the bigger challenges that SHM systems face is to provide useful but more important reliable information to help in the decision making. This can be observed in previous studies [11, 12], where the selected feature is not always able to track the growth of the damage. In this case, one can go into the virtual prototype and study the effect of each parameter individually by relating structural changes to the performance of the selected featured, in order words virtual prototypes will provide more understanding about the SHM system under study. Other important aspect in the development of SHM systems is the influence of the operational and environmental effects on the performance of SHM system. It is important to know if the deviation detected by the SHM systems is because of the damage or because other factors that influences the performance of the SHM system [13]. Similarly, as shown in [14], the observations measured in the repaired wind turbine blade experienced an irregularity and the damage indices did not follow the same pattern. Virtual prototypes rely on the data fusion and therefore data from weather conditions can possibly be taken into account to investigate its effects in the SHM performance.

Quantifying the avalue of the SHM systems is probably one of the most important aspects to be considered for the future of SHM. This aspect is the great interest for the industry and infrastructure's owners to make decisions about their interests. Having information about the life-cycle of a structure will add useful information towards the quantification of the value of SHM [16]. The concept of value of information (VoI) is currently presentend as a metric to quantify the value of SHM. It can be used to evaluate the total expected lifetime operation and maintenance costs for a wind turbine with SHM and without SHM [17]. The key factor of VoI is to include within the quantification of the cost of a SHM system not only the deterioration because of damage of the object, the failure of hardware system or the SHM's algorithm implemented but also the decisions to be made after the evaluation of the entire SHM system.

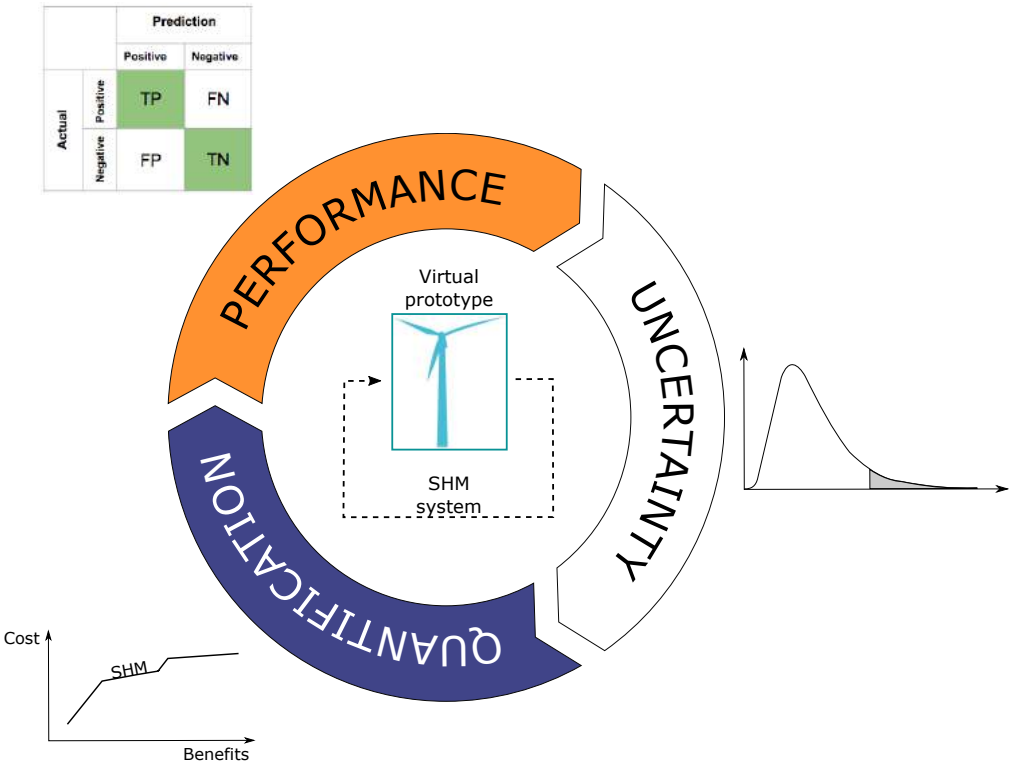


Figure 1: Conceptual representation of a Virtual Prototype for SHM systems

Other aspect that it is not directly included in the design of a SHM system but it is of great interest in the research community and industry is damage prognosis. Damage prognosis refers to the estimation of the remaining useful life of a component, structure, etc. and it is the real importance for life-safety and

economic benefits quantification. The estimation of the remaining useful life is based on the combination of the analysis of models, simulations findings and the knowledge from past and present towards future predictions [15]. The consideration of these virtual environments for damage prognosis will act as a detailed model of the object and they will be beneficial for the development of prognosis studies.

To summarise, it is of great potential develop virtual prototypes for assessing the performance and value of SHM systems. In possession of a virtual prototype, one can evaluate different SHM systems for the same structure with strong reliability. This will help to understand the philosophy of each SHM approach as well as identify the limitations and alternatives to improve it towards the evaluation of interest. Additionally, these technologies will help in the quantification of the value of SHM at different states such as proof of concept, industrial implementation, decision making and economic driven with the aim of awaken the interest of the industrial stakeholders.

3 Creation on a virtual prototype of the monitored blade

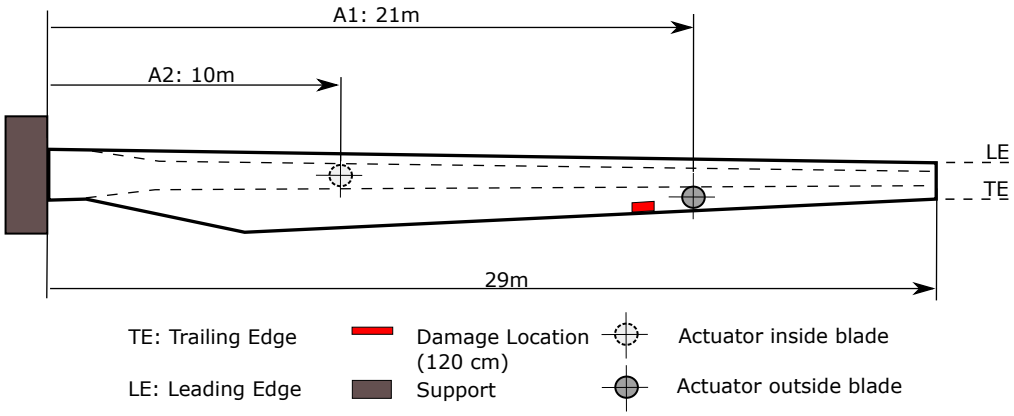
This study presents the intital steps of a numerical simulation of an actuator-based SHM system, which consists of an electromagnetic actuator and an array of accelerometers mounted on a wind turbine blade. Actuator's impact induce elastic waves that propagate along the blade; the response at different blade locations is measured by the accelerometers. Previous studies experimentally demonstrated that damage alters the vibration pattern and it can be used as a robust indicator of blade damage assessment [18]. The study presents the initial steps towards creating such a virtual prototype, namely simulation of the elastic wave propagation due to impact of the actuator. Similarly, for the same damage size and location, different actuation locations were studied.

3.1 Modelling and simulation details

This study is based on a numerical finite element model of a 34m wind turbine blade manufactured by SSP Technology A/S. The 34m wind turbine blade has extensively been studied both experimental and numerical at DTU Wind Energy [19, 20]. The blade was truncated at 29m in order to accommodate it in the blade test facility. A short description of the modelling considerations are described as follow. For further information refer to [20].

The model was simulated by MSC/PATRAN [21]. A volume representation of the geometry was required to use 20-noded layered continuum elements for modelling the blade structure. The outer geometry of the blade was modelled by 25 cross-section/aerodynamic profiles. The thickness of the laminates was represented according to the layup by the defined curves of the offset cross-sections. The individual cross-sections were connected by spline curves and interpolation surfaces to obtain a volume representation of the blade. This utilized 48 regions/solids to assign the different properties automatically by Blade Modelling Tool (BMT) developed by DTU Wind Energy. The approximate number of elements in this study was 40000. The composite layup was modelled with 15-44 plies though the thickness via BMT, and composite properties were assigned to layered 20-noded continuum elements. The blade was mounted on a test rig in a similar manner that it would be on a wind turbine hub. The rig is included as a spring/beam system, which is coupled to the blade via a MPC element in order to add some flexibility of the rig and therefore minimise its effect on the simulated eigenvalues and eigenvectors of the blade.

The model of the wind turbine blade was used to simulate the same experimental test campaign described in [18]. An electro-mechanical actuator was placed on the wind turbine blade to introduce an impact. The rationale of the experiment was to measure the vibration response of the wind turbine blade by accelerometers along the trailing and leading edge in order to apply a SHM system for damage assessment.



(a)



(b)



(c)

Figure 2: Blade scheme geometry and the actuators' locations. a) Blade scheme. b) Actuator location A1 c) Actuator location A2.

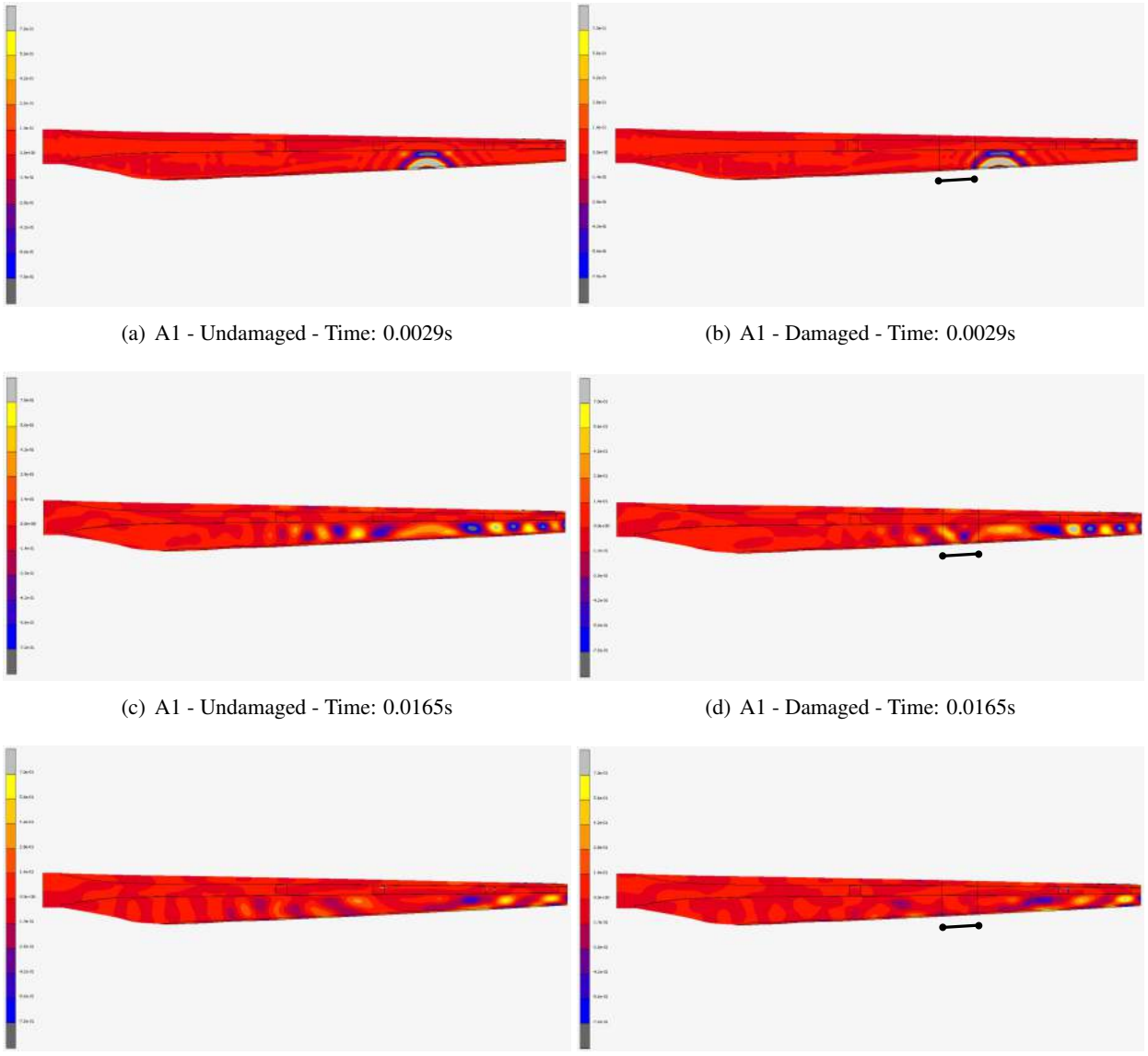
Therefore, the idea of this study is to create a virtual prototype of blade and hence simulate the experiment in a finite element model of the wind turbine blade. The simulation was first done in the undamaged wind turbine blade (no disbonding of the upper and lower shells in the trailing edge) and secondly in the damaged blade (with disbonding of the upper and lower shells in the trailing edge). The size of the damaged was 120 cm and it was in a location at approximately $\frac{2}{3}$ from the root and in the Trailing edge as shown in Figure 2(a). The simulation was done separately for two different actuator locations. First for the actuation location A1 and then for the actuator location A2 as it can be observed in Figure 2(b) and 2(c) respectively.

The propagation of the elastic waves is a transient phenomenon and it was simulated by MARC with its advanced nonlinear solver of MSC software [22]. The transient analysis was performed for a period of 0.1 seconds after the actuator impact and the accelerations in the vertical direction only were calculated for 2000 intermediate time steps. The impact was introduced in the closest node to the actuator under study.

4 Results and Discussions

This section presents the results, reflections and discussions found in the simulation of the experiment presented in Figure 2. The initial study of this research is to compare two different actuator locations for a fixed damage location and size of 120 cm. Figure 3 presents the elastic waves (EW) on undamaged and damaged blade at different times for an excitation in the actuator location A1. It can be observed that at 0.0029s after the impact of the actuator the EW on the damaged and undamaged blade have the same patter as the EW did not reach the damage region yet (see Figure 3(a) and 3(b)). Therefore, before the EW interact with the

damage region, there is not difference between both blade scenarios. However, once the EW interact with the damage region, there is a clear change in phase and amplitude as it can be observed by comparing Figure 3(c) and 3(d). At this time (0.0165s), the first EW arriving to the tip does not have any direct interference with damage. The comparison of the EW for undamaged and damaged blade did not present any clear visual change in the phase and it seems to travel at the same frequency without any visual delay. It might be seen a slight change in the amplitude but very small.



(a) A1 - Undamaged - Time: 0.0029s

(b) A1 - Damaged - Time: 0.0029s

(c) A1 - Undamaged - Time: 0.0165s

(d) A1 - Damaged - Time: 0.0165s

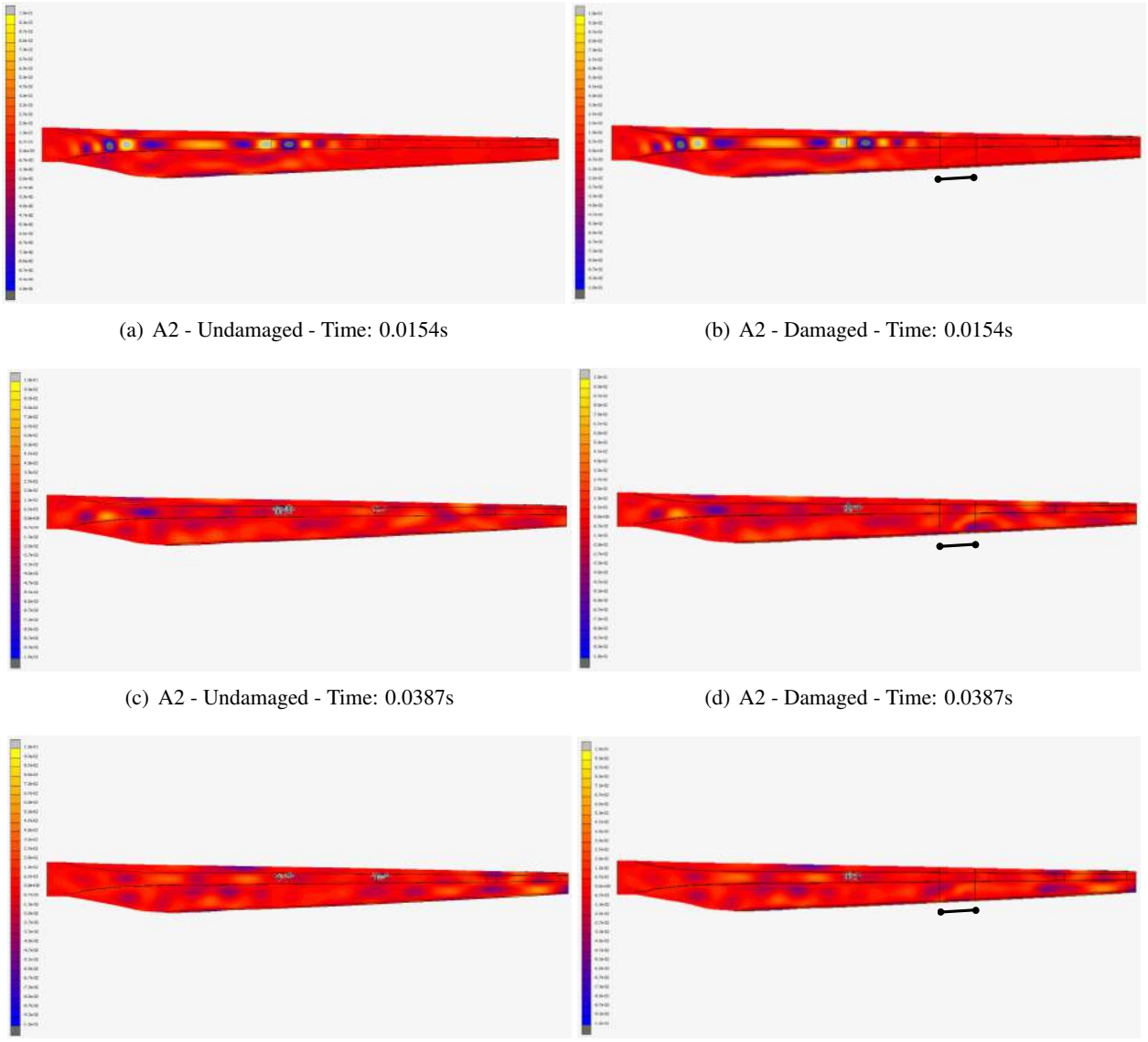
(e) A1 - Undamaged - Time: 0.0265s

(f) A1 - Damaged - Time: 0.0265s

Figure 3: Undamaged and Damaged wind turbine blade for Actuation location A1. The damage location and extend is defined with a black line.

However, looking at the root-direction, it can be observed that the EW clearly interact with the damage region and it clearly shows a significant difference between undamaged and damaged blade. The EW breaks its normal pattern and split after the damage, this was also observed in [23]. At time 0.0265s, the reflection of the EW after interacting with the damage region travels towards the tip of the blade. A small difference in amplitude can be better observed between undamaged and damaged blade (see Figure 3(e) and 3(f)). Again for this time, in the direction towards the root, the vibration pattern is still significantly different between both blade scenarios.

Therefore, it can said that when the EW interacts directly or indirectly with the damage region a change in the vibration pattern was clearly observed. Following this assumption, any accelerometers located along the trailing edge will be able to detect some irregularities/differences. However, the differences in the leading edge are not very clear and therefore accelerometers located along leading edge might not be able to detect the damage.



(a) A2 - Undamaged - Time: 0.0154s

(b) A2 - Damaged - Time: 0.0154s

(c) A2 - Undamaged - Time: 0.0387s

(d) A2 - Damaged - Time: 0.0387s

(e) A2 - Undamaged - Time: 0.0449s

(f) A2 - Damaged - Time: 0.0449s

Figure 4: Undamaged and Damaged wind turbine blade for Actuation location A2. The damage location and extend is defined with a black line.

As for the actuator location A1 is presented in Figure 4 for undamaged and damaged blade at different times for an excitation in the actuator location A2. At 0.0154s after the impact of the actuator, the EW move towards the root and tip of the blade as it occurred by the actuation in the location A1. However, a clear observation can be made already at this short time - the EW got trapped in the spar beam and therefore most of the energy transmitted to the blade will dissipate inside the spar beam (see Figure 4(a) and 4(b)). Some of the EW were able to scape from the spar beam and travelled towards the trailing and leading edge as it can be observed in Figure 4(c) and 4(d) at time 0.0387s. At this time, the EW interacts for the first time with the damage region and it can be observed that the vibration pattern changes when the undamaged and damaged blade were compared after the damage region towards the tip. Therefore, the assumption that the

interaction of elastic wave/damage provides information about damage presence by changing the vibration pattern is also observed. After the time 0.0449s, the difference in the vibration pattern between undamaged and damaged is very weak and there is not a visual difference between undamaged or damaged blade (see Figure 4(e) and 4(f)). As expected, there is not visual changes in the leading edge between undamaged and damaged for this actuation location. When the EW reach the damage region is already very weak and it will not contain enough energy to travel towards the leading edge with information about the presence of the damage.

5 Conclusion

This study presents the initial steps towards creating a virtual prototype of actuator-based SHM system, namely simulation of the elastic wave propagation due to impact of the actuator. It is shown that even this very initial investigation helps to understand the complex vibration pattern of the blade and how the presence of the damage alters it. The location of the actuator affects the wave propagation, as the interaction with the structural parts of the blade significantly complicates the vibration pattern before it actually reaches the damage region. The results obtained in the simulations clearly indicate that the actuator-based SHM system has a reasonable wave propagation and damage resolution ratio for damage diagnosis in large wind turbine blades.

Acknowledgements

The authors would like to thank Dr Valentina Ruffini for her work on the simulations during her stay in DTU Wind Energy. The work at DTU was supported by Innovation Fund Denmark through the Danish Centre for Composite Structures and Materials for Wind Turbines (DCCSM) (Grant no. 060300301B). The support is gratefully acknowledged.

References

[1] M. Martinez-Luengo, A. Kolios, L. Wang, *Structural health monitoring of offshore wind turbines: A review through the Statistical Pattern Recognition Paradigm*. Renewable and Sustainable Energy Reviews, Vol. 64, (2016), pp. 91-105.

[2] I. Antoniadou, N. Dervilis, E. Papatheou, A. E. Maguire, K. Worden, *Aspects of structural health and condition monitoring of offshore wind turbines*. Royal Philosophical Transactions A, Vol. 373, (2015), pp. 20140075.

[3] M. Luczak, B, Peeters, M. Döhler, L. Mevel, W. Ostachowicz, P Malinowski, Pawel, T. Wandowski, K. Branner, *Damage detection in wind turbine blade panels using three different SHM techniques* Structural Dynamics and Renewable Energy, Vol. 1 (2011), pp. 125-134.

[4] K. Worden, C. Farrar, G. Manson, G. Park, *The fundamental axioms of structural health monitoring*. Proceedings of the Royal Society of London A: Mathematical, Physical and Engineering Sciences, Vol. 463, (2007), pp. 1639-1664.

[5] M. McGugan, G. ereira, B. F. Sørensen, H. Toftegaard, K. Branner, *Damage tolerance and structural monitoring for wind turbine blades*. Royal Philosophical Transactions A, Vol. 373, (2015), pp. 20140077.

[6] D. García, D. Tcherniak, I. Trendafilova, *Damage assessment for wind turbine blades based on a multivariate statistical approach*. Journal of Physics: Conference Series, Vol. 628, (20015), pp. 012086.

[7] C. Farrar, K Worden, *An introduction to structural health monitoring*. Philosophical Transactions of the Royal Society of London A: Mathematical, Physical and Engineering Sciences, Vol. 365, (2007), pp. 303-315.

[8] E. Glaessgen, D. Stargel *The digital twin paradigm for future NASA and US Air Force vehicles*. Proceedings of 53rd AIAA/ASME/ASCE/AHS/ASC Structures, Structural Dynamics and Materials Conference 20th AIAA/ASME/AHS Adaptive Structures Conference 14th AIAA, (2012), pp. 1818.

[9] B. R. Seshadri, T. Krishnamurthy, *Structural health management of damaged aircraft structures using digital twin concept*. Proceedings of 5th AIAA/AHS Adaptive Structures Conference, (2017), pp. 1675.

[10] E. J. Tuegel, A. R. Ingraffea, T. G. Eason, S. M. Spottswood, *Reengineering aircraft structural life prediction using a digital twin*. International Journal of Aerospace Engineering, Vol. 2011, (2011).

[11] D. Tcherniak, L. L. Mølgaard, *Active vibration-based structural health monitoring system for wind turbine blade: Demonstration on an operating Vestas V27 wind turbine*. Structural Health Monitoring, Vol. 16, (2017), p. 536-550.

[12] A. G. González, S.D. Fassois, *A supervised vibration-based statistical methodology for damage detection under varying environmental conditions & its laboratory assessment with a scale wind turbine blade*. Journal of Sound and Vibration, Vol. 366, (2016), p. 484-500.

[13] L. D. Avendaño-Valencia, E. N. Chatzi, *Sensitivity driven robust vibration-based damage diagnosis under uncertainty through hierarchical Bayes time-series representations*. Procedia Engineering, Vol. 199, (2017), p. 1852-1857.

[14] D. Tcherniak, L. L. Mølgaard, *Active vibration-based SHM system: demonstration on an operating Vestas V27 wind turbine*. Proceedings of 8th European Workshop On Structural Health Monitoring (EWSHM 2016), (2016).

[15] C. R. Farrar, N. A. J. Lieven, *Damage prognosis: the future of structural health monitoring*. Philosophical Transactions of the Royal Society of London A: Mathematical, Physical and Engineering Sciences, Vol. 365 (20107), p.623-632.

[16] P. Omenzetter, U. Yazgan, S. Soyoz, M. P. Limongelli, *Quantifying the value of SHM for emergency management of bridges at-risk from seismic damage based on their performance indicators*. Joint workshop COST TU1402, COST TU1406, IABSE, (2017), p. 4-5.

[17] J. S. Nielsen, D. Tcherniak, M. D. Ulriksen, M, *Quantifying the value of SHM for wind turbine blades*. Proceedings of 9th European Workshop On Structural Health Monitoring, (2018).

[18] D. Tcherniak, L. L. Mølgaard, *Vibration-based SHM system: application to wind turbine blades*. Journal of Physics: Conference Series, Vol. 628, (2015), p. 012072.

[19] M.A. Eder, K. Branner, P. Berring, F. Belloni, H. Stensgaard Toft, J.D. Sørensen, A. Corre, T. Lindby, A. Quispitup,T.K. Petersen. *Experimental Blade Research - phase 2*. DTU Wind Energy, report no. E-0083, (2015), p. 108.

[20] G. C. Larsen, P. Berring, D. Tcherniak,P. H. Nielsen, K. Branner, *Effect of a damage to modal parameters of a wind turbine blade*. Proceedings of 7th European Workshop On Structural Health Monitoring, (2014).

[21] MSC/PATRAN. MSC Software Corporation: Patran. Available from: http://www.mscsoftware.com/product/patran.

[22] MSC/MARC. MSC Software Corporation: Marc. Available from: http://www.mscsoftware.com/product/marc.

[23] F. Szlaszyński, P. Omenzetter, *Numerical simulations of medium and high frequency elastic waves for damage detection in composite wind turbine blades*. Proceedings of SMAR 2017: 4th International Conference on Smart Monitoring, Assessment and Rehabilitation of Civil Structures, (2017).

Experimental damage detection on small wind turbines through vibration and acoustic analysis

F. Castellani [1], **D. Astolfi** [1], **M. Becchetti** [1], **F. Berno** [1]
[1] University of Perugia - Department of Engineering, Via G. Duranti 93 - 06125 Perugia (Italy)
e-mail: **francesco.castellani@unipg.it**

Abstract

Dynamical control system optimization and noise and vibration mitigation are particularly pressing issues as regards horizontal-axis small wind turbines. A peculiarity of this technology is that the generator constitutes a non-negligible fraction of the total mass and therefore the electromechanical coupling is relevant. Condition monitoring of small wind turbine generators is an overlooked topic in the literature and in the operation of these systems. This work is devoted to damage diagnosis on a permanent magnet generator of a horizontal-axis wind turbine having 3 kW of maximum power and 2 meters of rotor diameter. The experimental analysis is conducted through wind tunnel tests and on a generator test rig where a damaged and an undamaged generators have been driven at different rotational speeds. The test rig data are useful for studying the low-frequency tail of the spectrum, where the characteristic frequencies of the bearing are located. A fault in the cage of the bearing supporting the generator is diagnosed using the spectral coherence analysis.

1 Introduction

Small wind turbine technology [1] is characterized by a considerable range of criticality, basically dictated by the fact that it is expected to be targeted for domestic use. This implies that the size of the devices should be sufficiently small for the possible use in urban environment, that the material should be cheap enough in order that the price on the market is affordable for domestic investment, that the control system should be simple enough in order that the device can be exploited by users without technical expertise, that the efficiency of wind kinetic energy conversion should be high enough to counteract public opinion prejudices according to which this kind of technology performs poorly [2].

Optimizing power extraction means, especially for horizontal axis small wind turbines (HAWT), rotational speed up to several hundreds of rotor revolutions per minute (rpm). This implies that the control system has a crucial role and this is especially true in urban environment [3], where the resource is particularly characterized by gustiness, severe unsteadiness, meandering direction.

For these reasons, noise and vibration issues [4, 5, 6] are very common as regards small HAWT. The mechanical behavior of small HAWTs is strongly affected by the importance of the electromechanical couplings [7], due to fact that the generator constitutes a remarkable fraction of the total mass of the device. Therefore, the generator can transmit to the structure powerful contributions, possibly causing unexpected disturbing vibrations at high frequency. The literature about condition monitoring of generators of small wind turbines is remarkably missing. An inspiring paper for the objectives of this work is [8] where mechanical faults of a 500 W permanent magnet generator are studied. Two cases are considered: ball bearing outer race defect and rotor imbalance. One of the points of [8] is that a test rig has been developed in order to perform condition monitoring for varying shaft speed. A set of methods (continuous wavelet transform, short-time Fourier transform, order analysis, wavelet power spectrum) is shown to be effective for the objectives of the work.

On these grounds, the present work is devoted to the condition monitoring of a generator of a small HAWT

(horizontal axis wind turbine) having 2 meters of rotor diameter with a maximum power of 3 kW [9]. The test wind turbine has no gears and it is equipped with a permanent magnet generator (PMG).

The experimental analysis of the whole device has been performed through wind tunnel tests in the "R. Balli" (www.windtunnel.unipg.it) wind tunnel at the University of Perugia and a generator test rig has been used to analyze the PMG driven at different rotational speeds.

The general lesson from this case study is that, despite the simplicity and the cheap manufacturing of a small HAWT, the condition monitoring for this kind of systems requires sophisticated measurements and signal processing techniques. In particular, it arises that the vibrational and acoustic measurements in the wind tunnel resulted to be appropriate for identifying the main features of the spectra. The diagnosis of the anomaly has been possible using the test rig measurements, because these measurements are more appropriate for the study of the low-frequency spectrum where the characteristic frequencies of the bearings are located. In particular, the spectral coherence analysis has resulted to be a powerful technique because it clearly highlights the frequency content of ciclostationary signals [13] and the contributions to spectrum that arise are interpretable in light of the theoretical characteristic frequencies of the bearing. Finally, therefore, The general lesson from this case study is that, despite the simplicity and the cheap manufacturing of a small HAWT, the condition monitoring for this kind of systems requires sophisticated measurements and signal processing techniques. In particular, it arises that the vibrational and acoustic measurements in the wind tunnel resulted to be appropriate for identifying the main features of the spectra. The diagnosis of the anomaly has been possible using the test rig measurements, because these measurements are more appropriate for the study of the low-frequency spectrum where the characteristic frequencies of the bearings are located. In particular, the spectral coherence analysis has resulted to be a powerful technique because it clearly highlights the frequency content of ciclostationary signals [13] and the contributions to spectrum that arise are interpretable in light of the theoretical characteristic frequencies of the bearing. Finally, therefore, a suspect damage at the cage of the bearing has been identified.

The structure of the manuscript is as follows: in Section 2, the test case is described; the methods are presented in Section 3 and the results are collected in Section 4. Finally, conclusions are drawn in Section 5.

2 The test case

The wind turbine under investigation has 2 meters of rotor diameter and the maximum producible power is 3 kW. It has fixed pitch and the rotational speed varies from 200 to 800 rpm and the blades are made of a glass-fiber-reinforced polymer. The wind turbine has full electric load control, and the yawing is provided by the tail fin. For this study, it was controlled using a rpm-power curve extracted from wind tunnel experiments at steady state. The wind turbine is shown in Figure 1.



Figure 1: The front view of the wind turbine in the wind tunnel with the recovery test section on the background.

The wind tunnel is a closed-loop configuration, driven by a 375 kW electric motor. The air can be accelerated up to a maximum speed of 47 m/s. The inlet section of the open test chamber has 5 m^2 of area, and the recovery section is 7 m^2. Two Pitot tubes and a cup anemometer measure the wind speed blowing on the test section and a control station in the testing room measures the real-time static air pressure, temperature and relative humidity. It is possible to generate wind time histories that are variable in time, because the wind tunnel fan is controlled through an inverter.

During the wind tunnel tests, vibration measurements are collected through a radial accelerometer near the rear bearing of the shaft. At the same time also the rotational speed of the rotor and the noise are measured respectively through a tachometer and a microphone placed laterally 2 m far from the rotor (out of the wind flow). The sampling frequency is 5 kHz.

The test rig is displayed in Figure 2 where the position of the accelerometers used for the experimental analysis can be appreciated. On the generator, uni-axial accelerometers have been fixed in radial positions, in order to be aligned with front and rear bearings. A tri-axial accelerometer has been fixed on the front shell, just above the shaft hole; anyway the results revealed, as expected, that radial measurements near the bearing are the most meaningful for fault diagnosis. A torque meter was installed on the shaft from the motor to the generator, while rpm were measured thanks to an optical tachometer. Also electrical parameters (tension and current) were monitored on the brake circuit on the DC resistive load in order to estimate the power output from the generator. The sampling frequency is 5 kHz.

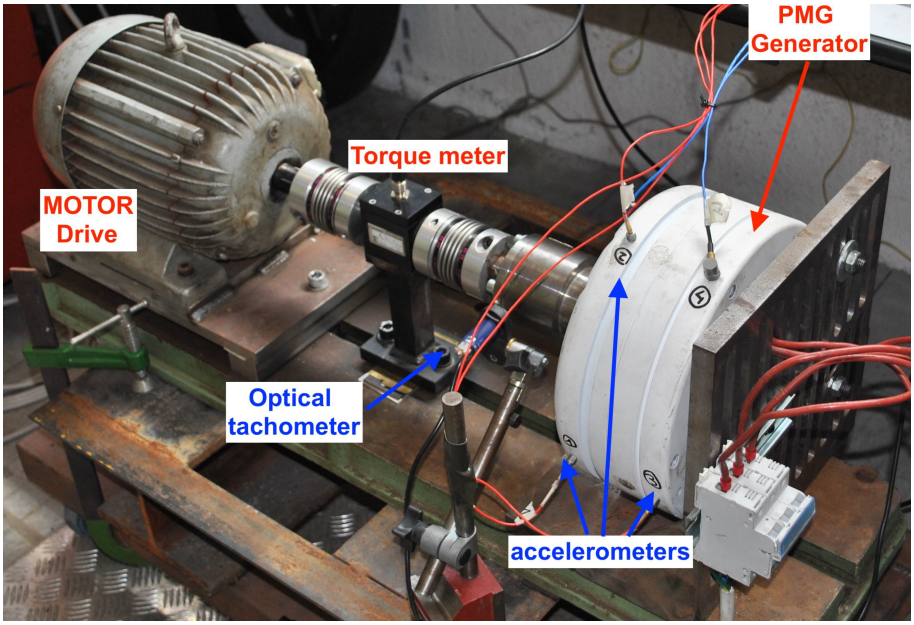


Figure 2: Test rig for the electric generator.

3 The methods

Two 1800 W PMGs were tested collecting mechanical and electric data both with wind tunnel ramp and steady test, as well as driving the generator on a test rig. The two electric generators are exactly the same model, but one of them revealed a faulty behavior resulting in vibration and poor performances. This can be appreciated as follows.

In the test rig, the driving torque was provided by an electric motor (see Figure 2), applying on the generator circuit side a resistive load in the same way as in the tunnel tests. Using the measurements from the torque meter and the optical tachometer, it is possible to calculate the mechanical power incoming in the generator, thanks to the relationship $P_{mec} = C_m\omega = C_m\frac{2\pi N}{60}$. About the electric side of the test rig, three-phases power was transformed into direct-current thanks to a rectifier and both the voltage and current intensity were measured in order to calculate the electric power produced by the generator as $P_{el} = Vi$. Therefore, the efficiency of the generator can be calculated as $\eta = \frac{P_{el}}{P_{mec}}$ and the results for different working conditions are reported in Table 1. It arises that the faulty generator is indeed clearly under-performing.

rpm	healthy (%)	faulty (%)
300	96.55	95.68
400	97.21	96.98
500	97.80	96.67

Table 1: Mean efficiency η at different rpm for healthy and faulty generator.

Several tests have been performed, with constant rpm and increasing ones. In particular, stationary tests have been performed at 300, 400 and 500 rpm and ramps tests from 300 to 500 rpm have been conducted. Electrical load was managed through a rheostat, where the electrical power produced was dissipated. For the ramp tests, the value of resistance was fixed, while the frequency to the inverter was increasing. The post-processing has been performed using Matlab.
Since the generator is gearless, the suspected fault causing the under-performance should be in the bearings

and this motivates the comprehension of this kind of systems, in order to interpret properly the experimental data.

3.1 Bearing characteristic frequencies

In order to interpret the frequency content of the acquired vibration signals, it is necessary that the possible contribution from a fault on each of the bearing components is clear. The literature about bearing faults comes at hand [14] at this aim. The bearing parameters are indicated as follows: f_r is the number of rpm of the shaft (Hz), D_b is the diameter of the rolling elements, D_p is the mean diameter of the bearing (pitch diameter), Z is the number of the rolling elements, α is the contact angle. The characteristic frequencies of possible faults are:

- damage on the inner race (BPFI, Ball Pass Frequency on Inner ring): $f_i = Z\frac{f_r}{2}\left\{1 + \frac{D_b}{D_p}\cos(\alpha)\right\}$
- damage on the outer race (BPFO, Ball Pass Frequency on Outer ring): $f_o = Z\frac{f_r}{2}\left\{1 - \frac{D_b}{D_p}\cos(\alpha)\right\}$
- damage on the rolling elements (BSF, Ball Spin Frequency): $f_r = \frac{f_r}{2}\frac{D_p}{D_b}\left\{1 - \left[\frac{D_b}{D_p}\cos(\alpha)\right]^2\right\}$
- damage on the cage (FTF, Foundamental Train Frequency): $f_c = \frac{f_r}{2}\left\{1 - \frac{D_b}{D_p}\cos(\alpha)\right\}$

In this case, we have $\alpha = 0$, $Z = 9$, $D_b = 0.0111$ m., $D_p = 0.0549$ m. and so we get the following frequencies:

damaged component	order (-)
inner race	5.4098
outer race	3.5902
rolling elements	2.3719
cage	0.3989

Table 2: Characteristic frequencies for bearing faults.

3.2 Data analysis

The measurements collected in the test rig and in the wind tunnel through accelerometers and microphone can be analyzed basically in the time domain or in the frequency domain.

As regards the time domain, several are the possible metrics for feature extraction. The squared Mahalanobis distance [10, 11] is commonly employed to measure the distinction between the characteristic vectors and has been shown to be effective in identifying the component looseness at different locations of rotating machinery. In this work, it has been used as follows: the selected time series are two from the healthy generator and one of the faulty generator. The test rig is run at the same working conditions and one healthy time series is taken as reference with respect to which computing the Mahalanobis distance for the remainder healthy time series and for the faulty one. Other features in the time domain are investigated [12], as for example, the kurtosis and the skewness.

As regards the frequency domain, the spectral analysis of ciclostationarity [13] has emerged in the last decades as a powerful approach for characterizing certain types of non-stationary mechanical signals, as for example from rotating machines like wind turbines. The autocorrelation function of a ciclostationary signal

contains all the information, but the frequency domain is the most powerful point of view for interpreting it. The spectral correlation is defined as

$$S_{XX}(\alpha, f) = \lim_{T\to\infty} \mathbb{E}\left\{X_T\left(f + \frac{\alpha}{2}\right) X_T^*\left(f - \frac{\alpha}{2}\right)\right\}, \tag{1}$$

where $X_T(f)$ is the Fourier transform of the signal $x(t)$ over an interval T. If the modulation of the signal is periodic, the spectral correlation is continuous in f and discrete in α: it is non-zero only at those frequencies that are multiple of fundamental modulation frequency. This technique is therefore powerful to extract the frequency content of a ciclostationary signal.

4 The results

4.1 Wind tunnel results

In Figure 3, the waterfall plot of the radial vibrations under the ramp wind time series is reported, when the faulty generator is adopted. The most evident contribution to the spectrum is 48P and 96P that are due to the electromechanical coupling (as discussed also in [7]).

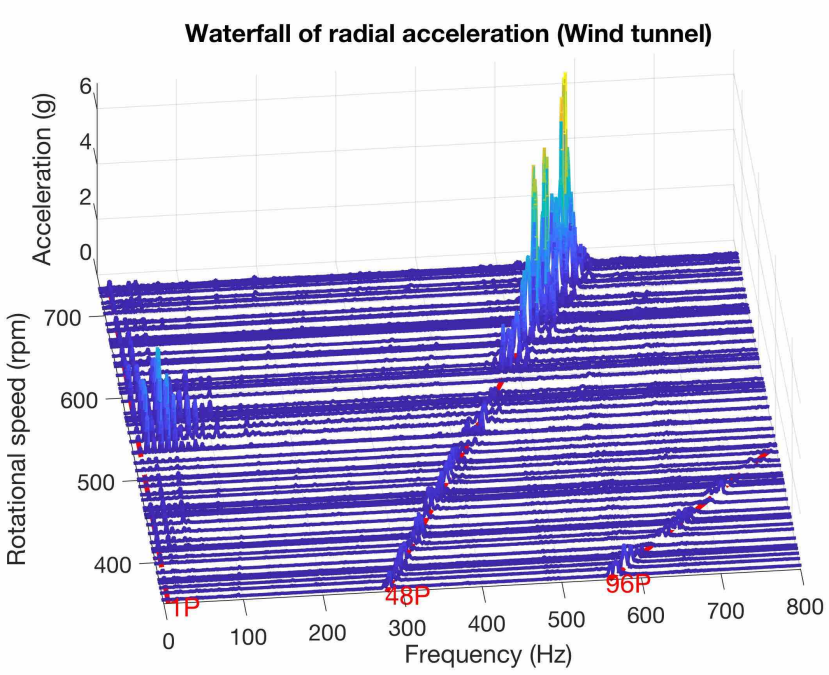


Figure 3: The waterfall plot of radial vibrations: faulty generator.

Figure 3 is indecisive as regards bearing fault detection and, for this reason, a waterfall plot focused on the low frequencies is reported in Figure 4 for the faulty generator and in Figure 5 for the healthy generator.

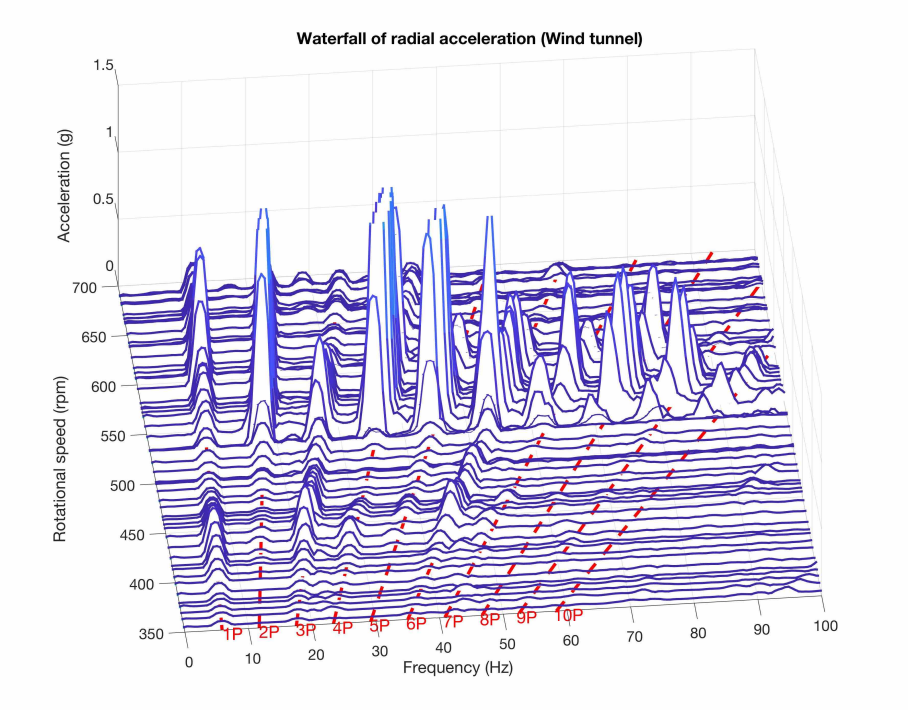


Figure 4: The waterfall plot of low frequency radial vibrations: faulty generator.

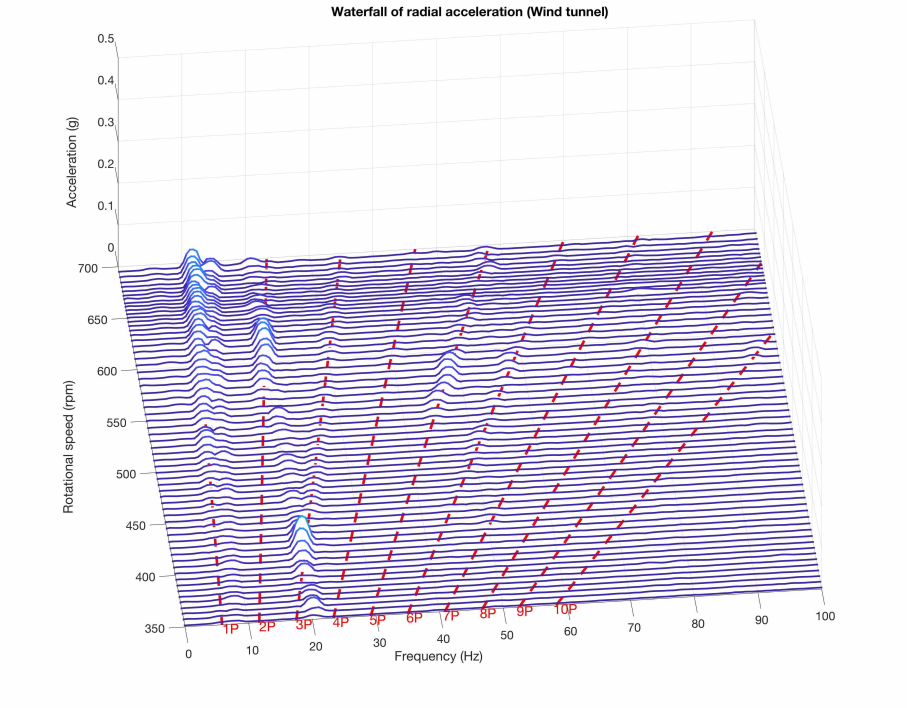


Figure 5: The waterfall plot of low frequency radial vibrations: healthy generator.

Comparing Figure 4 to 5, it is evident that the low-frequency vibration spectrum of the faulty generator has different features with respect to the healthy one, as regards amplitude and frequency contributions.

On these grounds, a further investigation on the faulty generator can be provided through the acoustic analysis. The advantage of acoustic analysis is the fact that it is not linked to the positioning on the damaged component; this can indeed be also a downside because an aerodynamic perspective might not be decisive for diagnosing a localized fault inside a wind turbine component. In Figures 6, the waterfall plot of the signal collected by the microphone is reported. It is remarkable that the electromechanical coupling is clearly visible in the acoustic spectrum. Furthermore, the spectrum is dominated by the contributions around the 3P frequency and this is consistent with the fact that acoustic measurements are sensitive most of all to the aerodynamics of the cyclic motion of the wind turbine.

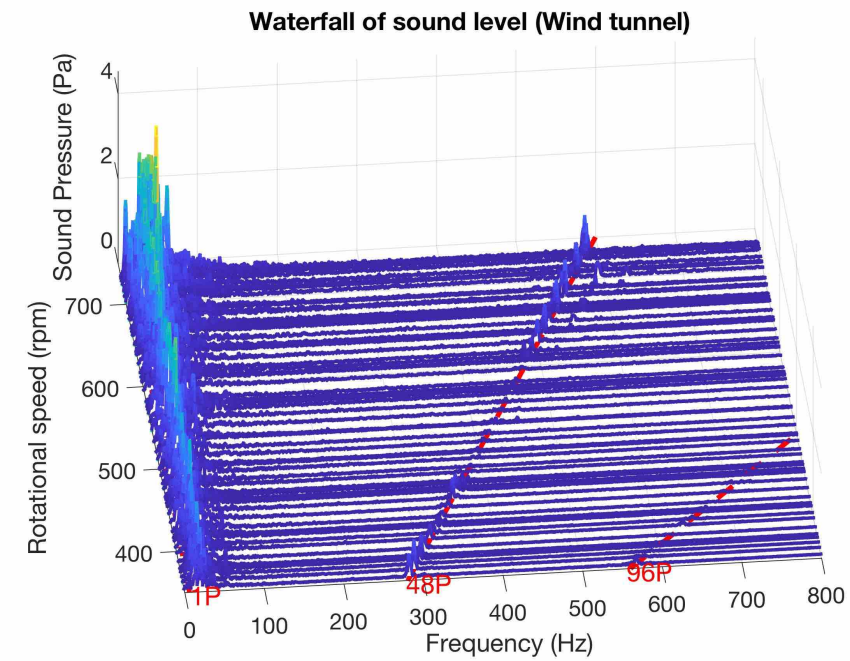


Figure 6: The waterfall plot of acoustic vibrations: faulty generator.

In Figure 7, the low-frequency waterfall plot is reported: it is interesting to notice the contribution around a 0.4P frequency at very high rotational regimes.

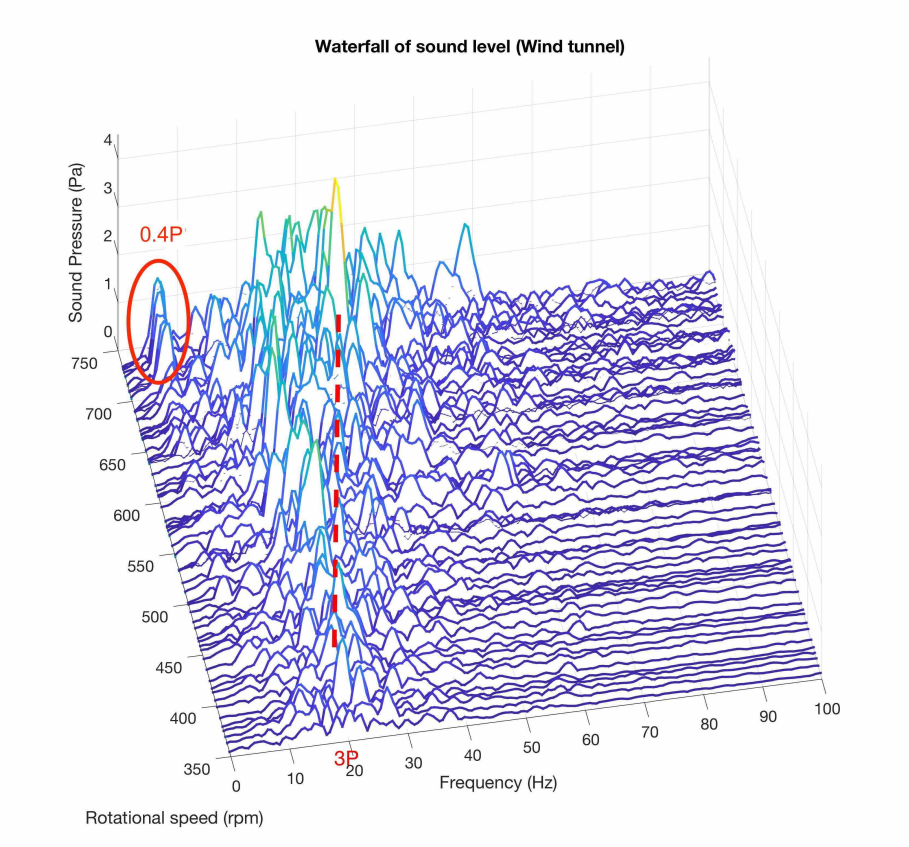


Figure 7: The waterfall plot of low-frequency acoustic vibrations: faulty generator.

Finally, a spectral coherence analysis has been performed on the radial accelerometer signal and the results for the two generators are plotted in Figure 8 and Figure 9.

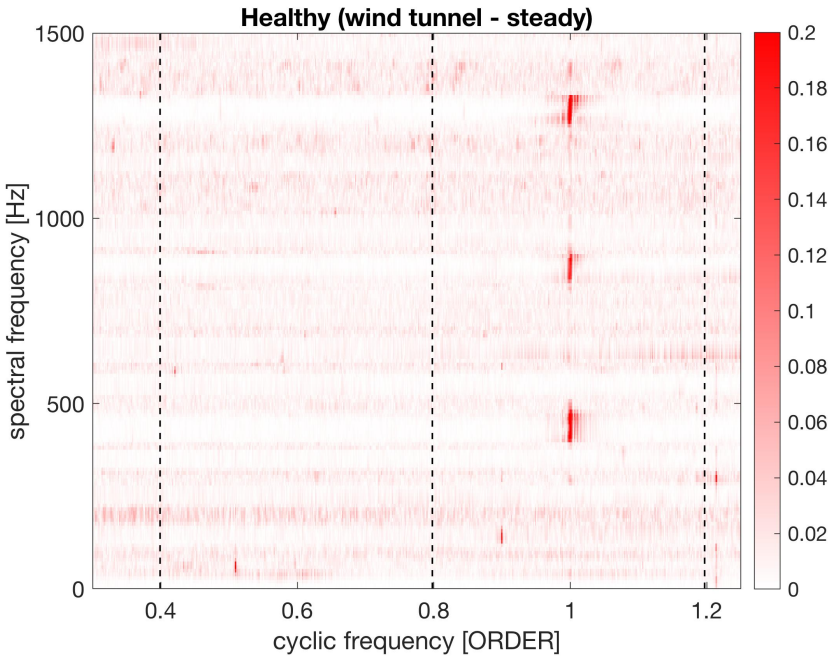


Figure 8: Spectral coherence analysis: healthy generator.

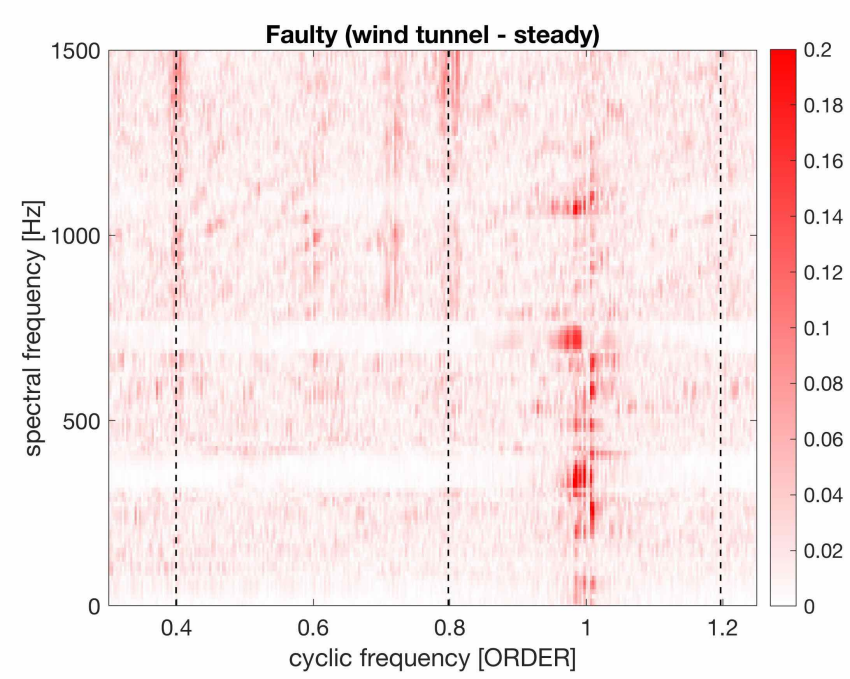


Figure 9: Spectral coherence analysis: faulty generator.

Comparing the two figures, it arises that Figure 9 is noisier with respect to Figure 8 and that a contribution at 0.4P (and second harmonic) is visible: it corresponds to the characteristic frequency of the cage (see Table 2). This points to a possible detection of the damage, as shall be supported by the results for the test rig data analysis.

4.2 Test rig results

In Figure 10, results are reported for the study of unprocessed data in the time domain. Tests at 400 rpm are selected and one time series from the undamaged generator is taken as reference. The target time series are collected as well at 400 rpm and one is taken from the undamaged generator and one from the damaged. The Mahalanobis distance between target and reference is computed and, from Figure 10, no clear indications arise for distinguishing the damaged from the undamaged generator.

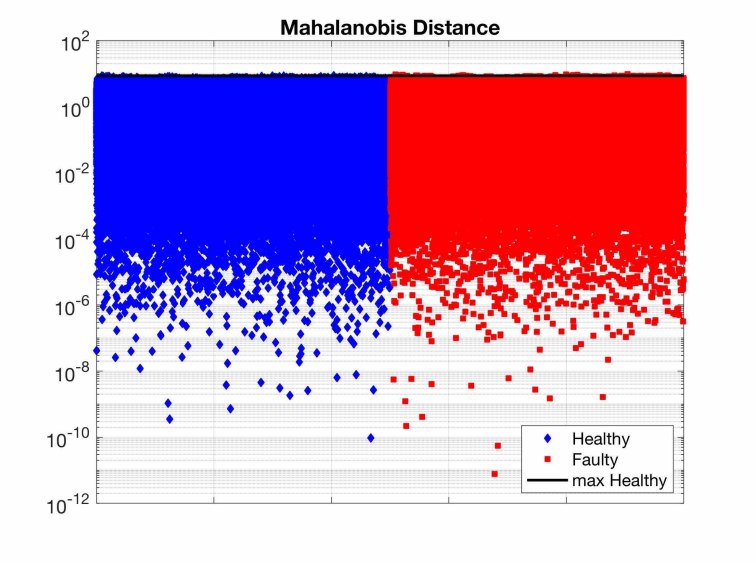


Figure 10: Mahalanobis distance between reference time series of undamaged generator and target time series of undamaged (blue) and damaged (red) generator. Tests at 400 rpm.

For this reason, data have subsequently order tracked around the characteristic frequencies of the bearing (Table 2) and sample results are reported in Figures 11 and 12 respectively for the cage and inner track frequency.

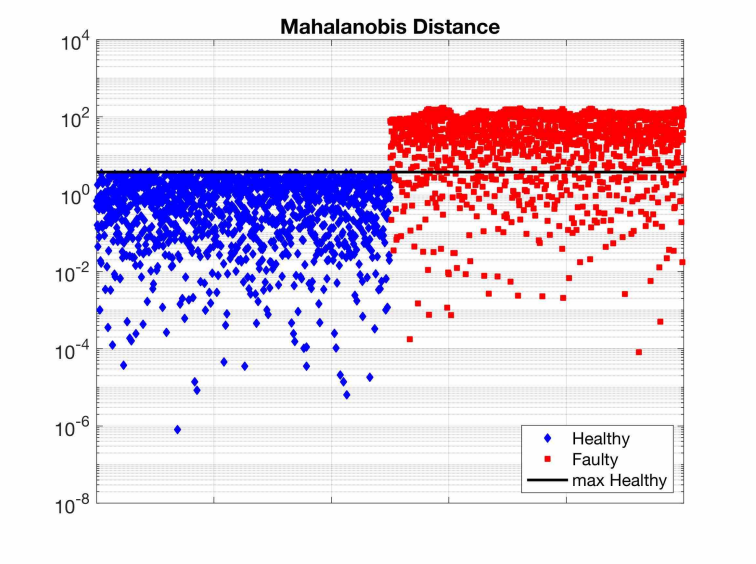


Figure 11: Mahalanobis distance between reference time series of undamaged generator and target time series of undamaged (blue) and damaged (red) generator. Data are order-tracked around the cage characteristic frequency. Tests at 400 rpm.

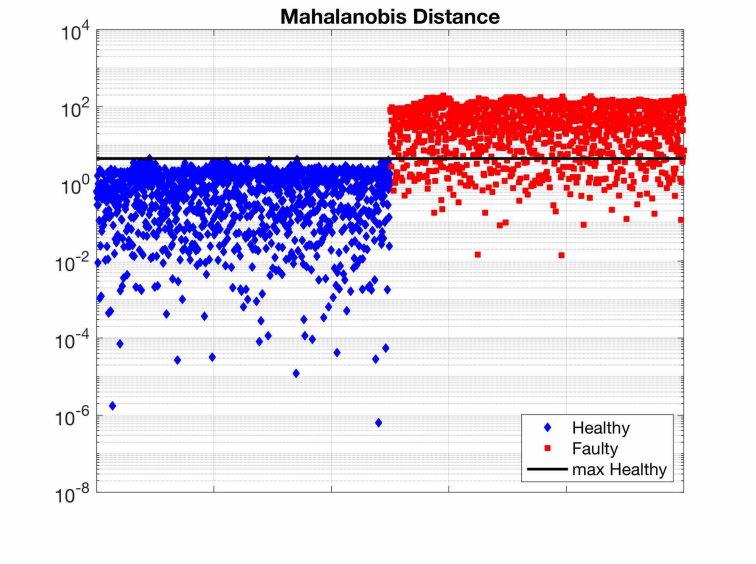


Figure 12: Mahalanobis distance between reference time series of undamaged generator and target time series of undamaged (blue) and damaged (red) generator. Data are order-tracked around the inner race characteristic frequency. Tests at 400 rpm.

In these cases, it clearly arises that the Mahalanobis distance is a responsive metric for distinguishing the damaged from the undamaged generator and it is evidently confirmed the intuitive expectation that the suspect damage regards the generator bearing. The missing information at this stage is the precise location of the damage in the bearing and, for this reason, the further analysis of the frequency content through the spectral coherence method can be decisive. The spectral coherence analysis for the test rig measurements at 400 rpm is represented in Figure 13 and Figure 14, using the data collected by a radial accelerometer.

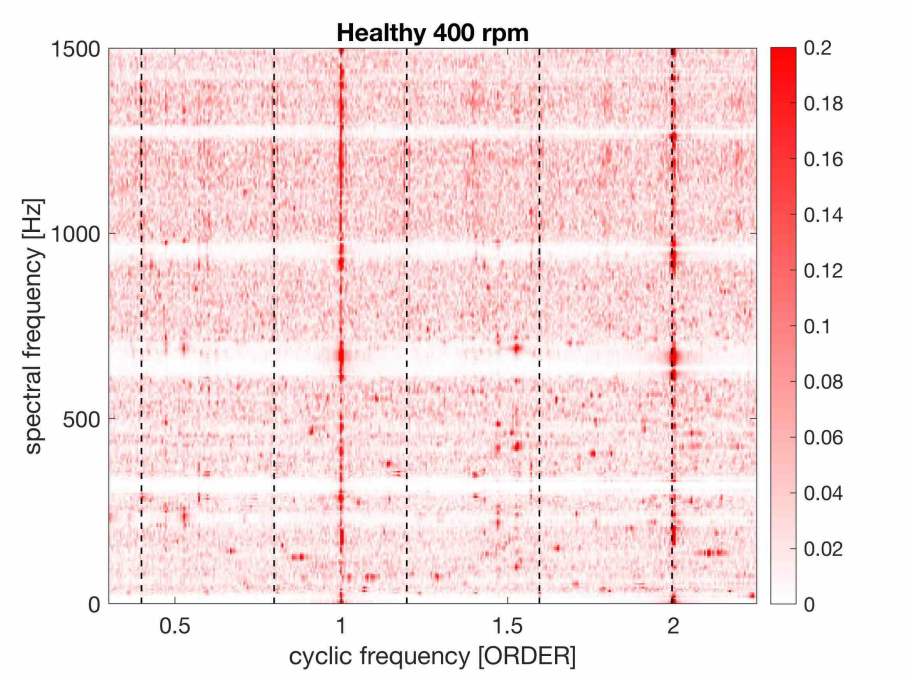


Figure 13: Spectral coherence analysis: healthy generator.

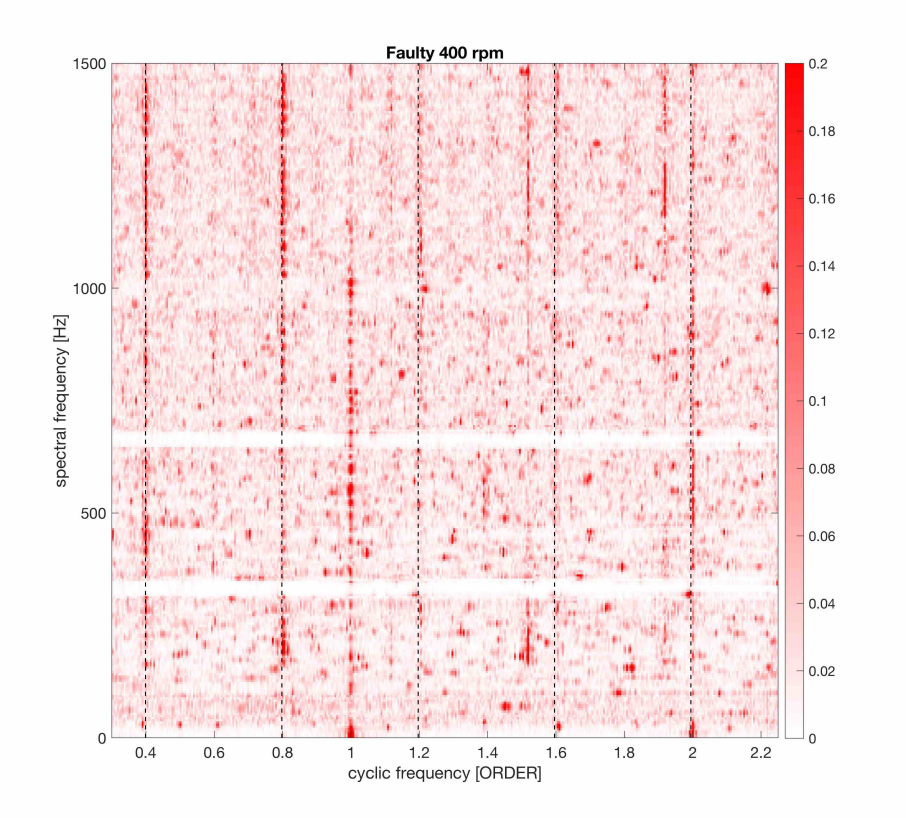


Figure 14: Spectral coherence analysis: faulty generator.

Comparing Figure 14 to 13, once again it arises that, in the spectral correlation of the faulty generator,

contributions at 0.4P and harmonics arise and this can be interpreted as due to a damage in the cage of the bearing (Table 2).

5 Conclusions

This work was devoted to the experimental analysis of a permanent magnet generator of a small HAWT with the aim of developing condition monitoring and damage diagnosis techniques. It is remarkable that this topic is quite overlooked in the scientific literature, despite the peculiarity of small HAWTs (small dimensions and high rotational speed) call for sophisticated analysis techniques and despite that the topic is quite pressing for the successful exploitation of small wind turbine technology, in order to mitigate noise and vibration issues.

The test case of this work was a 1800 W PMG, that has been adopted on a HAWT having 2 meters of rotor diameter and 3 kW of maximum producible power. Previous studies have been conducted on the dynamic behavior of this wind turbine [7] demonstrating a strong importance of the electromechanical coupling.

Experimental data have been collected in the wind tunnel through accelerometers and acoustic measurement campaigns; steady and ramp tests have been conducted. Furthermore, the generator suspected of being damaged has been driven on a test rig and measurements have been collected through accelerometers aligned with front and rear bearings. The test rig campaign has been particularly useful because it is more powerful for distinguishing the performances of the damaged generator with respect to an undamaged identical one.

Since the generator is gearless, the analysis has been focused on the bearings and the characteristic frequencies associated to damages on the different parts have been identified. The test rig data have been particularly useful for the diagnosis of the damage, because the low-frequency tail of the spectrum can more easily be interpreted with respect to what happens with the wind tunnel tests, involving the generator and the wind turbine operating jointly.

The lesson from this test case is that, despite the analysis in the time domain provides some indications of the anomaly, the damage can be better localized using signal analysis techniques devoted to ciclostationary phenomena. The spectral correlation analysis revealed a frequency content compatible with a damage on the cage of the bearing.

The general lesson from this study is that the cheap technology, commonly adopted for small HAWT in order to reduce the costs and spread this technology for domestic use, can be troublesome as regards performances and noise and vibration issues. The condition monitoring of this kind of devices requires complex techniques, whose study should be encouraged in the academia and whose adoption should be boosted in the industry for the successful use of this kind of clean energy conversion systems.

Acknowledgements

This research activity was partially supported by Italian PRIN funding source (Research Projects of National Interest - Progetti di Ricerca di Interesse Nazionale) through a financed project entitled SOFTWIND (Smart Optimized Fault Tolerant WIND turbines).

References

[1] D. Wood *Small Wind Turbines. Analysis, Design, and Application* Springer Verlag, London (2011).

[2] P. A. B. James, M.F. Sissons, J. Bradford, L.E. Myers, A.S Bahaj, A. Anwar, S. Green *Implications of the UK field trial of building mounted horizontal axis micro-wind turbines* Energy Policy, Vol. 38, No. 10, Elsevier (2010), pp. 6130-6144

[3] L. Battisti, M. Ricci *Wind Energy Exploitation in Urban Environment. TUrbWind 2017 Colloquium* Springer International Publishing, Cham (2018).

[4] S. Lee, S. Lee *Numerical and experimental study of aerodynamic noise by a small wind turbine* Renewable energy, Vol. 65, Elsevier (2014), pp. 108-112.

[5] E. Mollasalehi, Q. Sun, D. Wood. *Contribution of small wind turbine structural vibration to noise emission.* Energies, Vol. 6, No. 8, Elsevier (2013), 3669-3691.

[6] J. Taylor, C. Eastwick, C. Lawrence, R. Wilson (2013). *Noise levels and noise perception from small and micro wind turbines.* Renewable Energy, Vol. 55, Elsevier (2013), pp. 120-127.

[7] F. Castellani, D. Astolfi, M. Becchetti, F. Berno, F. Cianetti, A. Cetrini. *Experimental and Numerical Vibrational Analysis of a Horizontal-Axis Micro-Wind Turbine.* Energies, Vol 11, No. 2, MDPI (2018)

[8] H. Cai, Q. Sun, D. Wood. *Condition monitoring and fault diagnosis of a small permanent magnet generator* Wind Engineering, Vol 40, No. 3, Sage (2017), pp. 270-282.

[9] L. Scappaticci, N. Bartolini, F. Castellani, D. Astolfi, A. Garinei, M. Pennicchi. *Optimizing the design of horizontal-axis small wind turbines: From the laboratory to market* Journal of Wind Engineering and Industrial Aerodynamics, Vol. 154, Elsevier (2016), pp. 58-68.

[10] S.D. Wu, C.W. Wu, T.Y. Wu, C.C. Wang. *Multi-Scale Analysis Based Ball Bearing Defect Diagnostics Using Mahalanobis Distance and Support Vector Machine* Entropy, Vol 15 No. 2, Mdpi (2013), pp. 416-433.

[11] T.Y Wu, Y.L. Chung, C.H. Liu *Looseness diagnosis of rotating machinery via vibration analysis through Hilbert–Huang transform approach* Journal of Vibration and Acoustics, Vol 132 No. 3, American Society of Mechanical Engineers (2010).

[12] W. Caesarendra, T. Tjahjowidodo *A Review of Feature Extraction Methods in Vibration-Based Condition Monitoring and Its Application for Degradation Trend Estimation of Low-Speed Slew Bearing* Machines, Vol 5 No. 4, Mdpi (2017).

[13] J. Antoni *Cyclic spectral analysis in practice* Mechanical Systems and Signal Processing, Vol 21 No. 2, Elsevier (2007), pp. 597-630.

[14] W. Qiao, D. Lu *A survey on wind turbine condition monitoring and fault diagnosis—Part I: Components and subsystems* IEEE Transactions on Industrial Electronics, Vol 62 No. 10, IEEE (2015), pp. 6536-6545.

Gear tooth crack detection in a wind turbine drive train

Ch v h Gayatri[1], A.S. Sekhar[1]
[1]IIT Madras, Department of Mechanical Engineering
Chennai-600036, India
e-mail: **as_sekhar@iitm.ac.in**

Abstract
The vibration characteristics of the gear system change when gear tooth crack occurs during operating conditions and the system has to be monitored continuously to prevent the damage. A tooth crack model is developed with the mean gear mesh stiffness for external spur gear pair with different crack propagating lengths. Here, potential energy is used to obtain the analytical expression for the mean gear mesh stiffness and mean mesh stiffness with crack is incorporated into the wind turbine gear box and the dynamic analysis is performed with and without crack. The loads acting on the wind turbine drive train considered here are random in nature. The responses of wind turbine drive train in time and frequency domain are used to study the effects of gear tooth crack. The results showed the sidebands at tooth defective frequency in frequency domain and are found to be more sensitive than the gear mesh frequency and its harmonics. Hence the developed crack model is able to predict the presence of gear tooth crack in vibration response.

1 Introduction

The chances of failure of wind turbine components like gearbox are more before the rated life. This is due to the fact that these components are subjected to severe stochastic loads at the wind turbine site. If the gearbox fails, the operational and replacement costs associated with the gear or bearing are more since these components are located at certain height above the ground. There exists a great need in developing condition monitoring system such that if the gearbox component fails the fault can be able to be identified in turbine running condition itself without making the forceful shutdowns of the machine. Wind turbine gearboxes are used to increase the rotor speed to a speed suitable for the generation of electricity and operate under varying load conditions. The planetary gear boxes provide higher gear ratios and load carrying capacity compared to parallel arrangement. The existing studies considered the gear boxes with one planetary gear stage and two parallel gear stages [1-5]. In order to account for high capacity wind turbines, the present dynamic model is developed with gear box having two planetary gear stages and one parallel gear stage. Ji and Song [6] conducted the dynamic analysis of wind turbine drive train using harmonic balance method for multi-stage gearbox. Nejad [7] conducted the torsional dynamic analysis of 3 stage gear box with 2 planetary and one parallel stage and the vulnerability map for gear box is developed. Zhao [8] conducted the torsional dynamic behavior of wind turbine gear box with two planetary and one parallel gear stage. This model included time-varying mesh stiffness, damping, static transmission error and gear backlash. It is concluded that the mesh stiffness has more influence than the static transmission error. Chaari [9] proposed analytical method for the estimation of total mesh stiffness by considering only bending, fillet and Hertzian contact stiffness for gear tooth with and without fault. Chen and Shao [10] first proposed a crack model propagating along both tooth width and crack. The stiffness for gear tooth is obtained by considering the bending, axial, shear, fillet foundation and Hertzian contact stiffness for the gear pair and became the basis for the gear tooth stiffness calculation. Srikanth and Sekhar [11] modeled the tooth breakage phenomenon and derived the gear mesh stiffness for different percentages of breakage. Further the dynamic analysis of wind turbine drive train is performed using different tooth breakage stiffness values. Numerous studies have been carried out by various researchers in predicting gear tooth crack propagation. Lewicki [12] used FEM method with principles of Fracture

Mechanics to predict the crack propagation paths and suggested that the crack propagation paths are continuous, smooth and straight with slight curvature. Wu *et al* [13] simplified the crack propagation model by assuming the crack propagation path to be a straight line and constant crack angle of 45 degrees. Yogesh Pandya and Anand Parey [14] derived the mesh stiffness for the tooth crack by assuming the crack propagation as straight line and curved for various levels of crack. The time-varying mesh stiffness for crack growth in the tooth root was proposed by Zhou et al. [15] using an improved potential energy method. Hui Ma [16] obtained time varying mesh stiffness using analytical method for healthy spur gear pair and cracked gear tooth pair propagating as line and parabolic curve and are compared with FEM. Xihui Liang [17] derived the time varying mesh stiffness for the planetary gear set and proposed the crack propagation model when crack is present in planet or sun gears. In the present study, the dynamic characterization and fault detection is carried out on gearbox which consists of two planetary and one parallel gear stage subjected to stochastic loads.

2 Modelling of wind turbine drive train

Figure 1 shows major components of a wind turbine drive train. A two stage planetary with each stage consisting of three planets, sun and ring fixed and a single stage parallel gear box is typically considered here. All the gears assumed are to be spur. Rotor is the input, where the driving torque is applied and then subsequently transferred to the planet carrier of first planetary stage which rotates the planets that are symmetrically positioned at an angle. Planets then rotate the sun gears which are in mesh with sun. Hence in both stages of planetary, the output will be at the sun gear. The output at the 2nd stage planetary of sun gear is transferred to low speed gear of the parallel stage. The final output is at the high speed gear of the parallel stage and then to generator.

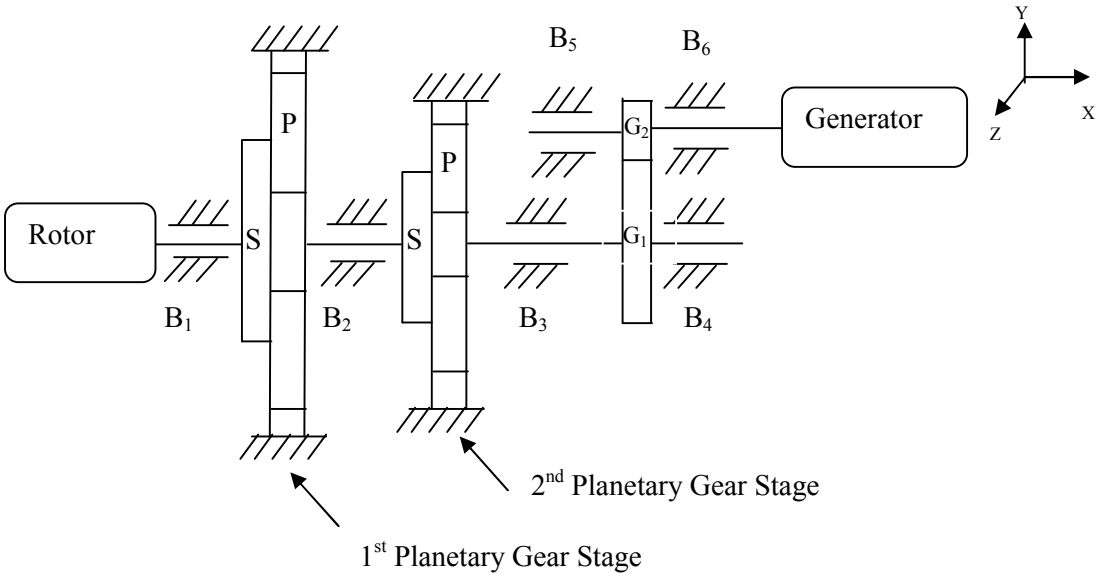


Figure 1: Components of wind turbine drive train

The details of the modelling done by the authors in [18] are followed in the present study. Gears, bearings and shafts are considered flexible with carrier as rigid based on rigid multi body modelling with discrete flexibility. A lumped parametric model is used to represent the flexibility of components. This approach contributes ten rotational and twelve transverse DOF for the entire drive train. The general coordinates vector for representing the degrees of freedom are:

$$\{q\}=\{\phi_1\ \phi_2\ \phi_3\ \phi_4\ \phi_5\ \phi_6\ \phi_7\ \phi_8\ \phi_9\ \phi_{10}\ y_{p1}\ z_{p1}\ y_{s1}\ z_{s1}\ y_{p2}\ z_{p2}\ y_{s2}\ z_{s2}\ y_{g1}\ z_{g1}\ y_{g1}\ z_{g1}\}^T. \quad (1)$$

Where ϕ_i (i=1,2,… 10) are the rotor, carrier1, planet1, sun1, carrier2, planet2, sun2, gear1, gear2, and generator absolute rotational DOF respectively and $y_{p1}, z_{p1}, y_{s1}, z_{s1}, y_{p2}, z_{p2}, y_{s2}, z_{s2}, y_{g1}, z_{g1}, y_{g1}, z_{g1}$ are the transversal degrees of freedom of planets of low and high speed planetary stages, gear1 and gear2 transverse in y and z directions respectively.

The system differential equations of motion are obtained using Lagrange's technique. The kinetic energy (K.E) of gears is given as,

$$\begin{aligned}K.E=&\frac{1}{2}J_1\dot{\phi}_1^2+\frac{1}{2}(J_2+3m_{p1}r_{c1}^2)\dot{\phi}_2^2+\frac{1}{2}(3J_3)\dot{\phi}_3^2+\frac{1}{2}J_4\dot{\phi}_4^2+\frac{1}{2}(J_5+3m_{p2}r_{c2}^2)\dot{\phi}_5^2+\\&\frac{1}{2}(3J_6)\dot{\phi}_6^2+\frac{1}{2}J_7\dot{\phi}_7^2+\frac{1}{2}J_8\dot{\phi}_8^2+\frac{1}{2}J_9\dot{\phi}_9^2+\frac{1}{2}J_{10}\dot{\phi}_{10}^2+\frac{3}{2}m_{p1}\dot{y}_{p1}^2+\frac{3}{2}m_{p1}\dot{z}_{p1}^2+\frac{1}{2}m_{s1}\dot{y}_{s1}^2+\\&\frac{1}{2}m_{s1}\dot{z}_{s1}^2+\frac{3}{2}m_{p2}\dot{y}_{p2}^2+\frac{3}{2}m_{p2}\dot{z}_{p2}^2+\frac{1}{2}m_{s2}\dot{y}_{s2}^2+\frac{1}{2}m_{g1}\dot{y}_{g1}^2+\frac{1}{2}m_{g1}\dot{z}_{g1}^2\\&+\frac{1}{2}m_{g2}\dot{y}_{g2}^2+\frac{1}{2}m_{g2}\dot{z}_{g2}^2\end{aligned} \quad (2)$$

The total potential energy (P.E) terms in Lagrange's technique are due to the flexibility of Gears, bearings and shafts considered above.

A transmission error occurs while meshing of gears because of the gear deformations and is given in the reference [1]. The time varying gear mesh stiffness contributes for P.E and is given as,

$$P.E_1=\frac{1}{2}\sum_{i=1}^{n}k_{r1p1i}\delta_{r1p1i}^2+\frac{1}{2}\sum_{i=1}^{n}k_{s1p1i}\delta_{s1p1i}^2+\frac{1}{2}\sum_{i=1}^{n}k_{r2p2i}\delta_{r2p2i}^2+\frac{1}{2}\sum_{i=1}^{n}k_{s2p2i}\delta_{s2p2i}^2+\frac{1}{2}k_{g1g2}\delta_{g1g2}^2 \quad (3)$$

Where k_{r1p1}, k_{s1p1}, $k_{s1p1}, k_{s1p1}, k_{g1g2}$ are the ring-planet, planet-sun of 2 stage planetary and parallel stage gear pinion mesh stiffness and $\delta_{r1p1}, \delta_{s1p1}, \delta_{r2p2}, \delta_{s2p2}, \delta_{g1g2}$ are the fixed ring-planet, sun-planet of 2 stages of planetary and external gear-pinion dynamic transmission errors which consists of gear deformations in y and z directions respectively.

The P.E due to bearing stiffness is given by,

$$P.E_2=\frac{1}{2}\sum_{j=1}^{5}k_{bj}(y_{bj}^2+z_{bj}^2) \quad (4)$$

Where k_{bj} represents bearing stiffness, y_{bj} and z_{bj} represent lateral displacements of bearings in y and z directions respectively.

The P.E associated with shaft stiffness is given as,

$$P.E_3=\frac{1}{2}k_{rc1}(\phi_2-\phi_1)^2+\frac{1}{2}k_{s1c2}(\phi_5-\phi_4)^2+\frac{1}{2}k_{s2g1}(\phi_8-\phi_7)^2+\frac{1}{2}k_{g2ge}(\phi_{10}-\phi_9)^2 \quad (5)$$

Where $k_{rc1}, k_{s1c2}, k_{s2g1}, k_{g1g2}$ represents the stiffness of shaft between rotor and carrier of 1st stage, sun of 1st stage and carrier of 2nd stage, sun of 2nd stage and gear1 of parallel stage,gear2 of parallel stage and generator respectively.

The wind modelling details done by Srikanth and Sekhar [19] are used in the present study. The rotor aerodynamic torque (T_R) is obtained from the total wind load which is sum of mean (u_m), ramp ($u_r(t)$), gust ($u_g(t)$) and turbulent components ($u_t(t)$) which is represented as,

$$u(t) = u_m + u_g(t) + u_r(t) + u_t(t) \tag{6}$$

$$T_R = \frac{1}{2\omega_R}\pi\rho R^2 u(t)^3 C_p(\lambda,\beta) \tag{7}$$

The generator torque is evaluated using,

$$T_G(t) = \frac{T_R(t)}{GR} \tag{8}$$

Where GR is the gear ratio of the gear box.

The proportional damping obtained by Rayleigh's approach is considered in the present dynamic model. The values of damping constants are evaluated using the first and second natural modes of frequencies and assuming 5% damping ratio as given in reference [20].

Using the Lagrange's approach, the equations of motion of the system are obtained as,

$$[M]\{\ddot{q}\} + [C(t)]\{\dot{q}\} + [K(t)]\{q\} = \{T_0(t)\} \tag{9}$$

Where $[M]$, $[C(t)]$ and $[K(t)]$ represent the mass, time dependent damping and stiffness matrices and $\{T_0(t)\} = \{T_R(t),0,0,0,0,0,0,0,0,-T_G(t),0,0,0,0,0,0,0,0,0,0,0,0\}$

The equations of motion are solved for responses in time domain using Newmark time integration algorithm, the results of which are given in section 4.

3 Gear tooth crack modelling

Gear tooth cracks are caused by many reasons, such as inappropriate operating conditions, material defects and manufacturing errors. Depending on the gear geometry and the applied torque on the gear, the crack often propagates either along the tooth root or along the rim. The tooth crack influences the change in the mesh stiffness and therefore produces abnormal vibration responses, such as impact and high frequency noise. Presence of gear tooth crack will reduce the effective thickness of a gear tooth carrying the load. Consequently, it will cause a reduction in the mesh stiffness. This change of vibration can be characterized through dynamic simulation of a gearbox and processed further to detect the crack severity and location. The general analytical approach for the calculation of gear tooth mesh stiffness is given in [10] where the effective mesh stiffness is a sum of axial, shear, bending, Hertzian contact stiffness's and fillet foundation stiffness. In the present study, the analytical approach given in [10] is used for the calculation of gear

mesh stiffness in the case of gear tooth crack and the fault is studied in the gear 2 which is attached to the generator since it experiences huge vibrations because of high rotational velocity.

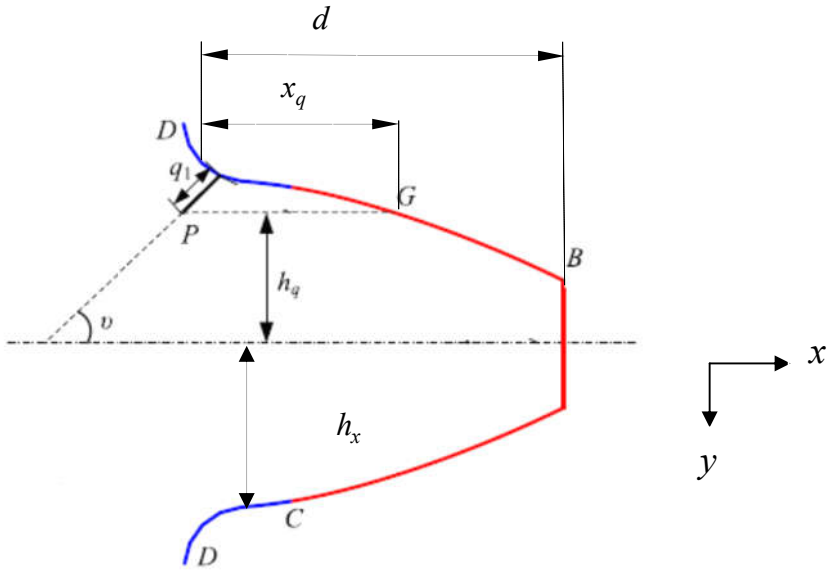


Figure 2: Cross section of Gear tooth crack [10]

Figure 2 represents the geometrical parameters of the crack (q_1,υ) in which $q_1$denotes the crack depth, and υ denotes the crack angle. Assume that there exists a crack of length $q_1$at the root of the gear 2.The crack path is assumed to be a straight line and start at the root of the pinion and then proceeds as shown in Figure 2. The intersection angle υ between the crack and the central line of the tooth is set at a constant 45^o. The crack length q_1 grows from zero with an increment size of 0.2 mm until the crack reaches the tooth's central line. At that point, q_1 reaches its maximum value of 17.96 mm. The mesh stiffness's are estimated for different propagating lengths of tooth root crack of the gear 2 teeth. With the influence of crack, the Hertzian contact stiffness will still be a constant since the work surface of the tooth has no defect and the width of the effective work surface W will always be a constant. The axial compressive stiffness will be considered the same with that under the perfect condition in that the crack part can still bear the axial compressive force as if no crack exists. The bending stiffness and shear stiffness, however, will change due to the change in effective area of cross-section.

The presence of a tooth root crack will cause a reduction in the effective tooth thickness and the part of the tooth material with respect to the crack is defined as the dead zone. This portion is removed from the tooth in calculating the gear mesh stiffness. The dead zone consists of the tooth profile, tooth crack, and the limit line. This limit line is through the crack tip and parallel to the center line of tooth simultaneously i.e. at point G, irrespective of the crack dimensions, which are shown in Figure 3 for different crack propagating lengths. As the crack length (q_1) changes, the length of the limiting line (x_q) also changes which result in the change in the effective area of cross-section.

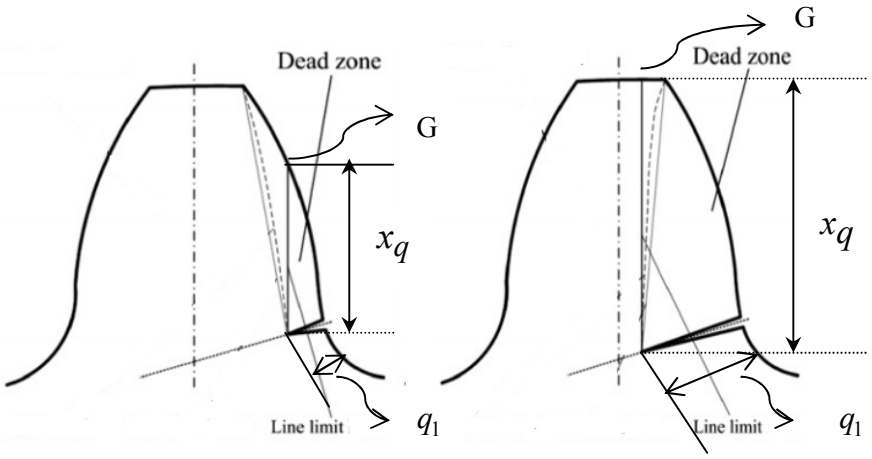


Figure 3: Limiting lines in Gear tooth crack

The effective area moment of inertia and area of the cross-section at the position of x can be calculated as:

$$I = \begin{cases} \frac{1}{12}(h_q + h_x)^3 W & 0 < x < x_q \\ \frac{1}{12}(2h_x)^3 W & x_q < x < d \end{cases} \tag{10}$$

$$A = \begin{cases} (h_q + h_x)W & 0 < x < x_q \\ (2h_x)W & x_q < x < d \end{cases} \tag{11}$$

where h_q is the distance from the root of the crack to the central line of the tooth, which corresponds to point G on the tooth profile, and h_q can be calculated by:

$$h_q = h_c - q_1 \sin\upsilon \tag{12}$$

Here h_c is the tooth thickness at the root circle, υ is the crack angle

Hence the total gear tooth mesh stiffness with crack K_{t_crack} is given by the following equation,

$$\frac{1}{K_{t_crack}} = \frac{1}{K_{ap}} + \frac{1}{K_{sp_crack}} + \frac{1}{K_{bp_crack}} + \frac{1}{K_{bg}} + \frac{1}{K_{ag}} + \frac{1}{K_{sg}} + \frac{1}{K_{fp}} + \frac{1}{K_{fg}} + \frac{1}{K_h} \tag{13}$$

Where K_{sp_crack} and K_{bp_crack} denotes the bending and shear gear mesh stiffness with crack.

The mean mesh stiffness obtained from the above equation is used for the generation of time varying gear mesh stiffness which is used for the dynamic characterization of drive train with presence of crack. The parameters of the typical wind turbine drive train are taken from [7] for the present dynamic analysis. The dynamic analysis is carried out for different percentages of gear tooth crack on gear2 (see fig. 1.) and the obtained results are plotted in the next section.

4 Results and discussion

The important parameters for the dynamic analysis and fault detection are taken from Nejad [7] and are considered for the present study. (See table 1-3)

Parameter	Specification
Type	Upwind/three blades
Rated power (MW), Rated wind speed (m/s)	5, 11.4
Rated rotor speed (rpm) ,Diameter(m)	12.1, 126
Rotor mass (×1000 kg), Rotor Inertia (kg-m^2), Generator Inertia(kg-m^2)	110, 2.183×10^8, 534.116
Gear ratio	96.354

Table 1: Wind turbine specifications

Parameter	First stage	Second stage	Third stage
Type	Planetary	Planetary	Parallel
Normal module (mm)	45	21	14
Normal pressure angle (degrees)	20	20	20
Number of teeth, Sun/pinion, Planet/gear, Ring gear	19,17,56	18,36,93	24,95
Pitch diameter (mm) sun/pinion, Planet/gear, Ring gear	855,765,2520	378,756,1953	336,1330,—
Mass (Kg) Sun/Pinion, Planet/gear	1900,1500	380,1500	180,1800
Inertia (Kg-m^2) Sun/Pinion, Planet/gear, Planet carrier	244,168,4180	9.5,143,820	3.8,475,—
Mean gear contact stiffness (N/m)	9×10^9	1.5×10^9	9.0246×10^8
Contact Ratio Ring-planet, Sun-planet, Gear-pinion	1.5354,1.5293,—	3.927,1.611,—	—,1.7243

Table 2: Details of gear box

Component	Value
Torsional stiffness of Main shaft, First- stage second shaft, Second stage-third shaft, High speed shaft (N-m/rad)	8.67×10^8, 5.68×10^8, 1.689×10^8, 0.181×10^8
Linear stiffness of Bearing 1,2,3,4,5,6 (N/m)	1.5×10^8, 1.2×10^8, 1.2×10^8, 5×10^8, 8.2×10^8, 8×10^8

Table 3: Specifications of Shafts and Bearings

Based on the above specifications of the wind turbine and gearbox, the important parameters for the dynamic characterization and fault detection are calculated and are given in table 4.

Parameter	Specification
First natural torsional frequency	2.28Hz
Mean gear mesh stiffness for 10 % and 40 % crack (N/m)	8.802×10^{8}, 7.6974×10^{8}
Gear mesh frequency of parallel gear stage	466.1Hz
Gear tooth defective frequency (running frequency)	19.4Hz

Table 4: Important parameters for fault detection

The modelling of gear tooth crack for wind turbine gear box and the calculation of mean mesh stiffness in the case of gear tooth crack is discussed in the previous section. The time varying gear mesh stiffness is represented in terms of Fourier series with mean gear mesh stiffness, gear mesh frequency and contact ratio [21]. Figures 4(a) and 4(b) represents the time-varying gear mesh stiffness plots without and with tooth crack for the gear2 respectively.

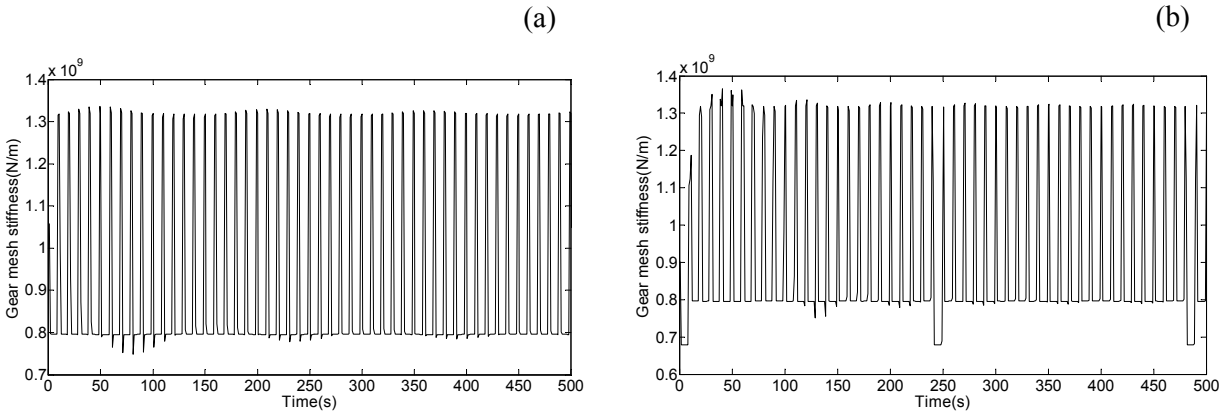


Figure 4: Time varying gear mesh stiffness (a) without crack (b) with 40% gear tooth crack

In fig. 4(b) the periodicity in gear mesh stiffness variation is observed for every 24thcycle which indicates the number of teeth on gear 2. Dynamic analysis is performed with and without existence of tooth crack and figure 5(a) and 5(b) represents the rotational vibration acceleration responses of gear2 without and with crack in frequency domain. In the case of healthy gear pair, FFT has only peaks at gear mesh frequencies as given in table 4 where as in case of crack the FFT has peaks at multiple number of gear tooth defective frequency i.e. 19.4Hz along with peaks at gear mesh frequencies and are shown in Figure 5(b) and 5(c). In the frequency domain representation, fault information is not clearly identified at lower percentages of fault as in the case of 10% gear tooth crack. Hence power spectral density is used to represent the fault information even at lower percentage of fault and is shown in figure 6 (b) along with higher severity of 40% in figure 6(c).

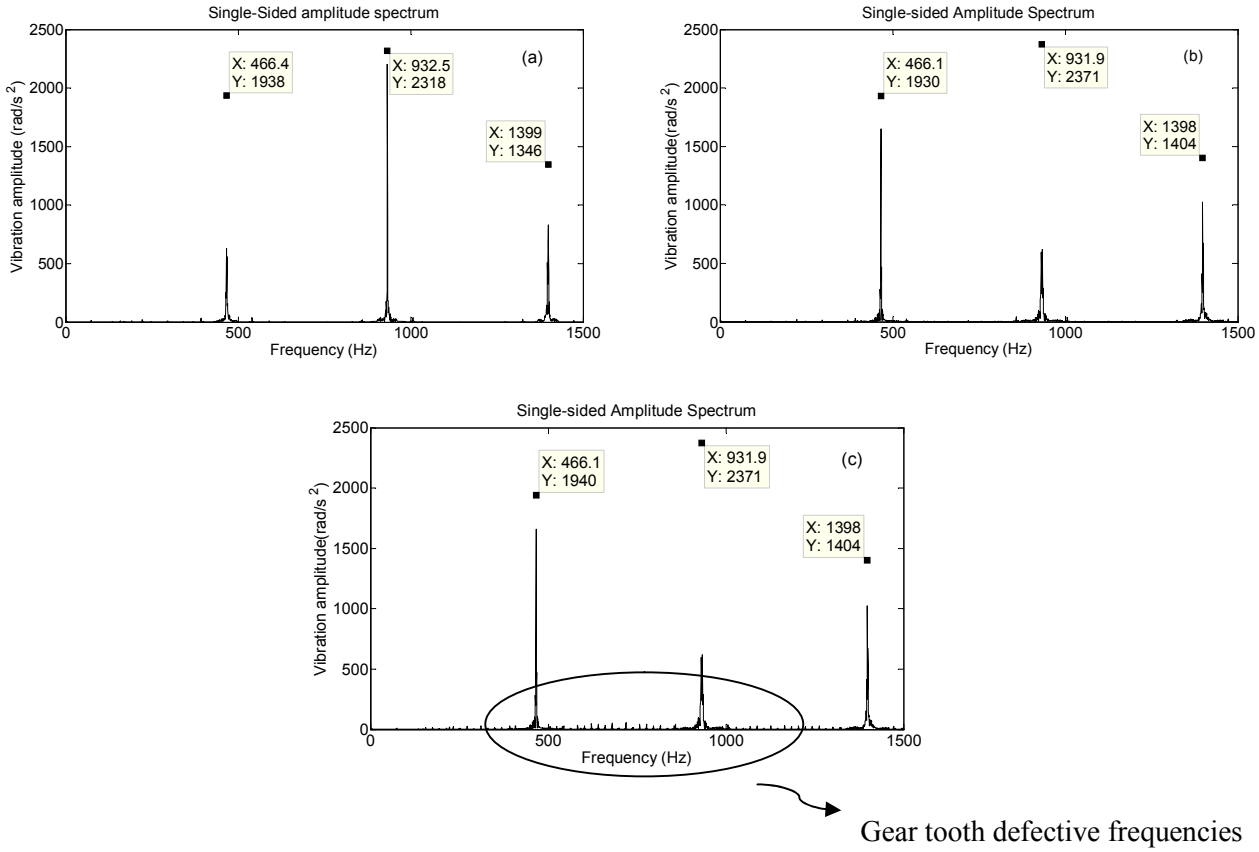
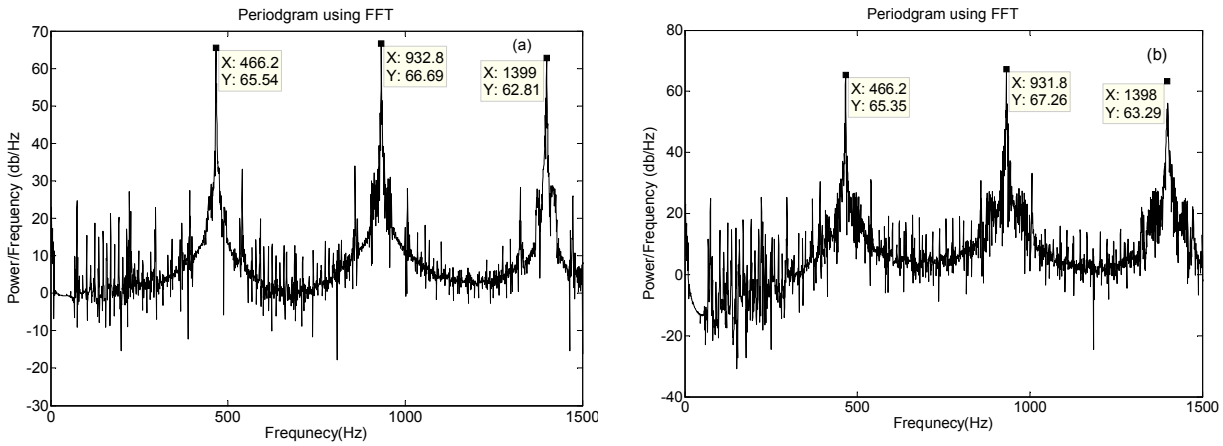


Figure 5: Frequency domain representation of gear 2 (FFT) (a) without crack (b) with 10% gear tooth crack (c) with 40% gear tooth crack



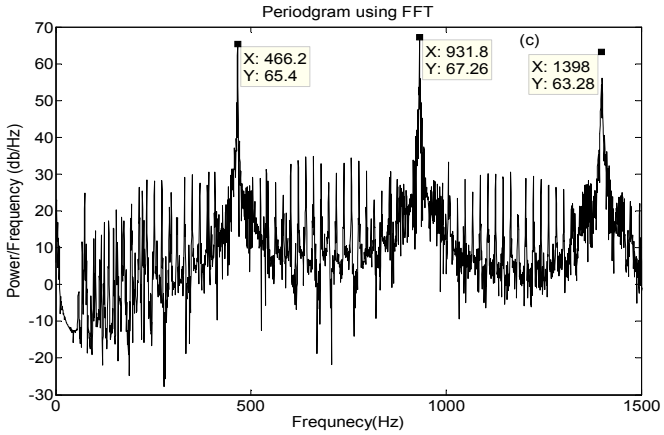


Figure 6: Frequency domain representation (PSD) of gear 2 (a) without crack (b) with 10% gear tooth crack (c) with 40% gear tooth crack.

5 Conclusions

The gear tooth crack due to the catastrophic failures in the wind turbine is modeled in the present work based on the literature data. The gear tooth crack effect is captured by evaluating the variation in the mean gear mesh stiffness due to the fault. The dynamic acceleration responses of gear2 without and with crack are obtained in the frequency domain (i.e. FFT and PSD) where the multiple numbers of peaks at tooth defective frequencies are identified in the case of gear tooth crack. This study is thus useful for fault detection in gearbox of wind turbine drive train.

References

[1] D. Qin, F. Tang, *Study on dynamic characteristics of gear transmission system of wind turbine*, in: 13th World Congress in Mechanism and Machine Science 2011, Guanajuato, Mexico.

[2] X. Wang, S. Wu, *Nonlinear dynamic modeling and numerical simulation of the wind turbines gear train*, in: International Conference on Electrical and Control Engineering 2011, IEEE Xplore, Yi Chang, 2011, pp. 2385–2389.

[3] M. Todorov, G. Vukov. *Parametric torsional vibrations of a drive train in horizontal axis wind turbine*, in: Proc. of the 1ère Conférence Franco-Syriennesur les Energies Renouvelables, Damas, Syrie, 2010, pp. 1–17.

[4] Y. Guo, J. Keller, R. Parker, *Dynamic Analysis of Wind Turbine Planetary Gears Using an Extended Harmonic Balance Approach*: Preprint, National Renewable Energy Laboratory (NREL), Golden, CO, 2012.

[5] Y. Yu, H. Yuan, Z. Huang, *Dynamic characteristics of gear transmission system for wind turbine gearbox*, Adv. Mater. Res. 2012 (482–484) (2012) 2327–2330

[6] D.D. Ji, Y.M. Song, J. Zhan, *Dynamics of gear train set in wind turbine*, Mater. Sci. Forum 698 (2012) 701–705.

[7] A.R.Nejad,*Developement of a 5 MW reference gearbox for offshore wind turbines*, Wind energy 2015.19:1089-1106 Wiley online library.

[8] Zhao, M.; Ji, J.C. *Nonlinear torsional vibrations of a wind turbine gearbox*. Appl. Math. Model. 2015, 39, 4928–4950.

[9] Chaari F, Fakhfakh T, Haddar M. *Analytical modeling of spur gear tooth crack and influence on gear mesh stiffness*. Euro J Mech A/Solids 2009;28:461–8.

[10] Chen ZG, Shao YM. *Dynamic simulation of spur gear with tooth root crack propagating along tooth width and crack depth*. Eng Fail Anal 2011;18:2149–64.

[11] P. Srikanth and A.S. Sekhar ,*Effect of gear tooth breakage on the dynamic response in a wind turbine drive train subjected to stochastic load excitation*,9th IFTOMM international conference on rotordynamics, September,22-25,2014,Milan, Italy.

[12] Lewicki DG. *Gear crack propagation path studies-guidelines for ultra-safe design*, NASA/TM-2001-211073, ARL-TR-2468.

[13] Wu S, Zuo MJ, Parley A. *Simulation of spur gear dynamics and estimation of fault growth*. J Sound Vib 2008;317:608–2

[14] Pandya Y, Parey A. Simulation of crack propagation in spur gear tooth for different gear parameter and its influence on mesh stiffness. Eng Fail Anal 2013;30:124–37.

[15] Zhou XJ, Shao YM, Lei YG, et al. *Time-varying meshing stiffness calculation and vibration analysis for a 16dof dynamic model with linear crack growth in a pinion*. J Vib Acoust 2012;134.011011-1-11.

[16] Hui Ma and Song *Time-varying mesh stiffness calculation of cracked spur gears*. Engineering Failure Analysis Volume 44, September 2014, Pages 179-194.

[17] Liang XH, Zuo MJ, Pandey M. *Analytically evaluating the influence of crack on the mesh stiffness of a planetary gear set.* Mech Mach Theory 2014;76:20–38.

[18] Ch v h Gayatri and A.S.Sekhar, *Dynamic analysis and characterization of wind turbine drive train using two stage planetary gear box,* The 5th International Conference on Kinematics, Mechanics of Rigid Bodies, and Materials 2017, Yogyakarta ,Indonesia.paper ID: 102

[19] P.Srikanth and A.S. Sekhar, *Wind turbine drive train dynamic characterization using vibration and torque signals*. Mechanism and Machine Theory 98 (2016) 2–20

[20] S. Chauhan, M.H. Hansen, D. Tcherniak*, Application of operational modal analysis and blind source separation/independent component analysis techniques to wind turbines*, Conference nd Exposition on Structural Dynamics IMAC-XXVII, 9–12 February 2009, Orlando, Florida, USA, 2009.

[21] Helsen J and Vanhollebeke F. *Insights in wind turbine drive train gathered by validating advanced models on a newly developed 13.2MWdynamically controlled test rig*. Mechatronics 2011; 21: 737–752.

Passive vibration control of offshore wind turbines using structure-immittance approach

Yi-Yuan Li [1], **Sara Ying Zhang** [1], **Jason Zheng Jiang** [1], **Simon Neild** [1], **Ian Ward** [2]
[1] University of Bristol, Department of Mechanical Engineering,
Senate House, Tyndall Avenue, Bristol, BS8 1TH, UK.
e-mail: **z.jiang@bristol.ac.uk**;

[2] SNC-Lavalin Atkins,
Epsom, Surrey, UK.

Abstract
Offshore wind turbines are growing in popularity due to the steady, high speed and environment friendly offshore wind resources. However, the wind and wave excitations can result in excessive vibration and hence destroying the structural integrity. To avoid this, the inerter-based vibration absorber, which is a reaction mass connected to the system with the combinations of springs, dampers and inerters, is employed in this study to suppress the vibration. Both monopile and spar-buoy offshore wind turbines are investigated in this paper by establishing limited degree-of-freedom models based on FAST. The structure-immittance approach is used to obtain the optimal absorber configurations with corresponding element values, by minimising the standard deviation of the tower top displacement. It will be shown that compared with the traditional tuned mass damper, the performance of the inerter-based absorber is superior. Moreover, with the same performance as the tuned mass damper, the mass of the inerter-based absorber can be significantly reduced.

1 Introduction

Offshore wind turbines (OWTs) are growing in popularity due to the steady, high speed and environment friendly offshore wind resources. However, the combined multiple hazards such as wind and wave excitations can result in excessive vibration and fatigue load, hence destroying the structural integrity, shortening the service life and increasing the energy production cost of the turbines. In order to prolong its lifespan, passive structural control strategy, which is widely used due to its simplicity and zero power input, is employed in this paper for the vibration suppression of the OWTs.

The most commonly used passive structural control device is the tuned mass damper (TMD). Murtagh et al. [1] studied the vibration mitigation of a blade coupling wind turbine model by using a TMD under the along-wind force; Lackner et al. [2] included a TMD into the FAST code [3], a fully coupled aero-hydro-servo-elastic code developed by National Renewable Energy Laboratory (NREL) to simulate the loads and performance of OWTs; Later Stewart et al. [4] optimised the parameter values of a TMD based on the limited degree-of-freedom (DOF) models; Stewart et al. [5] also investigated the effects of misalignment for the OWTs with a TMD in the nacelle; Specifically, Si et al. [6] investigated the vibration suppression of a spar-type floating OWT by employing a TMD in the platform. Even though the performance of the TMD will be improved as the mass of the TMD increasing, due to the space and weight limitation, performance of the TMD is limited. In order to enhance the vibration suppression capability of the TMD, a passive mechanical element, the inerter, is employed in the present study.

The inerter was first introduced by Smith [7]. It is a two-terminal device with the property that the force

generated is proportional to the relative acceleration across its two terminals. With inerter, the force-current analogy [8] between mechanical and electrical systems can be fully achieved, with mechanical elements springs, dampers and inerters corresponding to the electrical elements inductors, resistors and capacitors, respectively. For passive electrical networks, using the Bott-Duffin theorem [9], it has been shown that any positive-real functions can be realised as the driving-point immittance of a network consisting only of resistors, capacitors and inductors. Hence, mechanical networks consisting of dampers, inerters and springs can also synthesise all positive-real functions characterising force-velocity properties. In general, two approaches are applied to identify beneficial passive vibration absorber, the structure-based approach and the immittance-based approach. For the structure-based approach, network layouts, such as the TID [10] and the TMDI [11], are first proposed. Parameter values for the constituent elements are then selected based on performance criteria. With this approach, the complexity and topology of the absorber is pre-determined. However, only one network layout can be considered at a time even though there are large number of possible layouts, which inevitably limits the achievable performance of the proposed absorber. On the other hand, with the immittance-based approach, such as the application proposed by Wang et al. [12] and Li et al. [13], a positive-real immittance function which is capable of providing the optimum performance of the system is first obtained. Then, the corresponding network layout and element values can be identified using network synthesis theory. However, without pre-restricted complexity and topology of the network, undesirable networks with very complicated layouts may occur. To overcome the disadvantages of structure-based and immittance-based approaches, a novel structure-immittance approach was proposed by Zhang et al. [14] for passive vibration absorber identification. With this approach, a new class of structural immittance functions can be obtained, which can cover a full set of network layouts with explicit information of all topology possibilities; meanwhile, the number of each element type can be pre-determined, and the element values can be fixed or constrained.

In this paper, the NREL 5MW offshore wind turbine [15] is considered. An inerter-based absorber (IBA) is used to investigate the vibration suppression for both a fixed-bottom monopile and a floating spar-buoy platform. The structure-immittance method is employed to obtain the optimum absorber, which is a reaction mass connected to the nacelle at a single point using a combination of one inerter, one damper and two springs. This paper is constructed as follows: In Section 2, the structure-immittance method for one inerter, one damper and two springs case is briefly summarised; In Section 3, the limited DOF Matlab models of monopile and spar-buoy are established and the structure parameters are identified; In Section 4, the IBAs' layouts and corresponding parameter values are obtained for monopile and spar-buoy, respectively. The potential of mass reduction is also investigated in this section. Finally, conclusions are drawn in Section 5.

2 Structure-immittance method

By utilising the force-current analogy, the structure-immittance method can be applied both on mechanical and electrical networks. The transfer function of the mechanical network is defined as

$$Y(s) = \frac{F(s)}{V(s)} \tag{1}$$

where $F(s)$ and $V(s)$ are the force and relative velocity across the two terminals in Laplace domain, respectively. s is the complex frequency parameter of the Laplace transform. Mapping it to electrical system, the transfer function corresponds to the admittance of electrical networks, which is

$$Y(s) = \frac{I(s)}{U(s)} \tag{2}$$

where $I(s)$ and $U(s)$ are the current and voltage across the two terminals in Laplace domain, respectively. One-port (two-terminal) mechanical networks are taken into consideration to develop structure-immittance method in this paper. The definition of structural-immittances, which include all the possible arrangements

of a set number of elements, are given as the transfer functions from force to velocity. In this section, a mechanical system including one inerter, one damper and two springs as well as its structural-immittances are demonstrated.

For the case of one inerter, one damper and two springs, there are totally 18 absorber layouts. By using the structure-immittance method, two networks, termed Q_1 and Q_2, that contain all the 18 possible layouts, can be obtained. There are totally 4 steps needed to obtain the final networks Q_1 and Q_2 [14], for compliance these are summarised here. It should be noted that at most two springs are present for the networks obtained in each step.

Step 1: Two generic sub-networks M_1 and M_2 are constructed as shown in step 1 of Figure 1 . One is an inerter based sub-network and the other is a damper-based sub-network.

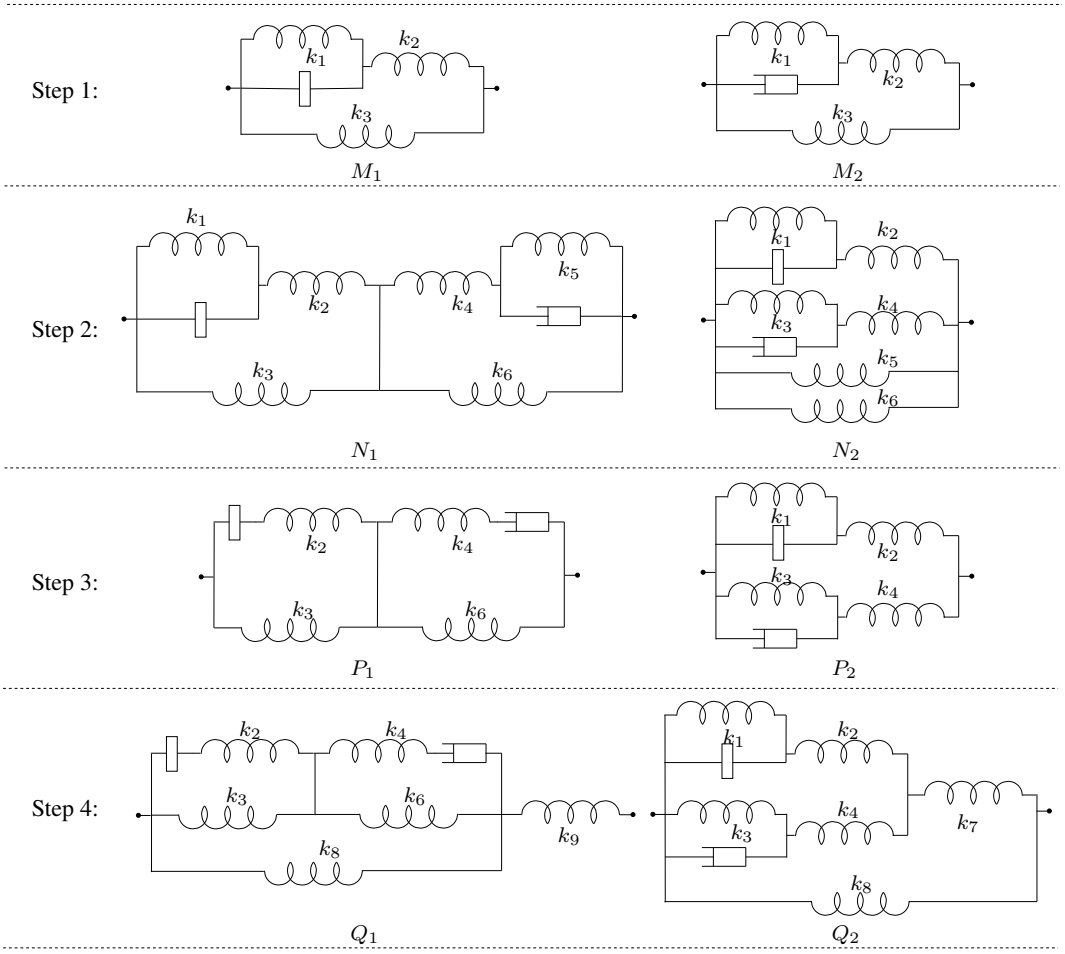


Figure 1: The networks obtained for 1 damper, 1 inerter and 2 springs

Step 2: Two sub-networks M_1 and M_2 are connected to each other both in parallel and in series to form two new networks N_1 and N_2, as shown in step 2 of Figure 1 .

Step 3: Since in networks N_1 and N_2, some of the springs are redundant and can produce the same effect on the network, redundancy of the springs in networks N_1 and N_2 need to be checked with springs removed if possible. For example, for k_1 in network N_1, the layout with k_1 and k_2 present can be realised by k_3 and k_4; the layout with k_1 and k_3 present can be realised by k_3 alone; the layout with k_1 and k_4 present is equivalent to that with k_3 and k_4; the layout with k_1 and k_5 present can be realised by k_3 and k_6; the layout with k_1 and k_6 present equals that with k_3 and k_6. Therefore, k_1 is redundant and can be removed. All of the springs in N_1 and N_2 should be checked one by one to guarantee that there is no redundancy left in the networks. As a result, two simplified networks P_1 and P_2 can be obtained, as shown in step 3 of Figure 1 .

Step 4: Springs are now added to the network to form the final networks. The adding rule is: a spring is first added in series and the redundancy is checked for this added spring. Then, another spring is added in parallel and the redundancy is checked. This process is repeated until any further addition of a spring in series or in parallel is redundant. Thus, the final networks can be constructed. Follow the adding rule, final networks, Q_1 and Q_2, are obtained, see step 4 of Figure 1 .

The structural-immittances of networks Q_1 and Q_2 are:

$$Y_i(s) = \frac{n_i(s)}{m_i(s)} \quad (i = 1, 2), \tag{3}$$

where

$$\begin{aligned}
n_1(s) =& bc(k_3/k_2 + k_8/k_2 + k_6/k_4 + k_8/k_4 + 1)s^3 + b(k_6 + k_8)s^2 + \\
& c(k_3 + k_8)s + k_3k_6 + k_3k_8 + k_6k_8, \\
m_1(s) =& s\big[bc(1/k_2 + 1/k_4 + 1/k_9)s^3 + b(k_3/k_2 + k_6/k_2 + k_6/k_9 + k_8/k_9 + 1)s^2 + \\
& c(k_3/k_4 + k_3/k_9 + k_6/k_4 + k_8/k_9 + 1)s + k_3 + k_6\big], \\
n_2(s) =& bc(1/k_2 + 1/k_4)s^3 + b(k_3/k_2 + k_3/k_4 + k_8/k_2 + k_8/k_7 + 1)s^2 + \\
& c(k_1/k_2 + k_8/k_4 + k_1/k_4 + k_8/k_7 + 1)s + k_1 + k_3 + k_8, \\
m_2(s) =& s\big[bc(1/(k_2k_4) + 1/(k_2k_7) + 1/(k_4k_7))s^3 + b(1/k_2 + 1/k_7)s^2 + \\
& c(1/k_4 + 1/k_7)s + k_1/k_2 + k_1/k_7 + k_3/k_4 + k_3/k_7 + 1\big].
\end{aligned} \tag{4}$$

$Y_1(s)$ and $Y_2(s)$ include all the possibilities of one inerter, one damper and two springs combinations. For $Y_1(s)$, only two of $1/k_2$, k_3, $1/k_4$, k_6, k_8 and $1/k_9$ are positive and all the others are equal to zero. For $Y_2(s)$, only two of k_1, $1/k_2$, k_3, $1/k_4$, $1/k_7$ and k_8 are positive and all the others are equal to zero. These transfer functions can be used, along with the constraints listed here to find the optimal one inerter, one damper and two springs configuration for a given system and objective function.

3 Limited DOF offshore wind turbine models

The ideal way to identify the IBA configurations and their corresponding parameters would be to carry out the optimisation within FAST. However, the inerter and the structure-immittance approach have not been included in FAST so far. Besides, FAST is expensive in terms of the computations needed since the simulation time in FAST for a 60 s simulating is around 60 s, and to find the optimum values, thousands of function calls might be needed. As a feasibility study, following [4], a limited DOF linear Matlab model for each type of OWT is established in this section.

3.1 Monopile

Considering the monopile, the tower fore-aft bending mode is responsible for most of the fatigue loading. Hence two DOFs are considered here: the tower fore-aft bending DOF and the IBA's mass DOF. The model is shown in Figure 2 (a). Applying the small angle approximation, equations of motion of the system are given as:

$$\begin{cases} m\ddot{x}_r = & mg\theta_t - Y\dot{x}_r - mR\ddot{\theta}_t \\ I_t\ddot{\theta}_t = & m_tgR_t\theta_t + RY\dot{x}_r - k_t\theta_t - c_t\dot{\theta}_t + mgx_r \end{cases} \tag{5}$$

where m_t is the turbine's total mass and m is the absorber's mass. The angle that the tower has deflected from vertical is denoted by θ_t. Nacelle of the OWT is considered as a reference frame and the displacement of the

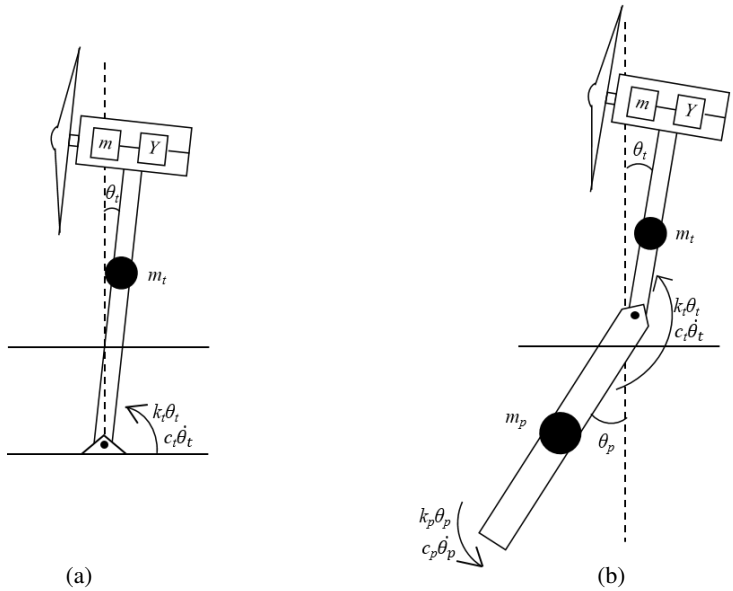


Figure 2: Limited DOF offshore wind turbine model inspired by [4]: (a) monopile; (b) spar-buoy.

absorber is relative to the nacelle, which is denoted as x_r. So the term $mR\ddot{\theta}_t$ exists due to the non-inertial reference frame. R and R_t are the distances from the tower hinge to the absorber and the centre of the turbine total mass, respectively. k_t and c_t are the rotary stiffness and rotary damping constants at the tower base. Y is the representation of the admittance function of absorbers consisting of inerters, dampers and springs. The absorber's mass m is taken to be equal to 20,000 kg for consistence with [4] and it is approximately 2% of the turbine's total mass m_t.

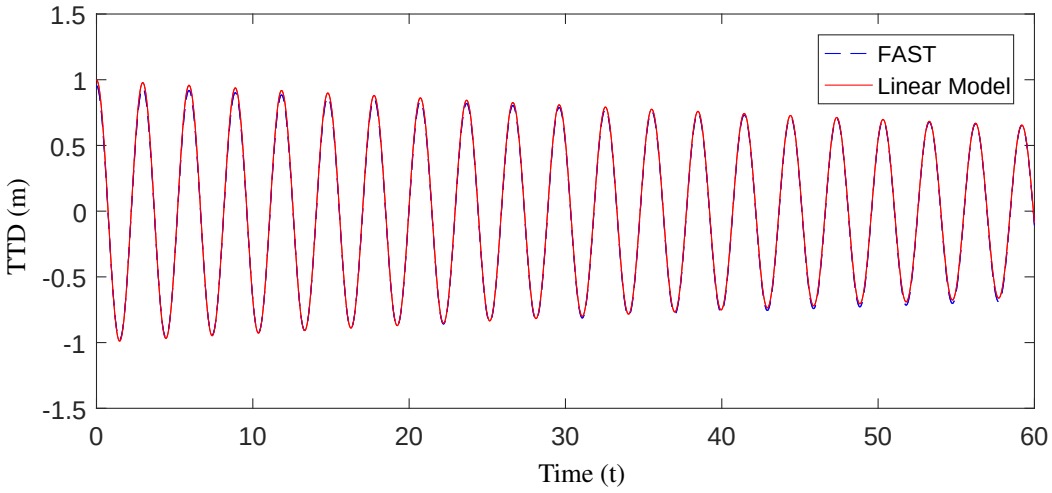


Figure 3: Response comparison of linear model and FAST for monopile

In order to use the linear model to obtain the optimal absorber's configuration, model parameters must be determined first. I_t, m_t, R_t and R can be obtained from [16, 17] and the FAST input files. The rotary stiffness k_t and the rotary damping constants c_t need to be determined by matching the linear model response to FAST output with the same input conditions. In this paper, a step input of the tower top displacement (TTD) equal to 1 m is used, which is the amount of tower bending in meters measured at the top of the tower. The response of the linear model is fitted into the FAST output in Matlab where the plot of the fit of the TTD for the monopile model is shown in Figure 3 . The monopile TTD starts at 1 m and oscillates at a frequency of approximately 0.337 Hz. It can be observed from Figure 3 that the responses of the limited DOF monopile Matlab model and the FAST output are very close to each other. The resulting rotary stiffness and rotary

damping values are $k_t = 2.52 \times 10^{10}$ kN·m/rad and $c_t = 7.75 \times 10^7$ kN·m·s/rad, respectively. The obtained parameters are listed in Table 1 .

Properties	Values
Hub mass	56780 kg
Nacelle mass	240000 kg
Rotor mass	110000 kg
Tower and monopile mass	522617 kg
Turbine total Mass m_t	929397 kg
absorber's mass m	20000 kg
Tower inertia I_t	5.43×10^9 kg·m^2
Turbine's height R	107.6 m
Mass centre to the bottom R_t	76.4 m
Rotary stiffness constant k_t	2.52×10^{10} kN·m/rad
Rotary damping constant c_t	7.75×10^7 kN·m·s/rad

Table 1: Monopile model parameters

3.2 Spar-buoy

For the spar-buoy, the tower fore-aft bending mode and the platform pitch angle mode are responsible for most of the fatigue loading. Therefore, there are three DOFs that are of concern: the tower fore-aft bending DOF, the platform pitch DOF and the absorber's mass DOF. The model is shown in Figure 2 (b) . Similarly, applying the small angle approximation and considering the absorber in the non-inertial reference frame, the equations of motion of the system are given as:

$$\begin{cases} m\ddot{x}_r = mg\theta_t - Y\dot{x}_r - mR\ddot{\theta}_t \\ I_t\ddot{\theta}_t = m_t g R_t\theta_t + RY\dot{x}_r - k_t(\theta_t - \theta_p) - c_t(\dot{\theta}_t - \dot{\theta}_p) + mgx_r \\ I_p\ddot{\theta}_p = -m_p g R_p\theta_p + k_t(\theta_t - \theta_p) + c_t(\dot{\theta}_t - \dot{\theta}_p) - k_p\theta_p - c_p\dot{\theta}_p \end{cases} \tag{6}$$

where m_p is the mass of the platform; θ_p is the angle that the platform has bent from vertical; R_p is the distance from the tower hinge to the centre of the platform mass; k_p and c_p are the rotary stiffness and damping constants of spar-buoy platform, which are the summation of hydrostatic and mooring line effects and so on. All the other parameters have the same values as those used in the monopile linear model.

Again, the model parameters must be determined first. Similarly, m_t, I_t, m_p, R, R_t and R_p can be obtained from [18] and the FAST input files. The tower and platform rotary stiffness and damping constants k_t, c_t, k_p and c_p, respectively, will be identified by comparing the model to FAST outputs in Matlab. In addition, the platform inertia I_p needs to be identified, this is because inertial effect of the water must also be considered in I_p. The platform inertia shown in the FAST input file is the true platform inertia, whereas for the simplified model, since the platform is under the sea, this effect is significant. For the spar-buoy type OWT, a step input of the platform pitch angle equal to 5° is used to obtain the FAST monopile model output. Figure 4 (a) and (b) show the plot of the fit for the TTD and the platform pitch angle (PPA) for the spar-buoy model in Matlab. Since the TTD reflects the tower bending condition, TTD is relative to the platform coordinate system. This means if the platform is pitched while there is no bending of the tower, then the TTD is zero. The spar-buoy PPA starts at 5° with the frequency of approximately 0.019 Hz and the TTD starts at 1 m with the frequency of approximately 0.377 Hz. It can be observed from Figure 4 that the fit between the limited DOF spar-buoy model and the FAST output is reasonable. The inaccuracies in the model are because the spar-buoy damping constant c_p includes many sources of hydrodynamic damping, wave radiation and viscous damping. These terms are nonlinear, and so are only approximated in the linear damping constants used in the low order linear model. The resulting rotary stiffness and damping constants of tower and

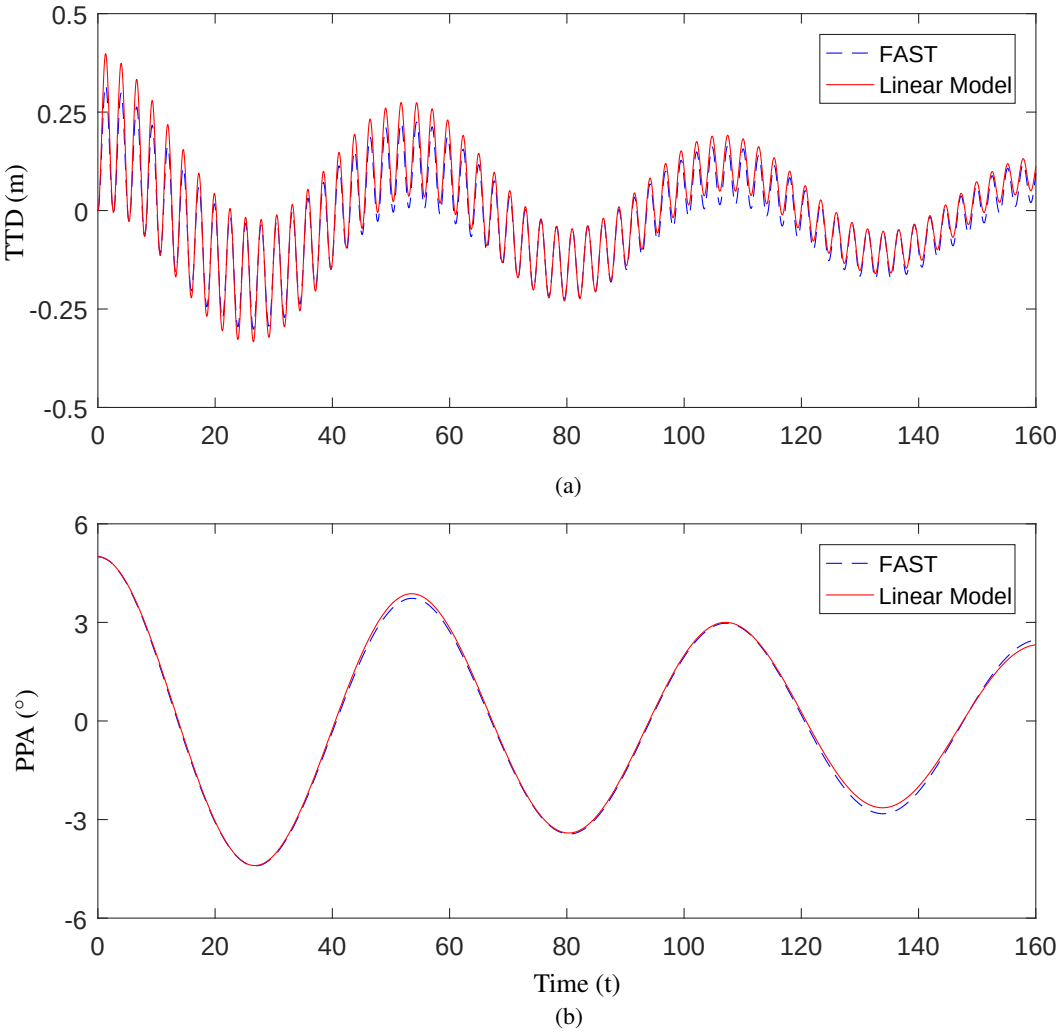


Figure 4: Response comparison of linear model and FAST for spar-buoy: (a) TTD; (b) PPA.

platform are $k_t = 1.56 \times 10^{10}$ kN·m/rad, $c_t = 5.32 \times 10^7$ kN·m·s/rad, $k_p = 6.00 \times 10^7$ kN·m/rad and $c_p = 5.42 \times 10^9$ kN·m·s/rad, respectively. The obtained parameter values are listed in Table 2 .

4 Applications of the inerter-based absorber

The proposed IBA involves connecting a reaction mass to the nacelle of the turbine at a single point via a combination of one inerter, one damper and two springs. In this paper, the initial condition is considered as the input for optimisation. Since the tower base bending moment is crucial to the tower fatigue life, the TTD is taken as the performance index, similar to [2]. Therefore, the objective function is defined as the standard deviation of the TTD:

$$J = std(\text{TTD}) \tag{7}$$

In order to identify the absorber's optimum layout and parameter values, objective function J is optimised using a combination of $patternsearch$ and $fminsearch$ in Matlab with $fminsearch$ refining the results obtained via $patternsearch$. The optimum configuration of the IBA is compared with the TMD to show its effectiveness.

Properties	Values
Hub mass	56,780 kg
Nacelle mass	240,000 kg
Rotor mass	110,000 kg
Tower mass	249,718 kg
Total turbine mass m_t	656,498 kg
Tower inertia I_t	2.73×10^9 kg·m^2
Platform mass m_p	7,466,330 kg
platform inertia I_p	5.01×10^{11} kg·m^2
Turbine's height to the tower hinge R	77.6 m
Turbine mass centre to the tower hinge R_t	64.5 m
Platform mass centre to the tower hinge R_t	-99.9155 m
Rotary stiffness of the tower k_t	1.56×10^{10} kN·m/rad
Rotary damping of the tower c_t	5.32×10^7 kN·m·s/rad
Rotary stiffness of the platform k_p	6.00×10^7 kN·m/rad
Rotary damping of the platform c_p	5.42×10^9 kN·m·s/rad

Table 2: Spar-buoy model parameters

4.1 Improvements with same absorber mass

In this section, the absorber's mass is taken to be 20000 kg for both TMD and IBA, with their optimum performances compared.

For the monopile case, the input load for optimisation procedure is an initial condition of TTD equal to 1 m. By using structure-immittance approach, the optimum IBA configuration and the corresponding parameter values are obtained. For the IBA case, the minimum value of the objective function is $J = 0.1782$ with $k_1 = 80.00$ kN/m, $k_2 = 7.21$ kN/m, $b = 1519$ kg, $c = 1.17$ kNs/m. For the TMD case, Y represents the velocity to force relation of a spring and a damper connected in parallel. The minimum value of the objective function is $J = 0.1909$ with $k = 82.60$ kN/m, $c = 8.393$ kNs/m. The performance improvement of the IBA is 6.65% compared with the TMD. Results are shown in Table 3 . The free decay responses of the monopile TTD with TMD and IBA in the nacelle are shown in Figure 5 .

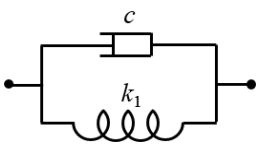
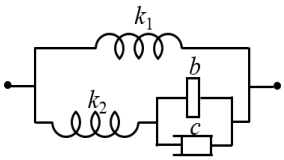
Optimal parameter values and layouts	Vibration Absorber	
	TMD	2-springs IBA
J	0.1909	0.1782
Performance improvement	/	6.65%
Layouts		
b	/	1519 kg
c	8.39 kNs/m	1.17 kNs/m
k_1	82.60 kN/m	80.00 kN/m
k_2	/	7.21 kN/m

Table 3: Optimisation results for monopile model

Similarly, for the spar-buoy case, the input load is an initial condition of tower TTD equal to 1 m. By using structure-immittance approach, the optimum IBA configuration and the corresponding parameter values are obtained. For the IBA case, the minimum value of the objective function is $J = 0.1667$ with $k_1 = 99.16$ kN/m, $k_2 = 9.26$ kN/m, $b = 1566$ kg, $c = 1.37$ kNs/m. The minimum value of the objective

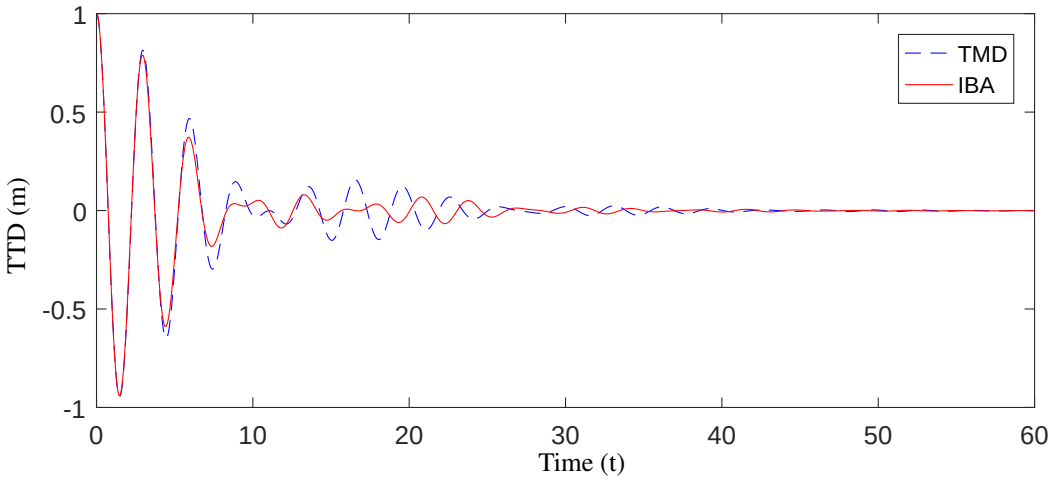


Figure 5: Free response of monopile TTD

function is $J = 0.1784$ with $k = 102.50$ kN/m, $c = 9.50$ kNs/m. The improvement of the IBVA is 6.56% compared with the TMD. The results are shown in Table 4. The free decay response of the spar-buoy tower top displacement and platform pitch angle with TMD and IBVA in the nacelle are shown in Figure 6 .

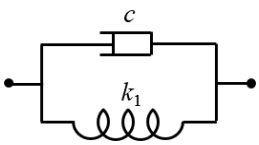
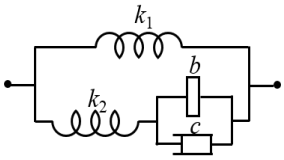
Optimal parameter values and layouts	Vibration Absorber	
	TMD	2-springs IBA
J	0.1784	0.1667
Performance improvement	/	6.56%
Layouts		
b	/	1566 kg
c	9.50 kNs/m	1.37 kNs/m
k_1	102.5 kN/m	99.16 kN/m
k_2	/	9.26 kN/m

Table 4: Optimisation results for spar-buoy model

4.2 Performances with different mass values

To assess the effect of mass on the optimum performance for TMD and IBA, mass values are taken as 10,000 kg, 20,000 kg and 40,000 kg, which are approximately 1%, 2% and 4% of the total mass of the monopile OWT. Using this information, compared with TMD of which mass value equals 20,000 kg, the possible mass reduction of the IBA while retaining the same level of performance is investigated.

For monopile, the input load for the optimisation procedure is the initial condition of TTD equal to 1 m. The monopile performance across a range of absorbers' mass values is shown in Figure 7 (a). It can be seen that as the mass value improves, the performance for both TMD and IBA are improved. However, the improvements of IBA is larger than that of the TMD. Moreover, compared to TMD with a 20,000 kg mass, the mass of IBA can be reduced to 16,785.7 kg (i.e. a 16.1% reduction) while achieving the same performance in terms of the cost function given in Eq. (7).

For spar-buoy, the input load for optimisation procedure is also the initial condition of TTD equal to 1 m. Relationships of the monopile performance with different absorbers' mass values is shown in Figure 7 (b).

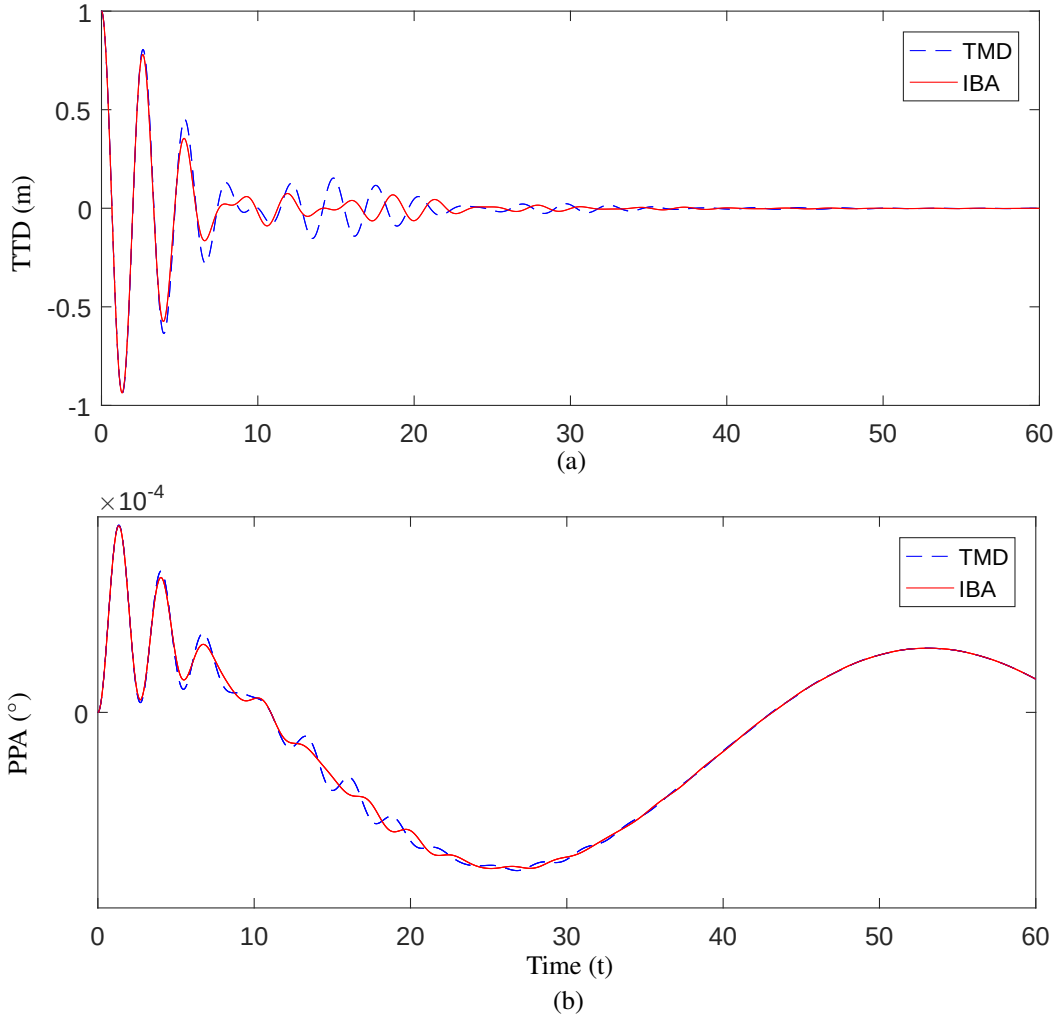


Figure 6: Free response of spar-buoy: (a) TTD; (b) PPA

Compared to TMD with a mass of 20,000 kg, the mass of IBA can be reduced to 14,996.9 kg (i.e. a 25.0% reduction) while achieving the same performance.

5 Conclusion and future work

In this paper, inerter-based absorbers are introduced in offshore wind turbine system to suppress its vibration. The absorber has a reaction mass connected to the nacelle at a single point using a combination of pre-determined number of inerters, dampers and springs. The concept of structure-immittance method is reviewed, which will facilitate the identification of the optimum absorber's layout and parameter values. The limited DOF Matlab models of monopile and spar-buoy are established, respectively, for the optimisation procedure. Since the tower bottom bending moment is the most fatigue loading, the standard deviation of tower top displacement is chosen as the reference index. The results show that the inerter-based absorber is superior to TMD in terms of reducing the tower top displacement. The reduction is 6.65% and 6.56% for monopile and spar-buoy, respectively, compared with TMD. Moreover, the relationship of performance with different mass values is also investigated. Compared with TMD, the mass can be reduced by 16.1% and 25.0% for monopile and spar-buoy, respectively, when employing an inerter-based device, while matching the performance of the TMD.

In our future work, the realistic wind and wave loads will be applied to the offshore wind turbine models in

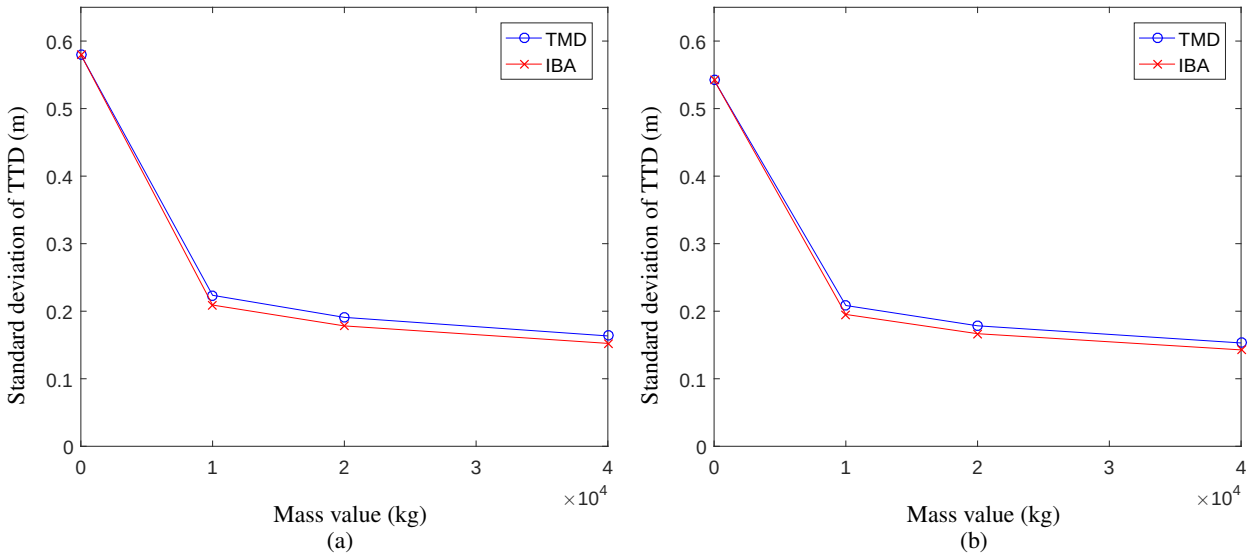


Figure 7: Performances for TMD and IBA with different mass values: (a) monopile; (b) spar-buoy

Matlab to further verify the efficiency of inerter-based absorbers in mitigating vibrations of turbines. Then the inerter and the structure-immittance method will be included in FAST for further optimisation to identify the most beneficial absorbers' layouts and their parameter values.

Acknowledgements

The authors would like to acknowledge the support of the University of Bristol, EPSRC and the Royal Society; Y-Y. L. is funded by the Dean's Scholarship of Engineering Faculty; S. Y. Z. and J. Z. J are supported by the EPSRC grant EP/P013546/1; J. Z. J is also supported by a Royal Society project IE151194; S. A. N is supported by EPSRC fellowship EP/K005375/1.

References

[1] PJ. Murtagh, A. Ghosh, B. Basu, BM. Broderick, *Passive control of wind turbine vibrations including blade/tower interaction and rotationally sampled turbulence*, Wind Energy, Vol. 11, (2008), pp. 305-317.

[2] MA. Lackner, MA. Rotea, *Passive structural control of offshore wind turbines*, Wind Energy, Vol. 14, (2011), pp. 373-388.

[3] JM. Jonkman, ML. Buhl, *FAST User's Guide*, TP-500-38230, NERL, Golden, CO., (2011).

[4] G. Stewart, M. Lackner, *Offshore wind turbine load reduction employing optimal passive tuned mass damping systems*, IEEE Transactions on Control Systems Technology, Vol. 21, No.4, (2013), pp. 1090-1104.

[5] GM. Stewart, MA. Lackner, *The impact of passive tuned mass dampers and wind–wave misalignment on offshore wind turbine loads*, Engineering Structures, Vol. 73, (2014), pp. 54-61.

[6] Y. Si, HR. Karimi, H. Gao, *Modelling and optimization of a passive structural control design for a spar-type floating wind turbine*, Engineering Structures, Vol. 69, (2014), pp. 168-182.

[7] MC. Smith, *Synthesis of mechanical networks: the inerter*, IEEE Transactions on Automatic Control, Vol. 47, No. 10, (2002), pp. 1648-1662.

[8] FA. Firstone, *A new analogy between mechanical and electrical systems*, The Journal of the Acoustical Society of America, Vol. 4, No. 3, (1933), pp. 249-267.

[9] R. Bott, RJ. Duffin, *Impedance synthesis without use of transformers*, Journal of Applied Physics, Vol. 20, No. 8, (1949), pp. 816.

[10] IF. Lazar, SA. Neild, DJ Wagg, *Using an inerter-based device for structural vibration suppression*, Earthquake Engineering and Structural Dynamics, Vol. 43, No. 8, (2014), pp. 1129-1147.

[11] L. Marian, A. Giaralis, *Optimal design of a novel tuned mass-damper-inerter (TMDI) passive vibration control configuration for stochastically support-excited structural systems*, Probabilistic Engineering Mechanics, Vol. 38, (2014), pp. 156-164.

[12] FC. Wang, MR. Hsieh, HJ Chen, *Stability and performance analysis of a full-train system with inerters*, Vehicle System Dynamics, Vol. 50, (2012), pp. 545-571.

[13] Y. Li, JZ. Jiang, NA. Neild, *Inerter-based configurations for main-landing-gear shimmy suppression*, Journal of Aircraft, Vol. 54, (2014), pp. 684-693.

[14] SY. Zhang, JZ. Jiang, SA. Neild, *Passive vibration control: a structure-immittance approach*, Proceedings of the Royal Society, Vol. 473, (2017), 20170011.

[15] J. Jonkman, S. Butterfield, W. Musial, G. Scott, *Definition of a 5-MW reference wind turbine for offshore system development*, TP 500-38060, NREL, Golden, CO., (1997).

[16] J. Jonkman, S. Butterfield, P. Passon, T. Camp, J. Nichols, et al., *Offshore Code Comparison Collaboration within IEA Wind Annex XXIII: Phase II Results Regarding Monopile Foundation Modelling*, IEA European Offshore Wind Conference, Berlin, Germany, December 4-6, (2007).

[17] J. Jonkman, W. Musial, *Offshore code comparison collaboration (OC3) for IEA Task 23 offshore wind technology and deployment*, TP-5000-48191, NREL, Golden, CO., (2010).

[18] J. Jonkman, *Definition of the Floating System for Phase IV of OC3*, TP-500-47535, NREL, Golden, CO., (2010).

Novel phase-bound magnetic vibration absorber for improved NVH performance of a wind turbine gearbox

B. Mrak [1,2], **R. Adduci**[2,3], **S. Weckx**[1], **W. Driesen** [1], **W. Desmet**[2,3]
[1] Flanders Make vzw,
Celestijnenlaan 300 D, B-3001, Heverlee, Belgium

[2] KU Leuven, Department of Mechanical Engineering,
Celestijnenlaan 300 B, B-3001, Heverlee, Belgium

[3] DMMS core lab, Flanders Make, Belgium
e-mail: **branimir.mrak@flandersmake.be**

Abstract
We propose a novel phase bound magnetic vibration absorber based on parallel combinations of magnetic springs. The corresponding design methodology is based on magnetic spring toolchain consisting of FE simulations of magnetic spring and 1D models together with system dynamics model. This approach is applied to an industrially relevant vibration reduction problem of gear meshing, specifically for wind turbine applications. In order to capture the relevant gearbox dynamic a semi-analytical Cai-Hayashi formulation of the gear stiffness is used in combination with ISO 6336 norm for spur gear capacity. We compare the modeling results to a state-of-the-art tuned mass damper approach, addressing the issues of tonalities in wind turbines. As opposed to the frequency bound vibration absorbers, the novel magnetic spring vibration absorber is order-selective, similarly to centrifugal pendulum absorbers, with the added value of a virtually infinite lifetime, no de-tuning issues, and feasible high-order vibration absorbers

1 Introduction

With increasing energy demands and ever-improving measures against global warming, renewable energy sources such as wind turbine generators are always in need of more robust and standardized performance. When it comes to noise emission issues, gearboxes in wind turbines are a significant source of torsional vibration [1] in the drivetrain that subsequently propagates to the supporting structure causing the unwanted noise emissions or premature fatigue failure. Specifically, varying contact forces resulting from variable mesh stiffness in gears propagates from gear to the housing due to the reaction forces in gears. The meshing modes have been linked to tonal noise peaks previously in earlier research [2]. A strong testimony to the importance of the tonal noise caused by the gearbox is the fact that the first two tonal peaks are the limit to which the turbine drivetrains producers have to minimize to satisfy the government regulations [3], but also the studies performed on perceived level of annoyance resulting from tonal noise sources as compared to broadband noise. In order to alleviate the noise emission levels, there is a need for improved torque ripple reduction methods for a wide operational range.

State-of-practice solutions for torque ripple reduction like single flywheels and dual-mass-flywheels deal with torsional vibrations only for a specifically targeted frequency range and as such are not a robust solution for a wind turbine for a full velocity-load range. Centrifugal pendulum dampers [4] are successful at noise reduction for a broader bandwidth, however, their effective achievable order is limited by the geometries to

low orders, while the gear meshing excitation is normally significantly higher. In the research community, phase fixed compensation solutions based on cam-spring combinations have been studied, especially targeting torque ripple in internal combustion engines (ICE). However, these solutions result in overly complex designs and are prone to lifetime issues and high friction [5]. In the field of hybrid automotive drivetrains, a similar issue with torque ripple that can be somewhat compensated (as reported in [6]) actively by using the vector controlled torque of an electrical motor. However, this method reduces the energy efficiency of the drivetrain and results in a reduced operational range for the electrical motor. Additionally, for high orders resulting from gear meshing torque bandwidth of the electrical motor allows only for limited compensation.

	Bandwidth	Max Order	Lifetime	Weight	Complexity	Efficiency
Flyhweel	+	++	+	- -	++	+
Linear TMD	–	++	0	0	0	0
Active control	+	+	+	0	-	-
Pendulum absorber	++	-	0	+	-	+
Magnetic absorber	++	+	++	+	+	+

Table 1: Overview of different vibration reduction approaches for torque ripple reduction

In the following pages we present a novel phase bound magnetic vibration absorber (PBMVA) based on torsional magnetic springs as defined and studied in [7].

Magnetic spring is a magnetic device that exhibits stiffness characteristic of a non-linear spring; it has a position-dependent passive force or torque characteristic (whether rotational or translational). Although the functionality of the magnetic spring can be compared to that of a mechanical spring, the underlying physical principles are different. Due to this difference magnetic springs do not succumb to fatigue failure, even after a very long operational lifetime. Additionally, magnetic springs intrinsically possess of sinusoidal characteristics and although the spring characteristic can be tuned in a similar, yet different periodical shapes, sinusoidal torques have been proven to result in the most efficient designs[7].

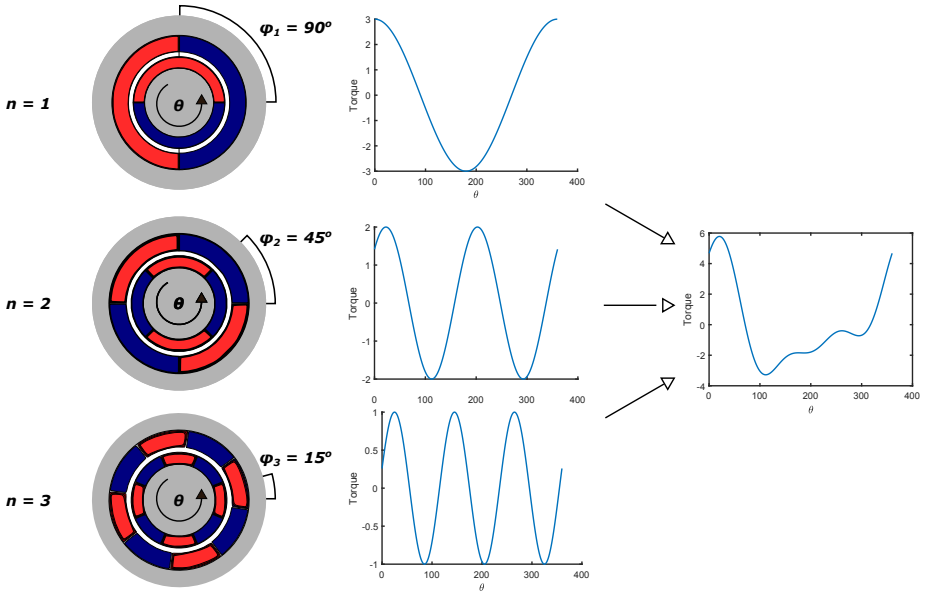


Figure 1: Magnetic spring based vibration absorber - fixed phase achieved by combining multiple magnetic spring in parallel with rotors rigidly connected to the input shaft of a gearbox

2 Capturing relevant gearbox dynamics

Geared mechanical systems are widely used in aeronautic, robotic and automotive industries to transfer motion and power between a driver and a driven axes located in space. An accurate model description of the reality, often known as digital twin, is required in model based design, control or analysis of gearboxes, for instance to predict the failure of the system components due to fatigue. In the automotive industry, hybrid and electric vehicles require special care for transmission design since noise from the internal combustion engine, masking the gear noise, is no longer present.

The growing power of the electronic devices is helping the engineering community to perform heavy simulations in reasonable smaller timeframe w.r.t the last decay. Although, for particular models where a lot of DOFs are needed to correctly describe the dynamic of the analyzed system, the best tradeoff between fast and accurate simulations is still a challenge to be solved. In first analysis, Lumped Parameter (LP) models are often used in literature with few degrees of freedom [10] to cope with this issue because of their modularity. It allows the user to plug-and-play different model complexity as well as they are good candidate for real time simulation. In this work a LP model of a spur gear pair is considered where the main focus is to qualitatively capture its dynamic response under specific working conditions, see fig. 2. A common parameter used to analyze the gear performances is the Transmission Error (TE) that is a measure of the deviation of the actual gears configuration w.r.t. the ideal gears kinematics, for both static and dynamic conditions, defined as follow:

$$TE = r_{B2} \cdot \theta_2 - r_{B1} \cdot \theta_1 \tag{1}$$

Several authors [11, 12, 13, 14], analyzed the phenomena occurring while two gears engages in both static and dynamic conditions. Assuming that the effects of the surrounding structures are negligible (i.e. bearings, shafts, etc.), the transmission error is considered as one of the main causes of dynamic excitation as well as the gear.

2.1 Semi-analytical model of variable non-linear meshing stiffness for single gear pair

In the following work a one degree of freedom non-linear LP model of a gear pair is considered. The global gear pair flexibility is lumped along the line of action accounting for both local and global teeth compliance whereas the gear body flexibility is considered negligible. The considered gears have the same geometry and their specifications have been chosen according to the model proposed by R. G. Parker work [15]. The gear inertias J_1 and J_2, and base circle radius r_{b1}, and r_{b2}, as shown in fig. 2. The gear specifications are summarized in tab.2. The variable static and dynamic TE are induced by the non-linear contact stiffness along the line of action due to three main reasons:

1. Variable *teeth stiffness* throughout contact
2. Variable *local stiffness* of the contacting tooth pair within the meshing cycle
3. Variable *number of teeth in contact* within the meshing cycle

The gear contact stiffness is modeled as a combination of the semi-empirical Cai-Hayashi formulation [9] and the ISO 6336-1:2006 [8]. The first allows to define the normalized gear contact stiffness in (eq. 2 and 3) depending on the gear contact ratio while the second computes the integral average stiffness (eq. 4). It is important to note that no torque dependency of the variable contact stiffness and gear geometry modifications have been taken into account.

For spur gear pair Cai and Cai-Hayashi introduced a semi-empirical description of the normalized gear contact stiffness accounting for variable meshing teeth. In particular eq. 2 describes the normalized stiffness

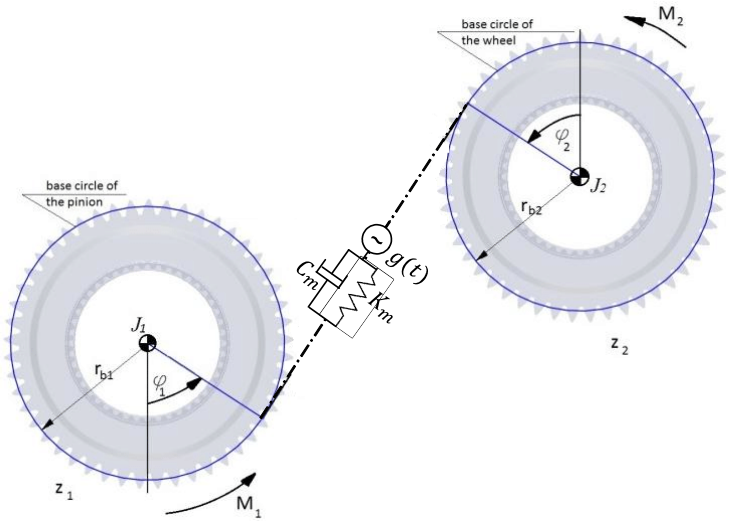


Figure 2: Lumped parameter non-linear gear pair model

for one tooth in contact while eq. 3 for two teeth in contact since the number of teeth in contact generally varies between one and two for spur gears.

$$K_{n1} = \frac{-1.8 \cdot \left(\frac{\theta_{mod}}{\theta_{cont}}\right)^2 + 1.8 \cdot \frac{\theta_{mod}}{\theta_{cont}} + 0.55}{0.85 \cdot \epsilon} \tag{2}$$

$$K_{n2} = K_{n1} + \frac{-1.8 \cdot \left(\frac{\theta_{mod} + \tau_1}{\theta_{cont}}\right)^2 + 1.8 \cdot \frac{\theta_{mod} + \tau_1}{\theta_{cont}} + 0.55}{0.85 \cdot \epsilon} \tag{3}$$

Where ϵ is the contact ratio that is function of the gear geometries, with θ_{mod}, θ_{cont} and τ_1 described in eq. 6-8 while the integral average stiffness is computed as follow:

$$K_{ave} = cp_{th} \cdot C_M \cdot C_R \cdot C_B \cdot w \cdot (0.75 \cdot \epsilon + 0.25) = 451.47 kN/m \tag{4}$$

Here cp_{th}, C_M, C_R and C_B are coefficients computed according to the ISO 2008 and w is the the working face width of the meshing gears.

$$K_m = \begin{cases} K_{ave} \cdot Kn_2, & \theta_{mod} < (\theta_{cont} - \tau_{pinion}) \\ K_{ave} \cdot Kn_1, & \theta_{mod} \geq (\theta_{cont} - \tau_{pinion}) \end{cases} \tag{5}$$

$$\theta_{mod} = mod(\theta_1, \tau_1) \tag{6}$$

$$\theta_{cont} = \epsilon \cdot \tau_1 \tag{7}$$

$$\tau_1 = \frac{2 \cdot \pi}{Z_1} \tag{8}$$

The resulting variable contact stiffness is shown in fig. 3 confirming the quality of the semi-analytical variable contact stiffness formulation w.r.t. the experimental curve reported in R. G. Parker work [15] despite the mentioned limitations.

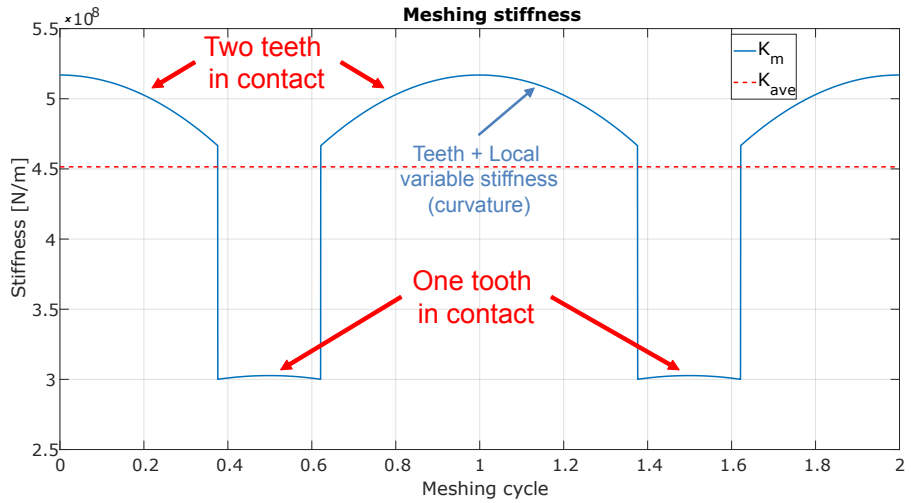


Figure 3: Variable contact stiffness K_m and average contact stiffness K_{ave} of a single gear pair for the reference mode

2.2 Wind turbine case - operational conditions and drivetrain topology

The speed ratio between the fast shaft and the slow shaft in wind generators predominantly used in large wind farms is around 100, with rotor with the impeller nominally rotating at around $20RPM$ and generator having its nominal speed at $2000RPM$. To achieve such high transmission rations, usually, at least one planetary stage is used alongside one or several helical stages, while a combination of multiple planetary and helical gears is not uncommon. The dominant force excitations causing tonal noise in windturbines are usually corresponding to the lower harmonics, usually 1st and 2nd harmonic, of the low speed stage[3].

Symbol	Reference Model	Wind Turbine Case	Model Parameter
Z_1	50	120	pinion teeth count
Z_2	50	25	wheel teeth count
$w_1 = w_2$	$20mm$	$20mm$	gear width
mn	$3mm$	$8mm$	normal module
ρ	$7700kg/m^3$	$7700kg/m^3$	material density
J_1	$7.7 \cdot 10^{-3}kgm^2$	$12.84kgm^2$	pinion inertia
J_2	$7.7 \cdot 10^{-3}kgm^2$	$24.2 \cdot 10^{-3}kgm^2$	wheel inertia
α	$20°$	$20°$	contact pressure angle
ζ	0.08	0.707	gear contact damping ratio
ϵ	1.75	1.74	contact ratio
T_{load}		$15000Nm$	load reaction torque
n_n		$1000rpm$	nominal speed
J_{s1}		$85kgm^2$	pinion shaft inertia
J_{s2}		$1kgm^2$	wheel shaft inertia

Table 2: Gear model parameters

To properly analyze the dynamic behaviour of the wind turbine drivetrain it is neccesary to understand the behaviour of the system in the following specific scenarios:

- start-up - velocity ramp up from stand-still to nominal speed where the variable contact stiffness dynamically excite the system
- nominal conditions - most prevalent mode, in which the wind turbine is generating electrical energy (50%-100% nominal torque and 50%-100% nominal speed)

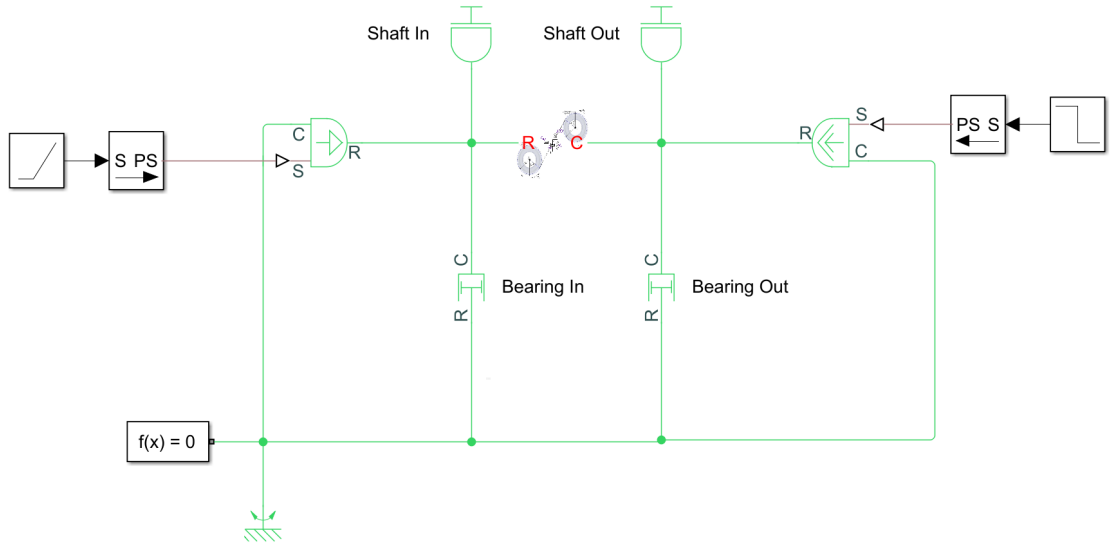


Figure 4: Block model of a single gear pair with driven by the ideal velocity source on the input shaft and with a constant ideal torque load on the output shaft

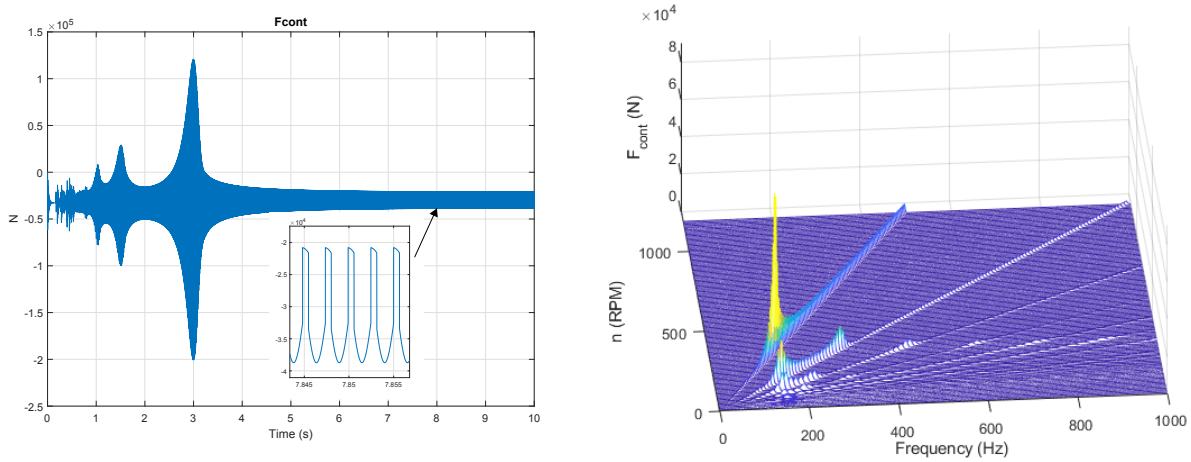
Of the above mentioned, the most criticial operational condition for NVH performance is by far the operation in nominal conditions when the wind turbine is generating electrical energy. Therefore, our efforts will focus on reducing the vibration due to the contact force variability in that specific range while making sure that for other scenarios the system functionality is not compromised. A numerical model was made using a commercial bond graph package Simscape (fig. 4). For a ramp-up 0-1250 RPM contact forces when speed source is applied can be seen in fig. 5a

3 Phase bound torque ripple absorber based on torsional magnetic springs

To reduce the torque ripple in drivetrains, a single magnetic spring with sinusoidal characteristic can be connected in parallel with the input or output shaft of a gearbox, in order to subtract a specific torsional order. Although, high-speed shaft is usually preferred due to lower order excitation and lower peak torques, which make the design of the vibration absorber easier. The proposed PBMVA consists of multiple magnetic springs with rotors rigidly coupled to the drivetrain shaft and stator rigidly connected to the housing of the gearbox, as shown in fig. 1. This way multiple orders can be compensated with various amplitude and phase alignment. Selecting the pole pair number of the magnetic spring n determines the frequency of the spring torque relative to the shaft rotation, while the orientation of the spring stator defines the phase ϕ of the superimposed sinusoidal torque (eq. 9) as schematically illustrated in fig 1. This formulation is coincidentally equivalent to the Fourier series decomposition with the DC component $A_0 = 0$ of a desired torque characteristic.

$$T_{PBMVA} = \sum_{n=1}^{N_{max}} A_n \cdot sin(n \cdot \theta + \phi_n) \tag{9}$$

Ideally, by infinite order Fourier decomposition, any periodic torque or force characteristic can be generated. In reality, only finite orders are feasible with a required design efficiency of a magnetic spring within a given space. Therefore, the feasible PBMVA characteristics are limited to lower order harmonic content i.e.



(a) Time series

(b) Waterfall plot

Figure 5: Modelled gear contact force with an ideal speed source on input shaft for ramp-up of 0-1250 RPM

continuous torque profiles with a max order of N_{max} finite order feasibility as a result of Gibbs phenomenon of the Fourier decomposition. Maximum achievable order of a magnetic spring that can be realized in a realistic design with limited space can be compared to the maximum magnetic gear reduction ratios found in the literature. Rather than limiting the pole pair number to a fixed value, we can say that the maximum efficient pole pair number is linked to the diameter of the magnetic array.

$$N_{max} \propto d_{ag} \tag{10}$$

where d_{ag} is the diameter of the magnetic air gap of a magnetic spring under consideration.

In [16]., the authors present a magnetic gear with 22 pole pairs at the size diameter of 44mm. Therefore, we assume that for application in MW powertrains, pole pairs numbers up to 100 or even higher are rather feasible. Using the above mentioned Fourier decomposition approach, and the models of the vibration absorber and the drivetrain, it is possible to investigate the optimal tuning of the magnetic spring that form the optimal vibration absorber for a given gear design (fig. 6).

Based on the operational conditions of the system, a virtual experiment is defined where the system is operating in quasi-steady-state while being driven by a motor with a PID speed controller, in order to find an optimal design of a magnetic spring at nominal loads. The load distribution, in this case, is somewhat different than the one considered in section 2. where a speed source is used on the input shaft. When searching for an optimal tuning of PBMVA, it is neccesary to apply a torque source for both the reaction torque and the input torque (generator torque). Such a model is closer to the operation of the physical system where the oscillating energy of the nonlinear gear contact is distributed between the input and output shaft inertia. Magnetic spring size and cost is proportional to the energy that can be stored within. More precisely, In [7] a theoretical energy density was established based on physical insight into energy stored in permanent magnets, which can be used as a simplistic 1D magnetic spring scaling model. The 1D model consists of the above described stiffness characteristic and the inertia which can be calculated from the energy density (eq. 11) assuming a fixed aspect ratio of a magnetic spring and an equal distribution of magnet volume between the rotor and the stator.

$$J_n = \frac{\rho_{NdFeB}}{2.93 \cdot \sqrt[3]{k_{AR}}} \cdot \left(\frac{2 \cdot A_n}{n \cdot E_{max}} \right)^{4/3} \tag{11}$$

Here, $E_{max} = 403.8kJ/m^3$ is the maximum realistic energy density of the magnetic spring [7], k_{AR} is the

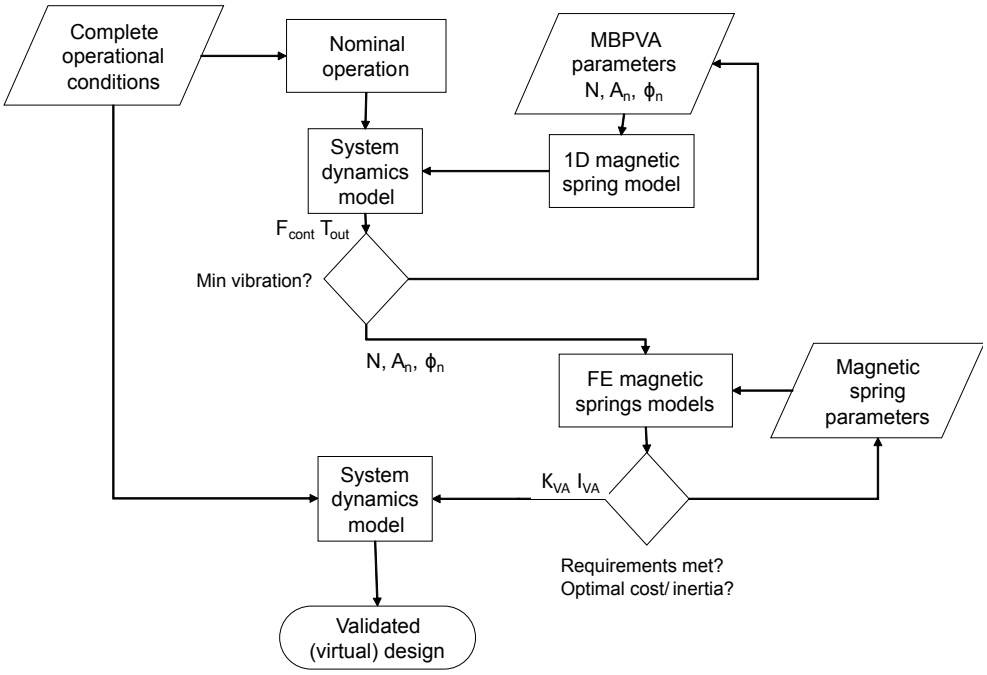


Figure 6: Design approach for multiple order PBMVA

ratio of the axial length and the air gap radius of the magnetic spring and $\rho_{NdFeB} = 7550kg/m^3$ is the density of NdFeB magnets.

Within the first optimization loop, a simplex solver is used to iteratively find the set of magnetic springs that minimizes the vibration. Using simplex solver (e.g. NOMAD) does not require the cost function gradients although it is computationally more expensive. Therefore, a hot start of the optimization using a good initial guess, based on Fourier decomposition of the input torque of the original system, limits the number of model evaluations necessary for convergence of the optimization algorithm. The decision variables are the number of the springs used in parallel, together with the amplitude and the phase of the each magnetic spring. The cost function is defined as a peak-to-peak force oscillation level at a given virtual experiment. Once the optimal design of the absorber is found within the system design optimization loop, the required order i.e. pole pair number, frequency, and phase can be used as input to the component loop optimization. The optimal PBMVA parameters can be used as an input for component design optimization loop [7], where detailed magnetic spring geometry, material selection and the exact topology can be optimized resulting in a realistic magnetic spring component set that forms the PBMVA. The component optimization loop also yields the exact stiffness and inertia matrices of the PBMVA.

As a last step in the virtual design exercise, the PBMVA resulting from component optimization can be plugged back into the dynamic model for a virtual validation of the design (fig. 8).

4 Optimization results and the impact on gear dynamics

The goal of the system level optimization is to find a PBMVA that will reduce vibration level for the single operational point at nominal conditions. Through use of PBMVA the speed variation on input shaft can be amplified while the transmitted torque oscillation can be minimized, also reducing the reactive forces in gearbox bearings which have been identified as a major excitation of tonalities in wind turbine drivetrain. The impacts of optimal different orders PBMVA on vibration level at the nominal conditions, for different orders, can be compared in tab. 3. It is visible that the first gear meshing order contribution is dominant and that, if focusing on a single order abosrber, the biggest reduction (60%) can be achieved here at nominal

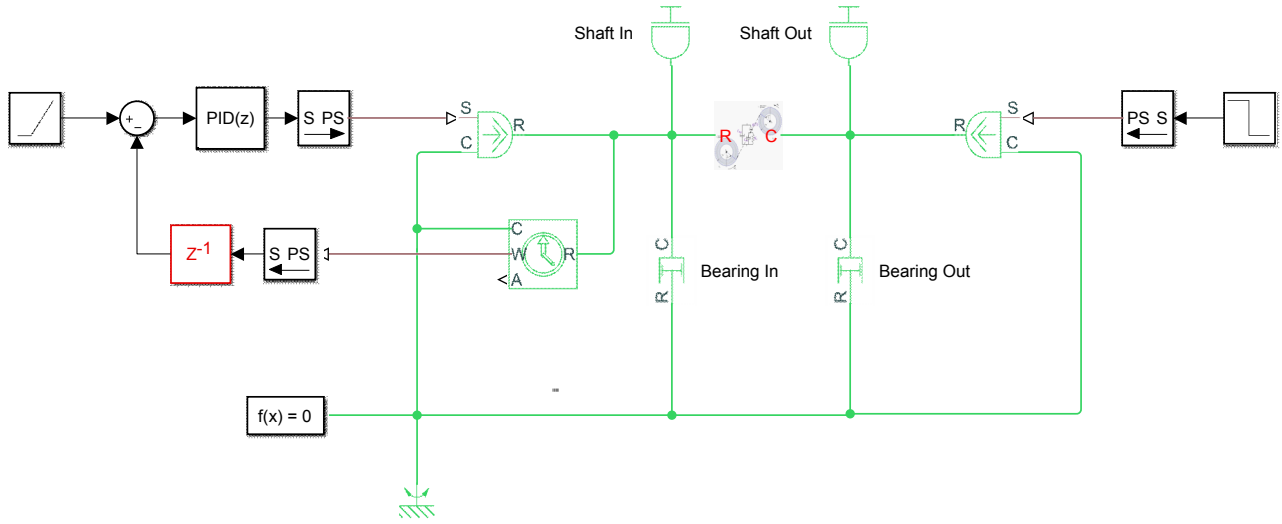


Figure 7: Model with added motor-generator with a feedback speed controller and a PBMVA on the fast shaft

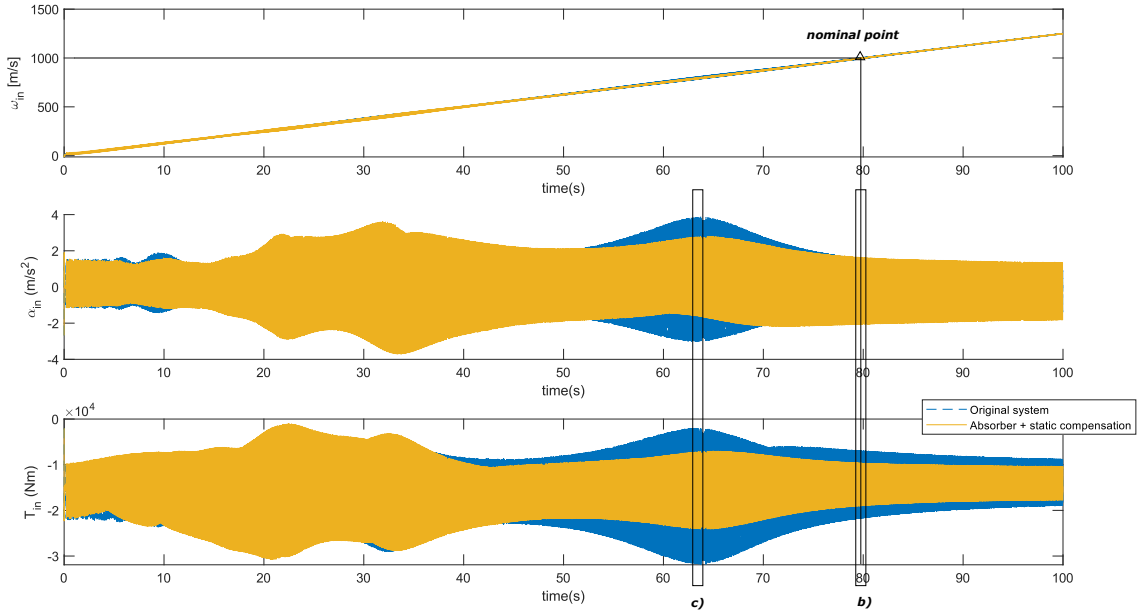
conditions. However, an additional 5-15% vibration reduction is feasible through surpression of the higher orders.

No. of parallel springs	1			2			3
Ripple reduction (%)	60.76	5.12	9.54	64.09	9.55	62.14	64.36
n - absorber order	25	50	75	25,50	50,75	25,75	25,50,75
$A_N(Nm)$	1237	1787	2402	1094 1107	1268 2120	0 2518	1073 2840 740
$\phi_N(rad)$	3.718	0.8349	3.9468	3.15 3.23	3.20 3.24	3.56 2.31	3.12 3.25 3.24

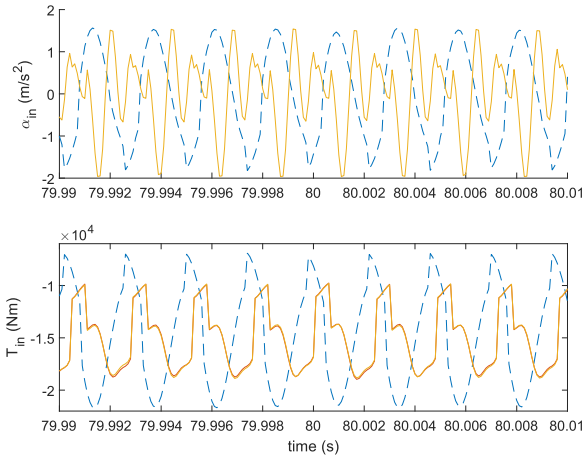
Table 3: Achieved torque ripple reduction at nominal conditions with PBMVA for first three gear meshing orders

A similar effect can, however, also be achieved by the use of conventional approaches such as linear tuned mass dampers (TMD). For purposes of this study, the TMD was tuned at nominal speed $n = 1000rpm$ using the Den Hartog tuning [17] for the first meshing order $f_0 = 25 \cdot n/60 = 416Hz$ where the selected TMD parameter tuning is $J_{TMD} = 0.9378kgm^2$, $c_{TMD} = 254.22Nms/rad$ and $K_{TMD} = 4.638 \cdot 10^6 Nm/rad$.

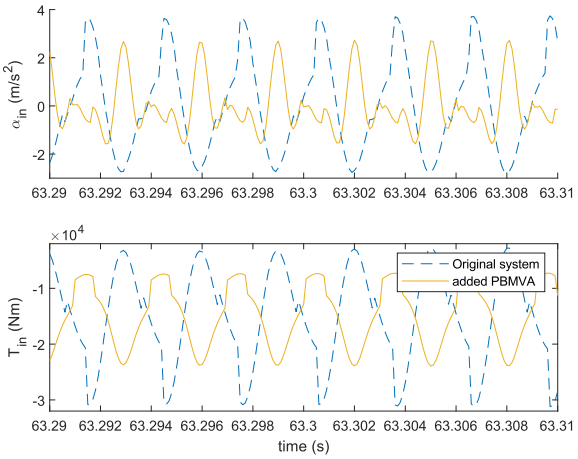
The main difference between the two described approaches lies in the performance outside of the nominal point for which the system was optimized. It can be seen in fig. 9, that PBMVA as an order targeting method, has a broadband effect in reducing the vibration while TMD is effectively targeting only a narrow frequency band. This is especially obvious when looking at higher orders at nominal conditions when TMD is used. Moreover, due to the intrinsic nature of the TMD it is in fact amplifying the undesired dynamic effect in other frequency regions, i.e. shifting the resonance to a lower frequency. At the nominal design point, $T_{load} = 15000Nm$ and $n_n = 1000rpm$, the system is not in resonance, therefore the PBMVA is reducing the forced response as expected: amplifying the primary shaft inertia oscillations in order to reduce the transmitted torque oscillation and consequently the contact force oscillation. The surprising effect of PBMVA occurs at system resonances (fig 8.c), where, although the resonance of the system has not been



(a) Full run of speed ramp-up from 0-1250 rpm



(b) Effect of PBMVA at nominal design point - forced response of the system

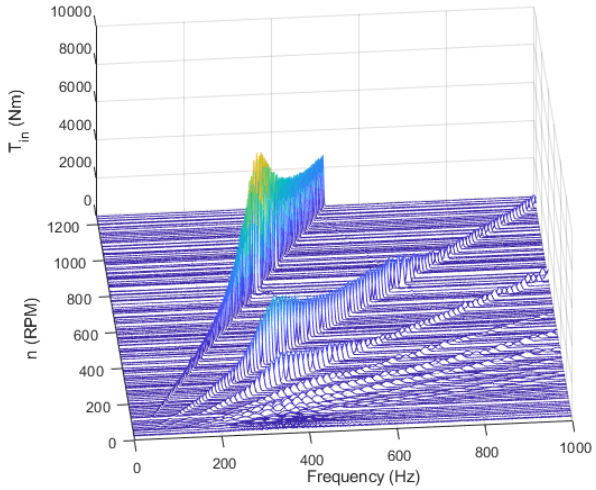


(c) Effect of PBMVA at resonance- natural response of the system

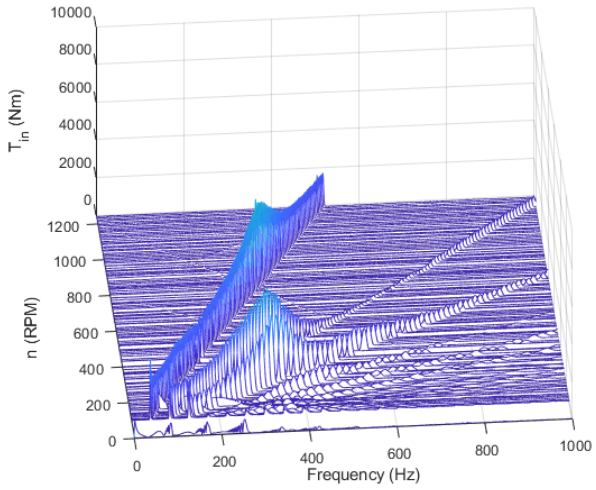
Figure 8: Validation run of 3 order tuned PBMVA for nominal conditions $T_{load} = 15000Nm$ and $n_n = 1000rpm$

shifted, due to the non-linear excitation reduction, both the acceleration and transmitted force are reduced simultaneously.

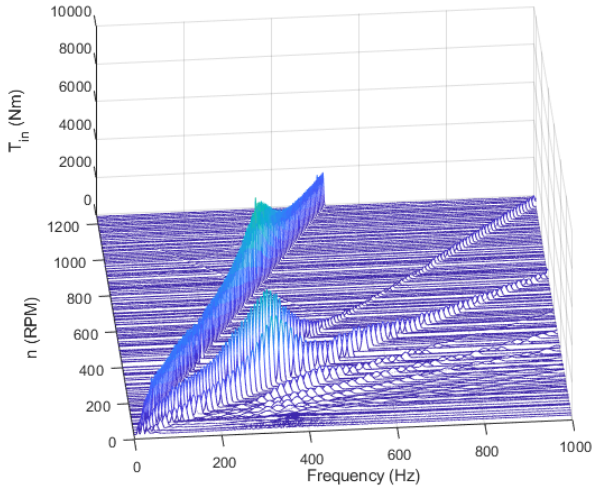
If we observe the drivetrain with a single gear contact under constant reaction load and generator torque, we can write the dynamics equation as a quasi-static model with linear dynamics contained in constant stiffness, damping and inertial matrices excited by the nonlinearity as a disturbance force - input. Further on, we can decompose the disturbance force to a Fourier series of the nonlinearity and try to correlate these with the orders appearing in transmitted torque as well as the optimal tuning of the PBMVA. Therefore, it is clear why a phase bound order targeting approach is more efficient, limiting the oscillating forces for the entire operational regime (50% to 100% nominal speed) of the proposed study case.



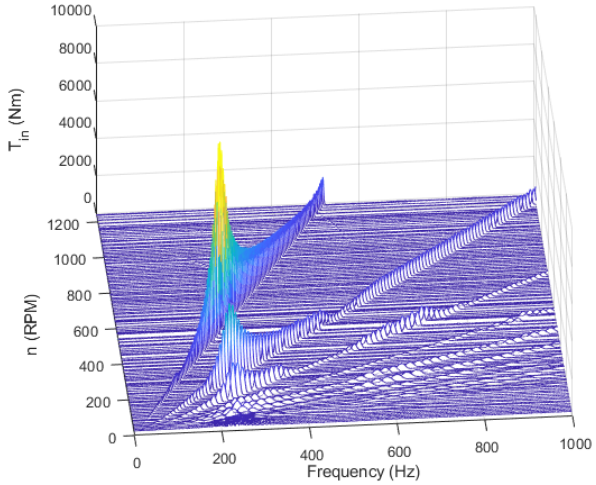
(a) original system



(b) 1-3 meshing order PBMVA



(c) 1-3 meshing order PBMVA with low speed active torque ripple suppresion



(d) Den Hartog tuned TMD

Figure 9: Waterfall plot of a validation run-up for all of the studied systems

5 Conclusions

A novel phase bound magnetic vibration absorber has been studied for a single gear pair, with the goal to compensate for vibration caused by the first three gear meshing orders. The modeling approach shows a vibration reduction of up to 64.46% for a spur gear at nominal conditions. In the worst case scenario, the resulting vibration reduction is lower with respect to the optimum. Nevertheless, PBMVA consistently reduces the vibration level in the entire operational range, unlike a linear TMD that was used to benchmark the novel approach. Considering that the variable contact stiffness of the helical gears is smoother compared to the spur gears (i.e. dominant low order excitations), PBMVA should be more performant in that case. PBMVA is suitable for wide bandwidth vibration reduction i.e. the phase bound nature of the absorber makes it more performant than frequency bound vibration reduction approaches for the phase-bound excitation.

Future work includes a fully coupled dynamic model of drivetrain and magnetic spring 6DOF model to study the added transfer path through the absorber, although the magnetic spring contribution in secondary DOF is expected to be negligible. A more detailed study with industrially relevant data of industrially used

gearboxes, where multiple stages are considered together with space constraints could answer questions about the practical limitations of the studied approach. Influence of material and modal damping on optimal tuning has been identified as a critical parameter for the optimal design of the PBMVA, therefore, better damping models should be used alongside measurement data.

Acknowledgements

This research was partially supported by Flanders Make, the strategic research centre for the manufacturing industry.

References

[1] Vanhollebeke, F., Helsen, J., Peeters, J., Vandepitte, D., Desmet, W., *Combining multibody and acoustic simulation models for wind turbine gearbox NVH optimisation*, in *Proceedings of the International Conference on Noise and Vibration Engineering ISMA, Leuven, Belgium 2012*, Leuven (2012), pp.44634477.

[2] Vanhollebeke, F., Peeters, P., Helsen, J., Di Lorenzo, E., Manzato, S., Peeters, J., Vandepitte, D., Desmet, W. *Large Scale Validation of a Flexible Multibody Wind Turbine Gearbox Model*, Journal of Computational and Nonlinear Dynamics,Vol 10 no.4, ASME (2015), pp. 041006-041006.

[3] Vanhollebeke, F. *Dynamic Analysis of a Wind Turbine Gearbox Towards Prediction of Mechanical Tonalities*, KU Leuven.Faculteit ingenieurswetenschappen, Leuven 2015

[4] Haris, E. Motato, M. Mohammadpour, S. Theodossiades, H. Rahnejat, M. O Mahony, A.F. Vakakis, L.A. Bergman, D.M. McFarland, *On the effect of multiple parallel nonlinear absorbers in palliation of torsional response of automotive*, International Journal of Non-Linear Mechanics,Vol 96, Elsevier BV (2017), pp. 2235.

[5] Versteyhe, M.R.J., Duchene T.E. *Torque ripple compensating device*, US Patent, US 20140261282

[6] Z. Zhong, S. Jiang, Y. Zhou and S. Zhou, *Active torque ripple reduction based on an analytical model of torque*, IET Electric Power Applications, Volume: 11, Issue: 3, pp. 331-341, 3 2017.

[7] Mrak, B., Driesen W., Desmet W. *Optimal Design of Magnetic Springs; Enabling High Life Cycle Elastic Actuators*, in *International Symposium on Magnetic Bearings ISMB16, Beijing, China 2018*, (In Print)

[8] *ISO Standard 6336-1:2006*,

[9] Cai, Y., Hayashi, T. *The Linear Approximated Equation of Vibration of a Pair of Spur Gears (Theory and Experiment)*, Journal of Mechanical Design,Vol 116, ASME (1994), pp. 558564.

[10] H. N. Ozguven, D. R. Houser *Mathematical models used in gear dynamics A review* Journal of Sound and Vibration, Vol. 121, No. 3 (1988), pp. 383-411.

[11] J.D. Smith *Gear noise and vibration* Marcel Dekker, Cambridge (2003)

[12] Litvin, F. L. Fuentes A. *Gear geometry and applied theory* Cambridge University Press, Cambridge (2004).

[13] S.L. Harris *Dynamic loads on the teeth of spur gears* Proceedings of the Institution of Mechanical Engineers, Vol. 172 (1958), p. 87.

[14] Shweiki, S. Korta, J. Palermo, A. Adduci, R. Mundo, D. *Combining finite element analysis and analytical modelling for efficient simulations of non-linear gear dynamics* in *VII European Congress on Computational Methods in Applied Sciences and Engineering Crete Island, Greece, 510 June 2016*

[15] Parker, R.G. and Vijayakar, S.M. *Non-linear dynamic response of a spur gear pair: modelling and experimental comparisons* Journal of Sound and Vibration, 237(3), 435-455.

[16] Jungmayr, G. Loeffler, J. Winter, B. and Jeske, F. and Amrhein, W. *Magnetic Gear: Radial Force, Cogging Torque, Skewing, and Optimization*, IEEE Transactions on Industry Applications, Vol 52, IEEE (2016), pp. 3822–3830.

[17] Den Hartog, J. P. *Mechanical Vibrations, 4th ed.* Dover Books on Engineering, 1985.

Fatigue stress estimation of offshore wind turbine using a Kalman filter in combination with accelerometers

N. Noppe [1], **K. Tatsis** [2], **E. Chatzi** [2], **C. Devriendt** [1], **W. Weijtjens** [1]
[1] Vrije Universiteit Brussel, Department of Mechanical Engineering, Acoustics And Vibrations Group, Pleinlaan 2, B-1050, Brussel, Belgium

[2] ETH Zürich, Institute of Structural Engineering,
Stefano-Franscini-Platz 5, 8093, Zürich, Switzerland

Abstract
An accurate stress or strain history at fatigue critical locations is often needed for a fatigue assessment. Unfortunately it is not feasible to install strain gauges as these fatigue hotspots. This contribution compares two techniques to obtain a reliable stress history at any location of the turbine structure, one is based on modal decomposition and expansion, the other is based on a Kalman filter. Both techniques will be validated and compared using data from an offshore wind turbine monitored by OWI-lab. The monitored turbine is instrumented with strain gauges at the interface between transition piece and tower and accelerometers at multiple levels. The installed strain gauges allow to validate the proposed techniques with respect to the reality.

1 Introduction

As wind farms are growing older, an accurate fatigue assessment of the turbines and their foundation becomes more valuable. A fatigue assessment is needed when deciding on a possible life time extension. Moreover, it can also be used to decide upon maintenance strategies and to improve the design of future turbines and their foundations.
Performing an accurate fatigue assessment of the support structure often requires measurements of the load history ([1],[2],[3],[4]). As some locations within the structure are more affected by loads, the fatigue induced by the load history at these hotspots is most valuable. Unfortunately, these hotspots are located below water level or subsoil. Therefore it is unfeasible or impossible to mount sensors at these critical locations. To resolve this limitation OWI-lab has worked on the concept of virtual sensing. Virtual sensing allows to estimate stresses at hotspots using measurements taken at more accessible locations within the structure such as on the tower structure. In particular accelerometers are favored as sensors, due to the ease of installation and their reliability on the long term. However, low frequency thrust loads cannot be captured using accelerometers. [5] introduced the idea to combine a thrust load estimation and accelerometers in order to estimate the full band stresses in the structure using a modal decomposition and expansion based virtual sensing technique. One of the drawbacks of this approach was the discontinuity in the frequency spectrum, since the signal was splitted in three frequency bands. A clear drop in accuracy around the frequency limits was observed.
An alternative course for tackling the problem of fatigue estimation on the basis of a limited number of vibration sensors has been taken by Papadimitriou et al. [6]. Such a course consists in fusing the available measurements with a Kalman filter for extrapolating the response at unmeasured locations. Within that context, a number of Kalman-type algorithms, able to operate on systems with unknown inputs, has been proposed and recently validated [7] under experimental conditions. Although such filters are subjected to

certain sensor requirements [8], their effectiveness on WT structures has been already demonstrated [9] on the basis of acceleration and inclination measurements. Alternatively, Naets et al. [10] proposed the use of dummy displacement measurements in order to stabilize the performance when only accelerations are available while in a recent contribution, Dertimanis et al. [11] extended the implementation to include the estimation of unknown system parameters.
This contribution will validate both approaches and compare the results.

2 Measurement Setup

The techniques proposed in this contribution will be validated using measurements taken at an offshore wind turbine located in the middle of the Belgian offshore wind farm Belwind, 46 km off the Belgian coast. This Vestas 3MW V90 turbine is installed on a monopile foundation and was instrumented with additional accelerometers and strain gauges. A total of eight accelerometers were installed at four different levels in the turbine tower (two per level) in order to capture vibrations in both X and Y direction. Additionally six strain gauges were installed on the lowest level, being the interface between tower and transition piece. An overview of the location of the sensors is given in Figure 1. The accelerations measured at all levels together with the thrust load will be used to predict the strains measured at the tower-TP interface and finally to predict the strains at hotspots located below the water level.

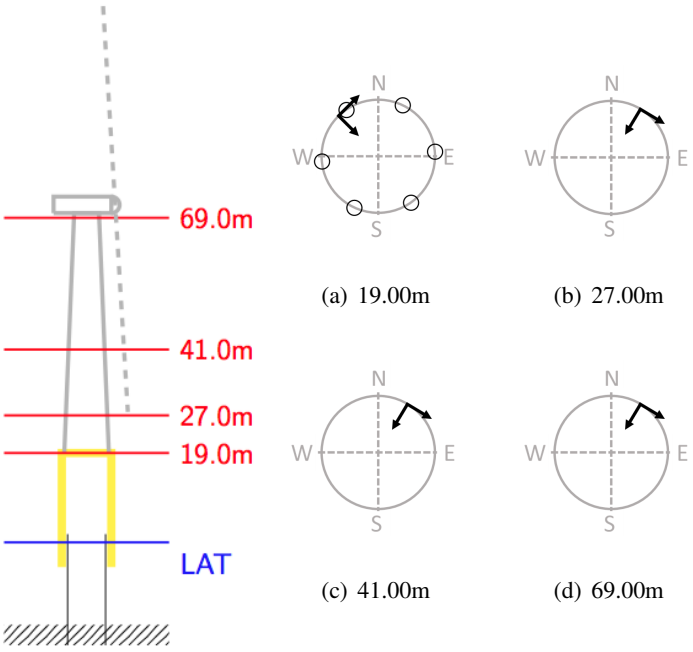


Figure 1: Locations of the additional sensors at of BBC01 wind turbine at the Belwind farm. The circles in (a) represent a strain gauge; the arrows in (a-d) represent an accelerometer.

In order to simplify the validation of both techniques presented in this paper, the thrust load signal used for this validation is obtained from the measured strain signal. To derive the thrust load signal from the strain measurements, the measured strains are transformed into a fore-aft and side-side bending moment. Additionally the low-frequent part (0 to 0.2 Hz) of the fore-aft bending moment is transformed into the acting thrust load using the distance between the location of the sensor and the hub. Ultimately the thrust load signal can be obtained using 1s SCADA data instead of strain measurements, as explained in [12].

3 Multi-band virtual sensing based on modal decomposition and expansion

The main goal of virtual sensing is to estimate the stresses at the fatigue-sensitive hotspots without the need of mounting sensors at these exact locations. This section will summarize the multi-band virtual sensing technique based on modal decomposition and expansion as explained in [5]. This technique combines measurements with a tuned finite element model (FEM) of the structure to predict stresses at any location of the structure. The FEM is created using pipe elements with the as design dimensions of the turbine. This FEM is tuned to match the modal properties obtained experimentally. More information about the finite element model and the tuning can be found in [5] and [13]. Figures 2 and 3 show the resulting structural and strain mode shapes respectively.

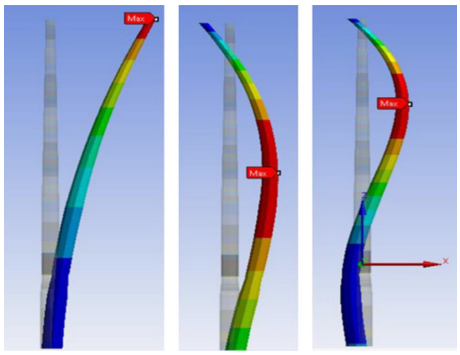


Figure 2: First three structural mode shapes of an offshore wind turbine. The first mode is captured best using the top accelerometer, while the second and third mode are captured better using the lower sensors.

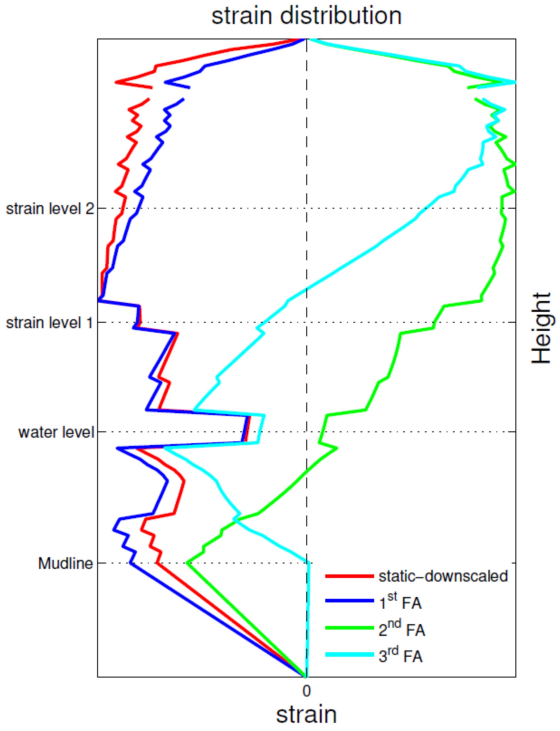


Figure 3: The static strain mode shape together with the strain mode shapes of the first three modes.

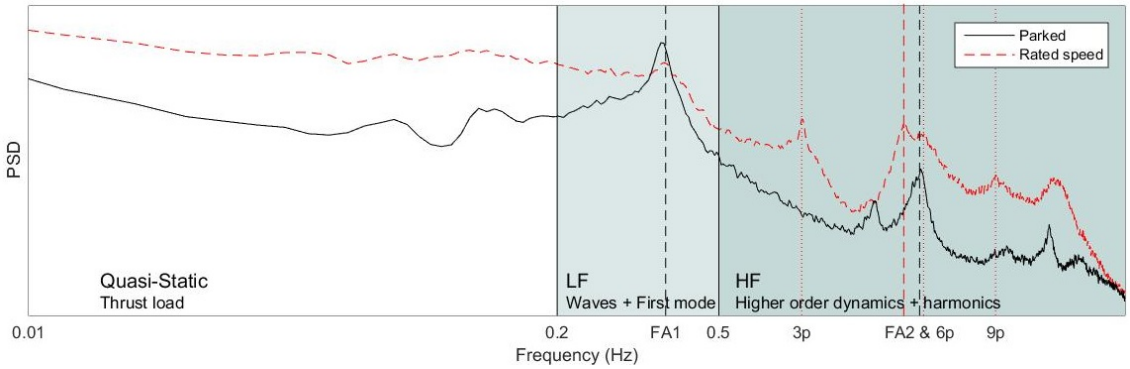


Figure 4: Frequency spectrum of the different loads acting on an offshore wind turbine in parked conditions and at rated rotor speed. The quasi-static load is dominated by the thrust load induced by variations in wind. Dynamic variations are induced by waves, structural dynamics and rotor harmonics.

The stresses observed at any location in the structure are induced by a variety of loads, each acting in a different frequency range. This can be seen in Figure 4. Since the structure responds differently to quasi-static loads then to dynamic loads, the resulting stresses are obtained differently.
The quasi-static thrust load (0 to 0,2 Hz), as induced by the variations in wind, is combined with the static strain mode shape obtained from the tuned FEM (Figure 3), to predict the quasi-static strains.
The dynamic part of the prediction is based on the modal decomposition and expansion technique. Each deflection of the structure is considered a combination of deflection caused by the excitation of different modes. Based on the acceleration measurements and the acceleration mode shapes a modal decomposition is performed. This is visualized by Figure 5. The resulting "acceleration" modal coordinates are then double integrated to obtain displacement modal coordinates. Multiplication of the displacement modal coordinates with the corresponding strain mode shapes from the tuned FEM (Figure 3) results in the dynamic strain prediction.
For this contribution, the dynamic frequency band was divided into the low frequency band (0,2 to 0,5 Hz) dominated by waves and first mode and the high frequency band (above 0,5 Hz) dominated by higher order dynamics and rotor harmonics. The difference in calculation between both bands is the number of considered modes. Since the low frequency band is dominated by the first mode, only one mode is considered. For the high frequency band, also the second and third mode are considered.
As both quasi-static loads and dynamic, both low and high frequency, loads are acting simultaneously, all predictions are superposed.

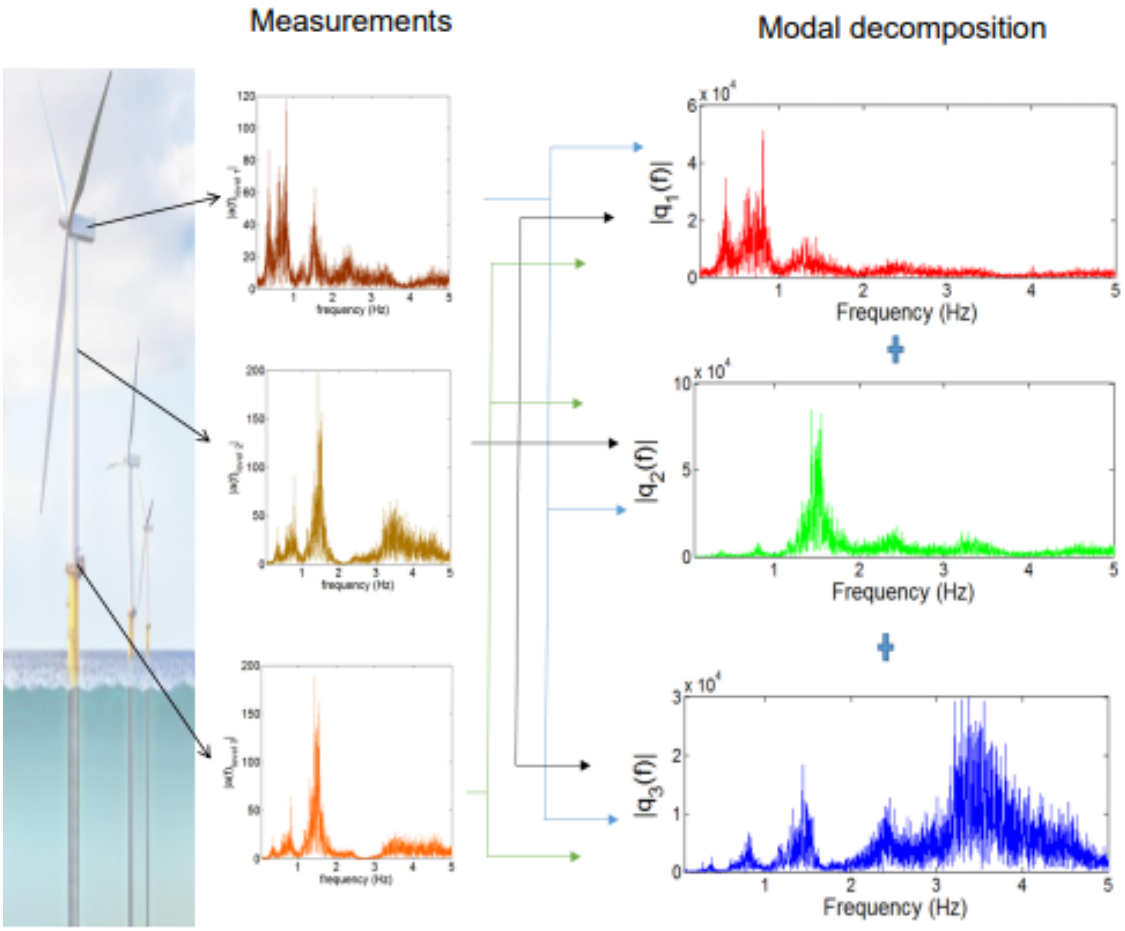


Figure 5: "Acceleration" modal coordinates are obtained based on accelerations measured at various locations in the tower and known acceleration mode shapes.

4 Kalman Filter

The starting point for implementing a Kalman filter towards state estimation on WTs, is the continuous-time linear system of dynamic equations of motion, which is transformed to a discrete-time modally reduced state-space system. Such an approach is widely reported in the literature and herein it is only briefly elaborated since the entire formulation and notation is adopted from [14]. In this sense, the system and measurement equations may be written as

$$\boldsymbol{\zeta}_{k+1} = \mathbf{A}\zeta_k + \mathbf{B}\mathbf{p}_k + \mathbf{w}_k \tag{1}$$

$$\mathbf{y}_k = \mathbf{G}\zeta_k + \mathbf{J}\mathbf{p}_k + \mathbf{v}_k \tag{2}$$

where $\boldsymbol{\zeta}_k \in \mathbb{R}^{n_\mathrm{s}}$ is the state vector containing modal displacements and velocities, $\mathbf{y}_k \in \mathbb{R}^{n_\mathrm{y}}$ is the output vector, $\mathbf{p}_k \in \mathbb{R}^{n_\mathrm{p}}$ is the input force vector and $\mathbf{w}_k \in \mathbb{R}^{n_\mathrm{s}}$ along with $\mathbf{v}_k \in \mathbb{R}^{n_\mathrm{p}}$ are zero-mean white processes, with covariance matrices $\mathbf{Q} \in \mathbb{R}^{n_\mathrm{s}\times n_\mathrm{s}}$ and $\mathbf{R} \in \mathbb{R}^{n_\mathrm{y}\times n_\mathrm{y}}$, representing the system and measurement noise, respectively. Finally, $\mathbf{A} \in \mathbb{R}^{n_\mathrm{s}\times n_\mathrm{s}}$ and $\mathbf{B} \in \mathbb{R}^{n_\mathrm{s}\times n_\mathrm{p}}$ are the system matrices while $\mathbf{G} \in \mathbb{R}^{n_\mathrm{y}\times n_\mathrm{s}}$ and $\mathbf{J} \in \mathbb{R}^{n_\mathrm{y}\times n_\mathrm{p}}$ are the output and feedthrough matrices. These matrices are based on a modal model, composed of the first six, three fore-aft and three side-to-side, vibration modes. These modes are obtained from a simple Finite Element (FE) model which is tuned in order to be in accordance with the identified modal properties, i.e. frequencies, damping ratios and mode shapes.

In the absence of information with respect to the driving forces, the state of the system may be augmented with the input vector, so that $\boldsymbol{\zeta}_k^a = \mathrm{vec}([\boldsymbol{\zeta}_k \ \ \mathbf{p}_k]) \in \mathbb{R}^{n_\mathrm{s}+n_\mathrm{p}}$, in order to form the so-called augmented state-space model

$$\boldsymbol{\zeta}_{k+1}^a = \mathbf{A}^a\boldsymbol{\zeta}_k^a + \mathbf{w}_k^a \tag{3}$$

$$\mathbf{y}_k = \mathbf{G}^a\boldsymbol{\zeta}_k^a + \mathbf{v}_k \tag{4}$$

where superscript^a designates the augmented quantities. By doing so, the evolution of input is dictated by the augmented system matrix $\mathbf{A}^a \in \mathbb{R}^{(n_\mathrm{s}+n_\mathrm{p})\times(n_\mathrm{s}+n_\mathrm{p})}$, whereby it is postulated that the input can be captured by a random-walk process.

$$\mathbf{p}_{k+1} = \mathbf{p}_k + \boldsymbol{\eta}_k \tag{5}$$

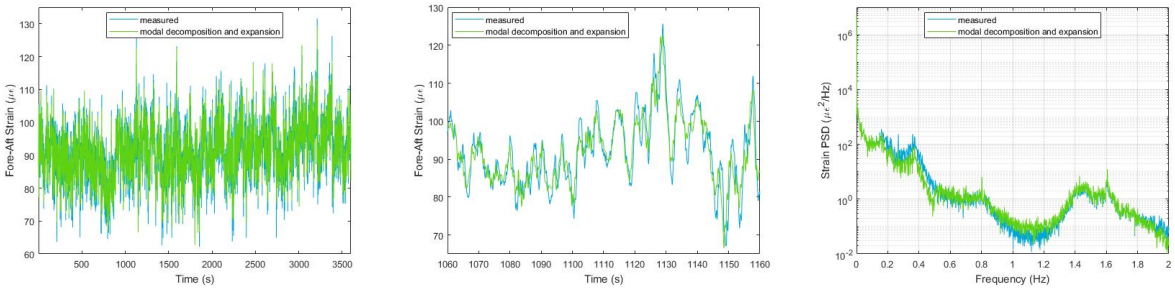
with $\boldsymbol{\eta}_k$ being a zero-mean white Gaussian process with covariance matrix $\mathbf{S} \in \mathbb{R}^{n_\mathrm{p}\times n_\mathrm{p}}$. Within this context, both input and state may be estimated recursively through the standard Kalman filter operating on the augmented state-space model.

As stated in Section 2, the measured response quantities of the considered WT comprise accelerations at four different elevations with a sampling rate of 20Hz, as well as the thrust force with a sampling rate of 1Hz. Due to this difference in the sampling rates, the above-described filter is employed in a multi-rate fashion which is materialized with the use of time-varying measurement noise. Considering that the lack of measurements is equivalent to optimal filtering with large measurement errors [15] and hence zero gain, the measurement noise corresponding to the thrust is set to an arbitrarily large value when thrust measurements are not available and it is reset to the tuned value as soon as thrust is measured again.

The estimation is subsequently performed assuming that the dynamics of the turbine are driven by the thrust force, applied on the tower top, and an equivalent wave force exerted at the hydrodynamic center. In contrast with the modal decomposition and expansion technique, the estimation using the Kalman filter does not assume any explicit distinction between quasi-static, low frequency and high frequency regimes. Instead, the quasi-static part of the response is captured by the thrust force, sampled at a rate of 1Hz, and the higher frequency dynamics are dictated by the acceleration measurements.

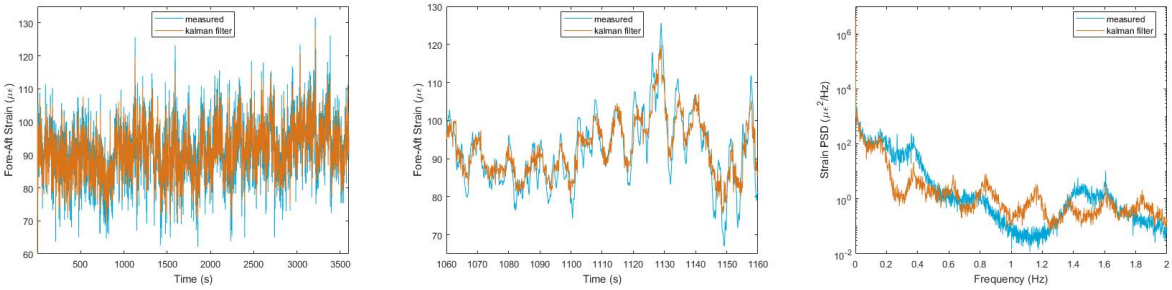
5 Results

Both proposed techniques are applied on the same case study, as presented in Section 2. Figure 6 shows the measured and predicted strain signal for the technique based on modal decomposition and expansion for one hour of measurements. Figure 7 does the same for the technique based on the kalman filter.
In general, the predicted signals by both techniques match the measurements good in time domain. This is also represented by a fairly low value of mean absolute error between measurement and prediction of 2,73$\mu\epsilon$ and 2,89$\mu\epsilon$ for the technique based on modal decomposition and expansion and the one based on the kalman filter respectively.
In the frequency domain both techniques can estimate quasi-static strain signals up to 0,2 Hz almost perfectly, while for higher frequencies the differences are clearly higher. In case of the modal decomposition and expansion technique, the signals seem to match pretty well, although the first mode is slightly underestimated.
Moreover, a drop can be observed around 0,2 Hz and more clearly around 0,5 Hz. These frequencies coincide with the limits at which the signal is divided to determine the different contributions to the resulting strain signal (quasi-static, low frequent and high frequent). This means the accuracy of the predicted signal reduces at the chosen limits in frequency for the different frequency bands. At those frequencies not only one of the possible loads dominates the response but an interaction between multiple loads results in the actual response. However, the prediction only captures one load, the one presumingly dominating the response.



(a) Time series of 1 hour (b) Zoom of 100 s (c) Frequency spectrum

Figure 6: Multi-band virtual sensing based on modal decomposition and expansion validated for a period of 1 hour. The blue line represents the actual measured signal and the green line the predicted signal. A mean absolute error between measured and predicted signal (of one hour) of 2,73$\mu\epsilon$ is found for the technique based on modal decomposition and expansion.



(a) Time series of 1 hour (b) Zoom of 100 s (c) Frequency spectrum

Figure 7: Multi-band virtual sensing based on a Kalman filter validated for a period of 1 hour. The blue line represents the actual measured signal and the red line the predicted signal. A mean absolute error between measured and predicted signal (of one hour) of 2,89$\mu\epsilon$ is found for the technique based on the kalman filter.

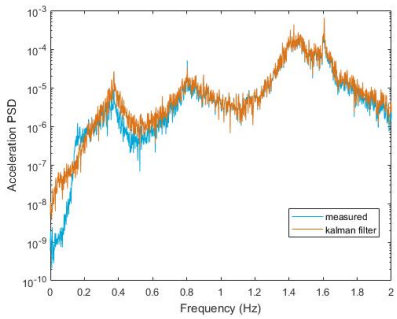


Figure 8: Frequency spectrum of the predicted and measured accelerations at the level of 19.0m using the Kalman filter.

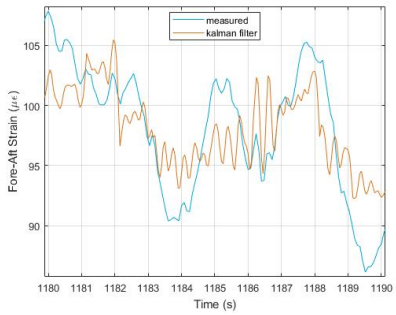


Figure 9: A drop in predicted strain is observed around 1182 s due to the discontinuous updating of the thrust force signal.

As seen in Figure 7, the measurement setup based on the Kalman filter provides sufficiently good response estimation, which additionally does not suffer from instability issues, as is usually the case in acceleration-only setups [10]. However, in terms of the frequency domain of the strain signal the match is not as good as for the results obtained using modal decomposition and expansion.
It should be underlined that despite the straight-forward way of fusing different types of measurements, tuning of the covariance matrices is always the key feature in obtaining an optimal estimation using Kalman-type filters. This is herein achieved by firstly adjusting the system and measurement covariances, so that the predicted accelerations show good agreement with the measured ones. This is highlighted in Figure 8, through the frequency domain representation of the two signals, which are well matching. Finally, once the two covariance matrices are adjusted, the input process is tuned using the L-curve.
Although the frequency spectrum of measured and predicted acceleration signal is well matching (Figure 8), this didn't result in a similar match between both strain signals. The predicted strain signal by the Kalman filter is based on acceleration measurements at the lower three levels. The top level acceleration signal is dominated by the first mode and therefore out of phase to the other acceleration signals. Such an effect is heuristically seen to work at the expense of the stress estimates and as as result the top acceleration was not used in the filter.
Another possible explanation for the mismatch in frequency domain is the lower measurement frequency of the thrust signal. This causes the prediction to be updated at some intermediate timestamps and results in big jumps in the predicted signal, as shown in Figure 9.

6 Conclusions

This contribution compared two possible techniques to reconstruct a strain history at fatigue critical locations of monopile foundations of offshore wind turbines. Both techniques combine measured accelerations and a

measured thrust load signal. The first technique is based on modal decomposition and expansion, the second is based on a Kalman filter. For both techniques a good match is obtained in time domain. However in frequency domain, the technique based on modal decomposition and expansion showed better results than the Kalman filter.

Acknowledgements

The authors would like to gratefully acknowledge the support of the European Research Council via the ERC Starting Grant WINDMIL (ERC-2015-StG #679843) on the topic of Smart Monitoring, Inspection and Life-Cycle Assessment of Wind Turbines as well as the financial support by the Institute for the Promotion of Innovation by Science and Technology in Flanders (IWT) in the framework of the VIS OWOME Project and by the Research Foundation - Flanders. The authors would also like to gratefully thank the people of Parkwind and Belwind for their continuous support.

References

[1] C. Loraux, E. Brhwiler, *The use of long term monitoring data for the extension of the service duration of existing wind turbine support structures*, J. Phys. Conf. Ser., 753, 072023, https://doi.org/10.1088/1742-6596/753/7/072023TS3, 2016

[2] A. Iliopoulos, W. Weijtjens, D. Van Hemelrijck, C. Devriendt, *Fatigue assessment of offshore wind turbines on monopile foundations using multi-band modal expansion*, Wind Energy, 20, 14631479, 2017

[3] M. Schedat, T. Faber, A. Sivanesan, *Structural health monitoring concept to predict the remaining lifetime of the wind turbine structure*, Domestic Use of Energy (DUE), 2016 International Conference on the IEEE, 15, 2016

[4] L. Ziegler, U. Smolka, N. Cosack, M. Muskulus, *Brief communication: Structural monitoring for lifetime extension of offshore wind monopiles: can strain measurements at one level tell us everything?*, Wind Energ. Sci., 2, 469476, https://doi.org/10.5194/wes-2-469-2017, 2017

[5] N. Noppe, A. Iliopoulos, W. Weijtjens, C. Devriendt, *Full load estimation of an offshore wind turbine based on SCADA and accelerometer data*, J Phys Conf Ser, 753 (2016), p. 72025, 10.1088/1742-6596/753/7/072025

[6] C. Papadimitiou, C.P. Fritzen, P. Kraemer, E. Ntotsios, *Fatigue predictions in entire body of metallic structures from a limited number of vibration sensors using Kalman filtering*, Structural Control and Health Monitoring, 18 (2011), 554-573.

[7] S. E. Azam, E. Chatzi, C. Papadimitriou, A. Smyth, *Experimental validation of Kalman-type filters for online and real-time state and input estimation*, Journal of Vibration and Control (2016), 1-26.

[8] K. Maes, E. Lourens, K. van Nimmen, E. Reynders, G. De Roeck, G. Lombaert, *Design of sensor networks for instantaneous inversion of modally reduced order model in structural dynamics*, Mechanical Systems and Signal Processing, 27 (2012), 446-460.

[9] K. Tatsis, V. Dertimanis, I. Abdallah, E. Chatzi, *A substructure approach for fatigue assessment on wind turbine support structures using output-only measurements*, Procedia Engineering, 199 (2017), 1044-1049.

[10] F. Naets, J. Cuadrado, W. Desmet, *Stable force identification in structural dynamics using Kalman filtering and dummy-measurements*, Mechanical Systems and Signal Processing, 50-51 (2015), 235-248.

[11] V. Dertimanis, E. Chatzi, S. E. Azam, C. Papadimitriou, *Output-only fatigue prediction of uncertain steel structures*, 8th European Workshop on Structural Health Monitoring (EWSHM), 2016.

[12] N. Noppe, W. Weijtjens, C. Devriendt, *Modeling of quasi-static thrust load of wind turbines based on 1s SCADA data*, Wind Energ. Sci., 3, 139-147, https://doi.org/10.5194/wes-3-139-2018, 2018

[13] A. Iliopoulos, R. Shirzadeh, W. Weijtjens, P. Guillaume, D. Van Hemelrijck, C. Devriendt, *A modal decomposition and expansion approach for prediction of dynamic responses on a monopile offshore wind turbine using a limited number of vibration sensors*, Mechanical Systems and Signal Processing, 68-69 (2016), 84-104

[14] K. Tatsis, E. Lourens, *A comparison of two Kalman-type filters for robust extrapolation of offshore wind turbine support structure response*, Proceedings of the 5th International Symposium on Life-Cycle Engineering, Delft, Netherlands, (2016), pp. 209-216.

[15] A. Gelb, *Applied Optimal Estimation*, MIT Press, Cambridge, 1974.

Experimental measurement of value and associated uncertainty of wave speed in Hopkinson bars with an accurate and robust method

D. Brizard [1]
[1] Univ Lyon, Universit Claude Bernard Lyon 1, IFSTTAR, LBMC UMR_T9406, F69622, Lyon, France
e-mail: **denis.brizard@ifsttar.fr**

Abstract
Post processing the strain waves in the measurement bars of Split Hopkinson Bars (SHPB) to get the stress-strain in the sample requires the knowledge of the longitudinal wave velocity c_0. In the context of metrology, we need to assess the measurement uncertainty in the value of c_0. The most intuitive way of getting the velocity c_0 relies on the measurement of the length of the bar and of the time shift between multiple reflections of a stress pulse in the bar. This method however faces some difficulties which increase the uncertainty in c_0. In this paper, we rather use a method based on the frequency spectrum of an impact test on a single bar and on the expression of longitudinal resonance frequencies. The relative uncertainty on the obtained velocity c_0 is also assessed and is lower than $0.04\,\%$: it is mainly related to the uncertainty in the length of the bar. A precise value of the velocity c_0 and of the associated measurement uncertainty is an important step in the context of SHPB to precisely assess the final uncertainty in SHPB test results, which is scarcely ever done.

1 Introduction

Split Hopkinson pressure bars is an experimental device for measuring the stress-strain relationship of materials in the intermediate range of strain rate ($100\,\mathrm{s}^{-1}$ to $10\,000\,\mathrm{s}^{-1}$) [1]. The device is composed of a striker and two measuring bars [2]. The sample lies between the two measuring bars and the striker hits the first measuring bar at a given velocity. A strain pulse propagates down the first measuring bar: part of the pulse is reflected at the interface with the sample and part of the pulse crosses the sample and propagates through the second measuring bar. The strain history in each bar is recorded with a strain gauge, this strain gauge is commonly placed in the middle of the bar to avoid overlay between the incident and reflected pulses. The stress and strain in the sample are computed from the incident, reflected and transmitted pulses in the bars.

The value of c_0 is important in the posttreatment of the SHPB tests because it is used to get the strain rate and the strain in the sample with the following equations [3]

$$\dot{\epsilon}_s(t) = \frac{-2c_0}{l_s}\epsilon_r(t) \tag{1}$$

$$\epsilon_s(t) = \frac{-2c_0}{l_s}\int_0^t \epsilon_r(\tau)d\tau \tag{2}$$

where l_s is the initial length of the sample and $\epsilon_r(t)$ is the reflected pulse measured in the input measuring bar.

In the context of quality in measurement, it is also necessary to determine the uncertainty in c_0 as it is involved in the final uncertainty in the stress and strain in the sample.

Of course it is possible to deduce c_0 from the measurement of E on a tensile testing machine and of the measurement of ρ. However, getting the value of c_0 directly from a test made on the SHPB device is appealing, especially if one does not have easily access to other facilities.

Because a SHPB device is designed to perform impact tests, an intuitive method to get c_0 would consist in the following steps: measure the length of the bar; perform an impact test on a single bar; and finally measure the time shift between multiple reflections of the stress pulse in the bar. This method however faces some major difficulties:

- because of the –non zero– rise time of the pulse, it is not perfectly square and precisely identifying a specific point on the pulse is difficult. Possibly noisy measurement can make this task even harder;
- the propagation in bars of finite diameter is dispersive [4] and so the shape of the pulse travelling down the bar is affected. It is also hard to find the time shift between two pulses with slightly different shape.

That is why in this article we introduce a method from precisely determining the velocity c_0, still from an impact test, but using the impact spectrum rather than the impact time series. Indeed, there is a link between the resonance frequencies –which appear in the impact spectrum– and the velocity of the bar c_0.

This article is organised as follows. The first part (Section 2) recalls the computation of the longitudinal resonance frequencies of a finite length rod. In Section 3, we derive the expression of the velocity as function of resonance frequencies and also compute the associated uncertainty. Finally, in Section 4 we show the efficiency of the proposed method on a concrete example.

2 Longitudinal modes of a finite length rod

Let L be the length of the bar, d the diameter of the bar. Let E, ρ and ν be respectively the modulus of elasticity, the density and the Poisson's ratio of the bar. In the following, the strain gauge is supposed to be positioned right in the middle of the bar. This should not theoretically be a restriction of the proposed method, only the antiresonances would differ. However, our strain gauges were glued in the middle of the bars in order to minimize pulse overlay between the incident and reflected waves.

2.1 1D solution

The wave equation of longitudinal waves in thin rods is [5] (pp77, (2.1.7)))

$$\frac{\partial^2 u}{\partial t^2} + \frac{E}{\rho}\frac{\partial^2 u}{\partial x^2} = 0 \tag{3}$$

where $u(x,t)$ is the displacement at coordinate x and time t. We can define the velocity of the bar $c_0 = \sqrt{E/\rho}$.

Stationary solution $u(x,t) = U(t)\Phi(x)$ and

$$\ddot{U}\Phi + c_0^2 U\Phi" = 0 \tag{4}$$

where the dot denotes derivative with respect to the time variable t and the prime denotes the derivative with respect to the space variable x.

$$\frac{\ddot{U}}{U} = -c_0^2\frac{\Phi"}{\Phi} = -\omega^2, \qquad \forall x,\ \forall t \tag{5}$$

where ω is the circular frequency. The longitudinal modes are the solutions of

$$\Phi" - \frac{\omega^2}{c_0^2}\Phi = 0 \tag{6}$$

Let $\lambda^2 = \omega^2/c_0^2$. The solutions of Eq. 6 are of the form

$$\Phi(x) = A\sin(\lambda x) + B\cos(\lambda x) \tag{7}$$

$$\Phi'(x) = \lambda A\cos(\lambda x) - \lambda B\sin(\lambda x) \tag{8}$$

where the constants A and B are determined from the boundary conditions, which are a null strain at $x = 0$ and $x = L$

$$\Phi'(0) = \lambda A \tag{9}$$

$$\Phi'(L) = -\lambda B\sin(\lambda L) \tag{10}$$

A null strain at the ends of the rod implies $A = 0$ and if we seek a non trivial solution (ie. $B \neq 0$) Eq. 10 becomes $\sin(\lambda L) = 0$. The longitudinal modes of the rod must therefore satisfy

$$\lambda_n = \frac{n\pi}{L},\ n \in \mathbb{N} \tag{11}$$

The eigenfrequencies of the rod are

$$f_n = \frac{nc_0}{2L},\ n \in \mathbb{N} \tag{12}$$

2.2 Antiresonances

Since the strain gauges are placed right at the middle of the bars, we need to identify the modes that also correspond to antiresonances. The additional condition for a mode to also be an antiresonance is

$$\Phi'(L/2) = 0 \tag{13}$$

From Eq. 8 a non trivial solution still implies $\sin(\lambda L/2) = 0$. The antiresonances therefore verify

$$\lambda = \frac{2n\pi}{L},\ n \in \mathbb{N} \tag{14}$$

The corresponding frequencies of the antiresonances are

$$f_{2n} = \frac{(2n)c_0}{2L},\ n \in \mathbb{N} \tag{15}$$

2.3 Observable resonances

In the case of a strain gauge located right in the middle of the rod, from Eq. 12 and Eq. 15 we can deduce that the observable resonances of the rod are

$$f_{2n+1} = \frac{(2n+1)c_0}{2L},\ n \in \mathbb{N} \tag{16}$$

2.4 1D solution with Love correction for the dispersion effects

The effect of the lateral inertia of the bar can be taken into account in the wave equation of the bar (see [6]; or [5], page 120: Love's equation of motion (2.5.61)). This leads to the following dispersive wave equation

$$\frac{\partial^2 u}{\partial x^2} + \frac{\nu^2 \rho J}{EA} \frac{\partial^4 u}{\partial x^2 \partial t^2} = \frac{\rho}{E} \frac{\partial^2 u}{\partial t^2} \tag{17}$$

where A is the section of the rod and J the polar moment of inertia. Let $\alpha^2 = \frac{\nu^2 \rho J}{EA}$ and still $c_0^2 = \frac{E}{\rho}$. In the case of a circular cross section with diameter d, we have $\alpha^2 = \frac{\nu^2 d^2}{8 c_0^2}$. Looking for a stationary solution of the form $u(x,t) = U(t)\Phi(x)$, Eq. 17 becomes

$$U\Phi" + \alpha^2 \ddot{U}\Phi" = \frac{1}{c_0^2} \ddot{U}\Phi \tag{18}$$

It is rewritten as

$$\frac{\ddot{U}}{U} = \frac{\Phi"}{\Phi/c_0^2 - \alpha^2 \Phi"} = -\omega^2, \qquad \forall x,\ \forall t \tag{19}$$

Solving this equation the same way as in section 2.1, we get the following condition for the resonances

$$\lambda = \frac{\omega}{c_0 \sqrt{1 - \omega^2 \alpha^2}} = \frac{n\pi}{L},\ n \in \mathbb{N} \tag{20}$$

Again, if we keep only the observable resonances and substitute the expression of α^2 into Eq. 20, we can get the value of c_0

$$c_0 = f_{2n+1} \sqrt{\left(\frac{2L}{2n+1}\right)^2 + \frac{(\pi \nu d)^2}{2}},\ n \in \mathbb{N} \tag{21}$$

3 Compute c_0 velocity and associated uncertainty from impact test

3.1 Velocity from impact test spectrum

The main idea of this article is that by performing an impact test on a bar of the SHPB device it is possible to get the value of c_0 and the associated uncertainty.

3.1.1 1D rod theory for longitudinal modes

If we consider the observable resonances of Eq. 16, we can deduce the velocity c from the f_{2n+1} peaks in the spectrum of the impact response of the bar

$$c(f_{2n+1}) = \frac{2L f_{2n+1}}{2n+1},\ n \in \mathbb{N} \tag{22}$$

This is indeed a way to get the velocity of waves at discrete frequencies f_{2n+1}, and not c_0, since in reality the wave propagation in the bar is dispersive ([4], [7]): the different wavelengths do not travel down the bar at the same speed and the velocity is therefore frequency dependent.

3.1.2 1D rod theory with Love correction for longitudinal modes

When we take the radial inertia into account, and contrary to the post-treatment with Eq. 22, it is possible to deduce the value of c_0 from the observable resonance frequencies f_{2n+1}

$$c_0 = f_{2n+1}\sqrt{\left(\frac{2L}{2n+1}\right)^2 + \frac{(\pi\nu d)^2}{2}},\ n \in \mathbb{N} \tag{23}$$

Note that removing the correction term $\pi\nu d^2/2$ in the previous equation leads to Eq. 22 for the simple 1D theory.

Of course Eq. 23 is only acceptable in low frequency: as the frequency increases, the correction for radial inertia is no longer sufficient and the resulting dispersion curve moves away from the Pochhammer dispersion curve (see figure 4 of [6] for a comparison of Pochhammer and Love dispersion curves).

3.2 Uncertainty in the value of the velocity

In the following, we use the notations defined in the GUM (guide to the expression of measurement uncertainty [8]) and the VIM (international vocabulary of metrology [9]). Let $u(x_1)$ denote the standard –in the sense of standard deviation– measurement uncertainty in x_1, it will be abbreviated as "uncertainty in x_1". The standard relative measurement uncertainty in x_1 is therefore $u(x_1)/x_1$, it will be abbreviated as "relative uncertainty in x_1".

The general rule for computing the uncertainty in the output of a functional relationship $y = f(x_i)$, with the assumption of uncorrelated inputs, is given in [8] (section 5.1.2, equation 10)

$$u^2(y) = \sum_{i=1}^{N}\left(\frac{\partial f}{\partial x_i}\right)^2 u^2(x_i) \tag{24}$$

3.2.1 1D rod theory for longitudinal modes

Eq. 22 is a functional relationship between input quantities L and f_{2n+1} and the output quantity $c(f_{2n+1})$. In [10], the reader can find a set of rules (see table 2 in [10]) for the most common functional relationships; this set of rules is only the application of Eq. 24. In the case of a fractionnal relationship of the type

$$y = \frac{Ax_1}{Bx_2} \tag{25}$$

where A and B are constants with no uncertainty, the uncertainty in the output is

$$\left[\frac{u(y)}{y}\right]^2 = \left[\frac{u(x_1)}{x_1}\right]^2 + \left[\frac{u(x_2)}{x_2}\right]^2 \tag{26}$$

Applying the rule of Eq. 26 to Eq. 22 gives the relative uncertainty in the computed velocity

$$\left[\frac{u(c)}{c}\right]^2 = \left[\frac{u(L)}{L}\right]^2 + \left[\frac{u(f_{2n+1})}{f_{2n+1}}\right]^2 \tag{27}$$

3.2.2 1D rod theory with Love correction for longitudinal modes

The equation of the velocity with Love correction (Eq. 23) is slightly more complicated when it comes to evaluate the associated uncertainty. Using the set of rules defined in table 2 of [10] is not sufficient and it is necessary to also use the primary definition Eq. 24.

In the case of a power relationship of the type

$$y = x_1^A \tag{28}$$

where A is a constant with no uncertainty the uncertainty in the output y is

$$\frac{u(y)}{y} = |A| \frac{u(x_1)}{x_1} \tag{29}$$

Writing Eq. 23 as $c_0 = f\sqrt{(\Gamma)}$ and using the rules of Eq. 26 and Eq. 29 we get

$$\left[\frac{u\left(c_0\right)}{c_0}\right]^2 = \left[\frac{u\left(f_{2n+1}\right)}{f_{2n+1}}\right]^2 + \frac{1}{4}\left[\frac{u\left(\Gamma\right)}{\Gamma}\right]^2 \tag{30}$$

We then need the general definition Eq.24 to write

$$u^2(\Gamma) = \left(\frac{2L}{2n+1}\right)^4 4L^2u^2(L) + \left(\frac{\pi d}{2}\right)^4 4\nu^2u^2(\nu) + \left(\frac{\pi\nu}{2}\right)^4 4d^2u^2(d) \tag{31}$$

Finally, combining Eq. 31 and Eq. 30 gives

$$\left[\frac{u\left(c_0\right)}{c_0}\right]^2 = \left[\frac{u\left(f_{2n+1}\right)}{f_{2n+1}}\right]^2 + \frac{1}{\left[\left(\frac{2L}{2n+1}\right)^2 + \left(\frac{\pi\nu d}{2}\right)^2\right]^2}\left[\left(\frac{2}{2n+1}\right)^4 L^4\left[\frac{u\left(L\right)}{L}\right]^2 + \left(\frac{\pi d}{2}\right)^4 \nu^4\left[\frac{u\left(\nu\right)}{\nu}\right]^2 + \left(\frac{\pi\nu}{2}\right)^4 d^4\left[\frac{u\left(d\right)}{d}\right]^2\right] \tag{32}$$

4 Application to 17-4PH steel bars

4.1 Impact test conditions

The present method is applied on the specific SHPB device designed and built at our laboratory, LBMC UMR_T9406 (Iffstar/UCLB). The measuring bars are made of Armco 17-4PH precipitation-hardening steel.

The Poisson's ratio of 17-4PH steel is $\nu = 0.291$ according to the manufacturer. The uncertainty on ν concerns its last significant digit (0.29**1**) and following [11] (Rule 1, page 23), the absolute uncertainty on ν is taken as $u(\nu) = 0.0005$.

The diameter of the bars is $d = 31.75\,\text{mm}$, the bars were centerless ground to obtain a precise diameter, a good cylindricity and a low surface roughness. The diameter is measured at several points and ranges from $31.71\,\text{mm}$ to $31.76\,\text{mm}$, so the absolute uncertainty on the diameter is taken as $u(d) = 0.025\,\text{mm}$.

The end surfaces of the bars were machined on a lathe. The length of the bars is $3058\,\text{mm}$, it is measured with a class II measuring tape. Directive 2014/32/EU [12] (Annex X, Chapter 1) gives the maximum permissible error (MPE) between two consecutive scale marks as $a + bL_r$, where $a = 0.3\,\text{mm}$, $b = 0.2$ and L_r is the value of the length rounded to the next whole metre ($L_r = 4\,\text{m}$ here).

The test for determining the value of c_0 is a single bar test: the strain wave is therefore reflected back and forth at the free ends of the bar. The steel impactor has a cylindrical shape; its diameter is $30.0\,\text{mm}$ and

Parameter x	unit -	value -	uncertainty $u(x)$	relative uncert. $u(x)/x$
L	m	3.058	0.0011	0.36×10^{-3}
d	mm	31.75	0.1	6.30×10^{-3}
ν	-	0.291	0.0005	1.72×10^{-3}
f_{2n+1}	Hz	-	5.23	-

Table 1: Summary of the SHPB setup characteristics

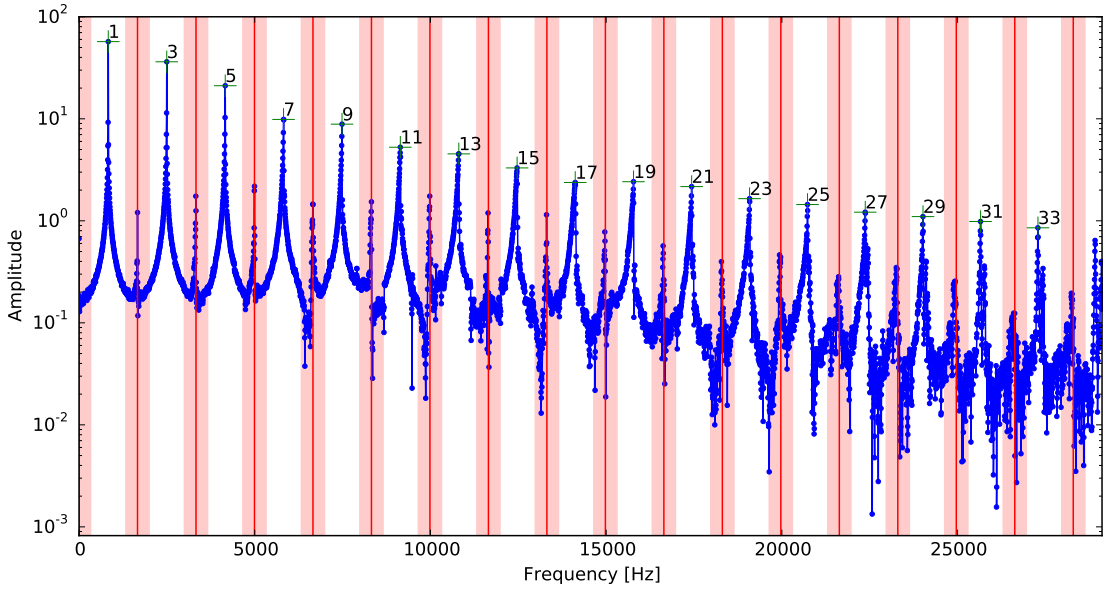


Figure 1: Frequency spectrum of the impact test (+: identified f_{2n+1} peaks with the corresponding value of $2n+1$; |: rough frequency f_{2n} of antiresonances; : discarded peak search zone)

its length is 94.2 mm. Using a short impactor is a way to have a high frequency content in the strain wave generated by the impact. The speed of the impactor just before impact is $23\,\mathrm{m\,s^{-1}}$; this parameter is indeed not important for the determination of c_0 as changing the striker velocity does not change the duration of the pulse.

The useful part of the signal is the part which contains the multiple reflections of the pulse in the bar. Its duration is 191 ms and during the time interval the pulse travels approximately 160 times the length $2L$.

Table 1 summarizes all the parameters values and uncertainties.

4.2 Peaks detection in frequency spectrum

Figure 1 illustrates the frequency spectrum of the impact test. The resonances are clearly visible. The peaks are automatically detected as the points with maximum amplitude between two antiresonances. The antiresonances are roughly determined using a first estimate of the velocity c_0 and Eq. 15. Because the spectrum becomes noisy as the frequency increases, especially around antiresonances, the peak search zone is reduced to 60 % of the frequency interval between two successive antiresonances by avoiding the light red bands (see Figure 1).

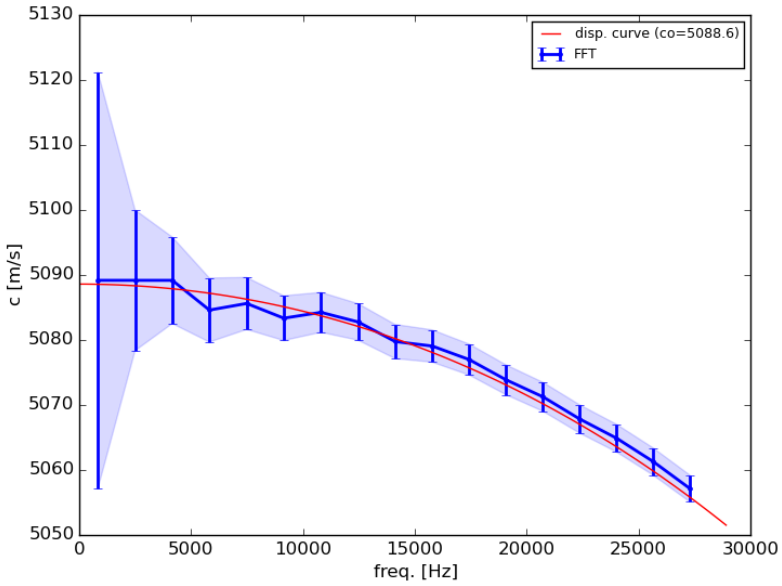


Figure 2: Velocity of the longitudinal waves and associated uncertainty with respect to frequency. The red curve is the exact dispersion curve computed with $c_0 = 5088.6\,\mathrm{m\,s^{-1}}$.

4.3 Velocity with 1D approach

Figure 2 illustrates the posttreatment of the impact spectrum with the 1D approach (see Eq.22). We also computed the numerical solution to the Pochhammer equation (red curve on Figure 2, see [13] for details on the computation) and it stays inside the corridor defined by the measurement uncertainty. This shows that we indeed computed $c(f_{2n+1})$ –and not c_0– as it is very close to the dispersion curve.

The uncertainty on the velocity decreases as the frequency increases (see Figure 3). This is due to the frequency term in Eq. 27: $u(f_{2n+1})$ is constant and taken equal to the frequency resolution in the frequency domain; it is inversely proportional to the duration of the time window of the impact signal. On the contrary, $\left[\frac{u(L)}{L}\right]^2$ is constant whatever the considered peak. From Eq. 27 it is clear that the uncertainty in c tends asymptotically to the value of the uncertainty in L as the frequency increases.

4.4 Velocity with Love correction approach

Figure 4 illustrates the posttreatment of the impact spectrum with the 1D approach with Love correction (see Eq.23). The Love correction removes the dispersive effect due to the finite diameter of the bar [5], that is why we can directly obtain the velocity c_0 from this graph.

Considering the uncertainty corridor, the points in Figure 4 are remarkably well aligned. That is why the velocity c_0 is computed by averaging the celerities $c_0^{(2n+1)}$ weighted by their respective inverse uncertainties (ie. $1/u(c_0^{(2n+1)})$). From the impact test posttreated with Love correction, the average velocity is $5088.63\,\mathrm{m\,s^{-1}}$. The uncertainty on the last point (highest frequency) is $u(c_0) = 2.07\,\mathrm{m\,s^{-1}}$. The relative uncertainty is $u(c_0)/c_0 = 0.41 \times 10^{-3}$, which is very close to the relative uncertainty in the length of the bar (which can also be observed in Figure 3).

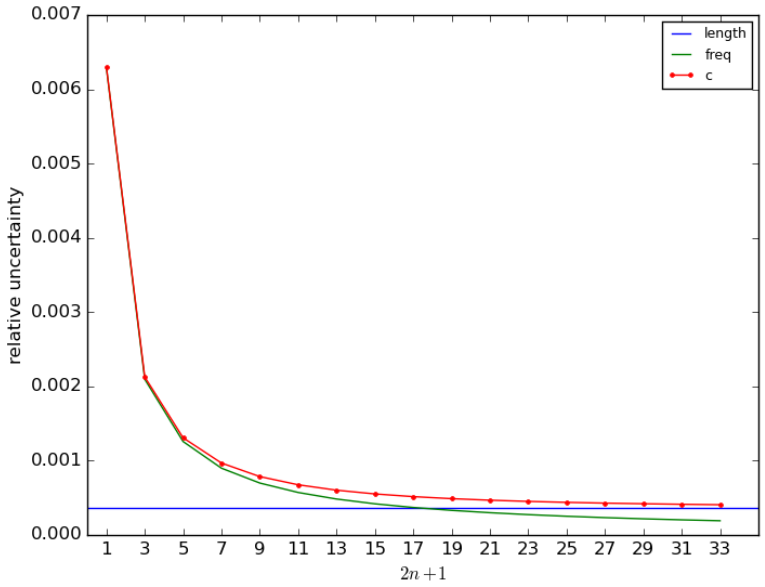


Figure 3: Values of the relative uncertainty in the velocity $u(c)/c$, in the frequency $u(f_{2n+1})/f_{2n+1}$ and in the length $u(L)/L$ with respect to the frequency index $2n+1$

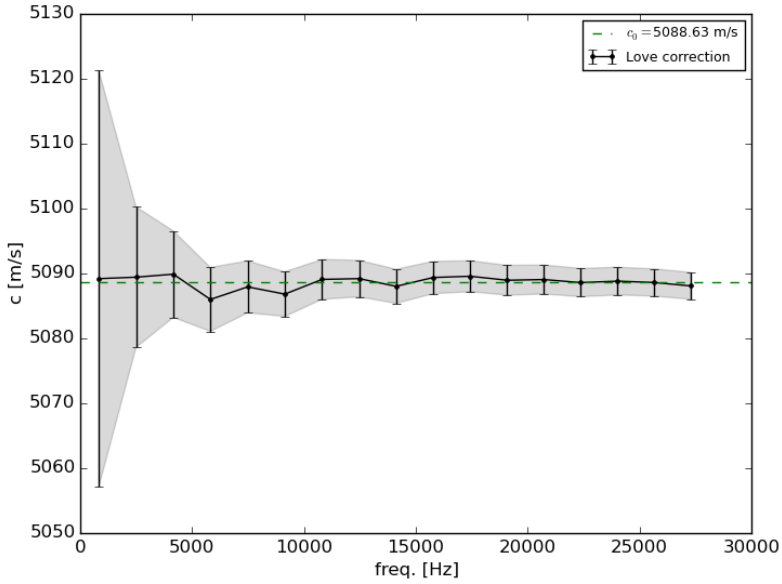


Figure 4: Velocity c_0 and associated uncertainty. Posttreatment of the impact test with Love correction.

5 Conclusion

We introduced a method for the precise determination of the velocity c_0 of SHPB measurement bars. This method is based on a simple impact test on a single bar, which is –of course– an easy experiment to perform on SHPB device. By working on the spectrum of this impact test, it is possible to easily identify sharp peaks that correspond to the resonance frequencies of the bar. The longitudinal modes of the bar give the relationship between the frequency of these peaks and the velocity c_0. We also expressed the uncertainty in the measurement of c_0 and showed in our case the relative uncertainty in c_0 is close to the uncertainty in the length of the bar, ie. around $0.04\,\%$. In the context of quality in measurement with SHPB, this is an important first step which then enables to assess the uncertainty in the strain and strain rate in the sample.

References

[1] Howard Kuhn. *ASM Handbook: Volume 8: Mechanical Testing and Evaluation*, volume 8. ASM International, 10 edition, September 2000.

[2] Bazle A Gama, Sergey L Lopatnikov, and John W Gillespie. Hopkinson bar experimental technique: A critical review. *Applied Mechanics Reviews*, 57(4):223, 2004.

[3] Zhouhua Li and John Lambros. Determination of the dynamic response of brittle composites by the use of the split Hopkinson pressure bar. *Composites Science and Technology*, 59(7):1097–1107, May 1999.

[4] Dennison Bancroft. The Velocity of Longitudinal Waves in Cylindrical Bars. *Physical Review*, 59(7):588–593, 1941.

[5] Karl F. Graff. *Wave Motion in Elastic Solids*. Dover Publications, June 1991.

[6] Simon P. Anderson. Higher-order rod approximations for the propagation of longitudinal stress waves in elastic bars. *Journal of Sound and Vibration*, 290(1):290–308, February 2006.

[7] R. M. Davies. A Critical Study of the Hopkinson Pressure Bar. *Philosophical Transactions of the Royal Society of London A: Mathematical, Physical and Engineering Sciences*, 240(821):375–457, January 1948.

[8] Evaluation of measurement data – Guide to the expression of uncertainty in measurement. JCGM 100: 2008 (GUM 1995 with minor corrections), BIPM Joint Committee for Guides in Metrology, Paris, 2008.

[9] International vocabulary of metrology – Basic and general concepts and associated terms, 3rd edn. JCGM 200: 2008 (VIM), BIPM Joint Committee for Guides in Metrology, Paris, 2008.

[10] Ian Farrance and Robert Frenkel. Uncertainty of Measurement: A Review of the Rules for Calculating Uncertainty Components through Functional Relationships. *The Clinical Biochemist Reviews*, 33(2):49–75, May 2012.

[11] Les Kirkup and Bob Frenkel. *An Introduction to Uncertainty in Measurement: Using the GUM (Guide to the Expression of Uncertainty in Measurement)*. Cambridge Universtity Press, Cambridge, 2006.

[12] Directive 2014/32/EU of the European Parliament and of the Council of 26 February 2014 on the harmonisation of the laws of the Member States relating to the making available on the market of measuring instruments (recast), February 2014.

[13] D. Brizard, S. Ronel, and E. Jacquelin. Estimating Measurement Uncertainty on Stress-Strain Curves from SHPB. *Experimental Mechanics*, 57(5):735–742, June 2017.

Experimental study of vibration uncertainty of multilayered timber beams assembled through wood dowels

T. A. Bui[1], P. Lardeur[2], M. Oudjene[1]
[1] Université de Lorraine, INRA LERMAB, F-88 Epinal, France
E-mail: **marc.oudjene@univ-lorraine.fr**

[2] Université de Technologie de Compiègne, Laboratoire Roberval
Centre de recherches de Royallieu, CS 60319, 60203 Compiègne Cedex, France

Abstract
This paper presents an experimental study of the vibration variability of adhesive free multi-layered timber beams (AFLTB). AFLTB are obtained by stacking several oak layers assembled through normal wood dowels (NWD) or compressed wood dowels (CWD). The mechanical properties of these natural materials, namely the elasticity moduli and the density which drive the vibration behaviour, exhibit large variability. Moreover, the assembly process may induce an additional source of variability. Consequently, taking into account variability in the analysis and design of AFLTB seems relevant and necessary. All the vibration tests were done using an impact hammer, under free-free conditions. First of all, variability of mass, FRFs, damping and frequencies of individual layers were measured. Then, after assembly, the variability of vibration characteristics of three-layer AFLTB was assessed and analyzed. In addition, finite element models for AFLTB are developed to assess the vibration characteristics of such beams.

1 Introduction

Nowadays, environmentally-friendly options are fully integrated in the design process of products and structures, and gained more and more interest in the actual context of global warming. Even if timber as a natural material is becoming a more competitive building material due to its environmentally-friendly and aesthetic aspects, timber construction has some drawbacks related to the use of high degree of petrochemical (adhesives) within Engineered Wood Products (EWPs), such as glulam and Cross Laminated Timber (CLT). In the last ten years, environmental and economic issues are driving an increasing need for sustainability in the construction sector around the world. In this context, a consortium with partners from six European countries was formed throughout a joint research project supported by the Northwest European Interreg Programme, called Adhesive Free Timber Buildings (AFTB), to develop more environmentally-friendly joining method as a substitute for adhesives and metallic fasteners. As a part of the AFTB project, it was proposed to use compressed (densified) wood dowels (CWD) as a joint element to connect timber laminates to produce adhesive free multi-layered beams and CLT panels.

The research work presented herein aims to assess the variability of dynamic properties of adhesive free laminated timber beams (AFLTB) assembled through wood dowels. The connection system proposed, to substitute the adhesive, is a set of wood dowels to connect timber laminates (without using adhesive). Such AFLTB are not covered by the Eurocode 5 and consequently an experimental investigation is required in order to use safely the design guidelines.

In particular, the dynamic characteristics of adhesive free structural elements, such as beams and cross-laminated panels, assembled through wood dowels are a key point for their vibrational comfort assessment. Moreover, both the variability involved in the timber material as well as the variability

induced by the construction of AFLTB are an important aspect and worthy of investigation for the vibrational comfort assessment of such new structural systems.

The present study focusses on the experimental study of the variability involved in AFLTB assembled using wood dowels. The study includes variability involved in the timber material itself as well as the variability involved in the multi-layer beams. The variability study includes: frequencies, damping, elastic modulus, density as well as intra-variability induced by the environmental conditions, namely the moisture content. Finally, a finite element model, using ABAQUS software, to simulate the dynamic characteristics of AFLTBs is presented.

2 State of the art

The use of wood dowels as joint material is not new. Hardwood dowels have been successfully used to connect structural members in timber frames for thousands of years. Unfortunately, hardwood dowels (not densified) suffer from creepage and loss of stiffness over time. The use of CWD could overcome above problems, as compressed wood has much better mechanical properties by controlling its density and moisture content (MC) during the manufacturing process [1].

Even if compression (or densification) of wood does not show extensive research in recent years, it has attracted many researchers in the past. This technology has been initiated in Germany since 1930 under the trade name of Lignostone and in England it has been known as Jicwood and Jablo [2, 3].

In the last ten years, many attempts have been undertaken to demonstrate the benefits of CWD as a joint element for structural bearing uses [2, 4-7].

In timber construction, vibration serviceability of timber floors is a key performance issue, since light weight timber floors are more prone to annoying vibrations induced by human activities than heavy concrete floors [8]. In the EU, the design criteria and methodology for vibration of timber floors are generally performed based on the Eurocode 5 [9]. Several studies dealing with serviceability vibration performance of cross-laminated timber floors are available in the literature [10-17]. However, at our best knowledge vibration performance of timber structural elements assembled through CWD is not described by any standard and has not been published elsewhere. Thus, this study focusses on the modal analysis of adhesive free multi-layered beams (AFLTB). Vibration performance of AFLTB has been recently studied by the authors [18], where the results in terms of frequencies and damping were compared to the conventional similar glued beams showing good vibration performance of AFLTB. This paper deals mainly with the vibration variability of AFLTB. The AFLTB were connected either using 68% compressed spruce dowels or using uncompressed oak dowels for comparison purpose.

3 Wood dowels and beam construction

3.1 Materials

Oak timber has been used in this study to manufacture the timber layers. The density mean value of the oak layers was 623 kg/m^3. The wood dowels used as connecting elements were made either from compressed spruce or uncompressed oak. CWD were obtained from compressed spruce timber blocks, having initial density of 437 kg/m^3, in the radial direction up to compression level of about 68% (also known as compression ratio CR). The normal wood dowels (NWD) made of oak, with density of 633 kg/m^3, were used for comparison purpose.

3.2 Production of compressed dowels

Free defects spruce timber blocks were conditioned at about 8% MC and 20°C prior to the densification process. The densification of the spruce timber blocks was done using a hot pressing machine with a maximum pressure force of 1500 kN (Figure 1).

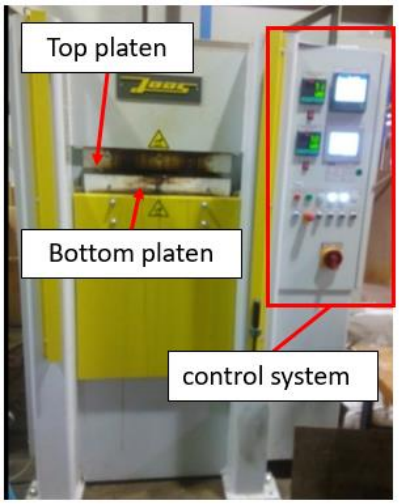


Figure 1: Hot pressing machine used for the wood densification

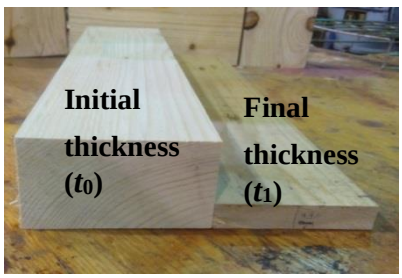
The hot pressing machine as shown in Figure 1 consists of two main parts: two hot metallic pressing apparatus and pressure/temperature control system.

The typical shape of spruce timber before and after densification process in the radial direction can be seen in Figure 2. Once the spruce timber blocks were densified in the radial direction at a level of compression of about 68%, they were cut and planned to obtain plates with a desired thickness of 16 mm (Figure 2a).

The compression ratio (densification level) may be calculated, based on the initial thickness (t_0) and the final thickness (t_1), by means the following relation [8]:

$$CR(\%) = \frac{t_1 - t_0}{t_0} \times 100 \tag{1}$$

From the obtained densified plates, rounded CWD with 16 mm diameter were produced (Figure 2b).



(a)



(b)

Figure 2: (a) Typical thickness before and after densification, (b) Typical rounded 16 mm CWD

It is worth noting that all spruce blocks were weighed before and after the densification process to obtain information on the increase of the density.

3.3 Construction of three-layer timber beams

Different types of adhesive free beams were manufactured by stacking three layers having the following dimensions: 70 mm x 22.5 mm x 1450 mm. All the laminates were weighed and moisture content (MC) measured prior to testing to obtain information about the density. The dowels were either made of 68% compressed spruce or uncompressed oak timber with 16 mm diameter (d =16 mm).

First, the laminates were drilled to obtain one row holes with 16 mm diameter. After that, they were stacked, pressed using clamping devices (Figure 3) and assembled by hammer insertion of the wood dowels.



Figure 3: Assembly of three-layer timber beams by hammer insertion of the dowels

4 Experimental modal analysis

4.1 Hammer impact excitation

The experimental data were recorded and analysed using the LMS Test Lab system.

All beams were tested under free–free conditions. The free–free conditions were achieved thanks to the mineral wool system placed at the two end supports as shown in Figure 4. The stiffness of the mineral wool is very low, which ensures free–free conditions [10]. The beams were excited by hammer impact at 11 points regularly spaced. One sensor was fixed at the beam end. Responses at these points were obtained using the reciprocity theorem.

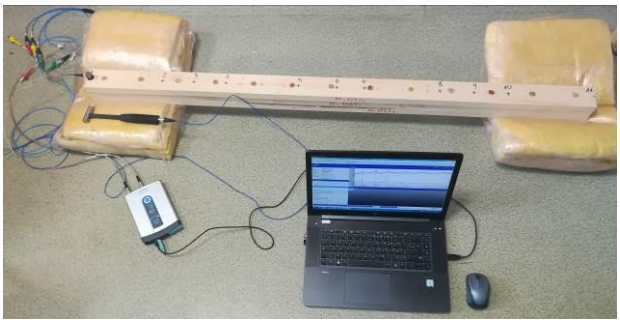


Figure 4: Experimental set-up under free – free conditions

4.2 Repeatability test

Figure 5 shows an example of FRF for one beam which was subjected to two series of hammer impacts. Each series of test contains five hammer impacts. Each curve displayed in Figure 5 represents the mean FRF for the five hammer impacts. It can be seen from this Figure that the mean FRF for the two series of impacts are close to each other, it can be therefore, concluded that the measurement uncertainty is negligible. It proves that results from experiments are stable and reliable.

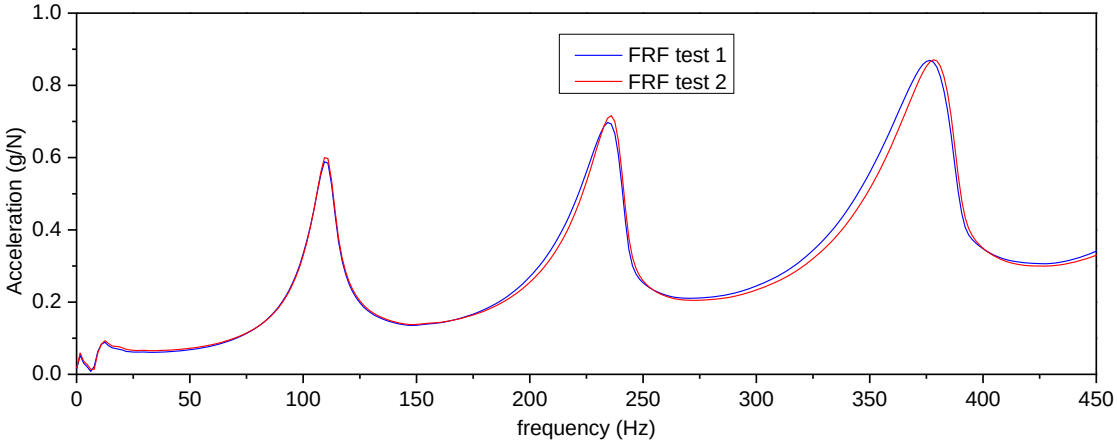


Figure 5: FRFs from 1 beam - repeatability test

5 Variability study

There are many sources which may cause variability of AFLTB. On the one hand, the mechanical properties, namely the elasticity properties and the density of timber material, which govern the vibration behavior, exhibit high variability. Moreover, the manufacture imperfections between theoretically identical beams and the mode of construction of dowelled AFLTB may induce an additional source of variability. The variability derived from all these aspects is called “inter variability”. On the other hand, the environmental conditions (in particular the moisture content) can also greatly affect the elastic properties of the timber layer as well their density values, which in turn may induce large variability. This is referred to as “intra variability”.

In order to assess the variability levels, the tests were performed on theoretically identical but physically different specimens. Inspired by a hierarchical approach, some measurements were made on AFLTB but also on the two main subsystems: individual layers and dowels. First of all, variability of mass, FRFs, damping and frequencies of individual layers, as well as variability of wood dowels density, were measured. Then, after assembly, vibration characteristics of AFLTB were extracted.

5.1 Inter variability

In order to have a better understanding of the inter variability, the first three vibration frequencies have been measured on the single layer beams and the three-layer dowelled beams. This also allows to compare the variability propagation mechanisms between the single layer beams and the three-layer beams.

5.1.1 Single layer beams and dowels

Sixteen oak single layer beams with dimensions of 70 mm × 22.5 mm × 1450 mm were, first, analyzed using the hammer impact excitation system.

The FRFs at an edge point of the sixteen single layer beams are depicted in Figure 6, where variability is clearly visible.

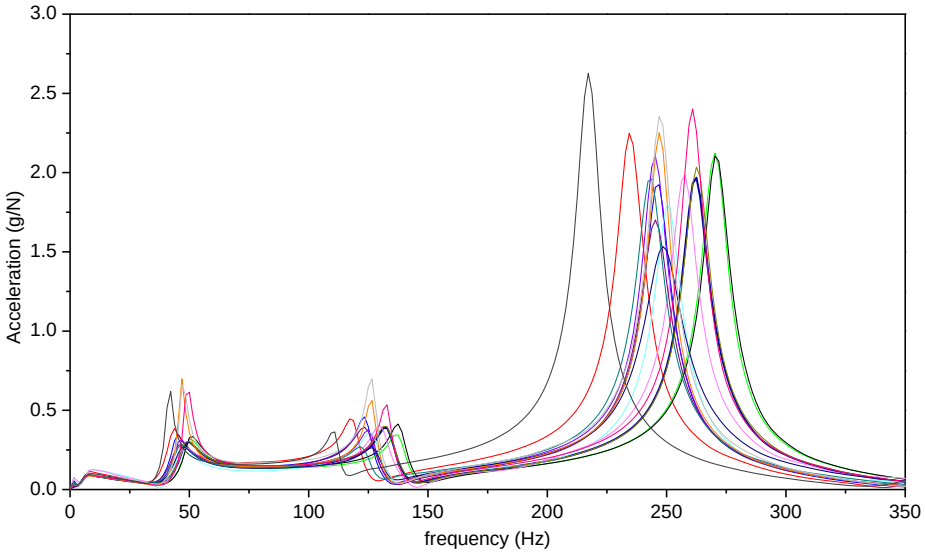


Figure 6: FRFs for 16 single layer oak beams

The frequency values as well as their corresponding variability for the sixteen oak single layer beams, are summarized in Table 1.

			Min	Max	Mean	CoV
	Mode 1	frequency (Hz)	41.6	49.6	46.5	4.80%
		damping (%)	2.5	4.5	3.7	8.10%
	Mode 2	frequency (Hz)	111.2	138.3	127.8	5.20%
		damping (%)	1.7	2.1	1.9	7.20%
	Mode 3	frequency (Hz)	217.7	270.9	250.4	5.10%
		damping (%)	1.5	2.2	1.8	10.30%

Table 1: Dynamic properties and corresponding variability for the oak single layer beams

All single layer beams were weighed to calculate the density. The longitudinal Young modulus of each single layer beam was extracted from the analytical expression of the frequencies according to the classical thin beam theory:

$$f_n = \frac{a_n}{2\pi L^2}\sqrt{\frac{EI}{A\rho}} \tag{2}$$

where:

$$a_1 = \left(\frac{3\pi}{2}\right)^2 ; a_2 = \left(\frac{5\pi}{2}\right)^2 ; a_3 = \left(\frac{7\pi}{2}\right)^2$$

I is the second moment of inertia, ρ is the mass density, A and L are the section area and the length of the specimen, respectively. The density values and their corresponding variability for the sixteen single layer beams as well as for the dowels are reported in Table 2. The values of the longitudinal elasticity modulus, calculated from frequency 1, are shown in Table 3 including the corresponding variability. From a theoretical point of view, the modulus can be calculated exploiting any mode. Equation (2) was also used for modes 2 and 3, the results obtained are consistent with those presented in Table 3. The variability level of the density of oak layers (and oak dowels) is moderate, while that of compressed dowels is high. It can be seen also that the variability level of the elastic modulus of layer is high.

Species		Min	Max	Mean	CoV
Oak layer	ρ (kg/m^3)	543.8	671.3	623.9	6.5%
Oak dowel	ρ (kg/m^3)	537.9	758.9	633.2	6.9%
Compressed dowel	ρ (kg/m^3)	891.6	1525.2	1172.5	13.0%

Table 2: Density and corresponding variability for single layer beams and dowels

	Min	Max	Mean	CoV
E_L	7.94 GPa	13.97 GPa	11.38 GPa	13.60%

Table 3: Elastic longitudinal modulus for single layer beams and corresponding variability

5.1.2 Dowelled three-layer beams

Figure 7 shows FRFs at an edge point for the five studied three-layer beams assembled using 27 NWD. As for single layer beams, the variability of FRF is significant for three-layer beams assembled with NWD.

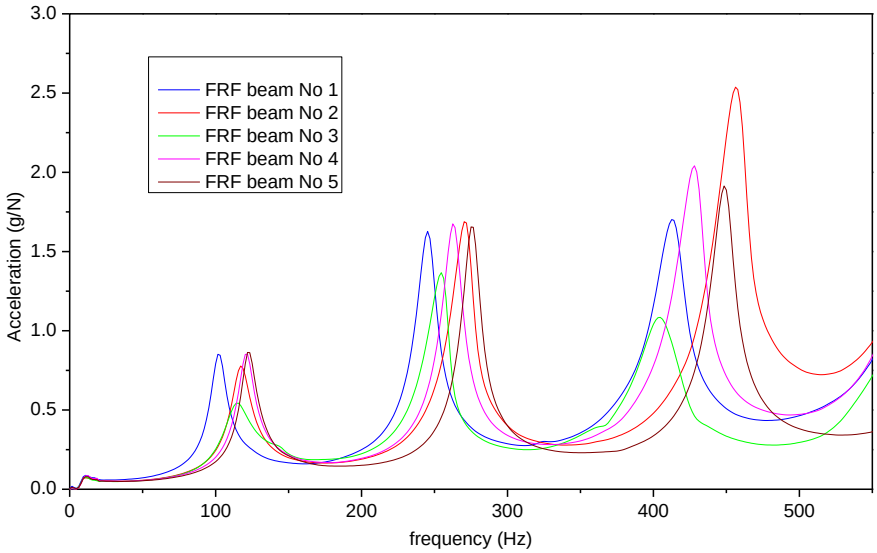


Figure 7: FRFs of three-layer oak beams assembled through 27 NWD

The variability of frequencies and damping ratios are summarized in Table 4. The variability of frequencies is close to that observed for the single layer beams. It can be observed that the variability of damping is much higher as compared to the variability of mass and frequencies. Also the variability of damping increases as the frequency increases.

		Min	Max	Mean	CoV
Mass (kg)		3.93	4.78	4.50	6.5%
Mode 1	freq (Hz)	102.0	122.4	115.4	6.3%
	damp (%)	4.1	6.3	5.1	14.9%
Mode 2	freq (Hz)	246.4	276.5	263.2	3.9%
	damp (%)	2.0	4.0	2.6	27.4%
Mode 3	freq (Hz)	406.3	461.6	432.8	4.8%
	damp (%)	1.4	3.3	2.0	36.8%

Table 4: Dynamic properties and corresponding variability for the three-layer beam assembled with 27 NWD

Figure 8 displays the FRFs for the five three-layer beams assembled through 27 CWD. The variability level of FRF is also significant for three-layer beams assembled with CWD and comparable with variability observed on three-layer beams assembled with NWD.

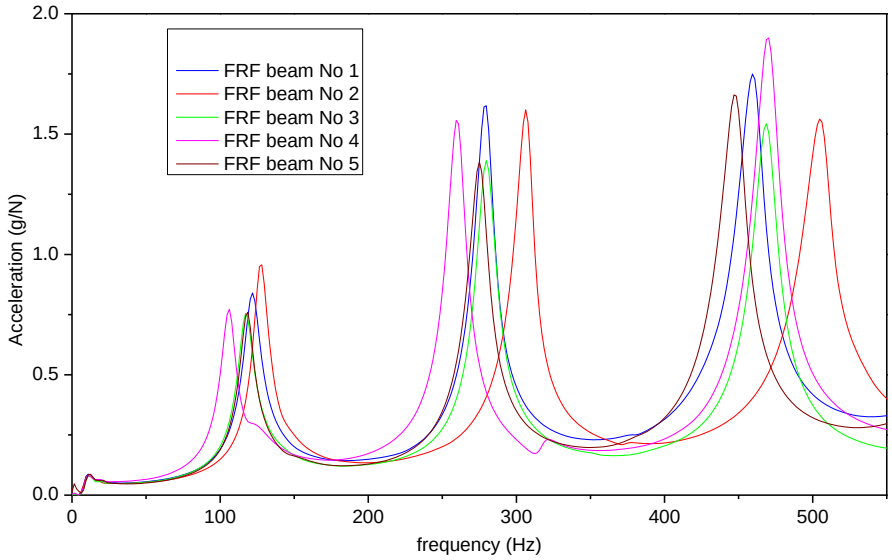


Figure 8: FRFs of three-layer oak beams assembled through 27 CWD

Table 5 summarizes the dynamic properties and the corresponding variability. In general, three-layer beams assembled by CWD have higher frequencies but lower damping ratio than three-layer beams assembled by NWD. It can be seen that the variability for both mass and frequencies is quite similar to that observed for the three-layer beams assembled with NWD, while the variability of the damping ratios is greatly reduced. This phenomenon can be attributed to the moisture-dependent swelling of the compressed wood dowels providing a better tight fitting of the connections which in turn reduces the uncertainties involved in the connection system.

		Min	Max	Mean	CoV
Mass (kg)		4.20	5.13	4.64	6.7%
Mode 1	freq (Hz)	105.9	127.5	118.2	6.0%
	damp (%)	3.7	4.7	4.3	9.0%
Mode 2	freq (Hz)	261.7	307.4	281.0	5.3%
	damp (%)	2.0	2.3	2.1	4.6%
Mode 3	freq (Hz)	449.4	507.4	471.1	4.2%
	damp (%)	1.6	2.4	1.9	13.7%

Table 5: Dynamic properties and corresponding variability for the three-layer beam assembled with 27 CWD

5.2 Intra variability

As for the inter variability quantification and for the same reasons, the first three vibration frequencies have been measured on both the single layer beams and the three-layer dowelled beams.

5.2.1 Single layer beams

To study the effect of the moisture variation on the vibration frequencies of beams, several moisture contents (MC) were considered: 9%, 12%, 15% and 18%. The first three frequencies for the single layer beam were measured for each MC level; results are displayed in Figure 9. In addition to experimental measurements, the theoretical relation (2) was used to calculate the frequencies as a function of the MC, where the elastic modulus and the mass were updated using equations (3) and (4), respectively.

$$\frac{E_{12}}{E_H} = \left[1 + \frac{1.5(H-12)}{100}\right] \tag{3}$$

$$M_H = M_{12}\frac{1+H}{1+12\%} \tag{4}$$

where E_{12} and M_{12} are the values of the modulus of elasticity and the mass at 12% MC, respectively. E_H and M_H are the values of the modulus of elasticity and the mass at MC level H%, respectively. It can be observed a fairly good agreement between the experimental measurements and the theoretically predicted frequencies. All the first three frequencies decrease linearly when the MC increases due to the decrease of the ratio E/M, which is the main source of variability (see equation (2)). It is worth noting that identical results were obtained in the case of similar conventional glued three-layer beams.

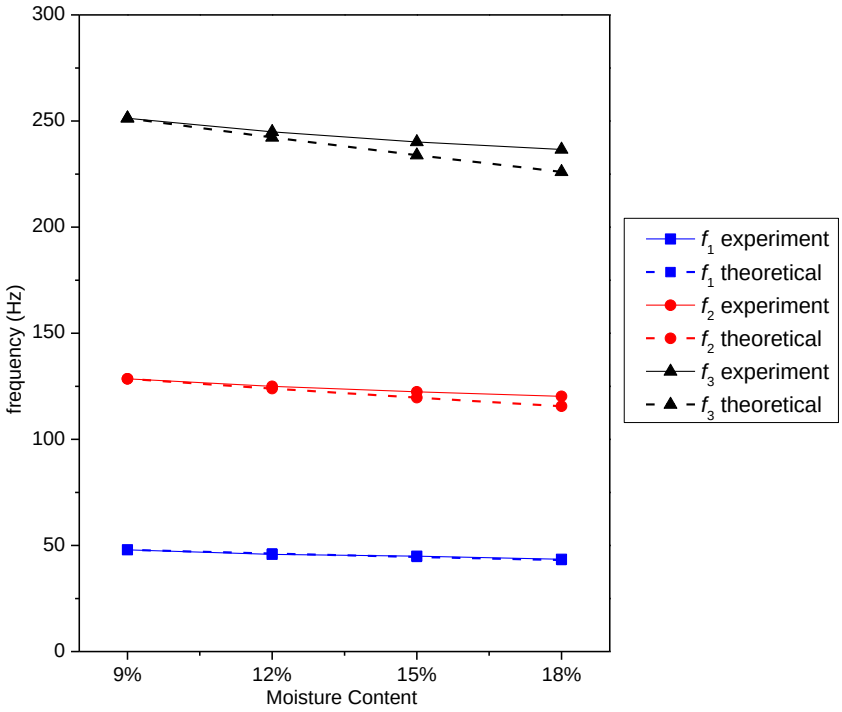
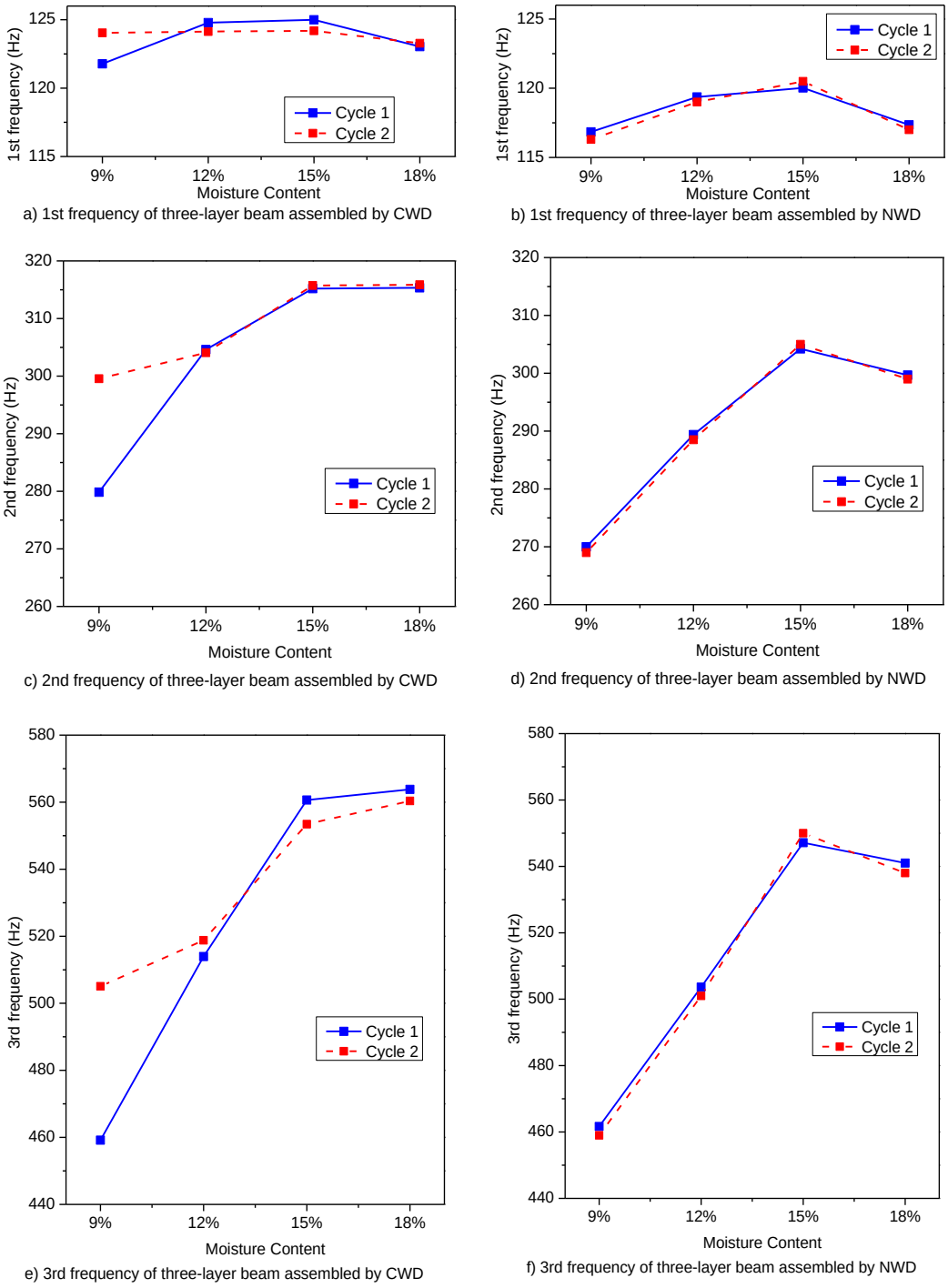


Figure 9: Effect of MC on frequencies for the single layer beam

5.2.2 Dowelled three-layer beams

Figure 10 shows the evolution of the first three frequencies of the three-layer beam assembled with NWD or CWD, as a function of MC.

The beams were subjected to two cycles of humidity variation. As in the case of single layer beam, the MC varies between 9% and 18% for each cycle. A first observation is that intra variability of the dowelled three-layer beams is relatively high by comparison to that observed in the case of single layer beams. Both dowelled three-layer beams show nonlinear variation of the frequencies when subjected to an increase of the MC.



a) 1st frequency of three-layer beam assembled by CWD

b) 1st frequency of three-layer beam assembled by NWD

c) 2nd frequency of three-layer beam assembled by CWD

d) 2nd frequency of three-layer beam assembled by NWD

e) 3rd frequency of three-layer beam assembled by CWD

f) 3rd frequency of three-layer beam assembled by NWD

Figure 10: Effect of MC on the first three frequencies of the dowelled three-layer beam

The first three frequencies of three-layer beams, assembled using NWD or CWD, exhibit an increase up to about 15% MC followed by a decrease between 15% and 18% MC. This phenomenon can be explained by the fact that in the case of dowelled AFLTB there are two main sources of variability acting concurrently during the moisture increase. The first source is the ratio *E/M* and the former one is the moisture-dependent swelling of compressed wood dowels which improves the tight fitting of the connections when MC increases. Moreover another phenomenon is observed. The results for the three-layer beams assembled using NWD seem to be independent on the number of humidity cycles, while for the three-layer beams assembled using CWD the first frequency significantly increases during the second cycle of humidity. In fact, in the case of virgin wood (uncompressed), the moisture-dependent swelling is

reversible during the dry process, while in the case of compressed wood the moisture-dependent swelling presents reversible and irreversible parts [20], leading to a permanent swelling (also known as shape memory effect) which in turn leads to a better and permanent tight fitting of the assemblies. CWD improve the performance of connections but also reduce the intra variability.

6 Finite element model

A finite element (FE) model to simulate the dowelled three-layer beams was built using Abaqus Standard [16]. The objective is to develop a numerical and predictive approach for multilayered timber beams assembled through wood dowels. Once FE models are verified against typical tests covering extreme cases and possibly an intermediate case, systematically-designed parametric studies can be undertaken using validated numerical models, avoiding extensive experimental campaigns. These studies should be capable of identifying the influence of materials properties, moisture content, stacking sequences, dowel patterns and boundary conditions on the serviceability vibration performance of the dowelled AFLTB. As a result, the identification of optimum dowelled beam systems can be carried out efficiently and cost-effectively. In addition, variability aspects can be taken into account in the finite element model, the Modal Stability Procedure (MSP) [21] will be tested in this context.

Hexahedral solid elements were used to mesh both the timber layers and dowels. The longitudinal modulus of elasticity of layers was taken from the results gathered from the experimental modal analysis carried out on the single layer beams. The other elastic properties have been taken from the literature [18, 19]. Verification and Validation methodology [17] was applied to evaluate the performance of the FE model.

6.1 Model verification

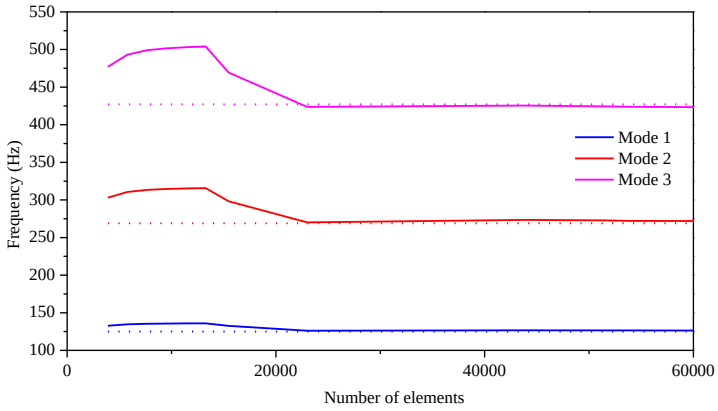


Figure 11: Convergence study of the first three frequencies

Figure 11 shows the mesh-size dependency of the first three frequencies. It can be observed that the higher order frequencies require much more elements for the convergence by comparison to the first frequency. By using about 23000 elements, the first three frequencies become stable.

6.2 Model validation

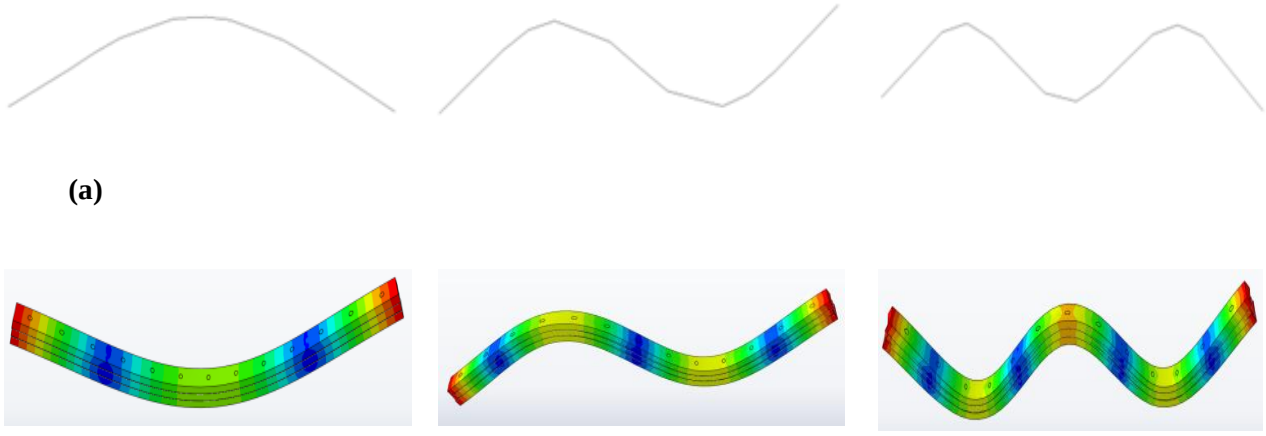
For one given three-layer oak beam the comparison between the experimental measurements and the numerically predicted results is presented hereafter.

Table 6 depicts the error values on the vibration frequency from the FE model when compared to the experimental values. It can be seen a fairly good agreement.

Further, the mode shapes predicted numerically are displayed in Figure 12. The experimental mode shapes for the three-layer beam are similar to that observed experimentally (Figure 12). The correlation between the numerically predicted mode shapes and the experimental ones was evaluated using the modal assurance criterion (MAC) values which are given in Table 6. The MAC values are close to 1, so a very good agreement exists between numerical and experimental mode shapes.

	Simulation	Experiment	Difference	MAC
f_1	125.5 Hz	122.4 Hz	2.5%	0.997
f_2	268.3 Hz	276.5 Hz	-3.0%	0.986
f_3	427.1 Hz	449.3 Hz	-4.9%	0.963

Table 6: Comparison between simulation and experimental results for a three-layer beam



a) Mode 1 b) Mode 2 c) Mode 3

Figure 12: The first three mode shapes: (a) experimental and (b) numerical

7 Conclusion

The aim of this paper is to assess the variability of vibration performance of adhesive free three-layer beams assembled using wood dowels to substitute the traditional adhesive (conventional glulam). Several adhesive free three-layer beams, made from oak timber and assembled using either normal oak dowels or 68% compressed spruce dowels, have been tested. Natural frequencies, mode shapes, and damping ratios were measured thanks to an experimental modal analysis under free-free conditions, using the impact hammer technique. Variability of these quantities of interest has been quantified.

First of all, single layer beams have been weighed to obtain information on the density and related variability. Then they were tested using a hammer impact under free-free conditions. Variability of frequencies and damping has been assessed. The variability of frequencies is moderate (about 5%), while

the variability of the damping ratio is relatively high (about 10%). The variability of frequencies for the three-layer beams assembled using NWD or CWD is close to that measured for the single layer beams. For the three-layer beams assembled with NWD, the variability of damping ratio is significantly higher compared to that observed for the single layer beams. It is worth noting that the variability of the damping ratio for the three-layer beams assembled using CWD is close to that observed for the single layer beams.

In addition to the inter-variability, intra-variability was also assessed. The frequencies of the single layer beams decrease monotonically as the moisture content increases. However, the tendency is significantly different in the case of three-layer beams assembled using wood dowels (NWD or CWD). In this case evolution of frequencies according to the moisture content is much more complicated and leads to high intra variability levels.

The comparison between results observed on single layer beams and three-layer beams highlight the fact that connections using wood dowels play an important role in the mechanical behavior of multilayered beams and in the variability quantification of their dynamic behavior.

Numerical modelling using the finite element method will be developed further to study numerically the variability of AFLTB. In particular the Modal Stability Procedure (MSP) will be exploited for the numerical study of variability of AFLTB.

Acknowledgements

The authors gratefully acknowledge the funding provided by the European Regional Development Fund via Interreg NWE grant 348 “Towards Adhesive Free Timber Buildings” (AFTB). The financial support from the Vietnamese government is also gratefully acknowledged.

References

[1] Z. Guan, W. Komatsu, K. Kitamori, K. Jung, *Structural characteristics of beam-column connections using compressed wood dowels and plates, Proceedings of 11th World Conference on Timber Engineering, Riva del Garda, Italy, 2010 June 20-24,* Riva del Garda (2010).

[2] M. Madhoushi, M. Gray, T. Tabarsa, *Influence of wood densification on withdrawal strength of fasteners in eastern cottonwood (populus deltoides), Proceedings of 11th World Conference on Timber Engineering, Riva del Garda, Italy, 2010 June 20-24,* Riva del Garda (2010).

[3] E-V. Kultikova, *Structural and properties relationships of densified wood*, Virginia Polytechnic Institute and State University, (1999).

[4] K. Jung, A. Kitamori, K. Komatsu, *Evaluation on structural performance of compressed wood as shear dowel*, Holzforschung, Vol. 62(4) (2008), pp. 461-467.

[5] I. Hassel, P. Berard, K. Komatsu, *Development of wooden shear Wall-Improvement of stiffness by utilizing elements of densified wood*, Holzforschung, Vol. 62(5) (2008), pp. 584-590.

[6] I. El Houjeyri, M. Oudjene, M. Khelifa, Y. Rogaume, A. Sotayo, Z. Guan, *Structural performance of timber connections and multilayered beams assembled through compressed wood dowels*, *World Conference on Timber Engineering, Korea, 2018 August 20-23,* Seoul (2018).

[7] T-A. Bui, M. Oudjene, P. Lardeur, M. Khelifa, Y. Rogaume, *Vibration performance of multilayered timber beams assembled through compressed wood dowels*, *World Conference on Timber Engineering, Korea, 2018 August 20-23,* Seoul (2018).

[8] B. Anshari, Z. Guan, K. Komatsu, A. Kitamori, K. Jung, *Explore novel ways to strengthen glulam beams by using compressed Japanese cedar, Proceedings of 11th World Conference on Timber Engineering, Riva del Garda, Italy, 2010 June 20-24,* Riva del Garda (2010).

[9] EN 1995-1-1:2004. Eurocode 5: design of timber structures – Part 1.1: general rules and rules for buildings. European Committee for Standardization, Brussels, Belgium (2004).

[10] J. Weckendorf, E. Ussher, I. Smith, *Dynamic response of CLT plate systems in the context of timber and hybrid construction*, Composite Structures, Vol. 157 (2016), pp. 412-423.

[11] K. Jarnerö, A. Brandt, A. Olsson, *Vibration properties of a timber floor assessed in laboratory and during construction*, Engineering Structures, Vol. 82 (2016), pp. 44-54.

[12] E-S. Bernard, *Dynamic serviceability in lightweight engineered timber floors*, J. Struct. Eng. ASCE 134 (2008), pp. 258-268.

[13] B. Zhang, A. Kermani, T. Fillingham, *Vibrational performance of timber floor constructed with metal web joists*, Eng. Struct. 56 (2013), pp. 1321-1334.

[14] E. Meier, *Wood-identifying and using hundreds of woods worldwide*, 2015-10-10, Hardcover– 1803.

[15] D. A. L. Silva, F. A. R. Lahr, O. B. Faria, E. Chahud, *Influence of wood moisture content on the modulus of elasticity in compression parallel to the grain*, Materials Research, Vol. 15 (2012), pp. 300 – 304.

[16] Abaqus 6.14, Dassault Systèmes Simulia Corp., (2014).

[17] W. L. Oberkampf, G. T. Timothy, C. Hirsch, *Verification, validation, and predictive capability in computational engineering and physics*, Appl Mech Rev, Vol. 57(5), (2004), pp. 345-384.

[18] E-M. Meghlat, M. Oudjene, H. Ait-Aider, J-L. Batoz, *A new approach to model nailed and screwed timber joints using the finite element method*, Construction and Building Materials, Vol. 41 (2013), pp. 263-269.

[19] V-D. Tran, M. Oudjene, P-J. Méausoone, *FE analysis and geometrical optimization of timber beech finger-joint under bending test*, International Journal of Adhesion & Adhesives, Vol. 52 (2014), pp. 40-47.

[20] J. Blomberg, *Mechanical and Physical Properties of Semi-Isostatically Densified Wood*. PhD. Thesis, Luleå University of Technology, LTU Skellefteå, Division of Wood Science and Technology, 2006:28, ISSN-1402-15444, (2006).

[21] É. Arnoult, P. Lardeur, L. Martini, *The modal stability procedure for dynamic and linear finite element analysis with variability*. Finite Elements in Analysis and Design, Vol. 47 (2011), pp. 30-45.

Fatigue analysis of wind excited structures with structural parameters affected by uncertainties described by interval variables

F. Giunta[1], G. Muscolino[1] and A. Sofi[2]
[1]University of Messina, Department of Engineering,
Villaggio S. Agata, Messina 98166, Italy.

[2]University "Mediterranea" of Reggio Calabria, Department of Architecture and Territory,
Salita Melissari, Feo di Vito, 89124, Reggio Calabria Italy.
e-mail: **alba.sofi@unirc.it**

Abstract
In this paper, the fatigue analysis of linear structures with uncertain-but-bounded parameters subjected to stationary multi-correlated stochastic excitations is addressed. To perform this analysis, approximate expressions of the bounds of the interval spectral moments of stress quantities are first evaluated. Since the definition of the interval stress spectral moments involves double occurrences of interval variables, a novel approach is here presented in order to overcome the so-called *dependency phenomenon*, which often leads to an overestimation of the interval solution width unacceptable from an engineering point of view. Then, the bounds of the *expected fatigue life* are evaluated by combining the method proposed by Benasciutti and Tovo [1] with the *improved interval analysis* via *extra unitary interval*, recently developed by the last two authors [2].

1 Introduction

Fatigue is recognized as one of the primary causes of failure of many structures and mechanical components. Since fatigue failures happen without any warning, they can have catastrophic consequences. The approach commonly adopted is to first convert the load into a set of fatigue cycles by using a cycle counting method, and then to evaluate the total damage by a proper damage accumulation rule (e.g. Palmgren–Miner rule) as a sum of single cycle damage contributions [3]. Practically, counting methods are algorithms, which identify fatigue cycles by appropriately combining maxima and minima for calculating the total damage as an appropriate summation of damage increments associated with each counted cycle. It is recognized that time domain counting algorithms are very expensive and represent the most time consuming part of the overall fatigue analysis; thus, other approaches that reduce the time needed for stress evaluation are clearly used. For stochastic stationary Gaussian excitations, the frequency-domain approach is more suitable. The principal advantage of the frequency-domain approach is the capability to produce analytical expressions to estimate cycle distribution and fatigue damage under a given counting procedure without requiring knowledge of each stress or strain time-history.

In the framework of frequency-domain approaches, the *rainflow counting* (*RFC*) method is undoubtedly the most popular and used counting algorithm. It has been recognized that it is the most accurate in identifying damaging events amongst all counting algorithms (see e.g., [4]). In fact, this algorithm extracts cycles on the basis of the material memory mechanisms. It is well known that, for a *very narrow-band* (*VNB*) stress process, it is reasonable to state that a stress cycle is formed by a peak and the following symmetrical valley, and the amplitude equals the value of peak if the process has zero mean. Therefore, the peak counting, level-crossing counting, range-mean counting and rainflow counting methods result in the same cycle distribution. Furthermore, the probability distribution of amplitude is identical to that of the peaks, and follows a Rayleigh distribution (see e.g., [5]). It has been recognized that the Rayleigh

distribution is too conservative and alternative methods have been proposed [1,6,7]. Recently, by performing both experimental and numerical tests, it has been demonstrated [8] that the solution proposed by Benasciutti and Tovo [1] is the most accurate one.

Uncertainties affecting structural parameters have traditionally been modeled in the context of the classical probability theory as random variables or random fields. Well-established probabilistic methods have been developed to analyze the effects of uncertainties on structural performance. However, available data are often insufficient to build credible probabilistic distributions of the uncertain parameters, especially in early design stages. Over the last decade, a number of non-probabilistic approaches [9] have gained much popularity as alternative tools for quantifying and processing uncertainties described by fragmentary or incomplete data. In this context, the interval model, originally developed on the basis of the interval analysis [10,11], is widely used when only bounds are known for the parameters involved in the engineering problem. To the best of the authors' knowledge, few studies have been devoted to fatigue analysis of structures with uncertain parameters modeled within a non-probabilistic context [12].

In this study, the solution proposed by Benasciutti and Tovo [1] is adopted and extended to fatigue analysis of linear discretized structures with interval parameters subjected to multi-correlated stationary Gaussian random excitation. The proposed procedure efficiently evaluates the lower and upper bounds of the fatigue life using appropriate combinations of the bounds of the interval mean-value and spectral moments of the selected interval stress components.

It has to be emphasized that, in the framework of interval analysis, the main drawback in the evaluation of the range of selected interval stress components is the so-called *dependency phenomenon* [13] which often leads to an overestimation of the interval solution width unacceptable from an engineering point of view. This phenomenon occurs when an expression contains multiple instances of one or more interval variables due to the inability of the classical interval arithmetic to keep track of the dependency between interval variables throughout calculations. Since the evaluation of interval stresses involves double occurrences of the same interval variable, interval stresses are more sensitive to this phenomenon than the displacements. In this paper, a novel approach is presented to limit the effects of the *dependency phenomenon*. The proposed approach evaluates the bounds of the mean-value and spectral moments of the selected interval stress process by applying the *improved interval analysis* (*IIA*) via *extra unitary interval* (*EUI*) [2] in conjunction with the so-called *Interval Rational Series Expansion* (*IRSE*) [14-18].

To assess the accuracy and computational efficiency of the proposed method, fatigue analysis of a truss structure with interval Young's modulus under wind excitation is performed. Appropriate comparisons with the *vertex method* solutions are presented.

2 Fatigue damage evaluation of linear structures under stationary stochastic excitation

Amongst all damage rules, the Palmgren-Miner linear damage model [3] is the most popular and used, due to its simplicity. According to this model, derived for constant amplitude tests, fatigue strength is quantified by the number of cycles to failure, N, under repeated sinusoidal cycles with amplitude y. For many materials, this relation is explicitly given as a straight line in a double-logarithmic diagram (Y-N curve):

$$y^k N = C \tag{1}$$

where k and C are material parameters and N is the number of cycles to failure at a given stress of constant amplitude y. For stationary stress processes, under the Palmgren-Miner rule [3] (ignoring mean-value), the *expected damage per unit of time* (or *mean damage intensity*) is a constant quantity and can be evaluated as:

$$\mathrm{E}\langle D_Y \rangle = \nu_{Y,a}\, C^{-1} \int_0^\infty y^k\, p_Y(y)\mathrm{d}y \tag{2}$$

where $p_Y(y)$ is the amplitude distribution of counted cycles, $\nu_{Y,a}$ is the rate of occurrence of counted cycles (i.e. *counted cycles/*s*)* given as (see e.g., [5]):

$$\nu_{Y,a} = \frac{1}{2\pi}\sqrt{\frac{\lambda_{Y,4}}{\lambda_{Y,2}}}; \quad \lambda_{Y,m} = \int_0^\infty \omega^m G_{YY}(\omega)\mathrm{d}\omega \tag{3}$$

where $\lambda_{Y,m}$ is the spectral moment of order *m* and $G_{YY}(\omega)$ is the one-sided *Power Spectral Density* (*PSD*) function of the stationary random stress process $Y(t)$. For stationary excitations, the *expected time to failure* (i.e. the *expected fatigue life*) can be estimated as:

$$T_\mathrm{F} = \frac{1}{\mathrm{E}\langle D_Y \rangle}. \tag{4}$$

Hence, for a given stationary random process $Y(t)$ (i.e. for a given spectral density), the *mean damage intensity* $\mathrm{E}\langle D_Y \rangle$ and the *expected fatigue life* T_F depend on the expected rate of occurrence of cycles $\nu_{Y,a}$ as well as on the amplitude distribution $p_Y(y)$. Unfortunately, because of the complicated procedure of peak–valley pairing, at present no explicit analytical solution is available for the amplitude distribution as well as for the *mean damage intensity* and *expected fatigue life*. For this reason, all methods existing in the literature are only approximate. In fact, the amplitude distribution $p_Y(y)$ depends by the counting method adopted. Thus, different choices of this amplitude distribution cause different damage. Here amplitude distribution is evaluated according to the *rainflow counting* (*RFC*) method, which is undoubtedly the most popular and used method (see e.g., [4]). In the framework of the *RFC* method, for a *very narrow-band* (*VNB*) stress process $Y(t)$, it is reasonable to state that a stress cycle is formed by a peak and the following symmetrical valley, and the amplitude equals the value of peak if the process has zero mean. Therefore, the peak counting, level-crossing counting, range-mean counting and rainflow counting methods result in the same cycle distribution [5]. Furthermore, the distribution of amplitude is identical to that of the peaks, and follows a Rayleigh distribution. Then, the number of cycles per unit time ($\nu_{Y,a}$) can be taken as the occurrence rate of up crossings at mean level $(\nu_{Y,0})$, and the *mean damage intensity*, $\mathrm{E}\langle D_{Y,VNB} \rangle$, in the *VNB* approximation, is evaluated as [5,19]:

$$\mathrm{E}\langle D_{Y,VNB} \rangle = \nu_{Y,0}\, C^{-1}\left(\sqrt{2\lambda_{Y,0}}\right)^k \Gamma\left(1+\frac{k}{2}\right); \quad \nu_{Y,0} = \frac{1}{2\pi}\sqrt{\frac{\lambda_{Y,2}}{\lambda_{Y,0}}} \tag{5}$$

where $\Gamma(\bullet)$ is the gamma function.

If the process $Y(t)$ is actually not narrow-band, the *mean damage intensity* predicted by Eq. (5) is too conservative. Hence, according to the *RFC* method, some authors proposed approximating *mean damage intensity*, $\mathrm{E}\langle D_{Y,RFC} \rangle$, by reducing the *VNB* solution [1,6,7]. Here the solution proposed by Benasciutti and Tovo [1] is adopted. Indeed, it has been recently demonstrated [8] that, for small values of the *Y-N* exponent (*k*~3), for larger *k* (*k*~7) as well as for an extreme value of *k* (~12), the Benasciutti and Tovo [1] solution gives acceptable results. According to this method, the *mean damage intensity* $\mathrm{E}\langle D_{Y,RFC} \rangle$, can be evaluated as:

$$\mathrm{E}\langle D_{Y,RFC} \rangle = \frac{\lambda_{Y,0.75}^2}{\lambda_{Y,0}\lambda_{Y,1.5}}\mathrm{E}\langle D_{Y,VNB} \rangle. \tag{6}$$

Substituting Eq.(6) into Eq.(4), the evaluation of the *expected fatigue life* T_F, yields:

$$T_{\mathrm{F}} = \frac{\pi C}{\sqrt{2^{(k-2)}}\,\Gamma\left(1+\frac{k}{2}\right)} \frac{\lambda_{Y,1.5}}{\lambda_{Y,0.75}^{2}} \sqrt{\frac{\lambda_{Y,0}^{3-k}}{\lambda_{Y,2}}}. \tag{7}$$

3 Linear structures with uncertain-but-bounded parameters under multi-correlated stationary stochastic excitations

3.1 Interval uncertainty modeling

The interval model, originally developed from the interval analysis [10], is the most used non-probabilistic approach to handle uncertainties occurring in engineering problems. The underlying idea is to represent the generic uncertain-but-bounded parameter as an interval variable ranging between its lower and upper bounds. Denoting by IR the set of all closed real interval numbers, let $\boldsymbol{\alpha}^I = \left[\underline{\boldsymbol{\alpha}}, \overline{\boldsymbol{\alpha}}\right] \in \mathrm{IR}^r$ be a bounded set-interval vector of real numbers such that $\underline{\boldsymbol{\alpha}} \le \boldsymbol{\alpha} \le \overline{\boldsymbol{\alpha}}$. The apex *I* means interval variable, while the symbols $\underline{\boldsymbol{\alpha}}$ and $\overline{\boldsymbol{\alpha}}$ denote the lower bound (*LB*) and upper bound (*UB*) vectors. According to the classical interval arithmetic, the *i*-th real interval variable $\alpha_i^I = \left[\underline{\alpha}_i, \overline{\alpha}_i\right]$ is characterized by the midpoint value (or mean), $\alpha_{0,i}$, and the deviation amplitude (or radius), $\Delta\alpha_i$, given by:

$$\alpha_{0,i} = \frac{1}{2}\left(\underline{\alpha}_i + \overline{\alpha}_i\right); \quad \Delta\alpha_i = \frac{1}{2}\left(\overline{\alpha}_i - \underline{\alpha}_i\right). \tag{8a,b}$$

The real numbers $\alpha_i \in \alpha_i^I = \left[\underline{\alpha}_i, \overline{\alpha}_i\right]$, collected into the vector $\boldsymbol{\alpha} \in \boldsymbol{\alpha}^I = \left[\underline{\boldsymbol{\alpha}}, \overline{\boldsymbol{\alpha}}\right]$, are here assumed to represent the dimensionless fluctuations of the uncertain structural parameters around their midpoint values. In the sequel, $\boldsymbol{\alpha}_0$ and $\Delta\boldsymbol{\alpha}$ will denote the vectors listing the midpoint values (or mean values) and the deviation amplitudes (or radii), $\alpha_{0,i}$ and $\Delta\alpha_i$, respectively, of the interval parameters α_i^I $(i = 1,\ldots,r)$. The main drawback of the *classical interval analysis* is the so-called *dependency phenomenon* [13] which often leads to an overestimation of the interval solution width unacceptable from an engineering point of view. This phenomenon occurs when an expression contains multiple instances of one or more interval variables due to the inability of the classical interval arithmetic to keep track of the dependency between interval variables throughout calculations. To limit the effects of the *dependency phenomenon*, recently the so-called *improved interval analysis* (*IIA*) *via extra unitary interval* (*EUI*) has been proposed. The key feature of this approach is the introduction of the *EUI*, $\hat{e}_i^I \in \left[-1,+1\right]$, $(i = 1,2,...,r)$, which does not follow the rules of the *classical interval analysis* [2]. According to the *IIA* via *EUI*, the following *affine form* definition for the i-th interval parameter α_i^I is assumed:

$$\alpha_i^I = \alpha_{0,i} + \Delta\alpha_i \hat{e}_i^I, \qquad (i = 1,2,\ldots,r). \tag{9}$$

In structural engineering, the dimensionless fluctuations of the uncertain-but-bounded parameters around their nominal values can be reasonably modelled as symmetric intervals, i.e. $\alpha_i^I \in \left[\underline{\alpha}_i, \overline{\alpha}_i\right]$ with $\overline{\alpha}_i = -\underline{\alpha}_i$, so that $\alpha_{0,i} = 0$ and $\Delta\alpha_i = \overline{\alpha}_i = -\underline{\alpha}_i$. Under this assumption, Eq. (9) reduces to:

$$\alpha_i^I = \Delta\alpha_i \hat{e}_i^I. \tag{10}$$

Furthermore, to assure physically meaningful values of the uncertain structural properties, the deviation amplitudes $\Delta\alpha_i$ should satisfy the conditions $\Delta\alpha_i < 1$. In this paper, it is assumed that the uncertainty affects elastic moduli. Here the uncertain Young's modulus of the i-th structural element is expressed as $E_i^I = E_{0,i}\left(1 + \Delta\alpha_i \hat{e}_i^I\right)$, with $E_{0,i}$ denoting the nominal value.

3.2 Equations of motion

Let us consider a quiescent *n*-DOF linear structure with r uncertain-but-bounded parameters subjected to a stationary multi-correlated Gaussian stochastic process $\mathbf{F}(t)$. The equations of motion can be cast in the following form:

$$\mathbf{M}\ddot{\mathbf{U}}^I(t)+\mathbf{C}^I\dot{\mathbf{U}}^I(t)+\mathbf{K}^I\mathbf{U}^I(t)=\mathbf{F}(t) \tag{11}$$

where $\mathbf{M}$ is the $n\times n$ mass matrix, herein assumed deterministic; $\mathbf{C}^I\equiv\mathbf{C}(\boldsymbol{\alpha}^I)$ and $\mathbf{K}^I\equiv\mathbf{K}(\boldsymbol{\alpha}^I)$ are the $n\times n$ damping and stiffness matrices of the structure which depend on the dimensionless interval parameters collected into the vector $\boldsymbol{\alpha}\in\boldsymbol{\alpha}^I$ of order *r*; $\mathbf{U}^I(t)\equiv\mathbf{U}(\boldsymbol{\alpha}^I,t)$ is the stationary Gaussian vector process of displacements; and a dot over a variable denotes differentiation with respect to time t. The Rayleigh model is herein adopted for the interval damping matrix, i.e.:

$$\mathbf{C}^I=c_0\mathbf{M}+c_1\mathbf{K}^I \tag{12}$$

where c_0 and c_1 are the Rayleigh damping constants having units s^{-1} and s, respectively. For the sake of simplicity, in the present study, the constants c_0 and c_1 are taken coincident with those pertaining to the nominal structure. The external load vector $\mathbf{F}(t)$ in Eq. (11), modeled here as a stationary multi-correlated Gaussian random process, is fully characterized, from a probabilistic point of view in the frequency domain, by the mean-value vector, $\boldsymbol{\mu}_{\mathbf{F}}=\mathrm{E}\langle\mathbf{F}(t)\rangle$, and the one-sided *PSD* function matrix, $\mathbf{G}_{\mathbf{FF}}(\omega)$ [5,21].

The interval stationary Gaussian stochastic response process $\mathbf{U}^I(t)$ of structures with uncertain-but-bounded parameters is completely characterized in the frequency domain by the interval mean-value vector, $\boldsymbol{\mu}_{\mathbf{U}}^I\equiv\boldsymbol{\mu}_{\mathbf{U}}(\boldsymbol{\alpha}^I)$, and the one-sided interval *PSD* function matrix, $\mathbf{G}_{\mathbf{UU}}^I(\omega)\equiv\mathbf{G}_{\mathbf{UU}}(\boldsymbol{\alpha}^I,\omega)$ [14,16-18]. As known, the generic response quantity of practical interest, $Y^I(t)\equiv Y(\boldsymbol{\alpha}^I,t)$ (e.g. displacement, strain or stress at a critical point), can be determined from the displacement vector $\mathbf{U}^I(t)\equiv\mathbf{U}(\boldsymbol{\alpha}^I,t)$ by means of the following relationship:

$$Y(\boldsymbol{\alpha}^I,t)=\mathbf{q}^{\mathrm{T}}(\boldsymbol{\alpha}^I)\,\mathbf{U}(\boldsymbol{\alpha}^I,t) \tag{13}$$

where $\mathbf{q}(\boldsymbol{\alpha}^I)\equiv\mathbf{q}^I$ is a vector collecting the combination coefficients relating the response process $Y^I(t)$ to $\mathbf{U}^I(t)$. The vector $\mathbf{q}^I$ in Eq. (13) may depend on the uncertain parameters. Double occurrences of the same interval variable into Eq.(13) amplify the effects of the *dependency phenomenon*. This phenomenon occurs due to the inability of the classical interval arithmetic to keep track of the dependency between interval variables throughout calculations [13]. In the framework of interval analysis, the *dependency phenomenon* often leads to an overestimation of the interval solution width unacceptable from an engineering point of view. Consequently, it is the main drawback arising when the bounds of interval stress quantities are evaluated. In the next section, a novel approach to limit the effects of the *dependency phenomenon* will be presented.

The complete probabilistic characterization of the interval stationary Gaussian random process, $Y^I(t)=\mu_Y^I+\tilde{Y}^I(t)$, requires the knowledge of the interval mean-value, μ_Y^I, and the interval one-sided *PSD* function, $G_{\tilde{Y}\tilde{Y}}^I(\omega)\equiv G_{YY}^I(\omega)$ of the zero-mean random process $\tilde{Y}^I(t)$. The interval mean-value, μ_Y^I, that, without loss of generality, is herein assumed positive $(\mu_Y^I>0)$, can be evaluated taking the stochastic average of both sides of Eq. (13), i.e.:

$$\mu_Y^I=\mathrm{E}\langle Y^I(t)\rangle=\mathbf{q}^{\mathrm{T}}(\boldsymbol{\alpha}^I)\boldsymbol{\mu}_{\mathbf{U}}^I=\mathbf{q}^{\mathrm{T}}(\boldsymbol{\alpha}^I)\left(\mathbf{K}^I\right)^{-1}\boldsymbol{\mu}_{\mathbf{F}} \tag{14}$$

with $\mathrm{E}\langle\bullet\rangle$ denoting the stochastic average operator and $\boldsymbol{\mu}_{\mathbf{U}}^{I}$ the interval mean-value of the displacement vector $\mathbf{U}^{I}(t)$. Based on Eq. (13), the interval *PSD* function of the zero-mean response process $\tilde{Y}^{I}(t)$ reads [14]:

$$G_{\tilde{Y}\tilde{Y}}^{I}(\omega)=\mathbf{q}^{\mathrm{T}}(\boldsymbol{\alpha}^{I})\mathbf{G}_{\mathbf{UU}}^{I}(\omega)\mathbf{q}^{\mathrm{T}}(\boldsymbol{\alpha}^{I})=\mathbf{q}^{\mathrm{T}}(\boldsymbol{\alpha}^{I})\mathbf{H}^{*}(\boldsymbol{\alpha}^{I},\omega)\mathbf{G}_{\tilde{\mathbf{X}}_{\mathbf{F}}\tilde{\mathbf{X}}_{\mathbf{F}}}(\omega)\mathbf{H}^{\mathrm{T}}(\boldsymbol{\alpha}^{I},\omega)\mathbf{q}^{\mathrm{T}}(\boldsymbol{\alpha}^{I})\equiv G_{YY}^{I}(\omega) \tag{15}$$

where the asterisk denotes complex conjugate; $\mathbf{G}_{\tilde{\mathbf{X}}_{\mathbf{F}}\tilde{\mathbf{X}}_{\mathbf{F}}}(\omega)$ is the *PSD* function matrix of the zero-mean stationary Gaussian stochastic process, $\tilde{\mathbf{X}}_{\mathbf{F}}(t)$, describing the random fluctuation of the input process, i.e. $\mathbf{F}(t)=\boldsymbol{\mu}_{\mathbf{F}}+\tilde{\mathbf{X}}_{\mathbf{F}}(t)$; $\mathbf{H}^{I}(\omega)\equiv\mathbf{H}(\boldsymbol{\alpha}^{I},\omega)$ is the interval *frequency response function* (*FRF*) matrix (also referred to as *transfer function matrix*), defined as:

$$\mathbf{H}^{I}(\omega)\equiv\mathbf{H}(\boldsymbol{\alpha}^{I},\omega)=\left[-\omega^{2}\mathbf{M}+\mathrm{j}\omega\mathbf{C}^{I}+\mathbf{K}^{I}\right]^{-1} \tag{16}$$

with $\mathrm{j}=\sqrt{-1}$ denoting the imaginary unit.

4 Bounds of interval normal stress characteristics of truss structures

4.1 Interval mean-value

In the case of truss structures, having *n*-DOFs, composed of *s* bar elements, indicating with $\rho_j=E_jA_j/L_j$ the axial stiffness of the *j*-th bar element, assuming that $r\le s$ elements possess uncertain-but-bounded axial stiffness and denoting with $\Delta\alpha_j$ the symmetric fluctuation of the uncertain axial stiffness around the nominal value $\rho_{0,j}=E_{0,j}A_{0,j}/L_{0,j}$, one gets

$$\rho_j^{I}=\rho_{0,j}(1+\Delta\alpha_j\hat{e}_j^{I}) \tag{17}$$

where $j=1,2,\ldots,r\le s$ and $\hat{e}_j^{I}$ is the *EUI*. It follows that the $n\times n$ stiffness matrix can be defined as:

$$\mathbf{K}^{I}\equiv\mathbf{K}(\boldsymbol{\alpha}^{I})=\mathbf{K}_0+\sum_{j=1}^{r}\Delta\alpha_j\hat{e}_j^{I}\ \mathbf{w}_j\mathbf{w}_j^{T} \tag{18}$$

where $\mathbf{w}_j=\mathbf{l}_j\mathbf{S}$, with $\mathbf{l}_j$ denoting a vector of order *s* with only the *j*-th element equal to $\sqrt{\rho_{0,j}}$ and the other ones equal to zero, and $\mathbf{S}^{T}$ being the $n\times s$ equilibrium matrix. In Eq.(18), $\mathbf{K}_0=\sum_{j=1}^{s}\mathbf{w}_j\mathbf{w}_j^{T}$ is the nominal stiffness matrix. Notice that the product $\mathbf{w}_j\mathbf{w}_j^{\mathrm{T}}$ gives a change of rank one to the nominal stiffness matrix.

Let us denote now with $Y_h(\boldsymbol{\alpha}^{I},t)$ the stationary normal stress process in the *h*-th bar element of the truss structure. According to Eq.(13), it can be written as [21]:

$$Y_h(\boldsymbol{\alpha}^{I},t)\equiv Y_h^{I}(t)=\mathbf{q}^{\mathrm{T}}\left(\alpha_h^{I}\right)\mathbf{U}(\boldsymbol{\alpha}^{I},t)=(1+\Delta\alpha_h\hat{e}_h^{I})\frac{\rho_{0,h}}{A_{0,h}}\mathbf{s}_h^{\mathrm{T}}\mathbf{U}(\boldsymbol{\alpha}^{I},t) \tag{19}$$

where $\mathbf{s}_h^{\mathrm{T}}$ is the *h*-th row of the compatibility matrix $\mathbf{S}$. The interval mean-value of the stationary normal stress process $\mu_{Y_h}^{I}\equiv\mu_{Y_h}\left(\boldsymbol{\alpha}^{I}\right)=\mathrm{E}\left\langle Y_h(\boldsymbol{\alpha}^{I},t)\right\rangle$ is given by :

$$\mu_{Y_h}^I = \mathbf{q}^{\mathrm{T}}\left(\alpha_h^I\right)\mathbf{K}^{-1}\left(\boldsymbol{\alpha}^I\right)\boldsymbol{\mu}_{\mathbf{F}} = \left(1+\Delta\alpha_h\hat{e}_h^I\right)\frac{\rho_{0,h}}{A_{0,h}}\mathbf{s}_h^{\mathrm{T}}\,\mathbf{K}^{-1}\left(\boldsymbol{\alpha}^I\right)\boldsymbol{\mu}_{\mathbf{F}} \tag{20}$$

where $\boldsymbol{\mu}_{\mathbf{F}}$ is the mean-value vector of the stationary multi-correlated Gaussian stochastic process $\mathbf{F}(t)$. To evaluate the inverse of the interval stiffness matrix, the *Interval Rational Series Expansion* (*IRSE*) [14] can be applied. According to the *IRSE*, once the deviation of the interval stiffness matrix $\mathbf{K}^I$, with respect to the nominal value $\mathbf{K}_0$, is written as superposition of rank-one matrices (see Eq. (18)), the following relationship is obtained:

$$\mathbf{K}^{-1}(\boldsymbol{\alpha}^I) = \left(\mathbf{K}_0 + \sum_{i=1}^{r}\Delta\alpha_i\,\hat{e}_i^I\mathbf{w}_i\,\mathbf{w}_i^{\mathrm{T}}\right)^{-1} \approx \mathbf{K}_0^{-1} - \sum_{i=1}^{r}\frac{\Delta\alpha_i\,\hat{e}_i^I}{1+\Delta\alpha_i\,\hat{e}_i^I d_i}\mathbf{D}_i = \mathbf{K}_0^{-1} + \sum_{i=1}^{r}\left(\tilde{a}_{0,i} - \Delta\tilde{a}_i\,\hat{e}_i^I\right)\mathbf{D}_i \tag{21}$$

where:

$$d_i = \mathbf{w}_i^{\mathrm{T}}\mathbf{K}_0^{-1}\mathbf{w}_i > 0\,; \qquad \mathbf{D}_i = \mathbf{K}_0^{-1}\mathbf{w}_i\,\mathbf{w}_i^{\mathrm{T}}\mathbf{K}_0^{-1}. \tag{22a,b}$$

while $\tilde{a}_{0,i}$ and $\Delta\tilde{a}_i$ are given by [14]:

$$\begin{aligned}\tilde{a}_{0,i} &= \frac{\left(\Delta\alpha_i\right)^2 d_i}{1-\left(\Delta\alpha_i\,d_i\right)^2} > 0;\\ \Delta\tilde{a}_{0,i} &= \frac{\Delta\alpha_i}{1-\left(\Delta\alpha_i\,d_i\right)^2} > 0.\end{aligned} \tag{23a,b}$$

By substituting Eq.(21) into Eq.(20), the following relationship is obtained:

$$\mu_{Y_h}^I = \left(1+\Delta\alpha_h\hat{e}_h^I\right)\frac{\rho_{0,h}}{A_{0,h}}\mathbf{s}_h^T\left[\mathbf{K}_0^{-1} + \sum_{i=1}^{r}\tilde{a}_{0,\mathrm{i}}\mathbf{D}_i - \sum_{i=1}^{r}\Delta\tilde{a}_i\hat{e}_i^I\mathbf{D}_i\right]\boldsymbol{\mu}_{\mathbf{F}}. \tag{24}$$

It is worth observing that the interval mean-value of the stationary normal stress process $\mu_{Y_h}^I$ is more affected by the *dependency phenomenon* than the interval displacement vector $\mathbf{U}^I(t)$ due to the double occurrence of the *EUI*, $\hat{e}_h^I$, associated with the h-th uncertain parameter [22]. In order to limit the effects of the *dependency phenomenon*, Eq. (24) is rewritten in the following form:

$$\mu_{Y_h}^I = \mathrm{mid}\left\{\mu_{Y_h}^I\right\} + \mu_{Y_h}^{\mathrm{D}}\hat{e}_h^I - \left(1+\Delta\alpha_h\hat{e}_h^I\right)\frac{\rho_{0,h}}{A_{0,h}}\mathbf{s}_h^T\sum_{\substack{i=1\\ i\neq h}}^{r}\Delta\tilde{a}_i\hat{e}_i^I\mathbf{D}_i\boldsymbol{\mu}_{\mathbf{F}} \tag{25}$$

where the midpoint of the interval mean-value $\mu_{Y_h}^I$ of the random interval normal stress process $Y_h^I(t)$, $\mathrm{mid}\left\{\mu_{Y_h}^I\right\}$, and $\mu_{Y_h}^{\mathrm{D}}$ are defined as:

$$\begin{aligned}\mathrm{mid}\left\{\mu_{Y_h}^I\right\} &= \frac{\rho_{0,h}}{A_{0,h}}\mathbf{s}_h^T\left[\mathbf{K}_0^{-1} + \sum_{i=1}^{r}\tilde{a}_{0,i}\mathbf{D}_i - \Delta\alpha_h\Delta\tilde{a}_h\mathbf{D}_h\right]\boldsymbol{\mu}_{\mathbf{F}};\\ \mu_{Y_h}^{\mathrm{D}} &= \frac{\rho_{0,h}}{A_{0,h}}\mathbf{s}_h^T\left[\Delta\alpha_h\mathbf{K}_0^{-1} + \Delta\alpha_h\sum_{i=1}^{r}\tilde{a}_{0,i}\mathbf{D}_i - \Delta\tilde{a}_h\mathbf{D}_h\right]\boldsymbol{\mu}_{\mathbf{F}}.\end{aligned} \tag{26a,b}$$

By applying the philosophy of the *IIA* via *EUI* to Eq.(25), the *LB*, $\underline{\mu}_{Y_h}$, and the *UB*, $\overline{\mu}_{Y_h}$, of the interval mean-value $\mu_{Y_h}^I$ of the random normal stress process are evaluated adding to its midpoint, $\mathrm{mid}\left\{\mu_{Y_h}^I\right\}$, the minimum and maximum, respectively, among all possible combinations of other quantities depending on the *EUI*s, once the contribution of the h-th uncertain parameter is isolated from the remaining ones [22]. It can be easily proved that these bounds can be evaluated, respectively, as

$$\begin{aligned}\underline{\mu}_{Y_h} &= \mathrm{mid}\left\{\mu_{Y_h}^I\right\} + \min\left\{-\mu_{Y_h}^{\mathrm{D}} + (1-\Delta\alpha_h)\Delta\mu_{Y_h}^{\mp},\quad \mu_{Y_h}^{\mathrm{D}} + (1+\Delta\alpha_h)\Delta\mu_{Y_h}^{\mp}\right\};\\ \overline{\mu}_{Y_h} &= \mathrm{mid}\left\{\mu_{Y_h}^I\right\} + \max\left\{-\mu_{Y_h}^{\mathrm{D}} + (1-\Delta\alpha_h)\Delta\mu_{Y_h}^{\mp},\quad \mu_{Y_h}^{\mathrm{D}} + (1+\Delta\alpha_h)\Delta\mu_{Y_h}^{\mp}\right\}\end{aligned} \tag{27a,b}$$

where the symbols $\min\{\bullet\}$ and $\max\{\bullet\}$ mean minimum and maximum value of the quantity into curly parentheses, respectively, and

$$\Delta\mu_{Y_h}^{\mp} = \mp\Delta\tilde{a}_i \frac{\rho_{0,h}}{A_{0,h}} \sum_{\substack{i=1\\ i\neq h}}^{r} \left|\mathbf{s}_h^T \mathbf{D}_i\, \boldsymbol{\mu}_{\mathbf{F}}\right|. \tag{28}$$

In this equation, the symbol $|\bullet|$ means absolute value, while the superscript minus or plus is related to the sign of the summation of absolute values.

4.2 Interval spectral moments

Approximate expressions of the interval spectral moments $\lambda_{Y_h,\ell}^I \equiv \lambda_{Y_h,\ell}\left(\boldsymbol{\alpha}^I\right)$ of the stationary random normal stress process, $Y_h^I(t)$, along with their bounds are evaluated in this section. According to the definition by Vanmarcke [23], the interval spectral moments of ℓ-th order of the stationary random interval stress process $Y_h^I(t)$ is defined as:

$$\lambda_{Y_h,\ell}^I = \int_0^\infty \omega^\ell G_{Y_hY_h}^I(\omega)\,\mathrm{d}\omega = \rho_{0,h}^2\left(1+\Delta\alpha_h\hat{e}_h^I\right)^2 \int_0^\infty \omega^\ell\, \mathbf{s}_h^{\mathrm{T}}\, \mathbf{H}^*\left(\boldsymbol{\alpha}^I,\omega\right)\mathbf{G}_{\tilde{\mathbf{X}}_{\mathbf{F}}\tilde{\mathbf{X}}_{\mathbf{F}}}(\omega)\mathbf{H}^{\mathrm{T}}\left(\boldsymbol{\alpha}^I,\omega\right)\mathbf{s}_h\,\mathrm{d}\omega. \tag{29}$$

In order to evaluate this integral, first an approximate analytical form of the interval *FRF* function matrix $\mathbf{H}^I(\omega)$ is derived by applying the *IRSE* [14,15]. To this aim, taking into account the decomposition (18) of the interval stiffness matrix, the interval damping matrix in Eq.(12) can be decomposed as:

$$\mathbf{C}^I \equiv \mathbf{C}(\boldsymbol{\alpha}^I) = \mathbf{C}_0 + c_1 \sum_{j=1}^{r} \Delta\alpha_j \hat{e}_j^I \mathbf{w}_j \mathbf{w}_j^{\mathrm{T}}, \tag{30}$$

where $\mathbf{C}_0 = c_0\mathbf{M} + c_1\mathbf{K}_0$ is the nominal damping matrix. By applying the *IRSE* [14,15], the following approximate explicit form of the interval *FRF* is obtained:

$$\mathbf{H}^I(\omega) \equiv \mathbf{H}(\boldsymbol{\alpha}^I,\omega) = \left[\mathbf{H}_0^{-1}(\omega) + p(\omega)\sum_{i=1}^{r}\Delta\alpha_i\,\hat{e}_i^I\,\mathbf{w}_i\;\mathbf{w}_i^{\mathrm{T}}\right]^{-1} \approx \mathbf{H}_{\mathrm{mid}}\left(\omega\right) + \mathbf{H}_{\mathrm{dev}}(\boldsymbol{\alpha}^I,\omega) \tag{31}$$

where $\mathbf{H}_{\mathrm{mid}}(\omega)$ and $\mathbf{H}_{\mathrm{dev}}^I(\omega)$ are two complex function matrices listing the midpoint and the interval deviation of the elements of $\mathbf{H}(\boldsymbol{\alpha},\omega)$, respectively, defined as:

$$\begin{aligned}\mathbf{H}_{\mathrm{mid}}\left(\omega\right) &= \mathbf{H}_0(\omega) + \sum_{i=1}^{r} a_{0,i}(\omega)\mathbf{B}_i(\omega);\\ \mathbf{H}_{\mathrm{dev}}^I\left(\omega\right) &\equiv \mathbf{H}_{\mathrm{dev}}(\boldsymbol{\alpha}^I,\omega) = -\sum_{i=1}^{r}\Delta a_i(\omega)\hat{e}_i^I\mathbf{B}_i(\omega),\end{aligned} \tag{32a,b}$$

$a_{0,i}(\omega)$ and $\Delta a_i(\omega)$ being complex functions, given respectively, by:

$$\begin{aligned}a_{0,i}(\omega) &= \frac{\left(p(\omega)\Delta\alpha_i\right)^2 b_i(\omega)}{1-\left(p(\omega)\Delta\alpha_i\, b_i(\omega)\right)^2};\\ \Delta a_i(\omega) &= \frac{p(\omega)\Delta\alpha_i}{1-\left(p(\omega)\Delta\alpha_i\, b_i(\omega)\right)^2}.\end{aligned} \tag{33a,b}$$

and

$$p(\omega) = \left(1 + \mathrm{j}\omega c_1\right); \quad b_i(\omega) = \mathbf{w}_i^{\mathrm{T}} \mathbf{H}_0(\omega)\, \mathbf{w}_i; \quad \mathbf{B}_i(\omega) = \mathbf{H}_0(\omega)\, \mathbf{w}_i\ \mathbf{w}_i^{\mathrm{T}} \mathbf{H}_0(\omega). \tag{34a-c}$$

In the previous equations, $\mathbf{H}_0(\omega)$ is the nominal *FRF* matrix. Under the assumption of classically damped nominal structural system, the *FRF* matrix $\mathbf{H}_0(\omega)$ can be conveniently evaluated as:

$$\mathbf{H}_0(\omega) = \mathbf{\Phi}_0\, \mathbf{H}_{0,\mathrm{m}}(\omega) \mathbf{\Phi}_0^{\mathrm{T}} \tag{35}$$

where $\mathbf{\Phi}_0$ is the nominal modal matrix of order $n \times m$ ($m \le n$) collecting the first m eigenvectors normalized with respect to the mass matrix $\mathbf{M}$. The matrix $\mathbf{\Phi}_0$ is obtained as solution of the following eigenproblem:

$$\mathbf{K}_0 \mathbf{\Phi}_0 = \mathbf{M} \mathbf{\Phi}_0\, \mathbf{\Omega}_0^2; \quad \mathbf{\Phi}_0^{\mathrm{T}} \mathbf{M} \mathbf{\Phi}_0 = \mathbf{I}_m \tag{36a,b}$$

where $\mathbf{\Omega}_0^2 = \mathbf{\Phi}_0^{\mathrm{T}} \mathbf{K}_0 \mathbf{\Phi}_0$ is the spectral matrix of the nominal structural system, say a diagonal matrix listing the squares of the natural circular frequencies of the structure for the nominal values of the uncertain parameters. Furthermore, in Eq. (35) $\mathbf{H}_{0,\mathrm{m}}(\omega)$ denotes the modal *FRF* function matrix of the nominal structure that is a diagonal matrix given by:

$$\mathbf{H}_{0,\mathrm{m}}(\omega) = \left[-\omega^2 \mathbf{I}_m + \mathrm{j}\omega \mathbf{\Xi}_0 + \mathbf{\Omega}_0^2 \right]^{-1} \tag{37}$$

where $\mathbf{\Xi}_0 = c_0 \mathbf{I}_m + c_1 \mathbf{\Omega}_0$ is the generalised damping matrix. Substituting the interval *FRF* function matrix written in the form (31) into Eq.(15), where $Y^I(t) \equiv Y_h^I(t)$, and neglecting higher order terms, the interval *PSD* function matrix of the normal stress, $G_{Y_h Y_h}^I(\omega)$, can be expressed in approximate form as follows [14]:

$$\begin{aligned} G_{Y_h Y_h}^I(\omega) = \left(1 + \Delta\alpha_h \hat{e}_h^I\right)^2 \frac{\rho_{0,h}^2}{A_{0,h}^2} \mathbf{s}_h^{\mathrm{T}} \Big\{ & \mathbf{H}_{\mathrm{mid}}^*(\omega) \mathbf{G}_{\tilde{\mathbf{X}}_\mathbf{F} \tilde{\mathbf{X}}_\mathbf{F}}(\omega) \mathbf{H}_{\mathrm{mid}}^{\mathrm{T}}(\omega) \\ & + \sum_{i=1}^{r} \left[\mathbf{H}_{\mathrm{mid}}^*(\omega) \mathbf{G}_{\tilde{\mathbf{X}}_\mathbf{F} \tilde{\mathbf{X}}_\mathbf{F}}(\omega) \mathbf{R}_i^{\mathrm{T}}(\omega) + \mathbf{R}_i^*(\omega) \mathbf{G}_{\tilde{\mathbf{X}}_\mathbf{F} \tilde{\mathbf{X}}_\mathbf{F}}(\omega) \mathbf{H}_{\mathrm{mid}}^{\mathrm{T}}(\omega) \right] \hat{e}_i^I \Big\} \mathbf{s}_h \end{aligned} \tag{38}$$

where $\mathbf{R}_i(\omega)$ is the complex matrix defined as:

$$\mathbf{R}_i(\omega) = -\Delta a_i(\omega) \mathbf{B}_i(\omega). \tag{39}$$

Also the interval *PSD* function matrix of the normal stress, $G_{Y_h Y_h}^I(\omega)$, is more affected by the *dependency phenomenon* than the one of the interval displacements, due to the double occurrence of the *EUI*, $\hat{e}_h^I$, associated with the h-th uncertain parameter. In order to limit the effects of this phenomenon, Eq. (38) is rewritten in the following form:

$$\begin{aligned} G_{Y_h Y_h}^I(\omega) = & \operatorname{mid}\left\{ G_{Y_h Y_h}^I(\omega) \right\} + \hat{e}_h^I\, G_{Y_h Y_h}^{\mathrm{D}}(\omega) \\ & + \left(1 + \Delta\alpha_h \hat{e}_h^I\right)^2 \frac{\rho_{0,h}^2}{A_{0,h}^2} \mathbf{s}_h^{\mathrm{T}} \left\{ \sum_{\substack{i=1 \\ i \ne h}}^{r} \left[\mathbf{H}_{\mathrm{mid}}^*(\omega) \mathbf{G}_{\tilde{\mathbf{X}}_\mathbf{F} \tilde{\mathbf{X}}_\mathbf{F}}(\omega) \mathbf{R}_i^{\mathrm{T}}(\omega) + \mathbf{R}_i^*(\omega) \mathbf{G}_{\tilde{\mathbf{X}}_\mathbf{F} \tilde{\mathbf{X}}_\mathbf{F}}(\omega) \mathbf{H}_{\mathrm{mid}}^{\mathrm{T}}(\omega) \right] \hat{e}_i^I \right\} \mathbf{s}_h \end{aligned} \tag{40}$$

where the following quantities have been introduced:

$$\begin{aligned}\operatorname{mid}\left\{G^I_{Y_hY_h}(\omega)\right\} &= \frac{\rho^2_{0,h}}{A^2_{0,h}}\mathbf{s}_h^{\mathrm{T}}\Big\{\left(1+\Delta\alpha_h{}^2\right)\mathbf{H}^*_{\mathrm{mid}}(\omega)\mathbf{G}_{\tilde{\mathbf{X}}_\mathbf{F}\tilde{\mathbf{X}}_\mathbf{F}}(\omega)\mathbf{H}^{\mathrm{T}}_{\mathrm{mid}}(\omega)\\ &\quad + 2\Delta\alpha_k\left[\mathbf{H}^*_{\mathrm{mid}}(\omega)\mathbf{G}_{\tilde{\mathbf{X}}_\mathbf{F}\tilde{\mathbf{X}}_\mathbf{F}}(\omega)\mathbf{R}^{\mathrm{T}}_k(\omega)+\mathbf{R}^*_k(\omega)\mathbf{G}_{\tilde{\mathbf{X}}_\mathbf{F}\tilde{\mathbf{X}}_\mathbf{F}}(\omega)\mathbf{H}^{\mathrm{T}}_{\mathrm{mid}}(\omega)\right]\Big\}\mathbf{s}_h;\\ G^{\mathrm{D}}_{Y_hY_h}(\omega) &= \frac{\rho^2_{0,h}}{A^2_{0,h}}\mathbf{s}_h^{T}\Big\{2\Delta\alpha_h\,\mathbf{H}^*_{\mathrm{mid}}(\omega)\mathbf{G}_{\tilde{\mathbf{X}}_\mathbf{F}\tilde{\mathbf{X}}_\mathbf{F}}(\omega)\mathbf{H}^{\mathrm{T}}_{\mathrm{mid}}(\omega)\\ &\quad +\left(1+\Delta\alpha_h{}^2\right)\left[\mathbf{H}^*_{\mathrm{mid}}(\omega)\mathbf{G}_{\tilde{\mathbf{X}}_\mathbf{F}\tilde{\mathbf{X}}_\mathbf{F}}(\omega)\mathbf{R}^{\mathrm{T}}_h(\omega)+\mathbf{R}^*_h(\omega)\mathbf{G}_{\tilde{\mathbf{X}}_\mathbf{F}\tilde{\mathbf{X}}_\mathbf{F}}(\omega)\mathbf{H}^{\mathrm{T}}_{\mathrm{mid}}(\omega)\right]\Big\}\mathbf{s}_h.\end{aligned} \tag{41a,b}$$

By applying the philosophy of the *IIA* via *EUI* to Eq.(40), the *LB*, $\underline{G}_{Y_hY_h}(\omega)$, and the *UB*, $\overline{G}_{Y_hY_h}(\omega)$, of the interval *PSD* function $G^I_{Y_hY_h}(\omega)$ of the random stationary normal stress process can be evaluated adding to its midpoint, $\operatorname{mid}\left\{G^I_{Y_hY_h}(\omega)\right\}$, the minimum and maximum, respectively, among all possible combinations of other quantities depending on the *EUI*s, once the contribution of the h-th uncertain parameter is isolated from the remaining ones. Then, after some algebra, these bounds can be evaluated as:

$$\begin{aligned}\underline{G}_{Y_hY_h}(\omega) &= \operatorname{mid}\left\{G^I_{Y_hY_h}(\omega)\right\}+\min\left\{-G^{\mathrm{D}}_{Y_hY_h}(\omega)+(1-\Delta\alpha_h)^2\Delta G^{\pm}_{Y_hY_h}(\omega),\quad G^{\mathrm{D}}_{Y_hY_h}(\omega)+(1+\Delta\alpha_h)^2\Delta G^{\pm}_{Y_hY_h}(\omega)\right\};\\ \overline{G}_{Y_kY_k}(\omega) &= \operatorname{mid}\left\{G^I_{Y_hY_h}(\omega)\right\}+\max\left\{-G^{\mathrm{D}}_{Y_hY_h}(\omega)+(1-\Delta\alpha_h)^2\Delta G^{\pm}_{Y_hY_h}(\omega),\quad G^{\mathrm{D}}_{Y_hY_h}(\omega)+(1+\Delta\alpha_h)^2\Delta G^{\pm}_{Y_hY_h}(\omega)\right\}\end{aligned} \tag{42a,b}$$

where

$$\Delta G^{\pm}_{Y_hY_h}(\boldsymbol{\alpha},\omega) = \pm\frac{\rho^2_{0,h}}{A^2_{0,h}}\sum_{\substack{i=1\\ i\neq h}}^{r}\left|\mathbf{s}_h^{\mathrm{T}}\left[\mathbf{H}^*_{\mathrm{mid}}(\omega)\mathbf{G}_{\tilde{\mathbf{X}}_\mathbf{F}\tilde{\mathbf{X}}_\mathbf{F}}(\omega)\mathbf{R}^{\mathrm{T}}_i(\omega)+\mathbf{R}^*_i(\omega)\mathbf{G}_{\tilde{\mathbf{X}}_\mathbf{F}\tilde{\mathbf{X}}_\mathbf{F}}(\omega)\mathbf{H}^{\mathrm{T}}_{\mathrm{mid}}(\omega)\right]\mathbf{s}_h\right|. \tag{43}$$

Finally, taking into account Eq.(29), the *LB*, $\underline{\lambda}_{Y_h,\ell}$, and the *UB*, $\overline{\lambda}_{Y_h,\ell}$, of the interval spectral moment $\lambda^I_{Y_h,\ell}\equiv\lambda_{Y_h,\ell}\left(\boldsymbol{\alpha}^I\right)$ of the random normal stress process can be evaluated, respectively, as:

$$\begin{aligned}\underline{\lambda}_{Y_h,\ell} &= \operatorname{mid}\left\{\lambda^I_{Y_h,\ell}\right\}+\min\left\{-\lambda^{\mathrm{D}}_{Y_h,\ell}+\left(1-\Delta\alpha_h\right)^2\Delta\lambda^{\pm}_{Y_h,\ell},\quad \lambda^{\mathrm{D}}_{Y_h,\ell}+\left(1+\Delta\alpha_h\right)^2\Delta\lambda^{\pm}_{Y_h,\ell}\right\};\\ \overline{\lambda}_{Y_h,\ell} &= \operatorname{mid}\left\{\lambda^I_{Y_h,\ell}\right\}+\max\left\{-\lambda^{\mathrm{D}}_{Y_h,\ell}+\left(1-\Delta\alpha_h\right)^2\Delta\lambda^{\pm}_{Y_h,\ell},\quad \lambda^{\mathrm{D}}_{Y_h,\ell}+\left(1+\Delta\alpha_h\right)^2\Delta\lambda^{\pm}_{Y_h,\ell}\right\}\end{aligned} \tag{44a,b}$$

where:

$$\begin{aligned}&\operatorname{mid}\left\{\lambda^I_{Y_h,\ell}\right\} = \int_0^\infty\omega^\ell\operatorname{mid}\left\{G^I_{Y_hY_h}(\omega)\right\}\mathrm{d}\omega;\\ &\lambda^{\mathrm{D}}_{Y_h,\ell} = \int_0^\infty\omega^\ell\,G^{\mathrm{D}}_{Y_hY_h}(\omega)\,\mathrm{d}\omega;\\ &\Delta\lambda^{\pm}_{Y_h,\ell} = \pm\frac{\rho^2_{0,h}}{A^2_{0,h}}\sum_{\substack{i=1\\ i\neq h}}^{r}\left|\int_0^\infty\omega^\ell\left[\mathbf{s}_h^{\mathrm{T}}\mathbf{H}^*_{\mathrm{mid}}(\omega)\mathbf{G}_{\tilde{\mathbf{X}}_\mathbf{F}\tilde{\mathbf{X}}_\mathbf{F}}(\omega)\mathbf{R}^{\mathrm{T}}_i(\omega)+\mathbf{R}^*_i(\omega)\mathbf{G}_{\tilde{\mathbf{X}}_\mathbf{F}\tilde{\mathbf{X}}_\mathbf{F}}(\omega)\mathbf{H}^{\mathrm{T}}_{\mathrm{mid}}(\omega)\mathbf{s}_h\right]\mathrm{d}\omega\right|.\end{aligned} \tag{45a,c}$$

4.3 Interval expected fatigue life

In this study, it is assumed that the linear structural system subjected to multi-correlated stationary Gaussian random excitation is affected by uncertainties in structural parameters. These uncertainties are modeled as interval quantities. It follows that the structural response is a multi-correlated stochastic stationary process characterized by interval mean-value and interval *PSD* function matrix. Since the interval model is adopted to describe the uncertain structural parameters, the *expected fatigue life* is an

interval quantity too, T_{F}^{I}, with a *LB* (the worst case), $\underline{T}_{\mathrm{F}}$, and an *UB*, $\overline{T}_{\mathrm{F}}$. The interval *expected fatigue life* for the selected response process, $Y_h^I(t)$, is here evaluated considering an appropriate combinations of the bounds of the pertinent interval spectral moments by extending the solution proposed by Benasciutti and Tovo [1] in the case of deterministic structural parameters. According to Eq.(7), since in practical applications $k > 3$, in the framework of the *IIA* via *EUI*, the *LB* and *UB* of the interval *expected fatigue life*, T_{F,Y_h}^{I}, for the h-th stress random process $Y_h^I(t)$ can be evaluated as:

$$\underline{T}_{\mathrm{F},Y_h} = \frac{\pi C}{\sqrt{2^{(k-2)}}\,\Gamma\left(1+\frac{k}{2}\right)} \frac{\underline{\lambda}_{Y_h,1.5}}{\overline{\lambda}^{2}_{Y_h,0.75}} \sqrt{\frac{\overline{\lambda}^{3-k}_{Y_h,0}}{\overline{\lambda}_{Y_h,2}}};$$
$$\overline{T}_{\mathrm{F},Y_h} = \frac{\pi C}{\sqrt{2^{(k-2)}}\,\Gamma\left(1+\frac{k}{2}\right)} \frac{\overline{\lambda}_{Y_h,1.5}}{\underline{\lambda}^{2}_{Y_h,0.75}} \sqrt{\frac{\underline{\lambda}^{3-k}_{Y_h,0}}{\underline{\lambda}_{Y_h,2}}} \tag{46a,b}$$

where the bounds of the interval spectral moments of the selected stress quantity, $\lambda_{Y_h,\ell}$ ($\ell = 0, 0.75, 1.5, 2$), are defined by Eqs.(44).

Notice that, since the mean-value and the spectral moments of the response are monotonic functions of the generic uncertain parameter α_i^I, the exact bounds of the *expected interval fatigue life*, T_{F,Y_h}^{I}, can be evaluated by applying the *vertex method*. As already mentioned, such combinatorial procedure is time consuming and becomes soon unfeasible as the number of uncertainties increases. Indeed, it requires 2^r stochastic analyses of the structure to compute response statistics corresponding to all possible combinations of the endpoints of the r interval parameters α_i^I. Conversely, the proposed approach allows one to handle an arbitrary number of uncertain parameters since it evaluates the bounds of the interval mean-value and spectral moments by handy formulas without resorting to any combinatorial procedure.

5 Numerical application

The proposed procedure is here applied to the 24-bar truss structure depicted in Figure 1 subjected to turbulent wind loads in the x-direction. The constituent material of the truss is steel with nominal Young's modulus $E_0 = E_{0,i} = 2.1\times10^8$ kN/m^2 ($i = 1,2,\ldots,24$), ultimate strength $Y_u = 725$ MPa and parameters of the *Y-N* curve (1), $k = 3.324$ and $C = 1.934\times10^{12}$ MPa^k [24]. The cross-sectional areas of all the bars of the nominal structure are the same and equal to $A_0 = A_{0,i} = 5\times10^{-4}$ m^2. The nominal lengths of the bars $L_{0,i} = L_i$, $i = 1,2,\ldots,24$ can be obtained from Figure 1, where $L = 3$. Moreover, the nominal lumped mass pertaining to each node is $m_{0,j} = m_0 = 500$ kg. The modal damping ratio for the first and third mode of the nominal structure is $\xi_0 = 0.05$, as a result the Rayleigh damping constants, c_0 and c_1, have been taken as $c_0 = 3.51790$ s^{-1} and $c_1 = 0.000547$ s, respectively.

As shown in Figure 1, the nodes 4, 7 and 10, located at three different levels z_i ($i = 4,7,10$), are subjected to the nodal forces $F_{x,i}$ ($i = 4,7,10$) in the along-wind direction [25]:

$$F_{x,i} = \frac{1}{2}\rho C_D A_i W^2(z_i,t) = F_{x,i}^{(s)} + \tilde{F}_{x,i}(z_i,t) \approx \frac{1}{2}\rho C_D A_i w_s^2 + \rho C_D A_i \tilde{W}(z_i,t) \quad (i = 4,7,10) \tag{47}$$

where $F_{x,i}^{(s)}$ and $\tilde{F}_{x,i}(z_i,t)$ denote the mean and random fluctuating component of wind loads, respectively; ρ is the air density; C_D is the drag coefficient; and A_i is the tributary area of the *i*-th node.

The following values of the parameters appearing in Eq. (47) are assumed: $\rho = 1.25\ \text{kg/m}^3$, $C_D = 1.2$, $A_4 = 9\,\text{m}^2$, $A_7 = 9\,\text{m}^2$, $A_{10} = 4.5\,\text{m}^2$. Moreover, in Eq.(47) $w_s(z) = w_{s,10}(z/10)^{\beta}$ with $w_{s,10}$ denoting the mean wind speed measured at height $z = 10\,\text{m}$, and $\tilde{W}(z,t)$ is the fluctuating component which is modeled as a zero-mean stationary Gaussian random process, fully described from a probabilistic point of view by the one-sided *PSD* function proposed by Davenport [26,27]:

$$G_{\tilde{W}\tilde{W}}(\omega) = 4K_0 w_{s,10}^2 \frac{\chi^2}{\omega\left(1+\chi^2\right)^{4/3}} \tag{48}$$

where $\chi = b_1\omega/(\pi w_{s,10})$. In this numerical application, when not otherwise specified, it is assumed $w_{s,10} = 25\,\text{m/s}$, $K_0 = 0.03$, $b_1 = 600\ \text{m}$ and $\beta = 0.3$. The 3-variate zero-mean stationary Gaussian random process $\tilde{\mathbf{W}}(t)$ collecting wind velocity fluctuations at the wind-exposed nodes (4, 7, 10) of the truss structure (see Figure 1) is fully characterized from a probabilistic point of view by the *PSD* function matrix $\mathbf{G}_{\tilde{\mathbf{W}}\tilde{\mathbf{W}}}(\omega)$ herein defined as reported in Ref. [14].

Young's moduli of the material of the $r = 7$ bars highlighted in Figure 1 are modeled as interval variables, i.e. $E_i^I = E_0(1+\Delta\alpha\hat{e}_i^I)$, ($i = 10,12,14,16,18,21,22$). Attention is herein focused on the evaluation of the range of the interval *expected fatigue life* $T_{F,\sigma_{16}}^I$ for the normal stress random process of bar 16 $Y_h^I(t) \equiv \sigma_{16}^I(t)$.

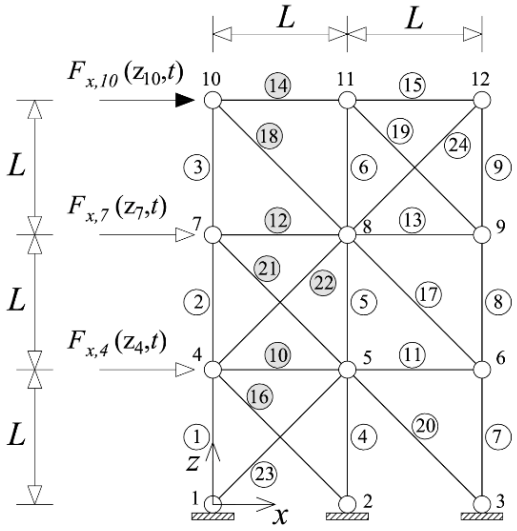


Figure 1 Truss structure under turbulent wind excitation.

First, the accuracy of the proposed approximate explicit expression of the *PSD* function $G_{\sigma_{16}\sigma_{16}}^I(\omega)$ of the interval random stress process $Y_h^I(t) \equiv \sigma_{16}^I(t)$ in Eq. (38) derived by applying the *IRSE* is assessed. To this aim, all the uncertain parameters are set simultaneously to their *UB*, i.e. $\hat{e}_i^I = +1$ ($i = 10,12,14,16,18,21,22$). Figure 2 displays the comparison between the exact *PSD* function and the approximate one provided by Eq. (38) for two different deviation amplitudes of the uncertain parameters, $\Delta\alpha = 0.1$ and $\Delta\alpha = 0.2$. A very good agreement is observed. The *PSD* function pertaining to the nominal structure is also plotted. It can be seen that the *IRSE* enables to capture the deviation of the *PSD* function from the nominal value.

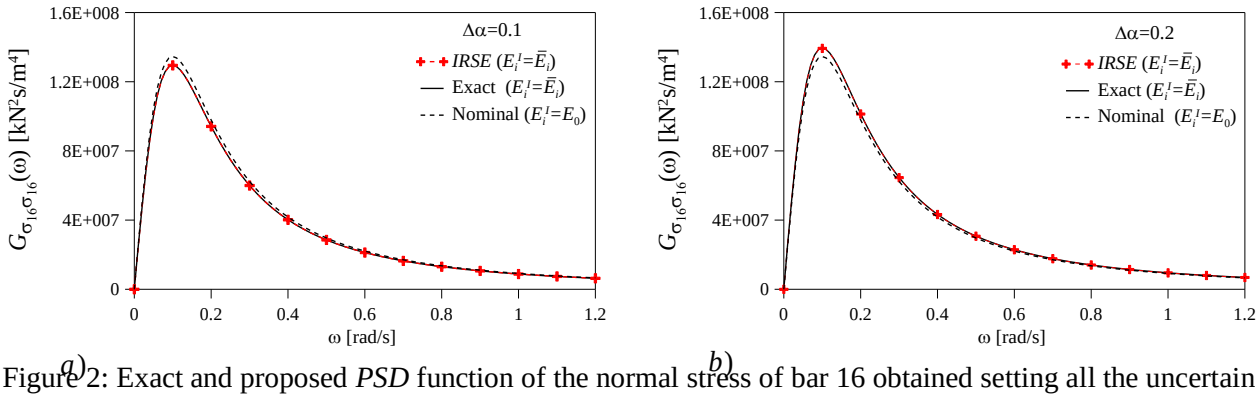


Figure 2: Exact and proposed *PSD* function of the normal stress of bar 16 obtained setting all the uncertain parameters to their *UB* for a) $\Delta\alpha = 0.1$ and b) $\Delta\alpha = 0.2$, along with the nominal *PSD* function.

Figure 3a shows the proposed bounds of the interval *expected fatigue life* $T^I_{F,\sigma_{16}}$ and the exact ones provided by the *vertex method* versus the deviation amplitude of the uncertain parameters. The nominal value of the *expected fatigue life* is also reported. Notice that the *LB* of the interval *expected fatigue life* is always smaller than the nominal value and decreases as the deviation amplitude of the uncertain parameters increases. This implies that assuming the nominal values of Young's moduli, i.e. neglecting uncertainty, may lead to serious overestimation of the fatigue life. By inspection of Figure 3a, it is observed that a very good match between the proposed and the exact bounds of $T^I_{F,\sigma_{16}}$ is achieved even when the degree of uncertainty increases. Indeed, the percentage errors affecting the proposed estimates of the bounds of the *expected fatigue life* $T^I_{F,\sigma_{16}}$, herein omitted for conciseness, are acceptable from an engineering point of view. In particular, the largest absolute percentage error affecting the *LB*, which is the quantity of interest for design purposes, is equal to 3.39% and is achieved for $\Delta\alpha = 0.2$. Furthermore, it is worth remarking that the proposed method overestimates the *LB* of the *expected fatigue life* $T^I_{F,\sigma_{16}}$ which implies a safe design.

Finally, in Figure 3b, the bounds of the interval *expected fatigue life* $T^I_{F,\sigma_{16}}$ versus the mean wind speed $w_{s,10}$ are plotted. As expected, the *LB* and the *UB* decrease as the mean wind speed $w_{s,10}$ increases, which implies that the structure is more prone to fatigue failure.

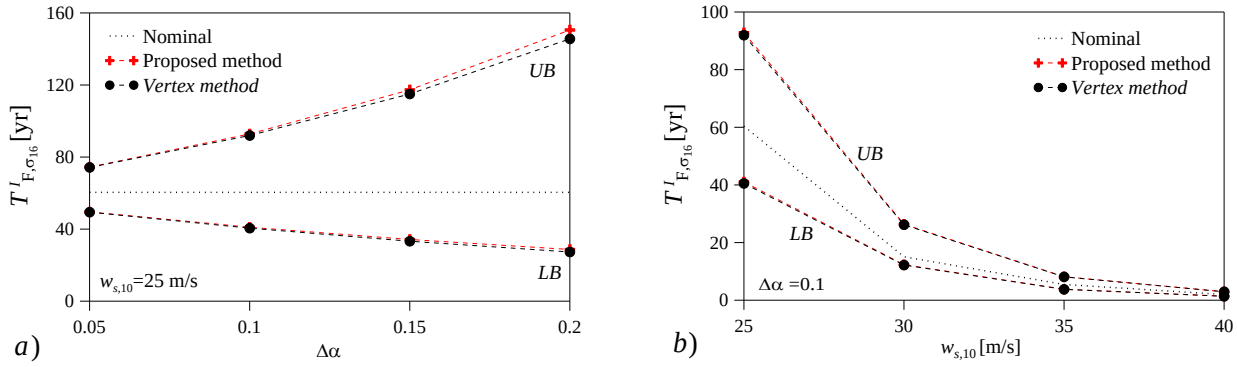


Figure 3: *LB* and *UB* of the *expected fatigue life* $T^I_{F,\sigma_{16}}$ provided by the *vertex method* and the proposed method versus a) the deviation amplitude of the uncertain parameters and b) the mean wind speed.

6 Conclusions

A novel method for estimating the region of the interval *expected fatigue life* of linear structures with uncertain-but-bounded parameters subjected to stationary multi-correlated stochastic excitations has been proposed. Without loss of generality, attention has been focused on truss structures with uncertain axial stiffness of the bars. The key idea of the proposed method is to derive the *Power Spectral Density* (*PSD*) function of a selected random stress process in approximate explicit form by applying the so-called *Interval Rational Series Expansion* (*IRSE*) [14] and then evaluate the bounds of the associated spectral moments. Specifically, in order to limit the overestimation, a novel procedure for estimating the bounds of the spectral moments has been developed in the framework of the *improved interval analysis* via *extra unitary interval* (*IIA* via *EUI*) [3]. Finally, the bounds of the interval *expected fatigue life* are evaluated by combining the method proposed by Benasciutti and Tovo [1] with the *IIA* via *EUI*.

A remarkable feature of the proposed method is the capability to provide very accurate estimates of the bounds of the spectral moments of the selected stress processes. Indeed, the evaluation of the range of stress related quantities is a quite challenging task in the framework of interval structural analysis. Furthermore, numerical results have highlighted the significant influence of the uncertain parameters on the *expected fatigue life*, which can be seriously overestimated when the nominal values of material parameters are assumed.

Acknowledgements

Support to this research by the PRIN2015, project No 2015TTJN95 entitled ‘‘Identification and monitoring of complex structural systems’’, is gratefully acknowledged.

References

[1] Benasciutti D., Tovo R., *Comparison of spectral methods for fatigue analysis of broad-band Gaussian random processes*, Probabilistic Engineering Mechanics, Vol. 21, No. 4, Academic Press (2006), pp 287-299.

[2] Muscolino G., Sofi A., *Stochastic analysis of structures with uncertain-but-bounded parameters via improved interval analysis*, Probabilistic Engineering Mechanics, Vol. 28, Academic Press (2012), pp. 152-163.

[3] Crandall S. H., Mark W. D., *Random Vibration in Mechanical Systems*, Academic Press, New York (1963).

[4] Dowling N.E., *Fatigue failure predictions for complicated stress–strain histories*, Journal of Materials, JMLSA, Vol. 7, No. 1 (1972), pp. 71–87.

[5] Lutes L.D., Sarkani S., *Random Vibrations: analysis of structural and mechanical system*, Elsevier Butterworth-Heinemann, Massachusetts (2004).

[6] Lutes L., Larsen C., *Improved Spectral Method for Variable Amplitude Fatigue Prediction*, Journal of Structural Engineering, Vol. 116, No. 4, ASCE (1990), pp. 1149-1164.

[7] Larsen C., Lutes L., *Predicting the Fatigue Life of Offshore Structures by the Single-Moment Spectral Method*, Probabilistic Engineering Mechanics, Vol. 6, No. 2, Academic Press (1991), pp. 96-108.

[8] Larsen C.E., Irvine T., *A review of spectral methods for variable amplitude fatigue prediction and new results*, Procedia Engineering, Vol. 101, Academic Press (2015), pp 243-250.

[9] Elishakoff I., Ohsaki M., *Optimization and Anti-Optimization of Structures under Uncertainty*, Imperial College Press, London (2010).

[10] Moore R. E., *Interval Analysis*, Prentice-Hall, Englewood Cliffs (1966).

[11] Moore R.E., Kearfott R.B., Cloud M.J., *Introduction to Interval Analysis*, SIAM, Philadelphia (2009).

[12] Zhu Y., Tian Y., *Fatigue evaluation of linear structures with uncertain-but-bounded parameters under stochastic excitations*, International Journal of Structural Stability and Dynamics, Vol. 18, No. 3, World Scientific (2018), pp. (1850045-1)- (1850045-32).

[13] Moens D., Vandepitte D., *A survey of non-probabilistic uncertainty treatment in finite element analysis*, Computer Methods in Applied Mechanics and Engineering, Vol. 194, No. 12-16, Academic Press (2005), pp. 1527–1555.

[14] Muscolino G., Sofi A., *Bounds for the stationary stochastic response of truss structures with uncertain-but-bounded parameters*, Mechanical Systems and Signal Processing, Vol. 37, No. 1-2, Academic Press (2013), pp. 163-181.

[15] Muscolino G., Santoro R., Sofi A., *Explicit frequency response functions of discretized structures with uncertain parameters*, Computers & Structures, Vol. 133, Academic Press (2014), pp. 64-78.

[16] Muscolino G., Santoro R., Sofi A., *Explicit sensitivities of the response of discretized structures under stationary random processes*, Probabilistic Engineering Mechanics, Vol. 35, Academic Press (2014), pp. 82-95.

[17] Muscolino G., Santoro R., Sofi A., *Explicit reliability sensitivities of linear structures with interval uncertainties under stationary stochastic excitations*, Structural Safety, Vol. 52, Part. B, Academic Press (2015), pp. 219–232.

[18] Muscolino G., Santoro R., Sofi A., *Reliability analysis of structures with interval uncertainties under stationary excitations*, Computer Methods in Applied Mechanics and Engineering, Vol. 300, Academic Press (2016), pp. 47-69.

[19] Spanos P.D., Sofi A., Wang J., Peng B., *A Method for Fatigue Analysis of Piping Systems on Topsides of FPSO Structures*, Journal of Offshore Mechanics and Arctic Engineering, Vol. 128, No. 2, ASME (2006), pp. 162-168.

[20] Li J., Chen J.B., *Stochastic Dynamics of Structures*, John Wiley & Sons, Singapore (2009).

[21] Impollonia N., Muscolino G., *Interval analysis of structures with uncertain-but-bounded axial stiffness*, Computer Methods in Applied Mechanics and Engineering, Vol. 200, No. 21-22, Academic Press (2011), pp. 1945–1962.

[22] Sofi A., Romeo E., *A novel Interval Finite Element Method based on the improved interval analysis*, Computer Methods in Applied Mechanics and Engineering, Vol. 311, Academic Press (2016), pp. 671–697.

[23] Vanmarcke E.H., *Properties of spectral moments with applications to random vibration*, Journal of the Engineering Mechanics Division, Vol 98, No. 2, ASCE (1972), pp. 425-446.

[24] Mršnik M., Slavič J., Boltežar M., *Frequency-domain methods for a vibration-fatigue-life estimation – Application to real data,* International Journal of Fatigue, Vol. 47, Academic Press (2013), pp 8-17.

[25] Simiu E., Scanlan R., *Wind effects on structures*, John Wiley & Sons, New York (1996).

[26] Davenport A. G., *The spectrum of horizontal gustiness near the ground in high winds*, Quarterly Journal of the Royal Meteorological Society, Vol.87, No. 372, Wiley-Blackwell (1961), pp. 194-211.

[27] Davenport G., *Note on the distribution of the largest value of a random function with application to gust loading*, Proceeding of the Institution of Civil Engineers, Vol. 28, No. 2, Ice publishing (1964), pp. 187-196.

Efficient bolted joint modeling for industrial applications - empirical and analytical approaches

K.-A. H. Hoppe [1], **P. Langer** [1], **S. Marburg** [1]
[1] Technical University of Munich, Faculty of Mechanical Engineering,
Chair of Vibroacoustics of Vehicles and Machines
Boltzmannstraße 15, D-85748 Garching bei München, Germany
e-mail: **alexander.hoppe@tum.de**

Abstract

Bolted joint modeling is a challenge that connects research to industrial applications. Past research has produced various analytical solutions for a bolt's effect on the response of a structure. A common industrial approach to the finite element method (FEM) solution is to couple the nodal displacement of a joint's opposing interfaces. This approach can be combined with empirical studies investigating the pressure cone diameter found in typical assemblies. At this point, an adaption of the modeling approach can be appropriate. The greatest challenge might be to find an acceptable trade-off between accuracy and applicational effort while maintaining a strong connection to the real physical effects. This paper aims to create awareness for the modeling uncertainties regarding bolted joint models for industrial use and to evaluate options that make model application more efficient. The application of completed empirical research to industrial models is investigated. A current industrial model is reviewed and compared to a new empirical-analytical model.

1 Motivation

With high production volumes and one single variant, Ford's Model T and the early Apple iPhone models may be considered as economical benchmarks. However, customer markets eventually demand increasing personalization. Expanding the product line demands either new designs or the creation of new products using existing designs. Impeding efficiency and driving costs, this is where complexity, the counterpart to the desirable simplicity, arises. Complexity in industrial production has been treated in different ways by the world's leading enterprises. SpaceX builds the Falcon Heavy from three modified 1^{st} stages of the Falcon 9 instead of coming up with one larger design. For this example, we can assume that the lower design costs outweigh the reduced revenue constituted by the lower payload capabilities compared to a more efficient new design. This concept is called modularity. Most automotive OEMs use vehicle platforms, a special case of modularity, to increase their product portfolio while controlling design costs. German car manufacturers tend to use the same drivetrain modules for several vehicle types within one category and build distinct bodies around the invariant drivetrain. This approach can lead to excessive connecting elements. Part of the japanese approach is to construct different vehicles from different categories with the same modules, but on a smaller scale. Examples are door-locks, keys, seals, and many others. The japanese approach additionally pays special attention on yet one lower level, the interface-level. The number of approved fasteners engineers can use is stated to be as low as 200 in some cases. Engineers have to file extra forms if they want to use a fastener that is not pre-approved. Comparing the number of fasteners per vehicle, the number of vehicles sold, and lastly the estimated approved number of fasteners yields how many applications one fastener model finds. This motivates engineers to determine the fastener's properties and its effect on the connected structures as accurately as possible.

Because the properties of fasteners are still challenging to predict, extensive research-effort goes towards

model-development. Ewins [5] analyzes simplifications, approximations, assumptions, and selections made in modeling processes. He discusses two types of uncertainty, aleatoric and epistemic. The first "relates to imprecision or a lack of knowledge of the precise numerical values of individual parameters", while "epistemic uncertainty refers to the inadequacy or incompleteness of a set of parameters that are used to describe behavior". He describes the appropriate modeling of joints as a major challenge within structural analysis. Ewins [5] criticizes model updating for a lack of predictability due to it being based on observed behavior and not on a description of the physical system. As has become apparent to the broader public in recent years through the hype of machine learning and artificial intelligence, additional issues that can arise within model updating are under- and over-testing. As joints present a significant epistemic uncertainty issue, the completed research notes that excessive detailing within a joint model will not necessarily be effective. The modeling process is not limited in terms of computational power, but rather through a lacking understanding of the underlying physics. Ewins [5] lists possibly missing features in current joint models as follows: non-flatness of jointed surfaces, micro-wear effects, and assembly-sequence. Hence, a focus on model-upgrading instead of model-updating is proposed.

The core idea behind this paper is to evaluate, whether there is a feasible modeling substitution for bolts. Omitting the bolt, static load-cases, as well as contact-mechanical investigations promises to save time. Data that are lost through this omission are the bolt's mass and moments of inertia, the bolt's stiffness and damping properties, its interaction with the joint members' surfaces, and the pre-stress effect. Each of these aspects will be treated in 2.

Since Weck [15] and Oexl [10] find that high-grade surface finishes promote high contact stiffnesses in the normal direction k_{N}, and since Schulz [14] acknowledges that the stiffness in tangential direction k_{T} is proportional to surface roughness, it seems plausible that these two stiffnesses could be linked with the friction coefficient μ. The authors would like to propose the following approach for replacing a part of a virtual assembly and applying its stiffness to the surfaces of the neighbouring bodies it interacts with in the real assembly:

$$k_{\mathrm{N}}(1+\mu) = k_{\text{analyt.}} \quad \text{and} \quad k_{\mathrm{T}} = \mu \cdot k_{\mathrm{N}} \tag{1}$$

where k_{N} is the normal stiffness, k_{T} is the tangential stiffness, and $k_{\text{analyt.}}$ is the calculated analytical stiffness in the load-direction of the substituted part.

2 Identification and Quantification of Joint Stiffness

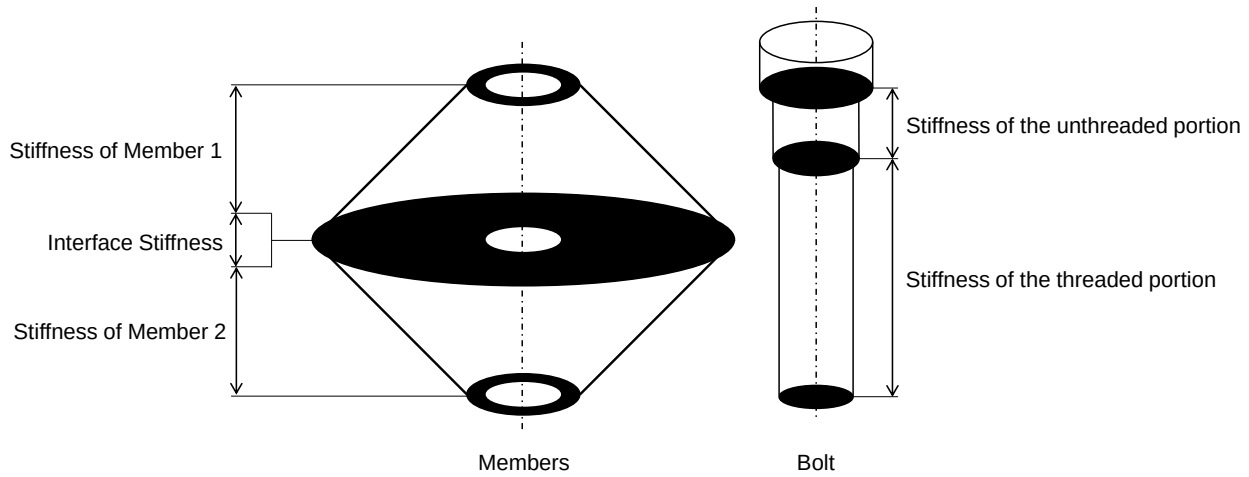


Figure 1: Stiffness components of a bolted joint. The members and the interface act as springs in series, as do the threaded and unthreaded portion of the bolt, respectively. The bolt and the member compound then act as springs in parallel. The interface stiffnesses corresponding to the contact area between bolt head and the upper member, as well as to the contact area between the threads and the lower member for tapped joint configurations, are neglected in this sketch for clarity's sake.

A lot of research is conducted in order to obtain member stiffnesses from models assuming smooth surfaces in contact. These analytical models take into account for contact at the joint interface, which is described by the clamping length, the pressure cone's starting diameter, and the pressure cone angle. Essentially, the volume under the influence of pre-stress caused by the bolt's clamping force is regarded as monolithic, while the remaining areas are assumed to be out of contact and to have no influence on additional stiffness introduced to the system through bolts. Because the surfaces in contact are modeled to be smooth, these models only put out normal stiffness, in contrast to e.g. tangential stiffness. Shigley [4] presents the commonly accepted model following up on Rötscher's [13] theories. Nawras [9] presents an improved model taking into account non-symmetrical problems as well as partially developed pressure cones, which can be caused by comparably slender beams.

Since we want to model the members and substitute the bolt, we are interested in the analytical bolt stiffness here. According to Shigley [4], the axial stiffness of the bolt can be modeled as two springs in series, composed of the threaded and the unthreaded portion of the bolt within the grip. The stiffness of the threaded region of the fastener is given as $k_\mathrm{t} = \frac{A_\mathrm{t} E}{l_\mathrm{t}}$, while the stiffness of the unthreaded region of the fastener is given as $k_\mathrm{d} = \frac{A_\mathrm{d} E}{l_\mathrm{d}}$. Hence, the overall bolt stiffness is $k_\mathrm{b} = \frac{A_\mathrm{d} A_\mathrm{t} E}{A_\mathrm{d} l_\mathrm{t} + A_\mathrm{t} l_\mathrm{d}}$.

3 Experiments

3.1 Description of test specimen

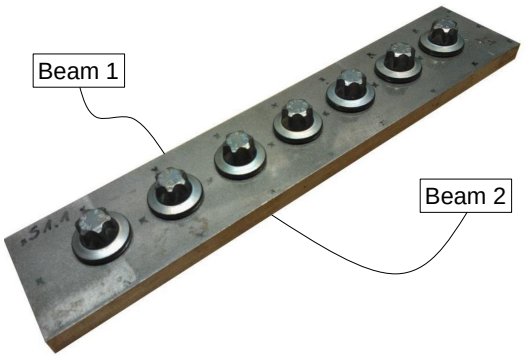


Figure 2: Test Specimen - tool steel (C45); The beams, measuring $0.2\text{m}\times0.04\text{m}\times0.004\text{m}$, are assembled via tapped joints using seven $\text{M}10\times16-10.9$ metric bolts with a nominal bolt diameter d of 0.01m, a bolt length l of 0.016m, a tensile strength R_m of $1000\,\text{N}\,\text{m}^{-2}$, and a yield strength of $900\,\text{N}\,\text{m}^{-2}$.

Figure 2 shows the investigated structure. The assembly consists of two beams that are joined by seven bolts. No washers or nuts are used in this assembly, thus we speak of a tapped joint configuration.

3.2 Experimental Modal Analysis

Experimental modal analysis (EMA) creates a linear model of a non-linear physical structure. The experimental procedure consists of the excitation, the detection, and the evaluation, according to Ewins [6]. An impulse, which is generally generated by a modal hammer and covers a frequency band up to 10 kHz, is utilized for the present structure's analysis. A laser detects the structure's surface speed, one single measurement point suffices to determine a natural frequency. However, in order to identify the corresponding mode shape, one has to include additional measurement points. By interpolating between the measurement points, the spanned sections and eventually an entire model solution can be obtained. The bolted asembly and the individual beams are analyzed with a laser Doppler vibrometer (LDV). For this purpose, a Polytec Scanning Vibrometer PSV-400 Scanning Head is used together with the PSV-Data-Acquisition-Analyser software. The data evaluation is performed by a Polytec OFV-5000 Vibrometer Controller coupled with the Polytec Data Management System and PSV-Evaluation by Polytec, as well as ME'scopeVES by Vibrant Technology.

3.3 Pressure Distribution

To visualize the pressure distribution, a two-ply FUJIFILM PRESCALE pressure measurement film for the $10\text{-}50\,\text{MPa}$ range is used. The real pressure distribution caused by a tightening torque M_A of $30\,\text{N}\,\text{m}$ is shown in pink color, cf. Figure 3. A dark pink color indicates a pressure level of around $50\,\text{MPa}$.

3.4 Sensitivity analysis - joint parameter variations

After we have established the joint properties that ought to be modeled, the sensitivities of these joint parameters are of interest. First we investigate the variation of the pre-load force and then the reproducibility of the dynamic model behaviour after loosening and tightening.

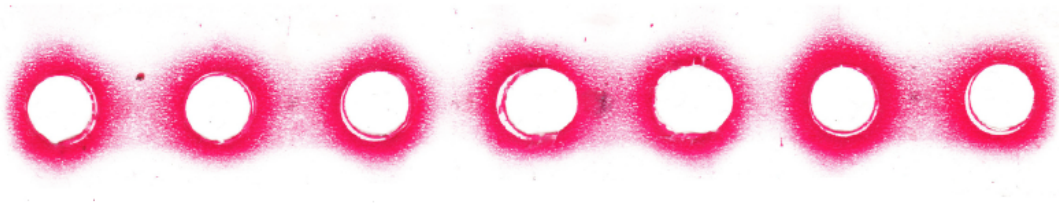


Figure 3: Visualisation of the real surface pressure distribution via two-ply FUJIFILM PRESCALE pressure measurement film.

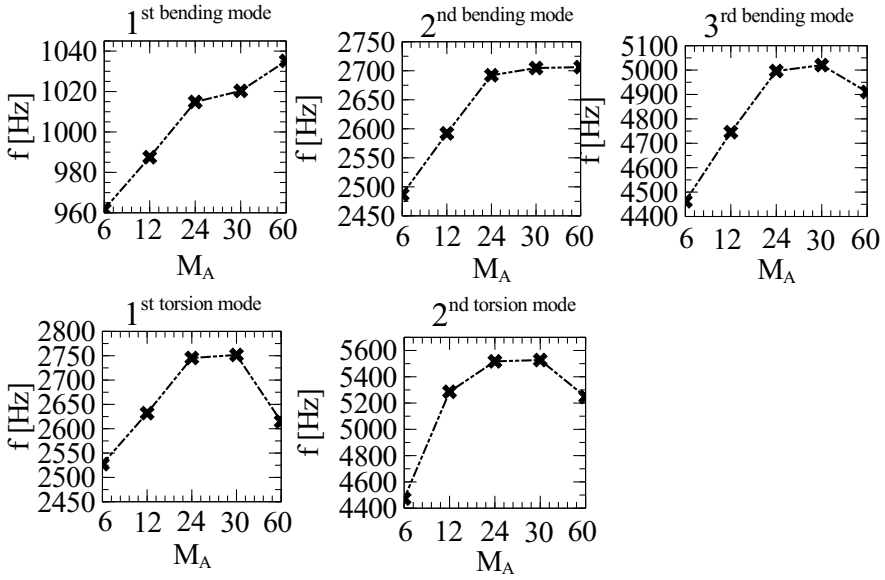


Figure 4: While the eigenfrequencies corresponding to the bending modes rise together with increasing tightening-torque, the latter seems to lower the eigenfrequencies corresponding to the torsional modes for torques M_A greater than $30\,\mathrm{N\,m}$, cf. Langer et al. [12].

Concerning the repeatability, the first three bending frequencies of the bolted beam structure are considered. The members are first separated and then re-joined after each measurement series. The positions of the bolts remain unchanged. In a second series of measurements, the bolt positions are arbitrarily varied. Ten measurements of the bolted structure are performed within each series. Figure 5 shows the results of the two series. The arithmetically averaged relative deviations over 10 samples ε_m of the first three bending modes are calculated with (2):

$$\varepsilon_\mathrm{m} = \left(\frac{f_\mathrm{max} - f_\mathrm{min}}{f_\mathrm{m}} - 1 \right) \times 100\,, \tag{2}$$

where f_max and f_min are the maximum and minimum eigenfrequencies in one measurement series and f_m is the eigenfrequency averaged over ten measurements. The shaded regions indicate the overall measurement uncertainty, cf. Figure 5. The relative deviation rises with higher eigenfrequencies and reaches a maximum ε_P of $0.51\,\%$. This shows a very high reproducibility and little sensitivity towards fastener positions. It is worth noting that the variations of the natural frequencies are also within the given overall uncertainty of the measurement.

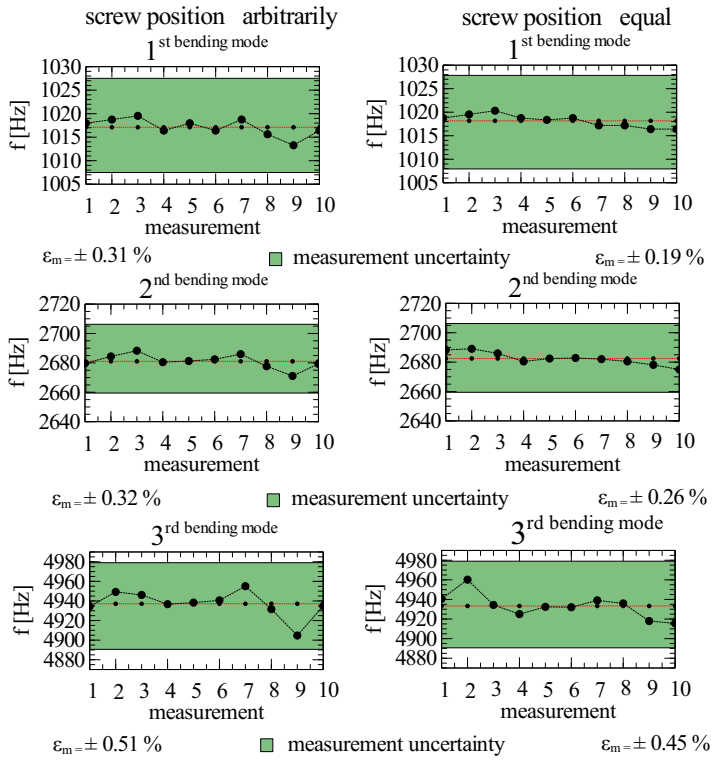


Figure 5: EMA - Measurement uncertainties resulting from ten assembly-disassembly-cycles for arbitrary and constant bolt positions, cf. Langer et al. [12].

4 State of the art model description

The search for a good bolt model is complicated and intricate. By which standard may we judge a model as ”good”? Looking to automotive tire models suggests that both empirical as well as physically-based nonlinear models are wide-spread. *TMeasy* is a semi-physical model that represents handling based on a three-dimensional slip approach. *FTire* is a non-linear model based on structural dynamics that describes the tire belt as a flexible ring approximated by elements with bending stiffness. While the required calculation time determines the application (*TMeasy* is real-time capable and can be used during a race, while *FTire* is not and finds application during tire development and ride comfort simulations), these models do share important traits. Both have a good relative trade-off between computational time and quality of the results, and both are easy to understand and use.

The industry’s vision is that the fastener manufacturer delivers an accurate simulation model to the OEM together with ordered physical fasteners.

Wentzel [16] remarks, ”A good joint model should be as simple as possible and still capture all the important physical properties of the actual joint.” He considers the force-displacement behaviour, the hysteresis, the damping, and the influence of velocity as the most important properties of a joint model.

Rohaizat et al. [11] list the use of the solid bolt model, the spider bolt model, the bolt stiffness value, and a linearized version of Hertzian contact theory as FE models to represent bolted joints. Concerning modeling approaches for joint interfaces, Rohaizat et al. [11] mention spring-damper compounds, Jenkins elements, and the Iwan model. Rohaizat et al. [11] uses CBEAM elements for the bolt shanks, RBEs for the bolts’ heads and nuts, and CELAS elements for the interface model.

Wentzel [16] names six joint modeling techniques found in the literature meaningful. The linear visco-elastic model and the linear complex stiffness model are mentioned first. These aim to match the energy

dissipation to the expected frictional dissipation in the joints. Wentzel [16] treats models that replace the actual joint next. The Iwan networks model, a spring-slider network calibrated to mimic the dissipative force-displacement relations, replaces the joint. More complicated, the Valanis model employing a first order differential equation reflects plasticity can be tuned to reproduce the force-displacement characteristics. The Bouc-Wen model uses sign functions in addition to the time derivatives. Wentzel [16] concludes that a detailed FE model can be used to simulate the micro-slip in the joint.

Bograd et al. [2] compare three different modeling methods. They use a Jenkins friction element for node-to-node contact simulation, a thin layer element employing hysteretic damping and linear stiffness, as well as a zero thickness element with nonlinear normal and tangential stiffness. They recommend the thin layer element approach for large structures and for use with currently available commercial FE software. Bograd et al. [2] report that the calculation times of the approach using zero thickness elements with an impulse response simulation in time and frequency domain following a preloading step are "extremely long". While some of the above approaches, namely Jenkins elements and hence also the Iwan model are used to model micro- and macro-slip, this may not be essential for selected industrial applications. Bograd et al. [3] point out that for typical applications, the joint pressure is high enough in order to ensure that macro-slip is avoided entirely in order to fulfill functionality requirements like leakage minimization in case of a cylinder head and crankcase compound. The exclusion of macro-slip drastically decreases the amoung of dissipated energy in the joint.

In the following, the authors would like to present a list of existing models that set the benchmark for the developed joint model.

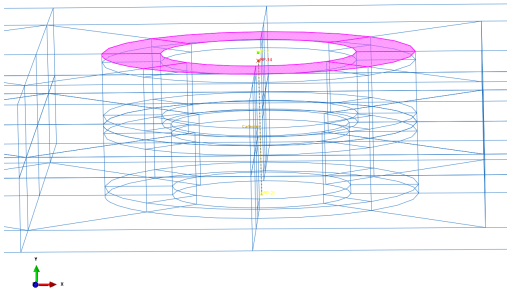
Model Type	1	2	3
Description	Tie constraint, full interface	Tie constraint, 2xD	Abaqus/CAE 6.13-1

Table 1: Overview of the model types.

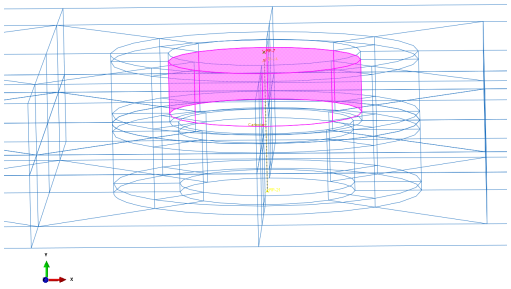
- Type 1: Here, a constraint is applied to the entire interface. The simplest approach is to kinematically tie all nodes on the opposing joint interfaces.
- Type 2: A refinement is to apply a tie constraint twice the size of the bolt head's diameter. The industry's state of the art approach for modal analysis is to kinematically tie the members' interfaces with anulli twice the diameter of the bolt head concentric to the bolt holes.
- Type 3: Abaqus/CAE 6.13-1 offers a range of built in functionalities that can be used to model joints. For this model type, all bodies are modeled with their geometrical and material properties, and their interactions are simulated. In an effort to exhaust the existing features, a tie constraint couples the bolt head and the upper member, a numerical contact model simulates joint interface interaction, another simulates the contact between the threads and the lower member. The thread simulation requires intial clearance values and contact directions at the slave nodes fot the small-sliding formulation. Other parameters for the threads' contact simulation within the static load step are the half-thread angle α, the pitch ρ, and the bolt major thread diameter d or bolt mean thread diameter d_{m}. The estimated pre-load force also acts as an input for a static load case. This force can be calculated analytically from the tightening torque, as demonstrated by Roloff and Matek [8]. With M_{A} equal to $30\,\mathrm{N\,m}$ and the friction coefficient's uncertainty, the lower and upper boundaries for the pre-load force are 11 and $19\,\mathrm{kN}$, respectively. The static step introduces stiffness to the model as contact pairs form and non-linearities occur. With the newly formed contact pairs and other sources of stiffening through pre-load, the modal analysis can ensue.

4.1 Developed FE-model

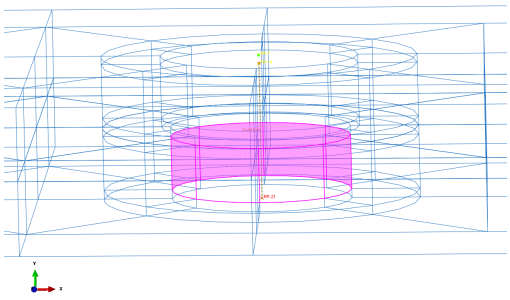
The introduction instigated thought about how a structural part of an assembly could be replaced by application of its properties to the neighbouring parts in a physically meaningful way. To stay true to this cause, the authors radically reduce the modeling parameters of the joint. There is no geometrical model of the bolt, the stiffening pre-load effect is neglected, and all contact interactions are neglected. The proposed model accounts for the bolt's mass, its stiffness, and the contact area of the joint interface. The experimentally determined contact area, cf. Figure 3, is kinematically tied, cf. Figure 6d. The mass of each bolt is added with a point mass on a reference point, cf. Figure 6b. This reference point is fixed to a partition with the size of the bolt head diameter on the upper member by Continuum Distributing Couplings. This simplification is reasonable, as the center of mass can be found almost exactly underneath the head of the bolt. The calculation of the axial bolt stiffness assuming "short" bolt dimensions, reduces itself to $k_{\text{analyt.}} = \frac{A_t E}{l_t}$, cf. Shigley [4]. This analytical axial stiffness is then, aided by the friction coefficient μ, split into tangential and normal components as proposed in the introduction: $k_N(1+\mu) = k_{\text{analyt.}}$ and $k_T = \mu \cdot k_N$. A wire holds a Cartesian Connector that uses stiffness in three degrees of freedom as input. The Connector uses values for the bolt stiffness in the normal and tangential directions. These components are subsequently applied to the joint members, the lower and the upper beam. With Continuum Distributing Couplings, two reference points are fixed to the area of contact between the bolt head and the upper member, and the bolt's threads and the lower member, respectively, cf. Figures 6a and 6c. The size of the partitions are determined by the bolt head on the one side, and the threads' length on the other.



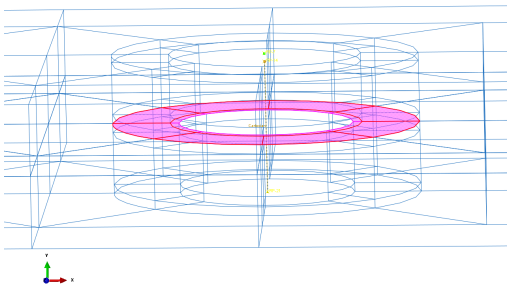
(a) Continuum distributing coupling (CDC) - upper member



(b) Continuum distributing coupling (CDC) for the bolt's mass, where the bolt's head connects to the upper member.



(c) CDC - lower member



(d) Interfacial tie constraint

Figure 6: Visualization of the model's components. The 3-dimensional bolt stiffness is applied to a Cartesian Connector linking the reference points corresponding to the CDCs on the upper and lower member cf. Figure 6a and 6c.

5 Results

For our calculations, we use the following system of consistent units:

ton	mm	s	N	MPa

Table 2: System of consistens units.

The interfacial contact diameter is experimentally determined as $17.6\,\mathrm{mm}$, cf. Figure 3. The mass of each bolt is $14\,\mathrm{g}$.
The length l_t of the threaded fastener shaft in axial direction is roughly $8.3\,\mathrm{mm}$. According to Shigley's [4] tabular overview, the cross-sectional area of the threaded portion in grip, the tensile-stress area A_t, is $58\,\mathrm{mm}^2$ for the used screws. Assuming "short" bolt dimensions, one bolt's relevant stiffness $k_\mathrm{analyt.} = \frac{A_\mathrm{t} E}{l_\mathrm{t}}$ calculated with Shigley's [4] method is hence $1.47 \times 10^6\,\mathrm{N\,mm^{-1}}$. Using $\mu = 0.3$ and with (1), $k_N = 1.13 \times 10^6\,\mathrm{N\,mm^{-1}}$ and $k_T = 0.44 \times 10^6\,\mathrm{N\,mm^{-1}}$.

Single beams	**Length** l [mm]	**Height** h [mm]	**Width** w [mm]
Beam 2	200.20	4.00	40.10
Beam 1	200.20	3.95	40.05

Table 3: Averaged geometrical data of the physical single beam structures under influence of measurement uncertainty according to Bär [1].

Single Beams	**Young's modulus** E [MPa]	**Density** ρ [kg/cm^3]	**Poisson's ratio** ν [-]
Beam 2	212170.00	7.83E-03	0.26
Beam 1	210700.00	7.84E-03	0.27

Table 4: Physical single beam structure's resulting material data averaged corresponding to measurement uncertainty according to Bär [1].

Property	**Young's modulus** E [MPa]	**Density** ρ [kg/cm^3]	**Poisson's ratio** ν [-]	**Mass** [g]
Value	210000.00	7.90E-03	0.29	14

Table 5: Material data for each of the seven tool steel M10 bolts with a metric ISO thread.

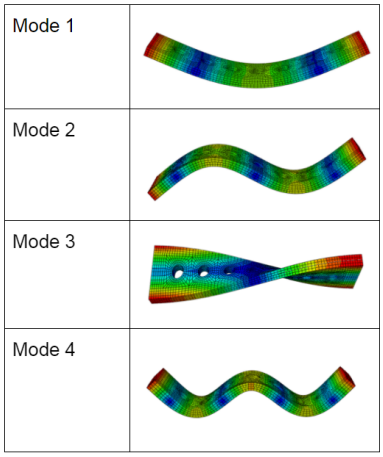


Figure 7: Visualization of mode shapes resulting from numerical modal analysis, cf. Langer et al. [7].

Mode shape	Experiment	Proposed Model	Type 1	Type 2	Type 3
1^{st} bending	1020	903	992	961	1041
2^{nd} bending	2705	2308	2724	2465	2690
1^{st} torsional	2752	1829	2738	1845	2421
3^{rd} bending	5020	4122	5294	4402	4738

Table 6: First four eigenfrequencies from the physical experiments and four virtual models of the double-beam assembly [Hz].

The deviations of the proposed model with respect to the experimental results shown in Table 6 are expected. The areal density of the joints makes the assembly very stiff and even close to the analytical solution for monolitical beams. In most engineering applications, the joint stiffness has less influence on the assembly's global modes. The results show that the proposed model is lacking in stiffness with regard to the torsional mode. Here, the authors are able to observe significant penetration at the joint interface.

6 Concluding remarks and recommendations

The authors proposed a bolted joint model based on the interfacial contact radius, the analytical axial fastener stiffness, the bolt mass, and the members geometrical and material properties. The analytical fastener stiffness was applied to the upper and lower members partially in axial and partially in tangential direction. The modeling effort was comparable to that of the industrial standard. However, the proposed technique additionally took into account the real contact radius and the physical properties of the bolt.

The results showed that especially torsional modes lacked stiffness. Towards the beams' outer borders, model collisions were observed. While a contact model could mitigate this inaccuracy, it would make non-linear analysis and contact search algorithms necessary.

An alternative modeling approach is to use thin-layer-elements or zero-thickness-elements without a contact model. This approach may solve collision issues and the corresponding stiffness matrix may still be reasonable to populate.

References

[1] J. Bär. Material and geometrical data of samples. *Digital register of results*, 2014.

[2] S. Bograd, P. Reuss, A. Schmidt, L. Gaul, and M. Mayer. Modeling the dynamics of mechanical joints. *Mechanical Systems and Signal Processing*, 25(8):2801–2826, 2011.

[3] S. Bograd, A. Schmidt, and L. Gaul. Joint damping prediction by thin layer elements. *Proceedings of the IMAC 26th Society of Experimental Mechanics Inc. Bethel, CT*, 2008.

[4] R. Budynas and J. Nisbett. *Shigley's Mechanical Engineering Design*. McGraw-Hill, New York, 9th edition, 2011.

[5] D. Ewins. Exciting vibrations: the role of testing in an era of supercomputers and uncertainties. *Meccanica*, 51(12):3241–3258, 2016.

[6] D. J. Ewins. *Modal testing: theory and practice*, volume 15. Research studies press Letchworth, 1984.

[7] P. Langer, A. Hoppe, C. Guist, and S. Marburg. Bolted joints: Eigenfrequencies from non-linear fe-models and experimental modal analysis. *INTER-NOISE and NOISE-CON Congress and Conference Proceedings*, 255(5):2967–2977, 2017.

[8] D. Muhs, H. Wittel, D. Jannasch, and J. Voßiek. *Roloff/Matek Maschinenelemente: Normung, Berechnung, Gestaltung-Lehrbuch und Tabellenbuch*. Springer-Verlag, 2007.

[9] H. M. Nawras, S. Obeed, and M. Jawad. Mathematical representation of bolted-joint stiffness: A new suggested model. *Journal of mechanical science and technology*, 25(11):2827–2834, 2011.

[10] S. Oexl. *Untersuchungen zum dynamischen Verhalten normalbelasteter Schraubverbindungen*. Der Andere Verlag, 2003.

[11] R. Omar, M. N. A. Rani, W. I. I. W. I. Mirza, M. A. Yunus, and M. H. Othman. Finite element modelling and updating for bolted lap joints. 2017.

[12] C. G. P. Langer and S. Marburg. Efficient modeling of vibroacoustic systems with consideration of and comparison with experimental measurements. In W. Kropp, O. v. Estorff, and B. Schulte-Fortkamp, editors, *Proceedings of the 45th International Congress and Expositionon Noise Control Engineering*, volume CD, pages 7683–7690. Institute of Noise Control Engineering, Aug 2016.

[13] F. Rötscher. *Maschinenelemente*. Springer, Berlin, 1927.

[14] T. Schulz. Modelling of contact stiffness in linear structural dynamic systems. Master's thesis, Karlsruher Institut für Technologie, 2011.

[15] M. Weck. *Werkzeugmaschinen 2: Konstruktion und Berechnung*. Springer-Verlag, 2006.

[16] H. Wentzel. Modelling of frictional joints in dynamically loaded structures: a review. 2006.

Experimental application of random matrix theory to quantify modal uncertainty in aircraft t-tails

A. Vishwanathan [1], **G. Vio** [1]
[1] University of Sydney, School of Aerospace, Mechanical and Mechatronic Engineering
Camperdown, 2006, Sydney, Australia
e-mail: **aditya.vishwanathan@sydney.edu.au**

Abstract
Quantifying experimental and human errors have not been a large focus within the uncertainty quantification research field, particularly when considering large scale commercial structures such as an aircraft. Recently the non-parametric method utilizing Random Matrix Theory (RMT) and the Marchenko-Pastur (MP) density formulation have received a surge in interest due to their suitability in modelling a variety of stochastic systems. This paper will aim to evaluate RMT and the MP density against numerical and experimental modal tests for six identically designed aircraft T-tails. Modal testing is conducted using an impulse hammer test under controlled environments. Results are compared with the stochastic finite element method, where known sources of parametric uncertainty are accounted for via pre-defined assumptions for material and geometric variability. After this analysis, this study aims to place some statistical bound on the modal uncertainty that results from experimental and human factors which can arise during construction and testing.

1 Introduction

Uncertainty quantification (UQ) has started to see wide adoption across a plethora of fields [1–3]. One such field is structural dynamics, where the traditional approach was to optimize a system using baseline parameters due to the limitations of early computational methods [4], and then implement extremely conservative margins of safety to compensate, leading to inefficient and costly designs [5]. Recent improvements in computing power have resulted in increased design productivity and analytical fidelity, however a reluctance to consider stochastic parameters within industry persists [6]. This is perhaps due to the inherent challenges faced when dealing with UQ since a large number of variabilities can occur in physical systems. Adhikari [7] summarizes three overarching categories that uncertainties can fall into:

- Parametric uncertainty in geometric parameters (length, width, thickness), material properties (Young's modulus, Poisson's ratio), and loading conditions.
- Model uncertainty (e.g. non-linear damping characteristics) that arise from a priori unknown system.
- Experimental and manufacturing errors that percolate into the system.

Parametric uncertainties are typically considered using the stochastic finite element method (SFEM), which has seen a huge rise in popularity due to spectacular growth in computing power and parallel processing [8, 9]. Since probabilistic *priori* can be assumed for the inputs, several approaches have been suggested to derive a measure of structural robustness. These include; perturbation based methods [10], projection based methods [11, 12], and Monte Carlo Simulations (MCS). Uncertainty due to modelling error has received comparatively less attention and can arise due to non-linearities in the equation of motion, the damping, and modelling of structural joints [7]. Since no explicit system parameters can be used to propagate these effects, a non-parametric method [13] utilising random matrix theory (RMT) was proposed.

RMT was introduced by Wigner in 1951 [14] and has been utilized in a wide variety of fields. In particular, it has been justified as a viable approach to quantify parametric and non-parametric uncertainties in structural dynamics [15–18]. As the name implies, the method involves representing all stochastic behaviour in a corresponding random matrix within the system of equations. The output response is characterised by non-dimensional *dispersion parameters*, which greatly reduces the number of unknowns within a given problem. Early studies showed RMTs suitability in predicting static displacement and uncertain frequency response for a cantilevered flat plate [18, 19]. More recent works have also successfully analyzed stochastic frequency response function (FRF) characteristics and determined changes in modal behaviour for uncertain pier dynamics [20], and 2D wings [21]. Another use for RMT has been in studying random undamped eigenvalue problems. It was shown that a simple approximation called the Marchenko-Pastur (MP) density function [22] provides a reasonable approximation of the analytical and experimental eigenvalue density for stochastic systems of varying complexity [23]. This study will contribute to literature by validating the MP density function for a finite element model (FEM) for an aircraft T-tail, and quantifying the manufacturing errors that went into building full scale aircraft T-tails.

Quantifying sources of error that percolate into experimental studies, such as human error in the construction of a structure, has received very little attention. Conducting completely controlled UQ experiments relies on nominally identical samples of the same structure [7], which is a significant deterrent from conducting these studies for large scale systems. The general approach thus far has been to quantify uncertainty through numerical simulation, or use simplified structures with well defined analytical formulations (e.g. a cantilevered plate or beam [7, 23]). UQ has been undertaken on a similar T-tail previously [24], however that study used one T-tail and was focussed on the differences exhibited from a numerical model as opposed to variations between nominal structures. Some notable experimental investigations outside of the aerospace field include Kompella and Bernhard [25], who studied structure-borne noise via analysis of driver microphone data for different pickup trucks, and Fahy [26], who measured the FRFs for 41 identical beer cans.

This paper is an experimental case study involving six aircraft T-tails which were made in the school of Aeronautical, Mechanical and Mechatronic Engineering (AMME) at University of Sydney. Each T-tail was constructed as part of an undergraduate unit of study, being supervised by qualified aircraft technicians. As such, it serves as an insight into the typical errors and sources of uncertainty that might be seen in a practical setting. Modal testing of each structure is conducted using an impulse hammer test, and the differences in modal behaviour are noted. For comparison, an FEM is also analysed, with known sources of parametric uncertainty controlled for. RMT is utilized as a tool to quantify the uncertainty that remains, and place some statistical bound on the unknown errors that percolate in the experimental study. A numerical study is also undertaken with the FEM to evaluate the suitability of the MP density function. The outline of the paper is as follows; the RMT formulation is outlined in Section 3, the experimental method is described in Section 4, the analysis and comparison of both sets of results is in Section 5, and finally a summary of the paper and key contributions are provided in Section 6. test the system with approximately

2 RMT Formulation

2.1 Optimal Wishart Parameters

For a damped *n*-degree-of-freedom linear dynamic system, such a system can be described using Equations (1) and (2):

$$\mathbf{M}\ddot{q}(t) + \mathbf{C}\dot{q}(t) + \mathbf{K}q(t) = \mathbf{f}(t) \tag{1}$$

$$\mathbf{H}(\omega) = [-\omega^2\mathbf{M} + i\omega\mathbf{C} + \mathbf{K}]^{-1} \tag{2}$$

where $\mathbf{f}(t)$ is the forcing vector, and $\mathbf{q}(t)$ is the response vector. Matrices $\mathbf{M}$, $\mathbf{C}$, and $\mathbf{K}$ represent the mass, damping and stiffness respectively, and are Wishart random matrices [27]. $\mathbf{H}(\omega)$ is the frequency response function (FRF), where ω is the input frequency. For modal analysis problems, damping is assumed to be

minimal, and the FE analysis software MSC.Nastran [28] is utilized to yield mass normalized eigenvalues and eigenvectors. As such, the baseline model can be reduced to a stiffness matrix $\mathbf{K_0}$. The *dispersion parameter*, which is analogous to the normalized standard deviation for a given random matrix, is shown below:

$$\xi_K^2 = \frac{E[||\mathbf{K} - \mathbf{K}_0||_F^2]}{||\mathbf{K}_0||_F^2} \tag{3}$$

where $||\cdot||_F$ and $E[\dots]$ denote the Frobenius norm and mean operators respectively. The dispersion parameter is assumed to be deterministic in RMT formulations, and in this paper is calculated using SFEM. This parameter alone, along with the baseline stiffness $\mathbf{K_0}$, is required to sample from the Optimal Wishart distribution [19] as below:

$$\mathbf{K} \sim W_n(p, \mathbf{\Sigma}) = \left[2^{\frac{1}{2}np}\Gamma_n\left(\tfrac{1}{2}p\right)|\mathbf{\Sigma}|^{\frac{1}{2}p}\right]^{-1} |\mathbf{K}|^{\frac{1}{2}(p-n-1)} e^{\mathrm{tr}\left(-\frac{1}{2}\mathbf{\Sigma}^{-1}\mathbf{K}\right)} \tag{4}$$

where

$$p = n + 1 + \theta \tag{5}$$

$$\mathbf{\Sigma} = \frac{\mathbf{K}_0}{\alpha} \tag{6}$$

and

$$\theta = \frac{1}{\xi_K^2}(1 + \gamma_K) - (n+1) \tag{7}$$

$$\gamma_K = \frac{[\mathrm{Tr}(\mathbf{K}_0)]^2}{\mathrm{Tr}(\mathbf{K}_0^2)} \tag{8}$$

$$\alpha = \sqrt{\theta p} \tag{9}$$

2.2 Marchenko-Pastur density

The random undamped eigenvalue problem is described below in Equations (10) and (11):

$$\mathbf{K}\phi_j = \lambda \mathbf{M}\phi_j,\ j = 1, 2, \dots, n \tag{10}$$

$$\mathbf{\Xi} = \mathbf{M}^{-1/2}\mathbf{K}\mathbf{M}^{-1/2} \tag{11}$$

In Equation 10, λ and ϕ_j represent the eigenvalues and mass-normalized eigenvectors for the system respectively, while Equation 11 is an equivalent matrix representation of the problem. Studying the shifts in individual eigenvalues yields invaluable information on the dynamical response of the system under uncertainty. For random processes, an emphasis is also placed on the probability distribution of eigenvalues [23, 29]. This is due to a phenomena known as modal veering [30], where the loci of individual eigenvalues cross over each other. Soize [31] showed that this overlap can be significant for large dimensionality systems exhibiting moderate uncertainty.

For a general analytical solution of the eigenvalue density for a linear stochastic system, the reader is referred to [23]. Another point of interest is the limiting behaviour of this eigenvalue density, which is difficult to solve analytically, and requires numerical computation. A simplification which is often made in structural mechanics is to assume that the density profile is asymptotically 'flat', which leads to a formulation known as the Marchenko-Pastur (MP) density [22]:

$$p(\lambda) = \frac{c}{2\pi a^2 \lambda} \begin{cases} \sqrt{(a^+ - \lambda)(\lambda - a^-)}, & \lambda \in [a^-, a^+] \\ 0, & \lambda \notin [a^-, a^+] \end{cases} \tag{12}$$

where

$$c = \left(\frac{\omega_{\text{max}} + \omega_{\text{min}}}{\omega_{\text{max}} - \omega_{\text{min}}} \right)^2 \tag{13}$$

$$a = \frac{\omega_{\text{max}} + \omega_{\text{min}}}{2} \tag{14}$$

Equation 12 is valid for the domain $\lambda \in [a^-, a^+]$, where a^- and a^+ are the lowest and highest eigenvalues of the baseline system; $\omega^2_{0_{min}}$ and $\omega^2_{0_{max}}$, respectively. The MP Density is an extremely promising and yet seemingly ambitious result, claiming that the limiting eigenvalue density is a function of only the first and last natural frequencies of the system. This is in contrast to traditional finite element methods, where the complete collection of eigenvalues are required to model the underlying probability density function. The validity of function in relation to numerical or experimental engineering models has not received much attention to the best of this author's knowledge. Adhikari et al. [23] recently concluded that the MP density yielded reasonable approximations for a cantilevered plate with randomly attached springs, and also for a numerical model of a helicopter tail boom which contained 13,116 DOFs. To give further exposure, this study shall compare the results obtained via the MP density with the FE eigenvalue distribution from the aircraft T-tail.

3 Experimental Setup

Figure 1 depicts the experimental setup which was used to conduct the hammer testing of the six T-tails. Equipment specifications are summarized in Table 1. The T-tails are suspended from a rigid structure and are free to translate and rotate in space. Two six channel Bruel and Kjaer Model 3160-A-042 systems are utilized to acquire the data. An impulse hammer (with an aluminium tip) is used to strike normal to the surface in 39 pre-defined locations (24 along the horizontal tail, and 15 along the vertical). This is clarified in Figure 2 which depicts the node numbering scheme used. Two tri-axial accelerometers are placed on the horizontal and vertical tails (seen in Figures 1a and 1b respectively) to obtain data. A 6400 Hz bandwidth was chosen with 0.125 Hz resolution, resulting in 51201 spectral lines.

Role	**Model No.**	**Sensitivity**	**Channel(s)**	**Node(s)**
Accelerometer	B&K 4535 B	0.9935 mV/(m/s^2)	2-4	1
Accelerometer	B&K 4535 B	0.9935 mV/(m/s^2)	6-8	31
Impact Hammer	B&K 8206	22.7 mV/N	1	1-39

Table 1: Equipment Specifications

4 Results

4.1 Experimental Results

Figure 3 shows the results from the hammer testing for all six T-tails. Data beyond the first 100Hz is omitted due to low coherence of the signal. The stable vibrational modes were determined via the Polymax algorithm [32] which was applied to the mean FRFs. Large discrepancies are noted between the FRFs, highlighting the significant manufacturing errors that took place during construction. Similarities are noted through the first stable mode which is found at around 50Hz, and the grouping of modes between 80Hz-100Hz. Some T-tails such as T1 and T6 possess additional modes in the 50Hz-70Hz range which are not seen in the other structures, which can perhaps be attributed to the presence of a loose bolt of joint. To ensure valid comparison between the T-tails and an FE model, a modal assurance criteria (MAC) [33] is utilized, and



(a) Positioning of Accelerometer 1 (b) Positioning of Accelerometer 2

Figure 1: Experimental setup of T-tail

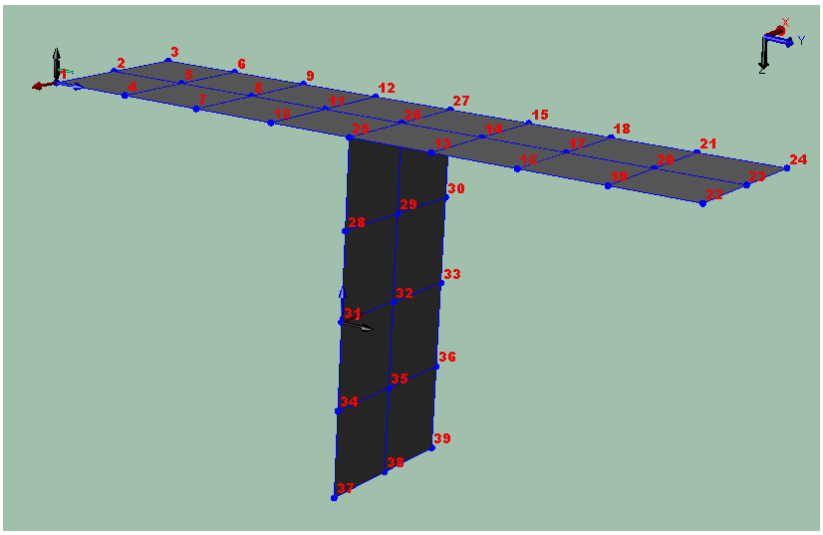


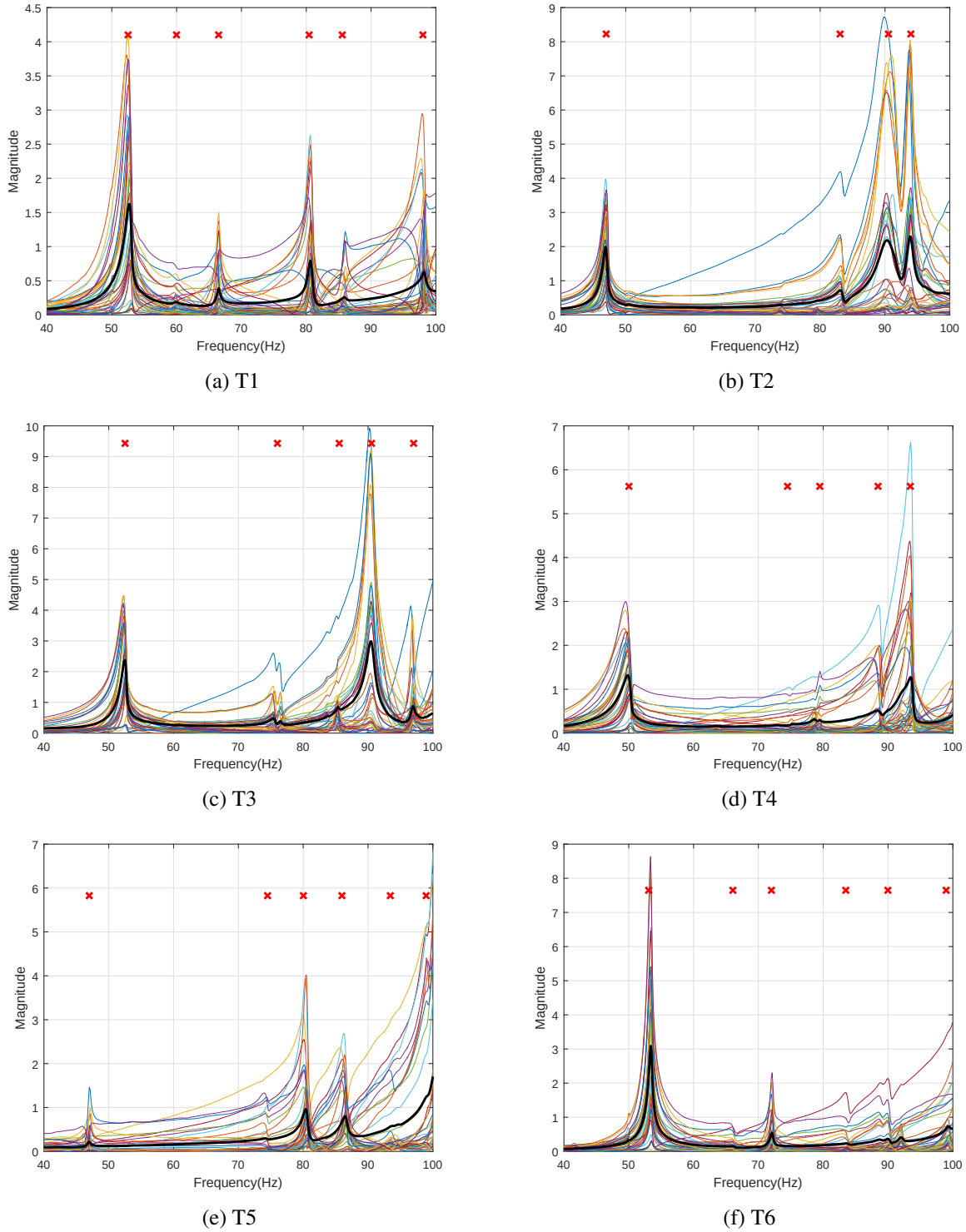
Figure 2: T-tail schematic showing the node numbering.

mode shapes are also visualized in Figure 4 via plotting the experimental eigenvectors and computational analysis in MSC.Nastran. A summary of the common vibrational modes is provided in Table 2.

Ttail	Mode 1(Hz)	Mode 2(Hz)	Mode 3(Hz)	Mode 4(Hz)
1	52.5	80.5	85.5	98
2	47	79.5	90.5	95
3	52.5	85.5	90.5	97
4	50	79.5	88.5	93.5
5	47	80	86	93.5
6	53	83.5	90	92
FE	50.07	75.7	101.2	110.15

Table 2: Common vibrational modes found in all six T-tails and the FE model

Since the goal of this study is to quantify the non-parametric effects, a measure of the parametric uncertainties



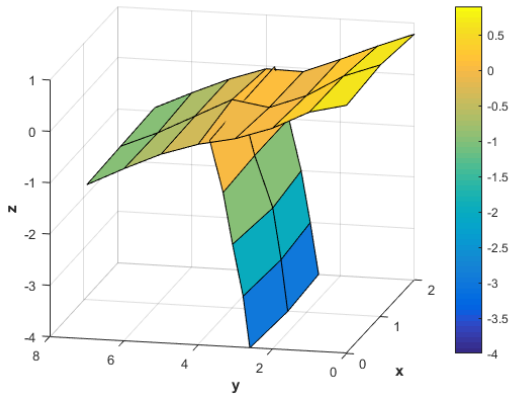
(a) T1 (b) T2

(c) T3 (d) T4

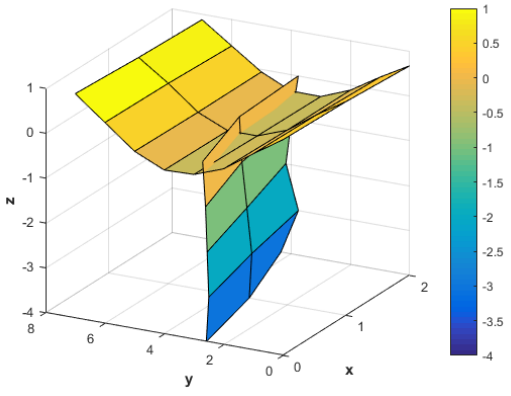
(e) T5 (f) T6

Figure 3: Experimental FRFs of six T-tails for all 39 nodes. The black lines are the mean FRFs, and the red crosses are the stable vibrational modes.

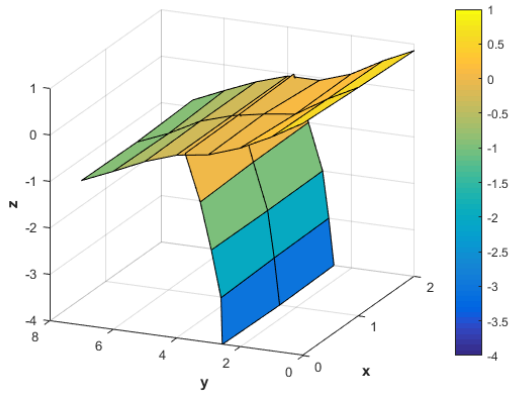
that exist within the T-tail is first estimated. A dimensional tolerance of 5mm along the wing span and chord, and 5% standard deviation in Young's modulus is assumed. These variabilities were suggested by University of Sydney in-faculty aircraft technicians, who oversaw construction of each T-tail, and can arise primarily due an even tension distribution along the aluminum skin when attached to the construction jig [11]. Using repeated sampling of the above random parameters, a dispersion parameter $\xi_k^2 = 0.12$ is obtained using



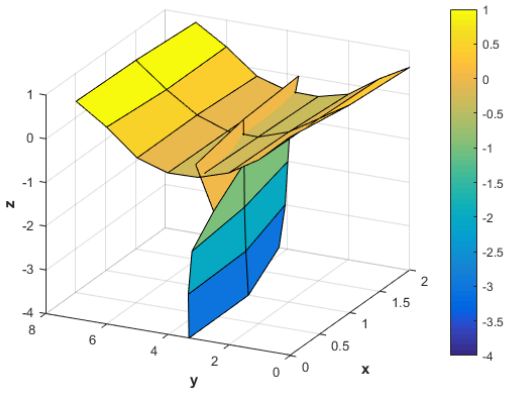
(a) T1: single bending mode at 52.5Hz



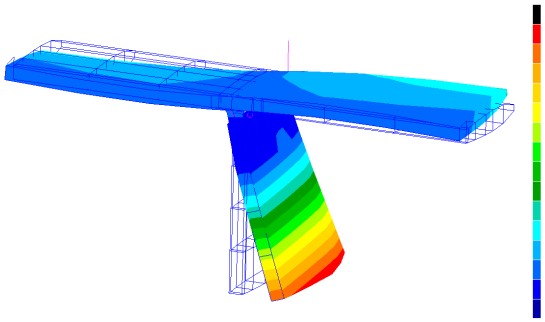
(b) T1: symmetric bending mode at 80.5Hz



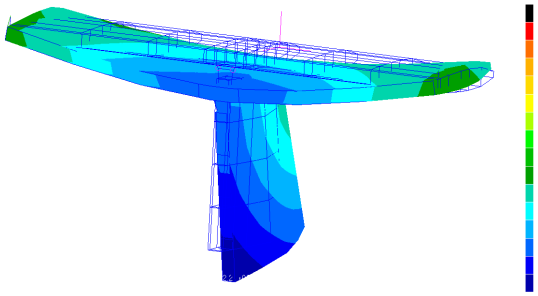
(c) T4: single bending mode at 50Hz



(d) T4: symmetric bending mode at 79.5Hz



(e) FE model: single bending mode at 50.07Hz



(f) FE model: symmetric bending mode at 75.7Hz

Figure 4: Two consistent modes found between T1, T4, and the FE model

Eqn. (3). We now use this along with the baseline stiffness of the FE model to generate random samples from the Wishart distribution in Eqn. (4). A total of 10,000 samples are taken in order to obtain a 95% confidence interval (CI) for each mode, which is shown in Figure 5. Note that the intervals are plotted on top of the experimental means to visualize the scatter in the physical systems. As expected, dispersion from the parametric sources alone underestimate the width of the CIs for modes 1 and 2, displayed by the red and blue regions respectively. It does however appear to cover the CIs for modes 3 and 4, however this is most likely biased due to the low number of experimental samples. From an aeroelastic stability point of view, an accurate understanding of how the first few modes shift due to uncertainty is vital.

An ad-hoc increase of the dispersion parameter is undertaken to ensure sufficient coverage of the experimental scatter. Figure 6 shows an adjusted CI plot where $\xi_k^2 = 0.155$, resulting in a 29% increase on top of the parametric effects alone. The CIs for modes 1 and 2 are now adequate to cover the range of samples. Therefore, a simple quantification of non-parametric effects has been obtained, and provides motivation to expose random matrix methods to more large scale UQ problems.

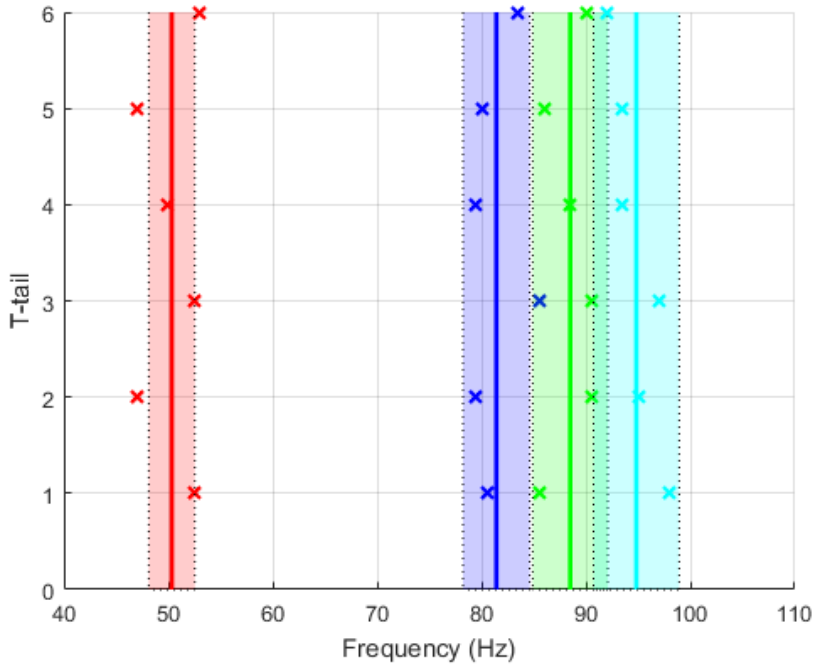


Figure 5: 95% CI of modes 1 to 4 symbolized by the shaded red, blue, green and cyan regions respectively. The thick lines are the mean values, and the crosses are the individual T-tail modal frequencies.

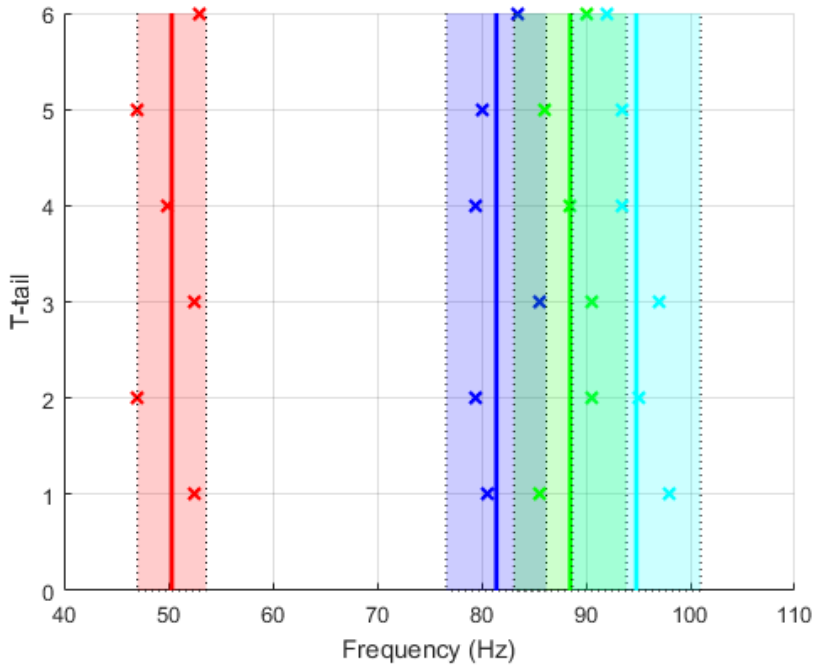


Figure 6: 95% CI with 20% increased dispersion parameter

4.2 MP Density Results

Another formulation covered in Section 2.2 was the limiting eigenvalue density called the Marchenko-Pastur Density or MP density, which arises from RMT. Since a large amount of eigenvalues are required, the coherence in the experimental data makes the determination of a limiting eigenvalue density difficult to obtain. As such, this study shall propagate the parametric uncertainty through the baseline FE model, and compare results with the analytical MP Density. Figures 7 and 8 show the PDFs for the baseline system, the mean stochastic FEM, and the MP density. Figure 7 is generated using all 730 eigenvalues, while Figure 8 uses only 500. Similar to the conclusion made by Adhikari et al. [23], a lower amount of eigenvalues shows greater discrepancy between the analytical MP density and the FE model. Interestingly, this discrepancy is only significant in the low to medium frequency range, and the tails of the distributions match extremely well. Increasing the number of eigenvalues improves the approximation, seen by the relative closeness of the PDF peaks. Overall, this result supports literature findings that the MP density can accurately model large random mechanical systems.

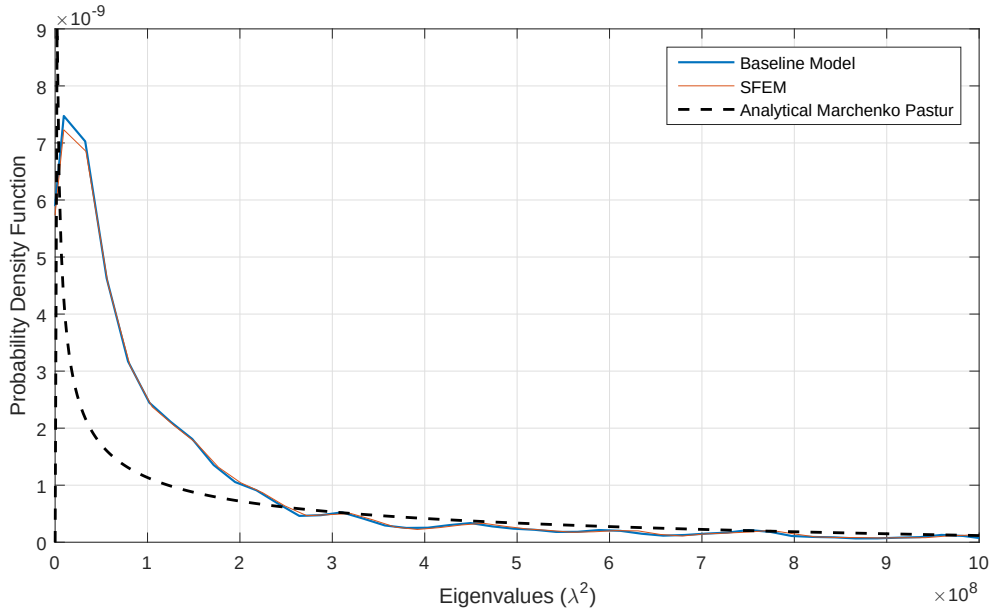


Figure 7: PDFs of the baseline model, mean SFEM realization, and the MP density approximation generated with 730 eigenvalues

5 Conclusion

This paper considers RMT as a possible means to quantify the experimental and model uncertainty for an aircraft T-tail. Six nominally designed structures underwent hammer testing to retrieve their natural frequencies. Parametric uncertainty in the length and width dimensions, and Young's modulus of the T-tail was propagated through a numerical FE model to obtain a normalized standard deviation of the stiffness matrix, or dispersion parameter. A confidence interval was obtained for the previously determined modes. It was found that the parametric variability alone did not account for the total uncertainty observed in the experiments, and this was particularly the case for the first and second modes. Increasing the dispersion parameter by 29% resulted in a widened interval which had adequate coverage over the experimental observations. Hence, we can provide a simple lower bound quantification of the unknown errors that permeated the experiment. This study is clearly limited via the number of T-tails tested, however provides a basis for UQ to be conducted on a much larger experimental scale. An additional aim of the paper was to evaluate the suitability of the Marchenko-Pastur (MP) Density function to approximate the eigenvalue distribution of a

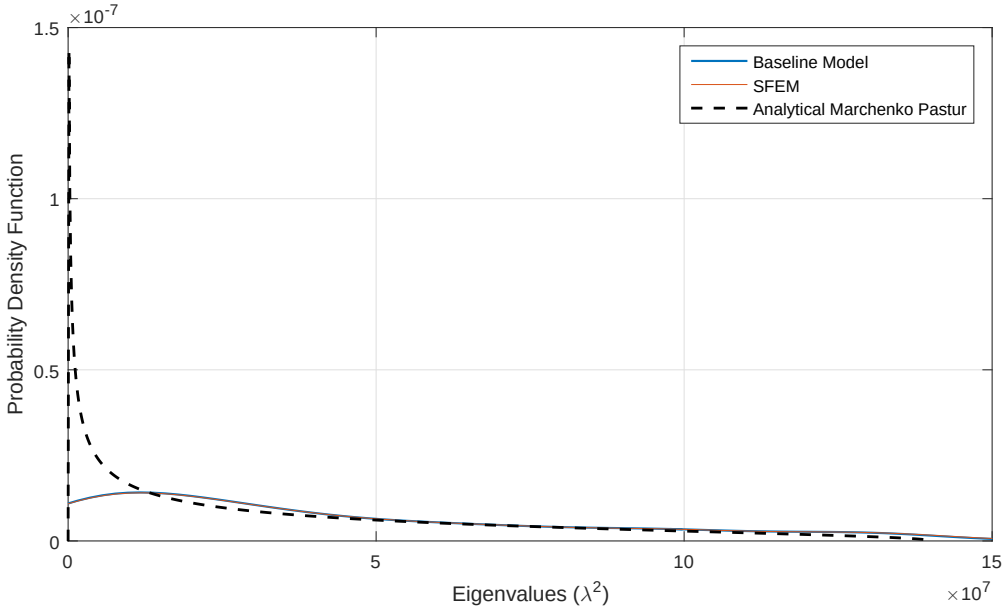


Figure 8: PDFs of the baseline model, mean SFEM realization, and the MP density approximation generated with 500 eigenvalues

linear perturbed T-tail model. Unfortunately due to limitations of the experiment, the physical T-tail results were not considered, however the MP density proved an accurate model for the behaviour of the numerical T-tail model when parametric uncertainty was applied.

Acknowledgements

The authors would like to thank Kim White for providing support with the FE model of the T-tail, and Gavin Lackey for supervising the construction of the T-tails.

References

[1] M. Avramova and K. Ivanov, "Verification, validation and uncertainty quantification in multi-physics modeling for nuclear reactor design and safety analysis," *Progress in Nuclear Energy*, vol. 52, pp. 601–614, sep 2010.

[2] Y. Qian, C. Jackson, F. Giorgi, B. Booth, Q. Duan, C. Forest, D. Higdon, Z. J. Hou, and G. Huerta, "Uncertainty quantification in climate modeling and projection," *Bulletin of the American Meteorological Society*, vol. 97, pp. 821–824, may 2016.

[3] A. Cunha, J. Felix, and J. Balthazar, "Quantification of parametric uncertainties induced by irregular soil loading in orchard tower sprayer nonlinear dynamics," *Journal of Sound and Vibration*, vol. 408, pp. 252–269, nov 2017.

[4] J. Kim, J.-C. Yoon, and B.-S. Kang, "Finite element analysis and modeling of structure with bolted joints," *Applied Mathematical Modelling*, vol. 31, pp. 895–911, may 2007.

[5] R. Beaulieu, *Margin of safety definition and examples used in safety basis documents and the USQ process*. Nuclear Operations Directorate, 2013.

[6] C. L. Pettit, "Uncertainty quantification in aeroelasticity: Recent results and research challenges," *Journal of Aircraft*, vol. 41, pp. 1217–1229, sep 2004.

[7] S. Adhikari, M. Friswell, K. Lonkar, and A. Sarkar, "Experimental case studies for uncertainty quantification in structural dynamics," *Probabilistic Engineering Mechanics*, vol. 24, pp. 473–492, oct 2009.

[8] V. Papadopoulos, *Stochastic Finite Element Methods*. Springer, 2017.

[9] G. Stefanou, "The stochastic finite element method: Past, present and future," *Computer Methods in Applied Mechanics and Engineering*, vol. 198, pp. 1031–1051, feb 2009.

[10] F. Yamazaki, A. Member, M. Shinozuka, and G. Dasgupta, "Neumann expansion for stochastic finite element analysis," *Journal of Engineering Mechanics*, vol. 114, pp. 1335–1354, aug 1988.

[11] P. Cheema, D. J. Munk, N. F. Giannelis, and G. A. Vio, "Experimental validation of polynomial chaos theory on an aircraft t-tail," in *18th AIAA Non-Deterministic Approaches Conference*, American Institute of Aeronautics and Astronautics, jan 2016.

[12] A. Vishwanathan, P. Cheema, and G. Vio, "Multi-particle swarm optimization used to study material degradation in aeroelastic composites including probabalistic uncertainties," in *2017 IEEE Congress on Evolutionary Computation (CEC)*, IEEE, jun 2017.

[13] C. Soize, "A nonparametric model of random uncertainties for reduced matrix models in structural dynamics," *Probabilistic Engineering Mechanics*, vol. 15, pp. 277–294, jul 2000.

[14] E. P. Wigner and P. A. M. Dirac, "On the statistical distribution of the widths and spacings of nuclear resonance levels," *Mathematical Proceedings of the Cambridge Philosophical Society*, vol. 47, p. 790, oct 1951.

[15] C. Soize, "Maximum entropy approach for modeling random uncertainties in transient elastodynamics," *The Journal of the Acoustical Society of America*, vol. 109, pp. 1979–1996, may 2001.

[16] M. Arnst, D. Clouteau, H. Chebli, R. Othman, and G. Degrande, "A non-parametric probabilistic model for ground-borne vibrations in buildings," *Probabilistic Engineering Mechanics*, vol. 21, pp. 18–34, jan 2006.

[17] M. Mignolet and C. Soize, "Nonparametric stochastic modeling of linear systems with prescribed variance of several natural frequencies," *Probabilistic Engineering Mechanics*, vol. 23, pp. 267–278, apr 2008.

[18] S. Adhikari, "Uncertainty propagation in linear systems: An exact solution using random matrix theory," in *48th AIAA/ASME/ASCE/AHS/ASC Structures, Structural Dynamics, and Materials Conference*, American Institute of Aeronautics and Astronautics, apr 2007.

[19] S. Adhikari, "Generalized wishart distribution for probabilistic structural dynamics," *Computational Mechanics*, vol. 45, pp. 495–511, jan 2010.

[20] M. Biklaryan, M. A. Lotfollahi-Yaghin, M. H. Aminfar, and A. Mojtahedi, "Comparative study of random matrices capability in uncertainty detection of piers dynamics," *Journal of the Persian Gulf (Marine Science)*, vol. 5, 2014.

[21] A. Vishwanathan, D. Munk, and G. Vio, "Frequency response characteristics of 2d wings in uncertain environments: A random matrix theory approach," in *12th World Congress on Structural and Multidisciplinary Optimization*, 06 2017.

[22] V. A. Marčenko and L. A. Pastur, "Distribution of eigenvalues for some set of random matrices," *Mathematics of the USSR-Sbornik*, vol. 1, pp. 457–483, apr 1967.

[23] S. Adhikari, L. Pastur, A. Lytova, and J. D. Bois, "Eigenvalue density of linear stochastic dynamical systems: A random matrix approach," *Journal of Sound and Vibration*, vol. 331, pp. 1042–1058, feb 2012.

[24] P. Cheema, G. Matthews, and G. A. Vio, "Probabilistic surrogate modeling for uncertainty quantification and bayesian inferencing on a t-tail," *AIAA Journal*, vol. 56, no. 3, pp. 1185–1197, 2018.

[25] M. S. Kompella and R. J. Bernhard, "Measurement of the statistical variation of structural-acoustic characteristics of automotive vehicles," in *SAE Technical Paper Series*, SAE International, may 1993.

[26] F. J. Fahy, *Foundations of Engineering Acoustics*. Academic Press, 2000.

[27] J. Wishart, "The generalised product moment distribution in samples from a normal multivariate population," *Biometrika*, vol. 20A, p. 32, jul 1928.

[28] MSC Software, *NASTRAN: Multidisciplinary Structural Analysis*.

[29] M. Mehta, *Random Matrices*. San Diego, CA: Academic Press, 2nd ed., 1991.

[30] J. L. du Bois, S. Adhikari, and N. A. J. Lieven, "On the quantification of eigenvalue curve veering: A veering index," *Journal of Applied Mechanics*, vol. 78, no. 4, p. 041007, 2011.

[31] C. Soize, "Random matrix theory and non-parametric model of random uncertainties in vibration analysis," *Journal of Sound and Vibration*, vol. 263, pp. 893–916, jun 2003.

[32] B. Peeters, H. V. der Auweraer, P. Guillaume, and J. Leuridan, "The PolyMAX frequency-domain method: A new standard for modal parameter estimation?," *Shock and Vibration*, vol. 11, no. 3-4, pp. 395–409, 2004.

[33] M. Pastor, M. Binda, and T. Harčarik, "Modal assurance criterion," *Procedia Engineering*, vol. 48, pp. 543–548, 2012.

Catastrophic event prediction associated with road vehicle dynamic responses and randomly uncertain suspension parameters

J.A. Gonzalez Anaya, J.F. Dunne
Department of Engineering and Design, University of Sussex,
Falmer, Brighton, BN19QT, United Kingdom.
e-mail: **j.f.dunne@sussex.ac.uk**

Abstract
A probabilistic approach is discussed for predicting rare, low-probability, catastrophic events associated with road vehicle dynamics. In particular, a Direct Integration method is compared with a Monte Carlo simulation for predicting road vehicle pitch displacements of sufficiently extreme magnitude to lead to non-linear catastrophic events such as flip-over. A 'Full-Car' simulation model, with 7-degrees of freedom, is used to represent the vehicle dynamic behaviour. The model assumes a bi-linear damper at each of the four suspension struts, where each damper has uncertainty described by a single unknown random parameter value. The vehicle is simulated following a straight-line path along in a deterministic roadway with sinusoidal undulations. The proposed method provides a fast, scatter-free nonlinear uncertainty propagation method that will allow suspension parameter studies to achieve safer vehicle design and operation.

1 Introduction

A vehicle moving over non-smooth terrain has the potential to dynamically reach a large amplitude of motion that could subsequently lead to an unstable catastrophic event. An example of just such a catastrophic event is flip-over, where a large pitch displacement creates the conditions of significant lift resulting in uncontrollable flipping of the vehicle. Manufacturers are interested in simulation tools that can be used to minimize such risks by influencing the design process to achieve high levels of operational safety.

Unfortunately, there have been several reported cases where catastrophic 'take-off' events have occurred as a consequence of intrinsic instabilities in the vehicle design [1-3] and most recently [4]. In a first study on the topic, Dominy et al. [1] undertook scaled-wind-tunnel tests with a typical LM-GTP car. They assessed the aerodynamic stability of a prototype car using design pitch and ground clearance conditions, and concluded that aerodynamic forces alone are unlikely to lead to dynamic instability. Similar findings have been independently arrived at by Katz [5], and Wright [2]. In considering the vehicle dynamic behaviour leading up to a catastrophe, the findings of [1][2] and [5], would suggest that there may be an unfavourable set of intrinsic suspension parameters that result from parameter variability in combination with the aerodynamic forces.

When the suspension parameters are unknown but modelled as random, predicting the probabilities of occurrence of a defined highly non-linear catastrophic event, usually requires lengthy Monte Carlo (MC) simulations. MC simulation however is always prone to some statistical scatter. A practical method that provides estimates of low-probability events without statistical scatter would be useful, the purpose being, to provide fast prediction of vehicle behaviour to improve operational safety. The prospect of being able to make such probabilistic predictions analytically is virtually impossible for such a non-linear system. Predicting the vehicle behaviour with intrinsically random parameters has been already studied in [6] and [7]. These studies have shown that the process require very substantial computational power, making them prohibitively expensive. On the other hand, an efficient extreme-value based Direct Integration (DI) bounding method is available in [8], creating the possibility of low-probability scatter-free predictions

without the need of MC simulations. The Direct Integration bounding method [8] has been used to study the dynamics of linear structures with uncertain parameters providing very accurate results with minimum computational expense. In this paper, an overview of a novel application of the statistical method [8] is given by using Extreme Value Theory to address a problem in vehicle dynamics. The objective is to demonstrate the computational accuracy and efficiency in predicting the cumulative distribution of an event that is associated with non-linear vehicle dynamics with randomly uncertain damping parameters, for a vehicle driven over a (deterministic) spatially-varying sinusoidal road surface.

2 Predicting vehicle response with intrinsic random parameters in the suspension

Consider a road vehicle in which there are N random physical parameters, e.g. stiffness and damping of the suspension sub-system, tyre temperature, weight of the car, etc. These N parameters can be represented by a vector: $\mathbf{X} = [\mathrm{X}_1, \mathrm{X}_2, \ldots \mathrm{X}_\mathrm{N}]^\mathrm{T}$ having an assumed joint probability density function f(**X**). This type of variability will create randomness within the entire vehicle response, meaning that variability in the suspension system can create a random motion event as a result of traversing a deterministic roadway.

Focusing on the vehicle dynamics response, an extreme value distribution can be associated with the random response variable: $M_N = \max\{Y1, Y2, \ldots., Y_N\}$ where Y_i are assumed to be independent and identically distributed variables. The variable Y_i represents the absolute magnitude for any dynamic response of interest, such as displacement, velocity, or spatially-averaged energy. The distribution of the maximum response M_N (in N realizations) is given [9] as:

$$\Pr(\mathrm{M_N} \leq \mathrm{Y}) = \mathrm{F_N(Y)} = \mathrm{F(Y)^N} \tag{1}$$

The magnitude of the response associated with a set of N uncertain vehicle responses is defined in terms of the percentage quantile $\mathrm{Z_P}$ associated with the distribution of $\mathrm{M_N}$ i.e. $\Pr(\mathrm{M_N} \leq \mathrm{Z_p})$ [9]. The bound $\mathrm{Z_P}$ can be then be expressed as:

$$\mathrm{F_N}(\mathrm{Z_p}) = \mathrm{p} \tag{2}$$

where p is the probability of the distribution for the quantile $\mathrm{Z_p}$

2.1 Response predictions assuming Log-normal vehicle body displacements

For the choice of random parameters, in most cases it is not possible to analytically construct the distribution F(y) associated with a vehicle response. There is however good evidence to suggest that for high levels of randomness, the probability density function associated with the displacement, for example, is log-normal [10]. In fact, according to R. Langley et al. [10], there is good reason to assume that the distribution for any type of absolute magnitude of response is approximately lognormal, including displacement, velocity or energy.

A lognormal variable can be defined by considering a continuous transformation to a standard normal variable $U=(\ln(Y)-\mu)/\sigma$ [9], where $Y > 0$, and where the parameters μ and σ are the mean and the standard deviation of ln(Y). From the moment function [9]: Variable Y under such a transformation has the following lognormal distribution with a 2-parameter density function:

$$\mathrm{f_Y(Y)} = \frac{1}{\mathrm{Y}\sigma\sqrt{2\pi}}\mathrm{e}^{\frac{-[\ln(\mathrm{Y})-\mu]^2}{2\sigma^2}} \tag{3}$$

and where

$$E(Y^r) = e^{r\mu+\frac{1}{2}r^2\sigma^2} \tag{4}$$

For the r^{th} moment of Y, explicit expressions for the parameters μ and σ in (3) can be obtained in terms of the mean μ_y and variance σ_y^2 of the lognormal variable Y as follows:

$$\mu = \ln\left(\frac{\mu_y}{\sqrt{1+\frac{{\sigma_y}^2}{{\mu_y}^2}}}\right) \tag{5}$$

$$\sigma^2 = \ln\left(1+\frac{{\sigma_y}^2}{{\mu_y}^2}\right) \tag{6}$$

By making the lognormal assumption for the absolute response magnitudes of interest for each realised ground vehicle, a set of identical, independent random variables Y_i then exist, each with a lognormal density given by equation (3).

There exist different routes to analytically calculate the mean and variance of the absolute magnitude for the vertical displacement of a ground vehicle with one or more random parameters. When these moments correspond to a lognormal variable, they can be associated with the moments μ_y and variance σ_y^2 used in equations (5) and (6), to obtain the distribution parameters. This being a lognormal density function given by equation (3) which can then be used in equation (1) to construct the quantile Z_P satisfying equation (2) to provide a statistical bound of the magnitude of the response of the N independent random vehicles that forms the focus of the study. In this paper, we have chosen to calculate the mean μ_y and the variance σ_y^2 via Direct Integration owing to its advantageous computational capabilities.

To do this for any set of random uncertain parameters, the magnitude of the response y=g(**X**) is a function of the random parameter vector **X**. Therefore, there is no statistical scatter for the function g(**X**). If the pdf f(**X**) is known, the mean and variance can be obtained from:

$$\mu_y = E(y) = E\big(g(\mathbf{X})\big) = \int_{-\infty}^{\infty}\dots\int_{-\infty}^{\infty} g(\mathbf{X})f(\mathbf{X})d\mathbf{X} \tag{7}$$

and

$$\sigma_y^2 = E(g(\mathbf{X})^2) - E\big(g(\mathbf{X})\big)^2 \tag{8}$$

noting that:

$$E(g(\mathbf{X})^2) = \int_{-\infty}^{\infty}\dots\int_{-\infty}^{\infty} g(\mathbf{X})^2 f(\mathbf{X})d\mathbf{X} \tag{9}$$

Equations (10 to (9) will now be applied to data generated by a simulation model. In particular, the simulation model will be used to generate the deterministic function g(**X**) used in equations (7) to (9). First the 'Full Car' vehicle dynamic simulation model will be described.

3 Full-Car model

The model used for the simulations is a 7- degree of freedom system. A diagram representing the system is shown in Figure 1. The vehicle has 4 independent suspension sub-systems with tyre damping and stiffness taken into account.

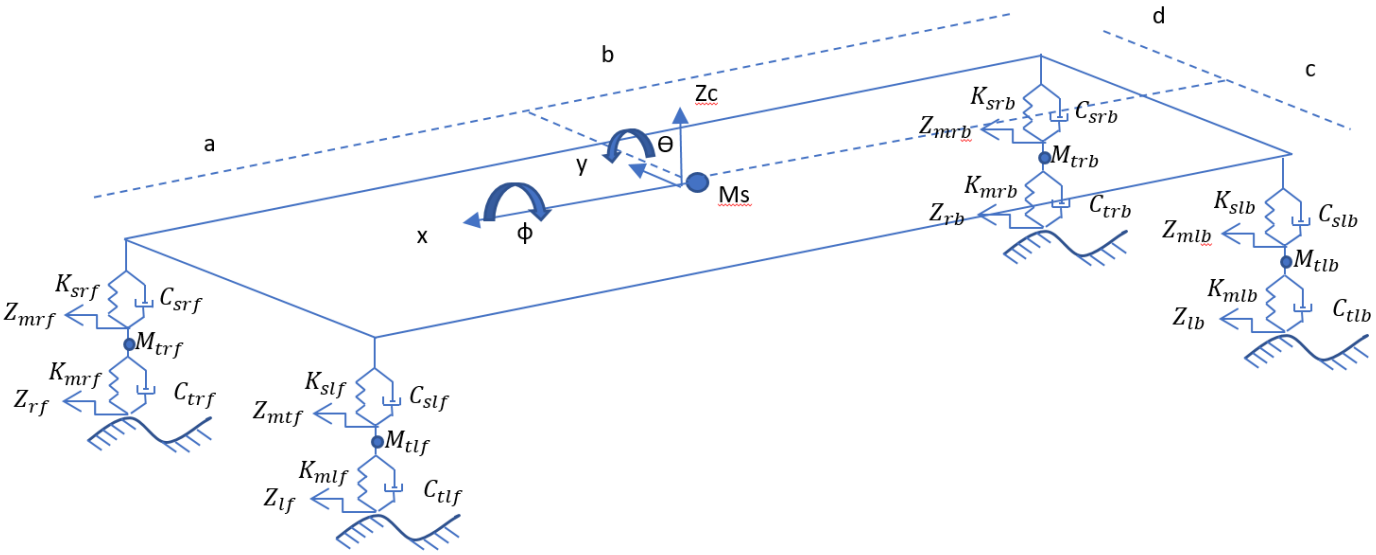


Figure 1. Full-Car model

The equations of motion that describe the car dynamic displacements can be represented as follows:

For the main body:

$$
\begin{aligned}
M_s\ddot{Z}_C = {} & \left(-K_{srf} - K_{slf} - K_{srb} - K_{slb}\right)Z_c \\
& + \left(-C_{srf} - C_{slf} - C_{srb} - C_{slb}\right)\dot{Z}_c \\
& + \left(K_{srf}a + K_{slf}a - K_{srb}b - K_{slb}b\right)\theta \\
& + \left(C_{srf}a + C_{slf}a - C_{srb}b - C_{slb}b\right)\dot{\theta} \\
& + \left(K_{srf}c - K_{slf}d + K_{srb}c - K_{slb}d\right)\phi \\
& + \left(C_{srf}c - C_{slf}d + C_{srb}c - C_{slb}d\right)\dot{\phi} \\
& + K_{srf}Z_{mrf} + K_{slf}Z_{mlf} + K_{srb}Z_{mrb} \\
& - K_{slb}Z_{mlb} + C_{srf}\dot{Z}_{mrf} + C_{slf}\dot{Z}_{mlf} \\
& + C_{srb}\dot{Z}_{mrb} + C_{slb}\dot{Z}_{mlb}
\end{aligned}
\tag{10}
$$

For pitch motion:

$$
\begin{aligned}
I_{yy}\ddot{\theta} &= \left(K_{srf}a + K_{slf}a - K_{srb}b - K_{slb}b\right)Z_c \\
&+ (C_{srf}a + C_{slf}a - C_{srb}b - C_{slb}b)\dot{Z}_c \\
&+\left(-K_{srf}a^2 - K_{slf}a^2 - K_{srb}b^2 - K_{slb}b^2\right)\theta \\
&+ (C_{srf}a^2 - C_{slf}a^2 - C_{srb}b^2 - C_{slb}b^2)\dot{\theta} \\
&+\left(-K_{srf}ac + K_{slf}ad + K_{srb}bc + K_{slb}bd\right)\phi \\
&+ (-C_{srf}ac + C_{slf}ad + C_{srb}bc - C_{slb}bd)\dot{\phi} \\
&-K_{srf}aZ_{mrf} - K_{slf}aZ_{mlf} + K_{srb}bZ_{mrb} \\
&+K_{slb}bZ_{mlb} - C_{srf}a\dot{Z}_{mrf} - C_{slf}a\dot{Z}_{mlf} \\
&+C_{srb}b\dot{Z}_{mrb} + C_{slb}b\dot{Z}_{mlb}
\end{aligned} \tag{11}
$$

For rolling motion:

$$
\begin{aligned}
I_{xx}\ddot{\phi} &= \left(K_{srf}c - K_{slf}d + K_{srb}c - K_{slb}d\right)Z_c \\
&+ (C_{srf}c - C_{slf}d + C_{srb}c - C_{slb}d)\dot{Z}_c \\
&+\left(-K_{srf}ac + K_{slf}ad + K_{srb}bc - K_{slb}bd\right)\theta \\
&+ (C_{srf}ac + C_{slf}ad + C_{srb}bc - C_{slb}bd)\dot{\theta} \\
&+\left(-K_{srf}c^2 - K_{slf}d^2 - K_{srb}c^2 - K_{slb}d^2\right)\phi \\
&+ (-C_{srf}c^2 - C_{slf}d^2 - C_{srb}c^2 - C_{slb}d^2)\dot{\phi} \\
&-K_{srf}cZ_{mrf} + K_{slf}dZ_{mlf} - K_{srb}cZ_{mrb} \\
&+K_{slb}bd - C_{srf}c\dot{Z}_{mrf} + C_{slf}d\dot{Z}_{mlf} \\
&-C_{srb}c\dot{Z}_{mrb} + C_{slb}d\dot{Z}_{mlb}
\end{aligned} \tag{12}
$$

The suspension sub-system Front Right tyre can be expressed as:

$$
\begin{aligned}
M_{trf}\ddot{Z}_{mtf} &= K_{srf}(Z_c - Z_{mrf} - a\theta - c\phi) \\
&+C_{srf}\left(\dot{Z}_c - \dot{Z}_{mrf} - a\dot{\theta} - c\dot{\phi}\right) \\
&+K_{mrf}\left(Z_{rf} - Z_{mrf}\right) - C_{trf}\left(\dot{Z}_{mrf} - \dot{Z}_{rf}\right)
\end{aligned} \tag{13}
$$

The suspension sub-system Front Left tyre can be expressed as:

$$
\begin{aligned}
M_{tlf}\ddot{Z}_{mlf} &= K_{slf}(Z_c - Z_{mlf} - a\theta + d\phi) \\
&+C_{slf}\left(\dot{Z}_c - \dot{Z}_{mlf} - a\dot{\theta} + d\dot{\phi}\right) \\
&+K_{mlf}\left(Z_{lf} - Z_{mlf}\right) - C_{tlf}(\dot{Z}_{mlf} - \dot{Z}_{lf})
\end{aligned} \tag{14}
$$

The suspension sub-system of the Rear Right tire:

$$\begin{aligned} M_{trb}\ddot{Z}_{mrb} &= K_{srb}(Z_c - Z_{mrb} + b\theta - c\phi) \\ &+C_{srb}\left(\dot{Z}_c - \dot{Z}_{mrb} + b\dot{\theta} - c\dot{\phi}\right) \\ &+K_{mrb}(Z_{rb} - Z_{mrb}) - C_{trb}(\dot{Z}_{mrb} - \dot{Z}_{rb}) \end{aligned} \quad (15)$$

The suspension sub-system of the Rear Left tire:

$$\begin{aligned} M_{tlb}\ddot{Z}_{mlb} &= K_{slb}(Z_c - Z_{mlb} + b\theta + d\phi) \\ &+C_{slb}\left(\dot{Z}_c - \dot{Z}_{mlb} + b\dot{\theta} + d\dot{\phi}\right) \\ &+K_{mlb}(Z_{lb} - Z_{mlb}) - C_{tlb}(\dot{Z}_{mlb} - \dot{Z}_{lb}) \end{aligned} \quad (16)$$

where the relevant distances from Centre of Gravity (CG) are represented in equations (10) – (16) as follows: *a* is the distance from CG to front wheel, b is the distance from CG to the rear wheel, c is the distance from CG to right wheel, d is the distance from CG to left wheel. For the parameters in the suspension: Cslf is the damping coefficient of the front-left damper, Cslb is the damping coefficient of the rear-left damper, Csrf is the damping coefficient of front-right damper, Csrb is the damping coefficient of back-right damper, , Kslf is the spring stiffness of front-left suspension, Kslb is the spring stiffness of the back-left suspension, Ksrf is the spring stiffness of the front-right suspension, Ksrb is the spring stiffness of back-right suspension, Kmlf is the spring stiffness of front-left tire, Kmlb is the spring stiffness of back-left tire, Kmrf is the spring stiffness of front-right tire, Kmrb is the spring stiffness of back-right tire, Mmlf is the mass of front-left wheel, Mmlb is the mass of back-left wheel, Mmrf is the mass of front-right wheel, Mmrb is the mass of back-right wheel, Zmlf is the displacement of the front-left wheel, Zmlb is the displacement of the back-left wheel, Zmrf is the displacement of front right wheel, Zmrb is the displacement of the back-right wheel. The moments of the body are:Ixx is the moment of inertia about X-X axis, Iyy is the moment of inertia about Y-Y axis. MS is the mass of vehicle, Zc is the displacement of centre of the vehicle body. The road inputs are described as: Zlf road input to the front-left wheel, Zlb is the road input to the back-left wheel, Zrf is the road input to front-right wheel, and Zrb is the road input to back-right wheel.

An appropriate set of deterministic suspension parameters are selected for the vehicle dynamic motion equations presented in equations (10)-(16), except the damping values. These damping parameters are adapted from a passive non-linear damper, taking into account that the compression ('bump') and rebound coefficients for a typical passive shock absorber are (by design) different, depending on the direction of travel i.e. whether 'bump' or 'rebound'. A set was chosen of uniformly distributed random bi-linear damping parameter values. Figure 2 shows the damper characteristic resulting from an example of 50 different parameter values being used to define a bi-linear shock-absorber depending on the cycle position. Additional complexity such as variability of the shock absorber resulting from frequency and temperature dependence, has not be considered in this paper.

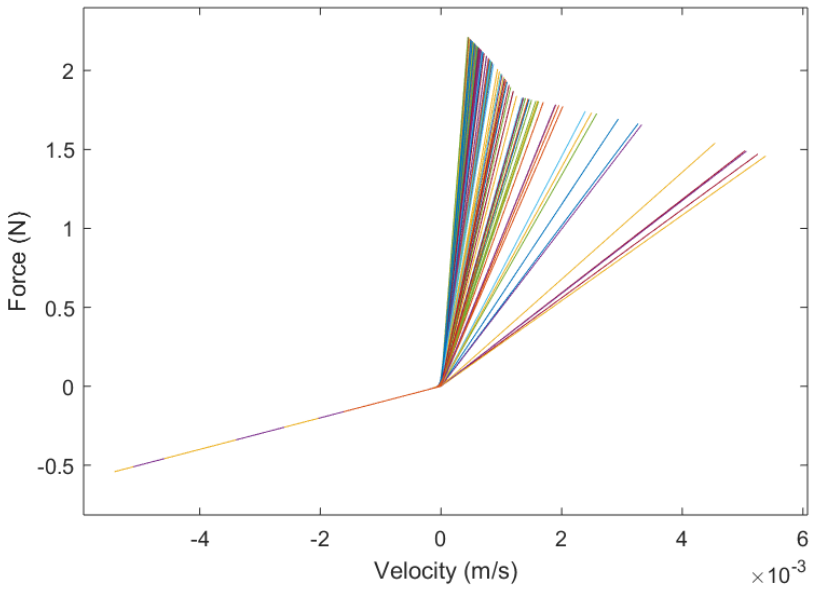


Figure 2. The first 50 simulations for random bi-lineal damper parameters

The road surface elevation in equations (10)–(16) is assumed to be a sinusoidal function of fixed amplitude and wavelength. This assumption is without loss of generality because any deterministic description of the road surface could be used to examine the uncertainty propagation. To obtain the function g(**X**) for use in equations (7) - (9), the system of equations (10) - (16) need to be integrated numerically to obtain the entire response. The Matlab Runge Kutta function *ODE45* [11] has been used to do this. In the particular, for application of the Direct Integration method considered in this paper, the computed deterministic function g(**X**) is 4-dimensional.

4 Monte Carlo simulation and use of the Direct Integration Method

4.1 Monte Carlo Simulation

The Monte Carlo simulation is chosen to be run as a representative description of the vehicle dynamics. Owing to its practical feasibility and reliability, the chosen Monte Carlo simulation method is based on Latin Hypercube Sampling (LHS) [12] stemming from the multidimensional nature of the problem which involves optimizing the choice of random values for the 4 different parameters.

The simulation was repeated 10000 times for vehicle response of 30 seconds and in each one, a different random value for the rebound of the suspension damper was chosen. The maximum vertical displacement of the front of the car was then recorded. This is chosen because the angle of attack and ground clearance are considered the main factors that create the conditions for the aerodynamic forces to cause vehicle lift-off. Figure 3 shows a histogram of the simulation results.

4.2 Direct integration Method

With the bi-linear damping model chosen to simulate the random variations, i.e. selected for just one of the damping coefficients (in each of the 4 dampers), this combination of parameters creates a 4-dimensional scatter-free response function g(**X**) for use in equations (7) and (9), which in turn can be used in equation (3) to obtain the required density function.

The probabilistic density function (pdf) of a uniform distributed set of variables is [9]:

$$f(X_i) = \frac{1}{2u} \tag{17}$$

where $u = \sqrt{3}\,\sigma_x$, and σ_x is the variance of the variable X_i. This probability density function is applied to every dimension of g(**X**). Direct Integration uses a variant of the standard trapezoidal rule using equi-spaced intervals of the variate in each of the discrete set of the 4 random damping parameters. In general, the computational demand in conventional multidimensional integration increases with the power of the number of dimensions. Some computational efficiency improvement can be found using quadrature techniques, or Monte Carlo Integration methods but are not within scope here.

5 Results and Discussion

The Monte Carlo simulation was repeated 10000 times. A histogram showing the results of the maximum height for the front part of the vehicle is given in Figure 3. These results were obtained by applying the LHS method in the Monte Carlo Simulation.

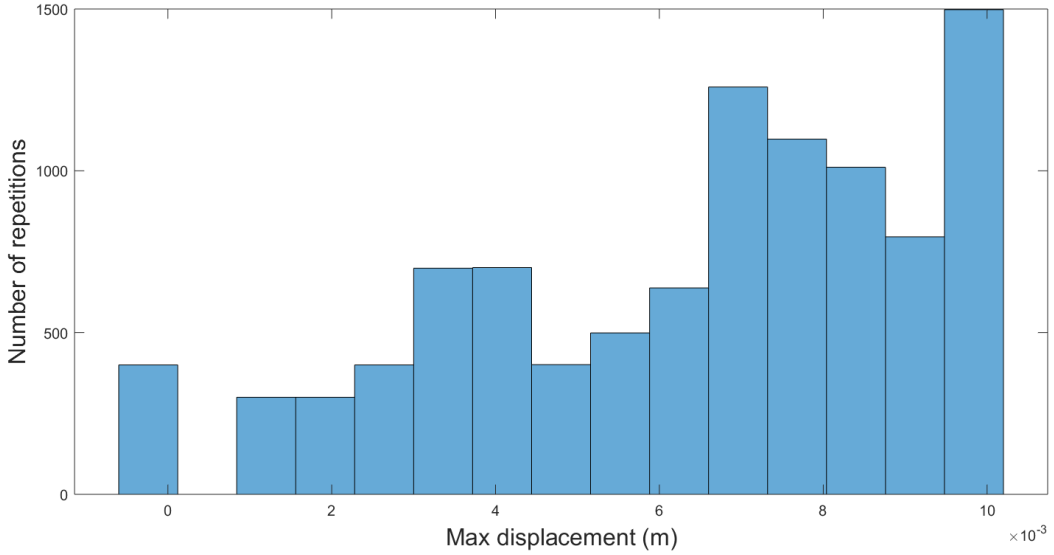


Figure 3. Histogram of 10000 repetitions of the Monte Carlo simulation

The Cumulative Distribution function can be calculated to obtain the Extreme Value response since it can be used to make predictions of the probability of a particular catastrophic event associated with a highly non-linear response such as a vehicle reaching a certain pitch height. A comparison is made between the Direct Integration method used in the adapted Extreme Value approach, and the Monte Carlo Simulation. Figure 4 shows the estimated Cumulative Distribution function for the Extreme Value responses comparing Direction Integration and Monte Carlo Simulation. This shows very good agreement between the

approaches but the important issue is the computational effort needed to achieve similar accuracy

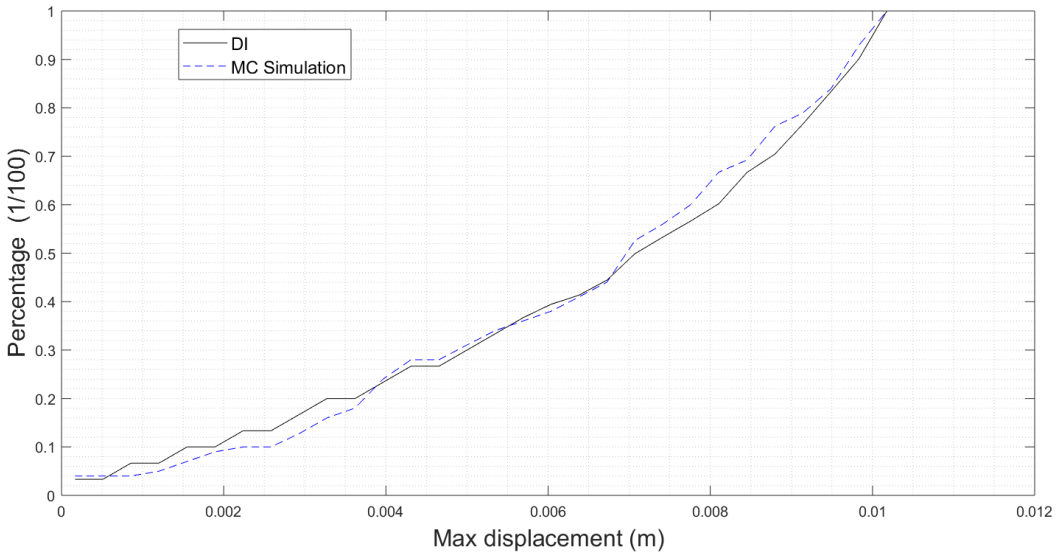


Figure 4. CDF comparative of Monte Carlo Simulation and the Direct Integration Method

To have the similar level of agreement shown in figure 4, the Direct integration method took 6 hrs 32 min, compared with Monte Carlo simulation which took 73 hrs and 3 minutes. The Direct integrations and the Monte Carlo simulations were run on an Intel Core i7 -6500U CPU PC at 2.50GHz.

The main benefits of the DI method are its simplicity and its computational efficiency. However, other integrations methods could produce better results when a higher number of dimensions is assessed. Monte Carlos simulations have been widely used for their accuracy. Yet, the computational power needed to run these simulations with an adequate sample size for a correct assessment is too high when the number of dimensions increase.

This paper, has not included within the full car model aerodynamic effects such as drag, lift, or ground effects that can have an important impact on vehicle stability. Results, similar to Figure 4, should actually be used to include angle-of-attack versus lift coefficients for specific cars. This is generally different for different car designs which have different lift coefficients as functions of angle of attack. These forces as reported in [1] - [5] can have of a high impact on vehicle behavior. It might also be possible to associate such probabilistic predictions with the particular stability of a car, such as reported in [5], i.e. to explain events that have occurred, such as at German Nürburgring event in May 2015 [3], or the Le Mans race meeting event in 2000 [2], or even the more recent SPA event in May 2018 [4].

A fast calculation method to predict the probability of such events could also be valuable for operation of autonomous vehicles when Level-5 autonomy [13] is reached, where a vehicle should be able to perform all critical driving functions, for all road conditions, totally autonomously (without any driver intervention).

6 Conclusions

A fast computational method using extreme value based uncertainty propagation has been adapted to provide the probabilistic information needed to predict rare catastrophically unstable vehicle dynamic events. The dynamics of the vehicle involve a nonlinear suspension system with random parameters. The adapted extreme value based method involves efficient multi-dimensional integration where the number of dimensions depends on the number of random variables chosen. Direct Integration has been compared with Monte Carlo simulation addressing a problem with 4 random parameters. The paper shows that 4-dimensional Direct Integration produces results of similar accuracy to the Monte Carlo simulation but, that

Direct Integration is an order of magnitude faster producing scatter-free results of similar accuracy. For problems involving substantially more than 4 random parameters, other integration techniques, such as Monte Carlo Integration, could however prove more appropriate than Direct Integration.

Acknowledgements

The authors wish to acknowledge the support of the Mexican Government research funding body CONACyT in enabling the first author: Mr Jesus Gonzalez, to undertake doctoral studies.

References

[1] R.G Dominy, A. Ryan, D.B. Sims-Williams, *The Aerodynamic Stability of a Le Mans Prototype Race Car Under Off-design Pitch Conditions*, SAE Technical Paper 2000-01-0872, 2000.

[2] P. Wright, *Cleared to take-off*, Race car Engineering, vol 9, N. 7, pp 16-18, 1999

[3] BBC Sport, *Spectator killed in Nürburgring endurance race accident*, www.bbc.co.uk/sport/motorsport/32100886 (Accessed: 27th April, 2018)

[4] Motosport.com, *SMP prepared to modify LMP1 car after airborne crash*, https://www.motorsport.com/wec/news/smp-prepared-to-modify-lmp1-airborne-crash-1035474/ *(Accessed: 10th May, 2018)*

[5] J. Katz, *Race Car Aerodynamics- Designing for Speed*, Pub. Robert Bentley, 1995

[6] W. Gao, N. Shang, J. Dai, *A stochastic quarter-car model for dynamic analysis of vehicle with uncertain parameters*, Journal of Vehicle System Dynamics, 46:12, 1159-1169, 2008.

[7] W. Gao, N. Shang, J. Dai, *Random displacement and acceleration responses of vehicle with uncertainty*, Journal of Mechanical Science and Technology, 25, 1221-1229, 2011.

[8] J. F. Dunne, and T. Cheepsomsong, *Accurate extreme-value-based frequency response bounding for structures with a small number of highly random parameters*, Journal of Sound and Vibration, 372,168-180, 2016.

[9] N.L. Johnson, S. Kotz, and N. Balakrishnan, 2nd Edition, *Continuous Unvariate Distributions*, Vol 1, Wiley Interscience, 207-220, 1994.

[10] R. Langley, J. Legault, J. Woodhouse, and E. Reynders, *On the applicability of the lognormal distribution in random dynamical systems*, Journal of Sound and Vibration 332, 3189-3302, 2013.

[11] Shampine, L. F. and M. W. Reichelt, *The MATLAB ODE Suite*, SIAM Journal on Scientific Computing, Vol. 18, 1–22, 1997.

[12] M. Keramat, and R. Kielbasa, Latin Hypercube Sampling Monte Carlo Estimation of Average Quality Index for Integrated Circuits, Analog Integrated Circuits And Signal Processing, vol. 14, pp. 131-142, 1997.

[13] Verband der Automobilindustrie, *Autonomy level reached*, www.vda.de (Accessed on 20th April 2018)

The influence of the uncertainty on dynamic soil properties on the prediction of railway induced vibration

M. Germonpré [1], **M. Papadopoulos** [1], **G. Degrande** [1], **G. Lombaert** [1]
[1] KU Leuven, Department of Civil Engineering, Kasteelpark Arenberg 40, B-3001, Heverlee, Belgium
e-mail: **matthias.germonpre@kuleuven.be**

Abstract

The growing recognition of railway induced vibration as an environmental issue increases the need for numerical prediction models. The development of these models is challenging, since they require substantial information on the model parameters of the track, soil and receiver. The soil, in particular, constitutes a significant source of uncertainty, while it has a dominant role in the prediction of ground-borne vibration. Therefore, this paper examines the sensitivity of railway induced vibration predictions to uncertain subsoil conditions. Based on the results of a measurement campaign conducted at a site in Belgium, models of the track, soil and building are developed. The measured and predicted response of the track, free field and building are compared and the influence of uncertain dynamic soil properties on the predicted response is investigated. It is found that this uncertainty has a large influence on the track-free field and track-building transfer functions, as well as on the free field and building response during train passages.

1 Introduction

The close proximity of existing and proposed railway tracks to residential areas results in public concern regarding noise and vibration produced by railway traffic. Railway induced vibration propagates through the soil and excites the foundations of nearby buildings. In the frequency range between 1 and 80 Hz, vibrations may cause disturbance of sensitive equipment and annoyance to people. At frequencies between 16 and 250 Hz, ground-borne vibration can cause re-radiated or structure-borne noise by vibrating walls and floors.

The growing recognition of railway induced vibration as an environmental issue has led to the development of numerical models for the prediction of the induced incident wave field as well as the structural response. However, given the complexity and the inherent uncertainty of the subproblems involved, in combination with the extended frequency range of interest, the accurate prediction of the response to railway induced vibration is challenging. Numerical models require substantial information on the model parameters of the track, the soil and the receiver, which requires extensive experimental investigation. Therefore, non-intrusive experimental methods have been developed to identify the track stiffness, the properties of shallow soil layers and the modal characteristics of structures, which can be utilized to calibrate numerical models.

The soil, in particular, constitutes a significant source of uncertainty in the numerical models, while it has a dominant role on the structural response to ground-borne vibration. Therefore, this paper examines the influence of uncertain subsoil conditions on the prediction of railway induced vibration. A measurement campaign was conducted at a site in Belgium where a railway track passes through a residential and office area. Measurements were taken on the track, in the free field and in a nearby office building during train passages. The dynamic properties of the track and subsoil at the site and the modal characteristics of the building were identified experimentally to facilitate numerical modeling. The measured and predicted response of the track, the free field and the building are compared and the influence of uncertain dynamic soil properties on the predicted response is discussed.

2 Description of measurement site

The measurement site located in Heverlee (Belgium) is shown in figure 1(a). The railway line L1390 between Leuven and Ottignies consists of two ballasted tracks on an embankment and is operated by passenger and freight trains. At 33 m from the track, the Blok D building of the administrative complex of KU Leuven is situated. This three-story building houses part of the administrative services of KU Leuven and provides temporary office space. Figure 1(b) shows a plan view of the floors. The foundation consists of individual footings and strip foundations. The Blok D building is part of a wider office building complex; the basement and the ground floor are interconnected with adjacent buildings by means of external walkways.

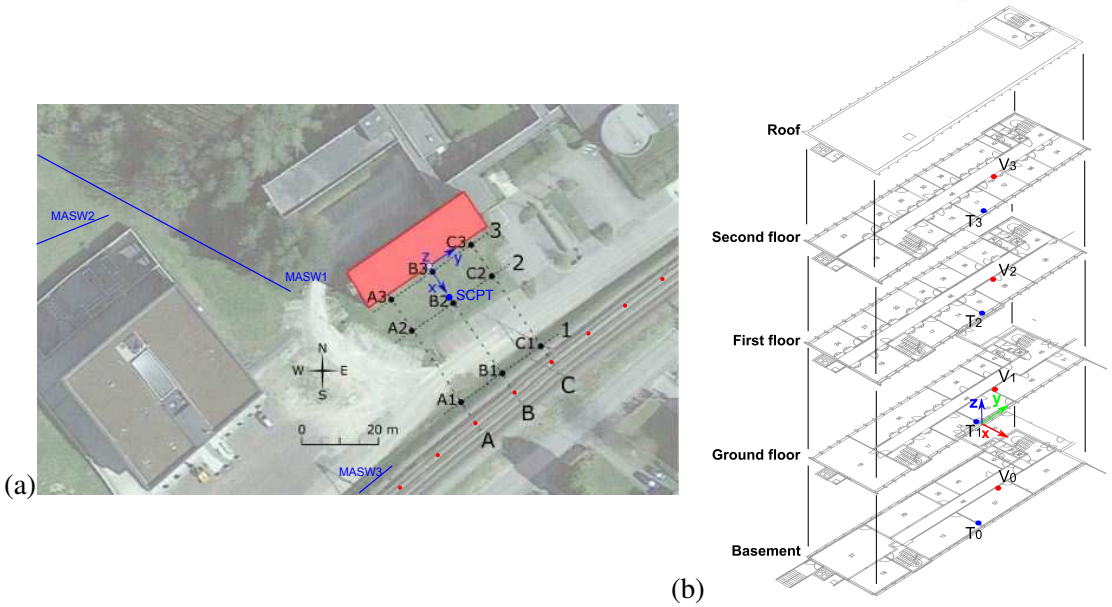


Figure 1: (a) Overview of the site in Heverlee and (b) plan view of the floors of the Blok D building. Receiver locations within the building V_k and T_k.

The dynamic response of the track, free field and building was measured during the passage of a high number of passenger and freight trains. The building response was measured at the basement, the ground floor, the first floor and the second floor at the receiver points T_k and V_k ($k = 0, .., 3$) (figure 1(b)). Free field vibration measurements were performed between the building and the railway track in 9 points (figure 1(a)). The three measurement points of line 1 are located at one meter from the foot of the embankment. The response in these points was measured in the x- and z-directions. On line 2, situated between the track and the building at 21 m from the embankment, the response was measured in the vertical direction only. On line 3, at one meter from the building, the response was measured in the x-, y- and z-directions. Measurement line B corresponds to the center of the building, lines A and C are located at 12 m from line B. Also, the vertical vibration velocity of ten adjacent sleepers centered around line B was monitored. By means of hammer impacts on these ten sleepers, sleeper receptance functions were identified. Also, transfer functions were obtained between a force on the sleepers located at lines A, B and C and the velocity in the free field and building receiver points.

Figure 2 shows the modeled cross section of the site, corresponding to line B. Although the cross sectional geometry is slightly different at lines A and C, the same cross section is assumed at the three measurement lines. Near the building, the soil is 1.85 m lower than at the foot of the embankment. The soil properties were determined by means of two multichannel analysis of surface waves tests [1, 2] (MASW1 and MASW2 in figure 1(a)) and one seismic cone penetration test (SCPT). At the location of MASW1 and MASW2, the soil surface is 1.85 m below the foot of the embankment (figure 2). Therefore, the results of these tests were used to determine the soil properties below this point. The SCPT was performed starting at z=0.85 m, one

meter higher than the MASW tests. The estimation of the soil properties between z=0.85 m and 1.85 m is only based on the SCPT results. To investigate the soil properties of the top 0.85 m, a third MASW test (MASW3 in figure 1) was performed between the track and the road. Due to the close proximity of the track, the results of this test did not allow to determine the properties of this part of the soil.

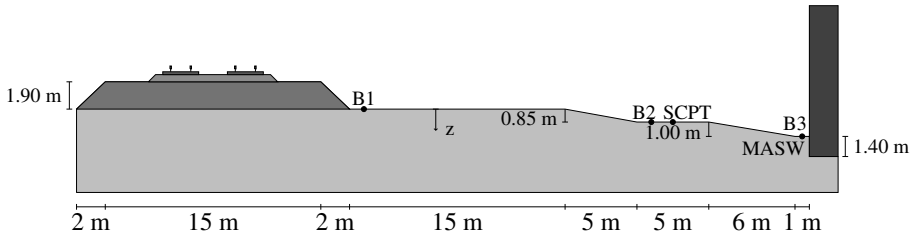


Figure 2: Cross section along measurement line B, with location of SCPT and MASW tests.

The modal characterstics of the building were identified experimentally. Ambient excitation data collected by fifteen wireless tri-axial accelerometers (GeoSIG units) placed on each floor, including the basement and the roof of the building, were processed in MACEC toolbox for MATLAB [3] to identify three global modes of the building; two lateral and one torsional. An additional modal test using combined ambient and forced vibration data was performed to identify the vertical modes of the building. Fifteen GeoSIG units and seven uniaxial accelerometers spread across the floors of the building were used. The forced vibration data were obtained by means of impact hammer excitation at the top two floors of the building. These data were also processed in MACEC resulting in eight identified vertical modes of the floors.

3 Numerical model

In order to predict free field and building vibrations during train passages, as well as to evaluate the effect of the uncertainty on the dynamic soil properties on the predicted results, a numerical model of the track, soil and building is developed. The measured track receptance functions, transfer functions between the track and the free field and the modal characteristics of the building are used to calibrate the track, soil and building models, respectively.

3.1 Soil model

The soil is modeled by a number of horizontal layers on top of a halfspace. The soil profile at Heverlee was determined using a Bayesian inversion procedure [4] that allows to combine data from different in situ tests. This procedure takes into account the uncertainties on the measurements and the horizontally layered soil model by means of likelihood functions. This probabilistic approach for the determination of the dynamic soil characteristics results in a MAP (Maximum A Posteriori Probability) profile, that can be considered as the soil profile that maximizes the posterior PDF of the soil parameters. This MAP profile is presented in table 1 and used to tune the track model. The top of the soil profile corresponds to the foot of the embankment in figure 2. The dynamic properties of the first soil layer are unknown.

The applied soil characterization method also results in an ensemble of soil profiles that are representative for the region of soil properties with high likelihood. These profiles are consistent with the measurement data and taking into account the measurement and model uncertainty, each of these profiles could be closer to the actual soil profile at the site than the MAP profile. These soil profiles are used in section 4 to investigate the effect of the uncertainty on the dynamic soil properties on the prediction of railway induced vibration. Figure 3 shows the soil properties of the MAP profile and the ensemble of 20 soil profiles. The largest variability on these 21 soil profiles is observed for the top layer and below 15 m. For the top soil layer, only

Layer	h [m]	C_s [m/s]	C_p [m/s]	β_s [-]	β_p [-]	ρ [kg/m^3]
1	0.85	-	-	-	-	-
2	1.0	141	282	0.044	0.044	1800
3	2.4	198	290	0.044	0.044	1800
4	4.2	168	368	0.021	0.021	1800
5	1.5	198	1835	0.029	0.029	1800
6	1.5	220	1835	0.043	0.043	1800
7	3.8	238	1835	0.055	0.055	1800
8	3.1	131	1835	0.062	0.062	1800
9	∞	317	1835	0.088	0.088	1800

Table 1: Dynamic soil characteristics in Heverlee (Belgium).

data from the SCPT are available, which makes it more difficult to accurately determine its properties. The SCPT was performed up to a depth of 15 m, so below this point only information from the MASW can be used. In this test, however, the waves in the soil only propagate below 15 m for low frequencies, so it is not possible to accurately determine the soil properties at this depth based on the MASW. The properties of the first 0.85 m are unknown.

3.2 Source model: ballasted track

The tracks consist of UIC60 rails with mass per unit length ρA = 60.2 kg/m and bending stiffness EI = 6.45 Nm^2, supported by resilient studded rubber rail pads connected to prestressed concrete monoblock sleepers. The rail pads are medium stiff, stiffness and damping properties of 150 $\times$ 10^6 N/m and 13.5 $\times$ 10^3 N/(m/s) are assumed. The sleepers have mass 300 kg and mass moment of inertia 157.3 kgm^2 and are 2.50 m long and 0.235 m wide with spacing L = 0.60 m. The sleepers are supported by a 0.40 m high porphyry ballast layer, for which a density ρ = 1800 kg/m^3, Poisson coefficient ν = 0.33 and damping β = 0.025 are assumed. The track is located on top of a 1.90 m high embankment. The soil characteristics are known from the second layer onward (below z=0.85 m). The dynamic properties of the ballast layer, the embankment and the first soil layer (above z =0.85 m) are unknown. Only the track closest to the building is taken into account.

To simulate the passage of a train on the track in Heverlee and to compute the resulting free field and building vibration, a numerical track model is developed. According to the findings in [5], a periodic track model is used to compute the track receptance and train-track interaction forces, while a 2.5D model is used to compute the propagation of vibration to the free field and the building. In the periodic track model, the embankment is modeled as an additional soil layer with the same properties. The inclination of the soil is neglected. The geometry of the 2.5D model corresponds to the cross section shown in figure 2, where the soil above z=1.85 m is modeled with finite elements and below this point by boundary elements. The presence of the building is disregarded.

The dynamic properties of the ballast layer, the embankment and the first soil layer, as well as the size of the sleeper-ballast contact area, are tuned based on the results of the measurements. Two contact areas with length l_c between the sleeper and the ballast located under the two rails are assumed. The tuning is performed based on a forward parametric study. The shear wave velocity C_s of the ballast and the size of the sleeper-ballast contact area are determined based on the measured sleeper receptance, using the periodic track model. The dynamic properties of the embankment and first soil layer are tuned based on the measured transfer functions between the track and the free field receiver points on the first measurement line, using the 2.5D model. For the length of the sleeper-ballast contact area, l_c = 0.30 m was found. The tuned values of the ballast, embankment and first soil layer are summarized in table 2.

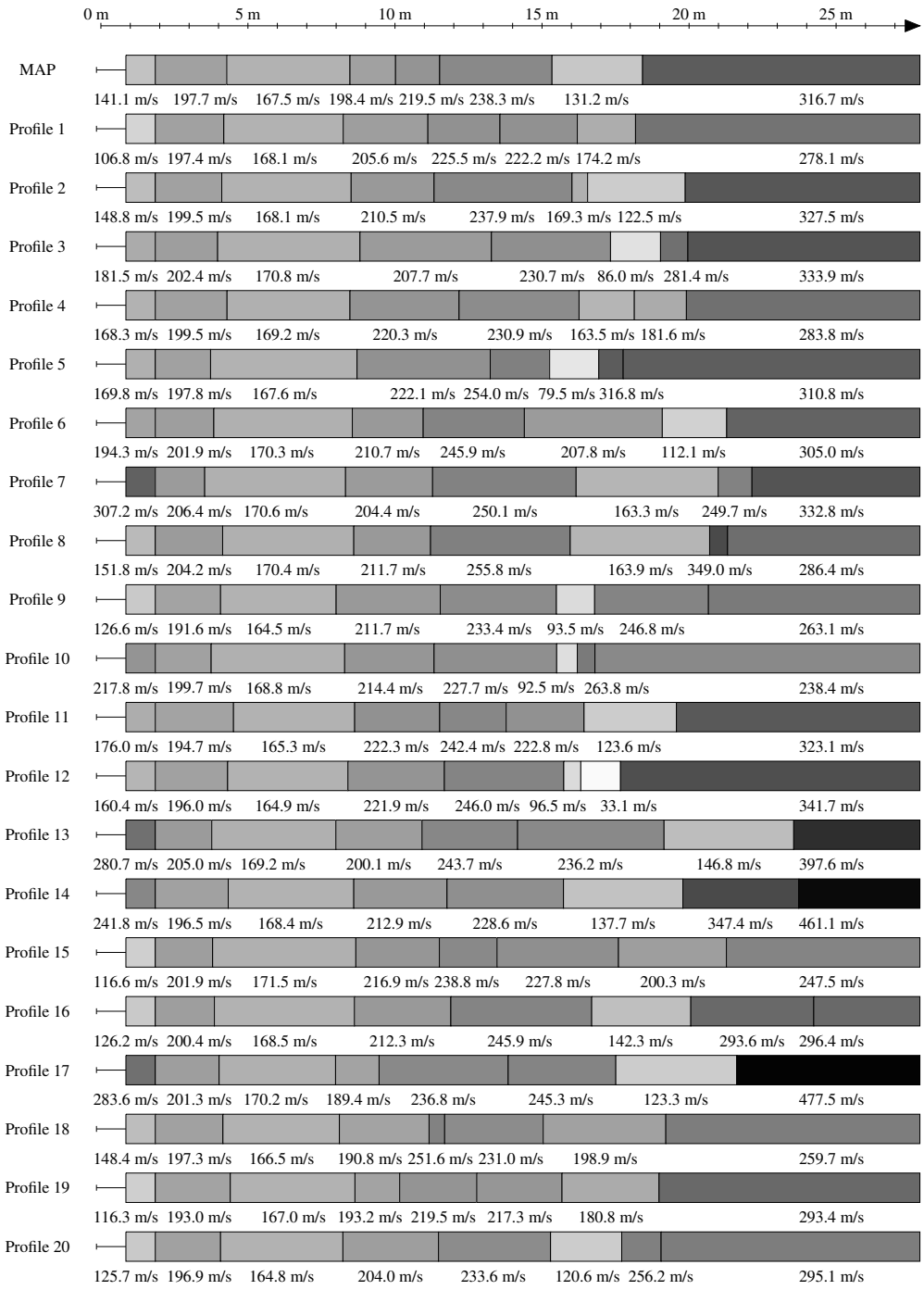


Figure 3: Dynamic soil properties of the MAP profile and an ensemble of 20 profiles representative for the region of soil properties with high likelihood.

	h [m]	C_s [m/s]	C_p [m/s]	β_s [-]	β_p [-]	ρ [kg/m^3]
Ballast	0.40	120	240	0.025	0.025	1800
Embankment	1.90	130	260	0.044	0.044	1800
Soil layer 1	0.85	141	282	0.044	0.044	1800

Table 2: Dynamic characteristics of the ballast, embankment and first soil layer.

Figure 4 shows the modulus of the measured sleeper receptance functions of the ten instrumented sleepers, as well as the computed track receptance function. The difference between the ten measured sleeper receptance functions is large. This is mainly due to the different support conditions of these sleepers: some are only supported by ballast on a small area underneath the rails, while others are supported by a larger ballast area. The computed receptance function after tuning lies within the ten measured functions.

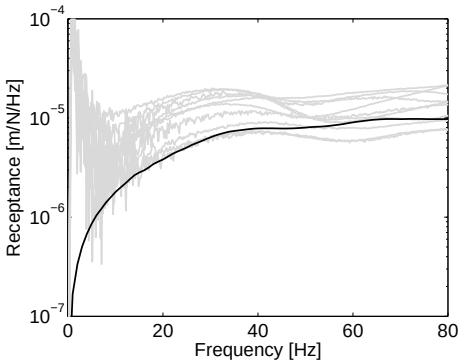


Figure 4: Modulus of measured (grey lines) and computed sleeper receptance after tuning (black line).

Figure 5 shows the modulus of the measured and computed track-free field mobility between the sleeper and the first and third measurement lines after tuning. The measured transfer functions correspond to the vertical free field velocity in a receiver point due to a vertical impulse load on the sleeper located at the same measurement line A, B or C. At line 1, the measured mobility shows a peak around 35 Hz. This peak is also present in the computed transfer function, although the mobility is slightly overestimated. Between 10 Hz and 20 Hz, the computed transfer function underestimates the vibration but in general, the computed transfer function agrees very well with the measurements. Also at line 3, a good agreement with the measurements is obtained, although the response is underestimated by the model between 20 Hz and 50 Hz.

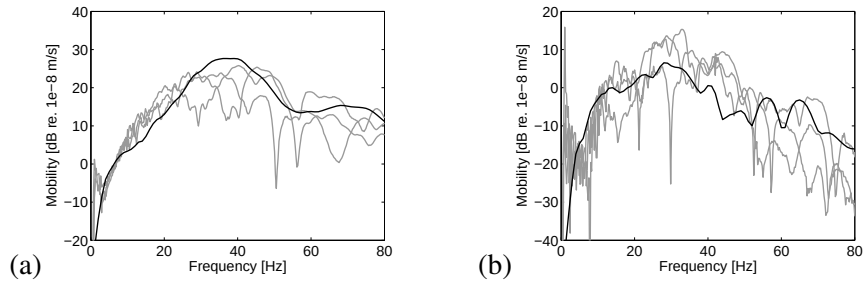
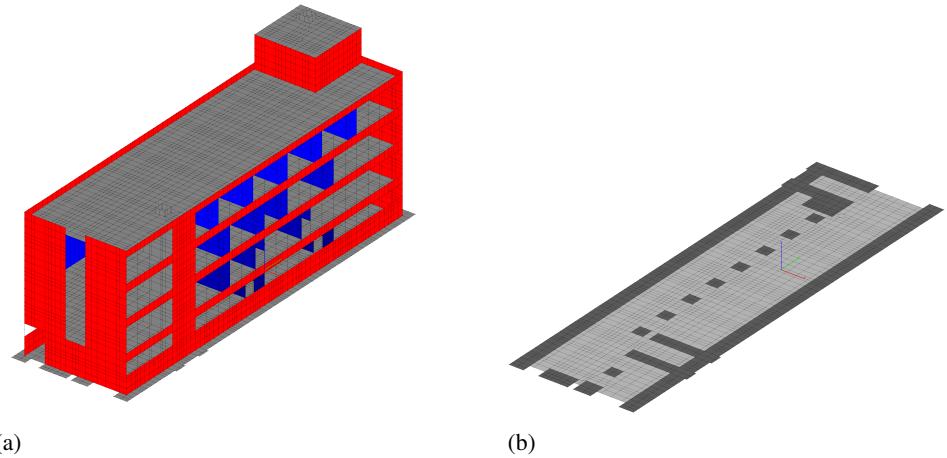


Figure 5: Modulus of the computed (black line) and measured (grey lines) transfer functions at lines A, B and C between a vertical force on the sleeper and the vertical velocity at the (a) line 1 (b) line 3.

3.3 Receiver model: Blok D building

Figure 6 shows the FE-BE model of the Blok D building. The model is based on the available structural and architectural drawings and on site inspections of the building. The finite element model is developed using the finite element software SAP2000 [6]. The walls, floors, footings and strip foundations are modeled with four-node shell elements and the beams and columns are modeled with two-node frame elements (figure 6a). The foundation of the Blok D building is modeled with boundary elements (figure 6b) disregarding the shallow embedment of the building in the surrounding soil. The MATLAB boundary element toolbox BEMFUN [7] is used to compute the dynamic stiffness of the surface foundation and the equivalent forces at the foundation due to incident wave fields. The boundary element mesh is conforming to the finite element mesh in order to facilitate the finite element-boundary element coupling (figure 6). The boundary element model is developed using the identified soil properties (section 3.1) after modification to account for the increased stress state underneath the building. A maximum finite element and boundary element size $l_{\mathrm{e}} = 0.60\,\mathrm{m}$ is chosen corresponding to 6 linear boundary elements per shear wave length at a frequency of $80\,\mathrm{Hz}$ for the mean soil properties used to compute the dynamic stiffness of the surface foundation.



(a) (b)

Figure 6: FE-BE model of the Blok D building. (a) FE mesh of the superstructure and (b) BE mesh of the surface foundation. The colors correspond to concrete (grey), masonry (red) and plasterboard walls (blue). The individual foundation footings and the strip foundations are shown in dark grey.

The non-structural elements can have a significant effect on the structural response and are, therefore, included as well in the finite element model of the building. Non-structural elements such as floor coverings and masonry infill walls contribute significantly to the mass and the stiffness of the building. In addition, lightweight elements with low stiffness such as plasterboard and plywood infill/partitioning walls are equally important. These walls introduce a weak coupling between degrees of freedom of successive floors which collectively can affect the vertical response of the floors. Hysteretic damping is assumed in the building with a hysteretic damping ratio $\eta = 0.03$.

The FE-BE model is calibrated using the experimentally identified modal characteristics. Table 3 summarizes the identified modal characteristics of the Blok D building. Dynamic SSI is a source of non-proportional damping leading to rather high modal damping ratios ξ^{exp} and low modal phase collinearity (MPC) values for almost all the identified modes. The MPC is a metric to quantify the coherence of a mode shape. A low MPC value can indicate a poorly or badly identified mode shape or, as in this case, it is the physical outcome of a non-proportionally damped system.

The stiffness and mass properties of the structural and non-structural elements of the building model are used as updating parameters to reduce the discrepancy between identified and predicted modal characteristics. The modal characteristics of the undamped coupled FE-BE model are computed using the static stiffness of the soil. Figures 7 and 8 show the predicted and identified global and vertical modes of the Blok D building.

Mode	$\boldsymbol{\varphi}^{\mathrm{exp}}$ (Figure)	$f_{\mathrm{r}}^{\mathrm{exp}}$ [Hz]	ξ^{exp} [−]	MPC [−]	Description
1	7a.1	3.37	0.032	0.91	Lateral y
2	7a.2	3.80	0.062	0.73	Lateral x
3	7a.3	5.12	0.023	0.90	Torsional
4	8a	9.14	0.032	0.94	Vertical
5	8b	10.70	0.013	0.79	
6	8c	11.18	0.027	0.93	
7	8d	12.57	0.029	0.78	
8	8e	15.59	0.043	0.80	
9	8f	15.98	0.020	0.76	
10	8g	16.43	0.040	0.87	
11	8h	20.14	0.027	0.72	

Table 3: Experimentally identified modal characteristics of the Blok D building.

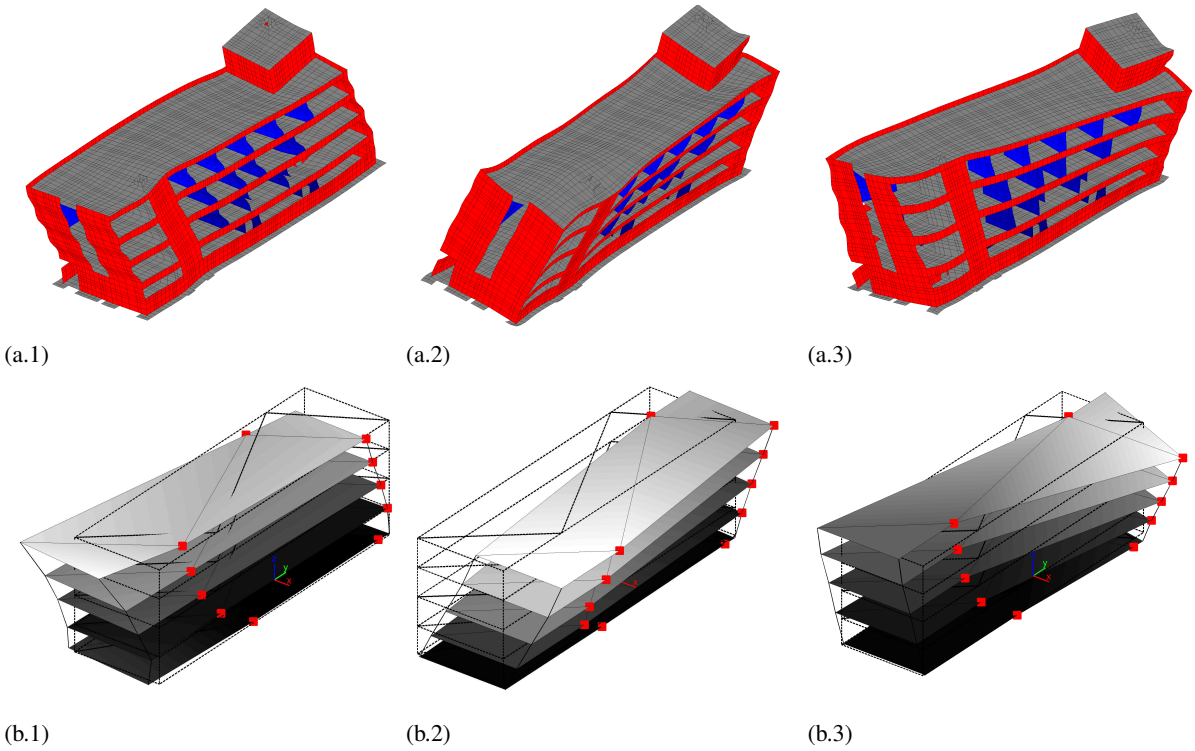


Figure 7: (a) Predicted mode shapes $\boldsymbol{\varphi}_j$ and (b) experimentally identified mode shapes $\boldsymbol{\varphi}_j^{\mathrm{exp}}$ of the Blok D building: (1) First lateral (y-direction) mode shape, (2) second lateral (x-direction) mode shape and (3) first torsional mode shape. The actually observed locations are marked with a red rectangle, the mode shapes $\boldsymbol{\varphi}^{\mathrm{exp}}$ were extrapolated to unobserved locations assuming rigid body kinematics.

Figure 8 shows the experimentally identified and the predicted vertical mode shapes of the calibrated FE-BE model. Figure 9 shows the relative eigenfrequency errors $\Delta f_{\mathrm{r}j}$ and the corresponding MAC values between the identified and the predicted modes for the updated FE-BE model. The agreement between the identified and predicted global modes of the building is rather good. However, the updated FE-BE model underestimates the eigenfrequencies of most of the vertical modes. This could be due to modeling simplifications of the foundation or due to the possibly anistropic nature of the soil, behaving stiffer in the vertical than in the lateral direction.

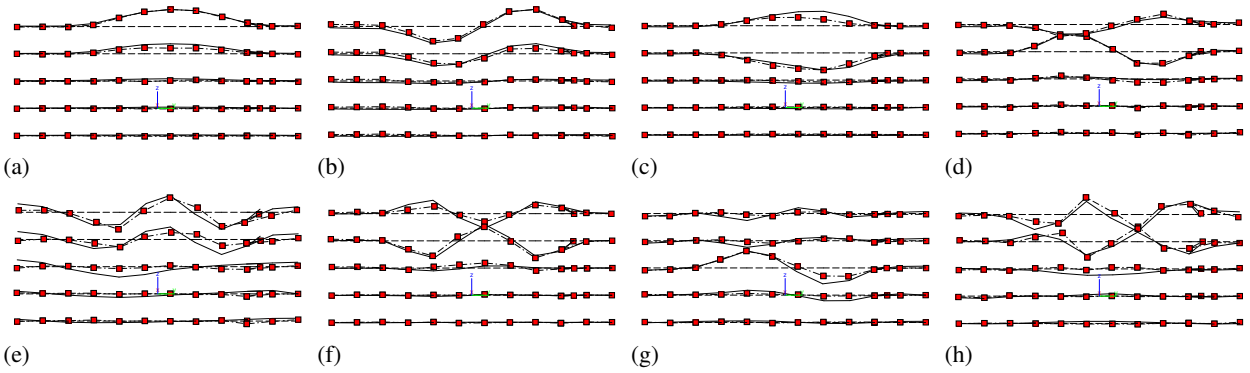
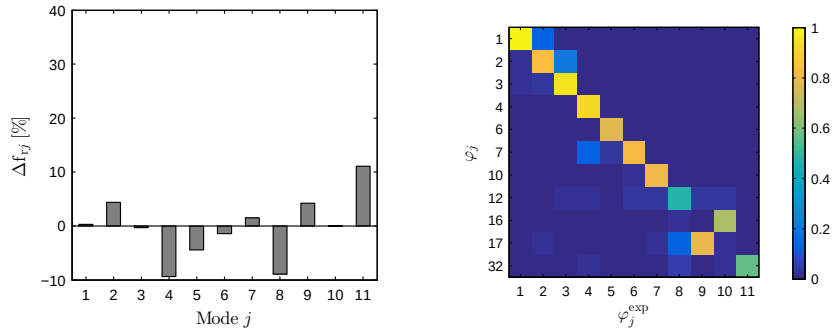


Figure 8: Identified vertical mode shapes $\boldsymbol{\varphi}^{\mathrm{exp}}$ (dashed-dotted lines) and predicted vertical mode shapes $\boldsymbol{\varphi}$ (solid lines) of the calibrated FE-BE model (solid lines) along the main corridor of the Blok D building. The actually observed locations of the identified $\boldsymbol{\varphi}^{\mathrm{exp}}$ are marked with a red rectangle.



(a) (b)

Figure 9: (a) Relative eigenfrequency error $\Delta f_{\mathrm{r}j}$ and (b) MAC values between the experimentally identified and the numerically predicted modes.

4 Effect of uncertainty on dynamic soil properties

4.1 Track receptance

The influence of the uncertainty on the dynamic soil properties on the track receptance is investigated in figure 10. The average receptance function shown in this figure is defined as the average receptance at each frequency for the computed sleeper receptances obtained with the 20 profiles from the ensemble. It is observed that the average receptance and the 5 % and 95 % quantiles are very close. Therefore, the uncertainty on the dynamic soil properties has only a very small influence on the track receptance.

4.2 Track-free field mobility

Figure 11 shows the influence of the uncertainty on the dynamic soil properties on the transfer functions between the vertical sleeper force and the free field response at the first and third measurement lines. The region between the 5 % and 95 % quantiles is large above 10 Hz, even up to 20 dB for line 3. The measured transfer functions lie almost entirely between the 5 % and 95 % quantiles. The influence of the uncertainty on the dynamic soil parameters on the prediction of the track-free field transfer function is very large, both at short and large distances from the track. The result obtained with the MAP profile is close to the average result obtained with the ensemble of 20 profiles, at both lines 1 and 3. The MAP profile is therefore representative of the average expected soil characteristics in Heverlee.

The largest difference between the 21 soil profiles in figure 3 is found between z=0.85 m and 1.85 m, where

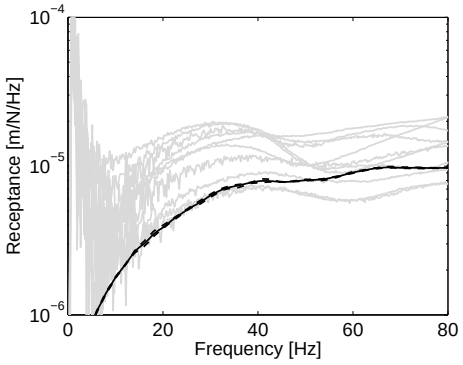


Figure 10: Modulus of the average (solid back line) and 5 % and 95 % quantile (dashed black lines) of the sleeper receptance computed with the ensemble of 20 profiles, compared to the measured sleeper receptance (grey lines).

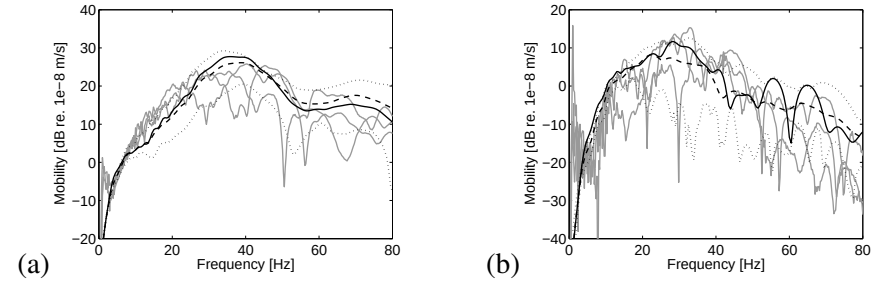


Figure 11: Modulus of the predicted transfer function between a vertical force on the sleeper and the vertical velocity at the (a) first and (b) third measurement line using the MAP profile (solid black line) and average (dashed back line) and 5 % and 95 % quantile (dotted black lines) of the transfer functions computed with the ensemble of 20 profiles. Comparison to the measured transfer functions (grey lines) at lines A, B and C.

the dynamic soil characteristics could not be determined using the MASW test results and are therefore only based on the SCPT, which leads to a larger uncertainty. Since the properties of this soil layer are also used for the first 0.85 m of soil in the track model discussed in section 3.2, they are of high importance for the prediction of the free field vibration. The influence of the properties of this soil layer on the vibration transfer is now discussed.

Figure 12 shows the transfer functions between the vertical sleeper force and the vertical response at the first and third measurement lines computed with the MAP profile and profiles 1 and 6 of the ensemble (figure 3). These three profiles are very similar, but the shear wave velocity C_s of the first layer differs largely: 141.1 m/s (MAP), 106.8 m/s (profile 1) and 194.3 m/s (profile 6). The effect of the stiffness of the first soil layer starts already at 10 Hz. Differences between the results obtained using the soft top layer and the stiff top layer up to 15 dB are observed.

4.3 Track-building mobility

Figures 13 and 14 show the measured and predicted transfer functions between the vertical force applied on the sleeper at line B and the velocities at the receiver locations T_k and V_k ($k = 0, .., 3$) inside the building (figure 1(b)). The receiver locations T_k are located close to the facade of the blok D building, a relatively stiff location, while the receivers V_k are located closer to the floor midspans which are more flexible in the vertical direction. The amplitude of the measured transfer functions generally decreases with increasing

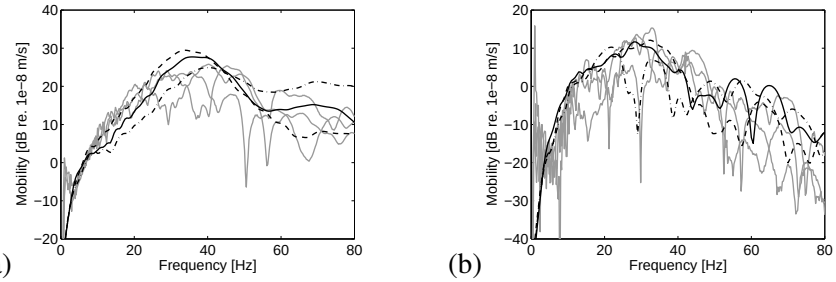


Figure 12: Modulus of the predicted transfer function between a vertical force on the sleeper and the vertical velocity at the (a) first and (b) third measurement line using the MAP profile (solid black line), profile 1 (dashed black line) and profile 6 (dash-dotted black line). Comparison to the measured transfer functions (grey lines) at measurement lines A, B and C.

frequency. The measured transfer functions attain their largest values in the frequency range between $10\,\mathrm{Hz}$ and $40\,\mathrm{Hz}$. The predicted and measured transfer functions are generally in the same order of magnitude. This is especially the case for the response up to $50\,\mathrm{Hz}$. The accuracy of the predicted transfer functions decreases as the frequency increases. Similarly to the measured transfer functions, the amplitude of the predicted transfer functions decreases significantly at higher frequencies. The realizations of the predicted transfer functions for different soil profiles suggest that significant part of the discrepancy between the predicted and measured transfer functions can be explained by uncertain subsoil conditions. Nevertheless, part of the discrepancy between the measured and the predicted transfer functions should be attributed to modeling uncertainty.

4.4 Train passage

The railway line between Leuven and Ottignies is operated by Desiro MS08 passenger trains. These electrically driven trains of the Desiro Main Line (ML) type consist of three cars and have a total length of 79.91 m. They were designed by Siemens Mobility and constructed partly by this company and partly by Bombardier Transportation. The center distance between two bogies is 18.61 m, the axle distance within one bogie is 2.30 m. The axles of the first and third cars are driving, those of the middle car are non-driving.

The train is modeled by means of six uncoupled bogie models (figure 15), consisting of seven degrees of freedom: the vertical displacements of the car body, bogie, two wheel sets and two wheel-rail contact points and the pitch rotation of the bogie. As the train and track are assumed to be symmetric, with one half of the train travelling on each of the rails, the bogie models only represent half of the train. The car body and bogie in figure 15 have mass m_{cb} and m_{b}, respectively, and are connected by the secondary suspension, modeled by a spring k_{s2} and damper c_{s2}. The bogie with moment of inertia I_{b} is connected to the wheel sets with mass m_{w} by the primary suspension, modeled by a spring k_{s1} and damper c_{s1}. The wheel sets are connected to massless wheel-rail contact points by linearised Hertzian springs k_{H}.

The simulated results are compared to the measured track, free field and building vibration during the passage of the same train at 81 km/h. The measured vibration is very similar for different passages of Desiro MS08 passenger trains. The train-track interaction forces are computed with a periodic track model and the MAP profile to characterize the soil, using the coupling algorithm described in [5]. The vibration transfer is computed by means of a 2.5D model with three soil profiles: the MAP profile and profiles 1 and 6 of the ensemble shown in figure 3, with soft and stiff top layer, respectively.

Figure 16 shows the measured and computed vertical vibration velocity at the first and third measurement lines in the free field. At line 1, good agreement between the measurements and simulations is observed. Between 16 and 63 Hz, the computed results slightly overestimate the measurements, but the difference

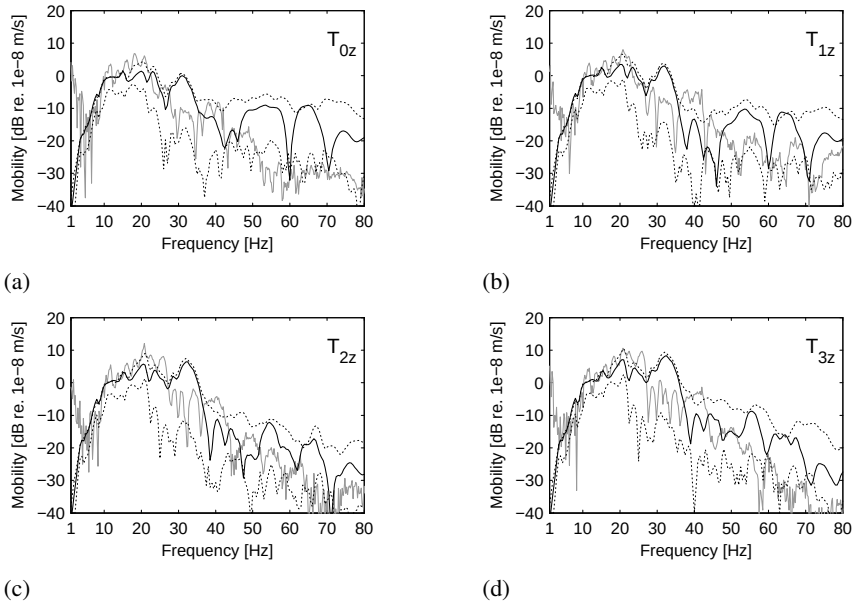


Figure 13: Modulus of the predicted transfer function between a vertical force on the sleeper and the vertical velocity at the receivers T_{kz} using the MAP profile (solid black line) and 5 % and 95 % quantile (dotted black lines) of the transfer functions computed with the ensemble of 20 profiles. Comparison to the measured transfer function (grey line).

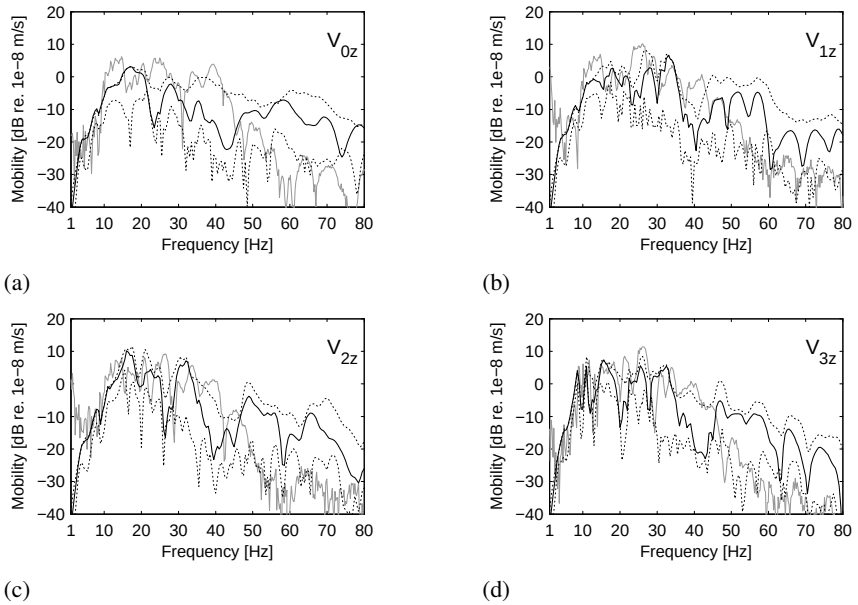


Figure 14: Modulus of the predicted transfer function between a vertical force on the sleeper and the vertical velocity at the receivers V_{kz} using the MAP profile (solid black line) and 5 % and 95 % quantile (dotted black lines) of the transfer functions computed with the ensemble of 20 profiles. Comparison to the measured transfer function (grey line).

remains below 5 dB in most frequency bands. At line 3, the simulations with the MAP profile underestimate the measured vibration below 5 Hz and give an overestimation above 16 Hz.

The computations with different soil profiles yield different results up to more than 10 dB. The measurements are almost for all frequencies in between the results obtained with the three soil profiles. At line 3, underestimation of the measurements at low frequencies is observed for all three soil profiles. Above 5 Hz,

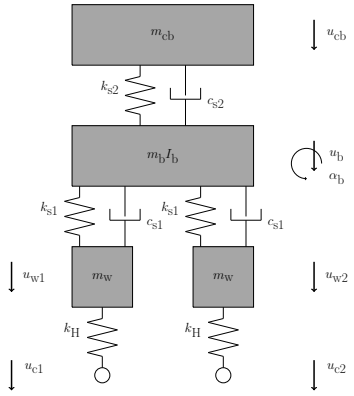


Figure 15: Vehicle model with seven degrees of freedom.

the measured results are almost for all frequencies in between the computed results. The largest effect of the uncertainty on the soil properties is observed between 8 Hz and 50 Hz, where the vibrations propagate mainly through the top soil layer, with differences up to 10 dB.

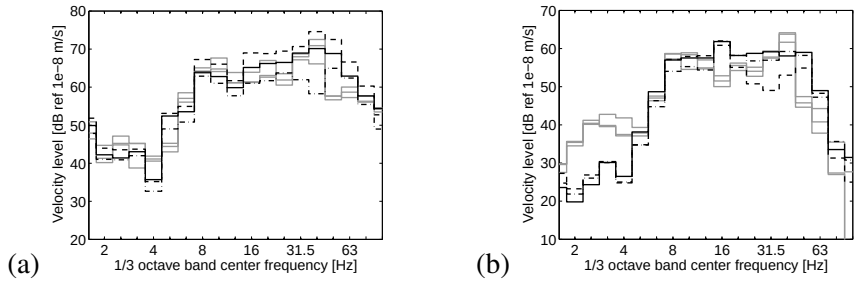


Figure 16: 1/3 octave band spectrum of the vertical free field velocity at the (a) first and (b) third measurement line during the passage of a Desiro MS08 passenger train at 81 km/h. Simulated results with MAP soil profile (solid black line), profile 1 (dashed black line) and profile 6 (dash-dotted black line) compared to measurement data (grey lines) at lines A, B and C.

Figures 17 and 18 show the measured and predicted response at the receiver locations inside the building. The predicted and measured response are generally in good agreement at frequencies higher than 8 Hz. The realizations of the predicted response for the three soil profiles show that the imperfectly known subsoil conditions affect the response to railway induced vibration and in particular at higher frequencies resulting in variation of the predicted response of up to 10 dB. The maximum response occurs in the frequency range between 8 Hz and 16 Hz corresponding to the frequency range of the identified vertical modes of the floors (table 3). Significant discrepancy of up to 30 dB between the predicted and measured response is only observed at frequencies lower than 8 Hz as well as at frequencies around 50 Hz. This discrepancy, however, can hardly be explained by the parametric uncertainty of the numerical models and should be attributed partially to the measurement error and partially to the modeling errors and simplifications.

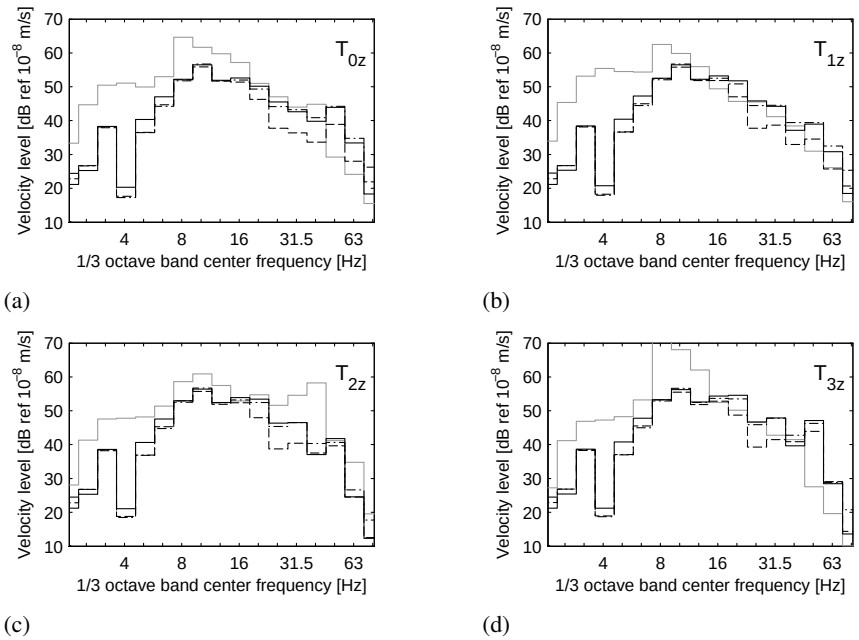


Figure 17: 1/3 octave band spectrum of the vertical velocity at the receivers T_{kz} during the passage of a Desiro MS08 passenger train at 81 km/h. Simulated results with MAP soil profile (solid black line), profile 1 (dashed black line) and profile 6 (dash-dotted black line) compared to measurement data (grey line).

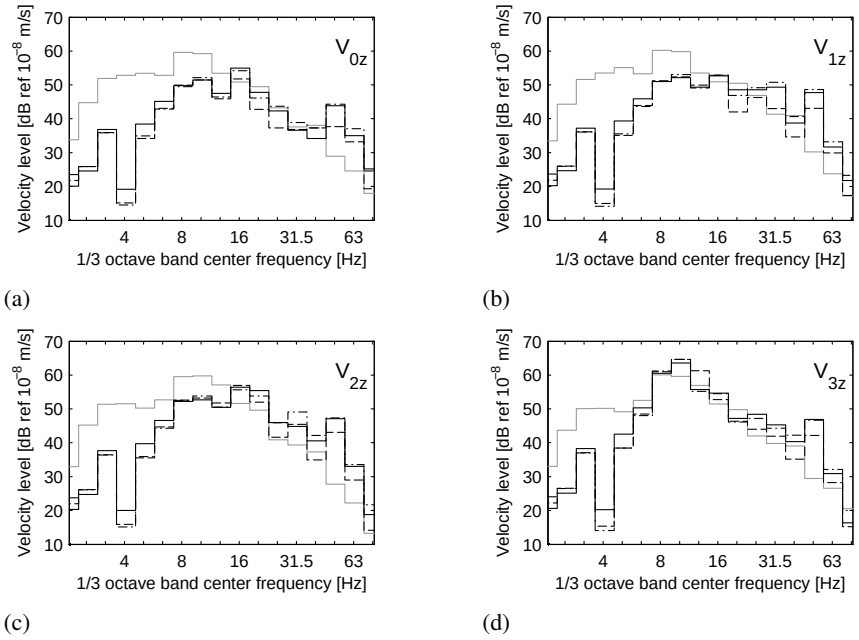


Figure 18: 1/3 octave band spectrum of the vertical velocity at the receivers V_{kz} during the passage of a Desiro MS08 passenger train at 81 km/h. Simulated results with MAP soil profile (solid black line), profile 1 (dashed black line) and profile 6 (dash-dotted black line) compared to measurement data (grey line).

5 Conclusions

This paper examines the sensitivity of railway induced vibration predictions to uncertain subsoil conditions. To this end, a numerical model of a track, soil and building are developed based on the results of an extensive measurement campaign conducted in Heverlee, Belgium. The measured and predicted track receptance, track-free field and track-building mobility functions as well as the free field and building response during a train passage are compared, and the sensitivity of the results to the uncertain soil properties is investigated.

The track receptance and, therefore, the prediction of the train-track interaction forces, are little sensitive to the uncertainty on the soil properties. The influence of this uncertainty on the track-free field transfer functions is very large, however, both at short and large distances from the track: differences up to 20 dB are observed for different soil profiles that are consistent with the results of the soil characterization tests.

Similarly to the track-free field transfer functions, the track-building transfer functions are particularly sensitive to the uncertainty on the soil properties, explaining to a significant extent the differences between the predicted and measured response. The predicted and measured response of the building to a train passage are generally in good agreement at frequencies higher than 8 Hz. The uncertainty on the subsoil properties results in variation of the predicted response of up to 10 dB, particularly at higher frequencies.

Acknowledgements

This research was performed within the framework of the project OT/13/59 “Quantifying and reducing uncertainty in structural dynamics” funded by the Research Council of KU Leuven. The first author is a PhD student supported by the Research Foundation Flanders (FWO) (Grant No. 11ZG817N). The financial support is gratefully acknowledged.

References

[1] VERACHTERT, R., AND DEGRANDE, G. Determination of the dynamic soil characteristics at site 1 next to the Blok D building of the administrative complex of KU Leuven. Report BWM-2017-03, Department of Civil Engineering, KU Leuven, October 2017.

[2] VERACHTERT, R., AND DEGRANDE, G. Determination of the dynamic soil characteristics at site 2 next to the Blok D building of the administrative complex of KU Leuven. Report BWM-2017-18, Department of Civil Engineering, KU Leuven, October 2017.

[3] REYNDERS, E., SCHEVENELS, M., AND DE ROECK, G. MACEC 3.3: a Matlab toolbox for experimental and operational modal analysis. Report BWM-2014-06, Department of Civil Engineering, KU Leuven, July 2014.

[4] VERACHTERT, R. Deterministic and probabilistic determination of dynamic soil characteristcs. PhD thesis, Department of Civil Engineering, KU Leuven, 2018.

[5] GERMONPRÉ, M., DEGRANDE, G., AND LOMBAERT, G. A study of modelling simplifications in ground vibration predictions for railway traffic at grade. Journal of Sound and Vibration 406 (2017), 208–223.

[6] COMPUTERS & STRUCTURES INC., CSI Analysis Reference Manual For SAP2000, ETABS, SAFE and CSiBridge - Release 16.1.1, January 2014.

[7] FRANÇOIS, S., SCHEVENELS, M., AND DEGRANDE, G. BEMFUN: MATLAB toolbox for boundary elements in elastodynamics. Report BWM-2009-26, Department of Civil Engineering, KU Leuven, December 2009.

Spectral and statistical evaluation of the properties of the vibration measured at the base of an automotive seat for non-Gaussian random noise synthesis

D. González [1], **R. López-Valcarce** [2]
[1] CTAG, Acoustics and Vibration Laboratory,
Pol. Ind. A Granxa, 249-250, 36400 Porriño, Spain
e-mail: **damian.gonzalez@ctag.com**

[2] University of Vigo, Department of Signal Theory and Communications,
Campus Lagoas-Marcosende, Rúa Maxwell, 36310 Vigo, Spain

Abstract
In this paper, we explore the properties of the vibration measured at the base of the driver seat when driving through different surfaces, with the purpose of defining a model for non-Gaussian random vibration testing. The recorded acceleration signals are first transformed to a 6 Degree of Freedom (DOF) space, and then segmented into stationary sections that are later analyzed. The non-Gaussian nature of the recorded vibration is demonstrated through different Gaussianity hypothesis tests, and the distribution of the third and fourth-order moments, as well as the crest factor, are computed and analyzed. The second-order spectral content reveals significant correlation at specific frequencies, while the significance of third-order polyspectra is checked through hypothesis testing. Based on our observations, a practical specification of the random process is proposed based on second-order spectral content, univariate kurtosis and crest factor levels.

1 Introduction

The usage of random vibration in mechanical testing of automotive components is a common technique, and has been applied in laboratories since many decades for the simulation of road-induced vibration. The spread of high-performance digital controllers allows accurate and repeatable control of Gaussian vibration profiles with desired power spectral density. One of the main advantages of using normal distributions is its solid theoretical foundations and the fact that many natural phenomena are well modelled through such distribution. Additionally, it is well known that a Gaussian stochastic process is completely characterized by its first and second-order statistics [1], *i.e.* mean and covariance. For a Gaussian zero-mean wide sense stationary (WSS) process, it suffices to give its autocorrelation sequence (or, equivalently, the coherence and variance). The spectral properties are then given by the Fourier transform of the autocorrelation function, which provides a convenient method for specifying the test conditions by means of the Power Spectral Density (PSD) or the Spectral Density Matrix (SDM), depending if the process is univariate or multivariate.

More recently, the focus in random vibration has moved to non-Gaussian processes, since field data suggests that significant deviation from Gaussianity can occur in many components, impacting its performance [2]. This results in higher complexity of the theoretical treatment and definition of the vibration problem. For non-Gaussian processes, the correlation function is not sufficient for fully characterising the process. A general definition must hence include the higher-order statistics (HOS), which consider the process statistics of order 3 and greater. As described in [3], these statistics are usually evaluated through the process cumulants and their Fourier transforms, known as polyspectra, which can be considered an extension of the second-order correlation function and classical power spectrum, respectively, to higher-orders. In general, the cumulants

for processes close to Gaussianity will be very small [3]. From a practical point of view, the usage of higher-order statistics for the definition of the non-Gaussian process has the following drawbacks:

1. Estimation of the second-order statistics (autocorrelation or power spectrum) with sufficient accuracy requires rather long signals, which is usually an issue due to the limited length of the test tracks used for the recording of the vibration signals, as well as to the lack of stationarity. This is even worse in the case of Multiple-DOF (MDOF) scenarios where, depending on the existing coherence between the different DOFs, the required record length for a given estimation accuracy may increase significantly. The estimation of the higher-order cumulants and polyspectra would require even larger records [3].

2. The complexity of the resulting model increases substantially. From an already large model consisting of a spectral density matrix (SDM) and joint first order probability density function (*pdf*), a new array would need to be introduced for each new HOS. In addition, the successive arrays will increase their dimensionality (second-order SDM is $N \times N$, third-order bispectrum is $N \times N \times N$, etc., with N the number of DOFs).

A simpler approach consists in specifying the non-Gaussian process through its moments, although, in general, many different distributions may fit a particular set of moments. Clearly, there is a trade-off between the degree of accuracy when specifying a statistical model and the resulting complexity and effort during the specification stage. For this reason, it is important to have an adequate understanding of the statistical properties of real-world vibration signals, in order to determine which ones are truly significant and should be considered when specifying the model.

In this paper we evaluate the spectral and statistical properties of the input vibration to the driver seat of a car, in order to explore a practical specification of the non-Gaussian vibration process. First, the measurement setup is described. Then, the post-processing of the recorded signals is presented, including the transformation to a 6-DOF space and the extraction of stationary segments from the data. A statistical analysis of the extracted segments is later performed, including the evaluation of Gaussianity and of the third and fourth-order normalized moments and crest factor. The process correlation and the joint distribution of the MDOF process are also evaluated. Finally, a spectral analysis is performed, with a focus in the bispectral content of the process. Based on our analyses, a proposal for the specification of the non-Gaussian multivariate process and the conclusions complete this paper.

2 Measurement setup

The measured vehicle is a VW Scirocco, with the characteristics shown in table 1.

Version	R-Line	Tyre	205/50 R17 93V
Engine	2.0 TDI	Front suspension	MacPherson strut
Gearbox	6 gear DSG	Rear suspension	Four-link

Table 1: Main vehicle characteristics.

The component selected for the measurements is the driver seat of the car. The acceleration input to the seat is recorded at the four fixing points with triaxial accelerometers, schematically shown in figure 1. This gives an overdetermined solution to the kinematics of the rigid body.

The fixing points of the seat are located symmetrically, which allows for the calculation of the Input Transform Matrix (ITM) from two distances, as indicated in figure 1. The specific values for the implemented instrumentation are 165 mm for length a, and 218.5 mm for length b.

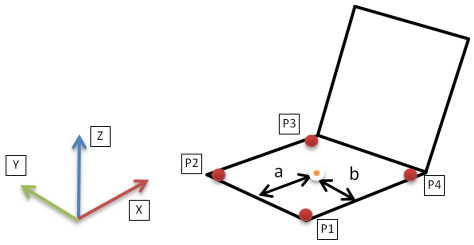


Figure 1: Location of the accelerometers.

The accelerometers used for the measurement are high sensitivity low mass ICP triaxial sensors (B&K type 4525 B and type 4535 B 001). A total of 12 acceleration signals, 5 GPS data streams and a video file are recorded per measurement. All the signals were sampled at 9600 Hz, applying a 4^{th} order Butterworth antialiasing filter with a -1dB cut-off frequency of 1000 Hz. The data acquisition systems used for the data recording are two HBM QuantumX MX840A, with external Somat ICP conditioning units.

A total of 4 scenarios are defined for measurement, as indicated in table 2. Most of the measured roads have sections of pavement in bad, fair and good condition. The roads used for the measurements are public roads. Hence, stability in the driving conditions was not guaranteed, and was subjected to the existing traffic.

Scenario	Surface	Road type	Average speed (km/h)	Length (km)
A	Asphalt	Highway	110	35.6
B	Asphalt	Conventional	52.5	124.2
C	Concrete	Conventional	70	4.2
D	Cobblestone	Town	30	0.5

Table 2: Measurement scenarios.

3 Signal post-processing

3.1 DOF transformation

The total 12 DOF measured at four points in X, Y and Z can be reduced to 6 DOF (X, Y, Z, Roll, Pitch and Yaw) without losing any information about the kinematics of the measured body. The transformation is performed through the Input Transform Matrix $[\mathcal{I}]$ [4], whose calculation is based on the distances shown in figure 1. The matrix $[\mathcal{I}]$ is computed so that the 6 DOF signals are obtained at the geometric center of the four measured points.

Figure 2 shows one of the recorded signals after transformation to the 6 DOF space. The transformation from a 12 DOF space to a 6 DOF space allows for halving the amount of data for post-processing.

3.2 Signal segmentation

Figure 2 illustrates the fact that the vibration process is in general non-stationary, although it can be considered approximately stationary over sufficiently short periods of time. Therefore, stationary segments are first extracted. The criterion for the segmentation is the extraction of the largest possible blocks of samples that can be considered stationary based on different statistical tests. For such purpose, an algorithm based on k-means clustering of the constant percentage bandwidth (CPB) spectra has been developed and applied

[5]. The segments of duration below 10 seconds, or with at least one of the blocks in the segment having null associated vehicle speed, or an average vehicle speed of the segment under 10 km/h, are all discarded.

Figure 2 illustrates the result of the segmentation for one of the measurements. The regions that were not assigned to a stationary segment are indicated in blue, while the different stationary segments are shown in different colors. The percentage of the total recorded signal that is retained after segmentation is 33%, the rest 67% being associated with transients. The supposedly stationary segments retained in this way are in general quite short, with most of them having durations under 20 seconds.

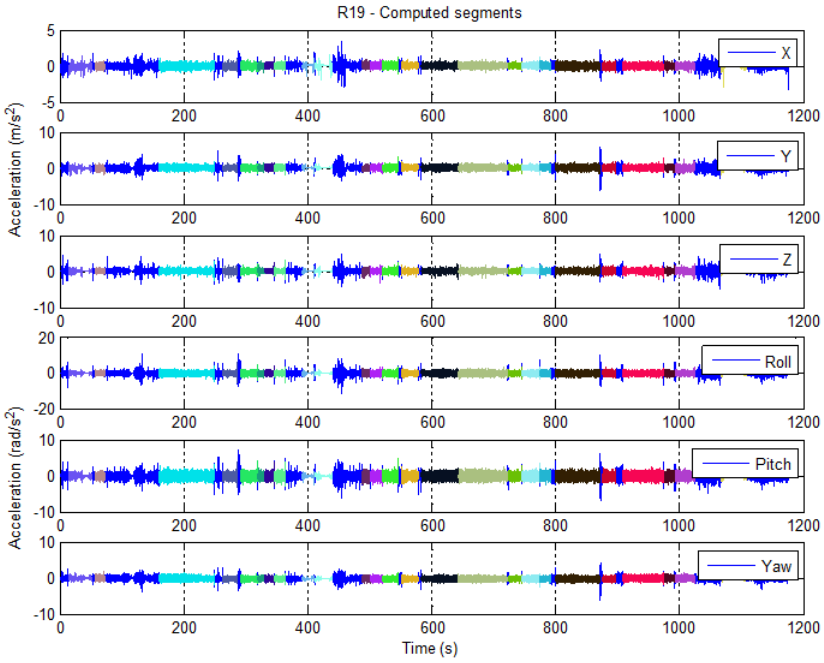


Figure 2: Result of the segmentation of one of the recordings. The regions not assigned to a stationary segment are shown in blue. The rest of the colors correspond to different segments extracted.

After the segmentation of the signals, two different stationarity tests are applied to each segment: runs test [6] and reversals test [6]. All these tests are applied individually to each of the 6 DOFs of the transformed process. A segment is considered stationary if all 6 DOFs pass the stationarity test.

Table 3 shows the percentage of segments passing stationarity tests respect to the total recorded signal, depending on the number of tests passed. Most of the recorded data corresponds to non-stationary segments and segments with no vibration. About 25% of the whole recordings, and nearly 80% of the extracted segments pass at least one of the stationarity tests while half of them pass both.

Description	Duration	Percentage of total duration	Percentage of extracted duration
Total length	3:52:14	100%	—
Extracted length	1:16:43	33%	100%
Stationary 2 crit.	0:30:36	13%	40%
Stationary 1 crit.	1:00:43	26%	79%

Table 3: Percentage of stationary segments depending on the number of stationarity tests that do not reject the stationarity null hypothesis, for a significance level of 0.05.

3.3 Gaussianity assessment

The assessment of the Gaussianity of each segment is done through four different tests: chi-squared [1], skewness, kurtosis and BHEP (Baringhaus-Henze-Epps-Pulley) [7] [8].

The univariate tests are applied to each DOF individually, and, for a given test, the process is considered Gaussian if all the DOFs pass the test. This does not imply that the process is jointly normal (counterexamples can be found in [1]). This latter condition is tested through the BHEP test, which is applied to the 6 DOF process. Table 4 shows the total cumulative duration of the segments that passed the different tests, as well as the percentage of duration of the extracted segments that pass the Gaussianity test. Although some DOFs in some segments can be considered Gaussian, in general the process fails to pass the tests. In particular, none of the extracted segments passes the multivariate BHEP test, evidencing the lack of Gaussianity of the process.

DOFs	Chi-squared		Skewness		Kurtosis		BHEP	
	Duration	%	Duration	%	Duration	%	Duration	%
1	0:11:56	16%	0:15:07	20%	0:12:22	16%	—	—
2	0:08:37	11%	0:17:24	23%	0:04:19	6%	—	—
3	0:06:23	8%	0:18:07	24%	0:04:23	6%	—	—
4	0:04:15	6%	0:11:21	15%	0:01:32	2%	—	—
5	0:00:00	0%	0:05:37	7%	0:00:00	0%	—	—
6	0:00:21	0%	0:00:22	0%	0:00:00	0%	0:00:00	0%

Table 4: Total cumulative duration of segments that pass the Gaussianity tests. The DOFs column indicate the number of DOFs that pass the test. The percentage columns correspond to the proportion of the duration of the extracted stationary segments that pass the test, for a significance level of 0.05.

4 Distribution of the moments and crest factor of the process

Since the process cannot be considered strictly Gaussian, we will now evaluate the statistical properties of the segments in order to check how distant from a normal distribution they are. Since moments of order 3 and 4 are fixed for a Gaussian process, we will focus on the skewness and kurtosis, defined as the third and fourth standardized moments. The first measures the asymmetry of the distribution, while the later quantifies the relative height of the tails.

$$\gamma = \mathbb{E}\left\{\left(\frac{X-\mu}{\sigma}\right)^3\right\} = \frac{\mathbb{E}\left\{(X-\mu)^3\right\}}{(\mathbb{E}\left\{(X-\mu)2\right\})^{3/2}} \tag{1}$$

$$\beta = \mathbb{E}\left\{\left(\frac{X-\mu}{\sigma}\right)^4\right\} = \frac{\mathbb{E}\left\{(X-\mu)^4\right\}}{(\mathbb{E}\left\{(X-\mu)^2\right\})^2} \tag{2}$$

Given the samples $\{x[n], n = 1, ..., N\}$, the sample skewness is computed as follows:

$$\hat{\gamma} = \frac{\sqrt{N(N-1)}}{N-2} \cdot \frac{\frac{1}{N}\sum_{n=1}^{N}(x[n]-\hat{m}_1)^3}{\left(\sqrt{\frac{1}{N}\sum_{n=1}^{N}(x[n]-\hat{m}_1)^2}\right)^3} \tag{3}$$

with $\hat{m}_1$ the sample mean. The estimator $\hat{\gamma}$ is unbiased [9]. As for the sample kurtosis, we have the following biased estimator:

$$\hat{\beta}_b = \frac{\frac{1}{N}\sum_{n=1}^{N}(x[n]-\hat{m}_1)^4}{\left(\frac{1}{N}\sum_{n=1}^{N}(x[n]-\hat{m}_1)^2\right)^2} \tag{4}$$

An unbiased alternative can be computed as [9]:

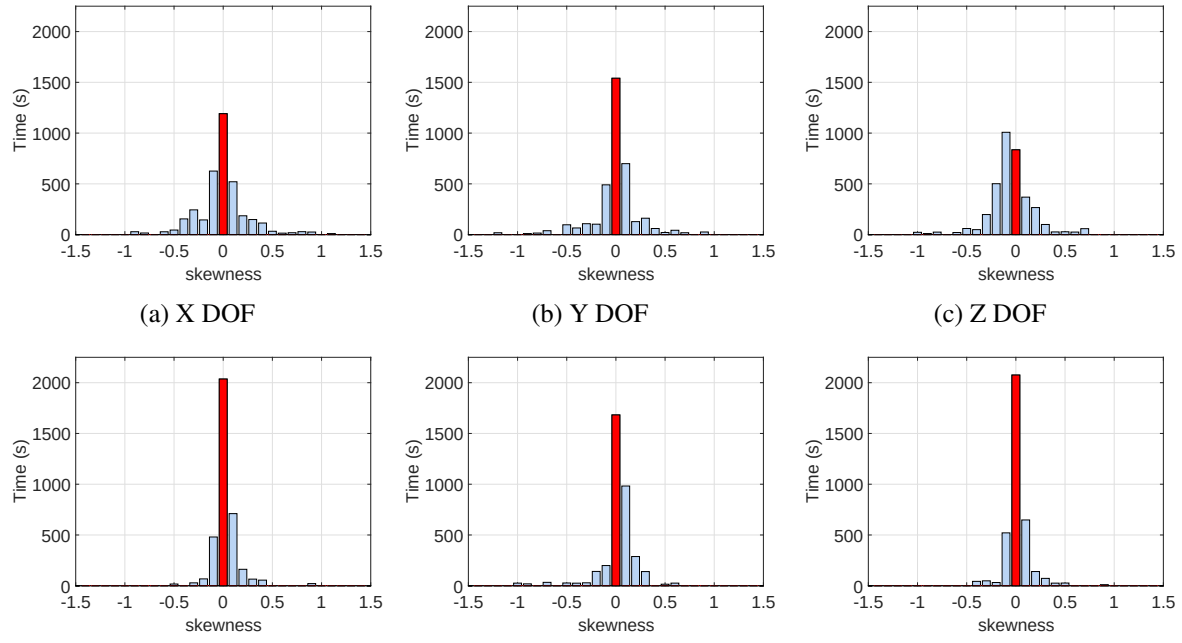
$$\hat{\beta}_u = \frac{N-1}{(N-2)(N-3)}\Big((N+1)\hat{\beta}_b - 3(N-1)\Big) + 3 \tag{5}$$

For the analysis of these two moments, we used the unbiased estimators.

It is well known that the variance of the sample estimators depends on the number of samples used for the estimation. Formulas are available that relate this variance to the number of samples under the assumption of independence between samples. In our case, the process is low-pass, which means that the samples are not independent. Under the assumption of weak dependence, we can compute a confidence interval for the sample estimators through the stationary bootstrap [10]. The values given here correspond to a coverage factor of K = 0.95.

4.1 Skewness

The histogram of the signal duration for different skewness levels is shown in figure 3. The skewness is estimated from all the samples within each segment, and only those passing at least one stationarity test are included in this analysis. These graphs confirm the fact that the skewness is most of the time very close to 0, showing a larger dispersion for the X and Z DOFs.



(a) X DOF (b) Y DOF (c) Z DOF

(d) Roll DOF (e) Pitch DOF (f) Yaw DOF

Figure 3: Total duration of stationary recorded signal for different skewness levels and DOFs. The Gaussian skewness level is highlighted in red.

Figure 4 shows the distribution of the size of the confidence interval of the skewness estimate as a function of the segment size. The uncertainty in the estimation of the skewness increases mainly with small segments. It is worth noting the significant level of uncertainty in the estimation for some of the segments, which

is reasonable taking into account the fact that the skewness is a third-order moment and the process is coloured. This has some practical implications, meaning that care must be exercised when considering a certain skewness level based on short recordings.

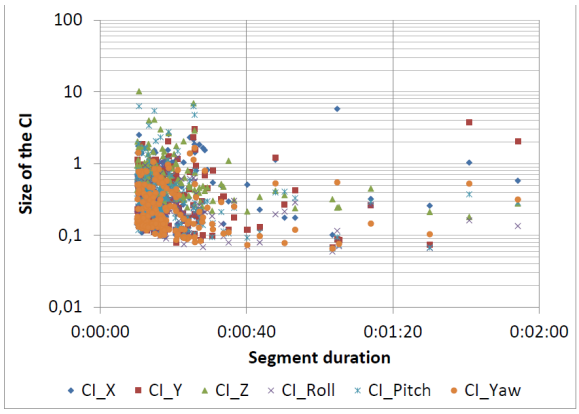


Figure 4: Size of the confidence interval of the skewness sample estimate, as a function of the segment size, computed through the stationary bootstrap for a coverage factor of 95%.

4.2 Kurtosis

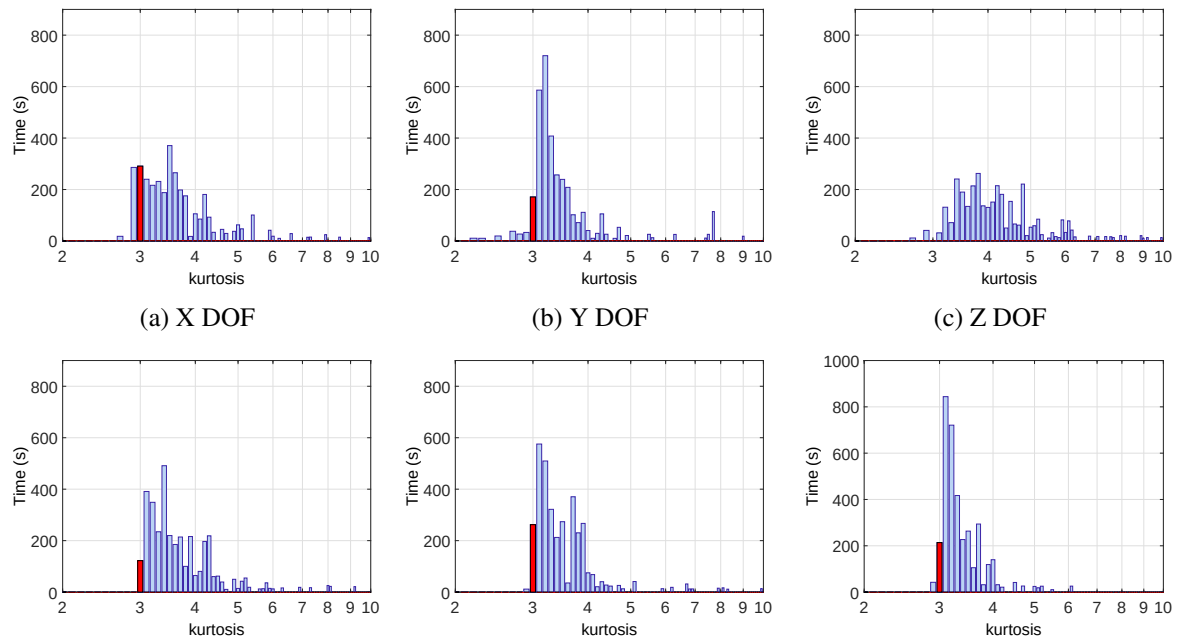
The distribution of the kurtosis level is shown in figure 5 for the different DOFs. As for the skewness, only the segments passing at least one stationarity test are included in this analysis. This graph confirms the fact that most of the recorded signals are very close to Gaussianity in terms of its kurtosis, although the distribution is skewed to the right, indicating that the values tend in general to be larger than for the Gaussian distribution. There is also a clear difference among the measured DOFs. There is a prevalence of large kurtosis values in Z direction, which is reasonable since it is the main direction of vibration input to the car. In all the cases the kurtosis levels are mostly above 3, indicating a clear leptokurtic behaviour.

As with the skewness estimate, one possible cause for the large dispersion in the kurtosis values for small segments may be the variability in the estimator when few samples are available. For small segment sizes (below 30 seconds) we find a significant increase in the distance between the upper and lower bounds of the confidence interval (CI). This can be observed in figure 6, showing the distribution of the size of the CI as a function of the segment size. The same shape as for the skewness is noticeable, indicating that the uncertainty in the estimation of the kurtosis increases mainly with small segments. Again, care must be exercised when considering a certain kurtosis level based on short recordings, due to the large uncertainty of the estimate under this condition.

4.3 Crest factor analysis

Although the Gaussian distribution is unbounded in the abscissa, real vibration processes are bounded due to physical constraints. This implies an additional deviation from Gaussianity in real-world processes, where the tails may present larger probabilities than the normal distribution, but will at a certain point fall to zero faster than normal. In practical vibration synthesis systems, for zero-mean processes this limitation is imposed through a signal clipping at a certain multiple of the standard deviation or RMS level, effectively limiting the crest-factor, but also producing a spectral distortion that can be compensated through post-filtering and closed-loop control techniques [11].

The crest factor (CF) of the stationary segments obtained from the field data is computed according to equation (6). The distribution of the CF is computed considering the duration of the road data, *i.e.*, the cumulative time with a CF in a certain range. The resulting histograms are shown in figure 7.



(a) X DOF (b) Y DOF (c) Z DOF

(d) Roll DOF (e) Pitch DOF (f) Yaw DOF

Figure 5: Total duration of stationary recorded signal for different kurtosis levels and DOFs. The Gaussian kurtosis level is highlighted in red.

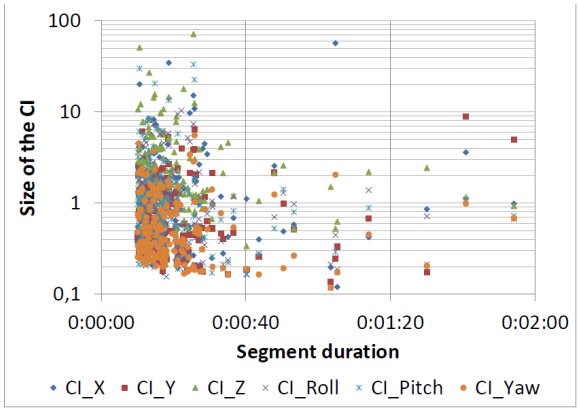
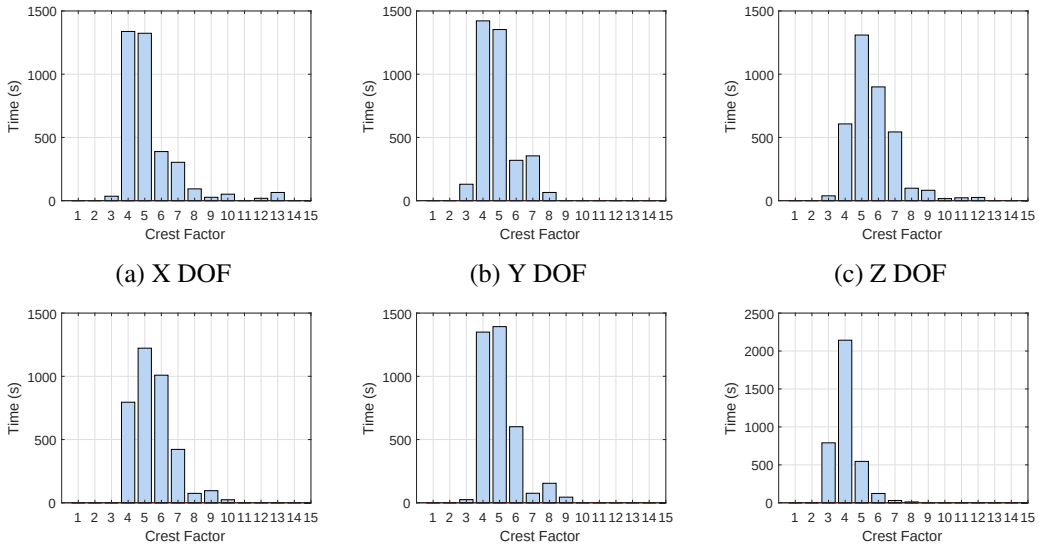


Figure 6: Size of the confidence interval of the kurtosis sample estimate, as a function of the segment size, computed through the stationary bootstrap for a coverage factor of 95%. Only segments that passed at least one stationarity test are shown.

$$\mathrm{CF} = \frac{|x|_{peak}}{x_{rms}} \tag{6}$$

In general, the CF spreads over a broad range starting close to 3 till more than 13. Most of the time the crest factor is near 5, which turns out to be a common CF for Gaussian random profile clipping in vibration testing, together with CF = 3.

From the previous analysis, it can be concluded that limiting the CF is a feature that is necessary if a realistic model of the vibration process is to be implemented, and should be considered also for random vibration tests using non-Gaussian processes.



(a) X DOF (b) Y DOF (c) Z DOF

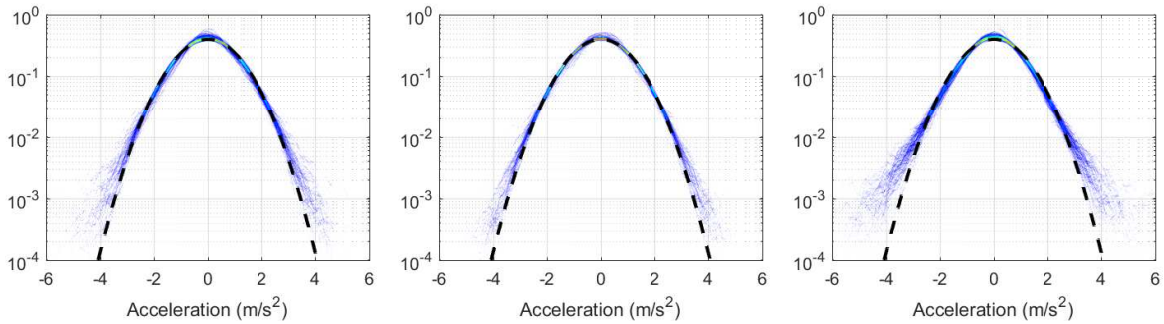
(d) Roll DOF (e) Pitch DOF (f) Yaw DOF

Figure 7: Total duration of stationary recorded signal for different crest factors (CF) and DOFs.

5 Marginal distributions

In this section we analyse the shape of the marginal distributions of the process. These probability density functions are estimated through the kernel density [12]. For better illustration, a histogram of the marginal distribution of the X, Y and Z DOF of the extracted segments is shown in figure 8. A similar result is obtained for the rotational DOFs (Roll, Pitch and Yaw). The following can be observed:

1. The *pdf* has a bell shape, clearly resembling a Gaussian distribution.
2. The distribution is different for each of the process DOFs. The tails of the marginal distribution for Z axis are significantly larger than for the X and Y axes, as shown in figure 8c, which is in agreement with the kurtosis values obtained for this axis in section 4.2.



(a) X DOF (b) Y DOF (c) Z DOF

Figure 8: Histogram of the normalised kernel estimate of the marginal distribution of the X DOF (a), Y DOF (b) and Z DOF (c) for all extracted segments. The dashed line corresponds to the normal distribution.

6 Process correlation and joint distribution

Before evaluating any joint distribution of the process, it is of interest to check the level of correlation between the different DOFs. We will first compute the matrix of correlation coefficients for the transformed 6-DOF process. This allows for checking the degree of linear dependence between the process DOFs, without considering the time dependence (this will be done later). The correlation coefficient matrix is computed for the unsegmented recordings and is shown in table 5. The correlation coefficients are very small but for the Y and Yaw DOFs.

Signal	**X**	**Y**	**Z**	**Roll**	**Pitch**	**Yaw**
X	1.00	0.01	-0.03	-0.02	-0.03	0.11
Y		1.00	-0.06	0.04	-0.12	-0.39
Z			1.00	-0.10	-0.04	-0.10
Roll				1.00	0.10	0.08
Pitch					1.00	0.05
Yaw						1.00

Table 5: Average correlation coefficients matrix for the 6 DOF process.

The previous analysis can be repeated considering the correlation structure of the process in the frequency domain. A simple way for observing such correlation is the calculation of the coherence function, defined in equation (7), where $G_{xx}(f)$ is the autospectral density of x, $G_{yy}(f)$ the autospectral density of y and $G_{xy}(f)$ their cross spectral density. According to this equation, given the autospectral density of the process, the coherence function can be used instead of the modulus of the cross-spectral density in the definition of the multivariate process. The Welch method is applied for the estimation of this function [6], using a Hanning window, spectral resolution of 1 Hz and no overlap.

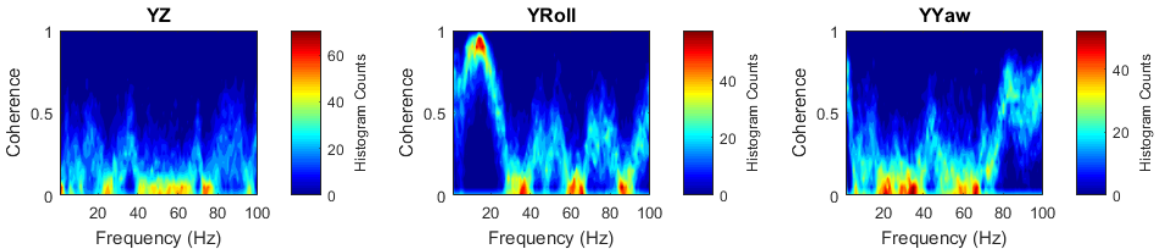
$$C_{xy}(f) = \frac{|G_{xy}(f)|^2}{G_{xx}(f)G_{yy}(f)} \tag{7}$$

In order to get further insight in the range of coherence levels that can be found in this particular case, we can plot a 3D histogram of the coherence function computed for the extracted segments. The result is shown in figure 9 for three different cases. The first one corresponds to two DOFs clearly showing low coherence in all the frequency range. A bivariate process consisting of these two DOFs is likely to be well modelled through two uncorrelated univariate signals. In figure 9b, we can observe a scenario showing large coherence around 15 Hz, which means that lateral motion at that frequency will most probably be accompanied by a Roll movement. Although Y and Yaw DOFs present the largest average absolute correlation coefficient in table 5, coherence between those two DOFs is in general low, with larger values only at frequencies above 80 Hz.

From the data in this section, we can conclude that significant correlation among the process DOFs can exist, even for stiff measurement points such as the seat base. This aspect would not be considered with the usage of uncorrelated noise for the simulation of multiaxial vibration processes.

The evaluation of the joint density of the process is done through the inspection of the kernel density estimate. Unfortunately, the inspection of the joint density is difficult or practically impossible for more than 3 DOFs. We will give here some representative examples for the 2 and 3 DOF case.

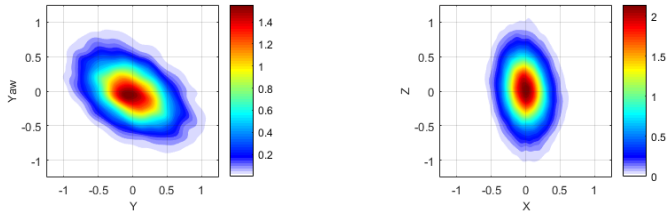
The analysis of the 2-DOF joint distribution reveal that all the joint densities have a clear elliptical shape. This aspect is better observed in figures 10a and 10b, corresponding to a contour plot of the kernel density estimate for two different segments and signals. The first one shows a clear correlation between the two DOFs, while the second figure indicates a lower correlation level. Another significant aspect is the shape of the kernel estimate at the tails of the density. In figure 10a the lower level contours are not perfectly elliptical,



(a) (b) (c)

Figure 9: Ordinary coherence histogram for two DOFs mostly uncorrelated (a), with coherent behaviour near 15 Hz (b) and with coherent behaviour at high frequency (c).

being the segment 14 seconds long. This irregular shape is due to the reduced number of samples at the tails. In figure 10b, the duration increases to 87 seconds, which means a larger number of samples at the tails and hence a better definition of the lower level ellipses. This point is significant in relation to the accuracy of the joint density estimate for higher dimensions. The low probability of having a significant number of points at the tails of the distribution will lead to the need for large sequences for an adequate estimate. Hence, a non-parametric estimation might be discouraged due to the large errors that may exist.



(a) (b)

Figure 10: 2-DOF joint density estimate for two different stationary segments.

The 3-DOF joint density is shown as a family of isosurfaces for one segment. Due to the large computational cost of the kernel density estimate for this number of DOFs, only two segments were evaluated in order to have an overview of the general shape of the distribution. The result is shown in figure 11. The same elliptical shape as for the bivariate case is observed. Now the tails are not as well defined as for the bivariate case. This is a consequence of the fact that, since the number of samples is limited, the number of them outside a certain isosurface reduces due to the larger available volume. That makes isolate kernels visible for the lowest level isosurface.

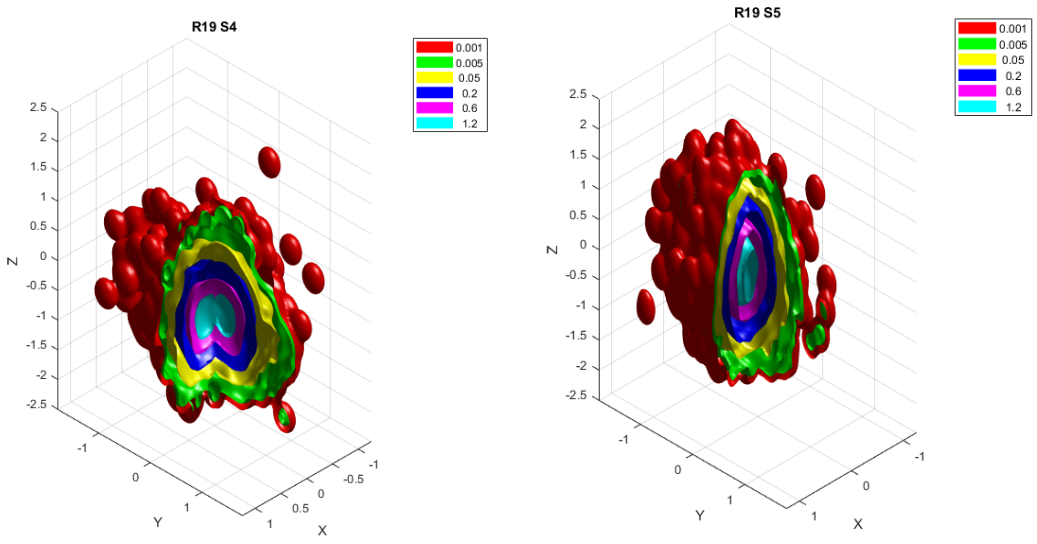
6.1 Process ellipticity

From the observation of the 2 and 3-DOF kernel density estimates, the process seems to have elliptical symmetry. In order to assess this property for different DOFs and larger dimensions, a multivariate ellipticity test is applied, based on [13]. The test is applied to each DOF separately, to a 3 DOF set consisting of $\{X, Y, Z\}$ and a 6 DOF set integrated by all available signals. The mean of the process is removed prior to the application of the test. In all cases a significance level of 0.05 is considered. For the case of individual DOFs, the test is unable to reject the null hypothesis of ellipticity. All the stationary segments under analysis present a symmetric distribution under univariate conditions. For the 3 DOF case, 45% of the duration of the stationary segments pass the ellipticity test, while the other 55% does not. Similar results are obtained for the 6 DOF case, with 44% of the signal duration passing the test, and 56% having the null hypothesis rejected.

A segment with rejected ellipticity and another one with the same hypothesis not rejected are evaluated

graphically in order to further analyse the overall shape of the estimated distribution. Both segments have a similar length. A kernel density estimate is performed for the 3-DOF case. Figures 11a and 11b show a 3D plot of the process distribution. From the observation of these graphs, no clear differences are noticeable that could indicate a lack of ellipticity of the analysed segments. This could indicate that the applied test might be too conservative when rejecting the ellipticity null hypothesis.

The results of the application of this ellipticity test are not conclusive, indicating that a significant percentage of the signal duration might present some amount of multivariate skewness.



(a) (b)

Figure 11: 3-DOF kernel density estimate for a segment with rejected (a) and accepted (b) ellipticity.

7 Spectral analysis

The spectral content of Gaussian processes can be properly specified through the Spectral Density Matrix (SDM), which includes the second-order spectra. For a 6 DOF process, this involves the specification of a 6×6 matrix with 6 autospectra and 30 cross-spectra. The calculation and structure of the SDM is well known in the field of vibration testing and is not shown here for brevity.

One of the main difficulties of using non-Gaussian distributions when modelling a vibration process is the need of higher-order spectra for the proper definition of the process.

An exploratory evaluation of bispectra is done in order to verify the departure from Gaussianity based on this higher-order spectrum. The analysis is based on the work by Hinich [14], while the test is applied based on an implementation by A. Swami [15]. Since Hinich's test checks the null hypothesis of the bispectrum being zero, a failure in rejecting such null hypothesis would reinforce the idea of the bispectrum not being strictly necessary for a practical definition of the non-Gaussian MDOF vibration process.

The test is applied to each of the stationary segments extracted from the measured data. The percentage of segments whose bispectrum can be considered null is indicated in table 6.

For a large percentage of the signal duration, the hypothesis of the bispectrum being null can not be rejected. Only the Z DOF shows a 19% of the measured time having a significant bispectral level, being the rest of the DOFs below 10%. This result reinforces the idea of not considering the higher-order spectra in the specification of the non-Gaussian vibration process, since the additional effort required for the process specification would not likely provide significant improvements in terms of model accuracy.

DOF	Total time	Hinich test	Fraction
X	01:16:43	01:09:32	91%
Y	01:16:43	01:11:20	93%
Z	01:16:43	01:01:48	81%
Roll	01:16:43	01:15:02	98%
Pitch	01:16:43	01:14:07	97%
Yaw	01:16:43	01:13:28	96%

Table 6: Hinich Gaussianity test for a significance level of 0.05.

8 Specification of the process

Two approaches can be considered for the specification of the multivariate non-Gaussian process. The first one is based on a strong assumption of non-Gaussianity, which would require the definition of the higher-order spectra and statistics, as well as the joint density of the process. This seems to be impractical, particularly when field data suggests that some simplifications can be reasonably made on the model in order to significantly reduce the necessary modelling and analysis effort. The second, more practical specification of the process is based on the results presented in this paper. The following elements are considered as part of the model, and are summarized in table 7.

1. Spectral Density Matrix, including autospectra and cross-spectra. The modulus of the cross-spectra can be replaced by an estimate of the process coherence.
2. Higher-order statistics: the specification of the process kurtosis is considered sufficient for most of the actual road vibration scenarios. Skewness is found to be very close to zero. The crest factor can provide useful information about the tail decay of the process distribution. These parameters should be specified for all the relevant DOFs.

The higher-order spectra are not considered for the process model, due to the following reasons:

- It was shown that, for the extracted stationary segments, the bispectra can be considered null in most of the cases.
- The complexity of the model would increase significantly when including the HOS, becoming impractical.

Property	Non-Gaussian	Proposed
SDM	Required	Required
Higher-order Spectra	Required	Not considered
Higher-order Statistics	Required	Univariate Kurtosis required. Skewness considered null.
Joint Density	Required	Not considered
Crest factor	Not required (implicit in joint density)	Recommended

Table 7: Process specification considering requirements under strong non-Gaussian conditions, and proposed simplified specification.

9 Conclusions

This paper describes field measurements performed on a car seat, with the purpose of providing an empirical background and a set of parameters for the proper definition of a non-Gaussian random process for vibration testing. The recorded signals are segmented into stationary sections for later analysis. The non-Gaussian nature of the recorded vibration is demonstrated through different Gaussianity hypothesis tests. It is found that, in general, the skewness is very close to zero, whereas the kurtosis is larger than that of a Gaussian. The crest factor was shown to cover a broad range of values. The marginals present in general a leptokurtic distribution. The inspection of the kernel estimates of the 2 and 3 DOF densities reveals elliptical symmetries. The application of a pseudo-Gaussian ellipticity test was not conclusive in rejecting this hypothesis. The second-order spectral content reveals significant correlation at specific frequencies, while third-order polyspectra can most of the time be considered null, reinforcing the lack of polyspectra in the specification of the process. A practical specification of the process is proposed based on second-order spectral content, univariate kurtosis and crest factor levels.

Acknowledgements

The work of R. López-Valcarce was partially funded by the Agencia Estatal de Investigación (Spain) and the European Regional Development Fund (ERDF) under project WINTER (TEC2016-76409-C2-2-R), and by the Xunta de Galicia (Agrupación Estratéxica Consolidada de Galicia accreditation 2016-2019; Red Temática RedTEIC 2017-2018) and the European Union (ERDF).

References

[1] A. Papoulis, S.U. Pillai, *Probability, random variables, and stochastic processes*, McGraw-Hill, (2002).

[2] D.O. Smallwood, *Generation of partially coherent stationary time histories with non-Gaussian distributions*, Technical Report, Sandia National Labs., Albuquerque (United States), (1996).

[3] J.M. Mendel, *Tutorial on higher-order statistics (spectra) in signal processing and system theory: theoretical results and some applications*, Proceedings of the IEEE, Vol. 79, No. 3, IEEE (1991), pp. 278-305.

[4] N. Fitz-Coy, V. Nagabhushan, M.T. Hale, *Benefits and challenges of over-actuated excitation systems*, Shock and Vibration, Vol. 17, No.3, Hindawi Publishing Corporation (2010), pp. 285-303.

[5] D. González , *Segmentation based on k-means clustering of CPB spectra*, Technical Report, TR-010-2014-B, Universidade de Vigo, (2014).

[6] J.S. Bendat, A.G. Piersol, *Random Data: Analysis and Measurement Procedures*, John Wiley & Sons (2011).

[7] A. Madansky, *Prescriptions for working statisticians*, Springer, New York (1988).

[8] N. Henze, *Invariant tests for multivariate normality: a critical review*, Statistical papers, Vol. 43, No. 4, Springer (2002), pp. 467-506.

[9] D.N. Joanes, C.A. Gill, *Comparing measures of sample skewness and kurtosis*, Journal of the Royal Statistical Society: Series D (The Statistician), Vol. 47, No. 1, Wiley (1998), pp. 183-189.

[10] D.N. Politis, J.P. Romano, *The stationary bootstrap*, Journal of the American Statistical Association, Vol. 89, No. 428, Taylor & Francis Group (1994), pp. 1303-1313.

[11] A. Steinwolf, *Shaker random testing with low kurtosis: Review of the methods and application for sigma limiting*, Shock and Vibration, Vol. 17, No. 3, Hindawi Publishing Corporation (2010), pp. 219-231.

[12] B.W. Silverman, *Density estimation for statistics and data analysis*, Chapman and Hall/CRC (1986)

[13] D. Cassart, *Optimal Tests for Symmetry*, PhD Thesis, Université Libre de Bruxelles (2007).

[14] M.J. Hinich, *Testing for Gaussianity and linearity of a stationary time series*, Journal of time series analysis, Vol. 3, No. 3, Wiley (1982), pp. 169-176.

[15] A. Swami, J.M. Mendel, C.L.M. Nikias, *Higher-order spectral analysis toolbox*, United Signals & Systems, Inc. (1993).

Uncertain quantification in nonlinear dynamics with an high-dimensional computational model

E. Capiez-Lernout [1], **C. Soize** [1]
[1] Université Paris-Est, Laboratoire Modélisation et Simulation Multi-échelle, MSME UMR 8208 CNRS, 5 bd Descartes, 77454 Marne-la-Vallée Cedex 02, France
e-mail: **evangeline.capiez-lernout@u-pem.fr**

Abstract
The present work concerns the dynamical analysis of an uncertain structure in the context of nonlinear dynamics. The structure is assumed to undergo large displacements and large deformations although the constitutive equations remain linearly elastic. The proposed strategy is compatible with the use of high-dimensional computational models, requiring to compute the random dynamical response from a stochastic nonlinear reduced-order model expressed in the time domain. With the proposed method, the uncertainty is introduced by replacing a deterministic chosen reduced-order basis with a stochastic projection basis, for which a new nonparametric probabilistic approach is used so that each realization of the projection basis respects some mathematical properties linked to the available information. The methodology is then applied on a computational model of a bi-clamped tridimensional beam structure.

1 Introduction

A major challenge in many research areas consists in developing advanced methodologies in order to construct predictive numerical simulation tools, which are representative of the observed dynamical behavior dynamical systems. In particular, it is important to quantify how inherent uncertainties propagate on the considered system. Furthermore, an essential aspect is to pay attention to the various nonlinear effects that can subsequently modify the dynamical response of the structure. There have been various researches concerning the development of computational strategies for constructing stochastic nonlinear reduced-order models that are able to accurately reproduce experimental dynamical structural responses that occur in nonlinear vibrational operating ranges. One one hand, a particular attention has to be paid on the construction of nonlinear deterministic reduced-order models [10, 1, 8, 7, 5], that have to be compatible with non intrusive computational strategies regarding existing industrial softwares. On the other hand, uncertainties can be implemented from the mechanical or geometrical parameters of a given deterministic computational model or with nonparametric probabilistic approaches which are parameterized by hyperparameters directly linked to the considered reduced-order models. We are interested in this latter strategy that allows both model and parameter uncertainties to be considered. In previous researches, uncertainty was introduced from the nonlinear reduced-operators issued from a given mean reduced-order model [9, 1, 3]. With the proposed method, the uncertainty is introduced by replacing the deterministic reduced-order basis with a stochastic reduced-order basis. This latter one is obtained by using a new nonparametric probabilistic approach [13, 6] so that each realization of the random projection basis respects some mathematical properties linked to the available information. Moreover, it is parameterized by a small number of hyperparameters. It is then used as the projection basis for constructing the stochastic nonlinear reduced-order model. With such uncertainty modeling, there is no need to construct the stochastic nonlinear reduced operators. The numerical effort is focused on the construction of the stochastic nonlinear reduced internal forces, which is explicitly carried out using the stochastic reduced-order basis combined with the finite element method. The paper is organized

as follows. In Section 2, the computational methodology is described. In particular, the computation of the mean nonlinear dynamical finite element response is used for constructing an adapted reduced-order basis with the proper orthogonal decomposition method. The stochastic nonlinear computational model is then written and the main steps concerning the computational resolution of the set of stochastic nonlinear differential equations are discussed. Section 3 is devoted to a numerical application consisting in a bi-clamped tridimensional beam subjected to a non symmetrical load and for which the uncertainty propagation of the dynamical nonlinear response is analyzed in details.

2 Description of the methodology

2.1 Context of the method

The present research is carried out in the context of the uncertainty propagation for elasto-dynamics structural systems that undergo geometrical nonlinear effects. In this field, a complete methodology has already been developed and a dedicated numerical tool that is adapted for large numerical computational models and that is non intrusive with respect to the industrial softwares has been constructed. More particularly, it has been experimentally validated in the context of the post-buckling of cylindrical shells [2] and applied to various numerical applications [3, 4]. Until now, the uncertainties were modeled through the nonparametric probabilistic approach for which a dedicated probability model issued from the maximum entropy principle [12] was directly implemented on the reduced operators of a mean nonlinear reduced-order model. In particular, such strategy requires the numerical construction of all linear, quadratic, and cubic operators issued from such nonlinear mean reduced-order model. As soon as the probability model is implemented, the numerical construction of the stochastic reduced nonlinear internal forces and of the stochastic tangent operator is then performed. Indeed it is required by the computational algorithms used for solving the stochastic nonlinear differential equations. In the present context, a nonparametric probabilistic approach on the model-form recently introduced in [13] is considered. In this approach, a dedicated probability model of random uncertainties is implemented on the projection basis used for constructing the mean nonlinear reduced-order model. As a consequence, the computational strategy has to be adapted. The main steps of this new methodology are summarized below and the related novel developments are explained in details.

2.2 Mean nonlinear finite element model of the structure

The considered structure is assumed to be fixed on a part of its boundary. In the context of the finite element method, a nonlinear finite element computational model that describes the nonlinear dynamical forced response of the considered structure is characterized in the time domain by the following set of nonlinear coupled differential equations such that

$$[\underline{M}]\ddot{\underline{\mathbf{U}}}(t) + [\underline{D}]\dot{\underline{\mathbf{U}}}(t) + [\underline{K}]\underline{\mathbf{U}}(t) + \underline{\mathbf{F}}^{\mathrm{NL}}(\underline{\mathbf{U}}(t)) = \underline{\mathbf{F}}(t) \quad , \tag{1}$$

$$[\underline{B}]^T \underline{\mathbf{U}}(t) = \mathbf{0} \tag{2}$$

in which the $\mathbb{R}^n$-vector $\underline{\mathbf{U}}(t)$ is the instantaneous displacement vector. In Eq. (1), the real matrices $[\underline{M}]$, $[\underline{D}]$, and $[\underline{K}]$ are the mass and damping, elastic stiffness $(n \times n)$ real matrices with symmetry positive definiteness property. The $\mathbb{R}^n$-vector $\underline{\mathbf{F}}(t)$ is issued from the finite element discretization of the external load and the $\mathbb{R}^n$-vector $\underline{\mathbf{F}}^{\mathrm{NL}}(\underline{\mathbf{U}}(t))$ describes the nonlinear finite element internal forces induced by the geometrical nonlinearities. In Eq. (1), the real $(n \times n_{\mathrm{BC}})$ matrix $[B]$ describes the n_{BC} constraint relations defining the Dirichlet conditions, verifying the relation $[\underline{B}]^T[\underline{B}] = [I_{n_{\mathrm{BC}}}]$. Since we are interested in analyzing the nonlinear vibrations of the structure, the external load is defined in the time domain for $t \in \mathbb{R}$ and a Fourier transform with respect to the time domain is performed on the nonlinear solution and allows then the nonlinear dynamical response in the frequency domain to be analyzed. In the present research, it is chosen to solve this set of nonlinear differential equations in order to construct the nonlinear dynamical response that

will be considered as the reference response. In this case, the nonlinear algorithms require to construct the nonlinear internal finite element forces and the related tangential operator with the finite element model. it should be noted that this calculation is particularly time consuming but is carried out once.

2.3 Construction of the projection basis

The construction of the mean nonlinear reduced-order model requires a projection basis. In the present work, such projection basis is computed from the nonlinear reference response with the proper-orthogonal decomposition method (POD-method), which is proved to be particularly relevant for nonlinear problems. Let $[A]$ be the $(n \times n)$ correlation matrix related to the nonlinear reference dynamical response $\underline{\mathbf{U}}(t)$. It is defined by

$$[\underline{A}] = [\underline{\mathbb{Y}}]^T [\underline{\mathbb{Y}}] \quad , \quad [\underline{\mathbb{Y}}]_{ij} = \underline{U}_i(t_j) \sqrt{\delta t} \quad , \tag{3}$$

in which δt is the constant sampling time step, and where t_j denotes the sampling time number j. The projection basis is defined by the eigenvectors $\underline{\boldsymbol{\varphi}}_\alpha$ related to the N most contributing eigenvalues $\underline{\lambda}_\alpha$, solution of

$$[\underline{A}]\, \underline{\boldsymbol{\varphi}}_\alpha = \underline{\lambda}_\alpha\, \boldsymbol{\varphi}_\alpha \quad \text{with} \quad \underline{\boldsymbol{\varphi}}_\alpha^T\, \underline{\boldsymbol{\varphi}}_\beta = \delta_{\alpha\beta} \quad , \tag{4}$$

in which $\delta_{\alpha\beta}$ is the Kronecker symbol set to 1 if $\alpha = \beta$ and to 0 otherwise. Note that in practice, for large computational models, the numerical construction of correlation matrix $[A]$ is difficult to achieve. In such a case, metrics $[A]$ is not computed and the eigenvalue problem is replaced by a singular value decomposition of metrics $[Y]$ or $[Y]^T$ (see Section 3.3).

2.4 Stochastic nonlinear reduced-order model

In this work, the nonparametric probabilistic approach of model-form uncertainties recently introduced in [13] is used. In such case, the probability model is directly implemented in the projection basis. Let $[\underline{\Phi}]$ be the $(n \times N)$ matrix whose columns are the eigenvectors $\underline{\boldsymbol{\varphi}}_1, \cdots, \underline{\boldsymbol{\varphi}}_N$. The matrix $[\underline{\Phi}]$ is then replaced by a stochastic matrix $[\boldsymbol{\Phi}(\boldsymbol{\alpha})]$, whose stochastic model and whose Monte Carlo numerical simulation procedure is found in [13]. It should be noted that the random vectors contained in random matrix $[\boldsymbol{\Phi}]$ verify the boundary conditions and orthonormality conditions

$$[\underline{B}]^T [\boldsymbol{\Phi}] = \mathbf{0} \quad , \quad [\boldsymbol{\Phi}]^T [\boldsymbol{\Phi}] = [I_N] \quad , \tag{5}$$

in which $[I_N]$ is the identity matrix with N order. The probability distribution of random matrix $[\boldsymbol{\Phi}]$ depends on a $\mathbb{R}^m$-valued hyperparameter $\boldsymbol{\alpha} = \{s, \beta, [\sigma]\}$, with $m = 0.5N(N+1)+2$. More specifically, s is a scalar which controls the global amount of uncertainty on the random basis, β is a scalar which controls the noise level around each projection vector basis and $[\sigma]$ is an $(N \times N)$ real upper triangular matrix which allows the correlations between the projection basis vectors to be controlled.

The stochastic computational model consists then in solving the set of stochastic nonlinear differential equations

$$[\boldsymbol{\mathcal{M}}]\ddot{\mathbf{Q}}(t) + [\boldsymbol{\mathcal{D}}]\dot{\mathbf{Q}}(t) + [\boldsymbol{\mathcal{K}}]\mathbf{Q}(t) + [\boldsymbol{\Phi}]^T \underline{\mathbf{F}}^{\mathrm{NL}}([\boldsymbol{\Phi}]\,\mathbf{Q}(t)) = [\boldsymbol{\Phi}]^T \underline{\mathbf{F}}(t) \quad , \tag{6}$$

in which $[\boldsymbol{\mathcal{M}}] = [\boldsymbol{\Phi}]^T\, [\underline{M}]\, [\boldsymbol{\Phi}]$, $[\boldsymbol{\mathcal{D}}] = [\boldsymbol{\Phi}]^T\, [\underline{D}]\, [\boldsymbol{\Phi}]$ and $[\boldsymbol{\mathcal{K}}] = [\boldsymbol{\Phi}]^T\, [\underline{K}]\, [\boldsymbol{\Phi}]$ are the full random mass, damping and stiffness matrices belonging to the set of positive-definite symmetric $(N \times N)$ real-valued matrices, and where $\mathbf{Q}$ is the $\mathbb{R}^N$-valued random vector of the generalized coordinates from which the $\mathbb{R}^n$-valued random vector of the physical solution $\mathbf{U}$ is reconstructed by

$$\mathbf{U} = [\boldsymbol{\Phi}]\, \mathbf{Q} \quad . \tag{7}$$

Regarding the numerical computation, the set of these stochastic nonlinear differential equations is solved in the time domain by using the Monte Carlo numerical simulation, using an implicit and unconditionally

stable integration scheme (Newmark method with the averaging acceleration scheme). For each sampling time, the nonlinearity is solved iteratively by using either the fixed point method or an arc-length-based algorithm, depending on the nonlinearity rate. Concerning the current strategy, the knowledge of the nonlinear reduced-order internal force vector is required by both nonlinear algorithms whereas the knowledge of the related reduced tangent operator (that is time consuming) is only required by the use of the arc-length-based algorithm. Practically, the contributions of both nonlinear reduced-order internal force and tangent reduced operator induced by each finite element are explicitly constructed with the finite element method. The assemblage over the finite elements is particularly quick because it only requires to sum each of these contributions. A posterior nonlinear dynamical analysis is performed from Eq.(7) in the frequency domain by computing the Fourier transform of the nonlinear dynamical response.

3 Numerical application

3.1 Description of the finite element computational model

The three-dimensional bounded domain Ω is a slender rectangular domain defined in a Cartesian system $(0, \mathbf{e}_1, \mathbf{e}_2, \mathbf{e}_3)$ such that $\Omega =]0, \underline{l}[\times]0, \underline{b}[\times]0, \underline{h}[$ with $\underline{l} = 8\,m$, $\underline{b} = 0.8\,m$, $\underline{h} = 0.6\,m$. Let Γ_0 and Γ_1 be the boundaries described as $\Gamma_0 = \{\mathbf{x};\, x_1 = 0\}$ and $\Gamma_1 = \{\mathbf{x};\, x_1 = \underline{l}\}$. The structure is assumed to be fixed on both boundaries so that we have a Dirichlet condition on $\Gamma_0 \bigcup \Gamma_1$. The structure is free on boundary $\partial\Omega \setminus \{\Gamma_0 \bigcup \Gamma_1\}$. The structure is subjected to an external point load applied along directions $\mathbf{e}_1$, $\mathbf{e}_2$ and $\mathbf{e}_3$ at the excitation node located at $(3.2, 0.4, 0.6)$. The Young modulus, the Poisson coefficient and the mass density of the homogeneous and isotropic linear elastic material are $\underline{E} = 2 \times 10^{11}\, N.m^{-2}$, $\underline{\nu} = 0.3$ and $\underline{\rho} = 8200\, Kg.m^{-3}$. A three dimensional finite element model is constructed with $40 \times 4 \times 3 = 480$ solid finite elements with 8 nodes. Therefore, the mean computational model has 820 nodes and $n = 2\,320$ degrees of freedom (see Fig. 1).

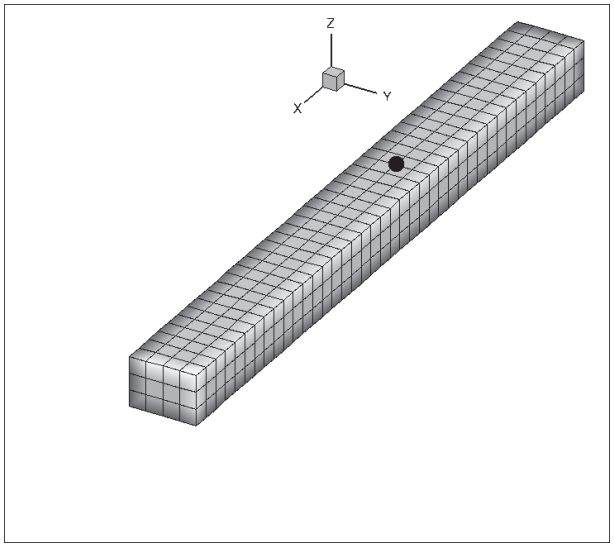


Figure 1: Finite element mesh of the structure - localisation of the excitation node (• symbol).

It should be noted that the fundamental eigenfrequency related to the linear undamped structure is $\nu_1 = 47.930\, Hz$. The frequency band of analysis is then chosen as $\mathbb{B} = [40\,,\, 2000]\, Hz$. The damping is then represented by a Rayleigh model $[D] = \alpha\,[M] + \beta\,[K]$ with $\alpha = 24.2$ and $\beta = 9.4 \times 10^{-6}$, which corresponds to a critical damping rate $\xi_1 = 0.040$ at fundamental frequency ν_1 and such that $\xi \in [0.015, 0.060]$ in frequency band $\mathbb{B}$. The chosen observation node is located at $(3.2, 0.4, 0.6)$, where the external point load is applied.

3.2 Description of the external loading

We are interested in analyzing the nonlinear dynamical forced response in frequency band $\mathbb{B}$. The chosen excitation frequency band is $\mathbb{B}_{exc} = [450\,,\,1200]\,Hz$. The load intensity is chosen as $f_0 = 18 \times 10^6\,N$ that corresponds to a consequent rate of geometrical nonlinearity for the numerical application presented. Consequently, it is no longer possible to directly compute the forced response in the frequency domain. The forced response is then computed in the time domain according to Eq.(1) and Eq. (2). The time dependent function $g(t)$ is defined with $\Delta\nu = 750\,Hz$ and $s = 1.1$. Practically, the computation is carried on a truncated time domain $\mathbb{T} = [t_{ini}, t_{ini} + T]$. The initial load is chosen as $t_{ini} = -4/\Delta\nu = -0.053\,s$ yielding a null initial load. The time duration T is then adjusted so that the system be returned at its equilibrium state within a given numerical tolerance for both linear and nonlinear computations. Even the fundamental eigenfrequency does not belong to excitation frequency band $\mathbb{B}_{exc}$, it ca be indirectly excited through the geometrical nonlinear effects. Time duration is chosen as $T = 0.234\,s$ which ensures the system to return to its equilibrium state with a relative tolerance $\tau = e^{-2\pi\xi_1\nu_1 T} = 6\%$ when fundamental eigenfrequency is excited. The sample frequency ν_e and the number of time steps are then chosen as $\nu_e = 35\,000\,Hz$ and $n_t = 8\,192$ yielding a constant sampling time step $\delta t = 2.857 \times 10^{-5}\,s$ and a constant sampling frequency step $\delta\nu = 4.272\,Hz$. It should be noted that the fundamental resonance that could possibly be excited would be nearly correctly represented with such computational choice. Let $t_\alpha = t_{ini} + \alpha\delta t\,, \alpha \in \{0, \cdots, n_t - 1\}$ and let $\nu_\beta = -0.5\nu_e + \beta\delta\nu\,, \beta \in \{0, \cdots, n_t - 1\}$. The Fourier transform $\widehat{g}(2\pi\nu)$ of function $g(t)$ is numerically estimated by using the Fast Fourier Transform since function $\widehat{g}(2\pi\nu)$ can be written as

$$\widehat{g}(2\pi\nu_\beta) = \exp\left(i\pi\, t_{ini}\nu_e\right)\, \exp\left(2i\pi\beta\delta\nu t_{ini}\right) \sum_{\alpha=0}^{n_t-1} (-1)^\alpha\, g(t_\alpha)\, exp(-2i\pi\alpha\beta/n_t) \quad . \tag{8}$$

Figure 2 displays the graphs of function $t \mapsto g(t)$ and $\nu \mapsto |\widehat{g}(2\pi\nu)|$.

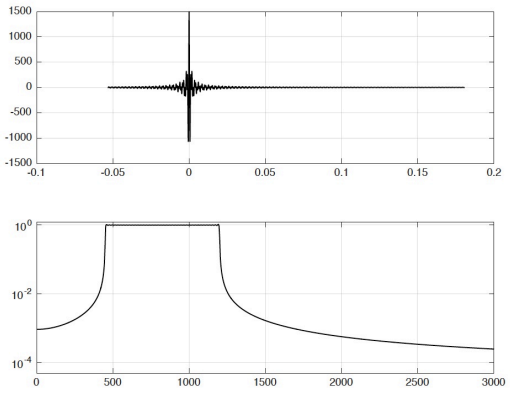


Figure 2: Representation of the time dependent load in the time domain and in the frequency domain : graphs of $t \mapsto g(t)$ (upper graph) and $\nu \mapsto |\hat{g}(2\pi\nu)|$ (lower graph).

3.3 Construction of the projection basis for the mean nonlinear reduced-order model

The dynamical response of the mean nonlinear finite element model is first calculated according to the algorithm described in Section 2.4. Figure 3 displays the graphs of both linear and nonlinear finite element dynamical responses at the observation node along the three dimensions in the time domain. It can be seen that the chosen load intensity yields subsequent geometrical nonlinear effects. Indeed, it can be seen that the dynamical response amplitudes are limited by the geometrical nonlinear effects. Moreover, the dynamical

system returns to its equilibrium state with a longer delay, in particular for the transverse directions. This means that the resonances that are located outside and below the excitation frequency band are indirectly excited by the geometrical nonlinearities. In order to quantify such geometrical nonlinear effects, a Fourier transform of both nonlinear and linear responses is carried out in the frequency domain. Figure 4 displays the graph of the response amplitude related to the observation node in the frequency domain for both nonlinear and linear cases. It is clearly seen that there exists a consequent contribution of resonances located in the very low frequency band outside the excitation frequency band.

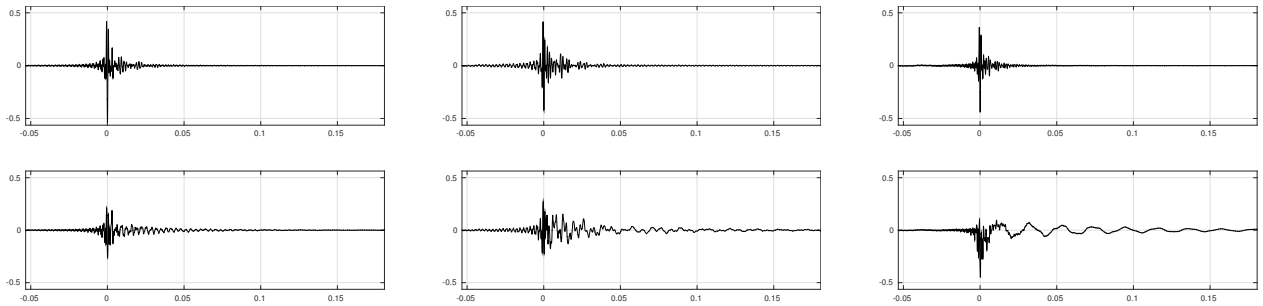


Figure 3: Time domain observation $t \mapsto u_{obs,1}(t)$ (left figure), $t \mapsto u_{obs,2}(t)$ (middle figure), $t \mapsto u_{obs,3}(t)$ (right graph) related to the linear (upper graph) and to the nonlinear (lower graph) finite element dynamical responses.

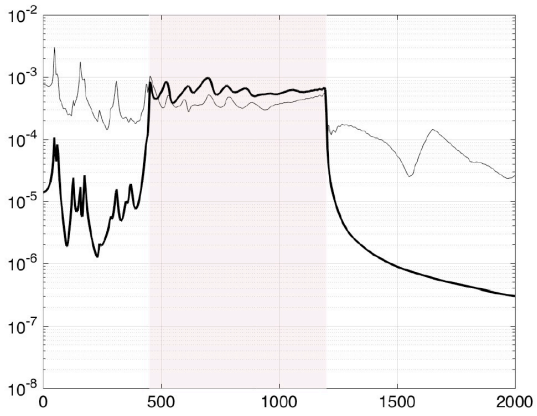


Figure 4: Frequency domain observation $\nu \mapsto ||\widehat{u}_{obs}(2\pi\nu)||$ related to the linear (thick black line) and to the nonlinear (thin black line) finite element dynamical responses for excitation frequency band $\mathbb{B}_{exc} = [450\,,\,1200]\,Hz$ (light red zone).

The mean nonlinear finite element dynamical response is then used for constructing the projection basis with the POD-method as described in Section 2.4. Practically, in the present case, since $n < n_t$, the projection basis is numerically calculated by using the single value decomposition of matrix $[\mathbb{Y}]^T$ whose singular values s_α are sorted by decreasing order and such tha $s_\alpha^2 = \lambda_\alpha$ and whose right-singular vectors corresponds to the basis vectors $\boldsymbol{\varphi}_\alpha$. Note that the projection basis strongly depends on the nature of the external load, which requires to be computed for each considered load case. Figure 5 displays several basis vectors issued from this POD decomposition. It is clearly seen that this projection basis presents local spatial displacements around the excitation node (that was expected), contrarily to a usual basis constituted of linear elastic eigenmodes.

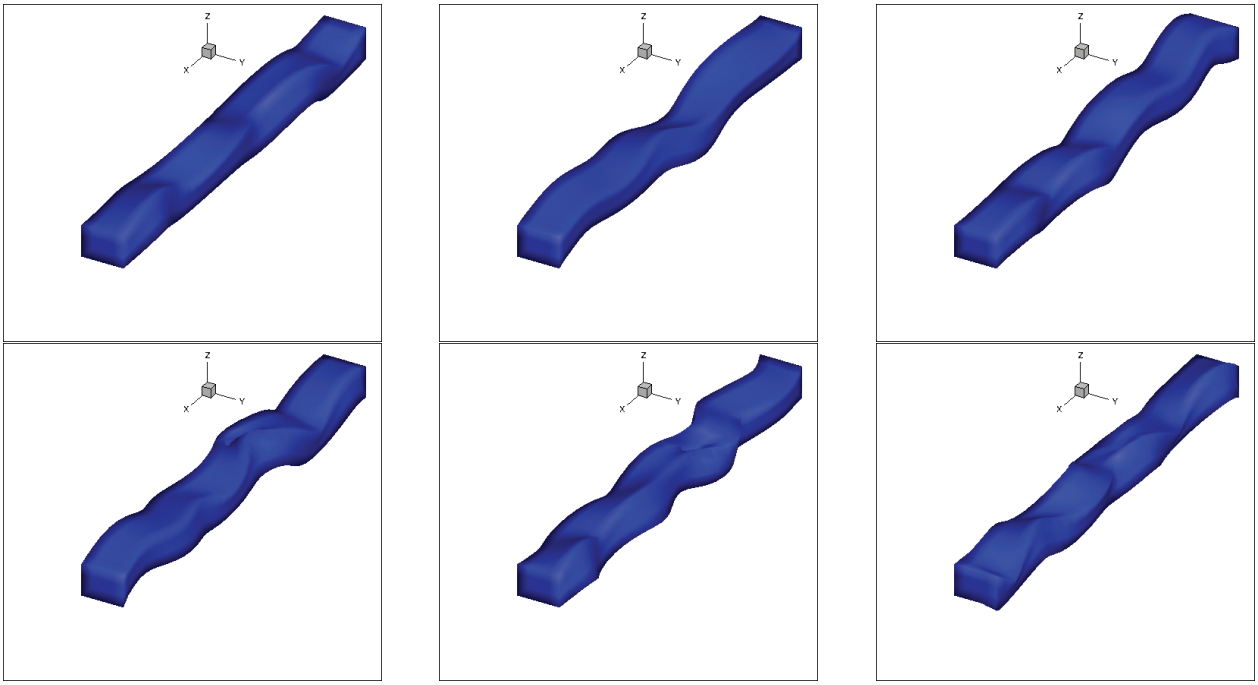


Figure 5: Representation of several basis vectors belonging to the projection basis computed with the POD method over the mean nonlinear finite element dynamical response.

3.4 Computational validation of the mean nonlinear reduced-order model

First a convergence analysis is performed in order to set the optimal order of the mean nonlinear reduced-order model that can accurately reproduce the nonlinear finite element response. Let $N \mapsto Conv_s(N)$ and $N \mapsto Conv_Q(N)$ be the convergence functions defined by

$$Conv_s(N) = \sqrt{\frac{\sum_{\alpha=1}^{N} s_\alpha^2}{\sum_{\alpha=1}^{n} s_\alpha^2}} \tag{9}$$

$$Conv_Q(N) = \sqrt{\frac{\displaystyle\int_0^{+\infty} ||\widehat{\mathbf{Q}}^N(2\pi\nu)||^2 \, d\nu}{\displaystyle\int_0^{+\infty} ||\widehat{\mathbf{U}}^{ref}(2\pi\nu)||^2 \, d\nu}} \quad . \tag{10}$$

Figure 6 displays the graph of function $N \mapsto Conv_s(N)$. Since the projection basis is orthonormal, it can easily be shown that $Conv_Q(n) = 1$. Figure 7 displays the graph of function $N \mapsto Conv_Q(N)$. It is seen that a good agreement is obtained for $N = 60$. From now on, we use $N = 60$ in the numerical application. In previous researches, the chosen projection basis was issued from nonlinear static calculations or from linear elastic modes which did not require the knowledge of the mean nonlinear finite element dynamical response. As a consequence, the systematic convergence analysis carried out with the mean nonlinear reduced-order model was converging towards a certain value yielding a converged value of N. But there was no computational proof that such converged value was the good one. In the present strategy, a computational effort for solving the mean nonlinear finite element model has been carried out. Consequently, it is computationally proved that the converged nonlinear dynamical response obtained with the mean nonlinear reduced-order model corresponds to the reference nonlinear finite element dynamical response.

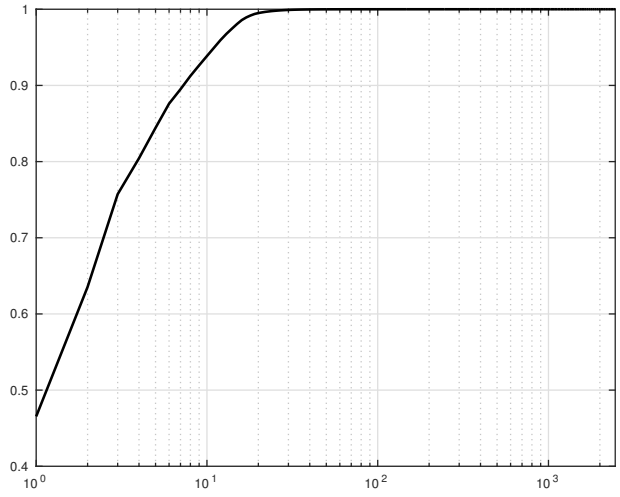


Figure 6: Convergence analysis for the mean nonlinear reduced-order model : graph of function $N \mapsto Conv_s(N)$.

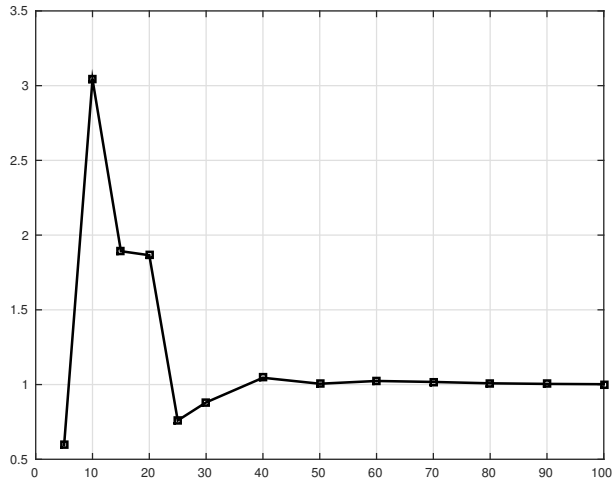


Figure 7: Convergence analysis for the mean nonlinear reduced-order model : graph of function $N \mapsto Conv_Q(N)$.

3.5 Stochastic nonlinear dynamical response

This Section is devoted to the stochastic nonlinear dynamical analysis of the structure. The computational results are presented for $s=0.003$, $\beta=0.0025$ and $[\sigma]$ an upper triangular matrix with N order for which the non-zeros entries are defined by $[\sigma]_{ii} = 10$, $[\sigma]_{i,i+1} = 5$ and $[\sigma]_{i,i+2} = 2.5$. The results are computed with $n_s=70$ Monte Carlo numerical realizations.

An experimental data basis is assumed to be available for the three observation dofs. Such experimental response is computed numerically as follows : The material properties $\underline{E}$, $\underline{\nu}$, $\underline{\rho}$ are replaced by stochastic fields $\mathbf{E}(\mathbf{x})$, $\boldsymbol{\nu}(\mathbf{x})$ and $\boldsymbol{\varrho}(\mathbf{x})$ yielding inhomogeneous materials along the length of the beam and we have then

$$\begin{aligned} \mathbf{E}(\mathbf{x}) &= \underline{E}(1+0.03\sum_{i=0}^{I} \boldsymbol{\xi}_i \sin\left(\frac{0.02\pi i}{\underline{\ell}}(x-0.5\underline{\ell})\right) \quad , \\ \boldsymbol{\nu}(\mathbf{x}) &= \underline{\nu}(1+0.03\sum_{i=0}^{I} \boldsymbol{\xi}'_i \sin\left(\frac{0.02\pi i}{\underline{\ell}}(x-0.5\underline{\ell})\right) \quad , \end{aligned} \tag{11}$$

$$\boldsymbol{\varrho}(\mathbf{x}) \quad = \quad \underline{\rho}(1+0.03\sum_{i=0}^{I}\boldsymbol{\xi}_i''\sin\left(\frac{0.02\pi i}{\underline{\ell}}(x-0.5\underline{\ell})\right) \quad ,$$

in which $\boldsymbol{\xi}_i$, $\boldsymbol{\xi}_i'$ and $\boldsymbol{\xi}_i''$ are independent truncated Gaussian random variables in order that $\forall \mathbf{x} \in \Omega$, $\mathbf{E}(\mathbf{x}) > 0$, $\boldsymbol{\nu}(\mathbf{x}) \in]0\,,1/2[$ and $\boldsymbol{\varrho}(\mathbf{x}) > 0$ almost surely. Note that the nonlinear stochastic computational model cannot reproduce this experimental data.

Let $\mathbf{u}_{exp}(2\pi\nu)$ be the vector of the experimental response. Figures 8 , 9 and 10 display the graph of function $\nu \mapsto |\mathbf{u}_{obs,i}(2\pi\nu)|$ (black dashed line), $\nu \mapsto |\mathbf{u}_{exp,i}(2\pi\nu)|$ (red line), and the graph of the confidence region of random function $\nu \mapsto |\mathbf{U}_{obs,i}(2\pi\nu)|$ of the observation with a probability level $p_c = 0.95$ related to the nonlinear reduced-order model for $i \in \{1,2,3\}$. First, it can be seen that unexpected resonances that are induced by the geometrical nonlinear effects and that are located in the low frequencies outside $\mathbb{B}_{exc}$ appear with subsequent amplitudes. Concerning the longitudinal displacement, it is seen that the proposed computational model captures well the nonlinear experimental dynamical behavior. Concerning the transverse displacements, we have a good agreement between the computational model and the experimental response except for the first resonance. It should be noted that the presented results have been obtained for a selected value of $\boldsymbol{\alpha}$, which does not correspond to an optimal value that would be obtained by solving an optimization problem allowing for minimizing the distance to the experimental target.

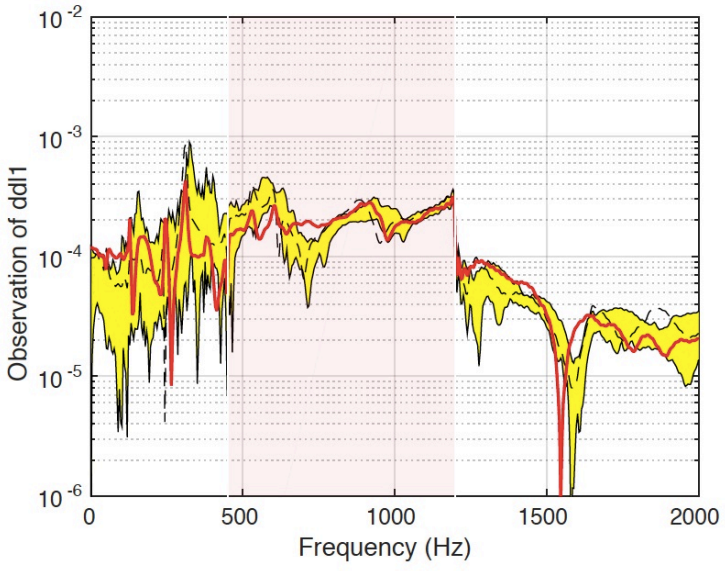


Figure 8: Graph of functions $\nu \mapsto |\mathbf{u}_{obs,1}(2\pi\nu)|$ (black dashed line) computed with the nonlinear finite element model, $\nu \mapsto |\mathbf{u}_{exp,1}(2\pi\nu)|$ (red line), graph of the confidence region of random function $\nu \mapsto |\mathbf{U}_{obs,1}(2\pi\nu)|$ computed with the nonlinear stochastic reduced-order model (yellow zone), localization of the excitation frequency band $\mathbb{B}_{exc} = [450\,,\,1200]\,Hz$ (light red zone).

4 Conclusion

In the context of structural dynamics with geometric nonlinearities, a computational methodology is presented for analyzing the propagation of uncertainties on the nonlinear dynamical response. A nonparametric probabilistic method for modeling model-form uncertainties, which is implemented from a given projection basis is used for constructing a stochastic computational nonlinear reduced-order model . A numerical application, which consists in a bi-clamped beam, is presented and shows the capability of the stochastic computational model to capture the unexpected resonances induced by the geometrical nonlinearities.

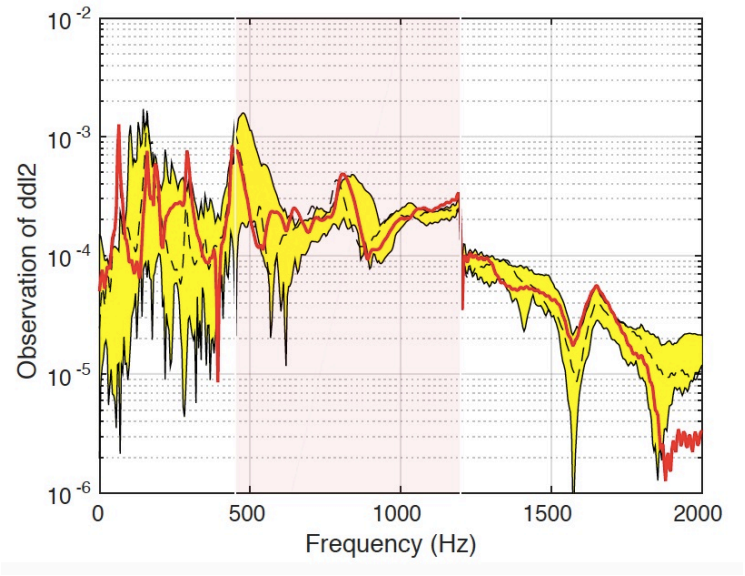


Figure 9: Graph of functions $\nu \mapsto |\mathbf{u}_{obs,2}(2\pi\nu)|$ (black dashed line) computed with the nonlinear finite element model, $\nu \mapsto |\mathbf{u}_{exp,2}(2\pi\nu)|$ (red line), graph of the confidence region of random function $\nu \mapsto |\mathbf{U}_{obs,2}(2\pi\nu)|$ computed with the nonlinear stochastic reduced-order model (yellow zone), localization of the excitation frequency band $\mathbb{B}_{exc} = [450\ ,\ 1200]\ Hz$ (light red zone).

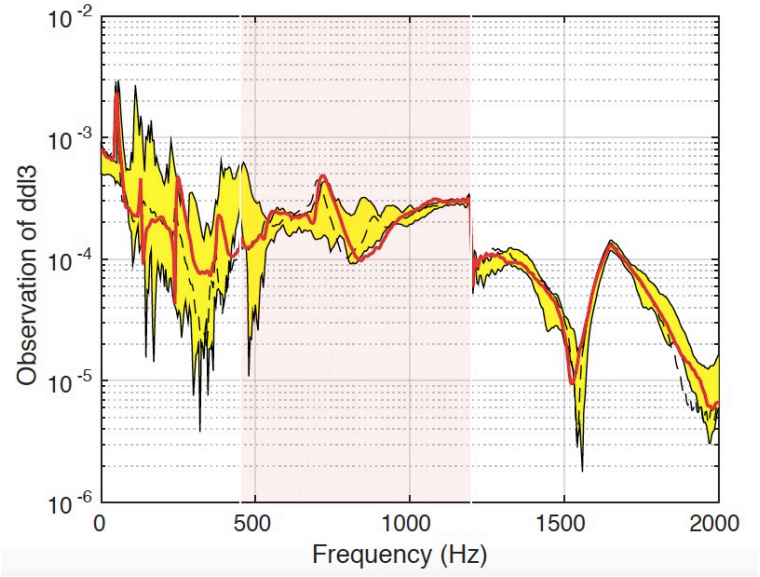


Figure 10: Graph of functions $\nu \mapsto |\mathbf{u}_{obs,3}(2\pi\nu)|$ (black dashed line) computed with the nonlinear finite element model, $\nu \mapsto |\mathbf{u}_{exp,3}(2\pi\nu)|$ (red line), graph of the confidence region of random function $\nu \mapsto |\mathbf{U}_{obs,3}(2\pi\nu)|$ computed with the nonlinear stochastic reduced-order model (yellow zone), localization of the excitation frequency band $\mathbb{B}_{exc} = [450\ ,\ 1200]\ Hz$ (light red zone).

References

[1] E. Capiez-Lernout, C. Soize, M.-P. Mignolet, Computational stochastic statics of an uncertain curved structure with geometrical nonlinearity in three-dimensional elasticity, *Computational Mechanics*, **49**

(1) 87-97 (2012).

[2] E. Capiez-Lernout, C.Soize, M.-P.Mignolet, Post-buckling nonlinear static and dynamical analyses of uncertain cylindrical shells and experimental validation, *Computer Methods in Applied Mechanics and Engineering*, **271**, 210-230 (2014).

[3] E. Capiez-Lernout, C. Soize, and M. Mbaye. Mistuning analysis and uncertainty quantification of an industrial bladed disk with geometrical nonlinearity. *Journal of Sound and Vibration*, 356(11):124–143, 2015.

[4] E. Capiez-Lernout and C. Soize. An improvement of the uncertainty quantification in computational structural dynamics with nonlinear geometrical effects. *International journal for Uncertainty Quantification*, 7(1):83–98, 2017.

[5] C. Farhat, P. Avery, T. Chapman and J. Cortial. Dimensional reduction of nonlinear finite element dynamic models with finite rotations and energy-based mesh sampling and weighting for computational efficiency. *International Journal for Numerical Methods in Engineering*, 98(9):625-662, 2014.

[6] C. Farhat, A. Bos, P. Avery and C. Soize. Modeling and quantification of model-form uncertainties in eigenvalue computations using a stochastic reduced model. *AIAA Journal*, 56(3):1198–1210,2018.

[7] A.K. Gaonkar and S.S. Kulkami. Model order reduction for dynamic simulation of beams with forcing and geometric nonlinearities *Finite Elements in Analysis and Design*, 76:50-62, 2013.

[8] M.-P. Mignolet, A. Przekop, S.A. Rizzi, and M.S. Spottswood. A review of indirect/non-intrusive reduced-order modeling of nonlinear geometric structures. *Journal of Sound and Vibration*, 332(10):2437–2460, 2013.

[9] M.-P. Mignolet and C. Soize. Stochastic reduced-order models for uncertain geometrically nonlinear dynamical systems. *Computer Methods in Applied Mechanics and Engineering*, 197:3951–3963, 2008.

[10] A.A. Muryavov and S.A. Rizzi. Determination of nonlinear stiffness with application to random vibration of geometrically nonlinear structures. *Computers and Structures*, 81:1513–1523, 2003.

[11] L. Sirovich. Turbulence and the dynamics of coherent structures *Quarterly of Applied Mathematics*, 45(3):561–571, 1987.

[12] C. Soize. *Stochastic Models of Uncertainties in Computational Mechanics*. Lecture Notes in Engineering Mechanics 2, American Society of Civil Engineers (ASCE), 2012.

[13] C. Soize and C. Farhat. A nonparametric probabiistic approach for quantifying uncertainties in low-dimensional and high-dimensional nonlinear models. *International Journal for Numerical Methods in Engineering*, 109(6):837-888, 2017.

Vibration analysis of a structure with an attachment at an uncertain location using parametric model order reduction with Krylov subspaces

S. Li[1], B. R. Mace[1], J. S. Dhupia[1]
[1] University of Auckland, Department of Mechanical Engineering
20 Symonds Street, Auckland 1010, New Zealand
e-mail: **sli183@aucklanduni.ac.nz**

Abstract
This paper presents an approach to calculate the response statistics of a structure comprising a main, host structure with an attachment for which there is uncertainty in the coupling location. The approach is based on a Krylov model order reduction method, which reduces the order of a finite element model of the structure enabling an efficient way to estimate the statistics of the structural response. The multi-point constraint method is used to connect the finite element models of the attachment and the structure. One (or more) analysis is performed for the attachment located at a given, position(s) to obtain the projection matrices. Afterwards, a Parametric Model Order Reduction method is applied to reduce the model order. Uncertainty in the location of the attachment is included in a Monte Carlo simulation. The method is described and a numerical example presented which illustrates the accuracy and efficiency of the proposed method.

1 Introduction

Uncertainty problems have attracted the attention of many researchers for some years. A large amount of research focuses on uncertainty in geometrical and/or material properties [1], damping [2], joints of the model [3] etc. However, uncertainty and variability in the physical locations of attachments have been considered much less frequently. During the early design stage, some of the properties and parameters may not be defined exactly, for example necessary componentry of various forms, referred to here as attachments, being added later. The problem concerned in this paper is about efficient analysis of the structure where there is uncertainty or variability in the physical locations of the points at which attachments are attached or connected. To include uncertainty and variability in the modelling process, repeated calculation is needed. However, re-analysis of large-scale FE models requires large computational effort which is time-consuming. This issue can be addressed by model order reduction (MOR) methods.

The general goal of MOR methods is to replace the original, high order model by another model which retains the main features of the model but is of lower complexity. Pade approximation related methods, also known as Krylov-based approximation methods, correspond to techniques developed for approximating the input and output behavior of the original system by a reduced system based on projection and moment matching. Such methods are widely used in the area of large electronic circuits [4]. In the development of this category of MOR methods, there are two broad approaches: Pade via Lanczos (PVL) and multipoint rational interpolation [5]. Feldmann and Freund [6] developed the PVL method, which builds the connection between Pade approximation and Krylov subspaces. In order to approximate the transfer function over a broad frequency range, the multipoint rational interpolation approach was developed to provide moment matching at selected frequencies [5]. Currently, research in Pade approximation related methods includes aspects of variable and uncertain parameters, such as physical and geometrical parameters. One of the important research directions in this category is parametric model order reduction (pMOR) which can preserve the original system parameters in the reduced model. In this

paper, a pMOR methods based on moment matching and projection is considered, in which two strategies can be used to obtain the projection matrices: using a single pair of fixed global basis matrices [7, 8], and interpolating multiple local matrices each considering different parameters [9, 10]. Although by using fixed global basis matrices the dimension of the projection matrices will increase through the increase of the number of parameters, the advantage is that there is no need to compute the reduced order model repeatedly for each different set of parameters. This strategy is suitable for a system with few uncertain parameters and repeated calculation is required for a large number of samples.

In this paper, pMOR is applied to the prediction of the frequency response of a mechanical dynamic system with an attachment, in which the location of the connection between the main system and the attachment are uncertain. In order to consider the uncertainty efficiently, the multi-point constraint (MPC) method is used to assemble the FE models of the main system and the attachment. Then pMOR is applied to model the system using a single pair of projection matrices for different attachment locations, and reduce the model order. The projection matrices are obtained through choosing some expansion frequencies and baseline positions. Based on the reduced order model, Monte Carlo simulation (MCS) is used to consider the influence of the uncertainty on the original structure.

The paper is organized as follows. The next section presents the basic problem setup, which is the system with an uncertain located attachment. The Krylov-based model order reduction and pMOR method used in this paper are described in Section 3. Next, numerical examples are presented in Section 4. Section 5 concludes.

2 Frequency response of the model with an attachment at an uncertain location

This situation is illustrated in Figure 1, in which the main structure is divided into two regions: Region 1 is the part of the structure in which the attachment cannot lie; Region 2 is the part of the structure to which the attachment is connected, but the location of that connection is uncertain. Both the main structure and the attachment are assumed to be modelled using the finite element (FE) method. The different FE models are assembled by MPCs. This section presents the response of the FE model and the model with attachments.

A time-invariant, single-input, single-output, system with an attachment can be written as a second order differential equation

$$\begin{aligned} \mathbf{M}(p)\ddot{\mathbf{x}}(t)+\mathbf{D}\dot{\mathbf{x}}(t)+\mathbf{K}(p)\mathbf{x}(t)=\mathbf{b}u(t) \\ y(t)=\mathbf{c}^T\mathbf{x}(t) \end{aligned} \tag{1}$$

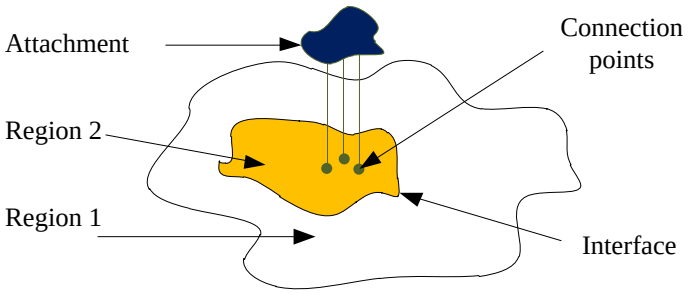


Figure 1 A structure with an attachment

where t is time, $\mathbf{x}(t)$ is a vector of the nodal coordinates of the FE mesh. $u(t)$ is the input force function and $y(t)$ is the output displacement function, $\mathbf{b} \in \mathbb{R}^{N\times 1}$ containing the input coefficients and $\mathbf{c} \in \mathbb{R}^{N\times 1}$ containing the output coefficients. $\mathbf{D}^{N\times N}$ is the damping matrix and $\mathbf{M}(p)^{N\times N}$ and $\mathbf{K}(p)^{N\times N}$ are the mass and stiffness matrices with the attachment, respectively, and variable parameter p models the uncertain location in Region 2.

Note that the influence of the attachment is evaluated by considering variations in the structure's mass and stiffness matrices, given by

$$\begin{aligned}\mathbf{M}(p) &= \mathbf{M} + \Delta\mathbf{M}(p)\\ \mathbf{K}(p) &= \mathbf{K} + \Delta\mathbf{K}(p)\end{aligned} \tag{2}$$

where $\Delta\mathbf{M}(p)$ and $\Delta\mathbf{K}(p)$ are mass and stiffness perturbation matrices, and $\mathbf{M}$ and $\mathbf{K}$ are the values of the system matrices independent of the parameter.

In the FE model, the simplest way to assemble two models is the node-by-node method, in which coincident meshes are required. If the attached location changes, modifications need to be applied to the meshes. In order to avoid remeshing the model, MPCs [11] are used here. The advantage is that the connection can be placed at any location without changing the meshes.

Considering uncertainty and taking the Laplace transform of Eq. (1), the input-output relation can be expressed as

$$H(s,p) = \bar{y}(s)/\bar{u}(s) = \mathbf{c}^T\left(s^2\mathbf{M}(p) + s\mathbf{D} + \mathbf{K}(p)\right)^{-1}\mathbf{b} \tag{3}$$

where $\bar{u}(s)$ and $\bar{y}(s)$ represent the Laplace transforms of $u(t)$ and $y(t)$.

Assuming a hysteretic damping matrix

$$\mathbf{D} = j\eta\mathbf{K}/s \tag{4}$$

proportional to the stiffness matrix, where $j = \sqrt{-1}$ and η is the loss factor, then Eq.(3) becomes

$$H(s,p) = \bar{y}(s)/\bar{u}(s) = \mathbf{c}^T\left(s^2\mathbf{M}(p) + \mathbf{K}(p)(1 + j\eta)\right)^{-1}\mathbf{b} \tag{5}$$

In practice, this transfer function can be obtained in various ways, such as modal decomposition, direct inversion, etc. The MOR objective of this paper is to approximate the original model by a reduced model, therefore Eq.(5) can be efficiently calculated many times. The pMOR method used is based on a rational two-sided Arnoldi algorithm in which two global constant projection matrices, $\mathbf{V}, \mathbf{W} \in \mathbb{R}^{N\times n}$ ($n \ll N$) are used, and yields reduced matrices and vectors, $\left(\tilde{\mathbf{M}}(p)\right)^{n\times n}$, $\left(\tilde{\mathbf{K}}(p)\right)^{n\times n}$, $\tilde{\mathbf{c}}^{n\times 1}$ and $\tilde{\mathbf{b}}^{n\times 1}$. The MOR methods involved are briefly reviewed in the following section.

3 Performing model order reduction

This section describes the model order reduction of a dynamic system using a pMOR method, which is based on a rational Krylov method, the rational two-sided Arnoldi algorithm [5]. A global basis is generated which allows all the different values of the parameter to be considered.

3.1 Rational Krylov model reduction for a second-order system

Krylov-based MOR was originally developed for the first-order system. However, second-order systems are common in engineering. The simplest way to apply Krylov-based methods to a second-order system is by transforming the system into a first-order one. Alternatively, methods of performing MOR directly in a

second-order system have been introduced [12, 13] which will be adopted in this work. Considering a specific parameter value p_k, Eq.(5) can be expressed as

$$H(s, p_k) = \mathbf{c}^T \left(s^2 \mathbf{M}(p_k) + \mathbf{K}(p_k)(1 + j\eta) \right)^{-1} \mathbf{b} \tag{6}$$

By using a two-sided Arnoldi method, a pair of orthogonal matrices $\mathbf{V}_m$ and $\mathbf{W}_m$ can be built though the subspaces [14]

$$\begin{aligned} &\mathbf{V}_m \text{ is a basis of } \mathrm{K}_m \left(\mathbf{K}(p_e)_{s_m}^{-1} \mathbf{M}(p_e), \mathbf{K}(p_e)_{s_1}^{-1} \mathbf{b} \right) \\ &\mathbf{W}_m \text{ is a basis of } \mathrm{K}_m \left(\mathbf{K}(p_e)_{s_m}^{-T} \mathbf{M}(p_e)^T, \mathbf{K}(p_e)_{s_1}^{-T} \mathbf{c} \right) \end{aligned} \tag{7}$$

where

$$\begin{aligned} \mathrm{K}_m \left(\mathbf{K}(p_e)_{s_m}^{-1} \mathbf{M}(p_e), \mathbf{K}(p_e)_{s_1}^{-1} \mathbf{b} \right) &= \mathrm{span} \left(\mathbf{K}(p_e)_{s_1}^{-1} \mathbf{b}, \cdots, \mathbf{K}(p_e)_{s_m}^{-1} \mathbf{M}(p_e) \cdots \mathbf{K}(p_e)_{s_1}^{-1} \mathbf{b}, \right) \\ \mathrm{K}_m \left(\mathbf{K}(p_e)_{s_m}^{-T} \mathbf{M}(p_e)^T, \mathbf{K}(p_e)_{s_1}^{-T} \mathbf{c} \right) &= \mathrm{span} \left(\mathbf{K}(p_e)_{s_1}^{-T} \mathbf{c}, \cdots, \mathbf{K}(p_e)_{s_m}^{-T} \mathbf{M}(p_e)^T \cdots \mathbf{K}(p_e)_{s_1}^{-T} \mathbf{c} \right) \end{aligned} \tag{8}$$

and $\mathbf{K}(p_e)_{s_m} = -\mathbf{K}(p_e) - j\eta \mathbf{K}(p_e) - s_m^2 \mathbf{M}(p_e)$ [15], s_k (k=1,2,…,m) are expansion frequencies, $\mathbf{V}_m, \mathbf{W}_m \in \mathbb{R}^{N \times m}$, and each base is orthonormal

$$\mathbf{V}_m^T \mathbf{V}_m = \mathbf{I}, \mathbf{W}_m^T \mathbf{W}_m = \mathbf{I} \tag{9}$$

These expansion frequencies s_k (k=1,2,…,m) are predetermined and fixed, and the same number of matched moments for each expansion frequency are selected. They will be determined by the frequency range of interest and *a priori* knowledge of the system such as the number of modes inside the frequency range. Some work has been done to investigate the selection of the expansion frequencies, for example, an procedure was proposed to choose the expansion frequencies iteratively [16] by optimizing the error of transfer function. As the parameters determined in the next section also influence the results, the calculation process will become tedious to select different sets of expansion frequencies for each value of the parameter chosen. Therefore, in this paper, expansion frequencies will be selected linearly in the frequency range of interest and they are the same for different values of the parameters.

3.2 Model reduction of the system with an attachment at random locations

The calculated projection matrices $\mathbf{V}_m$ and $\mathbf{W}_m$ in Section 3.1 are only exact for the specific parameter value p_e. In order to preserve the parameter in the matrices, two strategies can be considered: a global basis [17] or local bases [9]. While local bases methods perform interpolations between different local models, the global basis method can construct constant projection matrices V and W for an arbitrary parameter value, which is very suitable if the system has few parameters but repeated calculations are needed. In this work, the only parameter is the uncertain location of the attachment, so the first strategy is used.

Suppose we have a set of values $p_e, e = 1, \ldots E$, i.e. specific attachment locations, the corresponding local basis matrices $\mathbf{V}_1 \cdots \mathbf{V}_E$ and $\mathbf{W}_1 \cdots \mathbf{W}_E \in \mathbb{R}^{N \times m}$ can be calculated through the rational Krylov method in Section 3.1. A common way to obtain the global matrices is to concatenate the local basis matrices [18], written as

$$\begin{aligned} \mathbf{V}_n &= \left[\mathbf{V}_1 \ \mathbf{V}_2 \cdots \mathbf{V}_E \right] \\ \mathbf{W}_n &= \left[\mathbf{W}_1 \ \mathbf{W}_2 \cdots \mathbf{W}_E \right] \end{aligned} \tag{10}$$

However, directly combining these matrices together has a strong possibility to lead to rank-deficient global basis matrices. Thus a singular value decomposition (SVD) always follows the concatenation step to construct orthonormal columns.

Therefore, performing MOR to the transfer function in Eq.(5), we have

$$\tilde{H}(s,p)=\tilde{\mathbf{c}}^T\left(s^2\tilde{\mathbf{M}}_p+\tilde{\mathbf{K}}_p\left(\mathbf{I}+j\eta\mathbf{I}\right)\right)^{-1}\tilde{\mathbf{b}} \tag{11}$$

where $\tilde{\mathbf{M}}(p)=\mathbf{W}_n^T\mathbf{M}(p)\mathbf{V}_n$, $\tilde{\mathbf{K}}(p)=\mathbf{W}_n^T\mathbf{K}(p)\mathbf{V}_n$, $\tilde{\mathbf{c}}=\mathbf{c}\mathbf{V}_n$, $\tilde{\mathbf{b}}=\mathbf{W}_n^T\mathbf{b}$.

As the order of the transfer function is reduced, the computational cost for one single calculation will decrease significantly. Therefore, the MCS can be performed for a large number of samples at relatively low cost.

4 Numerical example

In this section a numerical example is considered to demonstrate the proposed method. The results are verified against a full FE analysis of the system. In the example, the attachment is considered as a point mass attached within a region of an otherwise homogeneous structure.

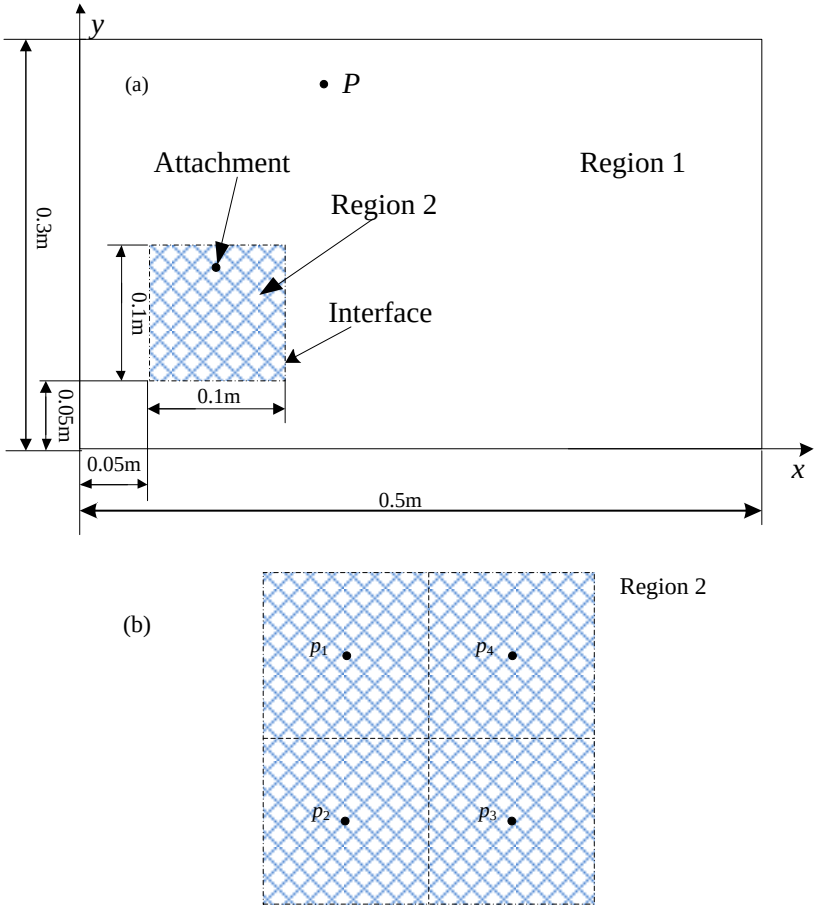


Figure 2 The plate divided into two regions: (a) the whole plate; (b) details of Region 2

4.1 Plate with uncertain located mass

The example comprises a 0.5m (L_x)$\times$0.3m (L_y) steel plate, 1.62×10^{-3}m thick, as shown in Figure 2. The density is 7520 kg m^{-3} and Poisson's ratio is taken as 0.33. The Young's modulus is taken to be 1.748GPa.

The boundary conditions are free and the input and output are located at point P (0.4 L_x, 0.83 L_y). A mass of 0.156 kg (8.5% of the plate mass) is attached at randomly selected points within Region 2.

In the numerical predictions Kirchhoff plate theory [19] is implemented in MATLAB. A 12×20 element mesh is used to construct the FE model. The position of the added mass in the x and y directions is assumed to obey a normal distribution, with the means at 0.2 L_x and 0.33L_y respectively, and the standard deviations being 0.045L_x and 0.042L_y respectively, with the mean being in the center of the square. The coordinates (x_m, y_m) of the m^{th} sample are independent of each other. The importance sampling method was used to sample 2000 points in Region 2, and the pMOR method was applied to perform the MCS. The values of the parameter in pMOR are selected where the added mass is located at the four locations p_1 (0.15L_x, 0.25L_y), p_2 (0.15L_x, 0.42L_y), p_3 (0.25L_x, 0.25L_y) and p_4 (0.25L_x, 0.42L_y). Loss factors are chosen as 0.004 for all the modes.

Assume that we are interested in the range of frequency between 100Hz and 200Hz. First two expansion frequencies, 120Hz and 180Hz, are chosen in this range of frequency. Thus we have $n=2\times4$, and the reduced matrices $\tilde{\mathbf{M}}, \tilde{\mathbf{K}} \in \mathbb{R}^{819\times8}$. Figure 3(a) shows the FRF of the system with the added mass located at the center of the plate (0.2L_x, 0.33L_y). The results of the FE-MPC method are the direct solution for the transfer function apart from the frequencies close to the expansion frequencies. Note that there are significant differences between the results of FE-MPC and pMOR. Now three expansion frequencies

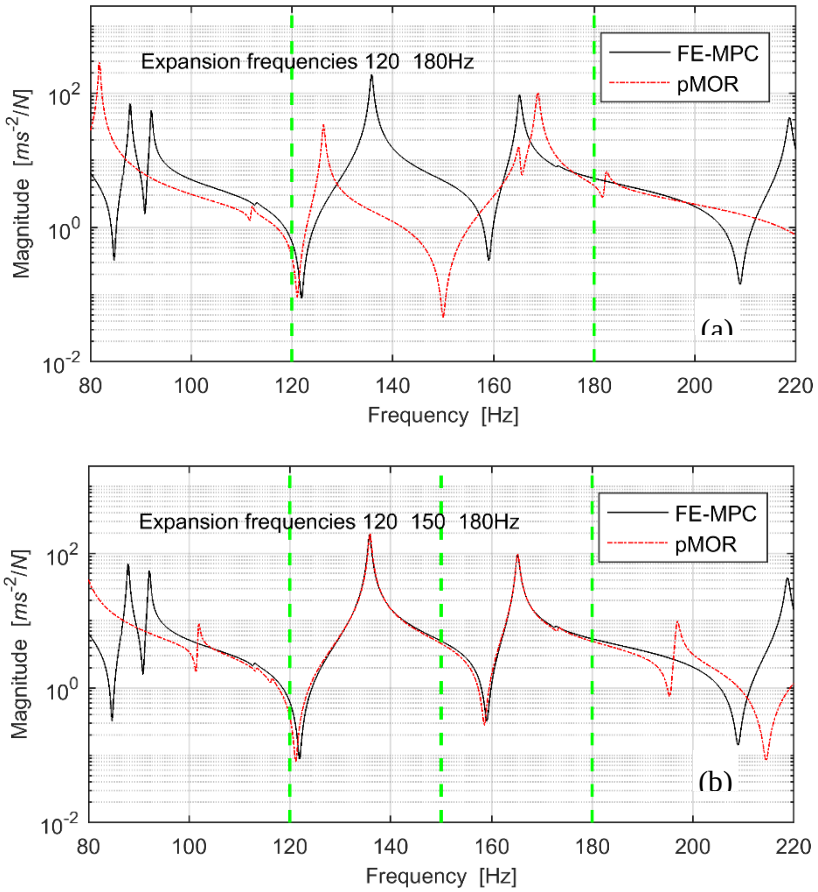


Figure 3 Comparison of FRF by full FE analysis and by pMOR: (a) two and (b) three expansion frequencies; mass attached at the centre of Region 2

(120Hz, 150Hz and 180Hz) are selected and the reduced matrices $\tilde{\mathbf{M}}, \tilde{\mathbf{K}} \in \mathbb{R}^{819\times 12}$. The FRF is shown in Figure 3(b), and shows good agreement between 110Hz and 190Hz.

Figure 4 shows the influence of selected parameter values. Instead of selecting four baseline values of the parameter, only three parameter values are considered (p_1, p_2 and p_3). The predictions of the FRF are less accurate than the results by using 4 baseline parameter values. Using more parameters and more expansion frequencies always yields more accurate results, but will result in larger projection matrices and subsequently increase the computation cost. Thus there is a balance between the accuracy and computation cost, and that is still an open question for this method. In this case, we choose four parameters and three expansion frequencies to achieve the projection matrices. The dimension of the original FE model is reduced from 819 to 12, the computational cost being reduced dramatically and the subsequent MCS for the estimation of response statistics becomes very cheap.

Then the MCS is performed using 2000 samples for the attachment location p. The FRF envelopes and mean FRF are presented in Figure 5 (note the different frequency range in the subplot). The expansion frequencies are selected as 120, 150 and 180Hz, and good agreement can be observed over a slightly wider frequency range. This is because the moments at the expansion frequencies are matched in the projection matrices. However the accuracy decreases as the frequency moves away from the expansion frequencies. Note that while the added mass introduces a larger variation in the FRF at higher frequencies (e.g. around 400-500Hz), the pMOR method can nevertheless approximate the response statics at these higher frequencies. It is believed that this is because the stochastic overlap is greater than 1 in this frequency range, so that the variability in a resonance peak across the ensemble becomes larger than the separation of adjacent resonances.

5 Conclusions

This paper discussed the effect of an attachment at an uncertain location on the vibrational response of a structure, and presented an efficient method to estimate the envelopes of the frequency response function (FRF) and mean FRF. Two projection matrices **V** and **W** are constructed by rational Krylov method-based parametric model order reduction (pMOR). These matrices are then applied to reduce the size of the system model significantly. Hence the computational cost of repeated calculation is reduced.

The main structure and the attachment are modelled by FE method and assembled using multi-point constraints to avoid remeshing of the FE model for each different location of the attachment. The rational Arnoldi method is used as the basic model order reduction method, then pMOR is applied to construct two global constant projection matrices. As the dimensions of the projection matrices are much smaller than the original model and can preserve the change of the parameter values, it enables us to build a reduced model for the structure with the uncertain located attachment. Thereafter, Monte Carlo simulation can be

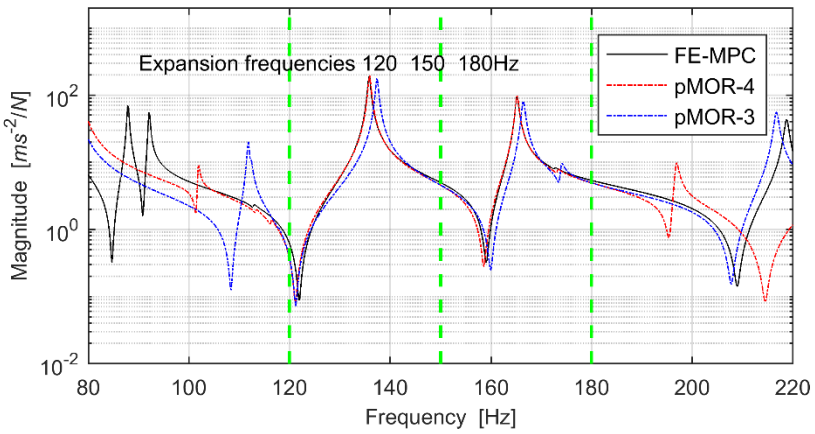


Figure 4 Comparison of FRF by full FE analysis and by pMOR: FE-MPC (Black), pMOR using 4 locations (Red) and pMOR using 3 locations (Blue); mass attached at the center of Region 2

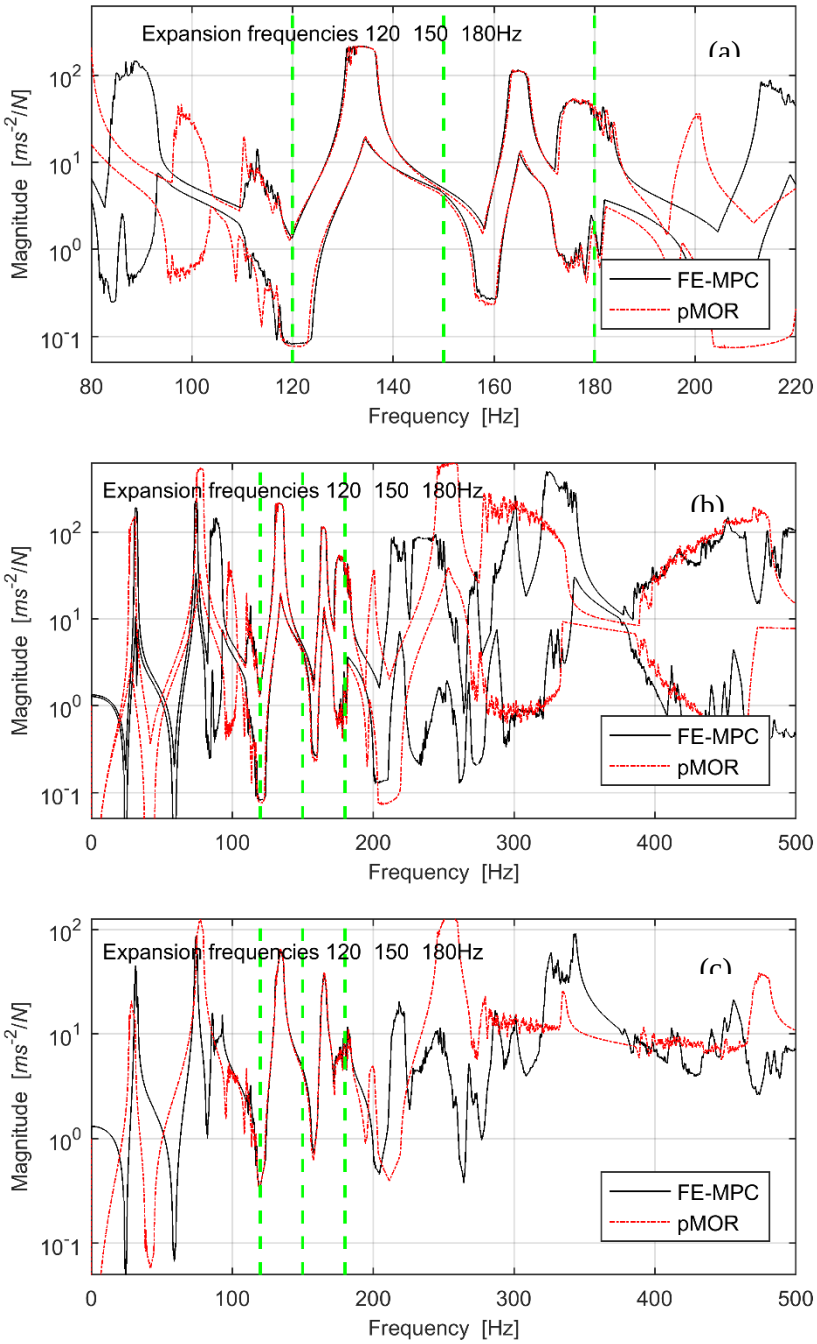


Figure 5 Comparison of FRF envelopes and mean FRF by full FE analysis and by pMOR: (a) envelopes (80-220Hz); (b) envelopes (0-500Hz); (c) mean FRF

performed cheaply in the frequency of interest.

The proposed method was verified numerically on an example structure of a plate with a point mass attached at random locations. It was seen that the accuracy of the predicted results is influenced by the number and location of selected expansion frequencies, and the number of selected values of the parameter at which the projection matrices are evaluated. The predicted envelopes of the FRFs using the proposed method are in good agreement with the results of the solving for the transfer function directly for the frequencies between the expansion frequencies. The approximations in the proposed method become less accurate as the frequency moves away from the expansion frequencies. The results show that the

proposed method reduces the model order of the structure significantly and leads to accurate results for both the FRF and their statistics in the presence of uncertainty.

Acknowledgements

The scholarship offered to the first author by China Scholarship Council (CSC) is gratefully acknowledged.

References

[1] Van den Nieuwenhof, B. and J.-P. Coyette 2003 Modal approaches for the stochastic finite element analysis of structures with material and geometric uncertainties *Computer Methods in Applied Mechanics and Engineering*, **192**(33–34): p. 3705-3729.

[2] Cortes Mochales, L., N.S. Ferguson, and A. Bhaskar 2012 Uncertainty propagation in locally damped dynamic systems. in *ISMA 2012 - Conference on Noise and Vibration Engineering*. Leuven, BE.

[3] Dohnal, F., B.R. Mace, and N.S. Ferguson 2009 Joint Uncertainty Propagation in Linear Structural Dynamics Using Stochastic Reduced Basis Methods *AIAA Journal*, **47**(4): p. 961-969.

[4] Besselink, B., et al. 2013 A comparison of model reduction techniques from structural dynamics, numerical mathematics and systems and control *Journal Of Sound And Vibration*, **332**(19): p. 4403-4422.

[5] Grimme, E.J. "Krylov projection methods for model reduction." Ph.D. Thesis, University of Illinois at Urbana-Champaign, 1997.

[6] Feldmann, P. and R.W. Freund 1994 Efficient linear circuit analysis by Pade approximation via the Lanczos process. in *Proceedings of the conference on European design automation*. Grenoble, France.

[7] Li, P., et al. *Modeling interconnect variability using efficient parametric model order reduction*. in *Proceedings of the conference on Design, Automation and Test in Europe-Volume 2*. 2005.

[8] Soll, T. and R. Pulch 2017 Sample selection based on sensitivity analysis in parameterized model order reduction *Journal of Computational and Applied Mathematics*, **316**: p. 369-379.

[9] Amsallem, D. and C. Farhat 2008 Interpolation Method for Adapting Reduced-Order Models and Application to Aeroelasticity *AIAA Journal*, **46**(7): p. 1803-1813.

[10] Amsallem, D. and C. Farhat 2011 An Online Method for Interpolating Linear Parametric Reduced-Order Models *SIAM Journal on Scientific Computing*, **33**(5): p. 2169-2198.

[11] Octavio de Alba Alvarez, R. "Vibration analysis of uncertain spot-welded structures." Ph.D. Thesis, University of Southampton, 2012.

[12] Eid, R., et al. 2007 Parametric order reduction of proportionally damped second-order systems *Sensors and Materials, Tokyo*, **19**(3): p. 149-164.

[13] Gugercin, C.A.B.a.S. *Krylov-based model reduction of second-order systems with proportional damping*. in *Proceedings of the 44th IEEE Conference on Decision and Control, and the European Control Conference*. 2005. Seville, Spain.

[14] Panzer, H.K. "Model Order Reduction by Krylov Subspace Methods with Global Error Bounds and Automatic Choice of Parameters." Ph.D. Thesis, Universität München, 2014.

[15] Rudy Eid , B.S., Boris Lohmann, *Parametric Order Reduction of Proportionally Damped Second Order Systems*, in *Technical Reports on Automatic Control*. 2006.

[16] Gugercin, S., A.C. Antoulas, and C. Beattie 2008 H_2 model reduction for large-scale linear dynamical systems *SIAM Journal on Matrix Analysis and Applications*, **30**(2): p. 609-638.

[17] Benner, P., S. Gugercin, and K. Willcox 2015 A Survey of Projection-Based Model Reduction Methods for Parametric Dynamical Systems *SIAM Review*, **57**(4): p. 483-531.

[18] Sturler, E.d., et al. 2015 Nonlinear Parametric Inversion Using Interpolatory Model Reduction *SIAM Journal on Scientific Computing*, **37**(3): p. B495-B517.

[19] Petyt, M. 2010 *Introduction to Finite Element Vibration Analysis*. 2nd ed, New York: Cambridge University Press. p. 127.

Outlier analysis under uncertainty: applications to structural health monitoring

R. Fuentes [1], **N. Dervilis**[1], **D. Tcherniak**[2], **K. Worden**[1], **E.J. Cross**[1]
[1] Dynamics Research Group, Department of Mechanical Engineering, University of Sheffield, Mappin St, Sheffield S1 3JD, UK
e-mail: **ramon.fuentes@sheffield.ac.uk**

[2] Innovation Group, Brüel & Kjær Sound & Vibration Measurement, Nærum, Denmark

Abstract
Outlier analysis is now standard practice when performing data-driven damage identification; the Mahalanobis squared-distance being one of the most fundamental tools in this context. In this setting, "observations" are rarely given as raw sensor data, but instead constitute the output of a estimator, such as an Auto Regressive (AR) or Fourier coefficient set. Whilst efficient computation of these type of estimators is now widespread, the advent of Bayesian inference now allows for the estimation of uncertainty of the outputs of these estimators, and this, in turn, helps to derive more informative damage-sensitive features. If the object one is observing is fundamentally uncertain, what is an appropriate measure of novelty? The issue is investigated from three different points of view. Results are demonstrated on a case study on damage identification in a wind turbine blade during operation, it is shown that taking the uncertainty of damage-sensitive features into account reduces false positive and negative rates.

1 Introduction

Outlier analysis often amounts to computing the distance between a measured object and a reference probability distribution. In the Gaussian case, this is usually given by the popular Mahalanobis squared-distance, between the mean of a reference distribution $\boldsymbol{\mu}$, and the observation in question $\mathbf{x}$ (Note bold notation is used as it is being assumed that features are multivariate, so $\boldsymbol{\mu}$ is a vector and $\boldsymbol{\Sigma}$ is a matrix),

$$d^2 = (\mathbf{x} - \boldsymbol{\mu})\boldsymbol{\Sigma}^{-1}(\mathbf{x} - \boldsymbol{\mu}) \tag{1}$$

where $\boldsymbol{\Sigma}$ is the covariance of the reference distribution. This distance has been shown to be a very effective measure of *novelty* in data, and hence it has been widely adopted in Structural Health Monitoring (SHM) to perform damage detection. The general requirement for damage identification to be successful is that $\mathbf{x}$ should be a *damage-sensitive* feature. When the dynamic response from a structure, such as vibration, is being measured, what constitutes a damage-sensitive feature has been widely investigated in the past [1–5]. The appropriate damage-sensitive feature depends on the context, but the general consensus is that useful damage-sensitive features include Auto-Regressive (AR) model coefficients, or Fourier-based coefficients, such as a power spectrum, Frequency Response Function (FRF), transmissibility, etc. All these are outputs from estimator, and more often than not, they are outputs of *linear* estimators.

Outlier analysis often involves both the estimation of a covariance, $\boldsymbol{\Sigma}_T$, from a reference training set, and evaluating d^2 on new observations $\mathbf{x}$ (the output of an estimator). Invariably, when carrying outlier analysis, it is assumed that each observation is perfect; no uncertainty about it is assumed. Is this a realistic assumption? This paper makes the case that it is indeed not, and there are simple instances where one might encounter real and quantifiable uncertainties over the observations.

Over the years, a large amount of machine learning research has focused around the issue of probabilistic estimation of unknown quantities, such as model parameters; this task is achieved relatively well through the machinery of Bayesian inference. Being able to quantify uncertainty in one's model parameters is useful, and provides a valuable additional layer of information that can be exploited for the purposes of outlier analysis.

Bayesian computation has also advanced the disciplines of signal processing and time series analysis, both fundamental to the extraction of damage-sensitive features. The result of this is that most useful damage-sensitive features can be derived through Bayesian inference, yielding a probabilistic output. It is no surprise that Bayesian parameter inference has made its way into structural dynamics [6, 7], and subsequently SHM problems [8–11].

A question then arises, how should one deal with this probabilistic output, to make the best use of damage-sensitive features that now include what is now a probability distribution over those features. Surprisingly, this issue has not been thoroughly addressed in the general setting of outlier analysis, and even less so in the case of SHM. The Bayesian paradigm is often addressed in terms of its ability to create better models, but with few exceptions [6], this probabilistic output is not carried forward into an outlier analysis process.

Two of the most widespread tools for feature extraction will be considered in this paper: AR models, and the Discrete Fourier Transform (DFT); their Bayesian computation is of interest. As such, they are both useful damage-sensitive features, but extensions and variations of them permit a host of other features to be derived from them. The pertinent question in this paper is: if, through Bayesian computation, one has arrived not just at a point estimate for $\mathbf{w}$, but at a full posterior distribution, given observed data $p(\mathbf{w}|\mathcal{D})$, what should be done with this posterior in terms of outlier analysis? This paper investigates this specific issue. Two problems need addressing. The first is that of learning an appropriate covariance matrix, when observations are uncertain. In this paper, a pragmatic approach is taken by training the model using the notion of a collapsed Gaussian mixture density. The second and more pressing issue is that of deriving appropriate novelty measures that deal with uncertainty. Section 3 discusses some potential appropriate novelty measures, based on error propagation, marginalisation and comparison of probability distributions. These measures are applied to a real world, and relevant case study of vibration-based damage detection of a wind turbine blade during operation in Section 4. An emphasis is placed in comparing the traditional Mahalanobis squared-distance, with the uncertainty-informed novelty measures discussed in Section 3. First, the next section will provide some motivation for outlier analysis under uncertain features, by describing the estimation of two common damage-sensitive features as a Bayesian linear regression problem.

2 Uncertainty in dynamic response features

This section discusses the idea of uncertain damage-sensitive features, and how probabilistic estimates of some common features can arise from Bayesian inference on simple linear problems. Particular attention is given to Auto Regressive (AR) models, as they are of interest to the study and practice of SHM. Due to the limited amount of space, the Bayesian linear regression formulation will not be dealt with in detail.

An autoregressive model describes any given point in a signal, y_t at time t, as a function of previously measured points,

$$y_t = \sum_{j=1}^{p} w_j y_{t-j} + \varepsilon, \qquad \varepsilon \sim \mathcal{N}(0, \sigma^2) \tag{2}$$

where j is the lag number, w_j is an autoregressive weight corresponding to the j^{th} lag, and ε is the signal noise, assumed to be Gaussian-distributed with zero mean and variance σ^2. This basic autoregressive model corresponds to the following linear regression problem,

$$\mathbf{y} = \mathbf{A}\mathbf{w} + \varepsilon \tag{3}$$

where $\mathbf{A}$ is a matrix containing p lagged versions of y along its columns, and $\mathbf{w}$ is a vector containing the autoregressive weights. The signal is also represented as a vector $\mathbf{y} = \{y_1, ...y_n\}$. At this point a solution

could be sought for $\mathbf{w}$ through standard least squares methods, and this is precisely what standard methods for estimating AR coefficients do, such as the Yule-Walker method. Extensions to this general idea are possible, and are widely used in practice in general system identification and also in SHM.

Other useful feature extraction models can be described in terms of this linear regression problem, a good example of this being the Discrete Fourier Transform (DFT). To see how this is the case, consider the matrix $\mathbf{A}$ (using the same notation, to draw the equivalence of the problem to AR estimation), with sine waves of k different frequencies along its columns, representing an N-point time history:

$$A_{kn} = e^{-\frac{2\pi kn}{N}} \tag{4}$$

The Fourier coefficients can then be recovered from the same linear regression problem as the one given in equation (3), with the $\mathbf{A}$ matrix given by equation (4), and where the weights, $\mathbf{w}$, now represent Fourier coefficients. In this paper, however, attention will be given to the autoregressive model.

2.1 Bayesian inference for linear regression

Given a data-set $\mathcal{D}$, and a set of candidate parameters from a reference model, encoded in a vector $\boldsymbol{\theta} = \{\theta_1, ..., \theta_n\}$, the philosophy behind Bayesian inference is to use Bayes' theorem to derive the conditional probability of the parameters given the data,

$$p(\boldsymbol{\theta}|\mathcal{D}) = \frac{p(\mathcal{D}|\boldsymbol{\theta})p(\boldsymbol{\theta})}{p(\mathcal{D}, \boldsymbol{\theta})} \tag{5}$$

In the case of linear regression, the model parameters consist of the weight vector $\mathbf{w}$. One of the issues with Bayesian inference is that the marginal distribution of the joint $p(\mathcal{D}, \boldsymbol{\theta})$ can often yield an intractable integral, requiring approximate methods to solve it. Tractable analytical solutions to the Bayesian inference problem can be derived through the use of conjugate distributions, and these are of interest to the authors due to their ease and cheapness of computation. The conjugate solution for the linear regression problem is in fact straightforward, and can be achieved by placing a Normal-Inverse Wishart prior over the model parameters. This yields a posterior distribution that is Gaussian, so $p(\mathbf{w}_i|\mathcal{D}) = \mathcal{N}(\boldsymbol{\mu}_i, \boldsymbol{\Sigma}_i)$. Note the use of the subscript, which is used later on to denote the model parameters of the i_{th} measurement. Unfortunately, writing down an analytical solution to the Bayesian linear regression problem takes too much space for this publication, so the reader is referred to textbooks such as [12, 13]. For illustration purposes, a solution using Bayesian linear regression, to AR and Fourier coefficients, for a half-second excerpt of wind turbine vibration data is shown in Figure 1, showing the resulting 3σ confidence intervals. The reader may be able to note that the confidence intervals shrink at the strongest coefficients.

3 Dealing with uncertain observations

The Mahalanobis squared-distance of equation (1), which is widely used in outlier analysis, does not account for the fact that the features in question, $\mathbf{x}$ can be fundamentally unknown, and, through Bayesian analysis, are given in terms of a posterior probability distribution $p(\mathbf{x}|\mathcal{D})$. Before carrying on, it is worth doing some notational book-keeping. Note that from here on, $\mathbf{x}$ will be used to denote a damage-sensitive feature, to account for the fact that this could be either a model parameter (for which $\mathbf{w}$ was used in Section 2.1), or it could in some instances refer to predictions directly over measured data.

The problem at hand is one of density estimation, where the inputs into the model are uncertain. There are two questions to answer. The first being, what is an appropriate method for training a model when inputs are uncertain? The second question is, what is an appropriate distance metric to use as a novelty score, to perform damage identification? In this paper, the answers to both of these questions will be greatly simplified through two major assumptions. The first is that the posterior distribution of the damage-sensitive features,

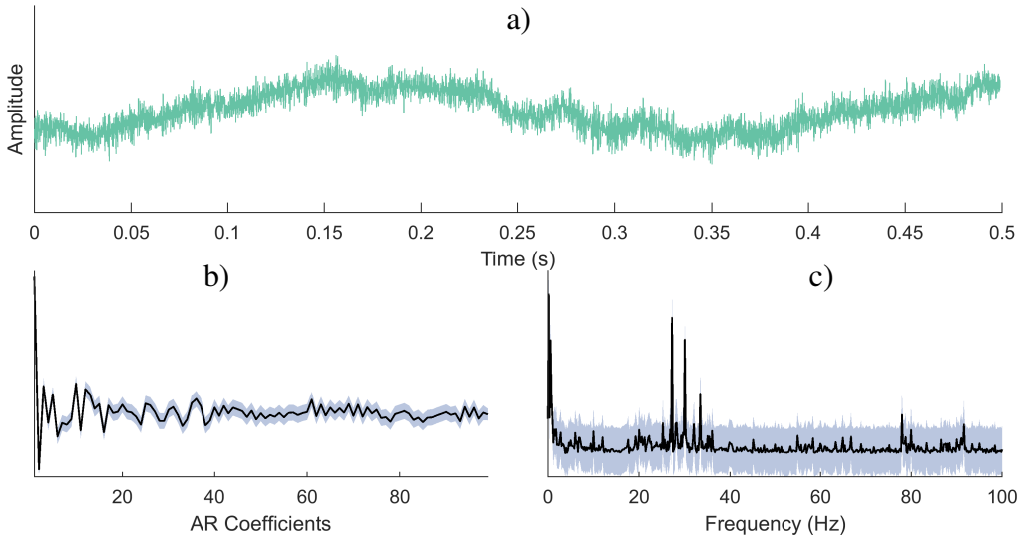


Figure 1: Illustration of two features derived from a short time history, showing a) time history from acceleration measurement of a wind turbine blade, b) AR features and c) Fourier features, both with 3σ confidence intervals derived using Bayesian linear regression.

$p(\mathbf{x}|\mathcal{D})$ is Gaussian distributed; this is not unreasonable if a conjugate Gaussian method is used to derive the posterior, as was the case in the Bayesian linear regression discussed in Section 2.1. More advanced regression methods such as Gaussian Processes (GPs), Relevance Vector Machines (RVMs) and Bayesian Neural Networks will, in their most common formulations, yield posterior predictive distributions in terms of a Gaussian distribution. The second assumption is that the training data will be Gaussian. The impact that this has is the inability of the outlier analysis methods to deal with data that contain multiple regimes, associated with a changing environment or operation. The argument here is that for the purposes of this paper, this is a useful and acceptable simplification, as the focus is placed largely on the introduction of new novelty measures. More complex density models could be used, such as Gaussian mixture models or Kernel density estimates, with relatively little additional effort.

3.1 Training

Under the Gaussian assumption, training involves learning the mean $\boldsymbol{\mu}_T$ and the covariance $\boldsymbol{\Sigma}_T$ of the undamaged data. Note that the subscript T on these parameters denote that they refer to training set. The procedure for learning these, through maximum likelihood, is well established and documented, and even simple Bayesian extensions exist which not only allow posterior distributions over both $\boldsymbol{\mu}_T$ and $\boldsymbol{\Sigma}_T$, but also permit doing so in a sequential, on-line fashion (see for example [14]).

A maximum likelihood solution for mean and covariance states that $\boldsymbol{\mu} = \frac{1}{N-1}\sum \mathbf{x}_i$ and $\boldsymbol{\Sigma} = \frac{1}{N-1}\sum (\mathbf{x}_i - \boldsymbol{\mu})^2$ (where $\mathbf{x}_i$ is the i^{th} observation), thus characterising both the average of the process and its average variation, respectively. Standard maximum likelihood estimation approaches do not normally consider the case where each individual data point has an uncertainty attached to it. It is easy to see why this is an unusual problem. When estimating mean and variance, one is already attempting to capture both the average of the process and its average scatter, so wouldn't computing the expectation and variance mean that the job is done? Unfortunately not. Each observation is itself a prediction, and is given in terms of a posterior distribution, characterised by a mean $\boldsymbol{\mu}_i$ and variance $\boldsymbol{\Sigma}_i$, and this issue needs addressing.

The problem is illustrated in Figure 2, where ten uncertain observations are shown. Each observation, $\mathbf{x}_i$ is specified in terms of a Gaussian probability density, $p(\mathbf{x}_i) = \mathcal{N}(\mathbf{x}|\boldsymbol{\mu}_i, \boldsymbol{\Sigma}_i)$.

General intuition about the problem indicates that if one has uncertain observations, the overall variance of the entire set $\mathbf{x} = \{\mathbf{x}_1, ..., \mathbf{x}_n\}$ should account for the variance in the mean (which is the maximum likelihood solution), as well as capture any increase in variance due to observation uncertainty. If there was high confidence in $\mathbf{x}$, manifested through low values of $\boldsymbol{\Sigma}_i$, one would expect the overall variance of the entire set, $\boldsymbol{\Sigma}_T$, to be close to the maximum likelihood solution. If, on the other hand, there is low confidence on the observations, this should lead to a higher overall variance $\boldsymbol{\Sigma}_T$.

The estimation of both $\boldsymbol{\mu}_T$ and $\boldsymbol{\Sigma}_T$ is in fact relatively simple and is, as always, simplified by the assumption of a Gaussian $p(\mathbf{x}_i)$. The overall density of all the uncertain observations could be viewed as the density of a (very large) Gaussian mixture model, where each observation corresponds to one mixture component, with an independent mean and covariance. The total density is simply the sum of individual densities, weighted by a factor describing the ratio of observations found in each component against the entire set. Because in this case, there is no reason to believe different observations have different weightings, this prior can be set to $1/N$, which yields an overall density,

$$p(\mathbf{x}) = \sum_{i=1}^{N} \frac{1}{N} \mathcal{N}(\boldsymbol{\mu}_i, \boldsymbol{\Sigma}_i) \tag{6}$$

This mixture density can be collapsed into a single Gaussian density which minimises the error between the above density and the resulting collapsed approximation, by simply taking its mean and covariance. These can be written, straight from Gaussian sum identities as,

$$\boldsymbol{\mu}_T = \sum_{i=1}^{N} \frac{1}{N} \boldsymbol{\mu}_i \tag{7}$$

$$\boldsymbol{\Sigma}_T = \sum_{i=1}^{N} \frac{1}{N} (\boldsymbol{\Sigma}_i^\top + \boldsymbol{\mu}_i \boldsymbol{\mu}_i - \boldsymbol{\mu}_T^\top \boldsymbol{\mu}_T) \tag{8}$$

Not surprisingly, the resulting mean is the same as the original mean of non-probabilistic observations. The covariance, on the other hand, combines the effects of the standard deviation from the mean as well as the added individual observation variance. The resulting covariance captures the desired intuition, and this is illustrated in Figure 2, using a synthetic example dataset. The covariance resulting from accounting for only individual means is shown in black, while the "corrected" covariance, that accounts for individual observation variance is shown in dashed blue. Note the slight increase in variance along the direction with most variance on the individual observations.

Collapsing a Gaussian mixture into a single Gaussian is obviously an approximation to the true density (only the first two moments are captured), but in this paper, it serves its purpose well; it allows a comparison between novelty scores from a Gaussian distribution where no observation uncertainty is placed against one where observations are assumed to be uncertain.

3.2 Prediction

Once a density has been estimated for the overall training set, taking into account any uncertainty in the observations, it is time to make some predictions about new observations. As with regular outlier analysis, the goal is to determine whether a new observation falls above or below an alarm threshold, and this will be done using an appropriate distance metric. As briefly introduced in Section 1, the Mahalanobis squared-distance is an appropriate discordance metric when the data being modelled can be safely assumed to be Gaussian-distributed. The Mahalanobis squared-distance, alone, is not an ideal distance to compare an uncertain observation against a reference density.

This issue has not been investigated in detail in the past, so the authors feel that a discussion of different approaches for tackling the problem is important. In the authors' view there are three different ways of tackling this problem: 1) as a problem of error propagation, 2) as a marginalisation problem and 3) as a problem

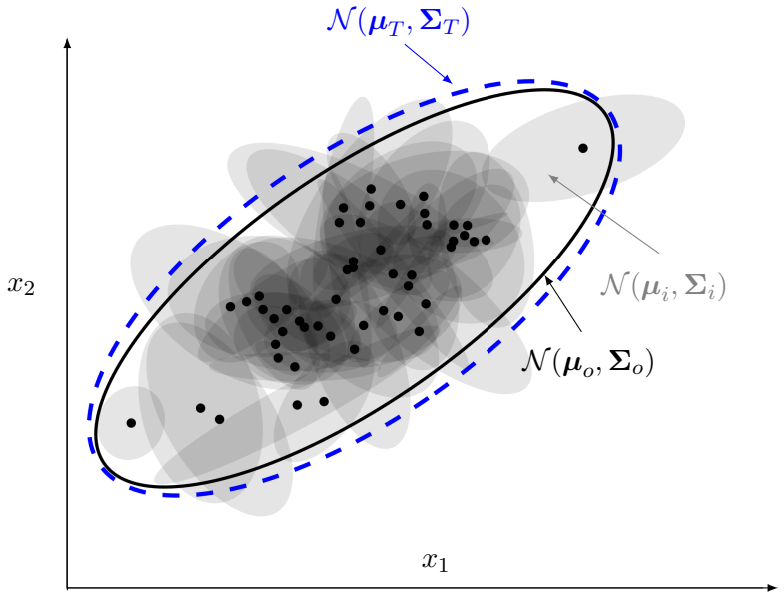


Figure 2: Illustration of problem of density estimation with uncertain observations. Shown are the covariances for the overall training set (blue), original (mean only) covariance, and observation individual covariance (grey).

of comparing distributions. Rather than presenting a single unified and "best" solution, the similarities, pros and cons of these formulations will be discussed.

3.2.1 Error propagation

Perhaps the most obvious way to approach this problem is by taking the Mahalanobis distance of equation (1), where $\mathbf{x}$ is assumed to be a point-estimate, and treating it instead as a random variable. Doing so, leaves one with a relatively simple problem of error propagation. To see this, let the difference between observations and the data mean be described by $\mathbf{v} = (\mathbf{x} - \boldsymbol{\mu})$. For clarity of presentation, it helps to work with the precision matrix, defined by the inverse of the covariance $\boldsymbol{\Sigma}^{-1} = \boldsymbol{\Lambda}$. The Mahalanobis squared-distance can thus be rewritten as,

$$d^2 = \mathbf{v}^\top \boldsymbol{\Lambda} \mathbf{v} \tag{9}$$

Unlike the original Mahalanobis squared-distance, the error term is now a probability distribution, since $\mathbf{x}$ is itself described by a distribution. Again, the fact that each observation $\mathbf{x}_i$ is described by a Gaussian distribution helps simplify things here, and allows for the entire error propagation to be written down analytically. It should be easy to see that the error term, $\mathbf{v}$, is the Gaussian describing the observation uncertainty, but offset by the mean of the training set, $\boldsymbol{\mu}_T$, so: $\mathbf{v} \sim \mathcal{N}(\boldsymbol{\mu}_i - \boldsymbol{\mu}_T, \boldsymbol{\Sigma}_i)$. The benefit of having Gaussian observation uncertainty, which reduces the error terms to a Gaussian density, now pays off, since equation 9 is a quadratic form for which there is a simple identity describing the expectation and variance,

$$\mathrm{E}[d^2] = \boldsymbol{\mu}_\mathbf{v}^\top \boldsymbol{\Lambda} \boldsymbol{\mu}_\mathbf{v} + \mathrm{Tr}(\boldsymbol{\Lambda}_T \boldsymbol{\Sigma}_i) \tag{10}$$

$$\mathrm{Var}[d^2] = \mathrm{Tr}[\boldsymbol{\Lambda}\boldsymbol{\Sigma}_i(\boldsymbol{\Lambda}_T + \boldsymbol{\Lambda}_T^\top)\boldsymbol{\Sigma}_i] + \boldsymbol{\mu}_\mathbf{v}(\boldsymbol{\Lambda}_T + \boldsymbol{\Lambda}_T^\top)\boldsymbol{\Sigma}_i(\boldsymbol{\Lambda}_T + \boldsymbol{\Lambda}_T^\top)\boldsymbol{\mu}_\mathbf{v} \tag{11}$$

Equations (10) and (11) above, now describe a distribution over the familiar Mahalanobis squared-distance, treating the error as a random variable, undergoing the square transform with the precision matrix of the training data. The result for the expectation is clear and intuitive; it is the standard Mahalanobis squared-distance, with a correction term that accounts for the fact that observations are in fact uncertain. The correction term, $\mathrm{Tr}(\boldsymbol{\Lambda}_T \boldsymbol{\Sigma}_i)$ equates to a sum (over the dimensions of $\mathbf{x}$) of the ratios of observation and training variances,

σ_i^2/σ_T^2. If the variance of a particular observation is low with respect to the training variance, the correction factor will be minimal, and vice-versa. Equation (11) applies the same concept to the average deviation, and thus allows for upper and lower confidence bounds to be placed around the mean novelty score.

This error propagation approach is relatively simple, given that all of the distributions involved are Gaussian. Under non-Gaussianity, the standard alternative would be to perform Monte Carlo simulations of $\mathbf{v}$, in order to arrive at a distribution for the resulting Mahalanobis squared-distance. This approach was taken in [15], though it should be noted that all distributions involved were also Gaussian.

The expectation over the squared Mahalanobis distance will tend to grow, with respect to an uncorrected d^2, whenever the variance of the observations is comparable to the training variance, both in the case of inliers and outliers, making this a fairly robust measure when features are uncertain. This is illustrated, in comparison with a simple d^2 and the other measures considered in the paper, in Figure 3. Furthermore, it is important to note that the Var$[d^2]$, described by equation (11), allows for the setting of confidence intervals around the expected Mahalanobis squared-distance. This is useful both in terms of aiding the decision making process, as well as determining appropriate and safer thresholds over training data.

3.2.2 Marginalisation

A slightly different way of analysing this problem is to treat it as a marginalisation task. The predictive distribution of a probabilistic model can often be expressed in terms of a simple marginalisation relationship. This has been previously done, for example, in the task of nonparametric, kernel-based regression methods in the presence of uncertain input data [16].

In the problem at hand, this is possible by considering the product of a Mahalanobis squared-distance and the Gaussian distribution that describes the uncertain observations, $\mathcal{N}(\boldsymbol{\mu}_i, \boldsymbol{\Sigma}_i)$. The integral over this product, with respect to $\mathbf{x}$ would represent the expectation of d^2,

$$\mathrm{E}[d^2] = \int (\mathbf{x} - \boldsymbol{\mu}_T)^\top \boldsymbol{\Lambda}_T (\mathbf{x} - \boldsymbol{\mu}_T) \mathcal{N}(\boldsymbol{\mu}_i, \boldsymbol{\Sigma}_i) d\mathbf{x} \tag{12}$$

It turns out that an identity exists for the integral in equation (12), and it takes the form,

$$\mathrm{E}[d^2] = (\boldsymbol{\mu}_i - \boldsymbol{\mu}_T)^\top \boldsymbol{\Lambda}_T (\boldsymbol{\mu}_i - \boldsymbol{\mu}_T) + \mathrm{Tr}(\boldsymbol{\Lambda}_T \boldsymbol{\Sigma}_i) \tag{13}$$

which is effectively equivalent to the expectation derived for d^2, through error propagation. This is a reassuring position to be in. A particularly interesting point to note is that this measure is no longer a distance, as it is asymmetric, due to the trace operator over $\boldsymbol{\Lambda}_T \boldsymbol{\Sigma}_i$, which as discussed above, yields a ratio between observation variance to training variance. This is the desired behaviour as one would like the novelty score to grow with large observation variance, and to shrink with large training variance. If these two terms were flipped, so that the trace operated over $\boldsymbol{\Lambda}_i \boldsymbol{\Sigma}_T$, the opposite would be true. Because the trace operator defines a dot product between two matrices, this also gives a relative measure of misalignment between the two matrices, so it will increase if the variance directions are significantly different.

As a point of discussion, it is interesting to see what would occur under marginalisation over the two distributions $\mathcal{N}(\boldsymbol{\mu}_i, \boldsymbol{\Sigma}_i)$ and $\mathcal{N}(\boldsymbol{\mu}_T, \boldsymbol{\Sigma}_T)$. Noting that these two distributions are Gaussian, their product will also be Gaussian-distributed with a normalisation constant C_c (parameters for this product are denoted with subscript c here). The marginal integral takes the form,

$$p(\mathbf{x}) = \int \mathcal{N}(\mathbf{x}|\boldsymbol{\mu}_T, \boldsymbol{\Sigma}_T) \mathcal{N}(\mathbf{x}|\boldsymbol{\mu}_i, \boldsymbol{\Sigma}_i) d\mathbf{x} \tag{14}$$

$$= \int C_c \mathcal{N}(\boldsymbol{\mu}_c, \boldsymbol{\Sigma}_c) d\mathbf{x} \tag{15}$$

The constant inside the integral can be taken outside, and the term $\int \mathcal{N}(\boldsymbol{\mu}_c, \boldsymbol{\Sigma}_i) d\mathbf{x}$ disappears as it is a Gaussian distribution (and thus integrates to one), leaving only the normalisation constant. The resulting

density (which contains the relevant distance metric) can therefore be evaluated using C_c. This constant can, in turn, be written down using standard Gaussian identities, which yields,

$$p(\mathbf{x}) = \frac{1}{\sqrt{\det(2\pi(\boldsymbol{\Sigma}_i + \boldsymbol{\Sigma}_T))}} \exp\left(-\frac{1}{2}(\boldsymbol{\mu}_i - \boldsymbol{\mu}_T)^\top (\boldsymbol{\Sigma}_i + \boldsymbol{\Sigma}_T)^{-1}(\boldsymbol{\mu}_i - \boldsymbol{\mu}_T)\right) \tag{16}$$

which is a standard Gaussian distribution over $\mathbf{x}$, with one key difference; the total covariance is now simply a sum of the individual training and observation covariances. The measure of interest is the quadratic form inside the exponent, which effectively gives a Mahalanobis squared-distance. Unlike the integral over the quadratic form of equation (12) which yields an asymmetric measure, the resulting density of equation (16) is symmetric with respect to the observation and training distributions. In terms of outlier analysis, this may be an undesired behaviour. A simple sum of observation and training variance is too simplistic, and this is clear if one considers the situation when one is evaluating an outlying observation, for which a large distance is desired. If the observation variance of an outlier is lower than the training variance, this symmetric measure would still produce a large distance (it would hardly be any different from equation (1)). However, as the observation variance grows, the resulting symmetric measure will *decrease*, by virtue of the overall variance growing. Effectively what happens is that the observation variance dominates the training variance. This would lead to any uncertain observations being flagged as inliers, which is potentially disastrous. However, this is only a problem if observation variance is greater than training variance. The distance specified by this marginal integral is similar in principle to the Bhattacharyya distance, discussed later.

3.2.3 Comparison of probability distributions

A third way to approach this problem is to ask: how different is the distribution of the observations from the distribution describing the training data. The last of the three approaches (of this paper) for analysing the problem of deriving relevant measures of novelty when faced with the problem of observations that contain uncertainty is to consider the comparison between probability distributions.

There are a multitude of methods to do so, but here the discussion will focus on two methods: one distance and one divergence. The difference between a distance and a divergence is symmetry, and as has been discussed above, symmetry (or a lack of), generates certain behaviours when it comes to identifying outliers. In this section the Kullback-Leibler (KL) divergence will be compared against the Battacharyya distance as a novelty measure under uncertain observations. Given that both of these measures are relatively well known in the literature, the discussions shall be kept brief and narrowly centred around the issue of outlier analysis.

3.2.4 Kullback-Leibler divergence

The KL divergence, $\mathrm{KL}(p|q)$, between two distributions p and q, is given by the following integral:

$$\mathrm{KL}(p|q) = \int p(\mathbf{x}) \log\left(\frac{p(x)}{q(x)}\right) d\mathbf{x} \tag{17}$$

It is widely used in statistical inference, and has roots in information theory [17, 18], as it is a useful measure of information gain. It effectively measures how much knowledge about $q(\mathbf{x})$ will increase one's knowledge about $p(\mathbf{x})$. It is important to note that the KL divergence is not a distance, as it is an asymmetric measure in the sense that $\mathrm{KL}(p|q) \neq \mathrm{KL}(q|p)$. When considering the outlier analysis problem under uncertain data, $q(\mathbf{x})$ takes the role of the training distribution, and $p(\mathbf{x})$ assumes the role of the observation distribution. The premise is that if q does not add a significant amount of information to p, then p is an inlier. This is not a symmetric measure, so it is fair for the reader to ask, why not use the divergence the other way around? The simplest explanation is provided by writing down the KL divergence for the two Gaussian distributions of interest (that is training and observation). When both $p(\mathbf{x})$ and $q(\mathbf{x})$ are Gaussian, the problem can be

described in terms of means and covariances of both distributions, and the standard form for this is given by

$$2\text{KL}\left(\mathcal{N}(\boldsymbol{\mu}_i, \boldsymbol{\Sigma}_i)|\mathcal{N}(\boldsymbol{\mu}_T, \boldsymbol{\Sigma}_T)\right) = (\boldsymbol{\mu}_T - \boldsymbol{\mu}_i)^\top \boldsymbol{\Lambda}_T(\boldsymbol{\mu}_T - \boldsymbol{\mu}_i) + \text{Tr}(\boldsymbol{\Lambda}_T\boldsymbol{\Sigma}_i) + \log\left(\frac{|\boldsymbol{\Sigma}_T|}{|\boldsymbol{\Sigma}_i|}\right) - D \quad (18)$$

where D is the dimension of $\mathbf{x}$, and the expression is given as $2KL(p|q)$ in order to simplify the terms on the right. The expression for the KL divergence above is the standard d^2 relationship with two "correction terms" that effectively account for uncertainty of the observations. It is important to note that in this form, the KL divergence weights the squared error between the two means with the precision of the *training data*. It should be simple to see that if the KL divergence were to be used the other way around, this term would weight the squared error with the precision of the observation distribution, which would bear no significance to the outlier analysis problem.

The expression is similar to that of the expectation of d^2 through both error propagation and marginalisation. The correction terms, however, differ from those of equations (10) and (13), and so play slightly different roles. Note that trace term in equation (18) is effectively the same as the trace operator in equation (10) that gives an expression for $\text{E}[d^2]$.

The key difference between the KL divergence and $\text{E}[d^2]$ is the addition of a (log) ratio of determinants. This quantifies the volume ratio between training and observations, and it provides a small balance to the trace term (very small in fact due to the log operator). Its effect may seem counter-productive for the purpose of outlier analysis, since it will mean that the overall distance will increase as training variance increases, and as observation variance decreases. This term only helps in the case of a potential inlier, but with very high variance, as it measures how much the training covariance lies inside the observation covariance. This case is illustrated in Figure 3b. Overall, the trace operator will tend to overpower the log-volume ratio in the KL divergence.

3.3 Bhattacharyya distance

The last novelty measure discussed in this paper, as a measure of novelty for uncertain observations, is the Bhattacharyya distance [19], which can be viewed as a generalisation of a Mahalanobis squared-distance for distributions. In the statistical inference literature, it is also a popular measure of distance between distributions, and in contrast with the KL divergence, it is symmetric. Before delving into this small discussion, it is worth revisiting the formulation for the marginal distribution of $p(\mathbf{x})$ given uncertain observations as Gaussians, as given in equation (16). The Bhattacharyya *coefficient* is defined in terms of a similar marginalisation problem, inside a square root,

$$c_B(p, q) = \int \sqrt{p(\mathbf{x})q(\mathbf{x})}d\mathbf{x} \quad (19)$$

and the Bhattacharyya distance is then defined as the negative log of the coefficient,

$$d_B(p, q) = -\log(c_B(p, q)) \quad (20)$$

which simply takes the probability density defined by (19), and formulates it in terms of a useful distance measure. The Bhattacharyya distance for the case when both p and q are Gaussian yields (using training and observation subscripts),

$$d_B = \frac{1}{8}(\boldsymbol{\mu}_i - \boldsymbol{\mu}_T)^\top \boldsymbol{\Sigma}(\boldsymbol{\mu}_i - \boldsymbol{\mu}_T) + \frac{1}{2}\log\left(\frac{\det \boldsymbol{\Sigma}}{\sqrt{\det \boldsymbol{\Sigma}_i \det \boldsymbol{\Sigma}_T}}\right) \quad (21)$$

where $\boldsymbol{\Sigma}$ denotes the sum of variance terms, $\boldsymbol{\Sigma} = \frac{\boldsymbol{\Sigma}_i + \boldsymbol{\Sigma}_T}{2}$. It is straightforward to see what this distance is doing. It is averaging over the variances in order to compute a squared Mahalanobis distance between the means of both distributions, and it is enhancing this with a ratio of geometric mean volume to arithmetic mean volume. In effect, this correction term only plays a role when there is a large disparity between the two

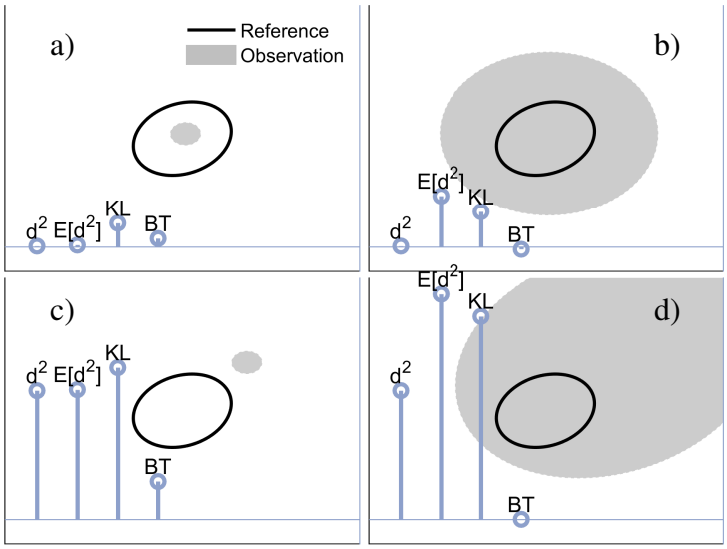


Figure 3: Illustration of the four distance metrics measuring novelty between reference distribution and observation distribution. Four cases are shown: a) inlier, low variance, b) inlier, high variance, c) outlier, low variance and c) outlier, high variance.

distributions. For outlier analysis, this only offers an advantage when the observation variance is small, as it will enhance confidence over the fact that an observation may be an inlier or outlier. At the limit of very small observation variance, the Bhattacharyya distance becomes a (scaled) Mahalanobis squared-distance. The total covariance, which also appears in the quadratic form does not discriminate between training and observation variance. If observation variance is high, the it will take over the term $\mathbf{\Sigma}$, and dominate the training variance. Therefore, it runs the risk of predicting small distances when observation variance is larger than training variance. This is both in the case of inliers and outliers, as illustrated in Figure 3b) and c).

The Bhattacharyya distance is a good measure of similarity between distributions, but one should be careful when interpreting the results if an observation has a higher variance than the training set.

3.4 Synthetic example

Figure 3 provides an illustration of the novelty measure that each novelty measure yields, using a synthetic example, consisting of inliers and outliers with low and high observation variance, with respect to a (two-dimensional) reference set. In the case of an inlier with low observation variance, all four novelty measures yield a low value, with the KL divergence showing a slightly higher value due to its log variance ratio term. The dissimilarities appear in the case of an inlier with high variance. In that setting, the expected Mahalanobis squared-distance and the KL divergence perform well: they both produce a high novelty index. The Bhattacharyya distance, on the other hand, produces a low novelty index, as the training distribution lies inside the observation distribution. When considering outliers, all novelty measures produce high scores when variance is low. When variance is high, however, $\mathrm{E}[d^2]$ produces the greatest discordance, followed by the KL divergence which is more conservative due to added log variance ratio term. The Bhattacharyya distance, fails to flag this as an outlier, again due to the high observation variance.

4 Case study: wind turbine blade damage detection

The concepts laid out in this paper were applied to a data-set originating from a field investigation on a Vestas V27 wind turbine. This investigation, together with an approach to damage detection using a Mahalanobis squared-distance, has been documented in detail in [20]. In this section the authors focus on a comparison between the various novelty measures discussed throughout this paper.

The data-set consists of acceleration measurements at 16 positions along one of the three blades, with recordings spread out across a three and a half-month period, during which three levels of damage were seeded, in the form of an artificial separation between the upper and lower surfaces of the blade, as they meet at trailing edge of the blade. In the original investigation of this dataset [20], three damage scenarios are used. In this paper, only the two lowest-severity damage cases are considered, of 15cm and 30cm crack lengths. The 15cm seeded crack along the trailing edge is illustrated in Figure 4, along with its position on the blade, relative to measurement channels. The blade was also instrumented with an actuator that provided an impulse excitation, as this enhances detectability of the different levels of damage when compared with the vibration resulting from the ambient excitation. In this paper, however, the authors consider only portions of data where the actuator *did not* impact the blade, so as to impose greater difficulty of detection. Also, a limited amount of data was considered; the original recordings capture 30 seconds of data, but only sections of data of 0.8 seconds are considered (taken at the beginning of every record). This is in order to replicate the realistic scenario where one may have years worth of data and would not be able to afford storing most of it. Furthermore, in the setting of a short data record, probabilistic estimates of damage-sensitive features are of greater value due to the relatively poor quality of the data, and hence the potential for poor estimates of features. The use of novelty measures that takes this into account makes greater sense in this setting.

The original sample rate of the acquired data was of 16384Hz, but this was down-sampled to 4096Hz, without a significant loss of information. The damage-sensitive features considered in this study were AR coefficients, derived using the Bayesian linear regression procedure outlined in Section 2.1, with a model order of 200 lags. There is an important aspect to note regarding AR model order and sample rate; they both had to be carefully selected so that the Mahalanobis squared-distance performed well as a detector. In contrast, the novelty measures that used the full Bayesian solution proved to be overall relatively insensitive to the model order and therefore sample rate.

The comparison of interest in this paper is between the outlier analysis procedures with and without the consideration of uncertainty, in the form of the full posterior distribution of the coefficients $p(\mathbf{w}|\mathcal{D})$. This involves both the training procedure and the evaluation of the novelty score. Without consideration for uncertainty, the outlier analysis procedure is the same as in the previous literature [1]. The mean and covariance of the features are computed using a standard maximum likelihood approach, using only the mean output from the Bayesian solution, $\boldsymbol{\mu}_i$. On the other hand, when uncertainty is taken into account, both $\boldsymbol{\mu}_i$ and $\boldsymbol{\Sigma}_i$ are used, from the posterior $p(\mathbf{w}|\mathcal{D})$ of each data recording. In this case, training involves the sum-of-Gaussians procedure outlined in Section 3.1. Then, three different prediction strategies are compared for measuring novelty with the full posterior distribution of the AR features: 1) the expectation of the Mahahalanobis squared-distance, $\mathrm{E}[d^2]$, from equation (10); 2) the KL Divergence using equation (18), and; 3) the Bhattacharyya distance using equation (20).

The reference distribution is Gaussian, and a comparison is being drawn between the uncertainty-informed novelty measures and a simple Mahalanobis squared-distance. It is therefore useful to analyse data that is fundamentally unimodal. For this reason, data originating from only one operating regime was considered, by taking only instances of recordings where the speed of the main rotor was within a range between 35rpm to 50rpm.

The available data was split into training, testing and damage subsets, and the results for predictions, based on the learned models from the training set, are shown in Figure 5 for both measurement channels considered. It may be useful to reiterate here that the reference model used for $\mathrm{E}[d^2]$, KL divergence and Bhattacharyya distance are all the same (derived from the training procedure outlined in Section 3.1). The reference model for

the Mahalanobis squared-distance, d^2, is thus different from the others as this was derived using maximum likelihood. The thresholds shown in Figure 5 have all been established using a 99^{th} percentile of the novelty measures inside the training set. The only exception to this is the expected Mahalanobis squared-distance. In this case, one also has confidence intervals available, and these can be used to better inform the threshold selection. In the case of $\mathrm{E}[d^2]$, the threshold was set using the 99^{th} percentile of its 3σ upper confidence interval, which can be evaluated using equation (11).

4.1 Discussion of results

In the particular case presented here, the Mahalanobis squared-distance has failed to generalise, as it has a poor performance in terms of false positive rates. One of the reasons for this, is that with an AR model order of 200, the quantity of training data (of 600 observations) is barely sufficient to yield a well-conditioned covariance matrix. Added to this is the fact that even though an attempt was made at selecting a single operating regime, other operational and environmental variables will mean the data density will be different between training and testing phases. The uncertainty-informed covariance, on the other hand is better conditioned; even in the setting of a low number of observations, its conditioning will not be as poor given that it is built on top of already well conditioned covariances (due to the use and choice of prior distribution in the Bayesian inference step). In other words, in the absence of a definition of spread, the average spread of individual posteriors for the observations will be used. This also helps to better summarise what could potentially be multimodal behaviour into a single Gaussian. The training procedure presented in Section 3.1 collapses both the mean and covariances of a potentially complex density into a single Gaussian, using information from both the individual observation mean and variance. On the other hand, performing a maximum likelihood estimate of mean and covariance (using no individual observation variance), effectively also collapses the density into a single Gaussian, but using only the information provided by the means. The point here is that the approximation of the variance given by adding the extra information contained in the posterior solution of individual features helps in terms of generalisation performance.

Figure 5, shows a marginal improvement in detectability from the uncertainty-informed novelty measures. The detection performance of each novelty measure depends on several factors. Two of these key factors are the size of the training set and the model order. A full investigation of these two factors is well outside the scope of this paper. However, more pertinent to the problem under investigation is the question of the *size* of each observation: the length of time used in the time history, to derive the damage-sensitive features. This matters because, in general, the variance of the posterior distribution of model weights will decrease as the data size increases - an indication of higher confidence in the model parameters (an AR model in this case). With very large data records, variance will be small, and if a good enough model is being used, one may as well use a standard outlier analysis approach that does not involve uncertainty in the observations. The value of including uncertainty in the novelty measures emerges in the limit of low data quality, and this can involve low quantity, high noise, or a bad fit against the assumed model. To illustrate this, in the limited amount of space given here, Figure 6 compares the False Positive Rates (FPR) and False Negative Rates (FNR) for each novelty measure, with increasing data sizes. Time histories ranging from 500 points up to 8000 points (with sample rate of 4096Hz) were used to carry out the parameter estimation step, and novelty measures resulting from these are subsequently computed.

It is clear from Figure 6 that using the expectation over d^2 gives the best balance of false positive and false negative rates. Overall, the Mahalanobis squared-distance is the worst performing, highlighting the point that including uncertainty in the outlier analysis process is useful.

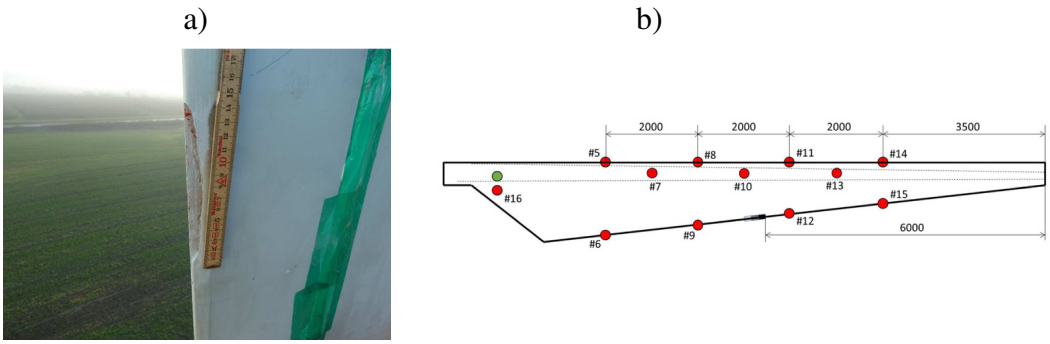


Figure 4: Illustration of a) 15cm damage to trailing edge and b) damage location within the blade, showing channel numbers and dimensions in millimetres [20].

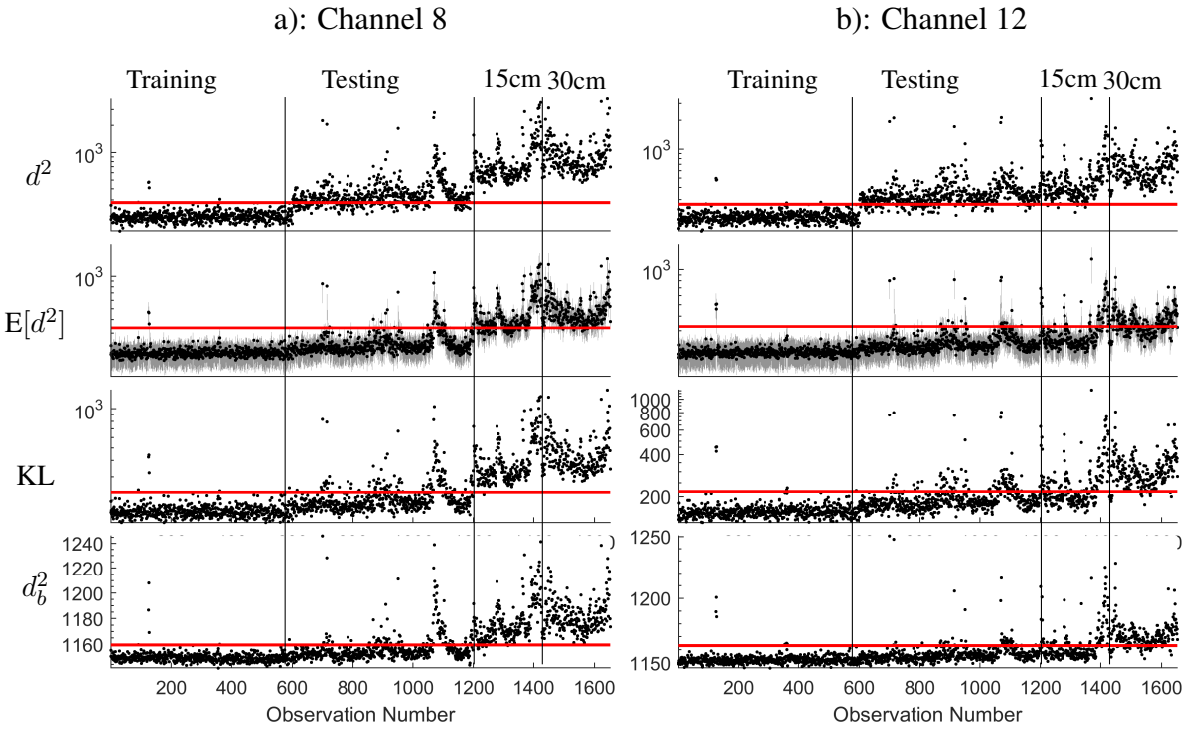


Figure 5: Resulting four novelty measures on training, testing, and damaged sets, consisting of 15cm and 30cm damage on blade training edge. The two channels shown correspond to a) the best and b) worst, damage predictors. Thresholds shown are 99^{th} percentiles of training sets for each measure.

5 Conclusions

This paper has presented a methodology for dealing with uncertain observations when performing outlier analysis, applied to the problem of damage identification from measured dynamic response data. Current outlier analysis methods do not deal with the problem of computing novelty measures when the object being observed is fundamentally uncertain. Such is the case when a probabilistic estimate is used to derive damage-sensitive features. This paper has addressed this issue by looking at the problem in three different ways: by applying error propagation through a Mahalanobis squared-distance, through marginalisation and through comparison of probability distributions. It has been shown that the error propagation approach yields effectively the same result as performing marginalisation of distributions. The output of this is an expectation and a variance over the traditional Mahalanobis squared-distance. On the other hand, the Kullback-Leibler (KL) divergence, and the Bhattacharyya distance are both discussed as potential candidates for comparing the probabilistic output of Bayesian estimates against reference probability densities from training data. These

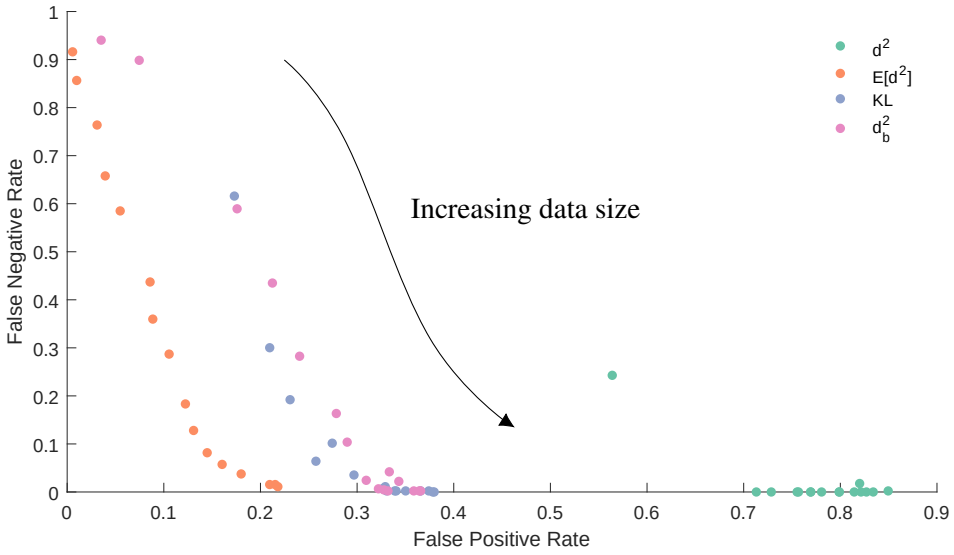


Figure 6: False positive and negative rates with increasing size of data used to derive damage-sensitive features (AR coefficients), compared for all novelty measures.

three novelty measures all take observation uncertainty into account in slightly different ways, and they are all compared against the traditional Mahalanobis squared-distance in a case study of damage identification using vibration measurements in a wind turbine blade in operation. A Bayesian AR model has been used as an example of a damage-sensitive feature, although it has been discussed how this methodology is applicable in the wider sense of features derived from linear estimators, such as Fourier features. Including uncertainty in the outlier analysis is of greater value when a limited amount of data is available, and hence greater uncertainty exists over damage-sensitive features. It has been shown that in the presence of uncertainty, all three novelty measures compared far outperform a squared Mahalanobis distance in terms of false positive and negative rates. This effect is exacerbated in the limit of damage-sensitive features derived from low and poor data quantities. Of the novelty measures investigated, the expectation over the Mahalanobis squared distance has proven to be the most robust in terms of acknowledging uncertainty in both inlying and outlying observations, with the added advantage that it is possible to place confidence intervals around it, which is useful in terms of robust threshold selection. Further use of this confidence intervals to aid the decision-making of whether an observation is an inlier or outlier is motivation for further extensions of this work.

Acknowledgements

This work has been funded by the UK Engineering and Physical Sciences Research Council (EPSRC) through grants EP/N018427/1: Autonomous Inspection in Manufacturing and Re-manufacturing (AIMaReM), and EP/R004900/1: A New Partnership in Offshore Wind.

References

[1] K. Worden, G. Manson, and N. R. J. Fieller, “Damage detection using outlier analysis,” *Journal of Sound and Vibration*, vol. 229, no. 3, pp. 647–667, 2000.

[2] H. Sohn, C. R. Farrar, N. F. Hunter, and K. Worden, “Structural Health Monitoring Using Statistical Pattern Recognition Techniques,” *Journal of Dynamic Systems, Measurement, and Control*, vol. 123, no. 4, p. 706, 2001.

[3] K. Worden, C. R. Farrar, G. Manson, and G. Park, "The fundamental axioms of structural health monitoring," *Proceedings of the Royal Society A: Mathematical, Physical and Engineering Sciences*, vol. 463, pp. 1639–1664, 2007.

[4] F. N. Catbas, M. Gul, and J. L. Burkett, "Conceptual damage-sensitive features for structural health monitoring: Laboratory and field demonstrations," *Mechanical Systems and Signal Processing*, vol. 22, pp. 1650–1669, oct 2008.

[5] A. Deraemaeker, E. Reynders, G. De Roeck, and J. Kullaa, "Vibration-based structural health monitoring using output-only measurements under changing environment," *Mechanical Systems and Signal Processing*, vol. 22, pp. 34–56, jan 2008.

[6] J. Ching, J. L. Beck, and K. A. Porter, "Bayesian state and parameter estimation of uncertain dynamical systems," *Probabilistic Engineering Mechanics*, vol. 21, pp. 81–96, jan 2006.

[7] K. Worden and J. Hensman, "Parameter estimation and model selection for a class of hysteretic systems using Bayesian inference," *Mechanical Systems and Signal Processing*, vol. 32, pp. 153–169, oct 2012.

[8] M. W. Vanik, J. L. Beck, and S. K. Au, "Bayesian Probabilistic Approach to Structural Health Monitoring," *Journal of Engineering Mechanics*, vol. 126, pp. 738–745, jul 2000.

[9] J. Ching, M. Muto, and J. L. Beck, "Structural Model Updating and Health Monitoring with Incomplete Modal Data Using Gibbs Sampler," *Computer-Aided Civil and Infrastructure Engineering*, vol. 21, pp. 242–257, may 2006.

[10] L. Bornn, C. R. Farrar, D. Higdon, and K. P. Murphy, "Modeling and diagnosis of structural systems through sparse dynamic graphical models," *Mechanical Systems and Signal Processing*, vol. 74, pp. 133–143, jun 2016.

[11] S. Mukhopadhyay, H. Lu, and R. Betti, "Probabilistic Structural Health Assessment with Identified Physical Parameters from Incomplete Measurements," *ASCE-ASME Journal of Risk and Uncertainty in Engineering Systems, Part A: Civil Engineering*, vol. 2, p. B4015003, sep 2016.

[12] C. M. Bishop, *Pattern recognition and machine learning*. Springer-Verlag New York, 2006.

[13] K. P. Murphy, *Machine Learning: A Probabilistic Perspective*. MIT Press, 2012.

[14] K. P. Murphy, "Conjugate Bayesian analysis of the Gaussian distribution," Tech. Rep. 7, 2007.

[15] C. C. Aggarwal and P. S. Yu, "Outlier Detection with Uncertain Data," in *SIAM International Conference on Data Mining*, 2008.

[16] A. Girard, C. E. Rasmussen, J. Quinonero-Candela, and R. Murray-smith, "Gaussian Process Priors With Uncertain Inputs Application to Multiple-Step Ahead Time Series Forecasting," in *Advances in Neural Information Processing Systems 15 (NIPS)*, 2002.

[17] T. M. Cover and J. A. Thomas, *Elements of Information Theory*. Wiley, 1991.

[18] D. J. C. Mackay, *Information Theory , Inference , and Learning Algorithms*. Cambridge University Press, 2003.

[19] A. Bhattacharyya, "On a Measure of Divergence between Two Multinomial Populations," *Sankhy: The Indian Journal of Statistics (1933-1960)*, vol. 7, pp. 401–406, 1946.

[20] D. Tcherniak and L. L. Mølgaard, "Active vibration-based structural health monitoring system for wind turbine blade: Demonstration on an operating Vestas V27 wind turbine," *Structural Health Monitoring: An International Journal*, vol. 16, pp. 536–550, sep 2017.

A stochastic multidomain approach for mid-frequency vibration problems

S. Adhikari [1], **M.I. Friswell** [1]
[1] College of Engineering, Swansea University Bay Campus,
Fabian Way, Swansea SA1 8EN, UK
e-mail: **s.adhikari@swansea.ac.uk**

Abstract

The consideration of uncertainty becomes increasingly necessary for complex engineering structures. For structural dynamic systems, the approach to model uncertainty often depends on the frequency of excitation. For low-frequency vibration problems, parametric uncertainty model is normally used. Random field or random variables can be used to model uncertain parameters and stochastic finite element method can be used to propagate uncertainty. For high-frequency vibration problems, nonparametric uncertainty model is normally used. Random matrix models, such as those based on Wishart random matrices, can be used for this purpose. However, in the majority of practical engineering problems, both types of uncertainties need to be modelled simultaneously as one expects a mixture of wavelengths. This paper proposes a new approach to consider multiple wavelength-scales by combining parametric and nonparametric uncertainty models.

1 Introduction

Complex dynamic structures such as aircraft and helicopters contain many distinct substructures, and for a given frequency of excitation, the wavelength of vibration in different substructures can be significantly different. For example, in the context of an aircraft fuselage, the ring girders will have significantly longer wavelength of vibration compared to the thin panels for a given frequency of excitation. For deterministic systems many methods of substructuring, such as component mode synthesis, have proved to be very efficient to compute the response of the assembled structure [1, 2, 3]. These methods retain degrees of freedom at the interfaces, but reduce the internal component degrees of freedom by projecting on various subspaces (for example the fixed interface modes). The reduced subsystem models are then used to build a model of the complete system. The approach is useful because computing the eigensystems of a number of smaller models is faster than computing a single eigensystem of a large model.

Mace and Shorter [4] used a perturbation method to evaluate the global modal properties and frequency response functions due to uncertainty in the local modal properties. Giannini and Hanss [5] used component mode synthesis and reduced order modelling to determine the fuzzy response of the assembled structure. The model reduction required significant computation and they tried to maximise the number of uncertain parameters at the joints and boundaries. Hinke et al. [6] extended substructuring methods by considering the local modal uncertainty in components, evaluated using perturbation (first order sensitivity) methods.

Jensen et al. [7] formulated a reanalysis procedure for assembled structures and applied this to uncertainty propagation. Sarsri et al. [8] presents a method using component mode synthesis and polynomial chaos to obtain the stochastic frequency response functions for the assembled structure, by projecting the component uncertainties onto a deterministic subspace. Chentouf et al. [9] considered both parametric and non-parametric uncertainties within a component mode synthesis approach, where the subspace used to project the substructure response accounted for the uncertainty. Pascual and Adhikari [10] considered the propagation of combined parametric and non-parametric uncertainties for two cases: when both uncertainties are

over the entire domain, and when different types of uncertainties occur over non-overlapping subdomains. The examples used random matrix theory and polynomial chaos expansion.

A simplified situation with two non-overlapping domains containing two different wavelength-scale will be considered. Domain 1 is related to long-wavelength vibration where uncertainty will be modelled by random fields. Domain 2 is related to small-wavelength vibration where uncertainty will be modelled by random matrices. Although a simple two-domain problem is considered, the proposed approach can be extended to multiple domains. The global equation of motion of dynamic equilibrium will be partitioned into two subdomains. Each subdomain is connected to each other by a certain common interface. The degrees of freedom corresponding to this common interface glues two different subdomains with two different types of uncertainty models. Once a smaller problem corresponding to this interface degrees of freedom is solved, the solution for the two stochastic subdomains can be performed independently. This forms the basis of the proposed numerical method.

2 Stochastic dynamical systems

The consideration of uncertainty becomes increasingly necessary for complex engineering structures. For structural dynamic systems, the approach to model uncertainty often depends on the frequency of excitation. For linear systems, this in turn is related to the wave-length scale of vibration.

For low-frequency vibration problems (longer wavelength), a parametric uncertainty model is normally used. Random field or random variables can be used to model uncertain parameters and stochastic finite element method can be used to propagate uncertainty. For high-frequency vibration problems (shorter wavelength), a non-parametric uncertainty model is normally used. Random matrix models, such as those based on Wishart random matrices, can be used for this purpose [11, 12]. In majority of practical engineering problems, one expects a mixture of wavelengths.

Possible sources of uncertainty include

- parametric uncertainty - e.g. uncertainty in geometric parameters, friction coefficient, strength of the materials involved.
- model uncertainty - arising from the lack of scientific knowledge about the model which is a-priori unknown.
- experimental error - uncertain and unknown errors percolate into the model when they are calibrated against experimental results.
- computational uncertainty - e.g. machine precession, error tolerance and the so called h and p refinements in finite element analysis

Parametric uncertainty is often used for low-frequency vibration problems, where only the first few vibration modes (typically few tens) participate in the dynamical response of interest. Uncertainty models such as random variables or random fields are used to represent uncertain parameters. Well established methods such as the stochastic finite element method (polynomial chaos, perturbation methods, spectral methods) exist in the literature.

The discretised equation of motion of a linear dynamical system can be expressed as

$$\mathbf{M}\ddot{\mathbf{u}}(t) + \mathbf{C}\dot{\mathbf{u}}(t) + \mathbf{K}\mathbf{u}(t) = \mathbf{f}(t) \tag{1}$$

where $\mathbf{M} \in \mathbb{R}^{n\times n}$ is the mass matrix, $\mathbf{C} \in \mathbb{R}^{n\times n}$ is the damping matrix, $\mathbf{K} \in \mathbb{R}^{n\times n}$ is the stiffness matrix, $\mathbf{u}$ is the response vector, and $\mathbf{f}$ is the forcing vector. Transforming to the frequency domain gives

$$\mathbf{A}(\omega)\mathbf{u} = \mathbf{f} \tag{2}$$

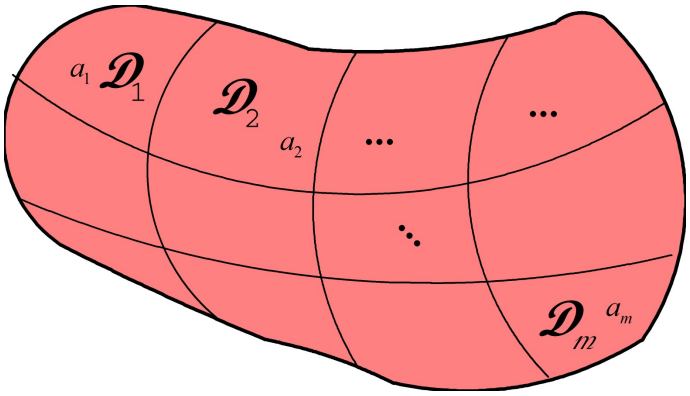


Figure 1: Domain decomposed into subdomains

where the dynamic stiffness matrix is given by

$$\mathbf{A}(\omega) = -\omega^2\mathbf{M} + i\omega\mathbf{C} + \mathbf{K} \in \mathbb{C}^{n\times n} \tag{3}$$

For the parametric uncertainty models, the dynamic stiffness matrix can be expressed as

$$\mathbf{A}(\theta_1) = \mathbf{A}_0 + \sum_{i=1}^{M} \xi_i(\theta_1)\mathbf{A}_i \tag{4}$$

where $\mathbf{A}_0$ is the baseline model, and $\xi_i(\theta_1)$ are random variables.

Non-parametric uncertainty is often used for high-frequency vibration problems, where many vibration modes (typically hundreds) participate in the dynamical response of interest. Uncertainty models such as random matrices can be used to represent the uncertain system matrices. Thus, a system matrix (and hence the dynamic stiffness) could be expressed as

$$\mathbf{A}(\theta_2) = W_n(\delta_A, \mathbf{A}_0) \tag{5}$$

where $\mathbf{A}_0$ is the baseline model, $\theta_2 \equiv \delta_A$ is a dispersion parameter, and W_n is a Wishart random matrix of dimension n.

3 Domain decomposition for multi-frequency scale problems

Domain decomposition was developed to solve a boundary value problem by splitting it into smaller boundary value problems on subdomains, as shown in Figure 1. The problems on the subdomains are independent, which makes domain decomposition methods suitable for parallel computing. These methods were originally developed for the numerical solution of partial differential equations (not explicitly for uncertainty quantification), and excellent and powerful computational tools are available.

To demonstrate the approach, only two domains are considered and the domains are assumed to have very different stiffnesses. Thus Domain 1 is flexible and corresponds to long wavelength responses, and in contrast Domain 2 is stiff with short wavelength responses, as shown in Figure 2. The analysis will subdivide the domain Ω into two non-overlapping domains, Ω_1 and Ω_2, as shown in Figure 3, with corresponding dynamic stiffness matrices

$$\text{Domain 1}: \quad \mathbf{A}^1(\theta_1) = \mathbf{A}_0^1 + \sum_{i=1}^{M} \xi_i(\theta_1)\mathbf{A}_i^1 \qquad (\text{dimension } n_1) - \text{parametric uncertainty} \tag{6}$$

$$\text{Domain 2}: \quad \mathbf{A}^2(\theta_2) = W_{n_2}(\delta_A, \mathbf{A}_0^2) \qquad (\text{dimension } n_2) - \text{nonparametric uncertainty} \tag{7}$$

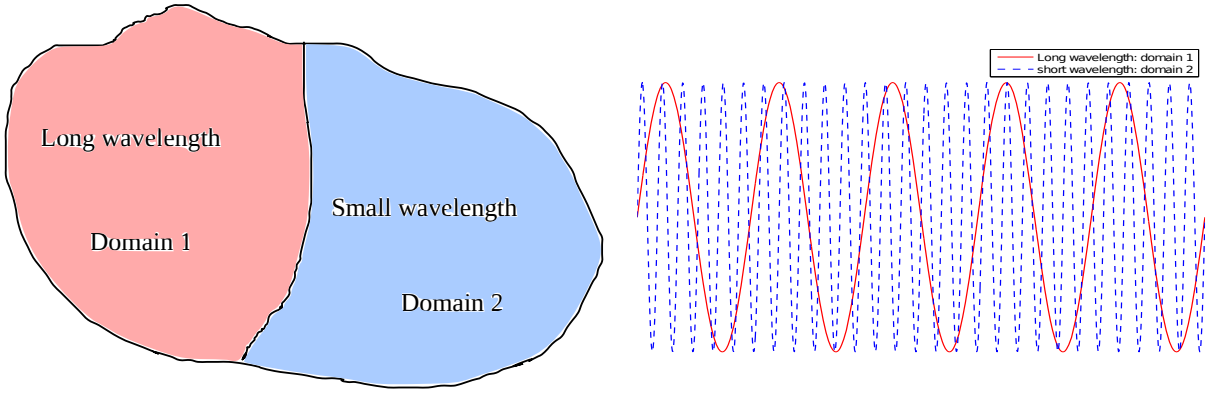


Figure 2: Decomposition into two subdomains of different stiffnesses

The equations of motion in the frequency domain of the complete system (i.e. over the whole domain Ω) was given in Eq. (2), and can be partitioned as

$$\begin{bmatrix} [\mathbf{A}^1_{II}]_{m_1\times m_1} & 0 & [\mathbf{A}^1_{I\Gamma}]_{m_1\times m_\Gamma} \\ 0 & [\mathbf{A}^2_{II}]_{m_2\times m_2} & [\mathbf{A}^2_{I\Gamma}]_{m2\times m_\Gamma} \\ [\mathbf{A}^1_{\Gamma I}]_{m_\Gamma\times m_1} & [\mathbf{A}^2_{\Gamma I}]_{m_\Gamma\times m_2} & [\mathbf{A}^1_{\Gamma\Gamma}+\mathbf{A}^2_{\Gamma\Gamma}]_{m_2\times m_2} \end{bmatrix} \begin{Bmatrix} \mathbf{u}^1_I \\ \mathbf{u}^2_I \\ \mathbf{u}_\Gamma \end{Bmatrix} = \begin{Bmatrix} \mathbf{f}^1_I \\ \mathbf{f}^2_I \\ \mathbf{f}^1_\Gamma + \mathbf{f}^2_\Gamma \end{Bmatrix} \tag{8}$$

where the subscripts I and Γ correspond to internal and interface degrees of freedom, respectively, and the generalised coordinates for both subdomains have been reordered to group internal and interface degrees of freedom together. The number of interface degrees of freedom is m_Γ, and the numbers of internal degrees of freedom in subdomains 1 and 2 are m_1 and m_2, respectively. From the definitions in Eqs. (6) and (7) we have $n_1 = m_1 + m_\Gamma$ and $n_2 = m_2 + m_\Gamma$.

This equation of motion can be rearranged into following explicit forms (interior and interface problems):

$$[\mathbf{A}^1_{II}]\{\mathbf{u}^1_I\} = \{\mathbf{f}^1_I\} - [\mathbf{A}^1_{I\Gamma}]\{\mathbf{u}_\Gamma\} \tag{9}$$

$$[\mathbf{A}^2_{II}]\{\mathbf{u}^2_I\} = \{\mathbf{f}^2_I\} - [\mathbf{A}^2_{I\Gamma}]\{\mathbf{u}_\Gamma\} \tag{10}$$

$$\begin{aligned} &[\underbrace{[\mathbf{A}^1_{\Gamma\Gamma}] - [\mathbf{A}^1_{\Gamma I}][\mathbf{A}^1_{II}]^{-1}[\mathbf{A}^1_{I\Gamma}]}_{\mathbf{S}_1} + \underbrace{[\mathbf{A}^2_{\Gamma\Gamma}] - [\mathbf{A}^2_{\Gamma I}][\mathbf{A}^2_{II}]^{-1}[\mathbf{A}^2_{I\Gamma}]}_{\mathbf{S}_2}]\{\mathbf{u}_\Gamma\} \\ &\quad = \underbrace{[\{\mathbf{f}^1_\Gamma\} - [\mathbf{A}^1_{\Gamma I}][\mathbf{A}^1_{II}]^{-1}\{\mathbf{f}^1_I\}]}_{\mathbf{F}_1} + \underbrace{[\{\mathbf{f}^2_\Gamma\} - [\mathbf{A}^2_{\Gamma I}][\mathbf{A}^2_{II}]^{-1}\{\mathbf{f}^2_I\}]}_{\mathbf{F}_2} \end{aligned} \tag{11}$$

The coefficient matrix $\mathbf{S} = \mathbf{S}_1 + \mathbf{S}_2$ is known as the *Schur complement* matrix.

4 Computational approach for uncertainty propagation

To demonstrate the stochastic domain decomposition on two subdomains, we consider the two system matrices, one with parametric uncertainty and one with non-parametric uncertainty. For the domain with parametric uncertainty (long wavelength scale),

$$[\mathbf{A}^1(\theta_1)]_{n_1\times n_1} = \begin{bmatrix} \mathbf{A}^1_{II}(\theta_1) & \mathbf{A}^1_{I\Gamma}(\theta_1) \\ \mathbf{A}^1_{\Gamma I}(\theta_1) & \mathbf{A}^1_{\Gamma\Gamma}(\theta_1) \end{bmatrix} = \mathbf{A}^1_0 + \sum_{i=1}^{M} \xi_i(\theta_1)\mathbf{A}^1_i \tag{12}$$

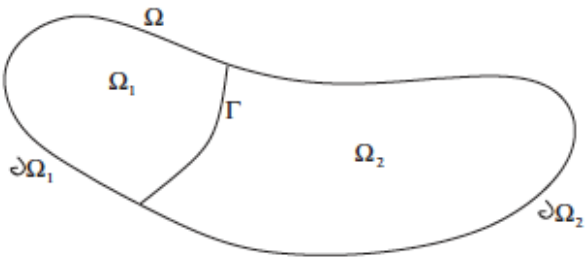


Figure 3: Decomposition into two ideal subdomains

with $n_1 = m_1 + m_\Gamma$. For the domain with nonparametric uncertainty (short wavelength scale),

$$\mathbf{A}^2(\theta_2)_{n_2\times n_2} = \begin{bmatrix} \mathbf{A}^2_{II}(\theta_2) & \mathbf{A}^2_{I\Gamma}(\theta_2) \\ \mathbf{A}^2_{\Gamma I}(\theta_2) & \mathbf{A}^2_{\Gamma\Gamma}(\theta_2) \end{bmatrix} = W_{n_2}(\delta_{A_2}, \mathbf{A}^2_0) \tag{13}$$

with $n_2 = m_2 + m_\Gamma$.

For the stochastic interface problem we have a system of (densely) coupled m_Γ complex stochastic equations given by

$$[\mathbf{S}_1(\theta_1) + \mathbf{S}_2(\theta_2)]\mathbf{u}_\Gamma(\theta_1, \theta_2) = \mathbf{F}_1(\theta_1) + \mathbf{F}_2(\theta_2) \tag{14}$$

where

$$\mathbf{S}_1(\theta_1) = \mathbf{A}^1_{\Gamma\Gamma}(\theta_1) - \mathbf{A}^1_{\Gamma I}(\theta_1)[\mathbf{A}^1_{II}(\theta_1)]^{-1}\mathbf{A}^1_{I\Gamma}(\theta_1) \tag{15}$$

$$\mathbf{F}_1(\theta_1) = \mathbf{f}^1_\Gamma - \mathbf{A}^1_{\Gamma I}(\theta_1)[\mathbf{A}^1_{II}(\theta_1)]^{-1}\mathbf{f}^1_I \tag{16}$$

and

$$\mathbf{S}_2(\theta_2) = \mathbf{A}^2_{\Gamma\Gamma}(\theta_2) - \mathbf{A}^2_{\Gamma I}(\theta_2)[\mathbf{A}^2_{II}(\theta_2)]^{-1}\mathbf{A}^2_{I\Gamma}(\theta_2) \tag{17}$$

$$\mathbf{F}_2(\theta_2) = \mathbf{f}^2_\Gamma - \mathbf{A}^2_{\Gamma I}(\theta_2)[\mathbf{A}^2_{II}(\theta_2)]^{-1}\mathbf{f}^2_I \tag{18}$$

Solving the interface problem we obtain $\mathbf{u}_\Gamma(\theta_1, \theta_2)$. This can used to calculate the interior solutions as

$$\mathbf{u}^1_I(\theta_1, \theta_2) = [\mathbf{A}^1_{II}(\theta_1)]^{-1}[\mathbf{f}^1_I - \mathbf{A}^1_{I\Gamma}(\theta_1)\mathbf{u}_\Gamma(\theta_1, \theta_2)] \tag{19}$$

$$\mathbf{u}^2_I(\theta_1, \theta_2) = [\mathbf{A}^2_{II}(\theta_1)]^{-1}[\mathbf{f}^2_I - \mathbf{A}^2_{I\Gamma}(\theta_1)\mathbf{u}_\Gamma(\theta_1, \theta_2)] \tag{20}$$

The most computationally intensive parts of the solution process is the calculation of $[\mathbf{A}^1_{II}(\theta_1)]^{-1}$ and $[\mathbf{A}^2_{II}(\theta_1)]^{-1}$ which involves the solution of m_1 and m_2 coupled complex stochastic equations. However, existing computational methods for uncertainty propagation, mode reduction and substructuring can be used, for example component mode synthesis [6].

4.1 Modal solutions

One approach to solve the stochastic interior problem for parametric uncertainty is to consider the modal decomposition, and recognise that only the lower modes will contribute significantly to the response. Recall that in the frequency domain

$$\mathbf{A}_{II}(\omega, \theta) = -\omega^2\mathbf{M}_{II}(\theta) + i\omega\mathbf{C}_{II}(\theta) + \mathbf{K}_{II}(\theta) \tag{21}$$

Assuming proportional damping model, we have

$$[\mathbf{A}_{II}(\omega, \theta)]^{-1} = \sum_{k=1}^{m} \frac{\phi_k(\theta)\phi_k^T(\theta)}{\omega_k^2(\theta) - \omega^2 + 2i\zeta_k\omega_k(\theta)} \tag{22}$$

Here ζ_k are the modal damping factors, which have been assumed to be deterministic in this case for simplicity, but could also be random. The eigenvalues and eigenvectors are obtained from

$$\mathbf{K}_{II}(\theta)\boldsymbol{\phi}_k(\theta) = \omega_k^2 \mathbf{M}_{II}(\theta)\boldsymbol{\phi}_k(\theta), \quad k = 1, 2, \cdots \tag{23}$$

Any existing methods for the random eigenvalue problem can be used (for example perturbation, polynomial chaos, Neumann series, ...).

4.2 Perburbation solutions

If the uncertainty has only a small effect on the system matrices, perturbation methods may be used, where the second and higher order terms in the uncertainty are neglected. Thus, using Eq. (12), the inverse in Eqs. (15) and (16) becomes

$$[\mathbf{A}^1_{II}(\theta_1)]^{-1} \approx [\mathbf{A}^1_{0,II}]^{-1} - \sum_{i=1}^{M} \xi_i(\theta_1)[\mathbf{A}^1_{0,II}]^{-1}\mathbf{A}^1_{i,II}[\mathbf{A}^1_{0,II}]^{-1} \tag{24}$$

and hence to first order Eqs. (15) and (16) become

$$\begin{aligned}\mathbf{S}_1(\theta_1) \approx{}& \mathbf{A}^1_{0,\Gamma\Gamma} - \mathbf{A}^1_{0,\Gamma I}[\mathbf{A}^1_{0,II}]^{-1}\mathbf{A}^1_{0,I\Gamma} \\ &+ \sum_{i=1}^{M} \xi_i(\theta_1)\left\{\mathbf{A}^1_{0,\Gamma I}[\mathbf{A}^1_{0,II}]^{-1}\mathbf{A}^1_{i,II}[\mathbf{A}^1_{0,II}]^{-1}\mathbf{A}^1_{0,I\Gamma} - \mathbf{A}^1_{i,\Gamma I}[\mathbf{A}^1_{0,II}]^{-1}\mathbf{A}^1_{0,I\Gamma} - \mathbf{A}^1_{0,\Gamma I}[\mathbf{A}^1_{0,II}]^{-1}\mathbf{A}^1_{i,I\Gamma}\right\}\end{aligned} \tag{25}$$

$$\mathbf{F}_1(\theta_1) \approx \mathbf{f}^1_\Gamma - \mathbf{A}^1_{0,\Gamma I}[\mathbf{A}^1_{0,II}]^{-1}\mathbf{f}^1_I + \sum_{i=1}^{M} \xi_i(\theta_1)\left\{\mathbf{A}^1_{0,\Gamma I}[\mathbf{A}^1_{0,II}]^{-1}\mathbf{A}^1_{i,II}[\mathbf{A}^1_{0,II}]^{-1} - \mathbf{A}^1_{i,\Gamma I}[\mathbf{A}^1_{0,II}]^{-1}\right\}\mathbf{f}^1_I \tag{26}$$

5 Numerical example: Coupled Euler-Bernoulli beams

The example consists of two coupled Euler-Bernoulli beams with stochastic elasticity, shown in Fig. 4. We study the deflection of the beam under the action of a point harmonic load on the interior of beam 1. The parameters of the beams are:

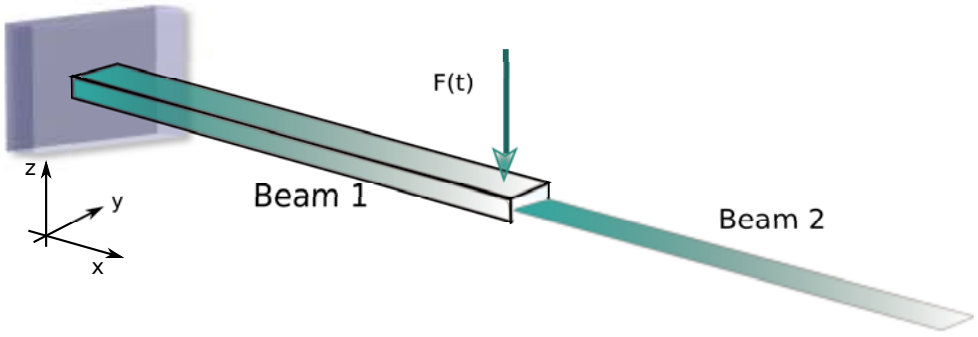


Figure 4: The example Euler-Bernoulli beam

$L_1 = 1$, $EI_{1_0} = 1/3$, $\rho A_1 = \pi^2/12$, $\zeta_1 = 0.04$
$L_2 = L_1$, $EI_{2_0} = EI_{1_0}/10^3$, $\rho A_2 = \rho A_1$, $\zeta_2 = \zeta_1/2$

Here L, EI_0, ρA and ζ denote the length, bending rigidity, mass density and the constant modal damping factor for both the beams.

The behaviour of the underlying deterministic system is considered first. The natural frequencies of the two Euler-Bernoulli beams are shown in Figure 5. Due to the difference in the stiffness values, beam 1 has less

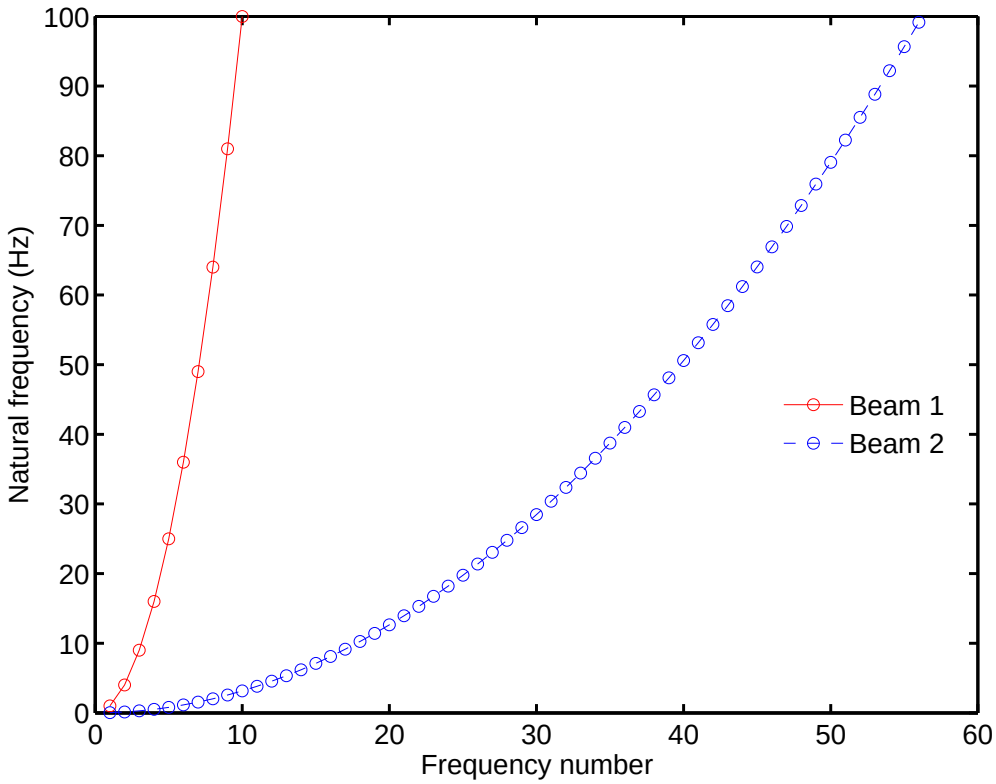


Figure 5: Natural frequencies of the two Euler-Bernoulli beams.

number of natural frequencies compared to beam 2 within a given frequency range (100 Hz in this case). The deterministic frequency response functions of the two beams in isolation (in the cantilever configuration with a point load at the end) are shown in Figure 6.

Now we consider the dynamics of the stochastic system. The following points should be noted for the stochastic case:

- The bending modulus of the first beam is modelled by two Gaussian random variables (a discretised random field with standard deviation $\sigma_a = 0.2$). The stiffness matrix is of the form

$$\mathbf{K}^1(\theta_1) = \mathbf{K}_0 + \xi_1(\theta_1)\mathbf{K}_1^1 + \xi_2(\theta_1)\mathbf{K}_2^1$$

- For the second beam, an Wishart random matrix model with $\delta = 0.2$ is considered.
- The mass matrix and the damping factors are deterministic for both beams.
- First-order perturbation is used for the interior random eigenvalue problems. A 1000-sample Monte Carlo Simulation (MCS) is used for the interface problem.
- For the numerical calculation we used $n_1 = 60$, $n_2 = 328$. In the domain decomposition approach, $m_1 = 58$, $m_2 = 336$ and $m_\Gamma = 2$.

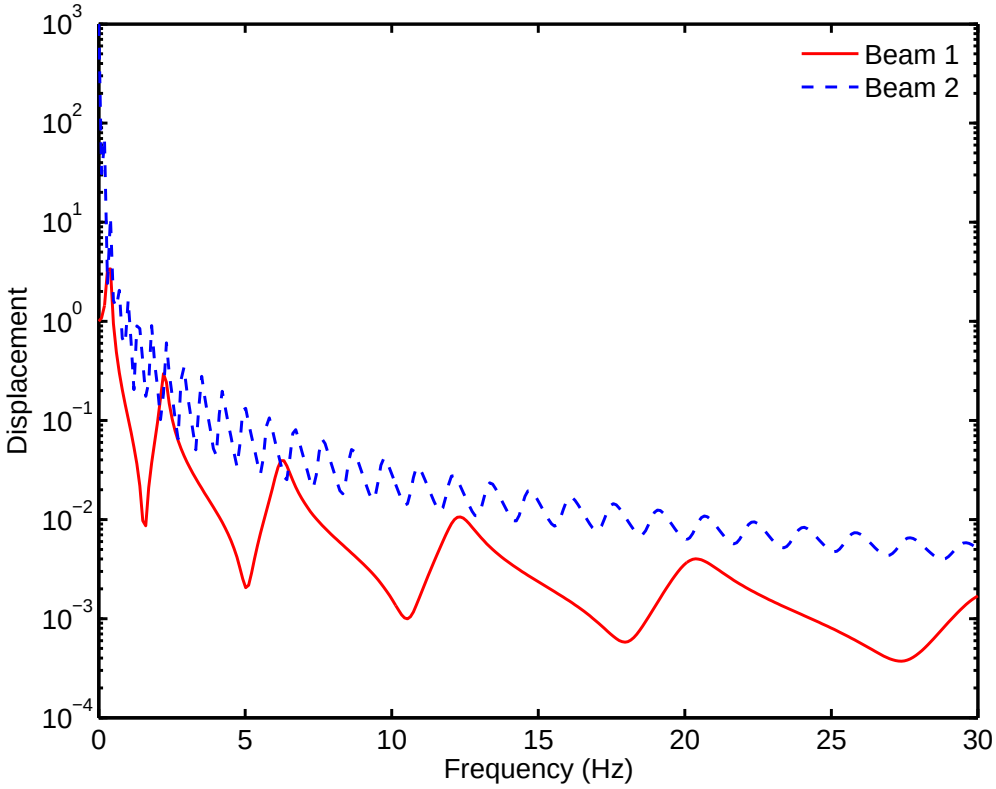


Figure 6: The deterministic frequency response functions of the two beams in isolation (in the cantilever configuration with a point load at the end).

The mean and the standard deviation of the coupled stochastic system at the driving point is shown in Figure 7. The mean and the standard deviation of the coupled stochastic system at the tip of the cantilever is shown in Figure 8. For both caseS we can observe that the mean response includes the characteristicS of both beams.

6 Conclusions

This paper investigates a new approach to consider multiple wavelength-scales by combining parametric and nonparametric uncertainty models. The main idea was to decompose the overall domain into two non overlapping sub-domains and subsequently utilise Schur complement matrices. The main features of the paper include:

- The objective was to consider large and small wavelength-scale vibrations simultaneously in conjunction with relevant stochastic models.
- A parametric uncertainty model is considered for large wavelength-scale vibrations (low frequency). Random field/random variable models can be used for this purpose.
- A non-parametric uncertainty model is considered for small wavelength-scale vibrations (high frequency). Random matrix models can be used for this purpose.
- The domain decomposition method (originally proposed for parallel computation of deterministic boundary problems) is used to ‘combine’ the two domains with two different uncertainty models.

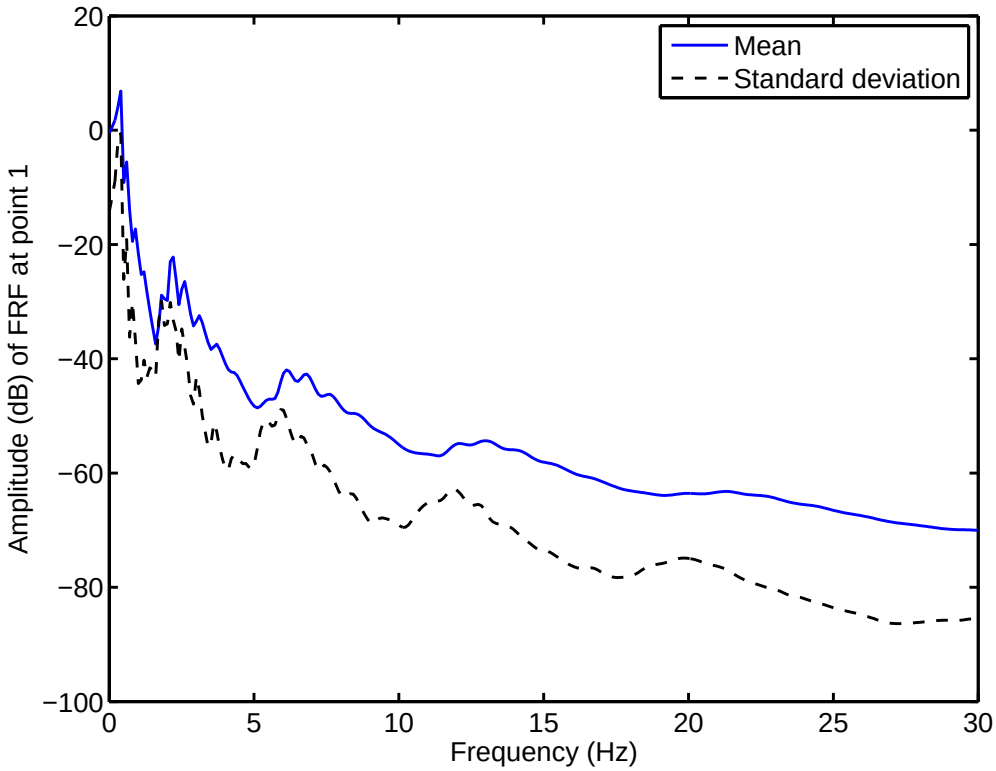


Figure 7: Response statistics of the coupled stochastic system at the driving point.

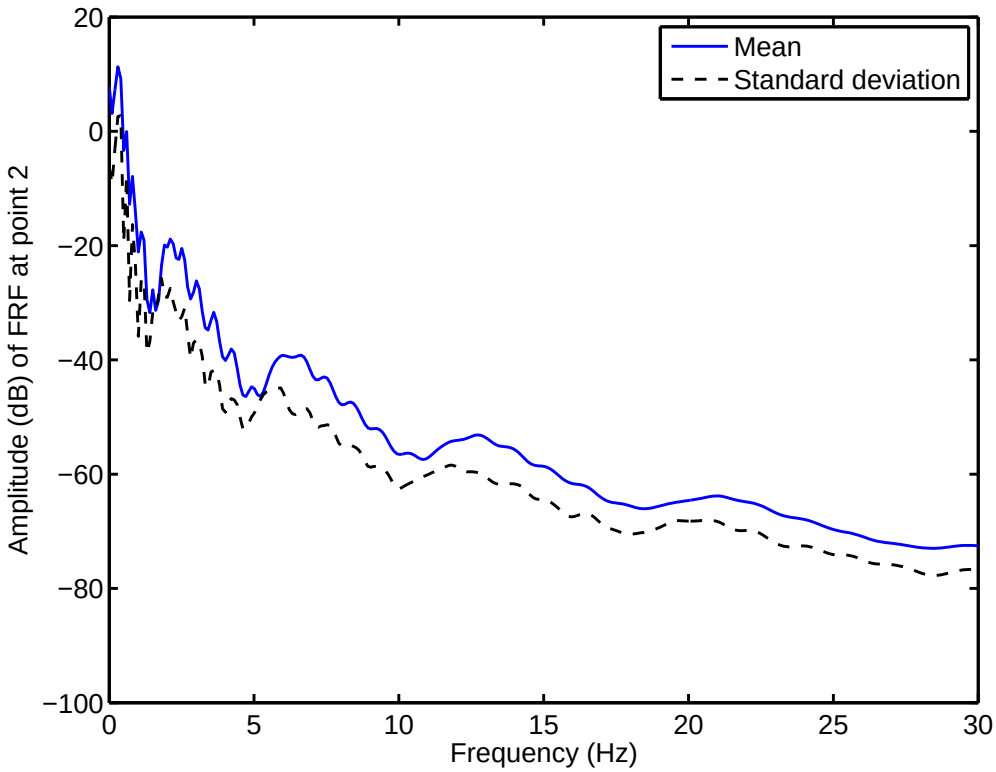


Figure 8: Response statistics of the coupled stochastic system at the tip of the cantilever.

- A simple numerical example with two wavelength-scale domains is used to illustrate the idea.

Future studies will considerer more physically realistic examples and reduced computational methods.

Acknowledgements

The authors acknowledge the support of the EPSRC Programme Grant on Digital Twins for Improved Dynamic Design, grant number EP/R006768.

References

[1] R. R. Craig, M. C. C. Bampton *Coupling of substructures for dynamic analysis*, AIAA Journal Vol. 6 (1968), pp. 1313-1319.

[2] R. R. Craig, *Structural Dynamics: An Introduction to Computer Methods*, Wiley, New York (1981).

[3] M. Petyt, *Introduction to Finite Element Vibration Analysis*, Cambridge University Press (1990).

[4] B.R. Mace, P.J. Shorter, *A local modal/perturbational method for estimating frequency response statistics of built-up structures with uncertain properties*, Journal of Sound and Vibration, Vol. 242, No. 5 (2001) pp. 793-811.

[5] O. Giannini, M. Hanss, *The component mode transformation method: a fast implementation of fuzzy arithmetic for uncertainty management in structural dynamics*, Journal of Sound and Vibration, Vol. 311 (2008), pp. 1340-1357.

[6] L. Hinke, F. Dohnal, B. R. Mace, T. P. Waters, N. S. Ferguson, *Component mode synthesis as a framework for uncertainty analysis*, Journal of Sound and Vibration, Vol. 324, No. 1-2 (2009), pp. 161-178.

[7] H. A. Jensen, V. A. Araya, A. D. Muñoz, M. A. Valdebenito, *A physical domain-based substructuring as a framework for dynamic modeling and reanalysis of systems*, Computer Methods in Applied Mechanics and Engineering, Vol. 326 (2017), pp. 656-678.

[8] D. Sarsri, L. Azrar, A. Jebbouri, A. El Hami, *Component mode synthesis and polynomial chaos expansions for stochastic frequency functions of large linear FE models*, Computers and Structures, Vol. 89 (2011), pp. 346-356.

[9] S.-A. Chentouf, N. Bouhaddi, C. Laitem, *Robustness analysis by a probabilistic approach for propagation of uncertainties in a component mode synthesis context*, Mechanical Systems and Signal Processing, Vol. 25 (2011), pp. 2426-2443.

[10] B. Pascual, S. Adhikari, *Combined parametricnonparametric uncertainty quantification using random matrix theory and polynomial chaos expansion*, Computers and Structures, Vol. 112-113 (2012), pp. 364-379.

[11] S. Adhikari, M. I. Friswell, *Random Matrix eigenvalue problems in structural dynamics*, International Journal for Numerical Methods in Engineering, Vol. 69, No. 3 (2007), pp. 562-591.

[12] S. Adhikari, *Wishart random matrices in probabilistic structural mechanics*, Journal of Engineering Mechanics, Vol. 134, No. 12 (2008), pp. 1029-1044.

Efficient random vibration analysis of nonlinear systems with long short-term memory networks for uncertainty quantification

D. A. Najera-Flores[1], A. R. Brink[2]
[1] ATA Engineering, Inc.
San Diego, CA, USA
e-mail: **dnajera@ata-e.com**

[2] Sandia National Laboratories
Albuquerque, NM, USA

Abstract
Complex mechanical structures are often subjected to random vibration environments. One strategy to analyze these nonlinear structures numerically is to use finite element analysis with an explicit solver to resolve interactions in the time domain. However, this approach is impractical because the solver is conditionally stable and requires thousands of iterations to resolve the contact algorithms. As a result, only short runs can be performed practically because of the extremely long runtime needed to obtain sufficient sampling for long-time statistics. The proposed approach uses a machine learning algorithm known as the Long Short-Term Memory (LSTM) network to model the response of the nonlinear system to random input. The LSTM extends the capability of the explicit solver approach by taking short samples and extending them to arbitrarily long signals. The efficient LSTM algorithm enables the capability to perform Monte Carlo simulations to quantify model-form and aleatoric uncertainty due to the random input.

1 Introduction

Random vibration is an important load environment to consider during the design of mechanical, aerospace and civil structures as it can lead to fatigue type failures. As the name implies, random vibration is a stochastic load that is best described in the frequency domain using a power spectral density function (PSD). For linear systems, the PSD of the response is calculated as

$$[S_X(\omega)] = [H(\omega)][S_F(\omega)][H^*(\omega)]^T, \tag{1}$$

where $S_X(\omega)$ is the response PSD, $H(\omega)$ is the frequency response function (FRF), $S_F(\omega)$ is the input PSD, and $[\cdot]^*$ is the complex conjugate [1]. An exhaustive discussion on random vibration of linear systems is found in [1] and [2]. In practice, it is rare to find a structure that behaves in a truly linear way. Often the nonlinearities are weak and do not contribute to the overall response, thus the linear assumption holds. However, there are applications and structures in which the nonlinearities play an important role, such as geometric nonlinearity in panel flutter [3], hysteretic nonlinearity in vehicle suspension [4], and nonlinear stiffness and damping from frictional joints [5]. Joint probability distribution functions (PDF) inclusive of the time varying nature of nonlinear systems can be numerically simulated using several existing techniques, such as perturbation techniques [6], equivalent linearization [7], multi-Gaussian closures [8], stochastic averaging [9], or seeking the solution to the Fokker-Planck equation for Markov vector processes [10], [11]. These techniques are only valid for narrow classes of vibration input, such as stationary Gaussian, and can only be reasonably solved for systems with limited degrees of freedom (DOF). The work presented in this paper is motivated by the need to develop an efficient method to calculate the structural response of nonlinear mechanical systems with a large number of DOF subjected to any class of random vibration excitations. Currently for large numerical models of complex structures, explicit time integration is

performed using finite element analysis (FEA). A major drawback of this method is that explicit solvers are conditionally stable because their smallest allowable time step is driven by the smallest characteristic element size of the finite element model (FEM). Since FEMs that include contact nonlinearities require high mesh refinement to accurately resolve conditions at interfaces, the stable timestep becomes small enough to make analysis of long duration signals intractable. As a result, random analysis is typically performed using a short realization of the random environment. This approach is problematic because the time signal statistics may not be captured by a short realization. Moreover, a single realization may not be representative of the worst case for a nonlinear structure where there is path dependency. These challenges motivate the need for a more efficient approach for obtaining structural response of nonlinear structures to random vibration inputs.

The technique presented in this paper aims to provide a novel and efficient methodology to conduct numerical analysis of nonlinear structures subjected to random inputs. The method consists of using machine learning techniques to accomplish the objective. In particular, the Long Short-Term Memory (LSTM) network is used to extend the structural response of a short duration random signal to a much longer time signal from which significant statistical features can be extracted. The remainder of this paper will introduce the mechanics of a LSTM neural network, then apply them to a system with a strong and weak contact nonlinearity.

2 Methodology

2.1 Long Short-Term Memory Networks

The field of deep learning has been applied with success to a broad set of applications in recent years [12]. The basis for deep learning is algorithms that learn from experience when exposed to data. A commonly used tool in deep learning is a deep neural network which is built by stacking sequential layers of parallel operations, referred to as units. The sequential traversal through the algorithm allows the program to refer to earlier operations. These units act as storage for state information and provide a structure to organize the network's processes. As such, deep neural networks learn both hierarchical representations of data, and the structural organization of the computer program that process the data.

A special case of deep neural networks is the recurrent neural network (RNN). RNNs are a family of neural networks specialized in processing sequential data [13]. The main advantage of an RNN over a traditional neural network is its ability to share model parameters across different timesteps. This capability allows the network to learn relations between timesteps. A more specialized type of RNN is the long short-term memory (LSTM) network. The LSTM, which is a type of gated RNN, was originally proposed by Hochreiter and Schmidhuber [14], and alleviates many of the computational challenges of the traditional RNN [15]. Using gates to control the flow of information through time, the LSTM has self-loops that allow it to "forget" or "remember" information about the past. Additionally, by using bidirectionality, the LSTM can also learn how the "future" affects the current state. LSTM networks have been successful in many applications, including speech recognition [16], handwriting recognition and generation [17], machine translation [18], image captioning [19], among others.

A diagram of a single LSTM cell can be seen in Figure 1.

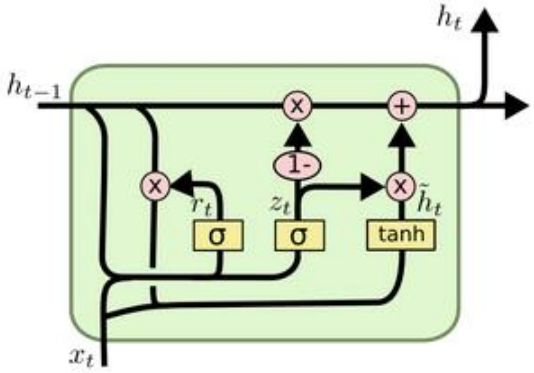


Figure 1. A single LSTM cell *[20]*.

The forget gate unit $f_i^{(t)}$(for timestep *t* and cell *i*) is computed as

$$f_i^{(t)} = \sigma\left(b_i^f + \sum_j U_{i,j}^f x_j^{(t)} + \sum_j W_{i,j}^f h_j^{(t-1)}\right), \tag{2}$$

where b_i^f, U_i^f, W_i^f are the biases, input weights and recurrent weights for the forget states, respectively. The input vector, represented by $x^{(t)}$ and $h^{(t)}$ (e.g., the input and output acceleration of a dynamic process), is the current hidden layer vector. The $\sigma()$ operator is the sigmoid function. The LSTM cell internal state is updated by

$$s_i^{(t)} = f_i^{(t)} s_i^{(t-1)} + g_i^t \sigma\left(b_i \ + \sum_j U_{i,j} x_j^{(t)} + \sum_j W_{i,j} h_j^{(t-1)}\right), \tag{3}$$

where b_i , U_i , W_i are the biases, input weights, and recurrent weights into the LSTM network. The nonlinear sigmoid operation is weighted by the external input gate. The external input gate is computed similarly to the forget gate but with its own set of parameters, such that

$$g_i^{(t)} = \sigma\left(b_i^g + \sum_j U_{i,j}^g x_j^{(t)} + \sum_j W_{i,j}^g h_j^{(t-1)}\right). \tag{4}$$

The output $h_i^{(t)}$ of the LSTM cell can be controller via the output gate $q_i^{(t)}$

$$h_i^{(t)} = \tanh(s_i^{(t)})\, q_i^{(t)}, \tag{5}$$

$$q_i^{(t)} = \sigma\left(b_i^o + \sum_j U_{i,j}^o x_j^{(t)} + \sum_j W_{i,j}^o h_j^{(t-1)}\right). \tag{6}$$

In the above equations, all parameters are learned through a process known as backpropagation through time (BPTT) [13]. BPTT is the process by which gradients are computed through the nodes of the computational graph with respect to a loss function. The loss function is typically the negative log likelihood function, where the current timestep is predicted from past and current inputs, and past outputs, such as

$$L^t = -logP\left(y^{(t)} | x^{(1)}, \ldots., x^{(t)}, y^{(1)}, \ldots., y^{(t-1)}\right). \tag{7}$$

2.2 Dropout and Model-Form Uncertainty

Dropout is a method of regularization typically used to reduce the model's generalization error [21]. It is usually implemented by masking certain hidden units chosen at random, based on a uniform probability defined by the user. The masked hidden unit is dropped, reducing the model's effective capacity. At each epoch, different units are dropped, which forces the model to be more resilient; each hidden unit must be able to perform well in the absence of other units. The implication is that the hidden units are optimized to perform well in many contexts, resulting in a more generalizable network [22].

Gal and Ghahramani [23] showed that dropout can be re-interpreted as performing approximate Bayesian inference in deep Gaussian processes. They developed the theoretical framework to show that performing backpropagation through a neural network is analogous to minimizing the Kullback-Leilbler divergence between an approximate distribution and the posterior of a deep Gaussian process. Therefore, a trained deep network with dropout included essentially functions as a deep Gaussian process. The implication is that activating dropout during analysis provides a stochastic prediction. A family of predictions can be obtained with a Monte Carlo simulation by performing numerous forward passes through the stochastic network. The resulting statistical distribution of predictions is an expression of the model-form error.

3 Case Studies

3.1 Intermittent Contact Problem

The contact problem under consideration in this section is a three degree of freedom (DOF) system, as illustrated in Figure 2. It consists of three differing masses connected by springs. A penalty spring was used to model contact between M_2 and M_3, with a small initial gap. An input random vibration acceleration was applied at one end while the other end remained fixed. Response was recovered at M_1. This location was chosen instead of M_2 to avoid contaminating the data with artificial peaks in the response due to the arbitrary penalty stiffness. The response of M_1 was still affected by the contact interaction but without the numerical artifacts of the contact algorithm. The masses and springs were set to arbitrary values such that there was significant contact throughout the excitation. The masses M_1, M_2, and M_3 were set to 1, 10, and 2, respectively. The spring stiffnesses K_1, K_2, and K_3 were set to 100, 2000, and 100, respectively.

The goal of this notional problem was to exercise nonlinear response due to intermittent contact interactions. The expectation is that the contact problem is harder to predict due to the non-smooth response associated with impact between the two masses. The objective is to predict the acceleration response at M_1, given the input random vibration. The three DOF system was implemented and solved in Matlab using ODE45.

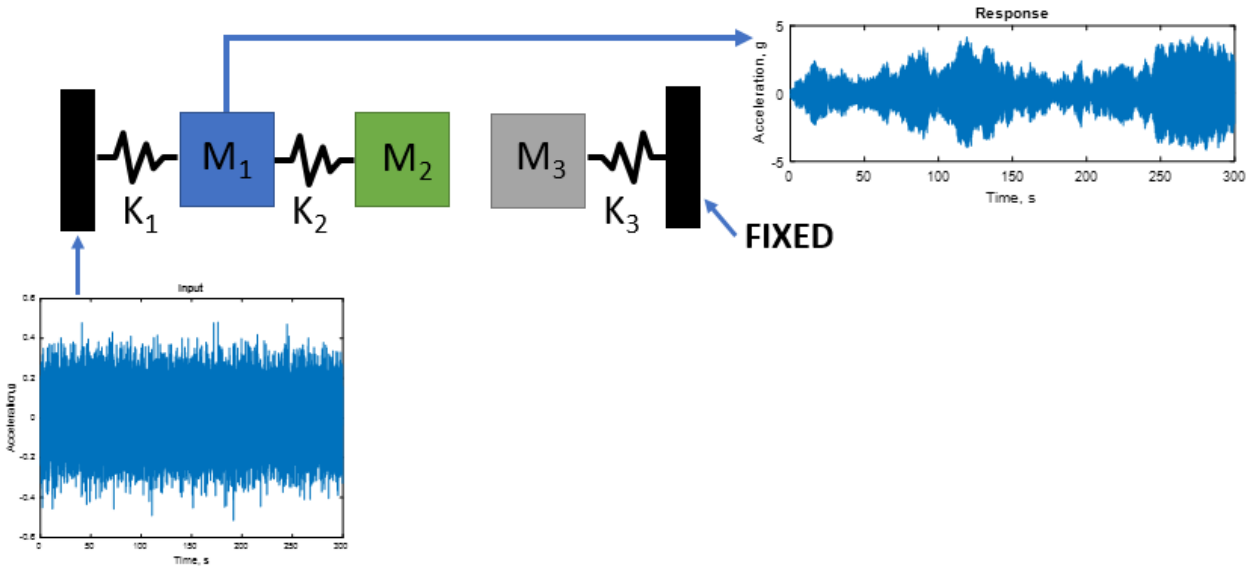


Figure 2. Diagram of the three DOF contact problem with boundary conditions indicated.

3.1.1 LSTM Architecture

The LSTM architecture used to model the contact problem was a deep bidirectional network with dropout layers, and a time distributed dense output layer. The data (input and response) was divided in *m* segments that were 100 points long (each point corresponding to a timestep). The LSTM was trained by using these 100-step segments. The input to the LSTM was a 2x100 vector containing the segment corresponding to the i^{th} step excitation and the segment corresponding to the response of the $(i\text{-}1)^{th}$ segment. The output to the LSTM was a 1x100 vector containing the segment corresponding to the i^{th} step response. Figure 3 shows an example of this process; the LSTM network takes in the excitation at the segment we are trying to predict and the response of the previous segment (blue) and outputs the response at the current segment (orange).

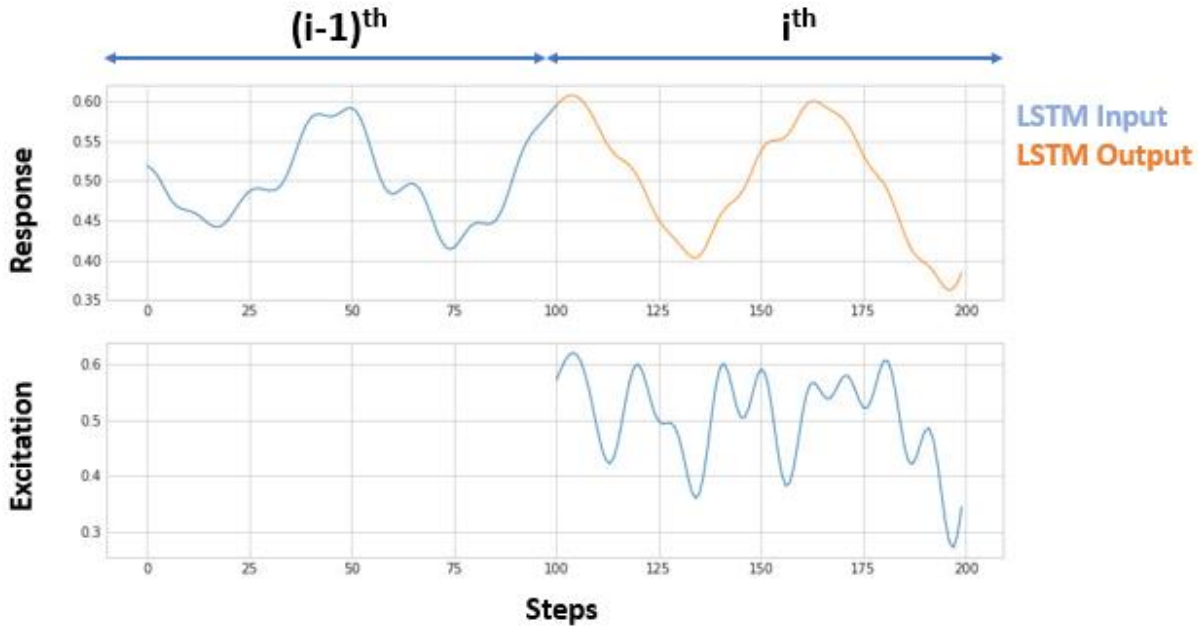


Figure 3. Typical input/output data used for training the LSTM network.

Figure 4 shows a diagram representing the LSTM architecture used. The *x* variables represent the input time history, while the *y* variables represent the output time history. The diagram shows the prediction of a single segment. In this case, the *T* superscript would be 100, representing the number of points in a segment. Each row of the diagram represents a layer. The general architecture used contained layers of bidirectional LSTMs, followed by forward LSTMs, followed by a time distributed dense output layer. The data was scaled to be between 0 and 1, so that rectified linear unit (ReLu) activation functions could be used throughout the network. After each layer, a dropout layer was added for regularization. As seen in the diagram, output of the LSTM units is shared across the entire network.

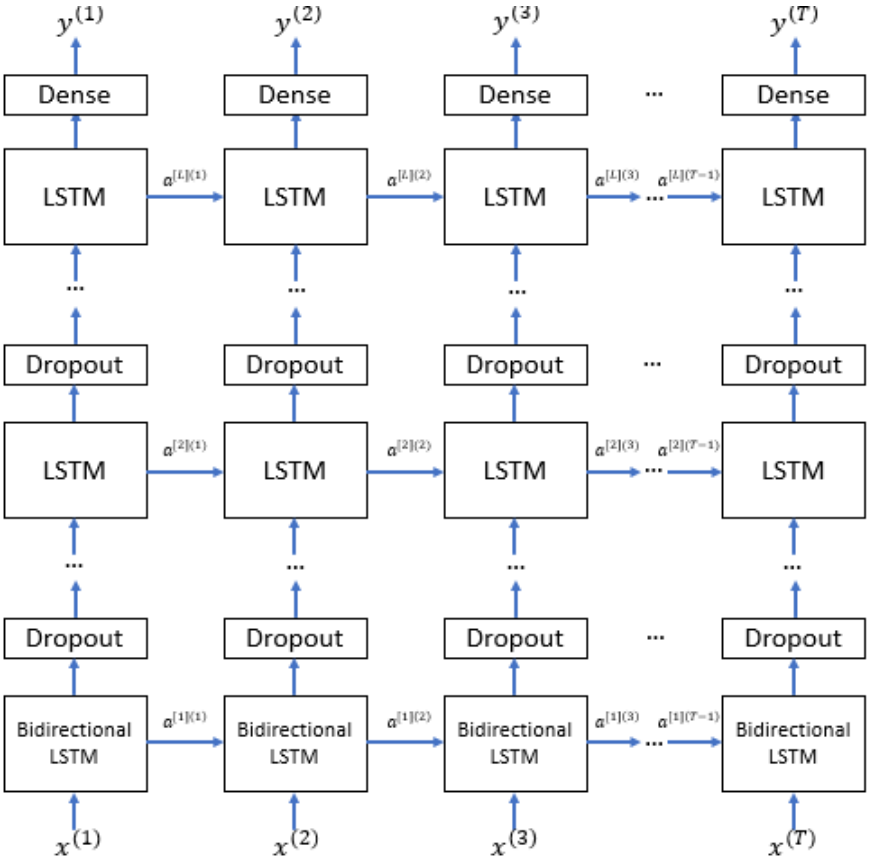


Figure 4. Schematic of the LSTM architecture used for the contact problem.

Each of the LSTM boxes in the diagram represents one of the LSTM cell of Figure 1. Each LSTM cell has *n* number of hidden units. The number of hidden units in the LSTM cell represents the degree of decomposition to which the incoming time sequence will be mapped. For example, an LSTM with 30 hidden units will decompose the two-dimensional input vector into 30 time sequences. Figure 5 shows the transformation of the input through every layer. The last layer shows the prediction (orange) and the actual response (black). In this example, the LSTM takes in two time sequences and transforms them into 30 time sequences. The LSTM then takes the input transformed into a high-dimensional space through a series of nonlinear operations, until they are combined into a single time sequence in the last layer. The transformations are determined by the weights of the hidden units. Each gate has different weights and they control the flow of information, as determined by Equations (2-6). These weights are applied to the input over the entire length (time wise) of the input. Since the input is 2 dimensional and the number of hidden weights is 30, the LSTM effectively maps the input from 2 to 30 dimensions. The input weights were represented by *W* in the equations above. The rest of the weights were represented by *U*. Physically, one could think of the high-dimensional representation of the input as representing a change of basis. In this interpretation, the program is able to generalize when it finds the proper basis representation of the signal, and the proper algorithm that transforms such basis representation into the output. There is no further compression or decomposition going from layer 1 to layer 2, hence the weight matrix is square. A desirable

property of the weight matrices is sparsity. Sparse weight matrices may indicate a reduction in redundancy in the feature representation, and consequently, better utilization of the network capacity [24]. Though no explicit effort has been taken to enforce sparsity, the matrices in Figure 5 show sparsity. This sparsity is likely a consequence of dropout.

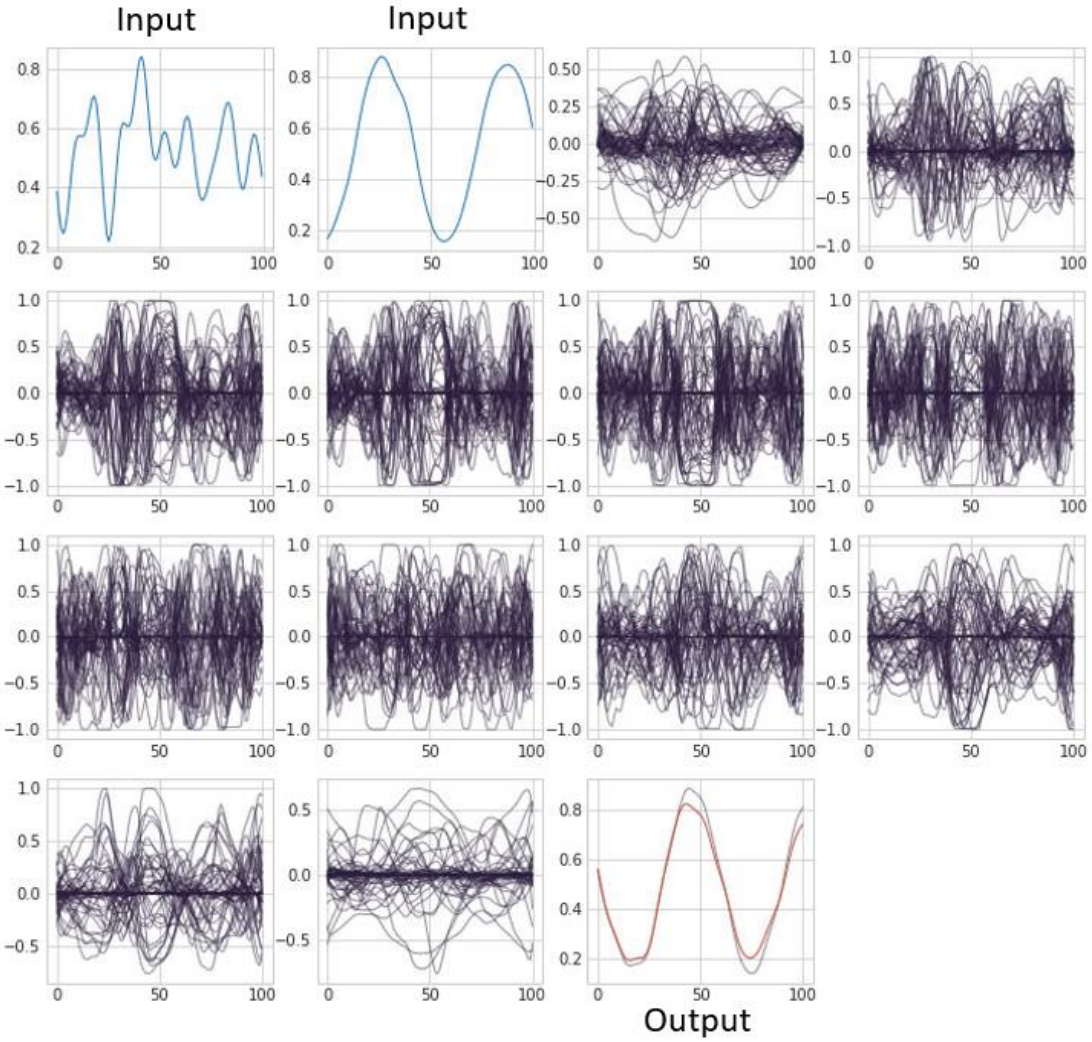


Figure 5. The transformed input signals as they traverse the depth of the LSTM network.

3.1.2 Results

The full network was trained using synthetic data generated in Matlab by solving the three DOF contact problem. Several time series realizations of a random vibration excitation were generated from a single PSD using the method of random phase. The time signals share statistical properties, but they are unique realizations. The network was trained on one of the realizations and tested on a completely different realization, called the test dataset.

Figure 6 shows the input random excitation (top) and the corresponding response (bottom). The response from direct numerical time integration is shown in red, and the neural network prediction is plotted in black. The initial data used to seed the prediction is shown in blue in the bottom plot. The blue portion of the bottom plot is the only information needed to perform the prediction after the network has been trained. It

can be seen that the overall shape of the response is captured by the prediction. Figure 7 shows a close-up of the prediction. As illustrated, the prediction is performed stochastically by performing a Monte Carlo simulation. In this case, 20 realizations of the response are shown in black. The variance in the predictions is a way to quantify the model-form error, as discussed in Section 2.2.

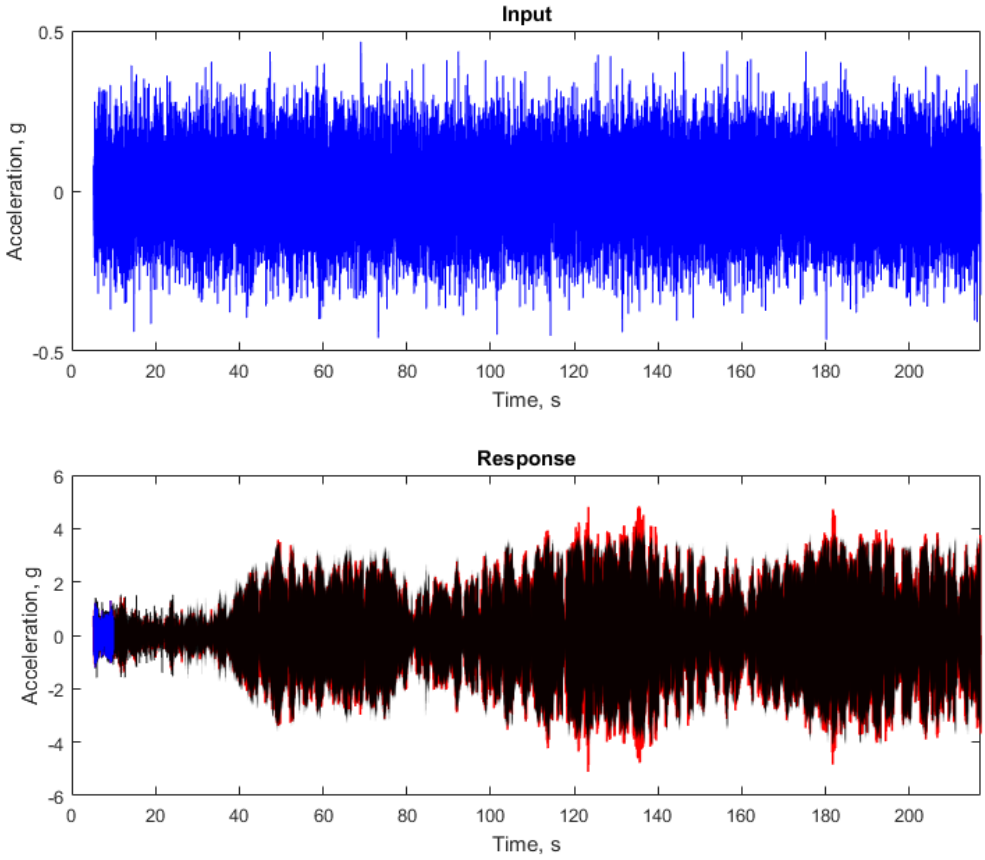


Figure 6. Input random vibration excitation (top) and response (bottom). In the bottom image, the actual response is shown in red, the network prediction is shown in black, and the "seed" use to generate the prediction is shown in blue.

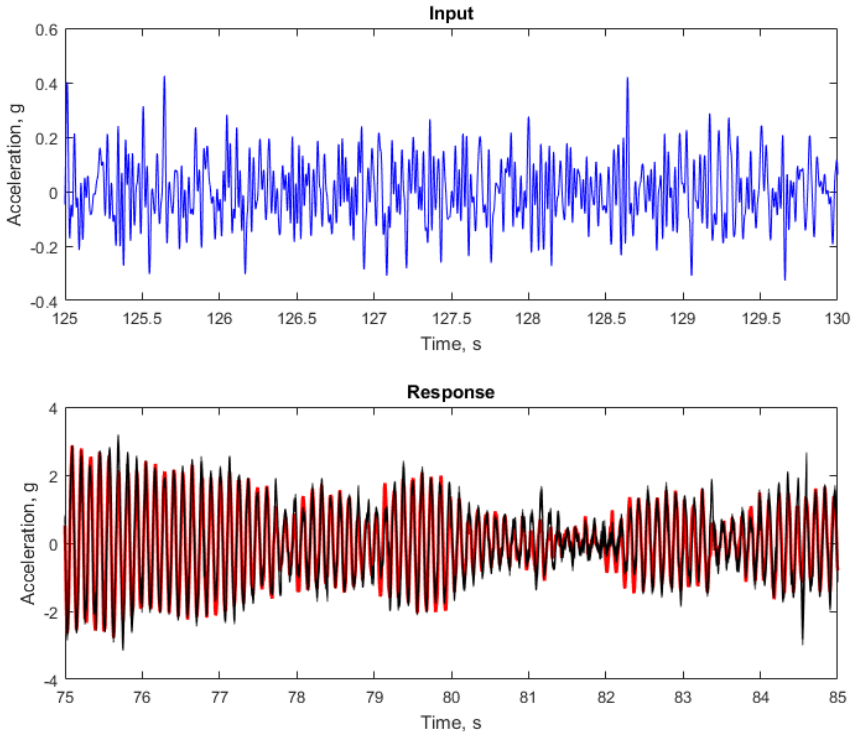


Figure 7. Close-up of input random vibration excitation (top) and response (bottom). In the bottom image, the actual response is shown in red, the network prediction is shown in black, and the "seed" use to generate the prediction is shown in blue.

Figure 8 shows the same comparison of PSDs in the frequency domain. The prediction envelopes the actual response and it matches the peaks well. Figure 9 shows the comparison using a spectrogram calculated with the Short-Time Fourier Transform. The spectrogram also shows a good match between the actual response and the prediction. The error is larger at lower frequencies. This error may be a consequence of the window size chosen to partition the signal in Section 3.1.1. A longer window would capture lower frequency content better but would decrease the number of training samples. More work is needed to determine an optimal window size.

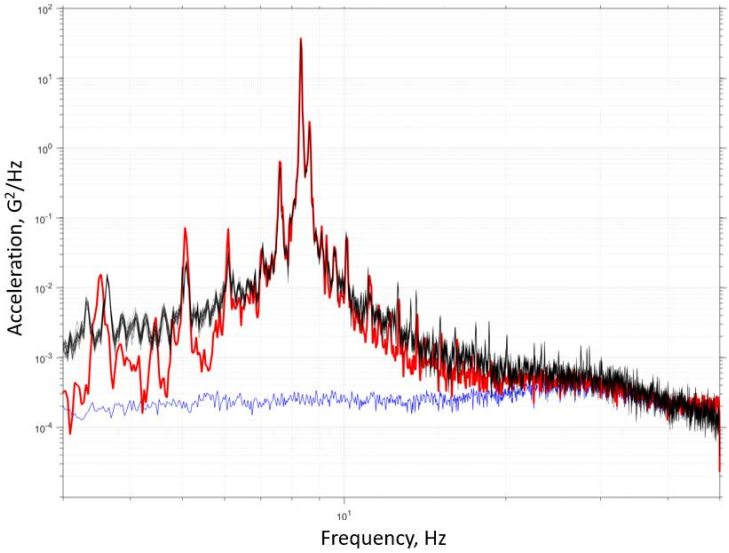


Figure 8. Power spectral density of input (blue), actual response (red), and prediction (black).

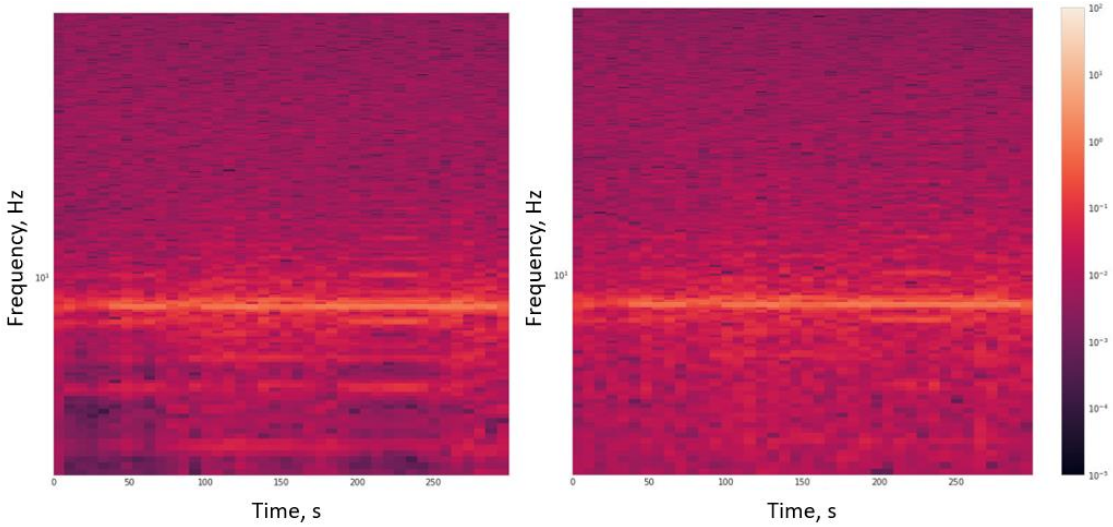


Figure 9. Spectrogram of actual response (left) and network prediction (right).

Lastly, the model parameters (K and M) were varied to study the effect of parametric uncertainty. The parameters were varied +/- 10% of their nominal value to model the uncertainty associated with these values. A few values were sampled from a uniform distribution in the +/- 10% range from the nominal values and their responses were evaluated with the Maltab model. A short "seed" from each evaluation was used to predict the long-term response using the LSTM network. Figure 10 shows the comparison between the actual response and the prediction. For the most part, the network is robust enough to capture small parametric variations. The effect of the change of parameters is embedded in the "seed" data, which the network is able to identify and accurately capture the evolution of the response. The multiple predictions correspond to different model realizations due to the network having been trained with dropout. The multiple realizations are an expression of model-form uncertainty.

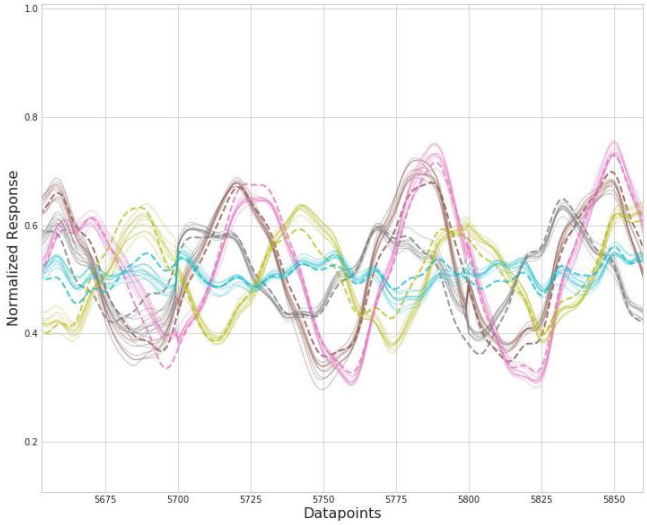


Figure 10. The response of five variations of the model parameters shown. The actual responses are shown with a dashed line and the predictions are shown with solid lines.

3.2 The Ministack

The Ministack assembly is a benchmark specimen that was developed at Sandia National Laboratories (SNL) to better understand the nonlinear damping and stiffness of a compression fit interface. The structure consists of an outer can that houses a subassembly of an aluminum slug that fits tightly in between two foam cups. For this work, a reduced-order model of the Ministack that was developed by Kuether and Najera [25] was used to generate training data. The reduced order model includes a nonlinear interface represented by an Iwan element. The Iwan element consists of a constitutive model that captures the microslip behavior and nonlinear dependence of damping and stiffness, as the amplitude of the response increases [26]. The Iwan element parameters corresponding to the Ministack frictional interface were found through optimization in [25]. Figure *11* shows the Ministack finite element model and the frictional interfaces that were reduced to Iwan elements. The random vibration input was applied at the base of the can and the response was recorded at the top of the slug.

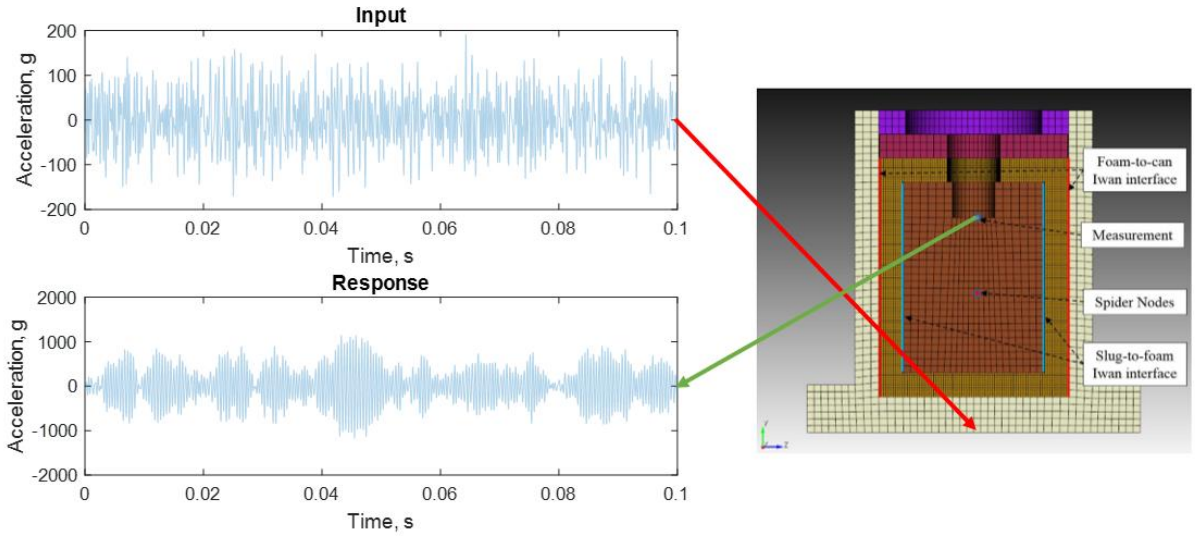


Figure 11. The Ministack finite element model with the interfaces that were reduced to Iwan elements with the random vibration input and response locations indicated.

3.2.1 LSTM Architecture

The LSTM architecture used to model the Ministack problem was a deep LSTM network with dropout layers, and a fully connected output layer. The architecture used was similar to that of the contact problem described in Section 3.1.1. One of the differences was that the Ministack LSTM was not bidirectional. It was found that the Ministack could be modeled without including bidirectionality. Another difference was the output layer. In the case of the contact problem, the output layer was time distributed while that was not the case for the Ministack. It was found that a static dense layer with multiple features representing the time dimension worked best for the Ministack. The exploration of the inner workings of the Ministack LSMT are not provided here but similar conclusions to the contact problem can be drawn. The LSTM network finds the appropriate basis representation of the signal, and the graph structure that best performs the mapping of input to output.

3.2.2 Results

The network was trained using synthetic data generated in Matlab using the reduced-order model described in [25]. As in the contact problem, the results provided in this section were generated using the test dataset.

Figure 12 shows the input random vibration (top) and the response (bottom). In the bottom plot, the actual response is shown in red, the prediction is shown in black, and the seed data used to generate the response with the LSTM network is shown in blue. The predicted and actual responses are nearly indistinguishable. Figure 13 shows a close-up of the data to illustrate the close match between prediction and actual. Since the LSTM network provides stochastic predictions, the prediction shown in Figure 13 represents the mean prediction.

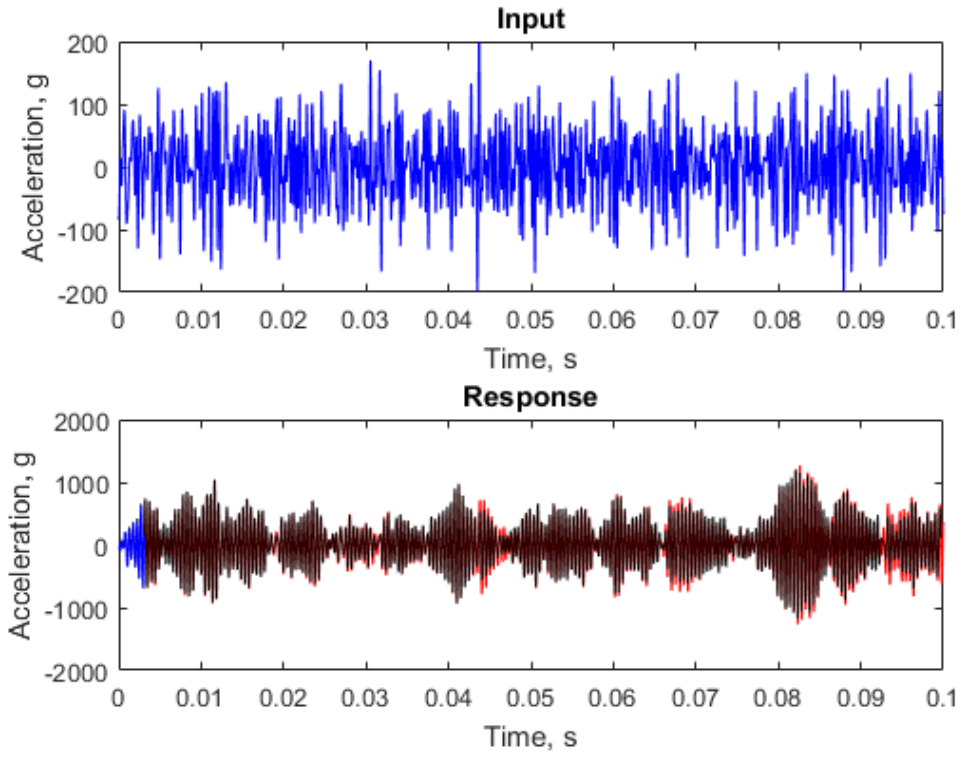


Figure 12. Input random vibration excitation (top) and response (bottom). In the bottom image, the actual response is shown in red, the network prediction is shown in black, and the "seed" use to generate the prediction is shown in blue.

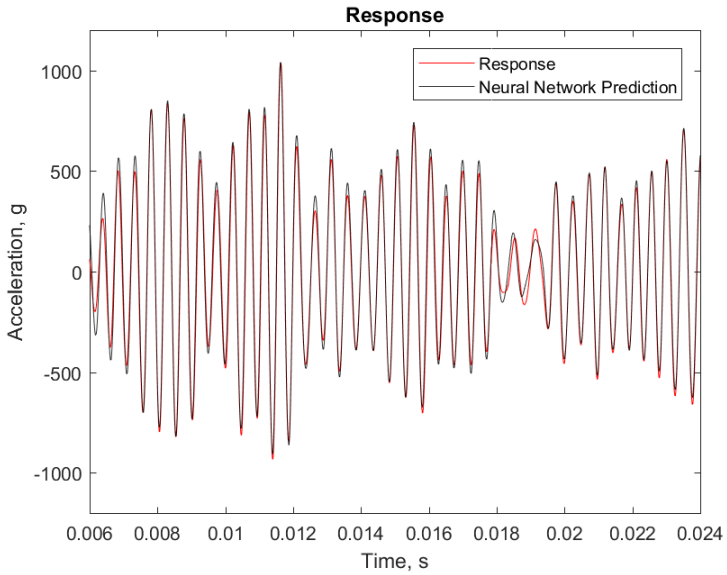


Figure 13. Close-up of Ministack actual response (red) and LSTM network predictions (black).

To illustrate the stochastic predictions of the LSTM network with dropout, Figure 14 shows multiple realizations of the prediction in black. Variance in the response can be used to quantify the epistemic uncertainty of the response, as described in Section 2.2. Uncertainty, represented by the range of predictions, tends to be larger in areas where the LSTM network error is larger (e.g., in areas the network did not encounter during training).

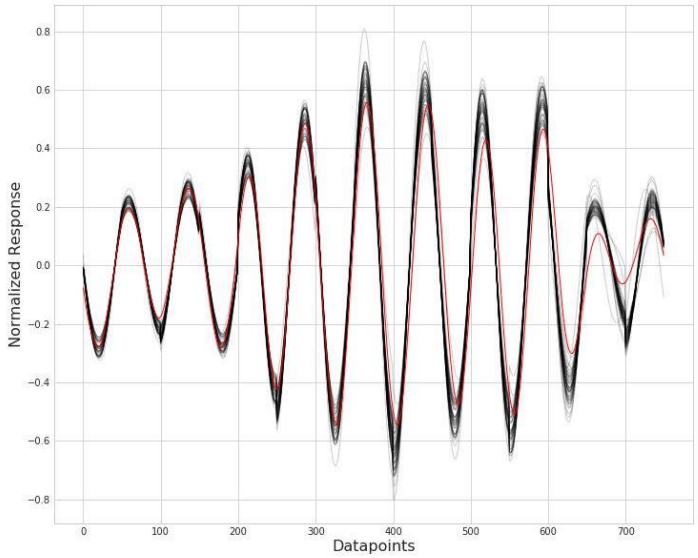


Figure 14 - Response including error

4 Conclusion

This paper presents a novel method using Long Short-Term Memory neural networks to predict the response of nonlinear systems subject to random broad-band excitation. By using the LSTMs ability to use past as well as future data in its prediction, accurate predictions of strong and weak nonlinearities are possible. Two typical nonlinearities in the form of intermittent contact and frictional sliding were used as baseline

examples, both of which were shown to be solvable with the LSTM neural network. Additionally, it was shown that by including dropout layers, the model becomes stochastic in form allowing it to predict epistemic and aleatoric uncertainty inherent to the analysis.

Acknowledgements

Sandia National Laboratories is a multimission laboratory managed and operated by National Technology & Engineering Solutions of Sandia, LLC, a wholly owned subsidiary of Honeywell International Inc., for the U.S. Department of Energy's National Nuclear Security Administration under contract DE-NA0003525.

References

[1] P. H. Wirsching, T. L. Paez and K. Ortiz, Random Vibration Theory and Practice, New York: John Wiley and Sons, Inc., 1995.

[2] T. L. Paez, "Random Vibration - A Brief History," Sound and Vibration, January 2012.

[3] J. Shoneman, C. Ostoich, L. Jarman, C. Van Damme and M. S. Allen, "Linear and Nonlinear Reduced-Order Modeling for Hypersonic Panel Flutter," AIAA SciTech Forum, 2018.

[4] C. R. Hua, Y. Zhao, Z. W. Lu and H. Ouyang, "Random Vibration of Vehicle with Hysteretic Nonlinerar Suspension under Road Roughness," Advances in Mechanical Engineering, vol. 10, no. 1, pp. 1-10, 2018.

[5] M. R. Brake, The Mechanics of Jointed Structures, Springer International Publishing, 2018.

[6] S. H. Crandall, "Perturbation Techniques for Rnadom Vibration of Nonlinear Systems," The Journal of the Acoustical Society of America, vol. 35, no. 11, 1963.

[7] J. B. Roberts and P. D. Spanos, Random Vibration and Statistical Linearization, New York: Wiley, 1990.

[8] G. K. Er, "Multi-Gaussian Closure Method for Randomly Excited Nonlinear Systems," International Journal of Nonlinear Mechanics, vol. 33, no. 2, 1998.

[9] R. Z. Khasminskii, "A Limit Theorem for the Solution of Differential Equations with Random Right-Hand Sides," Theory of Probability and its Applications, vol. 11, no. 3, 1966.

[10] H. Risken and F. Till, The Fokker-Planck Equation: Methods of Solution and Applications, Berlin: Springer-Verlag, 1996.

[11] S. Narayanan and P. Kumar, "Numerical Solutions of Fokker-Planck Equations of Nonlinear Systems Subjected to Random and Harmonic Excitations.," Probabilistic Engineering Mechanics, vol. 27, pp. 35-46, 2012.

[12] R. Vargas, A. Mosavi and L. Ruiz, "Deep Learning: A Review," Advances in Intelligent Systems and Computing, 2017.

[13] S. Haykin, Neural Networks, A Comprehensive Foundation, 2nd ed., Upper Saddle River: Prentice-Hall, Inc., 1999.

[14] S. Hochreiter and J. Schmidhuber, "Long Short Term Memory," Neural Computation, vol. 9, no. 8, pp. 1735-1780, 1997.

[15] S. Hockreiter, Y. Bengio, P. Frasconi and J. Schmidhuber, "Gradient Flow in Recurrent Nets: The difficulty of Learning Long-Term Dependencies," A Field Guide to Dynamical Recurrent Neural Networks, 2001.

[16] A. Graves, A.-R. Mohamed and G. Hinton, "Speech Recognition with Deep Recurrent Neural Networks," in IEEE International Conference on Acoustics, Speech and Signal Processing, Vancouver, 2013.

[17] A. Graces, M. Liwicki, S. Fernandez, R. Bertolami, H. Bunke and J. Schmidhuber, "A Novel Connectionist System for Improved Unconstrained Handwriting Recognitions," IEEE Transactions on Pattern Analysis and Machine Intelligence, vol. 31, no. 5, pp. 855-868, 2009.

[18] T. Luong, I. Sutskever, Q. V. Le, O. Vinyals and W. Zaremba, "Addressing the Rare Word Problem in Neural Machine Translation," arXiv: 1410.8206 [cs], 2014. [Online]. Available: https://arxiv.org/abs/1410.8206.

[19] J. Donahue, L. A. Hendricks, S. Guadarrama, M. Rohrbach, S. Venugopalan, K. Saenkno and T. Darrell, "Long-Term Recurrent Convolutional Networks for Visual Recognition and Description arXiv: 1411.4389," 2014. [Online]. Available: https://arxiv.org/abs/1411.4389.

[20] C. Olah, "Colah's Blog," 2015. [Online]. Available: http://colah.github.io/posts/2015-08-Understanding-LSTMs/.

[21] W. Zaremba, I. Sutskever and O. Vinyals, "Recurrent Neural Network Regularization arXiv:1409:2329," 2015. [Online]. Available: https://arxiv.org/abs/1409.2329.

[22] N. Srivastave, G. Hinton, A. Krizhevsky, S. Ilya and R. Salakhutdinov, "Dropout: A Simple Way to Prevent Neural Networks from Overfitting," Journal of Machine Leanring Research, vol. 15, pp. 1929-1958, 2014.

[23] Y. Gal and Z. Ghahramani, "Dropout as a Bayesian Approximation: Representing Model Uncertainty in Deep Learning," in Proceedings of the 33rd International Conference on Machine Learning, New York, 2016.

[24] S. Changpinyo, M. Sandler and A. Zhmoginov, "The Power of Sparsity in Convolution Neural Networks arXiv:1702.06257," [Online]. Available: https://arxiv.org/pdf/1702.06257.pdf.

[25] R. J. Kuether and D. A. Najera, "Modeling Nonlinear Energy Dissipation of the Ministack Assembly (SAND2017-10517)," Sandia National Laboratories, Albuquerque, 2017.

[26] D. J. Segalman, "A Four-Parameter Iwan Model for Lap Type Joints," Journal of Applied Mechanics, vol. 72, no. 5, pp. 752-760, 2005.

Multilevel Monte Carlo applied to a structural engineering model with random material parameters

P. Blondeel[1], **P. Robbe**[1], **C. Van hoorickx**[2], **G. Lombaert**[2], **S. Vandewalle**[1]
[1] KU Leuven, Department of Computer Science, NUMA Section
Celestijnenlaan 200A, 3001 Leuven, Belgium
e-mail: **philippe.blondeel@kuleuven.be**

[2] KU Leuven, Department of Civil Engineering
Kasteelpark Arenberg 40, 3001 Leuven, Belgium

Abstract
Practical structural engineering problems often exhibit a significant degree of uncertainty in the properties of the materials being used, in the dimensions of the modeled structures, in the magnitude of loading forces, etc. In this paper, a cantilever/doubly clamped beam with uncertainty in the Young's modulus under a static and a dynamic load is considered. The uncertainty is modeled by means of a random variable and by means of a random field. In order to compute the statistical quantities of the static deflection and frequency response function, Multilevel Monte Carlo is combined with a Finite Element solver. This recent sampling method is based on the idea of variance reduction, and employs a hierarchy of finite element discretizations of the structural engineering model. The computational cost of the method is compared to the cost of standard Monte Carlo, demonstrating a significant speedup of up to several orders of magnitude.

1 Introduction

There is an increasing need to accurately simulate and compute solutions to engineering problems whilst taking into account model uncertainties. Methods for such uncertainty quantification and propagation in structural engineering can roughly be categorized into two groups: non-sampling methods and sampling methods. Examples of non-sampling methods are the perturbation method and the Stochastic Galerkin Finite Element method. The perturbation method is based on a Taylor series expansion in order to approximate the mean and variance of the solution [1]. The method is quite effective, but its use is restricted to models with limited number of relatively small uncertainties. The Stochastic Galerkin method, first proposed in [2], is based on a spectral representation in the stochastic space. It transforms the uncertain coefficient partial differential equation (PDE) problem by means of a Galerkin projection technique into a large coupled system of deterministic PDEs. This method allows for somewhat larger numbers of uncertainties and is quite accurate. However, it is highly intrusive and memory demanding, making its implementation cumbersome and restricting its use to rather low stochastic dimensions.

Sampling methods, on the other hand, are typically non-intrusive. Each sample corresponds to a deterministic solve for a set of specified parameter values. Two particularly popular examples are the Stochastic Collocation Method [3] and the Monte Carlo (MC) method [4]. The former samples a stochastic PDE at a carefully selected multidimensional set of collocation points. After this sampling, a Lagrange interpolation is performed leading to a polynomial response surface. From this, the relevant stochastic characteristics can easily be computed in a post-processing step. However, as is also the case for Stochastic Galerkin, the Stochastic Collocation method suffers from the curse of dimensionality: the computational cost grows expo-

nentially with the amount of random variables considered in the problem. The Monte Carlo method on the other hand, selects its samples randomly and does not suffer from the curse of dimensionality. Its drawback is its slow convergence as a function of the number of samples. The convergence of Monte Carlo can be accelerated in a variety of ways. For example, alternative non-random selections of sampling points can be used, as in Quasi-Monte Carlo [5, 6], and Latin Hypercube [7] sampling methods. Also, variance reduction techniques such as Multilevel Monte Carlo (MLMC) [8] and its generalizations, see, e.g., [9, 10], can speed up the method. Note that there also exist hybrid variants which have both a sampling and non-sampling character. This type of methods combines, for example, the stochastic finite element (SFEM) methodology with Monte Carlo sampling or a multi-dimensional cubature method, see, e.g., [11, 12].

Monte Carlo methods have already been applied in the structural engineering domain, for example in problems of structural dynamics [13]. The focus of this paper is to apply the Multilevel Monte Carlo method to a structural engineering problem, discretized by means of the Finite Element Method. A comparison with the standard Monte Carlo method will show a significant reduction in computational cost. The structure of the paper is as follows. In section 2, we formulate the mathematical model, introduce the problem statement and describe how the uncertainty is modeled. Section 3 recalls the Multilevel Monte Carlo method, and provides some additional algorithmic implementation details. In Section 4, numerical results are presented. First, a performance comparison is made between standard Monte Carlo and Multilevel Monte Carlo for a static load case. Next, results showing the uncertainty propagation in function of the type of modeled uncertainty are presented for the static loading case and the dynamic loading case. The fifth and last section offers concluding remarks and details some paths for further research.

2 The mathematical model

2.1 A clamped beam with uncertainty in the Young's modulus

The considered engineering problem is the response of a two dimensional cantilever/doubly clamped concrete beam with a static or dynamic load. The dimensions of the beam are $2.5\mathrm{m}$ (length) by $0.25\mathrm{m}$ (height).The material parameters are selected as follows: the density is set to $2500\mathrm{kg}/\mathrm{m}^3$; the Poisson ratio is 0.15; the Young's modulus is subject to some uncertainty, and has a mean value of $30\mathrm{GPa}$. Two uncertainty models will be considered. The first case consists of a homogeneous Young's modulus characterized by means of a single random variable. The second case is a heterogeneous Young's modulus represented as a random field. For both cases, we will compute the stochastic characteristics of the static response (beam deflection) and the dynamic response (frequency response function). The two considered beam cases are shown in Fig.1.



Figure 1: Cantilever beam loaded on its right end (left) and doubly clamped beam loaded in the middle (right)

2.1.1 The homogeneous case

Following [14], we opt to describe the Young's modulus in the homogeneous case by means of a univariate Gamma distribution. This distribution is characterized by a shape parameter α and a scale parameter β:

$$f(x|\alpha,\beta) = \frac{1}{\beta^{\alpha}\Gamma(\alpha)} x^{\alpha-1} e^{\left(-\frac{x}{\beta}\right)}. \tag{1}$$

The corresponding mean value and variance can be computed respectively as $\mu = \alpha\beta$ and $\sigma^2 = \alpha\beta^2$. In this paper, we will select $\alpha = 7.1633$ and $\beta = 4.1880\text{E}9$, which are based on values coming from [15]. This leads to a mean of 30GPa and a standard deviation of 11.2GPa. The Gamma distribution is plotted in Fig. 2.

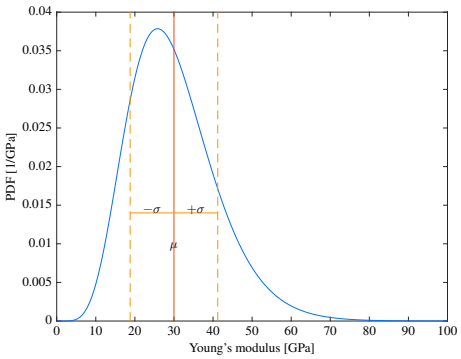


Figure 2: Probability density function (PDF) for Young's modulus with α = 7.1633 and β = 4.1880E9. Shown also is the mean μ and the standard deviation σ.

2.1.2 The heterogeneous case

The Young's modulus with spatially varying uncertainty will be represented by means of a (truncated) Gamma random field. The construction of this random field is done by means of a classical, two step process. First, a (truncated) Gaussian random field is generated, by means of a Karhunen-Loève (KL) expansion [16]. Next, this Gaussian random field is transformed into a Gamma random field by means of a memoryless transformation [17].

A Gaussian random field $Z(\mathbf{x}, \omega)$ with exponential covariance kernel is used here, i.e.,

$$C(x, y) := \sigma^2 \exp\left(-\frac{\|\mathbf{x} - \mathbf{y}\|_p}{\lambda}\right) . \tag{2}$$

We selected the 1-norm ($p = 1$), a correlation length $\lambda = 0.3$ and a standard deviation $\sigma = 1.0$. The corresponding KL expansion can then be formulated as follows

$$Z(\mathbf{x}, \omega) = \mathbb{E}[z(\mathbf{x}, .)] + \sum_{n=1}^{\infty} \sqrt{\theta_n}\xi_n(\omega)b_n(\mathbf{x}) . \tag{3}$$

$\mathbb{E}[z(\mathbf{x}, .)]$ denotes the mean of the field, and is set to zero. The $\xi_n(\omega)$ functions denote i.i.d. standard Normal random variables. The symbols θ_n and $b_n(\mathbf{x})$ denote, respectively, the eigenvalues and eigenvectors related to the covariance kernel (2). For the parameter values selected above, those eigenvalues and eigenvectors can be computed analytically [18, 2, 19, 20]. For a one-dimensional domain $[0, 1]$, they are given by

$$\theta_n^{1\text{D}} = \frac{2\lambda}{\lambda^2 w_n^2 + 1} \quad \text{and} \quad b_n^{1\text{D}}(x) = A_n \left(\sin(w_n x) + \lambda w_n \cos(w_n x)\right) . \tag{4}$$

The constants A_n are chosen in such a way as to normalize the eigenvectors: $\|b_n\|_2 = 1$. The constants w_n represent the real solutions, in increasing order, of the transcendental equation

$$\tan(w) = \frac{2\lambda w}{\lambda^2 w^2 - 1} . \tag{5}$$

For the two-dimensional case, the eigenvalues and vectors are obtained in tensorproduct way,

$$\theta_n^{2\text{D}} = \theta_{i_n}^{1\text{D}}\theta_{j_n}^{1\text{D}} \quad \text{and} \quad b_n^{2\text{D}}(\mathbf{x}) = b_{i_n}^{1\text{D}}(x_1)b_{j_n}^{1\text{D}}(x_2) \quad \text{with} \quad n = (i_n, j_n) . \tag{6}$$

In an actual implementation the number of KL terms in (3) is truncated to a finite value. This value depends on the magnitude and, more precisely, the decay of successive eigenvalues. Those eigenvalues are plotted in Fig. 3. Inclusion of the first 101 KL-terms is sufficient in order to represent 90 % of the variance of the random field. The percentage of the variance that is accounted for as a function of the number of included eigenvalues corresponds to the cumulative sum of the eigenvalues, and is also illustrated in the figure. A cumulative sum of 1 corresponds to 100% of the variance of the field being accounted for.

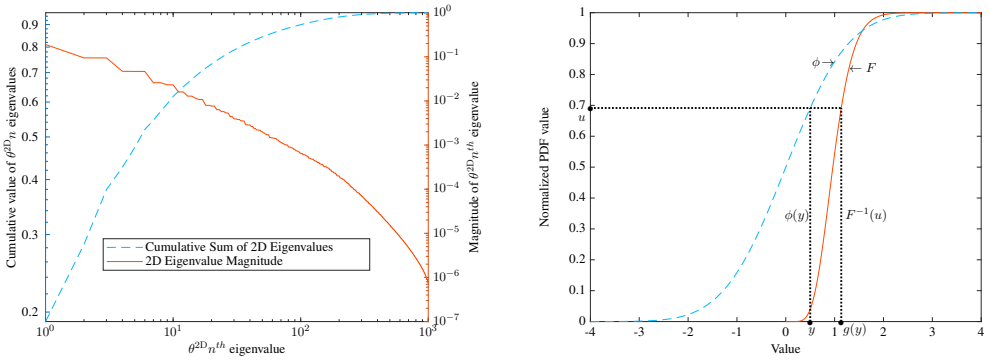


Figure 3: Left: Magnitude of the eigenvalues and their cumulative sum. Right: Memoryless transformation used to generate the Gamma random field.

Once the Gaussian field has been generated, a memoryless transformation is applied pointwise,

$$g(y) = F^{-1}\left[\phi(y)\right], \tag{7}$$

in order to obtain the Gamma random field [17]. Here, F denotes the marginal cumulative density function (CDF) of the target distribution and ϕ the marginal CDF of the standard Normal distribution. This transformation is depicted in Fig. 3 (right) with the full red line representing F, and the dashed blue line representing ϕ. Contour plots of a Gaussian random field and the corresponding Gamma random field are presented for illustration purposes in Fig. 4.



Figure 4: Gaussian random field (left) and the corresponding Gamma random field (right).

2.2 The Finite Element Method

The Finite Element method will be used to compute the static and dynamic response of the beam for the plane stress case. An equidistant, regular rectangular mesh is applied with bilinear quadrilateral elements. For the static case, this leads to the system equation of the form

$$\mathbf{K}\underline{\mathbf{u}} = \underline{\mathbf{f}}, \tag{8}$$

with $\mathbf{K}$ the global stiffness matrix, $\underline{\mathbf{f}}$ the global nodal force vector and $\underline{\mathbf{u}}$ the displacement. The global stiffness matrix and nodal force vector are obtained from the element stiffness matrices $\mathbf{K^e}$ and the element

force vectors $\underline{\mathbf{f}}^{\mathbf{e}}$. These are computed analytically by evaluation of the following integrals:

$$\mathbf{K}^{\mathbf{e}} = \int_{\Omega} \mathbf{B}^T \mathbf{D} \mathbf{B} d\Omega \quad \text{and} \quad \underline{\mathbf{f}}^{\mathbf{e}} = \int_{\Gamma_t} \mathbf{N}^T \bar{\mathbf{t}}_n d\Gamma_t. \tag{9}$$

The element nodal force vector $\underline{\mathbf{f}}^{\mathbf{e}}$ is modeled as a Neumann boundary condition, where $\bar{\mathbf{t}}_n$ stands for the surface traction specified as a force per unit area and $\mathbf{N}$ the element shape function matrix, integrated over the free element boundary Γ_t. The element stiffness matrix $\mathbf{K}^{\mathbf{e}}$ is obtained by integrating the matrix $\mathbf{B}^{\mathbf{T}}\mathbf{D}\mathbf{B}$ over the element's surface Ω. Matrix $\mathbf{B}$ is defined as $\mathbf{L}\mathbf{N}$ with $\mathbf{L}$ the derivative matrix specified below, and with $\mathbf{D}$ a 3x3 matrix containing the element wise material parameters,

$$\mathbf{L} = \begin{bmatrix} \frac{\partial}{\partial x} & 0 \\ 0 & \frac{\partial}{\partial y} \\ \frac{\partial}{\partial y} & \frac{\partial}{\partial x} \end{bmatrix} \quad \text{and} \quad \mathbf{D} = \frac{E}{1-\nu^2} \begin{bmatrix} 1 & \nu & 0 \\ \nu & 1 & 0 \\ 0 & 0 & \frac{1-\nu}{2} \end{bmatrix}. \tag{10}$$

For the dynamic response case the following equation is obtained,

$$\left(\mathbf{K} - (2\pi f)^2 \mathbf{M}\right) \underline{\mathbf{u}} = \underline{\mathbf{f}} \quad \text{with} \quad \mathbf{M}^e = \int_{\Omega} \mathbf{N}^T \rho \mathbf{N} d\Omega \,. \tag{11}$$

Matrix $\mathbf{M}$ denotes the system mass matrix obtained from the assembly of the element mass matrices $\mathbf{M}^{\mathbf{e}}$. f denotes the frequency and ρ the volumetric mass density of the material.

The assignment of random values to the Young's modulus matrix is done by means of the midpoint approach, i.e., the value is taken constant within each individual element and equal to the value of the random field at the center point of the element [21].

3 The Multilevel Monte Carlo method

3.1 Method overview

The Multilevel Monte Carlo method (MLMC) is an extension of the standard Monte Carlo (MC) method, see, e.g., [8, 22]. The method relies on a clever combination of many computationally cheap low resolution samples and a relatively small number of higher resolution, but computationally more expensive samples. The application of MLMC to our problem will be based on a hierarchy of nested finite element meshes. These meshes will be indexed from 0 to L, with 0 indicating the coarsest mesh and L the finest mesh. An example of such a hierarchy is shown in Fig. 5. It is common in the PDE setting to use a geometric relation for the number of degrees of freedom between the different levels, i.e., the number of finite elements for a mesh at level ℓ is proportional to $2^{d\ell}$, where d is the dimension of the problem.

Let $\mathbb{E}[P_L(\omega)]$, or $\mathbb{E}[P_L]$ for short, be the expected value of a particular quantity of interest P depending on a random variable ω, discretized on mesh L. The standard MC estimator for $\mathbb{E}[P_L]$ using N_L samples on mesh L, denoted as Q_L^{MC}, can be written as

$$Q_L^{\mathrm{MC}} = \frac{1}{N_L} \sum_{n=1}^{N_L} P_L(\omega^n) \,. \tag{12}$$

Multilevel Monte Carlo, on the other hand, starts from a reformulation of $\mathbb{E}[P_L]$ as a telescoping sum. The expected value of the quantity of interest on the finest mesh is expressed as the expected value of the quantity of interest on the coarsest mesh, plus a series of correction terms (or *differences*):

$$\mathbb{E}[P_L] = \mathbb{E}[P_0] + \sum_{\ell=1}^{L} \mathbb{E}[P_\ell - P_{\ell-1}] \,. \tag{13}$$

Each term in the right-hand side is then estimated separately by a standard Monte Carlo method with N_ℓ samples, i.e.,

$$Q_L^{\text{MLMC}} = \frac{1}{N_0}\sum_{n=1}^{N_0} P_0(\omega^n) + \sum_{\ell=1}^{L}\left\{\frac{1}{N_\ell}\sum_{n=1}^{N_\ell}\left(P_\ell(\omega^n) - P_{\ell-1}(\omega^n)\right)\right\}, \tag{14}$$

where Q_L^{MLMC} is the Multilevel Monte Carlo estimator for the expected value $\mathbb{E}[P_L]$, which is a discrete approximation of the continuous solution $\mathbb{E}[P]$. The mean square error (MSE) is defined as

$$\text{MSE}(Q_L^{\text{MLMC}}) \equiv \mathbb{E}\left[\left(Q_L^{\text{MLMC}} - \mathbb{E}\left[P\right]\right)^2\right] = \mathbb{V}\left[Q_L^{\text{MLMC}}\right] + \left(\mathbb{E}\left[Q_L^{\text{MLMC}}\right] - \mathbb{E}\left[P\right]\right)^2, \tag{15}$$

with $\mathbb{V}$ denoting the variance. The MLMC estimator in (14) can be written as a sum of $L+1$ estimators for the expected value of the difference on each level, i.e.,

$$Q_L^{\text{MLMC}} = \sum_{\ell=0}^{L} Y_\ell, \quad \text{where} \quad Y_\ell = \frac{1}{N_\ell}\sum_{n=1}^{N_\ell}\left(P_\ell(\omega^n) - P_{\ell-1}(\omega^n)\right). \tag{16}$$

where we defined $P_{-1} \coloneqq 0$.

Because of the telescoping sum, the MLMC estimator is an unbiased estimator for the quantity of interest on the finest mesh, i.e.,

$$\mathbb{E}[P_L] = \mathbb{E}[Q_L^{\text{MLMC}}]. \tag{17}$$

Denoting by V_ℓ the variance of the difference $P_\ell - P_{\ell-1}$, the variance of the estimator can be written as

$$\mathbb{V}[Q_L^{\text{MLMC}}] = \sum_{\ell=0}^{L}\frac{V_\ell}{N_\ell}. \tag{18}$$

In order to ensure that the MSE is below a given tolerance ϵ^2, it is sufficient to enforce that the variance $\mathbb{V}[Q_L^{\text{MLMC}}]$ and the squared bias $(\mathbb{E}[P_L - P])^2$ are both less than $\epsilon^2/2$. The condition on the variance of the estimator can be used to determine the number of samples needed on each level ℓ. Following the classic argument by Giles in [8], we minimize the total cost of the MLMC estimator

$$\text{cost}(Q^{\text{MLMC}}) = \sum_{\ell=0}^{L} N_\ell C_\ell, \tag{19}$$

where C_ℓ denotes the cost to compute a single realization of the difference $P_\ell - P_{\ell-1}$, subject to the constraint

$$\sum_{\ell=0}^{L}\frac{V_\ell}{N_\ell} \leq \frac{\epsilon^2}{2}. \tag{20}$$

Treating the N_ℓ as continuous variables, we find

$$N_\ell = \frac{2}{\epsilon^2}\sqrt{\frac{V_\ell}{C_\ell}}\sum_{\ell=0}^{L}\sqrt{V_\ell C_\ell}. \tag{21}$$

Note that if $\mathbb{E}[P_\ell] \to \mathbb{E}[P]$, then $V_\ell \to 0$ as ℓ increases. Hence, the number of samples N_ℓ will be a decreasing function of ℓ. This means that most samples will be taken on the coarse mesh, where samples are cheap, and increasingly fewer samples are required on the finer, but more expensive meshes. In practice, the number of samples must be truncated to $\lceil N_\ell \rceil$, the least integer larger than or equal to N_ℓ.

Using (21), the total cost of the MLMC estimator can be written as

$$\text{cost}(Q^{\text{MLMC}}) = \frac{2}{\epsilon^2}\left(\sum_{\ell=0}^{L}\sqrt{V_\ell C_\ell}\right)^2. \tag{22}$$

This can be interpreted as follows. When the variance V_ℓ decreases faster with increasing level ℓ than the cost increases, the dominant computational cost is located on the coarsest level. The computational cost is then proportional to V_0C_0, which is small because C_0 is small. Conversely, if the variance decreases slower with increasing level ℓ than the cost increases, the dominant computational cost will located on the finest level L, and be proportional to V_LC_L. This quantity is small because V_L is small. For comparison, the computational cost of a Monte Carlo simulation that reaches the same accuracy is proportional to V_0C_L.

In our numerical results presented next, we will compare the cost of the MLMC estimator to the cost of a standard MC simulation, both in actual runtime (seconds) and in some normalized cost measure. This cost is chosen such that the time needed to obtain a sample on the coarsest mesh (level zero) is equal to a cost of one unit. When using the standard geometric mesh hierarchy, the cost for a single sample on level ℓ is proportional to $2^{\gamma\ell}$. The factor γ is determined by the efficiency of the solver. The advantage of using this normalized cost is that it decouples the cost of the simulation from the specific computer hardware. This makes it easier to compare results coming from different machines. This is not the case when presenting the runtimes of the algorithm, which are machine dependent.

The second term in (15) is used to determine the maximum number of levels L. A typical MLMC implementation is level-adaptive, i.e, starting from a coarse finite element mesh, finer meshes are only added if required to reach a certain accuracy. Assume that the convergence $\mathbb{E}[P_\ell] \to \mathbb{E}[P]$ is bounded as $|\,\mathbb{E}[P_\ell - P]| = \mathcal{O}(2^{-\alpha\ell})$. Then, we can use the heuristic

$$|\mathbb{E}[P_L - P]| = \left|\sum_{\ell=L+1}^{\infty}\mathbb{E}[P_\ell - P_{\ell-1}]\right| \approx \frac{|\mathbb{E}[P_L - P_{L-1}]|}{2^\alpha - 1} \tag{23}$$

and check for convergence using $|\,\mathbb{E}[P_L - P_{L-1}]|/(2^\alpha - 1) \leq \epsilon/\sqrt{2}$, see [8] for details.

For completion, we now mention the central MLMC complexity theorem. We refer to [22] for a proof.

Theorem 1. *Given the positive constants $\alpha, \beta, \gamma, c_1, c_2, c_3$ such that $\alpha \geq \frac{1}{2}\min(\beta, \gamma)$ and assume that the following conditions hold:*

1. $|\mathbb{E}[P_\ell - P]| \leq c_1 2^{-\alpha\ell}$,
2. $V_\ell \leq c_2 2^{-\beta\ell}$ *and*
3. $C_\ell \leq c_3 2^{\gamma\ell}$.

Then, there exists a positive constant c_4 such that for any $\epsilon < \exp(-1)$ there exists an L and a sequence $\{N_\ell\}_{\ell=0}^{L}$ for which the multilevel estimator, Q_L^{MLMC} has an MSE $\leq \epsilon^2$*, and*

$$\text{cost}(Q^{\text{MLMC}}) \leq \begin{cases} c_4\epsilon^{-2} & \text{if} \quad \beta > \gamma \\ c_4\epsilon^{-2}\,(\log\ \epsilon)^2 & \text{if} \quad \beta = \gamma, \\ c_4\epsilon^{-2-(\gamma-\beta)/\alpha} & \text{if} \quad \beta < \gamma. \end{cases} \tag{24}$$

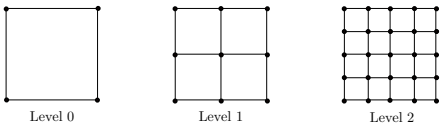


Figure 5: Illustrative example of a hierarchy used in the MLMC method

3.2 Implementation aspects

The MLMC method is non-intrusive. Only an interface between the Finite Element solver routine and the multilevel routine is necessary. All modules used in the simulation are written in MATLAB. All simulations have been run on a workstation equipped with 24 Intel Xeon E5645 CPU's, each clocked at 2.40 GHz, and a total of 49 GB RAM. Just as the classic MC method, the MLMC method is *embarrassingly parallel*, so parallel sampling is possible.

4 Numerical Results

In this section, we discuss our numerical experiments with the MLMC method. We consider the static and dynamic load case, using both a homogeneous and a heterogeneous uncertain Young's modulus.

4.1 Comparison between MC and MLMC

First, we compare the efficiency of MLMC and MC for the static response of the doubly clamped beam shown in Fig. 1 (right). The quantity of interest is the node with the maximum transversal deflection, which coincidently also corresponds to the node with the largest system variance. The coarsest finite element mesh (level 0) consists of 410 degrees of freedom, while the finest finite element mesh considered (level 4) consists of 83330 degrees of freedom.

Fig. 6 compares the actual simulation time needed to reach a certain tolerance ϵ on the root mean square error (RMSE) for both standard MC and MLMC, for a homogeneous (left) and heterogeneous uncertain Young's modulus (right). Our MLMC method consistently outperforms the standard MC method, with speedups up to a factor ten or more. In Tab. 1, we summarize the results expressed in actual simulation time and in standard cost. For MC, some values of the RMSE have been omitted. This is due to the long computation time, which is in the order of days. Also note that the MC simulation is run at the finest level L of the corresponding MLMC simulation, where L is chosen according to (23). This explains the sudden jump in the MC simulation time to the right of Fig. 6.

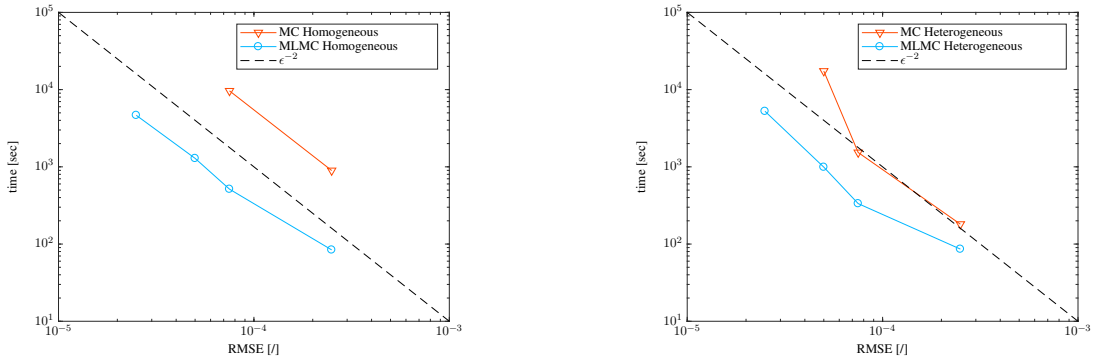


Figure 6: Actual simulation time in seconds as a function of the desired tolerance on the RMSE applied to the doubly clamped beam in Fig. 1 (right) for a homogeneous (left) and heterogeneous (right) Young's modulus.

RMSE [/]	Homogeneous Young's modulus				Heterogeneous Young's modulus			
	Times [sec]		Norm. Cost		Times [sec]		Norm. Cost	
	MLMC	MC	MLMC	MC	MLMC	MC	MLMC	MC
2.5E-4	84	896	4.75E3	8.43E4	86	181	2.55E3	1.28E4
7.5E-5	514	9632	5.38E4	9.84E5	334	1533	3.00E4	1.29E5
5.0E-5	1287	-	1.30E5	-	991	17380	1.09E5	1.99E6
2.5E-5	4650	-	5.14E5	-	5244	-	5.63E5	-

Table 1: Actual simulation time in seconds and normalized cost for MLMC and MC applied to the doubly clamped beam in Fig. 1 (right) for a homogeneous and heterogeneous Young's modulus.

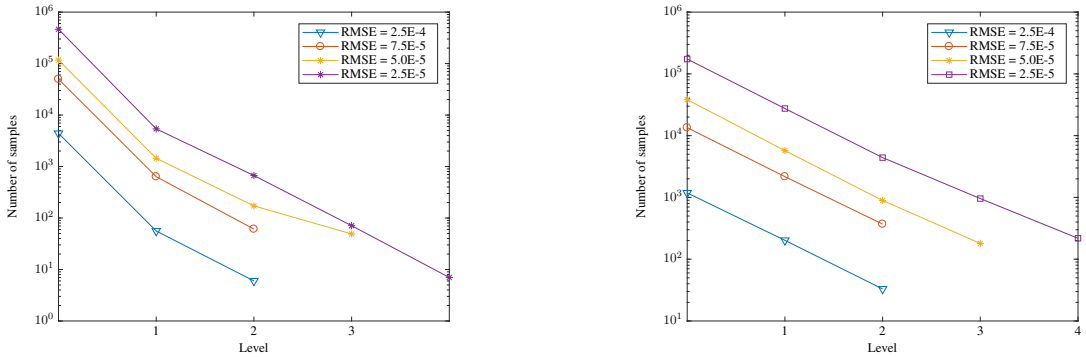


Figure 7: Total number of samples on each level for different tolerances ϵ on the RMSE using a homogeneous (left) and heterogeneous (right) Young's modulus.

RMSE [/]	Homogeneous Young's modulus							Heterogeneous Young's modulus						
	MLMC						MC	MLMC						MC
	level					equivalent	level	level					equivalent	level
	0	1	2	3	4	Max	Max	0	1	2	3	4	Max	Max
2.5E-4	4408	56	6	/	/	262	4651	1183	202	33	/	/	153	771
7.5E-5	49816	635	61	/	/	2697	49308	13477	2169	370	/	/	1568	6750
5.0E-5	116934	1446	172	49	/	1651	-	38322	5728	893	180	/	918	16700
2.5E-5	464180	5393	669	71	7	1091	-	173742	27492	4412	958	218	1374	-

Table 2: Number of samples for MLMC and MC

Fig. 7 shows the number of samples over the different levels in function of the desired tolerance. Note that the number of samples is decreasing as the level ℓ increases, as required. Numerical values for N_ℓ are repeated in Tab. 2. In order to make a better comparison between the cost of MC and MLMC, we also list the equivalent number of samples on the finest level L, that is, the number of samples on level L that would yield a cost equal to the MLMC cost. These results show a considerably lower sample size in favor of MLMC.

Comparing the actual number of samples of MLMC with MC, we notice that when the Young's modulus is homogeneous, the number of samples on the coarsest level in the MLMC simulation is of the same order of magnitude as the number of samples on the finest level L in the MC simulation. This makes it easier to estimate the amount of samples that would be needed for a MC simulation given the results of a MLMC simulation. However, when the Young's modulus is heterogeneous, this number of samples is not the same. The reason behind this stems from the fact that on this coarsest level a very rough approximation of the random field is used for the MLMC simulation, while the MC simulation uses a random field equal to the

random field corresponding to the finest level of MLMC. It is thus probable that on the coarsest level, the variability of the random field is not fully and adequately captured. In order to better illustrate this point, the same Gaussian random field at different resolution levels is shown in Fig. 8. As can be seen, a sufficiently high number of points is required to capture the variability.

In order to validate this hypothesis, MLMC simulations with a heterogeneous Young's modulus have been rerun with a finer coarsest level. The results are presented in Tab. 3.

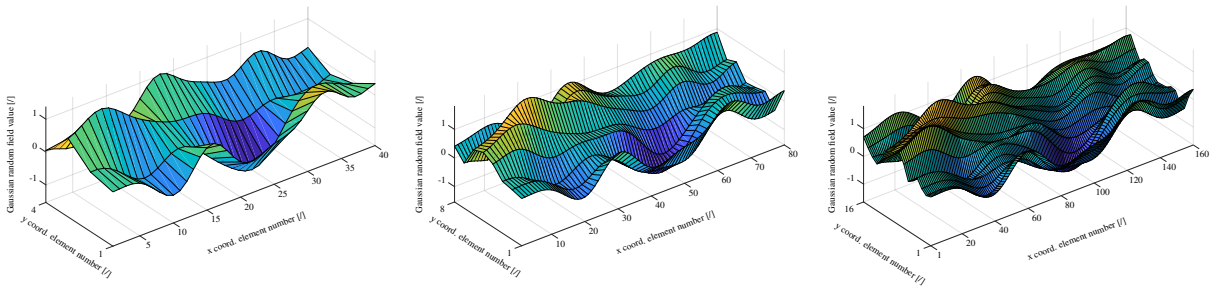


Figure 8: Realizations of a Gaussian random field on level 0 (left), level 1 (middle), level 2 (right).

RMSE [/]	MLMC level					MC level
	0	1	2	3	4	Max
2.5E-4	/	738	38	10	/	649
7.5E-5	/	8628	468	97	/	7178
5.0E-5	/	19477	969	234	/	15947

Table 3: Number of samples for MLMC and MC for a heterogeneous Young's modulus with a finer coarsest level

As can be seen from Tab. 3, the number of samples of MC is equal in magnitude to the number of samples on the coarsest level of MLMC.

4.2 Rate verification

In this section, we estimate the rates α, β and γ from Theorem 1, see Tab. 4. We list the online estimated rates for various tolerances ϵ on the RMSE, corresponding to the tolerances considered in Fig. 6. Following the results in this table, it is possible to estimate the asymptotic cost of the MLMC estimator, using the different regimes from Eq. (24). Since $\beta > \gamma$ in all cases, we expect an optimal cost proportional to ϵ^{-2}. This is indeed what we observe in the numerical experiments in Fig. 6.

RMSE [/]	Homogeneous Young's modulus			Heterogeneous Young's modulus		
	α	β	γ	α	β	γ
2.5E-4	1.97	4.38	2.09	2.18	3.22	2.03
7.5E-5	2.03	5.11	2.16	2.13	2.99	2.13
5.0E-5	1.88	4.03	2.10	1.86	3.08	2.30
2.5E-5	1.87	3.80	2.22	1.61	3.12	2.17

Table 4: Parameters for the MLMC algorithm

Fig. 9 shows the behavior of the expected value and the variance of the quantity of interest P_ℓ, and of the difference $P_\ell - P_{\ell-1}$, in case of a tolerance ϵ equal to 2.5E-5. Note that the mean and the variance of P_ℓ over the different levels remains constant while the variance and the mean of the differences between two successive levels continuously decreases. The rates α and β can be read off as the slope of the red lines.

In case where the Young's modulus is homogeneous, Fig. 9 (left), the variance corresponding to the finest level is lower than the variance on the previous levels. This phenomenon can be explained by looking at the amount of samples on that level, used to estimate the variance. Only seven samples where taken, if more samples would have been taken on this level, the variance would be equal to the variance on the other levels.

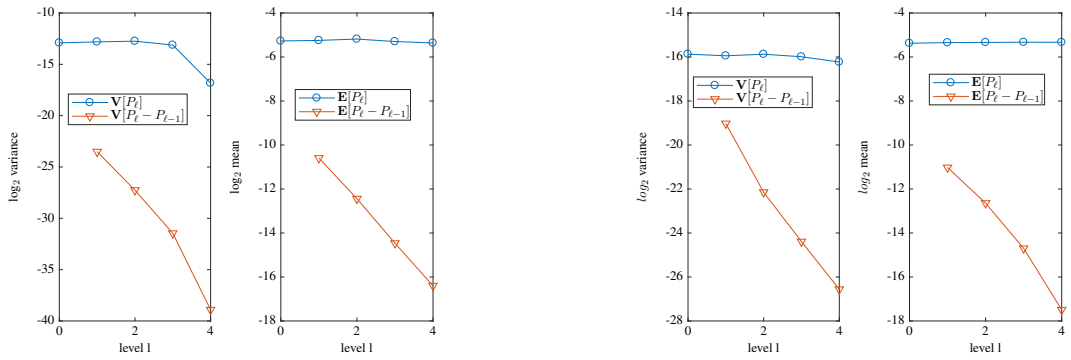


Figure 9: Rates for when the Young's modulus is homogeneous (left) and heterogeneous (right), in case of a tolerance ϵ equal to 2.5E-5

4.3 Visualization of the solution

In this part, the static response, i.e. the displacement of the beam, and the dynamic response, i.e. the frequency response functions (FRF) are shown. An important aspect to take into consideration is that in order to obtain the results for the static response only one Multilevel Monte Carlo run is required. This is in contrast to the solution for the dynamic response, which requires multiple independent Multilevel Monte Carlo runs, one run for each individual frequency.

Solutions that will be shown for the static response are the transverse displacements of the nodes along the top side op the beam. Solutions shown for the dynamic response are frequency responses functions for a single node of the finite element mesh. The node chosen for the representation of the FRF coincides with the one that has the largest variance of all the nodes which make up the mesh. This node also determines the optimal amount of samples per level computed according to (21). In case of the static response, the nodal displacement with the largest variance determines the optimal amount of samples per level.

4.3.1 Static Response

In this part we show the displacement of the beam under a static load including uncertainty bounds. The beam configuration is a doubly clamped beam which is loaded at mid span, as shown in Fig. 1 (right).

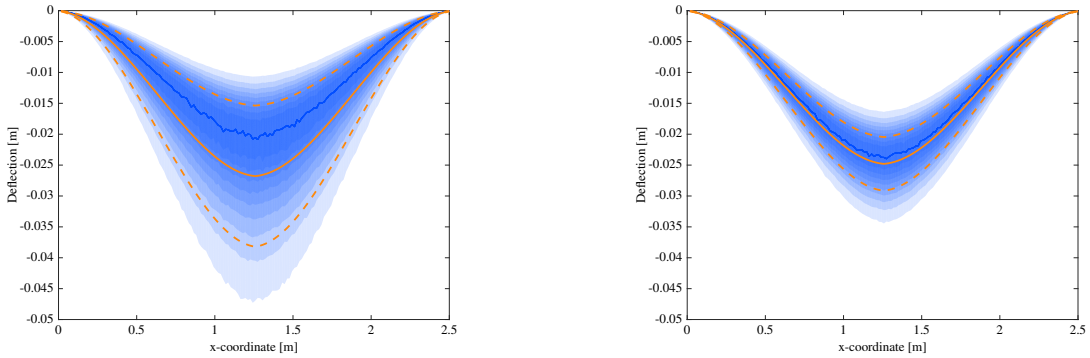


Figure 10: Deflection of the beam for when the Young's modulus is homogeneous (left) and heterogeneous (right)

Fig. 10 shows the deflection of the beam with a homogeneous Young's modulus (left) and with a heterogeneous Young's modulus (right). The full orange line represents the average of the displacement, the dashed orange lines are the 1σ bounds equidistant around the average, which of course only make sense in case of a Normal distribution. The shades of blue represent the PDF, with the dark blue line corresponding to the most probable value. As can be observed from Fig. 10 (right), the average value and the most probable value of the PDF tend to coincide for the heterogeneous case. Here, the PDF of the displacement closely resembles that of a Normal distribution. This is however not the case when the Young's modulus is homogeneous. Then the distribution of the solution has a non-negligible skewness.

Fig. 11 and Fig. 12 show a cut-through in order to better illustrate how the shades of blue represent the PDF.



Figure 11: Visualization of the PDF when the Young's modulus is homogeneous, AB cut-through (left), beam displacement (right)

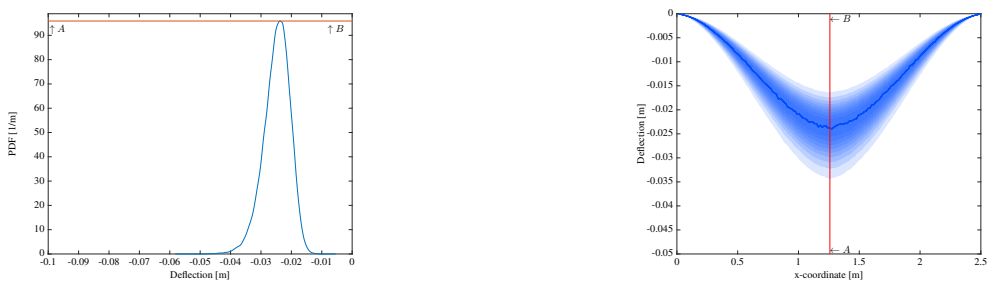


Figure 12: Visualization of the PDF when the Young's modulus is heterogeneous, AB cut-through (left), beam displacement (right)

4.3.2 Dynamic Response

For the dynamic response, the solution is a frequency response function (FRF). The beam configuration we consider, is a cantilever beam clamped on the left side and loaded on the right side, as shown in Fig. 1 (left), with a dynamic load. In order to ensure the correct representation of the dynamic response, and to determine the minimum number of finite elements required, the bending wavelength, $\lambda_{\min}$, must be evaluated for each frequency

$$\lambda_{\min} = \sqrt{\frac{2\pi}{f_{\max}}} \sqrt[4]{\frac{EI}{\rho A}}, \tag{25}$$

with E the mean Young's modulus, I the moment of inertia, A the area, ρ the density, $f_{\max}$ the highest simulated frequency, and $\lambda_{\min}$ the smallest obtained wavelength for that highest input frequency.

For the beam configuration used here, it has been checked that at least six elements are used to represent the wavelength on the coarsest grid for the highest simulated frequency, which in this case is 400 Hz.

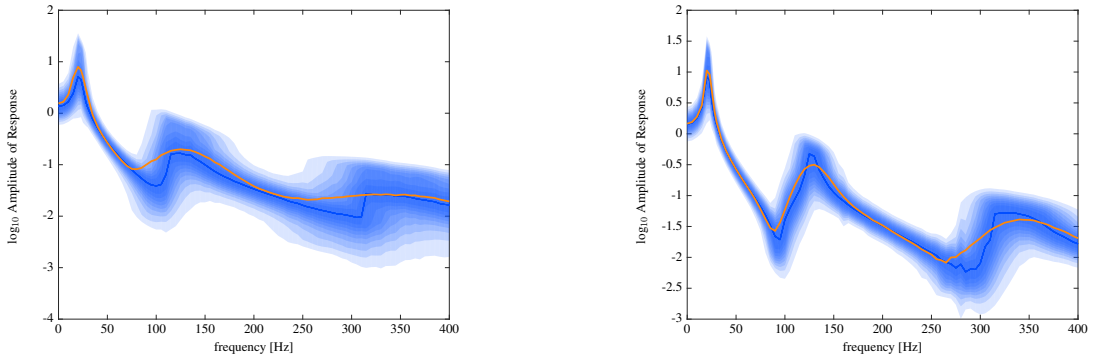


Figure 13: Dynamic Responses of the beam for when the Young's modulus is homogeneous (left) and heterogeneous (right)

The FRF results are presented in Fig. 13. As was the case for the static response, the shades of blue represent the PDF, with the blue line being the most probable value, and the orange line the average value. As can be observed, the uncertainty bounds for the FRF when the Young's modulus is homogeneous, Fig. 13 (left), are wider and more spread out than in the case of a heterogeneous Young's modulus, Fig. 13 (right). This discrepancy is due to the fact that in case of a homogeneous Young's modulus, the resonance frequency will be shifted for each different sample. Averaging all these samples gives rise to a broad and wide uncertainty bound. Fig. 14 shows the resulting FRF for ten realizations. In case of a heterogeneous Young's modulus, the different samples average out in each point. This gives rise to much smaller uncertainty bounds.

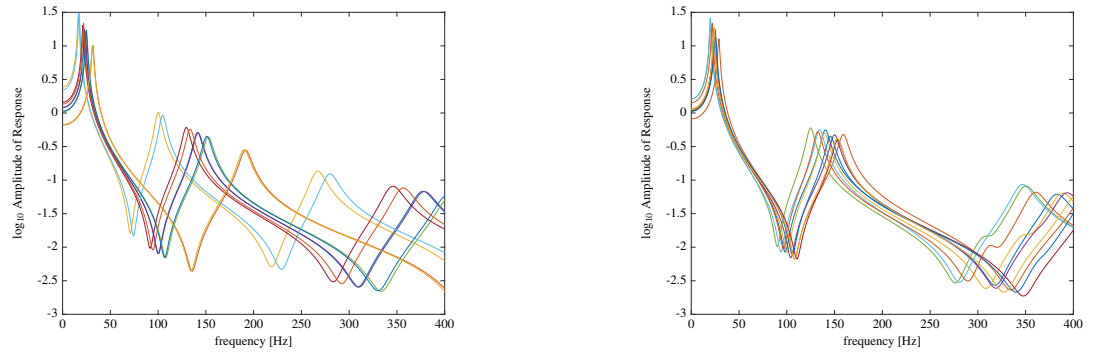


Figure 14: Ten different samples for when the Young's modulus is homogeneous (left) and heterogeneous (right)

An important inequality that must hold for MLMC to work well is

$$\mathbb{V}[P_1 - P_0] \ll \mathbb{V}[P_1]. \tag{26}$$

It has been observed empirically that (26) is not necessarily fulfilled for certain frequencies for the dynamic response in case of a heterogeneous Young's modulus. The reason for this phenomenon appears to be closely linked to the resolution of random fields on the different levels, as discussed in §4.1. In order to remedy this, we use the following strategy. Using a small number of samples, the magnitude of $\mathbb{V}[P_1] - \mathbb{V}[P_1 - P_0]$ is estimated. When the estimation is below a certain threshold T, the coarsest level is discarded and the algorithm is started on a finer mesh. We write this condition in a $\log_2$ base, in order not to lose consistency with Fig. 9, which depict the rates in a $\log_2$ base. The estimation after simplification is written as

$$\log_2 \left(\frac{\mathbb{V}[P_1]}{\mathbb{V}[P_1 - P_0]} \right) > \log_2 T. \tag{27}$$

For the experiments reported here, we selected the right-hand side of (27) heuristically to be equal to 2.3.

5 Conclusion

It this work, it has been demonstrated that the Multilevel Monte Carlo method provides a significant computational cost reduction and speedup in comparison with the standard Monte Carlo method for computing the stochastics of the response in a structural engineering problem. This has been show by means of actual computing times and normalized computational costs. Speedups are typically of the order of a factor ten for moderate accuracies and can be even much higher for higher accuracies. In addition, figures depicting the static response and the dynamic response have been presented with uncertainty bounds. To model the uncertainty in the Young's modulus, we considered both a homogeneous case, represented by a single random variable, and a heterogeneous case, modeled by means of a random field. Further paths of research will focus on non-linear test cases, and ways to exploit the similarities between the responses for neighboring frequencies.

Acknowledgements

This research was funded by project IWT/SBO EUFORIA: "Efficient Uncertainty quantification For Optimization in Robust desgn of Industrial Applications" (IWT-140068) of the Agency for Innovation by Science and Technology, Flanders, Belgium. The authors gratefully acknowledge the support from the research council of KU Leuven though the funding of project C16/17/008 "Efficient methods for large-scale PDE-constrained optimization in the presence of uncertainty and complex technological constraints".

References

[1] M. Kleiber, T. D. Hien, *The stochastic finite element method: basic perturbation technique and computer implementation*, Wiley, Chichester (1992)

[2] R. G. Ghanem, P. D. Spanos, *Stochastic Finite Elements: A Spectral Approach*, Dover Publications, New York (2003)

[3] I. Babuška, F. Nobile, R. Tempone, *A stochastic collocation method for elliptic partial differential equations with random input data*, SIAM Journal on Numerical Analysis, Vol. 45, No. 3, Society for Industrial and Applied Mathematics (2007), pp. 1005-1034.

[4] G. S. Fishman, *Monte Carlo: concepts, algorithms and applications*, Springer-Verlag, New York (1996).

[5] R. E. Caflisch, *Monte Carlo and quasi-Monte Carlo methods*, Acta Numerica, Vol. 7, Cambridge University Press (1998), pp. 1-49.

[6] H. Niederreiter, *Monte Carlo and quasi-Monte Carlo methods*, Springer, Berlin (2004).

[7] W.-L. Loh, *On Latin hypercube sampling*, The Annals of Statistics, Vol. 24, No. 5, Institute of Mathematical Statistics (1996), pp. 2058-2080.

[8] M. B. Giles, *Multilevel Monte Carlo Path Simulation*, Operations Research, Vol. 56, No. 3, Institute for Operations Research and the Management Sciences (2008), pp. 607-617.

[9] P. Robbe, D. Nuyens, S. Vandewalle, *A Multi-Index Quasi-Monte Carlo Algorithm for Lognormal Diffusion Problems*, SIAM Journal on Scientific Computing, Vol. 39, No. 5, Society for Industrial and Applied Mathematics (2017), pp. S851-S872.

[10] P. Robbe, D. Nuyens, S. Vandewalle, *A dimension-adaptive multi-index Monte Carlo method applied to a model of a heat exchanger* in P. Glyn and A. Owen, editors, *Proceedings of MCQMC2016, Monte Carlo and Quasi-Monte Carlo Methods* , Springer-Verlag, Berlin, 2018 (accepted for publication).

[11] R. Ghanem, *Hybrid stochastic finite elements and generalized Monte Carlo simulation*, Journal of Applied Mechanics (ASME), Vol. 65, No. 4, The American Society of Mechanical Engineers (1998), pp. 1004-1009.

[12] S. Acharjee, N. Zabaras, *A non-intrusive stochastic Galerkin approach for modeling uncertainty propagation in deformation processes*, Computers and Structures, Vol. 85, No. 5-6, Elsevier Ltd (2007), pp. 244-254.

[13] M. Shinozuka, *Monte Carlo solution of structural dynamics*, Computers and Structures, Vol. 2, Pergamon Press (1972), pp. 855-874.

[14] Y. Liu, M. D. Shields, *A direct simulation method and lower-bound estimation for a class of gamma random fields with applications in modelling material properties*, Probabilistic Engineering Mechanics, Vol. 47, Elsevier Ltd (2017), pp. 16-25.

[15] E. Simoen, *Uncertainty quantification in finite element model updating (PhD thesis)*, KU Leuven, Leuven (2013).

[16] M. Loève, *Probability theory*, Springer, New York (1977).

[17] M. Grigoriu, *Simulation of Stationary Non-Gaussian Translation Processes*, Journal of Engineering Mechanics, Vol. 124, No. 2, American Society of Civil Engineers (1998), pp. 121-126.

[18] K. A. Cliffe, M. B. Gilles, R. Scheichl, A. L. Teckentrup, *Multilevel Monte Carlo methods with applications to elliptic PDEs with random coefficients*, Computing and Visualization in Science, Vol. 14, No. 3, Springer (2011), pp. 3-15.

[19] R. Ghanem, *Probabilistic characterization of transport in heterogeneous media*, Computer Methods in Applied Mechanics and Engineering, Vol. 158, No. 3-4, Elsevier Ltd (1998), pp. 199-220.

[20] D. Zhang, Z. Lu, *An efficient, high-order perturbation approach for flow in random porous media via Karhunen-Loève and polynomial expansions*, Journal of Computational Physics, Vol. 194, No.2, Elsevier Ltd (2004), pp. 773-794.

[21] J. Li, J. Chen, *Stochastic Dynamics of Structures*, Wiley, Asia (2010)

[22] M. B. Giles, *Multilevel Monte Carlo methods*, Acta Numerica, Vol. 24, Cambridge University Press (2015), pp. 259-328.

On the non-parametric modelling of uncertain elastic joints in periodic structures

A.T. Fabro[1], **J.-M. Mencik**[2]
[1]Department of Mechanical Engineering, University of Brasilia, Campus Darcy Ribeiro, CEP 70910-900, Brasilia-DF, Brazil
e-mail: **fabro@unb.br**

[2]INSA Centre Val de Loire, Université d'Orléans, Université de Tours, Laboratoire de Mécanique Gabriel Lamé, 3 Rue de la Chocolaterie, 41034 Blois, France

Abstract

This work focuses on the analysis of periodic structures which are connected to elastic joints. Emphasis is on the use of non-parametric approaches to assess the reflection and transmission coefficients of waves in periodic structures which are connected to joints with uncertain mass, damping and stiffness matrices. The wave finite element method is used to model the periodic structures and the Craig-Bampton component mode synthesis procedure is used to model the joints. Several non-parametric approaches are proposed to assess the uncertainty in the scattering matrix of the joints. Parametric approaches are also proposed when the component modes of the joints are perturbed and when the material parameters of the joints are described in terms of random fields. Numerical experiments are carried out by considering two aluminium plates (waveguides), undergoing in-plane vibrations, connected to a composite plate (joint). For each approach, the effects of the randomness of the joint on the wave reflection and transmission coefficients are assessed.

1 Introduction

Structures often consist of mechanical components connected to elastic joints which can be a great source of uncertainties. These are related not only to the mechanical parameters of the joints, but also to the numerical model itself. Such uncertain joints include bolts, welds and connection angles, for instance, and can have a strong impact on the variability of the response of built-up structures. In addition, each type of joint or connection may involve different sources of uncertainty, hence adding extra complexity on engineering design [1].

The issue of identifying the dynamic behaviour of joints is not a new one and has been investigated in terms of energy flow [2], vibrational modes [3] and wave reflection and transmission coefficients [4]. The modelling of joints can be very challenging due to several local effects [5], which requires the inclusion of some level of uncertainty [1]. Typically, the mechanical properties of the joints are considered uncertain [6] and are usually handled by a parametric approach in which case a stochastic model of the parameters is used. On the other hand, the analysis of uncertainties in the numerical model requires a non-parametric approach [7], where random matrices are used to describe the mass, damping and stiffness matrices of the joints. Among the non-parametric approaches is the random matrix theory (RMT), which, for instance, has been used to model non-parametric uncertainties in dynamic substructuring [8, 9, 10].

This work focuses on the analysis of periodic structures which are connected to elastic joints. The periodic structures under concern are made up of identical substructures of arbitrary 2D or 3D shapes, which are assembled along a straight direction. Also, the joints can be of arbitrary shape and are usually described

with the finite element (FE) method. Such mechanical systems are frequently encountered in mechanical engineering, e.g., in the automotive industry (chassis frame). Emphasis is on the use of a non-parametric approach to assess the reflection and transmission coefficients of waves in periodic structures which are connected to joints with uncertain mass, damping and stiffness matrices. To achieve this task, the wave finite element (WFE) method is used to model the periodic structures and the Craig-Bampton (CB) component mode synthesis procedure is used to model the joints. The WFE method is an efficient numerical tool to assess the wave propagation in periodic structures [11, 12, 13] which has been applied to calculate the reflection and transmission coefficients in joints [14, 15]. The inclusion of parametric [16, 17, 18] and non-parametric uncertainties [19] has also been considered. Within the CB framework, the mass, damping and stiffness matrices of joints are projected on reduced vector bases of static modes and fixed-interface modes. As a result, the scattering matrix of the joints, which provides the reflection and transmission coefficients for the waves in the connected periodic structures, can be computed efficiently.

Hence, a numerical strategy is proposed to assess the uncertainty in the scattering matrices of the joints which results when the reduced mass, damping and stiffness matrices — i.e. those issued from the CB reduced bases — are described with random matrices. For comparison purpose, several parametric models of the joints are also investigated.

The rest of the paper is organized as follows. Section 2 presents the FE and CB modellings of the joints. Section 3 presents the strategy to compute the scattering matrix — i.e., a matrix with reflection and transmission coefficients — of the joints. Section 4 introduces the probabilistic modelling. Two non-parametric approaches which use random mass, damping and stiffness matrices for modelling the joints are presented. Also, three parametric approaches are proposed. The first two ones involve perturbating the component modes of the joints; the third one is commonly used and invokes random fields for describing the Young's modulus and the mass density of the joints. Numerical experiments are brought in Section 5. These concern two identical aluminium plates, undergoing in-plane vibrations, connected to a composite plate (joint). The statistics for some wave reflection and transmission coefficients are analyzed and discussed.

2 Joint modelling

Consider the FE model of an elastic joint which connects two (or more) periodic structures. In the frequency domain, the dynamic equilibrium equation of the joint is given by $\mathbf{D}\mathbf{q} = \mathbf{F}$, where $\mathbf{D}$ is the dynamic stiffness matrix (DSM) of the joint, expressed by:

$$\mathbf{D} = -\omega^2\mathbf{M} + \mathtt{i}\omega\mathbf{C} + \mathbf{K}, \tag{1}$$

where $\mathbf{M}$, $\mathbf{C}$ and $\mathbf{K}$ denote the mass, damping and stiffness matrices, respectively. Here, assumption is made that the damping matrix $\mathbf{C}$ is proportional to the stiffness matrices, i.e., $\mathbf{C} = \alpha\mathbf{K}$ where α is a positive small real number ($\alpha \ll 1$). Also, $\mathbf{q}$ and $\mathbf{F}$ are the displacement and force vectors, respectively. The dynamic stiffness matrix can be further partitioned into internal DOFs $(\mathtt{I})$ and interface DOFs $(\mathtt{B})$. By assuming that the internal DOFs are free from excitation sources, this yields:

$$\mathbf{D}\mathbf{q} = \begin{bmatrix} \mathbf{D}_{\mathtt{II}} & \mathbf{D}_{\mathtt{IB}} \\ \mathbf{D}_{\mathtt{BI}} & \mathbf{D}_{\mathtt{BB}} \end{bmatrix} \begin{bmatrix} \mathbf{q}_{\mathtt{I}} \\ \mathbf{q}_{\mathtt{B}} \end{bmatrix} = \begin{bmatrix} \mathbf{0} \\ \mathbf{F}_{\mathtt{B}} \end{bmatrix}. \tag{2}$$

Denote as $n_{\mathtt{I}}$ and $n_{\mathtt{B}}$ the numbers of internal and interface DOFs, respectively, and consider the so-called fixed-interface modes of the joint $\boldsymbol{\chi}_k^{\mathtt{fix}}$ $(k = 1, \ldots, n_{\mathtt{I}})$ which are solutions of the following generalized eigenproblem:

$$\mathbf{K}_{\mathtt{II}}\boldsymbol{\chi}_k^{\mathtt{fix}} = \omega_k^2\mathbf{M}_{\mathtt{II}}\boldsymbol{\chi}_k^{\mathtt{fix}}, \tag{3}$$

where ω_k^2 and $\boldsymbol{\chi}_k^{\mathtt{fix}}$ are the eigenvalues — i.e., the square of the eigenpulsations ω_k of the fixed-interface modes — and the eigenvectors of the matrix pencil $(\mathbf{K}_{\mathtt{II}}, \mathbf{M}_{\mathtt{II}})$, respectively. The related $n_{\mathtt{I}} \times n_{\mathtt{I}}$ matrix

of fixed-interface modes is written as $\mathbf{X}^{\mathtt{fix}} = [\boldsymbol{\chi}_1^{\mathtt{fix}} \cdots \boldsymbol{\chi}_{n_\mathtt{I}}^{\mathtt{fix}}]$. Also, define the so-called $n_\mathtt{I} \times n_\mathtt{B}$ matrix of static modes of the joint $\mathbf{X}^{\mathtt{st}}$, expressed by:

$$\mathbf{X}^{\mathtt{st}} = -\mathbf{K}_{\mathtt{II}}^{-1}\mathbf{K}_{\mathtt{IB}}. \tag{4}$$

Within the framework of the CB method, the displacement vector $\mathbf{q}_\mathtt{I}$ (internal DOFs) is expressed in terms of static modes and a reduced set of fixed-interface modes $\{\widetilde{\boldsymbol{\chi}}^{\mathtt{fix}}\}_{k=1,\ldots,m_\mathtt{I}} \subset \{\boldsymbol{\chi}^{\mathtt{fix}}\}_{k=1,\ldots,n_\mathtt{I}}$ with $m_\mathtt{I} \ll n_\mathtt{I}$. Denote as $\widetilde{\mathbf{X}}^{\mathtt{fix}}$ the $n_\mathtt{I} \times m_\mathtt{I}$ reduced matrix of fixed-interface modes expressed by $\widetilde{\mathbf{X}}^{\mathtt{fix}} = [\widetilde{\boldsymbol{\chi}}_1^{\mathtt{fix}} \cdots \widetilde{\boldsymbol{\chi}}_{m_\mathtt{I}}^{\mathtt{fix}}]$. Hence, the displacement vector $\mathbf{q}_\mathtt{I}$ can be approximated as follows:

$$\mathbf{q}_\mathtt{I} \approx \mathbf{X}^{\mathtt{st}}\mathbf{q}_\mathtt{B} + \widetilde{\mathbf{X}}^{\mathtt{fix}}\widetilde{\boldsymbol{\alpha}}, \tag{5}$$

where $\widetilde{\boldsymbol{\alpha}} = [\widetilde{\alpha}_1 \cdots \widetilde{\alpha}_{m_\mathtt{I}}]^T$ is to be understood as a vector of generalized coordinates. As a result, the displacement vector $\mathbf{q}$ is expressed by:

$$\mathbf{q} = \begin{bmatrix}\mathbf{q}_\mathtt{I} \\ \mathbf{q}_\mathtt{B}\end{bmatrix} \approx \widetilde{\mathbf{T}}\begin{bmatrix}\widetilde{\boldsymbol{\alpha}} \\ \mathbf{q}_\mathtt{B}\end{bmatrix} \quad \text{where} \quad \widetilde{\mathbf{T}} = \begin{bmatrix}\widetilde{\mathbf{X}}^{\mathtt{fix}} & \mathbf{X}^{\mathtt{st}} \\ \mathbf{0} & \mathbf{I}_{n_\mathtt{B}}\end{bmatrix}, \tag{6}$$

where $\mathbf{q}_\mathtt{B}$ is the displacement vector which concerns the interface DOFs. By introducing Eq. (6) in Eq. (2), and left-multiplying the resulting equation by $\widetilde{\mathbf{T}}^T$, this yields the following reduced matrix equation:

$$\widetilde{\mathbf{D}}\begin{bmatrix}\widetilde{\boldsymbol{\alpha}} \\ \mathbf{q}_\mathtt{B}\end{bmatrix} = \begin{bmatrix}\mathbf{0} \\ \mathbf{F}_\mathtt{B}\end{bmatrix} \quad \text{where} \quad \widetilde{\mathbf{D}} = -\omega^2\widetilde{\mathbf{M}} + \mathtt{i}\omega\widetilde{\mathbf{C}} + \widetilde{\mathbf{K}}. \tag{7}$$

Here, $\widetilde{\mathbf{M}}$, $\widetilde{\mathbf{C}}$ and $\widetilde{\mathbf{K}}$ are reduced $(n_\mathtt{B} + m_\mathtt{I}) \times (n_\mathtt{B} + m_\mathtt{I})$ mass, damping and stiffness matrices, which are given by:

$$\widetilde{\mathbf{M}} = \widetilde{\mathbf{T}}^T\mathbf{M}\widetilde{\mathbf{T}} \quad , \quad \widetilde{\mathbf{K}} = \widetilde{\mathbf{T}}^T\mathbf{K}\widetilde{\mathbf{T}} \quad , \quad \widetilde{\mathbf{C}} = \alpha\widetilde{\mathbf{K}}. \tag{8}$$

Notice that the fixed-interface modes can be normalized in such a way that $(\widetilde{\mathbf{X}}^{\mathtt{fix}})^T\mathbf{M}_{\mathtt{II}}\widetilde{\mathbf{X}}^{\mathtt{fix}} = \mathbf{I}_{m_\mathtt{I}}$, which also means that $(\widetilde{\mathbf{X}}^{\mathtt{fix}})^T\mathbf{K}_{\mathtt{II}}\widetilde{\mathbf{X}}^{\mathtt{fix}} = \mathtt{diag}\{\omega_k^2\}_{k=1,\ldots,m_\mathtt{I}}$. As a result, the reduced mass matrix $\widetilde{\mathbf{M}}$, Eq. (8), can be expressed as follows:

$$\widetilde{\mathbf{M}} = \begin{bmatrix}\mathbf{I}_{m_\mathtt{I}} & \widetilde{\mathbf{M}}_{\mathtt{B}\alpha}^T \\ \widetilde{\mathbf{M}}_{\mathtt{B}\alpha} & \widetilde{\mathbf{M}}_{\mathtt{BB}}\end{bmatrix}, \tag{9}$$

where

$$\widetilde{\mathbf{M}}_{\mathtt{B}\alpha} = (\mathbf{X}^{\mathtt{st}})^T\mathbf{M}_{\mathtt{II}}\widetilde{\mathbf{X}}^{\mathtt{fix}} + \mathbf{M}_{\mathtt{BI}}\widetilde{\mathbf{X}}^{\mathtt{fix}}, \tag{10}$$

$$\widetilde{\mathbf{M}}_{\mathtt{BB}} = (\mathbf{X}^{\mathtt{st}})^T\mathbf{M}_{\mathtt{II}}\mathbf{X}^{\mathtt{st}} + (\mathbf{X}^{\mathtt{st}})^T\mathbf{M}_{\mathtt{IB}} + \mathbf{M}_{\mathtt{BI}}\mathbf{X}^{\mathtt{st}} + \mathbf{M}_{\mathtt{BB}}. \tag{11}$$

Also, due to the property of the static modes (cf. Eq. (4)), the reduced stiffness matrix $\widetilde{\mathbf{K}}$, Eq. (8), can be expressed as follows:

$$\widetilde{\mathbf{K}} = \begin{bmatrix}\mathtt{diag}\{\omega_k^2\}_{k=1,\ldots,m_\mathtt{I}} & \mathbf{0} \\ \mathbf{0} & \widetilde{\mathbf{K}}_{\mathtt{BB}}\end{bmatrix}, \tag{12}$$

where

$$\widetilde{\mathbf{K}}_{\mathtt{BB}} = (\mathbf{X}^{\mathtt{st}})^T\mathbf{K}_{\mathtt{IB}} + \mathbf{K}_{\mathtt{BB}}. \tag{13}$$

Notice that $\widetilde{\mathbf{M}}$, $\widetilde{\mathbf{C}}$ and $\widetilde{\mathbf{K}}$ (Eq. (8)) are real symmetric matrices of size $\mu \times \mu$ where $\mu = m_\mathtt{I} + n_\mathtt{B}$. Also note that the matrix $\widetilde{\mathbf{M}}$ is positive definite, while the matrix $\widetilde{\mathbf{K}}$ is positive semidefinite. As it turns out, the ranks of the matrices $\widetilde{\mathbf{M}}$ and $\widetilde{\mathbf{K}}$ are μ and $\mu - \mu_{\mathtt{rig}}$, respectively, where $\mu_{\mathtt{rig}}$ stands for the number of rigid body modes.[1] As for the reduced damping matrix $\widetilde{\mathbf{C}}$, since $\mathbf{C} = \alpha\mathbf{K}$, it is positive semidefinite.

[1] $\mu_{\mathtt{rig}} \neq 0$ for a free joint — i.e., when the internal DOFs are not subjected to kinematic constraints —; $\mu_{\mathtt{rig}} = 6$ for a 3D free joint, while $\mu_{\mathtt{rig}} = 3$ for a 2D free joint.

Since the matrix $\widetilde{\mathbf{M}}$ is symmetric positive definite, it admits the following Cholesky decomposition:

$$\widetilde{\mathbf{M}} = \mathbf{R}_{\mathtt{M}}^T \mathbf{R}_{\mathtt{M}}, \tag{14}$$

where $\mathbf{R}_{\mathtt{M}}$ is a $\mu \times \mu$ upper triangular matrix. Also, since the matrix $\widetilde{\mathbf{K}}$ is symmetric positive semidefinite, the following Cholesky decomposition can be proposed [20]:

$$\mathbf{\Pi}^T \widetilde{\mathbf{K}} \mathbf{\Pi} = \mathbf{R}_{\mathtt{K}}^T \mathbf{R}_{\mathtt{K}} \quad \text{where} \quad \mathbf{R}_{\mathtt{K}} = \begin{bmatrix} (\mathbf{R}_{\mathtt{K}})_{11} & (\mathbf{R}_{\mathtt{K}})_{12} \\ \mathbf{0} & \mathbf{0} \end{bmatrix}, \tag{15}$$

where $(\mathbf{R}_{\mathtt{K}})_{11}$ is a $(\mu - \mu_{\mathtt{rig}}) \times (\mu - \mu_{\mathtt{rig}})$ upper triangular matrix, and $\mathbf{\Pi}$ is a permutation matrix, i.e., which is such that $\mathbf{\Pi}^T \mathbf{\Pi} = \mathbf{\Pi}\mathbf{\Pi}^T = \mathbf{I}_\mu$. As a result, the matrix $\widetilde{\mathbf{K}}$ can be decomposed as follows:

$$\widetilde{\mathbf{K}} = \mathbf{\Pi} \mathbf{R}_{\mathtt{K}}^T \mathbf{R}_{\mathtt{K}} \mathbf{\Pi}^T. \tag{16}$$

Also, the matrix $\widetilde{\mathbf{C}}$ admits the following Cholesky decomposition:

$$\widetilde{\mathbf{C}} = \alpha \widetilde{\mathbf{K}} = \alpha \mathbf{\Pi} \mathbf{R}_{\mathtt{K}}^T \mathbf{R}_{\mathtt{K}} \mathbf{\Pi}^T = \mathbf{\Pi} \mathbf{R}_{\mathtt{C}}^T \mathbf{R}_{\mathtt{C}} \mathbf{\Pi}^T, \tag{17}$$

where $\mathbf{R}_{\mathtt{C}} = \sqrt{\alpha} \mathbf{R}_{\mathtt{K}}$. A Matlab toolbox including this positive semidefinite Cholesky decomposition is available in [21].

3 Scattering matrix model

Let us consider, for the sake of clarity, an elastic joint which connects two periodic structures 1 and 2 as shown in Figure 1. It is worth recalling that the reduced DSM of the joint is given by $\widetilde{\mathbf{D}} = -\omega^2 \widetilde{\mathbf{M}} + \mathtt{i}\omega \widetilde{\mathbf{C}} + \widetilde{\mathbf{K}}$, which, from Eqs. (9) and (12), can be written in the following form:

$$\widetilde{\mathbf{D}} = \begin{bmatrix} \widetilde{\mathbf{D}}_{\alpha\alpha} & \widetilde{\mathbf{D}}_{\mathtt{B}\alpha}^T \\ \widetilde{\mathbf{D}}_{\mathtt{B}\alpha} & \mathbf{D}_{\mathtt{BB}} \end{bmatrix}. \tag{18}$$

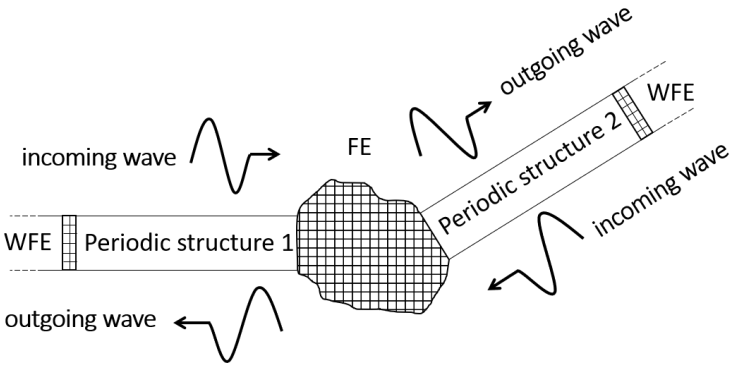


Figure 1: FE mesh of an elastic joint connecting two periodic structures with incoming and outgoing waves.

The periodic structures under concern are made of identical substructures which are assembled together along a certain straight direction. 2D or 3D substructures with arbitrary-shaped FE meshes can be dealt with. The WFE method constitutes an efficient numerical tool to assess the propagation of wave modes along such periodic structures. The key steps of the WFE method can be summarized as follows (see [13] for further details):

1. Express the DSM of a substructure;

2. Condense the DSM on the coupling (interface) DOFs;

3. Express the transfer matrix of the substructure from the condensed DSM;

4. Compute the eigenvalues (wave parameters) and eigenvectors (wave shapes) of the transfer matrix.

The wave parameters are usually denoted by $\mu_j = \mathtt{exp}(-\mathtt{i}\beta_j d)$, where β_j has the meaning of wavenumbers, while d represents the substructure length. Also, the wave shapes are denoted by $\boldsymbol{\phi}_j$ which can be further partitioned into displacement and force components as follows $\boldsymbol{\phi}_j = [\boldsymbol{\phi}_{\mathtt{q}j}^T \, \boldsymbol{\phi}_{\mathtt{F}j}^T]^T$.

Notice that the transfer matrix of a substructure is symplectic [22], which means that the eigenvalues come in pairs $(\mu_j, \mu_j^\star)$, where $\mu_j^\star = 1/\mu_j$. Let us denote by n the number of interface DOFs, between two consecutive substructures. Hence, the eigensolutions of the transfer matrix can be split into two sets, say n positive-going wave modes $(\mu_j, \boldsymbol{\phi}_j)$ defined so that $|\mu_j| < 1$, and n negative-going wave modes $(\mu_j^\star, \boldsymbol{\phi}_j^\star)$ where $|\mu_j^\star| = |1/\mu_j| > 1$.

In matrix form, the positive-going and negative-going wave modes can be written as follows:

$$\boldsymbol{\mu} = \mathtt{diag}\{\mu_j\}_{j=1,\ldots,n} \quad , \quad \boldsymbol{\mu}^\star = \boldsymbol{\mu}^{-1}, \tag{19}$$

$$\boldsymbol{\Phi} = \begin{bmatrix} \boldsymbol{\Phi}_{\mathtt{q}} \\ \boldsymbol{\Phi}_{\mathtt{F}} \end{bmatrix} \quad , \quad \boldsymbol{\Phi}^\star = \begin{bmatrix} \boldsymbol{\Phi}_{\mathtt{q}}^\star \\ \boldsymbol{\Phi}_{\mathtt{F}}^\star \end{bmatrix}, \tag{20}$$

where $\boldsymbol{\Phi}_{\mathtt{q}} = [\boldsymbol{\phi}_{\mathtt{q}1} \cdots \boldsymbol{\phi}_{\mathtt{q}n}]$, $\boldsymbol{\Phi}_{\mathtt{F}} = [\boldsymbol{\phi}_{\mathtt{F}1} \cdots \boldsymbol{\phi}_{\mathtt{F}n}]$, $\boldsymbol{\Phi}_{\mathtt{q}}^\star = [\boldsymbol{\phi}_{\mathtt{q}1}^\star \cdots \boldsymbol{\phi}_{\mathtt{q}n}^\star]$ and $\boldsymbol{\Phi}_{\mathtt{F}}^\star = [\boldsymbol{\phi}_{\mathtt{F}1}^\star \cdots \boldsymbol{\phi}_{\mathtt{F}n}^\star]$ are $n \times n$ matrices of wave shapes.

The scattering matrix — namely, $\mathbb{C}$ — of the joint which connects the periodic structures 1 and 2 can be formulated as follows [12, 16]:

$$\mathbb{C} = -[\widetilde{\mathbf{D}}^* \boldsymbol{\Psi}_{\mathtt{q}}^\star + \boldsymbol{\Psi}_{\mathtt{F}}^\star]^{-1} [\widetilde{\mathbf{D}}^* \boldsymbol{\Psi}_{\mathtt{q}} + \boldsymbol{\Psi}_{\mathtt{F}}], \tag{21}$$

where $\widetilde{\mathbf{D}}^*$ is the condensed DSM of the joint w.r.t. its interface DOFs, expressed by $\widetilde{\mathbf{D}}^* = \mathbf{D}_{\mathtt{BB}} - \widetilde{\mathbf{D}}_{\mathtt{B}\alpha} \widetilde{\mathbf{D}}_{\alpha\alpha}^{-1} \widetilde{\mathbf{D}}_{\mathtt{B}\alpha}^T$ (cf. Eq. (18)). Also, the matrices $\boldsymbol{\Psi}_{\mathtt{q}}$, $\boldsymbol{\Psi}_{\mathtt{q}}^\star$, $\boldsymbol{\Psi}_{\mathtt{F}}$ and $\boldsymbol{\Psi}_{\mathtt{F}}^\star$ are expressed as follows:

$$\boldsymbol{\Psi}_{\mathtt{q}} = \begin{bmatrix} \mathcal{L}_1(\boldsymbol{\Phi}_{\mathtt{q}})_1 & \mathbf{0} \\ \mathbf{0} & \mathcal{L}_2(\boldsymbol{\Phi}_{\mathtt{q}})_2 \end{bmatrix} \quad , \quad \boldsymbol{\Psi}_{\mathtt{q}}^\star = \begin{bmatrix} \mathcal{L}_1(\boldsymbol{\Phi}_{\mathtt{q}}^\star)_1 & \mathbf{0} \\ \mathbf{0} & \mathcal{L}_2(\boldsymbol{\Phi}_{\mathtt{q}}^\star)_2 \end{bmatrix}, \tag{22}$$

$$\boldsymbol{\Psi}_{\mathtt{F}} = \begin{bmatrix} \mathcal{L}_1(\boldsymbol{\Phi}_{\mathtt{F}})_1 & \mathbf{0} \\ \mathbf{0} & \mathcal{L}_2(\boldsymbol{\Phi}_{\mathtt{F}})_2 \end{bmatrix} \quad , \quad \boldsymbol{\Psi}_{\mathtt{F}}^\star = \begin{bmatrix} \mathcal{L}_1(\boldsymbol{\Phi}_{\mathtt{F}}^\star)_1 & \mathbf{0} \\ \mathbf{0} & \mathcal{L}_2(\boldsymbol{\Phi}_{\mathtt{F}}^\star)_2 \end{bmatrix}, \tag{23}$$

where $\mathcal{L}_1$ and $\mathcal{L}_2$ are rotation matrices whose purpose is to express the displacement and force vectors of the periodic structures 1 and 2 in the (global) coordinate system of the joint. Within the present framework, the local positive direction of each periodic structure is supposed to point towards the joint. In this sense, the positive-going wave modes are to be understood as incoming waves, while the negative-going wave modes represent outgoing waves. It should be emphasized that, to derive Eq. (21), the FE meshes of the periodic structures and the joint are assumed to be compatible at the coupling interfaces. Hence, the number of interface DOFs of the joint, $n_{\mathtt{B}}$, is expressed by $n_{\mathtt{B}} = n_1 + n_2$ where n_1 and n_2 are the numbers of substructure interface DOFs of the periodic structures 1 and 2, respectively.

The scattering matrix $\mathbb{C}$ can be partitioned as follows:

$$\mathbb{C} = \begin{bmatrix} \mathbb{C}_{11} & \mathbb{C}_{12} \\ \mathbb{C}_{21} & \mathbb{C}_{22} \end{bmatrix}, \tag{24}$$

where $\mathbb{C}_{11}$ is the $n_1 \times n_1$ matrix of reflection coefficients for the periodic structure 1, $\mathbb{C}_{22}$ is the $n_2 \times n_2$ matrix of reflection coefficients for the periodic structure 2, $\mathbb{C}_{12}$ is the $n_1 \times n_2$ matrix of transmission coefficients

from the periodic structure 2 to the periodic structure 1, and $\mathbb{C}_{21}$ is the $n_2 \times n_1$ matrix of transmission coefficients from the periodic structure 1 to the periodic structure 2.

Notice that the values of the reflection and transmission coefficients depend on the normalization of the wave shapes. A "physical" way to achieve this task is to normalize each wave shape w.r.t. the norm of its displacement component. This yields:

$$\boldsymbol{\Phi}_1 = \begin{bmatrix} (\boldsymbol{\Phi}_{\mathtt{q}})_1 \\ (\boldsymbol{\Phi}_{\mathtt{F}})_1 \end{bmatrix} \quad \rightarrow \quad \boldsymbol{\Phi}_1 / \mathtt{diag}\{\|(\boldsymbol{\phi}_{\mathtt{q}j})_1\|\}_{j=1,\ldots,n_1}, \tag{25}$$

$$\boldsymbol{\Phi}_2^\star = \begin{bmatrix} (\boldsymbol{\Phi}_{\mathtt{q}}^\star)_2 \\ (\boldsymbol{\Phi}_{\mathtt{F}}^\star)_2 \end{bmatrix} \quad \rightarrow \quad \boldsymbol{\Phi}_2^\star / \mathtt{diag}\{\|(\boldsymbol{\phi}_{\mathtt{q}j}^\star)_2\|\}_{j=1,\ldots,n_2}. \tag{26}$$

4 Probabilistic modelling of the reduced DSM

4.1 Available information and definition of the random matrix ensemble

This section aims at defining random matrices $\widehat{\mathbf{M}}$, $\widehat{\mathbf{C}}$ and $\widehat{\mathbf{K}}$, which are built from the baseline reduced matrices $\widetilde{\mathbf{M}}$, $\widetilde{\mathbf{C}}$ and $\widetilde{\mathbf{K}}$ of the joint. An important point in the application of the RMT for probabilistic modelling in structural dynamics is the proper definition of the random matrix ensemble. A poor choice can lead to results which are not physically meaningful [23]. Within this rationale, the Gaussian Orthogonal Ensemble (GOE) cannot be used to model $\widehat{\mathbf{K}}$ (and therefore $\widehat{\mathbf{C}}$) because $E\left\{\|\widehat{\mathbf{K}}^{-1}\|_F^2\|\right\} = +\infty$ ($E[\cdot]$ and $\|\cdot\|_F$ being the mathematical expectation and the Frobenius norm, respectively), i.e., there is no statistical convergence.

The available information used to properly define the random matrices is:

1. The random matrices $\widehat{\mathbf{M}}$, $\widehat{\mathbf{C}}$ and $\widehat{\mathbf{K}}$ are statistically independent.
2. The matrix $\widehat{\mathbf{M}}$ is positive definite; the matrices $\widehat{\mathbf{C}}$ and $\widehat{\mathbf{K}}$ are positive semidefinite.
3. The mean values of $\widehat{\mathbf{M}}$, $\widehat{\mathbf{C}}$ and $\widehat{\mathbf{K}}$ correspond to the nominal reduced matrices $\widetilde{\mathbf{M}}$, $\widetilde{\mathbf{C}}$ and $\widetilde{\mathbf{K}}$, respectively.
4. The second order moment of the response is finite. This condition is satisfied by imposing $E\left\{\|\widehat{\mathbf{M}}^{-1}\|_F^2\|\right\} < +\infty$, $E\left\{\|\widehat{\mathbf{C}}^{-1}\|_F^2\|\right\} < +\infty$ and $E\left\{\|\widehat{\mathbf{K}}^{-1}\|_F^2\|\right\} < +\infty$ [24].

Within the framework of the RMT theory [8], the random matrices $\widehat{\mathbf{M}}$, $\widehat{\mathbf{C}}$ and $\widehat{\mathbf{K}}$ are defined by:

$$\widehat{\mathbf{M}} = \mathbf{R}_{\mathtt{M}}^T \widehat{\mathbf{G}}_{\mathtt{M}} \mathbf{R}_{\mathtt{M}} \quad , \quad \widehat{\mathbf{C}} = \boldsymbol{\Pi} \mathbf{R}_{\mathtt{C}}^T \widehat{\mathbf{G}}_{\mathtt{C}} \mathbf{R}_{\mathtt{C}} \boldsymbol{\Pi}^T \quad , \quad \widehat{\mathbf{K}} = \boldsymbol{\Pi} \mathbf{R}_{\mathtt{K}}^T \widehat{\mathbf{G}}_{\mathtt{K}} \mathbf{R}_{\mathtt{K}} \boldsymbol{\Pi}^T, \tag{27}$$

Here, $\widehat{\mathbf{G}}_{\mathtt{M}}$, $\widehat{\mathbf{G}}_{\mathtt{C}}$ and $\widehat{\mathbf{G}}_{\mathtt{K}}$ are three symmetric positive definite matrices, of sizes $\mu \times \mu$, $(\mu - \mu_{\mathtt{rig}}) \times (\mu - \mu_{\mathtt{rig}})$ and $(\mu - \mu_{\mathtt{rig}}) \times (\mu - \mu_{\mathtt{rig}})$, respectively. The Cholesky decompositions of the random matrices $\widehat{\mathbf{G}}_{\mathtt{M}}$, $\widehat{\mathbf{G}}_{\mathtt{C}}$ and $\widehat{\mathbf{G}}_{\mathtt{K}}$ give:

$$\widehat{\mathbf{G}}_{\mathtt{M}} = \mathbf{R}_{\mathtt{G_M}}^T \mathbf{R}_{\mathtt{G_M}} \quad , \quad \widehat{\mathbf{G}}_{\mathtt{C}} = \mathbf{R}_{\mathtt{G_C}}^T \mathbf{R}_{\mathtt{G_C}} \quad , \quad \widehat{\mathbf{G}}_{\mathtt{K}} = \mathbf{R}_{\mathtt{G_K}}^T \mathbf{R}_{\mathtt{G_K}}, \tag{28}$$

where $\mathbf{R}_{\mathtt{G_M}}$, $\mathbf{R}_{\mathtt{G_C}}$ and $\mathbf{R}_{\mathtt{G_K}}$ are upper triangular matrix of sizes $\mu \times \mu$, $(\mu - \mu_{\mathtt{rig}}) \times (\mu - \mu_{\mathtt{rig}})$ and $(\mu - \mu_{\mathtt{rig}}) \times (\mu - \mu_{\mathtt{rig}})$, respectively.

The upper triangular matrix $\mathbf{R}_{\mathtt{G_M}}$, $\mathbf{R}_{\mathtt{G_C}}$ and $\mathbf{R}_{\mathtt{G_K}}$ are random matrices, defined such that:

1. For $k < l$, $[\mathbf{R}_{\mathtt{G_M,G_C,G_K}}]_{kl} = \sigma_{\mathtt{M,C,K}} U_{kl}$ where $\sigma_{\mathtt{M,C,K}} = \delta_{\mathtt{M,C,K}}(s+1)^{-1/2}$, U_{kl} is a real-valued standard normal random variable and s is the size of the random matrix (i.e., $s = \mu$ for $\mathbf{R}_{\mathtt{G_M}}$ and $s = \mu - \mu_{\mathtt{rig}}$ for $\mathbf{R}_{\mathtt{G_C}}$ and $\mathbf{R}_{\mathtt{G_K}}$); also, $\delta_{\mathtt{M,C,K}}$ is a dispersion parameter defined so that $0 < \delta_{\mathtt{M,C,K}} < \sqrt{(s+1)(s+5)^{-1}}$.

2. For $k = l$, $[\mathbf{R}_{\mathtt{G_M},\mathtt{G_C},\mathtt{G_K}}]_{kk} = \sigma_{\mathtt{M,C,K}}(2V_k)^{1/2}$ where V_k is a real-valued Gamma random variable with the following probability density function (PDF):

$$p_{V_k}(v) = \frac{v^{(s+1)/2\delta^2_{\mathtt{M,C,K}}-(1+k)/2}}{\Gamma\left[(s+1)/2\delta^2_{\mathtt{M,C,K}}) + (1-k)/2\right]} e^{-v}, \quad v > 0, \tag{29}$$

where $\Gamma[\cdot]$ is the Gamma function.

This definition allows a Monte Carlo (MC) procedure to be proposed. Hence, samples of the matrices $\mathbf{R}_{\mathtt{G_M},\mathtt{G_C},\mathtt{G_K}}$ can be generated while Eqs. (27) and (28) are used to assess the random reduced matrices $\widehat{\mathbf{M}}$, $\widehat{\mathbf{C}}$ and $\widehat{\mathbf{K}}$ of the joint, and further the random condensed DSM $\widehat{\mathbf{D}}^*$ and the random scattering matrix $\widehat{\mathbb{C}}$, Eq. (21).

4.2 Non-parametric probabilistic model

Two non-parametric approaches are proposed. The first one considers random matrices $\widehat{\mathbf{M}}$, $\widehat{\mathbf{K}}$ and $\widehat{\mathbf{C}}$ to assess the random scattering matrix of the joint, as explained in Section 4.1. In the second approach, small perturbations of the eigenpulsations ω_k are assumed while the matrices of fixed interface modes and static modes are supposed to be unperturbed [10]. In this framework, only the diagonal block terms $\widetilde{\mathbf{M}}_{\alpha\alpha} = \mathbf{I}_{m_\mathtt{I}}$, $\widetilde{\mathbf{C}}_{\alpha\alpha} = \alpha\,\mathtt{diag}\{\omega_k^2\}_{k=1,\ldots,m_\mathtt{I}}$ and $\widetilde{\mathbf{K}}_{\alpha\alpha} = \mathtt{diag}\{\omega_k^2\}_{k=1,\ldots,m_\mathtt{I}}$ of the matrices $\widetilde{\mathbf{M}}$, $\widetilde{\mathbf{C}}$ and $\widetilde{\mathbf{K}}$ (cf. Eqs. (9) and (12)) are subject to randomness. The matrices $\widetilde{\mathbf{M}}_{\alpha\alpha}$, $\widetilde{\mathbf{C}}_{\alpha\alpha}$ and $\widetilde{\mathbf{K}}_{\alpha\alpha}$ are positive definite, and admit the following Cholesky decompositions $\widetilde{\mathbf{M}}_{\alpha\alpha} = \mathbf{R}^T_{\mathtt{M}_{\alpha\alpha}}\mathbf{R}_{\mathtt{M}_{\alpha\alpha}}$, $\widetilde{\mathbf{C}}_{\alpha\alpha} = \mathbf{R}^T_{\mathtt{C}_{\alpha\alpha}}\mathbf{R}_{\mathtt{C}_{\alpha\alpha}}$ and $\widetilde{\mathbf{M}}_{\alpha\alpha} = \mathbf{R}^T_{\mathtt{K}_{\alpha\alpha}}\mathbf{R}_{\mathtt{K}_{\alpha\alpha}}$, where:

$$\mathbf{R}_{\mathtt{M}_{\alpha\alpha}} = \mathbf{I}_{m_\mathtt{I}} \quad , \quad \mathbf{R}_{\mathtt{C}_{\alpha\alpha}} = \sqrt{\alpha}\,\mathtt{diag}\{\omega_k\}_{k=1,\ldots,m_\mathtt{I}} \quad , \quad \mathbf{R}_{\mathtt{K}_{\alpha\alpha}} = \mathtt{diag}\{\omega_k\}_{k=1,\ldots,m_\mathtt{I}}. \tag{30}$$

Hence, random matrices $\widehat{\mathbf{M}}_{\alpha\alpha} = \mathbf{R}^T_{\mathtt{M}_{\alpha\alpha}}\widehat{\mathbf{G}}_{\mathtt{M}_{\alpha\alpha}}\mathbf{R}_{\mathtt{M}_{\alpha\alpha}}$, $\widehat{\mathbf{C}}_{\alpha\alpha} = \mathbf{R}^T_{\mathtt{C}_{\alpha\alpha}}\widehat{\mathbf{G}}_{\mathtt{C}_{\alpha\alpha}}\mathbf{R}_{\mathtt{C}_{\alpha\alpha}}$ and $\widehat{\mathbf{K}}_{\alpha\alpha} = \mathbf{R}^T_{\mathtt{K}_{\alpha\alpha}}\widehat{\mathbf{G}}_{\mathtt{K}_{\alpha\alpha}}\mathbf{R}_{\mathtt{K}_{\alpha\alpha}}$ can be generated using the strategy depicted in Section 4.1, which are fully populated. This yields a new random scattering matrix $\widehat{\mathbb{C}}$.

Care must be taken when defining the dispersion parameter δ for comparing both approaches. It controls the level of statistical fluctuation of the random matrices, and must be set so that $\sigma_{\mathtt{M,C,K}} = \sigma_{\mathtt{M}_{\alpha\alpha},\mathtt{C}_{\alpha\alpha},\mathtt{K}_{\alpha\alpha}}$, leading to:

$$\delta_{\mathtt{M}_{\alpha\alpha},\mathtt{C}_{\alpha\alpha},\mathtt{K}_{\alpha\alpha}} = \delta_{\mathtt{M,C,K}}\sqrt{\frac{m_\mathtt{I}+1}{\mu+1}}. \tag{31}$$

4.2.1 Parametric probabilistic model of the component modes of the joint

One of the main consequences of the non-parametric approaches is that some of the DOFs which are not connected in the deterministic model become coupled to each other, even though they are not spatially adjacent. This effect happens because of the fully populated matrices $\widehat{\mathbf{G}}_\mathtt{M}$, $\widehat{\mathbf{G}}_\mathtt{C}$ and $\widehat{\mathbf{G}}_\mathtt{K}$ (or $\widehat{\mathbf{G}}_{\mathtt{M}_{\alpha\alpha}}$, $\widehat{\mathbf{G}}_{\mathtt{C}_{\alpha\alpha}}$ and $\widehat{\mathbf{G}}_{\mathtt{K}_{\alpha\alpha}}$), which also leads to a fully populated random DSM [25, 26]. To overcome this issue, a parametric model can be proposed which uses the diagonal terms of $\mathbf{R}_{\mathtt{G_M},\mathtt{G_C},\mathtt{G_K}}$ only, such that both non-parametric and parametric approaches share the same level of uncertainty, i.e., for the diagonal terms of the random mass, damping and stiffness matrices.

Similarly to the non-parametric case, two approaches can be proposed. The first one invokes random matrices $\widehat{\mathbf{M}}$, $\widehat{\mathbf{C}}$ and $\widehat{\mathbf{K}}$ in the same way as Eq. (27):

$$\widehat{\mathbf{M}} = \mathbf{R}^T_\mathtt{M}\widehat{\mathbf{P}}_\mathtt{M}\mathbf{R}_\mathtt{M} \quad , \quad \widehat{\mathbf{C}} = \mathbf{\Pi}\mathbf{R}^T_\mathtt{C}\widehat{\mathbf{P}}_\mathtt{C}\mathbf{R}_\mathtt{C}\mathbf{\Pi}^T \quad , \quad \widehat{\mathbf{K}} = \mathbf{\Pi}\mathbf{R}^T_\mathtt{K}\widehat{\mathbf{P}}_\mathtt{K}\mathbf{R}_\mathtt{K}\mathbf{\Pi}^T. \tag{32}$$

where $\widehat{\mathbf{P}}_\mathtt{M}$, $\widehat{\mathbf{P}}_\mathtt{C}$ and $\widehat{\mathbf{P}}_\mathtt{K}$ are diagonal positive definite random matrices of sizes $\mu \times \mu$, $(\mu - \mu_\mathtt{rig}) \times (\mu - \mu_\mathtt{rig})$ and $(\mu - \mu_\mathtt{rig}) \times (\mu - \mu_\mathtt{rig})$, respectively. They are defined in a similar way as the non-parametric case by

$\widehat{\mathbf{P}}_{\mathtt{M}} = \mathbf{R}_{\mathtt{P_M}}^T \mathbf{R}_{\mathtt{P_M}}$, $\widehat{\mathbf{P}}_{\mathtt{C}} = \mathbf{R}_{\mathtt{P_C}}^T \mathbf{R}_{\mathtt{P_C}}$ and $\widehat{\mathbf{P}}_{\mathtt{K}} = \mathbf{R}_{\mathtt{P_K}}^T \mathbf{R}_{\mathtt{P_K}}$, where $[\mathbf{R}_{\mathtt{P_M,P_C,P_K}}]_{kk} = [\mathbf{R}_{\mathtt{G_M,G_C,G_K}}]_{kk} = \sigma_{\mathtt{M,C,K}}(2V_k)^{1/2}$, and $[\mathbf{R}_{\mathtt{P_M,P_C,P_K}}]_{kl} = 0$ for $k \neq l$.

The second approach involves perturbing the diagonal components of the matrices $\widetilde{\mathbf{M}}_{\alpha\alpha}$, $\widetilde{\mathbf{C}}_{\alpha\alpha}$ and $\widetilde{\mathbf{K}}_{\alpha\alpha}$. This yields the following random matrices:

$$\widehat{\mathbf{M}}_{\alpha\alpha} = \mathtt{diag}\left\{\frac{2\delta_{\mathtt{M}_{\alpha\alpha}}^2}{(s+1)}V_k\right\}_k, \; \widehat{\mathbf{C}}_{\alpha\alpha} = \alpha\,\mathtt{diag}\left\{\omega_k^2\frac{2\delta_{\mathtt{C}_{\alpha\alpha}}^2}{(s+1)}V_k\right\}_k, \; \widehat{\mathbf{K}}_{\alpha\alpha} = \mathtt{diag}\left\{\omega_k^2\frac{2\delta_{\mathtt{K}_{\alpha\alpha}}^2}{(s+1)}V_k\right\}_k, \tag{33}$$

Once the random matrices $\widehat{\mathbf{M}}$, $\widehat{\mathbf{C}}$ and $\widehat{\mathbf{K}}$ (or $\widehat{\mathbf{M}}_{\alpha\alpha}$, $\widehat{\mathbf{C}}_{\alpha\alpha}$ and $\widehat{\mathbf{K}}_{\alpha\alpha}$) have been generated, the random scattering matrix $\widehat{\mathbb{C}}$ can be assessed by following the strategy proposed in Section 3.

4.2.2 Parametric probabilistic model of the material properties of the joint

The most popular parametric approach involves modelling the material properties of the joint as random fields [27, 28]. Material properties in mechanical systems usually have non-negative values, which means that their PDF have a non-negative support. In this work, the Young's modulus and the mass density of the joint will be modelled as random fields [29, 28], i.e., $E(x,y) = E_0\left[1 + \delta_E H_E(x,y)\right]$ and $\rho(x,y) = \rho_0\left[1 + \delta_\rho H_\rho(x,y)\right]$, where E_0 and ρ_0 are nominal values of the Young's modulus and the mass density, respectively; δ_E and δ_ρ are dispersion terms, $H_E(x,y)$ and $H_\rho(x,y)$ are zero-mean, independent and unit standard-deviation random fields with correlation functions $R_E(\tau_x,\tau_y)$ and $R_\rho(\tau_x,\tau_y)$, respectively, where τ_x and τ_y are the distance between any two points in the x and y directions. Here, it is assumed that $R_\rho(\tau_x,\tau_y) = R_E(\tau_x,\tau_y) = e^{-(\tau_x^2+\tau_y^2)/l_c}$, where l_c is the correlation length. The Karhunen-Loeve (KL) expansion [28] can be used to represent the random fields as follows:

$$H_{E,\rho}(x,y) = \sum_{r=1}^{\infty}\sqrt{\lambda_r}\xi_r\varphi_r(x,y), \tag{34}$$

where λ_r and $\varphi_r(x,y)$ are the eigenvalues and eigenfunctions of the correlation kernel [28], respectively, and ξ_r are uncorrelated random variables. The series in Eq. (34) is truncated by considering a finite number of terms $N_{\mathtt{KL}}$, chosen to accurately describe the correlation functions [30]. As a rule of thumb, $N_{\mathtt{KL}}$ can be chosen such that $\lambda_j/\lambda_1 < 0.1$. In this work, the random field are chosen to be Gamma distributed and an iterative scheme is used to simulate Gamma random fields [31].

5 Numerical example

Let us consider two identical infinite aluminium plates undergoing in-plane vibration, i.e., displacement in the plane of the plate, connected to an isotropic composite short glass-fibre reinforced epoxy plate (joint) as shown in Figure 2. The composite plate is 1 mm thick with a width of 0.15 m, a length of 0.65 m, a Young's modulus of 13 GPa, a mass density of 1150 kg/m^3, a Poisson coefficient of 0.33 and a viscous damping coefficient $\alpha = 0.005$. The aluminium plates are 1 mm thick with a width of 0.15 m, a Young's modulus of 210 GPa, a mass density of 7800 kg/m^3, a Poisson coefficient of 0.33 and a viscous damping coefficient $\alpha = 0.005$. Both aluminium plates are modeled with the WFE method by considering the transfer matrix of a substructure (see Section 3) whose length is 0.02 m as shown in Figure 2.

The FE mesh of the joint involves 60×15 four-nodes plane-stress rectangular elements with 2 DOFs per node, leading to 1952 DOFs where 32 DOFs are used for each interface. As for the substructure used to model the aluminium plates, it is meshed with 2×15 four-nodes plane-stress rectangular elements with 32 interface DOFs. Here, a total number of $m_{\mathtt{I}} = 10$ fixed interface modes are used to model the joint (cf. Section 2).

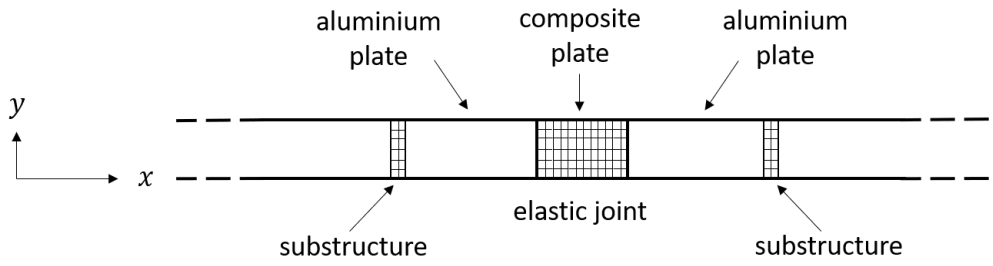


Figure 2: Two aluminium plates connected to a composite joint.

The composite plate (joint) has uncertain parameters and is modelled with the non-parametric and parametric approaches proposed in Section 4. Also, both aluminium plates have deterministic parameters and share the same wave modes. For the sake of simplicity, the present analysis will focus only on the first in-plane shearing wave mode of the plates. The deterministic/nominal values of the real parts of the reflection and transmission coefficients about this mode are displayed in Figure 3 on a frequency band $[1 - 40]$ Hz. It is worth noting that, due to the symmetry properties of the system, the reflection coefficients in plates 1 and 2 are identical, as well as the transmission coefficients, from plate 1 to plate 2 and from plate 2 to plate 1. It is seen in Figure 3 that the frequency evolution of the reflection and transmission coefficients is complex — i.e., it is neither constant nor slowly varying —, which can be explained for a two fold reason: (1) coupling which occurs between the considered wave mode and the vibrational modes of the joint; (2) mode conversion which occurs between the considered wave mode and the other wave modes of the waveguides.

The non-parametric approaches (Sections 4.1 and 4.2) are applied. The first approach involves considering the random matrices $\widehat{\mathbf{M}}$, $\widehat{\mathbf{C}}$ and $\widehat{\mathbf{K}}$ with $\delta_{\mathtt{M}} = \delta_{\mathtt{C}} = \delta_{\mathtt{K}} = 0.3$. The results are shown in Figure 4. The second one considers the random matrices $\widehat{\mathbf{M}}_{\alpha\alpha}$, $\widehat{\mathbf{C}}_{\alpha\alpha}$ and $\widehat{\mathbf{K}}_{\alpha\alpha}$, when the dispersion coefficients are computed by means of Eq. (31), see Figure 5. Here, the reflection/transmission coefficients issued from only one sample of random values of the non-parametric approaches are shown. It is seen that both non-parametric approaches generate transmission coefficients which meet the principle of reciprocity, i.e., which are identical from plate 1 to plate 2 and from plate 2 to plate 1. As for the reflection coefficients, it is seen that the non-parametric approach based on matrices $\widehat{\mathbf{M}}$, $\widehat{\mathbf{C}}$ and $\widehat{\mathbf{K}}$ generates reflection coefficients (for plates 1 and 2) which are not equal to each other as shown in Figure 4. This breaks somehow the symmetric nature of the problem. In contrast, it is seen in Figure 5 that the second non-parametric approach which uses the matrices $\widehat{\mathbf{M}}_{\alpha\alpha}$, $\widehat{\mathbf{C}}_{\alpha\alpha}$ and $\widehat{\mathbf{K}}_{\alpha\alpha}$ preserves the principle of reciprocity.

Also, the parametric approaches (Sections 4.2.1 and 4.2.2) are applied. The approaches based on the matrices $\widehat{\mathbf{M}}$, $\widehat{\mathbf{C}}$ and $\widehat{\mathbf{K}}$, and the matrices $\widehat{\mathbf{M}}_{\alpha\alpha}$, $\widehat{\mathbf{C}}_{\alpha\alpha}$ and $\widehat{\mathbf{K}}_{\alpha\alpha}$ yield reflection/transmission coefficients which meet the symmetry properties of the system as shown in Figures 6 and 7. The last parametric approach involves random fields for modelling the Young's modulus and the mass density (Section 4.2.2), when $\delta_E = \delta_\rho = 0.3$ and $l_c = 0.1L_x$, where L_x is the length of the joint. In this case, the generated random reflection coefficients show different values when compared to the previous cases (see Figure 8).

The statistics of the reflection and transmission coefficients can be highlighted using the MC method where $n_S = 1000$ simulations are considered. Figure 9 shows the mean values, the 5^{th} and the 95^{th} percentiles of the reflection and transmission coefficients obtained from the first non-parametric approach (Section 4.1). Note that the envelopes (5^{th} and the 95^{th} percentiles) of the reflection coefficients are identical between plates 1 and 2, unlike the individual sample case (Figure 4). Hence, it is seen that the random joint is symmetrical in an average sense, which agrees with the principle of reciprocity. Similar trends are found for the second non-parametric strategy as shown in Figure 10. Finally note that the non-parametric approaches lead to slightly different percentile bounds, which are due to the model assumptions.

Figures 11 and 12 show the mean values, the 5^{th} and the 95^{th} percentiles of the reflection and transmission coefficients issued from the parametric approaches described in Section 4.2.1. The first two approaches do not produce similar percentile bounds, which is especially highlighted for the transmission coefficients. It

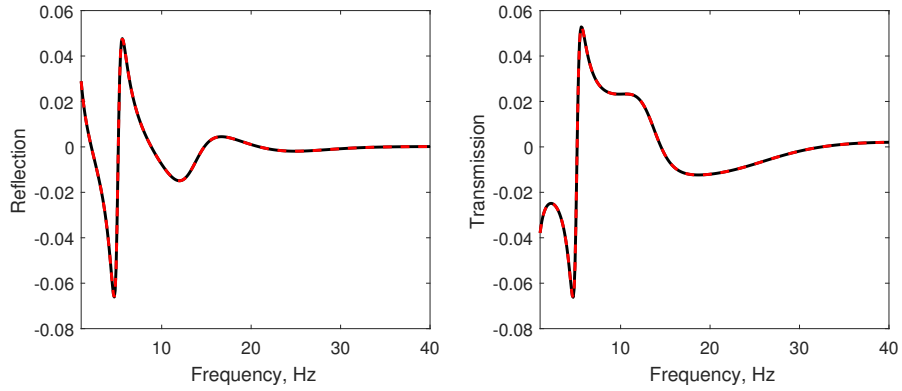


Figure 3: Nominal values (real parts) of the reflection coefficients (left) for plate 1 (black solid line) and plate 2 (red dashed line); Nominal values (real parts) of the transmission coefficient (right) from plate 1 to plate 2 (black solid line) and from plate 2 to plate 1 (red dashed line).

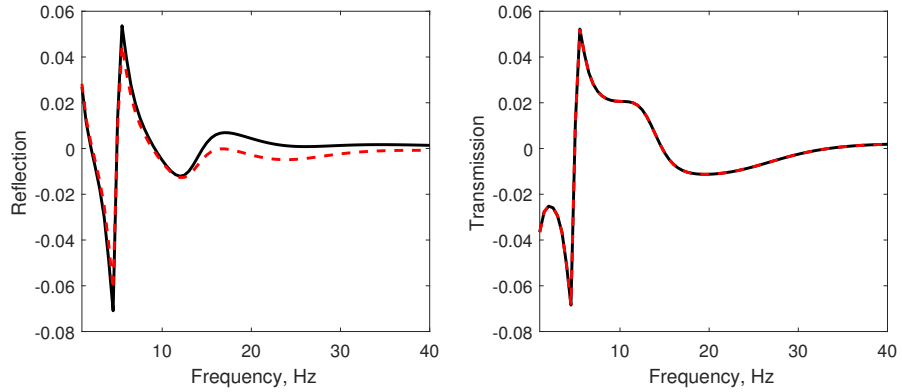


Figure 4: Real parts of the reflection coefficient (left) and transmission coefficients (right). One sample from the non-parametric approach with $\widehat{\mathbf{M}}$, $\widehat{\mathbf{C}}$ and $\widehat{\mathbf{K}}$.

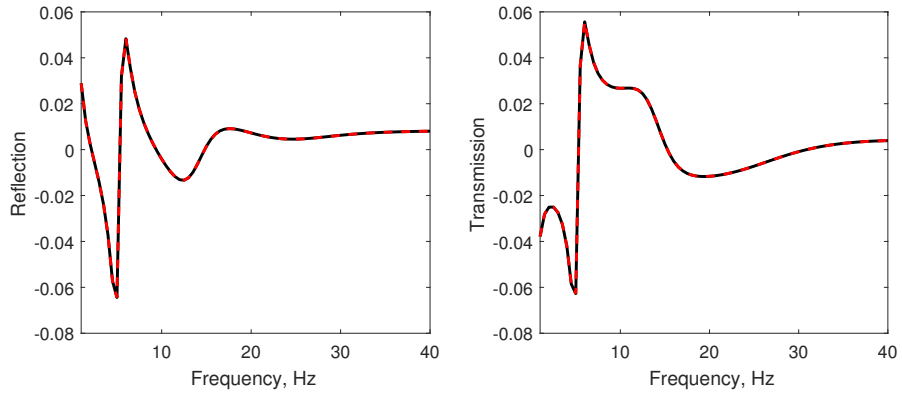


Figure 5: Real parts of the reflection coefficient (left) and transmission coefficients (right). One sample from the non-parametric approach with $\widehat{\mathbf{M}}_{\alpha\alpha}$, $\widehat{\mathbf{C}}_{\alpha\alpha}$ and $\widehat{\mathbf{K}}_{\alpha\alpha}$.

should be pointed out that the results displayed in Figure 12 are close to those in Figure 10. This gives credit to the non-parametric approach based on the random matrices $\widehat{\mathbf{M}}_{\alpha\alpha}$, $\widehat{\mathbf{C}}_{\alpha\alpha}$ and $\widehat{\mathbf{K}}_{\alpha\alpha}$ for modelling the joint. Also, this non-parametric approach appears to be robust in the sense that it provides upper and lower confidence bounds (Figure 10) which include those given by the first non-parametric approach (Figure 11).

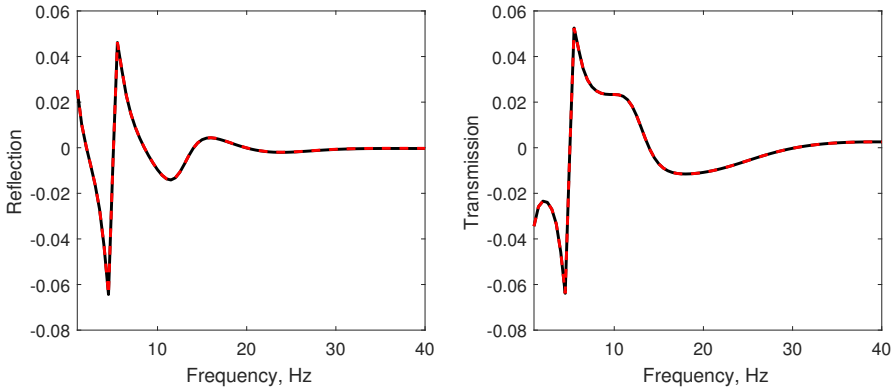


Figure 6: Real parts of the reflection coefficient (left) and transmission coefficients (right). One sample from the parametric model with $\widehat{\mathbf{M}}$, $\widehat{\mathbf{C}}$ and $\widehat{\mathbf{K}}$.

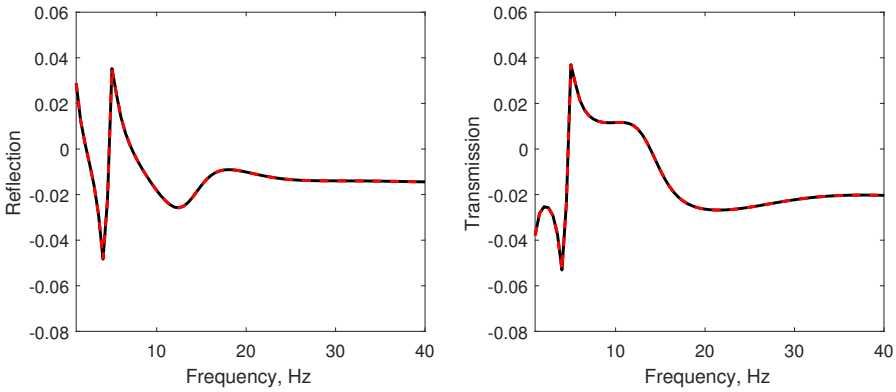


Figure 7: Real parts of the reflection coefficient (left) and transmission coefficients (right). One sample from the parametric model with $\widehat{\mathbf{M}}_{\alpha\alpha}$, $\widehat{\mathbf{C}}_{\alpha\alpha}$ and $\widehat{\mathbf{K}}_{\alpha\alpha}$.

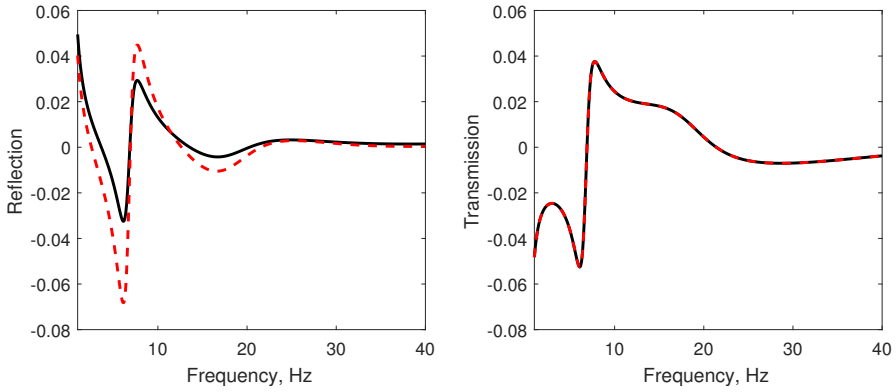


Figure 8: Real parts of the reflection coefficient (left) and transmission coefficients (right). One sample from the parametric model using random field properties with $\delta_E = \delta_\rho = 0.3$ and $l_c = 0.1L_x$.

Finally, Figure 13 shows the reflection and transmission coefficients issued from the parametric approach when the Young's modulus and the mass density of the joint are modelled with random fields (Section 4.2.2). Here, the results are clearly not compatible with the previous stochastic modelling strategies, not only in terms of overall percentile bounds but also in terms of frequency bands most affected by the randomness.

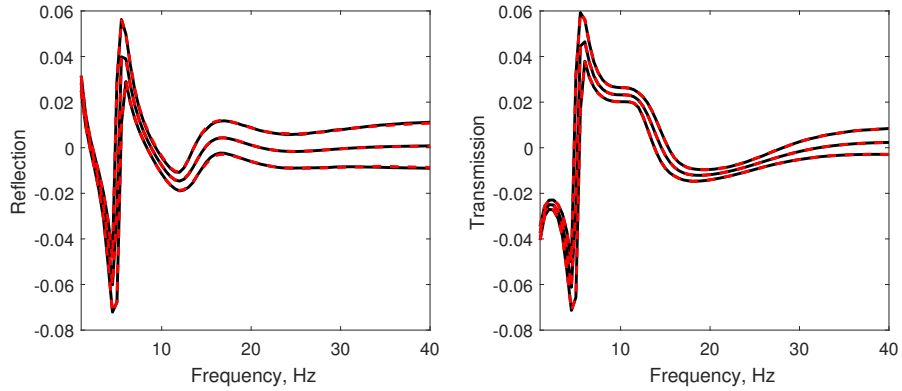


Figure 9: Real parts of the reflection coefficient (left) and transmission coefficients (right). Mean value, 95th and 5th percentiles issued from the non-parametric model with $\widehat{\mathbf{M}}$, $\widehat{\mathbf{K}}$ and $\widehat{\mathbf{C}}$.

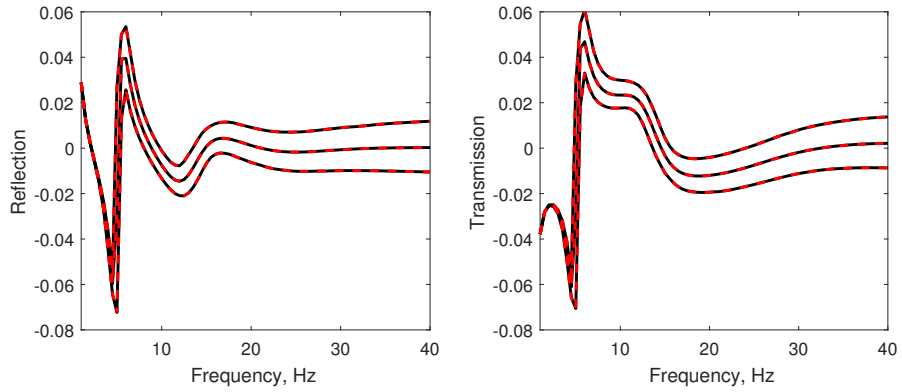


Figure 10: Real parts of the reflection coefficient (left) and transmission coefficients (right). Mean value, 95th and 5th percentiles issued from the non-parametric model with $\widehat{\mathbf{M}}_{\alpha\alpha}$, $\widehat{\mathbf{K}}_{\alpha\alpha}$ and $\widehat{\mathbf{C}}_{\alpha\alpha}$.

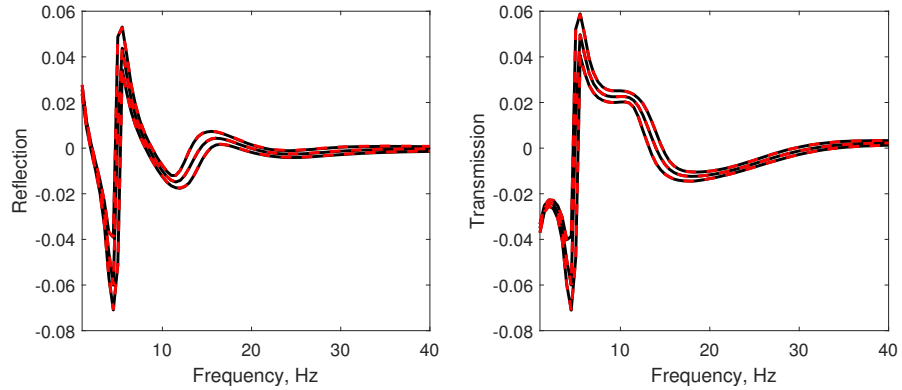


Figure 11: Real parts of the reflection coefficient (left) and transmission coefficients (right). Mean value, 95th and 5th percentiles issued from the parametric model with $\widehat{\mathbf{M}}$, $\widehat{\mathbf{K}}$ and $\widehat{\mathbf{C}}$.

6 Concluding remarks

In this work, a stochastic modelling of elastic joints connecting periodic structures has been proposed. The periodic structures are modelled using the WFE method, while the joints are modelled with the FE method and the CB reduction technique. The scattering matrix of the joints, which provides the wave reflection/transmission coefficients in the periodic structures, has been formulated. The statistical behaviour of

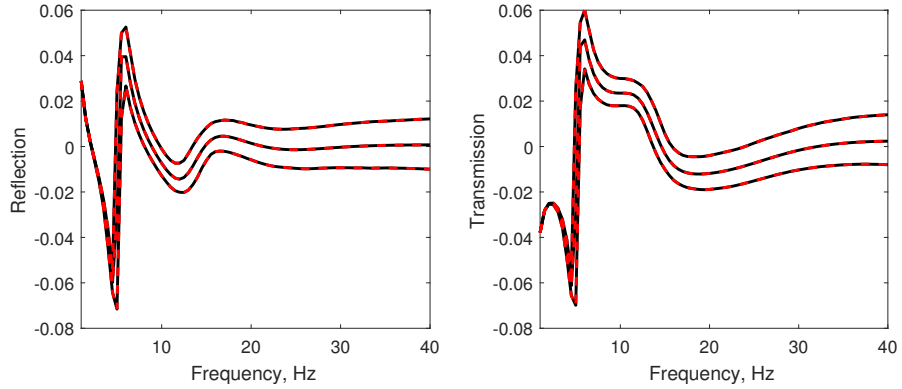


Figure 12: Real part of the reflection coefficient (left) and transmission coefficients (right). Mean value, 95th and 5th percentiles issued from the parametric model with $\widehat{\mathbf{M}}_{\alpha\alpha}$, $\widehat{\mathbf{K}}_{\alpha\alpha}$ and $\widehat{\mathbf{C}}_{\alpha\alpha}$.

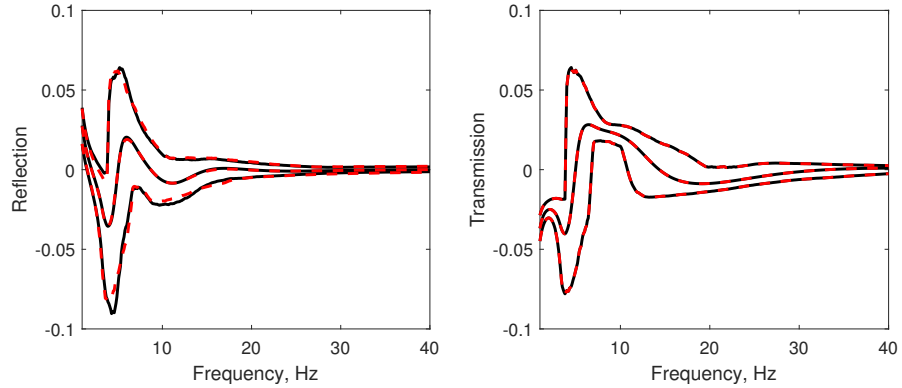


Figure 13: Real part of the reflection coefficient (left) and transmission coefficients (right). Mean value, 95th and 5th percentiles issued from the parametric model using random field properties with $\delta_E = \delta_\rho = 0.3$ and $l_c = 0.1L_x$.

the reflection/transmission coefficients has been analyzed. For this purpose, two non-parametric approaches have been investigated which use the RMT for modelling the joints. Also, three parametric approaches have been considered for modelling the joints. The first two ones involve perturbating the component modes of the joints. The last one uses a random field model of the material properties of the joints. It has been shown that the choice of a stochastic modelling impacts the determination of the reflection/transmission coefficients. One good and robust choice would consists in choosing the non-parametric approach which uses the CB matrices $\widehat{\mathbf{M}}_{\alpha\alpha}$, $\widehat{\mathbf{C}}_{\alpha\alpha}$ and $\widehat{\mathbf{K}}_{\alpha\alpha}$ of the joints. Future works will concern the stochastic modelling of the whole scattering matrix of joints with complex shapes.

Acknowledgements

The authors gratefully acknowledge the financial support of the Federal District Research Foundation (FAPDF) Process number 0193.001507/2017.

References

[1] R. A. Ibrahim, C. L. Pettit, Uncertainties and dynamic problems of bolted joints and other fasteners, Journal of Sound and Vibration 279 (3) (2005) 857–936. doi:10.1016/j.jsv.2003.11.064.

[2] M. Beshara, A. J. Keane, Vibrational energy flows in beam networks with compliant and dissipative joints, Journal of Sound and Vibration 203 (2) (1997) 321–339. doi:10.1006/jsvi.1996.0889.

[3] J. R. F. Arruda, J. M. C. Santos, Mechanical joint parameter estimation using frequency response functions and component mode synthesis, Mechanical Systems and Signal Processing 7 (6) (1993) 493–508. doi:10.1006/mssp.1993.1029.

[4] J. M. Muggleton, T. P. Waters, B. R. Mace, B. Zhang, Approaches to estimating the reflection and transmission coefficients of discontinuities in waveguides from measured data, Journal of Sound and Vibration 307 (1) (2007) 280–294. doi:10.1016/j.jsv.2007.07.007.

[5] R. Octavio de Alba Alvarez, Vibration analysis of uncertain spot-welded structures, phd, University of Southampton (May 2012).
URL http://eprints.soton.ac.uk/348956/

[6] F. Dohnal, B. R. Mace, N. S. Ferguson, Joint Uncertainty Propagation in Linear Structural Dynamics Using Stochastic Reduced Basis Methods, AIAA Journal 47 (4) (2009) 961–969. doi:10.2514/1.38974.

[7] C. Soize, A comprehensive overview of a non-parametric probabilistic approach of model uncertainties for predictive models in structural dynamics, Journal of Sound and Vibration 288 (3) (2005) 623–652. doi:10.1016/j.jsv.2005.07.009.

[8] Soize C., ChebliŁ H., Random Uncertainties Model in Dynamic Substructuring Using a Non-parametric Probabilistic Model, Journal of Engineering Mechanics 129 (4) (2003) 449–457. doi:10.1061/(ASCE)0733-9399(2003)129:4(449).

[9] M. P. Mignolet, C. Soize, J. Avalos, Nonparametric Stochastic Modeling of Structures with Uncertain Boundary Conditions/Coupling Between Substructures, AIAA Journal 51 (6) (2013) 1296–1308. doi:10.2514/1.J051555.

[10] F. F. Real, F. Fontanela, T. G. Ritto, A. Batou, C. Desceliers, A probabilistic model of uncertainties in the substructures and interfaces of a dynamical system: application to the torsional vibration of a drill-string, Archive of Applied Mechanics 87 (4) (2017) 685–698. doi:10.1007/s00419-016-1217-6.

[11] B. R. Mace, D. Duhamel, M. J. Brennan, L. Hinke, Finite element prediction of wave motion in structural waveguides, The Journal of the Acoustical Society of America 117 (5) (2005) 2835–2843. doi:10.1121/1.1887126.

[12] J. M. Mencik, M. N. Ichchou, Multi-mode propagation and diffusion in structures through finite elements, European Journal of Mechanics - A/Solids 24 (5) (2005) 877–898. doi:10.1016/j.euromechsol.2005.05.004.

[13] J.-M. Mencik, New advances in the forced response computation of periodic structures using the wave finite element (WFE) method, Computational Mechanics 54 (3) (2014) 789–801. doi:10.1007/s00466-014-1033-1.

[14] M. N. Ichchou, J.-M. Mencik, W. J. Zhou, Wave finite elements for low and mid-frequency description of coupled structures with damage, Computer Methods in Applied Mechanics and Engineering 198 (15-16) (2009) 1311–1326.

[15] J. M. Renno, B. R. Mace, Calculation of reflection and transmission coefficients of joints using a hybrid finite element/wave and finite element approach, Journal of Sound and Vibration 332 (9) (2013) 2149–2164. doi:10.1016/j.jsv.2012.04.029.

[16] J. M. Mencik, Model reduction and perturbation analysis of wave finite element formulations for computing the forced response of coupled elastic systems involving junctions with uncertain eigenfrequencies, Computer Methods in Applied Mechanics and Engineering 200 (45) (2011) 3051–3065. doi:10.1016/j.cma.2011.06.014.

[17] F. Bouchoucha, M. N. Ichchou, M. Haddar, Diffusion matrix through stochastic wave finite element method, Finite Elements in Analysis and Design 64 (2013) 97–107. doi:10.1016/j.finel.2012.09.008.

[18] M. A. B. Souf, M. Ichchou, O. Bareille, N. Bouhaddi, M. Haddar, Dynamics of random coupled structures through the wave finite element method, Engineering Computations 32 (7) (2015) 2020–2045. doi:10.1108/EC-08-2014-0173.

[19] S. Ben, O. Bareille, M. Ichchou, M. Haddar, The wave finite element method for uncertain systems with model uncertainty, Proceedings of the Institution of Mechanical Engineers, Part C: Journal of Mechanical Engineering Science 230 (6) (2015) 974–985. doi:10.1177/0954406215617197.

[20] N. Higham, Analysis of the cholesky decomposition of a semi-definite matrix, Reliable Numerical Computation, Oxford University Press, Oxford (1990) 161–185.

[21] N. J. Higham, The Matrix Computation Toolbox, —http://www.ma.man.ac.uk/ higham/mctoolbox—.

[22] W. X. Zhong, F. W. Williams, On the direct solution of wave propagation for repetitive structures, Journal of Sound and Vibration 181 (3) (1995) 485–501.

[23] C. Soize, Uncertainty Quantification - An Accelerated Course with Advanced Applications in Computational Engineering, 1st Edition, Interdisciplinary Applied Mathematics, Elsevier, 2017.

[24] C. Soize, Maximum entropy approach for modeling random uncertainties in transient elastodynamics, The Journal of the Acoustical Society of America 109 (5) (2001) 1979–1996. doi:10.1121/1.1360716.

[25] J. Legault, R. S. Langley, J. Woodhouse, Physical consequences of a nonparametric uncertainty model in structural dynamics, Journal of Sound and Vibration 331 (25) (2012) 5469–5487. doi:10.1016/j.jsv.2012.07.017.

[26] R. Sampaio, E. Cataldo, Comparing Two Strategies to Model Uncertainties in Structural Dynamics, Shock and Vibration 17 (2) (2010) 171–186, doi: 10.3233/SAV-2010-0505.

[27] G. I. Schuëller, H. J. Pradlwarter, Uncertain linear systems in dynamics: Retrospective and recent developments by stochastic approaches, Engineering Structures 31 (11) (2009) 2507–2517. doi:10.1016/j.engstruct.2009.07.005.

[28] R. Ghanem, P. D. Spanos, Stochastic Finite Elements: A Spectral Approach, revised Edition, Dover Publications, Minneola, N.Y., 2012.

[29] E. Vanmarcke, Random Field: Analysis and Synthesis, 2nd Edition, Word Scientific, Cambridge, MA, 2010.

[30] S. P. Huang, S. T. Quek, K. K. Phoon, Convergence study of the truncated KarhunenLoève expansion for simulation of stochastic processes, International Journal for Numerical Methods in Engineering 52 (2001) 1029–1043. doi:10.1002/nme.255.

[31] K. K. Phoon, S. P. Huang, S. T. Quek, Simulation of second-order processes using Karhunen-Loève expansion, Computers & Structures 80 (12) (2002) 1049–1060. doi:10.1016/S0045-7949(02)00064-0.

Vehicle model likelihood computation using a probabilistic complex FRF matrix statistical reduction

J. Reyes[1,2]**, C. Soize**[1]**, L. Gagliardini**[2]**, G. Brogna**[2,3]
[1] Laboratoire Modélisation et Simulation Multi Echelle, Université Paris Est Marne la Vallée
5 Boulevard Descartes, 77420 Champs-sur-Marne, France

[2] PSA Group, Centre Technique de Vélizy,
Route de Gisy, 78140 Vélizy-Villacoublay, France

[3] Laboratoire Vibrations Acoustique,Université de Lyon
F-69621, Villeurbanne, FRANCE
e-mail: **justin.reyes@mpsa.com**

Abstract

In a probabilistic context, improvement of vibroacoustic models prediction capabilities requires an adapted indicator to compare measurements with the predictions. The likelihood is used to perform such comparisons as soon as the probability of a given result may be estimated. Vibroacoustic analysis mainly relies on complex matrix-valued Frequency Response Functions that can be easily measured and computed. The likelihood of such matrices is investigated. A two stage statistical reduction is proposed in order to separate statisticaly independent components with random complex amplitudes. Their probability may be computed independently. The joint probability density fonction of the real and imaginary parts of each independent random variables is estimated using a nonparametric stochastic model implemented in MSC/NASTRAN and the Monte Carlo simulation method. The proposed statistical reduction presents many interesting properties including data reduction or related to the physical behavior of the studied system.

1 Introduction

In the automotive industry, computational vibroacoustic models are used for designing automobiles against noise.(see for instance [4, 15, 2]). However, the computational vibroacoustic models can have high dimension: the one considered in this paper has fifteen million of degrees-of-freedom (DOFs) for the structural part and the coupled acoustic cavity has about eight million of DOFs. This high dimension of the computational vibroacoustic model brings some difficulties that are mostly overpassed introducing the reduced-order computational vibroacoustic model (ROM) contructed with a modal projection.
Since automobiles are an industrial product, they are subjected to manufacturing uncertainties. Considering the use of simulation during the design process, unvoidable future changes may also be considered as uncertainties. Due to the introduction of simplifications in the modeling process, there are uncertainties in the computational vibroacoustic model, which have to be taken into account. The nonparametric probabilistic approach of uncertainties was introduced ten years ago to handle any kind of uncertainties in large computational vibroacoustic models such as the automotive ones.
In the vibroacoustic analysis, FRFs are widely used to control the structure-borne noise transmission in the case of multiple transmission paths. The advantage of the matrix-valued FRF is that, even for such complex structures such as automobiles, it always provides a simple linear relationship between one vector-valued in-

put (excitation) and one vector-valued output (observation). The computational vibroacoustic model allows an easy computation of FRF matrices for a given set of sampled frequencies. The FRF complex matrices can also be measured experimentally. FRF matrices can also be processed as a results of the stochastic computational vibroacoustic model using the realizations. In order to compare experimental measurements with the results given by the stochastic computational vibroacoustic model, we propose an approach based on the likelihood [11, 14], which was introduced in [5, 13]. In this work, we use the likelihood for quantifying the "distance" between the experiments and the stochastic computational vibroacoustic model. For this purpose, the quantity of interest is the complex matrix-valued FRF, $[\text{FRF}] = \{\omega \mapsto [\text{FRF}(\omega)]\}$. Both the parameters uncertainties and the model uncertainties induced by the modeling errors are taken into account by the nonparametric probabilistic approach of uncertainties [12, 4, 13, 9]. The principle of this approach consists in replacing the generalized matrices of the reduced-order vibroacoustic computational model by random matrices whose probability distributions are constructed [14] using the maximum entropy principle from Information Theory. A set of realizations of the random FRF matrices is obtained using the Monte-Carlo method [10]. Since the statistical estimates of the quantities of interest require a relatively large number of realizations to obtain convergence, the required storage space may be tremendous.
The proposed approach aims to quantifying the consistency of the stochastic comptational vibroacoustic model – described by a set of realizations – with the measurements. It is based on two successive statistical reductions that are constructed using Independent Component Analysis (ICA) [7]. These statistical reductions hopefully lead us to a high-data compression.
In this paper, we will first introduce the nonparametric probabilistic approach of uncertainties together with the FRFs computations. Then, the two statistical reductions will be presented and applied to a computational vibroacoustic model of a car. The "distance" between the predictions and the experiments is then computed using the likelihood function. Finally, some observations will be discussed and assessed.

2 Brief summary of the nonparametric probabilistic approach of uncertainties for computational vibroacoustic models

A computational vibroacoustic model is often constructed at early design stage in order to predict the response of the real system, which will be, later, manufactured from the design. The modeling process introduces two kinds of uncertainties : the system parameters uncertainties and the model uncertainties. To achieve some predictability, these uncertainties have to be taken into account. However, the usual parametric probabilistic approach does not consider the model uncertainties. We will use the nonparametric probabilistic approach of uncertainties [12, 4, 9, 14] which takes into account both kind of uncertainties. Let us now introduce all the notations that will be used along this paper. The nominal values (chosen as the mean values) of the generalized are replaced by random matrices. The probability distributions of these random matrices depend on six hyperparameters δ which control the level of uncertainties for each type of forces occuring in the computational vibroacoustic model. In this paper, uncertainties on the coupling matrix is not taken into account. The MSC/Nastran software, in which the nonparametic probabilistic approach has been implemented [8], is used to produce $n = 1, \ldots, N_{MC}$ realizations of the matrix-valued FRF, for which the values of the six hyperparameters δ are those given in [4].

2.1 Nonparametric probabilistic approach

In this paper we consider a linear elastoacoustic problem of a complex structure coupled with an internal acoustic cavity. The computational model is constructed using the finite element method (FEM) as shown in Fig.1. The problem is formulated in the frequency domain ω (angular frequency). We are interested in computing FRF of the system in the frequency band analysis noted $\mathcal{B}$ defined by $\mathcal{B} = [\omega_{min}, \omega_{max}]$ with $0 < \omega_{min} < \omega_{max}$ (with $\omega = 2\pi f$). The complex vector $\mathbf{u}(\omega)$ of the m_s degree of freedom (DOF) of the

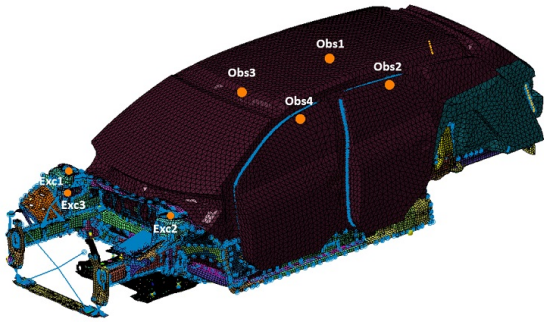


Figure 1: Finite element mesh of the computational model with the excitation and observation points The comptational model has 15 million structural DOFs and 8 million DOFs in the acoustic cavity

FEM, corresponding to the discretization of the displacements field. Let $\mathbf{p}(\omega)$ the complex vector of the m_f DOFs representing the discretization of the acoustical pressure field. The finite element model is considered as the mean model and is written in the frequency domain as

$$\begin{bmatrix} -\omega^2[M^s] + i\omega[D^s] + [K^s] & [C] \\ \omega^2\,[C]^T & -\omega^2[M^f] + i\omega[D^f] + [K^f] \end{bmatrix} \quad \begin{bmatrix} \mathbf{u}(\omega) \\ \mathbf{p}(\omega) \end{bmatrix} \quad = \quad \begin{bmatrix} \mathbf{f}^s(\omega) \\ \mathbf{f}^f(\omega) \end{bmatrix} \tag{1}$$

Where $[M^s]$, $[D^s]$, and $[K^s]$ are the $(m_s \times m_s)$ positive-defined symmetric real mass matrix, damping and stiffness matrices of the structure where m_s is the number of structural DOFs. And $[M^f]$, $[D^f]$, and $[K^f]$ are the $(m_f \times m_f)$ positive-defined symmetric real mass matrix, damping and stiffness matrices of the structure where m_f is the number of acoustical DOFs. The complex vectors $\mathbf{f}^s(\omega)$ and $\mathbf{f}^f(\omega)$ is related to the discretization of the external forces applied respectively on the structure and in the cavity. $[C]$ the coupling complex matrix between the structure and the acoustic cavity of dimension $(m_s \times m_f)$. For the complex dynamical structures of interest, the number of DOFs can be relatively high. The next step is to construct the nominal ROM which we will consider as the reduced mean computational model. It is constructed by the usual method of projection on subspace spanned by a set of elastic modes. such that,

$$([K^s] - \lambda^s[M^s])\psi^s = 0 \tag{2}$$
$$([K^f] - \lambda^f[M^f])\phi^s = 0 \tag{3}$$
$$\mathbf{u}(\omega) = [\Psi^s]\mathbf{q}^s(\omega), \tag{4}$$
$$\mathbf{p}(\omega) = [\Phi^f]\mathbf{q}^f(\omega), \tag{5}$$
$$\mathbb{F}^s(\omega) = [\Psi^s]^T\mathbf{f}^s(\omega), \tag{6}$$
$$\mathbb{F}^f(\omega) = [\Phi^f]^T\mathbf{f}^f(\omega), \tag{7}$$
$$[\mathcal{C}] = [\Psi^s]^T[C(\omega)][\Phi^f]. \tag{8}$$

Where $0 < \lambda_1^s \leq \ldots \leq \lambda_{n_s}^s$ are the eigenvalues associated with the eigenvectors $\psi_1^s, \ldots, \psi_{n_s}^s$. The same application is done for λ^f and ϕ^f. $[\Psi^s]$ reprensents the matrix of the eigenvectors such that $[\Psi^s] = [\psi_1^s, \ldots, \psi_{n_s}^s]$ and $[\Phi^f] = [\phi_1^f, \ldots, \phi_{n_f}^f]$. The nominal ROM is written as

$$\begin{bmatrix} -\omega^2[\mathcal{M}^s] + i\omega[\mathcal{D}^s] + [\mathcal{K}^s] & [\mathcal{C}] \\ \omega^2[\mathcal{C}]^T & -\omega^2[\mathcal{M}^f] + i\omega[\mathcal{D}^f] + [\mathcal{K}^f] \end{bmatrix} \quad \begin{bmatrix} \mathbf{q}^s(\omega) \\ \mathbf{q}^f(\omega) \end{bmatrix} \quad = \quad \begin{bmatrix} \mathbb{F}^s(\omega) \\ \mathbb{F}^f(\omega) \end{bmatrix} \tag{9}$$

The use of nonparametric probabilistic aproach of uncertainties yields, the following stochastic ROM,

$$\begin{bmatrix} -\omega^2[\mathbf{M}^s] + i\omega[\mathbf{D}^s] + [\mathbf{K}^s] & [\mathbf{C}] \\ \omega^2\,[\mathbf{C}]^T & -\omega^2[\mathbf{M}^f] + i\omega[\mathbf{D}^f] + [\mathbf{K}^f] \end{bmatrix} \quad \begin{bmatrix} \mathbf{Q}^s(\omega) \\ \mathbf{Q}^f(\omega) \end{bmatrix} \quad = \quad \begin{bmatrix} \mathbb{F}^s(\omega) \\ \mathbb{F}^f(\omega) \end{bmatrix} \tag{10}$$

Each random matrix $[\mathbf{A}]$ depends on the hyperparameter $\delta_A > 0$ written as,

$$\delta_A = \sqrt{\frac{E\{|||[\mathbf{G}_A] - [\underline{G}_A]||_F^2\}}{|||[\underline{G}_A]||_F^2}}, \tag{11}$$

in which $[\mathbf{G}_A]$ is the random matrix germ of random matrix $[\mathbf{A}]$.

2.2 Matrix-valued random frequency response function

For all ω fixed in the frequency band of analysis, $\mathcal{B}$, Eq. (9) has a unique solution

$$\begin{bmatrix}\mathbf{Q}^s(\omega)\\ \mathbf{Q}^f(\omega)\end{bmatrix} = \underbrace{\begin{bmatrix}-\omega^2[\mathbf{M}^s] + i\omega[\mathbf{D}^s] + [\mathbf{K}^s] & [\mathbf{C}]\\ \omega^2\,[\mathbf{C}]^T & -\omega^2[\mathbf{M}^f] + i\omega[\mathbf{D}^f] + [\mathbf{K}^f]\end{bmatrix}^{-1}}_{[\mathbf{Z}(\omega)]} \begin{bmatrix}\mathbb{F}^s(\omega)\\ \mathbb{F}^f(\omega)\end{bmatrix} \tag{12}$$

In this paper, it is assumed that $\mathbb{F}^f(\omega) = 0$. Consequently Eq. (12) yields

$$\mathbf{Q}^f(\omega) = [\mathbf{Z}_{21}(\omega)]\mathbb{F}^s(\omega) \tag{13}$$

in which, $[\mathbf{Z}_{21}(\omega)]$ the random block matrix. From Eqs. (5) and (6), we obtain

$$\mathbf{P}(\omega) = \underbrace{[\Phi^f][\mathbf{Z}_{21}][\Psi^s]^T}_{[\mathbf{H}(\omega)]}\mathbf{f}^s(\omega) \tag{14}$$

with $[\mathbf{H}(\omega)]$ is a random complex matrix of dimension $(N_e \times N_o)$. The output of Nastran can be chosen between the displacement, velocity or acceleration field for the structure and the acoustic pressure field for the internal cavity. The output represents directly the FRF. The finite element model that is used is presented in Fig. 1. The observation points (Obs.1-4) are located at the ears level of the persons in the vehicle. The structural excitations (Exc.1-3) are located to the supports of the engine.

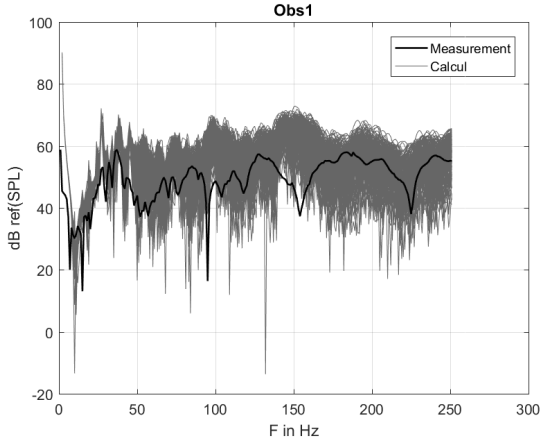


Figure 2: Two hundred realizations of a random FRF computed with stochastic ROM (grey), and corresponding FRF from an experimental measurement (black)

In Fig.2, we can see the N_{MC} realizations of the random FRF computed with Nastran and the corresponding experimental measurement. It can be noticed that the dispersion increases with the frequency. Indeed, it is widely known that the level of uncertainties increases with the frequency. In Fig.2, we can see that, in the low-frequency band $[0 - 15]$ Hz, the measurement is far from the realizations constructed with the stochastic ROM. That can be explained partly by measurement problems. This band will not be considered in the following.

3 Statistical reductions

In this section, we will propose two statistical reductions based on the use of the Independent Component Analysis (ICA). The main difference with the Principal Component Analysis (PCA) is that the generalized coordinates are statistically independent. This approach has been widely used [7]. The ICA allows for yielding a better physical interpretation of the extracted components as explained in Section 3.1. We will use the Joint Approximation Diagonalization of Eigen-matrices (JADE) algorithm as presented in [1], which uses the fourth-order moments. JADE computes the matrix such as the sum of all nondiagonal terms of the fourth-order moments matrix equal to zero.
Let $\mathbb{M}_{n,m}(\mathbb{C})$ be the set of all the $(n \times m)$ complex matrices. Let $\omega_1, \ldots, \omega_{N_f}$ be the frequency sampling. Let N_o be the number of observation DOFs, and let N_e be the number of excitation DOFs. The FRF complex random matrix is written as $[\text{FRF}(\omega_j)]$ with value in $\mathbb{M}_{N_o,N_e}(\mathbb{C})$, with $j = 1, \ldots, N_f$. Let be $N = N_o \times N_e$. The complex random matrix $[\text{FRF}(\omega_j)]$ is reshaped as the random vector $\mathbf{F}(\omega_j)$ with values in $\mathbb{C}^N$. Let $[\mathbf{Y}] = [\mathbf{F}(\omega_1), \ldots, \mathbf{F}(\omega_{N_f})]$ be the random matrix with values in $\mathbb{M}_{N,N_f}(\mathbb{C})$. The N_{MC} independent realizations of random matrix $[\mathbf{Y}]$ are denoted by $\{[Y_n], n = 1, \ldots, N_{\text{MC}}\}$ and are constructed with the stochastic ROM.

3.1 First statistical reduction based on ICA

The first statitical reduction based on ICA is devoted to the construction of a frequency basis by subbands for which the coordinates are statisticaly independent. We introduce

$$[R] = \frac{1}{N_{\text{MC}}} \sum_{n=1}^{N_{\text{MC}}} [Y_n]^* [Y_n] \quad \in \mathbb{M}_{N_f,N_f}(\mathbb{C}) \tag{15}$$

in which $[Y_n]^* = [\overline{Y}_n]^T$. The eigenvalue problem $[R]x^\alpha = \lambda_\alpha x^\alpha$, with $\alpha = 1, \ldots, N_f$, is solved for the Hermitian complex matrix $[R]$. The real eigenvalues are sorted in decreasing order. Matrix $[R]$ is represented with the first $N_p \leq N_f$ eigenvalues such that $[R] \simeq \sum_{\alpha=1}^{N_p} \lambda_\alpha x^\alpha (x^\alpha)^*$, that is rewritten as,

$$[R] = [x][\Lambda][x]^*, \tag{16}$$

in which $[\Lambda]$ is the diagonal matrix of the eigenvalues and where $[x] = [x^1, \ldots, x^{N_p}]$ is the matrix of the eigenvectors. It should be noted that

$$[x]^*[x] = [I_{N_p}], \tag{17}$$

It can easily be proven that each realization $[Y_n]$ can be written as

$$[Y_n] = [A_n][x]^* \tag{18}$$

in which, $[A_n] \in \mathbb{M}_{N,N_p}(\mathbb{C})$ is given by the projection on $[Y_n]$. Using Eq.(17),

$$[A_n] = [Y_n][x]. \tag{19}$$

Let

$$[c] = [x]^* \tag{20}$$

be the complex $(N_p \times N_f)$ matrix, for which its columns are denoted by c^j with $j = 1, \ldots, N_f$: $[c] = [c^1, \ldots, c^{N_f}]$. Let us introduce the random vector $\mathbf{c}$ with values in $\mathbb{C}^{N_p}$ whose realizations are $c^1, \ldots, c^{N_f}$. The Independent Component Analysis (ICA) of random vector $\mathbf{c}$ is carried out and yields,

$$[c] = [b][S], \tag{21}$$

in which $[b]$ is a $(N_p \times N_p)$ complex matrix and $[S]$ an $(N_p \times N_f)$ complex matrix whose columns $S^1, \ldots, S^{N_p}$ are independent. From Eqs.(18), (20),(21), it can be deduced that,

$$[Y_n] = [\widehat{A}_n][S], \tag{22}$$

in which $[\widehat{A}_n]$ is written as

$$[\widehat{A}_n] = [A_n][b] \quad \in \mathbb{M}_{N,N_p}(\mathbb{C}). \tag{23}$$

The frequency band analysis is $\mathcal{B} = [25, 250]Hz$. On the frequency basis $[c]$, there are N_p independent components. The threshold for the cumulative energy is fixed at 95%, which is sufficiently high to resynthesize the FRF by inverse step.

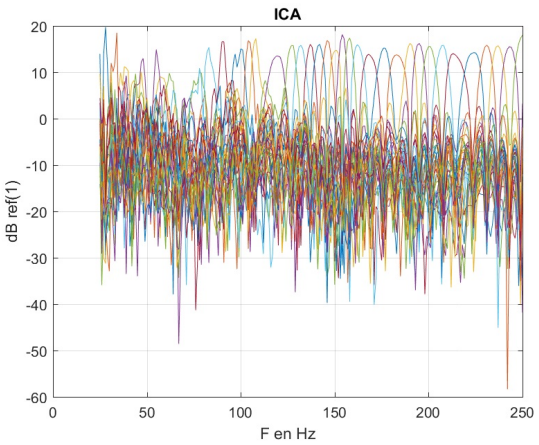


Figure 3: Frequential independent components from JADE algortihm with ICA

Figure 3 shows the N_p independent components issued from the ICA. We can see peaks all along the frequency band $\mathcal{B}$. It can be seen that each component has a different contribution over the frequency band. Consequently, for each subband of $\mathcal{B}$, only the components that have the main contributions are kept. This means that the reductions is performed by subband and not globally for all the frequency band of analysis. We take the frequency value at the maximum of each independent component from the first ICA statistical reduction from Fig. 3. It can be seen that the subbands are narrower for the lowest frequencies. As the frequency increases, the width of the subbands increases.

3.2 Second statistical reduction based on ICA

In the second statistical reduction, we construct a spatial basis over the observations and excitations DOFs. From the N_p independent components obtained from the first statistical reduction over the frequency band, we determine the components that have contributions on the spatial basis. We use exactly the same methodology that the one presented in section 3.1. The independent component analysis is reused for constructing a second statistical reduction of random matrix $[\widehat{\mathbf{A}}]$ whose realizations are $\{[\widehat{A}_n], n = 1, \ldots, N_{\text{MC}}\}$ that are defined by Eq.(23), and that allows for obtaining the following representation,

$$[\widehat{A}_n]_{k\alpha} = \sum_{\beta=1}^{\widehat{N}_p(\alpha)} [\widehat{F}]_{k\beta}[\chi_n]_{\beta\alpha} \tag{24}$$

with $k = 1, \ldots, N$ and $\alpha = 1, \ldots, N_p$, in which $\widehat{N}_p \leq N$, where $[\widehat{F}(\alpha)]$ and $[\chi_n(\alpha)]$ are complex matrices of dimension $(N \times \widehat{N}_p(\alpha))$ and $(\widehat{N}_p(\alpha) \times 1)$ respectively. The matrix $[\chi_n]$ represents the basis. Substituting

Eq. (24) into Eq. (22) yields

$$[Y_n]_{kj} = \sum_{\alpha=1}^{N_p} \sum_{\beta=1}^{\widehat{N}_p(\alpha)} [\widehat{F}]_{k\beta} [\chi_n]_{\beta\alpha} [S]_{\alpha j} \tag{25}$$

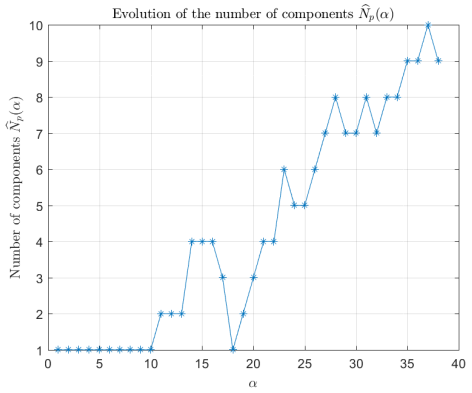


Figure 4: Number of component $\widehat{N}_p(\alpha)$ over the $\alpha = 1, , N_p$ of the first statistical reduction.

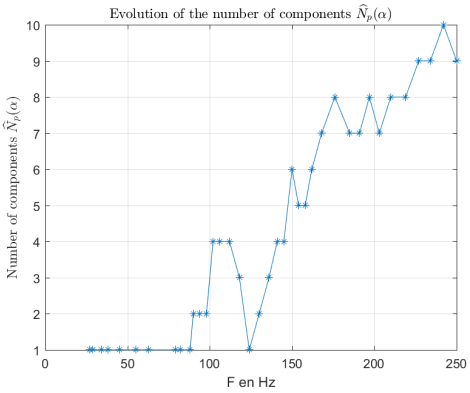


Figure 5: Number of component $\widehat{N}_p(\alpha)$ over the frequency value of the maximum of each α of the first statistical reduction

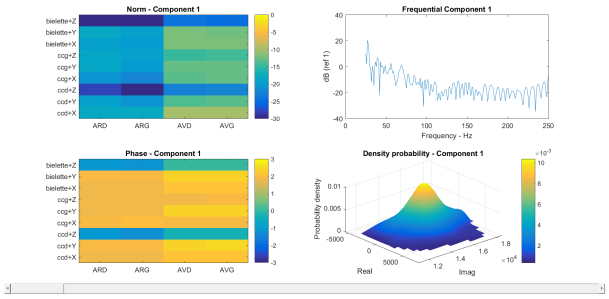


Figure 6: Norm (upper left), phase (bottom left), frequential component (upper right) and the probability density (bottom right) for $\gamma = 1$

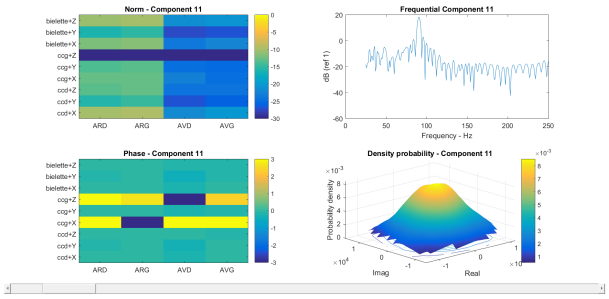


Figure 7: Norm (upper left), phase (bottom left), frequential component (upper right) and the probability density (bottom right) for $\gamma = 11$

This second statistical reduction is applied to each component obtained by the first statistical reduction. In Fig.4 and 5, it can be noticed that the number of components from the second statistical reduction increases with the frequency. This can be explained by the fact that the effects of the model uncertainties increase with the frequency. Figures 4 and 5 show that there is an analogy between the value of α and the frequency band. In fact, it can be seen in Fig. 3 that each component of the first statistical reduction has a contribution over the frequency subbands. The probability density function of the random variable $[\chi]_{\beta,\alpha}$ is estimated with its realizations $[\chi_n]_{\beta,\alpha}$. Such a probability density function is shown in the bottom right in Fig. 6 and Fig. 7. Moreover, Fig. 6 and Fig. 7 show the paticipation of each excitation point for each observation point (left figures up and bottom). The upper-right figure represents the frequential independent component of the first statistical reduction.

3.3 Projection of an experimental measurement

Only one experimental measurement is available and is projected using the two statistical reductions in order to obtain the $(\widehat{N}_p \times N_p)$ complex matrix $[\chi^{exp}]$. For all $\ell = 1, \ldots, \nu_{\text{exp}}$, let $[Y^{\text{exp}}]$ be the $(N \times N_f)$ complex

matrix related to the experimental measurement, which is written as

$$[Y^{\exp,\ell}] = [\widehat{A}^{\exp,\ell}][S]\,, \tag{26}$$

$$[\widehat{A}^{\exp,\ell}]_{k\alpha} = \sum_{\beta=1}^{\widehat{N}_p(\alpha)} [\widehat{F}]_{k\beta}[\chi^{\exp,\ell}]_{\beta\alpha}\,. \tag{27}$$

The projection of Eq. (26) yields

$$[\widehat{A}^{\exp,\ell}] = [Y^{\exp,\ell}][\mathscr{S}]\,, \tag{28}$$

in which $[\mathscr{S}] = [S]^*([S][S]^*)^{-1}$ is the right pseudo-inverse of $[S]$. For α fixed in $\{1,\ldots,N_p\}$, let $[\mathbb{H}(\alpha)]$ be the $(\widehat{N}_p(\alpha)\times\widehat{N}_p(\alpha))$ complex matrix defined by

$$[\mathbb{H}(\alpha)]_{\beta'\beta} = \sum_{k=1}^{N} \overline{[\widehat{F}]}_{k\beta'}[\widehat{F}]_{k\beta}\,. \tag{29}$$

The projection of Eq.(27) on $[\widehat{F}]$ yields, for α fixed in $\{1,\ldots,N_p\}$ and β' in $\{1,\ldots,\widehat{N}_p(\alpha)\}$, the expression of $[\chi^{\exp,\ell}]$ written as

$$[\chi^{\exp,\ell}]_{\beta'\alpha} = \sum_{k=1}^{N} [\widehat{\mathscr{F}}(\alpha)]_{\beta' k}[\widehat{A}^{\exp,\ell}]_{k\alpha}\,, \tag{30}$$

with $[\widehat{\mathscr{F}}(\alpha)]$ the left pseudo-inverse such that

$$[\widehat{\mathscr{F}}(\alpha)]_{\beta' k} = \sum_{\beta=1}^{\widehat{N}_p(\alpha)} [\mathbb{H}(\alpha)^{-1}]_{\beta'\beta}[\widehat{F}]_{k\beta}\,. \tag{31}$$

4 Maximum likelihood method

In this section, we use the maximum likelihood method as proposed in[13, 5]. The method consists in introducing a statistical reduction as done in Section 3.1. The likelihood function is estimated using the kernel density estimation method [6]. The statistical reduction is efficient if $\widehat{N}_p(\alpha) \ll N$. In order to decrease the computational effort, we use the two statistical reductions proposed in the Section 3. The family $\{[\chi]_{\beta\alpha},\ \alpha=1,\ldots,N_p,\ \beta=1,\ldots,\widehat{N}_p(\alpha)\}$ of random variables are gathered in a random vector $\mathbf{W} = (W_1,\ldots,W_{N_{\text{comp}}})$ with $N_{\text{comp}} = \sum_{\alpha=1}^{N_p} \widehat{N}_p(\alpha)$. The corresponding experimental values of $\mathbf{W}$ are denoted by $\{\mathbf{w}^{\exp,\ell}, \ell = 1\ldots,\nu_{\exp}\}$. Let $(w_1,\ldots,w_{N_{\text{comp}}}) \mapsto p(w_1,\ldots,w_{N_{\text{comp}}})$ be the probability density function on $\mathbb{R}^{N_{\text{comp}}}$. We use the following approximation $\mathscr{L}$ of the log-likelihood function of $\mathbf{W}$, which is written, for all $\gamma = 1,\ldots,N_{\text{comp}}$, as

$$\mathscr{L} = \sum_{\ell=1}^{\nu_{\exp}} \sum_{\gamma=1}^{N_{\text{comp}}} \mathscr{L}_{\gamma,\ell}\,, \tag{32}$$

with

$$\mathscr{L}_{\gamma,\ell} = 10\log_{10} p_{w_\gamma}(w_\gamma^{\exp,\ell})\,. \tag{33}$$

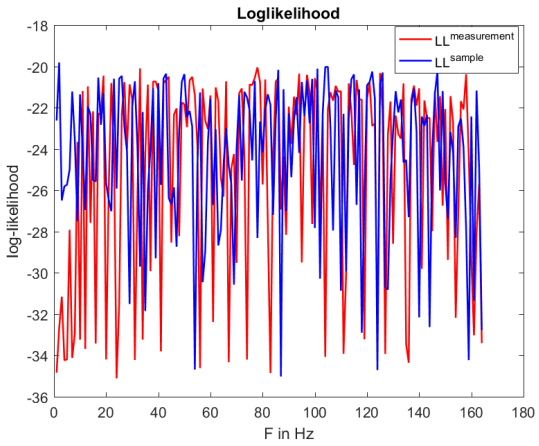


Figure 8: *Log-likelihood* $\mathscr{L}_{\gamma,\ell}$

To be able to visualize the log-likelihood of the components from the first statistical reduction, Eq.(32) are rewritten as function of the frequency,

$$\mathscr{L} = \sum_{\ell=1}^{\nu_{\exp}} \sum_{\alpha=1}^{N_p} \mathscr{L}_\alpha \tag{34}$$

with

$$\mathscr{L}_\alpha = \sum_{\beta=1}^{\widehat{N}_p(\alpha)} \mathscr{L}_\beta \tag{35}$$

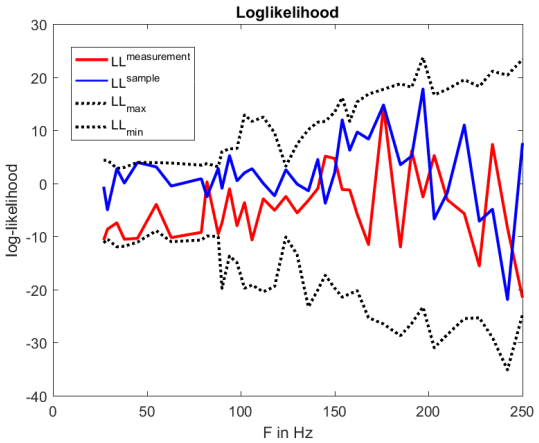


Figure 9: *Log-likelihood of the experimental measurement (red), a sample from Monte Carlo (blue), the minimum and the maximum of the stochastic basis (black dotted)*This example is with dispersion as written in [4]

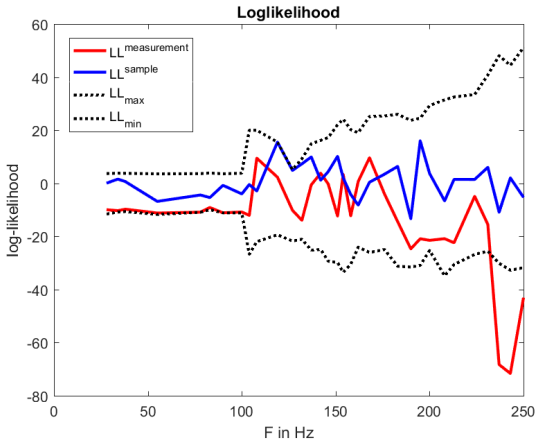


Figure 10: *Log-likelihood of the experimental measurement (red), a sample from Monte Carlo (blue), the minimum and the maximum of the stochastic basis (black dotted)*This example is with low dispersion

Figures.9 and 10 shows the maximum and the minimum of the log-likelihood for $[\chi]_{\alpha,\beta}$. It can be noticed that the realizations computed with the stochastic ROM are within the range of the maximum and the minimum. A verification step has been realized to make sure that all realizations are within the range. The experimental measurement is also within the range of the maximum and the minimum. We can interprete it as the model is sufficiently good.

5 Additional comments

In this section, we give some comments about the results presented. Using Eqs. (25) and (22), the FRF are resynthesized in the physical space. This allow us to check the threshold we imposed in the eigenvalue problem. With the threshold at 95%, $[Y_n]$ is computed and is compared with the initial input.

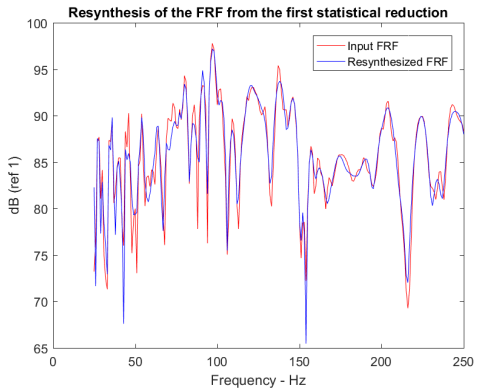


Figure 11: Resynthesized FRF from the first statistical reduction

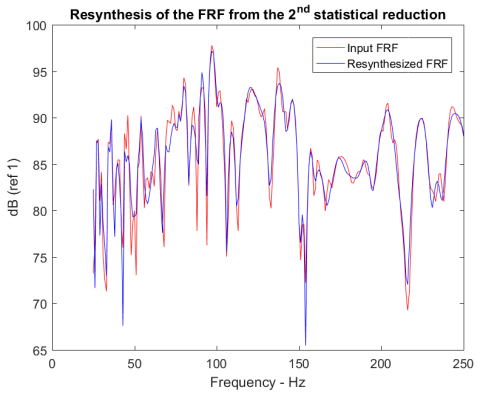


Figure 12: Resynthesized FRF from the second statistical reduction

Figures 11 and 12 show the resynthesized FRF with the corresponding input FRF. With the threshold at 95%, we can notice that we effectively have small differences compared to the input FRF. The slight difference comes from the reduced representation. Figures 13 and 14 correspond to threshold at 99%, for which the differences are very small. Moreover, the resynthesis from the first and the second statistical reduction gives the same results. This value of the threshold could be used for this analysis but the computation cost would be greater and the reduction factor, detailed hereinafter, would be worse.

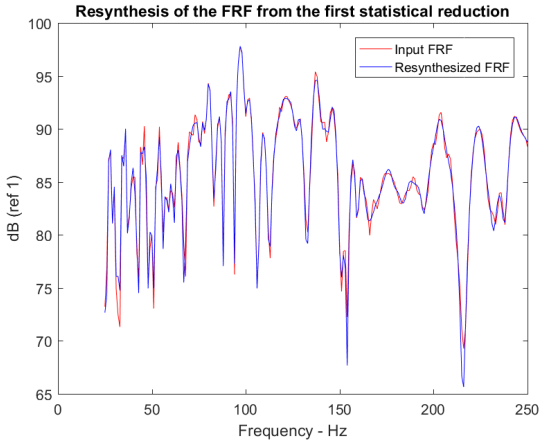


Figure 13: Resynthesized FRF from the first statistical reduction

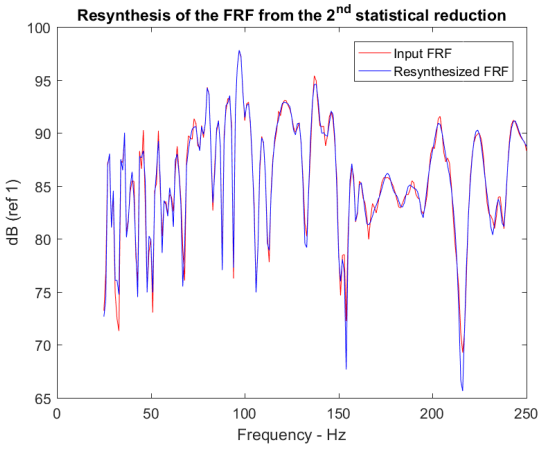


Figure 14: Resynthesized FRF from the second statistical reduction

The reduction factor noted F_{red} is given by

$$F_{red} = \frac{N \times N_f \times N_{MC}}{N_{\text{comp}} \times (N + N_{MC}) + (N_p \times N_f)} \tag{36}$$

Let τ the threshold of the cumulative energy. The value of F_{red} vary with τ.

Table 1 shows that the evolution of reduction factor depends on τ. When τ increases F_{red} decreases. The highest the input dimension, the highest the datad reduction.

τ	0.80	0.90	0.95	0.99
F_{red}	78	48	34	20

Table 1: F_{red} in terms of τ

The last comment is on the FRF with the maximum of the probability density function for each component $\gamma = 1, \ldots, N_{\text{comp}}$.

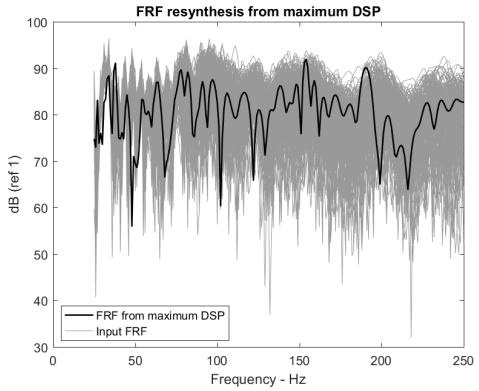


Figure 15: FRF resynthesis for the maximum of the PDF with $k = 1$

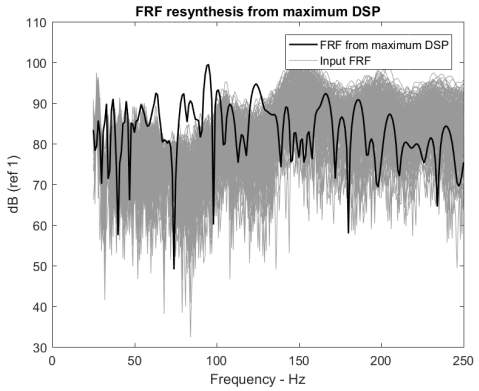


Figure 16: FRF resynthesis for the maximum of the PDF with $k = 26$

Figures $15 - 16$ show the FRF issued from the maximum of the probability density function. These figures show that, for each $k = 1, 36$, the synthesized FRF is almost always inside the grey region defined by the realizations.

6 Conclusion

In this paper, we have mostly presented a methodology for constructing a statistical reduction of a random complex matrix-valued FRF. The random FRF matrix is represented by a large collection of realizations computed using the Nonparametric Variability Modeling in MSC/NASTRAN. Since we consider the complex matrix-valued FRF, the use of two stages statistical reductions is efficient. The first stage provides a decomposition of the studied frequency range in independent subbands, while the second stage deals with the DOFs interaction in each of these subbands. Statistical independence of the reduction components is guaranteed by an Independent Component Analysis as implemented in the JADE algorithm. Once the components have been characterized, the PDF of their complex amplitude is determined, later allowing the likelihood computation. The model reduction is performed according to a requested precision: the lower the precision, the lower the number of components and the higher the reduction. This reduced representation has been validated by resynthesizing the complex matrix-valued FRF. Finally, the likelihood of a measurement on a full vehicle was computed and analyzed.

The proposed statistical reduction offers many perspectives in different fields. First, considering the data reduction capabilities, compressed model could be handled in NVH synthesis tools in order to propagate uncertainties for various vibration sources and operating conditions. Second, the deep physical meaning of the independent components have not yet been investigated. Results presented in the paper are very promising: automatic decomposition of the investigated frequency range, dominant phase relationship between DOFS... Further investigations are already in progress.

References

[1] J.-F. Cardoso, A. Souloumiac, *Blind beamforming for non-Gaussian signals*, IEEE Proceedings F (Radar and Signal Processing), Vol. 140, No. 6 (1993), pp. 362-370.

[2] R. Citarella, L. Federico (eds), *Advances in Vibroacoustics and Aeroacoustics of Aerospace and Automotive Systems*, Applied Sciences, MDPI, Basel, Switzerland (2018).

[3] R. Dony, *et al.*, *Karhunen-Loève transform*, The transform and data compression handbook, Vol. 1 (2001), pp. 1-34.

[4] J.-F. Durand, C. Soize, L. Gagliardini, *Structural-acoustic modeling of automotive vehicles in presence of uncertainties and experimental identification and validation*, Journal of the Acoustical Society of America, Vol. 124, No. 3 (2008), pp. 1513-1525.

[5] C. Fernandez, C. Soize, L. Gagliardini, *Sound-insulation layer modelling in car computational vibroacoustics in the medium-frequency range*, Acta Acustica United with Acustica (AAUWA), Vol. 96, No. 3 (2010), pp. 437-444.

[6] P. D. Hill, *Kernel estimation of a distribution*, Communications in statistics - Theory ad Methods. Vol. 14, No. 3 (1985), pp. 605-620.

[7] A. Hyvarinen, J. Karhunen, E. Oja, *Independant Component Analysis*, John Wiley and Sons, Hoboken, New Jersey (2004).

[8] *Mid-frequency acoustics*, chapter 12 of the Dynamic Analysis user guide, MSC Nastran, 2017. 2017.

[9] R. Ohayon, C. Soize, *Advanced Computational Vibroacoustics - Reduced-Order Models and Uncertainty Quantification*, Cambridge University Press, New York (2014).

[10] R. Y. Rubinstein, D. P. Kroese, *Simulation and Monte Carlo Method*, Second Edition, John Wiley and Sons, Hoboken, New Jersey (2008).

[11] R. J. Serfling, *Approximation Theorems of Mathematical Statistics*, John Wiley and Sons, Hoboken, New Jersey (1980).

[12] C. Soize, *A Nonparametric model of random uncertainties for reduced matrix models in structural dynamics*, Probabilistic Engineering Mechanics, Vol. 15, No. 3 (2000), pp. 277-299.

[13] C. Soize, E. Capiez-Lernout, J.-F. Durand, C. Fernandez, L. Gagliardini, *Probabilistic model identification of uncertainties in computational models for dynamical systems and experimental validation*, Computer Methods in Applied Mechanics and Engineering, Vol. 198, No. 1 (2008), pp. 150-163.

[14] C. Soize, *Uncertainty Quantification. An Accelerated Course with Advanced Applications in Computational Engineering*, Springer, New York (2017).

[15] E. Yuksel, G. Kamci, I. Basdogan, I. *Vibro-acoustic design optimization study to improve the sound pressure level inside the passenger cabin*, Journal of Vibration and Acoustics, Vol. 134, No. 6 (2012), pp. 061017.

High dimensional dependence via pair constructions for interval finite models

M. Faes[1], **D. Moens**[1]
[1] KU Leuven, Department of Mechanical Engineering,
Celestijnenlaan 300 B, B-3001, Heverlee, Belgium
e-mail: **matthias.faes [at] kuleuven.be**

Abstract
Classical (independent) interval analysis considers a hyper-cubic input space consisting of independent intervals. This stems from the inability of intervals to model dependence and might result in a serious over-conservatism as no physical guarantee of independence of these parameters exists. In a spatial context, dependence of one model parameter over the model domain is usually modelled using a series expansion over a set of basis functions that interpolate a set of globally defined intervals to local (coupled) uncertainty. However, such approach might prove to be too inflexible to model the dependence between a large number of model parameters. This paper therefore presents a flexible approach for the modelling of dependent intervals that is also applicable to high-dimensional problems. Specifically, it is proposed to construct the dependence structure in a similar approach to copula pair constructions, yielding a limited set of 2-dimensional dependence functions. The applied case studies indicate the flexibility and performance of the method.

1 Introduction

The calculations needed to perform a structural design usually involve the solution of sets of partial differential equations (PDE). The approximative solution of these PDE's is usually provided by means of a numerical model $\mathcal{M}(\boldsymbol{x})$, parametrized by a parameter vector $\boldsymbol{x}(\mathbf{r}) \in \mathcal{X} \subset \mathbb{R}^{d_i}$ with $\mathcal{X}$ the set of physically admissible parameters and $k \in \mathbb{N}$. For example, $\boldsymbol{x}(\mathbf{r})$ may contain inertial moments, clamping stiffness values or constitutive material parameters as a function of a spatial coordinate $\mathbf{r} \in \Omega \subset \mathbb{R}^d$ over the model domain Ω with dimension $d \in \mathbb{N}$. In case $\mathcal{M}(\boldsymbol{x})$ is constructed following a finite element approach, Ω is discretised by means of a set of finite elements, yielding d structural degrees of freedom (DOF). The model $\mathcal{M}(\boldsymbol{x})$ provides a vector of model responses $\boldsymbol{y}(\mathbf{r}) \in \mathcal{Y} \subset \mathbb{R}^{d_o}$, with $\mathcal{Y}$ the set of admissible model responses and $d_o \in \mathbb{N}$, through a set of function operators $m_i,\ i = 1, \ldots, d_o$, which are defined as:

$$\mathcal{M}(\boldsymbol{x}) : y_i(\mathbf{r}) = m_i(\boldsymbol{x}(\mathbf{r})) \quad i = 1, \ldots, d_o \tag{1}$$

with $m_i : \mathbb{R}^{d_i} \mapsto \mathbb{R}$ Note that the dependence of $\boldsymbol{y}$ on $\mathbf{r}$ is only valid when nodal or elemental responses are considered. This is for example not the case when $\boldsymbol{y}$ consists of eigenfrequencies.

One of the key challenges in the application of interval theoretical approaches for modelling uncertainty in finite element models, is the inability of intervals to account for dependence between multiple uncertain parameters. In the context of spatial dependence of a single parameter, recent work of the authors focussed on modelling spatial dependence via interval fields [1]. Following the method presented in [1], an interval field $\boldsymbol{x}^{\boldsymbol{I}}(\mathbf{r})$ is modelled as a series expansion, where local uncertainty is modelled using $n_b \in \mathbb{N}$ globally defined independent interval scalars $\boldsymbol{\alpha}^I \in \mathbb{IR}$ and basis functions $\boldsymbol{\psi}(\mathbf{r}) : \Omega \mapsto \mathbb{R}$:

$$\boldsymbol{x}^{\boldsymbol{I}}(\mathbf{r}) = \sum_{i=1}^{n_b} \boldsymbol{\psi}(\mathbf{r}) \cdot \alpha_i^I \tag{2}$$

with $\mathbb{IR}$ the domain of real interval scalars, $\mathbf{r} \in \Omega \subset \mathbb{R}^d$ a spatial coordinate over the model domain Ω with dimension $d \in \mathbb{N}$. This framework for the modelling of spatial uncertainty modelling was recently applied in the context of inverse uncertainty quantification [2, 3] and the modelling of various dynamic phenomena [4, 5, 6, 7], as well as additively manufactured plastic components [8].

However, while being very valuable for modelling spatial phenomena, when considering the dependence between multiple physical parameters of a dynamic model, such a weighting approach might not be appropriate. Typically, more flexibility is needed in this context since the dependence structure can differ greatly from parameter pair to parameter pair. Especially for high-dimensional problems, the accurate definition of a set of basis functions to model dependence between different model parameters proves to be highly challenging. In the context of probabilistic modelling of uncertainty, techniques based on Copula [10] are being applied widely, for instance in the modelling of dependence in system reliability [9]. Copula pair constructions further extend these concepts towards a flexible modelling of high-dimensional uncertainty [11].

This paper explores the application of vine copula approaches for the modelling of dependence between uncertain parameters of a dynamic FE model that are modelled as intervals. In section 2, a concise introduction to copula in a probabilistic context is presented. Then, section 3 proposes a new method to propagate high-dimensional interval uncertainty with dependence between the interval valued parameters. Section 4 and 5 present two case studies to illustrate these ideas. Conclusions are listed in section 6.

2 Copula in a probabilistic context

2.1 Copulas

Copula are functions that construct a joint distribution function $F_{1:d_i}(x_1, x_2, \dots x_{d_i})$, with $x_1, x_2, \dots x_{d_i} \in [0,1]^{d_i}$ starting from their one-dimensional marginals $F_i,\ i = 1, \dots, d_i$. As such, the modelling of the dependence is decoupled from the modelling of the non-determinism in the model parameters. The application of Copula on a bivariate distribution is based on Sklar's theorem [10]:

$$F_{1:d_i} = c_{1:d_i}\left(F_1\left(x_1\right), F_2\left(x_2\right), \dots, F_{d_i}(x_{d_i})\right) \tag{3}$$

with $c_{1:d_i} : [0,1]^{d_i} \mapsto [0,1]$ the copula function, which is unique if all $F_i,\ i = 1, \dots, d_i$ are continuous. Note that a copula is always contained between the Fréchet-Hoeffding bounds:

$$\max\left(1 - d_i + \sum_{i=1}^{d} x_i, 0\right) \leq c_{1:d_i} \leq \min(x_i) \tag{4}$$

which bound the dependence between the parameters and correspond to the probability mass lying on the principal diagonals of $[0,1]^{d_i}$.

However, it may not be physically accurate to use the same copula family (i.e., dependence structure) to model the dependence between all combinations of parameters since this dependence is in general not the same. Furthermore, sampling from a copula in $d > 2$ proves to be a daunting task [9].

2.2 Pair Copula Construction

To overcome the limitations of these *regular* copula, the d_i-dimensional density $f(x_1, \dots, x_{d_i})$ is constructed using a product of $d(d-1)/2$ bivariate (conditional) copula [11]. For instance, when considering 3 probabilistic parameters x_1, x_2 and x_3, the joint density $f(x_1, x_2, x_3)$ can be decomposed into a product of conditional densities as:

$$f(x_1, x_2, x_3) = f_{3|12}(x_3|x_1, x_2) \cdot f_{2|1}(x_2, x_1) \cdot f_1(x_1) \tag{5}$$

Then, by applying eq. (3), the bivariate densities can be written as:

$$f_{2|1}(x_2|x_1) = c_{12}\left(F_1\left(x_1\right), F_2\left(x_2\right)\right) \tag{6}$$
$$f_{3|2}(x_3|x_2) = c_{32}\left(F_3\left(x_3\right), F_2\left(x_2\right)\right) \tag{7}$$
$$f_{3|12}(x_3|x_1, x_2) = c_{13|2}(F_{1|2}(x_1|x_2), F_{3|2}(x_3|x_2)) \tag{8}$$

which yields:

$$\begin{aligned} f(x_1, x_2, x_3) = f_1(x_1) \cdot f_2(x_2) \cdot f_3(x_3) \cdot c_{12}\left(F_1(x_1), F_2(x_2)\right) \cdot c_{23}\left(F_2(x_2), F_3(x_3)\right) \\ \cdot c_{13|2}(F_{1|2}(x_1|x_2), F_{3|2}(x_3|x_2)) \end{aligned} \tag{9}$$

with $c_{ij|k}$ the bivariate copula linking F_i and F_j conditional on x_k. For higher d_i, a similar construction can be made. As such, the joint density $f(x_1, \ldots, x_{d_i})$ can be represented as the product of marginal densities and a product of bivariate (conditional) copula. This enables the modelling of dependence between two x_i with a much higher degree of flexibility, since different c_{ij} can be employed for all x_i.

As can be noted, a huge number of constructions can be contrived when d_i is large. Most commonly, therefore a set of nested trees is used to visualise and enumerate these constructions via graph theory. Such set of nested trees is also referred to as "vine copula". An extensive literature exists discussing many aspects of Copulas, Copula pair constructions and different types of vine copula. The interested reader is referred to [11] or the book of Mai and Scherer [12].

3 A copula based approach for interval finite element computations

3.1 Interval finite element method

The goal of an interval FE calculation is to find the bounds on the uncertainty in the model responses of eq. (1), given an interval description of the uncertainty in $\boldsymbol{x^I} \in \mathcal{X}^I \subset \mathbb{IR}^{d_i}$ For multiple parameters, the interval vector $\boldsymbol{x^I}$ is defined as the Cartesian product of the intervals x_i^I:

$$\boldsymbol{x^I} = x_1^I \times \ldots \times x_{d_i}^I \tag{10}$$

and as such spans a hypercubic set by definition [13]. The interval FE method can thus be expressed as finding the solution set $\tilde{\mathbf{y}}$:

$$\tilde{\boldsymbol{y}} = \left\{\boldsymbol{y} | \boldsymbol{y} = \mathcal{M}(\boldsymbol{x}); \boldsymbol{x} \in \boldsymbol{x^I}\right\} \tag{11}$$

Generally, $\tilde{\boldsymbol{y}}$ spans a non-convex manifold in $\mathbb{R}^{d_o}$, as the output responses y_i are (possibly non-linearly) coupled through the PDE of the FE model under consideration. Therefore, instead of calculating the *real* uncertain solution set spanned by $\tilde{\mathbf{y}}$, the uncertainty at the output of the FE model generally is approximated using an interval vector $\boldsymbol{y^I}$, which is usually calculated following a bounded optimisation problem, where the bounds $\underline{y}_i$ and $\overline{y}_i$ on each output quantity y_i of the solution interval vector $\mathbf{y}^I$ are determined by searching the domain, defined by $\boldsymbol{x^I}$ [13]:

$$\begin{aligned} \underline{y}_i &= \min_{\boldsymbol{x} \in \boldsymbol{x^I}} m_i(\boldsymbol{x}) \qquad i = 1, ..., d_o \\ \overline{y}_i &= \max_{\boldsymbol{x} \in \boldsymbol{x^I}} m_i(\boldsymbol{x}) \qquad i = 1, ..., d_o \end{aligned} \tag{12}$$

where $y_i^I = [\underline{y}_i; \overline{y}_i]$ is the result interval scalar for the i^{th} component of the solution interval vector of the model. Solution of equation (12) returns the smallest hyper-cubic approximation $\boldsymbol{y^I}$ of $\tilde{\boldsymbol{y}}$. Also methods that try to estimate $\tilde{\boldsymbol{y}}$ by its smallest convex set have been introduced in recent years [14, 15].

3.2 Dependence between intervals

In a bivariate context, the concept of dependence can be illustrated using figure 1. This figure shows two arbitrary parameters x_1 and x_2. The corresponding uncertainty is scaled for both parameters to the interval [0,1] for illustrational purposes, which is a straightforward operation on the data. In case no dependence between these parameters is taken into account, the space of admissible parameter combinations corresponds to the unit square $[0,1]^2$, which is also illustrated using the striped line. However, in case dependence is present between these two parameters, this can be modelled in an interval context by defining a set $\mathcal{D}_{12}$ that limits the range of admissible parameter combinations. The degree of dependence can then be computed as the relative area of $\mathcal{D}_{12}$ with respect to $[0,1]^2$ [3, 16].

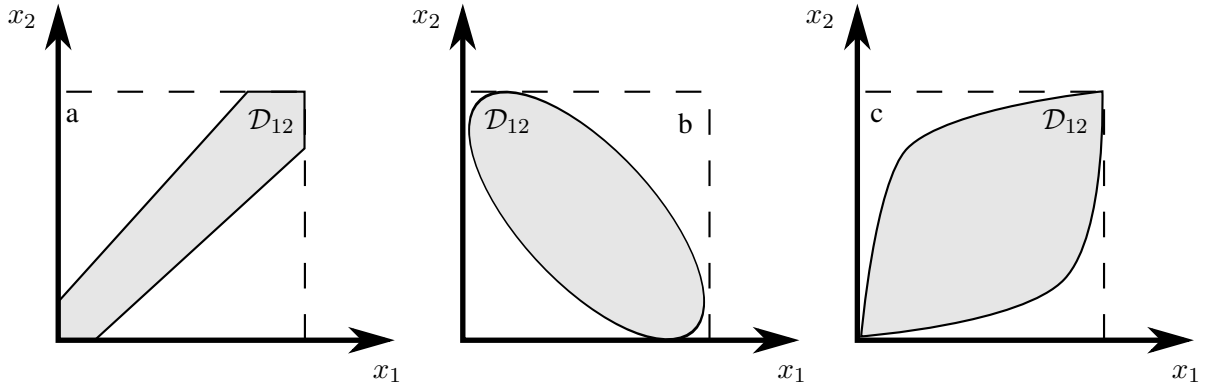


Figure 1: Illustration of dependence between two arbitrary parameters x_1 and x_2, modelled as a convex region $\mathcal{D}_{12}$.

The definition of $\mathcal{D}_{12}$ can be based on expert knowledge, first principle fundaments, joint measurements of the uncertain parameters, etc. $\mathcal{D}_{12}$ can take any shape within $[0,1]^2$, as long as it is physically relevant. In the specific case of figure 1, in a) a dependence is assumed that slightly decreases as x_1 and x_2 increase, figure b) illustrates a negative ellipse-shaped dependence. Finally figure c) illustrates a large dependence in the centre of $[0,1]^2$ and small dependence in the tails.

In case more than 2 parameters are considered, the definition of $\mathcal{D}$ might prove to be very cumbersome or even impossible. Therefore, a similar dependence pair construction is proposed to allow for a more flexible definition of the joint-dependence structure. Similarly to eq. (9), when considering the joint dependence between three intervals x_1^I,x_2^I and x_3^I, the joint dependence $\mathcal{D}(x_1^I, x_2^I, x_3^I)$ can be decomposed as:

$$\mathcal{D}(x_1^I, x_2^I, x_3^I) = x_1^I \cdot x_2^I \cdot x_3^I \cdot \mathcal{D}_{12} \cdot \mathcal{D}_{23} \cdot \mathcal{D}_{13|2} \tag{13}$$

with $\mathcal{D}_{ij}$ the bivariate dependence between x_i and x_j. Also here, the concept can easily be extended to general d dimensions. This concept is illustrated in figure 2. This figure shows the unit cube $[0,1]^3$, together with $\mathcal{D}_{12}$, $\mathcal{D}_{23}$ and $\mathcal{D}_{13|2}$. As can be noted, the set $\mathcal{D}_{13|2}$ is not necessarily constant over x_2, allowing for the definition of highly complicated dependence structures with a very limited set of parameters.

In the context of propagating this uncertainty through the numerical model, this decomposition serves as an equality constraint for the global optimisation that underlies the interval finite element model. Specifically, to infer the bounds on y, following set of constrained optimisation problems is solved:

$$\underline{y}_i = \min_{\boldsymbol{x} \in \boldsymbol{x}^I} m_i(\boldsymbol{x}) \qquad \text{s.t. } \boldsymbol{x} \in \mathcal{D}(x^I) \tag{14}$$

$$\overline{y}_i = \max_{\boldsymbol{x} \in \boldsymbol{x}^I} m_i(\boldsymbol{x}) \qquad \text{s.t. } \boldsymbol{x} \in \mathcal{D}(x^I) \tag{15}$$

where the optimiser checks whether the new candidate point lies inside $\mathcal{D}$. In case $\mathcal{D}$ consists only of convex dependence pairs, this reduces to a set of linear inequality constraints, which can easily be solved by any gradient-based or evolutionary optimisation solver.

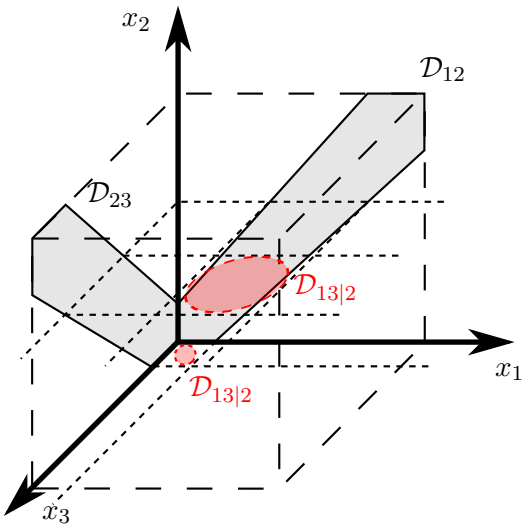


Figure 2: Decomposition of the $d = 3$-dimensional dependence using the proposed dependency pair decomposition.

Note that, while employing a similar decomposition structure as in a probabilistic context, the underlying meaning is fundamentally different. Instead of decomposing a high-dimensional density function, into its marginals and a set of bivariate copula, this method presents a way to limit the hypercube $x_1^I \times \ldots \times x_d^I$ of admissible values by a set of two-dimensional sets. While similar, still no inference of the likelihood of certain values within this set is made or aimed at. As such, the interval paradigm is not violated following this approach.

4 Case study 1: analytical function

As a first example, dependent interval uncertainty is propagated through a simple analytical equation having three parameters $x_i,\ i = 1, \ldots, 3$:

$$y = x_1 \cdot x_2 - 2 \cdot x_3 \tag{16}$$

with $x_1^I = [1, 4]$, $x_2^I = [2, 6]$, $x_3^I = [3, 5]$.

This function is constructed such that the extreme values for y do not correspond with either $\underline{x}$ or $\overline{x}$. The dependence between these parameters assumes following structure:

$$\mathcal{D}_{12} = \mathcal{H}(|x_2 + x_1 - 1| - \theta_1) \tag{17}$$
$$\mathcal{D}_{23} = \mathcal{H}(|x_1 - x_2| - \theta_2) \tag{18}$$
$$\mathcal{D}_{13|2} = x_{1|2}^I \times x_{3|2}^I \tag{19}$$

with $\mathcal{H}$ the Heaviside function, $||$ denoting the absolute value and $\theta_1 = 0.5$ and $\theta_2 = 0.15$.

Table 1 lists the results when the problem is solved both with and without taking this dependence into account. The $\hat{\bullet}$ operator indicates the interval that yields the extreme values for y. As can be noted, the results without dependence between the interval parameters are highly over-conservative with respect to the case when the dependence is taken into account following the proposed approach. The efficiency of the propagation is solely dependent on the used optimisation algorithm, which should be selected based on the topology of the objective function (i.e., the numerical model) at hand.

This dependence structure is illustrated in figure 3, which illustrates the shape of the sets $\mathcal{D}_{12}$ and $\mathcal{D}_{23}$, as well as the set D_{13} resulting from modelling the dependence as listed in eq. (17) to eq. (19). This visualisation is

Table 1: Results of the propagation of the interval uncertainty through eq. (16)

Problem	$\underline{\hat{\boldsymbol{x}}}$	$\overline{\hat{\boldsymbol{x}}}$	y^I
Independent	$[1, 2, 5]$	$[4, 6, 3]$	$[-8, 17.5927]$
Dependent	$[1.0005, 4.6792, 4.6344]$	[3.9916,4.0112,3.7096]	$[-4.5874, 8.5919]$

obtained by propagating a Sobol Sequence containing 50000 samples through the analytical function. Note that the latter set is not the one as defined in eq. (19), since it is not conditional on the value of x_2. Rather, it is a visualisation of all $D_{13|2}$ for all values of x_2.

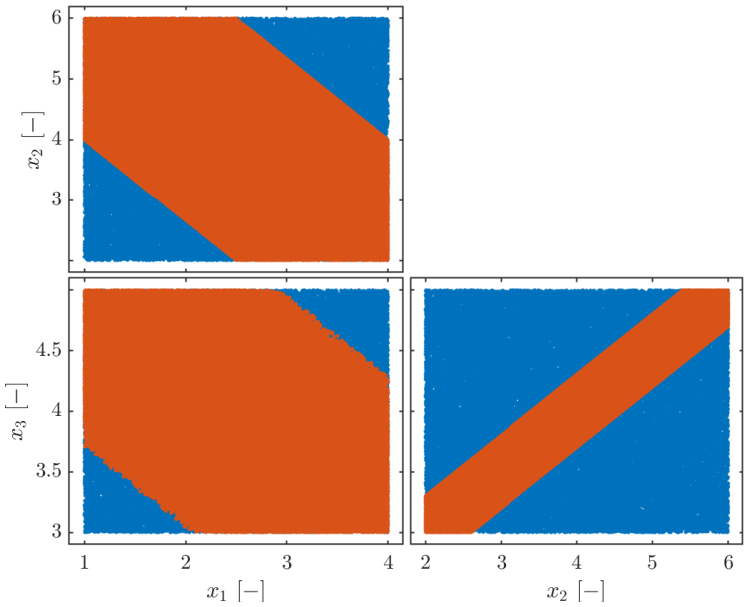


Figure 3: Illustration of the dependence structure of the analytical model, employed for the case study.

5 Case study 2: composite blade

The second case study concerns a finite element model of a long and slender blade. The structure has a total length of 30 m and the width is 1 m at the widest part. This blade is produced using a multilayer laminar composite material, with deterministic ply material properties $E_1 = 231\ GPa$, $E_2 = 77\ GPa$, $\nu_{12} = 0.31$ and $G_{12} = G_{23} = G_{13} = 42.7\ GPa$. Different lay-ups are placed in the structure, where close to the attachment of the blade (left-most), the lay-up is thicker as compared to at the end-point (right-most). The dynamic behaviour of the structure is modelled using a Finite Element model containing 621 nodes, 606 bilinear shell elements, 573 rigid connections, 10 concentrated masses and 132 rod elements. The finite element model of this structure is shown in figure 4.

The model is solved for its 10 first eigen-modes and corresponding resonance frequencies. Table 2 lists the result of the deterministic simulation. The effect of mode-crossover and -veering is accounted for by tracking the mode shapes via the modal assurance criterion. To limit the computational expense, 10 4-layer Artificial Neural Network with (4,6,4,1)-configuration are trained using Bayesian regulation back-propagation, based on a training data set containing 1750 samples. Furthermore, a validation data set of 750 specimens was used, indicating that the ANN are well capable of predicting the behaviour of the full FE model at highly reduced computational cost.

To illustrate the developed method, 4 parameters are considered uncertain, and they are modelled as de-

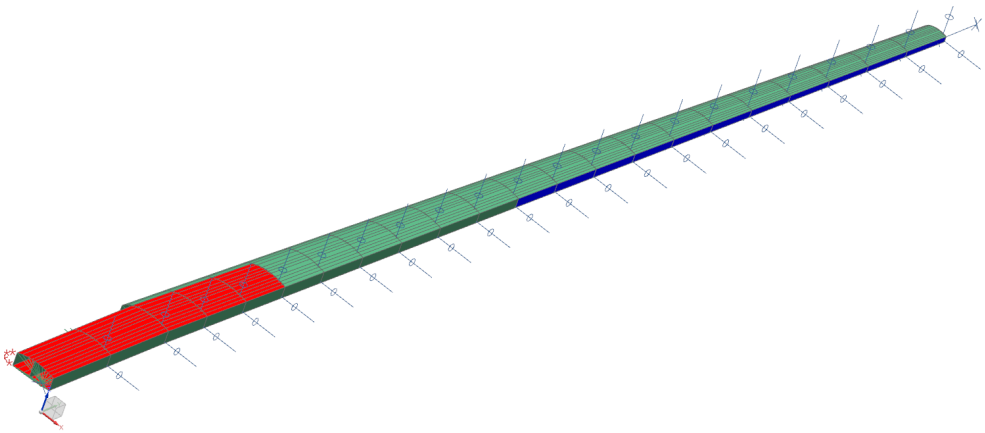


Figure 4: Finite element model of the composite blade

Table 2:

Mode number	description	f
1	1^{st} vertical bending	0.79 Hz
2	1^{st} horizontal bending	2.07 Hz
3	2^{nd} vertical bending	3.11 Hz
4	3^{th} vertical bending	7.72 Hz
5	2^{nd} horizontal bending	8.67 Hz
6	4^{th} vertical bending	14.45 Hz
7	3^{th} horizontal bending	21.68 Hz
8	5^{th} vertical bending	23.84 Hz
9	1^{st} torsion	26.76 Hz
10	6^{th} vertical bending	35.01 Hz

pendent intervals. Specifically, the primary and secondary Young's modulus (E_1 and E_2), as well as the thickness of two composite shells (t_1 and t_2, as indicated using respectively red and blue elements in figure 4) are considered for the analysis. For this 4-dimensional structure, the dependence is decomposed as:

$$\mathcal{D}(E_1, E_2, t_1, t_2) = E_1^I \cdot E_2^I \cdot t_1^I \cdot t_2^I \cdot \mathcal{D}_{12} \cdot \mathcal{D}_{23} \cdot \mathcal{D}_{34} \cdot \mathcal{D}_{13|2} \cdot \mathcal{D}_{24|3} \cdot \mathcal{D}_{14|23} \tag{20}$$

in analogy to eq. (13), and where subscripts $1, 2, 3, 4$ of $\mathcal{D}$ correspond to E_1, E_2, t_1, t_2 respectively. For notational simplicity, the dependence of D_{ij} on x_i and x_j is omitted. This specific decomposition structure is analogous to the D-vine representation of a pairwise copula construction. This construction is appropriate in this case, as it allows for the direct description of the dependence between E_1^I, E_2^I and t_1^I, t_2^I, whereas the higher order terms can be included to model dependence between these two sets of parameters.

As a first case study, the dependence between the intervals is specifically modelled as:

$$\mathcal{D}_{12} = \mathcal{H}(|E_2 + E_1 - 1| - \theta_1) \tag{21}$$
$$\mathcal{D}_{23} = E_2^I \times t_1^I \tag{22}$$
$$\mathcal{D}_{34} = \mathcal{H}(|t_1 - t_2| - \theta_2) \tag{23}$$
$$\mathcal{D}_{13|2} = x_{1|2}^I \times x_{3|2}^I \tag{24}$$
$$\mathcal{D}_{24|3} = x_{2|3}^I \times x_{4|3}^I \tag{25}$$
$$\mathcal{D}_{14|23} = x_{1|23}^I \times x_{4|23}^I \tag{26}$$

with $\theta = [0.95, 0.85]$. As a second case study, also dependence between E and t is included:

$$\mathcal{D}_{12} = \mathcal{H}(|E_2 + E_1 - 1| - \theta_1) \tag{27}$$
$$\mathcal{D}_{23} = \mathcal{H}(|t_1 - t_2| - \theta_2) \tag{28}$$
$$\mathcal{D}_{34} = \mathcal{H}(|t_1 - t_2| - \theta_3) \tag{29}$$
$$\mathcal{D}_{13|2} = x^I_{1|2} \times x^I_{3|2} \tag{30}$$
$$\mathcal{D}_{24|3} = x^I_{2|3} \times x^I_{4|3} \tag{31}$$
$$\mathcal{D}_{14|23} = x^I_{1|23} \times x^I_{4|23} \tag{32}$$

with $\theta = [0.95, 0.7, 0.85]$.

The cross-sections of this 4-dimensional convex dependence region are shown in figure 5. The blue area is the domain covered by the independent intervals, whereas the orange and yellow areas correspond respectively to cases 1 and 2. As can be noted, adding more terms to the dependence construction presented in eq. (20) further reduces the set of admissible parameter value combinations within the hypercube spanned by the intervals. Furthermore, in case 2, it is clear that no cross-dependence is present between the thickness and Young's modulus values. On the other hand, the inclusion of the cross-dependence term $\mathcal{D}_{23}$ in case 2 incorporates the dependence immediately for all combinations of the 4 parameters.

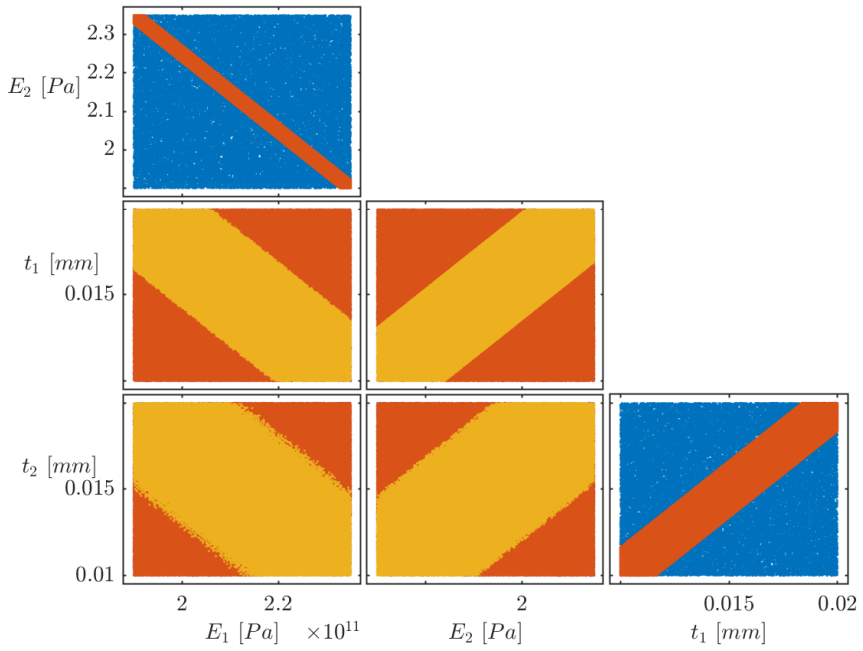


Figure 5: Two dimensional cross-sections of the 4-dimensional convex set of admissible values representing the dependent intervals. Blue indicates the full hypercube, orange corresponds to the first case (i.e., no cross-dependence between Young's modulus and the thickness) and yellow corresponds to the second case.

To illustrate the effect of the dependence between these parameters, these dependent intervals are also propagated through the numerical model of the composite blade. The result hereof is illustrated in figure 6. This figure shows two-dimensional cross-sections of the 10-dimensional result manifold, obtained by propagating 50000 Sobol samples from the dependent input parameters. Note that this is not a proper interval propagation technique. However, the main goal of this figure is to illustrate the solution manifold given the dependent intervals. As can be noted, when more dependence is included in the analysis, the solution manifold becomes smaller and smaller. Furthermore, also the dependence between the resonance frequencies is

impacted. Finally, note that increasing the dependence between the input intervals yields a solution manifold that is contained within the case of less dependence.

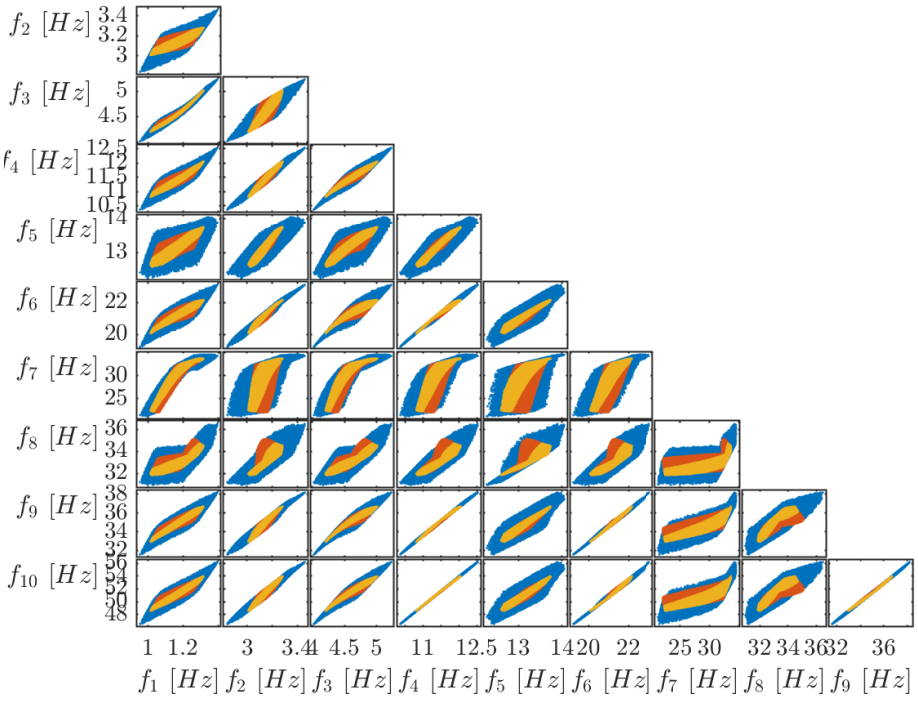


Figure 6: All combination of the 10 first eigenfrequencies, obtained by propagating the dependent intervals through the composite blade model.

6 Conclusions

Classical (independent) interval analysis considers a hyper-cubic input space consisting of independent intervals. This stems from the inability of intervals to model dependence and might result in a serious over-conservatism as no physical guarantee of independence of these parameters exists. In a spatial context, dependence of one model parameter over the model domain is usually modelled using a series expansion over a set of basis functions that interpolate a set of globally defined intervals to local (coupled) uncertainty. However, such approach might prove to be too inflexible to model the dependence between a large number of model parameters. This paper therefore presents a flexible approach for the modelling of dependent intervals that is also applicable to high-dimensional problems. Specifically, it is proposed to construct the dependence structure in a similar approach to copula pair constructions, yielding a limited set of 2-dimensional dependence functions. This definition of dependence also integrates well with the global optimisation approach. A first case study, where the developed method is applied to an analytical function is included to illustrate the main ideas. Application of a global optimisation algorithm also indicates that by introducing dependence between the model parameters, the width of the output interval is decreased significantly. The second case study applies the methodology to a realistic finite element model of a long, slender composite blade. Two different dependence structures are propagated and it is shown that the method is well capable of limiting the set of admissible parameter combinations, yielding tighter output sets. Future work will focus on applying higher-order dependence constructions for the propagation of interval uncertain parameters, as well as on the quantification of the dependence functions based on indirect measurement data.

References

[1] W. Verhaeghe, W. Desmet, D. Vandepitte, D. Moens, Interval fields to represent uncertainty on the output side of a static FE analysis, Computer Methods in Applied Mechanics and Engineering, **260**, 50-62 (2013)

[2] M. Faes, D. Moens, Identification and quantification of spatial interval uncertainty in numerical models, Computers & Structures,
textbf192, art.nr. 2017_331, 16-33 (2017)

[3] M. Faes, J. Cerneels, D. Vandepitte, D. Moens, Identification and quantification of multivariate interval uncertainty in Finite Element models, Computer Methods in Applied Mechanics and Engineering, **315**, 896-920 (2017)

[4] M. Broggi, M. Faes, E. Patelli, Y. Govers, D. Moens, and M. Beer, Comparison of Bayesian and Interval Uncertainty Quantification: Application to the AIRMOD Test Structure, IEEE Symposium Series on Computational Intelligence 2017 (2017).

[5] M., Imholz, D., Vandepitte, and D. Moens, Analysis of the effect of uncertain clamping stiffness on the dynamical behaviour of structures using interval field methods. In Applied Mechanics and Materials (2015), vol. 807, Trans Tech Publ, pp. 195–204.

[6] M., Imholz, D., Vandepitte, and D. Moens, Derivation of an Input Interval Field Decomposition Based on Expert Knowledge Using Locally Defined Basis Functions. In 1st ECCOMAS Thematic Conference on International Conference on Uncertainty Quantification in Computational Sciences and Engineering (2015), pp. 1–19.

[7] M., Imholz, D., Vandepitte, and D. Moens, Application of Interval Fields to fit experimental data on deepdrawn components.. In ICVRAM-ISUMA-UNCERTAINTIES 2018 (2018).

[8] M. Faes and D. Moens, Identification and quantification of spatial variability in the elastostatic properties of additively manufactured components. 19th AIAA Non-Deterministic Approaches Conference, (2017), pp. 1–13,.

[9] J. Behrensdorf, M. Broggi, M. Beer, Reliability analysis of networks interconnected with copulas.. In ICVRAM-ISUMA-UNCERTAINTIES 2018 (2018).

[10] A. Sklar, Fonctions de repartition a n dimensions et leurs marges, Publications de lInstitut de Statistique de lUniviversite de Paris, **8**, 229-231 (1959)

[11] K. Aas, C. Czado, A. Frigessi, H. Bakken, Pair-copula constructions of multiple dependence, Insurance: Mathematics and Economics, **44**, Issue 2, 182-198 (2009)

[12] J.F. Mai, M. Scherer, Simulating Copulas: Stochastic Models, Sampling Algorithms, and Applications, Series in Quantative Finance - Vol. 4, Imperial College Press (2009).

[13] D. Moens and M. Hanss Non-probabilistic finite element analysis for parametric uncertainty treatment in applied mechanics: Recent advances. Finite Elements in Analysis and Design 47, 1, 4–16, (2011).

[14] Hanss, M. The transformation method for the simulation and analysis of systems with uncertain parameters. Fuzzy Sets and Systems 130, 3, 277–289 (2002)

[15] Hanss, M. The extended transformation method for the simulation and analysis of fuzzy-parameterized models. International Journal of Uncertainty, Fuzziness and Knowledge-Based Systems 11, 06 (2003), 711–727.

[16] O. Giannini and M. Hanss, An interdependency index for the outputs of uncertain systems. Fuzzy Sets and Systems 159, 1292-1308 (2008).

A multi-fidelity approach for possibilistic uncertainty analysis

M. Mäck [1], **M. Hanss** [1]
[1] University of Stuttgart, Institute of Engineering and Computational Mechanics,
Pfaffenwaldring 9, 70569 Stuttgart, Germany
e-mail: {**markus.maeck, michael.hanss**}**@itm.uni-stuttgart.de**

Abstract

Possibilisitic uncertainty representation can be used to model a system in case of sparse data or incomplete information. This, however, comes along with a large number of deterministic model evaluations, which in case of a complex, large-scale model results in tremendous computational effort. Hence, special techniques should be applied to reduce the computational cost by simplification or model-order reduction techniques, or by building a computationally less expensive surrogate model. In this paper, a novel approach is introduced which combines the analyses of the expensive, high-fidelity model and the approximated, low-fidelity model in a multi-fidelity approach. For this purpose, a possibilistic correlation analysis is applied to estimate the conditional possibility of the high-fidelity output given the low-fidelity output. In this way, the possibilistically quantified uncertainty of the high-fidelity model output can be estimated using only a low number of expensive model evaluations.

1 Introduction

In numerical simulation, there is an increasing trend towards the explicit incorporation of uncertainty and on the prediction about uncertain processes or processes with uncertain conditions. The inclusion of uncertainty in the numerical analysis offers additional insights and supplemental options for the interpretation of the simulation results. While probabilistic methods are widely spread, well elaborated, and therefore, provide a useful tool for modeling stochastic processes and random behavior, in case of uncertainty based on a lack of knowledge and restricted information, more appropriate theories need to be used. Uncertainty quantification based on possibility theory has gained more and more attention because of its property of being able to model imprecise and even contradictory information [1]. For additional information and the measure-theoretical fundamentals of possiblity theory, see e.g. [2]. There exists a variety of numerical methods for possibilistic uncertainty quantification [3, 4] which are based on the direct link between possibility theory and fuzzy set theory [5, 6].
A general drawback of the possibilistic uncertainty quantification is that it requires a large number of deterministic model evaluations. In case of complex, large-scale models, here called high-fidelity models (HFMs), this results in tremendous computational effort. To reduce the computational cost, appropriate low-fidelity models (LFMs) need to be derived, which preferably provide a good approximation of the original model, but to lower computational costs. Besides simplification and model-order reduction, data driven surrogate models are state of the art in uncertainty quantification. An overview of different strategies, which are used in a probabilistic framework, is provided in [7]. In the context of possibilistic uncertainty representation and fuzzy sets, surrogates are used in [8] and [9]. Even if these methods lead to a significant reduction of the computation time, the overall effort may still be too high because the construction of the surrogate is based on multiple evaluations of the expensive HFM.
A different strategy to reduce the computational costs is the combination of the LFM and the HFM in a

multi-fidelity approach (MFA). A list of different multi-fidelity models and model management strategies is given in [10], and another survey on multi-fidelity modeling with some applications in [11]. Of course, this approach is not only restricted to uncertainty quantification, but it can also be applied to other fields which suffer from expensive numerical evaluations, such as optimization under uncertainty. In the context of probabilistic uncertainty quantification, there exist some works using Bayesian formulations in terms of Gaussian [12] and non-Gaussian processes [13], [14]. The probabilistic correlation and regression analysis between the LFM and HFM motivates the procedure of the possibilistic multi-fidelity analysis. For the compensation of the discrepancy between the results of the corresponding high- and low-fidelity models,which is deterministic, but unknown, rather than random and stochastic, a well-directed combination of their possibilistic analyses proves to be a promising approach. Explicitly, the data obtained by only a few evaluations of the HFM is used to analyze the possibilistic correlation to the LFM, whose computing time is considered to be significantly smaller. Based on that, the conditional possibility distribution of the corresponding models can be estimated using a possibilistic regression analysis. Finally, the marginal possibility distribution of the high-fidelity model can be computed using the estimated conditional possibility as well as the marginal possibility distribution of the low-fidelity model. It exists quite some literature where the conditioning in possibility theory is discussed. See for example [16], [17], [18], [19], and the overview paper [20] or the contribution in [21] which uses the conditional distribution in a Bayesian-like approach. In the listed literature, it is mainly discussed how to derive the conditional distribution for a given joint distribution. In the MFA, however, the joint distribution is deduced from an estimated conditional distribution.

2 Preliminaries

The following section provides a short introduction to possibility theory and its connection to fuzzy sets, serving as a basis for the latter approach. It introduces the fundamental expressions needed in this work. Additionally, the basic notions and ideas about multi-fidelity modeling are introduced.

2.1 Possibility Theory and Fuzzy Sets

Possibility theory is an uncertainty theory based on set functions, being capable of handling incomplete or inconsistent information. A possibility measure $\Pi : 2^{\Omega} \to [0, 1]$ on the universe of discourse Ω satisfies:

- $\Pi(\Omega) = 1, \quad \Pi(\emptyset) = 0$ and
- $\Pi\left(\cup_k A_k\right) = \sup_k \Pi(A_k) \quad$ if $A_k \subseteq \Omega$ and $\cap_k A_k = \emptyset$.

Let $\mathscr{P} = \left(\Omega, 2^{\Omega}, \Pi\right)$ be a possibility space, then a possibilistic variable ξ on $\mathscr{P}$ is defined as a mapping onto the real line $\mathbb{R}$, i.e. $\xi : \Omega \mapsto \Xi,\ \Xi \subseteq \mathbb{R}$. The possibility of an event A with its associated possibilistic variable ξ can be expressed by the possibility measure $\Pi(A = \xi^{-1}(X)) = \Pi_{\xi}(X)$ with $A \in \Omega$ and $X \in \Xi$. The joint possibility measure $\Pi_{\xi,\eta}$ of the possibilistic variables ξ and η is related to the conditional possibility measure $\Pi_{\xi|\eta}$ and the marginal possibility measures Π_{ξ} and Π_{η} of the respective variables ξ and η via

$$\Pi_{\xi,\eta}\left(X, Y\right) = \min\left[\Pi_{\xi|\eta}(X|Y), \Pi_{\eta}(Y)\right] = \min\left[\Pi_{\eta|\xi}(Y|X), \Pi_{\xi}(X)\right] \tag{1}$$

which is an analogon to the law of total probability [16]. The marginal distribution Π_{ξ} satisfies

$$\Pi_{\xi}(X) = \sup_{Y} \Pi_{\xi,\eta}\left(X, Y\right) \tag{2}$$

as a projection of ξ along η, which means that the dependency on η is eliminated. In case of total independency, it follows that $\Pi_{\xi|\eta}(X|Y) = \Pi_{\xi}(X)$, and therefore directly from Eq. (1)

$$\Pi_{\xi,\eta}\left(X, Y\right) = \min\left[\Pi_{\xi}(X), \Pi_{\eta}(Y)\right]. \tag{3}$$

To establish a direct link between possibility theory and fuzzy set theory, the event A is decomposed into a union $A = \bigcup_i a_i$ of its elementary events $a_i \in \Omega$. The possibility measure can be rewritten as

$$\begin{aligned} \Pi(A) = \Pi\left(\bigcup_i a_i\right) &= \sup_i \Pi(a_i) \\ &= \sup_{a \in A} \Pi(\{a\}) \\ &= \sup_{a \in A} \pi(a) = \sup_{a \in A} \pi_\xi(x = \xi(a)) \end{aligned} \tag{4}$$

with π as the so-called possibility distribution function.
A fuzzy variable is defined as the possibly infinite set of pairs

$$\tilde{p} = \{(x, \mu) \in \Omega \times [0,1] \,|\, \mu = \mu_{\tilde{p}}(x)\} \tag{5}$$

with the membership function μ as a mapping of x to the unit interval. Using Eq. (4) and the idea that the membership function induces a possibility distribution function, it yields

$$\mu_{\tilde{p}}(x) = \Pi(\{a \in \Omega \mid \tilde{p}(a) = x\}) = \pi_{\tilde{p}}(x), \tag{6}$$

which represents a family of nested confidence subsets [18] and where the fuzzy variable can be interpreted as a possibilistic variable. For further information, the reader is referred to e.g. [23] and [4].
Two important properties of fuzzy sets are the following. The *core* of a fuzzy set is defined as

$$\text{core}(\tilde{p}) = \{x \in \Omega \,|\, \mu_{\tilde{p}}(x) = 1\}, \tag{7}$$

and the *support*, which contains all elements with non-zero membership, as

$$\text{supp}(\tilde{p}) = \{x \in \Omega \,|\, \mu_{\tilde{p}}(x) > 0\}. \tag{8}$$

In this work, only so-called fuzzy numbers, as a special class of fuzzy valued variables are used, which exhibit the additional property that there exists only one $\bar{x}$ with $\mu_{\tilde{p}}(\bar{x}) = 1$. Hereinafter, the terms *membership function* and *possibility distribution function* are used interchangeably.

2.2 Multi-Fidelity Modeling

Generally, the models under consideration in possibilistic uncertainty quantification are of the form of (partial) differential equations, which are deterministic per se, but need to be evaluated multiple times if analyzed under uncertainty. Hence, they can be described as a mapping $f : \mathcal{X} \mapsto \mathcal{Z}$ which maps the input domain $\mathcal{X} \in \mathbb{R}^n$ to the output domain $\mathcal{Z} \in \mathbb{R}^m$ with n and m denoting the dimension of the input and output domain, respectively. A HFM with the mapping f_H provides the values $\boldsymbol{z}_\text{H}$ for the output of a quantity of interest $\boldsymbol{z}$, or in this case the possibility distribution function $\mu(\boldsymbol{z}_\text{H})$, for a required, problem-dependent accuracy. In general, the HFM can be large-scaled, complex and highly nonlinear, which entails tremendous computational effort. In case of a possibilistic uncertainty analysis, this can be challenging to be realized. The LFM with the mapping f_L provides the values $\boldsymbol{z}_\text{L}$ and $\mu(\boldsymbol{z}_\text{L})$, approximating the same output $\boldsymbol{z}$ with a lower accuracy, but also lower computational costs. Usually, the LFM is derived directly from the HFM, e.g. using model-order reduction techniques, surrogate models or by neglecting internal dynamics. The derivation of the LFM depends on the given application, and there are usually multiple possibilities to derive a LFM for a given problem. Of course data-fitted LFMs with sufficient evaluations of the HFM offer a good and acceptable approximation and can be used directly for the uncertainty analysis, but they may still be computationally too expensive.
The idea of using multi-fidelity models instead consists in combining the advantages of the models with different fidelity. It implies a trade-off between accuracy and computational cost of the evaluations. In [10],

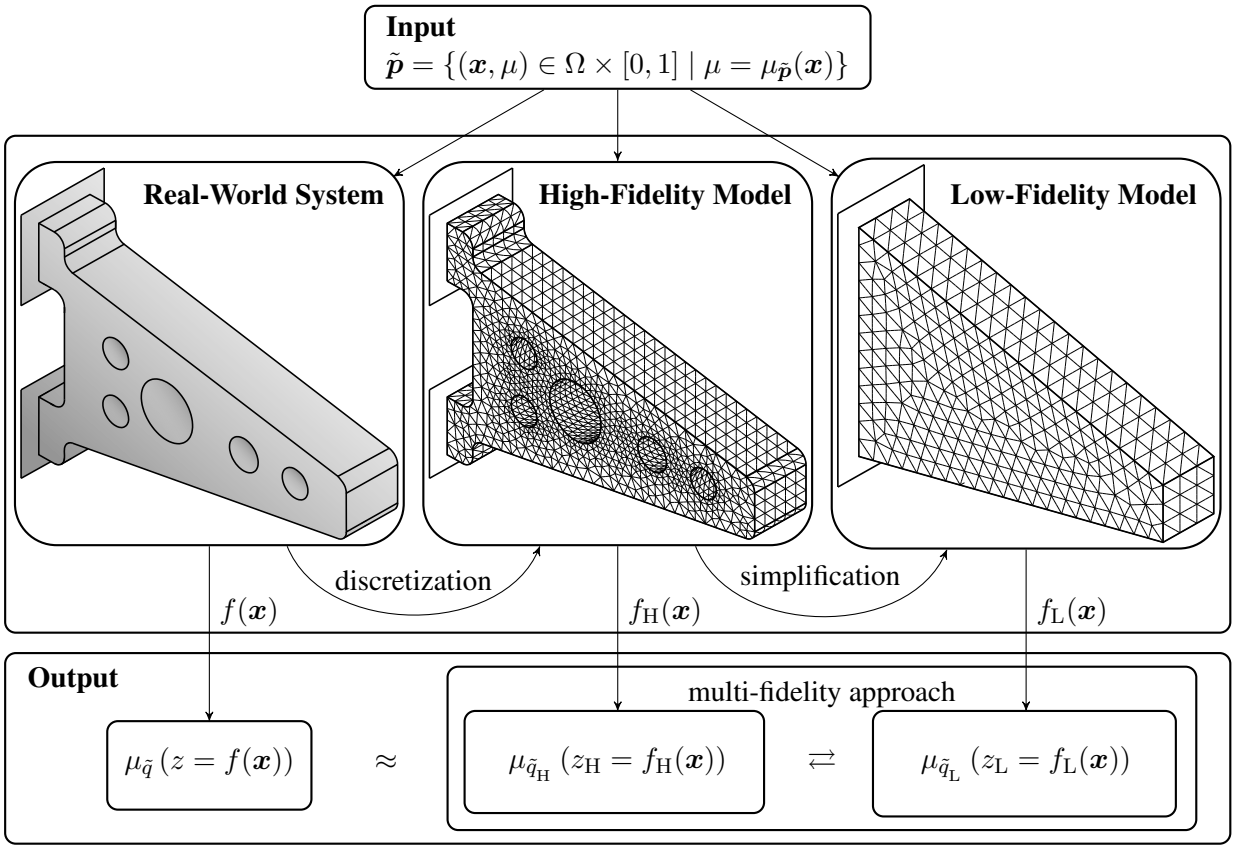


Figure 1: Models of different fidelity with one quantity of interest.

several ways of how to incorporate models with different fidelities are presented. In the present contribution, only a small number of HFM evaluations are combined with a large number of LFM evaluations to exploit their possibilistic correlation and predict the possibilistic quantities of the model with only low computational effort. The additional information gained by the evaluation of the HFM acts as a kind of correction factor for the low-fidelity solution. The approach is motivated by the work of *Biehler et al.* [14] who used a similar approach, but in a probabilistic framework, explained in detail in [15]. The relation between models of different fidelity is shown in Figure 1 using the example of a structural element, in anticipation of the application example in Section 5.

3 Propagating Possibility – Fuzzy Arithmetic

With the definitions introduced in the previous section it is possible to propagate imprecise information through a model. For this purpose, consider the mapping $f : \mathcal{X} \mapsto \mathcal{Z}$, which maps the input domain $\mathcal{X}$ onto the output domain $\mathcal{Z}$. The input parameter vector is given as a fuzzy variable $\tilde{\boldsymbol{p}}$. The membership function of the resulting fuzzy variable $\tilde{\boldsymbol{q}}$ can be obtained using the *extension principle* introduced by *Zadeh* in the form

$$\mu_{\tilde{\boldsymbol{q}}}(\boldsymbol{z}) = \begin{cases} \sup\limits_{\boldsymbol{x} \in f^{-1}(\boldsymbol{z})} \mu_{\tilde{\boldsymbol{p}}}(\boldsymbol{x}) & \text{if } \exists\, \boldsymbol{x} = f^{-1}(\boldsymbol{z}), \\ 0 & \text{else.} \end{cases} \tag{9}$$

The numerical implementation of fuzzy arithmetic is commonly based on the α-cut decompostition of fuzzy sets. The bounds of the α-cut intervals of the output quanities of interest can be determined by an α-cut optimization or special sampling-based methods like the *transformation method*, introduced in [4], resulting

in membership-dependent interval bounds. By using one of the mentioned methods, not only the α-cut decomposition of the fuzzy sets is needed, but also all the information gained by the model evaluation which does not result in the interval bounds is discarded. Besides, in the multivariate case, the α-cut formulation neglects potential dependencies between fuzzy sets, which may lead to an overestimated result.
A different approach for the numerical implementation of the extension principle which needs neither an α-cut discretization nor the discretization of the output domain is the *sampling method* [3]. The selection of the sample points from the parameter domain $\mathcal{X}$ is now moved to the beginning of the solution procedure and the restrictions of the α-cuts are discarded.
Consider an n-dimensional fuzzy input vector, then the samples are drawn from the input domain $\mathcal{X} \in \mathbb{R}^n$ which reads as

$$\{\boldsymbol{x}\} = \{\boldsymbol{x}^{[i]}\}_i^N,\ \boldsymbol{x}^{[i]} \in \mathcal{X},\ i \in \{1, \ldots, N\} =: \mathfrak{I} \tag{10}$$

with N denoting the number of sample points. The output domain of the mapping is defined as $\mathcal{Z} \in \mathbb{R}^m$. Performing a pointwise evaluation of $f(\{\boldsymbol{x}\})$ yields potential points of the membership curve

$$\{\mu_{\tilde{\boldsymbol{q}}}^{[i]}\}_i^N \left(\{\boldsymbol{z}^{[i]}\}_i^N = f(\{\boldsymbol{x}^{[i]}\}_i^N)\right) = \mu_{\tilde{\boldsymbol{p}}}\left(\{\boldsymbol{x}^{[i]}\}_i^N\right) \tag{11}$$

which need to be extracted. Here, the extension principle from Eq. (9) is applied in the form

$$\mu_{\tilde{\boldsymbol{q}}}^{[k]} = \max_{i \in \left\{\boldsymbol{z}^{[i]} = \boldsymbol{z}^{[k]}\right\}} \mu_{\tilde{\boldsymbol{q}}}^{[i]},\ k \in \mathfrak{K} \subseteq \mathfrak{I}, \tag{12}$$

resulting in a discrete, non-convex representation of the membership function. In the next step, the points on the membership curve are extracted, according to the convexity criterion, and finally, the membership can be reconstructed by

$$\mu_{\tilde{\boldsymbol{q}}}(\boldsymbol{z}) = \mathcal{I}\left(\{\boldsymbol{z}^{[j]}, \mu_{\tilde{\boldsymbol{q}}}^{[j]}\}\right),\ j \in \mathfrak{J} \subseteq \mathfrak{K} \tag{13}$$

using an interpolent $\mathcal{I}$, or taking the smallest convex fuzzy set which envelops $\mu_{\tilde{\boldsymbol{q}}}^{[k]}$. An important point is how to choose an appropriate sampling sequence $\{\boldsymbol{x}\}$. Of course, the schemes mentioned for the α-cut approaches can be adapted resulting in an optimizer-based sequence or a pattern-based sampling. The use of an optimizer-based sequence results in an iterative scheme which prohibits an efficient parallelization of the solution procedure. Another strategy is the use of randomly distributed samples. It combines the advantage of the parallel evaluation of $f(\boldsymbol{x})$ and $\mu(\boldsymbol{x})$ as well as the potential recovery of outliers in the solution. In this paper, only uniformly distributed samples are used in the form of

$$g\left(\boldsymbol{x}^{[i]}\right) \sim \mathcal{U}(0,1)^n, \tag{14}$$

where g denotes a mapping of the elements to the unit hypercube, which can be chosen without loss of generality. The generation of the samples can be further modified using importance sampling or Latin hypercube sampling, resulting in pseudo-randomly distributed points. A drawback of the random sequence is that N has to be large enough to get an appropriately reconstructed membership function. To reduce the computational cost to a minimum, all samples which result in $\mu_{\tilde{\boldsymbol{q}}}(\boldsymbol{z}) = 0$ can be discarded because they do not contribute to the membership function. This is important, especially in the case of strong dependency between fuzzy parameters. Keep in mind that the results based on the drawn samples do not yield any probabilistic significance and are just used to construct the membership function. This justifies the discard of those samples which, opposite to the probabilistic case, does not result in a biased distribution in the possibilistic case. Of course, the different types of generating samples can be combined, showing the flexibility of the sampling method.

4 Multi-Fidelity Modeling in Possibilistic Uncertainty Analysis

The introduced theories in the previous sections are sufficient to outline the MFA for the possibilistic uncertainty analysis based on fuzzy arithmetic. In the following, z_H denotes the output of the HFM and $\mu_{\tilde{z}_\mathrm{H}}(z_\mathrm{H})$ its possibility distribution function to be estimated. The output of the LFM is denoted by z_L and the corresponding possibility distribution function $\mu_{\tilde{z}_\mathrm{L}}(z_\mathrm{L})$, respectively. These outputs describe the same quantity of interest of the system, which can be for example stresses, energies or eigenfrequencies in mechanical systems. The LFM is hereby deduced from the HFM, for example by simplification or neglecting internal dynamics. Another possibility to deduce the LFM are data-fit models, for example a sparse-grid surrogate model of the HFM. To successfully apply the proposed approach, the computation time of the LFM has to be small in comparison to the HFM. Otherwise, it is more advisable to evaluate the HFM directly. And second, the multi-fidelity model has to show at least a small amount of possibilistic correlation or otherwise the approach fails. Since this approach is widely applicable, the formulations are kept rather general. An exemplary example is shown in Section 5. A connection between HFM and LFM can be established using Eq. (1) and Eq. (2) with the formulation of Eq. (6), resulting in

$$\mu_{\tilde{z}_\mathrm{H}}(z_\mathrm{H}) = \max_{z_\mathrm{L}} \min \left[\mu_{\tilde{z}_\mathrm{H}|\tilde{z}_\mathrm{L}}(z_\mathrm{H} \mid z_\mathrm{L}), \mu_{\tilde{z}_\mathrm{L}}(z_\mathrm{L})\right] \tag{15}$$

showing the interrelation of the distribution functions. Since the LFM can be a poor approximation of the HFM, the respective possibilistic quantities, i.e. $\mu_{\tilde{z}_\mathrm{L}}$ and $\mu_{\tilde{z}_\mathrm{H}}$, may differ significantly. Therefore, the formulation in Eq. (15) can be interpreted as applying a possibilistic correction factor based on the conditional membership function, and thus, of information about the HFM. Whereas $\mu_{\tilde{z}_\mathrm{L}}$ can be computed directly with the method of Section 3 in an inexpensive manner, the conditional distribution $\mu_{\tilde{z}_\mathrm{H}|\tilde{z}_\mathrm{L}}(z_\mathrm{H}|z_\mathrm{L})$ needs to be estimated using a possibilistic regression model. Therefore, both the LFM and HFM are to be evaluated at certain points

$$\begin{aligned} \{z_\mathrm{L}^{[j]}\} &= f_\mathrm{L}(\{\boldsymbol{x}^{[j]}\}) \\ \{z_\mathrm{H}^{[j]}\} &= f_\mathrm{H}(\{\boldsymbol{x}^{[j]}\}) \end{aligned} \tag{16}$$

with $j \in \mathfrak{I}$ so that the possibilistic correlation of the HFM and LFM can be evaluated. The points are chosen among the ones already used for the calculation of $\mu_{\tilde{z}_\mathrm{L}}$ and they should cover the whole support of the LFM solution. Hence, the estimation of the conditional distribution is strongly dependent on the selection of $\boldsymbol{x}^{[j]}$ and the number of the selected samples.

4.1 Estimating the Conditional Distribution

The conditional membership function can be estimated using a possibilistic regression model. Contrary to probabilistic regression models, all of the sample points need to be covered by the regression analysis. This is based on the maxitivity property of the possibility theory, because of which outliners can have a major influence on the solution. A possibilistic regression model which actually captures the data is shown by *Hose and Hanss* in [22]. It is based on a linear least-squares formulation. In case of a complex correlation between the HFM and LFM, this approach fails to provide an adequate model because of its global formulation. Therefore, the approach is extended and modified and a non-parametric least-squares formulation is introduced which is able to account for local features. Piecewise polynomials, so-called splines, can be used to approximate nonlinear functions and their coefficents can be estimated using least squares. The use of the truncated power basis leads to ill-conditioned matrices in the least-squares formulation. To overcome this difficulty, a B-spline basis can be introduced. A detailed explanation is beyond the scope of this work and the reader is referred to [24] for more information about splines and B-splines, as well as their construction. Given n data points in the form $\{(z_\mathrm{L}^{[j]}, z_\mathrm{H}^{[j]})\}_{j=1}^{n}$, the model to be approximated reads as

$$z_\mathrm{H}^{[j]} = \sum_{i=1}^{p+k+1} \beta_i B_{i,p}\left(z_\mathrm{L}^{[j]}\right) + \delta_j \tag{17}$$

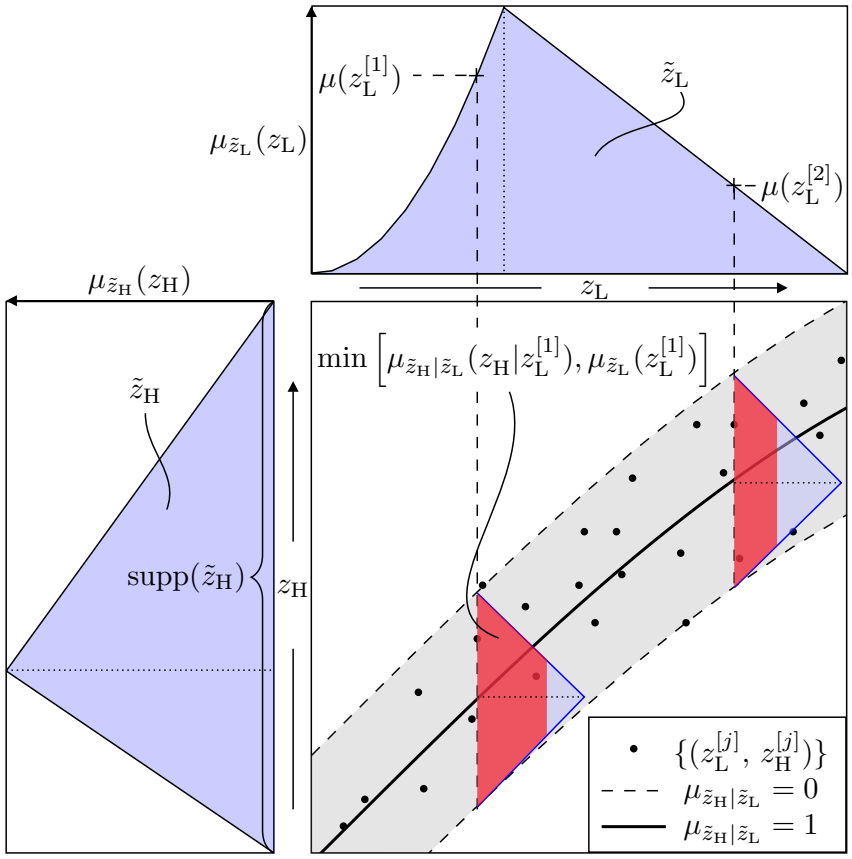


Figure 2: General procedure for the MFA in possibilistic uncertainty analysis

with k denoting the number of spline knots, δ_j denoting some deterministic perturbation, and p being the degree of the polynomia. This can be rewritten in the matrix form

$$\boldsymbol{z}_{\mathrm{H}} = \boldsymbol{\beta}\boldsymbol{B} + \boldsymbol{\delta} \tag{18}$$

which is again the common expression for linear least squares. The next step is to solve n elementary least-squares problems to find the parameters $\boldsymbol{\beta}^{[j]}$ which describe a function passing through the jth data point and achieving maximum compatibility with the remaining data. The solution for the elementary (linear) least-squares formulation with the given constraints reads as

$$\begin{pmatrix} \boldsymbol{\beta}^{[j]} \\ \lambda^{[j]} \end{pmatrix} = \begin{pmatrix} 2\boldsymbol{B}^{\mathsf{T}}\boldsymbol{B} & \boldsymbol{b}_j \\ \boldsymbol{b}_j^{\mathsf{T}} & 0 \end{pmatrix}^{-1} \begin{pmatrix} 2\boldsymbol{B}^{\mathsf{T}}\boldsymbol{z}_{\mathrm{H}} \\ z_{\mathrm{H}}^{[j]} \end{pmatrix} \quad \forall j = 1, \ldots, n \tag{19}$$

with the Lagrange parameter λ^j, and $\boldsymbol{b}_j$ denoting the jth row of $\boldsymbol{B}$, see [22]. The solutions

$$z_{\mathrm{H}}^{[j]} = \sum_{i=1}^{p+k+1} \beta_i^{[j]} B_{i,p}(z_{\mathrm{L}}) = S^{[j]}(z_{\mathrm{L}}) \quad \forall j = 1, \ldots, n \tag{20}$$

of this formulation can now be used to derive the bounds of the conditional membership function

$$\mathrm{supp}(\tilde{z}_{\mathrm{H}} \,|\, \tilde{z}_{\mathrm{L}}) = \left(\min_j \left[S^{[j]}(z_{\mathrm{L}}) \right], \max_j \left[S^{[j]}(z_{\mathrm{L}}) \right] \right) \tag{21}$$

as well as the progression of the nominal value

$$\mathrm{core}(\tilde{z}_{\mathrm{H}} \,|\, \tilde{z}_{\mathrm{L}}) = S^{[m]}(z_{\mathrm{L}}) \tag{22}$$

with the mth data point having the membership value $\mu(S^{[m]}) = 1$. The membership values between the support and the nominal value are initially approximated using linear interpolation. This provides the most simple approximation of the conditional membership function. Additionally, some information of the evaluated points can be exploited and the progression can be bounded tighter. Recalling Eq. (12) yields the estimation

$$\mu_{\tilde{z}_\mathrm{L},\tilde{z}_\mathrm{H}}\left(z_\mathrm{L}^{[j]}, z_\mathrm{H}^{[j]}\right) = \max_{l\in\{(x^{[l]},y^{[l]})=(x^{[j]},y^{[j]})\}} \mu^{[l]}_{\tilde{z}_\mathrm{L},\tilde{z}_\mathrm{H}}\left(z_\mathrm{L}^{[j]}, z_\mathrm{H}^{[j]}\right) \geq \mu^{[j]}_{\tilde{z}_\mathrm{L},\tilde{z}_\mathrm{H}}\left(z_\mathrm{L}^{[j]}, z_\mathrm{H}^{[j]}\right) \tag{23}$$

which can be used with Eq. (1). This means that the membership value of the ith sample not necessarily needs to be located on the membership curve. Here, two cases have to be analyzed. The first one,

$$\begin{aligned}\mu_{\tilde{z}_\mathrm{L},\tilde{z}_\mathrm{H}}\left(z_\mathrm{L}^{[j]}, z_\mathrm{H}^{[j]}\right) &= \min\left[\mu_{\tilde{z}_\mathrm{H}|\tilde{z}_\mathrm{L}}\left(z_\mathrm{H}^{[j]} \mid z_\mathrm{L}^{[j]}\right), \mu_{\tilde{z}_\mathrm{L}}\left(z_\mathrm{L}^{[j]}\right)\right] \\ &= \mu_{\tilde{z}_\mathrm{L}}\left(z_\mathrm{L}^{[j]}\right) \leq \mu_{\tilde{z}_\mathrm{H}|\tilde{z}_\mathrm{L}}\left(z_\mathrm{H}^{[j]} \mid z_\mathrm{L}^{[j]}\right) \leq 1, \text{ if } \mu_{\tilde{z}_\mathrm{L}|\tilde{z}_\mathrm{H}}\left(z_\mathrm{H}^{[j]} \mid z_\mathrm{L}^{[j]}\right) \geq \mu_{\tilde{z}_\mathrm{L}}\left(z_\mathrm{L}^{[i]}\right),\end{aligned} \tag{24}$$

only yields trivial information about the conditional membership. The second one,

$$\begin{aligned}\mu_{\tilde{z}_\mathrm{L},\tilde{z}_\mathrm{H}}\left(z_\mathrm{L}^{[j]}, z_\mathrm{H}^{[j]}\right) &= \min\left[\mu_{\tilde{z}_\mathrm{H}|\tilde{z}_\mathrm{L}}\left(z_\mathrm{H}^{[j} \mid z_\mathrm{L}^{[j]}\right), \mu_{\tilde{z}_\mathrm{L}}\left(z_\mathrm{L}^{[j]}\right)\right] \\ &= \mu_{\tilde{z}_\mathrm{H}|\tilde{z}_\mathrm{L}}\left(z_\mathrm{H}^{[j]} \mid z_\mathrm{L}^{[j]}\right) \leq \mu_{\tilde{z}_\mathrm{L}}\left(z_\mathrm{L}^{[j]}\right) \leq 1, \text{ if } \mu_{\tilde{z}_\mathrm{H}|\tilde{z}_\mathrm{L}}\left(z_\mathrm{H}^{[j]} \mid z_\mathrm{L}^{[j]}\right) \leq \mu_{\tilde{z}_\mathrm{L}}\left(z_\mathrm{L}^{[j]}\right) \\ &\overset{(23)}{\geq} \mu^{[j]}_{\tilde{z}_\mathrm{L},\tilde{z}_\mathrm{H}}\left(z_\mathrm{L}^{[j]}, z_\mathrm{H}^{[j]}\right)\end{aligned} \tag{25}$$

however, yields an additional estimation of the conditional membership dependent on the evaluated points which can be used to achieve a more accurate result. The first approximation of the conditional membership using only a linear interpolation between the support and the core can now be modified in order to fulfill the deduced condition. The modification of the membership function according to Eq. (25) with linear interpolation is shown in Figure 3.

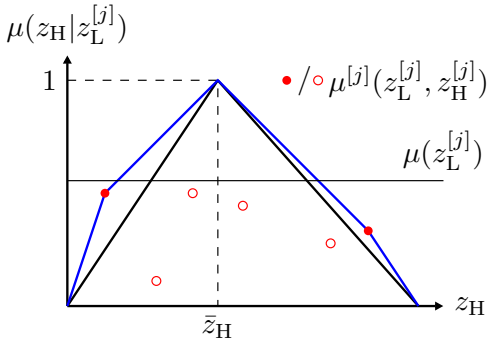


Figure 3: Modified membership function. Only the filled red circles contribute to the modification.

5 Application Example – Eigenvalue Analysis

The presented approach is now applied to the eigenvalue analysis of a linear dynamical system with uncertain parameters. The equation of motion of the crisp system, i.e. without uncertain parameters, with k degrees of freedom is defined by

$$\boldsymbol{M}\ddot{\boldsymbol{u}} + \boldsymbol{K}\boldsymbol{u} = \boldsymbol{0}, \quad \boldsymbol{M}, \boldsymbol{K} \in \mathbb{R}^{k\times k}, \tag{26}$$

where no damping is considered, and $\boldsymbol{M}$ and $\boldsymbol{K}$ are the positive definite mass and stiffness matrices, respectively. The eigenvalue problems read as

$$\left(\boldsymbol{K} - \omega_i^2 \boldsymbol{M}\right) \boldsymbol{\Phi}_i = \boldsymbol{0} \tag{27}$$

with the ith natural frequency ω_i and the corresponding eigenvector $\boldsymbol{\Phi}_i$, respectively. The solution of the eigenvalues can be determined by solving

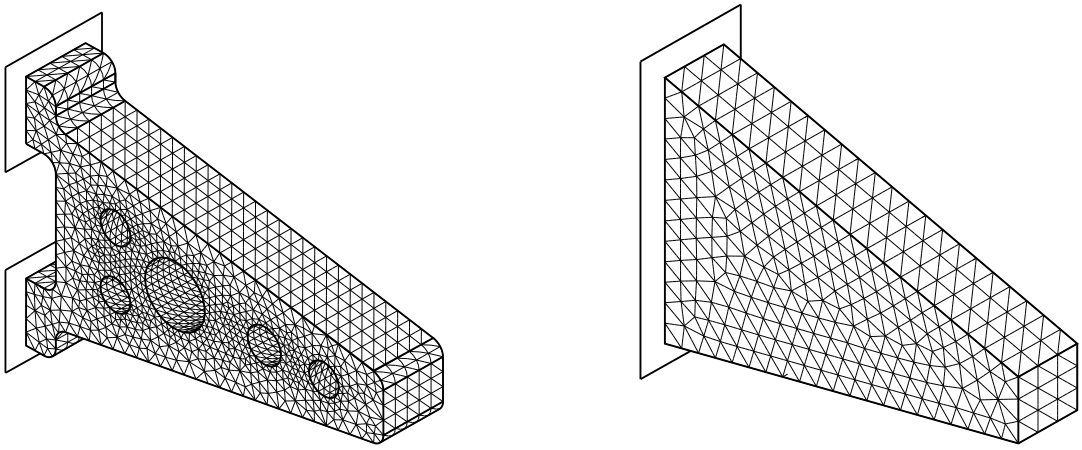
$$\det(\boldsymbol{K} - \omega_i^2 \boldsymbol{M}) = 0. \tag{28}$$

In the case of uncertain system parameters, the mass matrix $\boldsymbol{M} = \boldsymbol{M}(\tilde{\boldsymbol{p}})$ as well as the stiffness matrix $\boldsymbol{K} = \boldsymbol{K}(\tilde{\boldsymbol{p}})$ are dependent on the fuzzy parameter vector $\tilde{\boldsymbol{p}}$.
In this example, an fictitious structural element is investigated which is modeled by the finite-element method. The HFM of the structural element, which includes many geometrical details and a fine mesh, as well as the LFM, which is derived directly from the HFM by simplification of the structure and coarsening of the mesh are shown in Figure 4. The displacements and the rotation on the backside of the structural elements are set to zero. The isotropic material properties of the structural element are modeled by triangular fuzzy numbers with the properties summarized in Table 1. For the mass and stiffness matrix, this results in $\boldsymbol{M} = \boldsymbol{M}(\tilde{\rho})$ and $\boldsymbol{K} = \boldsymbol{K}(\tilde{\nu}, \tilde{E})$ with the uncertain density $\tilde{\rho}$, the uncertain Poisson ratio $\tilde{\nu}$ and the uncertain Young's modulus $\tilde{E}$.

Table 1: Material properties of the structural element modeled by triangular fuzzy numbers

	$\tilde{\rho}\ [\mathrm{kg/m^3}]$	$\tilde{\nu}[-]$	$\tilde{E}$ [GPa]
nominal value	7800	0.3	210
support	[7600, 8300]	[0.25, 0.35]	[205, 220]

For the finite-element analysis, the commercial software package Abaqus is used.



(a) High-fidelity model (b) Low-fidelity model

Figure 4: Structural element models of different fidelity.

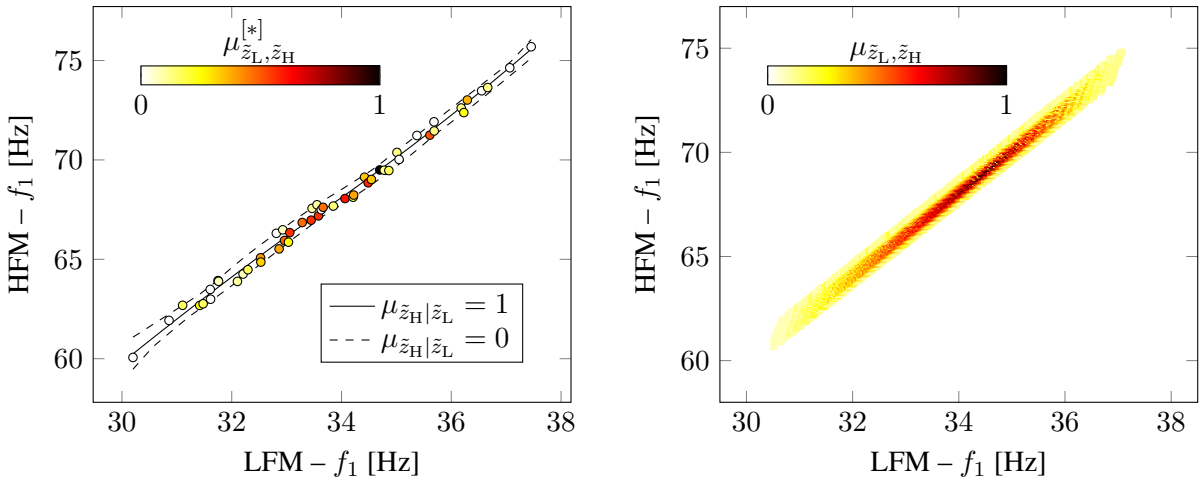
5.1 Results

In this particular case, the first eigenfrequency f_1 of the structural element model is defined as the quantity of interest, i.e. the membership function $\mu_{\tilde{f}}(f_1)$ is to be determined. The times for a single evaluation, using a 4-core Intel Xeon 3.3 GHz workstation with 129 GB RAM, are listed in Table 2 together with the numbers of degree of freedom. The LFM is evaluated $22^3 = 10648$ times in order to get a good representaion of

Table 2: Comparison of the individual HFM and LFM solutions

	HFM	LFM
solution time (one evaluation)	26.15s	8.34s
degrees of freedom	132687	21618

the LFM membership function. From these evaluations, 50 parameter configurations, which cover the entire support of the LFM membership function are picked randomly, and the HFM is evaluated with those as inputs. Using the approach described in Section 4, the conditional membership function is estimated and, in the end, the membership function of the HFM is deduced. The estimated conditional membership function and the resulting joint membership distribution of the first eigenfrequency are shown in Figure 5. Finally, the estimated HFM solution and the corresponding LFM solution are outlined in Figure 6. The comparison of the MFA, the reference solution, the LFM as well as their relative errors are listed in Table 3. For the description of the shape parameter of the membership function, the lower and upper expected value E_* and E^* [25] as well as the lower and upper bound of the membership function μ_* and μ^* and its cardinality are used as described in [3]. Although the LFM is a rather poor approximation, the presented approach provides a good approximation of the HFM with a speed-up factor of about three. An overview of the estimated conditional membership functions of the first six eigenfrequencies are shown in the Appendix.



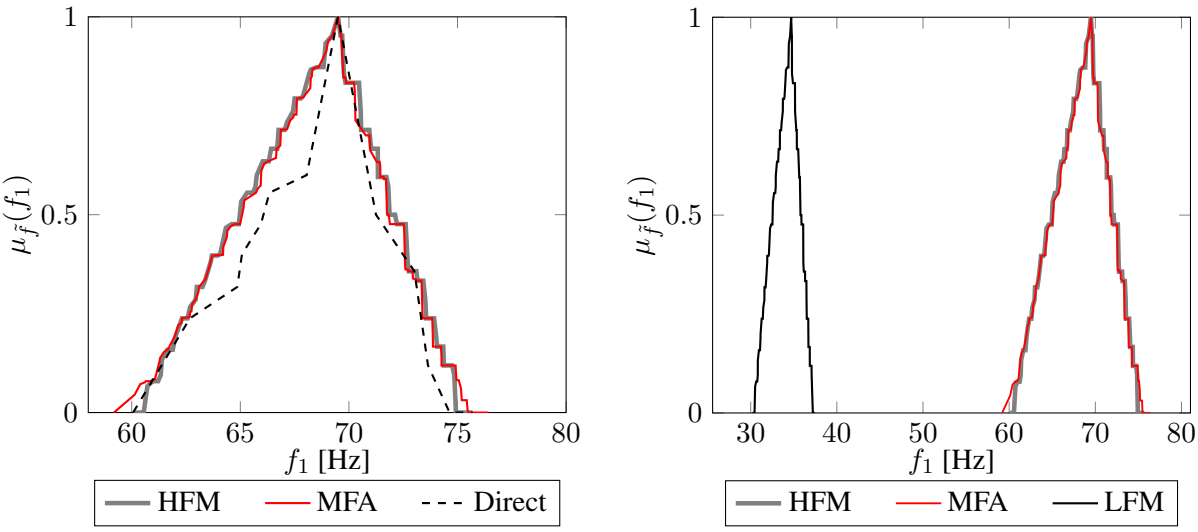
(a) Estimated conditional membership function $\mu_{\tilde{z}_\mathrm{H}|\tilde{z}_\mathrm{L}}$.

(b) Reconstructed joint membership function $\mu_{\tilde{z}_\mathrm{L},\tilde{z}_\mathrm{H}}$.

Figure 5: Structural element models of different fidelity

Table 3: Comparison of the HFM, MFA and the LFM solution

	HFM [Hz]	MFA [Hz]	LFM [Hz]	$\Delta^{\mathrm{rel}}_{\mathrm{MFA}}$	$\Delta^{\mathrm{rel}}_{\mathrm{LFM}}$
$\mu_*(\tilde{f})$	60.06	59.47	30.20	$1.0 \cdot 10^{-2}$	$9.9 \cdot 10^{-1}$
$\mu^*(\tilde{f})$	75.69	76.06	37.46	$4.8 \cdot 10^{-3}$	$1.0 \cdot 10^{0}$
$E_*(\tilde{f})$	64.92	64.93	32.52	$1.3 \cdot 10^{-4}$	$9.9 \cdot 10^{-1}$
$E^*(\tilde{f})$	72.18	72.12	35.90	$8.3 \cdot 10^{-4}$	$1.1 \cdot 10^{0}$
$\int \mu_{\tilde{f}} \, \mathrm{d}f$	7.26	7.19	3.38	$9.5 \cdot 10^{-3}$	$1.2 \cdot 10^{0}$



(a) Comparison of the reference HFM solution (gray) with the MFA solution (red) and the solution achieved by direct evaluation of the HFM using 50 sample points (dashed).

(b) Comparison of the reference HFM solution (gray) with the MFA solution (red) and the LFM solution (black).

Figure 6: Solution to the fuzzy eigenvalue problem of the structural element model.

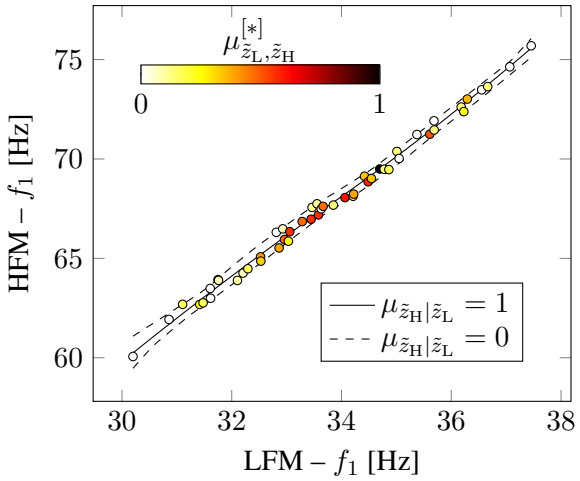
6 Conclusion

The proposed work shows a novel approach for possibilistic uncertainty quantification using models of different fidelity to reduce the computing time. Using a sample-based approach for fuzzy arithmetic, the conditional possibility distribution can be estimated by a non-parametric possibilistic regression model which results in an estimation of the HFM solution. Future work can deal with a more elaborated regression model for the estimation of the conditional distribution and with an advanced strategy for the selection of the samples for the regression analysis. Additionally, the applicability of this approach can be tested for more complex models from different fields of the engineering sciences.

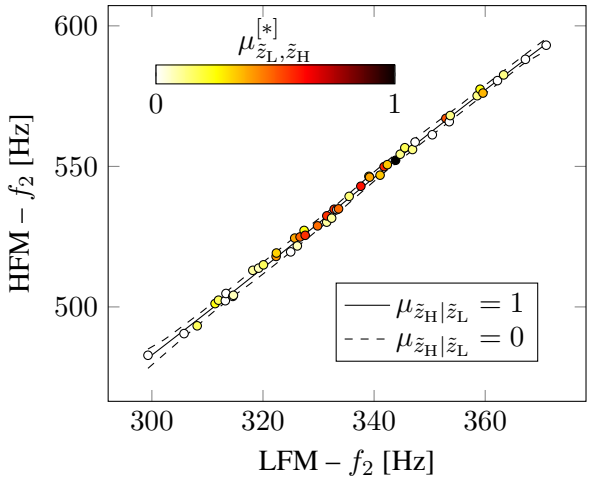
Acknowledgements

The authors gratefully acknowledge the support of this research by the German Research Foundation DFG in the framework of the priority programme 1886 *Polymorphic Uncertainty Modelling for the Numerical Design of Structures*.

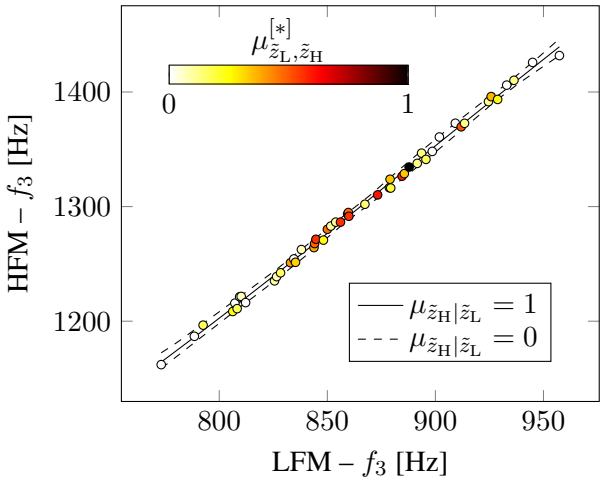
A – Appendix



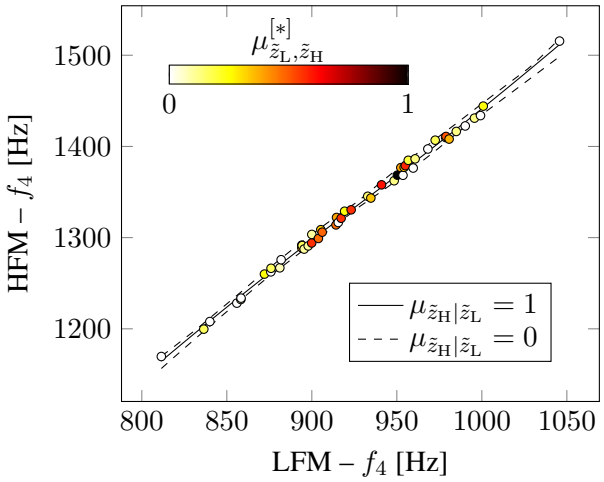
(a) Estimated conditional membership function of the 1st eigenfrequency.



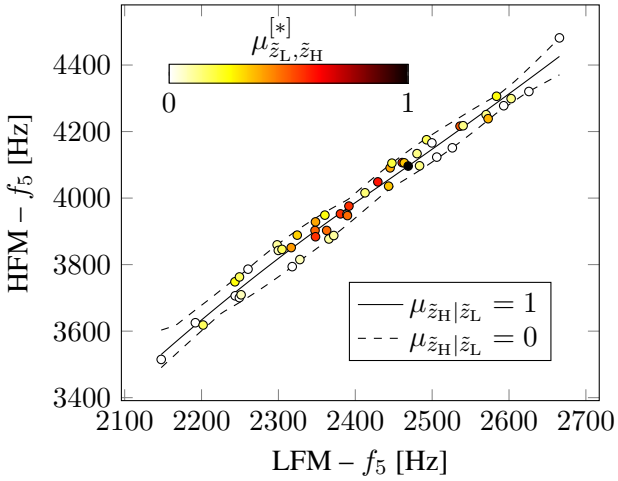
(b) Estimated conditional membership function of the 2nd eigenfrequency.



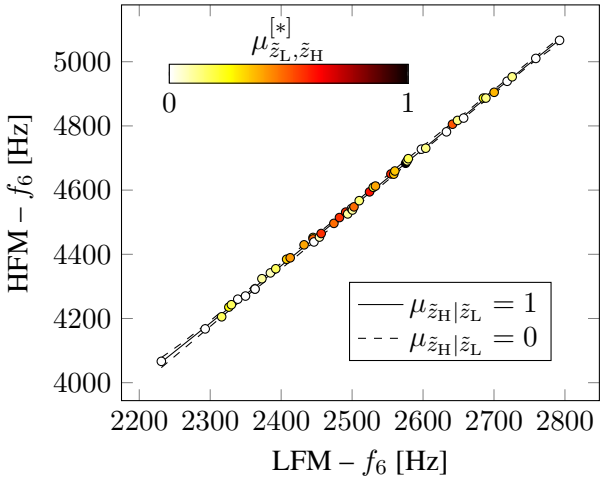
(c) Estimated conditional membership function of the 3rd eigenfrequency.



(d) Estimated conditional membership function of the 4th eigenfrequency.



(e) Estimated conditional membership function of the 5th eigenfrequency.



(f) Estimated conditional membership function of the 6th eigenfrequency.

References

[1] D. Dubois, H. Prade, *Possibility Theory: An Approach to Computerized Processing of Uncertainty*, Plenum Press, 1988.

[2] G. De Cooman, *Possibility Theory I: The Measure- and Integral-Theoretic Groundwork*, International Journal of General Systems, 25(4): 291–323, 1997.

[3] N. P. Walz, *Fuzzy Arithmetical Methods for Possibilistic Uncertainty Analysis*, PhD thesis, Universität Stuttgart, Aachen, 2016.

[4] M. Hanss, *Applied Fuzzy Arithmetic - An Introduction with Engineering Applications*, 2nd Edition, Springer, Berlin, 2010.

[5] L. Zadeh, *Fuzzy Sets as a Basis for a Theory of Possibility*, Fuzzy Sets and Systems, 1:3–28, 1978.

[6] D. Dubois, H. Prade, *Possibility Theory and Its Applications: Where Do We Stand?*, pages 31–60. Springer Berlin Heidelberg, Berlin, Heidelberg, 2015.

[7] M. Köppel, F. Franzelin, I. Kröker, S. Oladyshkin, G. Santin, D. Wittwar, A. Barth, B. Haasdonk, W. Nowak, D. Pflüger, and C. Rohde, *Comparison of Data-Driven Uncertainty Quantification Methods for a Carbon Dioxide Storage Benchmark Scenario*, Technical report, 2017.

[8] A. Klimke, K. Willner, and B. Wohlmuth, *Uncertainty Modeling Using Fuzzy Arithmetic Based on Sparse Grids: Applications to Dynamic Systems*, International Journal of Uncertainty, Fuzziness and Knowledge-based Systems, 12:745–759, 2004.

[9] N. P. Walz, M. Hanss, *Fuzzy Arithmetical Analysis of Multibody Systems With Uncertainties*, Archive of Mechanical Engineering, Vol. LX, No. 1, pp. 109- 125, 2013.

[10] B. Peherstorfer, K. Willcox, M. Gunzburger *Survey of Multifidelity Methods in Uncertainty Propagation, Inference, and Optimization*, SIAM Review, 2017.

[11] G. Fernandez, C. Park, N. Kim, R. Haftka, *Review of Multi-Fidelity Models*, arXiv preprint arXiv:1609.07196, 2017.

[12] M. C. Kennedy, A. O'Hagan, *Predicting The Output From a Complex Computer Code When Fast Approximations are Available*, Biometrika, 87(1):1–13, 2000.

[13] P. Koutsourelakis, *Accurate Uncertainty Quantification Using Inaccurate Computational Models*, SIAM Journal on Scientific Computing , 31:3274–3300, 2009.

[14] J. Biehler, M. W. Gee, W. A. Wall, *Towards Efficient Uncertainty Quantification in Complex and Large-Scale Biomechanical Problems Based on a Bayesian Multi-Fidelity Scheme*, Biomechanics and Modeling in Mechanobiology, 14(3):489–513, Jun 2015.

[15] J. Biehler, *Efficient Uncertainty Quantification for Large-Scale Biomechanical Models Using a Bayesian Multi-Fidelity Approach*, PhD thesis, Technische Universität München, München, 2016.

[16] E. Hisdal, *Conditional Possibilities Independence and Noninteraction*, Fuzzy Sets and Systems, 1(4):283 – 297, 1978.

[17] H. T. Nguyen, *On Conditional Possibility Distributions*, Fuzzy Sets and Systems, 1(4):299–309, 1978.

[18] D. Dubois, *Possibility Theory and Statistical Reasoning*, Computational Statistics & Data Analysis, 51(1):47 – 69, 2006.

[19] B. Bouchon-Meunier, G. Coletti, C. Marsala, *Conditional Possibility and Necessity*, in B. Bouchon-Meunier, J. Gutiérrez-Ríos, L. Magdalena, and R. R. Yager, editors, *Technologies for Constructing Intelligent Systems 2*, Springer, 2002, pp. 59–71.

[20] G. de Cooman. *Possibility Theory II: Conditional Possibility*, International Journal of General Systems, 25(4):325–351, 1997.

[21] S. Lapointe, B. Bobée, *Revision of Possibility Distributions: A Bayesian Inference Pattern*, Fuzzy Sets and Systems, 116(2):119 – 140, 2000.

[22] D. Hose, M. Hanss, *Fuzzy Linear Least Squares for the Identification of Possibilistic Regression Models*, Fuzzy Sets and Systems, 2018. (to appear)

[23] B. Liu, *Theory and Practice of Uncertain Programming*, Physica-Verlag, Heidelberg New York, 2002.

[24] K. Höllig, J. Hörner, *Approximation and Modeling with B-Splines*, Vol. 132, SIAM, 2013.

[25] D. Dubois, H. Prade, *The Mean Value of a Fuzzy Number*, Fuzzy Sets and Systems, Vol. 24, 279-300, 1987.

A sensitivity-based approach for the dynamic analysis of structures with uncertain-but-bounded parameters

F. Giunta[1], G. Muscolino[1] and A. Sofi[2]
[1]University of Messina, Department of Engineering,
Villaggio S. Agata, Messina 98166, Italy.

[2]University "Mediterranea" of Reggio Calabria, Department of Architecture and Territory,
Salita Melissari, Feo di Vito, 89124, Reggio Calabria Italy.
e-mail: **alba.sofi@unirc.it**

Abstract
The paper addresses the dynamic analysis of structures with uncertain-but-bounded material properties subjected to deterministic dynamic loads. The main purpose of the analysis is the evaluation of the bounds of stress time-history. A sensitivity-based approach is adopted in the context of finite element analysis to detect suitable combinations of the endpoints of the uncertain parameters for estimating the bounds of the stress field. To reduce the computational burden, the concept of *pseudo-static sensitivity* is exploited. Furthermore, only two combinations over the whole time-interval of interest are identified as the most common ones among those detected at each time instant. Numerical results demonstrate the accuracy of the proposed approach through comparison with the results provided by the classical combinatorial procedure.

1 Introduction

The main purpose of structural analysis is to evaluate response quantities, such as displacements, rotations, stresses etc., to perform reliability assessment of engineering systems. To this aim, not only external loads but also material properties need to be modeled with great accuracy. It has been widely recognized that parameters characterizing the mechanical behavior of structural materials are affected by uncertainties caused by measurement or manufacturing errors, or other factors. Experimental data available to define mechanical properties are often quite limited, so that the accuracy of the traditional probabilistic model becomes questionable [1]. Indeed, within a probabilistic framework, the uncertain parameters are modeled as random variables or random fields, under the assumption that complete information is available to define the pertinent probability density function (PDF). However, as highlighted by Ben-Haim and Elishakoff [2], even small variations deviating from the real values may cause relatively large errors of the probability distributions in the feasible region of the design space.

Non-probabilistic approaches can be alternatively used to treat uncertainties affecting material properties when only fragmentary or incomplete experimental data are available. In this framework, the interval model seems today the most suitable analytical tool when only range information or tolerance is known [2,3]. The interval model, which is based on the set theory, represents the uncertain parameters as interval variables with assigned *lower bound* (*LB*) and *upper bound* (*UB*) without requiring complete information on the distribution of the uncertainties between such bounds.

The main advantage of the *Classical Interval Analysis* (*CIA*) is that it provides analytically rigorous enclosures of the solution [4,5], but its application to practical engineering problems is not an easy task due to two main drawbacks commonly faced in the development of interval-based procedures for structural analysis: *i*) the drastic overestimation of the interval solution range due to the so-called *dependency phenomenon* [1,5]; *ii*) the high computational costs required by uncertainty propagation procedures, such as the classical combinatorial approach [1,6].

The dynamic equilibrium of structural systems with interval uncertainties is governed by interval *Ordinary Differential Equations* (*ODE*s). If such equations are solved using the *CIA*, the overestimation will progressively increase in the process of numerical iterations [7,8]. Several methods have been proposed in the literature to limit the overestimation of the solution of the set of interval *ODE*s governing linear or non-linear dynamic problems with interval uncertainties. In particular, the upper and lower bounds of the dynamic response were obtained by Chen et al. [9] using Taylor series expansion combined with a method based on matrix perturbation theory. Subsequently, the *Interval Perturbation Method* (*IPM*), which is based on Taylor series expansion and parameter perturbation, has been introduced to evaluate the dynamic response of structures subjected to deterministic [10-13] or stochastic excitations [14]. More recently, Gao et al. [15] presented the *interval factor method* to calculate the dynamic response of truss structures with interval parameters under interval loads. Rama Rao et al. [16] proposed two methods to obtain the transient response time-history of structures subjected to a sudden impact load: the first one is based on adaptive Taylor series expansion along with gradient method, while the second approach relies on direct optimization. Yang et al. [17] used the Laplace transform to convert the *ODE*s into a system of linear equations and the inverse Laplace transform to obtain the response time-history, once higher-order terms are removed by matrix perturbation technique in Laplace domain.

Though often less accurate than other methods, the *IPM* or, equivalently, the first-order interval Taylor series expansion, is the most widely used to obtain the *LB* and *UB* of the interval dynamic response. The main advantages of the *IPM* are the flexibility and the simplicity of the mathematical formulation. However, since the effect of neglecting higher-order terms is unpredictable, the effectiveness of this method is limited to uncertainties with small intervals. Furthermore, the computational burden associated with the *IPM* rapidly increases with the dimensions of structural systems and the number of uncertainties.

In this paper, attention is focused on a recently proposed procedure [18] for evaluating the bounds of the interval displacement time-history of structural systems with uncertain-but-bounded material properties under deterministic dynamic excitations. The key idea of this approach stems from the observation that, at each time instant, the dynamic response of a structural system is a monotonic function of the uncertain material properties. Hence, as customary in the context of interval static structural analysis [19,20], sensitivity analysis of the response can be performed to define suitable combinations of the endpoints of the uncertain parameters to be used for estimating the bounds of the dynamic response. In order to reduce the computational burden associated with the evaluation of response sensitivities at each time instant, the concept of *pseudo-static sensitivity* of the response is introduced. The definition of *pseudo-static sensitivities* involves just the evaluation of the nominal dynamic response time-history. Based on the results provided by the *pseudo-static sensitivity* analysis, two combinations of the endpoints of the uncertain parameters are identified for estimating the *LB* and *UB* of the response time-history. Such combinations are selected as the most common ones among those detected at each time instant. Then, response bounds can be estimated as the minimum and maximum among the deterministic dynamic responses pertaining to the most common combinations. Such responses can be evaluated by performing two parallel modal analyses. In the present paper, this procedure is further extended to evaluate the bounds of the time-history of interval stress components. As known, the prediction of sharp bounds of the interval stress field is a challenging task since stress variables are more affected by the *dependency phenomenon* [1,5] than the displacement field.

A 24-bar truss structure with uncertain Young's modulus of the material is analyzed. The accuracy of the proposed method is demonstrated through appropriate comparisons with the exact bounds provided by the classical combinatorial procedure, known as *vertex method* [21].

2 Problem statement

Let us consider a quiescent classically damped linear structural system subjected to a deterministic excitation. Assume that the structure is discretized into N finite elements (FEs) and that the resulting model has n DOFs. Without loss of generality, all structural parameters are assumed to be known deterministically, except Young's modulus of the material. Specifically, Young's modulus of each FE is modeled as an interval variable, i.e.:

$$E^{(\ell)I} = E_0\left(1+\alpha_\ell^I\right), \quad \left(\ell = 1,2,...,N\right) \tag{1}$$

where $\alpha_\ell^I \in \left[\underline{\alpha}_\ell, \overline{\alpha}_\ell\right] \in \mathrm{IR}$ is the dimensionless fluctuation of the $\ell-$th uncertain property around the nominal value, E_0, with IP denoting the set of all closed real interval numbers, while $\underline{\alpha}_\ell$ and $\overline{\alpha}_\ell$ are the *lower bound* (*LB*) and *upper bound* (*UB*) of α_ℓ^I, respectively.

Let the fluctuations be collected into the interval vector $\boldsymbol{\alpha}^I = [\alpha_1^I, \ \alpha_2^I, \ \ldots, \ \alpha_N^I]^T$ of order *N*, with the apex *T* meaning transpose operator. According to the *Classical Interval Analysis* (*CIA*) [4,5], the N uncertain-but-bounded parameters $\alpha_\ell^I \quad (\ell = 1,2,\ldots,N)$ are assumed to be independent and $\boldsymbol{\alpha}^I \in [\underline{\boldsymbol{\alpha}}, \overline{\boldsymbol{\alpha}}] \in \mathrm{IR}^N$ is a bounded set-interval vector of real numbers such that $\underline{\boldsymbol{\alpha}} \le \boldsymbol{\alpha} \le \overline{\boldsymbol{\alpha}}$, with the symbols $\underline{\boldsymbol{\alpha}}$ and $\overline{\boldsymbol{\alpha}}$ denoting the vectors collecting the *LB* and *UB* of the interval variables α_ℓ^I, respectively.

Following the *improved interval analysis* (*IIA*) [22], the $\ell-$th real interval variable α_ℓ^I can be expressed in the following *affine form*:

$$\alpha_\ell^I = \alpha_{0,\ell} + \Delta\alpha_\ell \, \hat{e}_\ell^I, \quad \left(\ell = 1,2,...,N\right) \tag{2}$$

where

$$\alpha_{0,\ell} = \frac{1}{2}\left(\underline{\alpha}_\ell + \overline{\alpha}_\ell\right); \quad \Delta\alpha_\ell = \frac{1}{2}\left(\overline{\alpha}_\ell - \underline{\alpha}_\ell\right) \tag{3a,b}$$

are the midpoint value (or mean), $\alpha_{0,\ell}$, and the deviation amplitude (or radius), $\Delta\alpha_\ell$; $\hat{e}_\ell^I \in \left[-1,1\right]$ is the so-called *Extra Unitary Interval* (*EUI*) [22] associated with the ℓ-th real interval variable α_ℓ^I.

Since α_ℓ^I denotes the dimensionless fluctuation of the ℓ-th uncertain Young's modulus around the nominal value, it can be reasonably modelled as a symmetric interval variable, that is $\overline{\alpha}_\ell = -\underline{\alpha}_\ell$. Under this assumption, $\alpha_{0,\ell} = 0$ and $\Delta\alpha_\ell > 0$, so that Eq. (2) reduces to:

$$\alpha_\ell^I = \Delta\alpha_\ell \hat{e}_\ell^I, \quad \left(\ell = 1,2,...,N\right) \tag{4}$$

where $\Delta\alpha_\ell < 1$ in order to ensure always positive values of the uncertain physical properties.

In the framework of interval symbolism, a generic interval-valued function f and a generic interval-valued matrix function $\mathbf{A}$ of the interval vector $\boldsymbol{\alpha}^I$ will be denoted in equivalent form, respectively, as:

$$\begin{aligned} f^I &\equiv f(\boldsymbol{\alpha}^I) \Leftrightarrow f(\boldsymbol{\alpha}), \quad \boldsymbol{\alpha} \in \boldsymbol{\alpha}^I = \left[\underline{\boldsymbol{\alpha}}, \overline{\boldsymbol{\alpha}}\right]; \\ \mathbf{A}^I &\equiv \mathbf{A}(\boldsymbol{\alpha}^I) \Leftrightarrow \mathbf{A}(\boldsymbol{\alpha}), \quad \boldsymbol{\alpha} \in \boldsymbol{\alpha}^I = \left[\underline{\boldsymbol{\alpha}}, \overline{\boldsymbol{\alpha}}\right]. \end{aligned} \tag{5a,b}$$

Taking into account Eq. (1), the constitutive matrix of the ℓ-th FE can be expressed as follows:

$$\mathbf{D}^{(\ell)}(\alpha_\ell^I) = \left(1+\Delta\alpha_\ell\hat{e}_\ell^I\right)\mathbf{D}_0 \tag{6}$$

where $\mathbf{D}_0$ is the nominal value.

Uncertainty affecting the elastic modulus of the material propagates to the response of the FE model which turns out to be described by interval quantities. Specifically, following the standard displacement-based finite element method (FEM) formulation, the interval displacement field within the ℓ-th FE can be related to the global nodal displacements collected into the interval vector $\mathbf{u}(\boldsymbol{\alpha}^I, t)$ as follows:

$$\mathbf{u}^{(\ell)}(\mathbf{x}, t; \boldsymbol{\alpha}^I) = \mathbf{N}^{(\ell)}(\mathbf{x})\mathbf{L}^{(\ell)}\,\mathbf{u}(\boldsymbol{\alpha}^I, t) \tag{7}$$

where $\mathbf{L}^{(\ell)}$ is the connectivity matrix; $\mathbf{N}^{(\ell)}(\mathbf{x})$ denotes the shape-function matrix; $\mathbf{x}$ is the position vector.

Strain-displacement equations yield the following expression of the interval strain field within the ℓ-th FE:

$$\boldsymbol{\varepsilon}^{(\ell)}(\mathbf{x},t;\boldsymbol{\alpha}^I) = \mathbf{B}^{(\ell)}(\mathbf{x})\,\mathbf{L}^{(\ell)}\,\mathbf{u}(\boldsymbol{\alpha}^I,t) \tag{8}$$

where $\mathbf{B}^{(\ell)}(\mathbf{x})$ is the strain-displacement matrix. Finally, the interval stress field can be expressed as follows:

$$\boldsymbol{\sigma}^{(\ell)}(\mathbf{x},t;\boldsymbol{\alpha}^I) = \mathbf{D}^{(\ell)}(\alpha_\ell^I)\,\boldsymbol{\varepsilon}^{(\ell)}(\mathbf{x},t;\boldsymbol{\alpha}^I) = \left(1+\Delta\alpha_\ell\hat{e}_\ell^I\right)\mathbf{D}_0\,\mathbf{B}^{(\ell)}(\mathbf{x})\,\mathbf{L}^{(\ell)}\,\mathbf{u}(\boldsymbol{\alpha}^I,t). \tag{9}$$

In analogy to the standard displacement-based FEM, Eqs. (7)-(9) express the interval displacement, strain and stress fields within the ℓ-th FE as interpolation of the nodal displacements. Notice that the interval stresses, collected into the vector $\boldsymbol{\sigma}^{(\ell)}(\mathbf{x},t;\boldsymbol{\alpha}^I)$, depend on the uncertain parameters both through the nodal displacements and the elastic matrix $\mathbf{D}^{(\ell)}(\alpha_\ell^I)$. This circumstance makes the interval stress field more sensitive to the *dependency phenomenon* than the displacement field.

The dynamic response of the FE modeled structure with uncertain Young's modulus is governed by the following set of interval second-order *Ordinary Differential Equations* (*ODE*s):

$$\mathbf{M}\,\ddot{\mathbf{u}}(\boldsymbol{\alpha},t) + \mathbf{C}(\boldsymbol{\alpha})\,\dot{\mathbf{u}}(\boldsymbol{\alpha},t) + \mathbf{K}(\boldsymbol{\alpha})\,\mathbf{u}(\boldsymbol{\alpha},t) = \mathbf{f}(t), \qquad \boldsymbol{\alpha}\in\boldsymbol{\alpha}^I = \left[\underline{\boldsymbol{\alpha}},\overline{\boldsymbol{\alpha}}\right] \tag{10}$$

where $\mathbf{M}$ is the $n\times n$ mass matrix; $\mathbf{K}(\boldsymbol{\alpha}^I)$ is the $n\times n$ interval stiffness matrix [20] of the structure; $\mathbf{f}(t)$ is the $n\times 1$ order time-dependent vector collecting the external loads; finally, a dot over a variable denotes differentiation with respect to time t. Moreover, the Rayleigh model is adopted for the damping matrix, so that the following relationship holds:

$$\mathbf{C}(\boldsymbol{\alpha}) = c_M\,\mathbf{M} + c_K\,\mathbf{K}(\boldsymbol{\alpha}), \qquad \boldsymbol{\alpha}\in\boldsymbol{\alpha}^I = \left[\underline{\boldsymbol{\alpha}},\overline{\boldsymbol{\alpha}}\right] \tag{11}$$

where c_M and c_K are the Rayleigh damping constants having units s^{-1} and s, respectively.

Adopting the interval formalism above introduced, the interval global stiffness matrix $\mathbf{K}(\boldsymbol{\alpha}^I)$ can be expressed as:

$$\mathbf{K}(\boldsymbol{\alpha}^I) = \mathbf{K}_0 + \Delta\mathbf{K}(\boldsymbol{\alpha}^I) = \mathbf{K}_0 + \sum_{\ell=1}^{N}\Delta\alpha_\ell\,\hat{e}_\ell^I\,\mathbf{K}_\ell \tag{12}$$

where $\mathbf{K}_0$ is the nominal global stiffness matrix, which is a positive-definite symmetric matrix of order $n\times n$ pertaining to the structure with $\boldsymbol{\alpha}=\mathbf{0}$, $\Delta\mathbf{K}(\boldsymbol{\alpha}^I)$ is the interval deviation of the stiffness matrix with respect to the nominal one and $\mathbf{K}_\ell$ is a semi-definite positive matrix given by:

$$\mathbf{K}_\ell = \left.\frac{\partial\mathbf{K}(\boldsymbol{\alpha})}{\partial\alpha_\ell}\right|_{\boldsymbol{\alpha}=\mathbf{0}}. \tag{13}$$

At each time instant, all possible solutions of the equations of motion in Eq. (10) obtained as the uncertain parameters α_ℓ^I vary independently over their ranges are contained within a solution set:

$$\Sigma(t) = \left\{\mathbf{u}(\boldsymbol{\alpha},t)\in\mathrm{R}^n \,\middle|\, \mathbf{M}\,\ddot{\mathbf{u}}(\boldsymbol{\alpha},t) + \mathbf{C}(\boldsymbol{\alpha})\,\dot{\mathbf{u}}(\boldsymbol{\alpha},t) + \mathbf{K}(\boldsymbol{\alpha})\,\mathbf{u}(\boldsymbol{\alpha},t) = \mathbf{f}(t),\ \boldsymbol{\alpha}\in\boldsymbol{\alpha}^I = \left[\underline{\boldsymbol{\alpha}},\overline{\boldsymbol{\alpha}}\right]\right\} \tag{14}$$

where $\left\{S(\boldsymbol{\alpha},t)\middle|P(\boldsymbol{\alpha},t)\right\}$ means "the set of quantities $S(\boldsymbol{\alpha},t)$ such that the proposition $P(\boldsymbol{\alpha},t)$ holds". As known, the exact evaluation of the solution set is very difficult. Therefore, within the interval framework, the solution of Eq. (10) is carried out by seeking, at each time instant, the *LB* and *UB* of the interval displacement vector, containing the solution set, which has the narrowest interval components, i.e.

$$\mathbf{u}(\boldsymbol{\alpha}^I,t) = \left[\underline{\mathbf{u}}(t),\overline{\mathbf{u}}(t)\right] \tag{15}$$

or in component form

$$u_j(\boldsymbol{\alpha}^I,t)=\left[\underline{u}_j(t),\overline{u}_j(t)\right],\quad (j=1,2,\ldots,n) \tag{16}$$

with

$$\begin{aligned}\underline{u}_j(t)&=\min\left\{u_j(\boldsymbol{\alpha},t)\middle|\ u_j(\boldsymbol{\alpha},t)\in \mathrm{R},\,\boldsymbol{\alpha}\in \mathrm{IR}^N\right\},\\ \overline{u}_j(t)&=\max\left\{u_j(\boldsymbol{\alpha},t)\middle|\ u_j(\boldsymbol{\alpha},t)\in \mathrm{R},\,\boldsymbol{\alpha}\in \mathrm{IR}^N\right\},\quad (j=1,2,\ldots,n)\end{aligned} \tag{17a,b}$$

where the symbols $\min\{\square\}$ and $\max\{\square\}$ mean minimum (inferior) and maximum (superior) value of the quantity between parentheses. In the next sections, a sensitivity-based procedure, recently proposed by authors [18], is briefly described and extended to the evaluation of the bounds of the time-histories of the interval stress field.

3 Pseudo-static sensitivity analysis

The interval sensitivity analysis of structural system response gives information on the impact of the change of an individual interval parameter on the generic output quantity of interest (displacement, rotation, stress etc.) [23]. Relying on the assumption that the response quantities are monotonic functions of the uncertain parameters, sensitivity analysis has been exploited in the literature to identify appropriate endpoints of the interval parameters for evaluating the approximate bounds of the static response [19,20]. Recently, the authors extended this approach to estimate the approximate time-dependent bound functions of the interval dynamic displacements [18]. The key idea of the proposed method is to reduce the computational effort required by sensitivity analysis introducing the definition of *pseudo-static sensitivity* function of the dynamic response with respect to the uncertain parameters.

At each time instant, *pseudo-static sensitivity* analysis enables one to predict the monotonic increasing or decreasing behaviour of the response and thus detect the combinations of the endpoints of the uncertain parameters to be used for evaluating the bounds of the response. Since considering different combinations at each time instant is computationally onerous, only two combinations are selected to estimate the *LB* and *UB* of the response over the whole time interval of interest. Such combinations are identified as the "most common" combinations among those detected at each time instant by performing a preliminary *pseudo-sensitivity* analysis. The aim of the present paper is to extend this approach to estimate the bounds of the interval stress field. For this purpose, in the sequel the definition of the *pseudo-static sensitivity* of both displacements and stresses is given.

3.1 Pseudo-static sensitivity of displacements

The vector collecting the *pseudo-static sensitivity* functions of the displacement time-history with respect to the ℓ -th uncertain parameter, $\alpha_\ell \in \alpha_\ell^I=\left[\underline{\alpha}_\ell,\overline{\alpha}_\ell\right]$, is given by the following explicit expression [18]:

$$\mathbf{s}_{\mathbf{u},\ell}(t)=\left.\frac{\partial \mathbf{u}(\boldsymbol{\alpha},t)}{\partial \alpha_\ell}\right|_{\boldsymbol{\alpha}=\mathbf{0}}=-\mathbf{K}_0^{-1}\mathbf{K}_\ell\mathbf{u}_0(t),\quad (\ell=1,2,\ldots,N) \tag{18}$$

where $\mathbf{u}_0(t)$ is the nominal displacement vector, i.e. for $\boldsymbol{\alpha}=\mathbf{0}$, and $\mathbf{K}_\ell$ is the semi-definite positive matrix given in Eq.(13). Equation (18) is obtained by direct differentiating the equations of motion (10) and then neglecting inertial and damping terms.

It is worth noting that the evaluation of the *pseudo-static sensitivity* of the displacement vector with respect to any of the N uncertain parameters just requires the solution of the *ODE*s governing the nominal displacement vector $\mathbf{u}_0(t)$:

$$\mathbf{M}\ddot{\mathbf{u}}_0(t)+\mathbf{C}_0\dot{\mathbf{u}}_0(t)+\mathbf{K}_0\mathbf{u}_0(t)=\mathbf{f}(t) \tag{19}$$

with $\mathbf{C}_0=c_M\mathbf{M}+c_K\mathbf{K}_0$. The solution of Eq. (19) can be performed by classical modal analysis. To this aim, the following coordinate transformation is introduced:

$$\mathbf{u}_0(t)=\boldsymbol{\Phi}_0\mathbf{q}_0(t) \tag{20}$$

where $\boldsymbol{\Phi}_0$ is the modal matrix of order $n\times m$ ($m\le n$ being a suitable integer) collecting the first m eigenvectors, normalized with respect to the mass matrix $\mathbf{M}$, solution of the following eigenproblem:

$$\mathbf{K}_0\boldsymbol{\Phi}_0=\mathbf{M}\boldsymbol{\Phi}_0\boldsymbol{\Omega}_0^2;\quad \boldsymbol{\Phi}_0^T\mathbf{M}\boldsymbol{\Phi}_0=\mathbf{I}_m \tag{21}$$

in which $\mathbf{I}_m$ is the identity matrix of order m; $\boldsymbol{\Omega}_0$ is a diagonal matrix of order m listing the first m natural circular frequencies, $\omega_{0,k}$, of the structural system with nominal values of the uncertain parameters, respectively. By applying the coordinate transformation in Eq. (20) to Eq.(19), the following set of decoupled second-order *ODE*s in the modal subspace is obtained:

$$\ddot{\mathbf{q}}_0(t)+\boldsymbol{\Xi}_0\dot{\mathbf{q}}_0(t)+\boldsymbol{\Omega}_0\mathbf{q}_0(t)=\boldsymbol{\Phi}_0^T\mathbf{f}(t) \tag{22}$$

with $\boldsymbol{\Xi}_0=c_M\mathbf{I}_m+c_K\boldsymbol{\Omega}_0$.

The j-th component, $s_{u_j,\ell}(t)$, of the *pseudo-static sensitivity* vector function, $\mathbf{s}_{\mathbf{u},\ell}(t)$, defined in Eq. (18), gives information about the change of the displacement $u_j(\boldsymbol{\alpha}^I,t)$ due to a variation of the ℓ-th uncertain parameter $\alpha_\ell\in\alpha_\ell^I=\left[\underline{\alpha}_\ell,\overline{\alpha}_\ell\right]$ around the nominal value. Specifically, within a small range around $\boldsymbol{\alpha}=\mathbf{0}$, at each time instant, $u_j(\boldsymbol{\alpha}^I,t)$ is an increasing or decreasing function of the parameter α_ℓ depending on whether $s_{u_j,\ell}(t)>0$ or $s_{u_j,\ell}(t)<0$, respectively. Then, based on the knowledge of the *pseudo-static sensitivity* functions $s_{u_j,\ell}$, $(\ell=1,2,\ldots,N)$, the combinations of the endpoints of the ℓ-th uncertain parameter providing the *LB* and *UB* of the j-th displacement component $u_j(\boldsymbol{\alpha}^I,t)$ at the time instant t, denoted by $\alpha_{j,\ell}^{(\mathrm{LB})}(t)$ and $\alpha_{j,\ell}^{(\mathrm{UB})}(t)$, can be estimated as follows:

$$\begin{aligned}
&\text{if}\quad s_{u_j,\ell}(t)>0,\quad \text{then}\quad \alpha_{u_j,\ell}^{(\mathrm{UB})}(t)=\overline{\alpha}_\ell,\quad \alpha_{u_j,\ell}^{(\mathrm{LB})}(t)=\underline{\alpha}_\ell;\\
&\text{if}\quad s_{u_j,\ell}(t)<0,\quad \text{then}\quad \alpha_{u_j,\ell}^{(\mathrm{UB})}(t)=\underline{\alpha}_\ell,\quad \alpha_{u_j,\ell}^{(\mathrm{LB})}(t)=\overline{\alpha}_\ell,\\
&\qquad\qquad (j=1,2,\ldots,n;\ \ \ell=1,2,\ldots,N).
\end{aligned} \tag{23a,b}$$

The functions $\alpha_{u_j,\ell}^{(\mathrm{LB})}(t)$ and $\alpha_{u_j,\ell}^{(\mathrm{UB})}(t)$ can be collected into the following time-dependent vectors of order N:

$$\begin{aligned}
\boldsymbol{\alpha}_{u_j}^{(\mathrm{LB})}(t)&=\left[\alpha_{u_j,1}^{(\mathrm{LB})}(t)\quad \alpha_{u_j,2}^{(\mathrm{LB})}(t)\quad \ldots\quad \alpha_{u_j,N}^{(\mathrm{LB})}(t)\right]^T;\\
\boldsymbol{\alpha}_{u_j}^{(\mathrm{UB})}(t)&=\left[\alpha_{u_j,1}^{(\mathrm{UB})}(t)\quad \alpha_{u_j,2}^{(\mathrm{UB})}(t)\quad \ldots\quad \alpha_{u_j,N}^{(\mathrm{UB})}(t)\right]^T,\quad (j=1,2,\ldots,n).
\end{aligned} \tag{24a,b}$$

3.2 Pseudo-static sensitivity of stresses

In order to quantify the influence of the change of the uncertain parameters on the interval stress field within the i-th FE, *pseudo-static sensitivity* analysis can be carried out. By direct differentiation of Eq. (9), the following expression of the vector collecting the *pseudo-static sensitivity* functions with respect to the ℓ-th uncertain parameter, $\alpha_\ell\in\alpha_\ell^I=\left[\underline{\alpha}_\ell,\overline{\alpha}_\ell\right]$, is obtained:

$$\mathbf{s}_{\boldsymbol{\sigma}^{(i)},\ell}(\mathbf{x},t)=\left.\frac{\partial\boldsymbol{\sigma}^{(i)}(\mathbf{x},t;\boldsymbol{\alpha})}{\partial\alpha_\ell}\right|_{\boldsymbol{\alpha}=\mathbf{0}}=\mathbf{D}_0\,\mathbf{B}^{(i)}(\mathbf{x})\mathbf{L}^{(i)}\left[\mathbf{u}_0(t)+\mathbf{s}_{\mathbf{u},i}(t)\right],\quad\text{for}\quad \ell=i\,;$$

$$\mathbf{s}_{\boldsymbol{\sigma}^{(i)},\ell}(\mathbf{x},t)=\left.\frac{\partial\boldsymbol{\sigma}^{(i)}(\mathbf{x},t;\boldsymbol{\alpha})}{\partial\alpha_\ell}\right|_{\boldsymbol{\alpha}=\mathbf{0}}=\mathbf{D}_0\,\mathbf{B}^{(i)}(\mathbf{x})\mathbf{L}^{(i)}\,\mathbf{s}_{\mathbf{u},\ell}(t),\quad\text{for}\quad \ell\neq i\quad(i,\ell=1,2,\ldots,N)\qquad(25a,b)$$

where $\mathbf{s}_{\mathbf{u},i}(t)$ is the *pseudo-static sensitivity* vector of the displacements given by Eq.(18). Based on the knowledge of the *pseudo-static sensitivity* functions $s_{\sigma_j^{(i)},\ell}(t)$, $(\ell=1,2,\ldots,N)$, the combinations of the extreme values of the ℓ-th uncertain parameter providing the *LB* and *UB* of the j-th stress component $\sigma_j^{(i)}(\boldsymbol{\alpha}^I,t)$ at the time instant t can be estimated as follows:

$$\begin{aligned}&\text{if}\quad s_{\sigma_j^{(i)},\ell}(t)>0,\quad\text{then}\quad \alpha^{(\mathrm{UB})}_{\sigma_j^{(i)},\ell}(t)=\overline{\alpha}_\ell,\quad \alpha^{(\mathrm{LB})}_{\sigma_j^{(i)},\ell}(t)=\underline{\alpha}_\ell;\\ &\text{if}\quad s_{\sigma_j^{(i)},\ell}(t)<0,\quad\text{then}\quad \alpha^{(\mathrm{UB})}_{\sigma_j^{(i)},\ell}(t)=\underline{\alpha}_\ell,\quad \alpha^{(\mathrm{LB})}_{\sigma_j^{(i)},\ell}(t)=\overline{\alpha}_\ell,\quad(\ell=1,2,\ldots,N).\end{aligned}\qquad(26a,b)$$

The functions $\alpha^{(\mathrm{LB})}_{\sigma_j^{(i)},\ell}(t)$ and $\alpha^{(\mathrm{UB})}_{\sigma_j^{(i)},\ell}(t)$ can be collected into the following time-dependent vectors of order N:

$$\begin{aligned}\boldsymbol{\alpha}^{(\mathrm{LB})}_{\sigma_j^{(i)}}(t)&=\left[\alpha^{(\mathrm{LB})}_{\sigma_j^{(i)},1}(t)\quad\alpha^{(\mathrm{LB})}_{\sigma_j^{(i)},2}(t)\quad\ldots\quad\alpha^{(\mathrm{LB})}_{\sigma_j^{(i)},N}(t)\right]^T;\\ \boldsymbol{\alpha}^{(\mathrm{UB})}_{\sigma_j^{(i)}}(t)&=\left[\alpha^{(\mathrm{UB})}_{\sigma_j^{(i)},1}(t)\quad\alpha^{(\mathrm{UB})}_{\sigma_j^{(i)},2}(t)\quad\ldots\quad\alpha^{(\mathrm{UB})}_{\sigma_j^{(i)},N}(t)\right]^T.\end{aligned}\qquad(27a,b)$$

3.3 "Commonest" combinations

Compared to the static case [19,20], the main difficulty in the application of the sensitivity-based approach to dynamic problems lies in the fact that the above defined combinations of the endpoints of the interval parameters are time-dependent ones. This implies that, to obtain the approximate *LB* and *UB* of the interval dynamic displacement component $u_j(\boldsymbol{\alpha}^I,t)$ or the interval dynamic stress component within the *i*-th FE $\sigma_j^{(i)}(\mathbf{x},t;\boldsymbol{\alpha}^I)$, the equations of motion of the structural system have to be integrated by a step-by-step algorithm replacing at each time step the values of the uncertain parameters collected into the vectors $\boldsymbol{\alpha}_p^{(\mathrm{LB})}(t)$ and $\boldsymbol{\alpha}_p^{(\mathrm{LB})}(t)$, respectively (with the subscript $p=u_j$ or $\sigma_j^{(i)}$). It can be readily inferred that this procedure is very cumbersome and requires high computational effort.

An efficient way to overcome this drawback is to find two combinations of the endpoints of the uncertain parameters which do not vary with time and give accurate estimates of the *LB* and *UB* of the response time-history. The key idea of the proposed approach is to define such combinations as the most common ones among those deduced over the whole time interval of interest based on the information provided by the above described *pseudo-static sensitivity* analysis. These combinations are collected into the time independent vectors $\underset{\sim}{\boldsymbol{\alpha}}_{\mathrm{C},j}$ and $\tilde{\boldsymbol{\alpha}}_{\mathrm{C},j}$, which can be evaluated simply by using the built-in function "Commonest" of Wolfram Mathematica, that is:

$$\begin{aligned}\underset{\sim}{\boldsymbol{\alpha}}_{\mathrm{C},j}&=\left[\underset{\sim}{\alpha}_{C,j,1}\quad\underset{\sim}{\alpha}_{C,j,2}\quad\ldots\quad\underset{\sim}{\alpha}_{C,j,N}\right]^T=\underset{0<t\le t_F}{\mathrm{Commonest}}\left\{\alpha^{(\mathrm{LB})}_{j,1}(t)\quad\alpha^{(\mathrm{LB})}_{j,2}(t)\quad\ldots\quad\alpha^{(\mathrm{LB})}_{j,N}(t)\right\};\\ \tilde{\boldsymbol{\alpha}}_{\mathrm{C},j}&=\left[\tilde{\alpha}_{C,j,1}\quad\tilde{\alpha}_{C,j,2}\quad\ldots\quad\tilde{\alpha}_{C,j,N}\right]^T=\underset{0<t\le t_F}{\mathrm{Commonest}}\left\{\alpha^{(\mathrm{UB})}_{j,1}(t)\quad\alpha^{(\mathrm{UB})}_{j,2}(t)\quad\ldots\quad\alpha^{(\mathrm{UB})}_{j,N}(t)\right\},\end{aligned}\qquad(28a,b)$$

$$(j=1,2,\ldots,n)$$

where $0 < t \le t_F$ is the time interval of interest. In the previous equations, $\underset{\sim}{\boldsymbol{\alpha}}_{\mathrm{C},j}$ and $\tilde{\boldsymbol{\alpha}}_{\mathrm{C},j}$ collect the most common extreme values of the uncertain parameters which, according to *pseudo-static sensitivity* analysis, provide the *LB* and *UB* of the displacement $u_j(\boldsymbol{\alpha}^I, t)$ or stress $\sigma_j^{(i)}(\mathbf{x}, t; \boldsymbol{\alpha}^I)$, respectively, over the time interval $0 < t \le t_F$.

4 Generalized interval modal analysis

As known, the main step in vibration analysis of structures is the evaluation of the natural frequencies and associated mode shapes to apply modal analysis which, for classically damped linear systems, leads to a set of decoupled second-order *ODE*s. For a structural system with interval stiffness parameters, the narrowest set of natural frequencies is obtained setting the uncertain parameters simultaneously to their *UB* and *LB* [24,25], that is assuming the so-called *trivial* combinations of the endpoints of the uncertain parameters. However, a modal analysis based on the narrowest set of natural frequencies does not always guarantee the narrowest interval of the response time-history. Indeed, numerical investigations on several structural systems have shown that the most common combinations provided by the *pseudo-static sensitivity* analysis (see Section 3) are often quite different from the *trivial* ones [18]. Then, the key idea behind the proposed approach is to perform a *generalized interval modal analysis* associated with the most common combinations of the endpoints of the interval parameters (see Eqs. (28a,b)) defined in the previous section. To this aim, first the following two deterministic eigenvalue problems are solved:

$$\begin{aligned} &\mathbf{K}\left(\underset{\sim}{\boldsymbol{\alpha}}_{\mathrm{C},j}\right)\underset{\sim}{\boldsymbol{\phi}}_{j,k} = \underset{\sim}{\lambda}_{j,k}\,\mathbf{M}\,\underset{\sim}{\boldsymbol{\phi}}_{j,k}\,; \quad \underset{\sim}{\boldsymbol{\phi}}_{j,k}^T\,\mathbf{M}\,\underset{\sim}{\boldsymbol{\phi}}_{j,\ell} = \Delta_{k\ell} \\ &\mathbf{K}\left(\tilde{\boldsymbol{\alpha}}_{\mathrm{C},j}\right)\tilde{\boldsymbol{\phi}}_{j,k} = \tilde{\lambda}_{j,k}\,\mathbf{M}\,\tilde{\boldsymbol{\phi}}_{j,k}; \quad \tilde{\boldsymbol{\phi}}_{j,k}^T\,\mathbf{M}\,\tilde{\boldsymbol{\phi}}_{j,\ell} = \Delta_{k\ell}\,, \quad (k,\ell = 1,2,\ldots n;) \end{aligned} \tag{29a,b}$$

where $\underset{\sim}{\boldsymbol{\alpha}}_{\mathrm{C},j}$ and $\tilde{\boldsymbol{\alpha}}_{\mathrm{C},j}$ are the vectors collecting the most common combinations defined in Eqs.(28a,b) to evaluate the approximate *LB* and *UB* of the time-history of the *j*-th displacement ($j = u_j$) or stress ($j = \sigma_j^{(i)}$) component, respectively; $\underset{\sim}{\lambda}_{j,k}$ and $\underset{\sim}{\boldsymbol{\phi}}_{j,k}$ are the *k*-th eigenvalue and eigenvector, solution of the eigenproblem in Eq. (29a) corresponding to $\boldsymbol{\alpha} = \underset{\sim}{\boldsymbol{\alpha}}_{\mathrm{C},j}$; $\tilde{\lambda}_{j,k}$ and $\tilde{\boldsymbol{\phi}}_{j,k}$ are the *k*-th eigenvalue and eigenvector, solution of the eigenproblem in Eq. (29b) corresponding to $\boldsymbol{\alpha} = \tilde{\boldsymbol{\alpha}}_{\mathrm{C},j}$. Notice that, since the two stiffness matrices $\mathbf{K}(\underset{\sim}{\boldsymbol{\alpha}}_{\mathrm{C},j})$ and $\mathbf{K}(\tilde{\boldsymbol{\alpha}}_{\mathrm{C},j})$ as well as the mass matrix $\mathbf{M}$ are real, symmetric and positive-definite matrices, the eigenvectors solution of both eigenproblems are real vectors, while the eigenvalues are real and positive quantities.

Once the eigenproperties are evaluated, the time-histories of the j-th displacement component corresponding to $\boldsymbol{\alpha} = \tilde{\boldsymbol{\alpha}}_{\mathrm{C},j}$ and $\boldsymbol{\alpha} = \underset{\sim}{\boldsymbol{\alpha}}_{\mathrm{C},j}$ can be evaluated by classical modal analysis performing the following two coordinate transformations:

$$\mathbf{u}(\underset{\sim}{\boldsymbol{\alpha}}_{\mathrm{C},j}, t) = \underset{\sim}{\boldsymbol{\Phi}}_j\,\underset{\sim}{\mathbf{q}}_j(t); \qquad \mathbf{u}(\tilde{\boldsymbol{\alpha}}_{\mathrm{C},j}, t) = \tilde{\boldsymbol{\Phi}}_j\,\tilde{\mathbf{q}}_j(t) \tag{30a,b}$$

where $\underset{\sim}{\boldsymbol{\Phi}}_j$ and $\tilde{\boldsymbol{\Phi}}_j$ are two $n \times m$ ($m \le n$ being a suitable integer) matrices whose columns are the eigenvectors $\underset{\sim}{\boldsymbol{\phi}}_{j,k}$ and $\tilde{\boldsymbol{\phi}}_{j,k}$, respectively; $\underset{\sim}{\mathbf{q}}_j(t)$ and $\tilde{\mathbf{q}}_j(t)$ denote the modal coordinate vectors associated with the most common combinations of the endpoints of the uncertain parameters, $\boldsymbol{\alpha} = \tilde{\boldsymbol{\alpha}}_{\mathrm{C},j}$ and $\boldsymbol{\alpha} = \underset{\sim}{\boldsymbol{\alpha}}_{\mathrm{C},j}$, to be used for the evaluation of the *UB* and *LB* of the *j*-th interval response, respectively.

Setting $\boldsymbol{\alpha} = \tilde{\boldsymbol{\alpha}}_{\mathrm{C},j}$ and $\boldsymbol{\alpha} = \underset{\sim}{\boldsymbol{\alpha}}_{\mathrm{C},j}$ in Eq.(10) and applying the coordinate transformations in Eqs. (30a,b), the following sets of $2m$ decoupled second-order *ODE*s are obtained:

$$\begin{aligned}\ddot{\underset{\sim}{\mathbf{q}}}_j(t)+\underset{\sim}{\Xi}_j\,\dot{\underset{\sim}{\mathbf{q}}}_j(t)+\underset{\sim}{\Omega}_j\,\underset{\sim}{\mathbf{q}}_j(t)=\underset{\sim}{\Phi}_j^T\,\mathbf{f}(t);\\ \ddot{\tilde{\mathbf{q}}}_j(t)+\tilde{\Xi}_j\,\dot{\tilde{\mathbf{q}}}_j(t)+\tilde{\Omega}_j\,\tilde{\mathbf{q}}_j(t)=\tilde{\Phi}_j^T\,\mathbf{f}(t)\end{aligned} \tag{31a,b}$$

with $\underset{\sim}{\mathbf{\Omega}}_j$ and $\tilde{\mathbf{\Omega}}_j$ two diagonal matrices whose *k*-th elements are $\underset{\sim}{\omega}_{j,k}^2 \equiv \underset{\sim}{\lambda}_{j,k}$ and $\tilde{\omega}_{j,k}^2 \equiv \tilde{\lambda}_{j,k}$, respectively; while $\underset{\sim}{\Xi}_j$ and $\tilde{\Xi}_j$ are two diagonal matrices too, having *k*-th elements $\underset{\sim}{\xi}_{j,k}=(c_M+c_K\,\underset{\sim}{\omega}_{j,k}^2)/2\underset{\sim}{\omega}_{j,k}$ and $\tilde{\xi}_{j,k}=(c_M+c_K\,\tilde{\omega}_{j,k}{}^2)/2\tilde{\omega}_{j,k}$, respectively, evaluated according to the Rayleigh condition (11).

4.1 Bounds of the displacements

According to Eqs.(17a,b), once the modal analysis pertaining to $\underset{\sim}{\boldsymbol{\alpha}}_{\mathrm{C},j}$ and $\tilde{\boldsymbol{\alpha}}_{\mathrm{C},j}$ with $j=u_j$ is performed by solving the set of *ODE*s (31a,b), the *LB* and *UB* of the j-th displacement component $u_j^I(t)$ are given by:

$$\begin{aligned}\underline{u}_j(t)=\min\left\{\sum_{k=1}^{m}\underset{\sim}{\phi}_{j,jk}\,\underset{\sim}{q}_{j,k}(t),\quad\sum_{k=1}^{m}\tilde{\phi}_{j,jk}\,\tilde{q}_{j,k}(t)\right\};\\ \overline{u}_j(t)=\max\left\{\sum_{k=1}^{m}\underset{\sim}{\phi}_{j,jk}\,\underset{\sim}{q}_{j,k}(t),\quad\sum_{k=1}^{m}\tilde{\phi}_{j,jk}\,\tilde{q}_{j,k}(t)\right\},\end{aligned} \tag{32a,b}$$

where $\underset{\sim}{q}_{j,k}(t)$ and $\tilde{q}_{j,k}(t)$ are the *k*-th elements of the vectors $\underset{\sim}{\mathbf{q}}_j(t)$ and $\tilde{\mathbf{q}}_j(t)$, respectively; while $\tilde{\phi}_{j,jk}$ and $\tilde{\phi}_{j,jk}$ are the j-th elements of the vectors $\underset{\sim}{\boldsymbol{\phi}}_{j,k}$ and $\tilde{\boldsymbol{\phi}}_{j,k}$, respectively.

4.2 Bounds of the stress

Similarly, once the modal analysis pertaining to $\underset{\sim}{\boldsymbol{\alpha}}_{\mathrm{C},j}$ and $\tilde{\boldsymbol{\alpha}}_{\mathrm{C},j}$ with $j=\sigma_j^{(i)}$ is performed by solving the set of *ODE*s (31a,b), the *LB* and *UB* of the j-th stress component within the *i*-th FE $\sigma_j^{(i)}(\mathbf{x},t;\boldsymbol{\alpha}^I)$ are given by:

$$\begin{aligned}\underline{\sigma}_j^{(i)}(\mathbf{x},t)=\min\left\{\left\langle\boldsymbol{\sigma}^{(i)}(\mathbf{x},t;\underset{\sim}{\boldsymbol{\alpha}}_{\mathrm{C},\sigma_j^{(i)}})\right\rangle_j,\quad\left\langle\boldsymbol{\sigma}^{(i)}(\mathbf{x},t;\tilde{\boldsymbol{\alpha}}_{\mathrm{C},\sigma_j^{(i)}})\right\rangle_j\right\};\\ \overline{\sigma}_j^{(i)}(\mathbf{x},t)=\max\left\{\left\langle\boldsymbol{\sigma}^{(i)}(\mathbf{x},t;\underset{\sim}{\boldsymbol{\alpha}}_{\mathrm{C},\sigma_j^{(i)}})\right\rangle_j,\quad\left\langle\boldsymbol{\sigma}^{(i)}(\mathbf{x},t;\tilde{\boldsymbol{\alpha}}_{\mathrm{C},\sigma_j^{(i)}})\right\rangle_j\right\}\end{aligned} \tag{33a,b}$$

where $\langle\bullet\rangle_j$ denotes the *j*-th element of the vector into angle parentheses, and

$$\begin{aligned}\boldsymbol{\sigma}^{(i)}(\mathbf{x};\underset{\sim}{\boldsymbol{\alpha}}_{\mathrm{C},\sigma_j^{(i)}},t)=\left(1+\underset{\sim}{\alpha}_{\mathrm{C},\sigma_j^{(i)},i}\right)\mathbf{D}_0\,\mathbf{B}^{(i)}(\mathbf{x})\,\mathbf{L}^{(i)}\,\mathbf{u}(\underset{\sim}{\boldsymbol{\alpha}}_{\mathrm{C},\sigma_j^{(i)}},t);\\ \boldsymbol{\sigma}^{(i)}(\mathbf{x};\tilde{\boldsymbol{\alpha}}_{\mathrm{C},\sigma_j^{(i)}},t)=\left(1+\tilde{\alpha}_{\mathrm{C},\sigma_j^{(i)},i}\right)\mathbf{D}_0\,\mathbf{B}^{(i)}(\mathbf{x})\,\mathbf{L}^{(i)}\,\mathbf{u}(\tilde{\boldsymbol{\alpha}}_{\mathrm{C},\sigma_j^{(i)}},t).\end{aligned} \tag{34a,b}$$

5 Numerical application

To validate the proposed method, the 2D truss structure with 18 DOFs and 24 bars depicted in Figure 1 is analyzed. The following geometrical and mechanical properties are assumed: $L = 3\text{m}$ (see Figure 1), nominal cross-sectional area of the bars $A_0 = A_{0,i} = 5\times10^{-4}\ \text{m}^2$, nominal Young's moduli $E_0 = E_{0,i} = 2.1\times10^8\ \text{kN/m}^2$, $(i = 1,2,\ldots,24)$, nominal mass lumped at each node, $m_{0,j} = m_0 = 500\ \text{kg}$ $(j = 4,5,\ldots,12)$. The Rayleigh damping constants, c_M and c_K, in Eq.(11) are taken as $c_M = 3.51790\ \text{s}^{-1}$ and $c_K = 0.000547\ \text{s}$, respectively, in such a way that the modal damping ratio for the first and second modes of the nominal structure is $\xi_0 = 0.05$. An impulsive load, acting along the x-direction $f(t) = f_0\,\delta(t) = 1200\,\delta(t)\ \text{N}$ is applied to node 10 of the truss (see Figure 1). Young's modulus of the material of the $r = 7$ bars highlighted in Figure 1 is assumed to be uncertain, i.e. $E_i^I = E_0(1+\Delta\alpha\hat{e}_i^I)$, $(i = 10,12,14,16,18,21,22)$. The normal stresses of bars 16 and 22, $\sigma_{16}^I(t)$ and $\sigma_{22}^I(t)$, are selected as response quantities of interest. The accuracy of the proposed procedure is assessed by comparison with the exact bounds provided by the *vertex method* [21]. The latter is a combinatorial approach which requires to perform as many deterministic dynamic analyses as are the possible combinations of the bounds of the r uncertain-but-bounded parameters, say 2^r, and then seek, at each time instant, the minimum and maximum among the computed responses.

The interval normal stress of the *i*-th bar, $\sigma_i(\boldsymbol{\alpha}^I,t)$, can be expressed as:

$$\sigma_i(\boldsymbol{\alpha}^I,t) = \frac{\rho_i(\alpha_i^I)}{A_{0,i}}\mathbf{c}_i^T\mathbf{u}(\boldsymbol{\alpha}^I,t) \tag{35}$$

where $\mathbf{c}_i^T$ is the *i*-th row of the compatibility matrix $\mathbf{C}$ of the truss structure, while $\rho_i(\alpha_i^I)$ is the interval axial stiffness of the *i*-th bar defined as:

$$\rho_i(\alpha_i^I) = \rho_{0,i}\left(1+\Delta\alpha_i\hat{e}_i^I\right) \tag{36}$$

$\rho_{0,i} = E_0A_{0,i}/L_i$ being the nominal value.

Based on Eq. (35), the *pseudo-static sensitivity* function of the normal stress of the i-th bar with respect to the ℓ-th uncertain parameter, $\alpha_\ell \in \alpha_\ell^I = \left[\underline{\alpha}_\ell, \overline{\alpha}_\ell\right]$, takes the following form:

$$\begin{aligned} s_{\sigma_i,\ell}(t) &= \left.\frac{\partial\sigma_i(\boldsymbol{\alpha},t)}{\partial\alpha_\ell}\right|_{\boldsymbol{\alpha}=\mathbf{0}} = \frac{\rho_{0,i}}{A_{0,i}}\mathbf{c}_i^T\left[\mathbf{u}_0(t)+\mathbf{s}_{\mathbf{u},i}(t)\right], \quad \text{for } \ell = i; \\ s_{\sigma_i,\ell}(t) &= \left.\frac{\partial\sigma_i(\boldsymbol{\alpha},t)}{\partial\alpha_\ell}\right|_{\boldsymbol{\alpha}=\mathbf{0}} = \frac{\rho_{0,i}}{A_{0,i}}\mathbf{c}_i^T\mathbf{s}_{\mathbf{u},\ell}(t), \quad \text{for } \ell \neq i \quad (i,\ell = 1,2,\ldots,r). \end{aligned} \tag{37}$$

Figures 2 and 3 display the time-histories of the *LB* and *UB* of the interval normal stresses $\sigma_{16}^I(t)$ and $\sigma_{22}^I(t)$ for $\Delta\alpha = 0.1$. The proposed bounds are compared with the exact ones obtained by applying the *vertex method*, which, in the present case, requires 2^7 deterministic dynamic analyses. The nominal stress is also plotted. Similar results are reported in Figures 4 and 5 for $\Delta\alpha = 0.15$. By inspection of these figures, it is observed that the proposed method provides very accurate estimates of the bounds of the interval normal stresses $\sigma_{16}^I(t)$ and $\sigma_{22}^I(t)$ for both the selected degrees of uncertainty. Furthermore, it can be seen that the bounds of the stresses significantly deviate from the nominal value due to uncertainty.

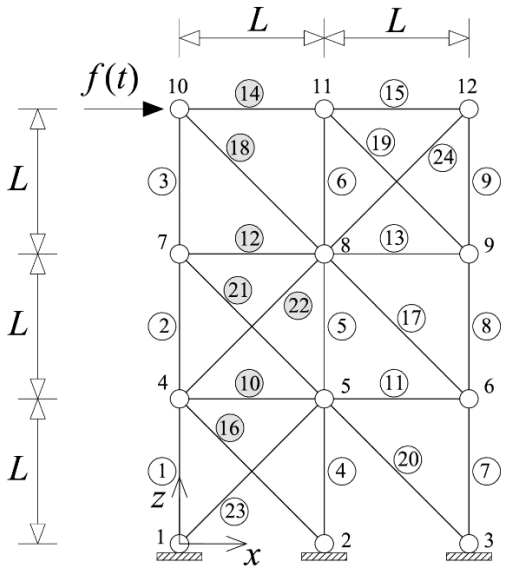


Figure 1: 24-bar truss structure subjected to an impulsive load.

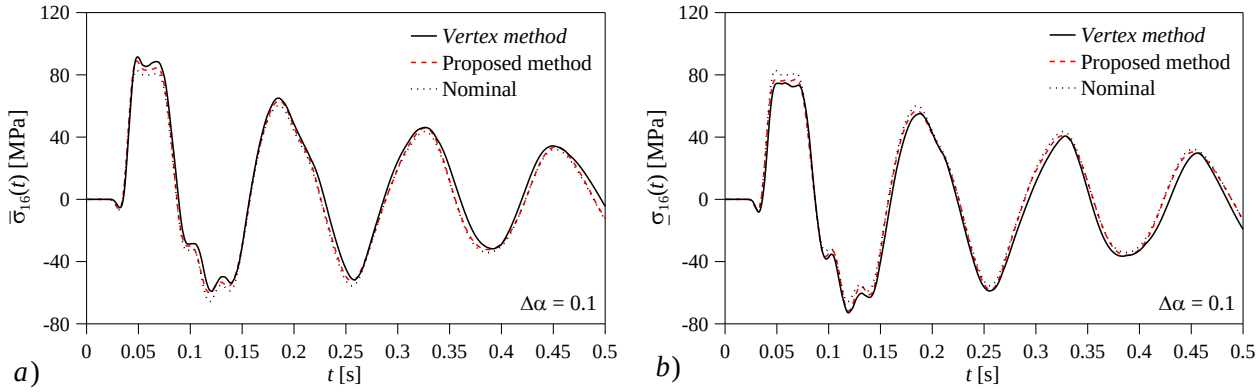


Figure 2: Time histories of the a) *UB* and b) *LB* of the interval normal stress $\sigma_{16}^{I}(t)$ of bar 16 provided by the *vertex method* and the proposed method for $\Delta\alpha = 0.1$.

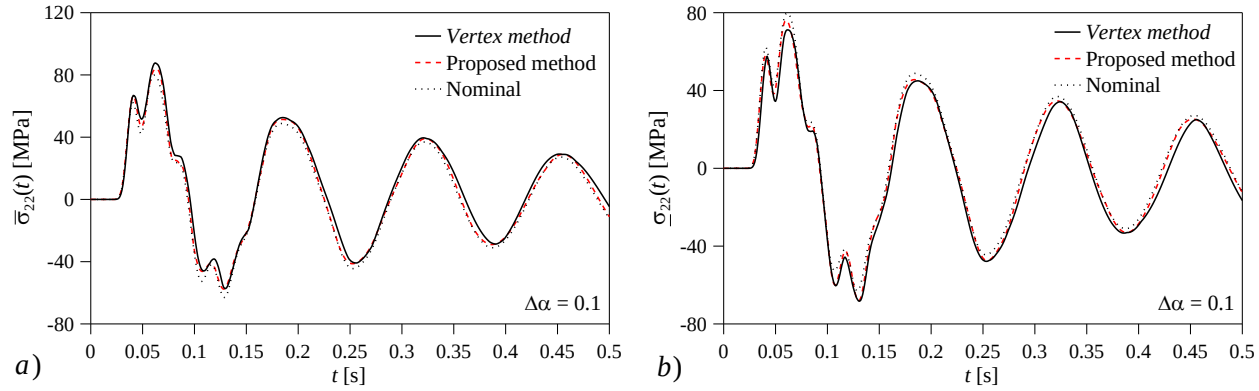


Figure 3: Time histories of the a) *UB* and b) *LB* of the interval normal stress $\sigma_{22}^{I}(t)$ of bar 22 provided by the *vertex method* and the proposed method for $\Delta\alpha = 0.1$.

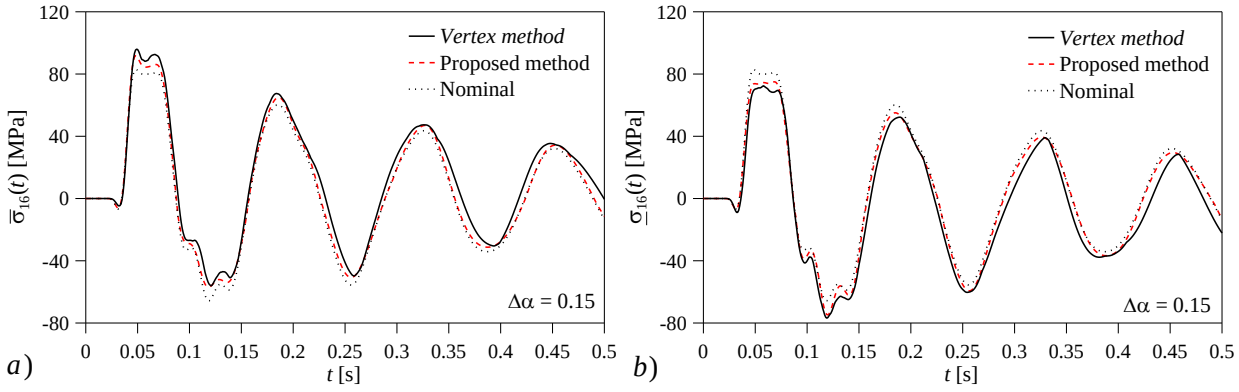


Figure 4: Time histories of the a) *UB* and b) *LB* of the interval normal stress $\sigma_{16}^{I}(t)$ of bar 16 provided by the *vertex method* and the proposed method for $\Delta\alpha = 0.15$.

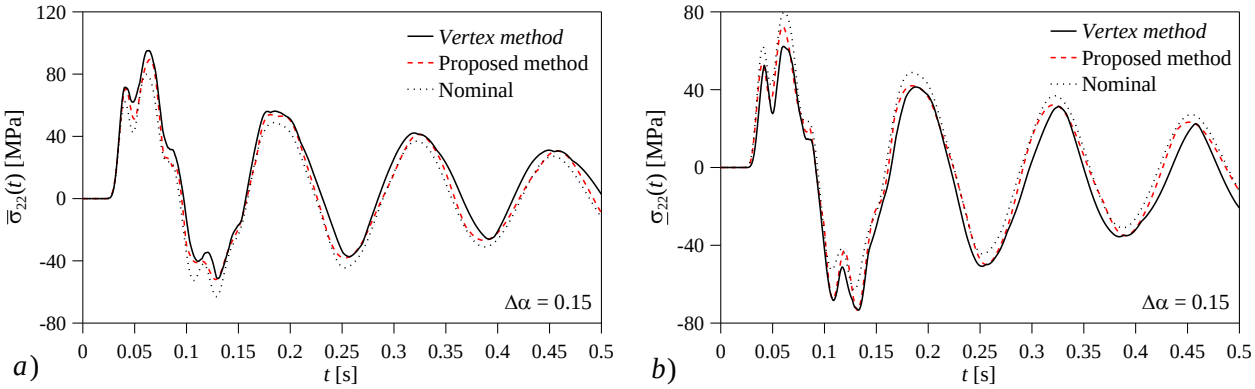


Figure 5: Time histories of the a) *UB* and b) *LB* of the interval normal stress $\sigma_{22}^{I}(t)$ of bar 22 provided by the *vertex method* and the proposed method for $\Delta\alpha = 0.15$.

For design purposes, it is of primary importance to accurately predict the maximum *UB* and minimum *LB* of stresses over the whole time-history. For the normal stress of the j-th bar, such quantities are defined as:

$$\overline{\sigma}_j^{(\max)} = \max_{0<t\le t_F}\left\{\overline{\sigma}_j(t)\right\}; \quad \underline{\sigma}_j^{(\min)} = \min_{0<t\le t_F}\left\{\underline{\sigma}_j(t)\right\}. \tag{38a,b}$$

Figure 6 shows the maximum *UB* and minimum *LB* of the interval normal stresses $\sigma_{16}^{I}(t)$ and $\sigma_{22}^{I}(t)$ versus the deviation amplitude of the uncertain parameters. Notice that the proposed estimates are very close to the exact values provided by the *vertex method*. The largest absolute percentage error, equal to 6.04%, is detected for the maximum *UB* of $\sigma_{22}^{I}(t)$ when $\Delta\alpha = 0.2$ (see Figure 6b). For the same stress component, the proposed method yields the exact minimum *LB*. Furthermore, it is observed that the region enclosed by the maximum *UB* and minimum *LB* of the selected stress components becomes wider as the degree of uncertainty increases.

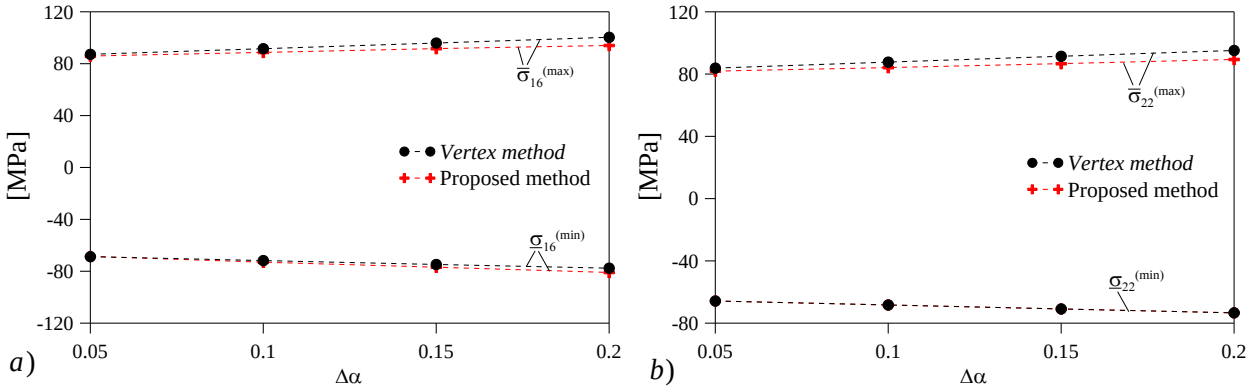


Figure 6: Maximum *UB* and minimum *LB* of the interval normal stress a) $\sigma_{16}^{I}(t)$ of bar 16 and b) $\sigma_{22}^{I}(t)$ of bar 22 provided by the *vertex method* and the proposed method versus the deviation amplitude of the uncertain parameters.

6 Conclusions

The dynamic analysis of linear-elastic structures with interval material properties subjected to deterministic dynamic excitations has been addressed. Attention has been focused on the evaluation of the time-histories of the lower and upper bounds of the interval stress field. To address this challenging task, a sensitivity-based procedure recently proposed by the authors for estimating the bounds of the dynamic displacements has been properly extended to deal with stress analysis as well.

The key idea of the proposed method is to perform two parallel deterministic modal analyses corresponding to two suitable combinations of the endpoints of the uncertain parameters identified by a *pseudo-static sensitivity* analysis. Then, the lower and upper bounds of the generic stress component are obtained seeking, at each time instant, the minimum and maximum among the stresses provided by the two modal analyses.

Unlike the widely used *Interval Perturbation Method*, the presented procedure provides accurate estimates of the range of the dynamic response in terms of displacements and stresses even for relatively large degrees of uncertainty. The main feature of the method is its non-intrusive nature which allows the integration into standard finite element codes.

Acknowledgements

The support to this research by the PRIN2015, project No 2015TTJN95 entitled “Identification and monitoring of complex structural systems”, is gratefully acknowledged.

References

[1] Moens D., Vandepitte D., *A survey of non-probabilistic uncertainty treatment in finite element analysis*, Computer Methods in Applied Mechanics and Engineering, Vol. 194, No. 12-16, Academic Press (2005), pp. 1527-1555.

[2] Ben-Haim Y., Elishakoff I., *Convex Models of Uncertainty in Applied Mechanics*, Elsevier Science Publishers, Amsterdam (1990).

[3] Elishakoff I., Ohsaki M., *Optimization and Anti-Optimization of Structures under Uncertainty*, Imperial College Press, London (2010).

[4] Moore R. E., *Interval Analysis*, Prentice-Hall, Englewood Cliffs (1966).

[5] Moore R.E., Kearfott R.B., Cloud M.J., *Introduction to Interval Analysis*, SIAM, Philadelphia (2009).

[6] Qiu Z.P., Wang X.J., *Vertex solution theorem for the upper and lower bounds on the dynamic response of structures with uncertain-but-bounded parameters*, Acta Mechanica Sinica, Vol. 25, No. 3, Springer (2009), pp. 367-379.

[7] Dimarogonas A.D., *Interval analysis of vibrating systems*, Journal of Sound and Vibration, Vol. 183, No. 4, Academic Press (1995), pp. 739-749.

[8] Wu J., Zhang Y., Chen L., Luo Z., *A Chebyshev interval method for nonlinear dynamic systems under uncertainty*, Applied Mathematical Modelling, Vol. 37, No. 6, Academic Press (2013), pp. 4578-4591.

[9] Chen S.H., Lian H.D., Yang X.W., *Dynamic response analysis for structures with interval parameters*, Structural Engineering and Mechanics, Vol. 13, No. 3, Techno-Press (2002), pp. 299-312.

[10] Qiu Z.P., Wang X.J., *Comparison of dynamic response of structures with uncertain-but-bounded parameters using non-probabilistic interval analysis method and probabilistic approach*, International Journal of Solids and Structures, Vol. 40, No. 20, Academic Press (2003), pp. 5423-5439.

[11] Qiu Z.P., Wang X.J., *Parameter perturbation method for dynamic responses of structures with uncertain-but-bounded parameters based on interval analysis*, International Journal of Solids and Structures, Vol. 42, No. 18-19, Academic Press (2005), pp. 4958-4970.

[12] Qiu Z.P., Wang L., Ma L., Wang X.., *Non-probabilistic interval analysis method for dynamic response analysis of nonlinear systems with uncertainty*, Journal of Sound and Vibrations, Vol. 319, No. 1-2, Academic Press (2009), pp. 531–540.

[13] Xia Y., Qiu Z.P., Friswell M.I., *The time response of the structures with bounded parameters and interval initial conditions*, Journal of Sound and Vibrations, Vol. 329, No. 3, Academic Press (2010), pp. 353–365.

[14] Muscolino G., Sofi A., *Response statistics of linear structures with uncertain-but-bounded parameters under Gaussian stochastic input*, International Journal of Structural Stability and Dynamics, Vol. 11, No. 4, World Scientific (2011), pp. 775-804.

[15] Gao W., Zhang N., Ma J., Wang X.B., *Interval dynamic response analysis of structures with interval parameters*, Proceedings of the Institution of Mechanical Engineers, Part C: Journal of Mechanical Engineering Science, Vol. 222, No. 3, SAGE (2008), pp. 377-385.

[16] Rama Rao M.V., Pownuk A., Vandewalle S., Moens D., *Transient response of structures with uncertain structural parameters*, Structural Safety, Vol. 32, No. 6, Academic Press (2010), pp. 449-460.

[17] Yang Y.W., Cai Z.H., Liu Y., *Interval analysis of dynamic response of structures using Laplace transform*, Probabilistic Engineering Mechanics, Vol. 29, Academic Press (2012), pp. 32-39.

[18] Muscolino G., Sofi A., Giunta F., *Dynamics of structures with uncertain-but-bounded parameters via pseudo-static sensitivity analysis*, Mechanical Systems and Signal Processing, Vol. 111, Academic Press (2018), pp. 1–22.

[19] Pownuk A., Efficient method of solution of large scale engineering problems with interval parameters. In: Muhanna, RL, Mullen RL (eds), Proc. NSF Workshop on Reliable Engineering Computing, September 15–17, 2004, Savannah, Georgia, USA (2004) pp. 305–316.

[20] Sofi A., Romeo E., *A novel Interval Finite Element Method based on the improved interval analysis*, Computer Methods in Applied Mechanics and Engineering, Vol. 311, Academic Press (2016), pp. 671–697.

[21] Dong W., Shah H., *Vertex method for computing functions of fuzzy variables*, Fuzzy Sets and Systems, Vol. 24, No. 1, Academic Press (1987), pp. 65–78.

[22] Muscolino G., Sofi A., *Stochastic analysis of structures with uncertain-but-bounded parameters via improved interval analysis*, Probabilistic Engineering Mechanics, Vol. 28, Academic Press (2012), pp. 152-163.

[23] Moens D., Vandepitte D., *Interval sensitivity theory and its application to frequency response envelope analysis of uncertain structures*, Computer Methods in Applied Mechanics and Engineering, Vol. 196, No. 21-24, Academic Press (2007), pp. 2486-2496.

[24] Modares M., Mullen R.L., Muhanna R.L., *Natural frequencies of a structure with bounded uncertainty*, Journal of Engineering Mechanics, Vol. 132, No. 12, ASCE (2006), pp. 1363-1371.

[25] Sofi A., Muscolino G., Elishakoff I., *Natural frequencies of structures with interval parameters*, Journal of Sound and Vibration, Vol. 347, Academic Press (2015), pp. 79-95.

A twin-mesh approach for random field analysis in high-dimensional dynamic models

S. G. Dastidar [1], **M. Faes** [1], **D. Moens** [1]
[1] KU Leuven, Department of Mechanical Engineering,
Jan De Nayerlaan 5, 2860, St.-Katelijne-Waver, Belgium
e-mail: **sabyasachi [dot] ghosh [at] kuleuven [dot] be**

Abstract
Non-deterministic methods such as the random field approach suffer from the curse of dimensionality from computational burden of industrially sized models. The computational complexity increases at high dimensions due to increased time complexity of eigenvalue computations, leading to the Karhunen-Loéve series expansion becoming intractable. This makes the corresponding propagation routines to become inviable. A novel methodology is proposed for efficient propagation of a random field by tackling this problem from the discretization perspective. The method uses a twin-model that efficiently discretizes a random field on a coarse mesh grid using a KL expansion, which is then propagated on a high-dimensional grid of the Finite Element model. A two-dimensional model of moderate-dimensionality with 10000 elements is used to illustrate the numerical efficiency of this approach through a convergence study focusing on the resolution of the twin-model when applied in a dynamic analysis. The method is also well suited for higher dimensions.

1 Introduction

In order to obtain an optimised reliable design, it is imperative to apply Uncertainty Quantification (UQ) in numerical models. Towards this end, non-deterministic approaches have been the subject of extensive studies over the past decades [1, 2, 3]. Specifically the current use of advanced materials and production processes in modern engineering has recently increased the need for spatial variability modelling. Historically, the main activity in this field has been in probabilistic approaches in which random fields have reached a high level of maturity, predominantly through the use of the Karhunen-Loève (KL) expansion scheme [4, 5]. Other methods such as the non-probabilistic interval field approach have also been introduced that quantify the local uncertainty objectively while with a reduced information requirement to do so [6, 7, 8].

However, when scaled to current high dimensional state-of-the-art industrial Finite Element (FE) models, these approaches significantly exceed the viable computational cost [9]. With an exponential increase in computing capabilities, such models with millions of degrees of freedom lead to a high number of non-deterministic variables. In the random field context, this leads to the Karhunen-Loeve expansion to become intractible. As a result, analysis of industrially sized problems become impractical which may lead to an analyst to resort to numerical compromises that affect accuracy of the approach.

To address these challenges, certain approaches have been proposed such as an extension of the Multi-Level Monte Carlo probabilistic approach [12]. In this work, Pisaroni et al. have drawn samples on several approximations of the complex numerical models on a hierarchy of nested computational grids containing different levels of discretization. In a following work, a method was proposed that estimated the optimal number of levels and the realisations required on each level, obtaining designs with decreased sensitivity to uncertain conditions [13]. The objective of this work is to study whether this efficient methodology could also be translated towards the discretization of a random field.

The computational complexity of a non-deterministic model using a random field increases at higher dimensions due to the increased time complexity of the eigenvalue computations, leading to intractiblity of the KL series expansion. This makes the corresponding propagation routines to become inviable. Normally, the deterministic FE mesh discretization is chosen for an accurate approximation of the model physics and is not tuned to the requirements of the probabilistic parameters. Therefore, in this paper a method has been developed that efficiently discretizes a random field on the high resolution Finite Element mesh. This has been accomplished by means of a low-resolution twin of the high-resolution FE mesh. A two-level grid hierarchy is considered, one for random field discretization with a KL expansion and the other for propagating the resultant random field. The former grid is a coarse mesh while the latter is considerably finer. This methodology is presented using the case study of a two-dimensional model of a plate that is subjected to global uncertainty in Young's modulus.

The structure of the paper is as follows. Section 2 first introduces the mathematical background of random fields and presents the twin-model approach. The applicability of the latter is where the main novelty of this work lies. In section 3, it is illustrated how a moderate-dimensional twin-mesh model has been constructed on the selected numerical model to demonstrate the efficiency and accuracy of the proposed approach. Finally, the conclusions are summarised in section 4.

2 Non-deterministic modeling of spatial non-determinism

2.1 Stochastic Finite Element Analysis

Consider a numerical model $\mathcal{M}(\boldsymbol{x})$ that is formulated using a FE approach, where its continuous domain of a finite dimension Ω is discretised through a set of finite elements producing t structural degrees of freedom (DOF). A vector of model responses $\boldsymbol{y}(\mathbf{r})$ is generated as a function of a spatial coordinate $\mathbf{r} \in \Omega \subset \mathbb{R}^d$ with dimension $d \in \mathbb{N}$ over Ω. Within this model, spatial uncertainty is introduced on one of its parameter vectors $\boldsymbol{x}(\mathbf{r}) \in \mathcal{X} \subset \mathbb{R}^k$, where $\mathcal{X}$ is the set of physically permissible parameters and $k \in \mathbb{N}$.

Such an uncertainty can be modelled as a random field $x(\mathbf{r}, \theta)$, which can be defined as a random function that describes a set of correlated random quantities for each location $\mathbf{r} \in \Omega \subset \mathbb{R}^d$. $\theta \in \Theta$ is a coordinate in the sample space Θ and (Θ, σ, P) is a complete probability space, with σ the sigma-algebra. The dimension of the resulting random field is the dimension of Ω. If the random quantity attached to each location $\mathbf{r}$ is a random variable $x(\theta)$, the random field is said to be univariate, which is the focus of this paper. If the random quantity is a random vector, the field is then referred to as multivariate. In addition, the discussion has also been restricted to isotropic random fields, which entirely defined by its mean function $\mu_x(\boldsymbol{r}) : \Omega \mapsto \mathbb{R}$ and its auto-covariance function $\boldsymbol{\Gamma}_x(\mathbf{r}, \mathbf{r'}) : \Omega \times \Omega \mapsto \mathbb{R}$. Mathematically, a random field is represented as a truncated series expansion, discretized over Ω by following a KL series expansion [5]. The expansion is based on a spectral decomposition of the autocovariance function of the field, and is depicted as follows:

$$\tilde{\boldsymbol{x}}(\mathbf{r}, \theta) = \mu_x(\mathbf{r}) + \sum_{i=1}^{m} \sqrt{\lambda_i} \boldsymbol{\psi}_i(\mathbf{r}) \xi_i(\theta) \tag{1}$$

where $\lambda_i \in [0, \infty)$ and $\boldsymbol{\psi}_i(\mathbf{r}) : \Omega \mapsto \mathbb{R}$ represent the eigenvalues and eigenfunctions respectively of the auto-covariance matrix. $\xi_i(\theta), i = 1, \ldots, m$ are standard uncorrelated random variables. The KL expansion can be approximated by sorting the eigenvalues λ_i and their corresponding eigenfunctions $\boldsymbol{\psi}_i(\mathbf{r})$ in a descending order and truncating the expansion after m terms [14]. The application of Mercer's theorem on the latter yields the spectral decomposition as follows:

$$\boldsymbol{\Gamma}_x(\mathbf{r}, \mathbf{r'}) = \sum_{i=1}^{m} \lambda_i \boldsymbol{\psi}_i(\mathbf{r}) \boldsymbol{\psi}_i(\mathbf{r'}) \tag{2}$$

Please note that the auto-covariance function $\mathbf{\Gamma}_x(\mathbf{r}, \mathbf{r'})$ is considered to be continuous, bounded, symmetric and positive definite. Hence, the eigenvalues λ_i are non-negative and the eigenfunctions $\boldsymbol{\psi}_i(\mathbf{r})$ satisfy the orthogonality condition $\int_\Omega \boldsymbol{\psi}_i(\mathbf{r})\boldsymbol{\psi}_j(\mathbf{r})d\mathbf{r} = \delta_{ij}$, with δ_{ij} denoting the Kronecker delta [16]. In such a case, the series expansion of eq. (2) converges and the random field can be expressed as in eq. (1). Based on this discretised field, N realisations are generated over Ω by using a Monte Carlo sampling approach to obtain samples from $\xi_i(\theta)$. Each of these realisations are then propagated over the numerical model $\mathcal{M}$.

When large scale problems containing multiple uncertain parameters are considered, non-determinstic model evaluations become substantially expensive which is referred to as the *curse of dimensionality*. This is because the computational efficiency of random field representations with the KL expansion relies on the solution of an eigendecomposition problem. Most of the algorithms for eigenvalue computations scale $\mathcal{O}(n^3)$, where $\mathcal{O}$ represents the computational time complexity and n is the dimension of the resulting covariance matrix. This makes the propagation routines at high-dimensions inviable.

This scenario is most evident in typical industrial FE models that can contain up to millions of degrees of freedom, which lead to the propagation of random fields on such models to be impractical. However, the deterministic FE mesh discretization is typically chosen such that it approximates the modelled physics accurately, and is not related to the definition of the probabilistic parameters. Therefore, it is proposed to define and propagate the random field parameters on a twin-model whose spatial discretization can be tailored to the specific needs of the random field definition.

2.2 Twin-mesh approach for random field analysis

Typically, high-fidelity models are used to describe a system with very high accuracy albeit with a trade-off in terms of computational cost. On the other hand, lower-fidelity models are computationally cheaper albeit with a reduced accuracy. In order to avoid the excessive computational demand due to the propagation routines mentioned in the previous section, the solution of UQ methods can be accelerated by multi-fidelity models that combine high-fidelity and low-fidelity model evaluations. The low-fidelity models approximate the same output quantities as high-fidelity models using methods such as model reduction, data-fit surrogates or simplified physics approximation methods. As a result, these Multi-Fidelity techniques ensure that the speedup of low-fidelity models are leveraged while taking into account the accuracy levels of the high-fidelity models.

While addressing the same problems as these techniques, our proposed twin-mesh method approaches the problem from the discretization perspective rather than from a propagation standpoint. The core objective is the development of a methodology that optimally discretizes a random field on the high-resolution FE mesh. This has been accomplished by considering a two-level grid hierarchy, one for random field discretization with a KL expansion and the other for propagating the resultant random field. The former grid is a coarse mesh while the latter is considerably finer. Figure 1 demonstrates the two levels of discretisation used in the low-resolution twin of the high-resolution FE mesh where the mesh used for propagating a random field is ten-times more coarse than the FE mesh.

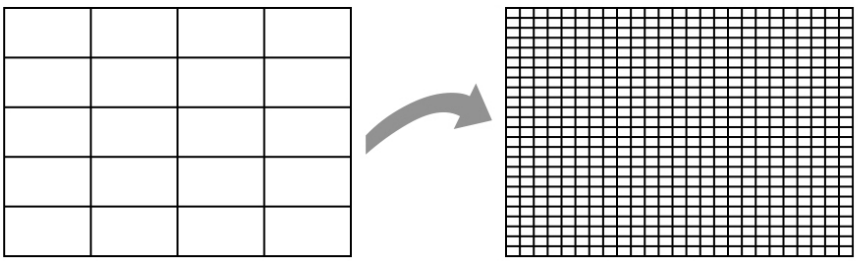


Figure 1: A twin-mesh model represented using a coarse mesh and a finely discretized mesh

The propagation of random fields on a continuous two-dimensional model domain using a twin-mesh approach requires discretization using two different mesh densities resulting in: 1) coarse mesh domain $\Omega_1 \subset \mathbb{R}^{d_1}$ with discretization $d_1 \in \mathbb{N}$; 2) fine FE mesh domain $\Omega_2 \subset \mathbb{R}^{d_2}$ with discretization $d_2 \in \mathbb{N}$. First, the uncertainty is defined over the coarse domain Ω_1, and the eigenfunctions $\boldsymbol{\psi}_i(\mathbf{r}) : \Omega_1 \mapsto \mathbb{R}$, are obtained by applying Mercer's theorem on the autocovariance function $\boldsymbol{\Gamma}(\mathbf{r}, \mathbf{r'})$. Secondly, the eigenfunctions $\boldsymbol{\psi}_i(\mathbf{r})$ are interpolated to obtain an approximation of the eigenfunctions $\boldsymbol{\psi}_i(\boldsymbol{t}) : \Omega_2 \mapsto \mathbb{R}$ over the FE mesh Ω_2 using a polynomial function:

$$y = \sum_{i=1}^{n+1} p_i x^{n+1-i} \tag{3}$$

where $n+1$ is the order of the polynomial which gives the number of coefficient parameters p_i approximated. The polynomial function is used to interpolate the eigenfunctions, obtained from Ω_1, to generate a response surface as demonstrated in Figure 2. The parameters p_i in eq. (3) are determined through least-squares regression, which calculates the partial derivatives of the coefficients and then minimises the sum of the squares of the residuals of predicted values from the actual values. Once an approximate model is obtained, the goodness-of-fit characterised by statistical evaluations such as the sum of squares due to error (SSE) determines if the approximated solution is satisfactory. SSE measures the total deviation of the approximated response values $\tilde{y}_i$ to the response values y_i of the coarse mesh, and is given by $\sum_{i=1}^{n} w_i(y_i - \tilde{y})^2$. The polynomial degree is deemed to be sufficient when the SSE is value close to 0, indicating that the model has a small random error component, and that the fit will be useful for prediction.

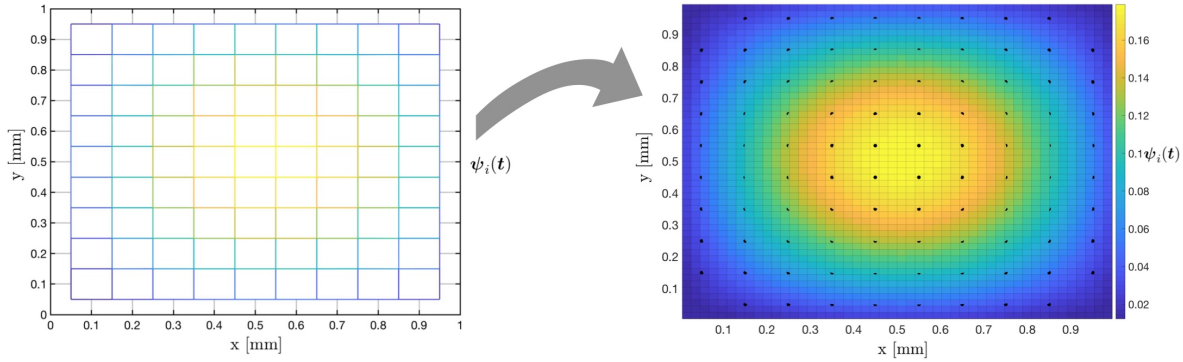


Figure 2: Approximation of $\boldsymbol{\psi}_i(\boldsymbol{t})$ over the FE mesh (right) obtained from $\boldsymbol{\psi}_i(\mathbf{r})$ of the coarse domain (left) using an interpolation scheme

Finally, these interpolated eigenfunctions $\boldsymbol{\psi}_i(\boldsymbol{t})$ are used to generate the random field on the FE mesh Ω_2 using eq. (1) to eq. (2). Furthermore, the random variables in this field are mutually correlated with a correlation length L. A smaller L leads to rough random fields which necessitates the FE mesh to be refined to accommodate the random field discretization. This is then followed by propagating the resultant realisations over the numerical model $\mathcal{M}$ that lead to a probabilistic definition $\boldsymbol{y}(\boldsymbol{t}, \theta)$ of the FE model's responses $\boldsymbol{y}(\boldsymbol{t})$:

$$\boldsymbol{y}\left(\boldsymbol{t}, \theta_i\right) = \mathcal{M}\left(\tilde{\boldsymbol{x}}\left(\boldsymbol{t}, \theta_i\right)\right) \quad i = 1, \ldots, N \tag{4}$$

3 Case study

The case study in this section aims at illustrating the efficiency and accuracy of the proposed twin-mesh approach by deploying it on a two-dimensional dynamic model of a plate. The model dimensions are 1

m by 1 m, with thickness 5 mm. Poisson's ratio and density are considered to be 0.3 and 7800 kg/m^3 respectively. The geometry of the plate is fully constrained on one of its edges, and is approximated using the FE method. The FE model domain Ω_2 is discretized into 10000 elements yielding 30603 degrees of freedom. Although this section focuses on Ω_2 with moderate dimensions, the methodology is also well suited for higher dimensional models.

In this model, the non-determinism arises due to the uncertainty introduced in Young's modulus over domain Ω_2, which is modelled using a probabilistic modelling approach. An isotropic random field with an exponential covariance kernel and correlation length of 30 cm is constructed. The field is considered to be two-dimensional, and is propagated over the FE mesh Ω_2. In this study, the global mean value of Young's modulus over the domain is 210 GPa, while the standard deviation of the random field is 50 GPa.

Application of random fields $x(\mathbf{r}, \theta)$ requires their discretization over the continuous model domain, as explained in section 2.1. A secondary coarse mesh Ω_1 is used for this discretization that can be obtained using the KL series expansion, as illustrated in section 2.2. The truncation order m has been considered as 100. The discretization d_1 of the coarse mesh is varied for determining the optimum value to minimize computational complexity while maintaining the level of accuracy, which will be explored later in this section. The basis functions $\sqrt{\lambda_i}\boldsymbol{\psi}_i(\mathbf{r})$ are obtained from spectral decomposition of the exponential covariance function. In this paper, this large symmetric eigenvalue problem has been solved using the Krylov–Schur method. Following this, these basis functions are interpolated over the finer FE mesh Ω_2 using a polynomial function, as shown in eq. (3). Finally, realisations of the random field are generated after obtaining 500 samples from $\xi_i(\theta)$ using a Monte Carlo sampling approach. Please note that to enable a fair comparison between the different cases in this chapter, the seed of the random number generator is kept constant.

The twin-mesh approach is evaluated with respect to the conventional random field analysis using a two-fold comparison of efficiency and accuracy. To quantify the efficiency, the analysis time that is required for the Matlab computations is investigated with respect to the discretization d_2 of the FE mesh Ω_2. In terms of accuracy, error metrics are obtained both at the input and output ends of the analysis. The objective is to substantiate that the basis functions and eigenfrequencies obtained from this approach are of the required level of precision. In addition, the effect of correlation length on the computational cost is also discussed.

3.1 Reduction in computational time

To highlight the computational gain from twin-mesh approach, its analysis time obtained from Matlab for evaluating the spectral decomposition is compared with that of the conventional random field approach, which drastically grows when scaled to higher dimensions. For the latter approach, the discretization of the KL expansion is considered equivalent to the one of the FE mesh. First, the computational time is plotted in figure 3 (blue curve) for several discretizations of the mesh domain Ω_2 from $d_2 = 25$ to 10000 using a conventional random field approach. Next, the corresponding computational times are plotted for the twin-mesh approach (red curve) using coarse discretizations of Ω_1: $d_1 = 25$, 100 and 400. For each of these coarse discretizations, the spectral decomposition is first computed over Ω_1, following which the interpolation scheme is employed for obtaining the polynomial response surface over the finer FE mesh domain Ω_2 for each discretization $d_2 = 25$ to 10000.

The resultant Figure 3 reveals a significant time gain. Please note that for these comparisons, it is imperative to consider the same truncation order m while computing the spectral decompositions. Figure 3 doesn't explictly elucidate the optimum discretization d_1 of the coarse mesh Ω_1 for the twin-model. However, this becomes comprehensible after investigation of the accuracy of spectral decomposition in the twin-mesh approach with respect to the conventional approach, as described in the next section.

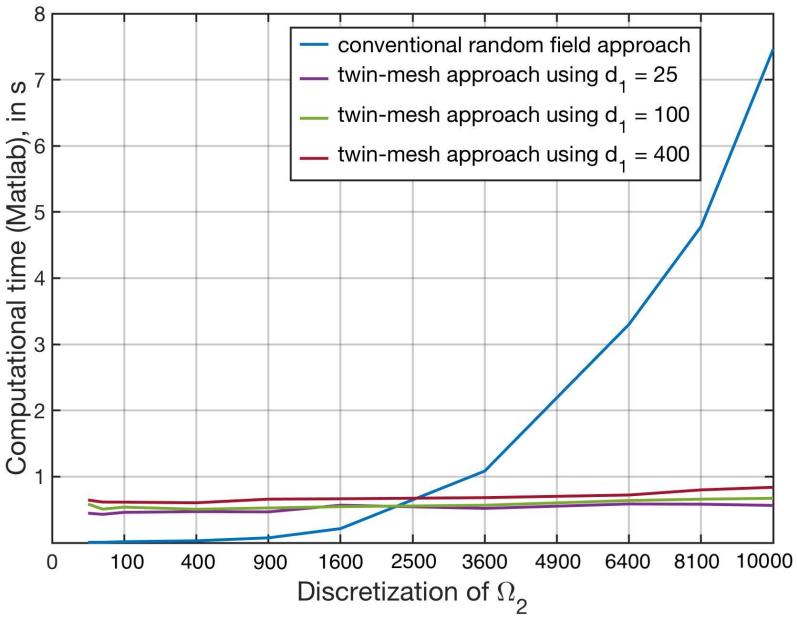


Figure 3: Computational time in Matlab with respect to discretization of Ω_2

3.2 Accuracy of the approach on the input side of analysis

In order to quantify the accuracy of this approach, comparisons have been performed on both input and output sides of the random field analysis. On the input side, two data sets have been used for comparison:

- **Reference case (conventional random field approach)**: Eigenfunctions $\psi_i(\mathbf{r})$ of the covariance matrix are obtained such that the domain used for spectral decomposition maintains the same level of discretization $d_1 = 10000$ as that of the FE mesh discretization $d_2 = 10000$ on which the random field is propagated.
- **Twin-mesh approach case**: Calculates the first hundred eigenfunctions $\psi_i(\mathbf{r})$ for different levels of discretizations of the coarse mesh Ω_1 from $d_1 = 25$ to 10000. $\psi_i(\mathbf{r})$ are then used to approximate the corresponding $\psi_i(\boldsymbol{t})$ for the finer FE mesh, as described in Section 2.2.

Next, the Root Mean Square (RMS) of pairwise differences between both these data sets containing each of their first ten corresponding basis functions $\sqrt{\lambda_i}\boldsymbol{\psi}_i(\mathbf{r})$ have been calculated. The resultant RMS value, referred to as "error" from here on, can serve as a measure of accuracy on the input side. Please note that this error is made relative with respect to the RMS value of the reference case. The error for the first ten eigenfunctions have been obtained with respect to the discretization of the coarse mesh Ω_1. Figure 5 demonstrates this using a plot for the first eigenfunction ψ_1. The plots for four of these eigenfunctions over the domain Ω_2 are illustrated in Figure 4.

From Figure 5, there are a couple of observations. First, there is an observed decrease in this error for each ψ_i when discretization of the coarse mesh Ω_1 is made finer. In particular, an abrupt and profound drop in the error can be observed at $d_1 = 100$. Further, the error continues to decrease rapidly till $d_2 = 900$. This observation is obtained in each of the first ten basis functions (figure 6). These show that beyond an optimal coarse mesh discretization between $d_1 = 100$ and 900, an increase in the mesh discretization doesn't necessarily add to the level of accuracy at the input side. In other words, beyond this optimal Ω_2 discretization level, the error converges rapidly towards zero.

Second, when the correlation length L of the analysis is gradually decreased from 0.3 to 0.001 m, the curves are observed to shift to the right (figure 7) indicating that the optimal level of discretization obtained

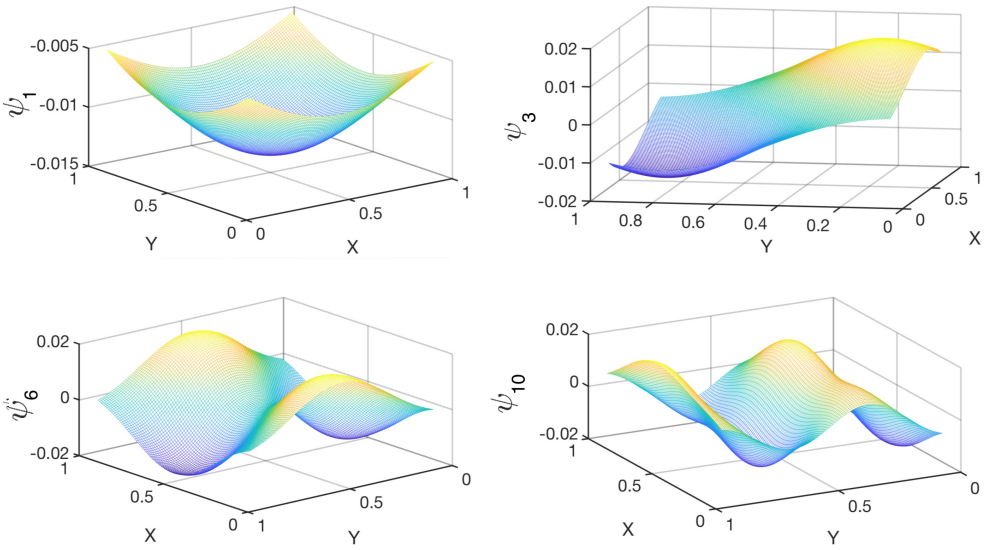


Figure 4: Plots for eigenfunctions ψ_1, ψ_3, ψ_6 and ψ_{10} over the domain Ω_2

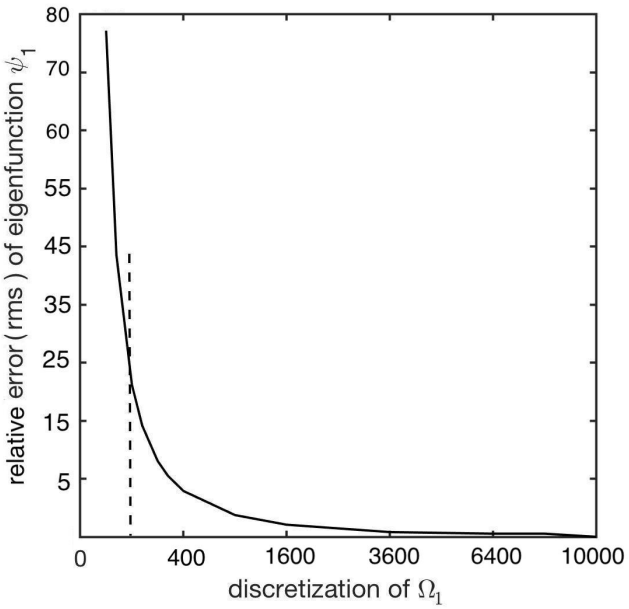


Figure 5: Dependance of error on the coarse mesh discretization Ω_1 obtained for the first eigenfunction ψ_1. A sudden drop, indicated at the striped line, demonstrates that an optimal mesh discretization can be achieved between this point, $d_1 = 100$, and $d_1 = 900$

above is dependant on the correlation length. This behavioural pattern becomes more profound when the correlation length is very low i.e., when $L = 0.001$. It is observed that for the correlation length of 0.3, the drop is observed to occur from d_1 = 100 to 400. With a decrease to 0.15, the corresponding drop is found from d_1 = 144 instead. Further, when it is decreased to 0.001, the drop occurs from d_1 = 320. This shift can be reasoned by the fact that a decrease in the correlation length L induces a decreased smoothening of the random field i.e., generates rougher fields. In the context of the twin-mesh approach, this entails that a higher level of KL discretization of the coarse mesh Ω_1 is required to characterize the fields with the equivalent error as that of cases with a lower L.

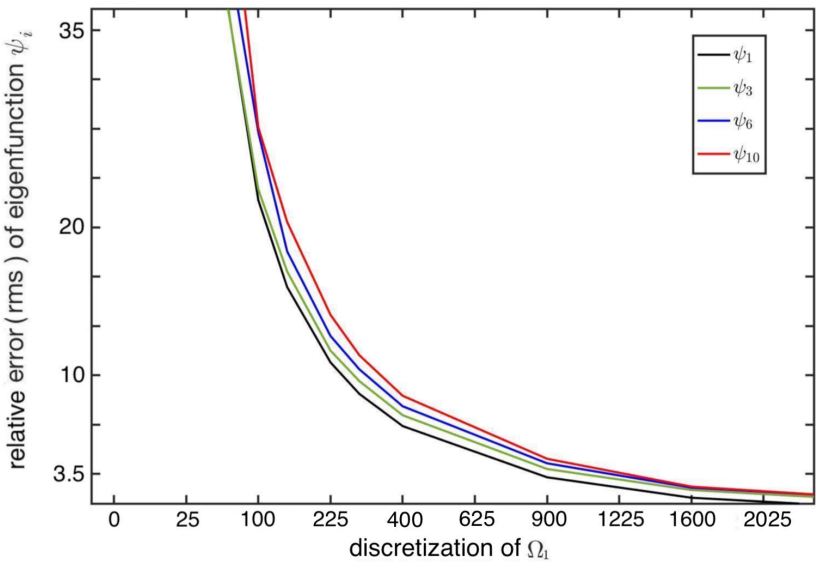


Figure 6: Dependance of error on the coarse mesh discretization Ω_1 obtained for four eigenfunction ψ_1, ψ_3, ψ_6 and ψ_{10}

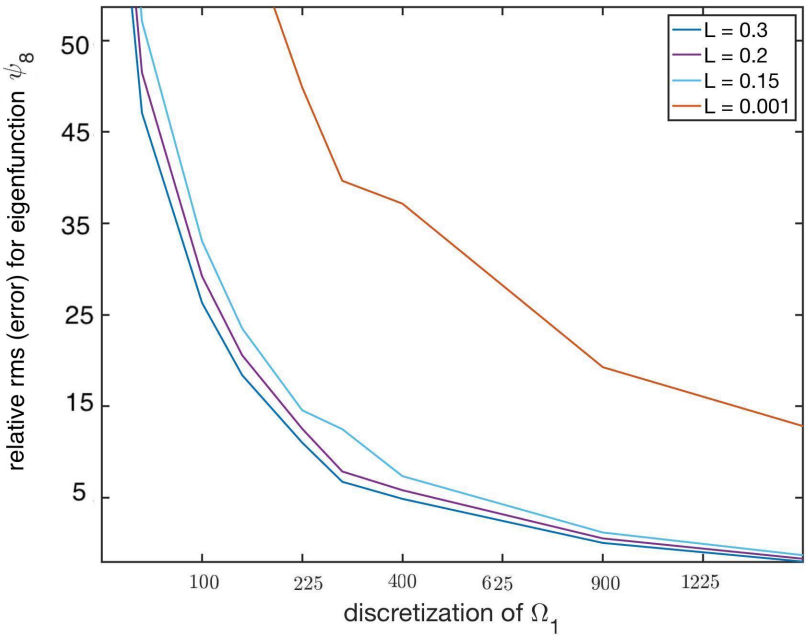


Figure 7: Dependance of the error on correlation length L

3.3 Accuracy of the approach on output side of analysis

To quantify the level of accuracy on the output side, eigenfrequencies ϕ_i of the first 10 eigenmodes have been obtained for 500 realisations of the random field. In this section, these ϕ_i for the following two cases will be compared:

- **Reference case (conventional random field approach)**: Uses the discretization $d_1 = 10000$ for propagating a random field through a FE model of discretization $d_2 = 10000$.

- **Twin-mesh approach case**: Calculates the eigenfrequencies using coarse mesh discretization varying from d_1 = 25 to 3600.

Of the first ten eigenmodes, the eigenfrequencies of the first three (ϕ_1, ϕ_2 and ϕ_3) for all 500 realisations have been plotted against ϕ_9 to create eigenfrequency clouds as illustrated in Figure 8. In this figure, the above clouds have also been generated for three different levels of discretization $d_1 = 100, 400$ and 3600. A comparison between these three levels show that with an increase in discretization, the clouds move closer indicating an increased accuracy of the twin-mesh approach case with respect to the reference case. Further, the clouds exhibit the same behaviour when the comparison is repeated for ϕ_{10} by plotting it against ϕ_1, ϕ_2 and ϕ_3, as shown in Figure 9.

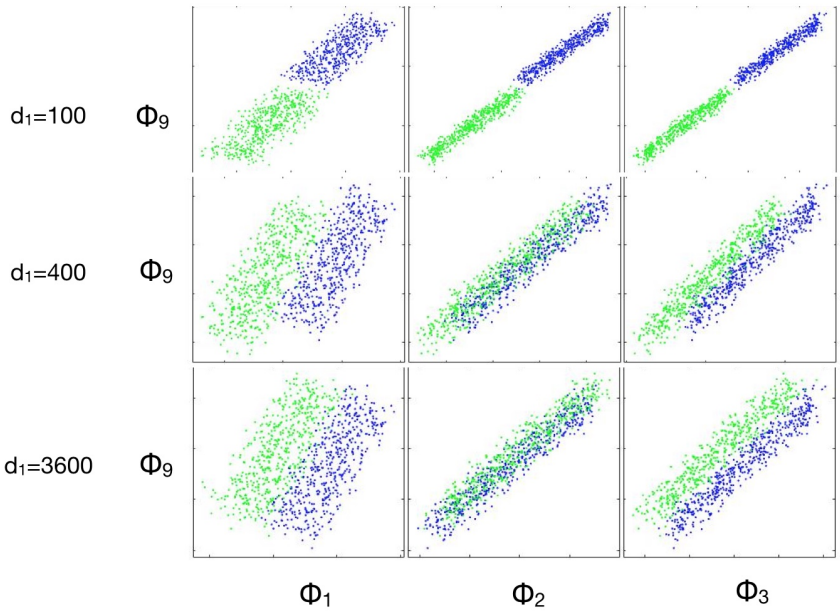


Figure 8: Clouds generated from eigenfrequencies ϕ_i for different discretizations d_1 such that ϕ_1, ϕ_2, ϕ_3 on the x-axis and ϕ_9 on the y-axis. Reference (blue) and twin-mesh cases (green) are compared.

To substantiate on the observation from these figures, the level of accuracy is accurately quantified using a statistical approach. For this, the generated eigenfrequencies of the first ten eigenmodes for all 500 realisations of the random field are stored in a 10 x 500 matrix. The distance between this matrix for both cases is calculated using Bhattacharya distance, which is a widely used metric to determine relative closeness between two probability distributions [17]. Additionally, two-by-two comparisons of eigenfrequencies have been made i.e., the realisations of two selected eigenfrequencies for both cases have been compared using Bhattacharya distance. In each of these comparisons, a distance closer to zero indicates high level of accuracy with respect to the reference case. Overall, three different two-by-two comparisons have been conducted, as shown in Figure 10.

From Figures 8 and 9, it was observed that when a coarse mesh Ω_1 is discretized with $d_1 = 100$, the twin-mesh approach generates eigenfrequency clouds with relatively low overlap with the corresponding ones from reference case. Hence, this can be considered a relatively bad correspondence level, which is quantified using Bhattacharya distance as 0.0267. For the discretizations $d_1 = 100$ to 400, the resultant observations highlight that there is a rapid decrease in distance within this interval followed by a steady decrease towards zero. This is indicative of the convergence of eigenfrequencies of the twin-mesh approach case with that of reference case. Based on this, it can be concluded that a low-dimensional twin of the FE mesh generates eigenfrequencies with a satisfactory level of accuracy at an optimal discretization $d_1 = 400$.

This is also illustrated in Figure 11 which plots the Bhattacharya distances between both cases for

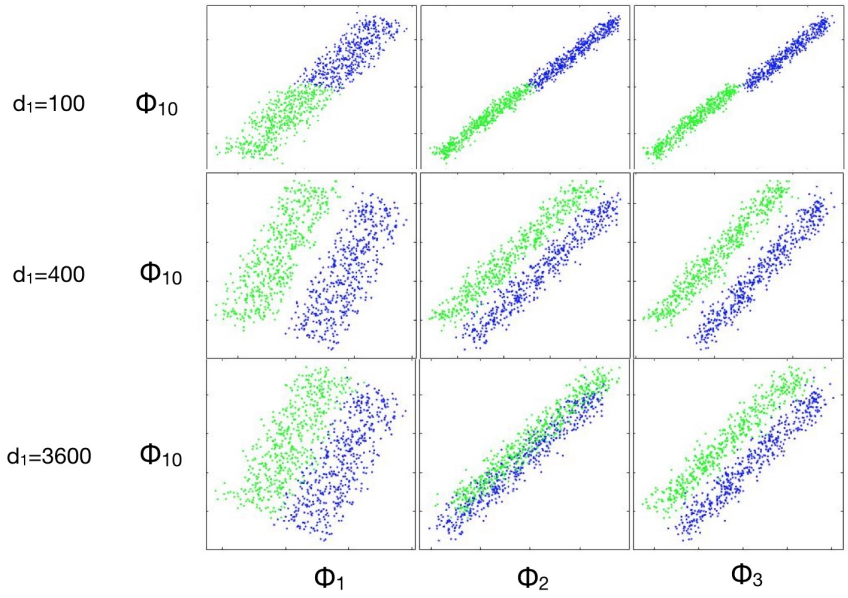


Figure 9: Clouds generated from eigenfrequencies ϕ_i for different discretizations d_1 such that ϕ_1, ϕ_2, ϕ_3 on the x-axis and ϕ_{10} on the y-axis. Reference (blue) and twin-mesh cases (green) are compared.

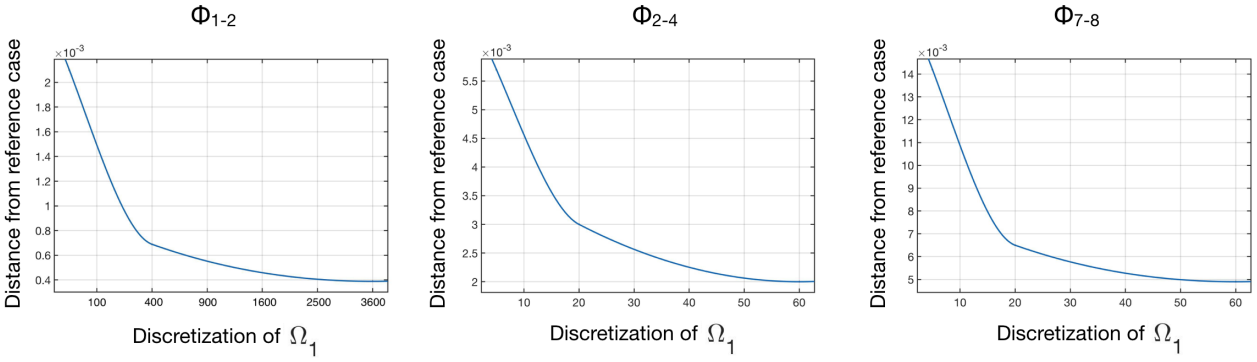


Figure 10: Bhattacharya distances generated for ϕ_{1-2}, ϕ_{2-4}, ϕ_{7-8} are plotted for different levels of discretization of Ω_1

eigenfrequencies of the first ten eigenmodes for 500 realisations of the random field. The figure also shows the corresponding computational time-dependence with discretization Ω_1 when such a twin-mesh approach is executed in Matlab. This time-dependance, which shows a quasi linear increase, illustrates a stark contrast with that obtained from the reference case as shown in Figure 3. Coupled with maintaining the level of accuracy at both the input and output sides of the analysis, this leads to a conclusion that the proposed approach indeed results in a reduction in computational time by requiring a reduced discretization of the grid for KL expansion between 10% and 20% of the FE grid (as shown in Figure 5).

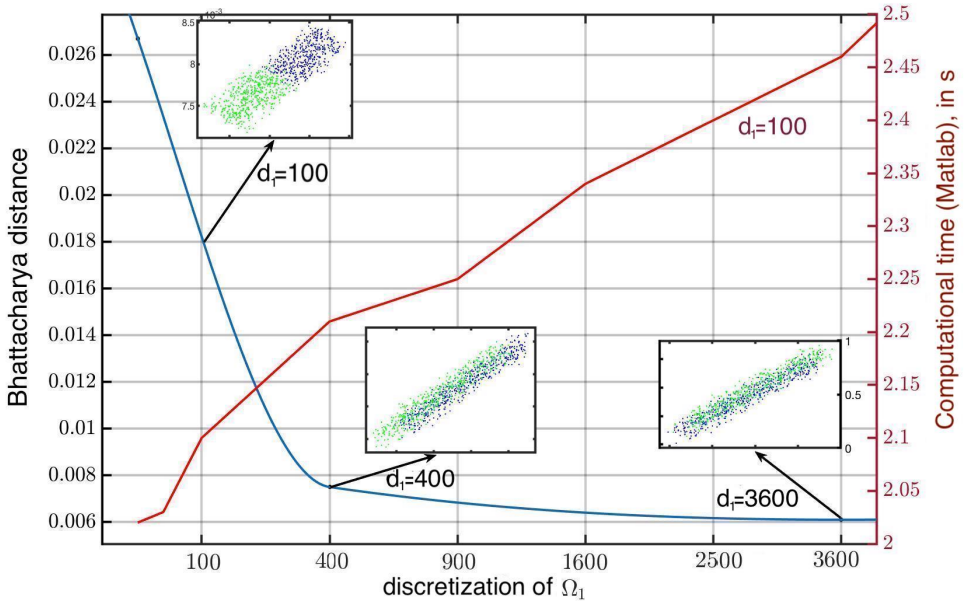


Figure 11: 1) Bhattacharya distance (blue curve) between the first 10 eigenfrequencies. 2) Computational time (red curve) in Matlab for running a twin-mesh model with discretization $d_1 = 100$.

4 Conclusions

Non-deterministic approaches, such as random field analysis, face significant computational challenges when analysing high-dimensional models required at the industrial scale. The computational efficiency of random field representations with the Karhunen-Loeve expansion relies on the solution of an eigendecomposition problem, which increases in complexity at high dimensions. A novel methodology has been presented for optimally propagating a random field on a high-resolution Finite Element model using a two-level grid hierarchy. More specifically, a twin-mesh approach is used to efficiently discretize a random field on a coarse mesh grid using a KL series expansion, which is then propagated on a high-dimensional grid of the FE model. The numerical efficiency and accuracy of this approach with respect to a conventional random field approach have been studied using a case study on a dynamic model of moderate-dimensionality. Overall, this study was successful in rendering a reduction in computational cost for evaluating the eigendecomposition by requiring a discretization for KL expansion of 10-20% of the FE grid, while keeping the accuracy at an acceptable level. Furthermore, the numerical accuracy after propagating the random field on the FE model is demonstrated using a convergence study, which shows that from a discretisation level of 20% of FE mesh, an acceptable accuracy is achieved by the low-dimensional twin model. In addition, it was illustrated that the optimal level of discretization of KL mesh is dependant on the correlation length. For future work, it is suggested to substantiate this study using more complex models. Finally, it is recommended to adapt this approach to other non-deterministic methods such as the interval fields.

Acknowledgements

The authors would like to acknowledge support of the Flemish Research Foundation (FWO) in the framework of the project ”HiDIF: High Dimensional Interval Fields” (project number G0C2218N).

References

[1] A. Haldar, S. Mahadevan, *Reliability assessment using stochastic finite element analysis*, John Wiley & Sons (2000).

[2] D. Moens, D. Vandepitte, *A survey of non-probabilistic uncertainty treatment in finite element analysis*, *Variability in the mechanical properties of laser sintered PA-12 components*, Computer methods in applied mechanics and engineering, 194.12-16 (2005), pp. 1527-1555.

[3] D. Moens, D. Vandepitte, *Recent advances in non-probabilistic approaches for non-deterministic dynamic finite element analysis*, Archives of Computational Methods in Engineering, 13.3 (2006), pp. 389–464.

[4] G.I. Schuëller, *Computational stochastic mechanics–recent advances*, Computers & Structures, 79.22-25 (2001), pp. 2225-2234.

[5] P. Spanos, R. Ghanem, *Stochastic finite element expansion for random media*, Journal of engineering mechanics, 115.5 (1989), pp. 1035–1053.

[6] W. Verhaeghe, W. Desmet, D. Vandepitte, D. Moens, *Identification and quantification of multivariate interval uncertainty in finite element models*, Computer Methods in applied mechanics and engineering, 260 (2013), pp. 50-62.

[7] M. Faes, Y. Wang, P. Lava, D. Moens, *Proceedings of Solid Free Form Symposium. Texas, August. 2015*, Texas (2015), pp. 10-12.

[8] M. Faes, J. Cerneels, D. Vandepitte, D. Moens, *Identification and quantification of multivariate interval uncertainty in finite element models*, Computer Methods in applied mechanics and engineering, 315 (2017), pp. 896-920.

[9] M. Faes, *Interval methods for the identification and quantification of inhomogeneous uncertainty in Finite Element models*, PhD Thesis, Katholieke Universiteit Leuven, Belgium (2017).

[10] B. Peherstorfer, K. Willcox, M. Gunzburger, *Survey of multifidelity methods in uncertainty propagation, inference, and optimization*, Technical Report TR-16-1, Aerospace Computational Design Laboratory, Department of Aeronautics and Astronautics, Massachusetts Institute of Technology, Cambridge, MA, USA (2016).

[11] K. Crombecq, *Surrogate modeling of computer experiments with sequential experimental design*, PhD Thesis, Ghent University, Belgium (2011).

[12] M. Pisaroni, *Multi Level Monte Carlo Methods for Uncertainty Quanti cation and Robust Design Optimization in Aerodynamics*, PhD Thesis, École Polytechnique Fédérale de Lausanne, Switzerland (2017).

[13] M. Pisaroni and F. Nobile and P. Leyland, *A Continuation Multi Level Monte Carlo (C-MLMC) method for uncertainty quantification in compressible inviscid aerodynamics*, Computer Methods in Applied Mechanics and Engineering, 326 (2017), pp. 20-50.

[14] W. Betz, I. Papaioannou, D. Straub, *Numerical methods for the discretization of random fields by means of the Karhunen-Loève expansion*, Computer Methods in Applied Mechanics and Engineering, 271 (2014), pp. 109–129.

[15] L. Parussini, D. Venturi, P. Perdikaris, G. E. Karniadakis, *Multi-fidelity Gaussian process regression for prediction of random fields*, Journal of Computational Physics, 336 (2017), pp. 36-50.

[16] S. P. Huang, S. T. Quek, K. K. Phoon, *Convergence study of the truncated Karhunen–Loeve expansion for simulation of stochastic processes*, International Journal of Numerical Methods in Engineering, 52 (2001), pp. 1029-1043.

[17] T. Kailath, *The Divergence and Bhattacharyya Distance Measures in Signal Selection*, IEEE Trasnactions on Communication Technology, 15 (1967), pp. 52-60.

Unstructured uncertainty modeling for coupled vibration systems

B. Dogančić[1], M. Jokić[1], N. Alujević[1], H. Wolf[1]
[1] Faculty of Mechanical Engineering and Naval Architecture, Zagreb, Department for Applied Dynamics
Ivana Lučića 5, 10002 Zagreb, Croatia
e-mail: **bruno.dogancic@fsb.hr**

Abstract
Unstructured uncertainty models are commonly used within robust control framework to cover unmodeled dynamics, particularly at high frequency. The resulting uncertain linear time invariant (LTI) models (i.e. models comprised of an LTI nominal model and an uncertainty model) are then used in robust controller synthesis procedure and have significant influence on the controller performance. This paper proposes a novel procedure for constructing unstructured uncertainty models for a class of mechanical vibration systems comprised of a number of interconnected (coupled) vibration subsystems. As the result of the proposed procedure, we are able to significantly reduce conservatism of the resulting uncertain LTI models of the individual subsystems, thus improving the performance of subsequent robust control strategies. We illustrate the results on a numerical example comprised of a series of simply-supported beams coupled with a set of springs.

1 Introduction

Dynamical systems today are complex and made of many interconnected and mutually interacting individual dynamical subsystems. Such systems form a class of spatially distributed dynamical systems and have gained significant importance in science and engineering in recent history. In order for them to perform the prescribed function they are often made up of elements that can act upon different physical laws - examples include active car suspension, multi-agent robotic systems, networks of embedded systems, smart structures and so on. Modeling, analysis and control of spatially distributed systems have gained significant importance in science and engineering and it is being recognized as a challenging task. As such it has attracted notable research interest [1].

This paper is focused on a particular class of mechanical vibration systems comprised of a number of passive and dissipative interconnected (coupled) vibration subsystems. Passivity and dissipativity, together with relevant stability criteria, play an important role in modern control theory. Many mechanical systems can be characterized in this manner. Typical examples include discretized infinite-dimensional structural systems such as beams, rods, plates and/or shells mutually interconnected with various elastic and damping components. For such a complex system there is a high demand in terms of robustness, efficiency and performance. When dealing with robust control of such systems, particularly when applying decentralized control strategies [2], each subsystem requires an approximation by an appropriate discretized model, as well as a corresponding uncertainty model [3]. It is of significant importance that the uncertainty model captures all neglected dynamics (e.g. possible nonlinearities, high order dynamics, discretization error etc.) and that the uncertainty set is as small as possible. In order to achieve the desired controller performance, it is necessary to reduce conservatism of the uncertainty model. On the other hand, it is convenient to use as coarse discretization as possible in order to reduce the controller order (size). This results in a situation where a compromise has to be made since we are faced with two essential modeling issues:

1) What discretization level (i.e. accuracy) to choose?
2) How to construct the least conservative uncertainty model?

In an attempt to answer the given questions, a case study is carried out in this paper. From the results obtained by a case study it can be observed that a part of individual subsystem uncertainty can be discarded since it does not influence the dynamic behavior of the assembled system. An example is considered in the form of a spatially distributed vibrational mechanical system comprised of a series of simply supported Euler beams coupled with springs, as shown in following sections.

2 Mathematical model

In this case study we consider vibrations of a mechanical system comprised of a finite number of simply supported Euler beams. The beams are mutually interacting and are coupled with springs as shown in Figure 1. Each beam has a circular cross-section and is defined by the geometric and material properties given in Table 1, where l is length, d is the diameter of the cross-section, E is the modulus of elasticity and v is Poisson's coefficient. Each beam is connected to two neighboring beams at one third and two thirds of their lengths with a spring of stiffness k, also given in Table 1.

l [m]	d [mm]	E [GPa]	v [-]	k [N/m]
0.6	1	210	0.3	500

Table 1: Subsystem properties

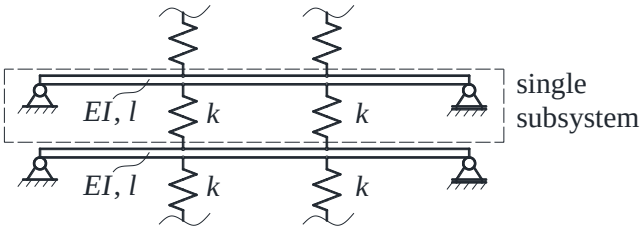


Figure 1: Spatially distributed mechanical system comprised of simply supported Euler beams coupled with springs

Each beam is modeled using finite element method and for each beam a series of successively finer discretizations are made. A beam is discretized with 3, 6, 12, 24, 48 and 96 finite elements. For each discretization, a proportional Rayleigh damping matrix is constructed such that modal damping ratio is approximately 0.05 for the first 6 beam vibration modes. Discretized beams are then connected with springs at specified points in order to obtain a series of successively finer dynamical models. Discretized subsystem models consisting of a single beam and springs is then converted into a linear time-invariant (LTI) descriptor state space (DSS) model with two inputs and two outputs. Inputs are displacements of two spring ends and outputs are beam deflections at one third and two thirds of its length. Based on the obtained LTI models we construct a nominal model and a series of uncertainty models corresponding to each discretization, as follows.

Nominal subsystem model is obtained by reducing the 96 finite element model, that is, nominal model is the reduced most accurate LTI model available. The reduction of the model is obtained by means of a balanced truncation. The criteria for reducing the model is removing all states that have Hankel singular values less than a prescribed value of 10^{-2}. This results in reducing the 576 number of states for the full model (obtained from 96 finite elements) to 19 states for the reduced model. The reduced model is suitable to be used as a nominal model for constructing unstructured uncertainty weights as it will be shown in the next section. By using model reduction, we increase efficiency of numerical modeling.

Perhaps the most widely used tools in robust control design are weights. Weights allow a control designer to capture the system uncertainties and to determine over what frequency ranges the performance is desired. Weights can be viewed as a way to tune the control design to achieve a desired level of performance and robustness without having to explicitly consider the system stability. "The design of a robust and high-performance control system relies heavily on the choice of weights used in the design. [3]". We start our analysis by considering uncertainty caused by unmodeled dynamics and assume that the real plant is obtained by combining the nominal plant $\boldsymbol{P}_{\text{sys}}$ with a transfer function of the kind $\boldsymbol{W}_1\Delta\boldsymbol{W}_2$. Where Δ is uncertainty block and $\boldsymbol{W}_1$ and $\boldsymbol{W}_2$ are frequency weights that adjust the amount of uncertainty at each frequency. Such kind of uncertainty is denoted as unstructured. The procedure of constructing unstructured uncertainty models for the presented case is as follows.

2.1 Unstructured uncertainties for single subsystem

For each discretization level (including the 96 FE level), input multiplicative error models are constructed. An input multiplicative error model consists of an unstructured uncertainty block Δ of a unit-gain and a diagonal, stable, minimum-phase shaping frequency weights $\boldsymbol{W}_1$ and $\boldsymbol{W}_2$. The described input multiplicative model is schematically shown in Figure 2a. At each input denoted by *w*, a frequency weight is constructed such that the response from *w-th* input to *z-th* output covers the relative error between nominal model and discretized model. Throughout the procedure an order (number of states) of frequency weights has been kept constant at each input. In order to make the size of the uncertainty model small, we used a low order of 8 for diagonal entries in weight $\boldsymbol{W}_1$ at each input, whereas weight $\boldsymbol{W}_2$ is a scalar of magnitude 1. $\boldsymbol{P}_{\text{sys}}$ is an interconnection transfer matrix function such that a linear fractional transformation with uncertainty block yields input multiplicative uncertainty model. Input multiplicative uncertainty [4] is expressed by:

$$\boldsymbol{G} = \boldsymbol{P}_{sys}(\boldsymbol{I} + \boldsymbol{W}_1\Delta\boldsymbol{W}_2), \tag{1}$$

where $\boldsymbol{G}$ is an uncertain system obtained by using the input multiplicative uncertainty model to alter the response of a system $\boldsymbol{P}_{\text{sys}}$.

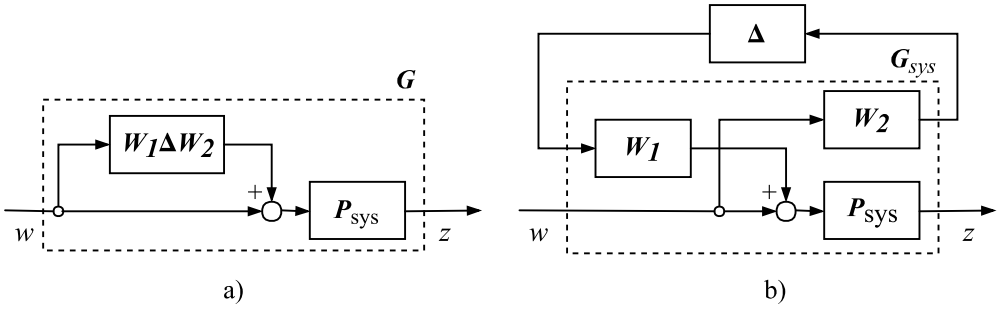


Figure 2: Input multiplicative uncertainty model: a) a subsystem, b) linear fractional representation of a subsystem

In a different study made in [5] the authors obtained similar results by using an additive uncertainty model. In a similar fashion they constructed Δ with norm equal to 1 but used a scalar weight $\boldsymbol{W}$. Additive uncertainty model is usually used to model an absolute error or to model a modest difference in responses of two systems. Scalar weights are used to cover the net response from each input to each output of the error between the nominal model and the discretized model. Uncertainty modeling using scalar weights is more conservative than using a weight at each input of the system. A less conservative uncertainty model can be obtained by using diagonal weights. We stress that, by different choice of $\boldsymbol{P}_{\text{sys}}$, different uncertainty models can be used in a straightforward fashion. In robust control theory we want to obtain a system in linear fractional transformation (LFT). For constructing LFT it is important to separate a normed uncertainty part Δ and connect it in feedback to a nominal LTI system. For input multiplicative error model, uncertainty separation can be done as it is shown in Figure 2b. By doing so we now consider a

system $\boldsymbol{G}_{\text{sys}}$ that has an uncertainty block Δ connected in feedback. In the next section we show how to refine the uncertainty model by examining a coupled system.

2.2 Subsystem coupling and uncertainty refinement for coupled system

Up until now we only considered modeling uncertainty for a single subsystem. We stress that this series of successively better subsystems models are essentially local since we didn't take into the account that the overall system is comprised of a series of coupled individual instances. To address this issue, we propose a procedure for modeling uncertainty weights for a single subsystem that takes into the account the neighboring subsystems coupling. Information about the coupled neighboring subsystems is used to further reduce the previously obtained uncertainty weights. A reduction of required uncertainty weights means a reduction in conservatism of an uncertain system. Since we are analyzing passive and dissipative coupled system we are assuming that a portion of individual subsystem uncertainty is damped by the neighboring subsystems and may be discarded. It needs to be kept in mind that this reduction of uncertainty might not be the case for spatially distributed system in general. Reduction of uncertainty using this presented approach may even vary for different passive and dissipative systems depending on the system structure and properties. The procedure for obtaining unstructured uncertainty for a single subsystem can be used with a minor extension in a following manner.

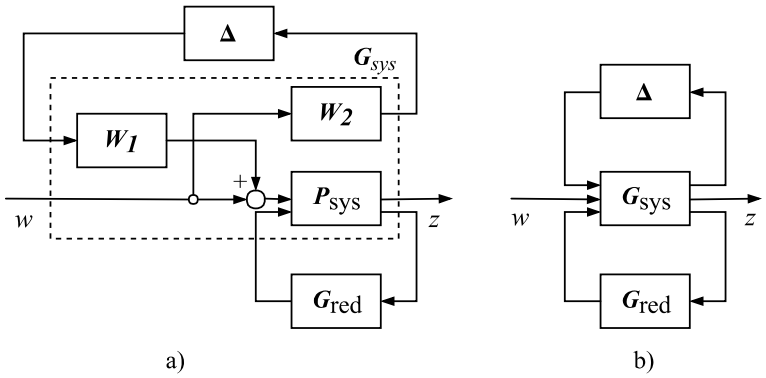


Figure 3: Input multiplicative uncertainty model: a) subsystem $\boldsymbol{G}_{\text{sys}}$ coupled with reduced model of neighboring subsystems $\boldsymbol{G}_{\text{red}}$, b) representation as a general framework for an uncertain feedback system

First, we need to take into the account the neighboring systems. The neighboring systems are series of a final number of previously obtained reduced nominal models. If we further reduce this series, we obtain a reduced model $\boldsymbol{G}_{\text{red}}$ that represents the neighboring systems. For reduction of a series we use balanced truncation with same criteria used for obtaining the nominal (single subsystem) model. Finally, we complete our modeling by connecting $\boldsymbol{G}_{\text{red}}$ into feedback loop with the uncertain individual subsystem $\boldsymbol{G}_{\text{sys}}$ as shown in Figure 3a. The resulting model can be viewed as a general framework for robust control, where an uncertain feedback system (i.e. $\boldsymbol{G}_{\text{sys}}$ with delta in feedback) has $\boldsymbol{G}_{\text{red}}$ as a controller on a system as shown in Figure 3b. With this model we can study the effect of neighboring systems on unstructured uncertainty model refinement by essentially changing the number of surrounding systems in $\boldsymbol{G}_{\text{red}}$. We stress that the number of neighboring systems needed for this certainly depends on the problem at hand. For this case study we chose that the number of surrounding subsystems change, i.e. we connect a different number of reduced nominal models in a feedback loop. For each number of neighboring subsystems, that is 1,3, 5 or 10 reduced nominal models, we recompute input multiplicative frequency weights $\boldsymbol{W}_1$ and $\boldsymbol{W}_2$ in a similar fashion as we did for a single subsystem. It is important to note that $\boldsymbol{G}_{\text{red}}$ for each number of neighboring systems becomes bigger in size but is nevertheless kept reasonably low. $\boldsymbol{G}_{\text{red}}$ has 19, 25, 29 and 40 states for 1, 3, 5 and 10 neighboring systems, respectively. With the complete mathematical model, we present results as shown in next chapter.

3 Results and discussion

To keep the size of a nominal model small, we reduce the most accurate system (i.e. the one with 96 FE). The response of a 96 FE model and that of a reduced model is shown in Figure 4 where it can be seen that the reduced model accurately describes the response of the full model.

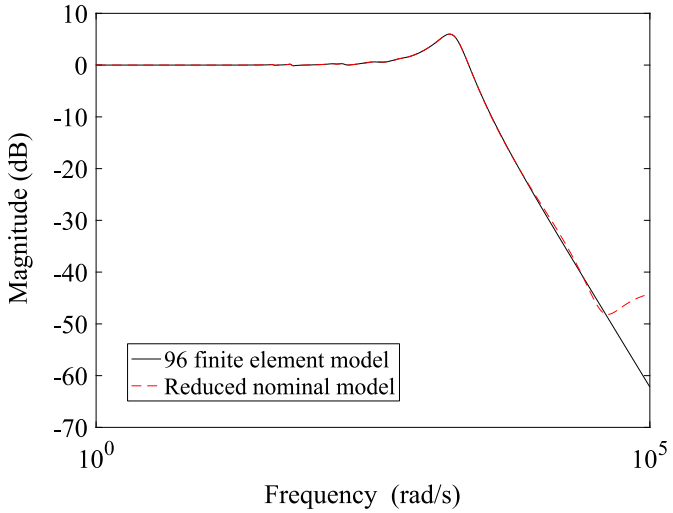


Figure 4: Frequency response of the most accurate model from 96 FE and a nominal reduced model

First, we study frequency weights obtained for single subsystem. A comparison of H_∞ norms of frequency weights for each discretization level is shown in Figure 5. As expected, the frequency weights norm decreases with finer discretization. This provides us quite straightforward criteria for deciding which discretization should be used. For example, a criterion could be such that the frequency weight norm is less than some prescribed value.

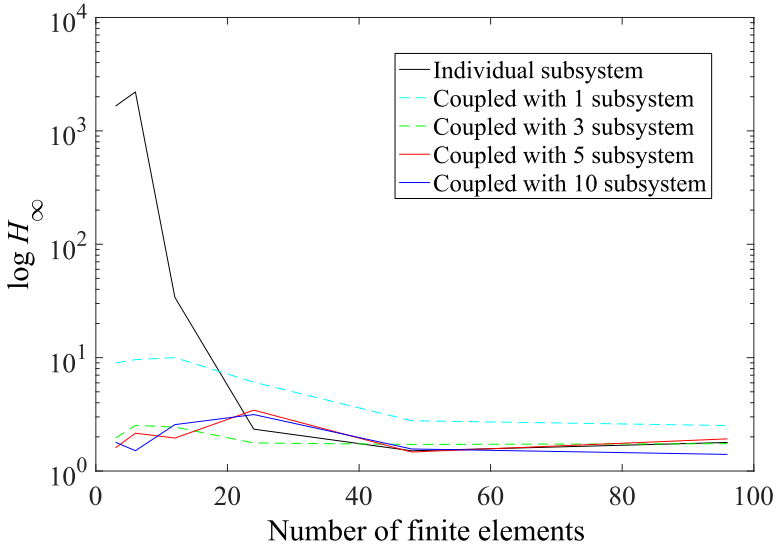


Figure 5: Comparison of H_∞ norms of frequency weights for a single subsystem and a different number of coupled subsystems for each discretization level

Next, we compare H_∞ norms for coupled subsystems when we add 1, 3, 5 and 10 neighboring subsystems. A comparison of H_∞ norms of frequency weights for both single and coupled subsystems for different levels of discretization is shown in Figure 5 as well. It is evident that new H_∞ norms obtained for coupled dynamical systems are decreasing. Most prominent decrease can be seen for low discretization levels.

When analyzing obtained frequency weights for individual subsystem and coupled subsystem it is seen that the newly obtained frequency weights for coupled subsystem have lower magnitude of the frequency response in wide frequency ranges as shown in Figure 6. In other words, the frequency weights of individual uncertainty models are "scaled" such that the uncertainty information that does not affect the overall system dynamics is discarded.

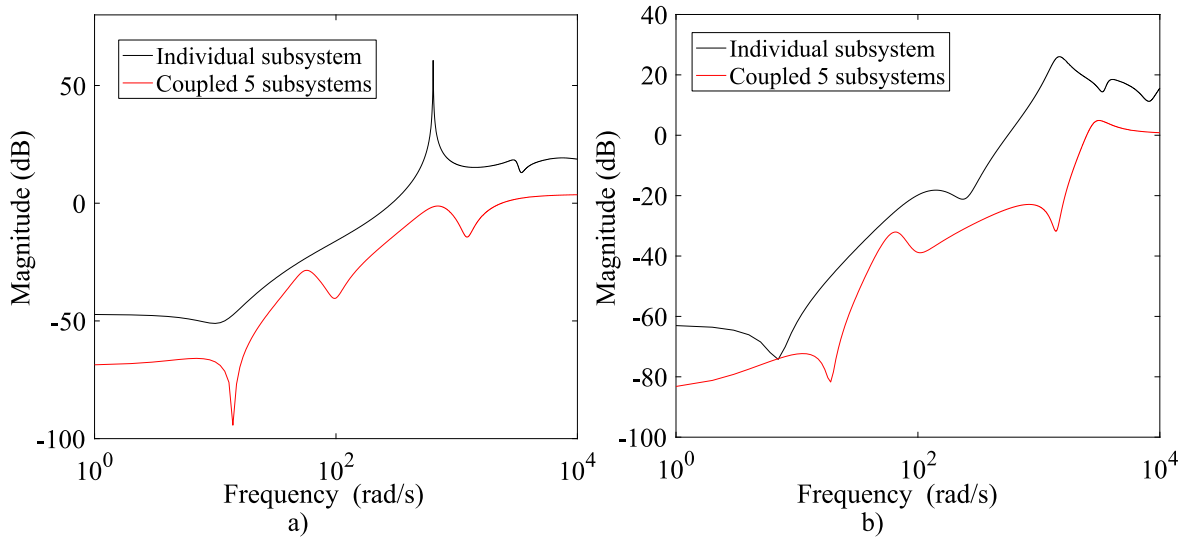


Figure 6: Comparison of frequency response of frequency weights for a single subsystem and a coupled subsystem for: a) 3 FE model, b) 12 FE model

When changing the number of surrounding systems (i.e. by adding more neighboring subsystems), uncertainty model can be further reduced, but this time only in a specific spectrum, as seen in Figure 7. For this example, higher frequency dynamics at around 10^3 rad/s is discarded from uncertainty model when adding more neighboring subsystems.

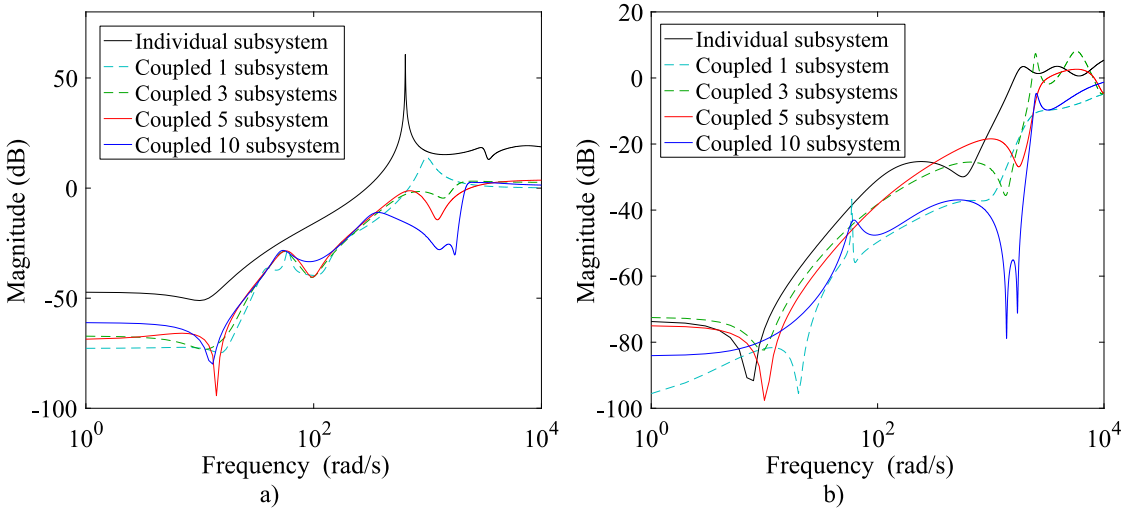


Figure 7: Comparison of frequency response of frequency weights for a single subsystem and a different coupled subsystem for: a) 3 FE model, b) 24 FE model

Numeric algorithm used for obtaining input multiplicative uncertainty weights calculates optimal weights on a frequency grid. It is interesting to investigate how well different order of weights covers the relative error between the nominal system and the LTI model for some discretization as it is shown in Figure 8. An increase in order of weights from 8 to 10 and then to 16 results in higher order weights more closely matching the response of relative error. This increase in weight order comes at cost of increase in size of the uncertain model and an increase in numeric calculation times.

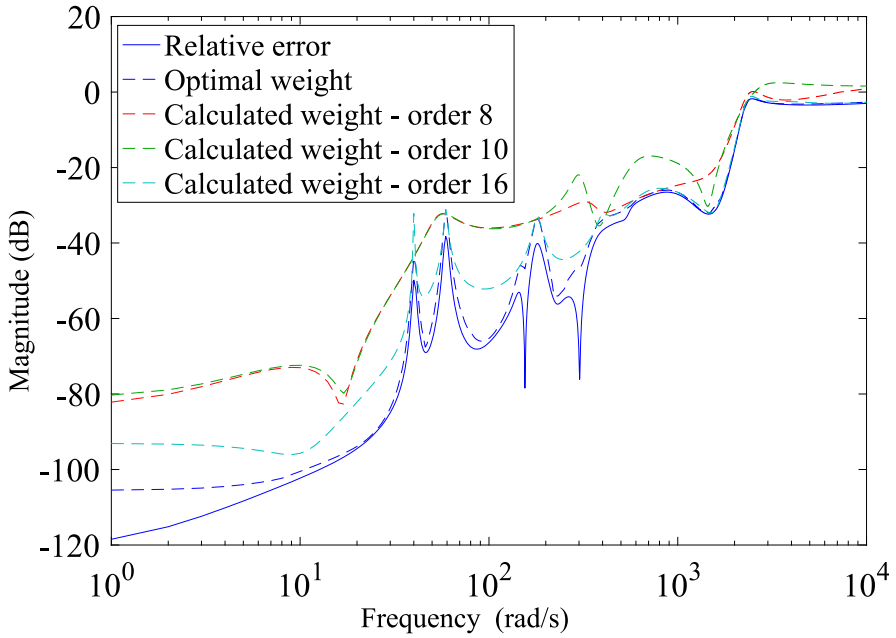


Figure 8: Comparison of frequency response of frequency weights for coupled subsystem and a different order of weights for 12 FE

An interesting observation is made when applying ν-gap analysis by Vinnicombe [6]. For the problem at hand a reduced series of neighboring systems can be viewed as a controller on an uncertain system as shown in Figure 3b. It is thus interesting to observe upper bounds on the Vinnicombe gap and distances between each controller model when we increase the number of neighboring systems. That is, we measure upper bounds on ν and ν-gap between one system connected as a controller and 3 systems connected as a controller on an uncertain system, and so on. It was shown that even controller models obtained by adding 1 subsystem and 2 subsystems in feedback are far apart in the sense that ν-gap is approximately 0.96. Between each other combination of controllers ν and ν-gap are practically equal to 1 which translates into systems being far apart. Also, to exclude possible errors in ν and ν-gap calculation instead of using reduced controller, analysis was carried out on a full model as well and yielded identical results. It would be interesting to further investigate these results as well.

4 Conclusion

The paper presents the results on the modeling of unstructured uncertainty for spatially distributed (coupled) vibration systems. Finite element mesh refining technique is used to obtain a series of successively finer spatial discretizations of an infinite dimensional vibrational mechanical system. This refining provides enough information for constructing a series of successively better uncertain linear time-invariant models. The resulting uncertain linear time-invariant model of a single subsystem can be further refined for a special class of passive and dissipative vibration systems by taking into account that it is coupled with a small number if neighboring subsystems that are passive and dissipative as well. By increasing the number of neighboring systems, it was shown that the magnitude in frequency response of required uncertainty on the single subsystem is decreasing. This reduces conservatism of the uncertainty model of individual subsystem which improves performance when dealing with robust control of passive and dissipative coupled dynamical vibration systems.

References

[1] M. R. Jovanović, *Modeling, analysis and control spatially distributed systems*, PhD Thesis, University of California, Santa Barbara (2004).

[2] P. Gardonio, N. Alujević, *Double panel with skyhook active damping control units for control of sound radiation*, The Journal of the Acoustical Society of America, Volume 128, Issue 3, (2010), pp. 1108-1117.

[3] S. Zhou, J. C. Doyle, K. Glover, *Robust and Optimal Control*, Prentice Hall (1996).

[4] U. Mackenroth, Robust Control Systems, Springer-Verlag Berlin Heidelberg (2004).

[5] M. Jokić, B. Dogančić, A. Jokić, M. Lobrović, *Uncertainty Modeling of Spatially Invariant Distributed Dynamical Systems*, in S. Perroto, P. Díez, editors, *Proceedings of International Conference on Adaptive Modeling and Simulation ADMOS 2017 Barcelona: CIMNE, 2017, June 26-28*, Italy, Verbania (2017), pp. -.

[6] G. Vinnicombe, Measuring Robustness of Feedback Systems, PhD Dissertation, Department of Engineering, University of Cambridge, (1993).

An efficient strategy to describe the propagation of variation through multi-stage metal forming processes

B.M. de Gooijer[1], J. Hazrati-Marangalou[1], H.J.M. Geijselaers[1], A.H. van den Boogaard[1]
[1] University of Twente, Chair of Nonlinear Solid Mechanics
Drienerlolaan 5, 7522 NB, Enschede, The Netherlands
e-mail: **b.m.degooijer@utwente.nl**

Abstract

In this work an efficient strategy to describe the propagation of uncertainty throughout a production process is proposed and validated. A two-stage metal forming process is used to demonstrate the proposed strategy. A metamodel of the first stage is built using a singular value decomposition combined with multiquadric radial basis functions. The strategy is validated by comparing the propagated results from the first stage, of both the metamodel and a finite element model, to a second stage finite element model for a new set of validation points. Using the proposed strategy, it will be possible to efficiently optimize multi-stage processes under uncertainty.

1 Introduction

When the uncertainties in a production process are in the same order of magnitude as the desired product tolerances, these uncertainties must be taken into consideration in order to design products that meet a required accuracy [1, 2]. Robust optimization is commonly used to design products or processes whilst taking into account the manufacturing variability. However an efficient strategy to optimize multi-stage processes is still lacking.

In robust optimization one can distinguish two types of variables [3, 4]: noise variables that cause process uncertainty (e.g. material scatter, machine dynamics or temperature changes) and design variables that can be set by a designer or operator (e.g. tooling geometry or machine settings).

The goal of robust optimization is to find the set of design variables that minimizes the uncertainty in an objective function. However, with an increasing number of process stages, the dimensionality of the problem at hand increases as well. Because of this high dimensionality, optimizing all process stages at once will not be efficient. One solution is to optimize each process stage separately. However, as shown by Suri & Otto [5] this approach will most certainly not lead to the global optimum after the last process stage. Thus, in order to be able to solve the robust optimization problem at hand, variation must be propagated from one stage to the next. To do so efficiently, numerical techniques such as metamodeling and decomposition methods can be applied.

The first attempt in optimization of a multi-stage metal forming process, although deterministic, was done by Roy et al. [6]. In their work all process stages are optimized simultaneously. In this approach the entire production chain is treated as a single stage. Other deterministic optimizations that use a simultaneous approach can be found in [7-10]. Kusiak, Jarosz et al. [11, 12] separate the simultaneous approach into sequential deterministic optimization of each stage for different levels of aggregation. Steffes-lai [13] and Sun [14] et al. show the importance of taking into account the forming history by comparing physical experiments with computer analyses. Du & Chen [15] propose two different approaches for describing the propagation of uncertainty through the process stages, which are an extreme condition approach and a statistical approach.

In this work, an efficient strategy to describe the propagation of uncertainty throughout the production process is proposed and validated. In Section 2, a general description of a production process is suggested

first. After that, a strategy is proposed to describe the propagation of uncertainty from one process stage to the next as low-dimensional as possible. In Section 3, a demonstrator process is introduced to validate the proposed strategy. The results of the first stage of the demonstrator process, of both a metamodel and a finite element model, are propagated to the second stage finite element model for a new set of validation points. Using the proposed strategy, it will be possible to efficiently optimize multi-stage processes under uncertainty.

2 Strategy for describing the propagation of variation

2.1 General description of a multi-stage production process

Before describing the strategy for propagation of variation, first a general description of a production process is suggested. A schematic representation of a two stage production process is given in Figure 1. Note however, that the description can be extended to an indefinite number of stages.

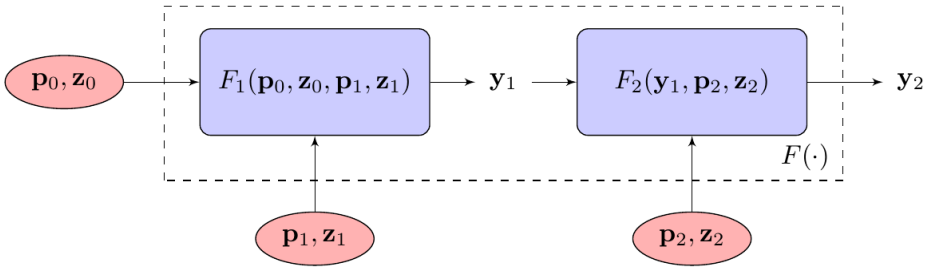


Figure 1: Schematic representation of a two stage production process.

When describing a production process two types of input variables can be distinguished: noise variables and design variables, denoted with z and p respectively. The vectors containing all noise and all design variables corresponding to process stage i are denoted with $\mathbf{z}_i$ and $\mathbf{p}_i$ respectively. Each process stage is a function of the output of the previous stage $\mathbf{y}_{i-1}$ and its noise and design variables, hence $F_i(\mathbf{y}_{i-1}, \mathbf{p}_i, \mathbf{z}_i)$. One exception for this is the first stage, where the process stage is a function of the initial variables, indicated with subscript 0, and its corresponding noise and design variables. Initial design variables are generally discrete, e.g. material type or thickness [1]. Noise variables are usually continuous and can be modelled with different types of distributions, e.g. normal, uniform or skewed distributions. Note that if there is a noise variable in the input, the output of all subsequent stages has to be considered as noise with an undetermined distribution. This output distribution can be determined by means of e.g. Monte Carlo sampling or analytical methods as proposed by Nejadseyfi et al. [16].

The goal of a robust optimization is to find the set of design variables $\{\mathbf{p}_i, \dots, \mathbf{p}_N\}$ that minimizes the sensitivity of the objective with respect to the noise variables or that minimizes an objective function under the constraint of sufficient robustness. The objective function will be a function of the output of the final stage $f_{obj}(\mathbf{y}_N)$, e.g. attaining a geometrical requirement or preventing defects such as wrinkling or fracture. Besides approaching each stage as a separate function $F_i(\cdot)$, one can define a function describing the entire production process $F(\cdot)$. In this simultaneous approach, all stages are combined to one single stage with a large number of design and noise parameters. Due to the high-dimensionality of the problem at hand, it will be infeasible to find an optimum using this simultaneous approach. Hence, in order to analyze the variation at the final stage and optimize the multi-stage production process under uncertainty, one needs to efficiently describe each process stage.

2.2 Efficiently propagating variation through multi-stage production processes

To efficiently describe a process stage, the variation in output of the stage must be captured as low-dimensional as possible. The strategy to efficiently describe the output of stage i consists of 3 steps:

1. Obtain training set of stage i

Based on a sampling method or a combination of sampling methods, a set of K sample points $\{\mathbf{z}_i, \mathbf{p}_i\}^{(k)}$ needs to be generated. Examples of sampling methods are full/fractional factorial design, central composite design, Latin hypercube sampling or a Halton/Sobol sequence. At each point k in the set the stage i model must be evaluated to obtain the output training data.

2. Reduce output of stage i

To find the dominant behavior in the training data of the i^{th}-stage output, a singular value decomposition (SVD) is applied. In a SVD a new geometric space is sought that maximizes the variation along its new axes [17]. In order to apply SVD, each output in the set of training data of stage i must be stored in a column vector $\mathbf{y}_i^{(k)}$. All K column vectors are collected in a so-called snapshot matrix $\mathbf{Y}_i$ [16, 17]:

$$\mathbf{Y}_i = \begin{bmatrix} \mathbf{y}_i^{(1)} & \cdots & \mathbf{y}_i^{(K)} \end{bmatrix} \tag{1}$$

Now the snapshot matrix can be decomposed using SVD:

$$\mathbf{Y}_i = \boldsymbol{\Phi}\mathbf{S}\mathbf{V}^T \tag{2}$$

Herein $\mathbf{S}$ is a diagonal matrix containing the K real positive singular values s_k in descending order, $\boldsymbol{\Phi}$ is a matrix with the left-singular vectors $\boldsymbol{\varphi}_k$ as its columns and $\mathbf{V}$ is a matrix with the right-singular vectors $\mathbf{v}_k$ as its columns. Note that $\boldsymbol{\Phi}$ has the same size as $\mathbf{Y}_i$, whereas $\mathbf{V}$ has size K by K. A new truncated basis $\bar{\boldsymbol{\Phi}}$ can be constructed from the first N_s right-singular vectors.

As $\boldsymbol{\Phi}$ is an orthogonal matrix, the amplitudes $\mathbf{A}$ corresponding to the K outputs vectors can be found by projecting the snapshot matrix $\mathbf{Y}_i$ in the new basis:

$$\mathbf{A} = \bar{\boldsymbol{\Phi}}^T\mathbf{Y}_i \tag{3}$$

Now each output in the training set can be approximated by multiplying the truncated basis with the corresponding column of the amplitude matrix $\mathbf{a}^{(k)}$ consisting of the N_s amplitudes corresponding to sample point k.

$$\mathbf{y}_i^{(k)} \approx \bar{\boldsymbol{\Phi}}\mathbf{a}^{(k)} \tag{4}$$

3. Build metamodel of output stage i

In order to build a metamodel of the i^{th}-stage output, the N_s amplitudes need to be interpolated. This can be done using e.g. Kriging, Radial Basis Functions or Response Surface Methods.

Using the obtained metamodel the output of stage i can be propagated to the next stage efficiently. This strategy can be repeated until the last stage is reached. When the metamodels of all stages are obtained, they can be used to solve the robust optimization problem.

3 Two-stage demonstrator process

To demonstrate the strategy proposed in the previous Section, a two-stage metal forming process is considered. A nonlinear, plane strain Finite Element (FE) model of both stages is constructed using the FE software MSc Marc and its preprocessor Mentat. In the first process step a sheet metal workpiece is bent downwards, where after it is bent upwards in the second step. A schematic representation of the FE model is presented in Figure 2. The sheet metal is meshed using 1200 quadrilateral elements (N_{elem}) and 1296 nodes (N_{nod}). The elements are fully integrated using four integration points ($N_{ip} = 4 \cdot N_{elem} = 4800$).

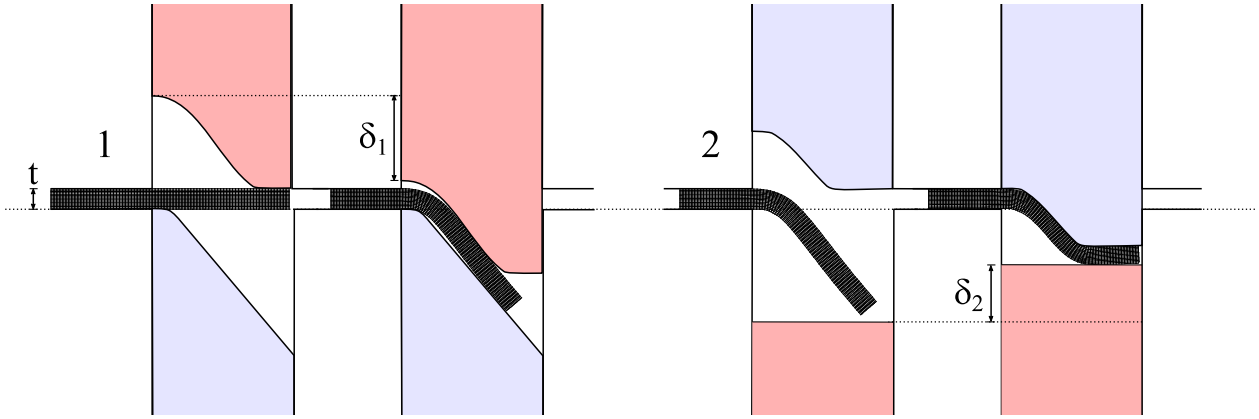


Figure 2: Schematic representation of the two stage FE model.

Following the general description as suggested in Section 2.1, there are only three parameters of interest among all model parameters. The vector with initial noise parameters $\mathbf{z}_0$, only contains the thickness t of the sheet metal. Hence:

$$\mathbf{z}_0 = \{\mathrm{t}\} = 0.300 \pm 0.005 \text{ mm} \tag{5}$$

The vector with the design parameters of the first stage $\mathbf{p}_1$, only contains the punch end distance δ_1:

$$\mathbf{p}_1 = \{\delta_1\} = 1.55 \pm 0.05 \text{ mm} \tag{6}$$

For ease of notation the noise and design parameter are combined to a 2 dimensional parameter space:

$$\mathbf{x} = \{\mathrm{t}, \delta_1\} \tag{7}$$

In the second stage no noise parameters are considered. Note however, that the uncertainty from the initial noise parameter will propagate to the second stage through the output $\mathbf{y}_1$. The vector with the design parameters of the second stage $\mathbf{p}_2$, only contains the punch end distance δ_2:

$$\mathbf{p}_2 = \{\delta_2\} = 2.1 \pm 0.1 \text{ mm} \tag{8}$$

3.1 Obtaining the first stage training set

To sample the first stage, a Latin hypercube sampling is used. According to Steffes-Lai [13] the number of training points needed in a D-dimensional parameter space can be calculated using:

$$K = 2\left[2 + D + \frac{D(D+1)}{2}\right] \tag{9}$$

Which results in 14 training points $\mathbf{x}^{(k)}$ for the first stage. The FE model is evaluated at these training points to obtain the output training data. In order to propagate the variation to the second stage FE model the nodal displacements ($\mathbf{u}$ in x-direction and $\mathbf{v}$ in y-direction), the equivalent plastic strain ($\boldsymbol{\varepsilon}_{eq}^{p}$, in each integration point) and the stress tensor ($\boldsymbol{\sigma}_{nn}$, in each integration point) are needed as output. Note that due to the plane strain FE analysis two components of the stress tensor $\boldsymbol{\sigma}_{23}$ & $\boldsymbol{\sigma}_{31}$ are zero.

3.2 Reducing the first stage output

In order to construct the snapshot matrix the output data from the FE simulation of the first stage corresponding to sample point $\mathbf{x}^{(k)}$ is stored in a $\left(2 \cdot N_{nod} + 5 \cdot N_{ip}\right) = 26592$ by 1 column vector:

$$\mathbf{y}_1^{(k)} = \left\{\mathbf{u} \quad \mathbf{v} \quad \boldsymbol{\varepsilon}_{eq}^{p} \quad \boldsymbol{\sigma}_{11} \quad \boldsymbol{\sigma}_{22} \quad \boldsymbol{\sigma}_{33} \quad \boldsymbol{\sigma}_{12}\right\}^T \tag{10}$$

All column vectors $\mathbf{y}_1^{(k)}$ are collected in the $(2 \cdot N_{nod} + 5 \cdot N_{ip})$ by K snapshot matrix $\mathbf{Y}_1$. This snapshot matrix is normalized between -1 and 1 based on the minimum and maximum value in each row, where after the singular value decomposition is applied. The contribution f_k of each singular value s_k to the snapshot matrix is suggested by Skillicorn [17] as:

$$f_k = \frac{s_k^2}{\sum_{i=1}^{r} s_i^2} \tag{11}$$

Where r is the rank of the snapshot matrix. When all contributions are displayed in a Pareto chart (see Figure 3) on can see that selecting N_s = 3 singular values will retain 80% of the information in the snapshot matrix. Hence, the new basis is truncated to 3 singular values only.

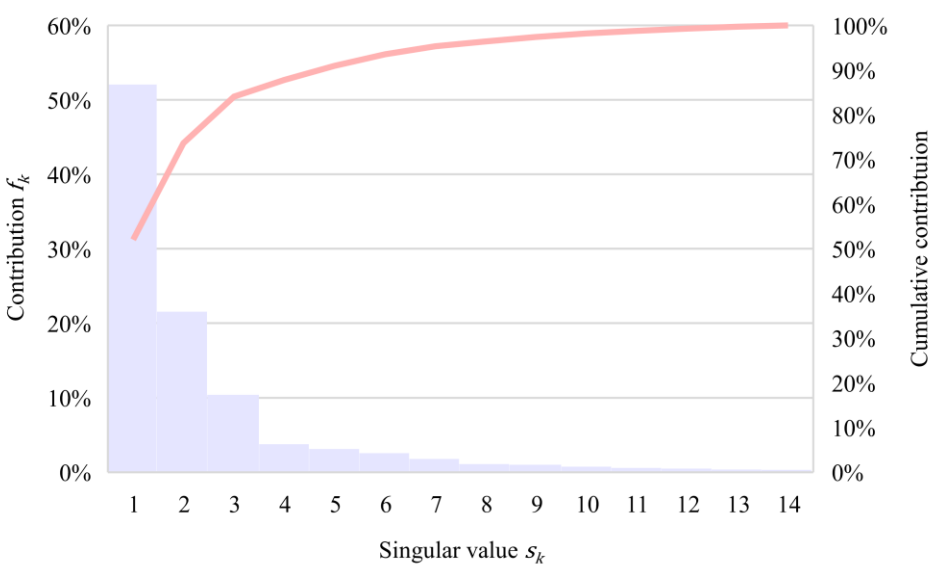


Figure 3: Pareto chart of the contribution of each singular value

After finding the amplitudes as proposed in equation (3) the output the FE simulation corresponding to sample point $\mathbf{x}^{(k)}$ can be approximated by multiplying the left-singular vector with its corresponding amplitude scalar and adding the results:

$$\mathbf{y}_1^{(k)} \approx \boldsymbol{\varphi}_1 \mathrm{a}_1^{(k)} + \boldsymbol{\varphi}_2 \mathrm{a}_2^{(k)} + \boldsymbol{\varphi}_3 \mathrm{a}_3^{(k)} \tag{12}$$

3.3 Building the first stage metamodel

To construct a continuous metamodel of the first stage, the amplitudes corresponding to the training points $\mathbf{a}^{(k)}$ are interpolated using multiquadric radial basis functions (MQ-RBF). A multiquadric radial basis function has the following form:

$$\psi(r) = \sqrt{c_{(k)}^2 + \|\boldsymbol{\theta}(\mathbf{x}^{(k)} - \mathbf{x})\|^2} \tag{13}$$

Resulting in the following SVD MQ-RBF metamodel of the first stage:

$$\hat{\mathbf{y}}_1(\mathbf{x}) = \boldsymbol{\varphi}_1 a_1(\mathbf{x}) + \boldsymbol{\varphi}_2 a_2(\mathbf{x}) + \boldsymbol{\varphi}_3 a_3(\mathbf{x}) \tag{14}$$

To test the quality of the obtained the metamodel a Latin hypercube sampling is used to generate a set of $M = 23$ validation points $\mathbf{x}^{(m)}$. In Figure 4 the displacement field of a validation point is evaluated using both the FE model and the metamodel. In the figure the blue circle is the target, hence the FE model, while the red dot is the result of the metamodel. The displacement field of the metamodel is good agreement with the displacement field of the FE-model. In the zoomed panel the region with the largest deviations is

displayed. In this region, the values from the metamodel are in proximity of the FE-model, however there are still opportunities for further enhancement.

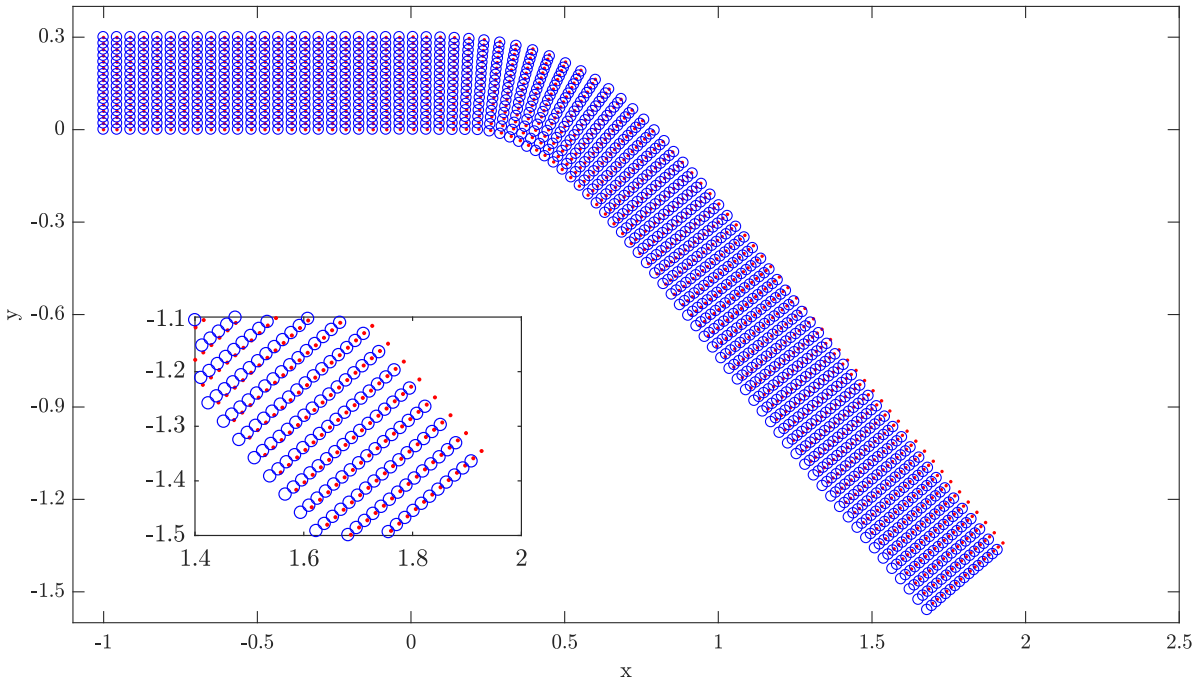


Figure 4: Output of the displacement field $\{\mathbf{u}, \mathbf{v}\}$ from both the first stage SVD MQ-RBF metamodel ($\cdot$) and the FE model (o). The zoomed panel shows the region with the largest RMSE.

A root mean square error (RMSE) can be calculated by subtracting the metamodel evaluated at a validation point $\hat{\mathbf{y}}_1\left(\mathbf{x}^{(m)}\right)$ from the actual FE results $\mathbf{y}_1^{(m)}$:

$$RMSE = \sqrt{\frac{1}{M}\sum_{m=1}^{m}\left(\mathbf{y}_1^{(m)} - \hat{\mathbf{y}}_1(\mathbf{x}^{(m)})\right)^2} \tag{15}$$

The RMSE is calculated for the different types of output data. The relative error in the different types of output data is calculated by dividing the RMSE by the absolute average. All error values are collected in Table 1. Although the relative errors for both $\boldsymbol{\sigma}_{11}$ and $\boldsymbol{\sigma}_{12}$ seem extremely large, the RMSE of all stresses is in the same order as the stresses itself. These first stage results will now be propagated to the next stage.

Output	Average value	RMSE	Relative error
$\mathbf{u}$	-0.1943	0.001166	0.600%
$\mathbf{v}$	-0.4840	0.001529	0.316%
$\boldsymbol{\varepsilon}_{eq}^{p}$	0.02776	9.092e-4	3.28%
$\boldsymbol{\sigma}_{11}$	-11.54	15.74	136%
$\boldsymbol{\sigma}_{22}$	-95.16	12.23	12.9%
$\boldsymbol{\sigma}_{33}$	-38.92	12.43	31.9%
$\boldsymbol{\sigma}_{12}$	1.936	9.139	472%

Table 1: Error values based on metamodel results of 23 validation points.

3.4 Propagating first stage results to the second stage

The results from the validation points $\mathbf{x}^{(m)}$ presented in the previous section from both the first stage SVD MQ-RBF metamodel and the first stage FE model are propagated to the second stage FE model. Unfortunately some of the second stage FE evaluations failed to converge, resulting in a set of $M = 14$ validation points $\mathbf{x}^{(m)}$ only. In Figure 5 the displacement field of a validation point is evaluated using both the FE model and the metamodel. Again the blue circle is the target, hence the first stage FE model propagated to the second stage FE model, while the red dot is the result of the metamodel propagated to the second stage FE model. Again, the displacement field of the metamodel seems in good agreement with the displacement field of the FE-model. Even in the region with the largest deviations the values from the metamodel are in close proximity of the FE-model.

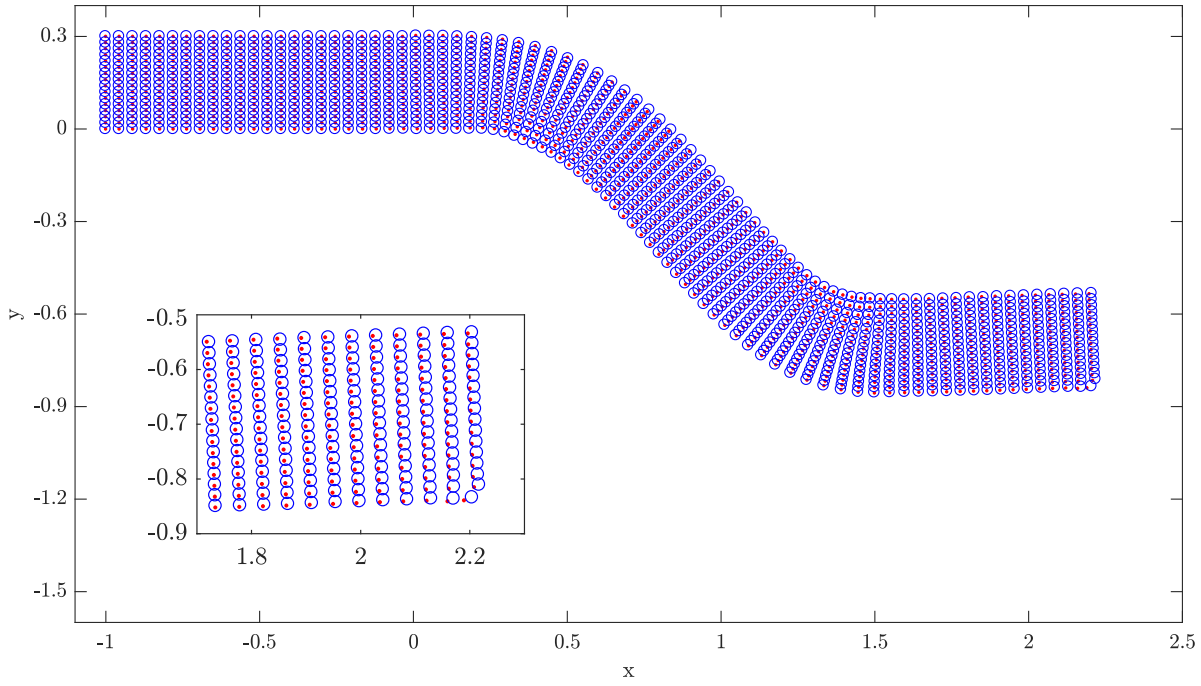


Figure 5: Output of the displacement field $\{\mathbf{u}, \mathbf{v}\}$ from both the first stage SVD MQ-RBF metamodel combined with the second stage FE model (·) and when both stages are modeled using the FE model (o). The zoomed panel shows the region with the largest RMSE.

Output	Average value	RMSE	Relative error
$\mathbf{u}$	-0.1271	0.006360	5.00%
$\mathbf{v}$	-0.3707	0.01279	3.42%
$\boldsymbol{\varepsilon}_{eq}^{p}$	0.05891	0.002258	3.83%
$\boldsymbol{\sigma}_{11}$	-12.35	21.20	172%
$\boldsymbol{\sigma}_{22}$	-94.88	15.36	16.19%
$\boldsymbol{\sigma}_{33}$	-77.01	18.61	24.17%
$\boldsymbol{\sigma}_{12}$	-0.4207	11.71	2785%

Table 2: Error values based on propagated results of 14 validation points

The RMSE of the validation points is calculated for the different types of output data of the second stage. All error values are collected in Table 2. The extremely large error in the metamodel of the $\boldsymbol{\sigma}_{12}$ component of the stress tensor, can be classified as an artificial error. Due to the low average value a change in sign will lead to a large RMSE and therefore a large relative error. The average relative error of the nodal displacements and the equivalent plastic strain is only 2,29% in the first stage and 3,96% in the second stage. Comparing Table 1 and Table 2 one can see that the error in the metamodel will propagate and increase with every stage.

4 Conclusion

The strategy proposed in this work has been used to feasible propagate output data to a subsequent stage. The propagated results after the second stage of both the displacement and equivalent strain fields are in good agreement with the finite element model. The stresses show relatively large deviations.

In future work the same strategy will be used to efficiently describe the second stage output in order to optimize the multi-stage production process.

Acknowledgements

This research project is part of the 'Region of Smart Factories' project and is partially funded by the 'Samenwerkingsverband Noord-Nederland (SNN), Ruimtelijk Economisch Programma'.

References

[1] M. H. A. Bonte, "Optimization Strategies for Metal Forming Process," University of Twente, 2007.
[2] J. H. Wiebenga, "Robust design and optimization of forming processes," University of Twente, 2014.
[3] G. Taguchi, *Introduction to Quality Engineering: Designing Quality into Products and Processes*. Quality Resources, 1986.
[4] M. S. Phadke, *Quality Engineering Using Robust Design*. Prentice Hall, 1989.
[5] R. Suri and K. Otto, "Manufacturing System Robustness Through Integrated Modeling," *J. Mech. Des.*, vol. 123, no. 4, p. 630, 2001.
[6] S. Roy, S. Ghosh, and R. Shivpuri, "A new approach to optimal design of multi-stage metal forming processes with micro genetic algorithms," *Int. J. Mach. Tools Manuf.*, vol. 37, no. I, pp. 29–44, 1997.
[7] H. J. Bong, F. Barlat, J. Lee, M.-G. Lee, and J. H. Kim, "Application of central composite design for optimization of two-stage forming process using ultra-thin ferritic stainless steel," *Met. Mater. Int.*, vol. 22, no. 2, pp. 276–287, 2016.
[8] L. Monostori and Z. J. Viharos, "Hybrid, AI- and simulation-supported optimisation of process chains and production plants," *CIRP Ann. - Manuf. Technol.*, vol. 50, no. 1, pp. 353–356, 2001.
[9] Y. Abe, K. Mori, and O. Ebihara, "Optimisation of the distribution of wall thickness in the multistage sheet metal forming of wheel disks," *J. Mater. Process. Technol.*, vol. 125–126, pp. 792–797, 2002.
[10] B. Denkena and H. Henning, "Multicriteria dimensioning of hard-finishing operations regarding cross-process interdependencies," *J. Intell. Manuf.*, vol. 23, no. 6, pp. 2333–2342, 2012.
[11] J. Kusiak, P. Morkisz, P. Oprocha, W. Pietrucha, and Ł. Sztangret, "On Aggregation of Stages in Multi-criteria Optimization of Chain Structured Processes," in *Lecture Notes in Artificial Intelligence 9692*, vol. Part I, Springer International Publishing Switzerland, 2016, pp. 411–419.
[12] P. Jarosz *et al.*, "A Methodology for Optimization in Multistage Industrial Processes : A Pilot Study," *Math. Probl. Eng.*, vol. 2015, 2015.
[13] D. Steffes-Lai, "Approximation Methods for High Dimensional Simulation Results Parameter Sensitivity Analysis and Propagation of Variations for Process Chains," University of Cologne, 2014.
[14] D. Sun, F. Andrieux, and M. Feucht, "Simulation of the process chain from forming to crash taking

into account stochastic aspects," *LS-DYNA Forum, Bamb. 2010*, pp. 1–10, 2010.
[15] X. Du and W. Chen, "Efficient Uncertainty Analysis Methods for Multidisciplinary Robust Design," *AIAA J.*, vol. 40, no. 3, pp. 545–552, 2002.
[16] O. Nejadseyfi, H. J. M. Geijselaers, and A. H. Van Den Boogaard, "Efficient calculation of uncertainty propagation with an application in robust optimization of forming processes," *AIP Conf. Proc.*, vol. 1896, 2017.
[17] D. Skillicorn, *Understanding Complex Datasets: Data Mining with Matrix Decompositions (Chapman & Hall/Crc Data Mining and Knowledge Discovery Series)*. 2007.
[18] V. Buljak, "Proper Orthogonal Decomposition and Radial Basis Functions Algorithm for Diagnostic Procedure Based on Inverse Analysis," *FME Trans.*, vol. 38, no. 3, pp. 129–136, 2010.
[19] A. Chatterjee, "An introduction to the proper orthogonal decomposition," *Curr. Sci.*, vol. 78, no. 7, pp. 808–817, 2000.

On inverse fuzzy arithmetical problems in uncertainty analysis

D. Hose, M. Hanss
University of Stuttgart, Institute of Engineering and Computational Mechanics,
Pfaffenwaldring 9, 70569 Stuttgart, Germany
e-mail: **{dominik.hose, michael.hanss}@itm.uni-stuttgart.de**

Abstract
This contribution proposes an intuitive and easy-to-compute method for the solution of inverse problems in fuzzy arithmetic. The surprisingly perspicuous main result is motivated and thoroughly discussed. An illustrative application to parameter identification based on modal analysis is provided.

1 Introduction

By now, fuzzy arithmetic, i.e. the forward propagation of uncertainties in a possibilistic context, has become a relatively well-explored discipline. Several methods exist for determining (or approximating) the possibilistic output distribution of a fuzzy variable according to the extension principle [1] if this output variable is dependent on a number of fuzzy input variables via a functional relationship. To name a few, for example the exact solution by optimization, the transformation method or interval arithmetic can be used, each with its own advantages, limitations and drawbacks. An overview of these methods is given in [2]. Yet, the inverse problem, i.e. inferring input distributions from a given output, has not received much attention even though being equally important.

Inverse problems typically arise in many scientific areas, usually where a set of parameters (lumped or concentrated) is to be estimated [3]. Common examples are medical imaging applications, the identification of physical or non-physical parameters resulting from simplifications in mechanical models, e.g. stiffness, damping or friction coefficients, or feasibility problems, where design specifications have to be met [4].

Generally, two scenarios where inverse problems play a major role have to be distinguished:

As an analogon to statistics in the probabilistic framework, the first scenario is concerned with inferring possibility distributions from crisp samples either directly or in order to determine e.g. regression model parameters. In this case, the output distribution is not given directly; instead, it has to be inferred in the process itself. These problems are treated e.g. in [5], [6], [7] or [8]. In the second scenario, the membership function of the output is given directly and the distributions of the input variables have to be inferred.

The present contribution is concerned with the latter scenario. The authors are only aware of one line of research that has dealt with finding those inverse distributions. In [9], Hukuhara introduces the Hukuhara or H-difference for set-valued functions which Bede and Stefanini use in [10] to propose a generalized differentiability of fuzzy-valued functions. To be able to define a difference quotient, they need to define the difference of two fuzzy sets, which is essentially the inverse to the addition operator. This approach is further generalized in [11] where an inverse to the multiplication is presented.

A solution procedure for fuzzily stated optimization problems has already been described in [12] where – among other things – fuzzy feasible sets are identified. However, it can be extended to solve more general inverse problems in fuzzy arithmetic. This contribution attempts to motivate the general solution and to prove its usability in estimation problems.

Notably, the presented results suggest that inverse fuzzy arithmetic is much more intuitive than its forward counterpart. The proposed solution can be obtained under minimal assumptions and without formulating and solving costly optimization problems, and it is described by the intelligible Eq. (13) in Section 4 forming the core of this contribution. To some extent, it is even capable of mitigating wrongful assumptions about the independence of the output distributions in question, and by introducing a relaxation to the inverse problem it can overcome certain problems of ill-posedness.

2 Fuzzy Variables in Possibility Theory

Fuzzy variables are the possibilistic counterpart to stochastic random variables. However, they can be motivated entirely by themselves. In contrast to classical set theory, fuzzy set theory allows gradual memberships of elements to a (fuzzy) subset $\widetilde{Y}$ of the universal set $\mathcal{Y}$ (here $\mathcal{Y} = \mathbb{R}^n$). Its membership function

$$\mu_{\widetilde{Y}} : \mathcal{Y} \to [0, 1] \tag{1}$$

is a generalization of the characteristic function in classical, ordinary set theory and uniquely defines the fuzzy set in terms of which elements belong fully, partially or not at all to it. The set of all fuzzy sets on $\mathcal{Y}$ is denoted $\mathcal{F}\mathcal{Y}$.

The support

$$\operatorname{supp}\left[\widetilde{Y}\right] = \operatorname{cl}\left(\left\{y \in \mathcal{Y} : \mu_{\widetilde{Y}}(y) > 0\right\}\right) \tag{2}$$

of a fuzzy set $\widetilde{Y} \in \mathcal{F}\mathcal{Y}$ is the closure of the set of all its elements with non-zero membership.

It is a special case of the α-cuts

$$\operatorname{cut}_\alpha\left[\widetilde{Y}\right] = \left\{y \in \mathcal{Y} : \mu_{\widetilde{Y}}(y) \geq \alpha\right\} \tag{3}$$

denoting the set of all its elements with membership α or higher.

Several operations on fuzzy sets can be defined consistently with their classical counterparts if the characteristic function acts as the fuzzy membership function. In particular, a fuzzy set $\widetilde{Y} \in \mathcal{F}\mathcal{Y}$ is said to be included in the fuzzy set $\widetilde{Z} \in \mathcal{F}\mathcal{Y}$, i.e. $\widetilde{Y} \subseteq \widetilde{Z}$, if the respective membership functions satisfy

$$\mu_{\widetilde{Y}}(y) \leq \mu_{\widetilde{Z}}(y) \qquad \forall y \in \mathcal{Y}\,. \tag{4}$$

Their intersection $\widetilde{X} = \widetilde{Y} \cap \widetilde{Z}$ is given by the element-wise minimum of the respective membership values

$$\mu_{\widetilde{X}}(y) = \min\left\{\mu_{\widetilde{Y}}(y), \mu_{\widetilde{Z}}(y)\right\} \qquad \forall y \in \mathcal{Y}\,. \tag{5}$$

Furthermore, it is important to distinguish between independent and dependent fuzzy variables. The (univariate) fuzzy variables $\tilde{x}_1, \ldots, \tilde{x}_n \in \mathcal{F}\mathbb{R}$ are called independent if the membership function $\mu_{\tilde{\boldsymbol{x}}}$ of the (multivariate) fuzzy variable $\tilde{\boldsymbol{x}} \in \mathcal{F}\mathbb{R}^n$ satisfies

$$\mu_{\tilde{\boldsymbol{x}}}(\boldsymbol{x}) = \min_{i=1,\ldots,n}\left\{\mu_{\tilde{x}_1}(x_1), \ldots, \mu_{\tilde{x}_n}(x_n)\right\} \qquad \forall\, \boldsymbol{x} \in \mathbb{R}^n\,, \tag{6}$$

where $\mu_{\tilde{x}_1}, \ldots, \mu_{\tilde{x}_n}$ are the marginal distributions of $\tilde{x}_1, \ldots, \tilde{x}_n$, respectively. To distinguish one from the other, the membership function $\mu_{\tilde{\boldsymbol{x}}}$ is also called the *joint* membership function.

For a thorough review of fuzzy set theory refer to [2].

In [13], Zadeh shows that fuzzy set theory serves as a basis for an alternative to probability theory for the computerized processing of uncertainty, namely possibility theory, which is thoroughly explained in [14].

A possibility measure is any measure $\operatorname{Pos} : 2^{\mathcal{X}} \to [0, 1]$ on the universe of discourse $\mathcal{X}$ satisfying

1. $\mathrm{Pos}(\mathcal{X}) = 1$,
2. $\mathrm{Pos}(\emptyset) = 0$ and
3. $\mathrm{Pos}(A \cup B) = \max\{\mathrm{Pos}(A), \mathrm{Pos}(B)\}$ for two disjunct subsets $A, B \subseteq \mathcal{X}$.

One interpretation of this measure is that it quantifies the feasibility or ease with which an event occurs as opposed to e.g. the frequentist interpretation of probability theory. For instance, the possibility (ease) of a sprinter beating the world record is fundamentally different from the probability (frequency) of the same event.

From the definition, it follows that a possibility measure is defined by its behavior on the elementary events of $\mathcal{X}$ according to

$$\mathrm{Pos}(A) = \sup_{x \in A} \mathrm{Pos}(\{x\}) \qquad \forall\, A \subseteq \mathcal{X} \tag{7}$$

just like probability theory. This allows to define a possibility distribution $\pi : \mathcal{X} \to [0, 1]$ given by

$$\pi(x) = \mathrm{Pos}(\{x\}) \qquad \forall x \in \mathcal{X}\,. \tag{8}$$

Consequently, one obtains

$$\mathrm{Pos}(A) = \sup_{x \in A} \pi(x) \qquad \forall\, A \subseteq \mathcal{X}\,. \tag{9}$$

Now, let $\mathcal{X} = \mathcal{Y} = \mathbb{R}^n$. The fuzzy membership function $\mu_{\tilde{\boldsymbol{x}}}$ of a (multivariate) fuzzy variable $\tilde{\boldsymbol{x}} \in \mathcal{F}\mathbb{R}^n$ can be interpreted as a possibility distribution function

$$\pi(\boldsymbol{x}) = \mu_{\tilde{\boldsymbol{x}}}(\boldsymbol{x}) \tag{10}$$

inducing a possibility measure similar to how a probabilistically distributed stochastic variable induces a probability measure.

3 Forward Fuzzy Arithmetic

Fuzzy arithmetic, i.e. the forward propagation of fuzzy sets through deterministic mappings, is fundamentally based on the extension principle formulated by Zadeh in [1].

Let $f : \mathbb{R}^n \to \mathbb{R}^m$ be a mapping and let $\tilde{\boldsymbol{x}} \in \mathcal{F}\mathbb{R}^n$ be a fuzzy set with the membership function $\mu_{\tilde{\boldsymbol{x}}}$. The membership function $\mu_{\tilde{\boldsymbol{y}}}$ of the fuzzy output $\tilde{\boldsymbol{y}} \in \mathcal{F}\mathbb{R}^m$ defined by

$$\tilde{\boldsymbol{y}} = f(\tilde{\boldsymbol{x}}) \tag{11}$$

is then given by

$$\mu_{\tilde{\boldsymbol{y}}}(\boldsymbol{y}) = \sup_{\boldsymbol{x}:\boldsymbol{y}=f(\boldsymbol{x})} \mu_{\tilde{\boldsymbol{x}}}(\boldsymbol{x})\,. \tag{12}$$

If f is not surjective, it is not possible to find an $\boldsymbol{x}$ satisfying $\boldsymbol{y} = f(\boldsymbol{x})$ for all $\boldsymbol{y} \in \mathbb{R}^m$. In this case, the membership of the respective element $\boldsymbol{y}$ is simply zero. A proof of the extension principle employing possibilistic arguments is given by Liu in [15].

Naturally, the evaluation of the extension principle can prove rather difficult as it requires the solution of a (possibly non-convex) optimization problem. Consequently, many approaches to a more efficient computation of $\tilde{\boldsymbol{y}}$ have been proposed. A broad overview on the available techniques – including standard fuzzy arithmetic, interval arithmetic, arithmetic with L-R or discrete fuzzy numbers, and finally the transformation method – is given in [2].

In contrast, it will be shown that inverse fuzzy arithmetic yields a much more straightforward solution.

4 Inverse Fuzzy Arithmetic

Given a possibilistic output variable $\tilde{\boldsymbol{y}} \in \mathcal{F}\mathbb{R}^m$ and a function $f : \mathbb{R}^n \to \mathbb{R}^m$, the corresponding inverse problem is to find the membership function $\mu_{\tilde{\boldsymbol{x}}}$ of the possibilistic input variable $\tilde{\boldsymbol{x}} \in \mathcal{F}\mathbb{R}^n$.

Throughout this section, it will be shown for various cases that the solution $\tilde{\boldsymbol{x}}$ to the inverse problem which requires minimal assumptions is given by

$$\mu_{\tilde{\boldsymbol{x}}}(\boldsymbol{x}) = \mu_{\tilde{\boldsymbol{y}}}(f(\boldsymbol{x})) \qquad \forall\, \boldsymbol{x} \in \mathbb{R}^n\,. \tag{13}$$

The most intuitive requirement for the solution of the inverse problem is that the solution ought to be consistent with the extension principle. However, this requirement alone is not sufficient to uniquely determine the solution $\tilde{\boldsymbol{x}}$, and thus the problem is generally ill-posed.

Example 1. *Let $f : x \mapsto x^2$ and $\tilde{y}$ be given by*

$$\mu_{\tilde{y}}(y) = \begin{cases} 1 - |y - \frac{1}{2}| & \forall\, y \in [0, \frac{3}{2}], \\ 0 & \text{else} \end{cases} \tag{14}$$

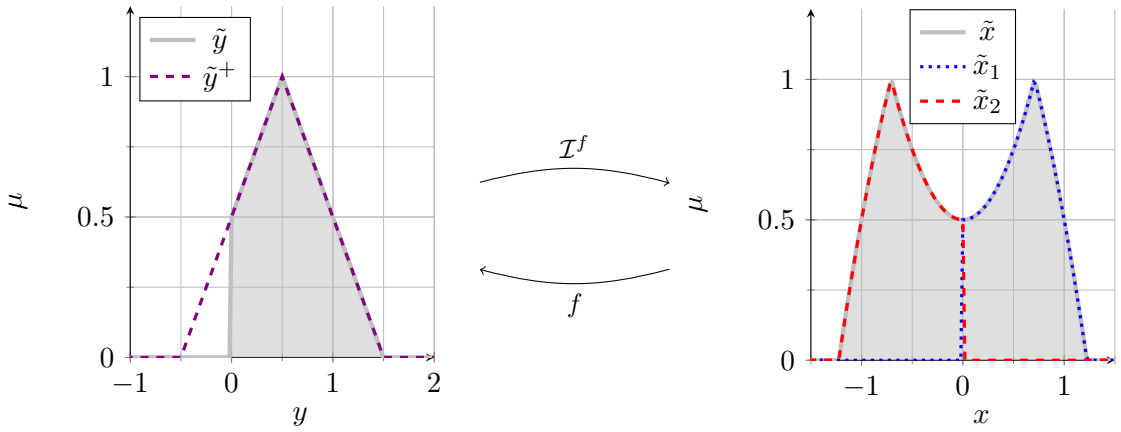
as shown in Fig. 1a. One possible input variable $\tilde{x}_1$ is given by the membership function

$$\mu_{\tilde{x}_1}(x) = \begin{cases} 1 - |x^2 - \frac{1}{2}| & \forall\, x \in [0, \frac{\sqrt{3}}{2}], \\ 0 & \text{else.} \end{cases} \tag{15}$$

However, the input variable $\tilde{x}_2$ given by the membership function

$$\mu_{\tilde{x}_2}(x) = \begin{cases} 1 - |x^2 - \frac{1}{2}| & \forall\, x \in [-\frac{\sqrt{3}}{2}, 0], \\ 0 & \text{else} \end{cases} \tag{16}$$

also satisfies the extension principle (cf. Fig. 1b). Since $\tilde{y} = f(\tilde{x}_1) = f(\tilde{x}_2)$, it is not clear which solution is the 'correct' one.



(a) Reference outputs $\tilde{y}$ and $\tilde{y}^+$.

(b) Inverse solutions $\tilde{x}_1$, $\tilde{x}_2$ and $\tilde{x}$.

Figure 1: Illustration of Examples 1–4.

In the general case, an infinite number of solutions exists. The extension principle merely provides an upper bound on the membership function of $\tilde{\boldsymbol{x}}$ since the equation

$$\mu_{\tilde{\boldsymbol{y}}}(\boldsymbol{y}) = \sup_{\boldsymbol{x}:\boldsymbol{y}=f(\boldsymbol{x})} \mu_{\tilde{\boldsymbol{x}}}(\boldsymbol{x}) \tag{17}$$

implies that for all $\boldsymbol{x}$ satisfying $\boldsymbol{y} = f(\boldsymbol{x})$ their membership value is bounded by $\mu_{\tilde{\boldsymbol{y}}}(\boldsymbol{y})$, i.e.

$$\mu_{\tilde{\boldsymbol{x}}}(\boldsymbol{x}) \leq \mu_{\tilde{\boldsymbol{y}}}(\boldsymbol{y}) \qquad \forall\, \boldsymbol{x}, \boldsymbol{y} \,:\, \boldsymbol{y} = f(\boldsymbol{x}) \;, \tag{18}$$

which can be rewritten to

$$\mu_{\tilde{\boldsymbol{x}}}(\boldsymbol{x}) \leq \mu_{\tilde{\boldsymbol{y}}}(f(\boldsymbol{x})) \qquad \forall\, \boldsymbol{x} \;. \tag{19}$$

In the previous example, this bound is given by $\mu_{\tilde{x}}$, the point-wise maximum of $\mu_{\tilde{x}_1}$ and $\mu_{\tilde{x}_2}$ (cf. Fig. 1b). All admissible distributions are located underneath, but *without further information, it is not justifiable to choose one over the other*.

For the motivation of the solution given in Eq. (13) consider the following: If $\tilde{y}$ was a crisp number $\tilde{y} = y$, the solution had to be expressed as $x = \pm\sqrt{y}$. This can be interpreted as selecting the upper bound $\tilde{x}$ from before as the general solution and motivates the choice of Eq. (13) which will be called the most general solution to the inverse problem.

The operator producing the most general solution to the inverse problem of fuzzy arithmetic shall be denoted

$$\mathcal{I}^f : \mathcal{F}\mathbb{R}^m \to \mathcal{F}\mathbb{R}^n \tag{20}$$

and is defined by

$$\mu_{\mathcal{I}^f(\tilde{\boldsymbol{y}})}(\boldsymbol{x}) = \mu_{\tilde{\boldsymbol{y}}}(f(\boldsymbol{x})) \qquad \forall\, \boldsymbol{x} \in \mathbb{R}^n. \tag{21}$$

Example 2 (Example 1 revisited)**.** *Let f and $\tilde{y}$ be defined as in Example 1. Then, the most general solution $\tilde{x} = \mathcal{I}^f(\tilde{y})$ possesses the membership function (cf. Fig. 1b)*

$$\mu_{\tilde{x}}(x) = \begin{cases} 1 - |x^2 - \frac{1}{2}| & \forall\, x \in [-\frac{\sqrt{3}}{2}, \frac{\sqrt{3}}{2}], \\ 0 & \text{else.} \end{cases} \tag{22}$$

Notice that finding the most general solution to the inverse problem only requires one evaluation of f for each element as opposed to the theoretically infinite number of evaluations required to solve the forward propagation problem.

In the case where f is bijective (injective and surjective), the inverse operator is given by $\mathcal{I}^f = f^{-1}$, and thus the most general solution operator is equivalent to a fuzzy arithmetical evaluation of

$$\tilde{\boldsymbol{x}} = f^{-1}(\tilde{\boldsymbol{y}}) \,. \tag{23}$$

Example 3 (Example 1 revisited once more)**.** *Let f, $\tilde{y}$ and $\tilde{x}_1$ be defined as in Example 1, but f restricted to input arguments from the negative reals $f : \mathbb{R}_0^- \to \mathbb{R}_0^+$. Then the inverse of f is given by $f^{-1} : y \mapsto -\sqrt{y}$, and accordingly the unique solution $\tilde{x}_2$ to the inverse problem is given by (cf. Fig. 1b)*

$$\tilde{x}_2 = -\sqrt{\tilde{y}}. \tag{24}$$

However, Eq. (13) does not guarantee that the extension principle is actually fulfilled in the general case. The fundamental question is whether the support of $\tilde{\boldsymbol{y}}$ is contained in the image of f. If the support of $\tilde{\boldsymbol{y}}$ is not contained therein, the most general solution to the inverse problem can still be computed, but it is not the true inverse solution anymore in the sense that it fulfills the extension principle. Instead, it becomes the maximum possible inverse solution whose forward propagation

$$f\left(\mathcal{I}^f(\tilde{\boldsymbol{y}})\right) \subseteq \tilde{\boldsymbol{y}} \tag{25}$$

is a fuzzy subset of the reference output.

To show this, let $\tilde{\boldsymbol{y}}^{\text{in}}$ and $\tilde{\boldsymbol{y}}^{\text{out}}$ be defined as the partition of $\tilde{\boldsymbol{y}}$ with the support contained inside the image of f and outside of it, respectively. Then, the most general inverse solution to $\tilde{\boldsymbol{y}}^{\text{in}}$ can be computed, yielding $f\left(\mathcal{I}^f\left(\tilde{\boldsymbol{y}}^{\text{in}}\right)\right) = \tilde{\boldsymbol{y}}^{\text{in}}$. However, for each $\boldsymbol{y} \in \operatorname{supp}\left(\tilde{\boldsymbol{y}}^{\text{out}}\right)$ it is impossible to find an $\boldsymbol{x}$ such that $\boldsymbol{y} = f(\boldsymbol{x})$ and thus

$$\mu_{\tilde{\boldsymbol{y}}^{\text{out}}}(\boldsymbol{y}) = 0 \qquad \forall\, \boldsymbol{y} \in \mathbb{R}^m\,. \tag{26}$$

In summary,

$$\mu_{f\left(\mathcal{I}^f(\tilde{\boldsymbol{y}})\right)}(\boldsymbol{y}) = \begin{cases} \mu_{\tilde{\boldsymbol{y}}}(\boldsymbol{y}) & \text{if } \boldsymbol{y} \in \operatorname{supp}\left(\tilde{\boldsymbol{y}}^{\text{in}}\right) \\ 0 & \text{else,} \end{cases} \tag{27}$$

and thus

$$\mu_{f\left(\mathcal{I}^f(\tilde{\boldsymbol{y}})\right)}(\boldsymbol{y}) \leq \mu_{\tilde{\boldsymbol{y}}}(\boldsymbol{y}) \qquad \forall\, \boldsymbol{y} \in \mathbb{R}^m. \tag{28}$$

The following example will further illustrate this.

Example 4 (Example 1 revisited again)**.** *Let f be defined as in Example 1 and $\tilde{y}^+$ be given by the membership function*

$$\mu_{\tilde{y}^+}(y) = \begin{cases} 1 - |y - \frac{1}{2}| & \forall\, y \in [-\frac{1}{2}, \frac{3}{2}], \\ 0 & \text{else} \end{cases} \tag{29}$$

The support of $\tilde{y}^+$ is the interval $[-\frac{1}{2}, \frac{3}{2}]$ and is therefore not contained in the image of f which is composed of only the positive reals $\mathbb{R}_0^+$. The most general solution $\tilde{x} = \mathcal{I}^f(\tilde{y}^+)$ is still given by Eq. (22)*, but one observes that $\tilde{y} = f(\tilde{x}) \neq \tilde{y}^+$. Instead $\tilde{y}$ is contained in $\tilde{y}^+$, i.e. $\tilde{y} \subseteq \tilde{y}^+$ (cf. Fig. 1a). In order to solve this problem, one would have to admit complex arguments of f.*

Notice that this is again consistent with the crisp case where e.g. $x^2 = -1$ cannot be solved if only real values $x \in \mathbb{R}$ are admissible.

So far, it has been assumed that only one output vector $\tilde{\boldsymbol{y}}$ is given, i.e. a joint membership function for all of the outputs. However, this requires knowing the interdependence among the fuzzy output variables beforehand. Instead, it seems more intuitive that the marginal memberships of the outputs $\tilde{y}_i$ for $i = 1, \ldots, m$ are known individually, without any assumptions about possible dependencies.

In the general case, it is not guaranteed that $\tilde{x}$ is a normalized fuzzy variable in the sense that its membership function attains one for some element. As illustrated below, this degree of consistency of a subnormalized possibility distribution [16]

$$\operatorname{cons}(\tilde{\boldsymbol{x}}) = \sup_{\boldsymbol{x}} \mu_{\tilde{\boldsymbol{x}}}(\boldsymbol{x}) \tag{30}$$

is useful for assessing the well-posedness of the inverse problem, i.e. how consistent the chosen model f and the fuzzy output $\tilde{y}$ are.

From just the marginal memberships it is not possible to infer the underlying joint distributions – they have to be assumed to be independent. The maximum consistent inverse solution $\tilde{\boldsymbol{x}}$ to the corresponding inverse problem in fuzzy arithmetic is given by constructing $\tilde{\boldsymbol{y}}$ as an independent multivariate output distribution from the marginal outputs according to

$$\mu_{\tilde{\boldsymbol{y}}}(\boldsymbol{y}) = \min_{i=1,\ldots,m} \mu_{\tilde{y}_i}(y_i) \qquad \forall\, \boldsymbol{y} \in \mathbb{R}^m \tag{31}$$

and then finding the corresponding maximum possible inverse solution for

$$f : \boldsymbol{x} \mapsto \begin{pmatrix} f_1(\boldsymbol{x}) \\ \vdots \\ f_m(\boldsymbol{x}) \end{pmatrix}\,. \tag{32}$$

If $\tilde{z}_i = f_i(\tilde{\boldsymbol{x}})$, then

$$\begin{aligned}
\mu_{\tilde{z}_i}(z_i) &\overset{\text{Ext. Prin.}}{=} \sup_{\boldsymbol{x}\in\mathbb{R}^n\,:\,z_i=f_i(\boldsymbol{x})} \mu_{\boldsymbol{x}}(x) \\
&\overset{(13)}{=} \sup_{\boldsymbol{x}\in\mathbb{R}^n\,:\,z_i=f_i(\boldsymbol{x})} \mu_{\tilde{\boldsymbol{y}}}(f(\boldsymbol{x})) \qquad\qquad \forall\, i=1,\dots,m \\
&\overset{(31)}{=} \sup_{\boldsymbol{x}\in\mathbb{R}^n\,:\,z_i=f_i(\boldsymbol{x})} \underbrace{\min_{j=1,\dots,m} \mu_{\tilde{y}_j}(f_j(\boldsymbol{x}))}_{\leq \mu_{\tilde{y}_i}(f_i(\boldsymbol{x}))} \\
&\leq \sup_{\boldsymbol{x}\in\mathbb{R}^n\,:\,z_i=f_i(\boldsymbol{x})} \mu_{\tilde{y}_i}(f_i(\boldsymbol{x})) \qquad = \mu_{\tilde{y}_i}(z_i)
\end{aligned} \tag{33}$$

and thus $\tilde{z}_i \subseteq \tilde{y}_i$. Hence, the forward propagation of $\tilde{\boldsymbol{x}}$ yields a fuzzy subset of the marginal reference output

$$f_i(\tilde{\boldsymbol{x}}) \subseteq \tilde{y}_i \qquad \forall\, i=1,\dots,m\,. \tag{34}$$

In an engineering context, this makes sense because in this way the resulting outputs will always have memberships below the specified feasibility and are therefore guaranteed to not exceed any limits, leading to robust inverse solutions.

Example 5. *Let f be a mapping*

$$\begin{aligned} f : \mathbb{R} &\to \mathbb{R}^2\,, \\ x &\mapsto \begin{bmatrix} x^2 \\ \frac{1}{2}x \end{bmatrix} \end{aligned} \tag{35}$$

and let the marginal distributions of $\tilde{y}_1$ and $\tilde{y}_2$ be given by the membership functions (cf. Fig. 2a)

$$\mu_{\tilde{y}_1}(y_1) = \begin{cases} 1-y_1 & \forall\, y_1 \in [0,1], \\ 0 & \text{else} \end{cases} \tag{36}$$

and (cf. Fig. 2b)

$$\mu_{\tilde{y}_2}(y_2) = \begin{cases} 1-\frac{4}{3}|y_2| & \forall\, y_2 \in [-\frac{3}{4},\frac{3}{4}], \\ 0 & \text{else.} \end{cases} \tag{37}$$

The respective solutions $\tilde{x}^1 = \mathcal{I}^{f_1}(\tilde{y}_1)$ and $\tilde{x}^2 = \mathcal{I}^{f_2}(\tilde{y}_2)$ are given by

$$\mu_{\tilde{x}^1}(x) = \begin{cases} 1-x^2 & \forall\, x \in [-1,1], \\ 0 & \text{else} \end{cases} \tag{38}$$

and

$$\mu_{\tilde{x}^2}(x) = \begin{cases} 1-\frac{2}{3}|x| & \forall\, x \in [-\frac{3}{2},\frac{3}{2}], \\ 0 & \text{else.} \end{cases} \tag{39}$$

Consequently, the final solution $\tilde{x}$ is given by the membership function (cf. Fig. 2c)

$$\mu_{\tilde{x}}(x) = \begin{cases} 1-\frac{|x|}{2} & \forall\, |x| \leq \frac{1}{2}, \\ 1-x^2 & \forall\, \frac{1}{2} \leq |x| \leq 2, \\ 0 & \text{else,} \end{cases} \tag{40}$$

which is shown in Fig. 2c. In Figs. 2a and 2b, it also becomes apparent that the forward propagation of the inverse solution is only a fuzzy subset of the reference output, i.e.

$$f_1(\tilde{\boldsymbol{x}}) \subseteq \tilde{y}_1 \qquad \textit{and} \qquad f_2(\tilde{\boldsymbol{x}}) \subseteq \tilde{y}_2. \tag{41}$$

From the example it can be deduced that this is equal to constructing $\tilde{\boldsymbol{x}}$ from the m marginal inverse solutions

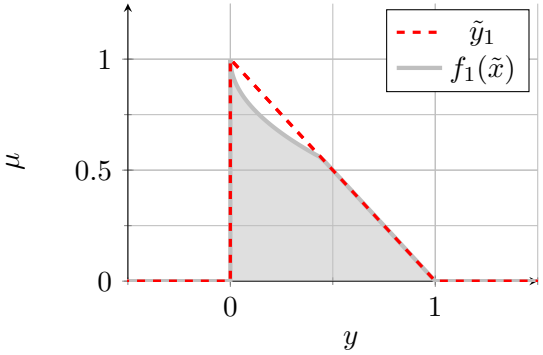
$$\tilde{\boldsymbol{x}}^i = \mathcal{I}^{f_i}\left(\tilde{y}_i\right) \qquad \forall\, i = 1, \ldots, m \tag{42}$$

by the fuzzy set intersection

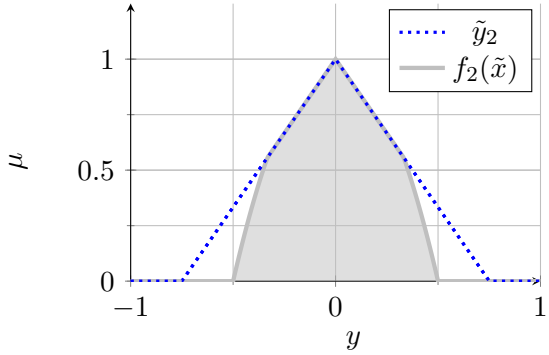
$$\tilde{\boldsymbol{x}} = \bigcap_{i=1,\ldots,m} \tilde{\boldsymbol{x}}_i \,, \tag{43}$$

which again makes sense since the difficulty of solving a problem is generally determined by the maximum difficulty of any subtask that is needed for the overall solution. If a soccer team has to beat several opposing teams to win a tournament, the possibility of becoming the champion is generally determined by the strength of the best opponent (neglecting other effects such as exhaustion etc.).

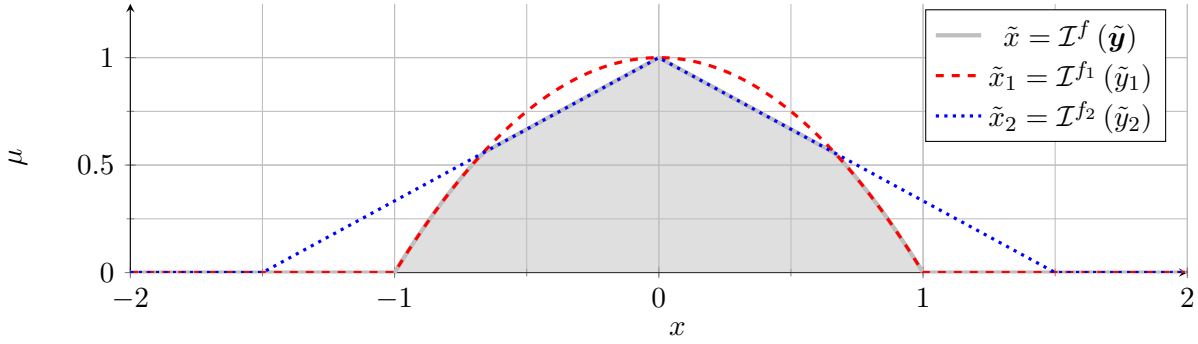
The application in Section 5 will show that this form of relaxing the problem can actually overcome certain problems of ill-posedness that typically arise in inverse problems.



(a) Reference output $\tilde{y}_1$ and forward propagation of the maximum consistent input distribution.



(b) Reference output $\tilde{y}_2$ and forward propagation of the maximum consistent input distribution.



(c) Intermediate solutions $\tilde{x}_1$ and $\tilde{x}_2$ and maximum consistent input distribution $\tilde{x}$.

Figure 2: Illustration of Example 5.

5 Application

As mentioned above, one instance where inverse problems arise is the estimation of model parameters. The presented solution can be employed in scenarios where the present uncertainties do not arise due to stochastic noise, but rather from incomplete knowledge of the system.

For example, consider a two-mass oscillator consisting of two masses m_1 and m_2 attached to one another, as well as to two walls, by means of three springs with the stiffnesses c_1, c_2 and c_3 as shown in Fig. 3. The

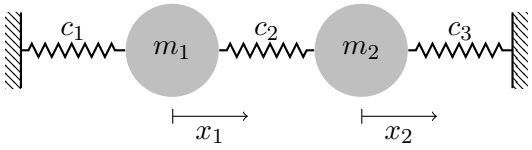


Figure 3: Setup of the two-mass oscillator.

equations of motion governing the dynamics of the two masses, i.e. their displacements $\boldsymbol{x} = \begin{bmatrix} x_1 & x_2 \end{bmatrix}^{\mathrm{T}}$, is given by the second-order linear time-invariant differential equation

$$\underbrace{\begin{bmatrix} m_1 & 0 \\ 0 & m_2 \end{bmatrix}}_{\boldsymbol{M}} \ddot{\boldsymbol{x}} + \underbrace{\begin{bmatrix} c_1 + c_2 & -c_2 \\ -c_2 & c_2 + c_3 \end{bmatrix}}_{\boldsymbol{K}} \boldsymbol{x} = \boldsymbol{0} \,. \tag{44}$$

Furthermore, let

$$f \;:\quad (m_1, m_2, c_1, c_2, c_3) \mapsto (\omega_1, \omega_2) \tag{45}$$

be the operator that produces the eigenfrequencies of the system depending on the system parameters, i.e. the positive solutions $\omega_{1,2}$ of

$$\det\left(\boldsymbol{K} - \omega^2 \boldsymbol{M}\right) = \left(c_1 + c_2 - \omega^2 m_1\right)\left(c_2 + c_3 - \omega^2 m_2\right) - c_2^2 \stackrel{!}{=} 0 \,. \tag{46}$$

For identification purposes, an experiment by simulation with the parameter values and initial conditions given in Table 1 is performed.

Table 1: Parameter values of the two-mass oscillator.

Masses		Stiffnesses			Initial Conditions			
m_1	m_2	c_1	c_2	c_3	$x_{1,0}$	$x_{2,0}$	$\dot{x}_{1,0}$	$\dot{x}_{2,0}$
2.1 kg	1.9 kg	150.0 N/m	100.0 N/m	50.0 N/m	−0.1 m	0.0 m	0.0 m/s	0.0 m/s

The mass m_1 is initially displaced and released. Its position can be measured by a sensor which is perturbed by some white noise (zero mean, $\sigma^2 = 1.0 \cdot 10^{-4}\,\mathrm{m}^2$ variance). Samples are collected for a time period of $T = 20\,\mathrm{s}$ at a sampling frequency of $\nu_\mathrm{s} = 100.0\,\mathrm{Hz}$. The measured output is depicted in Fig. 4.

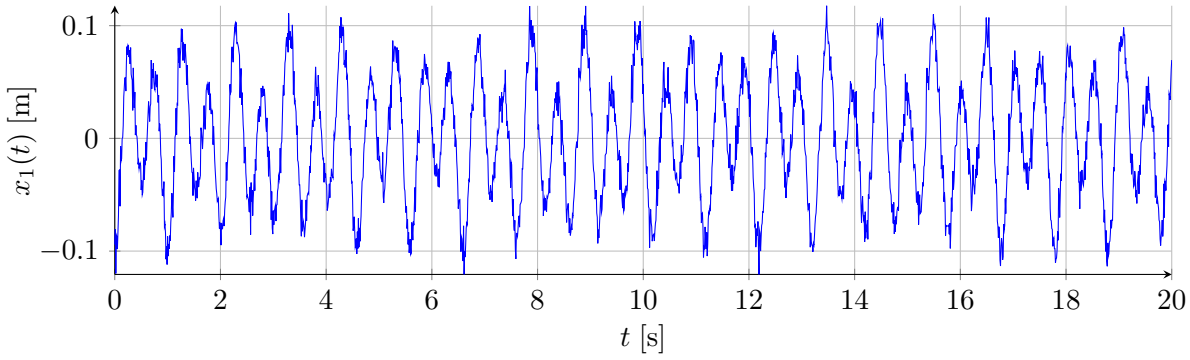


Figure 4: Measured displacement x_1 of mass m_1.

The frequency spectrum presented in Fig. 5 shows that the true eigenfrequencies of the system are not exactly deducible from the Fourier analysis. Below, it will furthermore be shown that the peaks are not

even consistent in the sense that no set of identified parameters would be able to exactly reproduce these eigenfrequencies. They are suitable initial guesses but some uncertainty regarding their exact values remains.

This uncertainty primarily stems from the time-discrete sampling – which is not something to be explained by stochastic perturbations, etc. The actual white noise contained in the measurement signal does not affect the spectrogram much. Yet, by taking samples and applying the discrete Fourier transform, information is clearly being lost. Accordingly, the resulting uncertainty is not aleatory but stems from the lack of knowledge induced by the finite sampling frequency and is thus epistemic. Reasoning with inverse fuzzy arithmetic provides a method to recover some of the lost information as shown below.

Since the Fourier coefficients a_k can be interpreted as the (not yet scaled) membership of the respective frequency to the closest eigenfrequency, the two fuzzy membership functions of the fuzzy eigenfrequencies $\tilde{\omega}_1$ and $\tilde{\omega}_2$ are constructed from these coefficients. First, the frequency spectrum is divided into two parts, the coefficients pertaining to the first and the second eigenfrequency, respectively. The peaks in these intervals are assumed to be the nominal values – they are the most plausible choices – and accordingly, all Fourier coefficients are rescaled to lie within the interval $[0, 1]$, yielding the membership functions in Fig. 6.

In order not to presuppose any a-priori interdependencies of $\tilde{\omega}_1$ and $\tilde{\omega}_2$, the fuzzy output vector $\widetilde{\boldsymbol{\omega}}$ is constructed as their independent joint possibility distribution according to Eq. (31).

Having found the fuzzy output vector $\widetilde{\boldsymbol{\omega}}$ and given the corresponding map f, three possible problems in parameter estimation shall be considered. Throughout these examples, the spring coefficients c_1, c_2 and c_3 are assumed to be known.

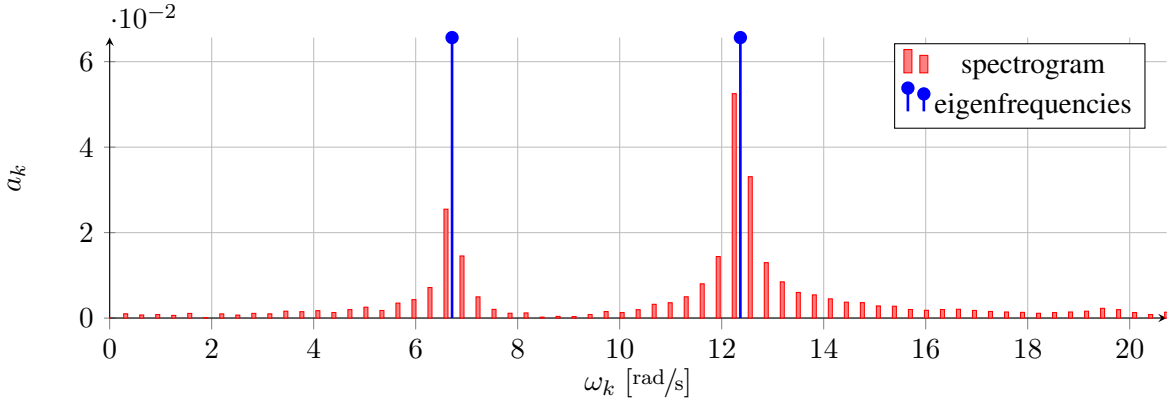


Figure 5: Frequency spectrum of $x_1(t)$.

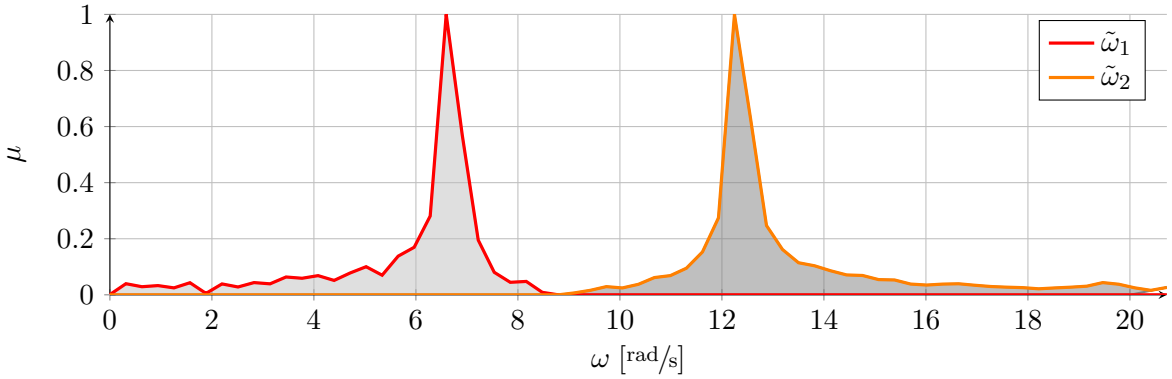


Figure 6: Assumed membership functions of the fuzzy-valued eigenfrequencies $\tilde{\omega}_1$ and $\tilde{\omega}_2$.

5.1 Estimation of One Mass

In the first scenario, only one mass is identified. For instance, if the mass m_2 is actually known, the map f reduces to

$$f^1(\theta) = f(\theta, m_2, c_1, c_2, c_3) \tag{47}$$

and only $\theta = m_1$ remains to be estimated. Computing

$$\tilde{m}_1 = \mathcal{I}^{f^1}(\widetilde{\boldsymbol{\omega}}) \tag{48}$$

yields the membership function shown in Fig. 7a. The same procedure is performed analogously for estimating m_2 given m_1 in Fig. 7b.

Evidently, the estimates with the highest memberships lie very close to the true values of the masses. However, their membership values do not reach one, revealing that an estimate based on the crisp frequencies with the largest Fourier coefficients would have been infeasible as no mass exists that can exactly reproduce these frequencies given the other parameters. For $\tilde{m}_1$ and $\tilde{m}_2$, the degrees of consistency are $\mathrm{cons}(\tilde{m}_1) = 0.89$ and $\mathrm{cons}(\tilde{m}_2) = 0.92$, meaning that only in α-cuts located beneath these levels feasible masses can be found in. The high degrees of consistency indicate that the problem is well-chosen, i.e. that the model f is suitable for reproducing the constructed fuzzy output $\widetilde{\boldsymbol{\omega}}$. By relaxing the problem, the ill-posedness of the (crisp) nominal inverse problem is overcome, feasibility is reintroduced and clearly a suitable estimate is provided.

5.2 Estimation of Two Masses

In the second scenario, it is assumed that both masses $\boldsymbol{\theta} = \begin{bmatrix} m_1 & m_2 \end{bmatrix}^{\mathrm{T}}$ are unknown and need to be estimated, thus the map f^2 is given by

$$f^2(\boldsymbol{\theta}) = f(\theta_1, \theta_2, c_1, c_2, c_3)\ . \tag{49}$$

The computation of

$$\tilde{\boldsymbol{m}} = \mathcal{I}^{f^2}(\widetilde{\boldsymbol{\omega}}) \tag{50}$$

yields the joint possibility distribution of the two uncertain masses, shown in Fig. 8.

Again, the true parameter values of the two masses lie within the region where $\mu_{\tilde{\boldsymbol{m}}}$ attains its maximum with a very high degree of consistency $\mathrm{cons}(\tilde{\boldsymbol{m}}) = 0.93$. However, it is clear that this time there is a second region where the parameter is equally plausible to be located. The result suggests that further information would be necessary to better determine the true masses as the uncertainty is too high to draw meaningful conclusions.

5.3 Estimation of a Surrogate Mass

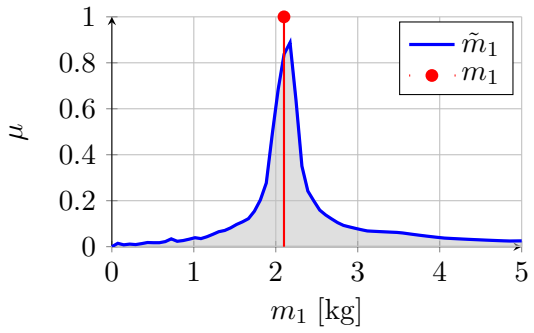
The last scenario is perhaps the most illustrative. The true masses m_1 and m_2 only differ by ten percent which could be assumed to stem from irregularities in manufacturing etc. Thus, one might not wish to identify them individually, but rather to find a good surrogate mass $\theta = m_1 = m_2$. The map to be inverted is then given by

$$f^3(\theta) = f(\theta, \theta, c_1, c_2, c_3)\ . \tag{51}$$

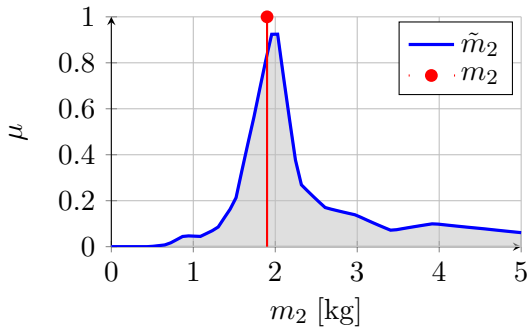
The uncertainty that any estimate would yield is evidently a result from a lack of information encoded in the model f^3, namely the disparity of the masses, which is not included therein.

The evaluation of

$$\tilde{m} = \mathcal{I}^{f^3}(\widetilde{\boldsymbol{\omega}}) \tag{52}$$



(a) Membership function of the estimated mass $\tilde{m}_1$ compared to the true value m_1.



(b) Membership function of the estimated mass $\tilde{m}_2$ compared to the true value m_2.

Figure 7: Results from estimating the masses $\tilde{m}_1$ and $\tilde{m}_2$.

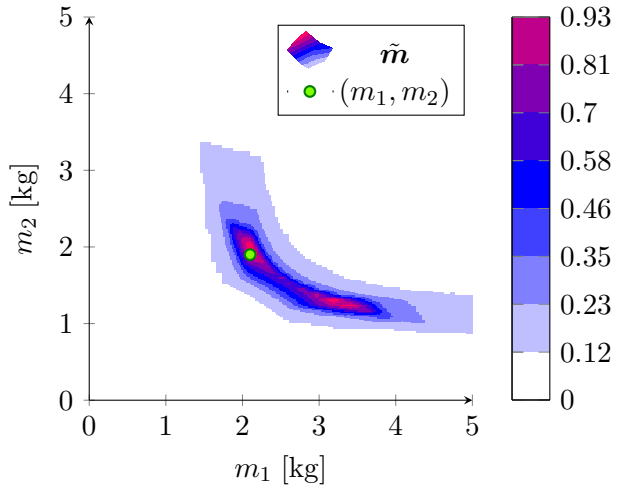


Figure 8: Joint membership function of the estimated mass vector $\tilde{\boldsymbol{m}}$ compared to the true value (m_1, m_2).

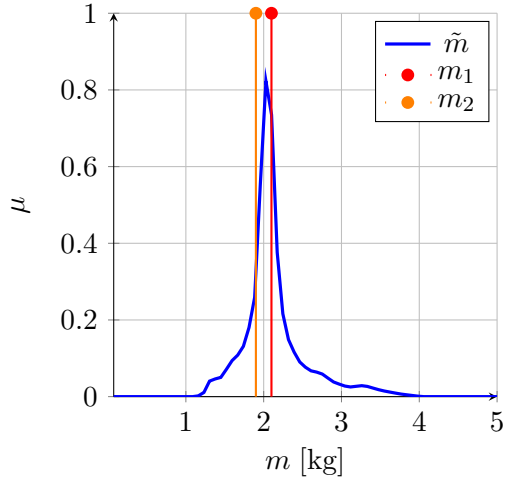


Figure 9: Membership functions of the surrogate mass $\tilde{m}$ compared to the true values m_1 and m_2.

yields the membership function $\mu_{\tilde{m}}$ shown in Fig. 9.

Again, the maximizer of the membership function lies close to the actual values m_1 and m_2, yet it would have been impossible to find a surrogate mass that exactly reproduces the frequencies with maximal Fourier coefficients. The relatively high degree of consistency $\mathrm{cons}\,(\tilde{m}) = 0.82$ is an indicator for the validity of the assumption that the masses can indeed be replaced by the surrogate mass even though an individual estimation (see above) provides a more consistent possibility distribution.

A forward propagation of $\tilde{m}$ through f^3, as presented in Fig. 10, shows that $\tilde{m}$ is able to reproduce $\tilde{\omega}_1$ and $\tilde{\omega}_2$ reasonably well, and their peaks manage to predict the true eigenfrequencies – especially the second one – a little better than the spectrogram. One could also argue that by making the membership functions – in particular the first one – tighter, it allows for a more precise prediction of the region where the true eigenfrequencies lie.

6 Conclusions

In this contribution, a formalized procedure for the solution of inverse problems in fuzzy arithmetic has been proposed. Even though a lot of nomenclature has been introduced, the basic principle is always the

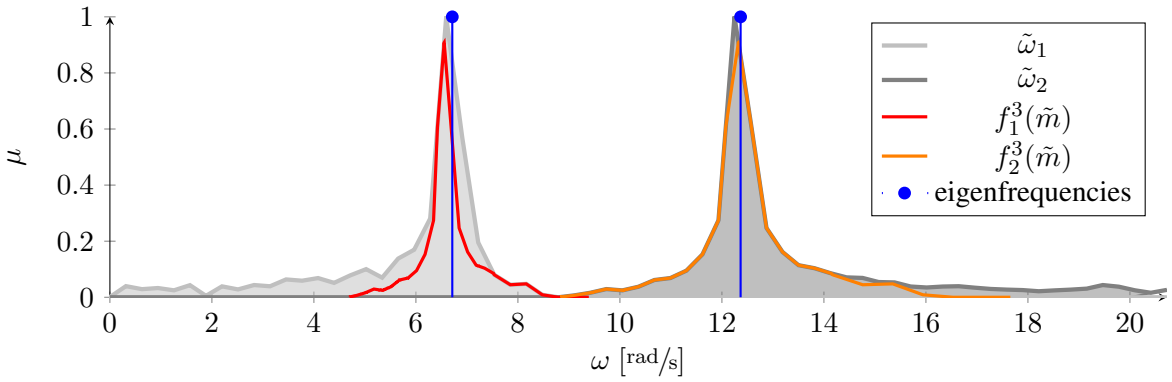


Figure 10: Forward propagation of the identified surrogate mass $\tilde{m}$ through f^3 compared to the assumed reference outputs $\tilde{\omega}_1$ and $\tilde{\omega}_2$.

same. Given a map f and a joint output distribution $\tilde{\boldsymbol{y}}$, Eq. (13) can be evaluated to determine the input distribution $\tilde{\boldsymbol{x}}$.

The presented approach has several advantages over other propositions. Most importantly, it is intuitive and easy to evaluate as opposed to possibly non-convex constrained optimization problems and the like. From a computational point of view, the question of how to effectively determine e.g. the support of the inverse solution to enable further sampling etc. still remains. The authors have already obtained satisfying results by employing sparse grids for the representation of the distribution.

As motivated throughout the paper, the presented results are exceptionally – but not solely – well suited to support engineers in estimation tasks where e.g. the measured output cannot be inverted exactly. By relaxing the problem in a sensible way and admitting some uncertainty, feasibility can be achieved even in cases where the crisp problem proves infeasible and – as supported by the example – the best guess with the highest degree of membership is often a promising estimate and very close to reality.

Acknowledgements

The authors gratefully acknowledge the support provided by the German Research Foundation (DFG) in the framework of the research project no. 319924547.

References

[1] Lotfi A Zadeh. The concept of a linguistic variable and its application to approximate reasoning - I. *Information Sciences*, 8(3):199–249, 1975.

[2] Michael Hanss. *Applied Fuzzy Arithmetic - An Introduction with Engineering Applications*. Springer, Berlin, 2010.

[3] Arun K Tangirala. *Principles of System Identification: Theory and Practice*. Crc Press, 2014.

[4] Dieter Bestle. *Analyse und Optimierung von Mehrkörpersystemen: Grundlagen und rechnergestützte Methoden*. Springer-Verlag, 2013.

[5] Thomas Haag, Jan Herrmann, and Michael Hanss. Identification procedure for epistemic uncertainties using inverse fuzzy arithmetic. *Mechanical Systems and Signal Processing*, 24(7):2021–2034, 2010.

[6] Hideo Tanaka. Fuzzy data analysis by possibilistic linear models. *Fuzzy Sets and Systems*, 24(3):363–375, 1987.

[7] Hisao Ishibuchi and Manabu Nii. Fuzzy regression using asymmetric fuzzy coefficients and fuzzified neural networks. *Fuzzy Sets and Systems*, 119(2):273 – 290, 2001.

[8] Dominik Hose and Michael Hanss. Fuzzy linear least squares for the identification of possibilistic regression models. *Fuzzy Sets and Systems*, 2018. (to appear)

[9] Masuo Hukuhara. Integration des applications mesurables dont la valeur est un compact convexe. *Funkcial. Ekvac*, 10:205–223, 1967.

[10] Barnabás Bede and Luciano Stefanini. Generalized differentiability of fuzzy-valued functions. *Fuzzy Sets and Systems*, 230:119–141, 2013.

[11] Luciano Stefanini. A generalization of hukuhara difference and division for interval and fuzzy arithmetic. *Fuzzy sets and systems*, 161(11):1564–1584, 2010.

[12] Richard E Bellman and Lotfi A Zadeh. Decision-making in a fuzzy environment. *Management Science*, 17(4):B–141, 1970.

[13] Lotfi A Zadeh. Fuzzy sets as a basis for a theory of possibility. *Fuzzy Sets and Systems*, 100, Supplement 1:9–34, 1999.

[14] Didier Dubois and Henri Prade. *Possibility theory: an approach to computerized processing of uncertainty*. Plenum Press, 1988.

[15] Baoding Liu. *Theory and practice of uncertain programming*. Springer, 2002.

[16] Didier Dubois. Possibility theory and statistical reasoning. *Computational Statistics & Data Analysis*, 51(1):47–69, 2006.

Bayesian model updating using stochastic distances as uncertainty quantification metrics

S. Bi[1], M. Broggi[1], M. Beer[1], Y. Zhang[2]
[1] Leibniz Universität Hannover, Institute for Risk and Reliability
CallinStr. 34, 30167 Hannover, Germany
e-mail: **sifeng.bi@irz.uni-hannover.de**

[2] Beijing Institute of Technology, School of Aerospace Engineering
Zhongguancun South Str. 5, 100081 Beijing, China

Abstract
Uncertainty quantification metrics are critical in the campaign of stochastic model updating, by provide an elaborate measurement of the uncertainty in both simulations and experiments. In this work, the Bhattacharyya distance is proposed as a comprehensive model updating metric for two samples considering their probabilistic properties. The updating process employs a two-steps Bayesian framework where the Bhattacharyya distance is well embedded and its performance is compared with the Euclidian distance. The Euclidian distance is utilized as metric in the first step where the geometry distance between the center points of the numerical and experimental samples are calculated. The posteriori distributions of the means are subsequently transferred to the second step where the Bhattacharyya distance is utilized as metric with the main effort to update the distributional coefficients of parameters. The feasibility of the overall two-step framework and the advantage of the Bhattacharyya distance metric are demonstrated in a simulated example.

1 Introduction

Uncertainty analysis has been generally acknowledged as a critical issue in computational mechanics engineering, where topics like stochastic model updating [1], verification and validation require more and more quantifiable uncertainty information in both simulations and experiments [2,3]. The development of a quantitative, comprehensive, and uniform metric for uncertainty information between two sets of simulated/measured data becomes one of the key aspects of uncertainty quantification (UQ).

By providing an absolute geometry distance between two single points, the Euclidian distance is probably the most common metric especially in deterministic updating approaches. Alternatively, the Bhattacharyya distance is a stochastic metric between two samples considering their probabilistic distributions. The Bhattacharyya distance is clearly more comprehensive for uncertainty treatment, however, its application on model updating is quite limited, to our knowledge, in the current literatures. Consequently, this work focuses on generalizing the application of the Bhattacharyya distance as a universal metric for stochastic model updating, by developing a Bayesian updating framework, in which the Bhattacharyya distance is fully embedded and actively operated.

The limitation of the Bhattacharyya distance's application in stochastic model updating is not only caused by the huge calculation cost; more critically, it is caused by the stochastic properties when evaluating the distance between two random samples. Bi et al. [4] performed a comprehensive comparison among the Euclidian, Mahalanobis, and Bhattacharyya distances as updating metrics via a direct Monte Carlo approach. However, this approach is essentially based on a single and non-directional searching technique with low efficiency. In the case of complex problems with high-dimensional parameter space, this approach would fail to search the global solutions.

To solve this issue, in this paper, a stochastic Bayesian updating approach is proposed, employing the transitional Markov chain Monte Carlo (TMCMC) algorithm [5] as an efficient updating tool. Thanks to a customized likelihood function, the Bhattacharyya distance is well embedded in the updating framework as a UQ metric. The customized likelihood is of first importance, since it acts as a convenient connection between the Bayesian updating tool and the statistical distance metric. The overall updating framework proposes a two-step strategy to employ the Euclidian distance and the Bhattacharyya distance as updating metric, successively. This strategy is intended to compare the effect and performance of these two distances, and thus a general guideline for metric selection is concluded. A simulated example on a spring-mass system is proposed to demonstrate the feasibility of the overall Bayesian updating approach along with the proposed Bhattacharyya distance metric.

2 Stochastic Bayesian updating and UQ metrics

2.1 Mathematic description of the uncertain system and Bayes' theorem

In the stochastic model updating approach, the investigating system is represented by the three components: input parameters x, output features y, and the numerical model $f(\cdot)$:

$$\begin{aligned} \mathbf{y} &= f(\mathbf{x}); \\ \mathbf{y} &= [y_1, y_2, \dots, y_m]^T; \\ \mathbf{x} &= [x_1, x_2, \dots, x_n]^T \end{aligned} \tag{1}$$

where **x** and **y** are respectively the input and output vectors; m and n are the number of output and input quantities, respectively. The numerical model $f(\cdot)$ can be either a complicated code package (e.g. finite element model) or a simplified functional relationship (e.g. response surface model).

In the deterministic updating scenario, it is not rare that only a single experiment is performed. The discrepancy between this single data and the model prediction is employed as the objective function, and the model parameters are updated through sensitivity-based methods [6] to minimize the discrepancy. However, because of the lack of knowledge and randomness of environment/human factors, both epistemic and aleatoric uncertainties are inevitable in parameterization and modelling, and the experiment processes. Consequently, in stochastic updating scenario, a multi-analysis-multi-experiment strategy is necessary, which leads to multiple samples of model inputs and outputs. The uncertainty information, implied in these samples, can be represented in various forms, such as intervals, fuzzy sets, and probabilistic distributions.

Suppose the size of the analytical samples is N_a, the model evaluation is executed N_a times to generate the analytical feature sample $\mathbf{Y}_a \in \mathbb{R}^{N_a \times m}$:

$$\mathbf{Y}_a = \begin{bmatrix} y_{11} & \cdots & y_{1m} \\ \vdots & \ddots & \vdots \\ y_{N_a 1} & \cdots & y_{N_a m} \end{bmatrix} \tag{2}$$

In addition to the analytical features, the experimental feature sample is obtained after multiple test. Suppose the number of experiments is N_e, the experimental feature sample has the similar structure as Eq. (2), while only the number of rows is changed: $\mathbf{Y}_e \in \mathbb{R}^{N_e \times m}$. Now the objective of stochastic model updating can be expressed as to minimize the discrepancy between $\mathbf{Y}_e$ and $\mathbf{Y}_a$, by calibrating the uncertain information of the sample of model inputs: $\mathbf{X}_a$. Note that, not only the means of the model parameters are calibrated, but also other uncertainty properties, i.e. variance and distribution form, need to be updated in the stochastic model updating process.

The stochastic nature of the Bhattacharyya distance (described in the following Sec. 3) makes it difficult to be employed in the classical deterministic approach [4]. Therefore, the well-known Bayesian updating framework is proposed in this work to employ the Bhattacharyya distance as a UQ metric. The foundation of Bayesian updating is

$$P(\mathbf{X}|\mathbf{Y}_e) = \frac{P_L(\mathbf{Y}_e|\mathbf{X})P(\mathbf{X})}{P(\mathbf{Y}_e)} \tag{3}$$

with the key elements in Bayes' theorem:

- $P(\mathbf{X})$ is the prior distribution of the inputs, representing the initial knowledge of $\mathbf{X}$;
- $P(\mathbf{X}|\mathbf{Y}_e)$ is the conditional distribution of the inputs, which is also known as the posterior distribution after Bayesian model updating based on the experimental data;
- $P(\mathbf{Y}_e)$ is the so-called "normalization factor", which guarantees the integral of the conditional distribution $P(\mathbf{X}|\mathbf{Y}_e)$ is normalized;
- $P_L(\mathbf{Y}_e|\mathbf{X})$ is the likelihood function of the experimental features $\mathbf{Y}_e$, for an instance of the parameters $\mathbf{X}$.

Among the above elements, the likelihood $P_L(\mathbf{Y}_e|\mathbf{X})$ is critical, since it represents the possibility of the experimental data under each investigating instance of the updating parameters $\mathbf{X}$. And thus the principle of Bayesian updating is expressed as: To find the specific parameters $\mathbf{X}$, which allows the exiting experimental observations to possess the largest probability, i.e. allows the likelihood function $P_L(\mathbf{Y}_e|\mathbf{X})$ to reach the maximum.

2.2 Customized likelihood function and TMCMC algorithm

Considering the application of the Bhattacharyya distance as a UQ metric, it is natural to propose a customized likelihood function, involving the information of discrepancy between the experimental and analytical outputs. In this work, the likelihood function is defined as

$$P_L(\mathbf{Y}_e|\mathbf{X}) = \frac{1}{\sigma\sqrt{2\pi}} exp\left\{-\frac{d(\mathbf{Y}_e, \mathbf{Y}_a)^2}{2\varepsilon^2}\right\} \tag{4}$$

where $d(\mathbf{Y}_e, \mathbf{Y}_a)$ is the distance metric representing the discrepancy between the experimental and analytical outputs; ε is the so-called width factor, which is a pre-defined coefficient controlling the centralization degree of the posterior distribution of the parameter $\mathbf{X}$. Lots of tests on different applications suggest the interval of ε fall within $[10^{-1}, 10^{-3}]$. A smaller σ gains a more peaked posterior distribution which is more likely to concentrate to the true value, however, requires more calculation effort by nature. What's more, an excessive small ε results in the consequence that the integration and sampling from the very peaked posterior distribution would be very difficult or even intractable.

The above discussion reveals a difficulty of the Bayesian updating approach, which is relative to the normalization factor $P(\mathbf{Y}_e)$. Indeed, the direct integration of the posterior distribution over the whole parameter space is quite difficult in practical application [7]. To solve this iuuse, the Transitional Markov Chain Monte Carlo (TMCMC) [5] algorithm along with the Metropolis-Hasting algorithm [8] are employed in this work as an effective updating tool. About this well-known TMCMC algorithm, Refs. [5,9] are suggested for more details, and more applications of this algorithm can be found in fields from stochastic model updating [10,11] to structural health monitoring [12].

3 A two-step strategy using Euclidian and Bhattacharyya distances

The overall updating framework proposes a two-step strategy, where the Euclidian distance and the Bhattacharyya distance are respectively utilized as updating metrics, by constructing the customized likelihood function following Eq. (4). This strategy is specially designed to compare and reveal the merit and demerit of the Euclidian and Bhattacharyya distances, and thus a general selection guideline of these metrics is concluded.

The Euclidian distance is an absolute geometry distance between two points. Considering the experimental and analytical output samples, $\mathbf{Y}_e \in \mathbb{R}^{N_e \times m}$ and $\mathbf{Y}_a \in \mathbb{R}^{N_a \times m}$, the operable manner to evaluate the Euclidian distance between these two samples is focusing on their mean values:

$$d_E(\mathbf{Y}_e, \mathbf{Y}_a) = [(\overline{\mathbf{Y}_e} - \overline{\mathbf{Y}_a})(\overline{\mathbf{Y}_e} - \overline{\mathbf{Y}_a})^T]^{1/2} \tag{5}$$

where $\overline{\mathbf{Y}_\blacksquare}$ is a row vector of the means of the matrix. The Euclidian distance contains only means of the matrices, while more information of the sample such as variance, covariance, and distribution is ignored. Consequently, it is more generally used in the deterministic updating methodologies where a single-simulation-single-observation procedure is utilized.

In the presence of random samples, a more comprehensive metric considering not only the mean but also the probabilistic or distributional information is desired. The Bhattacharyya distance is consequently proposed herein as a stochastic metric quantifying the degree of overlap between the distributions of two variables. The Bhattacharyya distance has the theoretical expression as

$$d_B(\mathbf{Y}_e, \mathbf{Y}_a) = -\log\left\{\int_{\mathbb{Y}} [P_e(y)P_a(y)]^{1/2} \mathrm{d}y\right\} \tag{6}$$

where $P_\blacksquare(y)$ is the probability density function (PDF) of the sample; $\int_{\mathbb{Y}} \blacksquare \mathrm{d}y$ denotes the integration over the whole output space. Note that, for most applications, there are more than one output quantities, i.e. $m > 1$, and thus the integration is performed on multi-dimension joint PDFs. It means, despite multi-output, the Bhattacharyya distance can always present as a uniform scalar taking the correlation among these multiple outputs into account, because of the multi-dimension joint PDF. This is one of the advantages of the Bhattacharyya distance.

To calculate the Bhattacharyya distance, a necessary step is to estimate the PDF based on the observation sample of the output variables. Classical techniques such as kernel density estimation [13] can be used in this step. However, this technique requires a large number of samples to achieve a converged estimation of the PDF. However, this requirement is usually infeasible, since number of observations is always limited, especially for applications where experiments are difficult or expensive. Instead of estimating an approximate PDF, a more practical method, named as the binning algorithm [4], is proposed to evaluate the probability mass function (PMF) of a discrete distribution. This algorithm contains the following steps:

1) Determine the public interval I_i of both $\mathbf{Y}_e$ and $\mathbf{Y}_a$ according to the i^{th} output $\mathrm{y}_i, \forall \mathrm{i} = 1, \dots, m$;
2) Decide the number of bins n_{bin} in the output variable space;
3) Count the joint probability mass for each bin.

Subsequently, the Bhattacharyya distance between two discrete distributions is evaluated as

$$d_B(\mathbf{Y}_e, \mathbf{Y}_a) = -\log\left(\sum_{k=1}^{N_{bin}} \sqrt{PM_e^{(k)} PM_a^{(k)}}\right) \tag{7}$$

where $PM_\blacksquare^{(k)}$ is the probability mass of the k^{th} bin. An advantage of this binning algorithm is that it makes the evaluation process independent to the actual distribution form of the variables. This makes it especially appropriate for stochastic model updating where the feature distributions cannot be exactly determined.

However, the Bhattacharyya distance's comprehensiveness makes its quantification on the means is not as direct as the Euclidian distance. For the extreme situation where the two investigating samples are too far to have any overlap, the Bhattacharyya distance value becomes infinite. This is the drawback of the Bhattacharyya distance, which is also the motivation to design this two-step strategy such that the geometry distance between the samples can be firstly reduced by the Euclidian distance metric, and thus the Bhattacharyya distance can be safely operated in the second step. The effect of this strategy is demonstrated in the follow example section.

4 Demonstration on a spring-mass system

4.1 Problem description

As shown in Fig. 1, a four degree-of-freedom (dof) spring-mass system is proposed in this section to demonstrate feasibility of the overall two-step Bayesian updating framework, where the Euclidian distance and the Bhattacharyya distance are utilized as UQ metrics in the first and second step, respectively. This numerical system contains four masses and eight springs, implying totally 12 parameters. In this example, the first four stiffness coefficients k_1-k_4 are regarded as uncertain parameters to be investigated. the remaining parameters (i.e. the four masses m_1-m_4 and the last four stiffness coefficients k_5-k_8) are treated as constant without uncertainty. The prescribed values of these constants are: m_1=0.7kg, m_2=0.5kg, m_3=0.3kg, m_4=0.5kg, and $k_{5\text{-}8}$=5.0N/m.

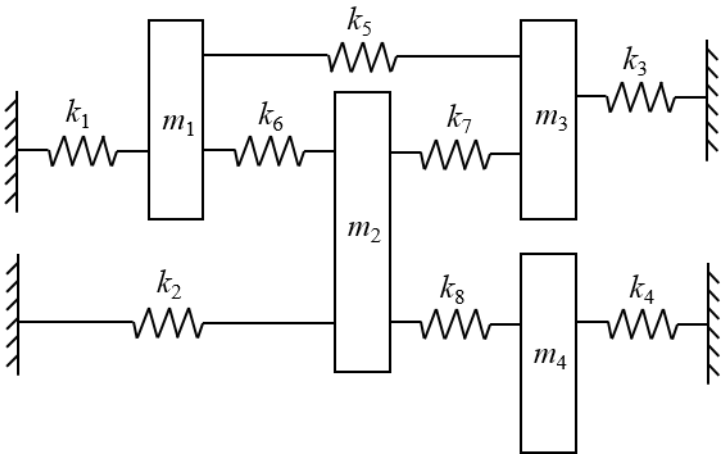


Fig. 1: The proposed 4 dof spring-mass system

The uncertainty properties of k_1-k_4 are detailed in Table 1, where both epistemic and aleatoric uncertainties are represented. k_1-k_4 are assumed as independent variables, obeying Gaussian or uniform distribution, which represents the aleatoric uncertainty. what's more, the distributions are not fully determined, since their probabilistic coefficients (e.g. the mean, variance, or boundary) are not fully known constant but lying within the given intervals, as shown in Table 1, representing the epistemic uncertainty due to the lack of knowledge. Instead of simple intervals of the parameters in the deterministic updating framework, the above assumption results in uncertainty spaces of the parameters under the probabilistic sense. Consequently, the stochastic updating problem in this example is more challenge than the classical deterministic updating procedure, since the task herein is no longer to calibrate the parameter itself, but to reduce the uncertainty space of the parameter by calibrating its distributional coefficients. By reducing and calibrating the uncertainty space of the parameters, the uncertainty space of system outputs is finally reduced and tuned close to the experimental data.

The four natural frequencies of the system f_1-f_4 are selected as the investigating outputs, whose uncertainty spaces are driven by the uncertainty spaces of k_1-k_4. A set of target values of distributional coefficients is given in Table 1, which can be used to generate the "simulated" experimental data. Assume the size of the experimental sample is 100, the parameters are randomly sampled 100 times based on the distributions along with the target coefficients. Subsequently, 100 samples of outputs are available which will be served as target in the updating procedure.

The last column of Table 1 presents the initial values of the distributional coefficients, which are set to be different from the target values. Considering the output samples, Fig. 2 presents the positional relationship between the initial and target data scatters, in the plane of f_1 and f_4. The Gaussian mixture modelling technique (with two Gaussian components) is utilized to estimate the joint PDFs of these two output variables. A set of contours of this estimated PDF is illustrated on each corresponding scatter as shown in

Fig. 2. Because the input parameters in Table 1 have different distribution forms, the evaluated system outputs present a distribution which is neither Gaussian nor uniform. Fig. 2 clearly shows the objective of this problem is not only to shift the initial sample toward the target sample, but also, more important, to reshape the initial sample such that the updated sample has the similar distribution as the target. To achieve this objective, both the Euclidian and Bhattacharyya distances are employed as metrics in the Bayesian updating procedure.

Parameter	Uncertainty characteristic	Target value	Initial value
k_1	Gaussian, $\mu_1 \in [3.0, 7.0], \sigma_1 \in [0.0, 0.5]$	$\mu_1 = 4.0, \sigma_1 = 0.1$	$\mu_1 = 7.0, \sigma_1 = 0.25$
k_2	Uniform, $a_2 \in [1.0, 4.0], b_2 \in [6.0, 9.0]$	$a_2 = 3.0, b_2 = 6.5$	$a_2 = 4.0, b_2 = 9.0$
k_3	Gaussian. $\mu_3 \in [3.0, 7.0], \sigma_3 \in [0.0, 0.5]$	$\mu_3 = 3.5, \sigma_3 = 0.5$	$\mu_3 = 7.0, \sigma_3 = 0.25$
k_4	Uniform. $a_4 \in [1.0, 4.0], b_4 \in [6.0, 9.0]$	$a_4 = 2.0, b_4 = 8.0$	$a_4 = 4.0, b_4 = 9.0$

Table 1: Uncertainty properties of the input parameters

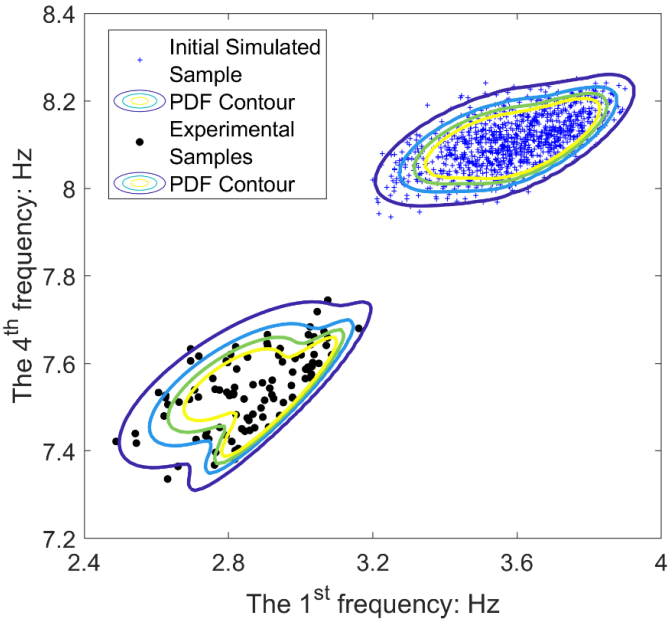


Fig. 2: Initial simulated and target experimental scatters

4.2 Step I: Updating with the Euclidian Distance Metric

There are eight distributional coefficients relative to the four parameters k_1-k_4 in this problem, and all prior distributions of these eight values are set to be uniform within the prescribed intervals as shown in Table 1. In the following context, the eight distributional coefficients are also termed as parameters. The Euclidian distance between the target sample and the simulated outputs sample is utilized to construct the likelihood function following Eq. (4). The width factor ε is set as 0.005, and 8 iteration steps are performed in the TMCMC algorithm before the convergence.

The posterior distributions of the eight parameters are illustrated in Fig. 3. After this updating step, most parameters (e.g. σ_1, σ_3, a_4, and b_4) have posterior distributions which are still nearly uniform, implying the updating step for these parameters is ineffective. Exceptionally, the posterior distributions of μ_1 and μ_3 are obviously different for their prior uniform distribution. The updated values of μ_1 and μ_3 are consequently available by calculating the means of the final sample of the updated inputs. The updated values of μ_1, a_2, b_2, and μ_3 are listed in Table 2, while the values of other parameters are omitted because their posterior distributions are still nearly uniform.

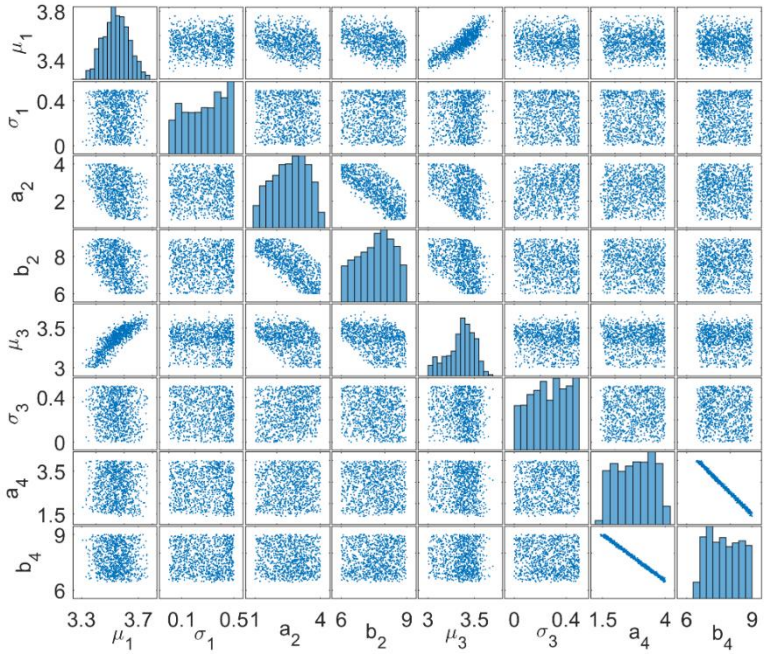


Fig. 3: The posterior distributions of the eight inputs after updating with Euclidian distance

A more intuitionistic representation of the effect of the first updating step is revealed by Fig. 4, where the positional relationship between the updated sample (named as Sample-ED in the figure) and the target experimental sample is illustrated. The centre points of the updated sample and the experimental sample are conincident with each other. However, the contour of the updated sample is remain the same as the one of the initial sample in Fig. 2, and thus obviouly different from the contour of the experimental sample. This phenomenon represents the effect of the first updating step is only to shift the initial sample toward the experimental sample, whithout any change on the shape of the sample. This result is cinsistent with the principle that the Euclidian distance only measures the geometry distance between the centre points of samples, while the disperion and distribution information of the samples is omitted. Consequently, a more comprehensive metric is required in the second updating step to further reduced the discrepancy between Sample-ED and the target experimental sample.

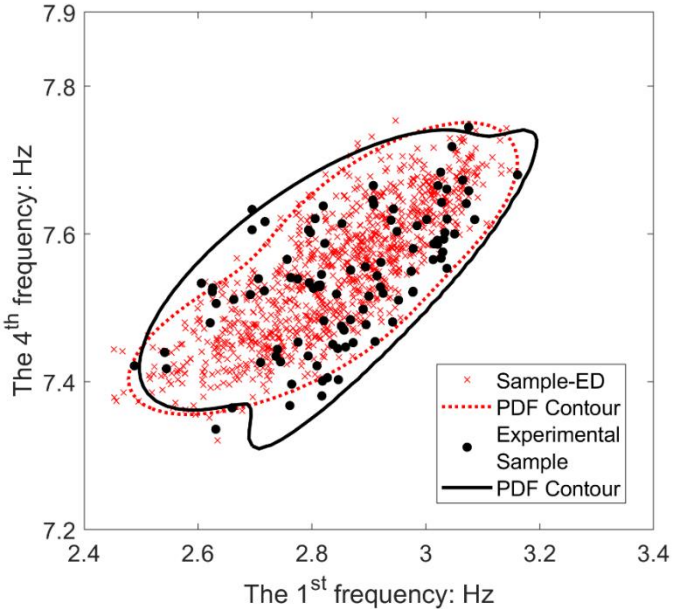


Fig. 4: Updated samples with the Euclidian distance mertic

Input	Target value	Updated value	
		with Euclidian metric	with Bhattacharyya metric
μ_1	4.0	3.5427 (-11.4%)	3.8647 (-3.38%)
σ_1	0.1	--	0.1226 (22.6%)
a_2	3.0	2.5906 (-13.6%)	2.2296 (-25.7%)
b_2	6.5	7.5797 (16.6%)	7.3763 (13.5%)
μ_3	3.5	3.3560 (-4.12%)	3.4104 (-2.56%)
σ_3	0.5	--	0.4731 (-5.38%)
a_4	2.0	--	1.9791 (-1.04%)
b_4	8.0	--	8.3170 (3.96%)
Absolute Mean Error		11.45%	9.763%

Table 2: Updated inputs using different distance metrics (percent errors in the parentheses)

4.3 Step II: Updating with the Bhattacharyya Distance Metric

In the second updating step, the Bhattacharyya distance is utilized as UQ metric to measure the discrepancy between the samples. Note that, this updating step is not performed on the initial output sample in Fig. 2, but performed on the updated sample after the first step (i.e. Sample-ED in Fig. 4). Therefore, the posterior distributions of the parameters are taken as prior distributions in this step. The width factor ε is set as 0.1, and the final convergence is reached after 12 iteration steps in the TMCMC algorithm. Fig. 5 illustrates the further updated posterior distributions of the eight input parameters, which are clearly different from the ones in Fig. 3. As shown in Fig. 5, all posterior distributions of the parameters are updated to concentrate to a single pole, implying the second updating step is effective for all parameters. Means of these posterior distributions are listed in the last column of Table 2. It is shown that the updated values are quite close to the target. The comparison between these updated PDFs and values in the first and second steps is further discussed in the next subsection (Sec. 4.4).

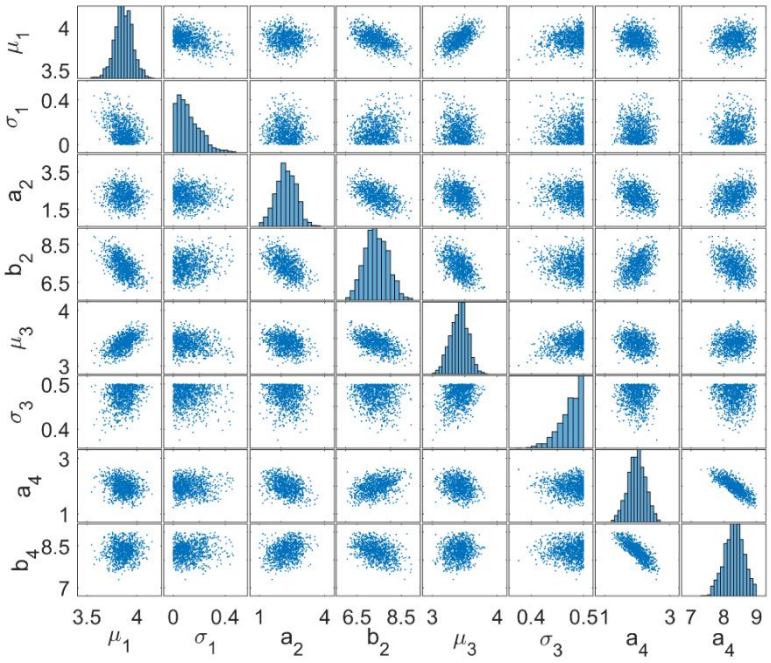


Fig. 5: Posterior distributions of the six inputs after updating with Bhattacharyya distance

A vivid representation of the updating process of the sample distributions is illustrated in Fig. 6. The final output sample updated using the Bhattacharyya distance metric is named as Sample-BD in the figure. The contour of Sample-BD is clearly calibrated from the contour of Sample-ED (referring to Fig. 4), and the finally updated contour of the sample is similar as the one of the experimental sample. After the iterative updating process, the final sample appears to coincide with the target sample, no matter on the position or on the shape, implying the Bhattacharyya distance metric is capable of updating of the uncertainty space of the outputs, and thus the input parameters.

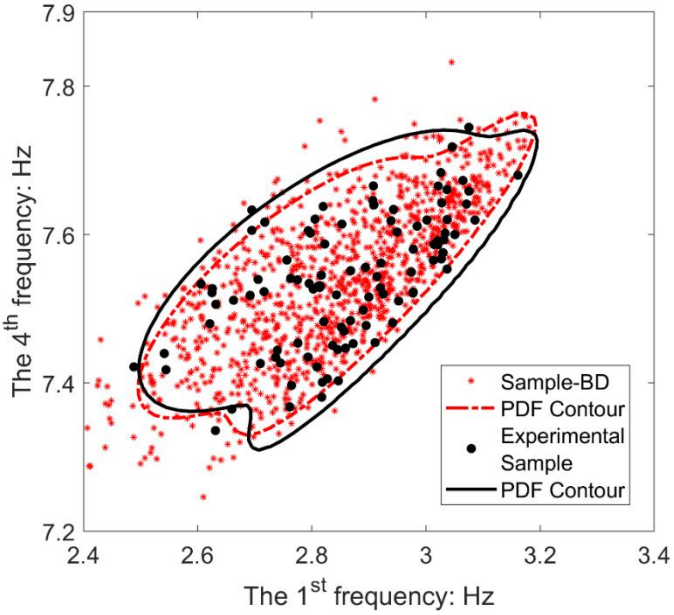


Fig. 6: Updated samples with the Bhattacharyya distance metric

4.4 Comparison between the results of the two steps

A detailed comparison between the posterior PDFs of the input parameters in these two updating steps is presented in Fig. 7. As mentioned above, the updated values of the parameters are estimated by calculating the mean of the updated samples, and these values are listed in Table 2, with the relative error compared with the target values in the parentheses. In order to obtain a comprehensive comparison of the results, a combined investigation on Fig. 7 and Table 2 is performed in the following discussion.

As shown in Fig. 7, the first updating step with the Euclidian distance is effective on only μ_1 and μ_3. Furthermore, only μ_3 has the similar posterior PDFs in these two steps. Refer to Table 2, the errors of μ_3 in both steps (-4.12% and -2.56%) are quite small, imply a good updating effect for this parameter. For μ_1, a clearly centralized PDF is obtained after the first step, however, this PDF is different from the one after the second step. The second step has a better updating effect for μ_1, since Table 2 shows that the error of the updated μ_1 with Bhattacharyya metric is much smaller than the one with the Euclidian metric. For the other parameters except μ_1 and μ_3, Fig. 7 clearly shows the posterior PDFs after the first step are still nearly uniform, while the posterior PDFs after the second step are obviously centralized to a single pole. The updated parameter values with the Bhattacharyya distance metric in Table 2 have an absolute mean error no more than 10%, which is even smaller the mean error of the only four available values with the Euclidian metric. This demonstrates that the Bhattacharyya distance utilized in the second updating step has a comprehensive advantage on distributional coefficient updating.

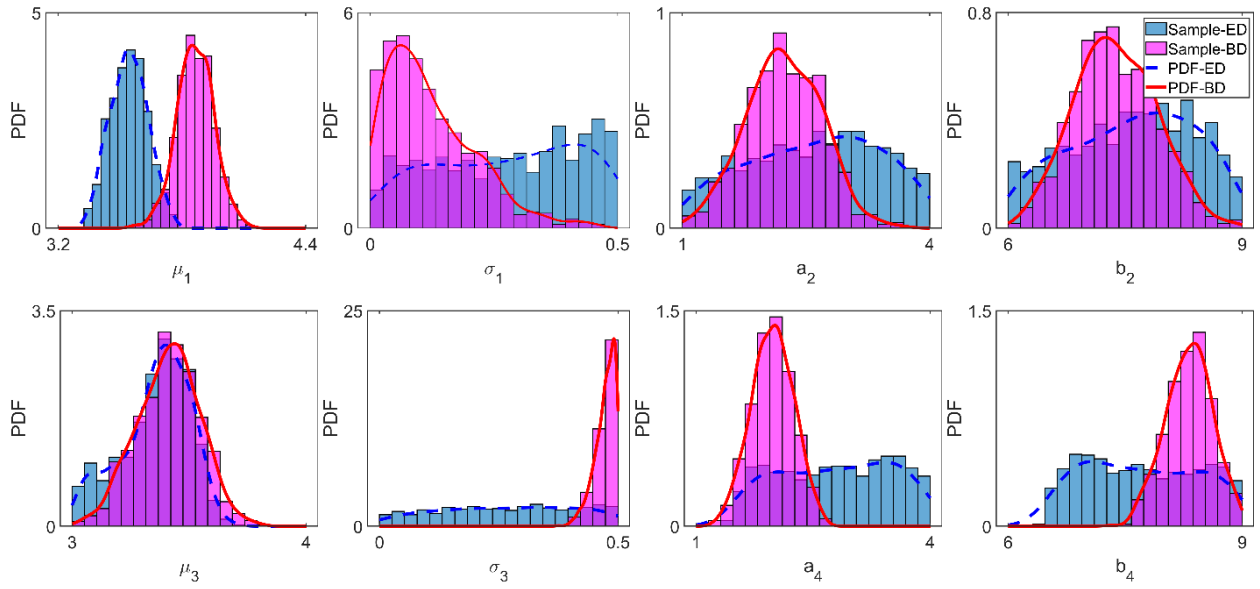


Fig. 7: Comparison of the posterior PDFs using different distance metrics

However, despite the comprehensive advantage, it is important to state that the Bhattacharyya distance is not suitable to be utilized as the exclusive metric without the assistant of the Euclidian distance metric. As discussed in Sec. 3, a significant drawback of the Bhattacharyya distance is the infiniteness when the investigating data samples are too far from each other. As an example, Fig. 2 illustrates this extreme situation, where the initial sample are completely apart from the experimental sample; that is to say, when the distributions of these two samples have no superposition. In this situation, the value of Bhattacharyya distance is always infinite regardless the varying discrepancies between these two samples. Consequently, the two-step strategy is specially designed to overcome this drawback of the Bhattacharyya distance by employing the Euclidian distance in the first step to shift the initial sample toward the observation sample, and then to reshape the sample in the second step.

5 Conclusions and perspectives

In this work, a stochastic Bayesian model updating approach employing the TMCMC algorithm and a customized likelihood function is proposed. This approach contains a two-step strategy where the Euclidian distance and the Bhattacharyya distance are utilized as the UQ metric, successively. These two steps have the uniform framework and the only difference between them is the customized likelihood function in Bayes' theorem is constructed using the Euclidian or Bhattacharyya distance.

During the updating procedure, the Euclidian distance is utilized as an absolute geometry distance considering only the means of samples. Comparatively, the Bhattacharyya distance is demonstrated to be more comprehensive because of the capability to calibrate not only the mean but also distributional coefficients of the samples. Consequently, it is a potential UQ metric which is more desirable for uncertainty treatment.

However, the spring-mass system example provides a special case where a direct and exclusive application of the Bhattacharyya distance is defective, since the infiniteness evaluation of the distance between the initial sample and the target sample. This demonstrates that the deterministic updating should be the precondition of any stochastic updating. In other words, the classical Euclidian distance metric using nominal parameters together with data means should be kept as the backbone in any stochastic updating procedure.

Acknowledgements

This work is supported by the Alexander von Humboldt Foundation, which is greatly appreciated by the first author.

References

[1] Z. Deng, S. Bi, S. Atamturktur, *Stochastic model updating using distance discrimination analysis*, Chinese Journal of Aeronautics, Vol. 27, No. 5, (2014).

[2] J. Zhang, J. Jin, Z. Liu, *Adaptive Spacecraft Attitude Tracking and Parameter Estimation with Actuator Uncertainties*, Journal of Aerospace Engineering, Vol. 27, No. 5, (2014).

[3] B. Yan, X. Zhang, Y. Luo, Z. Zhang, S. Xie, Y. Zhang, *Negative impedance shunted electromagnetic absorber for broadband absorbing: Experimental investigation*, Smart Materials and Structures, Vol. 23, No. 12, (2014).

[4] S. Bi, S. Prabhu, S. Cogan, S. Atamturktur, *Uncertainty Quantification Metrics with Varying Statistical Information in Model Calibration and Validation*, AIAA Journal, Vol. 55, No. 10, (2017).

[5] J. Ching, Y.-C. Chen, *Transitional Markov Chain Monte Carlo Method for Bayesian Model Updating, Model Class Selection, and Model Averaging*, Journal of Engineering Mechanics, Vol. 133, No. 7, (2007).

[6] J.E. Mottershead, M. Link, M.I. Friswell, *The sensitivity method in finite element model updating: A tutorial*, Mechanical Systems and Signal Processing, Vol. 25, (2011).

[7] J.L. Beck, S.-K. Au, *Bayesian updating of structural models and reliability using Markov Chain Monte Carlo simulation*, Journal of Engineering Mechanics-ASCE, Vol. 124, No. 4, (2002).

[8] W.K. Hastings, *Monte Carlo sampling methods using Markov chains and their applications*, *Biometrica*, Vol. 57, No. 1, (1970).

[9] J.L. Beck, S.-K. Au, *Bayesian Updating of Structural Models and Reliability using Markov Chain Monte Carlo Simulation*, Journal of Engineering Mechanics, Vol. 128, No. 4, (2002).

[10] E. Patelli, Y. Govers, M. Broggi, H.M. Gomes, M. Link, J.E. Mottershead, *Sensitivity or Bayesian model updating: a comparison of techniques using the DLR AIRMOD test data*, Archive of Applied Mechanics, Vol. 87, No. 5, (2017).

[11] C. Safta, K. Sargsyan, H.N. Najm, K. Chowdhary, B. Debusschere, L.P. Swiler, M.S. Eldred, *Probabilistic Methods for Sensitivity Analysis and Calibration in the NASA Challenge Problem*, Journal of Aerospace Information Systems, Vol. 12, No. 1, (2015).

[12] R. Rocchetta, M. Broggi, Q. Huchet, E. Patelli, *On-line bayesian model updating for structural health monitoring*, Mechanical Systems and Signal Processing, Vol. 103, (2018).

[13] S.J. Sheather, M.C. Jones, *A reliable data based bandwidth selection method for kernel density estimation*, Journal of the Royal Statistical Society, Vol. 53, No. 3, (1991).

Identification of a stochastic model for bolted joints

H. Jalali[1], H. Haddad Khodaparast[1], M. I. Friswell[1]
[1] Swansea University, College of Engineering, Bay Campus, Fabian Way, Crymlyn Burrows, Swansea, SA1 8EN, United Kingdom
e-mail: **hassan.jalali@swansea.ac.uk**

Abstract
In this paper an FE model of the contact interface in a bolted structure is considered. The paper demonstrates how the uncertainty may be represented in the contact interfaces and investigates these uncertainty effects in the dynamic responses of the structure, e.g. natural frequencies. The contact interface is modelled using stochastic material properties to account for the variability in contact parameters, i.e. surface roughness and preload effects. A simplified stochastic dynamic model is then used, and the parameters of the uncertain joint model are identified based on simulated data. The maximum likelihood method is used for identification.

1 Introduction

Frictional contact interfaces are commonly used in many applications in engineering. Due to the lack of information about the various parameters of the contact interfaces- such as contact stiffness and damping and surface roughness - they introduce uncertainty in the dynamic responses of assembled structures. Measurement, quantification and modelling of this uncertainty is a step forward in engineering structural design.

Gangadharan et al. [1] identified the stochastic welded joint model parameter in a car body by employing two coupled and uncoupled models. Lopez et al. [2] considered the connection between two substructures of a space structure as random springs and investigated the uncertainty in structural responses such as FRFs due to the uncertainty in joint parameters. Guo and Zhang [3] identified the uncertainty in joint model parameters by using updating approaches. Castelluccio and Brake [4] employed FE simulation to investigate the model input and form uncertainties in threaded fasteners. They characterized the source of uncertainty and variability in modelling fasteners as uncertainty in geometry, materials, mechanics and methodology.

In this paper uncertainty modelling in the contact interface of a lap-joint is considered. First, a stochastic equivalent thin layer model for the contact interface is proposed. The proposed model is then used in a 3D FE model of an assembled structure and variability in the natural frequencies due to the variability in contact interface parameters is simulated. The simulated natural frequencies are then employed and uncertainty in the parameters of a simplified stochastic joint model is identified. A hybrid analytical-FE modelling approach is also proposed to obtain the natural frequencies of the simplified dynamic model of the structure.

2 Theoretical background and development

Mechanical joints introduce flexibility into assembled structures due to the normal and tangential stiffnesses of their contact interfaces. The overall stiffness of two surfaces in contact in the normal and tangential directions has been addressed by many researchers in the past [5-7]. The contact interfaces are one of the

main sources of uncertainty in the assembled structure [8]. A main source of variability in contact parameters is the randomness in the contact surface characteristics such as preload and surface finish. In the next section, a thin layer with stochastic material properties is proposed to model contact surfaces based on the randomness in contact surface parameters.

2.1 Stochastic thin layer

In this section, two rough surfaces in contact with each other, as shown in Figure 1, is considered. From a microscopic point of view, the real profile of a surface $z(x, y)$ can be considered as a random process being described by the height statistical distribution function $\varphi(z)$ and the autocorrelation function $\mathcal{R}(\lambda)$ [9].

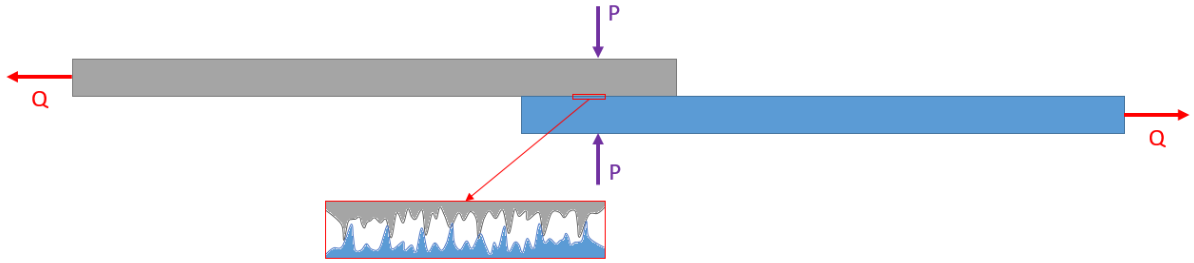


Figure 1: Contacting rough surfaces in a typical lap-joint application

The contact interface is loaded in normal and tangential directions as shown in Figure 1. Following the approximation made by Greenwood and Williamson [10] and to derive the tangential stiffness corresponding to the contact surfaces shown in Figure 1, we consider a smooth rigid surface in contact with a rough elastic surface as shown in Figure 2(a). We also consider the contact between two surfaces as the contact between widely spaced asperities.

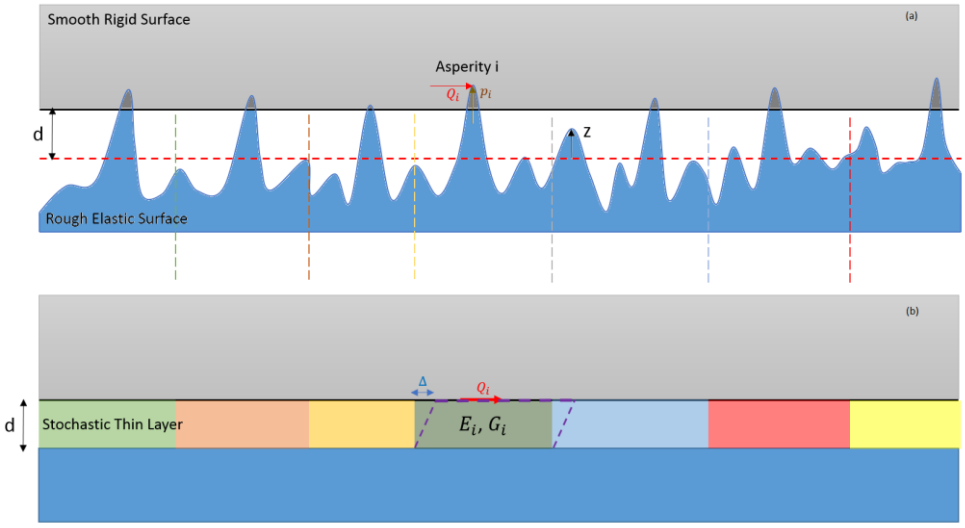


Figure 2: Contact between two rough surfaces (a) and the equivalent thin layer (b)

Based on Hertzian contact theory [11] the pressure distribution around asperity i with radius of curvature R_i carrying the normal load P_i can be approximated by [12],

$$p(r_i) = \left(\frac{6P_i E^{*2}}{\pi^3 R_i^2}\right)^{1/3} \sqrt{1 - \left(\frac{r_i}{a_i}\right)^2} \tag{1}$$

where r_i is a radial coordinate centered on asperity i. a_i and E^* are the radius of the contact patch and the equivalent modulus of elasticity of the contacting pair respectively. They are given by,

$$a_i = \left(\frac{3P_iR_i}{4E^*}\right)^{1/3},\ E^* = \frac{E}{1-\upsilon} \tag{2-3}$$

where E is the Young's modulus and υ is the Poisson's ratio of the contact surfaces. The contact surfaces are considered identical in this paper. This makes it possible to assume that the asperities are initially in stick regime (e.g. no slip takes place) when the contact interface is loaded tangentially. Therefore, the distribution of shear force around asperity *i* is given by [11],

$$q(r_i) = \frac{Q_i}{2\pi {a_i}^2\sqrt{1-\left(\frac{r_i}{a_i}\right)^2}} \tag{4}$$

where Q_i is the shearing force applied to asperity i. The tangential stiffness of asperity *i* can be expressed as [13],

$$\kappa_i^T = \frac{Q_i}{\Delta} = 8a_i\left(\frac{G}{2-\upsilon}\right) = 4a_i\left(\frac{E}{(2-\upsilon)(1+\upsilon)}\right) \tag{5}$$

where Δ is the relative tangential displacement of the contacting bodies and G is their shearing modulus. Since the asperities are randomly distributed and therefore have random parameters, Equation (5) indicates a random distribution of tangential stiffnesses in the contact interface.

The linear behaviour of contacting asperities - i.e. prior to slippage- can be analyzed by simulating the contact interface of Figure 2(a) as a thin layer shown in Figure 2(b). It can be ideally assumed that the thin layer is divided into N sections, each corresponding to one asperity in contact. Therefore, since the contacting asperities have a stochastic distributed function $\varphi(z)$, the thin layer has consequently stochastic distributed material properties.

The shear stress for the section of thin layer corresponding to asperity i with shear modulus G_i can be expressed as [14],

$$\tau_i = G_i\gamma \approx G_i\frac{\Delta}{d} \tag{6}$$

The shear stress can also be calculated by using the tangential force Q_i and the area of the contact patch A_i corresponding to asperity *i*,

$$\tau_i = \frac{Q_i}{A_i} \tag{7}$$

By combining equations (6) and (7) and using the definition of tangential stiffness in equation (5) one obtains,

$$\kappa_i^T = \frac{Q_i}{\Delta} = \frac{1}{d}A_iG_i \tag{8}$$

Finally, by using equation (5) and (8) the shear modulus for the section of thin layer corresponding to asperity i is obtained as,

$$G_i = 8d\left(\frac{G}{2-\upsilon}\right)\frac{a_i}{A_i} = 4d\left(\frac{E}{(2-\upsilon)(1+\upsilon)}\right)\frac{a_i}{A_i} \tag{9}$$

Equation (9) indicates that the contact interface can be modelled as a thin layer having randomly distributed material properties. Therefore, the shear modulus of the stochastic thin layer is considered as,

$$G_{TL} = G_0\big(1+\varepsilon\varphi_G(z)\big) \tag{10}$$

where G_0 is the mean value of the distributed shear modulus and $\varphi_G(z)$ is a zero-mean stationary field. The ratio between the normal and tangential stiffnesses of two similar contact surfaces is a function of the Poison's ratio [13, 15], i.e. $\kappa^N/\kappa^T = f(\upsilon)$. Since the normal stiffness of the contact interface can be directly related to the Young's modulus E_{TL} of the stochastic thin layer, we also assume,

$$E_{TL} = E_0\big(1+\varepsilon\varphi_G(z)\big) \tag{11}$$

where E_0 is the mean value of the distributed elastic modulus of the contact interface. If the behaviour of the contact interface in the normal and tangential directions is assumed to be decoupled, then equations (10) and (11) can fully describe the behaviour of the stochastic thin layer, otherwise, based on Hook's law a

constant Poisson's ratio υ_0 is defined for the stochastic thin layer which satisfies $G_0 = E_0/2(1+\upsilon_0)$. The concept of the contact interface model using a stochastic thin layer is used in the following sections to simulate the behaviour of an assembled structure. First, simulation of the material properties over the contact interface as a 2D random field is considered in the next section.

2.2 Simulation of stochastic material properties in 2D

We consider the distribution of the material properties over the contact interface, i.e. G_{TL} and E_{TL}, as spatial processes which are characterized by $\varphi_G(z)$ as defined in equations (10) and (11). $\varphi_G(z)$ contains a set of random variables $\{\varphi_t, t \in \mathrm{T}\}$ where T, the index set, is some subset of the 2-dimensional Euclidian space $\mathbb{R}^2$. φ_t is a random quantity defining the randomness in the shear modulus associated with a spatial position t in the contact interface. The state space of the special process is defined as the set of possible values of φ_t. Since FE modeling of the contact interface is considered in the next sections and, therefore, discrete number of material properties are assigned to a discrete number of elements to model a continuous contact interface, $\{\varphi_t, t \in \mathrm{T}\}$ is a special process with discrete index set and continuous state space. The Gaussian random field $\varphi_G(z)$ at a set of discrete points $t_1, \dots, t_r$ in $\mathbb{R}^2$ over the contact interface is defined as,

$$\varphi_G(z) = \left(\varphi_{t_1}, \dots, \varphi_{t_r}\right)^T \sim N(\mu_t, \Sigma_{s,t}) \tag{12}$$

where $\mu_t = \mathbf{E}\varphi_t$ is the expectation function and $\Sigma_{s,t} = \boldsymbol{cov}(\varphi_t, \varphi_s)$ is the covariance function. The Gaussian process is stationary if the expectation function is constant and the covariance function does not change under translation, i.e. $\boldsymbol{cov}(\varphi_{t+u}, \varphi_{s+u}) = \boldsymbol{cov}(\varphi_t, \varphi_s)$.

In the following, simulation of the stationary Gaussian process $\varphi_G(z)$ on a $n \times m$ rectangular grid representing the FE mesh grid corresponding to the stochastic thin layer is investigated. We consider the covariance function between two points $\{s\} = [x_s, y_s]$ and $\{t\} = [x_t, y_t]$ in the rectangular grid to depend on the Euclidean distance, i.e.

$$\boldsymbol{cov}(\varphi_t, \varphi_s) = \rho(\{s\} - \{t\}) = e^{-\frac{1}{b}\sqrt{(x_s - x_t)^2 + (y_s - y_t)^2}} \tag{13}$$

It is noteworthy that the random field is isotropic, i.e. the distribution remains the same under rotation, if $\rho(s-t) = \rho(\|s-t\|)$. Let Ω be an $mn \times mn$ symmetric block-Toeplitz covariance matrix where $mn = m \times n$. The covariance matrix Ω can be uniquely characterized by its first block row $(R_1, \dots, R_n)$ where each block $R_k, k = 1, \dots, n$ is also characterized by its first row and column. Having Ω, the $\overline{mn} \times \overline{mn}$ block-circulant matrix Σ where $\overline{mn} = (2m-1) \times (2n-1)$ is constructed. The procedure for constructing Ω and Σ is described in [1]. After diagonalizing the block circulant matrix as $\Sigma = \mathrm{P}^* diag(\gamma)\mathrm{P}$, matrix Γ is formed by using eigenvalues $\gamma_k, k = 1, \dots, (2m-1) \times (2n-1)$. By defining a complex Gaussian matrix Z with entries $\mathrm{Z}_{j,k} = \mathrm{U}_{j,k} + i\mathrm{V}_{j,k}$ where $\mathrm{U}_{j,k}, \mathrm{V}_{j,k} \sim N(0,1)$, the realization of the Gaussian field φ_G is obtained from the two-dimensional fast Fourier transform (FFT2) of $\sqrt{\Gamma} \odot \mathrm{Z}$ where square root is applied to each component of Γ and $\odot$ denotes component-wise multiplication [16]. Some realizations of φ_G are shown in the left hand-side of Figure 3. In the right hand-side of Figure 3, the distributions of φ_G are shown which indicate a random distribution.

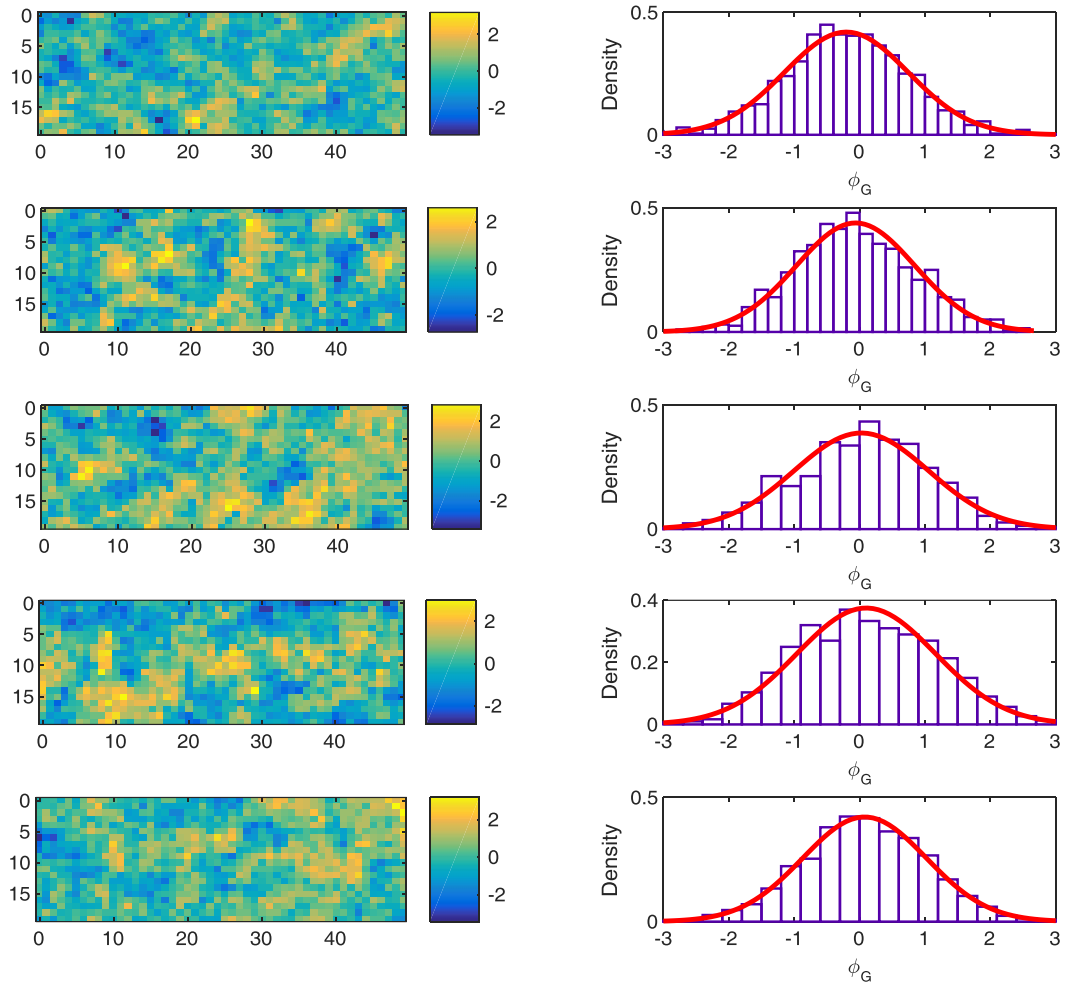


Figure 3: Some realizations of φ_G

2.3 Stochastic modeling of a bolted structure

In this section the dynamic model of an assembled structure is considered. We first describe how to model the stochastic interface joint model and later the model will be used to identify the joint model parameters based on simulated data. A bolted structure as shown in Figure (4) is considered. The structure contains two beam substructures connected through a frictional contact interface provided by a bolted lap joint.

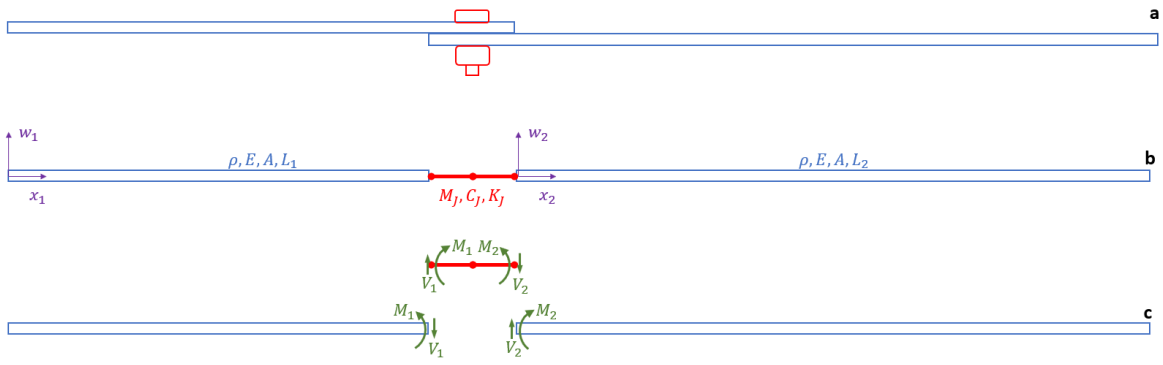


Figure 4: Schematic of the joined structure (a), hybrid FE-Analytical modeling method (b) and internal forces at the joint boundaries (c)

The equations governing the beam sections of the structure shown in Figure 4(b) can be written as,

$$EIw_1'''' + \rho A\ddot{w}_1 = 0, \quad 0 \le x \le L_1 \tag{14}$$

$$EIw_2'''' + \rho A\ddot{w}_2 = 0, \quad 0 \le x \le L_2 \tag{15}$$

The boundary conditions and compatibility requirements are,

$$w_1''(0,t) = w_1'''(0,t) = w_2''(L_2,t) = w_2'''(L_2,t) \tag{16-19}$$

$$EIw_1''(L_1,t) = M_1,\ EIw_1'''(L_1,t) = V_1,\ EIw_2''(0,t) = M_2,\ EIw_2'''(0,t) = V_2 \tag{20-23}$$

The equations governing the dynamic response of an FE model representing the joint section can be written as,

$$\left[\boldsymbol{M_J}\right]\{\ddot{\boldsymbol{d}}_{\boldsymbol{J}}(\boldsymbol{t})\} + \left[\boldsymbol{C_J}\right]\{\dot{\boldsymbol{d}}_{\boldsymbol{J}}(\boldsymbol{t})\} + \left[\boldsymbol{K_J}\right]\{\boldsymbol{d_J}(\boldsymbol{t})\} = \{\boldsymbol{f_J}(\boldsymbol{t})\} \tag{24}$$

where,

$$\{\boldsymbol{d_J}(\boldsymbol{t})\} = \begin{bmatrix} w_1(L_1,t) & w_1'(L_1,t) & \{\bar{d}\}_{q-4\times1}^T & w_2(0,t) & w_2'(0,t) \end{bmatrix}^T \tag{25}$$

$$\{\boldsymbol{f_J}(\boldsymbol{t})\} = \begin{bmatrix} V_1 & M_1 & \{0\}_{q-4\times1}^T & V_2 & M_2 \end{bmatrix}^T \tag{26}$$

In equations (25) and (26), $q = 2\bar{n} + 2$ is the number of DOFs of FE model and $\bar{n}$ is the number of elements used for modeling the joint section. Since free vibration response of the structure is considered we have,

$$w_i(x,t) = Y_i(x)e^{j\omega t}, i = 1{,}2 \quad \{\boldsymbol{d_J}(\boldsymbol{t})\} = \{\boldsymbol{X}\}e^{j\omega t} \tag{27,28}$$

From equations (20-23) and (26-27) one may deduce,

$$\{\boldsymbol{f_J}(\boldsymbol{t})\} = \{\boldsymbol{F}\}e^{j\omega t} \tag{29}$$

By using equations (4), (28) and (29) one obtains,

$$[\boldsymbol{D}]\{\boldsymbol{X}\} = \{\boldsymbol{F}\} \tag{30}$$

where $[\boldsymbol{D}] = \left[\boldsymbol{K_J}\right] + j\omega\left[\boldsymbol{C_J}\right] - \omega^2\left[\boldsymbol{M_J}\right]$.

By rearranging equation (30) in the following form,

$$\begin{bmatrix} (D_{11})_{2\times2} & (D_{12})_{2\times q-4} & (D_{13})_{2\times2} \\ (D_{21})_{q-4\times2} & (D_{22})_{q-4\times q-4} & (D_{23})_{q-4\times2} \\ (D_{31})_{2\times2} & (D_{32})_{2\times q-4} & (D_{33})_{2\times2} \end{bmatrix} \begin{Bmatrix} X_1 \\ \bar{X}_j \\ X_2 \end{Bmatrix} = \begin{Bmatrix} F_1 \\ 0 \\ F_2 \end{Bmatrix} \tag{31}$$

From the second equation in (31), $\bar{X}_j$ is obtained as,

$$\bar{X}_j = -D_{22}^{-1}(D_{21}X_1 + D_{23}X_3) \tag{32}$$

By substituting equation (32) into equation (31), the shear forces and bending moments at the joint boundaries can be obtained as,

$$\begin{Bmatrix} V_1 \\ M_1 \\ V_2 \\ M_2 \end{Bmatrix} = \begin{bmatrix} D_{11} - D_{12}D_{22}^{-1}D_{21} & D_{13} - D_{12}D_{22}^{-1}D_{23} \\ D_{31} - D_{32}D_{22}^{-1}D_{21} & D_{33} - D_{32}D_{22}^{-1}D_{23} \end{bmatrix} \begin{Bmatrix} Y_1(L_1) \\ Y_1'(L_1) \\ Y_2(0) \\ Y_2'(0) \end{Bmatrix} \tag{33}$$

By substituting equations (27) and (28) into equations (14-23), solving the resultant equations and satisfying boundary conditions and compatibility requirements, the natural frequencies of the system can be obtained.

The joint section in Figure 4(b) is modelled by using 2-noded generic elements [17]. The generic joint model is employed to obtain the stiffness matrix of the joint elements. To consider the randomness in the joint contact surfaces described in previous sections, the joint parameters are considered as random fields. The stiffness matrix of the generic joint element is then considered as,

$$\left[\boldsymbol{k_j}(\boldsymbol{\theta})\right] = k_1(\theta)\{\boldsymbol{u_1}\}\{\boldsymbol{u_1}\}^T + k_2(\theta)\{\boldsymbol{u_2}\}\{\boldsymbol{u_2}\}^T \tag{34}$$

where $k_{\mathrm{i}}(\theta) = k_{\mathrm{i0}}(1 + \varepsilon_i f_i(\theta))$ $(i = 1,2)$. k_{i0} and $0 < \varepsilon_i \ll 1$ (i=1,2) are the mean values and deterministic constants and $f_i(\theta)$ is a zero mean random field describing the variability in the joint parameters. In equation (34) $\{\boldsymbol{u_1}\}$ and $\{\boldsymbol{u_2}\}$ are defined as,

$$[\overline{\boldsymbol{u}}] = \begin{bmatrix}\{u_1\}^T \\ \{u_2\}^T\end{bmatrix} = \begin{bmatrix}2/L & 1 & -2/L & 1 \\ 0 & -1 & 0 & 1\end{bmatrix} \tag{35}$$

The mean values and scaling factors in equation (34) can be identified by using experimental results which is described in the next section.

2.4 Maximum likelihood method

Identification of the stochastic joint model parameters described in the previous section is considered by using natural frequencies and employing the maximum likelihood method as described in this section. The natural frequencies can be related to the joint parameters by,

$$\mathbf{y} = \mathbf{f}(\mathbf{x}) \tag{36}$$

where $\mathbf{x} = [k_1, k_2]^T$ is the vector of joint parameters and $\mathbf{y} = [\omega_1, \dots, \omega_{\mathrm{m}}]^T$ is the vector of natural frequencies. If the distribution of natural frequencies is known, our goal is to identify the distribution of the parameters by using the maximum likelihood method. For identification purposes, we assume X as the distribution function of the parameters which belongs to a specific distribution family, i.e. $X \sim \mathrm{O}(\theta_x)$. where θ_x is a random vector with mean vector $\{\boldsymbol{\mu_x}\}$ and covariance matrix $[\boldsymbol{\Sigma_x}]$ which need to be identified. Uncertainty propagation methods such as perturbation or Monte-Carlo can be used to calculate the probability distribution of the natural frequencies $f(y|\theta_x)$ for a given θ_x.

For a set of N independent response measurements (i.e. natural frequencies) $\left[y'_{(1)}, \dots, y'_{(N)}\right]$, the log likelihood is given by,

$$l(\theta_x) = log(f(y'_{(1)}, \dots, y'_{(N)}|\theta_x)) = \sum_{i=1}^{N} \log(f(y'_{(i)}|\theta_x)) \tag{37}$$

The optimum value of θ_x can be identified by maximizing equation (37) which can be done by using optimization approaches. In this paper the perturbation method [18] is used to estimate equation (37). In the next sections, a numerical example is used to demonstrate the modeling and identification methods.

3 Application to a numerical example

Proper identification of model uncertainties in real structures is always limited by the number of response samples available. To overcome this limitation, in this section variability in the contact interface of an assembled structure is simulated by using an FE method. The FE model makes it possible to generate many samples which will be used in the uncertainty identification of the joint model parameters. First, simulation of the variability in the contact interface is considered.

3.1 FE modelling and experimental simulation results

To investigate the applicability of the modelling methods described in the previous sections, in this section a simulated example is considered. A bolted structure is modelled in Ansys as shown in Figure 5. The structure is composed of two beam sections (400 mm and 300 mm in length) being connected by a 20 mm × 50 mm contact interface. The structure is modeled in Ansys by using SOLID186 element. The contact interface is modeled using a layer of 1000 solid elements of dimension $1 \times 1 \times 0.125$ mm. The thin layer elements have distributed material properties as described in the previous sections. The beam sections are made of steel (i.e. $E_s = 210$ GPa, $\rho_s = 7800 \frac{\mathrm{kg}}{\mathrm{m}^3}$ and $\upsilon_{\mathrm{s}} = 0.3$). The material distribution of the contact

interface is defined based on equation (11) such that $E_0 = 50$ MPa, $\upsilon_0 = 0.3$ and $\varepsilon = \frac{1}{3}$. Figure 5 also shows a realization of distributed material properties over the contact interface,

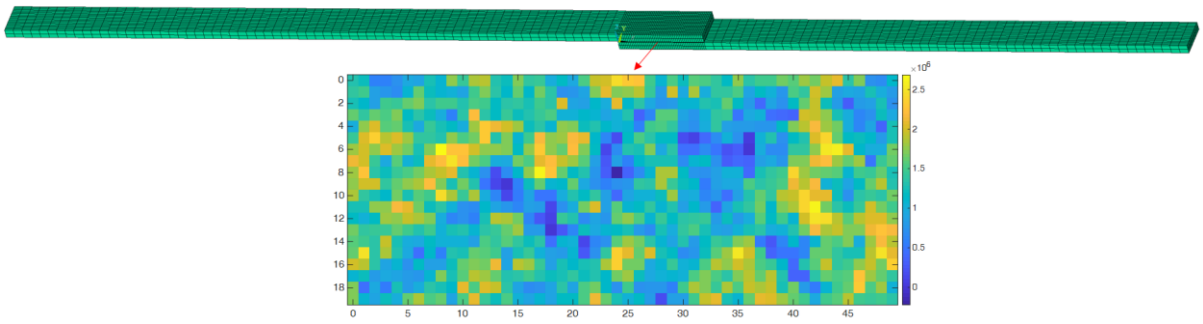


Figure 5: FE model and realization of the contact interface material properties

To generate sufficient samples for uncertainty identification of the joint model parameters, 8000 samples for the distribution of material properties of the contact interface is considered and for each sample the FE model is analyzed, and the natural frequencies are obtained. The distribution of different natural frequencies is shown in Figure 6. Figure 6 shows a reasonable distribution in natural frequencies for the first four bending modes in the XZ-plane. The distribution of natural frequencies for these modes are used in the next section and uncertainty in the joint model parameters are identified.

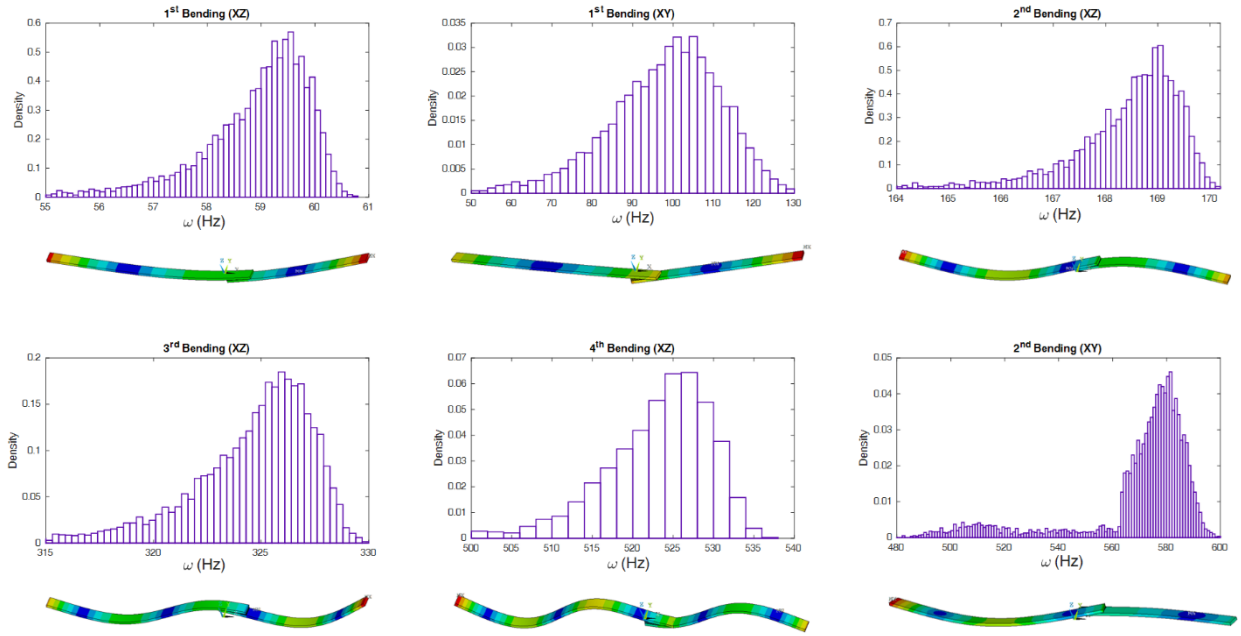


Figure 6: Distribution of natural frequencies due to randomness in contact interface parameters

The results presented in Figure (6) indicate that the distribution of natural frequencies is a negatively skewed (skewed-left) distribution.

3.2 Dynamic modeling and parameter identification

To identify the uncertainty in the parameters of the contact interface, a dynamic model based on Figure 4(b) is constructed for the structure. The beam sections are modelled by using equations (14) and (15). 5 joint elements defined by equation (34) are used to model the joint section of the structure in equation (24). Since the undamped natural frequencies will be used to identify the joint parameters, the damping matrix of the joint model in equation (24) is ignored, i.e. $[C_J] = 0$. By considering some values for joint parameters k_1

and k_2, the natural frequencies can be estimated by employing the modeling method described in previous sections.

To identify the mean values and deterministic constants of the joint model parameters defined in equation (34), maximization of the log likelihood estimator given by equation (37) by employing a uni-directional search optimization approach is utilized. The initial joint parameter values of the stochastic model, i.e. k_{i0} and ε_i (i=1,2), in the identification procedure are estimated by updating a deterministic model using mean values of the first four natural frequencies, i.e. $\bar{\omega}_i, i = 1, \dots, 4$, corresponding to the bending modes in the XZ plane. The deterministic model is obtained by choosing $k_i(\theta) = \bar{k}_i, i = 1,2$ in equation (34). The deterministic model is updated by using the natural frequency sensitivity approach. The identified deterministic joint model parameters and the accuracy of the identified deterministic model are reported in Table 1.

	$\bar{\omega}_1$	$\bar{\omega}_2$	$\bar{\omega}_3$	$\bar{\omega}_4$
Simulated	58.9	168.5	324.6	519.8
Updated	59.1	167.4	322.0	522.7
Error (%)	0.49	-0.59	-0.73	0.95

Table 1: Updating of the deterministic model ($\bar{k}_1 = 46.4$, $\bar{k}_2 = 7017.0$)

The initial mean values of the stiffness parameters, i.e. $k_{i0}, i = 1,2$, are set as the identified parameters reported in Table 1. The initial deterministic constants, i.e. $\varepsilon_i, i = 1,2$, are chosen as 30% of the initial mean values of the stiffness parameters. After selecting the initial values, the identification of stochastic model is carried out by maximizing equation (37). Two different distribution functions are considered for the joint parameters $k_1(\theta)$ and $k_2(\theta)$: normal distribution and Weibull distribution functions.

Based on the assumed distribution functions, populations of joint parameters are generated. The natural frequencies are calculated at each set of joint parameters from the generated populations by solving the characteristic equation, i.e $|H(\omega)| = 0$, which finally results in a distribution for each natural frequency, i.e. $[\, y_{(1)}, \dots, y_{(N')}]$. The parameters of the Normal distribution for the joint parameters are fine tuned such that the likelihood estimator defined in equation (37) is maximized. By using perturbation method, the likelihood estimator for the normal distribution is obtained as,

$$l(\{\mu_x\}, [\Sigma_x]) = -\frac{1}{2}\Big(Nm\ log\ 2\pi + N \log|\Sigma_y| + \sum_{i=1}^{N}\big(\{y\}'_{(i)} - \{\mu_y\}\big)^T [\Sigma_y]^{-1}\big(\{y\}'_{(i)} - \{\mu_y\}\big)\Big) \quad (38)$$

where $\{\mu_x\}$ and $[\Sigma_x]$ are the mean vector and covariance matrix of the joint parameters, $\{y\}'_{(i)}$ is the vector of simulated natural frequencies shown in Figure 6 and $\{\mu_y\}$ and $[\Sigma_y]$ are the mean vector and covariance matrix of the distribution of natural frequencies described above. A diagonal covariance matrix is considered in this paper which is equivalent to using the *normlike* command of Matlab. Figure 7 shows the identified joint parameters based on a normal distribution function and in Figure 8 the distribution of the simulated and identified natural frequencies are compared.

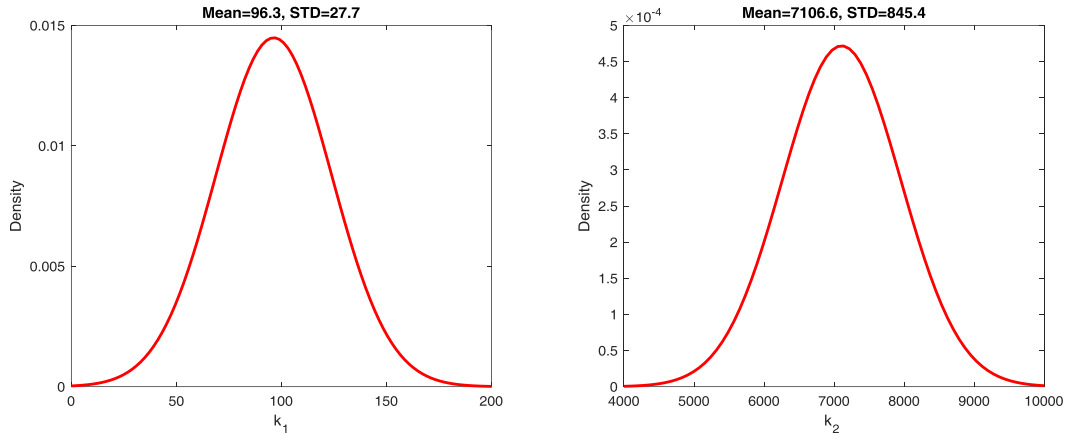


Figure 7: Identified joint parameters based on Normal distribution function

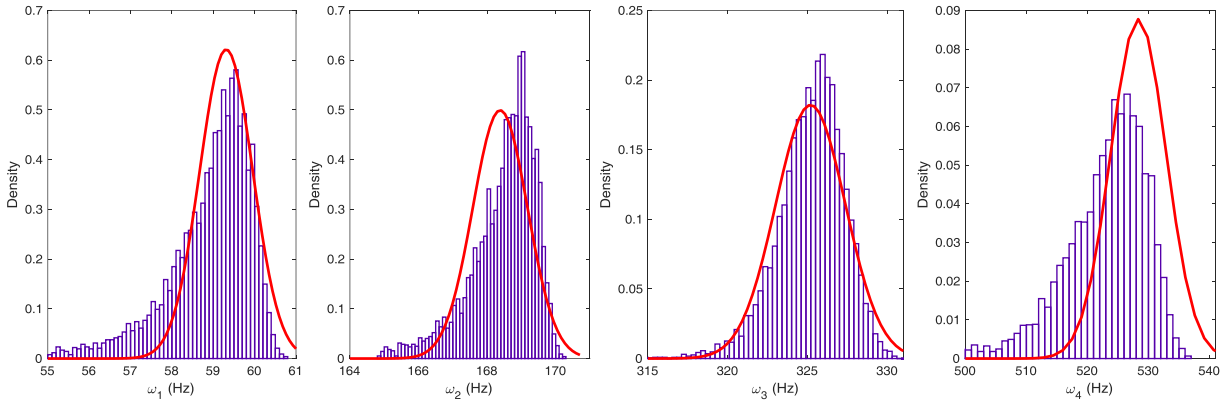


Figure 8: Simulated (bars) and identified (lines) natural frequencies

Having the simulated natural frequencies $[y'_{(1)}, \dots, y'_{(N)}]$ and the generated natural frequencies $[y_{(1)}, \dots, y_{(N')}]$, the Weibull log-likelihood is estimated by using *wbllike* command of Matlab to compute equation (37) which is maximized to obtain the joint parameters. In Figure 9 the identified joint parameters based on a Weibull distribution function are shown. The distribution of the simulated and identified natural frequencies based on a Weibull distribution function are compared in Figure 10.

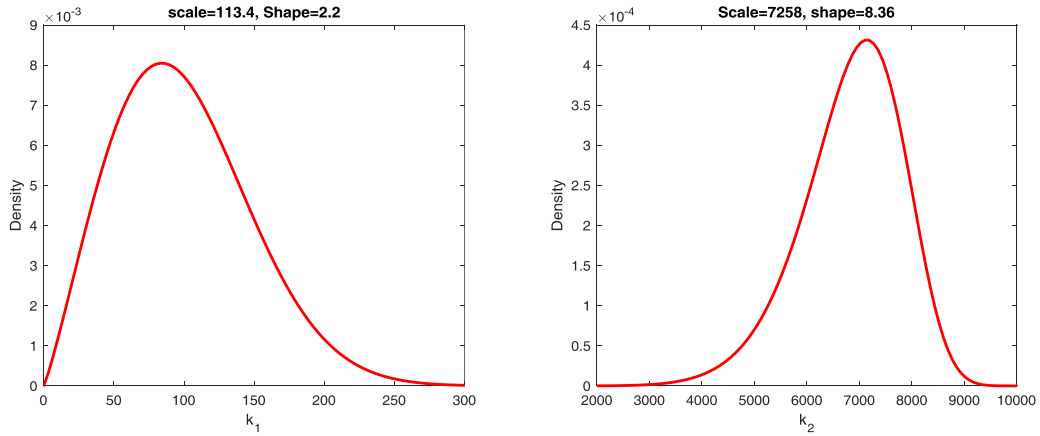


Figure 9: Identified joint parameters based on Weibull distribution function

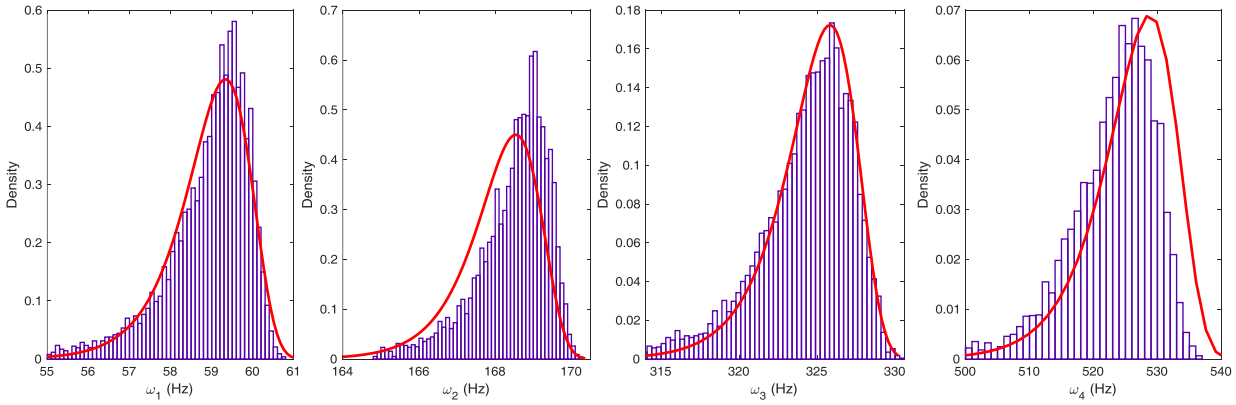


Figure 10: Simulated (bars) and identified (lines) natural frequencies

The presented results in Figure 8 and 10 indicate that although for two considered distribution functions the identification is successful, the Weibull distribution function ends in better identification results.

4 Conclusions

In this paper simulation of the variability in the contact interfaces of bolted lap-joints and identification of uncertainties in parameters of a stochastic joint model was considered. First, a stochastic thin layer was proposed to simulate the randomness in the parameters of the contact interface by stochastic material properties. Then an FE model of assembled structure was constructed, and the contact interface was represented by stochastic thin layer and variability in natural frequencies resultant from the variability in contact interface material properties was investigated. The results show that although the distribution of the contact parameters is normal, the distribution of the natural frequencies is more like a beta distribution. Finally, uncertainty in the parameters of a simplified joint model was identified by using the maximum likelihood method.

Acknowledgment

This research is funded by the Engineering and Physical Sciences Research Council through Grant no. EP/P01271X/1.

References

[1] S. N. Gangadharan, E. Nikolaidis, R. Haftka, *Probabilistic system identification of two flexible joint models*, AIAA Journal, Vol. 29, No. 8, (1991), pp. 1319-1326.

[2] C. Lopez, A. Baldomir, E. Menga, S. Hernandez, C. Cid, D. Freire, *A study of uncertainties in dynamic properties of assembled aircraft structures*, in International Conference on Noise and Vibration Engineering - International Conference on Uncertainty in Structural Dynamics ISMA2016-USD2016, Leuven, Belgium, 2016.

[3] Q. T. Guo and L. M. Zhang, *Identification of the Mechanical Joint Parameters with Model Uncertainty*, Chinese Journal of Aeronautics, Vol. 18, No. 1, (2005), pp. 47-52.

[4] G. M. Castelluccio, M. R. W. Brake, *On the origin of computational model sensitivity, error, and uncertainty in threaded fasteners*, Computers and Structures, Vol. 186, (2017), pp. 1-10.

[5] R. A. Onions, J. F. Archard, *The contact of surfaces having a random structure*, Journal of Applied Physics, Vol. 6, (1973), pp. 289-304.

[6] H. A. Sherif, S. S. Kosa, *Relationship between normal and tangential contact stiffness of nominally flat surfaces*, Wear, Vol. 151, (1991), pp. 49-62.

[7] M. L. Raffa, F. Lebon, G. Vairo, *Normal and tangential stiffnesses of rough surfaces in contact via an imperfect interface model*, International Journal of Solids and Structures, Vol. 87, (2016), pp. 245-253.

[8] D. J. Segalman, D. L. Gregory, M. J. Starr, B. R. Resor, M. D. Jew, J. P. Lauffer, N. M. Ames, *Handbook on Dynamics of Jointed Structures*,, Albuquerque: Sandia National Laboratories, (2009).

[9] G. P. Petropoulos, C. N. Pandazaras, J. C. Davim and H. West, *Surface texture characterization and evaluation related to machining*, London: Springer-Verlag, (2010).

[10] J. A. Greenwood and J. P. B. Williamson, *Contact of nominally flat surfaces*, Proceedings of the Royal Society of London. Series A, Mathematical and Physical Sciences, Vol. 295, No. 1442, (1966), pp. 300-319.

[11] K. L. Johnson, *Contact Mechanics*, Cambridge : Cambridge University Press, 1985.

[12] S. Medina, D. Nowell and D. Dini, *Analytical and Numerical Models for Tangential Stiffness of Rough Elastic Contacts*, Tribology Letter, Vol. 49, (2013), pp. 103-115.

[13] R. D. Mindlin, *Compliance of elastic bodies in contact*, Journal of Applied Mechanics, Vol. 16, (1949), pp. 259-268.

[14] C. Erlich, A. Schmidt and L. Gaul, *Microslip joint damping prediction using thin-layer elements*, Dynamics of Coupled Structures, vol. 1, (2014), pp. 239-244.

[15] S. Akarapu, T. Sharp and M. O. Robbins, *Stiffness of contacts between rough surfaces*, Physical Review Letters, vol. 106, (2011), 204301.

[16] D. P. Kroese and Z. I. Botev, *Spatial process simulation*, in Stochastic Geometry, Spatial Statistics and Random Fields, Springer, 2015, p. 369–404.

[17] H. Ahmadian and H. Jalali, *Generic element formulation for modelling bolted lap joints*, Mechanical Systems and Signal Processing, vol. 21, No. 5, (2007), pp. 2318-2334.

[18] J. R. Fonseca, M. I. Friswell, J. E. Mottershead and A. W. Lees, *Uncertainty identification by the maximum likelihood method*, Journal of Sound and Vibration, vol. 288, (2005), pp. 587–599.

A Bayesian filtering approach to operational modal analysis with recovery of forcing signals

T. J. Rogers [1], **K. Worden** [1], **G. Manson** [1], **U. T. Tygesen** [2], **E. J. Cross** [1]
[1] Department of Mechanical Engineering, Mappin Building,
Mappin Street, Sheffield, S1 3JD, UK
e-mail: **trogers3@sheffield.ac.uk**

[2] Ramboll Energy, Bavnehøjvej 5, DK-6700 Esbjerg Denmark

Abstract
Operational Modal Analysis (OMA) remains a difficult and active area of research, especially when unmeasured loads on a structure, are harmonic and close to the resonant frequencies in the presence of light damping. This situation arises across engineering, one example is in the offshore energy industry where wave loads are commonly a narrowband loading close to the resonant frequencies of the structure. This paper presents a *grey-box* approach to the OMA problem, where a physical model of the system dynamics is combined with a technique from machine learning. A Latent Force Model (LFM) is used to represent the loading acting on a structure where the forcing is assumed to be a Gaussian Process (GP). The model is transformed into a state-space formulation and inference is performed simultaneously over the system parameters and the hyperparameters of the GP via a Markov-Chain Monte-Carlo method. This is gives distributions over the system parameters and produces a good prediction of the latent forces acting on the system.

1 Introduction

Experimental modal analysis of linear systems is a well established area of interest within structural dynamics. Techniques for inferring the system parameters of linear systems where input and output data are present are now mature and can be found in any good undergraduate textbook, for example see [1]. In a wider sense, the handling of second order linear time-invariant (LTI) systems, of which physical dynamic systems are a subset, is also well covered in the literature [2]. Unfortunately, for many structures which are encountered by engineers, it is not possible to gather information regarding the input to the system — the forcing. This is due to two important factors; first, it is not possible to place sensors in the load path to some structures such as buildings undergoing base excitation from earthquakes. Second, it can be prohibitively expensive to design and fit sensors which can withstand the environmental conditions in which the structure operates. This is the case in the offshore energy industry where wave loading presents a phenomenon which is difficult to measure and which produces an environment in which sensors must be very robust.

The current solution to this is to use techniques in operational modal Analysis (OMA), or output-only modal analysis. Reviews of some techniques which may be used can be found in [3, 4], however, a common problem encountered is the identification of modal behaviour when the loading has significant harmonic components which are close to the modes of the structure and when the structure is lightly damped. In this case it becomes very difficult to separate the narrow peaks in the frequency domain due to the harmonic loads and those from the resonances of the structure.

This paper makes use of a state-space form of the system which is a common approach in OMA techniques and one that has been shown to be effective for state/input estimation [5, 6]. It has become commonplace to use the Extended Kalman Filter (EKF) formulation where the parameters of the model are included as

additional states. In this way recursive estimates of the system parameters can be made within the Bayesian filtering setting [7]. Lourens *et. al* [8] show a Kalman filter based formulation for estimation of the states of the structure and the forcing signal based on fixed parameter sets from a reduced order finite element (FE) model.

This paper aims to incorporate a novel use of the machine learning Latent Force Model [9] in a state space formulation [10] to allow efficient inference with a nonparametric prior over the forcing function. Alongside this, Bayesian estimates of the system properties can be obtained using MCMC inference over the state space model, this avoids the linearisation present in the EKF formulation for parameter estimates. Being a Bayesian model of the full system, this methodology returns distributions over the parameters and also the forcing function which give indication of the uncertainty in both the inputs and also the parameters. This can be carried forward into further uncertainty quantification analysis or used for heuristic assessment of model quality.

The layout of the paper is as follows: the theoretical foundations of the model are laid out in Sections 2 to 4 covering an introduction to Gaussian Processes, state-space modelling, and the Latent Force Model. The application of this model to the problem of OMA is discussed in Section 5, including the need to constrain the model with informative prior distributions. Section 6 presents results from use of this procedure on a simulated dataset and conclusions are made in Section 7.

2 Gaussian Process Regression

Gaussian Processes (GPs) [11, 12] are a popular non-parametric Bayesian machine learning technique. The most interpretable explanation is as a distribution over functions, so each random draw from a GP is a function from a functional family defined by the covariance function and specified by the data that has been used to train the process. In this section we adopt notation from within the GP community which is in line with that in [12], and which presents the general case for any GP, in the rest of the paper the notation will be consistent with the usual practice in state-space models for clarity.

A Gaussian Process is fully defined in terms of its mean function $m(\boldsymbol{x})$ (the mean is commonly assumed to be zero and this convention is adopted here although addition of an explicit mean function is trivial) and its covariance function $k(\boldsymbol{x}, \boldsymbol{x}')$, see Eq. (1). The covariance function allows the computation of the covariance between any two data points $\boldsymbol{x}_i$ and $\boldsymbol{x}_j$ such that the element in the covariance matrix K_{ij} is given by $k(\boldsymbol{x}_i, \boldsymbol{x}_j)$. This allows the covariance matrix for any finite number of data points to be calculated analytically.

$$f(\mathbf{x}) \sim \mathcal{GP}\left(m(\mathbf{x}), k(\mathbf{x}, \mathbf{x}')\right) \tag{1}$$

Assuming there is a finite set of observed training data $\mathcal{D}$ with N observations of input-output pairs: $\mathcal{D} = \{\boldsymbol{x}_i, y_i\}_{i=1}^{N}$ where $y_i = f(\boldsymbol{x}_i) + \varepsilon$, $\varepsilon \sim \mathcal{N}\left(0\,,\ \sigma_n^2\right)$. This states that there is some underlying functional relationship between $f(\boldsymbol{x})$ where the observations y are corrupted by white Gaussian noise. Then the GP distribution collapses to a Multivariate Normal distribution in N dimensions, Eq. (2).

$$\boldsymbol{y} \sim \mathcal{N}\left(\mathbf{0}\,,\ K\left(X, X\right) + \sigma_n^2 \mathbb{I}\right). \tag{2}$$

Where $\boldsymbol{y}$ is the vector of all observed noisy outputs and X the matrix of all observed inputs in $\mathcal{D}$. When a new input point $\boldsymbol{x}^\star$ or number of input points $X^\star$ is observed the covariance with the training data can be calculated as a joint Gaussian formed between the training and test data, Eq. (3).

$$\begin{bmatrix} \mathbf{y} \\ \mathbf{f}_\star \end{bmatrix} \sim \left(\mathbf{0}, \begin{bmatrix} K(X, X) + \sigma_n^2 \mathbb{I} & K(X, X^\star) \\ K(X^\star, X) & K(X^\star, X^\star) \end{bmatrix}\right). \tag{3}$$

The predictive distribution over $\boldsymbol{f}^\star$ can be computed by considering the conditional distribution $p\left(\boldsymbol{f}^\star \mid \boldsymbol{x}^\star, X, \boldsymbol{y}\right)$. Since the joint is Gaussian this can be computed analytically, where it itself is a Gaussian, and the equations for the predictive mean and variance are given in Eq. (4).

$$\boldsymbol{f}^\star \sim \mathcal{N}\left(\mathbb{E}\left[\boldsymbol{f}^\star\right],\ \mathbb{V}\left[\boldsymbol{f}^\star\right]\right), \tag{4a}$$

$$\boldsymbol{f}^\star = k(\mathbf{x}^\star, X)\left[K(X,X) + \sigma_n^2\mathbb{I}\right]^{-1}\mathbf{y}, \tag{4b}$$

$$\mathbb{V}\left[\boldsymbol{f}^\star\right] = k(\mathbf{x}^\star, \mathbf{x}^\star) - k(\mathbf{x}^\star, X)\left[K(X,X) + \sigma_n^2\mathbb{I}\right]^{-1}k(X, \mathbf{x}^\star). \tag{4c}$$

3 Bayesian State-Space Models

This paper focuses on linear Gaussian state-space models. The notation, from this section onwards, is $\boldsymbol{x}(t)$ is used to represent the state vector, and $\boldsymbol{y}(t)$ the observations in the model for the continuous case or $\boldsymbol{x}_t$ and $\boldsymbol{y}_t$ for the discrete time case. $\boldsymbol{u}(t)$ and its discrete time counterpart $\boldsymbol{u}_T$ is a known input to the system at time t. It is normally most convenient to form a continuous time state-space model since differential equations readily convert into this form. The continuous time state-space transition is defined as,

$$\frac{\mathrm{d}\boldsymbol{x}(t)}{\mathrm{d}t} = F\boldsymbol{x}(t) + G\boldsymbol{u}(t) + Lw(t). \tag{5}$$

Here, F is the continuous state transition matrix, G the continuous input matrix, and L the continuous time process noise matrix when $w(t)$ is a white noise process with spectral density q. Since observation of physical systems happen in discrete time it is usual that analysis is carried out with a discrete model, the observation model is added at this point.

$$\boldsymbol{x}_{t+1} = A\boldsymbol{x}_t + B\boldsymbol{u}_t + Q, \tag{6a}$$

$$\boldsymbol{y}_t = C\boldsymbol{x}_t + R, \tag{6b}$$

with A being the discrete time transition and B the discrete time input. Q is the process noise, C the observation matrix and R the observation noise. Since the solutions to models of this form are in discrete time it is necessary to convert a continuous time transition model into its corresponding discrete time representation, i.e. find A and B from F and G. This procedure is well documented, for example see [2], and is shown here for completeness.

$$A = \exp_m\left(F\,\Delta t\right), \tag{7a}$$

$$B = F^{-1}\left[\left(A - \mathbb{I}\right)G\right]. \tag{7b}$$

$\exp_m$ is the matrix exponential operator. Δt is the sampling period when discretising the continuous time model. The continuous time noise process $Lw(t)$ must also be discretised to perform inference over the model.

$$Q = \int_0^{\Delta t} \Phi\left(\Delta t - \tau\right) LqL^\mathsf{T}\Phi\left(\Delta t - \tau\right)\mathrm{d}\tau, \tag{8}$$

where, $\Phi(\tau) = \exp_m\left(F\tau\right)$. Once discretised, it is now possible to recover the filtering distributions $p\left(\boldsymbol{x}_t \mid \boldsymbol{y}_{1:t}\right)$ and the smoothing distributions $p\left(\boldsymbol{x}_t \mid \boldsymbol{y}_{1:T}\right)$, for a time point t in a data record that is T time points long, using the Kalman filtering equations [13] and the Rauch-Tung-Striebel (RTS) smoother [14].

4 The Latent Force Approach

The Latent Force Model (LFM) [9, 15] is an approach for combining GPs with a mechanistic model where the GP is used to represent the forcing experienced by the system. In this way the output of the GP can include modelling of the dynamics of a system. This model is a form of *grey-box* where known physical processes are augmented with machine learning technology to improve model performance. Of most interest, from the point of view of structural dynamics is a second order LFM which has the familiar form of a R degree of freedom linear dynamical system.

$$M\ddot{\boldsymbol{x}} + C\dot{\boldsymbol{x}} + K\boldsymbol{x} = F. \tag{9}$$

Additionally, in the LFM, F is defined as a set of independent Gaussian Processes in time.

$$\begin{aligned} p\left(F \,|\, \boldsymbol{t}\right) = \prod_{r=1}^{R} \boldsymbol{f}_r = \prod_{r=1}^{R} \mathcal{N}\left(\mathbf{0}\,,\; K\left(\boldsymbol{t}_r, \boldsymbol{t}_r\right)\right), \\ \boldsymbol{f}_r \sim \mathcal{GP}\left(\mathbf{0}, k(t,t')\right), \end{aligned} \tag{10}$$

where the covariance of each of the latent forces in time is defined by the covariance function $k(t,t')$ giving rise to the covariance matrix $K_{\boldsymbol{f}_r,\boldsymbol{f}_r}$ which is the covariance between the latent forces at all points in time $K\left(\boldsymbol{t}_r, \boldsymbol{t}_r'\right)$ with $\boldsymbol{t}_r$ being the vector of all time points when the output is observed. While this model has produced some very promising results in modelling, the main challenge in implementing this form of model is the computational complexity which is $\mathcal{O}\left(N^3R^3\right)$ where R is the number of dimensions (degrees of freedom) and N the number of observed training points, which here is the length of the signal in time. This issue can be addressed using sparse methodologies that have become popular within the GP literature, good reviews can be found in [16, 17], more specifically [18] shows how a multiple output GP such as the one in the LFM can be computed in a sparse manner reducing the computational complexity from $\mathcal{O}\left(N^3R^3\right)$ to $\mathcal{O}\left(N^3R\right)$ using the partially independent training conditional (PITC) sparse approximation.

However, work by Hartikainen and Särkkä [19] has shown that, for GPs where the input is temporal and the covariance function is stationary, the inference procedure can be converted into a linear time-invariant (LTI) stochastic differential equation (SDE) which has a state-space formulation. This state space model can be solved, for certain cases, exactly using a Kalman filter [13] and Rauch-Tung-Striebel (RTS) smoother [14]. This methodology computes in $\mathcal{O}\left(NR^3\right)$ which is a significant improvement given that, usually, $N \gg R$.

For example, if a GP is defined to have a Matérn covariance [20] between any two points in time. Since it is a stationary covariance it is defined in terms of the absolute difference between the two input points, $r = |t - t'|$.

The Matérn class of covariance functions are governed by a smoothness parameter which gives rise to a number of special cases. Setting $\nu = 1/2$ gives rise to the exponential covariance function which equivalent to an Ornstein-Uhlenbeck process and as $\nu \to \infty$ the popular Squared Exponential (SE) covariance function [12] which is also referred to as the Gaussian kernel. Choosing values of $\nu = p + 1/2$ for p as any non-negative integer lead to simple expressions for Matérn covariance functions. In the case with smoothness parameter $\nu = 3/2$, the covariance function can be written as,

$$k(t,t') = \left(1 + \frac{\sqrt{3}r}{\ell}\right) \exp\left(-\frac{\sqrt{3}r}{\ell}\right). \tag{11}$$

Following Hartikainen and Särkkä [19] and converting the covariance function into an LTI SDE requires the spectral density, by taking the Fourier transform. Setting $\lambda = \sqrt{2\nu}\Big/\ell$ and $\nu = p + 1/2$, in the Matérn class of covariance functions it can be seen that,

$$S(\omega) \propto \left(\lambda^2 + \omega^2\right)^{-(p+1)}. \tag{12}$$

This can be factorised simply, as in Eq. (13), to recover the transfer function needed to convert to a state-space model.

$$H\left(\mathrm{i}\omega\right) = \left(\lambda + \mathrm{i}\omega\right)^{-(p+1)}. \tag{13}$$

An LTI SDE of order m has the form shown in Eq. (14) where $f(t)$ is a random process of interest, $\boldsymbol{a}$ are some set of coefficients and $w(t)$ is a white noise process which has a spectral density $S_w(\omega) = q$.

$$\frac{\mathrm{d}^m f(t)}{\mathrm{d}t^m} + a_{m-1}\frac{\mathrm{d}^{m-1} f(t)}{\mathrm{d}t^{m-1}} + \ldots + a_1\frac{\mathrm{d}f(t)}{\mathrm{d}t} + a_0 f(t) = w(t). \tag{14}$$

Rearranging this into a state-space model is possible by constructing a vector $\boldsymbol{f(t)} = \left[f(t)\frac{\mathrm{d}f(t)}{\mathrm{d}t}\ldots\frac{\mathrm{d}^{m-1}f(t)}{\mathrm{d}t^{m-1}}\right]$ which gives rise to a first order vector Markov process.

$$\frac{\mathrm{d}\boldsymbol{f(t)}}{\mathrm{d}t} = F\boldsymbol{f(t)} + Lw(t), \tag{15}$$

where,

$$F = \begin{pmatrix} 0 & 1 & & \\ & \ddots & \ddots & \\ & & 0 & 1 \\ -a_0 & \ldots & -a_{m-2} & -a_{m-1} \end{pmatrix}, \qquad L = \begin{pmatrix} 0 \\ \vdots \\ 0 \\ 1 \end{pmatrix}. \tag{16}$$

The coefficients $a_0, \ldots, a_{m-1}$ (Eq. (16)) are the coefficients of the polynomial in the denominator of the transfer function which are given by $H(\mathrm{i}\omega)$ (Eq. (13)), $h_0, \ldots, h_{m-1}$. The spectral density of the white noise process $S_w\left(\omega\right) = q$ is equal to the constant in $S\left(\omega\right)$ (**??**) which is,

$$q = \frac{2\,\sigma_f^2\,\pi^{1/2}\lambda^{(2p+1)}\Gamma\left(p+1\right)}{\Gamma\left(p+1/2\right)}. \tag{17}$$

For the case of the Matérn covariance with $\nu = 3/2$ as in Eq. (11) the equivalent state-space model is shown in Eq. (18).

$$\frac{\mathrm{d}\boldsymbol{f(t)}}{\mathrm{d}t} = \begin{pmatrix} 0 & 1 \\ -\lambda^2 & -2\lambda \end{pmatrix}\boldsymbol{f(t)} + \begin{pmatrix} 0 \\ 1 \end{pmatrix} w(t). \tag{18}$$

It is then possible to convert this continuous time state-space model to a discrete time form and solve with a Kalman filter and RTS-smoother [2]. Since the LFM model contains a temporal Gaussian process as the latent function, and the mechanistic portion of the model has a simple state-space representation, it is natural to form a state-space representation of the LFM and this was shown in [10].

In this paper the methodology is shown for a single degree of freedom (SDOF), oscillator as the mechanistic model, although it can be easily extended to the multi-degree of freedom (MDOF) case — or indeed systems with different order ordinary differential equations (ODEs). First, the equation of motion is converted to its state space form, which is again a first order vector Markov process.

Taking the SDOF equation of motion,

$$m\ddot{x} + c\dot{x} + kx = F, \tag{19}$$

dividing through by m, and setting $x_1 = x$, $x_2 = \frac{\mathrm{d}x_1}{\mathrm{d}t} = \dot{x}$ in a state vector $\boldsymbol{x}$, recovers a state-space representation of the oscillator:

$$\begin{bmatrix}\dot{x}\\ \ddot{x}\end{bmatrix} = \begin{pmatrix}0 & 1\\ -\frac{k}{m} & -\frac{c}{m}\end{pmatrix}\begin{bmatrix}x\\ \dot{x}\end{bmatrix} + \begin{pmatrix}0\\ \frac{1}{m}\end{pmatrix}F. \tag{20}$$

The formulation shown in Eq. (20) is useful where there are known external inputs to the system F and the effect of the forcing on the system is through the input matrix $B = [0,\ -1/m]^{\mathsf{T}}$. In the case of OMA these inputs are unknown but can be considered as one or more additional latent states in the model, when the transition for f is linear and described by the matrix F_f this would be written,

$$\begin{bmatrix}\dot{x}\\ \ddot{x}\\ \dot{\boldsymbol{f}}\end{bmatrix} = \begin{pmatrix}0 & 1 & 0\\ -\frac{k}{m} & -\frac{c}{m} & \frac{1}{m}\\ 0 & 0 & F_f\end{pmatrix}\begin{bmatrix}x\\ \dot{x}\\ \boldsymbol{f}\end{bmatrix} + Lw(t). \tag{21}$$

The number of additional states that are introduced is dependent upon the model chosen for the transition of f, which is now also in first order vector Markov process form. When using the LFM, it is clear from Eqs. (13) and (16) that the choice of covariance function for the GP chosen to represent F will affect the number of additional states required. Stein [21] suggests that Matérn kernels are a more appropriate choice of covariance function since the Squared Exponential imposes an unrealistic smoothness assumption. A choice of $\nu = 3/2$ as in Eq. (11), is a common choice which appears to perform well, this leads to the addition of two states to the model as in Eq. (18). This procedure leads to the full four dimensional state space model shown in Eq. (22).

$$\begin{bmatrix}\dot{x}\\ \ddot{x}\\ \dot{f}\\ \ddot{f}\end{bmatrix} = \begin{pmatrix}0 & 1 & 0 & 0\\ -\frac{k}{m} & -\frac{c}{m} & \frac{1}{m} & 0\\ 0 & 0 & 0 & 1\\ 0 & 0 & -\lambda^2 & -2\lambda\end{pmatrix}\begin{bmatrix}x\\ \dot{x}\\ f\\ \dot{f}\end{bmatrix} + Lw(t). \tag{22}$$

The model including the noise $Lw(t)$ must now be discretised to perform inference.

At this point any observation model for the observed variable y can be adopted in the process, for instance if measuring displacement it is simply Eq. (23a), or if measuring acceleration it is Eq. (23b), for both the observation matrix is multiplied by the discrete states. If other observations were available these could also be incorporated if a suitable observation model could be formed.

$$y = \begin{bmatrix}1 & 0 & 0 & 0\end{bmatrix}\begin{bmatrix}x_t\\ \dot{x}_t\\ f_t\\ \dot{f}_t\end{bmatrix} + \sigma_n^2. \tag{23a}$$

$$y = \begin{bmatrix}-\frac{k}{m} & -\frac{c}{m} & \frac{1}{m} & 0\end{bmatrix}\begin{bmatrix}x_t\\ \dot{x}_t\\ f_t\\ \dot{f}_t\end{bmatrix} + \sigma_n^2. \tag{23b}$$

Now, in possession of a model which can represent the system, attention turns to the problem of inference. While methods such as expectation maximisation exist for this form of model [22], these maximum likelihood solutions do not give information about the parameter uncertainties in the model. Instead, in this paper, a fully Bayesian solution is adopted using Markov Chain Monte Carlo (MCMC) to perform inference over the

system parameters and the GP hyperparameters. MCMC is an inference method with guaranteed convergence to the true posterior distribution of interest in the limit [23]. The parameter vector for this model, therefore, is $\boldsymbol{\theta} = \left[m, k, c, \sigma_f^2, \ell\right]$. It is assumed that the process noise in the dynamics is small (the system is well described by a linear dynamic model) and that the observation noise is known.

The likelihood of the parameters in the model given the data observed for T time points, $p\left(\boldsymbol{\theta} \mid \boldsymbol{y}_{1:T}\right)$, is related to a quantity called the energy function $\varphi_T\left(\boldsymbol{\theta}\right)$ through a proportionality relationship.

$$p\left(\boldsymbol{\theta} \mid \boldsymbol{y}_{1:T}\right) \propto \exp\left(-\varphi_T\left(\boldsymbol{\theta}\right)\right). \tag{24}$$

The energy function $\varphi_T\left(\boldsymbol{\theta}\right)$ can be well approximated by the following recursion as the filter runs [24],

$$\varphi_t\left(\boldsymbol{\theta}\right) \simeq \varphi_{t-1}\left(\boldsymbol{\theta}\right) + \frac{1}{2}\log|2\pi S_t(\boldsymbol{\theta})| + \frac{1}{2}\boldsymbol{v}_t^{\mathsf{T}} S_t^{-1}\boldsymbol{v}_t. \tag{25}$$

$\boldsymbol{v}_t$ and S_t are defined as,

$$\boldsymbol{v}_t = \boldsymbol{y}_t - C\left(A\boldsymbol{x}_{t-1}\right), \tag{26a}$$

$$S_t = C\left(AP_{t-1}A^{\mathsf{T}} + Q\right)C^{\mathsf{T}} + R, \tag{26b}$$

when P_{t-1} is the state covariance at $t-1$. The recursion for φ_T is started at $\varphi_0 = -\log p\left(\boldsymbol{\theta}\right)$. Inference can then be performed using the standard MCMC Metropolis random walk algorithm, which for this problem is shown in Algorithm 1.

Algorithm 1 MCMC Metropolis Random Walk for Parameter Inference in State-Space LFM

$n_b, n_s \leftarrow$ Length of burn in and desired number of samples
$\boldsymbol{\theta}_0 \leftarrow \left\{m_0, k_0, c_0, \sigma_{f0}^2, \ell_0\right\}$ ▷ Set Start Points for Markov Chain
$n_a \leftarrow 0, k \leftarrow 0$ ▷ Number of accepted $\boldsymbol{\theta}$, Number of Steps
$p\left(\boldsymbol{\theta}' \mid \boldsymbol{\theta}_k\right) = \mathcal{N}\left(0\,,\ \Sigma_p\right)$ ▷ Proposal is random walk with diagonal matrix Σ_p
$p\left(\boldsymbol{\theta} \mid \boldsymbol{y}\right) \propto \exp\left\{-\varphi_T\left(\boldsymbol{\theta}\right)\right\}$ ▷ Posterior Likelihood is Proportional to the Energy Function
while $k < (n_b + n_s)$ **do**
  Sample $\boldsymbol{\theta}'$ from $p\left(\boldsymbol{\theta}' \mid \boldsymbol{\theta}_k\right)$
  Calculate $\varphi_T\left(\boldsymbol{\theta}'\right)$ ▷ Eq. (25)
  $\log\left(\alpha\right) = \min\left\{-\varphi_T\left(\boldsymbol{\theta}'\right) + \varphi_T\left(\boldsymbol{\theta}_k\right), 0\right\}$ ▷ Log Acceptance Ratio
  $\boldsymbol{\theta}_{k+1} \leftarrow \begin{cases} \boldsymbol{\theta}', & n_a{+}{+} \quad \text{with probability } \alpha \\ \boldsymbol{\theta_k}, & \text{otherwise} \end{cases}$
  $k \leftarrow k + 1$
end while

In this way, it is possible to generate samples from the true posterior of the parameter vector $\boldsymbol{\theta}$. These samples can be used for further uncertainty quantification steps or can be used for model scrutiny. The strength of this method, alongside recovering Bayesian posteriors over the system properties, is to recover, as a latent state of the system, the time series of the forcing signal applied to the system.

5 Application to Operational Modal Analysis

It is clear from the formulation that this model is directly applicable to the problem of modal analysis. One of the strengths of the model presented here is the flexibility available due to the non-parametric form of the

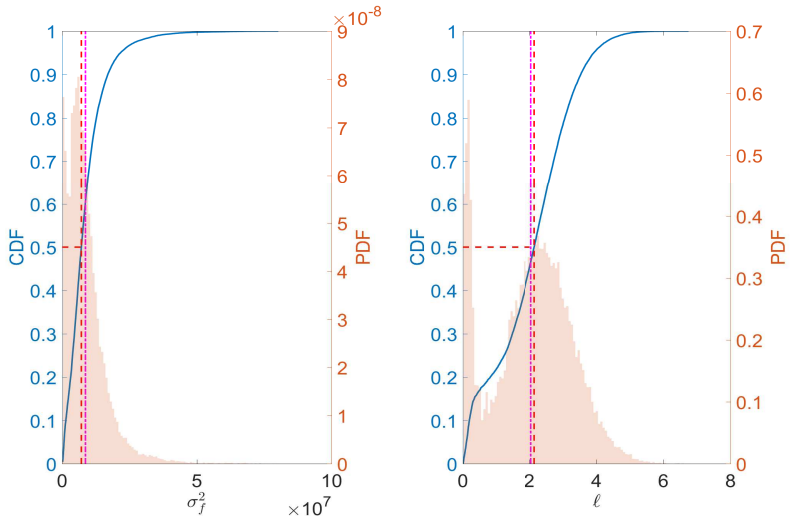


Figure 1: Plots showing the histograms and CDFs for the parameters being inferred when system parameters are known. The mean values are shown with the dot-dash $(\cdot-)$ line in magenta, and the values estimated from the empirical CDF with the dashed $(--)$ line in red.

forcing function as defined by the GP. This also presents a problem in the practical application of the model. As well as the normal system identification problems with the scaling of the mass, stiffness, and damping parameters which lead to non-identifiability in the model when the forcing level is unknown; the ability of the GP to model behaviour very similar to the dynamics (it is not restricted to a Gaussian white noise form) means that it can mask dynamics in the system. For this reason it is necessary to place prior distributions over the system parameters. Prior distributions can also be placed over the hyperparameters of the GP model to control its behaviour without breaking the Bayesian paradigm within which the model has been set up.

In the current work it is necessary to constrain at least one of the system parameters to a fixed value to resolve these problems. In this case it is assumed that one of the system parameters is known with certainty *a priori*, this can be interpreted as a delta prior on that parameter. The other prior distributions can be elicited from knowledge of the system. This could be from a finite element (FE) model where if necessary reduced order modelling techniques can be employed. It should be noted that when using MCMC for inference there is no restriction on the distribution of these priors, therefore, empirical distributions can be used.

The choice of prior over the hyperparameters of the GP poses a more difficult problem as they are less interpretable in a physical sense. It is possible to set a formal uniform prior, for example $p\left(\sigma_f^2\right) = 1$ which is a form of improper prior. However, it can be helpful to set the prior over the signal variance σ_f^2 around the expected variance of the loading and the length-scale ℓ based upon the expected frequency content of the loading.

6 Results

The results presented in this paper are from a simulated SDOF system response to a measured wave force input where the parameters of the model are chosen such that the natural frequency of the system is close to the narrowband loading frequency. The wave loading data was measured as a part of the Christchurch Bay project in the UK [25]. This represents the initial work into the application of LFM state-space models for OMA.

The parameters of the SDOF model are chosen to be: $m = 2000$ kg, $k = 100$ N m^{-1} and $c = 5$. These values correspond to modal parameters $\omega_n = 0.2$ Hz and $\zeta = 0.0079$. This presents a problem that is normally

Parameter	True Value	Prior Mean	Posterior Mean	CDF Estimate
$\sigma_f^{2\,*}$	-	-	8.64×10^6	7.12×10^6
ℓ^*	-	0.693	1.760	2.148

Table 1: Table showing results for the GP hyperparameters when the system parameters are known and fixed. (* denotes that the true values for these parameters are unknown.)

difficult in a OMA setting where the loading frequency is close to the resonant frequency of a lightly damped mode.

All of the parameters of the model must take only positive values for them to be valid, therefore, the random walk of the Markov-Chain must take place in a transformed space which ensures this. The values in the transformed space are denoted $\hat{(\cdot)}$, with the transformation defined as:

$$\theta = \log\left\{\exp\left(\hat{\theta}\right) + 1\right\}, \tag{27}$$

where θ is the parameter of interest. Prior probability distributions over the system parameters are chosen with a random perturbation on the mean values in the system parameters to simulate priors elicited from an incorrect model (e.g. an uncalibrated FE model). To constrain the problem it is assumed that the mass of the system is known *a priori* and as such this is modelled with a delta prior for all tests.

Inference was performed as in Algorithm 1 with the burn-in set to 1×10^3 samples and the total number of samples as 1×10^5. Since the distributions may be non-Gaussian, and the distributions over the Gaussian Process hyperparameters are expected to be multimodal, the parameter estimates used to calculate the example force are taken to be the values when the empirical cumulative density function (CDF) is equal to 0.5.

6.1 LFM With Known System Parameters

As an initial test the model is run with the system parameters fixed at the true values to demonstrate the ability of the LFM to model the input to the system. The priors for this are summarised below:

$$p\left(\hat{\sigma}_f^2\right) = 1, \tag{28a}$$
$$p\left(\hat{\ell}\right) = \mathcal{N}\left(0\,,\ 2\right), \tag{28b}$$
$$p\left(m\right) = \delta\left(2000\right), \tag{28c}$$
$$p\left(k\right) = \delta\left(100\right), \tag{28d}$$
$$p\left(c\right) = \delta\left(5\right). \tag{28e}$$

Using this procedure, samples from the posteriors over the signal variance and length-scale hyperparameters were drawn. Plots of the PDF normalised histogram and CDFs are shown in Fig. 1 along with mean estimates and CDF estimates of the values. A summary of the results is shown in Table 1. GP modelling the latent force on the system, the signal variance of the forcing σ_f^2 is assumed unknown and a uniform prior is used, the length-scale parameter has a prior to discourage very long or short length-scales. Long length-scales will cause the function in the forcing to become very smooth, the extreme of which is that it remains at the mean, in this case the signal variance increases and the solution returned is one in which all the forcing is considered noise. This, although a valid solution, is not helpful in the setting of modal analysis where retrieval of the forcing time series adds a significant amount of valuable information. If the length-scale is allowed to become very small, then the GP will attempt to model the noise in the signal as if it were functional, this is

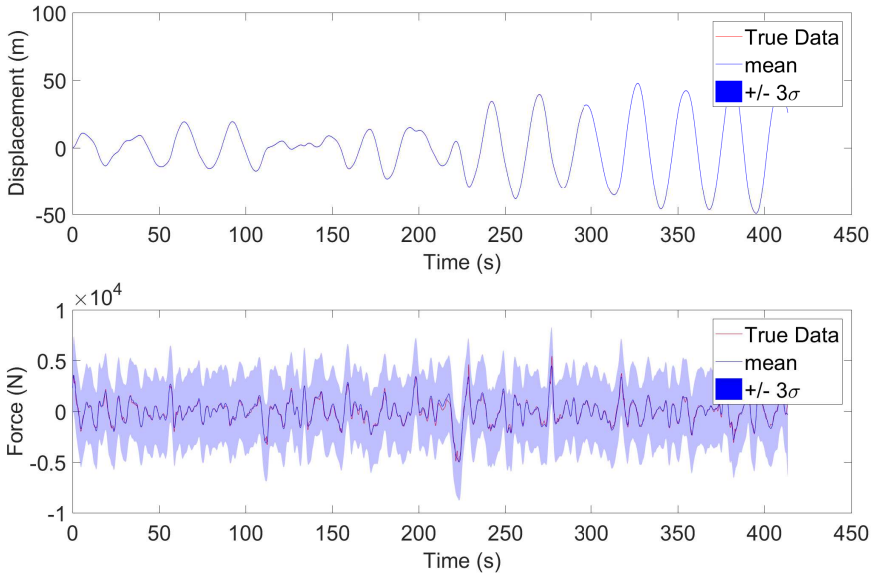


Figure 2: Smoother estimate of displacement and forcing signal on the system when m, k, and c are known. True values are shown in red, mean estimates as a solid blue line and three standard deviation confidence in the shaded regions

also clearly not a desirable situation. Since the distributions are skewed and multi-modal, the mean estimates are not a good value to take and instead the CDF estimate is used to predict the forcing experienced by the structure. Figure 2 shows the smoother prediction over the forcing as well as the observed state. As expected the prediction over the displacements is modelled well with very small variance. The prediction over the forcing is good, and there is a 3.3% normalised mean square error value with the mean prediction, however, one of the strengths of this model is that in addition to this there are also confidence intervals which represent the uncertainty in the forcing.

6.2 OMA With The LFM

For the case of performing OMA with the GP LFM, the priors used in this model are shown below:

$$p\left(\hat{\sigma}_f^2\right) = 1, \tag{29a}$$

$$p\left(\hat{\ell}\right) = \mathcal{N}\left(0\,,\ 2\right), \tag{29b}$$

$$p\left(m\right) = \delta\left(2000\right), \tag{29c}$$

$$p\left(\hat{k}\right) = \mathcal{N}\left(105.9\,,\ 2500\right), \tag{29d}$$

$$p\left(\hat{c}\right) = \mathcal{N}\left(4.8\,,\ 6.25\right). \tag{29e}$$

When running the model where only the mass is known, samples are generated from the posteriors over the GP hyperparameters and the system parameters, k and c. Plots of the histograms and CDFs of the parameters are shown, as before, in Fig. 3 and a summary of the results is shown in Table 2. It can be seen that the parameter estimates of the system parameters are within 2% for both the mean values of the distributions and the CDF estimates, this would indicate that the distributions are uni-modal and are not heavily skewed. When the values from the CDF estimates are used to run the filter-smoother over the full dataset, the predictions

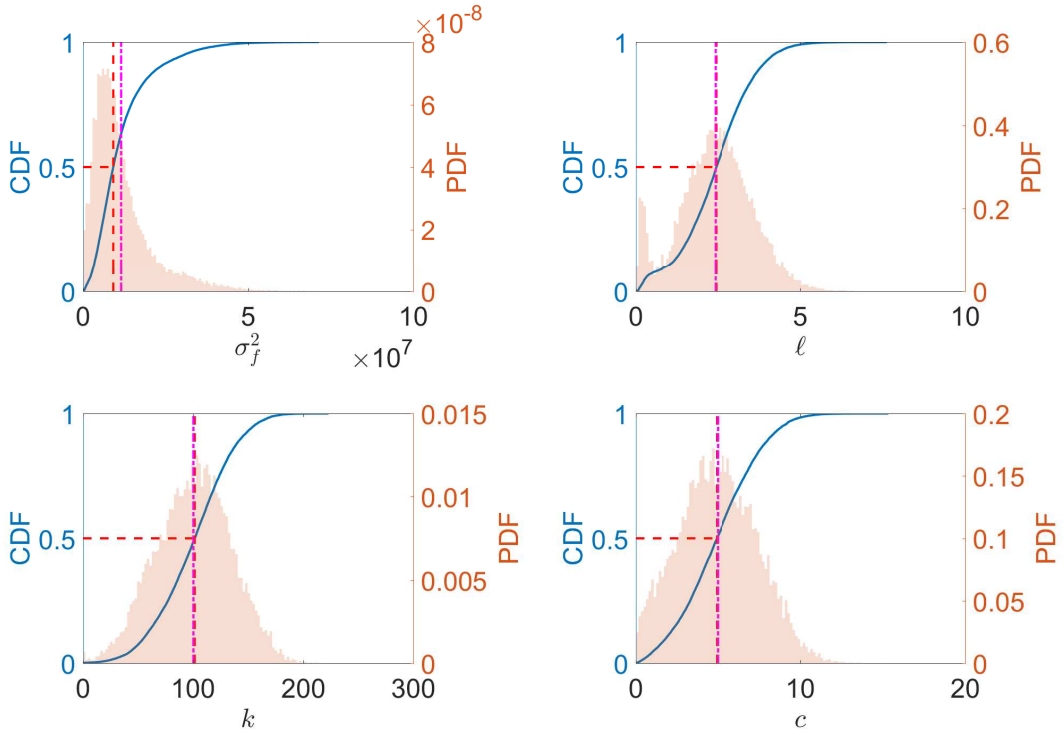


Figure 3: Plots showing the histograms and CDFs for the parameters being inferred in the full LFM OMA procedure. The mean values are shown with the dot-dash $(\cdot-)$ line in magenta, and the values estimated from the empirical CDF with the dashed $(--)$ line in red.

Parameter	True Value	Prior Mean	Posterior Mean	CDF Estimate
$\sigma_f^{2\,*}$	-	-	1.153×10^7	9.154×10^6
ℓ^*	-	0.693	2.283	2.443
k	100	105.9 (5.9%)	100.2 (0.2%)	101.4 (1.4%)
c	5	4.81 (-3.8%)	4.91 (-1.8%)	4.93 (-1.4%)

Table 2: Table showing results from the full LFM OMA model, values in brackets denote the percentage error versus the true values. (* denotes that the true values for these parameters are unknown.)

in Fig. 4 are made. The prediction over the force continues to be accurate with a normalised mean squared error on the mean of the signal of 3.1%. This result is comparable to the results obtained when the system properties are known, which is unexpected and encouraging. It follows that the estimates of the signal variance and length-scales are similar for this model and the model with known system parameters. It is also reassuring that the values for the GP hyperparameters are similar to those from the case where the system is known. This would suggest that the solution is stable and that the use of priors has alleviated some of the identifiability issues arising from the flexibility of the GP prior.

7 Conclusions

The work presented here has demonstrated through application to a simple system, a single degree of freedom oscillator, the benefit of using a Gaussian Process Latent Force Model in the task of operationa modal analysis. Specifically, the state-space formulation of this model has allowed for efficient inference to be made and as

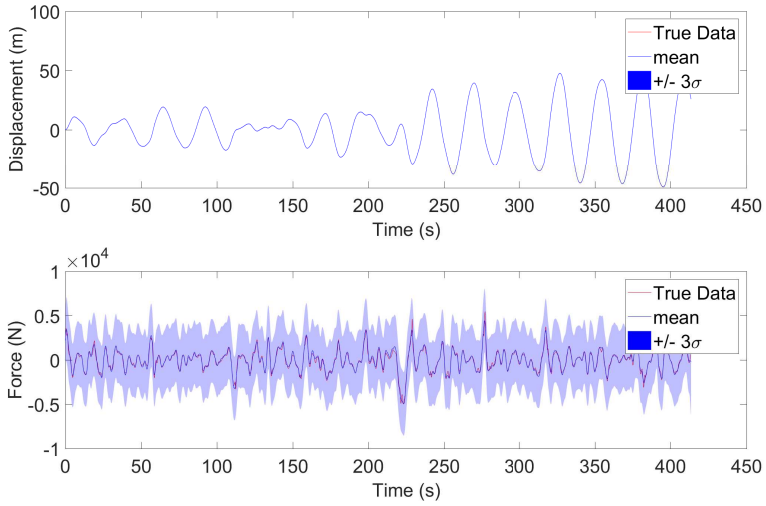


Figure 4: Smoother estimate of displacement and forcing signal from the LFM OMA on the system with true values shown in red, mean estimates as a solid blue line and three standard deviation confidence in the shaded regions

such Markov-Chain Monte-Carlo methods can be used to recover distributions over the system parameters and the GP hyperparameters. It has been shown that these distributions can be used to elicit accurate point estimates of the parameters and also of the loading, something that is normally not possible in an OMA setting.

It is worth noting, however, that the tasks shown here have been performed on simulated data under a number of significant assumptions. First it is assumed that the linear model of the system can represent the behaviour well with low process noise. Second the model is tested with a low level of artificial Gaussian white noise added. Thirdly there exist priors over the system parameters in which there is non-negligible probability mass at the true values. Finally, it is assumed that the mass of the system is known accurately *a priori*, this is required to constrain the unidentifiability inherent in the model. This unidentifiability stems from the scaling of the forcing and the system parameters by the mass, that is, a system with the same response can be recovered if all the system parameters are multiplied by some constant α and if the forcing magnitude is also scaled by α. The flexibility of the GP as a prior over the forcing function only increases this issue. By fixing the mass and placing informative priors over the system parameters the model can be constrained in such a way that it is more likely to converge to the true parameter posteriors.

Nevertheless, the authors believe that this represents a powerful *grey-box* approach to the problem of OMA. It is clear that the model is capable of returning good estimates of the forcing, and the system parameters under the constraints already discussed. The results presented here motivate further work into the use of GP LFM models in the modal analysis setting. This includes the extension of the current model to a multi-degree of freedom case. Additionally, in nonlinear systems where the structure of the nonlinearity is known (e.g. a cubic stiffness term), this model is also applicable although the Kalman filtering formulation must be replaced with a nonlinear counterpart. The last area of work is regarding the inference procedure; it is appealing to replace the MCMC inference used in this paper with a more efficient method which could be based on a state-augmentation approach or a two step identification process where the system parameters and forcing are iterated recursively.

Acknowledgements

T. J. Rogers wishes to thank Ramboll Energy for their ongoing support of this research.

References

[1] S. S. Rao and F. F. Yap, *Mechanical vibrations*. Prentice Hall Upper Saddle River, 2011, vol. 4.

[2] L. Ljung, *System identification*. Springer, 1998.

[3] B. Peeters and G. De Roeck, "Stochastic system identification for operational modal analysis: a review," *Journal of Dynamic Systems, Measurement, and Control*, vol. 123, no. 4, pp. 659–667, 2001.

[4] E. Reynders, "System identification methods for (operational) modal analysis: review and comparison," *Archives of Computational Methods in Engineering*, vol. 19, no. 1, pp. 51–124, 2012.

[5] S. E. Azam, E. Chatzi, and C. Papadimitriou, "A dual kalman filter approach for state estimation via output-only acceleration measurements," *Mechanical Systems and Signal Processing*, vol. 60, pp. 866–886, 2015.

[6] S. E. Azam, E. Chatzi, C. Papadimitriou, and A. Smyth, "Experimental validation of the kalman-type filters for online and real-time state and input estimation," *Journal of Vibration and Control*, vol. 23, no. 15, pp. 2494–2519, 2017.

[7] L. Ljung, "Asymptotic behavior of the extended kalman filter as a parameter estimator for linear systems," *IEEE Transactions on Automatic Control*, vol. 24, no. 1, pp. 36–50, 1979.

[8] E. Lourens, C. Papadimitriou, S. Gillijns, E. Reynders, G. De Roeck, and G. Lombaert, "Joint input-response estimation for structural systems based on reduced-order models and vibration data from a limited number of sensors," *Mechanical Systems and Signal Processing*, vol. 29, pp. 310–327, 2012.

[9] M. Alvarez, D. Luengo, and N. Lawrence, "Latent force models," in *Artificial Intelligence and Statistics*, 2009, pp. 9–16.

[10] J. Hartikainen and S. Sarkka, "Sequential inference for latent force models," *arXiv preprint arXiv:1202.3730*, 2012.

[11] A. O'Hagan and J. F. C. Kingman, "Curve fitting and optimal design for prediction," *Journal of the Royal Statistical Society. Series B (Methodological)*, pp. 1–42, 1978.

[12] C. E. Rasmussen and C. K. I. Williams, *Gaussian processes for machine learning*. Citeseer, 2006.

[13] R. E. Kalman, "A new approach to linear filtering and prediction problems," *Journal of basic Engineering*, vol. 82, no. 1, pp. 35–45, 1960.

[14] H. E. Rauch, C. Striebel, and F. Tung, "Maximum likelihood estimates of linear dynamic systems," *AIAA journal*, vol. 3, no. 8, pp. 1445–1450, 1965.

[15] M. A. Alvarez, D. Luengo, and N. D. Lawrence, "Linear latent force models using gaussian processes," *IEEE transactions on pattern analysis and machine intelligence*, vol. 35, no. 11, pp. 2693–2705, 2013.

[16] J. Quiñonero-Candela and C. E. Rasmussen, "A unifying view of sparse approximate gaussian process regression," *Journal of Machine Learning Research*, vol. 6, no. Dec, pp. 1939–1959, 2005.

[17] T. D. Bui, J. Yan, and R. E. Turner, "A unifying framework for sparse gaussian process approximation using power expectation propagation," *arXiv preprint arXiv:1605.07066*, 2016.

[18] M. Alvarez and N. D. Lawrence, "Sparse convolved gaussian processes for multi-output regression," in *Advances in neural information processing systems*, 2009, pp. 57–64.

[19] J. Hartikainen and S. Särkkä, "Kalman filtering and smoothing solutions to temporal gaussian process regression models," in *Machine Learning for Signal Processing (MLSP), 2010 IEEE International Workshop on*. IEEE, 2010, pp. 379–384.

[20] M. S. Handcock and M. L. Stein, "A bayesian analysis of kriging," *Technometrics*, vol. 35, no. 4, pp. 403–410, 1993.

[21] M. L. Stein, *Interpolation of spatial data: some theory for kriging*. Springer Science & Business Media, 2012.

[22] Z. Ghahramani and G. E. Hinton, "Parameter estimation for linear dynamical systems," Technical Report CRG-TR-96-2, University of Totronto, Dept. of Computer Science, Tech. Rep., 1996.

[23] A. Gelman, J. B. Carlin, H. S. Stern, D. B. Dunson, A. Vehtari, and D. B. Rubin, *Bayesian data analysis*. CRC press, 2013.

[24] S. Särkkä, *Bayesian filtering and smoothing*. Cambridge University Press, 2013, vol. 3.

[25] G. Najafian, R. Tickell, R. Burrows, and J. Bishop, "The UK Christchurch Bay compliant cylinder project: analysis and interpretation of Morison wave force and response data," *Applied Ocean Research*, vol. 22, no. 3, pp. 129–153, 2000.

Fuzzy Model Updating: covariance updating to estimate the interval radii of the updated parameters

D. Ricardo, T. A. N. Silva*
NOVA UNIDEMI, Department of Mechanical and Industrial Engineering,
Faculty of Science and Technology, Universidade NOVA de Lisboa,
Campus de Caparica, 2829-516 Caparica, Portugal.
email: **tan.silva@fct.unl.pt**

Abstract

Stochastic model updating techniques aim at reducing the epistemic uncertainty mainly related to the lack of knowledge. These techniques are usually computationally demanding and the use of non-probabilistic methods allows for the reduction of the computational effort, typically associated with stochastic model updating methods. This paper presents a fuzzy model updating method based on a convex joint fuzzy membership of all the experimental responses and on the sensitivity-based updating of the interval centre at each alpha-cut of the uncertain model parameters. Moreover, the covariance updating concept is used to estimate the interval radii of the referred intervals directly from the covariance matrix of the experimental response set. The developed method allows to achieve precise predictions of the intervals of the parameters with a reduced computational effort. A numerical example is given to evaluate the implementation and performance of the proposed fuzzy model updating method.

1 Introduction

Due to lack-of-knowledge or imprecise information, one may assume that the probabilistic structure of both the data and modelling parameters is not clear. Hence, rather than consider a probabilistic approach to uncertainty quantification, one may use a non-probabilistic approach to the problem of stochastic model updating. In this context, one may consider techniques based on interval arithmetic, although it is known that this kind of techniques tends to overestimate the parameters bounds, due to the fact that it is assumed that the parameters are uniformly distributed over the entire design space. This leads to the inability to distinguish regions inside the response intervals, and consequently inside the parameter intervals, which can be overcome using fuzzy logic. Detailed reviews on non-probabilistic model analysis can be found in [1–3], where a special focus on interval and fuzzy finite element (FE) model analysis is given.

The concept of fuzzy sets was introduced in [4], under the assumption that the membership assigned to a real world object is, in a given context, imprecise. In opposition to the classical set theory, where the membership of an object is determined in binary terms, the membership of an object to a fuzzy set is assigned by a membership function, where the membership levels (α-level) vary continuously between zero and one.

As the uncertainty can be often expressed in terms of real numbers, an object in a fuzzy set $\hat{P} \in \hat{\mathcal{P}}(\mathcal{R})$ is defined as a fuzzy number $\hat{p}$, iff it satisfies a set of conditions [5], from which the fuzzy set convexity condition is of paramount importance within the framework of model updating, as it allows for a decomposition of a fuzzy number into continuous intervals at each α-level, and therefore the fuzzy arithmetic can be reduced to interval arithmetic at each α-level.

Additionally, if a fuzzy set $\hat{P} \in \hat{\mathcal{P}}(\mathcal{R}^n)$ is considered and all the conditions listed above are satisfied, then a fuzzy vector is defined. Note that a fuzzy number is a particular case of a fuzzy vector, defined for $n = 1$.

From now on, a fuzzy set $\hat{P} \in \hat{\mathcal{P}}(\mathcal{R}^n)$ is referred to as a hyper fuzzy set, in the sense of its multiple dimensionality.

Concerning the use of fuzzy arithmetic, one can find several works exploiting the forward propagations of fuzzy numbers in order to assess the uncertainties in the model responses. This is the basic concept of stochastic FEA [6]. The authors of [7] discussed the computational efficiency of the Zadeh's extension principle when used to solve fuzzy modal analysis problems, and proposed to use Pad approximants to compute the extreme eigensolutions for each α-level set. A surrogate model was proposed in [8], the random sampling High-Dimensional Model Representation (RS-HDMR), which captures the input-output system relation in order to obtain the fuzzy description of the model responses at each α-level. Within the framework of the IWT-SBO project "The Fuzzy Finite Element Method" [9], the forward uncertainty propagation was extensively analysed, mainly for civil structures. Moreover, the fuzzy FEM model updating was also addressed [10]. In their work, the optimization problem solution is achieved considering that the fuzzy FEM can be applied as a multi-level interval analysis, using the Gradual α-level Decreasing (GαD) algorithm [11]. The work [12] assesses the performance of interval analysis at each α-level in order to built a fuzzy model response membership function based on optimized interval bounds for the modelling parameters.

Specifically concerning the fuzzy FEM model updating, few works have been published. Among the available fuzzy FEM model updating techniques, in [13], the authors proposed a fuzzy FEM model updating method based on a fuzzyfied objective function defined in terms of the eigensensitivities. The proposed method is used to update a bridge model using, as reference, data from a single modal test. Therefore, it means that the uncertainty in the measured data can only arise from measurement noise and thus the existence of epistemic uncertainty [14] is not considered. Within the same context, a fuzzy arithmetic based model updating procedure is proposed in [15], where the membership functions of each updating parameter are determined by minimising an objective function, using a hybrid global optimization strategy, based on the combined use of the genetic (GA) and particle swarm optimization (PSO) algorithms.

Regarding the uncertainty quantification in terms of epistemic or parametric uncertainty, which arises due to the lack of knowledge and therefore is reducible, Haag et al. identified a valid fuzzy model for a brake pad, considering experimental modal analysis (EMA) of just one brake pad specimen [16]. The epistemic uncertainty identification or quantification using inverse fuzzy arithmetic was previously considered in [17]. The authors considered the use of the reduced transformation method [5], whose application is limited to monotonic relations between model inputs and outputs. In [16], the monotonicity was investigated and it was assumed, due to the fact that the fuzzy membership functions of the outputs were linear and monotonous. Note that if monotonicity can be considered, the inverse fuzzy arithmetic problem, i.e., the inverse interval arithmetic problem at each α-level, can be solved using the vertex method [18]. However, when monotonicity is not verified, such as in the cases where mode shape data is to be included in the reference outputs, the applicability of approaches based on the vertex method is limited. A general solution for the inverse interval arithmetic was proposed in [19] and it consists in an interval model updating method based on the Kriging predictor sensitivity analysis.

All the referred works on fuzzy FEM model analysis consider a prior knowledge or, to be more precise, a prior assumption of the fuzzy membership functions of the modelling parameters. Taking some risk, all the already published works consider triangular or left-right (L-R) membership functions [5], as it can be concluded from a wide range of works. Chronologically, citing some selected works, [12, 20–25]. However, in real experiments it is unusual or even impossible to know beforehand the deterministic value or the statistical distribution of a certain model parameter. Nevertheless, experimental responses, such as natural frequencies and mode shapes, are readily available from EMA and the estimation of the uncertain model parameters via the inverse problem solution can be addressed as an approach to develop valid models. In this context, the idea of generating a hyper fuzzy membership, strictly based on the available reference data, namely experimental modal data and therefore of a completely inverse fuzzy model updating strategy was proposed in [26]. This fuzzy model updating strategy does not assume nor impose any kind of behaviour or structure regarding the updating parameters, instead the proposed fuzzy model updating process relies only on the fuzzy membership function constructed from a experimental data set, measured eigenfrequencies and/or eigenmodes.

Its implementation is based on the interval model updating method [19] applied at each α-level, taking as reference several cuts of a convex hyper membership function of the responses, and therefore a discretized fuzzy number is generated for each updating parameter.

In this work, the proposed implementation of a fuzzy model updating strategy is based on this basic idea of reducing the problem to a series of interval model updating problems, as mentioned. Here, one considers the construction of a convex joint fuzzy membership function containing the entire experimental data set, using the inverse Zadeh's extension principle, introduced in [26]. Moreover, it combines the concepts of covariance matrix updating given in [28] and the perturbation based interval updating proposed in [27]. This extends the work [27] to its application in the context of fuzzy model updating and introduces an efficient manner to compute the radii of the interval at each α-level.

2 Fuzzy model updating

If the modelling parameters and responses are fuzzy variables, a sensitivity-based model updating method can be framed by the well-known relation between the system responses and modelling parameters,

$$(\hat{\boldsymbol{z}}_m - \hat{\boldsymbol{z}}_j) = \hat{\mathbf{S}}_j \left(\hat{\boldsymbol{\theta}}_{j+1} - \hat{\boldsymbol{\theta}}_j \right) \tag{1}$$

where $\hat{\boldsymbol{z}}_m$ is the fuzzy vector of reference or measured responses and $\hat{\boldsymbol{z}}_j$ is its model counter-part; $\hat{\boldsymbol{\theta}}_j$ is a fuzzy vector of modelling parameters; and $\mathbf{S}_j$ is the sensitivity matrix, all these computed at the jth iteration of the model updating procedure.

Equation (1) can the recast to compute the updated fuzzy modelling parameters vector, in a least-squares sense, giving

$$\hat{\boldsymbol{\theta}}_{j+1} = \hat{\boldsymbol{\theta}}_j + \hat{\mathbf{T}}_j \left(\hat{\boldsymbol{z}}_m - \hat{\boldsymbol{z}}_j \right) \tag{2}$$

As previously referred, it is useful to consider the decomposition of the fuzzy vectors into interval variables at a given number of α-levels, allowing to treat the fuzzy model updating problem as a series of interval ones. Thus, a generic fuzzy number $\hat{x}$ is decomposed into an interval vector at each α-level as

$$\check{x}^{(\alpha)} = \mathrm{cut}_\alpha \hat{x} = [\underline{x}\,,\, \overline{x}]^{(\alpha)} \quad : \quad \left\{ \underline{x}^{(\alpha)} \leq x \leq \overline{x}^{(\alpha)},\ 0 \leq \alpha \leq 1 \right\} \tag{3}$$

and consequently eq. (2) is recast to form the interval model updating equation at each α-level,

$$\check{\boldsymbol{\theta}}_{j+1}^{(\alpha)} = \check{\boldsymbol{\theta}}_j^{(\alpha)} + \check{\mathbf{T}}_j^{(\alpha)} \left(\check{\boldsymbol{z}}_m^{(\alpha)} - \check{\boldsymbol{z}}_j^{(\alpha)} \right) \tag{4}$$

where $\check{\bullet}$ stand for a interval variable.

Concerning the fuzzy model updating, if an empirical hyper-membership function for the experimental/reference response set is already available, the updating process starts at $\alpha = 1$, aiming to find the centre of the parameters hyper-cube, which is the basis for the parameters initial interval. Note that the initial interval on the parameters space must lead to a solution hyper-space, encompassing the entire hyper-space of the experimental responses. With a feasible initial hyper-interval for the parameter set, the interval model updating is carried on at each α-level of the fuzzy membership. Details on the interval model updating method using the Kriging predictor can be found in [19].

In this work, the proposed implementation of a fuzzy model updating strategy is based on this basic idea of reducing the problem to a series of interval model updating problems, as mentioned. Moreover, it combines the concepts of covariance matrix updating given in [28] and the perturbation based interval updating proposed in [27].

Based on the perturbation method to define a random variable, in [28] it is shown that a stochastic model updating problem can be reduced to a deterministic one by transforming the covariance matrix of the reference data into the one of the modelling parameters after updating their means. This is attained by

$$\mathbf{cov}\left(\Delta\boldsymbol{\theta}_{j+1}, \Delta\boldsymbol{\theta}_{j+1}\right) = \tilde{\mathbf{T}}_j \mathbf{cov}\left(\Delta\boldsymbol{z}_m, \Delta\boldsymbol{z}_m\right) \tilde{\mathbf{T}}_j^T \tag{5}$$

where $\mathbf{cov}\left(\Delta\boldsymbol{\theta}_{j+1}, \Delta\boldsymbol{\theta}_{j+1}\right)$ is the covariance matrix of the updating parameters, while $\mathbf{cov}\left(\Delta\boldsymbol{z}_m, \Delta\boldsymbol{z}_m\right)$ is the one of the reference data set. $\tilde{\mathbf{T}}_j^T$ is the weighted/regularized pseudo-inverse of the sensitivity matrix computed for the mean values of the updating parameters.

In [27], the interval variables were defined by the perturbation method, using the centre and radius of the interval. Thus, the reference data vector can be cast as an interval variable at each α-level as

$$\tilde{\boldsymbol{z}}_m^{(\alpha)} = \tilde{\boldsymbol{z}}_m^{(\alpha)} \pm \delta\boldsymbol{z}_m^{(\alpha)} \tag{6}$$

where $\tilde{\boldsymbol{z}}_m^{(\alpha)}$ is the centre and $\delta\boldsymbol{z}_m^{(\alpha)}$ the radius of the interval reference data vector at a given α-level.

Recalling that the variance σ^2 of a generic continuous random variable x, uniformly distributed in a given interval, can be obtained from its bounds, one has,

$$\sigma^2 = \frac{(2\delta x)^2}{12} \tag{7}$$

where $2\delta x$ is the interval range of x.

Hence, if one considers the combined use of the concepts given in [27, 28], one can compute the interval radii of the updating parameters right after updating their centres, as the variance of the updating parameters is available from the diagonal of the updated covariance matrix (eq. (5)). Thus, the interval radii of the updating parameters can be computed as,

$$\delta\boldsymbol{\theta}_{j+1} = \sqrt{3}\,\boldsymbol{\sigma}_{j+1} \tag{8}$$

where $\boldsymbol{\sigma}_{j+1}$ is a vector with the updated variance values of the modelling parameters.

3 Numerical example

The numerical example considered is the 3 degree of freedom (DoF) mass-spring system shown in fig. 1. This is a simple example that has been used by several authors, e.g. [28]. In this work, the presented results (section 4) consider the case for which the updating parameters for the 3 DoF system are $\boldsymbol{\theta} = [\theta_1\ \theta_2\ \theta_3]^T = [k_1\ k_2\ k_5]^T$ and their reference values at the support are $\mu_{\alpha_{0.0}}\left(\hat{\theta}_i\right) = \left[\underline{\theta}_i\ \overline{\theta}_i\right] = [1.8\ 2.2]$ for $i = 1, 2, 3$. Note that the reference sample was generated using latin-hipercube sampling from a normal distribution with 30 observations and the correspondent reference response set is given by its fuzzy memberships. Here, the reference response set is $\hat{\boldsymbol{z}}_m = \left[\hat{z}_1 \cdots \hat{z}_4\right]^T = \left[f_1\ f_2\ f_3\ |\phi_{1,1}|\right]^T$, i.e. the first three eigenfrequencies and the modulus of the first element of the first eigenvector.

4 Results and discussion

In this section a set of results for the fuzzy model updating problem of the numerical example are discussed. The presented results summarize the outcome of the updating process in terms of the fuzzy memberships of the updating parameters. Note that in this case one can compare the updated results with the reference ones, as this is a numerical example. Recall that the reference response set contains 30 observed values for $\hat{\boldsymbol{z}}_m$. This is considered to be a fair simulation of an experimental data set that is usually obtained from a

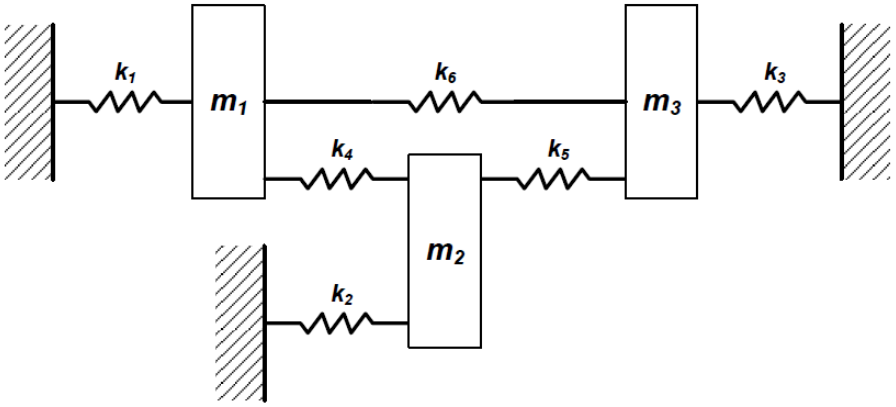


Figure 1: Three degree of freedom mass-spring system example.

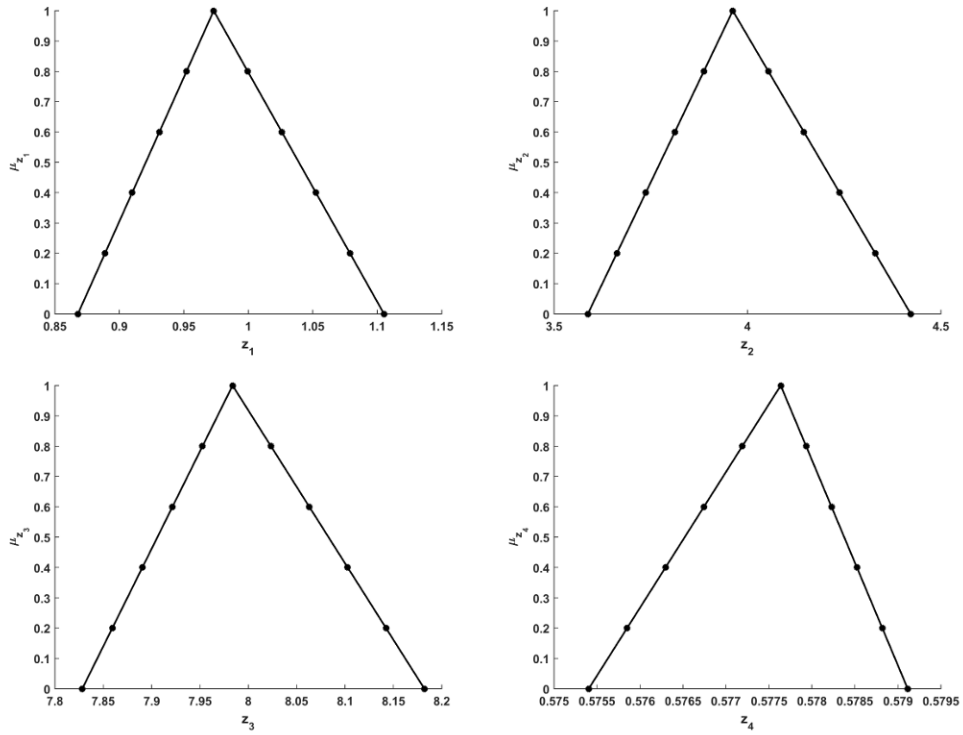


Figure 2: Triangular fuzzy membership of each reference response ($\mu_{\hat{\boldsymbol{z}}_m}$) (points at the intersections with the considered α-levels).

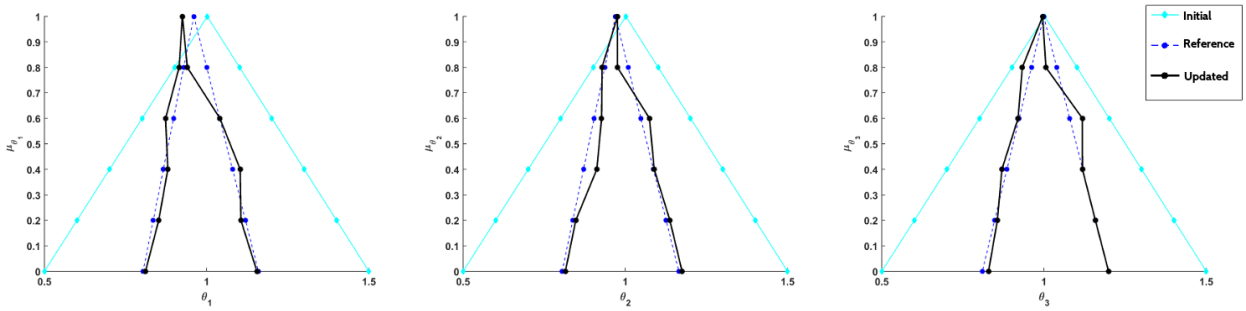


Figure 3: Fuzzy memberships of each updating parameter ($\mu_{\hat{\boldsymbol{\theta}}_i}$) - Case with reference triangular memberships (extension of the method of [27]).

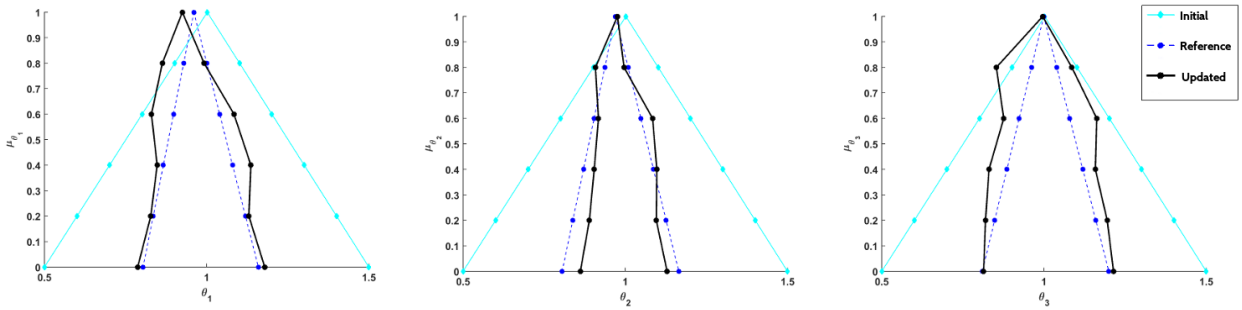


Figure 4: Fuzzy memberships of each updating parameter ($\mu_{\hat{\boldsymbol{\theta}}_i}$) - Case with reference triangular memberships (proposed method).

series of tests in identical structures. From the observed reference response set, the obtained triangular fuzzy membership of each reference response is given in fig. 2.

Using the interval updating procedure proposed in [27], one obtained the results given in fig. 3. In this implementation of the fuzzy model updating method, one must solve a two-steps interval optimization problem at each α-level. From fig. 3, one may observe a good agreement between the reference and the updated memberships, although the reference memberships are not recovered perfectly. Note that this example considered a sample with 30 observations for both reference and updating data sets.

If the same example case is solved with the fuzzy model updating method proposed in this work, the results are the ones of fig. 4. This results are overall worst that the ones of fig. 3, although there are significant differences between the two implementations and one should not expect that both methods perform equally in all situations. One must bear in mind that, in terms of updating, proposed method is completely based on the updating of the centre of the interval at each α-level only. In more detail, the proposed method only needs to solve a deterministic sensitivity-based updating of those centres, followed by a transformation of the covariance matrix of the reference data contained in each α-level to estimate each interval radius. By this, the results given in fig. 4 are in agreement with the difficulty of estimating the variance for a limited sample size. Note that the highest the memberships level the smaller the number of sampled values in each interval. In both implemented methods, the interval at $\alpha = 1$ is considered to be the crisp value, therefore at this level the updating method is reduced to update of the centre only. Note that the crisp values are as well updated by both methods.

In [26], it was shown that the use of empirical fuzzy memberships can enhance the updating outcomes. If the concept of empirical fuzzy membership is applied, the fuzzy memberships obtained for the reference responses are the ones shown in fig. 5, instead of the triangular ones used in the previous results (fig. 2).

Figures 6 and 7 show results for both implementation of the updating procedure for both types of fuzzy memberships considered. As the empirical memberships tend to encompass better the observed data, the intervals are more accurately updated for the same sample size. The membership of θ_2 is not recovered

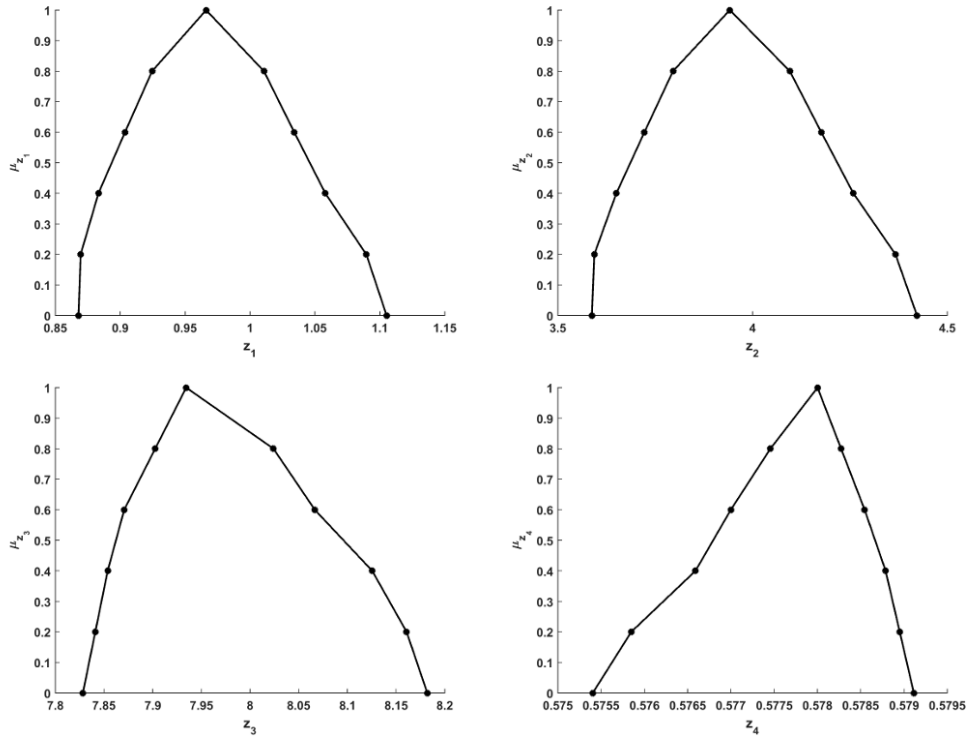


Figure 5: Empirical fuzzy membership of each reference response ($\mu_{\hat{\boldsymbol{z}}_m}$) - Case with reference empirical memberships (proposed method).

correctly by the proposed method (fig. 7), although the others are quite in agreement with the reference ones.

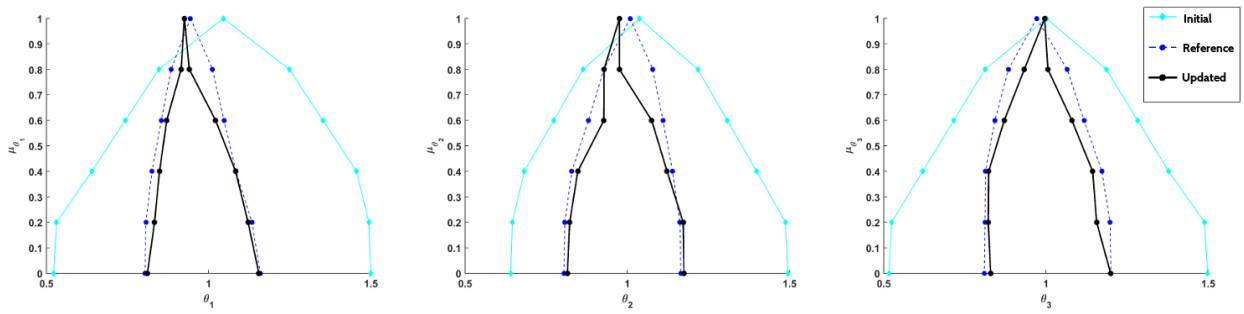


Figure 6: Fuzzy memberships of each updating parameter ($\mu_{\hat{\boldsymbol{\theta}}_i}$) - Case with reference empirical memberships (extension of the method of [27]).

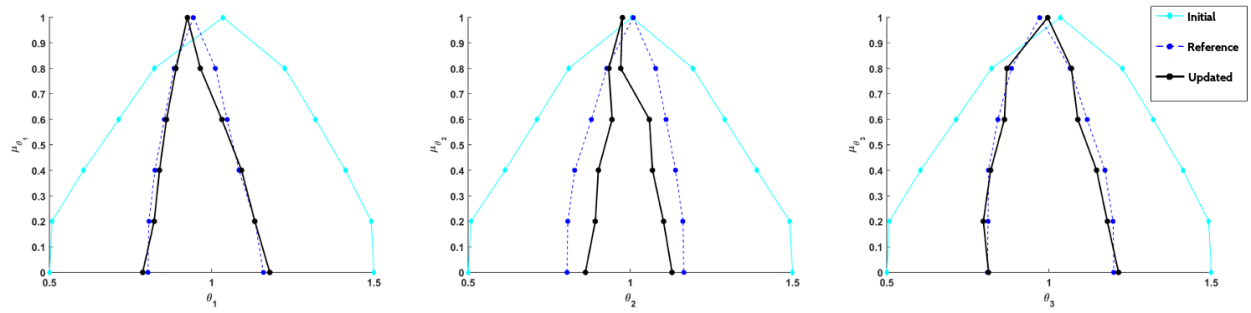


Figure 7: Fuzzy memberships of each updating parameter ($\mu_{\hat{\theta}_i}$) - Case with reference empirical memberships (points at the intersections with the considered α-levels).

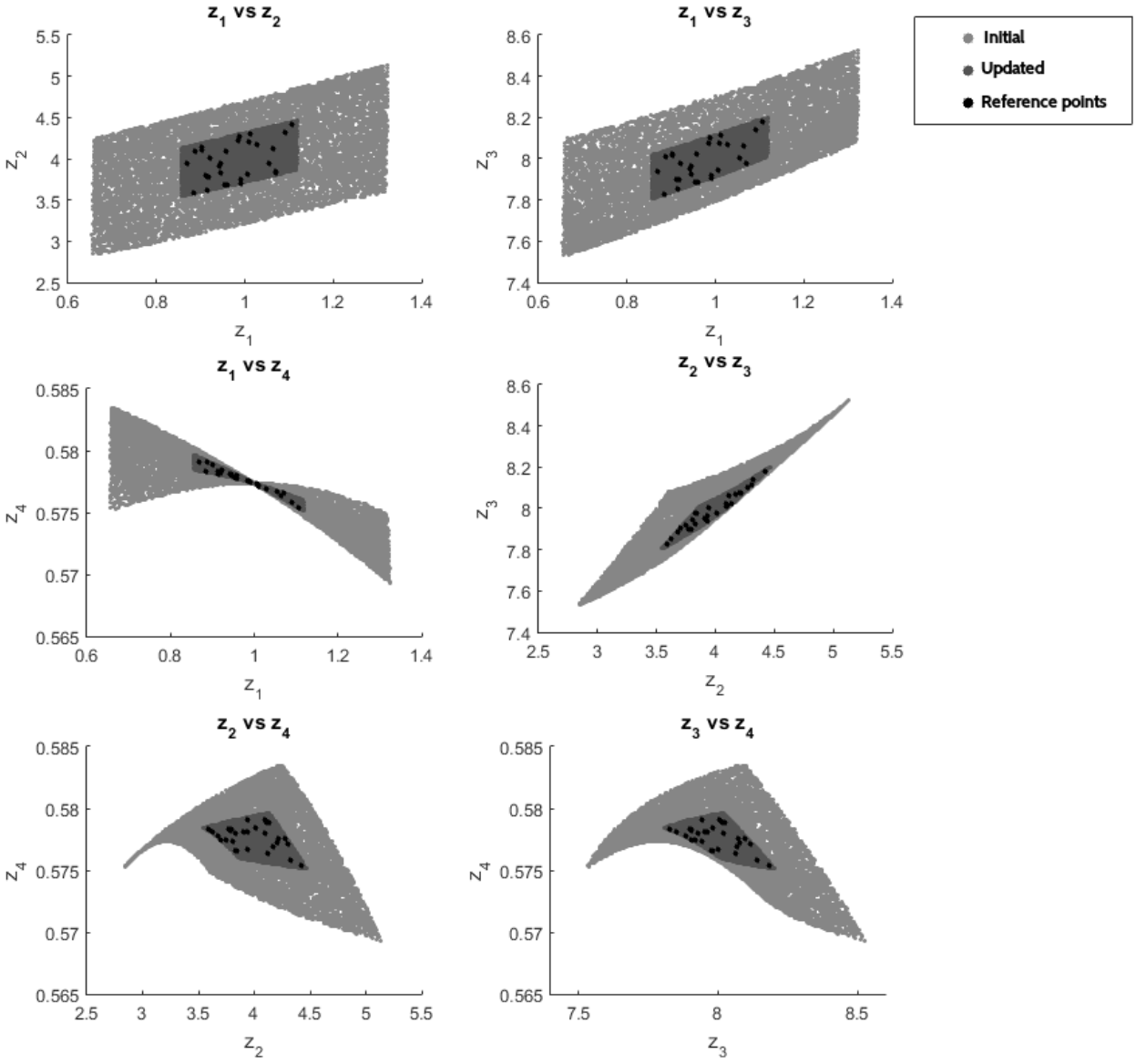


Figure 8: Response space in the hyper-planes defined by each pair of responses.

The response space obtained with the support of the updated parameters of fig. 7 is given in fig. 8. In fig. 8, it is possible to observe that all the reference points are contained within the space of updated solutions.

Regarding the issue with limited sample sizes, one knows that often it is unfeasible to acquire experimentally large sample, concerning the test of identical structures, for instance. However, for theses implementations it is advisable to work with samples as larger as possible in order to be able to estimate correctly the interval radii, as it is expected that for samples with higher the number of observations the estimation of the intervals is more accurate.

5 Conclusion

A purely inverse implementation of a fuzzy model updating method is proposed and its performance assessed using a numerical example. The method can be framed as a successive application of the interval model updating method at each α-level of a hyper-membership function of the reference response set. The method performs quite fast, as it is a backward implementation that avoids unnecessary forward propagation of the parameters through the model. Moreover, the accuracy of the predicted solutions is quite good, even for reference data samples of reduced dimension. Regarding the generation of the membership functions, one uses the inverse Zadeh?s extension principle, which is the key for the purely inverse implementation of the method. The major novelty of this work is the combined use of the successive application of the interval model updating at each α-level and the covariance matrix updating to estimate the each interval radius from its updated centre.

Acknowledgments

The authors acknowledge the support of the Portuguese Foundation for Science and Technology, FCT, under LAETA, through IDMEC, and the strategic project PEst-OE/EME/UI0667/2014 (UNIDEMI, FCT-NOVA).

References

[1] Moens, D. and Vandepitte, D., *A survey of non-probabilistic uncertainty treatment in finite element analysis*, Computer Methods in Applied Mechanics and Engineering, Vol. 194, No. 12-16, pp. 1527–1555, apr 2005.

[2] Moens, D. and Vandepitte, D., *Recent advances in non-probabilistic approaches for non-deterministic dynamic finite element analysis*, Archives of Computational Methods in Engineering, Vol. 13, No. 3, pp. 389–464, sep 2006.

[3] Moens, D. and Hanss, M., *Non-probabilistic finite element analysis for parametric uncertainty treatment in applied mechanics: Recent advances*, Finite Elements in Analysis and Design, Vol. 47, No. 1, pp. 4–16, jan 2011.

[4] Zadeh, L. A., *Fuzzy Sets*, Information and Control, Vol. 8, No. 3, pp. 338–353, 1965.

[5] Hanss, M., Applied Fuzzy Arithmetic, Springer-Verlag, Berlin/Heidelberg, 2005.

[6] Ghanem, R. G. and Spanos, P. D., Stochastic Finite Elements: A Spectral Approach, Dover Publications, Inc., rev. edn., 2012.

[7] Massa, F., Ruffin, K., Tison, T. and Lallemand, B., *A complete method for efficient fuzzy modal analysis*, Journal of Sound and Vibration, Vol. 309, No. 1-2, pp. 63–85, jan 2008.

[8] Chowdhury, R. and Adhikari, S., *Fuzzy parametric uncertainty analysis of linear dynamical systems: A surrogate modeling approach*, Mechanical Systems and Signal Processing, Vol. 32, pp. 5–17, oct 2012.

[9] Moens, D., *Fuzzy Finite Elements in Engineering: algorithms, implementation strategies and applications*, *International Conference on Uncertainty in Structural Dynamics - USD2012*, 2012.

[10] Simoen, E., Lombaert, G. and Roeck, G. D., *The Fuzzy FE method in Civil Engineering*, *International Conference on Uncertainty in Structural Dynamics - USD2012*, Leuven, Belgium, 2012.

[11] Degrauwe, D., Arman, E. O., Reynders, E., De Roeck, G. and Lombaert, G., *An efficient fuzzy calculation algorithm with application to finite element model updating*, *ISMA2006 International Conference on Noise and Vibration Engineering*, edited by Sas, P. and De Munck, M., pp. 4105–4116, 2006.

[12] Rao, M. V. R., Pownuk, A., De Munck, M. and Moens, D., *Fuzzy analysis of the moment of resistance of a doubly reinforced concrete beam with uncertain structural parameters*, Life Cycle Reliability and Safety Engineering, Vol. 2, No. 1, pp. 9–20, 2013.

[13] Liu, Y. and Duan, Z., *Fuzzy finite element model updating of bridges by considering the uncertainty of the measured modal parameters*, Science China Technological Sciences, Vol. 55, No. 11, pp. 3109–3117, sep 2012.

[14] Roy, C. J. and Oberkampf, W. L., *A comprehensive framework for verification, validation, and uncertainty quantification in scientific computing*, Computer Methods in Applied Mechanics and Engineering, Vol. 200, No. 25-28, pp. 2131–2144, jun 2011.

[15] Erdogan, Y. S. and Bakir, P. G., *Inverse propagation of uncertainties in finite element model updating through use of fuzzy arithmetic*, Engineering Applications of Artificial Intelligence, Vol. 26, No. 1, pp. 357–367, jan 2013.

[16] Haag, T., Carvajal González, S., Hanss, M., Moens, D., Haag, T., Carvajal González, S. and Hanss, M., *Model validation and selection based on inverse fuzzy arithmetic*, Mechanical Systems and Signal Processing, Vol. 32, pp. 116–134, oct 2012.

[17] Haag, T., Herrmann, J. and Hanss, M., *Identification procedure for epistemic uncertainties using inverse fuzzy arithmetic*, Mechanical Systems and Signal Processing, Vol. 24, No. 7, pp. 2021–2034, 2010.

[18] Dong, W. and Shah, H. C., *Vertex method for computing functions of fuzzy variables*, Fuzzy Sets and Systems, Vol. 24, No. 1, pp. 65–78, oct 1987.

[19] Khodaparast, H. H., Mottershead, J. E. and Badcock, K. J., *Interval model updating with irreducible uncertainty using the Kriging predictor*, Mechanical Systems and Signal Processing, Vol. 25, No. 4, pp. 1204–1226, may 2011.

[20] Hanss, M. and Willner, K., *A fuzzy arithmetical approach to the solution of finite element problems with uncertain parameters*, Mechanics Research Communications, Vol. 27, No. 3, pp. 257–272, may 2000.

[21] Anoop, M. B., Rao, K. B. and Gopalakrishnan, S., *Conversion of probabilistic information into fuzzy sets for engineering decision analysis*, Computers \& Structures, Vol. 84, No. 3, pp. 141–155, 2006.

[22] Massa, F., Lallemand, B. and Tison, T., *Fuzzy multiobjective optimization of mechanical structures*, Computer Methods in Applied Mechanics and Engineering, Vol. 198, No. 5-8, pp. 631–643, jan 2009.

[23] Quaranta, G., *Finite element analysis with uncertain probabilities*, Computer Methods in Applied Mechanics and Engineering, Vol. 200, No. 1, pp. 114–129, 2011.

[24] Schaal, C. and Hanss, M., *Fuzzy Arithmetical Assessment of Wave Propagation Models for Multi-Wire Cables*, *Special Topics in Structural Dynamics, Volume 6*, edited by Allemang, R., Clerck, J. D., Niezrecki, C. and Wicks, A., Vol. 1 of *Conference Proceedings of the Society for Experimental Mechanics Series*, chap. 18, pp. 177–185, Springer New York, 2013.

[25] Adhikari, S. and Khodaparast, H. H., *A spectral approach for fuzzy uncertainty propagation in finite element analysis*, Fuzzy Sets and Systems, Vol. 243, pp. 1–24, may 2014.

[26] Silva, T. A. N., Development and Implementation of Model Updating Techniques in Structural Dynamics, Ph.D. thesis, Instituto Superior Técnico, Universidade de Lisboa, 2015.

[27] Deng, Z., Guo, Z. and Zhang, X., *Interval model updating using perturbation method and Radial Basis Function neural networks*, Mechanical Systems and Signal Processing, Vol. 84, pp. 699–716, feb 2017.

[28] Silva, T., Maia, N., Link, M. and Mottershead, J., *Parameter selection and covariance updating*, Mechanical Systems and Signal Processing, Vol. 70-71, 2016.

Bayesian estimation of interval bounds based on limited data

M. Imholz [1], **D. Vandepitte** [1], **D. Moens** [1]
[1] KU Leuven, Department of Mechanical Engineering,
Celestijnenlaan 300 B, B-3001, Heverlee, Belgium
e-mail: **maurice.imholz@kuleuven.be**

Abstract
When conducting uncertainty quantification, probability methods are widely used to represent quantities of a variable nature. First, a type of probability density function has to be chosen, often based on initial assumptions and physical boundary conditions, defining a set of stochastically parameters. Because the available data is physically limited to a finite number, there will always be uncertainty on the exact value of these parameters. At some point, the amount of experiments will be too low for the estimated parameters to be of practical use. In the case of very low data availability, one can attempt to use intervals instead to quantify the variability. Because no probability density function is defined, intervals can be used in the presence of low data availability, leaving only an upper and lower bound to be defined. This paper will present a method to estimate interval bounds based on a limited set of experiments, trying to optimally use the information they contain and determine practically usable interval bounds.

1 Introduction

Interval estimation concerns the capturing of the variability of a quantity x by an upper and a lower bound that effectively limit the possible values that x can take. Besides this, we also assume that in between these bounds, all values have a finite nonzero possibility of occurring. However, we do not attempt to assign any probability to any value of x, except to those which fall out of the interval, as they have a probability equal to 0. Obviously, this means that before using interval quantitation, we should not be concerned with this probability. This is for example the case in a worst-case scenario analysis, where we only try to identify the lowest performing possible outcome of a non-deterministic system and attempt to ensure it is still sufficiently performing according to the demands. All quantities in our field of interest are theoretically bounded. Many quantities cannot drop below zero (eigenfrequencies, thicknesses, stiffnesses, etc.). However, their physical bounds are of greater interest, which are usually much narrower and therefore of greater practical use. Suppose we have a quantity x we want to estimate by an interval, on a total population of N. We have tested n samples ($n \ll N$) of this population and observed a minimal value and maximal value $\langle \widehat{x_m} | \widehat{x_M} \rangle$. We now which to estimate the minimal and maximal value of $\underline{x}$, and $\overline{x}$ within our entire population, and use this as bounds for our interval $x^I = \langle \underline{x} | \overline{x} \rangle$. Obviously, a first estimate could be to just take the observed bounds as estimate for the interval: $x^I = \langle \widehat{x_m} | \widehat{x_M} \rangle$, but for very small n, this will be possibly a very non-conservative result, with many samples in the total population falling out of the estimated interval. This renders the interval not usable for further reliability analysis, as too little variability of the quantity x is captured by the interval. We therefore look for a conservative result that still takes into account as much of the available information contained in the limited dataset as possible.

2 Bayesian updating

2.1 General definition

Bayesian inference or Bayesian updating is a widely used technique to incorporate (additional) experimental knowledge on a variable quantity to estimate the quantitys stochastic parameter (citeBayes). Starting from an initial guess on the parameter value θ, or prior distribution $p(\theta)$ (which may either be inferred from previous experiments or completely from theoretical assumptions), the posterior distribution incorporating the experimental knowledge $p(\theta D)$ can be calculated by multiplying with the likelihood function $p(F|\theta)$ in what is known as Bayes theorem:

$$p(\theta|D) = \frac{p(D|\theta)p(\theta)}{p(D)} \tag{1}$$

$p(D)$ serves as a normalizing constant so that $\int_{-\infty}^{\infty} p(\theta D)d\theta = 1$. Obviously, the posterior depends greatly on the choice of the prior, but also on the type of PDF and the associated parameter vector that is used. If the PDF is well chosen and enough data is available, performing Bayesian inference can lead to a posterior distribution that approaches a delta function located at the true parameter value. However, if the PDF is chosen badly the posterior may not converge or it may even converge to a wrong parameter value. Because of this, additional testing is often done to assess the goodness-of-fit. However, in the presence of little available data, these tests often fail. E.g. if we compare the maximum value of the likelihood given by the Gaussian distribution and the uniform distribution, for a set of 30 samples drawn from the standard normal distribution, the uniform distribution almost always scores better. One would need at least about 60 samples to be able to unambiguously distinguish the normal from the uniform distribution. And for PDF types that resemble the shape of the Gaussian distribution more closely, this number will be even higher.

2.2 non-possibilistic Bayesian updating

In the presence of low data availability, non-possiblistic approaches can be an answer. Interval estimation or, by extension, non-possibilistic parameter estimation using Bayesian approaches has not been subject to extensive research. Only recently, Yi et a al. proposed a Bayesian updating framework for intervals based on the definition of the Interval escape rate and interval coverage rate and defined a bayesian-like updating scheme. ([1]). Also quite recently, Hanselowski et al. proposed a Bayesian updating scheme based on fuzzy numbers ([2]), in which a fuzzy prior is defined directly on a limited data set. Through use of inverse fuzzy arithmetic the posterior fuzzy numbers are determined. The work in this paper is based on one major assumption: the interval concept is often used in the presence of low data availability and omits the need of defining a suitable PDF. However, we assume the interval does capture an unknown finitely bounded PDF, even though we cannot identify it properly. Instead we will introduce a continuous set of possible PDFs and define new interval bound estimators in a Bayesian framework. Through this a preliminary choice of PDF is no longer necessary, but much of standard Bayesian analysis is still applicable.

3 Bayesian Interval Estimation based on a generalized PDF shape

3.1 Extreme Value Distributions

Consider a PDF $f_x(x)$ for quantity x with parameter vector θ. Suppose we have a total population of N samples, with a maximum value $\overline{x}$ and a minimum value $\underline{x}$. If $f_x(x)$ is known, we can directly calculate the PDFs on the extreme values $\overline{x}$ and $\underline{x}$, which are dependent on the population size N and are given by:

$$M_x^{(N)}(\overline{x}, \theta) = N f_x(\overline{x}) \left(\int_{-\infty}^{\overline{x}} f_x(t)dt \right)^{N-1} \tag{2}$$

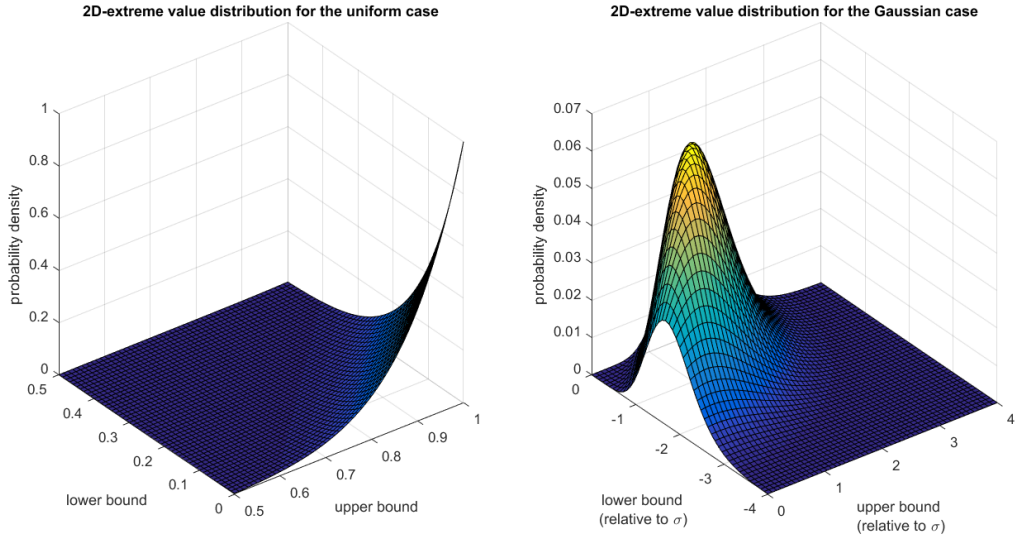


Figure 1: 2D extreme value distributions for the uniform and gaussian distribution

$$m_x^{(N)}(\underline{x},\theta) = N f_x(\underline{x}) \left(\int_{\underline{x}}^{\infty} f_x(t)dt \right)^{N-1} \tag{3}$$

Since these distributions depend on the prior determination of $f_x(x)$ and parameter vector θ, we can also interpret these extreme value PDFs as the conditional probability $p(\overline{x}\theta)$ and $p(\underline{x}\theta)$. These functions are known as the *extreme value distributions* ([3]). Some of these distributions are well known and have been applied in reliability analysis before, such as the Gumbel, Frchet and Weibull distributions. In the next step we can also define a 2-D PDF on the occurrence of an interval $x^I = \langle \underline{x} | \overline{x} \rangle$ as:

$$p(x^I = f_x(\underline{x}) f_x(\overline{x}) \left(\int_{\underline{x}}^{\overline{x}} f_x(t)dt \right)^{N-2}, \underline{x} \leq \overline{x} \tag{4}$$

Figure 1, shows an example of the 2D-extreme value distribution in case that $f_x(x)$ equals the uniform distribution and in case it equals the Gaussian distribution, for a sample size of 10. Note that these are all a priori-distributions that are only valid for a certain population size N.

3.2 Bayesian Inference for interval bounds

Consider n experimental samples with a maximum observed value $\widehat{x_M}$ and a minimum observed value $\widehat{x_m}$. What we are interested in now is an estimate for the populationwide extreme values given the observed extreme values, defined by $p(\overline{x}\widehat{x_M}, \widehat{x_m})$ and $p(\underline{x}\widehat{x_M}, \widehat{x_m})$. First, we assume the minimum observed value does not affect the populationwide maximum too much and vice versa, leading to $p(\overline{x}\widehat{x_M}, \widehat{x_m}) \approx p(\overline{x}\widehat{x_M})$ and $p(\underline{x}\widehat{x_M}, \widehat{x_m}) \approx p(\underline{x}\widehat{x_M})$. Now, we can apply Bayes theorem by writing these probabilities in terms of a prior distribution on $\underline{x}$ and $\overline{x}$ and an appropriate likelihood function (from now on, only the expressions for the maximum are given, the expressions for the minimum are quite similar):

$$p(\overline{x}|\widehat{x_M}) = \frac{p(\widehat{x_M}|\overline{x})p(\overline{x})}{p(\widehat{x_M})} \tag{5}$$

We now write the likelihood back in terms of a stochastic parameter vector θ as:

$$p(\widehat{x_M}|\overline{x}) = \int_S \int_\theta p(\widehat{x_M}|\theta) \cdot p(\theta\overline{x}) d\theta dS = \int_S \int_\theta M_x^{(n)}(\widehat{x_M},\theta) \cdot p(\theta\overline{x}) d\theta dS \tag{6}$$

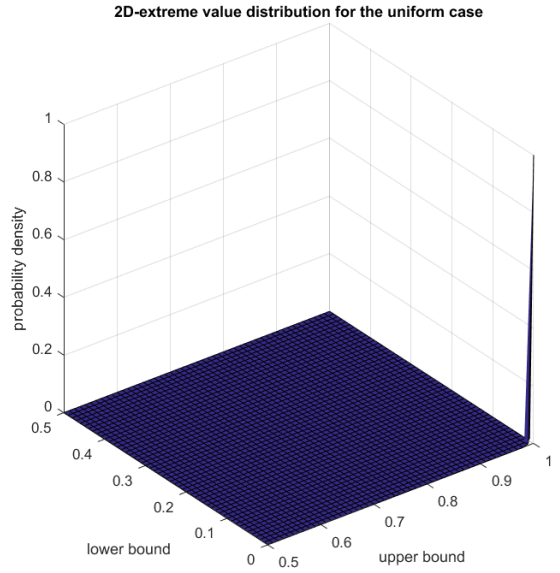


Figure 2: 2D extreme value distributions for the uniform distribution if $N = 500$

The S-integral refers to the fact that for equation 6 to be true, we need to integrate over all possible types of PDFs, and for each PDF integrate over all possible values of the corresponding parameter value θ. The second term in the integral $p(\theta\overline{x})$ we can also express using bayes theorem in terms of a likelihood function as:

$$p(\theta|\overline{x}) = \frac{p(\overline{x}|\theta)p(\theta)}{p(\overline{x})} \tag{7}$$

In equation 7, $p(\overline{x}|\theta)$ now describes the likelihood of obtaining a maximum value $\overline{x}$ in the entire population of size N, for a certain parameter value θ. If N is large enough, it can be proven that for PDFs with finite bounds this function will approach a delta function at $_{\overline{x}}$, a parameter value that defines a PDF with a maximum possible value equal to $\overline{x}$. This can be easily illustrated in the case of the uniform distribution: figure 2 show the likelihood p(x) for $N = 500$. This means the inner integral in equation 6 drops out:

$$p(\widehat{x_M}|\overline{x}) = \int_S \int_\theta M_x^{(n)}(\widehat{x_M}, \theta) \cdot \delta(\theta - \theta_{\overline{x}}) d\theta dS = \int_S M_x^{(n)}(\widehat{x_M}, \theta_{\overline{x}}) dS \tag{8}$$

Combining similar expressions for $p(\widehat{x_m}|\underline{x})$, we can write the *interval Bayesian inference* equation as:

$$p(x^I \widehat{x_M}, \widehat{x_m}) = \frac{\int_S M_x^{(n)}(\widehat{x_M}, \theta_{\overline{x},\underline{x}}) dS \cdot p(x^I)}{p(\widehat{x_M}, \widehat{x_m})} \tag{9}$$

In equation 9, all probabilities are 2D-PDFs. It expresses the conditional probability of an observed interval in terms of a prior distribution on the interval bounds and a likelihood function that incorporates the extreme value distributions.

3.3 Generalized PDF

For the outer integral, we still have to integrate over all PDFs with finite bounds equal to $\underline{x}$ and $\overline{x}$. For this we will parametrize the shape of the PDF. We assume the PDF is continuous, except at the bounds where it may have a probability density different from zero. Also, by definition, $\int_{-\infty}^{+\infty} f_x(x)dx = \int_{\underline{x}}^{\overline{x}} f_x(x)dx = 1$. We will use the following parametrization, given by equation 10:

$$f_x(x) = ax^4 + bx^3 + cx^2 + dx + e \tag{10}$$

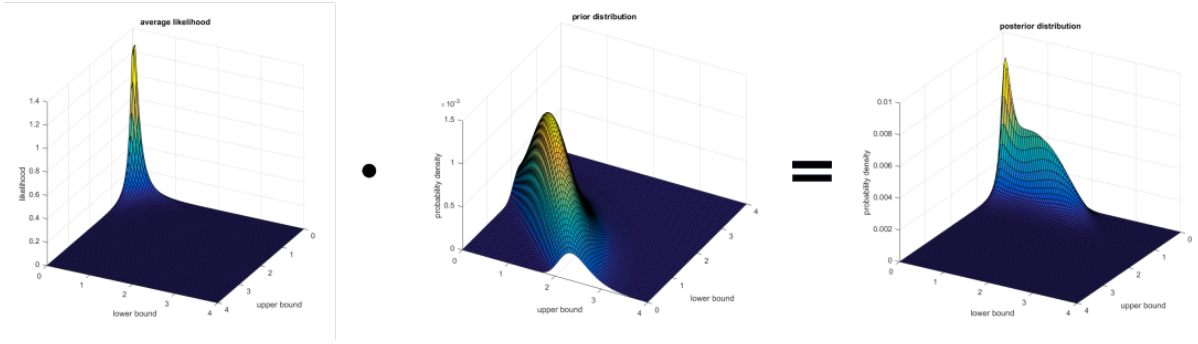


Figure 3: example of interval Bayesian inference for an experiment size of 10.

We define four adjustable parameters as given in table 1 The coefficients in equation 10 are linked to these

symbol	description
p_0	Probability density at $\underline{x}$
p_1	Probability density at $\overline{x}$
$\frac{df_x(x)}{dx}\Big\|_0$	first derivative of the PDF at $\underline{x}$
$\frac{df_x(x)}{dx}\Big\|_1$	first derivative of the PDF at $\overline{x}$

Table 1: parameters used to determine the PDF shape

parameters through (equation 11):

$$\begin{bmatrix} a \\ b \\ c \\ d \\ e \end{bmatrix} = \begin{bmatrix} -15 & -15 & -2.5 & 2.5 \\ 32 & 28 & 6 & -4 \\ -18 & -12 & -4.5 & 1.5 \\ 0 & 0 & 1 & 0 \\ 1 & 0 & 0 & 0 \end{bmatrix} \cdot \begin{bmatrix} p_0 \\ p_1 \\ \frac{df_x(x)}{dx}\Big|_0 \\ \frac{df_x(x)}{dx}\Big|_1 \end{bmatrix} + \begin{bmatrix} 30 \\ -60 \\ 30 \\ 0 \\ 0 \end{bmatrix} \tag{11}$$

Appropiate bounds on these parameters have been determined so that $f_x(x) > 0$ within the interval $\langle \underline{x} | \overline{x} \rangle$. This defines a wide set of PDFs (including asymmetrical ones) which allows us to evaluate the likelihood as defined in equation intervalBayesian. Figure 3 shows an example of the posterior distribution obtained using a prior that equals the EVD for a normal distribution with a total population $N = 1000$, and a sample set of 10.

4 Average likelihood and worst-case likelihood estimation

The likelihood used in equation 9 can be calculated in two ways:

- Equation 6 describes the *average likelihood estimate*, as it determines an average likelihood over a parametrized set of PDFs. The likelihood is simply calculated by explicitely evaluating the integral over thee parameters defined in table 1, thereby determining the average likelihood over a large set of possible PDF shapes.
- Another way to deal with the integration in equation 6, is not integrating at all, but instead determining the maximum value of $p(\widehat{x_M}, \widehat{x_m} | \overline{x}, \underline{x})$ over all possible PDFs, and use this quantity as an estimate for the likelihood function. This reasoning relates well to the concept of interval theory: assuming the true nature of the PDF is unknown, we let our likelihood be determined by the PDF that makes the observed

data the most likely, given certain bounds. This comes down to a sort of worst-case-likelihood and may fit better with the concept of intervals than the integrated likelihood estimate.

Figure 4 shows an example of both estimators for 5 randomly chosen points in the interval $\langle 0|1 \rangle$ and shows how the likelihood evolves with increasing interval size. To evaluate the validity of the use of the average

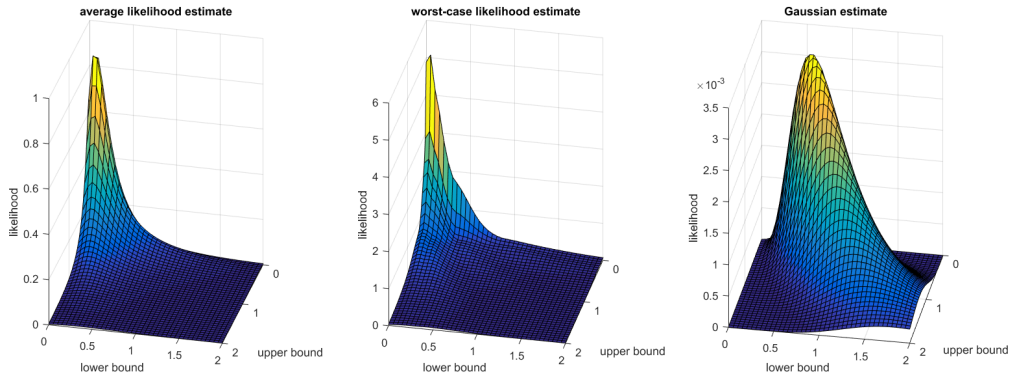


Figure 4: average and worst case likelihood for a sample size of 5

and worst-case likelihood estimators, their convergence rate for increasing data availability is compared to standard Bayesian estimation where the Gaussian distribution is assumed. An important requirement of an estimator is that once the amount of data approaches infinity, the estimator will converge to the actual value (i.e. an unbiased estimator), but preferably it will also converge monotonically and as fast as possible. First, a non-informative prior is considered for the interval bounds, i.e. a uniform distribution bounded by the observed extremes and six times the observed interval radius. Since the Gaussian distribution is not bounded, we will use the truncated Gaussian distribution truncated at $\pm 3\sigma$. The variable of interest is given a random PDF performing a 2D-polynomial transformation on a uniformly distributed germ variable. Figures 5, 6 and 7 show the evolution of the estimated 95%-confidence intervals on the interval bounds for an increasing number of samples. On th xx-axis the logarithm of the sample size is given, which ranges from 7 up to 270. The intervals are normalized so the desired interval equals $\langle 0|1 \rangle$. We clearly see that because of the (wrong) assumption of a Gaussian distribution, the estimation of the bounds converge to a wrong value. Both the average likelihood and the worst case likelihood estimator converge to the right interval bounds and also outperform the Gaussian estimator in the case of small sample size. Also, we see that for a sample size bigger than 40, the average and worst case likelihood estimator almost coincide, and that for smaller sample size, the average likelihood tends to perform better.

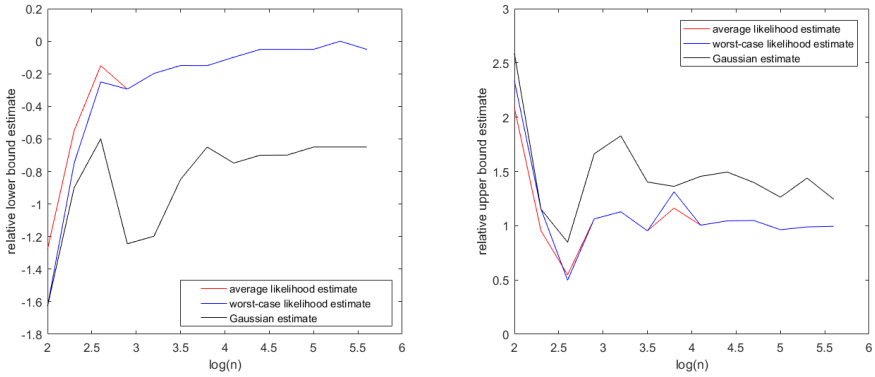


Figure 5: evolution of the 95%-confidence estimate on the lower and upper bound for increasing sample size (1) 5

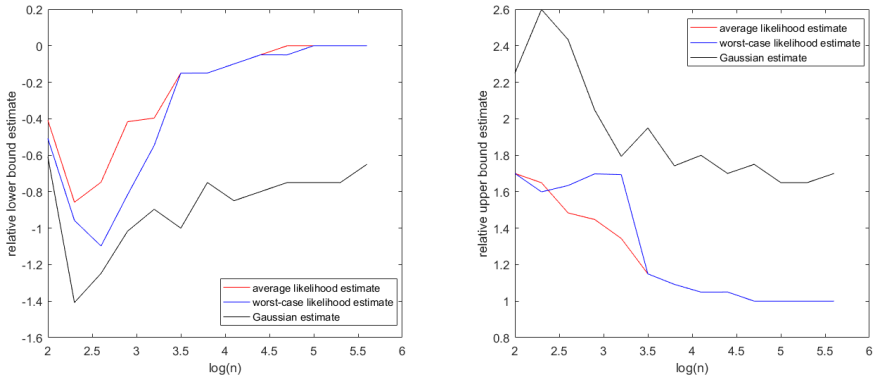


Figure 6: evolution of the 95%-confidence estimate on the lower and upper bound for increasing sample size (2)

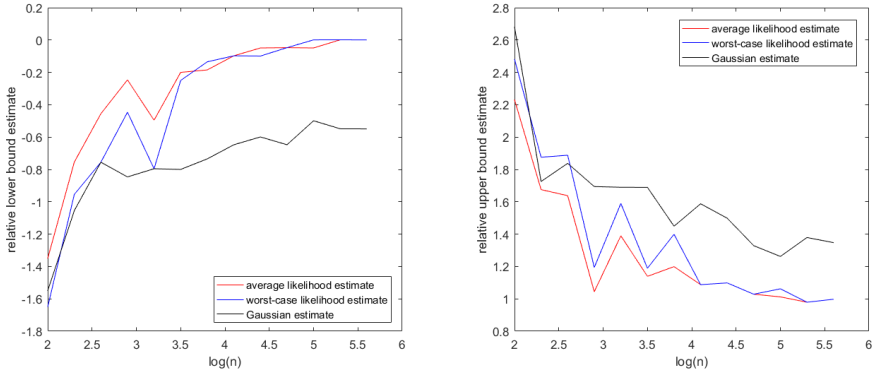


Figure 7: evolution of the 95%-confidence estimate on the lower and upper bound for increasing sample size (3)

5 Conclusions

This paper introduced a Bayesian inference scheme that can be used to determine interval bounds on small data sets where therre is high uncertainty on the exact type of distribution, Bayes' theorem was adapted to an interval-equivalent form and the resulting likelihood is determined, including a large set of possible PDFs in the calculation, thereby increasing the robustness of the final result. The likelihood can either be estimated by averaging over the entire set of PDFs, or by taking the worst-case likelihood, further increasing robustness in the case of low data availability. Initial numerical experiments show that the method is better capable of estimating the true interval bounds than the Gaussian distribution estimate.

Acknowledgements

The KU Leuven fund and the FWO fund for scientific research are hereby graciously acknowledges.

References

[1] Y. Li, X. Wang, C. Wang, M. xu, L. Wang, *Non-probabilistic Bayesian update method for model validation*, Applied Mathematical Modelling, vol 58, Elsevier inc. (2018), pp. 388-403

[2] A.. Hanselowski, S. Ihrle, M. Hanss *A Fuzzy model updating technique motivated by Bayesian Inference*, *Proceedings of The 2015 Thematic Conference on Uncertainty Quantification in Computer Sciences and Engineering, Hersonissos, Greece, 2015 May 25-27*, Hersonissos(2015), pp. 548-559

[3] S. Kotz, S. Nadarajah, *Extreme Value Distributions: Theory and Applications*, London: Imperial college press, 2000

[4] D. Kelly, C. Smith, *Bayesian Inference for Probabilistic Risk Assessment: A Practitioner's Guidebook*, Springer-Verlag, London, 2011

Stochastic analysis of the natural frequencies of rectangular plates under random temperature distributions

R. A. Borges[1], **L. F. F. Rodovalho**[2], **D. A. Rade**[3]
[1] Federal University of Goiás – Mathematics and Technology Institute – School of Industrial Mathematics, Catalão, GO, Brazil

[2] Federal University of Uberlândia, School of Mechanical Engineering, Uberlândia, Brazil.

[3] Aeronautics Institute of Technology, Division of Mechanical Engineering, São José dos Campos, Brazil, e-mail: **rade@ita.br**

Abstract
It has been shown in the literature that temperature variations can induce modifications of the static and dynamic characteristics of beam-like and plate-like structures, due to the so-called *stress-stiffening effect*. In most cases of practical interest, temperature variations associated to environmental and operational conditions are very difficult to control and can be rationally considered as random quantities. In this context, the present paper addresses the propagation of uncertainties affecting the temperature on the natural frequencies of thin rectangular plates. A Rayleigh-Ritz-based dynamic model is first derived for the bending vibrations of plates, accounting for the presence of thermal stresses. This model is combined with a Karhunen-Loève expansion (KL), used to discretize the temperature distribution, which is modeled as a Gaussian random field. The results enable to quantify the influence of temperature randomness on the thermal stresses, and evaluate the sensitivities of the natural frequencies with respect to such randomness.

1 Introduction

Many problems of structural engineering, particularly those related to structural dynamics, are prone to the influence of temperature variations. These later can be associated to either environmental conditions or thermal effects induced by the operation of the structural system. Notable cases are those involving viscoelastic materials, the mechanical properties of which (stiffness and damping) are known to be strongly dependent on temperature [1]. Similar dependence is exhibited by mechanical systems containing viscous dampers, whose damping effectiveness depends directly on the viscosity of the fluid used in these devices, which, on its turn, depends on temperature. In both examples, temperature variations can be due to modifications of the ambient temperature and, very often, to self-heating effects resulting from energy dissipation mechanisms within the material [2].

Less obvious, yet equally important, is the influence of thermal stresses, which are comprehensively covered in [3]. The occurrence of thermal stresses can induce significant modification of the apparent stiffness of structures, which is known as *stress-stiffening effect*. In fact, non-uniform temperature distributions and/or constrained thermal dilatations can induce thermal stresses, the distribution of which depends on the spatial variation of temperature over the structure, and also on boundary conditions. The stress-stiffening effect is more pronounced in beam-like and plate-like structures, whose bending stiffness, buckling loads and modal characteristics can be strongly affected by the presence of thermal stresses. As pointed-out by Cui and Hu [4], the structural components of high-speed aircrafts and space vehicles can be subject to temperature increase due to aerodynamic heating and/or solar radiation.

Many research works reported in the literature address the influence of thermal stresses on the buckling and/or vibration behavior of structural systems and components. In spite of not dealing directly with thermal stresses, Dickinson [5] investigated the free lateral vibrations of simply-supported rectangular plates subject

to normal and shear in-plane forces, using, for this purpose, the semi-analytical Rayleigh-Ritz method. Results are presented for plates with different aspect ratios and various in-plane load conditions.

Porter Goff [6] investigated, both analytically and experimentally, the influence of residual stresses induced by welding on the natural frequencies of a rectangular plate under free boundary conditions. The study shows that the presence of residual stresses reduces the natural frequencies of the plate, and that this effect is more pronounced on the natural frequencies associated to torsional modes than on those related to flexural modes. In addition, it was found out that this effect is less significant for higher-order modes.

In the work of Mead [7], consideration was given to the natural modes and frequencies of a free rectangular Kirchhoff plate subjected to in-plane stresses generated by prescribed non-uniform surface temperature distributions. Based on Rayleigh-Ritz approach, combined with the use of an Airy's stress function, a discrete model was derived and used to formulate the vibration and buckling eigenproblems. Results and discussion clarify how the knowledge of the actual thermal stress distribution can lead to the understanding of its effect on plate modes and frequencies.

More recently, Cui and Hu [4] investigated the thermal buckling behavior and natural vibration characteristics of a uniformly heated rectangular thin plate with two adjacent in-plane frictional sliding edges. Besides thermal stresses, temperature dependencies of material properties and friction coefficients were taken into consideration. The authors concluded that it is possible to adjust the in-plane forces and the clearances in the edges in order to improve the mechanical performance of heated rectangular plates.

All previous investigations described above consider time-invariant temperature and thermal stress distributions, which presupposes thermal equilibrium. Although this can be a reasonable assumption is certain cases, it cannot be applicable to (possibly the majority of) other cases of practical interest. This is particularly true in situations in which the structure is subjected to a combination of heat transfer mechanisms with the surrounding media (conduction, natural or forced convection, and radiation). In such cases, temperature can hardly be controlled and, due to the large number of factors that might intervene in the heat transfer mechanisms, it becomes meaningful to consider temperature variations as random. As a result, thermal stresses and also the static and dynamic properties of the structure should be considered as being random as well.

The theoretical foundations and numerical approaches for modeling uncertainties in structural dynamics have been addressed by many authors in the last few decades. Although various approaches for dealing with uncertainties have been developed, those based on probability theory are far more popular than the others [8-9].

Under this motivation, in this paper, an approach for evaluating the influences of random temperature variations onto the modal characteristics of thin rectangular plates is suggested and evaluated. Such an approach employs a stochastic Rayleigh-Ritz approach, consisting of the combination of the classical Rayleigh-Ritz method with the Karhunen-Loève expansion (KL). This later is used to discretize the random part of the temperature distribution over the surface of the plate, which is modeled as a Gaussian random field.

In the sections that follow, the derivation of thermal stresses from a prescribed two-dimensional temperature field based on the concept of Airy's stress function is first presented. Then, a deterministic Rayleigh-Ritz-based dynamic model for the bending vibrations of rectangular plates, accounting for the presence of thermal stresses, is formulated following the procedure suggested in [7]. After revisiting the formulation underlying the discretization of the random temperature field based on KL expansion, numerical simulations are performed for a particular steel plate under free boundary conditions, considering different levels of uncertainty affecting two different nominal temperature distributions. The simulation results provide the statistics of the first five natural frequencies of the plate, which are discussed.

2 Theory

In this section the theoretical foundations of three main aspects explored in this paper are reviewed, namely: a) the derivation of thermal stresses induced by a given temperature distribution; b) the derivation of the equations of the transversal motion of plates accounting for the presence of in-plane stresses; c) the discretization of two-dimensional random fields based on Karhunen-Loève expansion, which will be used to model the temperature distribution over the plate surface.

2.1 Computation of thermal stresses

Consider a thin rectangular plate of dimensions *a*, *b* and *h* illustrated in Fig. 1. Under the hypotheses of material homogeneity and isotropy, and plane stress state, given a prescribed temperature field imposed on the plate surface, $T(x,y)$, the resulting stress components are obtained by solving the following bi-harmonic differential equation for the associated Airy's stress function $\phi(x,y)$ [3]:

$$\nabla^4\phi(x,y) + E\alpha\nabla^2 T(x,y) = 0 \tag{1}$$

$$\sigma_x(x,y) = \frac{\partial^2\phi(x,y)}{\partial y^2}, \sigma_y(x,y) = \frac{\partial^2\phi(x,y)}{\partial x^2}, \tau_{xy}(x,y) = \frac{\partial^2\phi(x,y)}{\partial x\partial y} \tag{2}$$

where E and α are, respectively, the material Young's modulus and linear thermal dilatation coefficient, which are assumed to be independent on the temperature, $\nabla^2(.) = \frac{\partial^2(.)}{\partial x^2} + \frac{\partial^2(.)}{\partial y^2}$ is the Laplace operator and $\nabla^4(.) = \frac{\partial^4(.)}{\partial x^4} + \frac{\partial^4(.)}{\partial y^4} + 2\frac{\partial^4(.)}{\partial x^2\partial y^2}$ is the bi-harmonic operator.

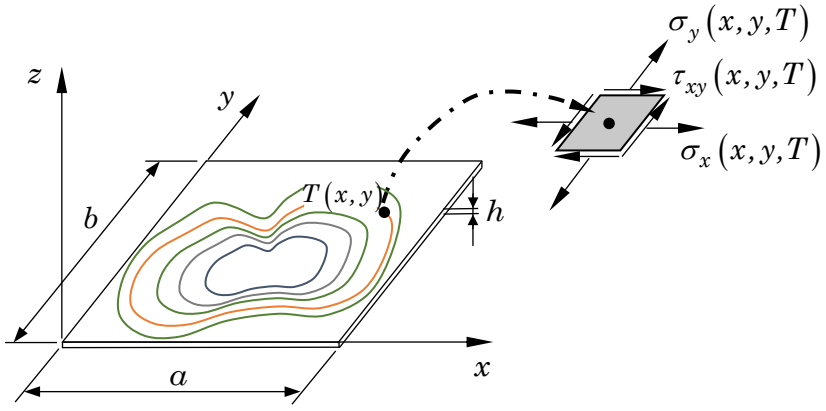


Figure 1. Illustration of a rectangular plate under non-uniform temperature distributions and thermal stresses.

The Airy's stress function $\phi(x,y)$ must satisfy the stress boundary conditions on the edges of the plate. In the present study, free boundary conditions are assumed for the four edges. Hence, the solution of Eq. (1) must satisfy:

$$\begin{aligned}
\sigma_x &= \frac{\partial^2 \phi}{\partial y^2} = 0, \text{ at } x = 0, x = a, \\
\sigma_y &= \frac{\partial^2 \phi}{\partial x^2} = 0, \text{ at } y = 0, y = b, \\
\tau_{xy} &= \frac{\partial^2 \phi}{\partial x \partial y} = 0, \text{ at } x = 0, x = a, \ y = 0, y = b.
\end{aligned} \tag{3}$$

The approximate solution to Eq. (1) can be obtained by expressing $\phi(x,y)$ as a double truncated series of the form:

$$\phi(x,y) = \sum_{m=1}^{M} \sum_{n=1}^{N} A_{mn} f_m(x) g_n(y), \tag{4}$$

where $f_m(x)$ and $g_n(y)$ are chosen as eigenfunctions of uniform, clamped-clamped Euler-Bernoulli beams. It can be easily seen that, under these conditions, the stress boundary conditions (3) are fully satisfied.

For a given temperature distribution $T(x,y)$, the computation of the coefficients A_{mn} is carried-out by adopting a Galerkin-type scheme, which consists in introducing Eq. (4) into Eq. (2), multiplying both sides successively by $f_m(x) g_n(y)$, m=1 to M, n=1 to N, and integrating both sides of the resulting equation on the domain $0 \le x \le a, 0 \le y \le b$. The computation of the integrals is greatly facilitated by the orthogonality of the beam eigenfunctions. This approach leads to a set of $M \cdot N$ linear equations, which must be solved to obtain the coefficients A_{mn}. Then, the thermal stresses can be obtained by associating Eqs. (2) and (4).

2.2 Equations of bending motion of plates subjected to in-plane stresses

The equations of motion for the undamped bending vibration of free-free plates subjected to in-plane stresses are derived herein by using the Rayleigh-Ritz method [10], which consists in approximating the transverse displacement field of the plate by the double truncated series of the form:

$$w(x,y,t) = \sum_{r=1}^{R} \sum_{s=1}^{S} W_{rs}(t) \psi_r(x) \psi_s(y), \tag{5}$$

where $\psi_r(x)$ and $\psi_s(y)$ are the eigenfunctions of uniform free-free Euler-Bernoulli beams.

Based on the hypotheses of the Kirchhoff plate theory, the kinetic and potential energies of the plate, this latter accounting for the in-plane stresses, are given, respectively, by:

$$T(t) = \frac{1}{2} \rho h \int_0^b \int_0^a \left(\frac{\partial w}{\partial t} \right)^2 dx dy, \tag{6}$$

$$U(t) = U_{bend}(t) + U_{stress}(t), \tag{7.a}$$

where

$$U^{(bend)}(t) = \frac{1}{2} D \int_0^b \int_0^a \left\{ \left(\frac{\partial^2 w}{\partial x^2} + \frac{\partial^2 w}{\partial y^2} \right)^2 - 2(1-\nu) \left[\frac{\partial^2 w}{\partial x^2} \frac{\partial^2 w}{\partial y^2} - \left(\frac{\partial^2 w}{\partial x \partial y} \right)^2 \right] \right\} dxdy, \tag{7.b}$$

$$U^{(stress)}(t) = \frac{1}{2} h \int_0^b \int_0^a \left\{ \sigma_x \left(\frac{\partial w}{\partial x} \right)^2 + 2\tau_{xy} \frac{\partial w}{\partial x} \frac{\partial w}{\partial y} + \sigma_x \left(\frac{\partial w}{\partial x} \right)^2 \right\} dxdy, \tag{7.c}$$

where ρ and ν are, respectively, the mass density and Poisson's coefficient of the material, and $D = Eh^3 \big/ 12\left(1-\nu^2\right)$.

According to the Rayleigh-Ritz method, the equations of motion are obtained by first introducing the approximate solution (5) into Eqs. (6) and (7), which leads to expressions of $T(t)$ and $U(t)$ as functions of $W_{rs}(t)$. By applying Lagrange's Equations considering $W_{rs}(t)$ as generalized coordinates, the equations of motion for the free bending vibrations of the plate are found under the form:

$$\mathbf{M}\ddot{\mathbf{w}}(t) + \left(\mathbf{K}^{(bend)} + \mathbf{K}^{(stress)} \right) \mathbf{w}(t) = \mathbf{0}, \tag{8}$$

where $\mathbf{w}(t) = \left[W_{11}(t) \quad W_{12}(t) \quad \cdots \quad W_{RS}(t) \right]^T$ is the vector of generalized coordinates, $\mathbf{M}_{(R\cdot S \times R\cdot S)}$ is the mass matrix, $\mathbf{K}^{(bend)}_{(R\cdot S \times R\cdot S)}$ is the bending stiffness matrix, which depends on the plate dimensions and material properties, while $\mathbf{K}^{(stress)}_{(R\cdot S \times R\cdot S)}$ is the geometric stiffness matrix, which depends on the plate dimensions and on the distribution of thermal stresses.

From Eq. (8), the eigenvalue problem the solutions of which provide the natural frequencies and mode shapes of the plate, is expressed as:

$$\left(\mathbf{K}^{(bend)} + \mathbf{K}^{(stress)} - \omega_i^2 \mathbf{M} \right) \mathbf{W}_i = \mathbf{0}, \tag{9}$$

It should be pointed-out that the dependence of the eigensolutions on the temperature distribution comes from the fact that $\mathbf{K}^{(stress)}$ depends on the distribution of the thermal stresses.

3 The Karhunen-Loève expansion

The Karhunen-Loève (KL) expansion provides a continuous representation of the temperature distribution over the surface of the plate as a superposition of random variables weighted by deterministic orthogonal functions defined on $0 \le x \le a; 0 \le y \le b$, as follows [11]:

$$T(x,y,\theta) = \bar{T}(x,y) + \sum_{r=1}^{R} \sqrt{\lambda_r}\, f_r(x,y)\, \zeta_r(\theta), \tag{10}$$

where θ belongs to the sample space Ω of the associated probability space $(\Omega, \Im, P)$, and the deterministic functions $f_r(x,y)$ and the zero-mean random variables $\zeta_r(\theta)$ are orthogonal, i.e.,

$$\int_0^b \int_0^a f_r(x,y)\, f_s(x,y)\, dx\, dy = \delta_{rs}, \quad r,s = 1,2,... \tag{11.a}$$

$$E\left[\zeta_r(\theta)\right] = 0,\ r = 1,2,... \tag{11.b}$$

$$E\left[\zeta_r(\theta)\zeta_s(\theta)\right] = 0,\ r,s = 1,2,... \tag{11.c}$$

In Eq. (10), the functions $f_k(x,y)$ and the scalar values λ_r are, respectively, the eigenfunctions and eigenvalues of the covariance function $C(x_1, x_2, y_1, y_2)$, hence satisfying:

$$\int_0^b \int_0^a C(x_1,x_2,y_1,y_2) f_r(x_1,y_1)\, dx_1 dy_1 = \lambda_r f_r(x_2,y_2),\ r = 1,2,... \tag{12}$$

The properties of the covariance function (positive-definiteness and symmetry) ensure that the eigenvalues a real-valued and positive, and that the eigenfunctions are linearly independent.

As mentioned in [11], analytical solutions exist for a very limited number of types of covariance functions. For the sake of simplicity, one of those cases are considered here, which consists in adopting, under the assumption of stationarity of the random field, an exponential covariance function defined as

$$C\left[(x_1,y_1),(x_2,y_2)\right] = C\left[(x_1-x_2),(y_1-y_2)\right] = \exp\left(-\frac{x_1-x_2}{L_x} - \frac{y_1-y_2}{L_y}\right), \tag{13}$$

where L is the correlation length and the domain of definition is $0 \le x_1 \le a, 0 \le x_2 \le a, 0 \le y_1 \le b, 0 \le y_2 \le b$.

For the exponential covariance function, the eigensolutions of Eq. (12) are [11]:

- For r and s even :

$$\lambda_r = \frac{2c_x}{\omega_r^2 + c_x^2},\ f_r(x) = \frac{\cos(\omega_r x)}{\sqrt{a + \frac{\sin(2\omega_r a)}{2\omega_r}}},$$
$$\bar{\lambda}_s = \frac{2c_y}{\bar{\omega}_s^2 + c_y^2},\ f_s(y) = \frac{\cos(\bar{\omega}_s y)}{\sqrt{b + \frac{\sin(2\bar{\omega}_s b)}{2\bar{\omega}_s}}} \tag{14}$$

where $c_x = 1/L_x$, $c_y = 1/L_y$, and ω_r and $\bar{\omega}_s$ are the roots of the following transcendental equations:

$$c_x - \omega_r \tan(\omega_r a) = 0,\ c_y - \bar{\omega}_s \tan(\bar{\omega}_s b) = 0. \tag{15}$$

- For r and s odd :

$$\lambda_r = \frac{2c_x}{\omega_r^2 + c_x^2},\ f_r(x) = \frac{\sin(\omega_r x)}{\sqrt{a + \frac{\sin(2\omega_r a)}{2\omega_r}}},$$
$$\bar{\lambda}_s = \frac{2c_y}{\bar{\omega}_s^2 + c_y^2},\ f_s(y) = \frac{\cos(\bar{\omega}_s y)}{\sqrt{b + \frac{\sin(2\bar{\omega}_s b)}{2\bar{\omega}_s}}} \tag{16}$$

where ω_r and $\bar{\omega}_s$ are the roots of the following transcendental equations:

$$\omega_r + c_x \tan(\omega_r a) = 0,\ \bar{\omega}_s + c_y \tan(\bar{\omega}_s b) = 0. \tag{17}$$

4 Numerical results

In this section two sets of results obtained from numerical simulations are presented and discussed: the first considers a deterministic doubly quadratic temperature distribution, which is the same considered in [7]. The second set comprises results from stochastic analysis using the Karhunen-Loève expansion.

4.1 Deterministic analysis of the influence of temperature distribution on the plate natural frequencies

One considers the following two-dimensional quadratic temperature distribution:

$$T(\xi,\eta) = 16T_0\left(\xi - \xi^2\right)\left(\eta - \eta^2\right). \tag{18}$$

where $\xi = x/a$, $\eta = y/b$, $0 \le \xi \le 1, 0 \le \eta \le 1$.This distribution, normalized by T_0, is illustrated in Fig. 2.

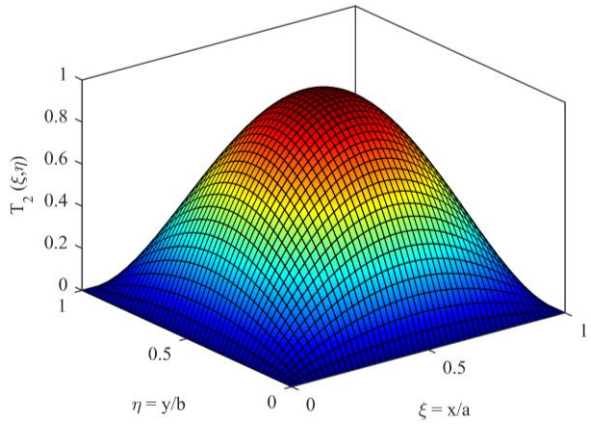


Figure 2. Two-dimensional representation of the temperature distribution over the plate.

Figure 3 depicts the distributions of dimensionless normal and shear stresses ($\sigma_x/E\alpha T_0$, $\sigma_y/E\alpha T_0$, $\tau_{xy}/E\alpha T_0$) for the temperature distribution over the surface of a plate with aspect ratio $a/b=2$, while Fig. 4 shows the distributions of those stresses along the midlines $\eta=0.5$ and $\xi=0.5$. It should be pointed-out that, as can be seen in the formulation presented in Section 2.1, the magnitude of the stress components depend linearly on the temperature scaling factor T_0.

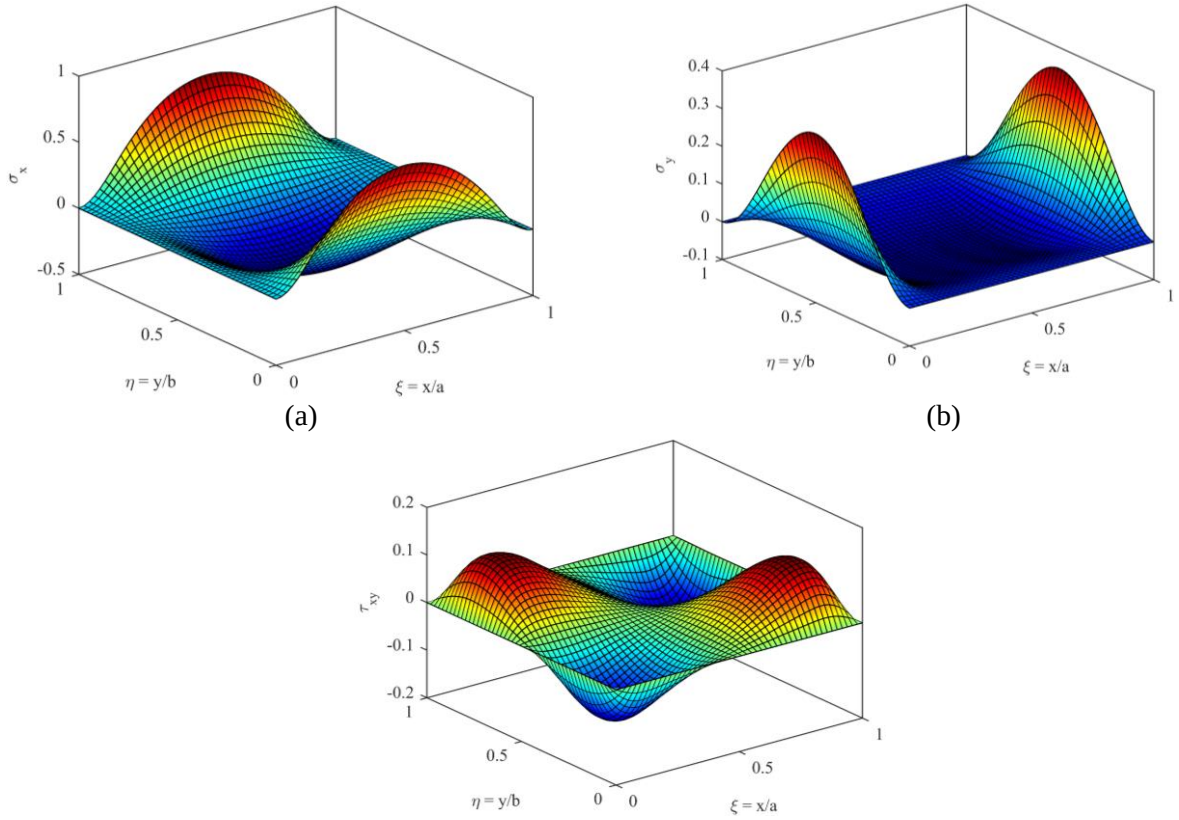


Figure 3 – Distributions of non-dimensional stress components for the temperature field considered in Eq. (18): (a) distribution of $\sigma_x/E\alpha T_0$; (b) distribution of $\sigma_y/E\alpha T_0$; (c) distribution of $\tau_{xy}/E\alpha T_0$. Aspect ratio $a/b=2$.

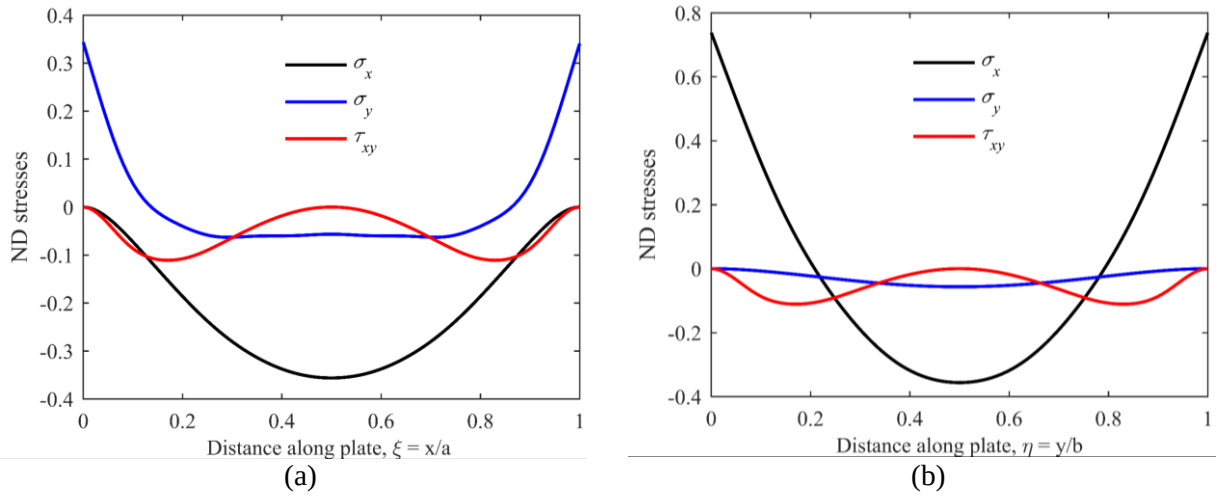


Figure 4 – Distributions of non-dimensional stress components $\sigma_x/E\alpha T_0$, $\sigma_y/E\alpha T_0$, $\tau_{xy}/E\alpha T_0$ for the temperature field considered: (a) distributions along the centerline $\eta = 0.5$; (b) distributions along the centerline $\xi = 0.5$. Aspect ratio $a/b = 2$.

Although, for a given temperature distribution, the magnitudes of the thermal stresses vary linearly with the scaling factor T_0, the same dependency cannot be expected for the natural frequencies of the plate, since the temperature intervenes only in $\mathbf{K}^{(stress)}$ in Eq. (9), so that T_0 cannot be factored-out of the stiffness matrix.

The effect of the temperature on the first five non-dimensional natural frequencies of the plate, considering the non-dimensional temperature distribution, is illustrated in Fig. 5. The non-dimensional temperature and natural frequencies are defined, respectively, as $T_{ND} = T_0 \alpha a b \left(1-\nu^2\right)/h^2$, $\Omega_{ND} = \omega\sqrt{\rho h a^4/D}$.

It is worth mentioning that the null values achieved for the first natural frequency indicate buckling of the plate.

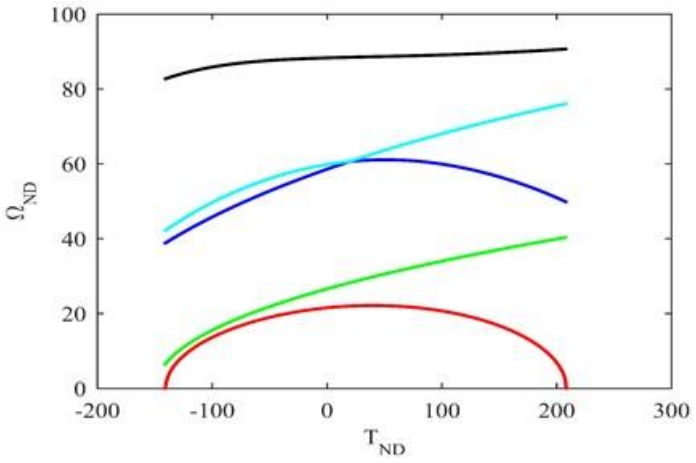


Figure 5 – Variations of non-dimensional natural frequencies Ω_{ND} of the plate with non-dimensional temperature T_{ND}.

4.2 Stochastic analysis of the influence of temperature distribution on the plate natural frequencies

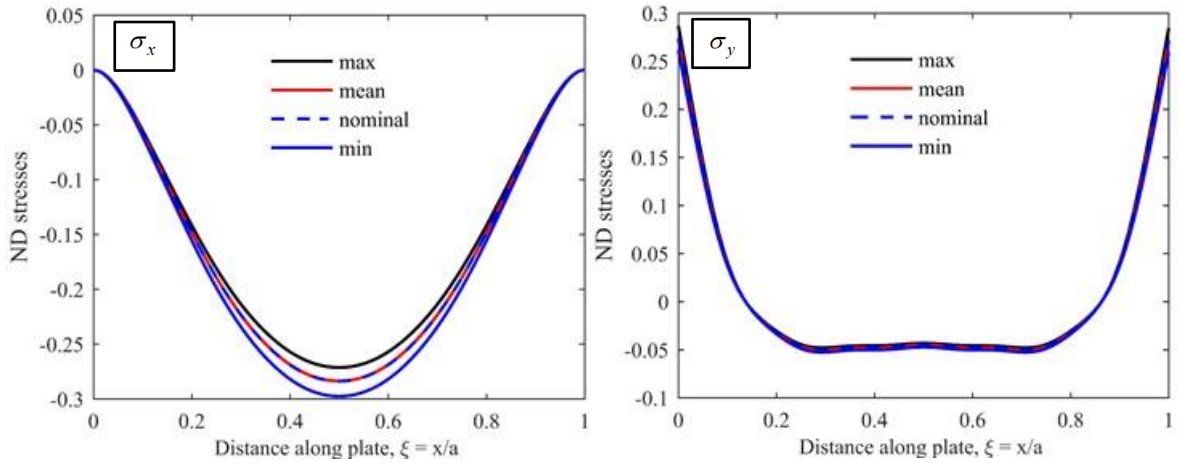
Using the Karhunen-Loève expansion expressed by Eq. (10), assuming the mean temperature distribution given by Eq. (18), the two-dimensional random field representing the stochastic temperature distribution is expressed as:

$$T(\xi,\eta,\theta)=\left(\xi-\xi^2\right)\left(\eta-\eta^2\right)\left[16T_0+\sum_{r=1}^{R}\sqrt{\lambda_r}f_r(\xi,\eta)\zeta_r(\theta)\right] \tag{19}$$

The meaning of the quantities appearing in Eq. (19) has been previously stated in Sec. 3.

To obtain the results presented next, the temperature random field of Eq. (19) with $T_{ND}=100$ was discretized using six zero-mean normal variables $\zeta_r=N\left(0,\sigma_r^2\right), r=1,2,...,6$ with different values of standard deviations. These random variables were sampled (with 500 samples) using a random number generator. For each sample, the temperature field was reconstructed according to Eq. (19), and used to compute the corresponding thermal stresses. These later were then introduced in the Rayleigh-Ritz model to compute the samples of the first five natural frequencies.

Figures 6 and 7 show graphically the statistics of the thermal stress distributions along the plate midlines $\eta=0.5$ and $\xi=0.5$, for two values of the standard deviations ascribed to the random variables ζ_r, namely $\sigma_r=0.03$ and $\sigma_r=0.1$, while Figs. 8 and 9 illustrate the histograms of the first five natural frequencies. In addition, Tab. 1 indicates the statistics of the natural frequencies.



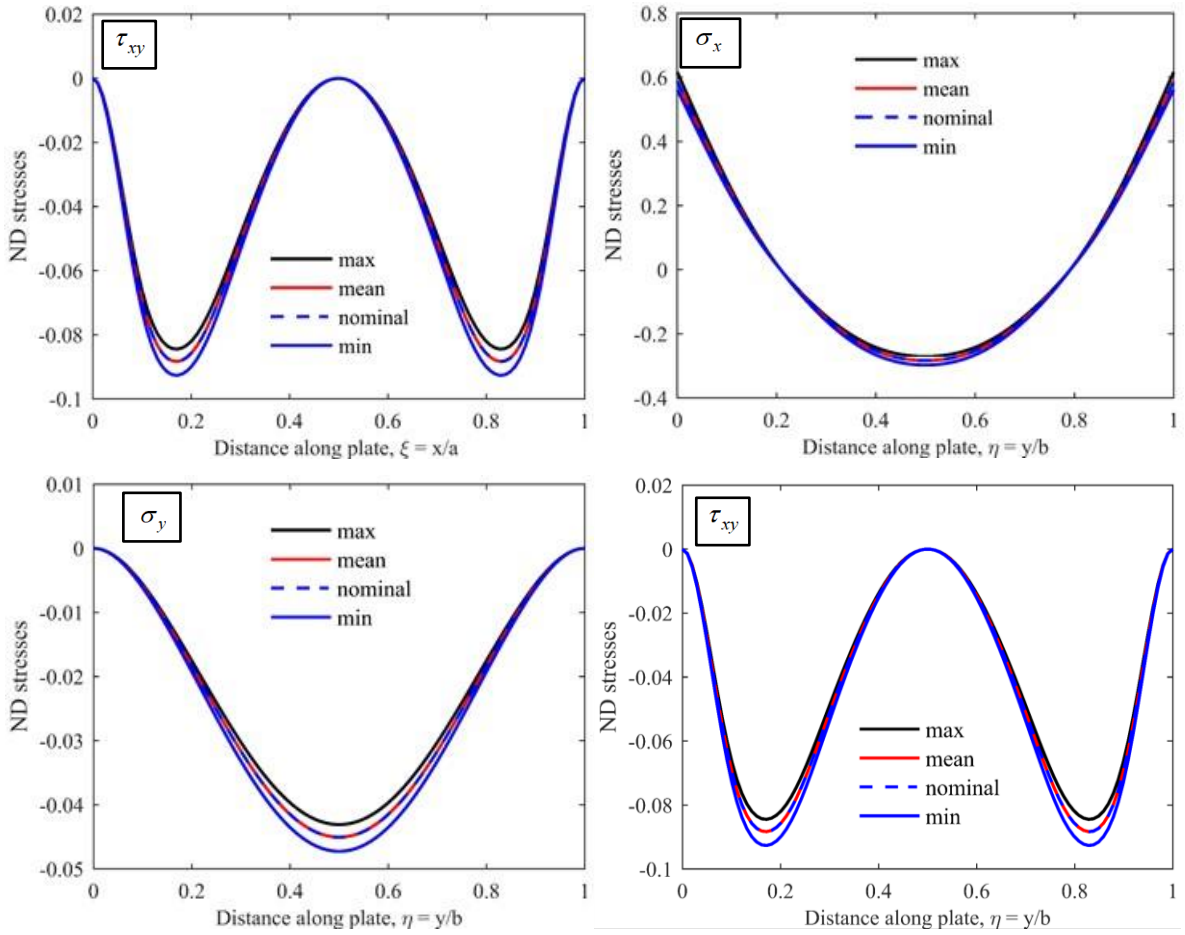
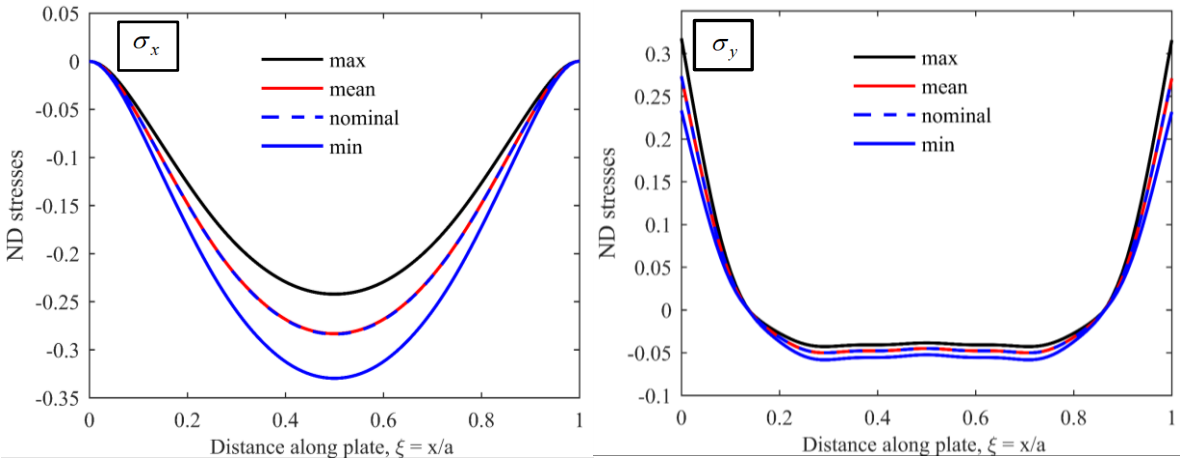


Figure 6 – Statistics of the random thermal stress distributions for $T_{ND} = 100$ and $\sigma_r = 0.03, r = 1, 2, ..., 6$



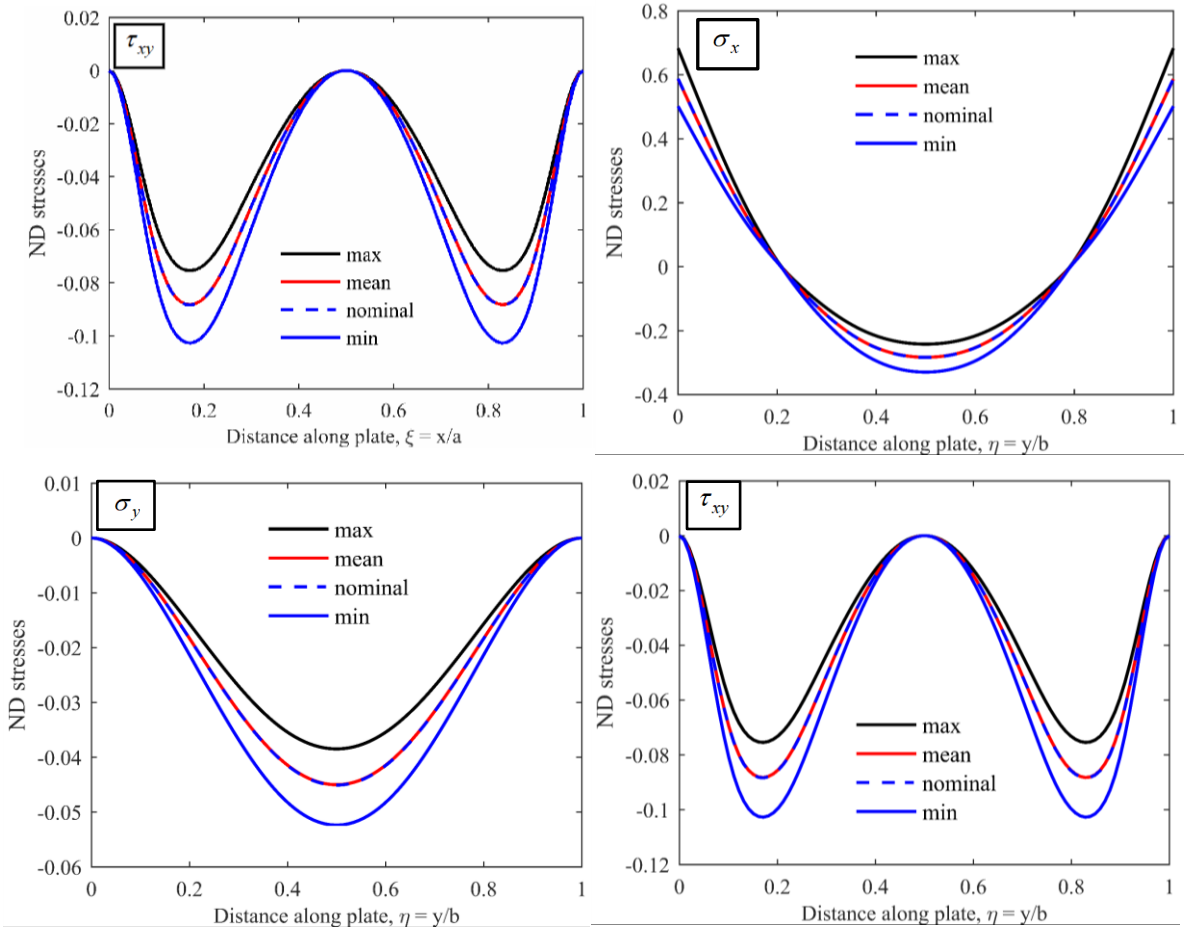
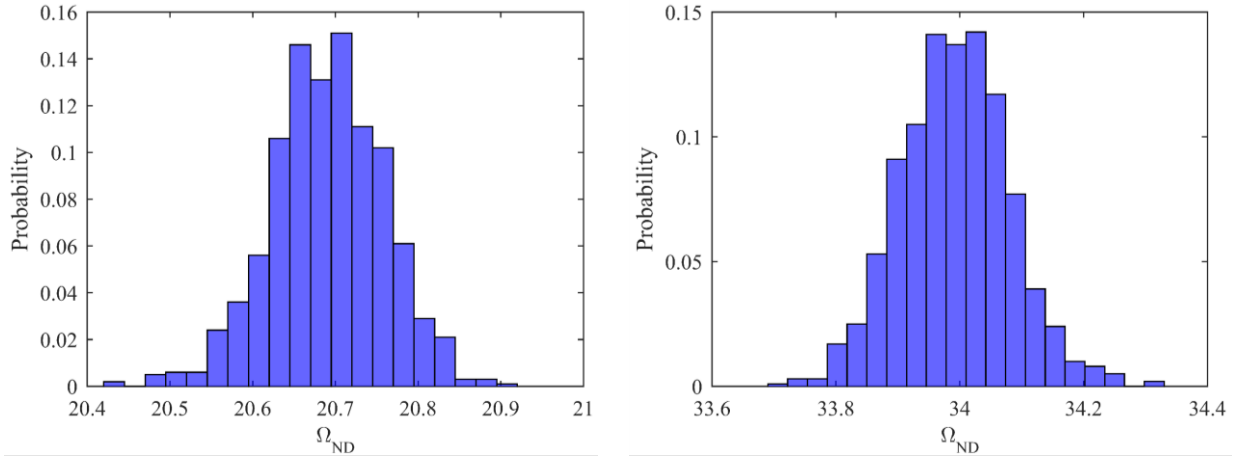


Figure 7 – Statistics of the random thermal stress distributions for $T_{ND} = 100$ and $\sigma_r = 0.10, r = 1, 2, \ldots, 6$



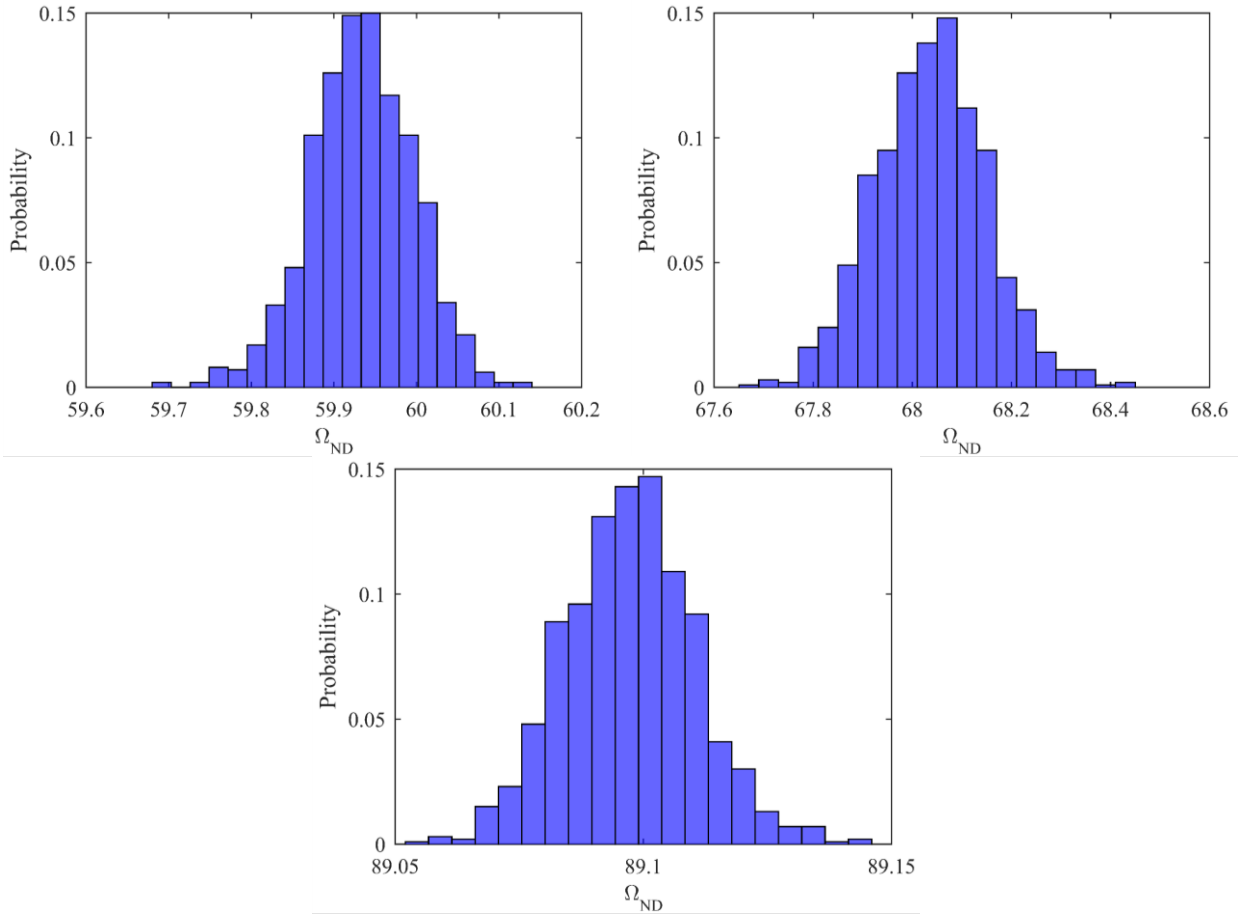
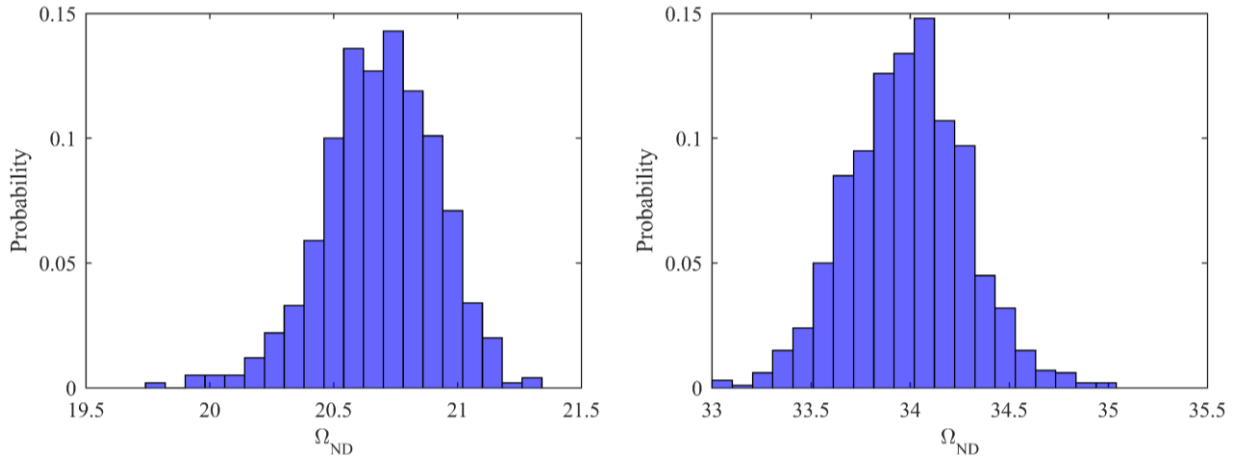


Figure 8 – Histograms of the first five natural frequencies for $T_{ND} = 100$ and $\sigma_r = 0.03, r = 1, 2, ..., 6$.



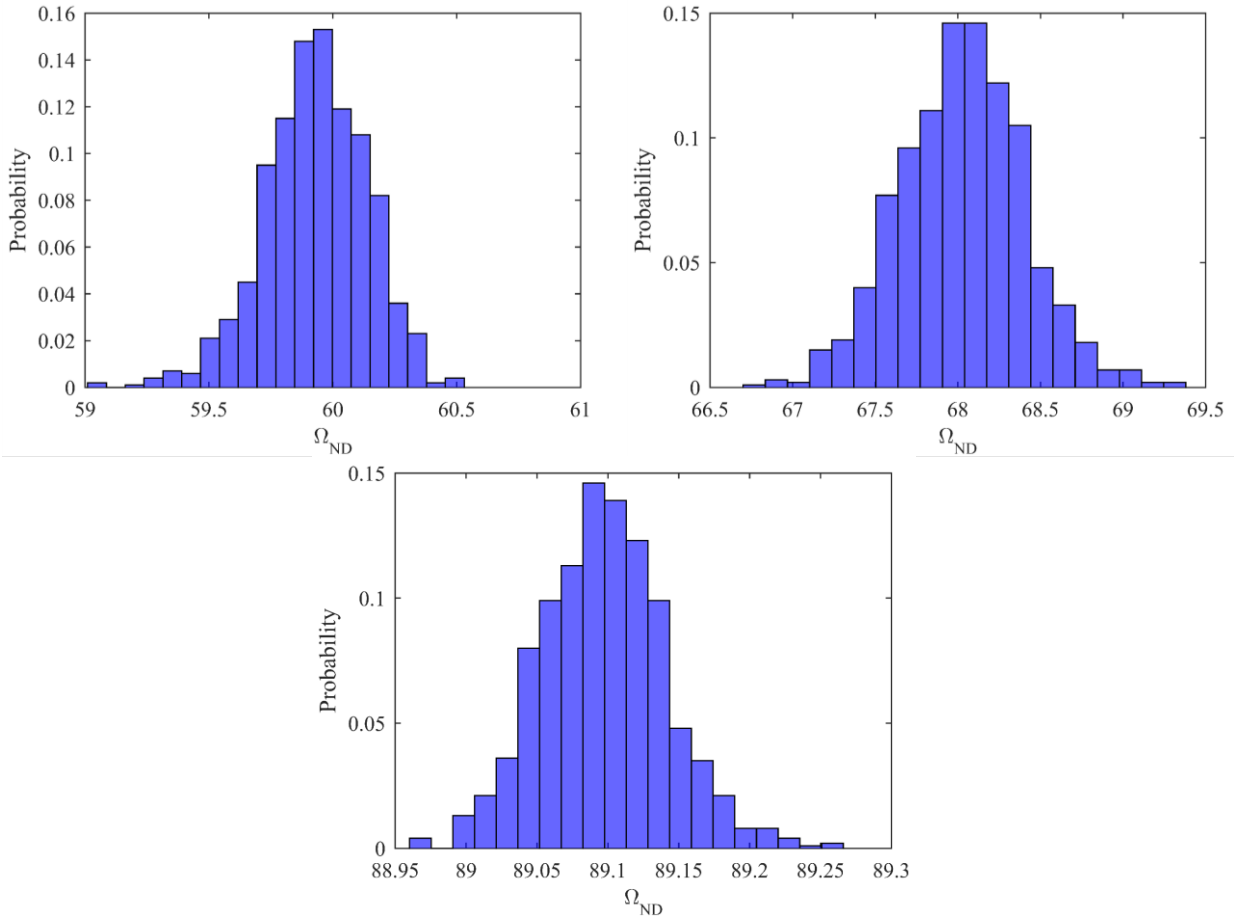


Figure 9 – Histograms of the first five natural frequencies for $T_{ND} = 100$ and $\sigma_r = 0.10, r = 1,2,...,6.$

Table 1 – Statistics of the first five natural frequencies of the plate for $T_{ND} = 100$ and $\sigma_r = 0.03, r = 1,2,...,6.$.

Non-dimensional frequencies	Ω_1	Ω_2	Ω_3	Ω_4	Ω_5
Sample mean value	20.69	33.99	59.93	68.037	89.097
Sample standard deviation	0.068	0.088	0.063	0.11	0.013
Sample coefficient of variation	0.0033	0.0026	0.0010	0.0017	0.00015
Minimum value	20.43	33.71	59.70	67.67	89.06
Maximum value	20.90	34.31	60.13	68.44	89.15

Table 2 – Statistics of the first five natural frequencies of the plate for $T_{ND} = 100$ and $\sigma_r = 0.10, r = 1,2,...,6.$

Non-dimensional frequencies	Ω_1	Ω_2	Ω_3	Ω_4	Ω_5
Sample mean value	20.69	33.98	59.93	68.026	89.097
Sample standard deviation	0.23	0.29	0.21	0.38	0.043
Sample coefficient of variation	0.011	0.0087	0.0035	0.0056	0.00049
Minimum value	19.74	33.03	59.07	66.80	88.96
Maximum value	21.33	35.03	60.51	69.37	89.27

The results shown above enable to verify the influence of the randomness of the temperature distribution on the values of thermal stresses and the natural frequencies of the plate. In Figs. 8 and 9 one can clearly see that, as expected, the dispersions of the stress distributions increase with the dispersion of the temperature field, which are indicated by the values of the standard deviations ascribed to the random variables

$\zeta_r = 0.10, r = 1,2,...,6$. Dispersion increase is also observed for the natural frequencies, as indicated by the sample standard deviations given in Tabs. 1 and 2.

Interesting to notice is that the sensitivity of the natural frequencies to the temperature randomness, which are indicated by the sample coefficients of variation presented in the third lines of Tabs. 1 and 2, vary substantially from one mode to the other.

Conclusions

The stochastic analysis of the natural frequencies of thin rectangular plates under random temperature variations has been addressed. For this purpose, a modeling procedure based on the combination of the Rayleigh-Ritz method, duly adapted to account for the presence of thermal stresses, and the Karhunen-Loève, used to discretized the random part of the temperature random field. Under the hypotheses adopted, the modeling strategy has proved to be effective in characterizing the random influences of temperature variations on the natural frequencies of plates. In fact, it was possible to quantify the relations between the dispersion levels affecting the temperature field and the dispersions of natural frequencies. It could be seen that these later vary significant to a particular natural frequency to the other.

Although the variations of the natural frequencies associated to the randomness of temperature were found to be small for the cases examined, it is believed that those variations can be much larger in other situations (other boundary conditions and larger variability of the random temperature field). In such cases, those sensitivities can be high enough to justify the consideration of thermal stresses on the modeling of the dynamic behavior of plates.

Acknowledgements

R. A. Borges is thankful for the Mathematics and Technology Institute, Federal University of Goiás. L. F. F. Rodovalho acknowledges the Brazilian Ministry of Education (CAPES Foundation), the Brazilian Research Council for Science, Technology and Innovations (CNPq), the Federal University of Uberlândia and the Structural Mechanics Laboratory (LMEst). D. A. Rade gratefully acknowledges the São Paulo State research agency FAPESP (grant # 2015/20363-6) and CNPq (grant # 310633/2013-3) for the financial support to this research work.

References

[1] A.D. Nashif, Jones, D.I.G., Henderson, J.P., Vibration Damping, John Wiley & Sons, New York, 1985.

[2] De Cazenove, J., Rade, D.A., de Lima, A.M.G., Araújo, C.A., A numerical and experimental investigation on self-heating effects in viscoelastic dampers. Mechanical Systems and Signal Processing, v. 27, p. 433-445, 2012.

[3] Boley, B.A., Wiener, J.H., Theory of Thermal Stresses, Dover Publications, Inc., 1960.

[4] Cui, D., Hu, H., Thermal buckling and natural vibration of a rectangular thin plate with in-plane stick-slip-stop boundaries. Journal of Vibration and Control, vol. 22, p. 1-17, 2016.

[5] Dickinson, S.M., Lateral vibration of rectangular plates subject to in-plane forces. Journal of Sound and Vibration, vol. 16, p. 465-472, 1971.

[6] Porter Goff, R.F.D., The effect of self-equilibrating stresses on the natural frequencies of a free-free rectangular plate, Journal of Sound and Vibration, vol. 47, p. 85–94, 1976.

[7] Mead, D.J., Vibration and buckling of flat free-free plates under non-uniform in-plane thermal stresses. Journal of Sound and Vibration, vol. 260, p. 141-165, 2003.

[8] Smith, R.C., Uncertainty Quantification. Theory, Implementation, and Applications. Society for Industrial and Applied Mathematics, 2014.

[9] Soize. C., Uncertainty Quantification: An Accelerated Course with Advanced Applications in Computational Engineering (Interdisciplinary Applied Mathematics), Springer, 2017.

[10] Craig Jr., R.R., Kurdila, A.J., Fundamentals of Structural Dynamics – 2nd Edition.Wiley, 2006.

[11] Ghanem, R.G., Spanos, P.D., Stochastic Finite Elements: A Spectral Approach, Revised Edition. Dover, 2012.

Robust identification of parameters uncertainty in stochastic finite element model updating

N. Sharma[1], S. V. Modak[1]
1 Department of Mechanical Engineering, Indian Institute of Technology,
Delhi, Hauzkhas, New Delhi, 110016, India

Abstract
The stochastic model updating methods seek to determine the variability of the parameters of the model from the variability of the measured output. The experimental data measured on several samples of the test structure is influenced not only by variability associated with different test structures but also by measurement noise. In the first part of this paper some of the methods for statistical identification of structures are compared to identify the variability of the model parameters with and without the presence of measurement noise. Many of the current methods like perturbation based approaches cannot distinguish between the variability due to parameter variability and measurement noise. In the second part of the paper, a methodology for stochastic FE model updating is presented to obtain a robust estimate of the variability of model parameters. It is formulated to take into account data from multiple dynamic tests conducted on each sample of the test structure. The proposed methodology is validated on a simulated cantilever beam.

1 Introduction

Finite Element (FE) Models are widely used for analysis of engineering structures. A finite element model that accurately represents the dynamic behavior of a system is very useful for structural dynamic design and analysis, damage detection, structural health monitoring and vibration control [1]. Despite the high sophistication of FE modeling, prediction of dynamic characteristics using FE models often shows considerable discrepancies with respect to the experimental measurements. These discrepancies may arise due to modeling inaccuracies associated with material properties, boundary conditions, joints, damping and due to the idealization and simplifications made in the modeling [1, 2]. Measurement noise may also contribute to these discrepancies. FE model updating is now considered an acceptable approach to improve the correlation between analytical predictions and the experimental data. Usually, experimental data consists of modal frequencies, mode shapes, and frequency response functions. During past three decades, a lot of research has been carried out on development and application of model updating algorithms, such that the updated model is able to reproduce the measured data as closely as possible [2 - 4].

The conventional approach to FE model updating is typically deterministic in nature, which means that the experimental data is obtained from a single test piece and therefore the measured data does not have any variability. However, such a deterministically updated model cannot predict the dynamics of a lot of sample of structures manufactured to a same nominal design [9, 10]. This happens because the dynamic characteristic of a population of samples of the structure has a variability associated with it, while the dynamic characteristics associated with the deterministically updated model are inherently single valued.

The variability in the measured dynamic characteristics occurs due to inherent variation in the material properties, geometry and manufacturing from specimen to specimen. Variability may also arise due to measurement noise [7, 8], environmental effect, damage [5], disassembly and reassembly of the same structure [11] and material degradation over a period of time. Many of the sources of variability like that due to variation in boundary conditions, joint properties, material properties, damping cannot be easily measured or quantified. This has led to the notion of what has come to be known as stochastic finite element model updating in which the idea is to identify and quantify these sources of variability through an inverse approach based on measured variability of dynamic characteristics [6].

The work by Collins et al. [8] first time proposed a statistical method for the treatment of measurement noise in the model updating. In this, a linearized sensitivity based approach is adopted and the statistics of the unknown parameters are determined from the noisy vibration measurements using minimum variance approach. Friswell [7] modified this method by incorporating the correlation between the measured data and the updating parameters. In the above methods, the uncertain parameters are identified on the basis of the measurements, which are noisy, from a single test piece. But variability due to material, geometry, and manufacturing arising from a number of nominally identical test samples is not considered [9]. Mares et al. [9] uses the regression analysis to obtain a linearized model in which optimization take place by gradient method for the treatment of test structure variability. Some other statistical approaches that have been applied for the stochastic model updating include maximum likelihood method by Fonseca et al. [12] and Bayesian methods (Beck and Katafygiotis [13, 14], Dwight et al. [15], Boulkaibet et al. [16]).

However, the stochastic model updating methods are computational intensive due to the involvement of randomized updating parameters. Thus there is a need for developing computational efficient methods. Hua et al. [5] developed a mean centered perturbation method for statistical identification of uncertain model parameters by using the statistics of measured modal data. In this method, the first order perturbation approach is applied on the sensitivity based FE model updating method, which leads to two recursive system of equations that allows estimating the mean and variance of the updating parameters [5]. This method requires calculation of second order sensitivities, which is computationally expensive [6]. Khodaparast et al. [6] developed a perturbation method which can be approximated by omitting the correlation between updated parameters and the measured data leading to an approximate but computationally simpler version of the method. In the simplified method, only first order sensitivities are required. The Perturbation methods offer computational superiority in comparison with Bayesian and MC-based methods, but also have some limitations. These are related to the assumption that the parameters should follow Gaussian distribution and that the initial parameters estimate should be close to their true values.

In this paper, the methods proposed by Collins et al. [8], Friswell [7], and Hua et al. [5] are compared for their effectiveness to identify the variability of model parameters from the measured modal characteristics in the presence of noise. The results are also compared with the Monte-Carlo simulation (MCS) method. The limitations of the methods are identified. A new methodology for robust stochastic FE model updating is then proposed. All the methods are evaluated through a numerical study on a cantilever beam structure.

2 A brief description of stochastic model updating methods

A brief description of the four methods (Collins et al. [8], Friswell [7], Hua et al. [5], and MCS) considered for the study is given in this section. For brevity, the first three of these methods are referred in this paper as, methods of Collins, Friswell, and Hua respectively. Methods of Collins and Friswell are formulated for dealing with uncertainty due to measurement noise, while the method of Hua is a perturbation approach formulated for dealing with variability associated with test-structure specimen.

FE model updating is a kind of optimization problem, which starts with the determination of the correlation between the test data and the corresponding FE model data. If the correlation is not acceptable, then the difference between the two needs to be minimized by updating the chosen uncertain parameters of the model. The objective function of the optimization problem is defined as,

$$\text{Min } J_\theta = \varepsilon^T W \varepsilon = \left\| W^{1/2} \left(z_m - z(\theta) \right) \right\|_2^2 \tag{1}$$

where $\varepsilon_{n\times 1}$ is the vector of the residue of modal data, $z_{m_{n\times 1}}$ and $z(\theta)_{n\times 1}$ are the measured and the analytical vectors of the modal data with $n = n_{fm} \times \left(1 + n_{\phi m}\right)$. n_{fm} and $n_{\phi m}$ are the number of measured natural frequencies and measured mode shapes respectively. $\theta_{m\times 1}$ is the vector of updating parameters, and the $W_{n\times n}$ is the diagonal weighting matrix. The modal data is generally a highly nonlinear function of the updating parameters and therefore the optimization problem is defined by Eq. (1) is nonlinear in nature. The problem is often solved in an iterative way with the gradient based optimization method, in which the nonlinear

function is linearized at the current value of the updating parameters. The solution of Eq. (1) is found iteratively using following equations.

$$\theta^{(k+1)} = \theta^{(k)} + \Delta\theta^{(k)} \tag{2}$$

$$\Delta\theta^{(k)} = \left[S^T S\right]^{-1} S^T W^{1/2} \left[z_m - z\left(\theta^{(k)}\right)\right] \tag{3}$$

where $\Delta\theta^{(k)}$ is the vector of parameters changes at the kth iterations step, $\varepsilon = \left[z_m - z\left(\theta^{(k)}\right)\right]$ is the vector of discrepancy between the measured and the analytical modal parameters at the kth iteration step, $[S]$ is the modal sensitivities matrix.

2.1 Minimum variance method of Collins et al. (1974)

In the method of Collins et al. [8], it is assumed that both the measured data and the updating parameters have errors which may be specified by their variances. In this method, the unknown updating parameters are assumed to be normally distributed with mean values

$$E\left(\theta^{(k)}\right) = \bar{\theta}^{(k)} \tag{4}$$

and, covariance matrix

$$\mathrm{Cov}\left(\theta^{(k)}, \theta^{(k)}\right) = V^{(k)} \tag{5}$$

It is assumed that updating parameters value at next iteration, θ^{k+1} may be updated using previous estimate $\theta^{(k)}$ as

$$\theta^{(k+1)} = \theta^{(k)} + T\left(z_m - z^{(k)}\right) \tag{6}$$

where T is an unknown transformation matrix to be determined. It is also assumed that the error vector $\varepsilon = z_m - z$ (z is the expected (mean) value of output predicted by FE model) follows joint normal distribution with mean

$$E[\varepsilon] = 0 \tag{7}$$

and covariance matrix

$$\mathrm{Cov}(\varepsilon, \varepsilon) = E\left[\varepsilon^T \varepsilon\right] = V_\varepsilon \tag{8}$$

Since transformation matrix T in (6) is deterministic, the following equation can be written

$$E\left(\theta^{(k+1)} - \theta^{(k)}\right) = TE\left(z_m - z^{(k)}\right) = \{0\} \quad \Rightarrow \quad E\left(\theta^{(k+1)}\right) = E\left(\theta^{(k)}\right) = \bar{\theta} \tag{9}$$

The mean value of the parameters estimate gives the solution of the model updating problem. The best estimate of the mean will occur when the variance of the parameters is minimized. To obtain parameters with minimum variance, the variance matrix of the updated parameters must be calculated

$$V^{(k+1)} = E\left[\left(\theta^{(k+1)} - \theta\right)\left(\theta^{(k+1)} - \theta\right)^T\right] \tag{10}$$

Which is further expanded as

$$V^{(k+1)} = V^{(k)} + \left(D^{(k)} - V^{(k)}\left(S^{(k)}\right)^T\right)T^T + T\left(\left(D^{(k)}\right)^T - S^{(k)}V^{(k)}\right) + TV_z^{(k)}T^T \tag{11}$$

where $V_z^{(k)}$ is given by

$$V_z^{(k)} = S^{(k)} V^{(k)} \left(S^{(k)}\right)^T - S^{(k)} D^{(k)} - \left(D^{(k)}\right)^T \left(S^{(k)}\right)^T + V_\varepsilon \tag{12}$$

The matrix T is obtained by minimizing the expression for the variance matrix given in equation(11). Thus the expression for the matrix T which gives the minimum variance for the updated parameters is

$$T = \left(V^{(k)} \left(S^{(k)}\right)^T - D^{(k)}\right) \left(V_z^{(k)}\right)^{-1} \tag{13}$$

The expression of matrix T requires the variance of the current parameter estimates and also the correlation between the current parameters and the measurement noise. Therefore these matrices must be updated at every iteration step. The updated variance matrix may be obtained from Eq.(11), and the updated correlation matrix may be calculated from its definition and equation (6) and(13), as follows,

$$D^{(k+1)} = E\left(\theta^{(k+1)}, \varepsilon^T\right) \quad \Rightarrow \quad D^{(k+1)} = D^{(k)} - \left[V^{(k)} \left(S^{(k)}\right)^T - D^{(k)}\right] \left(V_z^{(k)}\right)^{-1} \left[S^{(k)} D^{(k)} - V_\varepsilon\right] \tag{14}$$

In Collins's method the correlation between the updated parameters and the measurement noise is ignored by setting the correlation matrix to zero at each iteration. This gives two recursive system of equations which is used for the estimation of mean and covariance of the updating parameters, are

$$\theta^{(k+1)} = \theta^{(k)} + V^{(k)} \left(S^{(k)}\right)^T \left[S^{(k)} V^{(k)} \left(S^{(k)}\right)^T - V_e\right]^{-1} (z_m - z^{(k)}) \tag{15}$$

$$V^{(k+1)} = V^{(k)} - V^{(k)} \left(S^{(k)}\right)^T \left[S^{(k)} V^{(k)} \left(S^{(k)}\right)^T + V_e\right]^{-1} S^{(k)} \left(V^{(k)}\right)^T \tag{16}$$

2.2 Minimum variance method of Friswell (1989)

Friswell corrected the assumption regarding omission of correlation between the updating parameters and the measured modal data. In Friswell's approach, the correlation between updating parameter and the measured data is accounted for and is defined as

$$Cov(\theta^{(k)}, z_m) = \begin{cases} 0 & if \quad k = 1 \\ D^{(k)} & if \quad k = 2,3,4..... \end{cases} \tag{17}$$

Now three recursive system of equations are obtained for the estimation of parameters, variances of parameters and the correlation matrix.

$$\theta^{(k+1)} = \theta^{(k)} + \left[V^{(k)} \left(S^{(k)}\right)^T - D^{(k)}\right] \left(V_z^{(k)}\right)^{-1} \left[z_m - z^{(k)}\right] \tag{18}$$

$$V^{(k+1)} = V^{(k)} - \left[V^{(k)} \left(S^{(k)}\right)^T - D^{(k)}\right] \left(V_z^{(k)}\right)^{-1} \left[V^{(k)} \left(S^{(k)}\right)^T - D^{(k)}\right]^T \tag{19}$$

$$D^{(k+1)} = D^{(k)} - \left[V^{(k)} \left(S^{(k)}\right)^T - D^{(k)}\right] \left(V_z^{(k)}\right)^{-1} \left[S^{(k)} D^{(k)} - V_\varepsilon\right] \tag{20}$$

2.3 Perturbation method of Hua et al. (2008)

Hua et al. considered the stochastic model updating problem by perturbation approach. In Hua's approach the mean value and the covariance predicted from the FE model are converged upon the experimentally measured data and by doing so first two statistical moments of the uncertain parameters are determined. When uncertainty in modal parameters are considered in updating, the updating parameters in each iteration become random, and the model updating problem becomes more complicated. In Hua's approach it is

assumed that the measured vector z_m is defined by summation of a deterministic part (mean value) $\overline{z}_m$ and a random part X_i i.e.

$$z_m = \overline{z}_m + X_i \tag{21}$$

Where the term X_i (with zero mean), referred to as basic random variable (BRV), represents the uncertainty in the measured modal parameters due to test structure variability and the measurement noise. Now using first order perturbation technique, the terms in Eq.(3), namely the change in structural parameters, modal sensitivity S, and error $\varepsilon = z_m - z$, at the kth iteration step will be expanded as linear function in terms of BRVs around mean value point, i.e.

$$S^{(k)} = \overline{S}^{(k)} + \sum_{i=1}^{n} \frac{\partial S^{(k)}}{\partial X_i} X_i \tag{22}$$

$$\Delta\theta^{(k)} = \Delta\overline{\theta}^{(k)} + \sum_{i=1}^{n} \frac{\partial \Delta\theta^{(k)}}{\partial X_i} X_i \tag{23}$$

$$\varepsilon^{(k)} = \overline{\varepsilon}^{(k)} + \sum_{i=1}^{n} \frac{\partial \varepsilon^{(k)}}{\partial X_i} X_i \tag{24}$$

Substitution Eq. (22)-(24) into Eq. (3) and comparing the zeroth order and first order terms of X_i leads to two recursive systems of deterministic equations as,

$$\overline{S}^{(k)} \Delta\overline{\theta}^{(k)} = \overline{\varepsilon}^{(k)} \tag{25}$$

$$\overline{S}^{(k)} \frac{\partial \Delta\theta^{(k)}}{\partial X_i} = \left(\frac{\partial \varepsilon^{(k)}}{\partial X_i} - \frac{\partial S^{(k)}}{\partial X_i} \Delta\overline{\theta}^{(k)} \right) \quad \Rightarrow \quad \overline{S}^{(k)} \frac{\partial \Delta\theta^{(k)}}{\partial X_i} = \left(\frac{\partial z_m{}^{(k)}}{\partial X_i} - \frac{\partial z^{(k)}}{\partial X_i} - \frac{\partial S^{(k)}}{\partial X_i} \Delta\overline{\theta}^{(k)} \right) \tag{26}$$

Where the partial derivative of $z^{(k)}$ and $S^{(k)}$ with respect to X_i at each iteration step are evaluated by

$$\frac{\partial z^{(k)}}{\partial X_i} = \frac{\partial z^{(k)}}{\partial \theta^{(k)}} \frac{\partial \theta^{(k)}}{\partial X_i} \tag{27}$$

$$\frac{\partial S^{(k)}}{\partial X_i} = \sum_{j=1}^{m} \frac{\partial S^{(k)}}{\partial \theta_j{}^{(k)}} \frac{\partial \theta_j{}^{(k)}}{\partial X_i} \tag{28}$$

$$\frac{\partial \theta^{(k)}}{\partial X_i} = \frac{\partial \left(\theta^{(k-1)} + \Delta\theta^{(k-1)} \right)}{\partial X_i} \quad \Leftrightarrow \quad \frac{\partial \theta^{(0)}}{\partial X_i} + \sum_{j=1}^{k-1} \frac{\partial \left(\Delta\theta^{(j)} \right)}{\partial X_i} \tag{29}$$

In the above equations, $\partial z^{(k)} / \partial \theta^{(k)}$ and $\partial S^{(k)} / \partial \theta_j{}^{(k)}$ are the first and the second order modal sensitivities respectively. Note that the starting estimate for the $\partial\theta / \partial X_i$ in Eq. (29) is zero at the first iteration. On sequentially solving Eq. (25) to Eq. (29) one can get the mean of the change in structural parameters and the derivatives of the change in structural parameters with respect to BRV. Repeating the computation over all BRVs, one can obtain the matrix of $\left[\partial \Delta\theta^{(k)} / \partial X \right]$ and $\left[\partial \theta^{(k)} / \partial X \right]$ needed for the computation of the covariance matrix. In practice, the mean and variance of the updating parameters are often needed which will be obtained by following equations.

$$\overline{\theta}^{(k+1)} = \overline{\theta}^{(k)} + \Delta\overline{\theta}^{(k)} \tag{30}$$

$$\begin{aligned}\mathrm{Var}\left(\theta^{(k+1)},\theta^{(k+1)}\right) &= \mathrm{Var}\left(\theta^{(k)},\theta^{(k)}\right)+\mathrm{Var}\left(\theta^{(k)},\Delta\theta^{(k)}\right)+\mathrm{Var}\left(\Delta\theta^{(k)},\theta^{(k)}\right)+\mathrm{Var}\left(\Delta\theta^{(k)},\Delta\theta^{(k)}\right)\\ &= \left[\frac{\partial\theta^{(k)}}{\partial X}\right]\mathrm{V}_{z_m}\left[\frac{\partial\theta^{(k)}}{\partial X}\right]^T+\left[\frac{\partial\theta^{(k)}}{\partial X}\right]\mathrm{V}_{z_m}\left[\frac{\partial\Delta\theta^{(k)}}{\partial X}\right]^T+\left[\frac{\partial\Delta\theta^{(k)}}{\partial X}\right]\mathrm{V}_{z_m}\left[\frac{\partial\theta^{(k)}}{\partial X}\right]^T\\ &+\left[\frac{\partial\Delta\theta^{(k)}}{\partial X}\right]\mathrm{V}_{z_m}\left[\frac{\partial\Delta\theta^{(k)}}{\partial X}\right]^T\end{aligned} \tag{31}$$

where V_{z_m} is the covariance of the measured data. In this way, the Eq.(30) and the Eq. (31) gives the means and the covariance of the updating parameters respectively at the k^{th} iteration step.

2.4 Monte Carlo simulation (MCS) method

In the MCS method, the statistical measured data is sampled giving N number of samples of measured data. Then deterministic model updating is performed for each samples of the measured data. When this is done for all the samples of measured data we get N sets of identified values of updating parameters, from which the statistics or variability of the updating parameters can be computed. Thus the MCS approach essentially is a repeated application of deterministic model updating.

3 A comparative study of some of the existing stochastic FE model updating methods

The case study considered here for comparison is that of updating of an undamped finite element model of a simple but representative cantilever beam structure, as shown in Fig. 1, using simulated experimental data. The dimensions of the beam are 600 x 50 x 5 mm. The modulus of elasticity and density are assumed to be 200 x 10^9 N/m^2 and 7800 kg/m^3 respectively. The beam is modeled using 12 noded beam finite elements. The displacements in y direction and the rotation about the z-axis are taken as two degrees of freedom at each of the nodes. This FE model is considered as a baseline model of the cantilever beam which will be later updated.

Another FE model with the same topology as the baseline model is constructed to provide the simulated experimental modal data by introducing certain known discrepancies in the thickness of all the finite elements with respect to the baseline model. In the simulated experimental FE model, every three consecutive finite elements were grouped together, giving a total of 4 groups, in which discrepancies are introduced as detailed in Table 1.

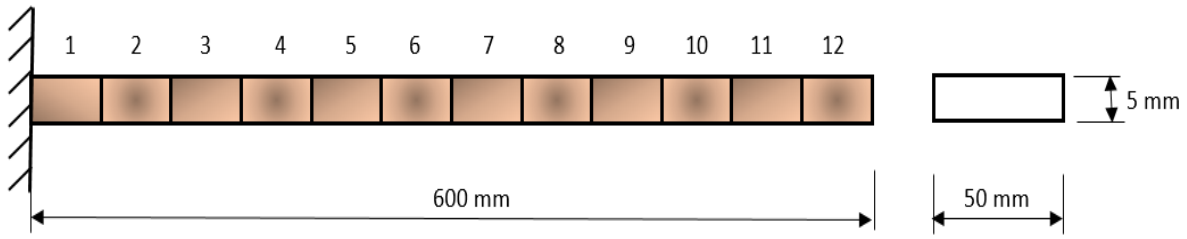


Figure 1: Cantilever beam structure

Group No.	Element grouping	Thickness of baseline model (mm)	% deviation in mean thickness in the simulated exp. FE model
1	1-3	5	+ 20
2	4-6	5	+ 40
3	7-9	5	+ 10
4	10-12	5	+ 40

Table 1: Discrepancies between baseline and the simulated experimental model with uncertain updating parameters.

In this work, the study is divided into three different cases according to the source of uncertainties in the measured modal parameters.

- Case-1: Uncertainties arise only due to the measurement noise
- Case-2: Uncertainties arise only due to test structure variability
- Case-3: Uncertainties arise due to both the test structure variability and the measurement noise

In first two cases, the comparison of statistics of the updating parameters are identified using Collins's method, Friswell's method, and Hua's method. The results are also verified with MCS method. In third case only Hua's method is compared with MCS. In all numerical studies, eigenvalues of the first six modes are assumed to be available as measured modal data.

Case 1 - Uncertainties due to measurement noise

It is assumed that 1% Gaussian, zero mean and uncorrelated random noise is present in each modal data. Updating using MCS method is performed by generating 500 samples of the simulated measured eigenvalues with noise. For updating using Collins's and Friswell's method an initial parameter coefficient of variance (COV, ratio of the standard deviation to the mean) of 0.15 was used for all the parameters. Table 2 gives a comparison of percentage error in the mean values of the updating parameters obtained using the four methods while Fig. 2 (A) shows a comparison of the mean value of the updating parameters before and after updating. It is observed that the mean value of updating parameters obtain by the methods of Collins, Hua, and MCS are very close to the simulated value and thus the percentage error after updating in the mean value is nearly zero. It is seen that the method of Friswell shows a significant error in the mean values. It is observed that the performance of the Friswell's method is sensitive to the choice of initial variance of the parameters.

Updating parameters	Before updating	After Updating			
		Collins et al. (1974)	Friswell (1989)	Hua et al. (2008) *	MCS *
t_1	-16.66	-0.05	-6.99	-1.50E-08	0.17
t_2	-28.57	0.14	-6.33	6.51E-09	-0.12
t_3	-9.09	-0.02	-6.46	7.89E-09	-0.04
t_4	-28.57	-0.04	-1.69	1.07E-09	0.13

Table 2: Percentage error in updating parameters before and after updating

Table 3 and Fig. 2 (B) give a comparison of the COV of the updating parameters after updating using the four methods. It is noted that methods marked with '*' do not require any initial estimate of variance of the uncertain updating parameters. It is observed that the magnitude of COV obtained by methods of Collins and Friswell are very small as compared to that obtained by Hua and MCS methods. It is because the former methods are the minimum variance methods which minimize the variance associated with the updating parameters, while the later methods associate the variability of the measured data to the variability of the parameters.

COV	Before updating	After Updating			
		Collins et al. (1974)	Friswell (1989)	Hua et al. (2008) *	MCS *
t_1	0.15	1.17E-03	2.18E-03	7.61E-02	1.51E-02
t_2	0.15	2.79E-03	1.94E-03	4.53E-02	3.63E-02
t_3	0.15	6.50E-04	1.33E-03	5.40E-02	7.84E-03
t_4	0.15	1.78E-03	7.30E-03	2.65E-02	2.24E-02

Table 3: COV of updating parameters before and after updating

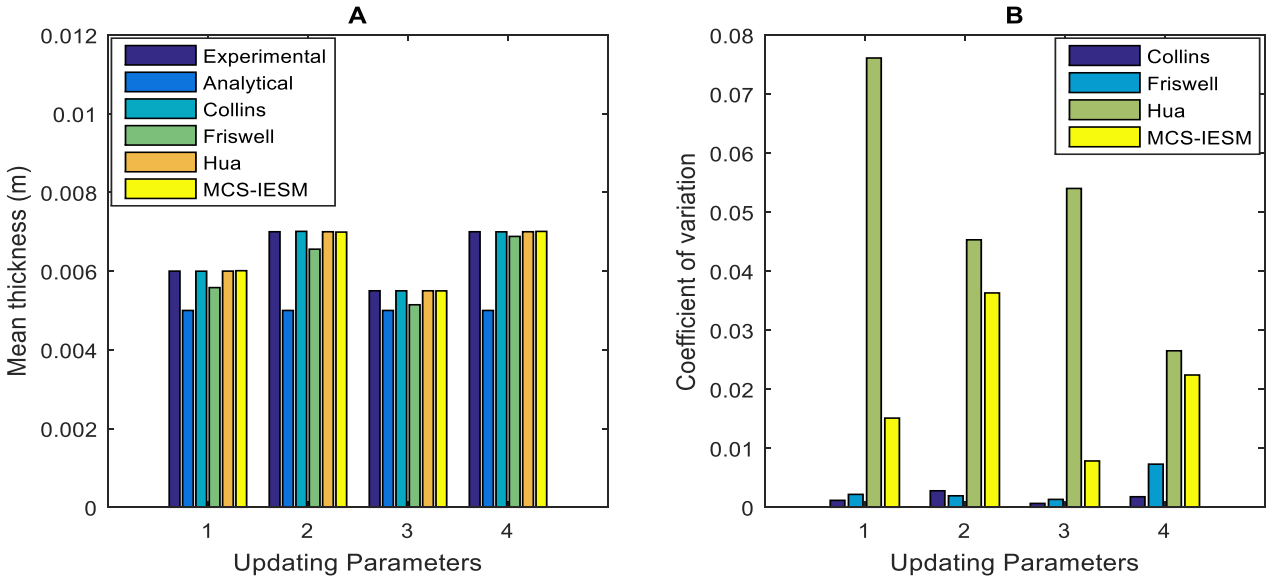


Figure 2: Comparison of the mean of updated parameters (A) and the COV of updated parameters (B)

It should be noted that the COV of the updated parameters (extracted from the updated covariance matrix) in this case does not indicate variability in the updating parameters but only gives an idea of confidence one can have in the identified mean values of the updating parameters.

Case -2 Uncertainties arise only due to test structure variability

In this section, the performance of the methods of Collins, Friswell, and Hua are compared with the MCS, in presence of test structure variability. In order to simulate the test structures, it is assumed that the each updating parameter is a statistically independent random variable having COV of 0.1. In this study, 500 samples of the test-structures are generated. The uncertainty in the simulated modal data is obtained by forward propagation using MCS method. For updating using Collins's and Friswell's method an initial

parameter COV of 0.15 was used for all the parameters. Model updating using MCS method is performed using both random and Latin Hypercube Sampling (LHS). The key idea behind LHS is to divide parameter space into equal probability space. This sampling technique, ensures a better coverage of random parameter space. In this case, as both the mean and covariance of updating parameters are known, the performances of model updating methods in identifying the statistics of updating parameters can be evaluated. Table 4 and Fig. 3 (A) gives a comparison of the percentage error in the mean value of the updating parameters after updating using the four methods while Table 5 and Fig. 3 (B) gives a comparison of COV of the updating parameters and % errors in COV respectively. It is seen that the method of MCS is performing very well for estimation of both the mean and variance of the updating parameters. The performance is even better using Latin Hypercube Sampling. Method of Hua is giving significant error in estimation of mean and COV of updating parameters. It is observed that in an earlier study [5] Hua's method yielded better results on account of the fact that the forward propagation is done using perturbation approach which assumes the correct knowledge of the mean value of the measured data. However, in reality this is not so as the statistics of the measured data needs to be derived from a discrete set of measurements on a given number of test structures. The method followed in the present study closely simulates this process of generation of statistics of measured data. This inevitably gives rise to some error in the estimate of the mean and variance of the measured modal data. This is the reason why the estimates of the mean of the updating parameters obtained by the Hua's method are in error. In nutshell it can also be said that while the Hua's method reduces the whole sample space in terms of values of mean and covariance and uses this data for identification, the MCS method, on the contrary, uses whole sample space to perform identification. Finally it is observed that the minimum variance methods of Collins and Friswell are not formulated for identifying the uncertainties of the stochastic updating parameters and hence the variances of the updating parameter identified from these method cannot be interpreted as estimate of the parameter variabilities. These methods are applicable only when variability arises solely due to measurement noise.

Updating parameters	Before updating	After Updating				
		Collins et al. (1974)	Friswell (1989)	Hua et al. (2008) *	MCS *	
					Random	LHS
t_1	-16.66	-0.06	-1.23	-1.45	0.15	0.012
t_2	-28.57	-0.03	-9.65	2.65	-0.32	0.004
t_3	- 9.09	0.02	1.33	-0.61	0.80	0.006
t_4	-28.57	-0.15	-9.27	-2.12	-0.22	0.006

Table 4: Percentage error in updating parameters before and after updating

Updating parameter	COV in the simulated experimental model	After Updating				
		Collins et al. (1974)	Friswell (1989)	Hua et al. (2008) *	MCS *	
					Random	LHS
t_1	0.1	7.25E-03	0.08	0.11	0.091	0.10
t_2	0.1	7.32E-03	0.09	0.10	0.102	0.10
t_3	0.1	7.67E-03	0.07	0.10	0.099	0.10
t_4	0.1	7.95E-03	0.06	0.10	0.105	0.10

Table 5: COV of updating parameters after updating

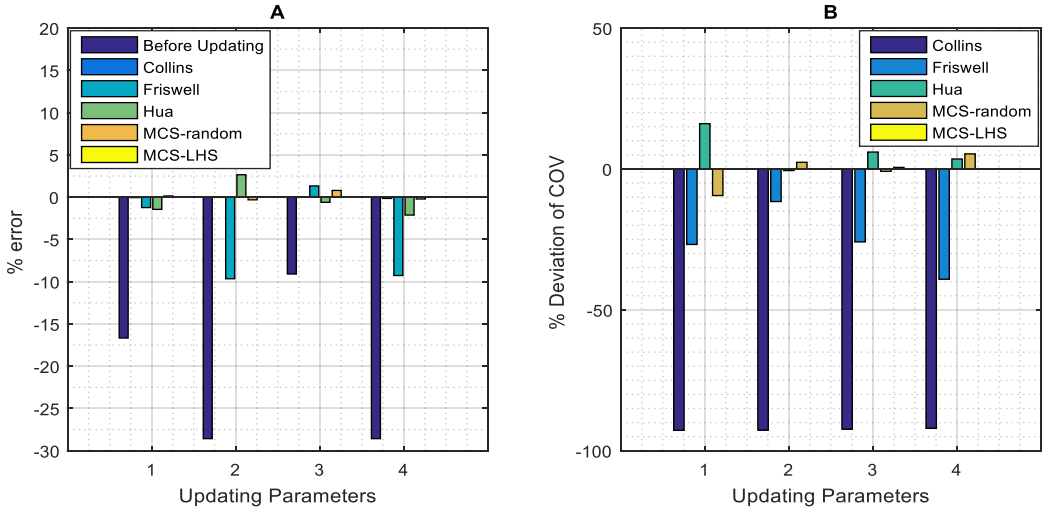


Figure 3: Comparison of the % error in mean (A) and COV of updated parameters (B)

Fig. 4 shows a scatter of the first two natural frequencies corresponding to simulated experimental and analytical model at first and last iteration in case of updating using MCS. It is seen that at the end of first iteration the scatter of the natural frequencies corresponding to the analytical model is large and it converges upon the scatter of natural frequencies corresponding to the simulated experimental model at convergence. This shows the success of the MCS method.

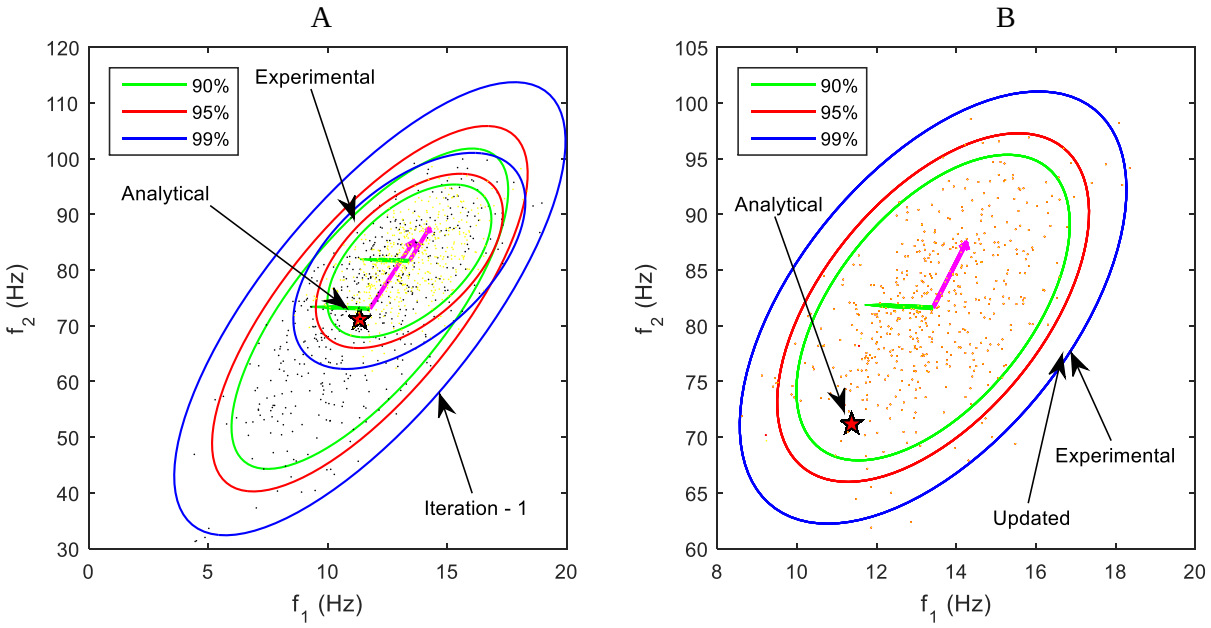


Figure 4: 2-D confidence ellipse at 1st iteration (A) and after updating (B) on a plane of f_1 and f_2

Thus, for case - 2, the MCS method performs best while the performance of the Hua's method is closed to that of MCS. The methods of Collins and Friswell should not be used for identifying variability.

Case - 3 Uncertainty due to test-structure variability and measurement noise

In this section, the performance of the method of Hua is compared with the MCS, in the presence of test structure variability and measurement noise. As already stated in case -2 the method of Friswell and Collins are not capable of handling test structure variability and hence these are not considered for study in case-3.

To simulate the test structures, it is assumed that each updating parameter is a statistically independent random variable having a COV of 0.1. In this study, 500 samples of the test-structures are simulated. In this case, the variability in the experimental modal data is simulated into two steps. First of all simulated modal data corresponding to each structure is obtained by forward propagation using MCS method. Then it is assumed that only one test is performed on each sample of the test-structure in the presence of 1% Gaussian random noise in the modal data. The process of performance of one test on a sample in the presence of noise is simulated by randomly picking a sample of the measured data from its Gaussian distribution having mean equal to the nominal value of the measured data for the sample and covariance equal to the simulated noise (of 1% in this case).

Model updating using MCS method is performed using both random and Latin Hypercube Sampling (LHS). Table 6 gives a comparison of percentage error in mean values of the parameters after updating while Table 7 gives a comparison of COV of updated parameters and Fig 5 shows the comparison of % error of COV of updated parameters from the simulated experiments. The % error in the COV of the updating parameters estimated by the Hua's method is much larger than those found using MCS. It is observed that the result obtained using MCS method in this case have somewhat deteriorated over case -2 due to presence of measurement noise in the data. The Hua's method shows little higher error as compared to MCS due to the reason explained in case 2.

Updating parameters	Before updating	Hua et al. (2008) *	MCS *	
			Random	LHS
t_1	-16.66	-1.27	-0.16	0.14
t_2	-28.57	2.59	-0.67	-0.07
t_3	- 9.09	-0.75	0.46	-0.06
t_4	-28.57	-2.07	0.46	0.12

Table 6: Percentage error in updating parameters before and after updating

Updating parameters	COV in the simulated experimental model	Hua et al. (2008) *	MCS *	
			Random	LHS
t_1	0.1	0.14	0.10	0.10
t_2	0.1	0.11	0.11	0.11
t_3	0.1	0.12	0.10	0.10
t_4	0.1	0.11	0.10	0.10

Table 7: COV of updating parameters after updating

Fig. 6 shows a scatter of the first two natural frequencies corresponding to simulated experimental and analytical model at first (A) and last iteration (B) in case of updating using MCS. It is seen that at the end of first iteration the scatter of the natural frequencies corresponding to the analytical model is large and it converges upon the scatter of natural frequencies corresponding to the simulated experimental model at convergence. Unlike case-2, in this case, the cloud of the updated modal natural frequencies are not wholly overlapped on the cloud of the measured natural frequencies. This is due to the presence of measurement noise in the modal data.

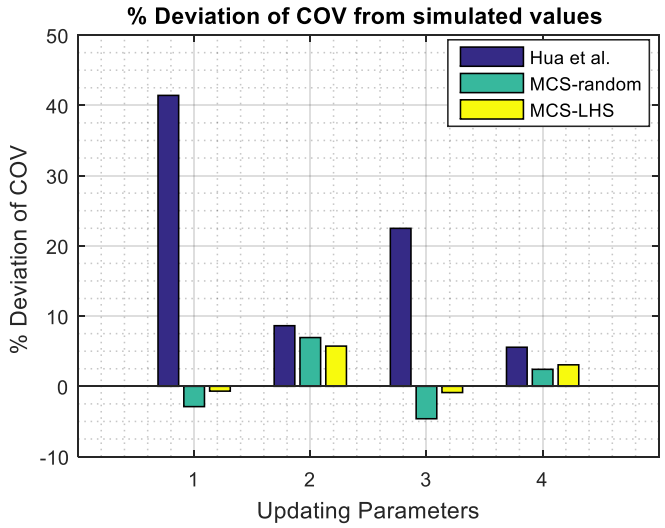


Figure 5: Comparison of % deviation of COV of updated parameters from simulated experiments

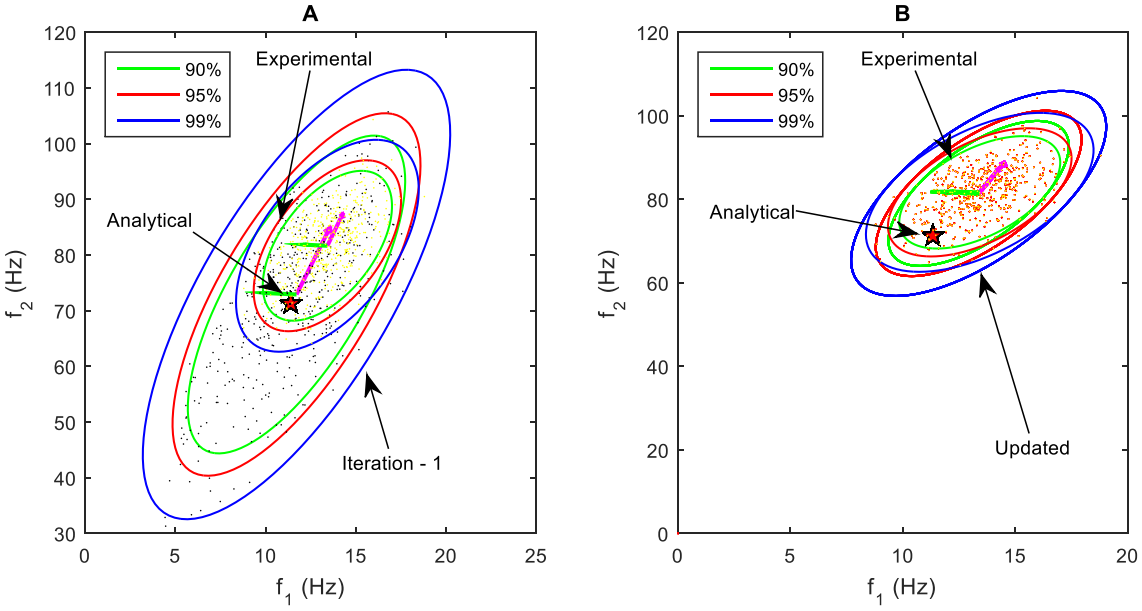


Figure 6: 2-D confidence ellipse at 1st iteration (A) and after updating (B) on a plane of f_1 and f_2

4 Robust parameter identification in stochastic FE model updating

In case-3 of section 3, variability of the measured data arises due to both test-structure variability as well as measurement noise. In stochastic FE model updating, variability of the measured data is obtained by test on the multiple samples of the test-structure. Typically a single test is performed on each sample. However, this approach leads to statistics of the measured data which though captures the variability of the test-structures but are also affected by measurement noise. The parameter identification through stochastic FE model updating using such a data will also be influenced by the measurement noise and hence not accurate and robust. This approach is referred as non-robust approach in further discussion in this paper.

To deal with this problem an approach is proposed in this paper to perform robust identification of the uncertain parameters through stochastic FE model updating. In this method, multiple tests are proposed to be performed on each sample. The variability of the measured data on this sample is solely due to

measurement noise alone and hence this variability is removed by statistical averaging. This yields an estimate of the mean value of the measured data corresponding to this sample. This process is repeated for other samples yielding mean value of the measured data corresponding to them. In this way, the mean value of the measured data corresponding to various samples are free of measurement noise and are used for parameter identification using a stochastic FE model updating approach. This would form a robust procedure as the parameter identification is not affected by the measurement noise. This approach is referred as robust approach in further discussion in this paper.

In the numerical study presented here, to be realistic, 20 samples of the test-structures are simulated. The uncertainty in the simulated modal data is obtained by forward propagation using MCS method. To simulate experiments, 10 number of tests are assumed to be carried out on each sample and a measurement noise of 4% is added to the modal data of each sample. The procedure as explained above is followed to perform stochastic FE model updating using MCS and Hua's method by both non-robust and robust approaches. Table 8 gives a comparison of percentage error in mean value of updating parameters obtained using the proposed robust method with non-robust method. Similarly Table 9 gives a comparison of COV of updating parameters. Fig 7 gives the percentage error in the COV identified in the robust and non-robust approaches. It is observed that the mean value and the COV of the updating parameters obtained using the robust approach are closer to the true values than those obtained using the non-robust approaches. This shows that the stochastic updated model is able to reproduce the statistics of the measured modal data very closely without being affected by measurement noise of the test procedures. This shows the robustness of the proposed stochastic model updating approach.

Updating parameters	Before updating	Using non-robust approach		Using robust approach	
		Hua et al. (2008) *	MCS* (Random)	Hua et al. (2008) *	MCS* (Random)
t_1	-16.6	0.31	2.39	-0.25	1.92
t_2	-28.57	5.03	-1.37	6.01	0.89
t_3	- 9.09	1.84	5.16	2.22	3.45
t_4	-28.57	-0.66	1.25	-1.39	1.41

Table 8: Comparison of % error in updating parameters using non-robust and robust approach

Updating parameters	COV in the simulated experimental model	Using non-robust approach		Using robust approach	
		Hua et al. (2008) *	MCS* (Random)	Hua et al. (2008) *	MCS* (Random)
t_1	0.1	0.22	0.15	0.18	0.13
t_2	0.1	0.22	0.18	0.105	0.11
t_3	0.1	0.18	0.14	0.13	0.12
t_4	0.1	0.14	0.095	0.092	0.10

Table 9: Comparison of COV of updating parameters using non-robust and robust approach

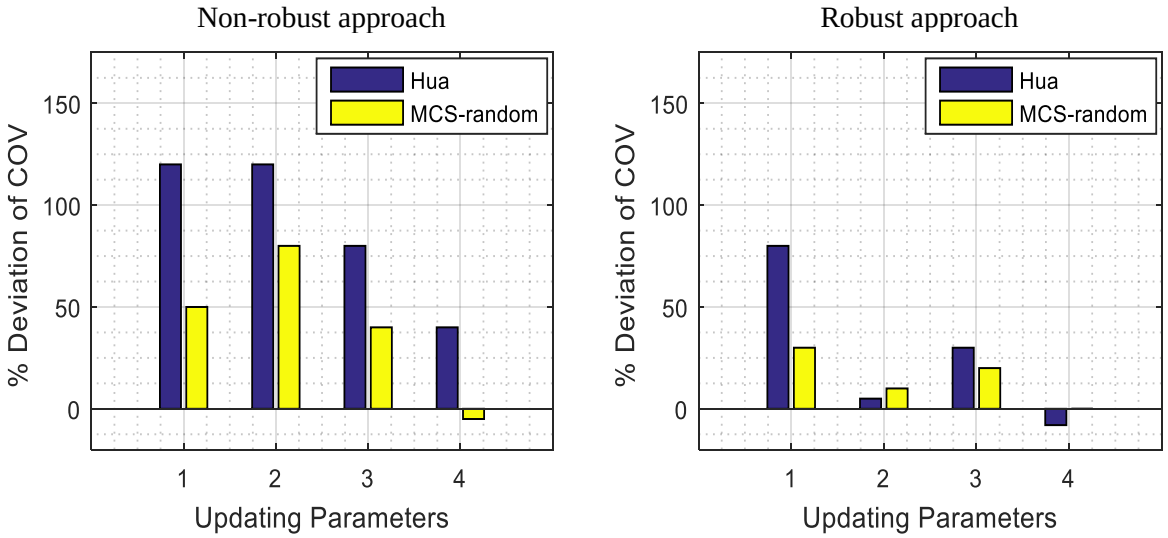


Figure 7: Comparison of % deviation of COV of updated parameters from simulated experiments

Conclusion

A comparative numerical study of the existing stochastic FE model updating methods in the presence of three different type of uncertainties are presented in this paper. On the basis of comparative studies for the case-3 in which uncertainties due to measurement noise and the test-structure variability both are present, it is concluded that the existing methods do not yield satisfactory results of the statistics of the updating parameters. An improved or the robust method for the identification of the statistics of the uncertain updating parameters is proposed in this paper. To demonstrate the performance of the robust parameter identification approach, a comparative numerical study is carried out between robust and non-robust approach, and it is found that the statistics of the parameters found by the proposed robust approach are closer to their true values than what is obtained from the non-robust approach.

Acknowledgements

The financial support for this work provided by Aeronautics Research and Development Board (Structures panel), Ministry of defense, Government of India, is gratefully acknowledged.

References

[1] M. I. Friswell, J. E. Mottershead, *Finite Element Model Updating in Structural Dynamics*, Kluwer Academic Publishers, Boston (1995).

[2] J. E. Mottershead, M. I. Friswell, *Model updating in structural dynamics: a survey*, Journal of sound and vibration, Vol. 167, No. 2, (1993), pp. 347–375.

[3] M. Imregun, W.J. Visser, *A Review of Model. Updating Techniques*, Shock and Vibration Digest, Vol. 23, (1991), pp.19-20.

[4] N. A. Z. Abdullah, M. S. M. Sani1, M. M. Rahman, I. Zaman, *A review on model updating in structural dynamics, Proceedings of Materials Science and Engineering in IOP Conference Series 3rd International Conference of Mechanical Engineering Research, the Kuantan, The Malaysia, 2015 August 18-19*, The Kuantan (2015), Vol 100, No. 1. .

[5] X. G. Hua, Y. Q. Ni, Z. Q. Chen, J. M. Ko, *An improved perturbation method for stochastic finite element model updating*, International journal for numerical methods in engineering, Vol. *73*, (2008) pp. 1845–1864.

[6] H. H. Khodaparast, J. E. Mottershead, M. I. Friswell, *Perturbation methods for the estimation of parameter variability in stochastic model updating*, Mechanical Systems and Signal Processing, Vol. 22, No. 8, (2008), pp. 1751–1773.

[7] M. I. Friswell, *The adjustment of structural parameters using a minimum variance estimator*, Mechanical Systems and Signal Processing, Vol. 3, No. 2, (1989), pp. 143–155.

[8] J. D. Collins, G. C. Hart, T. K. Hasselman, B. Kennedy, *Statistical identification of structures*, Journal of American Institute of Aeronautics and Astronautics, Vol. 12, No. 2, (1974), pp. 185–190.

[9] C. Mares, J.E. Mottershead, M.I. Friswell, *Stochastic model updating: Part 1 - Theory and simulated example*, Mechanical Systems and Signal Processing, Vol. 20, No. 7, (2006), pp. 1674–1695.

[10] J. E. Mottershead, C. Mares, S. James, M. I. Friswell, *Stochastic model updating: Part 2 – application to a set of physical structures*, Mechanical Systems and Signal Processing, Vol. 20, No. 8, (2006), pp. 2171–2185.

[11] Y. Govers, H. H. Khodaparast, M. Link, J. E. Mottershead, *A comparison of two stochastic model updating methods using the DLR AIRMOD test structure*, Mechanical Systems and Signal Processing, Vol. 52-53, (2015), pp. 105–114.

[12] J. R. Fonseca, M. I. Friswell, J. E. Mottershead, A. W. Leesa, *Uncertainty identification by the maximum likelihood method*, Journal of Sound and Vibration, Vol. 288, (2005), pp.587–599.

[13] J. L. Beck, L. S. Katafygiotis, *Updating Models and their Uncertainties. I: Bayesian Statistical Framework*, Journal of Engineering Mechanics, Vol. 124, No. 4, (1998), pp. 455–461.

[14] L. S. Katafygiotis and J. L. Beck, *Updating Models and their Uncertainties. II: Model identifiability*, Journal of Engineering Mechanics, Vol. 124, No. 4, (1998), pp. 463–467.

[15] R. P. Dwight, H. H. Khodaparast, J. E. Mottershead, *Identifying structural variability using Bayesian inference*, International Conference on Uncertainty in Structural Dynamics, the Leuven, The Belgium, 2012 September 17-19, The Leuven (2012), pp. 4681–4695.

[16] I. Boulkaibet, T. Marwala, L. Mthembu, M. I. Friswell, S. Adhikari, *Sampling Technique in Bayesian Finite Element Model Updating*, Proceeding of the Society for Experimental Mechanics, Vol. 29, (2012), pp. 75-83.

On the efficacy of random matrix theory to quantify uncertainty in topology optimisation

A. Vishwanathan [1], **G.A. Vio** [1]
[1] School of Aerospace, Mechanical and Mechatronic Engineering, The University of Sydney
NSW 2006, Australia
e-mail: **aditya.vishwanathan@sydney.edu.au**

Abstract
A popular approach for dealing with randomness in Topology Optimisation (TO) is using a Reliability-Based Topology Optimisation (RBTO) routine. The First-Order Reliability Method (FORM) is a widely adopted approximation used for RBTO due to its simplicity, however is in itself another optimisation problem which scales relatively poorly with the number of stochastic variables. An efficient and novel approach for dealing with uncertain material properties in RBTO is provided in this paper using the Random Matrix Theory (RMT). RMT is particularly powerful since all uncertainties are encapsulated within one random matrix, thereby reducing the complexity of the problem. Numerical simulations are conducted on a cantilevered rectangular plate with uncertain Young's modulus and Poisson's ratio, optimised for volume with a reliability constraint placed on compliance. Results corroborate well with Monte-Carlo simulations and showcase the potential for RMT being applied to more complex TO problems.

1 Introduction

Structural topology optimisation (TO) routines using finite element analysis evaluations are extremely computationally demanding due to the large order of design variables typically required in a mesh. The inclusion of uncertainties in the optimisation problem further exacerbates this issue, perhaps explaining why the majority of works within TO have dealt with deterministic behaviour [1]. However, it is clear that uncertainties in material properties, loading, and boundary conditions must be taken into account to ensure reliable and practical final designs, and therefore efficient inclusion of stochastic parameters within traditional TO algorithms is needed [2, 3].

Two formulations which are commonly used for uncertainty quantification (UQ) within TO are Robust Topology Optimisation (RTO) and Reliability-Based Topology Optimisation (RBTO) [4]. The goal of RTO is to optimise for a deterministic objective, while minimising its sensitivity with respect to random parameters. This can be achieved relatively simply through incorporating a weighted sum of the mean and standard deviation in the objective function [5–7]. Efficient determination of the statistical moments has been undertaken using perturbation methods such as Taylor and Neumann expansion [8, 9], and polynomial chaos theory [1], which in particular has shown to be effective in various engineering optimisation problems due to its non-intrusive implementation [10, 11]. Perhaps the more realistic formulation within TO however is RBTO, which considers uncertainty in the constraint through a probability of failure. Early implementations of Reliability-Based Design focused on sizing and shape optimisation [12], or discrete truss systems [13]. The first examples of RBTO on continuous structures can be seen in works by Maute and Fragopol [14], and Wang et al. [15]. Both studies utilised the First-Order Reliability Method (FORM), and specifically the Performance Measure Approach (PMA), which is generally viewed as the robust alternative to the conventional Reliability Index Approach (RIA) [16]. FORM has since been validated to provide acceptable approximations for the probability of failure, seen through an numerical benchmark result [17], and other notable

works [18–20]. However, aside from the accuracy limitations of FORM when dealing with highly non-linear limit state functions, it also necessitates a nested non-linear optimisation problem to locate the Most Probable Point (MPP). A single-loop method [20,21] has been suggested to alleviate the associated computational cost, however it remains largely untested for problems with a high number of uncertain variables. Additionally, with the exception of Jalalpour et al. [22], dealing with material uncertainties in RBTO remains unexplored, perhaps due to the aforementioned difficulties in dealing with a large number of stochastic parameters.

This study presents an efficient and novel method at dealing with material uncertainties in RBTO through Random Matrix Theory (RMT), and more specifically, via Soize's non-parametric method [23]. Random matrices have shown great promise in quantifying uncertainty for a variety of structural dynamics applications [24–26], however it has yet to be applied in a TO framework. This approach amalgamates all parametric uncertainties into one *dispersion parameter* which is analogous to the normalized standard deviation of the stochastic stiffness matrix. We shall examine the suitability of using this parameter alone to characterise the material uncertainties in RBTO. A numerical study is undertaken on a cantilevered plate with deterministic loading conditions, and uncertain material properties (Young's modulus and Poisson's ratio). The optimization objective is to minimize volume, while ensuring the probability of failure with respect to maximum compliance meets a pre-defined reliability. Final topologies using the non-parametric method are compared with Monte-Carlo simulations (MCS) to validate the results.

2 Methodology

2.1 Deterministic TO formulation

The deterministic optimisation routine is described in Eqn. 1. The volume V is the objective to be minimised, and the constraint enforces that compliance C of the structure should not exceed a maximum value C_{max}. The decision variables x_i represent the densities of the discretised finite elements (ne total elements). Lastly, the system obeys the linear structural equation $KD = F$, where K is the stiffness matrix, D is the displacement, and F is the applied load.

$$\begin{aligned} \underset{x}{\text{minimise}} \quad & V = \sum_{i=1}^{ne} x_i \\ \text{subject to} \quad & C - C_{max} \leq 0 \\ & x_i = x_{min} \text{ or } 1 \\ & KD = F \end{aligned} \tag{1}$$

A modified Solid Isotropic Material with Penalisation (SIMP) algorithm [27] is utilised in this study to ensure efficient computation in MATLAB. This involves discretising the design domain into square finite elements, and assigning each element a density x_i, where its Young's modulus E_i obeys the following equation:

$$E_i = E_{min} + x_i^p (E_0 - E_{min}) \tag{2}$$

where E_0 is the baseline stiffness of the material, E_{min} is a negligible non-zero stiffness value assigned to void regions in order to prevent singularities, and p is the penalisation factor. Due to the large number of design variables encountered in continuous TO problems, Svenberg's Method of Moving Asymptotes (MMA) [28] is used to conduct efficient gradient-based optimisation. This requires knowledge of the objective and constraint sensitivities with respect to the design variables, which are described below in Eqns. 4 and 5;

$$\frac{\partial V}{\partial x_i} = 1 \tag{3}$$

$$\frac{\partial C}{\partial x_i} = -p x_i^{p-1} (E_0 - E_{min}) d_e^T K_e d_e \tag{4}$$

where d_e and K_e are the element displacement and stiffness respectively. In order to prevent formation of checker-board patterns, a sensitivity filter is implemented to modify the compliance sensitivities as such;

$$\frac{\partial \hat{C}}{\partial x_i} = \frac{\sum_{j \in S} H_j x_j \frac{\partial C}{\partial x_j}}{\sum_{j \in S} H_j x_j} \tag{5}$$

where S defines the set of elements surrounding element i within a center-to-center distance r_{min}, and H_i is a weighting factor equal to the center distance subtracted from r_{min}. The reader is referred to Andreassen et al. [27] for specific details on the MATLAB implementation.

2.2 Reliability analysis

The deterministic optimisation described in Eqn. 1 can be modified to obtain an RBTO formulation seen in Eqn. 6;

$$\begin{aligned} \underset{x}{\text{minimise}} \quad & V = \sum_{i=1}^{ne} x_i \\ \text{subject to} \quad & P(g(y) \leq 0) \leq R \\ & g(y) = C_{max} - C(y) \\ & x_i = x_{min} \text{ or } 1 \\ & K(y)D(y) = F \end{aligned} \tag{6}$$

where y represents the stochastic variable(s), and $g(y)$ is called the limit state function. The deterministic limit on maximum compliance has now changed to a constraint on the probability of failure $P_f = P(g(y) \leq 0)$ being less than a specified upper bound R. This is termed the "reliability" of the solution. It is very difficult to determine an analytical representation of P_f, and instead most practical applications of RBTO rely on the FORM approximation. In FORM, the probability of failure P_f is characterized by a reliability index β, which is the distance from the origin to the most probable point (MPP) of failure in the standard normal space u. This requires a mapping of the random variables y to the probabilistic space u. The limit state function $g(u)$ can then be integrated at the MPP to determine P_f as such;

$$P_f \approx \Phi(-\beta) \tag{7}$$

where Φ is the standard normal cumulative distribution function. A drawback of FORM is that it requires a nested non-linear optimization to locate the MPP, which can be formulated using either the conventional RIA approach, or PMA approach. It has been shown by Lee et al. [16], and argued by Maute and Frangopol [14], that the PMA approach is the more robust alternative for TO problems since the mean design can be quite far from the failure surface, leading to no valid solutions to the RIA optimisation problem. PMA uses a pre-defined target reliability index β_t which can be back-calculated using Eqn. 7 for a given reliability constraint. It then assumes the MPP is located at this distance from the origin, and finds the point u^* which minimizes the value of the limit-state function. The overall FORM procedure can be summarized by replacing the reliability constraint in Eqn. 6 with a PMA optimisation routine as in Eqn. 8.

$$\begin{aligned} \underset{u}{\text{minimise}} \quad & g(u) = C_{max} - C(u) \\ \text{subject to} \quad & \sqrt{u^T u} = \beta_t \end{aligned} \tag{8}$$

It is noted that if there is only one random variable, the optimisation routine in Eqn. 8 reduces to an analytical solution $u^* = \beta_t$. Sensitivity analysis for PMA is simplified by assuming that the derivative of the limit state is independent of the random variable at the MPP [14], and therefore reduces down to the compliance sensitivity calculated at u^* as in Eqn. 9.

$$\frac{\partial g}{\partial x_i} = \frac{\partial C}{\partial x_i}\Big|_{u^*} \tag{9}$$

As a means of validation, MCS will also be conducted to compare against the FORM results. In MCS, P_f can be estimated by taking n samples for the random variable(s) and determining the frequency of failure. This is described mathematically using an indicator function I, which is equal to 1 when the constraint fails, and 0 otherwise. Due to the discontinuity of this function, an approach described in [1] is used to replace it with a smooth approximation;

$$I(g(y)) = \frac{1}{2}\left(\tanh(\frac{g(y)}{\epsilon}) + 1 \right) \tag{10}$$

where $\epsilon > 0$ is a small number which controls the width of the 0-to-1 transition. Using Eqn. 10 both the probability of failure and its sensitivity can be determined using MCS;

$$P_f = \frac{1}{2n}\sum_{j=1}^{n}\left(\tanh(\frac{C_j - C_{max}}{\epsilon}) + 1 \right) \approx \frac{n_{C>C_{max}}}{n} \tag{11}$$

$$\frac{\partial P_f}{\partial x_i} = \frac{1}{2n\epsilon}\sum_{j=1}^{n}\frac{\partial C_j}{\partial x_i}\left(1 - \tanh^2(\frac{C_j - C_{max}}{\epsilon}) \right) \tag{12}$$

2.3 RMT implementation

The reliability analysis can be greatly simplified by representing all uncertainty within a random matrix. In TO problems, a logical choice is to choose the stiffness matrix K from the linear structural equation. The stochastic system is then modelled with a mean stiffness matrix K_0, and a mean-normalized standard deviation ξ_K, which is called the *dispersion parameter*. The former is characteristic of the baseline parameters, and the latter is determined using Eqn. 13;

$$\xi_K^2 = \frac{E[||K - K_0||_F^2]}{||K_0||_F^2} \tag{13}$$

where $E(.)$ and $||.||_F$ are the mean and Frobenius norm operators respectively. Implementation of Eqn. 13 necessitates sampling of the random parameters, and repeatedly formulating the associated stiffness matrices. For isotropic structures, the dispersion of the element stiffness matrix K_e is equivalent to the full stiffness matrix, therefore allowing for fast computation of Eqn. 13 even for a large number of samples. Furthermore, since the element stiffness matrix is independent of the decision variables, ξ_K can be pre-computed before the optimisation routine.

In FORM the random variable space y must be transformed to the standard normal space u, where the PMA optimisation described in Eqn. 8 is performed. This routine can be expensive for a large number of random variables, however notably has an analytical solution if there is only one variable. As such, using RMT significantly reduces the computational complexity of RBTO since all uncertainty is confined to K. We shall assume the input material uncertainties are normally distributed, allowing for the following expressions for the probabilistic transform and inverse transforms respectively;

$$u = \frac{K - K_0}{\xi_K K_0} \tag{14}$$

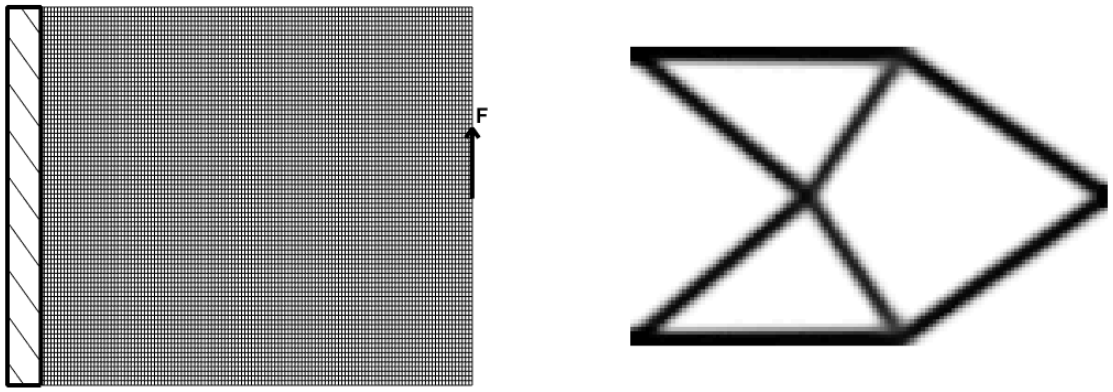
$$K = u\xi_K K_0 + K_0 = (1 + u\xi_K)K_0 \tag{15}$$

Using Eqns. 13- 15, any number of random variables can be simplified to a one-dimensional standard normal space. The suitability of this method will now be examined through a numerical example.

3 Numerical example: Cantilevered plate

A cantilevered rectangular plate with the left edge clamped, and a vertical load on the right edge is visualised in Figure 1a. The example is adapted from Kim et al. [18], where the resolution of the model has been

increased to 80×128 finite elements for greater clarity in the final topology. The vertical load $F = 300$N, and the baseline material properties of the plate are; Young's modulus $E = 2.07 \times 10^5$Pa, Poisson's ratio $\nu = 0.3$, and thickness $t = 0.05$m. A SIMP routine was utilised with a maximum compliance constraint $C_{max} = 1200$N/m to derive a deterministic result, seen in Figure 1b.



(a) Finite element model of plate

(b) Deterministic optimised topology

Figure 1: Cantilevered plate with applied load is optimised using deterministic SIMP to obtain a topology with final volume fraction $V^* = 0.19$.

3.1 One random parameter

We first consider a simple validation case with only a random Young's modulus, which follows a Gaussian distribution as follows;

$$E \in \mathcal{N}(\mu_E, \sigma_E) \tag{16}$$

where $\mu_E = 2.07 \times 10^5$Pa and $\sigma_E = 0.15\mu_E$. To provide motivation for considering RBTO instead of Deterministic Topology Optimisation (DTO), the topology in Figure 1b is re-tested with 10^5 samples for the random Young's modulus, resulting in a probability of failure $P_f = 0.4980$, i.e. the compliance exceeds the maximum limit for approximately half the samples. This is clear undesirable, and hence RBTO should be used to maximise the reliability of the final structure.

RBTO is formulated using MCS, FORM, and RMT as per the methodologies described in Section 2. For RMT, random sampling from the Young's modulus distribution is first performed to yield the dispersion parameter $\xi_k^2 = 0.0225$ using Eqn. 13. This value is also equal to the mean-normalized variance of the Young's modulus distribution, which makes sense since K_e is proportional to E. For this reason, both FORM and RMT will yield the same solutions for one random parameter. Figure 2 shows the optimized topologies yielded for various reliabilities R, and Table 1 summarizes the corresponding volume fractions V^* and probabilities of failure P_f when the structures were re-tested with 10^5 samples from Eqn. 16. As expected, using a high order MCS yields a slightly better optimum in terms of volume while satisfying the constraint. Visually however, few differences are exhibited between both sets of structures, and that is also corroborated by small differences in volume fractions and probabilities of failure. With increasing reliability, the cross braces and the edges of the structure become thicker, which is similar to the results produced by Kim et al. [18]. Another way to visualize the probabilistic results is to plot the PDFs of the structures when re-tested, which is seen in Figure 3. The poor performance of the deterministic structure under random stiffness is illustrated through almost half its PDF extending beyond the failure line, resulting in $P_f = 0.4980$. In contrast, the reliable PDFs are shifted left and upwards with increasing reliability, meaning less of the curve falls in the failure region. The MCS and FORM/RMT curves can barely be distinguished from one and other, highlighting that they provide excellent approximations for one random parameter.



(a) MCS $R = 10^{-1}$



(b) FORM/RMT $R = 10^{-1}$



(c) MCS $R = 10^{-2}$



(d) FORM/RMT $R = 10^{-2}$



(e) MCS $R = 10^{-3}$



(f) FORM/RMT $R = 10^{-3}$

Figure 2: RBTO topologies yielded from MCS and FORM/RMT for varying values of R, for an uncertain Young's modulus

	$\mathbf{R = 10^{-1}}$		$\mathbf{R = 10^{-2}}$		$\mathbf{R = 10^{-3}}$	
Method	V^*	P_f	V^*	P_f	V^*	P_f
MCS	0.2120	0.1000	0.2457	0.0099	0.2857	0.001
FORM/RMT	0.2179	0.0998	0.2538	0.0098	0.2860	0.001

Table 1: Volume fractions V^* and probabilistic of failure P_f for topologies yielded from MCS, and FORM/RMT for varying reliabilities R, when considering a random Young's modulus.

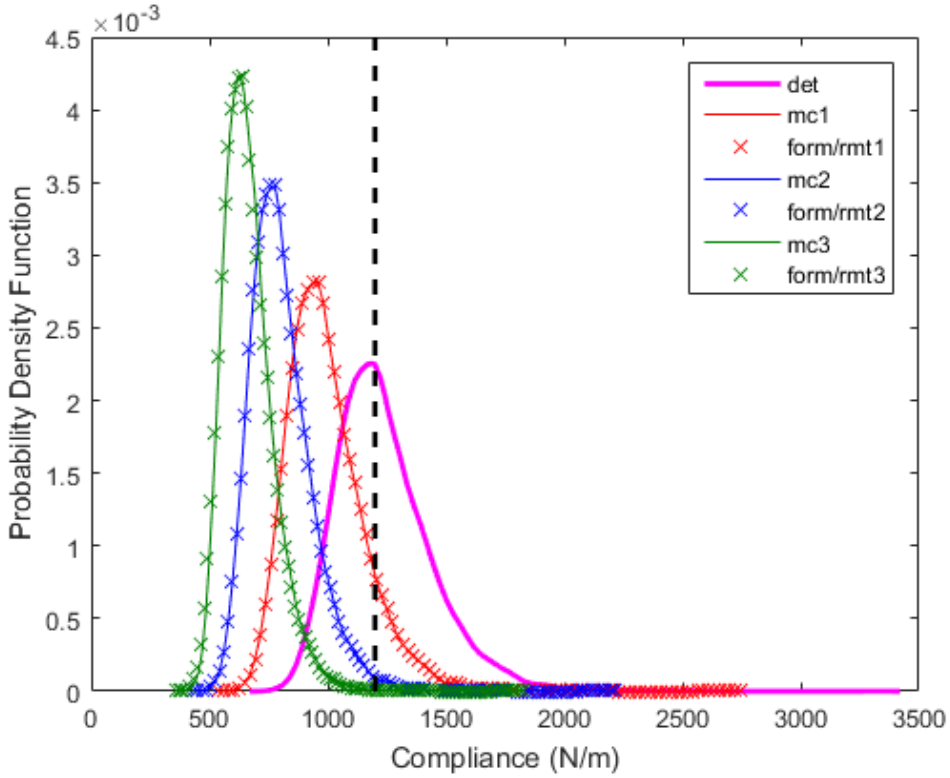


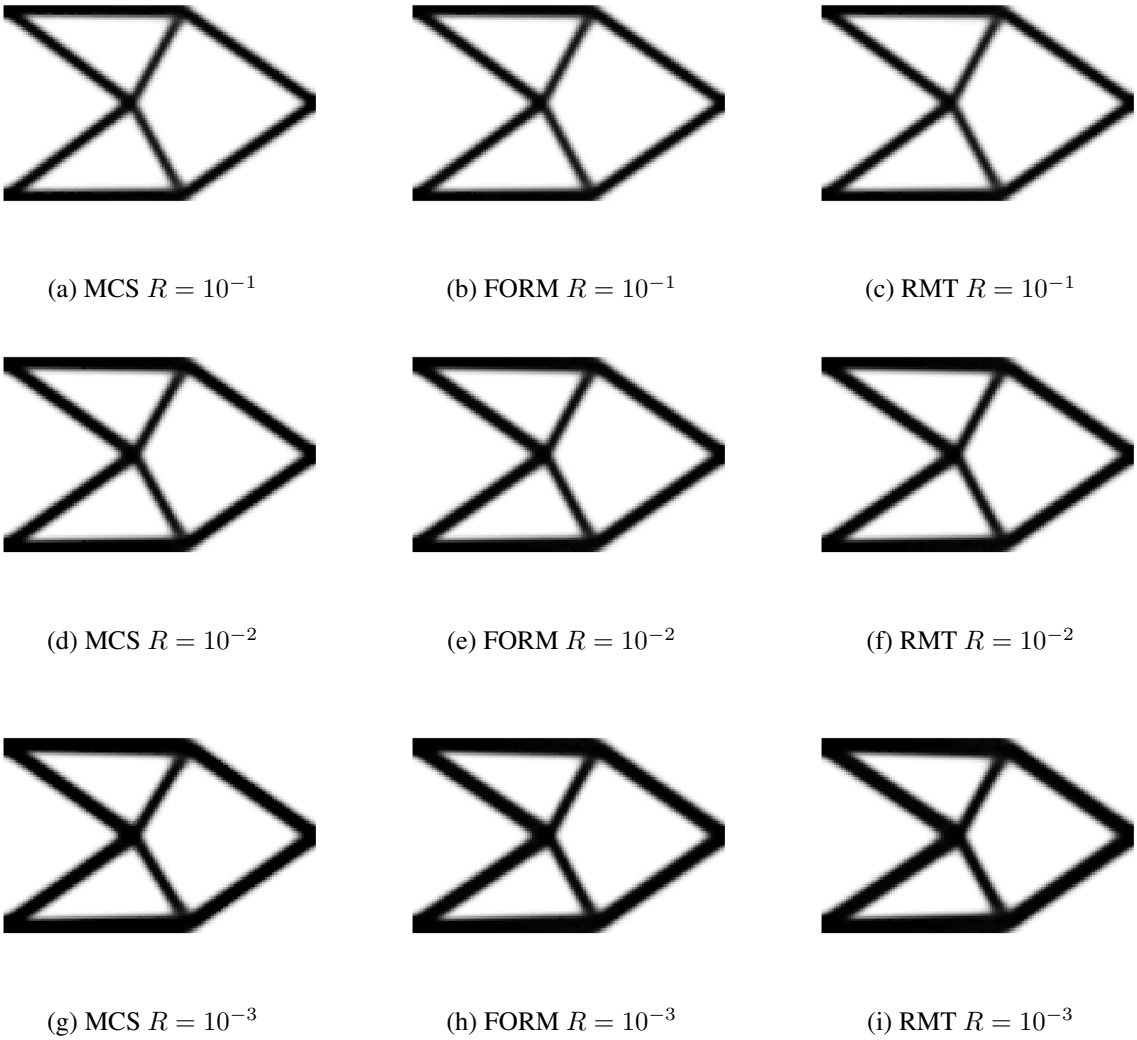
Figure 3: Compliance PDFs considering uncertain Young's modulus of optimised topologies using deterministic SIMP, MCS RBTO, and FORM/RMT RBTO. The numbers 1, 2, and 3 after the legend descriptions represent the reliability values $R = 10^{-1}, R = 10^{-2}$, and $R = 10^{-3}$ respectively. The dashed black line visualizes the compliance constraint C_{max}.

3.2 Two random parameters

We now extend the problem from Section 3.1 by introducing a random Poisson's ratio ν. The two random parameters are defined as follows;

$$E \in \mathcal{N}(\mu_E, \sigma_E) \tag{17}$$
$$\nu \in \mathcal{N}(\mu_\nu, \sigma_\nu) \tag{18}$$

where $\mu_\nu = 0.3$, $\sigma_\nu = 0.15\mu_\nu$, and the Young's modulus distribution is the same as Section 3.1. By randomly sampling both parameters, a dispersion parameter $\xi_k^2 = 0.0253$ is determined for the elemental stiffness matrix K_e, implying that uncertainty in E contributes significantly more to the dispersion than ν, since including the extra uncertain parameter only increased ξ_k^2 by 12%. This new dispersion parameter is then used within the RMT formulation, while MCS and FORM follow their standard approaches as dictated by Sections 2.1 and 2.2. The resulting topologies are seen in Figure 4 and the corresponding volume fractions and probabilities of failure are tabulated in Table 2.



(a) MCS $R = 10^{-1}$ (b) FORM $R = 10^{-1}$ (c) RMT $R = 10^{-1}$

(d) MCS $R = 10^{-2}$ (e) FORM $R = 10^{-2}$ (f) RMT $R = 10^{-2}$

(g) MCS $R = 10^{-3}$ (h) FORM $R = 10^{-3}$ (i) RMT $R = 10^{-3}$

Figure 4: RBTO topologies yielded from MCS, FORM, and RMT for varying values of R, for an uncertain Young's modulus and Poisson's ratio

	$\mathbf{R = 10^{-1}}$		$\mathbf{R = 10^{-2}}$		$\mathbf{R = 10^{-3}}$	
Method	V^*	P_f	V^*	P_f	V^*	P_f
MCS	0.2158	0.0991	0.2496	0.0098	0.2880	0.001
FORM	0.2179	0.0984	0.2542	0.0098	0.2947	0.001
RMT	0.2204	0.0862	0.2607	0.0067	0.3089	0.0005

Table 2: Volume fractions V^* and probabilistic of failure P_f for topologies yielded from MCS, FORM, and RMT for varying reliabilities R, when considering a random Young's modulus and Poisson's ratio

As foreshadowed by the small change in dispersion, we see very similar trends as Section 3.1 for all sets of topologies with increasing reliability. Of note however are the RMT results which appear noticeably thicker than MCS and FORM. Table 2 confirms that RMT provides a conservative volume fraction, with a significantly lower probability of failure. This is also corroborated by the PDFs of the re-tested structures in Figure 5, and the zoomed in section of the failure region in Figure 6, where RMT is increasingly shifted to the left and upwards of the MCS and FORM results for increasing R, therefore exhibiting less failure. The RMT result is clearly sub-optimal, but yields greater reliability and requires far less computational time to

compute. This is due to FORM solving a 2D optimization problem each iteration, while RMT only requires 1 function evaluation each iteration due to the analytical solution for a 1D PMA problem as discussed in Sections 2.2 and 2.3. This also means less information needs to be known about the relative effects of each random parameter to the limit-state function, which greatly simplifies sensitivity analysis. Additionally the random sampling that needs to be performed to determine ξ_k^2 can be done prior to the optimization loop, and for isotropic structures only requires formulating the elemental stiffness K_e, therefore not adding significant computational burden.

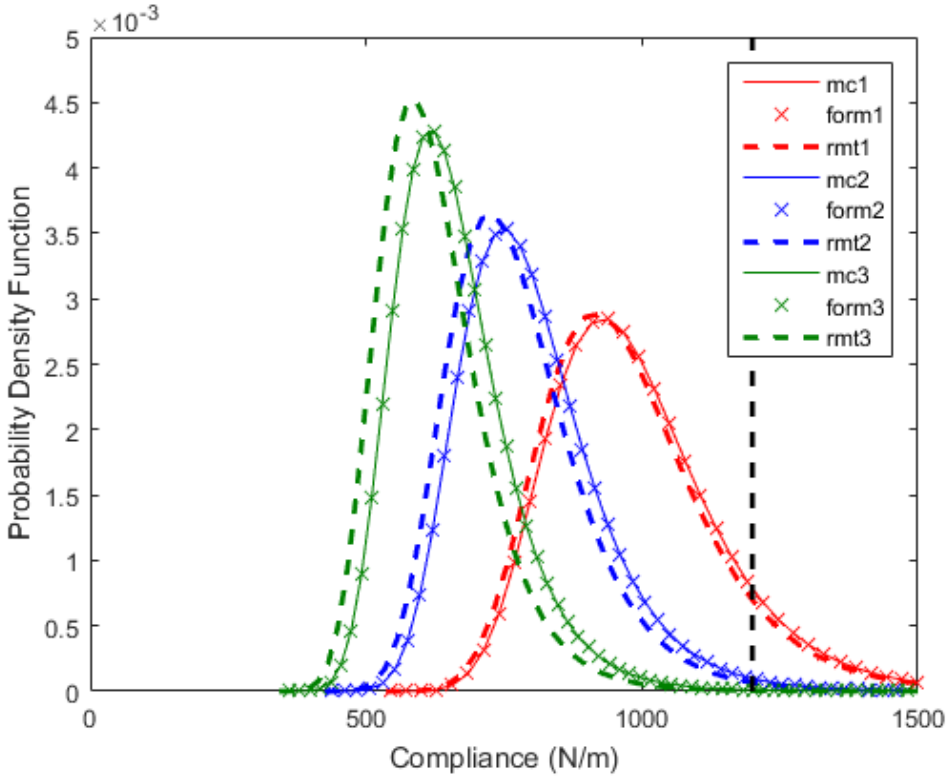


Figure 5: Compliance PDFs considering uncertain Young's modulus and Poisson's ratio of optimised topologies using MCS, FORM, and RMT. The numbers 1, 2, and 3 after the legend descriptions represent the reliability values $R = 10^{-1}, R = 10^{-2}$, and $R = 10^{-3}$ respectively. The dashed black line visualizes the compliance constraint C_{max}.

4 Conclusion

The efficacy of using RMT to reduce the dimensionality of an RBTO routine is investigated in this paper. A cantilevered plate with random Young's modulus and Poisson's ratio is optimized for volume, with a reliability constraint imposed on compliance. It is shown that the RMT results produce slightly sub-optimal topologies, with a significantly lower probability of failure, at much less computational expense. This is due to amalgamating all material uncertainty into one dispersion parameter which corresponds to the random stiffness matrix. These results provide motivation to evaluate RMT in more complex RBTO problems.

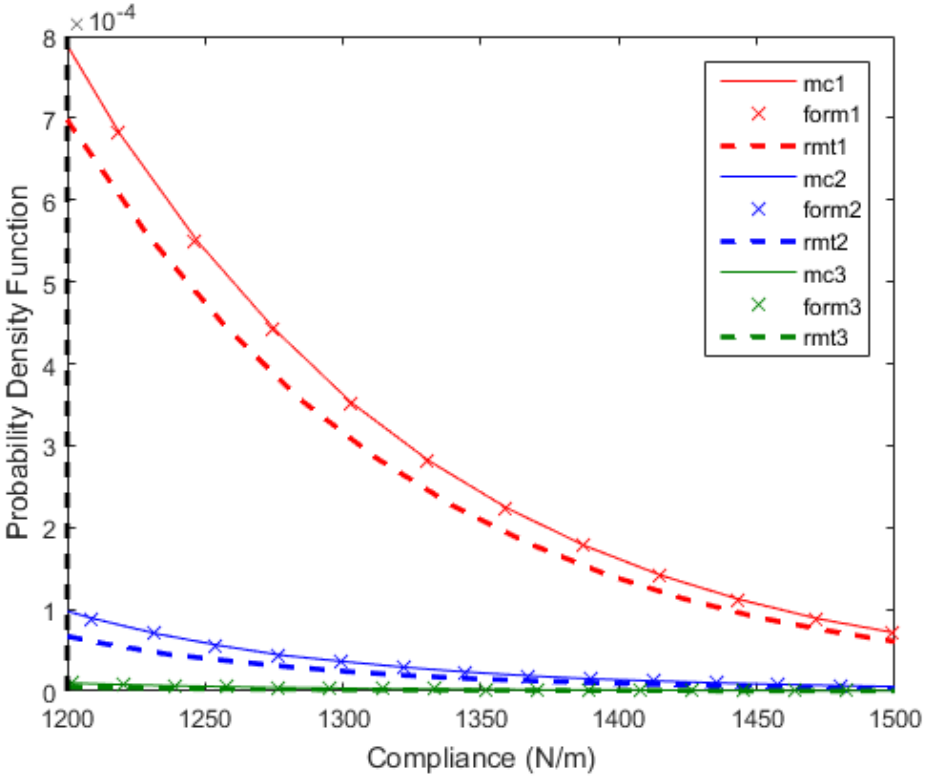


Figure 6: Zoomed section of compliance PDFs showing failure region $C > C_{max}$

References

[1] V. Keshavarzzadeh, F. Fernandez, and D. A. Tortorelli, "Topology optimization under uncertainty via non-intrusive polynomial chaos expansion," *Computer Methods in Applied Mechanics and Engineering*, vol. 318, pp. 120–147, may 2017.

[2] O. Sigmund and K. Maute, "Topology optimization approaches," *Structural and Multidisciplinary Optimization*, vol. 48, pp. 1031–1055, aug 2013.

[3] D. J. Munk, G. A. Vio, and G. P. Steven, "Topology and shape optimization methods using evolutionary algorithms: a review," *Structural and Multidisciplinary Optimization*, vol. 52, pp. 613–631, may 2015.

[4] K. Maute, "Topology optimization under uncertainty," in *Topology Optimization in Structural and Continuum Mechanics*, pp. 457–471, Springer Vienna, 2014.

[5] J. Zhao and C. Wang, "Robust topology optimization under loading uncertainty based on linear elastic theory and orthogonal diagonalization of symmetric matrices," *Computer Methods in Applied Mechanics and Engineering*, vol. 273, pp. 204–218, may 2014.

[6] X. S. Zhang, E. de Sturler, and G. H. Paulino, "Stochastic sampling for deterministic structural topology optimization with many load cases: Density-based and ground structure approaches," *Computer Methods in Applied Mechanics and Engineering*, vol. 325, pp. 463–487, oct 2017.

[7] K. Shintani, Y.-C. Chan, and W. Chen, "Robust multi-material topology optimization for lattice structure under material uncertainties," in *Advances in Structural and Multidisciplinary Optimization*, pp. 1110–1123, Springer International Publishing, dec 2017.

[8] M. Jansen, G. Lombaert, and M. Schevenels, "Robust topology optimization of structures with imperfect geometry based on geometric nonlinear analysis," *Computer Methods in Applied Mechanics and Engineering*, vol. 285, pp. 452–467, mar 2015.

[9] Z. Fu, C. Wang, and J. Zhao, "Truss topology optimization under uncertain nodal locations with proportional topology optimization method," *Mechanics Based Design of Structures and Machines*, vol. 45, pp. 190–206, apr 2016.

[10] A. Vishwanathan, P. Cheema, and G. A. Vio, "Multi-particle swarm optimization used to study material degradation in aeroelastic composites including probabalistic uncertainties," in *2017 IEEE Congress on Evolutionary Computation (CEC)*, IEEE, jun 2017.

[11] P. Cheema and G. A. Vio, "A non-intrusive polynomial chaos method to efficiently quantify uncertainty in an aircraft t-tail," *Applied Mechanics and Materials*, vol. 846, pp. 512–517, jul 2016.

[12] K.-Y. Lin and D. M. Frangopol, "Reliability-based optimum design of reinforced concrete girders," *Structural Safety*, vol. 18, pp. 239–258, jan 1996.

[13] Y. Murotsu and S. Shao, "Optimum shape design of truss structures based on reliability," *Structural Optimization*, vol. 2, pp. 65–76, jun 1990.

[14] K. Maute and D. M. Frangopol, "Reliability-based design of MEMS mechanisms by topology optimization," *Computers & Structures*, vol. 81, pp. 813–824, may 2003.

[15] S. Wang, H. Moon, C. Kim, J. Kang, and K. K. Choi, "Reliability-based topology optimization (RBTO)," in *Solid Mechanics and Its Applications*, pp. 493–504, Springer Netherlands, 2006.

[16] J.-O. Lee, Y.-S. Yang, and W.-S. Ruy, "A comparative study on reliability-index and target-performance-based probabilistic structural design optimization," *Computers & Structures*, vol. 80, pp. 257–269, feb 2002.

[17] G. I. N. Rozvany and K. Maute, "Analytical and numerical solutions for a reliability-based benchmark example," *Structural and Multidisciplinary Optimization*, vol. 43, pp. 745–753, mar 2011.

[18] C. Kim, S. Wang, K. ryun Rae, H. Moon, and K. K. Choi, "Reliability-based topology optimization with uncertainties," *Journal of Mechanical Science and Technology*, vol. 20, pp. 494–504, apr 2006.

[19] K. H. Cho, J. Y. Park, S. P. Ryu, J. Y. Park, and S. Y. Han, "Reliability-based topology optimization based on bidirectional evolutionary structural optimization using multi-objective sensitivity numbers," *International Journal of Automotive Technology*, vol. 12, pp. 849–856, nov 2011.

[20] M. Silva, D. A. Tortorelli, J. A. Norato, C. Ha, and H.-R. Bae, "Component and system reliability-based topology optimization using a single-loop method," *Structural and Multidisciplinary Optimization*, vol. 41, pp. 87–106, may 2009.

[21] T. H. Nguyen, J. Song, and G. H. Paulino, "Single-loop system reliability-based topology optimization considering statistical dependence between limit-states," *Structural and Multidisciplinary Optimization*, vol. 44, pp. 593–611, jul 2011.

[22] M. Jalalpour and M. Tootkaboni, "An efficient approach to reliability-based topology optimization for continua under material uncertainty," *Structural and Multidisciplinary Optimization*, vol. 53, pp. 759–772, nov 2015.

[23] C. Soize, "Random matrix models and nonparametric method for uncertainty quantification," in *Handbook of Uncertainty Quantification*, pp. 219–287, Springer International Publishing, 2017.

[24] S. Adhikari, "Matrix variate distributions for probabilistic structural dynamics," *AIAA Journal*, vol. 45, pp. 1748–1762, jul 2007.

[25] H. Xiao, J.-X. Wang, and R. G. Ghanem, "A random matrix approach for quantifying model-form uncertainties in turbulence modeling," *Computer Methods in Applied Mechanics and Engineering*, vol. 313, pp. 941–965, jan 2017.

[26] A. Vishwanathan, D. Munk, and G. A. Vio, "Frequency response characteristics of 2d wings in uncertain environments: A random matrix theory approach," in *Advances in Structural and Multidisciplinary Optimization*, pp. 799–813, Springer International Publishing, dec 2017.

[27] E. Andreassen, A. Clausen, M. Schevenels, B. S. Lazarov, and O. Sigmund, "Efficient topology optimization in MATLAB using 88 lines of code," *Structural and Multidisciplinary Optimization*, vol. 43, pp. 1–16, nov 2010.

[28] K. Svanberg, "The method of moving asymptotes—a new method for structural optimization," *International Journal for Numerical Methods in Engineering*, vol. 24, pp. 359–373, feb 1987.